Virtual

IUTAM International Union of Theoretical and Applied Mechanics

25th International Congress of Theoretical and Applied Mechanics

August 22-27, 2021

BOOK OF ABSTRACTS

Editor: **Alberto Corigliano**

ISBN number: **978 -83-65550-31-6**

under the auspices of

POLITECNICO MILANO 1863

UNIVERSITÀ DI PAVIA

www.ictam2020.org

ICTAM Milano 2020+1 Virtual

Sponsorship Acknowledgement

Silver Sponsors

life.augmented

Tetra Pak®

Other Sponsors

CAMBRIDGE UNIVERSITY PRESS

OXFORD UNIVERSITY PRESS

Springer

frontiers in Materials

INDEX

ORGANIZATION

President
Alberto Corigliano
Solid and Structural Mechanics
Politecnico di Milano

Secretary General
Umberto Perego
Solid and Structural Mechanics
Politecnico di Milano

AIMETA Representative
Carlo Cinquini
Solid and Structural Mechanics
Università di Pavia

EXECUTIVE LOCAL ORGANIZING COMMITTEE

Massimiliano Cremonesi, Solid and Structural Mechanics, Politecnico di Milano

Aldo Ghisi, Solid and Structural Mechanics, Politecnico di Milano

Valentina Zega, Solid and Structural Mechanics, Politecnico di Milano

LOCAL ORGANIZING COMMITTEE

Ferdinando Auricchio, Solid and Structural Mechanics, Università di Pavia

Paolo Biscari, Applied Mathematics, Politecnico di Milano

Carlo Bottasso, Solid and Fluid Mechanics, Technische Universität München

Annalisa Buffa, Applied Mathematics, CNR-IMATI- Pavia / Ecole Polytechnique Fédérale de Lausanne

Federico Cheli, Applied Mechanics, Politecnico di Milano

Gabriele Dubini, Biomechanics, Politecnico di Milano

Roberto Frassine, Materials Mechanics, Politecnico di Milano

Alberto Guadagnini, Fluid Mechanics, Politecnico di Milano

Carlo Lovadina, Applied Mathematics, Università di Milano (formerly Università di Pavia)

Anna Pandolfi, Solid and Structural Mechanics, Politecnico di Milano

Paolo Pennacchi, Applied Mechanics, Politecnico di Milano

Maurizio Quadrio, Fluid Mechanics, Politecnico di Milano

Alfio Quarteroni, Applied Mathematics, Politecnico di Milano / Ecole Polytechnique Fédérale de Lausanne

Alessandro Reali, Solid and Structural Mechanics, Università di Pavia

ORGANIZATION

EXECUTIVE COMMITTEE OF THE IUTAM CONGRESS COMMITTEE FOR THE PERIOD 2016-2020

Alberto Corigliano
President of the ICTAM 2020 + 1 Congress
Politecnico di Milano
Milan ITALY

Bruno Eckhardt
Philipps-Universität
Marburg, Germany

Nadine Aubry
President IUTAM
and of the Congress Committee
Tufts University, Boston, USA

Jacques Magnaudet
Institut de Mecanique des Fluides
de Toulouse, France

Robert M. McMeeking
Secretary of the Congress Committee
University of California Santa Barbara, USA

Gabor Stepan
Budapest University of Technology
and Economics, Hungary

Leslie Banks-Sills
Tel Aviv University
School of Mechanical Engineering
Ramat Aviv ISRAEL

EXECUTIVE COMMITTEE OF THE IUTAM CONGRESS COMMITTEE FOR THE PERIOD 2020-2024

Alberto Corigliano
President of the ICTAM 2020 + 1 Congress
Politecnico di Milano
Milan ITALY

Shiyi Chen
Southern University of Science
and Technology
Shenzhen CHINA

Norman Fleck
President IUTAM and of the
Congress Committee
Cambridge University - Department
of Engineering
Cambridge UK

Heuy Dong Kim
Andong National University
- Department of Mechanical
Engineering
Andong-si, Gyeongsangbuk-do
KOREA

Sanjay Mittal
Secretary of the Congress Committee
Indian Institute of Technology Kanpur-
Department of Aerospace Engineering
Kanpur INDIA

Paul Linden
University of Cambridge - Department
of Applied Mathematics and
Theoretical Physics
Cambridge UK

Leslie Banks-Sills
Tel Aviv University
School of Mechanical Engineering
Ramat Aviv ISRAEL

ORGANIZATION

MEMBERS OF THE CONGRESS COMMITTEE IUTAM

Prof. P. (Pilar) Ariza (Spain) 2020/2024
Prof. Nadine Aubry (USA) 2020 Chair of CC and XCCC (ex officio)
Prof. E. (Ellen) Arruda (USA) 2024
Prof. L. (Leslie) Banks-Sills (Israel) 2020/2024 member of XCCC
Prof. D. (Davide) Bigoni (Italy) 2022
Prof. L.C. (Catherine) Brinson (USA) 2024
Prof. S. (Shiyi) Chen (China) 2020 / 2024 member of XCCC
Prof. A. (Alan) Cocks (UK) 2022
Prof. A. (Alberto) Corigliano (Italy) 2020/2024 member of XCCC
Prof. A. (Anne) De Wit (Belgium) 2022
Prof. Bruno Eckhardt (Germany) 2020 member of XCCC
Prof. Horacio Espinosa (USA) 2020
Prof. N.A. (Norman) Fleck (UK) 2024 Chair of CC and XCCC (ex officio)
Prof. J.M. (Maciej) Floryan (Canada) 2020 / 2024
Prof. S. (Samuel) Forest (France) 2024
Prof. P. (Peter) Frick (Russia) 2024
Prof. Huajian Gao (USA) 2020
Prof. M.D. (Michael) Gilchrist (Ireland) 2022
Prof. E. (Elisabeth) Guazzelli (France) 2024
Prof. S. (Stefan) Hartmann (Germany) 2024
Prof. Patrick Huerre (France) 2020
Prof. P. (Peter) Hunter (New Zealand) 2020 / 2024
Prof. A. (Anne) Juel (UK) 2022
Prof. H.D. (Heuy Dong) Kim (Korea, Republic of) 2024 member of XCCC (ex officio)
Prof. Ann Karagozian (USA) 2020
Prof. Djimedo Kondo (France) 2020
Prof. P.F. (Paul) Linden (UK) 2022/ 2024 member of XCCC
Prof. D. (Detlef) Lohse (Netherlands) 2022
Prof. Tianjian Lu (China) 2020
Prof. Jacques Magnaudet (France) 2020 member of XCCC
Prof. Valery Matveenko (Russia) 2020
Prof. Robert M. McMeeking (USA) 2020 Secretary of CC and XCCC
Prof. G. (Gareth) McKinley (USA) 2024
Prof. S. (Sanjay) Mittal (India) 2022/2024 Secretary of CC and XCCC
Prof. H. (Henryk) Petryk (Poland) 2020/ 2024
Prof. S. (Stéphane) Popinet (France) 2024
Prof. G. (Gherhardt) Ribatski (Brazil) 2024
Prof. M.V. (Maria Vittoria) Salvetti (Italy) 2020 / 2024
Prof. Eric Shaqfeh (USA) 2020
Prof. Gábor Stépán (Hungary) 2020 member of XCCC
Prof. A. (Alfredo) Soldati (Austria) 2024
Prof. K.J. (Kathleen) Stebe (USA) 2024
Prof. S. (Shu) Takagi (Japan) 2022
Prof. Jens Walther (Denmark) 2020
Prof. W.-C. (Wei-Chung) Wang (China-Taipei) 2022
Prof. J.-X. (Jianxiang) Wang (China) 2022
Prof. H. (Hiroshi) Yabuno (Japan) 2020/ 2024
Prof. X.J. (Xiaojing) Zheng (China) 2024

ORGANIZATION

ITALIAN STEERING COMMITTEE

General Mechanics

- **Nicola Bellomo,** Politecnico di Torino
- **Franco Brezzi,** Institute for Advanced Studies IUSS Pavia
- **Angelo Morro,** University of Genova
- **Mario Primicerio,** University of Firenze

Applied Mechanics

- **Enrico Ciulli,** University of Pisa
- **Giovanni Legnani,** University of Brescia
- **Vincenzo Parenti Castelli,** University of Bologna

Fluid Mechanics

- **Alessandro Bottaro,** University of Genova
- **Emilio Fortunato Campana,** CNR - INSEAN
- **Maurizio Pandolfi,** Politecnico di Torino
- **Renzo Piva,** University of Roma La Sapienza
- **Roberto Verzicco,** University of Roma Tor Vergata

Solid and Structural Mechanics

- **Davide Bigoni,** University of Trento
- **Antonio De Simone,** International School for Advanced Studies (SISSA) Trieste
- **Luigi Gambarotta,** University of Genova
- **Giulio Maier,** Politecnico di Milano
- **Paolo Podio Guidugli,** University of Roma Tor Vergata
- **Giuseppe Rega,** University of Roma La Sapienza
- **Bernhard Schrefler,** University of Padova
- **Fabrizio Vestroni,** University of Roma La Sapienza

Message of IUTAM President

Dear IUTAM colleagues, Dear Friends,

On behalf of IUTAM, including the Congress Committee and the Executive Committee, we write to extend a very warm welcome to you as participants of ICTAM2020+1. As we all realise, this Congress is unique in the history of IUTAM in many ways, and we have every expectation that it will be long remembered in IUTAM history as extraordinary in quality and impact in addition to its unique nature. It is, for example, the first ICTAM that has straddled the time of office of two IUTAM presidents, and so this welcoming address is a double-act.

We are extremely grateful to the local organisers who have worked tirelessly for several years on the project of bringing ICTAM to Milano, and although many of us are not be able to travel to Italy at this time, nonetheless we can be present together, in real-time, for many of the events of ICTAM2020+1. Mechanics in Italy is thriving, and so it is exciting for this large international congress in mechanics to gravitate to Milano. The organisers have overcome many challenges in these uncertain times, and we are deeply appreciative of their dedication and agility in organising such a large virtual gathering.

It requires only a glance at the program to realise that ICTAM2020+1 has a very fine collection of presentations across an enormous range of topics in mechanics. It is particularly pleasing to see participation by a highly diverse group of scientists, over at least 16 hours of difference in time-zone.

We wish you a very successful ICTAM2020+1, and would like to ask that you participate as fully as you can. Once again, we wish to recognize the organising team, in particular Professor Alberto Corigliano, as President of the Congress, and Professor Umberto Perego, as Secretary-General of the Congress, for all their hard work and commitment without which the congress would not have been possible. Many thanks to them, and a warm welcome to you!

With our best wishes for a most enjoyable and productive ICTAM2020+1,

Nadine Aubry
IUTAM President (2016-2020),
IUTAM Vice President (2020-2024)

Norman Fleck
IUTAM President (2020-2024)

Message of AIMETA President

On behalf of the Italian Association of Theoretical and Applied Mechanics (AIMeTA), welcome to the 25th International Congress of Theoretical and Applied Mechanics ICTAM 2020+1 in Milano. After Stresa in 1960, the ICTAM is back to Italy, and the Italian community of mechanics is proud of this and very happy to host you.

Mechanics in Italy has a long and important tradition, with giants in the past and major scholars and relevant contributions nowadays. We are very active, perfectly integrated in the international environment, which recognize the quality of our work. We are doing research in all fields of mechanics, in traditional and new frontiers area, and we are ready for future challenges.

Unfortunately, the pandemic forced the organizers to go online, which is the best that could have been done. As a consequence, you will be missing the occasion to visit Milano and Italy, with their lovely atmosphere, climate, culture, history, and science! But I am sure you will have soon the opportunity to visit us in person.

In spite of the very unwanted situation, the organizers "accepted the challenge" and showed their resilience and flexibility, organizing this event in the best possible way. The fact that a very large number of colleagues from all parts of the world, many more than what expected for an online congress, confirmed their submissions is the proof of the success of the organizers, as well as of the importance of ICTAM for the international community. Thanks to them and to all of you for attending this very special conference, which I am sure you will remember in any case.

Enjoy ICTAM now and Milano in the nearest future..

Stefano Lenci

President of AIMeTA

Welcome message of the 25° ICTAM President

The 25th ICTAM was initially scheduled from 23 to 28 August 2020 and should have taken place in Milano, Italy. Due to the covid-19 pandemic, the Organizing Committee decided to postpone this important event by one year and finally decided to transform the 25th ICTAM into a fully virtual Congress. This decision was considered to be the most reasonable for the organization of an ICTAM Congress, maximizing the active participation of Authors with high quality scientific works. This virtual meeting has the full support of both the President of IUTAM and the Executive Committee of the Congress Committee who very much look forward to the event.

In view of the high number of registered participants and the 1500 extended abstracts included in this book, that decision seems to have been the right one.

Participation in the 25th ICTAM-Virtual will allow you to appreciate the high quality scientific program that has been setup by the IUTAM Congress Committee, full of very interesting and innovative contributions on all aspects of Mechanics.

I hope you will enjoy the various ways in which you will be able to reach and take advantage of the scientific content of the Congress. For instance, you can explore the on-demand area, where you will find the pre-recorded full presentations that will remain available until the end of the year. You can also participate in the live sessions, where you will have the possibility to interact with Authors. Furthermore, you can make use of the chat lines to further interact with Colleagues. Finally, I hope you will appreciate the wonderful set of live Plenary and Sectional Lectures given by top scientists in the field of Mechanics.

The 25th ICTAM is a big event, and can only exist and can only be organized as a result of the numerous institutions and persons that work hard for the final result.

At an international level, IUTAM, the IUTAM Congress Committee (CC) and, more specifically, the Executive Committee of the Congress Committee (XCCC) and the Bureau have fully supported all phases of the Congress Organization. The International Paper Committee (IPC) reviewed more than 3400 extended abstracts in two successive calls. We all owe them a debt of gratitude.

Due to the change of dates, a new IUTAM President and new member of IUTAM Committees were appointed while the congress organization was in progress. Therefore, the responsibility of the 25th ICTAM is shared between the two Presidents, Nadine Aubry and Norman Fleck, the two Secretaries of the CC, Robert McMeeking and Sanjay Mittal, and all members of the previous and current Committees and Bureau. To all of them my special thanks for the great help received, in particular during the initial phases of the Congress organization. A special mention goes to Bruno Eckhardt, a valuable member of the XCCC, who unexpectedly passed away in the summer of 2019. He will always remain in my memory.

At a National level, the organization of 25th ICTAM was supported by AIMETA, the Italian Association of Theoretical and Applied Mechanics, in collaboration with Politecnico di Milano and Università di Pavia, which provided the highly experienced and motivated Local Organizing Committee. Politecnico di Milano also provided a motivated group of young researchers who integrated into the staff of the local organizing committee.

The technical organization was managed by the team of the professional congress organizer AIM Group International, who provided an excellent service.

To the organizing teams of AIMETA, Politecnico di Milano, Università di Pavia and AIM Group, I would like to express my most sincere thanks for the continuous support during the preparation of the Congress.

Finally, I would also like to thank my Colleagues Umberto Perego, Secretary General of 25th ICTAM and Carlo Cinquini, representative of AIMETA, for their constant support and collaboration given to this enterprise starting from the initial idea to submit a bid to IUTAM.

On behalf of the Local Organizing Committee and of the IUTAM Congress Committee, I would like to convey to you my warmest welcome to the 25th ICTAM.

Milano, August 2021

Alberto Corigliano
25th ICTAM President

TOPICS

MS01 - Modeling and controlling turbulent shear flows

MS02 - Local mechanics of climate processes

MS03 - Biological fluid-structure interaction at the microscale

MS04 - Nonlinear dynamics for design

MS05 - Mechanics of additive manufacturing

MS06 - Mechanics of C-allotropic materials and structures

FM01 - Biological Fluid Mechanics

FM02 - Boundary Layers

FM03 - Combustion and Flames

FM04 - Compressible Flows

FM05 - Convection

FM06 - Drops, Bubbles and Interfaces

FM07 - Multiphase and Particle-Laden Flows

FM08 - Flow Instability and Transition

FM09 - Thin Film Flows

FM10 - Geophysical and Environmental Fluid Dynamics

FM11 - Low-Reynolds-number flows and suspensions

FM12 - Micro- and Nano-fluidics

FM13 - Non-Newtonian and Complex Fluids

FM14 - Computational Fluid Dynamics

FM15 - Turbulence

FM16 - Vortex Dynamics

FM17 - Waves in Fluids

FM18 - Electro- and Magneto- Hydrodynamics

SM01 - Biomechanics and Biomaterials

SM02 - Tribology - Contact and Friction

SM03 - Damage Mechanics

SM04 - Elasticity

SM05 - Fracture Mechanics

SM06 - Geophysics and Geomechanics

SM07 - Impact Mechanics and Wave Propagation

SM08 - Multi-component, Composites and Hierarchical Materials

SM09 - Phase Transformations and Thermomechanical Phenomena

SM10 - Sizescale Effects in Materials

SM11 - Multibody and Vehicle Dynamics

SM12 - Nanostructures and MEMS

SM13 - Plasticity, Viscoplasticity and Creep

SM14 - Stability and Instability of Materials and Structures

SM15 - Computational Solid Mechanics

SM16 - Vibrations and Control of Structures

SM17 - Soft Materials and Extremely Deformable Structures

SM18 - Metamaterials

FS01 - Acoustics

FS02 - Exascale Computing

FS03 - Experimental Methods in Mechanics

FS04 - Nonlinear Dynamics and Pattern Formation

FS05 - Porous Media

FS06 - Fluid Structure Interactions

FS08 - Granular Materials and Flows

FS09 - Foams and Cellular Materials

FS10 - Optimization for Solids and Fluids

FS12 - Education in Mechanics

TIMETABLE

CITY	San Francisco (USA)	Greenwich (UK)	Rome (IT)	Beijing (PRC)	Sydney (AUS)	Sunday 22 August	Monday 23 August	Tuesday 24 August	Wednesday 25 August	Thursday 26 August	Friday 27 August
Time Zone	PDT	GMT	CEST	CST	AEST						
Coordinated Universal Time Greenwich Mean Time	UTC/GMT -7	UTC/GMT	UTC/GMT +2	UTC/GMT +8	UTC/GMT +10						
45'	4.00-4.45	11.00-11.45	**13.00-13.45**	19.00-19.45	21.00-21.45			VIRTUAL EVENT SHOW COOKING	VIRTUAL EVENT SHOW COOKING	VIRTUAL EVENT SHOW COOKING	VIRTUAL EVENT ADI MUSEUM
15'	4.00-4.45	11.45-12.00	**13.45-14.00**	19.45-20.00	21.45-22.00						
60'	5.00-6.00	12.00-13.00	**14.00-15.00**	20.00-21.00	22.00-23.00	IUTAM GENERAL ASSEMBLY	OPENING CEREMONY	ORAL DISCUSSION	PRIZE PLENARY LECTURE The 2020 Batchelor Prize in Fluid Mechanics	ORAL DISCUSSION	ORAL DISCUSSION
60'	6.00-7.00	13.00-14.00	**15.00-16.00**	21.00-22.00	23.00-00.00 (+1)		OPENING LECTURE	ORAL DISCUSSION	PRIZE PLENARY LECTURE The 2020 Rodney Hill Prize in Solid Mechanics	ORAL DISCUSSION	ORAL DISCUSSION
15'	7.00-7.15	14.00-14.15	**16:00-16:15**	22.00-22.15	00.00-00:15 (+1)		*BREAK*				
45'	7.15-8.00	14.15-15.00	**16.15-17.00**	22.15-23.00	00.15-01:00 (+1)		MINI SYMPOSIA KEYNOTE LECTURES	SECTIONAL LECTURES	POSTER DISCUSSION / IUTAM GENERAL ASSEMBLY	SECTIONAL LECTURES	MINI SYMPOSIA KEYNOTE LECTURES
15'	8.00-8.15	15.00-15.15	**17:00-17:15**	23.00-23.15	01.00-01:15 (+1)		ORAL DISCUSSION	SECTIONAL LECTURES		SECTIONAL LECTURES	CLOSING LECTURE
30'	8.15-8.45	15.15-15.45	**17:15-17:45**	23.15-23.45	01.15-01:45 (+1)						
15'	8.45-9.00	15-45-16.00	**17:45-18:00**	23.45-00.00 (+1)	01.45-02:00 (+1)			*BREAK*		*BREAK*	
15'	9.00-9.15	16.00-16.15	**18:00-18:15**	00.00-00:15 (+1)	02.00-02:15 (+1)		*BREAK*	ORAL DISCUSSION		POSTER DISCUSSION	*BREAK*
15'	9.15-09.30	16-15-16.30	**18.15-18.30**	00.15-00:30 (+1)	02.15-02:30 (+1)		ORAL DISCUSSION		*BREAK*		CLOSING CEREMONY
60'	9.30-10.15	16-30-17.15	**18.30-19.15**	00.30-01:15 (+1)	02.30-03:15 (+1)				ORAL DISCUSSION		
15'	10.15-10.30	17.15-17:30	**19.15-19:30**	01.15-01.30 (+1)	03.15-03:30 (+1)		VIRTUAL EVENT SHOW COOKING COCKTAIL				
30'	10.30-11.00	17:30-18.00	**19.30-20.00**	01.30-02.00 (+1)	03.30-04:00 (+1)				VIRTUAL EVENT PRADA FOUNDATION TOUR		
30'	11.00-11.30	18.00-18.30	**20.00-20.30**	02.00-02.30 (+1)	04.00-04:30 (+1)						

LEGEND	PLENARY	SECTIONAL LECTURES	MINI SYMPOSIA KEYNOTE LECTURES	ORAL DISCUSSION	POSTER DISCUSSION	GENERAL ASSEMBLY	SOCIAL EVENTS

PLENARY OPENING LECTURE

PL118206

BIOINSPIRED NANOMECHANICS: A CONTRIBUTION FOR THE CENTENARY OF THE GRIFFITH'S THEORY

Nicola Maria Pugno
Laboratory for Bioinspired, Bionic, Nano, Meta, Materials & Mechanics, Department of Civil, Environmental and Mechanical Engineering, University of Trento, Via Mesiano, 77, 38123 Trento, Italy
School of Engineering and Materials Science, Queen Mary University of London, Mile End Road, London E1 4NS, United Kingdom;
(nicola.pugno@unitn.it, extended abstract of the opening plenary lecture of the XXV ICTAM)

Summary The Italian artist, inventor and scientist Leonardo da Vinci (1452-1519) can probably be considered the father of bio-inspired design, as illustrated for example by his artificial wings and flying machines, based on bird observation and dissection. Five centuries from his death, bioinspiration is attracting widespread attention worldwide, both in academia and industry. This paper, related to the planned opening plenary lecture at XXV ICTAM, provides 3 new ideas in line with Griffith's theory of Linear Elastic Fracture Mechanics (LEFM): (i) a simple proposal to further generalize Dynamic/Quantized Fracture Mechanics theory and thus LEFM; (ii) the introduction of multiscale 3D Ashby's plots, to account for the role of size-effects on material properties for an improved material/structural selection and comparison; (iii) a new fundamental toughening mechanism that we -with Massimiliano Fraldi and colleagues- believe could be the key to better understand the fracture of bones, including related diseases (e.g. osteoporosis) and treatments; it is based on the evidence of stress alternating in sign in lamellae, thanks to symmetry breaking and hierarchy, simultaneously helping the crack opening needed for bone remodeling and the crack arrest needed for preserving its integrity and thus life, also suggesting new bio-inspired designs for tough composites. The inspiration for this work derives not only from Nature (and from da Vinci), but also from fundamental papers published by estimated colleagues of our community, all of whom I cannot mention here for brevity, starting from A. A. Griffith, who 100 years ago published his seminal paper. The following considerations thus represent my contribution for the centenary of Griffith's theory.

GRIFFITH/GENERALIZED DYNAMIC QUANTIZED FRACTURE MECHANICS

In 1921 Griffith published his seminal paper, submitted in 1920, basically describing the theory of Linear Elastic Fracture Mechanics (LEFM) [1], Fig. 1.

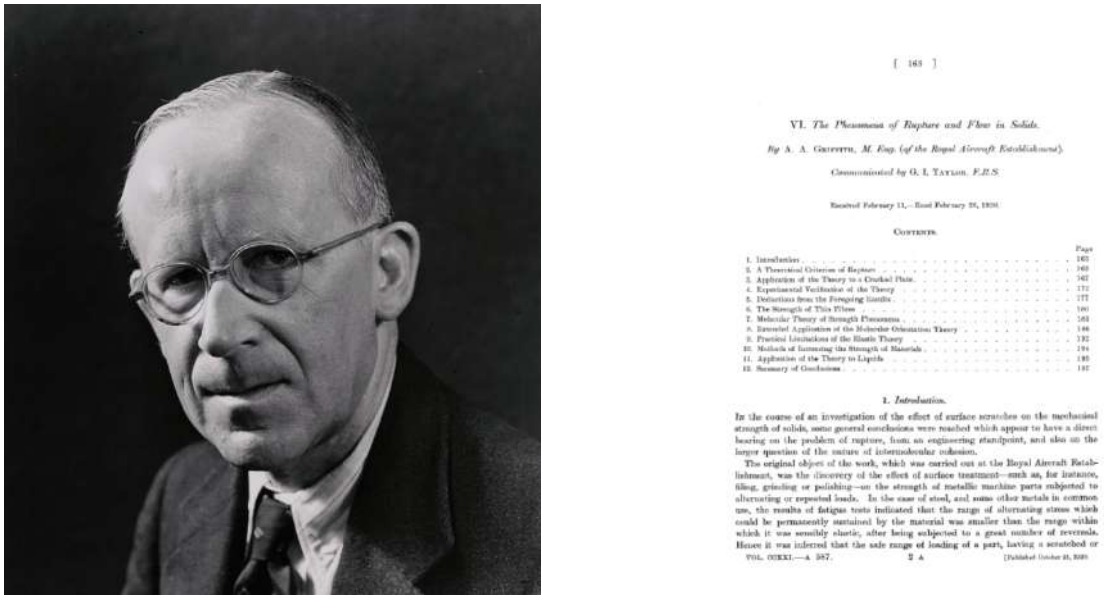

Figure 1. (left) Sir A. A. Griffith published his pioneering paper 100 years ago: The phenomena of rupture and flow in solids. Philosophical Transactions of the Royal Society of London. Series A, Containing Papers of a Mathematical or Physical Character. 1921 IV. 221: 163-198. (right) The first page of his pioneering paper.

According to LEFM, not the (maximal) stress but the energy release rate, or equivalently the stress intensity factor, must reach a critical value for the onset of crack propagation. In order to solve some limitations of LEFM, including the remaining paradox of infinite strength for vanishing crack length, I extended LEFM by introducing Quantized Fracture Mechanics (QFM, [2]): mathematically, differentials are simply substituted by finite differences in Griffith's energy balance. This corresponds to considering the onset of crack propagation not when the energy release rate reaches a critical value (the fracture energy per unit area of the material) but when its mean value along a fracture quantum of crack surface area ΔA -the previously introduced finite difference- reaches the material fracture energy. Equivalently, it is not the

stress intensity factor (for the different crack propagation modes) $K \equiv K_{LEFM}$ that must reach a critical value (the fracture toughness of the material, K_C) for crack propagation, but instead the square root of the mean value of the square of the stress intensity factor along a fracture quantum, which is by definition the quantized stress intensity factor K_{QFM}. This theory is thus based on the removal of the hypothesis of continuous crack growth, i.e. on the existence of a quantum of energy dissipation/crack advancement, as postulated in the stress-analogue approach by Novozhilov [3]. In dynamic fracture, and considering the existence of a quantum of action, the mean value must be considered also along a quantum of time Δt -thus defining the dynamic quantized stress intensity factor K_{DQFM} [4]- as introduced again by the Russian's School in the stress-analogue incubation time fracture mechanics approach [5].

The exponent of 2 can in principle be generalized to a positive real number α, thus proposing a Griffith/Generalized (Dynamic) Quantized Fracture Mechanics (GQFM), predicting crack propagation according to:

$$K_{GQFM}^{(\alpha,\Delta A,\Delta t)} \equiv \sqrt[\alpha]{\frac{1}{\Delta A \Delta t}\int_{t-\Delta t}^{t}\int_{A}^{A+\Delta A} K(A,t)^{\alpha}\mathrm{d}A\mathrm{d}t} = K_C \qquad (1)$$

Note that $K_{GQFM}^{(\alpha,\Delta A=0,\Delta t=0)} = K_{LEFM}$, $K_{GQFM}^{(\alpha=2,\Delta A,\Delta t=0)} = K_{QFM}$, $K_{GQFM}^{(\alpha=2,\Delta A,\Delta t)} = K_{DQFM}$ and $K_{GQFM}^{(\alpha=1,\Delta A=0,\Delta t)} = K_{ITFM}$, where K_{ITFM} is the equivalent stress-intensity factor according to the incubation time fracture mechanics [5]. Accordingly, all these limiting-case theories, which have been proved to capture experimental observations that LEFM cannot describe, are recovered and thus the correspondence principle is satisfied, as expected in the limit of vanishing fracture energy and action quanta.

The generalized stress intensity factor in (1) could also extend stress-intensity factor based laws such as those of fatigue, as proven for $\alpha = 2$ to capture both long and short crack behaviours even in fatigue (thus from the Wöhler to the Paris regimes) [6]. With the criterion (1), apparent R-curve behaviours and strain-rate effects emerge naturally as a consequence of the existence of fracture and time quanta, rendering fracture toughness no longer, or less crack-length and strain-rate dependent, and thus a more realistic material property, as it must be by definition. This could also help in the formulation of more realistic Ashby's plots.

MULTISCALE 3D ASHBY'S PLOTS

Asbhy's plots are fundamental for material selection [7]. As is well known, simply assuming in Griffith's theory a crack length $a \propto l^k$, where l is the structural size, would result in a scaling law for the strength of the type $\sigma \propto l^{-k/2}$, as similarly predicted by Weibull's statistics [8] or by other interpretations, e.g. fractal geometry [9]. I do not wish to comment here about the details of size-effect laws, but rather to emphasize that with the advent of nanotechnology, it is not infrequent to see papers reporting the fabrication of a new material using an Ashby's plot, even if it has been tested at a smaller size-scale. The need to adopt different Ashby's plots at the micro- and nano-scales has already been highlighted [10]. Here, I propose to use 3D Asbhy's plots for an improved multiscale representation, material/structural selection and comparison.

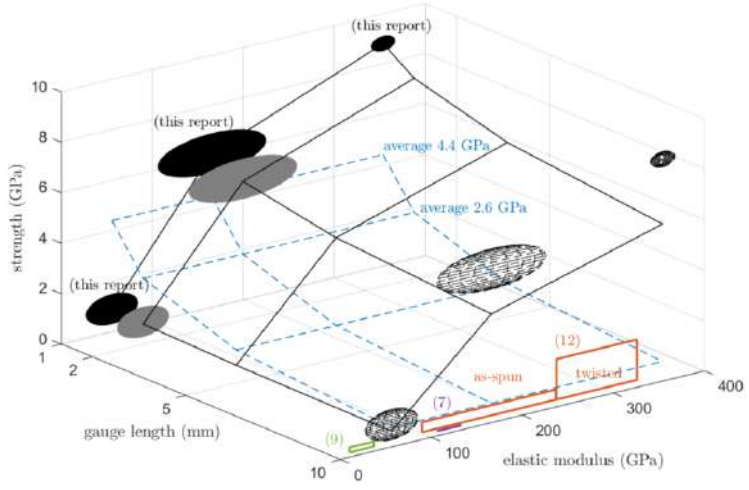

Figure 2. The black ellipses represent the strength vs elastic modulus data collected by the authors in [11] corresponding to samples with 1-mm gauge length (their fig. 4B). The overall average of this data is 4.4 GPa, while I have computed a total average of 2.6 GPa for the data at 2-mm gauge length (their fig. 3A). The corresponding scaling law, considering in a first approximation the independence of the elastic modulus, is of the type $\sigma \propto l^{-k/2}$ with a large value of $k/2 \cong 0.75$ (blue dashed lines). This scaling law predicts strength values comparable to those taken from the literature (green, purple or red areas, 1-cm gauge length). When considering the low- and high-strength regions (peaks in their fig. 3A), the average for the ellipse centred at a strength of 6.2 GPa for 1-mm gauge length falls to 5.6 GPa for a 2-mm gauge length, thus giving a scaling law with $k/2 \cong 0.15$ (black solid lines). The dashed ellipses are the projections at 10-mm gauge length of those at 1-mm gauge length, as reported in [11], whereas mean or maximal predictions at 10-mm are those reported with the blue dashed or black continuous lines, respectively. This case study must be considered just a preliminary example, such as the deduced size-effects.

As an example, I treat the case reported in Figure 2, where nanotube bundles are considered according to the paper in [11]. Asbhy's plot presented by the authors was inevitably classical, i.e. 2D, without considering the role of the bundle/gauge length, even if these authors perfectly recognized the role of size-effects and thus tested samples at different gauge lengths. A 3D Asbhy's plot, with a new axis corresponding to the size-scale (here gauge length) could thus be a better choice for comparison with other experiments, as described in Fig. 2. The experiments from the literature reported for comparison in [11] where performed at a gauge length of 1 cm, which I have considered in the 3D plot. I have also reported their experiments [11], not in the same plane but in their correct positions (1-mm or 2-mm gauge length planes). According to the same authors' experiments at different gauge lengths and assuming the simple mentioned scaling law of $\sigma \propto l^{-k/2}$, I could predict mean or maximal strength values expected at larger gauge lengths, including 10 mm, as reported respectively with the blue dashed or black solid lines.

The need for multiscale 3D Asbhy's plots is thus evident if we wish to move towards a standardization in material property comparisons. Regarding fracture toughness, the use of criterion (1) could further help the standardization, as previously mentioned. In general, the understanding of the toughness mechanisms is fundamental in Nature and Engineering. We believe that we have discovered a new fundamental one in bones.

A RECENTLY DISCOVERED TOUGHENING MECHANISM IN BONES

Bone tissue is a hybrid material made of an inorganic calcium phosphate phase nucleated into a collagenous matrix and organized hierarchically, from nanofibrillary components, to osteons (hundreds of micrometers in size), up to the cortical/trabecular macrostructure. It behaves as a complex composite able to adapt its internal organization to optimize the mechanical response under externally applied loads, contemporarily minimizing weight and resisting severe impacts and fatigue stress cycles by exhibiting surprising and not yet completely understood crack arresting mechanisms to avoid catastrophic fracture. In particular, it seems to be suitably designed to resist fracture at multiple size scales, thus achieving remarkable strength and toughness. However, the exceptional mechanical properties of bone can deteriorate with ageing and/or diseases: therefore, it is necessary to fully understand the mechanisms that confer these properties, also to develop therapies able to preserve or even rescue tissue functionality. Osteons, the fundamental bone units (Fig. 3a), are nearly hollow cylinders made of several concentric layers (lamellae) comprising helically arranged fibres wrapped nearly alternately clockwise and counterclockwise. With the Basic Multicellular Unit (BMU) osteocytes sense mechanical signals and activate and coordinate osteoblasts and osteoclasts for bone remodelling, i.e. resorption of preexisting bone by osteoclasts followed by *de novo* bone formation by osteoblasts (this process being impaired during ageing and diseases). It is ascertained that micro-damaging occurring across the scales plays a crucial role in bone mechanobiology, the micro-cracks opening at the osteon-matrix interfaces and within osteons working to trigger the BMU activities and the level of damage being an indicator of the need to locally increase mineral content through bone remodelling processes. However, how the crack propagation is triggered and arrested nearly simultaneously, both in compression and in tension (and thus also in bending) in such a stiff material, is still a partially unsolved enigma.

The most recognised hypothesis to explain the crack stopping/slowing phenomenon is based on the material inhomogeneity and anisotropy and the layered architecture of osteons: after nucleating, cracks would be halted when radially travelling across the osteon lamellae since they encounter the nearly alternating and in any case different arrangement of the wrapped fibres that make them decelerate at the lamellar interfaces and deviate along the circumferential direction. This leads to the dissipation of energy by increasing the length of the crack path, as well as by breaking micro-bridge elements and encountering a number of micro-voids and discontinuities generating micro-cracking. This mechanism surely plays an important role in arresting cracks in bone, but both theoretical calculations to estimate stress intensity factors at the crack tips and numerical analyses simulating crack propagation within osteons under static/cyclic loads as well as experimental findings [12], highlight that this is not sufficient to hinder fracture, suggesting that some yet undiscovered mechanisms should cooperate with (or exploit) bone hierarchy to halt crack progression [13]. Theoretical results also suggest that tensile hoop stresses in the lamellae, responsible for micro-crack opening in the radial direction, would occur only in case of compressive loads, while experimental observations show diffuse radial micro-cracks generated by tensile loads too [14].

Motivated by these incomplete and somehow contradictory results, we (the authors of ref. [15]) deeply explored an additional crack opening and stopping thus smart toughening mechanism with respect to those widely accepted in the literature, for which we have now clear theoretical evidences as well as experimental confirmation on 3D printed artificial hierarchical bones. For the occasion of this XXV ICTAM conference, we have rendered the paper public in the *Arxiv* [15]. Our results, obtained from an accurate mechanical model (Fig. 3a) of elastic anisotropy (Fig. 3b), show a counterintuitive radially distribution alternating in sign of both hoop and shear stresses in the lamellae and sub-lamellae (Fig. 3c,d), which could simultaneously act to open and halt cracks (Fig. 3e) thanks to hierarchy and symmetry breaking (Fig. 3f). This could also better stimulate the osteocyte activity by amplifying the mechanical signal, thus finally producing a "perfect" system capable to work both under compression or tension and thus bending.

Accordingly, this indeed unveils a powerful crack opening and simultaneously arresting mechanism, mediated by both the helical microstructure of the collagen fibrils in lamellae and sub-lamellae and the currently neglected small discrepancy in the nearly symmetric staggered angles of their wrapping in adjacent lamellae/sub-lamellae. The latter symmetry breaking generates this mechanism of Alternating Stresses in Lamellae (ASL, Fig. 3f), also occuring in sub-lamellae (ASL2) and hierarchy is shown to further enhance its power (Fig. 3c,d). Thus if ASL plays a fundamental role in bone toughening, its disappearance could be strictly related with bone ageing and common bone degenerative diseases, such as osteoporosis. Therefore, investigating the mechanosignaling pathways linking ASL to cellular response(s) and

tissue remodelling could have important and wide-ranging implications for both the comprehension of bone disorders and the conception of new therapies, essentially based on the idea of restoring ASL when lost. Additionally, with this ASL*n*-based toughening mechanism, a new design of bio-inspired *n*-level hierarchical composites is envisioned, e.g. in the next generation of self-healing materials where both crack opening and arrest could be required.

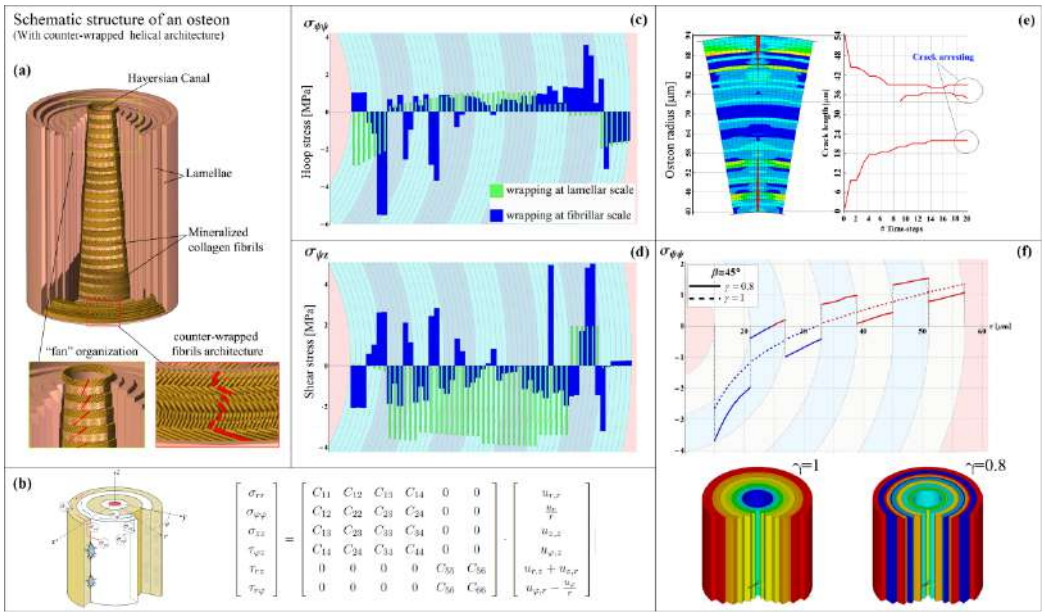

Figure 3. a) Osteon schematic structure. b) Anisotropic (monoclinic) elastic global equations resulting from the local helicoidal transversal isotropy (5 elastic constants). c)-d) Alternating in sign hoop and shear stresses without or with the presence of sub-lamellae, with stress jump amplification in the latter hierarchical case. e) Numerically (finite element) simulated crack progression and halting across osteon lamellae. f) Alternating in sign hoop and shear stresses in adjacent lamellae with fibril wrapping angles of β and $-\gamma\beta$ respectively and related stress jump amplification for symmetry breaking ($\gamma \neq 1$). For details see [15].

CONCLUSIONS

To celebrate the centenary of Griffith's theory (1921), in this paper -related to the opening plenary lecture at XXV ICTAM- I have presented 3 new concepts in the field of fracture: (i) a new extension of Griffith's theory, following the previous proposals by the author on Dynamic/Quantized Fracture Mechanics; (ii) the proposal of multiscale 3D Asbhy's plots, to include in these plots the fundamental role of the size-scale on the strength and in general on the mechanical properties of materials, for an improved material/structural selection and comparison; (iii) a new fundamental bone toughening mechanism, deriving from evidence of stress alternating in sign in osteon lamellae, emerging from the rupture of the symmetry of fibrils and empowered by hierarchy of sub-lamellae, suggesting also inspired solutions in Leonardo da Vinci's spirit [16].

As our lamellae, alone we are fragile but altogether we are resilient: this is why the pandemic is not stopping us, thanks to the new frontiers of Science and Technology and especially solidarity among peoples.

References

[1] Griffith, A. A. The phenomena of rupture and flow in solids. *Philosophical Transactions of the Royal Society of London*. Series A, Containing Papers of a Mathematical or Physical Character. IV. **221**: 163-198, 1921.
[2] Pugno N. M., Ruoff R. Quantized Fracture Mechanics. *Philosophical Magazine* **84**: 2829-2845, 2004.
[3] Novozhilov V. On a necessary and sufficient criterion for brittle strength, *Prik. Mat. Mek.* **33**: 212-222, 1969.
[4] Pugno N. M. Dynamic Quantized Fracture Mechanics. *International Journal of Fracture* **140**: 159-168, 2006.
[5] Petrov Y. and Morozov N. On the Modeling of Fracture of Brittle Solids, *Journal of Applied Mechanics* **61**: 710-712, 1994.
[6] Pugno N. M., Cornetti N., Carpinteri A. New unified laws in fatigue: from the Wöhler's to the Paris' regime. *Engineering Fracture Mechanics* **601**: 595-601, 2007.
[7] Ashby M. F. A first report on deformation-mechanism maps. *Acta Metallurgica* **20**: 887-897, 1972.
[8] Weibull W. A statistical distribution function of wide applicability. *Journal of Applied Mechanics* **18**: 293-297, 1951.
[9] Carpinteri A., Pugno N. M. Are the scaling laws on strength of solids related to mechanics or to geometry? *Nature Materials* **4**: 421-423, 2005.
[10] Zou, Y. Materials selection in micro- or nano-mechanical design: Towards new Ashby plots for small-sized materials, *Materials Science and Engineering: A* **680**: 421-425, 2017.
[11] Koziol K., Vilatela J., Moisala A., Motta M., Cunniff P., Sennett M., Windle A. High-Performance Carbon Nanotube Fiber. *Science* **318**, 1892-1895, 2007.
[12] Sabet F., Najafi A., Hamed E., Jasiuk I. Modelling of bone fracture and strength at different length scales: a review. *Interface Focus* **6**: 20150055, 2016.
[13] Ritchie R. O. The conflicts between strength and toughness. *Nature Materials* **10**: 817-822, 2011.
[14] Yeni Y. N., Hou F., Ciarelli T., Vashishth D., Fyhrie D. P. Trabecular shear stresses predict in vivo linear microcrack density but not diffuse damage in human vertebral cancellous bone. *Annals of Biomedical Engineering* **31**: 726-732, 2003.
[15] Fraldi M., Cutolo A., Carotenuto A., Palumbo S., Bosia F., Pugno N. M. Alternating in sign lamellar stresses, thanks to symmetry breaking and hierarchy, provide a new fundamental bone toughening mechanism, *Arxiv,* August 2021.
[16] Pugno N. M. The commemoration of Leonardo da Vinci. *Meccanica* **54**: 2317-2324, 2019.

PLENARY CLOSING LECTURE

PL118207

RHEOLOGY OF DENSE GRANULAR SUSPENSION

Élisabeth Guazzelli
Matière et Systèmes Complexes, CNRS, Université de Paris, France

Summary Suspensions consisting of mixtures of particles and fluids are materials with broad applications both in natural phenomena and in industrial processes. The present talk focusses on the rheology of concentrated suspensions of non-colloidal particles and shows that it can be tackled by a diversity of approaches depending on the flow configuration and on the parameters that one wishes to describe.

INTRODUCTION

Suspensions are composed of mixtures of particles and fluid and are ubiquitous in many natural phenomena (e.g. sediment transport in rivers and oceans, landslides, debris and lava flows) and in industrial processes (e.g. food and cosmetic, pulp and paper, materials for civil and petroleum engineering), see e. g. [1]. Due to their relevance to so many common situations, it is of utter importance to understand their response to imposed forces or motions at their boundaries. The problem is then to determine the rheological properties of these media (usually considered as equivalent homogeneous materials) from a knowledge of the mechanics of the particles and the interstitial fluid. In other words, the issue is to understand the relationship between the macroscopic or bulk properties of the flowing medium and its microscopic structure, see e. g. [2] .

This talk concerns the rheology of non-Brownian suspensions, meaning that the particles of interest are sufficiently large (i.e. have radius much larger than a micrometer) for Brownian or colloidal forces (such as electric double layer or van der Waals forces) to be ignored. It is mostly restricted to the condition of vanishingly small Reynolds numbers. It also focusses on the dense regime of large particle concentrations which is far from being completely deciphered. The major impediment to this understanding stems from the complex nature of the interactions between the particles. The grains can interact both by hydrodynamic interactions through the liquid but also by direct mechanical contact as the concentration increases. This is why these suspensions have been coined 'dense granular suspensions' as they somehow belong to an intermediate regime between pure Stokesian (inertialess) suspensions for which long-range hydrodynamics interactions or lubrication forces between the particles are essential and granular flows for which only direct contact interactions are present, see e. g. [3].

There are multiple avenues to study dense suspension rheology. Dense suspensions can be seen as a fluid with effective rheological properties but also as a two-phase system wherein the fluid and particles can experience relative motion. They can be described with constitutive laws in which the control parameter is the normal stress imposed to the particle phase rather than the volume fraction. This alternative description inspired by the frictional approach of dry granular media is particularly suited to yield examination of the rheology close to the jamming transition. Also, when the suspensions are confined, e.g. by interfaces, the discrete nature of the suspension comes into play.

THE SUSPENSION VIEWED AS A SINGLE EFFECTIVE FLUID

Provided the length scale of the flow is large compared with the average spacing between the particles, the suspension may evidently be regarded as a continuous effective fluid. It is well known since the seminal work of Einstein [4, 5] that the effect of adding particles results in an increase of the viscosity of the mixture above that of the suspending fluid. For the simplest case of a suspension of monodisperse hard spheres under simple shear, see figure 1 (a), the shear stress, τ, scales linearly with the shear rate, $\dot{\gamma}$, in the Stokes regime of vanishingly small Reynolds numbers. In other words, the scaling of the stress is viscous, $\tau = \eta_s \eta_f \dot{\gamma}$, where η_f is the viscosity of the suspending fluid and η_s is the relative viscosity of the suspension. This suspension viscosity, η_s, only depends on the particle volume fraction, ϕ, and increases with increasing ϕ. It is seen to diverge at the jamming transition where the particle concentration reaches a maximum value, ϕ_c, for which the suspension ceases to flow. This maximum flowable volume fraction generally differs from the maximum close random packing fraction (≈ 0.64) and varies depending on the size distribution of the particles and also their surface interactions, more precisely their frictional interactions. In practice it may be difficult to flow a suspension for $\phi > 0.52 - 0.62$.

A viscous suspension of hard spheres can be seen as a quasi Newtonian fluid with a shear viscosity increasing with increasing volume fraction. This however does not account for the existence of normal stress differences, i.e. for normal stresses which are no longer isotropic under shear, which appear for non dilute suspensions. This non-Newtonian feature is intimately linked to the loss of isotropy of the suspension microstructure due to the irreversible dynamics (due to contact interactions between the rough spheres) that develop under shear. Similarly to the shear stress, normal stresses scale viscously in Stokes flows and are proportional to the modulus of the shear stress. They also present the same divergence as the shear stress when approaching the jamming transition. Normal stress differences are difficult to be measured as they happen to be much smaller than the shear stress at small ϕ. For suspensions of hard spheres, the second normal stress difference is observed to be negative and to increase with increasing ϕ while the first normal stress difference is much smaller and its sign more elusive, see e. g. [6, 7].

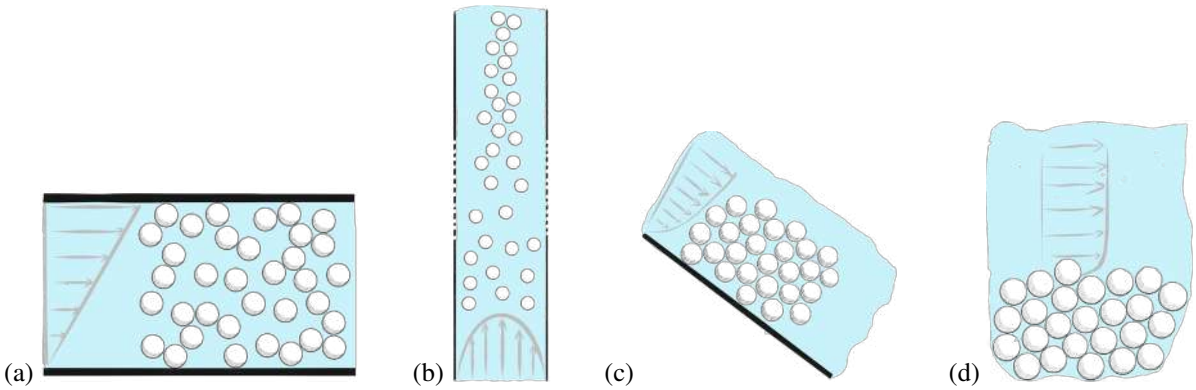

Figure 1: Some suspension flow configurations: (a) shearing flow of a suspension of neutrally-buoyant hard spheres between two plates, (b) shear-induced migration of neutrally-buoyant spheres in pressure-driven Poiseuille flow in a tube, (c) flows of immersed heavy particles down an inclined plane, (d) erosion of sedimented particles under the action of viscous fluid shearing flows.

BEYOND A SINGLE PHASE VIEW: TWO-PHASE SUSPENSION FLOWS

In many flow configurations, the fluid and the particles experience relative motion. It is then necessary to go beyond the single phase description presented in the preceding section and to consider two separate fluid and particle phases. An archetypal example is the phenomenon of shear-induced migration, e. g. the observed irreversible migration of neutrally-buoyant spheres in a pipe flow [8]. The particles have a tendency to move from the high shear region at the wall toward the low shear region at the centre line, see figure 1 (b). A key concept of the two-phase description is that of particle pressure. Whereas the whole suspension, i. e. the mixture of the particles and the fluid, is incompressible, the particle phase is not. There exists a pressure coming from the dispersed particulate phase that can develop in particular in the concentrated regime. It has been termed particle pressure (or more generally particle normal-stress) and has been considered an analog to the osmotic pressure exerted by colloidal particles or dissolved molecules and ions, where here the shear rate plays the role of the temperature to induce agitation and collisions between the particles. This particle normal stress P also scales viscously and is linear in the modulus of the shear rate. It can be written as $P = \eta_n(\phi)\,\eta_f\dot{\gamma}$ (where $\dot{\gamma}$ is conveniently defined in an invariant form as $\dot{\gamma} = \sqrt{2\,\mathbf{E}:\mathbf{E}}$ where $\mathbf{E}$ is the rate of strain). The dimensionless effective normal viscosity η_n is again a sole function of ϕ and presents the same divergence as $\eta_s(\phi)$ when approaching jamming at ϕ_c. Particle normal stress produces the driving force for the motion of the particles and is fundamental in the physical understanding of the migration process [9, 10, 11, 12].

AN ALTERNATIVE FRICTIONAL APPROACH

Up to now we have discussed situations where the control parameter is the particle volume fraction, ϕ. However, under some flow configurations, ϕ is not controlled and is a free adjustable parameter. This is the case of flows where gravity controls the level of stress experienced by the particle phase such as flows of heavy particles down an inclined plane [13] or transport of sedimented particles under the action of viscous fluid shearing flows [14, 15] depicted in figure 1 (c) and (d), respectively. The control parameter is then the stress imposed to the particle phase, P, and no longer the volume fraction, ϕ. This alternative description, coined 'pressure-imposed rheology' by contrast to the classical 'volume-imposed rheology' (see figure 2) is derived from the rheological approach developed to describe dry granular flows and hinges on a frictional view of the problem, see e. g. [16]. When the suspension is subjected to steady shear under a confining particle pressure P, there is only one dimensionless control parameter, a dimensionless shear rate which can be interpreted as the ratio of the time scale for particles to rearrange due to the pressure P to the time scale of the flow, $\dot{\gamma}^{-1}$. The effective friction coefficient $\mu = \tau/P$ and the volume fraction ϕ are sole function of this dimensionless number. In the case of suspensions for which viscous forces are dominant, the dimensionless number is $J = \eta_f\dot{\gamma}/P$ and is viscous in contrast to dry granular flows where it is inertial. Suspensions and granular materials can thus be described with a common frictional framework [17]. In the case of viscous suspensions, this frictional formulation is equivalent to the classical description of the rheology of suspensions in terms of effective viscosities discussed earlier: the shear, $\eta_s(\phi) = \tau/\eta_f\dot{\gamma} = \mu/J(\phi)$, and normal, $\eta_n(\phi) = P/\eta_f\dot{\gamma} = 1/J(\phi)$, relative viscosities where $J(\phi)$ is the inverse function of $\phi(J)$ which is perfectly defined since $\phi(J)$ is monotonic. This alternative frictional approach is particularly suitable to infer the singular rheological properties at the jamming transition as it circumvents the divergence observed in volume-imposed rheometry.

APPROACHING JAMMING

As the jamming transition is approached, particles form an extended network of contacts, and the rheology is then dominated by contact forces, even in the case of viscous suspensions for which contact interactions prevail over long-range

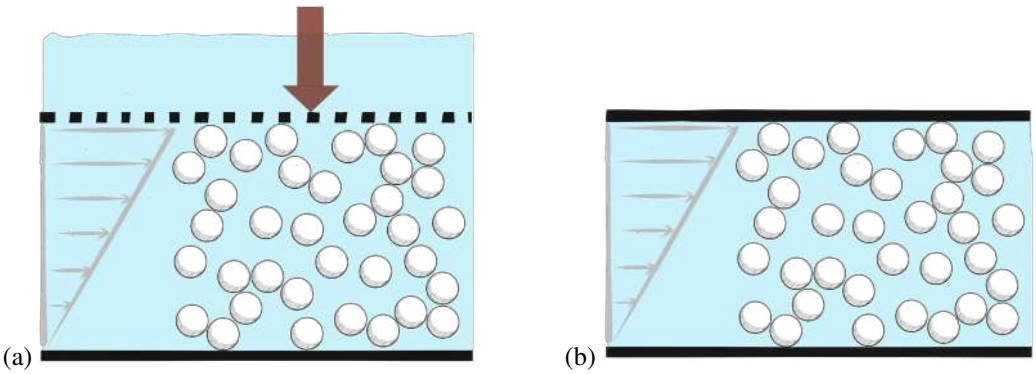

Figure 2: Pressure-imposed versus volume-imposed rheometry: (a) in pressure-imposed rheometry, the neutrally-buoyant particles are sheared at a given shear rate under a confining pressure applied to a top porous plate which enables the fluid to flow through it but not the particles (the height of the top plate can adjust in response to dilatation or compaction of the sheared suspension), (b) in volume-imposed rheometry, the neutrally buoyant particles are sheared at a given shear rate and constant volume fraction as the gap between the plates is kept constant.

hydrodynamics interactions or lubrication forces. There is not yet an accepted microscopic description of the transition and the current description, while remaining rather empirical, aims at understanding the properties of the contact network between the particles close to jamming [18, 19]. Experiments for suspensions of frictional spheres show similar algebraic divergences of the shear and normal viscosities in $(\phi_c - \phi)^{-2}$ close to the transition, see e. g. the pressure-imposed rheometry measurements of [17, 20]. This asymptotic behavior is not changed by an increase in particle roughness, or equivalently interparticle friction [21]. The quasistatic value of the effective friction coefficient, μ_c, is not significantly affected either. It is also similar to that obtained for dry granular spheres showing that hydrodynamic interactions are inconsequential and contact forces are prevailing in this quasistatic limit. Only the critical volume fraction at jamming, ϕ_c, is impacted as it decreases with increasing roughness. Conversely, the influence of the particle shape seems to have a profound impact on the singular behavior near the jamming transition. For suspension consisting of rod-like particles (i. e. fibers), the critical volume fraction, ϕ_c, decreases with increasing aspect ratio, A, and when rescaling with $\phi_c(A)$ is done, the shear and normal viscosities present a divergence in $(\phi_c - \phi)^{-1}$, in stark contrast with the divergence observed for spheres [22].

WHEN CONTINUUM BREAKS DOWN: SUSPENSIONS CONFINED BY INTERFACES

Not everything is yet elucidated but, as discussed in the preceding sections, the bulk flow rheology of granular suspensions is beginning to be well documented. Much less is known in the case of confined flows where the discrete nature of the suspension comes into play and the continuum description breaks down. In particular, suspensions confined by mobile interfaces raise new questions which are entirely unexplored.

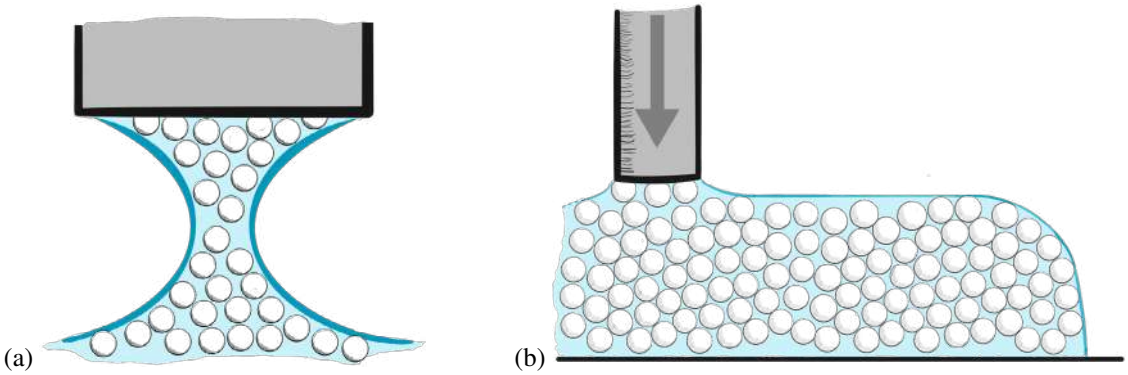

Figure 3: Two capillary flows of a suspension: (a) the pinch-off of a viscous suspension thread, (b) the wetting of a viscous granular suspension on a solid surface

Two classical capillary flow configurations are depicted in figure 3: (a) the pinch-off of a viscous suspension thread and (b) the wetting of a viscous granular suspension on a solid surface. Adding spheres to a viscous liquid thread has a drastic influence on its break-up. In the early stage of the pinch-off, the dynamics is independent of the size of the particles and the suspension behaves as an effective viscous fluid. But, there is a subsequent discrete regime in the late stage of the pinch-off, in which the thinning dynamics accelerates significantly and is dominated by discrete particle effects [23]. The spreading of a suspension on a solid surface also presents non-trivial behavior in particular in the vicinity of the moving contact line. The spherical particles remain at a finite distance from the contact line and there is consequently a region

devoid of particles in the vicinity of this contact line. This leads to an unexpected behavior as the apparent viscosity during spreading depends both on the size and volume fraction of the particles and thus profoundly differs from the bulk viscosity.

CONCLUSIONS

While long-range hydrodynamics interactions or lubrication forces are essential for dilute suspensions, contact interactions between particles become of fundamental importance for the understanding of concentrated suspension. This talk gives an overview of the different approaches that can be followed to tackle suspension rheology in this dense regime. Beyond the classical problem of the bulk flow of dense suspensions of hard spheres in a Newtonian fluid, there are entirely novel avenues of study concerning more complex mixtures of particles and fluid in more complex flowing geometries.

This work emanates from a long-term collaboration with O. Pouliquen on the rheology of granular suspensions at IUSTI (Aix Marseille Université and CNRS) and is part of the doctoral and postdoctoral studies of F. Boyer, E. Couturier, S. Dagois-Bohy, S. Hormozi, and F. Tapia. It also owes much to scientific interactions with J. F. Morris and P. R. Nott. Studies on sediment transport have been started with P. Aussillous and also come from collaboration with J. Chauchat, M. Médale, M. Ouriemi, M. Pailha, and Y. Peysson. Studies of fiber suspensions stem from a long-lasting collaboration with J. E. Butler (University of Florida) which has given rise to the jointly-advised doctoral studies of B. Snook, S. Shaikh, and S. Strednak. Finally, the more recent studies of granular suspensions confined by interfaces have been initiated with H. Lhuissier and M. Roché and are part of work undertaken with J. Château, L. Limat, M. Oléron, A. Pelosse, M. Zhao.

References

[1] Guazzelli É. and Morris J. F. A Physical Introduction to Suspension Dynamics. Cambridge University Press, 2012.
[2] Batchelor G. The stress system in a suspension of force-free particles. *J. Fluid Mech.* **41**: 545-570, 1970.
[3] Guazzelli É. and Pouliquen O. Rheology of dense granular suspensions. *J. Fluid Mech.* **852**: P1, 2018.
[4] Einstein A. Eine neue Bestimmung der Moleküldimensionen. *Ann. Phys.*, **19**: 289-306, 1906.
[5] Einstein A. Berichtigung zu meiner Arbeit: Eine neue Bestimmung der Moleküldimensionen. *Ann. Phys.*, **34**: 591-592,1911.
[6] Boyer F., Pouliquen O. and Guazzelli É. Dense suspensions in rotating-rod flows: normal stresses and particle migration. *J. Fluid Mech.* **686**:5-25, 2011.
[7] Couturier E., Boyer F., Pouliquen O. and Guazzelli É. Suspensions in a tilted trough: second normal stress difference. *J. Fluid Mech.* **686**: 26-39, 2011.
[8] Snook B., Butler J. E. and Guazzelli É. Dynamics of shear-induced migration of spherical particles in oscillatory pipe flow. *J. Fluid Mech.* **786**: 128-153, 2016 .
[9] Nott P. R. and Brady J. Pressure-driven flow of suspensions: simulation and theory. *J. Fluid Mech.* **275**: 157-199, 1994.
[10] Morris J. and Boulay F. Curvilinear flows of noncolloidal suspensions: The role of normal stresses. *J. Rheol.* **43**: 1213-1237, 1999.
[11] Lhuillier D. Migration of rigid particles in non-Brownian viscous suspensions. *Phys. Fluids* **21**: 023302, 2009.
[12] Nott P. R, Guazzelli É. and Pouliquen O. The suspension balance model revisited. *Phys. Fluids* **23**: 043304, 2011.
[13] Cassar C., Nicolas M. and Pouliquen O. Submarine granular flows down inclined planes. *Phys. Fluids* **17**: 103301, 2005.
[14] Ouriemi M., Aussillous P. and Guazzelli É. Sediment dynamics. Part 1. bed-load transport by laminar shearing flows. *J. Fluid Mech.* **636**: 295-319, 2009.
[15] Aussillous P., Chauchat J., Pailha M., Médale M. and Guazzelli É. Investigation of the mobile granular layer in bedload transport by laminar shearing flows. *J. Fluid Mech.* **736**: 594-615, 2013.
[16] Forterre Y. and Pouliquen O. Flows of dense granular media. *Annu. Rev. Fluid Mech.* **40**: 1-24, 2008.
[17] Boyer F., Guazzelli É. and Pouliquen, O. Unifying Suspension and Granular Rheology. *Phys. Rev. Lett.* **107**: 188301, 2011.
[18] Lerner E., Düring G. and Wyart M. A unified framework for non-Brownian suspension flows and soft amorphous solids. *Proc. Natl. Acad. Sci. USA* **109**, 4798-4803, 2012.
[19] Trulsson M., DeGiuli E. and Wyart, M. Effect of friction on dense suspension flows of hard particles. *Phys. Rev. E* **95**: 012605, 2017.
[20] Dagois-Bohy S., Hormozi S., Guazzelli É. and Pouliquen, O. Rheology of dense suspensions of non-colloidal spheres in yield-stress fluids. *J. Fluid Mech.* **776**: R2, 2015.
[21] Tapia F., Pouliquen O. and Guazzelli É. Influence of surface roughness on the rheology of immersed and dry frictional spheres. *Phys. Rev. Fluids* **4**: 104302, 2019.
[22] Tapia F., Shaikh S., Butler J. E., Pouliquen O. and Guazzelli, E. Rheology of concentrated suspensions of non-colloidal rigid fibres. *J. Fluid Mech.* **827**: R5, 2017.
[23] Château J., Guazzelli É., and Lhuissier H. Pinch-off of a viscous suspension thread. *J. Fluid Mech.* **852**: 178-198, 2018.
[24] Zhao M., Oléron M., Pelosse A., Limat L., Guazzelli É. and Roché M. to be published.

PRIZE PLENARY LECTURES

PP118204

MEASUREMENTS IN WALL-BOUNDED TURBULENCE

Alexander J. Smits
Department of Mechanical and Aerospace Engineering, Princeton University, Princeton NJ 08540, U.S.A.

Summary Our understanding of turbulent boundary layer scaling and structure has advanced greatly in the past 20 to 30 years. On the computational side, direct numerical simulations and large-eddy simulations have made extraordinary contributions as methods and computational resources have burgeoned, while on the experimental side major advances in instrumentation have made available imaging and quantitative techniques with unprecedented accuracy and detail. Here, I illustrate how our progress has been aided by the development of such experimental methods by reference to three particular questions on the scaling of turbulent boundary layers: (1) the similarity behavior in supersonic and hypersonic flows; (2) the structure of the outer layer in subsonic flows at high Reynolds number; and (3) the scaling of the turbulent stresses in the near-wall region. I close by discussing the likely role of computation and experiment in future studies.

TURBULENT BOUNDARY LAYERS IN SUPERSONIC AND HYPERSONIC FLOWS

There are two basic differences between boundary layers in subsonic and supersonic or hypersonic flows. First, there is always a region of subsonic flow near the surface, separated from the external flow by the point where the Mach number reaches one, that is, the sonic line. This region becomes smaller relative to the boundary layer thickness with increasing Mach and Reynolds number, but it also depends on the wall temperature in that it is larger on a heated wall than on a cooled one. Second, temperature gradients become important. For example, in a Mach 10.3 helium boundary layer over an adiabatic wall ($T_w/T_r = 1$), the temperature increases by a factor of about 33 across the boundary layer [1]. Hence the viscosity near the wall can be many times larger than that in the external flow, and a single Reynolds number no longer describes the flow state. As a result, the extent of the viscous layer as a fraction of the boundary layer thickness can increase significantly with Mach number. In addition, when the Mach number is high enough, the high temperatures experienced near the wall will lead to real gas effects including vibrational excitation, dissociation, and even ionization of the gas. Surface ablation effects may also become important. The onset of these real gas effects effectively marks the beginning of the hypersonic regime.

Prior to about 1985, it was generally believed that turbulence high-speed boundary layers was fundamentally different from that in subsonic flows. In particular, hot-wire measurements had shown that the level of the velocity fluctuations $\sqrt{\overline{u^2}}/u_\tau$ decreased with increasing Mach number, and that in the outer region of the boundary layer the turbulence was considerably less intermittent than in comparable subsonic flows [2, 3]. Flow visualization by schlieren or shadowgraph methods were not very helpful in this regard because they integrate across the flow, and do not generally give much information on the turbulent-non-turbulent interface. Also, the accuracy of hot-wire measurements in high-speed flows was often compromised by inadequate temporal or spatial resolution [4]. High-speed flow experiments make strict demands on hot wire anemometry in that the frequency content of the turbulent fluctuations is very high (100s of kHz), spatial resolution requirements are strict in that boundary layers are typically thin, and the aerodynamic loads on the wire can be severe. In addition, the calibration is complicated by the fact that the wire is sensitive to both density and velocity fluctuations [5].

The development of improved hot wire techniques in general [6], and in supersonic applications in particular [7, 8, 9, 10, 11] helped turn this around. In addition, the use of laser sheets and droplet seeding [12], and the development of filtered Rayleigh scattering methods [13, 14, 15] allowed planar visualizations of the flow field for the first time, as illustrated in figure 1. Superficially, therefore, a turbulent boundary layer in supersonic flow appears to behave much like its subsonic counterpart, in that its outer interface is highly intermittent, and it displays a large range of scales that increase with Reynolds number. The dynamic effects due to temperature gradients generally appear to be small, and over a large range of Mach numbers the mean velocity profile can be rescaled by accounting for the density changes induced by the temperature differences (as is the case for subsonic flows, the mean pressure across the boundary layer can be taken to be constant). This is the essence of the van Driest transformation, where, broadly speaking, the scaling variable for the velocity is taken to be $u^* = \sqrt{\tau_w/\rho}$ rather than the classic friction velocity $u_\tau = \sqrt{\tau_w/\rho_w}$.

A similar approach may be taken in scaling the turbulence profiles. It was Morkovin who first suggested using the local stress rather than the wall stress as a scaling variable [16], that is u^* rather than u_τ, and this is now known as Morkovin scaling. Recent PIV data obtained in a Mach 7.5 boundary layer confirms the usefulness of Morkovin scaling [4], as do DNS of similar flows [17]. These comparisons are given in figure 2.

As to the structure of the turbulence in high-speed flows, recent work suggests that, in contrast to previous understanding, it is largely independent of Mach number. For example, the streamwise length scales derived from velocity correlations were seen to decrease much more slowly with Mach number than suggested by older studies [4]. Similarly, the characteristic angle of inclination of the correlation contours of streamwise velocity is relatively insensitive to Mach number, whereas previous studies suggested that this angle increased with Mach number. These new observations also

Figure 1: (a) PLIF visualization of a Ma = 2.8 boundary layer (Re_θ = 81,900, $Re_\tau \approx$ 12,000). From [12]. (b) Two FRS images of a Ma = 7.5 boundary layer (Re_θ = 3310, Re_τ = 166). From [4]. Flow is from left to right.

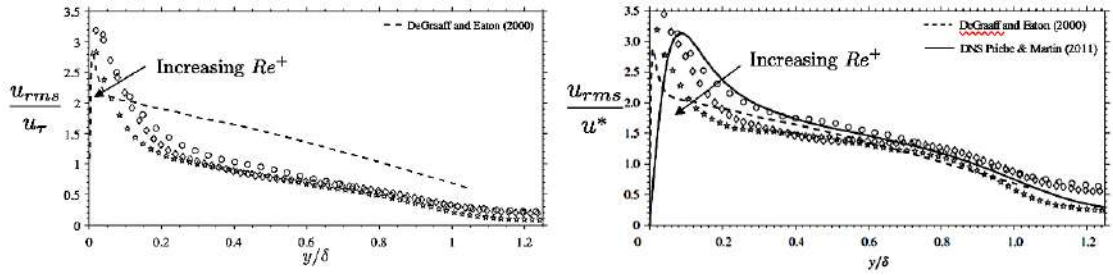

Figure 2: PIV turbulence data in Mach 7.5 air boundary layer, from [4]. (a) Classic scaling. (b) Morkovin scaling.

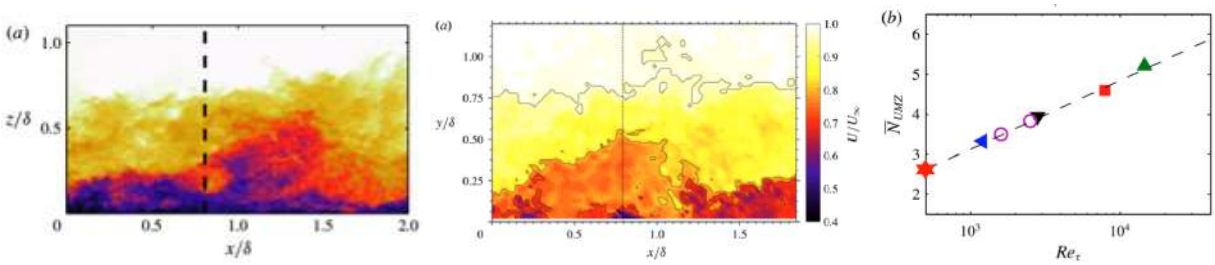

Figure 3: (a) Subsonic boundary layer streamwise velocity field [18]. (b) Mach 7.5 boundary layer streamwise velocity field, from [4]. (c) UMZ scaling with Reynolds number, adapted from [18]. The red star denotes the Mach 7.5 boundary layer.

imply that there are significant differences in the properties of velocity and density fields at high Mach number. Other measures, such as the number of Uniform Momentum Zones (UMZ), do not appear to demonstrate any Mach number dependence, and they appear to match the logarithmically scaling with Reynolds number observed for subsonic flows, as illustrated in figure 3.

SCALING OF THE OUTER LAYER

Despite many decades of work, it was not until relatively recently that the turbulence distributions in incompressible flows were accurately documented. For example, [19] collected a large number of experimental results on pipe flow, which illustrated the general lack of certainty in 2010 (see figure 4a). This lack of clarity has now largely been resolved by two major developments: the development of special-purpose, high-quality, high Reynolds number laboratory facilities, and major improvements in hot-wire anemometry.

We now consider the scaling of the outer layer, that is, the region where $y^+ > 100$. Townsend's [21] attached eddy hypothesis predicted that, in the overlap or logarithmic layer of the boundary layer at a sufficiently high Reynolds number, the streamwise turbulence intensity follows a logarithmic variation such that

$$\overline{u^{2+}} = B_1 - A_1 \ln(y/\delta) - V(y^+) \tag{1}$$

where the function $V(y^+)$ was introduced by Perry et al. [22] to account for viscous effects at lower Reynolds numbers. For the logarithmic term to emerge, it is clear that we need $V(y^+)$ to become negligible, which will only happen at high Reynolds number. Since the energy content in the outer layer is dominated by the larger scales of motion, any shortfall in either temporal or spatial resolution of the instrumentation is generally not the main issue, but high Reynolds numbers are essential. To develop high Reynolds number, high-quality boundary layers in conventional wind tunnels requires purpose-built large scale facilities, which are expensive. However, using high pressure as a means of increasing the unit Reynolds number is a cost-effective way to achieve very high Reynolds number flows (pipe or boundary layer). The Princeton Superpipe [23] yielded the results shown in figure 4b, up to $Re_\tau = 98,000$. The results for the outer layer are shown in figure 4c, and the logarithmic variation predicted by Townsend is clearly seen.

SCALING OF THE INNER LAYER

To reveal the scaling of the inner layer, in addition to having high Reynolds number facilities, we need instrumentation with sufficient temporal and spatial resolution to resolve the near-wall, small-scale motions accurately. Of these two, the

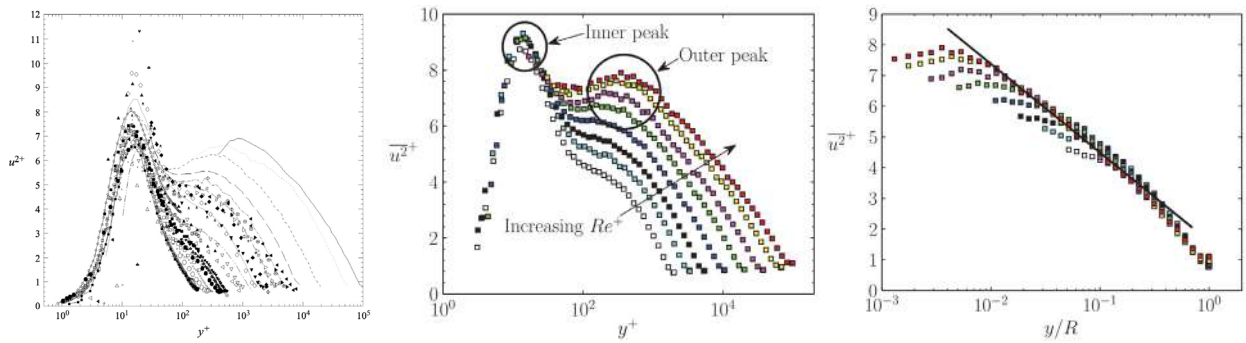

Figure 4: Streamwise turbulence intensity in pipe flow. (a) Data are from 13 experiments using LDV and hot wires. From [19], where sources are given. (b) Data from Superpipe in inner layer coordinates. From [20]. (c) Data from Superpipe in outer layer coordinates for $y^+ > 100$. The solid line is equation 1 with $A_1 = 1.25$, $B_1 = 1.61$. From [20].

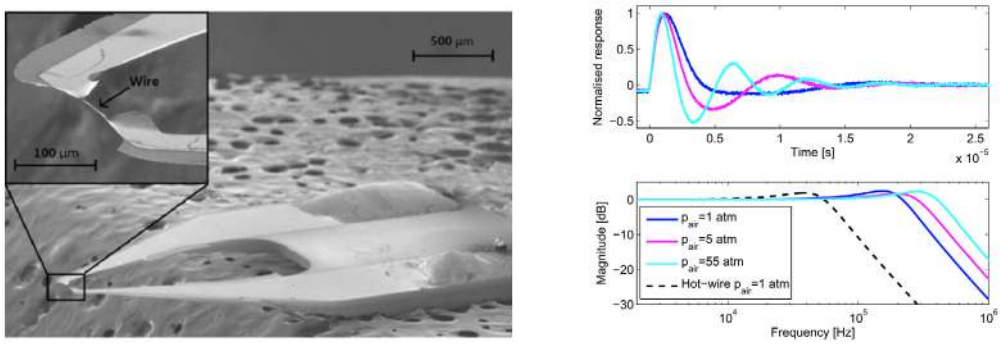

Figure 5: Configuration and performance of NSTAP ($\ell = 60$ μm, $w = 1$ μm, $t = 0.1$ μm). (a) Scanning electron microscope images. The probe is mounted on a wax substrate (seen in the background) for imaging. From [27]. (b) Temporal response of the NSTAP at different ambient air pressures. a) Square-wave response; (c) attenuation in signal with frequency (Bode diagram), where 0 dB indicates unity gain (estimated using square wave response). From [28].

spatial resolution was the more difficult criterion. It was widely held that hot wires or LDV with a maximum dimension $\ell^+ < 20$ would be sufficient to accurately measure the level of the near-wall peak in $\overline{u^{2+}}$, as long as $\ell/d \geq 200$ [24]. It was obvious, however, even from the data of [24] that the peak value continued to increase with decreasing ℓ^+ (see also [25]), as was made very clear by the work of Hutchins et al. [26].

In an effort to improve the spatial resolution of thermal anemometry, the NSTAP probes were developed at Princeton. These probes were made using MEMS techniques, and yielded ribbon-shaped sensors typically measuring 2 μm wide, 0.1 μm thick, and either 60 or 30 μm long (see figure 5)a. The sensors, therefore, have characteristic lengths about 10 times smaller than conventional hot wires, and, as evident from figure 5)b, they also have a typical frequency response about 10 times higher.

In this respect, the Superpipe data shown in figure 4b was taken using both 60 and 30 μm NSTAP probes, but even with these probes the peak could not be accurately resolved at the highest Reynolds number, despite corrections [29]. The measurements were, however, successful at unambiguously establishing the presence of the outer peak. It was not until NSTAPs were used in the Melbourne wind tunnel, where the boundary layer is about 350 mm thick, that measurements could be made in the near-wall region at high Reynolds number while maintaining $\ell^+ < 2.1$. The data are shown in figure 6, and they support a logarithmic correlation with Reynolds number, as also indicated by DNS.

SUMMARY

Our current understanding of turbulent boundary layers at all Mach and Reynolds numbers has been enabled by major advances in measurement techniques, especially in hot-wire anemometry and PIV. It is also clear that DNS and LES are beginning to take a leading role in the exploration of turbulence, and I expect that for canonical flows DNS will become the primary investigative tool within a decade.

References

[1] R.D. Watson, J.E. Harris, and J.B. Anders. Measurements in a transitional/ turbulent Mach 10 boundary layer at high Reynolds number. *AIAA Paper 73-165*, 1973.

[2] A.L. Kistler. Fluctuation measurements in a supersonic turbulent boundary layer. *Phys. Fluids*, 2:290–296, 1959.

[3] S.K. Robinson. Space-time correlation measurements in a compressible turbulent boundary layer. *AIAA Paper 86-1130*, 1986.

[4] O. J. H. Williams, D. Sahoo, M. L. Baumgartner, and A. J. Smits. Experiments on the structure and scaling of hypersonic turbulent boundary layers. *J. Fluid Mech.*, 834:237–270, 2018.

[5] L. S. G. Kovasznay. The hot wire anemometer in supersonic flow. *J. Aeron. Sci.*, 17:565–584, 1950.

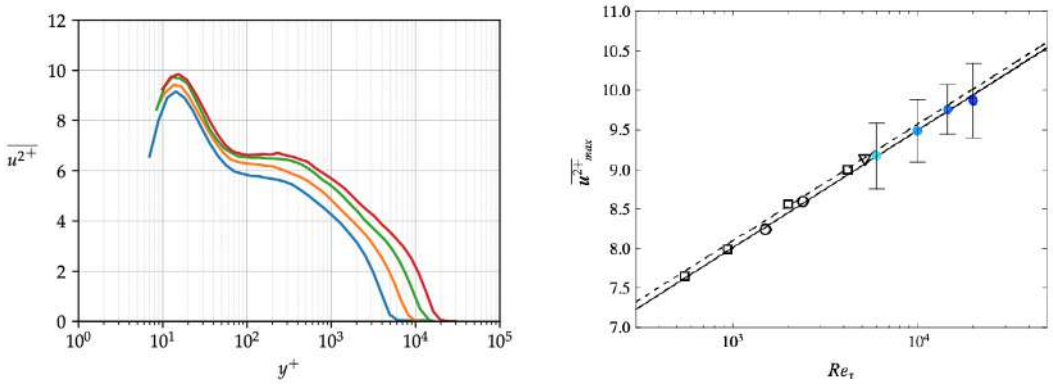

Figure 6: Left: Streamwise turbulence intensity in boundary layers for Re_τ = 6123, 10100, 14680, 19680. Data obtained using NSTAP with ℓ^+ = 2.5 to 3.5. Right: Dependence of unner peak magnitude on Reynolds number. ●, NSTAP; ○, DNS of turbulent boundary layer from [30]; □, DNS of channel flow from [31]; ▽, DNS of channel flow from [32]; ———, $\overline{u^{2+}_p} = 3.54 + 0.646\ln(Re_\tau)$; – – – –, $\overline{u^{2+}_p} = 3.66 + 0.642\ln(Re_\tau)$. From [33].

[6] A. E. Perry. Hot-Wire Anemometry. Oxford University Press, 1982.
[7] J. P. Bonnet and T. Alziary de Roquefort. Determination and optimization of frequency response of constant temperature hot-wire anemometers in supersonic flows. *Rev. Sci. Instrum.*, 51:234–239, 1980.
[8] D. Bestion and J. Gaviglio and J. P. Bonnet. Comparison between constant-current and constant-temperature hot-wire anemometers in high-speed flows. *Rev. Sci. Instrum.*, 54:(11) 1513-1524, 1983.
[9] A.J. Smits, K. Hayakawa, and K.C. Muck. Constant temperature hot-wire anemometry practice in supersonic flows. Part 1: The normal wire. *Exp. Fluids*, 1:83–92, 1983a.
[10] A.J. Smits and K.-C. Muck. Constant-temperature hot-wire anemometer practice in supersonic flows. Part 2: The inclined wire. *Exp. Fluids*, 2: 33–41, 1984.
[11] A.J. Smits and J.-P. Dussauge. Hot-wire anemometry in supersonic flow. *Chapter 5, AGARDograph 315*, 1989.
[12] M. W. Smith and A. J. Smits. Visualization of the structure of supersonic turbulent boundary layers. *Exp. Fluids*, 18:288–302, 1995.
[13] M. W. Smith and A. J. Smits. Cinematic visualization of coherent density structures in a supersonic turbulent boundary layer. *AIAA Paper 88-0500*, 1988.
[14] M. W. Smith, A. J. Smits, and R. B. Miles. Compressible boundary-layer density cross sections by UV Rayleigh scattering. *Optics Lett.*, 14: 916–918, 1989.
[15] R.B. Miles, J.N. Forkey, and W.R. Lempert. Filtered Rayleigh scattering measurements in supersonic/hypersonic facilities. *AIAA Paper 92-3894*, 1992.
[16] M.V. Morkovin. Effects of compressibility on turbulent flows. In A.J. Favre, editor, *Mécanique de la Turbulence*, pages 367–380. CNRS, 1962.
[17] S. Priebe and M. P. Martin. Direct numerical simulation of a hypersonic turbulent boundary layer on a large domain. *AIAA Paper 2011-3432*, 2011.
[18] C. de Silva, N. Hutchins, and I. Marusic. Uniform momentum zones in turbulent boundary layers. *J. Fluid Mech.*, 786:309–331, 2016.
[19] M. Hultmark, S. C. C. Bailey, and A. J. Smits. Scaling of near-wall turbulence in pipe flow. *J. Fluid Mech.*, 649:103–113, 2010.
[20] M. Hultmark, M. Vallikivi, S. C. C. Bailey, and A. J. Smits. Turbulent pipe flow at extreme Reynolds numbers. *Phys. Rev. Lett.*, 108(9):1–5, 2012.
[21] A. A. Townsend. *The Structure of Turbulent Shear Flow*. Cambridge University Press, Cambridge, UK, 1976.
[22] A. E. Perry, S. M. Henbest, and M. S. Chong. A theoretical and experimental study of wall turbulence. *J. Fluid Mech.*, 165:163–199, 1986.
[23] M. V. Zagarola and A. J. Smits. Mean-flow scaling of turbulent pipe flow. *J. Fluid Mech.*, 373:33–79, 1998.
[24] P.M. Ligrani and P. Bradshaw. Subminiature hot-wire sensors: development and use. *J. Phys. E: Sci. Instrum.*, 20:323–332, 1987.
[25] H. H. Fernholz and P. J. Finley. The incompressible zero-pressure-gradient turbulent boundary layer: an assessment of the data. *Prog. Aerospace Sci.*, 32:245–311, 1996.
[26] N. Hutchins, T. B. Nickels, I. Marusic, and M. S. Chong. Hot-wire spatial resolution issues in wall-bounded turbulence. *J. Fluid Mech.*, 635(-1): 103–136, 2009.
[27] M. Vallikivi, M. Hultmark, S. C. C. Bailey, and A. J. Smits. Turbulence measurements in pipe flow using a nano-scale thermal anemometry probe. *Exp. Fluids*, 51:1521–1527, 2011.
[28] M. Vallikivi and A. J. Smits. Fabrication and characterization of a novel nano-scale thermal anemometry probe. *J. Microelectromechanical Systems*, 23(4):899–907, 2014.
[29] A. J. Smits, J. Monty, M. Hultmark, S. C. C. Bailey, M. Hutchins, and I. Marusic. Spatial resolution correction for turbulence measurements. *J. Fluid Mech.*, 676:41–53, 2011.
[30] J. A. Sillero, J. Jiménez, and R. D. Moser. One-point statistics for turbulent wall-bounded flows at Reynolds numbers up to $\delta^+ \approx 2000$. *Phys. Fluids*, 25(10), 2013.
[31] A. Lozano-Durán and J. Jiménez. Effect of the computational domain on direct simulations of turbulent channels up to $Re_\tau = 4200$. *Phys. Fluids*, 26:011702, 2014.
[32] M. Lee and R. D. Moser. Direct numerical simulation of turbulent channel flow up to $Re_\tau \approx 5200$. *J. Fluid Mech.*, 774:395–415, 2015.
[33] M. Samie, I. Marusic, N. Hutchins, M. K. Fu, Y. Fan, M. Hultmark, and A. J. Smits. Fully resolved measurements of turbulent boundary layer flows up to Re_τ = 20,000. *J. Fluid Mech.*, 851:391–415, 2018.

PP118205

THE MECHANICS OF LIVING CELLS — ORDER AMONGST DISORDER

Vikram Deshpande
Cambridge University Engineering Department, Cambridge, United Kingdom

Summary Living cells evade thermodynamic decay aided by the exchange of nutrients with their environment and are quintessential examples of out-of-equilibrium systems. These nutrient exchanges also fuel large non-thermal fluctuations, but cells nevertheless maintain a homeostatic state over a timescale of hours to days. We use these observations to motivate a statistical thermodynamic theory for the "equilibrium" of adherent cells. Numerous, sometimes counterintuitive observations, of cell behavior can be rationalized using this formalism and we shall discuss phenomena where cells attain a specific type of order by maximizing their overall disorder. Examples that will form the focus of the talk include: (i) "contact guidance" — the widely known phenomenon of alignment of single cells induced by anisotropic environmental features and (ii) the spatial organization of cells within micro-tissues which serves as the precursor to morphogenesis.

INTRODUCTION

Cellular organization plays a crucial role in the micro-architecture of tissues and dictates their biological and mechanical functioning [1]. This organization is often the result of the response of cells to the anisotropy of their micro-environment, which induces cells to migrate preferentially along the direction of anisotropy - a phenomenon called contact guidance. Indeed, contact guidance is known to affect various downstream cell behaviors, including survival, motility, and differentiation. Uncovering the origins of cellular contact guidance is therefore critical, not only for understanding tissue morphogenesis and regeneration, but also for predicting disease progression such as cancer invasion.

METHODS

We aim elucidate the general biophysical mechanisms underlying contact guidance of individual cells. Various *in-vitro* chemical micropatterning approaches have been developed to study cellular contact guidance, as model systems to simplify the highly complex *in vivo* environments. We followed such an approach [2] and seeded a low density of myofibroblasts (specifically, Human Vena Saphena Cells; see Methods) on effectively rigid substrates microprinted with fibronectin stripes of widths w, ranging from greater than $1.5\ \text{mm}$ (resembling a homogeneous 2D substrate) to $50\ \mu\text{m}$ (Fig. 1a). This enabled us to investigate contact guidance as affected by ECM proteins in the absence of short-range cell-cell interactions and long-range interactions via substrate elasticity. Surprisingly, we observed that even in this highly simplified model system, contact guidance commences at stripe widths much greater than the average cell size.

To interpret our unanticipated experimental observations, we combined detailed morphometric analysis of cells (and their subcellular components) with a novel statistical framework [3] that models the non-thermal fluctuations of living cells (Fig. 1b). These fluctuations, fueled by the exchange of nutrients between the cell and the surrounding nutrient bath, allow the cell to explore a large number of morphological microstates. However, these fluctuations are constrained by the fact that the cell maintains a homeostatic state and by environmental cues such as, in our case, adherence to fibronectin stripes. In our approach, we assume that the distribution of observed microstates is the one that satisfies these constraints and contains the overwhelming number of morphological microstates (i.e., the distribution that maximizes the morphological entropy). Then the statistics of biological observables such as cell shape, orientations and spatial distributions of cytoskeletal proteins is derived from that maximum entropy distribution of morphological states of the cell.

RESULTS

To investigate the origins of cellular contact guidance, we seeded myofibroblasts on micropatterned fibronectin stripes of width w, ranging from $50\ \mu\text{m}$ to homogeneous substrates with $w \to \infty$. Outside the stripes, cell adhesion is prevented by treatment with a 1% solution of Pluronic F-127. A schematic illustration of our experimental setup is shown in Fig. 1a, where the fibronectin stripes are represented in maroon and the cells in green. The cells were fixed and stained for actin, vinculin and the nucleus 24 hours after seeding. Representative immunofluorescence images (from at least 50 observations over three independent experiments) of the actin cytoskeleton (green), nucleus (blue), and focal adhesions (vinculin in magenta) of cells on fibronectin (maroon) stripes of width $w = 50\ \mu\text{m},\ 160\ \mu\text{m}$ and $390\ \mu\text{m}$ are shown in Fig. 1c. These images suggest that while the orientation of the actin cytoskeleton and nucleus are reasonably coordinated to the cell shape, the focal adhesions

are spread nearly evenly throughout the cells. A picture that consistently emerges from these images is that cells align more on the narrower fibronectin stripes than on wider stripes, demonstrating the emergence of contact guidance due to the fibronectin micropatterns. In fact, contact guidance emerges at stripe widths much greater than the cell size

To understand the origins of this surprising observation, we combined morphometric analysis of cells and their subcellular components with a novel statistical framework [3] for modelling non-thermal fluctuations of living cells. This modelling framework is shown to predict (Fig. 1d) not only the trends but also the statistical variability of a wide range of biological observables including cell (and nucleus) shapes, sizes and orientations, as well as stress-fibre arrangements within the cells with remarkable fidelity. By comparing observations and theory, we identified two regimes of contact guidance: (i) guidance on stripe widths smaller than the cell size, which is accompanied by biochemical changes within the cells, including increasing stress-fibre polarisation and cell elongation, and (ii) entropic guidance on larger stripe widths, which is governed by fluctuations in the cell morphology. Overall, our findings suggest an entropy-mediated mechanism for contact guidance associated with the tendency of cells to maximise their morphological entropy through shape fluctuations.

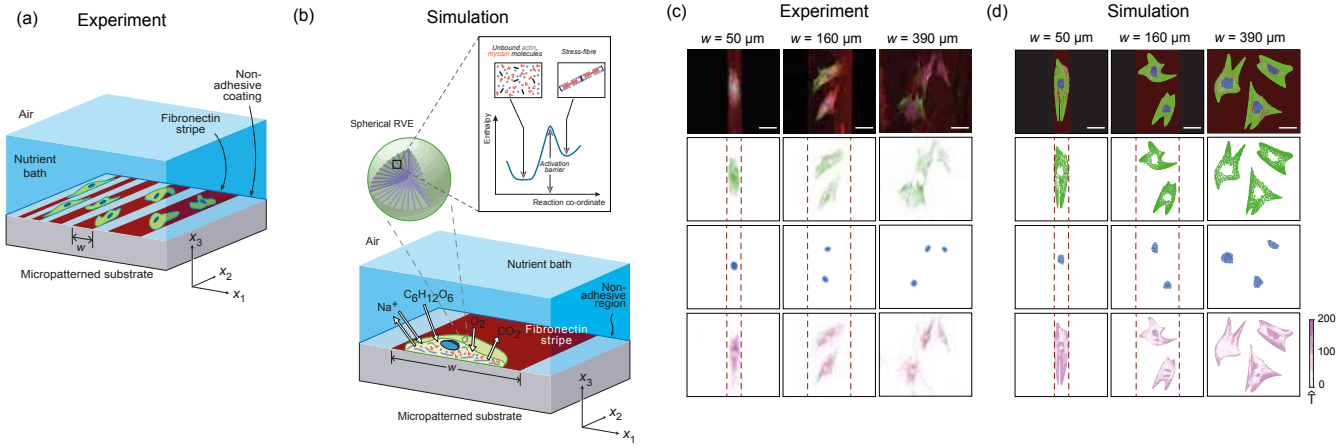

Figure 1: Experimental setup and representative images of the experimental data and simulations. (a) Sketch of the experimental setup of myofibroblasts seeded on a flat substrate micropatterned with fibronectin (red) stripes of width w. (b) An illustration of the cell model employed in the simulations using homeostatic mechanics framework. The sketch shows a section of a cell on a fibronectin stripe of width w and exchanging species with the nutrient bath. The inset shows a representative volume element (RVE) of the cell cytoplasm containing polymerized acto-myosin stress-fibers and the unbound proteins along with the energy landscape that governs the equilibrium of these proteins. (c) Immunofluorescence images of myofibroblasts on fibronectin stripes of 50, 160, and 390 μm showing the actin cytoskeleton (green), nucleus (blue), and focal adhesions (magenta); the edges of the stripes are indicated by dashed lines. (d) Corresponding predictions from the homeostatic mechanics framework with focal adhesions parameterized by the magnitude of the normalized traction $\hat{T}$. The scale bar in (c) and (d) $= 60$ μm and the width of the fibronectin stripes is indicated by the red dashed lines for the two narrowest stripes.

CONCLUSIONS

Most tissues in the human body exhibit a specific spatial organization of cells. This cellular organization plays a crucial role in the micro-architecture of tissues and dictates their biological and mechanical functioning. Despite the importance of cellular organization in all facets of tissue biology, the fundamental question of how a cell organizes itself in an anisotropic environment is still poorly understood. We show that similar to nematic ordering in liquid crystals, orientational ordering of cells on micropatterns is driven, rather counter-intuitively, by the tendency of cells to maximize morphological disorder. This finding reveals an alternative, entropy-mediated mechanism for explaining the response of cells to anisotropic environmental cues besides the often-invoked mechanisms that are predicated on very specific biochemical feedback pathways.

References

[1] K.R. Chien, I. J. Domian, and K.K. Parker. (2008) Cardiogenesis and the complex biology of regenerative cardiovascular medicine, *Science.* **322**:1494–1497.
[2] A.B.C. Buskermolen, H. Suresh, S.S. Shishvan, A. Vigliotti, A. DeSimone, N.A. Kurniawan, C.V.C. Bouten and V.S. Deshpande (2019), Entropic forces drive cellular contact guidance, *Biophysical Journal*, **116**, 1994-2008.
[3] S. Shishvan, A. Vigliotti and V.S. Deshpande (2018), The homeostatic ensemble for cells, *Biomechanics and Modeling in Mechanobiology*, **17(6)**, 1631-1662.

SECTIONAL LECTURES

SL109010

WHAT MAKES OCEAN WAVES GO ROGUE IN THE REAL WORLD?

Frédéric Dias
School of Mathematics and Statistics, University College Dublin, Ireland
Université Paris-Saclay, ENS Paris-Saclay, CNRS, Centre Borelli, 94235, Cachan, France

Summary The study of extreme ocean waves is a rapidly expanding area of research worldwide. Although much work in this area is based on modelling and experiments in controlled wave tanks, the starting point of all studies is wave observation in the natural world. During this talk, we will provide some evidence of extreme wave events, describe the main mechanisms for their generation and conclude with what we believe makes ocean waves go rogue in the real world.

INTRODUCTION

Extreme ocean waves occur under a variety of shapes and origins. First, we need to define what we mean by extreme. In this talk, the word "extreme" relates to wave events that the community cares about because of their potential destructive power. Extreme wave events are often linked to tsunamis, storm surges, storm waves, overtopping and freak waves. Extreme waves are often accompanied with wave breaking but in the past their study has often neglected wave breaking.

Extreme wave events occur worldwide on the ocean. They link together sailors, fishermen, marine officers, surfers, ship builders, coastal engineers, marine renewable energy developers, oceanographers, physicists and mathematicians around a common aim of understanding the formation, dynamics and impact of large ocean waves and currents. Tsunamis occur every year. There have been at least four major tsunamis in the last 20 years. The most recent ones are those of Krakatau (22 December 2018), which followed an eruption and partial collapse of the Anak Krakatau volcano in the Sunda Strait, and Sulawesi (28 September 2018), which was generated by a large earthquake and subsequent landslides. While the emphasis has been given to wave run-up and inundation to characterize tsunamis, the community has recently acknowledged the role of currents in evaluating the risk associated with tsunamis. The role of debris has also been emphasized. The swell generated by hurricane type storms can lead to waves larger than 20 meters in height. When these waves start feeling the sea bottom, extreme breakers that surfers try to surf can develop. Phenomenal barrels occur a few times every year in various locations around the world. The key ingredient is the local bathymetry for the focusing of wave energy. Storm's winds can push water onshore, causing a storm surge. Several times every year, catastrophic flooding can occur in low lying areas. On the other hand, it is less known that high lying areas such as cliff tops can also be temporarily flooded. Incident waves result in large runup amplifications at coastal cliffs. This is especially evident during storms in Ireland [1]. In the first part of the talk, we provide evidence of extreme wave events.

Freak waves are different in the sense that they are not necessarily associated with extreme conditions. Freak waves are localized both in space and in time. They can occur in calm seas as well agitated seas. The fact that they seem to be coming from nowhere is what makes them dangerous. Calm seas can mislead people that fish or walk dangerous rocky coasts: even in small seas, a single rogue wave can be enough to wash a person into the sea. After we give evidence of the type of rogue wave events described above, we review the physical mechanisms that can lead to rogue wave events.

OBSERVATIONS OF EXTREME OCEAN WAVES

Extreme ocean waves being rare events are difficult to observe or more precisely to measure accurately. When the waves are extreme, even if some instrument is available to measure them, there is always the possibility that the instrument is outside its normal range of operation. That means that it can either be damaged or not record the true value of the wave characteristics. After giving some evidence of carefully selected extreme wave events that have been measured by wave buoys, acoustic Doppler current profilers (ADCPs), satellite altimetry or lasers mounted on a bridge (the Andrea wave is one such example – see below), we will focus on the natural laboratory provided by the Aran Islands off the west coast of Ireland, where a lot of coastal boulder deposits (CBD) are present. These CBD, which are transported by waves at elevations above sea level and substantial distances inland, are markers for marine incursions. CBD on the Aran Islands are well-documented. Boulder transport was recorded using before-and-after photography (Figure 1), at surveyed sites for which elevation and inland distance were also measured. More than a thousand boulders, ranging in mass from 0.01 to 620 t, have been dislodged during the winter of 2013/2014 [2]. The 2013–2014 winter was the stormiest on record in the Ireland-UK region, with numerous Atlantic storms scourging the Irish seaboard. The winter-averaged significant wave height (H_s) was $\approx$ 40% higher than average, and off the west coast of Ireland there was a 5-fold increase (relative to the 67-year average) in the number of days with extreme sea states Central pressures for several events were <950 hPa (equivalent to category 3 hurricanes), and one reached as low as 927 hPa, putting it in the category 4 hurricane equivalent range. In combination with substantial storm duration and the large effective fetch, which predispose the North Atlantic region to extreme wave building, the stage was set for dramatic conditions. We will describe several scenarios that explain how CBD can be transported.

Figure 1. Examples of Aran Islands coastal boulder deposits that underwent change during the 2013–2014 winter storms. The photos A and B show repeat photography of a site on Inishmaan. The photos C and D show a site on Inishmore. The boulder weights about 210 t and from a starting location 10m above sea level 27m inland, it moved 22m in the 2013–2014 storms, to its current location 49m inland (adapted from [2]).

MECHANISMS OF EXTREME OCEAN WAVE GENERATION

The environment of the open sea involves multiple physical processes such as currents, dissipation, wind forcing and wave breaking. Aside from wave breaking, which is by nature nonlinear, currents, dissipation and wind forcing can be either linear or nonlinear. Despite this complexity, however, it has been possible to describe many aspects of large-amplitude ocean wave dynamics in regimes in which the physics is dominated by distinct linear or nonlinear mechanisms. For example, the linear processes of random wave superposition and dispersive focusing are both well-understood mechanisms that can lead to increased wave amplitude, and nonlinear focusing from modulation instability has been particularly studied because of its driving influence on wave localization and decay [3]. It is important to note, however, that although nonlinear focusing has certainly attracted much attention in the context of ocean rogue wave formation, determining the relative contribution of linear and nonlinear effects in driving extreme wave dynamics remains a subject of much study [4].

The characteristics of several extreme ocean wave events have been analysed in detail using an approach known as hindcasting. Such studies use archived meteorological and wave data at the location of the event under study to determine initial conditions for a forward-propagating wave model. The aim is to use the model to simulate the wave-field characteristics at later times and compare them quantitatively with a measured wave record. By varying the initial conditions and parameters of the model (particularly the directional wave energy spectrum), it is possible to draw conclusions as to which processes may be responsible for the emergence of the observed rogue waves. Studies of this type include the analysis of the maritime accidents of the fishing boat Suwa-Maru [5], the cruise ship Louis Majesty [6], the tanker Prestige [7], the merchant vessel El Faro [8], and modelling of the Draupner and Andrea waves and rogue waves generated during Typhoon Lupit in 2009 [9]. As an example, we illustrate the case of the Andrea wave, which, and its modelled profile using the hindcasting approach (Figure 2). The main conclusion of our work on extreme waves occurring in deep or intermediate water is that the wave shaping is found to be dominated by directional superposition, with a minor enhancement from the second order bound (Stokes) nonlinear contribution [10]. Modulational instabilities are ineffective and third-order resonant effects are negligible.

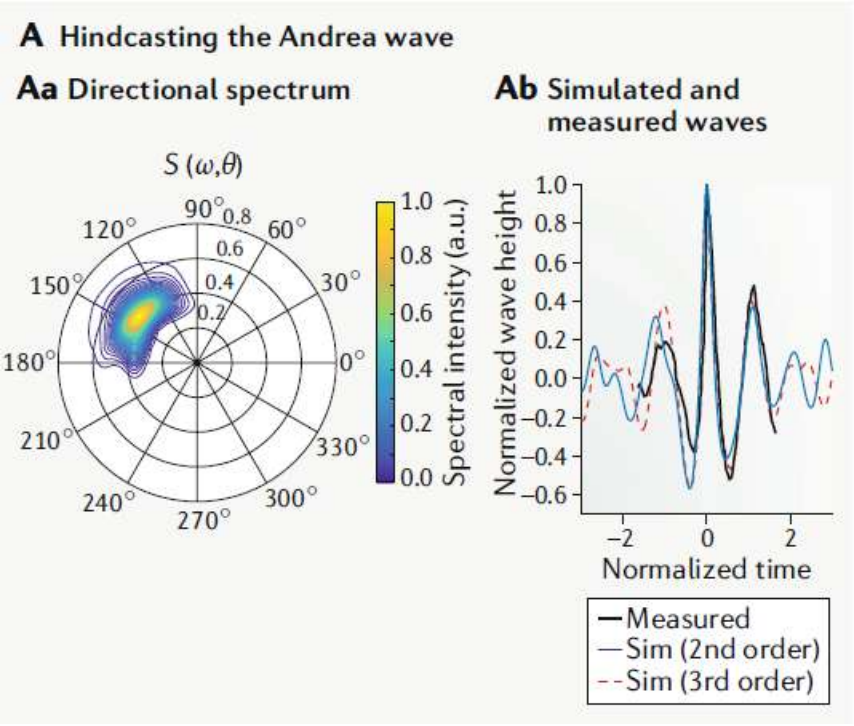

Figure 2. Hindcasting results for the Andrea wave. The directional wave energy spectrum $S(\omega,\theta)$ is used in numerical simulations, where ω is angular frequency and θ is direction in degrees (panel Aa). The measured Andrea wave (black) is compared with simulations including up to second order (blue) and third-order contributions (red) (panel Ab). The minor differences between the simulations point to a negligible role from third-order nonlinear focusing (adapted from [4]).

When it comes to extreme waves hitting the shoreline, the situation is even more complex. We also used hindcasting to recreate waves near the Aran Islands during the major storms of the 2013/2014 winter. The modelled wave heights are far from precise. They provide some sense of possible conditions at the coast but should be taken as indicator values only. Seas at some locations may have been more intense; other places will have seen lower wave activity. Bathymetric and topographic variation below the scale of the model will have focused and intensified wave heights in some areas and dampened them in others. The ways in which waves interact with the coast are determined not simply by the wave-generating mechanism, but also by complex interplay with bathymetry, and wave-wave interactions during shoaling. Infragravity waves and/or surf beat can add additional long-period components to storm-wave activity.

An interesting question is to compare the energy that tsunamis and storm waves can have to dislodge boulders. Our recent study [2] concludes that onshore flows generated by storm waves and by tsunami overlap considerably in terms of key parameters such as Froude number and flow-front velocity. Hydrodynamic equations have been derived to estimate the flow velocities required to move boulders both in the context of tsunamis and in the context of storm waves. We showed that these hydrodynamic equations systematically undervalue the power of storm waves. Therefore, while some CBD may indeed be tsunami deposits, or may have a tsunami component in their history, we emphasize that storms should be considered the default interpretation, which needs to be refuted, before a tsunami interpretation can be preferred.

DISCUSSION

Coming back to freak waves, we observe that a particular focus of the latest studies has been the relative contributions of linear and nonlinear effects in driving the emergence of rogue waves. However, although nonlinear focusing has been shown to be a dominant mechanism of rogue wave formation in wave tanks, it has not been possible to draw the same conclusion in the more complex environment of the ocean. As a result, our view is that it is not useful to focus on any single cause of all rogue waves. Rather, we believe that an objective interpretation of the current literature is that rogue waves on the ocean probably arise from several linear and nonlinear processes that contribute separately or in combination, depending on the ocean conditions at play.

We anticipate that progress in unravelling the complexity of ocean waves will require both more precisely targeted studies using wave tanks and improved in situ spatio-temporal measurements of ocean waves in their natural environment. We expect that wave tank experiments will be vital to continued efforts to understand dynamical processes such as dissipation, wave breaking and air–sea interaction, and will remain a major area of research for decades to come. Concerning the role played by nonlinearity, even in addition to potential contributions to rogue wave formation, much effort is still required to improve our understanding of how nonlinear focusing may contribute to phenomena such as wave run-up or wave overtopping.

We said above that we relate the word "extreme" to wave events that can have destructive power. Numerous marine structures are damaged by the violent impacts of extreme waves that are either breaking or very close to breaking. Design formulae for estimating the magnitude of the impulsive pressures generated by breaking waves are largely derived from the results of laboratory tests rather than from an in-depth analysis of the fundamental mechanics. Under extreme wave conditions, results are uncertain due to scale effects: the hydrodynamics requires different model scales and the influence of the various effects is difficult to infer from small-scale experiments. In the past ten years, a mathematical and computational modelling framework based on elementary loading processes (ELP) has been developed for the analysis of slamming of wave energy converters and inside the tanks of liquefied natural gas carriers [11] (Figure 3). Soon, we will use ELP to analyse overtopping.

Scaling remains the most important open question for all wave breaking impact applications. Impact pressures are strongly influenced by local phenomena such as local geometry, gas/liquid mixture and surface tension. Surface tension effects, which are quite subtle, have been largely ignored until now. Indeed, surface tension affects impact pressures not directly but indirectly. Surface tension leads to drastic changes in the geometry of the free surface.

Extreme breaking wave impacts belong to the class of extreme phenomena, such as freak waves. Extreme phenomena usually follow fat-tailed probability distributions. The topic of statistics/probability is clearly relevant to breaking wave impacts but is left aside in the present talk.

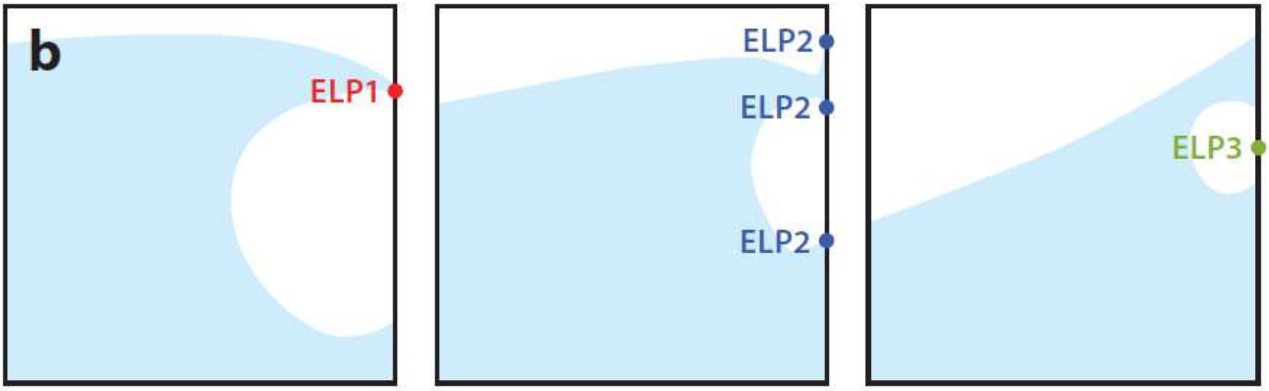

Figure 3. Qualitative description of the elementary loading processes (ELPs) that can occur when a wave hits a vertical wall. The contribution of each ELP is indicated: direct impact (ELP1, red), building jet (ELP2, blue), and compression of entrapped or escaping gas (ELP3, green) (adapted from [12]).

References

[1] O'Brien L., Renzi E., Dudley J. M., Clancy C. & Dias F. Catalogue of extreme wave events in Ireland: revised and updated for 14680 BP - 2017. *Nat. Hazards Earth Syst. Sci.* **18**, 729-758, 2018. doi:10.5194/nhess-18-729-2018

[2] Cox R., Ardhuin F., Dias F, Autret R., Beisiegel N., Earlie C, Herterich J., Kennedy A., Paris R., Raby A., Schmitt P. & Weiss R. Systematic review shows that work done by storm waves can be misinterpreted as tsunami-related, because commonly used hydrodynamic equations are flawed. *Frontiers in Marine Science* 2020

[3] Kharif, C. & Pelinovsky, E. Physical mechanisms of the rogue wave phenomenon. *Eur. J. Mech. B* **22**, 603-634, 2003.

[4] Dudley J.M., Genty G., Mussot A., Chabchoub A. & Dias F. Rogue waves and analogies in optics and oceanography. *Nature Reviews Physics* **1**, 675-689, 2019. doi: 10.1038/s42254-019-0100-0

[5] Tamura H., Waseda T. & Miyazawa Y. Freakish sea state and swell–wind sea coupling: numerical study of the Suwa-Maru incident. *Geophys. Res. Lett.* **36**, L01607, 2009.

[6] Cavaleri L. et al. Rogue waves in crossing seas: the Louis Majesty accident. *J. Geophys. Res. Ocean.* **117**, C00J10, 2012.

[7] Trulsen K., Borge J. C. N., Gramstad O., Aouf L. & Lefèvre J.-M. Crossing sea state and rogue wave probability during the Prestige accident. *J. Geophys. Res. Ocean.* **120**, 7113-7136, 2015.

[8] Fedele F., Lugni C. & Chawla A. The sinking of the El Faro: predicting real world rogue waves during Hurricane Joaquin. *Sci. Rep.* **7**, 11188, 2017.

[9] Fujimoto W., Waseda T. & Webb A. Impact of the four- wave quasi- resonance on freak wave shapes in the ocean. *Ocean. Dyn.* **69**, 101-121, 2019.

[10] Fedele F., Brennan J., Ponce de Leon S., Dudley J. & Dias F. Real world ocean rogue waves explained without the modulational instability. *Scientific Reports* **6**, 27715, 2016. doi: 10.1038/srep27715

[11] Dias F. and Ghidaglia, J.-M. Slamming: recent progress in the evaluation of impact pressures. *Annu. Rev. Fluid Mech.* **50**, 243–273, 2018. doi: 10.1146/annurev-fluid-010816-060121

[12] Lafeber W, Brosset L. & Bogaert H. Comparison of wave impact tests at large and full scale: results from the Sloshel project. *Proc. Int. Offshore Polar Eng. Conf.*, 22nd, 17–22 June, Rhodes, Greece, ed. JS Chung, I Langen, SY Hong, SJ Prinsenberg, pp. 285–99. Mountain View, CA: Int. Soc. Offshore Polar Eng, 2012.

SL118435

FRAGMENTATION VERSUS COHESION

Emmanuel Villermaux
Aix Marseille University, CNRS, Centrale Marseille, IRPHE UMR 7342, 13384 Marseille, France

LECTURE CONTENT

Capillarity is the familiar manifestation of the cohesion of liquids [1]. Since Laplace (1805), we know that intense attractive forces between the molecules *bridge the small with the large* as they shape liquid/vapor interfaces at the macroscopic scale through the concept of surface tension (menisci, drops, bubbles, puddles, liquid rise in tubes, etc...).

This lecture will concentrate on situations where liquids 'disgregate', following the neologism of R. Clausius (1862), meaning that they fragment by the action of deformations stresses whose intensity competes with that of cohesion forces. Various examples, including explosions, blow-ups, hard and soft impacts, and shears applied to liquid jets, sheets and drops will be reviewed. They concern applications ranging from liquid propulsion, agricultural spraying, to the formation of ocean spray, raindrops, and human exhalations by violent respiratory events.

In spite of their diversity, the various modes of fragment production share an ultimate common phenomenology – the ligament dynamics–, suggesting that the final stable droplets size distribution can be interpreted from elementary principles [2, 3].

The lecture will incorporate elements about:

- Origin and concept of surface tension. Founding idea of Laplace (1805).
- Tradeoff between cohesion and fragmentation: The shattered necklace example.
- Savart's sheets, bursting soap films and bubbles, receding rims and cusps.
- Paradigm of the corrugated ligament, inverse cascade of aggregations, fractional convolutions, Gamma distributions, fragments sizes, generalizations and analogies.
- Mechanisms for the formation of 'fines', direct cascades.

Figure 1: Rome, Piazza del Popolo, the lions of the central fountain expectorate a turbulent water sheet. Random velocity fluctuations and possible bubbles inclusions in the liquid nucleate holes which, driven by surface tension, grow and merge, leaving the sheet as a set of connected corrugated ligaments, which further breakup into a collection of disjointed droplets broadly distributed in size.

References

[1] Rowlinson, J. S. Cohesion. *Cambridge University Press*, 2002.
[2] Villermaux, E. Fragmentation Versus Cohesion. *J. Fluid Mech.* **898**, P1 (2020).
[3] Eggers, J. and Villermaux, E. Physics of Liquid Jets. *Rep. Prog. Physics* **71**, 036601 (2008).

SL118436

NONLINEAR DYNAMICS: A JOURNEY THROUGH EXPERIMENTS AND COMPUTATIONS

Balakumar Balachandran
Department of Mechanical Engineering, University of Maryland, College Park, MD 20742, USA

Summary Dynamics of a variety of mechanical and structural systems need consideration of nonlinearities. In this paper, a collection of experiments and computations conducted to further our understanding of nonlinear dynamics of a range of systems is presented. The experimental and computational findings are explained with the help of analytical studies. Grazing dynamics, energy localization, slow-scale and fast-scale decompositions, and buckling influenced oscillations are considered to illustrate the ubiquitous presence of nonlinearity influenced phenomena across length scales. The relevance of the work to different systems, including large scale structures, atomic force microscope systems, drilling systems, and rotary systems will be discussed.

INTRODUCTION

Nonlinear systems are ubiquitous across length scales, with representative examples including nano-scale systems [1], systems with flapping wings [2], manufacturing systems [3], and large scale aeroelastic systems [4]. While the sources of nonlinearities and the manifestations of nonlinear behaviour and nonlinear instabilities are different across these different systems, similar nonlinear phenomena have been observed in different physical systems. The elucidation of selected phenomena through experimental and computational means is one of the goals of this work. To that end, in the sections that follow, selected findings are drawn from the author's work with his collaborators.

SYSTEMS WITH SLOW AND FAST SCALE DYNAMICS

Dynamics of several systems can be described in terms of slow time scale and fast time scale components. These include flexible structural systems (e.g., [5-7]) and rotary systems (e.g., [8]). In these systems, sometimes, high-frequency input energy is transformed into a low-frequency response component (e.g., Figure 1), and in other instances, low-frequency input energy is transformed into a high-frequency response component (e.g., Figure 2). These systems have been extensively studied through experiments, computations, and analysis. For the nonlinear analysis, different singular

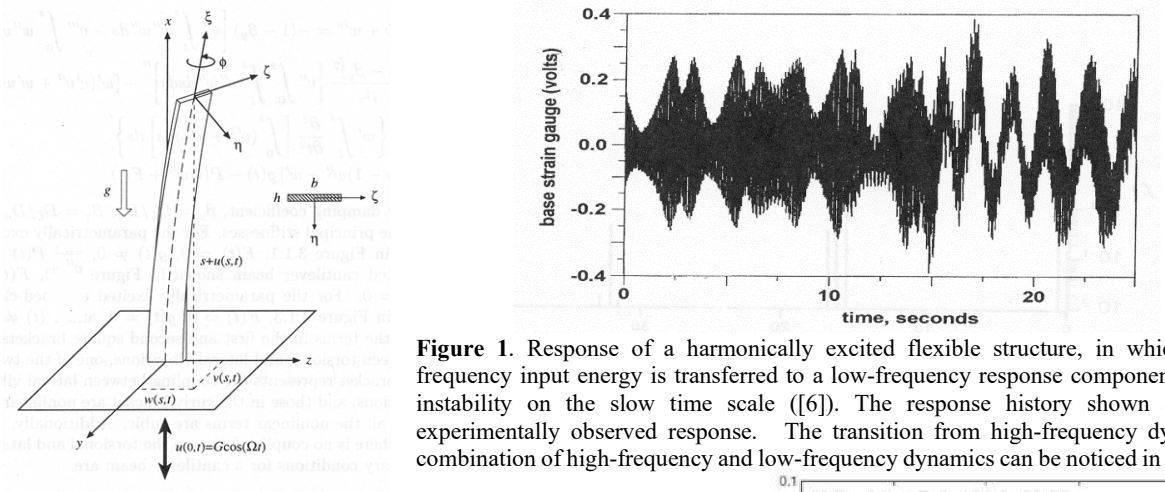

Figure 1. Response of a harmonically excited flexible structure, in which the high-frequency input energy is transferred to a low-frequency response component through an instability on the slow time scale ([6]). The response history shown above is an experimentally observed response. The transition from high-frequency dynamics to a combination of high-frequency and low-frequency dynamics can be noticed in the response.

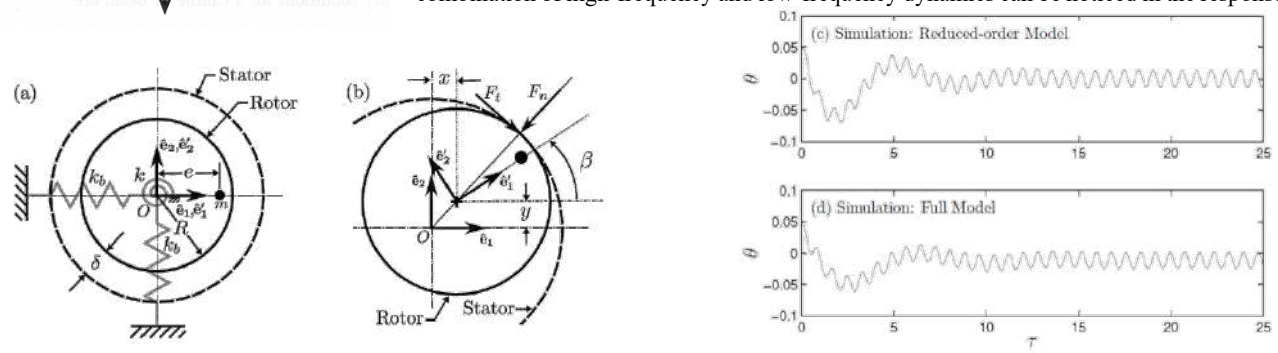

Figure 2. a) and b) Model used to torsional response of an extended, Jeffcott rotor. c) and d) Numerical results obtained by using the full system model and a reduced-order model [8]. The rotor is subjected to a low-frequency input. When a backward whirling instability occurs, the torsional response of the rotor includes a high-frequency component associated with backward whirling of the rotor. The presence of slow and fast scales can be discerned from the time histories. High-frequency backward whirling motion of a rotor subjected to a low-frequency input torque has been observed in laboratory scale experiments. This type of rotor dynamics studies is helpful for understanding drill-string dynamics.

SECTIONAL LECTURES

perturbation methods have been used, including the method of multiple scales and method direct partition of motions.

GRAZING DYNAMICS

Grazing dynamics can occur in many different scenarios, where is contact. Examples include metal cutting operations, rotor-stator dynamics, and tapping mode atomic force microscopy. For illustration, grazing contact is depicted in Figure 3.

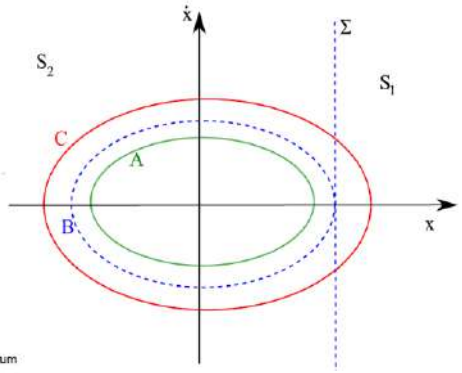

Figure 3. Orbits A, B, and C shown above are representative system responses, which are obtained as a scalar control parameter is quasi-statically varied. S_1 and S_2 are two regions separated by a boundary Σ, and orbit B represents the system response at grazing contact, which occurs when a periodic orbit grazes (makes tangential contact with a separating boundary). Post-grazing contact response can be a periodic oscillation, a quasi-periodic oscillation, a period added oscillation, or a chaotic oscillation.

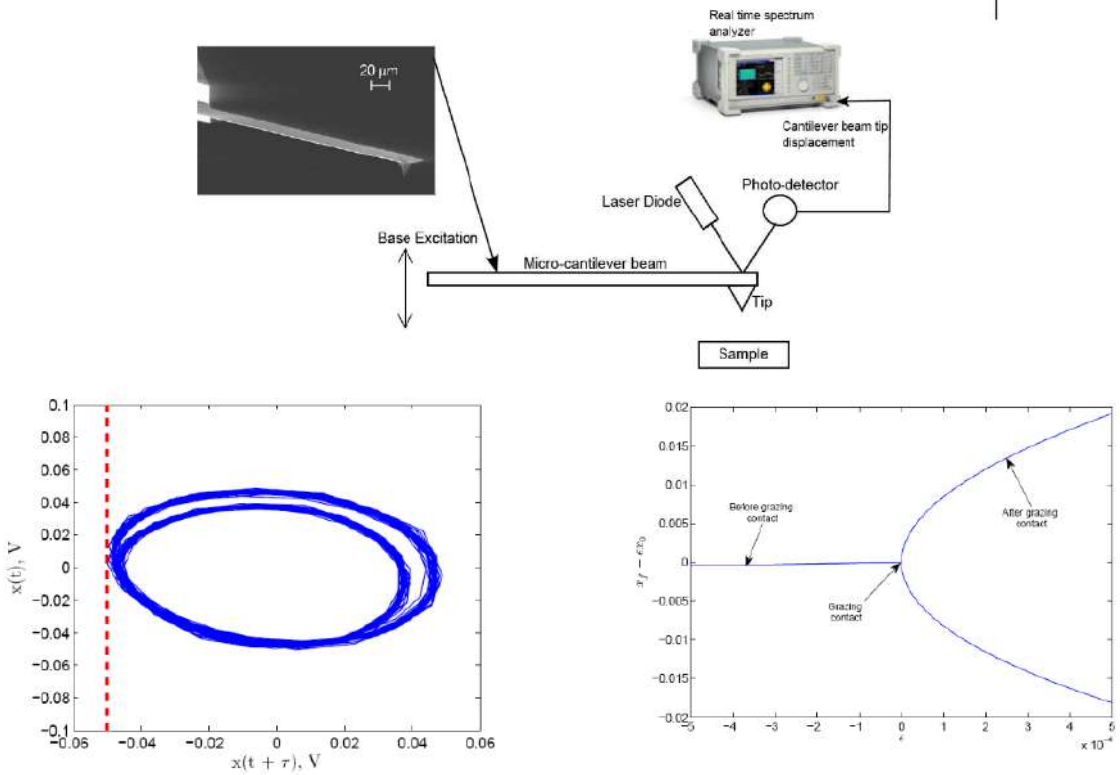

Figure 4. Experimental results obtained during tapping mode studies with a Silicon micro-cantilever are shown. When one taps delicate samples with a base excited cantilever, one would like to avoid damaging the sample. Typically, in these operations, the cantilever is excited at a frequency close to the cantilever's first natural frequency. From macro-scale studies [9], it is known that grazing contact is possible when the cantilever is excited at special frequency values between the first and second natural frequencies of the cantilever. Close to grazing contact, there is a period-doubling bifurcation in the system response. The macro-scale findings are applied to the micro-scale atomic force microscope cantilever. The corresponding experimental observation is shown in the left figure of the second row. In the right figure of the second row, results obtained from a discontinuity map analysis close to the grazing contact point are shown. A pitchfork structure can be seen emanating from the grazing contact point, supporting the occurrence of the period-doubling bifurcation observed in the experiments. Related work is reported in references [10, 11]. Based on these studies, it is conceivable that a nonlinear dynamics scheme can be used to detect near-grazing situations in experiments.

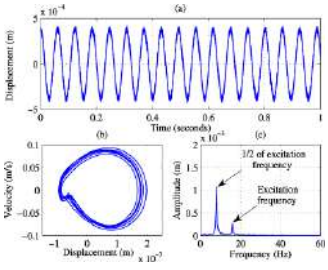

Figure 5. (a) Combined input with harmonic and noise components applied to the base of a cantilever. (b) Response phase portrait. (c) Response spectrum with a dominant peak at ½ of the input harmonic component frequency along with the input harmonic component frequency. When the noise component is turned off, the response spectrum contains only a component at the harmonic component frequency and the tip of the cantilever is contact free. The introduction of a low level of noise induces grazing contact and a period-doubling instability follows [12].

Noise can be used to influence contact dynamics, as discussed by Chakraborty and Balachandran [12].

DYNAMICS ABOUT A BUCKLED POSITION

Structures at different length scales can undergo a buckling instability. Here, an example is provided of a system a micro-scale. In Figure 6, a microelectromechanical system [14] is illustrated. This system has a curved cross-section as shown in the figure. Buckling of the microresonator results in a non-flat equilibrium position about which the system undergoes oscillations. This non-flatness is believed to be stress induced and it occurs due to the fabrication process. The corresponding modelling efforts are discussed in the work of the author and his collaborators [13, 14].

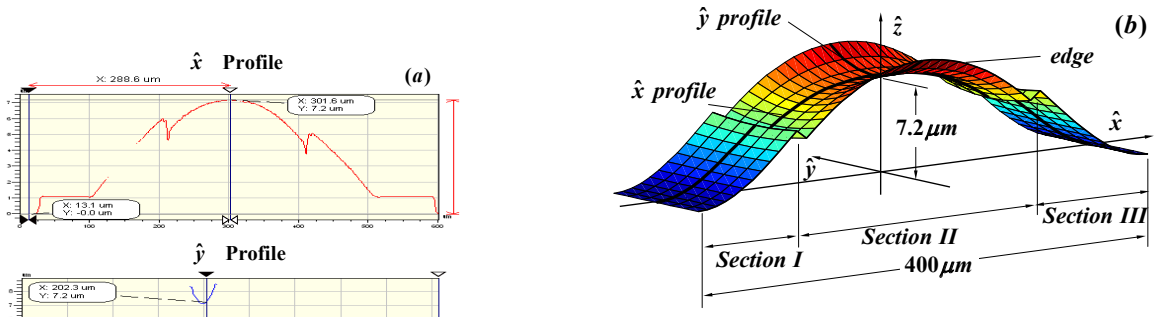

Figure 6. Static displacement profile of a 400 μm microresonator, which is essentially a clamped-clamped composite structure: (*a*) 2-D view of the measured 400 μm microresonator profile along *x*-axis and *y*-axis and (*b*) 3-D view of the resonator static profile showing that the structure has a saddle-shape displacement profile [14].

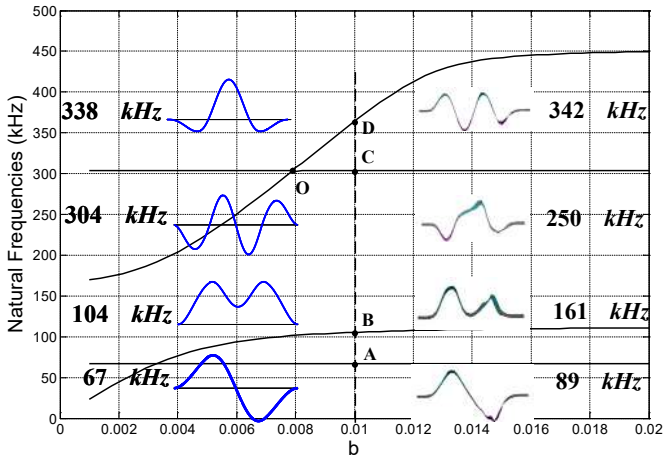

Figure 7. Forced oscillation displacement patterns of 400 μm piezoelectric resonator: predictions from model with rectangular cross-section are shown on the left and measured responses are shown on the right. The variations of natural frequencies with respect to the static non-flatness amplitude *b* are also shown in this figure. Locations A, B, C, D correspond to the predicted frequencies for the experimentally measured static amplitude *b* of 0.01 [14].

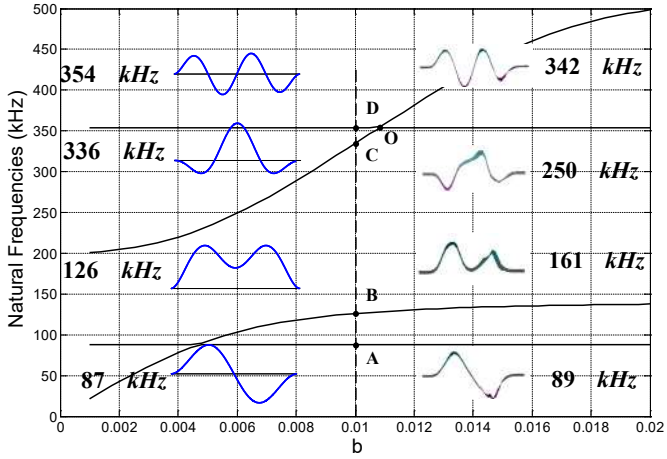

Figure 8. Free-oscillation response predictions for the 400 μm piezoelectric resonator are shown on the left and the experimental observations of spatial responses are shown on the right. The model takes curved cross-sections into account. The variations of natural frequencies with respect to the static non-flatness amplitude *b* are also shown in this figure. Locations A, B, C, D correspond to the predicted frequencies for the experimentally measured static amplitude *b* of 0.01 [14].

The experimentally observed spatial profiles of the considered resonator are shown in Figure 7 for different harmonic excitation frequencies. From the results shown in Figures 7 and 8, it is clear that if one were to just consider rectangular cross-sections, then, one cannot capture the experimentally observed spatial profiles. However, with consideration of the curved cross-section data from experiments, one can predict the spatial profiles observed in the experiments [14].

CONCLUSIONS

A collection of experimental and numerical results obtained for a range of nonlinear systems has been presented in this paper. In the talk, in addition to the nonlinear phenomena discussed here, additional phenomena will be presented and discussed.

References

[1] Postma, H. W. C., Kozinsky, I., Husain, A., Roukes, M. L. Dynamic Range of Nanotube and Nanowire-Based Electromechanical Systems. *Applied Phys. Letters*. **86**: 223105, 2005.
[2] Vanella, M., Fitzgerald, T., Preidikman, S., Balaras, E., Balachandran, B. Influence of Flexibility on the Aerodynamic Performance of a Hovering Wing. *Journal of Experimental Biology*. **212**: 95-105, 2009.
[3] Balachandran, B., Gilsinn, D. Nonlinear Oscillations of Milling. *Mathematical and Computer Modelling of Dynamical Systems*. **11**: 273-290, 2005.
[4] Noll, T. E., Brown, J. M., Perez-Davis, M. E., Ishmael, S. D., Tiffany, G. C., Gaier, M. Investigation of the Helios Prototype Aircraft Mishap. *NASA Report*. 2004.
[5] Balachandran, B., Nayfeh, A. H. Observations of Modal Interactions in Resonantly Forced Structures. *Nonlinear Dynamics*. **2**: 77-117, 1991.
[6] Anderson, T. J., Balachandran, B., Nayfeh, A. H. Nonlinear Resonances in a Flexible Cantilever Beam. *ASME Journal of Vibration and Acoustics*. **116**: 480-484, 1994.
[7] Anderson, T., Nayfeh, A. H., Balachandran, B. Coupling Between High-Frequency Modes and a Low-Frequency Mode. *Nonlinear Dynamics*. **11**: 17-36, 1996.
[8] Vlajic, N., Liu, X., Karki, H., Balachandran, B. Torsional Oscillations of a Rotor with Continuous Stator Contact. *International Journal of Mechanical Sciences*. **83**: 65-75, 2014.
[9] Balachandran, B. Dynamics of Elastic Structures Excited by Harmonic and Aharmonic Impactor Motions. *Journal of Vibration and Control*. **9**: 265-279, 2003,
[10] Chakraborty, I., Balachandran, B. Off-Resonance Cantilever Dynamics in the Presence of Attractive and Repulsive Tip Interaction Forces. *International Journal of Structural Stability and Dynamics*. **11**(4): 603-620, 2011.
[11] Chakraborty, I., Balachandran, B. Near-grazing Dynamics of Base Excited Cantilevers with Nonlinear Tip Interactions. *Nonlinear Dynamics*. **70**(2): 1297-1310, 2012.
[12] Chakraborty, I., Balachandran, B. Noise Influenced Elastic Cantilever Dynamics with Nonlinear Tip Interaction Forces. *Nonlinear Dynamics*: **66**(3): 427-439, 2011.
[13] Li, H., Preidikman, S., Balachandran, B., Mote Jr., C. D. Nonlinear Free and Forced Oscillations of Piezoelectric Resonators. Journal of Micromechanics and Microengineering. **16**: 356-367. 2006.
[14] Li, H., Piekarski, B., DeVoe, D., Balachandran, B. Nonlinear Forced Oscillations of Piezoelectric Microresonators with Curved Cross-Sections. *Sensors and Actuators A*.**144**: 194-200, 2008.

SL118437

MODELING FLOWS OVER NATURAL OR ENGINEERED SURFACES

Alessandro Bottaro
Department of Civil, Chemical and Environmental Engineering, Universit`a di Genova, Genova, Italy

Summary Natural and engineered surfaces are never smooth, but irregular, rough at different scales, compliant, possibly porous, liquid-impregnated or superhydrophobic. The correct numerical modeling of fluids flowing through and around them is important but poses problems. For media characterized by a periodic or quasi-periodic microstructure of characteristic dimensions smaller than the relevant scales of the flow, multiscale homogenization can be used to study the effect of the surface, avoiding the numerical resolution of fine-grained details. The homogenization strategy needed to model the interaction between a fluid in motion and regularly micro-textured, permeable or impermeable walls is revisited and examples are provided to demonstrate the accuracy and versatility of the approach.

INTRODUCTION

The study of the fluid motion above and through natural and engineered surfaces is a challenging task, particularly if the surface possesses small-scale features which exert some fluid-dynamics-related role, whose effect often cannot be captured directly by a numerical simulation because of the difficulty in addressing all the fine-grained details of the fluid/wall coupling. Such details might include the effect of the surface texture, its porosity, compliance and the interactions between the flow of the outer fluid and that of a different fluid which may be trapped within near-wall microcavities. It then becomes useful to employ an approach capable of replicating the important features near the wall at a fraction of the computational cost of a full, detail-resolving simulation; one such approach is multiscale homogenization. In the next section the mathematical description of the theory is limited to the case of rough surface, neglecting aspects related to the system porosity or elasticity, addressed, e.g., by Bottaro [1]. The equations are developed up to second order in terms of a small parameter, ϵ, to be able to account for those cases in which there is poor separation of scales.

MATHEMATICAL FORMULATION

A regularly structured three-dimensional rough wall is considered, with cartesian macroscale dimensionless coordinates $X_i = (X_1, X_2, X_3) = (X, Y, Z)$, Y being orthogonal to the mean surface plane. These independent variables are scaled by L, a characteristic macroscopic length. The surface $Y = 0$, tangent to the roughness elements, defines a fictitious wall on which *effective* boundary conditions should be imposed, as an alternative to the expensive alternative of computing all details of the flow field within the rough pattern. A unit cell is defined in a box which extends vertically from $y = y_{wall}(x, z)$ to $y \to \infty$; along the mean-wall parallel directions it is assumed that the representative roughness element is contained in a rectangular box, with periodic conditions which apply along x and z (cf. fig. 1). All microscale coordinates $x_i = (x_1, x_2, x_3) = (x, y, z)$ are normalized with a small length scale l and are thus dimensionless. The dependent variables are expressed as power series of the small parameter $\epsilon = l/L$, and denoted by

$$f = f^{(0)} + \epsilon f^{(1)} + \epsilon^2 f^{(2)} + ... \tag{1}$$

In general, capital letters will be used for macroscopic variables, and small letters will be employed for microscopic ones.

The whole physical domain is divided into two regions: a inner region goes from the wall to $y \to \infty$ and the outer region sits above, i.e. it goes from $Y = 0^+$ to $Y = Y_{max}$, with Y_{max} a function of the problem considered. In the inner region the equations are

$$\frac{\partial u_i}{\partial x_i} = 0, \tag{2}$$

$$\mathcal{R}\left(\frac{\partial u_i}{\partial t} + u_j \frac{\partial u_i}{\partial x_j}\right) = -\frac{\partial p}{\partial x_i} + \frac{\partial^2 u_i}{\partial x_j^2}, \tag{3}$$

and in the outer region they are

$$\frac{\partial U_i}{\partial X_i} = 0, \tag{4}$$

$$\frac{\partial U_i}{\partial t} + U_j \frac{\partial U_i}{\partial X_j} = -\frac{\partial P}{\partial X_i} + Re^{-1} \frac{\partial^2 U_i}{\partial X_j^2}. \tag{5}$$

In the equations above, $\mathcal{R} = \mathcal{U}l/\nu$ is the microscopic Reynolds number, $Re = U_{out}L/\nu$ is the macroscopic Reynolds number; the pressure in the near-wall region is normalized with the viscous pressure, $\mu\mathcal{U}/l$, and in the outer region the

SECTIONAL LECTURES

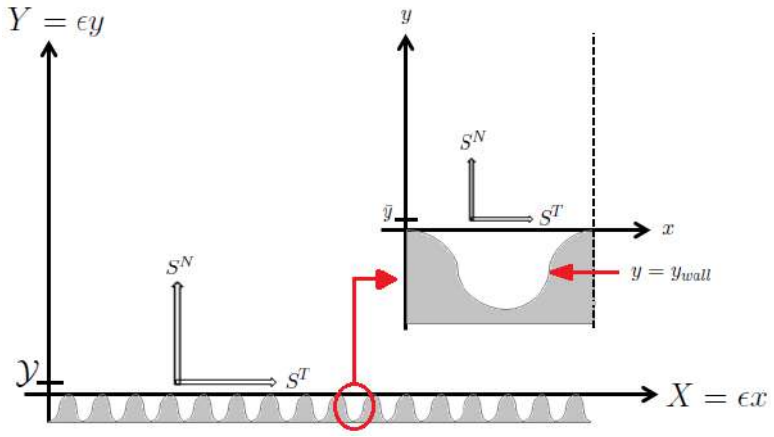

Figure 1: Sketch of regularly micro-structured rough wall, with close-up of a generic unit cell.

pressure scale is the dynamic pressure, ρU_{out}^2. Inner ($\mathcal{U}$) and outer (U_{out}) velocity scales are related by $\mathcal{U} = \epsilon U_{out}$; we also have $X_i = \epsilon x_i$. The two systems are matched at some interface plane (positioned for numerical purposes at a finite distance from the solid surface, in $y = y_\infty$, sufficiently far from the wall so that u_i and p there become independent of the microscale coordinates), and there it is imposed that velocity and traction are continuous, i.e.

$$U_i = \epsilon u_i, \tag{6}$$

$$-p\,\delta_{i2} + \frac{\partial u_i}{\partial x_2} + \frac{\partial u_2}{\partial x_i} = -Re\,P\,\delta_{i2} + \frac{\partial U_i}{\partial X_2} + \frac{\partial U_2}{\partial X_i}. \tag{7}$$

To simplify notations, the outer forcing terms will be denoted as follows:

$$S^{T_x} = \frac{\partial U}{\partial Y} + \frac{\partial V}{\partial X}, \tag{8}$$

$$S^{T_z} = \frac{\partial W}{\partial Y} + \frac{\partial V}{\partial Z}, \tag{9}$$

$$S^N = -Re\,P + 2\,\frac{\partial V}{\partial Y}. \tag{10}$$

For more details on formulation and scalings refer to Bottaro & Naqvi [2].

Equations at leading order

The problem at order ϵ^0 has already been addressed in several papers (see, e.g., [3, 4] and references therein), and will not be repeated here. The unknowns have the form

$$u_i^{(0)} = u_i^\dagger\,S^{T_x} + u_i^\ddagger\,S^{T_z}, \tag{11}$$

$$p^{(0)} = p^\dagger\,S^{T_x} + p^\ddagger\,S^{T_z} - S^N, \tag{12}$$

with the coefficients $u_i^\dagger$, $u_i^\ddagger$, $p^\dagger$ and $p^\ddagger$ function only of microscale variables. They arise out of Stokes problem, by considering alternatively S^{T_x} or S^{T_z} as forcing term.

Equations at first order

The equations at $\mathcal{O}(\epsilon)$ are:

$$\frac{\partial u_i^{(1)}}{\partial x_i} = \frac{\partial u_i^{(0)}}{\partial X_i}, \tag{13}$$

$$-\frac{\partial p^{(1)}}{\partial x_i} + \frac{\partial^2 u_i^{(1)}}{\partial x_j^2} = \frac{\partial p^{(0)}}{\partial X_i} - 2\,\frac{\partial^2 u_i^{(1)}}{\partial x_j \partial X_j}, \tag{14}$$

together with no-slip at the wall and no-traction at y_∞, i.e.

$$-p^{(1)}\,\delta_{i2} + \frac{\partial v^{(1)}}{\partial x_i} + \frac{\partial u_i^{(1)}}{\partial y} = 0. \tag{15}$$

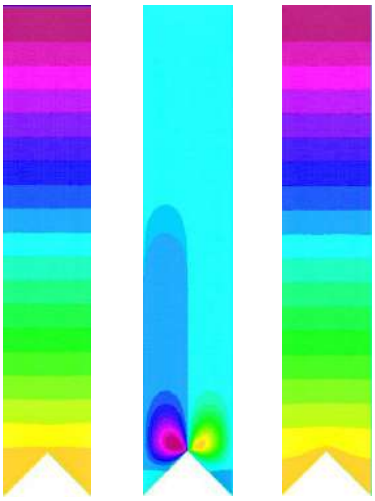

Figure 2: Order zero microscopic fields for riblets, computed for $y_\infty = 5$. From left to right, $u^\dagger$, $v^\dagger$ and $w^\ddagger$.

By using (11-12) we obtain:

$$\frac{\partial u_i^{(1)}}{\partial x_i} = -u_j^\dagger \frac{\partial S^{T_x}}{\partial X_j} - u_j^\ddagger \frac{\partial S^{T_z}}{\partial X_j}, \tag{16}$$

$$-\frac{\partial p^{(1)}}{\partial x_i} + \frac{\partial^2 u_i^{(1)}}{\partial x_j^2} = p^\dagger \frac{\partial S^{T_x}}{\partial X_j}\delta_{ij} + p^\ddagger \frac{\partial S^{T_z}}{\partial X_j}\delta_{ij} - \frac{\partial S^N}{\partial X_j}\delta_{ij} - 2\frac{\partial u_i^\dagger}{\partial x_j}\frac{\partial S^{T_x}}{\partial X_j} - 2\frac{\partial u_i^\ddagger}{\partial x_j}\frac{\partial S^{T_z}}{\partial X_j}. \tag{17}$$

The linear equations (16-17) admit a solution in the form

$$u_i^{(1)} = \hat{u}_{ij}\frac{\partial S^{T_x}}{\partial X_j} + \tilde{u}_{ij}\frac{\partial S^{T_z}}{\partial X_j} + \breve{u}_{ij}\frac{\partial S^N}{\partial X_j}, \tag{18}$$

$$p^{(1)} = \hat{p}_j\frac{\partial S^{T_x}}{\partial X_j} + \tilde{p}_j\frac{\partial S^{T_z}}{\partial X_j} + \breve{p}_j\frac{\partial S^N}{\partial X_j}, \tag{19}$$

so that three sets of auxiliary systems arise, one related to the gradient of S^{T_x} (and involving $\hat{\cdot}$ variables), one due to the gradient of S^{T_z} ($\tilde{\cdot}$ variables), and a last one induced by the gradient of S^N ($\breve{\cdot}$ variables). All of these microscopic problems involve inhomogeneous Stokes equations; for all, the boundary conditions are simply no-slip at y_{wall} and vanishing traction at y_∞, plus periodicity in x and z. Once these microscopic problems are solved, the solutions can easily be assembled to yield an *effective* condition for the macroscopic problem at $Y = \epsilon y_\infty$. It is very easy (and convenient) for this condition to be transferred onto the plane $Y = 0$, tangent to the roughness rims, as will be shown below for a representative case.

APPLICATION OF THE THEORY: RIBLETS

The case is now considered of longitudinal riblets, infinitely elongated in z. The unit cell becomes a simple two-dimensional domain in the (x, y) plane, with all microscopic variables invariant in z. As initially shown by Bechert and Bartenwerfer [5], the z-components of the microscopic equations reduce to the Laplace equation at leading order; at next order the problem in z is ruled by a set of Poisson equations. All equations at order zero and one have been solved accurately by the use of FreeFEM [6]. For the riblets displayed in fig. 2, the results of interest are reported in table 1; all the coefficients which are not reported in the table simply vanish.

It is simple to see that, up to a small error of order 10^{-5} the variables evaluated at the top boundary of the unit cell can be written, for any value of y_∞, as

$$u^\dagger = y_\infty + \lambda_x,$$
$$w^\dagger = y_\infty + \lambda_z,$$

Table 1: Microscopic variables evaluated at different y_∞'s.

y_∞	$u^\dagger$	$w^\ddagger$	$-\hat{u}_{21} = \breve{u}_{11}$	$\hat{u}_{12}$	$\tilde{u}_{32}$	$-\tilde{u}_{23} = \breve{u}_{33}$
4	4.07797	4.13965	8.31769	16.62980	17.13760	8.57542
5	5.07796	5.13966	12.89560	25.78570	26.41610	13.21510
6	6.07797	6.13965	18.47364	36.94172	37.69530	18.85470

$$
\begin{aligned}
-\hat{u}_{21} = \breve{u}_{11} &= \frac{1}{2}(y_\infty + \lambda_x)^2 + \beta_x, \\
\hat{u}_{12} &= (y_\infty + \lambda_x)^2, \\
\tilde{u}_{32} &= (y_\infty + \lambda_z)^2, \\
-\tilde{u}_{23} = \breve{u}_{33} &= \frac{1}{2}(y_\infty + \lambda_z)^2 + \beta_z.
\end{aligned}
$$

From table 1 we obtain $\lambda_x = 0.07797$, $\lambda_z = 0.13965$, $\beta_x = 0.00276$, and $\beta_z = 0.00706$. The results for the so-called *transverse* (λ_x) and *longitudinal* (λ_z) *protrusion heights* coincide with those given by Luchini et al. [7]. The additional coefficients β_x and β_z permit to correct the leading order solution when there is poor separation of scales.

The *effective* conditions

The *effective* conditions for the outer flow can be imposed by choosing any value of y_∞ and, in particular, they can be enforced at $\mathcal{Y} = \epsilon y_\infty \to 0^+$. In this case we end up with

$$U\big|_{\mathcal{Y}} = \epsilon\lambda_x \frac{\partial U}{\partial Y}\bigg|_{\mathcal{Y}} + \epsilon^2 \lambda_x^2 \frac{\partial^2 U}{\partial Y^2}\bigg|_{\mathcal{Y}} - \epsilon^2 Re \left(\frac{\lambda_x^2}{2} + \beta_x\right) \frac{\partial P}{\partial X}\bigg|_{\mathcal{Y}} + \mathcal{O}(\epsilon^3), \tag{20}$$

$$V\big|_{\mathcal{Y}} = -\epsilon^2 \left[\left(\frac{\lambda_x^2}{2} + \beta_x\right) \frac{\partial^2 U}{\partial X\, \partial Y}\bigg|_{\mathcal{Y}} + \left(\frac{\lambda_z^2}{2} + \beta_z\right) \frac{\partial^2 W}{\partial Y\, \partial Z}\bigg|_{\mathcal{Y}}\right] + \mathcal{O}(\epsilon^3), \tag{21}$$

$$W\big|_{\mathcal{Y}} = \epsilon\lambda_z \frac{\partial W}{\partial Y}\bigg|_{\mathcal{Y}} + \epsilon^2 \lambda_z^2 \frac{\partial^2 W}{\partial Y^2}\bigg|_{\mathcal{Y}} - \epsilon^2 Re \left(\frac{\lambda_z^2}{2} + \beta_z\right) \frac{\partial P}{\partial Z}\bigg|_{\mathcal{Y}} + \mathcal{O}(\epsilon^3); \tag{22}$$

Navier's slip holds at order ϵ, but effects related to the second derivatives of the slip velocity components and to the horizontal pressure gradient cannot be dismissed, particularly when ϵ and/or Re are not so small. Furthermore a transpiration velocity (blowing/suction) is present at $\mathcal{O}(\epsilon^2)$.

CONCLUDING REMARKS

The final macroscopic conditions (20-22) can be used to study the flow over riblets, without the need to carry out expensive feature-resolving simulations. These $\mathcal{O}(\epsilon^2)$ conditions remain valid under the same constraints which apply when using the simple Navier conditions, i.e. the riblets must be confined to the viscous sublayer of the turbulent boundary layer. The same applies to the case of a generic rough surface, for example with three-dimensional dimples. When the rough pattern protrudes outside the viscous sublayer, inertial terms cannot be neglected any longer. The effect of advection requires at the very least the extension of the theory to order three, when non-linear terms make their appearance in the equations [2]. This would also require the adoption of extended (wider and longer) unit cells over which to solve auxiliary problems. Further complications arise when considering some of the other effects (wall compliance, permeability, presence of a lubricant fluid, etc.) mentioned in the introduction of the present extended abstract, whose description is outside the scope of this brief contribution.

References

[1] Bottaro A. Flow over natural or engineered surfaces: an adjoint homogenization perspective. *J. Fluid Mech.* **877**: P1-P91, 2019.
[2] Bottaro A., Naqvi S. B. Effective boundary conditions at a rough wall: a high-order homogenization approach. Submitted 2020.
[3] Zampogna G., Magnaudet J., Bottaro A. Generalized slip condition over rough surfaces. *J. Fluid Mech.* **858**: 407-436, 2019.
[4] Jiménez Bolaños S., Vernescu, B. Derivation of the Navier slip and slip length for viscous flows over a rough boundary. *Phys. Fluids* **29**: 057103, 2017.
[5] Bechert D. W., Bartenwerfer, M. The viscous flow on surfaces with longitudinal ribs. *J. Fluid Mech.* **206**: 105129, 1989.
[6] Hecht, F. New development in freefem++. *J. Num. Math.* **20**: 251-266, 2012.
[7] Luchini P., Manzo D., Pozzi A. Resistance of a grooved surface to parallel flow and cross-flow. *J. Fluid Mech.* **228**: 87109, 1991.

SL118438

DYNAMICS OF COLLECTIVE CELLS AND BIOLOGICAL TISSUES

Xi-Qiao Feng
Institute of Biomechanics and Medical Engineering, AML, Department of Engineering Mechanics, Tsinghua University, Beijing 100084, China

Summary Experimental and theoretical efforts are directed toward studying the dynamic behaviours of biological tissues at multiple length scales. A modified cell division rule is proposed on the basis of comprehensive consideration of mechanical forces in the cell. Statistical laws of energies and velocities of collective cell migrations are derived. We find that the spontaneous oscillation of collective cells in such biological tissues as *Drosophila* amnioserosa stems from dynamic Hopf bifurcation induced by the feedback between mechanical strains and chemical cues. A nonlinear continuum mechanics theory is established to investigate the volumetric growth, surface wrinkling, and morphological evolutions of soft tissues (e.g., tumors) under physiological and pathological conditions.

INTRODUCTION

Most tissues and organs in our body are very soft and can undergo large deformation. This mechanical characteristic is advantageous for them to achieve a wealth of biological functions, such as motion, aspiration, metabolism, mass and energy transport. Physiological and pathological processes of soft tissues always involve complicated and coupled interactions among mechanical, physical, chemical, and biological factors. The rapidly developing mechanobiology integrates the experimental and theoretical methods in biology and mechanics to investigate the physiological and pathological responses of biological molecules, cells, and tissues to mechanical, physical and chemical factors at different length scales. In this paper, we briefly summarize some recent advances in the theoretical and experimental efforts toward understanding the biomechanical mechanisms underlying some important dynamic behaviours of cells and tissues.

DYNAMICS OF COLLECTIVE CELLS

Collective cell dynamics play a crucial role in vast physiological or pathological processes including embryo development, wound healing, tissue regeneration, and tumor invasion. It involves self-assembly and self-organization of intercellular cytoskeleton, regulation of biochemical signalling pathways, cell–cell and cell–microenvironment interactions. We combine experiments, theory, and simulations to study the division, migration, oscillation and other dynamic processes of collective cells in two-dimensional (2D) confluent cell monolayers and three-dimensional (3D) cell systems.

Cell division rule

Cell division is central for embryonic development, tissue morphogenesis, and tumor development. The well-known Hertwig's cell division rule suggests that cells tend to divide along their long axes. However, this rule was established merely on the basis of geometrical statistics, rather than the analysis of mechanical forces, and thus does not fit well with some experimental observations of cell divisions. Experiments have evidenced that mitotic cell division relies on instructive signals from cellular microenvironments to coordinate the division plane. However, it still remains unclear how the biophysical cues such as cell geometry and cell–cell junctions coordinate to steer spindle position and orientation along with other influencing factors. We establish a mesoscopic dynamic cell division model to explore the integrated regulations of cortical protein polarity, microtubule kinetics, cell deformability and boundary constraints. This model can correlate division-plane orientation with cell geometry and nucleus stress. Besides the effects of cell geometry, the concentration of cortical anchoring protein is also taken into account in our model. We show that through the mechanical linkage between cortical LGN/NuMA/dynein complex and astral microtubules, the intercellular cues induced by cell–cell junctions are transmitted into the spindle orientation machinery to steer cell division. Besides predicting spindle orientation and positioning with different cortical polarities, the dramatic morphological evolutions of cell rounding is also captured. The present model can not only explain various cell division phenomena observed in cell monolayers but also account for the effects of boundary constraints, demonstrating the extensive applications of our work. It is concluded that the final division plane is perpendicular to the maximal principal stress acting on the nucleus, consistent with all relevant experiments. This new rule of cell division is referred to as the maximal principal stress rule [1].

Thermal effects on cell division

Furthermore, we investigate the effects of heat stress on the divisions of human cancer cells [2]. Multipolar divisions of heated cells has long been thought to stem from centrosome aberrations of cells directly caused by heat stress. Through long-term live-cell imaging, we provide direct cellular evidences to demonstrate that heat stress can promote multiple multipolar divisions of, for instance, MGC-803 and MCF-7 cells. Our results show that, besides facilitating centrosome aberration, polyploidy induced by heat stress is another mechanism that causes multipolar cell divisions, in which

polyploid cancer cells engendered by mitotic slippage, cytokinesis failure, and cell fusion. Furthermore, we also find that the subsequent fates of theses polyploid cells depend on their experience of these events: the polyploid cells generated by mitotic slippage experience bipolar divisions with a higher rate than multipolar divisions, while those polyploid cells induced by both cytokinesis failure and cell fusion have a higher frequency of multipolar divisions than bipolar divisions. We also show that heat stress-induced multiple multipolar divisions of cancer cells usually produce aneuploid daughter cells, and might lead to genetically unstable cancer cells and facilitate tumor heterogeneity. These findings on the thermal effects on cell division should be helpful for the design of thermotherapy strategies of cancers.

Oscillation of Collective Cells

Nest, we investigate shape oscillations of collective cells which may occur in the morphogenesis and organogenesis of various tissues and organs. Owing to their collective nature, these processes require robustly coordinated dynamics of individual cells, which are often separated too distantly to directly communicate with each other through biomaterial transportation. Although it is known that the mechanical balance generally determines the morphologies of cell systems, it remains elusive whether and how the mechanical components may contribute to the collective cell morphodynamics. Taking the collective cell oscillation in *Drosophila* amnioserosa as an example, we study the dynamic features and underlying mechanisms of collective shape oscillations in 2D cell monolayers (Fig. 1) [3]. Considering the negative chemical–mechanical feedback between cell deformation and intracellular myosin activity (Fig. 1c), a chemomechanical model is established to describe collective morphodynamics in cell monolayers. Using this model, we study collective oscillations in *Drosophila* amnioserosa to elucidate the regulatory roles of mechanical components. The tensile stress is identified as a key activator that switches collective cell oscillations on and off. This regulatory role is shown analytically using the Hopf bifurcation theory. We find that the physical properties of the tissue boundary are directly responsible for synchronizing the oscillatory intensity and polarity of cells and for orchestrating the spatial oscillation pattern in the tissue.

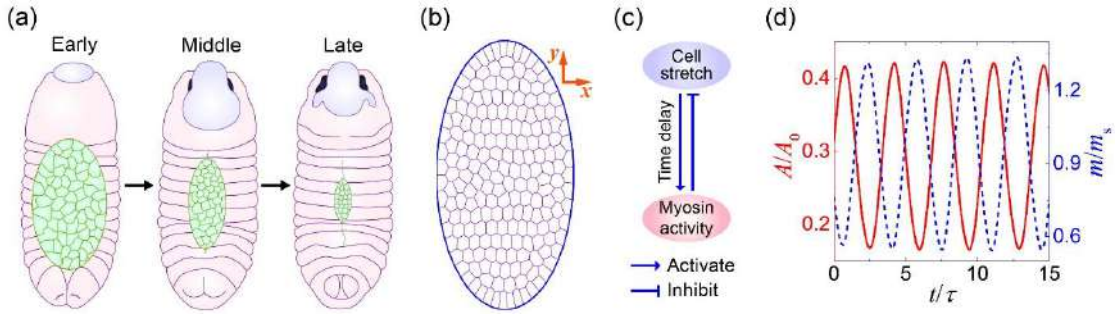

Figure 1. Collective cell oscillation in *Drosophila* amnioserosa. (a) Schematic of *Drosophila* dorsal closure. The central eye-shaped region is amnioserosa, surrounded by the lateral epidermis; (b) Geometric description of amnioserosa cells by connected polygons within an elliptic domain; (c) Interactive regulation between myosin activity and cell deformation; (d) Oscillations of normalized area (A/A_0) and myosin activity (m/m_0) of a representative cell, obtained from the chemomechanical model.

Migration of Collective Cells

Collective cell migration occurs in a diversity of physiological and pathological processes such as wound healing, cancer metastasis, and embryonic morphogenesis. In the collective context, cohesive cells may move as a translational solid, swirl as a fluid, or even rotate like a disk, with scales ranging from several to dozens of cells. By considering active cell motility and two typical social interactions among cells—local alignment (LA) and contact inhibition of locomotion (CIL), we establish an active vertex model to study collective cell migration on both planar and curved substrates. This model can well reproduce experimentally observed turbulent motion patterns in 2D cell monolayers. The regulating roles of LA and CIL on collective migration modes, characteristic scales, and density fluctuations are revealed. An intrinsic scale of cell monolayers is proposed to account for the mode transition of collective cell migration in confined spaces, and the corresponding patterns are attributed to the competition between the intrinsic scale of cell monolayers, geometric confinements, etc. A new dimensionless parameter, referred to as cell motility number, which involves the effects of cell motility, cell crowdedness, cell stiffness and confinement size, is defined to quantify the migration mode transition of collective cells.

For systems containing a large number of cells, the statistical features of forces, velocities, energies, shapes and other parameters at the meso scale are of significance for understanding the collective dynamics behaviours. To this end, we performed large-scale and long-time experiments to investigate the statistics of velocities and energies in diverse confluent cell monolayer systems that spontaneously orchestrate into mesoscale cell turbulence under certain conditions. We discover a linear relation between the variability and the mean of cell speeds as the monolayer matures, which reveals a time-invariant statistical rule. Through experimental and theoretical approaches, we demonstrate that cell velocities obey the non-canonical q-Gaussian statistics, with universality across different cell types and substrate stiffness. We further show that such universal velocity distribution statistics can be captured by the Tsallis statistical theory.

As to the energies of individual cells, the enstrophy is found to scale linearly with the kinetic energy as the monolayer matures, defining a characteristic length scale of vortices. The kinetic energies over time collapse to a family of probability

distributions, which deviate from the classic Maxwell–Boltzmann distribution and actually can be described by the q-Gaussian distribution of cell velocities. The energy spectra under larger wavenumbers exhibit a power-decaying law, with a scaling exponent markedly different from that in the classic 2D Kolmogorov–Kraichnan turbulence. Our experiments show that the obtained scaling relations of energies and velocities are nearly universal for all types of cells and substrates we measured. These findings provide physical insights into fundamental aspects of self-organization in biological tissues.

Furthermore, we investigate the relation between the collective motility and shape of human cancer cells under heat stress. Collective dynamics of MGC-803 cells in a confluent monolayer subjected to heat stress at 48 °C for 10 min are observed and analyzed using the long-term live imaging technique. It is found that the normal cell motions slow down with the increase in cell density and cell–cell adhesion, and the decrease in the average aspect ratio of cell shape and cell–substrate traction. Heat stress can speed up cellular motions accompanied with almost unchanged cell density, almost unchanged cell–cell adhesion, and the increase in the cell shape index and the tractions exerted by cells on the substrate. An approximately linear relation is revealed between the collective migration velocity and the shape index of the heated cells. This work provides inspirations for regulating cell motion with such factors as temperature.

THERMODYNAMIC MODEL OF TUMORS

In the recent years, continuum and discrete mechanobiological models have been proposed to investigate the mechanical properties and constitutive relations of soft tissues, e.g., brain and tumor. Our attention is focused on theoretical modelling of heterogeneous growth, angiogenesis, morphological and structural evolutions, invasion and metastasis of cancers. There are many mechanistic factors that might potentially collude with oncology to drive cancer progression. A solid tumor is an aggregate of cells, extracellular matrix (ECM), and interstitial space, where the cells and ECM provide mechanical integrity and act as a supporting skeleton, while the interstitial space is filled with fluids. Hence, a solid tumor is can be considered as a porous medium at the tissue level, and the theory of poroelasticity can be applied to characterize its mechanical behavior. The development and therapeutics of solid tumors are complex processes involving both biochemical regulations and mechanical interactions. We have developed a mechano-chemo-biological coupling poroelastic model to study some fundamental and clinical issues of tumors, e.g., volumetric growth, morphological evolution, vascular collapse, mechanical stiffening, and evaluation of therapeutic strategies.

In the initial development phase, a solid tumor is avascular and its growth induced by cell proliferation relies on the diffusion of oxygen and nutrients from surrounding host tissues. The gradients of these chemicals lead to heterogeneous tumor growth, which further engenders residual stresses. These stresses can modulate tumor growth both directly, by compressing tumor cells, and indirectly, by compressing the interstitial space and hinder nutrition diffusion. Based on the consideration of thermodynamics, a nonlinear poroelastic theory with a stress-modulated growth law is established to model the coupling among the mechanical, chemical, and biological mechanisms governing avascular tumor growth. The poroelastic theory can account for the interactions between the solid and fluid phases and reveal the regulating role of stresses on nutrient transport. The model shows that the mechano-chemo-biological coupling triggers anisotropic and heterogeneous growth, leading to the formation of a layered structure consisting of a necrotic core and a proliferative rim, in consistency with clinical observations. The inhibitory effect of external confinements on tumor growth is also verified by comparing the theoretical and experimental results for tumor growth under different conditions. For example, the model can reproduce the observation that there exists a steady state in which tumor growth is balanced by resorption and the effects of stresses on tumor growth may be, to some extent, reversible.

Tumor development is often accompanied with the evolution in mechanical properties. Although cancer cells generally have lower elastic moduli than the corresponding normal cells, experiments showed that tumor tissues are often stiffer than the surrounding tissues and can sustain higher compressive stresses. This contradiction is mainly attributed to the mechanical resistance capacity of tumor ECM. ECM is primarily composed of collagen fibrils and glycosaminoglycan (GAG) chains, where the collagen network maintains the mechanical integrity of ECM, and GAG chains can imbibe water and carry fixed negative charges, resulting in a gel-like phase. The poroelastic model is applied to study the chemo-mechanical behaviors of tumor ECM, which is treated as a polyelectrolyte consisting of a collagen network and GAG chains [4]. The deformation of collagen network is described by the eight-chain hyperelastic model, while the free energy due to the mixing of GAG chains and water is estimated by Flory-Huggins theory. The poroelastic model reveals that osmosis is primarily responsible for the compressive resistance of ECM. Considering that aggregated cells and collagen fibrils act as a solid skeleton and GAG chains immerse in fluids, this poroelastic model can be extended to the whole tumor tissue. The extended model fits well with the experimental data of tumor tissues under compression, and also reveals that over-expressed GAGs can stiffen the tumor tissue. Besides, GAG chains also influence the transient mechanical response of ECM and tumor tissues by modulating permeability.

As a novel anticancer strategy, nanomedicine uses nanoparticles for drug delivery. However, the transport of nanoparticles, whose sizes are normally tens or even hundreds of nanometers, may be hindered by a dense tumor ECM. Both collagen fibrils and GAG chains affect drug diffusion and fluid convection in the tumor ECM. By using the principle of maximum energy dissipation rate, we also propose a general thermodynamic framework of poroelastic solids with degradation effects [5]. This framework is specified to evaluate the enzymatic degradation of tumor ECM. The permeability of ECM is predicted by considering the hydraulic drags engendered by the collagen network and GAG meshwork, and the diffusivity of nanomedicines in ECM is estimated by considering the obstruction of collagen fibrils, which cause an increase in the diffusive length, and the frictions between GAG chains and nanoparticles. In consistency with experiments, our results reveal that the diffusion of nanoparticles in tumors is mainly hindered by collagen fibrils,

while the weakened fluid convection in ECM is due to GAG chains. Therefore, degradation of tumor ECM could be an effective strategy to improve the efficacy of drug delivery.

MORPHOMECHANICS OF SOFT TISSUES

Biological morphomechanics addresses the formation and evolution of morphologies induced by growth, deformation, damage and reshaping of various tissues and organs under physiological and pathological conditions. A challenging issue in biomechanics and medical engineering is to build the intrinsic relationship between biological specificity and mechanical principles in the morphogenesis of soft tissues. Using the growth-induced wrinkling theory and the pseudodynamic method we have investigated the surface instability and morphological evolution of soft tissues with different geometric configurations. First, the critical conditions for the buckling, period-doubling buckling, and creasing in such soft tissues as airway and esophageal mucosa are derived. The coupling mechanisms between mechanical and chemical factors (e.g., gene) underlying the morphogenesis of these soft tissues are unraveled. Pattern evolutions under different physiological and pathological conditions are predicted and experimentally verified.

Morphogenesis of tumors holds significant applications in biomedical engineering, treatment and diagnosis of cancers. During development, solid tumors and brains always stratify into layered or core-shell structures and evolve into diverse surface morphologies [6]. It is found that the surface wrinkling of spherical core–shell tissues exhibit complicated and 3D features, strong nonlinearity, and multiple pattern transitions. We derive the analytical solution for the critical buckling and pattern formation of spherical core–shell tissues due to differential growth. It is revealed that the spherical surface can buckle into a surface pattern consisting of pentagons and hexagons, named the buckyball-like mode. This wrinkling mode in core–shell structures has been further validated by the experiments. During subsequent morphological evolution, the buckyball-like wrinkling pattern can switch to labyrinth folding morphologies akin to animal brains. The energetic mechanisms underpinning the wrinkle-to-fold transition has been elucidated. In addition, the period-doubling folding, labyrinthine folding, and spiral wrinkling of cylindrical core-shell tissues are also identified. These findings provide a new perspective toward understanding the morphogenesis of brains and tumors.

The development of tissues and organs involve not only wrinkling and morphological evolution on their surfaces but also structural variation and instability in the interior. For a tumor beyond the avascular phase, for example, angiogenesis is required to supply more oxygen and nutrients needed by tumor growth and metabolism. However, blood vessels may buckle and even collapse, characterized as lumen closure, during cancer development. Vascular collapse may lead to hypoxia, which promote cancer metastasis, and hinder the delivery of drug. The buckling and collapse of blood vessels are closely associated with mechanical microenvironment in tumors, such as elevated interstitial fluid pressure, over-proliferation of perivascular cells, and abnormal osmotic pressure. It can be expected that, by exerting an outer pressure on the vessel wall, the overgrowth of perivascular cells and elevation of interstitial fluid pressure and osmotic pressure may lead to the buckling and collapse of blood vessels. We have investigated the stability of blood vessels embedded in a growing tumor, described by the biochemomechanical poroelastic model [7]. Linear stability analysis is first made to give the critical condition of vascular buckling. The analysis shows that interstitial fluid pressure tends to drive blood vessels to buckle with a lower buckling mode, while perivascular cell proliferation favors a higher mode. Furthermore, a nonlinear biochemomechanical finite element method is formulated to track the morphological evolution of blood vessels during postbuckling. The blood vessels with the second mode of buckling may readily evolve into a crack-like shape. This theory can reproduce the essential features of vascular collapse observed in *in vivo* tumors.

CONCLUSIONS

Physiological and pathological processes of living tissues involve complicated interactions of mechanical, biological and chemical cues at different length scales. Combined experimental and theoretical efforts are required to understand the dynamic behaviours of cells (e.g., deformation, division, motion, migration and oscillation) and tissues (e.g., growth, regeneration, reshaping, damage, morphogenesis). We have studied the division, migration, oscillation and some other dynamic behaviours of collective cells through the combination of experiments, theory and simulations. A biochemomechanical poroelastic model is established to investigate the stress-modulated avascular growth, surface wrinkling and vascular buckling in growing tumors, mechanical properties of cancerous tissues, and nanomedicine therapy. These models may not only deepen our understanding of evolutionary processes of cells and soft tissues but also hold promise for clinical applications.

References

[1] Zhao Z. L., Liu Z. Y., Du J., Xu G. K., Feng X. Q. A dynamic biochemomechanical model of geometry-confined cell spreading. *Biophys J*, **112**: 2377–2386, 2017.
[2] Chen S. Y., Liu M. Y., Huang H. M., Zhang Z. Y., Li B., Feng X. Q., Zhao H. P. The relation between the collective motility and shapes of human cancer cells under heat stress. *Appl Phys Lett*, **116**: 043703, 2020.
[3] Lin S. Z., Li B., Lan G. H., Feng X. Q. Activation and synchronization of the oscillatory morphodynamics in multicellular monolayer. *Proc Natl Acad Sci USA* **114**, 8157–8162, 2017.
[4] Lin S. Z., Ye S., Xu G. K., Li B., Feng X. Q. Dynamic migration modes of collective cells. *Biophys J*, **115**: 1826–1835, 2018.
[5] Xue S. L., Li B., Feng X. Q., Gao H. Biochemomechanical poroelastic theory of avascular tumor growth. *J Mech Phys Solids*, **94**: 409–432, 2016.
[6] Li B., Jia F., Cao Y. P., Feng X. Q., Gao H. Surface wrinkling patterns on a core–shell soft sphere. *Phys Rev Lett*, **106**: 234301, 2011.
[7] Yin S. F., Xue S. L., Li B., Feng X. Q. Bio-chemo-mechanical modeling of growing biological tissues: Finite element method. *Int. J. Non-Linear Mech*, **108**: 46–54, 2019.

SL118439

SIMPLE INVARIANT SOLUTIONS REPRESENTING FLUID TURBULENCE

Genta Kawahara
Graduate School of Engineering Science, Osaka University, Toyonaka, Osaka, Japan

Summary Theoretical approaches using simple invariant solutions (equilibrium and periodic solutions) to the Navier–Stokes equations are presented to the problems of subcritical transition and developed turbulence. Considering turbulent flows as dynamical systems, stable and unstable manifolds of invariant solutions could represent flow instability and thus turbulence dynamics, while the simple solutions themselves exhibit coherence in turbulent flows. In this paper we attempt to quantitatively characterize turbulent flow and its onset in terms of invariant solutions. Specifically, the intensity of turbulence-driven mean secondary flow in a square duct is evaluated using the three-dimensional steady traveling-wave solution (Uhlmann, Kawahara & Pinelli 2010), and the scaling law of the Nusselt number (dimensionless wall-to-wall heat flux) with the Rayleigh number observed in thermal convective turbulence is reproduced by the three-dimensional steady solution (Motoki, Kawahara & Shimizu 2020). The onset Reynolds number of transient turbulence is also determined by the first tangency of homoclinic orbits to the known three-dimensional periodic edge state (Kawahara & Kida 2001) in minimal plane Couette flow (Lustro *et al*. 2019).

1. INTRODUCTION

The motion of a viscous fluid is governed by the Navier–Stokes equations, i.e., a set of partial differential evolution equations, apparently implying that fluid flow is an infinite-dimensional dynamical system. However, the turbulent motion in a finite domain is considered to be finite-dimensional. The physical reason is that small-scale motions are smoothed by viscosity. There is a mathematical proof of the existence of approximate inertial manifolds for the Navier–Stokes equations, providing a relation between the dominant modes and the higher-order ones that can be truncated (see e.g. Foias 2001). Within such a manifold, the Navier–Stokes equations can be rigorously approximated by a finite-dimensional system of ordinary differential equations.

Dynamical systems theory suggests that coherent structures in turbulent flows may be thought of simple invariant sets in phase space, in the neighborhood of which the system spends a substantial fraction of time. Spatio-temporally organized structures appear when a turbulent state approaches such an invariant set. Possible simple invariant sets in phase space are a fixed point and a periodic orbit. Recently dynamical-systems approaches have been taken widely to the problems of subcritical transition (see e.g. Kerswell 2005; Eckhardt *et al*. 2007; Eckhardt *et al*. 2008) as well as to developed low-Reynolds-number turbulence (see e.g. Kawahara, Uhlmann & van Veen 2012). Many of recent studies in this approach are concerned with qualitative characterization of flow properties in transition and turbulence. In this paper, on the other hand, we shall attempt to quantitatively reproduce statistical properties of turbulent flows and evaluate the onset Reynolds number of transient turbulence using simple invariant solutions.

In section 2 three-dimensional steady traveling-wave solutions to the Navier–Stokes equation is presented for square-duct flow (Uhlmann, Kawahara & Pinelli 2010). This traveling-wave solution not only exhibits eight-vortex secondary flow consistent with that observed in turbulent square-duct flow but also reproduces a secondary flow intensity comparable with turbulence-driven secondary flow. We also discuss a three-dimensional steady solution to the Boussinesq equation for Rayleigh–Bénard convection in section 3 (Motoki, Kawahara & Shimizu 2020). This steady solution represents the scaling law of the Nusselt number Nu with the Rayleigh number Ra, $Nu \sim Ra^{0.31}$, commonly observed in turbulent thermal convection. In section 4 we identify the onset of transient turbulence eventually relaminarizing as the first tangency of a pair of distinct homoclinic orbits to the known periodic edge state (Kawahara & Kida 2001) in minimal plane Couette flow (Lustro *et al*. 2019). A brief summary and the outlook for future studies are given in section 5.

2. TRAVELING WAVE REPRESENTING MEAN SECONDARY FLOW

Mean secondary (cross-sectional) flow is widely observed in turbulent flow through straight ducts with non-circular cross-section. Theoretical interpretation of the generation of such (turbulence-driven) mean secondary motion of Prandtl's second kind has long been a significant issue in fluid mechanics. In this section we shall discuss turbulence-driven secondary motion in the flow through a square duct. The mean flow in the cross-section consists of four pairs of counter-rotating vortices on four walls (a total of eight vortices per cross-section). There are several phenomenological explanations of the formation of the secondary vortices based on inspection of the dominant terms in the averaged streamwise-vorticity equation (Gavrilakis 1992), identification of preferential locations of instantaneous quasi-streamwise vortices (Pinelli *et al*. 2010), and so on.

Here we theoretically interpret the generation of the mean secondary flow in terms of three-dimensional steady traveling-wave solutions to the Navier–Stokes equation (Uhlmann, Kawahara & Pinelli 2010). Figure 1 shows the flow field on the upper-branch traveling wave at the bulk Reynolds number $Re = 1404$ (see the cross on the blue curve in figure 2). It can be seen that a wavy low-speed streak as well as staggered streamwise vortices appear in the vicinity of all

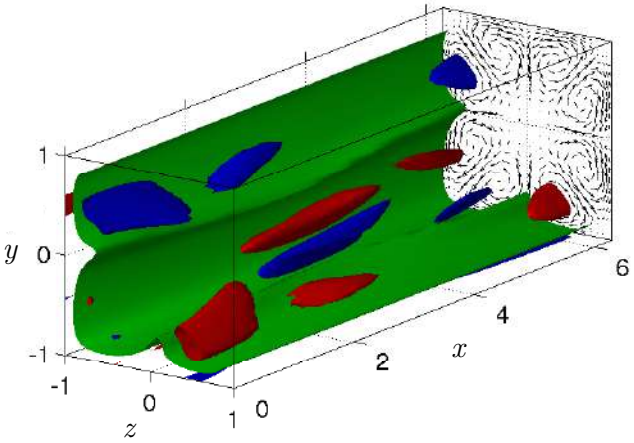

Figure 1: The upper branch of steady traveling waves (Uhlmann, Kawahara & Pinelli 2010) in pressure-driven square-duct flow at Reynolds number $Re = 1404$. The flow is visualized by green iso-surfaces of the streamwise velocity $0.55\,\max(u)$ and by red and blue iso-surfaces of the streamwise vorticity $\pm 0.65|\max(\omega_x)|$. The surfaces are cut away on one side of a diagonal of the duct cross-section for improved clarity. Streamwise-averaged velocity vectors are projected upon the cross-sectional plane of a square duct.

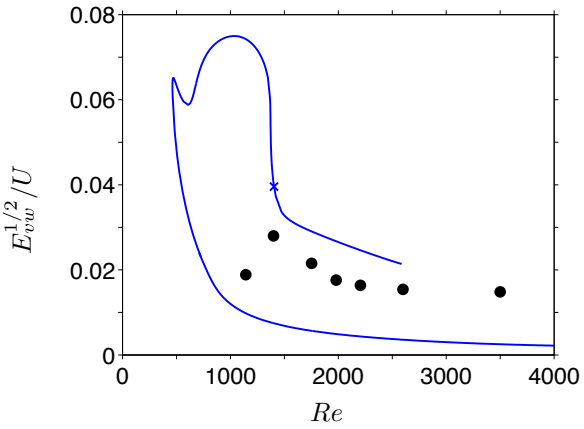

Figure 2: The intensity of the mean secondary flow $E_{vw}^{1/2}$ for Uhlmann, Kawahara & Pinelli's (2010) traveling waves normalized by the bulk velocity U as a function of the Reynolds number Re. $E_{vw} = \langle\langle v\rangle_x^2 + \langle w\rangle_x^2\rangle_{yz}$, where $\langle\cdot\rangle_m$ denotes the average with respect to m. The blue curve represents the upper- and lower-branch traveling-wave solutions on which the cross corresponds to the field visualized in figure 1. The closed circles stand for long-term averaged turbulent flow (Uhlmann *et al.* 2007).

four wall planes. The streamwise-averaged velocity of the traveling wave exhibits a secondary flow pattern with eight vortices, consistent with the mean secondary motion observed in turbulent square-duct flow. The traveling wave is quantitatively compared with turbulence data in figure 2, where the intensity of the secondary flow is shown as a function of the bulk Reynolds number Re. It is demonstrated that the upper-branch traveling wave has a comparable intensity with the turbulence-driven secondary flow at least up to $Re \approx 2500$, suggesting that the mean secondary flow can be identified as nonlinear equilibrium given by the invariant solution around which a turbulent system spends a substantial fraction of time.

3. STEADY SOLUTION REPRODUCING SCALING LAW IN TURBULENT CONVECTION

Rayleigh–Bénard convection is one of the most canonical turbulent flows. It is thermal convection driven by buoyancy, and dimensionless parameters in this system are the Rayleigh number Ra and the Prandtl number Pr. At low Ra wall-to-wall heat flux is given by thermal conduction. When Ra is increased, thermal convection arises and eventually convective turbulence appears to drastically enhance the heat flux. The dimensionless wall-to-wall heat flux normalized with thermal

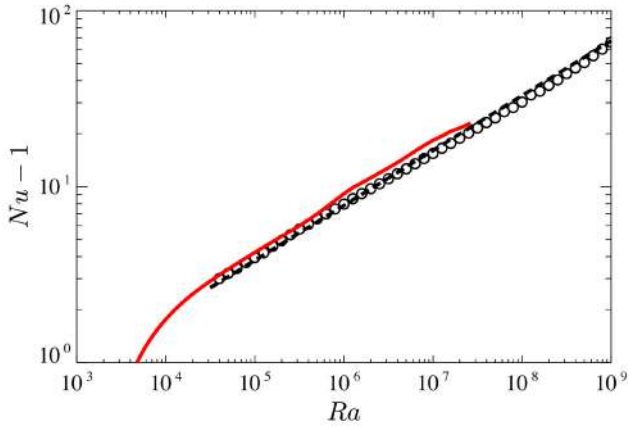

Figure 3: The Nusselt number Nu of Motoki, Kawahara & Shimizu's (2020) three-dimensional steady solution to the Boussinesq equation for $Pr = 1$ as a function of the Rayleigh number Ra. The red curve represents the invariant solution while the open circles denote the temporal average of the corresponding turbulent solution. The dashed line is the empirical correlation of the scaling law of Nu with Ra, $Nu - 1 = 0.105Ra^{0.312}$ (He *et al.* 2012).

conduction heat flux is the Nusselt number Nu. A large number of experiments and numerical simulations have been performed, and the scaling law $Nu \sim Ra^{0.31}$ has been commonly observed at $Ra \sim 10^8 - 10^{11}$ (see e.g. He *et al.* 2012). Grossmann & Lohse (2000) have proposed phenomenologically the scaling theory of Nu with Ra and Pr. Their theory gives us the scaling $Nu \sim Ra^{1/3}$ in the high-Ra range $Ra \sim 10^8 - 10^{14}$ for $Pr \sim 1$.

Here we aim at theoretically reproducing this well-known scaling law of Nu with Ra using a three-dimensional steady solution to the Boussinesq equation (Motoki, Kawahara & Shimizu 2020). Figure 3 shows the Nusselt number Nu of the steady solution for $Pr = 1$ as a function of the Rayleigh number Ra. In this figure the temporal average of Nu is also shown for a turbulent solution to the Boussinesq equation with consistent conditions with the steady solution. It is significant that Nu for the steady solution increases with increasing Ra, implying that at higher Ra, smaller-scale thermal plumes appear closer to the walls to enhance the wall heat flux in the simple invariant solution. It can be seen that the steady solution excellently reproduce the behavior of the corresponding turbulent solution, and what is remarkable in the figure is that the invariant solution exhibits the well-known turbulent scaling law $Nu \sim Ra^{0.31}$ (see e.g. He *et al.* 2012).

4. HOMOCLINIC TANGENCY LEADING TO TRANSIENT TURBULENCE

Recent studies have shown that transient turbulence eventually relaminarizing appears at the onset of subcritical transition to turbulence before (or without) the linear instability of laminar flow (see e.g. Eckhardt *et al.* 2008). It is indispensable for theoretical prediction of the transition to turbulence to determine the onset Reynolds number for such transient turbulence. Dynamical systems theory tells us that the onset of chaos can be identified by the emergence of the Smale horseshoe and that if transversal intersections of stable and unstable manifolds of a periodic orbit, i.e., homoclinic orbits, exist in our system, we can find a horseshoe map on its Poincaré section. Therefore, the onset of transient turbulence is rigorously determined as the first emergence of homoclinic orbits to a periodic edge state, i.e., the first homoclinic tangency.

Here we theoretically determine the onset Reynolds number of transient turbulence in minimal plane Couette flow by identifying the first homoclinic tangency to Kawahara & Kida's (2001) periodic edge state (Lustro *et al.* 2019). Figure 4 shows the two-dimensional projection of the two homoclinic orbits, which have been observed to exist down to the lowest (tangency) Reynolds number. Even at the highest Reynolds number $Re = 245$ the former of the two large-amplitude temporal oscillations are almost consistent between the two homoclinic orbits while the latter are significantly distinct (see figure 4 (*e*)). As Re is decreased these two homoclinic orbits get closer to each other and eventually merge to disappear in tangency at $Re \approx 240.88$. Below the tangency Reynolds number $Re \approx 240.88$ we have not observed transient turbulence eventually relaminarizing, implying that $Re \approx 240.88$ is the onset Reynolds number of transient turbulence in minimal plane Couette flow.

5. SUMMARY AND OUTLOOK

Recently dynamical-systems approaches have been taken to enrich our understanding of subcritical transition and developed turbulence with a focus on qualitative characterization of flow properties in transition and turbulence. In this paper, by using simple invariant solutions to the Navier–Stokes equations we have attempted to quantitatively reproduce the intensity of turbulence-driven secondary motion in square-duct flow and the scaling law of the Nusselt number with the Rayleigh number in turbulent Rayleigh–Bénard convection as well as to evaluate the onset Reynolds number of transient

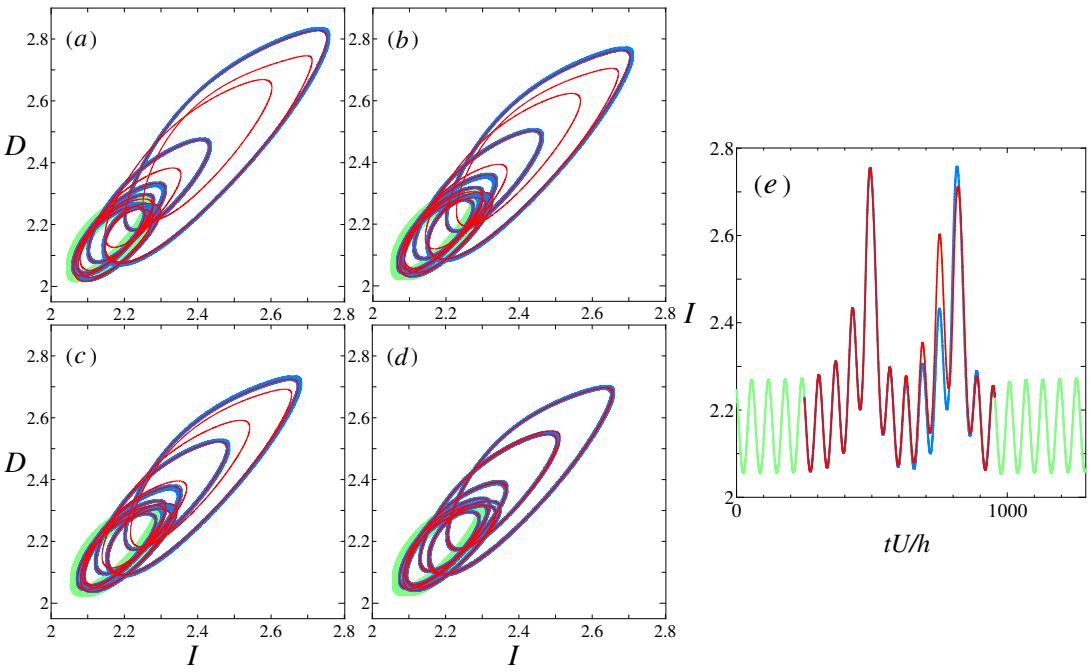

Figure 4: A pair of distinct homoclinic orbits that exhibit tangency in the two-dimensional projection defined by energy input rate I and energy dissipation rate D normalized with the corresponding laminar values. The light green line represents Kawahara & Kida's (2001) periodic edge state. The blue and red lines correspond to the family of homoclinic orbits. Starting from (a) the pair move closer to each other with decreasing Reynolds number until they merge to tangency at (d). (a) $Re = 245$, (b) $Re = 242.5$, (c) $Re = 241.4$, and (d) $Re \approx 240.88$. The value of I of the two orbits is shown as a function of time at $Re = 245$ in (e).

turbulence in minimal plane Couette flow. Such quantitative characterization in terms of simple invariant solutions to the Navier–Stokes equations could be the key to theoretical description of transition and developed turbulence. However, since the numerical computation of invariant solutions is much tougher at higher Reynolds numbers, representative statistical laws of turbulence, e.g., the inertial range in isotropic turbulence and the logarithmic layer in wall turbulence, are still beyond the quantitative characterization in terms of invariant solutions. In order to take a dynamical-systems approach to high-Reynolds-number turbulence using invariant solutions, we need to develop novel numerical schemes for invariant solutions and/or to obtain invariant solutions to the model equations for high-Reynolds-number turbulence, such as the LES (Large Eddy Simulation) equations, rather than the Navier–Stokes equations. More recently there are a few studies on the LES invariant solutions (see e.g. van Veen, Vela-Martín & Kawahara 2019 for an attempt on the inertial-range dynamics using a periodic solution to the LES equation).

References

[1] Eckhardt B., Faisst H., Schmiegel A., Scheider T. M. Dynamical systems and the transition to turbulence in linearly stable shear flows. *Phil. Trans. R. Soc. A* **366**: 1297–1315, 2008.
[2] Eckhardt B., Scheider T. M., Hof, B., Westerweel J. Turbulence transition in pipe flow. *Ann. Rev. Fluid Mech.* **39**: 447–468, 2007.
[3] Foias C., Manley O., Rosa R., Temam R. 2001. *Navier–Stokes Equations and Turbulence*. Cambridge Univ. Press, 1st ed., 2001.
[4] Gavrilakis S. Numerical simulation of low-Reynolds-number turbulent flow through a straight square duct. *J. Fluid Mech.* **244**: 101–129, 1992.
[5] Grossmann S., Lohse, D. Scaling in thermal convection: a unifying theory. *J. Fluid Mech.* **407**: 27–56, 2000.
[6] He X., Funfschilling, D., Nobach, H., Bodenschatz, E., Ahlers, G. Transition to the ultimate state of turbulent Rayleigh–Bénard convection. *Phys. Rev. Lett.* **108**: 024502, 2012.
[7] Kawahara G, Kida S. Periodic motion embedded in plane Couette turbulence: regeneration cycle and burst. *J. Fluid Mech.* **449**: 291–300, 2001.
[8] Kawahara G., Uhlmann M., van Veen L. The Significance of Simple Invariant Solutions in Turbulent Flows. *Ann. Rev. Fluid Mech.* **44**: 203–225, 2012.
[9] Kerswell R. R. 2005. Recent progress in understanding the transition to turbulence in a pipe. *Nonlinearity* **18**: R17–R44, 2005.
[10] Lustro J. R. T., Kawahara G., van Veen L., Shimizu M., Kokubu H. The onset of transient turbulence in minimal plane Couette flow. *J. Fluid Mech.* **862**: R2, 2019.
[11] Motoki S., Kawahara G., Shimizu M. Multiscale three-dimensional steady solutions in Rayleigh–Bénard convection. In preparation. 2020.
[12] Pinelli A., Uhlmann M., Sekimoto A., Kawahara G. Reynolds number dependence of mean flow structure in square duct turbulence. *J. Fluid Mech.* **644**: 107–122, 2010.
[13] Uhlmann M., Kawahara G., Pinelli A. Traveling-waves consistent with turbulence-driven secondary flow in a square duct. *Phys. Fluid* **22**: 084102, 2010.
[14] Uhlmann M., Pinelli A., Kawahara G., Sekimoto A. Marginally turbulent flow in a square duct. *J. Fluid Mech.* **588**: 153–162, 2007.
[15] van Veen L., Vela-Martín A., Kawahara G. Time-periodic inertial range dynamics. *Phys. Rev. Lett.* **123**: 134502, 2019.

SL118440

WHEN BIOLOGY INSPIRES FLUID MECHANICS

Eric Lauga
Department of Applied Mathematics and Theoretical Physics, University of Cambridge, Cambridge CB3 0WA, United Kingdom

Summary Research in fluid mechanics has long been motivated by the desire to understand the world around us. Biology, in particular, is dominated by transport problems involving fluids, from diffusion of nutrients and locomotion at the cellular level to flows around plants and the circulatory system of animals, and as such the biological realm is a constant source of inspiration for fluid mechanicians. In this talk I will highlight recent work in my group where fluid mechanics problems are inspired by small-scale biology. I will first focus on motile bacteria, from their individual and collective dynamics to their interactions with viruses. I will then highlight our research on the distribution of swimming speeds for eukaryotic organisms. Finally, I will show how cell locomotion can be used as a source of inspiration to design and optimise artificial swimmers and pumps.

INTRODUCTION

Fluid dynamics plays a crucial role in numerous biological processes, from the largest animals to the smallest cells, and research activity at the intersection of fluid dynamics and biology has been steadily growing since the pioneering work of Taylor in the 1950's. Over the last twenty years, fluid mechanics conferences and journals have seen a stark increase in research relevant to, or inspired by, biology.

An area of particular interest is the role of low Reynolds number flows in cellular life. Enabled by advances in microscopy and micromanipulation, experimental data have been used to inspire new models and enable hydrodynamic discoveries while in turn quantitative theories using fluid mechanics have been precisely tested. One area where this back and forth between theory and experiments has been very successful is the study of cell motility. Exemplified by the swimming of microorganisms such as bacteria and spermatozoa, this is an area where fluid dynamics has not only helped explain many natural phenomena but also one where biology has lead to a new understanding of hydrodynamics.

In this talk I will highlight recent work in my group where fluid mechanics problems are inspired by small-scale biology. I will first focus on motile bacteria, from their individual and collective dynamics to their interactions with viruses. I will then highlight our research on the distribution of swimming speeds for eukaryotic organisms. Finally, I will show how cell locomotion can be used as a source of inspiration to design and optimise artificial swimmers and pumps. Throughout the talk, I will attempt to focus on the basic mathematical modelling tools and emphasise the key physical ideas.

FLUID MECHANICS OF BACTERIA

Bacterial magneto-convection

Dense suspensions of swimming bacteria are known to self-organise and display unsteady dynamics. In work done in collaboration with the groups of Cécile Fradin and Kari Dalnoki-Veress from McMaster University, I will report on a new type of collective motion observed in a population of confined magnetotactic bacteria induced by application of a magnetic field perpendicular to the confining walls in a microfluidic setup. We find that a uniform distribution of bacteria

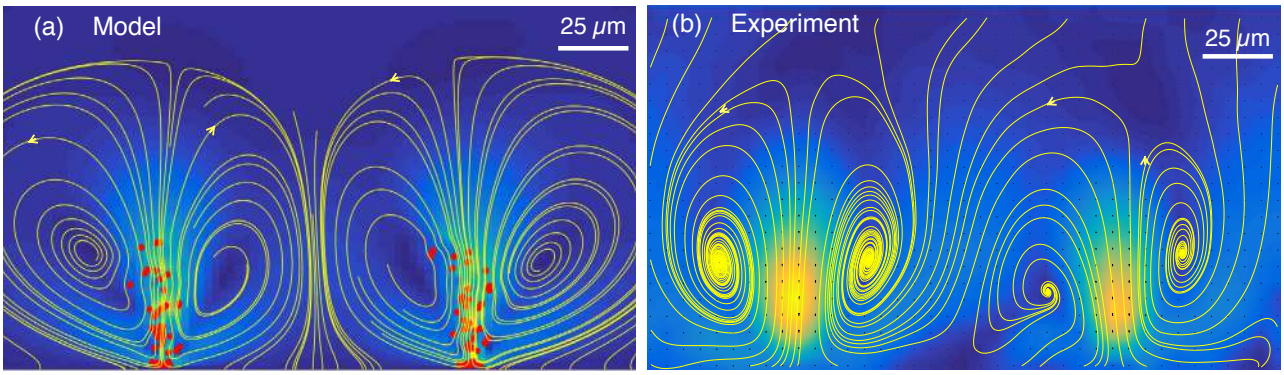

Figure 1: Convection cells created by two plumes in a 200 μm glass capillary. (a) Experimental measurements showing magnitude and streamlines of the flow field. (b) Convection cells and flow from theoretical model, where red dots represent cells [1].

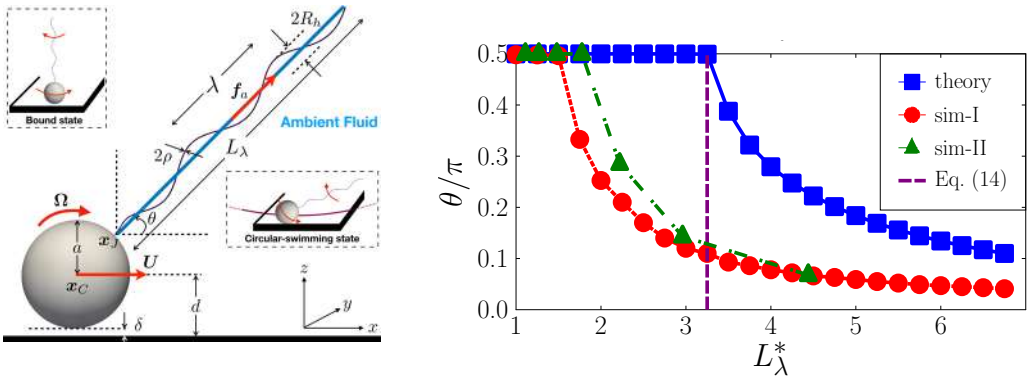

Figure 2: Left: Schematic diagram of a flagellated bacterium swimming near a plane surface. The cell body is modelled as a rigid sphere and the flagellar filament as a rigid right-handed helix rotating along its axis (numerical simulations) or a rod placed along the helix axis with an active force acting along it (theoretical model). The flagellum tilt angle is denoted by θ. The two possible final steady states of a bacterium near a surface are shown in the insets: the surface-bound state ($\theta = \pi/2$) and circular-swimming state ($\theta \neq \pi/2$). Right: Pitchfork bifurcation of the tilt angle, θ/π, plotted against the dimensionless flagellum axial length, L^*_λ, for the numerical simulations (red dashed lines/circles for sim-I and green dash-dotted lines/triangles for sim-II) and the theoretical model (blue solid lines/squares) [2]. The critical flagellum axial length below which bound state is possible is shown in purple dashed line for the analytical model.

self-organises spontaneously into bacterial plumes perpendicular to the wall, resulting in self-sustained flow convection cells (Fig. 1).

The observed plumes are reminiscent of bioconvection patterns and the flow generated resembles Rayleigh-Benard convection cells while the dynamics bears similarities with porous media flows. However, an essential difference exists between the phenomenon reported here and these well-studied instabilities. Both bioconvection and the Rayleigh-Benard instability rely on a density mismatch between layers of the fluids. In contrast, for the phenomenon reported here, no external forces are applied on the fluid and the magnetic field only exerts an external torque aligning magnetotactic bacteria with the field – the plumes result thus only from hydrodynamic interactions between the oriented cells and the confining walls.

Using a theoretical model based on hydrodynamic singularities, we are able to capture quantitatively the instability and the observed long-time growth of the plumes [1]. We use the model to show that the self-sustained state, which we term bacterial magneto-convection, results from the balance between the ordered state of the cells and both cell-cell and cell-wall hydrodynamic interactions.

Stability of bacteria bacteria near surfaces

It is well known that flagellated bacteria, such as the oft-studied *Escherichia coli*, swim in circles near surfaces. However, recent experiments have shown that a sulfide-oxidizing bacterium named *Thiovulum majus* can transition from swimming in circles to a dynamical surface-bound state where it stops swimming while remaining free to move laterally along the surface. In this bound state, the cell body continuously rotates around its centre in the direction perpendicular to the surface while its flagellar filaments point away from the surface, rotating in the opposite direction. Mathematically, we define the cell to be in the surface-bound state when the flagellum axis is perpendicular to the surface, i.e. $\theta = \pi/2$, and consequently, the radius of circular trajectory is $R = 0$ (see Fig. 2, left).

In the bound state, a small perturbation in the tilt angle of the flagellum is expected to destabilise the cell and cause it to swim parallel to the surface in circles. What makes this state stable? Using two different numerical simulations together with a theoretical analysis, we demonstrate the existence of a fluid-structure interaction instability that causes cells with relatively short flagella to become surface bound [2]. Specifically, we show that the flagellum of a freely swimming *T. majus* cell undergoes slow tilt angular dynamics near a rigid wall. If the distance between the cell's surface and the wall becomes sufficiently small, drag forces acting on the translating flagellum (which tend to align the flagellum parallel to the surface) are unable to compensate the large lubrication torque exerted on the cell body (which tends to align the flagellum perpendicular to the surface). In this case, the cell eventually points perpendicular to the wall and thus stops swimming, while the cell body and flagella continue rotating as seen in experiments. This bound state is stable only below a certain critical flagellum axial length, L_λ, normalised by the radius of the spherical cell body, a, consistent with experiments (see Fig. 2, right).

Hydrodynamics of bacterial phages

Bacteriophage viruses, one of the most abundant entities in our planet, lack the ability to move independently. Instead, they crowd fluid environments in anticipation of a random encounter with a bacterium. Once they land on the cell body of their victim, they are able to eject their genetic material inside the host cell. Many phage species, however, first attach to the flagellar filaments of bacteria. Being immotile, these so-called flagellotropic phages still manage to reach the cell

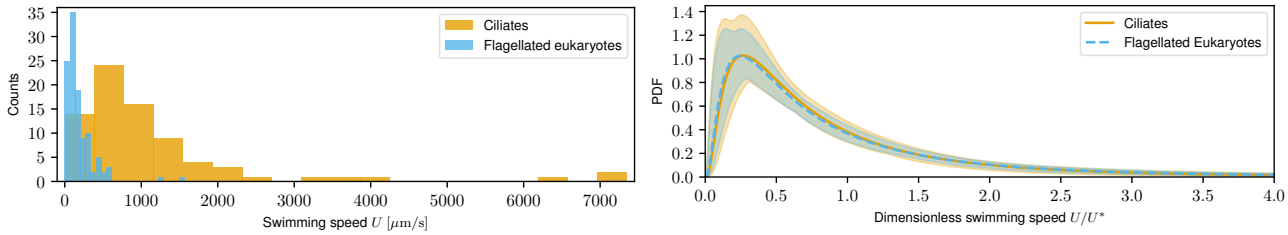

Figure 3: Left: Histograms of swimming speed for ciliates and flagellates demonstrate a similar character but different scales of velocities. Right: Test of rescaling hypothesis. Shown are the two fitted log-normal curves for flagellates and ciliates, each multiplied by the distribution median M, plotted versus speed normalized by M. The distributions for show remarkable similarity and uncertainty of estimation [5].

body for infection, and the process by which they move up the flagellar filament has intrigued the scientific community for decades. Back in 1973, Berg and Anderson [3] proposed the nut-and-bolt mechanism in which, similarly to a rotated nut that is able to move along a bolt, the phage wraps itself around a flagellar filament possessing helical grooves (due to the helical rows of flagellin molecules) and exploits the rotation of the flagellar filament in order to passively travel along it. One of the main pieces of evidence for this mechanism is the fact that immotile mutants of bacterial species such as *Escherichia coli* and *Salmonella typhimurium* equipped with straight, but rotating, flagellar filaments with a preserved helical groove structure are still infected by their relative phages.

Using two distinct theoretical approaches for the short-range interactions between phages and flagellar filaments, I will show the derivation of a first-principles theoretical model for the nut-and-bolt mechanism applicable to mutants possessing straight flagellar filaments [4]. Our model is fully analytical, is consistent with past experimental observations, and is able to predict the speed of translocation of a bacteriophage along a flagellar filament as a function of (i) the geometry of both phage and bacterium, (ii) the rotation rate of the flagellar filament and (iii) the handedness of the helical grooves.

FLUID MECHANICS OF EUKARYOTIC CELLS

Distribution of swimming speeds and a database of cell motility

One approach to quantifying biological diversity consists of characterising the statistical distribution of specific properties of a taxonomic group or habitat. Microorganisms living in fluid environments, and for whom motility is key, exploit propulsion resulting from a rich variety of shapes, forms, and swimming strategies. In joint work with the group of R. E. Goldstein in Cambridge, I will present our effort to explore the variability of swimming speed for unicellular eukaryotes based on published data (Fig. 3, left). The data naturally partitions into that from flagellates (with a small number of flagella) and from ciliates (with tens or more). Despite the morphological and size differences between these groups, I will show that each of the two probability distributions of swimming speed are accurately represented by log-normal distributions, with good agreement holding even to fourth moments. Scaling of the distributions by a characteristic speed for each data set leads in fact to a collapse onto an apparently universal distribution (Fig. 3, right). These results suggest a universal way for ecological niches to be populated by abundant microorganisms [5].

I will next present a thorough survey of the available experimental data produced to date on the characterisation of motile behaviour of unicellular microswimmers. We have assembled from the available literature empirical data on the motility of five broad categories of organisms: bacteria, archaea, flagellated eukaryotes, spermatozoa and ciliates. Whenever possible, we gathered the following parameters: species, geometry and size of the organisms, swimming speeds, actuation frequencies, actuation amplitudes, number of flagella and properties of the surrounding fluid. We analyse the results in the light of the established fluid mechanics principles for propulsion at low Reynolds numbers. We reproduce expected scalings for the locomotion of cells within the same taxonomic groups of organisms while demonstrating the variability for organisms of different species within the same group. We also obtain a number of new, unexpected scalings, for which we propose biophysical rationalisations. The material gathered in our work is a summary of the established knowledge in the domain, providing a convenient and practical reference point for future studies while highlighting uncharted territories [6].

FLUID MECHANICS OF ARTIFICIAL SWIMMERS

Quincke swimmers

Limitations in nanofabrication have thus far hindered the ability to design and program synthetic swimmers with the same abilities as self-propelled biological cells, so scientists have taken advantage of other physical mechanisms in order to design self-propelled artificial swimmers. Dielectric particles suspended in a weakly conducting fluid are known to spontaneously start rotating under the action of a sufficiently strong uniform DC electric field due to the Quincke rotation instability. This rotation can be converted into translation when the particles are placed near a surface providing useful

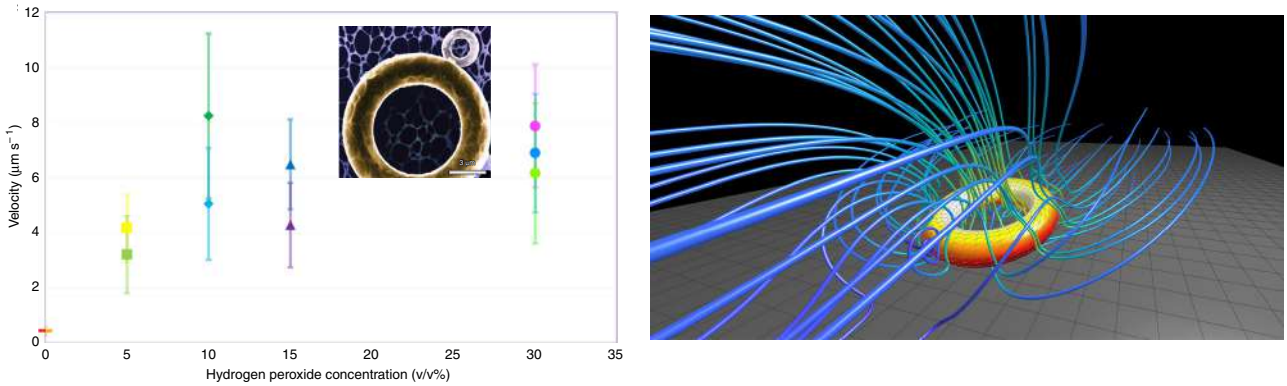

Figure 4: Left: Propulsion velocity of a catalytic Janus torus as a function on the concentration of hydrogen peroxide (Inset: High-resolution transmission electron microscope image of Janus torus; scale bar is 3 μm). Right: Flow streamlines and surface concentration of a steady gliding catalytic torus, at an angle of 12°, shown in the frame in which the torus is stationary [8].

model systems for active matter. Using a combination of numerical simulations and theoretical modeling, we demonstrate that it is possible to convert this spontaneous Quincke rotation into spontaneous translation in a plane perpendicular to the electric field in the absence of surfaces by relying on geometrical asymmetry instead [7].

Phoretic swimmers and pumps

Phoretic mechanisms, whereby gradients of chemical solutes induce surface-driven flows, have recently been used to generate directed propulsion of patterned colloidal particles. I first present experimental and theoretical work where, in collaboration with the groups of A. Sen and I. Aronson at Penn State, we encode multi-behavioural responses in microscopic self-propelled tori using nanoscale 3D printing. We show experimentally and theoretically that the tori continuously transition between two primary swimming modes in response to a magnetic field (see Fig. 4). The tori also manipulate and transport other artificial swimmers, bimetallic nano-rods, as well as passive colloidal particles, and have the potential to interact with biological active matter, e.g. bacteria or cells [8].

We next consider the case of confined phoretic flows, which provide efficient means to drive fluid motion on very small scales. Colloidal particles covered with chemically-active patches with nonzero phoretic mobility (e.g. Janus particles) swim using self-generated gradients and similar physics can be exploited to create phoretic pumps. In work carried in collaboration with the group of S. Michelin at Ecole Polytechnique (France), I will present a detailed analysis of the design principles of phoretic pumps and show that for a minimal phoretic pump, consisting of three distinct chemical patches, the optimal arrangement of the patches maximising the flow rate is universal and independent of chemistry [9].

In collaborative work in collaboration with the groups of E. Keaveny and D. Papageorgiou at Imperial College London and S. Michelin, I finally show theoretically that, in a mechanism analogous to Bénard-Marangoni convection, phoretic phenomena can create spontaneous and self-sustained wall-driven mixing flows within a straight, chemically-uniform active channel. Such spontaneous flows do not result in any net pumping for a uniform channel but greatly modify the distribution of transport of the chemical solute. The instability is predicted to occur for a solute Péclet number above a critical value and for a band of finite perturbation wave-numbers. We solve the perturbation problem analytically to characterise the instability, and use both steady and unsteady numerical computations of the full nonlinear transport problem to capture the long-time coupled dynamics of the solute and flow within the channel [10].

References

[1] Théry A., Le Nagard L., Ono-dit-Biot J.-C., Fradin C., Dalnoki-Veress K. and Lauga E.. Bacterial magneto-convection. Submitted, 2020.
[2] Das D. and Lauga E. Transition to bound states for bacteria swimming near surfaces. *Phys. Rev. E*, **100**, 043117, 2019.
[3] Berg H. C. and Anderson R. A. Bacteria swim by rotating their flagellar filaments. *Nature* **245**, 380, 1973.
[4] Katsamba P. and Lauga E. Hydrodynamics of bacteriophage migration along bacterial flagella. *Phys. Rev. Fluids*, **4**, 013101, 2019.
[5] Lisicki M., Rodrigues M. F. V., Goldstein R. E. and Lauga E. Swimming eukaryotic microorganisms exhibit a universal speed distribution. *eLife*, **8**, e44907, 2019.
[6] Lisicki M., Rodrigues M. F. V., Goldstein R. E. and Lauga E.. In preparation. 2020.
[7] Das D. and Lauga E. Active particles powered by Quincke rotation in a bulk fluid. *Phys. Rev. Lett.*, **122**, 194503, 2019.
[8] Baker R., Montenegro-Johnson T., Sediako A. D., Thomson M. J., Sen A., Lauga E. and Aronson I. S. Shape-programmed 3-D printed swimming microtori for the transport of passive and active agents. *Nature Comm.*, **10**, 4932, 2019.
[9] Michelin S. and Lauga E. Universal optimal geometry of minimal phoretic pumps. *Sci. Rep.*, **9**, 10788, 2019.
[10] Michelin S., Game S., Lauga E., Keaveny E. and Papageorgiou D.. Spontaneous onset of convection in a uniform phoretic channel. *Soft Matt.*, 2020 (accepted for publication).

SL118441

SIZE-EFFECTS IN POROUS METAL PLASTICITY

Christian F. Niordson
Department of Mechanical Engineering, Technical University of Denmark, Kgs. Lyngby, Denmark

Summary A model for the incorporation of micron scale size-effects in the plastic response of porous metals is proposed. Strain gradient plasticity theory is employed in a finite element setting in order to quantify size effects on the yield surface of porous metals. It is quantified how void growth on the micron scale is suppressed, and it is proposed to account for void-size effects in established conventional models by decreasing the sensitivity to porosity and mean stress. A simple simple transformation of conventional yield surfaces is proposed to obtain size-dependent yield surfaces.

MOTIVATION

Size-effects in metals have been confirmed in numerous small scale experiments. Whenever large strain gradients are imposed on micron scale samples, such as in torsion of thin wires or bending of thin films, the plastic response exhibits size-dependence with the general trend that 'smaller is stronger'. Similarly, micro- and nano-indentation tests show increased hardness for smaller indentation depths, where large densities of geometrically necessary dislocations accompany large plastic strain gradients.

Under macroscopically homogeneous deformation, size-effects may arise due to passivation layers or at internal microstructural interfaces causing inhomogeneous plastic strain. This includes the well known Hall-Petch effect where plastic strain gradients increase with decreasing grain size leading to higher yield strength. This paper focuses on how size-effects may be included in models for micron scale void growth and in homogenized theories of porous metal plasticity.

COMPUTATIONAL MODEL

The strain gradient plasticity theory by Gudmundson [1] is implemented in a finite element framework based on the minimum principles developed by Fleck and Willis [2] in finite strain generalization [3]. A homogeneous distribution of voids in layers (Figure 1b) with a hexagonal pattern (Figure 1a) is analysed using an axi-symmetric approximate representative volume element (RVE) (Figure 1c) of length L_c, radius R_c and with the void size R_v. Boundary conditions are imposed through displacements of the RVE sides (U_1 and U_2) such that a constant axi-symmetric stress ratio is maintained. For spherical voids the initial porosity is defined in terms of the RVE geometry by $f = 2R_v^3/(3R_c^2 L_c)$.

RESULTS

For equal in-plane and out-of-plane void spacing ($R_C = L_c$) and a porosity of $f = 0.04$ Figure 2a shows RVE predictions for macroscopic yield surfaces in mean stress - effective stress space (σ_m-σ_e space). The axes are normalized

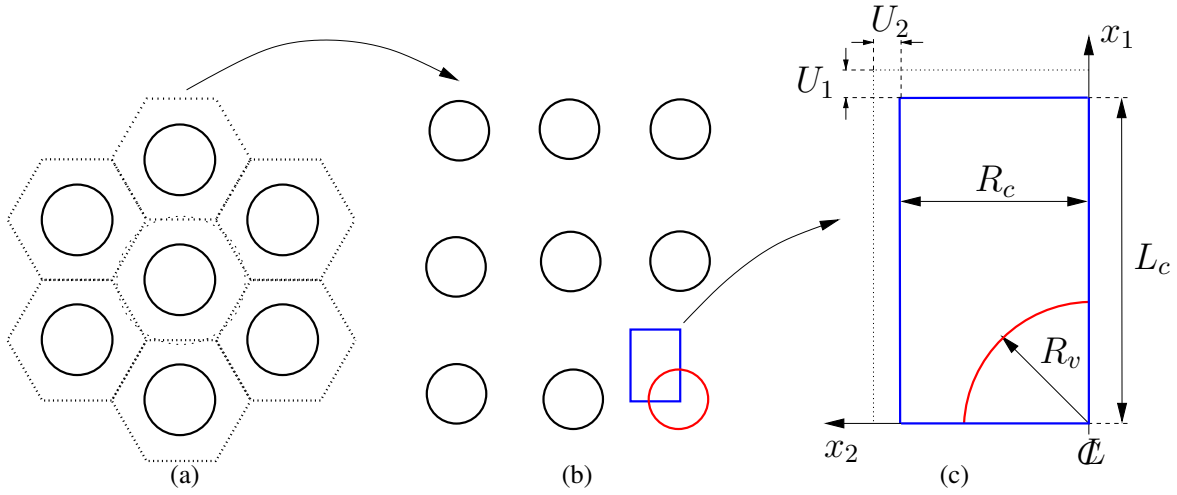

Figure 1: Hexagonal pattern of spherical voids (a) in layers (b). (c) Axi-symmetric representative volume element approximation including a single void.

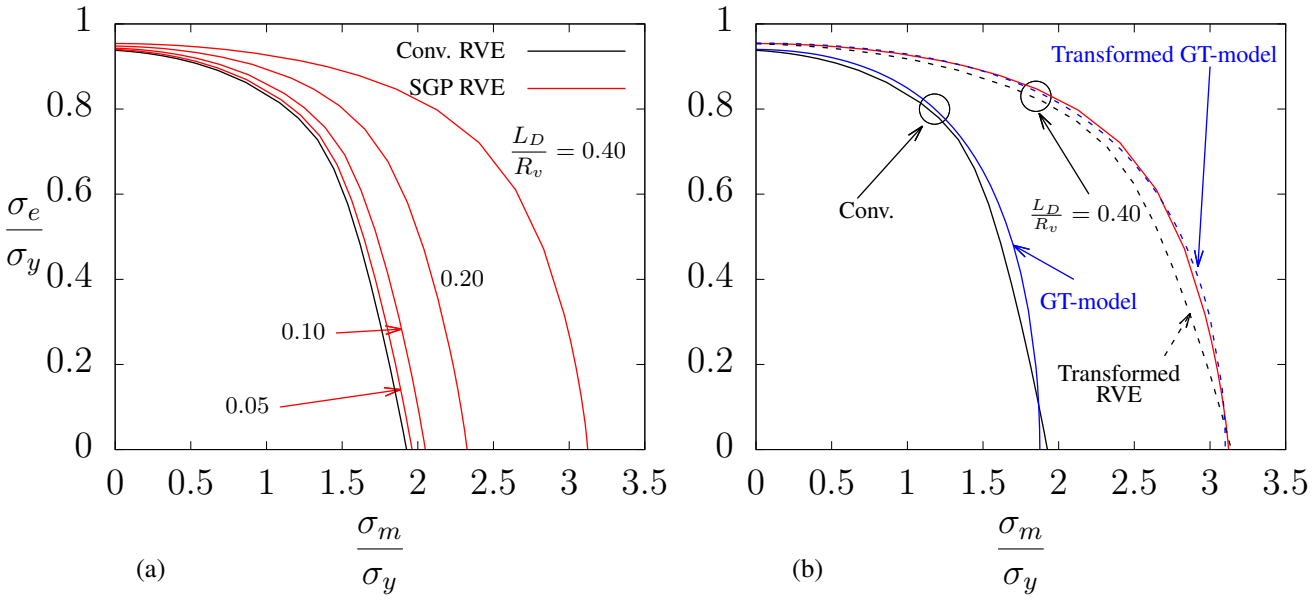

Figure 2: (a) Size dependence of yield surfaces. (b) Transformed conventional yield surfaces capture size effects well.

by the yield stress of the matrix material, σ_y. The black curve shows the conventional yield surface and the red curves show size-dependent yield surfaces for different ratios of the material length parameter in the strain gradient plasticity model, L_D, to void radius, R_v. For the fixed porosity of $f = 0.04$, the figure shows how the yield surface expands for decreasing void size. For each void size the yield surfaces presented may be expressed by yield functions of the form $F(\sigma_e, f, \sigma_m, \sigma_y) = 0$. Figure 2b shows the conventional yield surface and that for $L_D/R_v = 0.4$. Based on the notion that the yield surface of a size-dependent material corresponds to that of a conventional material with a smaller void volume fraction and a smaller mean stress sensitivity the yield surface for a conventional material may be transformed to that of the size-dependent material throug the transformation

$$F(\sigma_e, f, \sigma_m, \sigma_y) \rightarrow F(\sigma_e, Q_1 f, Q_2 \sigma_m, \sigma_y) \tag{1}$$

where $Q_1 \leq 1$ and $Q_2 \leq 1$ are positive parameters that depend on the size scale of the voids. By using $Q_1 = 0.75$ and $Q_2 = 0.67$ a yield surface for a conventional material may be transformed to be in close agreement of the size-dependent material for $L_D/R_v = 0.4$, as shown by the black dashed curve in Figure 2b. The figure also includes yield surfaces based on the conventional Gurson-Tvergaard model (GT-model) [4] (blue curve) and that of a transformed GT-model (dashed blue curve). It is seen that the same transformation parameters work well also for the Gurson-Tvergaard model.

CONCLUSIONS

Based on strain gradient plasticity investigations, it is shown how a simple transformation of yield surfaces (1) may be employed to transform yield surfaces conventional porous metals to the size-dependent scale. A systematic study shows that the transformation parameters may be well approximated by the following explicit expressions

$$Q_1 \approx \frac{0.364}{1 + 1.8\left(\frac{L_D}{R_v}\right) + 10\left(\frac{L_D}{R_v}\right)^2} + 0.636 \qquad Q_2 \approx \frac{1}{1 + 1.8\left(\frac{L_D}{R_v}\right)^{3/2}} \tag{2}$$

In the context of ellipsoidal voids the same transformation has also been found to give good predictions. However, care must be taken when choosing the relevant void size measures in the transformation.

References

[1] Fleck N. A., Willis J. R. , A Unified Treatment of Strain Gradient Plasticity. *J. Mech. Phys. Solids* **52**: 1379-1406, 2004.
[2] Gudmundson P., A mathematical basis for strain-gradient plasticity theory. Part II: Tensorial plastic multiplier. *J. Mech. Phys. Solids* **57**: 1045-1057, 2009.
[3] Niordson C. F., Tvergaard V., A homogenized model for size-effects in porous metals. *J. Mech. Phys. Solids* **123**: 222-233, 2019.
[4] Tvergaard V., On localization in ductile materials containing spherical voids. *Int. J. Fract.* **18**: 237-252, 1982.

SL118442

DATA-DRIVEN MECHANICS - THEORETICAL AND NUMERICAL ASPECTS IN THE CONTEXT OF INELASTIC MATERIAL BEHAVIOUR

Stefanie Reese*[1], Robert Eggersmann[1], Shahed Rezaei[1], Mauricio Fernández[2], Laurent Stainier[3], and Michael Ortiz[4,5]
[1]Institute of Applied Mechanics, RWTH Aachen University, Aachen, Germany
[2]Cyber-Physical Simulation Group, Technische Universitt at Darmstadt, Darmstadt, Germany
[3]Institute of Civil and Mechanical Engineering, Ecole Centrale de Nantes, Nantes, France
[4]Division of Engineering and Applied Science, California Institute of Technology, Pasadena, USA
[5]Hausdorff Center for Mathematics, Rheinische Friedrich-Wilhelms-Universit at Bonn, Bonn, Germany

INTRODUCTION

Due to the volatile development of storage capacities as well as suitable soft- and hardware, the amount of available data has increased by many orders of magnitude over the last decades. This influences almost all parts of practical life but also science and technology. In particular, the area of computational mechanics has a significant role in it, since it seeks for physically relevant models validated by meaningful data. The question arises as to whether the challenging step of setting up parametric constitutive models can be left out completely. Is it possible to represent and numerically predict the material behaviour purely by means of data? On the one hand, the presentation shall focus on data-driven approaches for inelastic material behaviour, where loading and unloading paths in a stress-strain diagram do not coincide. An important point is to clarify which data sets are needed to obtain a physically reasonable material description. What are today's limitations – also in comparison to standard continuum mechanical modelling? Another field of interest concerns the important question how the computational efficiency of such approaches can be improved. In the talk, several ideas to reduce the computational effort and to deal with large amounts of data are discussed. Of high significance are also connections to machine learning algorithms or other surrogate approaches including model order reduction.

DATA-DRIVEN INELASTICITY

A new paradigm in computational mechanics was recently introduced by Kirchdoerfer and Ortiz [1] as well as Conti et al. [2] which is called data-driven computing. The approach enables the usage of experimental data in the fundamental form of pairs of stress and strain directly in a computation. As a consequence, no explicit material law has to be formulated or fitted to experimental results. In this kind of data-driven approach the classical boundary value problem is reformulated by means of distances between states satisfying equilibrial and kinematic relations and states from a data set. The procedure started new ways of thinking and opened a new field of research.
One essential question concerning the extension to inelastic material behavior is answered by the authors in [3]. This formulation differs from data-driven problems in elasticity in that the material data set includes histories of prior stresses and strains or even history variables. As a result the relevance of a certain data point changes from one time step to another. As to mention a simple example of a data set which can represent time-dependent viscoelastic material behavior, we simply extend the data set in the following format: $D = \{\varepsilon_i^k, \sigma_i^k, \varepsilon_i^{k+1}, \sigma_i^{k+1}\}_{i=1}^N$. Here, the N stresses and strains

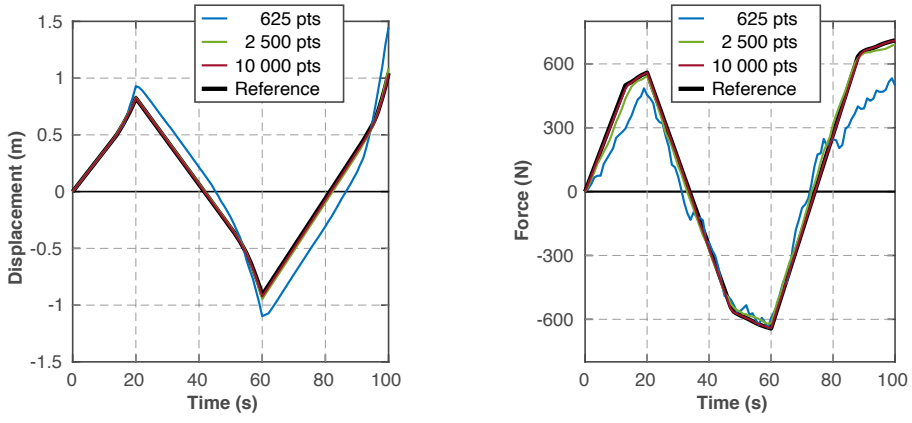

Figure 1: Plastic truss problem. Dependence of solution in dependence of number of data points per material point. Left: Displacement at a characteristic point over time. Right: Axial force (in a representative truss) over time.

*Corresponding author. E-mail: reese@ifam.rwth-aachen.de.

SECTIONAL LECTURES

indexed by $k+1$ are measured at time $t_{k+1} = t_k + \Delta t$ which is one time increment Δt after the measurements at time t_k. Further types of inelasticity, like elastoplasticity or viscoplasticity can be recovered in a very similar manner. As initially proven for elasticity, also for inelastic material behavior, the classical solution is approached with increasingly fine data sets (see Fig. 1). The central challenge for algorithms solving problems in inelasticity concerns the formulation of practical representational paradigms for the evolving material data set. An essential point to remain computationally efficient when handling large data sets is the usage of extremely fast search algorithms which interact with the solver. Further challenging issues arise from noisy data sets, see e.g. [4] and [5].

DATA-DRIVEN IDENTIFICATION OF MATERIAL RESPONSE

Meanwhile, a different field of research contrived, which can be understood as an inverse formulation of the data-driven paradigm. This field of research might solve a crucial issue. As the name suggests, the key in data-driven computing is the availability of large numbers of data. Leygue et al. [6] initially introduced an algorithm for solving inverse problems based on full-field strain measurements by digital image correlation (DIC). The goal is to identify the stresses which cannot be obtained by DIC. This is performed without the necessity to formulate a constitutive law a priori. The algorithm is based on minimizing the distance to a data set which is created during the solution procedure and is of a predefined size. In [7] and [8], among other examinations, the applicability to real experimental measurements is shown. In the present work we focus on a formulation that generalizes the initially proposed algorithm and makes it more robust, accurate and applicable to data sets of higher dimensions. The data are generated by means of a standard computation of the specimen plotted in Fig. 2. In the left part, the von Mises stress obtained from this computation is seen. These stress values are taken as reference. Fig. 2b and Fig. 2c show contour plots of the difference between the identified von Mises stress and the reference von Mises stress. It is clearly seen that the generalized identification algorithm reduces the error noticeably. Further investigations regarding noisy measurements and unknown Neumann boundary conditions show very promising results.

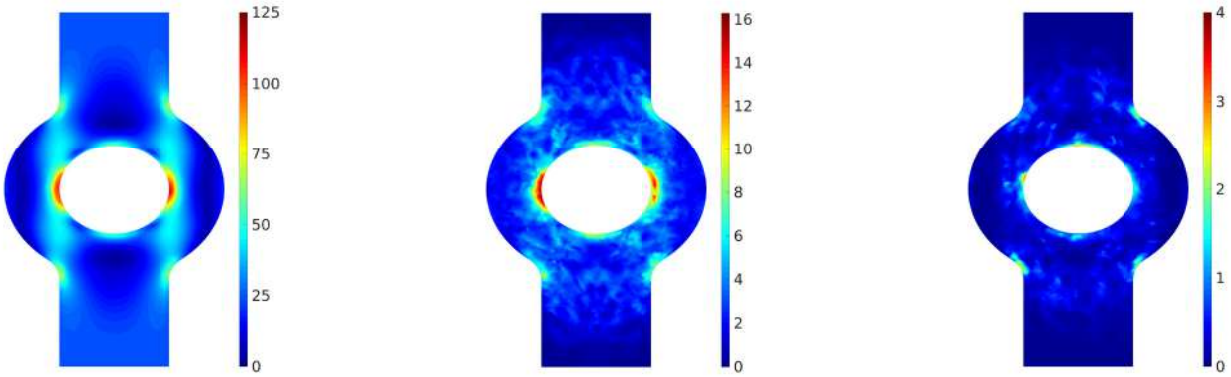

(a) (b) (c)

Figure 2: Stress identification problem: (a) reference von Mises stress [MPa], (b) stress error [MPa] of initially proposed identification algorithm, and (c) stress error [MPa] of generalized identification algorithm.

DATA-DRIVEN COMPUTATION ENHANCED BY TENSOR VOTING

Another important issue of data-driven computing occurs, when the amount of data is not high enough or the dimensionality of the data set is too high to sample the necessary phase space adequately. For these cases a new plug-in method for the data-driven solver is developed which makes use of local tangent spaces associated with each data point (see Fig. 3. Those tangents can be computed in an offline step by the tensor voting method introduced by Medioni and Mordohai [9]. Now, during the solution of a boundary value problem, in addition to the classically performed nearest neighbor search, the point in the local tangent space is computed which minimizes the actual distance. By this additional step, the convergence speed of the solver and the accuracy can be increased (see Fig. 4). The method shows promising results for data sets with homogeneous as well as for inhomogeneous data densities.

MULTI-SCALE COHESIVE ZONE MODELLING SUPPORTED BY MACHINE LEARNING

Grain boundary (GB) characteristics play an important role in the determination and prediction of material behavior, especially when it comes to nanocrystalline metals and ceramics (see [10] and [11]). Molecular dynamics simulations serve to gain deeper insight into the behavior of different grain boundaries. In the context of the present investigations of

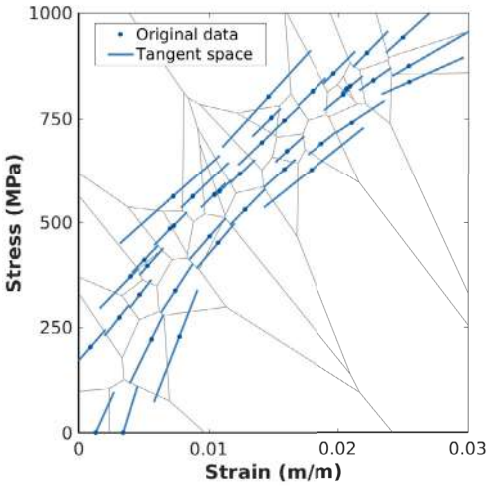

Figure 3: Voronoi tesselation of the phase space due to a given data set and corresponding tangent spaces computed by the tensor voting method.

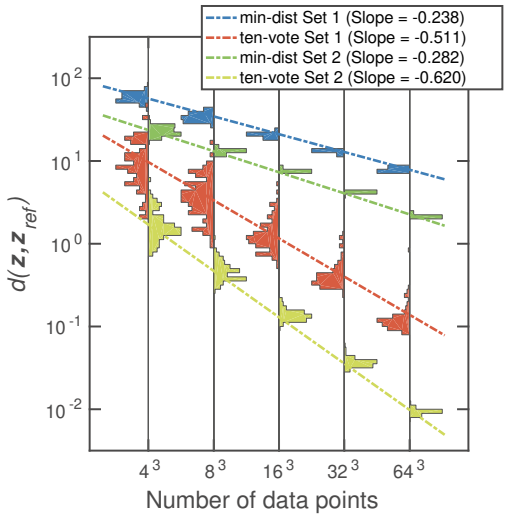

Figure 4: Comparison of convergence with respect to data set size of min-dist data-driven methods for noise-free data sets with random equally distributed (set 1) and random normally distributed (set 2) data points. Error histograms generated from 100 material set samples.

$\Sigma 5$ grain boundary of aluminum [12], it turns out that the behaviour in mode II differs noticeably from the one in mode I. In fact, the cyclic behaviour in mode II resembles rather elasto-plastic material behaviour than classical damage behavior. This shows that also the relations for the tractions in normal and shear direction must be chosen to be qualitatively different from each other.

It is, however, difficult to transfer the knowledge about the behavior at the atomistic level to a macroscopic cohesive zone formulation. For this purpose a new quantity called "traction density" is introduced. When it comes to the grain boundary (GB) behavior, the proposed methodology is able to represent intergranular fracture, grain boundary sliding as well as their mixed-mode behavior [13]. Interestingly, the calculations from current MD simulations show size-dependent traction-separation relation for the GB. By introducing a healing parameter in the new interface model, it is now possible to explain and predict possible GB size-dependent behavior. In order to cut short the scale transition, the traction-separation behavior at the atomistic scale can also be represented by means of artificial neural networks (see [14] and Fig. 5).

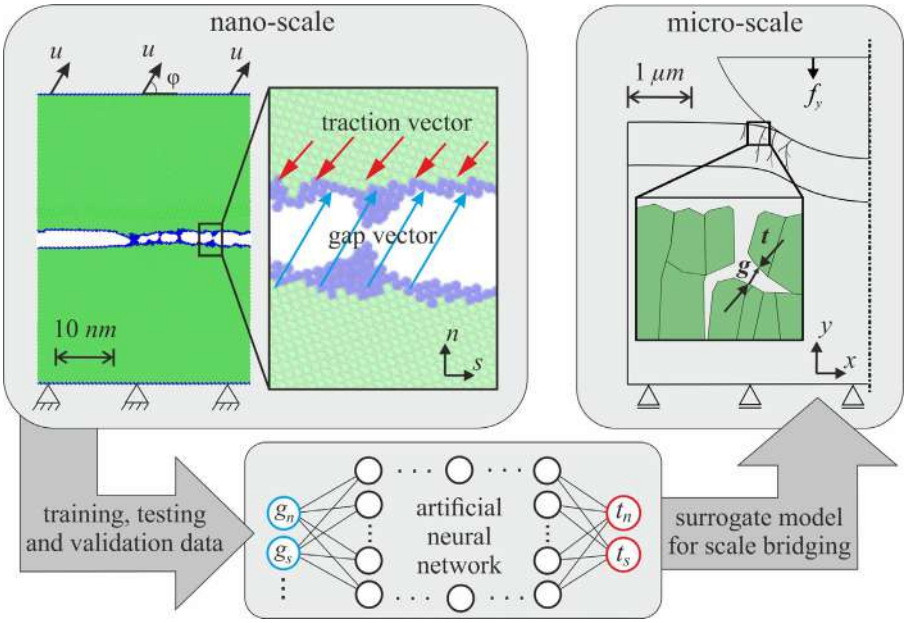

Figure 5: Scale bridging utilizing an artificial neural network trained by molecular dynamics simulation results.

Here, a Resnet like architecture with feed forward neural networks (FFNN) and a physics-guided model completion has been used. The approximation of the FFNN model is very good and can be also applied to temperatures and load angles which were not part of the training (see the results in Fig. 6). The next step is to implement the functions $t_n\,(g_n, g_t)$ and $t_t\,(g_n, g_t)$ directly into a macroscopic cohesive zone formulation.

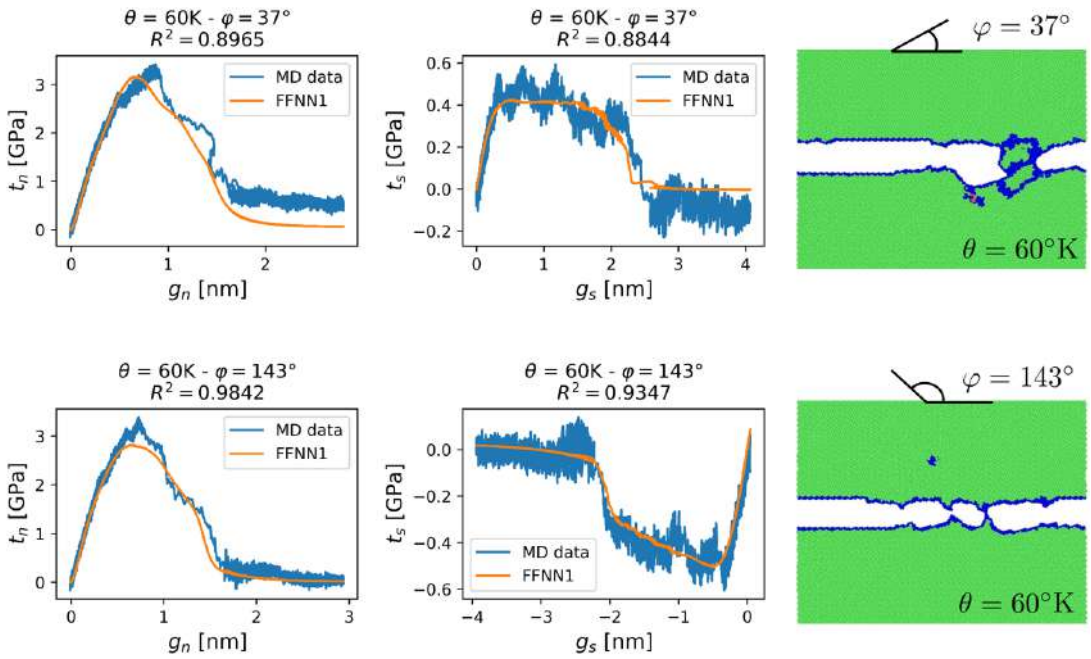

Figure 6: Evaluation of FFNN for unseen loading angles and temperature.

CONCLUSIONS

It is shown in the presentation that data-driven approaches are well suited to complement and improve constitutive modeling. This is carried out in various respects. One idea is to circumvent the development of complex phenomenological constitutive equations and to work only with the data available. Obviously, this requires sophisticated algorithms to reduce the CPU time effort of such data-based computations to an acceptable level. Another interesting application of data-driven mechanics is the identification of full-field stress data on the basis of measured strains. Having the complete information about the stress-strain behavior in complex structures available, might significantly support the development of constitutive models with good predictability. Finally, approaches such as machine learning can be well used to bridge scales. It is conceivable that for instance ANN models replace the classical microscopic boundary value problems in a homogenization procedure.

ACKNOWLEDGEMENTS

We acknowledge the support of F. Fritzen in discussions within the scope of machine learning. Also discussions with J. R. Mianroodi in conducting the molecular dynamics simulations are acknowledged.

References

[1] Kirchdoerfer T., et al. Data-driven computational mechanics. *Computer Methods in Applied Mechanics* and Engineering, **304**:81–101, 2016.
[2] Conti, S., et al. Data-driven problems in elasticity. *Archive for Rational Mechanics and Analysis*, **229**:79–123, 2018.
[3] Eggersmann, R., et al. Model-free data-driven inelasticity. *Computer Methods in Applied Mechanics and Engineering*, **350**: 81-99, 2019.
[4] Raissi, M., et al. Inferring solutions of differential equations using noisy multi-fidelity data. *Journal of Computational Physics*, **335**: 736-746, 2017.
[5] Ayensa-Jiménez, J., et al. A new reliability-based data-driven approach for noisy experimental data with physical constraints. *Computer Methods in Applied Mechanics and Engineering*, **328**: 752-774, 2018.
[6] Leygue, A., et al. Data-based derivation of material response. *Computer Methods in Applied Mechanics and Engineering*, **331**:184 – 196, 2018.
[7] Dalémat, M., et al. Measuring stress field without constitutive equation. *Mechanics of Materials*, **136**, 103087, 2019.
[8] Leygue, A., et al. Non-parametric material state field extracand tion from full field measurements. *Computational Mechanics*, **64**:501-509, 2019.
[9] Mordohai P., et al. Dimensionality estimation, manifold learning and function approximation using tensor voting. *Journal of Machine Learning Research*, **11**:411-450, 2010.
[10] Warner, D.H., et al. Atomistic based continuum investigation of plastic deformation in nanocrystalline copper. *International Journal of Plasticity*, **22**:754-774, 2006.
[11] Dahlberg, C.F.O., et al. A deformation mechanism map for polycrystals modeled using strain gradient plasticity and interfaces that slide and separate. *International Journal of Plasticity*, **43**:177-195, 2013.
[12] Rezaei, S., et al. Atomistically motivated interface model to account for coupled plasticity and damage at grain boundaries. *Journal of the Mechanics and Physics of Solids* **124**:325-349, 2019.
[13] Rezaei, S., et al. A nonlocal method for modeling interfaces: numerical simulation of decohesion and sliding at grain boundaries. *Computer Methods in Applied Mechanics and Engineering* **362**:112836, 2020.
[14] Fernández, M., et al. Application of artificial neural networks for the prediction of interface mechanics: a study on grain boundary constitutive behavior. *Advanced Modeling and Simulation in Engineering Sciences* **7**:1-27, 2020.

SL118443

EULERIAN FORMULATION OF INELASTICITY – FROM METAL PLASTICITY TO GROWTH OF BIOLOGICAL TISSUES

Miles Rubin
Faculty of Mechanical Engineering, Technion-Israel Institute of Technology, 32000 Haifa, Israel

Summary An Eulerian formulation of inelasticity is required to remove unphysical arbitrariness of choices of the reference configuration, an intermediate configuration, a total deformation measure and an inelastic deformation measure that are introduced in the Lagrangian formulation. It is shown that the Eulerian formulation can be used to model metal plasticity and growth of biological tissues.

INTRODUCTION

The need for an Eulerian formulation of inelasticity, in contrast to a Larangian formulation, can best be understood by Gillman's comment [5]

> "It seems very unfortunate to me that the theory of plasticity was ever cast into the mold of stress-strain relations because 'strain' in the plastic case has no physical meaning that is related to the material of the body in question. It is rather like trying to deduce some properties of a liquid from the shape of the container that holds it. The plastic behaviour of a body depends on its structure (crystalline and defect) and on the system of stresses that is applied to it . . . "

and the notion of an internal state variable by Onat [11] as a history-dependent variable that must be measurable in the current state of the material. Eckart [3] seems to be the first to propose an Eulerian evolution equation directly for an elastic deformation tensor for elastically isotropic solids, which was also done for polymeric liquids by Leonov [10].

The standard Lagrangian formulation introduces deformation tensors measured relative to a reference configuration or an intermediate configuration. For example, the total deformation gradient $\mathbf{F}$ from the reference configuration to the current configuration is determined by the evolution equation

$$\dot{\mathbf{F}} = \mathbf{L}\mathbf{F}\,, \tag{1}$$

where $(\dot{})$ denotes the material time derivative and $\mathbf{L}$ is the velocity gradient. The formulation proproped by Green and Naghdi [6] uses the right Cauchy-Green total deformation tensor $\mathbf{C} = \mathbf{F}^T\mathbf{F}$ and introduces a plastic deformation tensor $\mathbf{C}_p$ relative to a reference configuration by the evolution equation

$$\dot{\mathbf{C}}_p = \overline{\mathbf{A}}_p\,, \tag{2}$$

with $\overline{\mathbf{A}}_p$ being the inelastic deformation rate. The Bilby-Kröner-Lee multiplicative formulation [2, 8, 9] introduces a plastic deformation tensor $\mathbf{F}_p$ from a reference configuration to an intermediate configuration and an elastic deformation tensor $\mathbf{F}_e$ from the intermediate configuration to the current configuration by the evolution equation and definition

$$\dot{\mathbf{F}}_p = \mathbf{\Lambda}_p\mathbf{F}_p\,, \quad \mathbf{F}_e \equiv \mathbf{F}\mathbf{F}_p^{-1}\,, \tag{3}$$

where $\mathbf{\Lambda}_p$ is the inelastic deformation rate. Besseling [1] introduced an elastic deformation tensor $\mathbf{F}_e$ from an intermediate configuration to the current configuration directly by the evolution equation

$$\dot{\mathbf{F}}_e = (\mathbf{L} - \mathbf{L}_p)\mathbf{F}_e\,, \tag{4}$$

where $\mathbf{L}_p$ is the inelastic deformation rate. Also, Rodriguez et. al [13] modeled grow of biological tissues using the muliplicative formulation (3) by replacing p by g and identifying $\mathbf{F}_g$ as a growth tensor. However, letting $\mathbf{A}$ be an arbitrary second order tensor with positive determinant and $\mathbf{O}$ be an arbitrary proper orthogonal tensor, it follows that

$$\mathbf{F}_e = (\mathbf{F}\mathbf{A})(\mathbf{F}_p\mathbf{A})^{-1}\,, \quad \mathbf{F} = (\mathbf{F}_e\mathbf{O}^T)(\mathbf{O}\mathbf{F}_p)\,, \tag{5}$$

which demonstrates that the Lagrangian formulation exhibits arbitrariness in the choice of the reference configuration and the intermediate configuration, as discussed in [16]. This means that the tensors $\mathbf{F}, \mathbf{F}_e, \mathbf{F}_p$ and $\mathbf{F}_g$ are not internal state variables in the sense of Onat [11] since they exhibit unphysical arbitrariness that cannot be measured by experiments on identical samples of the material in its current state.

A FULLY ANIOSTROPIC ELASTIC-INELASTIC MATERIAL

In [16] it was proved that when the unphyiscal arbitrariness of the Lagrangian formulation is removed, the formulation must reduce to the Eulerian formulation in [14], which proposes evolution equations for a triad of linearly independent micostructural vectors $\mathbf{m}_i$

$$\dot{\mathbf{m}}_i = (\mathbf{L} - \mathbf{L}_p)\mathbf{m}_i \,, \tag{6}$$

that characterize elastic deformations and material orientations. Moreover, the elastic dilatation J_e and elastic metric m_{ij} are defined by

$$J_e = \mathbf{m}_1 \times \mathbf{m}_2 \cdot \mathbf{m}_3 > 0 \,, \quad m_{ij} = \mathbf{m}_i \cdot \mathbf{m}_j \,, \tag{7}$$

which satisfy the evolution equations

$$\dot{J}_e = J_e\,(\mathbf{D} - \mathbf{D}_p) \cdot \mathbf{I} \,, \quad \dot{m}_{ij} = 2(\mathbf{D} - \mathbf{D}_p) \cdot (\mathbf{m}_i \otimes \mathbf{m}_j) \,, \quad \mathbf{D} = \frac{1}{2}(\mathbf{L} + \mathbf{L}^T) \,, \quad \mathbf{D}_p = \frac{1}{2}(\mathbf{L}_p + \mathbf{L}_p^T) \,. \tag{8}$$

In these equations, $\mathbf{D}$ is the total deformation rate, $\mathbf{D}_p$ is the inelastic deformation rate, $\mathbf{I}$ is the second order identity tensor, $\mathbf{A} \cdot \mathbf{B} = \mathrm{tr}(\mathbf{A}\mathbf{B}^T)$ is the inner product betweeen two second order tensors $\mathbf{A}, \mathbf{B}$, and $\mathbf{a} \otimes \mathbf{b}$ denotes the tensor product of two vectors $\mathbf{a}, \mathbf{b}$. For later reference, $\mathbf{L}'$ and $\mathbf{D}'$ denote the deviatoric parts of $\mathbf{L}$ and $\mathbf{D}$, respectively.

Within the context of the purely mechanical theory, the strain energy function Σ per unit mass and the Cauchy stress $\mathbf{T}$ are given by

$$\Sigma = \Sigma(m_{ij}) \,, \quad \mathbf{T} = 2\rho \frac{\partial \Sigma}{\partial m_{ij}} (\mathbf{m}_i \otimes \mathbf{m}_j) \,, \tag{9}$$

where ρ is the current mass density and the usual summation convention is implied for repeated indices. Moreover, the microstructural vectors can be specified so that they form an orthonormal triad in any zero-stress state, with Σ restricted so that

$$\frac{\partial \Sigma}{\partial m_{ij}} = 0 \quad \text{and} \quad m_{ij} = \delta_{ij} \quad \text{whenever} \quad \mathbf{T} = 0 \,, \tag{10}$$

where δ_{ij} is the Kronecker delta. It also follows that the rate of material dissipation $\mathcal{D}$ requires inelastic deformation rate to be dissipative

$$\mathcal{D} = \mathbf{T} \cdot \mathbf{D} - \rho \dot{\Sigma} = \mathbf{T} \cdot \mathbf{D}_p \geq 0 \,. \tag{11}$$

Furthermore, it is noted that in the absence of inelastic deformation rate ($\mathbf{L}_p = 0$) the evolution equations (6) cause $\mathbf{m}_i$ to deform as material line elements so the constitutive equations (9) characterizes a general anisotropic hyperelastic material.

ELASTICALLY ISOTROPIC MATERIALS

For elastically isotropic materials it is not possible to distinguish between the microstructural vectors $\mathbf{m}_i$ so it is meaningful to use the work of Flory [4] to define the unimodular elastic distortional deformation tensor $\mathbf{B}'_e$ by

$$\mathbf{B}'_e = J_e^{-2/3} \mathbf{m}_i \otimes \mathbf{m}_i \,, \quad \det \mathbf{B}'_e = 1 \,. \tag{12}$$

In [15] an evolution equation was proposed directly for $\mathbf{B}'_e$ of the form

$$\dot{\mathbf{B}}'_e = \mathbf{L}'\mathbf{B}'_e + \mathbf{B}'_e\mathbf{L}'^T - \Gamma \mathbf{A}_p \,, \quad \mathbf{A}_p = \mathbf{B}'_e - \left(\frac{3}{\mathbf{B}'^{-1}_e \cdot \mathbf{I}} \right) \mathbf{I} \,, \quad \Gamma \geq 0 \,, \quad \mathbf{A}_p \cdot \mathbf{B}'^{-1}_e = 0 \,, \tag{13}$$

where Γ controls the inelastic deformation rate and $\mathbf{A}_p$ controls its direction, with $\mathbf{A}_p$ being restricted to ensure that $\mathbf{B}'_e$ remains unimodular. The two non-trivial invariants α_1 and α_2 of $\mathbf{B}'_e$ satisfy the equations

$$\alpha_1 = \mathbf{B}'_e \cdot \mathbf{I} \,, \quad \dot{\alpha}_1 = 2\mathbf{B}''_e \cdot \mathbf{D} - \Gamma \mathbf{A}_p \cdot \mathbf{I} \,, \quad \alpha_2 = \mathbf{B}'_e \cdot \mathbf{B}'_e \,, \quad \dot{\alpha}_2 = 4(\mathbf{B}'^2_e - \frac{1}{3}\alpha_2 \mathbf{I}) \cdot \mathbf{D} - 2\Gamma \mathbf{A}_p \cdot \mathbf{B}'_e \,, \tag{14}$$

where $\mathbf{B}''_e$ is the deviatoric part of $\mathbf{B}'_e$. Also, for isotropic materials the strain energy Σ and stress $\mathbf{T}$ are given by

$$\Sigma = \Sigma(J_e, \alpha_1, \alpha_2) \,, \quad \mathbf{T} = -p\,\mathbf{I} + \mathbf{T}'' \,, \quad p = -\rho J_e \frac{\partial \Sigma}{\partial J_e} \,, \quad \mathbf{T}'' = 2\rho \Big[\frac{\partial \Sigma}{\partial \alpha_1} \mathbf{B}''_e + 2 \frac{\partial \Sigma}{\partial \alpha_2} (\mathbf{B}'^2_e - \frac{1}{3}\alpha_2 \mathbf{I}) \Big] \,, \tag{15}$$

where p is the pressure, $\mathbf{T}''$ is the deviatoric part of $\mathbf{T}$ and the rate of material dissipation $\mathcal{D}$ requires

$$\mathcal{D} = \mathbf{T} \cdot \mathbf{D} - \rho \dot{\Sigma} = -p\,(\mathbf{D}_p \cdot \mathbf{I}) + \Gamma \left[\rho \frac{\partial \Sigma}{\partial \alpha_1} (\mathbf{A}_p \cdot \mathbf{I}) + 2\rho \frac{\partial \Sigma}{\partial \alpha_2} (\mathbf{A}_p \cdot \mathbf{B}'_e) \right] \geq 0 \,. \tag{16}$$

Moreover, Σ satisfies restrictions so that zero-stress states require

$$J_e = 1 \quad \text{and} \quad \mathbf{B}'_e = \mathbf{I} \quad \text{whenever} \quad \mathbf{T} = 0 \,. \tag{17}$$

Consequently, from (13) it follows that inelastic deformation rate causes a tendency for $\mathbf{B}'_e$ to approach the identity tensor, which causes a tendency for deviatoric stress to vanish. Also, it was shown in [15] that

$$\mathbf{A}_p \cdot \mathbf{I} \geq 0\,, \quad \mathbf{A}_p \cdot \mathbf{B}'_e \geq 0\,. \tag{18}$$

In the absence of inelastic deformation rate, the evolution equations (8) and (13) cause J_e to be the total dilatation and $\mathbf{B}'_e$ to be the unimodular part of the left Cauchy-Green deformation tensor $\mathbf{B} = \mathbf{F}\mathbf{F}^T$ from zero-stress states, so the constitutive equations model general isotropic hyperelastic response.

METAL PLASTICITY

For metal plasticity inelastic deformation rate is isochoric so that

$$\mathbf{D}_p \cdot \mathbf{I} = 0\,, \quad J_e = \frac{\rho_z}{\rho}\,, \tag{19}$$

where ρ_z is the zero-stress density. Moreover, following the work in [7, 12, 15, 19, 21], it is possible to develop a robust, strongly objective numerical integration algorithm for J_e and $\mathbf{B}'_e$. Specifically, consider a time step which begins at $t = t_n$, ends at $t = t_{n+1}$ with increment $\Delta t = t_{n+1} - t_n$. Given values of $J_e(t_n)$ and $\mathbf{B}'_e(t_n)$ at the beginning of the time step, the numerical algorithm produces estimates $J_e(t_{n+1})$ and $\mathbf{B}'_e(t_{n+1})$ at the end of the time step. Next, it is recalled that the relative deformation gradient $\mathbf{F}_r$, the relative dilatation J_r and the unimodular part $\mathbf{F}'_r$ of $\mathbf{F}_r$ satisfy the equations

$$\dot{\mathbf{F}}_r = \mathbf{L}\mathbf{F}_r\,, \quad J_r = \det \mathbf{F}_r\,, \quad \dot{J}_r = J_r\,(\mathbf{D} \cdot \mathbf{I})\,, \quad \mathbf{F}'_r = J_r^{-1/3}\mathbf{F}_r\,, \quad \dot{\mathbf{F}}'_r = \mathbf{L}''\mathbf{F}'_r\,, \quad \mathbf{F}_r(t_n) = \mathbf{F}'_r(t_n) = \mathbf{I}\,. \tag{20}$$

Then, using (19), the exact solution of the evolution equation (8) for J_e yields

$$J_e(t_{n+1}) = J_r(t_{n+1})J_e(t_n)\,. \tag{21}$$

Also, the elastic trial value $\mathbf{B}'^*_e$ and its deviatoric part $\mathbf{B}''^*_e$ are defined by

$$\mathbf{B}'^*_e = \mathbf{F}'_r\mathbf{B}'_e(t_n)\mathbf{F}'^T_r\,, \quad \mathbf{B}''^*_e = \mathbf{B}'^*_e - \frac{1}{3}(\mathbf{B}'^*_e \cdot \mathbf{I})\,\mathbf{I}\,, \tag{22}$$

where $\mathbf{B}''^*_e$ satisfies the evolution equation

$$\dot{\mathbf{B}}''^*_e = \mathbf{L}''\mathbf{B}'^*_e + \mathbf{B}'^*_e\mathbf{L}'' - \frac{2}{3}(\mathbf{B}'^*_e \cdot \mathbf{D}'')\,\mathbf{I}\,. \tag{23}$$

Next, from (13) it can be shown that the deviatoric part $\mathbf{B}''_e$ of $\mathbf{B}'_e$ satisfies the evolution equation

$$\dot{\mathbf{B}}''_e = \mathbf{L}''\mathbf{B}'_e + \mathbf{B}'_e\mathbf{L}'' - \frac{2}{3}(\mathbf{B}'_e \cdot \mathbf{D}'')\,\mathbf{I} - \Gamma\mathbf{B}''_e\,, \tag{24}$$

which can be approximated by

$$\dot{\mathbf{B}}''_e = \dot{\mathbf{B}}''^*_e - \Gamma\mathbf{B}''_e\,. \tag{25}$$

This equation yields the exact solution for elastic response ($\Gamma = 0$). Furthermore, using a backward Euler approximate of the derivative, (25) can be integrated implicitly do deduce that

$$\mathbf{B}''_e(t_{n+1}) = \frac{\mathbf{B}''^*_e(t_{n+1})}{1 + \Delta\Gamma}\,, \quad \Delta\Gamma = \Delta t\Gamma(t_{n+1})\,. \tag{26}$$

Once $\mathbf{B}''_e(t_{n+1})$ is known, the value of $\mathbf{B}'_e(t_{n+1})$ is determined by solving the cubic equation

$$\det \mathbf{B}'_e(t_{n+1}) = \det\left[\frac{1}{3}\alpha_1\mathbf{I} + \mathbf{B}''_e(t_{n+1})\right] = 1\,, \tag{27}$$

for α_1 as discussed in [7, 15]. Moreover, it was shown in [19] that this algorithm is simpler than the one for the evolution equation in [22]. Furthermore, this numerical algorithm is strongly objective to Superposed Rigid Body Motions ($SRBM$) since the quantities $J_e(t_{n+1})$ and $\mathbf{B}'_e(t_{n+1})$ transform like the exact values J_e and $\mathbf{B}'_e$ for all $SRBM$.

GROWTH OF BIOLOGICAL TISSUES

A unified theoretical structure for modeling interstitial growth and muscle activation in soft tissues was proposed in [17]. This model treats the tissue as an open system with a rate of mass supply, but with a single velocity for material

points in the tissue. Specifically, this model modifies the evolution equations for elastic dilatation and elastic distortional deformation of metals to take the forms [18]

$$\dot{J}_e = J_e \left[\mathbf{D}\cdot\mathbf{I} - \Gamma_m \ln\left(\frac{J_e}{J_h}\right) \right] , \quad \dot{\mathbf{B}}'_e = \mathbf{L}''\mathbf{B}'_e + \mathbf{B}'_e\mathbf{L}''^T - \Gamma \left[\mathbf{B}'_e - \left(\frac{3}{\mathbf{B}'^{-1}_e \cdot \mathbf{H}} \right) \mathbf{H} \right] . \tag{28}$$

For purely mechanical elastically isotropic response, the strain energy function Σ and the stress $\mathbf{T}$ take the forms (15). In contrast with the evolution equations for metal plasticity, the evolution equations (28) model the process of homeostasis which causes the elastic dilatation J_e to approach its homeostatic value J_h with the rate controlled by Γ_m and which causes the elastic distortional deformation $\mathbf{B}'_e$ to approach its homeostatic value $\mathbf{H}'$ with the rate controlled by Γ where

$$\mathbf{H}' = (\det \mathbf{H})^{-1/3}\mathbf{H} , \quad \det \mathbf{H}' = 1 . \tag{29}$$

The homeostatic values J_h and $\mathbf{H}'$ as well as the homeostasis rates Γ_m and Γ require constitutive equations. In particular, it is noted that the homeostatic value of stress need not be zero

$$\mathbf{T}(J_e, \mathbf{H}') \neq 0 , \tag{30}$$

which allows for modeling phenomena like the homeostatic value of tension in the skin as cells are being replaced over time.

In [17] equations were developed for growth of a fiber, growth of a material surface and volumetric growth. Also, in [20] structural tensors were used for anisotropic growth including torsion observed in early cardiac morphogenesis during c-looping.

CONCLUSIONS

It has been shown that the Eulerian formulation of inelasticity proposes evolution equations for elastic deformations based on internal state variables which are measurable by experiments on identical samples of a material in its current state. This formulation removes unphysical arbitrariness of choices of the reference configuration, an intermediate configuration, a total deformation measure and an inelastic deformation measure that are introduced in the Lagrangian formulation. The Lagrangian formulation of inelasticity is not necessarily incorrect but it has arbitrariness that can and should be removed.

References

[1] Besseling JF. A thermodynamic approach to rheology. *In: Irreversible Aspects of Continuum Mechanics and Transfer of Physical Characteristics in Moving Fluids* 16-53, 1968.
[2] Bilby BA , Gardner LRT, Stroh AN. Continuous distributions of dislocations and the theory of plasticity. *In: Proceedings of the 9th International Congress of Applied Mechanics. University de Brussels* **9**: 35-44, 1957.
[3] Eckart C. The thermodynamics of irreversible processes. IV. The theory of elasticity and anelasticity. *Physical Review* **73**: 373-382, 1948.
[4] Flory PJ. Thermodynamic relations for high elastic materials. *Transactions of the Faraday Society* **57**: 829–838, 1961.
[5] Gilman JJ. Physical nature of plastic flow and fracture. *In: Plasticity, Proc. 2. Symp. on Naval Structural Mechanics* 43-99, 1960.
[6] Green AE, Naghdi PM. A general theory of an elastic-plastic continuum. *Archive for Rational Mechanics and Analysis* **18**: 251-281, 1965.
[7] Hollenstein M, Jabareen M, Rubin, MB. Modeling a smooth elastic–inelastic transition with a strongly objective numerical integrator needing no iteration. *Computational Mechanics* **52**: 649–667, 2013.
[8] Kröner E. General continuum theory of dislocations and intrinsic stresses. *Archive for Rational Mechanics and Analysis* **4**: 273-334, 1959.
[9] Lee EH. Elastic-plastic deformation at finite strains. *Journal of Applied Mechanics* **36**: 1-6, 1969.
[10] Leonov AI. Nonequilibrium thermodynamics and rheology of viscoelastic polymer media. *Rheologica acta* **15**: 85-98, 1976.
[11] Onat ET. The notion of state and its implications in thermodynamics of inelastic solids. *In: Irreversible Aspects of Continuum Mechanics and Transfer of Physical Characteristics in Moving Fluids* 292-314, 1968.
[12] Papes O. Nonlinear continuum mechanics in modern engineering applications. *Ph.D. dissertation DISS ETH NO 19956* 292-314, 2013.
[13] Rodriguez EK, Hoger A, McCulloch AD. The constitutive equations for rate sensitive plastic materials. *Journal of BiomechanicsAspects of Continuum Mechanics and Transfer of Physical Characteristics in Moving Fluids* **27**: 455–467, 1994.
[14] Rubin MB. Plasticity theory formulated in terms of physically based microstructural variables - Part I. Theory. *International Journal of Solids and Structures* **31**: 2615-2634, 1994.
[15] Rubin MB, Attia AV. Calculation of hyperelastic response of finitely deformed elastic-viscoplastic materials. *International Journal for Numerical Methods in Engineering* **39**: 309-320, 1996.
[16] Rubin MB. Removal of unphysical arbitrariness in constitutive equations for elastically anisotropic nonlinear elastic–viscoplastic solids. *International Journal of Engineering Science* **53**: 38-45, 2012.
[17] Rubin MB, Safadi MM, Jabareen M. A unified theoretical structure for modeling interstitial growth and muscle activation in soft tissues. *International Journal of Engineering Science*. **90**: 1-26, 2015.
[18] Rubin MB. An Eulerian formulation of Inelasticity - From metal plasticity to growth of biological tissues. *Transactions of the Royal Society* **A377**: 20180071, 2019.
[19] Rubin MB, Cardiff P. Advantages of formulating an evolution equation directly for elastic distortional deformation in finite deformation plasticity. *Computational Mechanics* **60**: 703-707, 2017.
[20] Safadi MM, Rubin MB. A new approach to modeling early cardiac morphogenesis during c-looping. *International Journal of Engineering Science* **1177**: 1-19, 2017.
[21] Simo, JC. A framework for finite strain elastoplasticity based on maximum plastic dissipation and the multiplicative decomposition. Part II: computational aspects. *Computer Methods in Applied Mechanics and Engineering* **68**: 1-31, 1988.
[22] Simo, JC. Algorithms for static and dynamic multiplicative plasticity that preserve the classical return mapping schemes of the infinitesimal theory. *Computer Methods in Applied Mechanics and Engineering* **99**: 61-112, 1992.

SL118444

TRANSIENT SPRAY COOLING

Jan Breitenbach[1], Ilia V. Roisman[1], Fabian M. Tenzer[1], and Cameron Tropea*[1]
[1]Institute for Fluid Mechanics and Aerodynamics, Technische Universität Darmstadt, Germany

Summary Spray cooling is a very efficient technology, surpassing all other conventional cooling methods, especially those not involving phase change and not exploiting the latent heat of vaporization. However, the effectiveness of spray cooling is dependent on a large number of parameters, including spray characteristics like drop size, velocity and number density, the surface morphology, but also on the temperature range and thermal properties of the materials involved. Indeed, the temperature of the substrate can have significant influence on the hydrodynamics of drop and spray impact, an aspect which is seldom considered in model formulation. This process is extremely complex, thus most design rules to date are highly empirical in nature. Transient spray cooling adds complexity by the fact that the substrate temperature is continually cooling, thus the hydrodynamics occur in different thermodynamic regimes: film boiling, transitional boiling and nucleate boiling. On the other hand, significant theoretical progress has been made in recent years about the interaction of single drops with heated walls and improvements to the fundamentals of spray cooling can now be anticipated. The present contribution has the objective of summarizing some of these recent experimental and theoretical advances and to establish a framework for future development of more reliable and universal physics-based correlations to quantitatively describe and predict quantities involved in spray cooling.

INTRODUCTION

Spray cooling technology is a promising technique for the cooling of devices with very high heat flux densities [6, 7, 2], as encountered in the fields of metal production such as die forging and hot rolling, cooling of electronic modules, light-water reactors or of diode laser arrays. As shown by the large number of industrial applications spray cooling covers a wide variety of boundary conditions, e.g. the temperature range of spray cooling lies between cryogenic temperatures (80 K) to about 1300 K. An important demand in general, but in particular for spray cooling of electronic equipment, is the uniform heat removal from the surface and avoidance of hot spots. Compared to other heat transfer mechanisms, such as forced air or jet impingement, spray cooling has the highest heat transfer coefficient [9].

Current approaches, usually presented in the form of empirical correlations or developed as a simple superposition of single drop impacts, disregard to a large extent the physics of drop/spray wall interaction [4]. No universal model predicting the effectiveness of spray cooling over a significant range of operating parameters has been developed to date. The main difficulty in spray research is the fact that most sprays are usually polydisperse. Their behavior is governed by a large number of parameters which cannot be varied and controlled independently. Thus, it is not easy to identify the main influencing parameters or their combinations which define the problem.

The present study has the objectives to enhance the understanding of non-isothermal spray/wall interactions and to establish more reliable physics-based correlations for the various regimes in order to describe the quantities involved in the non-isothermal transient spray cooling process. For this purpose, non-isothermal single drop and spray impact experiments have been conducted leading to various physic-based theoretical considerations for the various heat transfer regimes.

HEAT FLUX MEASUREMENTS AND OBSERVATION OF SPRAY IMPACT

Figure 1 shows the evolution of the instantaneous heat flux $\dot{q}$ as a function of the surface temperature T_i for an exemplary spray cooling experiment. The results were obtained by solving the inverse heat conduction problem using temperature readings from thermocouples embedded in the target slightly below the surface where the spray impact takes place. The underlying spray parameters are: mass flux $\dot{m} = 1\,\mathrm{kg/m^2s}$, mean droplet diameter $D_{10} = 54\,\mu\mathrm{m}$ and mean droplet velocity $U = 7.6\,\mathrm{m/s}$. The substrate is initially heated to $450\,^\circ\mathrm{C}$, then the heating is switched off and the spray is turned on. Since the substrate continuously cools, the time t increases following the curve in Fig. 1 from right to left (or with decreasing surface temperature). The dashed part indicates the first instants of the cooling experiments when the precision of the results is not sufficient due to the temporal response of the thermocouples. The measured curve exhibits the well-known boiling regimes, in the order from high to low temperatures: film boiling regime at very high surface temperatures where the heat flux decreases in a linear fashion with decreasing surface temperature. This regime ends at the Leidenfrost point, corresponding to the minimum heat flux. The following transition boiling regime features an increasing heat flux until the maximum heat flux is reached (called the critical heat flux). Subsequently, in the nucleate boiling regime the heat flux again decreases until the surface temperature reaches the saturation temperature.

The images in Fig. 1 show pictures of the surface during spray impact and allow the identification of the corresponding hydrodynamic behavior. The equivalent instants are marked on the curve. At very high temperatures above the Leidenfrost point (right picture) we identify single drop impact onto a dry surface. The droplets impact at the surface, rebound or atomize and form secondary droplets due to inertia or thermal atomization [10]. In contrast to common expectations, a

*Corresponding author. E-mail: tropea@sla.tu-darmstadt.de.

SECTIONAL LECTURES

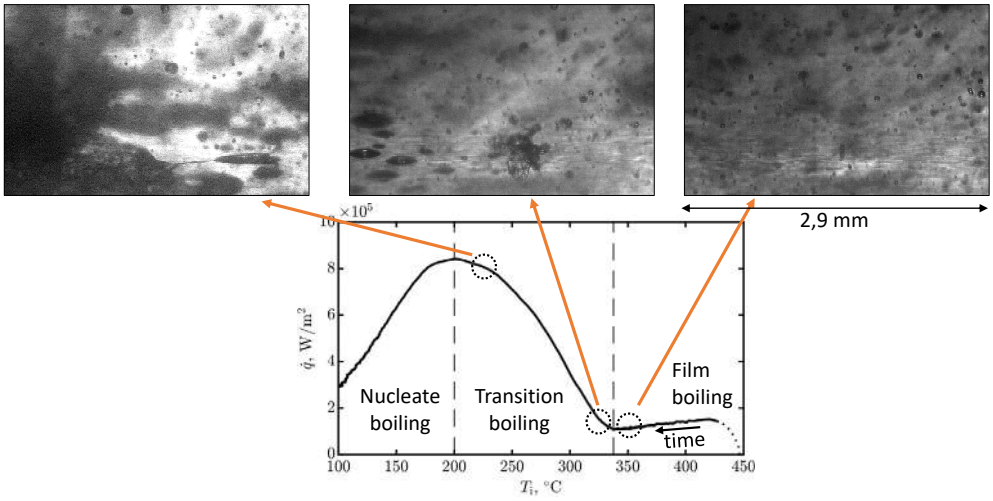

Figure 1: Heat flux as a function of the surface temperature. Images show pictures of the hydrodynamics during spray impact in different spray cooling regimes.

liquid film separated from the surface by a vapour layer cannot be observed [16]. Instead, spray impact can be regarded as a superposition of single drop impacts onto a dry wall [3]. At surface temperatures slightly below the Leidenfrost point (picture in the middle) we identify first small liquid patches on the surface. At even lower surface temperatures, approaching the critical heat flux, (left picture) the number of wetted patches increase, larger ligaments form and finally the entire surface is covered by liquid.

The broad variation of spray impact parameters (droplet diameter, droplet velocity and mass flux) - measured by a phase Doppler measurement system and a patternator - and substrate materials allows the validation of novel analytical models describing the heat transfer during spray cooling, which we present in the following section.

ANALYSIS AND MODELING OF HEAT TRANSFER

Film boiling regime

Consider the impact of a single liquid drop onto a flat solid substrate in the developed film boiling regime [3]. In this regime a vapor layer develops between the liquid and solid regions. Therefore, the heat transfer during film boiling includes heat conduction in an expanding thermal boundary in the solid wall, heat convection in an expanding thermal boundary in the liquid region and heat convection in the vapor layer. The heat flux is continuous at the solid/vapour interface. The jump in the heat flux at the vapor/liquid interface is caused by the energy required for evaporation and is described by the Stefan boundary condition. Solving the energy balance equation the heat flux of an impacting single droplet in the film boiling regime can be estimated, where ϵ_w is the thermal effusivity of the wall, T_w0 the the initial wall temperature and T_sat the saturation temperature

$$\dot{q}_1(t) = \frac{2G\,\epsilon_\mathrm{w}\,(T_\mathrm{w0} - T_\mathrm{sat})}{\sqrt{\pi}\,(K + 2G)\,\sqrt{t}}, \tag{1}$$

and the expression for the evolution of the vapor thickness is obtained in the form

$$h(t) = K\frac{\epsilon_\mathrm{w}\,(T_\mathrm{w0} - T_\mathrm{sat})}{\rho_l L}\sqrt{t}. \tag{2}$$

Here ρ_l is the density of the liquid, L the latent heat of evaporation and K a dimensionless coefficient, determined as

$$K = \sqrt{(B-G)^2 + \frac{4G}{\sqrt{\pi}}} - B - G, \tag{3}$$

with

$$G = \frac{\sqrt{\pi}\lambda_\mathrm{v}\rho_\mathrm{f} L}{2\,(T_\mathrm{w0} - T_\mathrm{sat})\,\epsilon_\mathrm{w}^2}; \quad B = \frac{\sqrt{5}\,(T_\mathrm{sat} - T_{f0})\,\epsilon_\mathrm{f}}{\sqrt{\pi}\,(T_\mathrm{w0} - T_\mathrm{sat})\,\epsilon_\mathrm{w}}. \tag{4}$$

Here the dimensionless parameter G is analogous to the inverse Stefan number, λ_v the thermal conductivity of the vapour, T_f0 the initial fluid temperature of the droplet and ϵ_f the thermal effusivity of the fluid. A comparison of the predicted model (2) for the vapor layer thickness with experimental data from [5] is shown in Fig. 2. The agreement between the data and the model is rather good, although no adjustable constant is used in the model. Noteworthy is the fact, that

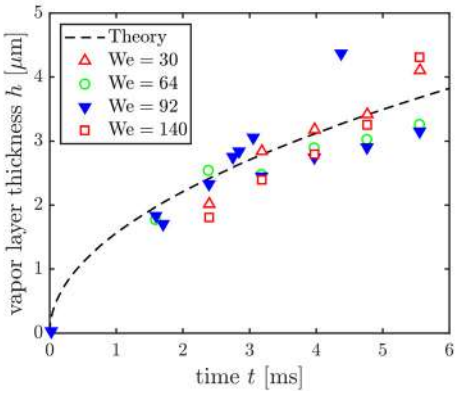

Figure 2: Vapor layer thickness $h(t)$ calculated with the theoretical predication (2) in comparison with experimental data obtained in [5] for an impacting water drop onto a hot saphire substrate at various impact Weber numbers. The drop diameter is constant for all cases.

the theoretical prediction (2) for the vapor layer thickness is not influenced by the impact velocity of the drop, again in excellent agreement with the experimental results.

The previously described model for single drop impact in the film boiling regime can be additionally extended to spray impact as shown in [3]. Additionally, neglecting drop-drop interaction and assuming a semi-infinite wall allows to derive a theory to predict the temporal evolution of the heat flux as well as the surface temperature during transient spray cooling of an initially homogeneously heated target. Some further simplifications and mathematical transformations lead to the following model for the dimensionless heat flux $\Phi(\xi)$ and dimensionless surface temperature $\Theta(\xi)$ as functions of the dimensionless time ξ, which can also be found in [15]:

$$\Phi(\xi) = -\int_0^{\xi} \frac{\Theta'(\zeta)}{\sqrt{\xi-\zeta}}\mathrm{d}\zeta, \quad \Theta'(\zeta) = \frac{1}{2}\sum_{i=1}^{\infty} a_i i \zeta^{i/2-1}, \quad \Theta(\xi) = 1 + \sum_{i=1}^{\infty} a_i \xi^{i/2}. \tag{5}$$

with a_i being a series that converges after a few steps i and the dimensionless quantities

$$\Theta = \frac{T_\mathrm{i}(t) - T_\mathrm{sat}}{T_\mathrm{w0} - T_\mathrm{sat}}, \quad \xi = t\pi S^2, \quad \zeta = \tau\pi S^2, \quad \Phi = \frac{\dot{q}}{S\epsilon_\mathrm{w}(T_\mathrm{w0} - T_\mathrm{sat})}, \tag{6}$$

and

$$S = 8.85\chi \frac{\dot{m}}{\rho_\mathrm{f} D_{10}^{1/2} U^{1/2}\left[1 - b + \sqrt{(1-b)^2 + w}\right]}, \quad w = \frac{8(T_\mathrm{i} - T_\mathrm{sat})\epsilon_\mathrm{w}^2}{\pi\lambda_\mathrm{v}\rho_\mathrm{f} L}, \quad b = \frac{2\sqrt{5}\epsilon_\mathrm{w}\epsilon_\mathrm{f}(T_\mathrm{sat} - T_\mathrm{f0})}{\pi\rho_\mathrm{f}\lambda_\mathrm{v} L}. \tag{7}$$

Here χ is a dimensionless fitting parameter depending, amongst others, on the surface properties approximately equal to unity. This predictive model obviously accounts for the different surface materials, spray properties (hydrodynamic and thermodynamic), spray temperatures and initial wall temperatures.

For validation, we calculate the dimensionless quantities for a variety of experimental data spanning the following ranges: $\dot{m} = 0.6 - 29.5\,\mathrm{kg/m^2 s}$, $D_{10} = 41 - 117\,\mu\mathrm{m}$, $U = 5.2 - 23.7\,\mathrm{m/s}$, $T_\mathrm{w0} = 300 - 462\,^\circ\mathrm{C}$ and $T_\mathrm{f0} = 18 - 23\,^\circ\mathrm{C}$. The corresponding measured evolution of the dimensionless surface temperature $\Theta(\xi)$ and dimensionless heat flux $\Phi(\xi)$ as

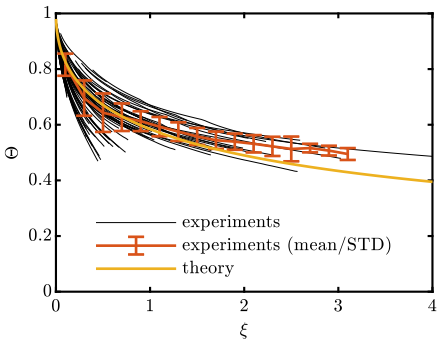

(a) Dimensionless surface temperature $\Theta(\xi)$.

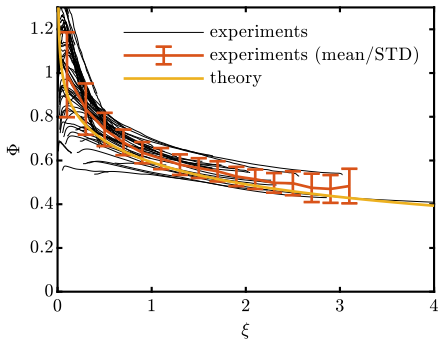

(b) Dimensionless heat flux $\Phi(\xi)$.

Figure 3: Evolution of the dimensionless quantities for the nickel target as a function of the dimensionless time ξ for experimental data in the film boiling regime compared to the theoretical solution.

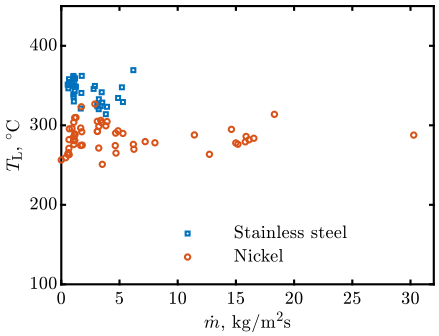

Figure 4: Dependence of the Leidenfrost temperature T_L on the mass flux $\dot{m}$ for different materials ([14].)

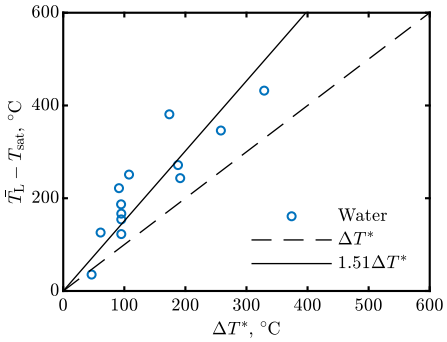

Figure 5: Mean substrate superheat at the Leidenfrost point $\overline{T}_L - T_{sat}$ as a function of ΔT^* for data from this study and from literature ([14].)

a function of the dimensionless time ξ for various experiments is shown in Fig. 3. Additionally, the single red line showing the experiments is the mean and standard deviation computed over all experiments and the yellow line corresponds to the theoretical prediction. We identify a very good agreement between experimental data and theory.

Leidenfrost point

The Leidenfrost point can be identified in experimental data as the minimum heat flux. Understanding and predicting the Leidenfrost point in sprays are of ongoing interest. There is some agreement that this point is influenced by the spray properties, having the mass flux as the main influencing factor [12, 11, 1]. However, the overall picture is rather diffuse [8]. Astonishingly, the present study leads to completely different results and insights into the Leidenfrost [14]. Figure 4 shows the dependence of the Leidenfrost temperature T_L on the spray mass flux $\dot{m}$ for two different substrate materials. Here the substrate material and not the mass flux is the major influencing factor. Spraying a nickel target, which has a higher thermal effusivity ϵ_w, results in a lower Leidenfrost temperature, whereas stainless steel, having a lower thermal effusivity, leads to a higher Leidenfrost temperature.

To explain this observation, imagine the appearance of a vaporization front between drop and wall, which expands along the surface immediately upon impact. This front develops instead of local nucleation bubbles if the surface temperature is sufficiently high. As derived in detail in [14], we can define a Reynolds number Re_v associated with the vaporization front and a characteristic superheat ΔT^*

$$Re_v = \frac{\epsilon_w \sqrt{\alpha_f}(T_{w0} - T_{sat})}{\nu_f L}, \quad \Delta T^* = \frac{\nu_f L}{\epsilon_w \sqrt{\alpha_f}}, \tag{8}$$

where α_f is the thermal diffusivity and ν_f the kinematic viscosity of of the fluid.

In Fig. 5 we plot the mean substrate superheat at the Leidenfrost point $\overline{T}_L - T_{sat}$ of the present experimental data and those found in literature as a function of the characteristic superheat ΔT^*. The literature data is based on experiments performed with various substrate materials from glass or ceramic, having very low thermal effusivities, to copper haven a very high one. The superheat associated with the Leidenfrost temperature follows a linear dependence on ΔT^*. The best fit of the data is $\overline{T}_L - T_{sat} = 1.51\Delta T^*$. This good agreement indicates a new understanding of the Leidenfrost point in sprays and allow the prediction of its temperature for various spray cooling applications.

Nucleate boiling

The temporal evolution of the heat flux and surface temperature indicate that the transition boiling regime lasts only a short time. Therefore, and based on the fact that the Leidenfrost point is the inception of wetting on the surface, we can image this regime to be replaced by a jump of the heat flux towards a very high value. For this reason we skip any further discussion of the transition boiling regime and move on to the nucleate boiling regime.

Upon wetting of the surface the contact temperature at the surface immediately decreases to the saturation temperature. Indeed, this corresponds to the hypothetical maximum cooling. Assuming again a semi-infinite target having the undisturbed initial temperature T_{w0} far away from the surface from where the spray impact takes place and the constant saturation temperature at the wetted surface, we can calculate the temporal evolution of the heat flux as [15]:

$$\mathcal{T} \equiv k \frac{\epsilon_w^2 \Delta T^2}{\pi \dot{q}(t)^2} \approx t - t_L. \tag{9}$$

Figure 6 shows $\mathcal{T} = k\epsilon_w^2 \Delta T^2 / \pi \dot{q}^2$, measured for various spray parameters and different initial substrate temperatures, as a function of $t - t_L$. Here t_L corresponds to the instant of the Leidenfrost point and is derived from the experimental data as the minimum heat flux, k is a constant which can be determined from the experiments and $\Delta T = T_{w0} - T_{sat}$. We can identify a very good agreement between experimental data and theoretical prediction. Furthermore, this leads to

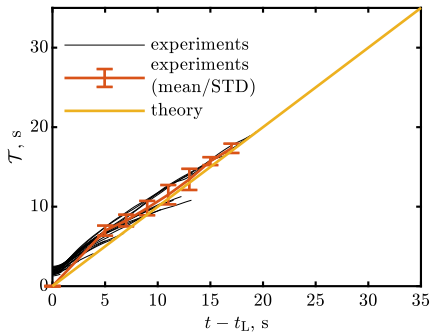

Figure 6: Scaling of the heat flux plotted as a function of time for the nickel target [13].)

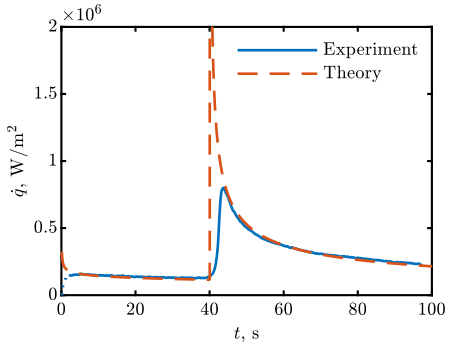

Figure 7: Exemplary comparison between one experiment and the theoretical prediction of the entire cooling process. Heat flux evolution with time [13].)

a new understanding of spray cooling in the nucleate boiling regime: The heat flux is independent of the spray properties and only depends on the substrate material, temperature difference and time. In other words, the heat flux is limited by the thermal inertia of the substrate material

CONCLUSIONS

The previously discussed overview of new models for the different regimes of transient spray cooling lead to new insights and provide a predictive capability to develop and improve spray cooling processes. As a conclusion Fig. 7 shows the application of the model for the film boiling and nucleate boiling regime to an example experiment. The Leidenfrost temperature was calculated from the experimental data. The excellent agreement between theory and experiment impressively illustrates the universality and performance of the developed models.

The authors gratefully acknowledge financial support from the Deutsche Forschungsgemeinschaft (DFG) in the framework of SFB-TRR 75 and the Industrieverband Massivumformung e.V.

References

[1] H. M. Al-Ahmadi and S. C. Yao. *Exp. Heat Transfer*, 21(1):38–54, 2008.

[2] J. Breitenbach. PhD thesis, Technische Universität, Darmstadt, 2018.

[3] J. Breitenbach, I. V. Roisman, and C. Tropea. *International Journal of Heat and Mass Transfer*, 110:34–42, 2017.

[4] J. Breitenbach, I. V. Roisman, and C. Tropea. *Exp. Fluids*, 59(3):55, 2018.

[5] W. Chaze. PhD thesis, Université de Lorraine, 2017.

[6] W.-L. Cheng, W.-W. Zhang, H. Chen, and L. Hu. *Renew. Sust. Energ. Rev.*, 55:614–628, 2016.

[7] J. Kim. *Int. J. Heat Fluid Flow*, 28(4):753–767, 2007.

[8] G. Liang and I. Mudawar. *Int. J. Heat Mass Tran.*, 115:1206–1222, 2017.

[9] S. K. Nayak, P. C. Mishra, and S. K. S. Parashar. *AEJ*, 55(3):1995 – 2004, 2016.

[10] I. V. Roisman, J. Breitenbach, and C. Tropea. *J. Fluid Mech.*, 842:87–101, 2018.

[11] N. Sozbir, Y. W. Chang, and S. C. Yao. *J. Heat Transf.*, 125(1):70, 2003.

[12] N. Sozbir, C. Yigit, R. J. Issa, S.-C. Yao, H. R. Guven, and S. Ozcelebi. *Atomization Spray*, 20(5):387–405, 2010.

[13] F. M. Tenzer. PhD thesis, Technische Universität, Darmstadt, 2020.

[14] F. M. Tenzer, J. Hofmann, I. V. Roisman, and C. Tropea. *Manuscript submitted for publication*, (arXiv:2001.05426), 2020.

[15] F. M. Tenzer, I. V. Roisman, and C. Tropea. *J. Fluid Mech.*, 881:84–103, 2019.

[16] J. Wendelstorf, K. H. Spitzer, and R. Wendelstorf. *Int. J. Heat Mass Tran.*, 51(19-20):4902–4910, 2008.

SL118485

ELECTRO–FLUID–MECHANICS OF THE HEART

Roberto Verzicco *[1,2,4], Valentina Meschini[3], Giulio Del Corso[4], and Francesco Viola[4]
[1]DII, Uniroma2, Roma, IT
[2]UTwente, Enschede, NL
[3]DM, DII, Uniroma2, Roma, IT
[4]GSSI, L'Aquila, IT

Summary We present the results from a multi–physics computational model capable of tackling the electrophysiology, the elasto–mechanics and the fluid dynamics of the heart, including their multi–way coupled interactions. The developed tool embodies accuracy, versatility and computational efficiency thus allowing cardiovascular simulations in realistic conditions without resorting to large–scale supercomputers. The model has been verified and validated through comparisons with the literature, ad–hoc experiments and clinical data. We show results for physiologic and pathologic configurations with the aim of assessing the reliability of the model and proving its predicting capabilities that could be used to anticipate the outcome of surgical procedures and to aid clinical decisions.

INTRODUCTION

The human heart is a hollow muscular organ that pumps blood throughout the body, to the lungs and to its own tissue. It drives the systemic–, the pulmonary– and the coronary–circulation, to bring oxygen and nutrients to every body cell and to remove the waste products. The heart achieves these fundamental goals by two parallel volumetric pumps, the right and the left, which beat approximately 10^5 times per day to deliver a continuous flow rate of about 5 l/min with an outstanding reliability. This is possible because of the highly cooperative and interconnected dynamics of the heart in which every element is key for the others. In a few words, each heart beat is triggered by specialized pacemaker cells that generate rhythmical electrical impulses propagating along well defined paths and with precise timings thus stimulating a sequence of contractions driving the blood from atria to ventricles and eventually to the arteries. The resulting hemodynamics yields shear stresses and pressure loads on the endocardium and on the valves, whose opening/closing ensures the correct flow direction across heart chambers: only the synchronized and synergistic action of the myocardium electrophysiology, mechanics of the tissues and hemodynamics allows the heart of an adult human to operate on a power of only 8 W, lifelong. Such a perfect and highly sophisticated mechanism, in which even a minor malfunctioning impairs its pumping efficiency, calls for a complete study on account of the scientific, social and economic implications.

Concerning the latter we note that cardiovascular disorders (CVD) are the main cause of population death and health care costs of developed Countries and, despite the advances of medical research, CVD expenditure projections for the next decades are predicted to become unsustainable. This scenario requires novel approaches that improve the effectiveness of the available diagnostic tools without concurrently increasing further the costs: computational science can be key for this purpose since it can add predicting capabilities and improve the precision of many evidence based [1] current procedures.

On the other hand, accurate and reliable CVD simulations involve the interconnected multi–physics dynamics of the whole heart and this is a formidable task from the modelling and computational point of view.

This paper shows the progress of the present research group towards the fully–coupled multi–physics computational model for the heart.

THE MODEL

The multi–physics computational model used in this study is thoroughly described in [2] where also verification and validation tests are reported; here only the main features are summarised.

One of the challenges of cardiovascular simulations is the definition of the initial configuration owing to the extreme variability among humans; even leaving apart differences related to gender, age, race or pathologies, also homogeneous cohorts of people (say male, adult, Caucasic, healthy) show differences. The two possible approaches are then either tackle a *patient specific* case or rely on an idealised setup which is representative of a broad class of people but of none in particular: the first approach is usually adopted when a particular case (such as a prosthesis implantation to a specific human) has to be anticipated while the second is preferred for research and development purposes.

In the present study we have adopted the latter possibility; starting from tens of high–resolution CT or MRI clinical images and medical atlas [3, 4] that have been ensemble–averaged and, relying on modeling software, the geometries for each heart chamber, valve and main vessel, have been built and assembled to form a 'standard' heart (figure 1a).

The hemodynamics is governed by the Navier–Stokes equations, which in non–dimensional form read:

$$\frac{\partial \mathbf{u}}{\partial t} + \mathbf{u}\cdot\nabla\mathbf{u} = -\nabla p + \nabla\cdot\tau + \mathbf{f}, \qquad \nabla\cdot\mathbf{u} = 0. \tag{1}$$

*Corresponding author. E-mail: verzicco@uniroma2.it.

SECTIONAL LECTURES

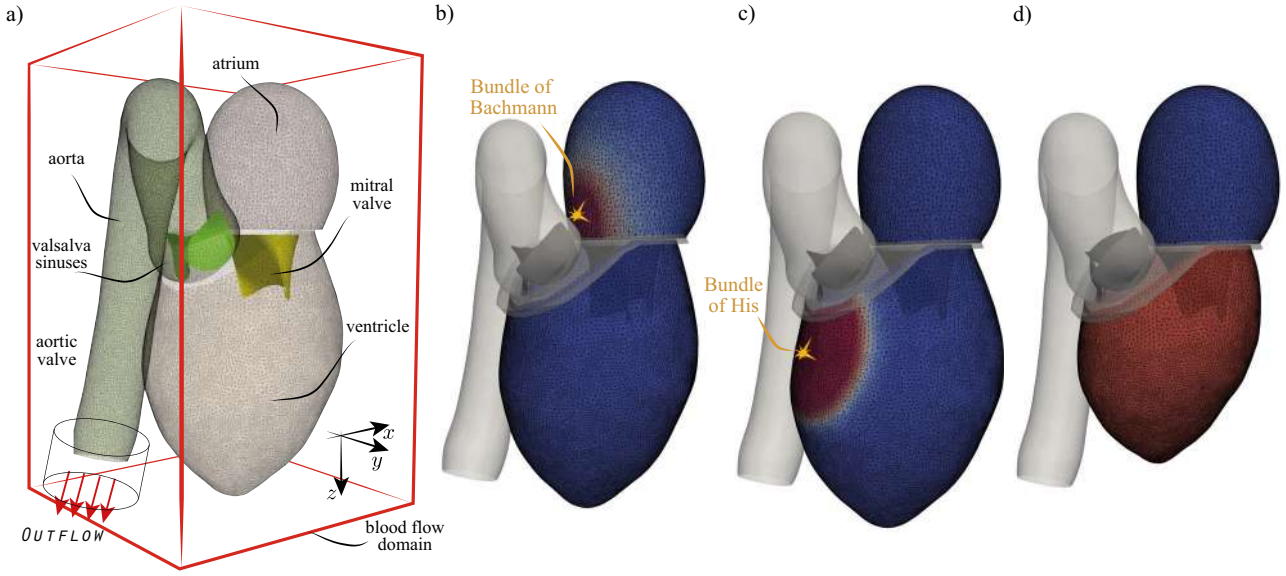

Figure 1: a) Geometry of the left heart assembly with ventricle, atrium, mitral and aortic valve and a tract of the aorta. All these deformable elements are anchored to rigid valvular planes that mimic the fibrous trine. b), c) and d) Snapshots of the transmembrane potential propagation in the left heart; the levels range from -85mV (blue) to $+20$mV (red). b) early atrial systole, corresponding to the time $t/T = 0.85$, c) early ventricular systole $t/T = 0.005$; d) peak ventricular systole $t/T = 0.23$. $T = 0.86$s is the heartbeat period.

Here $\mathbf{u}$ is the blood velocity and p the pressure; in the case of a Newtonian fluid, the viscous stress tensor τ is given by $Re^{-1}(\nabla\mathbf{u} + \nabla^T\mathbf{u})$, whereas non–Newtonian fluids call for more complex constitutive relations as done in [5]. The Reynolds number is defined as $Re = Ud/\nu$ being $d = 2.4$ cm the mitral annulus diameter, $U = 60$ cm/s the averaged velocity in the mitral annulus during diastole and $\nu = 4.8 \times 10^{-6}$ m^{2}s^{-1} is the effective kinematic viscosity for human blood with an hematocrit of 40%: the resulting Reynolds number is $Re = Ud/\nu = 3000$.

The dynamics of the heart tissues is integrated using the Fedosov's interaction potential approach [6, 7, 8]. Any structure is modeled as an elastic shell and discretized by triangular meshes. The mass is lumped at the nodes proportionally to the area of the triangles sharing a given node. Nodes sharing an edge are connected by elastic links oriented as the mesh edges and the former give back an in–plane force as a response to an in–plane stretching. Additionally, the bending stiffness is provided by torsional springs acting between two adjacent faces sharing an edge; the relative rotation of two adjacent triangles generates a restoring moment. When the hydrodynamics loads and the active muscular contraction (described below) are applied to the network, the latter deforms and generates internal elastic forces that are applied to the mesh nodes.

Although this model is typically used in the framework of linear elastic materials [9, 7], biological cardiac tissues are strongly nonlinear and anisotropic, thus requiring more complex constitutive relations. To simulate the response of an hyperelastic and orthotropic material, a Fung–type relation [10, 7] is adopted with the resulting tissue properties that are stiffer in the direction of the fibers than in the cross–fibre direction and an hyperelastic stress–strain behaviour.

The propagation of the electrophysiologic signal is obtained by modeling the myocardium as an intracellular and an extracellular overlapping continuum media (*bidomain* model) separated by the cell membrane which acts as an electrical insulator [11, 12]. The status of each domain is determined by its electrical potential whose gradient yields the electric field from which the current densities are computed. Considering the conservation of charges and the absence of external current sources, the transmembrane current is given by the gradient of the current density, which depends on the potential difference across the membrane (transmembrane potential) and on its permeability to the ions.

Once the activation potential at every point and every instant is available, the active tension τ_{act} of the tissue is computed [13] and translated in internal nodal active forces oriented as the local muscular fiber direction: according to the physiologic myocardium model by [14], here the fibers are assumed to spiral clockwise in the ventricle from the apex to the basis and back with a constant angle of $\pm 45^o$ while in the atrium fibers are aligned with its vertical axis.

The contraction and relaxation of the heart chambers along with the aorta and valve leaflets kinematics come from the dynamic balance between inertia, external and internal (passive and active) forces acting on each triangular vertex. For each node the second Newton law of motion, integrated twice in time, yields the instantaneous tissue configuration at each time step. The new geometry can then be used as input for the fluid and electrophysiology to to obtain the new active and external forces for the successive step.

Owing to the strongly interconnected dynamics of the three models it is not obvious whether they should be solved simultaneously or sequentially and, in the latter case, which one has to be integrated first.

Each of the two approaches (strong– or loose–coupling) have advantages and drawbacks and both have been implemented in the computational model. Unfortunately the most efficient choice depends on the specific problem and its

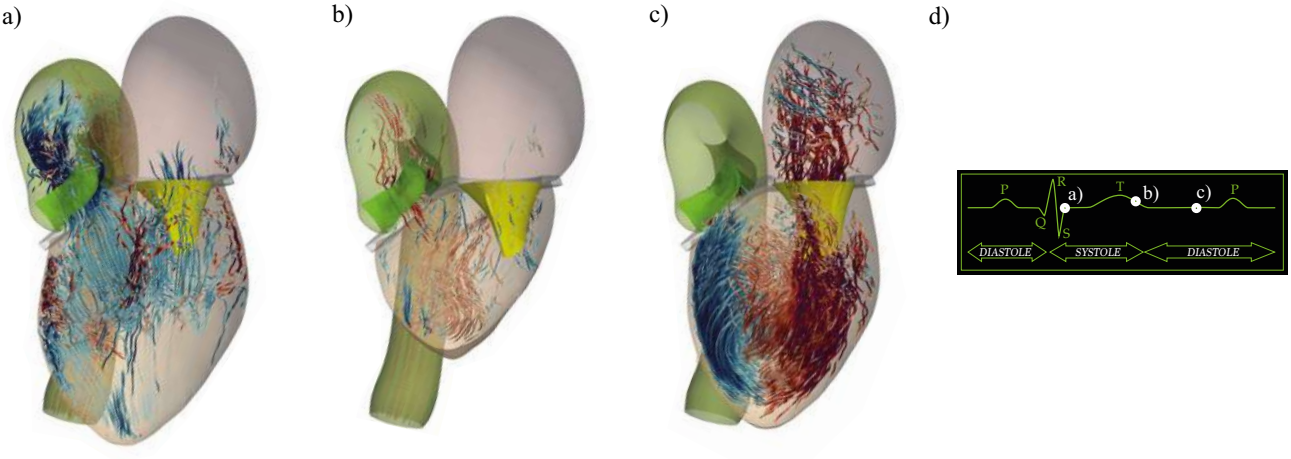

Figure 2: Instantaneous left heart configuration with streamtraces coloured by the local vertical velocity. The colour coding is -0.6 (dark blue), 0.6 (dark red). a) Snapshot at early ventricle systole $t/T = 0.14$, b) end of ventricle systole/beginning of isovolumic relaxation $t/T = 0.43$, c) early atrial systole (ventricle diastole) and passive filling phase $t/T = 0.60$. d) Sketch of an electrocardiogram with the instants of the three snapshots of the figure.

parameters; for the present cardiovascular simulations it appears that the time step size is physically limited by the elastic frequency of the stiffer tissue, the ventricle myocardium, rather than by the other physical systems or stability features of the integration scheme.

RESULTS

A series of preliminary simulations have been run to assess the time step and mesh needed for convergence. Eventually it was determined that the left–heart assembly of figure 1a could be properly simulated using a mesh of about 19 million nodes and 2 million time steps per heartbeat; more details about validations, comparison with experiments, other simulations and clinical data can be found in [2].

In the heart, each heartbeat is initiated by the sino–atrial node in the right atrium that 'sparks' an electrical impulse to initiate the propagation of the activation potential throughout the heart. This propagation occurs along specific directions and with precise timings and delays to allow the efficient filling and emptying of the various heart chambers.

Our computational model allows to consider the fully inhomogeneous and anisotropic electric conduction properties of the myocardium and therefore also the preferential directions and and different velocities of the signal propagation. However, since in this example we are considering only the left half of the whole organ, part of the 'electrical circuit' is not physically present and the activation potential has to be triggered separately at specific times and points. The latter are indicated in figure 1bc as Bundle of Bachmann and Bundle of His that are the position in which the fast conduction fibers intersect the left atrium and ventricle, respectively. Figure 1d finally shows the setup at the peak of the ventricular systole, when the electrical signal has fully propagated across the ventricle and activated the myocardium contraction that has reduced the volume of the chamber to about 30% of its initial value.

The asynchronous active contraction of the myocardium pushes the blood from the atrium to the ventricle and then to the aorta to feed the systemic circulation. The correct flow direction is assured by the heart valves that passively open and close owing to the hydrodynamic loads produced by the fluid structure interaction.

In figure 2 we report three representative snapshots of the blood motion within the left heart visualised by streamtraces coloured by the local value of the vertical velocity. Among the various features we note the large–scale recirculation generated in the relaxed ventricle by the mitral jet (figure 2c). This large vortex is very beneficial for the endocardium that, being constantly swept by the recirculating blood prevents its stagnation, especially within the trabeculae, and the formation of clots.

Although the results in figures 1, 2 are plausible and consistent with the mechanics of the heart, we can not consider them as a validation of the model since they are only qualitative and do not allow any quantitative comparison. In this respect, the graph of figure 3 is much more useful since it reports the time evolution of the pressure in the atrium, ventricle and aorta during a heart cycle. This is usually referred to as 'Wiggers diagram' and it is considered a standard of cardiac physiology to assess the health status of the organ. Our results show that not only the shape of the profiles but also the pressure value agree very well with the literature and this is particularly meaningful for the present computational model in which every quantity is obtained from the computation of the complex interconnected dynamics without imposing ad hoc conditions.

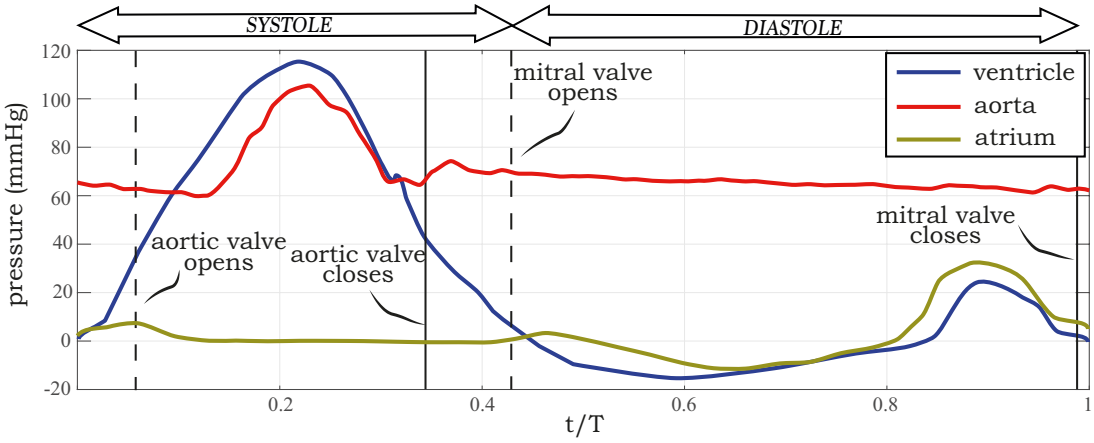

Figure 3: Wiggers diagram obtained by the present computational model.

CONCLUSIONS

In this paper we have presented a recently developed multi–physics model for cardiovascular simulations that has been used to simulate the full dynamics of the left heart. The model solves the three–dimensional incompressible hemodynamics coupled with the active contraction and passive deformation of the tissues via a fluid/structure interaction procedure. The active contraction, in turn, is activated by the electrophysiology that is computed by a bidomain electrophysiology model fully coupled with the other two.

The computational framework yields realistic results in terms of myocardium activation, hemodynamics and wall shear stresses (not shown here). Among the quantitative data we have computed the total volume variation of the ventricle in a cycle that gives an ejection fraction of about 60% and a cardiac output of 5.06 l/min, which are typical physiological values for the heart of a healthy adult.

Owing to the formidable computational effort required by this model, it has been parallelized using both, openMP and MPI directives and, more recently, also also GPU architectures; the parallelization strategies and the speed–up obtained are being reported elsewhere.

Another research activity is aimed at accounting the considerable variability of the input parameters; for this reason uncertainty quantification analysis is being performed either for evaluating the robustness of the model to errors affecting the inputs and for assessing the level of confidence to be given to the results.

Finally, the model is being extended to the full heart (left and right) to perform large simulation campaigns for inputs defined by probability distributions rather than deterministic values: the full set of simulations therefore could be considered as a virtual clinical trial to be analysed statistically.

References

[1] Sackett, D.L. Evidence–based medicine. *Semin. in Perinatology* **21**: 3–5, 1997.

[2] Viola, F., Meschini, V. & Verzicco, R. Fluid–Structure–Electrophysiology interaction (FSEI) in the left-heart: A multi–way coupled computational model, *Eur. J. Mech. B/Fluids* **79**, 212–232, 2020.

[3] Stouffer, G., Runge, M.S., Patterson, C. & Rossi, J. Netter's Cardiology. Elsevier Health Sciences, 2018.

[4] Carpentier, A., Adams, D.H. & Filsoufi, F. Carpentier's Reconstructive Valve Surgery. Elsevier Health Sciences, 2011.

[5] De Vita, F. and de Tullio, M. D. and Verzicco, R. Numerical simulation of the non-Newtonian blood flow through a mechanical aortic valve, *Theor. Comp. Fluid Dym.* **30**, 129–138, 2016.

[6] Fedosov, D.A, Caswell, B. & Karniadakis, G.E. Systematic coarse–graining of spectrin–level red blood cell models. *Comp. Meth. in Appl. Mech. Eng.* **199**: 1937–1948, 2010.

[7] de Tullio, M.D. & Pascazio, G. A Moving–Least–Squares Immersed Boundary Method for simulating the Fluid–Structure Interaction of elastic bodies with arbitrary thickness. *J. Comp. Phys.* **325**: 201–225, 2016.

[8] Spandan, V.A., Meschini, V., Ostilla–Mónico, R., Lohse, D., Querzoli, G., de Tullio, M D. & and Verzicco, R. A parallel interaction potential approach coupled with the immersed boundary method for fully resolved simulations of deformable interfaces and membranes. *J. Comp. Phys.* **348**: 567–590, 2017.

[9] van Gelder, A. Approximate simulation of elastic membranes by triangulated spring meshes. *J. Grap. Tools* **3**: 21–41, 1998.

[10] Hammer, P.E.,Sacks, M.S., Pedro, J. & Howe, R.D. Mass-spring model for simulation of heart valve tissue mechanical behavior. *Ann. Biomed. Eng.* **39**: 1668–1679, 2011.

[11] Tung L. A bi–domain model for describing ischemic myocardial dc potentials. *PhD Thesis*, Massachusetts Institute of Technology, Boston, 1978.

[12] Clayton, R.H. & Panfilov, A.V. A guide to modelling cardiac electrical activity in anatomically detailed ventricles. *Prog. Biophys. Mol. Bio.* **96**: 19-43, 2008.

[13] Göktepe, S. & Kuhl, E. Electromechanics of the heart: a unified approach to the strongly coupled excitation–contraction problem, *Comp. Mech.* **45**, 227–243, 2010.

[14] Torrent-Guasp, F., Kocica, M.J., Corno, A. Komeda, M., Cox, J., Flotats, A., Ballester–Rodes, M. & Carreras-Costa, F. Systolic ventricular filling. *Eur. J. Cardio-Thor. Surg.* **25**: 376–386, 2004.

SL118446

THEORETICAL ANALYSES OF CONFIGURATIONAL STABILITY OF CRACK PROPAGATION IN MIXED-MODE I+III OR I+II+III: A REVIEW

Jean-Baptiste Leblond*[1], Alain Karma[2], and Laurent Ponson[1]
[1]Institut Jean Le Rond d'Alembert, Facult des Sciences et Ingénierie, Paris, France
[2]Physics Department and Center for Interdisciplinary Research on Complex Systems, Northeastern University, Boston, Massachussetts, USA

Summary The instability of coplanar propagation of cracks loaded in mixed-mode I+III conditions, leading to splitting of the front and formation of small disconnected tilted facets, is well documented experimentally. This presentation reviews some recent analyses of this instability, based on (i) theoretical formulae of Gao and Rice (1986) and Movchan et al. (1998), providing general expressions of the stress intensity factors along the front of a semi-infinite crack slightly perturbed both within and out of its initial plane; (ii) a "double" propagation criterion, applied at all times all along the front, combining Griffith (1920)'s energetic condition and Goldstein and Salganik (1974)'s principle of local symmetry.

INTRODUCTION

Cracks loaded under mixed-mode I+III conditions are well known not to propagate along a plane, but in the form of small tilted facets, leading to splitting of the crack front. Figure 1 illustrates the behavior of this front, initially coinciding with the axis Oz, as it propagates under such conditions. The front splits into small facets of "type A" rotating around the direction Ox of propagation so as to minimize the mode III component of the local stress field, and facets of type B rotating in the opposite direction. Facets of type A are "privileged" over facets of type B in the sense that their length (in the direction of propagation) is larger (this is not represented in Figure 1 for legibility).

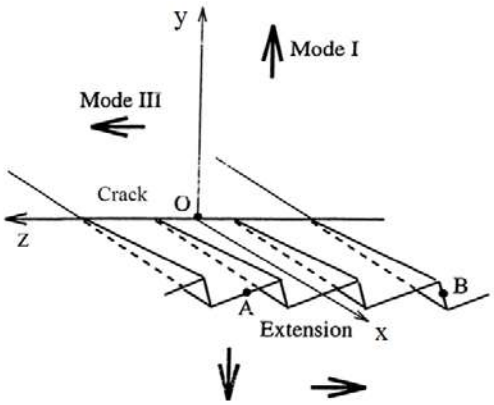

Figure 1. Schematic geometry of a crack propagating in mixed-mode I+III.

The aim of this presentation is to present and discuss some recent theoretical analyses of the formation of such twisted fracture facets under mixed-mode I+III loading conditions. These analyses were inspired by Pons and Karma's numerical simulations [1], based on a phase-field model, of crack propagation in mode I+III, which evidenced a "helical" instability of the propagating crack front. The common basis of these analyses consisted of two combined elements:

1) Theoretical formulae of Gao and Rice [2] providing the expressions of the first-order variations of the stress intensity factors (SIFs) along the front of a semi-infinite crack resulting from an arbitrary *in-plane* perturbation of the crack *front*; and of Movchan et al. [3] for the variations of the SIFs resulting from an arbitrary *out-of-plane* perturbation of the crack *surface*.
2) A "double" propagation criterion, which itself combined Griffith's energetic condition [4] and Goldstein and Salganik's "principle of local symmetry" (PLS) [5]. This criterion was assumed to apply at all times and all positions along the crack front.

The three analyses considered however differed in the hypotheses made on the loading and the fracture energy, as will be seen.

*Corresponding author. E-mail: jbl@lmm.jussieu.fr.

SECTIONAL LECTURES

GENERAL PRINCIPLES OF THEORETICAL STABILITY ANALYSES

A semi-infinite crack embedded within an infinite isotropic elastic body is considered in two configurations (Fig. 2). In the first, unperturbed one, the crack is planar and its front is straight. A Cartesian frame $Oxyz$ with axes oriented according to the standard convention is introduced. The crack is loaded under general mixed-mode I+II+III conditions, with uniform SIFs K_I^0, K_{II}^0, K_{III}^0 along the front. In the second, slightly perturbed configuration, the front of the crack is displaced in the direction x by a small distance $\phi_x(x,z)$ (Fig. 2, left), and its surface is displaced in the direction y by a small distance $\phi_y(x,z)$ (Fig. 2, right).

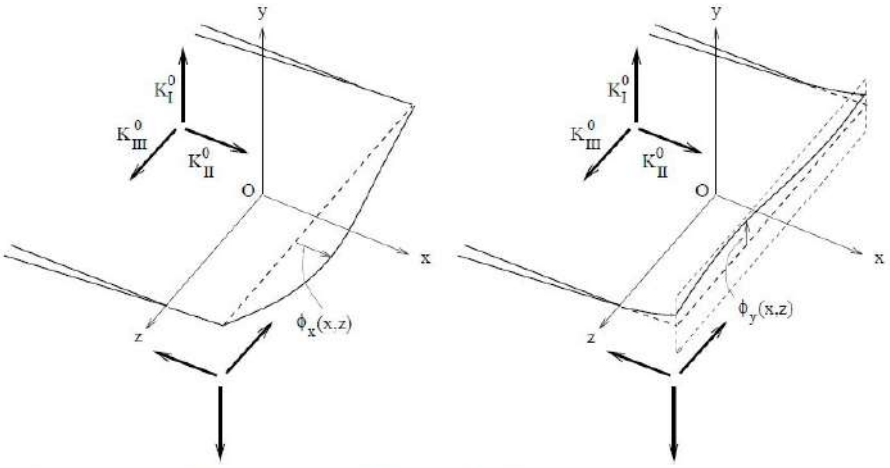

(a) In-plane perturbation of the crack front. (b) Out-of-plane perturbation of the crack surface.

Figure 2. Unperturbed and perturbed configurations of a semi-infinite crack loaded in mode I+II+III.

In this new configuration, the perturbation $\delta K_p(x,z)$ of the p-th SIF is given, to first order in the pair (ϕ_x, ϕ_y), by the formula $\delta K_p(x,z) = \delta_x K_p(x,z) + \delta_y K_p(x,z)$ where the contributions $\delta_x K_p(x,z)$ and $\delta_y K_p(x,z)$ arise from ϕ_x and ϕ_y, respectively. With some mildly restrictive hypotheses, the expressions of the contributions $\delta_x K_p(x,z)$ are given in the work of Gao and Rice [2], and those of the contributions $\delta_y K_p(x,z)$ in the work of Movchan et al. [3].

The prediction of the successive configurations of the crack, resulting from its mixed-mode propagation, are based on a double criterion enforced all along the crack front and at all instants during propagation, consisting of:

1) Griffith's condition [4] $G(x,z) = G_c(x,z)$ where $G(x,z)$ denotes the local energy-release-rate and $G_c(x,z)$ its local "critical value" inducing propagation of the front (that is, the fracture energy).
2) Goldstein and Salganik's PLS [5] according to which the local SIF $K_{II}(x,z)$ of mode II must be zero.

STABILITY ANALYSIS: BASIC VERSION

In the first, simplest version of the stability analysis [6], the loading is in mode I+III ($K_{II}^0 = 0$), and the fracture energy is assumed to be an absolute constant, depending only on the material. The instability mode (ϕ_x, ϕ_y) satisfying the double criterion is looked for in the form $\phi_x(x,z) = e^{\lambda x}\psi_x(z)$, $\phi_y(x,z) = e^{\lambda x}\psi_y(z)$ where λ (> 0) is an unknown parameter (the growth rate of the perturbation), and $\psi_x(z)$, $\psi_y(z)$ unknown functions (specifying the shape of the in-plane and out-of-plane perturbations).

The method used consists of introducing the Fourier transforms of all functions in the direction z of the unperturbed crack front, expressing the perturbations of the SIFs in Fourier's space for the perturbations of the crack front and surface considered, and then enforcing the double criterion. This yields a relation that ties together the Fourier transforms $\widehat{\psi_x}(k)$, $\widehat{\psi_y}(k)$ of $\psi_x(z)$, $\psi_y(z)$, plus a condition involving the "unperturbed mixity ratio" $\rho^0 = \frac{K_{III}^0}{K_I^0}$ and the "reduced growth rate" $\xi = \frac{\lambda}{|k|}$.

One finds that for the reduced growth rate ξ to be positive (as required for an instability mode), the unperturbed mixity ratio ρ^0 must be larger than some "critical value" given by

$$\rho^{cr} = \left[\frac{(1-\nu)(2-3\nu)}{3(2-\nu)-4\sqrt{2}(1-2\nu)}\right]^{1/2}$$

where ν denotes Poisson's ratio. This quantity is plotted as a function of ν in Fig. 3 below.

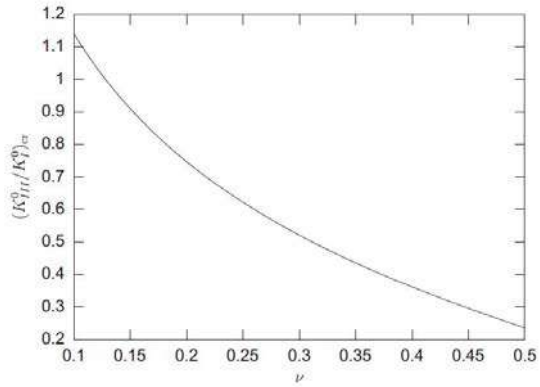

Figure 3. The critical mixity ratio as a function of Poisson's ratio.

Also, the geometry of instability modes - present when ρ^0 exceeds ρ^{cr} - is deduced from the relation connecting $\widehat{\psi_x}(k)$ and $\widehat{\psi_y}(k)$. It is found that the initially straight front becomes an elliptic helix the axes of which grow proportionally and exponentially with the distance x of propagation (Fig. 4). This result is fully compatible with the observations made numerically by Pons and Karma [1] using a phase-field model.

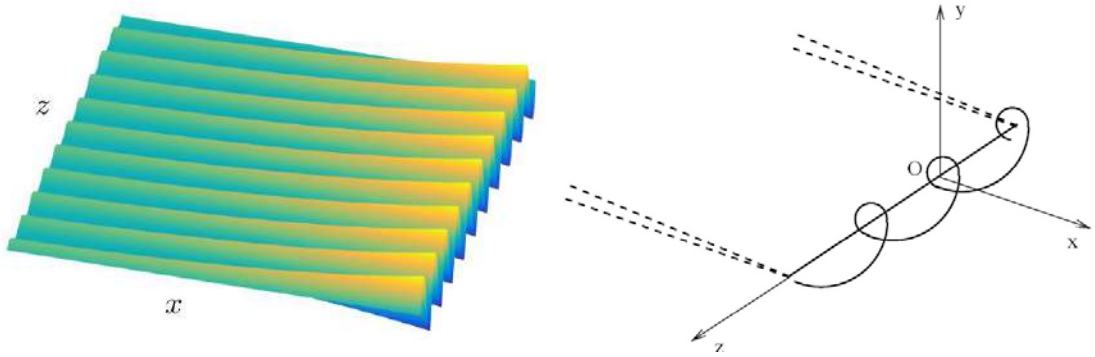

Figure 4. Geometry of the perturbed crack surface (left) and front (right).

STABILITY ANALYSIS: FIRST EXTENSION INCORPORATING A MODE-DEPENDENT FRACTURE ENERGY

One serious problem with the preceding analysis is that the value of the critical mixity ratio ρ^{cr}, being of the order of 0.5 for standard values of ν, is generally much larger than that actually observed, see for instance Sommer [7] and Pham and Ravi-Chandar [8].

One possible solution to this problem was proposed by Leblond et al. [9]. It consisted in heuristically assuming the local fracture energy $G_c(x,z)$ to be a function of the local "mixity ratio" $\rho(x,z) = \frac{K_{III}(x,z)}{K_I(x,z)}$, in agreement with some observations of Lin et al. [10]. The heuristic formula $G_c(\rho) = G_c^{\text{mode I}}(1+\gamma|\rho|^\kappa)$, with γ and κ being material parameters, was adopted by Leblond et al. [9].

Repeating the preceding analysis with this new hypothesis, Leblond et al. [9] found critical values ρ^{cr} of the unperturbed mixity ratio depending on γ and κ. With the values $\kappa = 2$ and $\gamma = 25$ providing a good fit of the heuristic formula for $G_c(\rho)$ with Lin et al.'s measurements [10], they found the value $\rho^{cr} \approx 0.1$, which is within the range of loadings considered in the experiments.

STABILITY ANALYSIS: SECOND EXTENSION INCORPORATING A SMALL MODE II LOADING COMPONENT

Small mode II loading components, arising from various imperfections, are bound to be present in actual experiments. It is therefore a natural idea to repeat the preceding analysis with such an extra loading component.

However the introduction of a small mode II components raises some new issues. The first arises from the resulting general kink of the crack, which is assumed to occur only once a certain position of the crack front is reached. We thus consider an initially flat semi-infinite crack obtained for instance through propagation in mode I fatigue. A static load including mode II and III components is applied henceforward. A general kink of the crack ensues, with possibly superimposed perturbations of the crack front and surface growing in an unstable manner.

Also, instability modes of the form $\phi_x(x,z) = e^{\lambda x}\psi_x(z)$, $\phi_y(x,z) = e^{\lambda x}\psi_y(z)$, with *real* parameter λ and *real* functions $\psi_x(z)$, $\psi_y(z)$, happen not to be compatible any more with continuous satisfaction of the double criterion. More general modes of the form $\phi_x(x,z) = \mathrm{Re}\left[e^{\lambda x}\psi_x(z)\right]$, $\phi_y(x,z) = \mathrm{Re}\left[e^{\lambda x}\psi_y(z)\right]$ with *complex* λ, $\psi_x(z)$, $\psi_y(z)$, must be considered. The calculations required to enforce the double criterion then become more complex, but still remain feasible.

The results are as follows. First, the presence of some mode II tends to stabilize the crack front in the sense that it slightly increases the value of the critical unperturbed mixity ratio ρ^{cr}. But the major effect is on the geometry of instability modes, which now *drift along the crack front as it propagates*. This motion is represented schematically in the left part of Fig. 5 (to be compared to the left part of Fig. 4). The right part of the same figure shows a photograph of a fracture surface recently observed by Vasudevan [11] in some experiment which involved small components of mode II and mode III. Ridges propagating obliquely with respect to the (vertical) main direction of propagation of the crack are apparent in this photograph; deciding whether or not this phenomenon may be explained by the theory developed requires further, more detailed investigations.

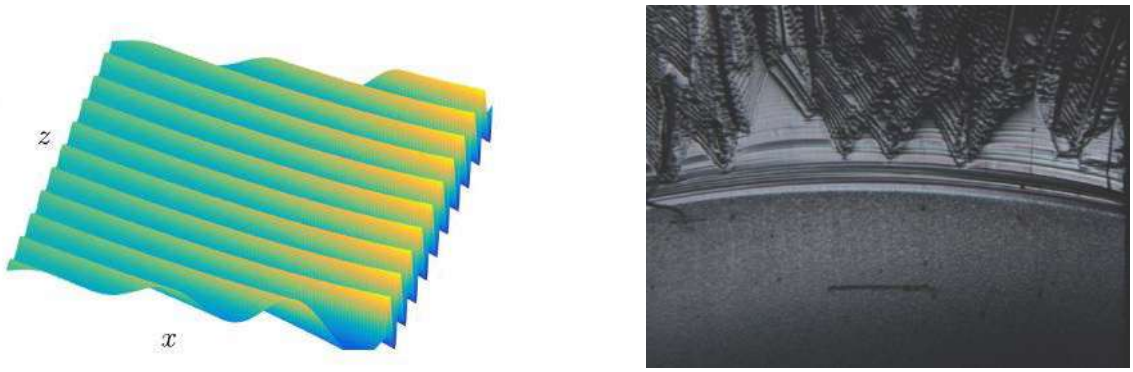

Figure 5. Drifting motion of instability modes in mode I+II+III. Left: theoretical predictions; right: experimental observations of Vasudevan [11].

References

[1] Pons A.J., Karma A. Helical crack-front instability in mixed-mode fracture. *Nature* **464**: 85-89, 2010.
[2] Gao H., Rice J.R. Shear stress intensity factors for planar crack with slightly curved front. ASME *J. Appl. Mech.* **53**: 774-778, 1986.
[3] Movchan A.B., Gao H., Willis J.R. On perturbations of plane cracks. *Int. J. Solids Structures* **35**: 3419-3453, 1998.
[4] Griffith A. The phenomena of rupture and flow in solids. *Phil. Trans. Roy. Soc. London Series A* **221**: 163-198, 1920.
[5] Goldstein R.V., Salganik R.L. Brittle fracture of solids with arbitrary cracks. *Int. J. Fracture* **10**: 507-523, 1974.
[6] Leblond J.B., Karma A., Lazarus V. Theoretical analysis of crack front instability in mode I+III. *J. Mech. Phys. Solids* **59**: 1872-1887, 2011.
[7] Sommer E. Formation of fracture "lances" in glass. *Engng. Fracture Mech.* **1**: 539-546, 1969.
[8] Pham K.H. and Ravi-Chandar K. Further examination of the criterion for crack initiation under mixed-mode I+III loading. *Int. J. Fracture* **189**: 121-138, 2014.
[9] Leblond J.B., Karma A., Ponson L., Vasudevan A. Configurational stability of a crack propagating in a material with mode-dependent fracture energy - Part I: Mixed-mode I+III. *J. Mech. Phys. Solids* **126**: 187-203, 2019.
[10] Lin B., Mear M.E., Ravi-Chandar K. Criterion for initiation of cracks under mixed-mode I+III loading. *Int. J. Fracture* **165**: 175-188, 2010.
[11] Vasudevan A. Deciphering triangular fracture patterns in PMMA : How cracks fragment in mixed-mode loading. *Ph.D. Thesis*, Sorbonne Université, Paris, France, 2018.

SL118447

MODELING DEMENTIA

Amelie Schafer[1], Mathias Peirlinck[1], Kevin Linka[1], Johannes Weickenmeier[2], Alain Goriely[3] and Ellen Kuhl[1]*
[1]Department of Mechanical Engineering, Stanford University, California, United States
[2]Department of Mechanical Engineering, Stevens Institute of Technology, New Jersey, United States
[3]Mathematical Institute, University of Oxford, United Kingdom

Summary Neurodegeneration will undoubtedly become a major challenge in medicine and public health caused by demographic changes worldwide. Recent studies have reinforced the hypothesis that the prion paradigm, the templated growth and spreading of misfolded proteins, could help explain the progression of a variety of neurodegenerative disorders. However, our current understanding of prion-like growth and spreading is rather empirical. Here we show that a physics-based reaction-diffusion model can explain the growth and spreading of misfolded protein in a variety of neurodegenerative disorders. We combine the classical Fisher-Kolmogorov equation for population dynamics with anisotropic diffusion and simulate misfolding across the human brain and use Bayesian approach to infer our model parameters from a longitudinal study of 76 human brains. Our continuum model correctly predicts amyloid-beta deposits and tau inclusions in Alzheimer's disease, alpha-synuclein inclusions in Parkinson's disease, and TDP-43 inclusions in amyotrophic lateral sclerosis. To reduce the computational complexity, we replace the continuous brain through a connectivity-weighted Laplacian graph created from 418 brains of the Human Connectome Project. Our brain network model simulates the key characteristic features of whole brain models at a fraction of their computational cost. Our results suggest that misfolded proteins in various neurodegenerative disorders grow and spread according to a universal law that follows the basic physical principles of nonlinear reaction and anisotropic diffusion. Our model has important clinical implications, from estimating the socioeconomic burden of neurodegeneration to designing clinical trials and pharmacological intervention.

More than 45 million people are living with dementia today and this number is expected to triple by 2050. A major challenge of age-related neurodegenerative diseases is that the initial symptoms of cognitive decline become noticeable only one or two decades after the first pathological abnormalities have started to affect the brain. For several decades, researchers have tried to establish early predictive indicators of neurodegeneration and identify common pathological themes of neurodegenerative disorders. Recent evidence suggests that the key to understanding common features of neurodegeneration could lie in the unusual biology of prion diseases [8]. Prions, proteinaceous infectious particles, are unconventional infectious agents that consist of misfolded proteins that act as corruptive seeds to initiate a chain-reaction of misfolding, growth, and spreading [2]. Prion diseases have some unique kinetic features: Disease progression is inevitable after initial seeding; the duration of the incubation period depends on both the initial seeding concentration and the rate at which prions amplify; and disease progression is characterized by a long, clinically silent incubation period during which prions grow and spread, followed by a brief and invariably fatal clinical disease [4]. Interestingly, these characteristics are similar to the progression of a wide variety of age-related neurodegenerative disorders including Alzheimer's disease, Parkinson's disease, and amyotrophic lateral sclerosis [9]. While the clinical and pathological symptoms of these disparate disorders may vary, at the molecular level, they share with prions the unique properties of nucleation, templating, growth, and spreading [3]. Each of these phenomena presents a potential target for therapeutic intervention; yet, our quantitative understanding of protein misfolding remains rather limited.

Here we illustrate how to model and simulate the spatio-temporal progression of neurodegenerative diseases within the human brain [5]. We have recently fit a network diffusion model based on a weighted Laplacian graph of the axonal connectome to longitudinal tau PET data of 46 subjects using a deterministic optimization approach [6]. We now use Bayesian hierarchical modeling to systematically infer the model paramters from longitudinal imaging data of 76 subjects from the Alzheimer's Disease Neuroimaging Initiative [7]. This probabilistic approach allows us to account for potential uncertainties in image acquisition and processing, and, at the same time, quantify the uncertainty in model calibration [1]. Identifying the uncertainty in our model parameters is essential to determine the accuracy of our personalized model predictions. Our results can have important implications in accurate study design and improved personalized diagnostics.

References

[1] Alber M, Buganza Tepole A, Cannon W, De S, Dura-Bernal S, Garikipati K, Karniadakis G, Lytton WW, Perdikaris P, Petzold L, Kuhl E. Integrating machine learning and multiscale modeling: Perspectives, challenges, and opportunities. *npj Digital Medicine*. 2:115, 2019.

[2] Fornari S, Schafer A, Jucker M, Goriely A, Kuhl E. Prion-like spreading of Alzheimer's disease within the brain's connectome. *J Royal Soc Interface*. **16**: 20190356. 2019.

[3] Goriely A, Kuhl E, Bick C. Neuronal oscillations on evolving networks: Dynamics, damage, degradation, decline, dementia, and death. *Phys Rev Lett*. 125:128102. 2020.

[4] Kuhl E. Connectomics of neurodegeneration. *Nature Neurosci*. **22**:1200–1202. 2019.

[5] Schafer A, Weickenmeier J, Kuhl E. The interplay of biochemical and biomechanical degeneration in Alzheimer's disease. *Comp Meth Appl Mech Eng*. **352**: 369-388. 2019.

[6] Schafer A, Mormino EC, Kuhl E. Network diffusion modeling explains longitudinal tau PET data. *Front Neurosci*. **14**:566876, 2020.

[7] Schafer A, Peirlinck M, Linka K, Kuhl E. Bayesian physics-based modeling of tau propagation in Alzheimer's disease. *Front Physiology*. doi:10.3389/fphys.2021.702975. in press. 2021.

[8] Weickenmeier J, Kuhl E, Goriely A. The multiphysics of prion-like diseases: progression and atrophy. *Phys Rev Lett*. **121**: 158101, 2018.

[9] Weickenmeier J, Jucker M, Goriely A, Kuhl E. A physics-based model explains the prion-like features of neurodegeneration in Alzheimer's disease, Parkinson's disease, and amyotrophic lateral sclerosis. *J Mech Phys Solids*. **124**: 264-281, 2019.

*Corresponding author. E-mail: ekuhl@stanford.edu

SL118448

MORPHING AND SHAPE CONTROL: FROM MECHANO-BIOLOGY TO ENGINEERING

Antonio De Simone

Locomotion strategies employed by unicellular organism are a rich source of inspiration for studying mechanisms for shape control. These strategies are particularly interesting because the organisms and the mechanisms they exploit are invisible to the naked eye, and offer surprising new solutions to the question of how shape can be controlled.
In recent years, we have studied locomotion and shape control in unicellular organisms using a broad range of tools ranging from theoretical and computational mechanics, to experiment and observations at the microscope, to manufacturing of prototypes. The physical models used to demonstrate the mechanisms exploited by biological organsism naturally suggest new solutions for adaptable and deployable structures, morphable devices, robotic applications, smart shape-shifting materials and structures. We will survey our most recent findings within this stream of research.

SL118449

DATA-DRIVEN MODELING OF FLUIDS

Clarence W. Rowley

Fluid flows can be extraordinarily complex, and even turbulent, yet often there is structure lying within the apparent complexity. Understanding this structure can help explain observed physical phenomena, and can help with the design of control strategies in situations where one would like to change the natural state of a flow. This talk addresses techniques for obtaining simple, approximate models for fluid flows, using data from simulations or experiments. We discuss and compare a number of methods for obtaining linear or nonlinear models, and apply the methods to several flows with complex behavior.

MINI SYMPOSIA

K107880 - MS01 - Modeling and controlling turbulent shear flows - Keynote

RESOLVENT ANALYSIS OF SEPARATED FLOWS OVER AIRFOILS

Kunihiko Taira* [1] and Chi-An Yeh[1]
[1] Department of Mechanical and Aerospace Engineering, University of California, Los Angeles, CA, USA

Summary Resolvent analysis, founded on transfer function from modern linear control theory, reveals the input-output characteristics of the base flow. This linear analysis technique is able to identify the most amplified flow structures and the required forcing input over a range of frequencies through the singular value decomposition of the resolvent operator. In this talk, we will discuss the use of resolvent analysis to study separated flow over a NACA 0012 airfoil. Examples will include the analysis of turbulent separated flows, active flow control, and transonic buffet over a range of Reynolds numbers. We will also discuss our efforts on incorporating data-science and network-science-based techniques to extend the applicability of resolvent analysis for fluid flows at higher Reynolds numbers and those with time-varying base states.

INTRODUCTION

A variety of aerodynamic flows exhibit sustained fluctuations about their base states, providing dynamical richness to the flow physics. Resolvent analysis offers the foundation to reveal the input-output relationship between the sustained perturbations and the flow response with respect to the base flow [1, 2]. As a companion to the global stability analysis that offers insights based on the homogeneous solution to initial value problems, the resolvent analysis describes the system response as the particular solution to the harmonic forced system [1, 3]. One of the key features of the resolvent analysis is its close connection to the pseudospectral analysis that captures the non-normality of the flow [1, 4].

In recent years, the refreshing perspective of McKeon and Sharma [5] has enabled the use of resolvent analysis for time-averaged turbulent base flows, assuming that the flow is statistical stationary. In their formulation, the nonlinear term in the Navier–Stokes equations is treated as intrinsic forcing in a feedback loop about the linearized operator. This perspective has enabled resolvent analysis to analyze turbulent flows, which has been a challenge for linearized techniques that assume small-amplitude perturbations about an equilibrium state. Resolvent analysis has in recent years been applied to reveal the input-output characteristics of a variety of flows [4]. In this presentation, we will focus on the applications of resolvent analysis on low and high-speed separated flows over a NACA 0012 airfoil. Towards the end of the talk, we discuss techniques to extend resolvent analysis to analyze complex high-Reynolds-number and time-varying base flows.

CHARACTERIZATION AND CONTROL OF SEPARATED FLOW

Resolvent analysis reveals the most amplified forcing or perturbation profile over a range of frequencies by performing the singular value decomposition (SVD) of the resolvent operator. The modal profiles determined from resolvent analysis can be used to develop control design metrics that can point to effective choices of control parameters, including forcing location, direction, and frequency. We consider the application of resolvent-based control to suppress flow separation over a NACA 0012 airfoil at Reynolds number of $23,000$, as shown in Fig. 1 [6]. For this flow, we take the resolvent modes to determine an effective control approach for enhancing mixing near the separation point to direct high-momentum fluid towards the airfoil surface. The guidelines developed from this resolvent-based approach are tested in full LES. The trend for control effectiveness predicted by the resolvent-based metric is found to be in excellent agreement with the results obtained from an exhaustive set of parametric LES runs. Because the present approach only requires the baseline flow and the discretized resolvent operator, the optimal set of control parameters can be found with significantly lower computational cost and time compared to a large number of LES cases.

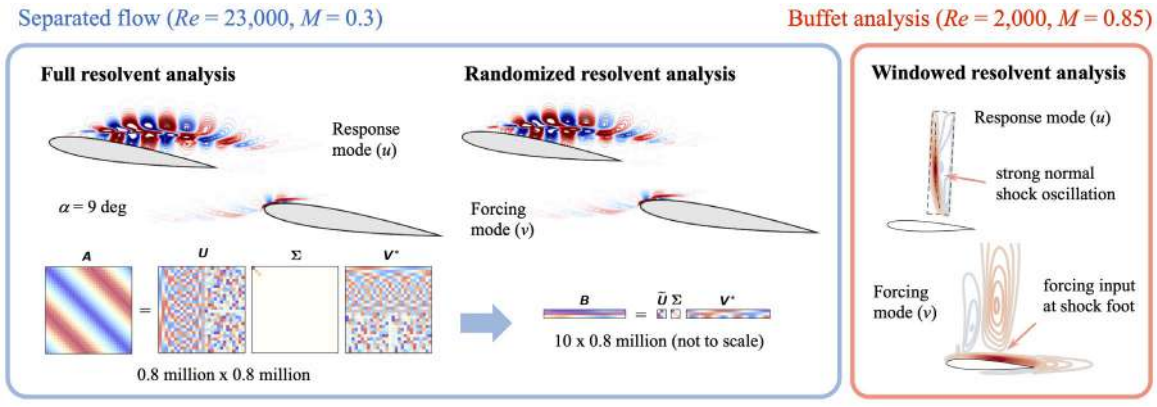

Figure 1: (Left) Resolvent analysis of turbulent separated flow over an airfoil at $Re = 23,000$ and $M = 0.3$. Comparison of full and randomized resolvent analysis shows excellent agreement. (Right) Resolvent analysis of transonic buffet at $Re = 2,000$ and $M = 0.85$ using spatial windowing revealing the source of 2D buffet at shock foot. This overview figure is compiled from [11, 8].

*Corresponding author. E-mail: ktaira@seas.ucla.edu

ANALYSIS OF TRANSONIC BUFFET

We can direct the focus of resolvent analysis to certain regions of the flow field to shed light on particular flow phenomena [7]. Spatial windowing can be incorporated into the resolvent formulation to identify the causal relations of particular flow phenomena. In this example, we apply spatial windowing to the region where standing shock appears over an airfoil in transonic flow to understand the origin of two-dimensional buffet [8], as shown in Fig. 1. Through this analysis, we reveal that the cause of the low-frequency buffet oscillation lies at the foot of the shock. What is noteworthy with this type of analysis is its ability to uncover such mechanism even for flow regimes that are not typically associated with buffet. The findings from the study is validated by actuating the transonic flow with the forcing mode profile to stimulate the predicted response in DNS. The results suggest that low-Reynolds number compressible flows encountered in Martian flight condition may be susceptible to buffet-induced low-frequency oscillations.

EXTENDING RESOLVENT ANALYSIS

Performing resolvent analysis requires the availability of the discretized Navier–Stokes operator, whose size is dependent on the spatial discretization scheme and the number of spatial grid points. The size of the resolvent operator becomes very large for turbulent base flows at high Reynolds numbers and for two- and three-dimensional base flows. To ease the handling of such high-dimensional resolvent operators and extend the applicability of resolvent analysis, we consider the use of randomized numerical linear algebra [9, 10, 11]. Randomized methods can provide a low-rank operator through a technique called sketching, which retains the dominant properties of the full operator. This reduction enables the use of the randomized singular value decomposition within the resolvent framework to achieve computational speedup and memory relief [11]. We provide guidelines on the use of randomized resolvent analysis and demonstrate its use for turbulent separated flows over the airfoils at $Re = 23,000$ and $500,000$ [11, 12], as shown in Fig. 1 for the lower Re. We also will discuss efforts to incorporate data-science and network-inspired inspired techniques into resolvent analysis to extract additional physical insights for complex fluid flows.

CONCLUSIONS

Resolvent analysis have become an invaluable modal analysis technique to reveal the input-output relationship for a variety of flows. One particularly attractive feature of resolvent analysis is its ability to analyze turbulent base flows, which has been an open question for global stability analysis. As many flows are under sustained perturbations or possess flow unsteadiness in turbulent conditions, resolvent analysis holds tremendous potential to analyze a range of flows for their characterization, modeling, and control.

This work was supported by the US Office of Naval Research (N00014-19-1-2460), US Air Force Office of Scientific Research (FA9550-18-1- 0040), and US Army Research Office (W911NF-17-1-0118). We acknowledge the insightful discussions with S. Benton, S. L. Brunton, D. Garmann, M. Kameda, Y. Kojima, J. Ribeiro, P. J. Schmid, and B. J. McKeon.

References

[1] Trefethen L. N., Trefethen A. E., Reddy S. C., Driscoll T. A., Hydrodynamic Stability Without Eigenvalues, *Science* **261**(5121): 578-584, 1993.
[2] Jovanović M. R., Bamieh B, Componentwise Energy Amplification, *J. Fluid Mech.* **534**: 145-183t, 2005.
[3] Taira K., Brunton S. L., Dawson S. T. M., Rowley C. W., Colonius T., McKeon B. J., Schmidt O. T., Gordeyev S., Theofilis V., Ukeiley L. S., Modal Analysis of Fluid Flows: An Overview, *AIAA J.* **55**(12): 4013-4041, 2017.
[4] Taira K., Hemati M. S., Brunton S. L., Sun Y., Duraisamy K., Bagheri S., Dawson S. T. M., Yeh C.-A., Modal Analysis of Fluid Flows: Applications and Outlook, *AIAA J.* available online, 2019.
[5] McKeon B. J., Sharma A. S., A Critical-Layer Framework for Turbulent Pipe Flow, *J. Fluid Mech.* **658**: 336-382, 2010.
[6] Yeh C.-A., Taira K., Resolvent-Analysis-Based Design of Airfoil Separation Control, *J. Fluid Mech.* **867**: 572-610, 2019.
[7] Jeun J., Nichols J. W., Jovanović M. R., Input-Output Analysis of High-Speed Axisymmetric Isothermal Jet Noise, *Phys. Fluids* **28**: 047101, 2016.
[8] Yoimi K., Yeh C.-A., Taira K., Kameda M., Resolvent Analysis on the Origin of Two-Dimensional Transonic Buffet, *J. Fluid Mech.* **885**: R1, 2020.
[9] Halko N., Martinsson P. G., Tropp J. A., Finding Structure with Randomness: Probabilistic Algorithms for Constructing Approximate Matrix Decompositions, *SIAM Rev.*, **53**(2): 217-288, 2011.
[10] Moarref R., Sharma A. S., Tropp J. A., McKeon B. J., Model-Based Scaling of the Streamwise Energy Density in High-Reynolds-Number Turbulent Channels *J. Fluid Mech.* **734**: 275–316, 2013.
[11] Ribeiro J. H. M.,Yeh C.-A., Taira K., Randomized Resolvent Analysis, *Phys. Rev. Fluids*, in review 2019.
[12] Yeh C.-A., Benton S. I., Taira K., Garmann D. J., Resolvent Analysis of a Laminar Airfoil Separation Bubble at $Re = 500,000$, *Phys. Rev. Fluids*, in review 2020.

LOW-COMPLEXITY MODELS FOR PASSIVE CONTROL OF WALL TURBULENCE

Andrew Chavarin, Christoph Efstathiou, Shilpa Vijay, and Mitul Luhar*
Department of Aerospace and Mechanical Engineering, University of Southern California, Los Angeles, USA

Summary The use of riblets is one of the most effective ways to reduce skin friction in wall-bounded turbulent flows. Recent simulations for anisotropic porous materials show promise as well. However, the design space for such functional surfaces is vast. We present a low-complexity modeling framework that enables efficient exploration of this design space for skin friction reduction. This framework uses a gain-based decomposition of the Navier-Stokes equations to identify a single mode that serves as a surrogate for the energetic near-wall cycle. Comparison against prior results shows that the gain of this one mode is a good predictor of performance for both riblets and porous materials. The framework is also able to predict when spanwise-coherent structures that lead to performance deterioration emerge over such surfaces. These developments provide a pathway for future optimization efforts.

INTRODUCTION

A great amount of effort has been expended on the development of passive skin friction reduction techniques for wall-bounded turbulent flows over the past few decades. Experiments and simulations have shown that streamwise-aligned *riblets* can yield as much as 10% skin friction reduction in wall-bounded flows [1, 5]. More recent efforts suggest that porous substrates with streamwise permeability (K_x) that is higher than the spanwise (K_z) or wall-normal permeability (K_y) could be even more effective than riblets. Direct numerical simulation (DNS) results show reductions in skin friction of up to 25% over idealized anisotropic permeable substrates [4]. It is generally accepted that the drag-reducing ability of riblets and permeable substrates arises from their anisotropy [6]. The mean flow is unimpeded in the riblet grooves and within streamwise-preferential permeable materials. However, turbulent cross-flows are blocked and displaced further from the wall. This weakens the quasi-streamwise vortices associated with the near-wall (NW) cycle and reduces turbulent momentum transfer in the wall-normal direction. Simple physical and theoretical arguments show that the initial decrease in skin friction over riblets and permeable materials depends on the difference between the effective slip length felt by the streamwise mean flow, l_x, and the spanwise turbulent cross-flow, l_z [6, 4]. For riblets l_x and l_z are determined by the shape and size. For porous materials, these slip lengths depend on the corresponding permeabilities, $l_x \sim \sqrt{K_x}$ and $l_z \sim \sqrt{K_z}$, though substrate thickness can also play a role. Skin friction reduction increases initially with increasing $(l_x - l_z)$. However, performance deteriorates beyond a certain riblet size or threshold permeability. For riblets, early studies attributed this deterioration of performance to the NW streamwise vortices lodging within the riblet grooves. Recent efforts suggest that a Kelvin-Helmholtz instability also plays a role in driving this deterioration of performance over riblets and porous materials [5, 3, 4].

In this talk, we present a unified low-complexity modeling framework that can (i) account for both riblet surfaces and anisotropic porous materials, (ii) determine whether riblets of specified geometry or porous materials with known permeability are likely to weaken or strengthen the NW cycle, and (iii) predict when Kelvin-Helmholtz type spanwise rollers emerge over such complex surfaces. These models require minimal computation, i.e., they can be implemented on standard laptop or workstation computers. As advances in manufacturing technology enable the development of increasingly complex functional materials and surfaces, such low-cost models can be very useful design tools.

MODELING FRAMEWORK

The low-complexity modeling framework is grounded in resolvent analysis [8]. For wall-bounded turbulent flows, the resolvent formulation interprets the Fourier-transformed Navier-Stokes equations as a forcing-response system. The nonlinear convective terms are interpreted as the forcing that acts on the remaining linear terms to generate a velocity and pressure response. For each wavenumber-frequency combination $\mathbf{k} = (\kappa_x, \kappa_z, \omega)$, a gain-based singular value decomposition of the forcing-response transfer function—the resolvent operator—yields a set of velocity and pressure response modes (singular vectors) that are ranked based on their forcing-response gain (singular values). These response modes, termed *resolvent modes*, are flow structures with streamwise and spanwise wavelength $\lambda_x = 2\pi/\kappa_x$ and $\lambda_z = 2\pi/\kappa_z$, respectively, traveling at speed $c = \omega/\kappa_x$. Previous work shows that the highest-gain (rank-1) resolvent modes obtained at specific $\mathbf{k}$ combinations serve as useful surrogates for energetic structures such as the NW cycle [7].

To account for the presence of riblets in this framework, we use a volume penalization method [3]. The presence of anisotropic permeable substrates is incorporated by extending the resolvent formulation to the volume-averaged Navier-Stokes equations, which include a generalized version of Darcy's law for flow through porous media [2]. The permeable medium is characterized by the porosity ϵ and a permeability tensor $\mathbf{K}$. Resolvent analysis proceeds as follows. First, the volume penalized or volume-averaged governing equations are Fourier-transformed and expressed as $[\mathbf{u_k}, p_\mathbf{k}]^T = H_\mathbf{k}\mathbf{f_k}$. Here, $\mathbf{u_k}$ and $p_\mathbf{k}$ denote the velocity and pressure fields, the forcing $\mathbf{f_k}$ represents the nonlinear terms, and $H_\mathbf{k}$ is the resolvent operator representing the linear forcing-response dynamics. Next, a singular value decomposition of the discretized resolvent operator is used to identify high-gain forcing and response modes as well as the forcing-response gain (singular values, $\sigma_\mathbf{k}$). Here, we focus on resolvent modes resembling the NW cycle (i.e., with $\mathbf{k}$ corresponding to $\lambda_x^+ = 10^3$, $\lambda_z^+ = 10^2$, and $c^+ = 10$) and spanwise-constant structures similar to Kelvin-Helmholtz vortices.

*Corresponding author. E-mail: luhar@usc.edu.

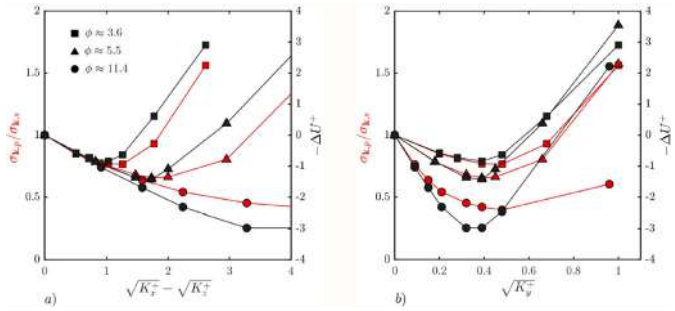

Figure 1: Comparison of the change in singular values for modes resembling the NW cycle (red) with the drag reduction observed in DNS (black; from [4]) over anisotropic porous materials. Symbols denote substrates with different anisotropy ratios, $\phi = K_x/K_z$.

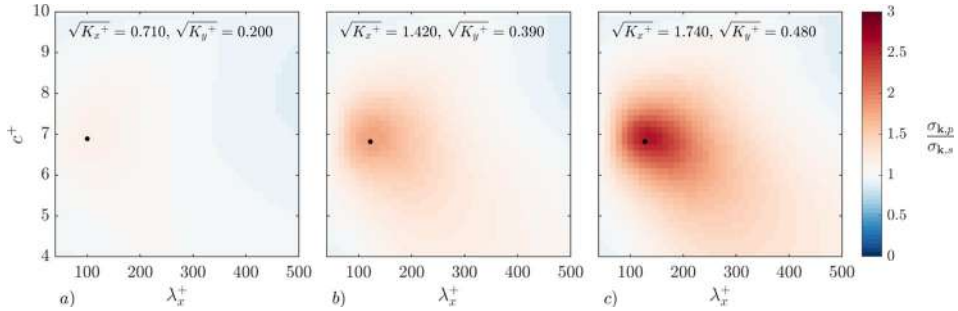

Figure 2: Change in singular values for spanwise-constant modes ($\kappa_z = 0$) of varying streamwise wavelength and mode speed. Wall-normal permeability $K_y(= K_z)$ increases from (a)-(c) but the anisotropy ratio is fixed, $\phi = K_x/K_z \approx 3.6$.

SAMPLE RESULTS AND DISCUSSION

The predictive power of the modeling framework is showcased by the sample results shown in Figs. 1-2 for flow over anisotropic porous materials with permeability $\mathbf{K} = \mathrm{diag}(K_x, K_y, K_z)$, where $K_y = K_z$. Fig. 1(a) shows that the forcing-response gain for the NW resolvent modes is a very good predictor of the friction reduction observed in DNS [4]. Material properties that lead to a suppression in gain relative to the smooth wall case ($\sigma_{\mathbf{k},p}/\sigma_{\mathbf{k},s} < 1$) yield an outward shift in the mean velocity profile ($-\Delta U^+ < 0$) and, hence, drag reduction in DNS. Further, the initial decrease in singular values is linearly proportional to $\sqrt{K_x} - \sqrt{K_z}$ across all cases, which is consistent with the slip length models proposed previously. Fig. 1(b) shows that the gain for the NW resolvent mode alone does not predict the exact conditions in which performance deteriorates. DNS data show that performance deteriorates as the wall-normal permeability increases beyond $\sqrt{K_y}^+ \approx 0.35$, irrespective of K_x and K_z. In DNS, this coincides with the emergence of spanwise-coherent rollers that resemble Kelvin-Helmholtz vortices and have a streamwise length scale of about 150 viscous units. Fig. 2 shows that the resolvent framework is able to predict the emergence of such structures as well. A region of high amplification is observed for spanwise-constant resolvent modes with $\lambda_x^+ \approx 100 - 150$ for the materials with $\sqrt{K_y}^+ \geq 0.39$. Results obtained for riblets are similarly encouraging [3].

The full presentation will include results for both riblets and anisotropic porous materials. Additional evaluation of model predictions against DNS results and a discussion of the predicted changes in flow structure will be provided as well. Time permitting, the presentation will also cover preliminary efforts on model-based geometry optimization and laboratory testing of such designed functional surfaces.

The authors thank Drs. Garcia-Mayoral and Gomez-de-Segura for sharing their DNS data. This work was supported by the US Air Force Office of Scientific Research under grants FA 9550-17-1-0142 and FA 9550-19-1-7027.

References

[1] Bechert, D., et al. Experiments on drag-reducing surfaces and their optimization with an adjustable geometry. *J. Fluid Mech.* **338**: 59-87, 1997.
[2] Breugem, W., B. Boersma, and R. Uittenbogaard. The influence of wall permeability on turbulent channel flow. *J. Fluid Mech.* **562**: 35-72, 2006.
[3] Chavarin, A., M. Luhar. Resolvent analysis for turbulent channel flow with riblets. *AIAA J.*, *to appear*, 2020.
[4] Gomez-de-Segura, G., R. Garcia-Mayoral. Turbulent drag reduction by anisotropic permeable substrates–analysis and direct numerical simulations. *J. Fluid Mech.* **875**: 124-172, 2019.
[5] Garcia-Mayoral, R., J. Jimenez. Hydrodynamic stability and breakdown of the viscous regime over riblets. *J. Fluid Mech.* **678**: 317-347, 2011.
[6] Luchini, P., F. Manzo, A. Pozzi. Resistance of a grooved surface to parallel flow and cross-flow. *J. Fluid Mech.* **228**: 87-109, 1991.
[7] Luhar, M., A. Sharma, B. McKeon. Opposition control within the resolvent analysis framework. *J. Fluid Mech.* **749**: 597-626, 2014.
[8] McKeon, B., A. Sharma. A critical-layer framework for turbulent pipe flow. *J. Fluid Mech.* **658**: 336-382, 2010.

RESTRICTED NONLINEAR MODELING FOR HIGH REYNOLDS NUMBER WALL-BOUNDED TURBULENCE

Dennice F. Gayme* [1] and Benjamin A. Minnick[1]
[1] Department of Mechanical Engineering, Johns Hopkins University, Baltimore, Maryland, USA

Summary The restricted nonlinear (RNL) model provides a reduced order representation of low to moderate Reynolds number wall-bounded turbulent flows that accurately predicts low-order statistics, spanwise energy spectra, and turbulent kinetic energy budgets at greatly reduced computational costs. Here, we introduce the additional large-scales required to capture higher Reynolds number behavior through an augmented RNL (ARNL) model. This flow representation permits additional nonlinear interactions in a manner consistent with generalized quasilinear (GQL) models, while enforcing the dynamical restrictions that maintain the computational benefits of the RNL framework. The ARNL model thus represents a hybrid approach that we show to be promising in representing wall-bounded turbulence at Reynolds numbers as high as $Re_\tau = 5200$.

BACKGROUND

The well-documented prevalence and importance of coherent motions in wall-bounded turbulent flows, see e.g. [1], has motivated the use of reduced order models to both isolate and interrogate the flow physics, see e.g. [2, 3]. The restricted nonlinear (RNL) model is one such approach that decomposes the flow field into large-scale $\mathbf{U}(y, z, t)$ streamwise constant (mean) dynamics and perturbations defined about that mean $\mathbf{u}(x, y, z, t)$. Order reduction is achieved through a dynamical restriction of its nonlinear interactions to those of the streamwise constant mean flow dynamics and interactions between perturbations that contribute to the mean. The model is parametrized by limiting the resulting linear perturbation equations to a small set of streamwise varying wavenumbers (nonzero streamwise Fourier coefficients $k_x \neq 0$) that maximize dissipation in the outer layer. This model reproduces low-order statistics, spanwise energy spectra, and turbulent kinetic energy budgets at $Re_\tau = 180$, even when restricted to a single nonzero streamwise mode interacting with the mean flow [2]. However, the RNL dynamics supported by only the small-scale streamwise varying modes associated with peak outer-layer dissipation are insufficient to capture the scale separation that emerges with increasing Reynolds number.

A similar reduction in accuracy has been seen with increasing flow complexity in closely related quasilinear (QL) models that are popular in the atmospheric sciences, see e.g. [4]. QL models employ a horizontally averaged large-scale and neglect the corresponding perturbation-perturbation nonlinearity, but do not parametrize the small-scale perturbations as in the RNL formulation discussed above. The fidelity of these models has been improved through the generalized QL (GQL) model which employs a spectral filter to define the 'mean' or large-scale dynamics rather than averaging, thereby allowing nonlinear interactions between non-zero streamwise and spanwise modes modes [5]. However, the improved predictions of the flow statistics are achieved at the cost of increasing computational expense due to the resulting energy scattering introduced through nonlinear modal interactions.

Here, we take a hybrid approach. The mean flow field is expanded to allow select non-zero modes to interact nonlinearly in the spirit of the GQL model, but the dynamics are limited to a small number of streamwise modes, saving computational resources as in the RNL model. We simulate these augmented (ARNL) dynamics supported by three non-zero streamwise modes, one scaling with the half-channel height that is treated as a large-scale, and two small-scale modes associated with the outer-layer peak of the surrogate dissipation spectra, see Figure 1. Our results demonstrate that the ARNL model reproduces low-order statistics and structural features of a channel flow at Reynolds numbers as high as $Re_\tau = 5200$, thereby increasing the range of applicability of the RNL modeling paradigm by a factor of 10.

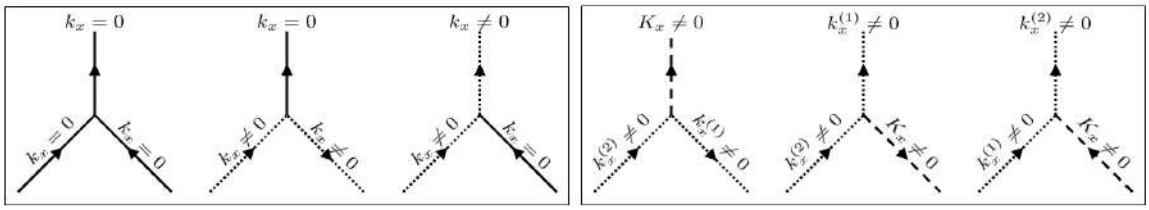

Figure 1: The nonlinear interactions between the streamwise varying ($k_x \neq 0$) modes retained in the RNL (left) and ARNL (both panels). The zero wavenumber ($k_x = 0$) is represented by the solid lines, small non-zero wavenumbers by dashed lines, and large non-zero wavenumbers by dotted lines. The wavenumbers used in the ARNL (right panel) triads are related by $k_x^{(2)} - k_x^{(1)} = K_x$, where K_x is a large-scale non-zero mode and $k_x^{(1)}, k_x^{(2)}$ are small-scale modes. In the ARNL convolution, K_x, $k_x^{(1)}$, and $k_x^{(2)}$ all interact with the zero wavenumber according to the left panel triads.

*Corresponding author. E-mail: dennice@jhu.edu

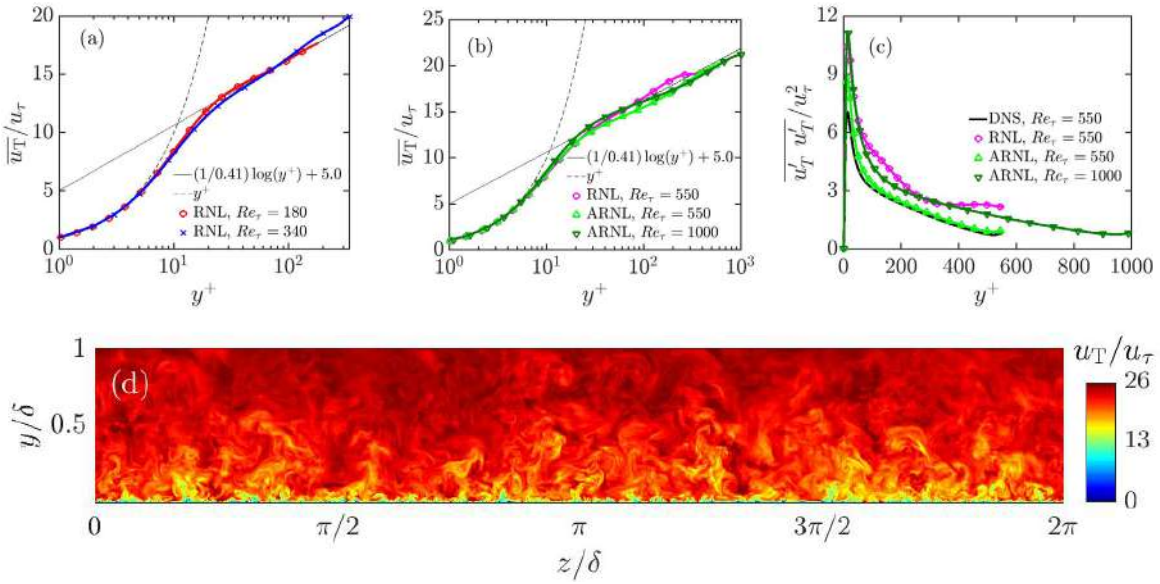

Figure 2: (a) RNL mean velocity profiles at $Re_\tau = 180$ ($k_x\delta = 0, 7$) and $Re_\tau = 340$ ($k_x\delta = 0, 14$). (b) Mean velocity and (c) streamwise Reynolds stress profiles from RNL simulations at $Re_\tau = 550$ ($k_x\delta = 0, 23$), and ARNL simulations at $Re_\tau = 550$ ($k_x\delta = 0, 7, 19.5, 26.5$), and $Re_\tau = 1000$ ($k_x\delta = 0, 7, 38.5, 45.5$). (d) An ARNL cross-plane snapshot at $Re_\tau = 5200$ ($k_x\delta = 0, 7, 214.5, 221.5$).

RESULTS

We consider a half-channel flow configuration of size $[L_x, L_y, L_z]/\delta = [4\pi, 1, 2\pi]$ with no-slip and stress-free boundary conditions imposed on the bottom ($y = 0$) and top ($y = \delta$) walls respectively, and periodic boundary conditions in the streamwise and spanwise directions. The RNL equations are solved using a modified version of the open source code LESGO (https://lesgo.me.jhu.edu) where wall-normal derivatives are discretized using second-order central finite differencing, and Fourier transforms de-aliased by the 3/2 rule are applied in the streamwise and spanwise directions. The temporal derivative is treated using the second-order Adams-Bashforth method.

The restriction placed on the RNL and ARNL dynamics significantly reduces perturbation-perturbation interactions between streamwise modes as shown in Figure 1. These limited interactions naturally permit simulating the governing equations in the streamwise Fourier space (k_x, y, z, t) where the simplified nonlinear term is treated as a convolution rather than performing a transformation to physical space, as is traditionally done. This framework is not only computationally efficient but also allows prescribes structures, represented as Fourier modes, to be isolated. In this manner, the dynamics of streamwise structures and their interactions can be readily studied, see [6] for further details of this implementation.

Figure 2 demonstrates the accuracy of the RNL mean velocity profiles at $Re_\tau = 180$ and 340 in panel (a), while panel (b) shows the decreased fidelity of the model at $Re_\tau = 550$. Panels (b) and (c) indicate that adding the energetic streamwise mode associated with the half channel height into the large-scale mean dynamics of the ARNL improves the low-order statistics at this Reynolds number and that they continue to be well represented at $Re_\tau = 1000$. Panel (d) provides a cross-plane snapshot of the instantaneous streamwise velocity of ARNL turbulence at $Re_\tau = 5200$, where the scale interactions typical of high Reynolds number wall-bounded turbulence are shown to be captured in this reduced order model. The computational savings of the ARNL simulations versus direct numerical simulations (DNS) represent a speed up by a factor of 26 at $Re_\tau = 550$, which increases to 200 at $Re_\tau = 5200$.

CONCLUSIONS

The ARNL modeling framework reproduces low-order statistics and structural features of high Reynolds number wall-bounded turbulence at vastly reduced computational cost over DNS. Ongoing work to better understand the required range of scale interactions will determine the full potential of the ARNL investigations of high Reynolds number flows.

This work is supported by ONR (N000141712649) and NSF (CBET 1652244).

References

[1] Smits A. J., McKeon B. J., & Marusic, I. High-Reynolds number wall turbulence. *Annual Rev. Fluid Mech.* **43** (1), 353-375, 2011.
[2] Gayme D. F. & Minnick B. A. Coherent structure-based approach to modeling wall turbulence. *Phys. Rev. Fluids* **4**, 110505, 2019.
[3] McKeon B. J., The engine behind (wall) turbulence: perspectives on scale interactions. *J. Fluid Mech.* **817**, P1, 2017.
[4] Farrell B. F. & Ioannou P. Structure and spacing of jets in barotropic turbulence. *J. Atmospheric Sciences* **64**, 3652-3665, 2007.
[5] Marston J. B., Chini G. P., & Tobias S. M. Generalized quasilinear approximation: Application to zonal jets. *Phys. Rev. Lett.* **116**, 214501, 2016.
[6] Bretheim J. U., Meneveau C., & Gayme D. F. A restricted nonlinear large eddy simulation model for high Reynolds number flows *J. Turbul.* **19**, 141-166, 2018.

EXPERIMENTS AND MODELLING OF SYNTHETIC JETS IN CROSS-FLOW

Bharathram Ganapathisubramani * [1], Girish Jankee[1], and Tim Berk[1]
[1] University of Southampton, UK

Summary The interaction between a synthetic jet actuator and a turbulent boundary layer is critically important in a variety of flow control applications. The ability to predict the trajectory of the jet in the presence of the cross flow will enable us to design flow control techniques for efficient and targeted usage of such actuators. In this investigation, we examine the effects of a synthetic jet issued into a crossflow from rectangular orifices through PIV and hot-wire measurements. Experiments are carried out over a large range of Reynolds numbers, jet exit geometries, frequencies and velocity ratios. An assessment of the trajectories obtained from experimental data results in identification of relevant non-dimensional numbers, the velocity ratio, momentum ratio and the Strouhal number, that dictate the behaviour of this interaction. There trajectories can be modelled using data-driven vortex models where the strength of the vortices are derived from data.

INTRODUCTION

Jets in crossflow have attracted considerable interest over the past decades with singular emphasis on flow control applications as they involve interaction of a jet with an incoming boundary layer. Knowledge of the jet trajectory is of paramount importance as it describes the depth of penetration as well as the streamwise range over which the actuator can be considered as effective. Jet trajectory can be computed using various parameters which include the positions of local velocity maxima, local scalar maxima, vorticity maxima or time-averaged streamline originating at the jet exit [1]. In this study, we focus on synthetic jet actuators and compute the trajectory based on the location of maximum velocity deficit.

The trajectory is commonly described using a power law:

$$\frac{y/D}{g(...)} = B(\frac{x/D}{g(...)})^n, \tag{1}$$

where y is the wall-normal trajectory (m), x is the streamwise location (m), D is the corresponding orifice dimension (m), $g(...)$ represents non-dimensional scaling factors and B and n are constants.

For steady jets, various scalings for $g(...)$ have been put forward and demonstrate that the jet trajectory depends on the velocity ratio and the diameter of the orifice [2, 3, 4]. However, [1] provides evidence that rd is not sufficient to scale such a wide range of data. Considerable variations in jet trajectories were observed, even for similar velocity ratios. This highlights that the velocity ratio and the orifice dimensions are not sufficient to completely describe the trajectory. Rather, it is important to account for the distribution of momentum in the jet and in the incoming boundary layer [5]. Additionally, synthetic jets are characterised by the forcing frequency which can take the form of a Strouhal number. However, there exists a certain level of ambiguity concerning the exact form of this Strouhal number. It is hypothesised that the Strouhal number could be either a function of the outer units of the boundary layer, the inner units of the boundary layer or the passing frequency of the crossflow over the jet [6]. In this study, we define a momentum ratio which uses the orifice dimensions and the momentum thickness of the boundary layer:

$$\mu = \frac{\rho \bar{U}^2 dl}{\rho U_\infty^2 d\theta} = r^2 \frac{l}{\theta} \tag{2}$$

where $\bar{U}$ is the jet exit velocity, U_∞ is the freestream velocity, l is the length of the orifice, d is the width of the orifice and θ is the momentum thickness of the boundary layer. In this study is to identify the parameters considered important for describing the synthetic jet trajectory in crossflow and determine the appropriate scaling factors. The investigation also considers constraints associated with the use of a single scaling law to describe the complete trajectory. These involve the interaction of vortical structures and the near field and far field regions of the flowfield. Finally, we examine the utility of vortex-based models in determining the trajectory of these flows with information about the strength/size of the vortices determined from experimental measurements.

EXPERIMENTAL SETUP

The study consisted of 2 experiments. High Reynolds number experiments were performed in the high-Reynolds-number boundary layer wind tunnel (HRNBLWT) at the University of Melbourne. A rectangular orifice with an aspect ratio of 13 was used and the actuator was operated over a range of frequencies between 60 and 400 Hz while the freestream velocity was varied between 10 and 25 m/s. Hot wire anemometry was used for velocity measurements from which the jet trajectories were derived. Experiments at lower Reynolds numbers were carried out in a 3 x 2 ft suction wind tunnel facility at the University of Southampton. Orifices with aspect ratios 3, 6 and 12 were tested between 100 and 600 Hz and velocity ratios of 0.25, 0.5 and 1.0. The freestream velocity was kept constant at 8 m/s. Planar- and stereo-PIV measurements were performed to capture the flowfield.

*Corresponding author. E-mail: G.Bharath@soton.ac.uk

RESULTS

Initial results demonstrated that the trajectory of a synthetic jet cannot be determined using a single scaling law. Rather, it is possible to categorise the flowfield of a synthetic jet and obtain appropriate scaling laws for each class by considering constraints such as vortex interaction, the near field behaviour, dominated by the synthetic jet or the far field behaviour which is defined by the crossflow properties.

There has been numerous attempts to define what constitutes the near-field or the far-field regions. Although [4] suggested a far-field definition of $x/r^2D > 0.3$, the threshold between the near-field and far-field behaviour still remains ambiguous. [7] defined a far field limited by $x \gg \sqrt{\pi D^2 4}$. However, application of this definition to the current datasets led to inconclusive results and a more adequate definition was needed, specifically for synthetic jet actuators. Using the gradient of the trajectory and the convergence of the fitting coefficients, the near field is found to occur when the jet is at an angle greater than 17° and the far-field region is defined by a jet angle less than 14° with the transition region lying in between. The following equation was subsequently derived for the streamwise location corresponding to the far-field:

$$\frac{x_{thresh}}{\delta} = 1.75\left(\frac{U_j}{U_\infty}\right)^{0.5}\left(\frac{fl}{U_j}\right)^{0.1}\left(\frac{l}{\delta}\right)^{0.4} \tag{3}$$

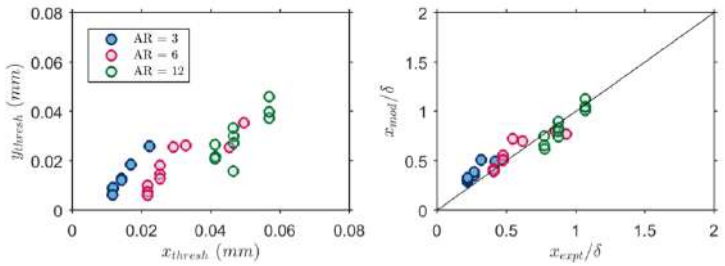

Figure 1: Left subplot shows the streamwise threshold values delimiting the far-field region for all the test cases. Right subplot compares the normalised experimental threshold values against the values derived from the model.

Application of the above-defined constraints leads to the emergence of four categories of synthetic jet behaviour, governed by different combinations of Strouhal numbers, velocity ratios and momentum ratios. In the presence of vortex interaction, in the near-field, the only parameters that are important are the velocity ratio and the jet-based Strouhal number ($St = fl/U_j$). In the far-field, together with the momentum ratio, it is observed that the Strouhal number now depends on the boundary layer thickness and the freestream velocity ($St = f\delta/U_\infty$). When there is no vortex interaction, the near field depends only on the velocity ratio and the crossflow-based Strouhal number while the far field trajectory is determined by a combination of the velocity ratio and the momentum ratio with the Strouhal number not significant. The talk will cover these and other aspects in greater detail.

References

[1] K. Mahesh, "The Interaction of Jets with Crossflow," *Annu. Rev. Fluid Mech.*, vol. 45, no. 1, pp. 379–407, jan 2013.

[2] J. F. Keffer and W. D. Baines, "The round turbulent jet in a cross-wind," *J. Fluid Mech.*, vol. 15, no. 04, p. 481, apr 1963. [Online]. Available: http://www.journals.cambridge.org/abstract_S0022112063000409

[3] A. R. Karagozian, "An analytical model for the vorticity associated with a transverse jet," *AIAA J.*, vol. 24, no. 3, pp. 429–436, mar 1986. [Online]. Available: http://arc.aiaa.org/doi/10.2514/3.9285

[4] S. H. Smith and M. G. Mungal, "Mixing, structure and scaling of the jet in crossflow," *J. Fluid Mech.*, vol. 357, p. S0022112097007891, feb 1998.

[5] S. Muppidi and K. Mahesh, "Study of trajectories of jets in crossflow using direct numerical simulations," *J. Fluid Mech.*, vol. 530, pp. 81–100, may 2005.

[6] T. Berk, N. Hutchins, I. Marusic, and B. Ganapathisubramani, "Trajectory of a synthetic jet issuing into high-Reynolds-number turbulent boundary layers," *J. Fluid Mech.*, vol. 856, pp. 531–551, dec 2018.

[7] J. E. Broadwell and R. E. Breidenthal, "Structure and mixing of a transverse jet in incompressible flow," *J. Fluid Mech.*, vol. 148, no. -1, p. 405, nov 1984. [Online]. Available: http://www.journals.cambridge.org/abstract_S0022112084002408

[8] H. Johari, "Scaling of Fully Pulsed Jets in Crossflow," *AIAA J.*, vol. 44, no. 11, pp. 2719–2725, nov 2006. [Online]. Available: http://arc.aiaa.org/doi/10.2514/1.18929

NETWORK-BASED RESOLVENT ANALYSIS FOR MODIFICATION OF ISOTROPIC TURBULENCE

Chi-An Yeh*[1], Muralikrishnan Gopalakrishnan Meena[1], and Kunihiko Taira[1]
[1] Department of Mechanical and Aerospace Engineering, University of California, Los Angeles, U.S.A.

Summary We present a network-based resolvent analysis that identifies the key dynamical paths along which perturbations amplify in a time-evolving isotropic turbulent flow. This formulation is built upon the Katz centrality, which reveals the flow structures that can effectively spread perturbations over a time-evolving network of vortical elements. Moreover, due to the resolvent form of the Katz function, we take the SVD of the resulting communicability matrix, complementing the resolvent analysis for fluid flows. The left-singular vector, or broadcast mode, gives insights into the hot spots from which perturbations can be effectively spread over the entire fluid-flow network when it evolves in time. This broadcasting structure infers that the opposite-sign vortex pairs, acting like local 'jets,' are the important structures in spreading perturbations. We observe that the forcing based on the broadcasting mode obtained from the longer time-horizon is more effective in modifying the evolution of the isotropic turbulence than that from the shorter time-horizon.

INTRODUCTION

Identifying structures that are significant in changing the dynamical evolution of a turbulent flow has been an important yet challenging task in fluid mechanics. A recent study by Jiménez [1] aimed to identify these structures as sub-volumes in 2D isotropic turbulence by blanking out sets of sub-volumes and tracking the change of the flow field evolution from that of the unperturbed flow. The sub-volumes that are flagged as significant structures contain strong vortices, rendering high levels of modification in turbulence evolution when these sub-volumes are blanked out.

Our goal is to identify these structures in 2D isotropic turbulence [2] using the modern toolsets of resolvent and network analyses. Resolvent analysis for fluid flows can be traced back to Trefethen et al. [3] and has been extended to turbulent flows by McKeon & Sharma [4]. Network analysis has demonstrated its strength in providing insights into the interactions amongst flow structures [2, 5, 6]. In this study, we seek a formulation that combines these two toolsets to identify the significant structures for modifying time-evolving 2D isotropic turbulence.

APPROACH

Network-based modeling of vortical interactions

We model the interaction dynamics of isotropic turbulence by a time-evolving network of vortical elements. In the turbulent flow field, the vorticity at each Eulerian grid point is treated as a vortical element, which constitutes a vertex of the network. The interactions between the vertices, or vortical elements, form the edges of the network. According to these interactions we construct the adjacency matrix $\boldsymbol{A} \in \mathbb{R}^{n\times n}$, where n is the number of Eulerian grid points and each edge-strength element a_{ij} in $\boldsymbol{A}$ quantifies vertex j's influence on vertex i.

The edge strength is defined in two manners. The first one is based on the induced velocity magnitude at i by j according to Biot–Savart's law and defines $a_{ij} = \omega_j \Delta s/2\pi|\boldsymbol{x}_i - \boldsymbol{x}_j|$, where Δs is the area of the cell. The second definition considers the perturbation perceived at $\boldsymbol{x}_i$ when a spatial vorticity pulse is introduced at $\boldsymbol{x}_j$ as $a_{ij} = |\,[\,\mathcal{N}(\omega + \epsilon\delta(\boldsymbol{x}_j)) - \mathcal{N}(\omega)\,]_i\,|/\epsilon$, according to the right-hand-side of the vorticity transport equation, $\partial_t\omega = \mathcal{N}(\omega)$. In what follows, we refer to the former as B–S (Biot–Savart) network and the latter as the N–S (Navier–Stokes) network. With a snapshot of vorticity field at time t_k, the adjacency matrices $\boldsymbol{A}_k$ can be determined using both definitions.

Katz centrality and network-based resolvent analysis

Network centralities deduced from adjacency matrices give valuable insights into important vertices to seed and broadcast information over the entire network. One of the centrality measures is called the Katz centrality [7]. This centrality can be viewed as a Markov chain process where a distributed piece of information, $\boldsymbol{f} \in \mathbb{R}^n$, is transferred through the vertices of a network by infinite amount of walks. Along each walk, the intensity of the information transferred from vertex j to i is characterized by the edge strength a_{ij} and a walk-downweighting parameter α as $\boldsymbol{q} = (\boldsymbol{I} + \alpha\boldsymbol{A} + \alpha^2\boldsymbol{A}^2 + \cdots)\boldsymbol{f}$. For the fluid-flow network, the information $\boldsymbol{f}$ can be interpreted as a forcing to be spread and amplified globally. Moreover, when α is chosen such that $\alpha < 1/\rho(\boldsymbol{A})$, where $\rho(\boldsymbol{A})$ is the spectral radius of $\boldsymbol{A}$, the infinite series converges as

$$(\boldsymbol{I} + \alpha\boldsymbol{A} + \alpha^2\boldsymbol{A}^2 + \cdots) = (\boldsymbol{I} - \alpha\boldsymbol{A})^{-1}. \tag{1}$$

With this formula, the traditional Katz broadcasting centrality is computed as $b_j = \Sigma_i(\boldsymbol{I} - \alpha\boldsymbol{A})^{-1}$, which quantifies vertex j's capability of broadcasting information to all other vertices in the network.

We note that the Katz function $(\boldsymbol{I} - \alpha\boldsymbol{A})^{-1}$ is in the form of a resolvent matrix of $\boldsymbol{A}$. It is also featured in the input–output process between $\boldsymbol{q}$ and $\boldsymbol{f}$. Therefore, instead of performing the column-sum to compute the broadcasting centrality, we follow the resolvent analysis in fluid flows [3, 4] and take the SVD of the Katz function as

$$(\boldsymbol{I} - \alpha\boldsymbol{A})^{-1} = \boldsymbol{Q}\boldsymbol{\Sigma}\boldsymbol{B}, \tag{2}$$

where we refer the leading right-singular vector $\boldsymbol{b}_1$ as the broadcasting mode. The broadcasting mode also complements the concept of forcing mode in resolvent analysis, as it identifies the most influential vertices, or sensitive regions, that can effectively spread perturbations over the vortical network.

*cayeh@seas.ucla.edu

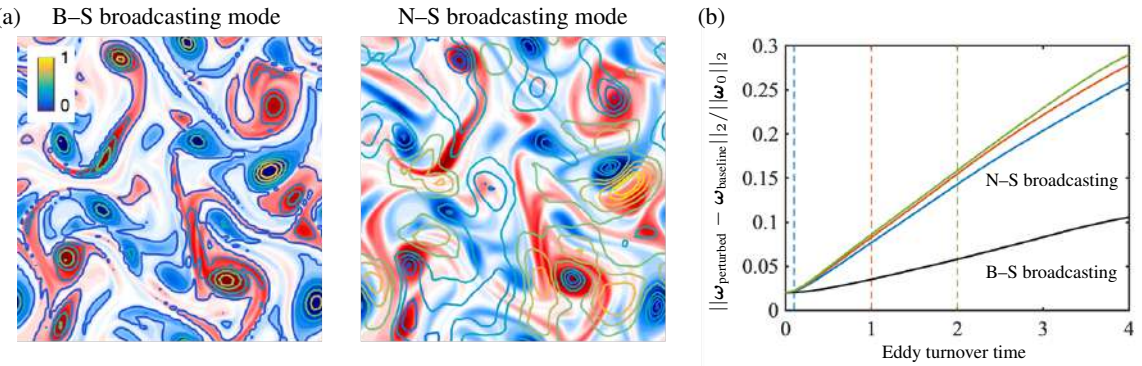

Figure 1: (a) B–S and N–S broadcasting modes (green-yellow contour lines) over the instantaneous vorticity field (blue-red solid contour). (b) Flow modifications using perturbations based on B–S and N–S broadcasting modes. For N–S network, three time-horizons, marked by the same-colored dashed lines, are examined in their influences on the flow modification.

Time-evolving network model

We aim to extract the broadcasting mode that further accounts for the time evolution of the vortical network. In a time-evolving network, the transfer of information over vertices can either kinematically occur in a time-frozen $\boldsymbol{A}$ or due to the time evolving nature of $\boldsymbol{A}$. This propagation of information over the time horizon $t \in [t_0, t_k]$ can be described as

$$\boldsymbol{q}(t_k) = \underbrace{(\boldsymbol{I} + \alpha \boldsymbol{A}_k + \alpha^2 \boldsymbol{A}_k^2 + \cdots)}_{t=t_k} \cdots \underbrace{(\boldsymbol{I} + \alpha \boldsymbol{A}_1 + \alpha^2 \boldsymbol{A}_1^2 + \cdots)}_{t=t_1} \underbrace{(\boldsymbol{I} + \alpha \boldsymbol{A}_0 + \alpha^2 \boldsymbol{A}_0^2 + \cdots)}_{t=t_0} \boldsymbol{f}(t_0), \tag{3}$$

where the identity matrix allows the information to 'stay' at the same vertex at a certain time instant [8]. Note that each infinite series can be further reduced to the associated Katz form. Similar to the walk-downweighting parameter α, we consider the formulation by Grindrod & Higham [9] where an age-downweighting parameter γ is introduced in

$$\boldsymbol{S}_{k+1} = \left[\boldsymbol{I} + e^{-\gamma \Delta t}(\boldsymbol{S}_k - \boldsymbol{I})\right](\boldsymbol{I} - \alpha \boldsymbol{A}_{k+1})^{-\Delta t} \tag{4}$$

to account for the decaying intensity of the information due to its aging in time. The communicability matrix $\boldsymbol{S}_k$ can be recurrently computed over the time horizon of $t \in [t_0, t_k]$. By taking the SVD of $\boldsymbol{S}_k = \boldsymbol{Q}\boldsymbol{\Sigma}\boldsymbol{B}$, we refer the leading right-singular vector $\boldsymbol{b}_1$ as the broadcasting mode for the time-evolving vortical network .

RESULTS

We show the broadcasting modes for the B–S and N–S networks determined for an instantaneous vorticity field in figure 1 (a). The B–S broadcasting mode suggests that the vortex cores, featured by high vorticity, are the regions of high broadcasting efficiency (yellow contour lines) in the 2D turbulence. This observation aligns with that made by Jiménez [1]. The N–S broadcasting mode tells an entirely different story. The volumes of high broadcasting efficiency are found to occupy the regions between opposite-sign vortex pairs. These vortex pairs locally build up highly oriented shear layers and act like local 'jets', which are known to be receptive to perturbations. Meanwhile, the vortex cores are the regions of the lowest broadcasting efficiency.

In the time-evolving network model, we choose the walk- and age-downweighting parameters $\alpha = e^{-\gamma t^*} = e^{-1}$, where t^* is the eddy turnover time at t_0. The broadcasting modes obtained from the time-evolving networks are found to be similar to their kinematic counterparts, highlighting the paths of either vortices or opposite-sign vortex pairs. To explore how these broadcasting modes can be used to target the sensitive regions in the turbulence, we add these broadcasting modes as initial vorticity disturbances, $\boldsymbol{\omega}(t_0) = \boldsymbol{\omega}_0 + \epsilon \boldsymbol{b}_1$, evolve the turbulent flow and track the differences from the unperturbed case in figure 1 (b). We find that the N–S broadcasting mode is more effective in modifying the turbulence, as its formulation is based on perturbation dynamics. Moreover, with the extended time-horizon over which the broadcasting modes are computed, higher levels of flow modification is achieved by the initial disturbances.

CONCLUSIONS

We perform network-based resolvent analysis of 2D isotropic turbulence and seek the broadcasting modes based on the Katz centrality as optimal initial disturbances. While the B–S and N–S broadcasting modes reveal different structures as the sensitive regions in 2D turbulence, the findings are physical intuitive and align with those from literature. The time-evolving network model shows that higher levels of modification can be achieved with the longer time-horizon, providing a framework to analyze time-varying base flows.

References

[1] Jiménez, J. Machine-aided turbulence theory. *J. Fluid Mech.* **854**: R1, 2018.
[2] Taira, K., Nair, A. G. & Brunton, S. L. Network structure of two-dimensional decaying isotropic turbulence. *J. Fluid Mech.* **795**: R2, 2016.
[3] Trefethen, L. N., Trefethen, A. E., Reddy, S. C. & Driscoll, T. A. Hydrodynamic stability without eigenvalues. *Science* **261** (5121): 578–584, 1993.
[4] McKeon, B. J. & Sharma, A. S. A critical-layer framework for turbulent pipe flow. *J. Fluid Mech.* **658**: 336–382, 2010.
[5] Nair, A. G. & Taira, K. Network-theoretic approach to sparsified discrete vortex dynamics. *J. Fluid Mech.* **768**: 549–571, 2015.
[6] Schlueter-Kuck, K. & Dabiri, J. O. Coherent structure colouring: identification of coherent structures from sparse data using graph theory. *J. Fluid Mech.* **811**: 468–486, 2017.
[7] Katz, L. A new status index derived from sociometric analysis. *Psychometrika* **18** (1): 39–43, 1953.
[8] Grindrod, P., Parsons, M. C., Higham, D. J. & Estrada, E. Communicability across evolving networks. *Phys. Rev. E* **83** (4): 046120, 2011.
[9] Grindrod P. & Higham D. J. A dynamical systems view of network centrality. *Proc. R. Soc. A* **470**: 20130835, 2013.

TRAVELING-WAVE PROPAGATION IN THE SWEPT LEADING-EDGE BOUNDARY LAYER AT HIGH REYNOLDS NUMBER

Aiko Yakeno *[1] and Shigeru Obayashi[1]
[1] Institute of Fluid Science, Tohoku University, Japan

Summary Transition characteristics around the leading-edge of a swept-back airfoil shape have been investigated numerically. We identified the generation of two coherent modes, i.e., the stationary and traveling waves in the swept direction. The existence of the traveling-wave mode has already been mentioned in previous studies, and we succeeded in observing that propagation through direct numerical simulations (DNS) in a swept-wing shape, at the practically high Reynolds number of $Re_c = 2.0 \times 10^6$ based on the chord length. Additionally, we analyzed the optimal transient-energy growth for the present leading-edge boundary layer. The wavelength of the optimal mode generated in a short-time and traveling in the swept direction corresponds to the results obtained through the DNS.

BACKGROUND

Commercial aircraft often have their main wing swept-back to suppress a shock wave. Around the swept wing, the boundary layer becomes three-dimensional and different types of laminar-turbulence transitions occur. Researchers have focused on studying the occurrence of turbulence, to increase viscous drag and delay transition [1, 2, 3, 4, 5]. Further, regarding the boundary-layer transition, several studies have been conducted both theoretically and experimentally. Most conventional-flow stability analyzes have discussed asymptotic behavior [6, 1]. In recent years, attention has been focused on the temporary energy amplification in finite time and transient growth due to a system's nonorthogonality [7, 8, 9]. Corbett and Bottaro (2001) analyzed the optimal perturbation in the Falkner–Skan–Cooke similarity solution and stated that the highest energy-amplification mode took the form of vortices and almost aligned with the external streamline to evolve streaks. Guegan *et al.* (2006, 2007) investigated the temporal energy growth based on the Görtler–Hämmerlin assumption for the swept Hiemenz flow and confirmed the spanwise traveling chordwise vortices as the most amplified instability mode at large Reynolds numbers. Discussion on the transition scenario is still ongoing, and not many examples exist for the application of the analysis to the actual flow field.

PROBLEM SETTINGS

We numerically investigated flow instabilities to cause a transition in the attachment-line boundary layer of a swept-back airfoil at the practically high Reynolds number of $Re_c = 2.0 \times 10^6$ based on the chord length of the airfoil. A DNS of the three-dimensional compressible Navier–Stokes equations was conducted for the leading-edge region of an airfoil shape, NACA0030, with swept angle $\alpha = 70$ [deg]. The Mach number was set to 0.2 in the present study; it was assumed to be incompressible. The schematic of the swept-back wing model and input flow direction, x, are shown in Fig.1. The original coordinate, (x, y, z), was rotated around the swept wing in the chord-wise, swept, and wall-normal directions, (x^*, y^*, z^*), respectively. The distributed random roughness was set at the wall to excite the flow instability in the swept upstream direction, which covers 20 [%] of the surface in the present study; it was switched on once and retained, similar to a step function. The governing equation was solved using the generalized curvilinear coordinates (ξ, η, ζ). At the ξ direction boundaries, we set a fixed pressure, which was obtained through a two-dimensional full wing computation at the same flow condition. The computational-grid number is $(470, 892, 179)$, in the ξ, η, and ζ directions, respectively, that is, 75 million in total.

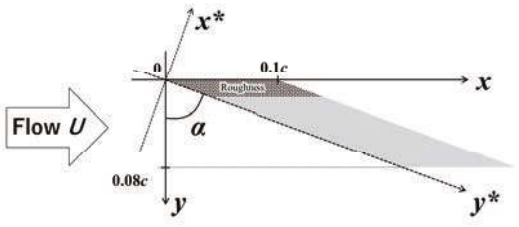

Figure 1: Top view of the swept wing and input flow direction. Distributed roughness is set at the wall in the swept upstream, covering 20 [%] of the surface.

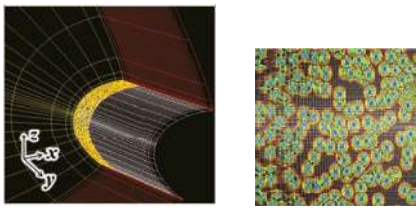

(a) (b)

Figure 2: (a) The grid at every 20 points. White grids represent the wall surface, while red and yellow grids are the boundaries at ξ and η, respectively. Local body force at the wall surface is shown as contour lines. (b) Body force distribution with a grid at every point.

STATIONARY- AND TRAVELING-WAVE PROPAGATIONS

The DNS results identify as many as two unstable modes around a swept wing: steady and traveling downstream. The steady mode is elongated in the external-flow directions, and the traveling mode moves in the sweep direction with a wavelength of approximately $\lambda_{y^*}/c = 0.008$, which is distributed to the upper and lower surfaces of the airfoil around an attachment line. The *two modes coexist*; this answers the question by Guegan *et al.*(2006, 2007) [4, 5] which mode is dominant based on the Görtler–Hämmerlin assumption for the swept Hiemenz flow.

*Corresponding author. E-mail: aiko.yakeno@tohoku.ac.jp

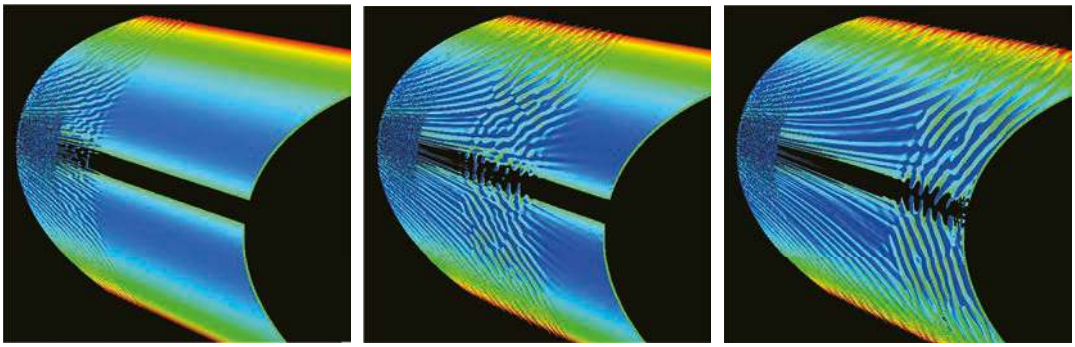

(a) $tU/c = t_0U/c + 2.5$ (b) $tU/c = t_0U/c + 7.5$ (c) $tU/c = t_0U/c + 12.5$

Figure 3: The traveling-wave propagation in the swept leading-edge boundary layer. The isosurface is the second invariant of deformation tensor $Q = 2.5$ with span-wise velocity v of -0.3(red) to 0.3(blue).

OPTIMAL TRANSIENT-ENERGY GROWTH

Next, we analyzed the optimal transient-energy growth for the leading-edge swept boundary layer. The temporal energy growth at target time τ is calculated as

$$G_{rate}(\tau) = E(\tau)/E(0) = \|\boldsymbol{u}'^*(\tau)\|^2 = (\boldsymbol{A}(\tau)\boldsymbol{u}_0'^*, \boldsymbol{A}(\tau)\boldsymbol{u}_0'^*) = (\boldsymbol{u}_0'^*, \bar{\boldsymbol{A}}(\tau)^T\boldsymbol{A}(\tau)\boldsymbol{u}_0'^*), \tag{1}$$

where the energy is defined as the kinetic energy of velocity perturbations, assuming that the flow is incompressible. This is the same as the inner vector with the self-adjoint operator, $\bar{\boldsymbol{A}}^{\boldsymbol{T}}\boldsymbol{A}$. Therefore, the maximum perturbation growth rate of $G_{max}(\tau)$ is described as the maximum eigenvalue of the self-adjoint operator:

$$G_{max}(\tau) \equiv \max_{\|\boldsymbol{u}_0'^*\|=1} E(\tau)/E(0) = \max_j \kappa_j, \quad \bar{\boldsymbol{A}}(\tau)^T\boldsymbol{A}(\tau)\boldsymbol{u}_j'^* = \kappa_j\boldsymbol{u}_j'^*, \quad \|\boldsymbol{u}_j'^*\| = 1. \tag{2}$$

Perturbations are of the following form when we assume periodicity in the swept x^* and chord directions y^*: $\boldsymbol{u}'^*(x^*, y^*, z^*, t) = \hat{\boldsymbol{u}}'^*(z^*, t)\exp(i\alpha x^* + i\beta y^*)$. We obtained initial value $\boldsymbol{u}_0'^*$ for the most amplified energy at each target time. The program code was validated by comparison with references ([7, 10]).

The energy growth for each target time are shown in Fig. 4. Two groups were realized: the short-time transient growth ($0.02 \leqq \tau U/c \leqq 0.08$) and the long-time exponential growth ($0.1 \leqq \tau U/c$); the optimal modes are $0.006 \leqq \lambda_{y*}/c \leqq 0.02$ and $\lambda_{y*}/c \approx 0.03$, respectively. Although G_{max} of the long-time exponential growth is much larger than that of short-time growth, its amplification takes significant time. In the short-time growth, the modes of $0.006 \leqq \lambda_{y*}/c \leqq 0.02$ grow much larger than that of $\lambda_{y*}/c \approx 0.03$, and the short-time optimal wavelength corresponds to the DNS results, $\lambda_{y*}/c \approx 0.008$. Therefore, we conclude that the traveling-wave generation in the present attachment-line boundary layer is strongly related to the short-time transient energy growth of the nonorthogonal basis.

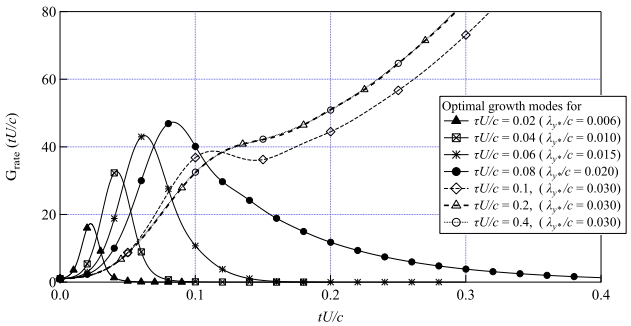

Figure 4: $G_{rate}(tU/c)$ of the short- and long-time optimal growth for each target times $\tau U/c$.

References

[1] P. Hall, M. R. Malik, and D. I. A. Poll. On the stability of an infinite swept attachment line boundary layer. *Proceedings of the Loyal Society of London*, 395:229–245, 1984.
[2] P. Corbett and A. Bottaro. Optimal linear growth in swept boundary layers. *Journal of Fluid Mechanics*, 435:1–23, 2001.
[3] D. Obrist and P. J. Schmid. On the linear stability of swept attachment-line boundary layer flow. Part 2. Non-modal effects and receptivity. *Journal of Fluid Mechanics*, 493(493):31–58, 2003.
[4] A. Guégan, P. J. Schmid, and P. Huerre. Optimal energy growth and optimal control in swept Hiemenz flow. *Journal of Fluid Mechanics*, 566:11–45, 2006.
[5] A. Guégan, P. Huerre, and P. J. Schmid. Optimal disturbances in swept Hiemenz flow. *Journal of Fluid Mechanics*, 578:223–232, 2007.
[6] P. G. Drazin and W. H. Reid. *Hydrodynamic Stability*. Cambridge University Press., 1981.
[7] K. M. Butler and B. F. Farrell. Three-dimensional optimal perturbations in viscous shear flow. *Physics of Fluids*, 4(8):1637–1650, 1992.
[8] L. N. Trefethen, A. E. Trefethen, S. C. Reddy, and T. A. Driscoll. Hydrodynamic Stability Without Eigenvalues. *Science*, 261:578–584, 1993.
[9] P. J. Schmid. Linear stability theory and bypass transition in shear flows. *Physics of Plasmas*, 7(5):1788–1794, 2000.
[10] D. Barkley, H. M. Blackburn, and S. J. Sherwin. Direct optimal growth analysis for timesteppers. *International Journal for Numerical Methods in Fluids*, 57:1435–1458, 2008.

FLOW-INDUCED MOTION OF A SINGLE BEAD AT SMALL SUPERCRITICAL SHIELDS NUMBERS

N. Topic[1], J. R. Agudo[1,2], G. Luzi[3], and A. Wierschem[1,3]
[1] Institute of Fluid Mechanics, Friedrich-Alexander-Universität Erlangen-Nürnberg (FAU), Erlangen,Germany
[2] Anton Paar Germany GmbH, Ostfildern, Germany
[3] LSTME Busan Branch, Busan, Republic of Korea

Summary We study the flow-induced motion of a single bead on regular substrates made of spherical particles at small particle Reynolds numbers. At near supercritical Shields numbers, the bead moves along the substrate. The average bead velocity increased approximately linearly with the Shields number and decreased as the spacing between substrate particles increases. We develop a model to describe the experimental findings. It shows good agreement with the experimental results and allows a collapse of the experimental data onto a master curve.

INTRODUCTION

Prediction of particle motion is important in a wide variety of industrial and natural processes like cleaning of surfaces, assembling of particles, conveying as well as sediment transport in rivers, granular beds erosion and dune formation [1]-[6]. Given its wide range of applications, onset of particle motion has been studied intensively during the last century. There have been many approaches to study flow induced particle motion at surfaces and in bedload transport, see e.g. [7] and references therein. Studying flow-induced motion of beads on regularly arranged monolayers of spheres as substrates, we found a strong impact of the substrate geometry on the incipient motion [1]-[3]. We proposed a model that takes into account the substrate geometry. It covers the entire range of angles of repose [3] and of size ratios between mobile beads and substrate spheres [6]. Although our study focusses on small particle Reynolds numbers, we remark that even in high Reynolds number flows, the particle Reynolds numbers may be of order one or smaller [7]. The particle motion is typically characterized by rolling, sliding, and bouncing [9], [10]. Here, we extend our study to the particle motion at small supercritical Shields numbers.

SYSTEM

We consider a single sphere of diameter D_P and density ρ_S deposited on a regular substrate and exposed to a steady shear flow (see Figure 1) with shear rate $\dot{\gamma}$ of a viscous incompressible Newtonian fluid of constant density ρ and kinematic viscosity ν. The substrate consists of a layer of fixed spheres of same size that are regularly arranged in quadratic configurations. In experiments, the spacing was achieved using sieves of different mesh size [1], [2], [6]. It has been shown that the shear flow penetrates slightly into the substrate [10]-[12]. Extrapolating the linear shear flow results in an effective zero level z_0 below substrate protrusions [3], [6].

We study the system at particle Reynolds numbers of about 1 and smaller, where the particle Reynolds number is given by $\mathrm{Re}_P = \dot{\gamma} D_P^2 / \nu$. The incipient motion is characterized by the critical Shields number θ_C, which compares the characteristic shear force acting on the particle to the resistant specific particle weight that retains the particle in its place. The Shields number is defined by $\theta = \nu\dot{\gamma} / \left[(\rho_S / \rho - 1) g D_P\right]$, where g is the acceleration of gravity.

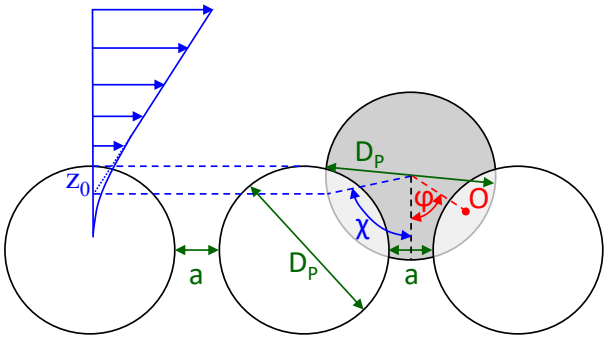

Figure 1. Sketch of the system: Single bead resting on a quadratic substrate exposed to a shear flow. D_P: particle diameter; a: substrate spacing; z_0: effective zero level below the top of the substrate; O: downstream contact point between mobile bead and substrate; ϕ: angle of repose; χ: angle between bead surface at effective zero level and vertical axis.

RESULTS

Beyond the critical Shields number, the bead leaves its equilibrium position in the substrate pocket and rolls along the substrate, slowly uphill and faster downhill. Figure 2(a) shows an experimental example at small supercritical Shields number. At larger Shields numbers, the modulation of the velocity diminishes. At the particle Reynolds numbers considered, the bead achieves a constant mean equilibrium velocity in the early stage of its motion. As the spacing between the substrate spheres increases, the mobile bead is located deeper in substrate. It has to climb steeper slopes and is stronger

shielded from the shear flow. This results in lower average velocities. Figure 2(b) shows this as a result of our model, where we scaled the average velocity with the settling velocity.

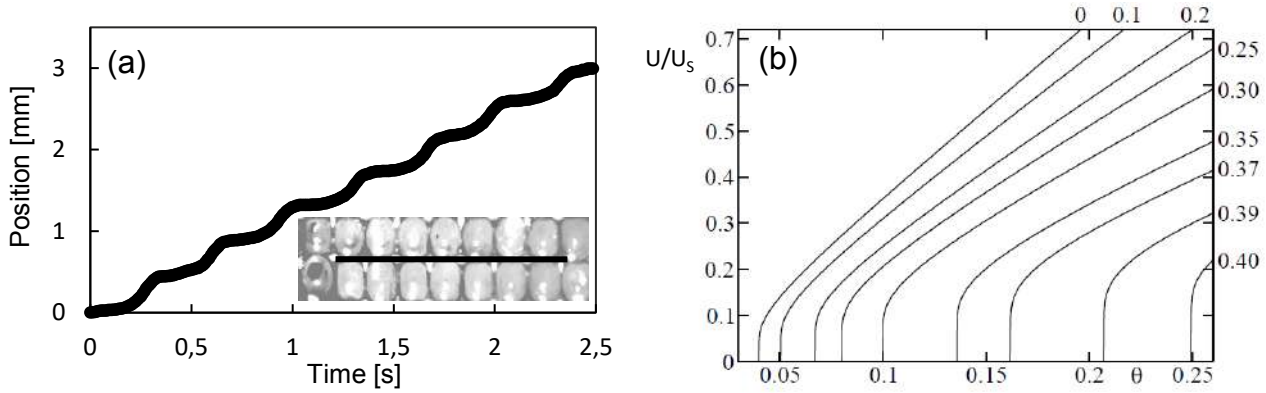

Figure 2. Experimental particle position during its motion along 7 substrate pockets on the quadratic substrate at $\theta/\theta_C = 1.3$ (a) and result of the model for the average bead velocity for different spacings a/D_P as a function of the Shields number (b). The respective values for a/D_P in (b) are printed at the end of the curves. The inset in (a) shows a top view of the path along the substrate; particle diameter: 0.4 mm.

To describe the experimental findings, we develop a model based on expressions for the forces and torques acting on the moving bead near a wall. Our model for the supercritical motion is an extension of the analytical description for the critical Shields number [3], [6]. It provides a quantitative description of the experimental results for the bead motion and allows a collapse of the experimental data onto a single curve. It also provides a threshold for detachment of the bead from the substrate.

CONCLUSIONS

At small supercritical Shields numbers, a bead exposed to the steady shear flow rolls along the substrates. Its velocity depends on the substrate geometry. It is modulated due to the local slope. The average bead velocity appears to be a linear function of the Shields number for all substrates studied. The slope of the curve and intercept depend on the substrate geometry. Our model recovers the experimental findings. It shows good quantitative agreement with the experimental results and allows a collapse of the experimental data onto a master curve. The master curve permits to forecast the bead velocity according to the sediment bed topography at low particle Reynolds numbers.

Acknowledgements

This study is supported by Deutsche Forschungsgemeinschaft through WI 2672/7-1, which is gratefully acknowledged.

References

[1] Agudo J. R., Wierschem A.: Incipient motion of a single particle on regular substrates in laminar shear flow. *Phys. Fluids* **24**: 093302, 2012.
[2] Agudo J. R., Dasilva S., Wierschem A.: How do neighbors affect incipient particle motion in laminar shear flow? *Phys. Fluids* **26**: 053303, 2014.
[3] Agudo J. R., Illigmann C., Luzi G., Laukart A., Delgado A., Wierschem A.: Shear-induced incipient motion of a single sphere on uniform substrates at low particle Reynolds numbers. *J. Fluid Mech.* **825**: 284-314, 2017.
[4] Agudo J. R., Luzi G., Han J., Hwang M., Lee J., Wierschem A.: Detection of granular motion using image processing with particular emphasis on rolling motion. *Rev. Sci. Instr.* **88**: 051805, 2017.
[5] Agudo J. R., Han J., Park J., Kwon S., Loekman S., Luzi G., Lichtenberger C., Delgado A., Wierschem A.: Visually based characterization of the incipient particle motion in regular substrates: From laminar to turbulent conditions. *J. Vis. Exp.* **132**: e57238, 2018.
[6] Topic N., Retzepoglu S., Wensing M., Illigmann C., Luzi G., Agudo J. R., Wierschem A.: Effect of particle size ratio on shear-induced onset of particle motion at low particle Reynolds numbers: From high shielding to roughness. *Phys. Fluids* **31**: 063305, 2019.
[7] Dey S., Ali S.Z.: Review Article: Advances in modeling of bed particle entrainment sheared by turbulent flow. *Phys. Fluids* **30**: 061301, 2018.
[8] Guazzelli E., Morris J. F.: A Physical Introduction to Suspension Dynamics. Cambridge University Press, 2012.
[9] Charru F., Mouilleron H., Eiff O.: Erosion and deposition of particles on a bed sheared by a viscous flow. *J. Fluid Mech.* **519**: 55-80, 2004.
[10] Ouriemi M., Aussillous P., Guazzelli E.: Sediment dynamics. Part 1. Bed-load transport by laminar shearing flows. *J. Fluid Mech.* **636**: 295-319, 2009.
[11] Mouilleron H., Charru F., Eiff O.: Inside the moving layer of a sheared granular bed. *J. Fluid Mech.* **628**: 229-239, 2009.
[12] Derksen J. J., Larsen R. A.: Drag and lift forces on random assemblies of wall-attached spheres in low-Reynolds number shear flow. *J. Fluid Mech.* **673**: 548-573, 2011.

STRUCTURE OF CONTROLLED FLOW SEPARATION

Curtis J. Peterson[1], Bojan Vukasinovic *[1], and Ari Glezer [1]

[1] Woodruff School of Mechanical Engineering, Georgia Institute of Technology, Atlanta, GA 30332-0405, USA

Summary Natural separation of turbulent flow by an adverse pressure gradient along a diverging surface within a duct is delayed using a spanwise array of surface-integrated fluidically-oscillating jets. The interaction of the jets with the local cross flow leads to the formation of a spanwise array of counter-rotating streamwise vortex pairs that are characterized by alternating induced downwash and upwash flows along the jet centerlines and between adjacent jets, respectively. The presence of the vortices delays separation proportionally to the magnitude of the actuation. In the presence of actuation induced vortices, the attached flow exhibits nominally spanwise-periodic turbulent structure in which enhanced turbulent kinetic energy as well as turbulent production and dissipation are coupled to the induced upwash and appear to be suppressed within the downwash domains.

The present experimental study focuses on the streamwise evolution of a surface vorticity layer that separates in an adverse streamwise pressure gradient along a diverging surface within a duct as flow attachment is incrementally extended by fluidic actuation of increasing intensity. Of particular interest is the spanwise structure of the attached flow in the presence of actuation with emphasis on the turbulent characteristics. The experiments are conducted within an open-return, subsonic wind tunnel with a square test section ($H = W = 127$ mm, and length $L = 660$ mm) implemented with a spanwise-uniform converging-diverging insert along the surface of the bottom wall (Figure 1a). The maximum cross stream protrusion of the insert is $H' = 17.6$ mm, and the Mach number at the upstream entrance of the test section is $M_o = 0.25$. The diverging insert contour is based on the suction surface of a VR-12 airfoil ($c = 62.2$ mm) at $\alpha = 13^o$, and a trip wire having diameter $d \approx 0.007c$ is placed upstream of the insert's apex at $x/c = 4.8$. Flow control actuation is effected using a spanwise array of 17 laterally oscillating fluidic actuator jets issuing nearly tangentially to the surface 7 mm apart at $x/c = 5.1$ and having rectangular orifices that measure 0.5 × 1 mm in the cross stream and spanwise directions, respectively (Peterson et al., 2019, Figure 1b). The jet thrust J is measured independently and is used to compute the jet momentum coefficient $C_\mu = J/(\rho_o A_o U_o^2)$. The cross-stream flow structure at multiple spanwise y-z planes is investigated using stereoscopic particle image velocimetry (SPIV) for which the CCD imagers are arranged as shown in Figure 1b and are traversed in the streamwise direction along with the laser sheet optics.

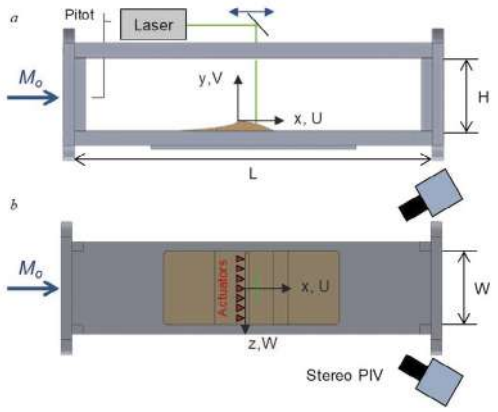

Figure 1. Side (a) and top (b) views of the flow insert in the bottom surface and the SPIV cameras and the laser sheet. The coordinate system is centered at the protrusion's apex.

The time-averaged flow over the ramp was investigated by Peterson et al. (2019) with emphasis on the characteristic features of separation and reattachment within a closed recirculation bubble. The flow structure ($M_o = 0.25$) is depicted in Figure 2 using raster plots of the time-averaged spanwise vorticity (overlaid with velocity vectors, 2a, c) and of the corresponding turbulent kinetic energy (TKE) (2b, d) in the absence (2a, b) and presence (2c, d) of actuation. In the absence of actuation (Figures 2a and b), the time-averaged flow exhibits the formation of a closed recirculating bubble that is bounded from above by a separating shear layer that originates at $x/c \approx 5.2$ downstream of the apex and its streamwise mixing and entrainment lead to cross stream spreading and transport of the spanwise vorticity and the formation of a hierarchy of vortical structures of decreasing scale as marked by TKE concentrations. The flow becomes reattached near the downstream edge of the field of view ($x/c \approx 6.4$), and the attached flow is characterized by a thick surface vorticity layer owing to separation. When C_μ is increased beyond some threshold, separation is streamwise-delayed progressively, and the respective length and width of the recirculating flow domain and the bounding vorticity layer diminish. When $C_\mu = 2.1 \cdot 10^{-3}$, the time-averaged flow becomes fully attached (Figures 2c and d) throughout the aft flow domain with significantly thinner surface vorticity layer that is characterized by much reduced TKE.

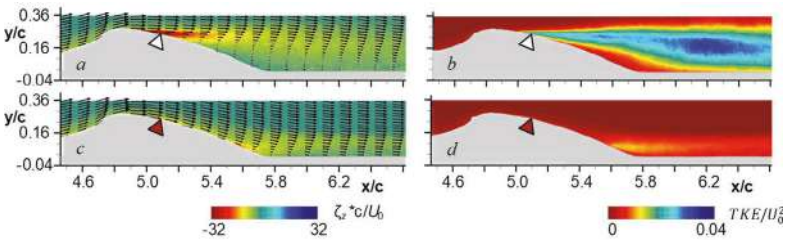

Figure 2. Color raster plots of (a, c) the time-averaged spanwise vorticity (overlaid with velocity vectors) and (b, d) the turbulent kinetic energy in the absence (a, b) and presence (c, d) of actuation: $M_o = 0.25$, $C_\mu = 2.1 \cdot 10^{-3}$.

*Corresponding author. E-mail: bojan.vukasinovic@me.gatech.edu

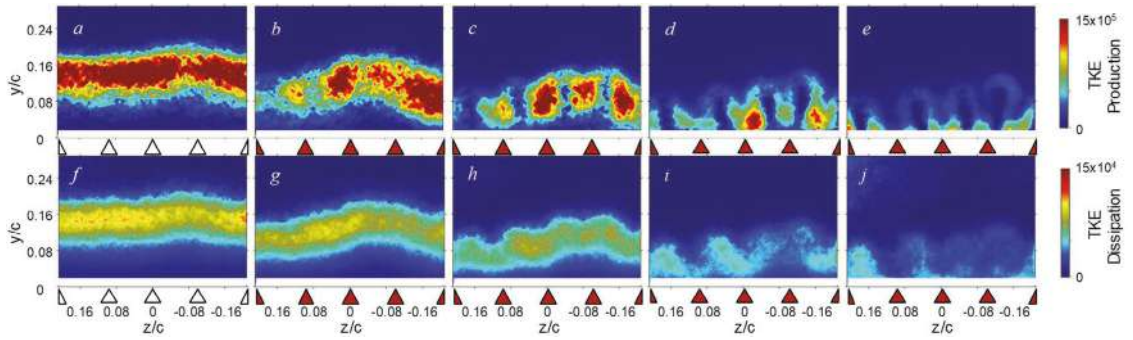

Figure 3. Color raster plots of turbulent production (a-e) and dissipation (f-j) in the absence (a, f) and presence (b-e, g-j) of actuation at the *y*-*z* plane $x/c = 5.72$ for $C_\mu \cdot 10^3 = 0.36$ (b, g), 0.96 (c, h), 1.5 (d, i), 2.1 (e, j). The respective spanwise positions of the inactive and active actuation jets are marked by white and red triangles.

The interaction of the actuation jets with the cross flow is assessed from stereo PIV (cf., Figure 1) measurements in the *y*-*z* plane at the streamwise location of separation in the absence of actuation ($x/c = 5.72$). The evolution of rates of turbulent production $-\langle u_i u_j \rangle \overline{S_{ij}}$ and dissipation $2\nu\langle s_{ij} s_{ij} \rangle$ with increasing levels of actuation $0 < C_\mu \cdot 10^3 < 2.1$ is shown using color raster plots in Figure 3 (since earlier measurements in the *y*-*x* plane indicated weak dependence on *x*, these estimates omit the variation with respect to *x*). As expected, Figures 3a and f show that the turbulent production and dissipation in the base flow are reasonably spanwise-uniform, peak within the separating shear layer and diminish precipitously towards the surface. The most salient features of the distributions of the turbulent production (b-e) in the presence of actuation is the formation of spanwise–regular concentrations that are roughly aligned with the centers of the actuation jets (marked by triangles in Figure 3) and move closer to the surface and weaken as the actuation level increases and the flow becomes more attached. It is noteworthy that as the flow becomes fully attached ($C_\mu = 2.1\ 10^{-3}$, Figure 3e), the production levels form discrete spanwise-periodic 'halo' patterns between the centers of the jets. As discussed in connection with Figure 4, these concentrations are associated with the formation of a spanwise array of alternating counter-rotating streamwise vortex pairs between adjacent actuation jets that are formed within the separating vorticity layer and are advected towards the surface as the actuation level is increased. The corresponding distributions of the dissipation show the evolution of higher concentrations between adjacent actuation jets that are nominally aligned with the centerlines of the vortex pairs and weaken as the flow becomes attached.

Spanwise alternating streamwise vortices that are induced by adjacent actuation jets are shown in Figure 4 along with the corresponding concentrations of TKE and turbulence production and dissipation. As noted in connection with Figure 3, jet actuation leads to the formation of a spanwise array of counter-rotating vortex pairs on each side of the jet orifice. The sense of these vortices is such that the induced vertical flow in the *y*-*z* plane is downwelling and upwelling along the center of and between adjacent jets, respectively (shown schematically in Figure 4). The downwelling flow along actuators' centerlines results in advection of entrainment of fluid from the high-speed side of the separating shear layer (cf., Figure 2a) and low-speed fluid from the near-wall region. The advection of the high-speed, low-turbulence fluid is marked by low TKE concentration above the jet centerline (Figure 5b) while the spanwise transport of low-speed fluid and its upwelling between the counter-rotating vortices results in halo-like concentrations between the jets. Figure 4c show shat turbulent production is primarily concentrated along the surface below and within the cores of the vortices, while dissipation (Figure 4d) is primarily associated with opposite spanwise motions at their upper edges coupled with shear with the higher speed streamwise flow above. The present investigations indicate that the actuation induced streamwise vortices within the nominally 2-D separating shear layer and their interactions with the layer's spanwise vortices result in enhanced entrainment from its low-speed side and thereby lead to gradual re-attachment of the surface vorticity layer that is able to overcome the increase in adverse streamwise pressure gradient.

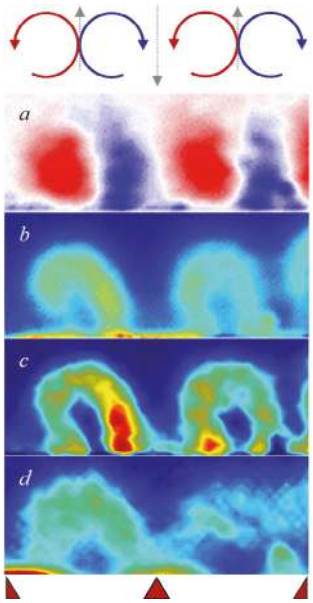

Figure 4. Color raster plots composite of the streamwise vorticity (*a*), TKE (*b*) and turbulent production (*c*) and dissipation (*d*) induced by neighboring actuation jets (marked by triangles) for $C_\mu = 1.5 \cdot 10^3$ at $x/c = 5.54$. The sense of rotation of the streamwise vortices is shown schematically at the top.

References

[1] Peterson, C.J., Vukasinovic, B., and Glezer. A. Control of a Closed Separation Domain in Adverse Pressure Gradient Over a Curved Surface. AIAA Paper 2019-1900, 2019.

CONTROL OF JET MIXING USING DEEP REINFORCEMENT LEARNING

Koichi Tsujimoto[1] and Tsubasa Tanoue[1]
[1] Division of Mechanical Engineering, Graduate School of Engineering, Mie University, Tsu, Mie, Japan

Summary In order to develop a new jet mixing procedure, we explore the possibility of DRL (deep reinforcement learning). First, we conduct some cases of open-loop control in which a main jet is manipulated by a pair of sub jet being actuated at the inlet of main jet, and examine the effect of actuating frequency on the mixing performance of main jet. Then, we select a DDPG (deep deterministic policy gradient) scheme among of the present DRL schemes, and apply it to the above-mentioned jet control problem. Compared the the results of DDPG with that of OLC (open-loop control), the DDPG scheme turns out the useful performance of jet mixing control, $i.e.$,both the entrainment of fluid from surroundings and statistical entropy are enhanced through the DRL while the main jet behaves like a flapping jet.

NUMERICAL PROCEDURE

Active flow control

The flow is assumed to be incompressible. Thus, the governing equations are the continuity and momentum equations. The Cartesian coordinate system is employed. Computational conditions such as the size of the computational domain, and Reynolds number are $(H_x, H_y) = (16D, 20D)$, where D is the nozzle diameter, Re = 100 , respectively. The spatial discretization involves a sine or cosine series expansion in the x direction and sixth-order compact scheme in the streamwise direction. Figure 1 is schematic drawing of the flow field. The inlet velocity distribution is assumed to be top-hat type. As well as the reference[1] a main jet is manipulated by a pair of sub jet being actuated at the inlet of main jet. Each sub jet is driven in opposite phase. In order to evaluate the results obtained by DRL, OLC (open loop control) is performed in which the sub jet is driven with a sine wave ($u_1 = -u_2 = u_0 sin(\omega t)$, ω: angular velocity).

DRL (deep reinforcement learning)

In reinforcement learning, learning is conducted with combining the concepts of environment (state), action, and reward. That is, under a certain environment, an action is selected based on a policy, and a state and a reward are obtained. The environment changes state due to action and rewards are immediately determined. It then finds a policy that maximizes rewards. In this study, such concepts are connected to the actual jet mixing control as follows; the action: the blowing of the sub jet at every moment, the policy: how to drive the sub jet, the state: the velocity of the main jet at monitoring locations and the reward: the entrainment due to the main jet. Although there are some proposals for the DRL scheme, DDPG (deterministic policy gradient) [2] is adopted because it is capable of dealing with continuous action such as blowing from sub jet. As shown in Fig, 2, DDPG consists of two networks, the critic network and the actor network, which promote learning while complementing each other. The distance between the sub jet and the location where mixing occurs are far apart. Therefore, there is a time lag between the state at the observation point and the action. In this study, the problem of time lag is solved by arranging multiple observation points at the downstream position. Specifically, a total of 20 observation points were arranged at a distance of 2D toward the downstream.

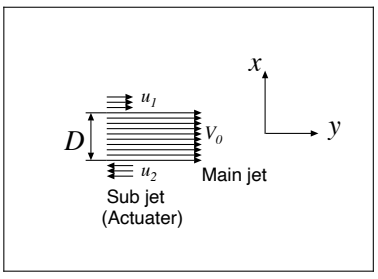

Figure 1. Active controlled jet

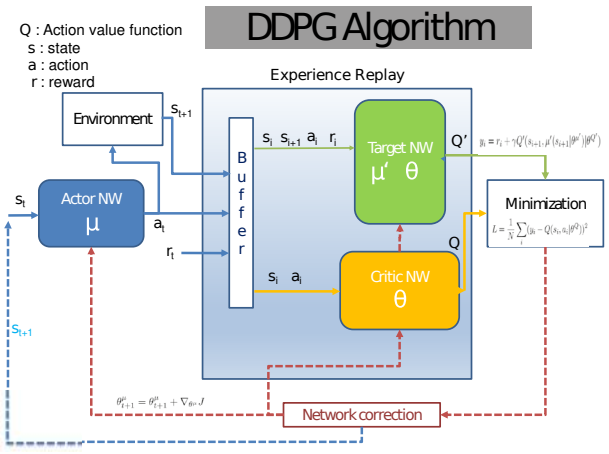

Figure 2. Algorithm of DDPG

a) Corresponding author. E-mail: tujimoto@mach.mie-u.ac.jp

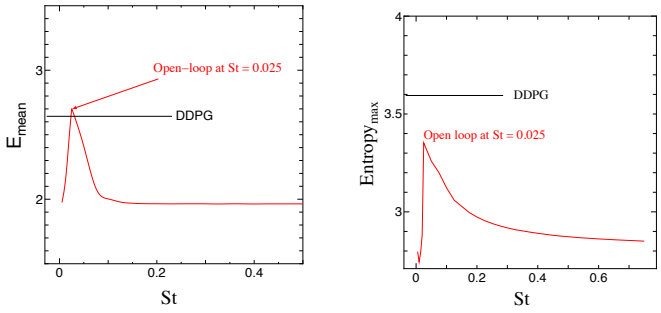

(a) entrainment (b) entropy

Figure 3. Comprison of mixing performance between OLC $v.s.$ DRL

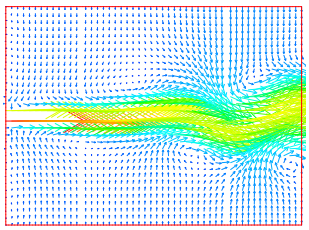

Figure 4. Instantaneous velocity vector plot

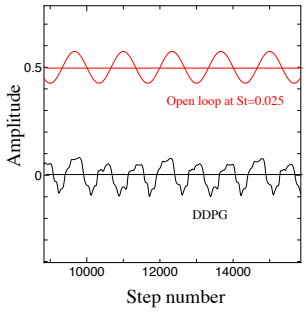

Figure 5. Amplitude of actuator input

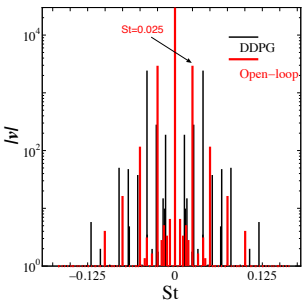

Figure 6. Frequency Characteristics with DMD

RESULTS

Entrainment of the surrounding fluid due to the main jet has been one of the measure of mixing performance. Figure 3 (a) shows the distribution of the entrainment E_{mean}. The red line in the figure is the result of OLC, and the black line is the value obtained by DRL. In the OLC, a peak appears at a low control frequency. In the literature[1], the same OLC is conducted, and St = 0.03 was shown as the optimal St number. This values is almost consistent with the results obtained in this OLC. At the same time, the value obtained by DRL is almost the same as the optimum value in the OLCs. Thus it reveals that the sufficient mixing performance is realized with the DRL. As another mixing meaure, Everson et al. [3] proposed a statistical entropy based on scalar concentration, and we verified this mixing measure based on the DNS data of active controlled jet[4]. Figure 3 (b) shows the distribution of statistical entropy. Similar to entrainment, the statistical entropy of the OLC is highest at St = 0.025, and the DRL shows higher mixing performance than that of OLC. Figure. 4 shows the instantaneous velocity vector field obtained by the DRL. Although the OLC induces the flapping jets due to the sub jets as shown in the literature[1], even in the DRL, the qualitatively similar structures are formed. Figure 5 shows the input waveform of the sub jet. In the case of OLC at St = 0.025, the waveform becomes a given sine waveform, while the distorted waveform is quasi-periodically generated in the DRL. We analyze the difference of the waveform using DMD (dynamic mode decomposition) method [5] which is easily capable of extracting the temporally periodic mode. Figure 6 shows the frequency characteristics. In the case of OLC at St = 0.025, first peak occurs at the control frequency, and second and third peaks occur at integer multiples of the first peak. On the other hand, in the DRL, the first peak has a higher frequency than the first peak of OLC, but the second and third peaks occur at lower frequencies than the primary frequency of OLC. Thus, unlike the OLC, obviously different frequencies are mixed in the DRL.

CONCLUSION

As a result of active control of jet mixing by open-loop control and DRL, there is an optimal control frequency at low frequency in OLC; the DRL results in the distorted waveforms that cannot be artificially determined. Furthermore, as a result of evaluating the entrainment and the statistical entropy, it was clarified that the DRL can achieve the same or better performance than the optimal mixing control in OLCs. From the jet structure, the mixing of DRL is activated by flapping, similar to that observed in the case of OLC. As a result of the analysis by DMD, the frequency characteristics of DRL show that the mode at the lower frequency is activated than the optimum result in the OLC, which is thought to contribute to the improvement of the mixing performance.

References

[1] Yuan, C.C.L., Krstic, M. and Bewley, T.R., *IEEE Proceedings - Control Theory and Applications*, **151**-6: 763 - 772, 2004.
[2] Lillicrap, T.P., Hunt, J.J., Pritzel, A., Heess, N., Erez, T., Tassa, Y., Silver, D., Wierstra, D., Int. Conf. Learn. Represent arXiv:1509.02971v5, 2016.
[3] R. Everson, D. Manin, and L. Sirovich, *AIAA J.* **36** : 121-127, 1998.
[4] K. Tsujimoto, S. Kariya, T. Shakouchi and T. Ando, *Int. Journal of Flow Control*, **1**-3: 213-225, 2009.
[5] S. J., Schmid, *J. Fluid Mech.*, **656**: 5-28, 2010.

A SPECTRAL POD–GALERKIN REDUCED–ORDER MODEL FOR TURBULENT SHEAR FLOWS

Aaron Towne [1]
[1] Department of Mechanical Engineering, University of Michigan, Ann Arbor, MI, USA

Summary Nonlinear reduced-order models for fluid systems are often obtained via Galerkin projection of the Navier-Stokes equations in a spatial inner product onto proper orthogonal decomposition (POD) modes. While popular, this approach has well-documented limitations, especially for turbulent flows. We develop an alternative approach based on a space-time Galerkin projection of the equations onto spectral proper orthogonal decomposition (SPOD) modes. By minimizing errors over a time window of interest, this approach has the potential to outperform and overcome limitations of standard POD-Galerkin models for turbulent shear flows.

INTRODUCTION

The high diensionality of the spatially discretized Navier-Stokes equations needed to simulate turbulent flows has spurred considerable effort to obtain reduced-order models capable of providing accurate approximate solutions at reduced computatinal cost. The most common approach used to obtained nonlinear reduced-order models of the Navier-Stokes equations is Galerkin projection [4]. In this approach, the discretized state vector $\boldsymbol{q}(t)$ is written as a summation of orthogonal spatial modes $\boldsymbol{\phi}_j$, each weighted by a time-varying expansion coefficient $a_j(t)$, i.e.,

$$\boldsymbol{q}(t) = \sum_{j=1}^{N} \boldsymbol{\phi}_j a_j(t). \tag{1}$$

A coupled set of nonlinear ordinary differential equations (ODEs) for the expansion coefficients is obtained by inserting (1) into the governing equations and subsequently projecting the governing equations onto the modes. Finally, a reduced order model is obtained by retaining only a subset of the modes, leading to a smaller set of coupled nonlinear ODEs for the remaining expansion coefficients.

While in general the modes could correspond to any orthogonal basis, they are most often chosen to be proper orthogonal decomposition (POD) modes [5]. A defining property of POD modes is that they optimally reconstruct the flow energy, computed in a spatial norm and averaged over time, for any order of the expansion in (1). However, this gaurentees neither optimality nor accuracy of the POD-Galerkin reduced-order model solution. In general, POD-Galerkin projection suffers from a number of well-known issues [4]. Errors within the approximation accumulate at every time step, leading to solutions that are often accurate only over short temporal horizons. Indeed, POD-Galerkin systems are sometime unstable.

METHOD

To alleviate these issues, several recent studies have proposed the use of various space-time reduced-order modeling approaches [1, 3]. In the present work, we develop a new framework for developing nonlinear reduced-order models based on a space-time Galerkin projection of the governing equations using spectral proper orthogonal decomposition (SPOD) modes [2, 7]. In place of (1), we consider the expansion

$$\boldsymbol{q}(t) = \sum_{j=1}^{N} \boldsymbol{\psi}_j e^{i\omega_j t} b_j. \tag{2}$$

Each SPOD mode $\boldsymbol{\psi}_j$ is associated with a single temporal frequency ω_j. SPOD modes are the solution of a space-time POD optimization problem for stationary flow, and therefore optimally capture the flow energy in a space-time norm [2, 7]. In this sense, they are the natural space-time equivalent of standard spatial POD modes. There exists a complete set of spatially orthogonal modes at each frequency, and the space-time modes $\boldsymbol{\psi}_j e^{i\omega_j t}$ are orthogonal in a space-time inner product. Physically, SPOD modes can be interpreted as coherent structures – portions of the flow that are self-correlated in space and time and uncorrelated with all other modes.

Using the expansion (2) and projecting the equations onto the modes using the space-time inner product leads to a set of coupled algebraic equations for the expansion coefficients b_j, which are time-independent scalars. This space-time projection of the equations naturally minimizes error over the full time window for which the modes are defined, providing a means to control the solution error over a desired time window and prevent the error accumulation and instability typical of POD-Galerkin methods. Additionally, we have developed a SPOD-Petrov-Galerkin variant that optimally captures linear amplification mechanisms with the Navier-Stokes equations.

*Corresponding author. E-mail: towne@umich.edu

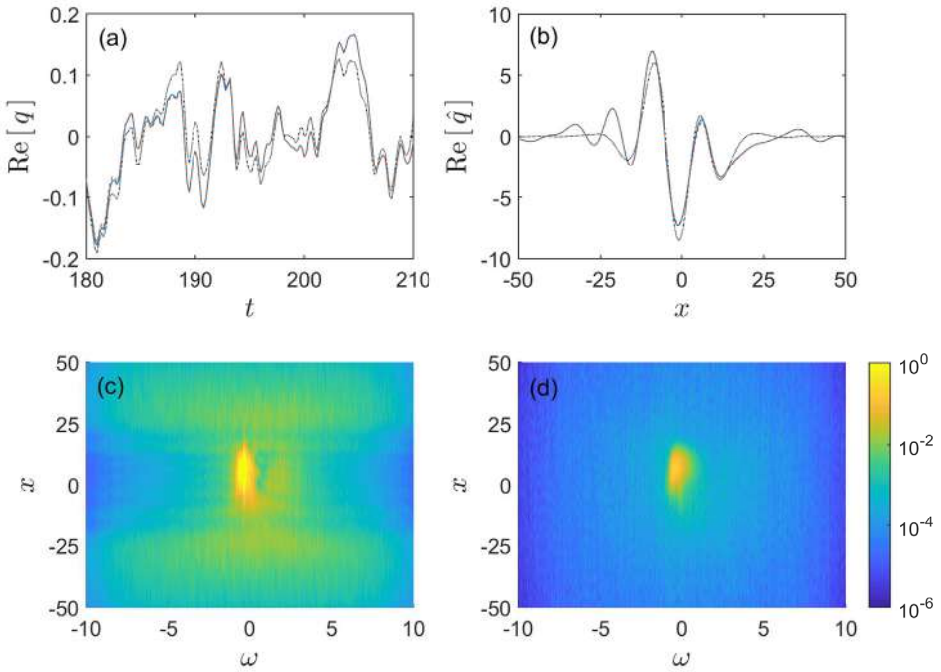

Figure 1: Results for the Ginzburg-Landau problem: (a) Sample time series for true solution (blue solid line), POD-Galerkin model (black dotted line), and SPOD-Galerkin model (dashed orange line); (b) Fourier mode of each solution (lines same as in (a)) at frequency $\omega = 1$; (c-d) PSD of error for the POD-Galerkin and SPOD-Galerkin modes, respectively. In all cases, the SPOD-Galerkin model yields lower error levels.

RESULTS

We demonstrate our method using two example problems. First, we consider the complex Ginzburg-Landau equation subject to random excitation [6]. This produces a simple model that mimics the non-normal energy amplification present in real shear flows and produces quasi-random time series reminiscent of turbulent flow. We construct both POD-Galerkin and SPOD-Galerkin reduced-order models, and choose the order of each model such that they have equal computational cost (i.e., we compare accuracy at fixed cost). Figure 1(a) shows an example time trace produced by the Ginzburg-Landau equation and the two reduced-order models, and Figure 1(b) shows the corresponding Fourier modes at a particular frequency, $\omega = 1$, as a function of the spatial coordinate x. In both cases, the POD-Galerkin solution contains noticeable errors, while the SPOD-Galerkin solution is essential indistinguishable from the true solution. Figure 1(c,d) shows the power spectral density of the error of the POD-Galerkin and SPOD-Galerkin reduced-order models, respectively, as a function of frequency and spatial location. The error for the SPOD-Galerkin model is consistenyly lower, by several orders-of-magnitude over most of the domain. In addition to the Ginzburg-Landau model, the conference presentation will include results for a turbulent channel flow.

CONCLUSIONS

Improved nonlinear reduced-order models are needed to enable low-cost prediction and control of turbulent shear flows. The proposed space-time SPOD-Galerkin projection approach has the potential to overcome issues commonly encountered when using traditional POD-Galerkin reduced-order models, such as error accumulation and instability, by minimizing errors over a desired time interval. While further testing is needed, our results demonstrate the considerable potential of the method to deliver accurate solutions at low computational cost.

References

[1] Y. Choi and K. Carlberg. Space–time least-squares Petrov–Galerkin projection for nonlinear model reduction. *SIAM J. Sci. Comput.*, 41(1):A26–A58, 2019.
[2] J. L. Lumley. *Stochastic tools in turbulence*. Academic Press, New York, 1970.
[3] E. J. Parish and K. T. Carlberg. Windowed least-squares model reduction for dynamical systems. *arXiv:1910.11388*, 2019.
[4] C. W. Rowley and S. T. M. Dawson. Model reduction for flow analysis and control. *Annu. Rev. Fluid Mech.*, 49:387–417, 2017.
[5] L. Sirovich. Turbulence and the dynamics of coherent structures. i. coherent structures. *Quart. Appl. Math.*, 45(3):561–571, 1987.
[6] A. Towne, A. Lozano-Durán, and X. Yang. Resolvent-based estimation of space-time flow statistics. *J. Fluid Mech.*, 883:A17, 2020.
[7] A. Towne, O. T. Schmidt, and T. Colonius. Spectral proper orthogonal decomposition and its relationship to dynamic mode decomposition and resolvent analysis. *J. Fluid Mech.*, 847:821–867, 2018.

INTERMITTENT TURBULENT STRUCTURES IN SUBCRITICAL TRANSITION OF ANNULAR COUETTE FLOW WITH/WITHOUT IMAGINARY DOMAIN

Kazuki Takeda[1] and Takahiro Tsukahara *[1]
[1] Department of Mechanical Engineering, Tokyo University of Science, Chiba, Japan

Summary In the subcritical transition of annular Couette flow (aCf), the global-stability Reynolds number Re_g increases with the decreasing radius ratio η, which is the ratio of inner- to outer radii. With low η, the small circumferential extent of the domain restricts the patterning of localized turbulence that may spread two-dimensionally. In such a case, the intermittently turbulent state settles down rapidly in the laminar state. However, aCf with an artificially-extended domain ($L_\theta > 2\pi$) exhibits two-dimensional patterns of localized turbulence by relaxing the circumferential confinement, even keeping a low η. The patterning and spreading of localized turbulence allows Re_g to be lower than that with the nominal domain of 2π. The newly found transitional process shows a good agreement with (1+1)-dimensional directed-percolation universality class.

INTRODUCTION

Annular Couette flow (aCf) is a wall-bounded shear flow between two concentric cylinders driven by a steady sliding motion of the inner cylinder, as illustrated in Fig. 1(a). This system is characterized by the radius ratio defined by the two radii of the inner and outer cylinders: that is, $\eta = r_{in}/r_{out}$. In aCf with $\eta \geq 0.1415$, the linear-stability Reynolds number Re_L goes to infinity and, even for $\eta = 0.1$, $\mathrm{Re}_L = 8.0 \times 10^5$ [1]. However, below Re_L, aCf can sustain turbulent state steadily. Especially, for low Reynolds numbers close to Re_g, the flow exhibits intermittently-turbulent structures of the localised turbulence that coexists with laminar regions. In plane Couette flow regarded as aCf with $\eta \to 1$, the intermittency shows two-dimensional pattern spreading in the streamwise and spanwise directions with a regular interval between oblique turbulent bands, the so-called turbulent stripe, near $\mathrm{Re}_g = 324$ [2]. The case with a low η can be regarded as a pipe flow and has actually exhibited a puff-like structure having the one-dimensional intermittency only in streamwise direction [3]. This fact indicates that spatial intermittency would be limited by the closed boundary condition of short circumferential extent. Recently, different types of directed percolation (DP) universality classes were found in various wall-bounded shear flows such as plane Poiseuille flow and Taylor-Couette flow with high η, by the experimental and DNS (direct numerical simulation) studies in huge domains [4, 6, 5]. In such flows, there occur splitting and decaying of localised turbulence frequently. The DP universality classes are characterized by some critical exponents about the spatiotemporal dimensions of the intermittency. For aCf with $\eta = 0.1$ and artificially-extended circumferential length ($L_\theta = 16\pi$) as the "imaginary domain", the subcritical transition revealed a trend of the DP universality class because of the relaxed closed boundary conditions [3]. The aCf with the imaginary domain is a good test system to investigate the competition between two effects of the closed circumferential length and the curvature.

In this study, we have performed DNS of aCfs at various η values to examine η-dependency of the intermittent structures, in particular the switching from stripe to puff. In addition, low-η aCfs with with imaginary domains have been also simulated to assess the intermittently-turbulent state as a DP universality class.

NUMERICAL METHOD AND CONDITION

We performed DNS of calculating the incompressible Navier-Stokes and continuity equations described in the cylindrical coordinate system, without using any turbulence model, for aCf with a huge computational domain. We calculated, from fully turbulent to laminar state in subcritical transition for low value of the radius ratio $\eta = 0.1$–0.3, aCf with a nominal domain ($L_\theta = 2\pi$) and that with a large enough imaginary domain for the circumferential direction ($L_\theta > 2\pi$) in order to relax the closed boundary condition in the circumferential direction. The details of computational conditions are summarized in Table 1. The control Reynolds number is $\mathrm{Re} = U_w h/4\nu$, where U_w is the speed of the sliding inner cylinder, h is the gap width between the concentric cylinders, and ν is the kinematic viscosity.

Table 1: Computational conditions. The superscript (*) represents a non-dimensionalized quantity by h.

	Nominal aCf (w/o imaginary domain)				aCf w/ imaginary domain			
η	0.1	0.15	0.2	0.3	0.1	0.15	0.2	0.3
$L_x^* \times L_r^*$	512×1	409.6×1			512×1	409.6×1		
L_θ	2π				128π		112π	96π
L_{out}^* $(= L_\theta\, r_{out}^*)$	7.0	7.4	7.9	9.0	446.8	473.1	439.8	430.8
L_{in}^* $(= L_\theta\, r_{in}^*)$	0.7	1.1	1.6	2.7	44.7	71.0	88.0	129.2
$N_x \times N_r$	2048×64							
N_θ	32		64		2048			

*Corresponding author. E-mail: tsuka@rs.tus.ac.jp

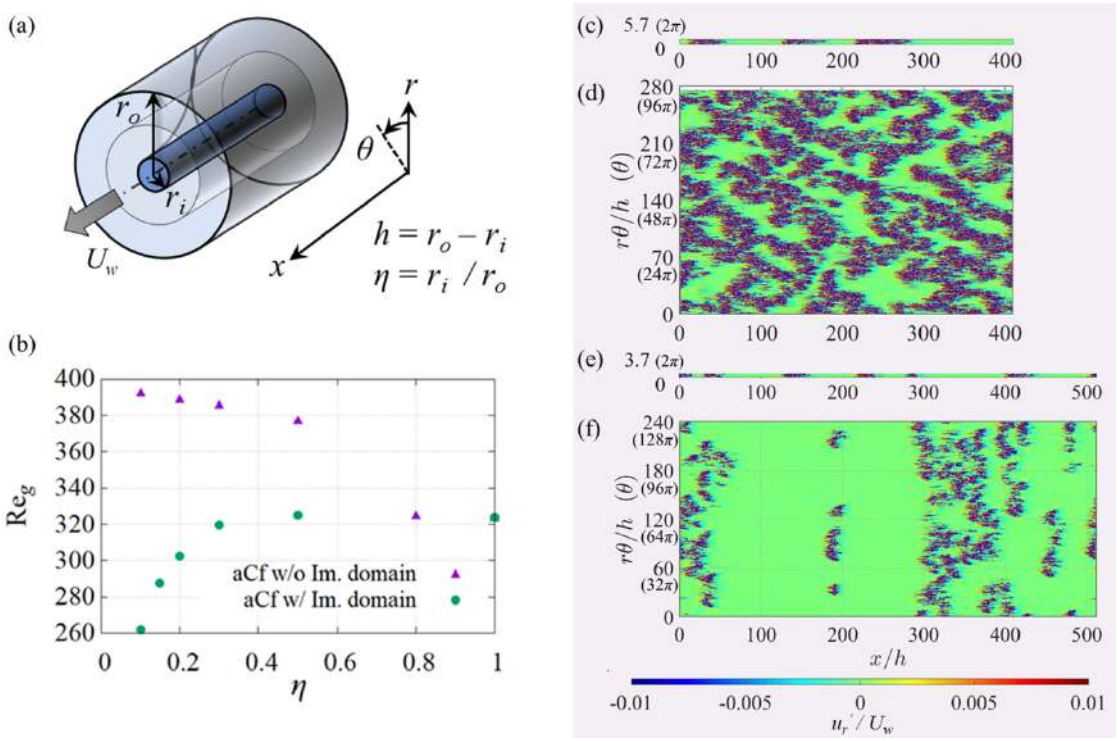

Figure 1: (a) Schematic of the annular Couette flow (aCf). The gray curved plane in the gap is the visualized (x, θ)-plane at the central gap $(r^* = (r^*_{in} + r^*_{out})/2)$. (b) Dependency of the global-stability Reynolds number Re_g on the radius ratio η, including the value at $\eta = 1$ cited from Duguet *et al.* [2], and from Kunii *et al.* for $\eta = 0.5, 0.8$ [3]. (c)–(f) Instantaneous flow fields with the intermittent structures of localized turbulence in aCf for $\eta = 0.3$; (c) without imaginary domain for $\mathrm{Re} = 388$, (d) with imaginary domain for $\mathrm{Re} = 325$ and $\eta = 0.1$; (e) without imaginary domain for $\mathrm{Re} = 402.5$, and (f) with imaginary domain for $\mathrm{Re} = 262.5$. Contours show radial (wall-normal) velocity fluctuation in the central gap $(x,\ \theta)$-plane, which is marked with a gray plane in (a). Red and blue as $|u_r^{'}/U_w| \geq 0.01$ indicate turbulent regions, while green as $|u_r^{'}/U_w| < 0.01$ corresponds to laminar region.

RESULTS AND DISCUSSION

In subcritical transition, for high η, the nominal aCf and artificial-extended aCf with an imaginary domain exhibit same intermittency with the stripe structure, while for low–middle η they have different structures of the puff-like and stripe structures. In the nominal aCf without an imaginary domain for $\eta < 0.7$, the intermittent structure cannot form the helical shape like the turbulent stripe and exhibits puff-like structures, as shown in Fig. 1(c,e). Figure 1(b) shows that Re_g increases from 324 for $\eta > 0.7$. On the other hand, in aCf with an imaginary domain, the stripe structures are not collapsed for $\eta \geq 0.3$: see Fig. 1(d). However, aCf with an imaginary domain and $\eta \leq 0.2$ forms the helical structure even far from Re_g, while near Re_g it collapses and forms turbulent spots that extend only in the circumferential direction, i.e., the transverse structures, as shown in Fig. 1(f). Interestingly, Re_g greatly decreases from 324, as plotted in Fig. 1(b).

We now introduce the turbulent fraction $F_t = (\text{Turbulent area})/(\text{Turbulent area} + \text{Laminar area})$ on the central gap plane. Although figure not shown, the temporal change of F_t and the Reynolds number dependency of time-averaged $\bar{F}_t$ can each be scaled with power laws: $F_t \sim t^{-\alpha}$ and $\bar{F}_t \sim (\mathrm{Re} - \mathrm{Re}_g)^{\beta}$. These scaling exponents show good agreements with the critical exponents of (1+1)d DP universality class; $\alpha_{\mathrm{DP}} = 0.159$ and $\beta_{\mathrm{DP}} = 0.276$. This result implies the universality in the turbulence spreading and developing.

CONCLUSIONS

We found the subcritical transition of annular Couette flows (aCf) with imaginary circumference domains exhibit different intermittent structures compared with the nominal aCf: for $\eta \geq 0.3$ the stripe structures form, while for $\eta \leq 0.2$ the transverse or spot structures occur. Re_g of the nominal aCf for $\eta < 0.8$ increases as η decreases ($\mathrm{Re}_g > 324$), while Re_g of aCf with imaginary domains for $\eta \leq 0.3$ decreases ($\mathrm{Re}_g < 324$).

The present work was partially supported by the Cyberscience Center of Tohoku University and by the Grants-in-Aid for Scientific Research (B) #19H02071 from the Japan Society for the Promotion of Science (JSPS).

References

[1] Gittler, P. Stability of axial Poiseuille-Couette flow between concentric cylinders. *Acta Mechanica* **101**: 1–13, 1993.
[2] Duguet, Y. *et al.* Formation of turbulent patterns near the onset of transition in plane Couette flow. *J. Fluid Mech.* **650**: 119–129, 2010.
[3] Kunii, K. *et al.* Laminar-turbulent coexistence in annular Couette flow. *J. Fluid Mech.* **879**: 579–603, 2019.
[4] Sano, M., Tamai K. A universal transition to turbulence in channel flow. *Nature Phys.* **12**: 249–253, 2016.
[5] Lemoult, G. *et al.* Directed percolation phase transition to sustained turbulence in Couette flow. *Nature Phys.* **12**: 254–258, 2016.
[6] Shimizu, M., Manneville P. Bifurcations to turbulence in transitional channel flow. *Phys. Rev. Fluids* **4**: 113903, 2019.

DATA-DRIVEN LINEAR ESTIMATORS FOR TURBULENT CHANNEL FLOW AT $Re_\tau = 2003$

Sean Symon *[1], Anagha Madhusudanan[1], Simon J. Illingworth[1], and Ivan Marusic[1]
[1] Department of Mechanical Engineering, University of Melbourne, Parkville, Australia

Summary We investigate the minimum number of flow measurements required to estimate the large scales of turbulent channel flow at a friction Reynolds number of $Re_\tau = 2003$. Time and space-resolved measurements, known at discrete wall-normal locations, serve as inputs to linear estimators based on the linearised Navier-Stokes equations. The nonlinear terms are treated as white noise in space and time forcing. The estimation is improved significantly when the input data are known at two wall-normal locations as opposed to a single wall-normal location. The estimated velocity fields are in good agreement with those of DNS in the buffer and logarithmic regions and can be used to infer statistics of the unknown nonlinear forcing terms.

INTRODUCTION

A practical limitation of controlling wall-bounded flows is the ability to measure them experimentally. The hardware needed to obtain measurements of high Reynolds number turbulence, for example, is costly in order to resolve the wide range of scales present. Recent work [1, 2] has focused on converting partially known measurements into estimates of flow states that are not measured. The work of Illingworth et al. [1] converted knowledge of time-resolved velocity measurements at one wall-normal location into estimates at other wall heights. This Kalman-filter-based approach relied on the linearised Navier-Stokes equations which, when linearised around the turbulent mean velocity profile, was able to reproduce key features of wall-bounded turbulent flows [3].

An alternative estimation technique is to relate the velocity field between two wall-normal planes using spectral linear stochastic estimation (SLSE) [2]. The performance of the linear estimator, however, was hindered by treating the unknown nonlinear terms as white in space and time forcing [4]. The linear estimator overemphasised small scales relative to large scales and overestimated the magnitude of velocity fluctuations below the measurement plane. In this work, estimation is improved by adding one additional measurement plane to counteract deficiencies of the linear model. It is also shown that a suitable nonlinear forcing can be derived from the input measurements to improve predictions of second-order velocity statistics and, consequently, estimates obtained from SLSE.

METHODS

Two methods are used to estimate turbulent channel flow: the Kalman filter and SLSE. Figure 1(a) outlines the components in the Kalman filter. The objective is to design a filter $\boldsymbol{F}(s)$ that minimises the error $\boldsymbol{e}$ between the estimated quantities $\boldsymbol{z}_e$ and filter estimate $\boldsymbol{z}$. The filter takes as input the measured quantities $\boldsymbol{y}$ contaminated by noise $\boldsymbol{n}$. The plant $\boldsymbol{P}(s)$ is derived from the linearised Navier-Stokes equations where $\boldsymbol{d}$ represents unmodelled nonlinear terms that are assumed to be white noise in space and time.

SLSE is illustrated in Figure 1(b) and provides an estimate at wall-normal location z_1 using a transfer kernel H_L and known input data at z_2. H_L is wavenumber-dependent and can be constructed from second-order velocity statistics $\boldsymbol{X}(k_x, k_y)$. In the first row (eLNS), the second-order statistics of the unknown forcing are assumed to be white in time and space, i.e. $\boldsymbol{S}_{\hat{d}\hat{d}} = \boldsymbol{I}$. The second row (sLNS) denotes the case when velocity correlations are known between multiple input planes. The unknown forcing statistics $\boldsymbol{S}_{\hat{d}\hat{d}}$ may be estimated from a projection-based approach [5] and used to compute updated velocity correlations $\boldsymbol{X}_f$ to improve estimation accuracy.

RESULTS

The linear estimators are tested on the large scales of turbulent channel flow at a friction Reynolds number of $Re_\tau = 2003$, which have been obtained by direct numerical simulation (DNS) [6]. In Figure 2, the DNS is compared to two

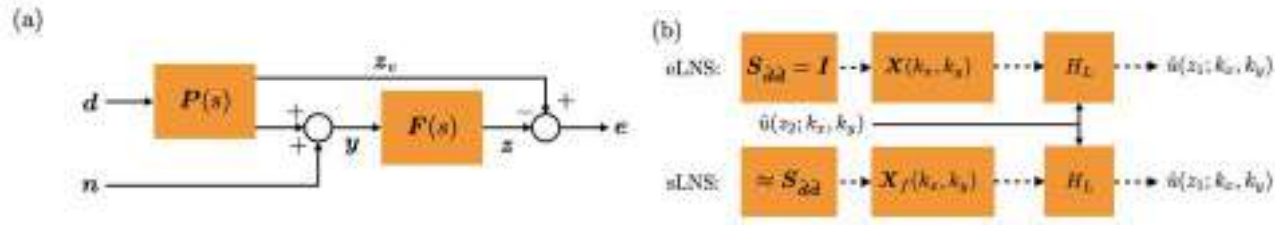

Figure 1: Schematic of the (a) Kalman filter and (b) SLSE-based linear estimators.

*Corresponding author. E-mail: sean.symon@unimelb.edu.au.

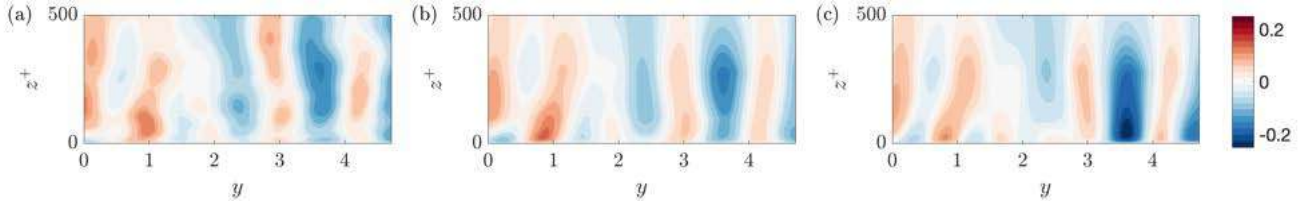

Figure 2: Streamwise velocity from (a) DNS, (b) Kalman filter using two input planes and (c) Kalman filter using one input plane.

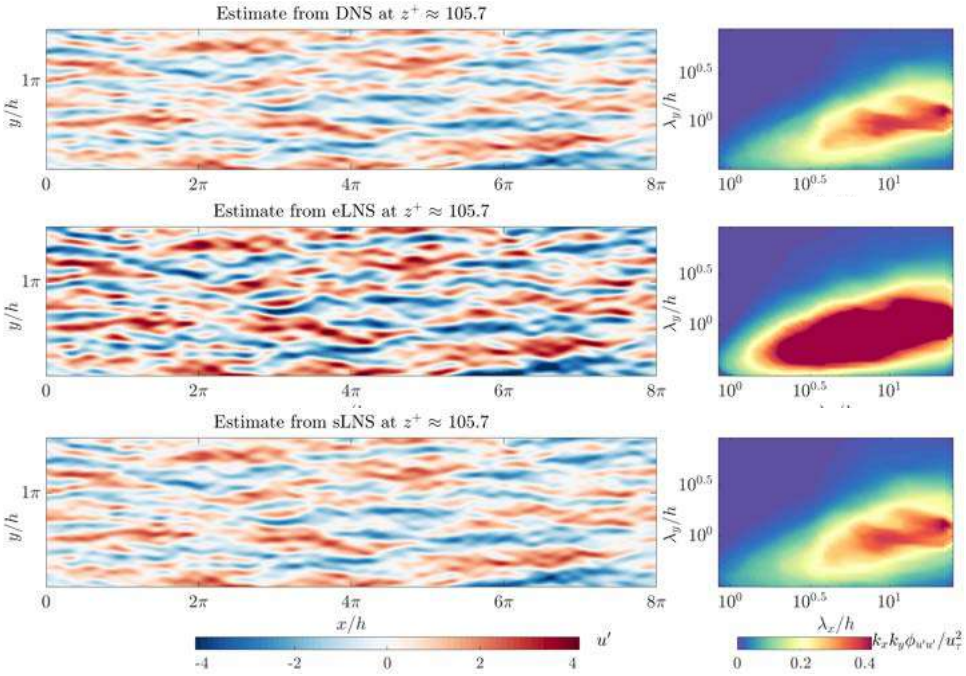

Figure 3: SLSE velocity estimates obtained from DNS (top), eLNS (middle) and sLNS (bottom).

Kalman filter-based estimators. The first, which will be referred to as the 2-plane case, has knowledge of the velocity field at two wall-normal locations: $z^+ = 100$ and $z^+ = 300$. The second has knowledge of the velocity field at $z^+ = 300$ only and will be referred to as the 1-plane case. There is good agreement between the DNS and 2-plane velocity fields in Figure 2(a) and (b) although it deteriorates above $z^+ = 500$. The 1-plane case in Figure 2(c) overestimates the velocity fluctuations near the wall. This is particularly apparent in Figure 2(c) where it can be seen that the 1-plane case predicts an intense $-u'$ fluctuation at $y = 3.5$. The addition of the second plane, therefore, is necessary to prevent overestimation near the wall.

Similar improvements can be observed in the estimates obtained using SLSE in Figure 3. Unlike the Kalman filter, SLSE does not yield the actual velocity field at the estimate location z_1. Instead, it predicts the velocity fluctuations that are coherent with the measurement plane at z_2 [2]. Hence, the best case scenario is referred to as the DNS estimate in Figure 3. eLNS, which assumes forcing that is white in time and space, overestimates the magnitude of fluctuations and overemphasises smaller scales relative to larger scales. sLNS, on the other hand, has limited knowledge of the forcing from the input measurements and is in very good agreement with the DNS estimate.

The financial support of the Australian Research Council is gratefully acknowledged and we thank the Fluid Dynamics Group of the Polytechnic University of Madrid (UPM) for the DNS dataset [6].

References

[1] Illingworth, S. J., Monty, J. P., and Marusic, I. Estimating large-scale structures in wall turbulence using linear models. *J. Fluid Mech.* **842**: 146-162, 2018.

[2] Madhusudanan, A., Illingworth, S. J. and Marusic, I. Coherent large-scale structures from the linearized Navier-Stokes equations. *J. Fluid Mech.* **873**: 89-109, 2019.

[3] McKeon, B. J. and Sharma, A. S. A critical-layer framework for turbulent pipe flow. *J. Fluid Mech.* **658**: 336-382, 2010.

[4] Symon, S., Illingworth, S. J. and Marusic, I. Large-scale structures predicted by linear wall-bounded turbulence *J. Phys. Conf. Ser.*, **1522**, 012006, 2020.

[5] Towne, A., Lozano-Durán, A. and Yang, X. Resolvent-based estimation of space-time flow statistics. *J. Fluid Mech.* **883**, A17, 2020.

[6] Vela-Martín, A., Encinar, M. P., García-Gutiérrez, and Jiménez, J. A second-order consistent, low-storage method for time-resolved channel flow simulations up to $Re_\tau = 5300$. *arXiv:1808.06461*, 2018.

MEAN MOMENTUM BALANCE IN ADVERSE PRESSURE GRADIENT TURBULENT BOUNDARY LAYERS

Sylvia Romero*, Spencer Zimmerman , Jimmy Philip, and Joseph Klewicki
Department of Mechanical Engineering, University of Melbourne, Parkville, Australia

Summary The mean momentum balance is used to analyze large eddy simulation data of adverse pressure gradient (APG) boundary layers (of Bobke et al., 2017), as well as newly acquired experimental data at higher Reynolds numbers. The structure of the mean momentum balance is compared relative to the zero pressure gradient case. Zero pressure gradient boundary layer data is obtained from the direct numerical simulations of Schlatter and Örlü, 2010 and Sillero et al., 2013, and experimental data from Zimmerman et al., 2019. Changes in the layered structure are seen to affect the emerged properties of the APG flow. We will discuss changes in the inner and outer interactions in terms of (for example) the location where the viscous force loses dominance, the skewness, and amplitude modulation.

Mean momentum balance

The mean momentum balance (MMB) is the time averaged statement of Newtons second law. We first consider the MMB for the channel flow since its force balance stucture is well-characterized (see [5], [6], and [7]). For channel flows the equation is a balance of three terms: viscous force (VF), turbulent inertia (TI), and pressure gradient (PG).

$$\underbrace{\frac{\partial^2 U^+}{\partial y^{2+}}}_{\text{VF}} - \underbrace{\frac{\partial \overline{uv}^+}{\partial y^+}}_{\text{TI}} - \underbrace{\frac{1}{\delta^+}}_{\text{PG}} = 0. \tag{1}$$

The VF term is the gradient of the viscous stress and the TI term is the gradient of the Reynolds stress. The zero-crossing of the TI term corresponds to the peak location of the Reynolds stress. Prior to the zero-crossing the TI term acts as a source, whereas after the zero-crossing the TI term becomes negative and acts as a momentum sink. The PG term is a function of Reynolds number and remains constant with wall-normal distance y. The superscript '$+$' denotes inner normalization.

For the two-dimensional zero pressure gradient boundary layer (ZPG BL) the equation is still a balance of three terms. Here, the PG term is replaced by the mean inertia (MI) term, which is still a function of Reynolds number, but no longer a constant in y or streamwise distance x.

$$\underbrace{\frac{\partial^2 U^+}{\partial y^{2+}}}_{\text{VF}} - \underbrace{\frac{\partial \overline{uv}^+}{\partial y^+}}_{\text{TI}} - \underbrace{[U^+\frac{\partial U^+}{\partial x^+} + V^+\frac{\partial U^+}{\partial y^+}]}_{\text{MI}} = 0. \tag{2}$$

Near the wall the VF and TI terms are dominant. Because of this the MMB structure for the ZPG BL and channel flow is very similar. The main difference is that a small outer peak forms in the MI and TI terms of the ZPG BL.

The MMB for the APG BL is comprised of four terms. Like the ZPG BL the mean momentum equation includes a non-constant MI term. Like the channel flow case, however the relevant equation also includes a constant PG term. For the APG BL this term is constant and negative, while for the channel flow it is positive.

$$\underbrace{\frac{\partial^2 U^+}{\partial y^{2+}}}_{\text{VF}} - \underbrace{\frac{\partial \overline{uv}^+}{\partial y^+}}_{\text{TI}} - \underbrace{[U^+\frac{\partial U^+}{\partial x^+} + V^+\frac{\partial U^+}{\partial y^+}]}_{\text{MI}} + \underbrace{U_\infty^+\frac{\partial U_\infty^+}{\partial x^+}}_{\text{PG}} = 0. \tag{3}$$

Due to the additional PG term the balance has changed from the ZPG BL to the APG BL as shown in Figure 1. For the APG BL, the VF term is now balanced by the PG term very near the wall, while away from the wall the PG term balances the MI term. Furthermore in the ZPG BL flow the position where the VF term loses leading order nominally coincides and scales with where the TI term crosses zero. In the APG BL flow, however, the TI term crosses zero beyond where the VF term loses dominance. Beyond the location where the VF term approaches zero, a new inertial balance emerges where the remaining three terms (the TI, MI, and PG) are balanced. This new structural feature suggests a change in the nature of the interaction between the inner and outer regions.

Experiments

The value of the Clauser pressure-gradient parameter $\beta = (\delta^*/\tau_w)(dP/dx)$, where δ^* is the displacement thickness, τ_w is the wall shear stress, and dP/dx is the streamwise pressure gradient, characterizes the boundary layer between ZPG: $\beta = 0$, APG: $\beta > 0$, and favourable pressure gradient (FPG): $\beta < 0$ cases. A boundary layer will behave differently depending on how rapidly β is changing and whether β is decreasing or increasing with Reynolds number. Large eddy simulation (LES) data of a quasi-equilibrium APG BL (where β is nominally constant) was studied. From direct numerical simulation (DNS) and LES data a range of low Reynolds numbers were analyzed for the ZPG BL ($670 \leq Re_\theta \leq 6.5\times10^3$)

*Corresponding author. E-mail: sylviar@student.unimelb.edu.au

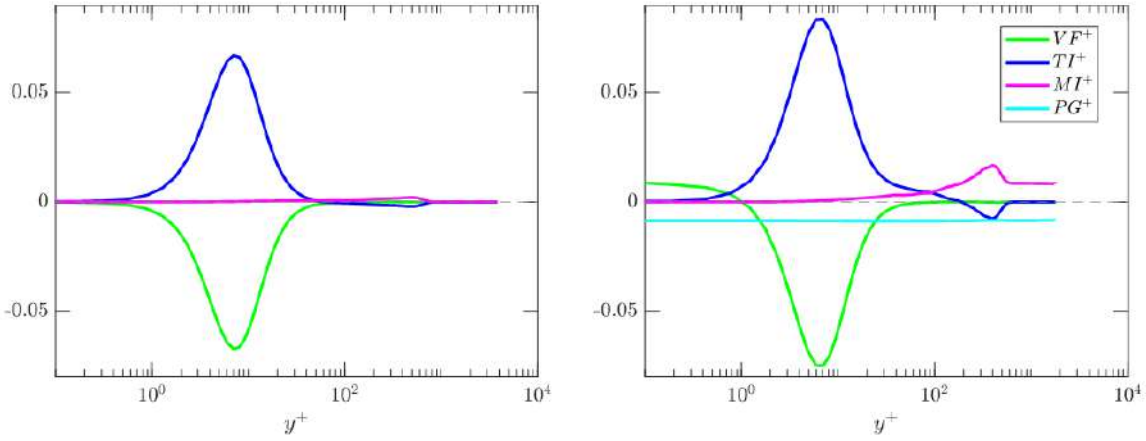

Figure 1: (Left) MMB of ZPG BL at $Re_\theta = 2000$, data from [2]. (Right) MMB of APG BL at $Re_\theta = 2000$, data from [1].

and APG BL cases ($1.3 \times 10^3 \leq Re_\theta \leq 3.2 \times 10^3$), respectively. To observe an APG BL at higher Reynolds numbers hot-wire anemometry experiments were conducted in the Flow Physics Facility (FPF) at The University of New Hampshire. A ramp structure was installed on the ceiling of the FPF. Extending approximately 15m downstream, this ramp creates a FPG region followed by a ZPG ramp (where the flow relaxes back to equilibrium), and that is followed by an APG ramp. The flow is then allowed to develop downstream of the ramp system back to equilibrium over a ∼20m fetch. Hot-wire measurements were taken in the region of the APG ramp as well as downstream of the ramp to observe this relaxation. In the APG region, the measured Reynolds numbers ranged from $2.1 \times 10^4 \leq Re_\theta \leq 2.7 \times 10^4$ and downstream of the ramp from $2.9 \times 10^4 \leq Re_\theta \leq 3.8 \times 10^4$.

Observations

From the APG BL LES the behavior of the VF term as it loses dominance remains largely the same as β changes from a ZPG case to mild quasi-equilibrium APG case. On the other hand, the peak in the Reynolds stress moves outwards, indicating an additional momentum source from the outer region. Despite this, the peaks of the Reynolds stress from the experimental measurements align better with the LES profiles with $\sqrt{\delta^+}$ scaling than with δ scaling. This suggests that the TI term zero-crossing still scales with $\sqrt{\delta^+}$ despite the additional PG term in the MMB.

Another indicator of inner and outer structural changes is the streamwise velocity skewness, S_u, which behaves similar to the amplitude modulation (AM) coefficient as seen in [8] and [9]. Owing to the application of an APG BL the extent of positive S_u increases. Given the connection between S_u and AM, this suggests that the AM has been modified. Similiar findings were seen by Harun et al., 2013, however AM was increased in the inner and outer regions. As the near-wall S_u increases the zero-crossing moves outwards. This was also noted for the AM in [10] at constant Reynolds number and increasing pressure gradient. Before the zero-crossing of the AM the small scales were positively correlated to large scale streamwise velocity fluctuations and afterwards negatively correlated. At high Reynolds numbers S_u commonly corresponds to the start of the inertial layer in the ZPG BL. A coupling of the S_u-zero-crossing and where the VF loses dominance was not observed in the APG BL experimental data.

Conclusion

The MMB under the addition of a pressure gradient suggests that inner and outer regions communicate differently from the ZPG BL flow. This is seen in the shift in the peak location of the Reynolds stress from where the VF loses dominance. Observations correlate with an increased S_u and amplitude modulation as the pressure gradient increases from a ZPG BL.

References

[1] Bobke A., et al. History effects and near equilibrium in adverse-pressure-gradient turbulent boundary layers. *J. Fluid Mech.* **820**: 667-692, 2017.
[2] Schlatter P., Örlü, R. Assessment of direct numerical simulation data of turbulent boundary layers. *J. Fluid Mech.* **659**: 116-126, 2010.
[3] Sillero J., Jiménez, J., Moser, R. One-point statistics for turbulent wall-bounded flows at Reynolds numbers up to $\delta^+ \approx 2000$. *Phys. Fluids* **25(10)**: 105102, 2013.
[4] Zimmerman S., Philip J., Monty J., Talameli A., Marusic I., Ganapathisubramani B., Hearst J., et al. A comparative study of the velocity and vorticity structure in pipes and boundary layers at friction Reynolds numbers up to 10^4. *J. Fluid Mech.* **869**: 182-213, 2019.
[5] Wei T., et al. Properties of the mean momentum balance in turbulent boundary layer, pipe and channel flows. *J. Fluid Mech.* **522**: 303-327, 2005.
[6] Fife P., Klewicki J., Wei T. Time averaging in turbulence settings may reveal an infinite hierarchy of length scales. *Discrete Contin. Dyn. Syst.* **24(3)**: 781-807, 2009.
[7] Klewicki J. A description of turbulent wall-flow vorticity consistent with mean dynamics. *J. Fluid Mech.* **737**: 176-204, 2013.
[8] Mathis R., Hutchins N., and Marusic I.Large-scale amplitude modulation of the small-scale structures in turbulent boundary layers. *J. Fluid Mech.* **628**: 311-337, 2009.
[9] Mathis R., Hutchins N., and Marusic I.The relationship between the velocity skewness and the amplitude modulation of the small scale by the large scale in turbulent boundary layers. *Phys. Fluids.* **23**: 121702, 2011.
[10] Harun Z., et al. Pressure gradient effects on the large-scale structure of turbulent boundary layers. *J. Fluid Mech.* **715**: 477-498, 2013.

THE MINIMAL SEED IN A BOUNDARY LAYER FLOW: A FREQUENCY-DOMAIN APPROACH

Georgios Rigas*[1], Denis Sipp [2], and Tim Colonius[3]
[1]Department of Aeronautics, Imperial College, London, United-Kingdom
[2]Department of Aerodynamics, Aeroelasticity and Acoustics, ONERA, Meudon, France
[3]Department of Mechanical and Civil Engineering, California Institute of Technology, Pasadena, CA, USA

Summary We identify the nonlinear optimal mechanisms at the edge of the turbulent regime through solution of the frequency-domain Harmonic-Balanced Navier-Stokes equations. Specifically, we seek the optimal harmonic or multi-harmonic forcing mechanisms that maximise the skin friction coefficient asymptotically in time, which can be viewed as *the minimal forcing seed in the frequency domain*. By retaining a small and finite number of harmonics that nonlinearly interact and distort the mean flow, but also transfer energy among them, a low-dimensional self-consistent dynamical description of the turbulent regime obtained. At the edge of turbulence, the skin-friction coefficient reaches the empirical turbulent values, and the velocity profiles depart from the law of the wall by developing a logarithmic region, as predicted by the model.

INTRODUCTION

For spatially developing flows of practical interest, such as boundary layer flows, nonlinear optimisation has been recently employed to find the most amplified initial condition of the governing Navier-Stokes equations that leads to turbulent dynamics. This is known in the literature as the *minimal seed* [1, 2]. By analog with the linear approaches, and specifically the frequency-response analysis, it is experimentally more natural to model transition from laminar to turbulent flow as a stationary process where disturbances are continually supplied to the system from the environment, i.e. to consider the nonlinear receptivity problem.

A natural generalization in order to calculate finite-amplitude perturbations in the frequency domain is to seek self-consistent solutions to the full Navier-Stokes equations under the form of an expansion consisting of a mean-flow solution, a fundamental mode and p harmonics of the fundamental. Using this framework, for a given forcing, the response of the system can be calculated in a self-consistent way. Subsequently, optimal nonlinear forcing mechanisms that lead to turbulence and maximise the skin-friction coefficient are calculated using a variational method and direct-adjoint looping.

THE MINIMAL FORCING-SEED AT THE EDGE OF TURBULENCE

By increasing the finite forcing amplitude, and repeating the nonlinear optimisation, we identified the frequency-domain minimal seed and the key-mechanisms that lead to turbulent dynamics. We found that for fundamental forcing, the nonlinearly most amplified disturbances correspond to a pair of oblique waves with frequency and spanwise wavenumber close to the linear optimal one. Nonlinearity is responsible for redistributing the energy to the streamwise uniform vortex component which leads to streak growth through the lift-up mechanism. Depending on the imposed spanwise symmetry, the low-speed streaks break down to turbulence through varicose oscillations (imposing reflectional symmetry in spanwise) or sinuous ones (no symmetry imposed in in spanwise), as shown in figure 1. In each case, hairpin vortices and quasi-streamwise vortices are observed prior to breakdown and the distinct regimes during the transition process can be summarised as follows:

- At the very early stages of transition, characterised by linear growth, the velocity profiles obey the linear wall law $u^+ = y^+$, as shown in figure 2. Transition has been triggered optimally with a pair of oblique waves.
- The second stage of transition is associated with the generation of streaks through nonlinear interactions of the oblique waves. At this regime the skin friction coefficient departs from the laminar Blasius values. This new regime is reflected as well through the modification of the local velocity profile for $y^+ > 10$, in accordance with the increase of the skin friction coefficient. Depending on the symmetry of the forcing, varicose Λ-shaped streaks (symmetry in z) or sinuous streaks (no symmetry in z) are identified for $Re_x > 260,000$.
- A third regime is observed where a distinct plateau is formed in the buffer region, $15 < y^+ < 30$ for all three cases. In the symmetric cases, hairpin-like vortical structures grow around the Λ-shaped low-speed streaks. In the case without symmetry, alternate quasi-streamwise vortices grow around the sinuous low-speed streaks. Immediately after the vortical structures are formed, the skin friction coefficient overshoots to the turbulent values.
- The final transition regime is associated with the breakdown of streaks. At this regime, the skin friction coefficient reaches the empirical turbulent values and energy is transferred to all the higher harmonics.

*Corresponding author. E-mail: g.rigas@imperial.ac.uk

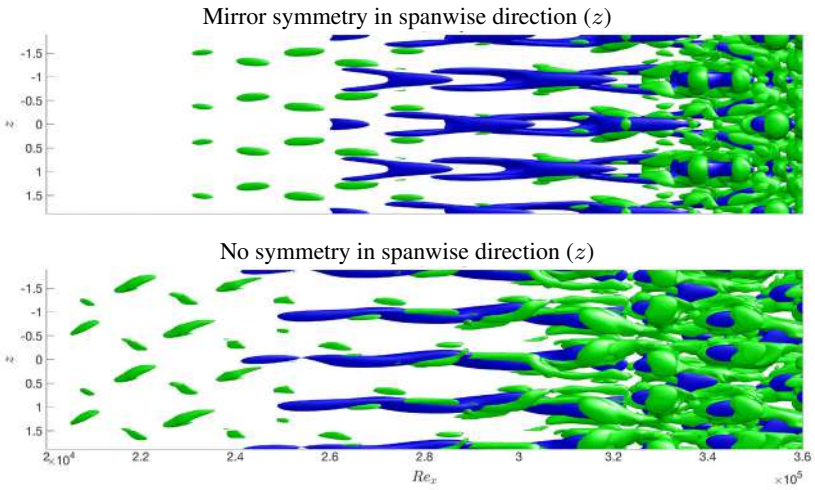

Figure 1: Nonlinear optimal response during laminar-turbulent transition on a plat plate boundary layer flow, triggered by a pair of oblique waves. Isosurfaces of low-speed streaks (blue) and vortical structures are shown. Solutions have been obtained with mirror-symmetry in z (top) and no symmetry (bottom), leading to varicose and a sinuous-like breakdown of the streaks, and the generation of hairpin and quasi-streamwise vortices, respectively.

For the case with no symmetry in z, the velocity profiles at the final stages of transition show characteristics similar to the ones observed in turbulent boundary layers. As shown in figure 2, the velocity profile appears to develops a nascent logarithmic region that extends in y^+ as Re_x increases. The skin friction coefficient, after an initial overshoot above the turbulent empirical values, drops to values close to the turbulent ones. For this specific case, we observed sinuous low-speed streaks, in contrast to the varicose streak instability that was observed for the symmetric case. The sinuous instability is a fundamental ingredient in the self-sustaining process (SSP) that has been identified in a variety of streamwise homogeneous flows [3].

The proposed *nonlinear input/output analysis* method identifies the most dangerous nonlinear mechanisms that lead to turbulent dynamics in the frequency domain, which can be viewed as *the minimal forcing seed in the frequency domain*. Advantages from the extension of the proposed framework to control applications will be discussed, specifically focusing on optimal passive geometric modifications and open-loop periodic forcing.

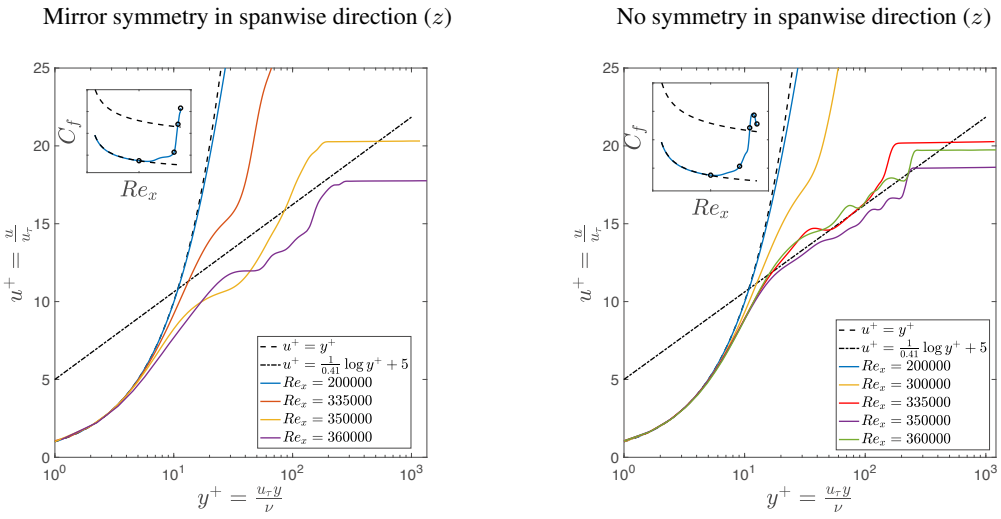

Figure 2: Mean velocity profiles during transition in innner units based on the local friction velocity u_τ. Linear (dashed) and log laws (dashed-dotted) are also shown. Then insets show the skin friction coefficient as a function of Re_x and the location where the velocity profiles are plot are marked with circles.

References

[1] Kerswell, R. R. Nonlinear nonmodal stability theory *Ann. Rev. Fluid Mech* **50**: 319–345, 2018.

[2] Cherubini, S. De Palma, P., Robinet, J.-C. & Bottaro, The minimal seed of turbulent transition in the boundary layer *J. Fluid Mech.* **689**: 221–253, 2011.

[3] Waleffe, F. On a self-sustaining process in shear flows *Phys. Fluids* **9**: 883–900, 1997.

TOWARDS A SELF-CONSISTENT RESOLVENT MODEL FOR TURBULENT JETS

Ethan Pickering *[1], Aaron Towne[2], Peter Jordan[3], and Tim Colonius[1]
[1] Department of Mechanical and Civil Engineering, California Institute of Technology, Pasadena, CA, USA
[2] Department of Mechanical Engineering, University of Michigan, Ann Arbor, MI, USA
[3] Institut Pprime, CNRS / Université de Poitiers /ENSMA, 86962 Futuroscope Chasseneuil, France

Summary Recent studies have shown that including a linear eddy-viscosity model significantly improves the match between modes predicted by resolvent analysis (linearized about the turbulent mean flow) and those educed from data (i.e. large eddy simulation) via spectral proper orthogonal decomposition. Given this agreement and the low-rank behavior of turbulent jets, we investigate whether a truncated resolvent basis accurately reconstructs turbulent statistics. In particular, we perform resolvent analysis of a turbulent jet using mean flow quantities found via a Reynolds-Averaged Navier-Stokes (RANS) simulation and determine if the associated RANS turbulent kinetic energy may be reconstructed, therefore constituting a self-consistent jet model. We present results for a Mach 0.4, isothermal, turbulent, round jet.

INTRODUCTION

Resolvent analysis [1] continues to provide a fruitful path for creating reduced-order models for turbulent flows, both among wall-bounded and free shear flow, yet complete models remain elusive, necessitating further refinement and/or modeling of turbulent forcing statistics. Recently, studies including an eddy-viscosity model in the resolvent operator in jets have shown striking improvements in alignment between resolvent modes and modes educed via SPOD [2, 3], the optimal basis for describing turbulent statistics[4]. Considering these improvements, we ask whether a self-consistent, reduced-order model for turbulent jets may be attained.

Self-consistent models of turbulent flow have been achieved through quasi-linear approaches in bluff bodies [5], channel flow [6], and turbulent boundary layers [7], and here we assess how well our current resolvent jet model may attain self-consistent behavior. We do so by reconstructing the one-point statistics from two target simulations. The first from a LES and the second from a RANS (i.e. tuned to match the LES meanflow quantities) for utility as a predictive jet modeling tool. The key advantage of reconstructing the one-point statistics of the LES first is the ability to decompose and compare LES and resolvent quantities at discrete frequency and wavenumber pairs, whereas RANS only provides an integrated mean quantity. For each frequency-wavenumber pair, alignment of SPOD and resolvent modes can then be optimized. With sufficient alignment, the resolvent models may be integrated in frequency and wavenumber to reconstruct the mean quantities associated with turbulent fluctuations, such as the TKE and acoustic field. Once demonstrated upon the LES database, we implement the same model using only RANS-based inputs, with a condition that the turbulent kinetic energy reconstruction be self-consistent – with the goal of producing a predictive, RANS-resolvent jet model.

METHODS

The resolvent operator, $\boldsymbol{R}$, takes the form of an input-output transfer function between flow responses, $\boldsymbol{q}$, and forcings, $\boldsymbol{f}$,

$$\boldsymbol{q} = \boldsymbol{R}\boldsymbol{f}, \tag{1}$$

where $\boldsymbol{R}$ is obtained from the linearized Navier-Stokes, continuity, and energy equations about a mean flow. In this study, stationary statistics in time and an axisymmetric geometry allow the resolvent operator to be defined at individual frequency and azimuthal wavenumber, $St - m$, pairs. Taking a singular value decomposition (SVD) of the resolvent operator, $\boldsymbol{R} = \boldsymbol{U}\boldsymbol{\Sigma}\boldsymbol{V}^*$, provides an orthogonal set of responses, $\boldsymbol{U}$, and forcings, $\boldsymbol{V}$, along with the diagonal matrix $\boldsymbol{\Sigma}$ whose entries denote the energetic amplification between the forcing and responses, ranked from largest to smallest.

The resolvent operator may also be viewed from a statistical perspective as described by Towne et al. [4], where the expectation of equation 1 times its complex conjugate,

$$\boldsymbol{S}_{qq} = \langle \boldsymbol{R}\boldsymbol{f}\boldsymbol{f}^*\boldsymbol{R}^* \rangle = \boldsymbol{R}\boldsymbol{S}_{ff}\boldsymbol{R}^* \tag{2}$$

gives the relationship between the two-point response statistics (i.e, the cross-spectral density tensor), $\boldsymbol{S}_{qq}$, and forcing statistics, $\boldsymbol{S}_{ff}$, through the resolvent operator. Expanding the resolvent operator then gives, $\boldsymbol{S}_{qq} = \boldsymbol{U}\boldsymbol{\Sigma}\boldsymbol{V}^*\boldsymbol{S}_{ff}\boldsymbol{V}\boldsymbol{\Sigma}\boldsymbol{U}^*$, and if $\boldsymbol{S}_{ff}$ is assumed to be a diagonal matrix of form $\alpha\boldsymbol{I}$, where α is a scalar constant which may be a function of frequency and wavenumber, the above equation reduces to $\boldsymbol{S}_{qq} = \alpha\boldsymbol{U}\boldsymbol{\Sigma}^2\boldsymbol{U}^*$. However, the form $\alpha\boldsymbol{I}$ assumes that the forcing is present at the same amplitude throughout the entire domain. Unfortunately, this assumption is poor for turbulent jets due to differences in spatial location of forcing mechanisms (i.e. Kelvin-Helmholtz, Orr, and Lift-Up) [8] and varied forcing amplitudes in those regions. Instead we replace $\boldsymbol{\Sigma}\boldsymbol{V}^*\boldsymbol{S}_{ff}\boldsymbol{V}\boldsymbol{\Sigma}$, with the diagonal matrix $\boldsymbol{B}$, whose diagonal entries represent the effective forcing amplitude for each resolvent mode.

SPOD directly decomposes $\boldsymbol{S}_{qq}$ as $\boldsymbol{S}_{qq} = \boldsymbol{\Psi}\boldsymbol{\Lambda}\boldsymbol{\Psi}^*$, where $\boldsymbol{\Psi}$ are orthogonal responses (from the LES) and $\boldsymbol{\Lambda}$ is a diagonal matrix denoting the energy of each response, showing that the assumption of a diagonal $\boldsymbol{B}$ is valid so long as $\boldsymbol{U} \approx \boldsymbol{\Psi}$. In the case that SPOD and resolvent modes are identically aligned the optimal model for $\boldsymbol{B}$ is $\boldsymbol{\Lambda}$. In these results we use $\boldsymbol{\Lambda}$ to inspire a functional form for $\boldsymbol{B}$, but determine the precise values by fitting the resolvent approximation to the one-point statistics. Finally, for reduced-order models, it also necessary to consider truncating the basis of resolvent modes, $\tilde{\boldsymbol{U}}$, and assess how closely the truncated basis reconstructs the statistics, $\tilde{\boldsymbol{S}}_{qq}$, as, $\tilde{\boldsymbol{S}}_{qq} = \tilde{\boldsymbol{U}}\tilde{\boldsymbol{B}}\tilde{\boldsymbol{U}}^*$.

*Corresponding author. E-mail: pickering@caltech.edu

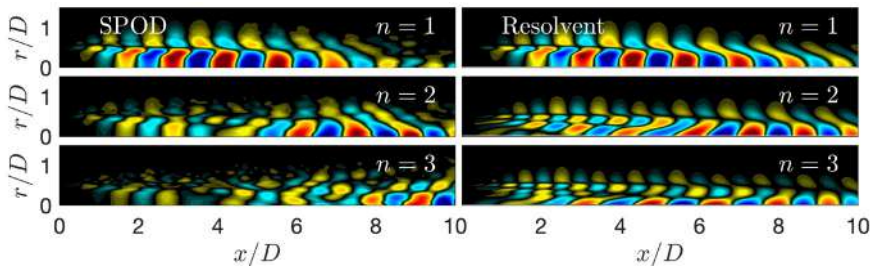

Figure 1: First three SPOD and resolvent modes (left and right columns respectively) of streamwise fluctuating velocity at $St = 0.6$, $m = 0$, for the $M_j = 0.4$ jet.

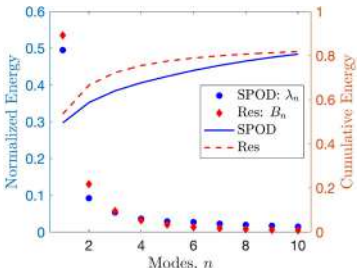

Figure 2: Normalized spectra of SPOD and fitted resolvent spectrum.

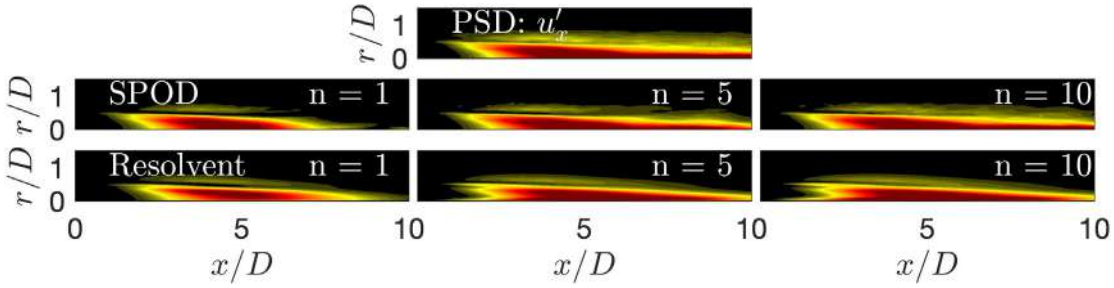

Figure 3: PSD of the LES data at $St = 0.6$, $m = 0$, for the $M_j = 0.4$ jet and the SPOD and resolvent reconstructions using 1, 5, and 10 modes from left to right.

RESULTS & OUTLOOK

The first three modes (fluctuating streamwise velocity) of the resolvent basis, found using the RANS eddy-viscosity resolvent model, are shown below for $m = 0$ and $St = 0.6$ for the $M_j = 0.4$ jet in figure 1 along with their associated SPOD modes. The resolvent modes show significant agreement with SPOD and present alignments of 92% 67% and 33% respectively. However, the resolvent spectrum suggests the first mode as containing $> 99\%$ of the energy due to the scalar forcing assumption. Therefore, we find the diagonal energy matrix $\tilde{\boldsymbol{B}}$ by performing a least-squares fit to the PSD of the chosen frequency $m - St$, by adjusting two parameters which model $\tilde{\boldsymbol{B}}$, $B_{i,i} = \alpha i^{-\beta}$. Figure 2 presents both the SPOD and modeled spectrum, each normalized by the total energy of the $St - m$ PSD. Both spectra are similar, which is expected as $\boldsymbol{U} \approx \boldsymbol{\Psi}$, however, we can also see $\tilde{\boldsymbol{B}}$ has values which are larger than the SPOD spectrum.

The resolvent and SPOD bases are then used to reconstruct the LES statistics at the given $St, m = [0.6, 0]$ pair and figure 3 presents the reconstructed PSD using a 1,5, and 10 mode basis. We can see that the first resolvent and SPOD modes account for a substantial amount of energy and reconstruct much of the overall PSD. We also see improvements in the reconstruction as further modes are added, although marginal.

We hypothesize that a truncated resolvent basis, and a simple form for the energy matrix $\tilde{\boldsymbol{B}}$, is sufficient for reconstructing the most energetic regions at each $m - St$ pair and may be integrated to construct the overall TKE field. In this talk we present the ability of the resolvent model to reconstruct the LES PSD across all $m - St$ pairs and subsequently expand the analysis to then reconstruct the overall RANS TKE. We present an optimization of the energy matrices $\tilde{\boldsymbol{B}}$ across the entire $m - St$ space constrained to best fit the RANS TKE and we discuss whether these matrices may be generalized for future RANS-resolvent predictive models.

References

[1] McKeon, B. J. & Sharma, A. S. 2010 A critical-layer framework for turbulent pipe flow. *J. Fluid Mech.* **658**: 336–382.

[2] Pickering, E., Rigas, G., Sipp, D., Schmidt, O.T. & Colonius, T. 2019 Eddy viscosity for resolvent-based jet noise models. *In 25th AIAA CEAS Aeroacoustics Conference*: 2454.

[3] Morra, P., Semeraro, O., Henningson, D. S. & Cossu, C. 2019 On the relevance of reynolds stresses in resolvent analyses of turbulent wall-bounded flows. *J. Fluid Mech.* **867**: 969–984.

[4] Towne, A., Schmidt, O. T., & Colonius, T. 2018 Spectral proper orthogonal decomposition and its relationship to dynamic mode decomposition and resolvent analysis. *J. Fluid Mech.* **847**: 821-867.

[5] Mantič-Lugo V., Arratia C., Gallaire F. 2014 Self-consistent mean flow description of the nonlinear saturation of the vortex shedding in the cylinder wake. *Physical review letters.* **20;113(8)**: 084501.

[6] Rosenberg, K. & McKeon, B.J., 2019 Computing exact coherent states in channels starting from the laminar profile: A resolvent-based approach. *Physical Review E*, 100(2), p.021101.

[7] Hwang, Y., & Eckhardt B., 2020 Attached eddy model revisited using a minimal quasi-linear approximation. *J. Fluid Mech.* Under consideration.

[8] Pickering, E., Rigas, G., Nogueira, P. A., Cavalieri, A. V., Schmidt, O. T., & Colonius, T. 2019 Lift-up, Kelvin-Helmholtz and Orr mechanisms in turbulent jets, *J. Fluid Mech.* Under consideration. preprint arXiv:1909.09737.

DIRECT CALCULATION OF EDDY VISCOSITY OF TURBULENT CHANNEL FLOW AT $Re_\tau = 180$

Danah Park*[1] and Ali Mani[1]
[1] Department of Mechanical Engineering, Stanford University, Stanford, USA

Summary This study presents an exact quantification of the eddy viscosity operator for the turbulent channel flow at $\mathrm{Re}_\tau = 180$ using a statistical technique, called macroscopic forcing method. Quantification of eddy viscosity is performed in the context of the generalized momentum transport equations which allow examination of mean momentum transport in a manner non-intrusive to the underlying transporting turbulent flow. Using these tools, we quantify the eddy viscosity in a tensorial kernel form. The results indicate the following: (1) the eddy viscosity is highly anisotropic, (2) its leading-order, obtained by neglecting spatial moments of the closure kernel, generates a non-symmetric Reynolds stress tensor, (3) the eddy viscosity operator acts on all components of the mean velocity gradient including mean rate of rotation, and (4) the eddy viscosity kernel is highly nonlocal.

INTRODUCTION

The Boussinesq approximation is common in the majority of the closure models for the Reynolds Average Navier Stokes equations (RANS). This approximation leads to an eddy viscosity coefficient which is a scalar field that locally describes the ratio between the deviatoric Reynolds stresses and the mean strain rate tensor. Similar to the notion of molecular mixing, Boussinesq assumes that the eddy viscosity is isotropic and local. There have been many demonstration of violation of these two assumptions in realistic flows, but quantitative measures of the non-Boussinesq effect are still lacking [1].

We have recently developed a new technique, called the macroscopic forcing method (MFM), [2] that allows the calculation of the exact RANS closure operator for any given flow. MFM measures turbulent momentum flux in response to different scenarios of mean momentum gradients obtained via forcing of the momentum transport equation. Exact eddy diffusivity operators can be obtained by careful assembly of such solutions. In this work, we present results of such calculation for the turbulent channel flow at $Re_\tau = 180$.

Eddy Viscosity Kernel

Equation 1 shows the fourth order tensorial kernel formulation of the RANS closure which is the most general representation of the eddy viscosity as an operator [3].

$$-\overline{u_j' u_i'}\,(\mathbf{x}) = \int D_{jilk}(\mathbf{x},\mathbf{y})\left.\frac{\partial U_k}{\partial x_l}\right|_{\mathbf{y}} \mathrm{d}\mathbf{y}. \tag{1}$$

Unlike the Boussinesq model, here the tensorial components in D_{jilk} capture anisotropy, while the integral form incorporates the nonlocal effects.

Macroscopic Forcing Method

The challenge with this general representation is quantification of the kernel itself, for which we applied MFM as follows. We first obtain the space-time resolved velocity field from a direct numerical simulation (DNS) and use it as a background velocity for additional DNS of a passive momentum transport equation, which we call the generalized momentum transport equation (GMT) as discussed in [2]. This way we gain two advantages. First, the GMT equation is a linear equation and thus can benefit from analysis using specific tools including superposition methods, combined with force response analysis. Second, this method is non-intrusive to the underlying turbulence that transports the momentum, and thus a RANS operator characterization based on GMT is exact for the given specific flow.

LEADING ORDER (LOCAL) APPROXIMATION

Starting with Equation 1, one can use the Taylor series expansion to expand the velocity gradient around $\mathbf{y} = \mathbf{x}$. If the velocity gradient is smooth, one may retain the leading term in this expansion. This will lead to a simplified representation of the eddy viscosity operator reduced to a local form $-\overline{u_j' u_i'}\,(\mathbf{x}) = D^0_{jilk}(\mathbf{x})\partial U_k/\partial x_l$, where D^0_{jilk} is the spatial integral of the kernel, effectively relegating the entire non-local kernel in 1 to a Dirac delta function. We use this approximate representation of eddy viscosity (essentially the zeroth order moment of the kernel) to assess the anisotropy of the closure oeprator.

In Figure 1(b), four components of the leading order eddy viscosity tensor are shown from the bottom wall to the top wall. D^0_{2121} corresponds to the standard eddy viscosity, which is commonly estimated by taking the ratio of Reynolds stress to the mean velocity gradient. Unlike such estimates, which essentially tune an inaccurate model form, here D^0_{2121} shows the exact leading-order eddy diffusivity coefficient. Conducting RANS solutions with this local eddy viscosity shows the error of the leading-order operator (neglecting the non-local effects) to be about 1.5 percent. This indicates that

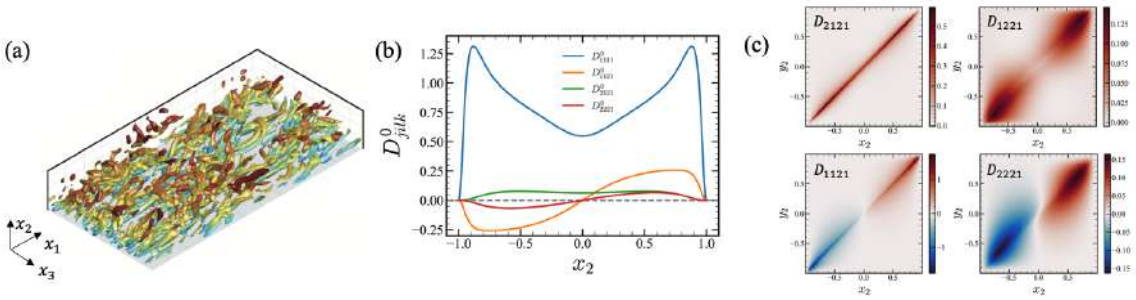

Figure 1: (a) The isocontour of the Q-criterion of the channel flow and its coordinates, (b) The distribution of the four elements in leading-order eddy viscosity tensor, and (c) the distribution of the eddy viscosity kernels.

the non-local effects are negligible for the $\overline{u_1 u_2}$ component of the Reynolds stress, which is the only important component when it comes to prediction of parallel channel flow.

Unlike parallel channel flows, spatially developing boundary layers, involve gradients in multiple directions and are thus sensitive to other components of the eddy viscosity. Using a scaling analysis, we determine four dominant eddy viscosity components which are shown in the figure. Here we use quantification of these components in the channel flow as a proxy to infer anisotropic effects in spatially developing flows. As shown, some components of the eddy viscosity tensor can be locally orders of magnitude larger than the nominal eddy viscosity, D^0_{2121} indicating drastic deviation from the Boussinesq limit.

In our presentation we will show that leading order eddy viscosity operator generates a non-symmetric Reynolds stress tensor. Moreover, our results suggest that leading-order Reynolds stress can be generated by both mean strain rate and mean rotation. This violates the mainstream modeling assumption of Reynolds stress to be only function of the mean strain rate tensor.

FULL KERNEL ANALYSIS

The capture of Reynolds Stress in the channel centerline requires the inclusion of nonlocal terms in the eddy viscosity operators. Hence, for a subset of these tensorial components, we calculated the full non-local eddy viscosity operator, specifically the kernel components that multiply $\mathrm{d}V_1/\mathrm{d}x_2$ in equation 1. We measure D_{ji21} as a function of both $x_2$and y_2. As shown in Figure 1(c), our results indicate that D_{2121} is highly local as the kernel is non-zero only when $\mathbf{x} \simeq \mathbf{y}$. This explains the earlier observation of small error of the leading-order approximation. In contrast, for other components of eddy viscosity, the results indicate significant nonlocality, which invalidate the intrinsic assumption in the Boussinesq hypothesis. Lastly, we confirm that incorporating the full kernel provides exact Reynolds Stresses recovering the symmetry that was lost in the leading order approximation.

CONCLUSION

In summary, we present an exact measurement of the eddy viscosity of the turbulent channel flow along with a quantification of non-Boussinesq effects, and its implications in modeling. For the parallel flow, only one Reynolds stress and one velocity gradient is important and hence anisotropy does not influence the predictions. In such case, the narrow kernel of D_{2121} indicates the validity of the local assumption. These two findings explain why Boussinesq approximation works well for parallel flows. However, our quantification suggests that this conclusion does not hold for spatially developing wall-bounded flows where the non-parallel effects become important. Our measurements reveal that the eddy viscosity is highly anisotropic and highly nonlocal, when it comes to components other than D_{2121} indicating a clear need to include non-Boussinesq effects in RANS models.

References

[1] Pope, S. B. A More General Effective-viscosity Hypothesis. *J. Fluid Mech.* **72.2**: 331-340, 1975.
[2] Mani A. and Park D. Macroscopic Forcing Method: a Tool for Turbulence Modeling and Analysis of Closures. **arXiv**:1905.0834, 2019.
[3] Hamba, F. Nonlocal Analysis of the Reynolds Stress in Turbulent Shear Flow. *Physics of Fluids* **72.11**: 115102, 2005.

*Corresponding author. E-mail: danah12@stanford.edu.

INPUT-OUTPUT ANALYSIS OF A TURBULENT SEPARATION BUBBLE VIA THE HARMONIC RESOLVENT

Alberto Padovan*[1] and Clarence W. Rowley[1]
[1] Department of Mechanical and Aerospace Engineering, Princeton University, Princeton, NJ, USA

Summary We study the input-output characteristics of a turbulent separation bubble at $Re_{\theta_0} = 490$ based on the momentum thickness. At these flow conditions, a low-frequency "breathing" mode is present, in addition to oscillations at higher frequencies, and we are interested in understanding their interplay. We perform a frequency-domain linearization of the dynamics about a time-periodic representation of the large, coherent structures that are observed in the flow. This allows us to compute the harmonic resolvent [3], which is a linear operator that governs the dynamics of time-periodic perturbations about a time-periodic base flow, in response to some external time-periodic input. The SVD of the harmonic resolvent shows that the low-frequency breathing mode interacts most strongly with perturbations at 3/2 and twice the breathing frequency, while perturbations at lower frequencies have little effect.

THE HARMONIC RESOLVENT

We apply the harmonic resolvent framework described in [3] to study the input-output characteristics of a turbulent separation bubble at $Re_\theta = 490$ based on the momentum thickness. The direct numerical simulations performed by Wu *et al.* [4] reveal the presence of three distinct unsteady motions: a low-frequency expansion/contraction (*breathing*) of the separation bubble, and two high-frequency modes associated with the shedding of spanwise vortical structures downstream of the separation bubble. For notational clarity, we henceforth let ω be the frequency associated with the breathing mechanism, while the frequencies of the downstream spanwise vortical structures are 2ω and $5\omega/2$.

In order to understand the nature of the coupling between the flow structures at the aforementioned frequencies, we proceed as follows. We write the velocity $\boldsymbol{u}$ and pressure p together in a single state variable $\boldsymbol{q} = (\boldsymbol{u}, p)$ and write the Navier-Stokes equation and continuity in the compact form

$$\frac{\mathrm{d}}{\mathrm{d}t}\begin{bmatrix}\mathbf{I} & 0\\ 0 & 0\end{bmatrix}\boldsymbol{q} = \boldsymbol{f}(\boldsymbol{q}), \tag{1}$$

where $\mathbf{I}$ is the identity matrix. We linearize the dynamics about a time-periodic base flow $\boldsymbol{Q}(t)$ over the set of frequencies $\Omega_b = \{-\frac{3}{2}\omega, -\omega, \ldots, \frac{3}{2}\omega\}$, and we consider time-periodic perturbations $\boldsymbol{q}'(t)$ over the set of frequencies $\Omega = \{-3\omega, -\frac{5}{2}\omega, \ldots, 3\omega\}$. It can be shown that performing the linearization in the frequency domain leads to an input-output system

$$\hat{\boldsymbol{q}}' = \mathbf{H}\hat{\boldsymbol{w}}' \tag{2}$$

where $\mathbf{H}$ is the harmonic resolvent. This is a frequency-domain, block, linear input-output operator that governs the dynamics of small perturbations about the time-periodic base flow, and it accounts for the leading-order coupling between structures at different frequencies. Here, $\hat{\boldsymbol{q}}' = \{\hat{\boldsymbol{q}}'_{k\omega/2}\}_{k=-6,\ldots,6}$ is a vector of all Fourier modes of the perturbed state, while $\hat{\boldsymbol{w}}'$ is a vector of all Fourier modes associated with perturbations (including nonlinearities) that feed back into the harmonic resolvent. We also point out that if we linearize about a steady base flow, then the harmonic resolvent reduces to the standard resolvent operator, for instance considered in [1, 2].

GLOBAL AND CROSS-FREQUENCY AMPLIFICATION MECHANISMS

Analyzing the structure of the harmonic resolvent sheds light on the underlying input-output characteristics of the flow. More precisely, we extract the global amplification mechanisms from the singular value decomposition of the harmonic resolvent. The left singular vectors are the (optimal) most amplified space-time response modes, and they identify the structures that are preferentially excited through the harmonic resolvent. The right singular vectors, on the other hand, are the optimal space-time forcing modes. These provide information about the spatio-temporal sensitivity of the flow and highlight the structures that are most effective at exciting an energetic response through the harmonic resolvent. We also perform an SVD of each block of the harmonic resolvent in order to extract information about the cross-frequency amplification mechanisms of the flow. We find the block singular values particularly informative, as they help identify the cross-frequency interactions that are dominant in the flow.

SELECTED RESULTS AND DISCUSSION

In this section we present the results for the harmonic resolvent evaluated about the previously described base flow. The time-periodic base flow is spanwise-averaged, and we consider two-dimensional perturbations about the base flow.

In figure 1 we show the singular values of the harmonic resolvent as well as the leading singular value computed for each individual block. First, we observe from figure 1a that the singular values quickly decay by more than one order of magnitude, suggesting that the amplification mechanisms about the base flow are low rank. Second, we notice from 1b

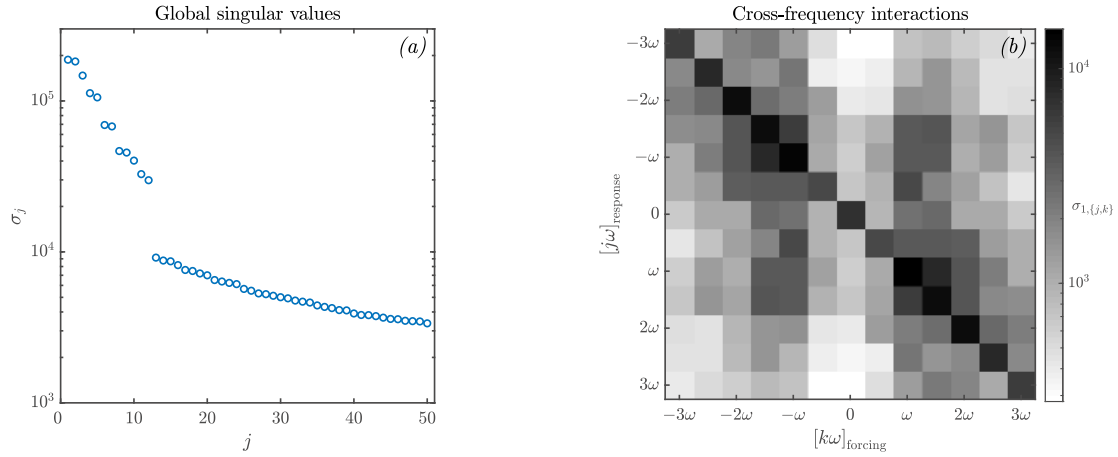

Figure 1: *(a)* singular values of the harmonic resolvent, and *(b)* first singular value, denoted $\sigma_{1,\{j,k\}}$, for each $(j\omega, k\omega)$ block of the harmonic resolvent. The block singular value identify the dominant cross-frequency input-output interactions.

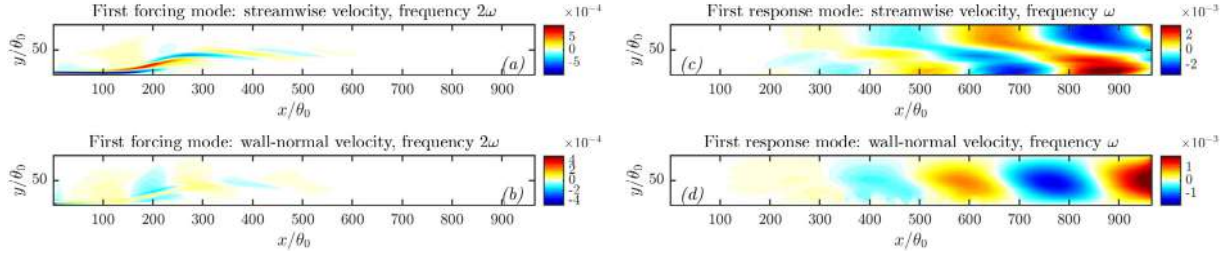

Figure 2: Real part of selected entries of the forcing and response modes associated with σ_1 in figure 1a. From the forcing mode we show *(a)* the streamwise velocity, and *(b)* the wall-normal velocity at frequency 2ω. From the response mode we show *(c)* the streamwise velocity, and *(d)* the wall-normal velocity at the breathing frequency ω.

that there is strong coupling across all frequencies. In particular, by looking at the ω row we find that the perturbations that most strongly couple to the breathing frequency are those at frequencies $3\omega/2$ and 2ω.

In figure 2 we present the optimal forcing and optimal response mode shapes associated with the $(2\omega, \omega)$ frequency pair. Figures 2a and 2b show the structures at frequency 2ω that are optimal at exciting a very energetic response through the harmonic resolvent. We observe that these structures are supported along the shear layer that forms as a consequence of separation, and we can therefore conclude that the shear layer is where this flow is most sensitive to disturbances at frequency 2ω. Figures 2c and 2d, on the other hand, show the most amplified structures at frequency ω that arise in response to a disturbance at frequency 2ω. Finally, we learn from the harmonic resolvent that the cross-frequency coupling between a disturbance at 2ω and the response at ω is sustained (linearly) by the base flow at $-\omega$.

CONCLUSIONS

We present selected results on the amplification mechanisms in a turbulent separation bubble obtained from the analysis of the harmonic resolvent. This is an input-output operator that governs the dynamics of perturbations about a time-periodic base flow in the frequency domain. We find that the flow is susceptible to perturbations along the shear layer that forms upstream of the separation bubble, and we identify the structures that form in response to perturbations along the shear layer. Furthermore, we learn that there is strong coupling across all frequencies, and that the breathing mechanisms is strongly affected by higher frequency structures that scatter back through the base flow.

This work was supported by the Air Force Office of Scientific Research, award FA9550-17-1-0084.

References

[1] Jovanović, M. R., Bamieh, B., Componentwise energy amplification in channel flow, *J. Fluid Mech.*, 2005, Vol. 534, 145–183
[2] McKeon, B. J., Sharma, A., A critical-layer framework for turbulent pipe flow, *J. Fluid Mech.*, 2010, Vol. 658, 336–382
[3] Padovan, A., Otto, S. E., Rowley, C. W., Amplification mechanisms and cross-frequency interactions in nonlinear flows via the harmonic resolvent, arXiv:1911.10179v1, 2019
[4] Wu, W., Meneveau, C., Mittal, R., Spatio-temporal dynamics of turbulent separation bubbles, arXiv:1908.10473v1, 2019

*Corresponding author. E-mail: apadovan@princeton.edu

BOUNDARY LAYER FLUX CONTROL USING KELVIN'S CATS' EYES

Giovanni Nino and Robert Breidenthal*
Department of Aeronautics and Astronautics, University of Washington, Seattle, USA

Summary Wind tunnel experiments are described to detect vortex position and to develop vortex actuators as part of an active control system. The position and strength of a vortex downstream from a vortex generator can be controlled by dielectric barrier discharge plasma jets and air jets at the swept leading edge of a vortex generator. It was found that the most effective location to place the actuators is on the vortex leading edge. Effects of the actuator topology on the level and type of control will be discussed.

BACKGROUND

In the free shear layer, entrainment had been thought to be controlled by small-scale nibbling at the "superlayer" edge [1]. The subsequent discovery of coherent structures revealed that entrainment instead is dominated by large-scale gulping in Roshko's engulfment tongues [2]. It was discovered that forcing the shear layer to form a regular array of vortices results in the entrainment rate going to zero [3]. Implausibly, the growth rate and the Reynolds stresses all essentially vanish when the vortices are equally spaced. Even the molecular mixing rate essentially vanishes as measured by Roberts and Roshko [4]. The vortices are rotating but accomplishing nothing. An idealized model of this behavior is Kelvin's cats' eye flow as shown in Figure 1, when a planar array of co-rotating point vortices of equal sign, strength, and spacing. The flow consists of external streamlines separated from internal streamlines about each vortex by a closed separatrix. The key concept is that the separatrix is a closed streamline, so that the outer flow is perpetually isolated from the inner flow.

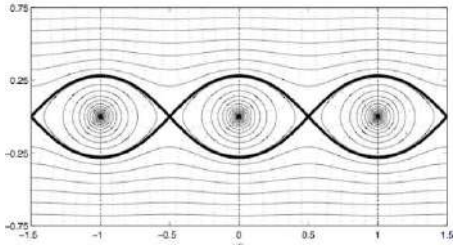

Figure 1. Kelvin's cats' eyes flow model.

A natural question is if such entrainmentless flow could be established for a boundary layer. If so, then all the wall fluxes would dramatically decline to their laminar values, which are much less than turbulent values at large Reynolds number. Based on the peculiar entrainment behavior of a vertical jet at a stratified interface, Cotel proposed that the entrainment rate due to a vortex near a surface should depend on the stationarity of that vortex [5]. If a large vortex is stationary near a solid wall, the wall fluxes would depend on the rotation period of the large vortex and be independent of any small-scale eddies. The wall fluxes would be laminar. This prediction was tested by adding large, streamwise vortices into a wall flow and attempting to stabilize them with a wavy wall, as suggested by Balle [6]. Water tunnel experiments have demonstrated that an initially turbulent boundary layer can be partially relaminarized by adding large, streamwise vortices to the flow and stabilizing them with large, streamwise grooves. The turbulent intermittency vanishes over about half the surface of the wavy wall when a streamwise vortex is deployed in a small "sweet spot" in the center of each groove. If the vortices are slightly mispositioned, the relaminarization effect disappears.

Just as the open-loop forcing of the free shear layer inhibits entrainment for only a short distance, open-loop forcing with a wavy wall relaminarizes the flow for only a short distance. Passive, open-loop control has only a limited range, as the vortices are unstable. It is natural to attempt to continuously stabilize the vortices over an entire surface with active vortex control using feedback. Such a vortex control strategy would exploit active control rather than a passive wavy wall to hold the streamwise vortices stationary. If achievable, it would in principle work for any arbitrary surface.

ACTIVE CONTROL APPROACH

With the aim to develop a boundary layer flux control over a flat or curved surface, a vortex-based active control concept has been divided in four parts: (i) vortex generator, (ii) vortex detection, (iii) actuators, and (iv) control logic. In this paper, we present recent experiments performed at the Kirsten Wind Tunnel on the vortex generation, detection and actuators. A vortex generator (VG) with a swept back leading edge was selected to be mounted on a flat plate and angled to the free stream to generate a vortex. This was the simplest and most effective way to produce reliable vortices. The angle of attack of the VG ranged from 10-25° with 5° increment for speeds between 20 m/s and 70 m/s.

Regarding the vortex detection (Figure 2), a method was developed based on the distribution of the pressure coefficients downstream of the VG. Dynamic pressures were collected with two electronic pressure scanner (Scanivalve ZOC33/64Px) modules over an array of pressure taps installed on a flat plate. The vortex center position is approximated by a fitted straight line on the pressure data using the least squares method. The resulting slope is used to calculate the vortex drift angle γ. This angle provides a good feedback to the controller.

The position and strength of a vortex downstream from a vortex generator can be controlled by actuators mounted on the VG itself. Two types of actuators were investigated: dielectric barrier discharge plasma jets and air jets. These devices are shown in Figure 3. It was found that the most effective location to place the actuators is on the vortex leading edge.

*Corresponding author. E-mail: breident@aa.washington.edu

The experiments reveal that the plasma induced electric wind results in a decrease of the vortex drift angle. It is believed that the induced body force displaces the center line of the induced vortex further away from the wall. Counter-intuitively, this corresponds to a reduction of the lift. Following the Kutta-Joukowski theorem, a reduction of the lift is associated with a reduction of the circulation and the vortex drift angle. On air jets, dynamic pressure cross sections were gathered at different stages behind a VG. Figure 4 shows the effects of air injection at three different ports on their associated dynamic pressure responses. It was found that the vortex position (direction and magnitude) changed in function of air pressure and injection location (i.e. port). For example, air injection at the lower position (Pos 1) of the VG leading edge produced a strong vortex displacement to the side. Air injection at other places (Pos 2 and 3) moved the vortex away of the surface. In addition, injectors topology affected the amount of displacement of the vortex. Divergent injectors produced longer vortex displacements than the one produced by circular injectors. It was clear, from these wind tunnel experiments, that air jets were more effective controlling the vortex position than dielectric barrier discharge plasma actuators. The next steps of the active control system are the development of the controller logic and the integration of the system.

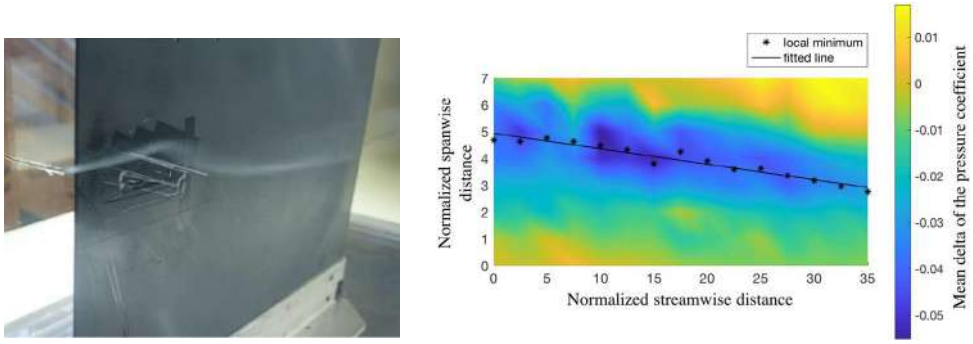

Figure 2. Vortex position location over a surface using pressure sensors. Smoke visualization (left) and vortex center fitted line based on coefficient of pressure distributions (right)

Figure 3. Actuators on vortex generators: plasma (left) and air jets (center and right).

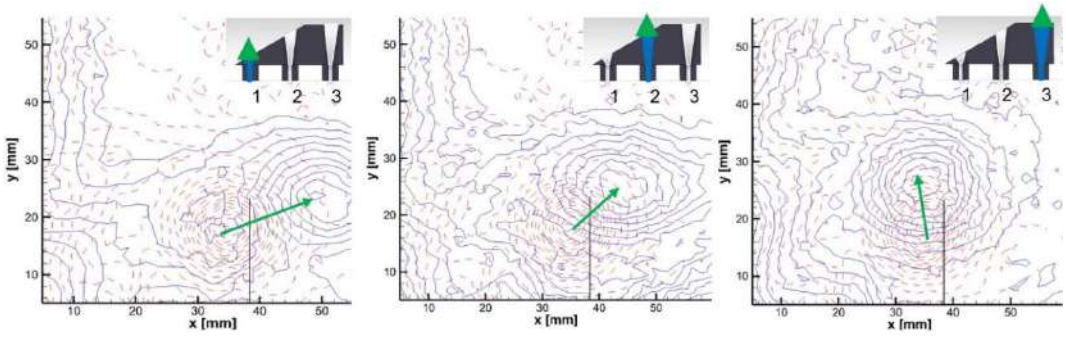

Figure 4. Dynamic Pressure Cross Sections for Different Injection Points: Initial position (red) and displacement (blue).

References

[1] Corrsin, S. & Kistler, A.L. 1955 Free-stream boundaries of turbulent flows, *NACA TR 1244*, Washington D.C.
[2] Brown, G.L. & Roshko, A. 1974 On density effects and large scale structure in turbulent mixing layers, *J. Fluid Mech.***64** 775-816.
[3] Oster, D. & Wygnanski, I. 1982 The forced mixing layer between parallel streams, *J. Fluid Mech.***123** 91-130
[4] Roberts FA, Roshko A (1985) Effects of periodic forcing on mixing in turbulent shear layers and wakes. *AIAA Shear Flow Control Conference*, Paper 85-0570
[5] Cotel, A.J. 2002 Turbulence inside a Vortex – Take Two, *Physics of Fluids*, **14** (8) 2933
[6] Balle, G.J. & Breidenthal, R.E. 2002 Stationary vortices and persistent turbulence in Karman grooves, *J. Turbulence* **3** 33-51

STUDY OF INTERMITTENT STRUCTURE IN ANNULAR COUETTE–POISEILLE FLOW FROM TURBULENT PUFF TO TURBULENT STRIPE

Hirotaka Morimatsu and Takahiro Tsukahara
Department of Mechanical Engineering, Tokyo University of Science, Chiba, Japan

We performed direct numerical simulations (DNS) of annular Couette-Poiseuille flow, focusing on intermittent structures in the subcritical transitional regime. For high radius ratios, we investigated the dependence of the intermittent structures on the pressure gradient, $F(p)$. For the radius ratio of $\eta = 0.8$, the pressure-gradient dependence of the intermittent structure was not observed. For $\eta = 0.5$, the intermittent structure changed dependently on $F(p)$: large $F(p)$ provided helical patterns of localized turbulence. For η of 0.3 and 0.1, we performed DNS with long computational domains and applied $F(p)$ at which the velocity gradient on the inner cylindrical wall surface becomes zero, in order to mimic the pipe flow. One-dimensional intermittency was observed, as seen in the pipe flow, and we found splitting from one puff to several puffs as well as decay of puff.

INTRODUCTION

In wall-bounded shear flow, it is known that the flow often shows characteristic intermittent structures of localized turbulence in the subcritical transitional regime. The characteristic intermittent structure exhibits a regular large-scale pattern in which laminar regions and turbulent regions coexist spatially. The intermittent structure differs depending on the channel shape. In planar flows, an intermittent structure called “turbulent stripe” or “turbulent band” that obliquely inclined to the main flow direction occurs. On the other hand, in the pipe flow, one-dimensional intermittency called a “turbulent puff”, where turbulent regions are localized only in the axial (streamwise) direction, occurs. It is reported that the turbulent puff in the pipe flow can be split from a single puff to two puffs [1]. These intermittent structures, such as turbulent stripe and turbulent puff, are known to also occur in annular flows. In the annular flow, since the channel shape changes with the radius ratio η of inner tube to the outer tube, the intermittent structure also changes according to the radius ratio. In the annular Poiseuille flow driven by a pressure gradient in the axial direction and the annular Couette flow driven by moving of the inner cylinder to the axial direction, one-dimensional intermittency like the turbulent puff in the pipe flow was found at low radius ratio, while high η provided the intermittency like the turbulent stripe such in planar flows [2]. At $\eta = 0.5$, a difference in the type of intermittent structure was found between the annular Poiseuille flow and the annular Couette flow. In the annular Poiseuille flow, turbulent stripe occurs. On the other hand, in the annular Couette flow, a characteristic intermittent structure does not occur, an irregular intermittent structure occurs [3].

In this study, we aim at a unified understanding of intermittent structures from turbulent puff to turbulent stripe by investigating intermittent structures in annular Couette-Poiseuille flows at various radius ratios. At high η, we studied the dependence of the intermittent structure on the given pressure gradient, represented by $F(p)$. At low η, our interest is in whether the turbulent puff-like intermittent structure that was observed in the annular flow can split and decay, like the puff in the pipe flow.

NUMERICAL METHODS

We performed direct numerical simulations (DNS) of annular Couette-Poiseuille flow. The flow is driven by moving of the inner cylinder to the axial direction and the pressure gradient in the axial direction. They are described by parameters of Re_w and $F(p)$. The Reynolds number is defined by $\mathrm{Re}_w = U_w h/\upsilon$, where U_w is the inner cylinder speed, h is the gap width between the cylinders, and υ is the kinetic viscosity. The magnitude of the non-dimensionalized pressure gradient is defined by $F(p) \equiv -\mathrm{d}P^*/\mathrm{d}x^* \cdot \mathrm{Re}_w$, where $\mathrm{d}P^*/\mathrm{d}x^*$ is the mean axial pressure gradient and μ is the viscosity. For radius ratios of $\eta = 0.8$ and 0.5, in order to investigate the $F(p)$-dependence of intermittent structures, we applied three different values of $F(p) = 4$, 8, and 16 in the flow path. For $\eta = 0.3$ and 0.1, we applied $F(p)$ at which the velocity gradient at the inner cylindrical wall surface becomes zero approximately.

The governing equations are the continuity equation and the Navier–Stokes equation in the cylindrical coordinate system. Periodic boundary condition is imposed in the main flow (x) and azimuthal (θ) directions, and non-slip condition is imposed on the wall surfaces. The computational domain size in the azimuthal direction is 2π. The axial domain size is adjusted to satisfy each purpose of the high- and low-η cases. For high $\eta = 0.8$ and 0.5, we performed DNS using the minimum computational domain ($L_x = 51.2h$), which can capture one wavelength of the turbulent stripe. For low $\eta = 0.3$ and 0.1, in order to capture multiple puffs, we performed DNS using very long computational domain ($L_x = 409.6h$) in the main flow direction.

RESULTS AND DISCUSSIONS

At first, we prepared a uniformly turbulent flow as an initial field for all cases, from which the Reynolds number was gradually decreased. For $\eta = 0.8$ and 0.5, we investigated the pressure-gradient dependences of the intermittent structure by applying three different $F(p)$. In the Couette-Poiseuille flow, the flow field can be classified according to whether or not there is a position of zero local shear rate in the cylinder gap. If there is no such position, the flow field is classified as Couette-type flow, otherwise (if there is such position) the flow field is classified as Poiseuille-type flow [4]. For $\eta =$

0.8, regardless of the flow type, helical turbulence occurred for all tested values of $F(p)$: see Figure 1. In the annular flow, higher the radius ratio, the higher the spatial freedom in the azimuthal direction. For high $\eta = 0.8$, the azimuthal computational domain is sufficiently large, so the helical turbulence occurred regardless of the magnitude of $F(p)$. For high $\eta = 0.5$, different intermittent structures occurred and depended on the $F(p)$. For $F(p) = 4$, where the flow field was Couette type, the helical turbulence did not occur, and an irregular intermittent structure occurred. On the other hand, for $F(p) = 8$ and 16 supplying Poiseuille-type flows, the helical turbulence occurred. However, the helical turbulence observed at $F(p) = 8$ was not steadily present, but repeatedly formed and collapsed. This is consistent with the fact that the stripe interval in the plane Poiseuille flow should be half of that of the plane Couette flow.

For the radius ratios of 0.3 and 0.1, we performed analysis that simulated the pipe flow by adjusting $F(p)$ to achieve the nearly zero shear rate at the inner-cylinder surface. For $\eta = 0.3$, one-dimensional intermittency like the turbulent puff in the pipe flow was observed at $\mathrm{Re_w} = 1470–1460$, as shown in Figure 2. Normalization of these Reynolds numbers using the hydrodynamic equivalent diameter and the bulk mean velocity reveals that those values correspond to approximately 2500. This Reynolds number is close to the value at which the turbulent puff occurs in the pipe flow. For $\eta = 0.1$, we observed one-dimensional intermittency as seen in the pipe flow at $\mathrm{Re_w} = 1600$. The normalized Reynolds number by the hydrodynamic equivalent diameter and the bulk mean velocity is approximately 2190. This Reynolds number is also close to the range of the turbulent puff in the pipe flow. Furthermore, these turbulent puffs observed in the present annular flows were found to split from one to several turbulent puffs as time progresses (Figure 3), and also decayed without maintaining the turbulence.

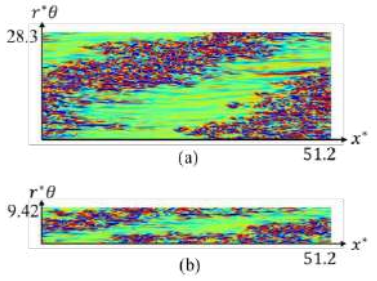

Figure 1. Instantaneous flow field in the (x, θ)-plane at the midgap for (a) $\eta = 0.8$, $F(p) = 4$ and (b) $\eta = 0.5$, $F(p) = 8$. The contour shows wall-normal fluctuation; red, $u_r' > 0.03U_w$; blue, $u_r' < -0.03U_w$.

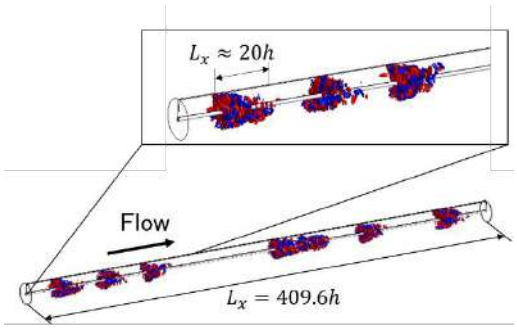

Figure 2. Three-dimensional visualization of the localized turbulent puffs for $\eta = 0.1$, $\mathrm{Re_w} = 1600$. The iso-surfaces show wall-normal fluctuation: red, $u_r' > 0.03U_w$; blue $u_r' < -0.03U_w$.

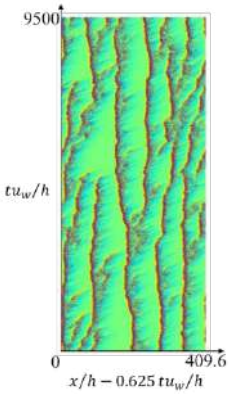

Figure 3. Space-time diagram of azimuthally-averaged wall-normal velocity $\langle u_r \rangle_\theta$ at the gap center for $\eta = 0.1$, $\mathrm{Re_w} = 1600$: red, positive value; blue, negative; green, zero.

CONCLUSIONS

We performed direct numerical simulations of annular Couette-Poiseuille flow for four different radius ratio. For the radius ratios of 0.8 and 0.5, we investigated the pressure-gradient dependences of intermittent structure by applying three different $F(p)$. By changing $F(p)$, the intermittent structures as well as the mean flow exhibited continuous variation between those in the Poiseuille-type and Couette-type flows: the helical turbulence can disappear at low $F(p)$ even with fixing $\mathrm{Re_w}$. For the radius ratios of 0.3 and 0.1, we simulated the pipe-flow-like system. In both η cases, we observed one-dimensional intermittency like the turbulent puff in the pipe flow. The one-dimensional intermittency exhibited split and decay of the turbulent puff. The present findings imply a smooth continuous transition from stripes to puffs in wall-bounded shear flows.

ACKNOWLEDGEMENTS

The present simulations were performed on an SX-ACE supercomputer at the Cybermedia Center of Osaka University and at the Cyberscience Center of Tohoku University.

References

[1] K. Avila, D. Moxey, A. de Lozar, M. Avila, D. Barkley, and B. Hof. The onset of Turbulence in pipe flow. *Science,* 333: 192-196, 2011.
[2] T. Ishida, Y. Duguet, and T. Tsukahara. Transitional structures in annular Poiseuille flow depending on radius ratio. *J. Fluid Mech.* **794**: R2, 2016.
[3] K. Kunii, T. Ishida, Y. Duguet, and T. Tsukahara. Laminar-turbulent coexistence in annular Couette flow. *J. Fluid Mech.* **879**: 579-603, 2019.
[4] K. Nakabayashi, O.Kitoh, and Y.Katoh. Similarity laws of velocity profiles and turbulence characteristics of Couette-Poiseuille turbulent flows. *J. Fluid Mech.* **507**: 43-69, 2004.

A SELF-SUSTAINING PROCESS THEORY FOR UNIFORM MOMENTUM ZONES AND INTERNAL INTERFACES IN TURBULENT SHEAR FLOWS

Brandon Montemuro[1,2], Chris White[3], Joe Klewicki[1,3,4], and Greg Chini *[1,3]
[1] Program in Integrated Applied Mathematics, University of New Hampshire, Durham, NH 03824 USA
[2] School of Oceanography, University of Washington, Seattle, Washington 98195 USA
[3] Department of Mechanical Engineering, University of New Hampshire, Durham, NH 03824 USA
[4] School of Electrical, Mechanical and Infrastructure Engineering, University of Melbourne, Parkville, VIC 3010 Australia

Summary The instantaneous streamwise velocity in turbulent wall flows exhibits a staircase-like profile, with uniform momentum zones (UMZs) separated by regions of concentrated spanwise vorticity (vortical fissures, or VFs) across which the streamwise flow speed jumps by a few multiples of the friction velocity. One challenge is to identify a mechanism that accounts for observed properties of the UMZ/VF profiles while respecting the constraints imposed by the mean momentum balance. Measurements show that outboard of the near-wall peak in the Reynolds stress: (i) the characteristic VF thickness decreases as the friction Reynolds number increases; and (ii) the mean momentum equation is inertially dominated. Supported by a new large-Re asymptotic analysis of the Navier-Stokes equations, a multiple spatial scale self-sustaining process for UMZs and VFs is proposed that satisfies these requirements.

SINGULAR NATURE OF TURBULENT WALL FLOWS

Meinhart & Adrian [1] were the first investigators to document that the wall-normal (y) structure of the instantaneous streamwise velocity in the turbulent boundary layer exhibits a staircase-like profile: regions of quasi-uniform momentum are separated by internal shear layers across which the streamwise velocity jumps by an O(1) amount when scaled by the friction velocity u_τ, as shown in Figure 1a. This sharply-varying instantaneous profile differs dramatically from the well-known long-time mean profile, which is logarithmic over much of the boundary layer, prompting Klewicki [2] to propose that the turbulent boundary layer is singular in two distinct ways. Firstly, spanwise vorticity and mean viscous forces are concentrated in a near-wall region of thickness $O(1/\sqrt{Re_\tau})$, where Re_τ is the friction Reynolds number. Secondly, in a turbulent boundary layer, spanwise vorticity and viscous forces are also significant away from the wall (in the inertial domain, i.e. outboard of the peak in the Reynolds stress), but *only* in spatially-localized regions (i.e. within the internal shear layers). This interpretation accords with a multiscale similarity analysis of the mean momentum balance for turbulent wall flows performed by Wei *et al.*[3]. In support of this notion, Cuevas Bautista *et al.* [4] demonstrate that the logarithmic profile and other higher-order statistcal features associated with the mean streamwise flow can be recovered by ensemble averaging staircase-like streamwise velocity profiles. The objective of the present investigation is to probe the governing Navier–Stokes equations in the limit of large Re_τ in search of a mechanistic self-sustaining process (SSP) theory that (i) can account for the emergent staircase-like profile of streamwise velocity in the inertial region and (ii) is compatible with the singular nature of turbulent wall flows.

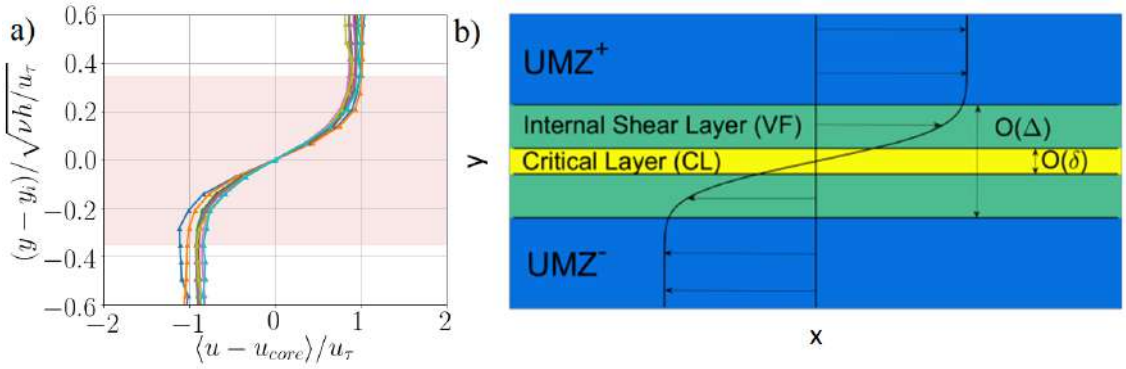

Figure 1: (a) Conditionally-averaged streamwise velocity through vortical fissures in the inertial region of a turbulent boundary layer flow (at $Re_\tau \approx 6000$) in the Flow Physics Facility at the University of New Hampshire. y_i indicates the wall normal location of the VF, u_{core} is the streamwise velocity at the center of the VF, and angle brackets indicate a conditional average. (b) Schematic diagram of the hypothesized three-region asymptotic structure in the fissure-normal direction centred on a fissure located at $y = 0$.

*Corresponding author. E-mail: greg.chini@unh.edu.

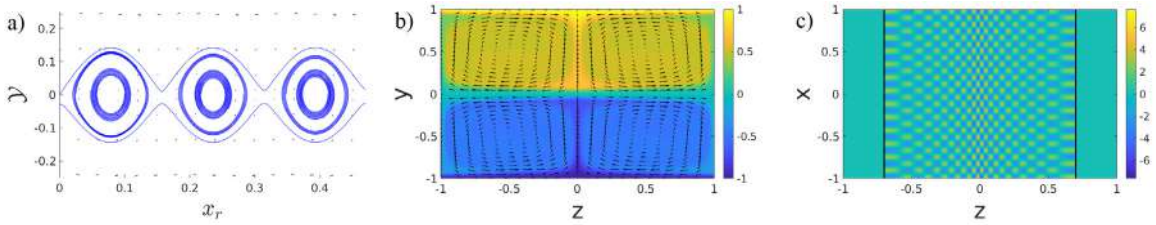

Figure 2: Two-dimensional projections of a new, inertial ECS exhibiting VFs coupled to adjacent UMZs in unbounded plane Couette flow at $Re_\tau \approx 8000$). (a) Close-up view of streamlines in a rotated-streamwise/wall-normal plane within the VF centred on $y = 0$, where the streamwise direction is rotated using Squire's transformation to highlight the appearance of the fine-scale Kelvin's cat's-eyes vortex pattern within the VF. (Arrows are also plotted to indicate in-plane velocity vectors.) (b) Mean velocity field in the fissure-normal/spanwise-plane. Color indicates the value of the streamwise-averaged streamwise velocity component while arrows show the roll velocity field. (c) Fissure-normal fluctuation velocity component in a streamwise/spanwise plane within the VF near $y = 0$. Color indicates the value of this component normalized by ${Re_\tau}^{-3/2}$. The solid black lines indicate caustics, which partition the plane into an 'illuminated region' ($-0.7 \leq z \leq 0.7$) and 'shadow zones' ($|z| \geq 0.7$).

A MULTISCALE SSP THEORY FOR INERTIAL REGION STRUCTURES

Plausible explanations for the formation and persistence of sharply-varying instantaneous streamwise velocity profiles all implicate quasi-coherent turbulent flow structures including streamwise roll motions that induce a cellular flow in the transverse (i.e. spanwise/wall-normal) plane. A possibility, explored here, is that these large–scale motions may be *directly* sustained via an inertial–layer SSP that is broadly similar to the near-wall SSP and closely-related vortex-wave interaction (VWI) theory developed by Waleffe [5] and Hall & Smith [6], respectively. It is argued that these theories cannot account for organized motions in the inertial domain, essentially because the rolls are predicted to be viscously dominated even at large Re_τ [7,8]. The target of the present investigation is an inherently multiscale SSP, in which inviscid streamwise rolls differentially homogenize an imposed background shear flow, thereby generating uniform momentum zones and an embedded internal shear layer (or 'interface'), and are sustained by Rayleigh instability modes having asymptotically smaller streamwise and spanwise length scales.

The Rayleigh mode is supported by the inflectional wall-normal profile of the streamwise–averaged streamwise velocity. Because the thickness of the internal shear layer varies comparably slowly in the spanwise direction, the Rayleigh mode is refracted and rendered fully three–dimensional. This three–dimensional mode is singular, necessitating the introduction of a critical layer within the shear layer within which the mode is viscously regularized. As in VWI theory, a jump in the spanwise Reynolds stress is induced across the critical layer, which ultimately drives the roll motions. This multiscale and three–region asymptotic structure (figure 1b) is efficiently captured using a complement of matched asymptotic and WKBJ analysis. In contrast to the near-wall SSP, the rolls are sufficiently strong to differentially homogenize the background shear flow, thereby providing a potential mechanistic explanation for the formation and maintenance of both UMZs and interlaced internal shear layers. Two-dimensional projections of a new exact coherent state (ECS) supported by the multiscale SSP and exhibiting this spatial structure are shown in figure 2.

CONCLUSIONS

In summary, a primary merit of the new SSP identified here is that it highlights the distinction between viscous and inertial ECS. The SSP also provides a plausible mechanism, derived directly from the NS equations, for the observed UMZ/VF profiles of streamwise velocity. In this mechanism, the VFs play a dynamically *active* role in the sustenance and persistence of the UMZs. Perhaps most significantly, the new SSP and associated ECS provide a concrete dynamical realization of the conceptual model of the singular nature of turbulent wall flows proposed by Klewicki, lending further support to the 'boundary-layers-within-*the*-turbulent-boundary-layer' paradigm.

References

[1] Meinhart C.D., Adrian R.J. On the existence of uniform momentum zones in a turbulent boundary layer. *Phys. Fluids* **7**: 694, 1995.
[2] Klewicki J.C. On the singular nature of turbulent boundary layers. *Proc IUTAM* **9**: 69-78, 2013.
[3] Wei T., Fife P., Klewicki J.C., McMurtry P. Properties of the mean momentum balance in turbulent boundary layer, pipe and channel flows. *J. Fluid Mech.* **522**: 303-327, 2005.
[4] Cuevas Bautista JC., Ebadi A., White C.M., Chini G.P. A uniform momentum zone-vortical fissure model of the turbulent boundary layer. *J. Fluid Mech.* **858**: 609-633, 2019.
[5] Waleffe F. Hydrodynamic stability and turbulence: Beyond transients to a self-sustaining process. *Stud. Appl. Math* **95**: 319, 1995.
[6] Hall P., Smith F. On strongly nonlinear vortex/wave interaction in boundary layer transition. *J. Fluid Mech.* **227**: 641-666, 1991.
[7] Chini G.P., Montemuro B., White C.M., Klewicki J. A self-sustaining process model of inertial layer dynamics in high Reynolds number turbulent wall flows. *Phil. Trans. Roy. Soc. A* **375**, 2017.
[8] Montemuro B., White C.M., Klewicki J.C., Chini G.P. A self-sustaining process theory for uniform momentum zones and internal shear layers in high Reynolds number shear flows. *J. Fluid Mech.* (2019, submitted).

AN ANISOTROPIC MODEL FOR THE TURBULENT SCALAR FLUX IN SHEAR FLOWS WITH DEEP LEARNING

Pedro M. Milani *[1] and John K. Eaton[1]
[1] Mechanical Engineering Department, Stanford University, Stanford CA, USA

Summary In the present paper, we consider a deep learning model for the closure of the turbulent scalar flux in the Reynolds averaged equations. This model utilizes a neural network with embedded rotational invariance to predict a tensorial turbulent diffusivity using mean flow quantities as inputs. Notably, the high fidelity data used for training do not explicitly contain a diffusivity tensor - the neural network architecture is designed to learn that information implicitly. The model is applied in an inclined jet in crossflow and shows significant improvement in predicting the streamwise evolution of the mean scalar concentration.

INTRODUCTION

Many turbulent shear flows of interest involve the transport of a passive scalar c by the velocity field u_i. One such example is the inclined jet in crossflow, in which a cylindrical jet releases a contaminant into the main flow. This configuration finds applications in turbomachinery film cooling [1], where the scalar concentration is analogous to temperature. To solve for the mean scalar concentration in practical flows, the Reynolds averaged equations are usually employed and closure models are needed for both the Reynolds stress (in the momentum equations) and the turbulent scalar flux (in the scalar transport equation).

Machine learning approaches have drawn increased attention in the community as means to formulate improved closure models [2]. For example, Ling et al. [3] developed the Tensor Basis Neural Network (TBNN), which is a neural network architecture to predict the Reynolds stress tensor with rotational invariance. Most authors focus on Reynolds stress modeling for the momentum equations; by contrast, the focus of the current work is on the turbulent scalar flux.

The most common model for the turbulent scalar flux is the simple gradient diffusion hypothesis, with an isotropic turbulent diffusivity prescribed via a fixed turbulent Schmidt number [4]. Milani et al. [5] explored machine-learned models for the turbulent Schmidt number field, and obtained some improvement; however, model form errors can be significant in 3D shear flows which makes this approach insufficient. A more comprehensive model form is shown in Eq. 1, which assumes that the turbulent scalar flux vector, $\overline{u_i' c'}$, is related to the mean concentration gradient via a tensorial diffusivity D_{ij}. This model is still local, but it allows different turbulent transport properties in different directions and cross-gradient transport (whereby, for example, gradients in the y direction affect the transport in the x direction).

$$\overline{u_i' c'} = -D_{ij} \frac{\partial \bar{c}}{\partial x_j} \tag{1}$$

Some authors have proposed algebraic models for the diffusivity tensor D_{ij} based on the Reynolds stress, but such models have not gained much traction in practical codes [4]. In the current work, we apply deep learning techniques to predict the diffusivity tensor based only on mean flow quantities in hopes that this could lead to a more practical model. In particular, we adapt the TBNN of Ling et al. [3] to the scalar modeling problem, with a modified architecture which we call TBNN-s (where 's' stands for scalar flux modeling). The model is developed using the highly resolved large eddy simulations (LES) of inclined jets in crossflow that are presented and validated in Milani et al. [6], shown in Fig. 1.

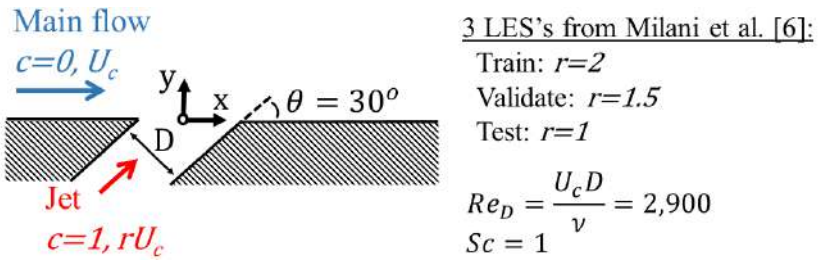

Figure 1: Schematic of the inclined jet in crossflow used in this study. This geometry is fully 3D, with a square channel main flow and a cylindrical jet. The flow is incompressible, U_c is the channel bulk velocity, and rU_c is the jet bulk velocity. Three highly resolved simulations are employed with the same Reynolds number (Re_D) and molecular Schmidt number (Sc), but different velocity ratios (r).

METHODOLOGY

The TBNN is designed to predict the Reynolds stress anisotropy tensor, which is a symmetric tensor explicitly available in the high fidelity data, as a function of the local mean flow variables. It employs a tensor basis expansion to guarantee that the turbulence model is invariant to any coordinate frame transformations. To use an analogous approach to model the turbulent scalar flux, we assume initially that it is a general function of $\mathbf{S}$ (the mean strain rate tensor), $\mathbf{R}$ (the mean rotation rate tensor), and $\nabla \bar{c}$ (the mean concentration gradient vector):

*Corresponding author. E-mail: pmmilani@stanford.edu.

$$\overline{\mathbf{u}'c'} = -\mathbf{f}(\mathbf{S}, \mathbf{R}, \nabla\bar{c}). \tag{2}$$

Then, we use an appropriate basis expansion to represent the function $\mathbf{f}$ with embedded rotational invariance. Zheng [7] shows that, for this particular case, there are 13 scalar invariants λ_i, which are ultimately the inputs to the neural network, and 6 vector elements in the integrity basis expansion, $\mathbf{t}^{(n)}$. The relevant vector basis is shown in Eq. 3:

$$\mathbf{t}^{(1)} = \nabla\bar{c}, \quad \mathbf{t}^{(2)} = \mathbf{S}\nabla\bar{c}, \quad \mathbf{t}^{(3)} = \mathbf{R}\nabla\bar{c}, \quad \mathbf{t}^{(4)} = \mathbf{S}^2\nabla\bar{c}, \quad \mathbf{t}^{(5)} = \mathbf{R}^2\nabla\bar{c}, \quad \mathbf{t}^{(6)} = (\mathbf{SR} + \mathbf{RS})\nabla\bar{c}. \tag{3}$$

Note that it is possible to factor out the mean concentration gradient $\nabla\bar{c}$ from each of the basis elements, such that they can be written as a 3x3 matrix multiplied by $\nabla\bar{c}$. Then, a weighted sum of the vector basis elements can be interpreted as a diffusivity tensor times the mean concentration gradient. Using a neural network architecture that explicitly recognizes this fact, it is possible to use high fidelity data with a known $\overline{u_i'c'}$ (but unknown turbulent diffusivity tensor D_{ij}) to train the network. The network learns a tensorial diffusivity that is most consistent with the given turbulent scalar flux and the invariance requirement. Then, for a new flow, we need only provide the quantities $\mathbf{S}$, $\mathbf{R}$, and $\nabla\bar{c}$ and the trained network is able to predict a turbulent diffusivity matrix.

RESULTS AND DISCUSSION

We train the proposed network architecture in the $r = 2$ LES and determine its hyperparameters through validation on the $r = 1.5$ LES. We use a deep neural network with 10 hidden layers and 30 nodes per layer. The network then predicts a turbulent diffusivity matrix in the $r = 1$ dataset, which is used to solve the Reynolds averaged scalar transport equation. The results are shown in Fig. 2.

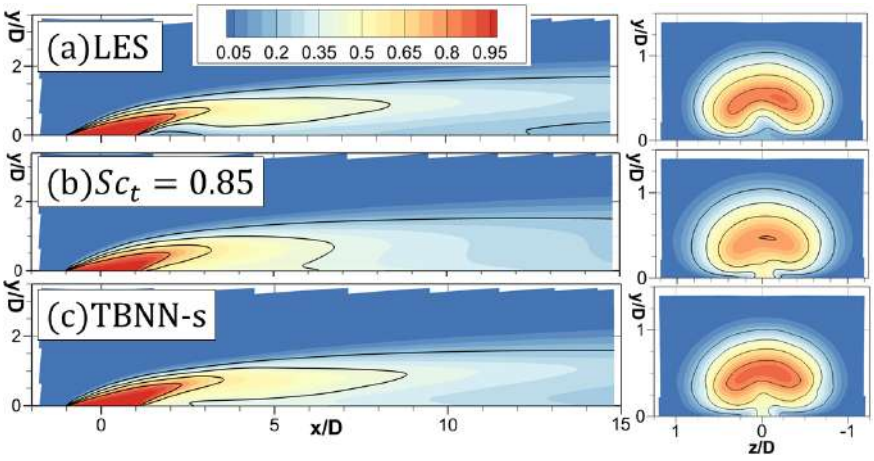

Figure 2: Mean scalar concentration in the $r = 1$ jet in crossflow. The left side shows centerplanes ($z = 0$) and the right side show axial ($y - z$) planes located at $x/D = 2$. (a) shows LES results, which are validated against experimental data. Both (b) and (c) are obtained by solving the Reynolds averaged scalar transport equation with the LES mean velocity field and distinct models for the turbulent scalar flux. (b) contains results from a baseline turbulence model, which is the isotropic gradient diffusion hypothesis with a fixed turbulent Schmidt number ($Sc_t = 0.85$). (c) shows results of the TBNN-s anisotropic model.

The resulting model is numerically stable after a simple post-processing step of the output diffusivity that forces it to be positive semidefinite. Interestingly, the TBNN-s model is able to significantly improve the mean scalar concentration field prediction in a flow that is has not been trained on. In particular, the network learns off-diagonal elements of the diffusivity matrix that are intuitively sound. So, this added cross-gradient capability of the model is able to better predict the streamwise decay compared to a baseline model. The results are also superior to those of a previously reported machine-learned isotropic model [5]. The TBNN-s proposed here can be readily applied to arbitrary 3D flows and meshes as long as relevant training data exist. Thus, future work could explore the application of this model in other turbulent flows where the concentration of a scalar contaminant is sought.

References

[1] D.G. Bogard, K.A. Thole Gas Turbine Film Cooling. *J. Propul. Power* **22**(2): 249-270, 2006.
[2] K. Duraisamy, G. Iaccarino, H. Xiao Turbulence modeling in the age of data. *Ann. Rev. Fluid Mech.* **51**: 357-377, 2019.
[3] J. Ling, A. Kurzawski, J. Templeton Reynolds averaged turbulence modelling using deep neural networks with embedded invariance. *J. Fluid Mech.* **807**: 155-166, 2016.
[4] D.P. Combest, P.A. Ramachandran, M.P. Dudukovic On the gradient diffusion hypothesis and passive scalar transport in turbulent flows. *Ind. Eng. Chem. Research* **50**(15): 8817-8823, 2011.
[5] P.M. Milani, J. Ling, J.K. Eaton Generalization of machine-learned turbulent heat flux models applied to film cooling flows. *J. Turbomach.* **142**(1): 011007, 2020.
[6] P.M. Milani, I.E. Gunady, D.S. Ching, A.J. Banko, C.J. Elkins, J.K. Eaton Enriching MRI mean flow data of inclined jets in crossflow with large eddy simulations. *Int. J. Heat Fluid Flow* **80**: 108472, 2019.
[7] Q.S. Zheng Theory of representations for tensor functions—a unified invariant approach to constitutive equations. *App. Mech. Rev.* **47**(11): 545-587, 1994.

OPTIMAL CONTROL FOR LARGE SYSTEM: A RESOLVENT-BASEDAPPROACH

Eduardo Martini*[1,2], Junoh Jung[3], André V. G. Cavalieri[1], Peter Jordan[2], Aaron Towne[3], and Lutz Lessahfft[4]
[1] Instituto Tecnológico de Aeronáutica, São José dos Campos/SP-Brazil
[2] Départemen tFluides,Thermique e tCombustion, Institut Pprime, CNRS, Université de Poitiers,ENSMA,86000 Poitiers, France
[3] Department of Mechanical Engineering, University of Michigan, Ann Arbor, MI 48109, USA
[4] Laboratoire d'Hydrodynamique, CNRS, Ecole Polytechnique, Institut Polytechnique de Paris, 91128 Palaiseau, France

Summary As fluid system typically have large numbers of degrees of freedom, classical control strategies typically need to be obtained using reduced order models (ROMs). Obtaining such models is often is the most costly process in the development of control strategies. Alternatives using response modes from resolvent analysis, PSE solutions, and data-driven methods have been proposed as an alternative. However, none of these approaches are generalizable to large class of problems, and are mostly restricted to flows dominated by convection, and to SISO control. An approach for optimal control of complex flows, without the construction of ROMs is proposed. The method has moderate computational cost, and a matrix-free approach makes it suitable for complex flows. Force colour, which is seen to be crucial for an accurate estimation of turbulent flows, is naturally handled by the method.

INTRODUCTION

Flow control has been an active research topic, with possible applications in aircraft noise and drag reduction. Classical control methods have been successfully used in many studies. Due to the large numbers of degrees-of-freedom of unsteady shear flows, reduced order models (ROMs) are typically constructed to obtain a system for which the solution of Ricatti equations is feasible. ROMs based on Galerkin projections using proper-orthogonal decomposition (POD) modes, balanced modes, and eigen-modes have been used. All of these can be computed from time marching schemes, however in some cases the number of modes required can be large, and the procedure is not always straightforward. Moreover, ROM accuracy may be fragile, and good representation of open-loop dynamics does not guarantee an accurate representation of the closed-loop behaviour. A posteriori tests are thus needed, which often requires some trial and error in the construction of a ROM.

Some alternatives have been proposed. Eigen-system realization algorithms have much lower computational cost, and are equivalent to a ROM based on balanced modes [1]. Optimal control and estimation gains for full systems can be obtained with iterative methods [2], which can be used directly for control (which is only feasible for simulations), or for constructing ROMs a posteriori. Both these methods are in practice restricted to low-dimensional inputs.

Another approach to estimation and control is the Wiener regulator. Martinelli [3] is, to the best of our knowledge, the only work using Wiener's method for flow control. The author realized that the method can potentially lead to large computational saving, as the most costly part of the calculation scales with the number of sensors and actuators, not with the dimensionality of the flow model. However, his application was limited to the use of one sensor and one actuator, probably due to the difficulties of solving the corresponding Wiener-Hopf problems.

METHODS

Estimation methods based on the resolvent operator have been proposed as an alternative to classical estimation tools [4, 5]. Building on these works, a previous work from from the authors [6] showed that the resolvent leads to optimal non-causal estimation, which minimizes the functional

$$\boldsymbol{J} = \int_{-\infty}^{\infty} \langle (\boldsymbol{u}(\boldsymbol{t}) - \tilde{\boldsymbol{u}}(\boldsymbol{t}))^{\dagger} (\boldsymbol{u}(\boldsymbol{t}) - \tilde{\boldsymbol{u}}(\boldsymbol{t})) \rangle \boldsymbol{dt}, \tag{1}$$

with $\langle \cdot \rangle$ representing the expected value, u the flow-state, and $\tilde{u}$ the flow state estimation obtained from low-rank flow measurements, $y(t)$. It is shown that the optimal estimate can be obtained for large systems using time marching of the adjoint and direct linearized Navier-Stokes equations, which naturally handles system disturbed by coloured forces. On a turbulent channel flow, the use of the correct force colour, with forces representing non-linear interactions [7], is crucial for obtaining accurate estimations with a low number of sensors, with estimation outperforming previous approaches [8]. Although typically unknown, force colour can be efficiently estimated using the method and an auxiliary set of sensors.

The method is extended to the development of control strategies: perturbations in certain flow regions, referred to as targets, $z(t)$, are minimized using flow actuation obtained via a convolution of a control law and flow readings, $a(t) = \Gamma(t) * y(t)$. This corresponds to minimization of the cost functional

$$\boldsymbol{J} = \int_{-\infty}^{\infty} \langle \boldsymbol{z}(\boldsymbol{t})^{\dagger} \boldsymbol{z}(\boldsymbol{t}) \rangle \boldsymbol{dt} + \int_{-\infty}^{\boldsymbol{0}} \boldsymbol{\lambda}(\boldsymbol{t}) \boldsymbol{\Gamma}(\boldsymbol{t}) \boldsymbol{dt}, \tag{2}$$

*Corresponding author. E-mail: emartini@ita.br

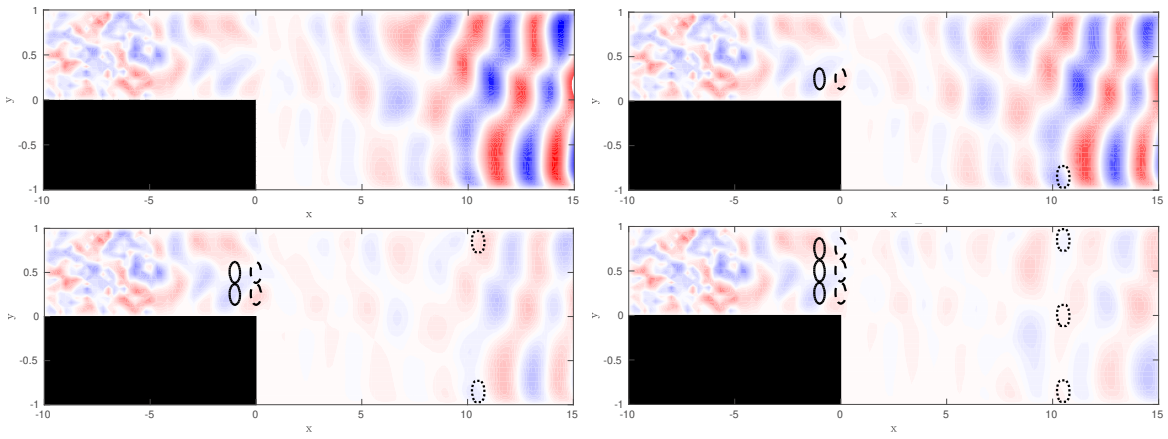

Figure 1: Flow perturbation snapshot for uncontrolled and optimally controlled systems. Colour map indicates streamwise velocity perturbations, with the same colour scale used in all plots. Solid, dashed and dotted circles represent sensors, actuators and targets used.

where the rightmost term corresponds to a Lagrange multiplier to enforce control law causality. A minimization of this functional leads to a Wiener-Hopf equation, due to the presence of the half-time-domain integral.

Solutions of Wiener-Hopf equations can be obtained with a kernel factorization as a multiplication of a causal and an anti-causal functions. Solving equation (2) requires the factorization of two kernels, of sizes $n_y \times n_y$ and $n_z \times n_z$, with n_y and n_z representing the number of sensors and targets used. Kernel factorization can only be obtained analytically for scalar kernels and special types of matrix kernels. In this work this is carried out with numerical solutions of the Fredholm equation of second kind [9]. Optimal causal control of large system is thus obtained with moderate costs, without requiring model reduction, for a system with assumed force and sensor noise statistics, via the resolvent operator: the method is thus refereed to as *Resolvent-based control*.

RESULTS

The method is applied for control of perturbations of a backward-facing step, with $Re = 500$, based on the channel width, and a unit step height. We work with the linearized Navier-Stokes system, driven by stochastic external disturbances. The spectral solver *Nek5000* is used for direct and adjoint computations. The configuration is similar to the that used by [10], where a single sensor and actuator were used to control low-rank disturbances using a data-driven approach. Here the problem is made considerably more challenging by making the external forces high rank, with spatiotemporal white forces used for $x < -5$. For this case multiple sensors and actuators are seen to be crucial for an effective control of flow disturbances, as seen in figure 1.

The proposed method is effective for developing control strategies, as the associated Wiener-Hopf equation scales with the number of sensors and targets, not with the dimensionality of the underlying problem. There is no need to form large system matrices, as all computations are carried out with the direct and adjoint time stepper. The method is thus directly applicable to complex, three-dimensional flows. The control law can easily incorporate coloured force statistics, which can be estimated using an approach proposed on a previous work [6].

References

[1] Zhanhua Ma, Sunil Ahuja, and Clarence W Rowley. Reduced-order models for control of fluids using the eigensystem realization algorithm. *Theoretical and Computational Fluid Dynamics*, **25(1-4)**:233–247, 2011.

[2] Onofrio Semeraro, Jan O. Pralits, Clarence W. Rowley, and Dan S. Henningson. Riccati-less approach for optimal control and estimation: An application to two-dimensional boundary layers. *Journal of Fluid Mechanics*, **731**:394–417, September 2013.

[3] Fulvio Martinelli. Feedback Control of Turbulent Wall Flows. *PhD thesis*, Politecnico di Milano, 2009.

[4] Samir Beneddine, Robin Yegavian, Denis Sipp, and Benjamin Leclaire. Unsteady flow dynamics reconstruction from mean flow and point sensors: An experimental study. *Journal of Fluid Mechanics*, **824**:174–201, 2017.

[5] Aaron Towne, Adrián Lozano-Durán, and Xiang Yang. Resolvent-based estimation of space–time flow statistics. *Journal of Fluid Mechanics*, **883**:A17, 2020.

[6] Eduardo Martini, André V. G. Cavalieri, Peter Jordan, Aaron Towne, and Lutz Lesshafft. Resolvent-based optimal estimation of transitional and turbulent flows [submitted]. *J. Fluid Mech.*, 2020.

[7] B. J. McKeon and A. S. Sharma. A critical-layer framework for turbulent pipe flow. *Journal of Fluid Mechanics*, **658**:336–382, September 2010.

[8] Mattias Chevalier, Jérôme Hœpffner, Thomas R Bewley, and Dan S Henningson. State estimation in wall-bounded flow systems. Part 2. Turbulent flows. *Journal of Fluid Mechanics*, **552**:167–187, 2006.

[9] V Daniele and G Lombardi. Fredholm factorization of Wiener-Hopf scalar and matrix kernels. *Radio Science*, **42(06)**:1–19, 2007.

[10] Aurelien Hervé, Denis Sipp, Peter J Schmid, and Manuel Samuelides. A physics-based approach to flow control using system identification. *Journal of Fluid Mechanics*, **702**:26–58, 2012.

ESTIMATION OF ROUGH WALLS BY THE ROUGHNESS HEIGHT AND STEEPNESS

Guozhen Ma[1], Chunxiao Xu[1] and Hyung Jin Sung[2], Weixi Huang *[1]
[1] Department of Engineering Mechanics, Tsinghua University, Beijing 100084, China
[2] Department of Mechanical Engineering, KAIST, Daejeon 34141, Korea

Summary Turbulent flows over three-dimensional sinusoidal rough walls are investigated by direct numerical simulations at $Re_\tau \approx 540$. By systematically varying the roughness height k^+ or wavelength λ^+, we introduce a new coupling scale $k^+ \cdot ES$ ($ES \sim k/\lambda$). By utilizing this scale, the roughness function collapses well to a single line. More importantly, the prediction model of wall resistance based on roughness function was established by defining a drag increasing ratio (*DI*). Thus we can estimate the wall drag coefficient directly from the given roughness height and steepness.

INTRODUCTION

The turbulent flow over a rough wall almost always produces higher drag than that of a smooth wall. The increase in drag is often quantified by the Hama roughness function ΔU^+, which reflects the downward shift of the streamwise mean velocity profile. In practice, the increase of drag usually brings a lot of harm and efficiency loss, and predicting the drag on a rough wall is therefore of crucial importance to most engineering problems. A central goal in the present study is to predict the roughness function directly from the given rough surface, and then predict the wall resistance.

The dependence of ΔU^+ on the roughness height k^+ and other geometric features, such as the density and shape has been explored in many studies (Jiménez, 2004; Flack & Schultz, 2010). Most of them mainly focused on investigating the influence of these two parameters separately. In this paper, a parameter $k^+ \cdot ES$ is defined which comprehensively considers the roughness Reynolds number and the steepness of the wall roughness, to parameterize the flow field statistics. *ES* is the mean absolute streamwise gradient of the surface (Napoli *et al*., 2008), and proportional to k/λ in the roughness form of our study.

COMPUTATIONAL SETUP

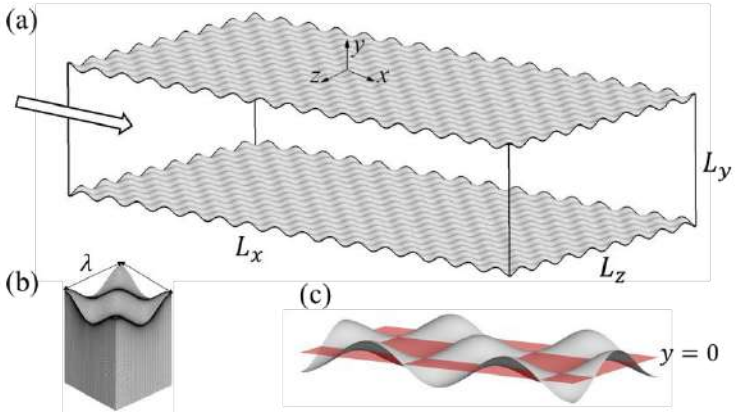

Figure 1. Schematics of the turbulent channel flow over three-dimensional sinusoidal rough walls.

The problem under consideration is the fully developed turbulent channel flow over 3D sinusoidal rough walls. The roughness form chosen is consistent with that of Chung *et al*. (2015). A schematic diagram of the channel is shown in Figure 1. A right-handed Cartesian frame fixed in the physical space is employed with *x*, *y* and *z* axes along the streamwise, vertical and spanwise coordinates, respectively. *k* is the semi-amplitude of the sinusoidal roughness and λ is the wavelength of the roughness elements. The mean height of the rough surfaces is set to zero, thus the coordinate $y = 0$ is used as the virtual origin of the bottom wall. The friction Reynolds number based on the friction velocity u_τ and the half channel height δ is about 540. The sizes of the computational domain is $2\pi\delta \times 2\delta \times \pi\delta$, and the corresponding grid number is 288×192×288. The grid sizes in the *x* and *z* directions are uniform with the resolution of $\Delta\xi_1^+ \approx 11$ and $\Delta\xi_3^+ \approx 5.5$, respectively. The grid points along the *y* axis follow a cosine distribution with $\Delta\xi_{2,min}^+ \approx 0.1$ and $\Delta\xi_{2,max}^+ \approx 8.9$. The no-slip condition is applied to the walls of the channel and a periodic boundary condition is applied in the *x* and *z* directions. The flow is driven by a mean pressure gradient, which is dynamically adjusted to keep the constant flow rate in time. We used the coordinate transformation to transform the irregular physical domain into a rectangular computational domain based on the boundary-fitted system. To identify the roughness effects, the phase average and triple decomposition are adopted in analysis of the flow fields. Further details of the numerical methods can be found in Zhang *et al*. (2019). In this work, three groups are chosen: (1) group A, k^+ is varied while k/λ is kept constant; (2) group B, λ^+ is varied while k^+ is kept constant; (3) group C, k^+ is varied while λ^+ is kept constant.

*Corresponding author. E-mail: hwx@mail.tsinghua.edu.cn.

NUMERICAL RESULTS

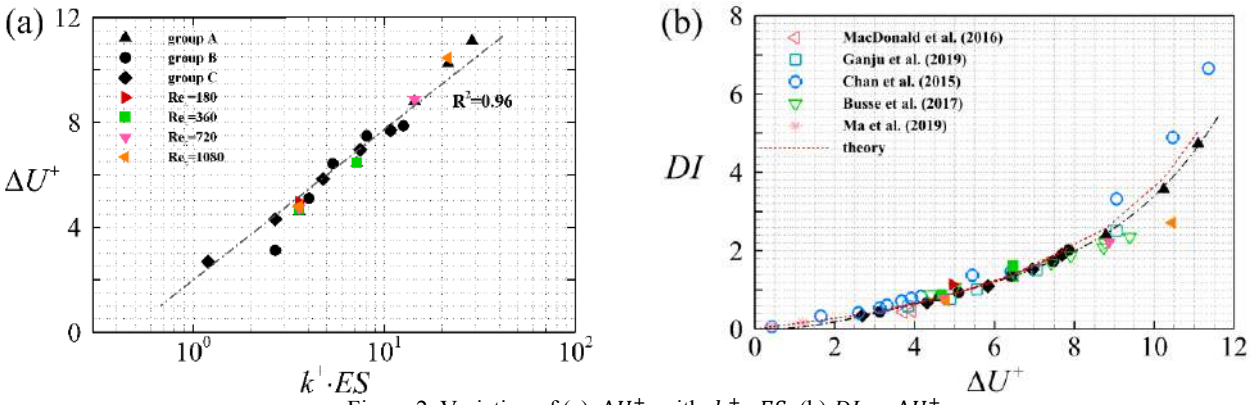

Figure 2. Variation of (a) ΔU^+ with $k^+ \cdot ES$; (b) DI *vs* ΔU^+.

A simple fitting of the present data is applied for the parametrization of ΔU^+ with k^+ and ES,

$$\Delta U^+ = 2.78 \cdot [log(k^+ \cdot ES)] + 1.35, \quad (1)$$

Figures 2(a) show the results of scaling of the roughness function ΔU^+ using new roughness paramater $k^+ \cdot ES$. All the data collapse well to a single line, that is, the rough walls constructed in different roughness heights and roughness wavelengths exhibit a similar behaviour by denoting $k^+ \cdot ES$. Here we add several cases to take into account the effect of Reynolds number. It's clear that the ΔU^+ only has to do with k^+, with little dependence on the Reynolds number. Figure 2(b) gives the prediction relationship between the drag coefficient C_f and ΔU^+. The y-axis is defined as the drag increase ratio as $DI = (C_f - C_{f,0})/C_{f,0}$, which is fitted by the fourth-order polynomial. Almost all data fall on the fitting asymptote, and the goodness-of-fit reaches 0.99. Note that C_f approaches the smooth wall result $C_{f,0}$ for $\Delta U^+ = 0$, namely DI tends to zero, which is reflected in the fit. Besides the fitting curve, DI can be derived according to its definition, i.e.

$$DI = \left(\frac{1}{1-\Delta U^+/U_{b,0}^+}\right)^2 - 1. \quad (2)$$

where $U_{b,0}^+$ denotes viscous-scaled bulk velocity of the smooth wall. The results of some published literature with different roughness forms are also putted in the figure to make comparisons, which show very good consistency.

CONCLUSIONS

In the present study, DNS with a body-conforming grid was performed for turbulent channel flow over three-dimensional sinusoidal rough walls. Three groups were chosen and the DNS data for a smooth wall was included for comparison. By systematically varying the roughness height k^+ and roughness steepness ES, we parameterize the effects of these two important parameters. The results showed the combination of k^+ and ES, i.e. $k^+ \cdot ES$, produces more reliable predictive schemes, which performs significantly better than just k^+ or ES individually. Then a resistance increasing ratio is defined to illustrate the predictive relationship between the total drag coefficient and the roughness function. The wall drag coefficient can be estimated directly from known roughness parameters of the surface, i.e. $C_f \sim f(k^+ \cdot ES)$, which is of great significance to our practical application. However, the scaling still exists the limitations. When ES is very large or small, there is a lack of the correct behaviour. This is related to the solidity of the roughness, and the current study is mainly applicable to the sparse regime.

Acknowledgments

The authors acknowledge funding support from the National Natural Science Foundation of China under Grants Nos. 11772172 and 91752205.

References

[1] Jiménez, J. (2004). Turbulent flows over rough walls. Annu. Rev. Fluid Mech., 36, 173-196.
[2] Flack, K. A., & Schultz, M. P. (2010). Review of hydraulic roughness scales in the fully rough regime. Journal of Fluids Engineering, 132(4), 041203.
[3] Napoli, E., Armenio, V., & De Marchis, M. (2008). The effect of the slope of irregularly distributed roughness elements on turbulent wall-bounded flows. Journal of Fluid Mechanics, 613, 385-394.
[4] Chung, D., Chan, L., MacDonald, M., Hutchins, N., & Ooi, A. (2015). A fast direct numerical simulation method for characterising hydraulic roughness. Journal of Fluid Mechanics, 773, 418-431.
[5] Zhang, W. Y., Huang, W. X., & Xu, C. X. (2019). Very large-scale motions in turbulent flows over streamwise traveling wavy boundaries. Physical Review Fluids, 4(5), 054601.

MODELING THE TURBULENT FLOW OVER AN ANISOTROPIC POROUS WALL USING DMD MODES AND DEEP LEARNING

Soledad Le Clainche[1], Marco Rosti[2], and Luca Brandt [3]
[1] School of Aerospace Engineering, Universidad Politécnica de Madrid, Madrid, Spain
[2] Complex Fluids and Flows Unit, OIST, Onna-son, Okinawa 904-0495, Japan
[3] Linné Flow Centre and SeRC, Department of Engineering Mechanics KTH, Stockholm, Sweden

Summary The main goal of this work is to model the flow near an anisotropic porous wall. Two databases have been analysed, where the drag increases or decreases compared to the case of an isotropic porous wall. Higher order dynamic mode decomposition (HODMD) is applied to identify the main spatio-temporal flow structures in the flow. As expected, the drag increase is related to the presence of spanwise elongated structures, so-called 'rollers', which are related to a KH-like instability, frequently reported over permeable substrates. On the contrary, the drag reduction mechanism is related with the presence of stronger streamwise correlated structures, so-called 'streaks'. Based on this, a group of DMD modes have been selected to model the wall shear stress. Combining these modes with linear and non-linear regression models, the evolution in time of the wall shear stress is predicted with noteworthy accuracy.

INTRODUCTION

Wall-bounded turbulent flows present a wall friction higher than laminar flows. Due to their widespread applications, in natural flows and in the industry, many researchers have studied in detail the flow over complex surfaces, especially over porous walls. In particular, researchers have paid special attention to the flow over isotropic porous walls [1], although more recently the community has started to consider the flow over anisotropic walls, as these can alter the near wall dynamics. Increasing the wall normal permeability, the drag increases compared to a standard isotropic wall [2,3]. This drag increase is related to a KH-like instability, identified by the presence of spanwise elongated structures, named 'rollers' [4]. On the other hand, decreasing wall-normal permeability and increasing the streamwise one, drag reduces and the flow is more correlated in the streamwise direction. The present work studies in detail two datasets obtained from numerical simulations of the turbulent flow over an anisotropic porous wall and compares the results with a third data set modelling the turbulent flow over an isotropic porous wall. In the first case, the wall normal permeability is increased, thus the drag increases, while in the second case, the permeability along the streamwise and spanwise direction is increased, thus the drag decreases when compared to the flow over a rigid wall [2].

METHODOLOGY

Higher order dynamic mode decomposition (HODMD) [5], an extension of dynamic mode decomposition (DMD) [6] introduced for the analysis of complex and noisy databases, is used to analyse two databases modelling a turbulent anisotropic porous wall [2]. The spatio-temporal HODMD analysis [7] have been carried out with the aim to identify the main mechanism producing the drag increasing or drag reduction in the flow. Once these mechanisms, have been identified by the DMD modes in form of coherent structures, the flow field, $\boldsymbol{v}_{rec}$, composed by the three components of the velocity, streamwise $\boldsymbol{u}_{app}$, wall-normal $\boldsymbol{v}_{app}$ and span-wise $\boldsymbol{w}_{app}$ components, is reconstructed using the M highest-amplitude (most-energetic) DMD modes, following the spatio-temporal DMD modal expansion (defined in time t and along spanwise coordinate z) as

$$\boldsymbol{v}_{rec} = \sum_{m=1}^{M} a_m \boldsymbol{u}_m e^{(\delta_m + i\omega_m)t + (\nu_m + i\beta_m)z},$$

where $\boldsymbol{u}_m$ and a_m, are the DMD modes and their corresponding amplitudes; ω_m, β_m are the frequency and wavenumber in the spanwise direction of the modes, and δ_m, ν_m are their corresponding temporal and spatial growth rates. A function modelling the wall shear stress, defined as $\tau = \mu \frac{\partial \boldsymbol{u}}{\partial y} + \boldsymbol{u}\boldsymbol{v}$, where μ is the fluid viscosity, is constructed using the previous approximation of the flow field, $\boldsymbol{u}_{app}$ and $\boldsymbol{v}_{app}$, as $\tau_{app} = \mu \frac{\partial \boldsymbol{u}_{app}}{\partial y} + \boldsymbol{u}_{app}\boldsymbol{v}_{app}$. Combining this wall shear function with linear and non-linear regression techniques, it is possible to minimize the difference between the real solution and the approximation, $\min 3|\tau - \tau_{app}|$, obtaining an efficient reduced order model for the wall shear stress evolution $\frac{d\tau_{app}}{dt}$. Integrating this model in time is then possible to predict the temporal history of the wall shear stress.

RESULTS AND FUTURE WORK

Figure 1 shows a three-dimensional reconstruction of two DMD spatio-temproral modes, with high and low frequency, in the drag reduction and drag increasing case analysed. In the drag increasing flow, it is possible to identify the spanwise elongated structures, the rollers, with $\beta = 0$ (related to a KH-like flow instability), nevertheless, in the drag reduction case, the structures are not spanwise correlated. More details about the physics of the problem will be presented at the time of the conference.

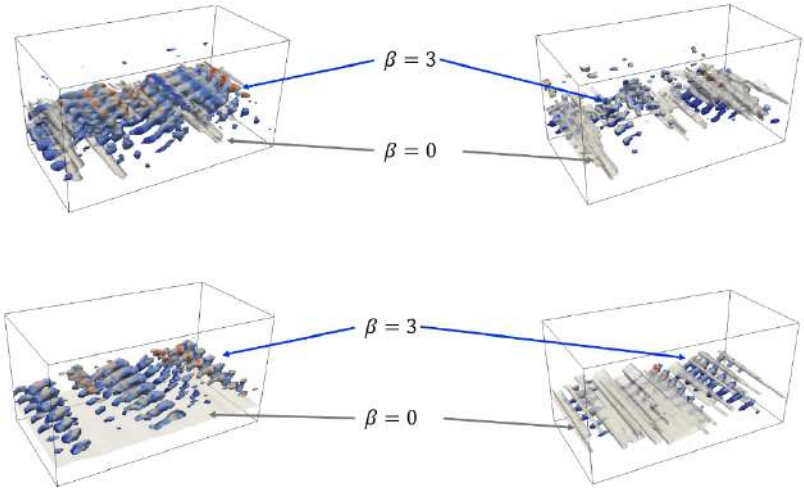

Figure 1: Three-dimensional reconstruction of two spatio-temporal DMD modes. Iso-surfaces of streamwise velocity in the module of the DMD modes. Left: low frequency mode. Right: high frequency mode. Top: drag increasing case. Bottom: drag reduction case.

Figure 2 shows the temporal evolution of the wall shear stress in the drag reducing case. The figure compares the model with the solution from the direct numerical simulations performed as described in [2]. The DMD analysis (training) is carried out in a group of data collected in the interval $t \in [0,200]$, while the prediction is carried out until the time $t \simeq 580$ with relative error smaller than 2%. More details about this model and these predictions will be presented at the conference. Similarly, a model for the shear stress in the flow of reduced drag will also be presented at that time.

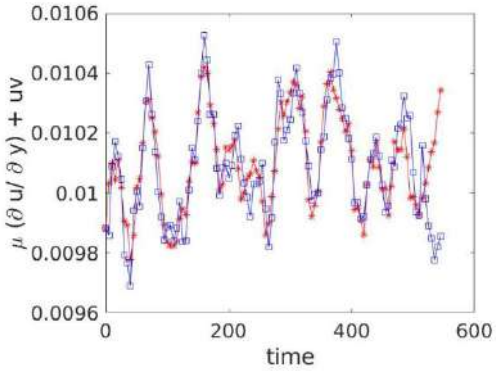

Figure 2. Temporal evolution of the wall shear stress in the drag reduction case. Blue and red lines correspond to the real solution and the model based on DMD combined with machine learning methods.

References

[1] Breugem W.P., Boersma B.J., Uittenbogaard, R.E. The influence of wall permeability on turbulent channel flow. *J. Fluid. Mech.* **562**: 35-72, 2006.
[2] Rosti, M., Pinelli A., Brandt L. Turbulent channel flow over an anisotropic porous wall-drag increase and reduction. *J. Fluid. Mech.* **842**: 381-394, 2018.
[3] Gómez de Segura G., García-Mayoral R. Turbulent draf reduction by anisotropic permeable substrates- análisis and direct numerical simulations. *J. Fluid. Mech.* **875**: 124-172, 2019.
[4] Jiménez J., Uhlmann M., Pinelli A., Kawahara G. Turbulent shear flow over active and passive porous surfaces. *J. Fluid. Mech.* **442**: 89-117, 2001.
[5] Le Clainche S., Vega J.M., Higher order dynamic mode decomposition, *SIAM J. Appl. Dyn. Sys.,* **16(2):**882-925, 2017.
[6] Schmid P. Dynamic mode decomposition for numerical and experimental data, *J. Fluid. Mech.* **656**: 5-28, 2010.
[7] Le Clainche S., Vega J.M., Spatio-temporal Koopman decomposition, *J. Nonlin. Sci..,* **28(3):**1-50, 2018.

SPATIO-TEMPORAL CHARACTERISTICS OF UNIFORM MOMENTUM ZONES THROUGH EXPERIMENTS AND MODELLING

Angeliki Laskari*[1], Charitha M. de Silva[3], Nicholas Hutchins[4], and Beverley J. McKeon[2]
[1] Department of Process & Energy, Delft University of Technology, Delft, The Netherlands
[2] Graduate Aerospace Laboratories, California Institute of Technology, California, US
[3] School of Mechanical and Manufacturing Engineering, University of New South Wales, Sydney, Australia
[4] Department of Mechanical Engineering, University of Melbourne, Melbourne, Australia

Summary The probability density function (pdf) of the instantaneous streamwise velocity can be used to extract information on the presence of uniform momentum zones (UMZs) in turbulent boundary layers [1]. In this work, we present new insight into the spatio-temporal characteristics of this pdf, using different experimental datasets with very long temporal and spatial domains. When the pdf is plotted over time, repeated transitions to lower velocities are observed, while similar trends can also be observed for increasing streamwise distance. In order to examine how these trends are linked to the underlying velocity field, a simple resolvent model is employed [2]. Results show that a single resolvent mode reproduces many of the observed patterns and highlights the importance of the wavelike nature and phase characteristics of the velocity structures involved.

EXPERIMENTAL RESULTS

Time-resolved planar Particle Image Velocimetry (PIV) data from a boundary layer at $Re_\tau = 5200$ in streamwise–wall-normal planes are first analysed [3]. The pdf of the streamwise velocity U, is constructed using the full streamwise extent of the field of view ($L_x|_{pdf} = 0.5\delta$) and all vectors within the turbulent region.

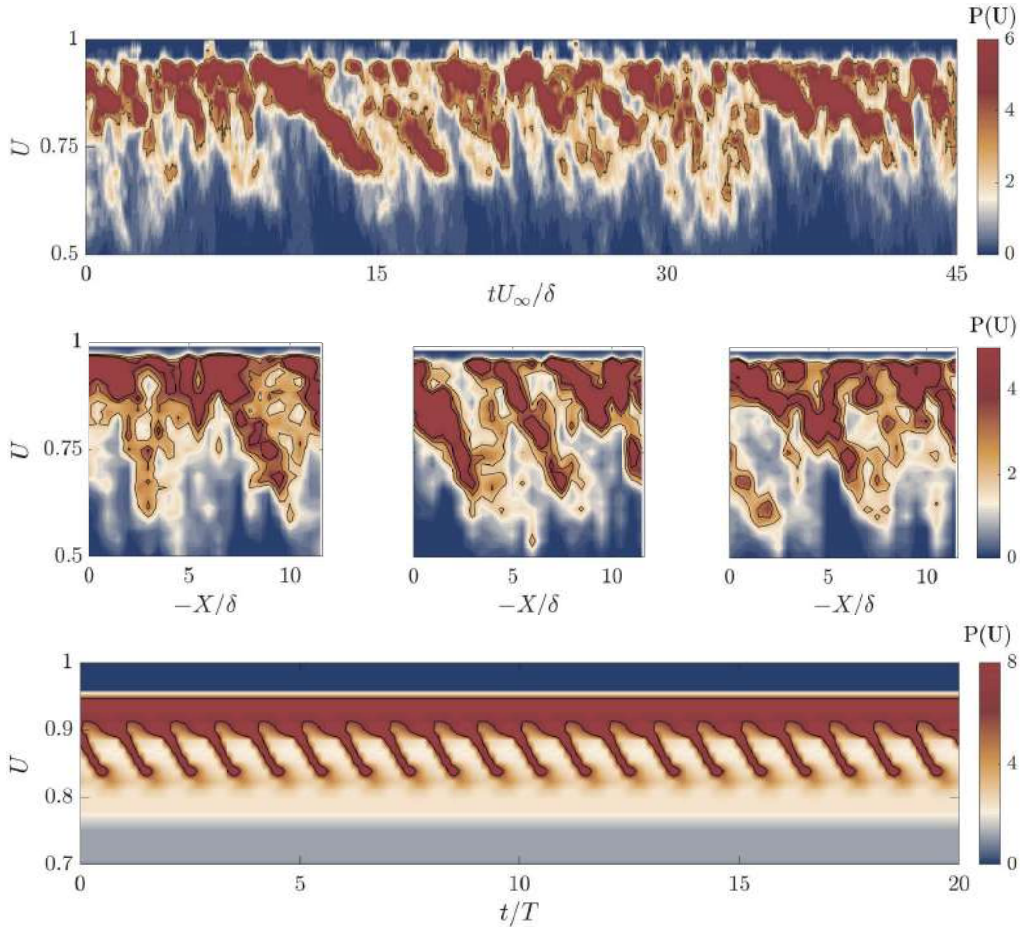

Figure 1: Contour plots of the probability density function, $P(U)$ of the full streamwise velocity, $U = u + \overline{U}$. Experimental measurements, temporal domain (Top, [3]). Experimental measurements, spatial domain, three independent snapshots (middle). Resolvent framework (Bottom, [2]).

*Corresponding author. E-mail: a.laskari@tudelft.nl.

The temporal evolution of the pdf indicates repeated transitions to lower velocities, while faster, more abrupt changes to higher velocities are also observed (figure 1, top). To quantify the rate of these temporal transitions, their slope with respect to time is estimated ($\tan\phi = \frac{\delta}{{U_\infty}^2}\frac{\Delta U_{min}}{\Delta t}$). Results show that these transitions are robust across all experimental datasets available, with $|\tan\phi_l| = 0.15\pm0.07$ and $|\tan\phi_h| = 0.35\pm0.11$, for the transitions to lower and higher velocities, respectively. When conditioned on these transitions, the number of zones present in the flow, N_{UMZ} shows a very distinct variation, increasing as $P(U)$ peaks at lower velocities, and decreasing when velocities close to the freestream are the most prominent in the flow. The corresponding velocity fluctuations also indicate a clear pattern of large-scale downstream leaning structures of alternating signs associated with both transitions observed in the pdf of U.

To compare this temporal pattern with the spatial evolution of the pdf, a second PIV dataset, with an extended streamwise field of view ($L_x = 12\delta$) at $Re_\tau = 2500$, is used. The pdf of U is computed over consecutive windows of $L_x = 0.5\delta$ along the streamwise direction of each snapshot. Preliminary results on the spatial evolution of the pdf indicate a similar trend for increasing streamwise distance as the one observed in the temporal domain (figure 1, middle).

SIMPLE RESOLVENT MODEL

In order to analyse the characteristics of the velocity structures leading to this spatio-temporal behaviour, we employ the resolvent framework [2]. Here, a simplified approach is followed where a single resolvent mode is used, located at the edge of the log region (centred at $y = 0.27$), with a wavelength λ_x and a wave period T. The mode amplitude profile for the streamwise velocity component is approximated by a Gaussian function (recently shown to be a very accurate representation of exact resolvent mode shapes in wall bounded turbulence, [4]), the phase variation in the wall-normal direction exhibits a $-\pi$ reversal across the critical layer) and the phase speed of the mode at the critical layer is $c_x = 0.89U_\infty$. The mean profile, which also informs the wall-normal extent and weighting of the mode, is from a channel flow at $Re_\tau = 15000$ (more details can be found in [5]).

Based on the temporal and spatial scales extracted from the experimental data, we select a streamwise extent $L_x|_{pdf} = 0.25\lambda_x$ for the model. The resulting temporal evolution of the pdf exhibits a very similar pattern of slower transitions to lower velocities and abrupt jumps to higher velocities as observed in the experiments, albeit periodic as expected (figure 1, bottom). Velocity fluctuations conditionally averaged on these transitions agree very well with the experimental results. Additionally, it is shown that the phase jump across the critical layer is crucial for reproducing the observed behaviour. The choice of the mode weighting with respect to the mean is another important factor in the resulting rate of these transitions and can be tuned accordingly, in order for the model to better match the experimental observations. To that end, increased complexity in the modelled pdf can also be achieved, by increasing the number of resolvent modes used, organised in a self-similar hierarchy ([6]).

CONCLUSIONS AND FUTURE WORK

Experimental datasets with long temporal and spatial domains allow a unique assessment of the evolution of the streamwise velocity pdf in wall-bounded flows, while the comparison of the dynamics observed in both space and time indicates the role and limitations of Taylor's hypothesis in connecting the two. We further exploit a simple model for the velocity fluctuations based on the resolvent approach to reproduce many of the experimental observations and highlight their link to the underlying wavelike nature and phase characteristics of the velocity structures involved.

ACKNOWLEDGEMENTS

This work was supported by the ONR under grant number N00014-17-1-3022.

References

[1] R. J. Adrian, C. D. Meinhart, and C.D. Tomkins. Vortex organization in the outer region of the turbulent boundary layer. *J. Fluid Mech*, 422:1–54, 2000.

[2] B. J. McKeon and A. S. Sharma. A critical-layer framework for turbulent pipe flow. *J. Fluid Mech*, 658:336–382, 2010.

[3] A. Laskari, R. de Kat, R.J. Hearst, and B. Ganapathisubramani. Time evolution of uniform momentum zones in a turbulent boundary layer. *J. Fluid Mech*, 842:554–590, 2018.

[4] S.T. Dawson and B.J. McKeon. On the shape of resolvent modes in wall-bounded turbulence. *J. Fluid Mech*, 877:682–716, 2019.

[5] B. J. McKeon. Self-similar hierarchies and attached eddies. *Phys. Rev. Fluids*, 4:082601(R), 2019.

[6] R. Moarref, A.S. Sharma, Tropp J.A., and B.J. McKeon. Model-based scaling of the streamwise energydensity in high-reynolds-number turbulent channels. *J. Fluid Mech*, 734:275–316, 2013.

A WALL-LAW FOR THE MEAN VELOCITY IN THE INNER PART OF TURBULENT BOUNDARY LAYERS AT ADVERSE PRESSURE GRADIENT AND APPLICATION FOR RANS TURBULENCE MODELLING

Tobias Knopp *[1], Nico Reuther[3], Matteo Novara[1], Erich Schülein[1], Daniel Schanz[1], Christian Willert[2], Andreas Schröder[1], Andreas Krumbein[1], Cornelia Grabe[1], and Christian J. Kähler[3]

[1] Institute of Aerodynamics and Flow Technology, DLR, Göttingen, Germany
[2] Institute of Propulsion Technology, DLR, Köln, Germany
[3] Institute for Fluid Mechanics and Aerodynamics, Universität der Bundeswehr München, Germany

Summary We present a strategy to modify turbulence models based on the Reynolds averaged Navier-Stokes (RANS) equations for flow separation on smooth surfaces due to an adverse pressure gradient. We describe two new turbulent boundary layer experiments to study the behaviour of the mean velocity profile at adverse pressure gradients and at high Re. We observe that the log-law in the mean velocity profile is a robust feature, but its region is much thinner than in zero-pressure gradient flows, and its slope is altered. A square-root law emerges above the log-law extending to the wall-ward distance the log-law typically occupies. Then we modify a differential Reynolds stress turbulence model. The modified model accounts for a change of the log-law slope and the formation of a square-root law at adverse pressure gradient, improving the agreement with the experimental data for both experiments.

GOALS, EXPERIMENTAL SETUP, AND MEASUREMENT TECHNIQUE

Turbulent boundary layers subjected to an adverse pressure gradient at high Reynolds numbers still pose many open questions regarding their statistically averaged mean flow, see [1]-[5]. At the same time, they have a high relevance in technical applications, e.g., in aerospace research. At high Re, turbulence resolving simulation methods like large-eddy-simulation (LES) and hybrid RANS/LES methods still need a near-wall model based on the RANS equations and statistical turbulence models for the foreseeable future. Therefore the prediction of flow separation on smooth surfaces due to an adverse pressure gradient is still not reliable. We pursue a strategy (i) to set-up a high-quality data base by new experiments, (ii) to find an empirical wall-law for the mean velocity in the inner layer, and (iii) to improve the turbulence models based on the empirical wall-law.

The first goal is to find a new wall-law for the mean velocity based on the following questions: Q1: Does a log-law region still exist at APG [1]-[5]? Q2: Does the slope of the log-law change with the streamwise pressure gradient in inner scaling $\Delta p_x^+ = (\partial P/\partial x)^+$, as proposed by [1]? Q3: Is there a sqrt-law region above the log-law, see e.g. [2], [3]? For this purpose we designed two new wind-tunnel experiments. The second goal is to use this knowledge of a wall law for the mean velocity to improve RANS turbulence models.

In the wind-tunnel experiments, the turbulent boundary layer flow develops on the side wall of the wind-tunnel and then follows a ramp and a long flat plate at almost zero pressure gradient. Then the flow enters into the adverse pressure gradient section, first along a curved surface and then on a flat plate, which is the focus region. The flat plate segment has an opening angle of 14.4° and 18.6° resp. relatively to the zero-pressure gradient section. The flow remains attached in the first experiment and separates in the second.

The experiments were performed at different Re by variation of the velocity up to $U_\infty = 36\,\mathrm{m/s}$. The focus region is at $8\,\mathrm{m} \leq x \leq 10.5\,\mathrm{m}$, where the test-section starts at $x = 0\,\mathrm{m}$. We obtain a significant adverse pressure gradient with $\Delta p_x^+ > 0.02$ and Rotta-Clauser pressure gradient parameter $\beta_{\mathrm{RC}} > 30$ for the first experiment and even larger values for the second, and Re_θ up to 50000 in the adverse pressure gradient region.

The measurement technique uses 2D2C large-scale particle image velocimetry (PIV) for characterising the streamwise evolution of the flow over a streamwise distance of 2.1 m or 15 boundary layer thicknesses. In the adverse pressure gradient focus region, we use 2D2C microscopic (2D μPTV) and 3D3C Lagrangian particle tracking (3D LPT) to measure the mean velocity and the Reynolds stresses down to the viscous sublayer. Oil-film interferometry is used for the complementary direct measurement of the wall shear stress.

RESULTS FOR THE MEAN VELOCITY AND DISCUSSION

For the mean velocity profile in the adverse pressure gradient region, we observe that the log-law in the mean velocity profile $u^+ = \log(y^+)/K_i + B_i$ is a robust feature, but its region is much thinner than in zero-pressure gradient flows, and its slope is altered. The value of the log-law slope coefficient K_i is found to be decreasing with increasing values of the pressure gradient parameter Δp_x^+. We find a value of $K_\mathrm{i} = 0.370 \pm 0.017$ for $\Delta p_x^+ = 0.018$, lower than for the von Kármán constant for zero pressure gradient boundary layers $\kappa = 0.4 \pm 0.02$, see Fig. 1 (a). A square-root law emerges above the log-law extending to the wall-ward distance the log-law typically occupies, see Fig. 1 (b), and the slope diagnostic function for the square-root law shows a plateau.

*Corresponding author. E-mail: Tobias.Knopp@dlr.de.

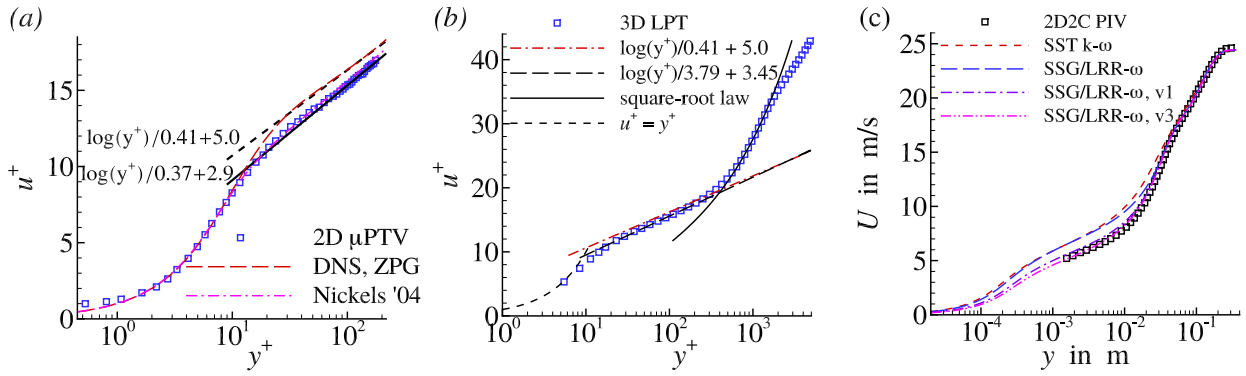

Figure 1: (a) Near wall profile of u^+ for $\Delta p_x^+ = 0.018$ and change of log-law slope. (b) Reduced extent of log-law region and square-root law for $\Delta p_x^+ = 0.011$. (c) RANS results for modified SSG/LRR-ω RSM using the square-root law modification (v1) and additional modification of the log-law slope (v3) at $\Delta p_x^+ = 0.027$.

The wall-distance, where the mean-velocity profile changes from the log-law to the square-root law, can be characterised by two similarity parameters, i.e., the pressure gradient parameter Δp_x^+ and the acceleration parameter $\Delta u_{\tau,x}^+ = (\partial u_\tau/\partial x)^+$, being the streamwise gradient of the wall shear stress velocity. Put in other words, we find mean-flow similarity in the inner layer for the present flow and other flows in the literature, provided that they are at the same values of Δp_x^+ and $\Delta u_{\tau,x}^+$ and provided that low-Re effects are small, i.e., $Re_\theta > 10000$. In the outer layer, the profiles can differ due to the different upstream history. Similarity in the inner layer and differences in the outer layer can be explained using the idea of the eddy turn over time.

RANS MODEL IMPROVEMENT FOR ADVERSE PRESSURE GRADIENTS

Then we present a RANS study for the two experiments using two popular models, i.e., the SST k-ω model and the differential Reynolds stress model (DRSM) SSG/LRR-ω. The SST model is based on the turbulent viscosity hypothesis. The SSG/LRR-ω model solves the transport equation for the Reynolds stress tensor using empirical models for redistribution and turbulent transport. For both, the dissipation ϵ is modelled using the specific dissipation rate ω, for which an additional empirical transport equation is solved. We observe that both models predict a too high velocity in the inner layer and cannot predict a square-root law, see Fig. 1 (c).

We apply the above findings for the mean velocity profile to modify the RANS models, extending the work in [5]. First, the coefficient which controls the slope of the log-law is made a function of the local value of Δp_x^+, instead of being a constant value in the standard model. Second, we add a model deficiency term so that the modified model gives a square-root law at adverse pressure gradient. The deficiency term is determined by analytical solution of an inverse boundary layer problem. Both modifications increase the dissipation in the inner part of the inner layer in agreement with the findings in [4]. This leads to a reduction of turbulent transport of momentum into the near-wall region, thus making the model more susceptible for flow separation. The modified model yields a much better agreement with the experimental data, see Fig. 1 (c).

CONCLUSIONS

In an analysis of two new turbulent boundary layer experiments, we find that the mean velocity profile at adverse pressure gradient in the inner layer shows a thin log-law region, whose slope is altered compared to the zero pressure gradient case, and a square-root law which emerges above the log-law extending to the wall-ward distance the log-law occupies at zero pressure gradient. These findings are used to modify a differential Reynolds stress RANS turbulence model to account for a change of the log-law slope and the formation of a square-root law at adverse pressure gradient, leading to improved agreement with the experimental data.

References

[1] Nickels, T. B. Inner scaling for wall-bounded flows subject to large pressure gradients. *J. Fluid Mech.* **521**: 217-239, 2004.
[2] Perry, A. E., Bell, J. B., and Joubert, P. N. Velocity and temperature profiles in adverse pressure gradient turbulent boundary layers. *J. Fluid Mech.* **25**: 299-320, 1966.
[3] Coleman, G.N., Rumsey, C. L., and Spalart, P. R. Numerical study of turbulent separation bubbles with varying pressure gradient and Reynolds number. *J. Fluid Mech.* **847**: 28-70, 2018.
[4] Kitsios, V., et al. Direct numerical simulation of a self-similar adverse pressure gradient turbulent boundary layer at the verge of separation. *J. Fluid Mech.* **829**: 392-419, 2017.
[5] Knopp, T., et al. Modification of the SSG/LRR-omega RSM for turbulent boundary layers at adverse pressure gradient with separation using the new DLR VicToria experiment. In: Proceedings of 21th STAB/DGLR Symposium 2018. Springer, 2019.

AMBIGUITY IN MEAN-FLOW-BASED LINEAR ANALYSIS

Ugur Karban*[1], Eduardo Martini[2], Benjamin Bugeat[3], Aaron Towne[4], André V. G. Cavalieri[2], Lutz Lesshafft[5], Anurag Agarwal[3], Peter Jordan [1], and Tim Colonius[6]
[1] Département Fluides, Thermique, Combustion, Institut Pprime, CNRS-University of Poitiers-ENSMA, France
[2] Instituto TecnolÓgico de Aeronáutica, São José dos Campos/SP, Brazil
[3] Department of Engineering, University of Cambridge, Cambridge, CB2 3AP, UK
[4] Department of Mechanical Engineering, University of Michigan, Ann Arbor, MI 48109, USA
[5] Laboratoire d'Hydrodynamique, CNRS / École polytechnique, Institut Polytechnique de Paris, Palaiseau, France
[6] Division of Engineering and Applied Science, California Institute of Technology, Pasadena, California 91125, USA

Summary The effect of a variable transformation on the linear operator that is obtained by linearizing a turbulent flow about its mean is investigated. It is shown that the characteristics of the linear operator are dependent on the state variables used and can be modified when the state vector is subjected to non-linear transformation and linearisation is not performed around a fixed point. This observation raises a uniqueness issue for mean-flow resolvent analyses. The effect of the variable transformation on the stability characteristics is demonstrated via some test cases, including a subsonic jet. The implications for the validity of mean-flow resolvent analyses and possibilities for optimizing resolvent-based approaches are discussed.

INTRODUCTION

Mean-flow-based linear analyses have been used since the 1970s to understand and model the dynamics of coherent structures in turbulent shear flow. The approach involves linearisation around the mean field and subsequent analysis of the resulting linear operator. Linear analysis performed using the mean flow has proved to be a useful way to study coherent structures in turbulent shear flows [1, 2, 3, 4, 5, 6]. However there is no rigorous mathematical justification for such a choice. The temporal mean is one of infinitely many non-fixed points about which one may linearise. This observation reveals an ambiguity in the roles that the linear operator and the remaining non-linear terms play. It is possible, for instance, to modify the linear operator via the introduction of an eddy-viscosity-based model in the linear part [7], or by directly changing the linearisation point, which change the characteristics of the linearised system.

In this paper, we discuss the validity of mean-flow resolvent analyses from the point of view of their uniqueness. By limiting ourselves to linearisation about the temporal mean, we show that, choosing two different variable sets that define a given flow yields two linearised systems with different characteristics, if the two variable sets are non-linearly related, as are, for example conservative and primitive variables. The formalisation is achieved by (*i*) considering a flow defined by Navier-Stokes equations written in two different variable sets that are non-linearly related, (*ii*) linearising the two systems around their temporal means, respectively, (*iii*) deriving a relation between the resulting linear operators.

METHODOLOGY AND RESULTS

Given a dynamical system, $\partial_t q = \mathcal{N}(q)$ with the state, q and the non-linear operator $\mathcal{N}$, linearising about the temporal mean of the state, $\overline{q}$ yields,

$$\partial_t q - \mathbf{A}_{\overline{q}} q' = f, \tag{1}$$

where q' is the fluctuating part of q, $\mathbf{A}_{\overline{q}} = \partial_q \mathcal{N}|_{\overline{q}}$ is the linear operator and f denotes the remaining non-linear terms. Given a non-linear transformation $\tilde{q}_T = \mathscr{H}(\overline{q})$, the relation between the linear operators of the original and transformed systems, $\mathbf{A}_{\overline{q}}$ and $\mathbf{A}_{\tilde{q}_T}$, respectively, is obtained as,

$$\mathbf{A}_{\tilde{q}_T} = \partial_q \mathscr{H}|_{\overline{q}} \mathbf{A}_{\overline{q}} \left(\partial_q \mathscr{H}|_{\overline{q}}\right)^{-1} + \partial_{qq} \mathscr{H}|_{\overline{q}} \left(\partial_q \mathscr{H}|_{\overline{q}}\right)^{-1} \mathcal{N}|_{\overline{q}}. \tag{2}$$

In (2), the first term on the right-hand-side denotes a similarity tranformation of $\mathbf{A}_{\overline{q}}$, which does not modify the eigenvalues. However, addition of the second term on the right-hand-side causes a change in eigenvalues. Note that second term is zero only if the transformation is linear ($\partial_{qq}\mathscr{H} = 0$) or linearisation is about a fixed point ($\mathcal{N}(q_0) = 0$). We first consider a model problem based on Ginsburg-Landau (G-L) equation, given as,

$$\partial_t q + U\partial_x q - \gamma \partial_{xx} q - \mu q = -\beta q|q|^2 + f_{ext}. \tag{3}$$

*Corresponding author. E-mail: ugur.karban@univ-poitiers.fr.

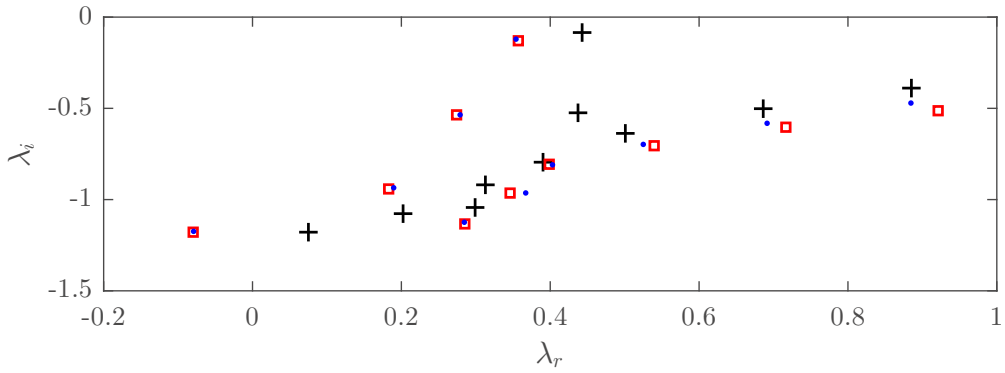

Figure 1: Eigenspectrum for the least unstable 10 eigenvalues of the original (black-plus), and the tranformed (red-square) systems and the first-order predictions of the corresponding transformed eigenvalues (blue-dot).

We limit the study to stationary systems, and bijective transformations between the variables.

The change in eigenvalues of the model problem due to a non-linear transformation of the state variable is shown in Figure 1. The transformation function used for this case has the form,

$$q_T = \frac{1}{q-a} + \frac{1}{a}, \tag{4}$$

where $a = 0.2$ is a free parameter. Eigenvalues in Figure 1 are significantly changed in the transformed system, and so are eigenfunctions. Note that $\tilde{q}_T$ does not correspond to the mean of the transformed state. We show that predicting the linear operator of the transformed system using the mean-flow information in the original system is only possible through a first-order Taylor-series expansion. In Figure 1, this first-order expansion is also shown to successfully predict the transformed eigenvalues.

CONCLUSIONS

The dependency of the characteristics of the linear operator defined for a dynamical system that is linearised about the temporal mean, (or any non-fixed point in general) on the state variables raises questions regarding the conditions for validity of mean-flow stability analysis. The validity of mean-flow resolvent analyses for jets have been justified based on the fact that for weakly non-parallel flow the resolvent of the linear operator will exhibit large gain separation [8], and associated large spatial separation between forcing and response modes, such that for the leading input-output pair the forcing is entirely localised at the upstream boundary [6]. However, we show in our analysis that using the same flow data, it is possible to obtain two different resolvent operators, with different gain separations and spatial supports for the corresponding modes. Having two different operators corresponding to the same flow indicates that one should take into account the non-linear terms for the validity of the mean-flow stability analysis, via, for instance, appropriate statistics for the forcing f in (1).

The final paper will include, in addition to discussion of the theoretical framework, demonstration of the issue using a model problem based on G-L equation, and a subsonic, compressible jet.

References

[1] Hwang Y.,Cossu C. Amplification of coherent streaks in the turbulent couette flow: an input–output analysis at low reynolds number. *J. Fluid Mech.* **643**: 333–348, 2010.
[2] Jordan P., Colonius T. Wave packets and turbulent jet noise. *Annu. Rev. Fluid Mech.* **45** (1): 173–195, 2013.
[3] Sharma A. S., McKeon B. J. On coherent structure in wall turbulence. *J. Fluid Mech.* **728**: 196–238, 2013.
[4] Towne A., Schmidt O. T., Colonius T. Spectral proper orthogonal decomposition and its relationship to dynamic mode decomposition and resolvent analysis. *J. Fluid Mech.* **847**: 821–867, 2018.
[5] Schmidt O. T., Towne A., Rigas G., Colonius T., Brès G. A. Spectral analysis of jet turbulence. *J. Fluid Mech.* **855**: 953–982, 2018.
[6] Cavalieri A. V. G., Jordan P. Lesshaft L. Wave-Packet Models for Jet Dynamics and Sound Radiation. *Appl. Mech. Rev.* **71** (2): 020802, 2019.
[7] Morra P., Semeraro O., Henningson D. S. Cossu C. On the relevance of Reynolds stresses in resolvent analyses of turbulent wall-bounded flows. *J. Fluid Mech.* **867**: 969-984, 2019.
[8] Beneddine S., Sipp D., Arnault A., Dandois J., Lesshaft L. Conditions for validity of mean flow stability analysis. *J. Fluid Mech.* **798**: 485–504, 2016.

HIERARCHY ANALYSIS OF LARGE-SCALE COHERENT STRUCTURES IN TURBULENT WALL-BOUNDED FLOWS

Guangyao Cui, Ido Ruhman, and Ian Jacobi
Faculty of Aerospace Engineering, Technion Israel Institute of Technology, Haifa, Israel

Summary Understanding the relationships between large- and small-scale coherent motions in turbulence is crucial for developing reduced-order models of turbulent flows. We implemented a novel, spatial wavelet-based approach for identifying hierarchies of coherent motions, utilizing insights from astrophysical galaxy cluster detection. The hierarchy detection method was validated against synthetic, turbulent super-structure data and then applied to new, experimental boundary layer measurements at high Reynolds number. The phase and amplitude relationships between different scale structures of momentum hierarchies were calculated and compared with the results of traditional filtering approaches.

Very large-scale regions of coherent, streamwise momentum have long been observed in measurements of the turbulent boundary layer [1] and are dynamically significant to its kinetic energy and Reynolds stresses [2]. Although these large-scale structures have been explored via spatial and temporal filtering of velocity fields, their interpretation has remained somewhat subjective: do they represent the superposition of smaller scale motions, in a 'bottom-up' construction [3, 4] or are these large structures the 'top-down' result of dynamics at the outer edge of the boundary layer [5]? Filtering-based analysis can describe the dynamics of these super-structures, but cannot determine whether a coherent region of momentum is best understood as a superposition of smaller motions or an independent larger motion. The answer to this question has important implications for analyzing scale interactions in turbulence and modeling canonical turbulent flows.

In order to examine the composition of very-large scale motions in wall-bounded flows, we need to identify hierarchies of coherent structures and establish their inter-relationships. To define such hierarchies objectively, we adopted an analytical tool from the world of astrophysics, traditionally used to identify clusters of galaxies from telescope imagery. A field of individual galaxies is typically obtained in the form of a binary field of points. Clusters are then determined by using a continuous wavelet transform of the field [6, 7]. A statistical comparison is performed between the resulting wavelet coefficients and the coefficients of a random ('no-clustering', null-hypothesis) field. Under this approach, a cluster of galaxies can be objectively defined as an isolated collection of binary points that are statistically unlikely to appear by chance over a given length scale (i.e. the wavelet size). We applied this technique in wall-bounded flows to avoid the subjectivity otherwise inherent in labeling long, meandering regions of high or low velocity as turbulent 'super-structures' (figure 1). In addition to identifying individual structures of momentum at different scales, the spatial wavelets were also used to establish a statistically significant hierarchy of these structures and then to study their spatial distribution and the dynamical (modulating) relationships present between scales within a single hierarchy.

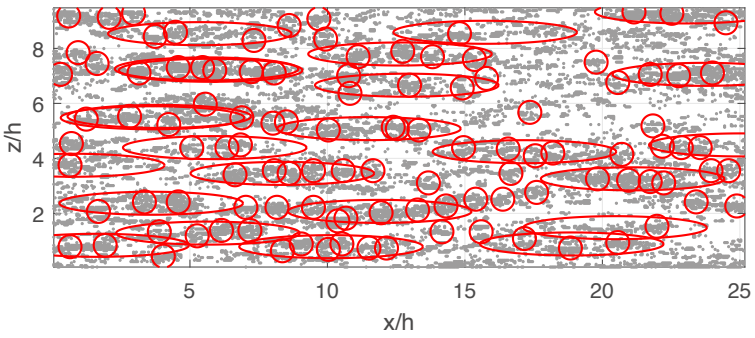

Figure 1: The wall parallel velocity field from a channel flow DNS (half-height h) [8] at $\mathrm{Re}_\tau = 1000$, sampled at $y^+ = 30$, binarized to represent the top 20% of velocities in the instantaneous PDF. Spatially coherent clusters of momentum are marked in red for wavelets with streamwise extent $0.8h$ and $6.6h$, identified with statistical significance level of 0.001 (here including overlaps), using the technique described below.

In this study, we developed a wavelet based hierarchy detection scheme for turbulent flow analysis, and applied it in two different environments: initial testing and validation of synthetic velocity fields and low Reynolds number DNS channel data; and primary application in new experimental measurements of a high Reynolds number boundary layer flow ($\mathrm{Re}_\tau \approx 6000$).

The initial validation study (figure 2) was performed using synthetic meandering velocity fields, representative of the super-structures observed in the logarithmic region of wall-bounded flows [1]. When applied to momentum measurements, the cluster detection process involved first segmenting the velocity field into binary fields (corresponding to uniform momentum zones) and transforming these fields via a continuous wavelet transform. The transform was calculated over all of the wavelet scales, aspect ratios, and orientation angles of dynamical relevance. The relative extrema of the wavelet-transformed field were then identified allowing for the detection of regions of high spatial density of coherent momentum [9]. However, the presence of a relative extremum alone does not necessarily represent a statistically significant spatial density of coherent momentum; in order to ascertain whether the extremum is significant, it must be compared with the magnitude of wavelet coefficient extrema that would be obtained via transformation of a uniform random process with the same number density as the momentum field. This statistical significance

*Corresponding author: ijacobi@technion.ac.il

thresholding was accomplished via an efficiently modeled version of a Monte-Carlo simulation. The thresholds were then applied to the extrema found in the transformed momentum field to identify statistically significant momentum clusters. The superposition of these clusters was then analyzed, under a similar statistical model, in order to group significant structures at different scales into hierarchies.

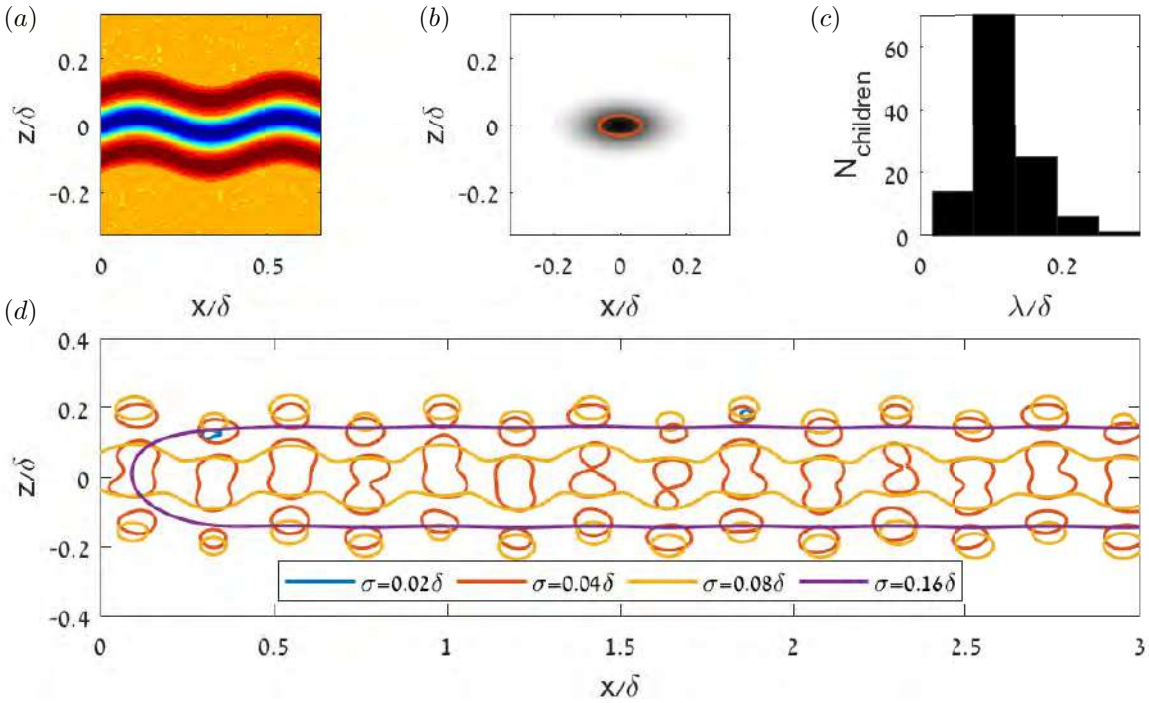

Figure 2: (a) Synthetic meandering streamwise velocity fields produced from [1]. (b) A Morlet wavelet with scale parameter $\sigma = 0.04\delta$ with a marked threshold level of three times the spatial RMS average of the wavelet coefficients. (c) For a given 'parent' $\hat{x}$-momentum structure of lengthscale $\lambda = 7\delta$, the distribution of 'child' structures that are contained within the parent hierarchy. (d) Contour levels corresponding to the coefficient-thresholded continuous wavelet transform of the velocity field, identifying a range of different physical scales of motion, in terms of the wavelet scales, from which the hierarchies were established.

Once the hierarchies were identified, the spatial phase and modulation relationships between 'parent' and 'child' members of each hierarchy were calculated using correlation analysis. However, unlike traditional scale modulation analysis, which involves filtering velocity signals to separate different scales of motion, after which the spatial relationships between scales are inferred [10], the statistical hierarchy approach outlined here naturally separates the scales and establishes their spatial relationships explicitly. The resulting scale-interactions were calculated between members of hierarchies using PIV measurements of a high Reynolds number boundary layer flow in a new, high speed water tunnel facility, and the ensemble averaged spatial scale-interaction relationships were compared with traditional filtering approaches.

A novel use of spatial wavelets and cluster-detection algorithms was shown to provide a new tool for the explicit identification of hierarchies of turbulent coherent structures and the study of scale interactions in wall-bounded flows.

The authors acknowledge the support of Israel Science Foundation grant number 1704/17.

References

[1] Hutchins, N. and Marusic, I., Evidence of Very Long Meandering Features in the Logarithmic Region of Turbulent Boundary Layers. *Journal of Fluid Mechanics* **579**: 1–28, 2007.
[2] Guala, M., Hommema, S. E., and Adrian, R. J., Large-scale and Very-large-scale Motions in Turbulent Pipe Flow. *Journal of Fluid Mechanics* **554**: 521–542, 2006.
[3] Saxton-Fox, T. and McKeon, B. J., Coherent Structures, Uniform Momentum Zones and the Streamwise Energy Spectrum in Wall-bounded Turbulent Flows. *Journal of Fluid Mechanics* **826**: 1-12, 2017.
[4] Adrian, R. J., Hairpin Vortex Organization in Wall Turbulence. *Physics of Fluids* **19**: 041301, 2007.
[5] Liu, H., Wang, G., and Zheng, X., Amplitude Modulation Between Multi-scale Turbulent Motions in High-Reynolds-number Atmospheric Surface Layers. *Journal of Fluid Mechanics* **861**: 585–607, 2019.
[6] Slezak, E. and Bijaoui, A. and Mars, G., Identification of Structures from Galaxy Counts: Use of the Wavelet Transform. *Astronomy and Astrophysics* **227**: 301–316, 1990.
[7] Langer, W. D. and Wilson, R. W. and Anderson, C. H., Hierarchical Structure Analysis of Interstellar Clouds Using Nonorthogonal Wavelets. *The Astrophysical Journal* **408**: 399–404, 1993.
[8] Data obtained from the JHTDB at **http://turbulence.pha.jhu.edu**.
[9] Escalera, E. and Mazure, A., Wavelet Analysis of Subclustering - An Illustration, Abell 754. *The Astrophysical Journal* **388**: 23–32, 1992.
[10] Mathis, R. and Hutchins, N. and Marusic, I., Large-scale Amplitude Modulation of the Small-scale Structures in Turbulent Boundary Layers. *Journal of Fluid Mechanics* **628**: 311–337, 2009.

ULTIMATE HEAT TRANSFER IN TURBULENT POISEUILLE FLOW BETWEEN PERMEABLE WALLS

Kenta Inada[1], Kentaro Tsugawa[1], Shingo Motoki *[1], Masaki Shimizu[1], and Genta Kawahara[1]
[1] Graduate School of Engineering Science, Osaka University, 1-3 Machikaneyama, Toyonaka, Osaka, Japan

Summary We study heat transfer in turbulent Poiseuille flow between permeable walls. The permeable wall model here assumes that the wall-normal velocity at the wall is proportional to the local pressure fluctuations. The temperature is treated as a passive scalar with a uniform heat generation and isothermal boundaries. As the bulk Reynolds number (or the permeability) increases, large-scale spanwise rolls appear, leading to turbulence promotion. Although the friction coefficient $C_f = \text{const.}$ is reached at high Reynolds number like a flow over rough walls, there is no flow separation near the permeable walls unlike rough walls. As a result, the similarity between momentum and heat transfer is maintained, and the Stanton number $St = \text{const.}$ is also achieved. The scaling implies the 'ultimate' state in which the heat flux is independent of the kinematic viscosity and the thermal diffusivity.

INTRODUCTION

The effect on the turbulent shear flow of wall surface properties is of great interest among many researchers in engineering and geophysics. In particular, flow over rough walls has been energetically investigated by experiments and numerical simulations. In turbulent flow, surface roughness leads to a significant increase in the flow resistance, and in the high-Reynolds-number region the friction factor becomes to be independent of the Reynolds number (i.e., independent of the kinematic viscosity), as seen in the so-called Moody diagram [1]. For smooth surfaces, the increase of skin-friction drag brings about the heat transfer enhancement because of the similarity between momentum and heat transfer [2]. For rough surfaces, however, the similarity breaks down since the increase of the flow resistance is attributed to the pressure drag due to the flow separation over the roughness elements [3, 4]. Thus, in terms of heat transfer enhancement, the introduction of surface roughness is not necessarily effective. The turbulent state in which the Stanton number is independent of the Reynolds number (i.e., the heat flux is independent of the viscosity and the thermal diffusivity) is related to the 'ultimate' state, which has been enthusiastically discussed in thermal convections [5]. However, it is still an open question whether or not the ultimate state can be achieved in convective turbulence even for rough surfaces [6, 7].

It is known that wall permeability remarkably increases the friction drag in turbulent plane Poiseuille flows [8, 9]. Although this is interpreted as due to the presence of large-scale spanwise rolls, originating from the Kelvin–Helmholtz-like instability, the Reynolds number dependence of the friction drag and heat transfer has not been clarified. In this study, we focus on momentum and heat transfer in a developed turbulent Poiseuille flow between parallel permeable walls.

FLOW CONFIGURATION

We conduct the direct numerical simulation (DNS) of turbulent forced convection in Poiseuille flow between two parallel permeable walls. The permeable walls are modeled assuming that the wall-normal velocity v at the walls (positioned at $y = \pm h$) is proportional to the local pressure fluctuations p', $v(y = \pm h) = \pm \beta p'/\rho$ (ρ is the mass density), and the no-slip condition is imposed on the walls (see [8]). The permeability coefficient β has the dimensions of an inverse velocity, and the flow between permeable walls is characterized by βu_b and the bulk mean Reynolds number $Re_b = 2hu_b/\nu$, where u_b is the bulk mean velocity and ν is the kinematic viscosity. The zero net mass flux through the wall is instantaneously ensured, and the blowing and suction are passively driven without an additional energy input. The temperature is treated as a passive scalar, and the advection-diffusion equation with a uniform heat generation and isothermal wall boundary conditions is solved. Periodic boundary conditions are employed in the streamwise (x-) and spanwise (z-) directions. The DNS is based on a Fourier–Chebyshev spectral method, and the time advancement is carried out with the implicit Euler scheme for the diffusion terms and the third order Runge–Kutta scheme for nonlinear terms, under a constant bulk mean velocity u_b and a constant bulk mean temperature θ_b.

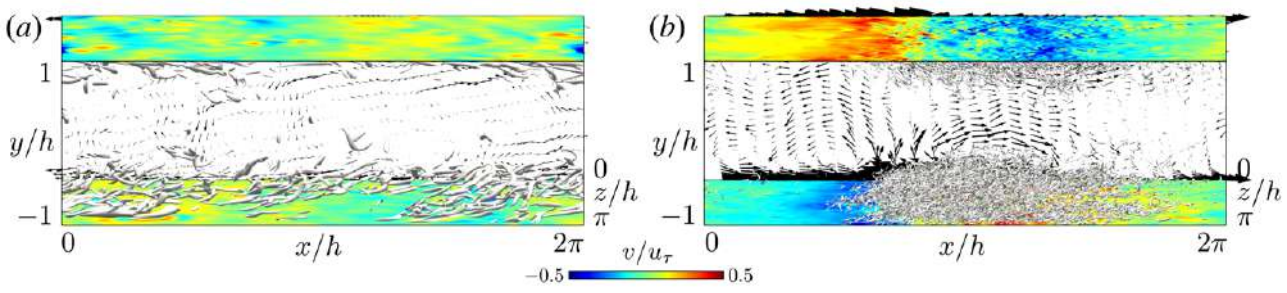

Figure 1: Instantaneous flow structures at (*a*) $Re_b = 8 \times 10^3$ and (*b*) $Re_b = 4 \times 10^4$ for $\beta u_b = 0.5$ and $Pr = 1$. The Gray objects show the vortex structures visualized by the isosurfaces of the positive second invariant of the velocity gradient tensor. The contours represent the wall-normal velocity v normalized by the friction velocity u_τ at the walls ($y = \pm h$). The vectors indicate the spanwise-averaged velocity fluctuations about the mean velocity, $(\langle u' \rangle_z, \langle v' \rangle_z)$.

*Corresponding author. E-mail: motoki@me.es.osaka-u.ac.jp

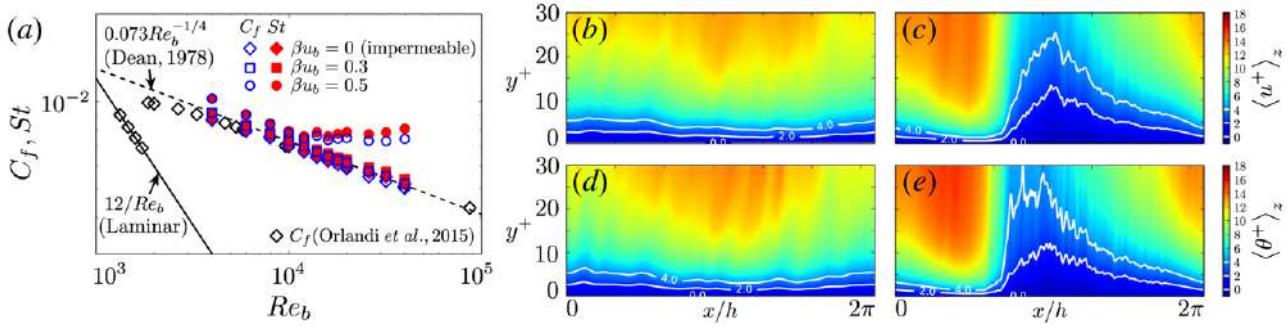

Figure 2: (*a*) Friction coefficient C_f and Stanton number St as a function of Re_b for $\beta u_b = 0, 0.3, 0.5$ and $Pr = 1$. The black open diamonds represent the DNS data for the impermeable plane Poiseuille flow [10]. The solid and dashed lines respectively indicate the laminar flow and the turbulent empirical correlation [11]. (*b-e*) Instantaneous spanwise-averaged streamwise velocity $\langle u^+ \rangle_z = \langle u/u_\tau \rangle_z$ and temperature $\langle \theta^+ \rangle_z = \langle \theta/\theta_\tau \rangle_z$. $y^+ = (y+1)/(\nu/u_\tau)$ is the distance from the wall normalized with the inner length scale. The white lines indicate the isolines of $0, 2, 4$.

RESULTS

In this paper, we present the results obtained in the domain $(L_x, L_y, L_z) = (2\pi h, 2h, \pi h)$ for the Prandtl number $Pr = 1$. Figure 1 shows the flow structures at $Re_b = 8 \times 10^3$ and 4×10^4 for $\beta u_b = 0.5$. At small Re_b (figure 1*a*), we see the turbulent structure similar to that in shear flows over impermeable walls, although it is accompanied by weak fluctuations of the wall-normal velocity v on the walls. In near-wall regions, quasi-streamwise vortices are distributed over the walls. At large Re_b (figure 1*b*), on the other hand, we can observe large-scale spanwise roll structures traveling downstream. The streamwise-traveling patterns in v on the walls are formatted, and small-scale vortex structures are localized in the blowing regions. The root-mean-square value $v_{\rm rms}(y = \pm h)$ is approximately 1% of u_b.

The friction coefficient $C_f = 2u_\tau^2/u_b^2$ and the Stanton number $St = 2u_\tau\theta_\tau/(u_b\theta_b)$ as a function of Re_b are shown in figure 2(*a*), where u_τ is the friction velocity and θ_τ is the friction temperature. At $Re_b \gtrsim 1.4 \times 10^4$ for $\beta u_b = 0.5$, we can observe $C_f = \text{const.}$ and $St = \text{const.}$, implying the ultimate turbulent state. In this range, St is maintained larger than C_f. For $\beta u_b = 0.3$, on the other hand, C_f and St are comparable to that in the impermeable cases even at $Re_b \approx 4 \times 10^4$, and they are almost the same due to the similarity between momentum and heat transfer. Although C_f and St gradually increase at any Re_b as the permeability βu_b increases, they have no effect on the scalings for small Re_b even at $\beta u_b = 0.5$. It is believed that the scalings $C_f = \text{const.}$ and $St = \text{const.}$ are attributed to the appearance of the large-scale spanwise rolls. Figures 2(*b-e*) show the spanwise-averaged streamwise velocity and temperature fields, $\langle u^+ \rangle_z = \langle u/u_\tau \rangle_z$ and $\langle \theta^+ \rangle_z = \langle \theta/\theta_\tau \rangle_z$, at $Re_b = 8 \times 10^3$ and 4×10^4 for $\beta u_b = 0.5$, corresponding to the instantaneous snapshots in figure 1. The white contour lines indicate $\langle u^+ \rangle_z = 0, 2, 4$ and $\langle \theta^+ \rangle_z = 0, 2, 4$, which exhibit the viscous and thermal diffusive sublayers. At $Re_b = 4 \times 10^4$ (figures 2*c,e*), significant fluctuations in both streamwise velocity and temperature fields can be observed in the near-wall region. However, there is no flow separation which causes an increase of pressure drag, and thus the similarity between momentum and heat transfer is maintained.

CONCLUSIONS

In turbulent Poiseuille flow between no-slip permeable walls, the scalings $C_f = \text{const.}$ and $St = \text{const.}$, implying the ultimate turbulent state, have been achieved. The wall permeability leads to large-scale spanwise roll structures which provide the significant promotion of turbulence mixing without flow separation.

References

[1] Moody L. F., *Trans. ASME* **66**: 671-684, 1944.
[2] Reynolds O., *Proc. Lit. Phil. Soc. Manchester* **14**: 7-12, 1874.
[3] Webb R. L., Eckert E. R. G. and Goldstein R. J., *Int. J. Heat Mass Transfer* **14**: 601-617, 1971.
[4] MacDonald M., Hutchins N. and Chung D., *J. Fluid Mech.* **861**: 138-162, 2019.
[5] Chillà F. and Schumacher J., *Eur. Phys. J. E* **35**: 58, 2012.
[6] Zhu X., Stevens R. J. A. M., Verzicco R. and Lohse D., *Phys. Rev. Lett.* **119**: 154501, 2017.
[7] Zhu X., Stevens R. J. A. M., Shishkina O., Verzicco R. and Lohse D., *J. Fluid Mech.* **869**: R4, 2019.
[8] Jiménez J., Uhlmann M., Pinelle A. and Kawahara G., *J. Fluid Mech.* **442**: 89-117, 2001.
[9] Suga K., Okazaki Y., Ho U. and Kuwata Y., *J. Fluid Mech.* **855**: 983-1016, 2018.
[10] Orlandi P., Bernardini M. and Pirozzoli S., *J. Fluid Mech.* **770**: 424-441, 2015.
[11] Dean R. B., *J. Fluids Engng* **100**: 215-223, 1978.

ATTACHED EDDY MODEL REVISITED WITH A QUASILINEAR APPROXIMATION

Yongyun Hwang*[1] and Bruno Eckhardt[2]
[1] Department of Aeronautics, Imperial College London, London, UK
[2] Fachbereich Physik, Philipps-Universität Marburg, D-35032 Marburg, Germany

Summary Townsend's model of attached eddies for boundary layers is revisited within a quasilinear approximation. The velocity field is decomposed into a mean and fluctuations. While the mean is obtained from the nonlinear equations, the fluctuations are modelled by replacing the nonlinear self-interaction terms with an eddy-viscosity-based turbulent diffusion and stochastic forcing. The stochastic forcing is subsequently determined self-consistently by solving an optimisation problem which minimises the difference between the Reynolds shear stresses from the mean and fluctuation equations. When applied to turbulent channel flow in a range of friction Reynolds number up to $Re_\tau = 20,000$, the resulting turbulence intensity profile and energy spectra exhibit exactly the same qualitative behaviour as DNS data throughout the entire wall-normal location, while reproducing the early theoretical predictions of Townsend within a controlled approximation to the Navier-Stokes equations.

INTRODUCTION

There has been a growing body of evidence that wall-bounded turbulence is composed of self-similar energy-containing eddies throughout the entire logarithmic region (i.e. attached eddy hypothesis) [1, 2, 3]: for example, the logarithmic wall-normal dependence of turbulence intensities of wall-parallel velocity components [4], the existence of self-similar self-sustaining coherent structures [5], and the self-similar linear modes and exact coherent states of the Navier-Stokes equations [6, 7, 8, 9]. Despite the important progress made over the last decade, the above observations are primarily on the existence of the self-similar energy-containing eddies in the logarithmic region (i.e. attached eddies). Therefore the issue of how they would have to be exactly reconciled for the prediction of turbulence statistics such as mean, fluctuaions and spectra still remains unresolved. In fact, the series of the early models developed by Townsend, Perry and their coworkers [1, 2, 3] are exactly on this issue: the linear superposition of second-order statistical moments of the self-similar energy-containing motions constant Reynolds shear stress predicts the general behaviour of turbulence intensity in the logarithmic region. The objective of the present study is to reformulate this idea by employing a controlled approximation to the Navier-Stokes equations. In particular, we will utilise a quasilinear approximation to the equations in a way that it can be directly compatible to the original attached eddy model [1].

QUASILINEAR APPROXIMATION

We consider a pressure-driven turbulent flow over a infinitely long and wide plane channel, where the upper and lower walls are located at $y = 0$ and $y = 2h$, respectively (y is the wall-normal coordinate). For the purpose of applying a quasilinear approximation, the velocity is decomposed into a mean and fluctuations (i.e. Reynolds decomposition): $\mathbf{u} = \mathbf{U} + \mathbf{u}'$, where $\mathbf{U}$ is the time-averaged mean velocity and $\mathbf{u}'(= (u', v', w'))$ is the velocity fluctuation with u', v' and w' being the streamwise, wall-normal and spanwise components, respectively. The full nonlinear equation is considered for the mean streamwise velocity, whereas the following form of linearised equations are considered for fluctuating velocity:

$$\frac{\partial \mathbf{u}'}{\partial t} + (\mathbf{U}\cdot\nabla)\mathbf{u}' + (\mathbf{u}'\cdot\nabla)\mathbf{U} = -\frac{1}{\rho}\nabla p' + \nu\nabla^2\mathbf{u}' + \mathcal{N} \quad \text{with} \quad \mathcal{N} = \nabla\cdot(\nu_t\nabla\mathbf{u}') + \mathbf{f}', \tag{1}$$

where ρ is the fluid density, ν the kinematic viscosity, p' fluctuating pressure, and $\mathcal{N}$ a minimal model for the self-interacting nonlinear term in the original full Navier-Stokes equations. The model for $\mathcal{N}$ is composed of an eddy-viscosity-based turbulent diffusion (ν_t is the eddy viscosity from [6]) and unknown stochastic forcing. Here, the former is introduced to model the energy cascade and turbulent dissipation, whereas the latter is to drive non-trivial turbulent fluctuations through (1) especially given the linearly stable nature of the typical mean velocity in turbulent channel flow.

If $\mathbf{f}'$ is set to be unknown, the mean equation and the fluctuation equations (1) are not able to be solved – the number of unknown is greater than the number of available equations. Therefore, we start by assuming that the mean velocity is available from a model or from an experimental measurement. Once mean is assumed to be known, the related Reynolds shear stress can be obtained from the mean equation. Then, for the fluctuation dynamics to be consistent with the mean, the Reynolds shear stress from (1) must be identical to the one from the mean equation. This poses the following optimisation problem for the determination of $\mathbf{f}'$:

$$\min_{\mathbf{f}'} \left\| \overline{u'v'} - \langle u'v' \rangle \right\|^2 \quad \text{subject to} \quad \text{sufficiently smooth spectrum of } \mathbf{f}', \tag{2}$$

*Corresponding author. E-mail: y.hwang@imperial.ac.uk.

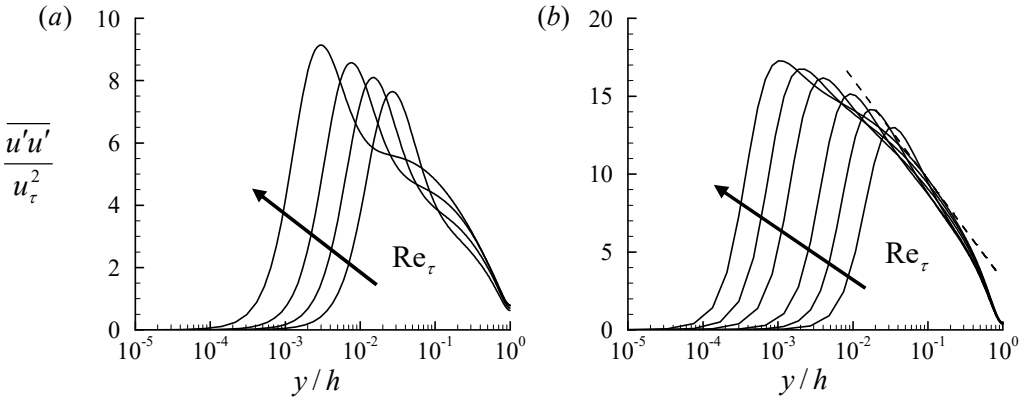

Figure 1: Streamwise turbulence intensity of (a) DNS at $Re_\tau = 543, 1001, 1995, 5186$ [10] and (b) QLA at $Re_\tau = 500, 1000, 2000, 5000, 10000, 20000$. In ($b$), the dashed line indicates the prediction of the original attached eddy model by Townsend. Here, Re_τ is the friction Reynolds number.

where $\overline{u'v'}$ are $\langle u'v' \rangle$ are the Reynolds shear stresses from the mean equation and the fluctuation equations (1), respectively, and $\|\cdot\|$ is an appropriate norm defined in the y-domain. Here, it should be mentioned that (1) admits the self-similar POD modes if the logarithmic mean velocity profile [6]. Given the linear nature of (1), this implies that the optimisation problem (2) can be solved by a linear superposition of such self-similar modes, the theoretical idea exactly the same as the one of Townsend [1]. In the final presentation, the full technical details on the solution procedure of (2) will be presented. From the solution to (2), $\mathbf{u}'$ can now be determined.

RESULTS AND DISCUSSION

Figure 1 compares streamwise turbulence intensity from direct numerical simulation (DNS) [10] with that from the present QLA in the outer-scaled wall-normal coordinate. It is found that the scaling behaviour of the streamwise turbulence intensity profiles of the QLA with Reynold number is strikingly similar to that of DNS at lower Reynolds numbers (up to $Re_\tau = 5186$). Furthermore, on increasing Reynolds number up to $Re_\tau = 20,000$, it becomes evident that the streamwise turbulence intensity gradually exhibits the logarithmic wall-normal dependence, as predicted by the classical attached eddy model of Townsend and Perry [1, 2]. It should be mentioned that this striking similarity to the DNS data also appears in the wall-normal and spanwise turbulence intensity profiles, while also exhibiting consistent behaviours with the classical predictions (not shown): in the logarithmic layer, the wall-normal turbulence intensity is obtained to be approximately constant and the streamwise one exhibits the logarithmic wall-normal dependence. Finally, spanwise wavenumber spectra for all the Reynolds stresses are also computed with QLA (not shown), and they also exhibit qualitatively identical behaviour to those from DNS.

CONCLUSIONS

In this work, we have presented a QLA for turbulent channel flow by formulating it in a way that it can be directly compatible to the attached eddy model of Townsend [1]. The reproduction of second-order turbulence statistics qualitatively identical to those of DNS evidently demonstrates the power of the original model of Townsend, while providing a new way to develop a predictive low-dimensional model for wall turbulence.

References

[1] Townsend, A. A., The structure of turbulent shear flow (2nd edition). Cambridge U. Press, 1976.
[2] Perry, A. E. & Chong, M. S., On the mechanism of turbulence. *J. Fluid Mech.* **119**: 173-217, 1982.
[3] Marusic, I. & Monty, J. P., Attached eddy model of wall turbulence *Annu. Rev. Fluid Mech.*, **51**: 49–74, 2019.
[4] Marusic, I., Monty, J. P., Hultmark, M. & Smits, A. J., On the logarithmic region in wall turbulence. *J. Fluid Mech.* **713**: R3, 2013.
[5] Hwang, Y., Statistical structure of self-sustaining attached eddies in turbulent channel flow. *J. Fluid Mech.* **723**: 264–288, 2015.
[6] Hwang, Y. & Cossu, C., Linear non-normal energy amplification of harmonic and stochastic forcing in the turbulent channel flow. *J. Fluid Mech.* **664**: 51–73, 2010.
[7] Moarref, R., Sharma, A. S., Tropp, J. A. & McKeon, B. J., Model-based scaling of the streamwise energy density in high-Reynolds-number turbulent channels. *J. Fluid Mech.* **734**: 275–316, 2013.
[8] Eckhardt, B. & Zammert, S., Small scale exact coherent structures at large Reynolds numbers in plane Couette flow. *Nonlinearity* **31**: R66–R77, 2018.
[9] Yang, Q., Willis, A. P. & Hwang, Y., Exact coherent states of attached eddies in channel flow. *J. Fluid Mech.* **862**: 1029–1059, 2019.
[10] Lee, M. K. & Moser, R. Direct numerical simulation of the turbulent boundary layer over a cube-roughened wall. *J. Fluid Mech.* **774**: 395-415, 2015.

A UNIFIED, VIRTUAL-ORIGIN FRAMEWORK FOR THE DRAG-REDUCING EFFECT OF TEXTURED SURFACES

Joseph I. Ibrahim[1], Garazi Gómez-de-Segura[1], Daniel Chung[2], and Ricardo García-Mayoral * [1]
[1] Department of Engineering, University of Cambridge, Cambridge, UK
[2] Department of Mechanical Engineering, University of Melbourne, Melbourne, Australia

Summary Certain surfaces with texturing of small size can reduce drag by generating different virtual origins for the mean velocity profile and the turbulent fluctuations, traditionally characterised by the streamwise and spanwise slip lengths. We generalise this idea by conducting direct simulations with different virtual origins for all three velocity components, using Robin, slip-length-like boundary conditions. We find that, for small slip lengths, the virtual origin for turbulence is actually set by, and can be easily computed from, the wall-normal and spanwise slip lengths. This origin affects directly the near-wall quasi-streamwise vortices, while the origin perceived by the near-wall streaks, in contrast, plays essentially no role in setting that for turbulence. We show that, other than by the shift in origin, turbulence remains essentially smooth-wall-like. The typical modifications of turbulent quantities discussed in the literature for controlled flows can then be reduced to a mere offset effect.

VIRTUAL ORIGINS IN WALL TURBULENCE

Certain textured surfaces, such as riblets or superhydrophobic surfaces, can reduce turbulent skin-friction drag. Like many turbulent-flow control techniques, including active ones, they aim to reduce friction by manipulating the near-wall cycle. The general idea is to impede the flow in the streamwise direction less than the cross flow. Quasi-streamwise vortices are then 'pushed' away from the surface relative to the mean flow, reducing the local transport of streamwise momentum and thus the skin-friction drag. When the texture is small, the flow perceives it in a homogenised fashion and the direct effect is confined to the near-wall region, with the change in drag manifesting as a constant shift of the mean velocity profile above, ΔU^+. For riblets, [9] proposed that the streamwise flow experiences a 'virtual origin' deeper than that of the spanwise flow, and that the change in drag depends on the difference between the two, $\ell_u - \ell_w$, where ℓ_u and ℓ_w are typically measured from the riblet-tip plane. It was later proposed that, for $\ell_u^+, \ell_w^+ \lesssim 1$, where '+' indicates viscous scaling, the extra mean velocity far from the wall was $\Delta U^+ \propto \ell_u^+ - \ell_w^+$ [7, 8].

Superhydrophobic surfaces exploit the same mechanism, with the overlying flow effectively slipping over the entrapped gas pockets. The streamwise and spanwise velocities experience the surface through their respective slip lengths, analogous to ℓ_u^+ and ℓ_w^+. When the spanwise slip length becomes larger than a few wall units, however, the drag-increasing effect of ℓ_w^+ on ΔU^+ saturates [1]. This saturation can however be accounted for through an 'effective' spanwise depth, $\ell_{w,eff}^+$, empirically defined as $\ell_{w,eff}^+ \approx \ell_w^+/(1+\ell_w^+/5)$ [2, 6]. The saturation is caused by slip-only surfaces being impermeable, which limits the extent to which quasi-streamwise vortices can approach the surface. [4, 3] argued that, to fully describe the effect of such textured surfaces on the flow, the virtual origins for all three velocity components should be considered. When the depth for the virtual origin of the wall-normal velocity is set equal to that of the spanwise velocity, $\ell_v^+ = \ell_w^+$, no saturation in the effect of the spanwise slip was observed. For intermediate values $0 < \ell_v^+ \leq \ell_w^+$, the virtual origin for the wall-normal velocity would act as the impermeable, reference plane, and turbulence would experience a virtual origin, ℓ_T^+, such that $\ell_v^+ \leq \ell_T^+ \leq \ell_w^+$, yielding

$$\Delta U^+ = \ell_U^+ - \ell_T^+, \tag{1}$$

where $y^+ = -\ell_U^+$ is the virtual origin experienced by the mean flow, and that for turbulence would be given by

$$\ell_T^+ \approx \begin{cases} \ell_v^+ + \dfrac{\ell_w^+ - \ell_v^+}{1+(\ell_w^+ - \ell_v^+)/5} & \text{if } \ell_w^+ > \ell_v^+, \\ \ell_w^+ & \text{if } \ell_w^+ \leq \ell_v^+. \end{cases} \tag{2}$$

RESULTS FROM DIRECT NUMERICAL SIMULATIONS

To assess the validity of (1) and (2), we carry out direct simulations of turbulent channels with virtual origins for all three velocity components, implemented through Robin boundary conditions, $u = \ell_x \partial u/\partial y$, $v = \ell_y \partial v/\partial y$ and $w = \ell_z \partial w/\partial y$, as proposed in [5]. Here ℓ_x, ℓ_y and ℓ_z are the 'slip' lengths in the streamwise, wall-normal and spanwise directions, respectively. We conduct simulations for a range of combinations of ℓ_x^+, ℓ_y^+ and ℓ_z^+, with ℓ_u^+, ℓ_v^+ and ℓ_w^+ defined a priori by locating the heights for which the Robin conditions are satisfied in smooth-wall rms fluctuation curves. The depth ℓ_T^+ is measured a posteriori by fitting the resulting Reynolds-stress curve to smooth-wall data, and shows good agreement with the predictions from (2). Results are shown in figure 1. When the wall-normal coordinate is measured from the virtual origin for turbulence, $y^+ = -\ell_T^+$, and u_τ is defined from the total-stress curve also at $y^+ = -\ell_T^+$, the

*Corresponding author. E-mail: r.gmayoral@eng.cam.ac.uk

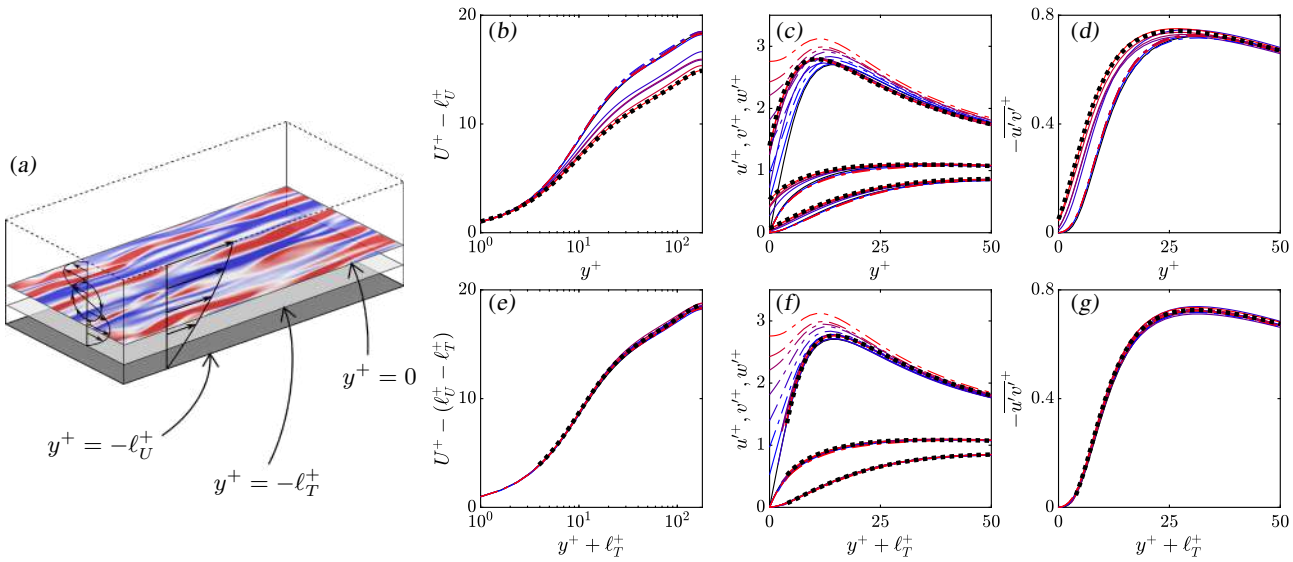

Figure 1: (*a*) Sketch illustrating the concept of virtual origins for turbulence, in light grey, and for the mean flow, in dark grey, below the reference plane $y^+ = 0$, where boundary conditions are numerically imposed, represented by isocontours of the streamwise fluctuating velocity. The cross-flow induced by quasi-streamwise vortices and the mean flow are represented with black lines. (*b-g*) Mean velocity, rms velocity fluctuations and Reynolds stress for simulations with slip and transpiration. Panels (*b-d*) portray results scaled with the conventional u_τ measured at $y^+ = 0$, while panels (*e-g*) portray results with y-origin at the origin for turbulence, $y^+ = -\ell_T^+$, and scaled with the u_τ value corresponding to that depth. Solid lines from blue to red, $(\ell_x^+, \ell_z^+, \ell_y^+) = (2,0,1.2), (2,2,1.2), (6,2,4.5), (4,4,1.2), (4,4,2.5), (4,6,1.5)$ and $(4,6,2)$; dash-dot lines from blue to red, $\ell_{x,f}^+ = 5, 10, 20, 50, 100$ and ∞ on the fluctuations and $\ell_{x,m}^+ = 0$ on the mean flow; black dotted line, $(\ell_{x,f}^+, \ell_z^+, \ell_y^+) = (4,6,2.2)$ on the fluctuations, but $\ell_{x,m}^+ = 10$ on the mean flow; solid black line, smooth-wall reference case.

cross-plane rms fluctuations and the Reynolds stress essentially collapse to smooth-wall data. The same is true for the mean velocity profile, save for a shift $\Delta U^+ = \ell_U^+ - \ell_T^+$, which is consistent with (1). This general collapse confirms that the near-wall dynamics remain smooth-wall-like, and that ℓ_T^+ captures the effect of the origin offset on turbulence.

The results also suggest that the virtual origin experienced by the mean flow is independent of that experienced by the streamwise fluctuations, and that the streamwise origin is relevant to ΔU^+ only through ℓ_U^+. One case in figure 1 has a larger slip length on the mean flow, $\ell_{x,m}^+ = 10$, than on the streamwise fluctuations, $\ell_{x,f}^+ = 4$. The resulting ΔU^+ is consistent with $\Delta U^+ = \ell_U^+ - \ell_T^+$, and $\ell_{x,m}$ has essentially no influence on the turbulence. To further test this, we run simulations with a slip length applied to the streamwise fluctuations only and no-slip on the mean flow. The results, also in figure 1, show that the peak value of the rms streamwise fluctuations exhibits a slight increase with increasing slip length, likely caused by the relaxation of the no-slip condition at $y = 0$, so that they effectively have an extended y-range over which to vanish. However, this has a negligible effect on the mean velocity profile, and ΔU^+ remains essentially zero.

References

[1] Busse A., Sandham. N. D. Influence of an anisotropic slip-length boundary condition on turbulent channel flow. *Phys. Fluids*, **24**:055111, 2012.
[2] Fairhall C. T., Abderrahaman-Elena N., García-Mayoral R. The effect of slip and surface texture on turbulence over superhydrophobic surfaces. *J. Fluid Mech.*, **861**:88–118, 2019.
[3] García-Mayoral R., Gómez-de-Segura G., Fairhall C. T. The control of near-wall turbulence through surface texturing. *Fluid Dyn. Res.*, **51**:011410 2018.
[4] Gómez-de-Segura G., Fairhall C. T., MacDonald M., Chung D., García-Mayoral R. Manipulation of near-wall turbulence by surface slip and permeability. *J. Phys. Conf. Ser.*, **1001**:012011, 2018.
[5] Gómez-de-Segura G., García-Mayoral R. Imposing virtual origins on the velocity components in direct numerical simulations. *Int. J. Heat Fluid Flow*, **86**:108675, 2020.
[6] Ibrahim J. I., Gómez-de-Segura G., Chung D., García-Mayoral R. The smooth-wall-like behaviour of turbulence over drag-altering surfaces: a unifying virtual-origin framework. Submitted to *J. Fluid Mech.*, arXiv:2006.16118.
[7] Jiménez J. On the structure and control of near wall turbulence. *Phys. Fluids*, **6**:944, 1994.
[8] Luchini P. Reducing the turbulent skin friction. In *Comput. Meth. Appl. Sci. '96*, pages 466–470. John Wiley & Sons Ltd., 1996.
[9] Luchini P., Manzo F., Pozzi A. Resistance of a grooved surface to parallel flow and cross-flow. *J. Fluid Mech.*, **228**:87–109, 1991.

O108233 - MS01 - Modeling and controlling turbulent shear flows - Oral

EXTRACTING NONLINEAR DYNAMICS OF LOW-DIMENSIONALIZED FLOWS

Kai Fukami* [1], Takaaki Murata[1], and Koji Fukagata [1]
[1] Department of Mechanical Engineering, Keio University, Japan

Summary Sparse identification of nonlinear dynamics (SINDy) is performed to obtain a governing equation of low-dimensinalized fluid flows. The SINDy with adaptive Lasso is applied to a flow around a cylinder at $Re_D = 100$ as an example of high-dimensional unsteady flow problems. To handle the cylinder flow with SINDy whose coefficient matrix is not suitable for a combination of a large number of variables, a convolutional neural network-based autoencoder (CNN-AE) is considered so that a high-dimensional data can be mapped into low-dimensional latent space while keeping the information of high-dimensional dynamics. The temporal evolution of the high-dimensional flow can be represented successfully by using the CNN-SINDy based modeling. At last, we also introduce the application to a nine-shear turbulent flow equation as a future perspective of SINDy based modeling.

INTRODUCTION

With a recent trend of uses of fluid *big data*, machine learning methods have been emerged as one of the prominent tools to analyze and understand complex and chaotic fluid flow phenomena [1]. Although a vast kind of machine learning methods has been proposed, a sparse identification of nonlinear dynamics (SINDy)[2] has been attracting attention due to its interpretable sense as a form of equation. Thus far, the SINDy has been utilized to various applications, e.g., reduced order modeling with sensor-based measurement [3], and shown its great potential. Here, we focus on two concerns with the use of SINDy for fluid dynamics: 1. influence of regression method and their parameters, and 2. applicability to high-dimensional complex flows. For the first problem, let us consider a typical regression problem $\boldsymbol{C} = \boldsymbol{D}\boldsymbol{\beta}$, where $\boldsymbol{C}$ and $\boldsymbol{D}$ are the response variable and the explanatory variable. We usually aim to obtain a coefficient matrix $\boldsymbol{\beta}$ with the use of SINDy, but we have a lot of regression choices and need to select appropriate parameters so as to obtain a desired equation. It must be useful to have a guideline for selecting these parameters for fluid dynamicists, since the uses of SINDy have been started as introduced above. Regarding the second problem, because the coefficient matrix of SINDy is composed by a combination of considered variables, it is relatively tough to apply to high dimensional problems. Here, we consider four regression methods of SINDy and a convolutional neural network-based autoencoder (CNN-AE), in order to address these aforementioned issues. In this paper, we focus on the discussion for the CNN-SINDy modeling and its future perspective, although the preliminary test for searching parameters is skipped.

METHODS

Sparse identification of nonlinear dynamics (SINDy)

Sparse identification of nonlinear dynamics (SINDy)[2] can identify a governing ordinary differential equation from a data set of temporal discretized observation. Temporal evolution of the state of dynamics $\boldsymbol{s}(t)$ in a typical dynamical system can be often formulated as $\dot{\boldsymbol{s}} = \boldsymbol{f}(\boldsymbol{s}(t))$. For the SINDy formulation, we first prepare a temporal discretized observation of state $\boldsymbol{X} = [\boldsymbol{s}(t_1), \boldsymbol{s}(t_2), ..., \boldsymbol{s}(t_n)]^T$ and its time derivations $\dot{\boldsymbol{X}} = [\dot{\boldsymbol{s}}(t_1), \dot{\boldsymbol{s}}(t_2), ..., \dot{\boldsymbol{s}}(t_n)]^T$, where n is the number of covered temporal snapshots and $\boldsymbol{s}(t) = \{s_1(t), s_2(t), ..., s_k(t)\}$ with k variables. The basic concept of the SINDy is to represent this $\dot{\boldsymbol{X}}$ using a library matrix $\boldsymbol{\Theta}(\boldsymbol{X})$ composed by a combination of the considered variables of $\boldsymbol{s}(t)$ and a coefficient matrix $\boldsymbol{\Xi}$ such that $\dot{\boldsymbol{X}}(t) = \boldsymbol{\Theta}(\boldsymbol{X})\boldsymbol{\Xi}$. The details can be seen in Brunton *et al.*[2]. Mathematically speaking, the procedure to obtain the coefficient matrix $\boldsymbol{\Xi}$ can be formulated as

$$\boldsymbol{\Xi} = \mathrm{argmin}||\dot{\boldsymbol{X}} - \boldsymbol{\Theta}(\boldsymbol{X})\boldsymbol{\Xi}||^2. \tag{1}$$

In this study, we consider four regression methods, i.e., thresholded least square algorithm (TLSA)[2], least absolute shrinkage and selection operator (Lasso) [4], elastic net (Enet)[5], and adaptive Lasso (Alasso)[6], for the aforementioned minimization manner. Although more details are skipped due to space limitation, we also check the effect of sparsity constant α, which plays a role in tuning a sparseness of coefficient matrix, with all covered regressions. We have found in the preliminary test using Van der Pol ossilator that Alasso can provide the correct number of equation terms with a wide range of sparsity constant α. In this paper, we utilize the Alasso following our preliminary test.

Convolutional neural network-based autoencoder (CNN-AE)

To handle a high-dimensional unsteady flow with SINDy, we utilize an autoencoder [7] constructed by using a convolutional neural network[8], which is one of the unsupervised machine learning methods. For construction of the autoencoder, target data set which we want to reduce a dimension are prepared as the input and output $\boldsymbol{q}$. The autoencoder $\mathcal{F}$ has usually intermediate lower-dimensional latent space $\boldsymbol{r}$ than its input or output $\boldsymbol{q}$ so that we can map a high-dimensional input data into the low-dimensional space while keeping the feature of high-dimensional data if the model $\mathcal{F}$ is able to output the same data as the input successfully. Internal procedure of the CNN-AE can be mathematically formulated as

$$\boldsymbol{q} \approx \mathcal{F}(\boldsymbol{q}) = \mathcal{F}_e(\mathcal{F}_d(\boldsymbol{r})), \tag{2}$$

where $\mathcal{F}_e$ is an encoder, which can map a data $\boldsymbol{q}$ into a latent space $\boldsymbol{r}$, and $\mathcal{F}_d$ is a decoder which can recover to original dimension. In other words, the latent vector $\boldsymbol{r}$ can be regarded as a low-dimensional representation of $\boldsymbol{q}$. Because the decoder is employed to remap a latent vector to the high-dimensional original space, we can represent the temporal evolution of high-dimensional dynamics by following only that of the latent vector obtaind by SINDy.

*Corresponding author. E-mail: kai.fukami@keio.jp

MINI SYMPOSIA

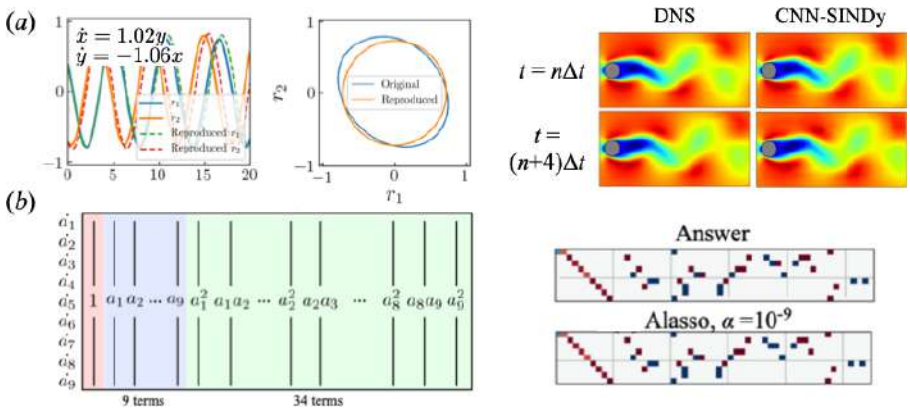

Figure 1: SINDy for (a) a cylinder wake with CNN-AE and (b) nine-shear turbulent flow equation.

RESULTS

As the example with high-dimensional data for the present modeling, a cylinder wake at $Re_D = 100$ is considered by numerically solving of a direct numerical simulation. The computational set up is the same as our previous study regarding the CNN-AE of unsteady flows[9]. The flow fields $\boldsymbol{q} = \{u, v\} \in \mathbb{R}^{384\times192\times2}$ are mapped into two dimensional latent space. We reported that the flow field can be mapped successfully thanks to nonlinear activation functions of the CNN-AE[9]. As introduced in methods, a temporal evolution of two latent values are followed by utilizing SINDy so that the high-dimensional dynamics can be also obtained with the present method. By using SINDy with Alasso, the sparse equation can be obtained, i.e., $\dot{x} = 1.02y$ and $\dot{y} = -1.06x$, and these are integrated successfully and stably, as presented in the time history and trajectory plots of figure $1(a)$. In addition, we see that the high-dimensional flow fields can be reconstructed well in time as shown in the right side of figure $1(a)$.

Through the cylinder wake example, we could demonstrate the great ability of the CNN-SINDy modeling. However, we also should care the remaining issue: applicability to turbulence. With the current autoencoder, it is tough to map complex turbulent flows into extremely low dimensional space, which is analogous to conventional linear theories[10]. Of course, with increasing a number of considerable variable, the size of coefficient matrix is also increased. Hence, our next suspicion here is whether SINDy can be applied if turbulence can be represented as low-dimensional manifolds. Here, let us consider a nine-shear flow equation[11] as the future perspective for SINDy modeling. In the nine-equation model, various statistics can be represented by using superposition of only nine Fourier modes $\boldsymbol{u}_j(\boldsymbol{x})$ and coefficients $a_j(t)$ such that $\boldsymbol{u}(\boldsymbol{x}, t) = \sum_{j=1}^{9} a_j(t)\boldsymbol{u}_j(\boldsymbol{x})$. The dynamics of coefficients is governed by the typical ordinary differential equation form $\dot{a} = f(a)$. We refer readers to Moehlis *et al.*[11] for details. Because the desired equation can be represented by 44 terms with a combination of up to 2nd order terms, we consider up to 2nd order terms of temporal coefficient to arrange a coefficient matrix as shown in figure $1(b)$. As shown in the right portion of figure $1(b)$, the dominant terms of the coefficient matrix can be caught perfectly by utilizing SINDy. It suggests that we may be able to present a machine-learning based reduced order modeling for turbulent flows with the interpretable sense as a form of equation, if well-designed model of mapping side can be constructed.

CONCLUSIONS

We performed SINDy to obtain governing equations of low-dimensionalized flow representations. Following our preliminary test not shown here, we used Alasso as the regression scheme for SINDy analysis. To handle a high-dimensional flow with SINDy, we also utilized a CNN-AE which can project a high-dimensional data into low-dimensional space. We found that the flow field can be reproduced successfully in time by utilizing the proposed model. At last, we further investigated the applicability of SINDy to turbulence using a nine-shear flow equation. The results implied that machine-learning based reduced order modeling for turbulent flows can be established with the interpretable sense as a form of equation, if a well-designed model on the mapping side can be constructed.

References

[1] Brunton S. L., Noack B. R., and Koumoutsakos P. Machine Learning for Fluid Mechanics. *Annu. Rev. Fluid Mech.* **52**: 477–508, 2020.
[2] Brunton S. L., Proctor J. L., and Kutz J. N. Discovering governing equations from data by sparse identification of nonlinear dynamical systems. *Proc. Natl. Acad. Sci.* **15**(113): 3932–3937, 2016.
[3] Loiseau J. C. *et al.* Sparse reduced-order modelling: sensor-based dynamics to full-state estimation. *J. Fluid Mech.* **844**: 459–490, 2018.
[4] Tibshirani R. Regression shrinkage and selection via the lasso. *J. R. Stat. Soc. Ser. B-Stat. Methodol.* **58**(1): 267–288, 1996.
[5] Zou H. and Hastie T. Regularization and variable selection via the elastic net. *J. R. Stat. Soc. Ser. B-Stat. Methodol.* **67**(2): 301–320, 2005.
[6] Zou H. The adaptive lasso and its oracle properties. *J. Am. Stat. Assoc.* **101**(476): 1418–1429, 2006.
[7] Hinton G. E. and Salakhutdinov R. R. Reducing the dimensionality of data with neural networks. *Science* **313**(5786): 504–507, 2006.
[8] LeCun Y. *et al.* Gradient-based learning applied to document recognition. *Proc. IEEE* **86**(11): 2278–2324, 1998.
[9] Murata T. *et al.* Nonlinear mode decomposition with convolutional neural networks for fluid dynamics. *J. Fluid Mech.* **882**: A13, 2020.
[10] Alfonsi G. and Primavera L. The structure of turbulent boundary layers in the wall region of plane channel flow. *Proc. R. Soc. A* **463**(2078): 593–612, 2007.
[11] Moehlis J., Faisst H. and Eckhardt B. A low-dimensional model for turbulent shear flows. *New Journal of Physics* **6**(56): 1–17, 2004.

INTERMEDIATE SCALING FOR STREAMWISE VELOCITY IN WALL TURBULENCE

Sourabh S. Diwan* [1] and Jonathan F. Morrison[2]
[1] Department of Aerospace Engineering, Indian Institute of Science, Bangalore-560012, India.
[2] Department of Aeronautics, Imperial College London, London-SW7 2AZ, UK.

Summary Here, we propose an intermediate scaling for the streamwise velocity in turbulent pipe and boundary layer (TBL) flows. Using an intermediate length scale (akin to the meso-layer scaling) and an associated velocity scale, we show that the mean-velocity defect and variance profiles achieve a Reynolds-number (Re) similarity in the intermediate region for both pipe and TBL. This reveals a Reynolds-number invariant log region in wall turbulence, in terms of the intermediate variables. As a consequence, the classical log law is seen to emerge only at sufficiently large Re and the Townsend-Perry 'constant' shows a systematic Re-dependence. These findings could have important implications for "attached-eddy modelling", in terms of choosing the scaling and form of the 'attached' eddies. It is plausible that such eddies scale on the intermediate variables which are local to the inertial sublayer.

INTRODUCTION

The logarithmic ("log") variation of the streamwise mean velocity (U) and variance ($\overline{u^2}$) in the inertial sublayer are two of the celebrated results in wall turbulence (Eq. 1).

$$U^+ = \frac{1}{\kappa}\ln(y^+) + C, \qquad \frac{\overline{u^2}}{u_\tau^2} = B_1 - A_1 \ln\left(\frac{y}{\delta}\right), \tag{1}$$

where u_τ is the friction velocity, y is the wall-normal distance and $^+$ indicates scaling on wall variables. δ is the boundary-layer thickness for the turbulent boundary layer (TBL) and pipe radius for the pipe flow. κ and A_1 in Eq. (1) are the well-known von Kármán and Townsend-Perry [1] 'constants' respectively; C and B_1 are the additive 'constants'. The log law for $\overline{u^2}$ is a consequence of the attached eddy hypothesis proposed by Townsend. This idea was further extended by Perry and Chong [2] in the form an attached eddy "model", which predicted the log variation of the mean velocity and variance (Eq. 1) as dual conditions. The attached-eddy model continues to provide a useful physics-based framework for understanding and interpreting the statistics of the energy-containing motions in wall turbulence [3].

Within the framework of the attached-eddy hypothesis, κ and A_1 are believed to be universal constants [1]. However, there remain open, central questions regarding the Reynolds-number invariance and universality of κ and A_1. This is partly because it is not entirely clear if u_τ and δ are the appropriate velocity and length scales for the energy-containing motions in the inertial sublayer [4]. In this work, we examine the scaling behaviour of the streamwise mean velocity and variance in an intermediate region between the inner and outer layers in wall turbulence. We propose that the length scale appropriate for the intermediate region is $y_m^+ \propto \sqrt{Re_\tau}$ ($Re_\tau = u_\tau\delta/\nu$), which is the typical "mesolayer" scaling; the velocity scale is chosen to be the rms turbulence velocity at $y = y_m$. Using these scales, the mean velocity defect and variance in the intermediate region show a Reynolds-number similarity in both pipe and TBL flows. The consequences of this finding for the Re-number behaviour of κ and A_1, and the attached-eddy modelling are discussed.

SCALING FOR THE INTERMEDIATE REGION

Here we use the turbulent pipe-flow data obtained in Princeton Superpipe using NSTAP [5] for $Re_\tau = 1985 - 98190$. For the TBL, we use two data sets - one obtained in the HRTF experiments at Princeton University [6] ($Re_\tau = 4635 - 72526$; VHS) and the other obtained in the HRNBLWT experiments at Melbourne University [7] ($Re_\tau = 2353 - 15685$; MHM). The intermediate length scale is defined as $y_m^+ = 3.5\sqrt{Re_\tau}$ and the velocity scale $u_m = \sqrt{\overline{u^2}}(y = y_m)$ (see [4]). Fig. 1 (a) and (b) show the mean velocity defect ($U - U_m$) and variance profiles scaled on u_m and y_m for the pipe and TBL; here U_m is the mean velocity at $y = y_m$. It is evident from the figure that the mean velocity defect and variance show a Reynolds number similarity, to an excellent degree, in the intermediate region (i.e. around $y/y_m = 1$) for Re_τ varying over two decades [8]. Moreover, the data for the pipe and TBL show a good collapse indicating a plausible "universal" behaviour for the streamwise velocity in the intermediate region of wall turbulence.

Note that the region above $y/y_m = 1$ typically corresponds to the inertial sublayer where the log scaling is expected to hold [1]. This implies that there exists a Reynolds-number invariant log law, in terms of the intermediate variables, for both mean velocity and variance for $y/y_m > 1$ (Eq. 2).

$$\frac{U - U_m}{u_m} = \frac{1}{\kappa_m}\ln\left(\frac{y}{y_m}\right) + C_m, \qquad \frac{\overline{u^2}}{u_m^2} = B_1^m - A_1^m \ln\left(\frac{y}{y_m}\right). \tag{2}$$

The log-law constants in Eq. (2) can be obtained by fitting a straight line through the data points in the intermediate region (figure 1). This has been done for the pipe and TBL separately to compare the individual constants. For the pipe data, the

*Corresponding author. E-mail: sdiwan@iisc.ac.in. We acknowledge financial support from ESPRC (Grant No. EP/I037938/1).

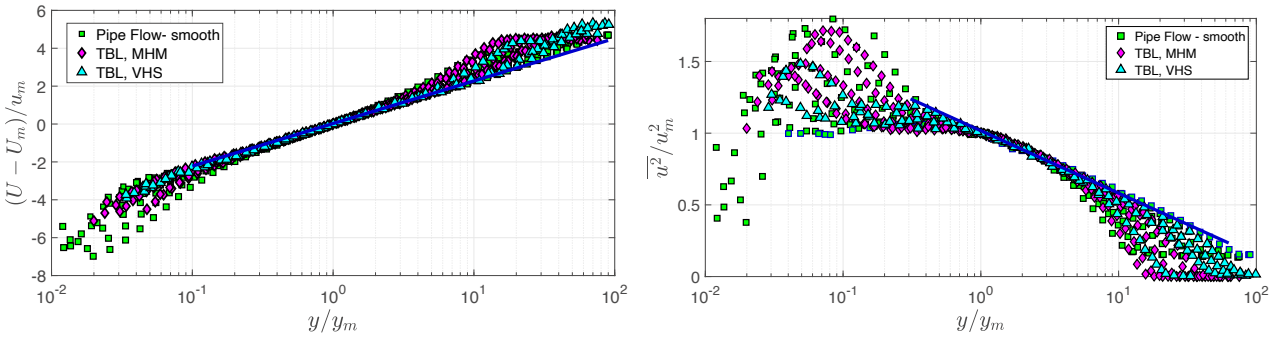

Figure 1: Profiles of (a) $U - U_m$ and (b) $\overline{u^2}$ scaled on y_m and u_m for the smooth-walled pipe [5] and TBL ([6],[7]) data. The extent of the log variation (indicated by a straight line) decreases with decrease in Reynolds number, for both mean velocity and variance.

extent of the log law is found to be $1.2 \leq y/y_m \leq 13$, whereas for the TBL it is $1.2 \leq y/y_m \leq 10$; the same interval is used for fitting the mean velocity and variance data for a given flow. Table 1 summarizes the numerical values of the constants in Eq. (2) obtained for the two flows. As can be seen from the table, the values for the log-law slopes, κ_m and A_1^m, are quite close to each other for the two flows, as expected from the good collapse among the data seen in figure 1. The averaged values of these constants are also included in table 1, which might represent, approximately, the plausible "universal" values for the constants. The straight lines shown in figures 1(a) and (b) represent the log fits to the mean velocity and variance data using the averaged values for the constants from table 1.

Table 1: Summary of the log-law constants for the pipe and TBL, along with averaged values for the two flows.

Case	κ_m	C_m	A_1^m	B_1^m
Turbulent pipe flow	1.034	0.0084	0.178	1.005
Turbulent boundary layer	1.015	0.044	0.200	1.028
Plausible "universal" values	1.025	0.0262	0.189	1.017

The log-law constants for the intermediate scaling (Eq. 2) can be readily related to the classical log-law constants (Eq. 1). The relations involve ratios u_m/u_τ and y_m/δ, which are functions of Re_τ [8]. We find that, for both pipe and TBL, κ has much higher values than can be associated with a log variation for $Re_\tau < 2 \times 10^4$, implying that a log law is untenable for lower Reynolds numbers [5]. For $Re_\tau > 2 \times 10^4$, κ falls in the range 0.4 ± 0.02 for the pipe and seems to asymptote to a value of 0.41 for the TBL. The Townsend-Perry 'constant' shows a systematic dependence on Reynolds number for both the flows, with $A_1 < 1$ for the smallest Re_τ, increasing to 1.24 for the highest Re_τ, consistent with [1].

The present findings have clear implications for the attached-eddy modelling. The work suggests that the energy containing eddies in the inertial sublayer, might scale better on u_m and y_m as compared to the classical scales, u_τ and δ. This is supported by the result that A_1 (Eq. 1) is a function of Re_τ, whereas A_m (Eq. 2) is Re-independent. Moreover, these eddies may not be physically attached to the wall [3], but rather, detached in some way. Some of these ideas need to be explored further in the context of the attached-eddy hypothesis. The choice of intermediate scales is being examined with reference to the kinetic energy balance around the outer peak [9].

CONCLUSIONS

We have shown that, using intermediate length and velocity scales, it is possible to achieve a Reynolds-number similarity in the intermediate region of wall turbulence. This implies existence of a Reynolds-number invariant logarithmic region, which seems to be "universal". As a consequence, the standard values of the Kármán 'constant' are realized only at sufficiently large Re_τ and that the Townsend-Perry 'constant' shows a systematic Re-dependence. The work can have important implications towards the attached-eddy modelling; more results on this will be presented during the talk.

References

[1] Marusic I., Monty J. P., Hultmark M., Smits A. J. On the logarithmic region in wall turbulence. *J. Fluid Mech.* **716**: R3, 2013.
[2] Perry A. E., Chong M. S. On the mechanism of wall turbulence. *J. Fluid Mech.* **119**: 173-217, 1982.
[3] Marusic I., Monty J. P. Attached eddy model of wall turbulence. *Ann. Rev. Fluid Mech.* **51**: 4974, 2019.
[4] Diwan S. S., Morrison J. F. Reynolds-number dependence of the Townsend-Perry 'constant' in wall turbulence. In *TSFP11 Digital Library Online, Begel House Inc.*, 2019.
[5] Hultmark M., Vallikivi M., Bailey S. C. C., Smits A. J. Turbulent pipe flow at extreme Reynolds numbers. *Phys. Rev. Lett.* **108**: 094501, 2012.
[6] Vallikivi M., Hultmark M., Smits A. J. Turbulent boundary layer statistics at very high Reynolds number. *J. Fluid Mech.* **779**: 371389, 2015.
[7] Mathis R., Hutchins N., Marusic, I. Large-scale amplitude modulation of the small-scale structures in turbulent boundary layers. *J. Fluid Mech.* **628**: 311337,2009.
[8] Diwan S .S., Morrison J. F. Intermediate Scaling and Logarithmic Invariance in Turbulent Pipe Flow. *arXiv:1909.11951*, 2019.
[9] Morrison J. F., Vicente J. F. The energy budget at the outer peak of $\overline{u^2}$ in turbulent pipe flow. APS DFD abstract: G11.00006, 2019.

SPATIAL ORGANIZATION OF WALL-COHERENT AND INCOHERENT STRUCTURES IN TURBULENT BOUNDARY LAYERS

Rahul Deshpande* [1], Jason P. Monty [1], and Ivan Marusic[1]
[1] Department of Mechanical Engineering, The University of Melbourne, Victoria 3010 Australia

Summary The study is aimed towards understanding the spatial organization of large coherent structures of the streamwise (u) velocity, in a zero pressure gradient turbulent boundary layer (ZPG TBL), by segregating the total flow into its sub-components: wall-coherent (WC) and incoherent (WI) structures. The decomposition is conducted by utilizing the spectral linear stochastic estimation (SLSE) technique [5]. Two datasets are considered, a low Reynolds number (Re_τ) DNS database of ZPG TBL [2], and a high Re_τ experimental database obtained via synchronous multi-point hotwire measurements of u. The instantaneous flow and mean statistics representative of the WC and WI motions are investigated for structure organization and scaling arguments, respectively. The eventual goal of this analysis is to propose a conceptual 3-D sketch of the large organized motions in TBL flow.

INTRODUCTION

Organized motions in canonical wall-bounded turbulent flows have been characterized into four principal elements [1], namely: near-wall streaks, hairpin vortices, large-scale motions (LSMs) and very-large-scale motions (VLSMs; superstructures or SS for external flows), with each of them being dominant at different wall-normal spacings. In the logarithmic (log) layer, the LSMs and VLSMs/SS constitute a majority portion of the Reynolds shear stress and kinetic energy [1]. The predominance of such large structures is evident in figure 1(a) which shows the instantaneous streamwise velocity (u) fluctuations in the wall-parallel (x-y) plane at the nominal start of the log-region ($z_o^+ \approx 2.6\sqrt{Re_\tau}$). The data are from the direct numerical simulation (DNS) of a ZPG TBL by Sillero et al. [2] at $Re_\tau \approx 2000$ (referred as $\mathcal{S}_1$ henceforth). Here, x, y and z refer to the streamwise, spanwise and wall-normal directions, respectively. Superscript '+' indicates normalization by viscous length (ν/U_τ) and velocity (U_τ) scales, while Re_τ refers to the friction Reynolds number calculated based on the boundary layer thickness, δ. The energetic predominance of the large structures is reflected via the premultiplied one-dimensional (1-D) streamwise and spanwise spectra of u shown in figure 1(b). Here, apart from the dataset $\mathcal{S}_1$, 1-D spectral estimates are also obtained from an experimental dataset of 2-D energy spectra for a $Re_\tau \approx$ 15,000 ZPG TBL (referred as $\mathcal{E}_1$ henceforth). These measurements were conducted in the High Reynolds Number Boundary Layer Wind Tunnel (HRNBLWT) at the University of Melbourne by following the same methodology as that of Chandran et al. [3]. In figure 1(b), the peaks at streamwise (λ_x) and spanwise (λ_y) wavelengths of 6δ and 0.7δ, respectively are observed for both the datasets and relate to the geometry and spatial organization of the δ-scaled SS [1].

The structures observed in the wall-parallel plane in figure 1(a) may be either wall-coherent (WC; i.e. they physically extend all the way down to the wall) or wall-incoherent (WI). The present study focuses on investigating these two sub-components of the ZPG TBL flow via instantaneous as well as statistical means. This is aligned with a recent upsurge in the interest towards understanding the WC motions, which have been found to be the principal candidates [4,5] for Townsend's 'attached' eddies. The study aims to revisit the spatial organization of large coherent structures, in the log-region of a ZPG TBL, after decomposing the total energy into WC and WI sub-components. Gaining new insights into the organization of WC and WI motions can help in clarifying several doubts/inconsistencies pertaining to the structural organization in the log-region, for example the meandering nature and formation of SS, etc.

ENERGY DECOMPOSITION USING SLSE

The decomposition is carried out by utilizing the scale-by-scale coupling between u-signals at two wall-normal locations, say z_o and z_r. Following Madhusudhanan et al. [6], the coupling is used to obtain a linear stochastic estimate (SLSE) of u at a given wall-normal location (z_o) based on measurement at another location (z_r). It is worth noting here that this approach enables estimation for only those scales that are coherent across z_o and z_r. The SLSE [5] essentially considers a scale-specific unconditional input to give a scale-specific conditional output following:

$$\widetilde{u}^E(z_o;\lambda_x,\lambda_y) = H_l(z_o,z_r;\lambda_x,\lambda_y)\widetilde{u}(z_r;\lambda_x,\lambda_y), \tag{1}$$

where $\tilde{u}(z_r;\lambda_x,\lambda_y) = \mathcal{F}[u(z_r)]$ is the 2-D Fourier transform of $u(z_r)$ in x and y. The superscript E represents the estimated quantity and H_l represents the scale-specific linear transfer kernel. The transfer kernel is computed from an ensemble of data following:

$$H_l(z_o,z_r;\lambda_x,\lambda_y) = \frac{\phi'_{uu}(z_o,z_r;\lambda_x,\lambda_y)}{\phi_{uu}(z_r;\lambda_x,\lambda_y)} = \mid H_l(z_o,z_r;\lambda_x,\lambda_y) \mid e^{i\psi(z_o,z_r;\lambda_x,\lambda_y)}, \tag{2}$$

with $\mid H_l \mid$ and ψ being the scale-specific gain and phase, respectively. To build the kernel we need ϕ'_{uu}, which is the 2-D cross-spectrum between $u(z_o)$ and $u(z_r)$, and $\phi_{uu}(z_r)$, which is the 2-D energy spectra at z_r. Both of these are available

*Corresponding author. E-mail: raadeshpande@gmail.com

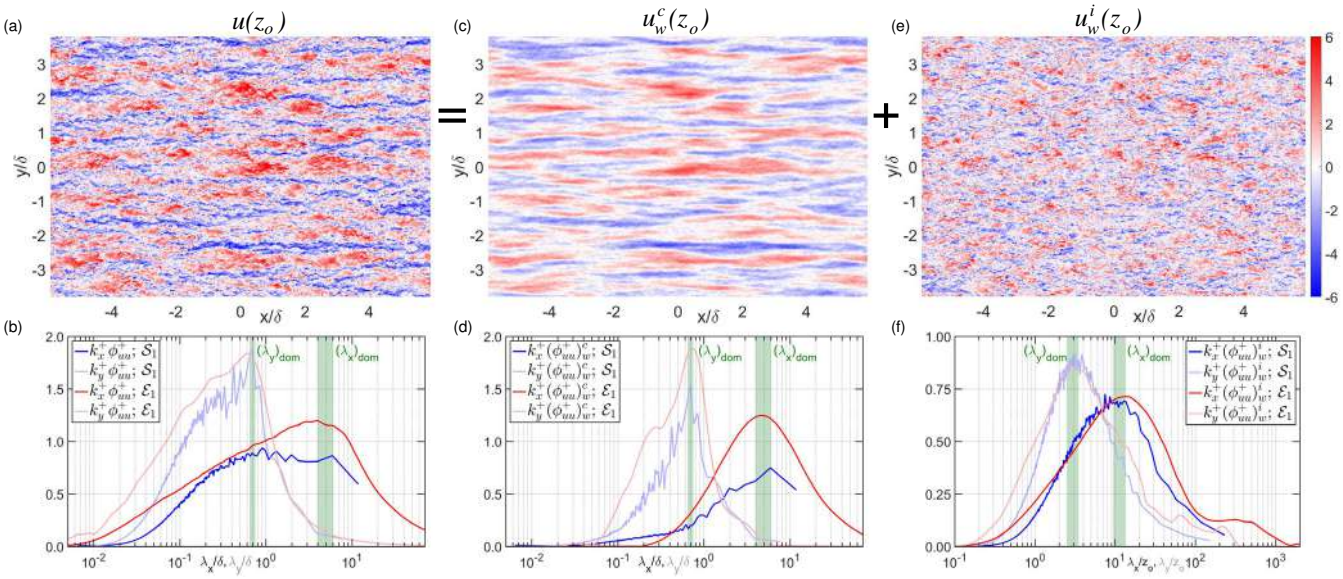

Figure 1: (a,c,e) The instantaneous streamwise velocity fluctuations from the $\mathcal{S}_1$ dataset at $z_o^+ \approx 2.6\sqrt{Re_\tau}$ with contributions from (a) all, (c) wall-coherent and (e) wall-incoherent structures. (b,d,f) Premultiplied streamwise (dark-shaded) and spanwise (light-shaded) energy spectra of the streamwise velocity component for $z_o^+ \approx 2.6\sqrt{Re_\tau}$ representing contributions from (b) all, (d) wall-coherent and (f) wall-incoherent structures. Data from $\mathcal{S}_1$ and $\mathcal{E}_1$ is plotted in blue and red, respectively while the green background is used to highlight the dominant streamwise and spanwise wavelengths.

for $z_o^+ \approx 2.6\sqrt{Re_\tau}$ and $z_r^+ \approx 15$ as part of the datasets $\mathcal{S}_1$ and $\mathcal{E}_1$. The linear stochastic estimate in the physical space, $u^E(z_o;x,y)$ can simply be obtained by inverse Fourier transforming the scale-specific estimate, $\widetilde{u}^E(z_o;\lambda_x,\lambda_y)$ obtained using equation 1. A stochastic estimate of the energy spectrum at z_o can be obtained from equation 1 following:

$$\phi_{uu}^E(z_o;\lambda_x,\lambda_y) = \mid H_l(z_o,z_r;\lambda_x,\lambda_y) \mid^2 \phi_{uu}(z_r;\lambda_x,\lambda_y). \tag{3}$$

Here, by considering z_r^+ at the wall (≈ 15), $u^E(z_o)$ and $\phi_{uu}^E(z_o)$ essentially represent the sub-components of $u(z_o)$ and $\phi_{uu}(z_o)$ that would include contributions from WC structures only. Accordingly, $u^E(z_o) \rightarrow u_w^c(z_o)$ and $\phi_{uu}^E(z_o) \rightarrow (\phi_{uu}(z_o))_w^c$ for z_r^+ near the wall. Following Baars and Marusic [5], the contributions from WI structures may be simply obtained by subtracting the WC contribution from the total, i.e. $u_w^i(z_o) = u(z_o) - u_w^c(z_o)$ and $(\phi_{uu}(z_o))_w^i = \phi_{uu}(z_o) - (\phi_{uu}(z_o))_w^c$. Availability of the instantaneous wall-parallel data at z_o^+ and z_r^+, as part of the dataset $\mathcal{S}_1$, allows estimation of u_w^c, u_w^i, $(\phi_{uu})_w^c$ and $(\phi_{uu})_w^i$ at z_o. On the other hand, only $(\phi_{uu})_w^c$ and $(\phi_{uu})_w^i$ can be computed from the high Re_τ $\mathcal{E}_1$ dataset. These estimates have been plotted in figure 1(c-f).

RESULTS

The decomposition of the full field (figure 1a) into WC (figure 1c) and WI (figure 1e) components leads to some noteworthy observations. In general, WC structures appear to be longer and wider compared to the WI motions. Further, the meandering behavior of the SS [1] is only seen in u_w^c, suggesting that the SS fall into the WC category. This is substantiated by the $(\phi_{uu})_w^c$ plots in figure 1(d), where both the streamwise and spanwise spectra peak at 6δ and 0.7δ, respectively unlike $(\phi_{uu})_w^i$. The peak in the spanwise spectra is consistent with the large-scale organization seen in u_w^c, wherein the low and high momentum fluctuations are arranged quasi-periodically (with period of the order of δ) along the spanwise direction. On the contrary, no such large-scale periodicity is discernible in u_w^i. Interestingly, the $(\phi_{uu})_w^i$ plots show that the dominant WI motions follow z_o-scaling, which is in contrast to the δ-scaling followed by the dominant WC motions. Future work would include investigating this behavior across the entire log-region, paving the way towards proposing a conceptual 3-D sketch of the large organized flow in the log-region.

References

[1] Smits, A.J., McKeon, B.J., Marusic, I. High–Reynolds number wall turbulence. *Annual Review of Fluid Mechanics* **43**, 2011.
[2] Sillero, J.A., Jiménez, J., Moser, R.D. Two-point statistics for turbulent boundary layers and channels at Reynolds numbers up to $\delta^+ \approx 2000$. *Physics of Fluids* **26(10)**: 105109, 2014.
[3] Chandran, D., Baidya, R., Monty, J.P., Marusic, I. Two-dimensional energy spectra in high-Reynolds-number turbulent boundary layers. *Journal of Fluid Mechanics* **826**, 2017.
[4] Hwang, J., Sung, H.J. Wall-attached structures of velocity fluctuations in a turbulent boundary layer. *Journal of Fluid Mechanics* **856**, 2018.
[5] Baars, W.J., Marusic, I. Data-driven decomposition of the streamwise turbulence kinetic energy in boundary layers. Part 1. Energy spectra. *Journal of Fluid Mechanics* **882**, 2020.
[6] Madhusudanan, A., Illingworth, S.J., Marusic, I. Coherent large-scale structures from the linearized Navier–Stokes equations. *Journal of Fluid Mechanics* **873**: pp.89-109, 2019.

ANALYTIC RESOLVENT ANALYSIS FOR WALL-BOUNDED FLOWS

Scott T. M. Dawson *[1] and Barbara Lopez-Doriga[1]
[1] Mechanical, Materials & Aerospace Engineering Department, Illinois Institute of Technology, Chicago, IL, USA

Summary This work presents an analytic approach for approximating the properties of the pseudospectra of linear operators related to wall-bounded turbulent shear flows, thus giving a means to predict the properties of energetically-dominant coherent structures at specific length- and time-scales. The method assumes that leading resolvent response modes (i.e. pseudoeigenmodes) of a given linear operator can be expressed as a sum of wavepackets with a given template shape, and then recasts the associated optimization problem as the minimization of a cost function over a low-dimensional space of parameters. In particular, we show how boundary conditions can be explicitly enforced within this framework through the use of "image" wavepackets on the opposite side of the boundary. This extends recent prior work that does not explicitly account for boundary conditions [1].

INTRODUCTION

While turbulent flows are highly nonlinear, evidence suggests that many of the underlying coherent features present in turbulent flows may be understood through linear mechanisms [2, 3]. In particular, shear-driven turbulent flows typically are associated with highly non-normal linearized operators, which can give rise to large transient growth and amplification of disturbances, even when the operator is asymptotically stable [7]. While the study of such operators can provide valuable insight into underlying mechanisms present in systems such as wall-bounded turbulence, the computational cost of such analysis is often a limiting factor. Indeed, it has been recently noted that "with current computational resources, [resolvent analysis of] fully inhomogeneous flows represent an unmet challenge" [5]. The present work provides an alternative pathway to such analysis motivated by wavepacket pseudomode theory [6, 4], which foregoes the need to form and decompose large discretized operators.

ANALYTIC RESOLVENT ANALYSIS

Analysis of linear amplification mechanisms for a dynamical system can be performed in the frequency domain using the resolvent formulation of the governing equations. Here, the Fourier-transformed (in time) state $\hat{\boldsymbol{x}}$ can be expressed as the result of applying the linear resolvent operator on $\hat{\boldsymbol{f}}$, which can represent nonlinearities and other unknown disturbances, through $\hat{\boldsymbol{x}} = (-i\omega\boldsymbol{I} + \boldsymbol{A})^{-1}\hat{\boldsymbol{f}}$. We are interested in finding the leading singular values and vectors in the singular value decomposition (SVD) of this resolvent operator. Under certain conditions, such modes are expected to resemble wavepackets that are local in both space and spatial frequency. Using this as motivation, rather than proceeding with numerical decomposition of the resolvent operator, we instead start with the assumption that the leading resolvent response mode (left singular vector) can be efficiently approximated by a small number of wavepackets of the form

$$\Psi(\boldsymbol{x}) = \sum_{j=1}^{r} c_j \exp\left(i\boldsymbol{k}_j^T(\boldsymbol{x}-\boldsymbol{x}_j) - (\boldsymbol{x}-\boldsymbol{x}_j)^T\boldsymbol{Q}_j(\boldsymbol{x}-\boldsymbol{x}_j)\right), \tag{1}$$

where $\boldsymbol{x}$ is the spatial coordinate.With this assumption, rather than computing the SVD numerically, we instead find the small number of coefficients that solve the minimization problem

$$\{\boldsymbol{c},\boldsymbol{k},\boldsymbol{Q},\boldsymbol{x}_0\} = \underset{\boldsymbol{c},\boldsymbol{k},\boldsymbol{Q},\boldsymbol{x}_0}{\operatorname{argmin}} \left\|(-i\omega\boldsymbol{I}+\boldsymbol{A})\,\Psi\right\|^2 := \underset{\boldsymbol{c},\boldsymbol{k},\boldsymbol{Q},\boldsymbol{x}_0}{\operatorname{argmin}} J(\boldsymbol{c},\boldsymbol{k},\boldsymbol{Q},\boldsymbol{x}_0;\omega), \tag{2}$$

where we analytically calculate the action of the linear operator on the template response mode shape. This was the approach taken in [1] for the case where $r = 1$, for systems with spatial homogeneity (and thus no localization) in the streamwise and spanwise directions. In this work, we consider the case with $r = 2$, which allows for the implementation of Dirichlet boundary conditions. For the purposes of exposition, here we focus on the simple operator $\boldsymbol{A} = -(iR)^{-1}D_{yy}+y$ in the vicinity of a boundary at $y = 0$, which is equivalent to the Squire operator with a linear mean velocity profile. Note in particular that this operator can be used in the understanding of the Orr mechanism in shear-driven turbulent flows. In order to satisfy the boundary conditions, we consider candidate response modes of the form

$$\Psi(y) = c\left\{\exp\left[ik_y(y-y_0) - q(y-y_0)^2\right] - \exp\left[-ik_y(y+y_0) - q(y+y_0)^2\right]\right\}. \tag{3}$$

For a specified frequency $\omega = \omega_r + i\omega_i$, we compute the cost function for this system to be

$$J(k_y,q,y_0;R,\omega) = \left[J_1 - qe^{\frac{k_y^2}{2q}+2qy_0^2}J_2 + J_3\right]\left(1 - 4k_yR^2e^{\frac{k_y^2}{2q}+2qy_0^2}\right)^{-1}, \tag{4}$$

*Corresponding author. E-mail: scott.dawson@iit.edu.

MINI SYMPOSIA

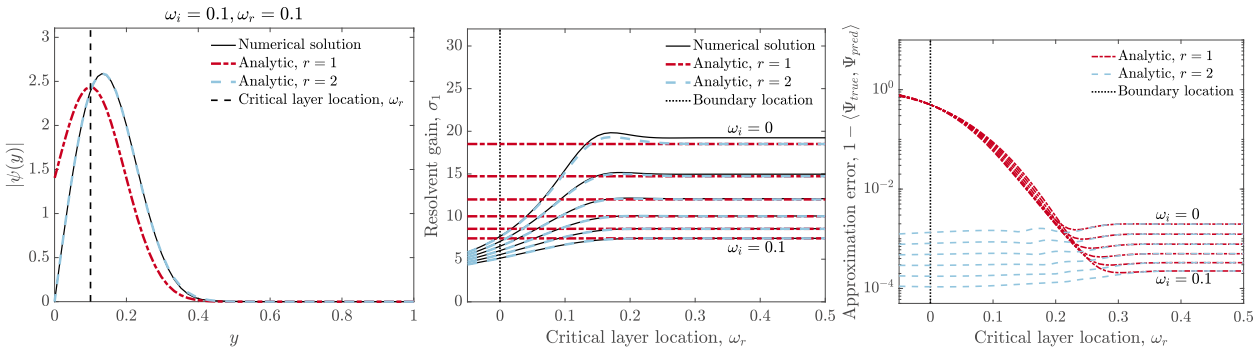

(a) (b) (c)

Figure 1: (a) Numerical and analytic mode shapes for a critical layer close to the wall at $\omega_r = 0.1$; (b) leading resolvent singular values; and (c) error between numerical and analytical modes for various complex frequencies. All results are for $R = 3000$, and compare analytic modes computed using a single wavepacket that does not account for boundary conditions ($r = 1$), and two wavepackets to ensure that boundary conditions can be satisfied ($r = 2$).

$$J_1 = 64q^6y_0^4 - 96q^5y_0^2 - 32q^4R\omega_i y_0^2 + 12q^4 + 16q^3Ry_0 + 4q^2R^2\omega_i^2 + 4q^2R^2y_c^2 + qR^2 - k_y^2R^2,$$
$$J_2 = \left(4q\left(3q^2 + 2q\left(3k_y^2 + R\omega_i\right) + k_y^4 + 2k_y^2R\omega_i + R^2\omega_i^2 + y_0^2 + y_c^2\right)\right) + 8qR(k_y - Ry_0y_c)\,\mathrm{erf}\left(\sqrt{2q}y_0\right) + R^2,$$
$$J_3 = 8q^3R\omega_i\,\mathrm{erfi}\left(\frac{k_y}{\sqrt{2q}}\right) + 4qk_yR^2y_c\,\mathrm{erfi}\left(\frac{k_y}{\sqrt{2q}}\right).$$

Figure 1 compares the performance of finding optimal mode shape parameters from this cost function to the mode computed from the numerical SVD, as well as to the analytic mode computed without enforcement of boundary conditions. We see using modes of the form given in equation 3 accurately captures both the shape and amplification of the numerically-computed leading resolvent mode even as the critical layer gets arbitrary close to the wall, which is not the case when only a single wavepacket is used.

CONCLUSION

The close agreement of the analytic and numerically-computed modes and singular values shows that the assumed form for the leading response mode shapes is valid. These results demonstrate the feasibility of extending this analytic analysis to more complex systems. Preliminary results suggest that this method can indeed extended to cases with multiple boundaries, multiple critical layers, and for the computation of suboptimal modes, though in some cases an exact closed-form expression for the cost function can be challenging to obtain. It is our goal to further extend this analysis towards systems where direct numerical computation of resolvent modes currently presents computational challenges (e.g. for cases with multiple directions of spatial inhomogeneity), particularly if needed for real-time modeling and control.

References

[1] S. T. M. Dawson and B. J. McKeon. On the shape of resolvent modes in wall-bounded turbulence. *Journal of Fluid Mechanics*, 877:682–716, 2019.

[2] Y. Hwang and C. Cossu. Linear non-normal energy amplification of harmonic and stochastic forcing in the turbulent channel flow. *Journal of Fluid Mechanics*, 664:51–73, 2010.

[3] B. J. McKeon and A. S. Sharma. A critical-layer framework for turbulent pipe flow. *Journal of Fluid Mechanics*, 658:336–382, 2010.

[4] D. Obrist and P. J. Schmid. Algebraically decaying modes and wave packet pseudo-modes in swept Hiemenz flow. *Journal of Fluid Mechanics*, 643:309–332, 2010.

[5] K. Taira, S. L. Brunton, S. T. M. Dawson, C. W. Rowley, T. Colonius, B. J. McKeon, O. T. Schmidt, S. Gordeyev, V. Theofilis, and L. S. Ukeiley. Modal analysis of fluid flows: An overview. *AIAA Journal*, pages 4013–4041, 2017.

[6] L. N. Trefethen and M. Embree. *Spectra and pseudospectra: the behavior of nonnormal matrices and operators*. Princeton University Press, 2005.

[7] L. N. Trefethen, A. E. Trefethen, S. C. Reddy, and T. A. Driscoll. Hydrodynamic stability without eigenvalues. *Science*, 261(5121):578–584, 1993.

THE EFFECT OF SETTLING INERTIAL PARTICLES ON HOMOGENEOUS TURBULENCE

Filippo Coletti*[1,2], Roumaissa Hassaini*[1]
[1] Department of Aerospace Engineering & Mechanics, University of Minnesota, Minneapolis, MN, USA
[2] Department of Mechanical and Process Engineering, ETH Zurich, Switzerland

Summary We report novel measurements of the effect of microscopic heavy particles on the turbulence in which they are suspended. We use a unique apparatus that generate a large volume of homogeneous air turbulence, and use laser imaging to simultaneously track the particle motion and the air velocity fields from the integral to the Kolmogorov scales in both space and time. It is the first time this is achieved experimentally for particles in a Stokes number range that produces clustering and enhanced settling. We systematically vary the volume fraction from 10^{-6} to $5*10^{-5}$, and report clear trends for the particle settling velocity and clustering, as well as for the air turbulence statistics. With increasing concentration, clustering and settling velocity of the particles is enhanced, turbulence kinetic energy is augmented, the dissipation rate is reduced, and the scale-by-scale distribution of the energy is profoundly altered by the particles.

BACKGROUND

Particle Laden turbulence occurs in natural processes such as rain, snow and sand. These flows are difficult to characterize in nature and even at small volume fraction the particles can modify the turbulence. Is the turbulence increased or inhibited? And what processes are causing such modifications? Answering these questions is still challenging for the scientific community, both numerically and experimentally, given the wide range of parameters and spatio-temporal scales involved [1,2].

EXPERIMENT

In the present work, we shed some light on these questions by tackling the problem at the laboratory scale. Well controlled experiments have been used, where the only changing parameter is the particle volume fraction. The latter is increased from below 10^{-6}, where it is verified that the turbulence is not affected by the particles (one-way coupling), up to $5*10^{-5}$, where major influence of the particles on the fluid is expected (two-way coupling). The experiments have been carried out in a 5 m^3 chamber. Homogeneous air turbulence with quasi-zero mean flow is generated thanks to 2 planes of 128 each random jets [3]. Size-selected glass micro-spheres (50 micron in diameter) fall into the chamber through a 3-m long vertical chute. Multi-scale imaging is implemented using 2 synchronized high speed cameras resolving from the Kolmogorov scale up to the integral scale. Particle Image Velocimetry (PIV) and Particle Tracking Velocimetry (PTV) are used simultaneously to follow respectively the flow and the 50 um glass beads particles. The particle Stokes number (based on the Kolmogorov time scale) is St =3.5 and the Reynolds number based on the Taylor microscale is Re_λ =300. We will briefly present in the following some of the main results from the study, showing the effect of the increasing volume fraction on both the particle transport and the air turbulence.

PARTICLE TRANSPORT

We investigated the change of the rate of gravitational settling thanks to the reconstructed velocity field of the particles. It appears that the mean fall speed of the particles is enhanced when the particle concentration is increased as plotted in Fig.1a. For the highest volume fraction the mean vertical velocity reaches almost $2W_0$, W_0 being the expected terminal velocity measured in one-way coupled regimes. Similar trends have been reported numerically, but much weaker in magnitude [4].

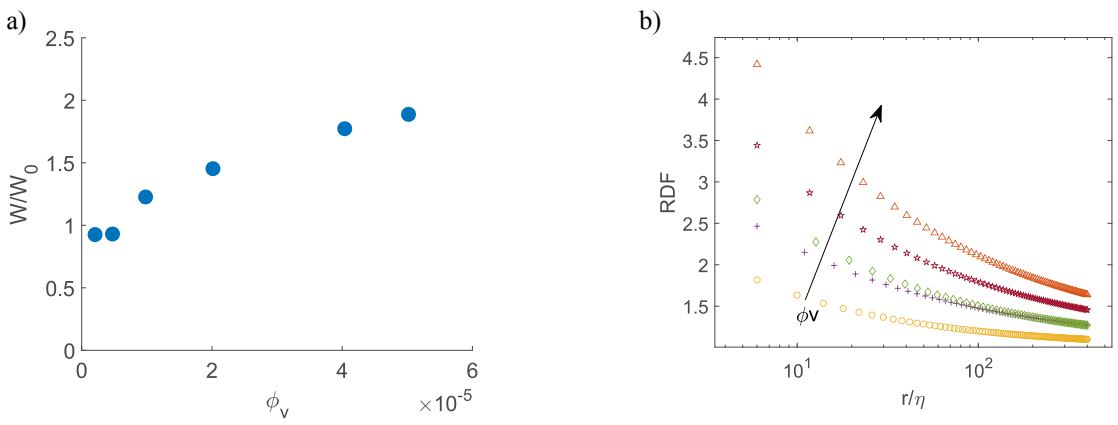

Figure 1. (a) Mean vertical velocity of the particles divided by W_0 versus the volume fraction. (b) RDFs of the particles in function of the scale r normalized by the Kolmogorov scale for different volume fractions.

*Corresponding author. E-mail: fcoletti@ethz.ch

At the present Stokes number, significant clustering of the particles is expected. To characterize such effect, Radial Distribution Functions (RDF) [5] are examined. As plotted in Fig1.b, the RDFs display significantly higher values as the volume fraction increases, which confirms an intensification of the clustering at all scales. Such effect, which we also confirm and explore via Voronoi tessellation (not shown), has never been documented experimentally before.

TURBULENCE MODIFICATION

The modification of the fluid by the particle-turbulence interaction is examined. The Turbulent Kinetic Energy (TKE) normalized by the unladen-case value is represented in fig2a, in function of the volume fraction, as retrieved from imaging at both small field of view (SFV) and large field of view (LFV). We observe a clear and major increase in the TKE. This turbulence augmentation is opposite to previous trends (turbulence modulation) observed in previous studies (e.g., Hwang & Eaton [6]) which considered much more inertial particles. We attribute the different behaviour to the important role of clustering and enhanced settling in the present regime.

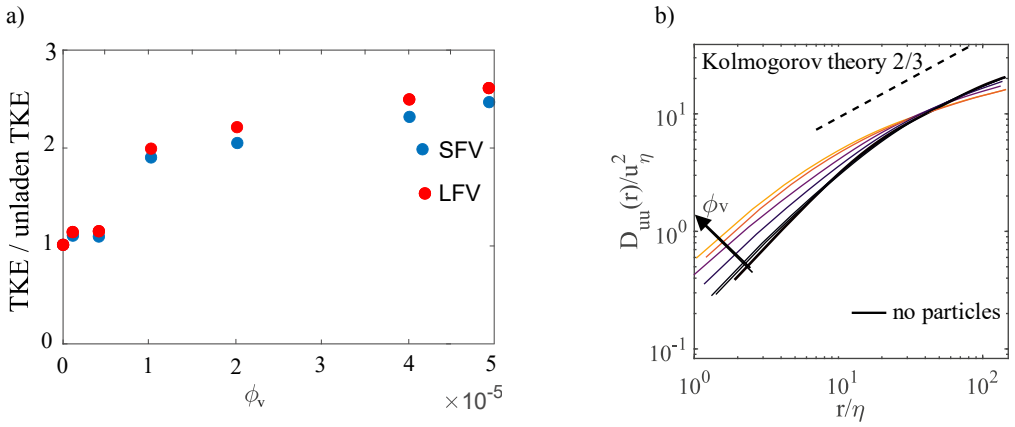

Figure 2. (a) Turbulent kinetic energy normalized by the unladen case in function of the volume fraction for the Small and Large Field of View. (b) Second-order velocity structure function versus normalized scale for the different volume fractions.

The energy distribution over the scales is of a great importance in turbulence. A quantity that can give us an insight to such distribution is the 2nd order velocity structure function, plotted in Fig 2b. As the volume fraction increases, we see a departure from the expected $r^{2/3}$ scaling predicted by Kolmogorov theory over the inertial scales. For significant loadings we have an excitement of the turbulence fluctuations at small scales whereas a modulation of these fluctuations is observed at larger scales. Such behaviour, termed pivoting, has been reported mainly numerically, and only sporadically experimentally [7,8]. The present systematic trend clarifies the picture and contributes to further our understanding of particle-turbulence interaction in the clustering regime.

References

[1] POELMA, Christian et OOMS, Gijs. Particle-turbulence interaction in a homogeneous, isotropic turbulent suspension. *Applied Mechanics Reviews*, 2006, vol. 59, no 2, p. 78-90.
[2] BALACHANDAR, S. et EATON, John K. Turbulent dispersed multiphase flow. *Annual Review of Fluid Mechanics*, 2010, vol. 42, p. 111-133.
[3] CARTER, Douglas, PETERSEN, Alec, AMILI, Omid, *et al.* Generating and controlling homogeneous air turbulence using random jet arrays. *Experiments in Fluids*, 2016, vol. 57, no 12, p. 189.
[4] BOSSE, T., KLEISER, L., & MEIBURG, E.. Small particles in homogeneous turbulence: settling velocity enhancement by two-way coupling. *Physics of Fluids*, 2006, 18(2), 027102.
[5] DE JONG, J., SALAZAR, J. P. L. C., WOODWARD, S. H., *et al.* Measurement of inertial particle clustering and relative velocity statistics in isotropic turbulence using holographic imaging. *International Journal of Multiphase Flow*, 2010, vol. 36, no 4, p. 324-332.
[6] HWANG, Wontae et EATON, John K. Homogeneous and isotropic turbulence modulation by small heavy ($ St\sim 50$) particles. *Journal of Fluid Mechanics*, 2006, vol. 564, p. 361-393.
[7] SUNDARAM, Shivshankar et COLLINS, Lance R. A numerical study of the modulation of isotropic turbulence by suspended particles. *Journal of Fluid Mechanics*, 1999, vol. 379, p. 105-143.
[8] PETERSEN, Alec J., BAKER, Lucia, et COLETTI, Filippo. Experimental study of inertial particles clustering and settling in homogeneous turbulence. *Journal of Fluid Mechanics*, 2019, vol. 864, p. 925-970.

LARGE-SCALE MODULATION OF AN EFFUSION FILM BY A TURBULENT BOUNDARY LAYER

Jeremy Basley *[1], Kevin Gouder[1], and Jonathan F. Morrison[1]
[1] Department of Aeronautics, Imperial College London, United Kingdom

Summary The evolution of a turbulent boundary layer injected with an effusion film is investigated for a range of film velocity over incoming velocity ratios, using Particle Image Velocimetry, visualisations, and hot-wire measurements. This work focuses on the momentum effects underlying the mixing of the effusion film. To that end, the geometry of a turbine blade is idealised in a large-scale facility, the upstream boundary layer is canonical and the effusion film is isothermal. The spectral content of the flow reveals that the effusion film first promotes near-wall turbulence until it separates above a critical velocity ratio and large-scale motions no longer penetrate the roughness sub-layer. Mixing is drastically altered by the injection of the film, as evidenced by amplitude modulation maps which feature intensified large-scale modulations of small-scale turbulence.

INTRODUCTION

In pursuit of higher efficiency in jet engines, the temperatures brought out in combustion chambers have to be maximised. As a result turbine blades located directly downstream of the combustion chamber endure harsh conditions, which must be alleviated by film or effusion cooling. Large velocity ratios are typically used to account for wide tolerances: typically VR $= U_f/U_\infty > 100\%$ up to 300%, where U_f and U_∞ are the characteristic velocities of the film and the incoming flow, respectively (see [1] for a review). This implies high flow rates are required for cooling, thus preventing further improvement of the engine's efficiency. A finer tuning of the film generation as well as minimised mixing must be achieved to maintain the integrity of the film and allow for lower velocity ratios to be used. This experimental study emulates the flow around a turbine blade using an idealised scaled-up configuration at low speed in order to get around the inherent constrains and challenges of internal flows in jet engines. This allows us to focus on the exchange mechanisms at play between the injected film and the incoming flow, and to concentrate on low velocity ratios (VR $< 40\%$).

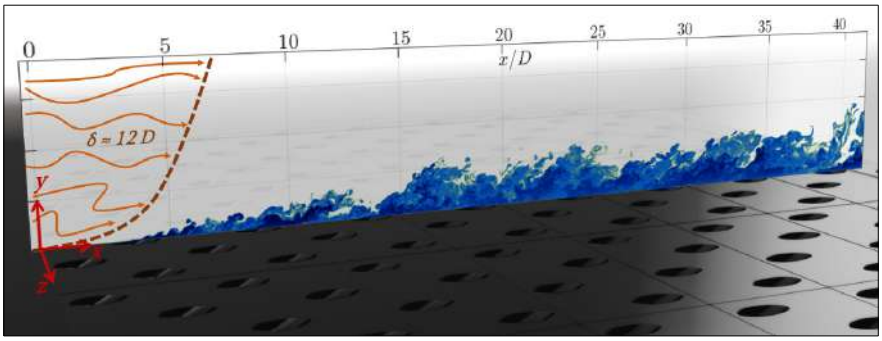

Figure 1: Illustration of the experimental set-up: rendered image of the effusion plate superimposed with a visualisation snapshot acquired in the plane aligned with the centre of effusion holes (for VR $= 26\%$).

EXPERIMENTS

The scaled-up effusion device consists of a plenum located directly underneath a thick plate with a staggered grid of inclined $D = 16$ mm diameter holes with a pitch of $5D$. This setup was placed in a self-similar turbulent boundary layer, tripped and developed over 15 m, yielding a Reynolds number between $2700 < u_\tau\delta/\nu < 4700$, with u_τ the friction velocity and $\delta \simeq 0.2$ m the boundary layer thickness upstream of the plate (Figure 1). Time-resolved planar PIV and visualisations were acquired in two streamwise wall-normal planes – one along the holes the other between two rows. A wide range of low velocity ratios were investigated, VR $< 40\%$ down to VR=0% whilst the holes remain open.

RESULTS & DISCUSSION

Power spectral densities were computed from stream-wise velocity fluctuations u. The spectral signature observed for VR=0% (Figure 2a) is consistent with high Reynolds number boundary layers [2]. It shows a scale separation between small-scale turbulence confined in the roughness sublayer – here generated by the perforated plate – and large-scale motions particularly intense in the log layer. Inserting the effusion film results in a broad-band increase of turbulence in the sub-layer, including large-scale motions (Figure 2b). Above a critical VR (around $15 - 20\%$) the separation of the film occurs and pushes away the large-scale motions outside the roughness sub-layer. This reduces the turbulent energy close to the wall but it generates a broad-band spike of large-scale fluctuations further around $y \approx 0.1\delta$ (Figure 2c).

*Corresponding author. E-mail: j.basley@imperial.ac.uk.

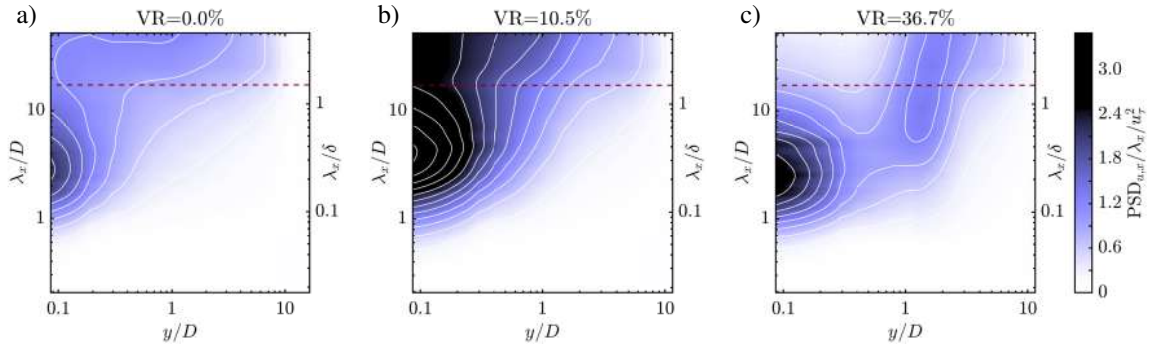

Figure 2: Pre-multiplied power spectral densities of stream-wise velocity $\mathrm{PSD}_{u,x}$ as a function of wavelength λ_x and wall distance y for three VR. Contour levels are shown every $0.3\,u_\tau^2$. The dashed lines mark the cut-off wavelength $\lambda_x = 1.5\delta$ used below.

The gap between small scales populating the roughness sub-layer and the large-scale motions allows for the decomposition of velocity fluctuations into $u = u_L + u_s$, where $u_L = u(\lambda_x > 1.5\delta)$ is the large-scale component obtained through stream-wise unbiased low-pass filtering, and u_s carries the remaining fluctuations at smaller scales. That decomposition has been used in numerous papers to quantify the amplitude modulation of small-scale turbulence by large-scale motions [3] via the coefficient AM, defined as the correlation between u_L and $(u_s^2)_L$, the large-scale envelope of small-scale fluctuations obtained by low-pass filtering u_s^2. Often restricted to temporal correlations of hot-wire measurements, AM has recently been extended to spatial correlations [4]. Here it is defined as

$$\mathrm{AM}(x_0, y_0, x, y) = \frac{\langle u_L(x_0, y_0) * (u_s^2)_L(x, y) \rangle}{\sigma_{u_L}(x_0, y_0)\, \sigma_{(u_s^2)_L}(x, y)},$$

where σ denotes a standard deviation. Contours of AM coefficient are shown in Figure 3. Inclined meandering large-scale motions modulate the amplitude of small scales in the roughness sub-layer, so that turbulence is intensified directly underneath at the front of these super-structures.

This mechanism which identifies inter-scale exchanges underlying the mixing within the boundary layer, is significantly altered by the presence of the effusion film. At low VR, modulations of small-scale turbulence are enhanced but remain confined near the wall. With increasing VR and the separation of the effusion film, large-scale motions no longer reach the inner layer. Instead the amplitude modulation occurs in the log layer at a much higher level. It is worth noting that such an evolution of AM is reminiscent of flat-plate boundary layers in adverse pressure gradients, which exhibit a similar separation of the inner sub-layer [5]. Further insight will be discussed in Milano, notably the extension of the large-scale modulation analysis to the concentration of injected fluid using synchronous velocity fields and visualisations.

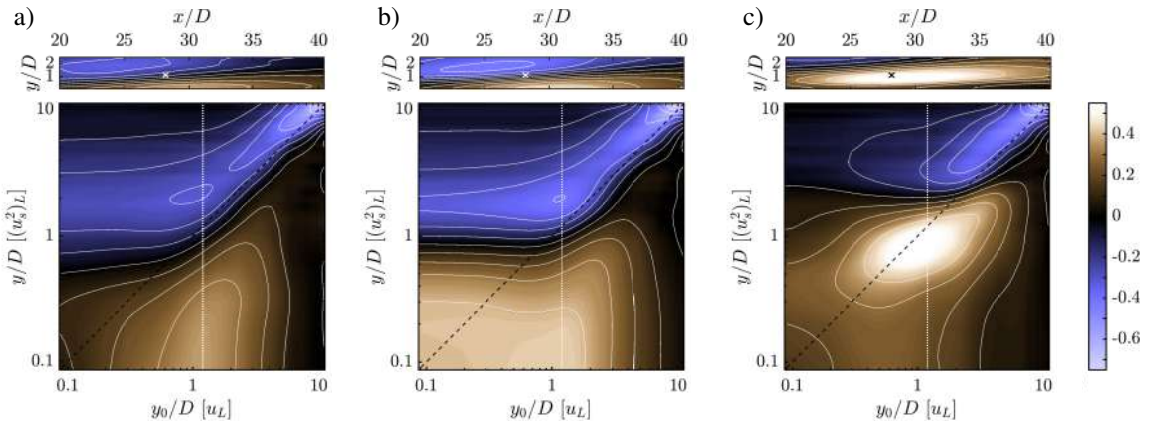

Figure 3: Amplitude modulation coefficient for (a) VR $= 0\%$, (b) VR $= 10\%$, and (c) VR $= 37\%$. (Top) single point correlation $\mathrm{AM}(x, y)$ at reference point $(x_0 = 28D, y_0 = 1.2D)$, and (bottom) two-point correlation profile $\mathrm{AM}(y_0, y)$ at $x_0 = 28D$. White dotted lines mark the intersections with top maps at $y_0 = 1.2D$ and black dashed diagonals mark the no-shift correlation ($y = y_0$).

References

[1] Krewinkel R., A review of gas turbine effusion cooling studies, *Int. Journal of Heat and Mass Transfer* **66**: 706–722, 2013.
[2] Squire D. T., Morrill-Winter C., Hutchins N., Schultz M. P., Klewicki J. C. & Marusic I., Comparison of turbulent boundary layers over smooth and rough surfaces up to high Reynolds numbers, *J. Fluid Mech.* **795**: 210–240, 2016.
[3] Mathis R., Hutchins N. & Marusic I., Large-scale amplitude modulation of the small-scale structures in turbulent boundary layers, *J. Fluid Mech.* **628**: 311–337, 2009.
[4] Basley J., Perret L. & Mathis R., Spatial modulations of kinetic energy in the roughness sublayer. *J. Fluid Mech.* **850**: 584–610, 2018.
[5] Harun Z., Monty J. P., Mathis R. & Marusic, I., Pressure gradient effects on the large-scale structure of turbulent layers, *J. Fluid Mech.*, **715**: 477–498, 2013.

CLOSED-LOOP CONTROL OF FORCED TURBULENT JETS

Igor A. Maia *[1], Peter Jordan[1], and André V. G. Cavalieri[2]
[1] Pprime Institute, CNRS, Université de Poitiers, ENSMA, Poitiers, France
[2] Divisão de Engenharia Aeronáutica, Instituto Tecnológico de Aeronáutica, São José dos Campos, Brazil

Summary We assess the possibility of performing closed-loop control of forced, turbulent jets through wave-cancellation. The study is motivated by the success of recent studies in applying wave-cancellation to control Tollmien-Schlichting waves in laminar boundary layers and Kelvin-Helmholtz instabilities in transitional mixing layers. Using a control law obtained through a system identification technique, here we demonstrate that wave-cancellation-based, closed-loop control is also possible in a fully turbulent jet.

INTRODUCTION

This work describes experiments involving closed-loop control of forced, turbulent jets. The strategy consists in eliminating disturbances through wave-cancellation. The technique assumes downstream propagation of disturbances to be linear and requires an estimation model capable of predicting their evolution in real-time. Wave-cancellation has been sucessfully applied in recent numerical studies to the control of Tollmien-Schlichting waves in laminar boundary layers [1], and Kelvin-Helmholtz instabilities in low-Reynolds-number, two-dimensional, transitional mixing-layers [2]. The results of these studies, which combine linear stability models and system identification, motivates the application of wave-cancellation to the control of disturbances in turbulent jets, which many recent studies have shown can be reasonably modelled using linear stability theory [3]. Kopiev et al. [4] have shown, in an open-loop configuration, that wave-cancellation of harmonic disturbances is possible. But wave-cancellation of stochastic disturbances in in a fully-turbulent jet, in a closed-loop configuration, has so far not been realised.

We tackle this issue experimentally. The goal of the forcing is to raise target axisymmetric disturbances above background turbulence levels, making them easier to control.

CONTROL STRATEGY

The control law design is based on that of Sasaki et al. [2] and Sasaki et al. [3]. We seek to eliminate a certain objective, z, which is given as a linear combination of sensor measurements, y, plus the actuation signal, u, which is itself dependent on the measurements. In the frequency-domain, this can be written as:

$$Z(\omega) = Y(\omega)H_{yz} + U(\omega)H_{uz}, \tag{1}$$

$$U(\omega) = K(\omega)\left(Y(\omega) + H_{uy}U(\omega)\right), \tag{2}$$

where Z, Y and U are the frequency-domain counterparts of z, y and u, H_{yz} and H_{uz} are the estimation and actuation transfer functions, respectively, and H_{uy} is a feedback transfer function. These are identified empirically, by computing the response of the jet to forcing and actuation separately. The control kernel, K is obtained by substituting Eq. 2 into Eq. 1, setting $Z = 0$ and solving for K. In the time domain, the control law is given by,

$$u(t) = \int_0^\infty k(\tau)y(t-\tau)\mathrm{d}\tau, \tag{3}$$

where k is the inverse Fourier transform of K.

The experiments were carried out in a jet with Mach and Reynolds numbers of $M = 0.05$ and $Re = 5 \times 10^4$, respectively, with the Reynolds number based on the jet diameter. The nozzle boundary layer was tripped at a distance of $2.5D$ (with D being the jet diameter) upstream of the exit plane, in order to ensure that the jet is turbulent.

Figure 1 shows a schematic of the experiment. The jet was forced at the nozzle lip by synthetic jets issuing from a 0.5 mm annular slot. The synthetic jets were generated by a system of eight loudspeakers acting in a synchronised manner so as to force axisymmetric wavepackets. The input measurements were provided by a ring of 6 microphones placed in the near pressure field of the jet at a streamwise distance of $0.3D$ from the nozzle exit. The actuators also consisted of synthetic jets generated by loudspeakers, and were placed at $1.4D$ downstream of the nozzle exit. The objective of the control law was to minimise the streamwise velocity fluctuations at the jet centerline, measured by a hot-wire placed at $2D$.

The jet was forced with band-limited stochastic signals in four different frequency bands: $0.3 \leqslant St \leqslant 0.45$, $0.3 \leqslant St \leqslant 0.65$, $0.3 \leqslant St \leqslant 0.85$ and $0.3 \leqslant St \leqslant 1$, where St is the Strouhal number, given by $St = fD/U_j$, with U_j being the jet exit velocity.

The closed-loop experiment is carried out using a LabVIEW software. The task of the sofwtare is to carry out the convolution given by Eq. 3 in real-time, using unsteady signals from the pressure measurements as input, y.

*Corresponding author. E-mail: igor.albuquerque.maia@univ-poitiers.fr

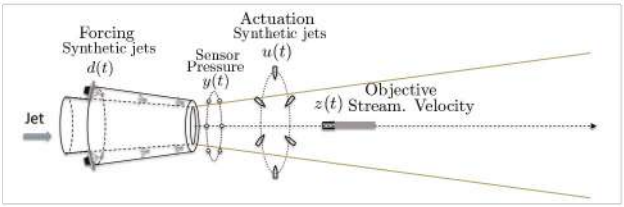

Figure 1: Schematic of closed-loop control experiment.

RESULTS

Linearity is a key feature for wave-cancellation. Here we use two-point coherence as a measure of the linearity of the system and a criterion for interpretation of the results. Control performance is dictated by two kinds of coherence: the coherence between sensor and objective, γ_{yz}, which we have found is a good proxy for the accuracy of the disturbance estimation; and the coherence between actuator and objective, γ_{uz}, found to be a good proxy for wavepacket generation.

Figure 2 shows streamwise velocity spectra of controlled and uncontrolled jets at the objective position. The spectra of the unforced jet is also shown for comparison. The coherences γ_{yz} and γ_{uz} associated with each control case are also shown. Two kinds of actuation were carried out: one whose gain was designed to reduce disturbance amplitude, named K_r and another designed to amplify disturbances, K_a, obtained by applying a π phase shift to K_r.

For the jet forced at the two narrowest frequency bands, control is effective in both reducing and amplifying the disturbances, thanks to the the high values of coherence. Reductions of up to 7dB can be observed in the frequency bands $0.3 \leqslant St \leqslant 0.45$ and $0.3 \leqslant St \leqslant 0.65$. At larger frequency bands, actuator performance is poor and nonlinear effects, reflected by the reduced coherence, γ_{uz}, degrade control authority.

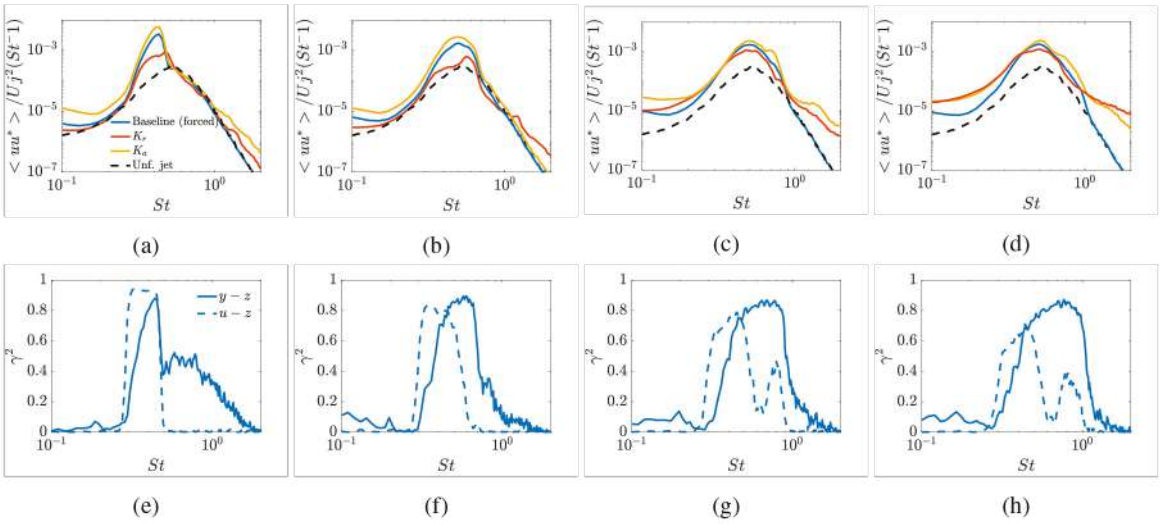

Figure 2: Streamwise velocity spectrum measured at the objective position of controlled an uncontrolled turbulent jets forced in the bands: (a) $0.3 \leqslant St \leqslant 0.45$; (b) $0.3 \leqslant St \leqslant 0.65$; (c) $0.3 \leqslant St \leqslant 0.85$; (d) $0.3 \leqslant St \leqslant 1$. Spectra of the unforced jet are also shown for comparison. The coherences corresponding to each case are shown on the bottom line.

CONCLUSIONS

We have shown that wave-cancellation is possible in a fully turbulent jet. This is the first time, to the best of our knowledge, that closed-loop control has been successfully applied to a turbulent jet. The performance of the control is shown to be largely underpinned by coherence between sensor and objective, on one hand, and actuator and objective on the other. These measures of coherence will thus be useful for the optimisation of actuation positioning.

References

[1] K. Sasaki, P. Morra, N. Fabbiane, A. V. G. Cavalieri, A. Hanifi, and D. Henningson. On the wave-cancelling nature of boundary layer flow control. *Th. Comp. Fluid Dyn.* **32**:593—616, 2018.

[2] K. Sasaki, G. Tissot, A. V. G. Cavalieri, F. J. Silvestre, P. Jordan, and D. Biau. Closed-loop control of a free shear flow: a framework using the parabolized stability equations. *Th. Comp. Fluid Dyn.*, **32**:765—788, 2018

[3] P. Jordan and T. Colonius. Wave packets and turbulent jet noise. *Ann. Rev. of Fluid Mech.*, **45**:176—195, 2013.

[4] V. F. Kopiev, I. V. Belyaev, M. Y. Zaytsev, V. A. Kopiev, and G. A. Faranosov. Acoustic control of instability waves in a turbulent jet. *Acoustical Physics*, **59(1)**:16—26, 2013.

A SIMPLE MODEL OF THE TURBULENT BOUNDARY LAYER BASED ON AN UNDERLYING BINARY FLOW STRUCTURE

Christopher M. White *[1], Alireza Ebadi1, Juan Carlos Cuevas Bautista[1], Greg Chini[1], and Joseph Klewicki[2]
[1] Department of Mechanical Engineering, University of New Hampshire, Durham, NH 03824, USA
[2] Department of Mechanical Engineering, University of Melbourne, Melbourne, Victoria, 3010, Australia

Summary Experimental and numerical studies over the past two decades reveal that as the Reynolds number becomes large the turbulent boundary layer is increasingly composed of large zones of uniform streamwise momentum segregated by narrow regions of high shear. Similarly, recent studies have shown that passive scalar fields in turbulent boundary layers also exhibit a binary spatial structure, namely, large uniform scalar zones separated by narrow regions of high gradient. Herein, a simple model of the turbulent boundary layer that exploits these essential binary elements of the boundary-layer structure is developed.

MODEL CONSTRUCTION

The present work focuses on recent studies in canonical smooth-wall flows, in which the momentum and passive scalar fields exhibit similar binary structures (extended regions of uniform quantity segregated by narrow regions of large gradient) [1, 2]. The target of the present work is to capture essential features of the momentum and scalar transport associated with this heterogeneous structure. This is achieved by employing a complementary set of theoretically educed and empirically observed findings to formulate a simple model for the streamwise velocity and passive scalar fluctuations in turbulent wall flows. In essence, this model leverages the physical space manifestation of scale separation between the extended regions of uniform quantity and narrow regions of large gradient. The model is informed specifically by analysis of the mean momentum equation and passive scalar transport equation.

Analysis of the mean momentum equation and mean passive scalar transport equation reveals the existence of a self-similar hierarchy of layers, on which the mean equation can be continuously rescaled into a single parameter-free form with all terms retaining leading-order significance [3, 4]. The width W^+ of each layer of the hierarchy, which is the characteristic length scale for the rescaling, is the average size of the turbulent motions responsible for the net flux towards the wall. The analysis shows that $W^+ = (-\frac{d^2U^+}{dy^{+2}})^{-\frac{1}{2}}$ and $W_\theta^+ = (-\frac{d^2\Theta^+}{dy^{+2}})^{-\frac{1}{2}}$ for the momentum and passive scalar fields, respectively. Here U is the mean streamwise velocity, y is the wall-normal direction, Θ is the mean scalar and a superscript $+$ denotes inner scaling.

In the present model a discrete version of the hierarchy layer structure is developed in which a region of uniform quantity and its adjacent region of large gradient are interpreted as one layer in the hierarchy. The model is constructed by first positioning a finite number of fissures (i.e. narrow regions of large gradient) across the boundary layer to create a master step-like profile. The wall-normal placement of the fissures are informed by analysis of the layer width profile W^+. In the inertial region of the boundary layer, this analysis is theoretically grounded while in the subinertial region it is primarily empirical. The master profile of velocity and passive scalar determined from the model are shown in figure 1 for a given Reynolds and Prandtl numbers. The fissures are then randomly displaced in the wall-normal direction following a minimal set of postulates, exchanging momentum and concentration as they move, to create instantaneous profiles of streamwise velocity and passive scalar concentration [5, 6]. This process is repeated to generate ensembles from which statistical moments are computed. The streamwise turbulent heat flux is computed by coupling the passive scalar model with the dynamical model.

RESULTS AND DISCUSSION

Figure 2 compares the statistical moments of the streamwise velocity and passive scalar computed from the model generated ensembles with the corresponding statistics extracted from channel flow DNS data [7, 8]. As evidenced by figure 2, the model is able to robustly predict the statistical moments of the streamwise velocity and passive scalar. Moreover, the streamwise turbulent heat flux is successfully reproduced by relating the motion of the thermal (passive scalar) fissures (TFs) to that of the vortical fissures (VFs), as determined by the model. The discrepancies in the near-wall region are attributable to the model restriction near the boundaries as described by [5]. Specifically, the fissures near the boundaries (wall and channel centerline) are fixed and not allowed to move (unlike other fissures). While allowing the near-boundary fissures to move improves the mean profile, it negatively impacts the higher statistical moments. In the absence of any analytical or physical justification, we did not attempt to tune the model parameters to produce more accurate results near the wall.

*Corresponding author. E-mail: chris.white@unh.edu

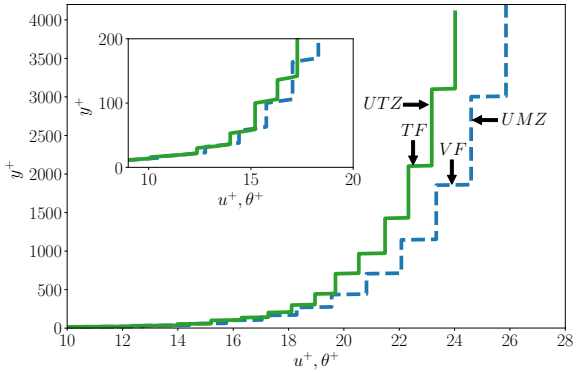

Figure 1: Discrete master temperature (solid lines) and velocity (dashed lines) profiles constructed from the model: uniform momentum zone (UMZ), uniform temperature zone (UTZ), vortical fissure (VF), thermal fissure (TF) at a friction Reynolds number $\delta^+ = 4088$ and Pr=1. Here the passive scalar is temperature. In the model, the VFs and TFs are randomly displaced to generate independent instantaneous profiles.

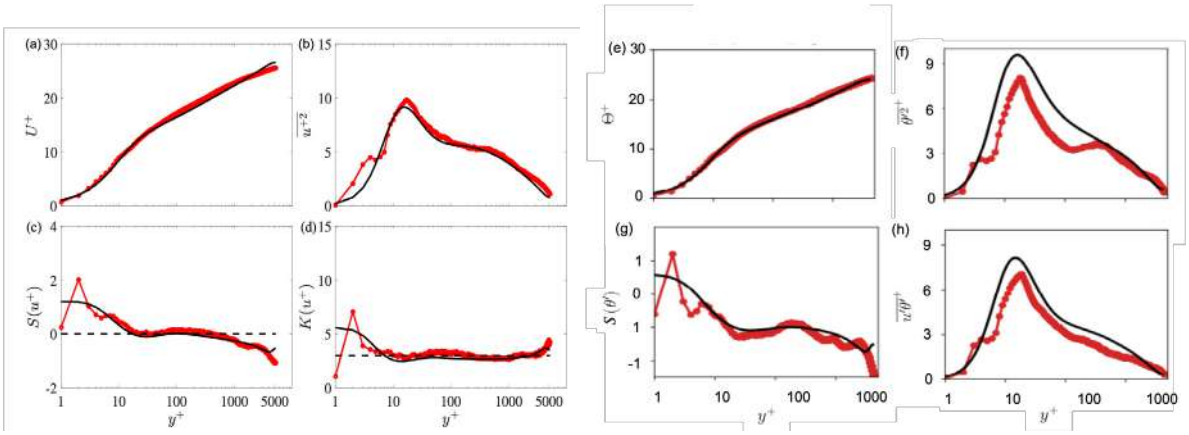

Figure 2: Statistical moments of the streamwise velocity and passive scalar (i.e. temperature) computed from the model. The profiles are (a) mean U^+, (b) variance $\overline{u'^{+2}}$, (c) skewness $S(u'^+)$ and kurtosis $K(u'^+)$ of the streamwise velocity u, (e) mean Θ^+, (f) variance $\overline{\theta'^{+2}}$, (g) skewness $S(\theta'^+)$ and (h) streamwise turbulent heat flux $\overline{u'\theta'}$ of temperature θ. The solid lines in (a – d) and (e – h) are computed from the DNS of [7] and [8], respectively.

CONCLUSIONS

A simple model to predict the statistical moments of the streamwise velocity and passive scalar in a turbulent boundary layer is developed. The formulation of the model begins with the analytical construction of master profiles that represent the most probable arrangement of the regions of large gradient (i.e. fissures). These master profiles are used in conjunction with a minimal set of postulated elements to randomly displace the fissures to generate realizations of the instantaneous streamwise velocity and passive scalar field, from which various statistics are computed. The model results are shown to agree remarkably well compared to statistics computed from DNS.

References

[1] Meinhart, C. D., Adrian, R. J. On the existence of uniform momentum zones in a turbulent boundary layer. *Phys. Fluids* **7**: 694-696, 1995.
[2] Eisma, H.E., Pollutant dispersion in wall-bounded turbulent flows: an experimental assessment. *PhD Thesis*, Delft University Technology, 2017.
[3] Wei, T., Fife, P., Klewicki, J., McMurtry, P. Properties of the mean momentum balance in turbulent boundary layer, pipe and channel flows. *J. Fluid Mech.* **522**: 303-327, 2005.
[4] Zhou, A., Pirozzoli, S., Klewicki, J., Mean equation based scaling analysis of fully-developed turbulent channel flow with uniform heat generation. *Int. J. Heat Mass Transf.* **15**: 50-61, 2017.
[5] Cuevas Bautista, J.C., Ebadi, A., White, C.M., Chini, G.P., Klewicki, J.C. A uniform momentum zone–vortical fissure model of the turbulent boundary layer*J. Fluid Mech.* **858**: 609-633, 2019.
[6] Ebadi, A., Cuevas Bautista, J.C., White, C.M., Chini, G.P., Klewicki, J.C. A heat transfer model of fully-developed turbulent channel flow *J. Fluid Mech.* **884**: R7, 2020.
[7] Lee, M., Moser, R.D. Direct numerical simulation of turbulent channel flow up to $Re_\tau \approx 5200$. *J. Fluid Mech.* **774**: 394-415, 2015.
[8] Pirozzoli, S., Bernardini, M., Orlandi, P. Passive scalars in turbulent channel flow at high Reynolds number. *J. Fluid Mech.* **788**: 614-639, 2016.

ASYMPTOTIC THEORY OF THIN TURBULENT SHEAR LAYERS

V.B. Zametaev*[1,2,3], A.R. Gorbushin[1,3] and I.I. Lipatov [1,3]
[1] Central Aerohydrodynamic Institute (TsAGI), 140180, Zhukovsky, Moscow Reg
[2] FRC "Computer Science and Control" of the RAS, 119333, 44 bldg. 2 Vavilov st., Moscow
[3] Moscow Institute of Physics and Technology (MIPT), 141701, Dolgoprudny, Mosc. reg., Russia

Summary Turbulent 2D thin shear layers of viscous incompressible fluid, namely boundary layer, mixing layer, free jet and channel flow were studied. To analyse the problem, an asymptotic method of multiple scales that is applied to the Navier-Stokes equations was used. Decomposition of the velocity as a sum of stationary and perturbation terms was introduced, which was applied instead of traditional summation of the mean-time value and fluctuation. A stationary flow inside the turbulent layer was identified using classical hypotheses. The basic flow was an entrainment of fluid from the external/core flow, which supplied the kinetic energy to the zone where turbulence was produced. The solution is applicable at the layer thickness scale and explains the 'turbulent viscosity' concept. The log-scale and Kolmogorov-scale regions do not influence this stationary solution in the main approximation.

MAIN ASSUMPTIONS

A stationary two-dimensional flow of a viscous incompressible fluid past a flat plate/in mixing layer/in jet/in channel of length L is considered; see Fig. 1. The characteristic time, size, and velocity of the incoming flow are equal to L/V_∞, L, V_∞, respectively. The pressure is introduced by the formula $\hat{p} = p_\infty + \rho V_\infty^2 p$, where ρ is the fluid density. All hydrodynamic functions, lengths and time are nondimensionalized via the traditional approach by using the specified flow parameters. The Reynolds number is introduced as $\mathrm{Re} = \rho V_\infty L/\mu$, which has a large value in this asymptotic study. In contrast to the external flow, the shear layer is assumed to be turbulent, considering the fluctuations of pressure and velocities relative to the sought-after basic profile of the streamwise flow velocity $u_0(x, y_1)$. The small dimensionless thickness of the turbulent shear layer has an order of magnitude of δ.

In this study, it is assumed that the amplitude of the perturbations is small in the main body of the shear layer; however, the squares of fluctuations (mean values of which are known as Reynolds stresses) should affect the basic flow. Estimates also must consider that, according to experiments by Schubauer & Klebanoff (1951) and Klebanoff (1955) and theory by Kolmogorov (1941), the main kinetic energy of fluctuations in the turbulent layer is contained in fast inviscid vortices whose characteristic dimensions on all axes are of the same order of magnitude and are comparable to the thickness of the layer δ; see Fig. 1. Such vortices belong to the 'inertial' range.

$$\left.\frac{\partial u'v'}{\partial y'} \sim u_0 \frac{\partial u_0}{\partial x};\quad x' \sim y' \sim z' \sim \delta\right\} \to v' \sim u' \sim w' \sim \delta^{1/2},\quad \delta \to 0$$

Based on the listed facts and assumptions, the asymptotic expansions of the solution in the main turbulent part of the shear layer should be sought at $\delta \to 0$, $\mathrm{Re} \to \infty$ in the form

$$u = u_0(x, y_1) + \delta^{1/2} u_1(x_1, y_1, z_1, t_1, x) + \delta u_2 + \ldots,\quad v = \delta^{1/2} v_1(x_1, y_1, z_1, t_1, x) + \delta v_2 + \ldots,\quad x - \text{slow variable}$$
$$w = \delta^{1/2} w_1(x_1, y_1, z_1, t_1, x) + \delta w_2 + \ldots,\ p = \delta^{1/2} p_1(x_1, y_1, z_1, t_1, x) + \delta p_2 + \ldots,\quad x_1 = \frac{x}{\delta}, y_1 = \frac{y}{\delta}, z_1 = \frac{z}{\delta}, t_1 = \frac{t}{\delta} - \text{fast variables} \qquad (1)$$

TECHNIQUES AND RESULTS

The analysis of the first and second approximations in (1) for the boundary layer/mixing layer [1]/free jet [2]/channel flow[3] is similar. However, unlike any laminar or averaged equations of motion for the main streamwise and vertical velocities in the shear layers, the main system in this analysis is the system of linear inviscid equations for perturbations of the vertical velocity v_1, pressure p_1 and main streamwise velocity u_0.

$$\nabla^2 p_1 + 2\frac{\partial u_0}{\partial y_1} \cdot \frac{\partial v_1}{\partial x_1} = 0,\quad \frac{\partial v_1}{\partial t_1} + u_0 \frac{\partial v_1}{\partial x_1} + \frac{\partial p_1}{\partial y_1} = 0 + O\left(\frac{1}{\mathrm{Re} \cdot \delta}\right) \qquad (2)$$

Fast perturbations dominate the stationary terms; however, a system of two equations (2) is not closed, thereby suggesting a solvability condition in next approximation. Furthermore, due to the linearity of the formulated problem, the solution for first-order perturbations, in the absence of a specified transverse flow, can be decomposed as a sum of slow two-dimensional stationary terms and fast three-dimensional non-stationary fluctuations:

laminar sublayer (on the Kolmogorov scale). This paper studies only the specified stationary velocities since it is possible to separate stationary and non-stationary problems in the first and second approximations. Due to linearity, the turbulence production zone and the Kolmogorov dissipation zone do not influence on the stationary solution in the main approximation.

It is possible to formulate the condition for the absence of secular terms (solvability condition) in the vertical velocity v_2, which results in a system of differential viscous equations for $v_{10}(x, y_1)$, $u_0(x, y_1)$, that depends on the vertical coordinate y_1:

$$\frac{1}{\mathrm{Re}\cdot\delta^{3/2}}\cdot v_{10}''' - v_{10}v_{10}'' + (v_{10}')^2 = 0, \qquad \frac{1}{\mathrm{Re}\cdot\delta^{3/2}}\cdot u_0'' - v_{10}\cdot u_0' + v_{10}'\cdot u_0 = 0 \tag{4}$$

System (4) admits the analytical solution for a mixing layer (see the comparison of this theory with the experiment, Fig.2), a 2D jet (Fig.3) and a turbulent boundary layer (Fig.4). The exact solution, which satisfies the impermeability condition on the wall, is the self-induced viscous stationary distributed entrainment of fluid into the turbulent boundary layer from the external flow. The parameter $Z_i = \mathrm{Re}\cdot\delta^{3/2}$ is excluded from equation (4.2) and $u_0(x, y_1)$ does not depend on Re: $v_{10} = -\dfrac{(-V_e(x))}{\mathrm{Re}\cdot\delta^{3/2}}\cdot(1-\exp(-Y))$, $u_0 = e^{-Y}\int_0^Y \exp(\eta - e^{-\eta})d\eta$, $Y = (-V_e)y_1$ $V_e(x) < 0$.

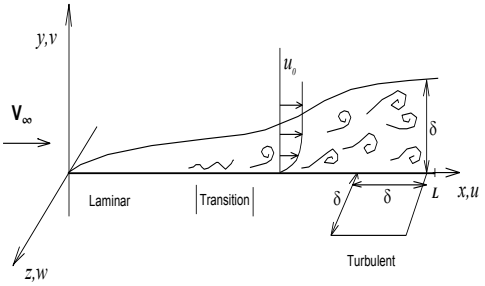

Figure 1. Sketch of TBL flow

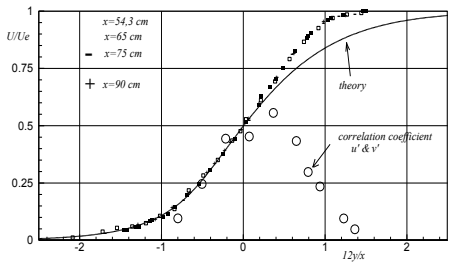

Figure 2. Mixing layer: Lipmann & Laufer 1947

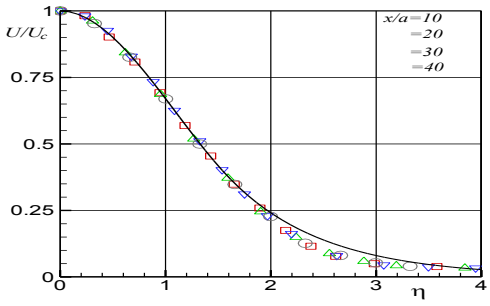

Figure 3. Jet: Miller & Comings 1957

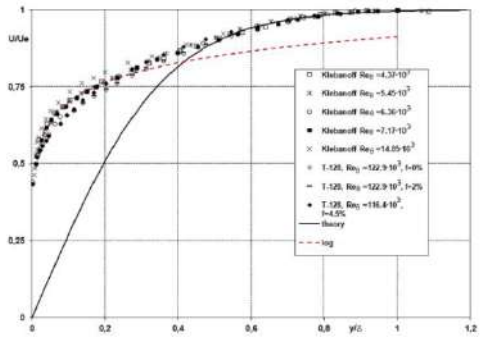

Figure 4. TBL: Klebanoff & Diehl 1952

CONCLUSIONS

Shear turbulent layers have a property of stationary entrainment, which defines the streamwise flow. The stationary flow (called secondary) is viscous throughout the entire thickness of the turbulent layer, which suggests a large-scale viscosity and substantiates the well-known physical concept of "turbulent viscosity". The self-induced entrainment of fluid into thin turbulent layer can be regarded as the mechanism of kinetic energy supply to the zone of production of turbulence, regardless of the type of production. The identified stationary solution does not depend on the turbulence production scale and the Kolmogorov scale in the main approximation.

ACKNOWLEDGEMENTS

This research was supported by the Russian Science Foundation (project number 20-11-20006) at MIPT. Computer support was provided by FRC CSC of the RAS and by TsAGI.

References

[1] Zametaev V.B., Gorbushin A.R., Lipatov I.I. Steady secondary flow in a turbulent mixing layer. *Int. J. Heat Mass T.* 132 . 655–661, 2019.
[2] Gorbushin, A.R., Zametaev, V.B., Lipatov, I.I. Steady secondary flow in a plane turbulent free jet. *Fluid Dyn.* V.54, N2,244–256, 2019.
[3] Zametaev, V.B. Modeling of the Turbulent Poiseuille–Couette Flow in a Flat Channel by Asymptotic Methods // *Computational Mathematics and Mathematical Physics*, 2020, Vol. 60, No. 9, pp. 1528–1538.
[4] Gorbushin, A.R. & Zametaev, V.B. Asymptotic Analysis of Viscous Fluctuations in TBL. *Fluid Dyn.*, V.53, No. 1, pp. 9–20, 2018.

TRANSIENT MODEL FOR EROSION MIXING PROCESS OF STRATIFIED LAYER CAUSED BY TURBULENT IMPINGING JET

Wooyoung Lee, Simon Song *[1], and Youngsoo Na, Jongtae Kim [2]
Department of Mechanical Convergence Engineering, Hanyang University, Seoul, Korea
Korea Atomic Energy Research Institute, Daejeon, Korea.

Summary The distribution and mixing of hydrogen gas in a containment building of a nuclear power plant in a severe accident can be characterized as the erosion mixing process of a stratified layer impinged by a turbulent jet. To predict the risk of a hydrogen explosion due to the erosion mixing, it is necessary to develop a transient model on the transient erosion mixing process over a long period of time. We experimentally and theoretically investigated the long-term erosion mixing process by the interaction between a stratified layer and a turbulent impinging jet. As a result, we proposed a transient model for predicting the interface displacement of the stratified layer and the mean axial velocity and half width of the jet. We found that the prediction results are in good agreement with experimental data when considering the density and pressure gradient of the stratified layer and the jet.

INTRODUCTION

An erosion mixing phenomenon of a stratified hydrogen layer by a vertically impinging jet is known to affect a safety of a containment building of a nuclear power plant under a severe accident. The hydrogen gas mixed with an air or a steam may cause combustion and explosion due to various ignition sources. To predict and prevent such a disaster, it is necessary to quantitatively analyze a detailed erosion mixing process over a long period of time because the mixing process determines thermo-hydraulic behaviours of the stratified hydrogen layer such as migration, mixing, heat transfer, and mass transfer. The transient behaviour of the interface of the stratified layer and the ambient gas is one of the important parameters for the quantitative evaluation of erosion mixing process. Nevertheless, most previous models on the erosion mixing have been developed to be valid for their initial state. We theoretically and experimentally investigated the erosion mixing process by interaction between a stratified layer and a turbulent impinging jet at a transient state. As a result, a theoretical model was developed for an interface displacement. The model prediction was validated against our own data in addition to other experimental data[1].

THEORETICAL BACKGROUND AND EXPERIMENTAL APPARATUS

We developed the theoretical model by applying the mass conservation law to the entrainment of the stratified layer into the impinging jet over a long elapsed time. According to the model, the interface displacement is affected by the elapsed time, ratio of the jet width to vessel size, and initial interfacial Froude number.

To validate the model, we performed experiments using a test facility for spray, aerosol, recombiner, and combustion (SPARC) built in Korea Atomic Energy Research Institute. The SPARC facility consisted of gas sampling pipes, a jet tube, and a helium injection tube contained in a cylindrical pressure vessel of 3.400 m in diameter, 9.532 m in height and 80 m^3 in volume. The erosion mixing was implemented by a vertical turbulent air jet onto a stratified helium layer formed at the upper part of the vessel. The helium concentration distribution in the vessel was measured at 13 vertical points along the vessel centreline by thermal conductivity analysis. The Reynolds number of experiments were 19,300 and 29,400 based on jet tube diameter, jet velocity at the tube exit.

RESULTS AND DISCUSSION

The interface displacement had a non-linear tendency with elapsed time where it increases rapidly at the initial state and then its growth rate decreases as time increases. In order to estimate its validity, the model proposed in this study was applied to the experimental data obtained under different conditions.[2] The prediction of the transient interface displacement by the theoretical model was in excellent agreement with the experimental data, demonstrating that the model would be useful for predicting the transient behaviors of an interface displacement of a stratified layer by an erosion mixing under various conditions as shown in Fig. 1a.
In addition, the mean axial velocity and width of the jet are modelled by considering a non-trivial density and pressure gradient in the stratified layer and jet unlike previous models. As a result, we found the prediction of current transient model are in good agreement with experimental data as shown in Fig. 1b.

*Corresponding author. E-mail: simonsong@hanyang.ac.kr

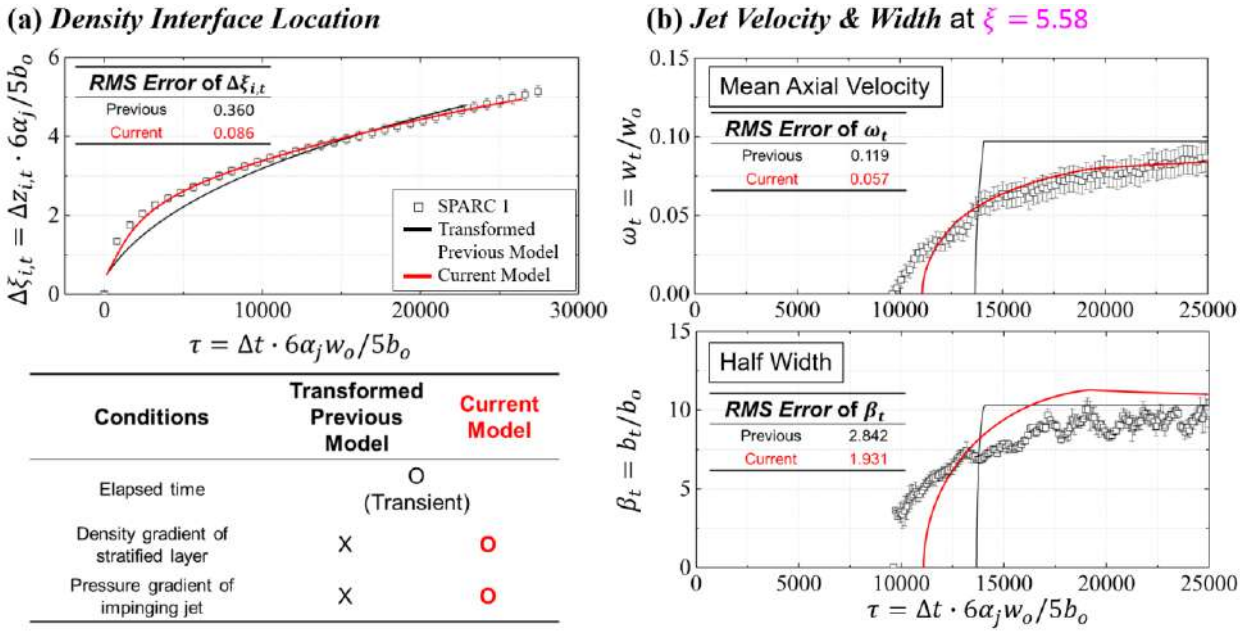

Conditions	Transformed Previous Model	Current Model
Elapsed time	O (Transient)	
Density gradient of stratified layer	X	O
Pressure gradient of impinging jet	X	O

Figure 1. Comparison of model prediction and experimental data.

CONCLUSIONS

We studied erosion mixing behaviours of a stratified layer impinged by a turbulent jet over a long period of time to develop a transient model for the erosion mixing. A novel theoretical model has been developed to be valid for a long period of time and its prediction on the interface displacement and the mean axial velocity and width of jet is compared with experimental data obtained in SPARC and other facilities reported in literature. We found that the prediction was in good agreement with the experimental data when considering both density and pressure gradients in the stratified layer.

References

[1] Kapulla R., Mignot G., Kapulla D.P., Proceeding of NURETH15, Pisa, Italy, May 12-17, 2013.
[2] Lee W., Song S., Na Y. S., and Kim J., International Journal of Heat and Mass Transfer, 141, 1159-1167, 2019.

MODAL ANALYSIS IN CURVILINEAR COORDINATES

Aadhy Parthasarathy[1], Siddhi Suri[1], and Theresa Saxton-Fox *[1]
[1] Department of Aerospace Engineering, University of Illinois at Urbana-Champaign, Illinois, USA

Summary Modal analysis techniques have proven useful in understanding and modeling turbulent phenomena [1]. However, these techniques are more efficient in parallel flows where Fourier transforms can be taken along homogeneous directions. We suggest that quasi-1D methods can be applied to mildly non-canonical flows by using a curvilinear coordinate system. For a given base flow, we identify a curvilinear coordinate system that allows the Fourier-transformed equations of motion to be simplified into a quasi-1D system that can be efficiently analyzed.

When performing reduced-order modeling or stability analysis in parallel flows, significant order reduction is possible using Fourier-transforms along the homogeneous directions [4, 1]. But when one transitions to a non-parallel flow, these order reductions are lost, and one instead must do a global analysis [2], requiring more intensive computation. Particularly for weakly non-parallel flows, the exact solution of modes using 1D analysis techniques may be possible if one changes the coordinate system within which the equations are written. We aim to formulate local stability and resolvent analyses using curvilinear forms of the Navier-Stokes equations by iteratively solving for an appropriate coordinate system given a particular base flow. We seek a coordinate system within which a Fourier transform can be usefully performed.

We define the following transformation between Cartesian coordinates (x^i) and orthogonal curvilinear coordinates (Z^i) such that,

$$Z^i = Z^i(x^1, x^2, x^3), \tag{1}$$
$$x^i = x^i(Z^1, Z^2, Z^3). \tag{2}$$

In the curvilinear coordinate system, we write the Navier-Stokes equations as,

$$\begin{gathered}\frac{\partial U_k}{\partial t} + U^h \frac{\partial U_k}{\partial Z^h} + U_j \Gamma^j_{hk} U^h = -\frac{1}{\rho}\frac{\partial P}{\partial Z^k} + \nu\left[\nabla^2 U_k - 2g^{ij}\Gamma^h_{jk}\frac{\partial U_h}{\partial Z^i} + U_h \frac{\partial}{\partial Z^k}\left(\frac{1}{\sqrt{g}}\frac{\partial}{\partial Z^i}(\sqrt{g}g^{ih})\right)\right], \\ g^{kk}\left(\frac{\partial U_k}{\partial Z^k} - U_h \Gamma^h_{kk}\right) = 0\end{gathered} \tag{3}$$

where U_i and U^i are the covariant and contravariant components of velocity respectively, ρ is fluid density, P is the scalar pressure, ν is fluid kinematic viscosity, g^{ij} is the metric tensor, and Γ^i_{jk} are the Christoffel symbols of the second kind [3]. The metric tensor and Christoffel symbols are additional variables introduced to keep track of the changing length and direction of the basis vectors at every point in a curvilinear coordinate system, whereas the basis remains constant everywhere in Cartesian coordinates.

At this point, a choice of the specific curvilinear coordinate system has not been made. The coordinate transformation should be chosen such that, when the governing equations are cast in a form appropriate to perform stability analysis or resolvent analysis, it will allow taking a Fourier transform along at least one of the non-parallel flow directions. To identify the suitable constraints on such a coordinate system, we decompose the flow as $U_i = \bar{U}_i + u_i$ and expand the curvilinear Navier-Stokes equations in these terms. $\bar{U}_i$ is the base flow for stability analysis or mean flow for resolvent analysis, and u_i is the fluctuation about the base flow. In equation 4, we show the left hand side of the resulting equation in the Z^1 direction for a two-dimensional flow, without including the terms containing only the base flow for the sake of compactness. Terms that contain only the base flow can be directly computed.

$$\begin{aligned}&\frac{\partial u_1}{\partial t} + \left[\bar{U}_1\frac{\partial u_1}{\partial Z^1} + u_1\frac{\partial \bar{U}_1}{\partial Z^1} + u_1\frac{\partial u_1}{\partial Z^1}\right]\sqrt{\frac{g^{11}}{g_{11}}} + \left[\bar{U}_2\frac{\partial u_1}{\partial Z^2} + u_2\frac{\partial \bar{U}_1}{\partial Z^2} + u_2\frac{\partial u_1}{\partial Z^2}\right]\sqrt{\frac{g^{22}}{g_{22}}} \\ &- \left[{u_1}^2 + 2\bar{U}_2 u_1\right]\sqrt{\frac{g^{11}}{g_{11}}}\left(\frac{1}{h_1}\frac{\partial h_1}{\partial Z^1}\right) - \left[{u_2}^2 + 2\bar{U}_2 u_2\right]\sqrt{\frac{g^{22}}{g_{22}}}\left(\frac{1}{h_2}\frac{\partial h_2}{\partial Z^1}\right) \\ &- \left[\bar{U}_1 u_2 + u_1\bar{U}_2 + u_1 u_2\right]\left(\sqrt{\frac{g^{11}}{g_{11}}}\left(-\frac{h_1}{{h_2}^2}\frac{\partial h_1}{\partial Z^2}\right) + \sqrt{\frac{g^{22}}{g_{22}}}\left(\frac{h_1}{h_2}\frac{\partial h_1}{\partial Z^2}\right)\right)\end{aligned} \tag{4}$$

To efficiently represent the fluctuating velocity field using a Fourier transform in the Z^1 direction, $\bar{U}_1$ and $\bar{U}_2$ must not be functions of Z^1. For example, consider the Fourier transform of a term in equation 4,

*Corresponding author. Email: tsaxtonf@illinois.edu

$$\int_{-\infty}^{\infty} \bar{U}_1 \frac{\partial u_1}{\partial Z^1} \cdot e^{-ik_1 Z^1} dZ^1 = \begin{cases} \bar{U}_1(-ik_1)\hat{u}_1, & \text{if } \bar{U}_1 \text{ is constant in } Z^1, \\ \text{does not simplify}, & \text{if } \bar{U}_1 \text{ is a function of } Z^1, \end{cases} \tag{5}$$

where $\hat{u}_1 = \hat{u}_1(k_1, Z^2, Z^2)$ is the Fourier transform of u_1 in the Z^1 direction. When $\bar{U}_1$ is not a function of Z^1, the expression on the left hand side of equation 5 simplifies to an algebraic expression.

To identify the appropriate coordinate system $(Z^1, Z^2) = (T, B)$ in which $\bar{U}_T$ and $\bar{U}_N$ are constant along T, we use an iterative scheme. Given a simple, non-parallel base flow initially defined in (x, y) such that $\bar{U} = [\bar{U}_x \;\; \bar{U}_y]'$ (schematically illustrated in Fig.1), we approximate the appropriate coordinate system (T, N) by defining curves along which $\bar{U}_x$, $\bar{U}_y$ are constant. With the approximate (T, N), we compute the components of our velocity field in the new coordinate directions, $\bar{U}_T, \bar{U}_N$. We iterate between defining the coordinate system (T, N) based on the components of the velocity field $\bar{U}_T, \bar{U}_N$ and defining the components of the velocity field based upon the coordinate system (T, N) until the process converges to a consistent coordinate system.

We will test our algorithm by re-deriving Cartesian and cylindrical coordinate systems for input parallel and axisymmetric base flows. We will report on the coordinate system found, and / or on the constraints that prevent the identification of such coordinate systems. We will additionally look for and report any assumptions that could be used to approximately use such coordinate systems, enabling approximate use of local analysis for non-parallel flows.

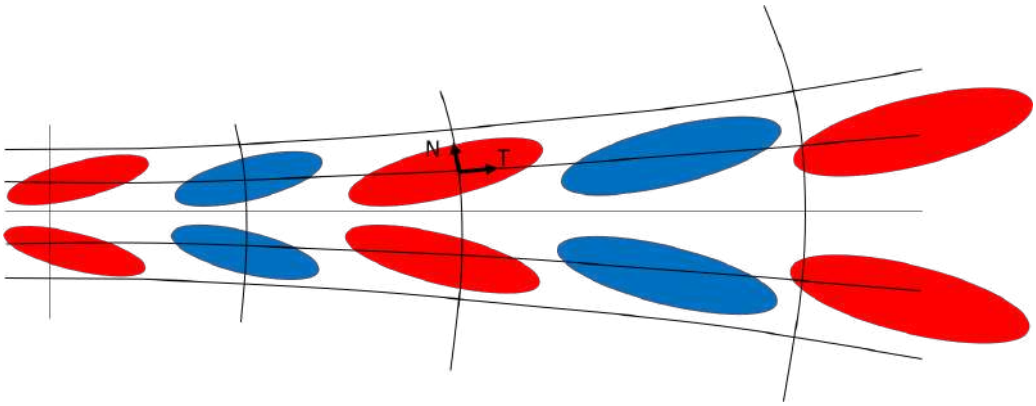

Figure 1: Illustration of modes following a curvilinear coordinate system.

References

[1] McKeon, B. J. The engine behind (wall) turbulence: perspectives on scale interactions. *Journal of Fluid Mechanics*, 817, 2017.

[2] Noack, B. R. and Konig, M. and Eckelmann, H. Three-dimensional stability analysis of the periodic flow around a circular cylinder. *Physics of Fluids*, 5:1279, September 1993.

[3] Surattana Sungnul. Transformation of the Navier-Stokes equations in curvilinear coordinate systems with maple. *Global Journal of Pure and Applied Mathematics*, 12(4):3315–3325, 2016.

[4] Yang, X. and Zebib, A. . Absolute and convective instability of a cylinder wake. *Physics of Fluids*, 1:689–696, April 1989.

EFFECT OF BI-MODAL EXCITATION PHASE ON A SHARP-EDGED IMPINGING JET

Basil Abdelmegied[1], and Ahmed Naguib *[1]
[1] Department of Mechanical Engineering, Michigan State University, East Lansing, USA

Summary In this study, we investigate the effect of bi-modal acoustic forcing on the flow structure of an impinging jet using flow visualization. The forcing scheme utilizes two frequencies: the fundamental instability frequency of the jet and its subharmonic. The focus of the work is to examine whether the phase angle between the two forced modes (the intermodal phase) has a significant effect on the vortical structure of the jet. Results reveal a striking outcome, whereby over a certain phase angle range, the initial development of the shear layer vortical structure is wake-like, leading to a significant growth in the shear layer and a corresponding reduction in the potential core.

INTRODUCTION

While there is a number of investigations utilizing bi-modal, two-frequency, axisymmetric forcing to control non-impinging jets [1-4], there is very little similar work done on the impinging counterpart. The two excitation frequencies employed in studies [2-4] are those of a fundamental instability (either the jet's preferred mode [2], or the initial shear-layer's instability [3-4]) and its subharmonic. [2] demonstrated that bi-modal forcing can lead to a more significant change in the jet flow than pure-harmonic excitation. [2-4] also showed that the phase angle difference between the fundamental and the subharmonic mode can have a substantial influence on the development of the vortical structures. For example, [4] demonstrated maximum enhancement of vortex pairing due to promoting subharmonic resonance [5] by having an optimum phase difference of $\pi/2$ *at the resonance streamwise location*. On the other hand, if the resulting phase difference at resonance is 0, pairing was suppressed. Overall, in comparison to single-frequency forcing, bi-modal forcing provides a larger number of degrees of freedom to affect the flow behaviour. In addition to the forcing level and frequency used in the former case, the latter approach presents opportunities for changing the jet behaviour through the phase difference and the amplitude ratio of the two modes. These opportunities remain largely unexplored for impinging jets. We found only one reference [6], which examined simultaneous excitation of an impinging jet using fundamental and subharmonic frequencies, where the authors employed both the first and the second subharmonic modes, each simultaneously with the fundamental mode. They found the first scenario to lead to enhancement of vortex pairing, and the second to promote amalgamation of three vortices. The authors did not undertake a systematic study of the intermodal phase influence. The present investigation is undertaken to study the effect of bi-modal acoustic forcing on an impinging jet with particular focus on the response of the jet flow structure to different values of the intermodal phase angle. Specifically, the forcing is defined as follows: $p'_a(t) = P_{a,f}\sin(2\pi f_0 t) + P_{a,s}\sin(2\pi f_0 t/2 + \phi)$; where, $p'_a(t)$ is the forcing acoustic pressure, $P_{a,f}$ and $P_{a,s}$ are the acoustic disturbance amplitude of the fundamental and subharmonic modes, respectively, f_0 is the fundamental mode frequency, and ϕ is the intermodal phase difference (where $0° \leq \phi \leq 180°$). In the present work, the overall root mean square of the disturbance $p'_{a,rms}$, the amplitude ratio $P_r = P_{a,s}/P_{a,f}$, and the fundamental frequency f_0 are maintained fixed while, ϕ is varied over its full range.

DESCRIPTION OF THE EXPERIMENTS

An axisymmetric air jet emerging from a sharp-edged opening is used in the present experiment. The jet diameter is $D = 12.7\ mm$ and the average jet exit velocity is $U_j = 5\ m/s$. The corresponding Reynolds number is $Re_D = 4{,}200$. A flat impingement wall is placed at a distance $H = 2D$ downstream of the sharp edge. To characterize the jet flow structure, flow visualization is utilized. This is accomplished by carefully seeding Polyethylene Glycol particles into two narrow slits on top and bottom of the plenum, upstream of the jet exit. Hot-wire measurements are used to check that the flow through the slits does not alter the main jet flow. The particles are illuminated using a laser sheet, and instantaneous images of the flow are captured using a CCD camera. The illuminated region spans the streamwise domain stretching between $0.5D$, downstream of the jet exit, to the impingement wall (as illustrated in the top left corner of Figure 1).

The fundamental forcing frequency is determined using spectra of the streamwise velocity close to the exit of the *unforced* jet, obtained from single-hot-wire measurements at the centre of the shear layer. The spectra exhibit a peak at a Strouhal number $St_D = f_0 D/U_j = 2.54$, which is utilized for the fundamental mode forcing. The amplitude ratio P_r is set to unity, and the overall sound pressure level is kept at $120\ dB$ (which corresponds to an acoustic velocity of approximately 1% of U_j). The intermodal phase ϕ is varied between 0° and 180° in steps of 15°. The characteristics of the forcing signal are verified using microphone measurements at $x/D = 0.75$.

RESULTS AND DISCUSSION

Figures 1a and 1b depict phase-averaged flow visualization images obtained at six phases of the subharmonic forcing cycle $\theta = 0°$ to 300° in steps of 60°. Each image is obtained from an average of 200 pictures captured by phase-locking triggering of the camera to the forcing signal, where $\theta = 0°$ corresponds to the start of the subharmonic cycle.

*Corresponding author. E-mail: naguib@egr.msu.edu.

Results for two intermodal phases are shown in Figure 1: $\phi = 0°$ and $\phi = 120°$. Other cases are not considered here due to space limitation. Comparing the two cases, the immediate impression is an apparent larger cross-stream spread of the seed particles towards both the centreline and the outside of the jet when $\phi = 120°$. This observation can be seen more easily by averaging the images over all cycle phases considered, leading to the images displayed in Figures 1c and 1d. The significant lateral spread of the jet when $\phi = 120°$, compared to $\phi = 0°$, is evident. Given that only the near-wall vortical fluid is seeded upstream of the jet exit, it is reasonable to interpret these observations as a significant influence of the bimodal phase on the spread rate of the jet shear layer and the development of the potential core.

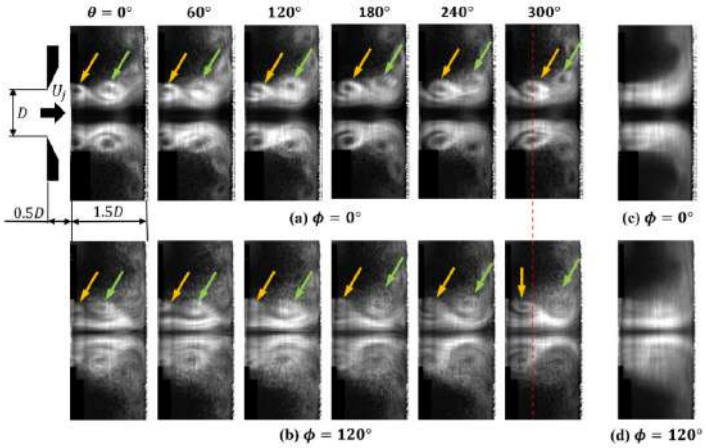

Figure 1. Comparison of the phase-averaged flow visualization images at six subharmonic-cycle phases for (a) $\phi = 0°$; (b) $\phi = 120°$. The corresponding cycle-averaged images are shown in (c) and (d) respectively.

Considering the evolution of the vortical structure in Figure 1, it takes approximately two subharmonic forcing cycles for a vortex to form and reach the impingement wall. In Figure 1, orange arrows are used to identify a single vortex ring as it evolves during the first cycle, and green arrows mark the vortex during the second cycle. Considering $\phi = 0°$ (Figure 1a), the organization, systematic evolution and coherence of the vortex ring due to forcing is evident. The vortex develops in the usual fashion for a shear layer, where the vortex consistently convects downstream from one image to the next as it grows in size. In comparison, for $\phi = 120°$, a notably different behaviour emerges, whereby during the first half of the first cycle ($\theta < 180°$), the vortex continues to roll-up (in the upper left corner of the flow) without translating significantly downstream. This behaviour is akin to vortex roll-up in the *wake* of a bluff body, in contrast to that expected in a jet's shear layer. Eventually, the vortex sheds and convects downstream. The surprising and fundamentally different initial vortex evolution is associated with other differences in the vortex characteristics. These include an apparently different vortex core size, vortex motion history (for example at $\theta = 300°$ in the first cycle, the vortex ring's streamwise position for $\phi = 120°$ lags behind that for $\phi = 0°$ by approximately $0.25D$; as may be visualized with the aid of the red broken line Figure 1), and larger vortex size at impingement (last image in the second forcing cycle).

CONCLUSIONS

Bi-modal excitation of a sharp-edged axisymmetric impinging jet at $Re_D = 4{,}200$ and jet-to-impingement-wall spacing of $2D$ revealed an intriguing effect of the intermodal phase angle on the jet vortical structure evolution. Specifically, the phase could alter the fundamental nature of the initial vortex evolution from being shear-layer to being wake like. This change is associated with differences in subsequent evolution and characteristics of the vortices, and the development of the jet shear-layer and potential core. Hot-wire and particle image velocimetery measurements will be carried out in future work to quantitatively characterize the observed change in the impinging jet behaviour.

ACKNOWLEDGEMENT

This work is funded by National Science Foundation (grant number CBET-1603720). Any opinions, findings, and conclusions or recommendations expressed are those of the authors and do not necessarily reflect the views of NSF.

References

[1] Arbey H., Ffowcs Williams J.E. Active Cancellation of Pure Tones in an Excited Jet. *J. Fluid Mech.* **149**: 445-454, 1984.
[2] Raman G., Rice E.J. Axisymmetric Jet Forced by Fundamental and Subharmonic Tones. *AIAA J.* **29**: 1114-1122, 1991.
[3] Paschereit C.O., Wygnanski I., Fiedler H.E. Experimental Investigation of Subharmonic Resonance in an Axisymmetric Jet. *J. Fluid Mech.* **283**: 365-407, 1995.
[4] Husain H., Hussain F. Experiments on Subharmonic Resonance in a Shear Layer. *J. Fluid Mech.* **304**: 343-372, 1995.
[5] Kelly R.E. On the Stability of an Inviscid Shear Layer which is Periodic in Space and Time. *J. Fluid Mech.* **27(4)**: 657-689, 1967.
[6] Vejrazka J., Tihon J., Marty Ph., Sobolík V. Effect of an External Excitation on the Flow Structure in a Circular Impinging Jet. *Phys. Fluids* **17**: 105102, 2005.

IMPACT OF COHERENT FLOW STRUCTURES ON TURBULENT TRANSPORT AND MIXING BEHIND A GENERIC GT SWIRLER. PIV/PLIF MEASUREMENTS

Vladimir Dulin*[1,2], Dmitriy Sharaborin[1,2], Aleskei Lobasov[1,2], and Dmitriy Markovich[1,2]
[1] Kutateladze Institute of Thermophysics, Novosibirsk, Russia
[2] Novosibirsk State University, Novosibirsk, Russia

Summary The present paper reports on the investigation of turbulent mixing for a model gas-turbine swirl burner (based on a design by TURBOMECA) under non-reacting flow conditions. Two different regimes of the model fuel (air with acetone) injection are compared. Namely, injection between vanes of the radial swirler to organize lean well-premixed combustion in a primary zone and supply of the model fuel from the swirler's ceneterbody as a central jet to organize a pilot flame. Stereoscopic PIV method, combined with tracer PLIF, is used to measure the velocity and concentration fields. A quantitative analysis of the impact of coherent flow structures on turbulent transport and mixing of the fuel is performed on the basis of POD of the PIV data and phase-averaging of the PLIF snapshots. Such data are important for development of efficient methods to supress unsteady combustion modes.

INTRODUCTION

Flame stabilization in combustion chambers of gas turbines is usually implemented by organizing flow swirl. A swirler in front of the combustion chamber produces rotating flow with a central recirculation zone, which ensures efficient flame ignition and combustion stability for a wide range of fuel and oxidizer flowrates, as well as a compact size of the combustion zone (Gupta et al. 1984, Weber and Dugue 1992). Meanwhile, turbulent flows with high swirl are usually featured by unsteady intensive velocity and pressure fluctuations, produced by large-scale vortex structures, including precessing vortex core. Since detailed measurements in full-scale combustion chambers of gas turbines are difficult and very expensive, the research on the fundamental aspects of the implementation of new technologies is carried out for laboratory-scale burners that adequately simulate important features of the operation of real devices with the possibility for detailed measurements of the physical and chemical processes. Since the use of contact measurement methods can lead to local perturbations of the flow and also significantly affect the conditions for the entire flame stabilization (Stricker 2002, Meier et al. 2004), optical methods have become widespread for studies of combustion processes.

In recent years, a number of studies have been published on the measurement of the instantaneous velocity fields in combustion chambers of gas turbines using particle image velocimetry (PIV), in order to study the effect of unsteady flow dynamics on flame stability and thermo-acoustic pulsations. To study the interaction of the velocity field with the flame front, the PIV method is applied simultaneously with planar laser-induced fluorescence (PLIF) (Stohr et al. 2009, Boxx et al. 2010). Such combination allows one to obtain the spatial distribution of velocity in a selected flow cross-section with a slice of the reaction zone. The analysis is often focused on the characteristics of coherent flow structures, which produce intensive velocity and pressure fluctuations, and on their relation with unsteady combustion modes. Proper orthogonal decomposition (POD) is used to extract the coherent structures and obtain phase-averaged shape of the reaction zone (e.g., Dulin et al. 2019). This information is important for development of efficient methods to control/alter unsteady mixing and combustion in swirl burners (Terhaar et al. 2014). However, non-intrusive experiments and quantitative analysis of the impact of the large-scale coherent structures on the fuel transport and mixing in combustion chambers are still scarce in the literature. The present study reports on such measurements for a model gas-turbine combustor by using a combined application of stereoscopic PIV and acetone PLIF.

EXPERIMENTAL SETUP

The experiments were performed for an optically accessible model gas-turbine swirl combustor at atmospheric pressure. The combustor consisted of a cylindrical plenum chamber, generic swirl nozzle (see Janus et al. 2007) and open combustion chamber with square observation windows (100x100 mm with the thickness of 4 mm) made of fused silica. 3D sketch of the swirl combustor and equipment used for the PIV/PLIF measurements are shown in Figure 1(a). The inset shows the design of the nozzle, which included a radial vane swirler and central pilot jet. The outlet diameter of the swirler nozzle was 37 mm. The swirl rate was approximately 0.7. The Reynolds number was Re = 30 000.

The model fuel could be supplied through the central jet or through holes between the vanes of the swirler. It was seeded by acetone vapour by bubbling the air flow through a heated tank with liquid acetone. The main air flow, supplied through the radial swirler, was seeded by TiO2 particles (with an average size of 0.5 um) by using a mechanical mixer. The flowrates were precisely controlled by mass flow meters (Bronkhorst High-Tech). Ratios of the volumetric flow rates of the main air and model fuel were chosen to simulate equivalence ratio 0.7 for the premixed mode. In the case of the pilot jet, the entire flow of the model fuel was injected through the central jet.

The PLIF system included a tunable pulsed dye laser (Sirah Precision Scan), pumped by a pulsed Nd:YAG laser (QuantaRay), was used to excite acetone fluorescence at approximately 283 nm (average energy of the pulses was 12 mJ).

*Corresponding author. E-mail: vmd@itp.nsc.ru.

Selection of the wavelength was conditioned by OH fluorescence experiments made at the same experimental setup. The laser beam was converted to a laser sheet by using a collimating optics and illuminated central plane of the flow. Intensity of the acetone fluorescence was captured by sCMOS camera (LaVision, 5 Mpix, 16 bit), connected to a UV-sensitive image intensifier (LaVision IRO). The image intensifier was equipped with a UV-lens and set of optical filters (with approximately 90% transmittance in the range 415–455 nm). The exposure time for each PLIF image was 200 ns. A set of images post-processing algorithms was used for subtraction of dark current and background intensity, correction for the laser-sheet intensity and spatial sensitivity of the sensor. To account for the non-uniformity of the laser fluence across the laser sheet and shot-to-shot variation of the pulses' energy, part (about 5%) of the laser beam was reflected by a fused silica plate into a calibration cuvette with a Rhodamine 6G solution. The spatial distribution of the fluorescence inside the cuvette was recorded by a CCD camera (ImperX Bobcat IGV-B4820, 16 Mpix, 12 bit).

The used stereoscopic PIV system included a pair of CCD cameras (ImperX Bobcat IGV-B2020, 4 Mpix, 8 bit) and double-head pulsed Nd:YAG laser (Quantel EverGreen 200, 6 ns pulses with 200 mJ at 532 nm). The cameras were equipped with lenses (Sigma 105 mm DG MACRO) and narrow-band optical filters, which transmitted light scattered by the tracer particles at 532 nm (± 5 nm). The laser beam was converted into a laser sheet by using a system of cylindrical and spherical lenses. Time separation between two PIV laser pulses was 20 μs. The PLIF images were captured almost in the middle of this interval. An in-house "ActualFlow" software was used to acquire and process the data.

SAMPLE RESULTS

Figure 1(b) shows the example of the instantaneous velocity and concentration snapshots. Large-scale vortex structures are highlighted by arrows. For the pilot jet mode, the flow mixing takes place in a highly unsteady manner with strong deflection of the central jet, since it flows against the central reverse flow. *The full paper will report on the Reynolds stresses and Reynolds fluxes distributions, their comparison with mean velocity and concentration gradients. The contribution of the coherent flow structures to the Reynolds stress and fluxes will be evaluated on the basis of the proper orthogonal decomposition.*

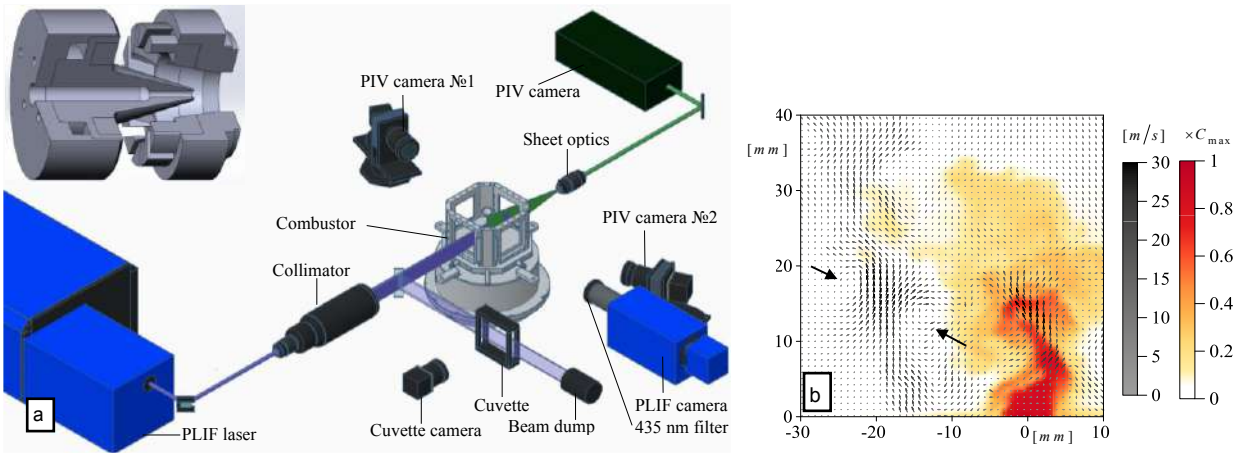

Figure 1. (a) Schematics of the PIV/PLIF setup and geometry of the swirler (inset). (b) Instantaneous velocity and (normalized) concentration fields for a piloted operation regime Large-scale vortex structure are indicated by arrows

The research is supported by Russian Science Foundation (grant № 19-79-30075).

References

[1] Gupta A., Lilley D., Syred N. Swirl Flows. Abacus Press, 1984.
[2] Weber R., Dugue J. Combustion accelerated swirling flows in high confinements. *Prog. Energy Combust. Sci.* **18**: 349–367, 1992.
[3] Meier W., Duan X.R., Weigand P. Temperatur-Messungen in turbulenten Drall-flammen: Thermoelemente im Vergleich zu Laser-Raman-Streuung. *Gaswarme Int.*, **53**: 153-158, 2004.
[4] Stricker W. Measurements of temperature in laboratory flames and practical devices. In Applied Combustion Diagnostics (Edited by K. Kohse-Hoinghaus and J. Jeffries), pp. 155-193, Taylor and Francis, 2002.
[5] Stohr M., Sadanandan R., Meier W. Experimental study of unsteady flame structures of an oscillating swirl flame in a gas turbine model combustor. *Proc. Combust. Inst.* **32**: 2925-2932, 2009.
[6] Boxx I., Stohr M., Carter C., Meier W. Temporally resolved planar measurements of transient phenomena in a partially premixed swirl flame in a gas turbine model combustor. *Comb. Flame* **157**: 1510-1525, 2010.
[7] Janus B., Dreizler A., Janicka J. Experiments on swirl stabilized non-premixed natural gas flames in a model gasturbine combustor. *Proc. Combust. Inst.* **31**: 3091-3098, 2007.
[8] Dulin V.M., Lobasov A.S., Chikishev L.M., Markovich D.M., Hanjalic K. On impact of helical structures on stabilization of swirling flames with vortex breakdown. *Flow, Turbul. Combust.* **103**: 887-911, 2019.
[9] Terhaar S., Reichel T.G., Schrödinger C., Rukes L., Paschereit C.O., Oberleithner K. Vortex breakdown types and global modes in swirling combustor flows with axial injection. *J. Propuls. Power* **31**: 219-229, 2014.

ON THE CONVERGENCE OF SPECTRAL PROPER ORTHOGONAL DECOMPOSITION

Diego C. P. Blanco *[1], Eduardo Martini[1,2], Kenzo Sasaki[1], and André V. G. Cavalieri[1]
[1] Divisão de Engenharia Aeroespacial, Instituto Tecnológico de Aeronáutica, 12228-900, São José dos Campos/SP - Brazil
[2] Département Fluides, Thermique et Combustion, Institut Pprime, CNRS, Université de Poitiers, ENSMA, 86000 Poitiers, France

Summary Spectral Proper Orthogonal Decomposition (SPOD) is a popular method of modal decomposition of flows due to its relationship with resolvent analysis, as a linear system forced with white noise should have SPOD modes identical to resolvent modes. SPOD may require long data sets due to the application of the Welch method, and a study of its convergence properties is lacking. Here, a linearized Ginzburg-Landau equation model with parameters set to mimic the dynamics of turbulent jets is considered. By computing SPOD modes of the white-noise forced equation, and comparing the result to the corresponding resolvent modes, convergence is studied. The error is shown to be related to the duration of blocks in the Welch method normalized by a convective time. Based on this finding, a method based on the convection velocity is proposed to further improve SPOD modes convergence. The proposed approach provides an order of magnitude improvement in convergence of the SPOD modes when compared to the classical method.

INTRODUCTION

Spectral Proper Orthogonal Decomposition (SPOD) method is a modal analysis, a Fourier space derivation of the homonym POD method, commonly used to identify coherent structures in data [1] as it provides an optimal orthonormal basis to represent coherent structures in space and time which contain most of the total data variance in the frequency domain, the method can be used to create a data-driven basis for the construction of reduced-order models from data. When applied to turbulent flows, the SPOD modes, and the associated eigenvalues, are related to the most energetic turbulent structures at each frequency for a chosen inner product norm.

The algorithm used to compute SPOD modes relies on the Welch method for spectral estimation. Therefore, the accuracy of computed gains λ and modes ψ is dependent on the appropriate choice of sampling parameters, number of flow snapshots/realizations N_t, time step between snapshots Δt, and estimations parameters, number of blocks N_b, snapshots per blocks N_{FFT}, overlapping between consecutive blocks O_{FFT} and windowing function. For a data set with given N_t and Δt (as in a given data set of experimental or numerical data), increasing N_b decreases N_{FFT} and *vice-versa*. Larger values of N_b penalizes frequency resolution and increases spectral leakage, whereas a larger value of N_{FFT} penalizes statistical convergence by reducing the number of averaging blocks. The proper compromise between these two types of error is often problem-dependent [2]. It is the purpose of this work to examine SPOD convergence in a model system, representative of fluid flows, and understand how SPOD errors scale as a function of sampling and estimation parameters.

METHODS

A model using the one dimensional linearized Ginzburg-Landau equation, $\frac{\partial q}{\partial t} = \left(-U\frac{\partial}{\partial x} + \mu(x) + \gamma\frac{\partial^2}{\partial x^2}\right)q + f$, where q and f are output response and input forcing respectively, is considered. When the system is forced with a spatially white forcing on a given frequency ω, the response SPOD modes, $\psi(x,\omega)$, are identical to the resolvent-analysis response modes, $\hat{u}(x,\omega)$ [2, 3]. We thus use such response mode, which is deterministic in nature, to quantify the SPOD estimation error of a the Ginzburg-Landau equation forced with a spatiotemporal-white forcing.

The parameters $\mu(x) = A(1 - x/10)$ and $\gamma = (1 - i)/10$ were set to mimic the system dynamics of jets [3]. Three distinct cases were investigated: $U = 10$ with $A = 0.6$, $U = 12$ with $A = 1$ and $U = 14$ with $A = 1.25$. Solutions were obtained using a Crank-Nicolson scheme for time marching, spatial discretization obtained using a grid spacing of $\Delta x = 0.1$ and a second-order non-centered finite difference scheme for $x \in [0, 30]$, having in total of $N_x = 300$ points. Because of the uniform grid, the inner-product matrix W is set to $I\Delta x$, where I is the identity matrix. Solutions were obtained for a time range of 500 time units and integration obtained using a time step of $\Delta t = 0.01$. A total of $N_t = 50000$ snapshots per case were generated. The N_{FFT} value is varied from 100 to 5000 in steps of 100, with $O_{FFT} = 75\%$ and number of blocks N_b set to comprise all N_t snapshots. This configuration ensures that all computations reach exactly the frequency $\omega = 2\pi$ rad/s in which SPOD and resolvent modes are compared. To reduce spectral leakage, an infinitely continuous windowing function [4] is applied on each block. The forcing is applied by setting the value at each grid point with a random complex number with uniformly distributed phase and amplitude at every timestep. To ensure that fluctuations are adequately resolved in frequency, we apply to the forcing signal a finite impulse response (FIR) low-pass filter of 30th order in time, with cut-off at 60% of the Nyquist frequency. The error ε between $\psi(x,\omega)$ and $\hat{u}(x,\omega)$ is calculated by $\varepsilon(\omega) = 1 - \frac{|\langle\psi,\hat{u}\rangle|}{||\psi||\,||\hat{u}||}$ with the operators $\langle .,. \rangle$ and $||.||$ being respectively the euclidean inner product and norm.

*Corresponding author. E-mail: diegodcpb@ita.br.

MINI SYMPOSIA

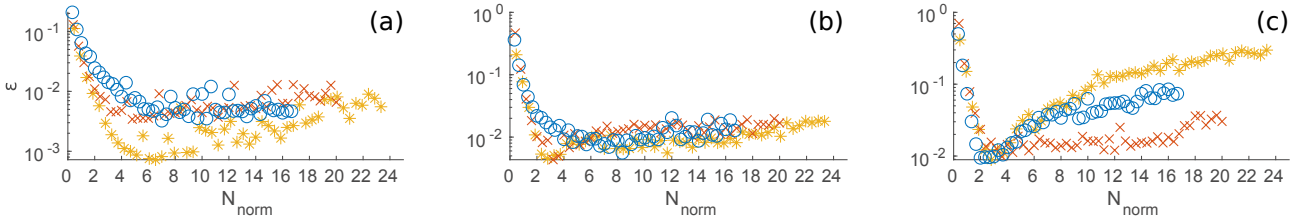

Figure 1: SPOD modes estimation error ε, at frequency $\omega = 2\pi$, plotted against the normalized window length $N_{norm} = N_{FFT}\Delta t/(x_{max}/U)$, with $x_{max} = 30$. The quantity x_{max}/U is the time taken to cross the entire domain based on the convection velocity. Legend: ($\circ$) $U = 10$, $A = 0.6$; ($\times$) $U = 12$, $A = 1$; ($*$) $U = 14$, $A = 1.25$ (a) Mode 1; (b) Mode 2; (c) Mode 3.

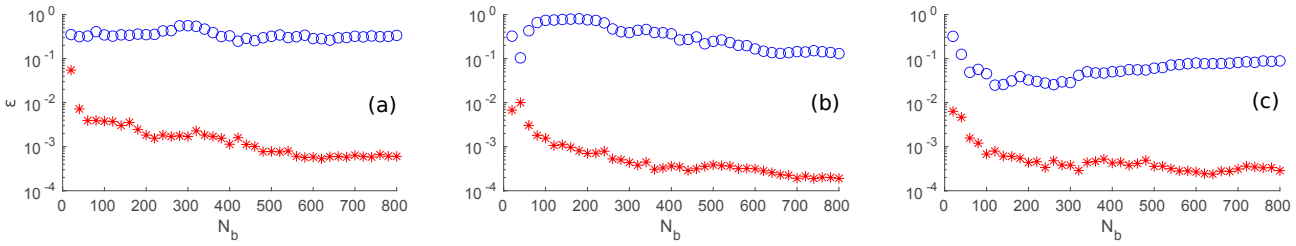

Figure 2: Estimation error ε of SPOD mode 1, at frequency $\omega = 2\pi$, plotted against number of blocks N_b using $N_{FFT} = 100$. Legend: ($\circ$) Non-shifted SPOD; ($*$) Shifted SPOD (a) $U = 10$, $A = 0.6$; (b) $U = 12$, $A = 1$; (c) $U = 14$, $A = 1.25$.

We anticipate that the error is related to the convection velocity U, which leads to a phase lag between lower and higher x with an apparent loss of coherence when the Welch method is applied with low N_{FFT} [5]. A proposed method to further reduce the total estimation error of the SPOD modes is to apply a temporal shift to the data as a function of the parameter U and position x. Considering a domain beginning at $x = 0$ and a matrix Q of realizations, with N_x rows and N_t columns, for each row i the columns are circularly shifted by $s_i = -\lfloor x_i/(U\ \Delta t)\rfloor$ positions. This maximises correlations and coherences between pairs of points, by application of the expected convection time as a delay to each spatial location. After application of the Welch method the i-th row of the resulting Fourier-transformed $\hat{Q}$ matrix, with N_x rows and N_b columns, is multiplied by $\exp(-j\omega s_i \Delta t)$ to correct the phase shift created by the temporal shift operation.

RESULTS

Using the total number of snapshots available, window size N_{FFT} and number of blocks N_b were varied and the estimation errors computed for the first 3 SPOD modes. The results shown in figure 1 indicate a relation between windows length, normalized by the domain size, and convection velocity U. For these cases, a normalized window size between 1 and 3 is a good compromise to achieve the best convergence across the first 3 SPOD modes. This provides a guideline for the selection of parameters for an accurate SPOD computation in convection-dominated flows.

In figure 2, we show that errors can be considerably reduced using applying a temporal shift, also based on the convection velocity U. Focusing on the window size considered, $N_{FFT} = 100$ (which corresponds to $N_{norm} < 0.5$ for all cases), errors obtained were significantly smaller, showing that convergence can be obtained using a fraction of the snapshots required by the classical method. The time shift method presented here is shown to provide a considerable reduction of the data needed for convergence of SPOD modes, which can be crucial for its application on datasets with short time lengths, as is typically the case in large experiments and simulations.

References

[1] SCHMIDT, O. T.; COLONIUS, T. Guide to spectral proper orthogonal decomposition. AIAA Journal, v. 58, n. 3, p. 1023–1033, 2020.

[2] TOWNE, A.; SCHMIDT, O. T.; COLONIUS, T. Spectral proper orthogonal decomposition and its relationship to dynamic mode decomposition and resolvent analysis. Journal of Fluid Mechanics, Cambridge University Press, v. 847, p. 821–867, 2018

[3] CAVALIERI, A. V. G.; JORDAN, P.; LESSHAFFT, L. Wave-packet models for jet dynamics and sound radiation. Applied Mechanics Reviews, ASME International, v. 71, n. 2, mar. 2019.

[4] MARTINI, E.; CAVALIERI, A. V. G.; JORDAN, P.; LESSHAFFT, L. Accurate Frequency Domain Identification of ODEs with Arbitrary Signals. *arXiv e-prints*, p. arXiv:1907.04787, 2020

[5] JAUNET, V.; JORDAN, P.; CAVALIERI, A. V. G. Two-point coherence of wave packets in turbulent jets. Physical Review Fluids, American Physical Society, v. 2, 024064, 2017.

DISCOVERING LOCALIZED, MULTIDIMENSIONAL, AND MULTISCALE STRUCTURE WITH DATA-DRIVEN WAVELETS

Daniel Floryan[1], Alex Guo[1], and Michael D. Graham [1]
[1] Department of Chemical and Biological Engineering, University of Wisconsin–Madison, Madison, WI 53706 USA

Summary Turbulence consists of localized structures that coexist at multiple scales. We combine the energy optimality principle of proper orthogonal decomposition with the localization and multiscale properties of wavelets to develop a method that can rationally extract the structures of interest. We will present the results of applying this method to a handful of turbulence datasets.

MOTIVATION

Turbulent fluid flows consist of localized concentrations of vortex motion that are coherent in space and time, and coexist at a wide range of scales. A great challenge is to rationally identify and analyze the constituent structures from a flow field. The most popular method to do so is proper orthogonal decomposition (POD), which builds a data-driven orthogonal basis whose elements are optimally ordered by energy content [1]. The application of POD has yielded many structural and dynamical insights into turbulence, but POD basis elements tend not to be localized in space. In fact, in statistically homogeneous directions, POD basis elements are Fourier modes. For certain flows (e.g., turbulent shear flows), spatial localization is a key feature of the constituent structures, one that we would like to capture.

DATA-DRIVEN WAVELET DECOMPOSITION

To address the shortcoming of POD, we recently developed the data-driven wavelet decomposition (DDWD) [2]. DDWD combines POD with wavelet theory. Wavelets build orthogonal bases whose elements are spatially localized and multiscale, two key features of turbulent structures. However, wavelets traditionally are not constructed from data. We built the energy optimality principle of POD into wavelets in order to build orthogonal bases whose elements are spatially localized, multiscale, and derived from data: data-driven wavelets. To represent multidimensional data, a tensor-product generalization of the one-dimensional method can be used [3]. This method has been applied to a number of datasets, including homogeneous isotropic turbulence, wind tunnel data on pipe flow turbulence, and the Kuramoto-Sivashinsky and Swift-Hohenberg models for pattern formation. In particular, when applied to a dataset of homogeneous isotropic turbulence [4, 5], DDWD yields a hierarchy of localized self-similar structures in the inertial subrange, shown in Figure 1 [2].

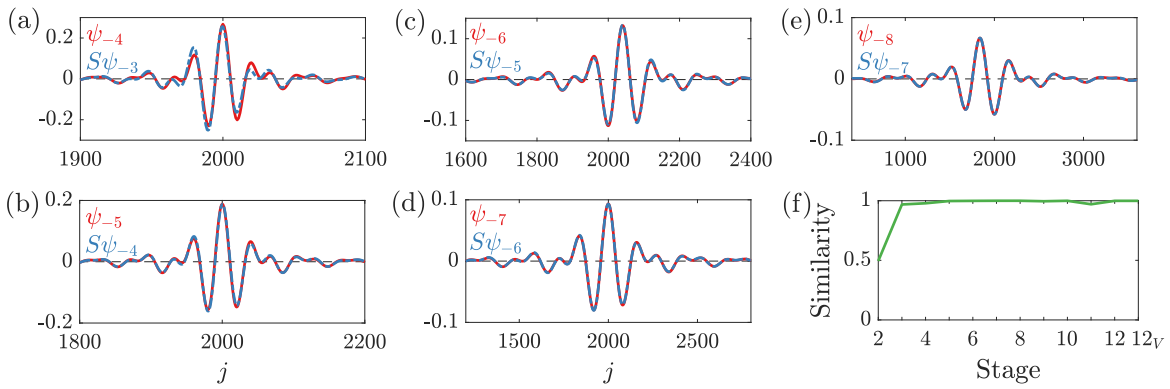

Figure 1: Data-driven wavelets computed from a dataset of homogeneous isotropic turbulence on a 4096^3 grid. Red curves show the computed wavelet at each stage, and blue curves show the wavelet from the previous stage dilated by a factor of 2.

References

[1] Holmes P., Lumley J. L., Berkooz G., and Rowley C. W. Turbulence, Coherent Structures, Dynamical Systems and Symmetry. Cambridge University Press, Cambridge 2012.
[2] Floryan D. and Graham M. D. Discovering multiscale and self-similar structure with data-driven wavelets. *PNAS*, 118(1) e2021299118, 2021.
[3] Frazier M. W. An introduction to wavelets through linear algebra. Springer Science and Business Media, New York 2006.
[4] Li Y., Perlman E., Wan M., Yang Y., Meneveau C., Burns R., Chen S., Szalay A., and Eyink G. A public turbulence database cluster and applications to study Lagrangian evolution of velocity increments in turbulence. *Journal of Turbulence*, **9**: 31, 2008.
[5] Perlman E., Burns R., Li Y., and Meneveau C. Data exploration of turbulence simulations using a database cluster. *Proceedings of the 2007 ACM/IEEE conference on Supercomputing*, 1–11, 2007.

*Corresponding author. E-mail: mdgraham@wisc.edu

GLOBAL STABILITY PROPERTIES OF THE CLIMATE: MELANCHOLIA STATES, INVARIANT MEASURES, AND PHASE TRANSITIONS

Valerio Lucarini[1,2,**]
[1] Department of Mathematics and Statistics, University of Reading, Reading, UK
[2] Centre for the Mathematics of Planet Earth, University of Reading, Reading, UK

Summary: In the current configuration, our planet is in a multistable regime - two asymptotic states can be realized. The warm state we experience in is in competition with the ice-covered snowball state. The bistability exists because of the positive ice-albedo feedback. Stochastically perturbing the parameter controlling the intensity of the incoming solar radiation the system perform transitions between the warm and the snowball state. The properties of the noise-induced escapes from the corresponding basins of attraction are studied in detail. We find the most probable paths for the transitions and show that the Melancholia states act as gateways. We also find evidence of a first order phase transition associated with the climate realized in the zero-noise limit.

For a wide range of values of the incoming solar radiation, the Earth has at least two competing attracting states, which correspond to different climates. The warm climate is similar to the present one; the snowball climate has global glaciation and conditions that can hardly support life forms. Paleoclimatic evidences indicate that in past our planet went through transitions between these two states. The main physical mechanism responsible for the multistability of the system is the ice-albedo feedback. In a previous work [1], we defined the Melancholia states unstable solutions that sit between the two climates. Such states live in the boundary between the two basins of attraction and are glaciated down to relatively low latitudes. Here, we study the global stability properties of the climate by introducing random perturbations as modulations to the intensity of the solar irradiance. We observe noise-induced transitions between the competing basins of attractions [2].

In the weak noise limit, large deviation laws can be used to express the invariant measure and the statistics of escape times. By empirically constructing the instantons, we prove that the Melancholia states are the gateways for the noise-induced transitions. An example is shown in Fig. (1). We also have that in the region of multistability, in the zero-noise limit, the measure is supported only on one of the competing attractors. For low (high) values of the solar irradiance, the limit measure is the snowball (warm) climate. The changeover between the two regimes corresponds to a first order phase transition in the system. Therefore, zero-noise limit and deterministic dynamics are not equivalent. What we propose seems of general relevance for the study of complex multistable systems. Finally, we propose a new method for constructing Melancholia states from direct numerical simulations, thus bypassing the need to use the edge-tracking algorithm [3].

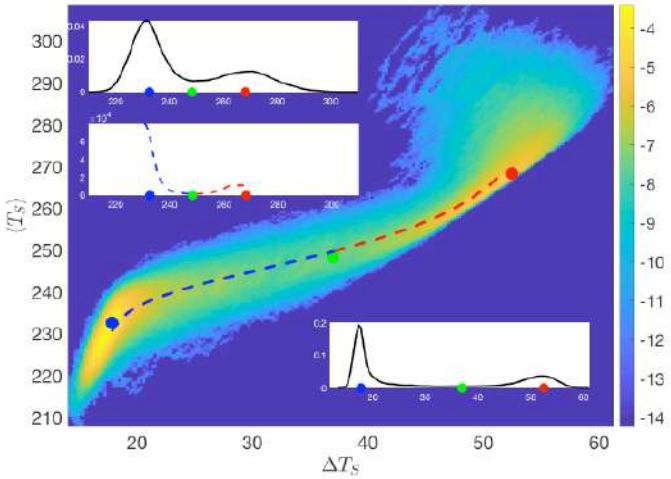

Figure 1. Main graph: invariant measure density in the projected phase space of equator-to-pole temperature difference (ΔT_S) vs globally averaged surface temperature ($\langle T_S \rangle$), with indication of the actual position of the warm attractor (red dot), snowball attractor (blue dot), Melancholia state (green dot) for standard conditions. The instantons are portrayed by the dashed lines.

References

[1] Lucarini V., Bódai T., *Nonlinearity* **30** R32 (2017)
[2] Lucarini V., Bódai T., Phys. Rev. Lett. **122**: 158701 (2019)
[3] Lucarini V., Bódai T., *Nonlinearity* **33** R59 (2020)

** Corresponding author. E-mail: **v.lucarini@reading.ac.uk**

SAMPLING EXTREME EVENTS AND PRECURSORS IN CLIMATE DYNAMICS USING MACHINE LEARNING AND RARE EVENT ALGORITHMS

Freddy Bouchet *[1], Corentin Herbert[1], Dario Lucente[1], and Francesco Ragone[1]
[1] Laboratoire de Physique, Ens de Lyon, Université Claude Bernard, Université de Lyon, CNRS, F-69342 Lyon, France

Summary Many key problems in climate dynamics require a huge computational effort. For instance, the study of extreme or rare events, the study of precursors of abrupt transitions to different climates, or the probabilistic prediction at the predictability margin, are three examples for which the computation of the relevant statistical quantities is impossible with reasonable computation resources, in comprehensive climate models. I will present several examples of new approaches we have developed, for instance using rare event algorithms and machine learning, for which we have solved these computational bottlenecks using concepts from statistical mechanics and dynamical systems.

The first application is the study of extreme heat waves using IPCC class climate models. For these models we have demonstrated a gain of several hundreds in the numerical cost for simulating extremely rare heat waves. We were able to compute return time plots for extreme heat waves with return times up to 10 000 years. Using the hundreds of simulated heat waves, we have exhibited global teleconnection pattern for extreme heat waves.

The second application is the computation of abrupt climate changes for Jupiter troposphere, and transitions to superrotating states for the Earth atmosphere dynamics.

The third application is a preliminary work on a simple model of El Nino to illustrate prediction at the predictability margin (prediction of interannual variability, beyond the Lyapunov time scale).

COMPUTING EXTREME HEAT WAVES USING RARE EVENT ALGORITHMS IN IPCC CLIMATE MODELS [3]

Studying extreme events and how they evolve in a changing climate is one of the most important current scientific challenges. Starting from complex climate models, a key difficulty is to be able to run long enough simulations to observe those extremely rare events. In physics, chemistry, and biology, rare event algorithms have recently been developed to compute probabilities of events that cannot be observed in direct numerical simulations. In this talk, we present such an algorithm, specifically designed for extreme heat or cold waves, based on statistical physics. This approach gives an improvement of more than two orders of magnitude in the sampling efficiency. We describe the dynamics of events that would not be observed otherwise. We show that European extreme heat waves are related to a global teleconnection pattern involving North America and Asia. This tool opens up a wide range of possible studies to quantitatively assess the impact of climate change. [3]

ABRUPT TRANSITIONS TO SUPERROTATION: WAVE-JET RESONANCE AND HADLEY CELL FEEDBACKS [1]

Strong eastward jets at the equator have been observed in many planetary atmospheres and simulated in numerical models of varying complexity. However, the nature of the transition from a conventional state of the general circulation, with easterlies or weak westerlies in the tropics, to such a superrotating state remains unclear. Is it abrupt or continuous? This question may have far-reaching consequences, as it may provide a mechanism for abrupt climate change in a planetary atmosphere, both through the loss of stability of the conventional circulation and through potential noise-induced transitions in the bistability range. We study two previously suggested feedbacks that may lead to bistability between a conventional and a superrotating state: the Hadley cell feedback and a wave–jet resonance feedback. We delineate the regime of applicability of these two mechanisms in a simple model of zonal acceleration budget at the equator. Then we show using numerical simulations of the axisymmetric primitive equations that the wave–jet resonance feedback indeed leads to robust bistability, while the bistability governed by the Hadley cell feedback, although observed in our numerical simulations, is much more fragile in a multilevel model. [1]

MACHINE LEARNING OF COMMITTOR FUNCTIONS FOR PREDICTING HIGH IMPACT CLIMATE EVENTS [2]

There is a growing interest in the climate community to improve the prediction of high impact climate events, for instance ENSO(El-Nino –Southern Oscillation) or extreme events, using a combination of model and observation data. In this talk we explain that, in a dynamical context, the relevant quantity for predicting a future event is a committor function. We explain the main mathematical properties of this probabilistic concept. We compute and discuss the committor

*Corresponding author. E-mail: freddy.bouchet@ens-lyon.fr

function of the Jin and Timmerman model of El-Nino. Our first conclusion is that one should generically distinguish between states with either intrinsic predictability or intrinsic unpredictability. This predictability concept is markedly different from the deterministic unpredictability arising because of chaotic dynamics and exponential sensibility to initial conditions. The second aim of this talk is to compare the inference of a committor function from data, either through a direct approach or through a machine learning approach using neural networks. We discuss the consequences of this study for future applications to more complex data sets. [2]

References

[1] HERBERT, C., CABALLERO, R., AND BOUCHET, F. Atmospheric bistability and abrupt transitions to superrotation: Wave–jet resonance and hadley cell feedbacks. *Journal of the Atmospheric Sciences 77*, 1 (2020), 31–49.

[2] LUCENTE, D., DUFFNER, S., HERBERT, C., ROLLAND, J., AND BOUCHET, F. Machine learning of committor functions for predicting high impact climate events. *arXiv preprint arXiv:1910.11736* (2019).

[3] RAGONE, F., WOUTERS, J., AND BOUCHET, F. Computation of extreme heat waves in climate models using a large deviation algorithm. *PROCEEDINGS OF THE NATIONAL ACADEMY OF SCIENCES OF THE UNITED STATES OF AMERICA 115*, 1 (JAN 2 2018), 24–29.

A BALANCED STATE CONSISTENT WITH PLANETARY-SCALE MOTION FOR QUASI-GEOSTROPHIC DYNAMICS

Woosok Moon *[1,2] and James Y-K. Cho[3]
[1] Nordic Institute for Theoretical Physics, Roslagstullsbacken 23, 106 91 Stockholm, Sweden
[2] Department of Mathematics, Stockholms universitet, SE-106 91 Stockholm, Sweden
[3] CCA, Flatiron Institute, New York, NY 10010, USA

Summary The role of planetary-scale zonally-asymmetric thermal forcing on large-scale atmospheric dynamics is crucial for understanding low-frequency phenomena in the atmosphere. Despite its paramount importance, good theoretical foundation for the understanding is still lacking. Here we address this issue by providing a general framework for including planetary-scale thermal forcing in large-scale atmospheric dynamics studies. This is accomplished by identifying two distinct geostrophic motions of horizontal length scale L in terms of the external Rossby deformation length scale L_D: *i*) $L \sim \epsilon^0 L_D$ and *ii*) $L \sim \epsilon^{1/2} L_D$, where ϵ is the Rossby number. In addition, via multi-scale analysis, we show that the large-scale atmospheric dynamics can be described by mutual interaction between the two scales. The analysis results in planetary geostrophic equations with large-scale thermal forcing that provide the basic balanced states for processes such as the growth of synoptic waves. In the long-time limit, the continuous growth and decay of synoptic waves provides the convergence of horizontal heat and vorticity fluxes, which contributes to the energy flux balance in the planetary geostrophic scale with planetary-scale advection and thermal forcing.

INTRODUCTION

The effects of zonally-varying thermodynamic or orographic forcing on large-scale atmospheric motions has been a main topic of investigation in atmospheric dynamics studies. This is because of the forcing's possible relationship to storm-tracks [1], large-scale atmospheric stationary waves [2] and low-frequency variability, such as the North Atlantic Oscillation [3] and Pacific North Atlantic mode [4]. However, despite this importance, adequate theoretical understanding is still lacking.

Zonally-*a*symmetric forcing poses a major challenge in dynamics studies. This is because obtaining a state in balance with an asymmetric thermal forcing is not trivial. For example, a radiative-convective equilibrium state with thermal wind balance does not automatically determine a basic balanced state for zonally-varying thermal forcing – as in the zonally-symmetric case. A possibility still exists for finding a statistically-stationary state with a zonally-asymmetric forcing. However, the connection between initial balanced state and subsequent growth of transient eddies is then lost.

Consider now the planetary scale, where the horizontal length-scale L_D is similar to the radius of Earth. The notion of planetary geostrophic motion has been introduced by [5] to explain the global thermocline structure of the ocean. Interestingly, the leading order PG equations are closed – i.e., it is not necessary to consider the next order to determine the leading order variables. In particular, the heat equation included in the leading order can take a global-scale thermodynamic forcing. Following this, planetary geostrophic motion for the large-scale atmosphere has been introduced by [6], wherein it is named 'geostrophic motion of type 2'. Significantly, in that study it is noted that large-scale flows would need to be forced to maintain the balance in the type 2 geostrophic motion. This suggests that the planetary geostrophic motion could serve in constructing a more physically realistic balanced state consistent with a zonally-asymmetric forcing. Indeed, in this paper we elucidate the relationship between planetary geostrophic (PG) and quasi-geostrophic (QG) motions and address how to deal with QG dynamics in the presence of planetary-scale zonally-asymmetric forcing.

TWO-SCALES IN LARGE-SCALE ATMOSPHERIC DYNAMICS

There are two different geostrophic motions in the large-scale atmosphere, which suggests that the large-scale atmospheric motions are shaped by the mutual interactions of the two scales. The two length-scales L and L_D for quasi-geostrophic and planetary geostrophic motion, respectively, have the ratio L/L_D whose order is $\epsilon^{1/2}$, where $\epsilon = U/(f_0 L_D)$. We will rely on this Rossby number for the planetary scale. The time-scale is chosen to be the advection time-scale. Hence, there are two time-scales $t \equiv L/U$ and $\tau \equiv L_D/U$, satisfying $\tau = \epsilon^{1/2} t$. A multi-scale analysis is applied to primitive equations based on the two scales with planetary-scale variables $\{X, Y, \tau\}$ and quasi-geostrophic scale variables $\{x, y, t\}$.

*Corresponding author. E-mail: woosok.moon@su.se

The leading equations in the multi-scale analysis are:

$$u_L = -\frac{\partial P_L}{\partial Y}, \quad v_L = \frac{\partial P_L}{\partial X}, \quad \rho_L = -\frac{1}{\rho_s}\frac{\partial}{\partial z}\left(\rho_s P_L\right) \tag{1a}$$

$$u_0 = -\frac{\partial P_0}{\partial y}, \quad v_0 = \frac{\partial P_0}{\partial x}, \quad \rho_0 = -\frac{1}{\rho_s}\frac{\partial}{\partial z}\left(\rho_s P_0\right) \tag{1b}$$

$$\frac{\partial w_L}{\partial z} + H w_L = \beta_L v_L \tag{1c}$$

$$\frac{\partial \Theta_L}{\partial \tau} + u_L\frac{\partial \Theta_L}{\partial X} + v_L\frac{\partial \Theta_L}{\partial Y} + w_L\left(\frac{\partial \Theta_L}{\partial z} + S\right) = -\left(\frac{\partial}{\partial t} + u_L\frac{\partial}{\partial x} + v_L\frac{\partial}{\partial y}\right)\Theta_0 - \frac{\partial}{\partial x}\left(u_0\Theta_0\right) - \frac{\partial}{\partial y}\left(v_0\Theta_0\right) - w_1\left(\frac{\partial \Theta_L}{\partial z} + S\right) + Q_L \tag{1d}$$

$$\frac{\partial}{\partial t}\nabla^2 P_0 + (u_L + u_0)\frac{\partial}{\partial x}\nabla^2 P_0 + (v_L + v_0)\frac{\partial}{\partial y}\nabla^2 P_0 + \beta v_0 = \left(\frac{\partial}{\partial z} + H\right) w_1\,, \tag{1e}$$

where the subscript 'L' refers to a planetary scale variable that depends only on X, Y, z and τ and the subscripts '0' and '1' represent quasi-geostrophic variables dependent on x, y, z and t. Note that the QG equations act as a short timescale forcing on the planetary scale. On the other hand, the PG motions provide a basic mean state satisfying the geostrophic and hydrostatic balance to the QG scale.

CONCLUSIONS

Large-scale atmospheric dynamics is controlled by processes of different scales and the interactions between them. Unravelling the interactions – and ultimately understanding the dynamics in full – requires a systematic approach. In this research, we have used an asymptotic approach to identify two separate scales in large-scale atmospheric dynamics and to understand the mutual interactions between them. Multi-scale analysis, in particular, is used in spatial and temporal domains to elucidate the interactions.

In this work, we have argued that the variation and structure of the large-scale atmospheric motion can be viewed in terms of the interaction of two geostrophic motions. One motion, the PG motion, can be interpreted as a balanced field directly forced by large-scale radiative-convective imbalance, as just noted; and, the other motion, aptly descried by the familiar QG vorticity equation, governs the lifecycle of synoptic waves that grow via the energy extracted from the balanced field.

Another significant perspective addressed through the multi-scale analysis is the construction of a statistically-stationary large-scale flow – i.e., PG motion forced by both the large-scale radiative imbalance and the QG eddies. Averaging the QG variables in time-domain shows the contribution of the QG motion to the slow time-evolution of the PG motion. The time-averaged horizontal heat flux convergence and vertically-integrated relative vorticity flux convergence act as forcing in the planetary heat equation. Then, the PG motion is balanced by the radiative imbalance and the heat and vorticity flux convergences.

References

[1] Chang, E. K., S. Lee, and K. L. Swanson, 2002: Storm track dynamics. *J. Climate*, **15(16)**, 2163–2183.

[2] Held, I. M., 1983: Stationary and quasi-stationary eddies in the extratropical troposphere: Theory. *Large-scale dynemical processes in the atmosphere*, 127–168.

[3] Marshall, J. and Coauthors, 2001: North Atlantic climate variability: phenomena, impacts and mechanisms. *Int. J. Climatol.*, **21(15)**, 1863–1898.

[4] Leathers, D. J., B. Yarnal, and M. A. Palecki, 1991: The Pacific/North American teleconnection pattern and United States climate. Part I: Regional temperature and precipitation associations. *J. Clim.*, **4(5)**, 517–528.

[5] Welander, P., 1959: An advective model of the ocean thermocline. *Tellus*, **11(3)**, 309–318.

[6] Phillips, N. A., 1963: Geostrophic motion. *Rev. Geophys.*, **1(2)**, 123–176.

THE ROLE OF WAVE BREAKING AND AIR-BUBBLES IN GLOBAL GAS TRANSFER

Luc Deike *[1,2]
[1] Department of Mechanical and Aerospace Engineering, Princeton University, Princeton, USA
[2] Princeton University, Mechanical and Aerospace engineering, Princeton, USA

Summary The transfer of gases at the ocean-atmosphere interface impacts weather and climate from local to global scales, with carbon dioxide (CO2) and oxygen key to marine ecosystems, and dimethylsulfide (DMS) affecting aerosols and atmospheric processes. Bubble mediated gas transfer by with breaking waves is a dominant term at high wind speed, but has remained poorly constrained, because of the wide range of scales involved, from wave statistics, to bubble dynamics. We present a multi-scale model that combines a statistical description of wave-breaking with a mechanistic model of air bubble entrainment by breaking coupled with a chemical model. This framework is validated against field measurements, and collapses all available CO2 and DMS gas transfer velocity data. We test implications of such sea-state dependent gas transfer model at regional and global scales for ocean and climate modeling.

INTRODUCTION

Physical processes at the ocean-atmosphere interface have a large effect on climate and weather by controlling the transfer of momentum and mass. Without wave breaking, transport between the ocean and the atmosphere is through slow conduction and molecular diffusion, while wave breaking is a transitional process from laminar to turbulent flow. When waves are breaking, the surface experiences dramatic changes, with sea spray ejection in the atmosphere and air entrainment into the ocean water. The complex dynamics and statistics of wave breaking in a particular ocean location depends mainly on the local wave state not the wind velocity, while current parameterizations for ocean-atmosphere interactions are based almost exclusively on the wind speed.

Ocean uptake accounts for approximatively 30% of the CO_2 released into the atmosphere. The gas transfer at the ocean-atmosphere interface is calculated from the gas concentrations in the air and water, expressed as a function of the gas solubility, α, and partial pressure in the water, p_w and in the air, p_a [1],

$$F = k_w \alpha (p_w - p_a), \tag{1}$$

where k_w is the gas transfer velocity which depends on the physicochemical properties (solubility and diffusivity D) of the gas and the atmospheric and oceanic conditions. State of the art ocean-atmosphere parameterizations for the transfer velocity, used in ocean and climate models [2], include a Schmidt number scaling (typically, $k_w \propto Sc^{-1/2}$, $Sc = \nu/D$, where ν is the kinematic viscosity) but depend solely on wind speed to account for turbulent and wave breaking induced transfers. Recent open ocean gas transfer velocity measurements of CO_2 and dimethyl sulfide (DMS) display very large scatter, when analyzed as a function of wind speed [2, 3, 4], exposing the failure of wind-speed parameterization at intermediate to high wind speeds that is associated with bubble-mediated gas transfer. Separating the contribution to the total flux into the bubble gas transfer and the diffusive transfer at an unbroken surface, bubble-mediated gas transfer had been introduced through the whitecap coverage [5], but was ultimately described by a function of the wind speed.

A SEA-STATE DEPENDENT GAS TRANSFER MODEL

We propose a general theoretical framework going consistently from the bubble scale to the final gas transfer velocity, elucidating its dependence on wind, wave parameters and physico-chemical parameters. Our approach accounts for the complex nature of wave breaking and air entrainment, a two-phase turbulent process, and the very large range of scales involved in the process, from wave statistics scales of order of km, O(1km), to wave breaking dynamics, O(1-10m), air entrainment, bubble generation and dissolution O(cm to μm), which is sketched on figure 1. We combine high fidelity direct numerical simulations, and laboratory measurement described in Deike et al 2016 [6], combined with the measured wave and wave breaking statistics top obtain a formulation for the volume flux of air entrained by breaking waves in the ocean, described in Deike et al 2017 [7]. The mass (gas) flux is then obtained by coupling the air flux formulation to a chemical gas transfer model [5], as presented in Deike and Melville 2018 [2], leading to a formulation for the bubble-mediated gas transfer due to breaking waves, taking into account processes at all scales. This theory is for the transfer of any gas and can be implemented in coupled wave-ocean-atmosphere and climate models, which should significantly reduce the uncertainties at moderate to high wind speeds.

The gas transfer velocity is first decomposed into the bubble and non-bubble components,

$$k_w = k_{nb} + k_b, \tag{2}$$

where the non-breaking gas transfer component, due to molecular diffusion enhanced by turbulence is given by $k_{nb} = A_{NB} u_* Sc^{-1/2}$ where $Sc = \nu/D$ is the Schmidt number, and A_{NB} a non-dimensional coefficient obtained from empirical

*Corresponding author. E-mail: ldeike@princeton.edu.

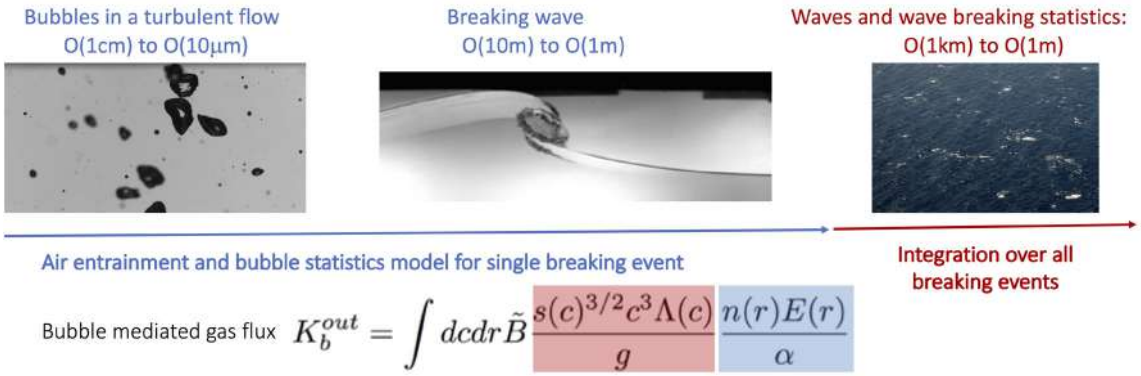

Figure 1: Sketch of the multi-scale modeling approach. The spectral model for the bubble mediated gas transfer depends on the size distribution of bubbles entrained by a breaking waves, determined from experiments and simulations. The gas transfer associated with these bubbles is estimated from a chemical diffusion model which accounts for the gas diffusivity, solubility and the bubble residence time. The gas transfer is then integrated over all the breaking wave statistics, itself related to the wave spectrum statistics and therefore the wind forcing conditions.

data on gas transfer at an unbroken interface [8]. The bubble mediated gas transfer k_b is given by a spectral formulation, integrating over the whole wave spectrum and the whole bubble size distribution [2],

$$k_b = \int dcdr\tilde{B}\frac{s(c)^{3/2}c^3\Lambda(c)}{g}\frac{n(r)E(r)}{\alpha}. \tag{3}$$

where $\Lambda(c)$ is the length of breaking crest distribution describing the breaking statistics as a function of wave speed c, $s(c)$ represents the slope spectrum, describing the saturation of the wave field and strength of air entrainment, g is gravity, $n(r)$ is the bubble size distribution (with r the bubble radius) under a breaking wave, α the gas solubility and $E(r)$ is the scale dependent efficiency transfer coefficient which depends on the bubble size, the gas solubility and diffusivity as well as the residence time of the bubble in the water. This model is validated against field measurements of the gas transfer velocity for CO_2 and DMS [4, 3] and very good agreement is observed [2].

We propose a simple parameterization for the cases of CO_2 and DMS, derived from the full equation, as a function of wind friction velocity u_* and wave height H_s, which capture the main wave effect, and solubility and diffusivity, that collapses all available data [2]. Such simple formulation can then be used to estimate globally the role of bubble mediated gas transfer, and evaluate the possible consequences on global modeling of biogeochemical cycle.

We use a global wave model, forced by realistic wind conditions to evaluate the global bubble contribution to air-sea gas exchange and identify the regions and seasons where such formulation could lead to improved accuracy when comparing to field measurements of gas transfer [9]. Finally, recent progress in wave modeling are now permitting to directly compute the breaking statistics [10], which will permit to investigate the role of the full wave complexity at high temporal and spatial resolution, capturing the wave field associated with storms with a high level of fidelity, and opening a pathway for more accurate models of ocean-atmosphere interaction, from gas transfer to spray generation, based on the present formulation.

References

[1] Rik Wanninkhof, William E Asher, David T Ho, Colm Sweeney, and Wade R McGillis. Advances in quantifying air-sea gas exchange and environmental forcing. *Annual Review of Marine Science*, 1:213–244, 2009.

[2] Luc Deike and W Kendall Melville. Gas transfer by breaking waves. *Geophysical Research Letters*, 45(19):10–482, 2018.

[3] S.E. Brumer, C.J. Zappa, B.W. Blomquist, C.W. Fairall, A. Cifuentes-Lorenzen, J.B. Edson, I.M. Brooks, and B.J. Huebert. Wave-related reynolds number parameterizations of CO_2 and DMS transfer velocities. *Geophysical Research Letters*, 44(19):9865–9875, 2017.

[4] T. G. Bell, S. Landwehr, S. D. Miller, W. J. Bruyn, A. H. Callaghan, B. Scanlon, B. Ward, M. Yang, and E. S. Saltzman. Estimation of bubble-mediated air–sea gas exchange from concurrent DMS and CO_2 transfer velocities at intermediate–high wind speeds. *Atmospheric Chemistry and Physics*, 17(14):9019–9033, 2017.

[5] Ralph F Keeling. On the role of large bubbles in air-sea gas exchange and supersaturation in the ocean. *Journal of Marine Research*, 51(2):237–271, 1993.

[6] L. Deike, W.K. Melville, and S. Popinet. Air entrainment and bubble statistics in breaking waves. *J. Fluid Mech.*, 801:91–129, 2016.

[7] L. Deike, L. Lenain, and W. K. Melville. Air entrainment by breaking waves. *Geophys. Res. Lett.*, (40):19, 2017.

[8] C.W. Fairall, M. Yang, L. Bariteau, J.B. Edson, D. Helmig, W. McGillis, S. Pezoa, J.E. Hare, B. Huebert, and B. Blomquist. Implementation of the coupled ocean-atmosphere response experiment flux algorithm with CO_2, dimethyl sulfide, and O_3. *Journal of Geophysical Research: Oceans*, 116(C4), 2011.

[9] Brandon Reichl and Luc Deike. Contribution of sea-state dependent bubbles to air-sea carbon dioxide fluxes. *Geophysical Research Letters*, Submitted, 2020.

[10] Leonel Romero. Distribution of surface wave breaking fronts. *Geophysical Research Letters*, 46(17-18):10463–10474, 2019.

TOWARDS A THEORY FOR THE OCEAN WAVE SPECTRUM

Anthony Bonfils *[1], Woosok Moon[1], Dhrubaditya Mitra[1], and John S. Wettlaufer[1,2,3]
[1] Nordic Institute for Theoretical Physics, Stockholm, Sweden
[2] Yale University, New Haven, USA
[3] Mathematical Institute, University of Oxford, UK

Summary The spectrum of surface gravity waves was measured in the sixties by Pierson and Moskowitz for a fully developed sea, however a theory explaining their observations has been lacking. The initial growth rate of waves is given by the linear theory of Miles which we compute using a new numerical scheme, solving the hydrodynamic Rayleigh equation for a general wind profile. Then, we compare it with analytical results obtained via the method of matched asymptotic expansions. However, there is a coupling between surface gravity waves and the turbulence of the wind that we believe plays an important role. Starting from the quasi-linear model of Janssen, we will consider the non-linear evolution of the ocean wave spectrum in a statistical mechanical framework, which might be useful for wave forecasting.

INSTABILITY OF A PARALLEL SHEAR FLOW OVER A FREE SURFACE

For centuries, scientists and sailors have been vexed by how the wind and the sea conspire to create the waves upon our oceans. Mathematically, the problem consists in calculating the spectrum of waves generated by a turbulent wind over a free surface. Phillips' theory [2] provides a good description of wave generation. Miles [3] proposed an instability mechanism for the growth of a mode traveling at the phase velocity c_0. His key assumption is that when the time scale of turbulent fluctuations is much smaller than the period of the wave, the wind profile $U(z)$ is logarithmic following the law of the wall (see figure 1). Since the density of air is much smaller than the density of water, their ratio $\epsilon = \frac{\rho_a}{\rho_w}$ is a natural small parameter. Thus, Miles could perturbatively solve the eigenvalue problem associated to the instability of a parallel shear flow over a free surface and calculate the initial growth rate:

$$\gamma = -\pi \epsilon c_0 \frac{U''(z_c)}{|U'(z_c)|} |\chi(z_c)|^2 \qquad \text{where} \qquad U(z_c) = c_0 \tag{1}$$

z_c is called the critical level and χ, the normalized perturbed vertical velocity, is solution of the Rayleigh equation

$$(U - c_0)(\chi'' - k^2\chi) - U''\chi = 0 \quad \text{with the boundary conditions} \quad \begin{cases} \chi(0) = 1 \\ \chi(z) \underset{+\infty}{\sim} e^{-kz} \end{cases} . \tag{2}$$

To compute γ, we developed a simple and efficient method for solving linear 2nd order boundary value problems with a regular singularity. Accuracy of the scheme has been checked by recovering the numerical results of Conte and Miles [4] for the dimensionless coefficient β (see its relation with γ in figure 2). We compare Miles' theory with four data sets of measurements of initial growth rates gathered by Plant [5]. It appears that the strength of wind-wave interaction, represented by the growth rate normalized by the frequency $\frac{\gamma}{f}$, is approximately proportional to the square of the wind forcing of waves $\frac{u_\star}{c_0}$. We study how this power law emrges from Miles' theory and show that it strongly depends on the wind parameter $\Omega = g z_0 \left(\frac{\kappa}{u_\star}\right)^2$. To do so, we solve equation (2) by asymptotic matching in the long and short wave approximations.

QUASI-LINEAR WIND-WAVE INTERACTION

Because the ocean wave spectrum $G(k,t)$ is continuous, each level above the surface can be seen as a critical one associated to a mode k of that spectrum. These critical layers interact in such a way that the wind profile gets modified. This can be seen as a analogous to wave turbulence. By a multiple-scale analysis, Janssen [6] established the following time evolution equation:

$$\frac{\partial U}{\partial t} = \frac{2\pi}{U^3(z,t)} \left|\chi_{k_c}(z,t)\right|^2 G(k_c,t) \frac{\partial^2 U}{\partial z^2} \quad \text{with } k_c(z,t) = \frac{1}{U(z,t)^2} \tag{3}$$

Miles' formula (1) still holds but the growth rate is now a function of time. Note that in the steady state, the wind profile should be linear. We numerically explore this model and extend our asymptotic methods, in order to understand the saturation of the waves.

*Corresponding author. E-mail: anthony.physth@gmail.com.

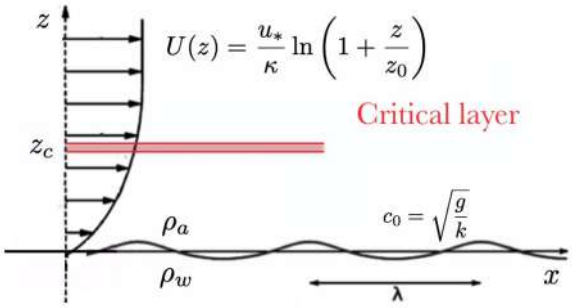

Figure 1: Schematic of a critical layer associated with a mode k that obeys the dispersion relation of surface gravity waves. In the law of the wall, κ is the von Karman constant, u_* the friction velocity and z_0 the roughness length.

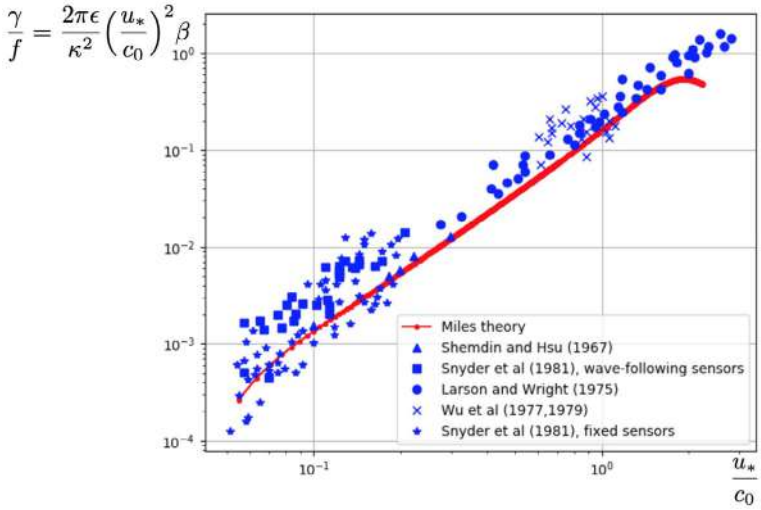

Figure 2: Comparison of Miles theory with experimental data. There is an approximate power law when β is a constant.

CONCLUSIONS

The small parameter ϵ introduces a scale separation in wind-wave generation. Whereas the evolution of gravity waves occurs on a short (fast) time scale, the energy transfer from the wind occurs on a long (slow) time scale. The feedback of growing surface waves on the wind profile occurs on an intermediate time scale. According to Miles' theory, waves can grow if the curvature of that profile is negative. Therefore, the vanishing of the curvature predicted by the model of Janssen will lead to the saturation of the waves, which is the first step in the transition towards a fully developed sea. It appears necessary to introduce stochastic methods in order to deal with the complexity of the non-linear interaction of waves through the wind in addition to the wave turbulence, which constitutes ongoing work.

References

[1] W. J. Pierson and L. Moskowitz. A proposed spectral form for fully developed wind seas based on the similarity theory of S.A. Kitaigorodskii. *J. Geophys. Res.* **69**: 51815190, 1964.
[2] O. M. Phillips. On the generation of waves by turbulent wind. *J. Fluid Mech.* **2**: 417445, 1957.
[3] J. W. Miles. On the generation of surface waves by shear flows. *J. Fluid Mech.* **3**: 185204, 1957.
[4] S. D. Conte and J. W. Miles. On the numerical integration of the Orr-Sommerfeld equation. *J. Soc. Indust. Appl. Maths* **7**: 361-366, 1959.
[5] W. J. Plant. A relationship between wind stress and wave slope. *J. Geophys. Res.* **87**: 19611967, 1982.
[6] P. A. E. M. Janssen. Quasilinear approximation for the spectrum of wind-generated water waves. *J. Fluid Mech.* **117**: 493506, 1982.

K106712 - MS03 - Biological fluid-structure interaction at the microscale - Keynote

HIGH-THROUGHPUT MEASUREMENT OF AN INDIVIDUAL'S RED BLOOD CELL SHEAR MODULUS DISTRIBUTION

Amir Saadat,[1] Diego A. Huyke,[2]† Diego I. Oyarzun,[2] Paulina V. Escobar,[4] Ingrid H. Øvreeide,[5] Eric S.G. Shaqfeh,[1,2,3] and Juan G. Santiago[2]
[1] Department of Chemical Engineering, [2] Department of Mechanical Engineering, [3] Institute of Computational and Mathematical Engineering Stanford University, Stanford, CA 94305, [4] Department of Mechanical Engineering, Pontificia Universidad Católica de Chile, 5 Department of Physics, Norwegian University of Science and Technology

Summary Red blood cell (RBC) deformability is critical in their flow through the microcirculation capillaries or the splenic sinusoids. To the best of our knowledge, this work is the first to measure the shear moduli of thousands of RBCs and is accomplished, thanks to a combined high-fidelity RBC numerical model and microfluidic system. There is no gold standard for shear modulus measurement using a microfluidic, high-throughput approach, which hampers the repeatability of microfluidic measurements across different labs. This work bridges this gap with figures of merit that are independent of operational and geometrical variables. Our results indicate excellent agreement with those measurements using "standard" optical tweezers or micropipette aspiration, however we take and analyze images of thousands of cells in several minutes.

INTRODUCTION

Deformability is a critical feature of red blood cells (RBCs) within their 100-120 day life-span through the blood circulation system, and it is a particularly important factor in their flow through the microcirculation capillaries or the splenic sinusoids. Deformability is affected by many pathological conditions and its alteration can impact the pathophysiology of many diseases. While primary reasons for altered deformability are hereditary, mutation, or parasite invasion, there are also many secondary biochemical pathways which influence RBC morphology, biochemistry, and biomechanics. As a result, RBC deformability is altered in many blood related diseases such as diabetes, sepsis, metabolic syndrome. For example, it was recently discovered that, even neurodegenerative diseases could be correlated to the deformability of RBCs due to the interrelation of neural activity and blood circulation.

Although the RBC structure is quite complex, the membrane is a few nanometers thick and therefore can be approximated with a 2D continuum sheet, defined by three main elastic moduli that describe its resistance to deformation; namely, the area dilatation, shear, and bending modulus (1, 2). The lipid bilayer as well as the spectrin network warrants an area inextensible sheet—the area expansion of the membrane is found to be negligible (3). In contrast, the ratio of bending to shear modulus of RBCs is very small which makes the bending resistance relatively inconsequential (2,4). As a result, RBC structure and deformability are largely governed by the membrane shear modulus.

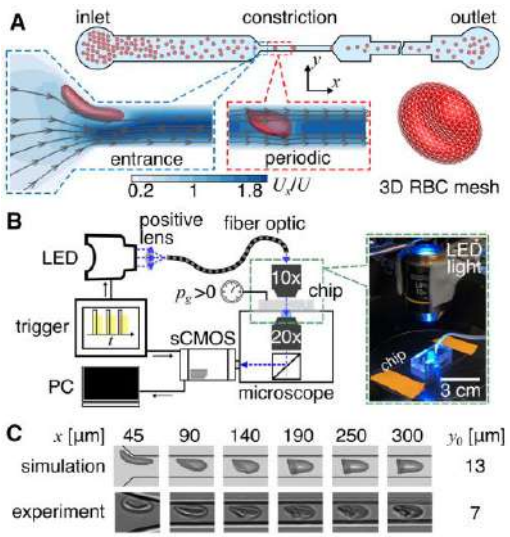

Figure 1. A schematic representation of our microfluidic chip design is shown in the top row of (A). Shown in the bottom row of (A) are the numerical simulation entrance and periodic domains and the mesh distribution over an individual RBC. In (B), a schematic and image of the experimental setup are shown. Panel (C) shows a qualitative comparison of simulation and experimental images of RBCs as they deform and approach a steady-state shape in a constriction with 7×7 μm2.

METHODS

Briefly, state-of-the-art methods to measure the shear modulus of RBCs are not high-throughput and, microfluidic platforms for high-throughput measurements of RBC mechanical properties have not yet enabled measurement of the shear modulus. These limitations challenge the development of diagnostic devices based on RBC shear modulus biomarkers. We demonstrate a high-throughput microfluidic platform, coupled with high-fidelity simulations to address this significant gap in technology. In contrast with existing technologies, this approach allows us to measure the shear modulus of individual RBCs and generate shear modulus distributions (for a given individual or multiple individuals) including measurements of thousands of cells in a few seconds of experimental data acquisition.

As shown in Figure 1A, immersed boundary simulations (5) were conducted near the entrance and in periodic channel domains to find the steady-state shape. We use the well-known Skalak model (55) for modelling the RBC membrane and we assume, as is usual, that these systems are largely surface incompressible. We then utilized the steady-state shapes to generate a surface for data interpretation relating the three important non-dimensional parameters: **the Taylor**

deformation (Ta) , the confinement (ϵ), and the capillary number (based on cell velocity) Ca_{cell}. Note the confinement is a geometric parameter that relates the square root of the projected area of the cell to the channel width, and is proportional to the surface to volume ratio of the RBC.

In conjunction with our high-fidelity simulations, we performed high-throughput experimental visualizations of RBCs under flow. The experimental setup consisted of a custom poly-dimethylsiloxane (PDMS) and glass microfluidic chip, as well as flow control and image acquisition instruments (Figure 1B). RBCs were imaged as they traveled through a $7\times7\times1000$ μm^3 constriction at velocities of 2-10 mm s^{-1} (Figure 1C). The experimentally measured, steady-state Taylor deformation of each RBC was compared to the aforementioned, computationally generated Taylor deformation versus confinement projection, and used to extract the nondimensional RBC capillary number.

RESULTS

From the simulations, we determined *Ta* at different values of ϵ and Ca_{cell} –the capillary number was selected in the range of 0.2-1.6 and the confinement levels were varied between 0.8-1.3. This parameter range is comparable to that which occurs physiologically in the microcirculation. We purposely selected values of ϵ and Ca_{cell} that guaranteed a static parachute shape. The values of *Ta* and ϵ were determined experimentally for every individual cell that is tracked in the microfluidic channels. One can then determine a unique Ca_{cell}, for specific values of *Ta* and ϵ. Then if one also measures the cell velocity, the modulus of the cell can be uniquely determined.

Figure 2 shows the shear modulus distribution for five different donors along with one sample that was "aged" for 5 weeks. We found that the distribution for each donor similarly follows a lognormal distribution. The mean shear moduli ranged from 16.6 to 27.2 μN/m. The standard deviations of shear moduli ranged from 8.6 to 20 μN/m. The results suggest that there are donor-to-donor differences in mean shear moduli as large as 10 μN/m. Moreover, the fresh blood distribution shows a mean shear modulus near 6.6 μN/m. After 5 weeks of storage, the mean shear modulus increases to 34 μN/m. The increase of the mean is expected due to the increase in the stiffness of the RBCs. All of our results are consistent with measurements made via micro-pipette aspiration or optical tweezers, except for the fact that we can make measurements of thousands of cells in minutes and thus determine distributions.

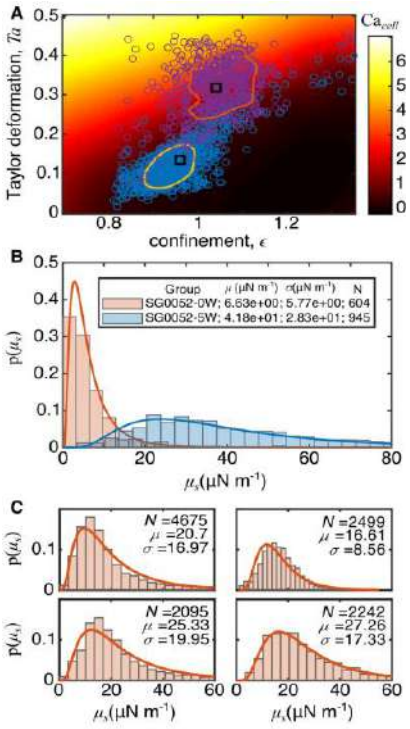

Figure 2. In (A) are shown experimentally Taylor deformation *Ta* versus confinement ϵ data for RBCs that were freshly withdrawn (purple, open circles) and 5-weeks stored in a 4°C fridge (blue, open circles). The solid lines enclose 50% of the experimental measurements. The scattered data is overlaid on the computationally generated *Ta* versus ϵ surface which results in a single capillary number of the cell Ca_{cell}. Panel (B) shows the shear modulus distributions corresponding to the same data set (fresh in orange and 5-weeks stored in blue). The shear modulus distributions (C) for four separate healthy donors was also found.

CONCLUSIONS

We have designed a high-throughput microfluidic platform for measuring the shear modulus and shear modulus distribution of an individual's blood sample. This was accomplished by fabricating microchannels with square cross-sections (7x7 μm^2) such that a steady-state parachute is formed after flow 300 μm downstream. We then determined the Taylor deformation parameter, *Ta*, using robust and automated single-cell tracking and shape quantification. Finally, we utilized our 3D computational method to construct a three-dimensional surface that is used to find the shear modulus and its distribution based on the experimentally measured values of *Ta*, confinement ratio, and cell velocity.

References

[1] J. Kim, H. Lee, S. Shin, Advances in the measurement of red blood cell deformability: A brief review. *J. Cell. Biotechnol.* **1**, 63–79 (2015).
[2] M. Dao, J. Li, S. Suresh, Molecularly based analysis of deformation of spectrin network and human erythrocyte. *Mater. Sci. Eng. C* **26**, 1232–1244 (2006)
[3] Y. Kim, K. Kim, Y. Park, Measurement Techniques for Red Blood Cell Deformability: Recent Advances https:/doi.org/10.5772/50698.
[4] C. Pozrikidis, Axisymmetric motion of a file of red blood cells through capillaries. *Phys. Fluids* **17**, 31503 (2005).
[5] Saadat, A., C. Guido, G. Iaccarino, E.S.G. Shaqfeh, ``An Immersed Finite Element Method for Deformable Particle Suspensions in Viscous and Viscoelastic Media", Phys. Rev. E 98(6), 063316 (2018)

SPATIAL DISTRIBUTION OF RED BLOOD CELLS IN PERIODIC MICROFLUIDIC NETWORKS

Adlan Merlo*[1], Maxime Berg*[1], Yohan Davit[1], Frédéric Risso[1], Paul Duru[1], and Sylvie Lorthois †[1]
[1] *Institut de Mécanique des Fluides de Toulouse (IMFT), Université de Toulouse, CNRS, Toulouse, France*

Summary The physics of blood flow in small vessel networks is dominated by the interactions between blood cells, plasma and blood vessel walls. This leads to strong couplings between the microvessel network architecture and the distribution of RBCs, which have been the object of a large amount of work. Most of them, however, consider complex microvascular architectures. Here, we present a series of experiments performed in both hexagonal and square periodic microfluidic networks, and gain physical insights on the results by comparison with discrete network models of RBC flow in the same configurations. We show that, despite the apparent simplicity of the geometries at hand, model predictions can differ significantly from experiments and are very sensitive to the network hierarchy, strongly suggesting that an improved description of blood flow at the local scale should be necessary.

INTRODUCTION

Microvascular networks are able to ensure adequate blood supply, feeding every cell in peripheral tissues with oxygen and nutrients under a wide range of physiologic conditions and varying metabolic needs. Their involvement in disease is also increasingly recognized [1, 2, 3]. Thus, since the very first observations of microvascular networks in small animals by Jean-Marie Poiseuille in the XVIIIth century, the blood microcirculation has been extensively studied. One of the most striking feature highlighted by the French physicist is the highly heterogeneous distribution of red blood cells (RBCs) throughout microvessel networks, with some vessels containing no blood cells and some others containing almost no plasma (suspending fluid) [4, 5, 6]. Because oxygen transported in the bloodstream is mainly stored within the RBCs, such heterogeneous distribution is likely to control the oxygenation of the surrounding tissue.

The physics of blood flow in these small vessel networks is dominated by the interactions between blood cells, plasma and blood vessel walls [7]. This leads to strong couplings between the microvessel network architecture and the distribution of RBCs. The emergence of such couplings has been the object of a large amount of work, from the scale of individual RBCs to the scale of the network (see [8] or [9] for recent reviews).

At network scale, in particular, a large variety of investigation tools, sometimes in combination, has been used, see, *e.g.*, [10, 11, 12, 13, 14, 15, 16, 17]: **a)** in vivo and in vitro experiments, **b)** network models where blood is described as an equivalent fluid with non-linear rheological properties, the RBCs being described by a volume fraction and their impact on larger scales being described by phenomenological descriptions, **c)** networks models coupled with simplified, discrete representations of the RBCs, as singular pressure drops, which are individually tracked, and **d)** more recently, direct numerical simulations resolving both the dynamics of the suspending fluid and of each individual RBC, as well as their large deformations, their interactions and the hydrodynamics of the suspending fluid.

Most of these works, however, consider complex microvascular architectures and vessel lengths and diameters distributed to match as closely as possible the *in vivo* distributions. This makes it difficult to isolate the contributions of local effects, such as cell partitioning at successive bifurcations [18], and large-scale couplings associated to the non-local nature of viscous flow in networks, even in the absence of any cell.

RED BLOOD CELL DISTRIBUTION IN SIMPLE PERIODIC NETWORKS

As far as we know, only the group of D. Obrist focused on simple generic model networks with channels of equal sizes and with periodic unit patterns [11, 17]. The first of these two works [11] was theoretical, based on the simplest possible Lagrangian network model of RBC flow, in order to reveal the underlying principles of RBC distribution at network scale, and considered square unit patterns, with 4-connectivity. One of their central theoretical result was the accumulation of RBCs in the network corners opposite to the inlet and outlet, *i.e.*, within the vessels exhibiting the smallest flow rates, as illustrated on Figure 1, left and middle pannels. This was a highly unexpected result.

In fact, previous *in vivo* experiments suggest that, on average, cell partitioning at individual bifurcations is highly biased toward the higher-flow pathway [18]. This results in strong spatial correlations between the volume fraction of RBCs (or hematocrit) and the flow velocity. In other words, vessels which exhibit higher flow velocities on average also exhibit higher hematocrits, which gives rise to the so-called tissue Fahraeus effect[1] [19].

Consistent with these previous works, the recent experimental results of Obrist's group [17], obtained with RBC suspensions flown through hexagonal, 3-connected, networks, display a preferential localization of the cells in the center of

*These authors have equally contributed to this work
†Corresponding author. E-mail: sylvie.lorthois@imft.fr

[1]The tissue Fahraeus effect denotes a reduction of the volume fraction of RBCs in the whole network by comparison to its discharge hematocrit (defined as the ratio between the RBC flow and the total flow). It is analogous to the the Fahraeus effect, *i.e.*, the reduction of the hematocrit within a single segment (tube hematocrit) by comparison to the discharge hematocrit, which results from the correlation between hematocrit and velocity within a single vessel cross-section [18].

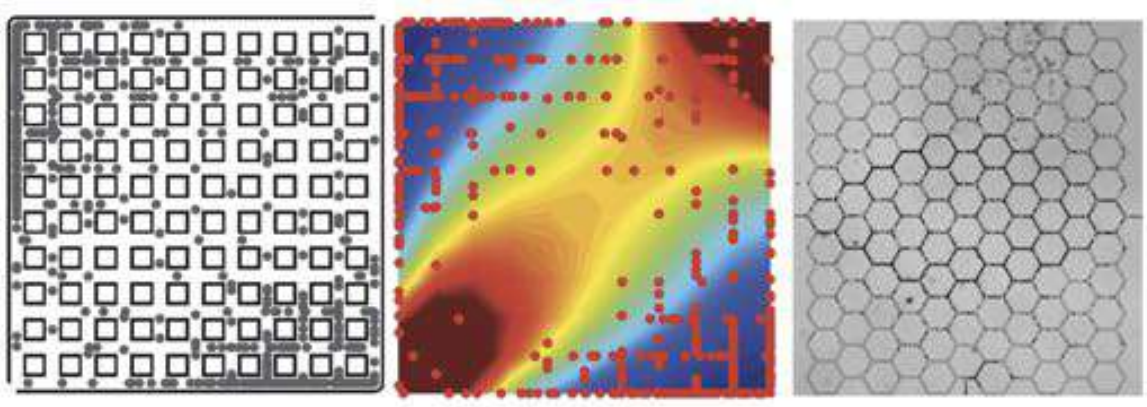

Figure 1: Spatial repartition of RBCs in a square microfluidic network with channels, as predicted by the discrete model with individually tracked RBCs proposed by [11]. Inflow is on the lower left corner and outflow is on the upper right corner. Channel radii are supposed sufficiently small for RBCs to flow in single line and follow the pathway of highest pressure drop at intersections. RBCs are displayed by dots in the figure panels. **Left**: Snapshot at 1.5 times the total network turnover time. **Middle**: Steady-state configuration. The colors indicate the average flow rate smeared out across the network (red, high velocities; blue, low velocities). The vessels are not shown. Reproduced with permission from [11]. **Right**: Human RBCs flowing from left to right in an hexagonal microfuidic network with channels of size $10\mu m$ x $10\mu m$ x $50\mu m$.

the network, whose channels have the highest velocities. By contrast, the network corners are almost devoid of RBCs. This raises several questions. For example, would the former theoretical prediction be supported by experiments performed in networks with square unit patterns? If yes, are there specific features of the studied configuration (*e.g.* channel diameters, connectivity) that sufficiently deviate from the subsequent experiments and typical *in vivo* conditions to explain the accumulation of RBCs in low flow vessels? What are the basic mechanisms and ingredients controlling the distribution of RBCs in simple generic networks with uniform vessel diameters?

To address these questions, we present a series of experiments performed in both hexagonal (*e.g.*, Figure 1, right panel) and square networks, and gain physical insights on the results by comparison with discrete network models of RBC flow in the same configurations. We show that despite the apparent simplicity of the geometries at hand, model predictions can differ significantly from experiments and are very sensitive to the network hierarchy, strongly suggesting that an improved description of blood flow at the local scale should be necessary.

References

[1] L.L Cooper et al. Microvascular function contributes to the relation between aortic stiffness and cardiovascular events. Circulation: Cardiovasc. Imaging. 9: e004979, 2016.
[2] L. Østergaard et al. Cerebral small vessel disease: capillary pathways to stroke and cognitive decline. JCBFM. 36: 302–325, 2016.
[3] J.C. Cruz Hernandez et al. Neutrophil adhesion in brain capillaries reduces cortical blood flow and impairs memory function in Alzheimer's disease mouse models. Nature Neuroscience. 22: 413-420, 2019.
[4] M. Desjardins et al. Aging-related differences in cerebral capillary blood flow in anesthetized rats. Neurobiol. Aging 35: 1947-1955, 2014.
[5] A. Pries et al. Blood-flow in microvascular networks - Experiments and simulation. Circ. Res. 67: 826–834,1990.
[6] A. Villringer et al. Capillary perfusion of the rat-brain cortex. An in vivo confocal microscopy study. Circ. Res. 75: 55-62, 1994.
[7] Y. C Fung. Biodynamics: Circulation. Springer, New York, 1984.
[8] T.W. Secomb. Blood Flow in the Microcirculation. Ann. Rev. Fluid Mech. 49:443-461, 2017.
[9] S. Lorthois, Blood suspension in a network. *In* Dynamics of blood cell suspensions in microflows. CRC Press, 2019.
[10] O. Forouzan et al. Passive recruitment of circulating leukocytes into capillary sprouts from existing capillaries in a microfluidic system. Lab Chip. 11: 1924, 2011.
[11] D. Obrist et al. Red blood cell distribution in simplified capillary networks. Phil. Trans. Royal Soc. A. 368: 2897-2918, 2010.
[12] A.R. Pries et al. Generalization of the Fahraeus principle for microvessel networks. Am. J. Physiol. 251: H1324-H1332, 1986.
[13] A.R. Pries et al. Structure and hemodynamics of microvascular networks: heterogeneity and correlations.Am. J. Physiol. 229: H1713-H1722, 1995.
[14] S.S Shevkoplyas et al. Prototype of an in vitro model of the microcirculation. Microvasc. Res. 65: 132-136, 2003.
[15] P. Balogh and P. Bagchi. Direct Numerical Simulation of cellular-scale blood flow in 3D microvascular networks. Biophys. J. 113: 2815-2826, 2017.
[16] P. Balogh and P. Bagchi. Analysis of red blood cell partitioning at bifurcations in simulated microvascular networks. Phys. Fluids. 30: 051902, 2018.
[17] A. Mantegazza et al. In vitro investigations of red blood cell phase separation in a complex microchannel network. Biomicroflu. 14: 014101, 2020.
[18] A. R. Pries et al. Red cell distribution at microvascular bifurcations. Microvasc. Res. 38: 81-101, 1989.
[19] A.R. Pries and P. Gaehtgens. Dispersion of blood cell flow in microvascular networks. *In* Microvascular Mechanics. Springer, NY, 1989.

MODELING THE COLLOIDAL HYDRODYNAMICS OF BIOLOGICAL CELL FUNCTION

Emma Gonzalez[1], Alp Sunol [1] Akshay Maheshwari[2], Drew Endy[2], and Roseanna N. Zia *[1]
[1] Department of Bioengineering, Stanford University, Stanford, California, U.S.A.
[2] Department of Chemical Engineering, Stanford University, Stanford, California, U.S.A.

Summary A physics-based computational model of a biological cell is presented, along with results from dynamic simulation of colloidal-scale biological processes. In a merging of biological modeling and physical modeling, biomolecules and their interactions are physically represented, individually and explicitly, in a representative voxel of translation molecules as well as a simple whole-cell confined model. With it, we show that an interplay between confinement, hydrodynamic interactions, Brownian motion, and interparticle forces qualitatively change particle dynamics. We find that colloidal-scale physics may be required to explain some life-essential biological processes in cells. The qualitative and quantitative influences of hydrodynamics, confinement and crowding, as well as the consequences of neglecting such influences, are discussed.

INTRODUCTION

Many mathematical representations of cellular behavior rely on abstractions that do not account for how macromolecules are organized and move within the crowded cell milieu. For example, linear algebra- and differential equation-based models typically do not represent individual biomolecules or their spatial position and motion. While atomistic modeling of biological cells is robust, structural biology modeling can evolve dynamics only over nanoseconds [figure 1(a)]. At the opposite end of the spectrum, systems biology abstracts space away entirely [figure 1(b)]. For many questions in biology these simpler models have been sufficient. However, a multitude of cellular processes occur between these two limits, at the colloidal scale [figure 1(c)]. I will discuss our progress in developing computational and theoretical tools to model biological processes in a simple model cell, by representing the cell as a spherically confined colloidal suspension, where biomolecules and their interactions are physically represented, individually and explicitly. By developing a more robust and physics-based model for how macromolecules interact within cells we can contribute to a more physically complete representation of living matter. A primary challenge in models of confined colloidal suspensions is the accurate and efficient representation of many-body hydrodynamic interactions, Brownian motion, and the enclosure itself. We have developed a "Cellular Stokesian dynamics" framework that accounts for spherically confined many-body hydrodynamic and lubrication interactions, Brownian motion, and active transport [2,3]. Utilizing this model, we study diffusion, hydrodynamic towing, confinement, and their impact on mRNA translation rates [3-5].

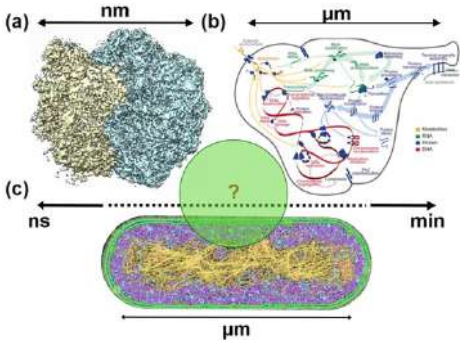

Figure 1 Presented work expands current range of modeling of biological cells. (a) Atomistic-scale modeling spans only nanoseconds. (b)Most whole-cell models are kinetics only with no spatial resolution. (c) Colloidal-scale processes are ubiquitous in cells, yet modeling them is emergent, partially owing to the difficulty in detailed representation of the relevant microscopic forces in low-Reynolds number flow. From [1].

METHOD OF SIMULATION

Our "Cellular Stokesian Dynamics" model [1] is utilized to represent a spherically confined colloidal suspension, fully modelling many-body hydrodynamic and lubrication interactions with an enclosing cavity and between particles. Brownian dynamics is also utilized to simulate a representative voxel of mRNA translation molecules. In both, the solvent is implicit. All biomolecules are represented as spheres of various sizes, relative to other biomolecules and relative to the enclosing cavity. The total packing fraction of solid to liquid of the model cell ranges from 50% to 5%; the degree of confinement ranges from a cavity 10 times to 400 times the size of the confined colloids. Hydrodynamic interactions are long-ranged and an infinitude of reflected interactions are fully accounted for by a novel set of mobility functions developed in our prior work [2]. We model coarse-grained interactions between proteins via a modified, continuous Kern-Frenkel model [6,7], which localizes attraction to an arbitrary number of patches on a protein's surface. Such a "patchy" model can capture the anisotropic nature of short-ranged attractions (e.g. hydrophobic interactions), as well as isotropic repulsions due to electrostatic interactions. Particle displacements, osmotic pressure, and reaction events are monitored throughout simulation, and utilized to compute self-diffusion and impact of entropic forces on relative transport rates during interactions between spheres representing translation molecules and other biomolecules.

INTERPLAY OF BROWNIAN MOTION, CONFINEMENT, POLYDISPERSITY, AND HYDRODYNAMICS

Study of particle volume fractions in the range between 0.05 and 0.40 reveals that confinement exerts a qualitative influence on particle dynamics, which in turn affects biomolecule association times in key biological cell processes. Confinement induces strong layered ordering [figure 3, left] and thus the mean-square displacement over all time scales depends on the position in the cavity [figure 3, center and right]. Additionally, at short times, the diffusivity is anisotropic,

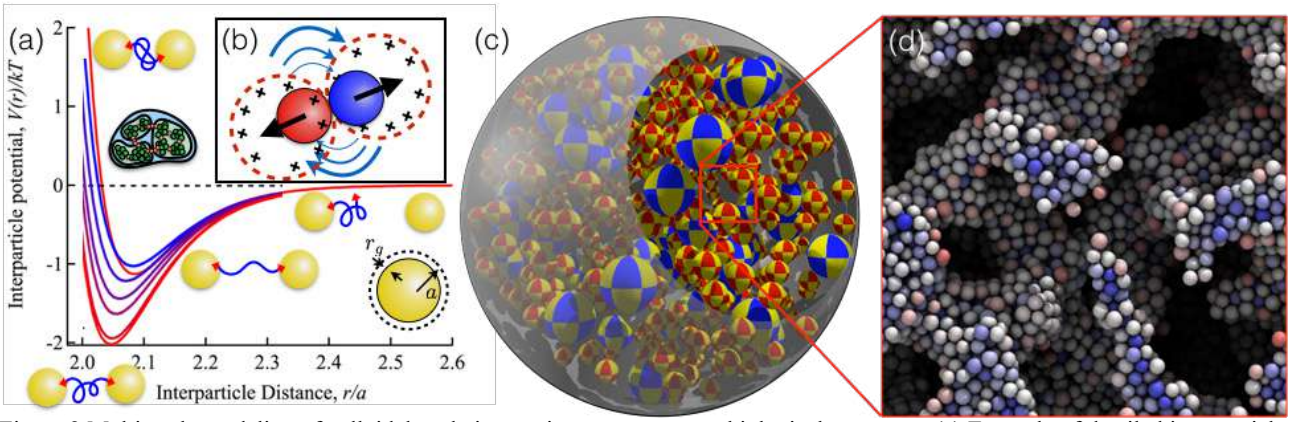

Figure 2 Multi-scale modeling of colloidal-scale interactions can represent biological processes. (a) Example of detailed interparticle potential. (b) Non-isotropic repulsive and attractive interactions of different ranges can be included in the model. (c) "Cellular Stokesian dynamics model of simple whole cell [1,2] includes many-body long-range reflected hydrodynamic interactions, lubrication interactions, Brownian motion, patchy interparticle attractions. (d) Colloidal gelation [8].

with diffusion along the cavity radius slower than diffusion tangential to the cavity wall, due to the anisotropy of hydrodynamic coupling and to confinement-induced spatial heterogeneity in particle concentration. The mean-square displacement is anisotropic at intermediate times as well and, surprisingly, exhibits super-diffusive and subdiffusive behaviours for motion along and perpendicular to the cavity radius respectively, depending on the suspension volume fraction and the particle-to-cavity size ratio. No long-time self-diffusive regime exists; instead, the mean-square displacement reaches a long-time plateau, a result of entropic restriction to a finite volume. In this long-time limit, the higher the volume fraction is, the longer the particles take to reach the long-time plateau, as cooperative rearrangements are required as the cavity becomes crowded.

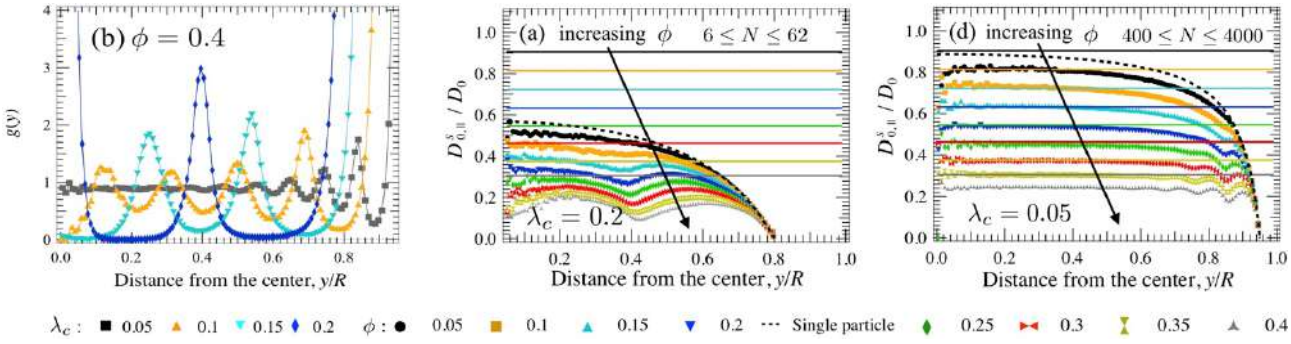

CONCLUSIONS

The ordered dynamical heterogeneity seen in our dynamic simulations promotes self-organization of particles based on their size and self-mobility, which is of particular relevance in biophysical systems [3]. Subsequent studies of polydispersity [4] reveal an important interplay with confinement that explains our results regarding the role of Brownian motion and reactions in processes in prokaryotic cells [5].

References

[1] Maheshwari A.M., Sunol A.M., Gonzalez E., Endy D. and Zia, R.N. Colloidal hydrodynamics of biological cells: A frontier spanning two fields. *Phys Rev. Fluids* **4** 110506 (2019).

[2] Aponte-Rivera C.A. and Zia R.N. Simulation of hydrodynamically interacting particles confined by a spherical cavity. *Phys. Rev. Fluids* **1** 023301 (2016).

[3] Aponte-Rivera C.A., Su Y., and Zia R.N.. Equilibrium structure and diffusion in concentrated hydrodynamically interacting suspensions confined by a spherical cavity. *J. Fluid. Mech.* **836**: 413-450 (2018).

[4] Gonzalez E., Aponte-Rivera C.A., and Zia, R.N. Impact of polydispersity and hydrodynamics on diffusion in spherically confined colloidal suspensions. In preparation for *J. Rheology.*

[5] Maheshwari A.M., Sunol A.M., Gonzalez E., Endy D. and Zia, R.N. Colloidal physics regulates tRNA supply to ribosomes during protein synthesis. In preparation for *Cell.*

[6] Kern N. and Frenkel D. Fluid-fluid coexistence in colloidal systems with short-range strongly directional attraction. *J. Chem. Phys.* **118** 9982-9989 (2003).

[7] Gögelein C., Nagele G., Tuinier R., Gibaud T., Stradner A., Schurtenberger P. A simple patchy colloid model for the phase behavior of lysozyme dispersions. *J. Chem. Phys*. **129** 085102 (2008).

[8] Zia R.N., Landrum B.J., and Russel W.B. A micro-mechanical study of coarsening and rheology of colloidal gels: Cage building, cage hopping, and Smoluchowski's ratchet. *J. Rheol.* **58**(5) 1121-1157 (2014).

DIURNAL VERTICAL MIGRATION OF *HETEROSIGMA AKASHIWO*

Li Zeng *[1], Tim Pedley[2], and Yu Yang[1]
[1] State Key Laboratory of Simulation and Regulation of Water Cycle in River Basin, China Institute of Water Resources and Hydropower Research, Beijing, China
[2] Department of Applied Mathematics and Theoretical Physics, University of Cambridge, Cambridge, UK

Summary Understanding the migration of *Heterosigma akashiwo* will make an important contribution to marine ecology. It is found that the fraction of helical and straight line motion modes changes greatly during the dark-light cycle. Cells' distribution exhibits three typical characteristics: stable accumulation at the top surface during the light period, the stable accumulation at both the bottom and upper surfaces during the dark period, and a non-equilibrium distribution during the transition between light and dark periods. The high concentration near the bottom is caused by downward swimming rather than sedimentation. It seems that cells' physiological rhythm rather than an asymmetrical mass distribution regulates the downward swimming. The Péclet number related to the vertical swimming velocity and translational diffusivity is found to vary with cells' vertical position.

INTRODUCTION

The migration of gyrotactic micro-organisms is quite significant for understanding many ecological phenomena in oceans. The type of gyrotactic micro-organism considered here is *Heterosigma akashiwo*, which is one typical species related to the harmful algal blooms occurring in coastal regions. Understanding the migration of *Heterosigma akashiwo* will make an important contribution to exploring the evolution of the marine ecosystem, especially the evolution of red tides. Regarding the migration of gyrotactic micro-organisms, there have been various theoretical, experimental, and computational investigations [1-7], with focus on swimming behaviours of individual swimmers, shear-triggered accumulation and trapping, bioconvection, etc. However, the diurnal migration of *Heterosigma akashiwo* is not well understood. Until now, the characteristics of swimming modes, detailed concentration distribution near the top and bottom surfaces, as well as the forces that drive the mean downward swimming during the whole dark-light cycle have been incompletely described. In this paper, therefore, we investigate the swimming modes of *Heterosigma akashiwo*, its concentration distribution, and the identification of potential factors to regulate the downward swimming during the dark-light cycle.

MATERIALS AND METHOD

Three groups of experiments were performed to investigate the diurnal vertical migration of *Heterosigma akashiwo*. The first experiment is to observe the migration in a confined micro-channel with height of 1 mm, width of 2.5 mm, and length of 50 mm. The objective is to explore the swimming modes and detailed concentration distribution near the wall during the whole dark-light period. The second experiment is to explore the diurnal vertical migration of *Heterosigma akashiwo* in one chamber with a height of 2 cm. The objective is to test whether similar behaviours still occur in the water body with larger spatial scale. The third experiment is to observe the distribution of *Heterosigma akashiwo* in the downward flow through a vertical tube. The objective is to explore whether the downward swimming in the dark period is caused by a change of relative positions of mass and buoyancy centers. The algal cells (GY-H24 *Heterosigma akashiwo* adopted in this work came from Zhoushan, Zhejiang, China, and were cultivated at the temperature of 25 $^{\circ}\mathrm{C}$ in a growth chamber with 12:12 light:dark photoperiod. The first experiment was carried out based on the MICRO-PIV system, and the second and third experiments were done based on the planar laser induced fluorescence (PLIF) technique.

RESULTS AND DISCUSSION

Experimental results showed that *Heterosigma akashiwo* can swim vertically upwards and downwards, on average, in still water. During the 1st hour (D1) to the 10th hour (D10) of the dark period, cells' downward swimming is stronger than their upward swimming, while, during the 3rd hour (L3) to the 11th hour (L11) of the light period, the upward swimming is dominant, as shown in figure 1. During the transition of dark to light or light to dark, there is no clear preference of swimming behaviour. The high concentration near the bottom wall is caused by cells' downward swimming rather than their sedimentation, since the mean swimming velocity of *Heterosigma akashiwo* in the dark period, approximately on the order of 100 $\mu\mathrm{m\ s}^{-1}$, is much greater than the sedimentation velocity, approximately 3 $\mu\mathrm{m\ s}^{-1}$.

Two typical swimming modes, helical motion and straight line motion, were observed during the dark-light cycle. The mean vertical swimming velocity of the straight line mode is approximately two times that of the helical mode. The fraction of swimming modes can change greatly during the dark-light cycle. It is found that the main swimming mode is straight line swimming in the dark period, while helical swimming dominates in the light period.

*Corresponding author. E-mail: lizeng@iwhr.com.

The accumulation of *Heterosigma akashiwo* near the top and bottom surfaces were also observed in the larger chamber with water depth of 3 cm, as shown in figure 2. The concentration distribution of *Heterosigma akashiwo* is not exponential, which means that the ratio of vertical swimming velocity and translational diffusivity near the wall is not constant. According to the balance of cells' flux contributed by the mean vertical swimming and translational diffusion in the vertical direction, the Péclet number based on the chamber depth, the mean swimming velocity and the translational diffusivity is found to vary with cells' vertical position. However, the separate variation of the mean swimming velocity and translational diffusivity is still not clear based on these data.

In general, bottom-heavy micro-organisms tend to swim upwards, while nose-heavy ones tend to swim downwards. It is well known that *Heterosigma akashiwo* is a bottom-heavy organism in still water during the light period [4], and their asymmetric mass distribution is beneficial in maintaining the upward swimming. Recent investigation has shown that a turbulent signal can trigger downward swimming by changing the relative position of the centers of mass and buoyancy [6]. The question arises as to whether downward swimming in still water is related to the change of relative position of the two centers? If it is, cells would swim towards the wall in the downward flow (with certain flow velocity) through a vertical tube during the dark period. However, our observation has shown that cells mainly accumulate in the central zone of the tube in the dark period as it did in the light period, which means that the downward swimming is not regulated by the asymmetrical mass distribution [1]. It appears that downward swimming is caused by the physiological rhythm of *Heterosigma akashiwo*.

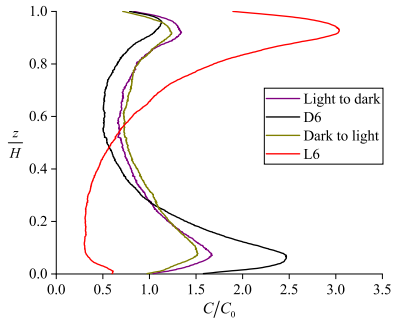

Figure 1: Variation of cells' concentration with z/H, where z is cells' vertical position, and H is the height of the confined micro-channel.

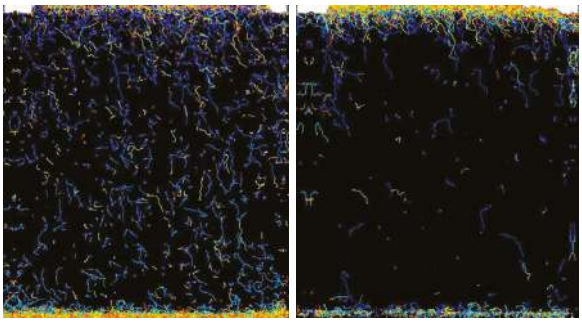

Figure 2: Instantaneous distribution of cells. Left figure corresponds to the dark period, and right figure corresponds to the light period

CONCLUSIONS

Distribution of *Heterosigma akashiwo* has distinct features in one dark-light cycle: stable accumulation on the top surface during the light period, and stable accumulation on both the bottom and top surfaces during the dark period. Detailed concentration structure of *Heterosigma akashiwo* has been identified for a time interval of 1 hour. The high concentration near the bottom is caused by cells' downward swimming rather than their sedimentation. It seems that the internal, physiological rhythm of *Heterosigma akashiwo* regulates the downward swimming. However, more evidence associated with both biology and fluid mechanics is required to further clarify this issue.

ACKNOWLEDGMENTS

This work is supported by the National Key R&D Program of China (grant no. 2016YFC0502202), and the IWHR Research & Development Support Program (grant nos. HY0145B402016 and HY0145B682017).

References

[1] Kessler J.O. Hydrodynamic Focusing Of Motile Algal Cells. Nature 313:218–220, 1985.
[2] Pedley T.J. Kessler J.O. Hydrodynamic Phenomena In Suspensions Of Swimming Microorganism. Annu. Rev. Fluid Mech. 24:313–358, 1992.
[3] Durham W.M. Kessler J.O. Stocker R. Disruption Of Vertical Motility By Shear Triggers Formation Of Thin Phytoplankton Layers. Science 323: 1067–1070, 2009.
[4] Bearon R.N. Grünbaum D. and Cattolico R. A. Relating Celll-evel Swimming Behaviors To Vertical Population Distributions In Heterosigma Akashiwo (Raphidophyceae), A Harmful Alga. Limnol. Oceanogr. 49:607–613, 2004.
[5] Schuech R., Menden-Deuer S. Going Ballistic In The Plankton: Anisotripic Swimming Behaviour Of Marine Protists. Limnol. Oceanogr. 4:1–6, 2014.
[6] Sengupta A., Carrara F., Stocker R. Phytoplankton Can Actively Diversify Their Migration Strategy In Response To Turbulent Cues. Nature 543:555–558, 2017.
[7] Zeng L., Pedley T.J. Distribution Of Gyrotactic Micro-organisms In Complex Three-dimensional Flows. Part I. Horizontal Shear Flow Past A Vertical Circular Cylinder. J. Fluid Mech. 852:358-397, 2018.

O0108365 - MS03 - Biological fluid-structure interaction at the microscale - Oral

EMERGENCE OF METACHRONAL WAVES IN ARRAYS OF INSTABILITY-DRIVEN BEATING CILIA

Chenglei Wang*[1], Simon Gsell[1], Umberto D'Ortona[1], and Julien Favier[1]
[1] Aix-Marseille Univ., CNRS, Centrale Marseille, M2P2, Marseille, France

Summary This research explores hydrodynamic interactions among an array of naturally curved cilia driven by a tip-concentrated follower force, i.e., a constant-magnitude force acting on the cilium tip and always aligned with the tip direction, in low Reynolds number flows. This fluid-structure interaction (FSI) problem is solved using a numerical framework based on the immersed boundary lattice Boltzmann method (IBLBM) and the finite element method (FEM). Simulation results show that when the Reynolds number, force magnitude, cilia spacing and domain size are properly chosen, hydrodynamic interactions can successfully result in metachronal waves (MCWs).

INTRODUCTION

Cilia are micro-scale hair-like organelles protruding from the surfaces of many eukaryotic cells. They undergo various oscillatory motions driven by numerous internal dynein molecular motors for fluid transport. When clustering in large domains, they usually coordinate with their neighbors to produce metachronal waves (MCWs) instead of beating in either random or synchronous manners. This amazing phenomenon was hypothesized to result from hydrodynamic interactions, and has been extensively explored in literature through various fluid-structure interaction (FSI) models [1,2]. In most of the existing works, it is assumed that cilia are actuated by regulating dynein motors through geometric feedback control schemes, such as the curvature-based feedback control [2].

Recently, Bayly and Dutcher proposed that such regulation may not be required since dynein motors can supply sufficiently large axial stresses to trigger dynamic buckling instability and induce sustained oscillations [3]. A later study demonstrated that the instability-driven cilia exhibit realistic asymmetric beating patterns when taking into account that cilia are expected to be curved in equilibrium states in nature [4]. This immediately leads to interesting questions: How do the cilia hydrodynamically interact when they are driven by this new kind of actuation strategy? Can metachronal waves emerge in this configuration? If so, what are they like and how are they influenced by some key parameters, such as the Reynolds number, actuation strength, cilia spacing and domain size? This work aims to address these questions through systematic numerical investigations.

PROBLEM DESCRIPTION AND METHODOLOGY

In this study, an array of cilia (N_x and N_y in the x- and y-directions, respectively) is placed in an initially quiescent flow contained in a domain with length L, height H and width W, as shown in Figure 1. The cilium diameter is described by D, and the spacings between cilia in the x- and y-directions are referred to as d_x and d_y, respectively. The cilia are assumed to exhibit a circular shape characterized by the arc length L_c and arc angle θ at rest. Cilium bases ($s = 0$, where s the Lagrangian coordinate along the cilium) are perpendicularly clamped at the bottom, whereas cilium tips ($s = L_c$) are set free. The axial stresses along each cilium are simplified as a compressive follower force $\boldsymbol{F}_T$ which is tangentially applied at the cilium tip. As the cilium deforms, the force magnitude is kept constant and its direction remains tangential to the cilium tip.

In nature, cilia are slender bodies, since their diameters are much smaller than their lengths. Herein, the diameter-to-length ratios are set as 0.1 to satisfy this slender-body condition. To simplify the problem, cilia are modeled as elastic filaments without internal damping effects, and they are only allowed to undergo in-plane deformations. As such, the governing equation for the dynamics of each cilium can be written as

$$\rho_c A \frac{\partial^2 \boldsymbol{X}}{\partial t^2} - \frac{\partial}{\partial s}\left[EA\left(1 - \left|\frac{\partial \boldsymbol{X}}{\partial s}\right|^{-1}\right)\frac{\partial \boldsymbol{X}}{\partial s}\right] + \frac{\partial^2}{\partial s^2}\left(EI\frac{\partial^2 \boldsymbol{X}}{\partial s^2}\right) = \boldsymbol{F}_f \tag{1}$$

where ρ_c is the cilium density, A the cross-section area of the cilium ($A = \pi D^2/4$), E the Young's modulus, I the moment of inertia ($I = \pi D^4/64$), $\boldsymbol{X}$ the cilium position, and $\boldsymbol{F}_f$ the fluid loading acting on the cilium.

The dynamics of the incompressible flow can be described by the continuity and momentum equations as follows

$$\nabla \cdot \boldsymbol{v} = 0 \tag{2}$$

$$\rho_f \frac{\partial \boldsymbol{v}}{\partial t} + \rho_f \boldsymbol{v} \cdot \nabla \boldsymbol{v} = -\nabla p + \mu \nabla^2 \boldsymbol{v} + \boldsymbol{f}_e \tag{3}$$

where ∇ is the gradient operator, $\boldsymbol{v}$ the flow velocity, ρ_f the fluid density, p the pressure, μ the dynamic viscosity, and $\boldsymbol{f}_e$ the external force per unit volume.

*Corresponding author. E-mail: chenglei.wang@univ-amu.fr.

MINI SYMPOSIA

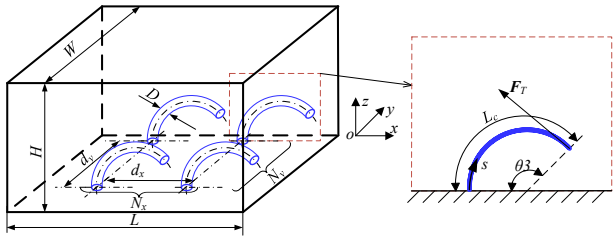

Figure 1: Schematic of an array of naturally-curved cilia located in the computational domain, where each cilium is actuated by a compressive follower force ($\boldsymbol{F}_T$) at its tip (not in scale). L, H and W are the length, height, width of the domain, respectively, L_c the cilium length, D the cilium diameter, d_x and d_y the x- and y-distances between two neighboring cilia, N_x and N_y the cilium numbers in the x- and y-directions, θ the cilium arc angle, and s the Lagrangian coordinate along the cilium.

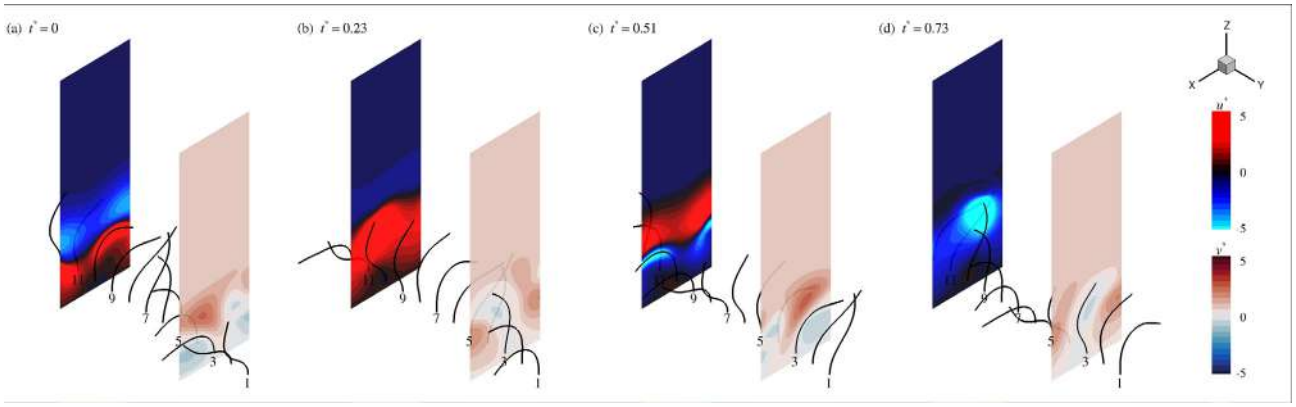

Figure 2: Snapshots of the cilia beating motion at instants $t^* = 0$ (a), 0.23 (b), 0.51 (c) and 0.73 (d), where $t^* = (t - t_r)\, EI/\mu L_c^4$ and t_r refers to the time for subfigure (a) in simulation. The four upper and lower contours display the dimensionless x- and y-velocities (u^* and v^*), respectively, where $u^* = u\mu L_c^3/EI$ and $v^* = v\mu L_c^3/EI$.

To study this FSI problem, the co-rotational finite element formulation is applied to solve structure dynamics. The multiple-relaxation-time (MRT) lattice Boltzmann method (LBM) is adopted as an alternative to simulate the three-dimensional fluid dynamics. To resolve the interplay between the flow and structure dynamics, the immersed boundary method (IBM) is incorporated so as to realize the no-slip boundary conditions on the structure surfaces as well as accurately evaluate the fluid loading.

RESULTS AND CONCLUSIONS

In this work, the collective behaviors of the one-and two-dimensional cilium arrays are explored over ranges of Reynolds number, force magnitude, cilium spacing and domain size. The simulation results reveal that all these parameters play important roles in the hydrodynamic interactions among cilia and the resulting collective behaviors. Particularly, various collective patterns, including metachronal waves, are observed. Herein, one representative case where a transverse metachronal wave emerges is briefly discussed for illustration.

In this case, a diaplectic row of cilia ($N_x = 1$ and $N_y = 12$) is evenly placed in the domain with the length $L = L_c$ and width $W = 3L_c$, corresponding to the x-distance $d_x = L_c$ and y-distance $d_y = L_c/4$, where L_c is the cilium length. The arc angle is set as $\theta = \pi/4$, and the magnitude of the follower force is $|\boldsymbol{F}_t| = 50EI/L_c^2$, where EI is the bending stiffness. The Reynolds number is $\mathrm{Re} = \rho_f EI/\mu^2 L_c^2 = 5$, where ρ_f is the fluid density and μ the dynamic viscosity. After a random initialization, a sustained wave formed by the 12 cilia with the wavelength of $3L_c$ emerges gradually, and it propagates along the positive-y direction, as shown in Figure 2. The x- and y-velocities of the flow fluctuate significantly around the cilia, whereas they remain relatively steady above the cilia, indicating that a more steady flow is generated in this region. Furthermore, the x- and y-velocities above the cilia are negative and positive, respectively, and they are nearly equal in magnitude. This implies that the global-flow-transport direction deflects from the ciliary beating direction by an angle of $\pi/4$, approximately.

References

[1] Chateau S., Favier J., D'ortona U., Poncet S. Transport efficiency of metachronal waves in 3D cilium arrays immersed in a two-phase flow. *J. Fluid Mech.* **824**, 931–961, 2017.
[2] Elgeti J., Gompper G. Emergence of metachronal waves in cilia arrays. *PNAS.* **110**, 4470–4475, 2013.
[3] Bayly, P., Dutcher S. Steady dynein forces induce flutter instability and propagating waves in mathematical models of flagella. *J R SOC INTERFACE.* **13**, 20160523, 2016.
[4] Ling F., Guo H., Kanso E. Instability-driven oscillations of elastic microfilaments. *J R SOC INTERFACE.* **15**, 22–24, 2018.

LINGERING DYNAMICS OF MICROVASCULAR BLOOD FLOW IN SYRIAN HAMSTERS

C. Wagner[1], A. Kihm[1],*, S. Quint[1], M. W. Laschke[2], M. D. Menger[2]
[1] Experimental Physics, Saarland University, Saarbruecken, Germany
[2] Institute for Clinical and Experimental Surgery, Campus University Hospital, Homburg, Germany

Summary *The microvascular networks in the body of vertebrates consist of the smalle vessels, such as arterioles, venules, and capillaries. The flow of red blood cells (RBCs) through these networks ensures the gas exchange in the tissues, as well as the transport of nutrients towards the tissues. Any alterations in this blood flow may have severe implications on the health state. Since the vessels in these networks obey dimensions similar to the diameter of RBCs, dynamic effects on the cellular scale play a key role.*
We present a detailed analysis of the shape alteration of RBCs while passing bifurcations and confluences as well as so called lingering effects. These lingering events of cells at the apex of bifurcating vessels affects the temporal distribution of cell-free areas in the branches and may even cause a partial blockage in severe cases.

Motivation and goals

Red blood cells obey an inner network of spectrin fibers, being responsible for their biconcave shape at rest. Due to the flexibility of this spectrin network, RBCs are able to pass through constrictions much smaller than their size at rest. However, not only constrictions alter the shape of RBCs, but also the intricate structure of the vascular network itself with its merging and bifurcating vessels. The shape of RBCs undergoes a characteristic deformation when approaching the apex of a bifurcation or a confluence, respectively. Whereas this alteration of the shape is due to increasing or decreasing confinements depending on the geometry, cells may even linger around the apex of a bifurcation, as shown in fig. (1) [2].

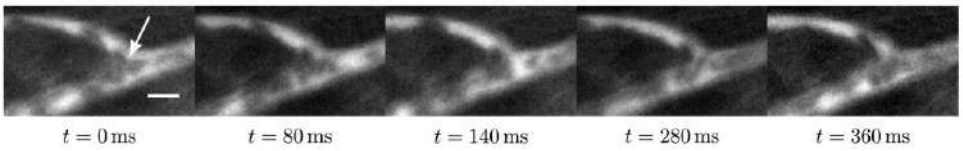

Figure 1. Time series of a lingering RBC at an arterial bifurcation for a time interval of 360 ms. At t=0 ms, an RBC is touching the apex of the bifurcation, marked by the arrow. The cell starts to deform and linger around this apex, leading to a partial blockage with decreased flow rate as can be seen in the upper branch of the daughter vessels for all subsequent images. Finally, the cell is detaching from the apex after 360 ms, exiting in the upper branch of the daughter vessels. Scale bar is 5 µm in width.

The steady progression in numerical modelling of RBCs even in complex networks has led to novel findings in the field of hemodynamics [2,3], especially concerning the impact and the dynamics of the lingering events. However, these results are yet unmatched by a detailed analysis of the lingering in experiments in vivo. To quantify this lingering effect in in-vivo experiments, we analyse branching vessels in the microvasculature of Syrian hamsters via intravital microscopy and the use of an implanted dorsal skinfold chamber (cf. Fig. (2)).

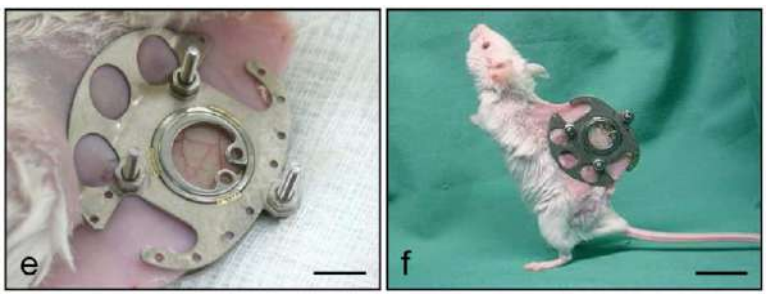

Figure 2. Stepwise preparation of a dorsal skinfold chamber in an anaesthetized balb/c mouse (e). Scale bar: 8 mm [1]. The animal tolerates the chamber well, as indicated by normal orientation behavior (f). Scale bar: 19 mm. After implantation, the blood vessels within the observation window can be investigated by means of intravital microscopy.

Using high-resolution objectives and high-speed cameras, the intravital microscopy provides insights into dynamic processes with single-cell resolution and is therefore perfectly suited to examine lingering in vivo.

Results and conclusions

The Hamster intravital images show various branching networks of vessels with different opening angles and diameter ratios. However, most of the observed topologies consist of only one or two bifurcations rather than multiple ones. Here we analyse as a typical example an area with 7 daughter branches in total (see fig. (3)).

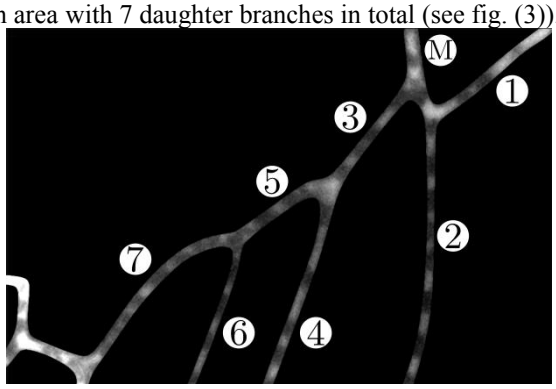

Figure 3. Branching arteriolar network. This geometry has been used for the detailed analysis shown in fig. 4. Blood flow is coming from the mother vessel (M) and exiting in all the other labelled branches. RBCs are black, in contrast to plasma or cell-free regions in white.

Using a self-written MATLAB image analysis script, we extract the temporal distribution of voids (cell-free regions) and RBCs in each branch. An exemplary time-signal of the measured intensities corresponding to these distributions is depicted in fig. (4). By normalising the void durations by the average passage time of a RBC, we are able to compare the void durations. We find that for distinctive pairs of branches, one vessel exhibits void durations of multiples of the RBCs passage time whereas the counterpart obeys rather short void durations. Interestingly, the lingering leads to substantially longer void durations in the branch of a bifurcation with the higher flow rate (branches #4,6). Several statistical measures will be presented that characterize the irregular flow dynamic of the network.

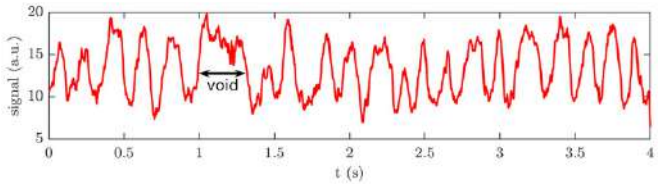

Figure 4. Intensity fluctuations along a line segment perpendicular to the vessel. Based on these findings, passage times of RBCs as well as temporal void lengths can be identified.

References

[1] M. W. Laschke, et al.: The dorsal skinfold chamber: window into the dynamic interaction of biomaterials with their surrounding host tissue, *European Cells and Materials* **22** (2011), 147-167.

[2] P. Balogh, and P. Bagchi: Direct Numerical Simulation of Cellular-Scale Blood Flow in 3D Microvascular Networks, *Biophys. J.* **12** (2017), 2815-2826.

[3] T. Ye, and L. Peng: Motion, deformation, and aggregation of multiple red blood cells in three-dimensional microvessel bifurcations, *Phys. Fluids* **31(2)** (2019).

STABILITY OF A RED BLOOD CELL IN A NARROWRECTANGULAR MICROCHANNEL

Naoki Takeishi*[1], Hiroaki Ito[2], and Shigeo Wada[1]
[1] Graduate School of Engineering Science, Osaka University, Toyonaka, Osaka, Japan
[2] Department of Physics Graduate School of Science, Chiba University, Chiba, Chiba, Japan

Summary The deformability of a red blood cell (RBC) highly affects the blood flow, both in large arteries and in the microcirculation, and hence it can be used to quantify the cell state. Despite numerous studies on the mechanical properties of RBCs much is still unknown about the relationship between deformability and the stable configuration of flowing cells in a confined rectangular channel. In this study, we numerically investigated the behavior of RBCs flowing at different $Capillary$ numbers (Ca) in a narrow rectangular microchannel that mimicked a microfluidic device. RBCs tend to exhibit asymmetrical shape for moderate Ca, while they show symmetrical shape for relatively low or high Ca. Since the slipper shape was only found at moderate Ca, measuring configurations of flowing cells will be helpful to quantify the cell state.

INTRODUCTION

It is well known that many blood-related diseases are associated with alterations in the geometry and membrane properties of red blood cells (RBCs) that result in reduced functionality [1]. Hence, cell deformability may be an important indicator of cell state, and might be used to diagnoses relevant blood diseases. Recent microfluidic techniques that are capable of high-throughput assay, and allows us to quantify the mechanical response of RBCs after spatial constriction in a confined microchannel [2]. Since the deformation of translating RBCs in the system is measured as projected two-dimensional configuration, a precise deformation especially in thickness direction of RBCs cannot be captured by means of the experimental observation. Along with the experimental study, recent computer simulation techniques have successfully been used to investigate aspects of cell dynamics [4, 5], where the RBC is modeled as a capsule than an inner fluid is enclosed by an elastic membrane. Since such numerical models allow us to investigate the effect of physical properties on cell behavior, the coupling of experimental and numerical approaches will be able to constitute a useful bioengineering strategy to quantify the cell state. The objective in this study, therefore, is to clarify the stable configuration of translating RBCs in a narrow rectangular microchannel. We numerically investigated the symmetry of the stable configuration of the deformed RBC for different Capillary number Ca, which is the ratio between the fluid viscous force and the membrane elastic force.

METHODS

We consider a cellular flow consisting of plasma and RBCs with radius a in a rectangular channel representing a microfluidic device with 10 μm $\times$ 3.5 μm along the wall-normal and span-wise directions, with a resolution of 16 fluid lattices per radius of RBC. The computational domain is shown in Fig.1(a) where the stream-wise length is set to be 50 μm. An RBC is modeled as a biconcave capsule, or a Newtonian fluid enclosed by a thin elastic membrane, with a major diameter 8 μm ($= 2a$), and maximum thickness 2 μm ($= a/2$). The membrane follows the Skalak constitutive law [3]. The flow was driven by a pressure gradient. Periodic boundary conditions were imposed on the inlet and outlet. To reproduce *in vivo* human RBC condition, the cytoplasmic viscosity was taken to be $\mu_1 = 6.0 \times 10^{-3}$ Pa·s, which is five times higher than the external fluid viscosity, $\mu_0 = 1.2 \times 10^{-3}$ Pa·s. Hence, the viscosity ratio λ ($= \mu_1/\mu_0$) was set to be 5. The problem was characterized by the capillary number $Ca = \mu_0 \dot{\gamma} a/G_s$, where G_s is the surface shear elastic modulus, and $\dot{\gamma}$ ($= U_m^\infty/H$) is the shear rate defined by the mean velocity of the external fluid without cell U_m^∞ and channel height H ($=$ 10 μm). The membrane was modeled as an isotropic and hyperelastic material that followed the Skalak constitutive law [3]. We used the lattice-Boltzmann method (LBM) coupled with the finite element method (FEM). These models were previously successfully applied to the analysis of cellular hydrodynamic interactions in channel flows [4]. More precise descriptions about numerical methods and model validations should be referred to our previous work [4, 5].

RESULTS & DISCUSSION

Figure 1(b) shows snapshots of a stable RBC configuration for different Ca at fully developed flow. The RBC demonstrated an almost unchanged (symmetrical) biconcave shape at small $Ca = 10^{-3}$, then shifted to an asymmetrical slipper shape as Ca increased. Such asymmetrical shape remains the same with twice the fluid mesh resolution [6]. Interestingly, similar asymmetrical shape can be also observed in the microfluidic device [6]. The RBCs finally attained a symmetrical parachute shape at further large Ca. To quantify the symmetry of the stable configuration of the deformed RBC, we propose a symmetry index ID_{sym}, which is defined by the volume ratio of two volumes that are divided by a plane parallel

*Corresponding author. E-mail: ntakeishi@me.es.osaka-u.ac.jp

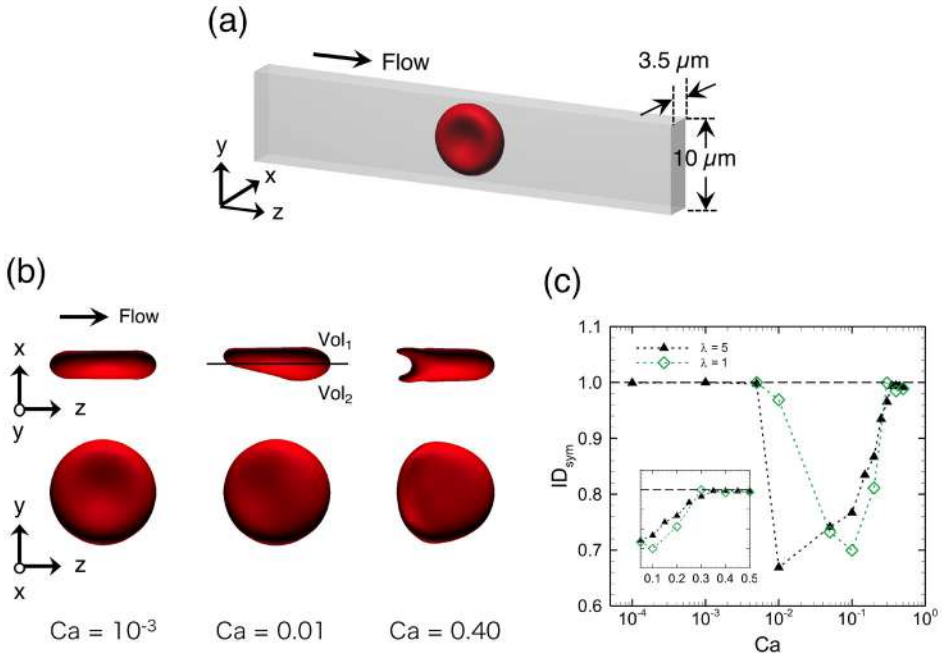

Figure 1: (a) Computational domain to reproduce a translating red blood cell (RBC) in the narrow rectangular microchannel. (b) Snapshots of a fully deformed RBC for different Ca at $\lambda = 5$, where the solid line denotes the center of the x-z-plane parallel to the flow direction, dividing the cell into the volume 1 (Vol_1) and volume 2 (Vol_2). (c) The symmetry index ID_{sym} as a function of Ca at $\lambda = 5$ (triangle) and 1 (diamond).

to the flow direction at the midline of the channel, as shown in Fig.1(b). Using volume 1 (Vol_1) and volume 2 (Vol_2), ID_{sym} is given as

$$ID_{sym} = \frac{MIN\,(Vol_1, Vol_2)}{MAX\,(Vol_1, Vol_2)}. \tag{1}$$

We show the results of ID_{sym} as functions of Ca in Fig.1(c). An asymmetrical parachute shape abruptly appeared for $Ca \geq 0.01$, but it gradually recovered and finally reached $ID_{sym} = 1$ for $Ca \geq 0.35$. These results suggest that there exists the following specific range of Ca that allows a RBC to deform into an asymmetrical slipper shape: $5 \times 10^{-3} < Ca < 0.35$. Figure 1(c) also showed that DI_{sym} was affected by λ. When λ decreased to unity (i.e., $\lambda = 1$), the membrane tended to assume a symmetrical shape even at relatively low $Ca = 0.01$. The most asymmetrical shape was found at at $\lambda = 5$, and the minimum $DI_{sym}|_{\lambda=1}$ shifted to larger $Ca \approx 0.1$ (Fig.1c). The value of DI_{sym} at $\lambda = 1$ started to recover beginning at $Ca = 0.1$, and finally almost reached ~ 1 at $Ca = 0.3$. Although we are not sure what perturbations are needed to destroy the stable symmetrical shape, identifying a stable mode of RBCs in a channel will be also helpful not only to understand the cell state but also to evaluate the blood rheology.

CONCLUSIONS

We numerically investigated the dynamics of translating RBCs in a narrow rectangular microchannel for different capillary numbers (Ca). Our numerical results showed that RBCs tend to exhibit asymmetrical shape for moderate Ca ($10^{-3} < Ca < 0.35$), while they show symmetrical shape for relatively low or high Ca ($Ca \leq 0.01$ or $0.35 \geq Ca$). The membrane deformation as a function of Ca remained the same even when the viscosity ratio λ decreased from physiological relevant value (λ = 5) to unity. If these shapes are found in diseased RBCs translating at specific velocities, the shapes will be an important indicator of cell state.

References

[1] Chen, S. Red cell deformability and its relevance to blood flow. *Annu. Rev. Physiol.* **49**: 177–192, 1987.
[2] Ito H., Murakami R., Sakuma S., Tsai C.-H.D., Gutsmann T., Brandenburg K., Poöschl J.M.B., Arai F., Kaneko M., Tanaka M. Mechanical diagnosis of human eryhrocytes by ultra-high speed manipulation unraveled critical time window for global cytoskeletal remodeling.*Sci. Rep.* **7**: 43134, 2017.
[3] Skalak R., Tozeren A., Zarda R.P., Chien S. Strain energy function of red blood cell membranes. *Biophys. J.* **13**: 245–264, 1973.
[4] Takeishi N., Imai Y., Nakaaki K., Takami Y., Ishikawa T. Leukocyte margination at arteriole shear rate. *Physiol. Rep.* **2**: e12037, 2014.
[5] Takeishi N., Rosti M. E., Imai Y., Wada S., Brandt L. Haemorheology in dilute, semi-dilute and dense suspensions of red blood cells. *J. Fluid. Mech.* **872**: 818-848, 2019.
[6] Takeishi N., Ito, H., Kaneko M., Wada S. Deformation of a red blood cell in a narrow rectangular microchannel. *Micromachines* **10**: 199, 2019.

MINUET DANSE OF TWO CAPSULES IN SHEAR FLOW

Xu-Qu Hu[1,2], Dominique Barthes-Biesel[1], and Anne-Virginie Salsac*[1]
[1] Biomechanics and Bioengineering Laboratory (UMR CNRS 7338), Université de Technologie de Compiègne, Alliance Sorbonne Université, Compiègne, France
[2] State Key Laboratory of Advanced Design and Manufacturing for Vehicle Body, College of Mechanical an Vehicle Engineering, Hunan University, Changsha, China

Summary We model the three-dimensional hydrodynamic interaction of a pair of spherical capsules freely suspended in a simple shear flow under Stokes flow conditions. The capsules are enclosed by a thin neo-Hookean elastic membrane and filled with a Newtonian liquid with the same density and viscosity as the suspending fluid. The motion and deformation of the capsules are modeled by means of a boundary integral technique coupled to a finite element method. Depending on their initial position and deformability, the two capsules may do a minuet danse: they oscillate about the flow gradient, get nearer to each other, finally interact strongly and separate. We identify the regions of space where simple crossing or minuet occur. This novel minuet motion leads to a significant capsule deformation (and potential damage), even when the interaction is initially weak.

INTRODUCTION

The hydrodynamics of pairwise interaction of deformable particles is a crucial topic for semi-dilute suspension rheology. The case of capsules (liquid drop enclosed by a thin elastic membrane) is complex because their motion and deformation result from non-linear fluid-structure interactions. Specifically, the capsules may be highly deformed as they cross each other, which may lead to potential damage of the membrane. This phenomenon is usually studied in a simple shear flow $\boldsymbol{v}^{\infty} = \{\dot{\gamma}\, x_2, 0, 0\}$ in a Cartesian reference frame centered on one capsule C_1, where $\dot{\gamma}$ is the shear rate. The center of the other capsule C_2 is initially positioned at $\boldsymbol{X}^{(0)} = \{X_1^{(0)}, X_2^{(0)}, X_3^{(0)}\}$. When the two capsules have their centres in the same shear plane ($X_3^{(0)} = 0$), C_2 is first displaced along the velocity gradient, 'jumps over' C_1 (*leap-frog motion*) and is shifted back towards the flow axis as it moves away (Figure 1a). The crossing leads to an irreversible trajectory shift along the x_2-direction. This phenomenon has been observed for initially spherical capsules (radius a) enclosed by a hyperelastic membrane [1, 2, 3, 4], for vesicles [5] and red blood cells [6]. The case of two capsules in different shear planes ($X_3^{(0)} \neq 0$) has been considered, since they are rarely in the same shear plane in practice: for a significant initial relative velocity ($|X_2^{(0)}| \geq 0.5a$), they do a sideways leapfrog motion [7, 5]. The objective of this paper is to investigate the three-dimensional motion of two capsules when their centroids are in or near the same x_1x_3-plane ($|X_2^{(0)}| < 0.2a$), a situation that has never been considered, but where close interaction and doublet formation may be expected to occur.

PROBLEM DESCRIPTION AND SOLUTION METHOD

We study the three-dimensional hydrodynamic interaction of a pair of identical, initially spherical capsules that are freely suspended in the simple shear flow $\boldsymbol{v}^{\infty}$ under Stokes flow conditions. The capsules are filled with a Newtonian liquid with the same density and viscosity μ as the suspending fluid. Their membranes are infinitely thin and satisfy the neo-Hookean constitutive law (surface shear modulus G_s), with negligible bending resistance. The relative flow strength is measured by the capillary number $Ca = \mu\dot{\gamma}a/G_s$. We concentrate on the case where the two capsule centres are initially located in two different shear planes ($X_1^{(0)} \neq 0, X_2^{(0)} = 0, X_3^{(0)} \neq 0$). The motion and deformation of the capsules are modeled by means of a boundary integral technique to compute the flow field, coupled to a finite element method to calculate the force exerted by the membranes on the fluids. We follow the motion and deformation of the capsules as they are convected towards each other after a sudden start of the shear flow.

MINUET DANSE VERSUS LEAPFROG

We first consider the situation where the two capsules are on the same streamline ($X_1^{(0)}/a = -8, X_2^{(0)} = 0, X_3^{(0)} = 0, Ca = 0.3$), in the shear plane where they remain under Stokes flow conditions. Although $X_2^{(0)} = 0$, the stresslet/rotlet disturbance created by C_1 displaces C_2 along the x_2-direction and thus convects it towards C_1. As shown in Figure 1a, the only way for C_2 to overpass C_1 is to 'leapfrog' over it in the x_1x_2-plane. Conversely, in the case $X_1^{(0)}/a = -2.6, X_2^{(0)} = 0, X_3^{(0)}/a = -2.6, Ca = 0.2$, capsule C_2 is located *off* the shear plane and can thus move freely in space. As shown in Figure 1b, C_2 catches up with C_1, interacts, overpasses C_1, reverses its motion and repeats the process twice before getting away: we call this process'minuet danse'. For successive close interactions (defined by $X_1 = 0$), the distance $|X_3|$ decreases (Figure 1b) and the capsule transient deformation increases (Figure 1c). The minuet danse may lead to damage

*Corresponding author. E-mail: anne-virginie.salsac@utc.fr.

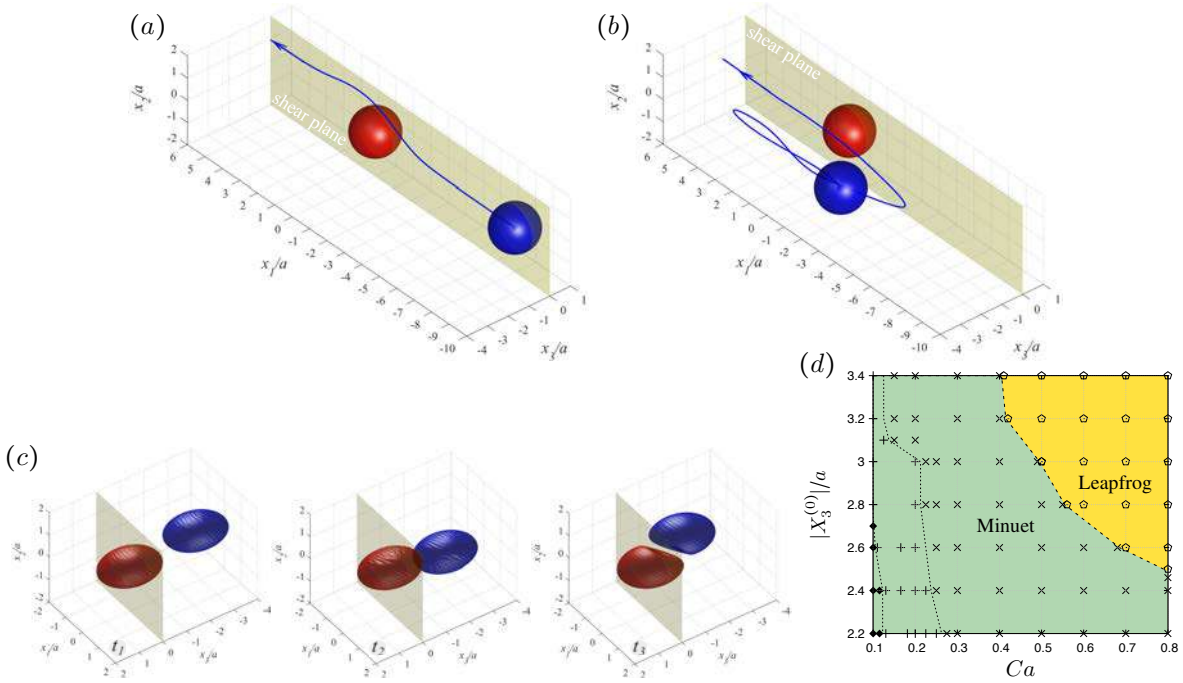

Figure 1: Trajectory of capsule C_2 (blue) in a reference frame centered on capsule C_1 (red). The two capsules are shown in their respective initial positions. (a) Leapfrog motion for $X_1^{(0)}/a = -8, X_2^{(0)} = 0, X_3^{(0)} = 0, Ca = 0.3$; (b) minuet danse with two reversions for $X_1^{(0)}/a = -2.6, X_2^{(0)} = 0, X_3^{(0)}/a = -2.6, Ca = 0.2$; (c) capsule profiles during close minuet interaction ($X_1 = 0$) at times t_1, t_2, t_3 in chronological order; (d) phase diagram showing the motion type as a function of position and deformability for $X_1^{(0)} = X_3^{(0)}$ and $X_2^{(0)} = 0$. The points represent the positions of C_2 at rest: × one oscillation, + two oscillations, ◆ three oscillations.

due to high transient deformation, whereas none was expected as the capsules were initially far apart (see the deformed profiles at the interaction time t_1 in Figure 1c). Depending on the capsule initial position and deformability, the minuet involves one, two or three reversals as shown in the phase diagram (Figure 1d). For non zero values of $|X_2^{(0)}|/a$ (less than 0.12), the boundary between leapfrog and minuet tends to occur for lower values of the distance $|X_3^{(0)}|$. This limited range of minuet motion explains why it had not been detected before. Note that if the capsules were pre-deformed to their steady profile in shear flow, they would take the same motion (leapfrog or minuet) as if they were initially spherical with only a small difference in the interaction times t_1, t_2, t_3. It follows that the minuet interaction is not restricted to the transient start of the flow of a suspension but is expected to occur steadily in a semi-dilute suspension under shear flow.

CONCLUSION

The situation that we have studied pertains to the pair interactions in a semi-dilute suspension of capsules. The novel aspect of our work is that we consider two capsules with their centres in (or near) the plane normal to the velocity gradient ($X_2^{(0)} \sim 0$). This configuration had never been studied before, because it entails long computations. The important results are (i) the pair can remain stable for a long time, while dancing a minuet, (ii) when they separate, the capsules can reverse direction, (iii) the less deformable the capsule, the more prone it is to do a minuet, (iv) this minuet dance progressively brings the capsules to closely interact and deform significantly: indeed, during the close interaction, the film thickness between the two capsules is of the order of $0.1a - 0.2a$. For small capsules, this may lead to physicochemical interaction.

Acknowledgments
This work was supported by the European Research Council (ERC) Consolidator grant (MultiphysMicroCaps, No. 772191) and by the China Scholarship Council (Visiting Scholar Grant of X.-Q. Hu).

References

[1] E. Lac, A. Morel, and D. Barthès-Biesel. *Journal of Fluid Mechanics*, 573:149–169, feb 2007.
[2] S. K. Doddi and P. Bagchi. *International Journal of Multiphase Flow*, 34(4):375–392, apr 2008.
[3] P. O. Olapade, R. K. Singh, and K. Sarkar. *Physics of Fluids*, 21(6):063302, 2009.
[4] P. Pranay, S. G. Anekal, J. P. Hernandez-Ortiz, and M. D. Graham. *Physics of Fluids*, 22(12):123103, 2010.
[5] P. Y. Gires, A. Srivastav, C. Misbah, T. Podgorski, and G. Coupier. *Physics of Fluids*, 26(1):013304, 2014.
[6] T. Omori, T. Ishikawa, Y. Imai, and T. Yamaguchi. *Journal of Fluid Mechanics*, 724:154–174, 2013.
[7] E. Lac and D. Barthès-Biesel. *Physics of Fluids*, 20(4):040801, 2008.

DEFORMATION AND STABILITY OF OSMOTICALLY-DEFLATED VESICLES UNDER A WIDE RANGE OF FLOWS

Vivek Narsimhan*[1], Charlie Lin [1], Dinesh Kumar [2], and Charles M. Schroeder [2]
[1] Davidson School of Chemical Engineering, Purdue University, West Lafayette, IN, USA
[2] Department of Chemical Engineering, University of Illinois–Urbana-Champaign, Urbana, IL, USA

Summary We perform boundary element simulations to describe the shape and stability of osmotically-deflated vesicles under a wide range of flows. The first half of this talk recaps vesicle dynamics in purely extensional flows, which are common in contractions, expansions, and/or suction flows. Above a critical flowrate, we find that find that moderately deflated vesicles undergo an asymmetric shape instability that is fundamentally different than droplet breakup. The physical origins of such shapes are discussed in detail and compared with microfluidic experiments. We will finish with simulations and experiments that describe vesicle shapes under general linear flows and large-amplitude oscillatory flows. The experiments will use a Stokes trap, a newly-developed technique that uses feedback control in a microfluidic device to trap particles under a given flow field for long periods of time.

OBJECTIVE

Vesicles are elastic and highly deformable sacs of fluid enclosed by a lipid bilayer. These entities are model systems to study physicochemical processes that occur in all cellular membranes. The shape and stability of vesicles are influenced by the type of flow, the elasticity of the membrane, as well the geometry of the flow channel. In turn, the shape of the vesicles influences their arrangement in the flow channel as well as the rheology of the medium. The conditions leading to vesicle fragmentation has been studied only in simple channel geometries and steady flows. A complete understanding of the physics of vesicle dynamics and stability under realistic non-equilibrium conditions is lacking, and achieving this knowledge will be invaluable for the manipulation of cells and vesicles in biomedical contexts. *The goal of this work is to use a combination of simulations, theories, and microfluidic experiments to investigate vesicle dynamics and stabilities under realistic flows (mixed- and time-dependent) and to understand how membrane elasticity confers stability.*

METHODOLOGY

Experiments: Vesicles are synthesized via electroformation, a technique where lipids on a conductive slide spontaneously swell upon addition of water and application of an AC electric field.[1,2] This procedure creates a polydisperse solution of unilamellar vesicles between 5-50 microns in size. To deflate the vesicles, an osmotic shock is applied through the addition of glucose, which is impermeable to the membrane. The lipids are a mixture of DOPC and a fluorescent dye for visualization (NBD-PC or rhodamine). Fig 1 shows snapshots of a osmotically-deflated DOPC vesicles at equilibrium. By visualizing the thermal fluctuations of the membrane, we can extract the membrane's bending modulus.[1,2]

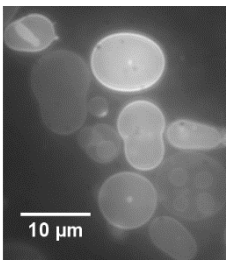

Fig 1: Osmotically deflated vesicles from electroformation[1]

The osmotically deflated vesicles are flowed into a Stokes trap,[1] a microfluidic cross-slot device with multiple inlet and outlet flows (Fig 2). By using an automated feedback loop on the inlet/outlet flowrates, one can generate a stagnation point in the device, as well as control the location, flow strength, and flow type of the stagnation point in real time. We use this device to hydrodynamically trap individual vesicles for up to a minute, and visualize their deformation over time. We use this information to understand what shapes the vesicles take in flow and identify shape instabilities that could lead to fragmentation.

Simulations: We model a vesicle as a droplet with a thin, elastic shell that represents the phospholipid bilayer. The elastic shell is area incompressible and has out-of-plane bending resistance. Thus, it is described by a Helfrich model with a bending modulus $\kappa \sim 5 - 50\ kT$. When placed under flow with a characteristic extension rate $\dot{\epsilon}$, there are several dimensionless groups that are important in describing the vesicle shape dynamics: (1) the viscosity ratio $\lambda = \mu_{in}/\mu_{out}$ between the fluid inside and outside the vesicle, (2) the reduced volume $\upsilon = 3\sqrt{4\pi}V/A^{3/2}$, where V and A are the volume and surface area of the vesicle, and (3) the bending capillary number $Ca = \mu_{out}\dot{\epsilon}a^3/\kappa$, which the ratio of viscous to bending forces on the surface, where $a = \sqrt{A/4\pi}$ is the vesicle's effective radius. The reduced volume tells the degree to which the vesicle is osmotically deflated. If the flow is time dependent and of mixed type (i.e., has vorticity + extension), there are additional dimensionless groups that describe the time scale of oscillation and the type of mixed flow.

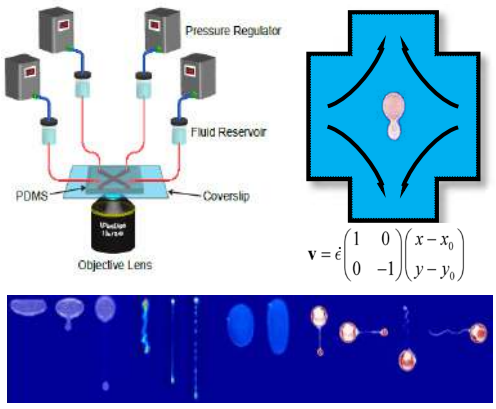

Fig 2: Top: schematic for Stokes trap. Bottom: pictures of vesicles stretched under planar extensional flow [1].

The simulations performed are based on the boundary integral formulation that has been used successfully to describe the flow physics of droplets, red blood cells, and vesicles. The technique uses

*Corresponding author. E-mail: vnarsim@purdue.edu

the fundamental solution to Stokes flow – the Green's function – to solve for the velocity on the vesicle surface due to the tension and bending forces. We discretize the vesicle surface into a triangular mesh and solve for the velocity field at each mesh point. Descriptions of the method are in references [3-5].

RESULTS

Fig 3 shows pictures of osmotically-deflated, DOPC vesicles under a planar extensional flow and corresponding simulation images. We have found that for moderately-deflated vesicles (reduced volume $0.60 < \nu < 0.75$), vesicles will stretch to an asymmetric dumbbell above a critical flowrate (i.e., critical bending capillary number). These shapes are fundamentally different than shapes observed during droplet breakup, and can be attributed to the incompressibility of the phospholipid bilayer. The physics of this shape transition can be shown to be a modified version of a classical Rayleigh-Plateau (i.e., capillary) instability,[3] with the following modifications: (a) the tension of the membrane is set by the flow, and (b) there is an additional bending resistance on the membrane.

When the vesicles are highly deflated and thread-like ($\nu < 0.60$), the vesicles stretch out symmetrically and sometimes form beads (i.e., 'pearls') in its central thread (Fig 4) [4]. These instabilities appear to be non-linear and hence depend on the initial conditions, especially in determining the number and size of beads formed. Again, we have been able to create phase diagrams that quantify these shape changes, and perform simulations to quantify the effects of different initial conditions [4].

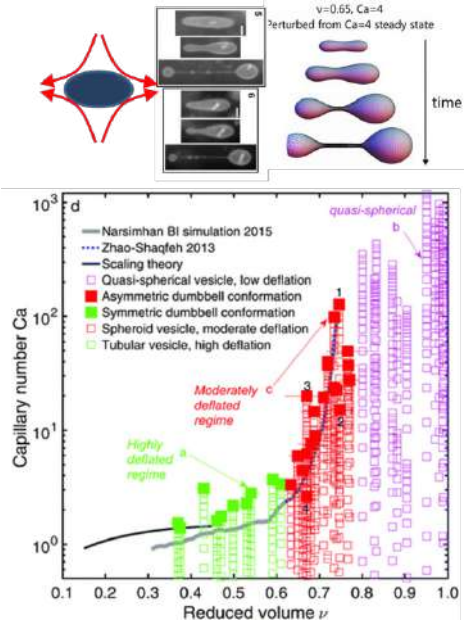

Fig 3: Top: Asymmetric dumbbell instability from experiments[2] and simulations[3]. Bottom: phase-diagram[1] of asymmetric and symmetric stretching modes under planar extensional flow.

Fig 4: Pearling instability and comparison to experiments [4] ($\nu = 0.38$, $Ca = 3.7$).

When the vesicle threads are stretched far from their initial shape and the flow is stopped, we can observe the vesicle relax to back to its original conformation. We observe two modes of relaxation – one associated with membrane tension and another associated with membrane bending. Interestingly, the volume of the vesicle appears to change after relaxation, which indicates that vesicles may undergo mechanoporation when subject to extreme strains. We are investigating the physics of this process in more detail.

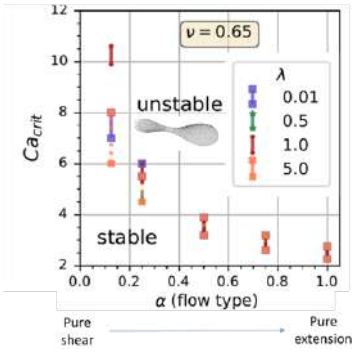

Fig 5: Onset of asymmetric instability vs. flow type for different viscosity ratios [5]

When vesicles are placed in a mixed linear flows (i.e., flows with vorticity and extension), we observe the asymmetric dumbbell instability depends greatly on the flow type [5]. Interestingly, vesicles do not appear to undergo shape instabilities under pure shear flow (Fig 5). This observation is vastly different than what is observed for droplets, which readily stretch and break up under shear. This phenomenon can be described using simple scaling/geometric arguments.[5]

Lastly, we will discuss some preliminary results for osmotically-deflated vesicles in time-dependent flows. We examine the deformation of giant, unilamellar vesicles under large amplitude, oscillatory extension (LAOE) to determine how their shapes evolve under time, and how these shapes play a role in non-linear rheology. We are in the process of developing phase diagrams that map different dynamical regimes for different flow rates and flow frequencies, for a wide range of reduced volumes. Interestingly, since vesicles experience compression during a half cycle of oscillatory flow, they can experience buckling (see Fig 6 for vesicle thread).

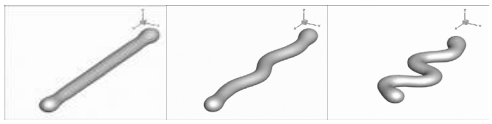

Fig 6: Vesicle thread buckling under planar compression from simulations

CONCLUSIONS

Vesicles and other cellular objects exhibit a rich set of dynamical behaviours under flow, due to the incompressibility of their phospholipid membrane and their non-spherical shapes when deflated. Observed shape instabilities include (a) asymmetric dumbbell stretching, (b) symmetric stretching, (c) pearling, and (d) wrinkling/buckling. We quantify the conditions under which many of these instabilities occur through simulation and microfluidic experiments, which hopefully will give better understanding on how to manipulate such biological objects under a wide range of contexts.

References

[1] D. Kumar, C.M. Richter, and C.M. Schroeder. *Soft Matter.* **16**: 337-347, (2020).
[2] J.B. Dahl, V. Narsimhan, B. Gouveia, E.S.G. Shaqfeh, and S.J. Muller. *Soft Matter*, **12**, 3787-3796, (2016).
[3] V. Narsimhan, A.P. Spann, and E.S.G. Shaqfeh. *J. Fluid Mech.*, **750**, 144-190, (2014).
[4] V. Narsimhan, A.P. Spann, and E.S.G. Shaqfeh, *J. Fluid Mech*, **777**, 1-26, (2015)
[5] C. Lin and V. Narsimhan, *Phys. Rev. Fluids*, **4**, 123606, (2019)

TRACKING THE SOURCE OF A PASSIVE SCALAR IN TURBULENCE

Rémi Monthiller *[1], Christophe Eloy[1], and Benjamin Favier[1]
[1] Aix Marseille Univ, CNRS, Centrale Marseille, IRPHE, Marseille, France

Summary How to find the source of an odour in a turbulent flow using only chemical cues? This problem is essential for the survival of plantkonic organisms since it affects feeding, mating and escaping predators. Darwinian selection has likely selected efficient solutions to solve this tracking problem, but the algorithms used by plankton are not yet known. In an attempt to reverse-engineer these algorithms, we have developed a 3D numerical environment, which allows us to simulate efficiently the advection-diffusion of a passive scalar together with the Lagrangian trajectories of active particles. To demonstrate the interest of this numerical environment, we address how sea slug larvae settle on coral reefs in response to chemical cues emitted by the coral [1].

CONTEXT: ODOUR TRACKING PROBLEMS

The survival of many organisms depend on their ability to locate targets (food, mate, predators) based on chemical cues [2]. Understanding this behaviour is needed to model ecosystems, but it also has applications to the conception of odour-tracking robots [3]. Copepods, that are millimetric crustaceans extremely abundant in fresh-water and marine environments, are model organisms to study this behaviour. Being blind, they use hydrodynamic and chemical sensing to detect preys, predator and mates [4]. To make the task even harder, copepods usually live in a turbulent flow. This flow not only stretches and stirs the chemical patches, but also induces a drift and a rotation of the copepods themselves. Yet, copepods have been very successful as species. Thus, they likely developed smart strategies to track odour in complex environments varying over space and time. However, these strategies and their fundamental properties are not fully understood.

APPROACH: DEVELOPMENT OF A VIRTUAL ENVIRONMENT

We have developed a 3D virtual environment to model the advection-diffusion of a passive scalar and the Lagrangian trajectories of active particles. The major challenge is to capture accurately the passive scalar field at each instant while remaining time-efficient. To address this challenge, we use kinematic simulations for the turbulent flow, the Diffusive Sheet Method (DSM) for the scalar field, and Jeffery's orbits for the active particles.

Our kinematic simulations aims to simulate homogeneous isotropic turbulence. It models the flow as a superposition of random Fourier modes varying in space and time over realisations [5]. These modes satisfy the incompressibility condition and their amplitude is chosen to match the Kolmogorov energy spectrum.

To track accurately the passive scalar in the turbulent flow, we use the Diffusive Sheet Method [6]. In turbulence, we expect the initial concentration to be stretched into an extremely thin convoluted sheet. This method is based on the Lagrangian tracking of this thin sheet with diffusion mainly occurring in the direction normal to its surface. Triangular surface elements are used to represent the advection and stretching of the sheet (Figure 1). To maintain an accurate resolution, triangulation is refined as the surface grows. Besides, the triangular elements whose concentration fall below a detection threshold are removed from the simulation, thus preventing the exponential blow-up of the number of triangular elements.

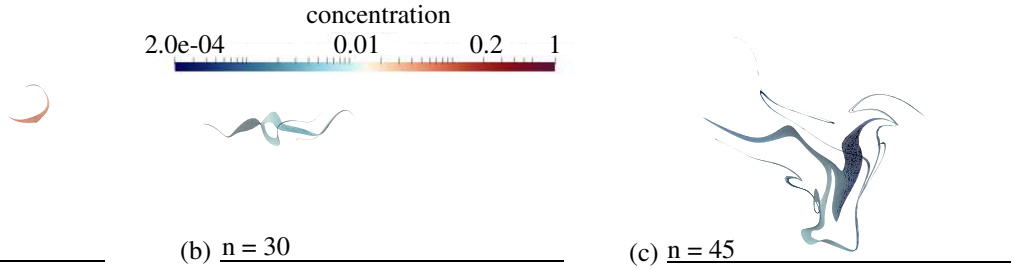

Figure 1: Illustration of the Diffusive Sheet Method [6] in a pseudo-turbulent flow. Initially a single triangular element is placed in the simulation box. The figure shows the advection and stretching of this initial distribution of passive scalar: (a) after 15 time steps, (b) after 30 time steps (c) after 45 time steps. The flow is simulated using kinematic simulation with 100 modes.

To complete this numerical environment, active particles are represented as ellipsoids smaller than the Kolmogorov length scale. Jeffery's orbits [7] are used to model how the flow affects the motion of the active particles. Thus, agents (1) drift with the local mean flow, (2) rotate with the vorticity, (3) rotate because of the strain components of the flow, and (4) actively swim in response to chemical sensing cues.

Using the previously described methods, the virtual environment is setup as an Open Source Library front-ended in Python. The complex and time-consuming algorithms are written in C++ to optimise performances.

*Corresponding author. E-mail: monthiller@irphe.univ-mrs.fr.

EXAMPLE: SEA SLUG LARVAE SETTLING ON CORAL REEFS

Before simulating the behaviours of complex organisms such as copepods, we first focus on a simpler problem. We address how sea slug larvae settle on corals based on the sensing of chemicals produced by the corals and transported by a turbulent flow. Koehl et al. [1] proposed a simple individual-based behavioural model of this problem where individual larvae have an on/off behaviour: when no chemical cue is detected, individuals swim and when the concentration is above a certain threshold, they stop swimming and sink because of their negative buoyancy. Based on a simple 2D numerical model, they showed that this simple individual behaviour is sufficient to increase significantly the success rate of settling on the corals.

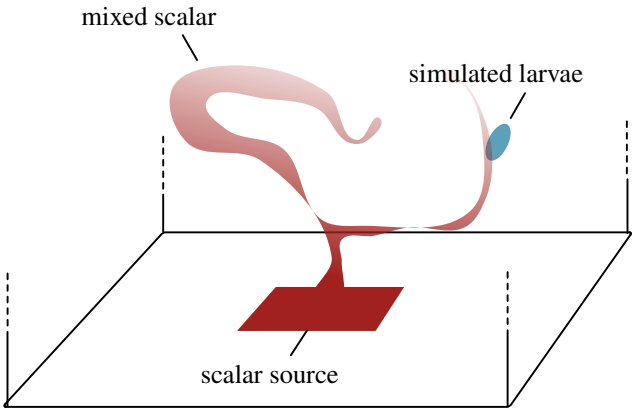

Figure 2: Illustration of the numerical setup in the example case.

We use our virtual environment to reproduce this specific tracking problem (Figure 2). Our aim is to assess the performance of the on/off behaviour and recover the results of Koehl et al. [1]. Besides, our model can be used to quantify the importance of the different parameters on the success rate (turbulence level, concentration threshold, swimming velocity, bottom-heaviness...) and thus inform us on how Darwinian evolution may have selected particular traits.

References

[1] Koehl, M. A. R., Strother, J. A., Reidenbach, M. A., Koseff, J. R., & Hadfield, M. G. (2007). Individual-based model of larval transport to coral reefs in turbulent, wave-driven flow: behavioral responses to dissolved settlement inducer. Marine Ecology Progress Series, 335, 1-18.
[2] Hein, A. M., Carrara, F., Brumley, D. R., Stocker, R., & Levin, S. A. (2016). Natural search algorithms as a bridge between organisms, evolution, and ecology. Proceedings of the National Academy of Sciences, 113(34), 9413-9420.
[3] Sousa, P., Marques, L., & de Almeida, A. T. (2008). Toward chemical-trail following robots. In 2008 Seventh International Conference on Machine Learning and Applications pp. 489-494. IEEE.
[4] Kiørboe, T. (2010). What makes pelagic copepods so successful?. Journal of Plankton Research, 33(5), 677-685.
[5] Kraichnan, R. H. (1970). Diffusion by a random velocity field. The physics of fluids, 13(1), 22-31.
[6] Martínez-Ruiz, D., Meunier, P., Favier, B., Duchemin, L., & Villermaux, E. (2018). The diffusive sheet method for scalar mixing. Journal of Fluid Mechanics, 837, 230-257.
[7] Jeffery, G. B. (1922). The motion of ellipsoidal particles immersed in a viscous fluid. Proceedings of the Royal Society of London. Series A, Containing papers of a mathematical and physical character, 102(715), 161-179.

IN VITRO ANALYSIS OF TIME-DEPENDENT RED BLOOD CELL PHASE SEPARATION IN A COMPLEX MICROCHANNEL NETWORK

Alberto Mantegazza *[1], Francesco Clavica[1,2], and Dominik Obrist[1]
[1] ARTORG Center for Biomedical Engineering Research, University of Bern, Bern, Switzerland
[2] Integrated Actuators Laboratory, Ecole Polytechnique Fédérale de Lausanne, Neuchâtel, Switzerland

Summary In this study we provided quantitative data on red blood cell (RBC) partitioning in 21 divergent bifurcations embedded in a complex *in vitro* network. In the majority of bifurcations the branch receiving a higher blood fraction received an even higher RBC fraction (*classical partitioning*). However, in some bifurcations the low-flow branch received a higher RBC flow fraction (*reverse partitioning*). Moreover, we found that the phase separation is strongly time-dependent and some selected bifurcations oscillated between the two types of partitioning.

INTRODUCTION

The topology of microvascular networks is complex and characterized by multiple diverging and converging blood vessels and the red blood cell (RBC) partitioning (i.e. *phase separation*) at diverging bifurcations is non-uniform. In our recent study [1], the RBC phase separation was investigated in a microvascular network model featuring many sequential symmetric bifurcations (Figure 1(a)). The time-averaged results (Figure 1(b)) confirmed that in most diverging bifurcations the branch with the higher blood flow fraction Φ received an even higher RBC flux fraction Ψ (*classical partitioning*). However, in agreement with computational results [2], an inversion of the classical phase separation behaviour (*reverse partitioning*) was observed for diverging bifurcations with skewed hematocrit profiles in the parent vessel. The hematocrit profile skewness (inset of Figure 1(b)) and the reverse partitioning were enhanced for high flow velocities.

In this study, we examined in detail the origin of these time-averaged phase separation results by investigating how cell partitioning evolves in time at specific bifurcations in the network (time-dependent phase separation).

MATERIALS AND METHODS

The PDMS microdfluidic device was fabricated via soft-lithography and replica molding. It embedded a network with 49 hexagonal elements and 176 microchannels. All microchannels dimensions (width $W = 10\ \mu m$, height $H = 8\ \mu m$ and length $L = 85\ \mu m$, Figure 1(a)) were inspired by the typical length scales found *in vivo*.

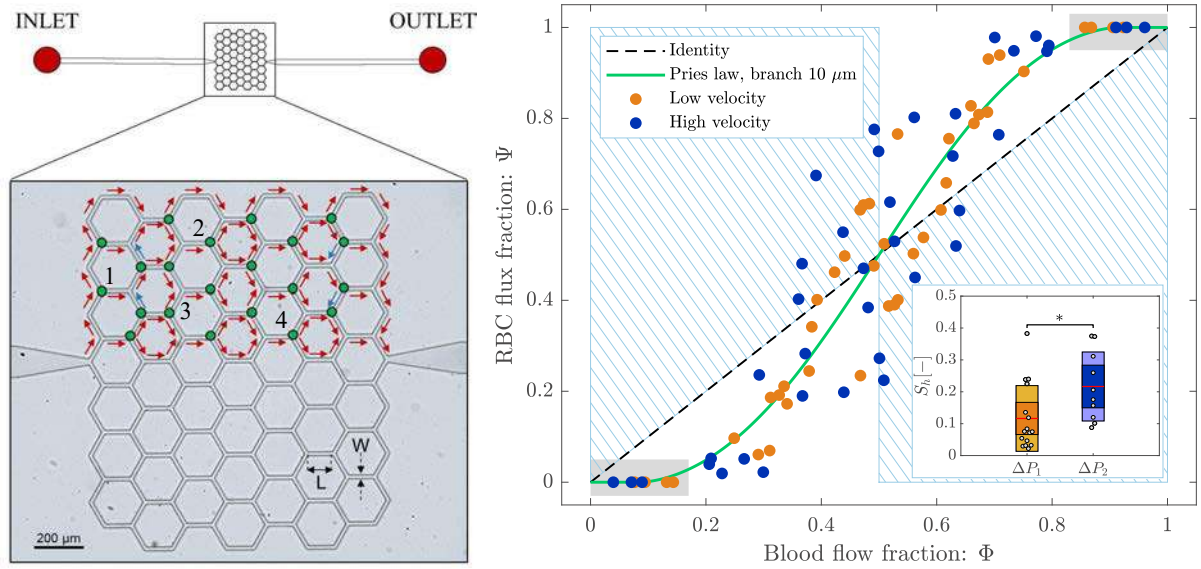

(a) (b)

Figure 1: (a) Microscope image of the microchannel network. Red and blue arrows indicate the direction of blood and plasma flow, respectively. Green dots represent diverging bifurcations considered in this study. (b) Phase separation results for the low (orange) and high (blue) velocity experiments (adapted from [1]). The green line is the empirical low from Pries [3]. The inset shows that the skewness hematocrit index (S_h) is statistically significantly ($p = 0.014$) higher for the high velocity experiment.

The working fluid was a suspension of RBCs at feeding hematocrit $H_f = 10\%$ dispersed in a water-based buffer fluid. The final solution matched the density and viscosity of physiological blood. The flow was controlled by setting a pressure

*Corresponding author. E-mail: alberto.mantegazza@artorg.unibe.ch.

MINI SYMPOSIA

difference between the fluid level in the reservoir and the device outlet ($\Delta P_1 = 35.3\ mbar$ and $\Delta P_1 = 47.1\ mbar$, hereafter referred as *low velocity* and *high velocity* experiments, respectively).

Particle Tracking Velocimetry (PTV) was performed on the image sequences to compute RBC velocity ($U_{rbc}[mm/s]$) and tube hematocrit ($H_t[-]$) in each channel of the top half of the network. Similarly to Mantegazza *et al.*[1], the RBC flux and the total blood flow rate in a Region Of Interest (ROI, $width = W_{ROI}$, $heigth = H_{ROI}$) were computed as

$$Q_{rbc}(t) = U_{rbc}(t) \times H_t(t) \times W_{ROI} \times H_{ROI}, \tag{1}$$

$$Q_{blood}(t) = U_{rbc}(t) \times W_{ROI} \times H_{ROI}. \tag{2}$$

The fractional RBC flux ($\Psi^i(t)$) and the fractional blood flow ($\Phi^i(t)$) in the daughter branch i were given by

$$\Psi^i(t) = \frac{Q^i_{rbc}(t)}{Q^P_{rbc}(t)}, \quad \Phi^i(t) = \frac{Q^i_{blood}(t)}{Q^P_{blood}(t)}, \tag{3}$$

where $i = 1, 2$ denotes the daughter branch 1 and 2 of a generic bifurcation and P denotes the parent branch.

RESULTS AND DISCUSSION

We found that the RBC fluxes $\Psi^i(t)$ and blood flow rates $\Phi^i(t)$ are strongly time-dependent (Figure 2(a)). Even if the time-averaged phase separation is classical (Figure 2(b)) or reverse (Figure 2(c)), the time-dependent phase separation is not constant and it can switch between the two types of partitioning (data are scattered above and below the identity lines in Figure 2(b) and (c)). In agreement with the computational results of Balogh and Bagchi [2], we report that in a complex microchannel network a bifurcation could have a classical partitioning with intermittent episodes of reverse partitioning or vice versa. The origin of these fluctuations may be connected to the temporary difference of the daughter branch resistances due to the passage of individual RBCs.

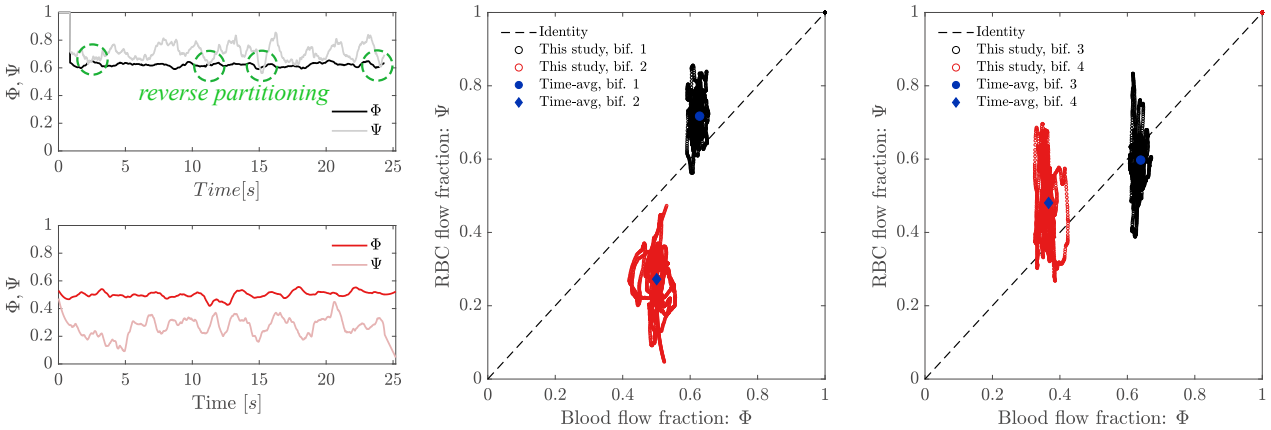

(a) (b) (c)

Figure 2: Time-dependent phase separation (high velocity experiment). (a) Time sequence of $\Phi^i(t)$ (black and red) and $\Psi^i(t)$ (grey and pink) for bifurcations 1 and 2 (cf. Figure 1(a)) exhibiting a time-averaged classical partitioning. (b) $\Phi - \Psi$ diagram for the sequences shown in Figure 2(a). The classical partitioning occurs when $\Psi^i(t) > \Phi^i(t)$ for $\Phi^i(t) > 0.5$ (and vice versa). (c) $\Phi - \Psi$ diagram for bifurcations 3 and 4 (cf. Figure 1(a)) exhibiting a time-averaged reverse partitioning. The reverse partitioning occurs when $\Psi^i(t) < \Phi^i(t)$ for $\Phi^i(t) > 0.5$ (and vice versa). The solid circles indicate the time-averaged results (cf. Figure 1(b)) corresponding to the bifurcations 1,2,3 and 4 indicated in Figure 1(a).

CONCLUSIONS

For the first time we provided *in vitro* quantitative data on the time-averaged and time-dependent RBC partitioning in a complex network and we showed that both time-averaged classical and reverse partitioning contemporary occurred in the network and that selected bifurcations can cycle between the two types of partitioning over time.

References

[1] Mantegazza A., Clavica F., Obrist D. In vitro investigations of red blood cell phase separation in a complex microchannel network. *Biomicrofluidics*. **14**, 014101, 2020. DOI: 10.1063/1.5127840.
[2] Balogh P., Bagchi P. Analysis of red blood cell partitioning at bifurcations in simulated microvascular networks. *Phys. Fluids*. **30**, 5, 2018.
[3] Pries A. R., Secomb T. W., Gaehtgens P., Gross, J. F. Blood flow in microvascular networks. *Circ. Res.*. **67**, 4, 1990.

DYNAMIC RESPONSE OF A FLAGELLATED ARTIFICIAL MICRO-SWIMMER ACTUATED BY ACOUSTIC POWER

Jinan Liu and Haihui Ruan *
Research Center for Fluid-Structure Interactions, Department of Mechanical Engineering, The Hong Kong Polytechnic University, Hung Hom, Kowloon, Hong Kong, China

Summary This work describes a theoretical study on a flagellated artificial micro-swimmer which consists of a rigid head and a flexible flagellum. We first clarified the dependence of head oscillation amplitude on acoustic pressure and frequency, and then employed the resistive force theory to relate the motility of a micro-swimmer and the dynamic response of the flagellum. The inertia and material damping were involved in the governing equation and the variable cross-section of a flagellum was also considered. We first validated the model by comparing the theoretical results with experimental results and then discussed the influences of several key nondimensional parameters and the results of optimization.

INTRODUCTION

The actuation and manipulation of micro-scaled robots have not been realized until the recent decade with the booming development of microfabrication. Among many potential applications, medical implementation could be the most significant impetus [1]. For example, it can be envisioned that a swarm of sperm-like micro-swimmers could be directed to the position of lesion under an external acoustic excitation, as shown in Figure 1(a).

However, the theoretical model of micro-swimmers is still lacking. Although acoustophoresis due to acoustic streaming has been well known, the particles that can be moved by sound is too small to carry medical functionalities. Recently, two new experiments on acoustic actuation have been reported in the open literature [2, 3]. These two works bring about an actuating mechanism different from the conventional acoustophoresis. It is observed that the dynamic response of the flagella of the artificial micro-swimmers described in these two works is similar to the wiggling of a biological flagellum [4], where the propulsive force can be determined based on the theories developed in the low-Reynolds-number regime [5]. In this regime, the resistive force theory (RFT) is widely adopted to explain the motion of microorganisms [6]. Therefore, the present study attempts to make clear the actuation mechanism of an acoustic wave that leads to the forward motion of a flagellum composed of a rigid head and a flexural tail. It should be noted that the inertia of the flagellum was not involved in most previous models of living microorganism based on RFT. Nevertheless, the foundation of the RFT is the Stokes equation, wherein only the inertia of fluid is neglected. In addition, the expression of the Reynolds number is related to the density of the fluid but irrelevant to that of a flagellum. Therefore, it is necessary to scrutinize the effect of inertia of a flagellum especially when the flagellum whips at a high frequency under external actuation. In order to make our model applicable in optimization an actual micro-swimmer design, we have further involved the effects of material damping and non-uniform flagellum cross-section in our analysis, which were not fully considered in previous theoretical works on flagellum propulsion.

MODELING AND RESULTS

Motion of the head

We denote the motion of the rigid head by the lateral displacement $u(t)$ and rotation $\theta(t)$. Under an acoustic actuation, it is intuitive to presume that both $u(t)$ and $\theta(t)$ should be periodic with the acoustic frequency f, that is $u(t) = u_0 \sin \omega t$ and $\theta(t) = \theta_0 \sin(\omega t + \varphi_h)$, where $\omega = 2\pi f$ is the angular frequency of the actuation, u_0 and θ_0 are the amplitude of the head oscillation. The phase angle difference between the translational and rotational motion is denoted by φ_h.

To understand the actuation mechanism, 3D finite element simulations for the head motion were carried out by using the software package COMSOL Multiphysics. Following Kaynak *et al*. [3], the head is assumed to be cone-shaped with two hemispherical ends, as depicted in Figure 1(b), where the white area is the head domain. It is featured by the radius r_1, r_2 ($r_1 > r_2$) of the end spheres and the distance d between their centers, and the line between the two centers is set to be the longitudinal axis of the head. The head is initially placed at the center of a box containing viscous fluids at room temperature. A transient sound pressure distribution is exhibited in Figure 1(b). In the simulation, the longitudinal motion of the head is constrained; the surface of the head is a sound hard wall; and a plane wave is incident from the lower boundary. The results confirm that the displacement and rotation of the head are both harmonic functions of time with frequencies identical to the acoustic frequency. The oscillating amplitude of the head is found proportional to the sound pressure p and the reciprocal of acoustic frequency $1/f$. The coefficients of proportionality can be extracted from the simulation results, which also tallies with the theoretical expectation of the case for an acoustic particle actuated by a plane wave [7]. These coefficients vary with the geometry of the head. It is found that the rotational motion strictly vanishes if a head is symmetric about a transverse plane (i.e., $r_1 = r_2$), but becomes nonnegligible for a droplet-like (i.e., $r_1 > r_2$) head. Noted that the phase angle difference φ_h is always 180° if the acoustic wave vector is normal to the longitudinal axis of the head. But it could slightly deviate from 180° if the incident wave is oblique.

*Corresponding author. E-mail: hhruan@polyu.edu.hk.

Dynamic response of the flagellum

We assume that the head of a micro-swimmer whips the flagellum in the plane of acoustic wave propagation. The length of the flagellum is denoted by L and the cross-section is assumed to be a circle of area A. The flagellum is treated as a cantilever Euler-Bernoulli beam agitated by the motion of the clamped end (i.e., the head), resulting in the dynamic response $z(x, t)$, where z and x are the transverse displacement and the coordinate along the flagellum. The Young's modulus, flagellum density and the second moment of area are respectively denoted by E, ρ and I. The material of the micro-swimmer is assumed to be a Kelvin-Voigt viscoelastic material, and we denote η as the viscosity. Based on the RFT, the fluid force perpendicular to the flagellum $F_\perp$ and the force parallel to the flagellum $F_\parallel$ can be considered proportional to the local transverse velocity $\partial z/\partial t$ and longitudinal velocity, respectively. The drag coefficients are denoted by $c_\perp$ and $c_\parallel$, respectively. Then, the terminal velocity v_{prop} can be estimated from the equation: $F\cos\psi - F_\perp \sin\psi = F_{\text{head}} + \int_L c\, v_{\text{prop}}$, where ψ is the slope angle of the flagellum and the fluid force of the head F_{head} depends on the head dimension. The Galerkin method is employed to solve the governing equations.

Some non-dimensional parameters are introduced for discussion. The motility of the micro-swimmer V_{cs} is defined as $V_{cs} = c\,\bar{v}_{\text{prop}}/(Lf)$, where $\bar{v}_{\text{prop}}$ is the time-averaged terminal velocity and the factor c reflects the relative resistance between the head and the flagellum. $\gamma = \eta\omega/E$ denotes the material damping coefficient. $w_0 = u_0/L$ is the non-dimensional head amplitude. For the case of a uniform flagellum, we have introduced the following two non-dimensional parameters: $S_p = L\sqrt[4]{2\pi c_\perp f/(EI)}$ and $\omega_{ns} = \omega L^2\sqrt{\rho A/(EI)}$, which are named the sperm number [8] and the resonance index, respectively. The sperm number indicates the relative importance of external fluidic drag to the internal elastic stress on a flagellum. The resonance index can be used to illustrate the effect of resonance on the motility. For the case of the non-uniform flagellum cross-section, we assume that the diameter D of the flagellum reduces from the root to the tip, which is expressed as: $D(x) = D_0\left[1 - K_s(x/L)^\Lambda\right]$, where K_s and Λ are constants, and D_0 represents the largest diameter at the root.

Since the tapered flagellum has been adopted in Kaynak *et al.*'s micro-swimmer [3], we prescribe the parameters based on an estimate of their work. Specifically, in Figure 1(c), we set D_0 = 25 μm, L = 180 μm, E = 10 MPa, ρ = 1200 kg/m^3, γ = 5, f = 4600 Hz, K_s = 0.9 and Λ = 1 along with a spherical head with the radius of 25 μm. The fluid viscosity is set to be 1 Pa·s. The geometric meaning of K_s = 0.9 is illustrated in the top-left inset of Figure 1(c), where the diameter of the root is 10 times that of the tip. The curve shown in Figure 1(c) demonstrates a reasonable agreement with the experimental results in [3]. Correspondingly, the calculated wiggling profiles of the flagellum for u_0 = 12 μm are shown in the bottom-right inset of Figure 1(c). The obtained profiles also resemble the experimental results. Other numerical results indicate that a large K_s and small Λ would be better in achieving a high motility. To explicate the effect of resonance and material damping on V_{cs} of a uniform elastic flagellum, we also explored the variation of V_{cs} in terms of S_p and ω_{ns} upon a prescribed head actuation. The numerical results indicate that the most efficient way to achieve a high motility is to design the flagellum that achieves resonance. We found that the higher motility generally comes with the narrower frequency bandwidth, and a large S_p or a moderate material damping is beneficial to broaden the bandwidth at resonance. In non-resonance regimes, the high motility can be achieved in a range of S_p; and the effect of a moderate γ is to shift this range of sperm number to the lower side. Undoubtfully, excessive γ reduces the motility of the micro-swimmer.

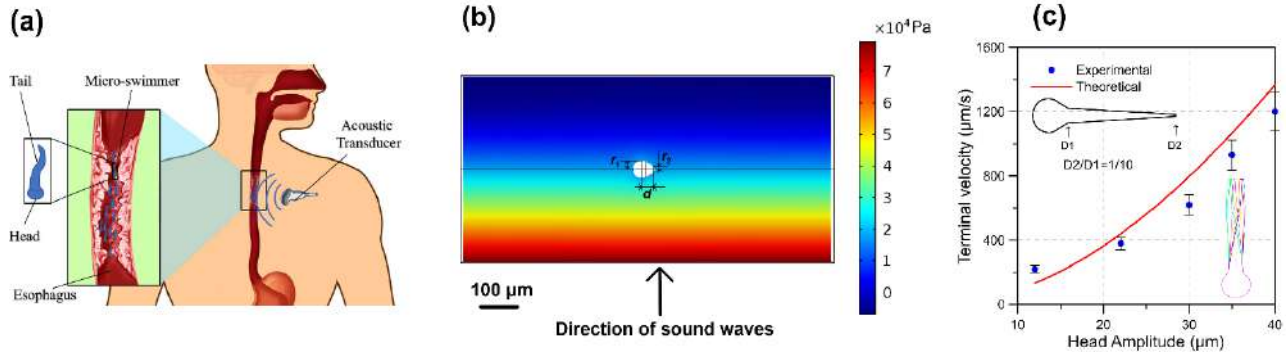

Figure 1. (a) A sketch of the application scenario; (b) instantaneous sound pressure distribution in the simulations; (c) the comparison between experimental [3] and theoretical results with the inset showing the wiggling profiles of the flagellum at u_0 = 12 μm.

References

[1] Cho, S., *Mini and micro propulsion for medical swimmers.* Micromachines, 2014. **5**(1): p. 97-113.
[2] Ahmed, D., et al., *Artificial swimmers propelled by acoustically activated flagella.* Nano letters, 2016. **16**(8): p. 4968-4974.
[3] Kaynak, M., et al., *Acoustic actuation of bioinspired microswimmers.* Lab on a Chip, 2017. **17**(3): p. 395-400.
[4] Gray, J., *The movement of sea-urchin spermatozoa.* Journal of Experimental Biology, 1955. **32**.
[5] Purcell, E.M., *Life at low Reynolds number.* American journal of physics, 1977. **45**(1): p. 3-11.
[6] Wiggins, C.H. and R.E. Goldstein, *Flexive and Propulsive Dynamics of Elastica at Low Reynolds Number.* Physical Review Letters, 1998. **80**(17): p. 3879-3882.
[7] Kinsler, L.E., et al., *Fundamentals of acoustics.* Fundamentals of Acoustics, 4th Edition, by Lawrence E. Kinsler, Austin R. Frey, Alan B. Coppens, James V. Sanders, pp. 560. ISBN 0-471-84789-5. Wiley-VCH, December 1999., 1999: p. 560.
[8] Lowe, C.P., *Dynamics of filaments: modelling the dynamics of driven microfilaments.* Philosophical Transactions of the Royal Society of London. Series B: Biological Sciences, 2003. **358**(1437): p. 1543-1550.

CELLULAR BLOOD FLOW SIMULATIONS FOR REDUCED-ORDER MODELS OF RED BLOOD CELL SPLIT IN COMPLEX GEOMETRIES

Timm Krüger *[1], Qi Zhou[1], Lowell Edgar[2], Romain Enjalbert[2], Peter Hoskins[1], and Miguel Bernabeu[2]
[1] School of Engineering, University of Edinburgh, Scotland, UK
[2] Usher Institute, University of Edinburgh, Scotland, UK

Summary Several diseases are related to haemodynamics and require a better understanding of blood flow and related transport mechanisms. The presentation will give an overview of recent work towards reduced-order models informed by cell-based blood flow simulations in complex geometries, such as segments of the retina. The reduced-order models depend on the spatial distribution of red blood cells in microvascular segments and their development along the flow axis via cell-cell interactions and lift forces. In the future, these models could be used to simulate organ-level blood flow with significantly reduced computational cost, making these models more attractive for clinical applications.

INTRODUCTION

Every year, millions of people worldwide are affected by blood-related diseases, such as malaria, cancer or sickle cell anemia. Understanding disease pathways, the role of blood flow and the effect on haemodynamics and solute/particle transport is crucial for the development of diagnostic tests and informing treatment options. Since in-vivo blood flow experiments are challenging, there has been a recent increase in modelling of blood flow in disease [1]. Blood flow modelling becomes particularly challenging at the scale of arterioles and capillaries where the diameters of blood vessels and red blood cells (RBCs) are similar. In these cases, computationally expensive cell–based models are still required to uncover suspension flow effects and predict cell distribution and tissue oxygenation. Deformable RBCs are typically modelled as hyperelastic or viscoelastic capsule–vesicle hybrids that are fully coupled to the ambient fluid flow and capture the cell deformation and dynamics on the micron level [2]. In order to enable more quantitative predictions in larger blood vessel networks (e.g. on the organ level), more efficient reduced models are required.

NOVELTY AND RESULTS

There has been recent effort to better understand cellular blood flow in complex geometries [3]. A key challenge is the distribution of RBCs at diverging bifurcations where the flow ratio of RBCs is usually different from the suspension flow ratio [4, 5]. This well-known effect is caused by the existence of the cell-free layer.

However, existing models [6] do not consider the finite recovery length of the RBC distribution after a perturbation (e.g. via an upstream bifurcation or constriction) and the resulting bias of the RBC split at downstream bifurcations. This effect is illustrated in Fig. 1. If consecutive bifurcations are sufficiently close, which often is the case in solid tumours, the RBC split bias can accumulate, therefore potentially affecting the organ-level perfusion and oxygenation.

The presentation will show results obtained via the highly parallelised lattice-Boltzmann-based code HemeLB from a) consecutive bifurcations (see Fig. 1), b) bifurcations after a geometric perturbation and c) retinal networks (see Fig. 2). Based on these microscopic results, I will sketch the development of a reduced-order model that is able to predict RBC split based on few parameters, such as distance between bifurcations and asymmetry of the cell-free layer. In the future this model will be consolidated to enable organ-level perfusion and oxygenation without the need to run computationally expensive RBC-level simulations. Until then, microscopic RBC simulations are still necessary to uncover the physics and delicate flow details responsible for RBC distribution in complex geometries.

References

[1] Sweeney P.W. *et al.* Modelling the transport of fluid through heterogeneous, whole tumours in silico. *PLOS Comput. Biol.* **15**: e1006751, 2019.
[2] Krüger T. *el al.* Crossover from tumbling to tank-treading-like motion in dense simulated suspensions of red blood cells. *Soft Matter* **9**: 9008–9015, 2013.
[3] Balogh P., Bagchi P. Direct Numerical Simulation of Cellular-Scale Blood Flow in 3D Microvascular Networks. *Biophys. J.* **113**: 2815–2826, 2017.
[4] Svanes K., Zweifach B.W. Variations in small blood vessel hematocrits produced in hypothermic rats by micro-occlusion. *Microvasc. Res.* **1**: 210, 1968.
[5] Fung Y.C. Stochastic flow in capillary blood vessels. *Microvasc. Res.* **5**: 34, 1973.
[6] Pries A.R. *et al.* Blood flow in microvascular networks. Experiments and simulation. *Circulation Res.* **67**: 826–834, 1990.

*Corresponding author. E-mail: timm.krueger@ed.ac.uk

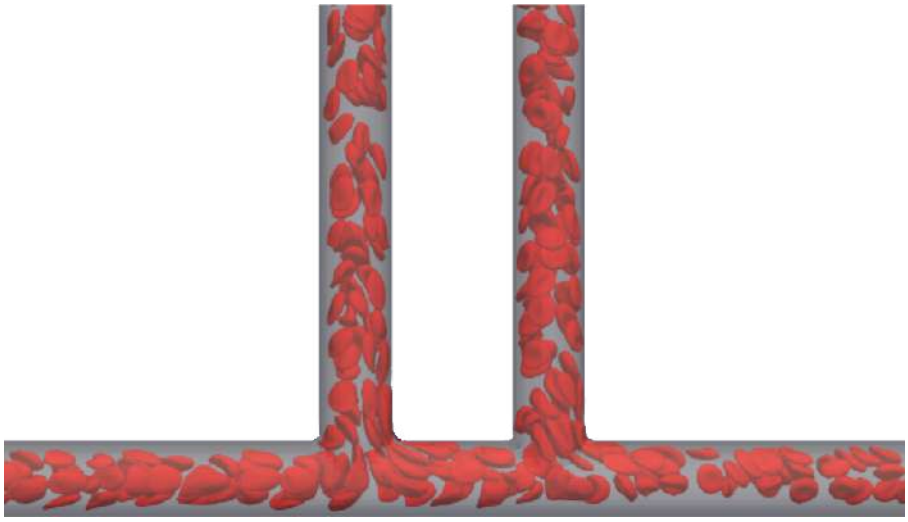

Figure 1: Simulated RBC flow through a double bifurcation (left to right) with emerging downstream asymmetry of the cell-free layer.

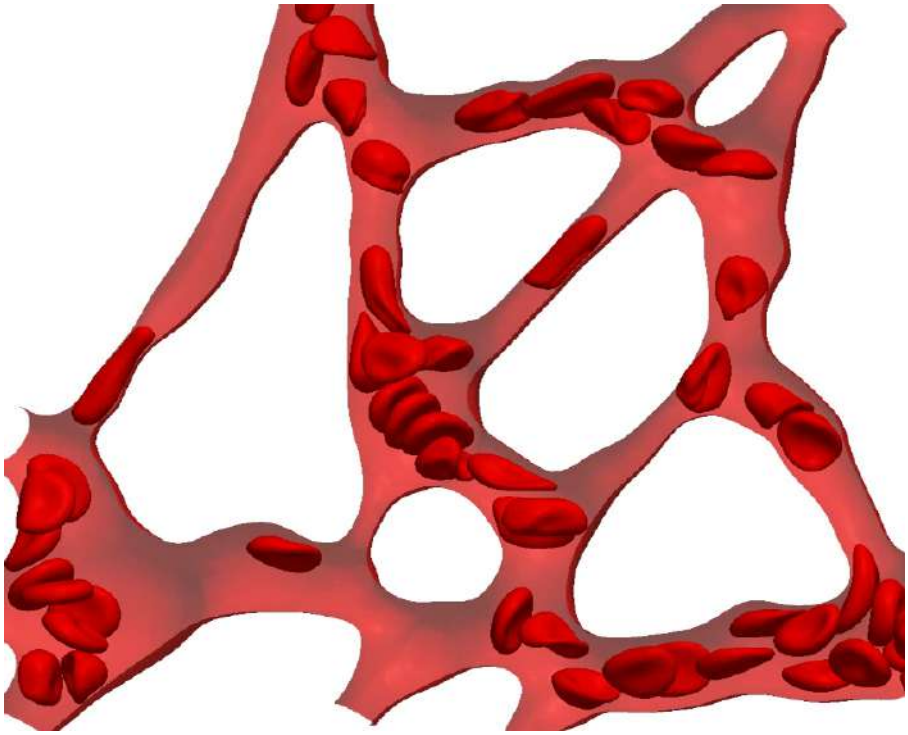

Figure 2: Simulation of RBCs flowing through a mouse retina segment with multiple inlets and outlets.

WICKING OF BIO-FLUIDS FOR PAPER BASED DIAGNOSTICS

Michael J. Hertaeg[1], Joseph D. Berry[2], Rico F. Tabor[3], and Gil Garnier *[1]
[1] Department of Chemical Engineering, Monash University, Clayton, Australia
[2] Department of Chemical and Biomolecular Engineering and the Particulate Fluids Processing Center, University of Melbourne, Parkville, Australia
[3] School of Chemistry, Monash University, Clayton, Australia

Summary The field of paper-based biodiagnostics has received attention recently for its potential to create fast, cheap and portable medical devices. However, much of the design of these devices is based on trial and error due to a lack of understanding of the controlling processes. This includes wicking from a finite source such as a droplet and the effect of biological components such as cells and surface active proteins, forming a complex fluid. Here, the radial wicking of a blood droplet and its components is investigated on a paper substrate using high speed photography and numerical modelling. The dominant effect blood components have on wicking is identified to be an intensifying of porosimetry hysteresis. This is due to an increase in the advancing contact angle caused by protein adsorption onto cellulose fibers in paper.

INTRODUCTION

The radial wicking of a droplet on paper is a complex fluid dynamics scenario. Here, absorption of the droplet into the paper a finite time after deposition causes a decrease in spreading rate that can be identified by plotting the stain area against time on a log-log scale (Figure 1). The two stages are observed and are referred to as stage one, where the drop is still present above the paper and stage two, where the drop has been completely consumed. Before the transition, spreading is driven only by the infiltration of pores near the edge of the stain. After the transition the reservoir of fluid vanishes and any further stain growth is caused by the redistribution of fluid from the large pores to the unfilled small pores at the edge of the stain. This occurs due to the greater magnitude of capillary force causing a low pressure in small pores [3]. In addition to droplet absorption, the stain growth transition was also shown to depend on a hysteresis effect because of differences between filling and emptying porous networks [4]. This effect is only relevant in the second stage as before stage transition, no pores are emptying. The cause of this hysteresis is poorly understood and is likely to be material and fluid dependent. However, the most likely causes are liquid entrapment due to poor interconnectivity, contact angle hysteresis and fiber swelling.

The effect that blood components such as cells and proteins have on wicking in paper is poorly described and understood. However, droplets containing blood proteins were shown to create lower equilibrium stain sizes on paper and to have a higher advancing contact angles on cellulose than simple fluids [2]. The objective of this study is to identify the primary impact blood components have on the radial wicking process.

METHODS

Droplets of whole blood and plasma were placed on paper substrates and their stain growth was monitored with high speed photography. These are compared with results of simple water-ethanol and water-glycerol solutions [1] to separate the effect of biological components from changes in viscosity and surface tension. An axisymmetric numerical model based on Richard's equation was developed, incorporating effects of hysteresis by expressing contact angle as a function of the temporal gradient of local volume fraction.

RESULTS

Figure 1 shows the evolution of the measured stain area with time for 20 μL droplets of different fluids analysed on both a linear and log-log scale. The log-scale is shown because the time of stage transition is clearly identified on this scale, and the local gradient in each stage is equivalent to the power dependence of the relationship of stain growth with time. Results from non-biological fluids varying in viscosity and surface tension [1] show that first and second stage gradients are constants independent of physical fluid properties. However, results from biological fluids reveal the second stage log-scale gradient to vary significantly between fluids. This indicates that biological components are responsible for the reduction in the log-scale gradient in the second stage but do not affect it in the first stage.

The difference between first and second stage gradients was previously shown to be caused by hysteresis [1], and modelling results indicate that an intensified hysteresis effect results in a lower second stage power. Therefore, the observed decrease in the second stage log-scale gradient of biological fluids is likely to be caused by an intensification of the hysteresis effect. In this case, the intensification is due to the higher advancing contact angles for biological fluids on cellulose.

*Corresponding author. E-mail: gil.garnier@monash.edu

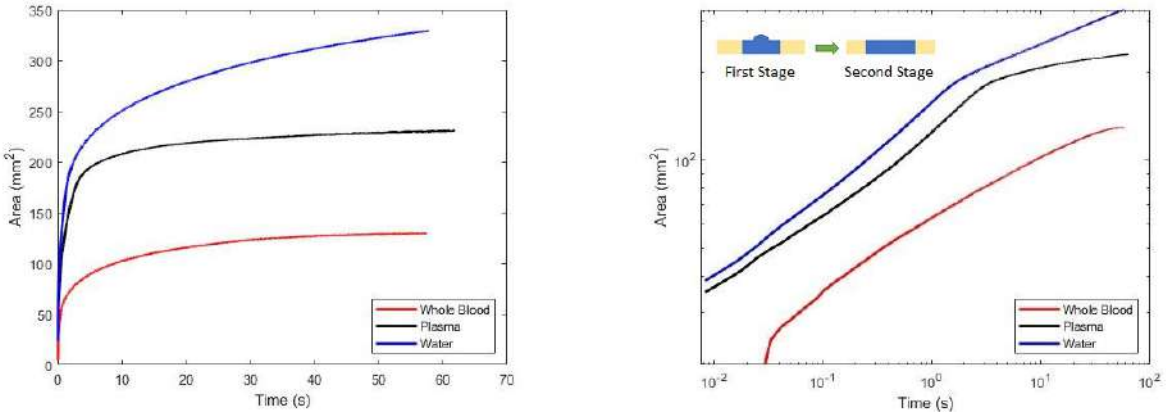

(a) (b)

Figure 1: Stain area as a function of time for several fluids (a) linear scale (b) log-log scale

Figure 2 shows visualizations created from simulation data compared to experimental results for a 17 μL water droplet on filter paper at three times. This emphasises the predictive ability of the model as well as inaccuracies introduced at later times due to slight fiber alignment present in most papers that is not included in the model.

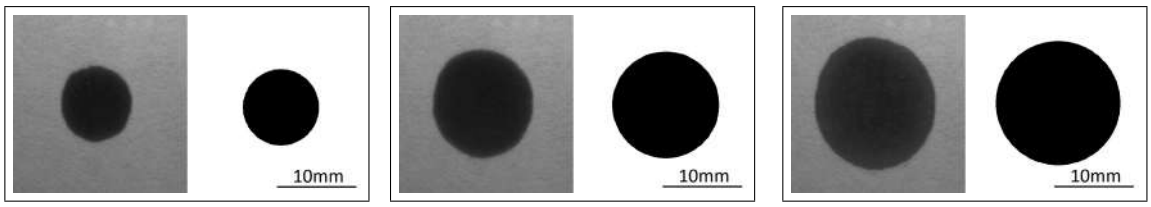

(a) 0.10 seconds (b) 0.85 seconds (c) 7.10 seconds

Figure 2: Stain images (left) and simulation result visualizations (right) at different times

CONCLUSION

Understanding the radial wicking of biological fluids is important for the design of paper-based diagnostic devices. Previously two stages have been identified. These stages are defined by whether or not the droplet is still present above the paper. As the majority of stain growth occurs in the second stage, this regime deserves particular attention. Porosimetry hysteresis coupled with absorption of the droplet into the paper have been identified as the causes of the observed stain growth transition where the log-scale gradient of stain growth with time changes abruptly. Hysteresis effects are intensified in biological fluids due to protein adsorption, and therefore the second stage behavior of such fluids is unique. A Richard's equation continuum model was developed, incorporating the effects of hysteresis. This can be used to aid design of the next generation of fast, cheap and portable paper based diagnostic devices.

References

[1] Hertaeg M. J., Tabor R. F., Berry J. D., Garnier G. Dynamics of stain growth from sessile droplets in paper. *Journal of Colloid and Interface Science*. **541**: 312-321, 2019.

[2] Hertaeg M. J., Tabor R. F., Garnier G. Effect of protein adsorption on the radial wicking of blood droplets in paper. *Journal of Colloid and Interface Science*. **528**: 116-123, 2018.

[3] Marmur A. Penetration and displacement in capillary systems of limited size. *Advances in Colloid and Interface Science*. **39**: 13-33, 1992.

[4] Kloubek J. Hysteresis in porosimetry. *Powder Technology*. **29** 63-73, (1981)

MODELLING OF THE DAMAGE OF A LIQUID-CORE CAPSULE UNDER SIMPLE SHEAR FLOWUNTIL INITIATION OF RUPTURE

Nicolas Grandmaison[1], Delphine Brancherie[2], and Anne-Virginie Salsac *[1]
1Biomechanics and Bioengineering Laboratory, CNRS - Université de Technologie de Compiègne, Compiègne, France
2Roberval Laboratory, CNRS - Université de Technologie deCompiègne, Compiègne, France

Summary Capsules are composed of a droplet surrounded by a deformable membrane of small thickness. When capsules are subjected to an external flow, the viscous forces can damage the capsule membrane and lead to its breakup. To study capsule damage until initiation of rupture, we develop the first fluid-structure interaction (FSI) model of a capsule in flow taking into account the damage of the membrane. We apply the framework of continuum damage mechanics and model the membrane with an isotropic brittle damage model. The problem of the membrane is solved with the finite element method and the internal and external fluid problems are solved with the boundary integral method. We study the influence of the dimensionless parameter governing the FSI which is the capillary number, ratio of the fluid viscous forces to the membrane elastic forces, and determine the criteria needed to control rupture.

INTRODUCTION

Capsules composed of a droplet surrounded by a deformable wall are used in numerous industrial applications to protect and ensure the controlled delivery of an active agent. When capsules are in flow, the viscous forces from the external flow can damage the capsules, potentially until breakup. Damage corresponds to the formation of microdefects in the wall which modify the properties of the capsule locally and thus the exchanges between the inner and the outer fluids. As a domino effect, it can lead to rupture as the accumulation of the microdefects can initiate a crack that propagates over the wall. The protection/release of the encapsulated agent is thus conditioned by the control of the damage of the capsule.

There are numerous contributions on the study of the dynamics of capsules in flow [1]. Few of them have, however, studied the rupture of capsules: the approach has only been experimental (see e.g. [2, 3]). The damage phase in the rupture process has thus never been studied. We propose to enrich a fluid-structure interaction model by modelling damage at the macroscale using the framework of continuum damage mechanics (CDM) (see e.g. [4] for a recent review), that offers a systematic approach of rupture for structures. In this work, we incorporate, for the first time, a CDM model into a fluid-structure interaction framework and study the damage process of a capsule in flow until the initiation of rupture.

MODEL

We consider an initially spherical capsule of radius a. The wall is assumed to be of very small thickness and is modelled as a membrane of mid-plane S and surface shear modulus G_s. The capsule is immersed in a simple shear flow of shear rate $\dot{\gamma}$. The internal and external fluids are the same incompressible Newtonian fluids of dynamic viscosity μ. Considering a capsule of microscopic size, the gravitational and inertial effects are negligeable compared to the viscous and elastic effects. Hence the only dimensionless parameter that governs the fluid-structure interaction is the capillary number $Ca = \mu a\dot{\gamma}/G_s$ that compares the fluid viscous forces to the membrane elastic forces.

The flows are governed by the Stokes equations. The boundary integral method [5] gives an explicit expression of the velocity $\underline{v}$ of the fluids on S as a function of the jump of viscous stresses $[\![\underline{\underline{\sigma}}]\!] \cdot \underline{n}$ across the membrane:

$$\forall \underline{x} \in S, \quad \underline{v}(\underline{x}) = \underline{v}^{\infty}(\underline{x}) - \frac{1}{8\pi\mu} \int_S \underline{\underline{J}}(\underline{x}, \underline{y}) \cdot [\underline{\underline{\sigma}}] \cdot \underline{n}(\underline{y}) \, \mathrm{d}S_{\underline{y}} \,, \tag{1}$$

where $\underline{v}^{\infty}$ is the velocity of the unperturbed simple shear flow and $\underline{\underline{J}}$ is the second order Oseen-Burgers tensor.

The membrane is at equilibrium at any instant. Hence, the principle of virtual works gives a relation between the internal tension tensor $\underline{\underline{T}}$ of the membrane and the external load vector $\underline{q}$ on the membrane:

$$\text{for any virtual displacement } \hat{\underline{u}} \,, \quad \int_S \underline{\underline{T}} : \underline{\underline{\varepsilon}}(\hat{\underline{u}}) \, \mathrm{d}S \; = \int_S \hat{\underline{u}} \cdot \underline{q} \, \mathrm{d}S \,, \tag{2}$$

where $\underline{\underline{\varepsilon}}(\hat{\underline{u}})$ is the symmetric part of the surface gradient of $\hat{\underline{u}}$.

The motions of the fluids and the membrane are coupled by imposing, on the interface S, the continuity of the velocities and the stresses (the jump of viscous stress $[\![\underline{\underline{\sigma}}]\!] \cdot \underline{n}$ is equal to the external load $\underline{q}$).

The damage of the membrane is modelled in the standard framework of CDM. The damage variable d is chosen to be a scalar that ranges from 0 (sound material) to 1 (macrocrack initiation). The choices for the free energy and for the damage criterion are given in Table 1. The expression of the damage criterion f is chosen from a model developped by Marigo [6] for brittle damage where we introduce the two parameters Y_D and Y_C representing an initial damage threshold

*Corresponding author. E-mail: a.salsac@utc.fr.

Table 1: Damage model of the membrane. ϕ_{NH} is the free energy of a Neo-Hookean material.

Surface density of free energy	$\phi = (1-d)\phi_{NH}$
Damage criterion	$f = -\dfrac{\partial \phi}{\partial d} - (Y_D + Y_C d)$

and a hardening modulus, respectively. Following the standard framework, we derive the damage evolution law from the normality law and the consistency condition:

$$\begin{cases} f < 0 \implies \dot{d} = 0 \\ f = 0 \implies d = (-\dfrac{\partial \phi}{\partial d} - Y_D)/Y_C. \end{cases} \tag{3}$$

NUMERICAL METHOD

We perform a Lagrangian tracking of the membrane. At the begining of a given time step, the current configuration of the membrane is known. We begin by solving the solid problem (eqs. (2), (3)) with the finite element method. First, we solve the local problem of damage evolution (eq. (3)) at the integration points. Then, we solve the global problem of equilibrium (eq. (2)) to find the external load at the nodes. Then we solve the fluid problem by computing the velocity of the fluids at the nodes from eq. (1). Finally, following the method developed by Walter *et al.* [5], the velocity is integrated explicitly by using a second-order Runge-Kutta scheme to determine the position of the nodes for the next time step.

RESULTS

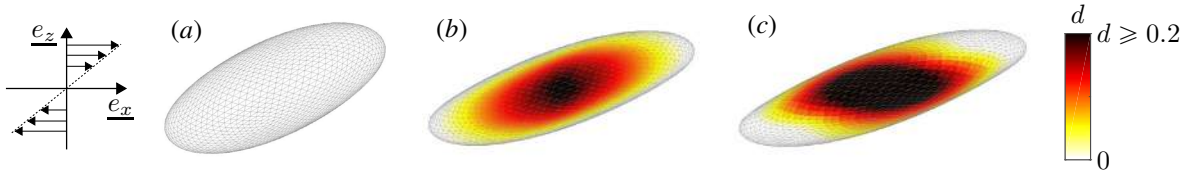

Figure 1: Damage of a capsule in simple shear flow observed, at steady state, in the shear plane ($\underline{e_x}$, $\underline{e_z}$) from the side, for (*a*) $Ca \leqslant Ca_c$ and (*b*) $Ca_c < Ca < Ca_\ell$, and (*c*) $Ca \geqslant Ca_\ell$ (shown at the instant of initiation of rupture, i.e. when $d = 1$ at the center of the capsule). Damage is symmetric with respect to the shear plane.

We have studied the damage process of a capsule as a function of the value of Ca for given values of the dimensionless damage parameters Y_D/G_s and Y_C/G_s. Damage occurs when Ca is larger than a critical value Ca_c and it leads to the initiation of rupture if Ca is larger than a limit value Ca_ℓ. When there is no damage ($Ca < Ca_c$), the motion of the capsule is known in the literature (see e.g. [5]): the capsule elongates in the flow strain direction, reaches a steady ellipsoidal shape and the membrane rotates around the vorticity axis (Figure 1a). When $Ca > Ca_c$, damage develops on the flanks of the capsule around the tip of the vorticity axis while the capsule elongates. If $Ca < Ca_\ell$, the capsule reaches a steady damaged state (Figure 1b), but when $Ca \geqslant Ca_\ell$, rupture is initiated when $d = 1$: it occurs at the tips of the vorticity axis (Figure 1c). The dimensionless damage parameters Y_D/G_s and Y_C/G_s influence the values of the thresholds Ca_c and Ca_ℓ and the intensity of damage.

In conclusion, the model proposed in this work enables to study the damage process and the criteria that control rupture of a capsule in flow.

Acknowledgements

This project has received funding from the European Research Council (ERC) under the European Unions Horizon 2020 research and innovation programme (Grant agreement No. ERC-2017-COG - MultiphysMicroCaps).

References

[1] Barthès-Biesel D. Motion and deformation of elastic capsules and vesicles in flow. *Annual Review of Fluid Mechanics* **48**: 25-52, 2016.
[2] Chang K.S., Olbricht W.L. Experimental studies of the deformation and breakup of a synthetic capsule in steady and unsteady simple shear flow. *J. Fluid Mech.* **250**: 609-633, 1993b.
[3] Koleva I., Rehage H. Deformation and orientation dynamics of polysiloxane microcapsules in linear shear flow. *Soft Matter* **13**: 3681-3693, 2012.
[4] Lemaitre J., Desmorat R. *Engineering Damage Mechanics*. Springer, 2005.
[5] Walter J., Salsac A.-V., Barthès-Biesel D., Le Tallec P. Coupling of finite element and boundary integral methods for a capsule in a Stokes flow. *Int. J. Numer. Meth. Engng.* **83**: 829-850, 2010.
[6] Marigo J. J. Formulation d'une loi d'endommagement d'un matériau élastique. *C. R. Acad. Sci. Paris* **292**: 1309-1312, 1981.

HOW FLOW DETERMINES RED BLOOD CELL MOTION AND BLOOD PLATELET FORMATION

Stephan Gekle[1]
[1] Biofluid Simulation and Modeling, Theoretische Physik VI, Universit at Bayreuth, Germany

Summary We use Boundary-Integral and Lattice-Boltzmann simulations to study two biologically relevant examples of fluid-structure interaction: red blood cell motion through narrow capillaries and the biogenesis of blood platelets. In the first scenario, we discover a pronounced bistability: the final shape of the red blood cell is not only determined by external parameters such as flow speed or channel geometry, but also depends crucially on the initial position in quantitative agreement with microfluidic experiments by our collaboration partners. In the second scenario, we show how platelet production in the blood stream is strongly accelerated by hydrodynamic forces in agreement with recent experiments. We explain the acceleration mechanism by an elasto-hydrodynamic instability closely related to the classical Rayleigh-Plateau mechanism of a liquid jet.

A fascinating example of cell mechanics is the deformation of cells in blood flow. Here, we elucidate two examples where the cell-flow interaction is particularly relevant. The common link between both scenarios is that cell behavior is determined by the cell membrane which is passively elastic in the first and biologically active in the second case.

In the first case, we investigate red blood cells flowing through capillaries which assume a wide variety of different shapes owing to their high deformability. Predicting the realized shapes is a complex field as they are determined by the intricate interplay between the flow conditions and the membrane mechanics. We construct the shape phase diagram of a single red blood cell with a physiological viscosity ratio flowing in a microchannel. We use both experimental in-vitro measurements by our cooperation partners as well as 3D Bounday-Integral simulations to complement the respective other one. Numerically, we have easy control over the initial starting configuration and natural access to the full 3D shape. With this information we obtain the phase diagram as a function of initial position, starting shape and cell velocity. Experimentally, we measure the occurrence frequency of the different shapes as a function of the cell velocity to construct the experimental diagram which is in good agreement with the numerical observations. Two different major shapes are found, namely croissants and slippers as illustrated in figure 1. Notably, both shapes show coexistence at low (< 1 mm/s) and high velocities (> 3 mm/s) while in-between only croissants are stable. This pronounced bistability indicates that RBC shapes are not only determined by system parameters such as flow velocity or channel size, but also strongly depend on the initial conditions [1].

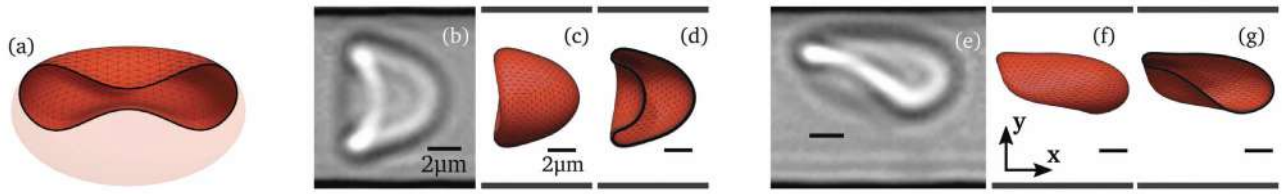

Figure 1: Typical RBC shapes from simulations and experiments. (a) The typical discocyte shape employed in some of the simulations as the starting shape. Half of it was made transparent for illustration purposes. Its horizontal diameter is $8\,\mu$m. (b) A typical croissant observed in the experiments when applying a pressure drop of $100\,$mbar (cell velocity $0.98(7)\,$mm/s). (c) A croissant with a velocity of $\approx 1.1\,$mm/s obtained from the numerical simulations. (d) The cross-section of the croissant from (c). (e) A slipper from the experiments at $500\,$mbar (cell velocity $5.16(11)\,$mm/s). (f) A typical slipper from the simulations with a cell velocity of $\approx 5.2\,$mm/s. (g) The cross-section of the slipper from (f). The black lines on the shapes from the simulations depict the mesh. The bottom and top black lines in all figures are the walls ($L_y \approx 12\,\mu$m apart), while the small black lines are scale bars of length $2\,\mu$m. The flow is in the positive x-direction (except in figure (a) where no flow exists).

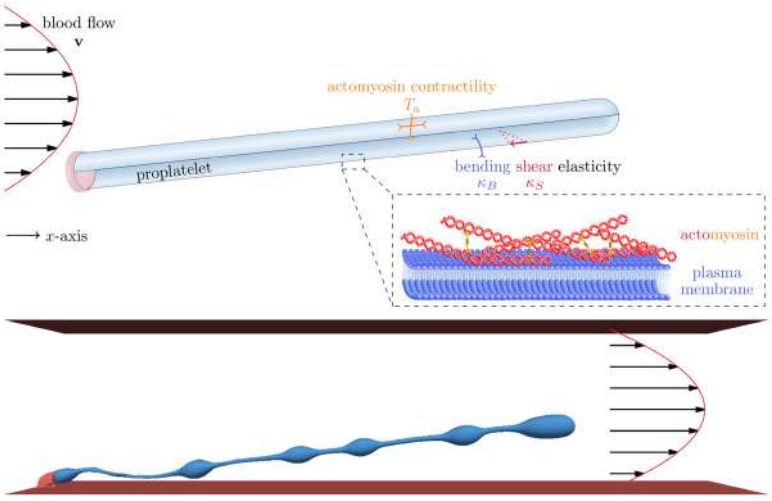

Figure 2: (a) Illustration of the simulation model for the proplatelet membrane. Plasma membrane and cortex (inlet) are treated together as elastic, active thin membrane. The membrane is endowed with bending κ_B and shear elasticity κ_S as well as actomyosin contractility T_a. We model the proplatelet as initially cylindrical membrane with one fixed end and one free end corresponding to the in-vivo situation. The proplatelet is subject to external blood flow. (b) A proplatelet forms periodic swellings in Poiseuille flow which rupture and lead to the release of platelets into the blood stream.

In the second case [2], we study blood platelets which are formed by fragmentation of long membrane protrusions (proplatelets) from bone marrow megakaryocytes in the blood flow. Using Lattice-Boltzmann/Immersed Boundary simulations we propose a biological Rayleigh-Plateau instability as the biophysical mechanism behind this fragmentation process. Our fully three-dimensional simulations, illustrated in figure 2 (a) highlight the crucial role of actomyosin contractility in the proplatelet cortex, which is required to trigger the instability, and illustrate how the wave length of the instability determines the size of the final platelets. The elasto-hydrodynamic origin of the fragmentation explains the strong acceleration of platelet formation in the presence of an external flow, which we observe in agreement with experiments [3] as illustrated in figure 2 (b). Our simulations then allow us to disentangle the influence of specific flow components: while a homogeneous flow leads to the strongest acceleration, shear flows can cause fusion events of two developing platelets leading to the release of larger structures which are observable as preplatelets in experiments. Together, our findings strongly point to a purely physical, rather than biochemical, regulation of platelet size and flow-accelerated platelet biogenesis.

References

[1] Guckenberger A., Kihm, A., John T., Wagner, C. and Gekle, S. Numerical-experimental observation of shape bistability of red blood cells flowing in a microchannel. *Soft Matter* **14**: 2032, 2018.

[2] Bächer, C., Bender, M. and Gekle, S. Flow-accelerated platelet biogenesis is due to an elasto-hydrodynamic instability. *To be submitted*

[3] Blin, A., Le Goff, A. Magniez, A., Poirault-Chassac, S., Teste, B., Sicot, G., Nguyen, K. A., Hamdi, F. S., Reyssat, M. and Baruch, D. Microfluidic model of the platelet- generating organ: beyond bone marrow biomimetics. *Sci. Rep.*, **6**: 21700, 2016

CRAWLING IN A FLUID

Alexander Farutin*[1], Jocelyn Etienne[1], Chaouqi Misbah[1], and Pierre Recho[1]
[1] *Univ. Grenoble Alpes, CNRS, LIPhy, 38000 Grenoble, France*

Summary There is growing experimental evidence that amoeboid cells can swim in bulk fluid medium. In this study, we analyze theoretically a model of an almost-spherical cell suspended in a fluid. The models couples the cortex mechanics with the flow in the fluids inside and outside the cell. We show that a spherically symmetric cell can undergo a spontaneous symmetry breaking, which results in polarization and swimming of the cell. The swimming velocity of the cell is obtained as an explicit function of the main parameters governing the cortex mechanics. We show that the symmetry breaking can occur as a sub- or supercritical pitchfork bifurcation, depending on the cortex properties. For some parameters, a Hopf bifurcation is observed, which results in coupled oscillations of actin and myosin distributions in the cortex and oscillatory swimming of the cell.

INTRODUCTION

Motility on a cellular scale is ubiquitous in nature and plays an important role in many physiological processes. A notable class is amoeboid cells, which are characterized by strong deformation of the cell body during the locomotion. Experimentally, these cells are usually studied while crawling on a substrate, when adhesion is indispensable for propulsion. However, *in vivo* these cells usually move in a complex medium made of fluid environment and elastic obstacles, like, for example, during motion of a cell in a tissue. The requirement of adhesive contact during this motion was challenged experimentally[1]. There is now growing experimental evidence that amoeboid cells can propel themselves in bluk fluid environment[2, 3, 4]. Motivated by these experiments, we have analyzed theoretically the motion of a spherical cell in a fluid[5]. We find that the cells can swim, provided that the retrograde flow of their cortex can be transmitted to the outside fluid. Several such transmission mechanisms have been proposed in the literature: (1) by deformations of the cell[2], (2) by recirculation of the phospholipid membrane[3], and (3), more recently, by transmembrane proteins[4].

MODEL

The model has two main ingredients: (1) a gel of actin filaments which constitute the cell cortex and (2) myosin motors which cross-link the actin filaments and create pulling stresses inside the cortex. The cortex is modeled as a compressible two-dimensional fluid covering the inner surface of the cell. The mechanical stress in the cortex can then be related to the distributions of concentrations of actin and myosin according to the active gel model. This stress generates cortex force, which is balanced by the viscous stresses in the fluids inside and outside the cell. Solving the force balance equations allows us to express the velocity of the cortex as a function of the distributions of actin and myosin along the cell surface. This is done analytically by expanding all distributions in spherical harmonics. The evolution of actin and myosin concentrations is governed by advection-diffusion equations on the cell surface, where we also add a turn-over term to account for the polymerization and depolymerization of actin. The resulting equations are non-linear because of the advection term and have to be solved numerically in general case but we also analyze analytically the linear stability of the homogeneous solution and use perturbation approach close to the instability point. Initially, we make no assumptions about the symmetry of the cell but eventually dynamics tends to an axisymmetric solution in all explored cases. The 3 main parameters of the model are: myosin contractility, compressional stiffness of the actin gel and the turn-over rate of actin, where cortex viscosity, cell size, and diffusion coefficient of myosin motors are set to 1.

RESULTS

We show that the spherically symmetric solution becomes unstable for high enough contractility. The mode becoming unstable corresponds to the first harmonic of the concentration fields. This results in accumulation of actin and myosin at the rear part of the cell and their depletion at the front (Fig.1). A self-sustained flow of actin appears from cell front to back, which is balanced by actin polymerization at the front and depolymerization at the rear. This flow of actin results in flow of the fluid outside the cell, which leads to autonomous self-propulsion of the cell. An interesting observation is that the propulsion speed is independent of the viscosity of the outer fluid, provided it is much lower than the cortex viscosity. We show that the symmetry breaking instability occurs supercritically for high turn-over rate of actin but can also occur subcritically if the turn-over rate is low enough. A bistability is observed in the latter case, where the motile solution and the symmetric one are both stable for the same parameters. For even lower rate of actin turn-over the spherically symmetric solution becomes unstable via Hopf bifurcation. This instability results in coupled oscillation of the distributions of actin and myosin, where the high-concentration spots move from one end of the cell to the other periodically. The cell swims back and forth in this case.

*Corresponding author. E-mail: alexandr.farutin@univ-grenoble-alpes.fr

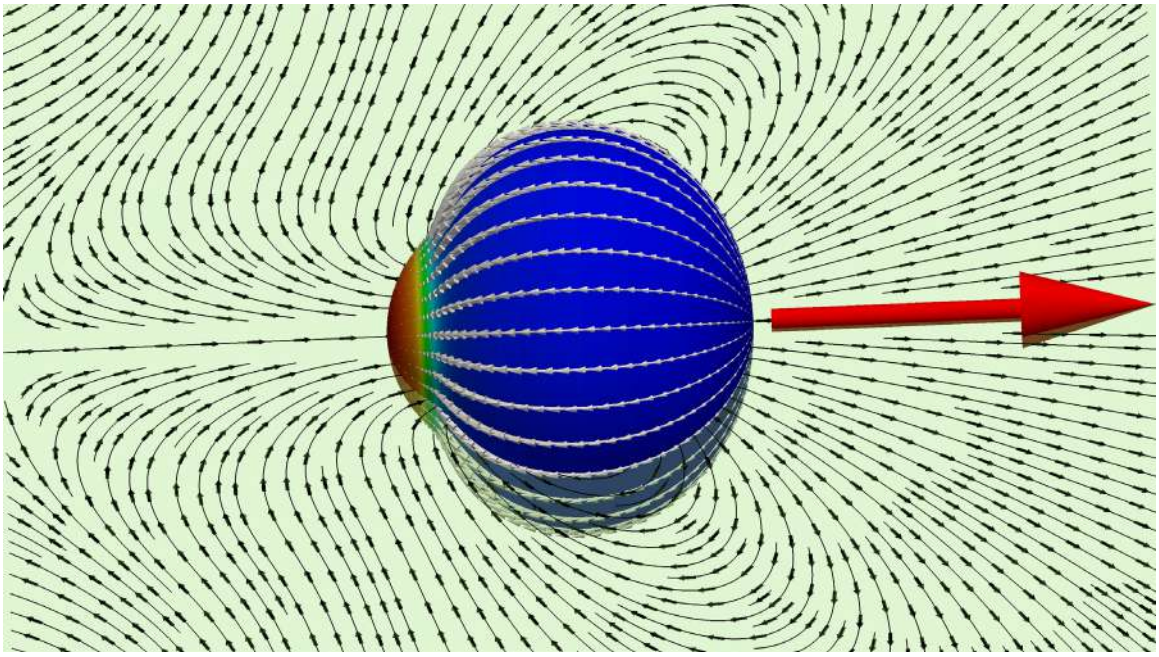

Figure 1: Flow lines around a swimming cell. Swimming direction is shown by a red arrow. Color code by actin distribution. Arrows on the cell surface show the retrograde flow.

Deformation of the cell is not a prerequisite of the motility in our model. Nevertheless, stresses in the cortex can lead to a non-spherical deformation of the cell. We have determined the shape of the cell that these stresses result in (Fig.1). Here we assume that the shape results from a balance of the cortex stresses, tension of the phospholipid membrane which encloses the cell, and a pressure surplus (due to osmosis) inside the cell. The resulting shapes are consistent with the shapes reported in earlier experiments.

More details can be found in [5].

ACKNOWLEDGMENTS

AF and CM thank CNES (Centre National dEtudes Spatiales) and the French-German University Programme Living Fluids (Grant CFDA-Q1-14) for financial support. JE and PR are supported by a CNRS Momentum grant, ANR-11-LABX-0030 Tec21 and IRS AnisoTiss of Idex Univ. Grenoble Alpes. All are members of GDR 3570 MecaBio and GDR 3070 CellTiss of CNRS. The computations were performed using the Cactus cluster of the CIMENT infrastructure, supported by the Rhne-Alpes region (GRANT CPER07 13 CIRA).

References

[1] Lämmermann T., Bader B. L., Monkley S. J., Worbs T., Wedlich-Söldner R., Hirsch K., Keller M., Förster R., Critchley D. R., Fässler R., Sixt M., *Nature* **453**: 51, 2008.

[2] Barry N. P., Bretscher M. S., *Proceedings of the National Academy of Sciences* **107**: 11376, 2010.

[3] O'Neill P. R., Castillo-Badillo J. A., Meshik X., Kalyanaraman V., Melgarejo K., Gautam N., *Dev. Cell.* **46**: 9, 2018.

[4] Aoun L., Nègre P., Farutin A., Garcia-Seyda N., Rizvi M. S., Galland R., Michelot A., Luo X., Biarnes-Pelicot M., Hivroz C., Rafaï S., Sibarita J.-B., Valignat M.-P., Misbah C., Theodoly O., *bioRxiv*, 2019.

[5] Farutin A., Étienne J., Misbah C., Recho P., *Phys. Rev. Lett.* **123**: 118101, 2019.

A HYDRODYNAMIC MODEL FOR SPIROPLASMA MOTILITY

Christian Esparza-Lopez[1] and Eric Lauga [1]
[1] Department of Applied Mathematics and Theoretical Physics, University of Cambridge. Wilberforce Road, Cambridge CB3 0WA, UK

Summary *Spiroplasma* is a tiny helical bacterium that swims and performs chemotaxis in a non conventional way. Based on experimental observations [1] and following a previous numerical approach [2], in this study we develop a hydrodynamic model to describe *Spiroplasma* motility. We obtain expressions for the total linear and angular displacements per stroke of the cell body. Observing that the swimming gait corresponds to a run-reverse motion, we can define an effective swimming speed, v_s, which we use to calculate the energy dissipated in one stroke, $\dot{W}$, and to define a hydrodynamic efficiency, $e = \dot{W}_0/\dot{W}$, where $\dot{W}_0$ is the power spent by a straight filament moving at speed v_s. We show that the helical shape that maximises both, v_s and e, is a helix of pitch angle ϕ close to that of *Spiroplasma* $\phi \simeq 35°$, in agreement with previous simulations and experimental observations [1, 2].

INTRODUCTION

Spiroplasma is a helical-shaped bacterium with no flagella, that swims by progressively shifting the chirality of its body. The change in geometry gives rise to a wall domain, a kink, which propagates along the cell body (see Fig. 1). The chirality is then reverted in a similar fashion completing a swimming stroke. It has been observed that the change in chirality occurs in the absence of external stress, therefore the body bends with an angle $\theta = \pi - 2\phi \simeq 110°$, where $\phi \simeq 35°$ is the pitch angle of the helical body [2]. A chirality transformation with the stress free constrain allows for two kind of kinematic modes, the "crankshafting" and the "speedometer cable" mode [4]. In the former, one of the domains revolve around the other, while in the later, both domains spin around their axes. Simple scaling arguments for the energy dissipated on each mode suggest that the "speedometer cable" transformations are predominant, as seen in experiments [1, 2]. The whole deformation is non reversible in time, therefore swimming is achieved at low Reynolds number and the bacterium moves in the direction opposite to the kink pair propagation. The time between strokes appears to be exponentially distributed, with rate $\lambda_k \simeq 1\ \mathrm{s}^{-1}$. The time between a kink pair follows a normal distribution with mean $\tau_p \simeq 0.26$ s. The kink pair propagates at an average speed $v_0 \simeq 10\ \mu$m/s which is linearly related to the swimming velocity $v_s \simeq 3.3\ \mu$m/s [1]. The total arc length of *Spiroplasma* is $L \sim 10\ \mu$m and its helical radius is $R \sim 0.5\ \mu$m, so that it can be therefore considered as a slender body and resistive-force theory can be applied to describe its motion.

MATHEMATICAL MODEL

Following experimental observations, we model *Spiroplasma* as a deformable rod which performs the swimming stroke shown in Fig. 1. The force acting on the body per unit length can be obtained using resistive-force theory as follows [3]

$$\mathbf{f} = -\zeta_{\parallel}\mathbf{v}_{\parallel} - \zeta_{\perp}\mathbf{v}_{\perp}, \tag{1}$$

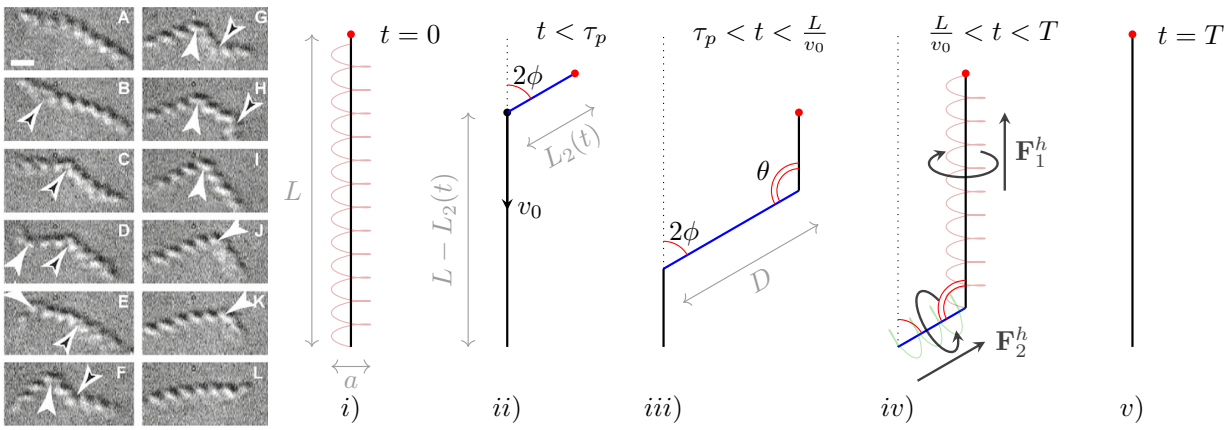

Figure 1: Spiroplasma swimming stroke (A-L) experiments [1] and (i-v) our model. (A,i): Initially the body has a right-handed helical shape. (B, C, ii): A kink appears at $t = 0$ and propagates from head (red circle) to tail along the body of length L at speed v_0. The deformed rod has two domains of size $L_2(t)$ and $L_1(t) = L - L_2(t)$. (D-H, iii): The second kink forms at $t = \tau_p$, the maximum distance between kinks is denoted by $D = v_0\tau_p$. (I-K, iv): The configuration is similar to that of ii), with reversed signs of the forces and torques acting on the body, the blue segment has left handed chirality and rotates clockwise, while the right handed segment rotates anticlockwise. The arrows represent the induced force. (L, v): The stroke finishes at $T = \tau_p + L/v_0$. The stroke is described in the frame of reference in which the tail is static.

*Corresponding author. E-mail: e.lauga@damtp.cam.ac.uk

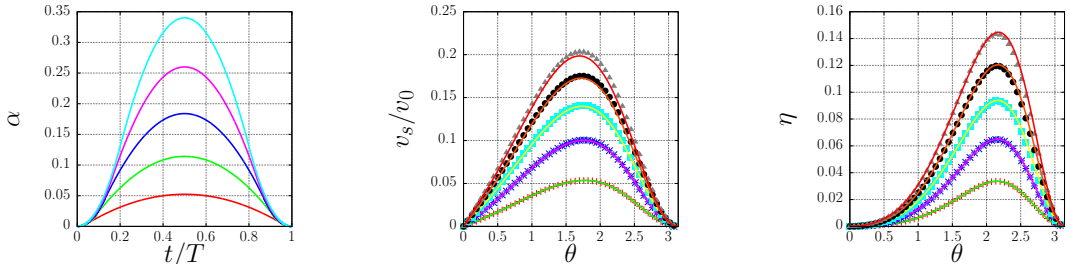

Figure 2: Angular displacement (left), swimming speed (center) and efficiency (right). Left panel shows that the body does not reorient after one cycle. The angle α is defined by $\cos\alpha \equiv \boldsymbol{\tau}(0)\cdot\boldsymbol{\tau}(t)$, where $\boldsymbol{\tau}(t)$ is the tangent vector to the "right-handed" domain. Center and right panels show a comparison between the full numerical solution and the asymptotic expansion of v_s and e at order d^2. The different curves in all panels correspond to increasing values of d (bottom to top) from 0.05 to 0.25 in steps of 0.05.

where $\zeta_{\parallel,\perp}$, $\mathbf{v}_{\parallel,\perp}$ are the parallel and perpendicular drag coefficients and swimming velocities respectively. The total force and torque acting on the body are given by $\mathbf{F} = \int \mathbf{f}\mathrm{d}s$ and $\mathbf{N} = \int \mathbf{x}\times\mathbf{f}\mathrm{d}s$, where $\mathbf{x}(s,t)$ is the position of a material point along the body at time t parametrised by the arc length s. We include the effects of helical geometry at a coarse-grained level by allowing the ratio of parallel to perpendicular drag coefficients, $\beta(\theta)$, to depend on the kink angle (or equivalently on the pitch angle ϕ) and by including external forces $\mathbf{F}_i^h$ (depicted in Fig. 1 iv), which account for the propulsion due to the rotation of the helical domains. We obtain the swimming velocity by considering the free swimming condition $\mathbf{F}+\mathbf{F}^h = \mathbf{0}$ and $\mathbf{N}+\mathbf{N}^h = 0$. The motion is symmetric under a half turn on the plane of motion and time reversal. Hence, by reversibility of Stokes flow, the body does not reorient at all after one cycle. This allows us to define an effective swimming speed as the ratio of the total linear displacement to the period of the stroke, that is

$$v_s^2 \equiv \frac{v_0^2}{(1+d)^2}\left(x_T^2+y_T^2\right), \tag{2}$$

where $d = v_0\tau_p/L$ is the ratio of the distance between kinks to the total length; x_T and y_T are the dimensionless components of the linear displacement $\mathbf{x}(t=T)/L$; and $T = L(1+d)/v_0$ is the period of the stroke. The energy dissipated in one stroke, $\dot{W}$, can be obtained by integrating the energy density, $\mathbf{f}\cdot\mathbf{v}$, along the body and over one period. We compare it to the energy dissipated by a straight filament moving at speed v_s, *i.e.* $\dot{W}_0 = \zeta\perp L v_s^2$. We finally define the hydrodynamic efficiency as

$$e \equiv \frac{\dot{W}_0}{\dot{W}} = \frac{T\zeta_\perp v_s^2}{\int_0^T\int_0^L \mathbf{f}(s,t)\cdot\mathbf{v}(s,t)\,\mathrm{d}s\,\mathrm{d}t}. \tag{3}$$

SUMMARY OF RESULTS

Despite the simplicity of the model, a full analytical solution seems impossible to obtain, due to the fact that the instantaneous swimming velocity $\mathbf{v}$ depends in a nonlinear way on β and θ. We can still make some progress by considering $d = D/L$ to be small. This assumption is supported by experiments, indeed according to Shaevitz et al. $v_0 \sim 10\ \mu$m/s, $\tau_p \sim 0.25\ s$ and $L \sim 10\ \mu$m hence $d \sim 1/4$ [1]. This approach is further justified by the fact that the numerical simulation shows that both v_s and e depend only weakly on d (see Fig. 2). We can therefore consider d small enough so that we can expand v_s and e in powers of d. Taking the first terms in the asymptotic expansion, it is found that the optimum kink angle lies between $\theta \simeq 100^\circ - 120^\circ$ which corresponds to a pitch angle of $\phi \simeq 30^\circ - 40^\circ$ in agreement with the experimental value $\phi \simeq 35^\circ$ [1].

CONCLUSIONS

In this work we develop a theoretical hydrodynamic model to describe the swimming of *Spiroplasma*. Our results show that the motility pattern corresponds to a run-reverse motion, as the body does not reorient after one stroke. Our theoretical model confirms that *Spiroplasma* optimises swimming efficiency at a maximum swimming speed.

References

[1] Shaevitz J. W., Lee J. Y. and Fletcher D. A. Spiroplasma Swim by a Processive Change in Body Helicity. *Cell* **122**: 941945, 2005.
[2] Wada H. and Netz R. R. Hydrodynamics of helical-shaped bacterial motility. *Phys. Rev. Lett.* **80**: 021921, 2009.
[3] Cox R. G. The motion of long slender bodies in a viscous fluid Part 1. General theory. *J. Fluid. Mech.* **44**: 791-810, 1970.
[4] Goldstein R. E., Goriely A., Huber G. and Wolgemuth C. W. Bistable Helices. *Phys. Rev. Lett.* **84**: 1631-1634, 2000.

MICROCIRCULATION OF RED BLOOD CELLS IN BIOMIMICKING SPLENIC SLITS

Anne Charrier [1], Alexis Moreau[1], Huije Lu[2], Emmanuèle Helfer[1], Zhangli Peng[2,3], and Annie Viallat*[1]
[1] Aix Marseille Univ, CNRS, CINAM, Marseille, France
[2] Department of Aerospace and Mechanical Engineering, University of Notre Dame, Notre Dame IN, USA
[3] Department of Bioengineering, University of Chicago at Illinois, Chicago IL, USA

Summary Red blood cells (RBC) are responsible for distributing oxygen throughout the body. To pass through the smallest blood capillaries, RBCs must be highly deformable. To ensure this property, RBCs undergo the most stringent test by passing through the interendothelial slits of the spleen. This test which is believed to filter RBCs by retaining the stiff ones is also known to play an important role in many diseases such as malaria or sickle cell disease. However, the mechanisms that govern the cell dynamics through the slits are still unknown. We have developed the first device replicating the physiological dimensions of the splenic slits and allowing the observation of RBC dynamics by optical video microscopy. Trapping and deformation, reported for the first time in in vitro submicron fenestrations, definitely underline the importance of strong cell confinement and deformation.

INTRODUCTION

Although their apparent simple morphology, red blood cells (RBCs) are very deformable with well-adjusted rheological properties enabling their fast, efficient and resilient transport into the microcirculation. In the spleen, RBCs pass the most stringent physical fitness test of the blood circulation, consisting in squeezing through submicronic slits where they undergo extreme deformations. This test which is believed to filter RBCs by retaining the stiff ones is known to play an important role in many diseases such as malaria or sickle cell disease. However, the mechanisms that govern the cell dynamics through the slits are still unknown and this is due to the lack of experimental tools. To answer this question, we have developed the first microfluidic device containing slits with submicron width replicating the physiological dimensions of splenic slits[1] where the RBC dynamics can be observed through the slits and recorded by optical microscopy.

BIOMIMETIC SPLENIC SLITS

We report the dynamics of RBCs as a function of the relevant external parameters (slit dimensions, pressure drop) and cell morphologies. Trapping and deformation, reported for the first time in in vitro submicron fenestrations, definitely underline the importance of strong cell confinement and deformation. The specific behaviours observed here shed light on the alteration of the mechanical properties of RBCs in disease. In particular, we show original modes of deformation with the formation of tips at the cell front. Conjointly, our collaborator (Zhangli Peng's group, University of Illinois at Chicago) developed numerical simulations that recover both RBC transit times and shape deformation. The comparison of experiments and simulations leads to a deep insight of the mechanisms of RBC transit through the slits.

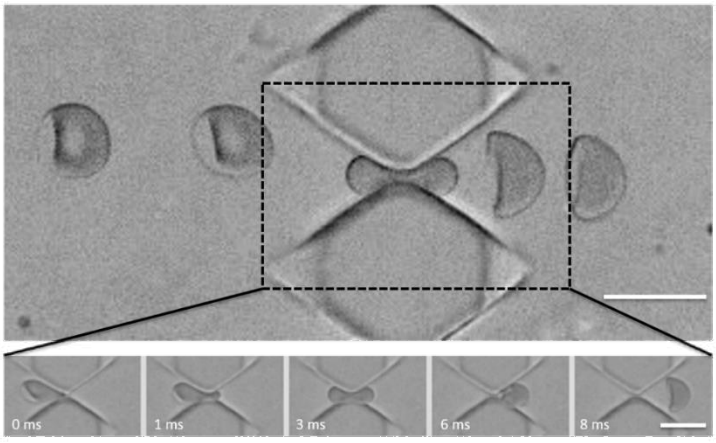

Figure 1. Superimposed images (top) and video sequences (bottom) of an RBC passing through slits of dimensions 0.67 x 1.9 x 4.7 μm^3. Scale bars: 10 µm. $\Delta P_{In/Out}$ = 10 mbar.

References

[1] Gambhire P., et al. *Small* **999b**: 991-996, 2017.

*Corresponding author. E-mail: **annie.viallat@univ-amu.fr**.
This work has been carried out thanks to the support of the A*MIDEX project (n° ANR-11-IDEX-0001-02) funded by the «Investissements d'Avenir» French Government program, managed by the French National Research Agency (ANR)

INFLUENCE OF RED BLOOD CELL DEFORMABILITY ON HEMODYNAMIC CHANGES IN PHYSIOLOGICALLY REALISTIC MICROVASCULAR NETWORKS

Prosenjit Bagchi[1], and Saman Ebrahimi
[1] Mechanical and Aerospace Engineering Department, Rutgers University, New Jersey, USA

Summary Microvascular networks are formed by capillary blood vessels and characterized by geometrically complex architecture of bifurcating, merging and winding vessels. Blood in such networks flows as a suspension of red blood cells (RBC) that are extremely deformable under healthy conditions. In many diseases, such as sickle cell disease, malaria, and diabetes mellitus, RBCs lose their deformability. Influence of the loss of deformability on hemodynamics at the scale of a microvascular network is poorly understood, and is the goal of this study. We use a 3D fluid-structure interaction model that accurately predicts deformation of every single RBC flowing through physiologically realistic microvascular networks. The model predicts that the loss of RBC deformability leads to a significant alteration to RBC distribution, and a significantly greater increase in vascular flow resistance in the vessels in the networks than isolated vessels. Physical mechanisms underlying these novel yet biologically important results are presented.

INTRODUCTION

Microvascular networks in human body are made of the smallest blood vessels, namely, capillaries, arterioles and venules. The architecture of a microvascular network is very complex and characterized by constantly bifurcating and merging vessels. The topology of networks can vary from organ to organ and also differ under healthy and disease conditions. Moreover, these vessels are not necessarily straight, and often highly winding. Blood in such small vessels behaves as a concentrated suspension primarily made of red blood cells (RBC) which are extremely deformable. Deformability of RBCs allows them to squeeze through the narrow capillaries with diameters less than their characteristic size.

Mathematical models of blood flow in such networks have treated the vessels as 1D straight segments neglecting the geometric complexity and details [1]. These models also do not consider the deformation and flow of individual red blood cell, and instead use empirical relations to prescribe blood viscosity and cell distribution at a vascular bifurcation. As such, these models cannot predict several hemodynamic processes and parameters that are of significant biological importance, such as formation of the plasma layer near the vessel wall, and wall shear stress gradient.

To overcome this limitation, we have developed a high-fidelity 3D, first-principle based, fluid--structure interaction model of blood flow in physiologically realistic microvascular networks [2]. The model retains the exact geometric details of the vasculature, e.g., 3D nature of the blood vessels and bifurcations, and vessel curvature. Deformation and flow of each individual red blood cell as they flow through the vessels are exactly simulated. The model does not assume any empirical viscosity law or bifurcation law; rather, these laws are predicted by the model. The model provides microscale details of hemodynamic quantities that are not readily available in experiments, and cannot be predicted by the traditional 1D network models, such as wall shear stress gradient and time-dependent red blood cell partitioning at bifurcations [3,4].

Of particular interest is the role of RBC deformability on network-scale hemodynamics. Many diseases, such as sickle cell disease, malaria and diabetes mellitus, are associated with a loss of RBC deformability. A detailed quantification of changes in network-scale hemodynamics under such conditions is lacking. Using the aforementioned high-fidelity model of RBC-resolved blood flow in capillary networks, here we provide the first-ever simulation results on the changes in network-scale blood flow under varying RBC deformability.

OVERVIEW OF MODEL

The numerical methodology is based on the framework of immersed boundary methods (IBM) for efficient fluid-structure interaction problems in conjunction with a 3D Finite Volume/Spectral fluid flow solver, and a Finite-Element solver for deforming interfaces. Two separate types of IBMs are employed to accommodate the wide variety of interfaces encountered in the cellular-scale blood flow, as follows. Blood cells are modelled as viscous drops surrounded by hyperelastic membranes with biconcave discoid resting shapes. The resistance of the cell membrane against shear deformation, bending and area dilation is modelled via appropriate constitutive relations. A Lagrangian mesh is fitted to the cell surface and is used to calculate the forces in the membrane due to deformation using the Finite Element Method. Cell deformation is coupled to the fluid flow, which is governed by the unsteady Stokes equations, via a continuous-forcing front tracking IBM. For rigid interfaces as defined by the walls of the blood vessels, and vascular bifurcations, a direct forcing sharp-interface ghost node IBM (GNIBM) is developed. With this, the no-slip boundary condition at the vascular wall is achieved by enforcing appropriate constraints on the fluid velocity at the Eulerian mesh nodes that are immediately outside the boundary (ghost nodes).

In silico microvascular networks are modelled from *in vivo* images and data using a standard CAD software, and maintaining the hierarchical structure and ordering as observed in physiological scenario (Fig. 1). The mesh defining the vessel surfaces is used in the context of the GNIBM to represent the nondeformable walls. Flow in the networks is driven by specifying inlet/outlet pressure or flow-rate boundary conditions corresponding to physiological values. The

present methodology is versatile, and can be used to simulate deformable cell motion in any capillary vessel networks, 3D or planar, of arbitrary complexity including cerebral, retinal and tumour microvasculature.

RESULTS

A visualization from one simulation is shown in Fig. 1a. The network geometry considered here covers a tissue area of about 450X300 μm^2. Generic characteristics of microvascular blood flow, such as heterogeneous distribution of blood cells and their highly deformed shapes including parachute/bullet/slipper shapes, are predicted by these simulations. Quantitative validations of hemodynamic parameters, such as vascular flow resistance and wall shear stress, against *in vivo* data were performed showing a good agreement.

We then simulate the flow of healthy and diseased RBCs through the networks to predict the influence of RBC deformability on network-scale hemodynamics. Diseased RBCs are modelled by increasing the cell membrane shear elastic modulus by a factor of ten. The most striking result is a significant redistribution of RBCs in the network upon their loss of deformability. This is shown in Fig. 1b where the percentage change in haematocrit in the vessels is shown. As can be seen here, while some vessels show as much as 30% increase in haematocrit, some show nearly similar range of decrease. Such altered distribution of blood cells has not been predicted before, and has significant biological implications in terms of oxygen delivery to tissues.

The physical mechanisms underlying such altered RBC distribution are identified, and attributed to the way RBCs are distributed to the daughter vessels as they flow through a bifurcation. We noted that the residence time of RBCs increased near the flow stagnation point at the bifurcations, a phenomenon we termed as 'lingering'. Because of this, a cell flowing through a bifurcation can either enter in to a daughter vessel which has a higher flow rate, or to the one that has a lower flow rate. The former is termed as the regular cell partitioning, while the latter as the reverse partitioning. We find that the reverse partitioning occurs less frequently, in a time-dependent sense, in presence of diseased RBCs than healthy RBCs, thereby resulting in the altered distribution of cells.

Fig 2c shows the changes in vascular flow resistance upon the loss of RBC deformability. A significant change is also noted here – while some vessels show a large increase in the flow resistance, some of them surprisingly show a drop in flow resistance. Also interesting to note is that when we simulate isolated vessels with diseased RBCs, the percentage increase in flow resistance is about 11—12% for vessels of 11—16 µm diameter. Thus the vessels in the networks impart additional resistance than isolated straight vessels in presence of diseased RBCs. The physical mechanism underlying such "excess" resistance is also the lingering event at bifurcations that causes large spikes in time-dependent flow resistance.

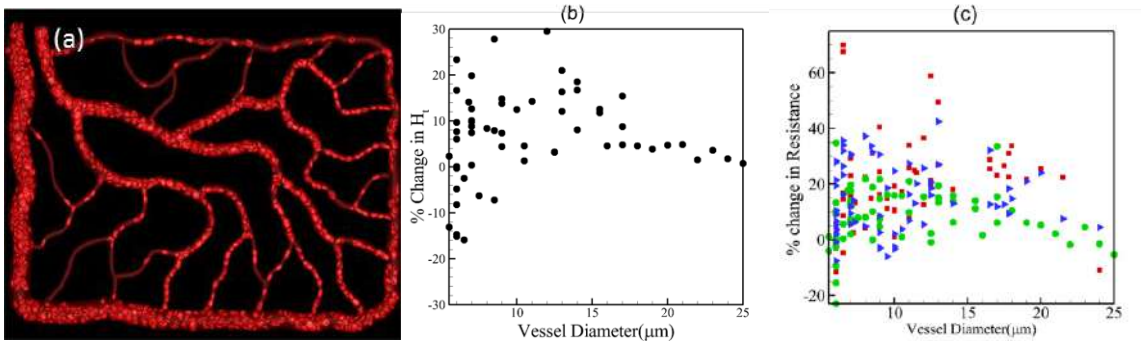

Figure 1. (a) An example fluid-structure interaction simulation of flow of many deformable blood cells through physiologically realistic microvascular networks. (b) Predicted change in haematocrit and (c) flow resistance due to loss of RBC deformability.

CONCLUSIONS

A high-fidelity, 3D fluid-structure interaction model is used to predict the changes in microvascular network-scale hemodynamics upon the loss of red blood cell deformability. The model accurately predicts the deformation of every single RBC flowing through physiologically realistic networks of capillary blood vessels comprising of multiple bifurcations and arbitrary vessel shapes. The simulations predict a significant alteration of RBC distribution upon loss of deformability; this result has biological implications in terms of oxygen delivery to tissues. Further, a significant increase in vascular resistance is also predicted for vessels in the networks, and is found to be higher than isolated vessels. The physical mechanisms underlying such changes are also identified.

References

[1] Fry B.C., Lee J, Smith N.P., Secomb T.W. (2012) Estimation of blood flow rates in large microvascular networks. *Microcirculation* 19: 530-538, 2012.
[2] Balogh P., Bagchi P. A computational approach to modeling cellular-scale blood flow in complex geometry. *J. Comput. Phys*. 334: 280-3, 2017.
[3] Balogh, P., Bagchi, P. The cell-free layer in simulated microvascular networks. *J. Fluid Mech*.. 864: 768-806, 2019.
[4] Balogh, P., Bagchi, P. Direct numerical simulation of cellular-scale blood flow in 3D microvascular networks. *Biophys. J*. 113: 2815-2826, 2017.

VERTICAL MIGRATION OF MICROCYSTIS COLONIES

Yu Yang, Li Zeng *, and Yihong Wu
State Key Laboratory of Simulation and Regulation of Water Cycle in River Basin, China Institute of Water Resources and Hydropower Research, Beijing, China

Summary Vertical migration of Microcystis colonies is significant for various ecological phenomena, especially for the harmful algal blooms. The trajectories of *Microcystis* colonies and the flow field around a *Microcystis* colony were measured by use of PLIF technique and PIV system. It is found that the migration direction of *Microcystis* colonies is subject to an Gaussian distribution. Two vortices are found to exist around *Microcystis* colonies, which differs from the flow pattern past a sphere at the same Reynolds number. An expression has been present to predict the vertical migration velocity of *Microcystis* colonies, based on Stokes' law.

INTRODUCTION

Blooms of *Microcystis*, occurring widespreadly in freshwaters, have received intensive concerns, due to its serious harms to aquatic ecosystem in terms of water quality deterioration, biodiversity reduction, massive death of fish, etc. [1]. Vertical migration of *Microcystis* colonies plays a significant role in blooms of *Mcirocystis*, in addition to nutrients, light, and temperature [2]. Regarding the vertical migration of *Microcystis* colonies, there have been various experimental and computational investigations, with focus on the velocity of vertical motion. Several empirical expressions have been presented to describe the relationship of migration velocity of *Microcystis* colonies and their size, based on the fields and laboratory observation [3-5]. However, these expressions are only valid for some specific conditions. Furthermore, hydrodynamic mechanisms of vertical migration of *Microcystis* are not been understood well. In this work, vertical migration of *Microcystis* colonies has been investigated, including the expression to calculate the vertical migration velocity and detailed flow structures around a *Microcystis* colony.

MATERIAL AND METHODS

The experimental system consists of a transparent test tube, an acrylic box, an imaging system, an injection system, and a planar laser device, as shown in Figure 1. The test tube (10mm×10mm×350mm, filled with BG-11 medium) was located in the acrylic box (100mm×100mm×400mm, filled with purified water) to prevent the convection due to the temperature difference of air and suspensions of *Microcystis* colonies. The 1.5 mm-thick pulse laser sheet was used to illuminate colonies in the centre-plane of the test tube. *Microcystis* (*aeruginosa,* FACHB1338), adopted in this work, came from the Freshwater Algae Culture Collection of the Institute of Hydrobiology, Wuhan, China, and was cultured in BG-11 medium at a temperature of 25℃ in a growth chamber of 12:12 light-dark cycle photoperiod. The trajectories of *Microcystis* colonies and flow fields around *Microcystis* colonies were measured by use of Planar Laser Induced Fluorescence (PLIF) technique and (Particle Image Velocimetry) PIV system.

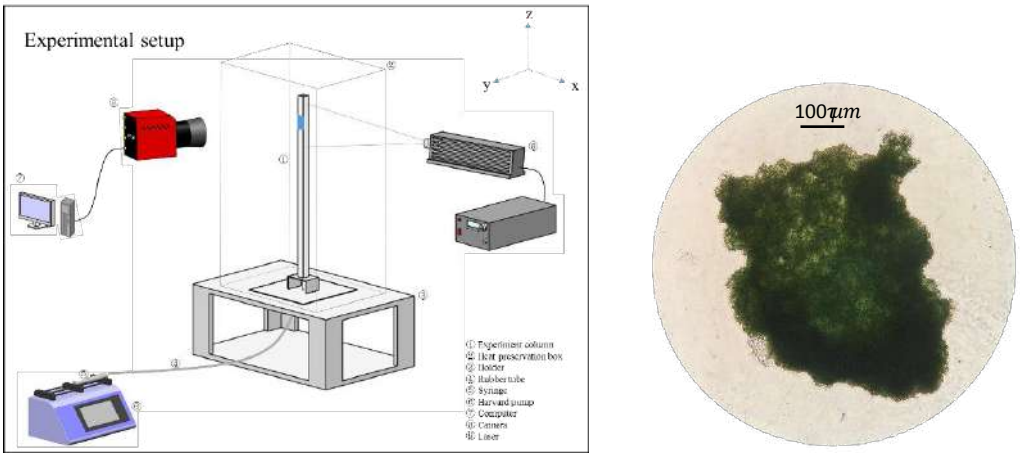

(a) (b)

Figure 1. Experimental setup (a) and a *Microcystis* colony (b).

RESULTS AND DISCUSSION

Trajectories of *Microcystis* colonies in the test tube were measured, with the diameter ranging from 10μm to 1054.5μm. It was found that *Microcystis* colonies migrate upward vertically, on average, while each colony migrates upward with a stochastic angle against the vertical direction, due to the irregular morphology of *Microcystis* colonies, especially massive pore structures, as shown in figure 2 (a). Statistical analysis showed that the migration direction is subject to an Gaussian distribution, as shown in figure 2 (b).

The flow field around *Microcystis* colonies was measured based on PIV. The Reynolds number, based on the equivalent diameter of a *Microcystis* colony and the mean stable vertical migration velocity, is approximately 0.3, much less than 1. The flow structure surrounding the colony differs from that around a sphere with the same Reynolds nubmer. There are two obvious vortices for the former, as shown in figure 3, while no vortices will occur for the latter.

In this work, we presented one expression to predict the vertical migration velocity of *Microcystis* colonies, based on Stokes' law. Figure 4 presented the relationship of vertical migration velocity and diameter. It shows that the vertical migration velocity of *Microcystis* colonies increases with their diameter.The density-size relationship of *Microcystis* colonies has been given, as shown in figure. 5. It is shown that the density of *Microcystis* colonies is the exponential function of their size.

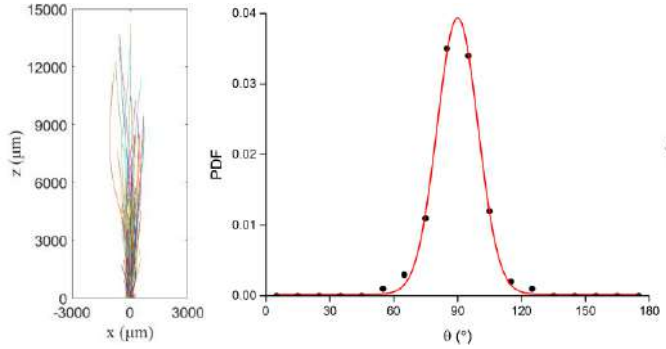

(a) (b)

Figure 2. Trajectories and migration direction distribution of colonies.

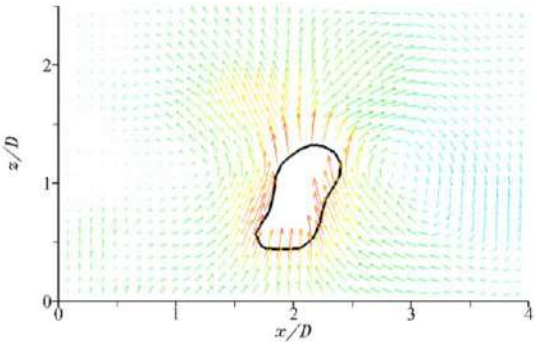

Figure 3. Flow field around a *Microcystis* colony

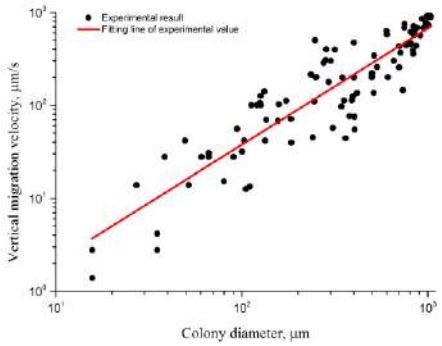

Figure 4. Variation of vertical migration velocity of *Microcystis* colonies with their diameter.

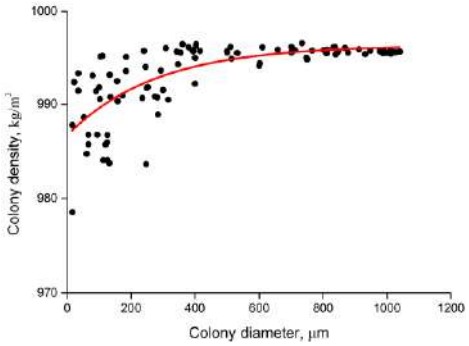

Figure 5. Variation of density of *Microcystis* colonies with their size.

CONCLUSIONS

The trajectories of *Microcystis* colonies and flow fields around them were measured by use of PLIF technique and PIV system. It is found that the migration direction of *Microcystis* colonies is subject to the exponential distribution. Two vortices are found to exist around one *Microcystis* colony, which differs from the flow pattern past a sphere with the same Reynolds number. An expression is presented to calculate the vertical migration velocity of *Microcystis* colonies, based on Stokes' law.

ACKNOWLEDGMENTS

This work is supported by the National Key R&D Program of China (grant no. 2016YFC0502202), and the IWHR Research \& Development Support Program (grant nos. HY0145B402016 and HY0145B682017).

References

[1] Huisman J., Codd G.A., Paerl H.W. Cyanobacterial blooms. *Nat. Rev. Microbiol.* **16**: 471-483, 2018.
[2] Visser P.M., Passarge J., Mur L.R. Modelling vertical migration of the cyanobacterium Microcystis. *Hydrobiologia*. **349**: 99-109, 1997.
[3] Nakamura T., Adachi Y., Suzuki M. Flotation and sedimentation of a single microcystis floc collected from surface bloom. *Wat. Res.* **27**: 979-983, 1993.
[4] Li M., Zhu W., Guo L.L., et al. To increase size or decrease density? Different Microcystis species has different choice to form blooms. *Sci. Rep.* **6**: 37056, 2016.
[5] Rowe M.D., Anderson E.J., Wynne T.T., et al. Vertical distribution of buoyant blooms in a Lagrangian particle tracking model for short-term forecasts in Lake Erie. *J. Geophys. Res. Ocean.* **121**: 5296-5314, 2016.

IN-SILICO CELL RHEOMETRY: MODELING OF ENDOTHELIAL CELLS UNDER STARTUP SHEAR CONDITIONS.

Konstantina Psaraki[1], Vlasis Mitsoulas[1], Yannis Dimakopoulos*[1], Stavros Pavlou[1], John Tsamopoulos[1]
[1] Laboratory of Fluid Mechanics and Rheology, Department of Chemical Engineering, University of Patras, Greece
Web: http://fluidslab.chemeng.upatras.gr/

Computational models of the endothelium, as well as experimental observations, can help in understanding the biomechanics of stress-induced cellular deformation, how mechanical stimuli are interpreted by endothelial cells, and important insights of disease progression. We present a new fluid-structure interaction model for the response of endothelial cell under startup shear conditions using an advanced Finite Element Method, while we introduce the poroelastic constitutive model for the rheological characterization of the cytoplasm. Since the mesh corresponds to the solid phase, forming a structure of solid net, we expect that the elasticity will differ from other works adopting hyperelastic models for the cell mechanics. We evaluate the rheological properties of the cell by implementing a benchmark compression experiment introduced by Caille et al.[1] and constructing force-deformation curves.

Introduction

Endothelial cells (ECs) form the basic barrier between blood vessels or capillaries and tissue, with the key function of controlling the flow of substances into and out of the underlying tissue ([2],[3]). Shear stress, which is the frictional force developed by blood stream above the endothelium, can elicit various responses with cell deformation, cytoskeletal rearrangement, and activation of signaling pathways, some of the principal ones [3]. Although the precise mechanisms of mechanical-chemical coupling in ECs exposed to shear-stress are not fully understood, the biochemical cascade for nitric oxide (NO) overproduction and calcium ions (Ca^{2+}) dynamics are linked to many harmful effects such as inflammations and induction of apoptosis [4]. This implies that we should deeply investigate the structural and chemical responses of endothelial cells under shear experiments and develop reduced biochemical models to provide accurate predictions with the minimum possible input.

Endothelial cells have mostly been modeled as “sacs” (cell wall) containing viscous fluids (cytoplasm) and a more viscous or even a solid nucleus ([1],[5-6],[10]). However, it is known that the nucleus is connected to the cell wall through numerous filaments that form a robust structure and act as the “skeleton” of the cell (cytoskeleton) [7-8]. Furthermore, the existence of a number of proteins throughout the cytoplasm, which are large biomolecules forming long chains of amino-acids, cannot confirm the Newtonian fluid notion [8]. In the present work, we implement a two-phase model for the characterization of the cytoplasm, which will consist of a viscous fluid (cytosol) flowing amongst the elastic solid structures (cytoskeleton) and thus constituting the “poroelastic” model. The other components of the cell, such as the nucleus, the cortex, the glycocalyx layer, the apical layer, and the cell wall, are modeled as elastic solids. A two-dimensional periodic model was developed for studying the dynamics described above and the kinematics of the surrounding blood plasma under startup flow conditions.

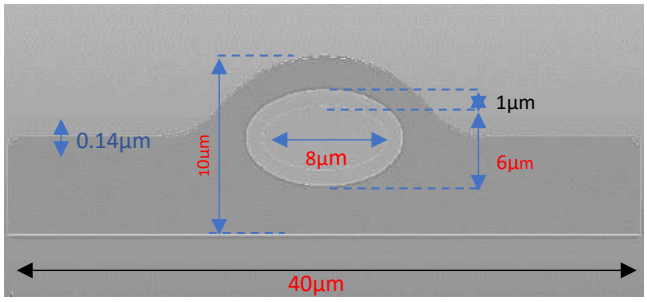

Organelle	Measure	Reference
Cell Length	40 μm	Tarbell et al.[10]
Maximum Cell Height	10 μm	Tarbell et al.[10]
Nucleus maximum radius	8 μm	Tarbell et al.[10]
Nucleus minimum radius	6 μm	Tarbell et al.[10]
Endoplasmic Reticulum thickness	1 μm	Lewis et al.
Cell Wall Thickness	0.14 μm	Philips et al.[11]
Cell to cell distance	1 μm	Jean et al.[9]

Figure 1. Geometrical Features of our Endothelial Cell. Its nucleus, endoplasmic reticulum, cytoplasm and cell wall are being depicted.

Results

In order to evaluate the parameters of the endothelial-cell model, we make a similar setup as Caille et al. [1], incorporating in our cell model only the poroelastic cytoplasm and the solid nucleus between two microplates, one moving and one fixed and compressing it with a downward velocity $u = 2.0 \cdot 10^{-6} m/s$. We calculated the force acted upon the cell due to the compression and plotted it versus the deformation of the cell to get a stress-strain curve. By comparing the results to those of Caille et al. (2002) [1], we retrieve the Young moduli of the cytosol and the cytoskeleton that will correspond to the modulus of their defined hyperelastic cytoplasm. We also simulated the compression of an isolated nucleus to find its elasticity and viscosity.

*Corresponding author. Email: dimako@chemeng.upatras.gr

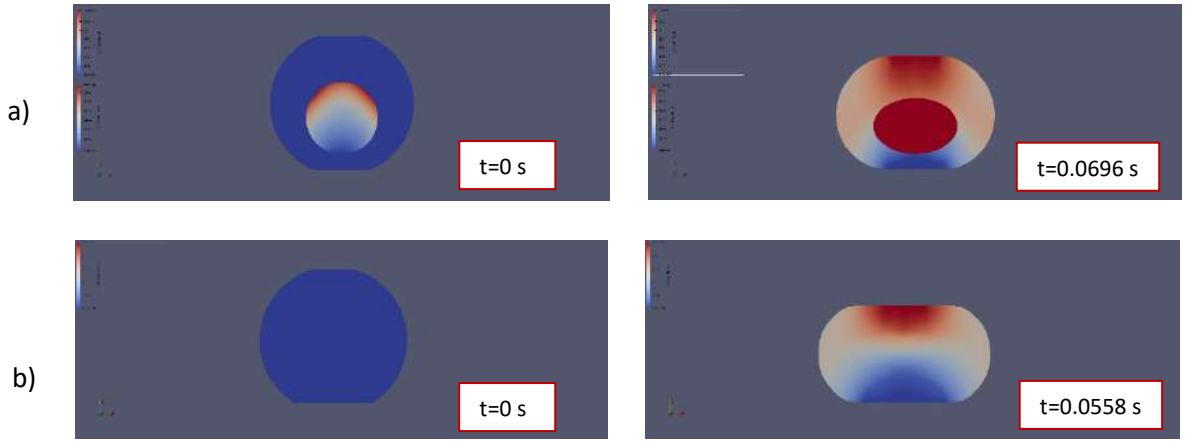

Figure 2 Compression of a round endothelial cell containing the solid nucleus ((a)). Compression of the solid nucleus ((b)) achieving a 27.6% deformation.

In our main analysis, we apply a constant shear velocity at the blood/plasma interface equal to $V_{x,CFL} = 53mm/s3$as a boundary condition. Under these conditions, our results indicate a significantly deformed endothelium, which in turn activates the biochemical cascade. These deformations are associated with tilting of the roundly extruded part of the endothelial cell towards the flow and even a slight movement and rotation of the nucleus.

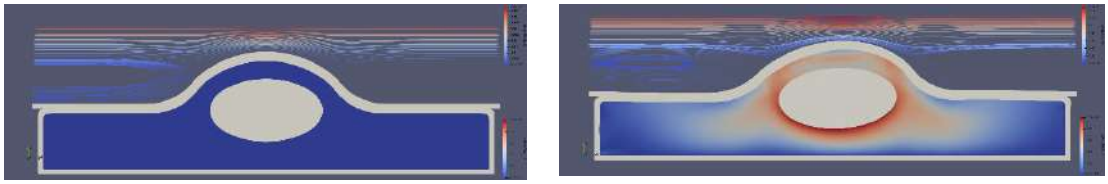

(a) t = 0 s (b) t = 0.09992 s

Figure 3. Startup shear simulation due to bloodstream's velocity. Initial configuration including the cell wall, the glycocalyx layer, the endoplasmic reticulum, the nucleus and the cytoplasm (a). Final configuration depicting the deformation of the cell due to the flow (b).

Conclusions

A two-dimensional model was developed for studying the rheological behavior of the endothelium under startup flow conditions featuring a Fluid-Structure Interaction (FSI) algorithm along with a novel poroelastic model which incorporates the material properties of the cytoplasm. In Fig. 3 we observe that the blood's flow strongly affects not only the endothelial cell's structure but also leads to a slight rotation of the nuclear domain. The proposed model was then validated by a compression benchmark experiment as in Caille et al. [1] where the cell is introduced amongst two microplates, one moving downwards and one fixed. The simulation was conducted for both a round cell, consisting of the nucleus and the surrounding cytoplasm, and for an isolated round nucleus. The compressive stresses spread throughout the cell and nucleus, achieving a noteworthy nuclear deformation.

Acknowledgment
The research work was supported by the Hellenic Foundation for Research and Innovation (H.F.R.I.) under the "First Call for H.F.R.I. Research Projects to support Faculty members and Researchers and the procurement of high-cost research equipment grant" .

References

[1] Caille N, Thoumine O, Tardy Y, and Meister JJ. *J Biomech.* 35(2):177-87 (2002).
[2] Félétou M. The Endothelium: Part 1: Multiple Functions of the Endothelial Cells—Focus on Endothelium-Derived Vasoactive Mediators. San Rafael (CA): Morgan & Claypool Life Sciences (2011).
[3] Fels J, Jeggle P, Liashkovich I, Peters W, and Oberleithner H. *Cell and tissue research* 355: 727-737 (2014).
[4] Pinton P, Giorgi C, Siviero R., et al. *Oncogene* 27: 6407–6418 (2008).
[5] Alt W, and Dembo M. *Math. Biosc.* 156 (1–2): 207-228 (1999).
[6] Mofrad M. *Ann. Rev. Fluid Mech.* 41(1), 433-453 (2009).
[7] Maniotis AJ, Chen CS, Ingber DE. *Proc. Natl. Acad. Sci. USA* 94: 849–854 (1997)
[8] Strychalski W, Copos C, Lewis O, Guy R. *J. Comp. Phys.* 282: 77-97 (2015).
[9] Jean RP, Chen CS, and Spector AA. *J Biomech. Eng.* 127 (4): 594-600 (2005).
[10] Dabagh M, Jalali P, Butler PJ, Randles A, and Tarbell JM. J R. Soc. Interface 14: 20170185 (2017).
[11] Milo, Ron, and Rob Phillips. Cell Biology by the Numbers. (2016).

*Corresponding author. Email: dimako@chemeng.upatras.gr

IN-SILICO RHEOMETRY OF GLYCOCALYX LAYER: INVESTIGATING THE EFFECT OF REAL PULSATILE PLASMA FLOW CONDITIONS AND MICROVESSEL DIASTOLE

Antonis Marousis[1], Vlasis Mitsoulas[1], Yannis Dimakopoulos *[1] and John Tsamopoulos[1]
[1] Labaratory of Fluid Mechanics and Rheology, Department of Chemical Engineering, University of Patras, Patras, Greece
Web: http://fluidslab.chemeng.upatras.gr/

The macromolecular layer covering the luminal surface of the vascular endothelium, known as the endothelial Glycocalyx layer (EGL), has a significant role in tissue hemostasis and mechanotransduction. In this study, we investigate the effect of the frequency of the pulsatile blood plasma flow as well as the capillary vasodilation-vasoconstriction on the behavior of the ESL. To this end, we perform 3D Fluid-Structure Interaction (FSI) simulations accounting for both blood plasma and endothelial glycocalyx (EG) body dynamics.

INTRODUCTION

The luminal surface of the vascular endothelium is covered by a network of membrane-bound proteoglycans and glycoproteins, forming the ESL. The ESL has been studied to a large extent over the years since it provides a vital role in vascular physiology and pathology [1], whereas its ability to control the capillary permeability may influence drug delivery processes [2]. However, the small scale of EG and its complex structure, especially in capillaries, makes it difficult for scientists to perform in vivo or in vitro experiments; hence most of the existing literature focuses on theoretical approaches. The blood plasma dynamics in ESL has been examined satisfactorily through hydrodynamic models, in which poroelastic walls have been considered [3]. Damiano & Stace [4] and Weinbaum et al. [5] attempted to evaluate the deformation and recovery time of EG after compression due to the passage of white blood cells, employing an electrohydrodynamic model and a mechano-electrochemical model, respectively. Accounting for the structure of EG, Squire et al. [6] identified that the glycocalyx fibers follow a quasi-periodic arrangement, findings which adapted by Weinbaum et al. [5] led to the development of an ideal periodic bush-structure model with hexagonal symmetry. More recently, Mitsoulas et al. [7] proceeded on a thorough analysis accounting for the mechanical and geometrical properties of EG through Fluid-Structure Interaction simulations (FSI).

In the present study, we investigate the effect of pulsatile blood flows with frequencies that do not correspond to normal heart rates on the ESL dynamical behavior. In addition, we account for a more realistic illustration of the capillary, in which the microvessel expands and contracts, and therefore the fiber-to-fiber distance variates with time. To address the problem, we consider the three-dimensional incompressible plasma flow perpendicular to the fibrous network, as shown in Fig. 1(a). Additionally, we adapt the minimal elementary domain of Mitsoulas et al. [7], see Fig. 1(b), which consists of two subdomains that correspond to fluid (blood plasma) and solid (EG fibers), respectively. The blood plasma has a Newtonian-fluid behavior, while the EG fibers are represented as hyperelastic solids. We solve the problem numerically using the Finite Element Method, while in order to account for the FSI solution, we implement the full monolithic coupling methodology with global unknowns. To better understand the dynamics of the coupled system, we evaluate the apparent permeability of ESL and dynamic characteristics such as the drag force and torque on a single fiber.

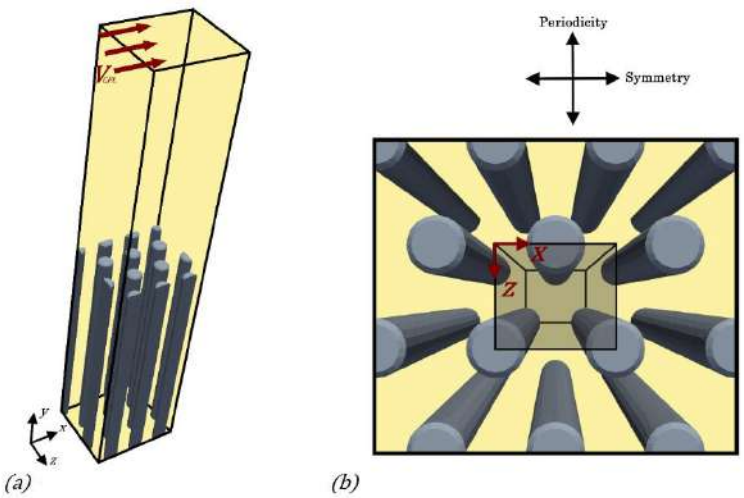

Figure 1. a) Side view of the 3D ESL periodical physical domain. b) Top view of the EG structure with unformed fibers. (The shaded area corresponds to the minimal elementary domain.)

*Corresponding author. E-mail: dimako@chemeng.upatras.gr (Prof. Y. Dimakopoulos)

RESULTS

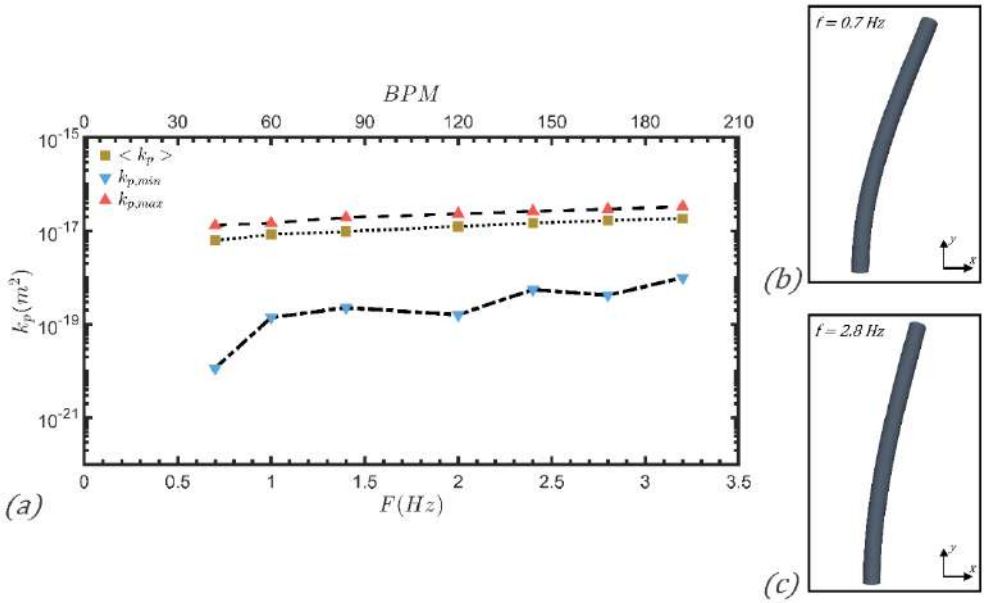

Figure 2. (a) Apparent permeability, k_p, as a function of frequency, F. The characters ■,▼, ▲ depict the mean, maximum and minimum value of k_p, respectively. (b),(c) Depiction of EG fiber in the fully deformed state for $f = 0.7Hz$ and $2.8Hz$, respectively.

We proceed with a parametric analysis concerning the frequency of the pulsatile plasma flow. In Fig. 2 (a), we present the evaluated minimum, maximum, and mean value of the apparent permeability of ESL, k_p, for various frequencies. Note that those results correspond to capillary diastole up to 15%. The minimum values of k_p correspond to the state when the EG fibers are fully deformed, and therefore the resistance to the flow is maximized. In conjunction, maximum k_p values arise when EG fibers are almost undeformed and flexible to move in the flow direction. By increasing the frequency, the maximum and minimum values of k_p become larger, with the latter exhibiting the largest increase. As shown in Fig. 2 (b), (c), which depicts the fully deformed state of the EG fiber for $f = 0.7$ and $2.8Hz$, the maximum deformation of the fiber is greater in the second case. In fact, in high frequencies, the rapid changes in the flow rate prevent the motion of EG fiber, which in turn causes smaller and time-limited deformations. As a result, it can be seen in Fig 2 (a) that the mean value of the transient apparent permeability is proportional to frequency.

CONCLUSIONS

In the present study, we examined the dynamical behavior of ESL through FSI simulations accounting for events that can take place in biological processes, such as variations in heart rate and capillary vasodilation-vasoconstriction. We found that the pulse frequency influences the behavior of EG, resulting in changes in the apparent permeability of ESL, more specifically, high-frequency pulsatile flows result in larger values of k_p.

Acknowledgments

The research work was supported by the Hellenic Foundation for Research and Innovation (H.F.R.I.) under the "First Call for H.F.R.I. Research Projects to support Faculty members and Researchers and the procurement of high-cost research equipment grant."

References

[1] A. R. Pries, T. W. Secomb, and P. Gaehtgens, "The endothelial surface layer," *Pflugers Arch - Eur J Physiol*, vol. 440, no. 5, pp. 653–666, Sep. 2000, DOI: 10.1007/s004240000307.
[2] D. Chappell, M. Jacob, K. Hofmann-Kiefer, P. Conzen, and M. Rehm, "A Rational Approach to Perioperative Fluid Management," *Anesthesiology*, vol. 109, no. 4, pp. 723–740, Oct. 2008, DOI: 10.1097/ALN.0b013e3181863117.
[3] E. R. Damiano, "The Effect of the Endothelial-Cell Glycocalyx on the Motion of Red Blood Cells through Capillaries," *Microvascular Research*, vol. 55, no. 1, pp. 77–91, Jan. 1998, DOI: 10.1006/mvre.1997.2052.
[4] E. R. Damiano and T. M. Stace, "A Mechano-Electrochemical Model of Radial Deformation of the Capillary Glycocalyx," *Biophysical Journal*, vol. 82, no. 3, pp. 1153–1175, Mar. 2002, DOI: 10.1016/S0006-3495(02)75474-X.
[5] S. Weinbaum, X. Zhang, Y. Han, H. Vink, and S. C. Cowin, "Mechanotransduction and flow across the endothelial glycocalyx," *Proceedings of the National Academy of Sciences*, vol. 100, no. 13, pp. 7988–7995, Jun. 2003, DOI: 10.1073/pnas.1332808100.
[6] J. M. Squire, M. Chew, G. Nneji, C. Neal, J. Barry, and C. Michel, "Quasi-Periodic Substructure in the Microvessel Endothelial Glycocalyx: A Possible Explanation for Molecular Filtering?," *Journal of Structural Biology*, vol. 136, no. 3, pp. 239–255, Dec. 2001, DOI: 10.1006/jsbi.2002.4441.
[7] V. Mitsoulas, S. Varchanis, Y. Dimakopoulos, J. Tsamopoulos, "In-silico rheometry of the glycocalyx layer: Start-up and pulsating shear experiments," submitted for publication in *Physical Review Fluids*.

NONLINEAR DYNAMICS FOR DESIGNING ANNULAR THERMOACOUSTIC SYSTEMS

Nicolas Noiray[1]*, Abel Faure-Beaulieu[1], Thomas Indlekofer[2], and James R. Dawson[2]
[1] Department of Mechanical and Process Engineering, ETH Zürich, Switzerland
[2] Department of Energy and Process Engineering, NTNU, Trondheim, Norway

Summary Annular combustors of modern aeroengines and gas turbines are subject to self-sustained azimuthal thermo-acoustic modes. These limit cycles are unwanted because the resulting intense acoustic field induces high-cycle fatigue of the combustor components. First, this paper presents a theoretical framework with a quaternion-based ansatz of the acoustic pressure for describing the slow-flow dynamics of the thermo-acoustic system. The associated variables define the state of an eigenmode, i.e. if it is purely standing or spinning, or a combination of standing and spinning waves, depending on the rotational and reflectional asymmetries of the annular system. Then, this framework is used to design interconnected nonlinear acoustic elements for controlling the thermo-acoustic dynamics.

One of the environmental challenges for civil aircraft transportation is the necessity to significantly reduce emissions of nitrogen oxides NO_x, which cause toxic pollution in the vicinity of airports and contributes to the formation of ozone in the high atmosphere. A technical solution for this problem is to burn lean fuel-air mixtures, which prevents near-stoichiometric hot-spots where NO_x are produced and reduces soot formation and unburned hydrocarbons. The problem is that the thermoacoustic stability is significantly reduced with these flames, because they are more sensitive to flow perturbations. In particular, they exhibit strong heat release rate response $\dot{Q}'$ to modulation of mixture composition or velocity field that result from the acoustic pressure field p'. Consequently, thermoacoustic instabilities, which are induced by the constructive coupling between the flames and the combustor acoustics, are more likely to occur. They yield high amplitude limit cycles which reduce the lifetime of the hot gas path parts because of the induced vibrations, or in the worst case destroy them during a sudden catastrophic event. In this context, numerous studies have been conducted about thermoacoustic instabilities in annular combustor geometries which are very common for land-based gas turbines and aeroengines, e.g. [1]. A fascinating aspect of thermoacoustic instabilities in annular combustion chambers is that they display pairs of azimuthal eigenmodes that yield standing or spinning thermoacoustic waves depending on the system symmetries as illustrated in Fig. 1.

In the present study, we propose a new low-order model of the thermoacoustic dynamics in annular combustors, which is used for designing interconnected nonlinear acoustic elements for controling the instabilities. In what follows, we briefly present the low-order model for idealized combustors exhibiting a mean low-Mach uniform swirling flow $\bar{\boldsymbol{u}} = U\mathbf{e}_\Theta + V\mathbf{e}_z$. A simple model with static nonlinearity is adopted for describing the heat release rate response to acoustic perturbations: $(\gamma-1)\dot{Q}' = \beta p' - \kappa p'^3$, where γ is the heat capacity ratio, and β and κ are real constants. It allows us to describe the phase space in the vicinity of supercritical Hopf bifurcations that are commonly encountered. This heat release rate model and a quaternion-based ansatz of the acoustic pressure are injected into the following acoustic wave equation

$$\left\{\frac{1}{c^2}\left(\frac{\partial^2}{\partial t^2} + 2\bar{\boldsymbol{u}}\cdot\nabla\frac{\partial}{\partial t}\right) - \nabla^2\right\} p' \;=\; \frac{\gamma-1}{c^2}\left(\frac{\partial \dot{Q}'}{\partial t} + \frac{U}{\mathcal{R}}\frac{\partial \dot{Q}'}{\partial \Theta}\right), \tag{1}$$

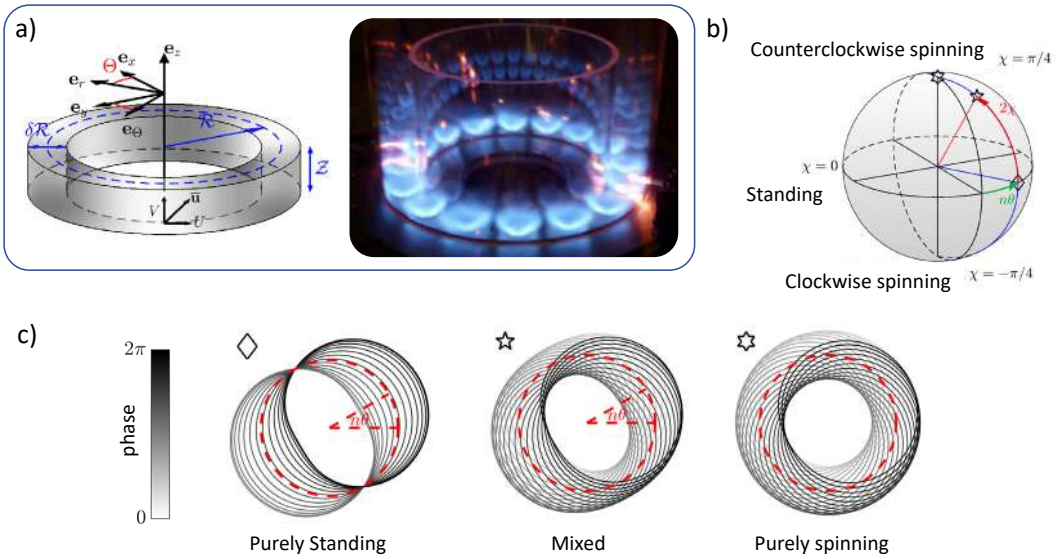

Figure (1) a) Sketch of an idealized annular combustor with coordinate system used in this work and picture of a lab-scale annular combustor [2]. b) Representation of the state of the thermoacoustic mode on the Bloch sphere, the markers correspond to the 3 cases displayed in c). c) Representation of the acoustic pressure in the chamber for 3 states of the first azimuthal mode: Standing mode with $\chi = 0$ and $\theta = \pi/6$, counterclockwise mixed mode with $\chi = \pi/6$ and $\theta = \pi/6$, and counterclockwise spinning mode with $\chi = \pi/4$.

*Corresponding author. E-mail: noirayn@ethz.ch

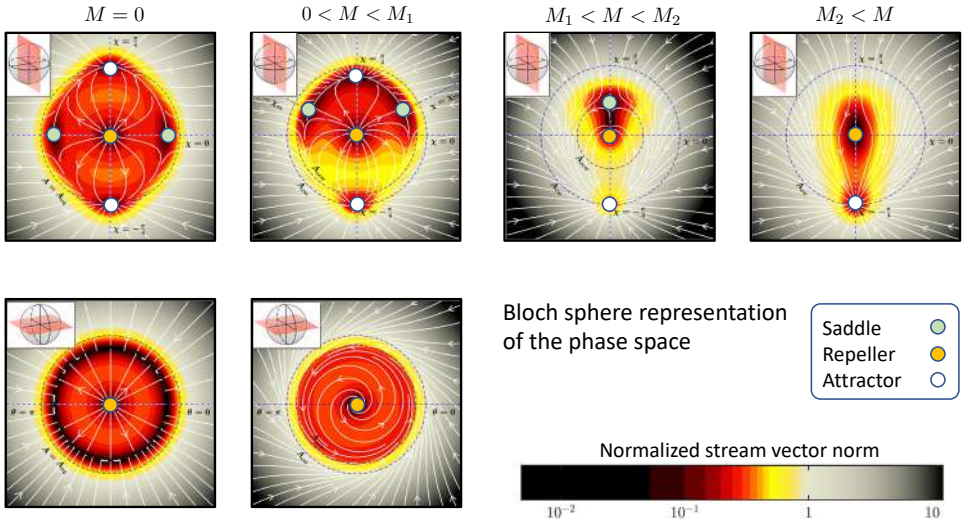

Figure (2) Streamlines describing the evolution of the phase space for a linearly-unstable azimuthal-thermoacoustic-mode, in the cases of a uniform distribution of the thermoacoustic feedback with and without uniform swirling mean flow. From left to right, the attractor landscape is modified when the Mach number $M = U/c$ of the azimuthal mean flow rises ($M = 0$, $M = 0.005$, $M = 0.02$ and $M = 0.1$). The other parameters are: $\beta = 160$ rad.s^{-1}, acoustic damping $\alpha = 155$ rad.s^{-1}, $\kappa = 0.5$ rad.s^{-1}Pa^{-2}, $\omega = 1167$ rad.s^{-1}.

where c is the speed of sound. The wave equation is then spatially and temporally averaged in order to obtain the system of differential equations, which governs the slow-flow phase-space variables [3]. In fact, the quaternion ansatz for the acoustic pressure $p' = \Re(\tilde{p})$ involves four real-valued variables that evolves slowly compared to the acoustic time scale $2\pi/\omega$. One has $\tilde{p}(\Theta, t) = A(t)\exp[i(\theta(t) - \Theta)]\exp[-k\chi(t)]\exp[j(\omega t + \varphi(t))]$, with i, j amd k the imaginary units of the quaternion algebra and with $(A, \theta, \chi, \varphi) \in \mathbb{R}^+\times]-\pi, \pi] \times [-\pi/4, \pi/4]\times]-\pi, \pi]$. The state of an azimuthal self-sustained thermoacoustic mode can then be graphically represented on a Bloch sphere with the first three slow-flow variables (A, θ and χ) taken as spherical coordinates as illustrated in Fig.1. Note that the temporal phase φ corresponding to slow drift of the fast oscillation frequency is not considered in this representation. The following dynamic system is then found for the slow-flow variables [3]:

$$\begin{cases} \dot{A} = \dfrac{1}{2}\Big(\beta\left[1 - M\sin(2\chi)\right] - \alpha\Big)A + \dfrac{3\kappa}{64}\Big(-5 - \cos(4\chi) + 4M\sin(2\chi)\Big)A^3, \\ \dot{\chi} = \dfrac{3\kappa}{64}A^2\Big(\sin(4\chi) + 6M\cos(2\chi)\Big) - \dfrac{M\beta}{2}\cos(2\chi), \\ \dot{\theta} = M\omega, \\ \dot{\varphi} = 0. \end{cases} \tag{2}$$

It allows us to describe the complex evolution of the phase space subject to explicit symmetry breaking associated to the presence of a mean swirling flow in the annular chamber (see Fig. 2). Indeed, the azimuthal Mach number $M = U/c$ breaks the symmetry between the two spinning waves. It is found that the counter-spinning modes have no longer the same frequency: $\omega(1 \pm M)$. Additionally, if the heat release occurs in a region where there is the uniform azimuthal mean flow, the spinning mode rotating against the swirl direction attracts the system with more strength than the co-rotating spinning mode. Beyond a critical azimuthal Mach number, a saddle-node bifurcation leads to a situation where the only attractor of the system is the spinning mode travelling against the mean swirl. Conversely, when the flames are not located in the convection zone, both counter-spinning modes are equally strong attractors (not presented in Eq. (2) nor in Fig. 2). The model predictions were recently confirmed experimentally [4], and this model can now be used to design interconnected nonlinear acoustic cavities for controlling the thermoacoustic instabilities in annular combustors. Indeed, taking advantage of these nonlinearities, unprecedented control will be achieved.

References

[1] Noiray, N. and Schuermans, B., On the dynamic nature of azimuthal thermoacoustic modes in annular gas turbine combustion chambers, *Proc. R. Soc. A* **469**: 10.1098/rspa.2012.0535, 2013.

[2] Bourgouin, J.-F., Durox, D., Schuller, T., Beaunier, J. and Candel, S., Ignition dynamics of an annular combustor equipped with multiple swirling injectors, *Comb. & Flame* **160**: 1398-1413, 2013.

[3] Faure-Beaulieu, A. and Noiray, N., Symmetry breaking of azimuthal waves: Slow-flow dynamics on the Bloch sphere, *Phys. Rev. Fluids* **5**: 023201, 2020.

[4] Indlekofer, T., Faure-Beaulieu, A., Dawson, J. R. and Noiray, N., Dynamics of azimuthal thermoacoustic modes in imperfectly symmetric annular geometries, *arXiv:2104.07380*

HARNESSING HYSTERESIS NONLINEARITIES IN MULTI-SCALE STRUCTURES

Walter Lacarbonara*
Department of Structural and Geotechnical Engineering, Sapienza University of Rome, Roma, Italy

Summary Different kinds of multiscale hysteresis material and geometric nonlinearities can be advantageously harnessed for tailoring high performance material systems such as damping material layers, vibration absorbers or metamaterial systems embedding arrays of hysteretic resonators. Hysteresis is a memory-dependent material nonlinearity that can be exhibited as inter-wire friction in wire ropes, inter-crystal friction in shape memory materials (SMA), frictional sliding between polymer crystals or chains and carbon nanotubes (CNT) in nanocomposite materials. Previous works addressed SMA wire ropes hysteresis in nonlinear vibration absorbers and isolators as well as nanoscale frictional phenomena in nanocomposite CNT/polymer materials. The main focus here is on high-performance metamaterials featuring a periodic distribution of highly tunable damped oscillators with geometric and hysteresis nonlinearities. The nonlinear wavefrequencies and waveforms away from internal resonances obtained via a Lie series-based perturbation technique exhibit a high nonlinear tunability which is a key for advanced applications.

HYSTERESIS IN ABSORBERS AND NANOSTRUCTURED MATERIALS

Previous efforts addressed the high nonlinear tunability of a hysteretic vibration absorber [1] made of a constrained moving mass subject to the restoring forces of assemblies of steel and SMA wire ropes with different constraining mechanisms for the ropes. Such tunability is manifested in the rich nonlinear frequency response function ranging from softening

O107079

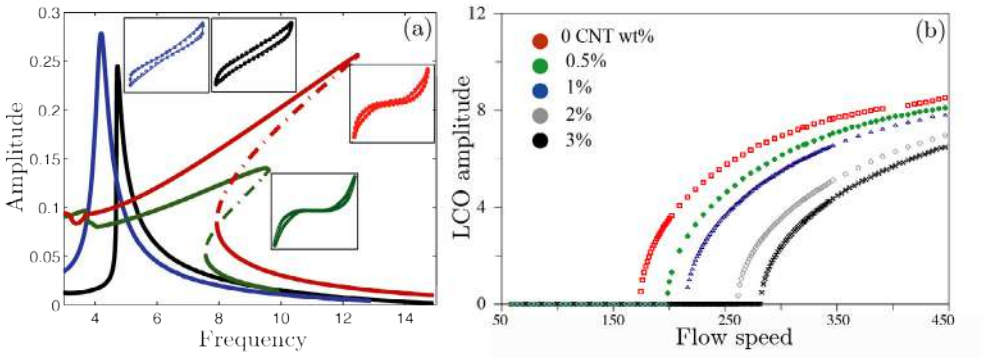

Figure 1: Two examples of high nonlinear dynamic tunability offered by (a) a vibration absorber with various hysteresis loops and frequency response functions, (b) supersonic flutter shift and LCO reduction vs. flow speed in a simply supported nanocomposite panel with different CNT weight fractions.

to hardening within the same multi-performance device (see Fig. 1a). Other applications dealt with isolators which combined the nonlinear hysteretic restoring forces of elastomers and SMA wires with the beneficial effects of a negative stiffness mechanism [2]. On a much different material scale, the frictional damping of carbonaceous nanofillers (here CNTs) [3, 4] dispersed in polymer hosting matrices was shown to lend itself to optimize high damping materials such as nanocomposite panels subject to supersonic flutter (see Fig. 1b). A multiple scales perturbation analysis proved that small CNT weight fractions can largely increase the flutter speed as well as control the limit cycle oscillation amplitude in the post-flutter range [3].

NONLINEAR WAVE PROPAGATION IN HYSTERETIC METAMATERIALS

A new hysteretic metamaterial is envisioned as an infinite one-dimensional periodic chain of stiff rings, each hosting a tunable *local resonator* with geometric and hysteresis nonlinearities [5].

The free propagation of nonlinear waves through such dissipative periodic lattice, by making use of the Floquet-Bloch theory for periodic structures, is governed by the following system of ODEs:

$$(1+\rho^2)\ddot{u}+\rho^2\ddot{w}+2l(\beta)u=0,\quad \rho^2\ddot{u}+\rho^2\ddot{w}+G(w,\dot{w})+F(w)=0 \tag{1}$$

where u and w denote the nondimensional displacement of the cell center of mass and of the resonator mass, respectively, $l(\beta):=(1-\cos\beta)/2)$ with β being the nondimensional wavenumber, (F,G) indicate the restoring forces in the springs and the hysteretic dashpot expressed as

$$F(w):=2w\left(\eta+(\mu-\eta)/\sqrt{1+w^2}\right),\quad G(w,\dot{w}):=\xi_1\dot{w}\left(1-\xi_2\exp(-\xi_3 w^2)\right) \tag{2}$$

*E-mail: walter.lacarbonara@uniroma1.it.

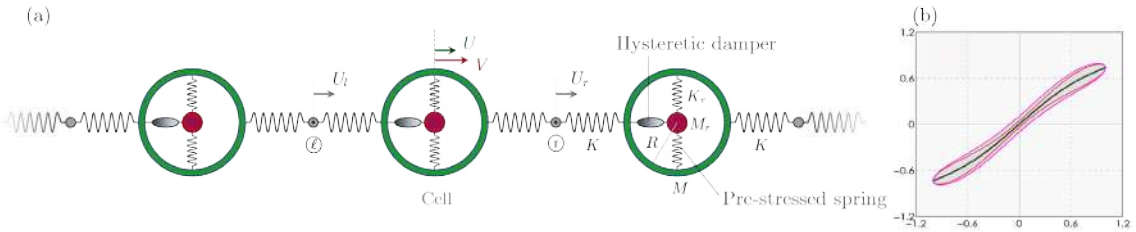

Figure 2: (a) 1D lattice of periodic cells (green) hosting nonlinear absorbers (red); (b) hysteresis loops of the cell response.

Moreover, ρ^2 is the mass ratio between the absorber and the ring, μ and η describe the nondimensional geometric and elastic stiffnesses of the secondary springs, and (ξ_1, ξ_2, ξ_3) are the coefficients regulating the hysteresis of the dampers. The third order Taylor series expansions of F and G yield $F(w) = 2\mu w - dw^3$ and $G(w, \dot{w}) = m\dot{w} + h\dot{w}w^2$ where $d := (\mu - \eta)$, $m := \xi_1(1 - \xi_2)$, $h := \xi_1\xi_2\xi_3$. Thus, d is the cubic stiffness coefficient (entailing a hardening nonlinearity if $d < 0$ or a softening nonlinearity if $d > 0$). On the other hand, while $m > 0$ is the linear damping coefficient, h scales the cubic part of the hysteresis damper force.

Equations (1) can be reduced to a first order form via a standard approach and then projected into the eigenvectors space. The four eigenvalues, for sufficiently small damping, are given by $\lambda_{1,2} = \alpha_1 \pm i\beta_1$, $\lambda_{3,4} = \alpha_2 \pm i\beta_2$, with $\alpha_{i,j}$ and $\beta_{i,j}$ both real. The Lie series operator approach to Hamiltonian perturbation theory is employed to yield the lowest order normal form in terms of time-dependent *action-angle* (I_j, ϕ_j)-variables (with $j = 1, 2$)

$$\dot{I}_j = 2I_j \left[M_{1,2}^{(j)} e^{2\alpha_1 t} I_1 + M_{3,4}^{(j)} e^{2\alpha_2 t} I_2 \right], \quad \dot{\phi}_j = \beta_j + \left[N_{1,2}^{(j)} e^{2\alpha_1 t} I_1 + N_{3,4}^{(j)} e^{2\alpha_2 t} I_2 \right] \tag{3}$$

which yield $\dot{\phi}_j = \beta_j + \left[N_{1,2}^{(j)} e^{2\alpha_1 t} I_1(0) + N_{3,4}^{(j)} e^{2\alpha_2 t} I_2(0) \right]$ on account of the fact that, to within leading order, $I_j(t) = I_j(0)$. The coefficients $N_{i,k}^{(j)}$ regulate the nonlinear frequency corrections of the acoustic $(j = 1)$ and optical $(j = 2)$ waves (see dispersion curves in Fig. 3a). The associated frequency corrections are softening (or hardening) depending on whether these coefficients are positive (or negative). Note that the coefficients depend on the mechanical parameters of the metamaterial, hence the waves can be largely tuned and made faster or slower on demand.

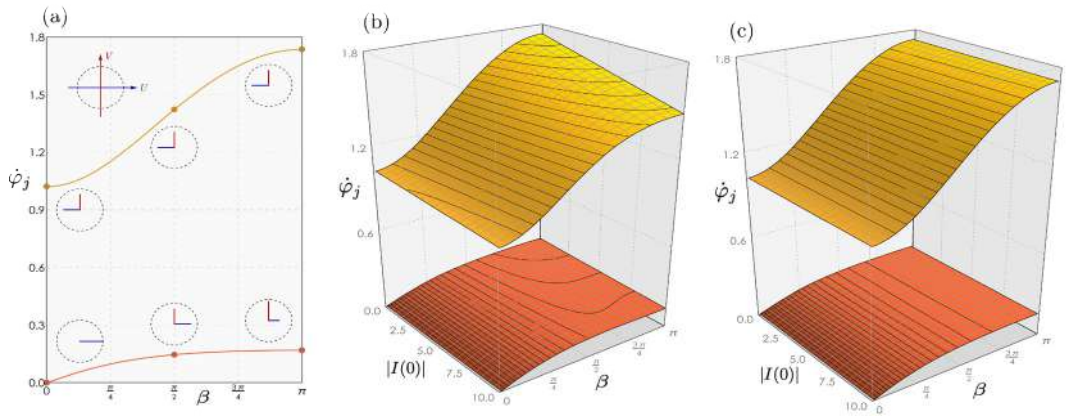

Figure 3: (a) Linear spectra for the acoustic and optical waves and snapshots of the nonlinear spectra with dissipation at different times: (b) $t = 0$ and (c) $t = 50$.

CONCLUSIONS

This paper discussed ways to harness multiscale hysteresis in multi-scale structures and metamaterials. The possibility of tailoring the metamaterial lattice properties to make the nonlinear waves faster or slower and of making these nonlinear effects more or less persistent over time depending on the hysteretic dissipation while allowing to fine tune the phases of the different waves is one of the key properties under investigation.

References

[1] Carboni B., Lacarbonara W. *Nonlinear Dyn.* **83**: 23–39, 2016.
[2] Salvatore A., Carboni B., Lacarbonara W. *Nonlinear Dyn.*, https://doi.org/10.1007/s11071-021-06666-y, 2021.
[3] M. Taló, G. Lanzara, B. Krause, A. Janke, W. Lacarbonara *ACS Appl Mat. Interf.*, DOI: 10.1021/acsami.9b12536, 2019.
[4] Formica G., Lacarbonara W. *Nonlinear Dyn.* **99**: 227–248, 2020.
[5] Fortunati A., Bacigalupo A., Lepidi M., Arena A., Lacarbonara. W. *Nonlinear Dyn.*, submitted, 2021.

ON NONLINEAR VIBRATION ISOLATION VIA QUASI-ZERO STIFFNESS CHARACTERISTIC: BENEFITS AND CHALLENGES

Ivana Kovacic[1]
[1] Centre of Excellence for Vibro-Acoustic Systems and Signal Processing, Faculty of Technical Sciences, University of Novi Sad, Novi Sad, Serbia

Summary This work summarizes some of author's results achieved in the field of vibration isolation from the viewpoint of the beneficial use of geometric stiffness nonlinearity. The focus is on two models that contain springs which incline as they extend, introducing geometric stiffness nonlinearity into the equations of motion. The systems under consideration have either one or two degrees of freedom. In both of them, springs' characteristics are tuned to intentionally achieve a quasi-zero stiffness characteristic, and the beneficial regions of systems' parameters for vibration isolation are determined. It is also shown that these systems can exhibit certain nonlinear dynamic phenomena, including multiple bending of the backbone curves, different types of bifurcation and detached outer or inner parts of the frequency-response curves.

INTRODUCTION

Passive vibration isolation is one of the routes for mitigating undesirable vibration [1]. Last several decades and especially the very last one, have opened some new avenues for progress in this respect via intentional use of geometric stiffness nonlinearity [2, 3]. This work summarizes some of author's related results [4-10] achieved mainly jointly with her colleagues, primarily M.J. Brennan, Universidade Estadual Paulista, Ihla Solteria, Brasil [4-8] and also with G. Gatti, University of Calabria, Cosenza, Italy [7, 8]. The focus is on the utilization of geometric nonlinearity in two physical configurations that include springs that incline as they extend and can be optimised to result in quasi-zero stiffness: (i) Model 1 has one degree of freedom and contains three springs, while (ii) Model 2 has two degrees of freedom and comprises a linear oscillator and a nonlinear attachment consisting of four springs. Besides emphasizing the exploited beneficial effects of geometric stiffness nonlinearity, certain challenges and potential issues brough into bear by systems' nonlinear dynamics are pointed out as well.

MODEL 1

It is known that in a harmonically excited linear mass-spring system, the lower its natural frequency, the wider the isolation region and the more advantageous its application. This low natural frequency can be achieved by low static stiffness, which undesirably causes a large static deflection. This disadvantage can be overcome by adding additional springs that become oblique as the system oscillates (Figure 1a), introducing geometric nonlinearity into the equation of motion. Moreover, acting as a negative stiffness, such oblique springs can be adjusted to result in zero dynamic stiffness, i.e. the so-called quasi-zero stiffness (QZS). The QZS mechanism can produce a smaller stiffness at larger displacements about the static equilibrium position than the system with the linear springs [4] and can also yield certain improvements of the transmissibility properties [5, 10]. However, it is found analytically and confirmed numerically that such a nonlinear vibration isolator under an asymmetric excitation comprising a constant and harmonic excitation can exhibit bifurcations related to different shapes of their frequency-response curves (FRCs), where five different regions I-V can be distinguished (Figure 1b). They are characterized by different bending of the FRCs, different number of multiple solutions in certain frequency regions and multiple amplitude jumps [6]. The example of the FRCs corresponding to the regions II and III are presented in Figure 1c. This system can also exhibit period-doubling bifurcations and chaos [9], which need to be taken into consideration when making a choice of a suitable operating regime.

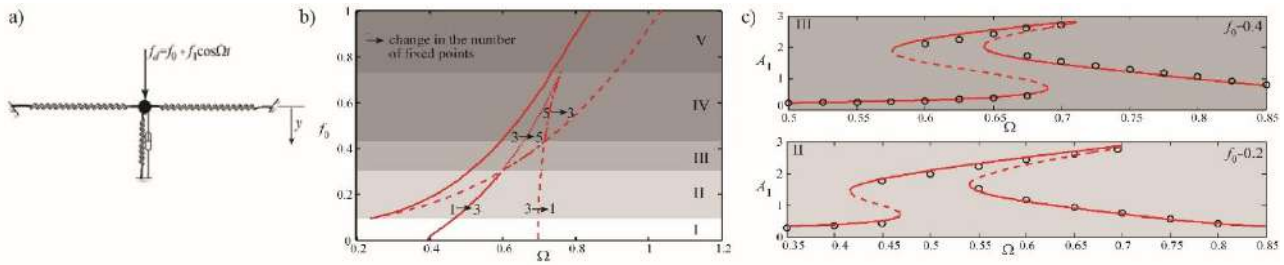

Figure 1. (a) Model 1 excited by a constant force f_0 and a time-varying force $f_1 \cos \Omega t$; (b) Saddle-node bifurcation set in the plane defined by the excitation frequency Ω and magnitude of the constant force f_0 (note that the set can be divided into five different regions labelled by I-V; (c) Typical shapes of the FRCs corresponding to the regions II and III (solid line – stable analytical results, dashed line – unstable analytical results, circles – numerical results).

Besides this physical configuration in which QZS is achieved via obliques springs, the presentation will also include the overview of other systems citing [4], but investigating the effects of QZS in the system whose design include magnets, X-shaped structures, cam-roller mechanisms, origami-inspired foldable cylinders, composite plates, etc. (Note that the number of citations of [4] is 224, source: SCOPUS, 3 Jan 2020, and the examples mentioned follow up [4]).

MODEL 2

Model 2 comprises a nonlinear oscillator attached and driven harmonically by an electro-dynamic shaker [7, 8]. The shaker is modelled as a linear oscillator and the nonlinear attachment consists of four springs (wires) [7], which incline as they extend (Figure 2a). The model is investigated in terms of the FRC of the relative non-dimensional displacement W, where the nonlinear attachment has a very small linear stiffness coefficient, which can be practically achieved by a very low tightening of the suspension springs during assembly of the mechanical rig, and this corresponds to a QZS configuration around the equilibrium position. It is found analytically and confirmed numerically that as a result of the change of the coefficient of pure cubic nonlinearity of the attachment, five different shapes of the FRCs can appear. Some of them are characterized by a two-part FRC, where a closed detached curve can appear outside or inside the main continuous resonance curve (Figure 2b). The latter is associated with a lower steady-state amplitude, and is, thus, desirable in practice. Experimental verifications of its existence are given in [11]. The presentation will include the overview of various methods (analytical, numerical and experimental) and the corresponding results completing the investigations of this system (Note that the number of citations of the related publications [7, 8] is 129, source: SCOPUS, 3 Jan 2020).

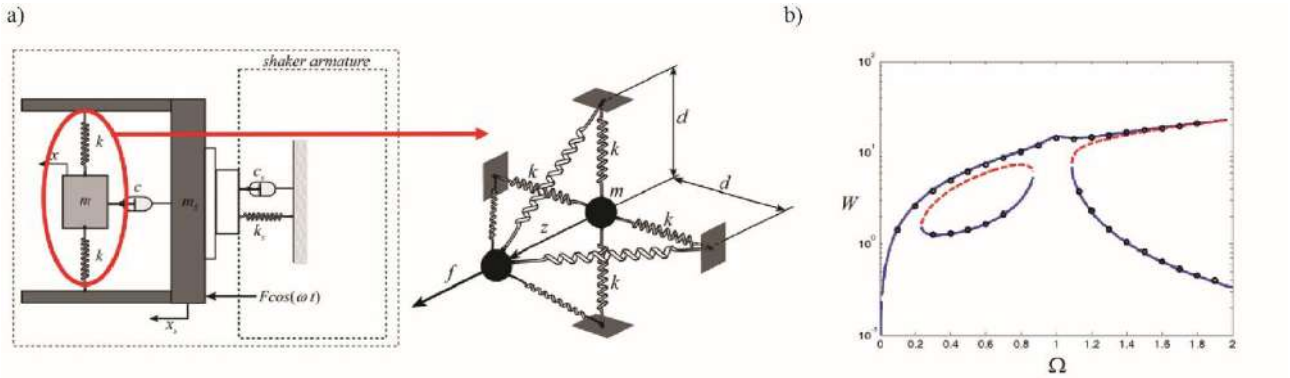

Figure 2. (a) Model 2 with the attachment comprising four springs; (b) One typical FRC with an inner detached part (solid line – stable analytical results, dashed line – unstable analytical results, circles – numerical results).

CONCLUSIONS

Two mechanical models comprising certain arrangements of springs whose deformations introduce geometric nonlinearities into the equation of motion have been presented. Certain characteristics of these springs can be adjusted to achieve a QZS configuration around the equilibrium position. The benefits of such configurations for nonlinear vibration isolation have been determined. In a system with one degree of freedom, these benefits involve widening the isolation region and achieving a smaller stiffness at larger displacements. In a system with two degrees of freedom, a detached part of the FRC appears inside the main continuous resonance curve, having a smaller steady-state amplitude than the co-existing stable solution at the same frequency. In both models, these beneficial effects are related to particular values of systems' parameters. It has also been demonstrated that variations of systems' parameters can lead to a diversity of nonlinear phenomena, which is a challenge to be taken care of in practical applications.

References

[1] Rivin E.I. Passive Vibration Isolation. ASME Press, New York 2003.
[2] Alabudzev P., Gritchin A., Kim L., Migirenko G., Chon V., Stepanov P. Vibration Protecting and Measuring Systems with Quasi-Zero Stiffness. Hemisphere Publishing, New York, 1989.
[3] Liu Ch.Ch., Jing X.J., Daley S., Li F.M. Recent Advances in Micro-Vibration Isolation. *Mech. Syst. Signal Pr.* **56–57**: 55-80, 2015.
[4] Kovacic I., Brennan M.J, Waters T.P. A Study of a Nonlinear Vibration Isolator with Quasi-Zero Stiffness Characteristic. *J. Sound Vib.* **315**: 700-711, 2008.
[5] Carrella A., Brennan M.J., Kovacic I., Waters T.P. On the Force Transmissibility of a Vibration Isolator with Quasi-Zero-Stiffness. *J. Sound Vib.* **322**: 707-717, 2009.
[6] Kovacic I., Brennan M.J., Lineton B. Effect of a Static Force on the Dynamic Behaviour of a Harmonically Excited Quasi-Zero Stiffness System. *J. Sound Vib.* **325**: 870-883, 2009.
[7] Gatti G., Brennan M.J., Kovacic I. On the Interaction of the Responses at the Resonance Frequencies of a Nonlinear Two Degree-of-Freedom System. Physica D **239**: 591-599, 2010.
[8] Gatti G., Kovacic I., Brennan M.J. On the Response of a Harmonically Excited Two Degree-of-Freedom System Consisting of Linear and Nonlinear Quasi-Zero Stiffness Oscillators. *J. Sound Vib.* **329**: 1823-1835, 2010.
[9] Kovacic I., Rega G., Zukovic M. On the Influence of a Constant Force on the Appearance of Period-Doubling Bifurcations and Chaos in a Harmonically Excited Pure Cubic Oscillator. *Chaos Solit. Fract.* **45**: 1531-1540, 2012.
[10] Kovacic I. On Some Performance Characteristics of Base Excited Oscillatory Systems with a Purely Nonlinear Restoring Force. *Int. J. Nonlinear Mech.* **65**: 44-52, 2014.
[11] Gatti G., Brennan M.J. Inner Detached Frequency Response Curves: an Experimental Study. *J. Sound Vib.* **396**: 246-254, 2017.

STABILITY AND STEERABILITY OF ROTARY STEERABLE SYSTEMS

Emmanuel Detournay *[1]
[1] Department of Civil, Environmental, and Geo- Engineering, University of Minnesota, USA

Summary Drilling geometrically complex boreholes in the subsurface has been made possible with the development of downhole tools that steer the bit. This paper outlines a model of borehole propagation that can be used to predict the bit trajectory and assess the conditions leading to abnormal situations, namely: the borehole tending to steer opposite to that intended with the steering tool; and a loss of directional stability leading to a limit cycle characterized by self-excited oscillations of the borehole attitude. Both the directional stability of the system and the counter-intuitive behaviors can be related to a key dimensionless group that can be interpreted as the ratio of a pseudo-stiffness characterizing the bit/rock interaction and the bending stiffness of the BHA.

INTRODUCTION

Drilling deep boreholes that weave complex trajectories in the subsurface has been made possible with the development of directional drilling, and in particular with the emergence of the *rotary steerable systems* (RSS) in the late 1990's. These servo-controlled downhole robots steer the bit by either applying a force on the borehole wall or by tilting the bit. Figure 1a sketches a typical rotary drilling structure, comprising a rig from which is suspended the *drillstring*. The rotary speed and the axial force (*hookload*) are imposed at the rig. The lower part of the drillstring is the *bottomhole assembly* (BHA), which is usually about one hundred meters long. It consists of heavier pipes and short elements of larger diameter, called *stabilizers*, which center the BHA in the borehole. The BHA or part of it is in compression in order to induce a sufficient *weight on bit*, the axial force transmitted to the bit at the lower extremity of the BHA. The RSS is located close to the bit. Such a semi-automated device works in association with sensors and downhole control units in order to steer the borehole. Considerations are restricted here to *push-the-bit* RSS, which apply a lateral force at a designated location on the BHA using a set of extensible pads that directly push on the borehole wall.

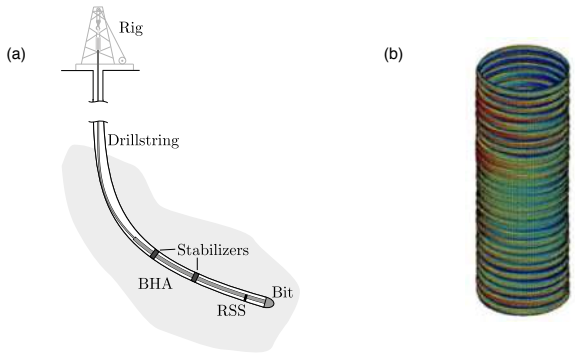

Figure 1: (a) Sketch of a drilling structure and (b) evidence of borehole spiraling from density log [8]

Study of this dynamical system is motivated by engineering issues, which include bit selection, designing the BHA to increase, maintain, or decrease the borehole inclination with or without the presence of a RSS [5], preventing borehole spiraling (Figure 1b) — an expression of self-excited limit cycle oscillations triggered by a directional instability of the drilling system and sustained by nonlinearities such as saturation of the bit tilt or intermittent contacts between the BHA and the borehole wall [4, 3], and devising an appropriate controller for the RSS to track a predefined well path [1, 2].

MATHEMATICAL MODEL

The borehole propagation model is constructed at the intermediate scale of the BHA, with boundary conditions capturing the processes at the two other scales [6, 7]. At the lower boundary, the bit is collapsed onto a point, with the details of the bit/rock interaction encapsulated into an interface law that relates the force and moment at the bit to penetration variables. At the upper boundary, the action of the drillstring is replaced by assumed known forces. All the dynamic and kinematic variables are averaged over many revolutions, implying that borehole propagation is a quasi-static process.

The directional propagation of the borehole depends on the force and moment at the bit; they are affected not only by the action of the RSS but also by the deformed configuration of the BHA, which is constrained by the stabilizers to espouse the existing borehole. The propagation of the borehole is thus governed by the interaction between a geometrical object, the wellbore, and a mechanical object, the drilling structure. The directional drilling model can be formulated by combining (i) a rate-independant *bit/rock interface law*, (ii) the *kinematic relationships* between the bit penetrations

*E-mail: detou001@umn.edu.

and the parameters characterizing the evolving geometry of the borehole, and (iii) the *beam model of the BHA* providing relationships linking the generalized forces at the bit to the geometry of the borehole and other external loads acting on the BHA. The equations governing the three elements of this model can be combined into two delay differential equations (DDEs), which represent the evolution equations for the borehole inclination and azimuth. The delays, corresponding to the positions of the stabilizers, capture the feedback of the borehole geometry on the transverse force applied at the bit.

Analysis of the propagation equations shows the existence of a critical dimensionless group $\eta\Pi = \eta W_a \ell_1^2/3EI$, which depends on several properties of the system: (i) lateral steering resistance η of the bit, a number that depends on the characteristics of the bit gauge; (ii) active weight on bit W_a, equal to the weight on bit reduced by the force transmitted by the wear surface of the bit; (iii) distance ℓ_1 between the first stabilizer and the bit; and (iv) bending stiffness EI of the BHA. Group $\eta\Pi$, typically of order $O(10^{-2} \sim 1)$, can be viewed as contrasting the resistance of the rock with the stiffness of the BHA, as the bit is tilted.

STABILITY AND STEERABILITY

The question of whether borehole spiraling occurs or not can be formulated as to whether a perturbation in the borehole trajectory is progressively amplified or dampened along the borehole, due to the geometric feedback embedded in the system, until a limit cycle is reached. A stability analysis of the governing DDEs indicates that there exists a critical value $\eta\Pi|_s$ of dimensionless group $\eta\Pi$, so that the system is unstable for $\eta\Pi < \eta\Pi|_s$, with the wavelength of the oscillations about equal to the distance between the bit and the first piece of equipment in contact with the wellbore — usually the first stabilizer. For a BHA with uniform mechanical properties, the bifurcation limit $\eta\Pi|_s$ depends essentially on the relative positions of the stabilisers. Although the BHA configuration can help make a system intrinsically more stable (*i.e.*, a system having a small $\eta\Pi|_s$), a system that is directionally stable initially may become unstable with increasing bit wear, higher rock strength, or reduced downhole weight on bit, all of which reduce the active weight.

The steerability of the drilling assembly also depends on $\eta\Pi$. Indeed, analysis of the DDEs indicate the existence of two particular values of that group, $\eta\Pi|_{\mathcal{V}}$, and $\eta\Pi|_{\mathcal{X}}$, that control the existence of different regimes of propagation. If $\eta\Pi = \eta\Pi|_{\mathcal{V}}$, the RSS is ineffective and the only possible solution is a vertical borehole; if $\eta\Pi = \eta\Pi|_{\mathcal{X}}$, gravity has no influence of the borehole trajectory. Thus $\eta\Pi|_{\mathcal{V}}$ characterizes the limit of steerability, as the borehole tends to steer opposite to that intended if $\eta\Pi \geq \eta\Pi|_{\mathcal{V}}$, while $\eta\Pi|_{\mathcal{X}}$ characterizes a holding tendency that marks, in the absence of a RSS, the transition between a dropping and a buiding assembly (respectively, negative and positive curvature of the trajectory).

The global response of the system to external loads is thus controlled predominantly by $\eta\Pi$ and the BHA configuration, on which the critical values depend. Noting that the steerability limit $\Pi|_{\mathcal{V}}$ is typically one order of magnitude larger than the stability limit $\eta\Pi|_s$, the directional drilling system should be designed in such a way that $\eta\Pi|_s < \eta\Pi < \eta\Pi|_{\mathcal{V}}$ so as to ensure both directional stability and steerability of the drilling assembly. Since $\eta\Pi$ is inversely proportional to D^4, with D the diameter of the BHA, small diameter BHAs are usually directionally stable, but could be prone to counter-intuitive drilling regimes. For large-diameter BHAs, the opposite is true: they are more at risk for directional instability, but less for a reversal of drilling regimes. The position of the first stabilizer is also influential as $\eta\Pi$ is proportional to ℓ_1^2.

CONCLUSIONS

The propagation of a borehole is governed by a set of delay differential equation in terms of the borehole inclination and azimuth, with the spatial delays corresponding to the position of the stabilizers on the BHA. Dimensionless group $\eta\Pi$, which measures the rock resistance against a tilt of the bit relative to the flexural rigidity of the BHA, is central to characterize the borehole trajectory. Indeed, the magnitude of $\eta\Pi$ relative to critical values that depend on the BHA configuration, defines different drilling regimes.

References

[1] Downton, G. and M. Ignova: 2011, 'Stability and response of closed loop directional drilling system using linear delay differential equations'. *Control Applications (CCA)*, pp. 893–898.

[2] Magaña, O. A. V., F. Monsieurs, E. Detournay, and N. van de Wouw: 2018, 'Robust output-feedback control of 3D directional drilling systems,'. *Int. J. of Robust and Nonlinear Control* **28**(18), 5915–5942.

[3] Marck, J. and E. Detournay: 2016, 'Spiraled Boreholes: An Expression of 3D Directional Instability of Drilling Systems'. *SPE Journal* **21**(02), 434–448.

[4] Pastusek, P. and V. Brackin: 2003, 'A model for Borehole Oscillations'. *Paper SPE* **84448**.

[5] Pastusek, P., V. Brackin, and P. Lutes: 2005, 'A Fundamental Model for Prediction of Hole Curvature and Build Rates With Steerable Bottomhole Assemblies'. In: *SPE Annual Technical Conference and Exhibition*. Dallas, Texas, U.S.A, pp. 1–7.

[6] Perneder, L., J. Marck, and E. Detournay: 2017, 'A Model of Planar Borehole Propagation'. *SIAM Journal on Appled Mathematics* **77**(4), 1089–1114.

[7] Shakib, M., E. Detournay, and N. van de Wouw: 2019, 'Nonlinear Dynamic Modeling and Analysis of Borehole Propagation for Directional Drilling'. *Journal of Non-Linear Mechanics* **113**, 178–201.

[8] Sugiura, J. and S. Jones: 2008, 'The Use of the Industry's First 3-D Mechanical Caliper Image While Drilling Leads to Optimized Rotary-Steerable Assemblies in Push-and Point-the-Bit Configurations'. In: *SPE Annual Technical Conference and Exhibition*. Denver, Colorado, USA.

EMERGENT SUBHARMONIC ATTENUATION ZONES IN NONLINEAR LOCALLY RESONANT METAMATERIALS: NUMERICAL MODELING AND EXPERIMENTS

Valentina Zega*[1], Priscilla B. Silva[1], Marc G.D. Geers[1] and Varvara G. Kouznetsova [1]
[1] Eindhoven University of Technology P.O. Box 513, 5600 MB Eindhoven, The Netherlands

Summary Locally resonant metamaterials are attracting increasing interest from the scientific community because of their extraordinary properties, in particular the subwavelength size of their unit cell. Recently, we theoretically proved a new mechanism for wave mitigation and control that exploits the nonlinear behaviour (i.e. autoparametric resonance) of the resonant components of the unit cells of a locally resonant metamaterial. It consists in the nonlinear interaction between propagating and evanescent waves and leads to the opening of subharmonic attenuation zones. Here, we present the design of a new single-material nonlinear locally resonant metastructure able to exploit such principle and we provide, to the best of our knowledge, the first experimental evidence of the discovered phenomenon. A good agreement between experiments and numerical prediction is also shown.

INTRODUCTION

Acoustic metamaterials and phononic crystals provide new possibilities for acoustic wave control and manipulation, as e.g. overcoming the traditional limits in focusing, wave guiding, and subwavelength sound and vibration insulation [1]. Recently, the consideration of nonlinearity in these engineered materials has opened up new possibilities [2]. In particular, we have recently theoretically shown the existence of a new mechanism for wave mitigation and control that consists in a nonlinear interaction between propagating and evanescent waves in a nonlinear elastic locally resonant metamaterial due to autoparametric resonance and discovered the consequent appearance of a subharmonic attenuation zone in the transmission diagram [3]. In the previous work [3], a simple mass-spring chain was considered to physically unraveil the phenomenon. Here we design a single-material nonlinear locally resonant metastructure, and we experimentally demonstrate the emergence of the subharmonic attenuation zone in the transmission diagram induced by autoparametric resonance. To the best of our knowledge, this represents the first experimental evidence of emergent subharmonic attenuation zones in nonlinear locally resonant metastructures. Numerical and analytical models supported the design process of the resonant unit-cell and show good agreement with the experiments.

NUMERICAL MODELLING

The proposed locally resonant metastructure consists of a chain of 50 unit cells (2.2 cm x 6.9 cm x 5 mm) made by an external frame and an inner mass connected to the frame through two pre-deflected arch beams (Figure 1), providing the required nonlinear coupling between the matrix and the resonator. The simple geometry and the use of a single material allows to manufacture the prototype using standard production. In the present design of the unit cell, quadratic nonlinearities, responsible of the emergence of subharmonic bandgaps induced by autoparametric resonance, appear because of the pre-deflection breaking the symmetry in the resonator, while cubic terms are related to the effect of the axial load on a clamped-clamped beam for large displacements of the mass [4].

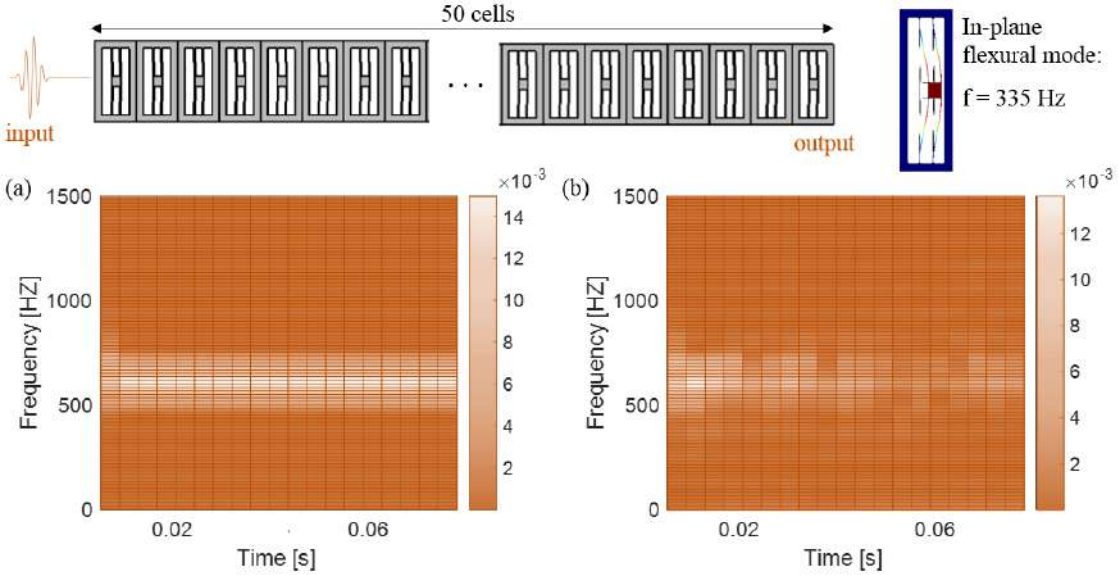

Figure 1. Nonlinear locally resonant metastructure and the first in-plane flexural mode of the unit cell. Spectrograms of the output signal computed at the right end of the chain in the (a) linear and (b) nonlinear regimes when a burst of 4 periods at around two times the natural frequency of the in-plane flexural mode of the resonator is applied as the input on the left side of the chain.

*Corresponding author. E-mail: zega.valentina@gmail.com.

As expected from the theory, the locally resonant metastructure shown in Figure 1 presents a bandgap in the longitudinal direction (only longitudinal waves are considered here for the sake of simplicity) around the natural frequency of the in-plane flexural mode of the inner resonator (f = 335 Hz from the modal analysis performed in COMSOLMultiphysics©). When an input signal at around two times the natural frequency of the inner resonator (700 Hz) is applied to the left side of the chain in the form of a prescribed 4-period burst displacement, on the right side of the chain full propagation (Figure 1a) is observed in the linear regime, while in the non-linear regime strong attenuation (Figure 1b) is obtained. Indeed, when the applied displacement is small, the autoparametric resonance does not activate and no attenuation outside of the bandgap frequency range is present. On the other hand, when the input displacement is sufficiently large to activate the nonlinear behaviour of the resonator, the autoparametric resonance induces the energy transfer mechanism between propagating and evanescent waves and a second attenuation zone emerges at two times the natural frequency of the resonator [3]. The numerical results reported in Figure 1 are obtained through 2D transient analyses in COMSOLMultiphysics© under the hypothesis of plane stress.

EXPERIMENTS

A prototype of the designed nonlinear locally resonant metastructure is fabricated from a single plate of AlMgSi1 alloy of 0.5cm thickness by electrical discharge machining (EDM). The employed experimental set-up is shown in Figure 2a: it consists of a shaker to apply the input displacements at the beginning of the chain, a laser vibrometer to detect the output displacements at the end of the chain and an acquisition board to transfer the signals to a computer for post-processing. The metastructure is suspended on wires to simulate free conditions on both top and bottom surfaces, as well as on one of the metastructure ends, thus avoiding any interaction with the table that could compromise the measurements.

The transmission diagram (20 $\log_{10}$ (output/input)) is measured in a wide range of frequencies for three different amplitudes of the input signal. When the amplitude input is small enough to not activate the nonlinear behavior of the resonator (red line in Figure 2b), the transmission diagram shows the expected linear behaviour with an attenuation in the proximity of the resonant frequency of the inner resonator and a full transmission at higher frequencies. When the input signal amplitude increases, a second attenuation zone emerges at two times the natural frequency of the inner resonator (blue and green lines in Figure 2b), as predicted by numerical analyses (Figure 1) and theoretical models [3].

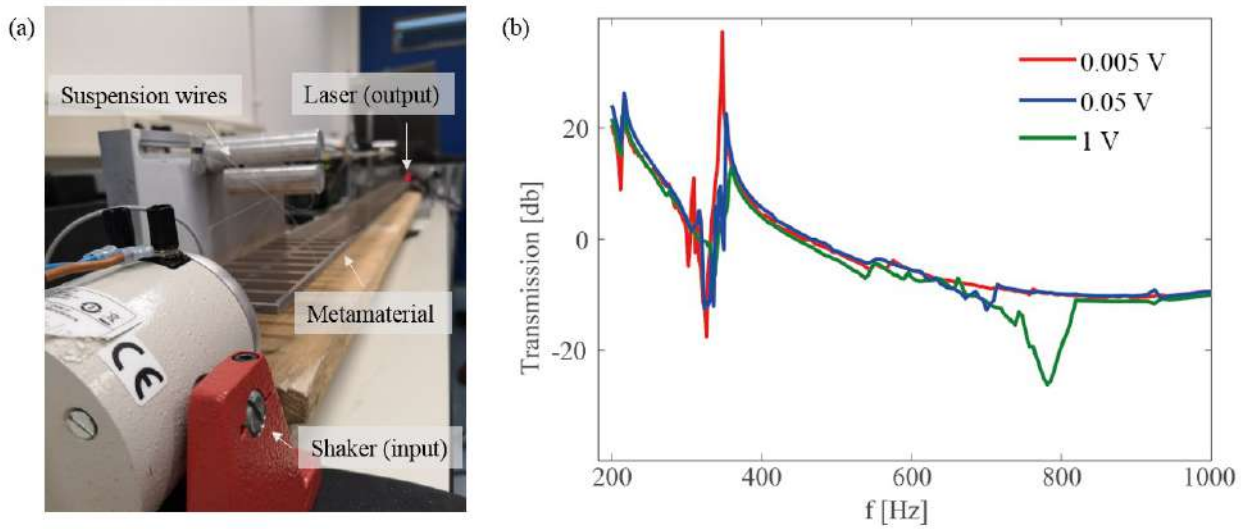

Figure 2. (a) Experimental set-up. (b) Transmission plot measured for different amplitudes of the input signal.

CONCLUSIONS

To the authors' knowledge, this work presents the first experimental evidence of the subharmonic attenuation zone induced by the autoparametric resonance energy exchange in a non-linear locally resonant metastructure. To this end, a new single-material nonlinear locally resonant metastructure has been designed and fabricated with standard processing techniques. Numerical simulations reveal an adequate agreement with experiments. This work exposes a new generation of nonlinear metastructures/metamaterials that can be employed in numerous potential applications.

References

[1] Monticone F et al Metamaterial, plasmonic and nonphotonic devices *Reports on Progress in Physics* **80**: (036401) 1-37, 2017.
[2] Fang X et al Ultra-low and ultra-broad-band nonlinear acoustic metamaterials *Nature Comm.* **8:** 1288, 2017.
[3] Silva, P.B. et al. Emergent subharmonic band gaps in nonlinear locally resonant metamaterials induced by autoparametric resonance *Ph. Rev. E* **99**: 063003, 2019.
[4] Ouakad H M et al The dynamic behavior of MEMS arch resonators actuated electrically *Int. J. Nonlin. Mech.* **45:** 704713, 2010.

BALLISTIC STUDY OF LONG ROD ERODING PROJECTILES AGAINST RHA AT OPTIMUM (L/D) RATIOS

Sana Zaki[1] and Dr Amir Mubasher [2]
[1] Department of Mechanical Engineering, SMME NUST, Islamabad
[2] Department of Mechanical Engineering, SMME NUST, Islamabad

Summary Long rod penetrators exhibit hydrodynamic behavior while striking against the target plates. Efforts of enhancing the target damage is the main purpose for upgrading the lethality of rounds. An experimental study is therefore devised controlling multiple variables like: change in penetrator length to penetration (P/L), optimizing length to diameter ratios (L/D) and material properties of TA rods. Every parameter has a unique contribution to the eroding pattern of projectiles which are later analyzed with numerical simulations in Abaqus. For optimization of parameters with the existing performance of rounds results from high speed camera are also accorded in the experimental study. It is found that the overall stability of eroding rod depends on smooth bore of heavy caliber gun, appropriate composition of charge bags (MCS and ACS), stable discarding of sabots and zero angle of attack while the long rod approaches to the target.

Introduction

Long rod kinetic energy rounds exhibit hydrodynamic behavior at their working velocities usually 1400-2000m/s. The eroding pattern of projectile into RHA at specified velocity, density and impact energy determines the damage done to Target. Several factors like increase in penetration to length (P/L), length to diameter (L/D) and material properties of penetrator are studied extensively and different combinations were subjected to test and trail to enhance the penetration. This hydrodynamic flow of Tungsten alloy penetrator in Target has been explained by various models, initially by the simplified Bernoulli equation [1] which is later on extended to modified equations by Tate [2,3,4] and Alekseevskii.

Fig 1. K.E rod approaching RHA at ordnance velocity (1500-2000m/s)

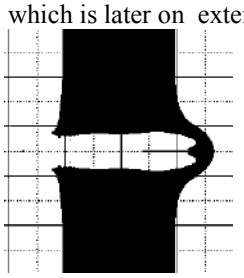

Fig 2. Numerical Simulation showing hydrodynamic flow of penetrator against the Target plate

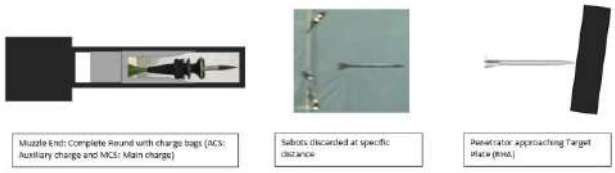

Fig 3. Experimental setup for long kinetic energy rods against RHA

Design parameters for 125mm smooth bore enhanced penetrator and corresponding sabot

Penetrator	Tensile Strength	R_m	1300	MPa
	Density	ρ_P	17.15	Kg/m^3
frustum	Ø at top	D_{FT}	8	mm
	Length frustum	L_{Fru}	95	mm
Cylindrical front part	Diameter	D_{FP}	24.5	mm
	Length	L_{FP}	114.5	mm
Buttress part	Buttress dia outside	D_{BO}	26.5	mm
	Buttress dia in the grooves	D_{BG}	23.8	mm
Rear part	Diameter	D_{RP}	26.0	mm
	Length	L_{RP}	28.0	mm
Tungsten	Length	L_P	661	mm
	Mean diameter	D_{mean}	25.7	mm
	Working length	L_w	631	mm
	Aspect ratio L/D	L/D	24.5	mm
	Mass	m_P	4.630	Kg
Target	Target density	ρ_T	7.850	Kg/m^3
	Brinell Hard. Number	BHNT	235	
	Obliquity NATO	θ	65	°

Analytical Tools

The perforation energy plays a vital role in achieving desired penetration of TA rod in RHA plate. Hence a projectile predictive model based on energy approaches is used [6]

$$E = kd^m t^n$$

Where,

$$m + n \approx 3$$

E: is the perforation energy
d: is the projectile diameter
t: is the plate thickness
k: is an empirically derived constant (as in figure 4)

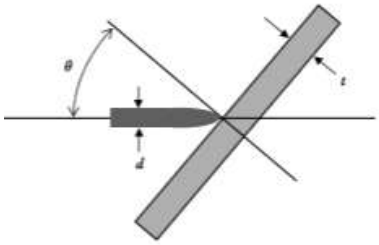

Fig 4. Impact Energy of projectile while approaching Target plate

MINI SYMPOSIA

Design Optimization

Case I: Change in Penetration with Penetrator Length (P/L)

The length of penetrator plays a vital role in ballistic study of long rod penetration.

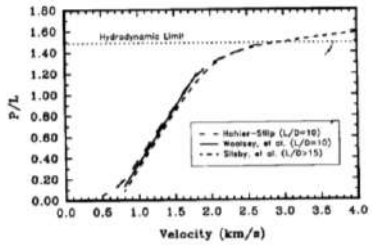

Fig 6. Hydrodynamic limit on penetration with change in (P/L) [9, 10, 11]

Case II: Change in Penetration with Length to Dia ratios (L/D)

In this study, the change in L/D has been examined both analytical and experimentally within $10 \leq L/D \leq 30$. Also there are certain analytical tools which verifies the depth of projectile in target plate. Lanz and Odermat [15] predicted an empirical formula that explicitly accounts the term L/D as shown in the below equation

$$\frac{d}{L} = \tau\left\{1 + \tau\frac{3.77}{L/D}\left[1 - tanh\left(\frac{L/D - 10}{6.89}\right)\right]\cdot\pi\left(\frac{\rho_t}{\rho_i}\right)^{0.745}\pi(\cos\theta)^{0.745}\cdot e^{-\frac{25.98}{\rho_t}V^2}\right\}$$

Case III: Change in Penetration with Penetrator Composition (W)

The overall functioning of kinetic energy rods are dependent on impact velocity, geometric parameters and material composition [16]. This process can be related with the below model

$$\sigma\tau = \varpi_s + \varpi_d \qquad \text{Eq (3.1)}$$

Experimental Results

Case I: Change in Penetration with Penetrator Length (P/L)

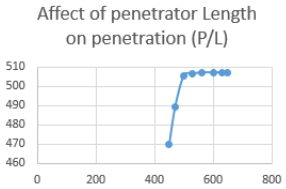

Graph 1. Increase in P/L with the variation in length in of projectile.

Case II: Change in Penetration with Length to Dia ratios (L/D)

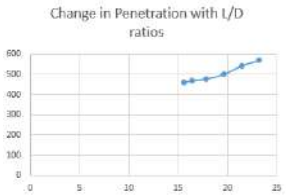

Graph 3. The change in depth of penetration with L/D ratios (10-20).

Case III: Change in Penetration with Penetrator Composition (W)

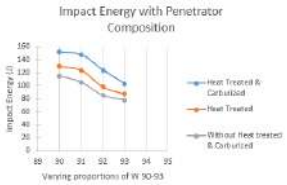

Graph 4. The change in penetration with increase in Impact Energy.

CONCLUSIONS

Long rod projectiles have multiple design variables that can increase target damage. In this study design optimization of 125mm APFSDS has been carried out and it is found that for a working range of L/D between 20-30 at ordnance impact velocity 1640m/s and impact energy 158J (W90-Ni-Cr-Fe) maximum penetration was achieved. It can also be concluded that at ordnance velocities the change of various variables like P/L and L/D is less significant than material composition related to its impact energy.

References

[1] A two-dimensional analysis of penetration by an eroding projectile, Int. J. Impact Eng #Vol. 15, No. 5, pp. 587-603, 1994 Elsevier Science Ltd
[2] A. Tate, A theory for the deceleration of long rods after impact. J. Mech. Phys. Solids 15, 287-399 0967).
[3] A. Tate, Further results in the theory of long rod penetration. J. Mech. Phys. Solids 17, 141-150 (1969).
[4] A. Tate, Long rod penetration models--Part II. Extensions to the hydrodynamic theory of penetration. Int. J. Engng Sci. 28:535-48 (1986).
[5] Analysis of the mechanics of perforation of projectiles in metallic plates, Int. J. Solids Structures, 1974, Vol. 10, pp. 671-684. Pergamon Press. Printed in Gt. Britain
[7] Ballistics- Theory and Design of Guns and Ammunition - Donald E. Carlucci, Second Edition
[8] Terminal Ballistics, Second Edition by Zvi Rosenberg and Erec Deckel, 2012.

……

MINI SYMPOSIA

NONLINEAR DYNAMICS AND CONTROL OF AN AEROELASTIC AIRFOIL MODEL WITH RANDOM NOISY FLUCTUATIONS

Yong Xu *[1, 2], Qi Liu[1], and Jürgen Kurths[3]
[1] School of Mathematics and Statistics, Northwestern Polytechnical University, Xi'an 710072, China
[2] MIIT Key Laboratory of Dynamics and Control of Complex Systems, Northwestern Polytechnical University, Xi'an 710072, China
[3] Potsdam Institute for Climate Impact Research, Potsdam 14412, Germany

Summary Uncertain fluctuations widely exist in practice, such as turbulence, crosswind, pressure fluctuations, etc. It is of significance and meaning to explore complex random dynamics and control for a conceptual airfoil model. In this work, we study an airfoil model subject to various random excitations, including Gaussian noises and narrow-band noise as primary approximations to model external random fluctuations. Therein, viscoelasticity of the airfoil models are also included. Theoretical analysis is implemented by averaging technique or multiple-scales method, and its correctness is verified. We uncover that the airfoil models can show multiple-values responses and stochastic transitions due to the existing of nonlinearities and random fluctuations, and sliding mode control is employed to achieve the vibration suppression. Moreover, a fixed-interval smoothing of the airfoil model is also addressed. All the results indicate that our works may provide a valuable support for the structural design of aircrafts.

INTRODUCTION

During the past few decades, nonlinear aeroelastic dynamics of typical airoil models has attracted widespread attention, which have also been a hot topic in the aerospace field. For example, Lee et al. [1] studied nonlinear behaviors of airfoil models with three common structural nonlinearity, namely, cubic, free-play and hysteresis. However, most of the studies only focus on the case without random fluctuations, and influences of complex external random factors are not considered. In fact, many uncertain fluctuations always exist in real environments, such as atmospheric turbulence, pressure fluctuation, random wind loading, etc [2]. The aeroelastic airfoil models, as typical nonlinear systems, can exhibit several complex nonlinear dynamic behaviors under random fluctuations, such as random flutter, stochastic bifurcation and jumps, etc. Therefore, it is of significance to study the nonlinear dynamic behaviors of the airfoil models with complex random disturbances. In recent years, nonlinear dynamics of airfoil models subject to different uncertain disturbances have been reported. For instance, random flutter of two-dimensional airfoil model was investigated by means of a probabilistic and statistical methods [3, 4]. In addition, stochastic bifurcation and early warning of a typical airfoil section were studied through experimental and numerical approaches [5]. However, most of the works are based on numerical simulations or experiments, and rarely focus on a theoretical analysis. It should be noted that coupling of the random disturbances and the nonlinear factors brings great difficulties and challenges to the analysis in theory. Consequently, this work attempts to review some of our advances on nonlinear dynamics of typical airfoil models with varying random fluctuations, including Gaussian white noise, Gaussian colored noise and narrow-band noise. Meanwhile, we also study the fixed-interval smoothing problem of the airfoil models, and accurate state and parameter estimations are obtained.

RESULTS

As we know, a typical airfoil section can be simplified as a conceptual two-degrees-of-freedom model which oscillates in the plunge and pitch directions [1, 3, 4, 5, 6, 7, 8, 9], as shown in Fig. 1. The pitch angle α is positive if nose-up; the plunge deflection h is positive in the downward direction. L and M are the aerodynamic lift and moment acting on the airfoil respectively, U represents the flow velocity, and b is the half-chord length. EA is the elastic axis, and G is the center of gravity. The elastic axis is located at the distance ab from the mid-chord where a is a constant, and the center of gravity is situated at the distance $x_\alpha b$ from the elastic axis where x_α is the dimensionless distance. Both distances are positive when measured towards the trailing edge of the airfoil. The simplified model can be employed to reveal mechanisms of some practical behaviors. In recent years, we have studied nonlinear dynamics of the stochastic airfoil models for three different cases, including Gaussian white, Gaussian colored and narrow-band noisy fluctuations, from the analytical and numerical perspective. First, a Gaussian white noise is considered as a primary approximation to model the external random fluctuation, and then a stochastic airfoil model with harmonic excitation is presented based on the deterministic airfoil system [6]. Therein, we assume that the airfoil model is provided with slight coupling and nonlinearity. A perturbation technique together with a stochastic averaging method is employed to obtain the amplitude-frequency responses of the proposed random airfoil model, and numerical simulation results are implemented to test correctness of the obtained approximate analytical solutions. In fact, the Gaussian white noise is only regarded as an ideal model, which cannot well describe the complex external environmental disturbances in comparison with the colored noise with a nonzero correlation time. For this reason, we extend the previous work [6] to the case of Gaussian colored

*Corresponding author. E-mail: hsux3@nwpu.edu.cn.

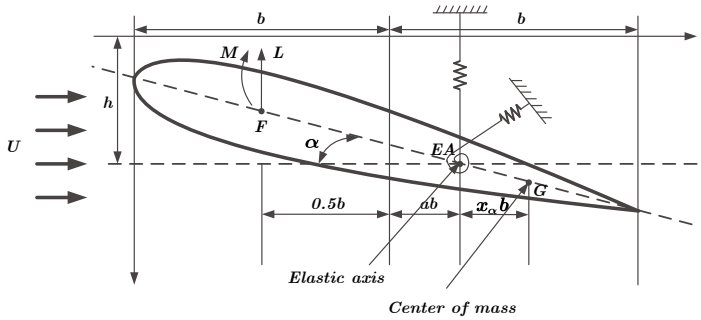

Figure 1: Structural model of a typical two-degrees-of-freedom airfoil section.

noise [7], and we find that intensity and correlation time of the colored noise excitations can all induce a stochastic jumps between high-amplitude and low-amplitude oscillations. The stochastic transitions between low-amplitude and high-amplitude oscillations are regarded as unwanted behaviors in aircraft flights, which can lead to fatigue and even damage of the airfoil structure. Hence, an effecitive sliding mode controller is designed for the proposed random airfoil model to achieve the stochasatic vibration suppression, and practical stability as a new concept is introduced to analyze stability of the controlled airfoil system. Furthermore, viscoelastic material propertis of the typical airfoil section are further explored [8, 9]. A fractional-order derivative is employed to describe the viscoelastic behavior of the airfoil material, and an averaging technique is applied to realize the theoretical analysis of the deterministic viscoelastic airfoil model [8]. Meanwhile, a fractional-order sliding mode control is implemented to study the vibration suppression of the introduced airfoil model. Besides, consider the effect of external random fluctuations, we further explore analytically the influences of random fluctuations as a narrow-band process on the airfoil model with viscoelastic terms [9]. Therein, the viscoelastic terms are characterized by a convolution integral over an exponentially decaying kernel function. The method of multiple scales are applied to obtain several approximate analytical solutions of the airfoil systems with random fluctuation and viscoelastic material property, including amplitude-frequency responses and steady-state moments. We uncover that the viscoelastic terms have a considerable influence on the system dynamical behaviors, which can simultaneously affect the structural damping and stiffness of the airfoil system. Similarly, stochastic jumps between high-amplitude and low-amplitude oscillations can be found due to narrow-band random fluctuations. In addition, a novel algorithm is introduced to explore the fixed-interval smoothing problem of the airfoil models from noisy measurement data. The results show that this algorithm can achieve accurate state and parameter estimations for the cases of Gaussian white or/and even more complex heavy-tailed measurement noises. Although both the airfoil models as mentioned above and the random noisy models are simplified, which are far from the engineering practice, we believe that these works can provide some valuable perspectives for the designers of the aircraft.

CONCLUSIONS AND FUTURE WORKS

In the present study, nonlinear dynamic behaviors of the airfoil models subject to Gaussian white, Gaussian colored and narrow-band noisy fluctuations are investigated theoretically by means of the stochastic averaging technique and the method of multiple scales method. The dynamic behaviors of the airfoil models will become more rich and complex due to the coupling effects of random and nonlinear factors. There are still several open problems worthing to further study as follows: **(1) More complex random excitation models must be considered.** Due to the synthesis of various environmental disturbances, several more complex cases such as Poisson noise, Lévy noise, etc., can be used to approximate the actual random fluctuations. **(2) Data-driven problems should be explored.** The present studies are based on the mathematical models established by physical mechanisms. However, with the rapid development of computer technology in recent years, data-driven problems and machine learning have caused widespread concern among scholars. Therefore, it is of more significance but difficulty to study the the airfoil models with complex random fluctuations from a data-driven perspective together with machine learning techniques, including response prediction, system identification, etc.

References

[1] Lee B. H. K , Price S. J., Wong Y. S. Prog Aerosp Sci. **35**: 205-334, 1999.
[2] Pettit C. J Aircr. **41**: 1217-1229, 2012.
[3] Poirel D. C., Price S. J. AIAA J. **39**: 1960-1968, 2001.
[4] Poirel D. C., Price S. J. J Fluids Struct. **18**: 23-42, 2003.
[5] Venkatramani J., Sarkar S., Gupta S. Nonlinear Dyn. **92**: 1225-1241, 2018.
[6] Xu Y., Liu Q., Guo G. B., et al. Nonlinear Dyn. **89**: 1579-1590, 2017.
[7] Liu Q., Xu Y., Xu C. Appl Math Modell. **64**: 249-264, 2018.
[8] Liu Q., Xu Y., Kurths J. J. Sound Vib. **432**, 50-64, 2018.
[9] Liu Q., Xu Y., Kurths J. Commun Nonlinear Sci Numer Simulat. **84**: 105184, 2020.

THE SIGNATURE OF NONLINEAR DYNAMIC SYSTEMSWITH DEGRADATION

Fabrizio Vestroni*[1] and Cristina Gatta[1]
[1]Department of Structural and Geotechnical Engineering, Sapienza University of Rome, Rome, Italy

Summary The characterization of the dynamic behaviour of linear systems are exhaustively described by frequency response curves (*frcs*). For nonlinear systems, which are prone to depend on response amplitude, at least one *frc* for each excitation intensity is required to characterize the dynamic behaviour. Nonlinear systems, mainly dealt with in the literature are invariant with respect to the deformation history: as a consequence, *frcs*, obtained with increasing and decreasing frequency, coincide. On the contrary, for many real systems, which suffer from their past experience, the *frcs* do not coincide. The steady-state response of a masonry wall, which is characterized by degrading restoring force, is considered to analyse the effects of decay on the fundamental signature of systems, the behaviour of which is strongly affected by their deformation history.

INTRODUCTION

Frequency response curves (*frcs*) are comprehensive in representing the dynamic behaviour of linear systems. The response of nonlinear systems depends on the amplitude of deformations undergone. Hence, focusing on the steady state response to harmonic excitations, a *frc* obtained for each excitation intensity is necessary to describe the system dynamic characteristics. Even if there is a wide variety of restoring force relationships, the overcome on the *frc* shapes are only marginal, whereas are more evident on higher order features, such as unstable branches, wrinkles, detached *frc*. Thus, the different *frcs* can be grouped in two large families (Fig. 1), single valued curves or curves with limited ranges of multiple solutions.

This topic has been touched by a few authors, starting from the *frcs* as a first fundamental step to a more in-depth analysis of the dynamic response of a nonlinear system [1, 2]. However, focus was on systems with restoring force relationships irrespective of the history, whereas most nonlinear constitutive relationships are considerably dependent on the previous deformation experienced, especially in the case of material nonlinearities. In this study for these latter cases, the modifications of the frequency response curves are investigated, with a view to understanding the extent to which the original signature of the curves remains meaningful in representing the core of the system dynamics.

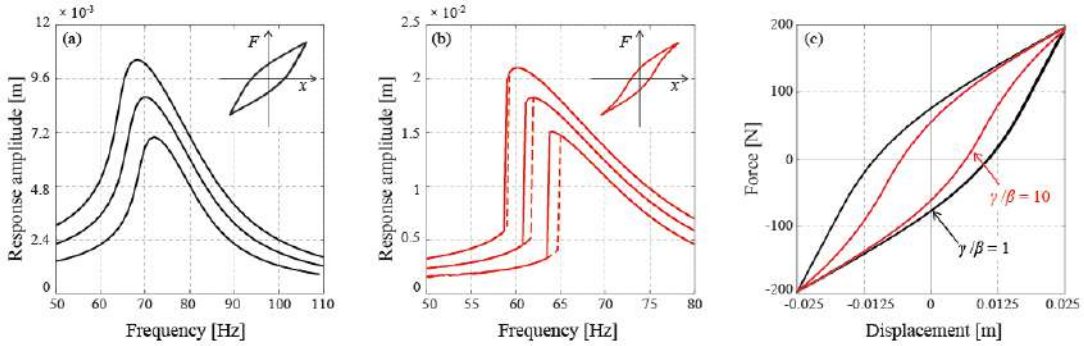

Figure 1. Single-valued (a) and multi-valued (b) *frcs* for fully ($\gamma/\beta = 1$) and reduced ($\gamma/\beta = 10$) hysteresis (c).

FREQUENCY RESPONSE CURVES OF A DEGRADING SYSTEM

The study addresses the dynamic behaviour of a slender masonry wall, restrained at the base. A non-local damage plastic model is proposed to analyse the behaviour of masonry structural elements [2]. The model, which adopts a macromechanical approach, captures strength and stiffness degradation with hysteretic dissipation characterizing the masonry response when it is subjected to a cyclic history beyond the elastic range. The stiffness recovery due to the crack closure, under cyclic loading conditions, is made possible by introducing, in the stress-strain constitutive law, two scalar damage variables, representing the damage in tension and compression, respectively. The cyclic response to an imposed displacement history is shown in Fig. 2a,b with the damage distribution, which is mainly concentrated at the base.

To validate the model, a real wall (Fig. 2c) has been realized and experimentally tested in the DISG Laboratory, Sapienza University. Shaking table tests were performed by imposing sinusoidal base accelerations with fixed frequency and increasing amplitudes. The numerical results are compared with the experimental outcomes which highlight that the wall response is strongly affected by the degrading mechanisms evolving in the panel, with a decrease of the wall natural frequency, due to the propagation of damage. It results that the model is able to capture the panel overall dynamic response, as both the actual resonance condition and the maximum reached displacement are satisfactorily matched.

*Corresponding author. E-mail: vestroni@uniroma1.it

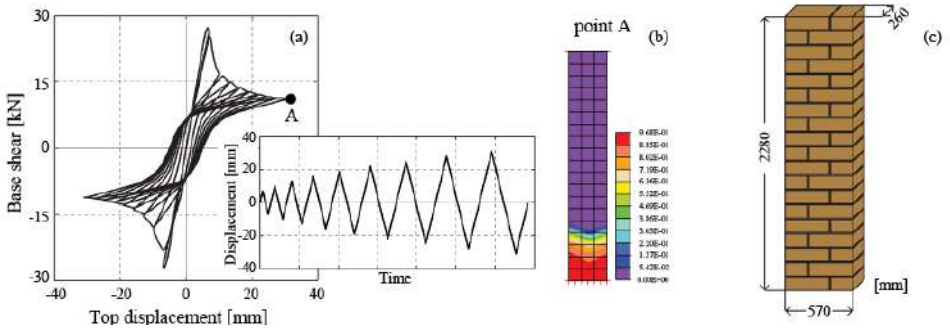

Figure 2. Cyclic load-displacement curve (a) and tensile damage distribution (b) for an example wall; experimentally tested wall (c).

The validated damage-plastic model has been used to numerically investigate the effect of mechanical properties evolution on the *frcs*, which are compared with those of a linear elastic system (Fig. 3). Horizontal harmonic base acceleration with slowly increasing (sweep 1) and decreasing (sweep 2) frequency, are applied at wall base, in the range [0.2 ÷1.5] of the initial frequency of the wall, for three acceleration intensities U/g = 0.04, 0.05, 0.06. For increasing excitation frequency (sweep 1), onset of damage leads to a decrease of wall natural frequency, while the forcing frequency increases. Thus, the wall suddenly leaves the resonance conditions, with a peak response attained at a frequency which slightly decreases with the increasing acceleration intensity, (Fig. 3a).

In the case of sweep 2, when the response curve leaves the elastic curve due to damage, the wall frequency decreases while the driving frequency also decreases and the response branch is bent on the left up to the resonance peak, just before falling down from the resonant to the non-resonant branch. A range of multiple solutions appears, which is clear by matching the curves obtained with sweep 1 and 2 (Fig. 3). This is consistent with the general results in [3]. For an assigned intensity, Fig. 3c shows the large difference between the two *frcs* for increasing and decreasing driving frequencies which is the impressive effect of the degrading properties of the wall. For this degrading system the multi-valuedness of the *frc* is not limited to a specific range, as occurs for the invariant restoring force relationships, but at any excitation frequency, the response oscillation amplitude is different as it depends on the history before reaching stationary oscillation.

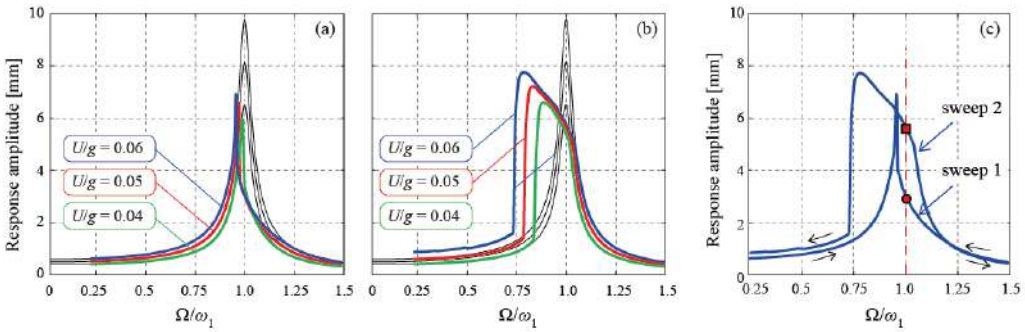

Figure 3. *Frcs* for sweep 1 (a) and sweep 2 (b): elastic response (black lines), damage-plastic response (green, red and blue lines corresponding to intensities U/g = 0.04, 0.05, 0.06, respectively); *frcs* for sweep 1 and 2 for U/g = 0.06 (c)

CONCLUSIONS

Frequency response curves are a fundamental tool to synthetically describe the dynamic response of a system. For invariant nonlinear systems *frcs* differ at different intensities, due to nonlinearity; however, for a given intensity only one curve describes the steady state response of the system, regardless of how an equilibrium point is reached. Here, the modification of this picture for a system characterised by mechanical properties which evolve with the deformation history, is given. Systems with degrading properties are common in the real world; explicit reference is made to a masonry wall for which a refined model has been validated by dynamic experiments on a shaking table. It is shown that the system is no longer represented by a unique *frc*, since any stable equilibrium point depends on the history followed to reach it.

References

[1] Cammarano A.,·Hill T. L., Neild S. A., Wagg D. J., Bifurcations of backbone curves for systems of coupled nonlinear two mass oscillator, *Nonlinear Dyn* 77:311–320, 2014

[2] Zhang G., Zang C., Friswell M. I., Measurement of multivalued response curves of a strongly nonlinear system by exploiting exciter dynamics, Mechanical Systems and Signal Processing, in press, https://doi.org/10.1016/j.ymssp.2019.106474

[3] Addessi D., Gatta C., Vestroni F., Dynamic response of a damaging masonry wall, X International Conference on Structural Dynamics, Eurodyn 2017, *Procedia Engineering*, 199, 152–157, 2017

[4] Gatta C., Addessi D., Vestroni F., Static and dynamic nonlinear response of masonry walls, *Int. J. Solids and Structures*, 155, 291–303, 2018.

[5] Capecchi D., Vestroni F., Periodic response of a class of hysteretic oscillators, *Int. J. Non Linear Mech.* 25, 309–317, 1990.

DETERMINISTIC DETECTION OF ISOLATED PERIODIC SOLUTION BRANCHES

Jörg Wallaschek*, Torsten Heinze, and Lars Panning-von Scheidt
Institute of Dynamics and Vibration Research, Leibniz University Hannover, Hanover, Germany

Summary The present study explores the relevance and detection of isolated periodic solution branches commonly encountered in nonlinear dynamical system analysis. Attention is drawn to the development of an entirely deterministic computational scheme for uncovering separated solution branches of systems with hysteretic forces. Based on a harmonic balance approximation a specific frequency domain nonlinearity smoothing is proposed, facilitating the application of the global terrain method as a candidate for deterministic global solution methods. Finally, a homotopy continuation transfers the solutions of the smoothed system to the non-smooth case.

RELEVANCE OF ISOLATED PERIODIC SOLUTION BRANCHES

Isolated periodic solution branches are known to exist for a variety of systems covering nonlinearities or piecewise linearities such as hysteretic forces, mechanical impacts, suspended cable structures, atomic-force microscopy, feedback control systems with deadband, nonlinear energy sinks, or nonlinear tuned vibration absorbers. Simultaneous self- and external excitation often provoke the separation of solution branches from the main solution branch. Furthermore, the deep connection of internal resonances and backbone curves to nonlinear frequency-response curves is uncovered. Extensive literature overviews provide the historical context as well as insight into further computational methods for isola detection [1, 2].

The relevance of isolated periodic solution branches is subsequently demonstrated using the single-degree-of-freedom system with a shape-memory alloy nonlinearity shown in Fig. 1a. For information on the exact parameter values, the reader is referred to the literature [1]. The system is pre-stressed such that the oscillation encloses the center of the hysteresis loop. It is solved using the harmonic balance method constrained to the fundamental harmonic and a vanishing static displacement leading to an algebraic set of two equations for three unknowns: the Fourier coefficients of the motion related to the cosine and sine component as well as the vibration frequency.

The results of interest that are commonly investigated during the design process are the nonlinear frequency-response curves depicted in Fig. 1b. Here the variation of the curves w.r.t. the excitation amplitude is illustrated. For a specific parameter regime isolated periodic solution branches exist. The stability estimation is based on Hill's method [3] and verified using time simulation rendering the system bistable, cf. Fig. 1c. Unfortunately, this isolated resonance curve is easily missed by local path continuation tools; thus, the danger of considering an incomplete solution set during the design process should be kept in mind. Note that this type of solution curve separation is not related to self-excitation as known for friction-damped systems.

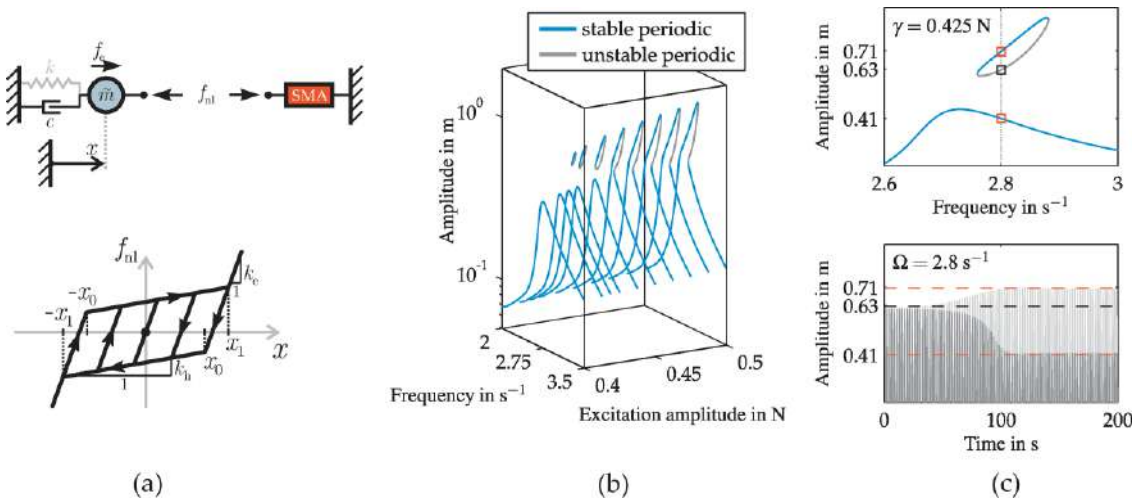

Figure 1. Periodic solutions of the single-degree-of-freedom shape-memory alloy model: (a) model definition and nonlinear force hysteresis, (b) merge of isola with main solution branch, (c) stability verification of harmonic balance solution using time integration [1].

ISOLA DETECTION METHODOLOGY

A global solution analysis for industrial purposes or possibly safety-relevant products should not compromise certainty in uncovering the complete set of solution branches. Therefore, the presented workflow relies solely on deterministic components to be given subsequently.

*Corresponding author. E-mail: joerg.wallaschek@ids.uni-hannover.de.

Nonlinearity smoothing

The employed global solution method requires C^2 continuous functions. The presence of the piecewise linearity of the hysteresis loop leads to deflections which are not continuously differentiable. Likewise, the harmonic balance approximation is not continuously differentiable as can be seen by plotting the squared norm of the harmonic balance residual, cf. Fig. 2a. The numerical treatment is performed using the alternating frequency/time domain method which relies on a time marching procedure to evaluate the nonlinear force law. In this study, we propose to modify the time marching procedure using a smoothed predictor-corrector scheme leading to a continuously differentiable nonlinear force term in the frequency domain, cf. Fig. 2b. Further details on the exact formulae and parameterization are provided in the literature [1].

Global terrain method

The set of unknowns is constrained by fixing the phase to yield distinct point solutions rather than branches. Since any isola covers a phase range of 360°, two points of each isola are within the set of solutions. As the nonlinearity is smoothed, the global terrain method can be applied [4]. It explores the squared norm of the residual in a structured way. In Fig. 2b the successful detection of all three solution points – one on the main branch and two on the isola – is shown. Note that only the relevant paths of the global terrain method connecting all three solution points are depicted. An extended variant with a specific search space scaling to overcome further discontinuity problems between solution points is presented in the literature [1].

Homotopy continuation

Finally, the found solution points of the smoothed residual function are transferred to the solution points of the non-smooth harmonic balance approximation using homotopy continuation. From these points, the entire isola can be computed using local path continuation. The feasibility of the homotopy continuation between two structurally equivalent functions – one smoothed and one non-smooth – is here presented for the shape-memory alloy system for the first time, cf. Fig. 2c.

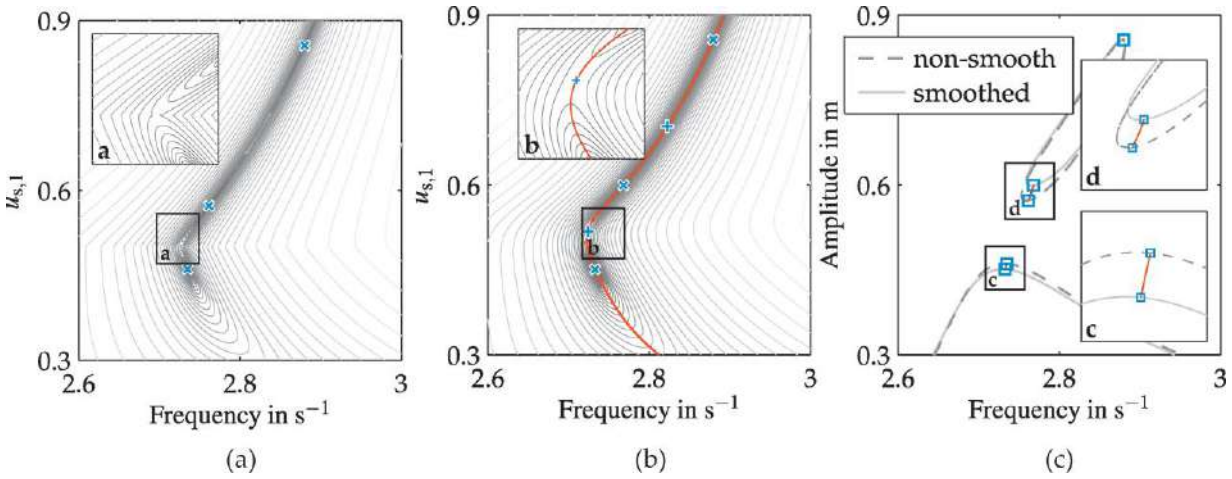

Figure 2. Deterministic detection of isola: (a) squared norm of non-smooth residual, (b) squared norm of smoothed residual and relevant subset of search paths of the global terrain method [1], (c) homotopy continuation between non-smooth and smoothed residual.

CONCLUSIONS

Within this study, the relevance of isolated solution branch detection was demonstrated. The proposed solution methodology enclosed a specific frequency domain nonlinearity smoothing within the harmonic balance method, a global solution method, and a homotopy continuation leading to the solutions of the non-smooth baseline system. A system with shape-memory alloy nonlinearity served as the test case for a successful application. The deterministic nature of the composing algorithms renders the overall detection methodology without the notion of uncertainty.

References

[1] Heinze T., Panning-von Scheidt L., Wallaschek J. Global detection of detached periodic solution branches of friction-damped mechanical systems. *Nonlinear Dyn*. (2019). **https://doi.org/10.1007/s11071-019-05425-4**.

[2] Habib G., Cirillo G.I., Kerschen G. Uncovering detached resonance curves in single-degree-of-freedom systems. *Procedia Engineering*. **199**: 649-656, 2017. **https://doi.org/10.1016/j.proeng.2017.09.116**.

[3] Groll G. von, Ewins D.J. The Harmonic Balance Method with Arc-Length Continuation in Rotor/Stator Contact Problems. *Journal of Sound and Vibration*. **241**: 223-233, 2001. **https://doi.org/10.1006/jsvi.2000.3298**.

[4] Lucia A., Feng Y. Global terrain methods. *Computers & Chemical Engineering*. **26**: 529-546, 2002. **https://doi.org/10.1016/S0098-1354(01)00777-3**.

REDUCED-ORDER MODELS FOR INCLINED ELASTIC CABLES WITH ARBITRARY SAG UNDER SUPPORT EXCITATION

Guilherme Jorge Vernizzi *[1,2], Stefano Lenci[2], and Guilherme Rosa Franzini[1]
[1] Offshore Mechanics Laboratory - LMO, Escola Politécnica, University of São Paulo, Brazil
[2] Università Politecnica delle Marche, Ancona, Italy

Summary This paper focuses on the study of the vibrations of inclined elastic hanging cables not limited to the small sag condition, under the action of boundary imposed motion. The problem is investigated using reduced-order models, which is not made in previous literature for this specific excitation in the case of arbitrary sag. The reduced model is obtained by a Galerkin procedure and allows the evaluation of the effect of different interpolation functions for the response and for how the top motion influence is distributed along the structure. The obtained results so far show good agreement with finite element simulations.

INTRODUCTION

The use of hanging cables as structural solution can be found in different engineering applications. They are present in stayed and suspended bridges, transmission lines, offshore oil exploration, mooring systems, among other uses. These elements are under dynamic solicitation from different sources and can exhibit a rich dynamical behaviour. This work focuses on one of the possible sources, namely the imposed motion on one of the boundaries.

A detailed study made with the method of multiple scales (MMS) for this kind of problem is described in [1]. A horizontal taut string is considered with its axial inertia neglected, under the action of transversal and longitudinal motions of one of the boundaries. Good agreement is shown between the obtained analytical solutions and experimental results. In [2], an inclined taut string under support excitation is investigated with a reduced-order model (ROM) based on modal decomposition. An analytical solution is presented for the steady-state amplitude of motion for some mode combinations.

In [3], the wind loading is also considered together with the support motion excitation on an inclined cable with small sag, nearing a taut string. The axial dynamics is condensed by neglecting axial inertia and the resulting equation is discretized via a Galerkin procedure. The model is used to investigate the instabilities the cable can undergo. Finally, in [4], a horizontal hanging cable is considered, also with the axial inertia neglected. A ROM is obtained with a Galerkin procedure using both in-plane and out-of-plane modes. An analytical solution is obtained with the MMS, followed by a series of investigations on the dynamic responses of the structure.

In the present work a ROM is obtained and discussed for a planar inclined hanging cable with arbitrary sag. In this case the axial inertia cannot be neglected, with the modes of vibration being coupled in the axial and transversal directions. ROMs for this type of configurations, considering support motions as the source of excitation, are not found in the literature to the best of the authors' knowledge. The investigations are intended to be carried in the same fashion of [5] in order to discuss gains, advantages and problems concerning projections functions used in the construction of ROMs.

MATHEMATICAL MODEL

An elastic hanging cable in still fluid is herein considered, with axial stiffness EA, immersed weight γ_s and axial and transversal masses per unit length m and m_t respectively. Added mass can then be easily included in the model with the different mass values for each direction. The horizontal and vertical distances between the hanging supports are d and h respectively. The tension $T_e\,(s)$ and the angle with the horizontal direction $\theta\,(s)$ in the static configuration are considered to be known, with s being the arclength coordinate. Taking now u and v as the axial and transversal displacements with respect to the static configuration, the equations of motion obtained from balance laws for a cable element (see [6] for example) are given as:

$$T_e'\left(\cos\gamma-1\right)-T_e\left(\theta'+\gamma'\right)\sin\gamma+T_d'\cos\gamma-T_d\left(\theta'+\gamma'\right)\sin\gamma=m\ddot{u} \tag{1}$$

$$T_e'\sin\gamma-T_e\theta'+T_e\left(\theta'+\gamma'\right)\cos\gamma+T_d'\sin\gamma+T_d\left(\theta'+\gamma'\right)\cos\gamma-\frac{1}{2}\rho D\overline{C_D}\dot{v}\left|\dot{v}\right|=m_t\ddot{v} \tag{2}$$

The hydrodynamic nonlinear damping is considered using Morison's model for the drag force in the transversal direction, while drag in the axial direction is disregarded since it usually is much smaller. The solution for the static equilibrium, which depends on γ_s, is already considered in the equations. T_d stands for the dynamic tension variation, γ is the dynamic variation of θ, ρ is the specific mass of the surrounding fluid, $\overline{C_D}$ is the mean drag coefficient and D is the external diameter of the structure. Primes denote differentiation with respect to s while dots represent differentiation with respect to time. The static strain is considered small, allowing the approximation $\varepsilon=\varepsilon_s+\varepsilon_d$, with the subscripts denoting the static and dynamic parts. The expression for the dynamic tension becomes $T_d=EA\varepsilon_d$. The compatibility relations are obtained by differential geometry as $\sin\gamma=\left(u\theta'+v'\right)/\left(1+\varepsilon_d\right)$, $\cos\gamma=\left(1+u'-v'\theta'\right)/\left(1+\varepsilon_d\right)$ and $\varepsilon_d=\sqrt{1+2\left(u'-v\theta'+uv'\theta'-u'v\theta'+\left(u'^2+v'^2+\left(u\theta'\right)^2+\left(v\theta'\right)^2\right)/2\right)}-1$. The obtained model can be applied

*Corresponding author. E-mail: guilherme.jorge.lopes@usp.br.

to vibrations in air by simply adjusting the parameters of the model. The ROM is obtained using a Galerkin procedure after expanding the equations up to third order terms, with the displacements written as:

$$\{u, v\} = \left\{ \eta(t)\,\phi_s(s) + \sum_{k=1}^{n} A_k(t)\,\phi_k(s)\,,\, \eta(t)\,\psi_s(s) + \sum_{k=1}^{n} B_k(t)\,\psi_k(s) \right\} \tag{3}$$

ϕ_k and ψ_k being the shape functions of the vibration modes of the cable in the axial and transversal directions respectively. In turn, ϕ_s and ψ_s are the functions used to describe a instantaneous distribution of the displacement of magnitude $\eta(t)$ along the cable. The expressions of the ROMs are not shown due to the size of this extended abstract.

COMPARISON WITH FINITE ELEMENT SOLUTION

A simple example is considered here with a comparison in the amplitude of response of transversal motion with a solution obtained by the finite element method (FEM). The data herein adopted are $EA = 2314$MN, $m = 108$kg/m, $m_t = 141.24$kg/m, $\gamma_s = 727$N/m and structural diameter $D = 0.2032$m. The distances between supports are given as $d = 1500$m and $h = 1800$m. The cable is subjected to a horizontal component of tension valued $T_h = 680550$N, and a total length of $L = 2452$m. For this abstract, the hydrodynamic damping is disregarded. For the ROMs, the inextensible static solution is used, giving a relative difference of only 1% in the natural frequency of the first mode with respect to the FEM solution. Two ROMs are used, ROM (i) uses the displacement field of a unitary static displacement at the top for the functions ϕ_s and ψ_s, while ROM (ii) uses a linear interpolation between supports. A comparison is made in the amplitude of response under a support motion in resonance with the first mode of vibration, with a structural damping ratio of 2% for the first mode. The comparison for the modal shape and the amplitude response curve are shown in Fig. 1. The amplitudes of motion are made dimensionless with D and the amplitude is taken on the point at $s = 1508$m, which is the peak of transversal motion of the first mode. It is possible to see that the modal shape function is in good agreement,

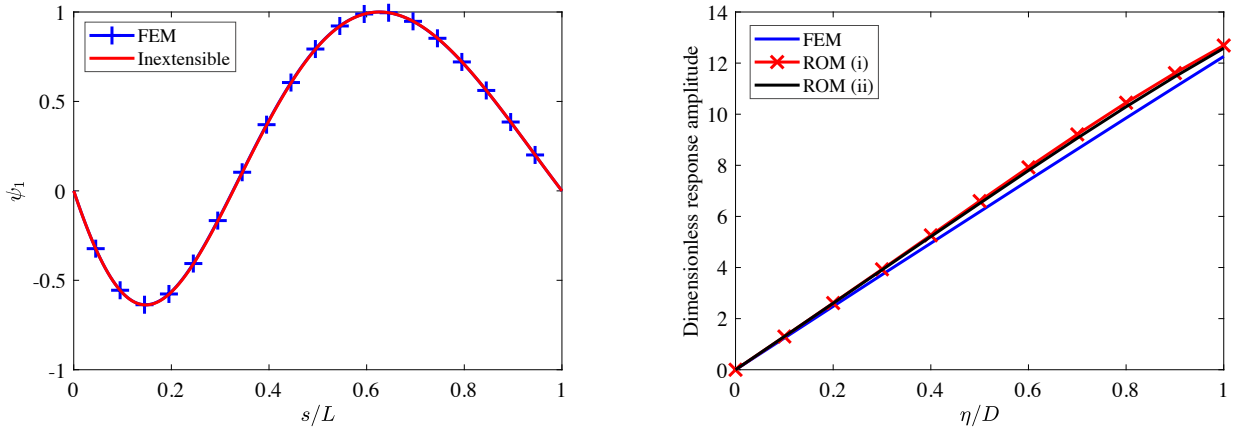

Figure 1: Left: Transversal shape function of the first mode for the FEM solution and the one using the inextensible static configuration. Right: Amplitude of response for the transversal displacement as a function of the excitation amplitude.

even with the use of the inextensible elastic configuration to calculate it. Also, it is possible to notice that, at least in the range shown, the use of a simple linear interpolation is able to give good quality results with respect to the FEM solution.

CONCLUSIONS

A reduced-order model (ROM) is developed using a Galerkin projection on the equations of motion of a hanging inclined cable. The projection contains a term for the contribution of the motion imposed to the boundary of the cable. The results show that the obtained model is in good agreement with finite element simulations. Further results and deeper investigations are intended for the conference, such as the use of more modes in the model, comparison of different ROMs for higher amplitudes of vibration and numerical tests with the effects of hydrodynamic damping.

Acknowledgements: The first author acknowledges the São Paulo Research Foundation (FAPESP) for research grants n. 2016/25457-1 and 2017/16578-2, the latter a financial support to his internship at Università Politecnica delle Marche.

References

[1] Nayfeh S.A., Nayfeh A.H., Mook D.T. Nonlinear response of a taut string to longitudinal and transverse end excitation. *J. Vib. Control* **1**: 307-334, 1995.
[2] Macdonald J.H.G. Multi-modal vibration amplitudes of taut inclined cables due to direct and/or parametric excitation. *J. Sound Vib.* **363**: 473-494, 2016.
[3] Luongo A., Zulli D. Dynamic instability of inclined cables under combined wind flow and support motion. *Nonlinear Dyn.* **67**: 71-87, 2012.
[4] Warminski J., Zulli D., Rega G., Latalski J. Revisited modelling and multimodal nonlinear oscillations of a sagged cable under support motion. *Meccanica* **51**: 2541-2575, 2016.
[5] Vernizzi G.J., Franzini G.R., Lenci S. Reduced-order models for the analysis of a vertical rod under parametric excitation. *Int. J. Mech. Sci.* **163**: 105122, 2019.
[6] O'Reilly O.M. Modeling nonlinear problems in the mechanics of strings and rods, the role of the balance laws. Springer International, 2017.

THREE-DIMENSIONAL ROCKING MOTION OF FREE-STANDING BLOCKS

Péter L. Várkonyi [1], Tamás Ther[1], and Tamás Baranyai[1]
[1] Department of Mechanics, Materials, and Structures, Budapest University of Technology and Economics, Budapest, Hungary

Summary Historical stone and masonry structures undergo rocking motion under earthquake excitation. Impacts during rocking motion absorb energy and may result in remarkable earthquake resilience. Simple models of rocking use deterministic impact models and assume two-dimensional motion. Nevertheless in reality, individual trajectories of rocking motion are unpredictable due to extreme sensitivity of impacts to geometric imperfections. In addition, imperfections may induce three-dimensional motion even is the excitation is planar. We develop a non-deterministic impact model, which is applicable to arbitrary 3-dimensional motion. Model parameters are fitted to statistical results of physical experiments. Our model can be integrated into a simulation engine in order to evaluate how three dimensional motion and imperfections affect the earthquake resistance of rocking blocks.

ROCKING BLOCKS

Rocking is a form of motion of (quasi-) rigid, heavy objects in unilateral contact with a support surface in the proximity of a state of stable rest. An important feature of 'rocking' is that episodes of roll motion are from time to time interrupted by impacts. Slip motion may be present in rocking but friction is often assumed to be large enough to prevent slip. Impacts are usually assumed to be inelastic, which eliminates the possibility of liftoff.

The simplest and widely studied example of rocking is the planar, small-amplitude motion of a cuboid-shaped slender block on a flat plane, which undergoes an impact whenever the resting position is reached. Housner [1] was the first to propose a model for these impacts. He assumed that the impact impulse is transmitted through the corner of the block, and slip motion does not occur. Using these assumptions, he defined the *velocity reduction factor* as the ratio of post- and pre-impact angular velocities $r = \omega^+/\omega^-$ and showed that r takes identical values in each impact of a given block. His model can be combined with Newton's laws to simulate the motion of the rocking block, and also to predict if the block will overturn in response to a given excitation. (Fig. 1).

HOUSNER'S MODEL AND REALITY

Experimental works revealed that Housner's model is an inaccurate description of real impacts. Most importantly, the value of r strongly varies from experiment to experiment, moreover the value predicted by Housner has a strong tendency to underestimate the empirically measured velocity reduction factors [2]. As a consequence, Housner's model often predicts overly optimistic results about the earthquake resistance of rocking blocks. Many works proposed improved

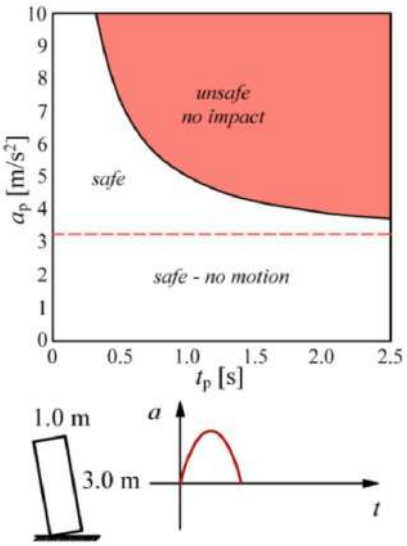

Figure 1: Overturning curve of a rocking block determined by numerical simulation using Housner's model. The horizontal acceleration of the ground is a half-sine pulse with peak acceleration a_p and duration t_p (bottom panel). If parameters fall into the shaded regions of the upper diagram, the block overturns, otherwise it stays upright.

*Corresponding author. E-mail: vpeter@mit.bme.hu.

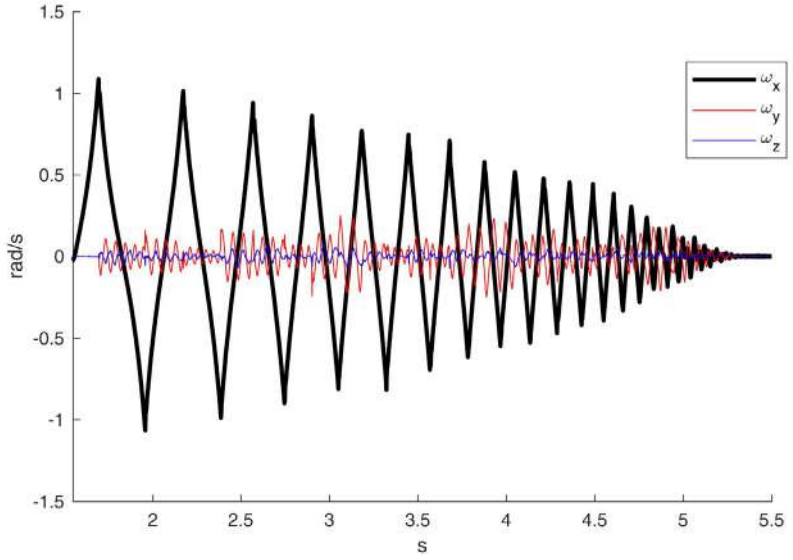

Figure 2: Angular velocitiy of a free-rocking stone block in a physical experiment (without excitation). The three curves show the components of the angular velocity in a coordinate frame with axes parallel to the edges to the block. Initially, the block rolls around an edge, and undergoes planar motion. Accordingly, $\omega_y = \omega_z = 0$. After the first impact, it undergoes three-dimensional motion, and all three components become non-zero

versions of the model that compensate for this tendency. Several authors have pointed out that the effect of geometric imperfections is responsible for the variability of r in experiments.

Sensitivity to imperfection is caused by the fact that in each impact, all points of the basal facet of the block reach the ground simultaneously. Contact forces can be transmitted to the block at any of these points during the (short) impact process and the net impulse resulting from these forces is not necessarily at the corner of the block. Indeed the whole process depends on small geometric imperfections of the base facet and of the underlying ground. In the limit of an ideally rigid block, an arbitrarily small imperfection may have finite effect.

THREE-DIMENSIONAL MOTION INDUCED BY IMPERFECTIONS

Imperfections may not only change the value of r, but they may also cause spontaneous symmetry breaking and the emergence of three-dimensional motion if the imperfections themselves are asymmetric. This is clearly visible in Fig. 2, which shows the angular velocity of a stone block measured in an experiment. Previous works did not study this effect and its consequences on earthquake resistence. Our aim is to fill this gap by developing an impact model and by integrating it into a numerical simulation engine.

DEVELOPMENT OF A NEW IMPACT MODEL

As first step we develop a parametrization of possible outcomes of the impacts as well as theoretical limits of the impact parameters dictated by physical laws (conservation of momentum, non-positive energy balance, etc.). Then, we measure probability distributions of the impact parameters two different ways including (i) physical experiments, and (ii) numerical simulations involving explicitly generated random imperfections. The parametrization and the measured distributions of impact parameters are combined into a non-deterministic impact model, which predicts post-impact angular velocities to be random values drawn from a certain probability distribution. We will later integrate the probabilistic impact model into a simulation engine, in order to perform systematic investigation of the behavior of blocks under earthquake excitation. Our ultimate goal is to produce (probabilistic) overturning curves (similar to Fig. 1), and to assess how the safety of blocks is affected by unpredictability and three-dimensional motion.

References

[1] Housner, G. W. (1963) The behavior of inverted pendulum structures during earthquakes. *Bulletin of the seismological society of America* **53**:403-417.

[2] Bachmann, J. A., Strand, M., Vassiliou, M. F., Broccardo, M., Stojadinović, B. (2018) Is rocking motion predictable? *Earthquake Engineering & Structural Dynamics* **47**:535-552.

NONPARAMETRIC IDENTIFICATION OF A MICRO PORTAL FRAME WITH 2:1 INTERNAL RESONANCE

Rodrigo T. Rocha[1], Feras Alfosail[1,2], Mohammad I. Younis*[1], and Sami F. Masri[3]
[1] King Abdullah University of Science and Technology - KAUST, Thuwal, Saudi Arabia
[2] Consulting Services Department, Saudi Aramco, Dhahran 31311, Saudi Arabia
[3] Department of Civil Engineering, University of Southern California, LA, California, USA

Summary This work presents a nonparametric identification method applied on a nonlinear micro portal frame. The frame has two dominant modes of vibration, vertical and horizontal directions. These are directly related to the symmetric mode (second mode) and the anti-symmetric mode (first, sway mode). Due to its geometric nonlinearities, the structure exhibits 2:1 internal resonance, causing the appearance of the saturation phenomenon when excited at the highest resonance frequency. This work aims to model the dynamics of the micro portal frame at the saturation phenomenon using a nonparametric identification method, which is shown to be very efficient in capturing the characteristics of complex nonlinear systems.

INTRODUCTION

Nonlinearities are important as they arise in many systems from geometric, material and external excitations effects. Based on these effects, the response of nonlinear systems increases in complexity and can involve multi-modal response. In particular, portal frames have been shown to have a geometric nonlinearity due to the shortening caused by bending of its flexible elements. In some cases, this may set the system to a 2:1 internal resonance between the symmetric and anti-symmetric modes, which has very rich and complex nonlinear dynamics. When the second primary resonance is excited in resonance of the symmetric mode, a saturation phenomenon occurs [1-3]. Therefore, there is a considerable advantage to model these kinds of systems so that nonlinear phenomena can be widely explored. However, the more complex is the dynamics, the more daunting is the challenge of developing an accurate mathematical model.

For this reason, identification techniques become increasingly important for formulating accurate models of complex nonlinear systems, generally classified into parametric and nonparametric. While parametric methods are used to obtain unknown parameters of a selected model class, the nonparametric methods can obtain a function from data measurements that can provide (partial) physical representations of a system [4-6], without prior knowledge of the system internal restoring forces or nonlinearities. This work aims to extend the application of the nonparametric identification technique demonstrated in [4] to identify the dynamic response of a micromachined nonlinear portal frame studied in [1,2] and through experiments.

MATHEMATICAL MODEL OF A PORTAL FRAME WITH 2:1 INTERNAL RESONANCE

The two-degrees-of-freedom 2-DOFs micro portal frame, shown in Fig. 1, is fabricated by the SOIMUMPs process of MEMSCAP [7]. It consists of a supported beam of length $L = 240\mu m$ attached to two columns with height $h = 133.1\mu m$ that are clamped in their bases. The beam and columns are considered as lumped masses, M and m, respectively. Their motions are described in two directions, vertical and horizontal. The coordinate u is related to the horizontal displacement of the mid-span of the beam, which is the anti-symmetric (sway) mode of vibration with natural frequency ω_1. The coordinate v is the vertical displacement of the mid-span of the beam, which is the symmetric mode with natural frequency ω_2. Geometric nonlinearity is introduced by considering the shortening due to bending of the columns and of the beam [1,2].

The microstructure is subjected to an electrostatic force through the electrode on top of the supported beam separated by a gap $d = 3.438\mu m$. The electrostatic force is considered as a harmonic cosine force $Q_{ext} = F\cos(\Omega t)$ in the mathematical model. The nodal displacements y and x are the vertical and horizontal motions for each lumped mass. Quadratic nonlinearities are included into the columns nodal displacements. Considering the generalized coordinates v and u as the motions of the mid-span of the supported beam, the dimensionless equations of motion of both horizontal and vertical motions are given, respectively, by

$$\begin{aligned} u'' + \omega_1^2 u + k_{31}u^3 + \mu_1 u' + \alpha_{11}uv + \alpha_{21}u^2u' + \alpha_{31}uu'^2 = 0 \\ v'' + \omega_2^2 v + k_{32}v^3 + \mu_2 v' + \alpha_{12}u^2 + \alpha_{22}v^2v' + \alpha_{32}vv'^2 + G = F\cos\Omega\tau \end{aligned} \quad (1)$$

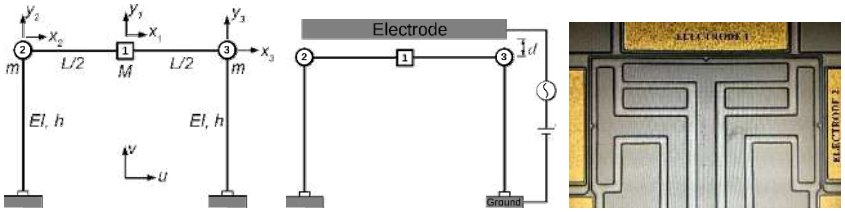

(a) (b) (c)

Figure 1. (a) Lumped physical model, (b) experimental scheme; and (c) picture of the fabricated micro portal frame.

This 2DOFs portal frame was studied in [1,2], in which the existence of 2:1 internal resonance was demonstrated, where the second natural frequency is twice the first one, i.e., $\omega_2 \approx 2\omega_1 + \sigma_1$, where σ_1 is a detuning factor. When the second mode is excited in resonance ($\Omega \approx \omega_2 + \sigma_2$), where σ_2 is a detuning factor, saturation phenomenon occurs [1-3].

*Corresponding author. E-mail: mohammad.younis@kaust.edu.sa.

Using the parameters of Table 1, Fig. 2a is generated showing the frequency-response of the system when saturation phenomenon is active. In the interval ($1.932 \leq \Omega \leq 2.064$), the second mode gets saturated, exchanging vibration energy and, consequently, exciting the first mode. In this situation, the first mode has a bigger amplitude of vibration than the vertical motion. For an experimental qualitative confirmation, the fabricated device is subjected to a $V_{dc} \approx 40$V and $V_{ac} = 0.5$V. Using a laser Doppler vibrometer and a vacuum chamber with pressure of 40mTorr to avoid squeeze-film damping [8], the data measured is plotted in Fig. 2b. It is noted that 2:1 internal resonance is triggered, where the vertical motion saturated, exchanging energy to the horizontal motion of the structure, proving the existence of saturation phenomenon as predicted by the mathematical model.

NONPARAMETRIC IDENTIFICATION METHOD AND APPLICATION

The nonparametric identification technique utilizes the state variables of a system to be identified, expressing its characteristics in terms of orthogonal functions [4]. The main purpose of the procedure is to find a restoring force using Chebyshev polynomials, making it possible to obtain physical characteristics of the dynamical system to be identified. However, in this case, the subject is related to a system of two-degrees-of-freedom with 2:1 internal resonance, in which the complexity increases due to cross and coupling terms. The restoring force of each coordinate can be defined as

$$\begin{aligned} f_1(u,u',v,v') &= -u'' \\ f_2(u,u',v,v') &= F\cos(\Omega\tau) - v'' \end{aligned} \tag{2}$$

It is important to mention that the restoring forces do not depend only on two variables; they depend on the variables related to their own variables and the coupling related ones. Due to the dependence on four variables, the Chebyshev function is selected to be in the form

$$f_a(u,u',v,v') = \sum_{i=0}^{n}\sum_{j=0}^{m}\sum_{k=0}^{o}\sum_{l=0}^{p} C_{ijkl}T_i(u)T_j(u')T_k(v)T_l(v'); \qquad a = 1,2 \tag{3}$$

Then, assuming the data points provided from Eq. (2) and using the experimental data without prior knowledge of the system restoring forces or nonlinearities, the least-squares fit between them and Eq. (3) yields the true restoring force. However, the convergence of the coefficients depends directly on the coefficients n, m, o and p. To have such convergence, the values must be, at least, $n = 3$, $m = 2$, $o = 3$ and $p = 2$, resulting in the values of line 2 of Table 1.

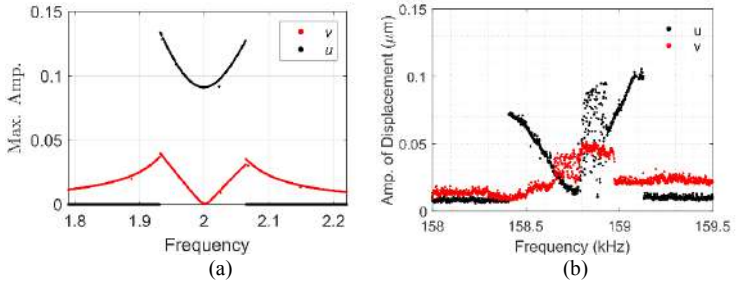

(a) (b)

Figure 2. Frequency responses of vertical and horizontal displacements of the mid-span of the beam; (a) analytical, (b) experimental.

Table 1. Comparison of the identified parameters with different number of data to the analytical (original) one.

Line	i	ω_i	k_{3i}	μ_i	α_{1i}	α_{2i}	α_{3i}	G	F
1 - Analytical	1	1	1.9151	0.00698	3.1918	0.0065	0.48	0	0
	2	3.9897	0.2705	0.02121	2.3938	0.0024	0.18	0.0049	0.010
2 – Full data identified	1	1	1.9151	0.00698	3.1918	0.0065	0.48	0	-
	2	3.9897	0.2705	0.02121	2.3938	0.0024	0.18	0.0049	-

CONCLUSIONS

This work presented the nonparametric identification of a 2DOFs micromachined nonlinear portal frame using data extraction from its mathematical model for the restoring force for data fitting. The method was efficient to identify both restoring forces with the nonlinear and coupling terms of the system without the need to assume a model class. For a future confirmation, we intend to utilize an error band of 5% for data fitting which increases the strength of the method.

References

[1] Rocha, R. T., Balthazar, J. M., Tusset, A. M., Piccirillo, V., Felix, J. L. Nonlinear piezoelectric vibration energy harvesting from a portal frame with two-to-one internal resonance. *Meccanica*, 52(11-12):2583-2602, 2017.
[2] Mazzilli, C. E., Brasil, R. M. Effect of static loading on the nonlinear vibrations of a three-time redundant portal frame: analytical and numerical studies. *Nonlinear Dynam.*, 8(3): 347-366, 1995.
[3] Nayfeh, A. H., Mook, D. T. Nonlinear oscillations. John Wiley & Sons, 2008.
[4] Masri, S. F., Caffrey, J. P., Caughey, T. K., Smyth, A. W., Chassiakos, A. G. A general data-based approach for developing reduced-order models of nonlinear MDOF systems. *Nonlinear Dynam.*, 39(1-2):95-112, 2005.
[5] Quaranta, G., Lacarbonara, W., Masri, S. F. A review on computational intelligence for identification of nonlinear dynamical systems. *Nonlinear Dynam.*, 1-53, 2020.
[6] Noël, J. P., Kerschen, G. Nonlinear system identification in structural dynamics: 10 more years of progress. *Mech. Syst. Signal Pr.* 83:2-35, 2017.
[7] MEMSCAP – SOIMUMPs, **http://www.memscap.com/products/mumps/soimumps**
[8] Younis M. I. MEMS linear and nonlinear statics and dynamics (Vol. 20). Springer Science and Business Media, 2011.

EXTREME SENSITIVITY FOR DELAY PARAMETER IN BIFURCATIONS OF CONTROLLED CONTINUA

Gabor Stepan*[1] and Li Zhang [2]
[1] Department of Applied Mechanics, Budapest University of Technology and Economics, Budapest, Hungary
[2] State Key Laboratory of Mechanics and Control of Mechanical Structures, Nanjing University of Aeronautics and Astronautics, Nanjing, China

Summary The control of continuum bodies is a difficult task especially when the damping is low and many high-frequency vibration modes are involved in the relevant dynamics of the system. This study presents a beam model that describes extreme sensitivity with respect to the time delays that appear in the feedback loop. It is shown that in undamped cases, the slightest variation of the time delay results in the abrupt loss of exponential asymptotic stability. In the presence of small damping, the loss of stability occurs via Hopf bifurcations. It is shown that the frequencies of the emerging self-excited vibrations are also extremely sensitive for the change of the delay parameter. The results draw the attention for the difficulties in the design of these systems and they also explain why spatial discretization techniques do not converge to the limit case of controlled continuum bodies.

MOTIVATION

The appearance of the so-called squeal in public address systems is an annoying and difficult-to-predict phenomenon. When it occurs, a wide range of frequencies can be experienced, and these are often varying, some frequencies die, some others get stronger. The variation of the locations of the microphones and loudspeakers has an essential effect on the occurrence of the phenomenon in the same way as the variation of the amplification and the time delay in the control loop [1].

In this study, the simplest mechanical model and the corresponding governing equations are given, which describe the sensitivity of the system dynamics with respect to the delay parameters, including the sensitivity of the vibration frequencies of the emerging self-excited vibrations.

MECHANICAL MODEL

The simplest possible mechanical model of the public address system is presented in Fig. 1. A prismatic elastic beam of length l is considered with modulus of elasticity E and uniform density ρ. The longitudinal displacement $u(x,t)$ of the beam cross section is given at the spatial location x at the time instant t. The feedback loop is characterized by the amplification K that can be considered as a proportional gain, the nonlinearity of the system is represented by the saturation of the control action. The time delay τ is an unavoidable part of any control loop, although the value of this parameter is often assumed to be negligible. In the present analysis, this delay τ and the gain K take the roles of the bifurcation parameters.

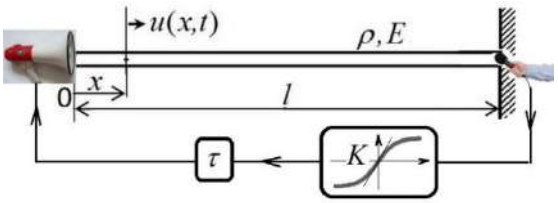

Figure 1. Simplified mechanical model of electroacoustic system

The governing equation of this system is the partial differential equation of the damped wave equation

$$\ddot{u}(x,t) - \eta c^2 \dot{u}''(x,t) - c^2 u''(x,t) = 0$$

where $c = \sqrt{E/\rho}$ is the speed of sound in the beam, and the parameter η characterizes the internal viscous damping in the beam. The corresponding two boundary conditions are of mixed typed and delayed:

$$u(l,t) = 0\,, \quad u'(0,t) = S \tanh\left(\frac{1}{S} K u'(l,t-\tau)\right)$$

where the saturation level of the actuation is set by the parameter S.

STABILITY AND BIFURCATIONS

In case of negligible damping $\eta = 0$, the stability analysis of the trivial solution can be carried out after the linearization of the second boundary condition: $u'(0,t) = K u'(l,t-\tau)$. The critical values of the time delay parameter are related to the time $T = l/c$ needed for the travelling wave to reach the end of the beam. By means of the general mathematical theorem of [2], one can prove that the system is exponentially unstable for any non-zero gain if the ratio τ/T is irrational.

Although from the continuous dependence of stability on parameters one might conclude that these systems are always unstable, this is not true in some infinite dimensional problems [3] like time delay systems. An analytical proof was given in [4] that there are thin exponentially stable parameter regions where the trivial solution is actually exponentially stable:

$$\tau/T = 4j-3, \quad 0 < K < \cos\left(\frac{2j-2}{4j-3}\pi\right) \quad \text{or} \quad \tau/T = 4j-1, \quad \cos\left(\frac{2j}{4j-1}\pi\right) < K < 0; \quad j = 1,2,\ldots.$$

These zero-measure stable regions become finite for positive damping $\eta > 0$. The stability boundaries are calculated with the help of computer algebra, and it is proved that there are Hopf bifurcations along the lobe structure of the stability boundaries. The corresponding stability chart is constructed in the plane of the delay and the gain parameters, but the fine fractal-like structure of the boundaries cannot be observed in Fig. 2 due to the limited resolution. It can be explored by zooming in numerically: the lobes intersect each other at several points resulting in double-Hopf bifurcations at the intersections.

FREQUENCIES OF SELF-EXCITED VIBRATIONS

The above described intricate stability properties are more apparent if the vibration frequencies of those self/excited vibrations are calculated, which appear at the Hopf bifurcations. These are presented in the panel below the stability chart of Fig. 2. Clearly, these frequencies are extremely sensitive even for the slight variation of the delay parameter. The frequencies belonging to certain lobes of the stability boundary jump from one mode to the other with varying delay, and at the double-Hopf points, quasi-periodic vibrations occur. Around the peaks/notches of the stability chart, three or even more vibration frequencies might be involved in the corresponding nonlinear vibrations.

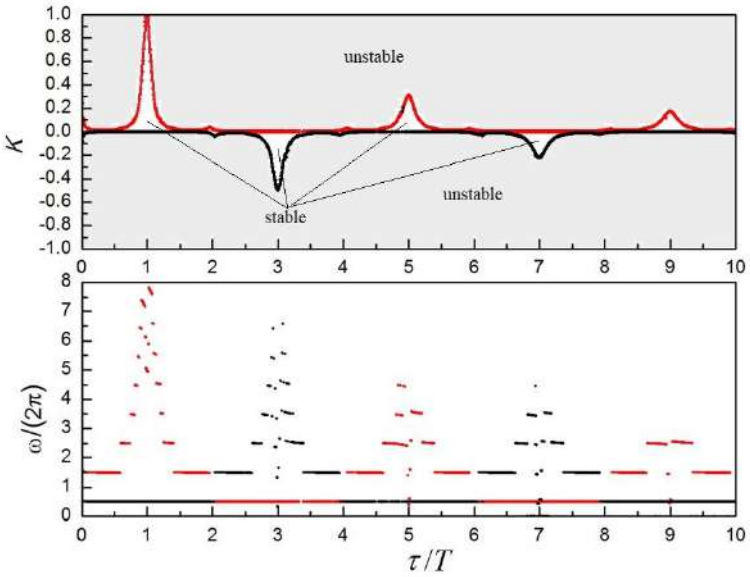

Figure 3. Vibration frequencies at the Hopf-type stability boundaries for damping parameter $\eta/T = 0.001$.

CONCLUSION

The mechanical model and its analysis draw the attention for the difficulties in the control design of systems involving continuum bodies. The results also explain why finite element techniques do not converge to the limit case of controlled continuum bodies. Similar phenomena are also observed in infinite dimensional problems [5]. The presence of time delay in continuum mechanical models result in infinite dimensional phase spaces with duplicate complexities.

Acknowledgement
This research was supported by the Hungarian-Chinese Bilateral Scientific and Technological Cooperation Fund under Grant no. 2018-2.1.14-TÉT-CN-2018-00008.

References

[1] Kuo S.M., Morgan D.R., Active noise control: a tutorial review, *Proceedings of the IEEE* **87** (1999) 943–973.
[2] Hale J.K., Lunel A.M.V., Strong stabilization of neutral functional differential equations, *IMA Journal of Mathematical Control and Information* **19** (2002) 5–23.
[3] Ito K., Turi J., Numerical methods for a class of singular integro-differential equations based on semigroup approximation, *SIAM Journal on Numerical Analysis* **28** (1991) 1698–1722.
[4] Zhang L., Stepan G., Exact stability chart of an elastic beam subjected to delayed feedback, *Journal of Sound and Vibration* **367** (2016) 219–232.
[5] Holmes P., Domokos G., Schmitt J., Szeberenyi I., Constrained Euler buckling: an interplay of computation and analysis, Computational Methods **170** (1999) 175-207.

STABILITY OF THE DRIVER-VEHICLE SYSTEM WITH THROTTLE CONTROL

Alois Steindl *[1], Johannes Edelmann[1], and Manfred Plöchl[1]
[1] Institute for Mechanics and Mechatronics, TU Wien, Vienna, Austria

Summary We investigate the stability of a controlled understeering vehicle along a steady-state cornering motion. To control the trajectory of the vehicle, the human driver is assumed to apply a constant front steering angle and a varying driving torque, which depends on the deviation of a point straight forward of the car at a fixed distance L_P from a reference circle. By varying the parameters of this feedback control we study the range of stable driving conditions and the system's dynamics after loss of stability.

VEHICLE MODEL

The basic two-wheel vehicle model with rear-wheel drive has been chosen to model the motion and stability properties of an automobile, Fig. 1. The state of the system is represented by the velocity of the vehicle v, the yaw rate $\dot{\psi}$, the vehicle side slip angle β, and the angular velocity of the driven rear wheel ω_R. The human driver (or a respective control system) applies a front steering angle δ_F and a drive torque M_R as input to the vehicle. The car's center of gravity lies on a height h above ground level. Thus, the equations of motion of the system read ([1])

$$m\dot{v}\cos\beta - m(\dot{\psi}+\dot{\beta})v\sin\beta = F_{xR} - F_{yF}\sin\delta_F, \qquad m\dot{v}\sin\beta + m(\dot{\psi}+\dot{\beta})v\cos\beta = F_{yR} + F_{yF}\cos\delta_F, \tag{1a}$$

$$I_\psi\ddot{\psi} = l_F F_{yF}\cos\delta_F - l_R F_{yR}, \qquad I_\omega\dot{\omega}_R = M_R - r_R F_{xR}, \tag{1b}$$

$$l_R F_{zR} - l_F F_{zF} = h(F_{xR} - F_{yF}\sin\delta_F), \tag{1c}$$

where $F_{zF} + F_{zR} = mg$. The tyre brush model [2] is applied to model the tyre characteristics, see Fig. 2, where the

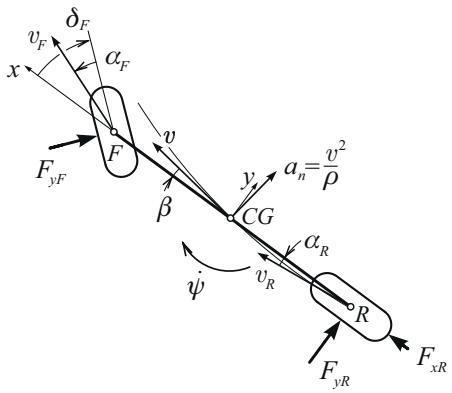

Figure 1: Two-wheel vehicle model.

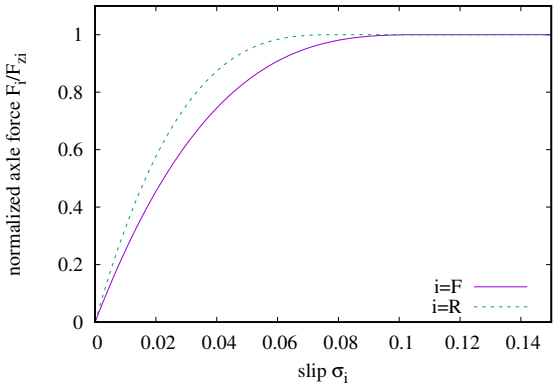

Figure 2: Normalized slip characteristics of front and rear simplified tyre/axle model at nominal loads.

mutual influence of the lateral and longitudinal force is considered.

Driver model

Our model for the driver assumes that during cornering the driver spots a point P straight ahead of the car at a distance L_P from the center of gravity, see Fig. 3. If the car drives along a circle with radius r_0 and center at the origin, the point P moves along a circle with radius r_{P0}. If the car leaves the circular path, the point P deviates from the circle and the driver adjusts the driving moment M_r accordingly. We apply the "simplified precision model" [3]

$$T_M\Delta\dot{M}_r(t) + \Delta M_r(t) = c_P\Delta r_P(t-\tau) + c_D\Delta\dot{r}_P(t-\tau), \tag{2}$$

with human reaction time τ and delay time T_M. For the preliminary results we use $\tau = T_M = 0$.

With $r_P = \sqrt{r^2 + 2L_P r\sin(\vartheta-\psi) + L_P^2}$ and $r_{P0} = \sqrt{r_0^2 + 2L_P r_0\sin\beta_0 + L_P^2}$, where r_0 and β_0 are the stationary values of (1), we obtain the first order approximation for the deviation

$$\Delta r_P \approx \frac{r_0 + L_P\sin\beta_0}{r_{P0}}\Delta r + \frac{L_P r_0\cos\beta_0}{r_{P0}}\Delta(\vartheta-\psi).$$

The position variables r and $\chi = \vartheta - \psi$ satisfy the differential equations

$$\dot{r} = v\sin(\chi-\beta), \qquad \dot{\chi} = \frac{v\cos(\chi-\beta)}{r} - \dot{\psi}. \tag{3}$$

*Corresponding author. E-mail: Alois.Steindl@tuwien.ac.at

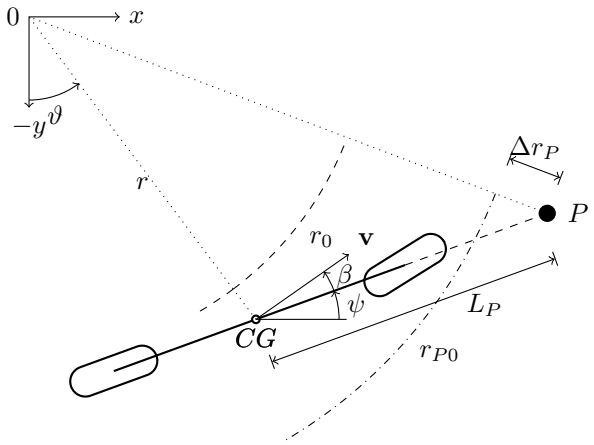

Figure 3: Geometric relations for the driver's preview model

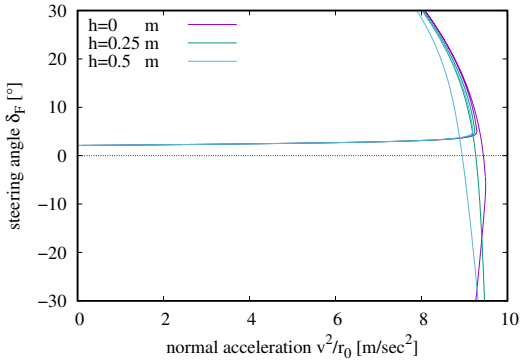

Figure 4: Handling diagram of the steady state vehicle model using $r_0 = 80\,\mathrm{m}$.

PRELIMINARY RESULTS

The handling diagram for the considered vehicle model is displayed in Fig. 4, which is computed for different heights h of the center of gravity and with constant curvature $r_0 = 80\,\mathrm{m}$. For normal accelerations $a_n = v^2/r_0 < 9\,\mathrm{m/sec^2}$ and small steering angles δ_F understeering behaviour ($\partial\delta_F/\partial a_n > 0$) is observed, In addition overdraw steering solutions and powerslide behaviour are visible. As expected, the regular steady state branch of the vehicle with fixed control parameters δ_F and M_r is throughout stable with one very small eigenvalue indicating singular perturbation behaviour.

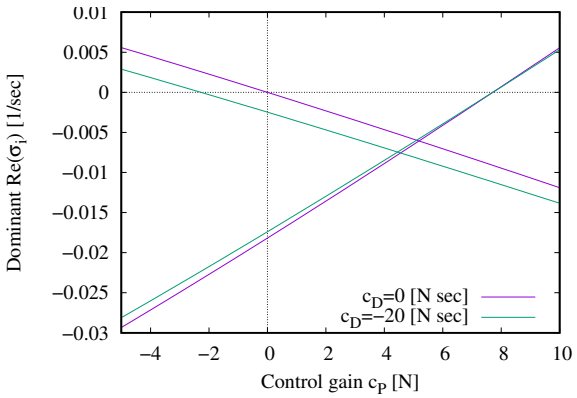

Figure 5: Evolution of the dominant eigenvalues for the linearized system (1–3) with $\tau = 0$, $T_M = 0$, $L_P = 20\mathrm{m}$, $h = 25\mathrm{cm}$, $r_0 = 80\mathrm{m}$ and $v_0 = 20\mathrm{m/s}$. For increasing control gains c_P the eigenvalues for the car position become stable, but the dominant eigenvalue becomes positive, leading to a strongly diverging system behaviour.

For the investigation of the driver's influence we choose the parameters corresponding to the steady state for $v_0 = 20\,\mathrm{m/sec}$. The variation of the real parts of the dominant eigenvalues can be seen in Fig. 5: For $(c_P, c_D) = (0, 0)$ a purely imaginary pair of eigenvalues occurs, because the car travels along a shifted circle, if it's initial position is perturbed. Increasing the gain c_P the purely imaginary eigenvalues become stable, but the weakly stable eigenvalue becomes unstable for sufficiently large values of c_P. For $c_D = -20\mathrm{N\,sec}$ the eigenvalues become a little bit more stable.

CONCLUSIONS

Adding to [4], our preliminary results indicate that carefully applied throttle control is able to stabilize the cornering motion of a vehicle and to track a desired curve. In the full paper a thorough analysis of the impact of several parameters of the simplified precision model will be given and a nonlinear stability analysis will be presented.

References

[1] Steindl, A., Edelmann, J., Plöchl, M.: Limit cycles at oversteer vehicle. Nonlinear Dynamics (2019). https://doi.org/10.1007/s11071-019-05081-8
[2] Pacejka, H.B.: Tire and vehicle dynamics. Butterworth-Heinemann, Oxford (2012)
[3] McRuer, D.T.; Graham, B.; Krendel, E.S.; Reisner, W.: Human Pilot Dynamics in Compensatory Systems, AFFDL-TR-65-15, 1965.
[4] Della Rossa, F.; Mastinu, G.: Straight ahead running of a nonlinear car and driver model – new nonlinear behaviours highlighted, Vehicle System Dynamics, 56:5, 753-768, 2018. DOI: 10.1080/00423114.2017.1422526

CHAOTIC SYNCHRONY OF PARAMETRIC PENDULUMS

Marek Balcerzak and Andrzej Stefanski
Division of Dynamics, Technical University of Lodz, Lodz, Poland

Summary We study the problem of complete synchronization of a pendulums' array attached to a common, externally forced structure. The presented analysis is focused on chaotic synchronization of the swinging, parametric pendulums. We propose a simplified criterion of synchronization for an arbitrary number of parametrically driven oscillators, which is based on the idea of a so-called *autonomous driver decomposition* and conditional Lyapunov exponents.

A pendulum is a classic example of a dynamical system, often used in mathematical and physical considerations. By means of pendulums one can model many engineering, technological systems and even dynamical processes from other branches of science. The antiphase correlation of oscillating two pendulum clocks was the first known case in history when the phenomenon of synchronization was observed and reported by Christian Huygens [1]. Over the three centuries after this fundamental report, plenty of studies on synchronized pendulums (also clocks, rotators etc.) have been published ([1–8] and references within). However, a vast majority of them concern systems of pendulums oscillating or rotating periodically. Recently, we have shown that introduction of an additional, intermediate structure between an external drive and a pair of pendulums causes their mutual coupling, which can lead to synchronization in a chaotic regime [9]. Here, this phenomenon is generalized for any number of pendulums. The novelty of the presented methodology consists in developing the *autonomous driver decomposition* [5] concept into a simple criterion of synchronization of any number of pendulums with a common parametric excitation. In general, the idea of this solution is based on separating a part of a dynamical system, which is treated as a master subsystem, and then duplicating the separated fragment. The duplicated part acts as a slave subsystem. Synchronous state between the master and the slave is stable if so-called conditional Lyapunov exponents, i.e. these connected with evolution of the slave subsystem, are negative.
In this Letter generalizes this phenomenon for any number of parametrically driven pendulums attached to the common structure and gives a criterion for its stability.

In this paper, a mechanical system of N+1 degrees of freedom, illustrated in Fig. 1, is analyzed. This structure is composed of a rigid beam of mass M_B and an array of N damped mathematical pendulums attached to it. The beam is harmonically driven (with an amplitude A and a frequency Ω) via a spring with stiffness K and externally damped (damping coefficient C). The pendulums have identical length l and it is assumed that for each of them the ratio between the damping coefficient c_i and its mass m_i (c_i/m_i ratio, i=1, 2, ..., N) is the same. As a result, taking $M = M_B + \sum_i^N m_i$ and $\omega = \sqrt{K/M}$ as the total mass and the reference frequency respectively, the following set of dimensionless equations describe the system:

$$\ddot{x} + \xi_y \dot{x} + x = q \sin \eta\tau - \sum_i^N \mu_i \left(\ddot{\phi}_i \sin\phi_i + \dot{\phi}_i^2 \cos\phi_i \right), \tag{1a}$$

$$\ddot{\phi}_i + (\ddot{x} + \gamma)\sin\phi_i + \xi\dot{\phi}_i = 0 \ , \tag{1b}$$

where x and ϕ_i are the dimensionless counterparts of the coordinates y, φ_i respectively (see Fig. 1), $\tau = \omega t$ is dimensionless time and $\mu_i = m_i/M$, $\xi_y = C/M\omega$, $\xi = c_i/m_i\omega l^2$, $q = A/l$, $\gamma = Mg/Kl$, $\eta = \Omega/\omega$ are dimensionless parameters. Consequently, in this representation, all the pendulums [Eq.(1b)] are identical even if they differ in masses or damping coefficients, as long as the ratio c_i/m_i is the same for each of them.

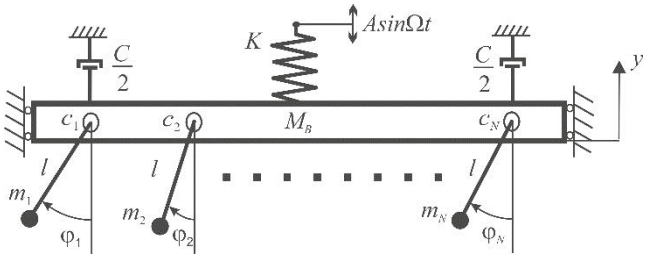

Figure 1.The analyzed system

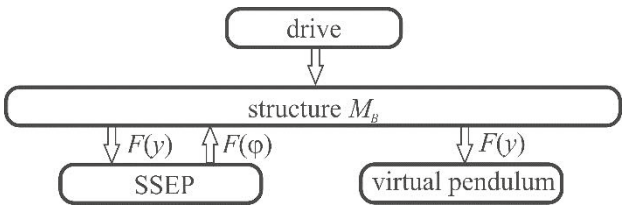

Figure 2.The scheme depicting the *autonomous driver decomposition* technique

The subject of our research is the phenomenon of complete synchronization (CS) of identical pendulums [Eq.(1b)]. In the synchronous regime ($\phi_i = \phi_j = \phi$), the array of pendulums (see Fig. 1) is reduced to a single, equivalent pendulum of the total mass $m = \sum_i^N m_i$ ($\mu = \sum_i^N \mu_i$) and the damping coefficient $c = \sum_i^N c_i$. Let it be called a *synchronous state equivalent pendulum* (SSEP). To rate the robustness of the synchrony, the *autonomous driver decomposition* technique [5] can be applied. The master subsystem is composed of the SSEP and the beam coupled mutually. On the other hand, "virtual pendulum" works as the slave subsystem. This pendulum plays the role of a synchronizability detector only and

does not affect the beam (see Fig. 2). Both pendulums are identical due to the same ratio $c/m = c_i/m_i$. If the CS between the SSEP and the virtual pendulum takes place, then the synchronous state of the pendulums' array reduced to the SSEP is stable. The condition for such stability is a negative value of the conditional Lyapunov exponents (CLE).

In Figs. 3(a)–3(c) bifurcation graphs generated for larger number of pendulums in the array (N=5, 10, 100), are presented. These pictures prove that synchronous state approach can be generalized for any number of parametrically driven pendulums. Independently of N, the synchronized chaotic swinging occurs in the same interval of the driving frequency ($0.941<\eta<0.966$), where the largest LE of the system is positive ($\lambda_1 > 0$) and the second LE, being the largest CLE, fulfills the condition $\lambda_2 = \lambda_C \le 0$. Increase of η over the threshold of negative λ_C (η >0.966) leads to synchrony loss, which is accompanied by the chaos–hyperchaos transition.

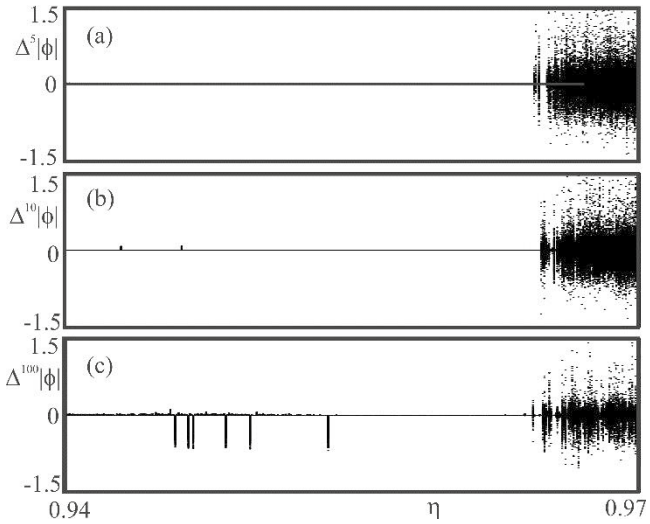

Figure 3. Bifurcation diagrams of the synchronization error $\Delta^N|\phi|$ versus driving frequency η: (a) N=5 – μ_i=0.1250, (b) N=10 – μ_i=0.0625, (c) N=100 – μ_i=0.00625.

In summary, the phenomenon of chaotic synchronization of dynamical systems under a common, parametric excitation has been demonstrated and its mechanism has been discussed. In this Letter, this phenomenon effect has been studied on the example of an array of pendulums attached to a driven structure. However, the same effect can occur, and the method of its detection can be applied, in other dynamical systems with an external (not only parametric) drive transmitted via a system component which is common for all receivers . In order to apply the presented method, an equivalent synchronous oscillator and its virtual replica, analogous to the SSEP and the virtual pendulum, respectively, should be modelled and used for detection of synchronization. Our research may shed a new light on the problem of controlling the dynamic behavior of parametric or externally driven oscillators. Introduction of an intermediate degree of freedom allows one to control the response of receivers even in the chaotic regime.

This Letter has been supported by the Polish National Centre of Science (NCN) under project No. 2017/27/B/ST8/01619.

References

[1] C. Huygens, *The Pendulum Clock*, Iowa State University Press, Ames, 1986.
[2] A Pikovsky, M. Rosenblum, J. Kurths, *Synchronization: A Universal Concept in Nonlinear Sciences*, Cambrige University Press, Cambrige, 2001.
[3] H. Fujisaka, T. Yamada, Stability theory of synchronized motion in coupled oscillator systems, *Progress of Theoretical Physics,* **69**: 32-47, 1983.
[4] T. Kapitaniak, Synchronization of chaos using continuous control, *Physical Review E* **50**: 1642-1644, 1994.
[5] L.M. Pecora, T.L. Carroll, Synchronization in chaotic systems, *Physical Review Letters,* **64**: 821-824, 1990.
[6] S. Boccaletti, J. Kurths, G. Osipov, D. L. Valladares, C. S. Zhou, The synchronization of chaotic systems, *Physics Reports,* **366**: 1-101, 2002.
[7] N. F. Rulkov, M. Sushchik, L. S. Tsimring , Generalized synchronization of chaos in directionally coupled chaotic systems, *Physical Review E,* **51**: 980-984,1995.
[8] M. Rosenblum, A. S. Pikovsky, J. Kurths, Phase synchronization of chaotic oscillators, *Physical Review Letters* **76**: 1804-1807, 1996.
[9] Karmazyn, M. Balcerzak, P. Perlikowski, A. Stefanski, Chaotic synchronization in a pair of pendulums attached to driven structure *Int. J. Non-linear Mech.* **104**: 261-270, 2018.

DESIGN OF A BASE-ISOLATED SINGLE-DEGREE-OF-FREEDOM SYSTEM WITH SYMMETRIC DEFORMABLE AND DISSIPATIVE CONSTRAINTS: A NUMERICAL STUDY

Giulia Stefani *[1], Maurizio De Angelis[1], and Ugo Andreaus[1]
[1] Department of Structural and Geotechnical Engineering, Sapienza University of Rome, Rome, Italy

Summary During strong earthquakes, base-isolated structures are expected to undergo large displacements, due to the increase in flexibility introduced by the isolation system. Such displacements can be accommodated by ensuring an adequate seismic gap around the structures. The limitation of these displacements, through the positioning of obstacles, allows to prevent the possible damage of the isolators, to the price of an increase in acceleration. In absence of an adequate gap, the effects of the impact with adjacent structures, as acceleration spikes, can be mitigated reducing the impact stiffness, to the price of an increase in displacement. These two conflicting problems were numerically investigated in this paper considering a single-degree-of-freedom system. Suitable combinations of selected parameters, which allow to reach a compromise between conflicting objectives, were identified.

INTRODUCTION

Base-isolated structures, when subjected to severe earthquakes, are expected to experience large displacements relative to the ground, due to the increase in flexibility introduced by the isolation system itself. Such displacements, that can be accommodated by ensuring an adequate seismic gap around the structures, can damage or reduce the efficiency of the isolation system [1]. In absence of a sufficient gap, the large displacements can lead to pounding with adjacent moat walls or structures [2]. These impacts can damage the structure and produce acceleration spikes which can be detrimental for sensitive equipment housed in the structures [3]. Based on these considerations, two conflicting control problems arise [4]. The first one concerns the control of excessive displacements. This can be done by inserting obstacles which limit the motion of the structure, to the price of an increase in acceleration. The second problem concerns the control of excessive accelerations that arise as a consequence of the impact between the structure and a rigid obstacle. This can be done by reducing the contact stiffness [5], and consequently, accepting an increase in the relative displacement. Considering a numerical model of a base-isolated single-degree-of-freedom (SDOF) system, symmetrically constrained by two obstacles (bumpers) and subject to a harmonic base excitation, the aim of this paper is to investigate the influence of selected dimensionless parameters, namely stiffness ratio between bumper and damper and dimensionless gap between mass and bumpers, on the dynamic response of the system and to identify suitable combinations of these parameters in order to reach a compromise between displacements and accelerations control.

NUMERICAL MODEL AND RESULTS

The system consists of a base-isolated mass, symmetrically constrained by two bumpers, excited by a harmonic base acceleration (forward and backward sine sweep signal). Both the isolation damper and the bumpers are modeled by an elastic element and a linear viscous damper arranged in parallel. The system is described in terms of dimensionless

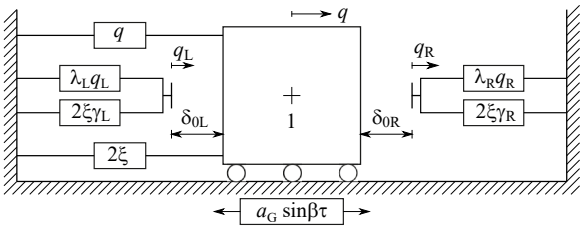

Figure 1: Numerical model of the SDOF system.

parameters, as shown in Figure 1, where q, q_j (j = R,L) are the dimensionless relative displacements, of the mass and of the Right and Left bumper respectively; β is the ratio between the circular frequency of the base excitation and the circular frequency of the isolated system; $a_G = 2\xi\sqrt{1-\xi^2}$ is the amplitude of the base acceleration; λ_j (j = R, L) is the ratio between the stiffness of the j-th bumper and that of the damper; γ_j (j = R, L) is the ratio between the damping coefficient of the j-th bumper and that of the damper; δ_{0j} (j = R, L) is the initial dimensionless gap, that is the initial distance between the mass and the j-th bumper. A value $\delta_{0j} = 0$ indicates that the bumpers are initially attached to the mass, a value $\delta_{0j} = 1$ indicates that the mass can only graze the bumpers without deforming them; if δ_{0j} takes values between 0 and 1, this indicates that the mass can beats and deforms the bumpers; the mass will be in the free flight condition for $\delta_{0j} > 1$.

*Corresponding author. E-mail: giulia.stefani@uniroma1.it.

The two control problems were studied assuming $\xi = 0.1$ and $\gamma_R = \gamma_L = \gamma = 5$ and investigating the influence of the stiffness ratio $\lambda_R = \lambda_L = \lambda$ and of the dimensionless gap δ_0 on the system response, represented in terms of maximum excursion of absolute acceleration η_a and relative displacement η_d of the mass in the forward sweep. This excursion was calculated as the difference between the maximum (positive) and the minimum (negative) values, evaluated at steady state resonance condition. Two different normalizations were adopted for the two problem. For the first problem (control of displacements) the normalization was made with respect to the free flight condition (η_{a0}, η_{d0}). For the second problem (control of accelerations) the normalization was made with respect to the case of rigid obstacle (η_{aR}, η_{dR}), conventionally assumed to occur for $\lambda = 100$. With reference to the first problem, from Figure 2(a), it can be observed that, compared to the free flight condition ($\eta_{a0} = \eta_{d0} = 1$), η_{d0} (blue lines) is always lower, while η_{a0} (red lines) is almost always greater, except for small values of both λ and δ_0. η_{a0} increases with increasing λ, while η_{d0} slightly decreases and remains almost constant for large values of λ. Furthermore, increasing δ_0 (increasing thickness of the lines), η_{a0} decreases while η_{d0} increases. The combination of small values of both λ and δ_0 appears to be a good choice which allows to realize a good compromise between reduction of displacement (primary objective) and limited increase in accelerations. With reference

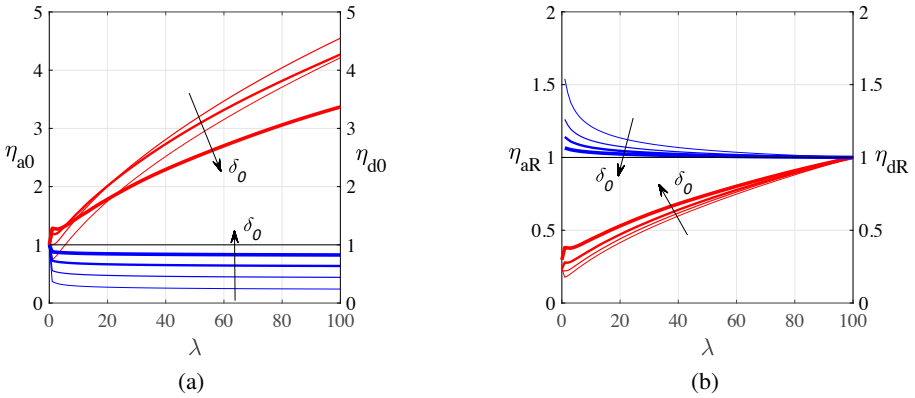

Figure 2: Maximum excursion of absolute acceleration (red lines) and relative displacement (blue lines) vs λ ($\xi = 0.1$, $\gamma = 5$): a) Problem 1; b) Problem 2.

to the second problem, from Figure 2(b), it can be observed that, compared to the rigid impact condition ($\eta_{aR} = \eta_{dR} = 1$), η_{aR} (red lines) is always lower, while η_{dR} (blue lines) is always greater. η_{aR} decreases with decreasing λ, while η_{dR} increases. Furthermore, increasing δ_0 (increasing thickness of the lines), η_{aR} slightly increases while η_{dR} decreases. The combination of small values of δ_0 and intermediate values of λ appears to be a good choice which allows to realize a good compromise between reduction of acceleration (primary objective) and limited increase in displacements.

CONCLUSIONS

In this paper a numerical study of the influence of selected dimensionless parameters on the dynamic response of a base-isolated SDOF system with symmetric deformable and dissipative constraints was performed. The response was represented in terms of maximum excursion of absolute acceleration and relative displacement of the mass. Two control problems, namely control of excessive displacements (Problem 1) and excessive accelerations (Problem 2) were considered, adopting two different normalizations. With reference to the Problem 1, it was observed that, compared to the free flight condition, the introduction of an obstacle allows to limit the displacement, with an increase in acceleration. However, by adopting small values of both dimensionless gap and stiffness ratio, it is possible to reach a good compromise between displacement reduction and not excessive acceleration increase. With reference to the Problem 2, it was observed that, compared to the case of impact with a very rigid obstacle (Problem 2), the interposition of a deformable obstacle allows to reduce the acceleration, to the price of an increase in displacement. However, by combining small values of dimensionless gap and intermediate values of stiffness ratio, it is possible to reach a good compromise between acceleration reduction and not excessive displacement increase.

References

[1] Ismail M., Rodellar J., Pozo F. Passive and hybrid mitigation of potential near-fault inner pounding of a self-braking seismic isolator. *Soil Dyn. Earthq. Eng.* **69**: 233-250, 2015.

[2] Masroor A., Mosqueda G. Experimental simulation of base-isolated buildings pounding against moat wall and effects on superstructure response. *Earthq. Eng. Struct. Dyn.* **41**: 2093-2109, 2012. https://doi.org/10.1002/eqe.2177.

[3] Reggio A., De Angelis M. Optimal design of an equipment isolation system with non-linear hysteretic behavior. *Earthq. Eng. Struct. Dyn.* **42**: 1907-1930, 2013.

[4] Andreaus U., De Angelis M. Influence of the characteristics of isolation and mitigation devices on the response of SDOF vibro-impact systems with two-sided bumpers and gaps via shaking table tests. *Struct. Control Health Monit.* 2020, in press.

[5] Andreaus U., De Angelis M. Nonlinear dynamic response of a base-excited SDOF oscillator with double-side unilateral constraints. *Nonlinear Dyn.* **84**: 14471467, 2016. https://doi.org/10.1007/s11071-015-2581-4.

MULTILEVEL DESIGN TOOLS FOR PARTICLE DAMPERS IN LIGHTWEIGHT MACHINES AND STRUCTURES

Robert Seifried * and Niklas Meyer
Institute of Mechanics and Ocean Engineering, Hamburg University of Technology, Hamburg, Germany

Summary Particle dampers are simple to manufacture damping devices. However, due to the complex nonlinear phenomena within the dampers, such as friction and impact, their efficient design and application is very challenging and nowadays mostly based on heuristic approaches. In this paper, a multilevel tool chain is presented to support a systematic investigation and design of particle dampers. Thereby various numerical models and experiments are used and coupled. The good agreement of the models and their efficiency for damper design are demonstrated on two application examples.

INTRODUCTION

In order to save resources, lightweight designs are becoming increasingly important these days. However, a smaller weight typically causes a decrease in stiffness and non-negligible vibration amplitudes. In recent years, the main focus of lightweight design techniques has been on increasing the stiffness of structures by design elements using shape or topology optimization. Damping is mostly not directly considered in these design strategies.
One type of promising damping devices to integrate in the lightweight designs are particle dampers. They are cheap and simply designed passive damping elements and can be seen as a derivative of single-mass impact dampers. Granular particles are embedded in a container attached to a vibrating structure. Due to structural vibrations, momentum is transferred to the granular material which interacts with each other. The mechanisms of energy dissipation are highly complex and involve impact and frictional phenomena. Due to these complex energy dissipation processes within the particle dampers, the dampers' efficiency depends on many design parameters such as material pairing, particle size, damper volume, and filling degree. Also, the working conditions, such as amplitude and frequency, have to be considered when designing appropriate dampers. While there have been already some very promising applications of particle dampers [1], the design process of such particle dampers is so far mostly heuristic and based on experimental trail-and-error strategies.
In this paper a systematic multilevel design methodology is presented, which is based on computational models as well as models derived from experiments. These models are not only useful for supporting the damper design and damper integration on the structure but also provide very useful insights into the processes, nonlinear effects and design parameters influencing the efficiency of the dampers.

MULTILEVEL MODELS FOR PARTICLE DAMPER DESIGN

For a meaningful understanding, and thus also for the design, of particle dampers investigations on different scales or levels are necessary using experiments and simulations, see Fig.1.
The first level is the single particle-particle and particle-wall interaction. Hereby, the energy dissipation in single impacts is of most interest. The energy dissipation is due to elasto-plastic or visco-plastic material behavior during impact. This energy loss is often described by the coefficient of restitution. Numerically these single impacts can be investigated in detail using finite element models of two impacting bodies [2]. Corresponding experimental investigations are performed for the impact of a sphere which is suspended by thin wires against a wall. Thus, the sphere can impact in a defined manner. The velocity of the impacting body is then measured by laser scanning vibrometer (LSV) PSV-500 from Polytec. By both methods the coefficient of restitution can be easily extracted for different impacting velocities.
The second level represents the investigation of an isolated particle damper and the determination of the energy dissipation for a given excitation frequency and amplitude. Hereby, dozens, hundreds or even several thousands of particles might be in one particle damper. Experimentally the testbed consists of a particle box with a free-free boundary condition that is excited by a controlled harmonic force via a shaker. The excitation force is controlled in such a way, that the frequency and acceleration magnitude of the box stays constant. With the used equipment this developed testbed allows the testing of a large frequency and acceleration range. Via the measured velocity of the box using the LSV and the measured force of the shaker, the complex power is determined [3]. By the complex power, the energy dissipation in one cycle and the loss factor can be calculated. Then characteristic diagrams are obtained, representing over acceleration and frequency the loss factor or energy dissipation, respectively. A similar setup is also used in the numerical model of the second level. Since simulations of dampers with many particles can be numerical burdensome finite element models are not useful here. Instead, a Discrete-Element-Model (DEM) is used. The spherical particles are rigid bodies and interact with each other and the particle box by continuous contact models. For the normal contact, these models are based on the contact law of Hertz and use modifications to introduce energy dissipation described by the coefficient of restitution obtained on the first level. Additionally, smoothed frictional forces are implemented. An efficient contact search algorithm based on the verlet list in combination with the link cell algorithm is used. For the time integration, a fifth order Gear predictor-corrector algorithm is applied. The damper model is excited by a harmonic motion using a rheonomic constraint. Then, from the reaction force and the acceleration of the damper the energy dissipation and loss factor can be determined again. Thus,

*Corresponding author. E-mail: robert.seifried@tuhh.de.

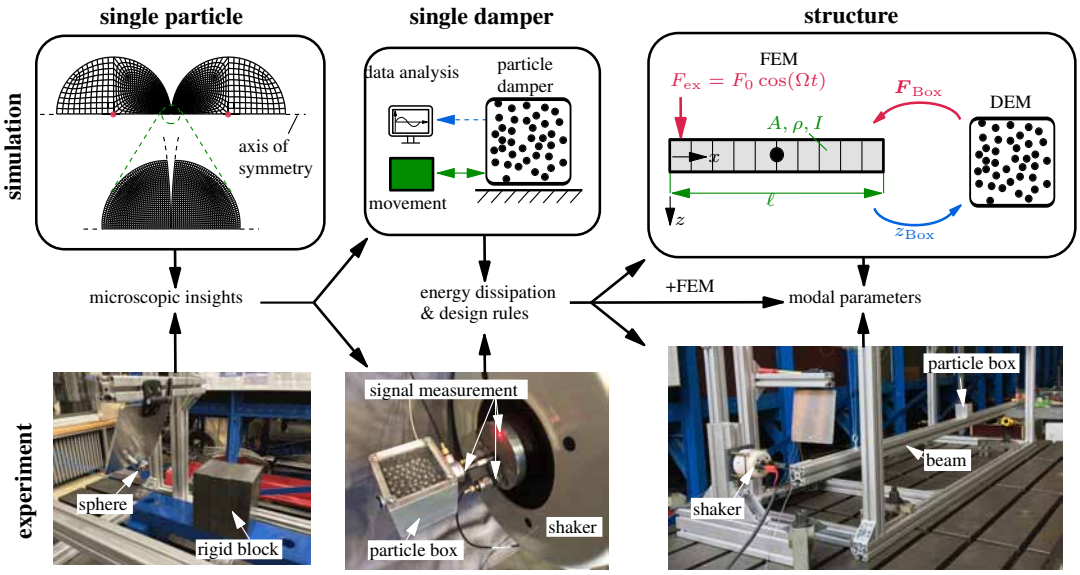

Figure 1: Tool chain for the analysis of particle dampers.

also by simulations characteristic diagrams for a given particle damper can be obtained. These diagrams can be stored and used on the third level for integration in a vibrating structure. Also, the characteristic diagrams and insights gained on the second level help to shorten the design phase for single particle dampers.
The third level represents the integration of one or several particle dampers in a vibrating structure or machine to evaluate their overall damping effect. Experimentally the testbed consists of a flexible structure supported by two soft cables, thus free-free boundary condition can be assumed. The structure is excited by a shaker and the excitation force is measured by a force sensor. The velocity profile of the structure is measured by the same LSV and analyzed with the software BK Connect providing the damping ratio. For the numerical investigations on the third level, two different approaches have been developed. In the first approach, the discrete element model from level two is coupled with a vibrating structure and simulated together. The flexible structure can be described e.g. by a continuous model, a reduced linear finite element model or a flexible multibody model. While this approach is very accurate and useful for verification purposes it is computationally very expensive, especially if a large frequency range should be investigated. Alternatively, the flexible structure can be coupled with the previously determined characteristic diagrams of the particle dampers. This coupling is easily implemented by a fixed point iteration and allows a fast simulation. Thus, different positioning and the application of several distributed dampers can be easily tested.
With models on these three levels, a holistic tool chain for the analysis of particle dampers is derived. This enables to design tailor made particle dampers at an early design stage of lightweight structures. On each level numerical models and experiments are available. On the one hand, in simulations many parameter variations can be computed yielding a good understanding of parameter sensitivities. On the other hand, the experiments are used once for the validation of the simulations. Also, from experiments one can get quickly a good impression of the behavior of some real possible particle combinations. Thus, numerical and experimental investigations should go hand in hand and on each level their results can be interchanged between experiments and simulations.

APPLICATION AND CONCLUSIONS

The efficiency of the developed multilevel tool chain is demonstrated using two applications. The first one is a simple beam-like structure where several distributed dampers are mounted. The second application example is a lightweight manipulator undergoing large working motion. This requires the modeling as flexible multibody system.
It is shown, that a very good qualitative agreement between the experiment and the numerical models are achieved on all three levels. Thus, the tool chain provides good and reliable insights to the complex mechanisms in particle dampers. For both systems different influence parameters on the damping behavior are analyzed, like the friction, particle radius, filling degree and material pairing. Finally, this allows optimized damper designs for either a certain defined excitation or a more broad excitation bandwidth.

References

[1] Panossian H., Structural Damping Enhancement via Non-obstructive Particle Damping Technique, *J. of Vibration and Acoustics* **114**, 1992
[2] Seifried R., Minamoto H., Eberhard P., Viscoplastic effects occurring in impacts of aluminum and steel bodies and their influence on the coefficient of restitution, *J. of Applied Mechanics* **77**, 2010.
[3] Yang M., Lesieutre G., Hambric S., Koopmann G., Development of a design curve for particle impact dampers, *Noise Control Eng. J.* **53**, 2005.

NON-LINEAR DYNAMIC AND QUASI-STATIC RESPONSES OF TWO-PHASE CERAMIC MATRIX AND METAL MATRIX COMPOSITES SUBJECTED TO COMPRESSION AND DEGRADATION

Tomasz Sadowski*[1], Eligiusz Postek [2], Daniel Pietras [1], Roman Gieleta[3], Leopold Kruszka[3]
[1] Department of Civil Engineering and Architecture, Lublin University of Technology, Lublin, Poland
[2] Institute of Fundamental Technological Research, Polish Academy of Science, Warsaw, Poland
[3] Military University of technology, Warsaw, Poland

Summary The paper presents modelling and experimental testing of non-linear degradation processes developing in two-phase ceramic matrix (CMCs) and metal matrix composites (MMCs) subjected to quasi-static and dynamic compressive loading. Modelling was performed by multiscale approach using both: (1) analytical and (2) numerical methods and selected Representative Volume Elements (RVE) based on SEM observations of composites. Both quasi-static and dynamic experimental tests were done applying standard MTS (100 kN) servo-hydraulic machine and Split Hopkinson Pressure Bar (SHPB) stand for impact tests with loading velocities 20 – 30 m/s. As a results we observed for CMCs in quasi-static loading failure mode by splitting of cylindrical samples, whereas for impact loading dynamic crushing process took place.

INTRODUCTION AND MOTIVATION

Quasi-static and dynamic degradation of semi-brittle ceramic matrix composites (CMCs) or metal matrix composites (MMCs) exhibit different mechanical response under uniaxial tension and uniaxial compression. In this paper we analysed cracking processes and failure under compression of two-phase CMC made of Al_2O_3 and ZrO_2 mixture and two-phase MMC built of WC grains and plastic Co matrix. The importance of these advanced composites results from their applications. The CMC is used as thermal barrier coatings (engines of aircrafts), whereas the MMC with addition nanoparticles is applied for modern cutting tools in different branches of engineering.

MULTISCALE MODELLING

Constitutive modelling of the analysed composites obeys description of: (1) elastic deformations of initially porous material, (2) limited plasticity and (3) cracks initiation and propagation. Description of polycrystalline composites with ceramic or metal matrixes behaviour at microscopic level is related to analysis of set of grains (RVE). The RVE is created with the help of SEM or μCT. In this paper we considered gradual degradation processes due to mechanical: quasi-static or dynamic loading. The basic elements of degradation are different defects growing inside polycrystal structure which includes: (1) dislocations or dislocation bands, (2) micro- and meso-cracks, kinked and wing cracks. To get macroscopic response of the material, one can calculate averaged values of stress and strain over the RVE with application of analytical approach or numerical one.

Analytical approach for quasi-static CMCs response

The constitutive equations for the considered CMC are the following:

$$\varepsilon_{ij} = S_{ijkl}(\sigma_{mn}, p, \omega^{(i)})\sigma_{kl}$$

where S_{ijkl} is the compliance tensor, ε_{ij} is the strain tensor, σ_{kl} is the stress tensor, p is the porosity parameter and $\omega^{(i)}$ are sets of parameters defining the presence of different kinds of defects "i" developing inside the material.

Cracks propagation mechanism is mainly along grain boundaries including defects kinking. It is strongly influenced by grain boundary porosity p_{gb}. Namely, any crack (straight or kinked one occupying grain boundaries) can propagate if the energy release rate G satisfies the following condition

$$G(\sigma_{ij}, \phi, p_{gb}) \geq \gamma_{gb}^{cr}(p_{gb}),$$

where ϕ describes orientation angle of cracks in RVE, γ_{gb}^{cr} is the critical value of the grain boundary surface energy.

Numerical approach for impact response of two-phase composites

Assessment of impact techniques is given in [1]. A basic model of MMCs is presented in [2]. The microstructures of Al_2O_3/ZrO_2 and WC/Co have different grain arrangement and their response is qualitatively different. In numerical models a low velocity impact of the two materials was investigated focusing attention on damage growth associated with microcracks and cracks initiation. We use finite element method (FEM) and meshless non-local peridynamics (PD), [3], Fig. 1. Further, the problems of binder modelling are different in both kinds of materials. In the WC/Co the binders are relatively thick and can be considered as elastic-plastic, while in the Al_2O_3/ZrO_2 the interfaces are thin and brittle. The

*Corresponding author. E-mail: sadowski.t@gmail.com or t.sadowski@pollub.pl.

grains in WC/Co are very hard, however, they are ductile as well [4]. The grains in Al_2O_3/ZrO_2 are both brittle. In the case of WC/Co the damage process develops rather along the binders, while in Al_2O_3/ZrO_2 the damage spread in both phases. A significant influence on crack initiation has initial voids, in particular in the CMC samples.

In case of WC/Co, the pulse duration was 10^{-7}s and the applied pressure level - 480 MPa. The proposed numerical model requires advanced FEM formulation including geometrical data and differet phenomena revealing inside of the RVE, like: (1) spatial distribution of the cermet constituents, (2) system of grain boundaries/binder interfaces modelled by interface elements, (3) rotation of brittle grains, (4) initiation and development of microcrakcs during loading process.

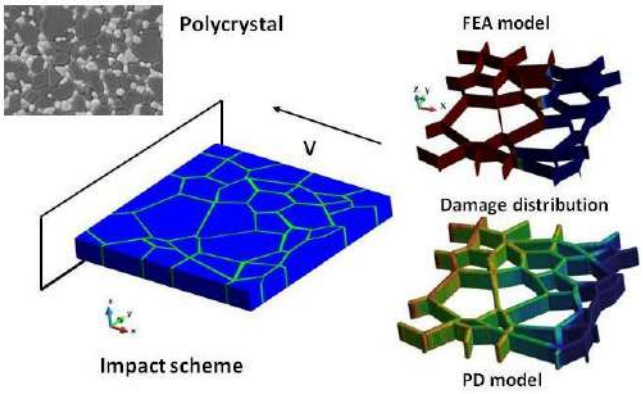

Figure 1. Numerical models in low velocity impact of CMC and MMC: FEM and PD.

RESULTS AND CONCLUSIONS

The obtained numerical results were compared with own experimental data for compression processes: under quasi-static loading using MTS (100 kN) and dynamic loading done with application of SHPB stand, Fig.2. The loading velocities were in the range 20 – 30 m/s.

Figure 2. Failure modes of CMC for: a) splitting in quasi-static loading (MTS) and 2) crushing during impact loading with SHPB.

Figure 2 presents qiute different failure modes for quasi-static loading and impact in case of CMC. We obtained splitting of specimens for quasi-static loading, wheras crushing took place during impact.

Similar phenomena were observed for the MMC. Its response due to pulse loading is significantly different in comparison to the quasi-static behaviour, i.e. the stress distributions and microcracking processes are quite different.

Comparison of the proposed models with experimental results lead to conclusion that theoretical models with good quality descrived non-linear behaviour of the two-phase composites under compression.

Acknowledgment

The results presented in this paper were obtained within the framework of research grant UMO/2016/21/B/ST8/01027 financed by the National Science Centre, Poland

References

[1] Kärger L., Baaran J., Gunnion A., Thomson R *Composites: Part B,* **71**: 40, 2009.
[2] Sadowski T., Hardy S., Postek E. *Materials Science Engineering A,* **230**: 424, 2006
[3] Silling S. A. *Journal of the Mechanics and Physics of Solids*, **175**: 48, 2000.
[4] Postek E., Sadowski T. *Int. J. Refractory Metals and Hard Materials*, **68**: 77, 2018.

NON-LINEAR DYNAMICS OF COMPOSITE LAMINATES WITH CURVILINEAR FIBERS UNDER SUPERSONIC AIRFLOW

Hamed Akhavan and Pedro Ribeiro*
DEMec/INEGI, Faculdade de Engenharia, Universidade do Porto, Porto, Portugal

Summary This research examines non-linear dynamics of variable stiffness composite plates, composed of curvilinear fibres in a polymeric matrix, exposed to a supersonic airflow. A reduced-order model obtained by sequentially applying static condensation and truncating to a selected number of modes of vibration is applied. The inclusion of a large-enough number of modes in the latter technique is essential for observation of the, often overlooked, rich dynamics of plates under airflows. Different scenarios, including LCOs with one dominant harmonic, period-*n* LCOs, and chaotic oscillations, are found in this self-excitation problem. Symmetry breaking bifurcations may introduce unstable LCOs and the aperiodic oscillations are preceded by period doubling bifurcations. The bifurcations and the stability status are affected by the curvilinear fibre paths, a feature that can be used in design.

INTRODUCTION

The non-linear dynamic behaviour of composite plates with curvilinear fibres and under a supersonic airflow is investigated in this work. A composite plate with curvilinear fibres is a type of variable stiffness composite laminate (VSCL) [1]; it can be manufactured using automated fibre placement technology [2]. Curvilinear fibres allow designers to achieve a load distribution or vibration characteristics that are more adequate to specific demands. There are a few works on dynamics of VSCLs (see, e.g., [1], [3] and references therein), but only limited investigations (e.g., Refs. [4] and [5]) are dedicated to non-linear aerodynamics of VSCL. This work intends to explore the latter issue in more detail.

A VARIABLE STIFFNESS PLATE SUBJECTED TO A SUPERSONIC AIRFLOW

In this research, a rectangular plate, with length a and width b is studied. A Cartesian coordinate system (x,y,z) with the origin located at the geometric centre of the undeformed plate is employed in the following equations. The reference curvilinear fibre path changes linearly from T_0 at the left edge to T_1 at the right edge, being its angle defined as $\theta(x) = (T_1 - T_0)(x + a/2)/a + T_0$. In order to define the other fibre paths in the lamina, the reference fibre path shifts in the y-direction. A displacement field, based on a third-order shear deformation theory is introduced as

$$\begin{aligned} u(x,y,z,t) &= u^0(x,y,t) + z\theta_y^0(x,y,t) - cz^3\left(\frac{\partial w^0(x,y,t)}{\partial x} + \theta_y^0(x,y,t)\right), \\ v(x,y,z,t) &= v^0(x,y,t) - z\theta_x^0(x,y,t) - cz^3\left(\frac{\partial w^0(x,y,t)}{\partial y} - \theta_x^0(x,y,t)\right), \\ w(x,y,z,t) &= w^0(x,y,t), \end{aligned} \tag{1}$$

where u^0, v^0, w^0 are mid-plane displacements components and t represents time. Rotations of a normal segment around the x and the y axis are represented by θ_y^0 and θ_x^0, respectively. These components are discretized using a p-version finite element as

$$r(x,y,t) = \mathbf{N}^r(x,y)^T \mathbf{q}_r(t), \tag{2}$$

where r can be $u^0, v^0, w^0, \theta_y^0$ or θ_x^0, $\mathbf{N}^r$ are vectors of shape functions and $\mathbf{q}_r$ are vectors of generalized coordinates.

Supersonic airflow is considered on one (front) side of the plate, while constant undisturbed air pressure is set at the other (back) side. The pressure difference between the plate surfaces due to a highly unsteady airflow (in x-direction) is defined using linear Piston theory as

$$\Delta p(x,y,t) = -\frac{2q}{\sqrt{M^2-1}}\left(\frac{M^2-2}{M^2-1}\frac{1}{U_\infty}\frac{\partial w(x,y,t)}{\partial t} + \frac{\partial w(x,y,t)}{\partial x}\right), \tag{3}$$

with q representing the dynamic pressure, M the Mach number and U_∞ the freestream velocity.

The principle of virtual work, in conjunction with equation (2), leads to the full-order model equations of motion, representing the self-excited vibrations of a VSCL under supersonic airflow. These equations have the following form [5]

$$\mathbf{M}\ddot{\mathbf{q}}(t) + \mathbf{F}_{unsteady}\mathbf{q}(t) + \left(\mathbf{K} + \mathbf{K}_n(\mathbf{q}(t)) + \mathbf{F}_{steady}\right)\mathbf{q}(t) = \mathbf{0}. \tag{4}$$

Matrices $\mathbf{M}$, $\mathbf{K}_\ell$ and $\mathbf{K}_{n\ell}(\mathbf{q}(t))$ are, respectively, the mass, linear and non-linear stiffness matrices [3]. Matrices $\mathbf{F}_{steady}$ and $\mathbf{F}_{unsteady}$ [5] are due to the interaction between the structure and the airflow. The order of the system of equations (4) is reduced first using static condensation, by neglecting membrane inertia, and then by transferring to a selected set of modal

*Corresponding author. E-mail: pmleal@fe.up.pt

coordinates. It is important to note here that more modal coordinates are employed than what is common practice in aeroelastic analyses [4], a factor that is important for the detection of bifurcations, the stability analyses and the computation of aperiodic oscillations. The reduced-order model is solved using Newmark's method and a shooting method.

RESULTS

Time histories (deflection ratio versus time), phase-plane plots (non-dimensional velocity versus deflection ratio) and positions of a point (u/h, v/h, w/h) during oscillation – where h is thickness of the variable stiffness plate - are displayed in Figure 1, for two aerodynamic loads. In this variable stiffness plate, a Hopf bifurcation occurs at a critical flutter speed (linear regime) corresponding to a non-dimensional dynamic pressure λ equal to 7.22 ($\lambda=2qa^3/\left(D\sqrt{M^2-1}\right)$, D represents a plate bending stiffness). For $\lambda>7.22$, oscillations with magnitude bounded by the geometrical non-linearity arise. The results shown in the sub-figure (a) are calculated when $\lambda=7.85$ and correspond to a periodic oscillation (an LCO), while in the sub-figure (b) the aperiodic oscillation that occurs at $\lambda=7.954$ is displayed. A symmetry-breaking bifurcation occurs around $\lambda=7.86$ and the stable LCO (shown in sub-figure a) becomes unstable, while two new stable branches are born. The aperiodic oscillation shown in sub-figure (b) is found after additional bifurcations on one of the latter branches.

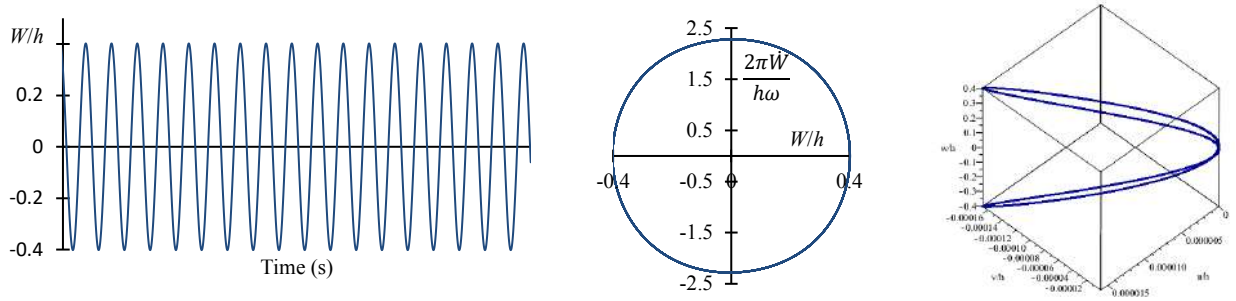

a) $\lambda=7.85$

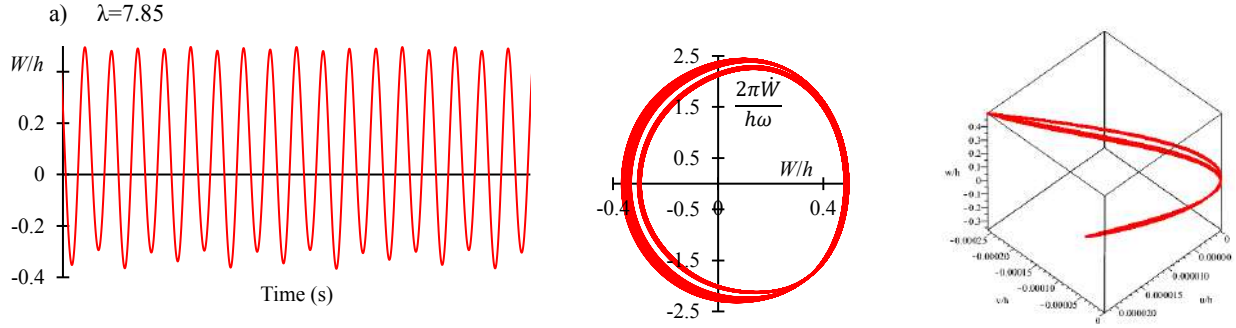

b) $\lambda=7.954$

Figure 1. Time histories, phase-plane plots and positions of a point at plate during oscillation, at two aerodynamic loads.

CONCLUSIONS

This investigation demonstrated how a stable LCO passes through bifurcations, which lead to other stable and unstable LCOs, and even to aperiodic solutions. These bifurcations happened during non-linear flutter of variable stiffness plates and their appropriate detection required that the number of degrees of freedom in the mathematical model was not severely reduced. Curvilinear fibre paths in laminated composites can be varied in order to – to a certain extent - avoid the occurrence of flutter due to Hopf bifurcations or additional bifurcations at large vibration amplitudes. Although variable stiffness plates are the chief interest here, the reduced-order model of the type employed, with a large-enough number of degrees of freedom, is capable of finding rich non-linear dynamics in other plates subjected to airflows.

ACKNOWLEDGEMENT

This research is carried out in the framework of project Nº 030348, POCI-01-0145-FEDER-030348, "Laminated composite panels reinforced with carbon nanotubes and curvilinear carbon fibres for enhanced vibration and flutter characteristics", funded by FEDER, through *Programa Operacional Competitividade e Internacionalização* – COMPETE 2020, and by National Funds (PIDDAC), through FCT/MCTES.

References

[1] Ribeiro P., Akhavan H., Teter A., Warminski J. A Review on the Mechanical Behaviour of Curvilinear Fibre Composite Laminated Panels. *J. Compos. Mater.* **48**: 2761-2777, 2014.
[2] Lukaszewicz D. H. J. A., Ward C., Potter K. D. The Engineering Aspects of Automated Prepreg Layup: History, Present and Future. *Compos. Part B-Eng.* **43**: 997–1009, 2012.
[3] Akhavan H. Non-Linear Vibrations of Tow Placed Variable Stiffness Composite Laminates. *PhD Thesis*, Univ. of Porto, Portugal, 2015.
[4] Akhavan H., Ribeiro P. Reduced-Order Models for Nonlinear Flutter of Composite Laminates with Curvilinear Fibers. *AIAA J.* **57**: 3026–3039, 2019.
[5] Akhavan H., Ribeiro P. Approximations by Reduced-Order Models for Nonlinear Flutter of Variable Stiffness Composite Plates. *SAMPE 2019,* Charlotte, NC, 2019.

NONLINEAR DYNAMICS OF PIEZOELECTRIC SCANNING MICROMIRRORS: MODELING AND EXPERIMENTAL VALIDATION

Andrea Opreni*[1], Nicolò Boni[2], Roberto Carminati[2], Massimiliano Merli[2], Gianluca Mendicino[2], and Attilio Frangi[1]
[1] Department of Civil and Environmental Engineering, Politecnico di Milano, Milan, Italy
[2] Analog and MEMS Group, STMicroelectronics, Milan, Italy

Summary Piezoelectric thin films have gained attention as key materials for the actuation of micro devices since they provide high drive forces, enhanced linearity, and improved reliability compared to electrostatic actuation. Here we address the simulation of piezo-micromirrors undergoing large rotations with reduced order models. We focus on obtaining a numerical estimate of the elastic energy term and of the piezo coupling coefficient starting from the Landau-Devonshire theory of ferroelectrics. The model is validated on a specific micromirror actuated with PZT patches.

INTRODUCTION

The development of optical Micro-Electro-Mechanical Systems (MEMS) is a direct result of market driven applications. Holographic lenses are becoming popular in the consumer industry, Head-Up-Displays are turning into a commodity of the automotive industry, and light manipulation is a requirement in most experimental scientific fields. Within the class of optical MEMS, scanning micromirrors provide excellent performance in terms of precision, compactness, and power consumption [1].
Piezoelectrically actuated micromirrors are subjected to both geometric and electromechanical nonlinearities. Concerning the latter, the theoretical work by Landau-Devonshire [2] shows that the strain experienced by piezoelectric materials upon the application of an external voltage is nonlinearly proportional to the polarization vector. Therefore, the linearized theory of ferroelectrics [3] holds for low values of applied voltages, hence it proves unreliable for modeling devices that require large drive voltages as scanning micromirrors.
In this work we develop a nonlinear piezoelectric model for the dynamic analysis of micromirrors actuated with Lead-Zirconate-Titanate (PZT) films. The model is validated on micromirrors with hardening behavior developed by STMicroelectronics. Preliminary results show a match between experimental data and the proposed model at oscillation amplitudes up to 21°.

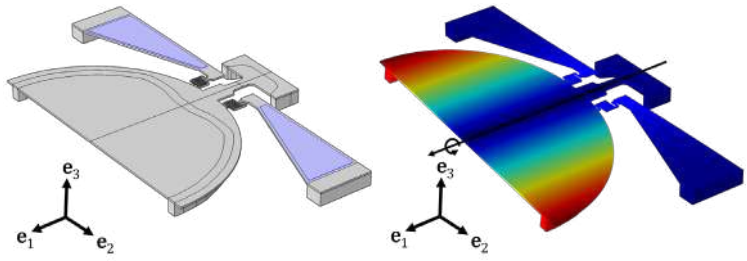

(a) (b)

Figure 1: Tested micromirror geometry (a), and torsional mode of the device (b).

MODEL

According to the theory of ferroelectrics developed by Landau-Devonshire, the polarization vector $\boldsymbol{P}$ induces inelastic deformation of the elementary cell of the piezoelectric crystal due to spontaneous polarization below the Courie temperature. Considering linearized elasticity, the Cauchy stress $\boldsymbol{\sigma}$ can then be additively decomposed in elastic and inelastic terms as:

$$\boldsymbol{\sigma} = \boldsymbol{\sigma}^{\varepsilon}[\boldsymbol{u}] - \boldsymbol{\sigma}^{P}[\boldsymbol{P}] \quad \text{where} \quad \boldsymbol{\sigma}^{\varepsilon}[\boldsymbol{u}] := \mathcal{C} : \boldsymbol{\varepsilon}[\boldsymbol{u}], \quad \boldsymbol{\sigma}^{P}[\boldsymbol{P}] := \mathcal{C} : \boldsymbol{\varepsilon}^{P}[\boldsymbol{P}] \tag{1}$$

where $\boldsymbol{\varepsilon}$ is the infinitesimal strain tensor, $\boldsymbol{u}$ is the displacement, $\mathcal{C}$ is the fourth-order elasticity tensor, and the superscripts $(\cdot)^{\varepsilon}$ and $(\cdot)^{P}$ define elastic and inelastic quantities. Neglecting active forces, the weak form of the linear momentum conservation equation for piezoelectric MEMS subjected to finite transformations reads:

$$\int_{\Omega} \rho \ddot{\boldsymbol{u}} \cdot \boldsymbol{w} \, \mathrm{d}\Omega + \int_{\Omega} (\boldsymbol{\sigma}^{\varepsilon} - \boldsymbol{\sigma}^{P}) : \mathrm{d}[\boldsymbol{w}] \, \mathrm{d}\Omega = 0 \tag{2}$$

*Corresponding author. E-mail: andrea.opreni@polimi.it.

where ρ is the density, $\boldsymbol{w}$ is the virtual displacement, $\mathbf{d}$ is the rate of deformation tensor, and Ω is the material volume. Equation (2) is projected on the subspace of the generalized coordinate θ representative of the system nonlinear motion [4]. By adding a damping term proportional to the system velocity we obtain a one degree of freedom model of the form:

$$J\ddot{\theta} + J\frac{\omega_0}{Q}\dot{\theta} + f(\theta) = c_{nl}V_0\cos(\omega t) \tag{3}$$

with J inertia, ω_0 resonance frequency of the mode of interest, Q quality factor estimated from experiments, $f(\theta)$ internal force vector evaluated with a nonlinear Finite Element model, V_0 drive voltage amplitude, ω excitation frequency, and c_{nl} piezoelectric coupling coefficient. If the piezoelectric patch is thin and deposited along the $\boldsymbol{e}_1\boldsymbol{e}_2$ plane, the electric field takes the form $\boldsymbol{E} = E\boldsymbol{e}_3$, thus if dielectric properties are isotropic $\boldsymbol{P} = P\boldsymbol{e}_3$. If we assume that the displacements of the piezoelectric material film are small, c_{nl} is then estimated by projecting the inelastic stresses on the mode of interest, and on the first cosine term of a Fourier basis:

$$c_{nl} = \frac{\omega}{\pi V_0}\int_0^T\int_{\Omega_P} P^2\Big[(\varepsilon_{11}[\boldsymbol{\phi}] + \varepsilon_{22}[\boldsymbol{\phi}])c_{31} + \varepsilon_{33}[\boldsymbol{\phi}]c_{33}\Big]\cos(\omega t)\,\mathrm{d}\Omega\,dt \tag{4}$$

where T is the period of the drive voltage, ε_{ij} are strain components, $\boldsymbol{\phi}$ is the linear mode basis, and c_{ij} are material constants.

NUMERICAL RESULTS AND EXPERIMENTAL VALIDATION

The proposed model was validated on micromirrors with hardening behavior developed by STMicroelectronics. The devices were made of monocrystalline silicon with (100) orientation actuated with PZT patches. The micromirrors geometry is reported in Figure 1a. The PZT patches are highlighted in light purple. The devices were actuated in their torsional mode. Its displacement field is reported in Figure 1b, highlighting that the PZT patches are subjected to small displacements. Preliminary results obtained for drive voltage amplitudes of 15 V and 20 V are reported in Figure 2. The charts show an excellent agreement between experimental data and proposed model.

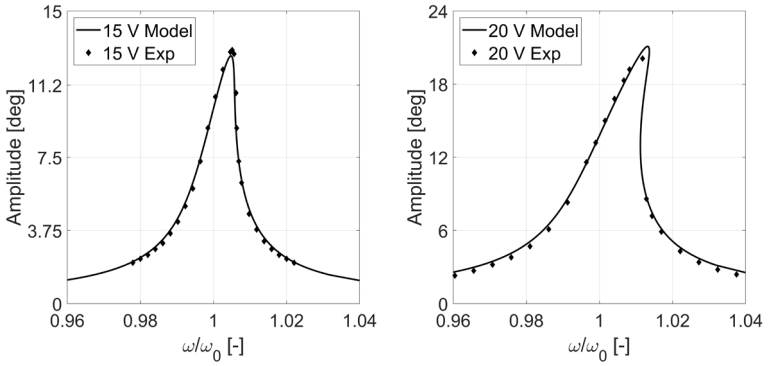

(a) (b)

Figure 2: Comparison between model and experimental data for actuation voltage amplitudes V_0 of 15 V (a) and 20 V (b).

CONCLUSIONS

We have developed a novel technique for the analysis of the nonlinear dynamic behavior of structures actuated using thin films of piezoelectric material. The model is based on the theory of ferroelectrics and it allows simulating devices subjected to geometrical and electromechanical nonlinearities on the sole basis of the polarization history of the piezoelectric material.

References

[1] A. Corigliano, R. Ardito, C. Comi, A. Frangi, A. Ghisi, S. Mariani, *Mechanics of Microsystems*, ISBN: 978-1-119-05383-5, Wiley, 2018
[2] A. F. Devonshire. Theory of ferroelectrics. *Advances in Physics*, 3(10):85–130, 1954.
[3] H.F. Tiersten, *Linear Piezoelectric Plate Vibrations: Elements of the Linear Theory of Piezoelectricity and the Vibrations Piezoelectric Plates*, ISBN: 978-1-119-05383-5, Springer, 2013
[4] A. Frangi, G. Gobat, Reduced Order Modelling of the non-linear stiffness in MEMS resonators, *Int. J. Non-linear Mechanics*, vol. 116, pp. 211-218, 2019

A MODIFIED NON-LINEAR ENERGY SINK FOR PARAMETRIC-INSTABILITY CONTROL OF A SPRUNG CYLINDER

Carlos E.N. Mazzilli*[1], Breno A.P. Mendes [1] and Eduardo A.R. Ribeiro [1]
[1] Department of Structural and Geotechnical Engineering, Escola Politécnica da USP, São Paulo, Brazil

Summary: This paper addresses the vibration control of a rigid cylinder constrained by a spring and a linear dashpot. Parametric excitation is assumed to cause a harmonic variation of the spring stiffness about an average value. The case of principal parametric instability is considered and the vibration control is provided by a mass attached to a linear spring, able to slide along a guiding bar placed within the cylinder. The guide is free to rotate about the cylinder longitudinal axis, although damped by a linear rotational dashpot. The assemblage plays the role of a non-linear energy sink, since there exists no linear rotational stiffness associated to the controller. This non-linear vibration absorber introduces a modification with respect to a similar assemblage studied in the literature, because it accounts for a variable distance of the rotational mass with respect to the cylinder axis. Preliminary results show that the modified system overall performs as a better controller.

PROBLEM MOTIVATION

The classical tuned-mass dampers attached to the main structure have proved to be effective in vibration control for narrowband excitations [1]. Non-linear vibration absorbers, like the so-called non-linear energy sinks (NES), are an interesting alternative [2]. With a damper and a non-linearizable stiffness, a NES is effective for a non-preferable suppression frequency. Such devices have been used in passive vibration control of buildings [3] and structures subjected to flow-induced loading [4].

This paper addresses the classic problem of the parametric excitation of a rigid cylinder with viscous-elastic constraints, characterised by a harmonic variation of its support stiffness about an average value. It is common knowledge that when the excitation frequency is twice the structure's natural frequency, the trivial solution of the otherwise unforced cylinder equation of motion becomes unstable, a phenomenon called principal parametric instability. This scenario comes about, for instance, in offshore risers, when waves impose heave motions to the floating rig to which the riser is attached, causing an almost-periodic modulation in its geometric stiffness. The present study is inspired by this problem, yet in a very simplified way. In [5], parametric-instability control by means of a rotational non-linear vibration absorber in a similar model has already been discussed. Yet, the novelty here is that the rotating mass is attached to a linear spring and slides along a guiding bar mounted inside the cylinder cross section (see Fig. 1). The guide is free to rotate, although damped by a linear dashpot. Therefore, the mass distance to the cylinder axis is not fixed, as in [5], bringing about the interesting problem of the self-adjustment of the rotation radius that seems to play a key role in the controller's efficiency.

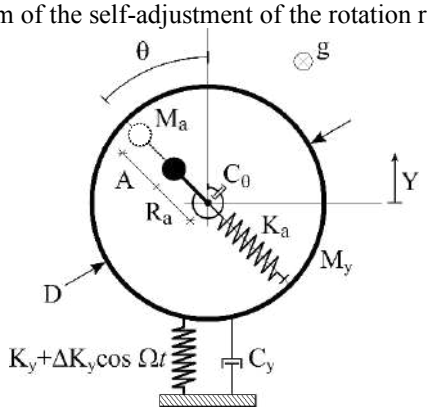

Figure 1. Cylinder with mounted NES.

$$y = \frac{Y}{D} \qquad a = \frac{A}{D} \qquad r = \frac{R_a}{D}$$

$$m = \frac{M_a}{M_y} \qquad \delta = \frac{\Delta K_y}{K_y} \qquad \tau = \omega_y t$$

$$\omega_y = \sqrt{\frac{K_y}{M_y + Ma}} \qquad n = \frac{\Omega}{\omega_y} \qquad \beta_1 = \frac{m}{(1+m)}$$

$$\beta_2 = \frac{C_y}{(M_y + M_a)\omega_y} \qquad \beta_3 = \frac{C_\theta}{3D^2 3M_a 3\omega_y} \qquad \beta_4 = \frac{K_a}{K_y}$$

Table 1. System variables and non-dimensional parameters.

MATHEMATICAL MODEL

The variables and non-dimensional system parameters are defined in Tab. 1, where Y is the cylinder displacement; A is the rotating mass radial displacement; D is the cylinder diameter; R_a is the NES radius for unstrained spring; M_y is the cylinder mass; M_a is the NES mass; K_y is the cylinder average stiffness; ΔK_y is the cylinder stiffness amplitude variation; K_a is the NES stiffness; ω_y is the cylinder reference natural frequency; Ω is the parametric-excitation frequency; C_y is the cylinder dashpot constant; C_θ is the NES rotational dashpot constant. It is worth mentioning that the NES unstrained spring length is assumed to be equal to the cylinder radius.

Hamilton's principle is used to obtain the set of non-linear differential equations that define the mathematical model:

$$y'' + \beta_2 y' + (1 + \delta \sin n\tau)y + \{\beta_1[a'' - (r+a)\theta'^2]\}\cos\theta - \{\beta_1[(r+a)\theta'' + 2a'\theta']\}\sin\theta = 0 \quad (1)$$

$$(a+r)^2\theta'' + [2(r+a)a' + \beta_3]\theta' - (r+a)y''\sin\theta = 0 \quad (2)$$

$$a'' + \frac{\beta_4}{\beta_1}a - (r+a)\theta'^2 + y''\cos\theta = 0 \quad (3)$$

*Corresponding author. E-mail: cenmazzi@usp.br.

where $(\ )' = \frac{d}{d\tau}$. Numerical integration of the system equations was performed using *Mathematica*® in different scenarios, whose results are briefly commented in the following. Firstly, the case of an infinitely-rigid NES spring precisely retrieves results found in [5], which is a necessary validation step. Next, it is seen that the less stiff is the NES, the more efficient it is, in the sense that the time required for full cylinder vibration suppression is smaller (see Fig. 2).

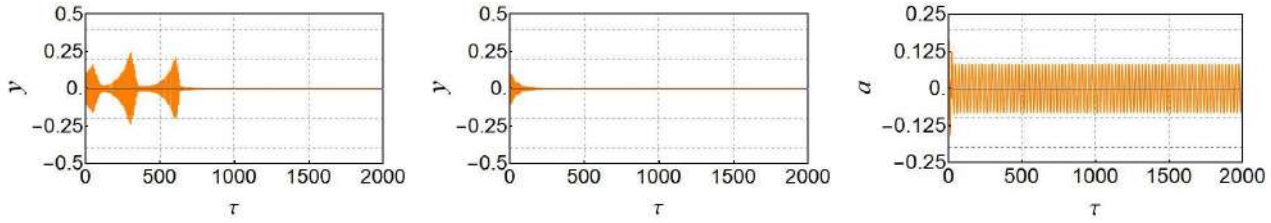

(a) Rigid NES ($\beta_4 \to \infty$) (b) Flexible NES ($\beta_4 = 0.01$)

Figure 2. Time responses for $r = 0.25$, $m = 0.15$, $\xi_y = 0.01$, $\xi_\theta = 0.05$, $\delta = 0.10$ and $n = 2$.

Even more evident is the NES' improved efficiency for the case depicted in Fig. 3, which shows that the infinitely-rigid NES is not able to control the parametric instability, whereas the one with a very low stiffness is.

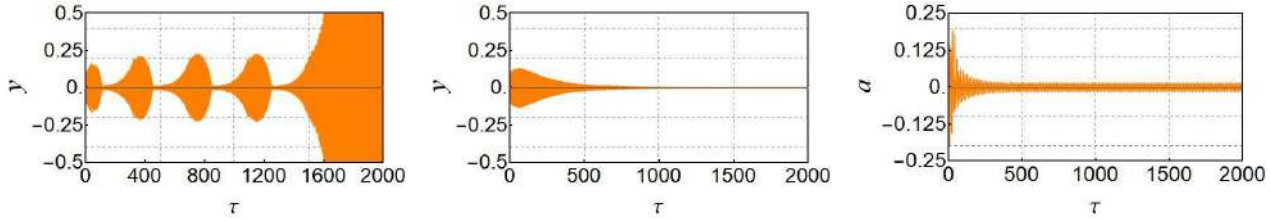

(a) Rigid NES ($\beta_4 \to \infty$) (b) Flexible NES ($\beta_4 = 0.01$)

Figure 3. Time responses for $r = 0.25$, $m = 0.05$, $\xi_y = 0.01$, $\xi_\theta = 0.05$, $\delta = 0.10$ and $n = 2$.

Fig. 4(a) is a NES's efficiency chart, for different choices of stiffness and mass parameters. Overall, there is an increase in the zone of controlled vibrations (blue) with respect to the rigid NES studied in [5]. Nevertheless, it is noteworthy that a thin unstable-response tongue (red) appears for $0.05 \leq \beta_4 \leq 0.15$, where the rigid NES performs better. Fig. 4(b) depicts the rotating mass vibration amplitude. Of course, meaningful maximum free-course sliding amplitudes $\hat{a}_{\max}$ should be smaller than one, where $\hat{a} = a/\left(\frac{1}{2} - r\right)$.

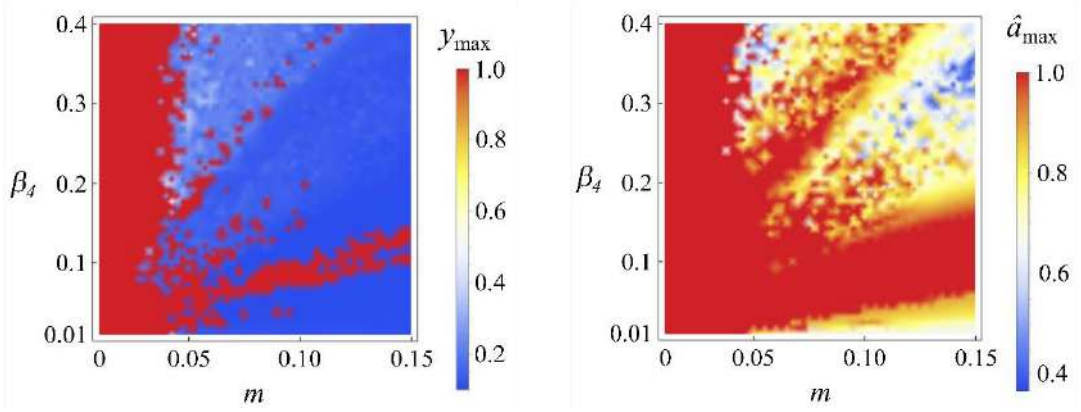

(a) $y_{\max}$ (b) $\hat{a}_{\max}$

Figure 4. NES efficiency chart for $\xi_y = 0.01$, $\xi_\theta = 0.05$, $\delta = 0.10$, $n = 2$ and $r = 0.25$.

CONCLUSIONS

Although this is still a work in progress, due to the high control-parameter-space dimension, it can already be seen that the optimization of the proposed modified rotating NES leads to a more efficient vibration controller.

References

[1] Den Hartog J.P. Mechanical vibrations. McGraw-Hill, 1956.
[2] Lee Y.S., Vakakis A.F., Bergman L.A., McFarland D.M., Kerschen G., Nucera F., Tsakirtzis S., Panagopoulos P.N. Passive non-linear targeted energy transfer and its applications to vibration absorption: a review. *J. Multi-body Dyn*, 222:77-134, 2008.
[3] Wierschen N.E., Hubbard S.A., Lu J., Fahnestock L.A., Spencer Jr. B.L., McFarland D.M., Quinn D.D., Vakakis A.F.,Bergman L.A. Response attenuation in a large-scale structure subjected to blast excitation utilizing a system of essentially nonlinear vibration absorbers. *J. Sound Vib*, 389: 52-72, 2017.
[4] Blanchard A.B., Gendelman O.V., Bergman L.A., Vakakis A.F. Capture into a slow-invariant-manifold in the fluid-structure dynamics of a sprung cylinder with a nonlinear rotator. *J. Fluids Struct*, 63: 155-173, 2016.
[5] Campedelli G.R., Franzini G.R., Mazzilli C.E.N. Further numerical studies on passive suppression of parametric instability using a rotative non-linear energy sink. *Enolides*, Novi Sad, 2018.

DESIGN OF STABILITY PRESERVING SIMULATION METHODS FOR THE PREDICTION OF ROCKFALL

Remco I. Leine *[1], Giuseppe Capobianco[1], Perry Bartelt[2], and Guang Lu[2]
[1] Institute for Nonlinear Mechanics, University of Stuttgart, Germany
[2] WSL Institute for Snow and Avalanche Research SLF, Davos Dorf, Switzerland

Summary The stability properties of a freely rotating rigid body are governed by the intermediate axis theorem, i.e. rotation around the major and minor principal axes is stable whereas and rotation around the intermediate axis is unstable. The stability of the principal axes is of importance for the prediction of rockfall. Current numerical schemes for 3D rockfall simulation, however, are not able to correctly represent these stability properties. In this paper we give a proof using Lyapunov functions of an extended intermediate axis theorem, which not only involves the angular momentum equations but also the orientation of the body. Inspired by the stability proof, we present a novel scheme which respects the stability properties of a freely rotating body and which can be incorporated in numerical schemes for the simulation of rigid bodies with frictional unilateral constraints.

INTRODUCTION

A full 3D simulation technique for rockfall dynamics, taking rock shape into account and using the state-of-the-art methods of multibody dynamics and nonsmooth contact dynamics, has been developed in [2]. The rockfall simulation technique is based on the nonsmooth contact dynamics method with hard contact laws. The rock is modeled as an arbitrary convex polyhedron and the terrain model is based on a high resolution digital elevation model. The developed numerical methods have been implemented in the code RAMMS:rockfall (Figure 1), which is being actively used in the natural hazards research community, and is to date the only 3D code which takes rockshape into account [1].

Field observations of natural rockfall events as well as high precision measurements with instrumented experimental rocks have shown that platy disc-shaped rocks have the tendency to roll and bump down the slope around their major principal axis. Simulations with the present implementation of RAMMS:rockfall, however, fail to represent the observed rolling phenomenon.

The intermediate axis theorem is a result of the Euler equations

$$\boldsymbol{\Theta}\dot{\boldsymbol{\omega}} + \boldsymbol{\omega} \times (\boldsymbol{\Theta}\boldsymbol{\omega}) = \mathbf{0}.$$

describing the movement of a rigid body with three distinct principal moments of inertia. The theorem describes the following effect: rotation of a rigid body around its minor and major principal axes is stable, while rotation around its intermediate principal axis is unstable. The classical intermediate axis theorem, however, only involves the Euler equations for the three components of the angular velocity. In this paper, we describe the dynamics of a freely rotating body in state-space form using as states the three angular velocity components $\boldsymbol{\omega}$ and an arbitrary parametrization of the orientation of the body with respect to the inertial frame, (i.e. the transformatiojn matrix $\boldsymbol{A}_{IK}$). Using the method

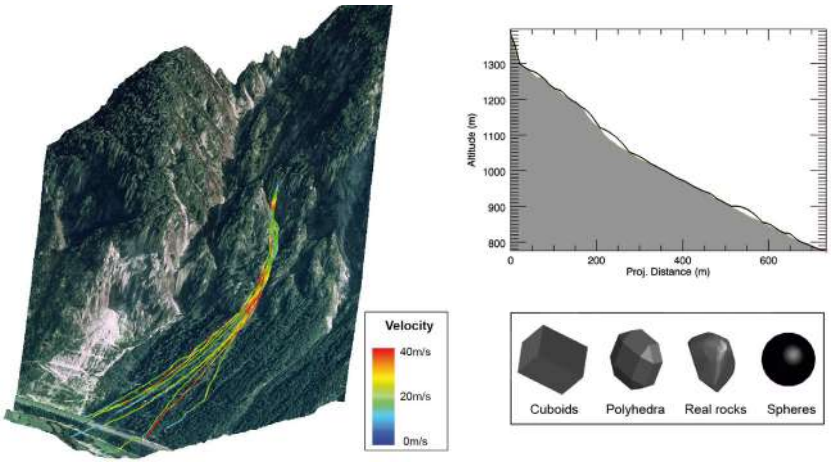

Figure 1: Graphical user interface of the RAMMS rockfall module.

of Lyapunov functions we rigorously prove an extended version of the intermediate axis theorem which considers the stability of the motion in the full state-space $(\boldsymbol{A}_{IK}, \boldsymbol{\omega})$.

In this paper we will show that the present scheme, which is fully explicit during flight phases of the rock, does not respect the intermediate axis theorem. Furthermore, we will present an implicit scheme which correctly describes the stability properties of a freely rotating body.

*Corresponding author. E-mail: leine@inm.uni-stuttgart.de

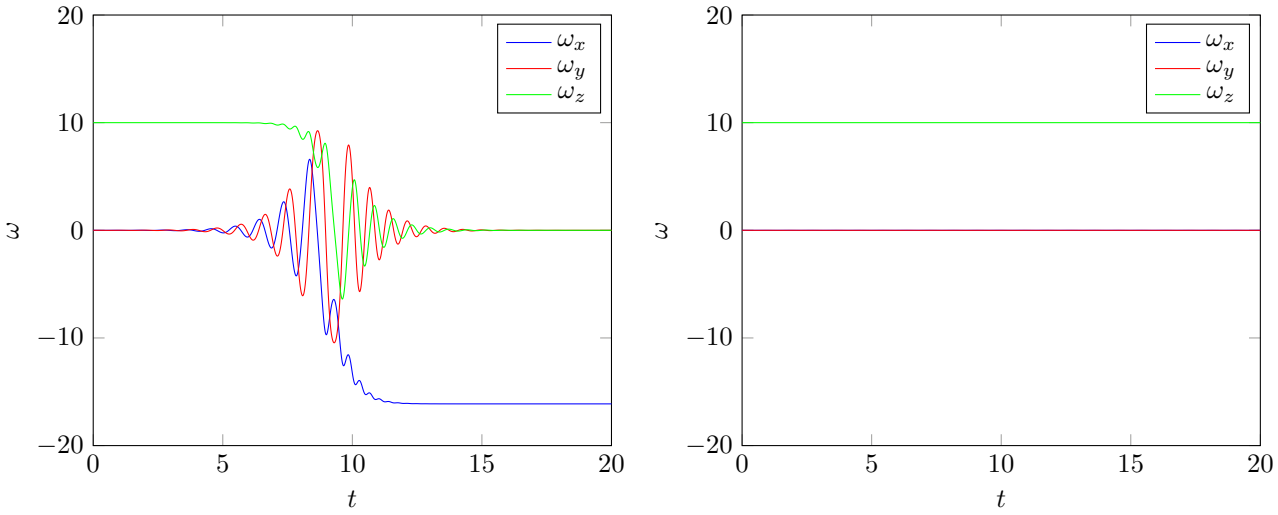

Figure 2: Angular velocities: left the explicit scheme, right the implicit scheme

A STABILITY PRESERVING IMPLICIT SCHEME

The alternative scheme for rockfall simulation is implicit and preserves the stability properties of the principal axes of rotation in accordance with the intermediate axis theorem. The implicit scheme consists of two parts:

1. as update rule for the angular velocity, we use the implicit scheme proposed by [3] which preserves the kinetic energy as well as the magnitude of the spin (i.e. the angular momentum with respect to the center of mass),

2. for update of the orientation parametrization, we propose a novel scheme which preserves the direction of the spin.

The stability properties of the implicit scheme are proven using the Lyapunov function which has been derived to prove the extended intermediate axis theorem.

NUMERICAL RESULTS

We compare the explicit and the implicit scheme on a numerical example by considering a cuboid with principal moments of inertia such that $A < B < C$. Rotation in the neighborhood of stationary rotation $\boldsymbol{\omega}_\star = \Omega \boldsymbol{e}_3$ around the major principal axis $\boldsymbol{e}_3$ is considered. We simulate 20 s using a time-step of $\Delta t = 0.01$ s using the explicit and implicit scheme. The results of both schemes are shown in Figure 2. The body initially rotates in the vicinity of the major principal axis with angular velocity $\omega_z = \Omega = 10$ rad/s, which is stable as follows from the extended intermediate axis theorem. However, in the numerical solution of the explicit scheme, the body deviates from stationary rotation around the major principal axis (approximately at $t = 10$ s) and tends to stable rotation around the minor principal axis with angular speed $\omega_x = -\sqrt{C/A}\Omega$. If a smaller time-step is taken in the explicit scheme, then the change of axis will be slower and will take place at a later point in time. The solution of the implicit scheme remains very close to the major principal axis, both in angular velocity and in orientation and is therefore much more accurate.

CONCLUSIONS

In this paper an extended intermediate axis theorem has been proven using Lyapunov functions. Using the same Lyapunov functions, we have given a rigorous proof that the implicit scheme presented in [3] respects the extended intermediate axis theorem. The computational cost per time-step is larger for the implicit scheme than the explicit scheme, as Newton iterations are needed to solve the implicit equations. However, numerical simulations show that the implicit scheme is far more accurate as it respects both the energy conservation and the invariance of the spin. The implicit scheme therefore allows to take larger time-steps without excessive error, making it a suitable scheme for rockfall simulation.

References

[1] M. Christen, Y. Bühler, P. Bartelt, R. Leine, J. Glover, A. Schweizer, C. Graf, B.W. McArdell, W. Gerber, Y. Deubelbeiss, T. Feistl, and A. Volkwein. Integral hazard management using a unified software environment: numerical simulation tool "RAMMS" for gravitational natural hazards. In G. Koboltschnig, J. Hübl, and J. Braun, editors, *Proceedings 12th Congress INTERPRAEVENT*, volume 1, pages 77–86, 2012.

[2] R. I. Leine, A. Schweizer, M. Christen, J. Glover, P. Bartelt, and W. Gerber. *Multibody System Dynamics*, 32:241–271, 2014.

[3] A. Schweizer. *Ein nichtglattes mechanisches Modell für Steinschlag*. PhD thesis, ETH Zurich, 2015.

TOWARDS NEW DYNAMICAL FUNCTIONALITIES WITH EXTREME PARAMETRIC OSCILLATORS

Alvaro Anzoleaga Grandi[1], Suzie Protière[1], and Arnaud Lazarus *[1]
[1] Institut Jean Le Rond d'Alembert, CNRS UMR7190, Sorbonne Université Paris, France

Summary Parametric instabilities can arise when the mechanical state of a structure is periodically modulated in time. It is often seen as a phenomenon to avoid for example with parametric rolling in ships but it can also be exploited, e.g. with parametric amplifiers in MEMS. One limitation in fully exploiting those dynamical instabilities is that inherent friction forces rapidly cancel sub harmonic parametric resonances. To overcome this drawback, we propose to extremely modulate the mechanical state of the system in order to enhance parametric instabilities. This original concept of "extreme" parametric oscillator is illustrated here through the numerical and experimental implementation of an electromagnetic pendulum. We find that it is possible to greatly enhance and control the number of sub harmonic instability regions which open the way for new promising design in structural dynamics.

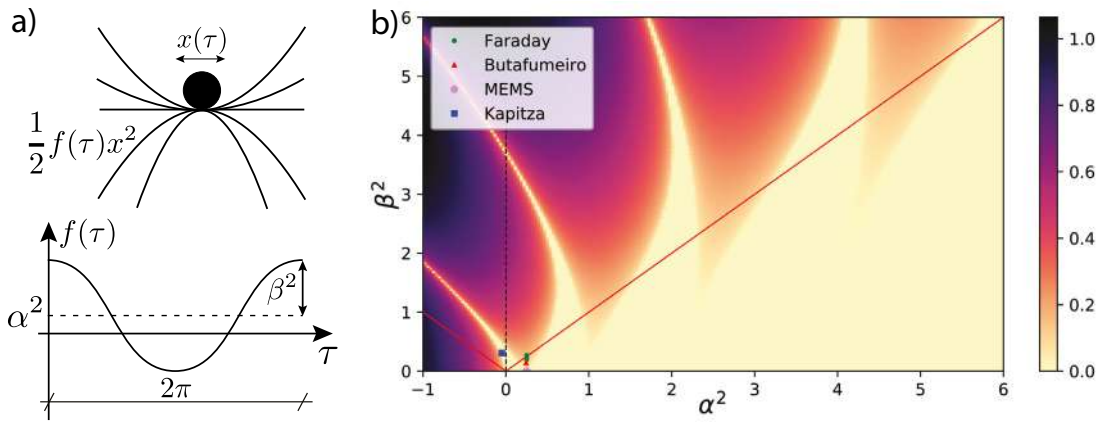

Figure 1: Linear stability analysis of parametric systems. a) A linear time-periodic system is an oscillator whose potential energy is periodically varied (here the modulation function is harmonic in time). b) Stability diagram of the parametric oscillator in the modulation parameters space α^2 and β^2. Darker regions are the so-called Mathieu's instability tongues. Parametric oscillators are usually used in a very restricted region of the modulation space as shown by the points around $\alpha^2 = \beta^2 = 0$.

Nowadays, from the use of buckling for folding [1] to the exploitation of fluttering piezoelectric flags for energy harvesting [2], instabilities eventually occurring in slender elastic structures are often seen as an opportunity to seize rather than a failure to avoid. Parametric instabilities, found in many engineering and physics problems [3, 4, 5], can be ultimately explained by the periodic modulation in time of the local potential energy of a dynamical system and described by archetypal instability tongues in the modulation parameters space (see Fig.1). Although this dynamical instability should theoretically offer a great freedom to design elaborate dynamical functionalities, it turns out practical parametric oscillators are often used at relatively low amplitude of modulations, because the modulation parameter is often a geometrical or mechanical parameters that is too cumbersome to effectively vary. Here, based on simple energetic concepts, we propose a first experimental proof of concept of an extreme parametric oscillator, a dynamical system whose potential energy can be easily and freely varied in time. In these type of systems, parametric instabilities are enhanced, even in the presence of frictional forces, and can be tailored to design interesting functionalities.

The proof of concept under study is the electromagnetic pendulum shown in Fig.2a). The experiment consists of a metallic pendulum that is symmetrically placed between two attracting electromagnets. When the electromagnets are OFF, the system is a simple pendulum, oscillating in the plane, that can be modeled by a mass in a harmonic potential well as shown in Fig.2b). When the electromagnets are ON, at a given input electrical current I, the energy landscape is varied (see Fig.2b)). When quasi-statically increasing the control parameter I, the natural frequency of the electromagnetic oscillator is decreasing (as is the local curvature of the potential), up to a particular value, $I = I_{max}$, where the metallic mass is no more naturally oscillating, but diverging (potential with a negative curvature), on the right or left electromagnet, depending on the imperfections in our system. This mechanical system is therefore an ideal candidate for what we coined an extreme parametric oscillator, because with a single parameter I, we are easily and drastically changing the state of our system, eventually from an oscillating to a diverging state. In classical parametric oscillators [3, 4, 5], this extreme modulation is hardly reachable because the geometrical of mechanical modulation parameters that come into play (length, gravity, height of the waves, etc...) are not easily varied on such scales.

*Corresponding author. E-mail: arnaud.lazarus@sorbonne-universite.fr

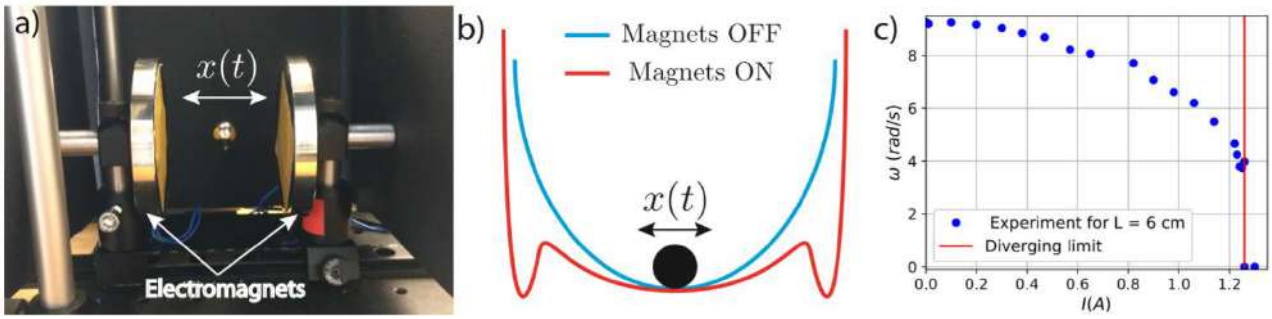

Figure 2: The electromagnetic parametric oscillator under study. a) A pendulum with a metallic mass is symmetrically placed between two identical attracting electromagnets that are periodically turned ON (red energy states in b)) and OFF (blue energy states in b)). b) Simplified "Particle in a time-varying potential well" model. c) Evolution of the natural frequency of the pendulum for various value of the electrical current I in the two electromagnets. Below $I < I_{max}$, the pendulum is naturally oscillating if perturbed. Eventually, for I close to the diverging limit I_{max} , the natural frequency goes down. Above I_{max} the mass is no more oscillating but diverging.

A parametric system is simply obtained by periodically turning the electromagnets ON or OFF in a square wave fashion as illustrated by the inset of Fig.3. The linear stability of such a system is supposed to be governed by the so called Meissner equation [6] that is a linear Ordinary Differential Equation with a piece-wise constant coefficient. Fig.3 shows the experimental stability charts of the electromagnetic pendulum represented in the Meissner modulation parameters space. The blue triangles indicate that the pendulum is dynamically stable, i.e. that the pendulum may be slightly vibrating but stay close to the trivial vertical state, in the middle of the electromagnetic box. The crosses indicate the modulation parameters for which the mass was parametrically unstable, i.e. dynamically impacting the electromagnets. The inset on the right side of Fig.3 representing Meissner's instability tongues in dark color shows that our experimental results are well predicted, at least for the two first parametric instability regions. But even more interesting is the main instability diagram of Fig.3: our dynamical system is able to trigger an unprecedented number of sub-harmonic parametric instability regions (here up to the 58^{th} regions when the current record demonstrated in a microelectromechanical device was found to be 28^{th} [5], thanks to ultra low damping). This ability to fully exploit the extended stability chart of parametric instabilities will be discussed for eventual new functionalities.

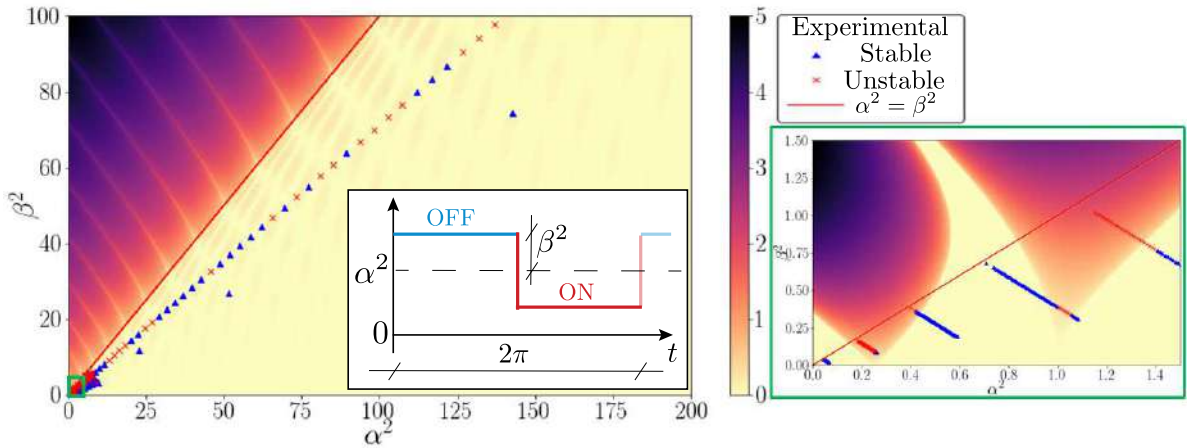

Figure 3: Extended stability chart showing the dynamical stability of the Meissner parametric system. Darker regions represent instability tongues. The blue triangles correspond to the experimental stable states and the red crosses correspond to the unstable ones. The red curve ($\alpha^2 = \beta^2$) represents the limit between systems that are naturally stable and systems naturally unstable (over the limit).

References

[1] A. Lazarus and P.M. Reis, Soft Actuation of Structured Cylinders through Auxetic Behavior, *Advanced Engineering Materials*, 17(6), 815-820, 2015.
[2] Pineirua, M., Michelin, S., Vasic, D. and Doaré, O., Synchronized switch harvesting applied to piezoelectric flags, Smart Materials and Structures, 25: 085004, 2016.
[3] B.C Chang, On the parametric rolling of ships using a numerical simulation method. *Ocean Engineering Science Direct* 447-457, 2008.
[4] S. Douady, Experimental study of the Faraday instability *J. Fluid Mech* ,Vol 221, pp383-409, 1990.
[5] Y. Jia, S. Du and A.A. Seshia, Twenty-Eight Orders of Parametric Resonance in a Microelectromechanical Device for Multi-band Vibration Energy Harvesting. *Scientific Reports* Vol 6, 30167, 2016.
[6] C. Sato, Correction of Stability Curves in Hill-Meissner's Equation. *Mathematics of Computation*, Vol 20, 93, 98-106, 1966.
[7] A. Lazarus, C. Maurini and S. Neukirch, Stability of discretized nonlinear elastic systems, in *Extremely Deformable Structures*, 1-53, Springer, 2015.

MODAL SUBSTRUCTURING USING NONLINEAR NORMAL MODES

Francesco Latini *[1], Jacopo Brunetti[2], Walter D'Ambrogio[2], and Annalisa Fregolent[1]
[1] Dipartimento di Ingegneria Meccanica e Aerospaziale, Università di Roma La Sapienza, Roma, Italy
[2] Dipartimento di Ingegneria Industriale e dell'Informazione e di Economia, Università dell'Aquila, L'Aquila, Italy

Summary Mechanical systems usually consist of many components connected together. The objective of this work is to define a coupling procedure based on Dynamic Substructuring to deal with coupled substructures jointed through nonlinear connections. It can happen that the nonlinearity at the connection is dominant with respect to those of the uncoupled components. Thus, it is possible to consider the latter as linear and account for the nonlinear effects of the connection. The connecting elements are thus considered as additional substructures included in the substructuring process. This is performed by setting the coupling procedure in the modal domain, considering the Linear Normal Modes (LNMs) for the linear substructures and the Nonlinear Normal Modes (NNMs) for the nonlinear connecting elements. The proposed method is used to couple two linear beams, connected through two cubic springs.

INTRODUCTION

Mechanical systems are in general made up of multiple components connected one to each other, thus each one affects the behaviour of the whole assembly. However, in many cases the connections themselves can have non negligible effects on the system's dynamics. The use of Finite Element Method (FEM) allows to get very accurate information regarding the system's behaviour, but the computational burden can largely increase if complex structures are under investigation. The need of reliable results in lesser time has led over the years to the development of other techniques, suitable to analize many situations. Among the others, Dynamic Substructuring [1, 2] has shown to be one of the most efficient in terms of computational time and accuracy of the achieved results. They have been first used to deal with linear systems [3], but some modifications have been made to account also for nonlinear phenomena. Although all the structures present nonlinearities, in some cases the nonlinear effects due to the connection are the most relevant. In such cases, the subsystems can be considered as linear, while the connection can be accounted in an additional nonlinear substructure to be included in the coupling process. This work aims at the definition of a substructuring-based procedure able to account for the nonlinear effects due to the connecting elements. Their nonlinear behaviour can be evaluated by computating their Nonlinear Normal Modes (NNM). They were first studied by Rosenberg [4] and later by Kerschen [5], who gave the definition for a nonlinear normal mode as the periodic response of a conservative nonlinear system which is characterized by energy dependent frequency and amplitude distribution. The coupling technique used here is based on the one proposed by Kuether and Allen [6], who managed to couple two nonlinear beams at their common interface. The procedure is performed in the modal domain, considering the Linear Normal Modes for the linear substructures and the Nonlinear Normal Modes for the substructures representing the nonlinear connecting elements. The NNMs of the coupled system achieved from the coupling can then be compared to the ones obtained by applying the Harmonic Balance (HB) [7] on the final assembly. This procedure was first applied to lumped parameter systems [8], providing very satisfactory results. The objective of this work is to evaluate the effectiveness of the method when linear continuous substructures connected through nonlinear springs are analyzed.

MODEL AND RESULTS

The model is composed of two linear beams coupled through two nonlinear cubic springs, as shown in Fig. 1. The parameters used for the analysis are listed in Table 1, where L is the length of the beams, t represents their thickness, w their width and n stands for the number of nodes considered for each beam. Fig. 2(a) shows the comparison between

L_A	w_A	t_A	L_B	w_b	t_B		ρ	E	n_A	n_B	k_l	k_{nl}
1000	10	2	1000	10	4	mm	7800 kg/m^3	205e9 Pa	21	21	1000 N/m	5e6 N/m^3

Table 1: Values of the physical and geometrical parameters of the model.

the first five NNMs obtained using the coupling procedure and the ones achieved applying the HB method. There is great correspondence between the curves, with an average error that is around 0.4% and being the maximum error below 0.7%, as shown in Fig. 2(b). Although it is not possible to retrace the presence of internal resonances, this is still a great result, because the main backbone of each NNM is reconstructed. Thus the method can be considered as reliable to investigate the dynamics of distributed parameter systems coupled with connecting elements, when the main behaviour of the structure needs to be analyzed.

*Corresponding author. E-mail: francesco.latini@uniroma1.it.

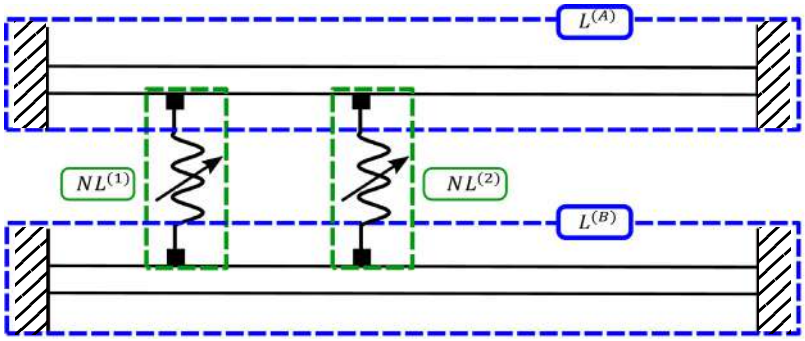

Figure 1: Sketch of the system model

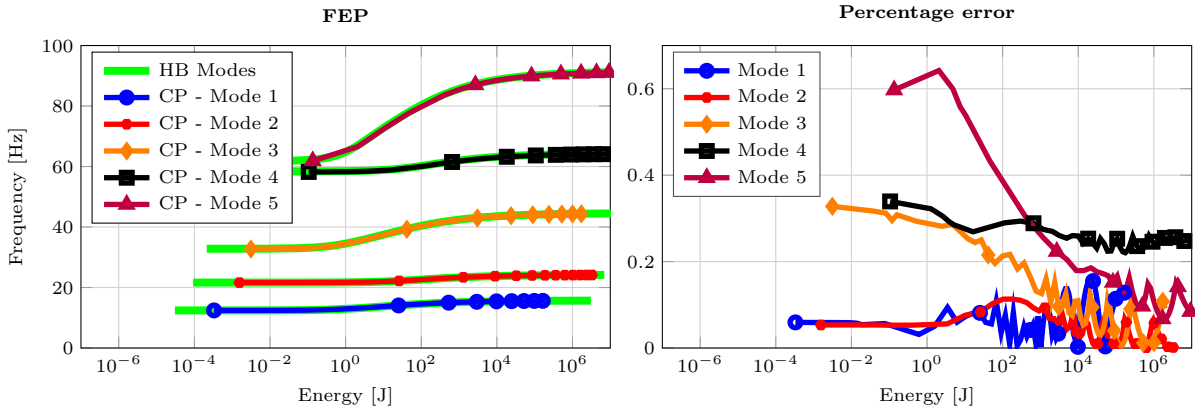

(a) Comparison of NNMs.

(b) Percentage Error.

Figure 2: Comparison between the NNMs obtained from the coupling procedure and Harmonic Balance

CONCLUSIONS

The coupling procedure presented here represents an alternative and fastmethod to analyze complex coupled structures in which the nonlinearities are only due to the presence of nonlinear connecting elements. The novelty of the approach is to consider the connections themselves as nonlinear substructures to be included in the coupling procedure. It is made possible by computing their NNMs to be used in the modal substructuring process. Further studies will be performed to evaluate the effects of modal truncation and see how the cut-off frequency affects the accuracy of the results.

References

[1] Hurty W., Dynamic analysis of structural systems using component modes, *AIAA Journal*, **Vol 3:** 678-685, 1965.

[2] Craig R., Bampton M. Coupling of substructures for dynamic analysis, *AIAA Journal*, 1968.

[3] de Klerk D., Rixen D. J., Voormeeren S. N., General Framework for Dynamic Substructuring: History, Review, and Classification of Techniques, *AIAA Journal*, 2008.

[4] Rosenberg R. M., The normal modes of nonlinear n-degree-of-freedom systems, *Journal of applied Mechanics*, **Vol 29:** 7-14, 1962.

[5] Kerschen G., Peeters M., Golinval J. Vakakis A. F., Nonlinear normal modes, Part I: A useful framework for the structural dynamicist, *Mechanical Systems and Signal Processing*, **Vol 23:** 170-194, 2009.

[6] Kuether R. J., Allen M. S., Nonlinear modal substructuring of systems with geometric nonlinearities, *54th AIAA/ASME/ASCE/AHS/ASC Structures, Structural Dynamics, and Materials Conference*, 2013.

[7] Krack M., Gross J., Harmonic balance for nonlinear vibration problems, *Springer*, 2019.

[8] Latini F., Brunetti J., D'Ambrogio W., Fregolent A. Substructures' coupling with nonlinear connecting elements. *Nonlinear Dynamics, Springer*, 2019.

DYNAMICS OF ROTATING COMPOSITE BEAM WITH NONLINEAR PIEZO-LAYERS

Jarosław Latalski *[1] and JerzyWarminski[1]
[1] Department of Applied Mechanics, Lublin University of Technology, Lublin, Poland

Summary The dynamics of a rotor consisting of a rigid hub with attached thin-walled active composite blade is presented. It's posed the beam is made of an orthotropic laminate with an embedded additional layer of piezoelectric material. When modelling the structural behaviour of the piezoceramics the higher order constitutive relations with respect to electric field have been adopted to properly capture the electromechanical properties of the transducer. Using the Hamilton's principle and next the Galerkin's method a system of mutually coupled nonlinear ordinary differential governing equations has been derived. A series of numerical simulations has been run to investigate the natural vibrations of the structure; next the forced vibrations excited by hub driving torque have been examined.

INTRODUCTION

The science of active structures, which is concerned with the interaction of electric/electromagnetic fields and elastic deformation of structures, has developed rapidly in the recent years. Typical applications of multifunctional designs range from civil structures, marine systems and MEMS to aerospace and aeronautics systems [1, 2]. Representative examples of active aerospace designs might be active rotors offering e.g. control of flutter and enhanced handling and maintenance. The topic of rotating smart composite beams is investigated worldwide by numerous research groups. Authors of the present submission contributed to this area presenting the mathematical model of the coupled behaviour of a laminate structure with an embedded active layer made of piezoceramics [3, 4].

STRUCTURAL MODEL AND PROBLEM FORMULATION

Let's consider an elastic single cell thin-walled beam with box shaped cross-section. The beam is clamped to the rigid hub rotating about fixed vertical axis CZ_0 – see Figure 1(a) driven by the external torque $T_{\mathrm{ext},z}$. The considered beam is made of unidirectional (UD) fibre reinforced composite material with additional structural layers of transversely isotropic piezoceramic material embedded onto opposite beam faces – Figure 1(b).

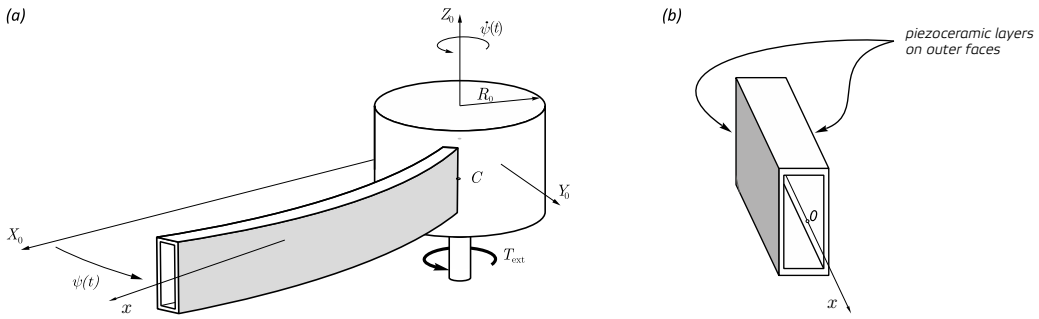

Figure 1: Model of the rotating hub—piezoelectric composite beam structure (a); placement of active material layers on the beam faces (b).

The mechanical equations of motion of the rotating hub/beam and a supplementary electric domain equation are derived according to the extended Hamilton's principle of the least action. In the presented research the higher-order constitutive relations of the piezoceramic material are postulated to extend the generality of the formulation and properly model the actual characteristics of active layers [4, 5]

$$\boldsymbol{\sigma} = \mathbf{C}\boldsymbol{\varepsilon} - \mathbf{e}\mathbf{E} - \hat{\mathbf{b}}\,\mathrm{sgn}(E_3)\mathbf{E}^2 \qquad \mathbf{D} = \mathbf{e}\boldsymbol{\varepsilon} + \boldsymbol{\xi}\mathbf{E} + \boldsymbol{\chi}\mathrm{sgn}(E_3)\mathbf{E}^2 \tag{1}$$

In the above relations—comparing to the classical linear ones—new terms are added where $\hat{\mathbf{b}}$ represents effective electrostrictive constants tensor and $\boldsymbol{\chi}$ is third order electric susceptibility tensor.

The system of coupled electromechanical partial differential governing equations is derived through standard variational calculus steps followed by adopting the derived orthogonality condition for complex bending-shear-torsional deformation of the beam. After transformation to the ordinary differential form and dimensionless notation one reads

$$\begin{gathered}\ddot{q} + \alpha_{12}\ddot{\psi} + \varsigma_1\dot{q} + \left(\alpha_{11} + \alpha_{13}\dot{\psi}^2\right)q + \alpha_{14}\dot{\psi}\dot{q}q + \alpha_{15}\mathrm{sgn}(q)q^2 = 0 \\ \left(1 + \widehat{J}_{\mathrm{h}} + \alpha_{h2}q\right)\ddot{\psi} + \alpha_{\mathrm{h}1}\ddot{q} + \varsigma_{\mathrm{h}}\dot{\psi} + \alpha_{\mathrm{h}3}\dot{q}\dot{\psi} = \mu_0 + \rho\sin\omega\tau\end{gathered} \tag{2}$$

*Corresponding author. E-mail: j.latalski@pollub.pl.

where the generalized coordinate q involves all three beam mechanical variables (flexural displacement, cross-section rotation and twist angle) and electrical one with different relative importance dependent on mode order and composite reinforcing fiber orientation. Symbol $\widehat{J}_{\mathrm{h}}$ stays for the relative mass moment of inertia and the driving torque is represented as a sum of a constant component μ_0 and a harmonic one with amplitude and frequency denoted by ρ and ω, respectively.

NUMERICAL RESULTS

A series of numerical simulation tests were performed to examine the dynamic performance of the system and to study the importance of nonlinear terms present in the piezoceramic material constitutive relations Eq. (1). Resonance curves around first natural frequency of the considered structure were plotted – see Figure 2 (a) and (b) for the beam and hub subsystem, respectively. The analysis was performed for different magnitudes of the dimensionless torque excitation amplitude ρ ranging from 0.001 up-to 0.01. Both resonance curves are bent to the left denoting a significant softening effect with stable and unstable regions highlighted by customary solid and dashed lines.

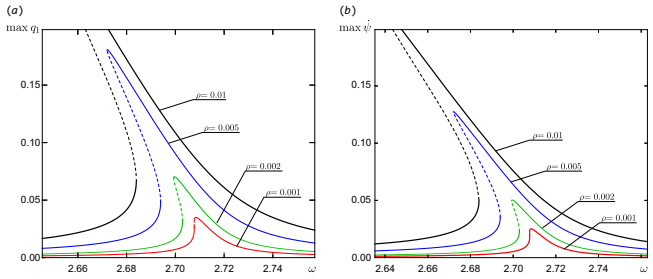

Figure 2: Resonance curves for the beam (a) and the hub (b) sub-systems around the first natural frequency with respect to excitation amplitude ρ. The solid (dashed) curves represent stable (unstable) solutions.

To confirm the results given in the above response diagrams time series plots were prepared — Figure 3. The envelopes of transient and steady state responses were shown with grey and blue colours corresponding to nonlinear and simplified (linear) piezoelectric effect, respectively. The results were obtained for the excitation amplitude $\rho = 0.01$ and frequency $\omega = 2.68$ for initial conditions matching lower branches of frequency response curves (Figure 2).

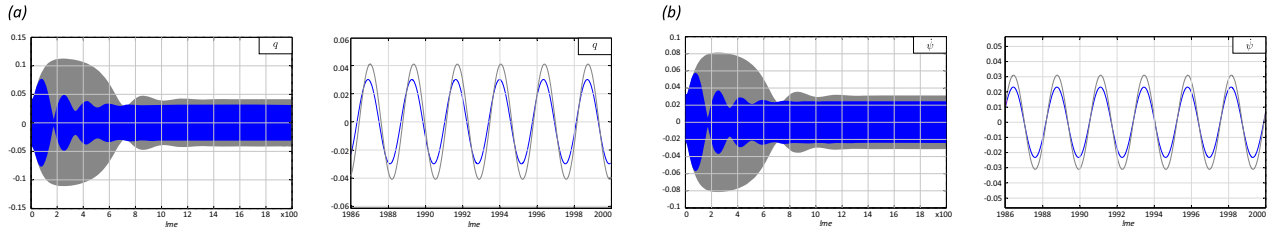

Figure 3: Envelopes of linear and nonlinear transient and steady state responses of the beam (a) and the hub (b) for excitation frequency $\omega = 2.68$ and amplitude $\rho = 0.01$; initial conditions: $q|_{\tau=0} = 0.04$, $\dot{q}|_{\tau=0} = 0$, $\Omega|_{\tau=0} = 0.005$. Colour code: gray – nonlinear piezoelectric effect, blue – linear piezoelectric effect.

FINAL REMARKS

The proposed mathematical model of the active rotor takes into account the nonlinear constitutive relations of the piezoceramic material beam layers. The performed numerical studies revealed the non-linear softening type frequency response of the system if driven by the torque applied to the hub. The important observation is the nonlinear features of the characteristics were present both for the beam and for the hub as well. Moreover, a significant difference in transient state was revealed when comparing nonlinear and linearized active beam response time series plots.

Acknowledgements
The work is financially supported by grant 2016/23/B/ST8/01865 from the National Science Centre, Poland.

References

[1] Chopra I., Sirohi J. Smart structures theory. Cambridge University Press, NY 2013.
[2] Smith R. C. Smart Material Systems. Model Development. Society for Industrial and Applied Mathematics, Philadelphia 2005.
[3] Latalski J. A coupled-field model of a rotating composite beam with an integrated nonlinear piezoelectric active element. *Nonlin. Dyn.* **90**(3), 2145–2162 2017
[4] Latalski J., Warminski J. Nonlinear vibrations of a rotating thin-walled composite piezo-beam with circumferentially uniform stiffness (CUS). *Nonlin. Dyn.* **98**(4), 2509–2529, 2019.
[5] Tiersten H. F. Electroelastic equations for electroded thin plates subject to large driving voltages. *J. Appl. Phys.* **74**(5): 3389–3393, 1993.

NONLINEAR FLEXURAL-FLEXURAL INTERACTIONS OF THE EXTENSIBLE SIMPLY SUPPORTED BEAM WITH AN AXIAL SPRING

Lukasz Kloda *[1,2], Stefano Lenci[2], and Jerzy Warminski[1]
[1] Department of Applied Mechanics, Lublin University of Technology, Lublin, Poland
[2] Department of Civil and Buildings Engineering and Architecture, Polytechnic University of Marche, Ancona, Italy

Summary In this paper large amplitude vibrations of the planar beam-spring system are studied. The model has linear behaviour of the material, inertia forces, linear viscous damping and nonlinear geometric deformations, and is subjected to an external excitation. The main goal is to investigate the first and second bending modes interactions which occurs not so close to primary (linear) resonance. Selected numerical results are compared with experimental tests and then the numerical analysis is extended beyond the experimental results.

INTRODUCTION

Structural systems based on simply supported beams are common in engineering applications. The study of the dynamic response of those structures is of great importance in stability and control analysis, and can have different behaviours. For instance the simply supported beam (when inertia terms are properly considered) has softening nature while the same structure with axially restrained ends has a hardening behaviour [1]. The boundary conditions at the beam's end can be controlled by an axial spring whose stiffness could be increased from 0 to ∞. Then, the system response changes continously his nature from softening to hardening phenomenon for the parametrically excited system [2] as well as the externally excited case [3]. The aim of this paper is to study the case of the primary resonance, when interaction between the first and the second bending modes occur for large amplitude oscillations. For this purpose a laboratory setup is built and based on experimental tests a numerical model is developed and used to match the experimental results

RESEARCH OBJECT

The beam-spring system consists of an initially straight beam mounted at the hinge (left) and the sliding support with axial compression spring (right), see Fig. 1a. The holder is screwed to a slip table, which enables tabletop periodic movement in the beam's flexible plane. The spring and beam can be replaced in order to vary the stiffnesses $EA(L)^{-1}/k_s$ which is a dimensionless parameter and correlate parameters of the beam-spring structure. The beam's dimensions are $L\times b\times h = 450\times 20\times 4.75$ mm, the hinge has mass moment of inertia $I_0 = 1.0928\times 10^{-5}$ kgm^2 and movable tip elements are reduced to mass moment of inertia $I_t = 7.556\times 10^{-6}$ kgm^2 together with concentrated tip mass $M_t = 0.155$ kg.

The prototype is modeled in ABAQUS_CAE© software by 100 equal-length linear beam elements $B21$ type placed in XZ plane (Fig. 1b). Boundary conditions are written $U(Z=0) = U(Z=L) = W(Z=0) = 0$, the axial spring is tied to node 101, and inertia elements are assigned to the beam nodes 1 and 101. Simulations are run in time domain, where frequencies of external excitation $\xi \sin \Omega T$ are gradually changed by sweep forward and backward to follow stable path solutions. The completed simulation is post-processed from the time domain to the domain of the excitation frequency and associated steady state motion amplitude $U_{max}(\xi, \Omega)$.

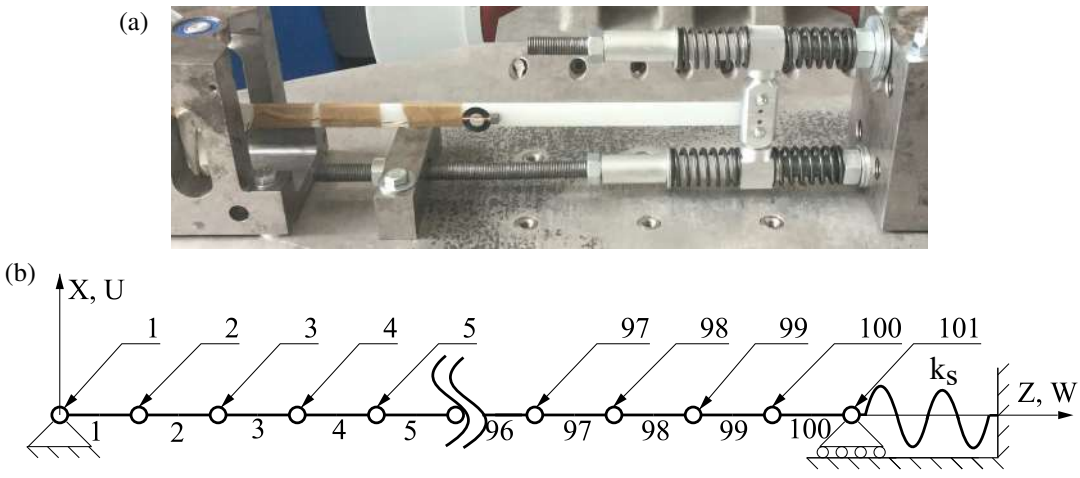

Figure 1: The hinged-simply supported beam with an axial spring: front view of experimental setup (a) and top view of finite element model (b).

*Corresponding author. E-mail: l.kloda@pollub.pl.

RESULTS AND CONCLUSIONS

Findings of the experimental and numerical investigations show a very good agreement for small amplitude of kinematic excitation $\xi = 1.0$ mm as well as large one $\xi = 2.5$ mm (Fig. 2a). Tests on Plexiglas beam with spring stiffness $k_s = 29254$ N/m $(EA(L)^{-1}/k_s = 0.042)$ present hardening nature with hysteresis and expose the interaction between the first and second bending modes (Fig. 2b), despite the fact that the second mode is not directly excited. It means that superharmonic resonance 1 to 3 between these modes occurs through nonlinearities and inertia terms, see Fig. 2c.

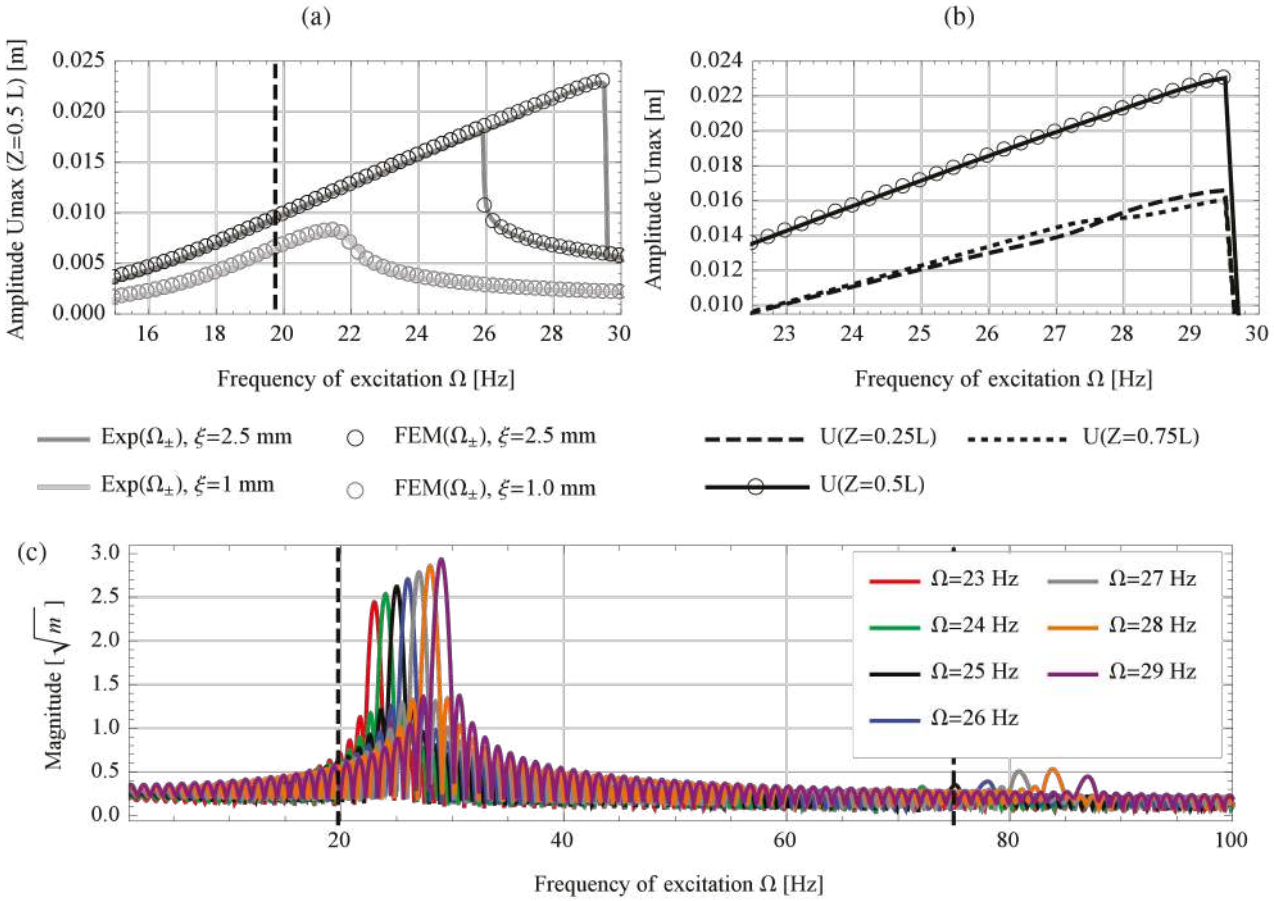

Figure 2: Frequency response curves for the beam: experiment vs finite element method (a), numerical simulations with modes interactions (b) and corresponding FFT analysis for node 26 (c). Black dashed vertical lines represent the natural frequencies.

In the future tests both flexural modes will be excited directly e.g. by concentrated force applied at $Z = 0.25L$ or periodic angular rotation of the hinge. In the proposed case presence of an additional stable solution is expected, different than in [4] where the response is significantly changed, rather as an imposition of a secondary resonance on a primary one with two solution hysteresies - wide and narrow [5].

ACKNOWLEDGEMENT

This work is part of the collaboration between Polytechnic University of Marche and Lublin University of Technology, which is aimed at developing a Joined Doctoral Programme.

The work is financially supported by grant No. 2019/33/N/ST8/026611 from the National Science Centre, Poland.

References

[1] Atluri S. Nonlinear Vibrations of a Hinged Beam Including Nonlinear Inertia Effects. *J. Appl. Mech.* **40**: 121-126, 1973

[2] Shibata A., Ohishi S., Yabuno H. Passive method for controlling the nonlinear characteristics in a parametrically excited hinged-hinged beam by the addition of a linear spring. *J. Sound Vib.* **350**: 111-122, 2015

[3] Kloda L., Lenci S., Warminski J. Hardening vs softening dichotomy of a hinged-simply supported beam with one end axial linear spring: experimental and numerical studies. *Int. J. Mech. Sci.* 1-22 (in press)

[4] Xiong, L., Tang, L., Mace, B.R. A comprehensive study of 2:1 internal-resonance-based piezoelectric vibration energy harvesting. *Nonlinear Dyn.* **91**: 1817-1834 (2018)

[5] Crespo Da Silva M.R.M., Zaretzky C.L. Non-linear modal coupling in planar and non-planar responses of inextensional beams. Int. J. Nonlin. Mech. **25(2-3)**: 227-239, 1990

ROLLING PENDULUMS ALONG CURVILINEAR TRACES AND SURFACES: COLLISION THEORY AND DYNAMICS OF VIBRO-IMPACT SYSTEMS

Hedrih (Stevanović) R. Katica[1,2]
[1] Mathematical Institute of Serbian Academy of Sciences and Arts, Belgrade, Serbia
[2] Faculty of Mechanical Engineering at University of Niš, Serbia

Summary An overview of the new derived nonlinear differential equations and phase trajectory equations of the body's rolling along curvilinear stationary and rotating curvilinear line - trajectories, as examples of rolling pendulums with one degree of freedom is done An appropriate system of coupled nonlinear differential equations for a homogeneous heavy ball rolling on an arbitrary surface with all elements of geometry, kinematics and rolling dynamics was performed. A generalization is given for the example of rolling a ball along the coordinate surfaces of functional nonlinear coordinate systems of curvilinear orthogonal coordinates, using the base vectors of the tangent space of the vector of the position of the contact point of the ball in rolling with the coordinate surface at which it rolls.
Based on Petrovic's theory Elements of Mathematical Phenomenology and Phenomenological Mapping, the theory of collisions between rolling bodies through geometry, kinematics and dynamics of impact and collision of balls in rolling is formulated, and examples of the dynamics of vibro-impact systems containing rolling balls are given.

ROLLING PENDULUMS ALONG STATIONARY OR ROTATE CURVILINEAR TRACES

1* We observe an axially symmetric body with one central plane of symmetry that is governed by the axis of symmetry of the body, Figure 1.a*. Let's propose that curvilinear trace of rolling is a curvilinear line defined by $y=f(x)$ in vertical coordinate plane $P(x, y=f(x))$. The rolling body, without slipping, has a degree of freedom movement along the curvilinear path, determined by generalized coordinate x . Nonlinear differential equation of dynamics of a rolling, heavy axial symmetric, with on a plane of symmetry, body along general curvilinear trace in vertical plane, is derived in the form: $\ddot{x}+\frac{1}{2}\dot{x}^2\frac{F'(x,r)}{F(x,r)}+\frac{g}{\kappa}\frac{f_C'(x,r)}{F(x,r)}=0$, (1) where coefficient of rolling $\kappa=\frac{\mathbf{J}_P}{Mr^2}=\frac{\mathbf{i}_P^2}{r^2}=\frac{\mathbf{i}_C^2}{r^2}+1=\kappa$. The first integral of the previous differential equation is equation of phase trajectory. A qualitative analysis of content of set of singular points, depending of the forms of curvilinear trace of rolling body is presented.

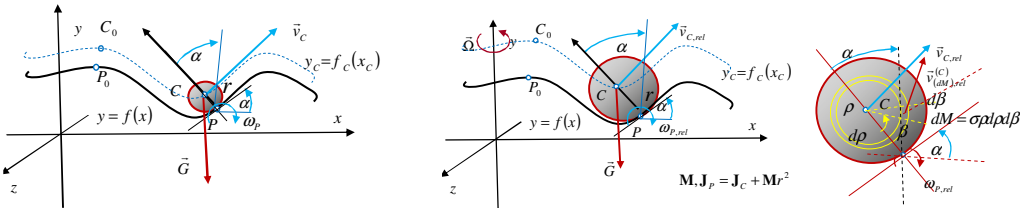

Figure 1. a* Geometric parameters of rolling of a rigid body along the curvilinear trace in a vertical plane; b* and **c*** Geometric parameters of rolling of heavy rigid thin discs on a rotating curvilinear trace in a vertical plane around a vertical axis

2* Nonlinear differential equation of rolling motion of a heavy thin rigid disk, without slipping with radius r, along rotate the curvilinear trace of the form $y=f(x)$, around vertical axis with constant angular velocity Ω, (see Fig.1.b* and c*), is: $\ddot{x}+\frac{1}{2}\dot{x}^2\frac{F'(x,r)}{F(x,r)}-\frac{r^2}{2}\Omega^2\frac{\mathbf{J}_z'(x,M,r)}{\mathbf{J}_P F(x,r)}+\frac{g}{\kappa}\frac{f'(x)}{F(x,r)}=0$, (2) . The first integral of the differential equation is phase trajectory equation and in the following form:

$$[\dot{x}(x)]^2=e^{-\int\frac{1}{F(x,r)}\frac{\partial F(x,r)}{\partial x}dx}\left[\Omega^2\int\left\langle\frac{r^2\mathbf{J}_z'(x,M,r)}{\mathbf{J}_P F(x,r)}\right\rangle e^{\int\frac{1}{F(x,r)}\frac{\partial F(x,r)}{\partial x}dx}dv-\frac{2g}{\kappa}\int\left\langle\frac{f'(x)}{F(x,r)}\right\rangle e^{\int\frac{1}{F(x,r)}\frac{\partial F(x,r)}{\partial x}dx}dv+C\right] \quad (3)$$

A Theorem is formulated. A qualitative analysis of stability of singular points and relative equilibrium positions on trace of rolling body is presented. Particular examples are presented in References [1-5].

ROLLING A HEAVY BALL OVER THE CURVE COORDINATE SURFACES OF ORTHOGONAL CURVILINEAR COORDINATE SYSTEMS

Suppose, we look at the coordinate surface of the functional nonlinear coordinate system, orthogonal curvilinear coordinate lines q^1, q^2 and q^3, with corresponding basic vectors $\vec{g}_i(q)$, $i=1,2,3$ each tangent to one of these coordinate line at considered point $P(q^1,q^2,q^3)$, see Fiig. 2.a*.. This coordinate surface is defined by two coordinate

*Corresponding author. E-mail: **khedrih@sbb.rs**, katicah@mi.sanu.ac.rs

lines q^1 and q^2 for $q^3 = const$, at considered point $P(q^1, q^2, q^3 = const)$, or by two basic vectors $\vec{g}_1(q)$ and $\vec{g}_2(q)$, in the tangent plane to the surface and third $\vec{g}_3(q)$ orthogonal to the tangent plane of the surface in corresponding point $P(q^1, q^2, q^3 = const)$. These coordinate lines q^1 and q^2 for $q^3 = const$ lie in that surface, that is, determine the shape of that surface. Suppose that a heavy rigid ball rolls over this coordinate surface. We denote with P point of the contact between ball's spherical surface and corresponding coordinate surface over which ball is in rolling. Assuming that there is no proper self-rotation, but only rolling, without slipping, then expression of the kinetic energy $\mathbf{E}_k$ is equal to: $\mathbf{E}_k = \frac{1}{2}\mathbf{J}_P\omega_P^2 = \frac{1}{2r^2}\mathbf{J}_P\left\langle g_{11}(\dot{q}^1)^2 + g_{22}(\dot{q}^2)^2\right\rangle + \frac{1}{2}\mathbf{J}_P\frac{g_{33}}{(|\vec{g}_3|)^2}\left(\dot{q}^1\frac{\partial|\vec{g}_3|}{\partial q^1} + \dot{q}^2\frac{\partial|\vec{g}_3|}{\partial q^2}\right)^2$, (4). As we adopted the generalized coordinates q^1 and q^2, by which we expressed kinetic $\mathbf{E}_k$ and potential $\mathbf{E}_p$ energy, now using the Lagrange differential equations of the second kind for independent generalized coordinates q^1 and q^2, we write two coupled nonlinear differential equations of rolling heavy ball over the coordinate surface.

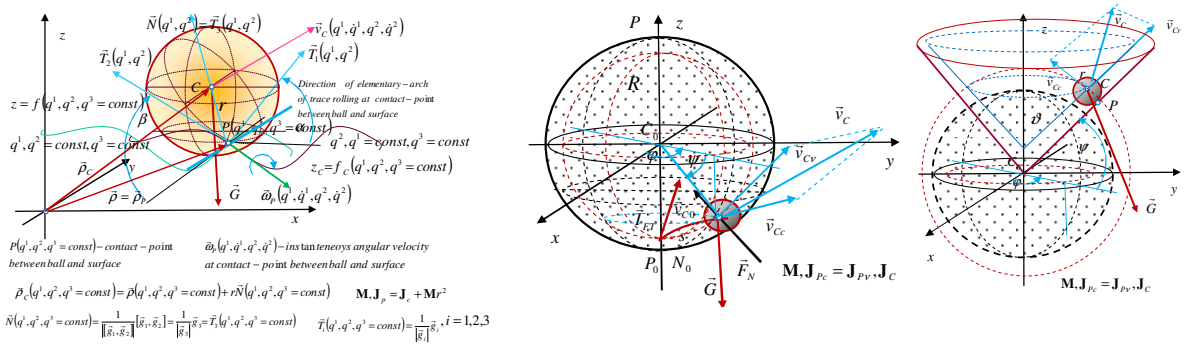

a* b* c*

Figure 2. a* Geometric parameters of rolling of a rigid ball along the coordinate surface of functional nonlinear coordinate system of orthogonal curvilinear coordinates; b* Kinetic elements of rolling heavy ball inside of coordinate sphere (b*) and inside of cne (c*)

COLLISION THEORY AMD DYNAMICS OF VIBRO-IMPACT SYSTEMS

Based on Petrovic's theory Elements of Mathematical Phenomenology and Phenomenological Mapping, the theory of collisions between rolling bodies through geometry, kinematics and dynamics of impact and collision of balls in rolling is formulated, and examples of the dynamics of vibro-impact systems containing rolling balls are given [2-5].

CONCLUSIONS

The corresponding systems of nonlinear differential equations of rolling the heavy ball along the coordinate surfaces of several functional nonlinear coordinate systems, including the spherical coordinate system, (Fig. b* and c*) is done. It has been proved that rolling the ball along a curved line is a system with one degree of freedom, and rolling the ball over the surface is a system with two degrees of freedom. Some examples of the vibro-impact dynamics are investigated.

Acknowledgement. Parts of this research were supported by the Ministry of Sciences of Republic Serbia trough Mathematical Institute SANU Belgrade Grants OI 174001" Dynamics of hybrid systems with complex structures".

References

[1] Hedrih (Stevanovic) K., (2019), Rolling heavy ball over the sphere in real Rn3 space, Nonlinear Dynamics, Springer, (2019) 97:63–82, https://doi.org/10.1007/s11071-019-04947-1. ISSN: 0924-090X (print version) ISSN: 1573-269X (electronic version)

[2] Hedrih (Stevanovic) K., (2019), Vibro-impact dynamics of two rolling heavy thin disks along rotate curvilinear line and energy analysis, **Journal** Nonlinear Dynamics, 98(4), 2551-2579, **DOI** 10.1007/s11071-019-04988-6; Springer; ISSN: 0924-090X (print version) ISSN: 1573-269X (electronic version); http://link.springer.com/article/10.1007/s11071-019-04988-6;

[3] Hedrih (Stevanovic) K., (2018), Non-linear phenomena in vibro-impact dynamics: Central collision and energy jumps between two rolling bodies, Dedicated to memory of Professor and important scientist Ali Nayfeh (December 21, 1933-March 27, 2017). **Nonlinear Dynamics,** February 2018, Volume 91, **Issue 3**, pp 1885–1907. https://doi.org/10.1007/s11071-017-3988-x. ISSN: 0924-090X (print version) ISSN: 1573-269X (electronic version) https://link.springer.com/article/10.1007/s11071-017-3988-x

[4] Hedrih (Stevanovic) K., (2017), Central collision of two rolling balls: theory and examples, Advances in Theoretical and Applied Mechanics, Vol. 10, 2017, no. 1, 33-79. https://doi.org/10.12988/atam.2017.765.

[5] Hedrih (Stevanović) K.,(2017), Dynamics of Impacts and Collisions of the Rolling Balls, Dynamical Systems: Theoretical and Experimental Analysis, Springer Proceedings in Mathematics & Statistics, Volume Number: 182, Chapter 13, pp. 157-168. © Springer, Part of Springer Science+Business , ISBN 978-3-319-42407-1. ISSN 2194-1009 ISSN 2194-1017 (electronic)

NONSTATIONARY RESPONSES OF MDOF NONLINEAR SYSTEMS UNDER RANDOM EXCITATIONS

Siu-Siu Guo *[1] and Qingxuan Shi[2]
[1] School of Civil Engineering,Institute of Mechanics and Technology, Xi'an University of Architecture and Technology, Xi'an, China
[2] School of Civil Engineering, Xi'an University of Architecture and Technology, Shaanxi, China

Summary The key to dynamical response analysis of MDOF structure under random excitation is generally to solve corresponding high-dimensional FP equation, which has been a great challenge for many years. A novel technique is developed for determining nonstationary solution of the FP equation. Specifically, the FP equation is reduced to a lower dimensional one through the state-space-split (SSS) technique. Then exponential-polynomial closure (EPC) method is applied to solve it. Monte carlo simulation (MCS) is conducted to verify the proposed solution procedure. A ten-degree-of-freedom nonlinear system under random excitations are studied to validate the effectiveness of the proposed procedure. It is found that obtained results agree well with the simulated ones. Moreover, computation time taken by the proposed procedure is only a smaller fraction of the one taken by the simulated method.

INTRODUCTION

Many systems are often modelled as multi-degree-of-freedom (MDOF) systems. They are generally subjected to stochastic loads, such as earthquake, wind or sea waves. Under these excitations, many systems experience inelastic deformation and exhibit nonlinearity. In the presence of the coupling of nonlinearity and randomness, stochastic response analysis becomes extremely difficult, especially for MDOF systems [1].

On the premise of Markov process, the response PDF is governed by Fokker-Planck (FP) equation. For a dynamical systems of dimension $2n$, corresponding FP equation is with $2n$ spatial dimensions and one time dimension. In this sense, MDOF systems results in high-dimensional FP equation. The FP equation has been explored for more than fifty years. Nonetheless, great challenges still exist for high-dimensional or multi-degree-of-freedom (MDOF) nonlinear stochastic systems.

In this paper, the SSS-EPC method is further improved to consider the time effect and makes nonstationary solutions of high dimensional FPK equations available. In this regard, random response analysis of MDOF nonlinear system becomes possible. The paper is organized as follows: the SSS technique is adopted to reduce the initial high dimensional FP equation to the interested lower one. Then the EPC method is employed to solve the treated one. Meanwhile, MCS is conducted to verify the proposed solution procedure. Finally, a ten-degree-of-freedom MDOF nonlinear system under external excitation is investigated to prove and validate the effectiveness of the proposed procedure.

SOLUTION PROCEDURE

MDOF system under random excitations are described in Ito's form as follows

$$\frac{d}{dt}X_i = f_i(\mathbf{X},t) + g_{ij}(\mathbf{X},t)W_j(t) \quad i = 1,2,...,n_x, j = 1,2,...,m \tag{1}$$

where X_i are components of the state vector $\mathbf{X}$; functions $f_i(\mathbf{X},t)$ and $g_{ij}(\mathbf{X},t)$ are generally nonlinear functions with deterministic forms. For the sake of simplifying the analysis, random normal excitations $W_j(t)$ are assumed to be independent of each other. They are characterized with power spectral densities

$$E[W_i(t)W_j(t+\tau)] = S_{ij}\delta(\tau), \quad i,j = 1,2,...m. \tag{2}$$

where $\delta(\cdot)$ is Dirac function, S_{ij} are constants.

Due to white noise excitations, the state vector is Markovian. As a result, the PDF $p(\mathbf{x},t)$ of the state vector is governed by the high-dimensional FP equation. With state space split technique, the whole state space $R_{\mathbf{X}}$ is divided into two parts $R_{\mathbf{X}_1}$ and $R_{\mathbf{X}_2}$. The first part $R_{\mathbf{X}_1}$ is related to interested state space $\mathbf{X}_1$, the other part $R_{\mathbf{X}_2}$ is the left space $\mathbf{X}_2$. Accordingly, the coefficients of the FP equation are divided into functions of only the interested state variables $\mathbf{x}_1$ characterized by PDF $p(\mathbf{x}_1,t)$ and functions with other state variables $(\mathbf{x}_1,\mathbf{x}_k)$ characterized by joint PDF $p_k(\mathbf{x}_1,\mathbf{x}_k,t)$. After a series of treatment, the high dimensional FP equation is finally reduced to a lower dimensional function of only few interested states [2]. With equivalent linearization technique, the lower dimensional FP function is further simplified as an approximated one.

With regard to the reduced approximated lower dimensional FP equation, traditional approximate methods becomes available. Herein the EPC method is utilized to solve nonstationary solutions of the treated FP equation [3].

On the other hand, since there is no exact solution to the high dimensional FP equation, MCS method with an sample size of 10^6 is conducted to verify the efficiency of the proposed solution procedure.

*Corresponding author. E-mail: siusiuguo@hotmail.com

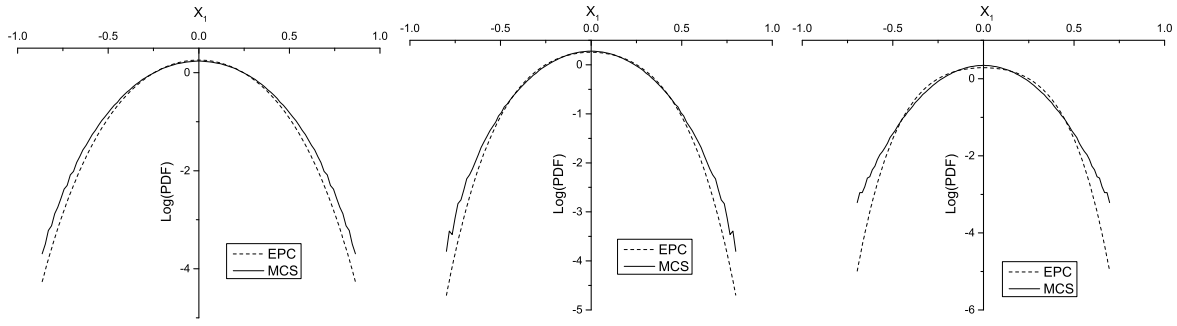

(a) t=1s (b) t=5s (c) t=7s

Figure 1: Log(PDF) of displacement x_1 at different time instants

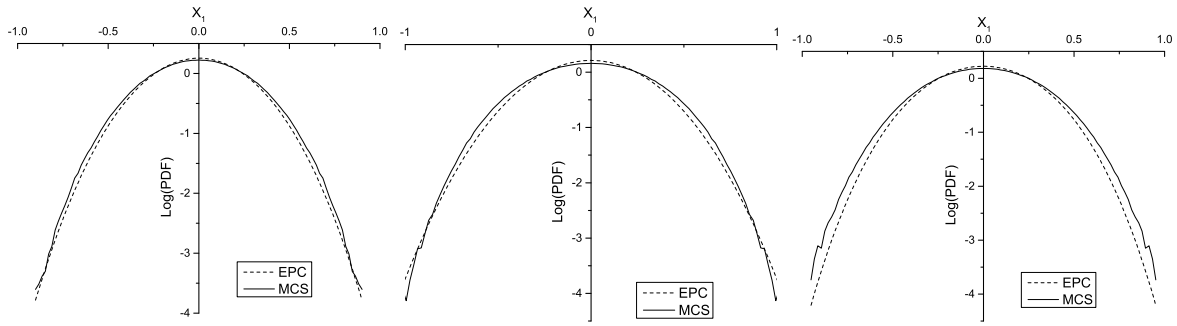

(a) t=1s (b) t=5s (c) t=7s

Figure 2: Log(PDF) of displacement x_{10} at different time instants

NUMERICAL EXAMPLES AND RESULTS DISCUSSIONS

Considering the following 10-degree-of-freedom nonlinear system under external excitation

$$\ddot{\mathbf{X}} + \mathbf{C}\dot{\mathbf{X}} + \mathbf{K}\mathbf{X} + \mathbf{H}(\mathbf{X};t) = f(t)\mathbf{I}W(t), \tag{3}$$

where $\mathbf{X}(t) = \{X_1, X_2, ...X_{10}\}$; $H(\mathbf{X};t) = \{X_1^3, X_2^3, ..., X_{10}^3\}$, $\mathbf{I} = \{1, 1, ..., 1\}^T$, $f(t)$ is of Amin and Ang type modulating function, $W(t)$ is Gaussian white noise process with power spectral density $E[W(t)W(t+\tau)] = 0.1\delta(\tau)$.

The results are shown in Figure 1 and Figure 2. By comparison, it is found that approximate solutions close to the simulated ones at different time instants.

Most importantly, it should be noticed that the computational time of the proposed procedure taken is greatly less than the one of the MCS method. For example, the time spent for the PDF results at time instants $t = 7s$ is about two seconds, while it is up to about half an hour for the MCS method.

CONCLUSIONS

In this paper, MDOF nonlinear systems under nonstationary random excitations are analyzed via high dimensional FP equation. It is solved by the generalized SSS-EPC method in a computationally efficient manner. Comparison with pertinent MCS results have demonstrated a relatively high accuracy degree of the proposed solution. Moreover, obtained results can be further utilized to conduct reliability analysis of engineering structures.

References

[1] Lin Y. K., Cai G. Q Probabilistic structural dynamics: advanced theory and applications. McGraw Hill, Singapore 1995.
[2] Er G. K. Methodology for the solutions of some reduced Fokker-Planck equations in high dimensions. *Ann. Phys. (Berlin)* **523**: 247-258, 2011.
[3] Guo S. S. Nonstationary solutions of nonlinear dynamical systems excited by Gaussian white noise. *Nonlinear Dyn.* **92**: 613-626, 2018.

A COMBINED LOCAL AND GLOBAL BIFURCATION APPROACH FOR NONLINEAR DYNAMICS BASED DESIGN OF A SELF-EXCITED INERTIA WHEEL PENDULUM

A. Zelman, S. Tsulker, R. Manikandan, A. Wolf and O. Gottlieb
Department of Mechanical Engineering, Technion – Israel Institute of Technology, Haifa, Israel

Summary: We consider a combined local and global bifurcation approach for nonlinear dynamics based design of a self-excited inertia wheel pendulum. The dynamical system can exhibit coexisting equilibria and periodic limit cycle oscillations culminating with possible nonstationary rotations which are an outcome of the implemented nonlinear feedback scheme. While a linear analysis is sufficient to for local stability of equilibria, an asymptotic analysis is required to determine if the Hopf threshold of periodic limit cycle oscillations is supercritical or subcritical and a global Melnikov approach is employed to obtain an estimate for the onset of transverse homoclinic rotations. We demonstrate our combined bifurcation approach via numerical integration and a desktop experiment.

INTRODUCTION

Self-excitation of restrained and freely oscillating rigid bodies are encountered in a variety of engineering applications including friction induced vibration, aeroelastic limit cycle oscillations and fluid-structure interaction. Stabilization of limit cycle oscillations has been proposed by several approaches including boundary feed forward control of a multi-tethered lighter-than-air sphere [1] and digital delayed feedback control of an aero-pendulum [2].While both translating internal attachments and internal rotating rigid-bodies have been shown to reduce the magnitude of oscillations of primary structures undergoing vortex-induced vibration, this reduction was documented for a specific set of control parameters (such as effective linear structural damping) and has been shown to lead to violent and non-stationary behaviour [3]. Of particular importance is the capability of an inertia wheel (or reaction wheel) with nonlinear feedback to obtain stable and robust limit-cycle oscillations in underactuated dynamical systems [4]. Thus, we consider here a planar pendulum augmented with a rotating inertia wheel (see Fig.1-left) where the unperturbed Hamiltonian system can be shown to exhibit a heteroclinic pitch phase plane with linear feedback (see Fig.1-middle) and a combined homoclinic and heteroclinic phase plane (see Fig.1-right) with nonlinear saturation [5].

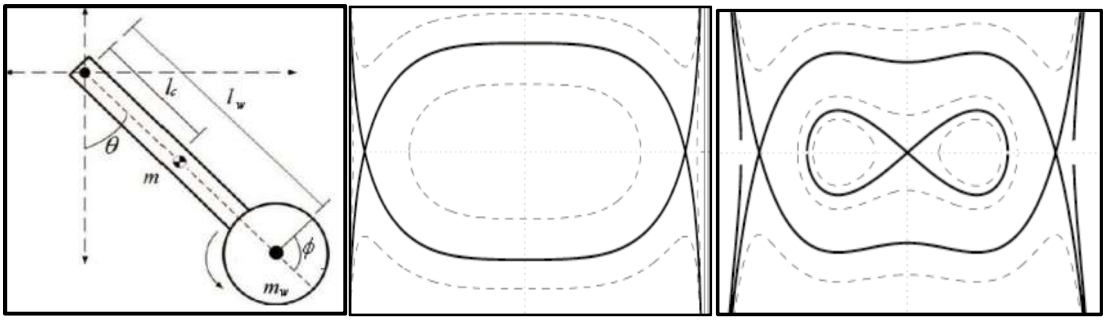

Figure 1. Inertia wheel pendulum coordinate system (left), heteroclinic (middle) and homoclinic (right) unperturbed Hamiltonian pitch phase planes with linear and nonlinear saturation based feedback respectively.

RESULTS

We summarize the local behaviour of the inertia wheel pendulum for the case of linear feedback with bifurcation diagrams for two sets of gains that enable a supercritical bifurcation about the zero equilibrium (Fig.2-left) and a subcritical bifurcation about the upright position (Fig.2-middle) respectively.

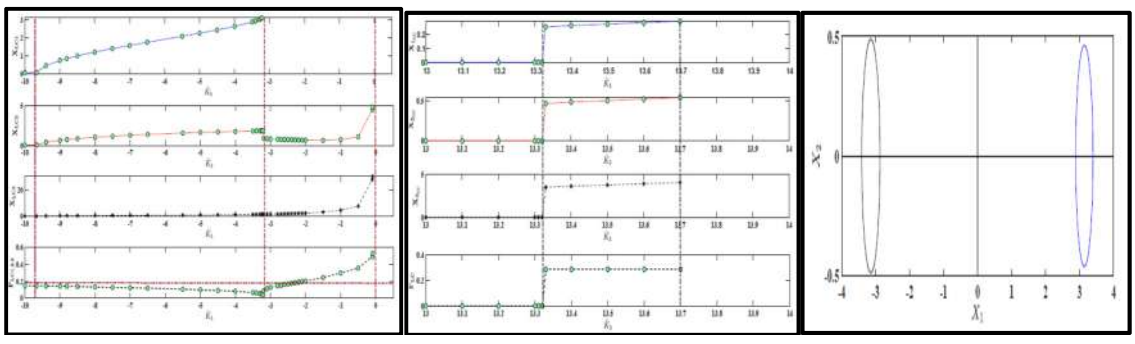

Figure 2. Supercritical (left) and subcritical (middle) bifurcation diagrams of stabilized inertia wheel dynamics as a function of wheel velocity gain and pitch phase plane (right) a pair of periodic limit cycles about the unstable upright position.

Numerical integration of the inertia wheel system with a gain set in the subcritical range reveals the anticipated pair of limit cycles about the upright position (Fig. 2-left). We employ a Melnikov based analysis [6] on a reduced third-order system obtained for a configuration with a cyclic coordinate for the inertia wheel position. The obtained threshold yields a bound on the gains required for periodic oscillations. The limitations of this approach consist of weakly nonlinear damping mechanisms for both pendulum and wheel friction bearings, and a sufficiently small gain for the pendulum angular velocity.

An investigation of the inertia wheel pendulum with nonlinear saturation feedback yields the addition of a pair of equilibria between the zero and upright positions. We make use of the local criteria to design a desktop experiment (Fig.3-left) where system parameters are obtained from a set of controlled free vibration decay experiments [7]. The latter reveal that a nonlinear dry friction Coulomb model is required to describe the system bearings. The estimated parameter set is incorporated into the model to yield a candidate set of gains for limit cycle oscillations about the upright position. We note that the nonstationary results portrayed in Fig.3 are possibly due to the implemented Arduino controller (not shown) which controls the speed of the motor driving the inertia wheel. The nonstationary time histories of the pendulum angle and velocity (Fig.3-middle) are sampled every positive zero-crossing of inertia wheel velocity to yield a wide spread Poincare' map (Fig.3-right).

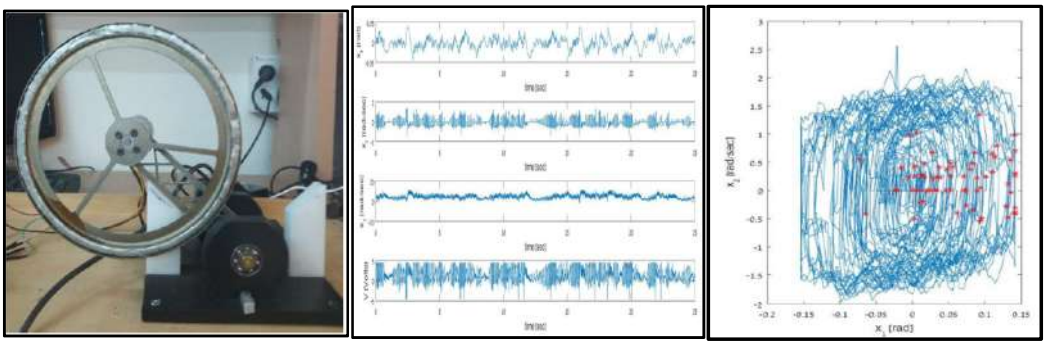

Figure 3. Inertia wheel experimental setup (left), nonstationary response (middle) and pitch phase plane overlaid with a Poincare' map (right).

CLOSING REMARKS

We consider a combined local and global bifurcation approach for nonlinear dynamics based design of a self-excited inertia wheel pendulum. The dynamical system can exhibit coexisting equilibria and periodic limit cycle oscillations culminating with possible nonstationary rotations which are an outcome of the implemented nonlinear feedback scheme. While a linear analysis is sufficient to for local stability of equilibria, an asymptotic analysis is required to determine if the Hopf threshold of periodic limit cycle oscillations is supercritical or subcritical and a global Melnikov approach is employed to obtain an estimate for the onset of transverse homoclinic rotations. We demonstrate our combined bifurcation approach via numerical integration and a desktop experiment. This combined approach implemented on a reduced third-order dynamical system can serve as a basis for comparison of different control strategies that exhibit a similar heteroclinic or homoclinic bifurcation structure.

References

[1] Mi L. and Gottlieb O., Nonlinear Dynamics, **93**:1353–1369, 2018.
[2] Habib G., Miklos A., Enikov E.T., Stepan G., and Rega G., Int. J. Dynamics and Control, 5: 629-643, 2017.
[3] Tumkur RKR, Pearlstein AJ, Masud A, Gendelman OV, Balnchard AB, Bergman LA, Vakakis AF, J Fluid Mechanics 828: 196-235, 2017.
[4] Haddad, N.K., Belghith, S, Gritli, H.and Chemori, A. Int. J. Bifurcation and Chaos**, 27**: 1750104, 2017.
[5] Spong M.W., Cork P., and Lozano R., Automatica, 37: 1845-1851, 2001.
[6] Wiggins S., and Holmes, P.J., SIAM J. Math Anal**. 18**: 612-629, 1987.
[7] Senesh M, Wolf A, Gottlieb O., J Vibration and Acoustics, 132: 011007, 1-12, 2010.

NONLINEAR DYNAMIC OPTIMIZATION OF HYSTERETIC NANOSTRUCTURED BEAMS

Giovanni Formica *[1] and Walter Lacarbonara[2]
[1] Department of Architecture, Roma Tre University, Rome, Italy
[2] Department of Structural and Geotechnical Engineering, Sapienza University of Rome, Rome, Italy

Summary The nonlinear dynamic response of carbon nanotube (CNT)/polymer nanostructured hysteretic beams is investigated with the aim of achieving optimal nonlinear material designs in terms of maximum multistability bandwidth. Leveraging on multistability is indeed regarded nowadays as an additional functionality for smart multifunctional structures in a variety of engineering applications, with the potential of promoting a growing aerodynamic morphing demand.
Optimal solutions are found employing asymptotically obtained Frequency Response Curves (FRC) over a certain range of excitation frequencies, by varying the meaningful nanostructured beams parameters, such as the CNT/polymer interfacial shear strength, the CNT volume fraction, direction and agglomeration, the CNT functionalization through the cross-section thickness.
Both accuracy and efficiency are attained through a nonlinear hysteretic beam model, obtained by reduction of a 3D mesoscopic theory, subsequently treated via the method of multiple scales to yield the asymptotic dynamic response.
The richness of the optimal solutions is induced by the unusual and unique combination of material and geometric nonlinearities, the former associated with the interfacial frictional sliding that yields hysteresis, the latter with stretching nonlinearities of the beam itself.

NONLINEAR NANOCOMPOSITE BEAM MODELS

The nonlinear 3D nanocomposite constitutive model capable of capturing the hysteretic nanostructural stick-slip behavior between the CNTs and the hosting polymer matrix, proposed and validated in previous works (see, e.g., [1, 2]), was reduced to accommodate the Saint-Venant plane bending kinematic state parametrized by the elongation of the centerline and the bending curvature. Following [3], where only the case of perfectly aligned CNTs was considered, the tension-elongation and moment-curvature relationships are obtained for generic CNT orientations according to an unusual derivation by which the tangent conditions in the CNT/polymer stick phase at the origin and past the onset of CNT slip are derived. The transition between these two states (namely, elastic and post-elastic phases) are assumed to be regulated by a hysteresis operator that mimics the Bouc-Wen model. Such approach yields the following moment-curvature relationship (M–κ):

$$M = \overline{EJ}^{(\mathrm{e})}[\delta\kappa + (1-\delta)\,\chi] \tag{1}$$

where $\delta := \frac{\overline{EJ}^{(\mathrm{p})}}{\overline{EJ}^{(\mathrm{e})}}$ is the ratio between the post-slip bending stiffness and the elastic bending stiffness, respectively, and χ is the hysteretic contribution to the bending curvature given in rate form by:

$$\dot{\chi} = \left[1 - \left(\bar{\beta} + \bar{\gamma}\,\mathrm{sign}(\chi\dot{\kappa})\right)|\chi|^n\right]\dot{\kappa} \tag{2}$$

with $(\bar{\beta}, \bar{\gamma}) = (\beta, \gamma)/\kappa_y^n$, where $\kappa_y = \frac{M^{(\mathrm{o})}}{(1-\delta)\overline{EJ}^{(\mathrm{e})}}$, while (β, γ, n) are the well-known Bouc-Wen parameters, and $M^{(\mathrm{o})}$ is the limit moment depending on the CNT/polymer interfacial shear strength $S^{(\mathrm{o})}$.

The mechanical beam parameters here introduced depend on Young's moduli and Poisson's ratios of the two material phases $\{E^{(i)}, \nu^{(i)}\}$ $(i = 1, 2)$, namely the CNTs and the polymer, and on the phase volume fraction ϕ, according to the "Equivalent Inclusion–Average Stress" approach [4, 5]. Such approach, in the average sense proposed by the Mori–Tanaka method, combines the equivalent stress-strain response of the CNTs treated as an inclusion, embedded in an hosting matrix phase (here the polymer), with the Eshelby theory of equivalent inclusion (see, for instance, [6]). Additionally, following [7], in the 3D continuum constitutive response (in whose setting the beam material response is derived) we introduce the effects of CNTs orientation (random or aligned along a preferential direction), and shape, geometry and variability of the CNTs length within the same nanocomposite.

Within such a theoretical framework, the considered mechanical parameters are condensed in the dependence of the bending stiffness coefficients on the above parameters. That is,

$$\left\{\overline{EJ}^{(\mathrm{e})}, \overline{EJ}^{(\mathrm{p})}\right\} = f\left(E^{(\mathrm{i})}, \nu^{(\mathrm{i})}, \boldsymbol{\varphi}, \bar{\phi}, \bar{A}\right) \tag{3}$$

where $\boldsymbol{\varphi}$ is the vector collecting the three Euler angles identifying the CNTs direction, $\bar{\phi}$ is the effective CNT volume fraction accounting for the CNT dispersion degree, and $\bar{A}$ is the CNT agglomerate area ratio.

*Corresponding author. E-mail: formica@uniroma3.it.

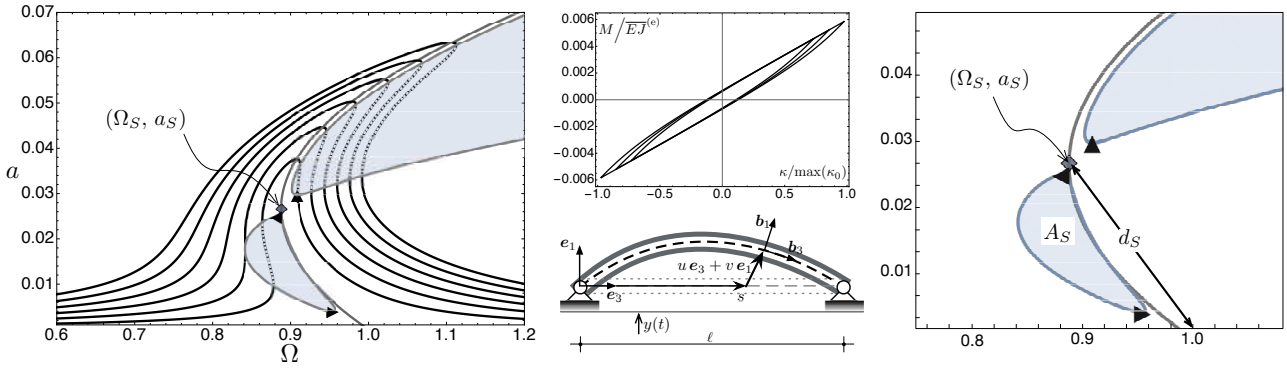

Figure 1: Typical FRC curve (on the left) showing deflection amplitude a vs. excitation-to-natural frequency ratio Ω of a simply supported beam (bottom center), and the moment-curvature hysteretic curves (top center). Within the regions bounded by the two grey lines, the softening or hardening responses are multi-valued and multi-stable (on the right, a zoom of the same FRC on the left).

OPTIMIZATION PROBLEM

The continuum beams incorporating hysteresis in the constitutive relationships are first discretized according to the approach proposed in [3]. To this end, the rate form of the moment-curvature relationship is integrated to yield a piece-wise closed-form representation for each of the four branches of the hysteresis cycles. The obtained piece-wise closed-form moment-curvature relationship is expanded in Taylor series and treated asymptotically in the context of the Galerkin discretization of the deflection field [3, 8, 9, 10, 11].

The ensuing piece-wise ODEs are then treated by the method of multiple scales to obtain the periodic responses to harmonic base excitations together with the frequency-response functions. In this way, the implicit form of the FRC, given in terms of deflection a and frequency ratio Ω, is obtained as:

$$\mathcal{G}(\Omega,\, a) = \mathcal{G}_1(a)\,\Omega^2 + \mathcal{G}_2(a)\,\Omega + \mathcal{G}_3(a) - \mathcal{G}_f(a)\,F^2 = 0. \tag{4}$$

where the coefficients $\mathcal{G}_k$ are explicitly given in terms of both mechanical and discretization parameters. The explicit form associated with (4) provides a simple explicit expression defining the backbone curves, determined as the loci of the peaks of the FRCs, *i.e.*, $\Omega = -\frac{\mathcal{G}_2(a)}{2\,\mathcal{G}_1(a)}$. Note that a qualitative switch of nonlinear behavior is observed in general nonlinear oscillators when the backbone curve exhibits a wiggle due to a change of bending so that the frequency response turns from hardening to softening or viceversa. The above transitions occur at threshold amplitudes where the local change of frequency with respect to the oscillation amplitude vanishes, that is, $\frac{d\Omega}{da} = 0$. This entails a linear response of the oscillator to within the sought order of approximation.

The interplay between the CNT/polymer nanostructural hysteretic nonlinearity and the geometric nonlinearity gives rise to rich and unexpected nonlinear behaviors with a remarkable tunability. By employing suitable fitness functions for maximum multistability bandwidth, such as the frequency bandwidth bounded by the switching point $(\Omega_S,\, a_S)$ and the linear frequency d_S, or the area enclosed by the instability regions A_S (see Figure 1 on the right), the optimization of the nansotructured beams is tackled thanks to the flexibility afforded by the asymptotic solution.

References

[1] Formica G., Milicchio F., Lacarbonara W. *Compos. Struct.* **194**: 633–642, 2018.
[2] Formica G., Milicchio F., Lacarbonara W. *Adv. Eng. Softw.* **125**: 126–135, 2018.
[3] Formica G., Lacarbonara W. *Nonlinear Dyn.* **99**: 227–248, 2020.
[4] Benveniste Y. *Mech. Mater.* **6**: 147–157, 1987.
[5] Odegard G. M., Gates T. S., Wise K. E., Park C., Siochi E. J. *Compos. Sci. Technol.* **63**: 1671–1687, 2003.
[6] Formica G., Lacarbonara W., Alessi R. *J. Sound Vib.* **329**: 1875–1889, 2010.
[7] Talò M., Krause B., Pionteck J., Lanzara G., Lacarbonara W. *Compos. Part B Eng.* **115**: 70–78, 2017.
[8] Nayfeh A., Mook, D. Nonlinear Oscillations. John Wiley & Sons, 1995.
[9] Rega G., Lacarbonara W., Nayfeh A., Chin C. *Int. J. NonLin. Mech.* **34**: 901–924, 1999.
[10] Lacarbonara W., Rega G., Nayfeh A. *Int. J. NonLin. Mech.* **38**: 851–872, 2003.
[11] Lacarbonara W., Arena A., Antman S.S. *Meccanica* **50**: 689–705, 2015.

O106829 - MS04 - Nonlinear dynamics for design - Oral

ANALYTICAL, NUMERICAL, AND EXPERIMENTAL INVESTIGATIONS OF A TUNED WEDGE DAMPER WITH SEGMENTED SMOOTH CONTACT SURFACES

Alexander Fidlin*[1], and Jimmy Aramendiz[1]
[1] Chair for Dynamics/Mechatronics, Karlsruhe Institute of Technology, Karlsruhe, Germany

Summary Diminishing detrimental vibrations directly influences the life span of machines and structures. Hence, vibration reduction alternatives have been intensively investigated, focusing either on vibration isolation, absorption or damping. This work proposes a damper, utilizing the last two vibration reduction mechanisms via dry friction and design of sliding contact surfaces. For low vibration amplitudes the damper acts as an absorber providing for almost perfect vibration annihilation, whereas for high vibrations it functions as a highly damped dissipation device. First, the minimal model of the damper is presented and simulated numerically, in order to gain a first insight into the system's dynamics. Then analytical investigations via averaging method are conducted in the vicinity of the resonance regimes. Finally, the numerical and analytical results are validated via experiments.

Vibration reduction has always been an essential aspect in the design of machines and structures [1]. Although, tuned mass dampers are a well-studied and broadly used, they do have their limitations. They can be tuned for an operating frequency; however additional resonance regimes are introduced into the system. Furthermore, in order to reach the operation frequency at least one structural resonance must be usually passed through. Alternatively, tuned mass damper parameters can be chosen in a broadband approach. In that case, however, the near-perfect vibration isolation at the tuned frequency is lost. An additional disadvantage of the common tuned mass damper is its lack of robustness. If the parameters of the tuned mass damper change due to wear or temperature, the tuning of the damper is lost and with it, the damper's effectiveness. The disadvantages of the tuned mass damper have forced engineers and researchers to investigate nonlinear dampers, in order to create robust, broadband, and effective solutions [2]. Friction based dampers have for years been an effective alternative in turbomachinery, railroad freight trucks, and civil engineering structures. In contrast to typical viscous dampers they do not require a complicated manufacturing or sealing and are robust with respect to environmental conditions. In general, friction based dampers with constant friction force are sensitive with respect to the excitation amplitude. However, this is circumvented by utilizing clamped contact surfaces with geometric variations. This alternative has been investigated in [3], in which a wedge damper was implemented to dampen the vibrations of a main structure.

Vibration reduction is mainly based on one of three mechanisms: vibration isolation, vibration absorption or vibration damping. This work proposes a nonlinear tuned wedge damper that utilizes the last two mechanisms. The damper is attached to a main system and improves the system's dynamics especially in the vicinity of the main system's structural resonance. Without loss of generality the main system is represented by a main spring c_1 and a main mass m_1. As an add-on solution the damper is attached to the main system, and is composed of an auxiliary mass m_2, an auxiliary spring c_2, two symmetrical contact surfaces and a third spring c_3, see Fig. 1(a). The third spring clamps the auxiliary mass between the symmetrical contact surfaces and has a small pre-stress displacement of $\Delta\ell$. The ratio of the contact forces between the auxiliary mass and the contact surfaces is described by the constant friction coefficient μ. Furthermore, the auxiliary mass is connected via the auxiliary spring and the contact surfaces to the main mass. The contact surfaces are mounted on the main mass in such a way that only horizontal forces are transmitted.

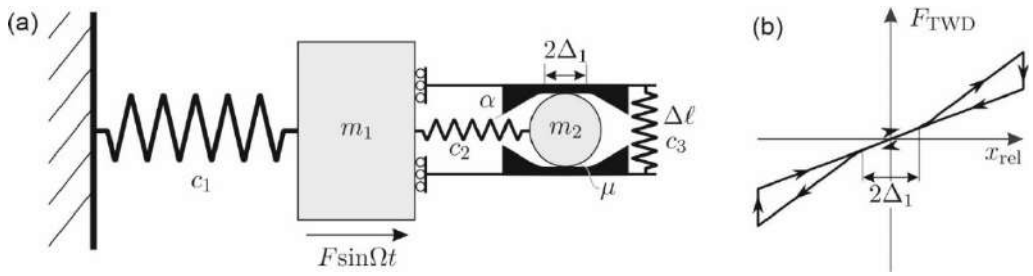

Figure 1: (a) The tuned wedge damper with segmented smooth contact surfaces. (b) The force characteristics of the damper

The novelty of this friction based tuned wedge damper lies in the design of the sliding contact surfaces. The surfaces are composed of five segments: a horizontal segment, two wedge segments, and two transition segments. The horizontal segment is parallel to the degrees of freedom and has the length $2\Delta_1$, whereas the wedge segments are rotated by the angle α with respect to the horizontal. The wedge segments are connected to the horizontal segment via the transition segments. Additionally, the transition segments are circular and are specifically chosen, in order to obtain a continuously differentiable contact area without impacts. Note that the friction coefficients for each section can be chosen separately. As mentioned above, the chosen design allows the damper to alternate between two vibration reduction mechanisms, vibration absorption and vibration damping. As long as the vibrations are sufficiently small the auxiliary mass oscillates within the Δ_1-range and, due to the proper choice of the pre-stress and friction coefficient, either minimal or no friction

*Corresponding author. E-mail: alexander.fidlin@kit.edu

MINI SYMPOSIA

affects the oscillations. Within this range, the damper operates as a vibration absorber and almost diminishing vibrations almost perfectly. If the relative vibration amplitude surpasses the Δ_1-threshold, the wedge and transition segments of the surfaces influence the damper's dynamics. This leads to a variable contact force and thus a variable friction force, which is proportional to the relative displacement between the masses. An exemplary damper force that acts on the main mass is depicted in Fig. 1(b). The damper force is composed of a dissipation free Δ_1-range and two outer dissipative sections.

The system's equations of motion are implemented and solved numerically. The discontinuities, which arise from the possible stick-slip-phases due to friction, are considered via event detection. For an appropriate choice of the system parameters (c_3<<1 & $\Delta\ell$=0), the numerical simulations give a first insight into the decoupling of vibration damping and vibration absorption, see Fig. 2(a). The outer wedge sections dampen vibrations with amplitudes larger than Δ_1, whereas vibrations with lower amplitudes remain completely undamped. The undamped vibrations are reduced via the absorption of the secondary spring and the absorber mass. A parameter study into the effect of the friction coefficient shows a reduction of the resonance peaks and an approximate invariance of the vibration absorption frequency for a large range of friction coefficient values. The system is effectively able to partially decouple the vibration reductions mechanisms as long as the vibration amplitude in the vicinity of the vibration absorption frequency are smaller than the displacement Δ_1. The angle α affects the effective stiffness and the effective damping outside of the Δ_1-range, whereas the length Δ_1 determines the change from vibration damping to vibration absorption. Variations of the pre-stress displacement $\Delta\ell$, show that this parameter determines if the system behaves predominantly as a one degree of freedom or a two degree of freedom system, similarly as in [3].

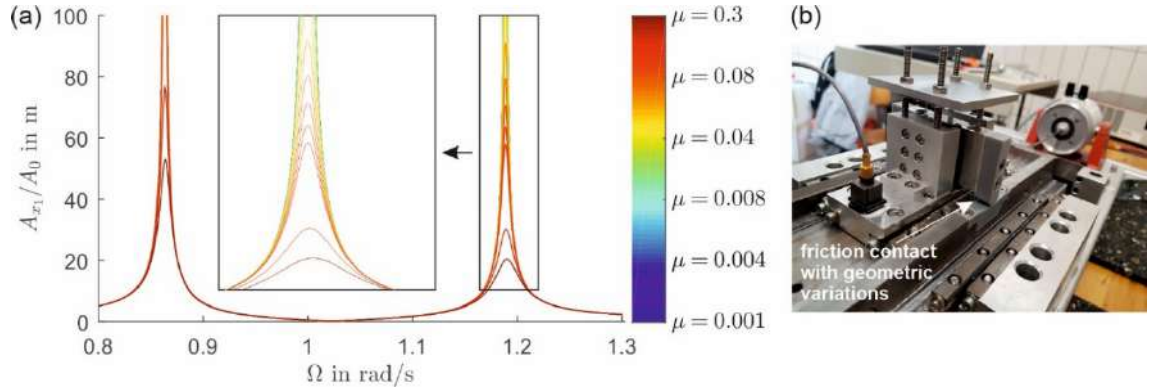

Figure 2: (a) Numerical investigation into the friction coefficient influence (b) Experimental setup of the tuned wedge damper

In order to obtain a deeper insight into the damper's dynamics it is investigated analytically. First, the equations of motion of the system are transformed into modal coordinates. Second, the coupled equations of motion are decoupled with the method proposed in [4]. Subsequently the resulting equations are analysed via averaging methods. The analytical solution concurs with the numeric results within the expected range of asymptotic methods.

The numerical and analytical results are validated via experiments with a setup described in [5]. The main structure is excited via a voice coil shaker that applies a sweep excitation with constant amplitude. Subsequently, the amplitude response functions of the system are derived for various excitations. The experimental results reflect qualitatively the numerical and analytical solutions and confirm the scalability of the effects with variating excitation amplitudes.

This work proposes a tuned wedge damper that decouples vibration damping and vibration absorption. It circumvents the disadvantages of the traditional tuned mass damper with regards to the sealing of the viscous component, robustness, and the trade-off between the damping and vibration absorption frequency. The proposed system is investigated numerically, analytically, and experimentally. These results give a first insight into the passive design of an effective damping device, and lay the foundation of a more complex implementation, e.g. in continuous or multibody systems.

References

[1] J. P. Den Hartog,. Mechanical vibrations. Courier Corporation. 1985

[2] Vakakis, A.F., Gendelman, O.V., Bergman, L.A., McFarland, D.M., Kerschen, G. and Lee, Y.S.: "Nonlinear Targeted Energy Transfer in Mechanical and Structural Systems", v. I and II, Springer, 2009.

[3] J. Aramendiz, A. Fidlin, and E. Baranowski, On the Dynamics of a Prestressed Sliding Wedge Damper. *Proceeding in Applied Mathematics and Mechanics*, 19(1), 2019, DOI: 10.1002/pamm.201900326

[4] J. Aramendiz, A. Fidlin, and K. Lei, Investigations on amplitude adaptive sequential friction-spring dampers. *ZAMM - Journal of Applied Mathematics and Mechanics/Zeitschrift für Angewandte Mathematik und Mechanik*. 2019, DOI: 10.1002/zamm.201800293

[5] A. S. Tan, J. Aramendiz, K. H. Ross, T. Sattel, and A. Fidlin, Comparative study between dry friction and electrorheological fluid switches for Tuned Vibration Absorbers. *Journal of Sound and Vibration*, 460, 2019, 114874.

MODELLING AND MITIGATION OF SLOSHING SYSTEMS USING PASSIVE ENERGY ABSORBERS

Maor Farid*[1], and Oleg Gendelman[2]
[1] Department of Mechanical Engineering, Massachusetts Institute of Technology, Cambridge, MA, USA
[2] Faculty of Mechanical Engineering, Technion – Israel Institute of Technology, Haifa, Israel

Summary This study treats oscillations of a liquid in partially filled vessel under horizontal harmonic ground excitation. When exposed to external disturbances, the liquid is divided into two portions: oscillating sloshing portion, and a-'static' non-sloshing portion, located at the bottom of the tank. Such excitation may lead to hydraulic impacts applied by the sloshing mass on the tank walls. Different equivalent mechanical models are suggested to mimic the liquid sloshing mass motion and essential dynamical regimes of the overall tank-liquid system, such as a series of pendula or mass-spring-dashpot systems which can impact the vessel walls. We use parameters of the equivalent mass-spring system for the well-explored case of cylindrical vessels. The hydraulic impacts are modelled by high-power potential function. Finite-Element (FE) method is used to determine and verify the model parameters and to identify dominant dynamical regimes, natural modes and frequencies. The tank failure modes and critical locations are identified. Mathematical relation is found between degrees-of-freedom (DOFs) motion and the mechanical stress applied in the tank critical section. This is the prior attempt to take under consideration large-amplitude nonlinear sloshing and tank structure elasticity effects for design, regulation definition and resistance analysis purposes. Both linear (tuned mass damper, TMD) and nonlinear (nonlinear energy sink, NES) passive energy absorbers (PEAs) contribution to the overall system mitigation is firstly examined. Dominant sloshing regimes, such as moderate amplitude, and vibro-impact (VI) violent sloshing are studied and described using reduced-order models and analytical methods.

INTRODUCTION

Partially filled liquid storage tanks of different shapes are used in many engineering fields, including vehicles, sea crafts, aircraft, for the storage of various, maybe hazardous, liquids. The term “sloshing” refers to oscillatory relative motion of the liquid with respect to the containing vessel. The liquid sloshing may be hazardous for the vessel safety, since dynamic loads related to the sloshing may have direct and rather strong calamitous effect on the vessel stability and robustness. So far, elaborated analytical studies are limited to small-amplitude sloshing in rectangular and cylindrical vessels. Thus, efficient numerical and analytic tools are desired for assessing the fluid loading on the structure and the coupling between their motions. While being most interesting and potentially hazardous, high-amplitude liquid sloshing in partially filled vessels still lacks complete analytic representation. The sloshing liquid has infinite number of degrees of freedom; boundary conditions on the free surface are nonlinear and time-dependent. It is noteworthy that the framework of the presented asymptotic analysis is not limited to specific tank shape. Any two dimensional tank shape with vertical walls in the free liquid surface zone can be treated. Moreover, we assume infinite roof height in order to eliminate both liquid spilling and interaction between the fluid and the tank roof.

REDUCED-ORDER MODEL DESCRIPTION

We introduce the equivalent mechanical model for liquid sloshing in cylindrical tank with the well explored TMD attached **[1]**. Parameters K and C are modal stiffness and damping of the vessel fundamental (1,1) beam-type mode, respectively. The tank is of radius R and height H and exposed to arbitrary external excitation of u_g.

The liquid static and dynamic portions heights and the combined tank-static liquid portion center of gravity height are denoted by h_0 and h_1, respectively. Parameters k_2 and k_3 represent the coupling stiffness associated with the TMD and NES, respectively. c_2 is the linear damping coefficient. The PEA installation height h_2 is determined by the designer. Masses $m_{\tan k}$ and m_0 are the tank shell mass and the liquid 'static' portion mass, respectively. The sloshing dynamics combines infinite number of sloshing modes with mass of m_n. However, as shown by Abramson **[2]**, the modal mass decreases rapidly with increasing mode number. Then, to reveal most important aspects of dynamics, one can take into account only the first sloshing mode and the static-like portion of the fluid in the mechanical equivalent model, as long as the excitation frequency is far from the natural frequencies of the higher modes. The normalized displacement coordinate of the sloshing mass m with respect to the tank axis is denoted by v. Impact takes place for the absolute value of v reaches unity. The liquid-structure interaction involves energy dissipation due to wave breaking and fluid viscosity, which exhibits VI behavior. Interaction between the sloshing mass and the tank walls is described by a strongly nonlinear power-form forces with high exponents potential and dissipation force functions **[3-5]**, fully-defined by empirical positive integers, which are going to be assessed both numerically and experimentally.

*Corresponding author. E-mail: faridm@mit.edu

Seismically-induced tank failure modes are explained extensively by Maekawa **[6]**. Based on the ROM, Von-Mises equivalent stresses were calculated in the tank critical point **P**.

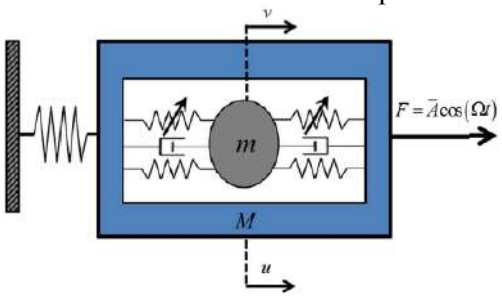

Figure1. System scheme-linear oscillator as the primary system and internal particle with both linear and cubic attachments. The displacements of the primary mass and the impacting mass are denoted as u and v, respectively

We separately apply both the well-known TMD and the cubic NES as vibration mitigation solutions. The following equations of motion are obtained for the overall tank-PEA system:

$$\begin{aligned}
&\ddot{u}+u+\varepsilon_1 v+Z\dot{u}+\varepsilon_1 Z\dot{v}-\varepsilon_2\left(1+\varepsilon_1\right)\beta_2^2 w-\varepsilon_2\kappa_2 w^3-2\varepsilon_2\beta_2\zeta_2\dot{w}=-\frac{\left(1+\varepsilon_1\right)^2}{R\Omega^2}u_{g,tt}\left(t\right)\\
&\ddot{v}+u+\left(\varepsilon_1+\left(1+\varepsilon_1\right)^2\beta_1^2\right)v+Z\dot{u}+\left(\varepsilon_1 Z+2\left(1+\varepsilon_1\right)\beta_1\zeta_1\right)\dot{v}-\varepsilon_2\left(1+\varepsilon_1\right)\beta_2^2 w-\varepsilon_2\kappa_2 w^3-2\varepsilon_2\beta_2\zeta_2\dot{w}+\left(1+\varepsilon_1\right)\kappa v^{4n+1}+\left(1+\varepsilon_1\right)\lambda\dot{v}v^{2n}=0\\
&\ddot{w}-u-\varepsilon_1\left(1+\left(1+\varepsilon_1\right)\beta_1^2\right)v+\left(1+\varepsilon_1\right)\left(1+\varepsilon_2\right)\beta_2^2 w+\left(1+\varepsilon_2\right)\kappa_2 w^3-Z\dot{u}-\varepsilon_1\left(Z+2\beta_1\zeta_1\right)v+2\left(1+\varepsilon_2\right)\beta_2\zeta_2 w-\varepsilon_1\kappa v^{4n+1}-\varepsilon_1\lambda v v^{2n}=0
\end{aligned}\tag{1}$$

While the TMD is examined, we take $\kappa_2=0$, when κ_2 is the parameter associated with the coupling between the NES and the tank structure, and in the same manner, when the NES is examined, we take $\beta_2=0$. The performances of both PEAs are evaluated with the help of two criteria; stress reduction and time of vibration decay. At this stage, the PEAs optimization is performed numerically; the TMD with mass about 10% of the total mass of the system allows up to 40% stress level reduction and 95% reduction of characteristic decay time in conditions of an optimal tuning.

CONCLUSIONS

ROM is used to describe main most hazardous dynamical regimes taking place in cylindrical tank subjected to horizontal ground excitation, and internal impact regime on particular. Additional TMD and NES vibration mitigation performances were primarily examined and exhibit promising results, in term of both decay time and stresses mitigation in the tank critical location.

References

[1] J.P. Den Hartog, Mechanical Vibrations, 1985.
[2] H.N. Abramson, The Dynamic Behavior of Liquids in Moving Containers. NASA SP-106, NASA Spec. Publ. 106 (1966).
[3] V.N. Pilipchuk, R.A. Ibrahim, The dynamics of a non-linear system simulating liquid sloshing impact in moving structures, J. Sound Vib. 205 (1997) 593–615.
[4] V. Babitsky, Theory of vibro-impact systems and applications. Springer Science & Business Media, 2013
[5] M.A. El-Sayad, S.N. Hanna, R.A. Ibrahim, Parametric Excitation of Nonlinear Elastic Systems Involving Hydrodynamic Sloshing Impact, Nonlinear Dyn. 18 (1999) 25–50.
[6] A. Maekawa, Recent Advances in Seismic Response Analysis of Cylindrical Liquid Storage Tanks, INTECH Open Access Publisher (2011).

TRANSIENT CHIMERA-LIKE STATES FOR FORCED OSCILLATORS

Dawid Dudkowski*[1], Jerzy Wojewoda[1], Krzysztof Czołczyński[1], and Tomasz Kapitaniak[1]
Division of Dynamics, Lodz University of Technology, Stefanowskiego 1/15, 90-924 Lodz, Poland

Summary We investigate the transient chimera-like states for the model of forced oscillators, realized in the form of physical double pendula hanged on an oscillating platform. We describe the dynamics of a single unit, uncovering different types of possible behaviors and discuss the properties of three such oscillators. Our results show, that the phenomenon of transient chimera-like states can arise and its lifetime is not straightforward, highly depending on possible uncertainties occurring in the system. The numerical study presented in this paper is confirmed by the experimental research, exhibiting that the described transient states have the same properties as the classical weak-chimeras and can be indistinguishable in real-world networks.

Chimera states occur widely in networks of identical oscillators as it has been shown in the recent extensive theoretical and experimental research. In such a state, different groups of oscillators can exhibit co-existing synchronous and irregular behaviors despite homogeneous coupling. Combining both coherent and incoherent types of responses, chimeras arise on the road to better understanding of the variety of phenomena occurring in nature. In our study we consider a star network, in which N identical peripheral end nodes are connected to the central hub node. The study is realized in the form of physical double pendula hanged on an oscillating platform, which have been shown in Fig. 1.

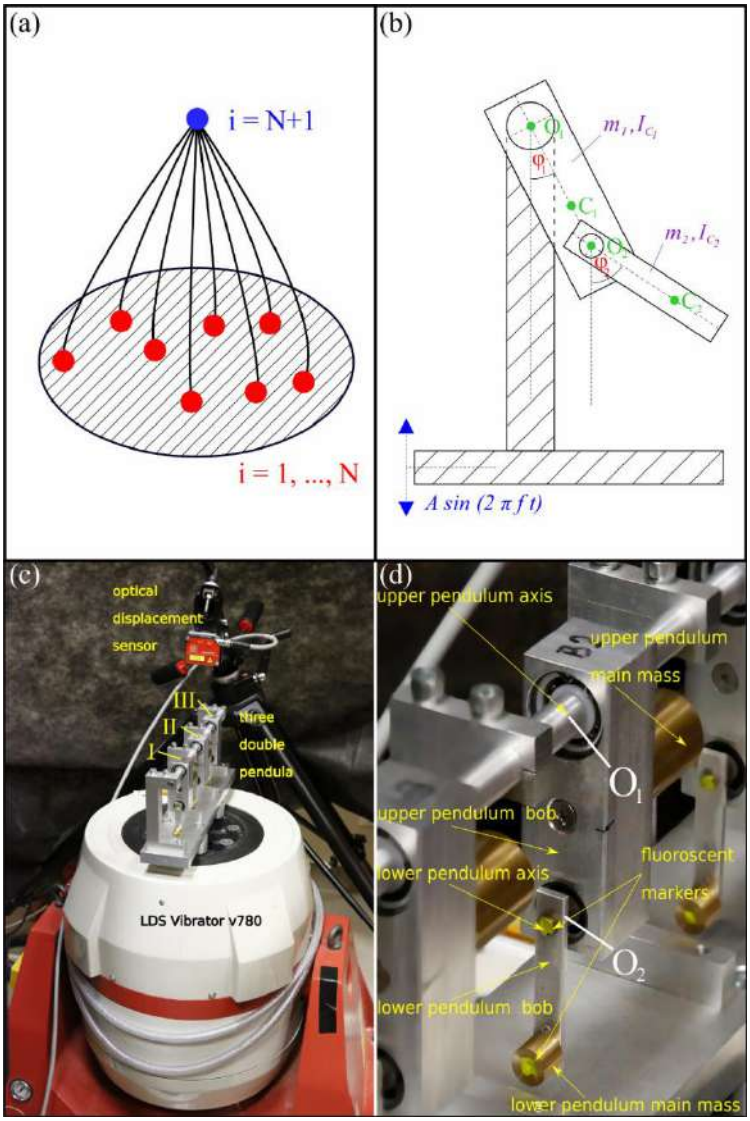

Fig. 1. In (a) a schematic model of a star network of N+1 nonlinear oscillator systems is shown, while in (b) a scheme of physical double pendulum used in the experimental research is presented. The experimental rig of three double pendula suspended on an oscillating platform and a zoom on a single double pendulum node are shown in (c) and (d), respectively.

*Corresponding author. E-mail: dawid.dudkowski@p.lodz.pl.

Each double pendulum shown in Figs. 1(b-c) consists of two elements, i.e., the larger pendulum (upper bob) which holds the smaller one (lower bob). The upper bob can rotate or oscillate around the axis O1 connected to the periodically oscillating platform and the lower bob can rotate or oscillate around the axis O2 as shown in Fig. 1(b) (both axis O1, O2 are perpendicular to the figure's plane). The upper and lower bobs have respectively masses m_1, m_2 [kg] and moments of inertia I_{C1}, I_{C2} [kgm^2] (around the perpendicular axes which crosses bob's mass centers C_1, C_2). The oscillations of the platform are described by the harmonic function $A\sin(2\pi ft)$, where A [m] and f [Hz] are respectively amplitude and frequency.

We describe the dynamics of a single unit, uncovering different types of possible behaviors and discuss the properties of three such oscillators. We find that if a single node exhibits transient chaotic behavior in the whole network, the pattern of transient chimera-like state, which persists for a significant amount of time, is created. Our results show, that the phenomenon of transient chimera-like states can arise and its lifetime is not straightforward, highly depending on possible uncertainties occurring in the system. The numerical study is confirmed by the experimental research, exhibiting that the described transient solutions can be observed in simple experiments with mechanical oscillators, which are controlled by elementary dynamical equations. Our finding suggests that transient chimera-like states have the same properties as the classical weak-chimeras and can be indistinguishable in real-world networks.

STRESSWAVES GENERATED DURING DYNAMIC FRACTURE OF A GLASS TUBE UNDER BENDING

Valentin van Gemmeren[1], Timothy Graf[1], and Jurg Dual *[1]
[1] Institute for Mechanical Systems, ETH Zurich, Zurich, Switzerland

Summary We experimentally induce dynamic fracture of a glass tube by focusing flexural waves. The resulting stress waves are modeled analytically by considering the diffraction of flexural waves at a partial crack. We observed the generation of both longitudinal and flexural waves during the dynamic fracture process. The crack rapidly traversed 85% of the cross section and then slowed down during the remainder of the cross section. Our work presents an experimental method for the generation of reproducible acoustic emissions and establishes a modeling approach.

INTRODUCTION

During fracture, stress waves are released that penetrate the surrounding bulk material. In the context of structural health monitoring, these stress waves are referred to as acoustic emissions and can provide valuable information about the presence, location, and size of cracks in a structure. Moreover, they are investigated in the context of fracture mechanics as they are a direct result of the failure mechanism. Among others, Schindler, Kinra, and Kolsky studied the stress waves released during fracture of glass rods under tension and four-point bending, and modeled their generation [1, 2, 3].

Recently, the authors have presented a method to produce precisely controlled dynamic fracture in a glass tube by focusing flexural waves [4]. Thereby, high loading rates were achieved and stress concentrations due to load transmission were avoided. In the present study, we investigate and model the acoustic emissions generated during the dynamic fracture due to flexural-wave focusing.

METHOD

Experimental setup

In the experiments, we induce dynamic fracture in a 1.5 m long glass tube with an outer diameter of 4 mm and a wall thickness of 0.5 mm. To induce fracture, a strong bending moment pulse with a duration of 100 ms is created in the middle of the beam through the constructive interference of two flexural-wave pulses propagating into opposing directions. The lateral deflection of the glass tube is measured on both sides of the fracture location with two laser Doppler vibrometers. The longitudinal motion of the tube is measured with laser Doppler vibrometer at the tip of the tube. Moreover, the fracture process is recorded with a high-speed camera at 252 kHz.

Modeling the generation of acoustic emissions

To model the generation of acoustic emissions, we compute the interaction of the two propagating flexural wave pulses with the gradual opening of a crack. We prescribe the crack depth with respect to time based on a piecewise linear function that was extracted from our experimental observations (see Figure 1). Further, we assume the crack surface to be traction-free and compute the resultant normal force, bending moment, and shear force of the transmitted and reflected wave pulses, respectively. We then simulate the propagation of the respective waves in the glass tube following Timoshenko beam theory for the flexural components [5], and cylindrical shell theory for the longitudinal components [6].

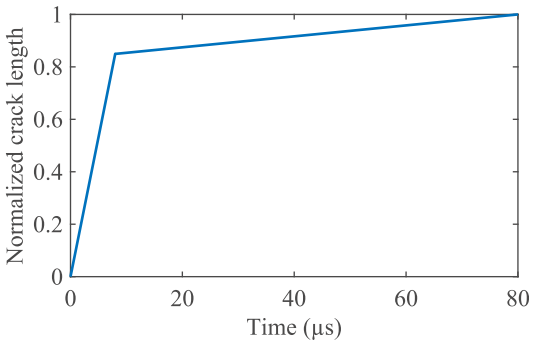

Figure 1: Model of the crack length with respect to time.

RESULTS AND DISCUSSION

Crack dynamics

With the help of the high-speed video recordings, we observed that the fracture process consists of two distinct stages. In the first stage that takes approximately 8 µs, the crack traverses 85% of the cross section with a relatively high velocity. In the second stage, the remainder of the cross section is traversed with at much lower speed. The fracture process in total takes about 80 µs (see Figure 1). In some instances when fracture does not occur directly at the focal point of the flexural waves, the crack turns slightly towards the axis of the tube.

*Corresponding author. E-mail: dual@imes.mavt.ethz.ch.

These observations agree to those of Kinra, Kolsky, and Schindler, who found the crack propagation under static bending to consist of a fast and a slow stage [2, 3]. In contrast, they observed the crack turning completely parallel to the axis of the tube and not traversing the remainder of the cross section at all. We attribute this difference in crack dynamics to our more load-controlled type of loading, compared to the displacement-controlled loading in three- and four-point-bending experiments.

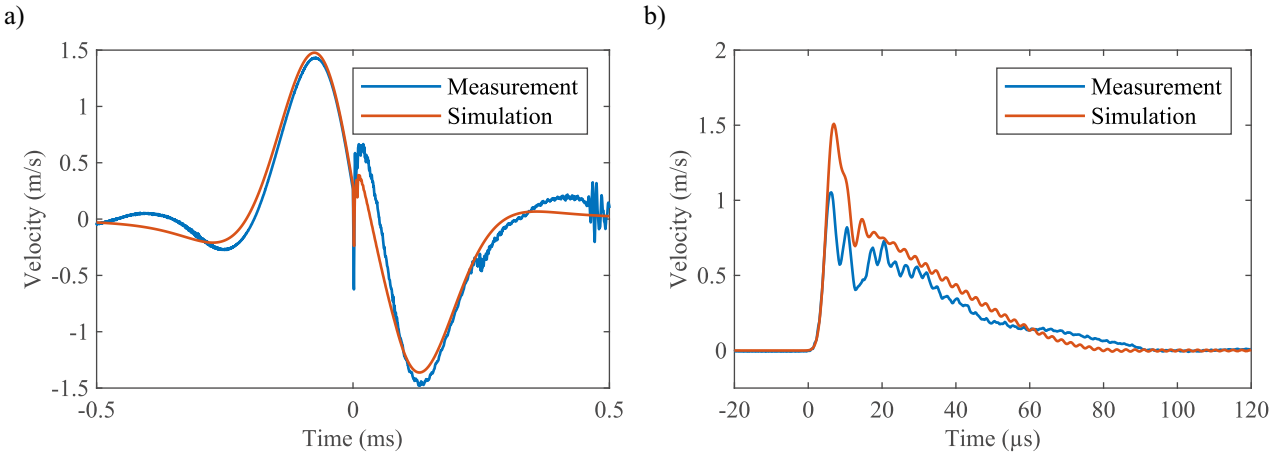

Figure 2: Measurement and simulation of the acoustic emissions generated during dynamic fracture under bending. (a) Flexural motion 10 mm next to the location of fracture. The sharp peak at 0 ms is generated during fracture. The sine-shaped motion before and after is mostly due to the flexural-wave focusing. (b) Longitudinal motion at the tip of the glass tube.

Acoustic emissions

Due to the asymmetry of the crack surface with respect to the axis of the tube, parts of the incident flexural waves are converted into longitudinal waves (see Figure 2b). The duration of the measured longitudinal wave pulse corresponds very well to the duration of the fracture process determined with the high-speed camera. The high-frequency ripples observed in measurement and simulation originate from the dispersion of the longitudinal waves in the tube. In the measurements of the lateral deflection of the glass tube, a sharp peak can be seen at the time instances where fracture occurs (see Figure 2a). This is due to the abrupt transition from wave transmission to wave reflection and is captured well by our simulation. However, the amplitude of the longitudinal wave pulse is overestimated by about 30%. We attribute this difference to our omission of modeling the stress waves ahead of the crack tip.

CONCLUSION

Our experiments show that the dynamic fracture of beams under bending can occur without the crack turning parallel to the beam, if the loading is load-controlled (produced by propagating flexural waves). The crack dynamics were approximated with a piecewise linear function and the normal and flexural components of the resulting acoustic emission were computed. This showed that the duration of the longitudinal pulse offers a good estimate of the duration of the fracture process. While our modeling already shows good results for the generated acoustic emissions, it would be interesting to further model the dynamic crack propagation to understand better the influence of different loading configurations. Our work provides an example of reproducible, experimental acoustic emissions that can be used to validate different modeling approaches.

References

[1] Kinra V. *Int. J. Solids Struct.* **12**: 803–808, 1976.
[2] Kinra V., Kolsky H. *Eng. Fract. Mech.* **9**: 423–432, 1977.
[3] Schindler H. J., Kolsky H. *J. Mech. Phys. Solid* **31**: 427–437, 1983.
[4] van Gemmeren V., Zybach B., Dual J. *Phys. Rev. Applied* **10**: 044021, 2018.
[5] Doyle J. F. Wave Propagation in Structures. Springer, New York, 1997.
[6] Mirsky I., Herrmann G., *J. Acoust. Soc. Am.* **29**: 1116–1123, 1957.

A COMPUTATIONAL PLATFORM FOR CONSTRAINED DESIGN OPTIMIZATION OF DYNAMICAL SYSTEMS

Mingwu Li[1] and Harry Dankowicz *[1]
[1] Department of Mechanical Science and Engineering, University of Illinois at Urbana-Champaign, Urbana, Illinois, USA

Summary A recent update to the MATLAB-based continuation package COCO supports modular construction of algebraic, differential, and integral equality and inequality constraints that define feasible regions on manifolds characterizing solutions to dynamical systems along which optimization may be performed. The implementation also encodes the construction of the adjoint necessary conditions for candidate extrema of scalar-valued objective functions in terms of corresponding Lagrange multipliers. Use of a nonsmooth complementarity function and auxiliary relaxation parameters allows such points to be located using a method of successive continuation. This paper demonstrates the application of this functionality to inequality-constrained problems in design optimization along families of periodic orbits of nonlinear differential equations and the optimal control of an inverted pendulum.

MOTIVATING EXAMPLE

Periodic solutions of the harmonically excited linear oscillator governed by the differential equation

$$\ddot{x} + \dot{x} + kx = f\cos(t+\theta) \tag{1}$$

in terms of the stiffness k, excitation amplitude f, and phase shift θ are given by

$$x_{\rm per}(t) = f\frac{(k-1)\cos(t+\theta)+\sin(t+\theta)}{(k-1)^2+1}. \tag{2}$$

For fixed f, local extrema of $\dot{x}_{\rm per}(0)$ under variations in k and θ are obtained with $\dot{x}_{\rm per}(0) = (-1)^n f$ at $k=1$ and $\theta = n\pi$. A global minimum for $f \leq f_0$ is then obtained at $f = f_0$ with $\dot{x}_{\rm per}(0) = -f_0$. We may locate this extremum through a method of successive continuation applied to a suitably formulated constrained design optimization problem in terms of a nonsmooth complementarity function and auxiliary Lagrange multipliers and relaxation parameters. Specifically, as explained in [1] and [2], with independent variables x, $\dot{x}$, k, θ, and f, candidate minima are obtained from periodic solutions of (1) with period 2π that satisfy the Karush-Kuhn-Tucker (KKT) conditions

$$\ddot{\lambda} - \dot{\lambda} + k\lambda = 0,\ \lambda(2\pi) - \lambda(0) = 0,\ \dot{\lambda}(2\pi) - \dot{\lambda}(0) - k\eta_v = 0, \tag{3}$$

$$\int_0^{2\pi} \dot{\lambda}(t)x(t)\,{\rm d}t + k\eta_k = 0,\ \int_0^{2\pi} \dot{\lambda}(t)f\sin(t+\theta)\,{\rm d}t + k\eta_\theta = 0,\ \int_0^{2\pi} \dot{\lambda}(t)\cos(t+\theta)\,{\rm d}t - k(\eta_f+\sigma_f) = 0, \tag{4}$$

with $\eta_v = 1$, $\eta_k = \eta_\theta = \eta_f = 0$, and $\sigma_f(f-f_0) = 0$ on $\{\sigma_f \geq 0,\ f \leq f_0\}$. These imply that

$$\lambda(t) = e^{t/2}\frac{\sin\left(\frac{\sqrt{3}}{2}(2\pi - t)\right) + e^{-\pi}\sin\left(\frac{\sqrt{3}}{2}t\right)}{\sqrt{3}(\cosh\pi - \cos\sqrt{3}\pi)},\ k=1,\ \theta=0,\ \sigma_f = 1,\ f = f_0, \tag{5}$$

consistent with the prediction above.

By the linearity and homogeneity of the KKT conditions (3)-(4), we may arrive at this optimal solution from an initial solution guess with $\lambda(t) \equiv 0$, $\eta_v = \eta_k = \eta_\theta = \eta_f = \sigma_f = 0$ along an intersecting sequence of one-dimensional manifolds corresponding to periodic solutions $x(t)$ to (1) with period 2π and solutions to (3)-(4) coupled to the nonsmooth complementarity equality condition

$$\sqrt{\sigma_f^2 + (f-f_0)^2} - \sigma_f + f - f_0 - \kappa_f = 0 \tag{6}$$

in terms of the relaxation parameter κ_f. For example, for fixed θ, $f > 0$, $\eta_k = 0$, and $\kappa_f \geq 0$, continuation from the initial solution guess yields a one-dimensional manifold with $\lambda(t) \equiv 0$, $\eta_v = \eta_k = \eta_\theta = \eta_f = \sigma_f = 0$, and a local minimum $\dot{x}_{\rm per}(0) = -f(1-\cos\theta)/2$ at $k = 1 + \cot\theta + \csc\theta$. A second one-dimensional manifold of solutions runs through this point and intersects the point with $\eta_v = 1$, $\eta_\theta = f\sin\theta/2$, $\eta_f = (1-\cos\theta)/2$, $\sigma_f = 0$, and $k = 1 + \cot\theta + \csc\theta$. This point lies on a third one-dimensional manifold obtained by allowing θ to vary and instead fixing $\eta_v = 1$. This manifold intersects the point with $\eta_\theta = 0$, $\eta_f = 1$, $\sigma_f = 0$, $k = 1$, and $\theta = \pi$. Provided that $\kappa_f > 0$ initially, a fourth manifold obtained by allowing f to vary and instead fixing $\eta_\theta = 0$ also intersects the point with $\eta_f = 0$, $\sigma_f = 1$, $k = 1$, $\theta = \pi$, and $f = f_0 + \kappa_f(2+\kappa_f)/(2+2\kappa_f)$. We arrive at the global minimum with $\kappa_f = 0$ by continuation along a one-dimensional manifold obtained by allowing κ_f to vary and instead fixing $\eta_f = 0$. If, in contrast, $\kappa_f = 0$ initially, continuation along the fourth manifold terminates at the singularity of (6) at $\sigma_f = f - f_0 = 0$.

*Corresponding author. E-mail: danko@illinois.edu.

SOFTWARE IMPLEMENTATION

The methodology in the previous section generalizes to arbitrary problems of constrained design optimization along families of solutions to integro-differential boundary-value problems, e.g., periodic and quasiperiodic orbits of nonlinear dynamical systems, including with delay (cf. [3]). The construction of algebraic, differential, and integral constraints, as well as of $\mathbb{R}^n$-valued inequalities, follows a systematic modular paradigm. This is supported in the COCO software platform and leveraged in the construction of production-ready toolboxes for common classes of equality constraints, e.g., multi-segment boundary-value problems. Indeed, a release of COCO from November 2017 also provides support for the associated construction of the corresponding contributions to the adjoint necessary conditions for stationary points in the absence of inequality constraints. As documented extensively in the tutorials accompanying this release, the modular construction paradigm allows, for example, for locating points of locally maximal curvature along a solution manifold.

In an unreleased recent update to COCO, full support is provided for the construction of the KKT conditions for a design optimization problem with both equality *and inequality* constraints. For general multi-segment boundary-value problems, including periodic and quasiperiodic orbits, the adjoint contributions to the KKT conditions are automatically constructed from a predefined library. In lieu of the typical complementarity conditions, the implementation uses one nonsmooth complementarity equality condition of the form (6) for each inequality constraint.

Switching between different one-dimensional solution manifolds, whether at a branch point or as a result of a change in the variables that are free to vary, is a common operation in COCO. In particular, in the former case, COCO stores a candidate direction that lies in the plane spanned locally by the two branches and approximately orthogonal to the original branch. For general multi-segment boundary-value problems, the new COCO update automatically extracts the components of this candidate direction needed in the construction also of the adjoint KKT conditions.

EXAMPLES

A nontrivial example of constrained design optimization solved using COCO is shown in Fig. 1. Here, a control input is sought to minimize an integral objective functional $\mathcal{J}$ in terms of the angular displacement, angular velocity, and control input along trajectories of an inverted pendulum, subject to an integral inequality $\mathcal{I} \leq 0$ on the angular and horizontal displacements. The figure shows the values of $\mathcal{I}$ and $\mathcal{J}$ at the initial and final points of the successive continuation paradigm, as well as along each distinct one-dimensional solution manifold constructed during the solution process.

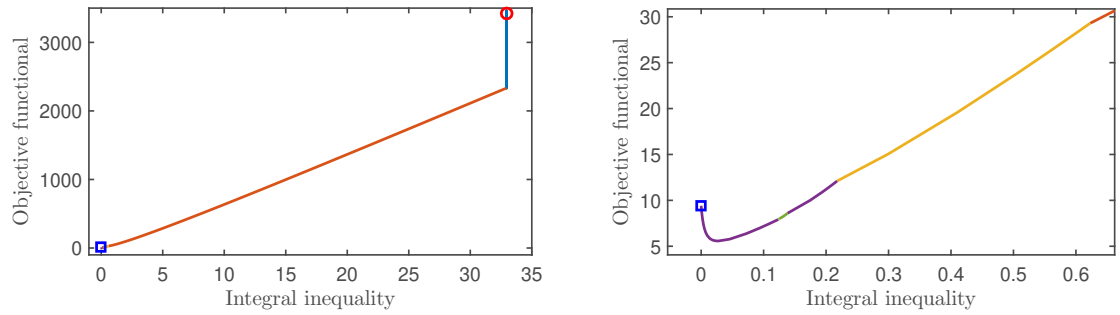

Figure 1: Projections of sequential continuation paths associated with a successive search for an optimal control input for an inverted pendulum. Feasible solutions correspond to nonpositive values of the integral inequality functional. The right panel shows a zoomed-in plot of the left panel around the located minimum (blue square). The initial point is denoted by the red dot in the left panel.

CONCLUSIONS

General-purpose support in the software package COCO for constrained design optimization with functional equality constraints and finite-dimensional inequality constraints is demonstrated using examples from nonlinear dynamical systems theory. While problem construction is straightforward, the specific application of the successive continuation paradigm is problem-dependent and nonunique. Importantly, as seen in both examples, the technique allows minima to be located with initial solution guesses also in the infeasible region.

References

[1] Li, M., Dankowicz, H. Staged Construction of Adjoints for Constrained Optimization of Integro-Differential Boundary-Value Problems. *SIAM J. Appl. Dyn. Syst.* **17(2)**: 1117-1151, 2018.

[2] Li, M., Dankowicz, H. Optimization with Equality and Inequality Constraints Using Parameter Continuation. *arXiv preprint.* arXiv:1909.01422, 2019.

[3] Ahsan, Z., Dankowicz, H., Sieber, J. Optimization along Families of Periodic and Quasiperiodic Orbits in Dynamical Systems with Delay. *Nonlinear Dyn.* https://doi.org/10.1007/s11071-019-05304-y, 2019.

SOBOL GLOBAL SENSITIVITY ANALYSIS ON A BISTABLE ENERGY HARVESTER

João Pedro C. V. Norenberg[1], Americo Cunha Jr *[2], Samuel da Silva[1], and Paulo Sérgio Varoto[3]
[1] Universidade Estadual Paulista - UNESP, Ilha Solteira, Brazil
[2] Universidade do Estado do Rio de Janeiro - UERJ, Rio de Janeiro, Brazil
[3] Universidade de São Paulo - USP, São Carlos, Brazil

Summary This work deals with a global sensitivity analysis in the nonlinear dynamics of a bistable piezo-magneto-elastic energy harvester. The objective is to evaluate the degree of influence of each input parameter variation, as well as their joint effect, on the system response. The global sensitivity analysis method used is the Sobol index, which is based on the idea of orthogonally decompose the total variance of the system response into a sum of conditional variances. The Monte Carlo-based analysis provides a detailed overview about the influence of the physical parameters on the energy recovering process in periodic and chaotic dynamic regimes.

INTRODUCTION

Piezoelectric energy harvesting technologies are considered a very appealing energy source to support low power electronic devices such as mobile phones or medical implants. Typically, it consists in an electromechanical system capable of capturing (mechanical) energy available for free in the environment and converting it into electrical potential. Several studies demonstrate that the introduction of nonlinearities in the system can optimize the electrical power harvested over a wide frequency range [1, 2, 3].

Global sensitivity analysis is a statistical tool that has been receiving great attention in the analysis of many engineering systems, providing a comprehensive approach on how an input variation can affect the underlying system response [4]. An application of these idea in the context of energy harvesting can be seen in the recent work of Aloui et al. [5]. The key point here is to evaluate the degree of influence of the input parameters, and their joint effect, on the system response. In the framework of nonlinear dynamical systems, is can be very useful tool to reveal the influence of each nonlinearity, especially because nonlinear systems, in general, present large sensitivity to variations on the input parameters.

In this work, a global sensitivity analysis based on Sobol' indices is conducted on a nonlinear dynamical system that emulates the behavior of a bistable piezoelectric energy harvester. This approach is based on the decomposition of the system output total variance in a summation of conditioned variances that quantifies the individual, and joint effect, of each model input variability on the system output power.

MATHEMATICAL BACKGROUND

The energy harvesting system studied is the piezo-magneto-elastic beam illustrated in Figure 1, proposed by Erturk et al. [2]. It consists of a cantilever ferromagnetic beam attached to a rigid base excited by a harmonic force, two magnets spaced from its free end causing bistable nonlinearity, and a piezoelectric transducer coupled to the structure with an electrical circuit.

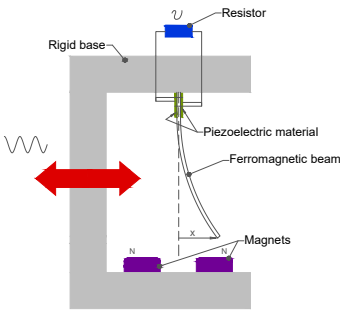

Figure 1: Schematic representation of the piezo-magneto-elastic energy harvesting system.

The electromechanical dynamical system evolves according to

$$\ddot{x} + 2\xi\,\dot{x} - 0.5x\,(1 - x^2) - \chi\,v = f\,\cos(\Omega t) \quad \text{and} \quad \dot{v} + \lambda\,v + \kappa\,\dot{x} = 0, \tag{1}$$

where x is the dimensionless tip displacement of the beam, Ω and f are the dimensionless frequency and amplitude of the harmonic force, respectively, ξ is a mechanical damping ratio, v is the dimensionless voltage, χ and κ are the mechanical

*Corresponding author. E-mail: americo@ime.uerj.br

and electrical piezoelectric coupling terms and λ is the reciprocal of the dimensionless time constant. The averaged output power delivered by this system is given by

$$P = \frac{1}{T}\int_{t_i}^{t_f} \lambda\, v(t)^2 \; dt, \tag{2}$$

being the main quantity of interest for the present study.

Now consider the mathematical model above in an abstract form $Y = \mathcal{M}(X)$, where X is a vector of k independent and uncertain parameters, and Y is a chosen scalar model output (quantity of interest). The Hoeffding-Sobol decomposition states that

$$Y = \mathcal{M}_0 + \sum_{i=1}^{k} \mathcal{M}_i(X_i) + \sum_{i<j}^{k} \mathcal{M}_{ij}(X_i, X_j) + \ldots + \mathcal{M}_{1,2,\ldots,k}(X_1, X_2, \ldots, X_k), \tag{3}$$

which is an orthogonal decomposition in terms of conditional expectations as defined by [4]. In this way, first-order Sobol' indices are defined as $S_i = Var[\mathcal{M}_i(X_i)]/Var[\mathcal{M}(X)]$, while the second-order Sobol' indices are $S_{ij} = Var[\mathcal{M}_{ij}(X_i, X_j)]/Var[\mathcal{M}(X)]$, etc. The total Sobol' indices are $S_{Ti} = 1 - S_{\sim i}$, by denoting $S_{\sim i}$ the sensitivity measure of all the variables excluding variable X_i.

NUMERICAL EXPERIMENTS

For all simulations reported here, the following dimensionless parameters used are: $\xi = 0.01$, $\chi = 0.05$, $\lambda = 0.05$, $\kappa = 0.5$ and $\Omega = 0.8$. Two set of values of f and initial conditions are considered, which produce two different dynamic behaviors: (i) $f = 0.083$ and $(x_0, \dot{x}_0, v_0) = (1, 1, 0)$ for periodic behavior; and (ii) $f = 0.115$ and $(x_0, \dot{x}_0, v_0) = (1, 0, 0)$ for chaotic behavior (see [3] for details). Sobol index analysis is performed based on the Monte Carlo (MC) method and the output parameter analyzed is the average power defined by Equation 2 by the interval $0 \leq t \leq 1000$. All parameters are considered independent with an uniform distribution centered in the nominal value with 20% of dispersion. Figure 2 show the first and second-order and total Sobol' indices for periodic (top) and chaotic (bottom) behaviors, considering the 5 most relevant second-order indices among the 15 possible.

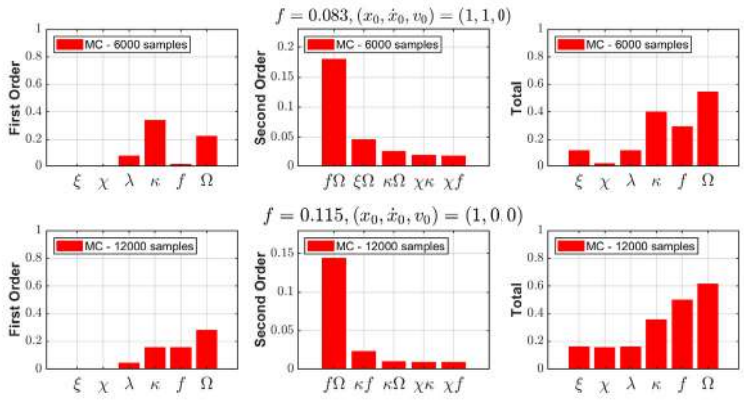

Figure 2: First, second-order and total Sobol' indices for the averaged output power, for periodic (top) and chaotic (bottom) behaviors.

Note that, for periodic regime, the piezoelectric coupling parameter κ, which controls the energy conversion, is the most influential parameter. Next, the excitation frequency Ω, the reciprocal time constant λ, for which the power is proportional, and finally the excitation amplitude f. Damping ratio and the mechanical piezoelectric coupling have negligible first-order influence, but the former has joint effect with κ. For chaotic behavior, an increase in the first-order influence of the mechanical parameters and f is observed, which may be explained by its high-sensitivity to variations.

FINAL REMARK

The global sensitivity analysis based on Sobol index is an adequate tool to describe the degree of influence of a nonlinear energy harvester parameters on amount of energy recovered for both, periodic and chaotic, dynamic regimes.

References

[1] Cottone F., Vocca H., Gammaitoni L. Nonlinear energy harvesting. *Phy. Review Letters* **102**:080601, 2009.
[2] Erturk A., Hoffmann J., Inman D. J. A piezomagnetoelastic structure for broadband vibration energy harvesting. *Appl. Phys. Lett.* **94**:254102, 2009.
[3] Lopes V.G., Peterson J.V.L.L., Cunha Jr. A. Nonlinear Characterization of a Bistable Energy Harvester Dynamical System. In: Belhaq M. (eds) Topics in Nonlinear Mechanics and Physics. Springer Proceedings in Physics, **228**. Springer, Singapore, 2019.
[4] Abbiati G , Marelli S. , Tsokanas N., Sudret B., Stojadinovic B. A Global Sensitivity Analysis Framework for Hybrid Simulation. 2019.
[5] Aloui R., Larbi W., Chouchane M. Global sensitivity analysis of piezoelectric energy harvesters. *Composite Structures* **228**:111317, 2019.

IMPACTS IN THE ROCKING OF MASONRY CIRCULAR ARCHES

Mario Como [1], Simona Coccia *[1], and Fabio Di Carlo [1]
[1] Department of Civil Engineering and Computer Science Engineering (DICII), University of Rome "Tor Vergata", via del Politecnico 1, 00133, Rome, Italy

Summary Analysis of the impacts occurring during the rocking of the masonry arch is the subject of the paper. Starting point is the study, in the context of the masonry Heyman's model, of the rocking motion of the arch along the two mechanisms u^- and u^+, having hinges mutually disposed at mirrored positions. Special attention is devoted to the instant in which the hinges of u^- become blocked: impacts and motion exchanges take place. A new impact model is proposed in the paper. The motion of the arch, just before and after impacts, is determined by application of the Principles of Conservation of linear and angular momentum. It is shown that the angular momentum of the arch evaluated around the hinges of the mechanism u^+ has to remain constant. The restitution factor is thus obtained.

Some recalls on the rocking of the column and of the masonry pier.

We consider some aspects of the alternate oscillations of the column based on a friction supporting plane π. Fig. 1a shows the column, rotating around the right corner O, just before colliding with π. At this instant all points of the base section, except the left corner O', touch without impact the plane π. The point O', on the other hand, that cannot cross the plane π, becomes instantaneously blocked. Impact occurs at O' and the impulse Pdt takes place (Fig. 1b). The column, continuing in its motion, rotates around the centre O' (Fig. 1c). Concluding, impact point matches the rotation centre of the succeeding motion. The case of the masonry pier is similar. The pier exhibits the typical diagonal cracks, testifying a past seismic event (Fig. 2 and Fig. 3). In this case, contacts occur along the diagonals except the base corners, that are at once rotation centres and impact points.

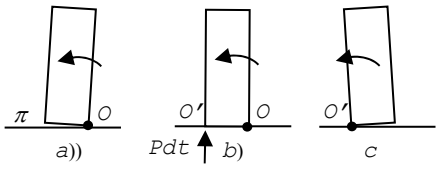

Fig. 1. The column.

Fig. 2. Diagonal cracks.

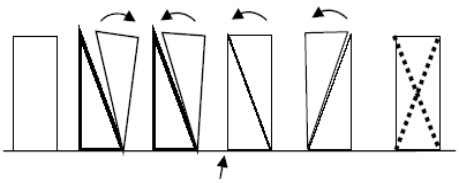

Fig. 3. The masonry pier.

The controversial position of impact points during the rocking of the masonry arch

The masonry arch, released from a defined configuration A, puts itself in motion along a single-degree-of-freedom mechanism u^-, the failure mechanism of the arch under a constant static distribution of horizontal forces. Fig. 4 shows the mechanism of the falling down arch. The arch continues its motion as far as the undeformed position is reached (Fig. 5). At this instant all hinges close and impacts take place. Just after the impacts, the arch continues to move still from the right to the left along the *reverse* mechanism u^+ that has a *mirrored hinges layout*, compared to u^- (Fig. 6). Tests made by DeJong et al. [1] confirm this assumption. Limit Analysis defines the positions of the hinges of mechanisms u^- and u^+ [2, 3]. The problem is the definition of the position of impact points.

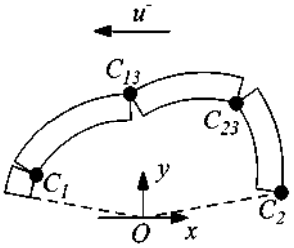

Fig. 4. The falling down motion.

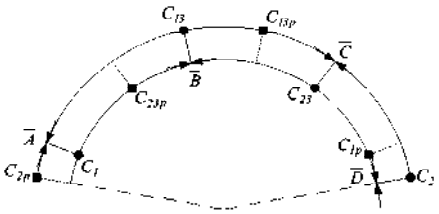

Fig. 5. The undeformed configuration.

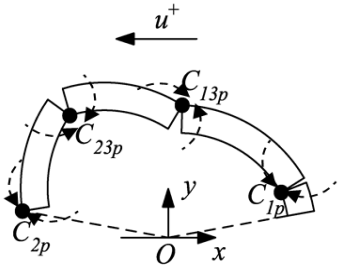

Fig. 6. The reverse mechanism.

In some studies, it is assumed that impacts occur at the same sections where the hinges of the first mechanism u^- are placed but on the opposite side [4]. This statement seems to come out from a questionable reading of what happens at the column base, above recalled. But the position of the impact point at O' in Fig. 1 does not derive from the fact that point O' of the base column is placed at the opposite side of the first centre O, but because O' is the rotation centre of the succeeding motion. Accordingly to the above assumption, we can distinguish, in all sections of the arch where the hinges C_1, C_2, C_{23} and C_{13} of the mechanism u^- are located but at the opposite sides, the assumed impact points $\bar{A}$, $\bar{B}$, $\bar{C}$ and $\bar{D}$. In Fig. 5 we can also see, marked with small squares, the hinges C_{1p}, C_{13p}, C_{23p} and C_{2p} of the succeeding mechanism u^+.

*Corresponding author. E-mail: coccia@ing.uniroma2.it

Concurrence of impacts points with the hinges of the succeeding mechanism u^+

Let us go back to Fig. 4 and let us consider the instant in which the hinges of the first mechanism u^- start to close. The facing sides of each hinge of u^- begin to go in contact. Consider, for instance, the left side of the arch. As soon as the hinge C_1 of the previous mechanism u^- closes, compressions transmit across the arch segment C_{13}-C_1, heading off to the left springer, while the hinges C_{2p} and C_{23p} take shape. Pushed by inertial forces the segment C_{2p}-C_{23p} starts to rotate counterclockwise around C_{2p}, so that the springing section of this segment at C_{2p} attempts to go across the rigid base plane of the left spring of the arch. The lower section of the segment C_{2p}-C_{23p} becomes suddenly blocked at C_{2p} and impact occurs at this point. The same stands for all facing sides of the other hinge sections of the segments C_{23p}-C_{13p} and C_{13p}-C_{1p}. Therefore, impacts occur at points C_{2p}, C_{23p}, C_{13p} and C_{1p} (Fig. 6). We conclude that in the masonry arch, such as in the column and in the masonry pier, impact points match the hinges of the succeeding mechanism u^+.

The new impact model

The velocity of all rigid segments in which the arch is subdivided just after the impact can be determined by applying the Principles of Impulse and of the Angular Momentum. As shown in Fig. 7, impulsive forces at internal post-impact hinges balance each other. Impulsive forces at external post-impact hinges, named F_1dt and F_2dt, and the rotational velocity immediately after the impact are unknown. A system of five equations is then required for a proper definition of the energy dissipation model. We can write two equations expressing the balance of the linear momentum of the entire arch along x and y directions and a third equation expressing the balance of the moment of momentum around the point O.

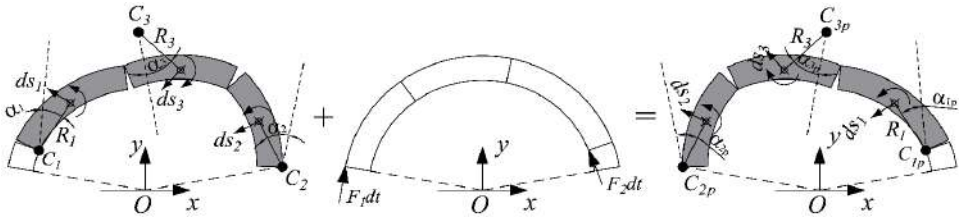

Fig. 7. Application of the Principle of Impulse to the whole system.

Let us go now to the fourth and fifth equations, referring to the conservation of the Angular Momentum around the points C_{23p} and C_{13p} as of the portions of the arch located *at the left* of the post-impact internal hinge C_{23p} (Fig. 8), as of the portion of the arch located at the right of the post-impact internal hinge C_{13p} (Fig. 9). The rotational equilibrium is written just around points C_{23p} and C_{13p} to eliminate the contribution of the unknown internal impulsive forces.

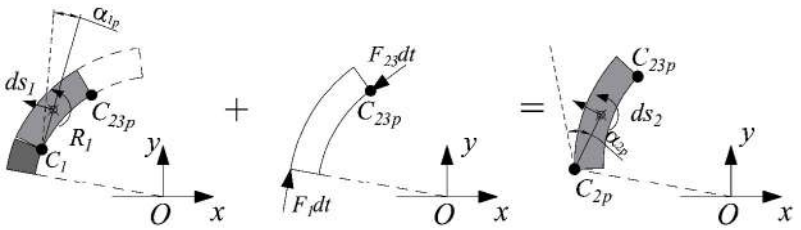

Fig. 8. Angular Momentum Principle on the portion of the arch located to the left of C_{23p}.

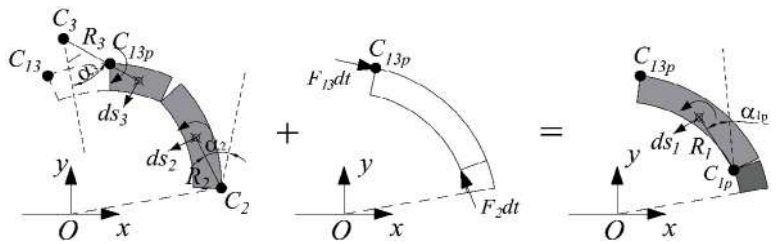

Fig. 9. Angular Momentum Principle on the portion of the arch located to the right of C_{13p}.

Numerical investigation is made to evaluate the corresponding restitution factor.

References

[1] DeJong M., De Lorenzis L., Adams S., Ochsendorf J.A. Rocking Stability of Masonry Arches in Seismic Regions. *Earth. Spec.* **24(4)**: 847-865, 2008.
[2] Heyman J. The stone skeleton. *Int. J. of Solids and Structures* **2(2)**: 249-256, 1966.
[3] Como M., Statics of Historic Masonry Constructions, 3rd ed., Springer, Heidelberg, 2017.
[4] De Lorenzis L., DeJong M., Ochsendorf J. Failure of masonry arches under impulse base motion. *Earth. Eng. and Struct. Dyn.* **36**: 2119-2136, 2007.
[5] Como M., Di Carlo F., Coccia S. Dynamic response of rocking cracked masonry walls. *Meccanica*, **54(3)**, 381-398, 2019.
[6] Housner G.W. The behaviour of inverted pendulum structures during earthquakes. *Bull. of the Seismological Society of America* **53(2)**: 403-417, 1963.

AGING AND SINGULAR PROBLEMS IN THERMO-VISCOELASTICITY AND MAGNETO-VISCOELASTICITY

Sandra Carillo *[1,2] and Claudio Giorgi[3]
[1] Dipartimento di Scienze di Base e Applicate per l'Ingegneria, Università di Roma LA SAPIENZA ,Rome, Italy
[2] I.N.F.N. - Sezione Roma1, Gr. IV - Mathematical Methods in NonLinear Physics, Rome, Italy
[3] Department DICATAM, Brescia, Italy

Summary The model of viscoelastic body is considered aiming to describe a wider variety of phenomenological situations. Accordingly, different concurring effects are coupled with viscoelasticity to take into account the combined mechanical response to different effects. Specifically, the classical model of viscoelasticity, is generalised to describe new magnetically sensible materials coupling the viscoelasticity with a magnetisation equation. Key property of the viscoelastic behaviour is the relaxation function G. The *classical* regularity assumptions are the framework to start with. A further generalisation consists in the introduction in the model of thermal effects. Indeed, a realistic description of the mechanical response of a material in most cases cannot disregard thermal effects further to mechanical and magnetic ones. In this framework, magneto-viscoelastic materials, for instance gels in which micro-particles magnetically sensible are inserted and thermo-magneto-viscoelastic ones, i.e. the same gels when also the thermal effects are taken into account, are considered. In such cases, the mechanical behaviour of the material, respectively, is influenced also by by an external magnetic field or also by the temperature.

INTRODUCTION

The mechanical response of a body termed *magneto-viscoelastic* is modelled via integro-differential equations in which the integral terms take into account the *deformation history* of the material. Specifically, a body is termed viscoelastic when its stress depends not only on the present status but also on its deformation history. It is termed thermo-viscoelastic if in addition its stress and thermal power depend on the temperature history. The kernels of the integral terms characterise the viscoelastic material to study: the relaxation functions $\mathbf{G}$ and c rule the dependence on the deformation and temperature histories, respectively. The combination of the viscoelastic behaviour with thermal or magnetic effects is introduced and scrutinised.

Viscoelastic body

The quantities suitable to describe the problem are: the *strain tensor*, denoted as $\mathbf{E} = \mathbf{E}(t)$, the *stress tensor* $\mathbf{T} = \mathbf{T}(t)$ the *relaxation modulus* $\mathbf{G} = \mathbf{G}(t)$, whose initial value is denoted as $\mathbf{G}_0 := \mathbf{G}(0)$.

The body is assumed to be homogeneous and isotropic so that the dependence on the spatial variable can be omitted when the viscoelastic behaviour of the body is described. Conversely, the dependence on time is not only through the present time, but also on the past (deformation) *history* of the material. The surrounding environment is assumed to be *passive*, that is, it is not affected by the presence of the viscoelastic body.

The quantities which describe the mechanical status of the viscoelastic body are related via *constitutive assumptions* which guaranty, the physical meaningfulness of the model [1]:

$$\mathbf{T}(t) = \int_0^\infty \mathbf{G}(\tau)\,\dot{\mathbf{E}}(t-\tau)\,d\tau \iff \mathbf{T}(t) = \mathbf{G}_0\mathbf{E}(t) + \int_0^\infty \dot{\mathbf{G}}(\tau)\ ,\ \mathbf{G}(t) = \mathbf{G}_0 + \int_0^t \dot{\mathbf{G}}(s)\,ds \tag{1}$$

where $\mathbf{E}^t(\tau) := \mathbf{E}(t-\tau)$ denotes the *strain past history*. In addition, $\mathbf{G}$ enjoys the *fading memory property*, that is

$$\forall \varepsilon > 0\, \exists\, \tilde{a} = a(\varepsilon, E^t) \in \mathbb{R}^+ s.t.\ \forall a > \tilde{a}, \left| \int_0^\infty \dot{\mathbf{G}}(s+a)\mathbf{E}^t(s)\,ds \right| < \varepsilon \tag{2}$$

The classical one-dimensional evolution problem reads

$$u_{tt} = G(0)u_{xx} + \int_0^t \dot{G}(t-\tau)u_{xx}(\tau)d\tau + f\ ,\ \text{i.b.c}: u(\cdot,0) = u_0,\ u_t(\cdot,0) = u_1 \text{ in } \Omega\,;\ u = 0 \text{ on } \Sigma = \partial\Omega \times (0,T) \tag{3}$$

wherein u denotes displacement and f external force which includes the history of the material. The classical assumptions the relaxation modulus satisfies are:

$$\dot{G} \in L^1(\mathbb{R}^+)\ ,\ G(t) = G_0 + \int_0^t \dot{G}(s)\,ds\ ,\ G(\infty) = \lim_{t\to\infty} G(t). \tag{4}$$

When, as commonly assumed, $G \in C^2(\mathbb{R}^+)$, then $\quad G(t) > 0, \qquad \dot{G}(t) \le 0, \qquad \ddot{G}(t) \ge 0, \qquad t \in (0,\infty).$ (5)

Under these assumptions, the problem (3) admits a unique solution as proved by Dafermos [2].

*Corresponding author. E-mail: sandra.carillo@uniroma1.it.

MAGNETO-VISCOELASTIC PROBLEM

The magneto-viscoelastic problem which models the behaviour of a viscoelastic body subject also to an external magnetic field, in the 1-dimensional case [3, 4], it is modelled by the nonlinear system

$$\begin{cases} u_{tt} - G(0)u_{xx} - \displaystyle\int_0^t G'(t-\tau)u_{xx}(\tau)d\tau - \frac{\lambda}{2}(\Lambda(\mathbf{m})\cdot\mathbf{m})_x = f\,, \\ \\ \mathbf{m}_t + \mathbf{m}\dfrac{|\mathbf{m}|^2-1}{\varepsilon} + \lambda\Lambda(\mathbf{m})u_x - \mathbf{m}_{xx} = 0\,, \end{cases} \quad \text{in } \Omega\times(0,T) \tag{6}$$

where $\Omega = (0,1)$ and $\mathbf{m} = (0, m_1, m_2)$, denotes the magnetization vector, orthogonal to the conductor, since $\mathbf{u} \equiv (u,0,0)$, when both quantities are written in $\mathbb{R}^3$. In addition, Λ is a linear operator defined by $\Lambda(\mathbf{m}) = (0, m_2, m_1)$, the scalar function u is the displacement in the direction of the conductor itself, here identified with the $x-$axis and λ is a positive parameter. In addition, the term f represents an external force which also includes the deformation history up to $t = 0$. Letting $\boldsymbol{\nu}$ be the outer unit normal at $\partial\Omega$, initial and boundary conditions are given as follows

$$u(\cdot,0) = u_0 = 0,\;\; \mathbf{m}(\cdot,0) = \mathbf{m}_0,\quad |\mathbf{m}_0| = 1 \quad \text{in } \Omega\,,\;\;,\;\; u = 0,\qquad \frac{\partial\mathbf{m}}{\partial\boldsymbol{\nu}} = 0 \qquad \text{on} \quad \Sigma = \partial\Omega\times(0,T)\,, \tag{7}$$

Under the assumptions $G(t) \in C^2(0,T)$, $u_0 \in H_0^1(\Omega)$, $u_1 \in L^2(\Omega)$, $\mathbf{m}_0 \in H^1(\Omega)$ and $f \in L^2(\Omega\times(0,T))$, the existence and uniqueness of the solution to the problem given by (6)-(7), is proved in [3]. The corresponding 3-dimensional problem is studied in [5].

MAGNETO-THERMO-VISCOELASTIC PROBLEM

Borrowing the arguments presented in [6], in a thermoelastic solid the stress–strain relation is given by

$$\mathbf{T}(t) = \mathbf{G}_0[\mathbf{E}(t) - \mathbf{E}^{\theta}(t)] + \int_0^{\infty} \dot{\mathbf{G}}(\tau)\,\mathbf{E}^t(\tau)\,d\tau$$

where $\mathbf{E}^{\theta}(t)$ is the *thermal strain*, whereas the *relative temperature* θ is ruled by the heat balance equation

$$c\,\dot{\theta}(t) + \int_0^{\infty} \gamma(\tau)\,\dot{\theta}\,(t-\tau)\,d\tau = \mathbf{B}\cdot\dot{\mathbf{E}}(t) - \nabla\cdot\mathbf{q}(t) + r(t).$$

In the isotropic Fourier case, $\mathbf{E}^{\theta}(t) = \alpha\,\theta(t)\,\mathbf{I}$ and the heat flux vector is given by $\mathbf{q} = -k\nabla\theta$. Then, the corresponding magneto-thermo-viscoelastic problem reads

$$\begin{cases} u_{tt} - G_0[u_{xx} - \alpha\theta_x] - \displaystyle\int_0^t G'(t-\tau)u_{xx}(\tau)d\tau - \frac{\lambda}{2}(\Lambda(\mathbf{m})\cdot\mathbf{m})_x = f\,, \\ c\,\theta_t + \gamma_0\theta + \displaystyle\int_0^t \dot{\gamma}(\tau)\,\theta\,(t-\tau)\,d\tau = \beta\,u_{xt} + k\,\theta_{xx} + g \\ \mathbf{m}_t + \dfrac{\mathbf{m}}{\varepsilon}(|\mathbf{m}|^2-1) + \lambda\Lambda(\mathbf{m})u_x - \mathbf{m}_{xx} = 0\,, \end{cases} \quad \text{in } \Omega\times(0,T) \tag{8}$$

where the term g includes the heat source r and the temperature history up to $t = 0$. System (8) is studied assigning *natural* initial and boundary conditions.

CONCLUSIONS AND PERSPECTIVES

The presented model systems are studied under the classical assumptions (4)-(5). Further generalisations to describe also the behaviour of new materials such as in [7], can be introduced when *singular kernel* problems are considered as in [9, 8]. Indeed, as discussed in [10], the classical assumptions are not suitable to describe many cases of interest in real materials, such as for instance, anti-seismic ones, or when damage effects are introduced to take into account the natural *aging* of materials.

References

[1] C. Giorgi, A. Morro, *Continuum Mech. Thermodyn.*, **4**, 151-165, 1992.
[2] C.M. Dafermos, *J. Diff. Equations*, **7**, 554-569, 1970.
[3] S. Carillo, V. Valente, G. Vergara Caffarelli, Applicable Analisys, 1791-1802, **(90) n.ro 12**, 2011.
[4] S. Carillo, **52**, (13), 2017, pp 3053–3060.
[5] S. Carillo, V. Valente, G. Vergara Caffarelli, Discrete and Continuous Dynamical Systems Series S. , 435 - 447 **(5) n.ro 3**, (2012).
[6] C. Giorgi, M.G. Naso, *Quart. J. Mech. Appl. Math.*, **53**, 363-374, 2000.
[7] Guo, Q., Zaïri, F., Guo, X. *International Journal of Plasticity*, **101**, 106-124, 2018.
[8] S. Carillo, M. Chipot, V. Valente, G. Vergara Caffarelli, Nonlinear Analysis Series B: Real World Applications, 35C (2017) pp. 200-210.
[9] S. Carillo, *Meccanica*, **50**, 603-615, 2015.
[10] S. Carillo, C. Giorgi, *Non-classical memory kernels in linear viscoelasticity*, Chapter 13 in "Viscoelastic and Viscoplastic Materials", M.F. El-Amin Editor, ISBN 978-953-51-2602-7, p 295-331 (2016) InTech.

ROBUST TRACKING OF PERIODIC SOLUTIONS IN EXPERIMENTS WITH CONTROL-BASED CONTINUATION

Sandor Beregi *[1], David A. W. Barton[1], Djamel Rezgui[1], and Simon A. Neild[1]
[1] Faculty of Engineering, University of Bristol, United Kingdom

Summary Characterising the dynamics of noise-polluted experimental systems can be often strenuous as measurement noise may conceal certain features of the deterministic system dynamics. In this study, we perform robust continuation of the steady-state periodic solutions of a nonlinear oscillator under noise-load. The periodic solutions of the system are traced by employing control-based continuation (CBC) while the experiment is contaminated with different levels of physical noise. The performance of the algorithm is then assessed with the help of parameter identification in the model of a Duffing-type oscillator, based on the acquired measurement data. By comparing the results to open-loop parameter sweeps, we demonstrate that CBC is more robust to random perturbations and, as a result, it can reveal the finer details of the system dynamics in the presence of noise.

INTRODUCTION

Extracting information from noise-polluted experiments is often a challenge as persistent random perturbations may obscure the finer details of the underlying deterministic system. In our study, we analyse the steady-state periodic solutions of a physical nonlinear oscillator featuring a bistable response (a parameter region where three steady-state solutions, two stable and one unstable, coexist). In traditional open-loop measurements, only the stable solutions can be detected; the unstable solutions must be inferred indirectly. Moreover, measurement noise may result in the system 'jumping' between the domains of attractions of the coexisting stable solutions potentially leading to a loss of information even from a part of the stable solutions [1, 2].

In case of nonlinear mathematical models, the widely used techniques of numerical bifurcation analysis are able to identify the steady-state solutions (e.g. equilibria, periodic orbits, invariant tori) of deterministic systems regardless of their stability. The method of control-based continuation (CBC) adapts the ideas of bifurcation analysis to experiments making it possible to trace both stable and unstable periodic solutions of the experimental rig. The method can also be employed in the presence of noise [3]. Our aim is to assess whether CBC is more robust in extracting information from the underlying deterministic system in noise-polluted experiments than standard open-loop measurements.

EXPERIMENTAL STUDY OF A FORCED NONLINEAR OSCILLATOR

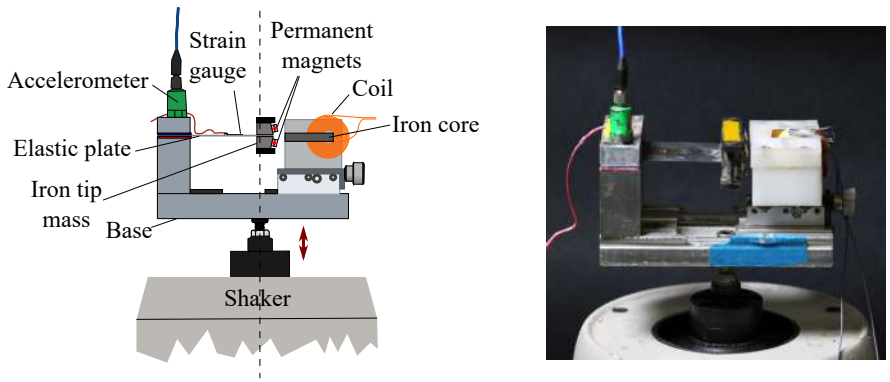

Figure 1: The nonlinear oscillator on the shaker providing forcing to the system. In the left panel, a schematic is presented while the experimental rig is shown in the right panel.

We studied the steady-state periodic solutions of the forced nonlinear oscillator (see Fig. 1) consisting of an elastic plate with an iron tip mass and permanent magnets and an electromagnetic coil. The device is designed such that the combination of the structural, inertial and electromagnetic forces result in a nonlinear restoring force while the experiment can be contaminated with physical noise by driving current through the coil.

We employ the technique of control-based continuation to trace the family of periodic solutions of the experimental rig for different forcing amplitudes at constant frequencies. Performing continuation in amplitude rather than frequency allows us to use a simplified version of the CBC algorithm [4]. Then we fit the model parameters of a Duffing-type oscillator to the acquired data considering odd order nonlinearities up to seventh order.

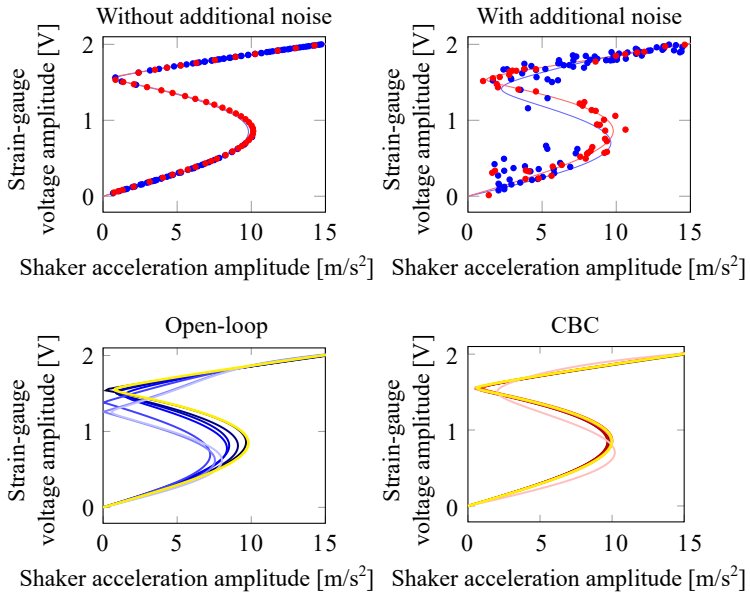

Figure 2: Top row: Amplitude response of the nonlinear oscillator at low and high noise-levels. The markers show the measurement data while the response of the fitted Duffing oscillator is indicated by the continuous lines. Bottom row: The amplitude-responses of the Duffing oscillator fitted to data acquired at different noise-levels. The response curves corresponding to measurements without noise added through the coil are highlighted in yellow. The blue markers and curves in each panel belong to parameter-sweeps while the red ones to CBC.

Robustness against noise

The parameter identification is used to characterise and quantify the resilience of the CBC algorithm against measurement noise (see Fig. 2). We traced the steady-state periodic solutions both using CBC and open-loop sweeps in the forcing amplitude while the experiment was physically polluted with different levels of additional noise through the coil. These tests indicate that while open-loop measurements can perform similarly at low noise levels as CBC, in the presence of a higher amount of noise the open-loop technique tends to fail to identify the location of the folds on the S-shaped response curve of the system whereas the deterministic response can be largely retained using CBC up to a noise level around 30 % of the largest vibration amplitude.

CONCLUSIONS

By performing experimental bifurcation analysis of a nonlinear oscillator, we demonstrated that CBC is capable to capture the underlying deterministic response even with a significant noise-load on the system. The steady-state response was captured both using CBC and standard open-loop parameter sweeps. By using the parameter-sweeps as benchmark, we established that CBC has the ability to extract finer details of the dynamics of the experimental rig than it was possible by open-loop approach. Thus, control-based continuation could be effectively used to investigate nonlinear systems experimentally where, beside the nonlinear effects, one has to deal with significant measurement noise.

Although our study focuses on forced vibrations, CBC can be generalised to study self-excited vibrations in autonomous systems such as in case of aeroelastic flutter [5]. In aeroelastic systems, the inherently unsteady airflow around oscillating aerofoils may results in a significant noise-load. Since the commonly used nonlinear mathematical models of these phenomena predict a complicated set of steady-state solutions [6] the robust experimental bifurcation analysis in aeroelastic systems may provide further novel results.

References

[1] Barkley D., Kevrekidis I.G., Stuart A.M. Adams J.A. (2006) The Moment Map: Nonlinear Dynamics of Density Evolution via a Few Moments *SIAM J. Applied Dynamical Systems*, Vol. 5. No. 3. pp. 403-434.

[2] Kuehn C. (2012), Deterministic Continuation of Stochastic Metastable Equilibria via Lyapunov Equations and Ellipsoids, *SIAM J. Sci. Comptut*, Vol. 34, No. 3, pp. A1635–A1658

[3] Schilder F., Bureau E., Santos I. F., Thomsen J. J., Starke J., (2015) Experimental bifurcation analysis—Continuation for noise-contaminated zero problems, *Journal of Sound and Vibration*, Vol. 358, pp. 251-266.

[4] Renson L., Shaw A.D., Barton D.A.W., Neild S.A. (2019), Application of control-based continuation to a nonlinear structure with harmonically coupled modes, *Mechanical Systems and Signal Processing*, Vol. 120, pp. 449-464.

[5] Tartaruga I., Barton D.A.W., Rezgui D., Neild S., (2019) Experimental bifurcation analysis of a wing profile, International Forum on Aeroelasticity and Structural Dynamics, IFASD 2019, 9-13 June 2019, Savannah, Georgia, USA

[6] Dimitriadis, G. (2017). Introduction to nonlinear aeroelasticity. John Wiley & Sons.

*Corresponding author. E-mail: sandor.beregi@bristol.ac.uk

A SIMPLE, REDUCED COMPLEXITY METHOD OF LYAPUNOV EXPONENTS ESTIMATION FOR DISCONTINUOUS SYSTEMS

Marek Balcerzak*[1], Artur Dabrowski[1] and Andrzej Stefanski[1]
[1] Division of Dynamics, Lodz University of Technology, Lodz, Poland

Summary According to the state-of-art algorithms, finding the whole spectrum of *n* Lyapunov Exponents (LEs) requires to integrate *n* orthogonal perturbations of the system under consideration. In this paper authors show that application of the novel method reduces the number of integrated perturbations to *(n-1)*. This applies to smooth systems, as well as non-smooth or even discontinuous ones. Important assets of the new algorithm are simplicity and ease of implementation. Authors shortly present the novel method and explain why it enables to skip integration of the last perturbation. Then, it is shown how the new approach can be adopted to discontinuous systems. Finally, application of the algorithm for estimation of LEs spectrum of an impact oscillator is described. Authors hope that the novel method is going to facilitate research in the field of dynamical systems, including discontinuous ones.

THE METHOD

Consider a dynamical system described by an ODE and the corresponding linearized equation which defines evolution of an infinitesimal perturbation of the system:

$$\dot{\boldsymbol{x}} = \frac{d\boldsymbol{x}}{dt} = \boldsymbol{f}(\boldsymbol{x}, t), \qquad \dot{\boldsymbol{z}}^1 = \boldsymbol{f}(\boldsymbol{x} + \boldsymbol{z}^1, t) - \boldsymbol{f}(\boldsymbol{x}, t) = \boldsymbol{J}(\boldsymbol{x}, t)\boldsymbol{z}^1 \tag{1}$$

where $\boldsymbol{x} \in \mathbb{R}^n$ is a state vector, $\dot{\boldsymbol{x}} = d\boldsymbol{x}/dt$, n is the order of the system, t is the time, $\boldsymbol{f}(\boldsymbol{x}, t)\colon \mathbb{R}^n \times \mathbb{R} \to \mathbb{R}^n$ is a vector field, $\boldsymbol{z}^1(t)$ is an infinitesimal perturbation and $\boldsymbol{J}_{ij} = \partial f_i/\partial x_j$ is the Jacobian matrix of the vector field $\boldsymbol{f}$ with respect to the state vector $\boldsymbol{x}$. Lyapunov Exponents (LEs) are numbers that specify exponential rates in which infinitesimal perturbations of a dynamical system change their lengths [1]. Almost any perturbation in the phase space has a component along a direction of the largest Lyapunov Exponent (LLE). Consequently, the LLE specifies the rate of change of the length of disturbances in most directions of the phase space. Analogously, most perturbations orthogonal to the direction of the LLE change their lengths according to the second LE. Generally, norms of perturbations orthogonal to the directions of the first *i* LEs evolve according to the *(i+1)*-th LE.

In the paper [2] it has been shown that LEs can be estimated by calculating the following formula in each integration step:

$$\lambda_i^*(t) = \frac{\boldsymbol{z}^i(t) \cdot \frac{d\boldsymbol{z}^i}{dt}(t)}{|\boldsymbol{z}^i(t)|^2} \tag{2}$$

The average of all $\lambda_i^*(t)$ approaches the *i*-th LE. Please note that the value (2) is independent from the length of the perturbation vector $|\boldsymbol{z}^i(t)|$. The first perturbation $\boldsymbol{z}^1$ is computed directly from (1) and not modified. Other perturbations $\boldsymbol{z}^i$ need to be continually orthogonalized with respect to $\boldsymbol{z}^1, \ldots, \boldsymbol{z}^{(i-1)}$ [1]. Note that $\boldsymbol{z}^i$, due to orthogonalization, is restricted to a subspace of the dimension *(n+1-i)*. Therefore, the last perturbation $\boldsymbol{z}^n(t)$ is confined to a 1-dimensional subspace (a line) in the phase space, so its direction is known solely from orthogonalization with respect to $\boldsymbol{z}^1, \ldots, \boldsymbol{z}^{(n-1)}$. This fact, for the case n=3, is illustrated in Figure 1.

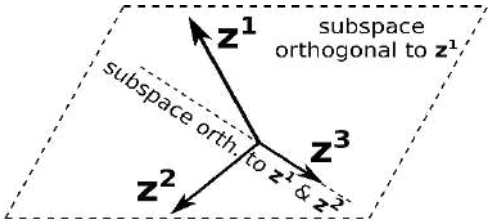

Figure 1. Perturbations and their subspaces for the case n=3. Direction of $\boldsymbol{z}^n$ is known solely due to orthogonalization.

As (2) is independent from perturbation's length, any vector in the subspace orthogonal to $\boldsymbol{z}^1, \ldots, \boldsymbol{z}^{(n-1)}$ (the line) can be used to calculate the last LE. Therefore, integration of the last perturbation is redundant.

If the system under consideration is discontinuous, the state and the perturbations may change instantaneously as the trajectory passes through a discontinuity. Assume that it is encountered at the times $t_1, \ldots, t_m$ and the transition

*Corresponding author. E-mail: marek.balcerzak.1@p.lodz.pl

rule, which defines transformation of perturbations at the discontinuity, can be presented in the form $\boldsymbol{z}^i(t_j+\epsilon) = \boldsymbol{T}[\boldsymbol{x}(t_j), t_j]\boldsymbol{z}^i(t_j-\epsilon)$ where $1 \le i \le n, 1 \le j \le m$ and ϵ is an arbitrarily small, positive number. The matrix $\boldsymbol{T}[\boldsymbol{x}(t_j), t_j]$ can be found using the method presented in the paper [3]. Then, the influence of the discontinuity on the values of LEs can be taken into account using the formula:

$$\lambda_i^{**}(t_j) = \lim_{\epsilon \to 0^+} \frac{1}{\Delta t} \ln \frac{\left|\boldsymbol{z}^i(t_i+\epsilon)\right|}{\left|\boldsymbol{z}^i(t_i-\epsilon)\right|} \tag{3}$$

where Δt is the integration step and $\boldsymbol{z}^i$ is orthogonalized with respect to the perturbations $\boldsymbol{z}^1, \ldots, \boldsymbol{z}^{i-1}$ both before and after passing through the discontinuity. It can be shown that in order to estimate the *i*-th LE in a system with discontinuity, one has to add the values (2) from each integration step, the values (3) computed during each transition through the discontinuity and divide the obtained sum by the number of integration steps.

NUMERICAL EXAMPLE

Consider the impact oscillator presented in Figure 2a. Its equations, in dimensionless form, are as follows:

$$\begin{gathered} \boldsymbol{x}' = \begin{bmatrix} x_1' \\ x_2' \end{bmatrix} = \boldsymbol{f}(\boldsymbol{x}, \tau) = \begin{bmatrix} x_2 \\ -x_1 - 2\beta x_2 + \cos(\eta\tau) \end{bmatrix}, x_1 < x_w \\ \lim_{\epsilon \to 0^+} \boldsymbol{x}(\tau_i + \epsilon) = \lim_{\epsilon \to 0^+} \boldsymbol{D}\boldsymbol{x}(\tau_i - \epsilon), \text{gdy } x_1(\tau_i) = x_w, \boldsymbol{D} = diag(1, -1) \end{gathered} \tag{4}$$

where $\boldsymbol{x} = [x_1, x_2]^T$ is the state vector and $\boldsymbol{x}'$ is its derivative with respect to the dimensionless time $\tau = t\sqrt{k/m}$, $\boldsymbol{f}$ is the vector field, $x_1 = kX/F$, $x_2 = \dot{X}\sqrt{mk}/F$, $\beta = c/(2\sqrt{mk})$, $\eta = \Omega\sqrt{m/k}$, $x_w = kX_w/F$, $\tau_i = t_i\sqrt{k/m}$ and $\boldsymbol{D}$ is the 2x2 diagonal matrix, which transforms the state vector $\boldsymbol{x}$ when a collision occurs (the position x_1 remains unchanged, whereas the sign of the velocity x_2 is reversed).

The presented method of LEs estimation has been applied for the system (4) with the following values of parameters: $\beta = 0.05, x_w = 2$. The non-dimensional forcing frequency η has been selected as a control parameter in the range $\eta \in [0.7, 0.76]$. The bifurcation diagram and LEs diagram are presented in Figure 2b. The LLE is marked with a solid line and the second LE with the dashed one.

a) b)

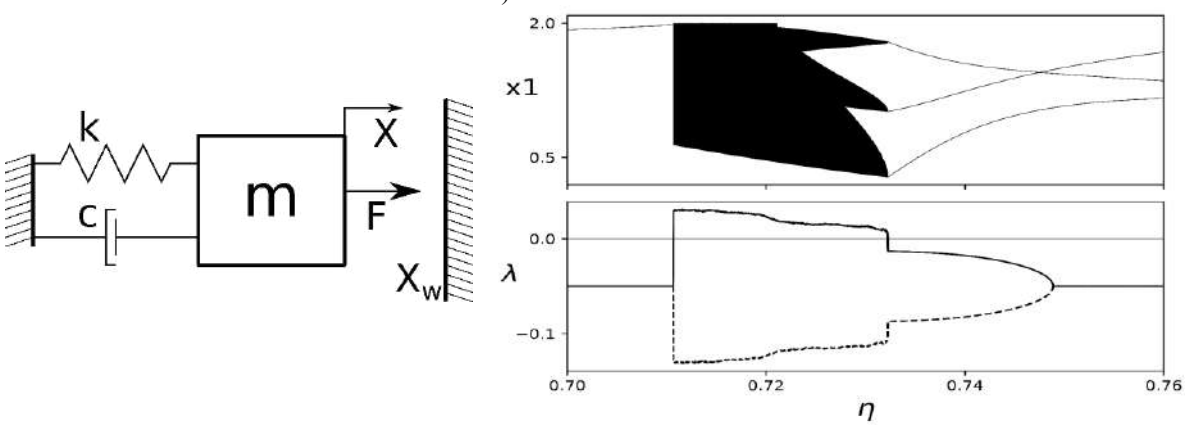

Figure 2. a) Scheme of the impact oscillator b) Bifurcation diagram and corresponding Lyapunov Exponents diagram

CONCLUSIONS

The presented results are in agreement with the publication [4]. Therefore, correctness of the presented method has been verified. Consequently, authors confirmed that it is possible to calculate the spectrum of n Lyapunov exponents of a non-smooth or discontinuous systems using only $n-1$ perturbations. It is expected that the presented method can simplify investigations of non-smooth dynamical systems and support research in this field.

References

[1] Parker T.S., Chua L.O. Practical Numerical Algorithms for Chaotic Systems. Springer-Verlag, Berlin 1989.
[2] Balcerzak, M., Pikunov, D., Dąbrowski, A.. The fastest, simplified method of Lyapunov exponents spectrum estimation for continuous-time dynamical systems. *Nonlinear Dyn.* **94(4)**: 3053-3065, 2018.
[3] Müller, P. C. Calculation of Lyapunov exponents for dynamic systems with discontinuities. Chaos Solitons Fractals **5(9)**: 1671–1681, 1995
[4] Balcerzak, M., Dąbrowski, A., Stefański, A., & Wojewoda, J. Spectrum of Lyapunov exponents in non-smooth systems evaluated using orthogonal perturbation vectors. In MATEC Web of Conferences Vol. 148, p. 10003. EDP Sciences, 2018

MULTIPLE-SCALE ANALYSIS OF A GEOMETRICALLY EXACT BEAM MODEL

Enrico Babilio*[1], Stefano Lenci[2], and Elio Sacco[1]
[1] Department of Structures for Engineering and Architecture, University of Naples "Federico II", Naples, Italy
[2] Department of Civil and Building Engineering and Architecture, Polytechnic University of Marche, Ancona, Italy

Summary Slender and highly flexible structures are frequently used as members in systems designed to meet high to extreme performances. Hence cables, ropes, yarns, hoses and pipelines, which are essential parts of such structures, play a relevant role in practically every engineering field. However, in real operating conditions, beams and beam-like structures exhibit responses often too complicated for current modeling tools. In this respect there is a continuous need for reliable models. In this area, the present contribution considers a beam model equipped with non-standard constitutive laws and, in particular, it is aimed at deriving approximate solutions of the equations of motion via asymptotic multiple scale expansion.

BASICS ON THE BEAM MODEL

We consider a geometrically exact beam model deduced by stipulating a relation between one- and three-dimensional formulations for initially straight beams undergoing planar and twist-less deformed states. Using comma notation for derivatives, the equations of motion derived in [1], to which we refer for any further detail, are written as

$$m_0\,u_{,tt} - m_1(\theta_{,t}^2\sin\theta - \theta_{,tt}\cos\theta) + c_0\,u_{,t} + c_1\theta_{,t}\cos\theta = \left(N(1+u_{,x})\sqrt{2\varepsilon+1} - \frac{Tv_{,x}}{\sqrt{2\varepsilon+1}}\right)_{,x} + q_1\,, \tag{1}$$

$$m_0\,v_{,tt} - m_1(\theta_{,t}^2\cos\theta + \theta_{,tt}\sin\theta) + c_0\,v_{,t} - c_1\theta_{,t}\sin\theta = \left(Nv_{,x}\sqrt{2\varepsilon+1} + \frac{T(1+u_{,x})}{\sqrt{2\varepsilon+1}}\right)_{,x} + q_2\,, \tag{2}$$

$$m_1(u_{,tt}\cos\theta - v_{,tt}\sin\theta) + m_2\,\theta_{,tt} + c_1(u_{,t}\cos\theta - v_{,t}\sin\theta) + c_2\,\theta_{,t} = M_{,x} - T\sqrt{2\varepsilon+1} + q_3\,, \tag{3}$$

where $u(x,t)$ and $v(x,t)$ stand for the axial and transverse displacements of the beam axis, $\theta(x,t)$ is the cross-sectional rotation, $m_k(x)$ and $c_k(x)$, $k=0,1,2$ are mass and damping coefficients, $q_i(x)$, $i=1,2,3$ are external loads, $N(x,t)$, $T(x,t)$ and $M(x,t)$ are axial, transverse and bending generalized stresses given by

$$N = \frac{\sin^2\gamma}{\sqrt{2\varepsilon+1}}\,K_S + \frac{\varepsilon}{\sqrt{2\varepsilon+1}}\,K_0 + \cos\gamma\left(\frac{3\varepsilon+1}{2\varepsilon+1}\right)\kappa\,K_1 + \frac{1+2\cos^2\gamma}{2\sqrt{2\varepsilon+1}}\kappa^2\,K_2 + \frac{\cos\gamma}{2(2\varepsilon+1)}\kappa^3\,K_3\,, \tag{4}$$

$$T = \sqrt{2\varepsilon+1}\,\frac{\sin 2\gamma}{2}\,K_S - \varepsilon\sin\gamma\,\kappa\,K_1 - \sqrt{2\varepsilon+1}\,\frac{\sin 2\gamma}{2}\,\kappa^2\,K_2 - \frac{\sin\gamma}{2}\kappa^3\,K_3\,, \tag{5}$$

$$M = \varepsilon\sqrt{2\varepsilon+1}\,\cos\gamma\,K_1 + \left(\varepsilon + (2\varepsilon+1)\cos^2\gamma\right)\,\kappa\,K_2 + \frac{3}{2}\sqrt{2\varepsilon+1}\,\cos\gamma\,\kappa^2\,K_3 + \frac{1}{2}\,\kappa^3\,K_4\,, \tag{6}$$

where $K_j(x)$, $j=0,1,\ldots,4$ and $K_s(x)$ are stiffnesses and $\varepsilon(x,t)$, $\gamma(x,t)$ and $\kappa(x,t)$ are axial, shear angle and bending strains, related to displacements and rotations.

Since their introduction, Eqs. (1-3) have been analyzed in some depth [2, 3, 4] mainly through numerical investigations. On the contrary, the present paper, following [5], is focused on analytical developments, based on the method of multiple scales [6]. In particular, to draw frequency-response curves as those reported in Fig. 1, the exact partial differential Eqs. (1-3) are analyzed around frequencies corresponding to certain natural modes.

A SUMMARY ON THE MULTIPLE-SCALE ANALYSIS

On introducing a small book-keeping parameter ϵ, the unknowns and their m^{th} time derivatives in Eqs. (1-3) can be expanded, up to the order r, as

$$w_i(x,t) = \sum_{j=1}^{r}\epsilon^j W_{ij}(x;\tau_0,\tau_1,\cdots,\tau_r)\,, \qquad \frac{\partial^m w_i}{\partial t^m} = \prod_{k=1}^{m}\sum_{j=0}^{r}\epsilon^j\frac{\partial w_i}{\partial\tau_j}\,, \qquad i=1,2,3 \tag{7}$$

where w_i are dummy functions such that $u=w_1$, $v=w_2$, $\theta=w_3$, $\tau_0=t$ is a fast time scale, $\tau_1=\epsilon t,\cdots,\tau_r=\epsilon^r t$ are slow scales and W_{ij} are unknown functions to be determined. From these equations and further assuming that c_0 and K_3 are at most order ϵ^2; m_1, c_1, c_2, and K_1 are at most ϵ^3; the loads q_2, of order ϵ^3, and q_1 and q_3, of order ϵ^4, are periodic functions whose frequencies are close to natural frequencies ω_i, that is

$$q_i(t) = P_i\cos(\Omega_i t) = P_i\cos(\omega_i\tau_0 + \sigma_i\tau_2)\,, \quad i=1,2,3 \tag{8}$$

*Corresponding author. E-mail: enrico.babilio@unina.it

being σ_i detuning parameters small of order of ϵ^2, after some algebra, the set of linear differential equations

$$m_0\, W_{1j,\tau_0\tau_0} - K_0\, w_{1j,xx} = \mathcal{P}_{1j}\,, \tag{9}$$

$$m_0\, W_{ij,\tau_0\tau_0} + K_S^{-1}\,(m_0\, m_2\, W_{ij,\tau_0\tau_0} - (m_0\, K_2 + m_2\, K_S)\, W_{ij,xx})_{,\tau_0\tau_0} + K_2\, W_{ij,xxxx} = \mathcal{P}_{ij}\,, \qquad i = 2,3 \tag{10}$$

with the index j spanning from 1 to the order of expansion, can be derived. Equations (9-10), and the expansion of proper boundary conditions, can be managed in cascade, taking into account, at any step, suitable solvability conditions to avoid that the solution contains resonant terms.

As a sketch of results, we report in Fig. 1 some frequency-response curves for a beam, which is supported by immovable hinges at both ends. The curves are drawn as a function of the detuning parameter σ_2, appearing in the transversal load, for four different values of K_4, namely 0, 2.5×10^{-4}, 1.0×10^{-3}, and 3.0×10^{-3}. Because of boundary conditions, the curves are hardening. Further, we see that the higher is the value of K_4, the more the corresponding frequency-response curve is bent. The response remains still nonlinear for $K_4 = 0$, as it can be seen from Eqs. (4-6) and from Fig. 1.

The next steps of this study will be aimed at comparing the behavior of the model we are dealing with to others existing in the scientific literature [7, 8, 9], as well as to numerical results.

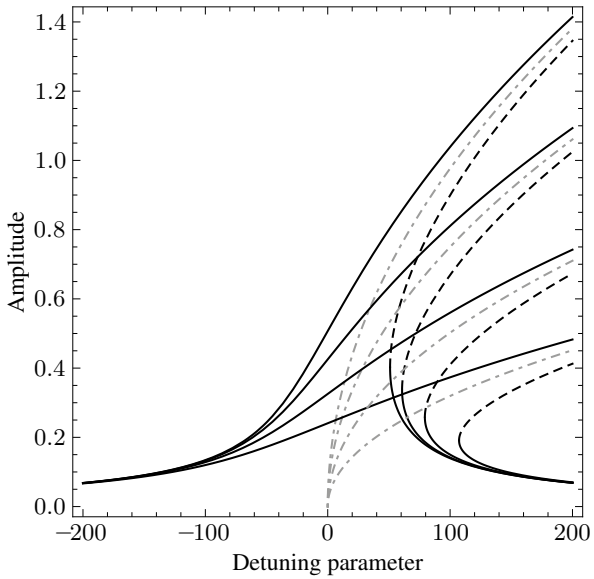

Figure 1: Stable (black solid lines) and unstable (black dashed lines) branches of frequency responses and backbone curves (gray dot-dashed lines) for four different values of the stiffness K_4, starting from 0 (corresponding to the less forward-bent curve) up to 3.0×10^{-3}.

CONCLUSIONS

The present contribution, which is part of an ongoing research focused on the analysis of a geometrically exact beam model with nonlinear constitutive relationships, reports about preliminary results from a multiple-scale analysis. The next steps, still in progress, will be focused on investigating the role played by parameters on the shape of frequency-response curves and comparing the present model with others and with results from numerical approaches available in the literature.

References

[1] Babilio E., Lenci S., On the notion of curvature and its mechanical meaning in a geometrically exact plane beam theory. *Int. J. Mech. Sci.*, **128-129**:277–293, 2017.

[2] Babilio E., Lenci S., Consequences of different definitions of bending curvature on nonlinear dynamics of beams. *Procedia Eng.*, **199**:1411–1416, 2017.

[3] Babilio E., Lenci S., A simple total-lagrangian finite-element formulation for nonlinear behavior of planar beams. *Proc. ASME Des. Eng. Tech. Conf.* DETC2018-85622. Quebec City, Quebec, Canada. August 26–29, 2018.

[4] Babilio E., Lenci S., On a geometrically exact beam model and its finite element approximation, I. Kovacic, S. Lenci, eds. *IUTAM Symposium on Exploiting Nonlinear Dynamics for Engineering Systems*, IUTAM Bookseries, Springer, **37**, 59–69, 2020.

[5] Kloda L., Lenci S., Warminski J., Nonlinear dynamics of a planar beam-spring system: analytical and numerical approaches. *Nonlinear Dyn.*, **94**(3):1721–1738, 2018.

[6] Nayfeh A.H., *Perturbation methods*. Physics textbook. John Wiley & Sons, 2000.

[7] Reissner E., On one-dimensional finite-strain beam theory: the plane problem. *Z. Angew. Math. Phys.*, **23**(5):795–804, 1972.

[8] Simo J.C., A finite strain beam formulation. The three-dimensional dynamic problem. Part I. *Comput. Method Appl. M.*, **49**(1):55–70, 1985.

[9] Irschik H., Gerstmayr J., A continuum-mechanics interpretation of Reissner's non-linear shear-deformable beam theory. *Math. Comp. Model Dyn.*, **17**(1):19–29, 2011.

HYSTERETIC MODELS IN FERROELECTRICS

Claudio Giorgi[1] and Angelo Morro *[2]
[1] DICATAM, University of Brescia, Brescia, Italy
[2] DIBRIS, University of Genoa, Genoa, Italy

Summary The paper deals with hysteresis in ferroelectrics and develops a constitutive model which seems to be a basic reference also for other hysteretic phenomena. Neither hysteresis operators nor superpositions of a linear component to rate-type law are involved. Instead, the approach is based on constitutive equations where both the polarization and the electric field are simultaneously independent variables so that the constitutive functions depend on both of them. Thermodynamic requirements are derived and a class of models is shown to be allowed. It is a conceptual advantage of the class so established that the behaviour of the material is described in a consistent scheme of constitutive equations. For definiteness some hysteresis loops are shown to arise from the constitutive model.

THERMODYNAMIC REQUIREMENTS ON UNDEFORMABLE FERROELECTRICS

For simplicity we restrict attention to undeformable ferroelectric materials. Let $\mathbf{E}$ be the electric field, $\mathbf{P}$ the dielectric polarization, θ the absolute temperature, η the entropy density, ε the internal energy density (per unit volume). The dielectric material is assumed to be undeformable and non-conductor. The balance of energy is then taken in the form $\dot{\varepsilon} = \mathbf{E}\cdot\dot{\mathbf{P}} + r$, the superposed dot denoting the time derivative while r is the energy supply. Let $\Phi = \varepsilon - \theta\eta - \mathbf{E}\cdot\mathbf{P}$,called free enthalpy density or Gibbs free energy density. The second-law inequality is considered in the form

$$\dot{\Phi} + \eta\dot{\theta} + \mathbf{P}\cdot\dot{\mathbf{E}} \leq 0.$$

Let Φ, η be functions of $\mathbf{E}, \theta, \mathbf{P}, \dot{\mathbf{E}}, \dot{\mathbf{P}}$. It follows that Φ is independent of $\dot{\mathbf{E}}, \dot{\mathbf{P}}$ and that $\eta = -\partial_\theta\Phi$ while

$$-(\mathbf{P} + \partial_{\mathbf{E}}\Phi)\cdot\dot{\mathbf{E}} - \partial_{\mathbf{P}}\Phi\cdot\dot{\mathbf{P}} \geq 0.$$

Assume $\mathbf{P}$ and $\mathbf{E}$ are collinear and let P, E be the components in the common direction. The thermodynamic restriction becomes

$$(P + \partial_E\Phi)\dot{E} + \partial_P\Phi\,\dot{P} \leq 0.$$

As a consequence, along any closed curve in the $E-P$ plane, as the time t runs over $[0,T]$, we have

$$0 \geq \int_0^T \{(P + \partial_E\Phi)\dot{E} + \partial_P\Phi\,\dot{P}\}dt = \int_0^T \{P\dot{E} + \dot{\Phi}\}dt = \int_0^T P\,\dot{E}\,dt.$$

The requirement $0 \geq \int_0^T P\,\dot{E}\,dt = \oint P\,dE$ implies that the closed curve is run in the counterclockwise sense. Further, the thermodynamic requirement is made explicit by letting

$$(P + \partial_E\Phi)\cdot\dot{E} + \partial_P\phi\cdot\dot{P} = -\xi|\dot{E}|, \qquad \xi \geq 0.$$

MODELLING OF FERROELECTRICS

Look at time intervals where $\dot{E} \neq 0$. It follows

$$\frac{\dot{P}}{\dot{E}} = -\frac{P + \partial_E\Phi}{\partial_P\Phi} - \frac{\xi}{\partial_P\Phi}\mathrm{sgn}\dot{E}.$$

Except at stationary points we can write

$$\frac{dP}{dE} = \chi_1 + \chi_2\mathrm{sgn}\dot{E}, \qquad \chi_1 = -\frac{P + \partial_E\Phi}{\partial_P\Phi}, \quad \chi_2 = -\frac{\xi}{\partial_P\Phi},$$

χ_1, χ_2 being functions of P, E and θ. Paraelectric materials are viewed as those with $\chi_2 = 0$; hence χ_1 is the positive slope of the polarization curve, that is the differential susceptibility. We then require that $\chi_1 > 0$, $|\chi_2| \leq \chi_1$.

To determine χ_1 and χ_2 we start from a characteristic non-decreasing function $\mathcal{P}$ (anhysteretic function) such that $P = \mathcal{P}(E) \iff \chi_2 = 0$. As a consequence, once a free enthalpy function Φ is chosen, the anhysteretic curve is given by

$$\frac{dP}{dE} = -\frac{P + \partial_E\Phi}{\partial_P\Phi} = \chi_1 =: g(E) \geq 0.$$

*Corresponding author. E-mail: angelo.morro@unige.it

Owing to the counterclockwise property of ferroelectric cycles the function χ_2 is required to satisfy

$$\chi_2(E,P) >=< 0 \quad \Longleftrightarrow \quad P >=< \mathcal{P}(E).$$

For definiteness let $\Phi(P,E) = \mathcal{L}(P-\mathcal{G}(E)) + \mathcal{F}(E) - PE$ where $\mathcal{F}, \mathcal{G}, \mathcal{L}$ are undetermined functions. By definition

$$\chi_1 = \frac{\mathcal{L}'(P-\mathcal{G}(E))\mathcal{G}'(E) - \mathcal{F}'(E)}{\mathcal{L}'(P-\mathcal{G}(E)) - E}, \qquad \chi_2 = -\frac{\xi}{\mathcal{L}'(P-\mathcal{G}(E)) - E}.$$

Letting $\chi_1 = g(E)$ we find $\mathcal{G}' = g, \mathcal{F}' = Eg$. To determine $\mathcal{L}$ we require $\chi_2[P-\mathcal{P}(E)] \le 0$, whence, since $\xi \ge 0$,

$$\frac{P-\mathcal{P}(E)}{\mathcal{L}'(P-\mathcal{G}(E)) - E} \ge 0.$$

Hence we let

$$\mathcal{L}'(P-\mathcal{G}(E)) = \alpha[P-\mathcal{G}(E)], \mathcal{P}(E) = \mathcal{G}(E) + E/\alpha.$$

As an example,

$$\Phi(P,E) = (\alpha/2)(P-\mathcal{G}(E))^2 + \mathcal{F}(E) - PE,$$

$$\mathcal{G}(E) = \int_0^E g(y)dy, \qquad \mathcal{F}(E) = \int_0^E y\, g(y)dy,$$

$$\chi_1 = g(E), \quad \chi_2 = -\frac{\xi}{\alpha[P-\mathcal{P}(E)]}, \quad \mathcal{P}(E) = \int_0^E [g(y) + 1/\alpha]dy.$$

Consistent with the meaning of anhysteretic differential permittivity, we let $g(E) \to 0$ as $|E| \to \infty$. The model is complete once g and ξ are selected.

Since the hysteretic behaviour occurs below the Curie temperature, $\theta_{\mathcal{C}}$, we let

$$\xi = \gamma(E,P)h(\theta),$$

where $h(\theta) = \max\{0, 1-\theta/\theta_{\mathcal{C}}\}$ and hence $h \to 0$ as $\theta \to \theta_{\mathcal{C}}$ from below. Among the possible functions γ we select $\gamma(E,P) = \gamma_0 g(E)[P-\mathcal{P}(E)]^2, \qquad \gamma_0 > 0$, where $g(E) = \mathcal{P}'(E) - 1/\alpha$. Let $\gamma_h(\theta) = \gamma_0 h(\theta)$; it follows that

$$\frac{dP}{dE} = g(E)[1 - \tau_h(P-\mathcal{P}(E))\mathrm{sgn}\dot{E}], \qquad \tau_h = \gamma_h/\alpha > 0.$$

Some hysteresis cycles are shown.

CONCLUSIONS

The same approach seems to be applicable to ferromagnetism, thus improving previous models [1, 2]. A further investigation is in order to apply the present ideas to plasticity.

References

[1] Fabrizio M., Giorgi C., Morro A. Phase transitions in ferromagnetism. *Internat. J. Eng. Sci.* **47**: 821-839, 2009.
[2] Coleman B.D., Hogdon M.L. A constitutive relation for rate-independent hysteresis in ferromagnetically soft materials. *Internat. J. Eng. Sci.* **24**: 897-919, 1986.

VIBRO-IMPACT SELF-PROPELLED CAPSULE IN MILLIMETRE-SCALE

Yang Liu*[1], Jiajia Zhang[1], Jiyuan Tian[1] Bingyong Guo[1], and Shyam Prasad [2]
[1] College of Engineering, Mathematics and Physical Sciences, University of Exeter, Exeter, UK
[2] Endoscopy Unit, Royal Devon and Exeter NHS Foundation Trust, Exeter, UK

Summary This work will study the prototype design of a vibro-impact self-propelled capsule endoscope for small-bowel diagnosis. Inspired by the nonlinear dynamics of nonsmooth dynamical systems [1], self-propulsion of a capsule endoscope can be achieved by employing an internal vibrational mass interacting with the main body of the capsule. In this work, we will show that the proposed concept has been implemented at the standard dimension of a market-leading capsule endoscope [2], which is 11 mm in diameter and 27 mm in length.

INTRODUCTION

Capsule endoscopy [3] has become established as the primary modality for examining the small intestinal mucosa. However, its reliance on peristalsis for passage through the intestine may cause variable locomotion speeds, which can result in incomplete visualisation of the mucosa and potentially missed pathology. Therefore, the current design is considered both time-consuming and burdensome for clinicians. Researchers have developed different propulsion methods for capsule endoscopy, and among many of them, the system driven by autogenous interactive forces using magnetic actuation [4] is a promising solution. In order to validate this concept, a millimetre-scale prototype of the capsule system will be presented in this paper.

THE PRINCIPLE, PROTOTYPE DESIGN AND EXPERIMENTAL SETUP

Physical model of the system and its prototype are presented in Fig. 1, where the rectilinear motion of the capsule is generated using a periodically driven permanent magnet (excited by external magnetic field) interacting with the capsule's main body as a hammer via the primary and the secondary constraints, in the presence of intestinal resistances. The external magnetic field is excited by a pulse-width modulation (PWM) signal, and the capsule can perform forward and backward progression by adjusting the amplitude, the frequency, and the duty cycle of the PWM signal.

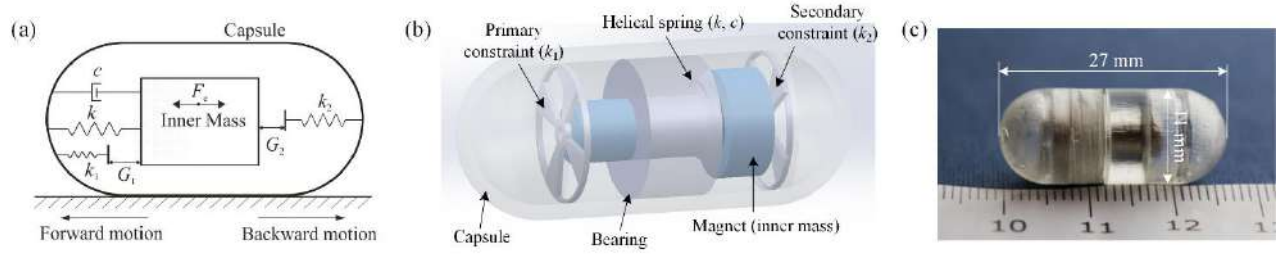

Figure 1. (a) Physical model, (b) conceptual design, and (c) 3D-printed prototype of the vibro-impact self-propelled capsule.

Schematics of the experimental setup and its photograph are shown in Fig. 2(a) and (b), respectively, where the coils are controlled by a drive circuit triggered by a pulse-width modulation (PWM) signal. A video camera was used to record the locomotion of the capsule, and the recorded video clip was analysed by using Tracker [5], a real-time tracking software for visualising the time histories of capsule's displacement as illustrated in Fig. 2(c) and (d).

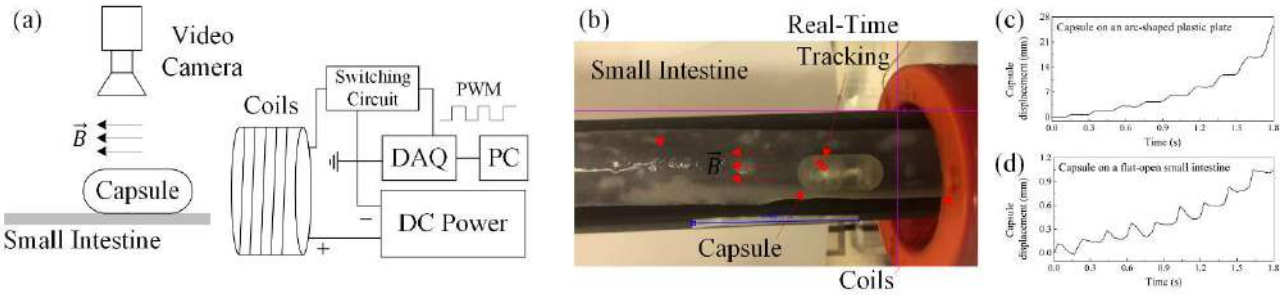

Figure 2. (a) Schematics and (b) photograph of the experimental setup. Time histories of capsule's displacement (c) on an arc-shaped plastic plate and (d) on a flat-open small intestine.

References

[1] Pavlovskaia E., Hendry D. C., and Wiercigroch M., Modelling of high frequency vibro-impact drilling, *Int. J. Mech. Sci.*, 91:110–119, 2015.
[2] PillCam™ SB 3 System, web site **http://www.medtronic.com/covidien/en-us/products/capsule-endoscopy/pillcam-sb-3-system.html**.
[3] Singeap A.M., Stanciu C., and Trifan A., Capsule endoscopy: the road ahead, *World J. Gastroenterol.*, 22:369–378, 2016.
[4] Liu Y., Pavlovskaia E., and Wiercigroch M., Experimental verification of the vibro-impact capsule model, *Nonlinear Dyn.*, 83:1029–1041, 2015.
[5] Tracker, web site **https://physlets.org/tracker/**

*Corresponding author. E-mail: y.liu2@exeter.ac.uk.

DYNAMIC IMPACT OF A CERAMIC SKELETON OF INTERPENETRATING PHASE COMPOSITES

Eligiusz Postek *[1], Tomasz Sadowski[2], Jarosław Bieniaś [2], Marek Boniecki[3]
[1] Institute of Fundamental Technological Research, Polish Academy of Science, Warsaw, Poland
[2] Department of Civil Engineering and Architecture, Lublin University of Technology, Lublin, Poland
[3] Institute of Electronic Materials Technology, Warsaw, Poland

Summary The paper presents modelling of a ceramic foam that works as skeleton of Interpenetrating Phase Composites (IPCs) before filling the preforms. The preforms are made of SiC or Al_2O_3. A dynamic analysis of an impact of such skeletons against rigid surface is performed. The results of the quasi-static analysis will serve as a reference to the dynamic analyses. The analysis of the IPCs skeleton is performed due to evaluation of the role of the skeleton in final product that is the filled IPCs.

INTRODUCTION AND MOTIVATION

Contemporary ceramic composites are used in many industries of strategic importance, such as the armaments industry, aviation, automotive [1] nuclear power [2] or space exploration, while in other areas they constitute the main source of technical progress [3]. In these applications, the material is often subjected to extreme loads, such as variable shock loads and high temperatures. In the presentation, we explore the degradation of an IPC skeleton.

In the last twenty years, the peridynamics that is a meshless non-local has been developed [4]. The method appears to be useful in analysis of brittle materials. The Metal-Ceramic composites are analysed in [5]. Metallic foams are analysed in [6].

NUMERICAL MODELLING

Problem statement

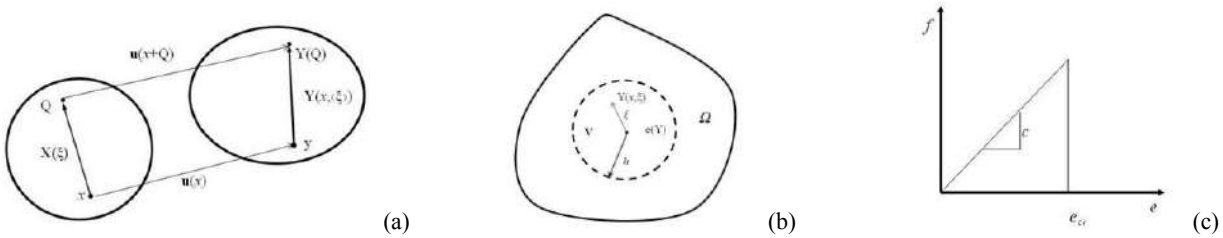

Figure 1. Peridynamics: state of deformation (a), integration over horizon (b), dependence of a force on stretch in a single bond (c).

When observing Fig. 1(a), x and Q are points in the undeformed body. It is a bond definition, $\xi = Q - x$. A reference state $\mathbf{X}$ is a function that acts on a bond, $\mathbf{X}(\xi)$. The deformation state depends on the new position of the coordinate x in the deformed configuration $y(x)$) as follows,$\mathbf{Y}(x, \xi) = y(x + \xi) - y(x)$. It yields $\mathbf{Y}(x, \xi) = y(Q) - y(x)$. The displacement state $U(x, \xi) = \boldsymbol{u}(x + \xi) - \boldsymbol{u}(\xi)$ yields $U(x, \xi) = \boldsymbol{u}(Q) - \boldsymbol{u}(x)$. Following Fig. 1(a), the scalar extension state $e(\boldsymbol{Y})$ is given as follows:

$$e(\mathbf{Y}) = |\mathbf{Y}| - |\mathbf{X}|$$

The scalar extension state is decomposed into its spherical e^i and deviatoric e^d parts:

$$e = e^i + e^d$$

The elastic force state $t(Y)$ is given in the form analogous to standard stress strain relation being the sum of the spherical and deviatoric parts as follows:

$$t(Y) = (3k\theta/m)\omega\underline{x} + \alpha\omega e^d$$

where k is the bulk modulus, θ is the dilatation, m is the weighted volume, ω is the influence function, $x = |\xi|$ is the basic scalar state, α is the coefficient related to the shear modulus $\alpha = (15\mu)/m$ where μ is the shear modulus.

The assumptions for the material failure model are as follows [7]. Bonds fail when their extension exceeds a critical value. Damage is caused by accumulation of broken bonds. Bonds failure is irreversible. A scheme for a single bond is shown in Fig 1(c) . The integration is over a domain V for all bonds. The dependence of force on its stretch in a bond is given in Fig. 1(b). It reads:

$$f = ce\zeta$$

where c is a constant depending on bulk modulus k and radius of the horizon h, $c = (18k)/(\pi h^4)$. Function is history dependent (time t) and takes value 1 when bond stretch is lower than critical stretch ζ or 0 otherwise. The damage d is defined s follows:

$$d(x,t) = 1 - \int_V \zeta(x,t,\xi)dV \Big/ \int_V dV$$

where *d* varies between 0 for primordial material and 1 for fully damaged material.

Physical model

The AL_2O_3 preforms are shown in Fig. 2(a) and Fig 2(b). The performs are of large pores and small pores, respectively. To obtain a numerical model, the CT scans of the performs are performed. The scans are shown Fig. 2(c) and Fig. 2(b). Basing on the CT scans, the hexadral discretizations are obtained. The initial discretizations stands for a base of finite element an peridynamics numerical models.

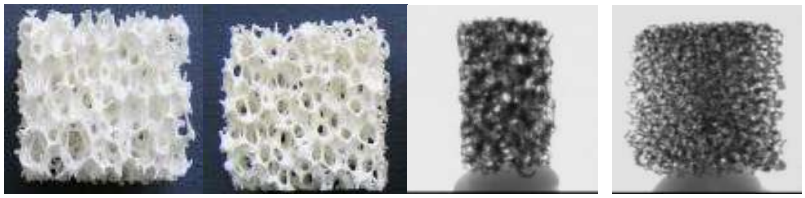

(a) (b) (c) (d)

Figure 2. Physical model: large pores sample (a), small pores sample (b), CT scan of large pores sample (c), CT scan of small pores sample.

Numerical model

The peridynamics models of the large and small pores samples are shown in Fig. 3. The impact scheme against the rigid surface is shown in Fig. 3(a). In this case, the impact velocity is 100 m/s. The damage development is shown in Fig. 3(b) and Fig 3(c) at time 9.5E-07 s. The difference in the range is clearly visible, the small pores sample is significantly more damaged than the large pores sample. The small pore sample is practically damaged in contrast to the large pores sample.

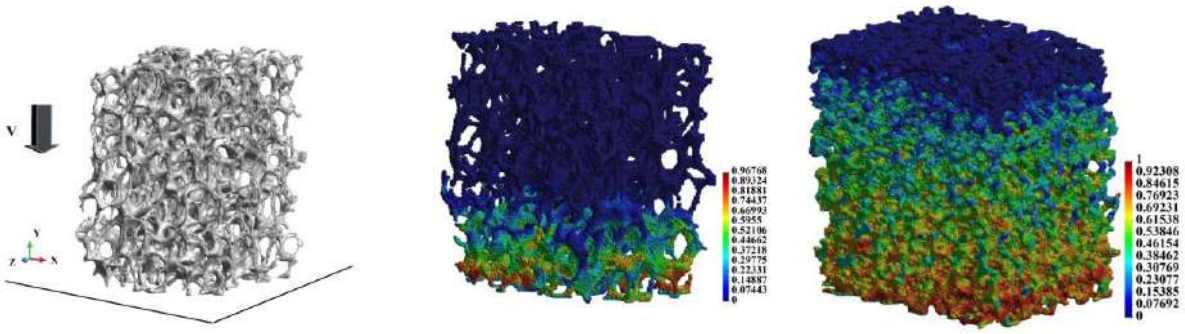

(a) (b) (c)

Figure 3. Damage distribution, impact velocity 100 m/s: a) impact scheme, b) large pores case, c) small pores case.

CONCLUSION AND FINAL REMARKS

We presented an application of peridynamics method for damage evaluation of the IPC skeleton. The damage development depends on porosity of the preforms strongly. It will be reflected in the final product as well. The calculations of the systems practically cannot be performed without application of High Performance Computing (HPC).

Acknowledgment

The results presented in this paper were obtained within the framework of research grant 2018/31/B/ST8/00601 financed by the National Science Centre, Poland. Calculations are performed using the "Okeanos" Cray CX40 system at the Interdisciplinary Centre for Mathematical and Computational Modelling in the University of Warsaw, Poland.

References

[1] Okada A. *Materials Science and Engineering B*, **161**: 182, 2009.
[2] Pittari J., Subhash G., Zheng J., Halls V., Jannotti P. *Journal of the European Ceramic Society*, **35**: 4411, 2015.
[3] Saberi Y., Zebarjad S.M., Akbari G.H. *Journal of Alloys and Compounds*, **484**: 637, 2009.
[4] Silling S. A. *Journal of the Mechanics and Physics of Solids*, **175**: 48, 2000.
[5] Sadowski T., Pankowski B. *Composite Structures,* **143:** 388, 2016.
[6] Postek E., Pęcherski R., Nowak Z. *Archives of Metallurgy and Materials*, **64**: 1603, 2019.
[7] Silling S.A., Epton M., Weckener O., Xu J., Askari E., *Journal of Elasticity,* **88**: 151, 2007.

MODE LOCALIZATION IN MECHANICALLY COUPLED MEMS RESONATORS

Hassen M. Ouakad[1], Saad Ilyas [2], and Mohamamd M. Younis*[2]
[1] Mechanical and Industrial Engineering Department, College of Engineering, Sultan Qaboos University, Al-Khoud, PO BOX 33, 123, Muscat, OMAN
[2] Physical Sciences and Engineering (PSE), King Abdullah University of Science and Technology, 23955-6900, Thuwal, KSA

Summary Mode localization is explored in a weakly mechanically coupled system comprising of two doubly-clamped microbeams mechanically linked with a coupling beam close to the anchors. The phenomenon is explored among the lower and higher order modes of vibration. An eigenvalue analysis is performed under different side-electrodes bias scenarios. A forced vibration analysis is then carried out to study the response of the system under different perturbation scenarios.

INTRODUCTION

The phenomenon of mode localization [1] in micro and nanoelectromechanical systems (MEMS and NEMS) coupled structures has emerged as a promising technology toward developing highly sensitive micro and nano sensors [2]. Various investigations have been carried out to understand mode localization and associated eigenvalue curve veering (avoided-crossing) [3], and exploit them for different sensing applications [2, 4]. This work focuses on investigating the dynamic characteristics of a MEMS coupled system exhibiting localization and veering at the higher order modes. This work aims to reveal the rich dynamics of the coupled systems at higher order modes and their potential towards developing highly sensitive MEMS sensors [5].

MECHANICALLY COUPLED MEMS RESONATOR DESIGN

A mechanically coupled MEMS resonator, Fig. 1, is designed through coupling two identical doubly-clamped primary (input and output) microbeams connected by a third (coupling) secondary microbeam. All the beams are assumed uniform and of rectangular cross-sectional shapes. Each primary microbeam is actuated by an electrode of identical dimensions located underneath it.

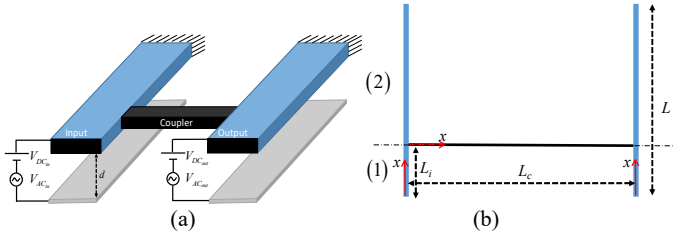

Figure 1. (a) 3D and (b) (2D) schematic of two doubly-clamped microbeams mechanically coupled through a third microbeam.

Table 1. Case Study

Parameter	Respective Value
Primary Microbeams Length L	600 μm
Primary Microbeams Width b	30 μm
Microbeams Thickness h	3 μm
Coupling Location	Vary
Coupling Microbeam Length L_c	300 μm
Coupling Microbeam Width b_c	10 μm
Electrodes Initial Gaps d	8 μm
Microbeams Young's Modulus E	169 GPa
Microbeams Mass Density ρ	2320 kg/m^3

FREE & FORCED VIBRATION ANALYSIS

First, the linear natural frequencies and mode shapes of the system consisting of two clamped-clamped microbeam (primary beams) coupled mechanically by a third microbeam (the coupler), Fig. 1, are computed. Then, the free vibration of the coupled resonator through solving both the eigenvalue problem with a linearized DC load electric forces only as well as the nonlinear dynamical responses of the resonator under DC and AC harmonic loads is investigated. Finally, we simulate the frequency-response curves of the mechanically coupled MEMS resonator when excited through its input microbeam by a DC load superimposed to an AC harmonic load of frequency near its lower and higher modes. In the dynamic analysis, long-time integration of the reduced-order model to obtain steady-state solutions needed to generate the frequency response curves of the coupled system is conducted.

SIMULATIONS & DISCUSSION

The variation of the eigenvalues (global natural frequencies of the system) considering different scenarios of the coupling location in order to capture the frequencies curve veering is first investigated. Figure 2 show the effect of varying the input microbeam static electrostatic load, assuming zero DC load on the output microbeam, on its lower: first/second (1/2) natural frequencies. Various coupling locations are chosen for different pair of modes for clear depiction of the mode localization phenomenon. One can clearly notice that the pairs of frequencies (1/2) do not intersect, their variation with the DC load simply showing two possible veering regimes near zero voltages, and then afterward at higher voltages that push up the lowest frequency due to the stretching effect toward the higher one. This portrayed veering phenomenon gets more and more distinctive as the coupling strength is further reduced to lower values among all lower and higher order modes. Coupling strength here is reduced as the coupling beam is moved closer to the anchor. It is observed that very weak coupling is required in order to notice these curve veering zones for higher-order modes, Figure 2.

Next, we explore the effect of the output microbeam electrode DC load $V_{DC,out}$ on the veering zones of the first/second frequencies pair, Figure 3. It is observed that through the DC bias of both input and output microbeams can be used as two independent tuning parameters that can shift the two veering zones upward or downward. The first veering zone

*Corresponding author. E-mail: mohammad.younis@kaust.edu.sa

(around small input beam DC load) whereas and the second veering zone (around higher input beam DC load) both show that the veering point frequency decreases with the increase of the output beam DC load.

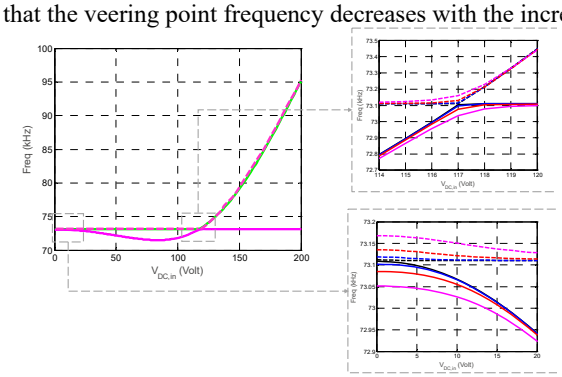

Figure 2. Variation of the first (continuous lines) and second (dashed lines) natural frequencies of the coupled resonator with $V_{DC,in}$ showing two veering zones and for: Black (L_c=20 μm), Blue (L_c =30 μm), Red (L_c =40 μm), and Magenta (L_c =50 μm).

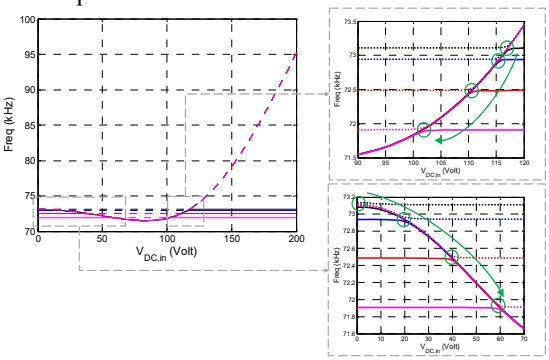

Figure 3. Variation of the first (continuous lines) and second (dashed lines) natural frequencies of the coupled resonator as varying the input bias voltage for L_c =40 μm and for: Black ($V_{DC,out}$ =0 Volt), Blue ($V_{DC,out}$ =20 Volt), Red ($V_{DC,out}$=40 Volt), and Magenta ($V_{DC,out}$ =60 Volt).

Next, we only consider the effect of the input beam DC bias. Figures 4a, and 4b show the steady-state dynamic frequency responses of the input beam and output beam, respectively, for different input beam DC load conditions as its AC input frequency is swept around the first and second global modes of the coupled resonator. It can be seen from Figure 4a that both pair of modes (1/2) show almost same amplitude for a small input DC load (at the first veering zone). Then as $V_{DC,in}$ is gradually increased, the modes start to exhibit localization. A stronger localization is observed in the first mode, where, more energy is confined into the input resonator, Figure 4a, which as a result vibrates with an amplitude much higher than the output beam. The localization becomes stronger for higher perturbation caused by high $V_{DC,in}$, Figure 4a. However, a slighter localization is observed in the second mode of vibration, where the energy is localized into the output resonator compared to the input resonator, Figure 4b. This is more evident for the case of $V_{DC,in}$ =20V in Figure 4.

Finally, we consider the case of direct excitation of the input beam (constant input DC load and varying AC input excitation frequency), and with perturbing the output beam overall stiffness through applying an output bias DC voltage, $V_{DC,out}$. Figures 5a shows that initially as the $V_{DC,out}$ is set to zero, the coupled system already exhibits localization due to the presence of $V_{DC,in}$. However, as $V_{DC,out}$ is increased, a similar localization behavior is observed, but now, the two modes swapped their roles, where second mode shows stronger localization compared to the first mode, Figure 5a (black).

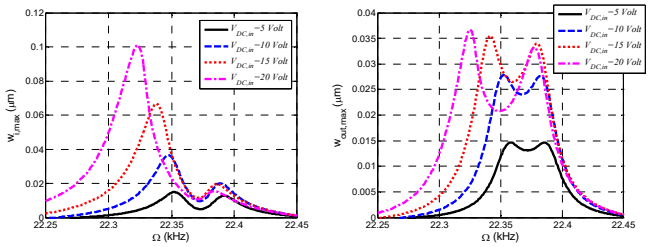

(a) Input Microbeam (b) Output Microbeam

Figure 4. Simulated frequency response curves of the mechanically coupled resonators of the coupled resonator with the actuating frequency swept around the pair of modes (1/2) assuming coupling location at 50 μm and with various DC bias voltages of the input resonator. Assumed parameters are $V_{AC,in}$=0.05 Volt, $V_{DC,out}$=0 Volt, and Q=500.

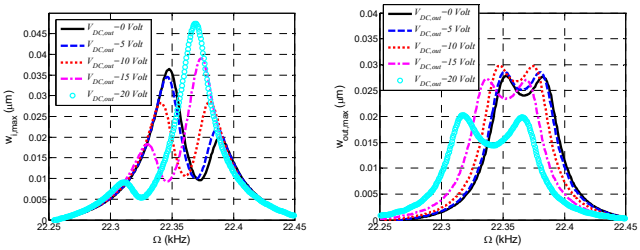

(a) Input Microbeam (b) Output Microbeam

Figure 5. Simulated frequency response curves of the mechanically coupled resonators of the coupled resonator with the actuating frequency swept around the pair of modes (1/2) assuming coupling location at 50 μm and with various DC bias voltages of the output resonator. Assumed parameters are $V_{DC,in}$= 10 Volt, $V_{AC,in}$=0.05 Volt, and Q=500.

CONCLUSIONS

In this work, a basic research of the phenomenon of mode localization was examined theoretically for mechanically coupled microbeams based MEMS resonator at lower and higher modes. It was observed from the eigenvalue problem that by controlling the coupling strength and location and strength of perturbation, the veering zones and their respective localization characteristics (frequency and amplitude) can be altered. Furthermore, the forced vibration analysis using frequency response curves shows that in order to exploit the phenomenon of mode localization, the choice of the resonator under excitation and the coupling beam location is extremely important. Finally, findings of this study encourage experimental research into the performance parameters, like sensitivity and resolution, for utilizing mode localization at higher order modes for developing smart sensors.

References

[1] C. Pierre and E. Dowell, Localization of vibrations by structural irregularity, *Journal of Sound and Vibration*, **114:** 549-564, 1987.
[2] C. Zhao, M. H. Montaseri, G. S. Wood, S. H. Pu, A. A. Seshia, M. Kraft, A review on coupled MEMS resonators for sensing applications utilizing mode localization, *Sensors and Actuators A: Physical*, **249**: 93-111, 2016.
[3] C. Pierre, "Mode localization and eigenvalue loci veering phenomena in disordered structures, *Journal of Sound and Vibration*, 126: 485-502, 1988.
[4] P. Thiruvenkatanathan, J. Woodhouse, J. Yan, A. A. Seshia, Manipulating vibration energy confinement in electrically coupled microelectromechanical resonator arrays, *Journal of microelectromechanical systems*, **20**: 157-164, 2011.
[5] F. Lochon, I. Dufour, D. Rebière, An alternative solution to improve sensitivity of resonant microcantilever chemical sensors: comparison between using high-order modes and reducing dimensions, *Sensors and Actuators B: Chemical*, **108**: 979-985, 2005/07/22/ 2005.

A THIN STRIP MECHANISM WITH NEGATIVE TORSIONAL STIFFNESS AND VARIABLE COMPRESSIVE STIFFNESS

Jinyou Li[1], Kangjia Fu[2], Yongpeng Gu[1], and Zhihua Zhao *[1]
[1] School of Aerospace Engineering, Tsinghua University, Beijing, China
[2] National Innovation Institute of Defense Technology (AMS), Beijing, China

Summary Negative stiffness mechanisms have great potential in different fields, such as vibration isolation, energy absorption and mesh antenna unfolding. In this study, inspired by a toy, we developed a novel type of compliant mechanism composed of thin strips, possessing negative stiffness property under torsion [1], while its compressive stiffness along the Z direction also varies with the torsion angle. Demonstrated with examples, it was shown that the proposed mechanisms could be combined to realize unusual torque-angle or variable force-displacement relationships, which can be used in different applications.

INTRODUCTION

Negative stiffness mechanisms that have great potential in different fields can be achieved in an active or passive way, in which the active way requires sensors and sophisticated control systems, making it more challenging in terms of size, cost and reliability. As for passive way, although numerous compliant mechanisms have been implemented in literature, few of them are designed based on structural or topological optimization, and the obtained structure is usually complex. Undoubtedly, there remains a number of unknown simple structures that can generate negative stiffness, and proposing an original design strategy may open a new avenue for the future inventions.

In this study, inspired by a toy that can be considered as a compliant mechanism named as “happy twist”, whose structure is pictured in Fig.1(A), we developed a novel type of compliant mechanism composed of thin strips, possessing negative stiffness property under torsion, while its compressive stiffness also varies with the torsion angle. Unlike most previous designs, which utilize planar curve beams and/or mechanical buckling, the proposed design is based on spatial curved beams and involves no buckling at all.

PARAMETRIC ANALYSIS OF THE CONFIGURATION

Figure 1(B) sketches the proposed compliant mechanism, which is a rotational symmetric assembly composed of several identical flexible strips and two rigid discs, in which the bottom disc is fixed on the ground, and the top disc is allowed to rotate but not to translate along the global Z-axis. For simplicity, the illustrated mechanism has three strips pre-stressed into a semicircle shape. The geometry of the proposed mechanism is fully depicted by four parameters – the disc radius r, the radius of the strip centerline R, the width b, and the thickness t of the rectangular cross section.

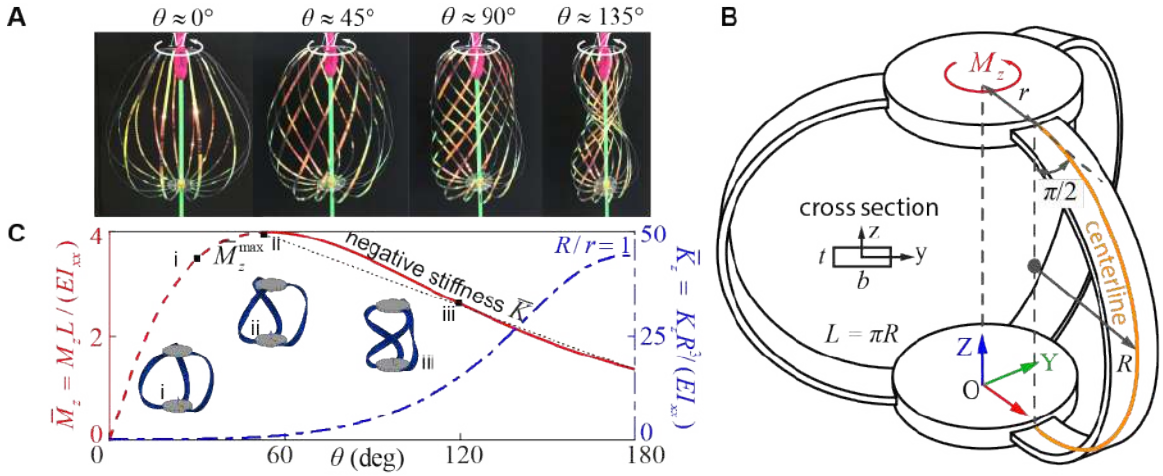

Figure 1: Compliant mechanism composed of thin strips.

To quantitatively describe the negative stiffness property, a numerical model was built based on our lab’s in-house code of flexible multibody dynamics [2]. Strips were uniformly meshed by geometrically-exact beam elements, whose deformations were shown in Fig. 1(C), and the torque $M_z(\theta)$ equaled the rotating reaction torque divided by the number of strips, the compressive stiffness $K_z(\theta)$ obtained the same way. The calculated $\bar{M}_z$ and $\bar{K}_z$ versus θ curve is plotted

*Corresponding author. E-mail: zhaozh@tsinghua.edu.cn

for $\theta \in [0, 180°]$, in which the nondimensionalized torque is defined as $\bar{M}_z \triangleq M_z L/EI_{xx}$, and the nondimensionalized axial stiffness is defined as $\bar{K}_z \triangleq K_z R^3/EI_{xx}$.

For a single strip of the designed mechanism, torque $M_z(\theta)$ and stiffness $K_z(\theta)$ are both functions of E, r, R, b and t, totally five mechanical and geometrical variables. The relationships between them and these parameters were analyzed through numerical simulations based on the well-known Buckingham π theory, whose results reveal that both relationships do not depend on t/r, weakly rely on b/t especially when $b/t > 10$, but vary significantly with different R/r. Thus, as an appropriate approximation, $\bar{M}_z(\theta)$ and $\bar{K}_z$ are sufficient to be considered as functions of R/r only. $\bar{K}_z$ varies in different trends with the value of R/r, which could be designed for different aims, and the negative stiffness of the torque from $\theta_{\max}$ to 180°, defined as $\bar{K}$, could be directly expressed as $\bar{K} = -0.409 - 1.658(R/r)^{-1.058}$.

SYNTHESIZED MECHANISMS FOR APPLICATION

Based on the proposed strip mechanism, unusual mechanisms could be constructed by combining it with other mechanisms in series or parallel. The mechanism shown in Fig. 2(A) is an example of the proposed strip mechanism in parallel with a helical spring. As shown in Fig. 2(B), the solid black line representing the total output of the elemental mechanism and the helical spring, gives a nearly constant torque within a certain range to produce a quasi-zero-stiffness mechanism, which has been frequently used in vibration isolation and energy absorption. Similarly, the mechanism in Fig. 2(C) is a series combination, which has lower positive stiffness but higher negative stiffness than the elemental mechanism alone, as shown in Fig. 2(D). As for the array mechanism in Fig. 2(G), its frame structures connecting the two-layer mechanisms can convert press into rotation, as shown in Fig.2(E)(F), so as to dynamically change compressive stiffness during the pressure process, which might be utilized to obtain gradient material to dynamically adjust the waveguide for acoustics.

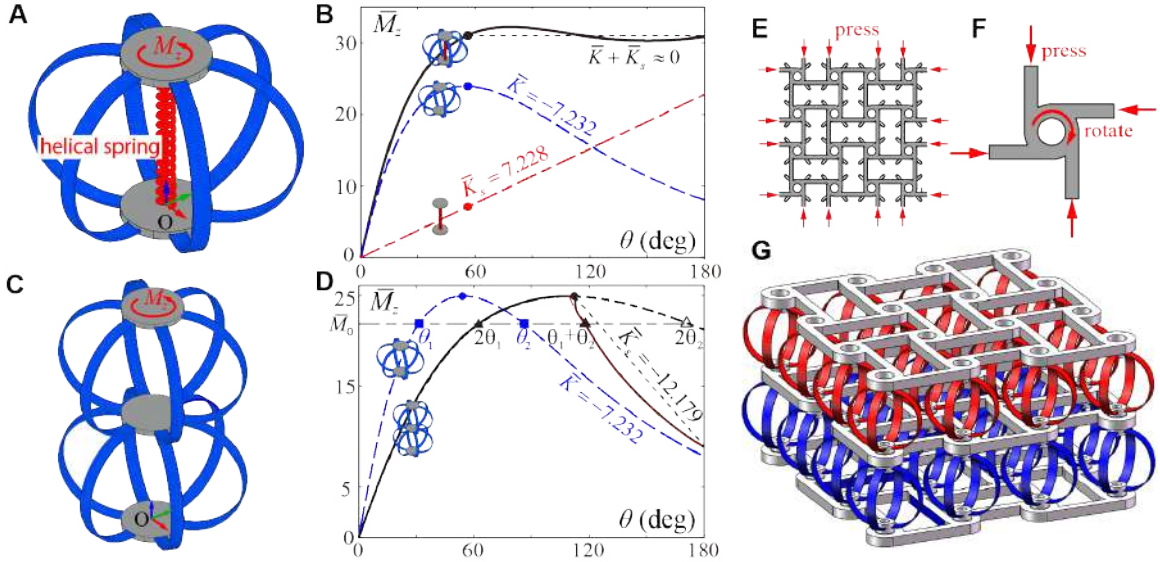

Figure 2: Synthesized mechanisms with unusual torque-angle relationships and adjustable compressive stiffness.

CONCLUSIONS

A novel type of compliant mechanism composed of thin strips was designed inspired by a toy named as “happy twist”. It generates negative torsional stiffness and variable compressive stiffness based on the spatial curved beams, which could be considered as a new path on designing mechanisms and might have application significance in different fields.

ACKNOWLEDGMENTS

This research was supported by the National Natural Science Foundation of China (Grant No. 11872221 and 11302114) and the Major State Basic Research Development Program (Grant No. 2012CB821203).

References

[1] Li J. Torsional negative stiffness mechanism by thin strips. Theoretical and Applied Mechanics Letters, 2019.
[2] Zhao Z. A quaternion-based formulation of Euler–Bernoulli beam without singularity. Nonlinear Dynamics, 2012.

ANALYSIS OF COUPLED BENDING-TORSION VIBRATION OF A RUB-IMPACT ROTOR SYSTEMS WITH GEAR COUPLING

Yuanhang Hou [1 2 3], Shuqian Cao *[1 2 3]
[1] Department of Mechanics, Tianjin University, Tianjin 300354, China
[2] Tianjin Key Laboratory of Nonlinear Dynamics and Control, Tianjin 300354, China
[3] National Demonstration Center for Experimental Mechanics Education, Tianjin University, Tianjin 300354, China

Summary The gear coupling is an important connection structure for aero-engines. While transmitting torque, it can also compensate for the axis of the two rotors being parallel to each other or being at different angles. Tooth side clearance between gear coupling is a key assembly feature parameter that affects the quality of the gear teeth. Reasonable backlash value is very important to reduce the vibration of the engine and improve the reliability of the aero engine.

INTRODUCTION

With the mass imbalance of the rotor and the backlash of the gear coupling considered, the bending-torsional coupling vibration response of the rotor system under rub-impact is studied in this paper. Firstly, the motion equation of bending-torsional coupling is derived from the Lagrange method of rub-impacting rotor system Then its nonlinear vibration features, such as the frequency spectra, poincaré section，and rotor orbit is primarily analyzed based on numerical techniques.

THE ROTOR MODEL OF THE GEAR COUPLING IS CONSIDERED

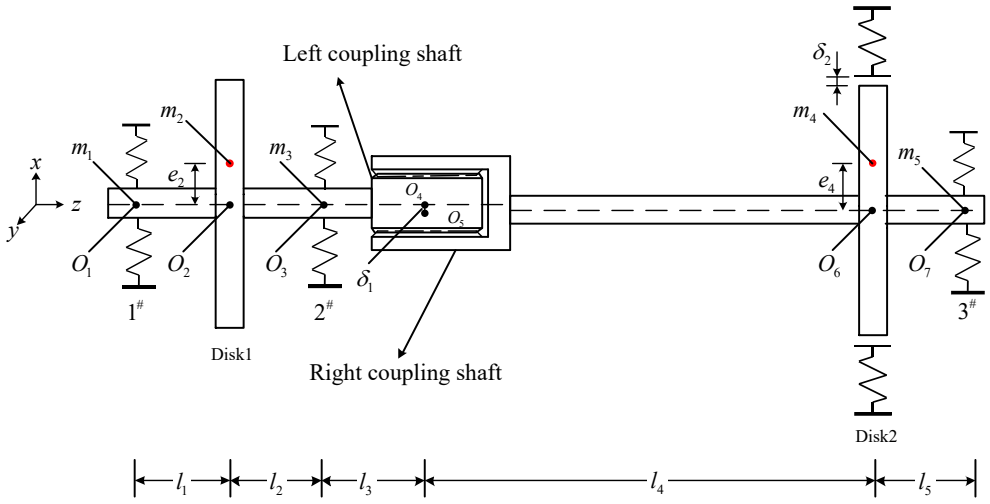

In this paper, the dynamic model of rotor system with gear coupling is established by using Lagrange equation.

$$M\ddot{q} \quad C\dot{q} \quad Kq \quad G + F_u + F_r + M$$

Among them, M , C , K , and are generalized mass matrix, damping matrix and stiffness matrix respectively; F_r is the rubbing force vector, G is the generalized gravity vector and F_u is the unbalanced vector.The driving torque of the turbine and the load torque of the compressor are considered, and the two are considered to be equal and opposite in steady motion.Obviously, the coupling of centroid coordinates and torsional coordinates in the unbalanced vector results in the coupled vibration of bending and torsional.

In the modeling of the gear coupling, the tooth side clearance of that is taken into account, and the nonlinear relationship between torque and torsion angle is obtained as follows:

$$f(u) = \begin{cases} u + cl & u < -cl \\ 0 & -cl < u < cl \\ u - cl & u > cl \end{cases}$$

Among them,u,cl3are torsion angle and tooth side clearance of gear coupling.

*Corresponding author. E-mail:hyhang@tju.edu.cn

MINI SYMPOSIA

CONCLUSIONS

The torsional stiffness of the system changes with the change of system load due to the existence of the tooth side clearance of the gear coupling, and the torsional vibration of the system has a rich frequency response at low speeds. As the speed increases, the influence of the tooth side clearance of the sleeve coupling on the vibration response of the system gradually decreases.

Acknowledgments This work is financially supported by the National Natural Science Foundation of China (No.11672201) and National Science and Technology Major Project（2017-IV-0008-0045）

References

[1] Li M, Yu L. Analysis of The Coupled Lateral Torsional Vibration of A Rotor-Bearing System with A Misaligned Gear Coupling [J]. Journal of Sound and Vibration, 243(2):283-300, 2001.
[2] Shuguo L, Yanhong M, Dayi Z. Studies on Dynamic Characteristics of The Joint in The Aero-Engine Rotor System [J]. Mechanical Systems and Signal Processing, 29: 120-136, 2012.
[3] Leen S B, Hyde T H, Ratsimba C H H. An Investigation of The Fatigue and Fretting Performance of A Representative Aero-Engine Spline Coupling [J]. The Journal of Strain Analysis for Engineering Design, 37(6): 565-583, 2002.
[4] Dewell D L, Mitchell L D. Detection of A Misaligned Disk Coupling Using Spectrum Analysis [J]. Journal of Vibration, Acoustics, Stress, and Reliability in Design, 106(1): 9-16, 1984.
[5] Lu W, Chu F. Radial and Torsional Vibration Characteristics of A Rub Rotor [J]. Nonlinear Dynamics, 76(1): 529-549, 2014.

NONPLANAR NONLINEAR VIBRATIONS OF AN IMPERFECT ELECTRICALLY ACTUATED BEAM

Kaio César Borges Benedetti and Paulo Batista Gonçalves*
Department of Civil and Environmental Engineering, Pontifical Catholic University, PUC-Rio, Rio de Janeiro, 22451-900, Brazil

Summary The last decades have witnessed a growing interest in the nonlinear dynamics of microelectromechanical systems (MEMS), in particular microbeams. In the analysis of the latter structures it is usually assumed that the beam is perfect and displays a planar behavior. The aim of the present work is to study the nonlinear nonplanar vibration of a clamped-free imperfect microbeam subjected to electrostatic and electrodynamic actuation and evaluate how the flexural–flexural–torsional motions are affected by the imperfections and external load. To describe the nonlinear vibrations of the system, nonlinear integro-differential equations of motion, including geometric, inertial and load nonlinearities, are adopted. A detailed parametric analysis shows the influence of imperfections on the structural response.

INTRODUCTION

The analysis of MEMS and NEMS under electrostatic and electrodynamic forces is a promising research area, which has been active for a few years [1]. These devices have beam used in filtering, communications, mass/gas sensing, signal processing, energy harvesting and sensors/actuators applications. Among MEMS devices slender microcantilevers have beam applied successfully in many engineering fields. However, this is an inherently nonlinear problem where instability can have either negative or positive effects on the structural response. This work aims to investigate the nonlinear static response and nonlinear nonplanar vibrations of an imperfect microbeam under electrical actuation in the main resonance region.

FORMULATION AND RESULTS

In order to analyze the nonplanar vibrations of the cantilever beam, the formulation proposed by Crespo da Silva and Glynn [2] for an inextensible beam, considering both geometric and inertial nonlinearities, based on Bernoulli-Euler hypotheses, is adopted, enabling the analysis of different types of internal resonances [3]. The formulation is modified to include the effect of initial geometric imperfections. The beam is subjected to an electric force $V \equiv V_{dc} + V_{ac}(t)$ where V_{dc} is the electrostatic voltage induced by the potential difference between the beam and the electrode and $V_{ac}(t)$ is the electrodynamic harmonic force. The distributed force and torque, considering a beam with a rectangular cross-section, are obtained by applying the classical parallel plate capacitor formulation [4]. They are written in terms of the flexural and torsional displacements and imperfection magnitudes. The linear flexural and torsional vibration modes are used as interpolation functions and the Galerkin projection is applied to obtain a reduced order model composed of a set of nonlinear coupled ordinary differential equations in terms of the modal amplitudes. Although the beam dynamics can be linearized considering small displacement and rotations, the applied forces are inherently nonlinear. The electrostatically actuated beam nonlinear response and pull-in instability are significantly affected by imperfections in the form of the flexural and torsional vibration modes. Fig. 1(a) displays the nonlinear static response of the electrostatically actuated imperfect cantilever for selected values of the angular imperfection γ_0. Up to four stable and three unstable solutions are obtained. These solutions are only physically meaningful for static deflections $w_s < 0.4$ and torsional amplitudes $|\gamma_s| < 0.026$, with the system pull-in occurring for higher displacements. The bifurcation diagrams of the dynamically excited beam are obtained using a continuation arc-length method at different actuation voltage levels and imperfections and instability and the corresponding bifurcation type are identified by the use of Floquet theory. Fig. 1(b) shows the resonance curves of the imperfect beam under alternating current for selected values of the forcing magnitude λ with an imperfection in the form of the flexural mode. The resonant response displays a softening behavior. In the main resonance region (at $\Omega/\omega_w=1.0$), a saddle-node bifurcation occurs along the non-resonant branch and a period-doubling bifurcation occurs along the resonant branch, leading to jumps in the beam response. A similar bifurcation pattern occurs at $\Omega/\omega_w=0.5$. A detailed parametric analysis is conducted, in order to highlight the effect of each parameter on the resonant dynamics of the system. Since the shape and magnitude of the imperfections are not known a priori, the influence of their uncertainties on the beam response is also evaluated.

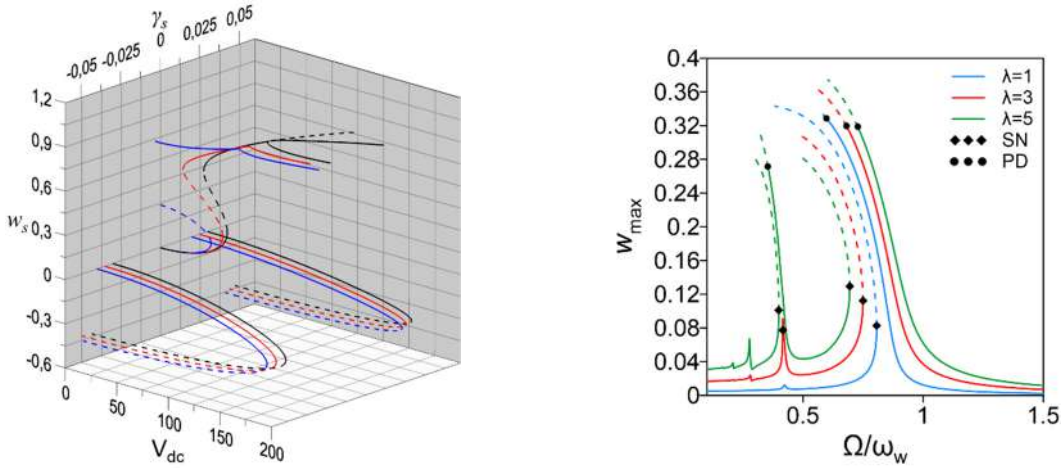

Figure 1. (a) Nonlinear static response of the electrostatically actuated imperfect cantilever (— perfect; — $\gamma_0 = 0.005$; — $\gamma_0 = 0.01$) ; (b) resonance curves of the imperfect beam under alternating current for selected values of the forcing magnitude λ with $V_{dc}=42, w_0=0.1, \gamma_0=0$ - SN: saddle-node bifurcation, PD: period-doubling bifurcation.

References

[1] Rhoads, J. F., Shaw, S. W., & Turner, K. L. Nonlinear dynamics and its applications in micro-and nanoresonators. *Journal of Dynamic Systems*, Measurement, and Control, **132(3)**: 034001, 2010.

[2] M. R. M. Crespo Da Silva and C. C. Glynn, "Nonlinear Flexural-Flexural-Torsional Dynamics of Inextensional Beams. I. Equations of Motion," *J. Struct. Mech.*, **6(4):** 437–448, 1978

[3] Carvalho, E. C., Gonçalves, P. B., Rega, G. Multiple internal resonances and nonplanar dynamics of a cruciform beam with low torsional stiffness. *International Journal of Solids and Structures*, **121**: 117-134, 2017.

[4] Younis, M. I. MEMS Linear and Nonlinear Statics and Dynamics, vol. 20. Boston, MA: Springer US, 2011

NONLINEAR VIBRATION RESPONSE AND BIFURCATION ANALYSIS OF FUNCTIONALLY GRADED MATERIAL PIEZOELECTRIC CYLINDRICAL SHELLS

Yunfei LIU *, Zhaoye QIN, and Fulei CHU
State Key Laboratory of Tribology, Department of Mechanical Engineering, Tsinghua University, Beijing. P.R. China

Summary The nonlinear forced vibrations of functionally graded material (FGM) piezoelectric cylindrical shells under multi-physics fields are studied. The FGM piezoelectric shells are subjected to electric-thermo-mechanical loads, and the porosity effect is considered here owing to the technical issues during the preparation of FGMs. An energy approach based on the Hamilton's principle is utilized to gain the nonlinear equations of motion. Afterwards, the Galerkin method is employed to transform the governing equations into multi-degree-of-freedom nonlinear ordinary differential equations, and subsequently the bifurcation analysis is conducted by using the pseudo-arclength continuation method. The effects of different parameters on the nonlinear dynamic response are investigated in this study.

INTRODUCTION

Piezoelectric materials, as a unique kind of smart materials, can generate electric fields due to mechanical deformation and also can cause mechanical deformations because of the electric fields' action. The inherent mechanical-electrical coupling effect of piezoelectric materials make them widely applied in engineering. Functionally graded piezoelectric materials (FGPMs) consist of two or more constituent phases with a continuous variation of material properties from one surface to another. As a consequence, FGPMs could solve the problems found in the traditional laminated composite materials such as matrix cracking, interlayer stress components jump, and interfacial debonding. Based on the above-mentioned advantages, a great deal of researchers studied the mechanical behavior of FGPM structures, while most studies only involve linear dynamics.

Investigation of the porosity effect, on the other hand, is limited in the literature. Owing to the technical issues during the preparation of FGMs, micro-voids or porosities usually occur within FGMs during the sintering preparation. The existence of micro-voids may change the structures' vibration frequency, reduce the mechanical strength, and even cause damage to the devices during operation. Therefore, in order to ensure the reliability of FGM structures, it is necessary to consider the porosity effect on vibration response at a design stage.

In practical engineering applications, the large amplitude vibration analysis is vital to assess the safety of structures, and several attempts have been made to obtain a solution for nonlinear vibration of structures [1–3]. It ought to be noted that, the nonlinear multiple internal resonance of piezoelectric materials, which may exhibit complex nonlinear dynamic responses, has not been studied in previous research.

Literature review shows that no study has been reported on nonlinear forced vibration and bifurcation analysis of FGM piezoelectric porous shells subjected to the electric-thermo-mechanical loads. Therefore, we focus on this novel issue and attempt to reveal the physics behind the numerical observations. The effects of different parameters on the nonlinear dynamic response are conducted in this study.

PROBLEM FORMULATION

Figure 1 presents a schematic diagram of FGM piezoelectric shells containing micro-voids. The material properties of the shells vary along the thickness direction, and the shells are subjected to electric-thermo-mechanical loads. It is assumed that micro-voids are dispersed evenly in the FGM structures here. The nonlinear governing equations are derived by using Donnell's nonlinear shallow-shell theory and Hamilton principle. Then, the system, a model involving forty-nine degrees of freedom, is discretized by the Galerkin method. Afterwards, the pseudo-arclength continuation method is employed to obtain numerical results.

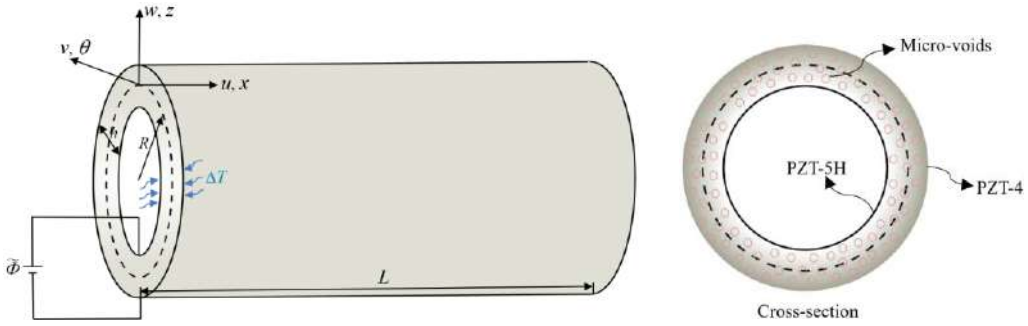

Figure 1. Schematic diagram of FGM piezoelectric cylindrical shells with micro-voids under multi-physics fields.

* Corresponding author. E-mail: yf-liu20@mails.tsinghua.edu.cn.

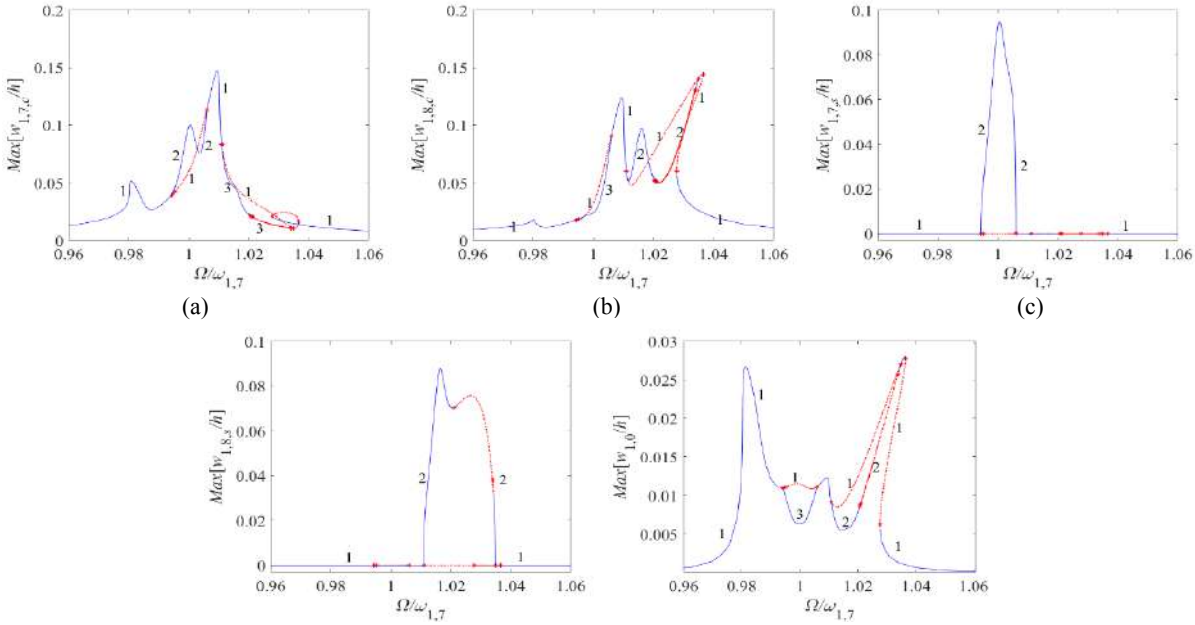

Figure 2. Frequency-response curves of FGM piezoelectric porous shells: (a) Maximum of $w_{1,7,c}/h$; (b) Maximum of $w_{1,8,c}/h$; (c) Maximum of $w_{1,7,s}/h$; (d) Maximum of $w_{1,8,s}/h$; and (e) Maximum of $w_{1,0}/h$ (blue solid line: stable solution; red dotted line: unstable solution).

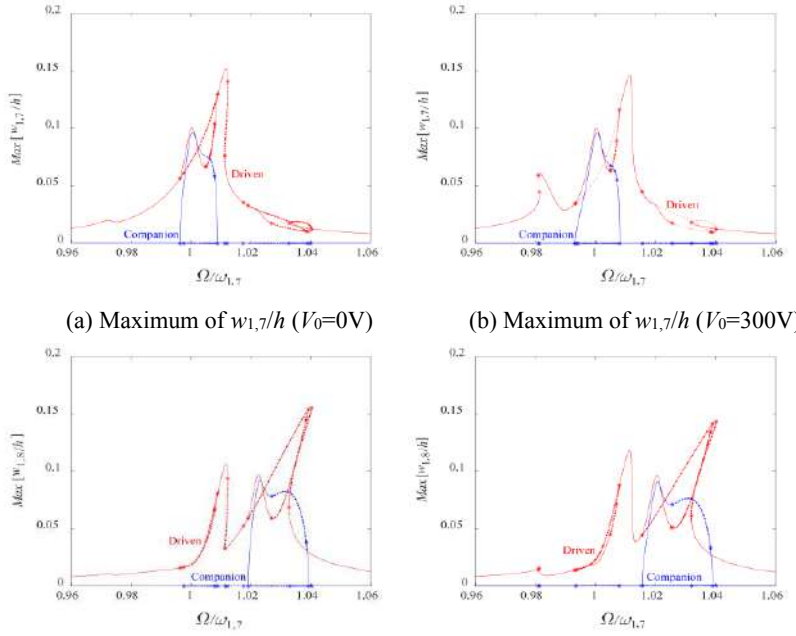

(a) Maximum of $w_{1,7}/h$ (V_0=0V) (b) Maximum of $w_{1,7}/h$ (V_0=300V)

(c) Maximum of $w_{1,8}/h$ (V_0=0V) (d) Maximum of $w_{1,8}/h$ (V_0=300V)

Figure 3. Frequency-response curves versus external applied voltages (red line: driven mode; blue line: companion mode).

CONCLUSIONS

The results show that the external applied voltage, temperature change, external excitation, power-law exponent, and porosity volume fraction play important role on nonlinear vibration response and bifurcation analysis of the FGM piezoelectric cylindrical shells with micro-voids. The nonlinear multiple internal resonance exhibits complex dynamic behaviors, and the frequency-response curves with different parameters are obviously different. Branch Point cycle, Pitchfork, and Neimark–Sacker bifurcations of the forced vibration responses arising from internal resonances are detected, showing complex nonlinear dynamics.

References

[1] J.N. Reddy, Mechanics of laminated composite plates and shells: theory and analysis, CRC press, 2003.
[2] R.I. Leine, H. Nijmeijer, Dynamics and bifurcations of non-smooth mechanical systems, Springer Science & Business Media, 2013.
[3] M. Amabili, Nonlinear mechanics of shells and plates in composite, soft and biological materials, Cambridge University Press, 2018.

OPTIMIZATION AND EVALUATION OF AM INFILL AND LATTICE STRUCTURES

Niels Aage[1], Morten Andersen[1], Jeroen Groen[1], Christian Rye Thomsen[2], Fengwen Wang[1], Yiqiang Wang[3], and Ole Sigmund *[1]
[1] Department of Mechanical Engineering, Technical University of Denmark, Lyngby, Denmark
[2] nTopology Inc., New York, United States of America
[3] State Key Laboratory of Structural Analysis for Industrial Equipment, Dalian University of Technology, Dalian, China

Summary This paper discusses optimization and evaluation of Additively Manufactured structures with infill or composed of lattice structures from a mechanical perspective. Much work has been done analytically and numerically on identifying stiffness optimal open and closed-walled microstructures. Specifically, many different isotropic or cubic symmetric microstructures have been identified that achieve the theoretical optimum given by the Hashin-Strikhman bounds. However, much less work has been devoted to microstructures that are optimal for non-isotropic loadings or to microstructures that simultaneous to high stiffness also have high compressive yield strength. Here, we discuss these challenges seen from a topology optimization view point and with the aim of providing more insight into the appropriate choice of infill and lattice structures for Additive Manufacturing.

ABSTRACT

For weight saving and stabilization during manufacturing purposes, Additive Manufacturing (AM) often makes use of so-called infill material. Infill is more or less systematically repeated microstructure in the interior of an AM part. Often pre-processing software for AM allows control of the infill to a certain extent, but this is mostly limited to the choice between a few standard honeycomb types and the infill volume fraction. Mostly, however, infill is far from optimal with respect to stiffness or other physical properties and hence, much can be gained in terms of weight savings or even stiffness or strength improvements if the infill can be systematically optimized and manufactured.

On the other hand, the large geometrical freedom allowed by AM has spurred a surge in the use and manufacturing of lattice structures; either open – henceforth referred to as truss lattice structures (TLS) or closed – henceforth referred to as plate lattice structures (PLS). Lattice structures in different forms may have superior or even optimal elastic, thermal, optical, hydraulic or other physical properties if designed appropriately. In connection with AM, lattice structures may be used as structures themselves or as porous infill in structures meant to have smooth and closed external surfaces.

It has long been known that PLS provide the optimal stiffness to weight ratio [1, 2] and achieve the Hashin Strikhman bounds. Near-optimal, single-scale isotropic PLS with maximum Young's modulus have been identified in [3, 4] and a systematic study shows how optimized PLS are always stiffer (up to 200%) than their TLS counterparts for arbitrary loading cases [5].

Local stresses in AM parts are seldomly isotropic and uniform and hence using uniformly distributed isotropic infill or lattice structures is a waste of efforts which can be avoided if one uses locally adapted, anisotropic microstructures. 2D multiscale topology optimization studies making use of knowledge of optimal microstructures and efficient projection approaches [6, 7] show that stiffness can be improved by more than 50% by using locally adapted infill. This work has recently been extended to 3D [8]. Here, we will use this approach to investigate the differences in using isotropic vs. anisotropic and TLS vs. PLS when considering optimal stiffness design of AM parts.

Despite all the analytical and numerical work spent on identifying stiffness optimal isotropic and anisotropic microstructures, very few works have considered yield or compressive strength of these microstructures. In principle, stiffness optimal microstructures should also be (near)optimal with respect to yield strength. However, considering that infill and lattice structures often have low volume fractions, chances are high that local or global instability will happen before yield. In previous work we have topology optimized 2D microstructures for maximum buckling strength [9], where the stability criterion was established based on Floquet-Bloch wave theory and finite element analysis of the unit cell. Here, we extend this approach to 3D and extract simplified geometrical 3D microstructures with near optimal stiffness and significantly increased buckling strength. These microstructures are compared to commonly used TLS and PLS with regards to stiffness, strength and manufacturability and they are used as basic building blocks for 3D projections as discussed above.

Our study provides insight and tools for the systematic design of manufacturable AM parts with superior stiffness and strength properties.

References

[1] R.M. Christensen. Mechanics of low density materials. *Journal of the Mechanics and Physics of Solids*, 34(6):563–578, 1986.
[2] O. Sigmund, N. Aage, and E. Andreassen. On the (non-)optimality of Michell structures. *Structural and Multidisciplinary Optimization*, 54:361–372, 2016.

*Corresponding author. E-mail: sigmund@mek.dtu.dk.

[3] J.B. Berger, H.N.G. Wadley, and R.M. McMeeking. Mechanical metamaterials at the theoretical limit of isotropic elastic stiffness. *Nature*, 543(7646):533–537, 2017.

[4] Y. Wang and O. Sigmund. Quasiperiodic mechanical metamaterials with extreme isotropic stiffness. *Extreme Mechanics Letters*, 2019. online.

[5] Y. Wang, J.P. Groen, and O. Sigmund. Simple optimal lattice structures for arbitrary loadings. *Extreme Mechanics Letters*, 29:100447, 2019.

[6] J.P. Groen and O. Sigmund. Homogenization-based topology optimization for high-resolution manufacturable microstructures. *International Journal for Numerical Methods in Engineering*, 113(8):1148–1163, 2018. (online since April 2017).

[7] J. Groen, J. Wu, and O. Sigmund. Homogenization-based stiffness optimization and projection of 2d coated structures with orthotropic infill. *Computer Methods in Applied Mechanics and Engineering*, 349:722–742, 2019. (also arXiv:1808.04740 August 2018).

[8] J. Groen, F.C. Stutz, N. Aage, J.A. Baerentzen, and O. Sigmund. De-homogenization of optimal multi-scale 3d topologies. *Submitted*, 2019. Uploaded on arXiv: arxiv.org/abs/1910.13002v1.

[9] C.R. Thomsen, F. Wang, and O. Sigmund. Buckling strength topology optimization of 2D periodic materials based on linearized bifurcation analysis. *Computer Methods in Applied Mechanics and Engineering*, 339:115–136, 2018.

IMMERSED BOUNDARY METHODS FOR SIMULATION IN ADDITIVE MANUFACTURING

Ernst Rank[1], Ferdinando Auricchio[2], Massimo Carraturo[2], John Jomo[2], Stefan Kollmannsberger[1], and Nina Korshunova[1], Alessandro Reali[2]
[1] *Chair for Computation in Engineering, Technical University of Munich, Germany*
[2] *Department of Civil Engineering and Architecture, University of Pavia, Italy*

Summary Immersed Boundary Methods have recently attracted much interest. In contrast to classical finite element methods they need only a very simple computational background grid instead of a boundary matching mesh. This advantage is particularly valuable in cases of complex geometry, where mesh generation is often one of the most time consuming working steps in a structural analysis, or in cases, where the geometry of a structure is significantly changing during a computation. Both situations frequently occur in problems of simulation of additive manufacturing. This presentation will begin with an introduction in immersed boundary methods and then show the opportunities of this approach for simulation of AM products and processes.

IMMERSED BOUNDARY METHODS

Immersed boundary methods are closely related to the finite element technique. Yet, they avoid meshing the domain of computation and instead embed an object in a larger, simply shaped domain, which is itself divided into a simple grid. The resulting 'elements' are non-conforming, i.e. cut by the boundary of the original domain. This seemingly simple modification of the original principle has many consequences. Several of the classical steps of FEM need to be redesigned, like the integration of element matrices, the definition of boundary conditions or the stabilization of equation systems. All these questions have been addressed with success during the last years in several variants of immersed boundary methods, like the Finite Cell Method (FCM, [1]), the CutFEM [2] or the cgFEM [3]. The FCM in particular, which is a high order immersed boundary method, can be directly connected to various types of geometric models without compromising computational efficiency or accuracy, yet with significant advantages over classical FEM. Furthermore, the capabilities of FCM have been extended by including the opportunity of local grid refinement as well as local increase of the approximation order of the shape functions.

The relief from the necessity of generating a boundary conforming mesh for a structure is particularly important for simulations in additive manufacturing, as will be shown in this contribution,. Two fields of application of the Finite Cell Method for AM technologies will be discussed in this presentation. The first addresses some problems from mesoscopic process simulation, the second virtual material characterization of complex porous structures obtained by additive manufacturing.

THE FINITE CELL METHOD FOR SIMULATION IN AM

Additive Manufacturing is adding material layer by layer to an already existing, evolving structure. Numerous process types have been developed over the past decades, and most of them involve multiple coupled physical phenomena. Thermo-mechanical and phase change problems are only mentioned as some of the most prominent ones. When FEM is used for a process simulation, the concept of 'element birth' is frequently used (e.g. [4]). Whenever a part of the structure is generated, one, several, or a full layer of elements is added to the structure and considered in the sequel of the coupled thermo-mechanical problem. In order to simplify the implementation of this transient process all 'unborn' elements are already generated before the start of the simulation, but activated only at the time of their 'birth'. One major disadvantage of this process is related to the multiscale nature of AM. The moving area of phase transition, being the computationally most demanding part of the domain is in general very small compared to the overall structure and requires a very fine mesh in order to achieve sufficient accuracy. Using FCM two remedies are available: The computational grid can be locally refined and unrefined, and only parts of finite cells can change their physical state during phase transition in the thermos-mechanical process. Both opportunities allow for a more precise and very efficient simulation of an AM process.

The second field of application of the Finite Cell Method addresses material characterization of additively manufactured products, whose mechanical properties highly depend on the AM process parameters. Slight changes in these parameters may lead, for example, to surface roughness, undesirable porosity or other microstructural defects. It is even more challenging to control parameters for AM *porous structures* in order to achieve a predefined nominal microstructure. Process-induced effects might deteriorate the mechanical properties of the final parts compared to conventionally manufactured ones. Therefore, the evaluation of the mechanical behaviour of AM components is one of the crucial tasks for defining their reliability and applicability. Yet, experimental mechanical testing of AM generated porous structures is limited by the high cost and time consumption, in particular, due to the need for a statistically significant number of

repetitions using the same type of specimens. Thus, the robust estimation of the mechanical characteristics of the final AM products through computational methods is a promising alternative. One important step in this *virtual material testing* is a precise structural simulation based on CT-scans of additively manufactured porous structures. When using finite element based techniques, an obvious challenge in this step is the generation of a finite element mesh for these complex structures. This crucial step can be avoided by using immersed boundary methods. We will show examples (see figure 1) of obtaining microscopic and macroscopic mechanical properties including homogenized elastic and elastoplastic parameters and compare them with experimentally obtained results.

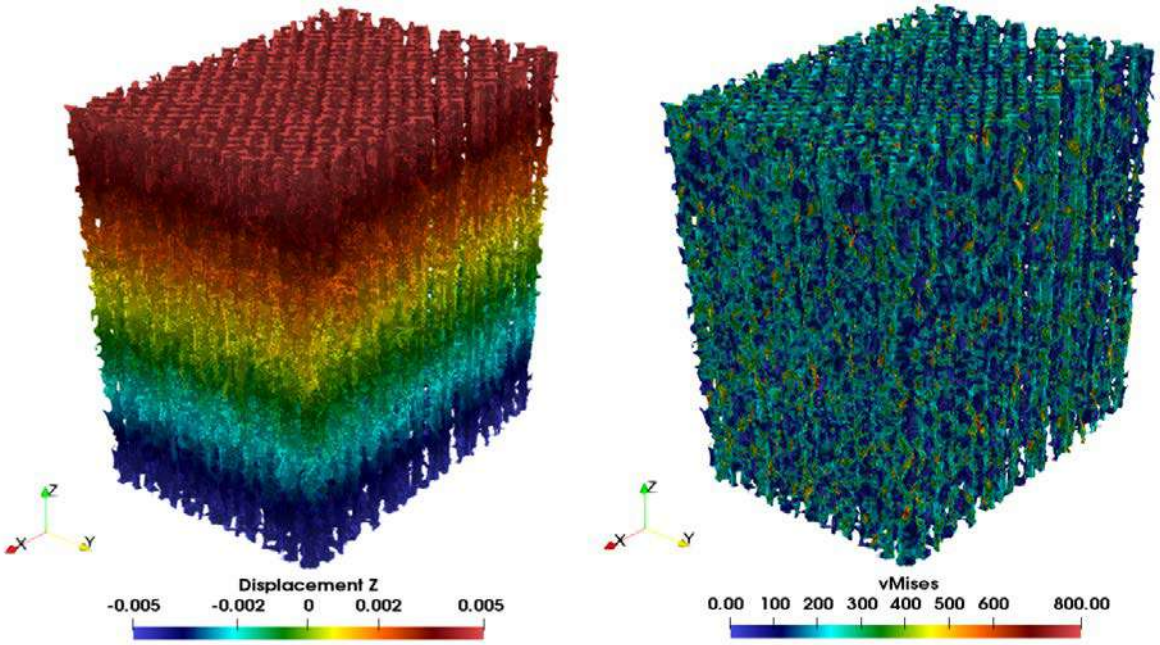

Figure 1. Displacement and von Mises stress fields of AM generated porous structure of Inconel 718 under uniaxial tension.

References

[1] The p-Version of the Finite Element and Finite Cell Methods. A Düster, E Rank, B Szabó, Encyclopedia of Computational Mechanics Second Edition, 1-35

[2] E. Burman, P. Hansbo, Fictitious domain finite element methods using cut elements: I. A stabilized Lagrange multiplier method. Comput. Methods Appl. Mech. Eng., 199: 2680-2686, 2010.

[3] E. Nadal Soriano, Cartesian grid FEM (cgFEM): High performance h-adaptive FE analysis with efficient error control. Application to structural shape optimization. PhD thesis, Universitat Politècnica de València, Valencia (Spain), 2014.

[4] Williams, R. J., Davies, C. M. and Hooper, P. A. A pragmatic part scale model for residual stress and distortion prediction in powder bed fusion, Additive Manufacturing, (2018), 22, 416-425.

NANOARCHITECTED MATERIALS: FROM TRUSS LATTICES TO PLATE- AND SHELL-BASED TOPOLOGIES

Lorenzo Valdevit*[1,2], Jens Bauer[2], Anna Guell Izard[2], Cameron Crook[1], Meng-Ting Hsieh[2], Marti Sala Casanovas[2]
[1] Department of Materials Science and Engineering, University of California, Irvine, CA, USA
[2] Department of Mechanical and Aerospace Engineering, University of California, Irvine, CA, USA

Summary This lecture presents recent results on the fabrication, mechanical performance and failure mechanisms of nanoarchitected ceramic materials with plate- and shell-based topologies. We first discuss the beneficial size effects on strength presented by nanoarchitected materials and review fabrication approaches that can capitalize on these effects. Subsequently, we discuss the mechanical benefits of plate- and shell-based architectures, compared to the well-established truss-based lattices. Finally, we demonstrate ceramic nanoarchitected materials with exceptional specific strength and discuss their deformation behavior.

EXPLOITING NANOSCALE SIZE EFFECTS IN CERAMIC ARCHITECTED MATERIALS

Ceramics are ideal engineering materials, by virtue of their high theoretical strength, high stiffness, low density, chemical stability and resistance to very high temperatures. According to linear elastic fracture mechanics, the fracture strength of a material scales as $\sigma_f \sim K_{Ic}/\sqrt{a}$, with K_{Ic} the fracture toughness of the material and a the size of the largest crack contained in the sample. Unfortunately, in most ceramic materials cracks can propagate easily, resulting in very low fracture toughness ($K_{Ic} \sim 1-10\ MPa\sqrt{m}$), and consequently low fracture strength. This drawback dramatically limits the use of ceramic materials in structural applications. At the macroscale, the sample dimension, t, is many orders of magnitude larger than the the size of the largest crack, resulting in a very mild size effect (Weibull theory); but as the sample dimension is reduced to the order of the crack size, the scaling changes to $\sigma_f \sim K_{Ic}/\sqrt{t}$. This significant smaller-is-stronger size effect persists until the theoretical strength of the material, σ_{th}, is achieved, after which further reduction in sample size have no effect on the strength of the material. As $\sigma_{th} \sim E/10$, with E the Young's modulus of the material, nanoscale ceramic materials can potentially exhibit strengths of the order of 10 GPa. Additionally, as brittle fracture is delayed, these materials can exhibit significant amounts of plasticity, when loaded in compression, even at room temperature (Fig. 1). Unfortunately, strengths on the order of σ_{th} are typically limited to the nanometer scale, and ultra-strong monolithic ceramics are hence unachievable in macroscale components. Architected materials have the potential to bridge this scale gap, by allowing fabrication of effective materials at the macroscale, but with individual geometrical features below a_{cr} [1].

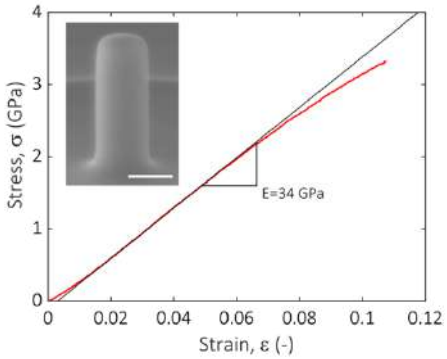

Figure 1. Compressive response of a pyrolytic carbon nanopillar (from [2]).

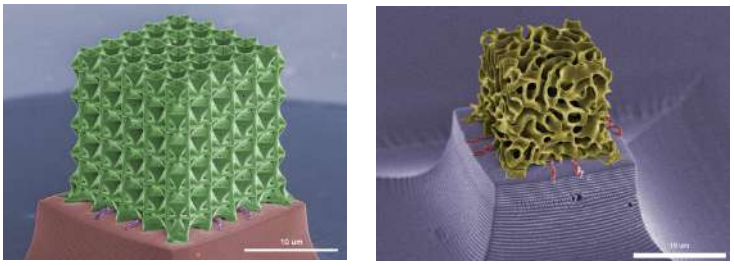

Figure 2. Carbon nanoarchitected materials with cube-octet plate and spinodal shell topologies.

THE MECHANICAL ADVANTAGE OF PLATE-BASED TOPOLOGIES

The vast majority of architected materials investigated over the past two decades have been truss lattices, by virtue of their relative ease of manufacturing and the simplicity in obtaining reasonably accurate analytical solutions for the mechanical and functional properties of interest. Over the past few year, remarkable progress in additive manufacturing technologies has opened the door to the investigation of more complex topologies. Two recent computational studies ([3], [4]) have predicted that closed-cell plate-based architected materials would be far superior to truss-lattices, with specific stiffness approaching the theoretical topological upper bound, while being virtually isotropic. Manufacturing challenges are very significant, though, as closed-cell topologies trap raw material, e.g. liquid monomer or powder, inside their cells. Here we demonstrate a fabrication process based on two-photon polymerization Direct Laser Writing followed by pyrolysis, resulting in closed-cell carbon plate-nanolattices. We demonstrate that these materials achieve the theoretical upper bounds in both stiffness *and* strength, and are the strongest cellular materials ever produced (Fig. 2). Details about their failure mechanisms are presented [5].

SHELL-BASED TOPOLOGIES DERIVED BY SPINODAL DECOMPOSITION

While we demonstrate that properly designed plate-based nanoarchitected materials achieve the theoretical upper bounds in both stiffness and strength, scalability for sample sizes beyond the micron-scale remains a challenge. This challenge may be overcome by adopting self-assembly techniques to generate shell-based topologies that approximate triply periodic minimal surfaces, with sample size at the macroscale, characteristic dimension at the micron scale and shell thickness at the nanometer scale. We computationally generate shell-based architected materials derived by spinodal decomposition of sacrificial constituents followed by postprocessing, and model their mechanical response. We show that these topologies are mechanically efficient while isotropic, and remarkably imperfection insensitive [6]. We fabricate nanoarchitected spinodal shell-based materials in carbon by two-photon polymerization direct laser writing of our computational designs, followed by pyrolysis [2]. While stochastic, these nanoarchitected materials are only slightly less efficient than the optimal plate-based materials discussed above (Fig. 2). When compressed beyond the elastic limit, these materials exhibit failure mechanisms that are strongly dependent on the wall thickness to unit cell size ratio: at small wall thicknesses, the crushing behaviour is progressive, with layer-by-layer fracture and significant energy absorption; at large wall thickness, the behaviour is catastrophic, with a single large crack destroying the entire sample at the same time. We explain this transition in terms of a competition between compressive and bending stresses in the shell sections. The implication is that, when properly designed, these architected materials can exhibit excellent energy absorption at low weight. Most importantly, these topologies are in principle amenable to scalable nanomanufacturing, when actual spinodal decomposition is used as a fabrication route. We will conclude with recent demonstrations of this approach [7].

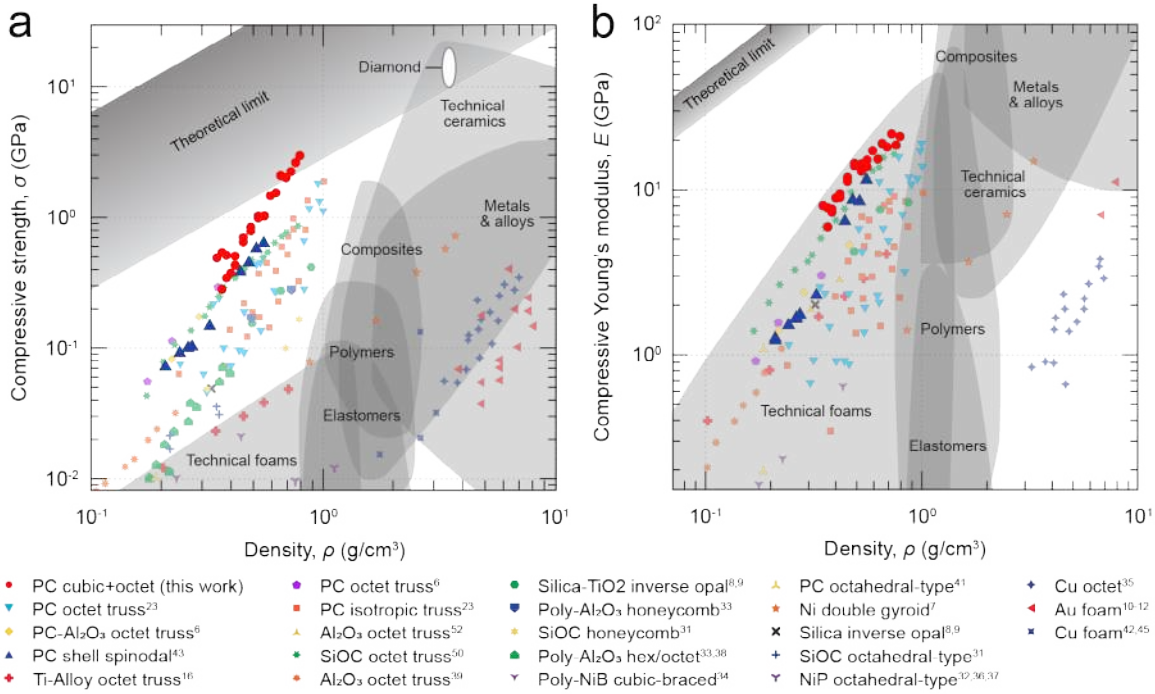

Figure 3. Strength/density and stiffness/density charts, showing the exceptional performance of plate (red) and shell (blue) carbon nano-architected materials compared to the universe of monolithic materials and other previously reported micro/nano-architected materials (modified from [5]).

ACKNOWLEDGMENTS

We gratefully acknowledge support from the Office of Naval Research (Grant No. N00014-17-1-2874, PM Dave Shifler) and the Air Force Office of Scientific Research (Grant No. FA9550-14-1-0352, PM Joycelyn Harrison).

References

[1] J. Bauer, L. R. Meza, T. A. Schaedler, R. Schwaiger, X. Zheng, and L. Valdevit, "Nanolattices: An Emerging Class of Mechanical Metamaterials," *Adv. Mater.*, 15, 1701826–1701850, 2017.
[2] A. Guell Izard, J. Bauer, C. Crook, V. Turlo, and L. Valdevit, "Ultrahigh Energy Absorption Multifunctional Spinodal Nanoarchitectures," *Small*, 466, 1903834–1903838, 2019.
[3] J. B. Berger, H. N. G. Wadley, and R. M. McMeeking, "Mechanical metamaterials at the theoretical limit of isotropic elastic stiffness," *Nature*, vol. 543, 7646, 533+, 2017.
[4] T. Tancogne-Dejean, M. Diamantopoulou, M. B. Gorji, C. Bonatti, and D. Mohr, "3D Plate-Lattices: An Emerging Class of Low-Density Metamaterial Exhibiting Optimal Isotropic Stiffness," *Adv. Mater.*, 30, 1803334–1803336, 2018.
[5] C. Crook *et al.*, "Plate-Nanolattices at the Theoretical Limit of Stiffness and Strength," *Nat. Commun.*, Accepted for publication, 2020.
[6] H. Meng-Ting, B. Endo, Z. Yunfei, J. Bauer, and L. Valdevit, "The mechanical response of cellular materials with spinodal topologies," *J. Mech. Phys. Solids*, 125, 401–419, 2019.
[7] A. E. Garcia *et al.*, "Scalable synthesis of gyroid-inspired freestanding three-dimensional graphene architectures," *Nanoscale Adv.*, 350, 1508–1513, 2019.

ON THE THERMO-MECHANICS OF DISLOCATION FIELDS IN TRANSIENT HETEROGENEOUS TEMPERATURE FIELDS

Manas V. Upadhyay*[1]
[1] Laboratoire de Mécanique des Solides, C.N.R.S., Ecole Polytechnique, IP Paris, 91128 Palaiseau, France

Summary During a metal/alloy additive manufacturing process, a molten material undergoes rapid solidification in a few milliseconds. Following this, it undergoes multiple heating-cooling cycles, i.e. Solid-State Thermal Cycling (SSTC), at varying temperature rates and amplitudes for the remainder of the build time. Thus far, most research efforts have focused on studying microstructure formation during solidification. There have been no coherent experimental/modeling efforts dedicated to study microstructure evolution during SSTC. During a series of recent in-situ TEM SSTC experiments by the author and colleagues, it has been shown that significant microstructure evolution occurs during SSTC. Based on these results, a novel thermo-mechanical model for dislocation dynamics due to transient heterogeneous temperature fields is proposed. Advantages/implications of the model are discussed.

MOTIVATION AND AIM

During an Additive Manufacturing (AM) or 3D printing process, just after deposition, a liquid material rapidly solidifies and spends rest of the building time being subjected to Solid-State Thermal Cycling (SSTC), at varying temperature rates and amplitudes, an illustration is shown in Fig. 1. During initial stages of SSTC, temperature amplitudes higher than annealing points and temperature rates as high as $10^6 K/s$ can be encountered. Consequently, large transient temperature gradients are formed, which result in strong transient thermal stresses due to internal and/or external constraints. Such rapidly varying temperatures and thermal stresses can result in significant changes in the microstructure, including dislocation structure evolution via dislocation dynamics. During later stages of SSTC, a nearly steady-state heat conduction occurs at relatively high temperatures with respect to room temperature. Such relatively high temperatures along with internal stresses due to a metastable microstructure can also result in additional dislocation dynamics.

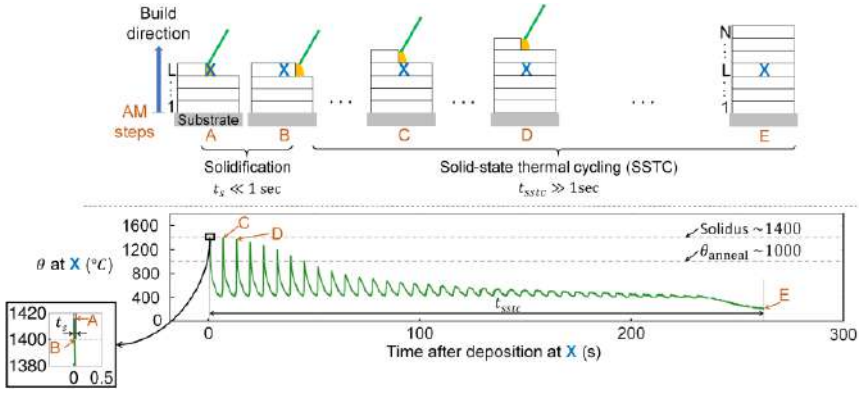

Figure 1: An illustration of temperature (θ) vs time (t) evolution at a material point X during additive manufacturing of a wall. t=0 corresponds to the moment the heat-matter interactions occur at X in a layer L<N, where N is the total number of layers.

Recently, a series of in-situ TEM SSTC experiments were performed on an AM 316L stainless steel by the author and colleagues (Dr. Lluis Yedra-Cardona, Dr. Eva Héripré) at the MSSMat Laboratory of CentraleSupélec. The experiments revealed significant changes to dislocation and precipitate structures (see Fig. 2). These results strongly motivate the need to better understand microstructural evolution during SSTC in order to have better control over the AM process. Here, the focus is on developing a model that allows studying dislocation dynamics due to SSTC during AM.

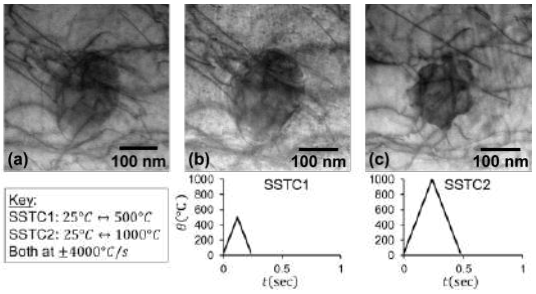

Figure 2: Results of a recent in-situ SSTC experiment in TEM on a lamella extracted from an AM 316L stainless steel sample. Bf-STEM snapshots show evolution of a precipitate and dislocation structure: (a) as-built, (b) after SSTC1, and (c) after SSTC2.

*Corresponding author. E-mail: **manas.upadhyay@polytechnique.edu**. Webpage: **https://www.manas-upadhyay.com**

Most existing dislocation dynamics models, both discrete and continuous kind, are designed to study dislocation motion and interactions under isothermal and/or adiabatic conditions. Indeed, there exist couplings between heat conduction and phenomenological elastic-plastic theory as well as between heat conduction and dislocation mechanics theory. However, none of the existing dislocation dynamics models account for temperature change induced crystallographic dislocation driving forces. To that end, a thermo-mechanically rigorous model of evolving dislocation fields under transient heterogeneous temperature fields is proposed [1]. In essence, this model is a strong coupling between the Field Dislocation Mechanics (FDM) model [2], theory of quasi-dislocations [3] and the heat conduction problem.

THE T-FDM MODEL

We consider a body $\mathcal{B}$ with surface $\partial\mathcal{B}$ to be a thermodynamically closed system. We shall assume that the local temperature θ at any material point in $\mathcal{B}$ is always below the solidus. Let θ_0 be the reference temperature. Next, we assume that $\mathcal{B}$ is a simply connected body without voids or cracks. Furthermore, we assume that $\mathcal{B}$ is a single crystal. Let $\mathcal{B}$ contain an arbitrary distribution of continuously represented dislocations represented via an areal dislocation density field $\boldsymbol{\alpha}^p$. Furthermore, we account for an areal defect density $\boldsymbol{\alpha}^\theta$ associated with incompatible thermal strains. The governing field equations of the geometrically linear T-FDM model [1] are:

$$\boldsymbol{U} = \boldsymbol{\nabla u} = \boldsymbol{U}^e + \boldsymbol{U}^p + \boldsymbol{\varepsilon}^\theta \tag{1}$$
$$\boldsymbol{\varepsilon}^\theta = \boldsymbol{\gamma}(\theta - \theta_0) \tag{2}$$
$$\dot{\boldsymbol{\alpha}}^{p,\beta} = -\boldsymbol{\nabla} \times \left(\boldsymbol{\alpha}^{p,\beta} \times \boldsymbol{v}^{p,\beta}\right) + \boldsymbol{S}^{p,\beta} \quad \text{and} \quad \boldsymbol{\alpha}^p = -\boldsymbol{\nabla} \times \boldsymbol{U}^p = \textstyle\sum_\beta \boldsymbol{\alpha}^{p,\beta} \tag{3}$$
$$\dot{\boldsymbol{\alpha}}^\theta = -\boldsymbol{\gamma}\left[\boldsymbol{\nabla}\dot{\theta} \cdot \mathbf{X}\right] \quad \text{and} \quad \boldsymbol{\alpha}^\theta = -\boldsymbol{\nabla} \times \boldsymbol{\varepsilon}^\theta \tag{4}$$
$$\dot{\boldsymbol{\alpha}} = \dot{\boldsymbol{\alpha}}^\theta + \dot{\boldsymbol{\alpha}}^p \quad \text{and} \quad \boldsymbol{\alpha} = \boldsymbol{\nabla} \times \boldsymbol{U}^e \tag{5}$$
$$\boldsymbol{\sigma} = \boldsymbol{C} : \boldsymbol{\varepsilon}^e - \boldsymbol{\beta}(\theta - \theta_0) \tag{6}$$
$$\boldsymbol{q} = -\boldsymbol{K} \cdot \boldsymbol{\nabla}\theta \tag{7}$$
$$\boldsymbol{V}^\beta = \tfrac{1}{B^\beta}\left(\boldsymbol{\sigma} \cdot \boldsymbol{\alpha}^{p,\beta}\right) : \mathbf{X} = \tfrac{1}{B^\beta}\left(\boldsymbol{\sigma} \cdot \boldsymbol{b}^\beta\right) \times \boldsymbol{l}^\beta \quad \text{for} \quad \boldsymbol{\alpha}^{p,\beta} = \tfrac{1}{V}\left(\boldsymbol{b}^\beta \otimes \boldsymbol{l}^\beta\right) \tag{8}$$
$$\boldsymbol{\nabla} \cdot \boldsymbol{\sigma} + \rho \boldsymbol{f} = \rho \ddot{\boldsymbol{u}} \tag{9}$$
$$\rho c_v \dot{\theta} = \boldsymbol{\nabla} \cdot (\boldsymbol{K} \cdot \boldsymbol{\nabla}\theta) + \boldsymbol{\mathfrak{T}} : \dot{\boldsymbol{U}}^p - \theta \boldsymbol{\beta} : (\dot{\boldsymbol{\varepsilon}} - \dot{\boldsymbol{\varepsilon}}^p) + \rho r \tag{10}$$

where $\boldsymbol{u}$: total displacement, $\boldsymbol{U}$: total distortion, $\boldsymbol{U}^{e/p}$: elastic/plastic distortion, $\boldsymbol{\varepsilon}^\theta$: thermal strain, $\boldsymbol{\gamma}$: thermal expansion coefficient matrix (assumed constant), $\boldsymbol{\alpha}$: Nye's dislocation density tensor, β: slip system, $\boldsymbol{\alpha}^{p,\beta}$: areal dislocation density, $\boldsymbol{b}^\beta$: Burgers vector, $\boldsymbol{l}^\beta$: dislocation line direction, V: volume over which dislocation density is averaged, $\boldsymbol{V}^\beta$: dislocation velocity, $\boldsymbol{S}^\beta$: dislocation source term, $\boldsymbol{\sigma}$: Cauchy stress, $\boldsymbol{C}$: elastic stiffness tensor, $\boldsymbol{\beta} = \boldsymbol{C} : \boldsymbol{\gamma}$: thermal moduli tensor, $\boldsymbol{q}$: heat flux vector, $\boldsymbol{K}$: heat conductivity matrix, B^β: dislocation drag term, $\boldsymbol{f}$: body force, ρ: material density, $\ddot{\boldsymbol{u}}$: acceleration, c_v: specific heat at constant volume, and ρr: heat loss term.

DISCUSSION AND CONCLUSIONS

In this work, a strong coupling between the FDM model, theory of quasi-dislocations and the heat conduction problem is developed to obtain the T-FDM model. The main motivation for developing this model is to study dislocation dynamics, interactions and structure evolution in crystalline solids experiencing transient heterogeneous temperature distributions such as those occurring due to SSTC during AM. Similar to most continuum models, the T-FDM model is based on the governing principles of rational thermodynamics: local thermodynamic equilibrium and Clausius-Kelvin-Planck formulation of the second law of thermodynamics. Since the T-FDM model is intended to be used to study dislocation dynamics under large temperature rates, it is crucial to verify that local thermodynamic equilibrium is always respected. Typically, the highest temperature rates occurring at a material point in a heat affected solid during an AM process are $\approx 10^6 K/s$, i.e. $10^{-6} K/picosecond$. Atomic fluctuations that accommodate thermal changes typically do so in timespans of $10^{-2} - 1 picoseconds$. Therefore, at the time scales at which temperature changes occur due to SSTC during AM, we can safely assume that they are instantaneously accommodated via atomic fluctuations. In other words, local thermal equilibrium is respected at any given instant in time. Furthermore, thermal stresses generated (if any) due to temperature gradients are also rapidly equilibrated resulting in mechanical equilibrium. If we assume that chemical equilibrium is also respected then the combined effect of these considerations is that for a system subjected to SSTC during AM, local thermodynamic equilibrium is respected at any given instant in time. The proposed model could be applied to study the dynamics of individual dislocations of any kind and/or their ensembles under any permissible combination of displacement, traction, temperature and heat flux boundary conditions.

Future work involves numerical implementation of the T-FDM model, extending it to a finite strain framework and up-scaling the model to the length scale of crystal plasticity approaches.

References

[1] M.V. Upadhyay, On the thermo-mechanical theory of field dislocations in transient heterogeneous temperature fields, JMPS 145 (2020) 104150.
[2] A. Acharya, A model of crystal plasticity based on the theory of continuously distributed dislocations, JMPS 49 (2001) 761–784.
[3] E. Kröner, Kontinuumstheorie der versetzungen und eigenspannungen, Ergebnisse Der Angewandten Mathematik. 5 (1958) 1–179.

ESTIMATING THERMOMECHANICAL RESIDUAL STRESSES IN FDM 3D PRINTED COMPOSITE PARTS

Camilo Suarez[1,3], Rémi Cornaggia[1,2], Aurélien Maurel-Pantel[1], Noël Lahellec*[1], Djaffar Boussaa[1], Hervé Moulinec[1], and Noelle Billon[4]
[1] Aix Marseille Univ, CNRS, Centrale Marseille, LMA, Marseille, France
[2] Inovsys, Marignagne, France
[3] University of Luxembourg, Esch-sur-Alzette, Luxembourg
[4] MINES ParisTech, CEMEF, Sophia Antipolis, France

Summary We implemented a two-step methodology to estimate the residual stresses induced by the FDM manufacturing process in 3D printed composite parts. The first step consisted in an analytical thermo-viscoelastic homogenization procedure to derive the effective behavior of the filament. The second step consisted in a coupled thermomechanical structural analysis of the part. The homogenization procedure was assessed by comparing its predictions to full-field FFT-based computations. The structural analysis was assessed by comparing its predictions to experimental results.

FRAMEWORK

We are interested in the capabilities and performances of 3D printed parts made of thermoplastic matrix reinforced by short (≈100 μm) to intermediate (≈1 mm) glass fibers. Our aim is to estimate the residual stresses induced by cooling these parts from extrusion to room temperatures, which is a critical requirement to design these parts, in particular their filament's deposition trajectory. This estimation is challenging because of the complexity of the material (thermo-visco-elastic composite) and that of the FDM process itself (Fig. 1).

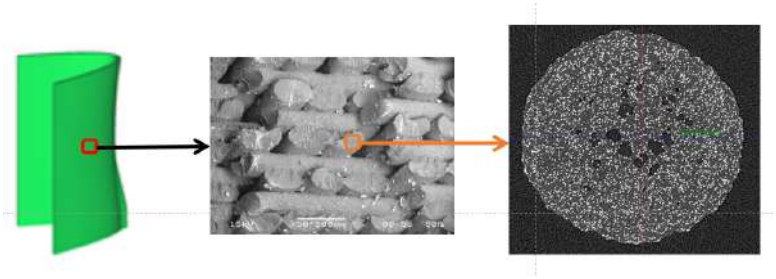

Figure 1: Three-scale configuration: printed part, fused filament structure and fiber-reinforced composite.

In the following, we provide some detail on each aspect of the methodology implemented.

HOMOGENIZATION OF REINFORCED POLYMER FILAMENTS

We estimated the FDM-induced residual stresses by using (i) a homogenization procedure to estimate the effective properties of the filament, and (ii) a coupled thermo-mechanical structural analysis. The homogenization procedure has two steps. The first step consisted in estimating the effective properties of the reinforced filament; the second step, in estimating the effective properties of the final 3D printed composite material.
The fibers of the filament were assumed to be elastic. Its matrix was assumed to be thermo-viscoelastic. Various mean-field methods were used to account for the fibers, and their predictions were compared with FFT-based full-field simulations. Finally, with these effective models at hand, the deflection and residual stresses in the whole part were estimated using an FEM code. Validation at the macroscale were then performed comparing FE simulations with experiments.

Thermo-viscoelastic modeling of the matrix The polymer matrix was assumed to be isotropic and its thermo-viscoelastic behavior to be described by an N-branch generalized Maxwell model, which is developed within the framework of generalized standard materials and characterized by the free energy $w(\boldsymbol{\varepsilon}, (\boldsymbol{\varepsilon}_v^i)_{i=1}^N, T)$ and the mechanical dissipation potential $\varphi((\dot{\boldsymbol{\varepsilon}}_v^i)_{i=1}^N, T)$, where $\boldsymbol{\varepsilon}$, $\boldsymbol{\varepsilon}_v^i$ are the strain and the viscous strain of branch i, respectively, and T is the temperature. For an N-branch model, these potentials can be written as

$$w(\boldsymbol{\varepsilon}, \boldsymbol{\varepsilon}_v^i, T) = \sum_{i=1}^{N} \frac{1}{2}(\boldsymbol{\varepsilon} - \boldsymbol{\varepsilon}_v^i) : \boldsymbol{L}^i : (\boldsymbol{\varepsilon} - \boldsymbol{\varepsilon}_v^i) + \sum_{i=1}^{N} (\boldsymbol{\varepsilon} - \boldsymbol{\varepsilon}_v^i) : \boldsymbol{L}^i : \boldsymbol{\alpha}(T - T_0) + c_0 \left[(T - T_0) - T \ln \frac{T}{T_0} \right] - \eta_0 T + e_0,$$

*Corresponding author. E-mail: lahellec@lma.cnrs-mrs.fr

and

$$\varphi(\dot{\boldsymbol{\varepsilon}}_v^i, T) = \sum_{i=1}^{N} \frac{1}{2} \dot{\boldsymbol{\varepsilon}}_v^i : \boldsymbol{L}_v^i(T) : \dot{\boldsymbol{\varepsilon}}_v^i,$$

where $\boldsymbol{L}^i$ and $\boldsymbol{L}_v^i$ are the elasticity and viscosity tensors of branch i, respectively, $\boldsymbol{\alpha}$ is the thermal expansion tensor, c_0 is the heat capacity at constant stress, and η_0 and e_0 are the initial entropy and internal energy, respectively. The number of branches and the tensors $\boldsymbol{L}^i$ and $\boldsymbol{L}_v^i$ were found using DMA and creep experiments at different temperatures.

Upscaling FEM calculations were used to solve the macroscopic coupled mechanical and thermal equilibrium equations for the macroscopic stress, strain and temperature. At each integration point, these quantities are the average over a representative volume element of their microscopic counterparts, which solve the local mechanical and thermal equilibrium equations given by:

$$\mathrm{div}\boldsymbol{\sigma}(\boldsymbol{x}, t) = 0, \quad \boldsymbol{\sigma}(\boldsymbol{x}, t) = \frac{\partial w}{\partial \boldsymbol{\varepsilon}}(\boldsymbol{x}, \boldsymbol{\varepsilon}, \boldsymbol{\varepsilon}_v^i, \overline{T}), \quad \frac{\partial w}{\partial \boldsymbol{\varepsilon}_v^i}(\boldsymbol{x}, \boldsymbol{\varepsilon}, \boldsymbol{\varepsilon}_v^i, \overline{T}) + \frac{\partial \varphi}{\partial \dot{\boldsymbol{\varepsilon}}_v^i}(\boldsymbol{x}, \dot{\boldsymbol{\varepsilon}}_v^i, \overline{T}) = 0. \tag{1}$$

$$\mathrm{div}\boldsymbol{q}(\boldsymbol{x}, t) = 0, \quad \boldsymbol{q}(\boldsymbol{x}, t) = -\boldsymbol{k}(\boldsymbol{x}).\boldsymbol{\nabla} T(\boldsymbol{x}, t), \tag{2}$$

where $\boldsymbol{q}$ and $\boldsymbol{k}$ are the heat flux and conductivity tensor respectively. It should be noted that the microscopic mechanical and thermal equations (1) and (2) are uncoupled because of the following: i) Only the average macroscopic, $\overline{T}$, is considered in the mechanical formulation (1). ii) The dissipated energy is taken into account at the macroscale, which simplifies the heat equation as shown in (2). The thermo-mechanical coupling is then achieved at the macroscopic scale. Equations (1) and (2) are supplemented with appropriate boundary conditions to enforce that $\overline{\boldsymbol{\varepsilon}}$ and $\overline{T}$ are the respective averages of the local fields $\boldsymbol{\varepsilon}(\boldsymbol{x})$, solution of (1), and $T(\boldsymbol{x})$, solution of (2).

Mean-field models to account for the fibers We used mean-field methods to estimate the average of the thermo-mechanical fields that solve the local equations (1) and (2). The used mean-field methods handle the complexity of the composite material (non-alignment of the fibers, thermo-viscoelasticity of the matrix, etc.).
Mean-field methods aim at determining closed-form approximations of the mean fields in each phase using simplifying assumptions (usually valid for low to medium densities of inclusions) and analytical results coming from Eshelby's equivalent inclusion method. We used several models to estimate the effective elasticity tensor of the filament, $\boldsymbol{L}_{\text{eff}}$, including the Interaction direct derivative model [4], which is characterized by the following equation:

$$\boldsymbol{L}_{\text{eff}} = \boldsymbol{L}_{\text{M}} + \left(\boldsymbol{I} - c_{\text{F}} \int_S f(\boldsymbol{n}) \Delta \boldsymbol{L}_{\text{F,M}}(\boldsymbol{n}) : \boldsymbol{A}_{\text{F,M}}(\boldsymbol{n}) : \boldsymbol{P}_{\text{F}}^{\text{D}}(\boldsymbol{n}) dS \right)^{-1} : \left(c_{\text{F}} \int_S f(\boldsymbol{n}) \Delta \boldsymbol{L}_{\text{F,M}}(\boldsymbol{n}) : \boldsymbol{A}_{\text{F,M}}(\boldsymbol{n}) dS \right) \tag{3}$$

where S is the unit sphere, c_{F} is the fibers' volume fraction, $\boldsymbol{n}$ is the fibers' orientation, f is the orientation probability density function, $\boldsymbol{A}_{\text{F,M}}$ is the localization tensor accounting for the fibers' shapes and material contrast, defined as $\Delta \boldsymbol{L}_{\text{F,M}}(\boldsymbol{n}) = \boldsymbol{L}_{\text{F}}(\boldsymbol{n}) - \boldsymbol{L}_{\text{M}}$, and $\boldsymbol{P}_{\text{F}}^{\text{D}}$ is Hill's tensor accounting for the fibers' spatial distribution.
In the case of linear viscoelastic constituents, Laplace-Carson transform is classically used which allows defining a linear symbolic elastic composite in the Laplace domain (the so-called correspondence principle [3]). This method cannot be used directly because of the temperature dependence of the viscous moduli of the matrix. To overcome this difficulty, we used an incremental formulation [1] that allows the Laplace-Carson transform to be used, provided that the moduli change slowly with the temperature.

VALIDATION

The proposed mean-field model was assessed by comparing its predictions in terms of effective moduli to those of FFT-based full-field simulations on representative volume elements (RVE). The proposed macroscopic structural analysis was assessed by comparing its predictions in terms of warping with the warping that develops within 3D printed asymmetric plates (plates with two deposition orientations: $0°$ and $90°$).

References

[1] Ricaud J.-M., Masson R. Effective properties of linear viscoelastic heterogeneous media: Internal variables formulation and extension to ageing behaviours *Int. J. of Solids and Struct.*, 46 (7-8) , pp. 1599-1606, 2009.
[2] Chatzigeorgiou G., Charalambakis N., Chemisky Y. and Meraghni F., Periodic homogenization for fully coupled thermomechanical modeling of dissipative generalized standard materials.*Int. J. of Plast.*, 2016,volume 81, pp. 18-39.
[3] Mandel, J. *Cours de Mécanique des milieux continus*, Gauthier–Villars, Paris, 1966.
[4] Müller, V. & Böhlke, T. Prediction of effective elastic properties of fiber reinforced composites using fiber orientation tensors, *Compos. Sci. Technol.*, 130 , 36-45, 2016
[5] Lahellec, N. and Suquet, P. Effective behavior of linear viscoelastic composites: A time-integration approach *Int. J. Solids Struct.*, 44, 507-529, 2007.

SELECTIVE LASER MELTING MANUFACTURING OF COPPER-GRAPHENE OXIDE COMPOSITES

Sara Residori[1§], Diego Corona[2§], Emanuele Sbardella[2], Mariano Zarcone[2], Gildo Di Domenico[2], Nicola Maria Pugno*[1,4] and Costantino Del Gaudio*[2]

[1] *Laboratory of Bio-Inspired, Bionic, Nano, Meta Materials & Mechanics, Department of Civil, Environmental and Mechanical Engineering, University of Trento, Trento, Italy*

[2] *Fondazione E. Amaldi, Rome, Italy*

[4] *School of Engineering and Materials Science, Queen Mary University of London, London, United Kingdom*

Summary 3D printing offers a valuable opportunity to design and fabricate ad hoc composites with tailored properties for several applications. Dealing with metal matrix components can pave the way to define novel and enhanced materials that positively affect not only the final characteristics, which is the expected result, but also the processing variables in the manufacturing stage. In this regard, the modification of 3D printed copper specimens with just 0.1% w/w graphene oxide (GO) provided a clear evidence of the optimal nanofiller content referred to density improvement and superior processability and hardness. A feasibility study was carried out following two different routes to disperse GO into Cu matrix, including nanofiller deagglomeration in bidistilled water or not, before to process the composite powder by selective laser melting (SLM) technique. Several working conditions were considered, setting the laser power at 175 W as the best input parameter resulted from a preliminary screening assessment. Reflectance measurements, density evaluation, scanning electron microscopy, Raman spectroscopy, and mechanical characterization, through indentation tests, were carried out to characterize each stage of the 3D printing process from the composite powders to the final specimens.

INTRODUCTION

Most metals and alloys are unsuitable for additive manufacturing (AM), but the development of this technology can benefit the production of metal matrix composites to reproduce of metal matrix composites can benefit from this technology to reproduce samples of complex geometry with high details and proper functional features [1]. It is well-known that 3D printed components often include several defects, as high porosity, that negatively affect mechanical properties. In this regard, the addiction of nanofiller can likely ameliorate this feature.

The presented study aims to prepare GO–based metallic composites, using copper as a matrix. The excellent thermal conductivity makes this metal particularly interesting for industry, but it is difficult to print for his high reflectance, that plays a key-role in the production process [2]. The potential of GO as a filler can provide a relevant contribution to the final composite if an effective filler-matrix interaction is obtained, but it can be also regarded as a supportive means to modify the processing variables and thus tailoring the entire experimental protocol. The SLM was here assessed as an adequate technique to fabricate 3D printed Cu-GO composites with the aim to investigate different processing conditions [3]. Density measurements, Raman analysis and mechanical indentation were therefore performed to characterize the 3D printed composites in order to evaluate their properties and critically correlate the collected findings to the computed porosity.

MATERIALS AND METHOD

Materials

Graphene oxide (GO; powder, oxidation: 4-10%) was supplied by Sigma-Aldrich (Milan, Italy). Deionized water was supplied by Carlo Erba Reagenti (Milan, Italy). Cu powder (99.9% purity, 4.8 g/cm3 apparent density) was purchased from ECKA Granules (Germany).

Composite fabrication

The composite powder was obtained following two different routes: mechanical mixing for 12 h through a custom-made epicyclical gear system (Route A); filler was ultrasonically disagglomerated in deionized water for 30 min and then mixed to Cu powder, water was finally removed in an oven at 100°C for 24 h (Route B).

Composites were fabricated by means of the 3D printer MySint100 (Sisma, Italy), a powder bed system equipped with a 200 W laser, 1070 ± 10 nm wavelength, and 30 µm focus beam diameter. The melting process was carried out in inert environment with nitrogen over-pressure. Box-shaped specimens (7x7x10 mm^3) were built on platforms of AISI316, setting a laser power of 175 W, scan speed of 600 mm/s and hatch distance of 0.06 mm and 0.04 mm. These variables were selected after a preliminary screening process.

The reflectance values of the Cu-GO powder were analysed by means of the Ulbricht integration sphere, equipped with a led source of 15 mW power and 940 nm wavelength. The detector was a PIN photodiode at 940 ± 150 nm.

*Corresponding author. E-mail: **nicola.pugno@unitn.it**.
*Corresponding author. E-mail: **costantino.delgaudio@fondazioneamaldi.it**
§Contributed equally to the work

The characterization of the 3D printed specimens was carried out by means of scanning electron microscopy (SEM; Philips XL30) to analyse the resulting morphology, Raman spectroscopy (InVia Raman microscope; Renishaw, UK) to investigate the GO distribution on the composite surface, and indentation tests (MTS Insight 5, USA) to assess the mechanical properties.

RESULTS AND DISCUSSION

The Cu-GO powder mechanically mixed was characterized by a reflectance value of 57.1%, while that obtained introducing the disagglomeration in an ultrasonic bath was 15.2%. The reflectance of the neat copper powder was 84.1%. These results confirmed that the addition of a carbon nanofiller can dramatically reduce the reflectance, even at very low concentration (0.1% w/w). It should be also noted that the possible formation of copper oxide might contribute to this result.

3D printed specimens were characterized by a quite large density distribution, which can be related to the energy density experienced by the powder during the fabrication process.

Surface morphology was analysed by SEM (Figure 1). Samples from Route A showed a rough surface, also revealing the presence of pores containing pristine copper powder. Instead, the Route B seemed to induce a slight modification of sample morphology, highlighting a more regular surface. This result can be related to the reflectance measurements since the composite powder prepared following the latter method seems to more efficiently interact with the laser source, thus inducing an enhanced melting of the powder.

Raman spectroscopy was carried out to evaluate the GO distribution within composites. A quite uniform filler distribution can be observed for all the investigated samples. Some quantitative indices were proposed, and the statistical analysis did not assess significant differences, confirming that the two experimental approaches led to a similar GO dispersion within the copper matrix.

Regarding the mechanical characterization, the indentation curves firstly showed a linear elastic region followed by a large plastic response with an almost constant slope up to the end of the test (Figure 2). Samples prepared following the Route B were characterized by a larger indentation force values in the plastic region compared to those from Route A. Generally, the mechanical response of a porous sample is related to the porosity degree of the structure, but in the present study, specimens with higher porosity showed better mechanical properties. This behaviour can be ascribed to the composite powder preparation: a preliminary filler deagglomeration in ultrasonic bath promoted an improved interaction with the copper powder, eliciting a competitive effect between the expected porosity weakness and the structural resistance. On the other hand, the GO mechanical dispersion failed to properly disagglomerate the as received nanofiller, leading to the presence of micro-aggregates as defects that added their negative role to the porosity level.

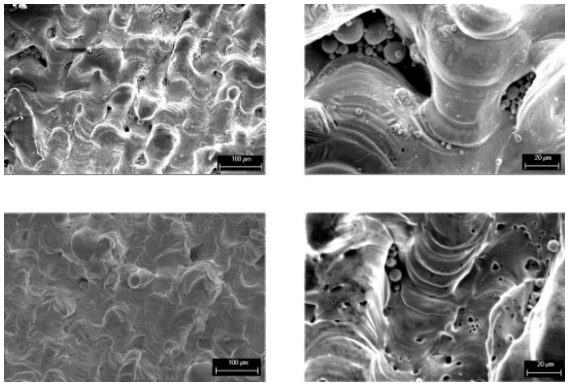

Figure 1. SEM micrographs of 3D printed composite samples fabricated following the Route A (upper panel) and the Route B (lower panel). Magnification: 200x (left column), 800x (right column)

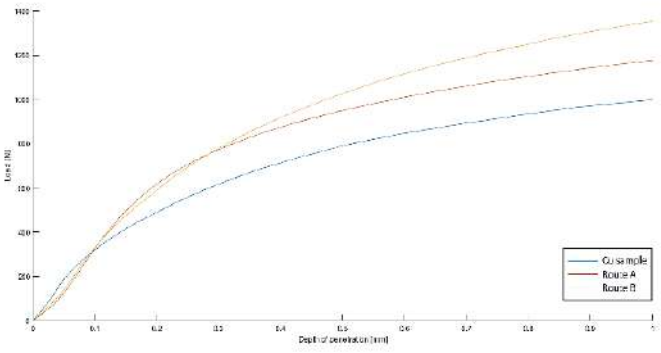

Figure 2. Representative indentation curves for 3D printed pure copper (blue), Route A (red) and Route B (yellow) specimens

CONCLUSION

3D printed metal matrix composites represent a valuable means to deal with components specifically designed to enhance required properties. CuGO composites, as an output of a SLM process, were here considered to evaluate the optimization of the fabrication protocol and the expected filler contribution. A mechanical reinforcement was measured for all the investigated composites when compared to pure copper specimens, the highest response being acquired from those specimens in which GO was disagglomerated by means of an ultrasonic bath. In order to counterbalance the negative effect related to the porosity degree, usually affecting 3D printed samples, the proposed approach could be an interesting option to be further exploited when specific structural properties are required.

References

[1] Murr L.E., Martuinez E., Amato K. N., Gaytan S. M., Harnandez J., Ramirez D. A., Shindo P. W., Medina F., Wicker R. B., Fabrication of Metal and Alloy Components by Additive Manufacturing: Examples of 3D Metal Science, Jmr&t, 2012, 42:54.

[2] Jadhav SD, Dadbakhsh S, Vleugels J, Hofkens J, Van Puyvelde P, Yang S, Kruth JP, Van Humbeeck J, Vanmeensel K. Influence of carbon nanoparticle addition (and impurities) on selective laser melting of pure copper. Materials. 2019; 12:2469. Cooler A. S. Binary Flow Systems. J. Fluid. Mech. 999: 991-996, 1999.

[3] Chu K, Wang X, Wang F, Li Y, Huang D, Liu H, Ma W, Liu F, Zhang H. Largely enhanced thermal conductivity of graphene/copper composites with highly aligned graphene network. Carbon. 2018; 127:102-112.

FIELD-ASSISTED 3D-PRINTING OF FUCTIONAL COMPOSITES

Tyler Ray[1], Drew Melchert[2], Rachel Collino[3], Neil D. Dolinski[2], Leanne Friedrich[2], Matthew Begley[2], and Dan Gianola[2]
[1] Department of Mechanical Engineering, University of Hawai'i at Mānoa, Honolulu, Hawai'i, USA
[2] Materials Department, University of California, Santa Barbara, Santa Barbara, California, USA
[3] MST-7 Engineered Materials, Division of Materials Science and Technology, Los Alamos National Laboratory Los Alamos, NM, USA

Summary Acoustic forces are an attractive pathway to achieve directed assembly for multi-phase materials *via* additive processes. Programmatic integration of microstructure and structural features during deposition offers opportunities for optimizing printed component performance. Here, we demonstrate that acoustic fields can effectively assemble conductive particles into networks within polymer matrices, whose configuration is modulated prior to curing, to produce 2-D conductive, 1-D conductive, or insulating materials on-demand, all using the same precursor ink. Furthermore, patterning efficient percolated networks in this manner increases conductivity an order of magnitude over conventional dispersed-fiber composites with an order of magnitude lower particle loading, improving printability and allowing versatile orthogonal control of other properties.

The ability to control particle alignment across volume fraction ranges would create new opportunities to print composite materials with engineered anisotropic properties (mechanical, electrical, thermal, and optical) [1]. A promising approach for achieving top-down control over microstructure is to combine field-assisted assembly with direct deposition. While electrostatic or electromagnetic fields are suitable for a narrow range of ink compositions and particle types, acoustic fields are broadly applicable to a wide class of colloids, spanning a broad range of composition, particle shape, and size. We demonstrate acoustic-field-assisted assembly of two-phase aligned composites, such as silver-coated fibers in a flexible polymer matrix, using microfluidic print nozzles (Fig. 1A) coupled to inexpensive piezoelectric actuators. Mechanical and electrical characterization of the flexible composite materials demonstrate the orthogonal control of material properties, such as conductivity and rigidity (Fig. 1B-D), enabled by field-assisted patterning.

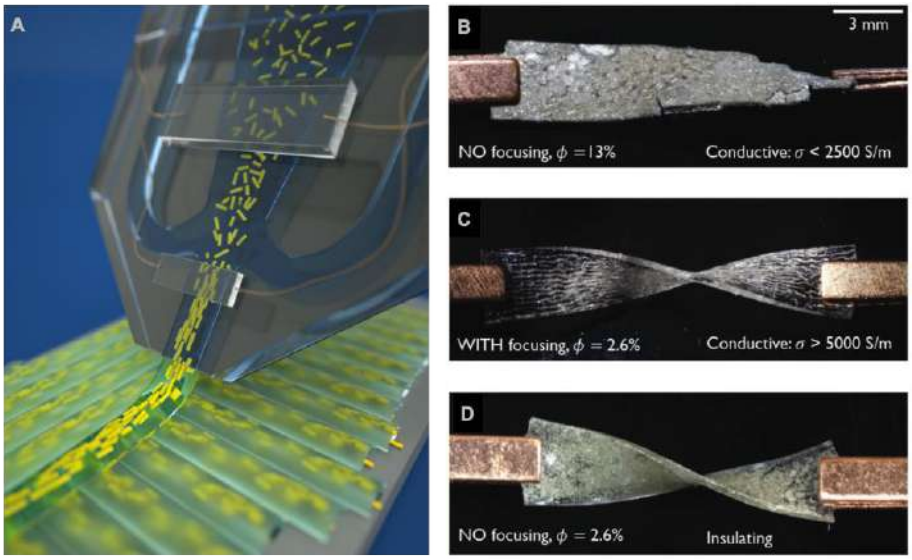

Figure 1: (A) Conceptual illustration of acoustic print nozzle. Piezoelectric actuation generates acoustic forces that align fibers during printing. (B-D) Photographs of silver-coated fiber elastomeric composites twisted to demonstrate gains in flexibility and conductivity via acoustic patterning. (B-D) Adapted with permission from [2].

Acoustic forces created by standing pressure waves are an attractive pathway to increasing the density and alignment of particles: they are active over large distances and relatively material agnostic (*i.e.*, they do not require specific surface functionalization, solution chemistries, or electromagnetic properties). In many applications, the particles are micron-sized or larger, such that the magnitude of easily achieved acoustic forces is much greater than those associated with fluid drag, implying that particles can be transported and assembled over relatively long distances on the order of seconds or less. These benefits create new opportunities to incorporate acoustic excitation in nozzles used for three-dimensional printing, to dramatically increase the density and alignment of particles relative to that of the 'ink'.

The acoustic nozzle schematic shown in Figure 1 illustrates the alignment of fibers in a viscoelastic matrix, which results from an applied acoustic force generated by piezoelectric elements mounted above the nozzle pathway. These nozzles are typically microfabricated in silicon or glass (150 µm deep) with a bonded glass capping layer according to the procedures in Ref. [3], with piezoelectric actuators bonded to the nozzle to generate standing waves in the channel.

Critically, acoustic focusing enables control of the microstructure of the deposited line by modulating acoustic excitation parameters, as demonstrated in Figure 1C for silver-coated fibers in a flexible polymer matrix. When the excitation frequency is tuned to induce focusing, fibers collapse to the acoustic nodes (tunable from 1 to N, frequency dependent). The patterned composite (Fig. 1C) exhibits conductivity at a particle volume fraction below the percolation threshold (Fig. 1C, unpatterned composite is insulating) due to structuring particles into percolated bundles rather than a

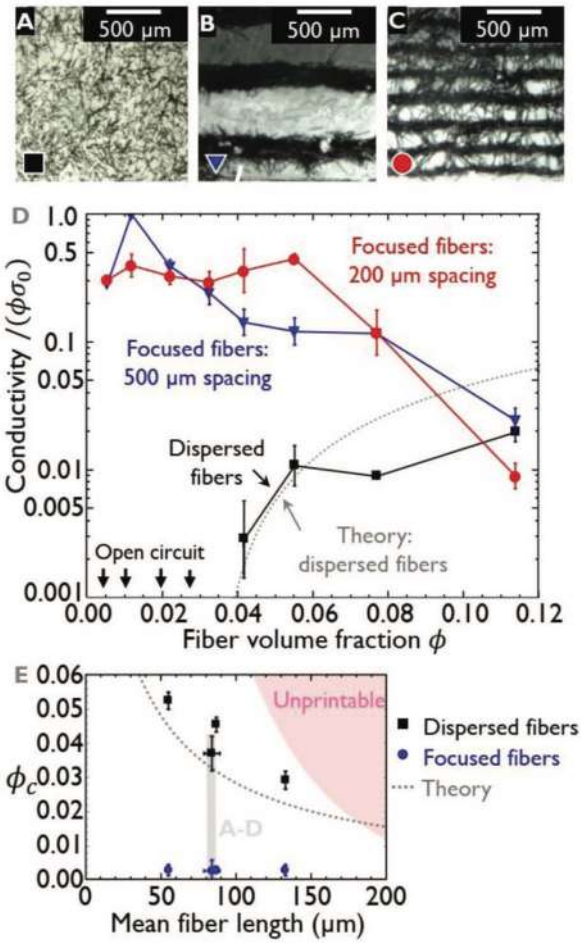

Figure 2: A) Image of a 0.5 vol% composite made without acoustic focusing. B) Images of 2.6 vol% composites made with acoustic focusing with 500 µm focused bundle spacing and C) 200 µm spacing. D) Electrical conductivity normalized by the conductivity of the fibers σ_0 and the volume fraction φ, which gives the volume fraction of fibers in the composite that contribute to the conductive network. Fiber alignment by shear flow, a factor especially apparent in the higher viscosity inks with high φ is expected to decrease conductivity below this model. E) The percolation threshold φ_c at which electrical behavior of composites transitions from insulating to conductive. Fiber alignment is expected to increase φ_c and high spread in the fiber length distribution is expected to decrease φ_c compared to the theoretical model shown here. [4] The "unprintable" region indicates approximately which volume fractions and fiber lengths clog the devices. Figure is adapted with permission from [2].

disconnected stochastic network. In order to achieve conductivity in the absence of patterning, a significantly higher particle loading volume is required (Fig. 1B), resulting in loss of mechanical flexibility.

Figure 2 illustrates the enhanced conductivity through acoustic focusing via assembly of carbon fibers dispersed in a UV-curable resin. The patterned composites in Figure 2B,C exhibit dramatically higher conductivity than Figure 2A as shown in Figure 2D. Below the percolation threshold for the dispersed-fiber composites φ_c, the patterned composites maintain high conductivity. Up to 97% of the fibers by volume contribute to the conductive network at φ = 1.2 vol% due to preferentially end-on-end stacking resulting from acoustic scattering forces [5]. At volume fractions up to 8%, the conductivity of the acoustically patterned composites is at least an order of magnitude higher than unpatterned, percolated composites from the same precursor ink. In contrast to the strong scaling in dispersed-fiber composites, conductivity in acoustically patterned composites is invariant from 1 to 10 vol%. This insensitivity to loading offers orthogonally control over material properties such as stiffness, strength, or thermal conductivity by tuning the filler loading.

The conductivity reported above is 1D, running parallel to the focused bundles of fibers, where bundles are insulated from each other. Control over conductivity in the perpendicular direction, however, is possible by tuning the applied pressure field. Modulating the focusing wavelength controls the bundle spacing, which in turn controls the number of fibers bridging between bundles: longer fibers are acoustically stable perpendicular to the focused bundles resulting in bridging. Controlling the focused line spacing modulates the electrical conductivity of the patterned composites between anisotropic or nearly isotropic. This response is suitable for on-the-fly modulation in a printing modality to allow programmable spatial control of electrical interconnects embedded in printed components.

These results are highly promising. Although the focus is on electrical conductivity, the approach described is extensible to other transport phenomena. As a relatively material agnostic technique for microstructural control, acoustic-focusing-assisted additive manufacturing greatly expands the library of printable multiphase inks. This technology demonstrates a novel approach to modulating material properties via microstructure control to pave the way for 3D printing components with embedded electrical circuits or other spatially modulated properties.

References

[1] Begley, M.R., Gianola, D.S., Ray, T.R. Bridging Functional Nanocomposites to Robust Macroscale Devices. Science **364**: eaav4299, 2019.
[2] Melchert, D. S., Collino, R. R., Ray, T. R., Dolinski, N. D., Friedrich, L., Begley, M. R., Gianola, D. S., Flexible Conductive Composites with Programmed Electrical Anisotropy Using Acoustophoresis. Adv. Mater. Technol. **4**: 1900586, 2019.
[3] Collino, R.R., Ray, T.R., Fleming, R.C., Cornell, J.D., Compton, B.G., Begley, M.R. Deposition of Ordered Two-Phase Materials using Microfluidic Print Nozzles with Acoustic Focusing. Extreme Mech Lett **8**: 37-46 96-106, 2016.
[4] Mutiso, R.M., Winey, K.I. Electrical Properties of Polymer Nanocomposites Containing Rod-Like Nanofillers. Prog. Polym. Sci. **40:** 63-84, 2015
[5] Collino, R.R., Ray, T.R., Fleming, R.C., Sasaki, C.H., Haj-Hariri, H., Begley, M. R. Acoustic Field Controlled Patterning and Assembly of Anisotropic Particles. Extreme Mech. Lett. **5**: 37-46, 2015.

MICROSTRUCTURE CONTROL THROUGH DEPOSITION PATTERN OPTIMIZATION IN DIRECT METAL DEPOSITION

Vibhas Mishra, Can Ayas, Matthijs Langelaar, Fred van Keulen
Mechanical, Maritime and Materials Engineering, Delft University of Technology, Delft, The Netherlands

Summary Direct Metal Deposition provides a unique capability to deposit material along a wide variety of deposition patterns. Deposition patterns affect the thermal history experienced by the produced parts. The thermal history at a particular point determines its microstructure. This opens up the possibility to tailor the microstructure at specific locations, by optimizing the deposition patterns. In this contribution, each material point in a given design is associated with a time variable, indicating its printing time. The deposition pattern is given by the ascending sequence of the time variables. Based on this deposition pattern, thermal simulation is performed to evaluate the thermal history of the critical points in the structure. Microstructure is linked to this thermal history. Thus, we show that through deposition time field optimization, specific microstructures can be achieved.

INTRODUCTION

Direct Metal Deposition (DMD) shows potential to economically produce large-scale structures such as ship propellers and aircraft structures. In the Direct Metal Deposition (DMD) process, the metal is melted and deposited simultaneously on a substrate using a robotic arm while following predefined deposition patterns or order. A unique capability of DMD is that various deposition paths, planes and order can be chosen for given part layout. The thermal history experienced by the part during manufacturing depends on the choice of deposition pattern. Moreover, The local thermal history determines the microstructure evolution therein [1]. For a specific engineering material such as High-Strength Low-Alloy steel, the temperature range between 800°C - 500°C is particularly important, since the cooling rate in this interval determines the constituent phases at a specific location [1]. For example, high cooling rates (>100°C/s) result in the hard and brittle martensitic phase, whereas low cooling rates (~1°C/s) form the soft and ductile pearlite phase mixture and intermediate cooling rates lead to the bainite phase [1]. The deposition patterns can be modified to change the thermal history experienced by the printed part [2]. Therefore, it is possible to change the deposition pattern in such a way that a desired thermal history and henceforth a desired microstructure can be realized at a location of interest.

OBJECTIVE

In a structure, locations with stress concentrations should comprise favourable metallurgical phases and morphology in order to mitigate crack initiation and propagation. We propose to control cooling rates and temperature history at these locations through optimizing the deposition pattern. For example, consider a block with a cylindrical hole subjected to uniaxial tension, as shown in Figure 1. The maximum stress concentration occurs at the highlighted points (labelled as 1 and 2). If the block is manufactured by the DMD process, the microstructure at these high-stress locations could be controlled by choosing a suitable deposition pattern which in turn adapt the cooling rates at these locations.

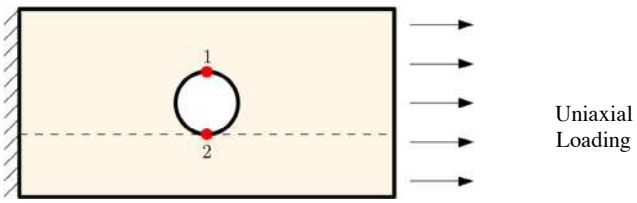

Figure 1 : Side view of a block with a cylindrical hole subjected to uniaxial loading. Highlighted points (1 and 2) in red are locations of stress concentration.

METHODOLOGY AND RESULTS

In order to achieve the objective, the structure will be discretized with Finite Elements (FE). At each FE a time variable is introduced which indicates when the associated material represented by the FE is printed; and the ascending order of the time variable represents the deposition pattern of the part. In order to maintain the continuity of the deposition pattern, continuity constraint proposed in [3] will be used. For every intermediate iteration during optimization, deposition patterns are obtained based on the time variable. The thermal history generated at the specific location through this deposition pattern can be evaluated by the element birth technique [4]. In the element birth technique, FEs are added sequentially in accordance with the time variable that represents the deposition pattern until the DMD process is completed.

Consider a solid block shown in Figure 2 which has been discretized with hexahedral elements. The block represents the lower region of the part shown in Figure 1 (region below the dashed line). Two basic raster strategies are shown in Figure 3. The corresponding thermal history generated at Point 2 of the block, as simulated for these two strategies, are shown in Figure 4. The graph shows temperature of Point 2 at every time step of transient simulation. Comparing the thermal profile obtained in the two basic strategies shows that the thermal history experienced by Point 2 is substantially different. Through optimization of the time field, the thermal history at points of interest can be modified such that desired

microstructures and material phases are obtained. The approach will be illustrated by several numerical examples. The optimized strategy to achieve a specific cooling rate at particular location in a structure will be presented.

Figure 2 : Lower region of the part shown in Figure 1, discretized with hexahedral elements

(a) (b)

Figure 3 : Two raster strategies with which the block (shown in Figure 2) can be produced (a) Raster X (b) Raster Y

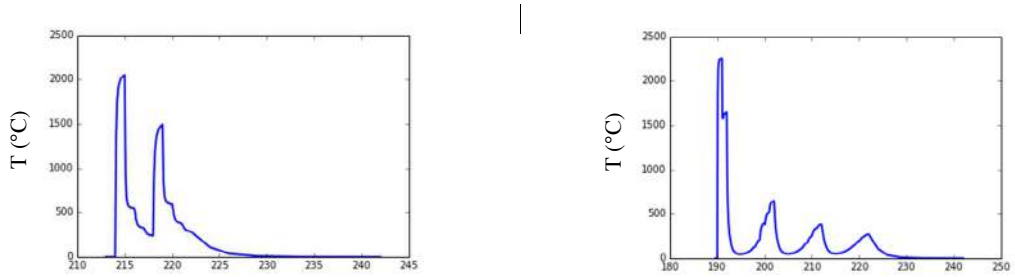

(a) (b)

Figure 4: The thermal profile (Temperature calculated at every time step) of Point 2 of the solid block (shown in Figure 2) produced by two raster strategies (a) Raster X (b) Raster Y

ACKNOWLEDGEMENTS

This research was carried out under project number S17024a in the framework of the Partnership Program of the Materials innovation institute M2i (www.m2i.nl) and the Technology Foundation TTW (www.stw.nl), which is part of the Netherlands Organization for Scientific Research (www.nwo.nl).

References

[1] Rodrigues, T. A., Duarte, V., Avila, J. A., Santos, T. G., Miranda, R. M., & Oliveira, J. P. (2019). Wire and arc additive manufacturing of HSLA steel: Effect of thermal cycles on microstructure and mechanical properties. *Addit. Manuf.*, 27, 440-450.

[2] Nickel, A. H., Barnett, D. M., & Prinz, F. B. (2001). Thermal stresses and deposition patterns in layered manufacturing. *Mater. Sci. Eng. A*, 317(1-2), 59-64.

[3] Wang, W., Munro, D., Wang, C. C., van Keulen, F., & Wu, J. (2019). Space-time topology optimization for additive manufacturing. *Struct. Multidiscip. Optim.*, 1-18.

[4] Schoinochoritis, B., Chantzis, D., & Salonitis, K. (2017). Simulation of metallic powder bed additive manufacturing processes with the finite element method: A critical review. Proceedings of the Institution of Mechanical Engineers, *Proc. Inst. Mech. Eng. B*, 231(1), 96-117.

PROCESS-STRUCTURE ANALYSIS FOR METAL ADDITIVE MANUFACTURING USING A MULTI-PHYSICS MODELING FRAMEWORK

Yanping Lian*[1], Feiyu Xiong[1], Chenyang Huang[1], Jiawei Chen[1], Wing Kam Liu[2], and Daining Fang [1]
[1] Institute of Advanced Structure Technology, Beijing Institute of Technology, Beijing, China
[2] Deparment of Mechanical Engineering, Northwestern University, IL, US

Summary In this study, we developed an integrated multi-physics modeling framework for additive manufacturing to offer highly-accurate simulations of the metal powder melting-solidification process. In this framework, discrete element method is used for the powder delivery simulation, finite volume method is proposed to solving for the mass, momentum, and energy conservation equations for the multi-physics phenomena involving fluid flow, heat transfer, surface tension at powder scale, while an improved cellular automaton method is developed for the grain structure evolution during the solidification. We conducted numerical examples, of which the results are in good agreement with experimental data. It is demonstrated that the proposed modeling framework is a powerful approach to simulate the metal AM processes and to address the process-structure relationship.

INTRODUCTION

Metal Additive Manufacturing (AM) has found potential to revolutionize the global part manufacturing landscape in recent years because of its ability to realize rapid fabrication, precise geometric control, and flexibility to create or repair metal parts without the use of any die or mold [1]. Because the AM process involves many different physical phenomena taking place at a variety of temporal and spatial scales, however, it is challenging to optimize the AM process parameters to minimize final product defects such as surface roughness, void formation, heterogeneous grain structures, etc. via the costly trial-and-error experiments. To comprehensively understand the AM process and guide the process parameters optimization, in this work we presented a multi-physics modeling framework. In this framework, powder spreading and thermal-fluid flow models are applied to predict the thermal history and defect formation in the multi-track and multi-layer build with different processing conditions; the space- and time-varying temperature field of these simulations is passed to a cellular automaton-based microstructure model [2,3] to predict the grain structure during the solidification. Through this framework, we study the effects of various process parameters on the resulting thermal features, defects, and grain structures of the build. The simulation results (e.g., melt pool shape and size, cooling rate, and grain structures) are in good agreement with experimental results from literature [4], demonstrating the appealing potential of the proposed modeling framework, which can be used to manipulate the "driving forces" behind the complex physical phenomena to obtain AM fabricated parts with desired qualities.

MODELING FRAMEWORK

The proposed integrated modeling framework is shown in Fig.1, taking the powder bed fusion as an example. It consists of three models. Based on the discrete element method (DEM), a powder spreading model is applied for the fractional contact and collisions between metal powders and the rake over the substrate. The output of the powder spreading simulation is passed to the finite volume method (FVM) thermo-fluid flow model to conduct the powder-scale multi-physics simulation, including heat transfer, fluid flow within the melt pool, and surface tension, where the volume of fluid scheme is used for free surface modeling. Based on a one-way coupling algorithm, we feed the temperature profiles and voids information from FVM results to the cellular automaton (CA) method for the grain structure simulation. CA method simulates the evolution of the external envelope of each dendritic grain rather than the details of the dendrite arms with simplified models based on the physical nucleation and growth kinetic laws. To model the epitaxial grain growth in AM, an enriched nucleation model and a restart calculation scheme for the multi-scan and multi-layer fabrication process are developed.

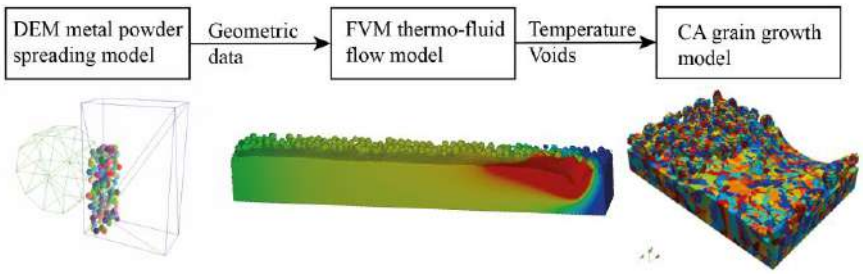

Figure 1 Integrated modeling framework for the process-structure relationship for additive manufacturing.

RESULTS AND DISCUSSION

Two sets of simulations are conducted to study the metal additive manufacturing with different process parameters. In the first set, we validated our modeling framework to the additive manufacturing benchmark (AM-Bench) experiments [4], AMB2018-02, by the National Institute of Standard Technology, USA. In AMB2018-02, melt pool geometry, cooling rates, surface topography, and grain structure in laser melted Inconel alloy IN625 bare plate were measured for three

*Corresponding author. E-mail: yanping.lian@bit.edu.cn

cases, which are Case A with laser power of 150 W and scan speed of 400 mm/s, Case B with 195 W and 800 mm/s, and Case C with 195 W and 1200 mm/s. The simulation results are compared with experimental data, as shown in Fig. 1 for the melt pool size and grain structure, Tale 2 for melt pool length and surface cooling rate, which demonstrate the performance of the modeling framework. In the second set, we conducted the simulations of the multiple-layer fabrication process in selective electron beam melting with different process parameters, i.e., electron beam power, layer thickness, and scan strategy, of which some results are shown in Fig. 3. It is revealed that the void formation between neighboring scans and layers due to the lack of fusion can be observed, and the surface roughness is related to the layer thickness with other process parameters given. Moreover, the obtained texture becomes stronger with the increase of deposited layers, and the completive grain growth is depicted by the thermal gradient distribution along the melt pool boundary, which leads to the complex grain structure, particularly within the overlap zone.

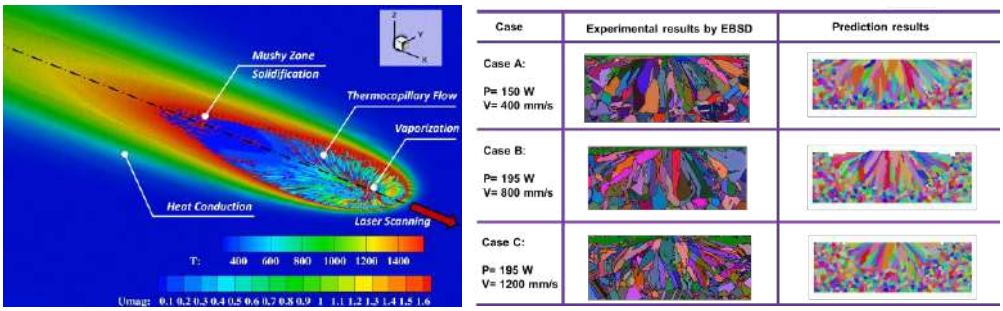

(a) (b)

Figure 2. Simulation results from the multi-physics modeling framework: (a) temperature distribution and streamlines within the melt pool for AMB-2018-02 Case B, (b) typical cross-sectional views of the grain structures for all 3 cases compared with the experimental results.

Table 1: Comparison of melt length and cooling rate between simulation results and experimental data

Case	Melt pool length (μm)			Surface cooling rate from 1563 K to 1273 K (K/s)		
	Experiment	Simulation	Difference	Experiment	Simulation	Difference
A	659±21	502	21%	$6.20\pm0.80\times10^5$	5.44×10^5	Match
B	782±21	772	Match	$9.35\pm1.43\times10^5$	7.59×10^5	19%
C	754±46	717	Match	$12.8\pm3.94\times10^5$	12.14×10^5	Match

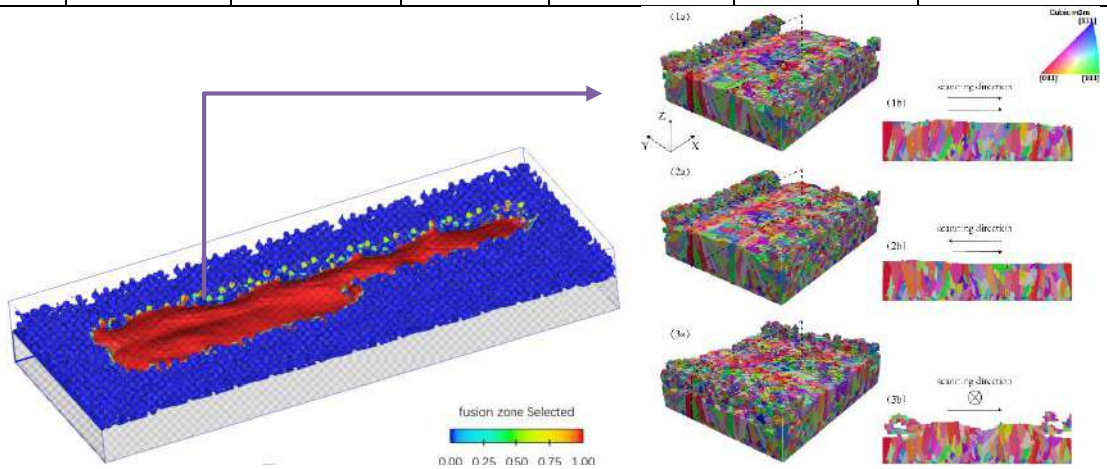

Figure 3. Simulation results with different scan strategies: (a) the 3D grain result and (b) cross-section view of (a) at the place marked by the dashed line. The scan strategies are Z-shaped, S-shaped and layer-wise rotation tracks for Case a, b, and c, respectively.

CONCLUSIONS

An integrated multi-physics modeling framework is developed for metal additive manufacturing (AM) processes. It is validated by the AMB2018-02 experimental results with three combinations of laser power and scan speed. Through this framework, the selective electron beam melting process is simulated at the powder-scale. The simulation results shed light on the effect of process parameters on the melt pool size, defect formation, and as-built grain structure. The modelling framework a powerful tool to guide the parameter optimization for AM.

References

[1] DebRoy T, Wei H, Zuback J, et al. Additive manufacturing of metallic components-process, structure and properties. *Progress in Materials Science*, **92**:112-224, 2018.

[2] Lian Y, Lin S, Yan W, Liu WK, Wagner G. A parallelized three-dimensional cellular automaton model for grain growth during additive manufacturing. *Computational Mechanics*, **61**:543-558, 2018.

[3] Lian Y, Gan Z, Yu C, Cats D, Liu WK, Wagner G. A cellular automaton finite volume method for microstructure evolution during additive manufacturing. *Materials & Design*, **169:** 107672, 2019.

[4] Lyle BL, Levine E. AMBENCH2018-description. web site **https://www.nist.gov/ambench2018-02-description.**

MINIATURE-SPECIMEN EXPERIMENTS FOR MECHANICAL ANALYSIS OF SLM TI6AL4V LATTICE MATERIALS

E. Hosseini*[1], S.A. Robmann[1,2], M. Fürer[1,2], D. Ghedalia[1,3], D. Greenfeld[1,2], A. Gillmann[1,3], M. Thalmann[1,2], S.R. Holdsworth[1], T. Lüthi[1], C. Affolter[1], D. Pasini[4], E. Mazza[1,2]

[1] Empa Swiss Federal Laboratories for Materials Science & Technology, 8600 Dübendorf, Switzerland
[2] ETH Zürich, Department of Mechanical and Process Engineering, 8092 Zürich, Switzerland
[3] ETH Zürich, Department of Materials, 8093 Zürich, Switzerland
[4] McGill University, Department of Mechanical Engineering, Montreal, QC, Canada

Summary The present work investigates the mechanical response of additively manufactured (AM) Ti6Al4V lattice materials. The size and built-orientation dependency of the deformation and fatigue response of selective laser melted (SLM) Ti6Al4V has been analysed based on the observations from a set of miniature-specimen experiments. The gauge length and diameter of the specimens were 2mm and 200-500µm, respectively, and were built with AM orientations of 0°, 30°, 45°, 60°, and 90°. The generated deformation data were employed for underpinning an anisotropic elastic-plastic constitutive model with isotropic hardening. Implementation of the material model into a finite element model provided experimentally consistent predictions for the mechanical behaviour of macroscale lattice specimens.

INTRODUCTION

Additive manufacturing (AM) enables the fabrication of orthopaedic implants with lattice materials of tailored mechanical properties and enhanced bone ingrowth [1]. Furthermore, tuning the compliance of the lattice materials enables minimizing stress shielding, a typical drawback of current implants, thus improving mechanical biocompatibility [2]. Furthermore, the long-term mechanical integrity of AM lattice materials is an important requirement to consider for the design of orthopaedic implants. The objective of the present study is to characterise the deformation and fatigue response of the AM material at a size-scale similar to that of the struts in the lattice materials. The generated data can ultimately be exploited for the development of mechanical solutions for assessment of the deformation and fatigue of lattice-structured biomedical implants.

EXPERIMENTS

Miniature-specimen experiments

In order to rationalize the behaviour of AM lattices, investigations were performed on miniature-specimens representing the differently oriented struts of the lattices. A set of miniature tensile tests for selective laser melted (SLM) Ti6Al4V specimens with a nominal gauge length of 2mm and nominal gauge diameters of 200, 300, 400, and 500µm, built with AM orientations of 0°, 30°, 45°, 60°, and 90° were performed. The test setup and examples of the observed strain-force curves are presented in Fig. 1a and b. Similarly, miniature-specimens with different build orientations and diameters were used for a set of tension-tension fatigue experiments with R-ratio of 0.1, Fig. 1c. The fatigue endurance data display a large scatter, indicate negligible dependency to the built orientation for 200µm specimens, and show a slightly better fatigue performance for 500µm thick specimens. Micro computed tomography (µCT) was used to reconstruct the geometry of the miniature-specimens and quantify the extent of AM under/oversizing for consideration in post-processing of the experimental records (Fig. 1d).

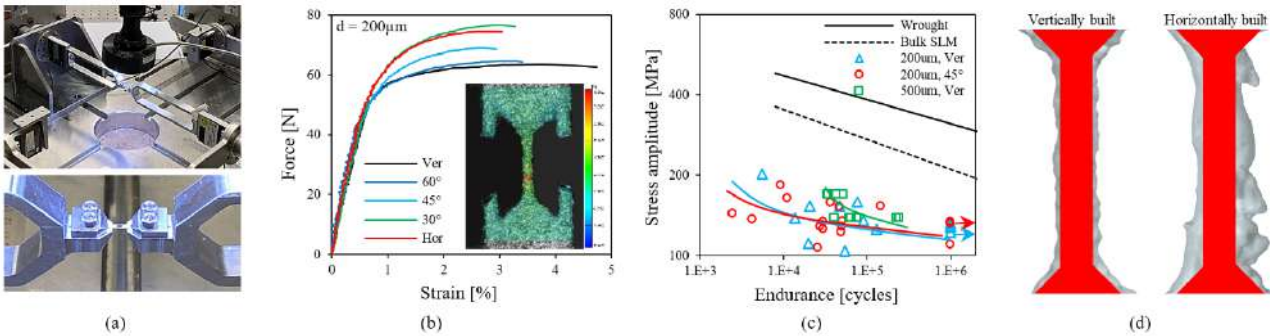

Fig. 1. a) Miniature-specimen testing setup equipped with digital image correlation (DIC) system for strain measurements, b) experimental strain-force curves for 200µm thick specimens with different AM orientations (inset: DIC analysis), c) fatigue endurance response of miniature-specimens compared with the reference lines for SLM and wrought Ti6Al4V, and d) comparison of the nominal and µCT reconstructed geometries for vertically and horizontally built miniature-specimens with diameter of 200µm.

Lattice-specimen experiments

A set of static tensile and tension-tension fatigue tests with R-ratios of 0.1 and -1.0 was conducted for the SLM Ti6Al4V lattices with tetrahedron cell topology and nominal porosity of 75% (Fig. 2). The observations from the fatigue experiments for the lattices indicated low fatigue to tensile strength ratios in the range of 0.04 - 0.05, as compared to

*Corresponding author. E-mail: ehsan.hosseini@empa.ch.

~ 0.3 and ~ 0.2 for wrought and bulk AM Ti6Al4V [3,4]. These observations highlight the need for further investigations on the fatigue response of AM lattices and careful use of such materials for cyclic loading applications. Similar to the miniature-specimens, µCT was employed to reconstruct the true geometry of the lattice specimens for consideration in subsequent finite element analyses (FEA).

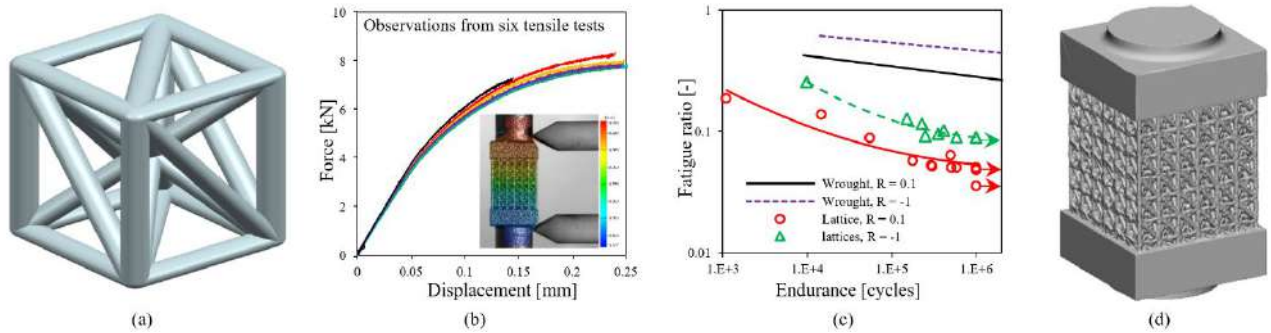

Fig 2. a) Tetrahedron cell topology, b) displacement-force curves for conducted tensile tests for SLM Ti6Al4V lattice specimens (inset: DIC analysis and side entry extensometer), c) fatigue endurance response of lattice specimens for R-ratios of 0.1 and -1.0 in comparison with reference lines for wrought Ti6Al4V, and d) an example for µCT reconstructed geometry of the examined lattice specimens.

CONSTITUTIVE MODEL DEVELOPMENT

The records from the miniature-specimen tensile experiments have been exploited for the development of an anisotropic material model for SLM Ti6Al4V. Due to the layer-by-layer manufacturing strategy, a transversely isotropic response is expected for SLM materials. This study, therefore, employed a transversely isotropic elastic-plastic model with isotropic hardening. An FE-based optimization strategy was utilised to derive the best set of model-parameters for representing the generated deformation data for miniature-specimens with different diameters and different built orientations. The designed FE model for the miniature-specimens used the µCT reconstructed geometries (e.g. Fig. 1d). The preliminary outcome of the optimization indicated a need for consideration of size effect in the material constitutive model and therefore the parameters of the proposed model were defined as a function of material-section thickness. Fig. 3a and b illustrate the representation of the developed constitutive model for different build orientations and section thicknesses, indicating a high stress level for the thicker and/or vertically built sections. The developed model was eventually used to describe the deformation response of the lattice specimens under tensile loading. As shown in Fig. 3c, the implementation of the constitutive model into FEA of the lattice specimens, based on the µCT reconstructed geometries (Fig. 2d), provided experimentally consistent predictions.

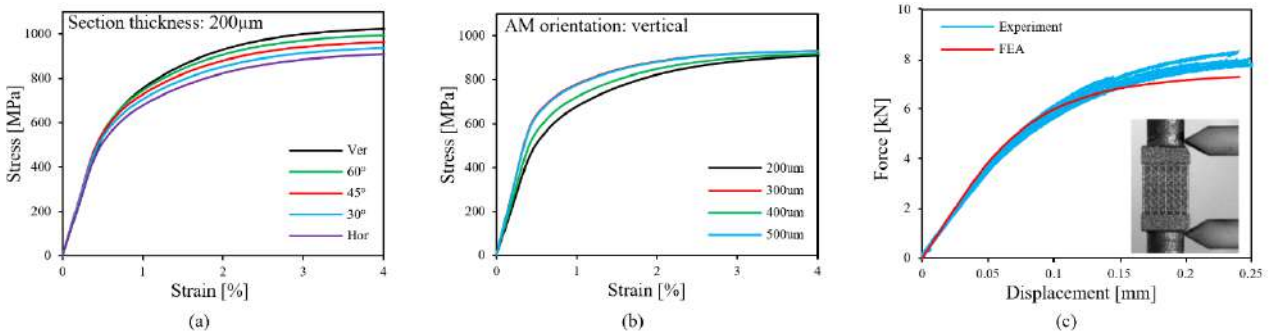

Fig 3. a) Model representation for the stress-strain response of SLM Ti6Al4V for a) different AM orientations and b) different section thicknesses. c) Comparison of experimental and model-predicted deformation response for the lattice specimens (inset: side entry extensometer for recording displacement).

CONCLUSIONS

Miniature-specimen experiments were employed to analyse the deformation and fatigue response of SLM Ti6Al4V at different AM build orientations and for specimens with different diameters. The observations were exploited for deriving a transversely isotropic elastic-plastic material constitutive model with isotropic hardening. The implementation of the developed material model into finite element models of the lattice specimens provided predictions consistent with the corresponding experiments.

References

[1] Arabnejad S., et al., Acta Biomaterialia 30 (2016), 345-356.
[2] Arabnejad S., et al., Journal of Orthopaedic Research 35.8 (2017), 1774-1783.
[3] Li P., et al., Internation Journal of Fatigue 85 (2016) 130-143.
[4] Gong H., et al., Materials & Design 86 (2015) 545-554.

PHASE-FIELD TOPOLOGY OPTIMIZATION FOR FUNCTIONALLY GRADED MATERIALS

Gianluca Alaimo1, Massimo Carraturo *[1], Alessandro Reali1, and Ferdinando Auricchio1
[1] Department of Civil Engineering and Architecture, University of Pavia, Pavia, Italy

Summary We present a numerical method to obtain topologically optimized functionally graded material (FGM) structures together with a possible pipeline to realize these kind of structural components using additive manufacturing (AM) technologies. In particular, we present a topology optimization routine based on phase-field approach FGM design together with a possible workflow to produce the resulting optimized components by means of different AM technologies.

INTRODUCTION

Functionally Graded Materials (FGMs) are characterized by a gradual spatial variation in composition and/or microstructure over the volume. Such a local variation allows to obtain global material properties in line with the functional requirements of the part. Accordingly, this class of materials introduces a radical shift from contour modeling to performance modeling since the performance-driven functionality is directly built into the material [1]. Additive manufacturing (AM) technologies drastically changed the approach to design, since the classical design for manufacturing is not required anymore and the designer can now focus on the function of the component itself. FGM design can be seen as a result of this change in the design perspective, where the component is optimized with respect to the specific application starting from its material microstructure. Nevertheless, even if recent AM technologies allow this possibility, the development of numerical methods suitable to generate FGM components is still an open issue for researchers. Moreover, implementations of automatized workflows from numerical results to final products are still an active field of research.

In the literature, we can find some numerical methods allowing to design FGM components. In particular, in [2] the mass of a structural component is minimized under stress constraints by means of the method of moving asymptotes, by optimally distributing the material density within a (fixed) initial domain. Our methodology has a similar objective, but additionally allows to obtain structures where also regions of voids can be accounted for, substantially introducing an additional degree of freedom within the design process.

FUNCTIONALLY GRADED MATERIAL TOPOLOGY OPTIMIZATION

FGMs are tightly connected with AM technologies since the high flexibility introduced into manufacturing processes allows to vary the material properties in an almost continuous fashion.

The presented topology optimization procedure aims at minimizing the compliance of FGM structures printed by means of AM processes, delivering component mechanical properties similar to periodic material structures, but employing less material. To this end, we exploit the possibility to obtain locally varying microstructures given by the most recent AM processes. Such a result is achieved by means of a phase-field topology optimization routine which is able to optimally distribute the material density parameter within the structure, allowing, at the same time, voids nucleations within the initial domain [3].

FROM SIMULATIONS TO 3D PRINTING

In order to convert the numerical results into printable data, we implemented the procedure described in Figure 1. The conversion procedure includes the following steps:

1. Choose the shape and the size of the microstructure cells;
2. Generate a Cartesian grid over the initial domain Ω with a constant size equal to the cell dimension;
3. Evaluate the average density value within each cell of Λ_ϕ and generate a cuboid (or any other geometric entity used to define the lattice cell) for each cell of Λ_χ;
4. By means of a simple boolean operation, subtracting Λ_χ to Λ_ϕ, we can obtain the final 3D virtual model ready to be printed.

The final structure is then printed and validated by means of experimental measurements [4]. Figure 2 shows the experimental setup for the three-point bending test.

*Corresponding author. E-mail: massimo.carraturo@unipv.it.

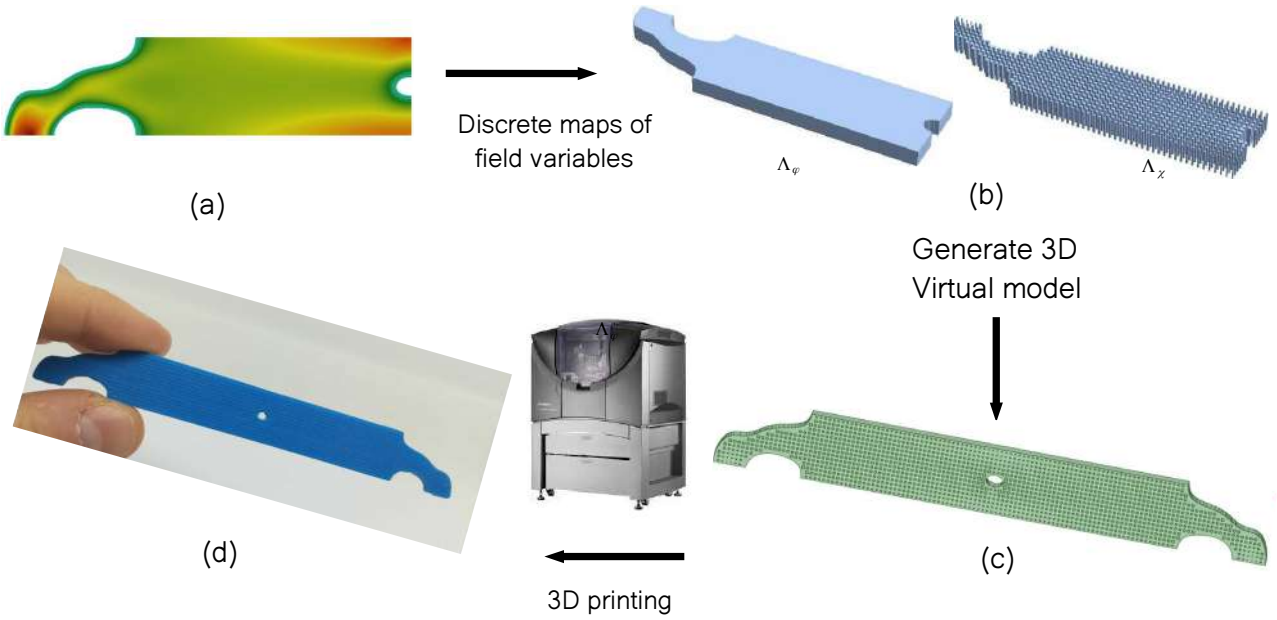

Figure 1: A complete pipeline from a continuously graded numerical solution to a 3D printed FGM structure; a) phase-field topology optimization, b) generation of 3D virtual model from the discrete maps of the field variables, c) finished 3D virtual model, d) 3D-printed part

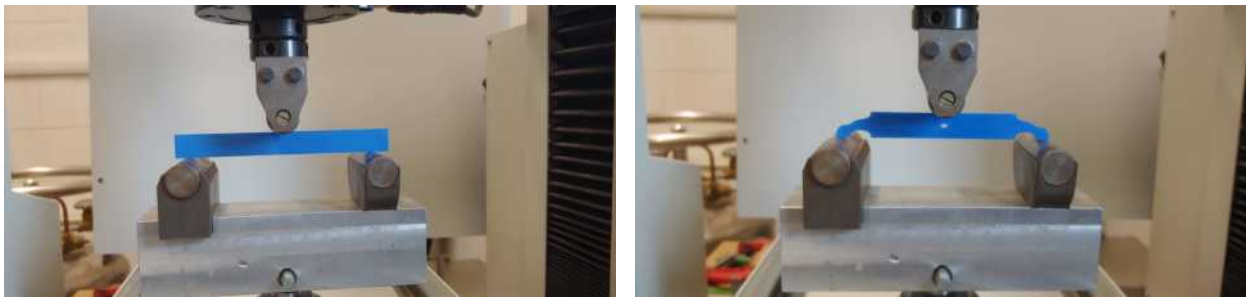

(a) Constant density specimen (b) FGM topologically optimized specimen

Figure 2: Experimental validation.

CONCLUSIONS

In this work, we employ the phase-field method together with asymptotic homogenization for the analysis and the topological optimization of FGM structures, whereas an *in-house* developed code is used to convert the density map into a 3D virtual model suitable for AM processes. Experimental evidences show the higher mechanical properties of optimized FGM components compared to similar lattice structures of the same weight but uniform density.

References

[1] Oxman N., Keating S., Tsai, E. Functionally Graded Rapid Prototyping. *Mediated Matter Group*, MIT Media Lab.. 2011.

[2] Cheng, L., Bai, J., To, A.C. Functionally graded lattice structure topology optimization for the design of additive manufactured components with stress constraints. *Computer Methods in Applied Mechanics and Engineering*, **344**: 334-359, 2019.

[3] Carraturo M., Rocca E., Bonetti E., Hömberg D., Reali A., Auricchio F. Graded-material design based on phase-field and topology optimization. *Computational Mechanics*. **64**: 1589-1600, 2019.

[4] Alaimo G., Carraturo M., Rocca E., Reali A., Auricchio F. Functionally Graded Material Design for Plane Stress Structures using Phase Field Method. *II International Conference on Simulation for Additive Manufacturing*, 2019.

A MICROMECHANICAL PHASE TRANSFORMATION MODEL FOR THE FINITE ELEMENT SIMULATION OF SELECTIVE LASER MELTING PROCESSES

Thorsten Bartel*[1], Isabelle Noll[1], and Andreas Menzel[1,2]
[1] Institute of Mechanics, Department of Mechanical Engineering, TU Dortmund, Dortmund, Germany
[2] Division of Solid Mechanics, Lund University, Lund, Sweden

Summary Additive manufacturing exhibits great potential for innovative industrial applications. The effect of the underlying process parameters on the properties of the final workpiece are, however, still rather vague. Thus, material and structural designs in order to obtain improved properties, in particular with respect to lifetime estimations, are rather based on empirical knowledge. This motivates the need for sophisticated material models and finite-element-based process simulations. In our contribution, the changes of state between the powder, molten, and re-solidified phase are modelled via a micromechanical phase transformation model based on energy minimisation. This model is embedded into a thermomechanically fully coupled FEM scheme for the simulation of selective laser melting processes. These simulations allow the prediction of, e.g., residual stresses and inherent strains.

THERMOMECHANICAL FRAMEWORK

The basic thermomechanical framework relies on a small-strain theory and the balance of linear momentum as well as the energy equation as global balance equations, viz.

$$\nabla_{\boldsymbol{x}} \cdot \boldsymbol{\sigma} + \boldsymbol{b} = \boldsymbol{0} \quad , \tag{1}$$

$$-\nabla_{\boldsymbol{x}} \cdot \boldsymbol{q} + r + \mathcal{D}_{\text{mech}} + \theta \, \frac{\partial}{\partial \theta} [\, \boldsymbol{\sigma} : \dot{\boldsymbol{\varepsilon}} - \mathcal{D}_{\text{mech}} \,] - \widetilde{c} \, \dot{\theta} = 0 \quad . \tag{2}$$

In these relations, $\boldsymbol{\sigma} := \partial \overline{\psi} / \partial \boldsymbol{\varepsilon}$ denotes the stress tensor derived from an energy density (to be specified later), $\boldsymbol{b}$ are volume-distributed forces, $\boldsymbol{q}$ is the heat flux vector, r symbolises heat sources, $\mathcal{D}_{\text{mech}}$ is the mechanical dissipation, θ is the absolute temperature, $\widetilde{c}$ reflects the effective thermal conductivity which stems from the specific constitutive model and $\dot{\bullet}$ denotes the time derivative. These two equations are transferred to their respective weak forms and subsequently discretised with respect to the underlying degrees of freedom — displacements $\boldsymbol{u}$ and temperature θ — in a straight-forward manner. The finite element modelling of the additive manufacturing process, however, requires some non-conventional aspects which shall be addressed in the following.

CONSTITUTIVE FRAMEWORK

The material model follows a micromechanical approach, where each possible state of the material — i.e. powder, molten, and re-solidified — is considered as an independent phase of the material; cf. [1] and references cited therein. Accordingly, we first introduce material models for each individual phase in terms of phase energy densities, to be specific

$$\psi_{\bullet} := \tfrac{1}{2} \left[\boldsymbol{\varepsilon}_{\bullet} - \boldsymbol{\varepsilon}^{\text{in}}_{\bullet} \right] : \mathbf{E}_{\bullet} : \left[\boldsymbol{\varepsilon}_{\bullet} - \boldsymbol{\varepsilon}^{\text{in}}_{\bullet} \right] + \psi^{\text{cal}}_{\bullet} \quad \text{with} \quad \bullet \in \{\text{pow}, \text{mel}, \text{sol}\} \, . \tag{3}$$

Here, $\boldsymbol{\varepsilon}_{\bullet}$ denotes the total strains in each phase where "pow" represents the powder phase, "mel" the molten phase, and "sol" the re-solidified phase. Moreover, $\boldsymbol{\varepsilon}^{\text{in}}_{\bullet}$ are the respective inelastic strain contributions in each phase, $\mathbf{E}_{\bullet}$ denote the underlying fourth order elasticity tensors, and $\psi^{\text{cal}}_{\bullet}$ reflect the caloric energy contributions. These phase energy densities define the averaged energy density $\overline{\psi}$ of the possible phase mixture by applying the mixture rule

$$\overline{\psi} := \xi_{\text{pow}} \, \psi_{\text{pow}} + \xi_{\text{mel}} \, \psi_{\text{mel}} + \xi_{\text{sol}} \, \psi_{\text{sol}} \quad , \tag{4}$$

wherein $\xi_{\bullet}$ denote the volume fractions of the respective phase.

In contrast to models which make use of one global inelastic strain tensor only, which frequently is referred to as inherent strain tensor, the present approach considers distinct and inelastic strain contributions specific for each phase. While no inelastic strains are considered in the powder material, the inelastic strains in the molten phase are decomposed as

$$\boldsymbol{\varepsilon}^{\text{in}}_{\text{mel}} := \boldsymbol{\varepsilon}^{\text{vi}}_{\text{mel}} + \boldsymbol{\varepsilon}^{\text{tr}}_{\text{mel}} \quad , \tag{5}$$

incorporating a viscous strain contribution, $\boldsymbol{\varepsilon}^{\text{vi}}_{\text{mel}}$, and a transformation strain contribution, $\boldsymbol{\varepsilon}^{\text{tr}}_{\text{mel}}$. Moreover, the inelastic strains in the solid phase are introduced as

$$\boldsymbol{\varepsilon}^{\text{in}}_{\text{sol}} := \boldsymbol{\varepsilon}^{\text{pl}}_{\text{sol}} + \boldsymbol{\varepsilon}^{\text{tr}}_{\text{sol}} + \boldsymbol{\varepsilon}^{\text{th}}_{\text{sol}} \quad , \tag{6}$$

*Corresponding author. E-mail: thorsten.bartel@udo.edu

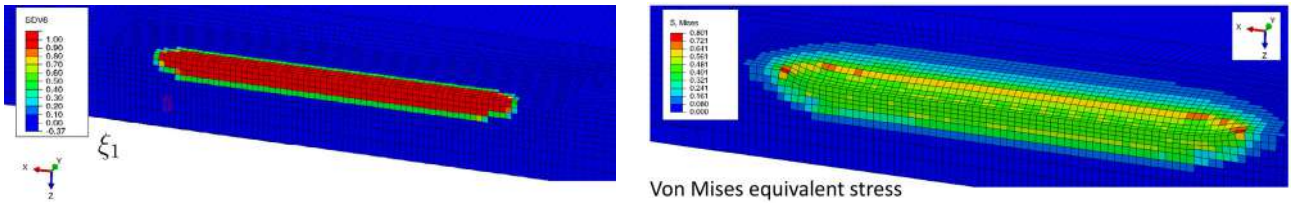

Figure 1: Selected results of the basic SLM process simulation after the addition of three layers. Left: Final distribution of the solid phase. The red parts symbolise purely solid regions with $\xi_{\text{sol}} = 1$, whereas blue regions illustrate the (still) powder material, and the apparent intermediate states (greenish colours) result from the interpolation algorithm used in Abaqus. Right: Illustration of the deformation and spatial distribution of the residual von-Mises equivalent stress.

which consist of a plastic part, $\varepsilon^{\text{pl}}_{\text{sol}}$, a transformation part, $\varepsilon^{\text{tr}}_{\text{sol}}$, and a thermal part, $\varepsilon^{\text{th}}_{\text{sol}}$. The transformation strains follow from the significant change in mass density, $\rho_\bullet$, and are defined as

$$\varepsilon^{\text{tr}}_{\text{mel}} := \frac{1}{3}\left[\frac{\rho_{\text{pow}}}{\rho_{\text{mel}}} - 1\right] \boldsymbol{I} \quad \text{and} \quad \varepsilon^{\text{tr}}_{\text{sol}} := \frac{1}{3}\left[\frac{\rho_{\text{pow}}}{\rho_{\text{sol}}} - 1\right] \boldsymbol{I} \quad , \tag{7}$$

wherein $\boldsymbol{I}$ denotes the second order identity tensor. The total strains $\boldsymbol{\varepsilon}_\bullet$ in each phase follow from the convexification of the multi-well potential defined in (4), which results in homogeneous stress states among the phases.

For the remaining internal state variables, namely ξ_{pow}, ξ_{mel}, ξ_{sol}, $\varepsilon^{\text{vi}}_{\text{mel}}$, and $\varepsilon^{\text{pl}}_{\text{sol}}$, thermodynamically consistent evolution equations are derived and solved at integration point level. The related inequality constrains, in particular the conservation of mass, are fulfilled and considered by so-called NCP functions (Nonlinear Complementarity Problem); see, e.g., [2] and references cited therein.

The heat conduction is modelled in terms of a Fourier-based formulation, i.e.

$$\boldsymbol{q} = -\,\widetilde{k}\,\nabla_{\boldsymbol{x}}\,\theta \quad \text{with} \quad \widetilde{k} := \left[\frac{V}{m}\left[\,\xi_{\text{pow}}\,\rho_{\text{pow}}\,k^{-1}_{\text{pow}} + \xi_{\text{mel}}\,\rho_{\text{mel}}\,k^{-1}_{\text{mel}} + \xi_{\text{sol}}\,\rho_{\text{sol}}\,k^{-1}_{\text{sol}}\,\right]\right]^{-1} \tag{8}$$

so that the averaged heat conduction coefficient $\widetilde{k}$ is obtained via homogenisation based on the respective heat conduction coefficients $k_\bullet$ of the individual phases. Moreover, the representation of the effective heat capacity results in

$$\widetilde{c} := -\,\theta\,\frac{\partial^2\overline{\psi}}{\partial\theta\,\partial\theta} = \frac{V}{m}\left[\,\xi_{\text{pow}}\,\rho_{\text{pow}}\,c_{\text{pow}} + \xi_{\text{mel}}\,\rho_{\text{mel}}\,c_{\text{mel}} + \xi_{\text{sol}}\,\rho_{\text{sol}}\,c_{\text{sol}}\,\right] \quad . \tag{9}$$

ALGORITHMIC IMPLEMENTATION

The material model addressed above is implemented into the Abaqus subroutine UMAT and UMATHT. An essential aspect of the subsequent Finite Element model is the modelling of the laser beam impact, in other words the specification of the heat source contribution r in (2). Here, we use a moving heat source according to [3] which can be incorporated into the Abaqus routine DFLUX.

FEM-BASED SIMULATION OF AN SLM PROCESS

The numerical example comprises a straight laser path and the addition of three powder layers to a solid base platform. This thermomechanically fully coupled simulation of a basic selective laser melting (SLM) process already provides important results, for example concerning the spatial distribution of the solid phase — which generally defines the geometry of the final workpiece — and the distribution and amplitudes of residual stresses after cooling, cf. Fig. 1.

It is remarked that the finite element simulations have been carried out by using an Updated Lagrange approach, where the configuration of the underlying system in the former time step is used as reference configuration for the current time step. This approach allows the use of a small strain theory with acceptable errors even though the occurring deformations, such as the change in width of the powder layer, is large.

References

[1] Bartel T., Guschke I., Menzel A. Towards the simulation of Selective Laser Melting processes via phase transformation models. Comp. Math. Appl. **78(7)**:2267-2281, 2019.

[2] Bartel T., Schulte, R., Menzel A., Kiefer B., Svendsen B. Investigations on enhanced Fischer-Burmeister NCP functions – application to a rate-dependent model for ferroelectrics. Arch. Appl. Mech. **89(6)**:995-1010, 2019.

[3] Goldak J., Chakravarti A., Bibby M. A new finite element model for welding heat sources. Metall. Trans. B **15**:299-305, 1984.

EFFECT OF THERMO–PHYSICAL PROPERTIES ON NUMERICAL SIMULATIONS OF HIGH SPEED STEEL LASER CLADDING

V. Tuninetti[1], R. T. Jardin *[2], H.-S. Tran[2], J. T. Tchuindjang[3], A. Mertens[3], L. Duchêne[2], A. M. Habraken [2]
[1] Department of Mechanical Engineering, Universidad de La Frontera, Temuco, Chile
[2] Department of ArGEnCo, MS F–MSM, University of Liège, Liège, Belgium
[3] Department of A&M–MMS, University of Liège, Liège, Belgium

Summary A sensitivity of the prediction of the melt pool shape and the temperature evolution with the thermo–physical properties in a high speed steel laser cladding process is investigated. The analysis is performed in the normal range of experimental errors in two finite element input data: the heat capacity and the thermal conductivity measurements. Significant effects for both a bulk and a thin–walled manufactured part are presented with their respective phenomena explanation. The process simulations with two and three dimensional finite element thermal models for each respective manufactured part shape consider a set of material parameters obtained from experimental data with both direct and inverse identification techniques. Microstructure prediction strongly depends on the pool size which is not only affected by the laser power but also by the variation of temperature dependent physical properties.

INTRODUCTION

Optimal cladding process parameters heavily rely on finite element (FE) simulations predicting melt pool size. However, the accuracy and the sensitivity of the FE results to the input thermo–physical material input properties are not often discussed, even if some validations are described. For instance, Chiumenti et al. [1] investigated the effect of preheating temperature on the thermal evolution and melt pool size. In the current work, a two (2D) and three dimension (3D) FE models are used to simulate the thermal evolution in both bulk and thin wall cladded samples, respectively. Previous studies conducted by Hashemi [2, 3] for high speed steel (HHS) bulk samples validate the substrate temperature and the melt pool size predictions. The thermal history accuracy is essential to explain the microstructure heterogeneity as shown by Jardin et al. [4]. The cladded samples studied hereafter are made by M4–HSS metal powder of 50 to 150 µm particle size. The bulk sample is composed by 36 layers with 27 parallel lines (tracks) each, giving a final parallelepiped shape of 40x40x27.5 mm. The targeted height per layer was 0.76 mm. The lines of the upper layers are printed with an offset to maintain contact with half of each of the two neighbouring lines of the lower layers. Temperature histories are measured by thermocouples located in the substrate at 10 mm from the sample in the direction of the lines and at 5 mm depth. The measured temperature level increases non–linearly with the number of the printed layers reaching a maximum global value. The temperature oscillations are correlated with the laser movements. Each oscillation observed in Fig. 1 (a) correspond to a layer deposit and the fourteen local maxima corresponds to the moment when the laser is closer to the thermocouple. More information about the cladding parameters applied to manufacture the thin wall and bulk samples are given in Table 1.

Table 1. Laser cladding process parameters selected for the samples manufacturing.

Sample	Laser beam speed (mm/s)	Laser power (W)	Preheating (°C)	Mass flow (mg/s)	Number of tracks per layer	Total number of layers
Bulk	6.67	1100	300	76	27	36
Thin wall	7.00	420	438	83	1	5

FE THERMAL MODEL FOR BULK AND THIN WALL LASER CLADDING PROCESSES

The FE code LAGAMINE developed at the University of Liège since 1985 is used to simulate both laser cladding processes (the bulk sample in 2D and the thin wall in 3D). The element birth technique is applied to model the addition of material within the processes. When a new layer is created and the laser beam moves, solid elements are activated with their respective surface elements for convection and radiation phenomena while the surface elements under this layer are deactivated. The bulk sample is modelled considering the vertical symmetry plane parallel to the laser movement during the tracks printing. The oscillations related to each track are consequently not captured by the 2D FE model. Considering the high temperature gradients, refinement of the mesh is performed in the cladding area to obtain accurate thermal history. Under the laser beam, the heat flux was applied through nodal input. At the surface, the energy balance equation is respected $k(\nabla T.n) = q_{laser} - h(T - T_0) - \varepsilon\sigma(T^4 - T_0^4)$, where k is the conductivity, n is the normal vector to the surface, ∇T is the temperature gradient, q_{laser} is the laser heat flux depending of the absorption factor (β) multiplied by the laser heat flux density distribution on the workpiece, h is the convection coefficient, σ is the Stefan–Boltzmann constant, ε is the emissivity coefficient and T_0 is the temperature of the environment. The temperature distribution for the cladded part is obtained from the three–dimensional heat conduction Eq. 1,

$$\frac{\partial}{\partial x}\left(k\frac{\partial T}{\partial x}\right) + \frac{\partial}{\partial y}\left(k\frac{\partial T}{\partial y}\right) + \frac{\partial}{\partial z}\left(k\frac{\partial T}{\partial z}\right) + Q_{int} = \rho c_p \frac{\partial T}{\partial t} \quad (1)$$

with $T(x,y,z,t)$ the transient temperature, Q_{int} the power per volume generated in the workpiece (phase transformation), ρc_p the heat capacity and t the time. More details regarding the model can be found in Tran et al. [5]. The parameters used in the reference boundary conditions for the two type of samples (Table 1) are inversely identified from experimental results shown in Figure 1 (a) and (d).

Table 1. Bulk and thin wall sample dataset inversely identified by correlating measurements and simulation results.

Sample	Convection (h) (W/m²K)	Emissivity (ε)	Absorption factor (β)
Bulk	230	1	0.067
Thin wall	10	0.8	0.44

ANALYSIS OF SIMULATION RESULTS AND CONCLUSIONS

Figure 1 (a) and (d) allows to validate the simulations of the cladding processes of bulk (bs) and thin wall (tw) samples. The range of variations for the sensitivity analysis is chosen within the accuracy of measurements associated with the experimental equipment used. The upper and lower bounds used hereafter are computed with the error variation of 3% for the specific heat, 7% for the thermal conductivity and 2% for the density. The numerical results presented in Figure 1 (b) and (e) show that a decrease of thermal inertia fraction produced by a lower heat capacity gives an increase in the temperature of the substrate of both samples. However, for the thin wall sample, the temperature is less sensitive to the increase of the ρc_p. This non–linear effect is explained by the low volume ratio between the clad and the substrate and by the relative high heat fraction related to the melting latent heat and the respective greater part of heat storage during superheating of the melt pool. The positive and negative variations of the conductivity shown in Figure 1 (c) and (f) yield quite symmetrical temperature differences compared to the curve associated with the reference conductivity value. However, an opposite behaviour appears between bulk and thin wall sample with the conductivity variations. The energy storage capacity within the melt pool has been found as the predominately driving feature of this behavior in the thin wall sample. Ongoing research validates this hypothesis and further details will be given in a future publication.

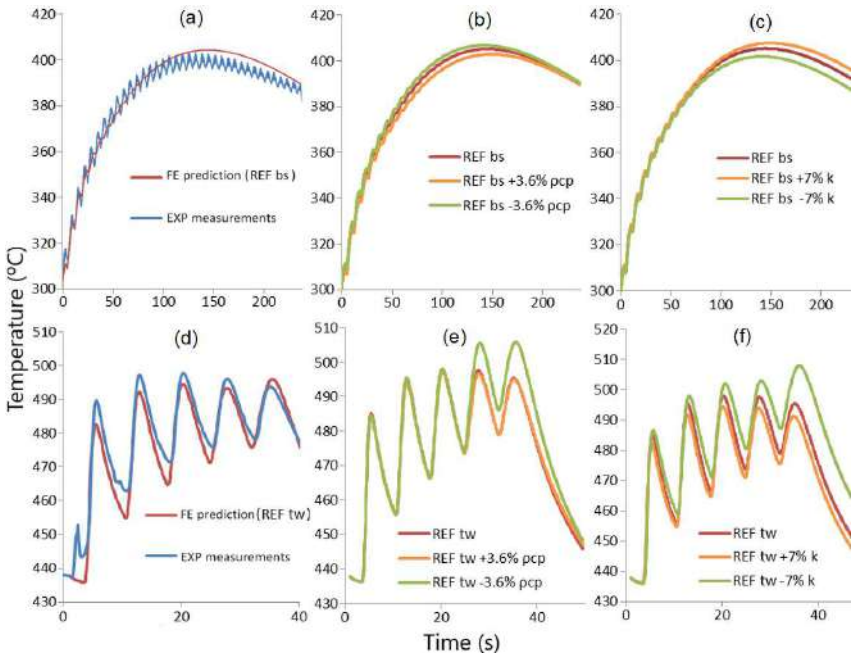

Figure 1. Experimental and predicted process thermal history at the local measurement points in the substrate of (a) bulk and (d) thin wall samples. Effect of the variations of ((b), (e)) heat capacity and ((c), (f)) conductivity on the computed temperature evolution.

Acknowledgments

The authors thank the cooperation agreement WBI/AGCID SUB2019/419031 (DIE19-0005), the Chilean Scientific Research Fund ANID FONDECYT 11170002 and the Belgian Scientific Research Fund FNRS for financial support.

References

[1] Chiumenti M., Lin X., Cervera M., Lei W., Zheng Y., Huang W. Numerical simulation and experimental calibration of additive manufacturing by blown powder technology. Part I: thermal analysis. *Rapid Prototyp. J.* **23**:448–463, 2017.

[2] Hashemi N. Study of high speed steel deposits produced by laser cladding: Microstructure-wear-thermal model, *Ph.D. thesis*. University of Liège, 2017.

[3] Hashemi N., Mertens A., Montrieux H.-M., Tchuindjang J.T., Dedry O., Carrus R., Lecomte-Beckers J. Oxidative wear behaviour of laser clad High Speed Steel thick deposits: Influence of sliding speed, carbide type and morphology. *Surf. Coatings Technol.* **315**:519–529, 2017.

[4] Jardin R.T., Tchoufang Tchuindjang J., Duchêne L., Tran H.-S., Hashemi N., Carrus R., Mertens A., Habraken A.M. Thermal histories and microstructures in Direct Energy Deposition of a High Speed Steel thick deposit. *Mater. Lett.* **236**:42-45, 2019.

[5] Tran H.-S., Tchuindjang J.T., Paydas H., Mertens A., Jardin R.T., Duchêne L., Carrus R., Lecomte-Beckers J., Habraken A.M. 3D thermal finite element analysis of laser cladding processed Ti-6Al-4V part with microstructural correlations. *Mater. Des.* **128**:130–142, 2017.

COMPREHENSION OF DISTORTION IN METAL ADDITIVE MANUFACTURING BASED ON ASSUMPTION OF CONSTRAINING FORCE INDUCED DISTORTION

Deqiao XIE[1], Jianfeng ZHAO *[2], Lida SHEN[2], Zongjun TIAN[2] and Yingdong Song[1]
[1] College of Energy and Power Engineering, University of Aeronautics and Astronautics, Nanjing, China
[2] College of Mechanical and Electrical Engineering, University of Aeronautics and Astronautics, Nanjing, China

Summary Metal additive manufacturing has exhibited attractive prospect in aerospace, medical, and automobile industries. However, the distortion of metal part has been an obstacle in widespread application of metal additive manufacturing. We proposed an assumption of constraining force induced distortion (CFID) so as to quantificationally explain the distortion in metal additive manufacturing. The distortion can be regarded as a result of a constraining force acting on a certain structure. The constraining force derives from the inconsistent shrinkage during the additive manufacturing process. And its direction is determined by laser scanning routine. Based on the CFID, we are able to comprehend the distortion as a whole, as well as to effectively predict and decrease the distortion in metal additive manufacturing.

Introduction

As a promising technology, metal additive manufacturing has been used in fabricating an integrated, lightweight, and complex-shaped structure, which has potential application in aerospace, medical, and automobile industries. Much attention has been paid on the mechanism of distortion in additive manufacturing, especially for metal parts. Mercelis [1] and Kruth [2] explained the distortion of metal additive manufacturing based on the thermal gradient mechanism (TGM). The qualitative TGM model states that the laser heats up solid material, which tends to expand. After the laser leaves, the irradiated zone will be cool and tends to shrink. The captured distortion images with Digital Image Correlation (DIC) [3] and the recorded distortion curves with Laser Displacement Sensor (LDS) [4] verified the distortion behavior in heating and cooling process predicted by TGM. However, some phenomena cannot be interpreted well by TGM, such as the link between temperature and distortion.

Assumption of constraining force induced distortion

Figure 1(a) illustrates the laser converging on the substrate; this melted the substrate and the incoming powder, forming a molten pool. After the laser was removed, the molten pool cooled and solidified, forming a one-track deposition. The molten pool shrunk due to the temperature decline after the laser was removed. The deposited metal all underwent the same melting-cooling process in the single track LMD, so the deposited track was assumed to shrink uniformly. In Figure 1b, l_d represents half the length of the deposited track at a high temperature. Δl_d is half the shrinkage of the deposited track at low temperature if there was no constraint. Nevertheless, the substrate at room temperature showed a little shrinkage. As a result, a balanced distribution of deformation was generated between the deposited track and the substrate. The deposited track was stretched by the substrate, while the substrate was compressed by the deposited track. Thus, the half shrinkage of the deposited track Δl_d could be restricted to Δl_s due to the substrate constraint. The interaction force along the longitudinal direction between the deposited track and the substrate was assumed to be F_{ds}.

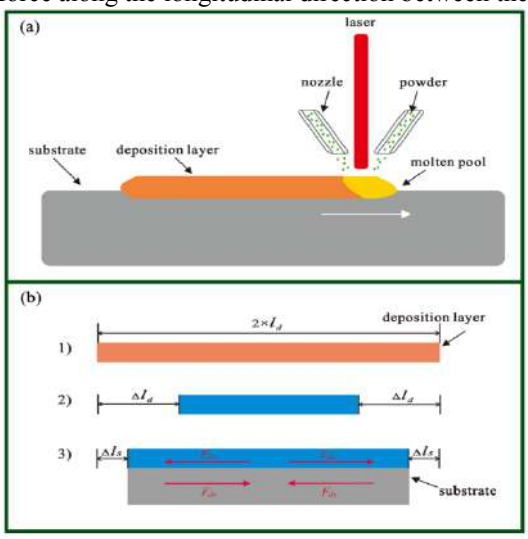

Fig. 1. Assumption of CFID.

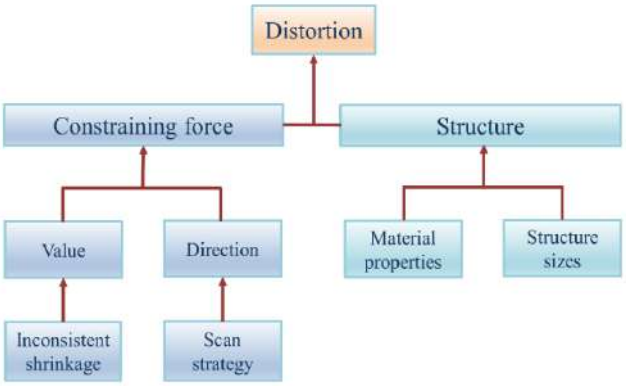

Fig. 2. Influencing factors of distortion.

Combined with melt-solidification process, the constraining force F_{ds} was expressed by Hooke's law as follows [5]:

$$F_{ds} = \frac{(\Delta l_d - \Delta l_d)}{l_d} \cdot E_d \cdot A_d = \frac{(\Delta l_d - \Delta l_d)}{\Delta l_d} \cdot \frac{\Delta l_d}{l_d} \cdot E_d \cdot A_d = k_{ds} \cdot \frac{\Delta l_d}{l_d} \cdot E_d \cdot A_d = k_{ds} \cdot (\alpha \cdot \Delta T + \beta_{pt}) \cdot E_d \cdot A_d$$

Distortion of thin-walled structure

Based on CFID, the longitudinal constraining force (LCF) in Fig. 3(b) is parallel to the longitudinal scan (LS) direction in Fig. 3(a), and the transverse constraining force (TCF) is also parallel to the transverse (TS). Fig. 4 shows that the side with LS was distorted. Besides, the side with TS was distortion-free. As a result, the assumption of CFID can be used to comprehend the distortion of thin-walled structure.

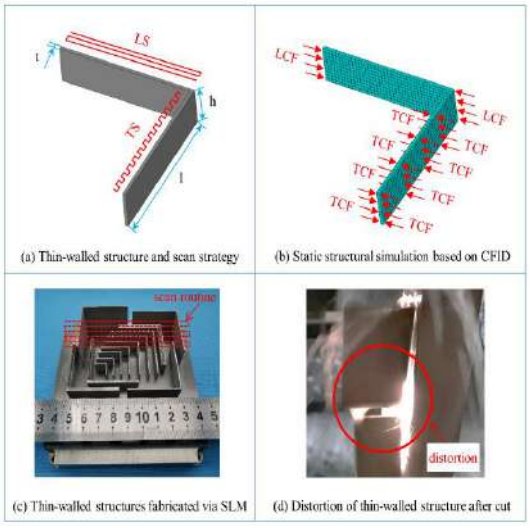

Fig. 3. Scan strategy of thin-walled structure via SLM.

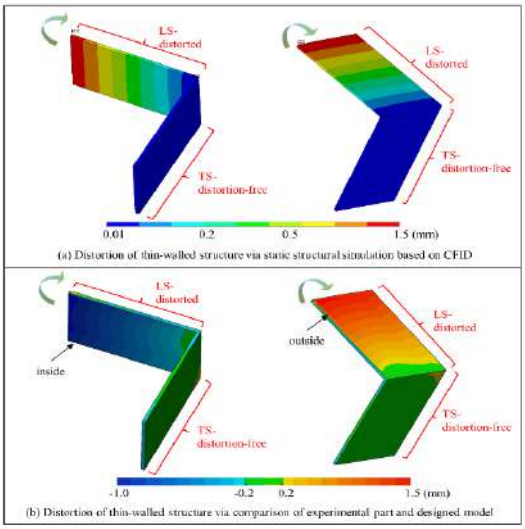

Fig. 4. Distortion of thin-walled structure.

Distortion of cantilever structure

Fig. 5 shows the assumed inconsistent shrinkage of cantilever structure based on CFID. It detailedly describes the evolution of inconsistent shrinkage. The experimental results validated the described inconsistent shrinkage, which impelled the distortion after the cantilever structure was cut from the substrate.

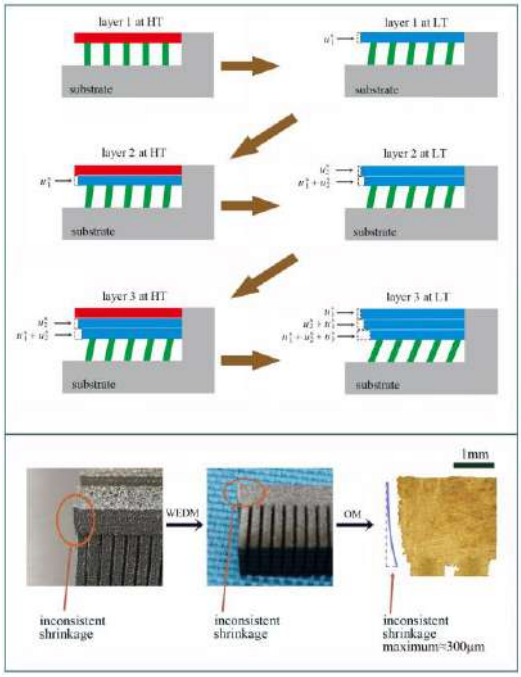

Fig. 5. Inconsistent shrinkage of cantilever structure.

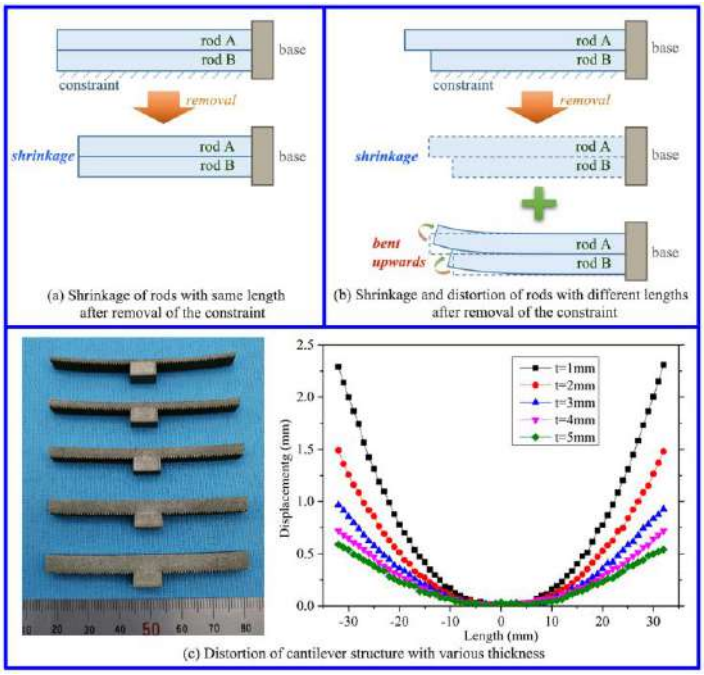

Fig. 6. Comprehension of distortion of cantilever structure.

Conclusions

We have proposed an assumption of Constraining Force-Induced Distortion (CFID) that offers a quantitative way to comprehend the distortion of additive manufacturing. The formula of constraining force pointed out the influencing factors of distortion as a whole. Based on the CFID, the distortion of typical structure, like thin-walled and cantilever structure, can be interpreted in detail.

References

[1] Mercelis, P.; Kruth, J.P. Residual stresses in selective laser sintering and selective laser melting. Rapid Prototyp. J. 2006, 12, 254–265.

[2] Kruth, J.-P.; Deckers, J.; Yasa, E.; Wauthle, R. Assessing Influencing Factors of Residual Stresses in SLM Using a Novel Analysis Method. Proc. IMechE Part B J. Eng. Manuf. 2012, 226(6):980-991.

[3] Biegler, M.; Graf, B.; Rethmeier, M. In-situ distortion in LMD additive manufacturing walls can be measured with digital image correlation and predicted using numerical simulations. Addit. Manuf. 2018, 20, 101–110.

[4] Denlinger, E.R.; Heigel, J.C.; Michaleris, P.; Palmer, T.A. Effect of inter-layer dwell time on distortion and residual stress in additive manufacturing of titanium and nickel alloys. J. Mater. Process. Technol. 2015, 215, 123–131.

[5] Xie, D.; Zhao, J.; Liang, H.; Tian, Z.; Shen, L.; Xiao, M.; Ahsan, M.N.; Wang, C. Assumption of constraining force to explain distortion in laser additive manufacturing. Materials 2018, 11, 2327.

MECHANICAL DESIGN IN ADDICTIVE MANUFACTURING: FROM 3D TO 4D PRINTING

Daining Fang*[1,2], Wei-Li Song [1], and Haosen Chen [1]
[1] Institute of Advanced Structure Technology, Beijing Institute of Technology, Beijing 100081, P. R. China
[2] State Key Laboratory for Turbulence and Complex Systems, College of Engineering, Peking University, Beijing, 100871, P. R. China.

Summary Development of addictive manufacturing technology has fundamentally exhibited great advantages, which provides an exclusive platform for manufacturing smart structures. Based on 3D printing added with additional dimension, either time or space, for manipulating shape, property or functions, in the present talk, I would initially analyse the key scientific issues in 4D printing technology as well as several examples based on our current studies for better understanding how 4D printing plays a significant role in designing and manufacturing smart structures and smart devices. The 4D printing technology is expected to open a novel strategy for substantially endowing the advanced structures with smartness and exceptionality.

Advanced manufacturing is one of the national strategies in China. Among the advanced manufacturing, addictive manufacturing technology holds the features of achieving complex arbitrary structures, typically in (1) integrating the materials and structures as well as (2) integrating design and manufacturing. Thus, these two features provide a new platform for mechanical structure design. There are three critical challenges in the addictive manufacturing. Challenge 1 is the mechanical design method and optimization theory toward addictive manufacturing. As is known, advantage extension upon layer-by-layer addictive manufacturing, while the appropriate mechanical design method is still incomplete. The second challenge is the mechanical modeling and simulation method for establishing relationship of "addictive manufacturing-design-performance prediction". It is a hot topic in structure design, process simulation and performance prediction separately, while integrating these three targets is still a great challenge. The third challenge is the advanced automatic equipment for developing addictive manufacturing via integrating design and manufacturing. For high-performance complicated structures in aerospace, addictive manufacturing equipment are required to develop for realizing the multi-yarn and pre-strengthening manipulation in promoting the effectiveness of the manufacturing. There are several critical factors in developing lightweight multi-functional materials and structures using addictive manufacturing, including design, equipment and manufacturing.

This presentation would focus on the mechanical design in the addictive manufacturing. In the mechanical design and manufacturing of 3D printing, there are three sections. In the first section, design methods for advanced 3D printed structures would be discussed on the design of zero expansion structures, chiral structures and auxetic structures. In the second section, design methods for shape retention in 3D printing would be included for alleviating two critical problems in the processing of addictive manufacturing. In the third section, design methods for property retention in 3D printing would be analysed to understand the microstructure regulating mechanism in the addictive manufacturing process.

Additionally, 4D printing technology would be systematically summarized. 4D printing uses an AM to create a 3D object with adding the dimension of shape change, property change or function variation over time and space. Initially, the background of 4D printing would be discussed. Subsequently, several demonstrations using 4D printing technology would be provided for better understanding the process. For example, swelling-driven 4D printed smart lattice structures could be established by the hetero-material printing based on the design lattice. Moreover, photo-polymerization-driven 4D printing would be realized via controlling the polymerization degree. Furthermore, active origami structures for reconfigurable antennas could be designed and constructed via multi-material printing and multi-stable origami design. In addition, stiff reconfigurable polygons for smart connecters could be assembled via two designed components. Also, precisely controllable smart chromatic films would be achieved via electrochemical manipulation.

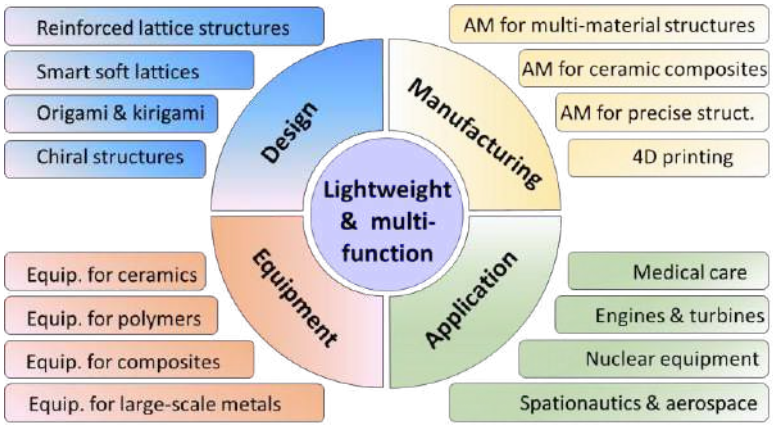

Figure 1. Schemes for illustrating the innovation R&D center for lightweight multi-functional structures

As shown in Figure 1, there is an innovation R&D center for lightweight multi-functional structures based on addictive manufacturing technology with range from design, manufacturing, equipment to applications. For a significant application

*Corresponding author. E-mail: fangdn@bit.edu.cn; fangdn@pku.edu.cn.

from addictive manufacturing technology, the very first all-printed metal satellite upon lattice structures was launched into the orbit. Such technology opens an era for designing & manufacturing key components for satellites using 3D lattice structures & addictive manufacturing, with great impacts on China's aerospace industry.

CONCLUSIONS

In conclusion, the core in the advanced manufacturing would be the mechanical design of structure unit cells for extending the concept of designing macrostructures, with expectation of breaking through the state-of-the-art of traditional materials and structures. With the assistant of mechanical design coupled with addictive manufacturing, various advanced structures with specific functions and applications would be expected to be achieved soon.

References

[1] Bao Y., Han Y., Yang L., Li N., Luo J., Qu W., Chen R., Jen A. K. Y., Li T., Chen H., Song W. L., Fang D. Bioinspired Controllable Electro-Chemomechanical Coloration Films. *Adv. Funct. Mater*. **29**: 1806383, 2019.

[2] Wang L. C., Song W. L., Zhang Y. J., Qu M. J., Zhao Z., Chen M., Yang Y., Chen H., Fang D. Active Reconfigurable Tristable Square-twist Origami. *Adv. Funct. Mater*. **30**: 1806383, 2020.

A THERMO-ELASTO-VISCOPLASTIC FINITE ELEMENT MODEL TO STUDY MICROSTRUCTURE EVOLUTION OF POLYCRYSTALS DUE TO INTRINSIC HEAT TREATMENT DURING METAL ADDITIVE MANUFACTURING

Nikhil Mohanan[1], Matthias Rambausek[1] and Manas Upadhyay*[1]
[1] Laboratoire de Mécanique des Solides, CNRS, Ecole Polytechnique, Institut Polytechnique de Paris, Route de Saclay, 91128 Palaiseau Cedex, France

Summary In this work, a strongly-coupled Thermo-Elasto-ViscoPlastic Finite Element (T-EVP-FE) crystal plasticity model is proposed. This model allows studying the elastic and plastic deformation of polycrystalline materials under the action of combined transient thermal and mechanical boundary conditions. These boundary conditions are obtained from a macroscale thermomechanical FE model that is used to simulate the building of AM samples. The simulated material is a 316L stainless steel. The role of single crystal elastic anisotropy and plastic heterogeneity on the intragranular and intergranular strains due to temperature/heat-flux boundary conditions is analysed and the key findings will be presented. Perspectives on comparison with experiments will also be presented.

MOTIVATION AND AIM

During an Additive Manufacturing (AM) or 3D printing process, just after deposition, a liquid material rapidly solidifies and spends rest of the building time being subjected to Solid-State Thermal Cycling (SSTC), at varying temperature rates and amplitudes, an illustration is shown in Fig. 1. During initial stages of SSTC, temperature amplitudes higher than annealing points and temperature rates as high as 10^6 K/s can be encountered. Consequently, large transient temperature gradients are formed, which result in strong transient thermal stresses due to internal and/or external constraints. Such rapidly varying temperatures and thermal stresses can result in significant changes in the microstructure, including dislocation structure evolution, recrystallization, phase transformation, etc. During later stages of SSTC, a nearly steady-state heat conduction occurs at relatively high temperatures with respect to room temperature. Such relatively high temperatures along with internal stresses due to a metastable microstructure can also result in dislocation recovery, grain growth, precipitation, etc.

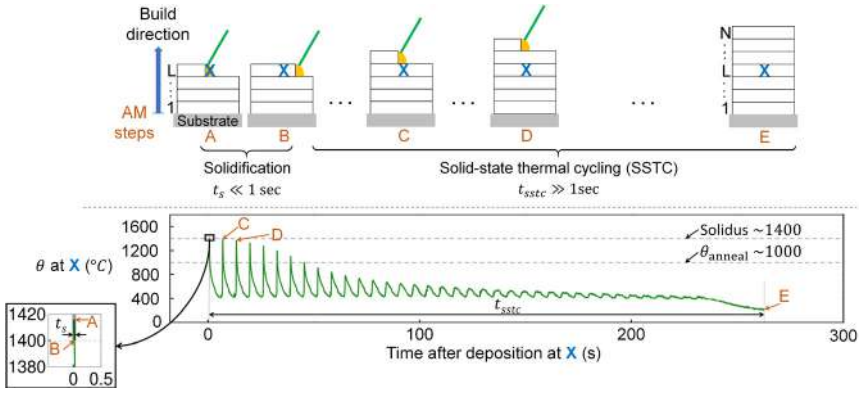

Figure 1: An illustration [1] of temperature (θ) vs time (t) evolution at a material point X during additive manufacturing of a wall. t=0 corresponds to the moment the heat-matter interactions occur at X in a layer L<N, where N is the total number of layers.

Currently, most research efforts in the field of modelling of microstructure evolution during metal AM are focused on understanding the microstructure formation during solidification. Thus far, very little efforts have been dedicated towards understanding the role of microstructure evolution due to SSTC during AM. In this work, we are interested in understanding what happens to the microstructure after it has solidified and until the end of the AM process, i.e. during the long period when it is subjected to SSTC.

Recently, Upadhyay [1] proposed the Thermal Field Dislocation Mechanics (T-FDM) model to study the dynamics of dislocations at the intragranular level under the action of transient temperature and heat flux boundary conditions. The focus of this work is at the polycrystalline level and our aim is to develop a crystal plasticity type modelling framework that captures the role of strong thermal gradients on the local and macroscopic elastic-plastic response of a material and that can be coupled/extended with other physics based-models, e.g. recrystallization/grain growth, to better capture microstructure evolution during SSTC.

To that end, we propose the Thermo-Elasto-ViscoPlastic Finite Element (T-EVP-FE) model to simulate the polycrystalline response due to SSTC during AM.

*Corresponding author. E-mail: **manas.upadhyay@polytechnique.edu**, Website: **https://www.manas-upadhyay.com**

THE T-EVP-FE MODEL

We consider a body $\mathcal{B}$ with surface $\partial\mathcal{B}$ to be a thermodynamically closed system. We shall assume that the local temperature θ at any material point in $\mathcal{B}$ is always below the solidus. We assume that $\mathcal{B}$ is a simply connected body without voids or cracks. We also assume that $\mathcal{B}$ is a polycrystal with intergranular interfaces (grain boundaries) such that the total displacement ($\boldsymbol{u}$) is continuous everywhere. The main set of governing equations of the geometrically linear T-EVP-FE model are:

$$\boldsymbol{U} = \boldsymbol{\nabla u} = \boldsymbol{U}^e + \boldsymbol{U}^p + \boldsymbol{\varepsilon}^\theta \tag{1}$$

$$\boldsymbol{\varepsilon} = \boldsymbol{sym}\,(\boldsymbol{U}),\ \boldsymbol{\varepsilon}^e = \boldsymbol{sym}\,(\boldsymbol{U}^e),\ \boldsymbol{\varepsilon}^p = \boldsymbol{sym}\,(\boldsymbol{U}^p),\ \boldsymbol{\varepsilon}^\theta = \boldsymbol{\gamma}(\theta - \theta_0) \tag{2}$$

$$\dot{\boldsymbol{\varepsilon}}^p = \sum_s \boldsymbol{m}^s \left(\dot{\gamma}_0^s \left(\frac{\boldsymbol{m}^s : \boldsymbol{\sigma}}{\tau_{crss}} \right)^n \operatorname{sign}(\boldsymbol{m}^s : \boldsymbol{\sigma}) \right) \tag{3}$$

$$\boldsymbol{\sigma} = \boldsymbol{\mathcal{C}} : (\boldsymbol{\varepsilon} - \boldsymbol{\varepsilon}^p) - \boldsymbol{\beta}(\theta - \theta_0) \tag{4}$$

$$\boldsymbol{q} = -\boldsymbol{K} \cdot \boldsymbol{\nabla}\theta \tag{5}$$

$$\boldsymbol{\nabla} \cdot \boldsymbol{\sigma} + \rho \boldsymbol{f} = \rho \ddot{\boldsymbol{u}} \tag{6}$$

$$\rho c_v \dot{\theta} = \boldsymbol{\nabla} \cdot (\boldsymbol{K} \cdot \boldsymbol{\nabla}\theta) + \boldsymbol{\sigma} : \dot{\boldsymbol{\varepsilon}}^p - \theta \boldsymbol{\beta} : (\dot{\boldsymbol{\varepsilon}} - \dot{\boldsymbol{\varepsilon}}^p) + \rho r \tag{7}$$

where bold font variables/symbols indicate vector/tensor (order ≥ 2) quantities, $\boldsymbol{U}$: total distortion, $\boldsymbol{\nabla}$: differential operator, $\boldsymbol{U}^{e/p}$: elastic/plastic distortion, $\boldsymbol{\varepsilon}^{e/p}$: elastic/plastic strain, $\boldsymbol{\varepsilon}^\theta$: thermal strain, $\boldsymbol{\gamma}$: thermal expansion coefficient matrix (assumed constant), θ_0: reference temperature s: slip system, $\boldsymbol{m}^s$: Schmid tensor, $\dot{\gamma}_0^s$: reference shear rate on a slip system s, τ_{crss}: critical resolved shear stress, n: power law exponent, $\boldsymbol{\sigma}$: Cauchy stress, $\boldsymbol{\mathcal{C}}$: elastic stiffness tensor, $\boldsymbol{\beta} = \boldsymbol{\mathcal{C}} : \boldsymbol{\gamma}$: thermal moduli tensor, $\boldsymbol{q}$: heat flux vector, $\boldsymbol{K}$: heat conductivity matrix, $\boldsymbol{f}$: body force, ρ: material density, $\ddot{\boldsymbol{u}}$: acceleration, c_v: specific heat at constant volume, ρ: density and ρr: heat loss term.

The model is implemented inside in the FEniCS [2] open-source software. The implementation is validated by comparing them with the predictions of a crystal plasticity fast Fourier transform model [3] under isothermal conditions and with analytical solutions for the heat transfer part. Next, the SSTC simulations using the T-EVP-FE model are driven using boundary conditions obtained from a macroscopic FE model that allows building AM structures. The results of these simulations will be presented. The role of single crystal elastic anisotropy and plastic heterogeneity on the intragranular and intergranular strains due to temperature/heat-flux boundary conditions is analyzed and the key findings will be presented. Finally, the different possibilities of comparison with experiments will be presented.

References

[1] Upadhyay, On the thermo-mechanical theory of field dislocations in transient heterogeneous temperature fields, Journal of the Mechanics and Physics of Solids, 145 (2020) 104150.

[2] Alnaes et al., The FEniCS Project Version 1.5, Archive of Numerical Software, vol. 3 (2015).

[3] Upadhyay et al., Study of lattice strain evolution during biaxial deformation of stainless steel using a finite element and fast Fourier transform based multi-scale approach, Acta Mat., 118 (2016) 28 – 43.

COMPUTATIONAL HOMOGENIZATION BASED ON THE MIXED TRANSFORMATION FIELD ANALYSIS: APPLICATION TO 3D-PRINTED MATERIALS

Elisabetta Monaldo *[1] and Sonia Marfia[1]
[1] Department of Engineering, Università degli Studi Roma Tre, Rome, Italy

Summary In this paper the Mixed Transformation Field Analysis, formulated for heterogeneous materials, is extended to the analysis of the mechanical behavior of the 3D-printed materials. In detail, a mixed-stress variational formulation of the elasto-plastic theory is considered. Under the assumption of periodic microstructure, a unit cell is identified and divided in subsets. In each subset, a self-equilibrated approximation of the stress and a constant plastic multiplier are assumed. The numerical results obtained are compared with some experimental evidence, available in literature, and with non-linear finite element (FE) analyses. The procedure allows to obtain effective results reducing the computing time usually associated to FE analyses.

INTRODUCTION

The 3D printing is a rapidly growing manufacturing technology that allows to make objects directly from a computer-aided design model. The ability to reproduce complex geometries, the rapid design-to-fabrication cycle times, the low maintenance costs and the lower amount of waste material generated are some of the advantages with respect to the conventional methods. Among the numerous methods, the fused deposition modelling is the most widely used. This technique, initially conceived as a process for making prototype, has found application as a manufacturing process for end-use parts. In order to be integrated as a part for serial production, the resulting 3D-printed components must possess the required mechanical properties. Several studies have shown that the process parameters, such as raster direction, layer thickness, and air gap, affect the mechanical properties of the resulting 3D-printed components by introducing anisotropy [1, 2]. Therefore, an open issue is the prediction of the 3D-printed parts behavior. Computational modelling techniques based on finite element (FE) method could be applied. Nevertheless, modelling the mechanical response of 3D printed structures taking into account the microstructural features by means of FE analyses requires a significant computational effort. Recently, in order to obtain efficient numerical homogenization procedures for heterogeneous materials characterized by plastic behavior, Reduced Order Models (ROM) heve been adopted [3]. Among ROM, the Mixed Transformation Field Analysis (MxTFA), based on a mixed stress variational approach considering an approximation of the inelastic strain based on a representation of the self-equilibrated stresses, results an effective approach as it reduces the number of macroscopic internal variables [4]. The aim of this paper is to determine the overall mechanical behavior of 3D-printed materials by means of the MxTFA. A numerical procedure is developed and verified with some numerical applications. The results obtained are compared with the experimental results available in literature and with FE-based reference solutions.

MATERIALS AND METHODS

The elasto-plastic homogenization problem is formulated in terms of the prescribed average strain and consists in finding the displacement field, the strain field, the inelastic strain field, and the stress field, which satisfy the compatibility, the constitutive and the equilibrium, with zero body forces, equations. In particular, the material is described as elasto-plastic and the classical Von Mises yield function is considered. Under the assumption of periodic microstructure, a unit cell (UC) composed by a printed fiber and voids is identified and divided into n non-overlapping subsets (see Fig. 1). The MxTFA defines an approximation of the stress and plastic multiplier over each subset. In detail, a self-equilibrated stress is considered introducing a constant, linear, or quadratic approximation and the plastic multiplier is assumed constant. Then, the inelastic strain approximation is derived through the flow rule. The MxTFA requires linear elastic pre-analyses, performed on a full discretization of the microscopic domain, in order to determine the localization operators necessary to recover the total strain in the typical point of the subset. The number of pre-analyses is related to the type of the selected stress approximation. The internal variables, i.e. the unknowns of the problem, are now the reduced stresses and the increment of the reduced plastic multipliers. They are obtained by enforcing the weak fulfilment of the compatibility equation and of the evolutive of the plastic multiplier over each subset. The evolutive of the reduced variables is solved employing a backward Euler algorithm with a return mapping technique. Finally, as usual in mixed stress formulations, the effective stress is evaluated directly from the reduced stress parameters defined in each subset that are obtained from the solution of the evolutive problem.

NUMERICAL APPLICATIONS

The effectiveness of the MxTFA-based homogenization procedure in the study of 3D-printed materials is verified by comparing numerical results with experimental results provided by [1] and with results recovered performing non-linear FE analyses. Since the problem is characterized by 3D displacement fields that do not vary along the fiber axis, the

*Corresponding author. E-mail: elisabetta.monaldo@uniroma3.it

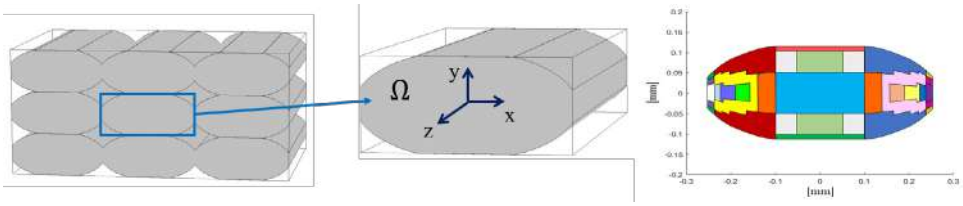

Figure 1: Periodic material, unit cell (UC), and subset discretization of the UC cross-section.

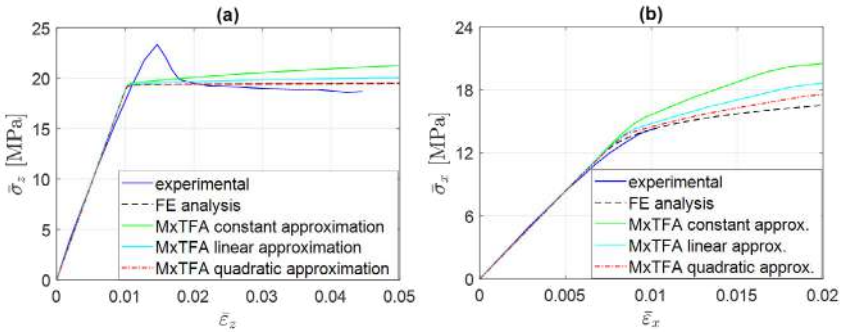

Figure 2: Macroscopic mechanical response of specimens with fiber orientation at $a = 0°$ (a) and $90°$ (b) subjected to tensile loading.

numerical analyses are performed on the UC cross section adopting a 3D-2D finite element with an enriched kinematic field. Both for the pre-analyses and for the micromechanical analysis, the UC is discretized with 2214 4-node 3D-2D quadrilateral finite elements and the homogenization procedure is realized considering a configuration with 22 subsets (see Fig. 1). The geometrical and mechanical parameters are chosen according to data provided by [1]. The mechanical response of specimens with unidirectional fiber orientation subjected to tensile loading is reproduced. In detail, denoting a the angle formed by the fiber axis with respect to the loading direction in a counter-clockwise rotation, specimens with $a = 0°$ and $90°$ are considered. Different analyses are carried out with constant, linear or quadratic stress approximation. Figure 2 shows the constitutive response of the equivalent homogenized materials together with the experimental response and with the FE solution. These results highlight that the MxTFA procedure is able to reproduce the both the elastic behavior and the plastic plateau of the material. Increasing the order of the stress approximation, the computed plastic response improves. Moreover, the MxTFA technique proves to be the most time-effective solution, drastically reducing the elapsed time in comparison to FE ones, also in the case with the highest order of stress approximation.

CONCLUSIONS

The Mixed Transformation Field (MxTFA) analysis is applied to compute the effective mechanical behavior of 3D-printed materials. The numerical applications have revealed the efficiency of the procedure and a good agreement with the reference results. Finally, the MxTFA analysis could represent an efficient tool for designing and prediction of the mechanical behavior of 3D-printed materials.

ACKNOWLEDGEMENTS

This study was funded by Italian Ministry of Education, projects PRIN2015 Multi-scale mechanical models for the design and optimization of micro-structured smart materials and metamaterials (CUP H32F15000090005) and PRIN2017 3D Printing: a bridge to the future: computational methods, innovative applications, experimental validations of new materials and technologies (CUP Project number 2017L7X3CS).

References

[1] Rodrìguez J. F., Thomas J. P., Renaud J. E. Mechanical behavior of acrylonitrile butadiene styrene (ABS) fused deposition materials. Experimental investigation. *Rapid Prototyp. J.* **7**: 148–158, 2001.

[2] Alaimo G., Marconi S., Costato L., Auricchio F., Influence of meso-structure and chemical composition on FDM 3D-printed parts. *Compos. Part B:Eng.* **113**: 371–380, 2017.

[3] Michel J., Suquet P., Nonuniform transformation field analysis, *Int. J. Solids Struct.* **40**: 6937–6955, 2003.

[4] Covezzi F., de Miranda S., Marfia S., Sacco E. Homogenization of elastic-viscoplastic composites by the Mixed TFA, *Comput. Methods in Appl. Mech. Eng.* **318**: 701–723, 2017.

SMOOTH TRIAXIAL WEAVING USING CURVED STRIPS

Pedro M. Reis *[1], Changyeob Beak[2], Alison G. Martin[3], Samuel Poincloux[1], Tian Chen[1,4], Yingying (Samara) Ren[4], Julian Panetta[4], and Mark Pauly[4]
[1] Flexible Structures Laboratory, Ecole Polytechnique Fédérale de Lausanne (EPFL), Lausanne, Switzerland
[2] Department of Mechanical Engineering, Massachusetts Institute of Technology, MA, USA
[3] Independent Artist, Via Ponte 3, 54013 Fivizzano, Italy
[4] Computer Graphics and Geometry Laboratory, EPFL, Lausanne, Switzerland

Summary Triaxial weaving is a craft technique commonly used to generate surfaces using tri-directional arrays of initially straight elastic strips. Traditional weaving uses discrete topological defects as building blocks for non-planar shaping. Taking an alternative point of departure, we introduce a novel approach for triaxial weaving that enables us to continuously span a variety of 3D shapes of the weave by tuning the natural in-plane curvature of the strips. We systematically explore the validity of our design strategy by quantifying the shape of experimental specimens with X-ray tomography in combination with continuum-based simulations. To demonstrate the potential of our design approach, we present a fullerene-like weave that is perfectly spherical, something that cannot be readily achieved using straight strips. Ellipsoidal and toroidal structures are also explored.

WEAVED STRUCTURES AS CURVED CRYSTALLOGRAPHIC SYSTEMS

Triaxial weaving (Fig. 1A) has long been loved by basket makers and artists seeking a combination of functional and aesthetically-pleasing structures. This ancient craft technique enables the generation of surfaces with tri-directional arrays of initially straight elastic strips. The design principles of traditional weaving are based on the observation that non-hexagonal topologies of strategically located unit cells impart out-of-plane shapes. In the realm of differential geometry, the weaving tradition is rooted in the concept of Euler characteristics through the Gauss-Bonnet theorem, with discrete topological defects being used as building blocks. The effect of topological charges in dictating the three-dimensional geometry of a surface is at the root of the morphology of many other curved crystallographic systems, as we have indicated in our previous work [1].

We take a unit-cell approach to revisit the study of traditional weaves using a combination of precision model experiments, computer simulations, and theory. As shown in the schematic diagram of Fig. 1B, each unit cell comprises n strips and n adjacent triangles. For simplicity, we focus on the case where the length, d, of all segments in the unit cell is uniform. The angle between two adjacent segment segments is α_i. In the first stage of the investigation, we start by considering strips that are straight in their rest (planar) configuration ($\kappa_g = 0$) and will then eventually relax this condition that possesses in-plane curvature ($\kappa_g \neq 0$) in their undeformed configuration, prior to weaving. For the particular case of $\kappa_g = 0$ and setting $\alpha_i = 2\pi/3$, the famous Gauss-Bonnet theorem states that the integrated Gaussian curvature of the unit cell is

$$\int \mathcal{K} \mathrm{d}A = \left(2 - \frac{n}{3}\right)\pi, \tag{1}$$

which is zero (planar weave) when $n = 6$ and can be varied in discrete steps of $\pi/3$ by modifying n. In Fig. 1C, we present: (top row) photographs of different instances of weaved unit cells for different values of n, (middle row) post-processed images obtained through X-ray micro computed tomography (μCT) including the computed Cosserat frame, and (bottom row) the corresponding simulated configurations using the finite element method (FEM). Excellent quantitative agreement is found between experiments and simulations. These topological defects are commonly used in traditional weaving to impart curvature on the structure (*e.g.,* at a corner), albeit with the drawback that curvature can only be injected discretely.

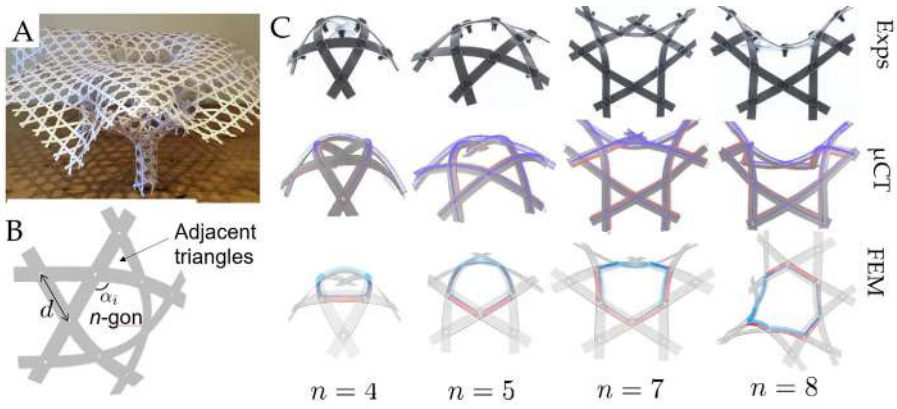

Figure 1: Weaving with straight strips. A. Weaved sculpture where the curvature is injected using topological defects into the lattice (credit: Alison Martin). B. Schematic of the unit cell. C. Shapes of the unit cell for different values of n. (Top) Experiments. (Middle) Reconstructed μCT images, onto which the measured Cosserat frame is superposed. (Bottom) Corresponding FEM simulations.

*Corresponding author. E-mail: pedor.reis@epfl.ch.

OBTAINING SMOOTH 3D WEAVES USING CURVED STRIPS

We now take an alternative point of departure toward circumnavigating the limitation mentioned above for traditional weaving, where the integrated Gaussian curvature of the structure can only be changed discretely by topological defects. We introduce a novel approach to triaxial weaving by considering strips that possess natural in-plane curvature. In other words, these curved strips relax the conditions on the zero geodesic curvature ($\kappa_g \neq 0$) and on the interior angles of the triangles ($\alpha_i \neq 2\pi/3$), such that the sum of their interior angles no longer adds up to π. Weaving with these curved strips allows for the integrated Gaussian curvature, $\int \mathcal{K} \mathrm{d}A$, to be varied continuously, as we detail next.

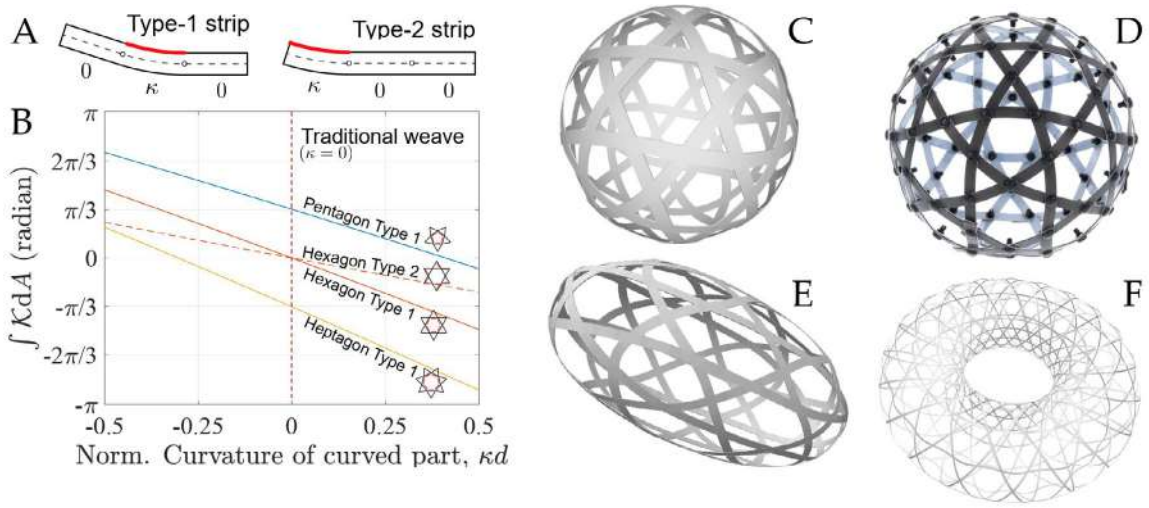

Figure 2: Weaving with curved strips. A. Our curved strips (in their rest configurations) can have either a constant curved portion in the center (Type-1) or at one of the extremities (Type-2). B. The integrated Gaussian curvature of unit cells with different topology can be varied continuously as a function of the normalized segment curvature, $\kappa^* = \kappa d$. C. Computational design of a spherical weave is achieved with strips with a sinusoidal geometry in their rest configuration. D. Photograph of corresponding experimental specimen. E and F. Our computational approach can yield design weaves with more complex geometries, such as ellipsoid and torus.

In Fig. 2A, we present schematics of the two types of curved strips that we consider in their rest (pre-weaved) configurations. These three-segment strips can either have a (constant) curved portion in their center (Type-1) or at one of their extremities (Type-2). We have systematically quantified the effect of the in-plane curvature, κ, in dictating the integrated Gaussian curvature of the unit cell, for different typologies. For convenience, we normalized the curvature of the curved segment as $\kappa^* = \kappa d$. The Gauss-Bonnet theorem yields the following prediction for the integrated Gaussian curvature:

$$\int_{\mathrm{n}} \mathcal{K}^I \mathrm{d}A = (2-n)\pi - n\kappa^* + n\left[\pi - \theta\left(\kappa^*\right)\right] \quad \text{and} \quad \int_{\mathrm{n}} \mathcal{K}^{II} \mathrm{d}A = (2-n)\pi + \frac{n\left[\pi - \theta\left(-\kappa^*\right)\right]}{2} + \frac{n\left[\pi - \phi\left(-\kappa^*\right)\right]}{2}, \quad (2)$$

for Type-1 and Type-2 strips, respectively, where θ and ϕ are the interior angles of the triangle adjacent to the curved part.

In Fig. 2B, we present predictions for $\int \mathcal{K} \mathrm{d}A$ as a function of κ^*, for Type-1 and Type-2 cells, with pentagonal, hexagonal, and heptagonal topologies. Importantly, we show that the curvature of the unit cell can be varied continuously by tuning the continuous variable κd, for each of these cases. For example, we can obtain a hexagonal unit cell with nonzero integrated curvature. We are in the process of validating these geometric predictions against experiments (using data obtained from X-ray tomography) and computer simulations. In our simulations, we use both FEM and the Discrete Elastic Rod (DER) method [3].

We have explored the geometric construction introduced above to design perfectly spherical fullerene-like weaves. Fig. 2C presents an optimized computed design with strips that, prior to weaving, have an in-plane sinusoidal geometry (*i.e.* they are not straight). Fig. 2D shows a photograph of the corresponding specimen realized experimentally, which deviates from a perfect sphere by at most 0.01% (standard deviation of the radial deflection from a sphere). Note that the resulting shape is strikingly smooth, despite the high-level of discreteness of the underlying unit cells. By contrast, following the classical topological approach of adding 12 pentagonal defects to a hexagonal weave using straight strips (as we did in the previous section), we would have obtained a far more faceted and non-smooth shape. We have leveraged our optimization-based computational approach to explore the weaving of more complex geometries. In Figs. 2E and F, we present examples for ellipsoidal and toroidal structures.

References

[1] M. Brojan,*et al*. "Wrinkling crystallography on spherical surfaces", *Proceedings of the National Academy of Sciences*, **112**(1), 14 (2015).
[2] P. Ayres, *et al.*, "Beyond the Basket Case: a principled approach to the modelling of Kagome weave patterns for the fabrication of interlaced lattice structures using straight strips" *Advances in Architectural Geometry*, 72–93 (2018).
[3] M. Bergou, *et al.*, "Discrete elastic rods", *ACM Transactions on Graphics*, **27**(3), 63 (2008).

ON THE CONTINUUM MECHANICAL MODELLING OF BILAYER GRAPHENE

Paolo Podio-Guidugli[1]
[1] *Accademia Nazionale dei Lincei, Roma, Italy*

Summary A macroscopic model accounting for combined shearing, bending, and slipping, of bilayer graphene is proposed. The idea is to think of bilayer graphene as a single elastic surface equipped with a director, that is, a vector capable of changes in length and orientation.

EXTENDED SUMMARY

C-allotropic materials and structures – under all respects, we dare say, the 21st century materials and structures – have attracted a tremendous attention during the past few years for their amazing mechanical, electrical, and thermal conductivity properties. However, their potentialities are far from being exploited, for one reason out of many because their continuum mechanical modelling is still not completely satisfactory.

Our present study is an attempt to move a step toward building a continuum model for bilayer graphene. Our point of departure is offered by three recent papers.

The first is [1], where the stretching and bending behavior of a single-layer graphene sheet is given a continuum description in terms of a postulated quadratic representation for the corresponding elastic energies, whose constitutive moduli - one more than in classical linear elasticity - are given an atomistically-informed expression. The energy representations are partly justified on the basis of a delicate analysis developed in [2]; the atomistic information is deduced by building on the discrete model for graphene developed in [3, 4], in which atomic interactions are governed by a harmonic approximation of a 2nd-generation Brenner potential depending on bond lengths, bond angles, and two types of dihedral angles. In the second paper [5], the continuum limit of a harmonic approximation of such a Brenner potential is deduced and a description of bent graphene sheets is achieved, including an analytical expression of their Gaussian stiffness, a parameter ruling their rippling. In the third paper [6], the connection between microscopic and macroscopic description is established within the general framework of homogenization theory, confining attention to the small displacements approximation. The bending behavior of a graphene sheet is accounted for by determining the variational limit - in the sense of Gamma-convergence - of a sequence of discrete energy functionals under a topology that guarantees the convergence of minimizers.

At the macroscopic scale of continuum mechanics, we think of bilayer graphene as a single elastic bending-and-shearing resistant surface equipped with a *director*, that is, in the present case, a vector capable of changes in length (so as to account for interlayer distance changes) and orientation (so as to account for interlayer shearing and slipping). Equilibria of such a two-dimensional system would be ruled by a potential once again consistent with the Brenner potentials mentioned above and featuring also a contribution of van der Waals type. In this connection, we mention that the role of van der Waals interactions in keeping together multilayer graphene, molybdenum disulfide, and hexagonal boron nitride, structures when they are bent has been studied in [7]. In the context of the model we envisage, the slip-length parameter introduced in that study might be connected to the angle of the director to the surface's tangent plane; in this connection, we mention that slip-mediated bending is the subject of [8]. Finally, having a director field at our disposal might permit a juxtaposition with the predictions made in [9] about interlayer interactions in multilayer graphene structures with the use of a registry-dependent Kolmogorov-Crespi type [10] combining long-ranged van der Waals and short-ranged anisotropic electronic contributions.

References

[1] Davini, C., Favata, A., Paroni, R. EPL **118**: 26001, 2017.
[2] Davini, C. Cont. Mech. Thermodyn. **26**: 95-113, 2014.
[3] Favata, A., Micheletti, A., Podio-Guidugli, P., Pugno, N.M. J. Elast. **125**: 1-37, 2016.
[4] Favata, A., Micheletti, A., Podio-Guidugli, P., Pugno, N.M. Meccanica **52**: 1601-1624, 2017.
[5] Davini, C., Favata, A., Paroni, R. J. Mech. Phys. Solids **104**: 96-114, 2017.
[6] Davini, C., Favata, A., Paroni, R. Arch. Rational Mech. Anal. **229**: 1153-1195, 2018.
[7] Wang, G., Dai, Z., Xiao, J., Feng, AZ., Weng, C., Liu, L., Xu, Z., Huang, R., Zhang, Z. Phys. Rev. Let. **123**: 116101, 2019 (suppl. mat. 1-16).
[8] Han, E., Yu, J., Annevelink, E., Son, J., Kang, D.A., Watanabe, K., Taniguchi, T., Ertekin, E., Huang, P.Y., van der Zande, A. Nat. Mat. https:doi.org/10.1038/s41563-019-0529-7, 2019.
[9] Wen,M., Carr, S., Fang, S., Kaxiras, E., and Tadmor, E.B. Phys. Rev. Lett. **123**: 116101, 2019.
[10] Kolmogorov, A.N., Crespi, V.H. Phys. Rev. B. **71**: 235415-1–235415-6, 2005.

NANO AND MICROSCALE ORIGAMI ENGINEERING: PRESENT AND FUTURE

Horacio Espinosa[1]*, Nicolas Alderete[1], Zhaowen Lin[1], Larissa Novelino,[2] Heming Wei[1], Glaucio Paulino,[2] and Sridhar Krishnaswamy[1]
[1] Theoretical and Applied Mechanics, Mechanical Engineering, Northwestern University, Evanston, USA
[2] Department of Civil Engineering, Georgia Tech, Atlanta, USA

Summary Origami structures have attracted considerable attention in recent years on account of their promise to yield deployable and tunable structures. Such properties are ideally suited for a variety of engineering applications from robotics to space exploration. Despite their potential, most efforts have been limited to macroscale demonstration. Therefore, research contributions for downscaling and expanding manufacturing capabilities are needed to achieve a broader spectrum of multifunctional capabilities stemming from morpho-functional transformations operating at micro and nanoscales. In this presentation, origami concepts combined with two-photon printing and *in situ* SEM mechanics analysis will be reported in the context of *microscale origami* exhibiting strong deformation anisotropy, auxeticity, and tunability of mechanical properties. Future research opportunities will be discussed.

INTRODUCTION

Origami, the ancient Japanese art form of paper (*Ori*) folding (*kami*) has established itself as a promising avenue for the design of deployable and highly tunable structures. Together with unusual mechanical properties, the stacking and space-filling capabilities of certain origami patterns make them formidable candidates for the design of architected metamaterials. Depending on the particulars of their geometry, these structures can give rise to a plethora of remarkable phenomena, including (but not limited to) mechanical anisotropy, shape recoverability, and multistability with high strength-to-density ratios. Notwithstanding, the complexities involved in their fabrication, regardless of lengthscale, still pose a substantial technical challenge and preclude the fruition of origami inspired engineering devices. At the macroscale, for example, the thermoset polymers used in additive manufacturing confer additional stiffness to the folds, which in turn requires the incorporation of a number of artifacts (e.g., flexible hinges) to attain the characteristic folding kinematics of origami. Likewise, often-complex geometric features present in origami designs and the requirement to accommodate multiple folding-unfolding cycles without structural damage, impose critical design constraints on both manufacturing and material selection. Unlike conventional metamaterials, the ability of origami principles to yield three-dimensional structures from planar forms (i.e., deployability) makes them especially attractive to applications where spatial economy is paramount (e.g., biomedicine, micro- and nanobotics, space exploration); a feature which also stresses the need to push origami engineering into the micro- and nanoscale realm. While translation of origami concepts into these scales presents inherent challenges pertaining to material handling, processing and metrology, their successful implementation opens the possibility of harnessing a wide range of phenomena inaccessible at the macroscale (e.g., size effects, quantum effects, photonics, phononics).

In an attempt to pave the way from macroscale to micro/nanoscale origami, we present results of two-photon polymerization 3D printing and *in situ* Scanning Electron Microscope (SEM) mechanical testing of micron-sized origami metamaterials resulting from the assembly of Miura-Ori tubes (Fig. 1a). The fabricated structures exhibit several unusual mechanical properties including anisotropic stiffness, configuration-dependent and reversible auxeticity, elastic mechanical instabilities and large degree recovery, a unique combination insofar absent from the portfolio of mechanical metamaterials. In this context, the potential of these Miura-Ori structures made of carbon allotropes will be theoretically explore.

MICROSCALE MIURA-ORI INSPIRED ORIGAMI METAMATERIALS

Two sets of origami metamaterials, with different dihedral angles, were investigated. The first set corresponds to a lattice comprised of Miura-Ori cells with folding angle ψ=55° (equivalent to 92.4% of the total extension of a Miura-Ori tube), and the second set corresponds to a folding angle ψ=40° (equivalent to 97.4% of the total extension of a Miura-Ori tube). Both configurations were fabricated via 3D direct laser writing (DLW), using a polymerization technique employing a two-photon liquid photoresist, tested with a nanomechanical platform inside an SEM, and analysed using Bloch theory and Finite Element Methods (FEM).

Stiffness Anisotropy and Elastic Instability

In situ SEM compression tests, with imposed oscillatory loading profiles, were performed along foldable directions of the origami structures to probe their stiffness as a function of compression level (Fig. 1b). The origami metamaterials exhibit pronounced stiffness anisotropy and tunability via compression along the X- and Y-directions (up to 200%). The relatively stable stiffness and the remarkable degree of recovery upon unloading and relaxation of these structures underscores their level of resilience (e.g., 93% recovery after 32% compression in the X-direction and 94% after 23% compression in Y-direction). The remaining direction of the origami structure, the stiff direction, was first approached via the Bloch Method in FEM to investigate potential elastic instabilities stemming from the restricted foldability and the

*Corresponding author. E-mail: espinosa@northwestern.edu

periodic arrangement of representative origami unit cells. Monotonic *in situ* SEM compression tests confirmed the predicted long wavelength critical load instability of the structure and revealed a subsequent cascading plastic collapse failure mode. Overall, the compression results along different directions point to a marked anisotropy and compression tunability, which makes these structures extremely appealing to load bearing, actuation, and sensing applications.

Poisson's Ratio Anisotropy and Reversible Auxeticity

The lateral expansion/contraction of the origami structures was measured for different combinations of compression/observation directions to uncover anisotropic behavior in Poisson's ratio. All directions presented marked anisotropic Poisson's ratio and marked auxeticity along certain directions (Fig. 1b). Moreover, origami structures with folding angle ψ=40° when tested along the X-direction revealed a switch in Poisson's ratio from positive to negative, constituting the first experimental observation of such phenomenon and unveiling the possibility of reversibly controlling the auxetic state of the metamaterial; a finding with profound potential implications in acoustic wave control.

FUTURE OF ORIGAMI ENGINEERING: THE ROLE OF C-ALLOTROPES

The future of origami engineering, as with most material and mechanical developments, lies undoubtedly at the micro and nanoscale. At the microscale, the micron-scale thickness of the origami panels, facilitated by manufacturing techniques like the one applied in our microscale origami structure, results in significantly reduced bending stiffnesses which enables folding without resorting to artificial hinges. At the nanoscale, folding of atomically thin sheets has been investigated in its capacity to perform programmed folding motions with or without the presence of external forces [1]. In this regard, the malleable nature of atomically thin graphene and its variants has made them forerunners in the pursuit of nanoscale origami and bottom-up techniques for engineering building blocks of more complex three-dimensional shapes and even nanoscale machines. Despite numerous computational studies on programmable graphene folding, experimental graphene origami remains elusive. Review of recent advances in graphene origami (Fig. 1c) and the prevailing technical challenges will be undertaken as the frontiers of origami engineering continues to be shaped.

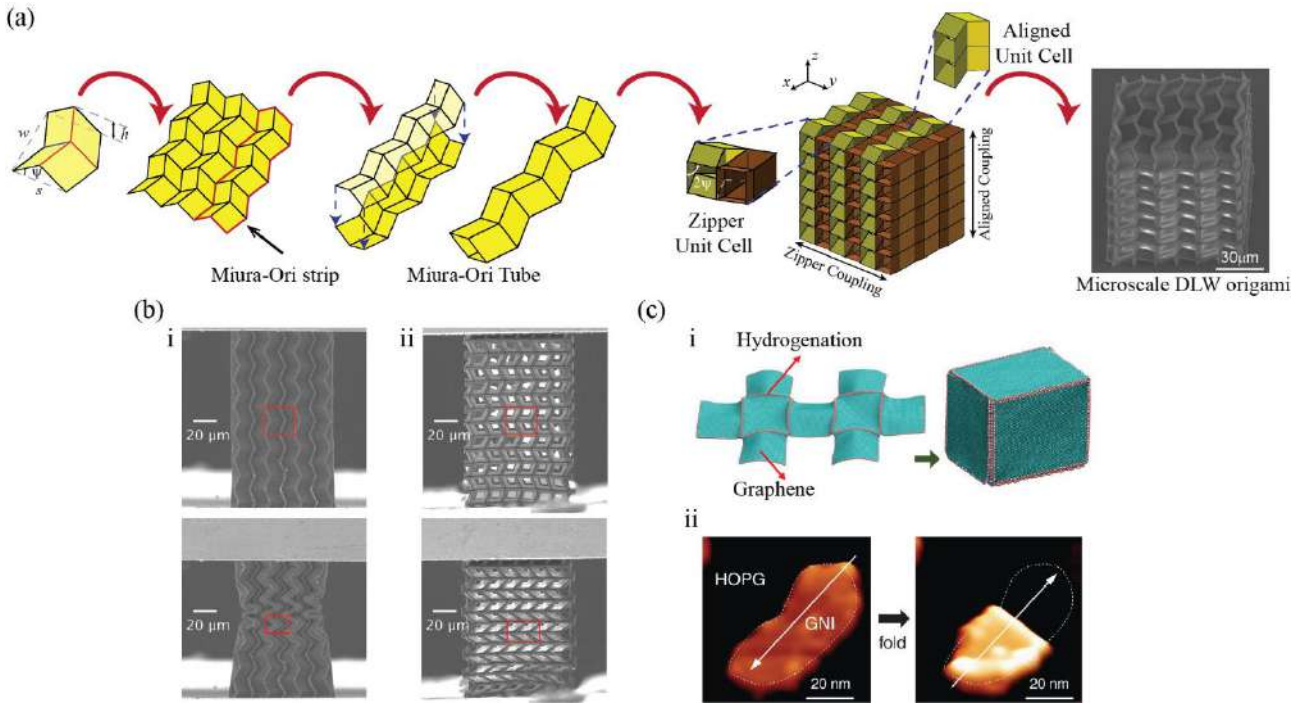

Figure 1. Micro and nanoscale origami engineering. (a) Origami structures based on assembly of Miura-Ori tubes. (b) Microscale two-photon lithography origami lattices (i: X-Direction, ii: Y-Direction). (c) Nanoscale origami prospects (i: Graphene origami cages via hydrogenation [2], ii: Experimental folding of graphene nanosheets [3]).

References

[1] Mu, J., Hou, C., Wang, H., Li, Y., Zhang, Q., Zhu, M., Origami-Inspired Active Graphene-Based paper for Programmable Instant Self-Folding Walking Devices, Science Advances, Vol.1, 2015.

[2] Zhu, S., Li, T., Hydrogenation-Assisted Graphene Origami and Its Application in Programmable Molecular Mass Uptake, Storage, and Release, ACS Nano 8(3), 2864-2872, 2014.

[3] Chen, H., Zhang, X., Zhang, Y., Wang, D., Bao, D., Que, Y., Xiao, W., Du, S., Ouyang, M., Pantelides, S., Gao, H., Atomically Precise Custom-Design Origami Graphene Nanostructures, Science 365(6457), 1036-1040, 2019.

FABRICATION, CHARACTERIZATION AND MECHANICAL PROPERTIES OF NANOARCHITECTED CARBON

Xuan Zhang*[1], Andrey Vyatskikh[2], Xiaoyan Li[3], Julia R. Greer[2], Huajian Gao[4]
[1] Leibniz Institute for New Materials, Saarbrücken, Germany
[2] Division of Engineering and Applied Science, California Institute of Technology, Pasadena, CA
[3] Department of Engineering Mechanics, Tsinghua University, Beijing, China
[4] School of Mechanical and Aerospace Engineering, College of Engineering, Nanyang Technological University, Singapore

Summary A long-standing challenge in material science and manufacture is to create porous materials that are simultaneously lightweight, strong, and resilient. Here we advanced a 3D microfabrication methodology to fabricate nanoarchitected pyrolytic carbon with lightweight densities ranging from 0.24 to 1.0 g/cm^3, GPa-level compressive strengths of 0.14 GPa to 1.90 GPa, and > 10% deformability before failure. The smallest characteristic length of the nanoarchitected carbons approaches the resolution limit of the available 3D additive manufacturing technologies, and their compressive strengths in this work approach the theoretical limits defined by the strengths of graphene and diamond.

INTRODUCTION

Porous, lightweight natural materials, such as bone, wood and diatoms, have been widely discovered and investigated. These natural materials have been shown to be both strong and resilient so that they are powerful in resisting high external loads and absorbing impact energy. Two design principles discovered in these natural materials lead to such excellent properties: (i) the flaw tolerance when the characteristic length scale of the material is below a critical value; and (ii) a hierarchical design which consists of multilevel architectures with dimensions ranging from macro- to nanoscale.

A long-standing challenge in material science and manufacture is to create porous materials that are simultaneously lightweight, strong, and resilient. Recent progresses in 3D microfabrication and additive manufacturing pave a promising way to achieve architected materials with delicate structural design and beneficial mechanical properties, like high specific stiffness and strength, good resilience/recoverability *et al*.

Here we achieved to fabricate nanoarchitected pyrolytic carbon with two prototype unit-cell geometries, octet- and iso-truss, and demonstrated a combination of their excellent properties with low density, high specific strength, imperfection insensitivity and good resilience.

RESULTS

We adopted a two-step method, using two-photon lithography (TPL) and pyrolysis in a vacuum at 900 °C, to fabricate two types of nanoarchitected carbon with octet- and iso-truss geometries, as shown in Figure 1. The octet architecture has cubic anisotropy and superior mechanical properties compared with other conventional porous architecture, including triangular, tetrahedral, or cubic trusses and stochastic foams. The iso architecture, based on the topological optimization, has been proven to be isotropic and possess the optimal stiffness compared with traditional truss topologies. After pyrolysis, each beam shrunk to 20-25% of its initial length dimension, and the final carbon trusses had unit-cell dimensions of ~2 μm, beam diameters ranging from 261 to 679 nm, and densities of 0.24 to 1.0 g/cm^3. The smallest diameter is much below the resolution limits of most available 3D lithographic technologies.

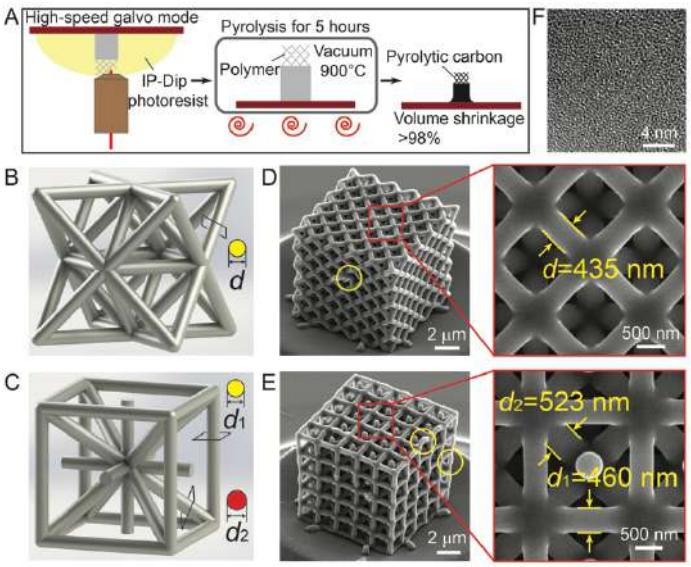

Figure 1. Fabrication and microstructural characterization of pyrolytic architected carbon of octet- and iso-truss.[1]

We performed uniaxial compressions on all pyrolytic architected carbon trusses. As the relative density ranged from 17% to 72%, Young's modulus of these carbon nanolattices increases from 2.28 GPa to 10.73 GPa, and the compressive strength increases from 0.14 GPa to 1.90 GPa. Elastic loading region persists up to an approximate 10-20% strain, then all pyrolytic carbon trusses are catastrophically failed via brittle fracture, which exceeds the value of reported carbon nano-/microlattices. The material property Ashby charts for Young's modulus and compressive strength versus density reveal that the moduli and strengths of these architected carbon are nearly one to two orders of magnitude greater compared with other micro-/nanolattices made up of vitreous carbon, alumina-polymer with comparable densities (Figure 2A).

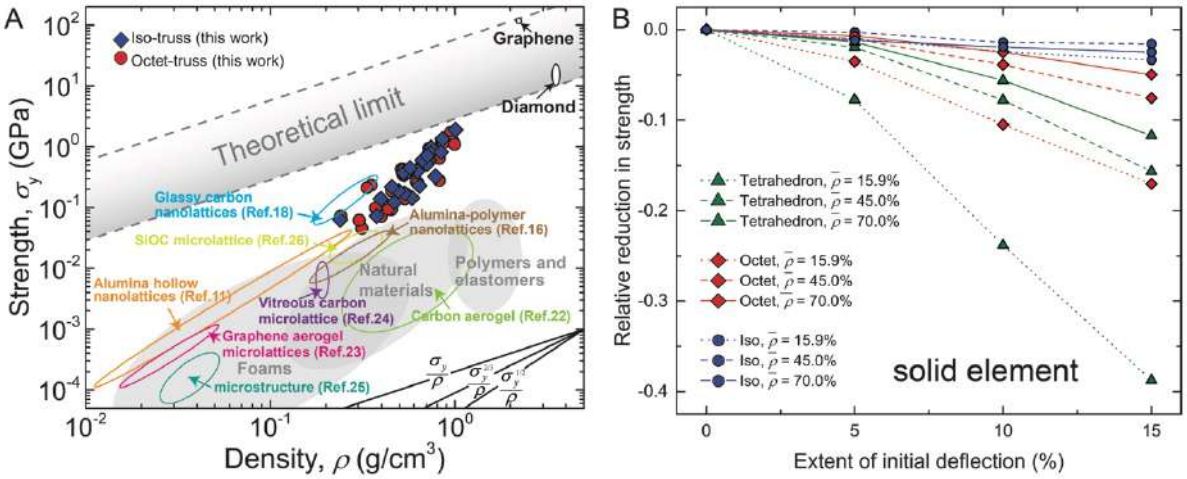

Figure 2. Ashby chart of compressive strength versus density and imperfection sensitivity of compressive strength in curvature of the structs.[1]

Besides, we observed some fabrication-induced defects in virtually all samples, including slight curvature of the struts, microvoids, and beam junction offsets or bulges. We performed finite-element (FE) simulations of the whole model to further investigate the influence of strut curvature imperfection on compressive strength. The FE simulation results show that for a given architecture, the nanolattices with higher densities experience smaller relative weakening associated with prebent imperfections; octet-truss and iso-truss unit cells for all densities are less susceptible to defects compared with tetrahedron-truss unit cells (Figure 2B).

CONCLUSIONS

We advanced a 3D microfabrication methodology to fabricate nanoarchitected pyrolytic carbon with lightweight densities below water density, GPa-level strengths, and larger than 10% deformability before failure. Departed from all existing work on micro/nanolattices reported before, the compressive strength of the nanoarchitected carbon in this work approaches the theoretical limits.

Reference

[1] Xuan Zhang, Andrey Vyatskikh, Huajian Gao, Julia R. Greer, Xiaoyan Li. Lightweight, flaw-tolerant and ultrastrong nanoarchitected carbon. *Proceedings of the National Academy of Sciences of the United States of America*, **201817309**, 2019.

THE NANOMECHANICS WHILE INTERFACING SINGLE-LAYER GRAPHENE

Y.J. Wei[1,4], Z.Q. Pang[1,4], J.T. Wu[1], H.Q. Yin[1], X.H. Shi[1], R.G. Yang[2] and M. Dresselhaus[3]
[1] LNM, Institute of Mechanics, Chinese Academy of Sciences, Beijing 100190, China
[2] Department of Mechanical Engineering and Materials Science and Engineering Program, University of Colorado, Boulder, CO 80309, USA
[3] Department of Physics and EECS, Massachusetts Institute of Technology, Cambridge, MA 02139, USA
[4] School of Engineering Sciences, University of Chinese Academy of Sciences, Beijing 100049, China

Summary In this talk, we will summarize the current advances on the mechanics while interfacing graphene in applications of different methods, including (1) the interface during making large-area single-layer graphene with patches of single-crystalline graphene; (2) dimension scale-up to make three-dimensional graphene honeycomb; (3) the influence of 3D morphology on adhension.

5-7 ring mechanics and Grain boundaries in graphene

Like most crystalline materials, two-dimensional materials exhibit rich mechanical behavior which heavily depends on their crystalline orientations and the arrangement existing defects. Here we illustrate in detail how the strength and the fracture behavior are influenced by crystalline orientations in pristine graphene. We reveal the crack kinking behavior as well as the orientation dependence of apparent fracture resistances. In addition, we show how typical defects like pentagon-heptagon rings in GBs would influence the strength of polycrystalline graphene and the behind mechanical mechanisms accounting for the observed behavior.

3-D architectured C-honeycomb

Although graphene has been broadly explored due to their outstanding mechanical properties, there exist significant challenges in retaining such properties of basic building blocks when scaling them up to three-dimensional materials and structures for many technological applications. The realized mechanical and thermal properties of 3-D carbon materials, by staggering graphene sheets or vertically grown carbon nanotube arrays, are significantly lower than those of individual graphene sheets or individual CNTs.The huge gap in mechanical properties between the low-dimensional carbon allotropes and their 3-D derivatives originates from the dissimilar bonding characteristics between carbon atoms within graphene or CNTs and the architectured 3-D engineering materials: The intra-structure bonding is covalent in nature, while van der Waals bonding dominates between different layers/tubes or with other materials1. Such heterogeneous bonding leads to property inheritance that is a mission impossible. We demonstrate the feasibility of constructing stable 3-D architectured C-honeycomb with covalent bonding. The specific strength of C-honeycomb could be the best in structural carbon materials. Its specific thermal conductivity is also much better than most metal and high thermal conductivity semiconductors. Its strong anisotropic Poisson's effect may be utilized to design multi-functional structures with applications ranging from biomedical engineering to energy and environment systems.

The statistic nature of graphene-substrate interaction

Given the out-of-plane deformation is of soft nature (see the figure below), wrinkles are easy to form (as seen in Figure 1). Whether such rich 3D morphology influences the interaction between graphene and other substrate? Is it possible to manipulate wrinkling patterns for possible engineering applications? The adhesion of a soft membrane plays a central role for the functionality of many biological and engineering systems, from cell adhesion to advanced materials. We revealed that the adhesion of a membrane-buffered interface could be significantly modulated due to thermally induced surface corrugations in the membrane. Not expected from classical mechanics theories, an enhancement of the adhesion range and a linear variation of the adhesion strength could be observed as temperature rises, which facilitates long-range adhesion between soft membranes like graphene sheets and lipid-bilayers with a substrate. Such surprising findings may pave the way to understand temperature-sensitive kinetics in many biological systems where the interaction of cell membranes with extra-cellular environments is pivotal.

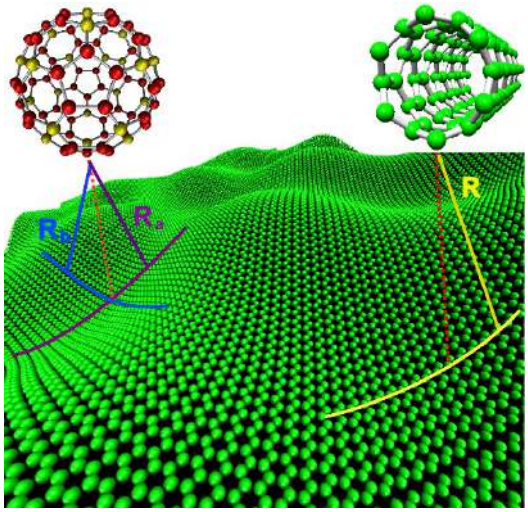

Figure 1. Illustration of the ultra-soft deformation in a graphene sheet and such a feature leads to the easy formation of fullerence and carbon nanotubes from graphene sheets. Such a process may involve the formation of defects in graphene which in turn alters the morphology and the deformation behavior of graphene.

CONCLUSIONS

High strength and ultra-low bending rigidity brings in uniqueness of graphene in contrast to other carbon allotropes. In this talk, we summarize the current advances on the mechanics while interfacing graphene in applications of different methods, including (1) the interface during making large-area single-layer graphene with patches of single-crystalline graphene, and how typical defects like pentagon-heptagon rings in grain boundaries would influence the strength of polycrystalline graphene; (2) during dimension scale-up to make three-dimensional graphene honeycomb using two-dimensional graphene, and what is the stable structure of those 3D carbon honeycomb and how is its mechanical properties; (3) given the out-of-plane deformation is of soft nature (see the figure below), wrinkles are easy to form. Whether such rich 3D morphology influences the interaction between graphene and other substrate.

References

[1] Chang, Yang, Wei, J. Mech. Phys. Solids **132**, 103697, 2019.
[2] Wei & Yang. Natl. Sci. Rev. **6**, 324–348 (2019).
[3] Gu, Wei, Li, Yang. Reviews of Modern Physics **90**, 041002, 2018.
[4] Pang et al. Nano Lett. **17**, 179–185, 2017.
[5] Yin, et al. Nano Lett. **15**, 1918–1924, 2015.
[6] Wang et al. Appl. Phys. Lett. **104**, 081902, 2014.
[7] Wei et al. Nano Lett. **13**, 26–30, 2013.
[8] Wei et al. Nature Materials **11**, 759–763, 2012.

ENHANCEMENT OF THE MECHANICAL PROPERTIES OF DIRECT-SPUN CARBON NANOTUBE MATS BY SUPERACID-ASSISTED DRAWING

Joe Stallard *, Wei Tan, Adam Boies, Norman Fleck.
Cambridge University Engineering Department, Trumpington St., Cambridge, CB2 1PZ, UK.

Summary: The mechanical behaviour of a direct-spun carbon nanotube mat is investigated upon fluid immersion. The elasto-plastic stress-strain response measured in air has significant orientation hardening and little in-plane anisotropy. Immersion in acetone, ethanol, toluene, NMP or chloroform reduces yield and failure strengths by up to 70%, without altering the ductility or shape of the stress-strain response. In contrast, chlorosulfonic acid immersion reduces tensile strength by almost 2 orders of magnitude, and increases ductility by over a factor of 5. Softening of the direct-spun mat upon chlorosulfonic acid infiltration is attributed to separation of bundled CNTs. Drawing in a chlorosulfonic acid solution followed by acid removal and drying increases the mat modulus by 2 orders of magnitude, and the tensile strength by a factor of 7, due to alignment of the nanotube bundle microstructure.

INTRODUCTION

Direct-spun carbon nanotube (CNT) mats and fibres are produced by drawing CNT aerogels from a floating catalyst chemical vapour deposition reactor [1]. The mat microstructure is a random interconnected network of CNT bundles, with a nodal connectivity of between 3 and 4. This microstructure deforms in a foam-like manner under macroscopic stress, with bending and shearing of CNT bundles, and so endows the mats with a typical tensile modulus of only a few GPa, much below that of CNT walls [2]. The modulus and strength of direct-spun mats and fibres are sensitive to the degree of alignment of the carbon nanotube bundle network [1]. Alignment may be enhanced through tensile drawing in the dry state, or whilst infiltrated with a polymer solution.

CNT-solvent solutions are also used to process nanotubes into mats and fibres. The van-der-Waals bonding between bundled CNTs prevents the formation of solutions in organic solvents, except at extremely dilute CNT volume fractions [3]. CNT dispersion is aided by sidewall modifications using oxidation or surfactants, yet relies upon sonication which reduces CNT length. CNTs separate when immersed in superacids, such as chlorosulfonic acid and oleum, forming a lyotropic mixture of isotropic and nematic liquid-crystalline phases [4]. Pultrusion of a CNT-superacid 'dope' into a bath of coagulating fluid creates an aligned CNT fibre, of modulus and strength up to 120 GPa and 1 GPa respectively [5]. Fibre properties vary with applied tension during coagulation, the choice of coagulating fluid, and CNT length.

The infiltration of organic solvents into direct-spun materials results in mechanical softening [6], yet the effect of superacid infiltration is hitherto unexplored, and forms the focus of this study. Herein, the stress-strain response of a typical direct-spun mat is measured in air, and whilst immersed in a range of organic solvents, chlorosulfonic acid, and solutions of chlorosulfonic acid and chloroform. Effects of immersion upon mechanical behaviour are discussed with relation to the mat microstructure. To increase alignment of the bundle microstructure, direct-spun mat samples are drawn whilst immersed in different fluids before fluid removal and drying; the enhancement in properties is then compared.

MECHANICAL PROPERTIES OF DIRECT-SPUN CNT MATS IN AIR AND UPON FLUID IMMERSION

The stress-strain response of direct-spun CNT mat samples (obtained from Tortech nanofibers Ltd.) were measured with a screw-driven tensile test machine at strain rate of $\dot{\epsilon} = 10^{-3}$ s^{-1} in air and whilst immersed in a range of liquids; the test setup is sketched in Figure 1(a). Load was applied with self-tightening wrapping grips; the strain state was measured optically by tracking the position of painted dots using a digital camera and image processing software.

Samples were submerged in acetone, toluene, NMP and chloroform for 3 hours before measurement of the stress-strain response whilst immersed; responses measured in air and in solvents are plotted in Figure 1(b). Whilst immersion in the solvents results in softening, the shape of the stress-strain response and ductility remain similar to that measured in air.

Now consider the influence of chlorosulfonic acid immersion upon the stress-strain response. After immersion in chlorosulfonic acid for a period of 5 minutes, the acid was drained and samples immersed in a solution of chlorosulfonic acid and chloroform; the volume fraction of acid f_{CSA} was varied between 0 (i.e. chloroform) and 1 (undiluted acid). Stress-strain responses measured whilst immersed in these solutions are plotted in Figure 1(c); the response measured when immersed in chloroform of Figure 1(b) is also included for comparison. The stress-strain response measured in chloroform after chlorosulfonic acid immersion is J-shaped with considerable hardening at nominal strains exceeding 0.4. Ductility rises and tensile strength reduces with increasing chlorosulfonic acid content.

EFFECT OF DRAWING UPON MECHANICAL PROPERTIES OF DIRECT-SPUN MATS

To increase their tensile modulus and strength, mat samples were drawn in air or whilst immersed in liquids as follows:

- **In air:** Samples were drawn to 80% of their nominal failure strength in air.
- **In chloroform:** Samples were drawn to 80% of their nominal failure strength in chloroform; the stress was maintained by application of a dead load whilst samples were dried in an oven at 70°C for one hour.

*Corresponding Author. E-mail: jcs202@cam.ac.uk

- **In chloroform and chlorosulfonic acid solutions:** Samples were immersed in chlorosulfonic acid for 5 minutes, then drawn in a solution of chlorosulfonic acid and chloroform of acid volume fraction $f_{CSA} = 1/64$ to a nominal stress of 10 MPa. The stress was maintained by application of a dead load whilst samples were rinsed in chloroform, acetone, and distilled water, and dried in an oven at 70°C for one hour, and 115°C for a further hour.

The stress-strain responses of drawn samples were then measured in air, with the same equipment and methods as described above. Results are plotted in Figure 2(a), alongside that of the original mat. The measured stress-strain behaviour of mats drawn in the presence of chlorosulfonic acid are elastic brittle. Images of the original and drawn mat microstructure in Figures 2(b) and (c) respectively reveal alignment of the bundle microstructure after drawing. The drawn sample modulus of approximately 55 GPa exceeds that of the original mat by two orders of magnitude. The stress-strain responses of mats measured after drawing in either air or chloroform absent acid are also above that of the original mat.

To establish the effects of fluid immersion in the absence of draw strain, samples were also immersed in identical fluids and dried for identical durations to those used to draw samples in the presence of chlorosulfonic acid, but without the application of any drawing strain. The mechanical properties of these samples were similar to those of the original direct-spun CNT mat. Thus, the enhancement in tensile strength and modulus is attributed to tensile drawing in the presence of chlorosulfonic acid, rather than to the influence of liquid infiltration and removal.

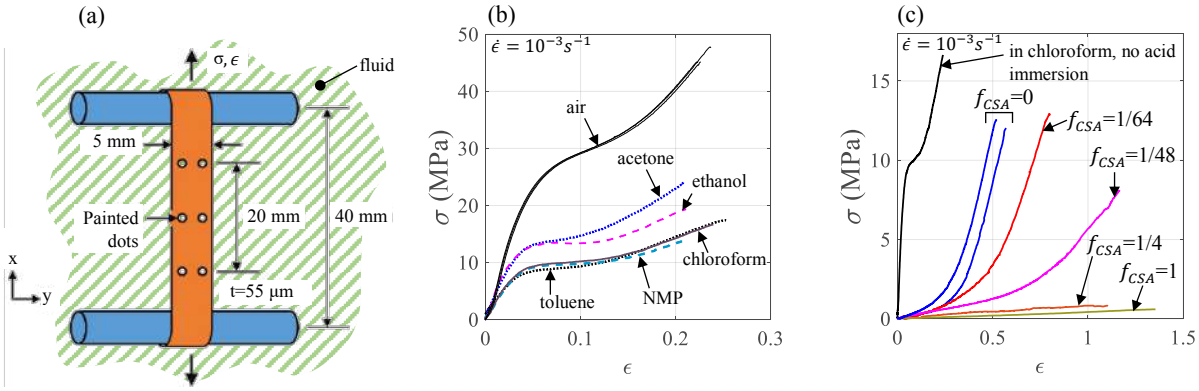

Figure 1: (a) Drawing response of immersed direct-spun mat samples. (b) The measured stress-strain response during drawing in air and organic solvents; (c) drawing response in solutions of chlorosulfonic acid and chloroform.

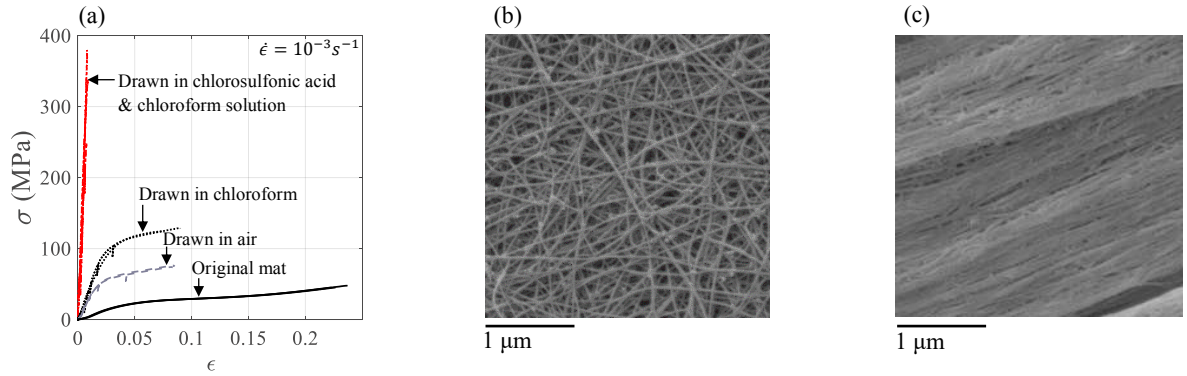

Figure 2: (a) Effect of drawing upon the stress-strain response of mat samples. (b) The CNT bundle microstructure of direct-spun mat in its original state; (c) the mat microstructure after drawing in a solution of chloroform and chlorosulfonic acid.

DISCUSSION & CONCLUSION

A network of tightly-packed CNT bundles forms the microstructure of direct-spun CNT mats. The reduction in tensile strength and increase in ductility measured upon chlorosulfonic acid immersion is attributed to the separation of bundled CNTs upon their exposure to chlorosulfonic acid, as described elsewhere in literature [4]. The influence of chlorosulfonic acid allows mat samples to be drawn to large strains, which facilitates microstructural alignment of the CNT bundle network. A drawing process was devised to enhance the mechanical properties of direct-spun CNT mat samples. Drawing in a chlorosulfonic acid solution increases the mat modulus by two orders of magnitude, and the tensile strength by up to a factor of 7. These enhancements are much above those obtained by drawing in air or in chloroform without acid.

References

[1] B. Alemán, V. Reguero, B. Mas, J.J. Vilatela. ACS Nano 9 (2015), pp. 7392-7398.
[2] J.C. Stallard, W. Tan, F.R. Smail, T.S. Gspann, A.M. Boies, N.A. Fleck. Extreme Mech. Lett. 21 (2018), pp. 65-75.
[3] S.D. Bergin, Z. Sun, D. Rickard, P.V. Streich, J.P. Hamilton, J.N. Coleman. ACS Nano 3 (2009), pp. 2340-2350.
[4] V.A. Davis et al. Nature Nanotechnology 4 (2009), pp. 830-834.
[5] N. Behabtu et al. Science 339 (2013), pp. 182-186.
[6] J. Qiu, J. Terrones, J.J. Vilatela, M.E. Vickers, J.A. Elliott, A.H. Windle. ACS Nano 7 (2013), pp. 8412-8422.

Thematic Session FM

K107279 - FM01 - Biological Fluid Mechanics - Keynote

OPTIMAL DESIGNS OF BIOLOGICAL NETWORKS: LUNGS AND ROOTS

Yeonsu Jung[1], Keunhwan Park[1], and Ho-Young Kim*[1]
[1] Department of Mechanical Engineering, Seoul National University, Seoul, Republic of Korea

Summary Airways in the lung and xylem of the root are network systems where both fluid transport and mass exchange with surrounding tissues occur simultaneously. Classical Murray's law, which explains the biological network design of cardiovascular systems and tree branches, is no longer valid in those systems involving mass exchange. Here we explore the design principles of the fluid-exchanging networks through the combination of theoretical and experimental approaches. This study not only elucidates the physical principles of general biological networks but also provides critical insights for artificial network systems.

INTRODUCTION

Natural creatures use various network systems to transport fluids within their bodies, which play essential roles in their metabolic activities. Those examples include cardiovascular system and lung airways in mammals, xylem, phloem and root networks in plants, and gills of fish. Because those networks have been evolved for millions of years to maximize their efficiency under constraints imposed by their surroundings, elucidating the physical principles behind their optimal structure can provide critical insights to enhance efficiency of artificial network systems. Here we consider two exemplary biological network systems, human lungs and plant roots.

BRANCHING RULES IN AIRWAYS OF HUMAN LUNG

The airway network of a human lung starts from conducting airways (from mouth to the 16th branching stage), which are connected to acinar airways surrounded by alveoli (from the 17th to 23rd branching stage) as shown in Fig. 1(a). The airway diameter gradually decreases through multiple branching, and the diameter reduction ratio in conducting and acinar airways is reported to be 0.79 and 0.94, respectively, as plotted in Fig. 1(b). The diameter reduction in the conducting airways, where no gas exchange with surrounding tissue occurs, was rationalized previously on the basis of classical Murray's law. Here, we mathematically show that the observed diameter reduction ratio in the acinar airway, where gas transfer between airway and alveoli arises, corresponds to the optimal value to maximize gas transfer rate per unit surface area under minimum cost for construction and maintenance of the organ [1].

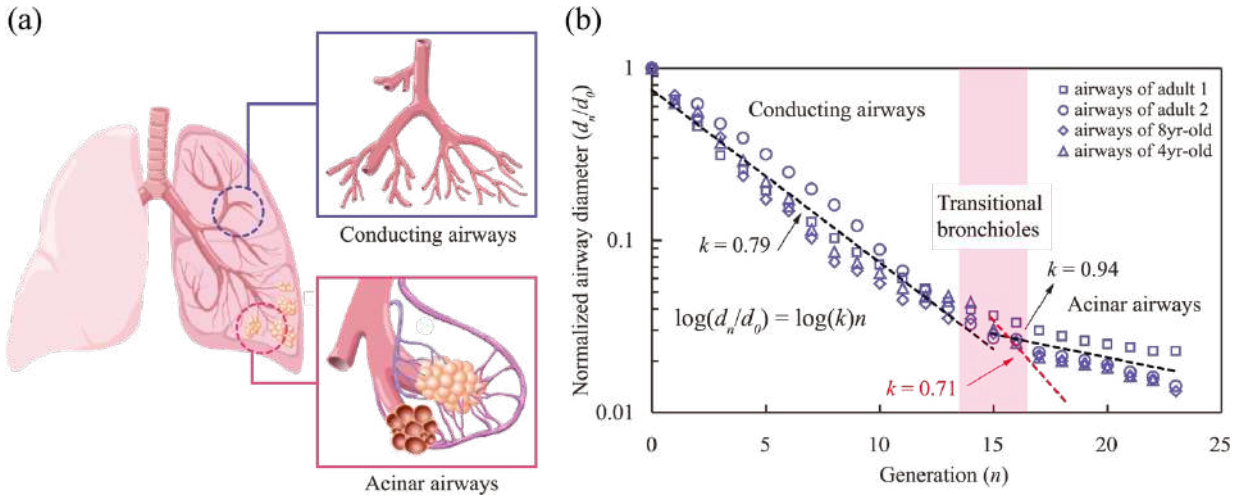

Figure 1. (a) Schematic of airways in human lung, consisting of conducting and acinar airways. (b) Reduction in normalized airway diameter along with airway generation. Adapted from Ref. [1].

*Corresponding author. E-mail: hyk@snu.ac.kr

ROOT LENGTH DISTRIBUTION OF PLANTS

Shaping a plant root into a structure optimized for water capture is increasingly important for the sustainability of agriculture in the era of global climate change. Although deep-reaching roots are favored by crop breeders and genetic engineers of plants, here we show that nature has apparently adopted a different strategy of shaping roots (see Fig 2a; roots are abundant over upper layers). We establish a mathematical model for optimal root length distribution by considering that plants seek maximal water uptake at the metabolic expenditure of root growth. Our theory finds a logarithmic decrease of root length density with depth to be most beneficial for efficient water uptake, which is supported by biological data as well as our experiments using root-mimicking network systems (see Fig 2b) [2].

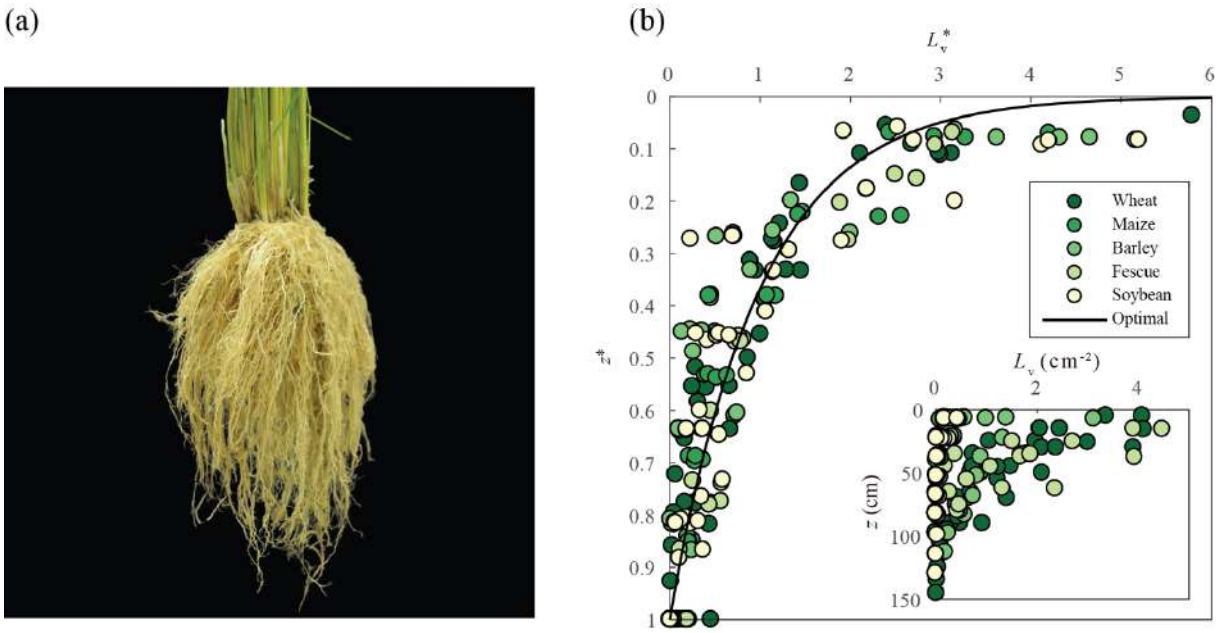

Figure 2. (a) Photograph of a rice plant (*Oryza sativa*). (b) Normalized root length distribution of various plants as a function of normalized depth. The solid line corresponds to the theoretical optimum distribution. Inset: dimensional raw data of the root length density. Adapted from Ref. [2].

References

[1] Park, K., Jung, Y., Son, T., Cho, Y.-J., Jeon, N.L., Kim, W., Kim, H.-Y. Optimal diameter reduction ratio of acinar airways in human lungs. *PLoS ONE* **14**: e0204191, 2019.

[2] Jung, Y., Park, K., Jensen K.H., Kim, W., Kim, H.-Y. A design principle of root length distribution of plants. *J. R. Soc. Interface* **16**: 20190556, 2019.

FLUID FLOWS SHAPING MORPHOLOGY

Karen Alim [1,2]
[1]Department of Physics, Technical University of Munich, Munich, Germany
[2]Max Planck Institute for Dynamics and Self-Organization, Göttingen, Germany

Summary Fluid flows can propagate information on large scales an essential feature during the development of an organism. What are the principal mechanisms of how fluid flows induce, transmit and respond to biological signals and thus control morphology? The role of fluid flows is particularly prominent during the adaptation of transport networks. Here, the network-forming slime mould *Physarum polycephalum* emerged as a model. Investigating the pivotal role of fluid flows in this live transport network we find that flows are patterned in a peristaltic wave thereby optimising transport. In fact, flows are hijacked by signals to propagate throughout the network promoting their own transport by invoking a propagating front of increased flow. This simple feedback of flows on morphology is sufficient to explain complex dynamics of the living network like finding the shortest path through a maze.

Flow networks are a fundamental building block of life, whether as blood vasculature, bronchioles in the lungs, nephron in the kidneys, intestines, lymphatic system or as the brain passages of the spinal fluid. How network architecture is controlled by the interaction with the flows flowing through it is still unclear, despite the broad significance of the question and an interest that has lasted almost a hundred years [14, 13]. Our research wants to open up the possibility to control network function and performance by identifying the physical principles that control the adaptation of the network architecture.

The ideal model system that allows to quantify the dynamics of fluid flows and network architecture in parallel is the network-forming slime mold *Physarum polycephalum*. *Physarum* is the model organism of the plasmodial slime molds, which forms a two-dimensional, tubular network as a single gigantic cell [11, 16]. We have established *Physarum* as a model system for the role of fluid flows in living matter by perfecting cell culture in liquid solution and on agar plates and introducing quantitative analyses. The reduced complexity of *Physarum* to a flow network alone allows a unique interaction of observed, quantified dynamics based on light microscopy data and hypothesis development in theoretical models.

Characteristic for *Physarum* is the periodic shuttle flow of the cytoplasm enclosed by the tubes [9, 10], which extends over the entire network. Each individual tube consists of a gel-like outer layer interspersed with an actin cortex which encloses the cytoplasmic fluid [6]. The actin cortex radially contracts the tube about every 100 seconds and thus drives the rhythmic pendulum flow [5, 19, 18, 2]. The quantifiable dynamics of the tube diameters therefore provide information about the coordination of the flows as well as network architecture - a unique basis for deciphering the physical coupling of network architecture and flow.

We have shown that the contractions of the tubes in *Physarum* are organized along the entire network in a peristaltic wave, which also dynamically adapts its wavelength to the size of the network [2]. The important innovative step towards the spatio-temporal measurement of the contractions along the 0.5-2cm networks was to measure the dynamics of the individual tubes of about $100\mu m$ diameter by the amount of light transmitted through the tubes. The decisive factor is that the large dynamic range of the microscope camera allows a fine resolution of the transmitted light quantity and thus of the contraction state of a tube and is not limited in resolution by the number of image pixels. Furthermore, we have shown that the flows follow the Stokes flow equations [4] and are thus completely determined by the contractions of the tubes in the entire network [2]. This step opens up unprecedented access to physical parameters such as the relative local pressure of the cytoplasm, which cannot be measured experimentally but which now follows from the theoretical calculation of the flow based on observed contraction patterns. Core for this insight was the development of simultaneous live imaging of fluid flows and network morphology using fluorescent tracer particles, which allows to resolve the different size scales of network and single tube. For this purpose, $1\mu m$ fluorescent tracer beads in the *Physarum* liquid culture [17] are integrated into the liquid cytoplasm.

The observation of actin-cortex contractions coordinated over centimeters now raises the question how the contractions can be coordinated on such large scales. Our theoretical work shows that the flow-driven transport of messenger substances, which themselves couple to the dynamics of the actin cortex, enables such long-range coordination of contractions [8]. However, the confirmation that calcium as actin cortex regulator fulfills this function is still pending.

Physarum is known for its ability to solve complex problems like the problem of the traveling salesman [20, 7, 12] or to find the shortest way through a maze [15]. *Physarum* solves these problems by adapting its network architecture to stimuli in its environment. We investigate how this complex behavior is achieved by transporting, processing and storing signals by means of the flow in the network [1]. We have discovered that a food stimulus releases a signal molecule in the cytoplasm. This signalling molecule is spread by fluid flows, but at the same time amplifies the flow by locally increasing the contraction amplitude during the journey through the network [3]. Thus, the signal molecule initiates a feedback, which amplifies its own propagation. This mechanism explains the ability of *Physarum* to find the shortest path between food sources in the maze.

*Corresponding author. E-mail: k.alim@tum.de.

References

[1] K. Alim. Fluid flows shaping organism morphology. *Phil Trans Roy Soc B*, 373:20170112, May 2018.

[2] K. Alim, G. Amselem, F. Peaudecerf, M. P. Brenner, and A. Pringle. Random network peristalsis in *Physarum polycephalum* organizes fluid flows across an individual. *Proc Natl Acad Sci USA*, 110(33):13306–13311, Aug. 2013.

[3] K. Alim, N. Andrew, A. Pringle, and M. P. Brenner. Mechanism of signal propagation in *Physarum polycephalum*. *Proc Natl Acad Sci USA*, 114(20):5136–5141, 2017.

[4] G. K. Batchelor. *An Introduction to Fluid Dynamics*. Cambridge University Press, Feb. 2000.

[5] M. Iima and T. Nakagaki. Peristaltic transport and mixing of cytosol through the whole body of *Physarum* plasmodium. *Math Med Biol*, 29(3):263–281, Sept. 2012.

[6] G. Isenberg and K. E. Wohlfarth-Bottermann. Transformation of cytoplasmic actin. Importance for the organization of the contractile gel reticulum and the contraction–relaxation cycle of cytoplasmic actomyosin. *Cell Tiss Res*, 173(4):495–528, Oct. 1976.

[7] A. Johannson and J. Zou. A Slime Mold Solver for Linear Programming Problems. In *How the World Computes*, pages 344–354. Springer, Berlin, Heidelberg, Berlin, Heidelberg, June 2012.

[8] J.-D. Julien and K. Alim. Oscillatory fluid flow drives scaling of contraction wave with system size. *Proceedings of the National Academy of Sciences*, 115(42):10612–10617, Oct. 2018.

[9] N. Kamiya. The rate of the protoplasmic flow in the myxomycete plasmodium I. *Cytologia*, 15(3-4):183–193, 1950.

[10] N. Kamiya. The rate of the protoplasmic flow in the myxomycete plasmodium. II. *Cytologia*, 15(1949):194–204, 1950.

[11] N. Kamiya. Physical and chemical basis of cytoplasmic streaming. *Annu Rev Plant Physiol*, 32:205–236, 1981.

[12] L. Liu, Y. Song, H. Zhang, H. Ma, and A. V. Vasilakos. Physarum optimization: A biology-inspired algorithm for the Steiner tree problem in networks. *IEEE Trans Comput*, 64(3):818–831, Jan. 2015.

[13] C. D. Murray. The physiological principle of minimum work: I. The vascular system and the cost of blood volume. *Proc Natl Acad Sci USA*, 12(3):207–214, Mar. 1926.

[14] C. D. Murray. The physiological principle of minimum work: II. Oxygen exchange in capillaries. *Proc Natl Acad Sci. USA*, 12(5):299–304, May 1926.

[15] T. Nakagaki, H. Yamada, and A. Tóth. Maze-solving by an amoeboid organism. *Nature*, 407:470, Sept. 2000.

[16] C. Oettmeier, K. Brix, and H.-G. Döbereiner. *Physarum polycephalum*—a new take on a classic model system. *J Phys D: Appl Phys*, 50(41):413001–12, Sept. 2017.

[17] C. Oettmeier, J. Lee, and H.-G. Döbereiner. Form follows function: ultrastructure of different morphotypes of *Physarum polycephalum*. *J Phys D: Appl Phys*, 51(13):134006–17, Mar. 2018.

[18] M. Radszuweit, S. Alonso, H. Engel, and M. Bär. Intracellular mechanochemical waves in an active poroelastic model. *Phys Rev Lett*, 110(13):138102, Mar. 2013.

[19] S. Takagi and T. Ueda. Emergence and transitions of dynamic patterns of thickness oscillation of the plasmodium of the true slime mold *Physarum polycephalum*. *Physica D*, 237(3):420–427, 2008.

[20] A. Tero, S. Takagi, T. Saigusa, K. Ito, D. P. Bebber, M. D. Fricker, K. Yumiki, R. Kobayashi, and T. Nakagaki. Rules for biologically inspired adaptive network design. *Science*, 327:439–442, Jan. 2010.

ROBOTIC CONTROL OF LIVE JELLYFISH SWIMMING IN THE LABORATORY AND ATLANTIC OCEAN

Nicole W. Xu[1]*, James Townsend[2,3], Jack Costello[2,3], Sean Colin[2,4], John O. Dabiri [5,6]
[1]Department of Bioengineering, Stanford University, Stanford, CA, USA
[2]Marine Biological Laboratory, Woods Hole, MA, USA
[3]Department of Biology, Providence College, Providence, RI, USA
[4]Department of Marine Biology and Environmental Science, Roger Williams University, Bristol, RI, USA
[5]Graduate Aerospace Laboratories (GALCIT), California Institute of Technology, Pasadena, CA, USA
[6]Department of Mechanical Engineering, California Institute of Technology, Pasadena, CA, USA

Summary Animal locomotion has the potential to expand the performance capabilities of robots by incorporating energy-efficient bioinpired designs. In addition, the robotic control of live animals enables further studies of entire organisms in more user-controlled, rigorous experiments for applications in animal-fluid interactions, robotics, and biology. This work presents a biohybrid jellyfish robot comprising a portable low-power microelectronic system embedded in live animals. Experiments in the laboratory to increase swimming frequency illustrate efficient enhanced swimming speeds of up to 2.8 times, dependent on bell kinematics that affect swimming hydrodynamics. This system was also deployed in the Atlantic Ocean to demonstrate the feasibility for future applications in ocean monitoring.

INTRODUCTION

A better of understanding of aquatic animal locomotion can potentially impact a wide range of fields, from addressing fundamental scientific questions about the ecology and evolution of basal organisms, to animal-fluid interactions [1], to applications in robotics and ocean monitoring [2-4]. In particular, *Aurelia aurita* (moon jellyfish) are a compelling model organism to study biological fluid dynamics and inspire more energy-efficient aquatic vehicles because of their low cost of transport (COT), the mass-specific metabolic energy expended to travel a unit distance [5]. The hydrodynamics and bell kinematics of natural *A. aurita* swimming have been well-characterized using flow visualization techniques such as particle image velocimetry (PIV) and image processing to track bell curvature. However, the application of embedded microelectronic systems to control their muscle contractions can further enable these tools to reveal fundamental biological and physical processes that cannot be understood by observation alone.

By directly inciting muscle contractions, robotic manipulation of jellyfish swimming enables systematic studies of how swimming frequency affects speeds, bell kinematics, and hydrodynamics. To do this, we incorporated a self-contained microelectronic system into live jellyfish to characterize the robotic control of jellyfish swimming in saltwater tanks in the laboratory, and field deployment of these biohybrid jellyfish robots in the Atlantic Ocean. Future applications could incorporate sensors and a closed-loop feedback mechanism to maneuver the biohybrid robot into targeted areas of the ocean to track temperature, pressure, etc. and collect data to monitor climate changes.

METHODS AND TECHNIQUES

Electrical stimulation using a square pulse wave, as illustrated in Fig. 1A, can reliably and robustly incite muscle contractions in live jellyfish [6]. A miniaturized system that encapsulates the microelectronic components in waterproof housing (Fig. 1B and C) enables free-swimming both in the laboratory [6] and *in situ*.

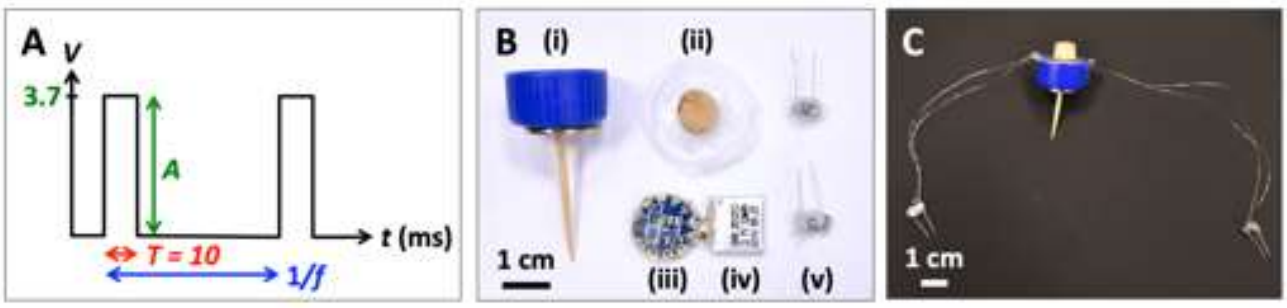

Figure 1. (A) Jellyfish muscle contractions can be externally controlled by using a square wave signal with an amplitude, A, of 3.7 V and pulse width, *T*, of 10 ms, set at frequencies, *f*, of 0.25, 0.38, 0.50, 0.62, 0.75, 0.88, and 1.00 Hz. (B) Components of a self-contained swim controller, which includes housing made from (i) a polypropylene cap with a wooden pin that embeds into the bell center, and (ii) a plastic film to waterproof the housing, both offset with stainless steel and cork weights to keep the device approximately neutrally buoyant. Microelectronics include (iii) a TinyLily mini-processor, (iv) lithium polymer battery, and (v) two platinum-tip electrodes with LEDs to visually indicate stimulation. (C) The fully assembled device, with the processor and battery encased in the housing. This figure is adapted from [1].

*Corresponding author. E-mail: nicolexu@stanford.edu

In the laboratory, free-swimming experiments were conducted using a self-contained two-electrode microelectronic system to demonstrate enhanced swimming speeds over a frequency range (0.25-1.00 Hz) in a 1.8-m vertical tank. Constrained experiments were also conducted to obtain oxygen consumption rates within this frequency range, to calculate COT values and determine whether enhanced propulsion was energy efficient or achieved at a metabolic cost to the animals. To track how bell kinematics and flow fields vary when the animals pulse at different frequencies, image processing techniques and 2D PIV were used in pinned animals, driven within this frequency range.

In the field, free-swimming experiments were conducted using the same self-contained two-electrode system to demonstrate the feasibility and robustness of the biohybrid robotic system as a proof of concept.

RESULTS: LOW-POWER BIOHYBRID ROBOTIC JELLYFISH CAN SWIM UP TO 2.8 TIMES FASTER

Fig. 2 illustrates the normalized swimming speeds (in body diameters s^{-1}) on the right ordinate axis over the swim controller frequency, from 0 Hz (inactive, swimming speed is due to the animals' natural pulses at 0.16 Hz) to 0.25 to 1.00 Hz (active swim control). The enhancement factor on the left ordinate axis is defined as the ratio of swimming speeds over the mean unstimulated swimming speeds (of $N = 6$ animals at 0 Hz). As shown, swimming speeds can be enhanced up to three times their natural animal counterparts, with a dependence on body morphology [6]. This trend has been similarly shown in a theoretical model, adapted from [7], to incorporate bell morphological parameters that mimic real animals. Enhancement factors increase as the aspect ratio of the bells increase (toward more prolate animals).

A noteworthy feature is the decrease in speeds when the animals are driven at higher frequencies, which is due to changes in the bell kinematics, in which the stimulation frequency increases beyond the limitation of natural jellyfish swimming (from biological constraints including contraction and relaxation stroke times). However, this difference in bell morphology has not been reported in literature. We will characterize the kinematics and fluid dynamics by using PIV to reveal how the bell kinematics change as a function of frequency.

Furthermore, this increase in swimming speeds does not create an undue metabolic cost on the animal and only comes at 10 mW of external power input to the microelectronics, which is 10 to 1000 times less external power per mass than existing aquatic robots in literature [6].

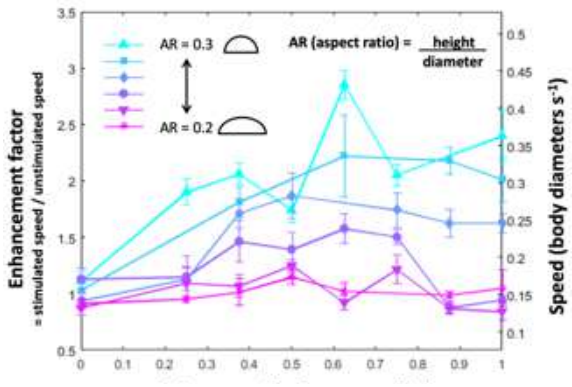

Figure 2. Enhancement factors and swimming speeds for jellyfish with external swim control from 0 to 1.00 Hz. Each animal ($N = 6$) is represented by a different color, with body geometry shown as an aspect ratio, or the bell height to diameter. Speed (in body diameters s^{-1}) is indicated on the righthand axis. Enhancement factor is defined as the speed scaled by the mean of the normalized 0 Hz speed for all 6 animals (in which the swim controller is embedded but inactive). This figure is adapted from [1].

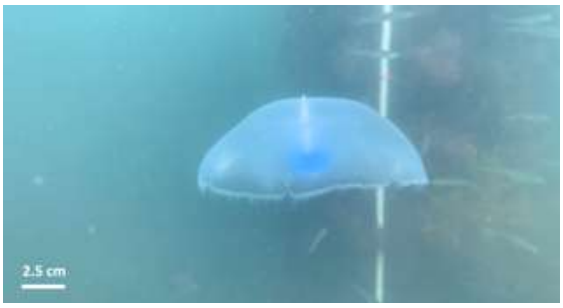

Figure 3. The biohybrid jellyfish robot was deployed in the Atlantic Ocean (at the Marine Biological Laboratory in Woods Hole, MA).

CONCLUSIONS

This biohybrid robotic jellyfish illustrates the capabilities of artificial control of aquatic animal locomotion. Enhanced propulsion has been demonstrated in laboratory conditions, and by successfully deploying this system in the Atlantic Ocean (Fig. 3), we demonstrate the robustness of this biohybrid system *in situ*. This suggests the potential for applications in sending biohybrid robots to collect data and monitor more sensitive areas of the ocean currently unexplored by other aquatic vehicles.

References

[1] J. O. Dabiri, S. P. Colin, J. H. Costello, M. Gharib, Flow patterns generated by oblate medusan jellyfish: field measurements and laboratory analyses. *J. Exp. Biol.* **208**, 1257–65 (2005).

[2] J. O. Dabiri. Optimal vortex formation as a unifying principle in biological propulsion vortex formation time: the dimensionless timescale during which vortex formation occurs. *Annu. Rev. Fluid Mech.* **41**, 17–33 (2009).

[3] Y. Tadesse, A. Villanueva, C. Haines, D. Novitski, R. Baughman, S. Priya, Hydrogen-fuel-powered bell segments of biomimetic jellyfish. *Smart Mater. Struct.* **21**, 045013 (2012).

[4] A. Villanueva, P. Vlachos, S. Priya, Flexible Margin Kinematics and Vortex Formation of *Aurelia aurita* and Robojelly. *PLoS One*. **9**, e98310 (2014).

[5] B. J. Gemmell, J. H. Costello, S. P. Colin, C. J. Stewart, J. O. Dabiri, D. Tafti, S. Priya, Passive energy recapture in jellyfish contributes to propulsive advantage over other metazoans. *Proc. Natl. Acad. Sci. U.S.A.* **110**, 17904–9 (2013).

[6] N. W. Xu, J. O. Dabiri. Low-power microelectronics embedded in live jellyfish enhance propulsion. *Sci. Adv.* **6,** eaaz3194 (2020).

[7] T. L. Daniel, Mechanics and energetics of medusan jet propulsion. *Can. J. Zool.* **61**, 1406–1420 (1983).

GPU ACCELERATED SIMULATIONS OF FLUID–STRUCTURE–ELECTROPHYSIOLOGY INTERACTION (FSEI) FOR THE HEART

Francesco Viola[1], Vamsi Spandan [2], Valentina Meschini[3], Joshua Romero[4], Massimiliano Fatica[4], and Roberto Verzicco *[5,6,1]
[1]Gran Sasso Science Institute, L'Aquila, Italy
[2]John A. Paulson School of Engineering and Applied Sciences, Harvard University, USA.
3Department of Mathematics, University of Rome Tor Vergata, Rome, Italy
[4]NVIDIA Corporation, 2701 San Tomas Expressway, Santa Clara, CA 95050, USA
5Department of Industrial Engineering, University of Rome Tor Vergata, Rome, Italy
[6]Physics of Fluids Group, Max Planck Center Twente for Complex Fluid Dynamics, MESA+ Research Institute, and J. M. Burgers Center for Fluid Dynamics

Summary The reliability of cardiovascular computational models depend on the accurate modeling of the hemodynamics, the realistic characterization of the tissues and the correct description of the fluid/structure interaction. The resulting multi-physics model thus requires an immense computational power and implies long time to get the results or to rely on external computational resources if multi–CPU processors are used (MPI acceleration). In the recent years, the graphics processing unit (GPU) has emerged as a popular platform for high performance computing and allows for considerable reductions of the time–to–solution. In order to develop a computational tool to support medical decision, our multi-physics solver [1] has been ported to GPU architectures using CUDA Fortran to tackle fast and accurate hemodynamics simulations of the human heart without resorting to large–scale supercomputers.

MOTIVATION

Each beat of the human heart is triggered by specialized pacemaker cells that generate rhythmical electrical impulses rapidly propagating through the heart, stimulating myocytes contraction and, in turn, pumping blood. The resulting hemodynamics yields shear stresses and pressure loads on the myocardium and on the valve leaflets, whose opening/closing ensures the correct flow direction across heart chambers. This highly sophisticated mechanism, however, can be affected by cardiovascular disorders (CVD) that reduce the pumping efficiency of the heart and can potentially yield life–threatening conditions. CVD are the main cause of death in developed countries and also one of the most relevant costs for health care systems (cost of 210 billion euro per year for the EU economy [2]). Computer simulations of the blood flow in the heart and arteries can be a precious tool to improve the predicting capabilities of diagnostics, to refine surgical techniques and test the performance of prosthetic devices. However, the reliability of cardiovascular simulations depends on the accurate modeling of the hemodynamics, the realistic characterization of the tissues and the correct description of the electro–fluid–structure interaction (FSEI).

THE MULTI–PHYSICS MODEL FOR THE LEFT–HEART

Our group has developed an innovative and versatile multi-physics model to simulate the left heart [1] In particular, the pulsatile and transitional character of the hemodynamics is obtained by solving directly the incompressible Navier–Stokes equations using a staggered finite differences method embedding various immersed boundary (IB) techniques to handle complex moving and deforming geometries. The structural mechanics is based on the Fedosov interaction potential method to account for the mechanical properties of the biological tissues, which are anisotropic and nonlinear [3]. The electrophysiology, responsible for the active potential propagation in the cardiac tissue triggering the active muscular tension, is incorporated by means of a bidomain model accounting for the different cellular models of the various portions of the heart [4]. All these models are three-way coupled with each other resulting into the FSEI as indicated in figure 1(a). The heart model is composed by realistic geometries of the left ventricle (figure 1b) and atrium whose active muscular contraction triggers a structural deformation of the endocardium that originates the hemodynamics, which, in turn, generates stresses on the surrounding cardiac tissue. The numerical framework also includes the bi-leaflet mitral valve, the three-leaflets aortic valve and the thoracic aorta, which are passive tissues experiencing continuous stretching and bending through the cardiac cycle. This computational framework is seen to provide realistic cardiovascular simulations both in terms of muscular activation, intraventricular hemodynamics and wall shear stresses. Figure 1(b) shows the instantaneous flow streamlines and the wall shear stress at the ventricle during the E-wave of the diastole, which is in qualitative and quantitative agreement with in-vivo and ex-vivo measurements [5].

In our model *the body kinematics comes as a result of the three-way FSEI* and a different cardiac configuration (e.g. cardiac output, heart rate, ventricle geometry, valve leaflets length and/or thickness) can be simply investigated by minimal modifications in the computational model [6]. The three-way FSEI makes the computational model predictive, thus opening the way to numerical experiments for virtually testing new prosthetic devices and surgical procedures.

*Corresponding author. E-mail: verzicco@uniroma2.it

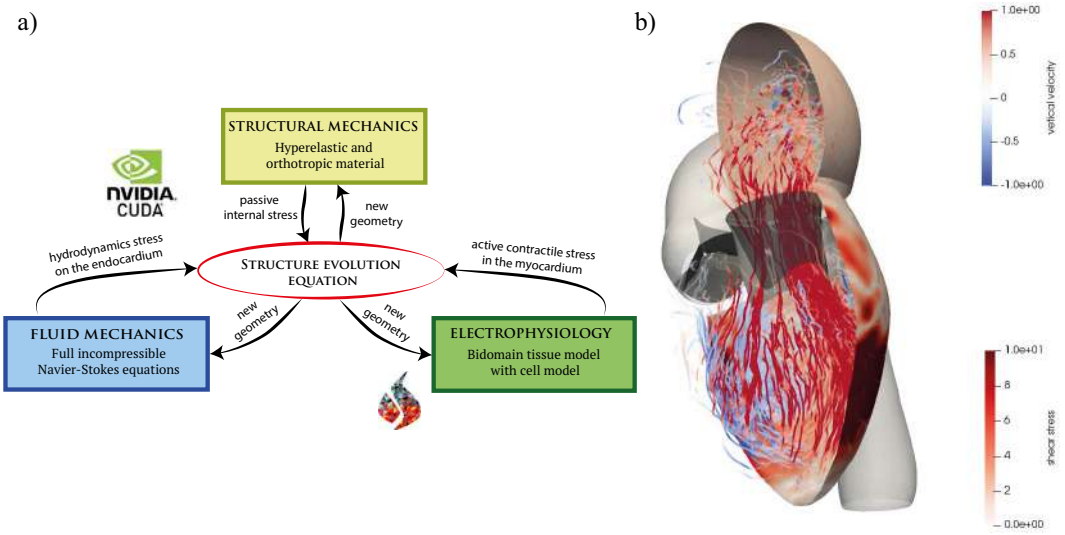

Figure 1: a) Sketch of the fluid–structure–electrophysiology (FSEI) coupling. b) Snapshot of streamlines coloured with the vertical velocity and wall shear stress on the tissue wet surface at the peak of the E–wave of the diastole.

PERFORMANCE BOTTLENECK OF THE MODEL

The fluid, structure and electrophysiology solvers are strongly interconnected and they may be solved simultaneously as a single large dynamical system through an iterative procedure (strong coupling) or sequentially where each model is used as input for the next one in a given order (loose coupling). Which of the two approaches is more efficient depends on the specific problem and its parameters. In the case the added mass phenomena or structures with reduced inertia do not play an important role the loose coupling is considerably faster than the strong one (computational time savings of the order of 50–70%). However, the time step size is physically limited by the elastic frequency of the stiff ventricle myocardium and a maximum time step of $2 \cdot 10^{-5}$ in nondimensional units (corresponding to $0.8\mu s$) is needed to ensure numerical stability. Such a small time step means that about *1 million time steps have to be run to integrate a single heart beat* and the computational model has to be highly optimized to resolve a heart beat within few hours in order to timely provide statistically converged results for clinical decision.

TOWARDS MEDICAL APPLICATION: GPU OPTIMIZATION

Efficient code parallelization and effective use of the computational resources are essential for clinical application where accurate and timely simulation results are needed. The current trends in high performance computing point towards GPU accelerators since this technology is well-suited to address problems where the same program can be executed on many data elements in parallel. Hence, the initial CPU code parallelized with MPI has been ported in CUDA Fortran with the extensive use of kernel loop directives (CUF kernels) in order to have a source code as close as possible to the original CPU version. The GPU accelerated multi-physics heart model shows good strong scaling characteristics, and the wall-clock time per step for the GPU version is in between one and two orders of magnitude smaller than for the CPU version of the code thus allowing for a timely solution of the intraventricular hemodynamics. Furthermore, since the main aim here is to provide an in silico tool to aid medical decisions we have tested the code not only on GPU clusters but also on a workstation mounting two Tesla V100 that could be easily installed in a hospital (on the contrary of a cluster). Due to the increased performance and efficient use of memory, the optimized GPU code on such workstation solves a single time step in 0.1 and 0.9 seconds on a 257^3 and 512^3 mesh, respectively thus reducing the time–to–solution of standard simulations to less than a day.

References

[1] Viola F., Meschini V., Verzicco R. Fluid–Structure–Electrophysiology interaction (FSEI) in the left-heart: A multi-way coupled computational model. *European J. of Mechanics / B Fluids*, 2020.
[2] Mittal R., et al. Computational modeling of cardiac hemodynamics: Current status and future outlook. *J. of Comp. Physics*, 305: 1065-1082, 2016.
[3] Fedosov D.A., Caswell B., Karniadakis G.E., Systematic coarse-graining of spectrin-level red blood cell models, *Comput. Methods Appl. Mech. Engrg*. 199 (29-32) 1937-1948, 2010.
[4] Tung L., A Bi-domain Model for Describing Ischemic Myocardial Dc Potentials (Ph.D. thesis), Massachusetts Institute of Technology, 1978.
[5] Viola, F., Jermyn, E., Warnock, J., Querzoli, G., & Verzicco, R. Left Ventricular Hemodynamics with an Implanted Assist Device: An In Vitro Fluid Dynamics Study. *Annals of biomedical engineering*, 1-16, 2019.
[6] Meschini, V., Viola, F., & Verzicco, R. Modeling mitral valve stenosis: A parametric study on the stenosis severity level. *J. of biomechanics*, 84, 218-226, 2019.
[7] Zhu X. et al. AFiD-GPU: a versatile Navier–Stokes solver for wall-bounded turbulent flows on GPU clusters. *Computer physics communications*, 229: 199-210, 2018.

CEREBROSPINAL FLUID MECHANICS IN THE BRAIN: MODELING

Jeffrey Tithof * [1,2], J. Brennen Carr[2], Jia Liu[2], Humberto Mestre[3,4], Ting Du[3], Maiken Nedergaard[3,4], John H. Thomas[2], Jessica Shang[2], and Douglas H. Kelley[2]

[1]Department of Mechanical Engineering, University of Minnesota, Minneapolis, MN, USA
[2]Department of Mechanical Engineering, University of Rochester, Rochester, NY, USA
[3]Center for Translational Neuromedicine, University of Rochester Medical Center, Rochester, NY, USA
[4]Department of Neuroscience, University of Rochester Medical Center, Rochester, NY, USA

Summary Recent breakthroughs with *in vivo* measurement techniques reveal cerebrospinal fluid flow through a network of "perivascular spaces" (PVSs) in the brain. PVSs are annular tunnels around the brain's vasculature and part of the recently discovered glymphatic system, an important waste removal pathway implicated in Alzheimer's disease. We have made multiple important advancements in modeling PVS flow. We introduce an improved geometric model of PVSs which we: (i) use to argue that PVSs are optimally shaped to maximize CSF flow and (ii) use to perform direct numerical simulations of microscopic PVS flow. We develop a hydraulic network model to obtain estimates of CSF flow speed, Reynolds, and Péclet numbers throughout the PVS network. These predictions may be tested in the future as experimental methods advance, and meanwhile can guide hypotheses about the glymphatic system.

INTRODUCTION

The brain is bathed in cerebrospinal fluid (CSF), a fluid primarily composed of water which provides the brain with shock absorption and buoyancy. A growing body of experimental evidence [1] has demonstrated that CSF also flows through the brain to remove toxic metabolic waste, such as amyloid-β, and that disruption of this clearance mechanism can lead to neurodegenerative diseases such as Alzheimer's. This clearance pathway, often referred to as the "glymphatic system," includes CSF flow through perivascular spaces (PVSs), which are annular tunnels surrounding the vasculature in the brain (Figure 1a). Numerical simulations offer great potential for gaining novel insights into this waste clearance system, but such simulations are still in their infancy, and the models that have been developed have reached conflicting conclusions, even regarding the direction of CSF flow in PVSs (see the review [2]). A substantial obstacle to developing accurate numerical simulations is the scarcity of experiments which provide model parameterizations and measurements for validation. However, we have recently performed *in vivo* measurements of CSF flow through PVSs [3] which provide a foundation for substantial advancements in modeling this waste clearance system unique to the brain.

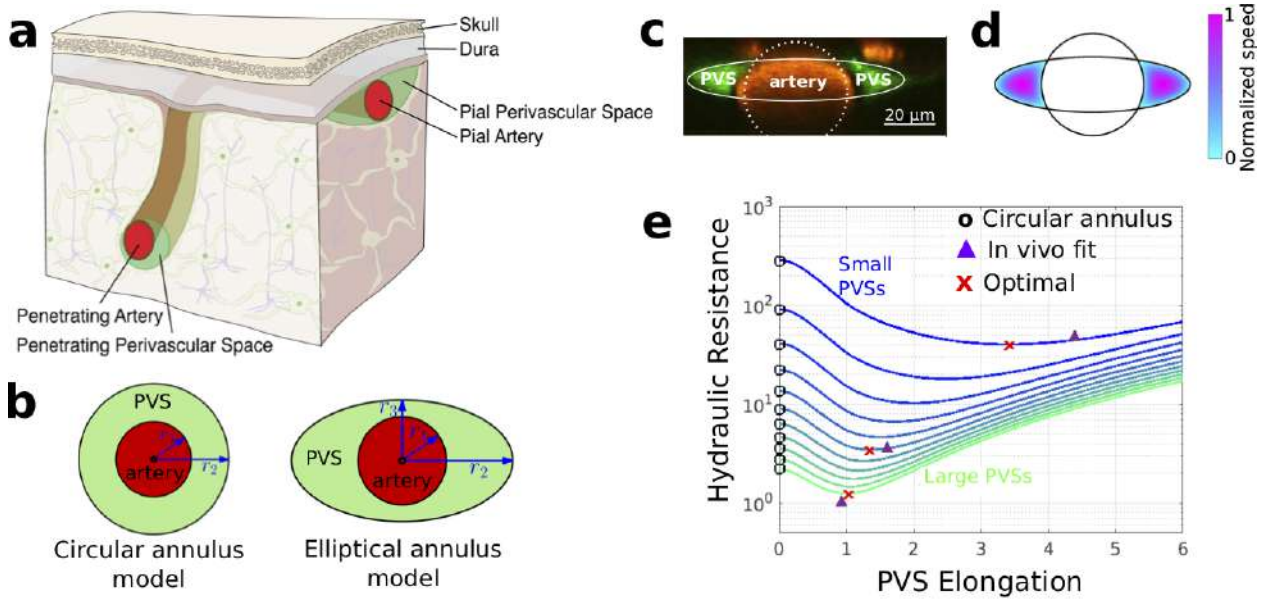

Figure 1: Improved modeling of perivascular spaces (PVSs) in the brain [4]. (a) A schematic illustrating PVSs as channels surrounding vasculature which contain flowing CSF. (b) All prior modeling studies have assumed the PVS has a circular annulus shape (left); we have introduced an elliptical annulus model (right). (c) An *in vivo* image of a PVS. (d) The speed profile computed for the optimal PVS shape which has the same cross-sectional area as the PVS shown in c. (e) Several curves of hydraulic resistance versus PVS elongation each with fixed PVS area. PVS shapes observed *in vivo* are nearly optimal, with hydraulic resistance much smaller than the circular annulus.

*Corresponding author. E-mail: j.tithof@rochester.edu.

IMPROVED MODELING OF PERIVASCULAR SPACES

All prior analytical and numerical models of CSF flow through PVSs have assumed that the PVS has a circular annulus shape (Figure 1b left). However, *in vivo* measurements [3] reveal that the outer boundaries of PVSs are often oblate and the arteries that form the inner boundary may be offset from the central axis (Figure 1c). Hence, we have proposed an improved model of the PVS which we refer to as the "elliptical annulus model" [4] (Figure 1b right). Using this model, we fit *in vivo* images of arteries and their PVSs to circles and ellipses, respectively, and then compute the velocity profile and hydraulic resistance for steady, laminar flow (Figure 1d). We find that for a fixed cross sectional area, the observed shapes of PVSs have hydraulic resistance that is lower than that of the circular annulus model by a factor ranging from 1.4 to 6.5. Furthermore, we find that the observed shapes of PVSs are very close to that of the optimal shape, defined as the shape which minimizes hydraulic resistance (minima of the curves in Figure 1e) and maximizes CSF flow. Our calculations demonstrate that the circular annulus assumed in all prior studies substantially overestimates the hydraulic resistance – and therefore underestimates the volume flow rate – in PVSs. We hypothesize that the nearly optimal shapes of PVSs may be a result of evolutionary optimization.

MICROSCOPIC AND MACROSCOPIC MODELS OF CSF TRANSPORT

The mechanism(s) driving CSF through PVSs is currently an open question. Although multiple hypotheses exist, most computational studies have pursued the hypothesis that flow is driven by arterial pulsations, a mechanism similar to peristalsis, which has the strongest experimental evidence [3]. We have performed direct numerical simulations (DNS) using finite element methods which capture the microscopic CSF transport due to arterial pulsations [5]. We employ the elliptical annulus model of the PVS, which is in contrast to all prior computational studies. We confirm that CSF is driven in the direction of the arterial pulse wave propagation (consistent with experimental observations [3]). We also find that an elliptical annulus gives rise to spanwise pressure gradients that drive azimuthal circulation (Figure 2a), an effect absent from prior simulations based on a circular annulus.

Since performing a DNS of the entire PVS network in the brain is not computationally feasible, we have developed a hydraulic network model (Figure 2b) based on the fluid flow analogue of Ohm's law: $dp/dz = Q\mathcal{R}$, where dp/dz is the pressure gradient along the streamwise direction, Q is the volume flow rate, and $\mathcal{R}$ is the hydraulic resistance. This model has been parameterized and validated using *in vivo* measurements and includes estimates of $\mathcal{R}$ based on realistic PVS shapes (Figure 1). Using this model, we obtain estimates of the pressure gradients, volume flow rates, flow speeds, Reynolds numbers, and Péclet numbers throughout the network. We also perform sensitivity analyses to set constraints on the potential volumetric flow rates deep within the brain, where high resolution experimental measurements are not yet feasible. Our results suggest the CSF flow through the brain's PVS network is strictly laminar and advection dominated for large molecules such as amyloid-β.

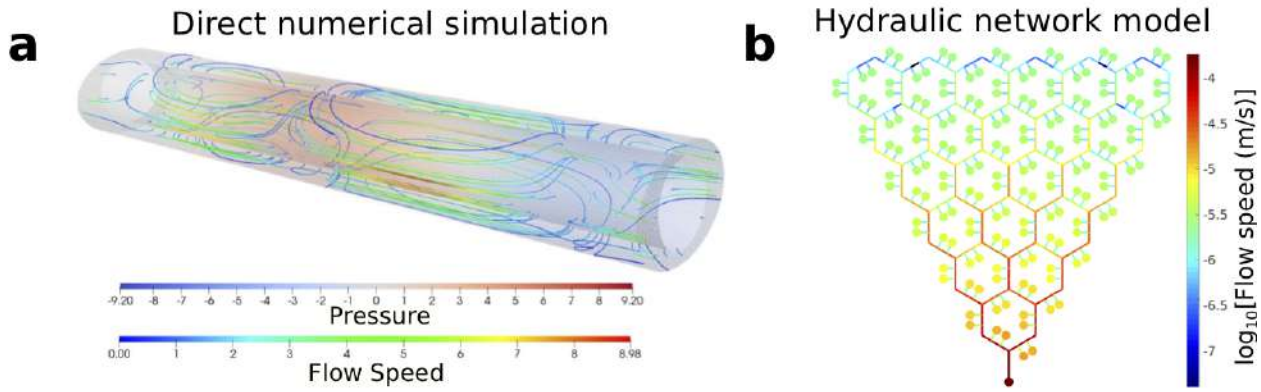

Figure 2: Microscopic and macroscopic simulations of CSF transport through PVSs. (a) Direct numerical simulation of arterial pulsation driven flow that captures microscopic CSF transport through a PVS. For an elliptical annulus, spanwise pressure gradients drive azimuthal circulation. (b) A hydraulic network model that captures the macroscopic CSF transport through the brain's PVS network. Each line or dot represents a pial or penetrating PVS (see Figure 1a), respectively, and the color coding indicates the flow speed. The hexagonal geometry is an idealized model of the vasculature at the surface of the brain [6].

References

[1] Plog B., Nedergaard M. *Annu. Rev. Pathol.-Mech.* **13**, 2018.
[2] Thomas J. H. *J. Roy. Soc. Interface*, **16**: 20190572, 2019.
[3] Mestre H., Tithof J., *et al. Nature Commun.* **9**: 4878, 2018.
[4] Tithof J. *et al. Fluids Barriers CNS* **16**: 19, 2019.
[5] Carr J. B. *et al. In preparation.*
[6] Blinder P. *et al. Proc. Nat. Acad. Sci.* **107**: 12670-12675, 2010.

SYNCHRONIZATION AND PROPULSION IN BUNDLES OF ROTATING HELICAL FILAMENTS

Maria Tătulea-Codrean[1] and Eric Lauga * [1]
[1]Department of Applied Mathematics and Theoretical Physics, University of Cambridge, Cambridge CB3 0WA, United Kingdom

Summary Multi-flagellated bacteria swim by rotating rigid helical filaments organised in bundles. The flagella within the bundle rotate in synchrony, and it has long been postulated that hydrodynamic interactions facilitate synchronization. Using a combined analytical (resistive-force theory) and computational approach (slender-body theory), we derive from first principles a dynamical system that explains the synchronization of two rotating helical filaments through hydrodynamic interactions. This is the first analytical model that accounts for the helical geometry of bacterial flagella, making a significant contribution to the mathematical understanding of a phenomenon revealed by computational studies more than a decade ago. We extend our analysis to self-propelling ensembles of N helical filaments and a spheroidal cell body, and we discover a novel and unexpected trade-off in propulsion.

INTRODUCTION

Bacterial motility is of fundamental interest to the scientific community, motivated not only by a desire to understand the oldest form of life on Earth, but also to draw inspiration from these resilient micro-organisms in order to design useful micro-robots capable of transporting cargo and navigating complex environments. Many species of bacteria propel themselves through viscous media by using an apparatus known as flagellum, which consists of a rigid helical filament actuated by a specialised rotary motor. In this work, we focus on bacteria that have multiple flagella and explore their environment using a strategy called "run-and-tumble" [1]. When a multi-flagellated bacterium starts to swim, the helical filaments are swept behind the cell body and rotate together in a coherent bundle, which leads to an interval of straight swimming called a "run". To change swimming direction, at least one motor must switch its sense of rotation, upon which the associated flagellum leaves the bundle and generates a torque on the cell body. The subsequent reorientation of the cell is called a "tumble". Recent advances in fluorescent microscopy have allowed the imaging of flagellar filaments whilst tracking swimming bacteria [2], allowing to probe open questions on the inner workings of a bundle of flagella and the reasons for having more than one flagellum. We address two aspects of this problem here: first the synchronization of helices within a bundle, and next the net propulsion they exert on the cell.

PROBLEM DEFINITION

We consider two parallel rigid filaments, with the same helical shape, rotating about their axes and separated by a distance d, as seen in Fig. 1(a). We model hydrodynamic interactions using Johnson's slender-body theory (SBT) with additional cross-helix interactions. The velocity of points along the centreline of helix k is expressed as

$$8\pi\mu\mathbf{u}_k(s) = \Lambda_k[\mathbf{f}_k](s) + \mathrm{K}_k[\mathbf{f}_k](s) + \sum_{l\neq k} \mathrm{J}_{kl}[\mathbf{f}_l](s), \tag{1}$$

where the functionals on the right-hand side represent integral expressions for the local (Λ_k) and non-local (K_k) part of SBT, and the interactions (J_{kl}) between helices [3, 4]. By using Legendre polynomials as an orthonormal basis for the force and velocity distributions along the filaments, Eq. (1) turns into an infinite linear system of equations which can be truncated and solved numerically. This numerical method is valid as long as the distance between the filaments $d \gg \epsilon$, the thickness of the filament. For distances $d \gg L$, the length of the filament, we further develop an asymptotic theory for calculating the interactions between the two filaments by hand. First, we calculate the single-helix resistance matrix, S_k, by integrating the force distribution along helix k, which we write as being proportional to the local velocity of the filament, according to resistive-force theory (RFT), i.e.

$$\mathbf{f}_k(s) = [c_\perp(\mathrm{I} - \mathbf{t}_k(s)\mathbf{t}_k(s)) + c_\parallel \mathbf{t}_k(s)\mathbf{t}_k(s)]\cdot[\mathbf{U}_k(s) - \mathbf{u}_\infty(\mathbf{r}_k(s))], \tag{2}$$

where $c_\perp$ and $c_\parallel$ are the local drag coefficients [5]. Once we know the behaviour of a single helix, we can calculate cross-helix interactions by noting that the leading-order flow induced by helix l at the position of helix k is a uniform flow coming from the far-field representation of helix l as a Stokeslet, which decays like the inverse of distance. Hence, the cross-interaction resistance matrix at order $\mathcal{O}(d^{-1})$ is

$$\mathrm{C}_{kl} = -\mathrm{S}_k^{1\leq j\leq 3}\cdot\left[\frac{\mathrm{I} + \hat{\mathbf{d}}_{kl}\hat{\mathbf{d}}_{kl}}{8\pi\mu|\mathbf{d}_{kl}|}\right]\cdot\mathrm{S}_l^{1\leq i\leq 3}, \tag{3}$$

*Corresponding author. E-mail: e.lauga@damtp.cam.ac.uk.

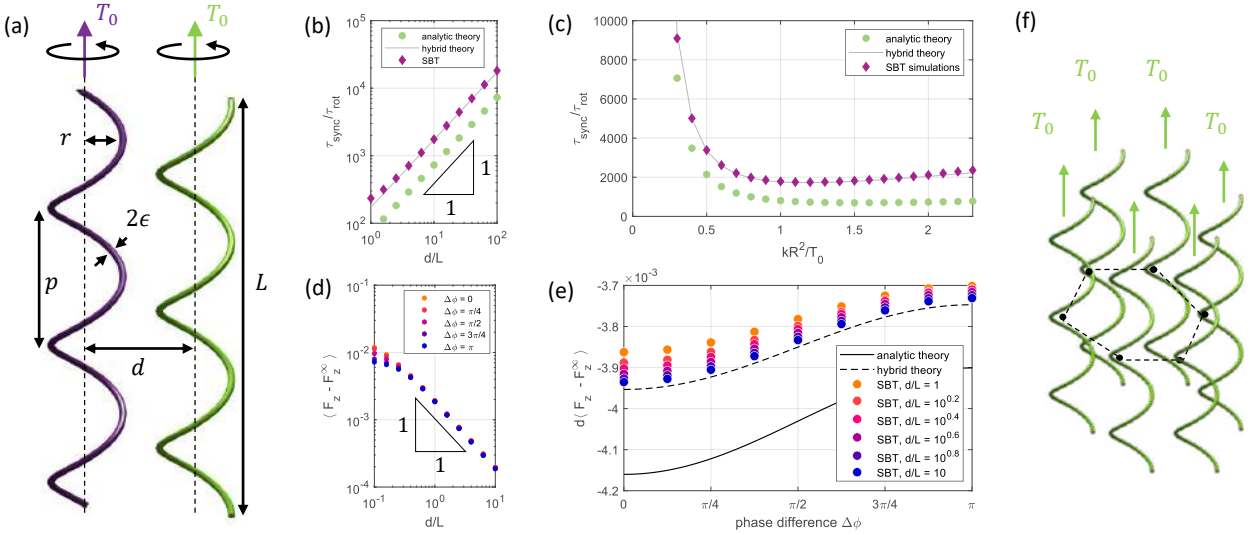

Figure 1: Synchronization and propulsion of rotating helical filaments. (a) Basic setup with two parallel rigid filaments of identical helical shape. (b) The time scale of synchronization increases linearly with the distance between the helices, and (c) achieves a minimum for intermediate values of the harmonic trap stiffness, k. (d) The deficit in propulsive force decreases with the inverse distance between the helices and (e) is largest when the helices are in phase. (f) Basic model for a bacterial flagellar bundle consisting of N rigid helical filaments in a regular polygonal arrangement.

where i and j indicate row and column numbers, and the vector $\mathbf{d}_{kl}$ is the separation between the two filaments. The matrices S_k and C_{kl} can be calculated by hand and, for simple cases, the full resistance matrix for the N-filament system can be inverted in order to find the linear and angular velocities of the filaments in terms of the forces and torques that are applied to them. This asymptotic theory, which we have further developed to include $\mathcal{O}(d^{-2})$ interactions, allows us to analyse the synchronization of a pair of identical parallel filaments through far-field hydrodynamic interactions.

RESULTS

Our analytical model for far-field interactions confirms the observation of previous computational studies [6, 7] that two rigid helical filaments driven by a constant torque cannot synchronize without some form of compliance – in our case, we consider the axes of the helical filaments being trapped in a harmonic potential. We derive a dynamical system for the phases and displacements of the two filaments, and we analyse this system analytically to determine the time scale of synchronization (Fig.1b,c) and the critical torque difference for which the filaments may still synchronize, at a non-zero phase difference which we determine. We also combine our far-field theory with SBT simulations to determine the loss in propulsive force on a rotating helical filament due to the presence of a second rotating helix at a distance d away from it (Fig.1d,e). We also consider a model of a bacterial flagellar bundle consisting of N helical filaments in a regular polygonal arrangement (Fig.1f). The challenge of extending our analytical framework to N filaments lies in the quadratic rise of computational time in our SBT simulations, and a greater complexity in the calculations we do by hand. Nevertheless, we succeed in quantifying the increase in synchronization speed with the number of flagella, and we discover a surprising phenomenon related to propulsion which has not been reported in the literature before.

CONCLUSIONS

Using an asymptotic calculation for the far-field hydrodynamic interactions between helical filaments, we develop the first analytical model that captures the synchronization of two rotating rigid helices in the presence of hydrodynamic interactions and elastic compliance. Our framework can easily be generalised to multiple body systems, which allows us to investigate synchronization and propulsion in realistic models of multi-flagellated bacteria. We complement our analytical theory with computations in order to compare the behaviour of such systems in the far vs. the near field.

References

[1] Berg H.C. *E. coli* in Motion. Springer, NY 1983.
[2] Turner L., Ryu W.S., Berg, H.C. Real-Time Imaging of Fluorescent Flagellar Filaments. *J. Bacteriol.* **182**: 2793-2801, 2000.
[3] Johnson R.E. An Improved Slender-Body Theory for Stokes Flow. *J. Fluid Mech.* **99**: 411-431, 1980.
[4] Tornberg A., Shelley M.J. Simulating the Dynamics and Interactions of Flexible Fibers in Stokes Flows. *J. Comp. Phys.* **196**: 8-40, 2004.
[5] Cox R.G. The Motion of Long Slender Bodies in a Viscous Fluid, Part 1. General Theory. *J. Fluid Mech.* **44**: 791-810, 1970.
[6] Kim M., Powers T.R. Hydrodynamic Interactions Between Rotating Helices. *Phys. Rev. E* **69**, 061910, 2004.
[7] Reichert M., Stark H. Synchronization of Rotating Helices by Hydrodynamic Interactions. *Eur. Phys. J. E* **17**: 493-500 , 2005.

THE HUMAN NASAL CAVITY: TOWARDS THE OPTIMAL SURGERY WITH CFD AND MACHINE LEARNING

Andrea Schillaci *[1], Luca Butera[2], Gianluca Romani[1], Carlotta Pipolo[3], Giovanni Felisati[3], Marcello Restelli[2], Giacomo Boracchi[2], and Maurizio Quadrio[1]

[1]*Dipartimento di Scienze e Tecnologie Aerospaziali, Politecnico di Milano, Milano, Italy*
[2]*Dipartimento di Elettronica, Informazione e Bioingegneria, Politecnico di Milano, Milano, Italy*
[3]*Unità di Otorinolaringoiatria, ASST Santi Paolo e Carlo, Dip. Scienze della Salute, Milano, Italy*

Summary Nasal breathing difficulties are a common condition, and their treatment often requires surgery. Unfortunately, procedures are designed and carried out mostly based on the surgeon's experience; data supporting surgical choices are lacking. Computational Fluid Dynamics (CFD), by naturally accessesing functional properties of the human nose, improves the understanding of its flow field. However, a detailed flow prediction alone does not immediately lead to identifying the best surgical maneuver. We intend to leverage Machine Learning (ML) to bridge this gap and infer functional information from CFD data. The present study is preliminary and uses rather crude anatomical and computational models; however, its results demonstrate the potential of a ML model trained on CFD data.

INTRODUCTION

Nasal breathing difficulties (NBD) are a commonly encountered condition in the clinical practice of the Ear, Nose and Throat (ENT) doctors, causing huge societal cost. For example, the overall annual economic burden of chronic rhinosinusitis in the U.S. alone is estimated at 22 billion USD per year [1]. Though a variety of techniques is available to ENT surgeons, consensus is lacking on the surgical approach for a specific patient. As a consequence, up to 50% of the patients undergoing common surgical procedures, as for example septoplasty, report that symptoms did not improve [2].

During the last years, Computational Fluid Dynamics (CFD) has successfully tackled increasingly complex geometries; the anatomy of the human nasal cavity has become affordable, and CFD is nowadays a further item in the toolbox of the ENT surgeons (Fig.1a). We have designed a computational procedure, described e.g. in [3], that starts from a CT-scan of the patient, and reliably computes the (mean and instantaneous) flow field in the nose via Direct Numerical Simulation. Our ambitious long-term goal is the development of a robust tool to support ENT surgeons in discriminating pathologies from the normal, often large anatomical variations, and in selecting the best surgical approach.

However, it remains non-obvious how to translate the wealth of information contained in a CFD solution into a rational selection of the best surgery for each patient [4]. In this work we describe our preliminary evaluation of Machine Learning (ML) towards this goal. We assess the inference capabilities of ML algorithms by estimating geometrical measures using only fluid dynamics features. We notice that our goal differs from the majority of the research that applies ML to fluid mechanics, where the efforts are devoted to the improvement of flow modeling, optimization and control [5].

METHODOLOGY

The preliminary nature of the work calls for a simplification of the problem, in terms of both the anatomies and the physical modeling, while at the same time maintaining its key features. For the CFD simulations, we employ a standard $k-\omega$ SST RANS turbulence model (tuned with preliminary Large Eddy Simulations), and a Gaussian process [6] is used for inference. From the anatomical standpoint, an original parametric CAD model of the upper airways is developed (Fig.1b) which replicates the main features of a real nasal cavity, but without the paranasal sinuses. The parametric model is then modified to mimic some of the most common anatomical variations observed in the ENT practice: 4 corresponding to asymptomatic variations of healthy noses, and 3 to pathological conditions typically leading to severe symptoms (anterior hypertrophy of the inferior turbinate, hypertrophy of the whole inferior turbinate, and anterior hypertrophy of the middle turbinate). Combinations of these parameters lead to 200 unique anatomies, which are used to generate a CFD dataset with the associated task of predicting the severity of single pathology expressed in terms of one parameter.

Adopting ML models over CFD output is not straightforward, since every CFD analysis produces large amounts of data. Even the relatively coarse RANS simulations considered here run on about one million cells, and each cell carries at least 7 real values (three spatial coordinates, three components of velocity and pressure). Learning on such highly-dimensional feature space requires an enormous amount of annotated data. Thus, CFD simulations cannot be directly an input for ML, and more compact descriptors are required. We resort to feature engineering, by devising a small number of features designed by experts, i.e. CFD engineers and ENT doctors. Examples of features are: a polynomial fit of pressure along the nose (Fig.2 a); a histogram of total travel times of tracers released at 200 specified locations (Fig2 b); the flow variables averaged over 5 specific cross-sections of the domain and smaller portions of these (Fig.2 c). In the end, the number of features is 342, which is still very high considering the number of samples.

*Corresponding author. E-mail: andrea.schillaci@polimi.it

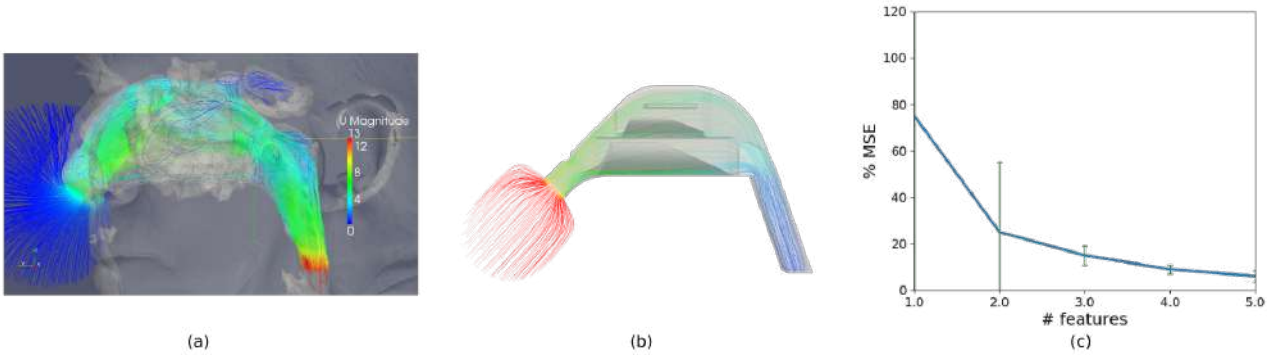

Figure 1: (a) Streamlines in the human upper airways (taken from [3]). (b) Streamlines in the simplified geometric model. (c) Mean square error of the prediction, versus the number of features. The vertical bar quantifies the variance.

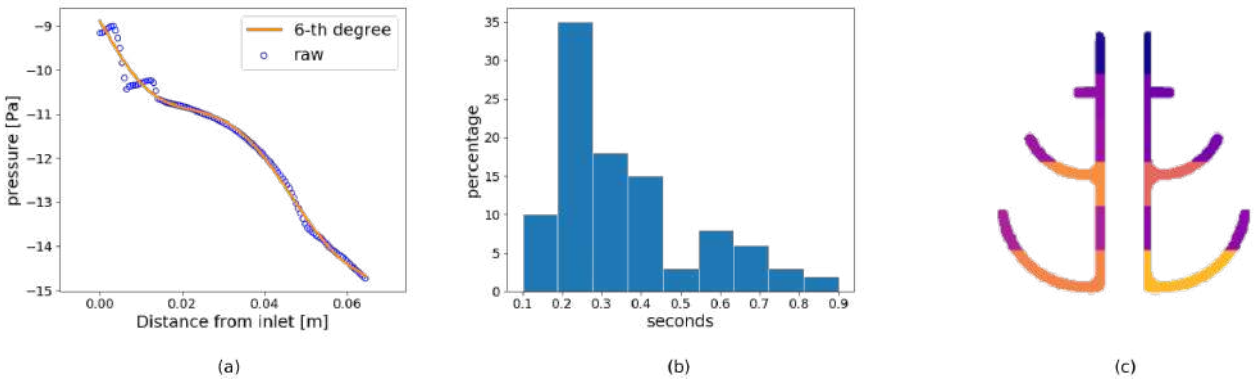

Figure 2: Example features. (a) Polynomially interpolated pressure. (b) Histogram of total travel times of tracers. (c) Flow variables averaged over 10 portions of a cross-section.

RESULTS AND CONCLUSIONS

Experiments performed by cross-validation over our dataset of 200 simulations, show that features extracted from CFD data can successfully infer the target measures of the CAD model. We performed feature selection to identify the most informative features, using both *Recursive Feature Elimination* and *Forward Feature Selection* by fitting *Extremely Randomized Trees* [7] as regression model. As an illustrative example, Fig.1c reports the results of a Gaussian Process trained on the most informative features for the anterior hypertrophy of the inferior turbinate, and shows that the mean square error of the prediction drops below 20%, when only 3 features are used. Remarkably, the *selected* features are often extracted from areas only indirectly affected by the geometrical modification, further indicating that CFD conveys important information. The most informative features are found to be the average flow values across the 5 slices.

CFD can have a large impact upon the ENT practice, as it provides functional *and* patient-specific information about the airflow in the human nose. In particular, our study indicates that features extracted from CFD data have the potential to identify pathologies even when accompanied by non-pathological variability. ML is thus a viable pathway to address those shortcomings that prevent CFD from being routinely deployed in clinical practice. The next step is to validate our study on more accurate CFD models (DNS), more realistic anatomies (CT scans of patients) and more realistic predictions (diagnosis of ENT specialists).

References

[1] Smith, K. A., Orlandi, R. R., & Rudmik, L. Cost of adult chronic rhinosinusitis: a systematic review. The Laryngoscope, 125(7), 1547-1556, 2015
[2] Sundh, C., & Sunnergren, O. Long-term symptom relief after septoplasty. Eur Arch Oto-Rhino-L, 272(10), 2871-2875, 2015
[3] Quadrio, M., Pipolo, C., Corti, S., Messina, F., Pesci, C., Saibene, A. M., Zampini, S. & Felisati, G. Effects of CT resolution and radiodensity threshold on the CFD evaluation of nasal airflow. Med Biol Eng Comput, 54(2-3), 411-419. 2016
[4] Quadrio, M., Pipolo, C., Corti, S., Lenzi, R., Messina, F., Pesci, C., & Felisati, G. Review of computational fluid dynamics in the assessment of nasal air flow and analysis of its limitations. Eur Arch Oto-Rhino-L, 271(9), 2349-2354, 2014
[5] Brunton, S., Noack, B., & Koumoutsakos, P. Machine learning for fluid mechanics. Annual Reviews of Fluid Mechanics, 2020.
[6] Rasmussen, C. E. Gaussian processes in machine learning. In Summer School on Machine Learning (pp. 63-71). Springer, Berlin, Heidelberg. 2003, February.
[7] Geurts, P., Ernst, D., & Wehenkel, L. Extremely randomized trees. Machine learning, 63(1), 3-42. 2006

A SIMPLE MODEL FOR FISH LOCOMOTION: FROM KINEMATICS TO PROPRIOCEPTIVE DRIVING

J. Sánchez-Rodríguez*[1], C. Raufaste [1], and M. Argentina [1]
[1]Université Côte d'Azur, CNRS, Institut de Physique de Nice, 06100 Nice, France

Summary We have developed an elementary model of self propelled locomotion from which we compute the locomotion velocity as function of the swimmer kinematics. In our model, these kinematics are reduced to the tail amplitude and its beating frequency. The influence of parameters characterising the surrounding flow and physical features of the swimmer are also quantified. Our results are in good agreement with previous works [1, 2]. We hypothesize that the kinematic parameters might be selected by driving the tail motion with a proprioceptive feedback. The simplest feedback would be that the tail motion to be linearly dependant on the normal force felt by its body. In parallel to this theoretical approach, we have constructed a robotic compliant fish which is attached to a force sensor. Our theoretical model accurately predicts these experimental outputs.

INTRODUCTION

Fish across many species and scales cruise in a relatively narrow range of Strouhal numbers, around 0.3 [1, 3, 4]. This dimensionless parameter, $St = Af/U$, is a simple combination of the swimming velocity U, tail-beat amplitude A and frequency f. The self propelled locomotion is modelled by accounting for the fluid-structure interaction and neglecting the biological aspects. In that sense, numerous artificial systems have been studied in experiments and models such as flapping foils [2, 5, 6] or compliant robots [7, 8].

We first consider theoretically and numerically a simple model of aquatic locomotion to study the influence of various parameters on the Strouhal number. The second law of Newton is applied to a slender airfoil-shaped two-dimensional body. The tail undulates with a prescribed harmonic motion defined by an amplitude A and a frequency f. The thrust and drag forces are derived within the Theodorsen's approach [9, 10], which postulates a perfect fluid. In a second step, we test a feedback to control the swimming gait of a robotic fish, based on a proprioceptive loop: the normal force felt by the robot drives the tail motion. We theoretically figure out the range of parameters that triggers self propulsion.

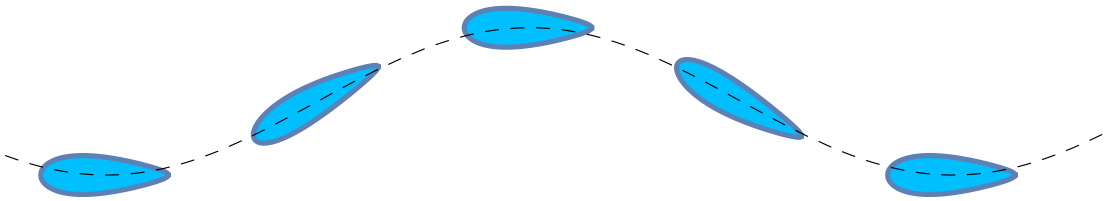

Figure 1: Orientation and trajectory of the swimming body predicted with the numerical simulation.

MODEL WITH KINEMATICS DRIVING

A simple model of aquatic locomotion is developed to analyze the effect of several parameters on the Strouhal numbers. These parameters are the tail-beat amplitude and frequency, the position of the center of mass in the swimmer body, the drag coefficient and the dimensionless added mass. We consider our swimmer to be a slender, airfoil-shaped, two-dimensional, rigid body performing a prescribed motion of amplitude A and frequency f in order to simulate the tail motion. Our theoretical approach assumes a two-dimensional, incompressible, irrotational and inviscid flow.

To assess the hydrodynamical forces acting on the swimmer, we follow the seminal paper of Theodorsen [9], and we take into account the pressure drag. The velocity potential of the flow is calculated with a conformal transformation, and the forces are written in the small amplitude regime. By balancing momentum, we deduce the equations describing the longitudinal and the transverse motion. The system is solved numerically, and we compute analytically solutions at the first orders in amplitude .

We show that the Strouhal number is strongly correlated with the drag coefficient c_d. With the values of c_d extracted from the literature, we forecast the Strouhal number belonging to the interval 0.1-0.3, in very good agreement with those measured on natural fish. The effect of the other parameters can be neglected up to the second order in amplitude and we obtain prediction for the phase delay between the heaving and pitching motions.

*Corresponding author. E-mail: jesus.sanchez@univ-cotedazur.fr

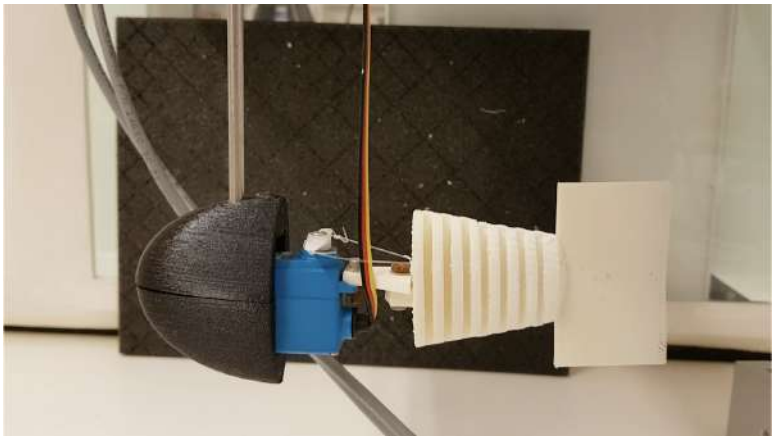

Figure 2: Picture of the compliant robotic fish.

MODEL WITH PROPRIOCEPTIVE DRIVING

We would like to take a step forward to understand which mechanism selects the parameter values. We postulate that swimming gait might be driven by a proprioceptive feedback, which would fix the amplitude and frequency. As a first guess, we assume that tail angle is proportional to the normal force felt by the swimmer. To explore this conjecture, we construct a robotic fish attached to a force sensor which detects both normal and longitudinal forces. We put this device in a water tunnel and we vary the value of the proportionality constant γ, which couples the normal force to the tail angle. For low values of γ, the system converges to a motionless phase, independently of the initial condition. For large γ, the robot oscillates periodically, and the undulation amplitude grows as γ increases, before to saturate to a constant value for larger values of the parameter. In between these two regimes, we experimentally predict the existence of a threshold in γ.

With our minimal model, we reproduce these results. Accurate modelling of the servo is essential to correctly mimic the tail movement observed in the experiments. The model presents excellent predictive properties: the threshold is accurately found, while the characteristics of the oscillation are perfectly captured, both numerically and theoretically.

References

[1] Gazzola M., Argentina M., Mahadevan L., 2014. Scaling macroscopic aquatic locomotion. Nature Physics 10, 758.
[2] Triantafyllou, G., Triantafyllou, M., Grosenbaugh, M., 1993. Optimal thrust development in oscillating foils with application to fish propulsion. Journal of Fluids and Structures 7, 205–224
[3] Taylor, G.K., Nudds, R.L., Thomas, A.L., 2003. Flying and swimming animals cruise at a Strouhal number tuned for high power efficiency. Nature425, 707–711
[4] Triantafyllou, M.S., Triantafyllou, G.S., Gopalkrishnan, R., 1991. Wake mechanics for thrust generation in oscillating foils. Physics of Fluids A: Fluid Dynamics 3, 2835–2837.
[5] M. Koochesfahani, "Vortical patterns in the wake of an oscillating airfoil," in 25th AIAA Aerospace Sciences Meeting, 1987.
[6] L. Schouveiler, F. Hover, and M. Triantafyllou, 2005. "Performance of flapping foil propulsion," Journal of Fluids and Structures 20, 949–959.
[7] Gibouin, F., Raufaste, C., Bouret, Y., Argentina, M., 2018. Study of the thrust–drag balance with a swimming robotic fish. Physics of Fluids 30, 091901.
[8] Zhu, J., White, C., Wainwright, D.K., Di Santo, V., Lauder, G.V., Bart-Smith, H., 2019. Tuna robotics: A high-frequency experimental platform exploring the performance space of swimming fishes. Science Robotics 4, eaax4615.
[9] Theodorsen, T., 1935. General theory of aerodynamic instability and the mechanism of flutter. report 496, National Advisory Committee for Aeronautics, Washington DC.
[10] Garrick, I.E., 1936. Propulsion of a flapping and oscillating airfoil. report 567, National Advisory Committee for Aeronautics, Washington DC.

NUMERICAL SIMULATION OF BLOOD FLOW IN THE THORACIC AORTA: STOCHASTIC SENSITIVITY ANALYSIS TO INLET VELOCITY SPATIAL DISTRIBUTION

Maria Nicole Antonuccio[1], Alessandro Mariotti[2], Simona Celi[1], and Maria Vittoria Salvetti *[2]
[1]BioCardioLab - Heart Hospital, Fondazione Toscana G. Monasterio, Massa, Italy
[2]Department of Civil and Industrial Engineering, University of Pisa, Pisa, Italy

Summary The effects of the spatial distribution of the inlet velocity in numerical simulations of the thoracic aorta are investigated. The velocity distribution is modeled through a truncated-cone shape, which well reproduces the in-vivo measured one in the systolic phase. The shape is changed by varying the ratio between the surfaces of the two bases. To carry out a systematic sensitivity analysis, a stochastic approach is adopted, in which the shape parameter is considered uncertain. This uncertainty is propagated through the numerical simulations and a continuous response of the output quantities of interest in the parameter space is obtained by means of generalized Polynomial chaos. The shape of the inlet velocity distribution has a significant influence on the velocity in the ascending aorta and hence on the wall shear stresses in this region, while the descending aorta is not affected.

INTRODUCTION

Blood flow and related stresses at the vessels walls play an important role in the initiation and progression of cardiovascular diseases such as in the case of ascending thoracic aortic aneurysms. Patient-specific in-vivo data can nowadays be obtained by 3D flow magnetic resonance (3D PC-MRI) imaging. However, MRI suffers of spatial and temporal resolution limitations and, thus, it is not able to provide quantitative flow indicators, such as wall shear stresses, with sufficient accuracy. A possible solution to obtain reliable and detailed information at a patient-specific level is to integrate in-vivo measurements with computational fluid dynamics (CFD), which can provide velocity, pressure and wall shear stresses with a resolution which is not presently attainable in experiments. On the other hand, different sources of uncertainties are present in CFD models, which might affect the accuracy of the results. Among others, a critical issue is given by inlet/outlet boundary conditions. In-vivo 3D PC-MRI data can be used to obtain indications on patient-specific boundary conditions for the simulations (see e.g. [4, 1]), reducing thus the uncertainty, as well as for comparison against numerical results, providing a cross validation.

The present work is part of a research activity towards the set-up and validation of a platform integrating in-vivo and in-vitro measurements with CFD simulations [2, 1]. We focus herein on the inlet conditions and, in particular, on the impact of the spatial distribution of velocity at the inlet on the blood flow and forces at the wall. The present analysis is motivated by previous studies in the literature [4, 3] and by the differences observed in the flow dynamics and wall shear stresses in simulations carried out by our group with plug flow at the inlet and with in-vivo measured inlet velocity respectively [5]. The inlet velocity profile is here analytically described by a truncated cone, which approximates reasonably well the measured velocity distribution in the systolic phase, which was observed in [5] to be the part of the cardiac cycle in which the flow variables were more sensitive to the inlet velocity distribution. The shape of the inlet velocity is then changed by varying the ratio between the surfaces of the two bases of the truncated cone, while the flow rate is always the same, equal to the in-vivo measured one. This analytic description of the inlet velocity distribution, together with a stochastic approach based on generalized Polynomial Chaos (gPC), allows the variability of the quantities of interest, i.e., velocity, pressure and wall shear stresses, with the shape of the inlet velocity profile to be systematically quantified.

COMPUTATIONAL SET-UP AND SENSITIVITY ANALYSIS

The considered aorta geometry and inlet flow rate are the same as in [1], obtained from MRI acquisitions performed on a healthy subject (28 years, male) with tricuspid aortic valve.

The open-source code *SimVascular* is used to carry out the hemodynamic simulations. The blood is considered as a Newtonian and incompressible fluid with density and kinematic viscosity. A finite-element method, including SUPG/PSPG stabilizing terms together with P1-P1 elements for both velocity and pressure, is used to discretize the governing equations. At the outflow boundaries, we use the 3-element Windkessel model [2]; on the arterial wall we impose a no-slip condition between the fluid and the wall and the effect of wall compliance is not taken into account in the simulations herein. As for the spatial distribution of the inlet velocity, the shape is assumed to be a truncated cone, which approximates rather well the measured inlet velocity distribution in the systolic phase (see Fig.1). The shape of the truncated cone depends on the ratio between the surfaces of the upper and the lower base, and thus the base area ratio $r = A_{top}/A_{base}$ is chosen as the uncertain parameter. It is varied in the range $r = [0.2 - 1]$, being $r = 1$ the plug flow condition. In order to obtain a continuous response surface of the quantities of interest with varying r, we use gPC, in which r is considered as a random variable with a given Probability Density Function (PDF) and the output quantities are obtained through a truncated orthogonal polynomial basis. We assume herein a uniform PDF of r on the given variation range because it is the least informative distribution with the highest variance in given intervals. The optimal polynomial

*Corresponding author. E-mail: maria.vittoria.salvetti@unipi.it

family for the gPC basis is thus given by Legendre polynomials. The polynomial expansion is truncated to third order and thus four quadrature points are needed to compute the coefficients of the expansion, which correspond to the following values of r: $0.256, 0.464, 0.736, 0.944$. Numerical simulations are carried out for these values of A_{top}/A_{base}. In all cases, the height of the truncated cone is calculated for each time instant in order to match the measured inlet flow rate.

RESULTS AND DISCUSSION

An example of the impact of the shape of the inlet velocity profile is given in Fig. 2(a−d), in which the distribution of wall shear stresses averaged over the cardiac cycle (TAWSS) is shown for the four deterministic simulations. By comparing Figs. 2(a−d) it is qualitatively evident that the TAWSS distribution in the ascending aorta and in the aortic arch changes with r, while it remains almost the same in the descending part. This observation is better summarized and quantified by the stochastic standard deviation of TAWSS obtained by means of gPC and reported in Fig. 2(e). This is a measure of the variability of TAWSS with r. The region of maximum variability of TAWSS indeed comprises the ascending aorta and the foremost part of the aortic arch.

The impact on the velocity field, pressure and flow rate waveforms at different sections has also been evaluated; it is not shown here for the sake of brevity, but it will be reported in the final paper. Possibly, in the final paper a similar analysis will be also shown by taking into account wall compliance.

References

[1] Boccadifuoco, A., Mariotti, A., Capellini, K., Celi, S. and Salvetti, M.V.: Validation of numerical simulations of thoracic aorta hemodynamics: comparison with in-vivo measurements and stochastic sensitivity analysis, *C*ardiovasc Eng Technol, **9**(4), 688–706, 2018.

[2] Boccadifuoco, A., Mariotti, A., Celi, S., Martini, N. and Salvetti, M.V.: Impact of uncertainties in outflow boundary conditions on the predictions of hemodynamic simulations of ascending thoracic aortic aneurysms, *C*omput Fluids, **1**65, 96–115, 2018.

[3] Youssefi, P. and Gomez, A. and Arthurs, C. and Sharma, R. and Jahangiri, M. and Figueroa, C.A.: Impact of patient-specific inflow velocity profile on hemodynamics of the thoracic aorta, *J*. Biomech. Eng., **140(1)**, 1011002, 2018.

[4] Morbiducci, U. and Ponzini, R. and Gallo, D. and Bignardi, C. and Rizzo, G.: Inflow boundary conditions for image-based computational hemodynamics: Impact of idealized versus measured velocity profiles in the human aorta, *J*. Biomech., **46(1)**, 102–109, 2013.

[5] Antonuccio, M.N., Mariotti, A., Celi, S. and Salvetti, M.V.: Effects of the distribution in space of the velocity-inlet condition in hemodynamic simulations of the thoracic aorta, to be published in Lecture Notes in Bioinformatics, Springer (2020).

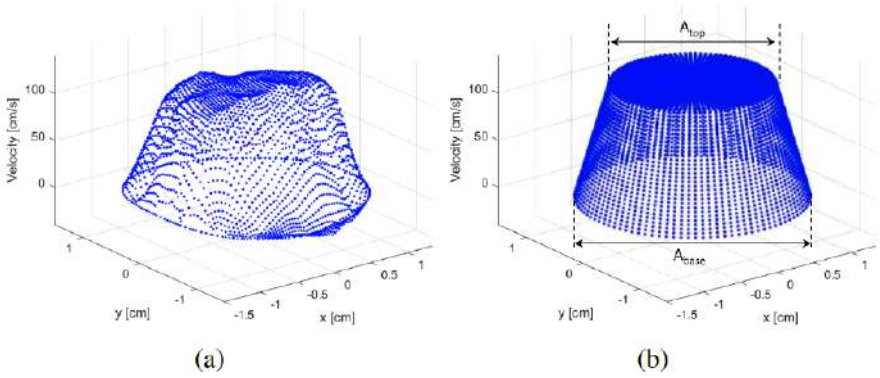

Figure 1: (a) Patient-specific inlet velocity at systolic peak, (b) modeled truncated-cone shape.

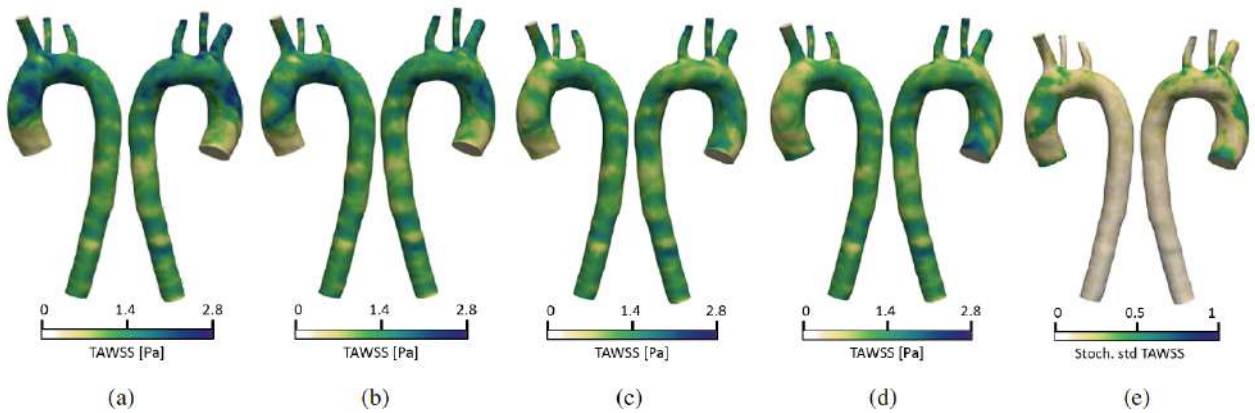

Figure 2: Effect of the base ratio on the TAWSS: (a) $r = 0.256$, (b) $r = 0.464$, (c) $r = 0.736$ and (d) $r = 0.944$. (e) Stochastic standard deviation of the TAWSS.

STRONGLY CONNECTED VASCULAR UNITS ARE FOUND IN FAT TISSUE PERFUSION

P. Kennel[1], J. Dichamp[1], C. Barreau[2], C. Guissard[2], L. Teyssedre[3], J. Rouquette[3], J. Colombelli[4], A. Lorsignol[3], L. Casteilla[3], and F. Plouraboue[1]
[1] Institut de Mécanique des Fluides de Toulouse (IMFT)-Université de Toulouse, CNRS-INPT-UPS, Toulouse
[2] CNRS 5273; UMR STROMALab, BP 84225, F-31 432 Toulouse Cedex 4
[3] ITAV, Université de Toulouse, CNRS, UPS, France.
[4] Advanced Digital Microscopy Core Facility, Institute for Research in Biomedicine (IRB Barcelona)

Summary We present an image-based blood flow perfusion modeling of a whole organ vascular network for analyzing both its structural and functional properties. By using Light-Sheet Fluorescence Microscopy (LSFM) and adapted image post-treatment workflow, we could segment and reconstruct the entire micro-vascular network composed of 1.7 million vessels, inside a $\sim 25 \times 5 \times 1 = 125\text{mm}^3$ volume of the mouse fat pad. Vascular graph clustering network analysis revealed the structural and functional organization of meso-scale tissue as strongly connected communities of vessels. These communities share a distinct heterogeneous core region and a more homogeneous peripheral one, consistently with known biological functions of fat tissue. This work shows the existence of strongly connected functional vascular units in fat tissue.

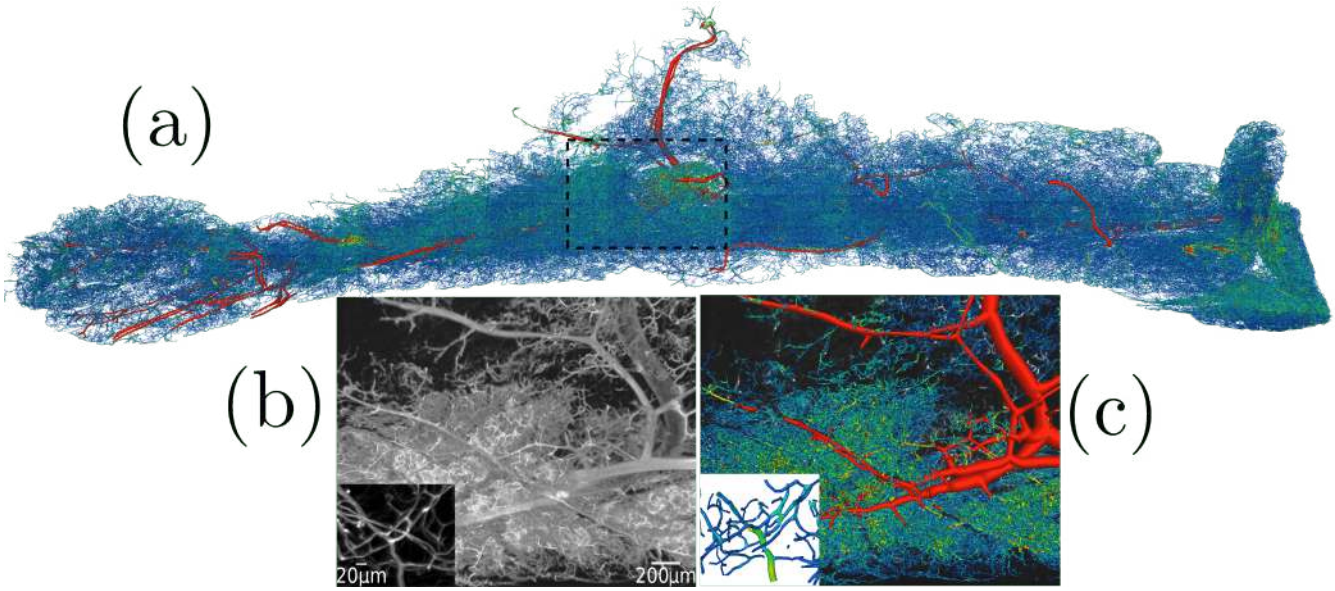

Figure 1: **All tissue vascular reconstruction** (**a**) The vascular network reconstructed from a $\sim 25 \times 5 \times 1 = 125\text{mm}^3$ volume of fat pad tissue based on image after various image post-processing. The vascular graph has $\sim 1.7.10^6$ edges and $\sim 1.2.10^6$ nodes. (**b**) Volume rendering of the maximal intensity projection of the original image of a small part of the tissue with another higher zoom level inside. (**c**) Corresponding reconstructed vascular graph highlighting the high resolution.

From LSFM imaging of mousse fat pad tissue, a complete reconstruction of the entire vascular network is performed, as illustrated in Fig. 1. Vascular perfusion is then computed over the entire network. Vascular graph clustering units are analyzed using graph clustering techniques with various graph weigths w_i, $i = 1, 4$ (see Fig. 2's legend for more details and [1]) so as to decipher the existence of functional units. The results are depicted in Fig. 2, showing the presence of strongly connected units. This work provides the proof of concept that in-silico all-tissue perfusion modeling can reveal new structural and functional exchanges between micro-regions in tissues, found from community clusters in the vascular graph.

References

[1] Blinder P, Tsai PS, Kaufhold JP, Knutsen PM, Suhl H, Kleinfeld D. Nat Neurosci. 2013;16(7):889–97.
[2] Schmid F, Kleinfeld D, Blinder P, Jenny P, Weber B. PLOS Comput Biol. 2016; p. 1–22.

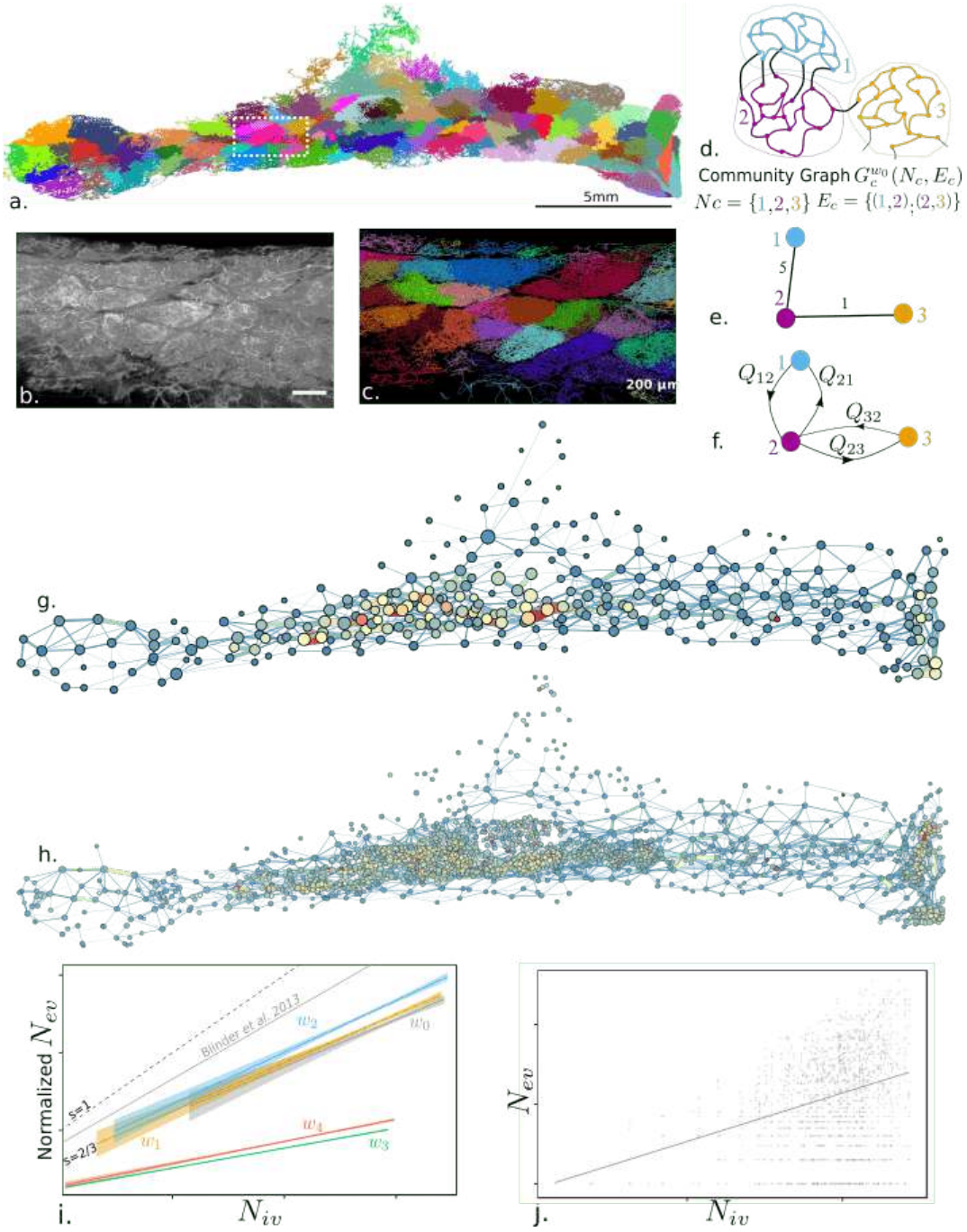

Figure 2: **Vascular graph clustering.** **(a)** Community clustering applied to the vascular network by using an unweighted vascular graph representation, w_0. Color codes for community membership. **(b)** and **(c)** Image volume rendering and the vascular graph segmentation, respectively, of a sub-volume (∼100m width) extracted in a dense and modular area of the tissue near the central lymph node (white dotted rectangle depicted in (a)). **(d)** Schematic illustration of vascular communities; **(e)** structural community graph, with the number of vessels connecting two communities as edges weights (5 and 1 here); and **(f)** bi-functional community graph with in/out fluxes Q_{ij} as edges weights. **(g)** Graph clustering of the communities for geometrical based weight (w_2, curvilinear distance) and **(h)** perfusion based weight (hydraulic resistance w_3); the disks are located in community centers projected in the (x, y) plane with sizes coding for volumes and color for vascular density (volumic ratio from 0% to 20%) illustrated with a cold-to-warm color scale. **(i)** Linear regressions of the scatter plot of number of vessels between each pair of communities N_{ev} versus number of vessels in the community N_{iv} (for each community in (d), number of colored edges vs. number of black edges). Full lines are the linear regressions for each clustering weight w_i. w_0 no weight (slope $s = 0.61$); w_1 Euclidean distance ($s = 0.62$); w_2 curvilinear distance ($s = 0.66$); w_3 hydraulic resistance (Cf. S2) ($s = 0.25$); w_4: hydraulic conductance (Cf. S2) ($s = 0.28$). The gray curve is the result of Blinder et al. [1] with $s = 0.83$. Dashed lines delimit the boundaries of weak communities (therefore having strong connections between units) with slopes $s = 2/3$ and $s = 1$. Shaded areas are the standard errors associated with each regression.

AN INVISCID MODEL FOR SELF PROPELLED SWIMMING OF UNDULATING BODIES

Damiano Paniccia * [1], Giorgio Graziani [1], Claudio Lugni [2], and Renzo Piva [1]
[1] Department of Mechanical and Aerospace Engineering, University of Rome La Sapienza, Rome, Italy
[2] CNR-INM: Italian Research Council Institute of Marine Engineering, Rome, Italy

Summary A two-dimensional inviscid potential model with vorticity release has been developed in order to investigate the self propelled swimming of undulating bodies. The body is free to move not only in the forward and lateral directions, but it can also rotate around its center of mass, according to the forces and moments induced by the flowfield generated by its own prescribed undulation. The numerical model is based on an unsteady potential panel code for deformable airfoil. The vortex shedding process is modeled by an unsteady Kutta condition. The model is able to predict the full kinematics of the undulating airfoil by expressing forces and moments in terms of hydrodynamic impulse.

MATHEMATICAL AND NUMERICAL MODEL

In recent years, much progress has been obtained for the study of fish self-propulsion, starting from the mathematical models for elongated flexible body proposed by Lighthill [1] and Wu [2], up to the numerical solutions of Navier-Stokes equations for incompressible and viscous flow about a deformable body. In the present paper, however, we adopt a simplified model, which seems to be more appropriate for a wide analysis of the relevant parameters. In fact, we developed a coupling model able to combine the dynamic evolution of the deformable body with the two-dimensional inviscid flow simulation accounting for vorticity generation and release.

Following Kanso [3], who considered only the massless case in the frame of pure potential flow, we solved the body dynamics problem through hydrodynamic impulse conservation considering an appropriate wake model which rises the complexity of both the body motion and the flow solution due to their intrinsic coupling.

Body kinematics and flow solution

The force on the body can be obtained via the hydrodynamic impulse formulation, i.e.

$$\mathbf{F} = -\rho \frac{d}{dt}\left[\int_{S_b} \mathbf{x}\times\mathbf{n}\times\mathbf{u}\, dS + \int_V \mathbf{x}\times\omega\, dV\right] \tag{1}$$

where S_b and V are the body surface and the fluid volume around the body, while $\mathbf{u}$ is the velocity field, ω is the vorticity and $\mathbf{n}$ is the outward normal on S_b (into V). A similar relation could be obtained for the moment M. The expression for the force and moments can be combined with the dynamics equations

$$\mathbf{F} = \frac{d}{dt}\left(m\mathbf{u}_b\right), \quad \mathbf{M} = \frac{d}{dt}\left(I\boldsymbol{\Omega}\right) \tag{2}$$

where $\mathbf{u}_b$ and $\boldsymbol{\Omega}$ are the body linear and angular velocity, to eliminate the time-derivatives and obtain a simple linear system like $\mathbf{AX} = \mathbf{B}$. Here the unknown vector $\mathbf{X}$ contains the locomotion linear and angular velocity components and $\mathbf{B}$ is the forcing term related to the prescribed shape deformation.

Flow solutions, i.e. $\mathbf{u}$ and ω, are computed using an unsteady potential panel code consistently modified to allow for the solution about deformable airfoil representig a fish. The vortex shedding process is modeled by an unsteady Kutta condition, through a wake panel attached to the trailing edge which is concentrated into a point vortex and shed into the wake. The vortex shedding requires an iterative scheme, due to the non-linearity of the problem.

NUMERICAL RESULTS

Here we present a typical case of neutrally buoyant ($\rho = 1$) fish's self propelled swimming, represented as a NACA0012 foil deformed through the undulation of its centreline

$$h(s,t) = a_0 A(s)\sin\left[2\pi\left(\frac{L}{\lambda}s - ft\right)\right] \tag{3}$$

This relation is used for the carangiform swimming [4], where the amplitude law is $A(s) = 1 - 0.825(s-1) + 1.625(s^2-1)$, $\lambda = 1$, $a_0 = 0.1$ and the frequency $f = 0.5$. The curve coordinate along the centreline, s, ranges from 0 to 1.

Fig.1 shows the wake visualization of the self propelled airfoil after 5 oscillation periods. The reverse Von Karman vortex street is found in the wake, as evidence of the thrust experienced by the foil.

From the comparison shown in fig.2a between the swimming velocity obtained with the pure potential model (as in [3]) and the vortex shedding model, we can see that the presence of vorticity release compensates the high velocity

*Corresponding author. E-mail: damiano.paniccia@uniroma1.it

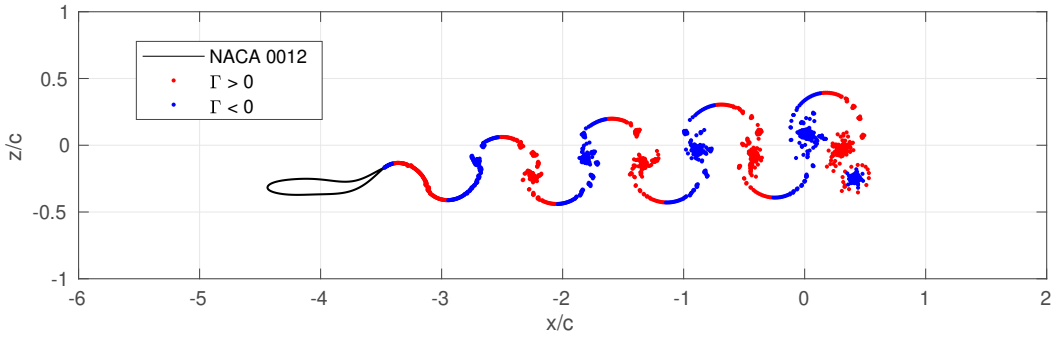

Figure 1: Swimming and wake visualization of a self-propelled deformable profile (NACA0012).

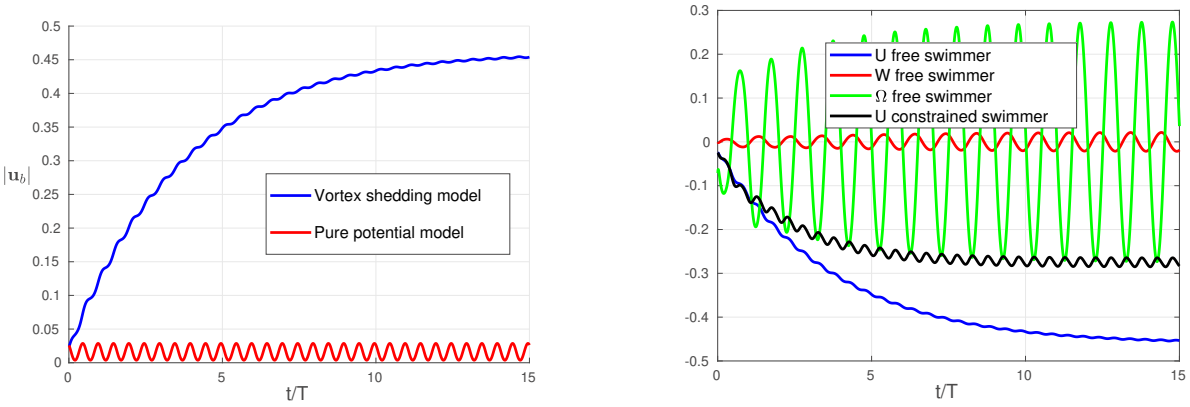

(a) (b)

Figure 2: (2a) Swimming speed obtained with pure potential and vortex shedding models - (2b) Horizontal U, lateral W and angular Ω velocity components. Constrained U is also shown in comparison.

oscillation predicted in the pure potential case. Moreover, the vortex shedding model reaches a steady state speed which is very close to the phase-velocity $\lambda f = 0.5$ of the traveling wave after a transient, while the pure potential model predicts a much lower velocity and reaches its steady state value since the beginning of the undulating motion.

Several studies about self-propelled swimming fish do not take care of lateral and angular kinematics of the airfoil, which is constrained to move along the horizontal direction only. Fig.2b shows the comparison between the obtained kinematics for a free swimmer and a constrained swimmer. The horizontal component of the swimming velocity U is about 35% higher when the airfoil is unconstrained. Therefore, forcing the airfoil to move along a fixed direction, or assuming that the fish's centre of mass is fixed to a point, leads to incorrect results both in terms of overall kinematics and energy and power consumption [5].

References

[1] Lighthill M. Note on the swimming of slender fish. *J. Fluid Mech.* **9(2)**: 305-317, 1960.
[2] Wu T. Y. Swimming of a waving plate. *J. Fluid Mech.* **10**: 321, 1961.
[3] Kanso E. Swimming in an inviscid fluid. *Theor. Comput. Fluid Dyn.* **24** 2010.
[4] Maertens A. P., Gao A. and Triantafyllou M. S. Optimal undulatory swimming for a single fish-like body and for a pair of interacting swimmers. *J. Fluid Mech.* **813**: 301-345, 2017.
[5] Carling J., Williams T. L. and Bowtell G. Self-propelled anguilliform swimming: simultaneous solution of the two-dimensional Navier-Stokes equations and Newton's laws of motion. *J. Exper. Biology* **201**: 3143-3166, 1998.

TURBULENT FLOW REDUCTION IN BILEAFLET MECHANICAL HEART VALVES

Hadi Zolfaghari[1], David Hasler[1], and Dominik Obrist * [1]
[1] ARTORG Center for Biomedical Engineering Research, University of Bern, Bern, Switzerland

Summary Bileaflet mechanical heart valves are successfully used for the replacement of stenotic aortic valves. Turbulent flow in the wake of these valves may be related to the formation of blood clots. Reduction of turbulent flow by natural laminar flow (NLF) is an established concept in aircraft design. It is our aim to apply this concept to heart valve design. Therefore, we study instability mechanisms leading to laminar-turbulent transition and discuss design optimization approaches to reduce turbulence.

BILEAFLET MECHANICAL HEART VALVES

The aortic valve is located between the left ventricle of the heart and the aorta. It opens during systole (contraction of the heart) and closes tightly during diastole (relaxation) to prevent blood from flowing back into the heart. At rest, the ejected blood stream reaches velocities of 1 to 2 m/s resulting in a Reynolds number of 3,000 to 6,000.

Aortic stenosis is a common disease of the aortic valve where the aortic valve does not fully open and creates a significant obstruction to the ejected blood stream [4]. In moderate to severe cases of aortic stenosis, the diseased valve is replaced by an aortic valve prosthesis. Especially in younger patients, mechanical heart valves are used because of their excellent durability. The most common design is the so-called bileaflet mechanical heart valve (BMHV) featuring two hinged valve leaflets which open and close during the heart beat (Figure 1a). However, it is known that unphysiological blood flow through BMHVs causes excessive viscous shear stresses which may lead to the formation of blood clots and blood trauma. For that reason, patients with BMHV are required to take life-long anti-coagulation medication which affects their quality of life. It is desirable to find ways to reduce the viscous shear stress levels in the flow past BMHVs and to obtain a more physiological blood flow.

Throughout systole, the flow past BMHVs is dominated by a turbulent wake. Next to its thrombogenic potential, turbulent blood flow may also be a factor in adverse aortic events (e.g. aortic dissection) because turbulent wall-shear stresses on the aortic wall may lead to endothelial damage. Moreover, turbulent viscous dissipation is a major contributor to the total pressure loss across the valve, which is one of the main performance parameters for artificial heart valves. In order to reduce turbulent shear levels, it is important to better understand the flow field past BMHVs and related instability mechanisms leading to laminar-turbulent transition. This allows to devise strategies to reduce turbulent flow as it has been successfully done in aircraft design by natural laminar flow (NLF).

METHODS

We investigate the flow past BMHVs by experimental and computational methods. For the experimental study, we use a pulsatile left heart flow loop and a tomographic particle image velocimetry (PIV) system as described in [1, 2]. It provides phase-averaged three-dimensional mean flow fields behind the BMHV. For the computational study, we perform direct numerical simulations (DNS) with a GPU-accelerated high-order Navier–Stokes solver [5]. The complex geometry of the BMHV is modeled by a sharp-interface immersed boundary method [3].

MEAN FLOW FIELD AND TURBULENT WAKE

Figure 1b shows the mean flow field past a BMHV at peak systole obtained with tomographic PIV [1]. The flow field comprises a complex configuration with multiple jets issuing from the three main orifices of the valve. As the jets widen in downstream direction, they reattach at the aortic wall about one valve diameter downstream of the valve orifice.

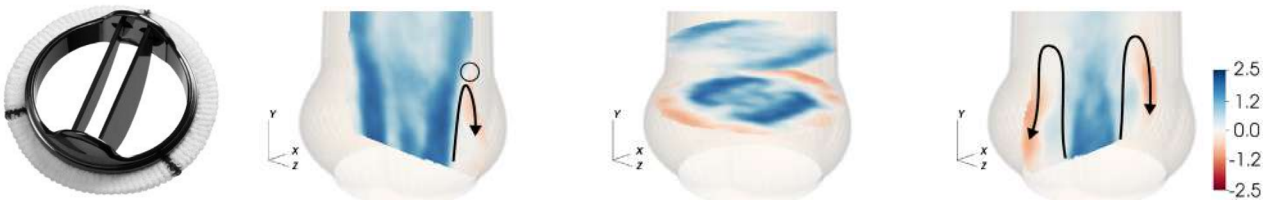

(a) (b)

Figure 1: (a) ST. JUDE REGENT bileaflet mechanical heart valve. (b) Axial velocities (in m/s) past a BMHV at peak systole (blue: positive axial velocity; red: negative velocity) [1].

*Corresponding author. E-mail: dominik.obrist@artorg.unibe.ch.

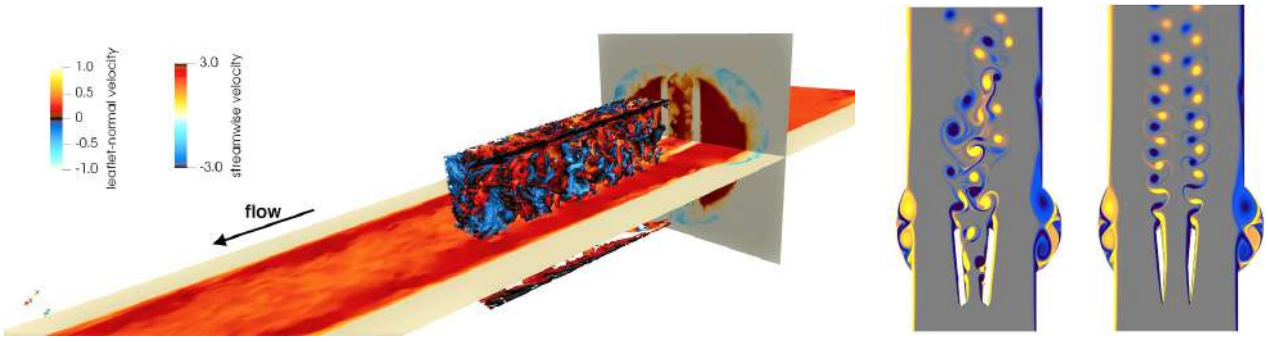

(a) (b) (c)

Figure 2: (a) DNS of the systolic flow past a BMHV with a turbulent wake (vortical structures visualized with the λ_2-criterion, $\lambda_2 = -0.1$). (b) Absolute instability between the leaflets leading to turbulent breakdown in the wake [6]. (c) Modified leaflet shape eliminating the primary instability [6].

Upstream of the reattachment points, there are two main regions of retrograde flow (recirculation) along the wall of the aorta.

The wakes and shear layers behind the two valve leaflets and between the forward and retrograde flow are unstable. This results in a strongly turbulent wake (Figure 2a). Although the flow in the sinus cavities (light blue regions in Figure 2a) is also unstable, it does not significantly contribute to the onset of turbulent flow behind the BMHV.

Quantitative analysis of the turbulent wake indicates high viscous shear stress levels beyond 10 Pa and turbulent viscous loss significantly contributing to the overall pressure loss across the valve. Furthermore, the analysis of velocity gradients along the aortic wall shows elevated levels of wall-shear stress as the turbulent wake attaches at the wall.

STRATEGIES FOR TURBULENT FLOW REDUCTION

Detailed analysis of the mechanisms leading to the turbulent wake indicates possible technical solutions for turbulence reduction, e.g. by shape optimization of the leaflet design. As it has been shown by Zolfaghari and Obrist [6], there exists an absolute instability close to the leading edge of the leaflets which leads to the breakdown of the Burgers vortex sheets in the wake of the two leaflets (Figure 2b). This primary instability can be suppressed by a slight modification of the leaflet shape (Figure 2c), i.e. by omitting the blunt leading edge of the leaflets which lead to an unstable impinging leading edge vortex (ILEV). This demonstrates the potential of design optimization for heart valve prostheses. Currently, a study on adjoint-based control of the ILEV instability is underway to identify optimal valve designs.

CONCLUSIONS

We have shown here that a detailed understanding of the flow past BMHVs can lead the way to better valve designs and less thrombogenicity. We have used modern experimental and computational tools to study the mean flow field and the turbulent wake of the valve. Tools of hydrodynamic stability theory were successfully applied to identify the origins of turbulent flow. Computational results suggest that NLF design concepts can be used to reduce turbulent flow past BMHVs.

References

[1] D. Hasler. *Experimental Investigation of the three-dimensional Flow Field in the Vicinity of Aortic Valve Prostheses*. PhD thesis, Universität Bern, 2017.

[2] D. Hasler, A. Landolt, and D. Obrist. Tomographic PIV behind a prosthetic heart valve. *Exp Fluids*, 57(5):80, 2016.

[3] R. Mittal, H. Dong, M. Bozkurttas, F. Najjar, A. Vargas, and A. von Loebbecke. A versatile sharp interface immersed boundary method for incompressible flows with complex boundaries. *J Comput Phys*, 227(10):4825 – 4852, 2008.

[4] V. T. Nkomo, J. M. Gardin, T. N. Skelton, J. S. Gottdiener, C. G. Scott, and M. Enriquez-Sarano. Burden of valvular heart diseases: a population-based study. *Lancet*, 368(9540):1005–1011, 2006.

[5] H. Zolfaghari, B. Becsek, M. G. Nestola, W. B. Sawyer, R. Krause, and D. Obrist. High-order accurate simulation of incompressible turbulent flows on many parallel gpus of a hybrid-node supercomputer. *Comp Phys Comm*, 244:132–142, 2019.

[6] H. Zolfaghari and D. Obrist. Absolute instability of impinging leading edge vortices in a submodel of a bileaflet mechanical heart valve. *Phys Rev Fluids*, 4(12):123901, 2019.

BIASED RE-ORIENTATION IN CHEMOTAXIS OF PERITRICHOUS BACTERIA

Tonau Nakai *[1], Taishi Ando [1], and Tomonobu Goto [1]
[1] Department of Engineering, Tottori University, Tottori, Japan

Summary Chemotaxis of peritrichous bacteria is caused by the suppression of the switching of the rotation of the flagellar motors. We investigated whether the chemotactic behavior would appear in the turn angle during the tumbles. It is found that the turn angle depends on the concentration gradient of a chemoattractant that the cell sensed just before the tumble. The distribution of turn angle is biased toward smaller value when the cell swims up the gradient, whereas the distribution is almost uniform (random direction) when swimming down the gradient. Upwardly swimming cells make the turn angle smaller by loosening fewer flagellar filaments from the bundle during tumbles, resulting in accumulation around a chemoattractant. Our numerical simulation based on the biased random walk model has revealed that this bias in angular distribution clearly affects the cell's behavior around an attractant.

BACKGROUND

The mechanism of bacterial chemotaxis has been intensely studied for peritrichous bacteria that have multiple flagella. Cells swim by rotating their helical flagella with flagellar motors at the proximal ends of the flagella. When each motor rotates counterclockwise (CCW) being viewed from the flagellum to the motor, flagella form a bundle and the cell propels itself straight (run). When the rotational direction of the motor switches to clockwise (CW), the corresponding flagellum is released from the bundle and the swimming direction of the cell changes (tumble) [1]. If a cell senses that the concentration of an attractant has increased, the cell decreases the switching frequency from CCW to CW, which causes longer run in swimming up the concentration gradient than swimming down. The longer run duration toward the attractant source has been actually observed for *E. coli* [2] and *Salmonella typhimurium* [3] cells.

The aim of this study is to demonstrate that the turn angle distribution depends on the swimming direction (up or down the concentration gradient). Recently, Sourjik et al. have predicted that chemotactic behavior of peritrichous bacteria can be seen in the turn angles during tumbles [4]. An observational study regarding flagellar filaments of *E. coli* cells during tumble revealed that the turn angle becomes smaller when the fewer number of filaments are released during a tumble [5]. The number of flagella released during a tumble can become fewer when the switching from CCW to CW is suppressed due to sensing a chemoattractant.

METHODS

A strain of peritrichous bacteria, *Salmonella typhimurium* SJW1103 was used. Cells were cultured in 3 mL of LB medium overnight at 30°C. Then, 0.1 mL of the bacterial suspension was put into 3 mL of the motility buffer (pH 7.0, 10 mM KH_2PO_4, 0.1 mM EDTA, 10 mM sodium lactate) and incubated for 3 hours at 30°C. The solution was centrifuged for 1 minute at 10000 rpm. The supernatant liquid of 0.9 mL was removed and the buffer of the same volume was added. One molar of L-serine with 0.3% agar was aspirated into the glass capillary with the internal diameter of 1 μm. To observe a single cell for a long time, only a few cells were poured into the preparation with a microinjection. Cells accumulating around an attractant were observed by an inverted microscope.

RESULTS

Trajectory of the trapped cell around an attractant

Figure 1 (a) shows an example of a swimming trajectory. The cell stays within 100 μm from the source of attractant for 5 minutes. Whether the swimming movement shows chemotaxis or just a random walk can be determined by calculating the mean square displacement (MSD). As shown in Fig. 1 (b), MSDs of samples I-IV reach plateau in the time region of 10-100 s, indicating that each cell is attracted to the capillary tip. Without an attractant, the MSD should increase linearly with time.

Turn angle

Difference in the distribution of the turn angle between swimming up and down the gradient is investigated. The relationship between the turn angle θ and the posture angle ϕ just before the tumble with respect to the attractant source is described in the following. Figure 2(a) shows the definitions of θ and ϕ, and Fig. 2 (b) shows a plot of θ and ϕ for all the 268 tumbles of the single cell. The posture angle $\phi < 90°$ for "up" swimming and $\phi > 90°$ for "down". The turn angle θ is distributed uniformly when $\phi > 90°$, whereas the distribution of θ is biased to smaller angle when $\phi < 90°$. This indicates that cells approaching the attractant source have smaller turn angle than receding cells. As shown in Fig. 2(c), this bias is clearly visualized by plotting the cumulative probability of θ for up ($\phi < 90°$) and down ($\phi > 90°$). If θ is observed at an equal probability at any angle (random direction), the cumulative probability would correspond to a dashed straight line. The distribution "down" is almost random and "up" is above "down", indicating that the directional change during a tumble after swimming up the gradient tends to be smaller.

*Corresponding author. E-mail: nakai@tottori-u.ac.jp.

Biased random walk simulation

How this observed bias in the turn angle affects the degree of the accumulation is investigated by the numerical simulation. The authors have developed a mathematical model for bacterial chemotaxis based on the biased random walk [6]. The modeled cell changes the tumble frequency and the turn angle depending on its moving direction of the adjacent steps. One cell was placed at the origin, and the calculation was performed in a 3 dimensional space. Calculated MSD was compared with the observation. Although the calculated MSD is 5 times larger than the measured MSD, but the cell stays around the origin only with the biased distribution of turn angle.

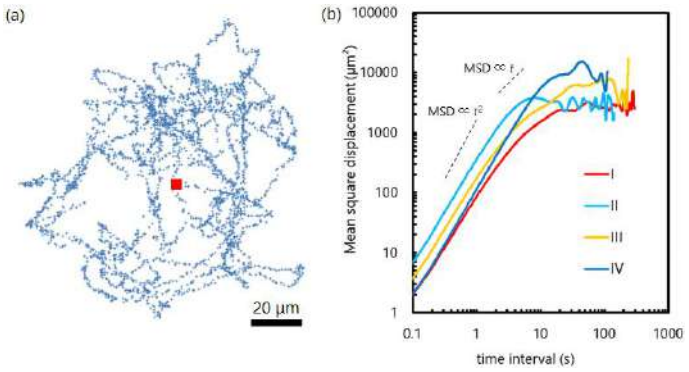

Figure 1. Single cell's behavior around the attractant source, (a) cell's trajectory, (b) mean square displacement of 4 cells.

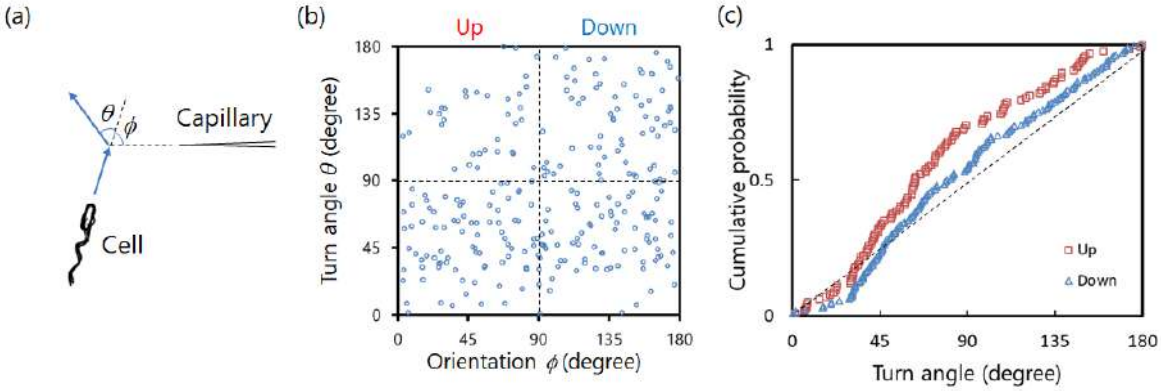

Figure 2. Turn angle distribution in a single cell, (a) definition of the turn angle θ and the orientation ϕ, (b) θ-ϕ plot, (c) cumulative probability of the turn angle.

CONCLUSIONS

We investigated the turn angle during the tumbles of peritrichous bacteria swimming in the concentration gradient of a chemoattractant. It is found that the turn angle depends on the concentration gradient that the cell sensed just before the tumble. The distribution of turn angle is biased toward smaller value when the cell swims up the concentration gradient, whereas the distribution of the angle is almost uniform (random direction) when swimming down the gradient. This behavior is reasonable because the nature of bacterial chemotaxis is changing the switching rate of flagellar motors according to the environment. Upwardly swimming cells make the turn angle smaller by loosening fewer flagellar filaments from the bundle during tumbles, resulting in accumulation toward higher concentration of the chemoattractant. How this observed bias in the turn angle affects the degree of the accumulation was investigated by the random walk simulation. In the concentration field where attractants diffuse concentrically from the point source, it was found that this angular distribution clearly affects the degree of accumulation of the cell.

Acknowledgements

This work was supported by JSPS Kakenhi Grant Numbers JP18K03950 and 19K04193.

References

[1] Silverman M., Simon M. Flagellar rotation and the mechanism of bacterial motility. *Nature* **249**: 73-74, 1974.
[2] Berg H.C., Brown D.A. Chemotaxis in *Escherichia coli* analyzed by three-dimensional tracking. *Nature* **239**: 500-504, 1972.
[3] Nakai T., Yoshino J., Goto T. Estimation of chemotaxis intensity of Salmonella cells by the capillary assay and biased random walk simulation. *J. Aero Aqua Bio-mech.* **8**: 63-68, 2019.
[4] Sourjik V., Wingreen N.S. Responding to chemical gradients: bacterial chemotaxis. *Curr. Opin. Cell Biol.* **24**: 262-268, 2012.
[5] Turner L., Ryu W.S., Berg H.C. Real-time imaging of fluorescent flagellar filaments. *J Bacteriol.* **182**: 2793-2801, 2000.
[6] Goto T., Nakai T. Steady distribution of cells in a one-dimensional biased random walk model of bacterial chemotaxis. *J. Biomech. Sci. Eng.* **11**: 15-00587, 2016.

MOTILITY AND AEROTAXIS IN SINORHIZOBIUM MELILOTI, A SOIL BACTERIUM

Julien Bouvard[1], Frédéric Moisy *[1], Carine Douarche[1], Nicolas Busset[2], Peter Mergaert[2], and Harold Auradou[1]
[1]Université Paris-Saclay, CNRS, FAST, 91405 Orsay, France
[2] Université Paris-Saclay, CEA, CNRS, Institute for Integrative Biology of the Cell (I2BC), 91198, Gif-sur-Yvette, France

Summary Aerotaxis is the ability of motile cells to move towards oxygen. Bacteria tracking and in-situ oxygen concentration measurements are used to characterize aerotaxis in *Sinorhizobium meliloti*, a motile nitrogen-fixing bacterium naturally present in the soil. Aerotaxis takes place in a sealed glass capillary closed at one end with an oxygen-permeable plug. Our results suggest that the oxygen dependence of the aerotactic velocity, $\propto \nabla c/c^2$, is stronger than the "logarithmic sensing" response ($\propto \nabla c/c$) found in other chemoattractants.

INTRODUCTION

Chemotaxis, the biased migration of a motile cell towards the source of a chemical gradient, is an ubiquitous phenomenon in nature. Yet, our understanding of the basic physical and hydrodynamical mechanisms behind chemotactic swimming in a liquid environment is still limited [1]. Among various chemoattractants, aerobic bacteria are sensitive to the oxygen content of the medium, a specific chemotaxis referred to as aerotaxis [2].

We are interested here in the aerotaxis of a motile nitrogen-fixing bacterium naturally present in the soil, *Sinorhizobium meliloti*, which forms a symbiotic association with some legume plants. Most experiments based on chemotactic/aerotactic assays for *S. meliloti* are qualitative, and do not provide quantitative information on its chemotactic response. A difficulty is to access simultaneously the dynamics of oxygen and bacterial concentrations.

Here oxygen concentration is measured using Ruthenium micelles, an oxygen-sensitive fluorescent dye encapsulated in phospholipid micelles to make it biologically inert [3]. We designed a simple experiment, shown in figure 1: a glass capillary, sealed at one end by a PDMS plug (which is permeable to oxygen) and at the other end by an oxygen-proof plug, is filled by a bacterial suspension mixed with Ruthenium micelles. Simultaneous measurements of oxygen concentration, bacteria concentration and bacteria swimming velocity are carried out to reconstruct the aerotactic response.

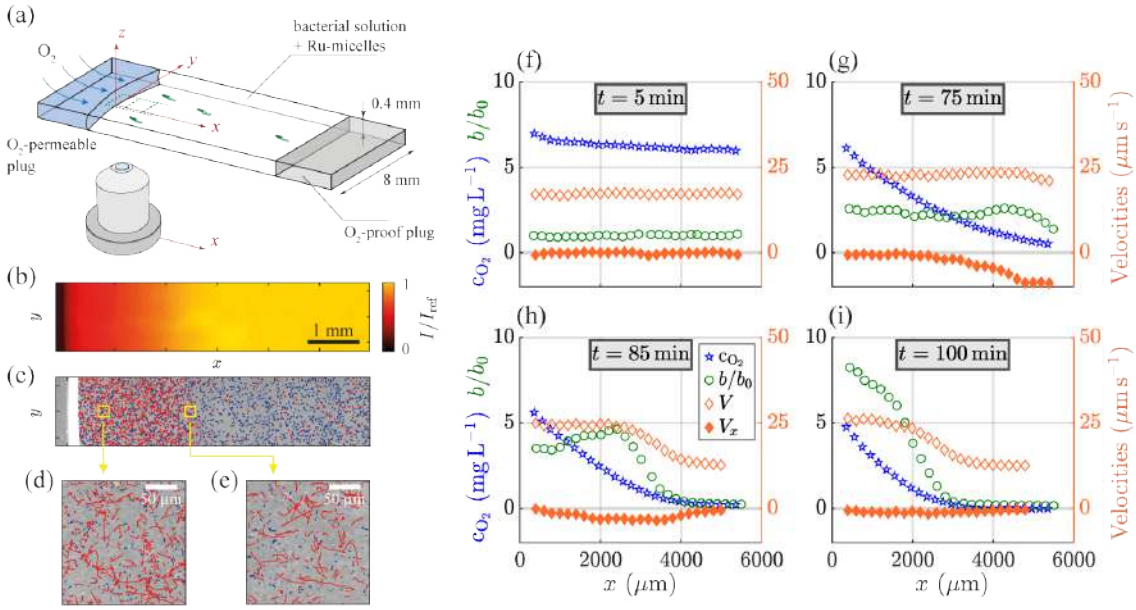

Figure 1: (a) Experimental setup: a glass chamber of rectangular section is filled with the bacterial suspension and Ruthenium micelles. One side of the capillary is sealed by pdms, permeable to oxygen, while the other side is sealed with an O_2-proof grease plug. (b) Fluorescence light intensity, mapping the oxygen concentration field (dark: high $[O_2]$). (c) Images of bacteria, superimposed to the bacteria tracks (non-motile and motile bacteria are in blue and red, respectively). (d), (e): Magnifications at two locations, showing the random and biased trajectories. (f), (g), (h) and (i): Variation of the local density of bacteria, oxygen concentration, magnitude of the swimming velocity of the bacteria and aerotactic velocity as function of the distance from the PDMS for four different times. The capillary is initially filled with an homogeneous suspension of bacteria at OD $= 0.05$.

*Corresponding author. E-mail: frederic.moisy@universite-paris-saclay.fr

RESULTS

Under usual conditions, a suspension of *S. meliloti* is composed of both non-motile and motile bacteria. Non-motile bacteria may be either attached to the substrate (on which they may form biofilms) or freely suspended in the liquid medium. We focus here on the motile population, swimming at a mean velocity of 20-25 $\mu\mathrm{m\,s^{-1}}$ and performing aerotaxis. Bacterial motion is observed using high-speed imaging under phase-contrast microscopy, and their trajectories are analysed by standard tracking methods using *ImageJ*.

Starting from an initial homogeneous concentration of bacteria and oxygen, oxygen consumption by the bacteria gradually produces an oxygen gradient near the oxygen-permeable PDMS plug, at $x = 0$. This oxygen gradient triggers the bacterial aerotaxis: Fig. 1 shows the propagation of a bacterial band escaping the low-oxygen region towards the oxygen source by swimming up the gradient. Reproducing this experiment with different initial concentrations yields the same qualitative result, on a time scale that depends on the initial bacterial concentration.

To infer the aerotactic response, we describe the bacterial concentration $b(x,t)$ using the standard one-dimensional Keller-Segel equation [4,5]:

$$\frac{\partial b}{\partial t} + \frac{\partial J_x}{\partial x} = 0, \qquad J_x = \chi(c) b \frac{\partial c}{\partial x} - \mu(c) \frac{\partial b}{\partial x}, \tag{1}$$

where c is the oxygen concentration, μ is the motility coefficient and χ the aerotactic sensivity coefficient. The averaged bacterial flux J_x has two contributions, aerotactic and diffusive. This equation assumes that the bacterial time response to changes in oxygen level is much faster than the dynamics of the propagating front, and that the mean run length is much smaller than the typical front width.

The flux in Eq. (1) is directly related to the averaged bacterial velocity V_x computed from the bacteria tracking through $J_x = bV_x$. This shows that the measured bacterial velocity V_x gives the aerotactic velocity $\chi(c)\partial c/\partial x$ only where b is uniform, *i.e.* at the location of the front or far from oxygen source, which severely limits the range of oxygen where $\chi(c)$ can be measured. Because of the large motility of *S. meliloti*, $\mu \simeq (8 \pm 2) \times 10^3\,\mu\mathrm{m^2\,s^{-1}}$, the diffusive flux represents a strong contribution to the total flux. Taking into account the diffusive flux term allows us to extend the range of oxygen concentration where the aerotactic sensivity coefficient $\chi(c)$ can be measured.

Our measurements show that the quantity $[V_x + (\mu/b)\partial b/\partial x]/(\partial c/\partial x)$ is indeed independant of x, t, and the initial bacterial concentration over a significant range of oxygen concentration, indicating that Equation (1) holds in the explored range of parameters. A power-law is found for the aerotactic sensitivity, $\chi(c) \propto 1/c^2$, over the whole range of oxygen concentration for which the cells are motile: between $0.3\,\mathrm{mg\,L^{-1}}$ (below which motility stops) and $5\,\mathrm{mg\,L^{-1}}$ (close to the saturation concentration). This scaling is compatible with the general form proposed by Lapidus and Schiller [6] and Rivero *et al.* [7], which applies when the dissociation constant of the considered chemoattractant (here oxygen) is much smaller than the ambiant attractant concentration.

Our results suggest that aerotaxis in *S. meliloti* is a very efficient process: the biased swimming towards oxygen is strongly enhanced in low-oxygen regions, with an oxygen dependence that exceeds the "logarithmic sensing" aerotactic response ($\chi \propto 1/c$) found in other species.

References

[1] J. B. Raina, V. Fernandez, B. Lambert, R. Stocker and J. R. Seymour. Nat. Rev. Microbiol. **17**, 284-294 (2019).
[2] R. Götz, N. Limmer, K. Ober and R. Schmitt. Microbiology, **128**(4), 789-798 (1982).
[3] C. Douarche, A. Buguin, H. Salman and A. Libchaber. Physical Review Letters **102**, 198101 (2009).
[4] E. F. Keller and L. A. Segel. Journal of theoretical biology **30**(2), 225-234 (1971).
[5] E. F. Keller and L. A. Segel. Journal of theoretical biology **30**(2), 235-248 (1971).
[6] I. R. Lapidus and R. Schiller. Biophysical journal **16**(7), 779-789 (1976).
[7] M. A. Rivero, R. T. Tranquillo, H. M. Buettner and D. A. Lauffenburger. Chemical engineering science **44**(12), 2881-2897 (1989).

GEOINSPIRED BIOREACTORS

Patrice Meunier *[1], Cyril Lefranc[1,2], Julien Roubach[2], Olivier Detournay[2]
[1] Institut de Recherche sur les Phénomènes Hors Equilibre, Université Aix-Marseille, Marseille France
[2] Planktovie, 45 av. Joliot-Curie, 13013 Marseille, France

Summary Inspired by the precession of the Earth, a new bladeless mixer has been designed, which consists of a tilted and rotating cylinder. While increasing the rotation of the cylinder, the flow transitions from laminar to turbulent with a perfect agreement between experiments and theory. It creates a strong mixing which is as efficient as using a classical Rushton turbine, but with a shear 20 times smaller. This soft mixer is particularly interesting for bioreactors which require an efficient mixing of oxygen and carbon dioxide but where a strong shear can damage fragile cells. Preliminary results obtained for the growth of microalgae in such photobioreactors suggest that it can be a technological breakthrough in biotechnologies.

INTRODUCTION

In biotechnology, the large scale production of fragile cells is severely limited by the weak supply of oxygen obtained in large bioreactors. The flux of oxygen is usually increased through an enhanced mixing created by bubbling or rotating blades. However, both bubbles and moving blades generate a strong shear which drastically lowers the growth of fragile cells. The need for a soft mixer without blades is thus required in many biological applications.

LAMINAR-TURBULENT TRANSITION IN A ROTATING TILTED CYLINDER

We present here a new type of mixer, patented under the name soft mixer, which consists of a rotating cylindrical container with an axis tilted with respect to the vertical (see figure below). The free surface remains horizontal which forces inertial (Kelvin) modes of azimuthal wavenumber m=1. The height of fluid is chosen such that the amplitude of the modes diverge because the forcing is located at the node of the mode [1]. This generates large steady motions even for small tilt angles with an amplitude scaling as the square root of the Reynolds number (due to Ekman pumping saturation). This steady inertial mode can in turn destabilize via a triadic resonance as in precessing or elliptic vortices [2]. The instability exhibits two inertial modes with azimuthal wavenumbers m=5 and m=6 satisfying the resonance condition. The wavenumbers and the viscous threshold of the instability can be predicted analytically with no adjustable parameters and show an excellent agreement with the experiment.

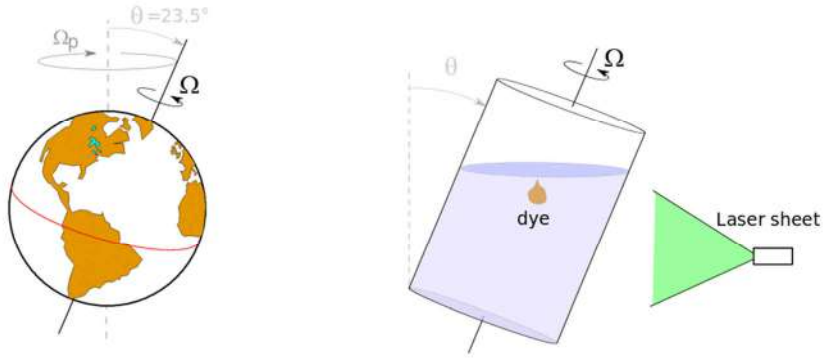

(a) (b)

Figure 1. (a) Precessing motion of the Earth inducing resonant motions inside the liquid iron core. (b) Resonant motion of a liquid inside a tilted rotating cylinder excited by the free surface. The mixing properties are measured using LIF visualisations with a fluorescent dye (Rhodamine B).

*Corresponding author. E-mail: patrice.meunier@univ-amu.fr.

The mixing time of this flow has been measured experimentally by introducing a fluorescent dye and by measuring its variance as a function of time. In the absence of instability, the dye is simply advected without large stretching (see Fig. 2a). However, in the presence of the instability, the dye is stretched and folded in the whole cylinder in a few rotation periods. It clearly shows that the tilt of the cylinder accelerates the mixing efficiency because it creates a turbulent flow through the instability (see Fig. 2c). For sufficiently large tilt (above 1 degree), the mixing inside this soft mixer is as efficient as for a Rushton turbine. However, the shear is an order of magnitude smaller which is extremely interesting for biological applications.

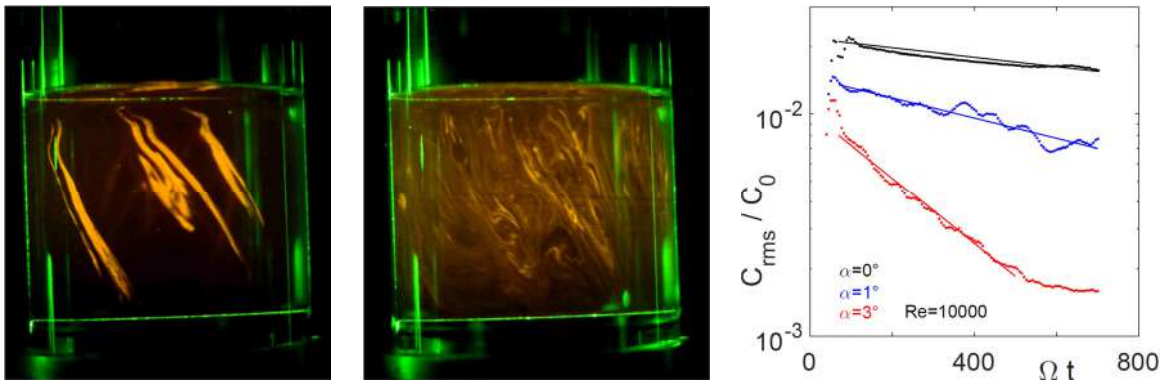

(a) (b) (c)

Figure 2. (a) Laminar dye patterns observed in the absence of the instability. (b) Strong mixing obtained in the presence of the instability. (c) Temporal decay of the variance of the dye concentration without tilting the cylinder (black), with a weak tilt (blue) and a large tilt (red).

A NEW GENERATION OF BIOREACTORS

A new type of bioreactor has been built based on the principle of the soft mixer. The rotating cylinder contains a nutritive liquid and is tilted with an angle of 3 degrees compared to the vertical (see Fig.3b). Shear sentitive microalgae (dinoflagellates Alexandrium, see Fig.3a) are introduced in the nutritive solution and grow with a duplication rate of about 2 to 3days to a very large concentration of about 20,000 cells/ml. This will allow to produce Saxitoxin which is naturally contained in the dinoflagellate. A large scale bioreactor of 150l is currently being tested for the production of these microalgae (see Fig. 3c).

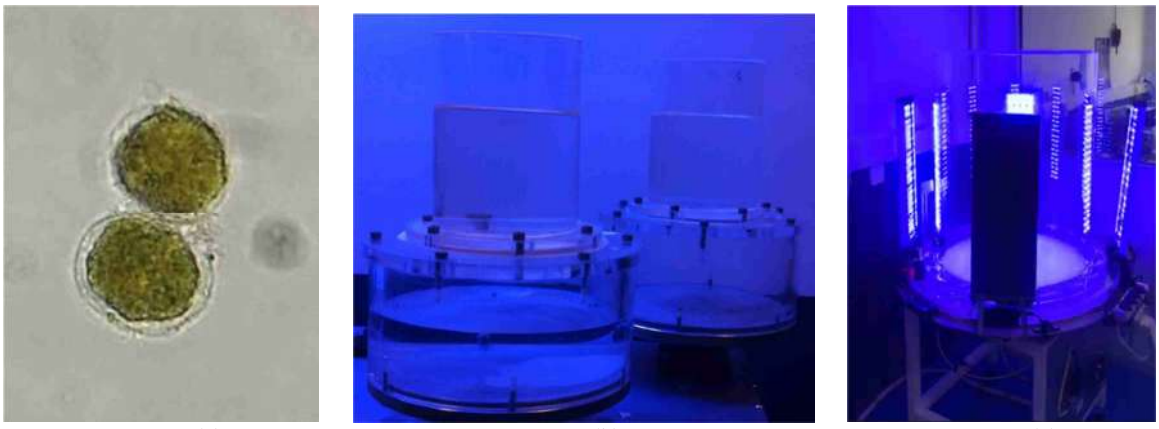

(a) (b) (c)

Figure 3. (a) Dinoflagellates produced in a soft mixer bioreactor. (b) 1 liter bioreactors tilted at an angle of 3degrees and rotating at 60rpm. (c) 150 liters bioreactor with 4 LED panels.

References

[1] Thompson R., Diurnal tides and shear instabilities in a rotating cylinder. *J. Fluid. Mech.* 40:737-751, 1970.
[2] Lagrange A., Meunier P., Nadal F., Eloy C., Precessional instability of a fluid cylinder. *J. Fluid Mech.* 666:104-145, 2011.

SYNCHRONISED STATES OF HYDRODYNAMICALLY COUPLED FILAMENTS AND THEIR STABILITY.

Smitha Maretvadakethope *[1], Yongyun Hwang [2], and Eric E. Keaveny[1]
[1] Department of Mathematics, Imperial College London, London, United Kingdom
[2] Department of Aeronautics, Imperial College London, London, United Kingdom

Summary Flagella and cilia exist throughout the natural world, whether as appendages to help micro-organisms swim or to pump fluid near tissues in highly viscous environments. A wide variety of synchronisation behaviours has been observed, expanding the full range from perfectly in-phase synchrony to completely anti-phase motion. Here, we use an elastic filament model to study the emerging synchronisation behaviours of two base-driven microfilaments. We quantify the synchronisation states that arise as the torque driving their motion is varied. Four synchronisation states are found, two of which are stable and the others unstable. A bifurcation and stability analysis is carried out using the power-method and a bisection method, and reveals that these states are non-trivially connected through pitchfork and saddle-node bifurcations.

INTRODUCTION

Cilia and flagella are slender, microscopic filaments used by single-celled organisms for motility and the tissues of large organisms for fluid transport. One example is the biflagellate algae *Chlamydomonas*, which consists of a cell body with two flagella protruding from its anterior. The flagella are observed to have two stable synchronised states: the anti-phase, breast-stroke during forward swimming, and the in-phase, parallel beating. Parallel beating is observed when the cell experiences a sudden stimulus at its anterior end, and attempts to quickly move away from the source [1]. Experimental studies of flagellar synchrony on *Chlamydomonas* have shown that synchronous behaviour can arise purely through hydrodynamic interactions [2], but also an additional elastic coupling between the bases of the flagella, known as basal coupling, can have a large effect on the type of synchrony which arises [3].

While simple models that treat systems of flagella as coupled 'bead-spring' oscillators with prescribed driving forces have produced initial results of synchronised states [4], more recent models capture the flagellum shape and elasticity and use ideas such as geometric switching to change the direction of flagellar motion [5] and generating synchonized states. It was found that for the case of two nearby, independently driven filaments, both in-phase and anti-phase synchrony can occur, and, over a particular range of parameter values, the bistability of these states exists.

THE MODEL

We make use of the elastic filament model developed by Schoeller et al. [6], modelling the flagella as inextensible Kirchoff rods with bending modulus, B, length l, and cross-sectional radius, a. The force and moment balances that arise in the model are discretised into $N = 19$ segments. The hydrodynamic interactions between these segments are accounted for through the Rotne-Prager-Yamakawa (RPY) approximation [7] that incorporates the effects of a nearby no-slip surface.

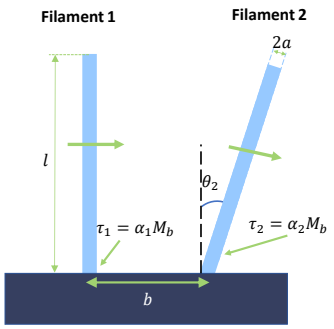

(a)

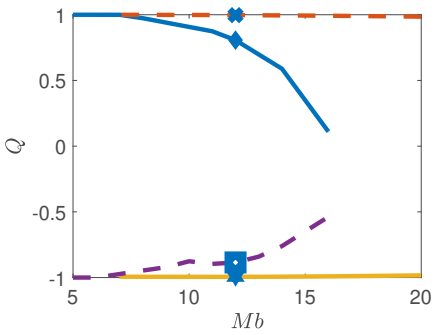

(b)

Figure 1: (a) Initial conditions of a simulation where $\alpha_1(0) = \alpha_2(0) = 1$, and $\theta_1(0) = 0$ and $\theta_2(0) = 0.01885$. (b) Bifurcation diagram of synchrony states for varying M_b. Stable branches are shown as solid lines, while unstable branches are indicated using dashed lines.

*Corresponding author. E-mail: sm6412@ic.ac.uk.

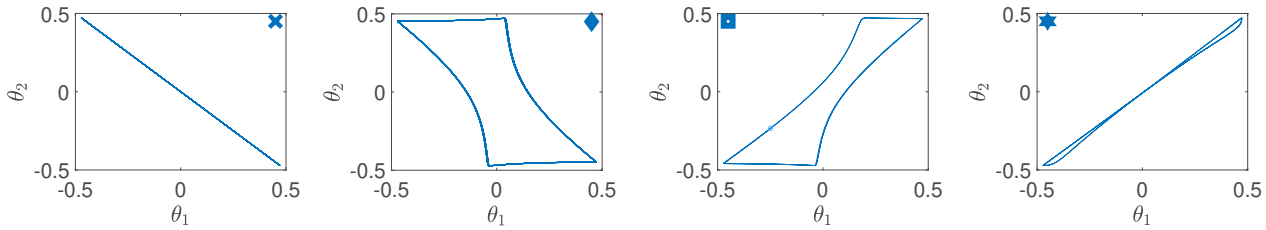

Figure 2: The phase diagrams plotting θ_1 versus θ_2 for the states indicated in Fig 1(a). The cases shown correspond to (a) the anti-phase synchrony, (b) the upper stable branch, (c) the intermediate unstable branch, and (d) the in-phase lower branch.

In our simulations, we consider two such flagella that are tethered to a planar surface a distance $b = l/2$ apart (see Fig. 1a). The filament $i = 1, 2$ is driven at its base by the torque $\tau_i = \alpha_i(t)M_b$, where M_b is the magnitude of the torque and $\alpha_i(t)$ controls the direction of the torque through a geometric switch. Specifically, the value of α_i transitions from 1 to -1 (or vice versa) when the filament base angle, θ_i, exceeds $\Theta = \pm 0.15\pi$ (see figure 1a).

To measure the synchrony of the system as it evolves, we compute the synchrony parameter,

$$Q = \frac{-1}{t_{end} - t_{start}} \int_{t_{start}}^{t_{end}} \alpha_1(t)\alpha_2(t)\mathrm{d}t. \tag{1}$$

If $Q = 1$, the filaments are perfectly anti-phase and if $Q = -1$ they are perfectly in-phase.

BIFURCATION ANALYSIS OF BISTABILITY

The recent work by Guo et al. [5] showed that there exists a region of bistability, by which the filaments can synchronise to two different stable states depending on the initial perturbation. In the present study, a total of four synchronisation states (including unstable ones) are computed, offering a complete description of the bistability. Figures 1 and 2 show a bifurcation diagram based on Q and M_b, and the phase diagram of each state depicted with $\theta_1(t)$ and $\theta_2(t)$, respectively. The upper-most branch is featured with the perfect anti-phase synchrony state (i.e. $Q = 1$; Fig. 2a), and becomes unstable through a supercritical pitchfork bifurcation near $M_b \simeq 7$. The intermediate stable state, emerged from this bifurcation, is continued with M_b, and reaches a turning point around $M_b \simeq 16$, at which it becomes unstable through a saddle-node bifurcation. Along the continued bifurcation curve, the phase diagram exhibits a continuous change (Figs. 2b and c). In particular, the two filaments are found not to be synchronised and their phase difference (i.e. $\theta_1 - \theta_2$) forms a limit cycle. Finally, the unstable intermediate state collides into the lower-most in-phase state at $M_b \simeq 5$ through a subcritical pitchfork bifurcation.

CONCLUSIONS

In this study, the bifurcation and stability of a system of two base-driven hydrodynamically interacting microfilaments have been fully described. These findings are particular important for biological systems such as swimming microorganisms. In particular, they underpin the statistical residence time of each state when the system is driven with stochastic noise. In this respect, characterising the stochastic dynamics of the system would be a natural step to pursue in the future.

References

[1] Wan K.Y., Goldstein R.E. Time irreversibility and criticality in the motility of a flagellate microorganism. *Phys. Rev. Let.*, **121** 05: 058103, 2018.
[2] Brumley D.R., Wan K.Y., Polin M., Goldstein R.E. Flagellar synchronization through direct hydrodynamic interactions.*Elife*, **3**: e02750, 2014.
[3] Goldstein R.E., Lauga E., Pesci A.I., Proctor M.R.E. Elastohydrodynamic synchronization of adjacent beating flagella, *Phys. Rev. Fluids*, **1** 7: 073201, 2016.
[4] Bruot N., Cicuta P. Realizing the physics of motile cilia synchronization with driven colloids. *Ann. Rev. Condensed Matter Phys.*, **7**:323–348, 2016.
[5] Guo H., Fauci L., Shelley M., Kanso E. Bistability in the synchronization of actuated microfilaments. *J. Fluid Mech.* **836**: 304-323, 2018.
[6] Schoeller S.F., Townsend A.K., Westwood T.A., Keaveny E.E. Methods for suspensions of passive and active filaments. *arXiv preprint* **arXiv**:1903.12609, 2019.
[7] Wajnryb E., Mizerski K.A., Zuk, P.J., Szymczak P. Generalization of the Rotne–Prager–Yamakawa mobility and shear disturbance tensors. *J. Fluid Mech.* **731**, 2013.
[8] Skufca J.D., Yorke J.A., Eckhardt B. Edge of chaos in a parallel shear flow. *Phys. Rev. Let.*, **96** 17: 174101, 2006.

CEREBROSPINAL FLUID MECHANICS IN THE BRAIN: EXPERIMENTS

Douglas H. Kelley *[1], Jeffrey Tithof[1,2], Humberto Mestre[3,4], Ting Du[3], John H. Thomas[1], and Maiken Nedergaard[3,4,5]
[1] Department of Mechanical Engineering, University of Rochester, Rochester, NY, USA
[2] Department of Mechanical Engineering, University of Minnesota, Minneapolis, MN, USA
[3] Center for Translational Neuromedicince, University of Rochester, Rochester, NY, USA
[4] Department of Neuroscience, University of Rochester, Rochester, NY, USA
[5] Center for Translational Neuromedicince, University of Copenhagen, Copenhagen, Denmark

Summary Fluid permeates the brain, not only providing buoyancy and cushioning, but also transporting neurotransmitters, wastes, and water as it passes around and through tissue. Waste removal is essential for avoiding diseases linked to its accumulation, like Alzheimer's. The glymphatic system is thought to drive fluid into brain tissue along spaces surrounding arteries, and we measure the velocity fields of such flows in live mice, finding evidence that flows are driven by the pulsing artery wall, as in peristalsis. We also show that high blood pressure alters the wave and weakens the flow. Water transport in an unhealthy brain can cause swelling that damages tissue, as in ischemic stroke. We present experimental studies of stroke in mice, including evidence that early swelling comes not from blood, as is canonical in medical education, but from cerebrospinal fluid surrounding the brain.

FLOW FOR WASTE REMOVAL: ARTERIAL PULSATION AND HYPERTENSION

The human brain makes up just 2% of body mass, but accounts for 25% of metabolic activity. Normal brain processes produce metabolic waste rapidly and in large quantities, and accumulation of waste products like amyloid-β and tau have been implicated in neurodegenerative disorders like Alzheimer's and Parkinson's diseases. Researchers have long been puzzled by the brain's apparent lack of lymph vessels, which sweep away cellular waste and excess fluid from most of the rest of the body. Recent identifications of lymph vessels in the periphery of the skull make the question more tantalizing: How is waste removed from the brain itself? Increasing evidence supports the hypothesis that waste is removed by cerebrospinal fluid (CSF) entering the brain along the perivascular spaces that surround arteries, then passing through brain tissue, a flow modulated by glial cells — dubbed the glymphatic system.

We present experimental studies of CSF flow in the brains of live mice. First, we focus on the perivascular spaces surrounding surface arteries, which we image with high spatial and temporal resolution (0.5 μm, 33 ms) using two-photon microscopy. Intravenous dye injections make arteries visible, and 1-μm polystyrene tracer particles infused into the cisterna magna track CSF flow, as shown in Fig. 1. We observe bulk flows that pulse in synchrony with the heart, proceeding on average in a direction parallel to the blood flow (not anti-parallel). The mean speed is 18.7 μm/s, so taking the width of the perivascular space as a characteristic length, we find the Reynolds number to be of order 10^{-3}: these flows are laminar. Using the diffusivity of amyloid-β, we find the Péclet number to be of order 10^2, so waste transport is dominated by advection here, though deep in the brain diffusion likely plays a larger role.

The fact that these flows pulse in synchrony with the heart is consistent with the existing hypothesis that CSF could be driven along perivascular spaces by a peristalsis-like mechanism as traveling mechanical waves deform the adjacent artery wall. If the hypothesis is true, then altering the traveling waves should change the resulting flow. To alter the

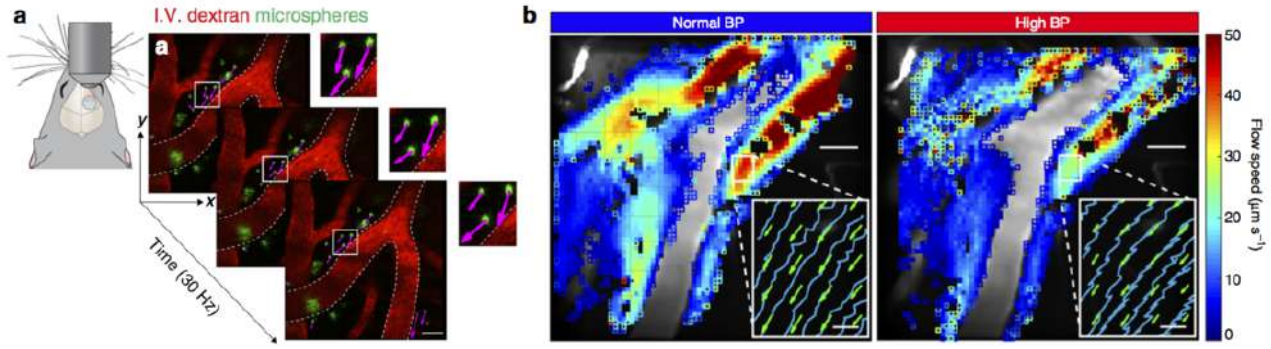

Figure 1: Flow of CSF in perivascular spaces for waste removal. (a), We record the motion of tracer particles in the perivascular spaces of live mice using two-photon imaging, then use automated particle tracking to make velocity measurements. (b), The mean flow of CSF (averaged over time) in the perivascular space near a bifurcation of the middle cerebral artery, before and after inducing high blood pressure. The flow has similar features in both cases but is slower on average when blood pressure is higher. Scale bars are 40 μm. Filled squares mark regions with > 20 measurements; open squares, < 20. Insets show mean flow (arrows) and paths of individual particles (blue), which display transitory backflow in the high-blood-pressure case. In insets, scale bars are 5 μm.

*Corresponding author. E-mail: d.h.kelley@rochester.edu.

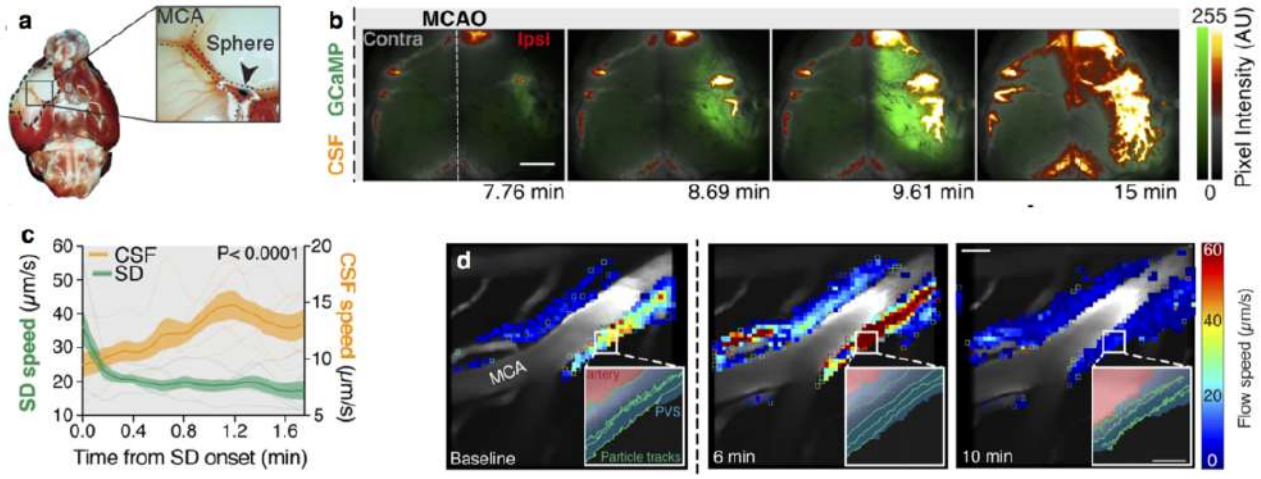

Figure 2: Flow of CSF during stroke. (a), We induce stroke by injecting a bead into the middle cerebral artery of a mouse, dramatically reducing blood flow to the surrounding tissue. (b), The canonical spreading depolarization wave (green) is followed by an inrush of dyed CSF (orange-white). The scale bar is 2 mm. (c), Front speed of spreading depolarization (SD) and dyed CSF. Pale curves show measurements from separate animals; bold curves and shaded regions show mean and standard error of the mean. (d), Fluid flow in the perivascular space surrounding the middle cerebral artery speeds up substantially after the artery is occluded, and pulsatility is nearly lost. Later, the flow slows and again becomes more pulsatile. Scale bar is 40 μm. Insets show particle tracks demonstrating changes in pulsatility. Scale bar is 5 μm.

waves, we use the drug angiotensin-II to quickly and significantly increase blood pressure. Because the volume of the circulatory system is tightly regulated, increased blood pressure causes muscular artery walls to stiffen, preventing changes in diameter. We expected wave propagation to differ in stiffened tissue, and confirmed this with measurements. We also found that mean flow in perivascular spaces is significantly slower in the high-blood-pressure case (Fig. 1), that artery wall velocity oscillations closely match CSF velocity oscillations, and that transitory backflow in the high-blood-pressure case correlates with rapid artery contractions that do not occur when blood pressure is normal. These observations support the hypothesis that artery pulsation drives CSF flow in perivascular spaces. Interestingly, early-onset high blood pressure is a risk factor for Alzheimer's disease in humans. Our findings [1] suggest that reduced CSF flow might be the cause.

FLOW DURING STROKE: SPREADING DEPOLARIZATION AND SWELLING

Ischemic stroke occurs when a cranial artery becomes blocked, depriving part of the brain of oxygen, energy, and nutrients (Fig. 2). Within minutes, nearby neurons are no longer able to maintain healthy gradients of ion concentrations across their cell membranes, so a chemical reaction-diffusion wave propagates across the brain; the process is known as spreading depolarization. Afterward, the tissue experiences severe swelling, the primary cause of irreparable damage during stroke. The canonical view is that the fluid causing this swelling comes from blood, but we present experimental evidence that, at least in early stages, it comes from CSF.

We induce stroke by injecting a bead into the middle cerebral artery. Working with mice genetically engineered such that their brain tissue fluoresces during neural activity, we observe spreading depolarization directly via transcranial imaging. We simultaneously observe the motion of dye in the CSF, finding that soon after the spreading depolarization wave passes, CSF rushes through perivascular spaces and into brain tissue, much faster than in healthy conditions. Tracking particles in perivascular spaces at much higher magnification confirms the findings: though flow pulsation is significantly reduced after occlusion, mean flow speed increases dramatically, then eventually slows (Fig. 2). Moreover, high magnification shows that arteries constrict violently as the spreading depolarization wave passes. Constriction could cause the flows we observe if CSF rushes in to fill the spaces formerly occupied by arteries. To test that hypothesis, we constructed a fluid dynamical model, based on a realistic artery map, in which we prescribed a spreading depolarization wave and corresponding artery constrictions. The model produced inflow similar to what we observe. Our MRI measurements show that large reservoirs of CSF in the skull are simultaneously drained; they are the sources. The discovery that swelling during stroke [2] comes substantially from CSF instead of blood may open the door for new treatments and improved patient outcomes.

References

[1] H. Mestre *et al. Nat. Commun.*, 9(1):4878, 2018.

[2] H. Mestre *et al. Under review.*

HOW INSECT WINGS AND PLANT LEAVES BLAST RAINDROPS

Sunghwan (Sunny) Jung *[1], Seungho Kim [1], Brian Wu [1], Ehsan Esmaili[1], and Jason J. Dombroskie [2]
[1] Department of Biological and Environmental Engineering, Cornell University, Ithaca, NY 14853, USA
[2] Department of Entomology, Cornell University, Ithaca, NY 14853, USA

Summary Many biological surfaces (e.g. bird feathers, insect wings, and plant leaves) are super-hydrophobic with physical morphology at different scales. However, it is not well understood how a raindrop impacts natural super-hydrophobic surfaces, and its significance of biological functions. In this present study, we found that a spreading drop at a high speed can generate wrinkled pattern (including shock-like waves) on a spreading liquid in the presence of surface morphology at the micro scale. Furthermore, the spreading drop is suddenly ruptured by growing holes followed by the shock waves, which leads to a decrease in contact time more than 50%. As a result, heat and momentum transfers are reduced by raindrops, which may lower the hypothermia risk of animals or less affect the stability of insect flights.

INTRODUCTION

In nature, many biological surfaces like bird feathers, insect wings, and plant leaves are super-hydrophobic with micro and nano structures [1, 2, 3]. Micro-structures cause a liquid-pinning behavior by allowing the liquid to penetrate into the gaps between the micro structures whereas nano structures hold air in between [4, 5]. The residence/contact time of a bouncing drop on superhydrophobic surfaces is predicted by balancing the inertia with capillarity [6, 7]. Hence, mass, momentum, and heat transfers strongly depend on its residence time of the drop on a substrate. There are a number of studies in terms of mass [8] and momentum transfers [9, 10, 11], but little attention has been paid to heat transfer aspects [12].

Drop impact on superhydrophobic structures is known to exhibit asymmetric spreading and retraction, a pancake-shaped rebouncing, finally leading to the rapid drop detachment with a significant decrease in the contact time. However, the role of micro-scale structures during drop impact was underestimated since most studies have focused on drop impacts at low speeds, quite lower than real raindrop impact speeds in natural events.

In this study, we will study how an impacting drop at high speeds can generate shock-like surface waves in the presence of surface morphology at the micro scale. The top air-liquid interface of the spreading liquid is perturbed due to the shock waves, and becomes vulnerable to film ruptures via hole nucleation. Finally, the holes grow in time and coalesce with each other. As a result, the contact time is reduced about 70%, and, correspondingly, the heat and momentum transfers of the impacting drop onto the substrate are reduced. Therefore, our findings may elucidate new functional benefits in terms of hypothermia risk, flight stability, spore dispersal of biological surfaces triggered by the micro-scale structures.

RESULTS

For details of the shock-like wave structure, we prepared two kinds of substrate with different wettability (contact angles). One substrate is a hydrophilic glass plate, and the other is a super-hydrophobic surface coated by hierarchical micro- and nano-structures using NeverWet coatings. On the smooth hydrophilic substrate, a drop merely spreads by forming a radially expanding rim as expected. No surface waves are observed. On the superhydrophobic glass, a drop spreads, retracts, and bounces at a low impact speed (fig. 1**b**), whereas a drop with a high impact speed exhibits shock-like surface waves and destructive break-up dynamics as in fig. 1**c**.

When a drop falls at a high speed, U, hundreds of shock-like surface waves were observed. Especially, these shock-like waves are formed only on top of micro-scale bumpy structures as in the second panel of fig. 1**c**. A drop spreads and then is suddenly ruptured, as holes are nucleated (see the third panel of fig. 1**c**). Eventually, the spreading drop breaks into smaller satellite droplets (the fifth panel) as the holes get bigger and coalesce. Therefore, we confirmed that, when a drop impacts hierarchical superhydrophobic surfaces with a high impact velocity, microscale bumpy structures interfere with the spreading drop to generate the numerous shock-like waves on the liquid-air interface and eventually break into smaller droplets.

CONCLUSIONS

In this talk, we showed that an impacting drop at high Weber numbers ($100 < \mathrm{We} < 1500$) generates interesting shock-like patterns and exhibits blasting fragmentation on hierarchical superhydrophobic surfaces. The shock-like waves are created only on topological bumps at the micro scale. Then, the interference of the shock-like waves triggers off hole nucleation and rupture, thereby breaking into small satellite droplets at earlier times. Such drop dynamics result in a decrease in the contact time up to 70%, which may indicate potential advantages of various biological surfaces to limit its heat transfer.

*Corresponding author. E-mail: sj737@cornell.edu.

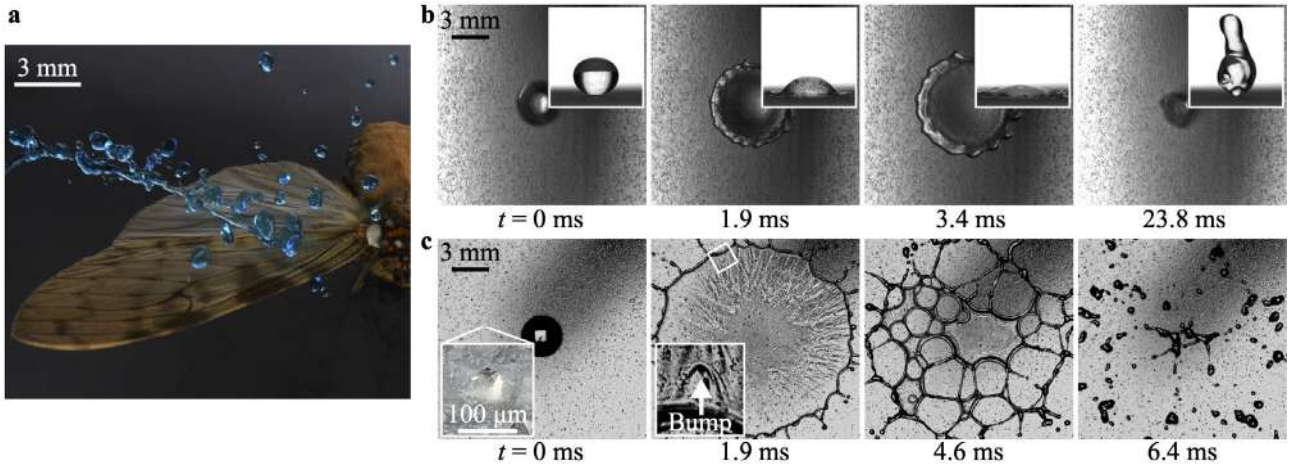

Figure 1: Dynamics of an impacting drop with 1.7 mm in radius on artificial surfaces. **a.** Drop impact on an insect wing at a high speed. **b.** Drop impact on a glass coated by hierarchical superhydrophobic structures at a low impact velocity, where [U, We] are [1.1 m/s, 60]. **c**. Drop impact on a glass coated by hierarchical superhydrophobic structures at a high impact velocity, where [U, We] are 3.8 m/s, 680], respectively. Insets in **b** represent the side-view image of drop impact achieved by a synchronized high-speed camera. Insets in **c** are magnified images of local area to clearly show the microbump, the shock-like wave on the microbump, and the nucleated hole followed by the shock-like wave, respectively. For low U, the impacting drop merely spreads, retracts, and rebounds, whereas, for high U, hundreds of shock-like waves are generated on the spreading drop, and then a number of holes are abruptly nucleated, which grow in time simultaneously (third panel). Finally, the contact time between the drop and the substrate gets shortened by breaking into smaller satellite droplets.

In nature, the exposure to cold rain can lower the body temperature of birds and destabilize flying insects [13]. The decrease in the drop-contact time and earlier fragmentation limit the heat and momentum transfer onto organisms. Our quantitative measurements and model predictions on various biological surfaces may unravel how birds lower hypothermia risks and how insects maintain flight stability as well as preserve regional heterothermy during rainfall. In addition, as an impacting drop is shattered into smaller satellite droplets, the droplets would spread plant pathogenic spores. It sheds light on a new spore dispersal mechanism based on satellite droplets besides recently discovered vortex-induced dispersal mechanism [8].

References

[1] W. Barthlott, M. Mail, B. Bhushan, and K. Koch. Plant Surfaces: Structures and Functions for Biomimetic Innovations. *Nano-Micro Letters*, **9**(23) (2017).

[2] H. Kang, P.M. Graybill, S. Fleetwood, J.B. Boreyko, and S. Jung, Seasonal changes in morphology govern wettability of Katsura leaves. *PloS one*, **13**(9), p.e0202900. (2018)

[3] K. Bhar, B. Chang, E. Virot, L. Straker, H. Kang, R. Paris, C. Clanet, and S. Jung, How localized force spreads on elastic contour feathers. *Journal of the Royal Society Interface*, **16**(160), p.20190267. (2019)

[4] Y. C. Jung, and B. Bhushan, Wetting transition of water droplets on superhydrophobic patterned surfaces. *Scripta Materialia* **57**, 1057–1060 (2007).

[5] D. Bartolo, F. Bouamrirene, E. Verneuil, A. Buguin, P. Silberzan, S. Moulinet, Bouncing or sticky droplets: Impalement transitions on superhydrophobic micropatterned surfaces. *EPL (Europhysics Letters)* **74**, 299–305 (2006).

[6] D. Richard, C. Clanet, D. Quéré, Surface phenomena: Contact time of a bouncing drop. *Nature* **417**, 811 (2002).

[7] J. C. Bird, R. Dhiman, H.-M. Kwon, K. K. Varanasi, Reducing the contact time of a bouncing drop. *Nature* **503**, 385–388 (2013).

[8] S. Kim, H. Park, H. A. Gruszewski, D. G. Schmale, S. Jung, Vortex-induced dispersal of a plant pathogen by raindrop impact. *Proceedings of the National Academy of Sciences* **116**, 4917–4922 (2019).

[9] A. K. Dickerson, P. G. Shankles, D. L. Hu, Raindrops push and splash flying insects. *Physics of Fluids* **26**, 027104 (2014).

[10] J.F. Louf, L. Nelson, H. Kang, P.N. Song, T. Zehnbauer, and S. Jung, How wind drives the correlation between leaf shape and mechanical properties. *Scientific reports*, **8**(1), p.16314 (2018)

[11] Y. Bhosale, E. Esmaili, K. Bhar, and S. Jung, Bending, twisting and flapping leaf upon raindrop impact, *Bioinspiration & Biomimetics* (2019).

[12] S. Shiri, J. C. Bird, Heat exchange between a bouncing drop and a superhydrophobic substrate. *Proceedings of the National Academy of Sciences* **114**, 6930–6935 (2017).

[13] R. Kennedy, Direct effects of rain on birds: a review. *British Birds* **63**, 401–414 (1970).

WAKE-MEDIATED INTERACTIONS BETWEEN SELF-PROPELLED TWO TANDEM FLEXIBLE FINS IN WALL EFFECTS

Young Dal Jeong[1], Jae Hwa Lee*[1] and Sung Goon Park[2]
[1] Department of Mechanical Engineering, Ulsan National Institute of Science and Technology, Ulsan, Korea
[2] Department of Mechanical and Automotive Engineering, Seoul National University of Science and Technology, Seoul, Korea

Summary It is known that self-propelled two tandem fins can take a hydrodynamic benefit. To analyze the wake–mediated interactions between two fins in wall effects, we perform a simulation for two tandem self-propelled flexible fins near a single wall (SW) or two-sided walls (TW). The vortex–vortex interaction near the wall for SW and TW greatly enhances a lateral flow, and synchronization of the strong lateral flow with a lateral motion of the follower reduces significantly the input power compared to that with no wall (NW). The follower for NW achieves large thrust using the interception mode to overcome a jet-like flow. However, the follower employs a mixed mode (i.e., combination of the interception mode and slalom mode) for SW and slalom mode for TW to maximize the benefit from the lateral flow since there is no need to generate a large thrust by the help of a negative horizontal flow.

INTRODUCTION

Collective motion is commonly observed in biological systems in nature (e.g., fish schooling and birds flocking). When the groups of active animals move in a fluid, each locomotion is influenced by the others through the wake–mediated interactions among them, and individuals in a schooling formation can take an energetic advantage in the light of hydrodynamics. Furthermore, flying/swimming organisms can take advantage of hydrodynamic benefits when they move near the wall. Although individual studies of self-propelled propulsors in a school (Zhu *et al*. 2014) and a single self-propelled propulsors in wall effects (Park *et al*. 2017), respectively, have performed, the hydrodynamic approach to the schooling behaviors under an influence of the walls have never been conducted simultaneously.

The objective of the present study is to examine the collective motion of self-propelled two tandem fins in wall effects. Introduction of the wall effects into dynamically moving fins in a school results in more complicated wake–mediated interactions between them than those without the wall effects (Zhu *et al*. 2014). To impose the wall effects on the wake–mediated interaction, two types of the walls are considered, i.e., one-sided single wall and two-sided walls on the bottom and top. Although one-sided single wall has been usually employed to examine the wall effects on the hydrodynamics of an isolated single fin thus far, the two-sided wall configuration has been also observed not only in the natural habitat of stream fish (e.g., rainbow trout) but also during the long distance migration of salmonid fish (e.g., Altantic salmon), when they swim near vertical structures such as stream margins, rock faces and large woody debris.

RESULTS & DISCUSSION

Figure 1 shows schematics of two self-propelled flexible fins in a tandem configuration with two coordinate systems, when the fins propel near a single one-sided wall (figure 1a) and between two-sided walls (figure 1b). The upstream and downstream fins are denominated as ‘leader’ and ‘follower’, respectively. Two fins are driven by harmonic plunging motions at the leading edge with a heaving amplitude (A_{head}) and flapping frequency (f) in the lateral direction, whereas the motion of the rest part is determined passively by the ambient fluid and nearby structures. In the horizontal direction, the fins are unconstrained, and thus they can move freely. The horizontal moving speed (i.e., cruising speed U_c) and the horizontal relative positions between the leader and follower (G_x) are determined spontaneously as a result of the interaction between the flexible fin and the ambient fluid. The lateral distance between the fin and the wall (d), which is important factor in determining the degree of wall effects, is prescribed using a mean lateral position of the leading edge when the fins are at the steady state. The fluid–flexible body interactions are modelled by solving the fluid and structure motion equations separately, and theses equations are coupled using an immersed boundary method (Huang *et al*. 2007).

Figure 2(a) shows schematics of the stable modes formed spontaneously for each case, i.e., interception mode for NW, mixed mode for SW and slalom mode for TW. $\boldsymbol{V_F}$=(u_{head}, v_{head}) and $\boldsymbol{V_T}$ denote the leading edge velocity and the vortex-induced velocity. In figure 2(a-i), the follower for NW takes the interception mode. The horizontal components of $\boldsymbol{V_F}$ and $\boldsymbol{V_T}$ at t^*/T=0 and 0.5 are opposite due to a jet-like flow generated by the leader, requiring a large thrust force for the follower. However, the lateral motion of the leading edge for the follower ($\boldsymbol{V_F}$) is in phase with the induced lateral flow by the leader ($\boldsymbol{V_T}$) in figure 2(a-i), and the synchronized flow in the lateral direction plays an important role as a ‘hydrodynamic puller’, leading to the reduction of the input power (Zhu *et al*. 2014). In figure 2(b-i), if the follower takes the slalom mode in the thrust wake as a stable spontaneous mode, both the horizontal and lateral components of $\boldsymbol{V_F}$ and $\boldsymbol{V_T}$ are opposite, leading to significant increase of the input power for thrust force of the follower.

In figure 2(a-ii), the follower for SW passes through the positive vortex, whereas it swims by slaloming beneath the negative vortex. Similar to the observation for NW, the horizontal component of $\boldsymbol{V_F}$ and $\boldsymbol{V_T}$ is opposite at t^*/T=0 and 0.5, while the lateral component of $\boldsymbol{V_F}$ and $\boldsymbol{V_T}$ is identical. However, the horizontal velocity during the upward motion is negative, because negatively induced horizontal velocity by the interaction between the main negative vortex and near-wall positive vortex (yellow arrow) is larger than the positively induced velocity by $\boldsymbol{V_T}$ at t^*/T=0. The horizontal velocity during the downward motion is positive due to the combined effects of the induced velocity by $\boldsymbol{V_T}$ and the induced velocity

*Corresponding author. E-mail: jhlee06@unist.ac.kr

between the main positive vortex and induced negative vortex near the wall (see t^*/T=0.5). In the lateral direction, the synchronized flows lead to the energy benefit for the follower. Particularly, the benefit from the lateral flow for the follower is strong during the upward motion (see the elliptic dashed line) under the significant influence of a vortex pair. As shown in figure 2(b-ii), if the follower passes through the negative vortex and swims through a region beneath the positive vortex as an another mixed mode, the horizontal and lateral directions of the velocity $\boldsymbol{V_F}$ are opposite to those of $\boldsymbol{V_T}$, leading to significant energy consumption of the follower over all flapping period. Given that the negative vortices are located above the trajectory of the follower due to the ascending motion of the vortex pair (figure 2a-ii) and the prescribed lateral movement of the follower near the wall (i.e., Eq. 4), an optimal trajectory of the follower for a maximum benefit from the lateral flow is achieved by passing through the positive vortices at the maximum lateral position.

In the slalom mode adopted by the follower for TW in figure 2(a-iii), the horizontal component generated by the positive and negative vortices has negligible effect on the follower at t^*/T=0 and 0.5 near the centerline. However, when the follower passes a region near the wall, it experiences strong negative horizontal flow created by the interaction between the main vortex and induced vortex near the wall (yellow arrow along the trajectory), reducing drag force acting on the follower. The identical lateral component of $\boldsymbol{V_F}$ and $\boldsymbol{V_T}$ always contributes to the hydrodynamic benefit. When the follower for TW takes the interception mode in the aligned vortex street instead of the slalom mode, a possible trajectory for the follower is shown in figure 2(b-iii). The follower at four instants (t^*/T=0.125, 0.375, 0.625 and 0.875) with $\boldsymbol{V_F}$ and $\boldsymbol{V_T}$ is denoted by the bold black lines. The lateral component of $\boldsymbol{V_F}$ coincides with that of $\boldsymbol{V_T}$ at t^*/T=0.375 and 0.875. However, the lateral components of $\boldsymbol{V_F}$ and $\boldsymbol{V_T}$ are opposite at t^*/T=0.125 and 0.625. In figure 2(a-iii), the slalom mode of the follower along the aligned vortex street maximizes the benefit from the lateral flow, and this trajectory gives rise to extra benefit by the negatively induced horizontal velocity component near the wall (yellow arrow).

In the conference, we will discuss the propulsive mechanism of the schooling fins in wall effects with two main questions: i) How the follower interacts with the vortex structures generated by the leader under an influence of the walls and ii) how the flow–mediated interactions improve (or deteriorate) the propulsive efficiency of the schooling fins near the walls. The underlying mechanism will be documented through the time evolution of the vorticity, horizontal and lateral velocities along the lateral line at the leading edge, temporal input power, averaged lateral velocity of the fin and averaged lateral flow acting on the fin. Furthermore, investigation of the pressure distribution will provide an intuitive understanding of the relation between the wake–mediated interactions and the propulsive performance of the fins.

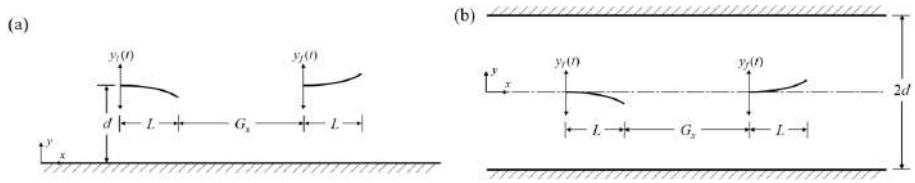

Figure 1. Schematic of two tandem flexible fins, when the fins propel (a) near the single wall and (b) between two parallel walls.

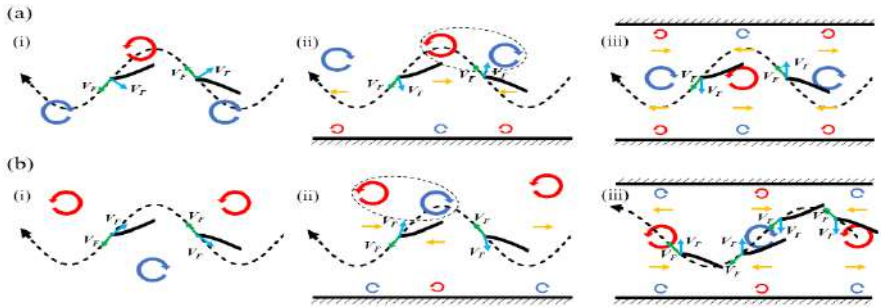

Figure 2. Schematics of (a) the stable spontaneous modes: (i) interception mode for NW, (ii) mixed mode for SW and (iii) slalom mode for TW. In (b), (i) slalom mode for NW, (ii) mixed mode for SW and (iii) interception mode for TW are shown as another stable modes for each case. $\boldsymbol{V_F}$ and $\boldsymbol{V_T}$ denote the leading-edge velocity for the follower and the vortex-induced velocity, respectively. In (ii) and (iii), upstream and downstream flows produced by main vortices (large circles) and induced vortices (small circles) near the wall are denoted by yellow arrows. In (a), (b-i) and (b-ii), bold black lines with $\boldsymbol{V_F}$ and $\boldsymbol{V_T}$ indicate the follower at t^*/T=0 and 0.5 (from right to the left). In (b-iii), bold black lines indicate the follower at t^*/T=0.125, 0.375, 0.625 and 0.875 (from right to the left). Bold dashed lines denote the trajectory of the leading edge for the follower. Red and blue circles with arrows indicate the positive and negative vortices, respectively. Elliptic dashed lines in (ii) indicate the vortex pairs.

ACKNOWLEDGEMENTS

This work was supported by the National Research Foundation of Korea (NRF) Grant funded by the Ministry of Science, ICT & Future Planning (NRF-2019R1A2C1083858).

References

[1] Huang, W.-X., Shin, S. J., Sung, H. J. Simulation of flexible filaments in a uniform flow by the immersed boundary method. *J. Comput. Phys.* **226**: 2206-2228.

[2] Park, S. G., Kim, B., Sung, H. J. Hydrodynamics of a self-propelled flexible fin near the ground. *Phys. Fluids* **29**: 051902, 2017.

[3] Zhu, X., He, G., Zhang, X. Flow-mediated interactions between two self-propelled flapping filaments in tandem configuration. *Phys. Rev. Lett.* **113**: 238105, 2014.

UNDERLYING STABILITY MECHANISMS OF SEMI-AQUATIC SNAKES ON FREE SURFACE: A BIO-INSPIRED APPROACH

Johann Herault * [1], Jonathan Brossillon[1], Vincent Lebastard[1], Frédéric Boyer[1], and Seth M. LaGrange[2]
[1] IMT Atlantique, LS2N, UBL, 44307 Nantes, France
[2] University of Illinois/INHS, Champaign-Urbana, Illinois, USA

Summary At the crossroad of mechanics, robotics, and biology, we report an investigation aiming to understand the underlying mechanisms of stability of water snakes on a free surface. To address this complex problem, a new theoretical model is developed to seek quickly the equilibrium configurations (position and orientation) of a continuous slender body with finite deformations (torsion and bending) relative to the water surface. The non-linear description of the body geometry relies on the geometrically exact approach introduced by Simo [1], where the orientations of the sections are parametrized by a continuous field of rotation matrices belonging to a Lie group. Then, a command law is introduced to achieve a static positioning of a continuous body thanks to controlled body deformations. Finally, a new bio-inspired robot named NATRIX will be presented. To stabilize its posture, this robot has a new actuation mechanism based on a controlled rolling motion of each body segment in order to achieve static and dynamic positioning. These new results pave the way for the next generation of autonomous bio-inspired robots designed for maritime exploration in extreme conditions.

INTRODUCTION

Snakes are fascinating animals that have colonized a wide variety of ecological niches by adapting their limbless locomotion strategy to the physical constraints of the local environment. Among these species, semi-aquatic snakes living near rivers, such as the grass snake (Natrix natrix) or the cottonmouth snake, have developed extraordinary capacities to maneuver on water surface [2]. Indeed, snakes deform significantly their body to maintain stable postures on water, while their head remains above the surface. Field observations (Fig.1) show that their body deformations are complex compositions of relative lateral and dorso-ventral flexions combined with torsions bof the spine chord. Interestingly, their capacities decline when they become tired. Consequently, snakes actively control their posture to achieve an overall balance between gravity and buoyancy forces. Understanding and reproducing the performances of these animals could lead to new insight into biological evolution and to new applications in maritime engineering and naval robotic.

Indeed, bio-inspired naval robots are promising technologies, which display exceptional maneuverability and low impact on ecosystem [3]. Despite their great potential, their slender body becomes a handicap at free surface due to their small axial inertia. Unlike aquatic snakes, their performances are strongly degraded by their uncontrolled rolling motions. Hence, our bio-inspired approach aims to solve the problem of robot stability thanks to our animal model: the semi-aquatic snake.

Figure 1: Pictures of a Cottonmouth snake (Agkistrodon piscivorus) stabilizing and chilling on water. These photos were taken in Southern Illinois (USA) by Seth M. LaGrange.

In the talk, I will present the theoretical framework to tackle the problem of surface stability of a slender body. First, I will introduce a model describing the body as a continuous Cosserat rods thanks to the exact geometrical approach introduced by Simo [1]. Then, I will present a new command law allowing for the stabilization of the head configuration (position and orientation) thanks to controlled body deformations. Finally, I will show how our theoretical results could be used in bio-inspired robotics. I will introduce our new robot named NATRIX capable of stabilizing its body thanks to a new mechanisms of actuation.

FROM THE MATHEMATICAL MODEL...

To predict the stable configurations (position and rotation) of a snake relative to a flat sea surface, we have developed an efficient and fast tool, called STAB [4], computing the equilibrium configurations of a buoyant body undergoing large deformations. To take into account finite rotations, our approach relies on the exact geometrical approach introduced by

*Corresponding author. E-mail: johann.herault@imt-atlantique.fr

Simo [1] consisting in parametrizing the orientation of each body section thank to rotation matrices $\mathrm{R}(s)$ taking value in the Lie group $\mathrm{SO}(3)$, and its position vectors $\mathbf{p}(s)$. The body is thus modeled by a Cosserat beam, which is described as a continuous stack of elliptical rigid sections of infinitesimal thickness.

Our code computes the position $\mathbf{p}_0(s=0)$ and the orientation $\mathrm{R}_0(s=0)$ of the head as a function of the body shape, which is given by the configuration of each body section relative to the head. To approach our animal model, this body shape is defined from the deformation fields (bending+torsion) given by $\vec{\kappa}(s) = (\kappa_1, \kappa_2, \kappa_3)$, which is the natural parametrization of the muskulo-skeletal system. The stable configuration of the head is found via a new optimization algorithm respecting the geometry of the non-linear manifold $\mathrm{SO}(3)$. Furthermore, we have decomposed the deformation field into Tchebyshev polynomials to reduce the computing time and achieve real time computation for robotic applications. Our results are then compared to experimental data with a very good agreement [4](error $< 3\%$).

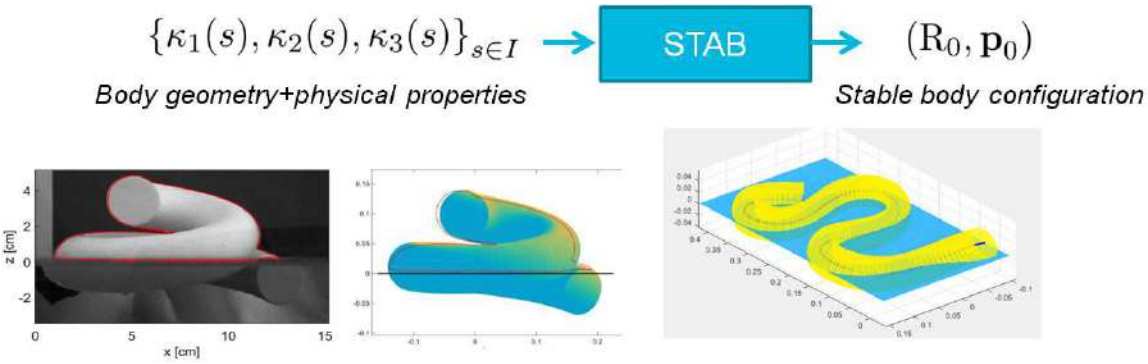

Figure 2: Top: principle of the code STAB. Bottom: experimental observation of a floating helical body (left), its numerical avatar (center) computed by STAB, and an illustration of stable configuration of a snake-like body.

From the code STAB, we are able to investigate the effect of the body deformations (bending and torsion) onto the stable configuration. This is the starting point of a control law imposing a desired configuration of the head $(\mathbf{p}_0, R_0)_{end}$ from an initial configuration $(\mathbf{p}_0, R_0)_{ini}$ thanks to a continuous evolution of the body deformation fields $\vec{\kappa}$. This complex inverse problem requires to find one body deformation among an ensemble of deformation fields $\{\vec{\kappa}\}$ corresponding to the same stable head configuration. Consequently, a new method is introduced to select the optimal deformation field for different criteria (minimal elastic energy, minimal time..etc) based on optimal control theory, paving the way for operational quasi-static positioning. Our results are then compared to observations of snakes to reveal the underlying strategy of these reptiles.

...TO THE BIO-INSPIRED ROBOT NATRIX

To translate these concepts into the physical world, we have developed a new serial robot with an innovative mechanical concept: a controlled and independent rolling motion for each segment. Previous bio-inspired robots have been designed to achieve anguilliform swimming, but they display poor stability. To achieve an active stability and an efficient swimming, our robot has a new degree of freedom so that each elliptical section can roll, independently and irrespectively of the net body orientation, to modify locally its immersed surface in order to control the buoyant effects. I will present the first tests of a three-links swimmer displaying 5 degrees of freedom (2 pivot joints, 3 rolling motion).

CONCLUSIONS

For the first time, we have investigated theoretically, numerically and experimentally the underlying stability mechanisms of semi-aquatic snakes on free surface. Our approach consists in developing new models of fluid-structure interaction, sufficiently concise to be exploited for maritime applications. By bringing together different disciplinary fields, our work aims to develop innovative and bio-inspired technological solutions to environmental issues.

References

[1] J. C. Simo, L. Vu-Quoc, On the dynamics in space of rods undergoing large motions: a geometrically exact approach, Computer methods in applied mechanics and engineering 66 (2) (1988) 125(161).
[2] C. Jayne, Swimming in constricting (Elaphe g. guttata) and nonconstricting (Nerodia fasciata pictiventris) colubrid snakes, Copeia, n 1 195-208, p. 1985
[3] A. J. Ijspeert, A. Crespi, D. Ryczko, J.-M. Cabelguen, From swimming to walking with a salamander robot driven by a spinal cord model, Science 315 (5817) (2007) 195(208)
[4] J. Herault. A geometrically exact approach for floating slender bodies with finite deformations, submitted in 2019.

RBC DYNAMICS UNDER SHEAR FLOW IN SICKLE CELL DISEASE. TOWARDS A MECHANICAL MARKER FOR MONITORING THE CLINICAL STATE OF PATIENTS

Emmanuèle Helfer[1], Maxime Sahun[1], Scott Atwell[1], Alexander Hornung[1], Emmanuelle Bernit[2], Isabelle Thuret[2], Ann Charrier[1], Catherine Badens[3], Annie Viallat[1]*
[1] Aix Marseille Univ, CNRS, CINAM, Marseille, France
[2] Assistance Publique des HÔpitaux de Marseille, Marseille, France
[3] Aix Marseille Univ, INSERM, MMG, Marseille, France

Summary Sickle Cell Disease (SCD), the most prevalent genetic disease in the world, is a haematological disorder in which red blood cell (RBC) rigidity is increased. This change results in problems of RBC circulation in narrow capillaries, leading to painful vaso-occlusive crises which are unpredictable and can be life-threatening. Here, we show that most RBCs from SCD patients have an impaired motion when submitted to a shear flow at low shear rate. We use this feature to propose a mechanical marker to follow the patient clinical state and to predict the very handicapping vaso-occlusive crises.

INTRODUCTION

The regimes of motion of red blood cells (RBCs) under shear flow have been extensively studied because they directly relate to the cell mechanical properties. In addition to tumbling and tank-treading motions, other regimes were recently discovered, such as swinging, flip-flopping, and rolling. Computational studies provide complex phase diagrams of motion that depend on λ, the ratio of RBC cytoplasm to external fluid viscosities, and on the capillary number Ca. Surprisingly, no experiments have been performed on RBCs from patients with sickle cell disease (SCD) which have altered mechanical properties, namely an increased rigidity due to mutated haemoglobin S that forms rigid fibers in the RBC [1].

RBC MOTION DYNAMICS UNDER FLOW

At very low shear rates, RBCs undergo tumbling-flipping motion and the orientation of their axis of symmetry with the flow direction, defined as the precession angle, is determined by the shear stress as a way to minimize energetically costly deformations [2]. The transition from tumbling to rolling undergone by RBCs as the shear rate is increased is a signature of their elasticity. At higher shear rates, the RBC enters in the tank-treading regime.
We show that the dynamics of RBCs under shear flow is modified in the SCD pathological condition. Though the tumbling - flip-flopping – rolling path observed by increasing the shear rate is not changed for SCD, the rolling-to-tank-treading threshold occurs at higher shear stress compared to healthy RBCs (Fig. 1).

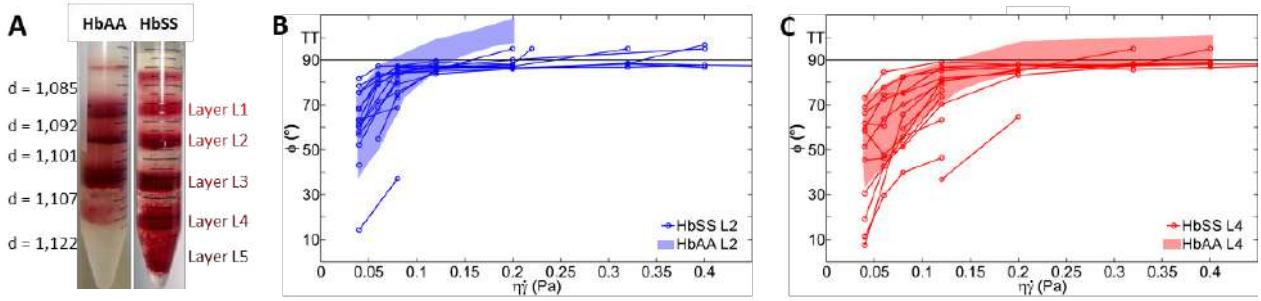

Figure 1. A) Density sorting of a healthy blood sample (HbAA) and of an SCD blood sample (HbSS). B-C) The evolution of the precession angle ϕ of RBCs with regards to the applied shear stress is shown for two density subpopulations of healthy and SCD blood samples.

A MECHANICAL PARAMETER OF SCD PATIENT STATE

Based on the above results we setup an experiment to measure the fraction of tank-treading RBCs, f_{TT}, in large cell populations from µL-size blood samples. As expected f_{TT} increases with increasing shear rate, moreover it is always

* Corresponding author. E-mail: **annie.viallat@univ-amu.fr**.
This work has been carried out thanks to the support of the A*MIDEX project (n° ANR-11-IDEX-0001-02) funded by the «Investissements d'Avenir» French Government program, managed by the French National Research Agency (ANR)

higher for healthy samples (Fig. 2). We show that f_{TT} depends on RBC density and state of hydration (internal water content), two parameters known to be critical in SCD. We thus propose f_{TT} as a mechanical marker of the average rigidity of blood samples that allows following the clinical state of SCD patients. We show that this marker is patient-dependent and is stable over time in the "out of crisis" period while it strongly varies during the course of a crisis. Our results pave the way to development for new inexpensive and easy-to-implement biological tests for monitoring the clinical status of SCD patients and for predicting the occurrence of disabling vaso-occlusive crises. Additionally, no treatment of SCD has been developed so far, due to the unpredictability of the vaso-occlusive events. Our assay can thus be used to test new pharmaceutical products as potential treatments.

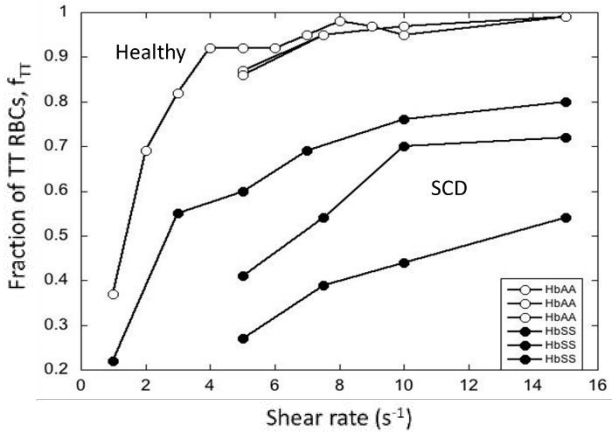

Figure 2. Fraction of tanktreading RBCs as a function of the applied shear rate for heathy and SCD samples.

References

[1] J. L. Maciaszek and G. Lykotrafitis, "Sickle cell trait human erythrocytes are significantly stiffer than normal.," *J. Biomech.*, vol. 44, no. 4, pp. 657–61, Feb. 2011.

[2] J. Dupire, M. Socol, and A. Viallat, "Full dynamics of a red blood cell in shear flow," *Proc. Natl. Acad. Sci. U. S. A.*, vol. 109, no. 51, pp. 20808–20813, Dec. 2012.

CONTRACTILE ACTIVITY, FLOWS AND NETWORK RESHAPING OF GIANT UNICELLULAR *P. POLYCEPHALUM* CONFINED IN ANNULAR GEOMETRY

Valentin Busson and Marc Durand *
Matière et Systèmes Complexes (MSC), UMR 7057 CNRS & Université de Paris, Paris, France.

Summary Slime mould *Physarum Polycephalum* is a giant unicellular organism that develops a tubular network in which oscillatory flows are generated by the contraction of the membranous layer surrounding the veins. We report the first experimental observation of contractile activity, flows and network reshaping of *P. Polycephalum* confined in a ring geometry. We show that spatial confinement orients the contractile waves and and main flow direction, and affects the network hierarchization. Stable contractile phase patterns are identified.

INTRODUCTION

Like *E. Coli*, *C. Elegans* or *Drosophila*, *Physarum Polycephalum* is a model organism intensively studied by the scientific community [1]. In its vegetative phase, called plasmodium, this organism is made of thousands of undifferentiated cells fusing in a single, multinuclear cell, and can reach macroscopic sizes (dozens of cm^2). This organism then develops a tubular network in which oscillatory flows (with period $\sim$ 1 minute) are generated by the contraction of the membranous layer surrounding the "veins". Hence, *P. Polycephalum* is likely the simplest organism developing a vascular network. This transport network has a twofold role: first, it supplies diffusive flows which are too slow to efficiently transport oxygen, nutrients, or waste through the giant cell. Second, this allows efficient transporting of the body mass during the growing stage or displacement of the cell. Such transport requires from this organism, deprived from central nervous system, a local control of the sol-gel transition of the cytoplasm, and a synchronization of the contractile activity in the whole organism in order to generate a contractile wave traveling from one side of the cell to the other.

In spite of its apparent simplicity, the growth of *P. Polycephalum* network shares common features with the development of vascular systems in higher organisms, or with the mechanisms that take place in the irrigation of tumors. In particular, one can clearly identify two stages in the development of the plasmodium: a growing phase during which *P. Polycephalum* explores its environment covering all the plane with a very dense and ramified tubular network. Then a reorganizing phase during which network becomes hierarchical and less and less reticulated [2, 3], with some veins growing at the expense of others which disappear. From a physicist's perspective, the plasmodium is an active gel that is able, at short times, to generate and adapt contractile waves along the veins to generate peristaltic flows, and at long times to control actively its sol-gel transition to modify the network architecture.

The present study focuses in particular in the interplay between contractile activity, fluid flows, and shaping of the organism in a spatially confined environment. Spatial confinement will orient the contractile waves and flows, and prevent growth of migration of the organism.

CONFINEMENT IN RING GEOMETRY

We built transparent, annular, chambers with varying perimeter and gap width (see Fig. 1), allowing us to probe the effects of spatial confinement on contractile activity and network reshaping. Both temperature and humidity are controlled. During all experiments, the organism is deprived of food and isolated from any other stimulus. Contractile activity is

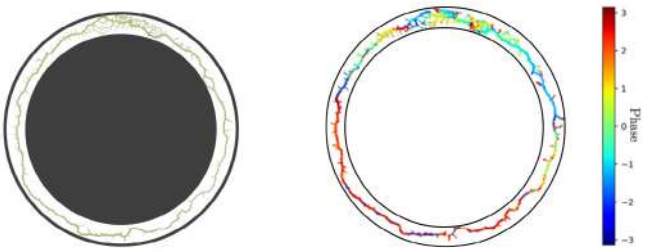

Figure 1: *P. Polycephalum* spatially confined in a ring chamber. Left: transmitted light imaging. Right: phase of the contraction wave.

recorded by transmitted light imaging. We then developed accurate image processing routines to extract properties from both the network architecture (vein lengths and widths, conductances) and contractile wave patterns (instantaneous phase, amplitude, wave-length, frequency, phase velocity). Additionally, from these measuring quantities we were also able to extract flow rates within the network.

*Corresponding author. E-mail: marc.durand@univ-paris-diderot.fr.

RESULTS

Short timescales: contractile modes

Different stable wave patterns are observed [4], which can be categorized in two main families (see Fig. 2):

- Peristaltic modes: they correspond to contractile propagating waves, with phase that varies linearly along the ring (in one direction or in another). Its wavelength is L/n, where L is the ring perimeter and n a positive integer. These modes generate non-zero net flow.
- Amphistaltic modes: they result from two contra-propagative contractile waves emanating from a pacemaker whose location changes with time. These modes do not generate net flow and appear to be more stable.

Asymetric modes, resulting from superposition of the two modes above, are also observed.

Our experimental results are also compared with existing theories [5]. In our experiments, we did not detect any noticeable drop of the characteristic wavelength for larger ring perimeters.

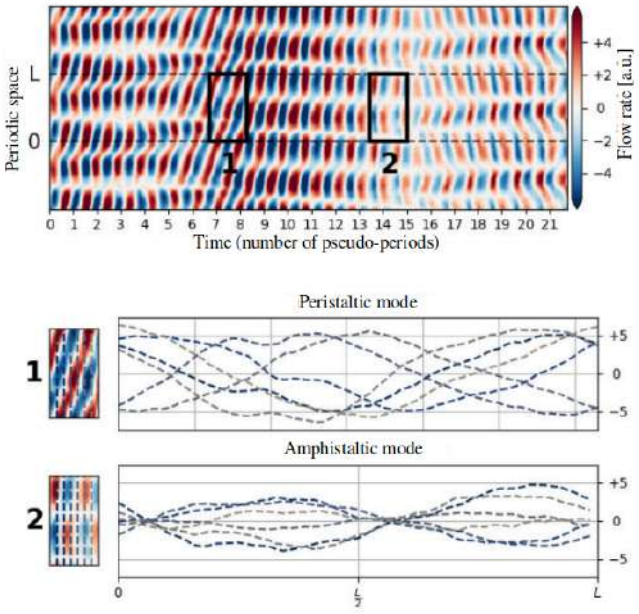

Figure 2: Top: Kymographs of flow rate around Physarum ring, where a transition from a peristaltic **(1)** to an amphistaltic **(2)** mode is observed. Bottom: for each mode, spatial variation of flow rate is plotted, for different times.

Long timescales: network hierarchization

On long timescales, network hierarchization is strongly affected by the confinement: veins at the middle of the ring and with orthoradial orientation expand, while peripheral veins shrink or disappear. Sometimes, the final network reduces to a single larger vein circling around the ring, as in Fig. 1. Most of the time however, small peripheral veins subsist, yielding a hierarchical, anisotropic network. We propose a simple model that reproduces these features, in which the evolution of a vein is related to the statistical flow going through it.

CONCLUSIONS

In summary, we report experimental observation of contractile activity, flows, and network reshaping of slime mould *P. Polycephalum* confined in an annular chamber. On short times, stable contractile modes are classified. On long times, we show that confinement strongly affects the network reshaping.

References

[1] C. Oettmeier, K. Brix, H.-G. Döbereiner, Physarum polycephalum – a new take on a classic model system. *J. Phys. D: Appl. Phys.* **50**: 413001, 2017.
[2] T. Nakagaki, H. Yamada, Á. Tóth, Maze-solving by an amoeboid organism. *Nature 407*, **470** (2000).
[3] A. Tero *et al.*, Rules for Biologically Inspired Adaptive Network Design. *Science* **327**, 439-442 (2010).
[4] V. Busson, M. Durand Contractive activity, flows and network reshaping of spatially confined slime mould. *In preparation*.
[5] J.-D. Julien, K. Alim, Oscillatory fluid flow drives scaling of contraction wave with system size, *Proc. Natl. Acad. Sci. USA* **115**: 10612-10617, 2018.

VARIATIONS OF OSCILLATING FLOW IN THE UPPER BRONCHIAL TREE

Katrin Bauer *[1], Thomas Janke [1], and Ruediger Schwarze[1]
[1] Institute of Mechanics and Fluid Dynamics, TU Bergakademie Freiberg, Germany

Summary There is still a lack of systematic analysis of the unsteady flow characteristics in the human airways. Thus, a realistic model of the human bronchial tree featuring the mouth throat region as well the bifurcating branches down to the 7th generation has been made from transparent silicone. By refractive index matching the oscillating flow inside the model geometry is visualized using Particle Image Velocimetry (PIV). Breathing parameters are varied from very low breathing activity up to breathing under heavy exercise. The results show that lower breathing velocities only lead to quantitative changes of the flow patterns during either in- or expiration. In contrast, at high breathing rates a remarkable qualitative change of the velocity profiles is observed during the expiration phase.

INTRODUCTION

Fundamental knowledge about flow characteristics in the human airways is crucial for the application of appropriate mechanical ventilation strategies as well as for efficient drug delivery within the lungs. Despite an increasing number of sophisticated flow investigations in the human bronchial tree, numerically as well as experimentally, systematic investigations aimed at understanding the flow physics in bifurcating airways, especially for higher Re, are rare and open questions remain. Banko et al.[1] investigated the three-dimensional, constant inspiratory flow at a realistic model of the upper bronchial tree for a typical breathing rate by means of Magnetic Resonance Velocimetry (MRV). At least for their specific model, representing a peak inflow situation, information about regional flow distortion and secondary flow strength could be given. The measurement technique of MRV was also carried out for investigating the inspiratory flow at a planar double bifurcation model for a large range of Reynolds numbers of Re = 100 - 5000 [3]. They could show that the secondary vortex intensity increases up to Re = 2000 and further decreases for larger Re. In 2018, Jalal et al. [2] extended their double bifurcation study by an oscillating flow at Re = 2000 and varying Womersley number Wo. At least for their parameter range they found stronger secondary flows for higher Wo during inhalation and weaker secondary flow during exhalation.

Recently, Janke et al. [4] presented PIV measurements at a realistic, patient specific upper airway (the SimInhale Benchmark Case) model for varying constant inflow conditions. Yet, unsteady flow measurements at such a realistic model have to the best of our knowledge not been done before and shall thus be presented here.

METHODS

The airway geometry represents the SimInhale Benchmark case [4, 5] which includes the mouth/throat passage and bifurcates down to the 7th generation (Fig. 1). For more information on model specifications see Lizal et al. [6]. This geometry has been 3D printed and surrounded by transparent silicone. After curing of the silicone, the model core has been dissolved in acetone and a transparent silicone block with the hollow lung geometry inside was received. The lung model was placed in a glass tank which is filled with a mixture of water and glycerin (mass ratio 42:58) in order to match the refractive index of the silicone. A linear motor generates an oscillatory motion of liquid through the model which mimics the appropriate breathing patterns. Flow similarity with breathing in air is maintained by considering Reynolds and Womersley similarity. The unsteady flow was measured phase averaged by planar PIV measurements at selected phase angles during the breathing cycle. The measurement plane was defined by a Nd:YAG Laser (Minilite) in the center of the main bifurcation. A total of 688 double images for each phase position were recorded by a PCO.1600 CCD camera. The recorded images were cross correlated by employing the software DaVis 8.4 from LaVision. The final window size was $16 \times 16\, px$ including $50\,\%$ overlap which corresponds to a spatial resolution of $0.5 \times 0.5\, mm^2$. Three different measurement settings were employed here with constant tidal volume of $500\, ml$ while the breathing frequency was varied. Thus, a low breathing situation (Re = 1100, Wo = 1.9), normal breathing (Re = 2200, Wo = 2.7) and breathing under exercise conditions (Re = 4400, Wo = 3.8) are compared here.

RESULTS AND DISCUSSION

Fig. 1 presents the color coded distribution of the averaged flow velocity. Shown are selected phase angles during the breathing cycle for low breathing (Re = 1100) and extensive breathing (Re = 4400) conditions. We refer here only to a change in Re since Janke et al. [7] have shown that a change in Wo in the same range as applied here has only neglectable influence on the flow.

During the inspiration phases, all breathing conditions are characterized by a strongly skewed velocity profile in the anatomical left main bronchus (right main branch in Fig. 1) and a large separation region.

*Corresponding author. E-mail: Katrin.Bauer@imfd.tu-freiberg.de.

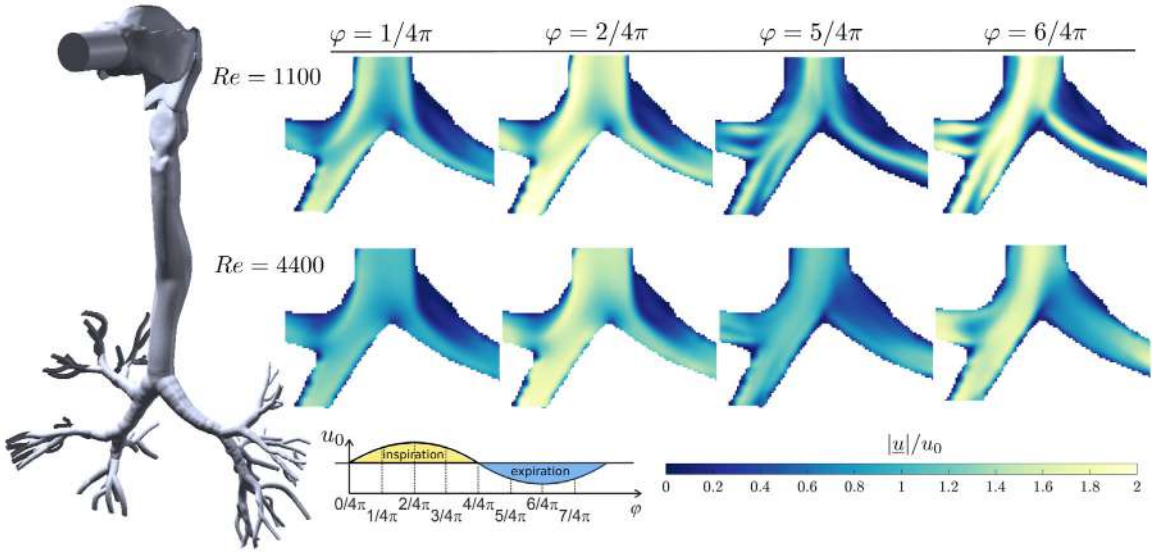

Figure 1: Lung geometry and velocity profiles at selected phase angles for low (Re = 1100) and normal breathing (Re = 4400) conditions.

Increasing Re from laminar to fully turbulent range only causes mild attenuation of the velocity profile skewness induced by turbulent fluctuations. Nevertheless, as reported by Jalal et al. [3], this turbulent diffusion already causes decreased secondary flow intensity. Considering the expiration, the streamwise flow has changed considerably. Besides a strong flow homogenisation, the location of high speed regions has changed, even from accelerated to peak expiration. Separation regions have completely vanished which suggests that secondary flows are not only strongly weakened but their location and structure has changed as well. 3D Particle Tracking Velocity (PTV) measurements at a generic lung model [7] in the range of Re = 250 - 2000 could already prove a displacement of helical flow structures during the expiration phase.

CONCLUSIONS

The results have shown that there occurs a change in flow structures during the expirational phase with increasing Re. This effect is universal for different lung geometries and will have a strong impact on flow distribution and particle transport. However, further 3D measurements are required to investigate the spatial development of helical structures, especially with regards to the secondary Dean structures in order to deduce transport pathways in more detail.

Acknowledgements

The authors gratefully acknowledge financial support of this project by the Deutsche Forschungsgemeinschaft DFG (grant No. BA 4995-2/3). We furthermore thank Dr. František Lizal, Brno Institute of Technology, for providing the lung geometry within the framework of SimInhale COST Action MP1404.

References

[1] A. J. Banko, F. Coletti, D. Schiavazzi, C. J. Elkins, and J. K. Eaton. Three-dimensional inspiratory flow in the upper and central human airways. *Experiments in Fluids*, 56(6):1–12, 2015.

[2] S. Jalal, T. V. de Moortele, A. Nemes, O. Amili, and F. Coletti. Three-dimensional steady and oscillatory flow in a double bifurcation airway model. *Physical Review E*, 103101:1–23, 2018.

[3] S. Jalal, A. Nemes, T. V. de Moortele, S. Schmitter, and F. Coletti. Three-dimensional inspiratory flow in a double bifurcation airway model. *Experiments in Fluids*, 57:148:11pp., 2016.

[4] T. Janke, P. Koullapis, S. C. Kassinos, and K. Bauer. PIV measurements of the SimInhale benchmark case. *European Journal of Pharmaceutical Sciences*, 133(February):183–189, 2019.

[5] P. Koullapis, S. C. Kassinos, J. Muela, C. Perez-Segarra, J. Rigola, O. Lehmkuhl, Y. Cui, M. Sommerfeld, J. Elcner, M. Jicha, I. Saveljic, N. Filipovic, F. Lizal, and L. Nicolaou. Regional aerosol deposition in the human airways: The SimInhale benchmark case and a critical assessment of in silico methods. *European Journal of Pharmaceutical Sciences*, 113(June 2017):77–94, 2018.

[6] F. Lizal, J. Elcner, P. K. Hopke, J. Jedelsky, and M. Jicha. Development of a realistic human airway model. *Proceedings of the Institution of Mechanical Engineers, Part H: Journal of Engineering in Medicine*, 226(3):197–207, 2012.

[7] T. Janke,R. Schwarze, and K. Bauer. Measuring three-dimensional flow structures in the conductive airways using 3D-PTV. *Experiments in Fluids*, 58(10):133, 2017.

A NUMERICAL STUDY OF OXYGEN TRANSFER FROM BLOOD IN PERMEABLE MICROCIRCULATION TO SURROUNDING TISSUE IN THE PRESENCE OF A MAGNETIC FIELD.

Alana Sankar-Ramkarran*[1], Sreedhara Rao Gunakala [1], and Donna M. G. Comissiong [1]
[1] Department of Mathematics and Statistics, The University of the West Indies, St. Augustine, Trinidad & Tobago

Summary Oxygen transfer from microcirculation to tissue through permeable vessel walls was examined in the presence of an external magnetic field. We considered a two-layered blood flow consisting of a core region as a particle-fluid suspension and a peripheral cell-free plasma layer. In the blood, oxygen is transported by molecular diffusion and convection while in the tissue region it depended on both molecular diffusion and its metabolic consumption. A Finite Element Method was used to solve the governing equations which arose with a fixed-point iterative technique being applied when treating with the nonlinear terms. The effects of varying haematocrit, core region thickness, magnetic field strength and wall permeability on oxygen transfer were examined. These results were subsequently interpreted and explained in terms of the physical situations in which they arise.

BACKGROUND OF STUDY

Oxygen (O_2) plays a key role in cellular energetics. Both oxidation and other forms of energy production are dependent on there being a steady supply of oxygen to the cells. When air enters the body (through the mouth or nose) it goes to the lungs where oxygen is extracted. This oxygen is then carried by the bloodstream through the circulatory system to tissues where it is utilized. Thus, in order to fully understand the regulation of blood flow, the physical mechanisms of oxygen transport throughout the pathway must be investigated [1]. The Finite Element Method is a useful tool in studying such problems since it can easily handle the flow geometry and boundary conditions. This method was used to study the transport of oxygen in the systemic capillaries and surrounding tissues, but wall permeability was not considered [2]. The magnetohydrodynamic blood flow through microcirculation with permeable walls was examined where a two-layered flow was used but oxygen transfer was not examined [3]. This study examined how oxygen is transferred through permeable microcirculation to tissue which is then used to predict the role that factors such as varied haematocrit, core region thickness, magnetic field strength and wall permeability will have on this process.

MATHEMATICAL FORMULATION

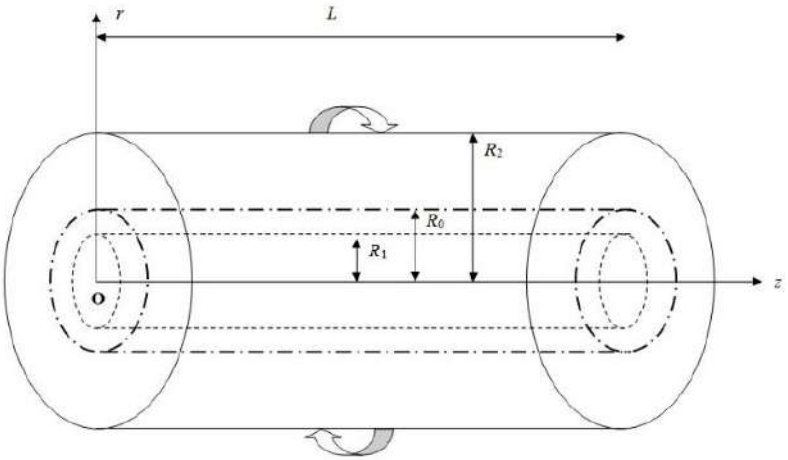

Figure 1. Geometry of the microcirculation in the presence of an external magnetic field.

Consider the laminar, axisymmetric, steady and fully developed blood flow through permeable microcirculation in the presence of an external magnetic field surrounded by a tissue region. The blood vessel is assumed to be circular, uniform and of semi-infinite extent. Radius, entrance, end and special wall effects are neglected since the length of the vessel is assumed to be much greater than its radius. In the presence of the Lorentz's force, a macroscopic two-phase model was used in the core region of radius R_1 while a Newtonian fluid is suitable for the peripheral layer (R_0-R_1) [3]. In both regions, oxygen transfer occurs through molecular diffusion and convection with haemoglobin and oxygen being in chemical equilibrium inside the red blood cells. In the tissue region, the transport of oxygen is assumed to depend on molecular diffusion with the rate at which oxygen is consumed following zero-order chemical kinetics. Proposed equations were non-dimensionalized and appropriate interface and boundary conditions were included. The velocity solutions were found and the Galerkin finite element method was used to obtain the solution for the mass transfer in the blood vessel region. Matlab code was written to generate any size mesh using eight node serendipity elements and this mesh was utilized in this study. A grid independence test and code validation were conducted, then graphs were generated to observe the partial pressure of oxygen (PO_2) in all three regions.

*Corresponding author. E-mail: alana.sankar@sta.uwi.edu

RESULTS

It was observed in Figure 2a that as hematocrit, C, increased, PO_2 was higher in all three regions. Thus, under conditions where the red blood cell count in the blood is lower than normal, for example in patients with plasma cell dyscrasias or Hb SS-sickle cell, there is less O_2 present which can be detrimental to the surrounding tissue which may become starved of O_2. Meanwhile, in patients with high hematocrit, for example those with polycythemia, there is a high O_2 concentration in the tissue which can lead to oxygen toxicity (hyperoxemia). This can result in twitching, dizziness, nausea, seizures and in severe cases can even be fatal. Another factor which increased O_2 is the thickness of the core region as shown in Figure 2b. An increased in the core region thickness corresponds to a thinning of the plasma layer. Hence as this peripheral layer thins, the oxygen content elevates in all regions.

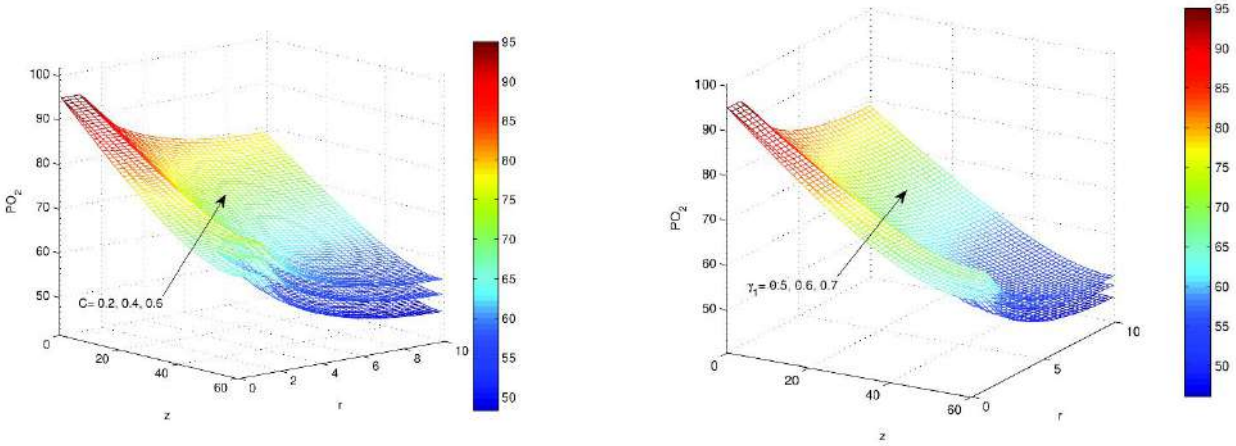

Figures 2a, 2b. Increased PO_2 observed on increasing haematocrit and core region thickness.

During Magnetic Resonance Imaging (MRI) scans and in the treatment of chronic pain and non-healing or slowly healing ulcers, human are subjected to magnetic fields. From Figure 3a, increasing the Hartmann number (magnetic field intensity) resulted in a decline in PO_2, thus high intensity magnetic fields should be avoided. Furthermore, some drugs administered can alter vessel wall permeability [2]. Hence incorporating wall permeability in O_2 transfer is important. Figure 3b showcased a decrease in PO_2 in all three regions as the vessel walls became more permeable with an increasing Darcy number. Therefore, the effect of medication (such as ACE inhibitors, beta blockers, calcium-channel blockers, decongestants, antihistamines, sildenafil, nonsteroidal and anti-inflammatory drugs) should be closely monitored.

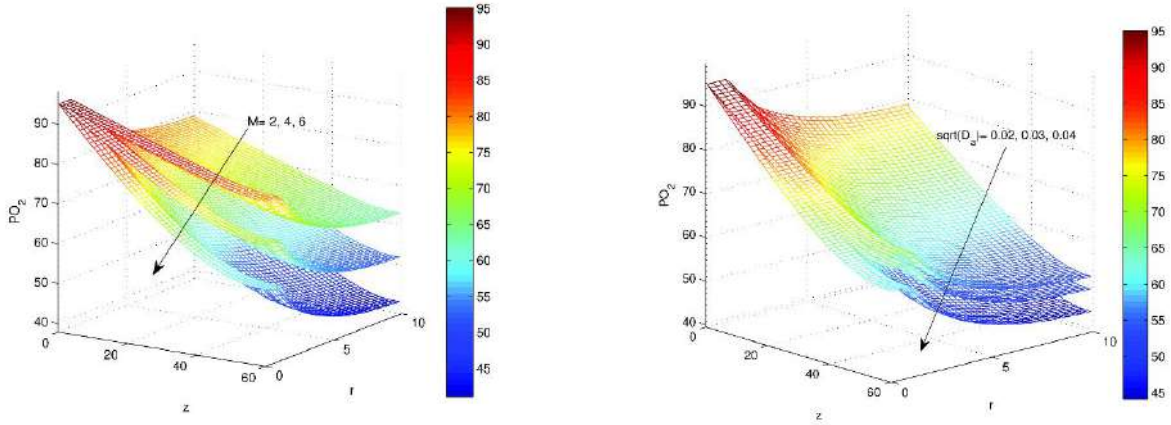

Figures 3a, 3b. Decreased PO_2 observed on increasing magnetic field strength and wall permeability.

CONCLUSION

In order to fully understand what occurs in microcirculation, it is important to examine how oxygen is transferred to tissues and what factors can affect this process. PO_2 increased on increasing haematocrit and core region thickness but decreased as the magnetic field strength and wall permeability were increased. Medical situations where these may arise were given and their effects discussed.

References

[1] Popel A.S. Theory of Oxygen Transport to Tissue. *Crit Rev in Biomed Eng.* **17**: 257-321, 1989.

[2] Scientific American 2014. web site **https://www.scientificamerican.com/article/common-prescription-drugs-alter-blood-s-flow/**

[3] Sharan M., Singh B., Singh M.P., Kumar P. Finite Element Analysis of Oxygen Transport in the Systemic Capillaries *IMA J Math Appl Biol Med Biol.* **8**:107-123, 1991.

[4] Sankar-Ramkarran A., Gunakala S.R., Comissiong, D. Magnetohydrodynamic Stenosed Blood Flow Through Microcirculation with Permeable Walls. *Int J Appl Comput Math.* **4**:1-17, 2018.

ORGANIZATION OF ACTIVE BACTERIAL SUSPENSION IN MICROFLUIDIC POISEUILLE FLOW

Axel Klein[1], Mathieu Jenny[1], Frédéric Jorand [2], and Nicolas Louvet*[1]
[1] Université de Lorraine, CNRS, LEMTA, F-54000 Nancy, France
[2] Université de Lorraine, CNRS, LCPME, F-54500 Nancy, France.

Summary We study the organization of a motile bacterial suspension under flow. Through pressure-driven flow microfluidic experiments and optical tracking techniques, we follow the Lagrangian trajectories of bacteria in a Poiseuille flow. From trajectories, we compute the bacteria orientations and concentration profiles as a function of the Peclet number, suspension concentration and walls confinement. Our first results highlight the strong influence of walls on the bacteria dynamics. Close to the wall, their orientations are isotropic as in the case of no applied flow.

INTRODUCTION

In their environment, wild type species of bacteria organize their motion as regular changes of direction to explore and harvest the environmental resources. To achieve its locomotion, the *Escherichia coli* (*E. coli*) bacterium regroups its flagella into a bundle and adopt a "Run & Tumble" swimming strategy. Under flow, bacteria are subject to hydrodynamic stresses that may cause changes in their swimming behaviour and thus lead to diversified transport properties [1]. We investigate experimentally the effect of flow strength and wall confinement on the organization of an active bacterial suspension.

MATERIALS AND METHODS

The wild type *E. coli* (ATCC9637) are suspended in motility medium (BMB) supplemented with 20 mM D-Glucose and 2:3 v/v Percoll. By computing the Mean Squared Displacement (MSD), from Lagrangian trajectories or using the Differential Dynamic Microscopy (DDM) technique, we measure bacteria swimming characteristics (i.e. the swim velocity V_b and the characteristic reorientation time t_b). In a fluid at rest and for a dilute suspension, V_b and t_b are, respectively, 12 µm/s and 1.5 s.

A pressure driven flow in microfluidic channel is used in order to manage the flow strength applied to the active suspension. The microfluidic device consists in a glass capillary connected to two syringes containing the bacterial suspension. The syringes are mounted on translating stages to adjust the height difference between the inlet and the outlet and thus impose the total pressure drop across the channel (Figure 1a). The channel has a rectangular cross section with high aspect ratio (width / height =10) which allows to discard effects due to lateral walls and consider a planar Poiseuille flow.

We use PIV and PTV techniques to measure fluid velocities and bacteria characteristics at different height in the channel (Figure 1b-c).

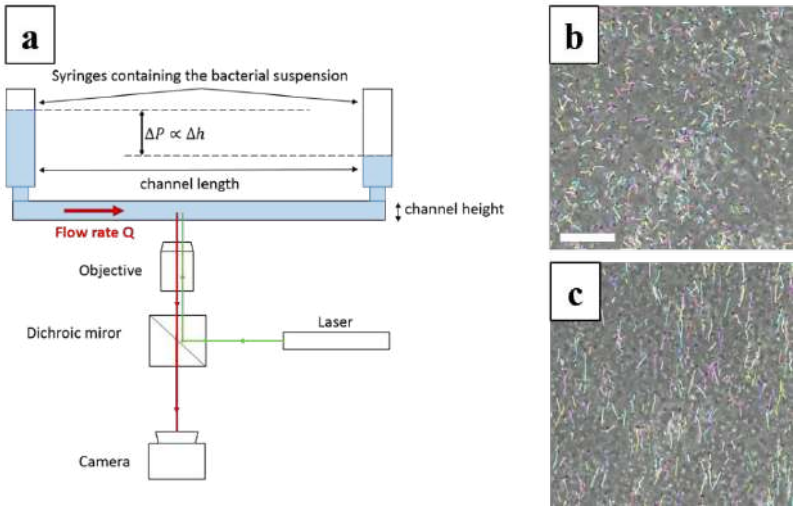

Figure 1: **a)** Experimental set-up used to track the bacteria behavior at various flow strength. **b) – c)** Bacteria trajectories close to the channel wall and at the mid channel height respectively. The pressure drop is 2 Pa corresponding to a maximum fluid velocity of 5 µm/s. The scale bar is 40 µm.

*Corresponding author. E-mail: nicolas.louvet@univ-lorraine.fr

FIRST RESULTS

From the bacteria trajectories measured by tracking technique, we compute the time and ensemble average of the bacteria orientation distribution. The results are plotted, Fig. 2, for two flow strengths at the wall and at the mid-height of the channel. We choose, as a reference, the case with no flow (black symbols) where the orientation is isotropic at both heights.

First results highlight the effect of the wall on the orientation distribution. In fact, in the near-wall region, the distribution of the bacteria swimming orientation is uniform meaning that a large part of bacteria swim upstream even at high flow strength (Fig.2 a-c). For the case (a) the Peclet number $Pe = \dot{\gamma}_w \cdot t_b$, with $\dot{\gamma}_w$ the wall shear rate, is close to 0.1 and the bacteria dynamic is not affected by the imposed flow. For larger Peclet numbers close to 1 (case (c)) we observe the same trend. In the middle of the channel bacteria are mostly oriented in the direction of the imposed flow (Fig.2 b-d). An increasing flow strength thus leads to a narrowing of the swimming orientation distribution. These results are in line with predicted Brownian simulations [2].

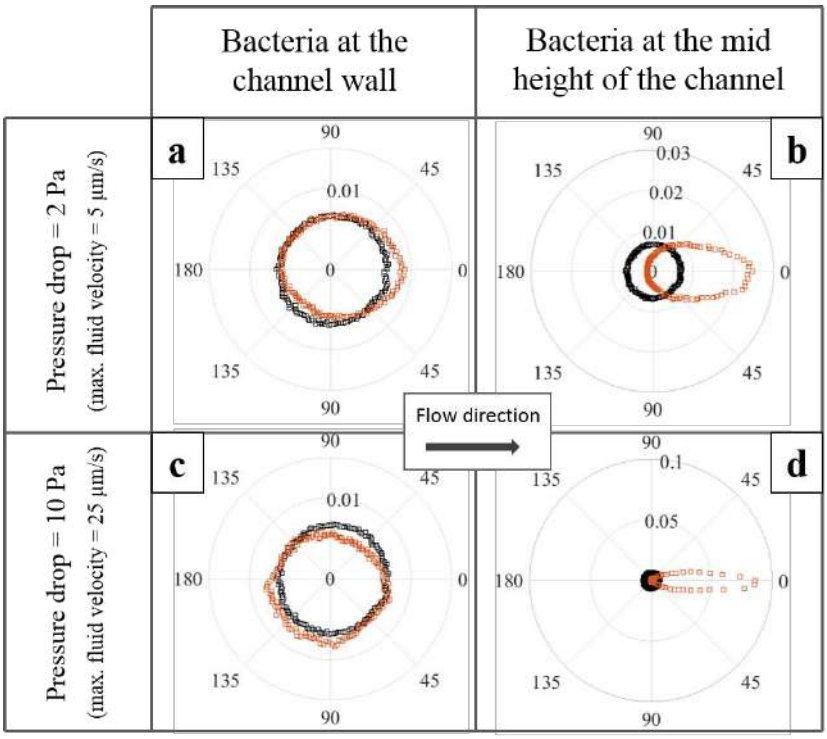

Figure 2: Polar representation of bacteria orientation under two flow strengths and two positions in the channel. The orange and black symbols are the cases with and without flow respectively. The bacteria concentration is 0.1 % vol.

CONCLUSION

We investigate the behaviour of motile bacteria under confinement at various flow strengths. We show that, in the near-wall region, upstream motions subsist, despite increasing Peclet number. However, in the mid-height of the channel, the flow strongly affects the bacterial behaviour and hinder upstream motions.

References

[1] B. Ezhilan and D. Saintillan, J. Fluid Mech. 777: 482-522, 2015.
[2] Mathijssen A. J. T. M., *et al.*, Nature communications 10: 3434, 2019.

RECONSTRUCTION OF A CORONARY ARTERY FLOW FROM IVUS MEDICAL IMAGES

Raz Hechter*[1], and Alexander Yakhot[1]
[1] Department of Mechanical Engineering, Ben-Gurion University, Beer Sheva, Israel

Summary Vascular lesions are usually accompanied by changes in arterial stiffness, attenuation, morphology and flow field. The objective of this work is to develop and test a new tool for assimilating clinical imaging to aid in finding and assessing pathologies resulting from lesions. The proposed tool utilizes the Kriging method, originally developed for spatial interpolation, in time as well, in conjunction with proper orthogonal decomposition to eliminate noise. The method was tested on an intravascular ultrasound clinical clip and yielded a flow field, which enables further calculation of hemodynamic properties as well as border detection.

BACKGROUND

Vascular lesions are usually accompanied by changes in arterial stiffness, attenuation, morphology and flow field. There is a gap between comprehensive useful information for physicians and achievable data through clinical imaging and measurement. To resolve this gap, many studies based on computational fluid dynamics (CFD) have suggested the use of simulations as a tool that completes the picture by adding upon the measured data. Since it is not suitable for patient-specific analysis, it cannot be accepted by the clinical community as a diagnostic tool. The objective of this work is to develop and test a new tool for assimilating clinical imaging to aid in finding and assessing pathologies resulting from lesions.

METHOD

The proposed tool utilizes the Kriging method, originally developed for spatial interpolation, in time as well. In conjunction with the proper orthogonal decomposition (POD), the approach has been applied for reconstruction of arterial flow field from patient-specific intravascular ultrasound (IVUS) images. The Kriging interpolation fills-in the gaps in the data, while the proper orthogonal decomposition eliminates noise.

RESULTS

The method was tested on an intravascular ultrasound (IVUS) clinical clip consisting of 48 frames (~7 sec). Figure 1 show a selected frame from the IVUS clip along with its reconstructed form. The reconstructed velocity field is quite smooth; the coronary artery wall border (in blue) is recognized.

CONCLUSION

The proposed Kriging space-time interpolation method yields a flow field, which enables further calculation of hemodynamic properties as well as border detection.

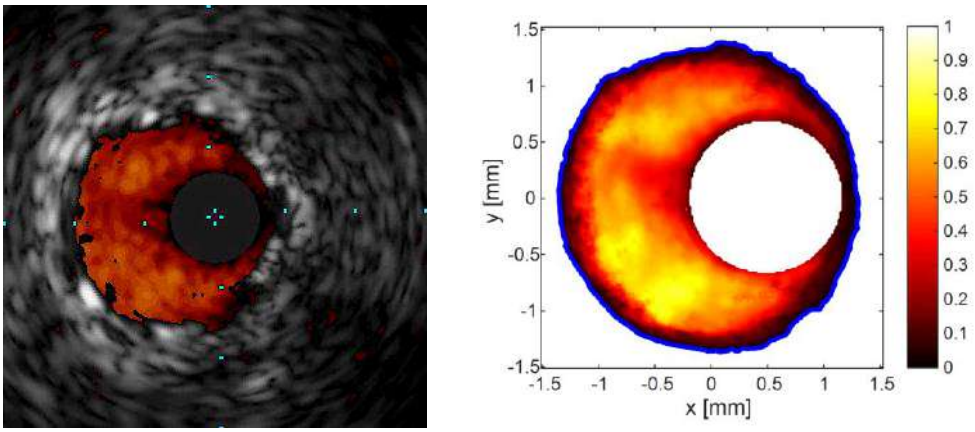

Figure 1. Left – IVUS image; right – reconstructed axial velocity field with the arterial border in blue.

References

[1] Lophaven, S., Nielsen, H. and Sondergaard, J., 2002, Matlab Kriging toolbox, Rep. IMM-REP-2002-12, Informatics and mathematical modeling, DTU.
[2] Yakhot, A., Anor, T. and Karniadakis, G. E., 2007, "A reconstruction method for gappy and noisy arterial flow data. Medical Imaging", IEEE Transactions on, 26(12), pp. 1681-1697.

*Corresponding author. E-mail: hechter@post.bgu.ac.il

STATISTICAL MODELLING OF CEREBRAL BLOOD FLOW AND TRANSPORT IN MICROVASCULAR NETWORKS

Florian Goirand *[1,2], Tanguy Le-Borgne[1], and Sylvie Lorthois[2]
[1] Geosciences Rennes, University Rennes 1, Rennes, France
[2] Toulouse Institute of Fluid Mechanics, UMR CNRS INPT UPS 5502, Toulouse, France

Summary Despite of the high dependency of brain cells function on the efficiency of blood transport throughout the micro-vasculature, only little is known about the physical processes that drive neural cell supply. Here, based on the statistical analysis of realistic blood flow computations in mouse brain micro-vascular networks, we develop a modular statistical framework allowing to integrate a growing number of flow and transport heterogeneities. In particular, this framework enables to capture the anomalous nature of the transport in brain micro-vascular networks. We further investigate the interplay between flow organization and vascular density decrease on the total amount of flow incoming in the network through random bond percolation.

GENERAL CONTEXT

The cerebral microvascular network and in particular its capillary bed is in charge of the local supply of vital chemical species (e.g. oxygen, nutrients) to brain cells and the removal of metabolic wastes (e.g. β-amyloid, τ-protein). Motivated by understanding the possible role of metabolic failure in diverse neurodegenerative disease, we analyse the organization of the blood flow at the microvascular level through various statistics from both Lagrangian and Eulerian point of views. The analysis is performed on the result of previous flow simulations performed in a 1 mm^3 of mouse cortex micro-vascular network ($\sim$ 14000 vessels) [1, 2] and provides key information to develop a statistical framework for blood flow and transport in such networks. On the other hand, a decrease of the cerebral blood flow associated to capillary vessel occlusions has been highlighted at early stage of Alzheimer disease [1]. Our numerical setup allowing a quantification of the consequences of network structure changes, we adapt classical percolation theory in dilute regime [3] aiming to predict the impact of such occlusions on global cerebral blood flow.

MAIN RESULTS

The Eulerian flow rate distribution shows two well-defined regimes: at high flow rates, the flow is ordered and reveals its dipolar nature induced by ponctual injection and pumping on the network. At low flow rates, the flow statistics are driven by the disordered organization of the network [4]. The analogy with dipole flows [5] and force distribution in random bead packs [6], akin to random aggregation theory, allows to derive analytical solutions for the Probability Density Functions (PDF) of flow in these two regimes.

From our analysis, we develop the first effective transport model based on micro-vascular structure and flow organization. Our transport model contains a deterministic part induced by the dipole structure and a stochastic component induced by the network disorder [7]. This approach allows to emphasize the ordering of the different transport properties on the observed statistics of travel times within the micro-vascular network. Comparison with simulated travel time distributions obtained by tracing the transport of passive particles through the network shows accurate predictions.

Furthermore, based on in vivo concentration measurements, we evaluate effective characteristic times of oxygen supply or β-amyloid removal. This evaluation indicates the importance of late time transport regime in the metabolic processes. In particular, this regime is characterized by a competition between the particle trajectory lengths and the heterogeneities of the velocity field as main drivers of the travel time variability within the micro-vascular network. Besides, this evaluation allows to identify critical transport times above which the metabolic processes might be significantly impacted (oxygen deprivation or accumulation of β-amyloid). We predict, in agreement with observations, that the weight of these critical regimes evolves non-linearly with cerebral blood flow decrease.

Eventually, we link massive variability of cerebral blood flow decrease induced by vessel occlusions to flow organization within a revisited dilute regime percolation theory. The latter allows to predict the non-linear evolution of the probability to experiment critically low global flow rates during the occlusion process.

Acknowledgements
This work has been funded by ERC BrainMicroFlow GA615102 & ReactiveFronts GA648377. F.G, T.L-B and S.L gratefully thank P. Blinder and P. Tsai for providing anatomical data.

*Corresponding author. E-mail: florian.goirand@imft.fr.

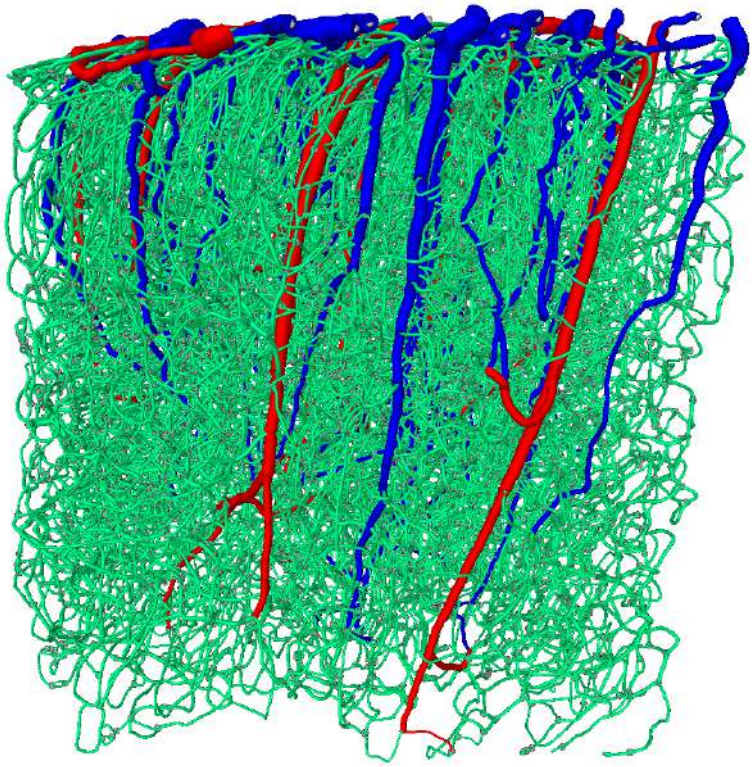

Figure 1: Sample of mouse brain micro-vascular network ($1mm^3$) with labelled vessel types: arterioles (red), venules (blue) and capillaries (green).

References

[1] Cruz-Hernndez J.C., et al. Neutrophil adhesion in brain capillaries reduces cortical blood flow and impairs memory function in Alzheimer's disease mouse models. *Nat. Neurosci.* **22.3**: 413, 2019.

[2] Berg M., et al. Modelling solute transport in the brain microcirculation: is it really well mixed inside the blood vessels?. *Journal of Fluid Mechanics*, 884, 2020.

[3] Kirkpatrick S. Percolation and conduction. *Rev. Mod. Phys.*, **45.4**: 574, 1973.

[4] Alim K., et al. Local pore size correlations determine flow distributions in porous media. *Physical review letters*, **119.14**: 144501, 2017.

[5] Kurowski P., et al. Anomalous dispersion in a dipole flow geometry. *Phys. Fluids*, **6.1**: 108-117, 1994.

[6] Liu C-H., et al. Force fluctuations in bead packs. *Science*, **269.5223**: 513-515, 1995.

[7] Dentz M., et al. Continuous time random walks for non-local radial solute transport. *Advances in water resources*, **82**, 16-26, 2015.

DYNAMICS OF A SMALL PEPTIDE SIMULATED IN WATER MODELS WITH VARYING VISCOCITY

Agnieszka M. Słowicka[1], Gouri S. Jas [2], and Krzysztof Kuczera [3]
[1] Department of Biosystems and Soft Matter, IPPT PAN, Warsaw, Poland
[2] Department of Pharmaceutical Chemistry, University of Kansas, Lawrence, KS, USA
[3] Department of Chemistry, University of Kansas, Lawrence, KS, USA

Summary The following paper concerns analysis of structure and dynamics of peptides in solution. We have studied the dipeptide N-acetyl-trypthophanamide (NATA) in water using molecular dynamics simulations, with solvent viscosity tuned by mass scaling. Increasing the viscosity of water had strong effects on the external and internal dynamics of NATA peptide. As expected, the rates of external peptide motions, describing overall translations and rotations, were inversely proportional to the effective solvent viscosity. Internal motions, representing conformational transitions, which may exhibited a more complicated pattern of change, will be studied in future work. Numerical results from molecular dynamics simulations were also compared with experimental measurements obtained by fluorescence anisotropy decay.

INTRODUCTION

The dynamics of small peptides have been considered numerically and experimentally [1-3]. The fundamental behavior of small peptides, like NATA, give us information about the internal and external dynamics of the basic biological protein systems immersed in the liquids with different viscosity. Interactions of biological particles with the solvent are manifested by a conformation changes of the molecule and its translation and reorientation in relation to the molecules of the solvent in which the particle is located [3]. The study of reorientation of the biological particles allows the recognition and isolation of the preferred behaviors of molecules in a contact with specific solvent. In this work, molecular simulations of peptide dynamics are compared with experimentally available measurements to verify the numerical results and microscopic effects that are difficult to investigate in the lab. The purpose of this analysis was to study the influence the solvent viscosity on the internal and external dynamics of the NATA peptide.

METHODS

Molecular dynamics (MD) simulations were used to study the behavior of NATA (see Fig.2) in a water-based liquid. Simulations of a single NATA molecule placed in water were performed using the GROMACS program with the OPLS/AA force field [4]. The TIP3P model was chosen for water modeling. Calculations of NATA peptide in a box of 1185 molecules of water were performed at the temperature T=300K using periodic boundary conditions in canonical ensemble (NVT) with the Nose–Hoover thermostat. To vary the viscosity of the liquid surrounding the peptide without changing the potential energy parameters, an artificial method of increasing the mass of the water molecule was used. With increasing the mass m in the molecular model, the viscosity of the modeled fluid increases proportionally to $m^{1/2}$. Numerical calculations were made for liquid models with viscosity $\eta = n \cdot \eta_0$, where n = 1,2,3,4,5 and η_0 is the basic viscosity of the the regular TIP3P model [7]. 200-nanosecond all-atom trajectories of NATA in water were generated with the five mass-scaled water models. The trajectories were analyzed by calculating peptide and solvent translational and rotational diffusion coefficients, as well as by following changes in internal structure like end-to-end distance and backbone and sidechain dihedral angles. Parameters calculated from the molecular dynamics simulations were compared with experimental measurements obtained for NATA in water [3].

RESULTS

Numerical studies of the peptide dynamics were concentrated on determining how the change of viscosity of the solvent effects peptide behavior. Studying this phenomenon, first of all, the viscosity of the solutions surrounding the peptide were calculated. According to the fact, that the water viscosity is proportional to the rotational orientation time τ for dipoles [2], we determined the reorientation time τ from simulations for different models of solvent comparing the results with the assumed relative viscosity of the solution η . As is shown on the graph (see Figure 1a), the dependence between the reorientation times τ and modeled viscosity of solvent is linear and reproduce very well the expected hydrodynamical relation between these parameters.

Analyzing the external dynamics of NATA in different solutions, the translational D_{tr} and rotational D_{rot} diffusion coefficients of the peptide were calculated and presented in Figure 1b and 1c. Taking into account the hydrodynamic correction due to the difference between the Stokes friction in an infinite system and in a system under periodic boundary conditions (PBC), the parameters were recalculated with respect to the following forms:

$D_{rot} = D^r_{PBC} + \frac{k_b T}{6\eta V}$ (1) and $D_{tr} = D^t_{PBC} + \frac{k_b T \xi}{6\pi\eta L}$ (2), where D^r_{PBC} , D^t_{PBC} are the diffusion coefficients from PBC simulations (rotational and translational respectively), k_B- Boltzmann constant, T – temperature, ξ=2.837297, η -

TIP3P water viscosity, V – volume of the calculated box and L –length of the simulated cell [5,6]. In Figure 1c, the red line represents D^{t}_{PBC} values obtained from simulations and the blue line D_{tr} after correction for PBC effects, illustrating relatively large influence of the geometry of the simulation box on the global diffusion coefficient values.

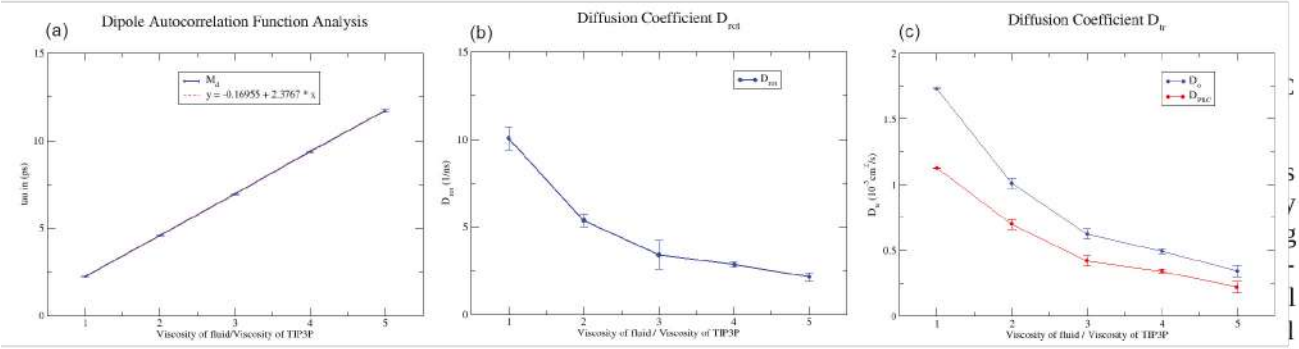

dynamics of NATA by proportional increasing of characteristic relaxation times. MD results are consisted with results obtained experimentally.

The natural follow-up question is, how does the internal dynamics of the peptide react to the increasing of the solvent viscosity. The detailed analysis of this problem will be realized in future studies based on results obtained from structural clustering of peptide conformers and investigation of the kinetics of transitions between preferred conformers of NATA in water-based solutions with different viscosity (Figure 2).

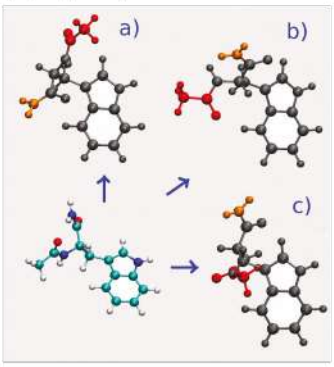

Figure 2. NATA molecule – typical conformations from MD simulation in TIP3P water (molecules of water not shown).

ACKNOWLEDGEMENTS

We acknowledge a partial support of project ITHACA (nr PPI/APM/2018/1/00045/U/001) founded by Polish National Agency for Academic Exchange. This project was partly supported by NSF Grant No. 1807852.

References

[1] Jas G. S., Childs E.W. and Kuczera K.Kinetic pathway analysis of an -helix in two protonation states: Direct observation and optimal dimensionality reduction. *J. Chem. Phys.* 150: 074902, 2019.
[2] Jas G. S., Middaugh C.R., and Kuczera K. Probing Selection Mechanism of the Most Favorable Conformation of a Dipeptide in Chaotropic and Kosmotropic Solution, *J. Phys. Chem. B*: 120, 6939−6950, 2016.
[3] Jas G. S., Rentchler E.C., Słowicka A.M., Hermansen J.R, Johnson C.K., Middaugh C.R., and Kuczera K. Reorientation Motion and Preferential Interactions of a Peptide in Denaturants and Osmolyte. J. Phys. Chem. B, 120: 3089−3099, 2016.
[4] Hess B., Kutzner C., van der Spoel D. and Lindahl E. GROMACS 4: Algorithms for highly efficient, load-balanced, and scalable molecular simulation, *J. Chem. Theory Comput.* 4: 435-447, 2008.
[5] Linke M., Köfinger J., and Hummer G. Rotational Diffusion Depends on Box Size in Molecular Dynamics Simulations, *J. Phys. Chem. Lett.* 9: 2874−2878, 2018,
[6] Yeh I-Ch. and Hummer G., System-Size Dependence of Diffusion Coefficients and Viscosities from Molecular Dynamics Simulations with Periodic Boundary Conditions. *J. Phys. Chem. B* 108: 15873-15879, 2004.
[7] Mao J. and Zhang Y. Thermal conductivity, shear viscosity and specific heat of rigid water models. *Chemical Physics Letters* 542: 37–41, 2012.

SPECTRAL PROPER ORTHOGONAL DECOMPOSITION FOR LOW-DIMENSIONAL MODELING OF THE FLOW IN ABDOMINAL AORTIC ANEURYSMS

Shahrzad Norouzi *[1], Giuseppe Di Labbio[1,2], and Lyes Kadem[1]
[1] Laboratory of Cardiovascular Fluid Dynamics, Concordia University, Montréal, Québec, Canada
[2] Laboratoire de Dynamiques des Fluides, Polytechnique Montréal, Montréal, Québec, Canada

Summary As an application of reduced-order modeling in cardiovascular flow analyses, spectral proper orthogonal decomposition (SPOD) is applied to velocity data of the flow inside idealized and compliant models of an abdominal aortic aneurysm (AAA) at different expansion ratios. The idea is to construct low-dimensional models of AAA flow and to identify the most important low-dimensional features of the flow.

INTRODUCTION

An abdominal aortic aneurysm (AAA) is referred to as a localized dilation of the aortic wall in the abdomen. The disease severity, represented in clinical practice by the maximal diameter in the expanded area, is correlated with flow features within the aneurysm sac, which vary depending on the size. Therefore, AAA flow dynamics analysis can provide insights into its progression and possibly lower the risk of sudden rupture that can be fatal up to 81%. In this context, a promising approach to more effectively analyze the abundant and high-dimensional experimental and numerical data is to construct data-driven reduced-order models that can facilitate the identification of the coherent structures in AAA flow and the development of predictive tools for the growth and risk of rupture of AAAs. In modeling AAA or any cardiovascular flows, two standard techniques, proper orthogonal decomposition (POD) and dynamic mode decomposition (DMD), can be used to generate low-dimensional models with their associated pros and cons. POD can provide the most energetically optimal model but fails in an accurate description of the dynamics of the flow. On the other hand, DMD can more efficiently extract and reproduce the dynamics of the flow, its performance is undermined in cardiovascular applications because of the transient, aperiodic and chaotic nature [1]. The optimality of POD in maximizing the total variance and the superiority of DMD in expressing temporal correlation are merged into an alternative method, spectral proper orthogonal decomposition (SPOD). With SPOD, data is decorrelated to spectral and energetic content, meaning that the modes at each frequency can preserve both the temporal and spatial coherence. In this experimental study, SPOD specific features are used in order to gain a better fundamental knowledge of the flow in AAAs and to derive reduced order models of the flow.

METHODOLOGY

To replicate the flow experimentally inside the abdominal aortic aneurysm, an *in vitro* simulator is designed that consists of elastic and optically clear silicone replica of AAAs. The pulsatile flow circulation at 1.05 Hz (63 bpm) within the experimental setup is obtained using a positive-displacement gear pump coupled with a motor and controlled through a LabVIEW interface. A mixture of water and glycerol (40% v/v) is used as the working fluid with a measured density and dynamic viscosity of 1160 kg/m^3, 4.1 cP. The flow is pumped from a higher reservoir and reaches an anatomical model of the aorta by passing along a trileaflet bioprosthetic aortic valve. The flow branches off to the renal arteries and the abdominal aorta encased in an acrylic chamber filled with the same fluid mixture to minimize optical distortion. The infrarenal flow rate is 1 ± 0.18 L/min with systolic and diastolic pressures of 153/95 (±3) mmHg, and the mean Reynolds and Womersley numbers are 344 ± 7 and 13.2, respectively. The experiments are carried out for 4 cases including a model with a nominal aortic diameter (2 cm) and 3 models of aneurysms with ratio of maximal to nominal diameters (d_r) of 1.5, 2 and 2.5. The flow in the AAA was captured using 2D time-resolved particle image velocimetry measurements over one cardiac cycle (T=0.952 s). The flow was seeded with polyamide paricles and illuminated with a 1 mm thick laser sheet formed by a double-pulsed Nd:YLF laser. Using a high-speed camera, 500 double-frame images were acquired 900 μs apart at an acquisition rate of 525 Hz. Finally, the images are post-processed and the velocity field snapshots are obtained with a spatial resolution of 0.6 mm $\times$ 0.6 mm. The measurements are performed on the plane bisecting the abdominal aorta, namely, the sagittal plane where AAA clinical *in vivo* measurements are often being performed. For each investigated case, the velocity snapshots from an ensemble of realizations of the flow is used to construct the input data matrix for SPOD implementation where a single PIV dataset is regarded as one block. The algorithm starts by performing a discrete-Fourier transform (DFT) on each block separately decomposing its related flow data into spatial structures associated with specific frequencies. Then at each frequency, the cross-spectral density tensor is estimated and used as the kernel for the POD eignevalue problem, which results in SPOD modes with their corresponding energy contents. Details on SPOD background and algorithm can be found in [2].

*Corresponding author. E-mail: norouzi.shahrzad@gmail.com.

RESULTS AND DISCUSSION

For each case and according to the number of realizations, decomposition yields a set of SPOD modes which are optimally ranked in terms of energy at each frequency. Considering the SPOD spectra (Figure1) and with POD intuition in mind, we see that for all the scenarios, there is a significant energetic difference between the first SPOD mode and the remaining modes (e.g., for the most dilated AAA, d_r=2.5, the energy fraction drops from 91.56% to 3.50% from the first to the second mode). Applying POD on the same velocity data will lead to a first mode that contains only 54% of the energy. So, the first mode is considered the leading mode to efficiently represent the flow at each frequency and

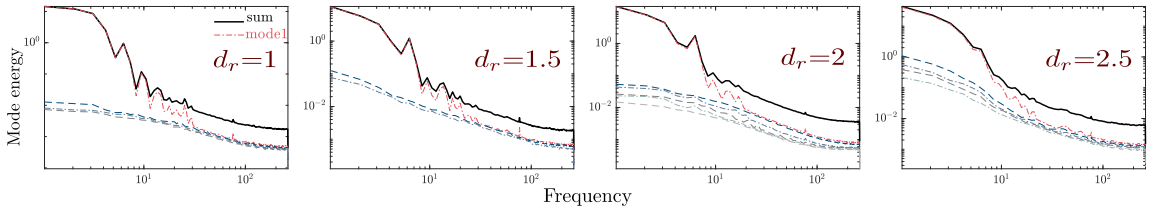

Figure 1: SPOD spectra for different AAA configurations as defined by the ratio of maximal to nominal diameters (d_r). Normal case d_r=1 and most severe case d_r=2.5.

identify the low-dimensional and essential features of the available flow field. To better illustrate this, the first SPOD mode at 5 primary harmonics (1.03-5.15) are visualized in Figure 2 for the most severe AAA, corresponding to d_r=2.5. SPOD is only applied to the fluctuating velocity components, and the temporal mean is subtracted. Since modes are mutually orthogonal on a spatiotemporal basis, we can say that the structures captured by a particular SPOD mode are temporally correlated with those extracted from the same mode at any other time within the flow field. This property of SPOD compared to POD where modes by definition cannot disclose any information on the flow history due to a lack of temporal correlation, makes it easier to interpret SPOD modes physically and correlate their shapes to the original flow field phenomena. Through qualitative visualization of the velocity snapshots, we can observe that the flow behavior, in this case, is characterized by the formation of an asymmetric vortex ring that travels downstream, pushing flow in its wake toward upstream. If we use the illustrated modes to reconstruct the initial velocity field, the structures extracted at the second harmonic (f=2.1) are reproducing the flow separation near the proximal neck followed by the retrograde flow of late deceleration and further propagation of the vortex, which can be noticed from the organization of the first SPOD mode streamlines at f=1.05. Therefore, this mode at six primary frequencies in the vicinity of the highest peak in the spectrum is used to illustrate the construction of a reduced-order model of the most complex aneurysmal flow being investigated in our study. Once the model is generated, by observing the instantaneous velocity, we can qualitatively say that the main features of the flow are well-reproduced. For further analysis and the significant contribution of the vortex ring to the flow dynamics in this AAA configuration, its presence and evolution over the entire cycle are quantified and compared to the original data in terms of vorticity. One snapshot of the vorticity field sampled from mid flow deceleration is plotted in Figure 2. We can notice that the strength of the vortex pair is very well-captured.

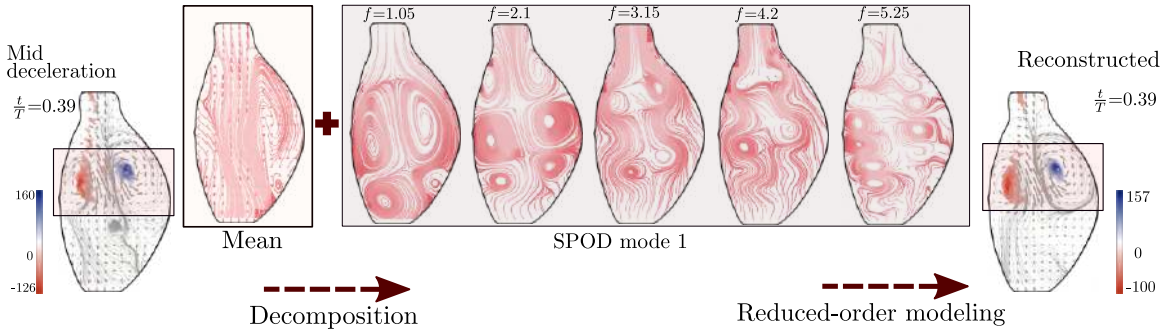

Figure 2: Decomposition and reconstruction of a low-dimensional model of the flow dynamics in a model of AAA with d_r=2.5.

Acknowledgments:The authors would like to thank Arnaud Le Floc'h for his help with MATLAB SPOD implementation.

References

[1] Taira, K., Brunton, S. L., Dawson, S. T., Rowley, C. W., Colonius, T., McKeon, B. J., ... Ukeiley, L. S. Modal analysis of fluid flows: An overview. *Aiaa Journal,* **55(12)**: 4013-4041, 2017.

[2] Schmidt, O. T., Colonius, T. Guide to spectral proper orthogonal decomposition. *AIAA Journal,* **58(3)**: 1023-1033, 2020.

COMPUTATIONAL STUDY OF HEMODYNAMIC NATURE IN CAROTID ENDARTERECTOMY PATIENTS: COMPARISON OF CLOSURE TECHNIQUES

Hyunwoo Jung[1], Taehak Kang[1], Dongik Kim**[2], Jaiyoung Ryu*[1,3]
[1] Department of Mechanical Engineering, Chung-Ang University, Seoul 06974, Republic of Korea
[2] Division of Vascular Surgery, Department of Surgery, Samsung Medical Center,Sungkyunkwan University of Medicine, Seoul 06351, Korea
[3] Department of Intelligent Energy and Industry, Chung-Ang University, Seoul 06974, Republic of Korea

Summary Carotid endarterectomy (CEA) is considered to be the golden standard to relieve stenosis conditions in both symptomatic and asymptomatic patients. Despite of numerous surgical techniques being developed in past few decades, superiority of one over another is still controversial. In this study, we present patient-specific results using computational fluid dynamics (CFD) to provide unbiased quantitative analysis of both primary closure (PC) and patch angiography (PA). Hemodynamic properties are calculated based on actual patient conditions to obtain values closer to the reality. As a result, pressure and flow rate match measurements and literature. WSS-related indicators show favorable outcomes for PC than PA, and PC technique may provide better postoperative consequences compared to PA.

INTRODUCTION

Carotid endarterectomy (CEA) has been the golden rule for treatment of moderate to severe carotid artery stenosis[1)]. Among various CEA techniques developed till date, two closing techniques are widely used, namely primary closure (PC) and patch angioplasty (PA). The superiority of these two techniques over one another is still undetermined and controversial while PA is preferred in clinical. This study aimed to compare the hemodynamic indicators of normal, PC, PA groups which influence atherosclerosis applying each patient's CTA image and Doppler Ultrasound data of common carotid artery (CCA). The total number of patients were 30, equally 10 people in each group. For clarifying the difference, 3D hemodynamic computational fluid dynamic (CFD) simulation was carried out. The hemodynamic indicators and flow parameter were quantified and compared. After that, the significance of the differences between groups was verified through a statistical method.

NUMERICAL METHOD

Unsteady hemodynamic simulations with patient-specific computational model were carried out for 30 carotid arteries using open - source CFD solver SimVascular[2)]. In all case, the modeling of 3D computational domain was conducted in same process. For virtual domains, a tetrahedral element mesh was generated. Also, prism layer using hexahedral mesh was adopted near vascular wall for measurement accuracy. Doppler ultrasound data were utilized to inlet boundary conditions. Due to inavailability of flow characteristic at arbitrary point, the outlet boundary conditions were assumed using windkessel lumped parameter model. Flowrates of internal carotid artery (ICA) and external carotid artery (ECA) were assumed to be 8 to 2 of CCA flowrate. For analyzing the results, 3 hemodynamic indicators which were time-averaged wall shear stress (TAWSS), oscillatory shear index (OSI), relative residence time (RRT) were calculated. After that, 3 indicators were converted to LSA for TAWSS, OSA for OSI and RTA for RRT which means the area with threshold-over indicators, called 'atherosclerosis prone area[3)]'. The thresholds were calculated with data of all cases referring literature[4)].

RESULTS AND DISCUSSION

Figure 1. showed the atherosclerosis prone area of 3 representative case of normal (a-c), PC (d-f), PA (g-i) group. Due to geometrical characteristic of each patient groups, flow becomes turbulent near bulb and lateral side of ICA. This turbulent flow changes hemodynamic nature of carotid artery. Among the CEA techniques, PA causes the larger enlargement of bulb than others. Due to this sudden enlargement, PA has most intense disturbed flow and the widest atherosclerosis prone area (low in TAWSS, high in OSI, RRT) in 3 representative cases. In figure 2, showing data of all cases, the same trend which were seen in representative cases can be confirmed in 3 patient groups. Case of PA group has wide severe area while PC group has similar trend with normal group. Although the PA was preferred in clinical environment, PC techniques provided more favorable hemodynamic nature of carotid artery.

*,** Corresponding author. Email: * jairyu@cau.ac.kr
** dongik.kim@samsung.com

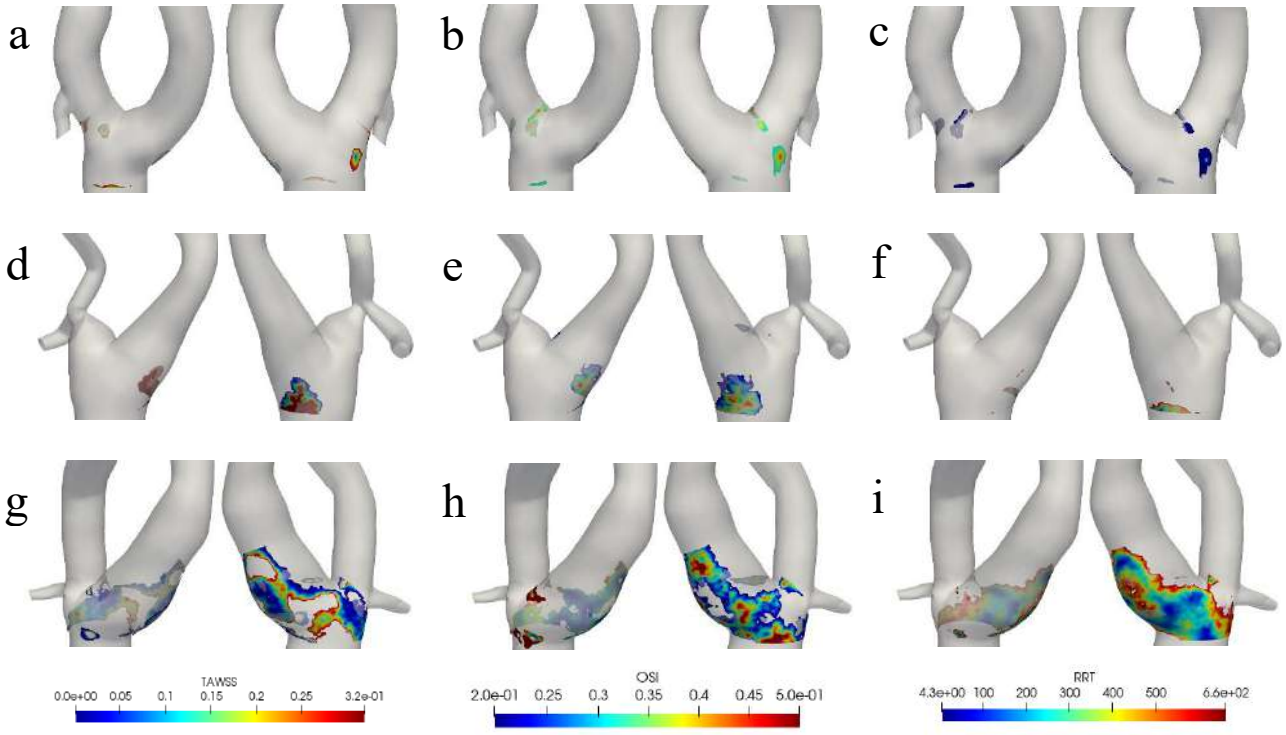

Fig 1. Atherosclerosis prone area of normal (a-c), PC (d-f), PA (g-i) case

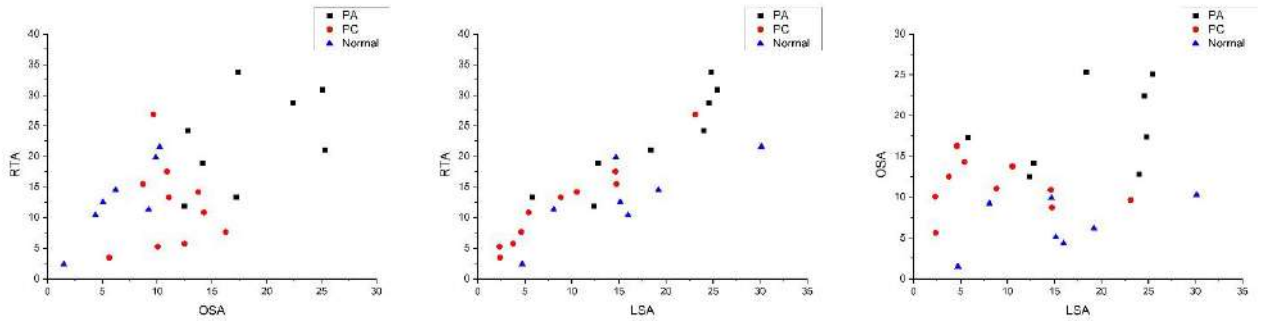

Fig 2. Scatter chart of atherosclerosis prone area in normal, PC, PA group

CONTRIBUTION

Conceptualization, Methodology, and investigation: H.J., D.K and J.R.; verification and writing-original draft preparation: H.J.; formal analysis, data curation, and visualization: H.J., T.K.; writing-review and editing, supervision, project administration, and funding acquisition: D.K and J.R. All authors have read and agreed to the published version of the manuscript.

References

[1] Swain, S., Turner, C., Tyrrell, P. and Rudd, A., 2008. "Diagnosis and initial management of acute stroke and transient ischaemic attack: summary of NICE guidance." Bmj, 337, p.786.
[2] Updegrove, A., Wilson, N.M., Merkow, J., Lan, H., Marsden, A.L. and Shadden, S.C., 2017. "SimVascular: an open source pipeline for cardiovascular simulation." Annals of biomedical engineering, 45(3), pp.525-541.
[3] Himburg, Heather A., and Morton H. Friedman. "Correspondence of low mean shear and high harmonic content in the porcine iliac arteries." (2006): 852-856.
[4] Stone, Peter H., et al. "Effect of endothelial shear stress on the progression of coronary artery disease, vascular remodeling, and in-stent restenosis in humans: in vivo 6-month follow-up study." *Circulation* 108.4 (2003): 438-444.

BIVENTRICULAR HEART MODEL WITH ELECTROMECHANICAL COUPLING

Nenad Filipovic*[1,2], Vladimir Geroski[1,2], Miljan Milosevic[1,2], and Milos Kojic[1,2]
[1]Faculty of Engineering, University of Kragujevac, Kragujevac, Serbia
[2] BioIRC Research and Development Center for Bioengineering, Kragujevac, Serbia

Summary In silico electro-mechanical model of heart is very important for better understanding of various diseases such as heart failure, cardiac arrhythmia, and cardiomyopathy. We have been developed a methodology for fluid-electro-mechanical model of heart tissue to provide mechanical response of the system. Some results for 3D biventricular heart model with constrains in septum zone are given. This model can give better understanding for real patient case for prediction of disease progression and development.

INTRODUCTION

It is very important to use detailed and complex model of heart electrical activity to understand disease progression as cardiomyopathy hypertrophic or dilated development. Muscles in the body are activated by electrical signals, transmitted from the nervous system to muscle cells, affecting the change of the cell membranes potentials. Additionally, calcium current and concentration inside the cell are main cause of generating active stress within muscle fibers. In electrophysiology, the goal is to determine the electrophysiological properties of all compartments and signal propagation characteristics within the body. For example, in heart electrophysiology, the fundamental advancements where achieved by designing the so called 'clamp' experiment [1] in order to determine characteristics of the membrane currents and constitutive relations for the conduction of currents. Following this break-through achievement, further important experiments were performed, with modifications and extension of the constitutive relations, e.g.[2-5]. Based on these experimental results, a large number of computational models related to electrical signal propagation within neural cells, along neural fibers-axons, and within extracellular space, have been introduced - in analytical and numerical (computational) form.

METHODS

Finite element model the patient parametric left ventricle has been modeling as fluid-structure interaction problem. The solid mechanics of the heart consist of two sources of stresses: the passive and active. The final stresses produced in the tissue are obtained adding the passive stresses and the active stresses. Passive stresses are a consequence of the structural properties of the cells and the connective tissues. We used model based on the recently available experimental investigation of Holzapfhel.

Boundary conditions for this model are: prescribed inlet velocity at mitral valve (right tube) and outlet aortic valve which was calculated as consequence of heart muscle contraction. As results we can see blood pressure and velocity distribution during whole heart cycle. Cardiac contractility is regulated by changes in intracellular Ca concentration. Normal function requires that Ca be sufficiently high in systole and low in diastole. Much of the Ca needed for contraction comes from the sarcoplasmic reticulum and is released by the process of calcium-induced calcium release.
Current flow through cell membrane contains ion currents of molecules such as sodium (Na^+), potassium (K) and calcium (Ca^{2+}), which are critically important for correct formulation of mathematical models for electrophysiology simulations. Additionally, calcium current and concentration inside the cell are main cause of generating active stress within muscle fibers.

RESULTS

Modelling such complex system is demanding in computational sense. In order to make computational models feasible for applications, we summarize our smeared methodology for modelling physical fields, so called composite smeared finite element (CSFE) for electrophysiology simulations [6]. In order to calculate calcium current and concentration within the cell, we coupled CSFE and OHara-Rudy (oRD) membrane model [7], a human ventricular action potential (AP) model formulated using undiseased human ventricular data which provide accurate ventricular myocyte electrophysiology and Ca^{2+} cycling validated over the entire range of physiological frequencies. Electrophysiology module is than coupled with muscle mechanics with widely used relation for heart muscle that connects calcium concentration and active stress along fibers [8].
Some of the results for coupled electro-mechanical simulation of 3D biventricular heart model with constrains in septum zone have been presented in the Figure 1. There is boundary conditions in the model (septum zone), fibers orientation from top viewpoint, fibers orientation from side viewpoint, displacements in coupled electro-mechanical model of biventricular heart for first cycle of electrical signal propagation.

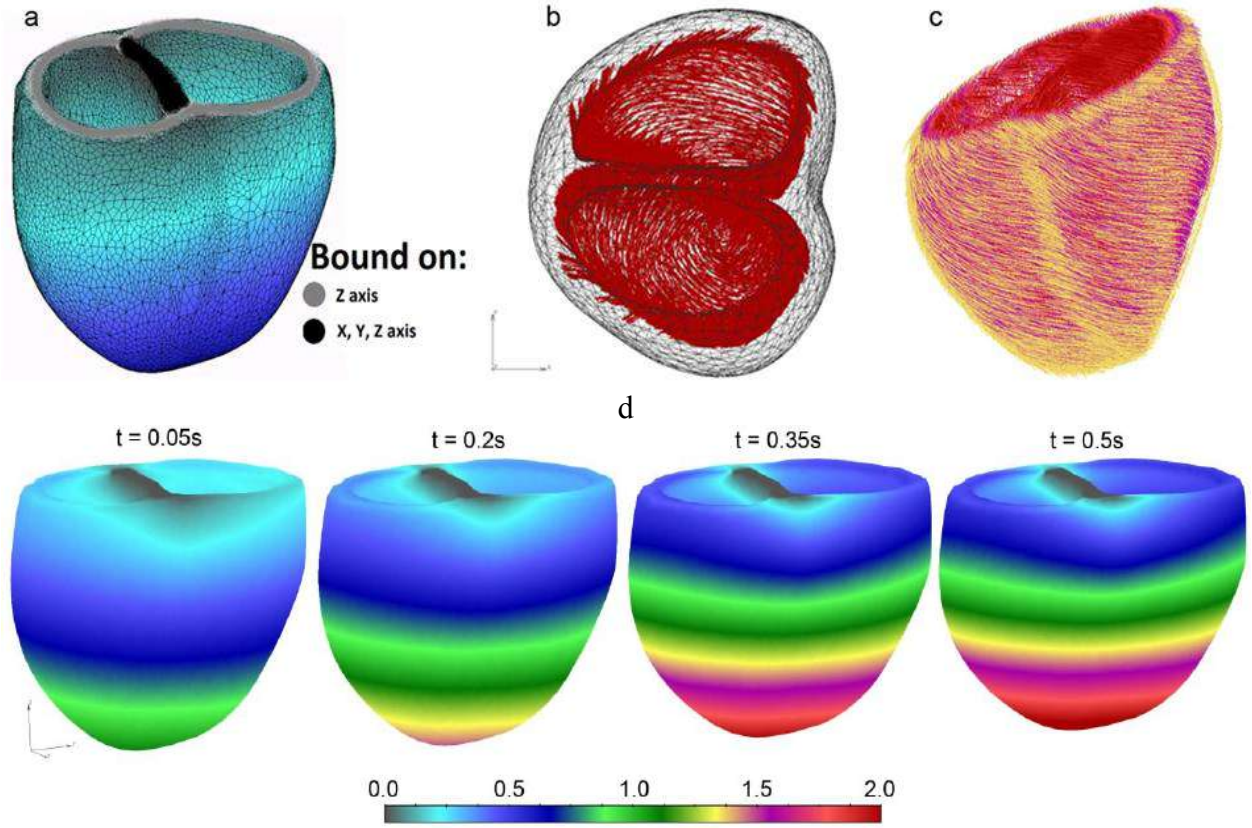

Figure 1. 3D biventricular heart model with constrains in the septum zone. a) Boundary conditions in the model (septum zone), b) Fibers orientation from top viewpoint; c) Fibers orientation from side viewpoint; d) Displacements in coupled electro-mechanical model of biventricular heart for first cycle of electrical signal propagation.

CONCLUSIONS

Coupled electro-mechanical model of heart failure, cardiac arrhythmia, and cardiomyopathy can give better insight in the everyday clinical practice. We presented our methodology for modelling physical fields, with composite smeared finite element (CSFE) for complex electrophysiology simulations. The prediction of disease development and progression is from crucial interest for a new patient specific medicine.

Acknowledgement: This research is supported by the Serbian Ministry of Education, Science and Technological Development (grant agreements III41007 and ON174028) and by the European Union's Horizon 2020 research and innovation programme under grant agreement No. 777204 - SILICOFCM. This article reflects only the author's view. The Commission is not responsible for any use that may be made of the information it contains.

References

[1] A.L. Hodkin, A.F. Huxley, A quantitative description of membrane current and its application to conduction and excitation in nerve, J. Physiology, 117 (1952) 500-544.
[2] D. Noble, A modification of the Hodgkin-Huxley equations applicable to Purkinje fibre action and pace-maker potentials, J. Physiolology, 160 (1962) 317-352.
[3] S.M. Baer, J. Rinzel, Propagation of Dendritic Spikes Mediated by Excitable Spines: A Continuum Theory, J. Neurophysiology, 65 (1991) 874-890.
[4] K.F. Decker, J. Heijman, J.R. Silva, T.J. Hund, Y. Rudy, Properties and ionic mechanisms of action potential adaptation, restitution, and accommodation in canine epicardium, Am J Physiol Heart Circ Physiol, 296 (2009) H1017–H1026.
[5] T. O'Hara, L. Virág, A. Varró, Y. Rudy, Simulation of the undiseased human cardiac ventricular action potential: Model formulation and experimental validation, PLoS Comput. Biol., 7 (2011) e1002061-e1002090.
[6] Milos Kojic, Smeared concept as a general methodology in finite element modeling of physical fields and mechanical problems in composite media, J. Serb. Soc. Comp. Mech., Vol 12, No.2, pp. 1-16, 2018.
[7] T. O'Hara, L. Virág, A. Varró, Y. Rudy, Simulation of the undiseased human cardiac ventricular action potential: Model formulation and experimental validation, PLoS Comput. Biol., 7 (2011)
[8] P.J. Hunter, A.D. McCulloch, H.E.D.J. ter Keurs, Modelling the mechanical properties of cardiac muscle, Progress in Biophysics & Molecular Biology 69, 289-331, 1998

RECENT RESULTS ON DROPLET TRANSMISSION IN THE UPPER AIRWAY LEADING TO SARS-COV-2 INFECTION AND AN ESTIMATION OF THE INFECTIOUS DOSE

Saikat Basu *[1, 2]

[1] Department of Mechanical Engineering, South Dakota State University, Brookings, United States

[2] Department of Otolaryngology / Head and Neck Surgery, The University of North Carolina – School of Medicine, Chapel Hill, United States

Summary How human respiratory physiology and inhaled airflow dynamics proceed to impact transmission of SARS-CoV-2, leading to the initial infection, is still an open question. An answer can help determine the susceptibility of an individual on exposure to a COVID-2019 carrier and can also quantify the still-unknown *infectious dose* for the disease. Synergizing computational fluid mechanics enabled tracking of respiratory transport in medical imaging-based anatomic domains, with sputum assessment data from hospitalized COVID-19 patients and earlier measurements of ejecta size distribution during regular speech – this study shows that the regional deposition of virus-laden inhaled droplets at the initial nasopharyngeal infection site peaks for the droplet size range of 2.5 – 19 μ and reveals that the number of virions that can establish an infection can remarkably be in the order of hundreds.

INTRODUCTION

As is well-known by now (11/2020), transmission of respiratory infections such as COVID-19 occurs through carriage of pathogens via droplets of different sizes produced during sneezing, coughing, singing, normal speech, and even, breathing [1]. Owing to perceptional ambiguities, this study does not insist on any nomenclatural distinction between "droplets" and "aerosols", and refers to all expiratory liquid-base particulates as *droplets*.

For tracking what range of droplet sizes might be more potent for transmission of SARS-CoV-2 (causative agent for COVID-19) and to eventually induce infection, it is key that we identify the initial infection sites. At least two recent studies [2, 3] reveal a striking pattern of relatively high SARS-CoV-2 infectivity in ciliated epithelial cells along the nasal passage lining in the upper airway, moderate infectivity in cells lining the throat and bronchia, and relatively low infectivity in lung cells. Such viral tropism is governed by the abundance of angiotensin-converting enzyme 2 (ACE2), a single-pass type I membrane protein that is exploited by viral spike protein binding as a gateway for cellular entry. ACE2 is abundant on ciliated epithelial cells, but is relatively scarce on the surface of lower airway cells. These findings are however for *in vitro* samples; deposition of virus-laden droplets along the anterior nasal airway might not be as effective at launching an infection despite the presence of ciliated cells, since the mucus layer provides some protection against virus

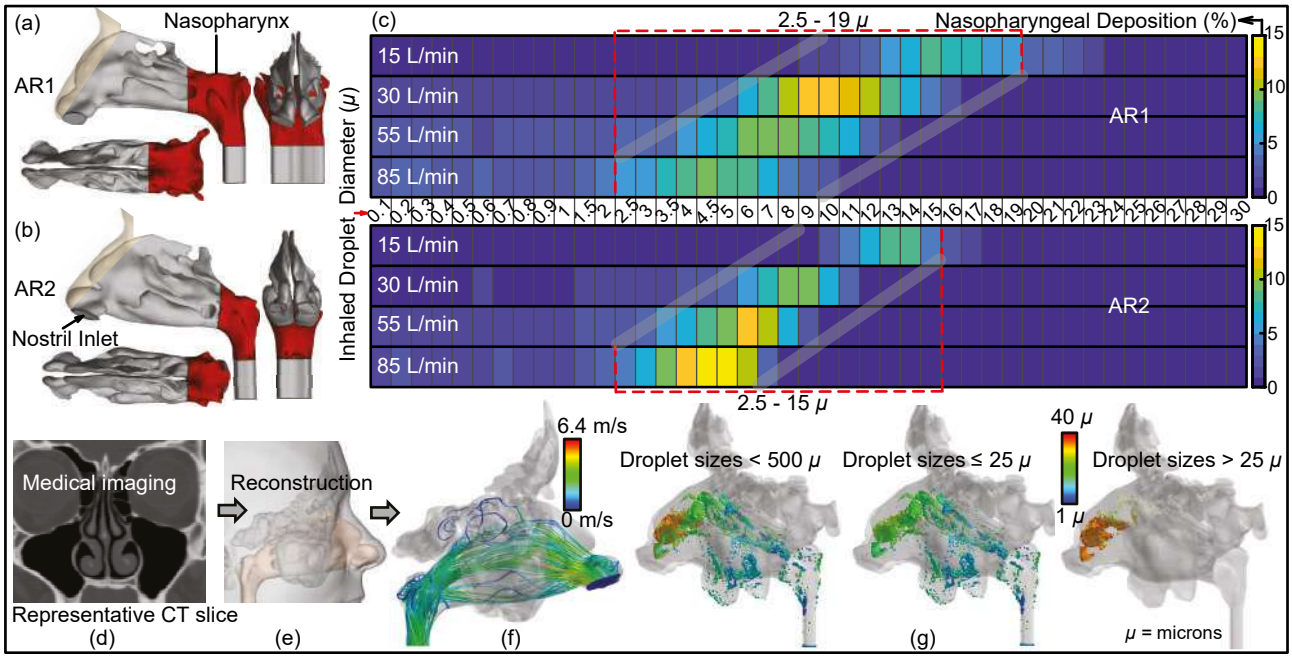

Figure 1: Panels (a)-(b) show sagittal, axial, and coronal views of the CT-based nasal domains, respectively in anatomic reconstruction 1 (AR1) and anatomic reconstruction 2 (AR2). Nasopharynx is marked in red. Panel (c) lays out the heat-maps for computational fluid dynamics (CFD) based inspiratory transmission, showing the percentage of inhaled droplets of each size undergoing nasopharyngeal deposition. Data for different breathing rates are arranged along separate rows. Tracked droplet sizes are along the horizontal axis (positioned between the two heat-maps). Nasopharyngeal landing peaks for droplets sized between 2.5 – 19 μ in AR1 and 2.5 – 15 μ in AR2. The patch bounded by the grey lines can be a definitive graphical technique to delineate the hazardous droplet sizes for various airborne transmissions. Panels (d)-(e) depict *in silico* geometry generation from medical grade scans. Panel (f) shows representative simulated streamlines during inhalation. Panel (g) characterizes intranasal regional deposition trends for sprayed droplets.

*Corresponding author. E-mail: Saikat.Basu@sdstate.edu; saikat_basu@med.unc.edu

invasion and infection. This points to the *nasopharynx* (region in the upper airway posterior to the septum and comprising the superior portion of the pharynx; see Fig. 1, Panels (a)-(b)) as the main *initial* infection site; it acts as the seeding zone for subsequent infection of the lower airway via aspiration of virus-laden nasopharyngeal fluid boluses. So at this point, a valid question to ask is: *what are the dominant inhaled droplet sizes that are making their way to the nasopharynx?*

METHODS

The study resconstructs two *in silico* anatomic geometries of the nasal airway from de-identified computed tomography (CT) scans. Use of the archived and anonymized medical records was approved with exempt status by the Institutional Review Board at the University of North Carolina. Test subjects include a 61 year-old female (subject for anatomic reconstruction 1, or AR1) and a 37 year-old female (subject for anatomic reconstruction 2, or AR2). The reconstructed geometries were meshed spatially into minute volume elements. Conforming with established mesh refinement-based protocols [4], each computational grid contained more than 4 million unstructured, graded tetrahedral elements.

Simulation of inhaled transport

Four different breathing rates were simulated, viz. 15, 30, 55, 85 L/min. The lower rate (i.e. 15 L/min) corresponds to comfortable resting breathing, and follows viscous-laminar steady-state flow physics. At higher flow rates commensurate with forceful breathing, shear layer separation from the tortuous cavity walls generates turbulence. For such flows, the study employs Large Eddy Simulations (LES), with Dynamic Kinetic Energy Subgrid-Scale Model for the small fluctuations. The numerical schemes implemented SIMPLEC pressure-velocity coupling and second-order upwind spatial discretization. On convergence of the airflow simulations, inhaled droplet dynamics were tracked (for each droplet size: 3015 droplets were tracked in AR1, 3000 in AR2) via Lagrangian-based discrete phase inert particle transport simulations.

RESULTS

Hazardous droplet sizes

Overall droplet size range of 2.5 – 19 μ registers the peak (see Fig. 1(c)) in terms of the percentage of droplets of each size that are deposited at the nasopharynx. The findings assume a post-dehydration density of 1.3 g/ml [5] for the respiratory droplets (expelled by the carrier and now being inhaled by the exposed individual). If there is little or no dehydration and as such the ejecta density remains at $\sim$1 g/ml, the hazardous size range for inhaled droplets revises to 3 – 20 μ; since the lighter droplets with lower Stokes numbers can now penetrate further into the intranasal airspace.

What could be COVID-19's infectious dose?

Infectious dose is a fundamental virological measure quantifying the number of virions that can go on to start an infection; the value of which is still not conclusively known for SARS-CoV-2, which is a single-stranded RNA virus. Sputum assessments [6] in hospitalized COVID-19 patients show an averaged viral load of 7×10^6 RNA copies/ml of oral fluid, with the peak load being 2.35×10^9 copies/ml. For the average load, probabilistic analysis shows that the chances for a dehydrated droplet of say 10-μ diameter to carry at least 1 virion is 13.6%. Subsequently, based on the new computations and the earlier reported range of droplet sizes emitted during normal speech [7], for a 5-minute exposure: the number of virions depositing at the susceptible individual's nasopharynx comes out to be 11.

To corollarily derive an *order-of-magnitude* estimate of the SARS-CoV-2 infectious dose, consider the March 2020 Skagit Valley Chorale superspreading incident, where a COVID-19 carrier infected 52 other individuals in a 61-member choir group, over an exposure time of 2.5 hours. The subjects were situated close to each other; which justifies ignoring the effect of spatial ventilation. Consequently, for an average RNA load, the number of virions depositing at a closely-positioned individual's nasopharynx in that duration approximates to $(11/5) \times 2.5 \times 60 \approx 330$. So, ~ 300 can be reckoned as a conservative upper estimate for the infective dose, the order agreeing with preliminary findings from other groups [8].

CONCLUSIONS

The quantitative estimate for the *still-elusive* infectious dose, together with this study's detection of the hazardous inhaled droplet sizes that target the infection-prone nasopharynx, can provide a key resource in COVID-19 mitigation.

Funding: This work is supported by a National Science Foundation (NSF) RAPID Grant 2028069 (PI: Basu) for COVID-19 research. Findings and opinions presented here are, however, author's and do not necessarily reflect NSF's views.

References

[1] Bourouiba L. Turbulent gas clouds and respiratory pathogen emissions: implications for COVID-19 transmission. *JAMA* **323**: 1837-1838, 2020.
[2] Hou Y. J. et al. SARS-CoV-2 reverse genetics reveals a variable infection gradient in the respiratory tract. *Cell* **182**: 429-446, 2020.
[3] Matheson N. J., Lehner P. J. How does SARS-CoV-2 cause COVID-19? *Science* **369**: 510-511, 2020.
[4] Basu S. et al. Numerical evaluation of spray position for improved nasal drug delivery. *Scientific Reports* **10**: 1-18, 2020.
[5] Stadnytskyi V. et al. The airborne lifetime of small speech droplets and their potential importance in SARS-CoV-2 transmission. *Proceedings of the National Academy of Sciences* **117**: 11875-11877, 2020.
[6] Wölfel R. et al. Virological assessment of hospitalized patients with COVID-2019. *Nature* **581**: 465-469, 2020.
[7] Xie X. et al. How far droplets can move in indoor environments – revisiting the Wells evaporation-falling curve. *Indoor Air* **17**: 211-225, 2007.
[8] Geddes L. Does a high viral load or infectious dose make COVID-19 worse? *New Scientist* **27**, 2020.

WALL-ATTACHED STRUCTURES IN AN ADVERSE PRESSURE GRADIENT TBL

Hyung Jin Sung*[1]
[1] Department of Mechanical Engineering, KAIST, Daejeon 34141, Korea

Summary The three-dimensional clusters of the streamwise velocity fluctuations (u) in turbulent boundary layers (TBLs) are explored from the perspective of the attached-eddy model. We extract the u clusters from the direct numerical simulation data of TBLs subjected to adverse pressure gradient ($\beta = 1.43$). The identified structures are decomposed into attached self-similar, attached non-self-similar, detached self-similar and detached non-self-similar motions with respect to the minimum distance from the wall (y_{min}) and the height (l_y) based on Townsend's attached-eddy hypothesis. The attached structures ($y_{min} \approx 0$) are self-similar and universal in the logarithmic region. The tall attached structures with $l_y = O(\delta)$ are non-self-similar and extended beyond 6δ in the streamwise direction, reminiscent of very-large-scale motions or superstructures.

INTRODUCTION

Townsend (1976) deduced that the energy-containing motions in the logarithmic region of wall-bounded turbulent flows can be understood as a linear superposition of self-similar eddies that are attached to the wall. The sizes of each eddy are proportional to the distance from the wall (y). Townsend's attached-eddy hypothesis predicts the turbulence statistics of the logarithmic region in terms of such structures, i.e., the logarithmic variation in the wall-parallel components of the Reynolds stresses. A typical feature of turbulent boundary layers (TBLs) subjected to adverse pressure gradients (APGs) is the enhancement in the large-scale energy above the logarithmic region. A strong outer peak is observed in the streamwise Reynolds stress, which results from long-wavelength motions in the energy spectra. The large-scale motions (LSMs) with sizes of $O(\delta)$ in the logarithmic region, where δ is the 99% boundary layer thickness, influence the small-scale motions through amplitude modulation and their footprints extend into the near-wall region. Recently, Hwang & Sung (2018) reported that the wall-attached structures of the streamwise velocity fluctuations (u) are self-similar and contribute to the presence of the logarithmic layer in a zero pressure gradient (ZPG) TBL. Therefore, research is required into the application of Townsend's attached-eddy hypothesis to APG TBLs, particularly through analysis of the wall-attached u structures in order to predict the influence on the turbulence statistics of strengthened LSMs. Although many studies of the turbulence statistics of APG TBLs have been performed, sufficient attention has not been paid to wall-attached structures despite their importance.

RESULTS

Identification of wall-attached structures

The coherent structures of u are defined as groups of connected points of $u(\mathbf{x}, t) > \alpha u_{rms}(y)$ and $u(\mathbf{x}, t) < -\alpha u_{rms}(y)$ in instantaneous flow fields, where α is the threshold and u_{rms} is the root mean square of u as a function of y. The percolation diagram for the identified u clusters enables the choice of α (not shown here). The percolation theory describes the statistics of the contiguous nodes in a randomly distributed system. In the present study, we select $\alpha = 1.5$ based on the percolation transition. To detect each u cluster, we use the connectivity of neighboring six-orthogonal grids at a given node in Cartesian coordinates (Moisy & Jiménez 2004). Figure 1(a) shows the number of u clusters per unit wall-parallel area as a function of y_{min} and y_{max}, which are the minimum and maximum distances from the wall. The u structures are divided into two groups: those are observed at $y_{min}^+ \approx 0$ and $y_{min}^+ > 0$, i.e. the wall-attached and wall-detached structures, respectively. Figure 1(b) shows iso-surface of u in an instantaneous flow field of the APG TBL. Two insets show a sample of the attached and detached u structures, respectively. The length scales of an individual cluster are defined as the dimensions of the box circumscribing the object, i.e., l_x, l_y and l_z are its streamwise, wall-normal and spanwise lengths, respectively. The wall-normal height (l_y) of clusters is defined as $l_y = y_{max} - y_{min}$.

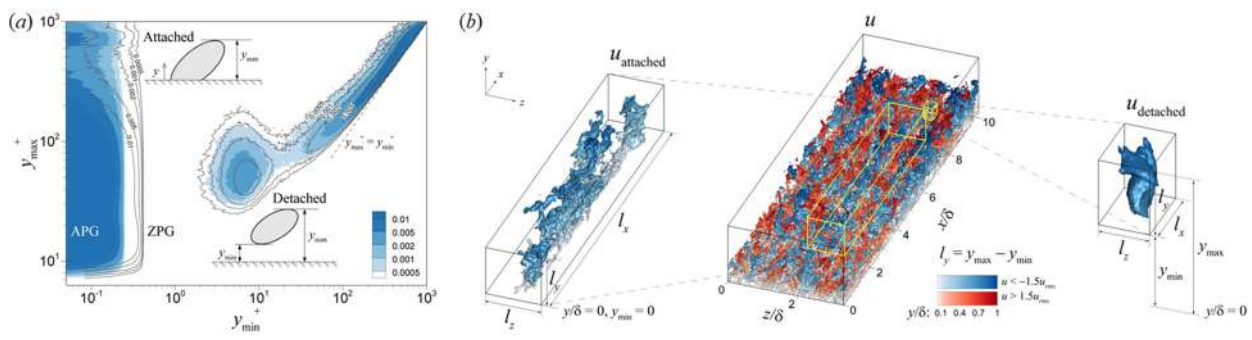

Figure 1. (a) The number of u clusters per unit wall-parallel area with respect to y_{min} and y_{max}. (b) 3D iso-surfaces of u in the APG TBL. Two insets show a sample of the attached and detached u structures, respectively.

*Corresponding author. E-mail: hjsung@kaist.ac.kr

attached structures

e examine the population density ($n_{attached}^*$) of attached u structures with respect to l_y. Here, $n_{attached}^*$ is defined as mber of attached u structures ($n_{attached}$) per unit wall-parallel area with respect to l_y. Figure 2(a) shows the utions of $n_{attached}^*$. There is a region for which $n_{attached}^*$ is inversely proportional to l_y, reminiscent of the hierarchical -scale distribution of attached eddies (Perry & Chong 1982). Beyond the upper limit of the inverse power-law ($l_y/\delta > 0.6$), $n_{attached}^*$ increases and a peak is observed at $l_y/\delta = 0.92$ ($l_y^+ = 710$). This behavior indicates the relative ance of tall attached structures with size δ, which is equivalent to the weighting for the large scales to satisfy the ty-defect law and the presence of low-wavenumber peak in the energy spectra in the model (Perry *et al*. 1986). We compose wall-attached structures into two types based on the height of the attached u structures: i.e., type A ($100 < l_y^+ < 0.6\delta^+$) and type B ($l_y/\delta > 0.6$). Figure 2($b$) shows the joint PDFs of l_x and l_z of the wall-attached u structures with t to l_y. The mean l_x of the type A structures ($100 < l_y^+ < 0.6\delta^+$) scales with l_y, following the power law $l_x \sim l_y^{0.74}$ w solid line). Above $l_y^+ > 0.6\delta^+$, the mean l_x rapidly increases and exhibits a constant value $l_x^+ \approx 3.5\delta^+$ for $l_y^+ > \delta^+$ horizontal line), which indicates that very tall structures (i.e., type B) are non-self-similar ($O(3-6\delta)$).

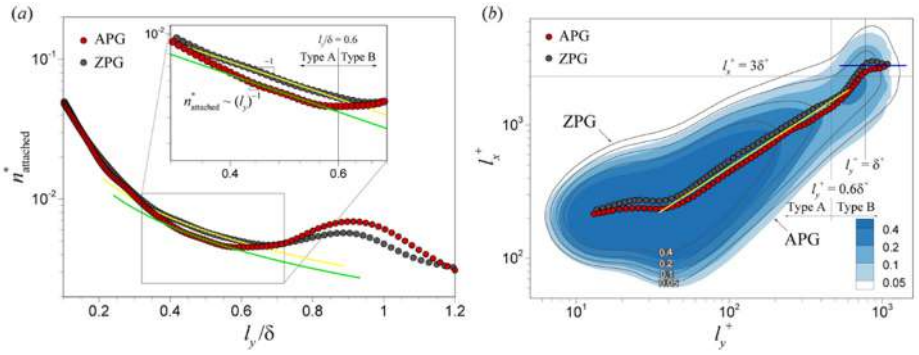

2. (a) The variation in $n_{attached}^*$ with l_y/δ. The inset shows an enlarged view of the region $l_y/\delta = 0.32-0.72$. (b) Joint PDFs of l_x and l_y. Circles indicate mean lengths. The yellow line in (b) represents $l_x \sim l_y^{0.74}$.

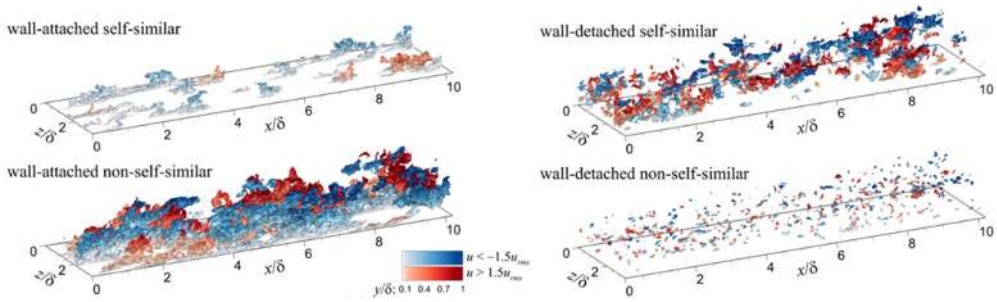

Figure 3. 3D iso-surfaces of the u clusters for the APG TBL

CONCLUSIONS

coherent u clusters have been explored from the perspective of the attached-eddy model. We extract the u clusters by he connectivity of six-orthogonal neighbors in Cartesian coordinates without any assumptions from DNS datasets for $\beta = 1.43$) and ZPG ($\beta = 0$) TBLs with $Re_\tau \approx 800$. The identified structures can be decomposed into attached self-similar, ed non-self-similar, detached self-similar and detached non-self-similar structures with respect to y_{min} and l_y (figure 3). zes of the attached self-similar structures ($100 < l_y^+ < 0.6\delta^+$) scale with l_y, and their population density is inversely tional to l_y in the region $l_y/\delta = 0.4-0.58$. They contribute to the logarithmic variation in the streamwise Reynolds stress the presence of the k_z^{-1} region in the pre-multiplied energy spectra of u. The attached self-similar structures are universal otions in the logarithmic region that are not dependent on the pressure gradient. The attached non-self-similar structures 0.6) are responsible for the enhanced large scales in the outer region in the presence of the APG. Their streamwise sizes $3-6\delta$), and some of them extend over 6δ in the streamwise direction and penetrate deeply into the near-wall region, scent of very-large-scale motions. In addition, wall-detached structures are also decomposed into self-similar and non-nilar ones. We establish new insights into coherent structures in TBLs and the development of the attached-eddy model.

ences

wnsend A. A. The Structures of Turbulent Shear Flow. Cambridge University Press, UK 1976.
vang J., Sung. H. J. Wall-Attached Structures of Velocity Fluctuations in a Turbulent Boundary Layer. *J. Fluid Mech.* **856**: 958–983, 2018.
oisy F., Jiménez J. Geometry and Clustering of Intense Structures in Isotropic Turbulence. *J. Fluid Mech.* **513**: 111–133, 2004.
rry A. E., Chong M. S. On the Mechanism of Wall Turbulence. *J. Fluid Mech.* **119**: 173–217, 1982.
rry A. E., Henbest S., Chong M. S. A Theoretical and Experimental Study of Wall Turbulence. *J. Fluid Mech.* **165**: 163–199, 1986.

EFFECT OF THE PRESSURE GRADIENT ON NEAR-WALL TURBULENT FLOW AND ITS CONSEQUENCES FOR THE BOUNDARY LAYER AND FOR PERTURBED FLOW OVER UNEVEN TERRAIN

Paolo Luchini *[1]
[1] Department of Industrial Engineering, Università di Salerno, Fisciano, Italy

Summary Our recent results have shown that long-claimed discrepancies between different (Couette versus Poiseuille, or plane versus cylindrical) geometries can be resolved when the velocity profile is suitably interpreted as the superposition of a universal law of the wall common to all geometries and a pressure-gradient depending law of the wake, the latter having a different shape for parallel flow than the one introduced by Coles for the boundary layer. A surprising consequence of these results is that the effect of pressure gradient upon a turbulent velocity profile is opposite in sign to its effect upon a laminar velocity profile. This observation offers an explanation for a) failed past attempts to include the effect of pressure gradient in turbulence models of a boundary layer, and b) the peculiar long-wave behaviour of perturbed flow over uneven terrain.

LAW OF THE WALL AND LAW OF THE WAKE

Despite its widespread adoption in research and in teaching, the classical scaling theory of the logarithmic velocity profile based after Prandtl, von Kármán and Millikan on the distinction between a wall layer and a defect layer, and particularly its universality, has been challenged by multiple discrepancies between this theory and both experiments and numerical simulations. Serious doubts were issued in the literature about the precise form of this law, leading to the formulation of alternate theories and hindering ongoing efforts to measure von Kármán's constant κ. Even among scientists who accept the validity of the logarithmic law

$$u^+ = A \log z^+ + B \tag{1}$$

(where $u^+ = u/u_\tau$, $z^+ = z u_\tau/\nu$, and $u_\tau = \sqrt{\tau_{\text{wall}}/\rho}$), many have surmised that either the additive factor B [1] or both $A = \kappa^{-1}$ and B [2] are not universal and change from one geometry to another.

The formulation of this theory introduced by Coles [3] takes the form of a pair of matched asymptotic expansions (incidentally providing a framework for the inclusion of higher-order terms), the leading order of which describes the mean velocity profile through two functions of one variable, traditionally named law of the wall and law of the wake:

$$u^+ = f(z^+) + G(Z) \tag{2}$$

($Z = z/h = z^+/Re_\tau$ being the normal coordinate in outer units, with h denoting the half-height of the duct and $Re_\tau = u_\tau h/\nu$ the shear-based Reynolds number). Coles proposed that not only the law of the wall $f(z^+)$ but also the law of the wake $G(Z)$ have a universal form, and proposed for the latter an S-shaped curve similar to the mixing layer of a wake, whence its name. It should be noted that the universality of $f(z^+)$ is rooted in theory, whereas the universality of $G(Z)$ is (and was presented as) an empirical observation useful to simplify boundary-layer calculations.

The connection between (1) and (2) is in that the logarithmic law (1) appears as the asymptotic form of $f(z^+)$ for $z^+ \to \infty$; nevertheless it should be clear when trying to extract the log law from (2) that also the behaviour of $G(Z)$ for

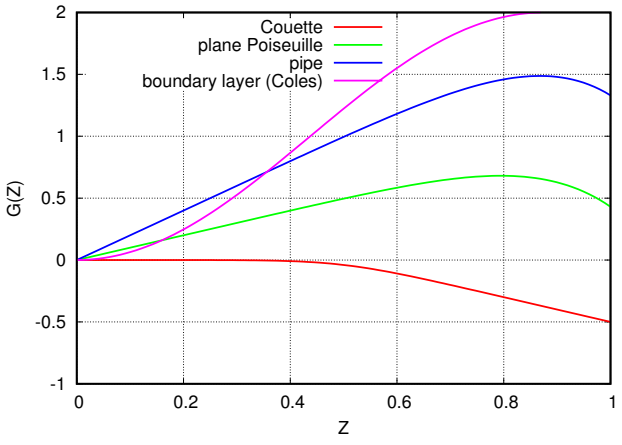

Figure 1: Wake functions of different geometries as extracted in [4].

*Corresponding author. E-mail: luchini@unisa.it.

$Z \to 0$ contributes to the velocity profile in the overlap layer $1 \ll z^+ \ll Re_\tau$. After devising an analytical method to separate $f(z^+)$ from $G(Z)$ by combining velocity profiles obtained in the same geometry at different Reynolds numbers [4], we could show that the law of the wall and the log law are indeed universal (with the same values of both κ and B) across plane Couette and Poiseuille flow and cylindrical pipe flow, but the law of the wake is different in each, and also different from the one determined by Coles for a boundary layer, in the way exhibited in figure 1 (taken from [5]).

In addition, the small-Z behaviour of $G(Z)$ is *linear* and proportional to the pressure gradient, as predicted in [6]:

$$u^+ = \underbrace{\kappa^{-1}\log(z^+) + B}_{f(z^+)} + \underbrace{A_1 g Z}_{G(Z)} \tag{3}$$

with $\kappa = 0.392$, $B = 4.48$, $A_1 = 1$, and $g = -p_x h/\tau_{\text{wall}}$ ($g = 0$ for Couette, 1 for plane Poiseuille, 2 for pipe flow).

THE OPPOSITE EFFECT OF PRESSURE GRADIENT IN LAMINAR AND IN TURBULENT FLOW

According to the above explanation, and also according to direct observation, the effect of pressure gradient pushes the velocity profile of turbulent plane Poiseuille flow upwards and *above* the velocity profile of turbulent plane Couette flow for the same wall shear stress (what you see when plotting both in wall units u^+ vs. z^+). This turbulent behaviour is strikingly opposite to laminar behaviour, where in wall units the velocity profile of Poiseuille flow is everywhere *below* Couette flow, as depicted in Figure 2 taken from [7] for an arbitrarily chosen Reynolds number $Re_\tau = 1000$.

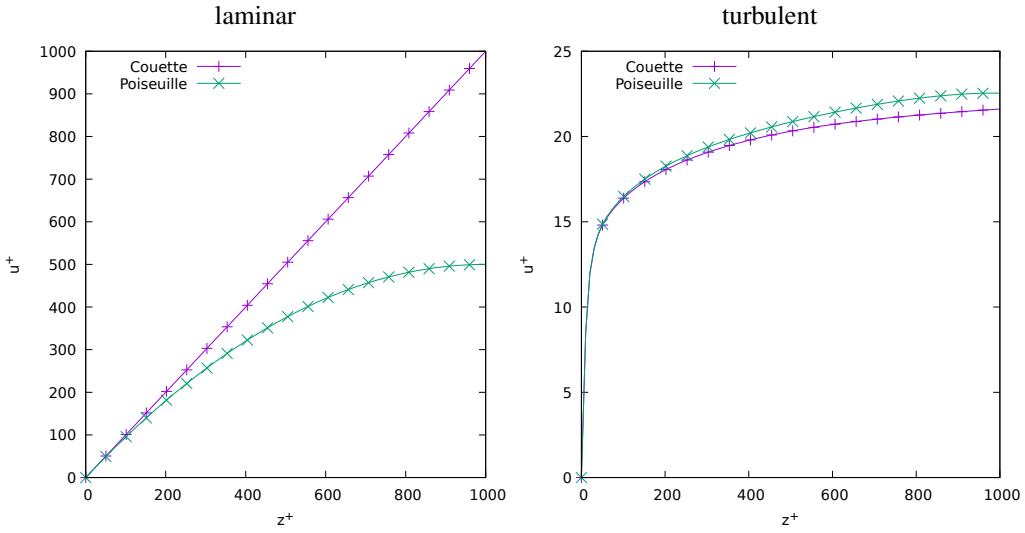

Figure 2: Couette and Poiseuille velocity profiles are oppositely situated in laminar and in turbulent flow.

This opposite effect explains why Johnstone *et al.* [8] found it inappropriate to model the action of pressure gradient upon the turbulent boundary layer as a change of the shear velocity from $u_\tau = \sqrt{\tau_{\text{wall}}/\rho}$ to $u_\tau = \sqrt{\tau(z)/\rho}$, which is in practice equivalent to adopting an eddy viscosity and predicts an effect of the pressure gradient of the same sign as laminar viscosity.

The phenomenon described in [7] is just as well consistent with the peculiar behaviour of perturbed flow over uneven terrain [9] in the large-wavelength regime, which again defeats description through an equivalent viscosity because the sign of the turbulent perturbation is opposite to laminar [10].

References

[1] Marusic I., McKeon B.J., Monkewitz P.A., Nagib H.M., Smits A.J., Sreenivasan K.R. Wall-bounded turbulent flows at high Reynolds numbers: Recent advances and key issues. *Phys. Fluids* **22**: 065103, 2010.
[2] Nagib H.M., Chauhan K.A. Variations of von Kármán coefficient in canonical flows. *Phys. Fluids* **20**: 101518, 2008.
[3] Coles D. The law of the wake in the turbulent boundary layer. *J. Fluid Mech.* **1**: 191–226, 1956.
[4] Luchini P. Structure and interpolation of the turbulent velocity profile in parallel flow. *Eur. J. Mech. B/Fluids* **71**: 15–34, 2018.
[5] Luchini P. Law of the Wall and Law of the Wake in Turbulent Parallel Flow. In: Örlü R., Talamelli A., Peinke J., Oberlack M. (eds) Progress in Turbulence VIII. iTi 2018. Springer Proceedings in Physics, vol 226. Springer, Cham, 2019.
[6] Luchini P. Universality of the turbulent velocity profile. *Phys. Rev. Lett.* **118**: 224501, 2017.
[7] Luchini P. An elementary example of contrasting laminar and turbulent flow physics. arXiv:1811.11877, 2018.
[8] Johnstone R., Coleman G.N., Spalart P.R. The resilience of the logarithmic law to pressure gradients: evidence from direct numerical simulation. *J. Fluid Mech.* **643**: 163–175, 2010.
[9] Luchini P., Charru, F. On the large difference between Benjamin2019s and Hanratty2019s formulations of perturbed flow over uneven terrain. *J. Fluid Mech.* **871**: 534–561, 2019.
[10] Luchini P. Immersed-boundary simulations of turbulent flow past a sinusoidally undulated river bottom. *Eur. J. Mech. B/Fluids* **55**: 340–347, 2016.

VERIFICATION AND CHARACTERIZATION OF PREDOMINANT INSTABILITIES OF SWEPT-WING BOUNDARY LAYERS

Y.S. Kachanov *[1], V.I. Borodulin[1], A.V. Ivanov[1], D.A. Mischenko[1], R. Örlü[2], A. Hanifi[2], and S. Hein[3]
[1] Khristianovich Institute of Theoretical and Applied Mechanics, SB RAS, Novosibirsk, Russia
[2] Department of Engineering Mechanics, KTH Royal Institute of Technology, Stockholm, Sweden
[3] Institute of Aerodynamics and Flow Technology, DLR, Göttingen, Germany

Summary The problem of identification and verification of the most important linear stability mechanisms of initial stages of laminar-turbulent transition in three-dimensional (3D) swept-wing boundary layers is discussed based on experimental and theoretical investigations performed, in particular, for real swept airfoil sections. Detailed analysis of all main boundary-layer stability characteristics with respect to the cross-flow (CF) instability modes and 3D Tollmien-Schlichting (TS) instability modes is carried out based on experimental data, as well as on computations within the framework of linear stability theories and the Parabolized Stability Equation (PSE) approach. The possibility of a very good agreement between all main measured and calculated stability characteristics is shown. Role of surface curvature and base-flow non-parallelism is discussed.

INTRODUCTION

Laminar-turbulent transition in 3D boundary-layer flows is of great scientific interest and significant importance for a wide range of technical applications. Its importance for aeronautical application has increased with the need for low-emission aircraft.

In general, there are several flow instability mechanisms which trigger transition in the swept-wing boundary layers, each having their own characteristics as well as sources of the disturbance excitation. The most significant of these instability mechanisms are: (*a*) the attachment-line instability, (*b*) the stationary and non-stationary cross-flow (CF) instability, (*c*) the Tollmien-Schlichting (TS) instability, and (*d*) the instability of separated shear layers that is important in presence of laminar separation zones.

The relative contribution of these modes to the transition process depends on the pressure gradient and the sweep angle. For instance, in case of a favorable, i.e., negative, streamwise pressure gradient (such as on the upper side of a long-laminar-run swept wing installed at a small positive or negative angle of attack) and a sufficiently large sweep angle, one may expect predominance of the stationary and/or traveling CF-instability modes inducing very specific transition scenarios. Meanwhile, in the case of nearly zero chordwise pressure gradients or weak adverse ones, the 3D TS-instability waves may prevail. Although the CF-mode instability of swept-wing boundary layers has been studied intensively for many years, the detailed qualitative agreement between all measured and calculated linear stability characteristics has not been obtained previously for real nonparallel boundary layers developing on curved surfaces of real swept airfoils. This is especially true for non-stationary CF-instability modes. For the 3D TS-instability characteristics of swept-wing boundary layers, the investigations are even rarer. This can be explained by the extreme complexity of accurate quantitative experimental investigations of these problems.

The present paper is devoted to description of the significant advancements in the described field achieved recently. These advancements are related to the CF- and TS-instability mechanisms.

EXPERIMENTAL AND THEORETICAL APPROACHES

The presentation starts with analysis of the problem and with description of recent steps directed towards its solution. In particular the present experimental approach is described. This approach is based on performing measurements in 3D boundary layers developing over a swept airfoil section equipped with specially designed contoured sidewalls helping to provide satisfaction of the sweep condition inherent for an infinite-span wing. In one of studies (called study '*A*'), an adverse chordwise pressure gradient was achieved at a negative angle of attack of the airfoil section. This gradient provided conditions favorable for predominance of the CF-instability mechanism. In another experiment (called study '*B*'), achieved at a positive angle of attack, the chordwise pressure gradient was very weak (close to zero one). The TS-instability mechanism was expected to be predominant in this case. The airfoil section was the same in the two studied cases, while the shapes of the sidewalls were different. The experiments were performed in Stockholm in the low-turbulence wind tunnel MTL of the Royal Institute of Technology (KTH).

All measurements were carried out at fully controlled disturbance conditions with excitation of either several oblique CF- or TS-modes of the frequency-spanwise-wavenumber spectrum or, alternatively, with excitation of spanwise-localized time-periodic wave trains of CF- or TS-instability modes. The excitation was carried out by specially designed disturbance sources representing either spanwise periodic or spanwise localized surface vibrators. The calculations consisted of two important steps: (*i*) the base-flow computations simulating the experimental conditions and (*ii*) the flow instability computations based on either locally-parallel linear stability theory or on the Parabolized Stability Equation (PSE) approach which took into account both the base-flow non-parallelism and the surface curvature. All main measurements were carried out by means of hot-wire anemometry, including two-component ones.

*Corresponding author. E-mail: kachanov@itam.nsc.ru .

SOME IMPORTANT RESULTS

The experiments have shown that almost all stability characteristics of instability modes, dominated in the boundary layer in cases '*A*' and '*B*', are dramatically different from each other. In particular, this is observed for dependences of amplification rates of modes of the frequency-wavenumber spectrum on the wave propagation angle θ* (Figure 1). The same is true for the spanwise-wavenumber distributions of the instability-mode phase velocities C^*_x calculated in the direction of the potential flow velocity vector at the boundary-layer edge (Figure 2).

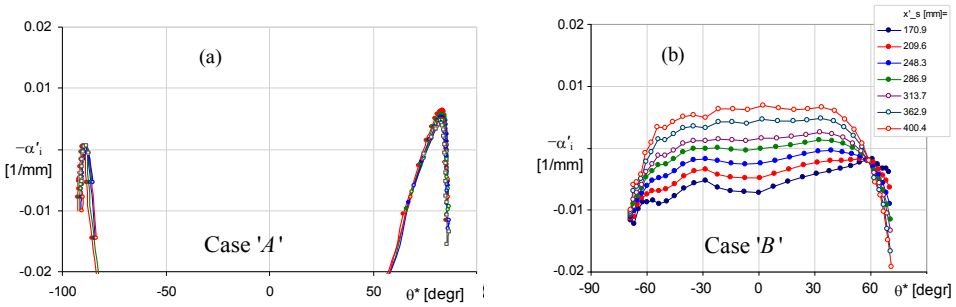

Figure 1. Radical difference of angular dependences of amplification rates of instability modes obtained in experiments '*A*' (*f* = 40 Hz, plot *a*) and '*B*' (*f* = 156 Hz, plot *b*).

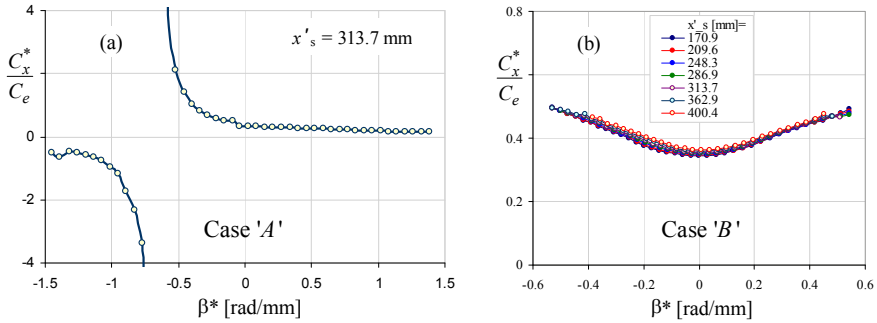

Figure 2. Radical difference of spanwise-wavenumber dependences of phase velocities of instability modes obtained in experiments '*A*' (*f* = 40 Hz, plot *a*) and '*B*' (*f* = 156 Hz, plot *b*).

Comparison of the measured and calculated stability characteristics has shown that in case '*A*' the CF-instability modes are predominant in the flow (see e.g. Figure 3), while in case '*B*' the TS-instability modes dominate.

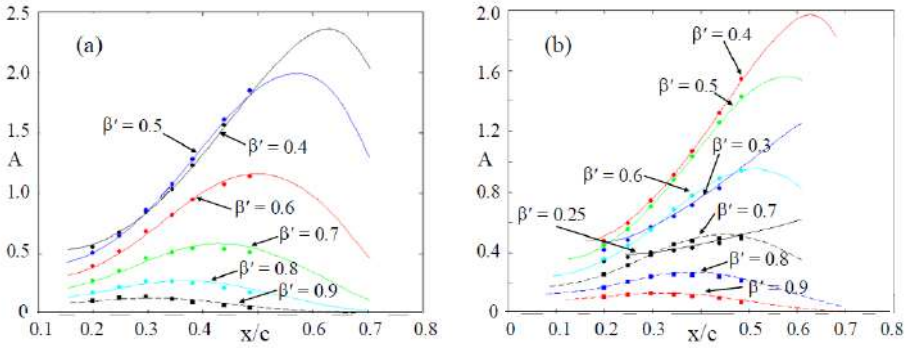

Figure 3. Comparison of measured amplification curves of boundary-layer disturbances, obtained in case '*A*' for frequencies *f* = 60 Hz (*a*) and 40 Hz (*b*), with those calculated for the CF-instability waves.

CONCLUSIONS

The present study resulted in clear identification of two types of the 3D boundary layer instability observed on a swept-wing model at two different angles of attack: (*i*) the CF-modes in case '*A*' and (*ii*) the TS-modes in case '*B*'. Their characteristics have been studied in detail and compared with each other. Very good agreement between all measured and calculated stability characteristics has been achieved, especially when the effects of the base-flow non-parallelism and the surface curvature were taken into account (in the framework of the PSE approach).

This work was supported by the European Commission through FP7 project RECEPT (grant agreement no. ACPO-GA-2010-265094) and by the Program of Fundamental Scientific Research of the Russian state academies of sciences in 2013-2020 (project No. AAAA-A17-117030610128-8).

INTERACTIONS OF WING TIP VORTEX AND DBD PLASMA ACTUATOR INDUCED FLOWS AND THEIR EFFECT ON THE AERODYNAMIC CHARACTERISTICS

Kozo Fujii *[1], Takumi Abe[1], Takuto Ogawa[1] and Makoto Yamamoto[1]
[1] Faculty of Engineering, Tokyo University of Science, Tokyo Japan

Summary Large eddy simulations (LES) for the flows over a rectangular wing with and without flow control by a dielectric barrier discharge plasma actuator (DBD-PA) are conducted. The DBD-PA is installed near the leading edge and burst mode actuation is applied. Wing tip effect on the flow control authority of the DBD-PA is investigated and efficient electrode length is discussed. The effect is evaluated based on the aerodynamic characteristics of the wing and analysis of the flow structure behind them. The authority of DBD-PA for a two-dimensional airfoil is confirmed to be effective for the low-aspect-ratio wing with the tip especially at post-stall conditions. Effective length of the electrode turns out to be different for the angles of attack higher and below the stall due to the complex interaction of tip vortex, location of the electrode edge and two-dimensional vortices induced by DBD-PA.

Introductions

Control of flow separation over an airfoil has great interest as flow separation is a critical phenomenon for aircraft. DBD-PA which comprises two thin electrodes with a dielectric between them have been shown to be very effective for the control of flow separations over an airfoil [1]. DBD-PA is easily attached to the airfoil or wing surface as shown in Fig. 1. DBD-PA induces weak jet flows (with the maximum speed of a few meters/second in general) in a small region near the wing surface when high alternating current (AC) voltage is imposed. Better control of separated flows was shown when duty cycle is applied (called burst mode) due to the interaction of two-dimensional vortices induced by DBD-PA and separated shear layers. Both the experimental and computational analysis showed that DBD-PA is very effective for flow separation control at the Reynolds numbers of the order 10^4-10^5 [2-6], which is the range of small UAV or recent drone flight. DBD-PA was also shown to be effective for improving aerodynamic characteristics at lower angles of attack [5]. Interestingly, DBD-PA in the burst mode promote transition to turbulent flows at above the stall angle, but delay transition at below the stall angle if proper actuation is used. When applying DBD-PA for better control of aircraft motion, it is necessary to confirm our knowledge for two-dimensional airfoils is applicable since there occurs interaction of wing tip vortices with the induced flows by DBD-PA, which may influence to the aerodynamic characteristics of the wing. The effect of the electrode length and its edge should also be evaluated. The objective of the present study is to find out how flow control authority is influenced by the wing tip. Physical phenomenon behind it is also discussed for better design of DBD-PA.

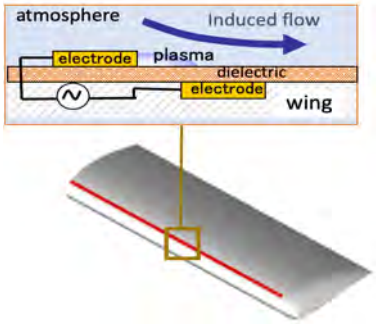

Fig.1 DBD-PA attached to a 3-D wing

Computational model and numerical approach

High fidelity implicit large eddy simulation (iLES) simulations for the flows over a rectangular wing having NACA0015 chordwise section of aspect ratio 2.0 with DBD-PA on and off are conducted under pre- and post-stall flow conditions. The Reynolds number is set to 63,000 ($c = 0.1$ [m] and $u_\infty = 10$ [m/s]), and the angles of attack are set to be 10, 12 and 14 degrees. Electrode of DBD-PA is attached from the root of the wing to 70%, 80%, 90% and 100% span location. An angle of attack of 14 degrees is the case above stall angle, 12 degrees just above stall, 10 degrees just below stall without DBD-PA. Three-dimensional compressible Navier-Stokes equations are solved with an iLES with a sixth-order compact differencing scheme for spatial discretization [2,3]. The body force terms of the DBDPA in the governing equations are those by the unsteady extension of the Suzen and Huang's model, which was validated in the previous studies [4,5]. The overset zonal method is adopted, and the total number of grid points is approximately 300 million. The former studies in the author's group showed the present grid system resolves a near-wall turbulence. The burst mode DBD-PA actuation with non-dimensional frequency of $F^+ = 6.0$ is used with the burst ratio BR to be 0.1. The DBD-PA is installed at 5% chord from the leading edge. Details of the numerical algorithm and the model of the DBD plasma actuator used here can be found in Ref. 6 and will be presented in the final manuscript.

Results and Discussions

Only the limited results are shown in this abstract. Figure 2 shows the spanwise lift-to-drag ratio (L/D) distributions for four different electrode length at angle of attack 14 degrees. Flow becomes totally separated without DBD-PA at this angle of attack. Remarkable increase of L/D is obtained for any case of DBD-PA/ON. If the electrode (therefore, DBD-PA induced flows) covers more than 80% of the span, L/D distributions do not show much difference. The L/D decreased

*Corresponding author. E-mail: fujii@rs.tus.ac.jp

toward the tip. There observed is strange reduction of L/D from 50% to 80% span region for the 70% span electrode. Figure 3 shows the top view of the flow structures over the upper surface of the wing at three different angles of attack for 90% span electrode. At α=14 degrees, two-dimensional spanwise vortices created by the DBD-PA promote turbulent transition and flow becomes attached except a small delay near the wing tip. Although not shown, surface Cp distributions and other information showed that DBD-PA recovers high suction peak near the leading edge by making the separation shear layer attached. Recovery of the suction peak increases the lift and early reattachment of the laminar separation bubble reduced the drag. Near the tip, effective angle of attack becomes lower due to the downwash of the tip vortex, and reattachment is delayed. This delay reduces the lift and increase the drag. This explains gradual decrease of L/D toward the tip, which is very different from what we expect from the typical elliptic lift loading of the square wing without PA. At α=12 and α=10 degrees, there appear two dimensional spanwise vortices in the inner part of the wing. Reference 6 showed that these stationary vortices are the key for drag reduction at angles of attack lower than the stall. At α=12 degrees which is slightly higher than the stall angle, inner part of the wing shows early transition similar to the result for α=14 degrees in Fig. 3(a). On the contrary, two-dimensional vortices stay downstream from 60% span to 90% span. Spanwise vortices covers much wider area at α=10 degrees shown in Fig. 3(c). This occurs because effective angle of attack becomes lower there by the downwash of the tip vortex. In Fig. 3(c), growth of disturbance seems to occur earlier near the tip and it gradually delayed from the tip toward the inner part of the wing. Edge of the electrode located at 90% span seems to be the reason for this region. Also, interaction with downwash of tip vortex would influence this phenomenon. Close-up view of the instantaneous flow structure of 70% span electrode is presented in Fig. 4 to explain the reason for the strange reduction of L/D from 50% to 80% span region in Fig. 2. Compared to 90% span electrode in Fig. 3(a), transition is delayed in this region. Longer laminar separation bubble exists in this region, which increase the drag in this region. Lift in this region decreases as a suction peak also reduces in this region. These explain strange reduction of L/D in this region in Fig. 2.

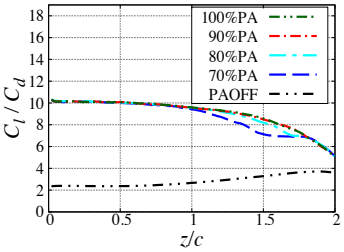

Fig.2 Spanwise *L/D* distributions for different electrode length. α= 14°

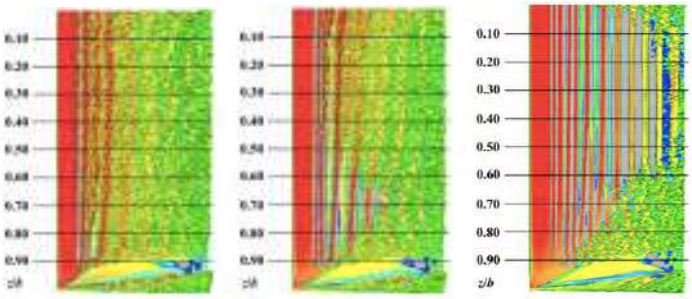

Fig.3 Instantaneous flow structures (Q-contours) at three angles of attack (90% span electrode)

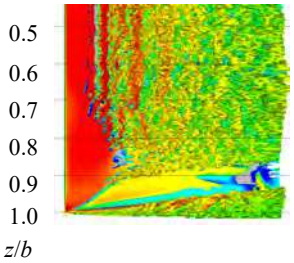

Fig.4 Close-up view of the flow structure at α=14° (70%span electrode)

Although not shown here due to the restriction of space, results for the angle of attack 10 degrees showed that DBD-PA is effective for increasing L/D at low angles of attack. Improvement of L/D for the wing remarkably reduced compared to that of two-dimensional airfoil (from L/D=22.0 to L/D=9.8) and the benefits of DBD-PA was not much. However, analysis of the flow structures indicated that reduction is mainly due to the interaction with wing tip and effect of electrode edge. Therefore, similar benefits should be obtained for a wing having larger aspect ratio.

Conclusion

Large eddy simulations (LES) for the flows over a rectangular wing with and without DBD-PA were conducted. Wing tip effect on the flow control authority of the DBD-PA was investigated and efficient electrode length was discussed. The authority of DBD-PA for two-dimensional airfoils was confirmed to be effective. Effective length of the electrode turned out to be different for angles of attack higher and below the stall due to the complex interaction of tip vortex, location of the electrode edge and two-dimensional vortices induced by DBD-PA.

Currently, additional simulations for a wing with large aspect ratio is underway. They will identify our speculative estimation for low angles of attack above to be confirmed. Also, snapshot POD and DMD analysis will be applied to the tip vortex flow field and flow region near the tip, which hopefully will separate the effect of tip vortex and the electrode edge. These will be included in the final manuscript with more precise discussion of the result shown in this abstract.

References

[1] Corke, T. C. et al., Annual Review of Fluid Mechanics, 42, 505-529 (2010).
[2] Sato M. Fujii K. et al., Physics of Fluids Vol. 27 (117101) 2015.
[3] Asada, K. and Fujii, K., Int. J. CFD, Vol. 29, pp. 215-229, 2015.
[4] Sekimoto, S. Nonomura, T. and Fujii, K., AIAA Journal, Vol. 55, No. 4, pp. 1385-1392, 2017.
[5] Fujii K., Philosophical Transactions A, The Royal Society, Vol. 372, Article ID 20130326, pp. 1471-2962, 2014.
[6] Fujii, K., Applied Science, 8 (4), 546, April 2018.
[7] Aono, H. Fujii K. et al., AIAA Journal, Vol.55, pp. 3789-3806, 2017.

EXTENDED WALL-ATTACHED STRUCTURES IN A DRAG-REDUCED FLOW

Min Yoon[1] and Hyung Jin Sung *[1]
[1] Department of Mechanical Engineering, KAIST, Daejeon 34141, Korea

Summary We define extended wall-attached structures in the vicinity of the wall ($y^+ < 100$). The three-dimensional (3-D) coherent structures of streamwise velocity fluctuations (u) in a turbulent channel flow are explored in an effort to assess the extended wall-attached u structures for drag reduction near the Navier slip wall. The mean shear carried by short wall-attached u structures is significantly reduced by the streamwise Navier slip. The number of vortical structures circumscribing the wall-attached structures remain almost unchanged, whereas their strengths are attenuated. The conditional statistics are performed to examine the extended wall-attached structures near the wall. The extended wall-attached structures play a major role in the frictional drag reduction.

INTRODUCTION

Townsend (1976) presupposed that the main energy-containing motions in the logarithmic region are self-similar with respect to their height and attached to the wall. Townsend's attached-eddy hypothesis can predict turbulence statistics through randomly superimposed attached eddies, which is rigorously applied to inviscid flow near the wall for high-Reynolds-number turbulent flow. Perry & Chong (1982) extended Townsend's attached-eddy hypothesis into the model using a hierarchy of self-similar vortex eddies, of which the population density is inversely proportional to the height. Recently, Hwang & Sung (2018) extracted wall-attached structures from the direct numerical simulation (DNS) data of a turbulent boundary layer. They reported that wall-attached u structures contribute to the presence of the logarithmic layer with the inverse power-law distribution and are physically anchored to the wall. Here, u is the streamwise velocity fluctuations. The near-wall turbulence dominantly influenced by the viscosity is closely related to the skin-friction reduction in drag-reduced flows. Hence, it is critical to explore the extended wall-attached structures near the wall ($y < 100\nu/u_\tau$) to explore the mechanism of drag reduction, where ν and u_τ are the kinematic viscosity and the friction velocity, respectively.

RESULTS

Identification of wall-attached structures

In the present study, the DNS data for turbulent channel flows ($Re_\tau \approx 550$) with the Navier and no-slip boundary conditions (Yoon *et al*. 2016) are used. The 3-D u clusters can be defined as groups of connected points satisfying $u(\mathbf{x}, t) > \alpha u_{rms}(y)$ and $u(\mathbf{x}, t) < -\alpha u_{rms}(y)$ in instantaneous flow fields. Here, α is the threshold, which is selected from the percolation diagram. Figure 1(a) represents the percolation diagram for all the identified u clusters. To detect u clusters, we choose $\alpha = 1.6$. Based on this condition, each u cluster can be detected by using the connectivity of six-orthogonal grids at a given node in Cartesian coordinate. Figure 1(b) shows the population density (n^*) of all the identified u clusters as functions of y_{max} and y_{min}, which are the maximum and minimum distances from the wall, respectively. Two distinct groups are observed at $y_{min}^+ \approx 0$ and $y_{min}^+ > 0$, where we classify the former as wall-attached structures and the latter as wall-detached structures (Hwang & Sung 2018). The characteristic lengths of each object can be defined as the box sizes circumscribing that: l_x (streamwise), l_z (spanwise) and l_y (wall-normal; height).

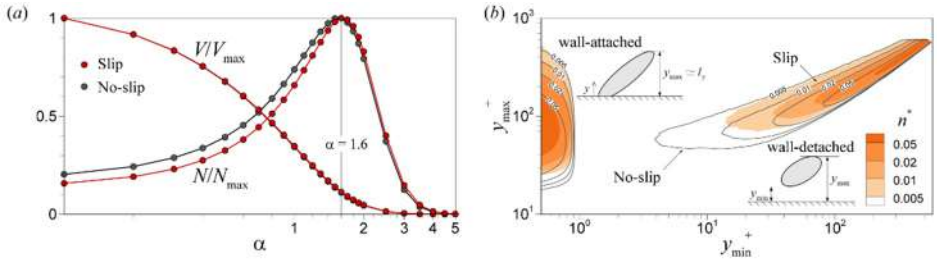

Figure 1. (a) The percolation diagram for the detected u clusters. Variations with α in the total volume (V) and total number (N) of clusters. (b) The number of u clusters per unit wall-parallel area (n^*) with respect to y_{min} and y_{max}.

Self-similarity of wall-attached structures

Figure 2(a) illustrates iso-surfaces of wall-attached structures ($u < 0$; blue, $u > 0$; red) and λ_{ci} clusters (yellow), where λ_{ci} is the swirling strength. For the slip, wall-attached structures are sparsely populated, but the numbers of the surrounding vortical structures per unit wall-attached structure remain unchanged. Figure 2(b,c) represents the joint probability density functions (PDFs) of l_x^+ and l_z^+ of wall-attached u structures with respect to l_y^+. The mean l_x^+ is proportional to l_y^+ with the power of 0.74 in the region of $l_y^+ > 100$, where the linear relationship $l_z \sim l_y$ is observed. As seen in the blue circles in figure 2(b,c), on the contrary, the mean l_x^+ and l_z^+ are not self-similar with l_y^+ in the region of $l_y^+ < 100$ and longer than

*Corresponding author. E-mail: hjsung@kaist.ac.kr

those of the no-slip, representing that the influence of the viscosity on wall-attached structures is dominant in the region of $l_y^+ < 100$ (i.e., $y^+ < 100$). The short wall-attached structures ($l_y^+ < 100$) are called the *extended* wall-attached structures in the present study.

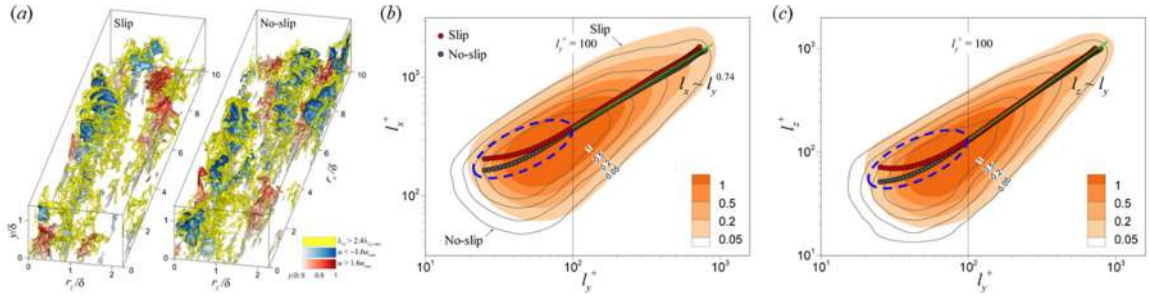

Figure 2. (*a*) 3-D iso-surfaces of λ_{ci} clusters (yellow) around wall-attached structures ($u < 0$; blue, $u > 0$; red) for the slip and no-slip cases. Joint PDFs of (*b*) l_x^+ and l_y^+ and of (*c*) l_z^+ and l_y^+ of wall-attached structures. Circles represent the mean lengths. The green line in (*a*) represents $l_x \sim l_y^{0.74}$ and in (*c*) $l_z^+ = l_y^+$.

Extended wall-attached structures

Figure 3(*a*) displays 3-D iso-surfaces of u carried by the wall-attached u structures in an instantaneous flow flied for the slip. All the wall-attached structures can be divided into the "extended" ($y^+ < 100$) and "self-similar" ($y^+ \geq 100$) (figures 2*b*,*c*). The 3-D iso-surfaces of u of the extended wall-attached structures ($u_{extended}$) below $y^+ = 100$ are illustrated in figure 3(*b*) for the slip and no-slip conditions. The streaks of negative $u_{extended}$ are more extended in the streamwise direction than those of positive $u_{extended}$, and the streamwise length of some structures are over 1δ. For the slip, empty spaces are observed more than those for the no-slip. Next, to examine the contribution of the extended wall-attached structures to the frictional drag, the skin friction (C_f) is decomposed into laminar ($C_{f,1}$) and turbulent ($C_{f,2}$) components using the FIK identity (Fukagata *et al*. 2002). C_f carried by the extended wall-attached structures ($C_{f,2a}$) can be examined through the conditional average. The tall wall-attached structures with the height of $l_y^+ \geq 450$ contribute half of $C_{f,2a}$. In particular, the skin-friction density of the extended wall-attached structures is over three times larger than the magnitude of total C_f over $l_y^+ = 30$.

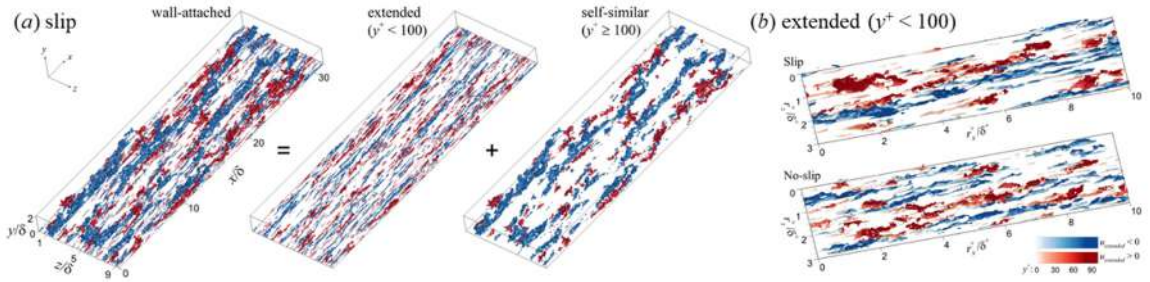

Figure 3. (*a*) 3-D iso-surfaces of wall-attached, extended ($y^+ < 100$) and self-similar ($y^+ \geq 100$) structures for the slip. (*b*) 3-D iso-surfaces of $u_{extended}$ at $y^+ < 100$ for the slip and no-slip cases.

CONCLUSION

We have examined structural features and statistics of extended wall-attached u structures and demonstrated the contributions to the frictional drag. We extract 3-D u clusters by using the connectivity of six-orthogonal neighbors in Cartesian coordinates from the DNS dataset for turbulent channel flows with the Navier slip wall ($Re_\tau = 470$) and no-slip wall ($Re_\tau = 577$) with the same Re_b. The skin-friction density of wall-attached u structures with the height of $l_y^+ = 100$ is approximately nine times of C_f. Moreover, the extended wall-attached u structures with the height above $l_y^+ = 100$ play a major role in the frictional drag reduction near the wall.

References

[1] Townsend A. A. The Structures of Turbulent Shear Flow. Cambridge University Press, UK 1976.
[2] Perry A. E., Chong M. S. On the Mechanism of Wall Turbulence. *J. Fluid Mech.* **119**: 173–217, 1982.
[3] Hwang J., Sung. H. J. Wall-Attached Structures of Velocity Fluctuations in a Turbulent Boundary Layer. *J. Fluid Mech.* **856**: 958–983, 2018.
[4] Yoon M., Hwang J., Lee J., Sung H. J., Kim J. Large-Scale Motions in a Turbulent Channel Flow with the Slip Boundary Condition. *Int. J. Heat Fluid Fl.* **61**: 96–107, 2016.
[5] Fukagata K., Iwamoto K., Kasagi N. Contribution of Reynolds Stress Distribution to the Skin Friction in Wall-Bounded Flows. *Phys. Fluids.* **14**(11): L73–L76, 2002.

ANALYSIS OF INTERSCALE ENERGY TRANSFER IN A BOUNDARY LAYER UNDERGOING BYPASS TRANSITION

Hanxun Yao *[1], Jean-Paul Mollicone[2], and George Papadakis[1]
[1] Department of Aeronautics, Imperial College London, London, UK
[2] Department of Civil and Environmental Engineering, Imperial College London, London, UK

Summary The Karman-Howarth-Monin-Hill Equation (KHMH) is employed to study the interscale energy transfer in a transitioning boundary layer due to forcing from free-stream turbulence. We consider different streamwise locations that cover the laminar, transitional and turbulent regions. The scale energy flux is presented on the (r_3, Y) plane, where Y is the wall-normal distance and r_3 is the spanwise separation. The results demonstrate how the scale energy is transferred in the physical space (wall-normal direction) and in the scale space, including forward and reverse cascade, during transition.

KARMAN-HOWARTH-MONIN-HILL EQUATION

The Karman-Howarth equation was originally derived for the second-order structure function $\langle \delta q^2 \rangle$ for homogeneous, isotropic turbulent flow [1, 2]. The structure function, $\langle \delta q^2 \rangle = \langle \delta u_i^2 \rangle = \langle (u_i^+ - u_i^-)^2 \rangle$, is defined using the velocity fluctuations, u_i, at two points indicated by $+$ and $-$ in Fig. 1 (left panel), where $\vec{X}$ denotes the mid-point and $\vec{r}$ the separation between the points. $\langle \delta q^2 \rangle$ can be considered as the energy contained in a length scale (eddy) of size $|\vec{r}|$. Hill [3] extended the Karman-Howarth equation to a generalised form that does not assume homogeneity or isotropy. The equation takes the form [4]

$$\frac{\partial \langle \delta q^2 \rangle}{\partial t} + \frac{\partial \boldsymbol{\phi_{s}}_i}{\partial x_i} + \frac{\partial \boldsymbol{\phi_{r}}_i}{\partial r_i} = \mathcal{P} - \epsilon \tag{1}$$

where the vector $\boldsymbol{\phi_{s}}_i = (\phi_x, \phi_y, \phi_z) = \langle U_i^* \delta q^2 \rangle + \langle u_i^* \delta q^2 \rangle + \langle 2 \delta u_i \delta p \rangle - \nu \frac{1}{2} \frac{\partial \langle \delta q^2 \rangle}{\partial x_i}$ is the energy flux in physical space, and the vector $\boldsymbol{\phi_{r}}_i = (\phi_{r1}, \phi_{r2}, \phi_{r3}) = \langle \delta u_i \delta q^2 \rangle + \langle \delta U_i \delta q^2 \rangle - 2\nu \frac{\partial \langle \delta q^2 \rangle}{\partial r_i}$ is the flux in scale space; $\mathcal{P} = -2 \langle \delta u_i \delta u_j \rangle \frac{\partial \delta U_j}{\partial r_i} - \langle (u_i^+ + u_i^-) \delta u_j \rangle \frac{\partial \delta U_j}{\partial r_i}$ is the production term and $\epsilon = 4\nu \left(\langle \frac{\partial \delta u_j}{\partial x_i} \frac{\partial \delta u_j}{\partial x_i} \rangle + \frac{1}{4} \langle \frac{\partial \delta u_j}{\partial r_i} \frac{\partial \delta u_j}{\partial r_i} \rangle \right)$ is the dissipation term.

INDICATIVE RESULTS

The bypass transitional flow field is obtained through DNS; transition is triggered by homogeneous, isotropic free-stream turbulence at the inlet. All the terms of the KHMH equation are calculated at different streamwise locations, shown in Fig. 1 (right panel). Due to lack of space, we present results on the (r_3, Y) plane only and plot the flux vector (ϕ_{r3}, ϕ_y). The normal component of the 6-dimensional flux vector, which does not have a projection on the (r_3, Y) plane, contributes to the net production, as in [5]. We fix $r_1 = 0, r_2 = 0$ and performed spanwise and time averaging.

Turbulent region We first validate our results at the fully turbulent region. The streamwise location is indicated by the black dash line in Fig. 1 (right panel). The flux vector (ϕ_{r3}, ϕ_y) and contours of the net production are shown in Fig. 2 (right panel). The production peak is located at the buffer layer, at $y^+ \approx 16$ or $Y \approx 2L_0$, where $^+$ indicates wall units and L_0 is the Blasius similarity variable at the inlet of the domain. This peak is related to coherent structures near the wall, which contribute to the near-wall regeneration cycle [6]. It is interesting to observe the flux arrows; they originate from the peak of the net source and then point to two sinks, one towards the wall and the other towards small r_3 scales (indicating forward cascade of energy). This behaviour is similar to that observed in channel flow [5]. However, reverse energy cascade (red arrows pointing to larger r_3 scales) can be observed above the energy peak; the flux vector then bends to approach the Y axis ($r_3 = 0$). These so-called spiral-like curves are also found in low-Reynolds number, wall bounded turbulent flows [5].

Laminar region As shown in Fig. 2 (left), the flux in the laminar region (green dashed line in the right panel of figure 1), is similar to the flux in the turbulent region, however, its production peak appears at a higher wall-normal location and at larger spanwise scale. The peak in the laminar region represents the average spacing of the so-called Klebanoff modes [7], which have a spanwise length scale of the order of the boundary layer thickness. Scale energy flux originates from the net production peak then points to different directions, meaning that scale energy is transferred mainly to smaller but also to larger streak sizes. The largest flux appears at the same height as the peak ($y^+ \approx 25$) and points to smaller spanwise scales. The spiral curves found in the turbulent region can not be observed at this location.

Transitional region We calculated the fluxes of Eqn. (1) at seven different streamwise locations, marked as the pink dash lines in Fig. 1 (right panel). From Fig. (3), we can observe how this scale energy transfer evolves from laminar-like to turbulent-like shape. The peak of production moves towards the wall and to smaller r_3. Two dissipation regions are maintained throughout the transition. The boundary layer grows (as indicated by the horizontal dashed line in all

*E-mail: h.yao17@imperial.ac.uk

figures) and energy flows away from the wall and to the small spanwise scales at the height above the production peak ($20 < y^+ < 100$). This indicates that the equilibrium boundary layer is forming gradually during the transition process.

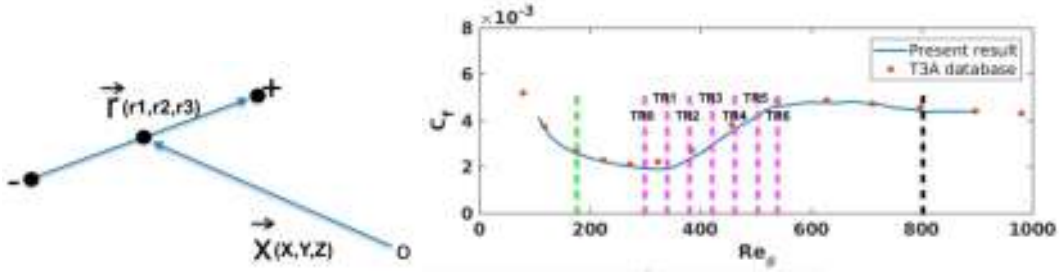

Figure 1: Schematic of points used to define a second order structure function (left); skin friction coefficient against Re_θ, where θ is the momentum thickness (right). The vertical dashed lines represent the calculation locations; from laminar (green), transitional (pink) to turbulent (black).

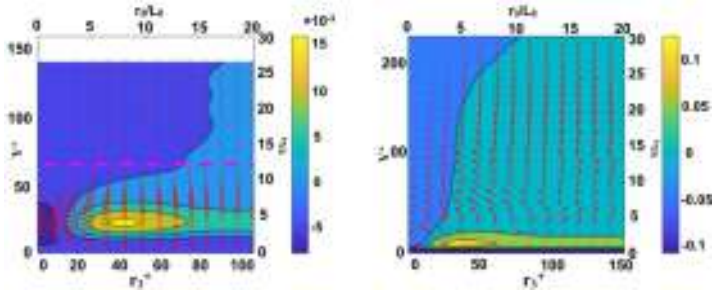

Figure 2: Energy flux (red arrows) on the (r_3, Y) plane at laminar region (left) and turbulent region (right). The contour is the net production and pink dash lines indicate the local boundary layer thickness.

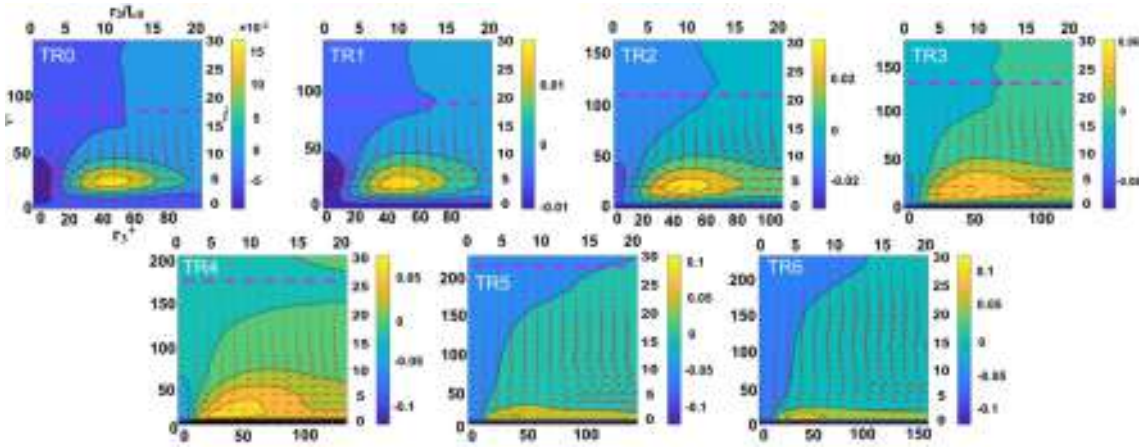

Figure 3: Evolution of energy flux (red arrows) and net production (contours) on (r_3, Y) plane in the transitional region at different streamwise locations, as indicated in Fig. (1, right)

References

[1] A. N. Kolmogorov, "Dissipation of energy in locally isotropic turbulence," in *Akademiia Nauk SSSR Doklady*, vol. 32, p. 16, 1941.
[2] T. De Karman and L. Howarth, "On the statistical theory of isotropic turbulence," *Proceedings of the Royal Society of London. Series A-Mathematical and Physical Sciences*, vol. 164, no. 917, pp. 192–215, 1938.
[3] R. J. Hill, "Exact second-order structure-function relationships," *Journal of Fluid Mechanics*, vol. 468, pp. 317–326, 2002.
[4] N. Marati, C. Casciola, and R. Piva, "Energy cascade and spatial fluxes in wall turbulence," *Journal of Fluid Mechanics*, vol. 521, pp. 191–215, 2004.
[5] A. Cimarelli, E. De Angelis, and C. Casciola, "Paths of energy in turbulent channel flows," *Journal of Fluid Mechanics*, vol. 715, pp. 436–451, 2013.
[6] J. Jiménez and A. Pinelli, "The autonomous cycle of near-wall turbulence," *Journal of Fluid Mechanics*, vol. 389, pp. 335–359, 1999.
[7] P. Klebanoff, "Effect of free-stream turbulence on a laminar boundary layer," in *Bulletin of the American Physical Society*, vol. 16, pp. 1323–+, AMER INST PHYSICS 1305 WALT WHITMAN RD, STE 300, MELVILLE, NY 11747-4501 USA, 1971.

SUPPRESSION OF BOUNDARY-LAYER SEPARATION BY ELEVATED FREE-STREAM VORTICAL DISTURBANCES

Dongdong Xu[1] and XuesongWu *[1,2]
[1] Department of Mechanics, Tianjin University, Tianjin 300072, China
[2] Department of Mathematics, Imperial College London, London SW7 2AZ,UK

Summary In this paper, we investigate the excitation of streaks or Görtler vortices by low-frequency free-stream vortical disturbances (FSVD) in a boundary layer subject to an adverse pressure gradient, and show that vortical disturbances of rather moderate level eliminate the separation which would occur in the absence of FSVD.

INTRODUCTION

A steady boundary layer subject to an adverse pressure gradient usually separates. Experiments found that FSVD of moderate level can reduce the size of the separation bubble, and may even eliminate it [1, 2]. Direct numerical simulations (DNS) showed that streaks in the boundary layer induced by FSVD act to inhibit the separation [3]. However, in DNS the free-stream and inlet disturbances are represented by continuous spectra of the O-S/Squire operators, which are non-physical [4]. Xu, Liu & Wu (2019) [5] presented a theoretical description of how physically realistic FSVD generate streaks or Görtler vortices in a boundary layer that is subject to a pressure gradient but remains attached. That work is now adapted to the case of a strong adverse pressure that would cause separation, and we show that the separation is eliminated by FSVD of moderate intensity.

FORMULATION: INITIAL-BOUNDARY-VALUE PROBLEM

The flow of interest is an incompressible boundary layer that develops over a semi-infinite flat or concave wall. Free-stream turbulence is represented by vortical disturbances superimposed on the incoming stream with velocity U_∞. The flow is described in a curvilinear system $x\hat{\boldsymbol{i}} + y\hat{\boldsymbol{j}} + z\hat{\boldsymbol{k}}$, normalized by Λ, the spanwise integral scale of turbulence. The dimensionless time variable $t = U_\infty t^*/\Lambda$ is introduced. The Reynolds number and Görtler number are defined as

$$R_\Lambda = U_\infty \Lambda/\nu \gg 1, \quad G_\Lambda = R_\Lambda^2 \Lambda/r_0^* \sim O(1). \tag{1}$$

The turbulent Reynolds number is defined as $r_t = \epsilon R_\Lambda \sim O(1)$, where $\epsilon \ll 1$ is a measure of the disturbance intensity. FSVD are assumed to have low frequencies, or long wavelength of $O(\Lambda R_\Lambda)$.

Governing equations Streaks or Görtler vortices induced by FSVD are fully developed in the region corresponding to $\hat{x} \equiv x/R_\Lambda = O(1)$ and $y = O(1)$, where the velocity and pressure, (u^*, v^*, w^*) and p^*, can be written as

$$(u^*, v^*, w^*)/U_\infty = (u, R_\Lambda^{-1} v, R_\Lambda^{-1} w), \quad p^*/(\rho U_\infty^2) = R_\Lambda^{-1}(P_B + R_\Lambda^{-1} p), \tag{2}$$

where P_B is the steady mean pressure. The rescaled velocity $\mathbf{u} \equiv (u, v, w)$ and pressure p are governed by the nonlinear boundary region equations (NBRE) [6],

$$\nabla \cdot \mathbf{u} = 0, \quad \mathbf{u}_{\hat{\tau}} + (\mathbf{u} \cdot \nabla)\mathbf{u} + G_\Lambda u^2 \mathbf{j} = (-P_{B\hat{x}}, -p_y, -p_z) + (\partial_{yy}^2 + \partial_{zz}^2)\mathbf{u}, \tag{3}$$

where $\hat{\tau} = t/R_\Lambda$, and $\mathbf{j}$ is the unit vector in the wall-normal direction.

In the previous work [5], the total flow field is decomposed as a sum of the unperturbed base flow and FSVD induced perturbation. This decomposition becomes inappropriate in the presence of a strong adverse pressure gradient that induces separation because the solution for the former terminates at a Goldstein singularity. In order to avoid this dead end, the flow is decomposed instead as a sum of the steady spanwise-averaged and the unsteady or spanwise-varying components,

$$\{u, v, w, p\} = \{U_B(\hat{x}, y), V_B(\hat{x}, y), W_B(\hat{x}, y), P_B(\hat{x})\} + \{\hat{u}, \hat{v}, \hat{w}, \hat{p}\}\,(\hat{x}, \eta, z, \hat{\tau}). \tag{4}$$

Initial and boundary conditions The oncoming FSVD are distorted by the nonuniform invisicd mean flow. This must be analysed in the outer region corresponding to $x = O(R_\Lambda)$ and $1 \ll y \ll O(a^*/\Lambda)$, where the base flow $(U_B, V_B) \approx (U_e(\hat{x}), -U_e'(\hat{x})y)$, while the disturbance can be written as (Xu, Liu & Wu 2019)

$$\epsilon R_\Lambda \big[(\bar{u}_0, \bar{v}_0, 0, \bar{p}_0)(\hat{x}, \hat{y}, \hat{\tau}) + (\hat{u}_0, \hat{v}_0, \hat{w}_0, \epsilon\hat{p}_1)(\hat{x}, y, z, \hat{\tau}) + \ldots\big], \tag{5}$$

where the far field variable $\hat{y} = y/R_\Lambda$. The terms $\bar{u}_0$, $\bar{v}_0$ and $\bar{p}_0$ represent the two-dimensional part induced by the displacement effect. Substitution of (5) into the N-S equations shows that $\bar{v}_0$ appears in the governing equations of the three-dimensional component $(\hat{u}_0, \hat{v}_0, \hat{w}_0, \hat{p}_1)$, indicating that the latter is also influenced by the viscous displacement effect. The coupling with $\bar{v}_0$ can be removed by the generalized Prandtl transformation (Xu, Liu & Wu 2019),

$$\bar{y} = U_e(\hat{x})y - \hat{\delta}(\hat{x}, \hat{\tau}) \quad \text{with} \quad \hat{\delta}_{\hat{\tau}} + U_e\hat{\delta}_{\hat{x}} = U_e\bar{\delta}_{\hat{x}}(\hat{x}, \hat{\tau}), \tag{6}$$

*Corresponding author. E-mail: x.wu@ic.ac.uk

where $\bar{\delta}$ is the spanwise averaged displacement thickness. In terms of $\bar{y}$, the governing equations for $(\hat{v}_0, \hat{w}_0)$ read

$$U_e\hat{v}_{0\bar{y}} + \hat{w}_{0z} = 0, \quad \mathcal{L}_{\mathcal{N}}\begin{pmatrix}\hat{v}_0\\ \hat{w}_0\end{pmatrix} + \begin{pmatrix}-U_e'\hat{v}_0\\ \hat{w}_0\end{pmatrix} = -\begin{pmatrix}U_e\hat{p}_{1\bar{y}}\\ \hat{p}_{1z}\end{pmatrix}, \tag{7}$$

where $\mathcal{L}_{\mathcal{N}} = \partial_{\hat{\tau}} + U_e\partial_{\hat{x}} + r_t(U_e\hat{v}_0\partial_{\bar{y}} + \hat{w}_0\partial_z) - (U_e^2\partial_{\bar{y}}^2 + \partial_z^2)$. The solution to (7) is obtained and then rewritten in terms of y using (6) to provide the boundary condition for (3).

On the other hand, in the upstream limits of (7) and (3) the respective solutions are obtained to specify the appropriate initial condition (Xu, Liu & Wu 2019).

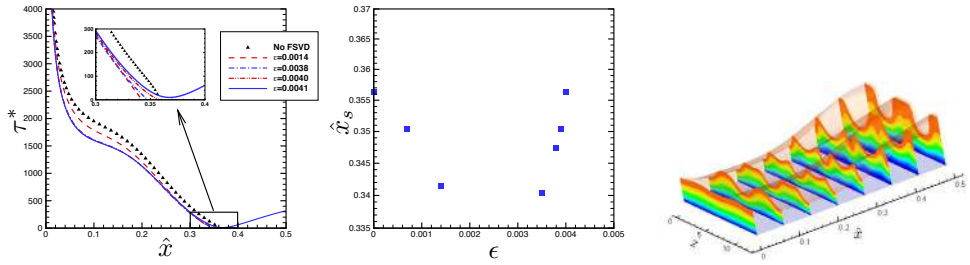

Figure 1: Flat-plate case ($G_\Lambda = 0$). Left: evolution of the minimum skin friction; middle: separation location $\hat{x}_s$ versus ϵ: right: nonlinear evolution of streaks ($\epsilon = 4.9 \times 10^{-3}$).

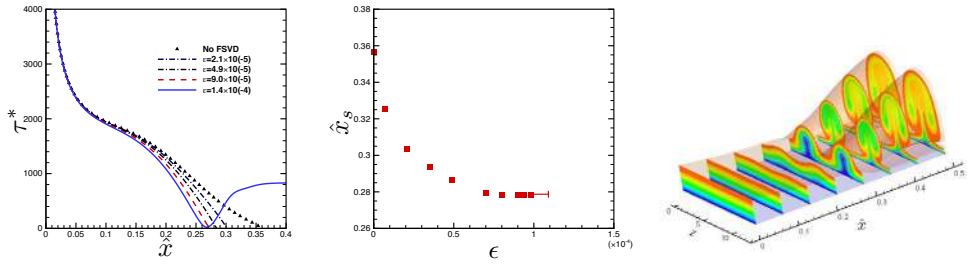

Figure 2: Concave-wall case ($G_\Lambda = 1501$). Left: evolution of the minimum skin friction; middle: separation location $\hat{x}_s$ versus ϵ: right: nonlinear evolution of Görtler vortices ($\epsilon = 1.4 \times 10^{-4}$).

MAIN RESULT: ELIMINATION OF SEPARATION

Calculations were performed for the slip velocity,

$$U_e(\hat{x}) = 1 + d\{\tanh^2[(\hat{x} - \hat{x}_0)\pi/L] - 1\} \text{ with } L = 0.5, \hat{x}_0 = 0.2, d = 0.112, \tag{8}$$

where d and L control the intensity and extent of the adverse pressure gradient respectively. Figure 1 shows the results for the flat-plate case. The boundary layer separates when the FSVD intensity $\epsilon = 0$ or small. As ϵ is increased, the separation first shifts upstream, but with further increase of ϵ, $\hat{x}_s$ increases and eventually approaches infinite when $\epsilon \approx 1.0 \times 10^{-3}$, which is critical intensity ϵ_c to eliminate the separation. The flow becomes attached when $\epsilon \geq \epsilon_c$. Figure 2 shows the results for the concave-wall case. As the FSVD level ϵ is increased, the separation moves upstream monotonically, and then no longer occurs when $\epsilon \geq \epsilon_c \approx 10^{-4}$. This critical intensity is much smaller than that in the flat-plate case, indicating that the centrifugal effect inhibits separation. Further results will be presented at the Congress.

References

[1] Zilli, J., Sutton, D. M., Lavoie, P. Effect of freestream turbulence on laminar separation bubbles and flow transition on an SD7003 airfoil at low Reynolds numbers. *AIAA Paper* 2017–0302, 2017.

[2] Istvan, M. S., Yarusevych, S. Effects of free-stream turbulence intensity on transition in a laminar separation bubble formed over an airfoil. *Exp. Fluids* **59** (3): 52, 2018.

[3] Hosseinverdi, S., Fasel, H. F. Numerical investigation of laminar–turbulent transition in laminar separation bubbles: the effect of free-stream turbulence. *J. Fluid Mech.* **858**: 714–759, 2019.

[4] Dong, M., Wu, X. On continuous spectra of the Orr-Sommerfeld/Squire equations and entrainment of free-stream vortical disturbances. *J. Fluid Mech.* **732**, 616–659, 2013.

[5] Xu, D., Liu, J., Wu, X. Streaks and Görtler vortices in boundary layer subject to pressure gradient: excitation by free-stream vortical disturbances, nonlinear evolution and secondary instability. *J. Fluid Mech. (Submitted)* 2019.

[6] Hall, P. The nonlinear development of Görtler vortices in growing boundary layers. *J. Fluid Mech.* **193**, 243–266, 1988.

UNSTEADY BOUNDARY-LAYER SEPARATION ON UPSTREAM MOVING WALL

A. I. Ruban *, A. Djehizian, and M. A. Kravtsova
Department of Mathematics, Imperial College London, UK

Summary This paper is concerned with unsteady boundary-layer separation during the stage when the separation point moves along the body surface in the downstream direction. Using the coordinate frame that moves with the separation point, one can reduce the problem to that of a steady flow separating from a wall moving parallel itself in the upstream direction. We assume the flow outside the boundary layer supersonic. First the problem is studied by means of numerical solution of the corresponding triple-deck equations, and then an analytical solution is given using asymptotic analysis. We found, surprisingly enough, that the separation takes place under the action of favourable pressure gradient that might be caused by an impinging Prandtl–Meyer expansion fan. We also found that the separation takes the form of what K. Stewartson termed 'collisional separation'.

PROBLEM FORMULATION

This is a long-standing fundamental problem of high-Reynolds-number flow theory, that attracted significan attention of various authors. The case of downstream moving wall was studied successfully by Vic. V. Sychev (see [1], [2]), with the supersonic version of his theory presented by Ruban *et al.* [3]. However, up to now, the separation on an upstream moving wall remained unresolved. This is, primarily, due to topological difficalties. It is well known that the boundary-layer separation on a motionless wall is identified by the condition of zero skin friction:

$$\left.\frac{\partial u}{\partial y}\right|_{y=0} = 0. \tag{1}$$

Here u is the longitudinal velocity component, and y is the coordinate measured perpendicular to the wall. In the case of downstream moving wall, the separation takes place at the point inside the boundary layer, where

$$u = \frac{\partial u}{\partial y} = 0. \tag{2}$$

In both cases, the velocity u is positive before the separation point. The conditions (1) and (2) identify the position where the flow reversal starts to form in the boundary layer. Contrary to that, for the upstream moving wall, a link between the flow reversal and boundary-layer separation does not exist. Indeed, even in unperturbed boundary layer on upstream moving wall there always exist a region near the wall where u is negative. Keeping this in mind we will identify the separation not by kinematic conditions, like by (1) and (2), but by the dynamic condition, namely, by the singularity in the solution of the governing equations.

To be specific, we consider, as an example, the boundary layer on the surface of a flat plate that is aligned with the oncoming supersonic flow. Our interest is in the incipience of the separation caused by an impinging shock or expansion wave. The later can be produced by an expansion ramp situated above the plate as shown in figure 1. It is convenient to perform the analysis in the coordinate frame that moves with the shock. In this frame the flow may be treated as steady.

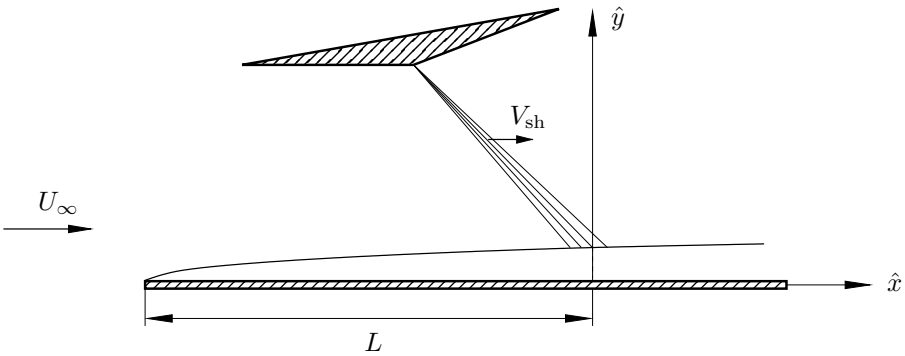

Figure 1: The flow layout.

NUMERICAL STUDY

We first assume that the shock speed $V_{\rm sh}$ is compatible with the triple-deck theory, that is $V_{\rm sh}/V_\infty = O(Re^{-1/8})$, where Re is the Reynolds number. The numerical solution of the triple-deck equations was conducted using the numerical technique described in Kravtsova *et al.* [4]. Both cases of impinging shock and expansion fan were analysed. We did not find any evidence of separation singularity in the case of the shock wave. So the main attention was payed to the boundary layer exposed to an expansion fan.

*Corresponding author. E-mail: a.ruban@imperial.ac.uk

An example of such calculations is displayed in figure 2. Here the wall speed is taken to be $U_w = V_{\rm sh}/V_\infty = -3.0$. We see two eddies forming in the flow; one lies downstream of the impinging expansion fan and the other upstream of the fan. The former was found to grows with U_w, while the latter becomes relatively smaller. This is the behaviour typical of 'collisional separation'.

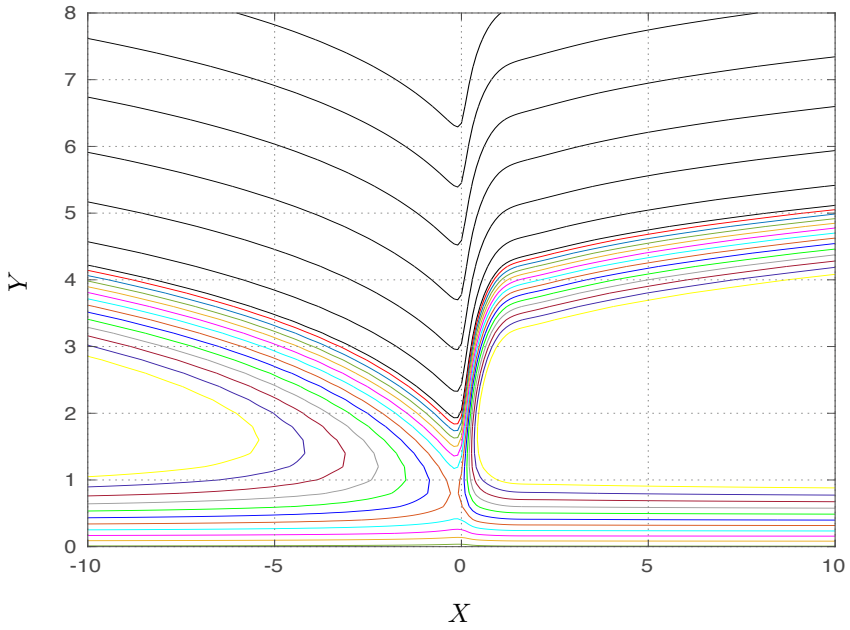

Figure 2: The streamline pattern in the boundary layer exposed to an impinging expansion fan.

THEORETICAL ANALYSIS

The theoretical analysis of the flow was conducted under the assumption that the impinging expansion fan speed satisfied the conditions $1 \ll V_{\rm sh}/V_\infty \ll Re^{-1/8}$. In this case the viscous lower tier of the triple-deck structure splits into the inviscid and viscous layers, and the pressure distribution along the interaction region can be found by analysing the interaction of the inviscid layer with the external supersonic flow. Still, to satisfy the no-slip condition on the body surface, one has to study the flow behaviour in the near-wall viscous later. This can be done analytically. We found that the solution in the viscous layer remains smooth in the case of impinging shock, but develops a singularity when the boundary layer is exposed to the expansion fan. A detailed analysis of the flow behaviour near the singularity shows that a new shorter region should be introduced in the vicinity of the separation point. An integro-differential equation for the pressure $P(X)$

$$\frac{1}{2} = \frac{d}{d\breve{X}}\left[2\int_{\breve{\Psi}_R}^{\breve{\Psi}_M} \frac{d\breve{\Psi}}{\sqrt{2\breve{\Psi} + e^{\chi(\breve{\Psi}+1)} - 2\breve{P}}}\right] + \frac{d\breve{P}}{d\breve{X}}\left[\int_{\breve{\Psi}_M}^{+\infty} \frac{d\breve{\Psi}}{\left[2\breve{\Psi} + e^{\chi(\breve{\Psi}+1)} - 2\breve{P}\right]^{3/2}} + \frac{1}{\sqrt{2\breve{\Psi}_M + e^{\chi(\breve{\Psi}_M+1)} - 2\breve{P}}}\right]$$

was deduced for this new region. Its solution shows that a collisional separation singularity forms in the flow at a finite position $\breve{X} = \breve{X}_0$ on the body surface, with the pressure behaving as

$$\breve{P} = \frac{\Lambda}{(\breve{X} - \breve{X}_0)^2} + \cdots \quad \text{as} \quad \breve{X} \to \breve{X}_0.$$

Conclusions

Thus we have established that (i) for the boundary layer to separate on an upstream moving wall, it should be exposed to a favourable pressure gradient, and (ii) the separation assumes the form of what was termed by K. Stewartson the 'collisional' separation.

References

[1] Sychev, Vic. V. 1979 Asymptotic theory of nonstationary separation. *Mekh. Zhid. Gaza* (6), 2132,
[2] Sychev, Vic. V. 1987 Analytical solution of the problem of flow near the boundary-layer separation point on a moving wall. *Prikl. Mat. Mekh.* **51** (3), 51952.
[3] Ruban, A. I., Araki, D., Yapalparvi, R. & Gajjar, J. S. B. 2011 On unsteady boundarylayer separation in supersonic flow. Part 1. Upstream moving separation point. *J. Fluid Mech.* **678**, 124155.
[4] Kravtsova, M. A., Zametaev, V. B. & Ruban, A. I. 2005 An effective numerical method for solving viscous-inviscid interaction problems. *Phil. Trans. R. Soc.* **A 363** (1830), 1157–1167.

VORTICAL STRUCTURES IN RELAMINARIZING BOUNDARY LAYERS

O. N. Ramesh*[1], Saurabh S. Patwardhan [2]
[1] Department of Aerospace Engineering, Indian Institute of Science, Bangalore, India
[2] Ansys India Pvt. Ltd, Pune, India

Summary In this work, we look at the evolution of vortical structures in relaminarizing turbulent boundary layers (TBL). A direct numerical simulation of relaminarizing TBL due to a favourable pressure gradient is carried out. Vortical structures are visualized using the λ_2 method proposed by Jeong and Hussain (1995). Two-point correlations of velocity and the near-wall streak structures are investigated. The weakened large-scale near-wall structures in a relaminarizing TBL progressively lean towards the wall. This is consistent with study of Dixit and Ramesh (2010) where a systematic decrease in the structure angle with FPG was observed. A new mechanism of stability of near-wall streaks in relaminarizing flows due to the kinematic action of wallward vertical velocity is proposed. A similar mechanism may also be operative during relaminarization due to strong suction.

NEAR-WALL COHERENT VORTEX STRUCTURES IN RELAMINARIZING FLOW

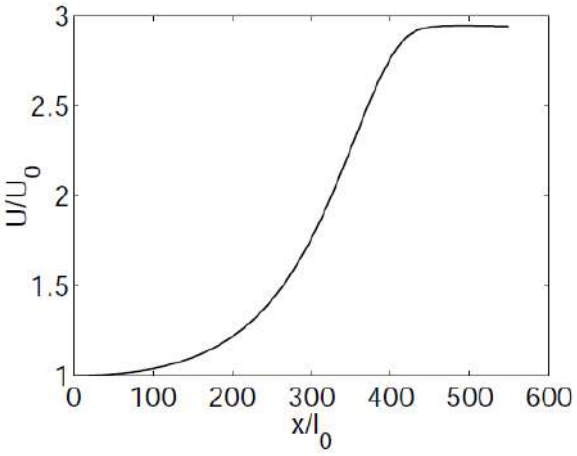

Figure 1 (a) Streamwise variation of U_∞

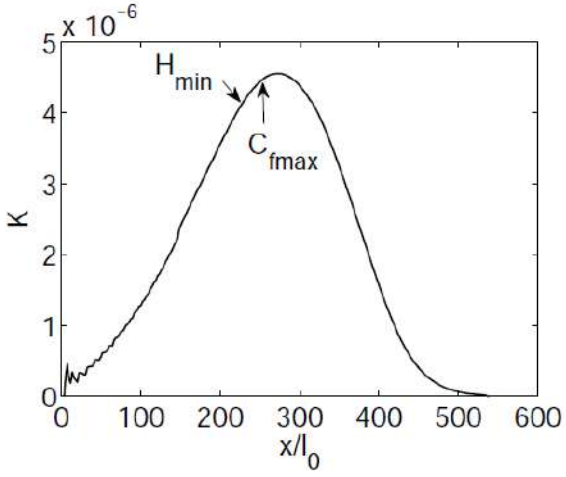

Figure 1 (b) Streamwise variation of K

In the present work, relaminarization of a zero pressure turbulent boundary layer at a Reynolds number of $\mathrm{Re}_\theta = 1000$ turbulent boundary layer, due to an imposed streamwise acceleration is investigated. This is a combined experimental and DNS study but presently only the computational results are presented. Details of the DNS study by a finite difference code and its validation by experiments will be discussed during the oral presentation and will not be presented here for brevity. Figure 1(a) shows the acceleration of the freestream velocity and the streamwise variation of the freestream acceleration parameter $K = \frac{\nu}{U_\infty^2}\frac{dU_\infty}{dx}$ is shown in figure 1(b). Studies in the literature (Narasimha and Sreenivasan 1973) have suggested the onset of relaminarization can be inferred to be either the location where the skin friction coefficient reaches a maximum or the shape factor reaches a minimum value. Both these locations are indicated in figure 1 (b) by arrows and they are seen to be very nearly the same; the relaminarization onset location can be taken to be $x/l_0 \approx 250$, where l_0 is a reference length scale. Figure 2 shows the visualisation of near-wall vortex structures in the initial turbulent region (fig. 2(a)) relaminarizing flow (fig. 2(b)) and the final retransition back to turbulence where streamwise acceleration (and K=0) (figure 2(c)). The vortex identification is based on the method proposed by Jeong & Hussain (1995). The value of λ_2 is -0.02 and is kept constant for the visualisation purpose at all locations. The vortex structures before the occurrence of relaminarization (fig. 2(a)) populate most of the boundary layer. The near-wall geometry is quasi-streamwise. As the pressure gradient increases, the vortices become fewer and the angle of inclination to the wall decreases (fig. 2(b)). This is expected as the favourable pressure gradient (FPG) stretches the streamwise vortex which increases the length of the vortex. After the pressure gradient is relaxed the flow retransitions. Figure 2(c) shows the retransitional structures which contain hairpin like vortices.

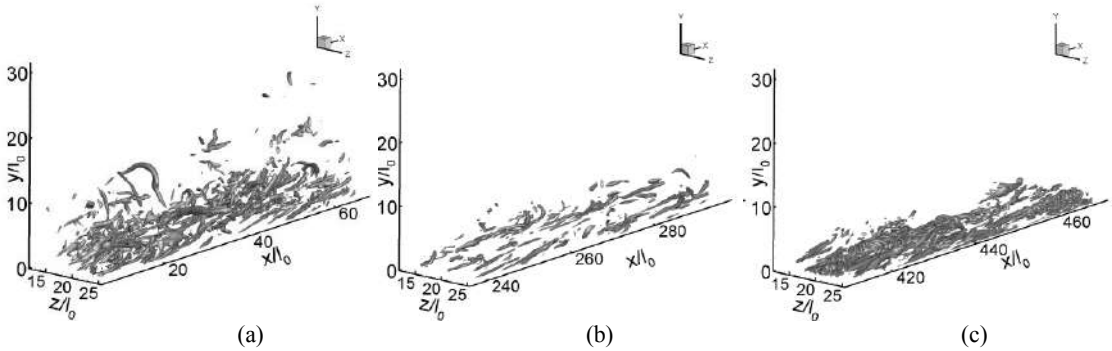

Figure 2. Near-wall vortex structures in relaminarizing flow

STREAK STABILISATION IN RELAMINARIZING BOUNDARY LAYER

The inner layer is known to play an important role in the process of relaminarization as it acts as a slip-boundary for the "Euler-like" outer region (Narasimha & Sreenivasan, 1973). Even though, the Reynolds shear stress is still relevant to the dynamics of the flow in the relaminarizing zone only in the inner layer, the turbulent intensity there decreases when scaled in inner as well as outer co-ordinates. We suggest that this occurs due to the stabilisation of lifted streaks in the near-wall region of the boundary layer. The decrease in the height of the crest along with the increased spanwise spacing of the streak results in a reduction of the streak flank angle. Figures 3(a) and 3(b) show a visualisation of the near-wall streaks in the relaminarizing flow. Figure 3(a) shows the streak view in the zone where the FPG is weak and figure 3(b) shows the streak view in the relaminarizing zone in the wall normal-spanwise plane (y–z plane). An important parameter which determines the stability of lifted streaks is the streak flank angle (Schoppa & Hussain, 2002). The streak flank angle is also a measure of wall-normal vorticity as $\omega_y = du/dz$. It was shown that larger the flank angle greater is the instability of the streak (Schoppa & Hussain, 2002). It is clear from the figures that the streak flank angle has decreased in the relaminarizing zone consistent with that expectation.

We believe the present study is crucial to understanding the near-wall structure of turbulent boundary layers – it is based on the expectation that one can understand the origin and cause of a structure better if we understand the condition under which such structures die out.

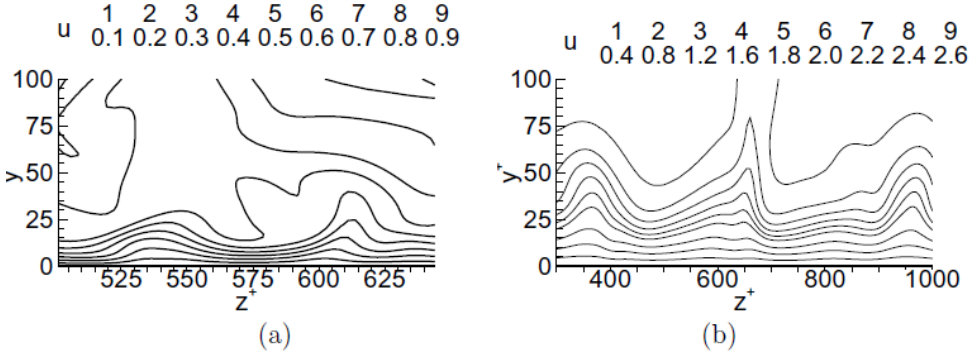

Figure 3. Near-wall streaks in relaminarizing flow

CONCLUSIONS

Near-wall vortex structures in relaminarizing flow become longer in the streamwise direction as the favourable pressure gradient increases. The angle made by the structures to the wall decreases. The structures become less populated in the near-wall region as relaminarization starts. Near-wall low speed streaks become longer and quieter. The spanwise spacing between the streaks also increases. A smaller flank angle of the lifted streaks in the relaminarizing zone results in the stability of these lifted streaks which in turn decreases the near-wall turbulent production. A decrease in turbulent production causes lower turbulent intensities. Strong wallward mean velocity appears to be the chief cause of the stability of lifted streaks. We believe that similar mechanism is prevalent in relaminarization caused due to intense wall suction.

References

[1] Jeong, J. & Hussain, F. On the identification of a vortex. *J. Fluid Mech*. **285**:69–94.
[2] Dixit S. A. Structure of sink flow boundary layers *PhD thesis*, Indian Institute of Science, Bangalore, 2010.
[3] Narasimha R. & Sreenivasan, K. R. Relaminarization in highly accelerated turbulent boundary layers. *J. Fluid Mech.* **61**:417-447.
[4] Schoppa W. & Hussain, F Coherent structure generation in near-wall turbulence. *J. Fluid Mech.***453**:57-108.

DIRECT NUMERICAL SIMULATION OF HYPERSONIC BOUNDARY LAYERS IN CHEMICAL NON-EQUILIBRIUM

Donatella Passiatore *[1,2], Luca Sciacovelli[2], Giuseppe Pascazio[1], and Paola Cinnella[2]
[1] DMMM, Politecnico di Bari, Bari, Italy
[2] DynFluid Laboratory, Arts et Métiers ParisTech, Paris, France

Summary The influence of high-temperature effects on compressible wall-bounded turbulence is investigated by means of a direct numerical simulation of a hypersonic, chemically out-of-equilibrium, turbulent boundary layer. The analysis aims at assessing the effects of chemical reactions on turbulence, also by comparing the results with those of a frozen flow. We will present a detailed analysis of the turbulent statistics and near-wall dynamics; the validity of some classical scalings and Reynolds analogy will also be discussed.

The investigation of turbulent hypersonic flows is a major subject for a wide range of applications, including reentry vehicles, spatial tourism or trans-atmospheric flights. The high temperatures reached in these regimes can cause chemical reactions (with characteristic times similar to those of the fluid motion), giving rise to a nonequilibrium chemical state. Such high-temperature effects have a strong impact on aerodynamic performance and heat transfer rates, but may also affect transition and turbulence dynamics [1].
In this work, we investigate the influence of finite-rate chemistry on compressible wall-bounded turbulence. More specifically, we carry out the direct numerical simulation of a hypersonic, chemically out-of-equilibrium, turbulent boundary layer, encompassing the laminar-to-turbulent transition, triggered by means of a suction-and-blowing forcing at the wall. The analysis aims at assessing the effects of chemical reactions on turbulence, also by comparing the results with those of a frozen flow (i.e. a flow with chemical reaction times much longer than the flow scales).
Flows under investigation are governed by the compressible Navier–Stokes equations for multicomponent chemically-reacting gases. Concerning the chemical modeling, the five-species (N_2, O_2, NO, O, N) model of Park [2] is considered. Thermodynamic quantities are determined using the contributions of the translational, rotational and vibrational modes of each species, whereas transport properties are computed by means of Blottner's model and Eucken's formula [3]. Finally, mass diffusion pheomenon is modeled following Hirschfelder's approximation [4].
The simulations are carried out by means of an in-house CFD code. The code is equipped with high-order finite-difference schemes (tenth order for convective fluxes and fourth order for viscous ones) and selective standard filters, supplemented with the Localized Artificial Diffusivity (LAD) method for shock capturing [5]; this technique consists in adding artificial transport properties to the physical ones, in order to smooth out discontinuities and/or strong unresolved dynamic, thermal and mass gradients. The time integration is carried out by means of a low-storage, explicit third-order Runge–Kutta algorithm. The direct numerical simulation strategy has been preliminary validated against literature results for two single-species boundary layer configurations at $M_\infty = 6$ [6] and $M_\infty = 2.25$ [7], whereas the chemical non-equilibrium model has been assessed against the configurations described in [8], [9] and [10].
The proposed work is carried out in the free-stream conditions of [10], representing a reference state widely used for stability studies; specifically, M_∞=10, T_∞=350 K, p_∞=3596 Pa and $T_w \approx 5400$ K. A computational grid of $\approx 3.2 \times 10^8$ points is considered, which ensures a good spatial resolution in all directions, i.e. $\Delta x^+ = 3$, $\Delta y_w^+ = 0.6$ and $\Delta z^+ = 2$, being x, y and z the streamwise, wall-normal and spanwise directions respectively. An instantaneous visualization of the chemically out-of-equilibrium simulation is shown in figure 1; the oxygen mass fraction varies of one order of magnitude, from the wall (where the temperature is the highest and the oxygen is highly dissociated) to the edge of the boundary layer, where it reaches the free-stream conditions.
Some quantitative results are reported in figure 2. The trend of the skin friction coefficient $C_f = 2\tau_w/(\rho_e U_e^2)$ is shown in figure 2(a): finite-reate chemistry little affects the skin friction distribution in the laminar and fully turbulent regions. Significant discrepancies are observed in the transition region, albeit the qualitative trends are close-by. This result is mainly due to the varying mixture composition in the chemically-reacting case. The root mean square values of the temperature are shown in figure 2(b). The results for the chemically-reacting simulation present lower values of temperature fluctuations; this is due to the endothermic nature of the reactions, which subtract energy from the system. Figure 2(c) presents the root mean square values of the mass fractions, for the chemically-reacting simulation. The strongest chemical activity is concentrated at the wall, where the temperature is the highest; however, the peaks of the fluctuations are shifted away from the wall and their position corresponds to the largest temperature fluctuations. The curves are plotted with respect to $y^+ = y\rho_w u_\tau/\mu_w$, at $Re_\tau = 180$.
In the final study, we will present a detailed analysis of first- and second- order statistics and near-wall dynamics. The validity of classical Reynolds analogy will be assessed and a skin friction decomposition will also be discussed.

*Corresponding author. E-mail: donatella.passiatore@poliba.it.

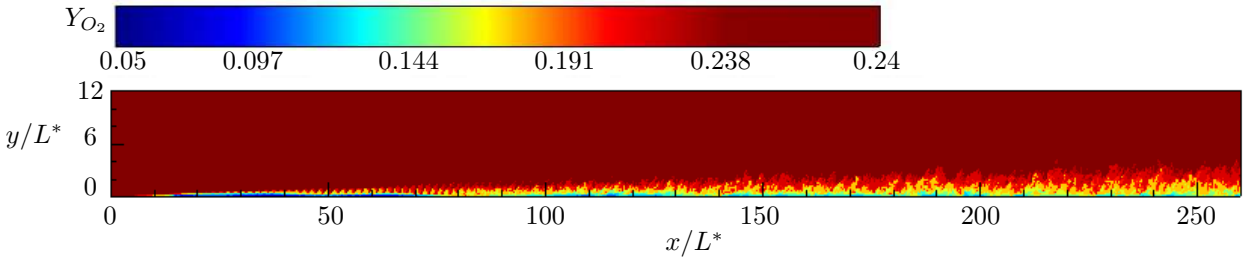

Figure 1: Isocontours of oxygen mass fraction Y_{O_2} in a (x,y) plane, with aspect ratio $x/y = 0.5$.

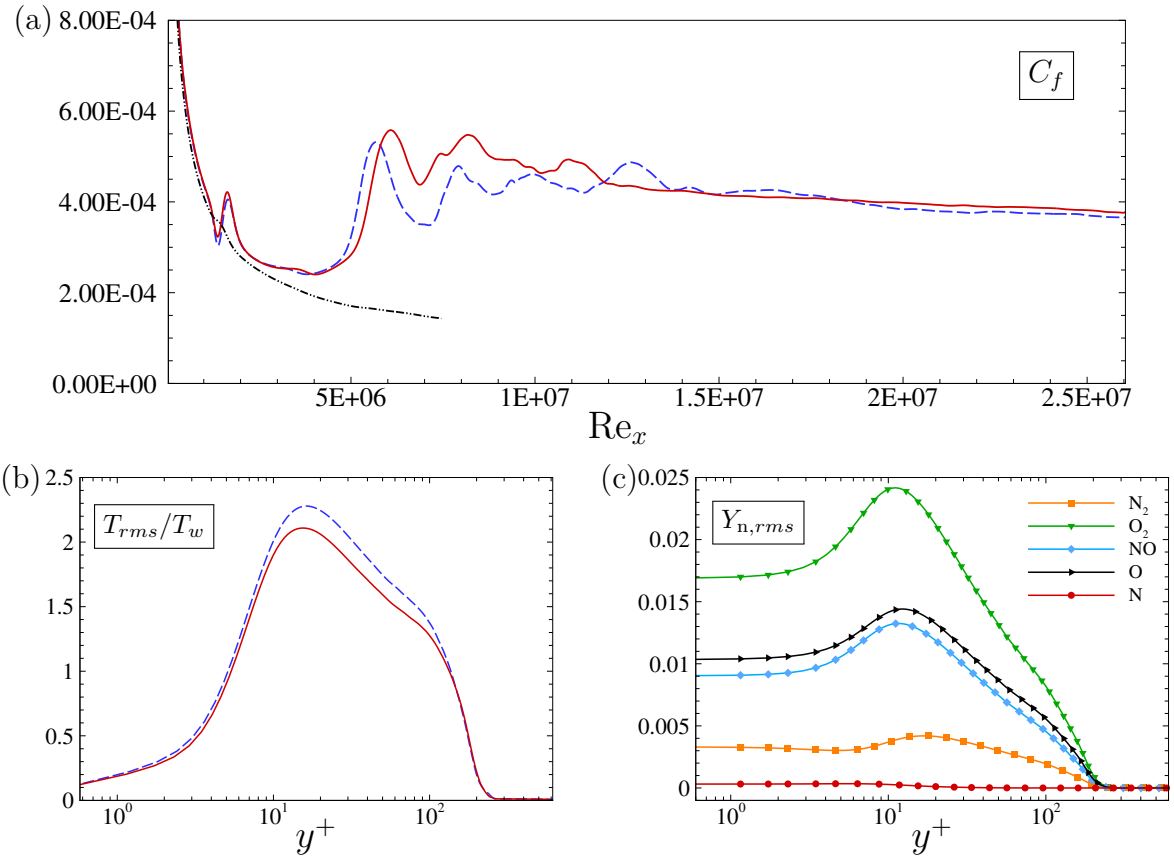

Figure 2: Skin friction coefficient (a), rms values of the temperature, normalized with wall temperature (b) and rms values of the mass fractions, for the chemically-reacting simulation (c). (- - - -) frozen simulation; (——) chemically-reacting simulation.

References

[1] G. Candler. Rate effects in hypersonic flows. Annual review of Fluid Mechanics, 51:379–402, 2019.
[2] C. Park. Review of chemical-kinetic problems of future NASA missions. I-Earth entries. Journal of Thermophysics and Heat transfer, 7(3):385–398, 1993.
[3] F. G. Blottner. Chemically reacting viscous flow program for multi-component gas mixtures. 1971.
[4] Joseph Hirschfelder, R Byron Bird, and Charles F Curtiss. Molecular theory of gases and liquids. 1964.
[5] S. Kawai, K. Santhosh, and S. K. Lele. Assessment of localized artifical diffusivity scheme for large-eddy simulation of compressible turbulent flows. Journal of computational physics, 229:1739–1762, 2010.
[6] K.J. Franko and S.K. Lele. Breakdown mechanisms and heat transfer overshoot in hypersonic zero pressure gradient boundary layers. Journal of Fluid Mechanics, 730:491–532, 2013.
[7] S. Pirozzoli and M. Bernardini. Turbulence in supersonic boundary layers at moderate Reynolds number. Journal of Fluid Mechanics, 688:120–168, 2011.
[8] B. Grossman and J. Garrett. A survey of upwind methods for flows with equilibrium and non-equilibrium chemistry and thermodynamics. In 24th Thermophysics Conference, page 1653, 1989.
[9] K. J. Franko, R. MacCormack, and S. K. Lele. Effects of chemistry modeling on hypersonic boundary layer linear stability prediction. In 40th Fluid Dynamics Conference and Exhibit, page 4601, 2010.
[10] F. Miró Miró, F. Pinna, E. S. Beyak, P. Barbante, and H. L. Reed. Diffusion and chemical non-equilibrium effects on hypersonic boundary-layer stability. In 2018 AIAA Aerospace Sciences Meeting, page 1824, 2018.

MANIPULATION OF WALL BOUNDED FLOWS WITH DENTICLES INSPIRED BY SHARK SKIN

Shane Nicholas*, Mohammed Omidyeganeh and Alfredo Pinelli
Department of Mechanical and Aeronautical Engineering, City, University of London. London, UK

Summary We have used Direct Numerical Simulation to analyse a pressure driven incompressible open channel turbulent flow bounded by a textured surface inspired by shark-skin-like denticles. The texture is obtained by combining a set of solid elements made out of a stem and a crown which are mounted uniformly on a solid wall. The resulting surface can be considered to be a realisation of an anisotropic porous wall allowing for differential wall-normal and wall-parallel permeability recently envisaged as a potential mean for skin friction drag reduction by a number of authors [1, 2]. The preliminary results show a non-trivial superposition of outer large-scale structures with others generated by the drag and the transpiration induced by the particular morphology of the canopy covering the wall.

INTRODUCTION

Viscous flows over surfaces covered with textured layers are ubiquitous in nature. In the last decades, many researches have dedicated their efforts in unveiling how these biological surfaces interact with fluid flows to deliver enhanced locomotion performances in terms of drag reduction and/or improved manoeuvrability. In particular, the great white shark capability of swimming at remarkable speed (almost 60 km/h) has motivated a number of experimental and numerical investigations focused on the eventual hydrodynamic advantages offered by the particular morphology of the skin of this large fish which is characterised by the presence of a dermal/tooth like structures acting as a permeable substrate. In particular, the whole skin is covered by denticle elements that can be modelled as the combination of three main geometrical features. A *stem* anchored to the impermeable surface of the skin holds on its tip a *crown* oriented in the streamwise direction (i.e. swimming direction). The crown also presents a series of *ridges* on its top. These striations of the crown have sparked the interest of many researches that inspired by these grooves have shown that the use of streamwise oriented roughness can effectively reduce the skin friction drag. In particular, the focus of the vast majority of the research has been focused on flat surfaces covered with riblets having a small protrusion height of few wall units ($y^+<15$) aligned in the streamwise direction of the flow that effectively act as an anisotropic roughness imposed on an impermeable wall. The experimental work of Berchert *et al.* [3], the theoretical analysis of Luchini et al. [4] and the numerical simulations of Choi *et al.* [5] are probably the most representative investigations striving to identify the physical mechanisms that promotes drag reduction and its breakdown for large values of the protrusion height. Indeed, the overall drag reduction produced by riblets is limited to a maximum of 10% with a non dimensionless riblet peak to peak spacing of about s^+=12-16. This maximum value of drag reduction attainable with a relatively simple streamwise oriented roughness is limited by the appearance of a linear instability that lead to the appearance of spanwise vorticity rollers also observed in other contexts when the value of the wall normal permeability is relaxed [6]. However, by assessing in detail the dermal structure of the skin of a smooth dogfish shark (*Mustelus canis*) using micro CT scans and gel-based surface profilometry methods, Ankhleyi *et al* [7] reported that the shark skin is fully covered with denticles that varied in size, shape, spacing, crown angle and presence/absence of ridges depending of the analysed portion of the body. However, while the presence of the stem and crown combination was a common characteristic that was observed throughout the whole shark skin, the ridges on the crowns were absent in its upstream portion of the body becoming a quite prominent feature in the rear part. This presence and absence of ridges led to the conjecture that the morphology of skin plays different hydrodynamic roles in different portions of the body, not only providing for a skin friction drag reduction mechanism. Recently, Bocanegra Evansa *et al* [8] conducted an experimental investigation looking at the possible role of the denticles on the control of boundary layer separation. Their observations confirmed that *ridgeless* denticles provide for a mitigation of the recirculation bubble in an adverse gradient turbulent boundary layer. On the other hand, Rosti *et al* [1] conducted numerical investigations on turbulent flows bounded by an anisotropic porous medium finding that the combination of vertical and in-plane permeability can potentially overcome the drag reduction limit of standard ribbletted surfaces. Similarly, more recently Gomez-de-Segura *et al* [2] conducted a stability analysis of turbulent flows over anisotropic porous walls, reporting that the formation of large spanwise roller which are due to a Kelvin Helmholtz like instability in standard ribbletted wall can be palliated enhancing the streamwise permeability as compared to the wall-normal one. The current study aims to explore the manipulation of turbulent wall bounded flows produced by the presence of denticles and the influence of their geometrical parameters on such manipulation in terms of either increase of local Reynolds stresses (i.e. separation control) or mitigation of skin friction drag.

PROBLEM FOMULATION

The current study has been carried out via a Direct Numerical Simulation approach using an in house developed incompressible Navier-Stokes Solver (SUSA). The governing equations are space discretised with a second order accurate, cell centred finite volume approach, while the time advancement is accomplished with a semi implicit, second order pressure correction scheme. The Poisson equation which enforces the continuity is solved directly with a fast solver exploiting FFTs in the periodic streamwise and spanwise directions. The MPI library is used in the framework of a domain

* Corresponding author. E-mail: shane.nicholas@city.ac.uk

decomposition approach to take advantage of parallel, memory distributed computer architectures. More information on the extensive validation campaign of the solver can be found in [10]. The denticles, which idealised model is shown at the bottom of figure 1, are modelled with the aid of a simplified Immersed Boundary method based on a Volume of Fluid (VOF) approach. In the current study, we have employed a denticle distribution of 32x16 in the streamwise and spanwise directions respectively, with an aligned arrangement which is reminiscent of the shark skin. Each denticle is fully resolved within the accuracy provided by the VOF formulation.

PRELIMINARY RESULTS

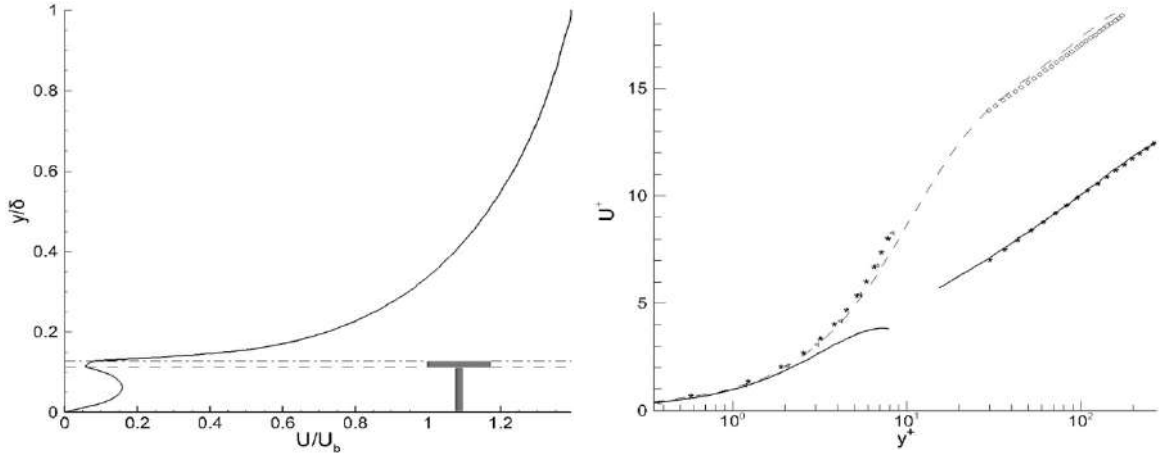

Figure 1. Mean velocity profile. On the left, the dashed line represent the position of the denticle crown. On the right, the dotted lines represent the logarithmic law whereas the dashed line represents, the canonical velocity profile of a channel flow at a nominal friction Reynolds number of $Re_\tau = 180$.

By inspecting the figure on the left showing the distribution of the mean velocity profile for denticles with spacing (s^+=13.6) distributed on the wall of an open channel with a nominal friction Reynolds number of $Re_\tau = 180$, it can be observed that there are three distinct flow regions, an outer layer which reminiscent of a canonical open channel turbulent flow, an inner shear layer that is formed underneath the denticle crown and a the wall layer in proximity of the zero velocity bottom surface. The outer flow continuously experiences an alternating boundary condition at the crown due to the transpiration that occurs by the voids between the adjacent denticles. The velocity profile formed in the inner layer bounded by the impermeable wall and the underside of the denticle crown is analogous to a parabolic function that characterises a laminar/transitional channel flow profile with a moving wall (i.e. a Poiseuille/Couette flow). Furthermore, the blocking effect of the denticle crown can clearly be evinced by the concavity of the inner profile. The overall shape of the mean profile resembles the one reported by Rosti *et al* [1] which could result in a drag reducing configuration. The figure on the right represents the mean velocity profile scaled by the inner and outer wall units. The outer flow was scaled by a friction velocity computed at the virtual origin. The latter can be interpreted as the location of the wall seen by the outer flow that can be deduced by inspection of the figure on the left side and can be explicitly determined to lay almost at the top of the denticle crown. The discontinuity of the profile is due to the second inner layer that is formed underneath the denticle crown with the complete modulation of the buffer layer dynamics.

CONCLUSIONS

To the authors knowledge the current investigation is the first attempt to produce a high-fidelity simulation of shark denticles from a viewpoint of a porous layer. Preliminary results have shed light on the various flow regimes. A complete discussion on the higher order statistics and pre-multiplied spectrum are presently ongoing and will be presented in the full paper. We would like to thank UKTC and EPSRC for providing computer time on Tier 2 CSD3, Cambridge.

References

[1] Rosti, M.E., Brandt, L. and Pinelli, A. Turbulent channel flow over an anisotropic porous wall – drag increase and reduction. Journal of Fluid Mechanics, 842, 2018.
[2] Gómez-de-Segura, G. and García-Mayoral, R. Turbulent drag reduction by anisotropic permeable substrates – analysis and direct numerical simulations. Journal of Fluid Mechanics, 875, 2019.
[3] Bechert, D.W., Bruse, M. and Hage, W. Experiments with three-dimensional riblets as an idealized model of shark skin. Experiments in Fluids, 28(5), 2000.
[4] Luchini P, Manzo F, Pozzi A. Resistance of a grooved surface to parallel flow and cross-flow. Journal of fluid mechanics. 228. 1991.
[5] Choi, H., Moin, P. and Kim, J. Direct numerical simulation of turbulent flow over riblets. Journal of Fluid Mechanics, 255(1), 1993.
[6] García-Mayoral R, Jiménez J. Drag reduction by riblets. Philosophical Transactions of the Royal Society A: Mathematical, Physical and Engineering Sciences., 369, 2011.
[7] Ankhelyi, M.V., Wainwright, D.K. and Lauder, G.V. Diversity of dermal denticle structure in sharks: Skin surface roughness and three-dimensional morphology. Journal of Morphology, 279(8), 2018.
[8] Bocanegra Evans, H., Hamed, A.M., Gorumlu, S., Doosttalab, A., Aksak, B., Chamorro, L.P. and Castillo, L.. Engineered bio-inspired coating for passive flow control. Proceedings of the National Academy of Sciences, 2018.

EFFECTS OF TWIN BOUNDARY ORIENTATION ON PLASTICITY OF BICRYSTALLINE COPPER MICROPILLARS: A DISCRETE DISLOCATION DYNAMICS SIMULATION STUDY [1]

DeAn Wei[1], Haidong Fan[2], Michael Zaiser[3], Guozheng Kang[1], Qianhua Kan[1], Xu Zhang *[1]
[1] School of Mechanics and Engineering, Southwest Jiaotong University, Chengdu, China
[2] Department of Mechanics, Sichuan University, Chengdu, China
[3] Institute of Materials Simulation WW8, FAU University of Erlangen-Nuremberg, Fürth, Germany

Summary Twin boundaries (TBs) constitute a special type of symmetric grain boundary (GB). TBs influence plastic deformation in a complex manner. In the present work, we propose a model for dislocation-TB interactions in the framework of discrete dislocation dynamics (DDD) simulations, which we use to investigate the mechanical properties of bicrystalline copper micropillars containing a TB. We systematically investigate how the compressive response depends on the orientation of the TB with respect to the micropillar cross-section. The simulations show significant strengthening effects for TB orientation angles less than 45º, where the interaction between mixed dislocations and TBs plays an important role. For angles larger than 45º, the interaction between screw dislocations and TB dominates, leading to weak strengthening. At 45º, dislocations on the dominant slip systems glide parallel to the TB and no strengthening is observed.

COMPUTATION MODEL AND DISLOCATION-TB INTERACTION MODEL

The simulated samples are bicrystalline micropillars in a form of rectangular hexahedra of size $750 \times 750 \times 1500 nm^3$. The orientations of the matrix and twin are shown by Thompson tetrahedra in Figure 1(a). The TB has an angle θ with respect to the micropillar cross-section; it is rotated about the direction $\mathbf{A^IB^I}$ ($\mathbf{B^IIA^II}$) which is aligned with the specimen *X*-axis. Three typical dislocation-TB interaction mechanisms obtained from molecular dynamics simulations [2] were introduced in DDD frame work Paradis [3] as shown in Fig. 1(b-e).

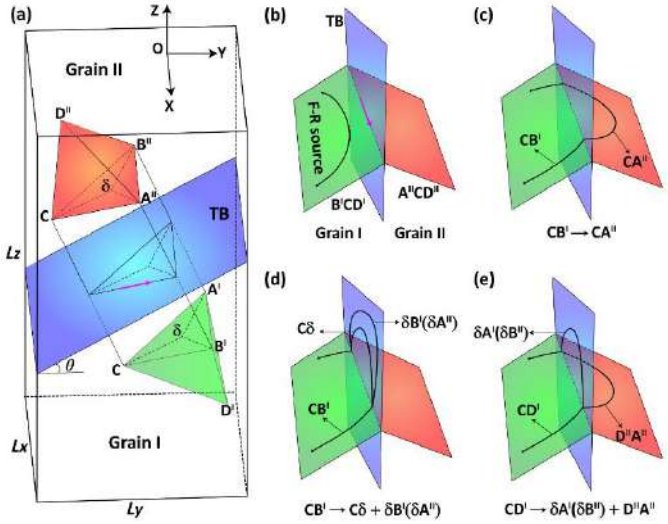

Figure 1. (a) A bicrystalline micropillar loaded along the Z-axis contains a TB. Schematic illustration of a dislocation approaching the TB. (c) Scenario 1: screw dislocation transmission through TB. (d) Scenario 2: screw dislocation absorption by TB. (e) Scenario 3: mixed dislocation penetration through TB.

MECHANICAL BEHAVIOURS

The overall stress-strain curves compiled in Fig 2(a) depends on TB angle. At angles from 0º to 15º, significant hardening is observed. As shown in Fig. 2(a), the yield stress is highest for θ= 0º. As the TB angle increases, the strength decreases and reaches a minimum at angles around 60º. Then the strength increases again as the orientation angle further increases. These findings, which are compiled in Fig. 2 (b), agree well with experimental results [4]. We can see that the yield stresses of the single crystals exhibit a similar trend as the bicrystal yield stress, which first decreases remarkably then increases. In addition, for orientation angles smaller than 45º the yield stress of the bicrystal is higher than that of the corresponding single crystals, indicating that the TB has a strengthening effect. For orientation angles larger than 45º, the bicrystals have comparable strength to the single crystals and their strength is intermediate between the two corresponding single-crystals, suggesting a weak hardening effect.

TB MICROSTRUCTURE EVOLUTIONS

Typical dislocation configurations are shown in Fig. 4. At $\theta = 0°$, mixed dislocations of multiple slip systems entangle

*Corresponding author. E-mail: xzhang@swjtu.edu.cn

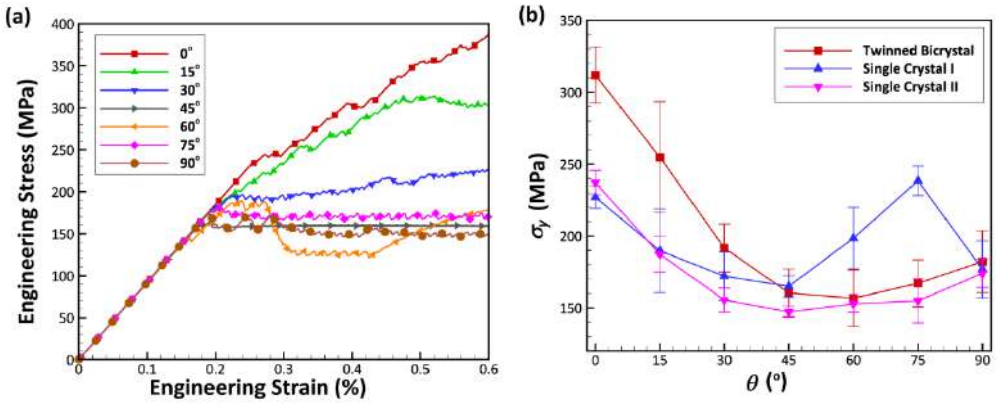

Figure 2. (a) Engineering stress-strain curves of bicrystals of various orientation angles. (b) Yield stresses of bicrystals and corresponding single crystals as a function of TB orientation.

as they pile up against the TB. At the orientation angle changed from15º to 45 º, the presence of the TB leads to a change in the deformation mechanism. Pilled-ups gradually disappears and free glide dislocations (slip parallel to TB) dominate plasticity. With a further increase of the orientation angle to 60º,), the $\mathbf{B^{II}C}$ dislocations then dissociate into two partial dislocations and glide on the TB, resulting in a high degree of twinning deformation and TB sliding. As the angle θ increases to 75° as shown in Fig. 4(f), screw dislocations $\mathbf{A^{II}C}$ and $\mathbf{B^{II}C}$ are activated and meet the TB, and the two phenomena – screw dislocation cross-slip and absorption by TB – can appear in the bicrystal at the same time. In the case of a 90º oriented TB, finally, all the active dislocations are screw dislocations. In this case, only dislocation transmission by cross-slips can be observed.

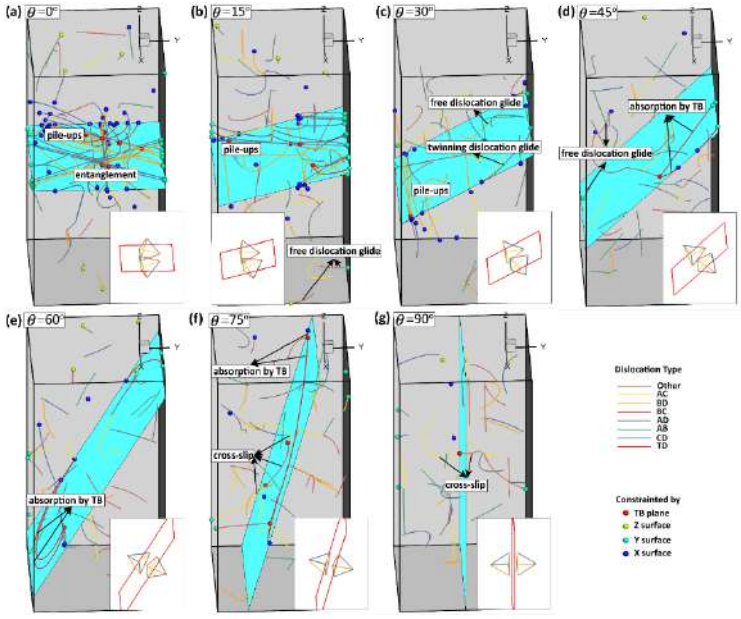

Figure 3 Typical dislocation configurations in the considered bicrystal micropillars at 0.6% total strain. (a) θ = 0º, (b) θ = 15º, (c) θ = 30º, (d) θ = 45º, (e) θ = 60º, (f) θ = 75º, (g) θ = 90º.

CONCLUSIONS

In this work, a dislocation-TB interaction model was introduced into DDD simulations to investigate the effect of TB orientation on the stress-strain response of axially loaded bicrystalline micropillars. The simulations show that the TB exhibits a strengthening effect, which however depends strongly on TB orientation. By changing the TB orientation with respect to the cross-section, the strengthening effect is found to be significant for angles less than 45º, but weak for angles larger than 45º. Especially at 90º, no strengthening effect is observed.

References

[1] D. Wei, M. Zaiser, Z. Feng, G. Kang, H. Fan, X. Zhang, Acta Mater., 176 (2019) 289-296.
[2] T. Zhu, J. Li, A. Samanta, H.G. Kim, S. Suresh, Proceedings of the National Academy of Sciences, 104 (2007) 3031-3036.
[3] A. Arsenlis, W. Cai, M. Tang, M. Rhee, T. Oppelstrup, G. Hommes, T.G. Pierce, V.V. Bulatov, Modelling and Simulation in Materials Science and Engineering, 15 (2007) 553.
[4] P.J. Imrich, C. Kirchlechner, C. Motz, G. Dehm, Acta Mater., 73 (2014) 240-250.

MARGINALLY SEPARATED BOUNDARY LAYER FLOWS: THE TRIPLE DECK STAGE

Dominik Kuzdas*[1] and Stefan Braun [1]
[1] TU Wien, Institute of Fluid Mechanics and Heat Transfer, Vienna, Austria

Summary High Reynolds number asymptotic theory is used to study laminar marginally separated boundary layer flows. From the asymptotic viewpoint, the bursting of a laminar separation bubble runs through various consecutive stages. The present work addresses triple deck equations governing the transient flow regime succeeding a finite time blow-up event in the solution of the fundamental equation of marginal separation theory. The numerical solutions of the corresponding Cauchy problem suggest the appearance of yet another finite-time blow-up, the associated break-down of the flow model and the formation of an Euler–Prandtl stage.

MOTIVATION

The transition from laminar to turbulent flow occurs in many engineering applications and still is not fully understood. In the present work we focus on the so-called 'by-pass' transition in localized boundary layer separation which typically may be observed in the flow past slender airfoils at small angles of attack or channel flows with suction. From a large Reynolds number point of view the bursting of a laminar separation bubble runs trough various consecutive stages. Each of them can be posed as a singular perturbation problem, Fig. 1.

The initial phase (i) is represented by a laminar wall-bounded shear layer on the verge of separation for which classical boundary layer theory ceases to provide an uniformly valid description. In the subsequent stage (ii) of so-called marginal separation viscous-inviscid interaction theory is capable of explaining the formation of closed, predominantly steady, reverse flow regions. However, the appearance of finite-time singularities in the numerical solution and the associated breakdown of the corresponding reduced model equations consequently leads to a spike formation stage (iii) which is governed by a fully nonlinear unsteady triple deck interaction. Although the Cauchy problem associated with this stage has been extensively studied in [1], a satisfactory numerical treatment of the suitably regularized problem is still lacking. In the present work we follow the achievements of [2] and [3] and aim for a reliable numerical solution of the triple deck stage (iii) to corroborate its terminal structure predicted by [1].

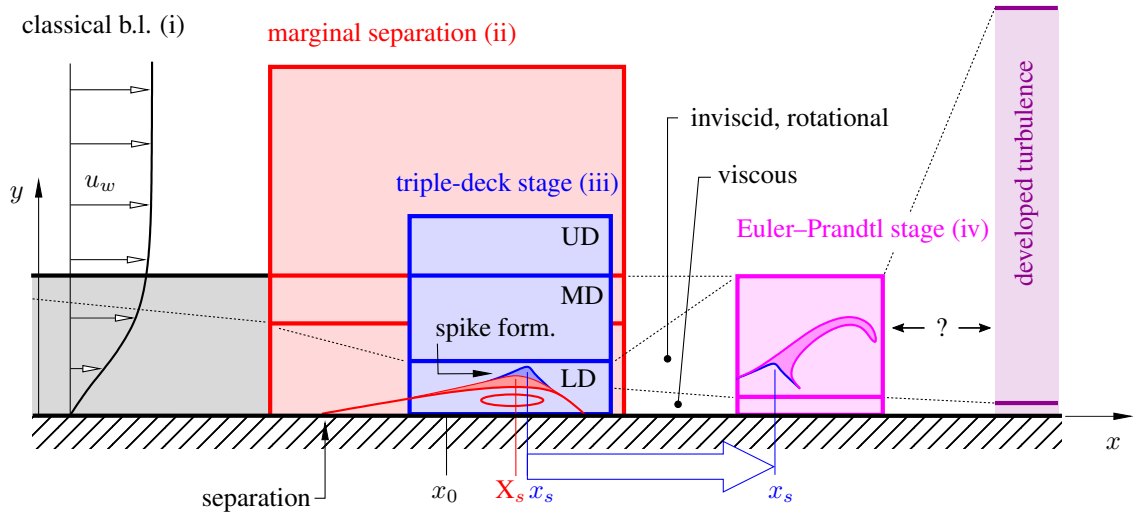

Figure 1: Asymptotic structure of the early stages of the laminar-turbulent transition process in laminar separation bubbles. Classical laminar boundary layer at the verge of separation (i), (black), composed of a viscous region (grey) and an inviscid outer flow (transparent). Consecutive interactive stages of marginal separation (ii) (red) and spike formation (iii) (blue), followed by self-induced vortex wind-up (magenta, shifted to the right for illustration) accompanied by finite-time blow-up events, here modelled up to the Euler–Prandtl (iv) stage. Continued bubble bursting finally leads to developed turbulent boundary layer flow (purple). Eventually a stage of fully developed turbulence may be reached.

SHORT OUTLINE

Based on the investigations regarding the finite time blow-up scenario of the marginal separation stage (ii) we want to address the consecutive triple deck stage (iii) numerically. For two-dimensional incompressible flows, the fundamental lower deck (LD) problem formulated in terms of the stream function $\psi(x,y,t)$, supplemented with the interaction law between the induced pressure $\mathcal{P}(x,t)$ and the displacement function $\mathcal{A}(x,t)$ from the upper deck (UD), reads

$$\frac{\partial^2\psi}{\partial y\partial t}+\frac{\partial\psi}{\partial y}\frac{\partial^2\psi}{\partial y\partial x}-\frac{\partial\psi}{\partial x}\frac{\partial^2\psi}{\partial y^2}=-\left(1+\frac{\partial\mathcal{P}}{\partial x}\right)+\frac{\partial^3\psi}{\partial y^3},\qquad \mathcal{P}=\frac{1}{\pi}\int_{-\infty}^{\infty}\frac{\partial\mathcal{A}/\partial\xi}{x-\xi}\mathrm{d}\xi. \tag{1}$$

*Corresponding author. E-mail: dominik.kuzdas@tuwien.ac.at.

Here x, y and t denote the stream-wise, the wall-normal coordinates and the time with all quantities being nondimensionalized and suitably scaled, [3]. Equations (1) are subject to the no-slip boundary conditions $\psi = \partial\psi/\partial y = 0$ at the solid wall $y = 0$, the far-field conditions $\psi \sim (y+A)^3/A + \ldots$ as $y \to \infty$ and $\psi \to y^3/6, (A, P) \to 0$, as $|x| \to \infty$. The initial or equivalently matching condition ensures the connection to the self-similar blow-up structure of the preceding marginal separation stage,

$$\begin{aligned}
\psi &\sim |t|^{\frac{1}{3}} \left(\frac{\hat{Y}^3}{6} + |t|^{-\frac{7}{9}} \hat{A} \frac{\hat{Y}^2}{2} + |t|^{-\frac{14}{9}} \hat{\psi} \right), \\
\hat{\psi} &\sim \left(\hat{\psi}_2(\hat{X}, \hat{Y}) + \hat{A}_1^2 \frac{\hat{Y}}{2} \right) + |t|^{-\frac{4}{9}} \left(\hat{\psi}_{e1}(\hat{X}, \hat{Y}) + \hat{A}_1 \hat{e}_1 \hat{Y} \right) + |t|^{-\frac{7}{9}} \left(\hat{\psi}_3(\hat{X}, \hat{Y}) + \hat{A}_1 \hat{A}_2 \hat{Y} + \hat{A}_1 \frac{\partial \hat{\psi}_2}{\partial \hat{Y}} + \frac{\hat{A}_1^3}{6} \right), \\
[\hat{A}, \hat{P}] &\sim [\hat{A}_1, \hat{P}_1](\hat{X}) + |t|^{-\frac{4}{9}} [\hat{e}_1, \hat{p}_{e_1}](\hat{X}) + |t|^{-\frac{7}{9}} [\hat{A}_2, \hat{p}_2](\hat{X}) + |t|^{-1} [\hat{e}_2, \hat{p}_{e_2}] + \cdots
\end{aligned} \tag{2}$$

as $t \to -\infty$ with the similarity scalings $x = |t|^{4/9}\hat{X}$ and $y = |t|^{1/9}\hat{Y}$. The leading order term $\hat{Y}^3/6$ represents the separation profile of the classical boundary layer and the (unique) blow-up profiles $[\hat{A}_1, \hat{P}_1]$ as well as $[\hat{e}_1, \hat{p}_{e_1}]$, etc. form Hilbert pairs according to the second equation (1). Further, $\hat{\psi}_2$, $\hat{\psi}_3$,... etc. are uniquely determined, the eigenfunctions $\hat{e}_1$, $\hat{e}_2$ with arbitrary amplitudes carry the history of the flow and enable the embedding of the local into a global solution.

To solve the initial value problem (1) and (2) for the intrinsic unknowns ψ, $\mathcal{A}$ and $\mathcal{P}$ the infinite (half space) domain of the asymptotic description is mapped onto a bounded domain and discretized with Chebyshev spectral collocation methods, [4]. In order to capture the singular behavior of ψ as $y \to \infty$ and the similarity properties as $x \to \pm\infty$ we use the ansatz $\psi(x, y, t) = (bd)^3\{[\eta + \mathcal{A}/(b^7 d)]^3/6 + g\}$, $\mathcal{A} = b^{-6}A$, $\mathcal{P} = b^{-10}P$ and the scalings $x = b^4\xi$, $y = bd\eta$ where the auxiliary functions $b(t)$, $d(\xi)$ exhibit the properties $b \sim |t|^{1/9}$ as $t \to -\infty$, $b \sim O(1)$ if $t \sim O(1)$ and $d \sim |\xi|^{1/4}$ as $\xi \to \pm\infty$, $d \sim O(1)$ if $\xi \sim O(1)$.

Time derivatives are formulated analytically based on the matching condition (2) in the asymptotic regime $-t \gg 1$ and otherwise approximated by a backward third order accurate finite differencing scheme capable of adaptive time stepping on a mapped domain. Finally, the nonlinear system of equations is solved using a modified Powell hybrid method.

The results of the numerical investigation are most conveniently depicted in terms of the boundary layer characteristics, namely displacement thickness $\delta^* - \delta_0^*(x_0) \propto Re^{-1/14}\mathcal{A}(x,t) + \cdots$ and wall shear stress $\tau_w \sim Re^{-1/14}\partial^2\psi/\partial y^2\,|_{y=0}$, Fig. 2. Special emphasis is placed on a proper start based on (2), see insert of Fig. 2(a). Although the terminal blow-up structure of (1) forwarded by [1] is not fully confirmed yet, the growing amplitudes in Fig. 2(b) strongly suggest a finite-time blow-up in the numerical solution of the triple deck equations (1) which triggers the subsequent Euler–Prandtl stage (iv).

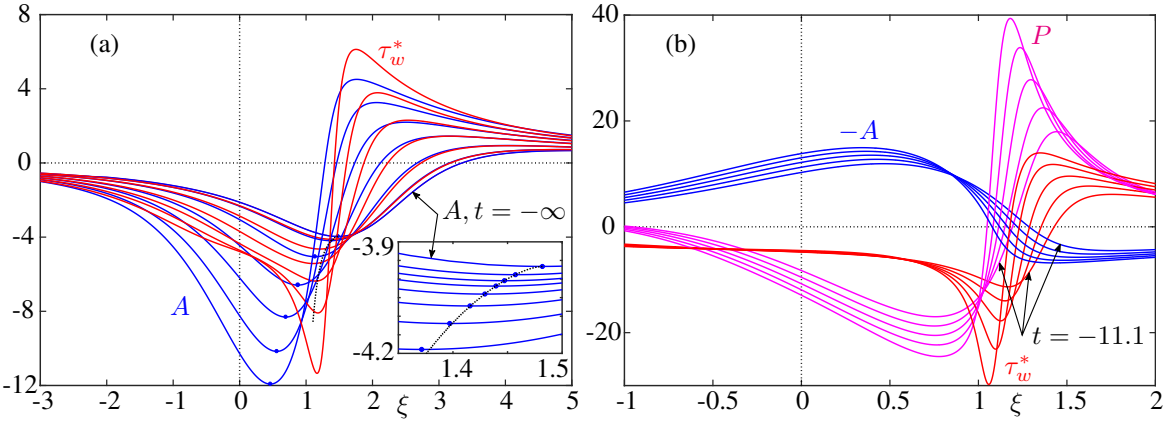

Figure 2: (a) Evolution of the displacement function $A(\xi, t)$ and the wall shear stress $\tau_w^*(\xi, t) = b^6\partial^2\psi/\partial y^2|_{y=0}$ for $t = -(\infty, 357, 58.2, 25.4, 17.0, 13.2, 11.1)$. Blue dots denote the minima of A according to (1) and the black dotted line the minimum of $\hat{A}$ in the limit as $t \to -\infty$, see eq. (2). Insert: Additional instants of time, $t = -(\infty, 6366, 3183, 2122, 1383, 889, 566, 357)$, confirm the connection to the preceding marginal separation stage. (b) Evolution of the induced pressure $P(\xi, t)$, $-A$ and τ_w^* for $t = -(11.1, 10.4, 9.75, 9.26, 8.83)$. The underlying polynomial approximation with the current resolution (n_ξ x $n_\eta \lesssim$ 230x115) fails to handle higher amplitudes for $t > -8.83$.

This work is supported by the Austrian Science Fund (FWF) (grant no. P31873-N32).

References

[1] Elliot J.W., Smith F.T. Dynamic stall due to marginal separation. *J. Fluid Mech.* **179**: 489-512, 1987.
[2] Scheichl S., Braun S., Kluwick A. On a similarity solution in the theory of unsteady marginal separation. *Acta Mech.* **201**: 153-170, 2008.
[3] Braun S., Scheichl S. On recent developments in marginal separation theory. *Phil. Trans. R. Soc. A* **372**: 1-16, 2014.
[4] Berrut J.-P., Trefethen L.N. Barycentric Lagrange Interpolation. *SIAM Rev.* **46**(3): 501-517, 2004.

MECHANISMS OF COHERENT AND RANDOM CONTRIBUTIONS TO DISSIMILAR HEAT TRANSFER ENHANCEMENT INDUCED BY TRAVELING WAVE-LIKEWALL BLOWING SUCTION

Arjun J. Kaithakkal *[1], Yukinori Kametani[1], and Yosuke Hasegawa[1,2]
[1] Institute of Industrial Science, The University of Tokyo, Japan
[2] Division of Applied Mathematics, Brown University, USA

Summary A turbulent channel flow (TCF) subjected to a traveling wave-like wall blowing and suction is studied using direct numerical simulations (DNSs). The turbulence fluctuation in the controlled flow contains some organized contribution due to the coherent nature of the control input, and hence can be decomposed into coherent and random contributions. The roles of the two key factors generating the dissimilar heat transfer, namely the fluid pressure and viscosity, are revealed through the budget analyses of the coherent and random contributions to the dissimilarity.

BACKGROUND

Due to the similarity between heat and momentum transfer, the 'Reynolds analogy'[1] predicts that an increase in heat transfer will be followed by a corresponding increase in momentum transfer. However, even if the governing equations of momentum and passive scalar are similar, their respective dynamics were found to show non-negligible dissimilarity for the canonical flow configurations. Indeed, it has been shown that a downstream traveling wave of wall blowing and suction can achieve significant dissimilarity[2,3]. The resulting dissimilarity can be quantified using the analogy factor $A = 2St/C_f$, where St and C_f respectively represents the non-dimensional heat and momentum flux, and dissimilar heat transfer enhancement is defined as $A > 1$. In the present paper, the dissimilar heat transfer enhancement achieved in a TCF using a traveling wave-like wall blowing and suction is studied through the budget analysis.

Numerical setup and Methodology

A fully developed TCF is numerically solved by DNS with a pseudo-spectral method[2]. A constant flow rate is imposed at a bulk Reynolds number of $Re = 2293$ and Prandtl number $Pr = 1$. The sinusoidal traveling wave of wall blowing and suction is given as, $v_w = \phi \sin\{2\pi/\lambda_x(x - U_p t)\}$. Here, ϕ, λ_x, and U_p represents the amplitude, wavelength, and phase-speed of the traveling wave, whereas t denotes the time. The root-mean-square value of the control input is set to be 5% of the bulk mean velocity. The wave parameters $(\lambda_x, U_p) = (1.12, 0.30)$ were found to achieve the maximum value for the analogy factor[3], and hence considered in the present study.

Following the previous studies[2,3], the contributions of the coherent and random components to dissimilarity can be quantified using, $D \equiv 2St - C_f = 3\int_{-1}^{1} y\overline{\tilde{v}(\tilde{\theta} - \tilde{u})}dy + 3\int_{-1}^{1} y\overline{v''(\theta'' - u'')}dy$, where $\tilde{(.)}$ and $(.)''$ denote the coherent and random components of turbulent fluctuations, respectively. Now, the generation of the coherent and random contributions to dissimilarity can be understood by analyzing the budget of $\overline{\tilde{v}(\tilde{\theta} - \tilde{u})}$ and $\overline{v''(\theta'' - u'')}dy$ as given by (1) and (2).

$$0 = \underbrace{\overline{\tilde{v}^2}\frac{\partial(\bar{\theta} - \bar{u})}{\partial y}}_{\text{production } (P_C)} \underbrace{- \overline{\widetilde{u_j''v''}\frac{\partial(\tilde{\theta} - \tilde{u})}{\partial x_j}}}_{\text{coupling term-1}(P_{C1_C})} \underbrace{- \overline{\{\widetilde{u_j''(\theta'' - u'')}\}\frac{\partial \tilde{v}}{\partial x_j}}}_{\text{coupling term-2 } (P_{C2_C})} + \underbrace{\frac{\partial}{\partial y}\left[\overline{(\tilde{\theta} - \tilde{u})\widetilde{v''v''} + \tilde{v}\{\widetilde{v''(\theta'' - u'')}\} + \tilde{v}\tilde{v}(\tilde{\theta} - \tilde{u})}\right]}_{\text{turbulent diffusion } (T_{D_C})}$$
$$\underbrace{-\frac{1}{Re}\frac{\partial}{\partial y}\left[\overline{\frac{\partial \tilde{v}(\tilde{\theta} - \tilde{u})}{\partial y}}\right]}_{\text{viscous diffusion } (V_{D_C})} \underbrace{- \overline{\left\{-(\tilde{\theta} - \tilde{u})\frac{\partial \tilde{p}}{\partial y} + \tilde{v}\frac{\partial \tilde{p}}{\partial x}\right\}}}_{\text{pressure-velocity-temperature correlation } (\Pi_C)} \underbrace{+ \frac{2}{Re}\overline{\frac{\partial \tilde{v}}{\partial x_j}\frac{\partial(\tilde{\theta} - \tilde{u})}{\partial x_j}}}_{\text{dissipation } (\epsilon_C)}. \quad (1)$$

$$0 = \underbrace{\overline{v''^2}\frac{\partial(\bar{\theta} - \bar{u})}{\partial y}}_{\text{production } (P_R)} \underbrace{+ \overline{\widetilde{u_j''v''}\frac{\partial(\tilde{\theta} - \tilde{u})}{\partial x_j}}}_{\text{coupling term-1 } (P_{C1_R})} \underbrace{+ \overline{\widetilde{u_j''(\theta'' - u'')}\frac{\partial \tilde{v}}{\partial x_j}}}_{\text{coupling term-2 } (P_{C2_R})} + \underbrace{\frac{\partial}{\partial y}\left[\overline{\tilde{v}\{\widetilde{v''(\theta'' - u'')}\} + v''v''(\theta'' - u'')}\right]}_{\text{turbulent diffusion } (T_{D_R})}$$
$$\underbrace{+\frac{1}{Re}\frac{\partial}{\partial y}\left[\overline{\frac{\partial v''(\theta'' - u'')}{\partial y}}\right]}_{\text{viscous diffusion } (V_{D_R})} \underbrace{- \overline{\left\{-(\theta'' - u'')\frac{\partial p''}{\partial y} + v''\frac{\partial p''}{\partial x}\right\}}}_{\text{pressure-velocity-temperature correlation } (\Pi_R)} \underbrace{+ \frac{2}{Re}\overline{\frac{\partial v''}{\partial x_j}\frac{\partial(\theta'' - u'')}{\partial x_j}}}_{\text{dissipation } (\epsilon_R)}. \quad (2)$$

*Corresponding author. E-mail: arjun@iis.u-tokyo.ac.jp

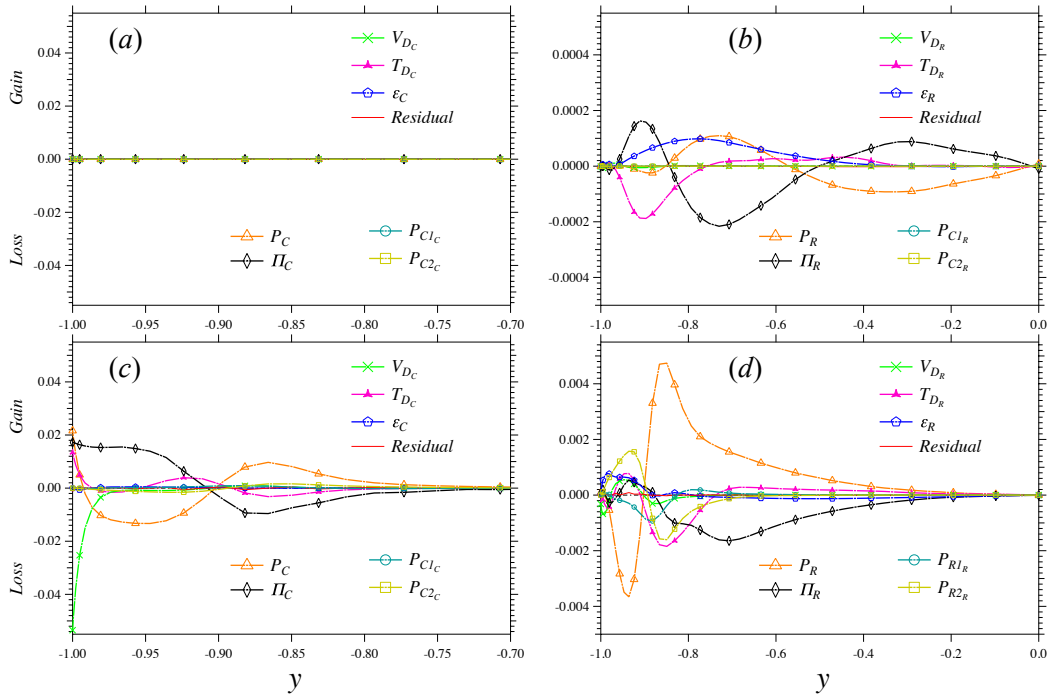

Figure 1: Terms in the budget equation for $-\overline{\tilde{v}(\tilde{\theta}-\tilde{u})}$ (a & c) and $-\overline{v''(\theta''-u'')}$ (b & d) for the uncontrolled (a & b) and controlled (c & d) channel flow.

RESULTS AND DISCUSSIONS

All the terms in the budget equation (1) and (2) are plotted in figure 1, for the uncontrolled and controlled channel flows (UCF and CF). The budget terms in the coherent contribution for the UCF and CF are respectively shown in figure 1(a) and 1(c). The absence of the coherent component in the UCF makes all the terms null as shown in figure 1(a). For the CF, on the other hand, the pressure fluctuation acts as the major factor causing dissimilarity in the coherent field. This can be confirmed from figure 1(c) by the dominant positive value of Π_C in the near-wall region where the coherent contribution becomes significant[3]. Π_C is balanced by P_C except in the near wall region. In the vicinity of the wall the positive contributions from Π_C, P_C, and T_{D_C} are balanced solely by the viscous diffusion term V_{D_C}, indicating the crucial role of viscosity in the dissimilar heat transfer process very close to the wall.

The plots of the budget terms in the random contribution to dissimilarity for the UCF and CF are respectively shown in figure 1(b) and 1(d). It is interesting to see that the budget of the random contribution to dissimilarity for the UCF is quite small, yet non-zero. This small contribution is caused by of the pressure fluctuation that affects only the dynamics of streamwise momentum. The vertical scale of figure 1(b) is one order of magnitude less than that of figure 1(d). Similarly, the range of the vertical axis in figure 1(d) is one order magnitude less than that of figure 1(c). It is worth noting, however, that the budget terms (production, diffusion, dissipation etc.) correspond to the 'fluxes' entering or leaving the system, and do not tell 'how much' remains in the system at an equilibrium state. Rather, the large budget terms (higher fluxes) of the coherent contribution in figure 1(c) should be interpreted as quick response of the coherent contribution, so that it can reach an equilibrium faster, while the random contribution is slower to reach an equilibrium (compare figure 1(c) and 1(d)). In figure 1(d), the term P_R represents a source term through the interaction of the mean component with the random component, and is found to be the most dominant term. Also, their positive and negative peaks agree well with those observed in the profile of the random contribution (not shown here). Since $\overline{v''^2}$ is always positive, the sign of is determined by the sign of $d(\bar{\theta}-\bar{u})/dy$. In fact it is found that the profile of $d(\bar{\theta}-\bar{u})/dy$ (not shown here) changes its sign between the respective peak locations.

In conclusion the analysis shows that the mechanism of the random contribution to dissimilarity depends on the indirect interaction between the coherent and random fields. This is in contrast to that of the coherent contribution to dissimilarity, where the correlation between velocity/temperature and pressure gradient, Π_C, is the dominant factor.

References

[1] Reynolds, *Proc. Lit Phil. Soc. Manchester* 14, 7-12, 1874.
[2] Hasegawa & Kasagi, J. Fluid Mech. 683, 57-93, 2011.
[3] Kaithakkal *et al.*, *J. Fluid Mech.* (accepted).

TOWARDS TURBULENT DRAG REDUCTION WITH PLASMA-BASED SPANWISE FORCING – A COMPARISON OF ACTUATION CONCEPTS

Marc T. Hehner[1], Jochen Kriegseis*[1], Nicolas Benard[2], Marios Kotsonis[3], Bettina Frohnapfel[1] and Davide Gatti[1]
[1] Institute of Fluid Mechanics (ISTM), Karlsruhe Institute of Technology (KIT), Karlsruhe, Germany
[2] PPrime Institute, University of Poitiers CNRS, Poitiers, France
[3] Faculty of Aerospace Engineering, Delft University of Technology, Delft, The Netherlands

Summary Three distinct concepts of spanwise flow forcing using plasma actuators are synthesised, implemented and compared in terms of their respective advantages and limitations. The three concepts involve either temporal or spatial oscillation of the plasma forcing, ultimately aimed at turbulent drag reduction. All experimental characterization efforts of the respective concepts are discussed in reference to the ISTM duct-flow facility in order to provide the comparison in physical dimensions (as relevant for actuator development and operation) and furthermore in viscous units (as relevant for the control concept in a turbulent channel flow).

BACKGROUND

Across the board of external and internal flow scenarios, the skin-friction drag is one of the key factors to determine the energy expenditure required to perform respective engineering applications. Consequently, numerous research efforts addressed the successful reduction of this contribution of drag and thus achieved meaningful energy savings. Among the different techniques towards turbulent drag reduction [1], Streamwise Traveling Waves (StTW) of spanwise wall velocity have established as one successful approach [2]. StTWs impose a transverse fluid motion on the mean flow by periodic oscillation of the surface, as shown in figure 1 (a). Additionally, the oscillation is periodically modulated along the streamwise direction. The achievable amount of drag reduction can be visualized for particular conditions of Re_τ in a (oscillation-) frequency (f), -streamwise wavelength (λ_x) plane [3]. Experimental studies have shown that StTWs favourably interact with near-wall turbulence and attain great potential for turbulent drag reduction and net energy savings (see e.g. [4-7]). However, the so-far proposed devices mainly involve physical oscillation of the wall, achieved through various mechanical means. These yield high complexity and limited control ability. Resonant effects or mechanical inertia of physically oscillating walls bound the maximum oscillation frequency, thus limiting applicability to a narrow range of typically relatively low Re_τ.

Plasma actuators are a type of electrical flow-control device of less complex structure than their mechanical alternatives. They can be configured to mainly induce wall-parallel momentum in the vicinity of the surface, providing a promising alternative to pure in-plane wall movement. Finally, they are based on electrical rather than mechanical principles, thus having the potential for high-frequency operation. Pioneering efforts by Wilkinson [8] and Jukes *et al.* [9] have laid the necessary foundations for advanced concepts to accomplish plasma-based drag reduction. Recent experimental proof-of-concept studies by Hehner *et al.* [10, 11] and Benard *et al.* [12] demonstrated the feasibility of concepts to produce particular kinds of virtual StTWs by a spanwise forcing; see figures 1 (b) and (c), respectively.

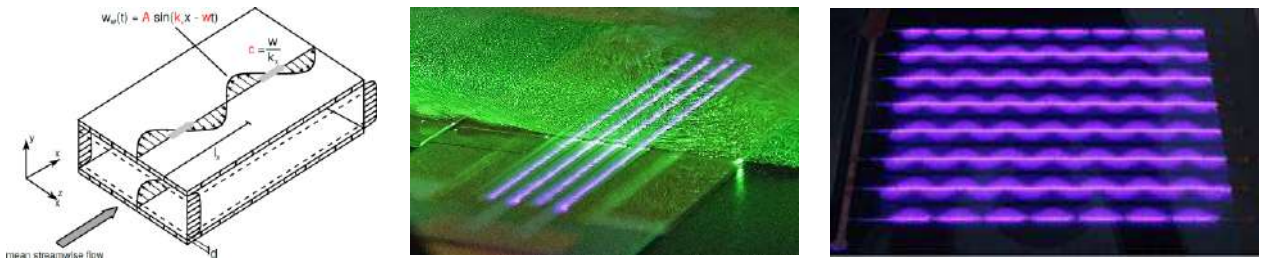

Figure 1: StTW of spanwise wall velocity. (a) Duct section and wall-velocity profile $w(x)$ of StTW. Reproduced from [6]. Spanwise forcing in (b) for virtual wall oscillation [10,11] and in (c) for (streamwise) standing waves [12] of virtual spanwise wall velocity.

OBJECTIVES

Due to the flexibility and large parameter space of plasma actuators, several concepts for efficient and effective StTW generation have been brought forward recently. The objective of the current work is to draw a comparison of the available actuation concepts for plasma actuators [10-12] through a well-documented common test case and elaborating advantages and disadvantages, relevant concept characteristics and Re_τ limitations. The drag-reduction map (f,λ_x-plane), presented by Gatti & Quadrio [6], spans two degrees of freedom for StTWs, which particularly lead to two special cases of (i) a purely temporal oscillation with $\lambda_x \rightarrow \infty$ and (ii) a standing wave in space without temporal oscillation, i.e. $f = 0$.

On the one hand this map provides a clear guideline for promising parameter combinations for successful flow control – on the other hand, however, this parameter space scales in viscous units, which closely relies on the considered test case

*Corresponding author E-mail: kriegseis@kit.edu

and, furthermore, requires a careful translation to physical dimensions, since the latter is the relevant parameter space for development, operation and control of either plasma-actuator concept. As such, the present contribution particularly elaborates the proper choice of control parameters from either perspective: flow requirements (in viscous units) and the actuator requirements (in physical units). This combined evaluation leads to a clear guideline for promising parameter combinations, which match the requirements from both perspectives. It is foreseen that all concepts are eventually applied, tested and evaluated in the ISTM duct-flow facility [6].

ACTUATION CONCEPTS FOR SPANWISE FORCING

Hehner *et al*. recently introduced two concepts for virtual wall oscillations with plasma actuators [10,11], both of which maintain a spanwise oscillatory forcing to virtually mimic wall oscillations. The so-called *burst* concept [10] individually operated various groups of electrodes in pulsed mode, where the duty-cycle (DC) and corresponding oscillation frequency f, and the force magnitude F can be adjusted precisely. The major drawback of the *burst* concept is the comparably fast material degradation of the dielectric due to continuous switch-on and -off events. The so-called *beat* concept is applied with the identical electrode array, but operated in a totally different way. In order to minimize the dielectric wear, the *beat* concept avoids any duty cycles, where all groups of electrodes receive a high-voltage signal at slightly different plasma frequencies, such that the resulting beat frequencies between the electrode groups lead to an effective duty-cycle frequency f. The advantage of a "mild" plasma operation comes with the price that the formerly independent control parameters of effective DC and forcing magnitude F are inherently coupled to the supplied high voltage for the beat concept. Benard et al. [12] introduced a plasma actuator that is capable of producing a virtually standing wave of spanwise velocity in the streamwise direction, as shown in figure 1 (c). This effectively *convective* oscillation concept works with steadily operated plasma discharges and only one group of high-voltage electrodes. In contrast to the electrical simplicity of this concept (at least in comparison with the *burst* and *beat* concepts), an accurately designed electrode shape along the main flow direction is of utmost importance for a successful operation of the *convective* concept. Particularly, the actuator design and operation have to match the optimal wavelength λ_x and forcing magnitude F for the respective Re_τ.

For the *burst* and *beat* concept the applicable Re_τ reaches an upper limit when the decreasing oscillation period cannot be compensated with an increase of the forcing magnitude. For the *convective* concept, Re_τ is limited by both a constructive and flow-characteristic confinement. The decreasing λ_x may lead to either too small geometric dimensions of the plasma actuator or to collapse of the induced standing wave. The main difference in the applicability of the three concepts is the adaptability of the control to the flow conditions. While for the standing wave the range of Re_τ at which drag reduction can be achieved is predetermined by the locked streamwise wavelength λ_x, the frequency of oscillation can be individually tuned for the *burst* and *beat* concept. Therefore, variable flow conditions can be considered for the latter applications, where a change of the oscillation frequency additionally requires an adjustment of the forcing amplitude.

Since all actuator concepts are scheduled to be evaluated in the channel-flow facility at ISTM [6], the actuator-parameter space will be converted into viscous units as apply for this wind tunnel, where skin friction is determined accurately via pressure-drop measurements. The test-section half height is $h = 12.6$ mm and the possible Reynolds number range is $200 < Re_\tau < 2500$.

The interplay of the influencing factors and control parameters will be comparatively discussed and evaluated along the drag-reduction map [3] as function of the possible Re_τ range of the ISTM test facility.

References

[1] Corke, T. C., Thomas, F. O. "Active and Passive Turbulent Boundary-Layer Drag Reduction". *AIAA J.* **56**, 3835-3847, 2018.

[2] Quadrio, M., Ricco, P., Viotti, C. "Streamwise-travelling waves of spanwise wall velocity for turbulent drag reduction," *J. Fluid Mech.* **627**, 161-178, 2009.

[3] Gatti, D., Quadrio, M. "Reynolds-number dependence of turbulent skin-friction drag reduction induced by spanwise forcing," *J Fluid Mech* **802**, 553-582, 2016.

[4] Auteri, F., Baron, A., Belan, M., Campanardi, G., Quadrio, M. "Experimental assessment of drag reduction by traveling waves in a turbulent pipe flow," *Phys. Fluids* **22**, 115103, 2010.

[5] Bird, J., Santer, M., and Morrison, J. F. "Experimental control of turbulent boundary layers with in-plane travelling waves," *Flow, Turbul. Combust.* **100**, 1015-1035, 2018.

[6] Gatti, D., Güttler, A., Frohnapfel, B. Tropea, C. "Experimental assessment of spanwise-oscillating dielectric electroactive surfaces for turbulent drag reduction in an air channel flow," *Exp. Fluids* **56**, 110, 2015.

[7] Choi, K.-S., Clayton, B. R. "The mechanism of turbulent drag reduction with wall oscillation," *Int. J. Heat Fluid Flow* **22**, 1-9, 2001.

[8] Wilkinson, S. P. "Investigation of an oscillating surface plasma for turbulent drag reduction," *AIAA paper* **2003-1023**, 2003.

[9] Jukes, T., Choi, K.-S., Johnson, G., Scott, S. "Turbulent drag reduction by surface plasma through spanwise flow oscillation," *AIAA paper* **2006-3693**, 2006.

[10] Hehner, M.T., Gatti, D., Kriegseis, J. "Stokes-layer formation under absence of moving parts – A novel oscillatory plasma actuator design for turbulent drag reduction," *Phys. Fluids* **31**, 051701, 2019.

[11] Hehner, M.T., Gatti, D., Mattern, P., Kotsonis, M., Kriegseis, J. "Beat-Frequency-Operated Dielectric-Barrier Discharge Plasma Actuators for Virtual Wall Oscillations", *AIAA J.*, October 2020.

[12] Benard, N., Bayoda, K.D., Bonnet, J. P., Moreau, E. "Non Homogeneous Streamwise Wall Forcing by Surface Plasma Actuator," *EDRFCM*, 2019.

IMPROVED EQUILIBRIUM WALL STRESS MODEL FOR TURBULENT BOUNDARY LAYERS WITH ZERO PRESSURE GRADIENT

Kevin Griffin,* Lin Fu, and Parviz Moin
Center for Turbulence Research, Stanford University, Stanford, CA 94305, USA

Summary In practice, there are two inconsistencies encountered when applying the equilibrium wall model (EQWM) for wall-modeled large-eddy simulation (WMLES): 1) the assumption of a constant stress layer is often not satisfied, and 2) the matching location is often outside the log layer. Herein, we propose two improvements to the classical EQWM: a) we explicitly account for the dependence of total stress on the distance from the wall, and b) we propose a modified eddy viscosity model that is applicable for the wake region of the boundary layer. These improvements greatly enhance the predictive capability of the EQWM, even when the matching location is at the edge of the boundary layer. This flexibility renders the new model much more suitable for WMLES of flows over complex geometries.

INTRODUCTION

The classical form of the EQWM begins with the one-dimensional RANS equation (neglecting the pressure gradient and advection terms) as

$$\frac{d}{dy}\left((\nu_t+\nu)\frac{dU}{dy}\right)=\frac{d\tau/\rho}{dy}. \tag{1}$$

Invoking the constant stress layer assumption, the term on the right-hand side vanishes. This ODE is then solved for $U(y)$ between the wall, where the no-slip condition is applied, and a matching location, where the LES solution is provided. In general, moving the matching location further away from the wall decreases the LES resolution requirements but also increases the reliance on the RANS model. To close this equation for $U(y)$, Cabot and Moin (2000) [1] employed the algebraic eddy viscosity model

$$\nu_t=\ell_m u_\tau,\quad \ell_m=\kappa y D,\quad D=(1-\exp(-y^+/A^+))^2, \tag{2}$$

where the turbulence eddy viscosity scales linearly with y for large y^+. Consequently, when coupled with the constant stress layer assumption, it recovers the log law away from the wall. This is, however, only appropriate when this model is deployed with a matching location in the log region. Large errors are generated if the matching location is in the wake region, where the constant stress layer and linear eddy viscosity assumptions are not valid.

NEW MODEL

In this work, we develop a new model which accounts for a non-constant stress layer, and we introduce an eddy viscosity form that is accurate regardless of the matching location.

Total stress distribution

For the classical EQWM, the built-in assumption is that the variation of the total stress between the wall and the matching location is negligible if the matching location is in the log layer (e.g. $\mathcal{O}(200\delta_\nu)$). When the matching location is any significant fraction of the boundary layer thickness, the assumption is invalid and typically the total stress is a function of wall-normal distance. Chen et al. [2] propose a model for the dependence of the total stress on the wall-normal distance. This model, i.e.

$$\tau(y)=\tau_w\left(1-\left(\frac{y}{\delta}\right)^{3/2}\right), \tag{3}$$

has been verified for a large range of Reynolds numbers [2]. Fig. 1a indicates that the prediction of this model agrees well with the DNS data [6]. With this model, we account for the right-hand side of Eq. (1) explicitly, rather than neglecting it as in the classical model.

Modified eddy viscosity model

Maise and McDonald (1968) [5] observed that the mixing length behaves like κy in the log region but plateaus in the wake region to a nearly universal value of $C_{max}\approx 0.09\delta$. This observation is robust to changes in Mach number and even moderate adverse pressure gradients. We design a hyperbolic tangent function for a mixing length model since it is a simple function that obeys the aforementioned linear and constant asymptotes. We replace the classical mixing length model, $\ell_m=yD$, with a new model,

$$\ell_m=C_{max}\tanh(\kappa y/C_{max})D. \tag{4}$$

While Cabot and Moin (2012) [1] take u_τ as the velocity scale in the classical model (which is consistent with a constant stress layer assumption), we propose to use the velocity scale $\sqrt{\tau(y)/\rho}$ instead. Fig. 1b and 1c indicate that these new models for ℓ_m and ν_t agree much better with DNS than the classical model.

*Corresponding author. E-mail: kevinpg@stanford.edu.

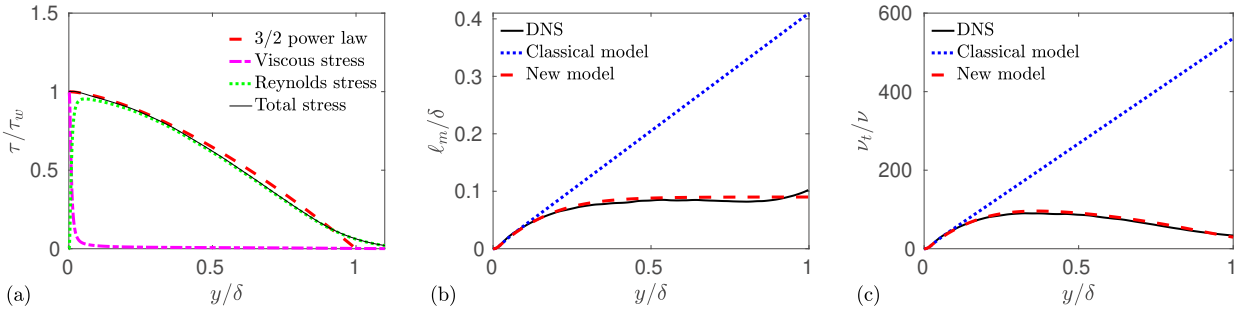

Figure 1: (a) The assumption of a constant total stress layer is not well motivated when the matching location $y_m/\delta > 0.2$. The new mixing length (a) and eddy viscosity (b) models agree well with DNS [6], unlike the classical models, which perform poorly in the outer layer ($Re_\theta = 4000$).

RESULTS

As shown in Fig. 2a, the new model correctly predicts the log law in the log region and also predicts the wake region well, whereas the classical model continues to predict a log law for all y. Fig. 2b with linear axes clearly shows the reduced prediction error in the outer layer from our new model. Fig. 2c shows that over a wide range of Re_θ from 300 (marginally turbulent) to 13000, the new model performs substantially better than the classical model.

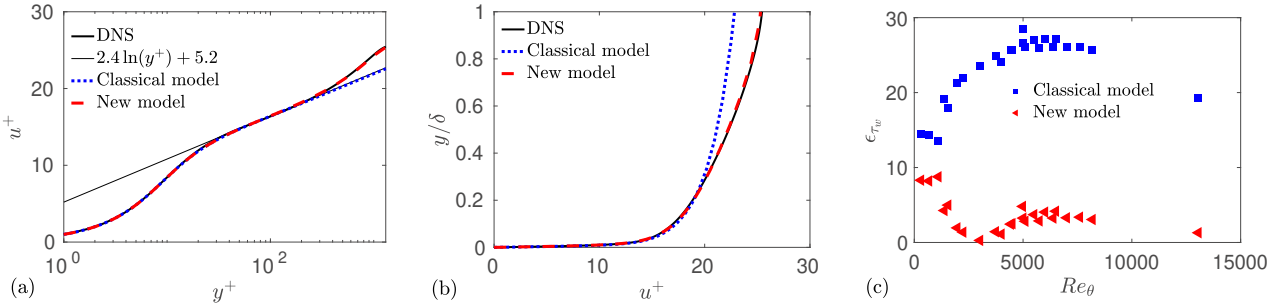

Figure 2: Velocity profiles for the new and the classical model on (a) semi-log and (b) linear scales show that the new model greatly improves the predicted mean velocity profile for the $Re_\theta = 4000$ case. (c) The percent error in wall shear stress, ϵ_{τ_w}, of the new model is much lower than that of the old model. Error is measured with respect to DNS, experiment, or WRLES [6, 4, 8, 3, 7].

CONCLUSIONS

We have improved the EQWM to accommodate a non-constant stress distribution and proposed a new eddy viscosity model for the wake region of turbulent boundary layers. These simple modifications greatly improve the predictive capability of the EQWM model and allow for setting the matching location for the model anywhere between the wall and the edge of the boundary layer. This flexibility in the choice of the matching location is essential for a robust deployment of the EQWM in complex geometries, since in such cases it is difficult and computationally expensive to guarantee that the matching location is in the log layer.

References

[1] W. Cabot and P. Moin. Approximate Wall Boundary Conditions in the Large-Eddy Simulation of High Reynolds Number Flow. *Flow, Turbul. Combust.*, 63:269–291, 2000.
[2] X. Chen, F. Hussain, and Z.-S. She. Non-universal scaling transition of momentum cascade in wall turbulence. *J. Fluid Mech.*, 871, 2019.
[3] G. Eitel-Amor, R. Örlü, and P. Schlatter. Simulation and validation of a spatially evolving turbulent boundary layer up to Re_θ = 8300. *Int. J. Heat Fluid Flow*, 47:57–69, 2014.
[4] J. Jiménez, S. Hoyas, M. P. Simens, and Y. Mizuno. Turbulent boundary layers and channels at moderate Reynolds numbers. *J. Fluid Mech.*, 657:335–360, 2010.
[5] G. Maise and H. McDonald. Mixing length and kinematic eddy viscosity in a compressible boundary layer. *AIAA J.*, 6(1):73–80, 1968.
[6] J. A. Sillero, J. Jiménez, and R. D. Moser. One-point statistics for turbulent wall-bounded flows at Reynolds numbers up to $\delta^+ \approx 2000$. *Phys. Fluids*, 25, 2013.
[7] A. J. Smits, E. F. Spina, A. E. Alving, R. W. Smith, E. M. Fernando, and J. F. Donovan. A comparison of the turbulence structure of subsonic and supersonic boundary layers. *Phys. Fluids A*, 1:1865–1875, 1989.
[8] P. R. Spalart. Direct simulation of a turbulent boundary layer up to R_θ= 1410. *J. Fluid Mech.*, 187:61–98, 1988.

ANTOMY OF DETERMINISITIC TURBULENT SPOTS+

Kwing-So Choi*[1], Yaxing Wang[1], Mike Gaster[2], Chris Atkin&[2], Yury Kachanov[3] and Vladimir Borodulin[3]
[1] Faculty of Engineering, University of Nottingham, Nottingham, UK
[2] School of Mathematics, Computer Science and Engineering, City, University of London, London, UK
[3] Institute of Theoretical and Applied Mechanics, Novosibirsk, Russia

Summary Experiments were carried out in a low-turbulence wind tunnel to study the initiation and development of deterministic flow structures in a laminar boundary layer over a flat plate under the excitation of broadband disturbances. Velocity measurements using a hot-wire probe revealed that the excited boundary layer developed well-organized events resembling turbulent spots. We found that these structures were highly reproducible until a very late stage of transition. Development of "deterministic" turbulent spots through a merger of low-speed structures is detailed here, which created a large delta-shaped lump accompanied by a thin positive velocity region near wall. Our investigation followed a recent experimental work on deterministic turbulence in order to study the anatomy of turbulent spots with a view to develop a strategy for controlling them for skin-friction drag reduction.

BACKGROUND

During the boundary layer transition, patches of turbulence, so-called turbulent spots can be observed as a part of the developing process leading to a fully developed turbulent boundary layer. Wygnanski et al [1] used electrical discharges to trigger a laminar boundary layer to generate turbulent spots for a detailed study of their structure. Gaster and Grant [2] used single-point impulses to excite a laminar boundary layer to create three-dimensional wave packets. Shaikh [3] used a sequence of broadband noise to excite the laminar boundary layer, where he found that the disturbance waves were modulated in a repeatable and deterministic manner. The subsequent generation of turbulent spots was similar to that observed in naturally excited situations. A similar wind tunnel investigation was performed by Borodulin and Kachanov [4] recently, who found that the boundary layer flow was deterministic until a very late transition stage where the turbulence statistics was similar to that of a fully developed turbulent boundary layer.

EXPERIMENTAL SETUP AND PROCEDURE

Experiments were carried out in a low turbulence wind tunnel at City, University of London. The wind tunnel test section had a dimension of 0.91 m (height) by 0.91 m (width) by 1.8 m (length), whose turbulence level was less than 0.005% for the frequency range of between 2 Hz and 2 kHz. The flat-plate test surface was made of aluminium cast tooling plate with a length of 1.5 m, which was vertically installed inside the test section. An excitation source consisted of 19 miniature speakers along the span. The cylindrical-shaped speakers of 12 mm in diameter, 9.5 mm high were embedded in the flat plate to excite the boundary layer through 19 small holes of 1 mm diameter. The excitation source was located at 325 mm from the leading edge, covering a span of 300 mm with a 15 mm interval. The wind tunnel speed was set at 18 m/s. The undisturbed baseline flow was set to zero-pressure gradient by adjusting the trailing edge flap and tab. The excitation signal was 400 ms long, which was repeated 20 times while the streamwise velocities were measured by a single hot-wire probe. The measurements were taken for a streamwise range from x = 350 mm to x = 1000 mm and over a spanwise range of z = ±60 mm across the whole boundary-layer thickness.

RESULTS AND DISCUSSIONS

The downstream change in the ensemble-averaged streamwise fluctuating velocity with a broad-band noise excitation from a point source is shown in Fig. 1. Here, the measurements were taken along the central line of the test plate between x = 330 mm and 700 mm. An early development of turbulent spots is seen only after 5 mm downstream of the excitation source, where a number of low-speed structures of approximately 1 mm high are seen at x = 330 mm. These are the precursor events to turbulence spots, which look like the heads of hairpin eddies. For example, five of such low-speed structures are seen at t = 110 ms at x = 330 (top figure), growing in size and strength as well as in number downstream. These low-speed structures will eventually "merge" together, creating a large delta-shaped lump accompanied by a thin positive fluctuating velocity region near wall, see the bottom figure at x = 500 mm. The contours of turbulent spots are highly reproducible in terms of their timing and duration as they are of relatively low frequency signal. This is in contrast to individual high-frequency spike signals (not shown here) within each turbulent spot, whose reproducibility is not very high. Therefore, the control strategy of "deterministic" turbulent spots must be developed based on the information of spot contour rather than individual low-speed hairpin structure within.

+ Supported by EPSRC grant EP/M028690/1
*Corresponding author. E-mail: kwing-so.choi@nottingham.ac.uk
&Currently at the University of East Anglia, UK

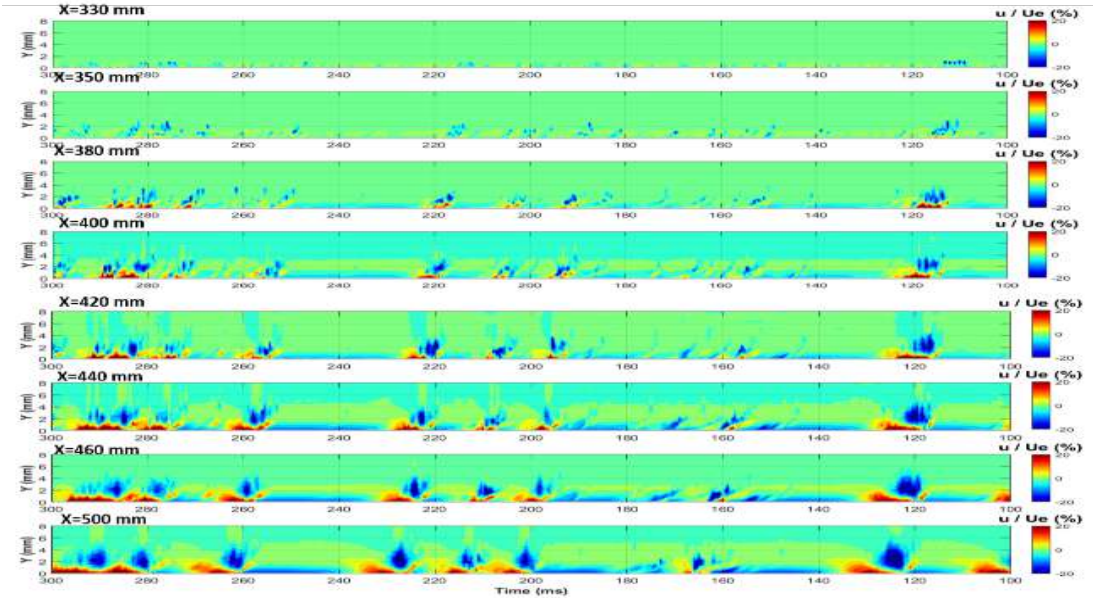

Figure 1. Contours of the streamwise velocity fluctuations, showing the downstream developments of boundary layer under a broadband excitation form a point source. The excitation source is at x = 325 mm from the leading edge.

Ensemble-averaged streamwise velocity contours of turbulent spots at x = 600 mm are given in Fig. 2 in t-z space. Here, the x-axis of the figure is represented by the negative time to show the spatial structure of turbulent spots from the temporal measurements. Here, we used Taylor's frozen flow hypothesis to convert time t to streamwise distance z using the measured convection velocity of turbulent spots. All turbulent spots are seen along the centreline (z = 0) of the flat-plate test surface. Turbulent spots are about 60 mm wide and 300 mm long at this streamwise location. Some turbulent spots are followed by another turbulent spot, while others are isolated. The number of turbulent spots does not seem to increase in the downstream, although the volume (length, width and height) of turbulent spots increased until they occupied all "empty" spaces. The turbulence level is high within the turbulent spots, increasing the intermittency downstream. At a wall-normal distance of y = 3.4 mm (bottom figure) only the wing-shape structure of negative velocity can be seen, suggesting that the leading edge of turbulent spots that is formed by the ejection of low-momentum fluid [5] is located further away from the wall. The wing-shaped structure is tallest at the centre (z = 0). At y = 1.0 mm (top figure), on the other hand, each wing of turbulent spots is followed by an oval-shaped high-velocity region. These high-velocity regions that are created by the downwash of high-momentum fluid [5] are always paired and are located closer to the wall. The coherent coefficient, a measure of the deterministic level of turbulence, across the span of turbulent spots is nearly constant.

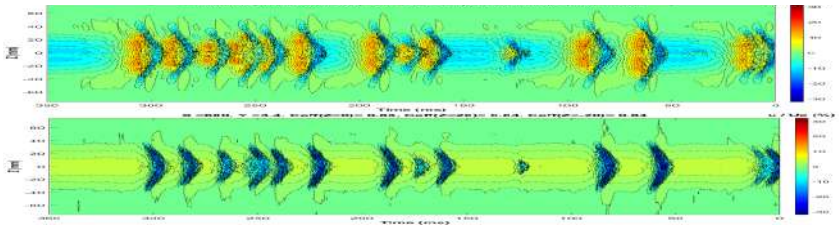

Figure 2: Contours of streamwise fluctuation velocity at x = 600 mm; y = 1.0 mm (top) and y = 3.4 mm (bottom).

CONCLUSIONS

Deterministic turbulent boundary layer was used to study the structure of turbulent spots in a low-turbulence wind tunnel. We were able to show that turbulent spots were initiated by hairpin-like structures that eventually merge to grow. They were highly reproducible, providing an opportunity for developing a control strategy for skin-friction drag reduction.

References

[1] Wygnanski I., Sokilov M., Friedman D. On a turbulent spot in a laminar boundary layer. *J. Fluid Mech.,* 78, 785-819, 1976.

[2] Gaster M., Grant I. An experimental investigation of the formation and development of a wave packet in a laminar boundary layer. *Proc. R. Soc. Lond. A* **430**, 253-269, 1975.

[3] Shaikh F.N. Investigation of transition to turbulence using white-noise excitation and local analysis techniques. *J. Fluid Mech.,* **348**, 29-83, 1997.

[4] Borodulin V.I., Kachanov Y.S. Experimental evidence of deterministic turbulence. *Eur. J. Mech., B/Fluids*, **32**, 5-11, 2013.

[5] Schroder A., J. Kompenhans J. Investigation of a turbulent spot using multi-plane stereo particle image velocimetry. *Exp.Fluids.* **36**, 82-90, 2004.

EXTENSION OF THE QSQH THEORY TO ALL VELOCITY COMPONENTS

Sergei Chernyshenko*
Department of Aeronautics, Imperial College London, London SW7 2AZ, UK

Summary An extension of the QSQH theory of the effect of large-scale structures on near-wall turbulence is proposed. It applies to all three components of the velocity and takes into account the fluctuations of the large-scale component of the wall friction. As an example of application, the dependence of the amplitude of fluctuations of the second moments of velocity on the Reynolds number is considered. The analysis explains why this dependence is particularly strong for the longitudinal and spanwise velocities. It also gives the shape of the increments of these two quantities with the Reynolds number as a function of the distance to the wall.

EXTENSION OF THE QSQH THEORY

According to the classical universality hypothesis, as the Reynolds number, Re, tends to infinity, the characteristics of the near-wall part of a turbulent boundary layer, if expressed in wall units, become independent of Re. It is now known that this hypothesis is not strictly accurate. The large-scale motions in the bulk of the boundary layer affect the near-wall flows [1]. This invalidates the classical universality hypothesis because the large-scale motions are Re-dependent in wall-units. The Quasi-Steady-Quasi-Homogeneous (QSQH) theory [2–4] describes the dominant features of the effect of large-scale motions. It has already been broadly confirmed, e.g. see [5–7]. The QSQH theory was originally formulated for the longitudinal velocity only, but recent comparisons [7] extend it to the spanwise and wall-normal velocity components, albeit without taking into account the fluctuations of the direction of large-scale wall friction. We will formulate the full extension of the QSQH theory and give an example of its application.

The QSQH theory presumes that any vector or scalar field can be represented as a sum of a large-scale and small-scale component. In particular, the wall friction $\boldsymbol{\tau}^*(t,x,z) = \boldsymbol{\tau}^*_L(t,x,z) + \boldsymbol{\tau}^*_L(t,x,z)$. We will use non-dimensional units based on the kinematic viscosity and the average large-scale friction velocity $\langle u^*_{\tau_L} \rangle = \langle \sqrt{|\boldsymbol{\tau}^*_L(t,x,z)|/\rho^*} \rangle$, where ρ^* is the density and the angular brackets denote averaging. Coordinate systems in figure 1 are related by the formulae $x_\theta = x\cos\theta - z\sin\theta$, $y_\theta = y$, $z_\theta = x\sin\theta + z\cos\theta$, $u = u_\theta\cos\theta + w_\theta\sin\theta$, $v = v_\theta$, and $w = -u_\theta\sin\theta + w_\theta\cos\theta$. The extended QSQH theory states that if $u_\theta(t,x_\theta,y_\theta,z_\theta,Re) = u_{\tau_L}\tilde{u}(\tilde{t},\tilde{x},\tilde{y},\tilde{z})$, $v_\theta(t,x_\theta,y_\theta,z_\theta,Re) = u_{\tau_L}\tilde{v}(\tilde{t},\tilde{x},\tilde{y},\tilde{z})$, $w_\theta(t,x_\theta,y_\theta,z_\theta,Re) = u_{\tau_L}\tilde{w}(\tilde{t},\tilde{x},\tilde{y},\tilde{z})$, and $\tilde{t} = tu^2_{\tau_L}$, $\tilde{x} = x_\theta u_{\tau_L}$, $\tilde{y} = y_\theta u_{\tau_L}$, $\tilde{z} = z_\theta u_{\tau_L}$, then the statistical properties of $\tilde{u}(\tilde{t},\tilde{x},\tilde{y},\tilde{z})$, $\tilde{v}(\tilde{t},\tilde{x},\tilde{y},\tilde{z})$, and $\tilde{w}(\tilde{t},\tilde{x},\tilde{y},\tilde{z})$ are independent of u_{τ_L}, θ, and Re. In general $u_{\tau_L} = u_{\tau_L}(\tilde{t},\tilde{x},\tilde{z})$ and $\theta = \theta(\tilde{t},\tilde{x},\tilde{z})$. If u_{τ_L} and θ were independent of time then u_{τ_L} would be equal to 1, the large-scale friction would be equal to the mean friction, our non-dimensional units would coincide with the wall units, and $\tilde{u},\tilde{v},\tilde{w}$ would be the velocity components in wall units. This highlights the physical meaning of the QSQH theory: the near-wall flow adjusts to the large-scale wall friction as if it were constant in time and homogeneous in space.

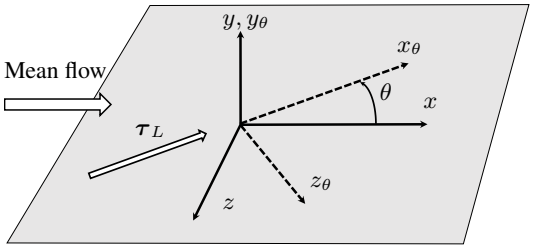

Figure 1: Coordinate x is in the mean flow direction, x_θ is in the direction of the large-scale component of the wall friction, y and y_θ are wall-normal, and z and z_θ are in the wall plane.

DEPENDENCE OF THE SECOND MOMENTS OF VELOCITY ON THE REYNOLDS NUMBER

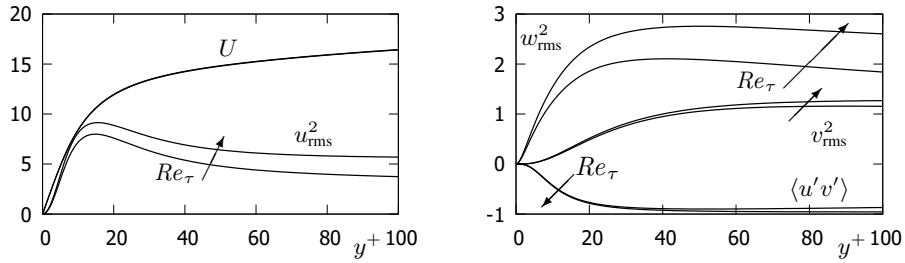

Figure 2: Data for plain channel at $Re_\tau = 950$ and 5200 from turbulence.oden.utexas.edu [8,9]. The curves for U overlap.

It is known that as Re changes, $u^2_{\rm rms} = \langle u'^2 \rangle$ and $w^2_{\rm rms} = \langle w'^2 \rangle$ vary much faster than $U(y) = \langle u \rangle$, $v^2_{\rm rms} = \langle v'^2 \rangle$, and $\langle u'v' \rangle$ (the primes denote fluctuations). But why is there such a difference? The very small variation of U with Re is explained in [3], and accounting for $\theta \neq 0$ adds little to it. We will concentrate on the second moments of velocity.

Applying the QSQH derivation technique described in [3] and assuming $\langle u'^2_{\tau_L} \rangle \ll 1$ and $\langle \theta^2 \rangle \ll 1$ gives the following expressions for the differences between the values at two Re:

$$\Delta u^2_{\rm rms} = \Delta\langle u'^2_{\tau_L} \rangle \left[\left(\frac{d\tilde{U}}{dy} \right)^2 + \frac{1}{2} \frac{d^2 y^2 \tilde{u}^2_{\rm rms}}{dy^2} \right] + \Delta\langle \theta^2 \rangle \left(\tilde{w}^2_{\rm rms} - \tilde{u}^2_{\rm rms} \right) + \ldots, \quad \Delta v^2_{\rm rms} = \frac{\Delta\langle u'^2_{\tau_L} \rangle}{2} \frac{d^2 y^2 \tilde{v}^2_{\rm rms}}{dy^2} + \ldots,$$

*Corresponding author. E-mail: s.chernyshenko@imperial.ac.uk.

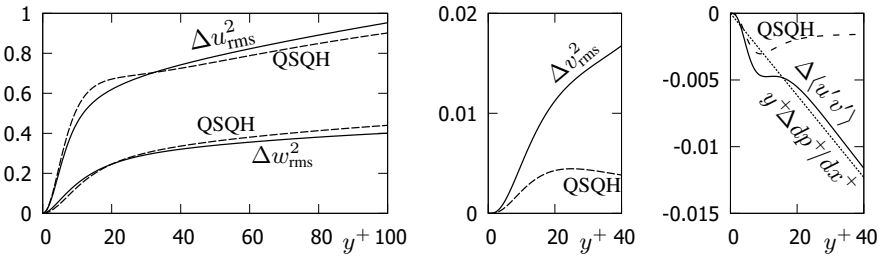

Figure 3: Increments of the second moments as Re_τ changes from 2000 to 5200: DNS ——, QSQH – – –, $y^+\Delta dp^+/dx^+$ ·····.

$$\Delta w^2_{\rm rms} = \frac{\Delta\langle u'^2_{\tau_L}\rangle}{2}\frac{d^2y^2\tilde{w}^2_{\rm rms}}{dy^2} + \Delta\langle\theta^2\rangle\left(\tilde{U}^2 + \tilde{u}^2_{\rm rms} - \tilde{w}^2_{\rm rms}\right) + \ldots, \quad \Delta\langle u'v'\rangle = \frac{\Delta\langle u'^2_{\tau_L}\rangle}{2}\frac{d^2y^2\tilde{\tau}_R}{dy^2} - \frac{1}{2}\langle\theta^2\rangle\tilde{\tau}_R + \ldots,$$

where $\tilde{U}(y) = \langle\tilde{u}\rangle$, $\tilde{u}^2_{\rm rms} = \langle\tilde{u}'^2\rangle$, $\tilde{v}^2_{\rm rms} = \langle\tilde{v}'^2\rangle$, $\tilde{w}^2_{\rm rms} = \langle\tilde{w}'^2\rangle$ and $\tilde{\tau}_R = \langle\tilde{u}'\tilde{v}'\rangle$. Since $\langle u'^2_{\tau_L}\rangle \ll 1$ and $\langle\theta^2\rangle \ll 1$, estimates can be done assuming that $\tilde{U} \approx U$, $\tilde{u}^2_{\rm rms} \approx u^2_{\rm rms}$, $\tilde{v}^2_{\rm rms} \approx v^2_{\rm rms}$, $\tilde{w}^2_{\rm rms} \approx w^2_{\rm rms}$, and $\tilde{\tau}_R \approx \langle u'v'\rangle$. The estimate shows that the terms with $\tilde{U}$ dominate. At $y^+ = 40$ for example, $(dy\tilde{U}/dy)^2 \approx 285$, while $u^2_{\rm rms} \approx 6$, and $U^2 \approx 203$, while $w^2_{\rm rms} \approx 2.4$. Dropping the much smaller terms gives that $\Delta u^2_{\rm rms} \approx \Delta\langle u'^2_{\tau_L}\rangle(dy\tilde{U}/dy)^2$, $\Delta w^2_{\rm rms} \approx \Delta\langle\theta^2\rangle\tilde{U}^2$, while $\Delta v^2_{\rm rms} \approx \Delta\langle u'v'\rangle \approx 0$. The physical mechanism of the term with $(dy\tilde{U}/dy)^2$ is the amplitude and wall-normal-scale modulation by the large-scale motions [2,3], while the term with $\tilde{U}^2$ is the effect of the fluctuations of the direction of the large-scale wall friction, which is introduced in the present work.

The precise values of $\langle u'^2_{\tau_L}\rangle$ and $\langle\theta^2\rangle$ and the statistics of the universal velocity depend on the definition of the large-scale filter. Assuming that a suitable filter exists one can adjust $\Delta\langle u'^2_{\tau_L}\rangle$ and $\Delta\langle\theta^2\rangle$ to fit $\Delta u^2_{\rm rms}$ and $\Delta w^2_{\rm rms}$. Taking $\Delta\langle\theta^2\rangle = 0.0016$ and $\Delta\langle u'^2_{\tau_L}\rangle = 0.0025$ for Re_τ changing from 2000 to 5200 gives the results shown in figure 3. The deviation of the QSQH predictions for $\Delta u^2_{\rm rms}$ and $\Delta w^2_{\rm rms}$ is not large and is of the same order of magnitude as reported in most cases in [3]. The QSQH predictions for $\Delta v^2_{\rm rms}$ and $\Delta\langle u'v'\rangle$ deviate considerably, by an order of magnitude, from the DNS results. This is because for these quantities the predicted QSQH effects are very small. The almost linear behaviour of $\Delta\langle u'v'\rangle$ for $y^+ > 20$ is suggestive. It is well-known that the dependence of the total shear stress on the distance to the channel wall is linear and in wall units is equal to $y^+dp^+/dx^+ = y^+/Re_\tau$, and that further away from the wall the Reynolds stress approaches the total stress. As Re_τ changes, so does the pressure gradient. The corresponding change in the total stress, equal to $\Delta y^+dp/dx = y^+(1/5200 - 1/2000)$, is shown with a dotted line in figure 2 and fits well the deviation between the QSQH prediction and DNS. Therefore, the deviation is due to the QSQH theory not taking into account the nonzero pressure gradient in a channel flow.

CONCLUSIONS

The proposed extension of the QSQH theory takes into account the fluctuations of the large-scale component of the wall friction. It describes the effect of large-scale motions on all three components of the velocity of near-wall turbulent flows. As an example of application, the extended theory explains the large sensitivity of the magnitudes $u_{\rm rms}$ and $w_{\rm rms}$ of the fluctuations of longitudinal and spanwise velocities to Reynolds number in comparison with the sensitivity of the mean velocity profile, the Reynolds stress, and the magnitude of the fluctuations of the wall-normal velocity. It is shown that the variation of $u_{\rm rms}$ with Re is largely caused by the variation of the amplitude and wall-normal-scale modulation by the outer, large-scale, Re-dependent motions, while the variation of $w_{\rm rms}$ is largely caused by the fluctuations of the direction of the large-scale, Re-dependent, component of the wall friction. The Re dependence of the other second moments is not dominated by these mechanisms because the mean universal wall-normal velocity is zero. In particular, the effect of the variation of the mean pressure gradient with Re is stronger than the QSQH mechanisms as far as the variation of the Reynolds stress with Re is concerned.

References

[1] R. Mathis, N. Hutchins, and I. Marusic. Large-scale amplitude modulation of the small-scale structures in turbulent boundary layers. *J. Fluid Mech.*, 628:311–337, 2009.
[2] S. I. Chernyshenko, I. Marusic, and R. Mathis. Quasi-steady description of modulation effects in wall turbulence, 2012. arXiv:1203.3714.
[3] C. Zhang and S. I. Chernyshenko. Quasisteady quasihomogeneous description of the scale interactions in near-wall turbulence. *Phys. Rev. Fluids*, 1:014401, May 2016.
[4] S. I. Chernyshenko, C. Zhang, H. Butt, and M. Beit-Sadi. A large-scale filter for applications of QSQH theory of scale interactions in near-wall turbulence. *Fluid Dyn. Res.*, 51(1):011406, jan 2019.
[5] L. Agostini and M. Leschziner. On the validity of the quasi-steady-turbulence hypothesis in representing the effects of large scales on small scales in boundary layers. *Phys. Fluids*, 28(4):045102, 2016.
[6] W. Baars, N. Hutchins, and I. Marusic. Reynolds number trend of hierarchies and scale interactions in turbulent boundary layers. *Phil. Trans. R. Soc. Lond.*, 375:20160077, 03 2017.
[7] L. Agostini and M. Leschziner. On the departure of near-wall turbulence from the quasi-steady state. *J. Fluid Mech.*, 871:R1, 2019.
[8] S. Hoyas and J. Jiménez. Scaling of the velocity fluctuations in turbulent channels up to $Re_\tau = 2003$. *Phys. Fluids*, 18(011702):1–4, 2006.
[9] M. Lee and R. D. Moser. Direct numerical simulation of turbulent channel flow up to Re_τ=5200. *J. Fluid Mech.*, 774:395–415, 2015.

DRAG REDUCTION BY TRANSVERSAL SURFACE WAVES IN SWEPT FLAT PLATE FLOW

Marian Albers *[1] and Wolfgang Schröder[1,2]
[1] Institute of Aerodynamics, RWTH Aachen University, Wüllnerstrasse 5a, 52062 Aachen, Germany
[2] JARA Center for Simulation and Data Science, RWTH Aachen University, Seffenter Weg 23, 52074 Aachen, Germany

Summary Large-eddy simulations of the drag reduction technique of traveling transversal surface waves at varying sweep angle in turbulent boundary layer flow over a flat plate are conducted. The results show only a moderate effect on the overall drag reduction for small sweep angles and downstream traveling waves. For a partially upstream traveling wave the effect is more diverse with increased viscous drag reduction but also strong additional pressure drag.

INTRODUCTION

The improvement of the aerodynamic efficiency of aircraft is one of the key methods for substantially lowered global CO_2 emissions. Since the drag of slender bodies moving in a fluid is to a large extent determined by viscous forces at the body surface, which are mainly determined by turbulent boundary layer flows developing along the surface, there is considerable interest to decrease the friction and pressure drag through control measures. Active flow control techniques, i.e., techniques where energy is introduced into the system, have proven to be capable of significantly reducing the wall-shear stress in turbulent wall bounded flows. For instance, spanwise wall oscillations [1] or streamwise oscillations of spanwise wall velocity [2] can strongly decrease the wall friction with limited control input such that also net power savings are achieved. Another technique, spanwise traveling transversal surface waves, has similar effects on the turbulent flow field [3, 4] by indirectly creating oscillating spanwise shear close to the wall. Many techniques for active drag reduction have a preferential direction of the actuation, e.g., spanwise or streamwise. However, in real flows a perfect alignment is not always guaranteed. Therefore, we investigate the influence of small to moderate angles of the propagation direction for transversal surface waves.

SETUP

Large-eddy simulations (LES) of spanwise traveling transversal surface waves in swept flat plate turbulent boundary layer flow are considered. The flow is investigated for a momentum thickness based Reynolds number of $Re_\theta = 1000$ at x_0, i.e., the location where the control region is initialized. The physical domain is discretized by a time-dependent curvilinear structured grid. A grid resolution of at least $\Delta x^+ = 10.7$, $\Delta y^+|_{\text{wall}} \leq 1.05$ and $\Delta y^+|_{\text{bl-edge}} = 13.2$, and $\Delta z^+ = 4.3$ in the streamwise, wall-normal, and spanwise direction is used which ensures the accurate approximation of all relevant flow scales and also of the curved boundary surface. On the surface, a time- and space-dependent no-slip condition is used. The y-coordinate of the wall in the interval $0 \leq x \leq 150$ is described by the function

$$y^+|_{\text{wall}}(\tilde{z}^+, t^+) = g(x)A^+ \cos\left(\frac{2\pi}{\lambda^+}\tilde{z}^+ + \frac{2\pi}{T^+}t^+\right), \tag{1}$$

where $\tilde{z} = z - \sin\varphi(x - x_0)$ is the propagation direction of the traveling wave and φ is the sweep angle between the spanwise direction z and the propagation vector $\tilde{z}$. A smooth transition from the non-actuated to the actuated region and vice versa is enabled by the piecewise-defined function $g(x)$. The parameters of the wave motion are the wavelength $\lambda^+ = \lambda u_\tau/\nu = 3000$, period $T^+ = Tu_\tau^2/\nu = 50$, and amplitude $A^+ = Au_\tau/\nu = 70$. These values showed high drag reduction in a previous investigation [4]. Sweep angles of $\varphi \in [0°, 10°, 20°, 30°]$ are considered for partially downstream traveling waves and $\varphi = 30°$ for upstream traveling waves.

RESULTS

A first impression of the near-wall flow field for one of the actuated cases can be obtained from Fig. 1 where streamwise velocity streaks are depicted for upstream traveling waves with a sweep angle of $\varphi = 30°$. In comparison to the incoming flow, i.e., non-actuated turbulent boundary flow, the near-wall structures show a mean inclination to the streamwise direction. Furthermore, the streaks appear to be larger with less structures in the high-wavenumber end of the spectrum.

The impact of the sweep angle on the pressure and viscous drag is illustrated in Fig. 2. The first column, which represents the baseline case $\varphi = 0°$, shows a purely viscous drag reduction of about 25 percent. Since lines of equal phase of the wave motion are perfectly aligned with the streamwise direction no additional pressure drag contribution is obtained. This changes when the sweep angle has non-zero values. For the second, third, and fourth columns, which

*Corresponding author. E-mail: m.albers@aia.rwth-aachen.de

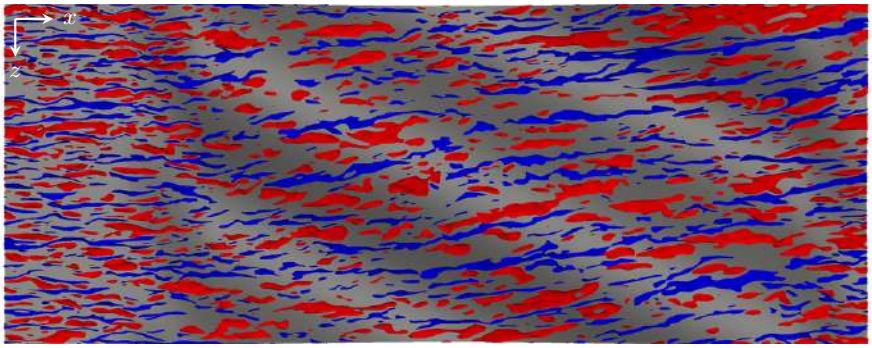

Figure 1: Contours of the random streamwise velocity fluctuations for $u''^{+} = -3$ (blue) and $u''^{+} = 3$ (red) in the streamwise interval $-20 \leq x \leq 145$ and in the near-wall region $0 < y^{+} < 20$ of the actuated upstream traveling wave case.

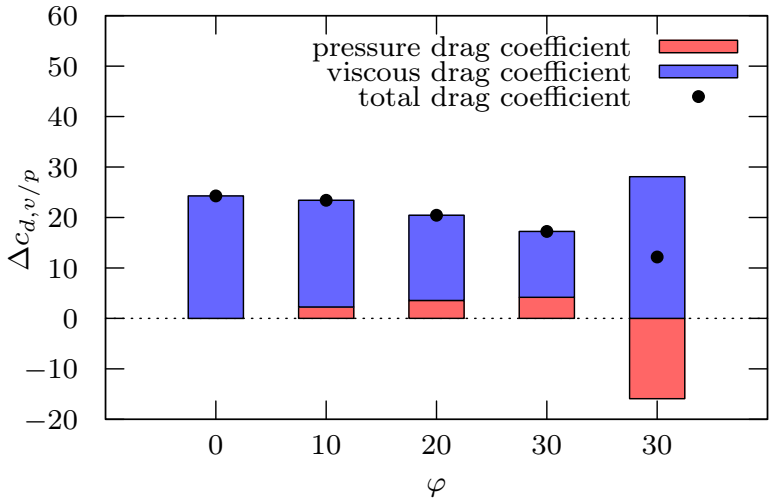

Figure 2: Variation of the viscous, pressure, and total drag coefficient.

represent increasing sweep angles for downstream traveling waves a decreasing viscous drag reduction and an additional favorable pressure drag contribution is observed. That is, the decrease of the overall drag reduction is damped since the pressure distribution generates thrust on the wavy surface. For the upstream traveling case, i.e., the fifth column, on the other hand a strong additional pressure drag diminishes the high viscous drag reduction such that the overall drag reduction is only moderate.

CONCLUSION

Large-eddy simulations of transversal traveling surface waves in turbulent boundary layer flow at a sweep angle were conducted. The results show a decrease of the overall drag reduction for non-zero angles. However, for small angles the effect is only on the order of a few percent since an additional positive pressure drag balances the decrease of the viscous drag reduction for downstream traveling waves. For upstream traveling waves the increased viscous drag reduction is diminished by a negative additional pressure drag. The detailed alterations of the turbulent flow field due to non-zero sweep angles will be presented at the conference.

References

[1] E. Touber and M.A. Leschziner, "Near-wall streak modification by spanwise oscillatory wall motion and drag-reduction mechanisms", *J. Fluid Mech.*, vol. 693, pp. 150-200, 2012.

[2] C. Viotti, M. Quadrio, and P. Luchini, "Streamwise oscillation of spanwise velocity at the wall of a channel for turbulent drag reduction", *Phys. Fluids*, vol. 35, p. 115109, 2009

[3] M. Albers, P. S. Meysonnat, and W. Schröder, "Actively reduced airfoil drag by transversal surface waves," *Flow Turbul. Combust.*, vol. 102, pp. 865–886, 2019.

[4] M. Albers, P.S. Meysonnat, D. Fernex, R. Semaan, B.R. Noack, W. Schröder, "Drag reduction and energy saving by spanwise traveling transversal surface waves for flat plate flow", *submitted to Flow Turbul. Combust.*, the preprint is available on *arXiv*, 2019

PARTICLE IMAGE VELOCIMETRY BASED EVALUATION OF COHERENT STRUCTURES AND SKIN-FRICTION DRAG REDUCTION BY SPANWISE WALL OSCILLATIONS

Kushal Kempaiah[1], Fulvio Scarano[1], Gerrit E. Elsinga[2] and Bas W. Van Oudheusden[1]
[1] Aerospace Engineering Department, TU Delft, Delft, the Netherlands
[2] Mechanical Engineering Department, TU Delft, Delft, the Netherlands

Summary The reduction of turbulent skin-friction drag over a fully developed canonical zero-pressure gradient turbulent boundary layer (ZPGTBL) subjected to spanwise oscillation is measured using planar particle image velocimetry (PIV). The experiments are conducted at Re_θ of 1000, the chosen range of spanwise oscillation amplitude and frequency is around the optimum reported in earlier studies ($T^+_{osc} = 100 - 700$, $A^+_{osc} = 50 - 150$). A high-resolution planar PIV set-up is employed to determine the drag reduction directly from wall shear stress measurement over the oscillating wall. Drag reduction, of up to 15% are quantified. A pronounced drop of turbulence production in the range $y^+ = 5 - 100$ is observed. The vorticity analysis indicates a distortion from the well-known hairpin-packet arrangement, suggesting that the drag-reduction mechanism lies in the inhibition of the hairpin auto-generation.

Introduction

Turbulent skin-friction drag plays a major role in energy consumption in the 21st century. Many techniques have been developed to reduce its detrimental effects. Spanwise wall oscillation is one such technique with a potential of achieving a significant skin-friction reduction. Several numerical (Jung et al. 1992) and experimental campaigns (Choi et al. 1998) have been undertaken with reductions of 45% in skin friction (Quadrio and Ricco 2004) being reported at optimum conditions. Experiments on drag reduction by spanwise wall oscillations reported in the literature have widely employed hot wire anemometry (HWA), given the high accuracy, small probe size and the high temporal resolution. Single-probe HWA measurements do not provide complete information on the behaviour of the different components of the Reynolds stresses which is important to quantify the variation in velocity fluctuations in the streamwise and wall-normal directions of the boundary layer. In addition, turbulent kinetic energy (TKE) production, which is related to the shear stress, can also explain the effects of the wall oscillation. Measurements with planar-PIV provide quantitative information on some components of the Reynolds stress tensor and the spanwise component of the vorticity vector.
Concerning the drag reduction mechanism, it has been proposed that the imposed spanwise wall motion affects the orientation of the streamwise vortices, which leads to a disruption in the lift-up mechanism, and thereby the production of turbulence (Touber and Leschziner 2012). This directly corresponds to a reduction in the ejection and sweep events, which are the drivers for wall-normal momentum transport. These ejections are associated with the formation of hairpin or horseshoe vortices, which are known to occur in packets and travel with similar velocities. It is therefore of practical interest to visualize and quantify the changes in the hairpin packets behaviour under the action of spanwise oscillations.
The present study investigates the applicability of planar PIV to determine skin friction drag reduction over a spanwise oscillating wall. The drag estimates are obtained by measuring the near-wall velocity gradient yielding an estimate of the wall shear. The method and its inherent uncertainties are discussed and compared with existing data. Moreover, velocity and vorticity visualizations are used to infer the large-scale organization of the turbulent structures, with a focus on hairpin packets and the modifications incurring when spanwise oscillations induce drag reduction.

Experimental setup and procedure

The experiments were conducted in an open-return low-speed wind tunnel (W-tunnel) at the Aerospace Engineering laboratory of Delft University of Technology. The tunnel features a contraction ratio of 9:1 with exit cross-section of $40 \times 40 cm^2$. For the current experiment, the turbulence intensity at the edge of the boundary layer at $33 m/s$ is below 1.4%. The flow at the exit is confined within a rectangular channel $1.63m$ long and a flat plate is installed $0.13m$ above the channel floor. The oscillations were obtained using a slider-crank mechanism with the system reaching up to 15 Hz oscillation frequency and peak-to-peak amplitude of 0.02 m. System vibrations were minimised by using a counterweight. The test section was realised in Plexiglas providing optical access for PIV imaging. The measurements are performed at two streamwise locations: ahead (-0.075) and over (0.85) the oscillating plate, at the positions indicated in Figure 1,

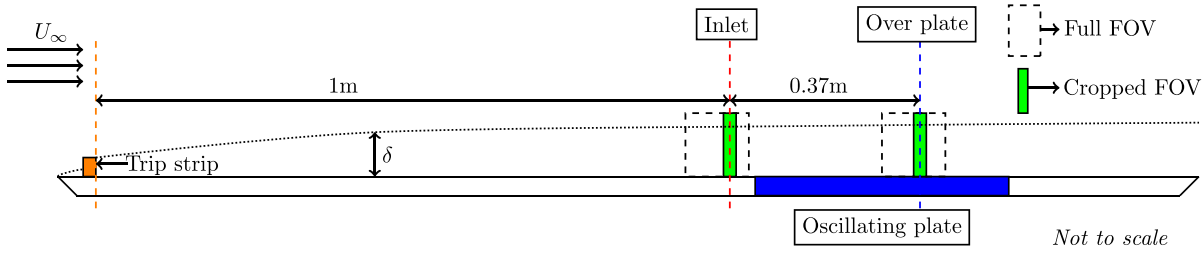

Figure 1: Schematic side-view of the plate with oscillating section. Regions of interest for the PIV measurements are highlighted in green

non-dimensionalization done with the length of the oscillating plate with its leading-edge as reference. For the near-wall measurements, the viscous sub-layer ($y^+ < 5$) is well resolved with 6 ($5y^+ = 0.5mm$) vectors, and data following a linear trend within a finite measurement interval.

Results

The slope $\left(\frac{\partial u}{\partial y}\right)_{y=0}$ at the wall is quantified and processed to provide the drag change with respect to the non-oscillating surface. Figure-2 depicts the boundary layer profile up to the wall, it can be seen clearly that the slope at the wall for the wall oscillated case is lower than that of the stationary wall. The results for the different experiments, with a varying value of the oscillation frequency and constant amplitude, are shown in Figure-3(Left). A peak reduction of 15% is obtained at $T^+_{osc} = 94$ and $A^+_{osc} = 100$ for $Re_\theta = 1000$. The non-dimensional wall velocity $(W^+_m = \pi A^+_{osc}/T^+_{osc})$ corresponding to the above case is $W^+_m = 3.34$ and the reported reduction from literature for a similar condition ($T^+_{osc} = 100$ and $W^+_m = 4.5$) is 17% from Quadrio and Ricco (2004).

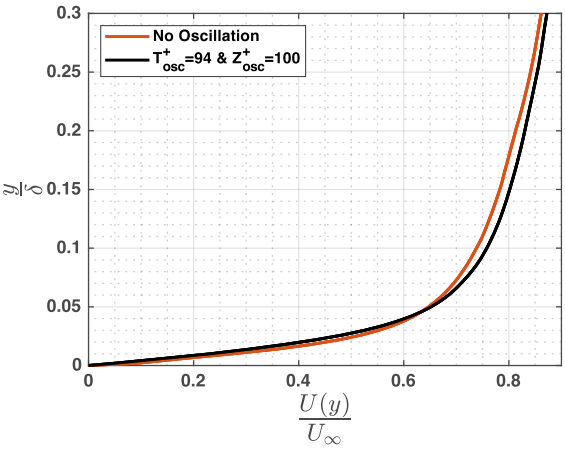

Figure 2:Scaled boundary layer profile

A hairpin packet signatures as described by Adrian (2007) features the presence of a packet of hairpin vortex heads aligned approximately along a 30-degree slope from the wall and separated by approximately 120-160 wall-units in the streamwise direction. They appear atop the low-speed streaks where they tend to auto-generate and lead to packets. For the stationary wall, hairpin packets of 2 to 4 vortices are most frequently observed; a marked difference from the case of the oscillating wall, where the range of organised structures varies between isolated hairpins and packets with more than 2 hairpins are only seldom observed. Figure-3 (Right) depicts this situation.

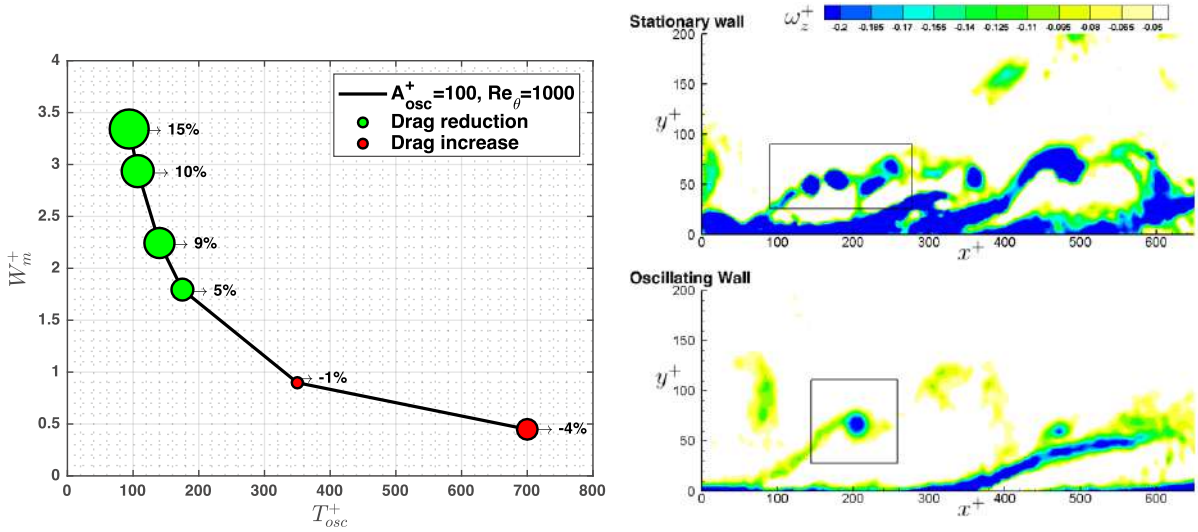

Figure 3: Drag reductions obtained from wall shear measurements(marker size represents magnitude(Left) and Vorticity fields(Right) with Hairpin packet signature (top) stationary wall (bottom) oscillating wall

References

[1] Jung WJ, Mangiavacchi N, Akhavan R. Suppression of turbulence in wall-bounded flows by high-frequency spanwise oscillations. *Physics of Fluids A: Fluid Dynamics* (1992)

[2] Choi KS, DeBisschop JR, Clayton BR. Turbulent boundary-layer control by means of spanwise-wall oscillation. *AIAA Journal* (1998)

[3] Quadrio, Maurizio and Pierre Ricco. Critical assessment of turbulent drag reduction through spanwise wall oscillations. *Journal of Fluid Mechanics* (2004)

[4] Touber, Emile and Michael A. Leschziner. Near-wall streak modification by spanwise oscillatory wall motion and drag-reduction mechanisms. *Journal of Fluid Mechanics* (2012)

[5] Adrian, Ronald J. Hairpin vortex organization in wall turbulence. *Physics of Fluids* (2007)

INVESTIGATION OF THE FLOW STRUCTURE BEHIND THREE-DIMENSIONAL AND TWO-DIMENSIONAL ROUGHNESS ELEMENTS ON A MODEL OF A FLYING WING

Alexandr Pavlenko*[1], Valeriia Kaprilevskaia[1], Victor Kozlov [1] and Mikhail Katasonov [1]
[1] Laboratory of Aerophysical researches of subsonic flows, Khristianovich Institute of Theoretical and Applied Mechanics of SB RAS, Novosibirsk, Russia

Summary The paper is devoted to the experimental studies of the development of stationary perturbations and the transition to turbulence behind a localized three-dimensional roughness element and two-dimensional roughness in the negative and positive pressure gradient region of a flying wing model. Panoramic flow structure were carried out by means of liquid crystal thermography technique with a heated surface by halogen lamp and oily covering visualization (mixture of oil, kerosene and titanium dioxide powder). Using hot-wire anemometry, the spatial characteristics of stationary perturbations were studied, and also the spectra of velocity pulsations spectra were obtained. It was found that the application of an acoustic field of 1 kHz leads to an increase in the amplitude of stationary structures behind the two-dimensional roughness element.

INTRODUCTION

Nowadays unmanned aerial vehicles (UAV) and drones are very popular types of aircrafts. Intensive development of unmanned aircraft leads to competition for the characteristics of aircraft. The most important indicators are autonomy, the minimum effective scattering area in the framework of the application of stealth technology. These requirements are fully satisfied by the concept of "flying wing" (figure 1). Reduction of aerodynamic resistance of the UAV by flow laminarization over stream-lined surfaces looks promising. The investigation of the flow structure over curved surfaces is a difficult challenge of the researchers. This work was aimed on investigation of the development of stationary perturbations behind a localized three-dimensional roughness element and two-dimensional roughness and of physical mechanisms of laminar-turbulent transition on the flying wing in the negative and positive pressure gradient region.
This work was supported by the project of Russian Science Foundation № 16-19-10330.

EXPERIMENTAL SETUP

Experiments were carried out in the test section of the T-324 low-turbulent wind tunnel of the ITAM SB RAS. The degree of free-stream turbulence was 0.04% in the range of 5-10000 Hz. The flow velocity was selected from the range 7.2 - 20 m/s and was controlled using a Pitot-Prandtl nozzle connected to an electronic micromanometer using a pneumatic track with an accuracy of 1%. Reynolds number was in range from $1.8*10^5$ for $U_o = 7.2$ m/s to $5*10^5$ for $U_o = 20$ m/s. In this experiment the main method of free-stream flow structure visualization was liquid crystal thermography. Visualization was made by thin-film liquid crystal coating which were placed in the research area. Then the coating was heated over than performance range. When exposed to the free-stream the film got cool and it allowed seeing the structure of the flow. The temperature range of the liquid crystal film used in the experiment was 30 - 32 °C.
Oil film technique was chosen as a second visualization method. Use was made of titanium dioxide mixed with kerosene. Having been covered in solution the wing was placed in wind tunnel working part. Exposed to the free-stream the solution became dry. After the experiment pictures of the flow were taken. Visualization made by oil film technique is illustrative of limiting streamline on the wing surface.
Qualitative measurements of boundary layer structure and its characteristics were carried out by constant-temperature hot-wire anemometry. Multilayer cylindrical roughness elements, cones and ribs were placed on the surface of the wing for excitation of stationary disturbances. Multilayer structure was chosen to investigate how roughness height influences on the disturbances. Total height was varied from 0.44 to 10 mm.
Investigations were carried out on the windward and leeward side of the model. The angle of attack was varied from -5 to 18 degrees.

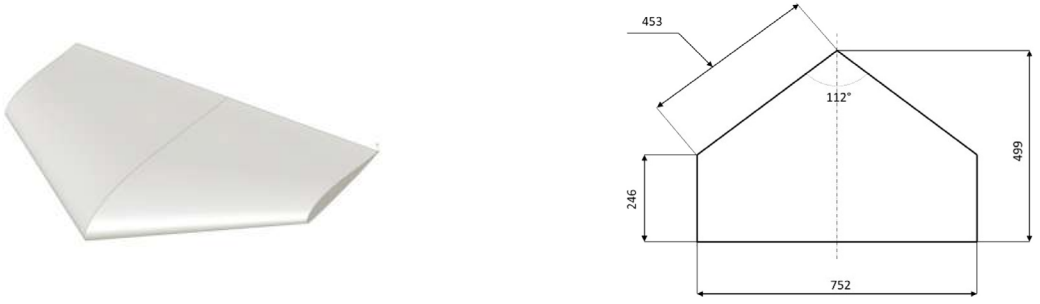

(a) (b)

Figure 1. Flying wing (a) and its parameters in mm (b).

*Corresponding author. E-mail: pavlyenko@gmail.com.

RESULTS AND DISCUSSIONS

The first series of experiments was devoted to the study of the flow over windward side of flying wing with disturbances' generators placed on its surface. These generators were made as three-dimensional (figure 2) and two-dimensional roughness elements, their height matching the boundary layer thickness. Visualization pictures of wall-adjacent flow were obtained in presence and absence of the three-dimensional roughness element by liquid crystal thermography. Using hot-wire it was possible to get quantitative data of boundary layer structure over a full range of speeds. It was shown that longitudinal structures are formed on the wing surface even in the absence of the roughness elements. These structures decrease in transverse size when free-stream velocity is increased. Influence of the three-dimensional roughness element height on the boundary layer structure was investigated. It was established that roughness greater than boundary layer thickness generates the most intensive longitudinal structure compared to minor roughnesses. Also area of the boundary layer maximum receptivity was found for the flying wing configuration. Being placed in this area roughness element leads to formation of the most intensive longitudinal structure. Location of this area is constant over a full range of free-stream velocity presented in this work. Visualizations of the flow behind three-dimensional roughness element (h_{3D} = 0.98 mm) were obtained in the area of maximum receptivity. It was found that longitudinal structure deflects and changes its form. Such form is probably a forepart of the general S-shaped form of the longitudinal structure moving downstream.

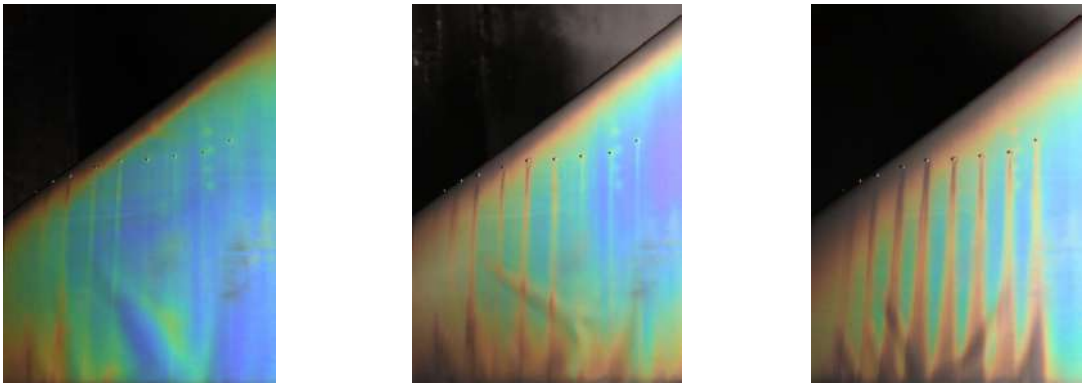

a) b) c)

Figure 2. Determination of the maximum susceptibility region: a) U_∞ = 7.2 m/s; b) U_∞ = 10.2 m/s; c) U_∞ = 15.1 m/s.

The second series of experiments was devoted to the study of the flow over leeward side of flying wing with cones and ribs on its surface. In the experiments performed on the model of a flying wing at low subsonic speeds, various flow options were found depending on the angle of attack. It is shown that the main types of flow around, previously known from experiments on the direct and sliding wings, are also realized on this type of wing. At small angles of attack, a laminar detachment bubble arises parallel to the leading edge, and with an increase in the angle of attack, a large-scale vortex flow gradually arises, which is characteristic of the case of flow around with a stall near the leading edge. It is shown that such a flow can be effectively controlled using cones and ribs near the leading edge of the wing (figure 3).

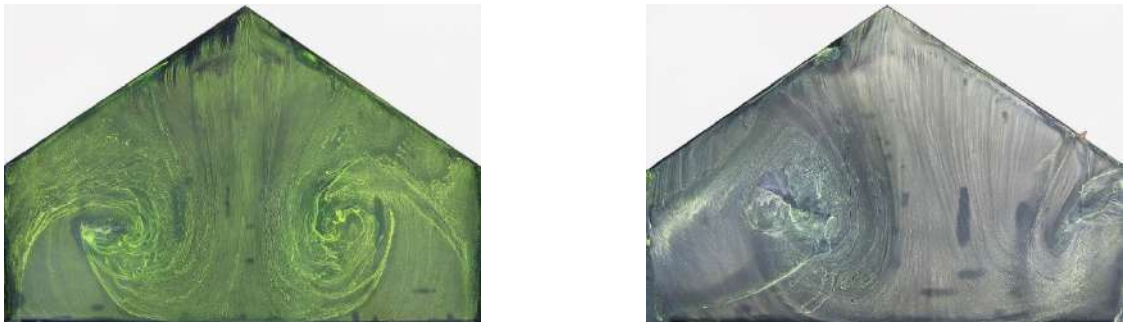

(a) (b)

Figure 3. Oil film visualization of flow on the wing at α=18°: a) smooth surface; b) one cone on the leading edge.

References

[1] Bippes H. Basic experiments on transition in three-dimensional boundary layers dominated by crossflow instability. *Progress in Aerospace Sciences* **35**: 363-412, 1999.

[2] Carpenter A.L., Saric W.S., Reed H.L. Roughness receptivity in swept-wing boundary layers experiments. *International Journal of Engineering Systems Modeling and Simulation* **2**: 128, 2010.

[3] Tolkachev S.N., Kaprilevskaya V.S., Kozlov V.V. The role of two-dimensional roughness element in the laminar-turbulent process in the favorable pressure gradient of the swept wing. *Vestnik NSU. Physics* **9**: 65-73, 2014.

[4] Pavlenko A.M., Zanin B.Yu., Katasonov M.M. Flow around a small-sized UAV model in a turbulent trace. *AIP Conference Proceedings.* https://doi.org/10.1063/1.5065278.

FLOW OVER SURFACES ROUGHENED BY CALCIUM CARBONATE DEPOSITION

T. A. Nascimento *[1], B. O. Temer[1], and J. B. R. Loureiro[1]
[1] Interdisciplinary Center for Fluid Dynamics (NIDF), Universidade Federal do Rio de Janeiro, Rio de Janeiro, Brazil

Summary Scaling formation over the internal surfaces of ducts, valves or heat exchangers is the main reason for the loss of efficiency in many industrial applications. The present work investigates the flow dynamics of calcium carbonate deposition in circular pipe flows. An experimental campaign is carried out to measure the deposition rate of calcium carbonate for different Reynolds numbers and fixed saturation index. The fouling thickness along the pipe is measured and the deposits characterized by scanning electron microscope and x-ray diffraction. The paper discusses the separate contributions for pressure losses as a result of the increase of surface roughness and the decrease in effective pipe diameter. The type of roughness created by the deposition process is also investigated. The growth direction of the roughness elements is correlated with the Reynolds number.

INTRODUCTION

Scaling is a problem typically found in many industrial applications, ranging from biomedical to oil exploration and production. Although many works have been devoted to the subject, the existing intricate relations between the thermodynamic predictions, the kinetics of the chemical reactions and the flow dynamics are still poorly understood (Zhang et al. 2001). Most of the data available in literature were obtained from small mixing vessels or capillary pipe flow experiments. Typically, these experimental results bare no dynamical similarity with real industrial applications.

The predictive models used by the oil industry rely essentially on thermodynamics and capillary tube blockage tests. The persistent high number of equipment failures due to fouling, specially in carbonate reservoirs oil fields, establishes an urgent need for research and improved technological solutions.

EXPERIMENT

Experiments were conducted on the Multipurpose Flow Loop of the Interdisciplinary Center for Fluid Dynamics (NIDF/UFRJ). A 70 m long and 11 mm internal diameter plexiglass pipe was used to simulate fully developed turbulent pipe flow. Solutions of 0.05 mol/l calcium chloride ($CaCl_2.2H_2O$) and 0.05 mol/l sodium bicarbonate ($NaHCO_3$) were prepared in separate reservoirs and mixed at the entrance of the flow loop, which operates in open circuit, as a illustrated in Fig. 1. The inlet flow rates were measured by electromagnetic flow meters; a Coriolis flowmeter was positioned at the outlet, prior to the discharge tank. The fourth tank was used to store the cleaning solution.

Figure 1: Sketch of the flow loop.

Four different total flow rates were investigated: 300, 450, 600 and 750 litres per hour. Each experimental run lasted for 90 minutes, after which the test sections were dried at ambient temperature and the cleaning solution was pumped into the flow loop.

RESULTS

Figure 2a illustrate the rough structure created by the deposition of $CaCO_3$ over the smooth pipe wall. Fig. 2a shows a fractal growth pattern. The smallest unity has a cubic shape, typical of calcite, the most stable form of $CaCO_3$. The structure grows from the wall as dendrites, probably from a nucleation site. The growth angle was measured for each visible structure and mean values have been calculated for positions 8.20 m and 62.20 m of the pipe length for the different flow rates. The results, shown in Fig. 2b, indicate a relation between the growth angle and the Reynolds number.

Figures 3a,b shows the deposition rate and the effective diameter along the pipe. The deposition rate was estimated by weighting the test sections in the beginning and at the end of experiment. It shows an exponential decay since in the inlet the solution saturation is maximum. Once precipitation and deposition begins, ions are consumed to form the crystals so that saturation decreases along the pipe. This fact also explains the profile of the effective diameter, as the thickness of

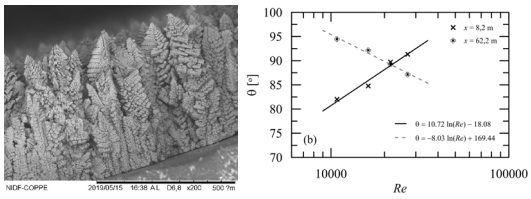

Figure 2: Illustration of the rough structures and the growth angle with respect to the pipe wall.

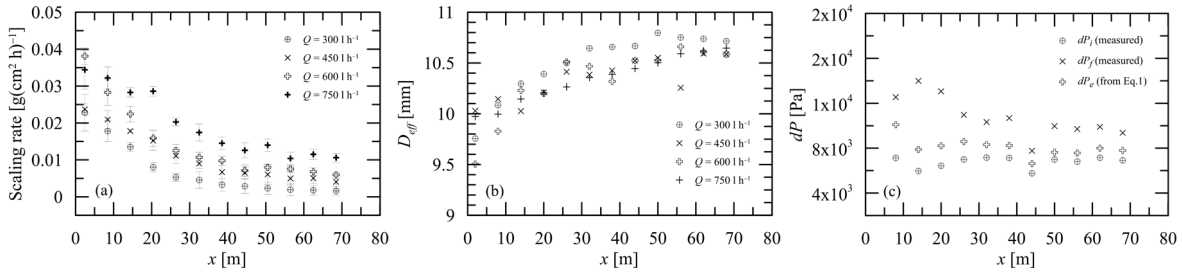

Figure 3: Deposition rate, effective diameter and differential pressure along the pipe.

fouling is higher in the entrance of the duct. The effective diameter reaches an almost constant value only at $x = 50$ m. It can also be noted that at the end of the test the inner wall of the pipe was fully covered by calcium carbonate.

The distribution of the differential pressure (dP) measurements for flow rate of $Q = 300$ lh^{-1} is shown in Fig. 3c, where dP_i denotes the values for the smooth pipe, measured at the beginning of the test, dP_f is the last measurement prior to the end of the run and dP_e was calculated from Eq. 1,

$$\frac{\Delta dP}{dP} = \frac{\Delta f}{f} - 5\frac{\Delta D}{D}, \tag{1}$$

where Δ denotes the changes between initial condition (subscript i, smooth pipe, D = 11 mm) and final condition (subscript f, roughened pipe, effective diameter shown in Fig. 3b).

Given a relative percentage change in the pipe diameter, this equation can be used to estimate dP for the final condition, considering that otherwise the inner wall would remain smooth (here denoted as dP_e). Figure 3c shows that the major contribution for the increase in pressure drop along the pipe is due to the surface roughness effects. The change in dP estimated from Eq. 1, due to the changes from nominal to effective diameter, is close to dP_i.

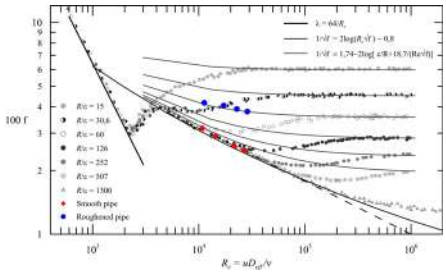

Figure 4: Moody chart illustrating the increase in drag caused by fouling.

The friction factor is shown in Fig. 4. At the start of the scaling experiments the pipe wall is smooth and f behaves as expected, following the Blasius equation. After 90 minutes, the inner surface has been fully covered by the $CaCO_3$ deposition; the blue dots represent the significant increase in wall friction due to pipe obstruction and, more importantly, due to increase in surface roughness.

References

[1] Zhang Y., Shaw H., Farquhar R., Dawe, R. The kinetics of carbonate scalingapplication for the prediction of downhole carbonate scaling. *J. Petroleum Sci. Eng.* **29**:85–95, 2001.

[2] Schlichting, H. Boundary layer theory. 817 pp, 1979.

*Corresponding author. E-mail: tiagon1712@gmail.com

EXPERIMENTAL INVESTIGATIONS OF BOUNDARY LAYER PERTURBATIONS GENERATED BY CONTROLLED LOCALIZED IMPACT OF THE ROUND MEMBRANE

Mikhail Katasonov*[1], Victor Kozlov[1], Alexandr Pavlenko[1] and Ivan Sadovskii[1]
[1] Laboratory of Aerophysical researches of subsonic flows, Khristianovich Institute of Theoretical and Applied Mechanics of the Siberian Branch of the Russian Academy of Sciences, Novosibirsk, Russia

Summary The spatial development of the flat plate boundary layer disturbances is experimentally investigated by the hot-wire anemometry. Controlled disturbances were introduced into the laminar flow by means of a membrane with a round form located on the surface of the model. The pulsed motion of a round membrane leads to the formation of longitudinal localized structures and wave packets in the boundary layer. Wave packets consist of a set of straight and oblique waves, differing in their propagation characteristics. The development of wave packets downstream is consistent with the linear theory of hydrodynamic stability.

INTRODUCTION

The laminar-turbulent transition in the boundary layer with an increased or moderate level of free-stream turbulence is associated with the development of disturbances generated by external flow perturbations [1]. It is known that the effect of large-amplitude incoming flow perturbations leads to the formation of longitudinally oriented localized structures (bands) in the boundary layer, consisting of regions with an excess and deficit of longitudinal velocity [2]. These structures are the primary instability and provide the necessary conditions for the development of high-frequency (secondary) wave disturbances, which under the favorable conditions evolve into turbulent spots. As recent studies have shown [3], the influence of incoming flow perturbations on the region of boundary layer incipience, in addition to streaky structures, can lead to the appearance of wave packets.

The present investigations are devoted to the study of the appearance and development of wave packets (precursors) and longitudinal localized structures. Wave packets form near the fronts of longitudinal localized structures where a sharp local change in the longitudinal velocity inside the boundary layer is observed.

EXPERIMENTAL TECHNIQUE

The measurements were carried out with a constant temperature hot-wire anemometer. The spatial structure of the studied disturbances was determined by the method of hot-wire anemometry visualization. Two-dimensional fields of the longitudinal components of the flow velocity were measured in various planes. Data collection was carried out synchronously with the moment of introduction of controlled disturbances. Artificial disturbances were generated in the boundary layer by means of high amplitude impulse deflection (0.3 mm) of a round membrane with a diameter of 18.7 mm, located on the surface of the model at a distance of 150 mm from its leading edge. As a model, we used a flat plate with a length of 1500, a width of 1000, and a thickness of 10 mm, on which a non-gradient Blasius flow was organized. The free-stream velocity was U_o = 21.5 m/s. The model was installed in a low-turbulent subsonic wind tunnel T-324 of ITAM SB RAS.

RESULTS

Papers in studies on the straight wing [4], the close attention of the experimenters to wave packets generated by localized action on the boundary layer attracted the fact of their rapid growth downstream. It turned out that the region of the unfavorable pressure gradient favors a strong increase in wave packets observed near the leading and trailing edges of longitudinal localized structures. An increase in the unfavorable gradient and further separation of the flow intensifies this process even more. In the region of a favorable pressure gradient, wave packets in the visualization patterns are not visible, since their intensity decreases here. In a nongradient flow, it was possible to increase wave packets downstream by increasing the Reynolds number to values greater than Re (δ^*)> 700. It was shown in [5] that if the frequencies of wave packets fall into an unstable region, they magnitude increase, that is, their behavior is consistent with the theory of hydrodynamic stability. A detailed study of the characteristics of wave packets [3] showed that they are very close to those observed for Tollmien-Schlichting wave packets.

These studies have established that the longitudinal structure arises due to local upward deviation of the model surface (membrane). Its length along the flow is determined by the time during which the membrane is in a deflected position. Wave packets occur during a short period of time when the membrane makes its movement up and back, down. The intensity of the localized longitudinal structure decreases downstream. Those observations are corresponds to the results of previous studies [2-5]. The amplitude of wave packets, in contrast, increases with increasing Reynolds number. It is experimentally shown that wave packets consist of straight and inclined waves. The straight waves increase faster than the inclined. The nature of their development is consistent with previous studies on the generation of wave packets by a point source on a plate [6], see figure 1.This figure shows the isocontours of the wave packet amplitude of present research in comparison with the isocontours of the amplitude of a typical wave train, obtained in

*Corresponding author. E-mail: mikhail@itam.nsc.ru.

[6]. The type of wave packets appeared as a result of the injection of a perturbation by the blowing-suction method and the method of controlled motion of the surface is fundamentally similar. The behavior of amplitude downstream of the wave packets is differing for the straight and oblique waves. The intensity of straight wave packets increases constantly downstream. At the same time, oblique wave packets grow sharply first and then their amplitude decreases.

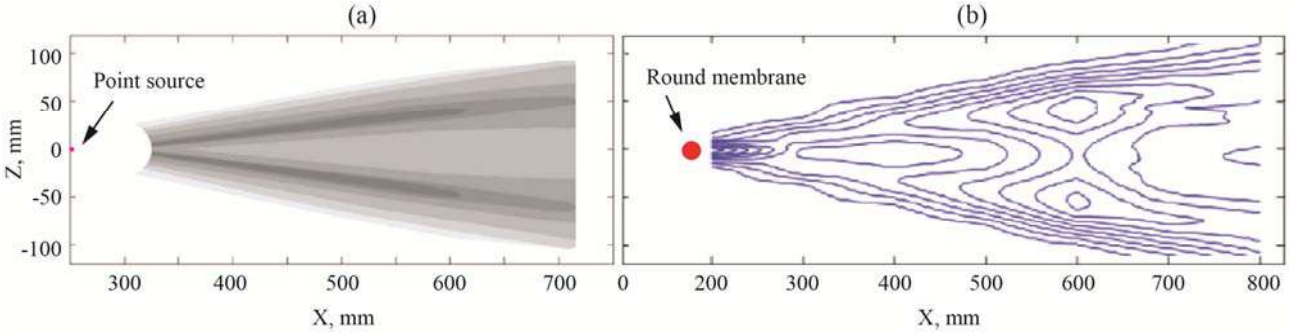

Figure 1. Isolines of the amplitude of the typical wave train generated by point source (a) and wave packet at the back front of the longitudinal localized disturbance (b) in the flat plate boundary layer.

CONCLUSIONS

Pulse movement of the round membrane with high amplitude in the boundary layer results in formation of disturbances of two types: longitudinal localized structures and wave packets near their fronts. Creating a source of modular perturbations allowed us to obtain data for high Reynolds numbers, where the wave packets become growing. Wave packets generated in this case consist of straight and oblique waves. The nature of their development is consistent with previous studies (generation of perturbations by a point source).

This work was supported by the project of Russian Science Foundation 16-19-10330.

References

[1] Morkovin M.V. Bypass Transition to Turbulence and Research Desiderata, Transition in Turbines, NASA-CP-2386, 1984

[2] Boiko A.V, Grek G.R, Dovgal A.V, Kozlov V.V The origination of turbulence in near-wall flows. Springer, Berlin Heidelberg NY. 2002

[3] Katasonov M.M., Kozlov V.V.,. Nikitin N.V, and Pavlenko A.M. The emergence and development of localized disturbances in a circular pipe and boundary layer, RIC NSU 2019 (in Russian).

[4] Chernorai V.G., Spiridonov A.N., Katasonov M.M., Kozlov V.V. Generation of perturbations by a localized vibrator in the boundary layer of a nonswept wing. *J Appl Mech Tech Phys,* 42(5), 765–772, 2001

[5] Katasonov M.M., Kozlov V.V., Pavlenko A.M. Experimental study of the disturbances generated by localized surface vibrations in the flat plate boundary layer *In: Proceedings of the XXV Conference on High-Energy Processes in Condensed Matter (HEPCM 2017): Dedicated to the 60th anniversary of the Khristianovich Institute of Theoretical and Applied Mechanics SB RAS (Russia, Novosibirsk, 5–9 Jun., 2017) : AIP Conference Proceedings.* –S.l.: AIP Publishing, 1893(1), 030093. doi: 10.1063/1.5007551, 2017

[6] Kozlov V.V., Ryzhov O.S. Receptivity of boundary layers: asymptotic theory and experiment. *Proc.* Roy. Soc. London Ser. A 429 341–373, 1990

INVESTIGATION OF THE EFFECT OF ROUGHNESS ELEMENTS ON THE BOUNDARY LAYER FLOW STRUCTURE OVER THE SWEPT WING SURFACE

Valeriia Kaprilevskaia[1]*, Alexandr Pavlenko[1], and Victor Kozlov[1]
[1] Laboratory of Aerophysical Research of Subsonic Flow, Khristianovich Institute of Theoretical and Applied Mechanics SB RAS, Novosibirsk, Russia

Summary The paper given represents the investigation results of stationary and secondary disturbances development behind two-dimensional roughness element. The experiment was carried out using liquid-crystal thermography and hot-wire anemometry. Lying upstream three-dimensional roughness element induced the disturbances which were affected by two-dimensional roughness lying further downstream. In this case the two-dimensional roughness caused the appearance of stationary structures. Excited by acoustics secondary perturbations took place within frequency range different from the case of excitement by three-dimensional roughness. Hot-wire helped to show that longitudinal structures started to form on the leading edge of the two-dimensional roughness element. The position of secondary disturbances was connected to the inflection points of transverse velocity distribution.

INTRODUCTION

Use of swept wings is required for transonic flight. However comparing them to a straight wing, the swept one has an additional instability mechanism due to the presence of the cross-flow. Such a mechanism results in laminar-turbulent transition in the favourable pressure gradient region. If modern aircraft manufacturers design a laminarized aircraft, it will provide a 15% reduction in fuel consumption. However there are a lot of problems since even micron-sized roughness can cause a localized area of laminar-turbulent transition in the transverse direction.

In [1 - 2], the investigations of transition caused by roughness were carried out in the neutral pressure gradient area. Single vortex forming on the edge of the roughness results in appearing of two modes of the secondary disturbances, followed by laminar-turbulent transition [1].

In paper [3] the investigations of the flow behind lengthy sticker are described. It was showed that the most destabilizing effect was caused by edges of the sticker led to stationary vortexes generation.

The variety of two- and three-dimensional roughness elements can be found on the surface of the modern wing: the joint of the slat is the perfect example of the two-dimensional roughness; natural surface roughness, vortex generators, insects and snow are considered as three-dimensional roughness elements.

EXPERIMENTAL SETUP

The experiment was carried out in the test section of the low-turbulent wind tunnel AT-324 of the ITAM SB RAS Figure1, (a). The test section parameters are 1000 × 1000 × 4000 mm. The free-stream velocity control was realized by the Pitot-Prandtl nozzle connected to an electronic manometer. Carrying out the experiment the values of free-stream velocity were 9.2 and 10.9 m/s.

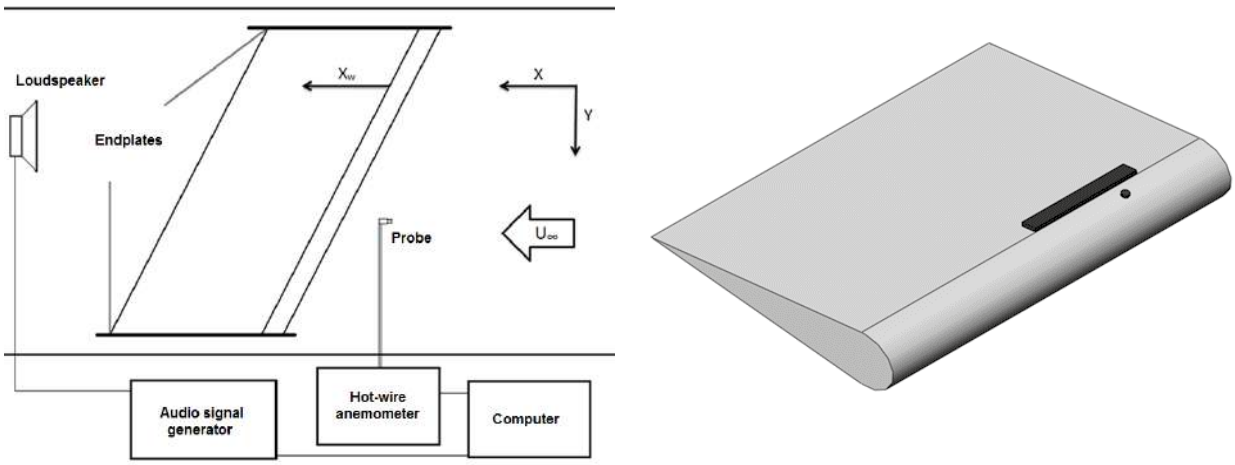

a b

Figure 1. Experimental set up (a) and the model of the wing with two-dimensional and three-dimensional roughness elements on its leading edge (b)

*Corresponding author. E-mail: valeria.kaprilevskaya@gmail.com

In the current work use was made of the wing formed by the cylinder with radius r = 40 mm and two converging planes Figure 1, (b). Chord is 400 mm and sweep angle is 45º. The angle of attack α = -12.3° was chosen to realize a favourable pressure gradient over the flat part of the wing profile.

Generation of the stationary disturbances was provided by three-dimensional cylindrical roughness element. The roughness involved had height of 0.8 mm and diameter of 1.6 mm. Two-dimensional roughness element was placed on the flat part of the wing; its width was 15 mm and length was 200 mm. It should be noted that two-dimensional roughness was multilayer and the thickness of the single layer was 0.13 mm. The total height could vary from 0 to 1.82 mm.

The secondary disturbances were excited by the loud speaker connected to the sound generator.

RESULTS

The results of the experiment were obtained using liquid-crystal thermography (LCT) and hot-wire anemometry. These techniques allowed receiving of qualitative and quantitative data of the flow over swept wing surface in presence of roughness elements. While carrying out the experiment, the two-dimensional roughness element was placed on the flat part of the wing. Figure 2 represents the influence of its height h_{2D} on the trace behind the cylindrical roughness element.

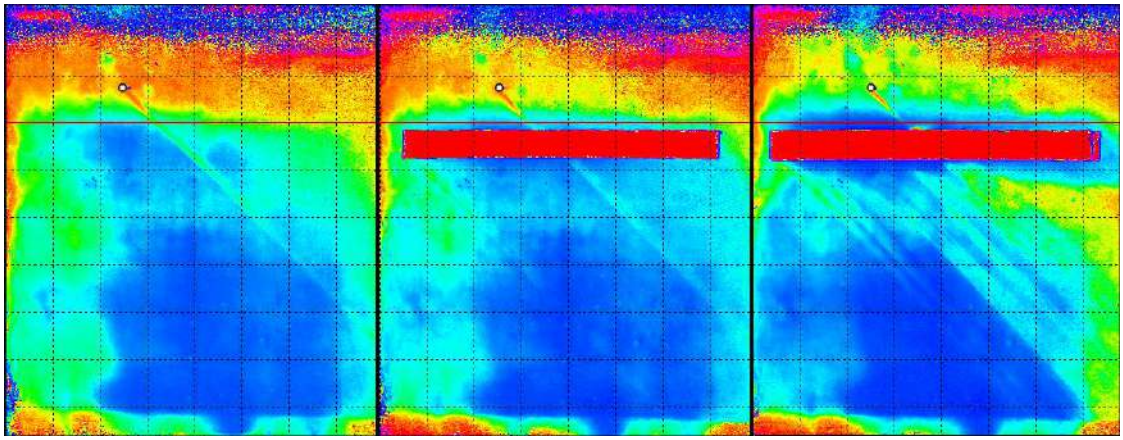

a b c

Figure 2. Visualization of the flow over wing's surface using LCT.
Height of the two-dimensional roughness element: a) 0mm; b) 0.52 mm; c) 1.56 mm

CONCLUSIONS

The two-dimensional roughness element destabilizes disturbances forming behind three-dimensional one and it also leads to decreasing of the boundary layer stability starting from h_{2D} = 0.52 mm. It was also found that two-dimensional roughness element generates stationary structures itself.

The acoustic influence significantly speeds up the development of the secondary disturbances. It causes the rapid growth of those disturbances and nonlinear development stage. The acoustics rebuilds the mean flow leading to multiplication and amplification of the stationary disturbances and increases the area of the turbulent flow regime too.

ACKNOWLEDGEMENTS

The reported study was funded by RFBR, project number 19-31-90018.

References

[1] Boiko A.V., Kozlov V.V., Syzrantsev V.V., Shcherbakov V.A. Experimental study of the transition to turbulence at a single stationary disturbance in the boundary layer of an oblique aerofoil *Journal of Applied Mechanics and Technical Physics* **36**: 67 – 77, 1995.

[2] Chernoray V.G., Dovgal A.V., Kozlov V.V., Lofdahl L. Instability of a swept-wing boundary layer disturbed by controlled roughness elements *Journal of Visualization* **13**: 251– 256, 2010.

[3] Boiko A.V., Kozlov V.V., Sova V.A., Shcherbakov V. A. Generation of the longitudinal structures in the boundary layer of the swept wing and their secondary instability *Thermophysics and Air Mechanics* **7**: 25-35 2000.

ABSENCE OF INERTIAL OVERLAP IN 2-D TURBULENT WALL JETS

Abhishek Gupta* [1,2], Harish Choudhary[1], A.K.Singh[2], Thara Prabhakaran [1] and Shivsai Ajit Dixit [1]
[1] Indian Institute of tropical meteorology, Pune, India
[2] Department of Physics, Institute of science, Banaras Hindu University, Varanasi, India

Summary The wall jet flow comprises of universal inner and outer scaling layers termed as the wall layer and the full-free jet layer respectively. Starting with this two-layer structure, theoretical arguments suggest that the overlap of these universal layers leads to a non-universal (Re_τ -dependent) power-law profile for mean velocity in the overlap layer. We define an intermediate variable $\eta\sqrt{Re_\tau}$, which absorbs this Re_τ-dependence of the overlap layer leading to a universal power-law overlap profile. Data indicate that there is no inertial overlap between the inner and outer scaling regions for the range of Reynolds numbers considered here.

INTRODUCTION

Wall- jet is a special kind of wall- bounded flow characterized by a non-monotone mean velocity profile with a velocity maximum (U_{max}) occurring close to the test surface. On either side of this maximum, velocity decreases in the wall normal direction (z). The study of wall-jet flow started way back in 1960's [1]. Several studies suggest that a wall jet could be considered to be made up of either a half free jet on top of a turbulent boundary layer or a jet layer overlapping with the inner wall layer. In the former, the boundary layer is considered to have its own overlap layer [2,3] while the latter is expected to exhibit an overlap consisting of a near-wall mesolayer and an inertial overlap layer further out [4]. Here, we are presenting some insights into the structure of wall-jet flow with the help of our own experiments and data from the literature. In particular, we show that the data do not exhibit occurrence of an inertial overlap in wall jets.

DATA AND RESULTS

The wall jet setup is constructed at the Fluid Dynamics Laboratory (FDL), Indian Institute of Tropical Meteorology (IITM), Pune, India. Mean velocity profiles at different streamwise (x) and spanwise (y) stations are measured, using a single hotwire probe, for two nozzle Reynolds numbers $Re_j = U_j b/\nu = 10244\ and\ 21228$ (P1 and P2 respectively); $\nu = 1.5 * 10^{-5} m^2 s^{-1}$(fluid kinematic viscosity) , b is nozzle height and U_j is the nozzle exit velocity. Wall shear stress is measured using Oil Film Interferometry.

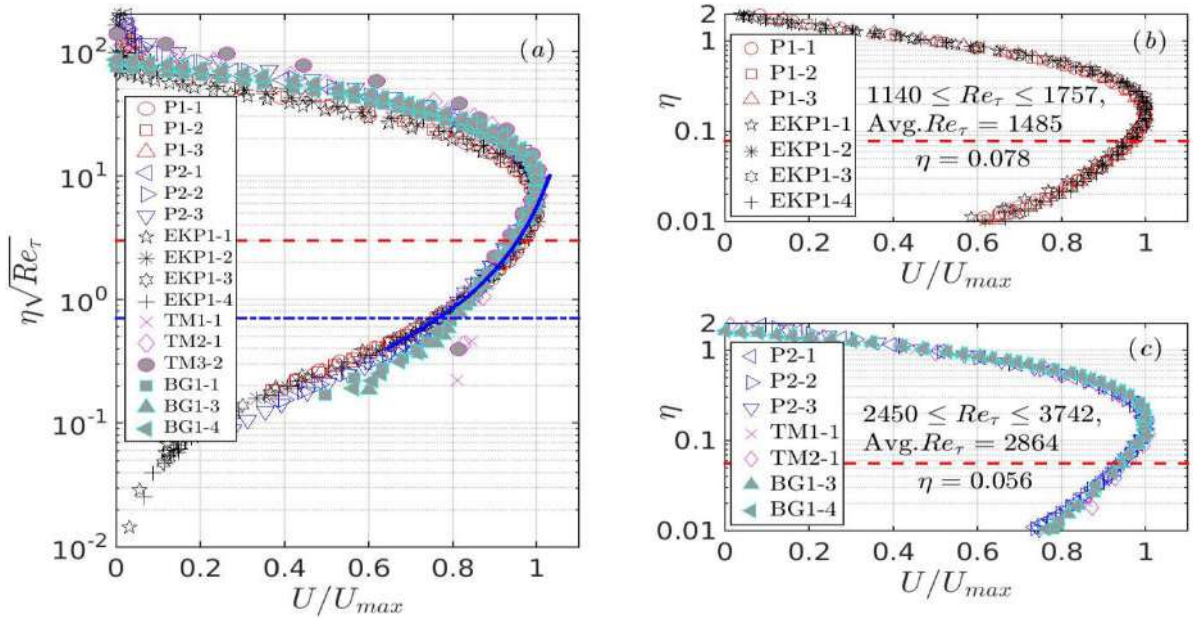

Fig 1: (a) Mean velocity profiles in the overlap layer scaling. Ordinate is the intermediate variable $\eta\sqrt{Re_\tau}$. Solid blue line is the least-squares curve fit of equation (1) to all data between the dashed and the dashed-dotted lines ($0.7 < \eta\sqrt{Re_\tau} < 3$). Our data is at $x/b =$ 49.5, 64.5 and 107. $Re_\tau = U_\tau * Z_T/\nu$ where, U_τ is the friction velocity, Z_T is the height from the wall above the velocity maximum where velocity equals $U_{max}/2$ and $\eta = z/Z_T$. (b) Outer scaling for high-Re wall jets with avg. $Re_\tau = 1485$ and (c) Outer scaling for high-Re wall jets with avg. $Re_\tau = 2864$.

*Corresponding author. E-mail: abhishek.gupta@tropmet.res.in

We have also included data from the literature such as Eriksson et al. 1998 (as EKP) [5], Bradshaw & Gee 1962 (as BG) [6] and Tailland & Mathieu 1967 (as TM) [7]. The detailed information about these datasets is given in their respective papers.

The wall jet flow comprises of universal inner and outer scaling layers termed as the wall layer and the full-free jet layer respectively. Starting with this classical inner and outer universal scaling (not shown), we have derived a universal overlap expression (derivation is not shown) in terms of an intermediate variable $\eta\sqrt{Re_\tau}$ of the form

$$\frac{U}{U_{max}} = K_o\left(\eta\sqrt{\mathrm{Re}_\tau}\right)^A - \frac{\beta}{U_{max}} \qquad (1)$$

where, K_o= −0.288, A = −0.535 and β/U_{max} = −1.115 are universal constants and obtained from the fitting of data used in fig-1(a) according to above equation .

All the data of fig-1(a) collapse remarkably well in the region where overlap is expected to occur. The collapse extends over the range $0.7 < \eta\sqrt{\mathrm{Re}_\tau} < 3$ i.e. approximately 40% of a decade in $\sqrt{\mathrm{Re}_\tau}$; the extent of this region is decided empirically by observation. Here, the position and extent of the mean-velocity overlap are fixed in $\eta\sqrt{\mathrm{Re}_\tau}$ and not in η or $z^+ = U_\tau * z/\nu$. In fact, with increasing Reynolds number, the position of the overlap layer is expected to shift towards the wall and its extent is expected to reduce in η coordinate; opposite is expected to be true for the z^+coordinate.

An interesting question that arises is whether there exists any inertial overlap layer between the inner and outer scaling regions. For this, we plot the mean velocity profile data by dividing it into two broad categories, low-Re_τ and high-Re_τ. Fig-1(b) and 1(c) are the plot with the average low-Re_τ= 1485 (for 1140 < Re_τ< 1757) and high-Re_τ= 2864 (for 2450 < Re_τ< 3742). From these plots, it is clear that beyond the outer limit (in η coordinate) of the mean-velocity overlap layer, data show remarkable collapse in outer scaling (up to η of 0.078 and 0.056 respectively). Exactly similar behavior is seen in inner scaling (not shown). This indicates that only the Re_τ-dependent (or mesolayer) mean velocity overlap of fig-1(a) exists in wall jets and the inertial overlap layer does not appear to exist, at least for the range of Reynolds numbers considered here. Also it may be noted that with increase in Reynolds number, the outer edge of the overlap layer in fig-1(c) shifts towards the wall in outer (η) coordinate as compared to fig-1(b). This indicates that the outer full-free jet flow progressively dominates the inner wall flow with increasing Reynolds number.

CONCLUSIONS

Experimental mean velocity data strongly support a two-layer structure of wall jets. An inner wall layer (scaling purely on wall variables) and an outer full free jet layer (scaling purely on outer variables). These scalings are universal i.e. independent of Re_τ. Analysis shows that these inner and outer descriptions lead to an Re_τ-dependent (non-universal) power-law velocity profile in the overlap layer of wall jets. An intermediate variable $\eta\sqrt{Re_\tau}$ absorbs this Re_τ-dependence and gives a universal power-law curve for approximately 40% of a decade in the intermediate variable over the range $0.7 < \eta\sqrt{Re_\tau} < 3$. Selective plotting of experimental data for low- and high-Re_τ ranges show that there is only Re_τ-dependent overlap between the universal inner and outer mean-velocity scaling descriptions; no inertial overlap appears to exist in wall jets for the range of Re_τ values presented here.

References

[1] Glauert, M. B. 1956 The wall jet. J. Fluid Mech. 1 (6), 625–643.
[2] Afzal, N. 2005 Analysis of power law and log law velocity profiles in the overlap region of a turbulent wall jet. Proc. Math. Phys. Eng. Sci. 461 (2058), 1889–1910.
[3] Gersten, K. 2015 The asymptotic downstream flow of plane turbulent wall jets without external stream. J. Fluid Mech. 779, 351–370.
[4] George,W. K., Abrahamsson, H., Eriksson, J., Karlsson, R. I., L¨ofdahl, L. & Wosnik, M. 2000 A similarity theory for the turbulent plane wall jet without external stream. J. Fluid Mech. 425, 367–411.
[5] Eriksson, J. G., Karlsson, R. I. & Persson, J. 1998 An experimental study of a two-dimensional plane turbulent wall jet. Exp. Fluids 25 (1), 50–60.
[6] Bradshaw, P. & Gee, M. T. 1962 Turbulent wall jets with and without an external stream. ARC R. & M. 3252, Her Majesty's Stationary Office.
[7] Tailland, A. & Mathieu, J. 1967 Jet pari´etal. J. M´ec. 6, 103–130.

MEAN PARAMETERS OF TURBULENT BOUNDARY LAYER WITH ZERO PRESSURE GRADIENT ON THE WALL OF THE WIND TUNNEL AT VERY HIGH REYNOLDS NUMBERS

Anton Gorbushin*[1,2], Svetlana Osipova [1,2], and Vladimir Zametaev [1,2]
[1] Central Aerohydrodynamic Institute, Zhukovsky, Russia
[2] Moscow Institute of Physics and Technology, Dolgoprudny, Russia

Summary Mean parameters of incompressible turbulent boundary layer (TBL) on a wind tunnel wall were acquired in the TsAGI T-128 Wind Tunnel (WT) in the range of $Re_\theta = 5.3\times10^4 – 2.9\times10^5$. The maximum Reynolds number $Re_\theta = 2.9\times10^5$ was 4.8 times higher in comparison with similar WT wall data published in scientific literature. At the maximum Reynolds number the record-high von Kármán number $\delta^+\sim1\times10^5$ was reached whereas the log law was applicable up to $y^+\approx 1.3\times10^4$. It confirmed different authors' suggestions about the universal profile of speed in outer region of layer. The acquired results were compared with other researchers' data and with known semi-empiric/analytical dependencies as well. The agreement between the shape factor at high Reynolds numbers was within $\Delta H = \pm0.012$ (±1%), and the local skin friction coefficient was $\Delta c_f = \pm0.000025$ (±1.7%).

INTRODUCTION

Studies of turbulent boundary layers (TBLs) at very high Reynolds numbers draw attention for two reasons: (i) they are of practical use for design of large aircraft and ships; (ii) researchers have always wondered what would happen with turbulent boundary layer at $Re \to \infty$. Incompressible TBLs with zero pressure gradient are of most interest. Many studies have described this canonical case. They can be divided into three groups: (i) studies on a flat-plate in wind tunnels or water tunnels; (ii) measurements on wind tunnel walls; (iii) atmospheric TBLs. Mean parameters of boundary layer acquired in test facilities at very high Reynolds numbers are defined in [1-3]. According to [1] the maximum Reynolds number $Re_\theta = 2.35\times10^5$ ($Re_\tau = 7.2\times10^4$) was reached on a flat-plate in WT, where θ is the momentum thickness of the boundary layer, $Re_\tau=\delta^+= \delta_{0.99}U_\tau/\nu$ is the von Kármán number, $U_\tau=U_e(c_f/2)^{1/2}$, ν is the kinematic viscosity of the air, c_f is the local skin friction coefficient, U_e is the local exterior flow speed. In water tunnels $Re_\theta = 1.5\times10^5$ ($Re_\tau = 5\times10^4$) was reached on a flat-plate [2]. The maximum Reynolds number reached on a WT wall was acquired in [3] and made $Re_\theta = 6\times10^4$.

This study supplements existing TBL data at very high Reynolds numbers with the results obtained on the wall of TsAGI transonic WT in the range of $Re_\theta = 5.3\times10^4 – 2.9\times10^5$.

TEST DESCRIPTION

Figure 1. Wind tunnel nozzle and rake installed on its upper wall.

The experimental studies conducted in the TsAGI T-128 transonic WT, which is a continuous variable-density closed-circuit test facility equipped with the four-stage compressor and the main drive with the power of 100 MW. Mach number range is M=0.15–1.4, total pressure range is P_t = 20–400 kPa. The facility is equipped with a 12-m adjustable nozzle. The size of test section is 2.75 × 2.75 m. The nozzle sidewall shape (Fig. 1) was chosen so that the zero pressure gradient could be provided over the length of 4 meters until the nozzle exit. The pressure gradient made dCp/dx= -0.006 m^{-1}, which corresponds to the local streamwise pressure gradient parameter [1] $K_p = \nu/U_e^2 \times dU_e/dx \approx 7\times10^{-10}$. The parameters of boundary layer were measured with a 0.2-m rake equipped with 26 total pressure probes, installed on the upper wall near the nozzle exit (Fig.1). The studies were conducted at M=0.2 (U_e ≈ 69 m/s; P_t≈100; 200; 300; 380 kPa), M=0.25 (U_e ≈ 86 m/s; P_t≈380 kPa), M=0.4 (U_e ≈ 140 m/s; P_t≈320 kPa).

RESULTS AND CONCLUSION

Clauser chart technique was used, where the log law $u^+ = {}^1/_k \ln y^+ + B$ was fitted to the velocity profiles using the von Kármán constant k=0.384 and additive constant B=4.127 recommended in [4]. Figure 2 shows mean velocity profiles in inner coordinates and the log law. The profiles are shifted on Y-axis by ΔU^+=2.5. At the maximum Reynolds number, the record-high von Kármán number $\delta^+\sim1\times10^5$ was obtained whereas the log law was applicable until $y^+\approx$

*Corresponding author. E-mail: gorbushin@tsagi.ru.

1.3×10^4. Figure 3 shows the comparison of non-dimensional velocity profiles with other studies confirming the conclusion (see [3], for example) that mean velocity profiles in the outer region of boundary layer show similarity i.e. independence of Reynolds number. The authors have found an analytical solution of Navier-Stokes equation $U/U_e = e^{-y}\int_0^y \exp(\eta - e^{-\eta})d\eta$ with the help of asymptotic methods at Re→∞ [5] that is also in good agreement with the experiment data beginning with $y/\delta_{0.99} \approx 0.6$.

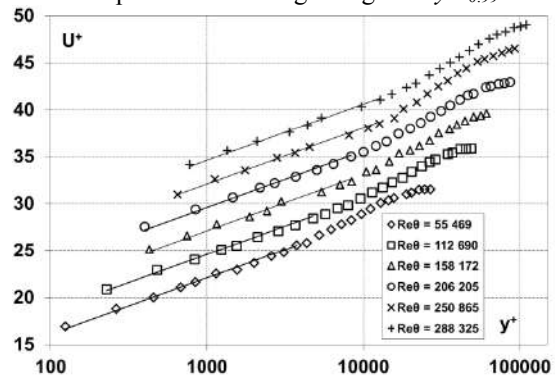

Figure 2. Mean velocity profiles in inner coordinates.

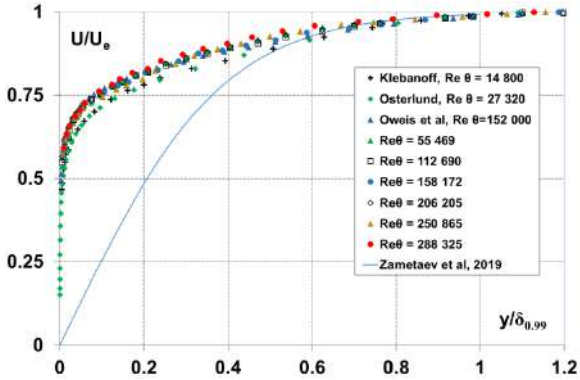

Figure 3. Comparison of non-dimensional velocity profiles with data of other studies.

Figure 4 shows the results as a dependency of the shape factor H on Re_θ in comparison with data of other studies. The agreement between the data at high Reynolds numbers is within $\Delta H = \pm0.012$ (±1%). The absolute value of derivative for this dependency considerably decreases beginning with $Re_\theta \approx 6\times10^4$. Figure 5 shows the results as a dependency of the friction coefficient c_f on Re_θ in comparison with data of other studies and known expressions defined by Schlichting, Coles-Fernholz, Falkner, Nikuradse, Prandtl-Kármán, Schultz-Grunow, Kármán-Schoenherr, Pirozzoli with constants recommended in [4]. The agreement between the skin friction coefficient at high Reynolds numbers is within $\Delta c_f = \pm0.000025$ (±1.7%). The relation between Re_θ and Re_x for these expressions was obtained basing on the analysis of study data published in scientific literature. Well known from literature compressibility corrections were applied to the shape factor in the form of multiplier 0.9775 (~2%) for M=0.25 and 0.946 (~5%) for M=0.4 and to the friction coefficient – 1.013 (~1%) for M=0.4.

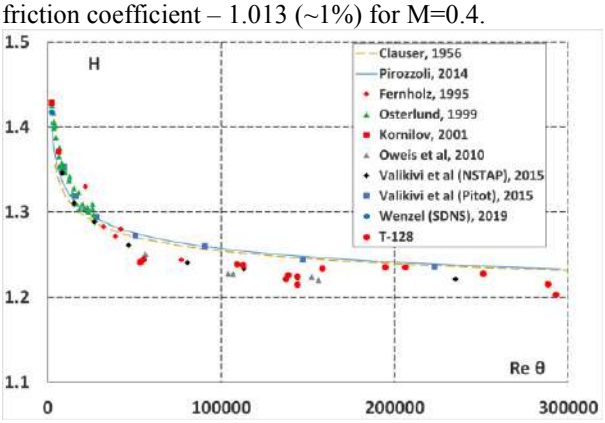

Figure 4. Shape factor H as a function of Re_θ.

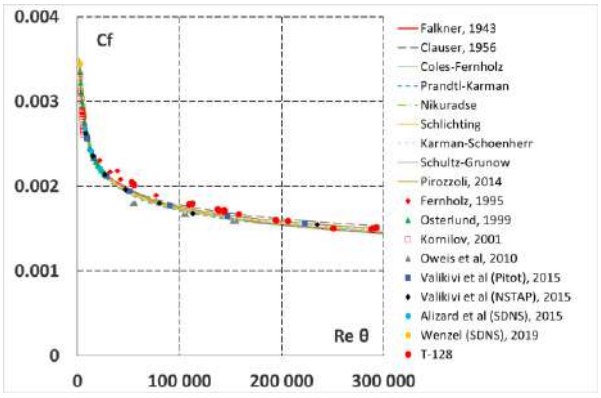

Figure 5. Skin friction coefficient c_f as a function of Re_θ.

The dependency $H = f(c_f)$ was compared with other authors' experimental results and with semi-empiric dependencies of Hama, Clauser and Pirozzoli. The change in the friction coefficient was shown for the same velocity profile with different values of the von Kármán constant published in scientific literature.

Funding: The reported study was funded by RFBR, project number 19-38-90296, and Russian Science Foundation, project number 20-11-20006.

References

[1] Vallikivi M., Hultmark M., Smits A.J. Turbulent boundary layer statistics at very high Reynolds number. *J. Fluid Mech* **779**: 371-389, 2015. https://doi:10.1017/jfm.2015.273

[2] Oweis G.F., Winkel E.S., Cutbrith J.M., Ceccio S.L., Perlin M., Dowling D.R. The mean velocity profile of a smooth-flat-plate turbulent boundary layer at high Reynolds number. *J. Fluid Mech* **665**: 357-381, 2010. https://doi:10.1017/S0022112010003952

[3] Fernholz H.H., Krause E., Nockemann M., Schober M. Comparative measurements in the canonical boundary layer at $Re_\theta \leq 6\times10^4$ on the wall of the DNW. *Phys. Fluids* **7**:1275–81, 1995. https://doi.org/10.1063/1.868516

[4] Nagib H.M., Chauhan K.A., Monkewitz P.A. Approach to an asymptotic state for zero pressure gradient turbulent boundary layers. *Phil. Trans. R. Soc. A* **365**, 2007. https://doi: 10.1098/rsta.2006.1948

[5] Zametaev V.B., Gorbushin A.R., Lipatov I.I. Steady secondary flow in a turbulent mixing layer. *International Journal of Heat and Mass Transfer* **132**, 655–661, 2019. https://doi.org/10.1016/j.ijheatmasstransfer.2018.12.012

CONCEPT OF VELOCITY AND TEMPERATURE FIELDS COMPARISON AT HEAT TRANSFER DETERIORATION UNDER WATER SUPERCRITICAL CONDITIONS

Vladyslav Filonov[1,2], Yuliia Filonova[1,2], and Victor Razumovskiy[2]
[1] IPP-CENTRE Ltd, Kyiv, Ukraine
[2] NTUU 'Igor Sikorsky Kyiv Polytechnic Institute', Kyiv, Ukraine

Summary. This paper presents one of the stages of creating reliable engineering methods for predicting deterioration heat transfer phenomenon for supercritical water reactors (SCWR) concept. This is the main problem for this type of fourth-generation reactor concept because a limited set of experimental data, the complexity of experimental studies, as well as multifactor nonlinearity of the process significantly complicate reliability of predicting the deterioration area by existing methods. The most advanced way to analyze deterioration conditions and characteristics is based on DNS strategy. Despite significant progress in recent years, it is still difficult to apply DNS to the engineering problems. A huge number of various turbulence models tests on existing experimental data indicate the prospect of adapting two-parameter models to predict deteriorated heat transfer. In this work DNS heat equation (DNSHE) procedure is considered, which will help in better understanding the mutual influence of speed and temperature in the boundary layer, based on model velocity and pressure fields, as well as on experimental data on heating wall temperature axial distribution. Obtained results will help to estimate the perspectives in adapting the temperature wall-functions for reliable nonlinear heat transfer characteristics prediction.

BACKGROUND AND INTRODUCTION

Moving towards supercritical water parameters in fourth-generation SCW reactors requires the solution of the main thermophysical problem - reliable heat transfer in the core. It is important to accurately predict the thermal loads limits in which there is no deteriorated heat transfer [1]. The majority of degraded heat transfer modes are characterized by the principal non-linearity of thermohydraulic processes in the core flow part due to the sensitivity of water properties to temperature.

Existing methods for predicting deteriorated heat transfer can be divided into two categories: analytical and differential. Analytical calculation methods are based on the use of empirical dependencies, together with the main parameters and additional balance relations form a system of transcendental equations. Sometimes, instead of balance relations, a one-dimensional momentum transfer equation is used. Nowadays are known several dozen of generalizing dependencies that are used to estimate the heat transfer coefficient [2].

Since analytical correlations and estimations cannot give an idea of the heat transfer deterioration processes complexity, an alternative and more fundamental approach is the use of CFD (differential methods). Many test calculations indicate the perspective of the eddy viscosity turbulence models adaptation. By varying the turbulent Prandtl number [3], better agreement between calculation and experiment can be achieved. Near-wall temperature function adaptation is perspective in prediction the deteriorated heat transfer, based on results of estimating the supercritical water flow pressure drop in one- and three-rod assemblies [4], as well as good agreement with experimental data regardless of the heat transfer regime.

The DNS application to predict deteriorated heat transfer [5] allows us to evaluate the flow structure near the heating wall, the ratio of forces, as well as changes in turbulence characteristics. These results can be used to calibrate engineering approaches that can be applied to more complex geometry and large-scale problems. Authors are working on the creation of reliable procedures that allow the use of eddy viscosity turbulence models together with near-wall functions on dynamically adaptive grids near a pseudo phase transition. In this paper authors suggest the procedure of velocity and temperature fields relationship finding in pseudo phase transition region.

EXPERIMENTS

Many experimental studies have been carried out in NTUU “KPI” at various test sections, which are presented in Fig.1. Screws were used for spacing of the rods in 3R and 7R assemblies, in addition, they provided the flow spin. Also, NTUU “KPI” has performed experiments in smooth vertical 600-mm heated-length tube A of outer diameter (OD) 8.11 and inner diameter (ID) 6.28-mm and vertical 600-mm heated-length tube B of 12.28/9.50-mm OD/ID (Figure 1).

For study external flowing around the rods bundle the NTUU “KPI” has performed experiments in a vertical 3 or 7 - rod bundle simulator made of 485-mm heated-length tubes of 5.2-mm OD and 4.5-mm ID with four helical ribs of 0.6-mm height and 1-mm width that were wound over the tubes with a 400-mm pitch. The bundle rods touching each other with the ribs formed the cage of regular triangles (Figure 1). 1-mm gap between the element ribs and a shaped dielectric displacer was provided with calibrated stainless steel fins of 0.1-mm thickness welded to the cylindrical surface of the rods in 7 cross-sections at 125, 185, 245, 305, 365, 425, and 485 mm from the entrance into the bundle.

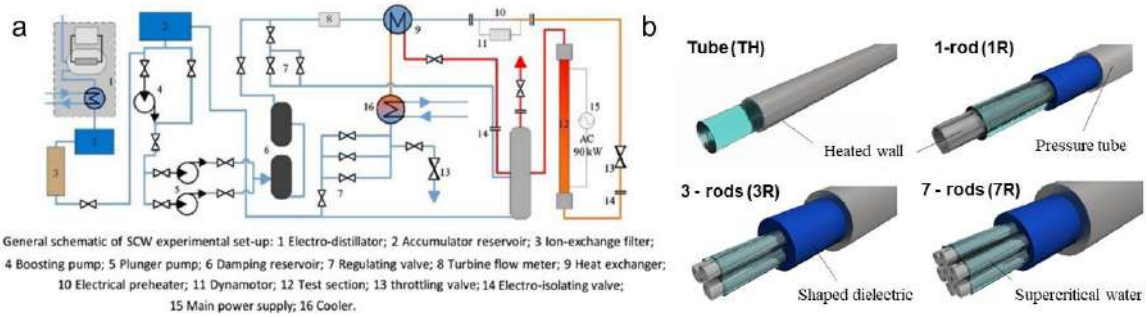

Figure 1. Scheme of the experimental set-up and test bundles.

DNSHE CONCEPTION

In a first approximation, the analysis of relationship between velocity- and temperature- near-wall functions can be carried out based on an energy equation numerical solution for the boundary layer (DNSHE). An axisymmetric formulation is considered (in the general case, an annular channel).

In this case, for representative modes with deteriorated heat transfer, model velocity and pressure fields are formed using CFD. The axial temperature distribution on the wall is formed as an interpolation function obtained based on experimental data. A numerical solution of the energy equation is carried out using FVM with a central differencing scheme in space on a locally adaptive Cartesian grid. The use of such meshes with wavelet algorithms makes it relatively easy to organize the mesh adaptation procedure near the pseudo phase transition point, as well as test various mesh refinement criteria. The general DNSHE concept is presented in Figure 2.

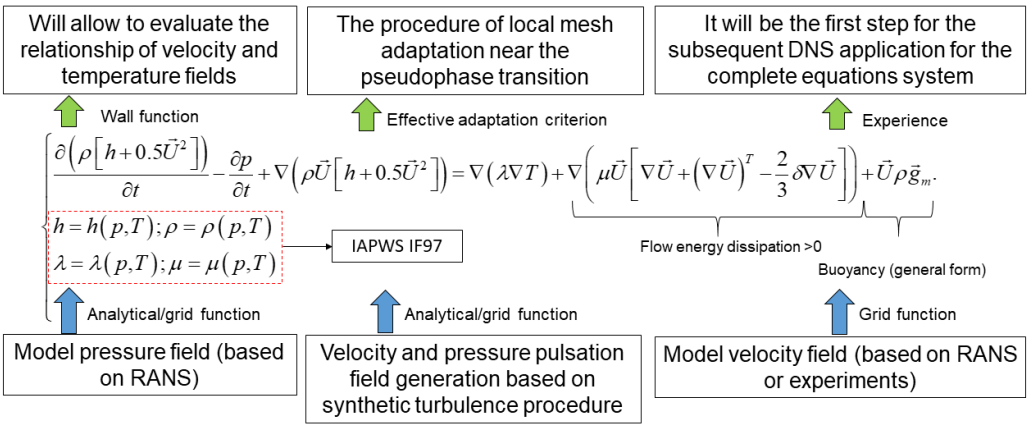

Figure 2. Chart of the DNSHE conception.

CONCLUSIONS

The application of DNSHE procedure together with the existing experimental data set for deteriorated heat transfer allow us to evaluate the relationship between the velocity- and temperature- fields in boundary layer. Also, this procedure is a great support to estimate the correctness of temperature near-wall functions adaptation for two-parameter turbulence models. In future works we will apply the experimental velocity fields instead of the modeling one, based on experimental instrumental measurements.

References

[1] Heat Transfer Behaviour and Thermohydraulics Code Testing for Supercritical Water Cooled Reactors (SCWRs): IAEA-TECDOC-1746.
[2] Eter A. Flow obstruction effects on heat transfer in channels at supercritical and high subcritical pressures. *PhD Thesis,* NTU Mech. Eng., Dept., Ottawa, 2016.
[3] Chiara Brogna. CFD modelling of heated ro bundles with water at supercritical pressure. *Magister Thesis*, UniPi, Pisa, 2017.
[4] Filonov V., On experimental investigation of heat transfer deterioration and hydraulic resistance in annular channel and SCWR 3 – rod bundle, ICONE26-81289, 2018.
[5] Jiaming Liu Analysis of heat transfer of supercritical water by direct numerical simulation of heated upward pipe flows. *Int. J. Thermal Silences.* DOI: 10.1016/j.ijthermalsci.2018.12.028, 2019.

APPLICATION OF CORRUGATED SURFACE TO CONTROL SKIN FRICTION NEAR THE SEPARATION

Artur Dróżdż, Paweł Niegodajew, Mathias Romańczyk and Witold Elsner
Czestochowa University of Technology, Armii Krajowej 21 42-200. Czestochowa, Poland

Summary The paper is about experimental analysis of a new passive skin friction control method applied to a high Reynolds number turbulent boundary layer close to separation. A proposed approach is based on the mechanism of scale interaction observed in the wall bounded flows known as amplitude modulation of small scales by large-scale motion. Results show that the small waviness of the surface can be use in an efficient way to postpone the turbulent boundary layer separation for high Reynolds numbers, where other methods based on roughness fails. This method introduces asymmetry between sweep and ejection events in the flow which results in positive skewness of streamwise fluctuations and additionally increases the momentum near the wall. The momentum is increased only in the inner part of boundary layer.

INTRODUCTION

Development of TBL in APG is accompanied with decrease in the wall shear in the streamwise direction and the separation usually takes place when τ_w reaches zero [1]. So, an effective separation postponing method should allow either to increase the τw locally (when the separation is expected to occur) or to reduce its decreasing rate within entire APG area.

Available literature offers a variety of different approaches allowing for flow separation delay which are generally classified as active or passive. The former ones involve a number of diversified solutions as dilution of polymer additives in flowing liquids [2,3], gas injectors [4,5], heating and cooling processes [6], moving wall systems [7,8] or exposing the flow to the action of electromagnetic field [9]. These methods are usually effective on one hand, on the other hand they require a consider-able energy input, which leads to higher energy consumption and reduction in the total efficiency. Consequently, a widespread attention is paid to the passive methods as they do not require an external energy source. Such methods may include, distributed roughness, blowing and suction or vortex generators.

The recent progress in both measuring and computational techniques has allowed acquiring a valuable data which ensured a better understanding of processes occurring in TBL. Particularly interesting is discovering of the amplitude modulation phenomenon discovered by Mathis [10], which relays on interaction between large scale motion (LSM), located in the outer region, with small structures close the wall. For relatively large Reynolds number LSM causes sequentially increase and decrease of the flow velocity close the wall, what surprisingly leads to increased net convection velocity of small structures and to increased wall-shear stress [11,12]. As it was showed further by Agostini and Leschziner [13] the small scales rather than LSM have a dominant contribution to the wall-share stress, however this is done though the amplitude modulation.

In the present study we would like to present a conceptual passive method, which relies on modification of the wall topology by waviness which shape is inspired by amplitude modulation process. This geometry was designed in a way ensuring an enhancement the amplitude modulation process by increasing the activity of pseudo-induced LSM in high speed zones on the crests of waviness and thus strengthen convection velocity of the small scales. Consequently, increased wall-shear stress and postponing of TBL separation is achieved. In particular, the study is focussed on searching for the optimal geometry of the wall including amplitude to period ratio of wavy surface. Worthy to note is that the re-search undertaken in this work has a pioneering character as such an attempt aimed at postponing separation at high Reynolds number has not been undertaken before.

EXPERIMENTAL SETUP

The experiment was performed in an open-circuit wind tunnel, where the TBL was developed along a flat plate, which was 5035 mm long, what allows to reach boundary layer thickness, $\delta = 95$ mm at the inlet to the test section. The wavy wall of different length was mounted just after the inlet plane (shown in Fig. 1). The specially design diffuser shape test section with a length of 1.835 m equipped with a perforated movable upper wall allows to generate the turbulent boundary layer on the bottom wall which is at the verge of the separation. The velocity measurements were performed with hot-wire anemometry Dantec Dynamics Streamline Pro apparatus. A single hot-wire probe of a diameter $d = 3$ μm and length $l = 0.4$ mm was used. The hot-wire bridge was connected to a 16-bit A/D converter. To have the verified reference friction velocity u_τ along the flow the CCCM technique was applied introduced by Niegodajew et al. 2019 [12]. The wavy wall was manufactured from a high-density polyurethane material which ensures a hydraulic smoothness of the surface right after mechanical processing. The amplitude of the wavy wall is changing in the streamwise direction to have the fixed ratio to the boundary layer thickness.

Fig. 1 Wavy-wall geometry. Streamwise direction from left to right.

RESULTS

The measurements were performed for the high inlet Reynolds number based on friction velocity Re_τ equal to 4000. Several different wavy surfaces were used during step by step optimisation characterised by different amplitude, length and period of wavy wall. At each step the velocity profile was measured at the fixed distance from the inlet (x = 1000 mm). The study showed that the applied method, with appropriately selected geometrical parameters ($A^+/(\lambda/\delta_{99,in}) \approx 110$, $\lambda/\delta_{99,in} = 1.71$ in Fig. 2), allowed obtaining a 13% increase in wall shear stresses at sepation relating to the value at the ZPG inlet and thus ensuring a delay of turbulent detachment of boundary layer.
In order to assess how the corrugated wall affects the boundary layer, the mean and fluctuation velocity profiles as well as the skewness factor at the certain location downstream the modified surface has been analysed. The effect of increased momentum is assigned either to modulation of convection velocity or/and to production of turbulent kinetic energy (TKE) in the location preceding recirculation zone. It means that the most affected area is the near-wall region. For corrugated wall the increased *uu* variance value is observed in the wall vicinity.

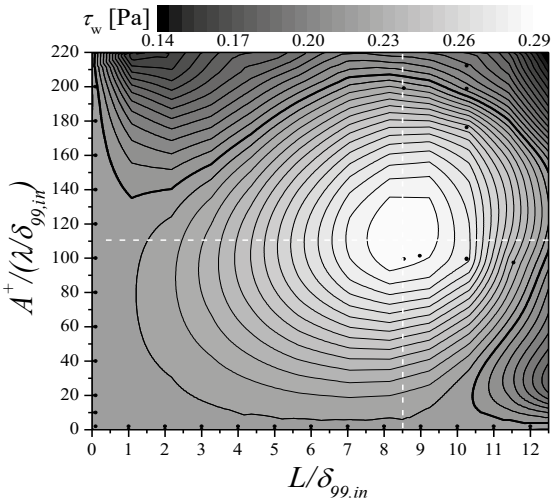

Figure 2. The wall shear stress at x = 1000 mm as a function of normalised both wave amplitude and length.

SUMMARY

It was demonstrated that for the specific amplitude, the period and the length of wavy wall the maximum of the skin friction value can be achieved when dealing with high Reynolds number turbulent boundary layer in adverse pressure gradient leading to separation. The undergoing results shows that the method can be used in an efficient way to postpone the turbulent boundary layer separation, where classical methods based on turbulizators fail. The optimized wavy wall shape substantially increases the momentum near the wall for high Reynolds number turbulent boundary layer and acts in similar way as the amplitude modulation mechanism leading to increase in convection velocity of turbulence. The significant increase of velocity is observed in the inner region of boundary layer (y<0.5δ), which coincides well with the area of the boundary layer where the effect of amplitude modulation is usually observed. Such reorganization of turbulence production introduces dominance of the sweep over the ejection. Increased sweep enhanced momentum transfer to the wall and cause the higher turbulence production downstream the flow.

ACKNOWLEDGMENTS

The investigation was supported by National Agency for Academic Exchange under Grant no. PPI/APM/2019/1/00062, National Science Centre under Grant No. DEC-2017/25/B/ST8/02480..

References

[1] M. Gad-el-Hak, D.M. Bushnell, Separation Control : Review, J. Fluids Eng. 113 (1991) 5–30.
[2] C.M. White, M.G. Mungal, Mechanics and Prediction of Turbulent Drag Reduction with Polymer Additives, Annu. Rev. Fluid Mech. 40 (2008) 235–256.
[3] X. Zhang, X. Duan, Y. Muzychka, Degradation of flow drag reduction with polymer additives — A new molecular view, J. Mol. Liq. 292 (2019) 111360.
[4] S.A. Mäkiharju, S.L. Ceccio, On multi-point gas injection to form an air layer for frictional drag reduction, Ocean Eng. 147 (2018) 206–214.
[5] X. Zhao, Z. Zong, Y. Jiang, T. Sun, A numerical investigation of the mechanism of air-injection drag reduction, Appl. Ocean Res. 94 (2020) 101978.
[6] H.O.G. Benschop, W.P. Breugem, Drag Reduction by Herringbone Riblet Texture in Direct Numerical Simulations of Turbulent Channel Flow, Phys. Fluids. (2017).
[7] M. Quadrio, Drag reduction in turbulent boundary layers by in-plane wall motion, Philos. Trans. R. Soc. A Math. Phys. Eng. Sci. 369 (2011) 1428–1442.
[8] N. Tomiyama, K. Fukagata, Direct numerical simulation of drag reduction in a turbulent channel flow using spanwise traveling wave-like wall deformation, Phys. Fluids. 25 (2013).
[9] V. Shatrov, G. Gerbeth, Magnetohydrodynamic drag reduction and its efficiency, Phys. Fluids. 19 (2007).
[10] R. Mathis, N. Hutchins, I. Marusic, Large-scale amplitude modulation of the small-scale structures in turbulent boundary layers, J. Fluid Mech. 628 (2009) 311–337.
[11] A. Dróżdż, W. Elsner, Amplitude modulation and its relation to streamwise convection velocity, Int. J. Heat Fluid Flow. 63 (2017) 67–74.
[12] P. Niegodajew, A. Dróżdż, W. Elsner, A new approach for estimation of the skin friction in turbulent boundary layer under the adverse pressure gradient conditions, Int. J. Heat Fluid Flow. 79 (2019) 108456.
[13] L. Agostini, M. Leschziner, The connection between the spectrum of turbulent scales and the skin-friction statistics in channel flow at Re τ ≈ 1000, J. Fluid Mech. 871 (2019) 22–51.

ON THE SEPARATED STRUCTURES IN TURBULENT FLOW AROUND OVAL-TRENCH DIMPLES

Aleksei Chulyunin*[1], Aleksei Sinyavin[1]
[1] Lomonosov Moscow State University, Research Institute of Mechanics, Moscow, Russia

Summary The mechanisms that determine the structure of the separated turbulent flow of an incompressible fluid around an oval-trench dimple which located on a flat wall transverse to the rectangular channel are discussed. In the case of short oval-trench dimples, including a spherical dimple, there are three equilibrium states of Reynolds-averaged flow: one symmetric state and two reflective asymmetric single vortex states. As the length of dimple increases, the symmetric state of the flow stabilizes, and the possible asymmetric equilibrium states become unstable. Further increases in the length of the dimple lead to the structural topology of the internal flows in the dimple becomes complicated.

INTRODUCTION

Study of the interaction between fluid flows and irregular surfaces is a common and significant problem of modern mechanics. A special place among such researches has dimpled channels. In these channels, the increase in heat transfer can be ahead of a rise in hydraulic losses [1, 2]. Based on the value of parameter Δ, shallow ($\Delta < 0.125$), moderate ($0.125 < \Delta < 0.25$), and deep ($\Delta > 0.25$) dimples are nominally distinguished. In the shallow dimples, the flow is unseparated. In contrast, in the moderate dimples, the characteristic vortex structures appear in the form of asymmetric two-cell region of the recirculation flow. The corresponding flows are observed in experiments and are well reproduced by URANS computational technologies. At this time, the calculation of deep dimples is complicated because the separated flow around them may have ambiguous structure and may be unsteady.

In paper [3], using the URANS computational technology, it is shown that, in the transition range from the moderate to the deep dimple $0.2 < \Delta < 0.26$, the uniqueness of the resulting flow is broken. This is exhibited in the fact that, for the same values of Δ and other constitutive parameters of the problem, the steady separated flow can look like both symmetric two-cell vortex structure and asymmetric single vortex structure. A more detailed study [4] of the turbulent flow around the spherical dimple ($\Delta = 0.26$, $Re_D = 40\,000$) with the LES computation technology confirmed the formation of separated asymmetric structure. However, in contrast to the URANS predictions, these structures appear to be unstable, and the flow patterns obtained by averaging the numerical solution to the problem demonstrate the existence of two alternating single vortex structures declined with respect to the main external flow by angles ±45°. In the same time, the long-term averaging provides the symmetric flow pattern around the dimple [4].

Recently, more and more works are devoted to the study of the characteristics of oval-trench dimples. In [5] it was shown that the total heat transfer from a channel with a long oval-trench dimple more than three times exceeds the heat transfer from a channel with a spherical dimple with the same spot area. In [5] dimples of small depth and, as a result, with steady structures are studied.

At the present study, based on the numerical modelling and partially by the experiment, the structures of the flow in deep oval-trench dimples are examined.

COMPUTATIONAL SETUP

A rectangular channel with an oval-trench dimple is considered. The dimensions of the calculation domain corresponded to the geometry of the channel with the dimple at the lower wall. The height of the channel was 0.83D. The distance from the channel side wall to the nearest trench edge was 1.5D for all λ. The entry boundary of calculation domain was at a distance of 4.5D from the front edge of the trench whereas the exit boundary was at a distance of 4.5D downstream the rear edge. In this study, we used two approaches to modelling turbulent flows. The first is based on the use of Reynolds averaged Navier-Stokes equations, which are closure using the two-parameter SST turbulence model. The second approach uses a modification of the method of detached eddies IDDES (The Improved Delayed Detached Eddy Simulation).

The unstructured mesh of polyhedral form applied for the discretization of the numerical domain into the control volumes. The average linear dimension of the cells inside the trenches was equal to 7×10^{-3} D and the dimension inside the flow core was 5×10^{-2} D. The near-wall step was prescribed equally to 10^{-4} D. A grid stretching normal to the wall is used to provide the sufficient near-wall grid resolution with $y^+<1$. A stretching factor normal to the wall is chosen to place several grid points into the viscous sublayer. The total number of control volumes was from 18 to 25 million, depending on the value of parameter λ. At the channel inlet boundary, a uniform profile of velocity head q was assigned. At the outlet boundary, the open boundary conditions with constant pressure $p = p_{out}$ were set, whereas no-slip boundary conditions were set on all rigid inner boundaries.

*Corresponding author. E-mail: chulyu-n@mail.ru.

RESULTS

The performed series of calculations show that with the increase of the length of the cylindrical part of the dimple from 0 to L = R, the flow stabilizes. Figure 1 presents the computer visualization of two characteristic states of the flow for $\lambda = 0.5$ with pronounced inclined single-core vortex structures beginning on the inner walls of trench end spherical rounding and emerging on the outer near-wall region of the flow near the opposite ends of the trench. Thus, the flow structure around the oval-trench dimple of small elongation is similar to the spherical dimple, but without a switch. The specific form of the steady-state flow structure depends on the initial conditions of the task. This result was obtained both numerically (URANS and DES technologies) and experimentally in the wind tunnel of the Research Institute of Mechanics of Lomonosov Moscow State University. As we move on to longer dimples, the pattern changes substantially. Instead of two equally possible asymmetric vortex structures (Figure 1, $\lambda = 0.5$), there remains a single symmetric two core structure beginning on the internal walls of end rounding and emerging in the outer flow through the central part above the rear edge of the trench (Figure 2a, $\lambda = 1.5$). The obtained flow in the trench of moderate length may be interpreted as the coincidence of two counter moving swirling jets flowing from the opposite ends of the trench.

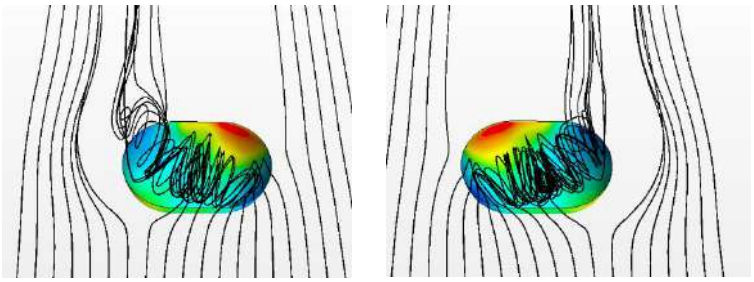

Figure 1. Single core asymmetric vortex structures of flow around a short trench at $\lambda = 0.5$.

An increase in parameter λ leads to the following qualitative variations in the structure of the flow around the oval-trench dimple (Figure 2b). The flow structure is symmetric but has qualitative differences from the previous case. Between the counter moving swirling jets propagating from the opposite ends of the trench, a buffer structure appears in the form of two secondary swirling jets propagating in different directions from the trench plane of symmetry. The flow rate in these secondary jets is fed from the external flow above the central part of the trench. Part of the shear layer turns back and enters in the trench, generating the vortex source in the trench plane of symmetry. As a result, the periphery swirling jets from the opposite ends of the trench come into collision not with each other, but with the countermoveing central jets. In the places of the collision of these jets at some distance to the left and the right from the trench plane of symmetry, they coalesce and turn back by 90° with the formation of two non-swirling jets flowing into the concurrent external flow.

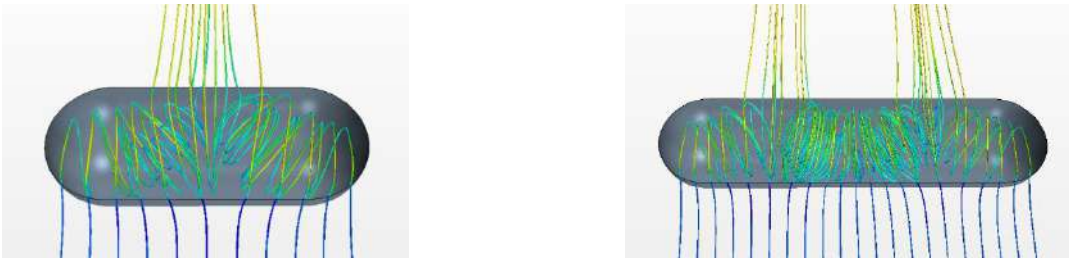

a) b)

Figure 2. Flow around an oval-trench dimples at length: a) λ=1.5, b) λ=3

Acknowledgements

This work is partially by supported by the Russian Foundation for Basic Research (project 19-01-00242).

References

[1] B.V. Dzyubenko, Y.A. Kuzma-Kichta, A.I. Leontiev, I.I. Fedik, L.P. Kholpanov, Intensification of Heat and Mass Transfer on Macro-, Micro-, and Nanoscales. Begell House, 2016, pp. 1–630.
[2] S. Rashidi, F. Hormozi, B. Sunden, O. Mahian. Energy saving in thermal energy systems using dimpled surface technology – A review on mechanisms and applications. *Appl. Energy*. **250**: 1491–1547, 2019.
[3] S. A. Isaev, A. I. Leont'ev, N. A. Kudryavtsev, I. A. Pyshnyi. The effect of rearrangement of the vortex structure on heat transfer under conditions of increasing depth of a spherical dimple on the wall of a narrow channel. *High Temp.* **41:** 229-232, 2003
[4] J. Turnow, N. Kornev, S. Isaev, E. Hassel. Vortex mechanism of heat transfer enhancement in a channel with spherical and oval dimples. *Heat Mass Transfer*. **47**: 301-313, 2011
[5] S.A. Isaev, A.I. Leontiev, O.O. Milman, I.A. Popov, A.G. Sudakov, Influence of the depth of single-row oval-trench dimples inclined to laminar air flow on heat transfer enhancement in a narrow micro-channel. *Intern. J. Heat and Mass Transfer*. **134**: 338-35, 2019.

SHOCK/BOUNDARY-LAYER INTERACTIONS: A COMPARISON BETWEEN SHOCK-CAPTURING AND SHOCK-FITTING SIMULATIONS

Alessia Assonitis *[1], Renato Paciorri[1], and Aldo Bonfiglioli[2]
[1] Department of Mechanical and Aerospace Engineering, Università La Sapienza, Roma, Italy
[2] Scuola di Ingegneria, Università degli Studi della Basilicata, Potenza, Italy

Summary Compressible viscous flows are often characterized by the interaction between shock-waves and boundary layers. The occurrence of shock/boundary-layer interactions (SBLI) within an high-speed flow can greatly affect the performance of a vehicle due to the presence of intense local heating and the loss of efficiency of the aerodynamic control surfaces. It is therefore of paramount importance to accurately predict the skin-friction and wall-heating distributions which, in turn, require the accurate modeling of the shock-waves. The proposed paper compares the reliability of two different numerical approaches which consist in modeling the shock-waves by either shock-capturing or shock-fitting, whereas in regions of smooth flow the governing PDEs are in both cases approximated using the same unstructured-grid CFD solver.

INTRODUCTION

Numerical models for compressible flows can be cast into two main categories: shock capturing (S-C) and shock-fitting (S-F). S-C methods, which are nowadays very popular due to their algorithmic simplicity, are built upon the integral, conservation-law form of the governing equations. No special treatment is required to handle the discontinuities, but these exhibit a finite thickness which is orders of magnitude larger than their physical one. Moreover, and, despite their great popularity, S-C schemes are known to be plagued by a variety of numerical problems that affect the accuracy and the quality of the computed solutions also downstream of the shocks [1].

The S-F technique, initially developed by Gino Moretti [2], relies on a different shock-modeling approach which consists in identifying and tracking the motion of the discontinuities, which are treated as internal boundaries of zero thickness that bound regions of the flow-field where a continuous solution of the governing PDEs exists. The motion of the discontinuities, and their upstream and downstream states, are computed by means of the Rankine-Hugoniot jump relations, whereas in the smooth-flow regions of the computational domain any gas-dynamic solver can be used to approximate either the conservation-law or non-conservative form of the governing PDEs [3].

The S-F approach overcomes most of the numerical troubles incurred by S-C methods, but it typically requires a major coding effort with respect to S-C algorithms.

In the proposed paper numerical simulations of different test-cases involving SBLIs have been performed using both the aforementioned approaches and, in particular, an improved version of S-F algorithm for unstructured grids proposed by Paciorri and Bonfiglioli [4]. The results will be mutually compared and also with experimental data available in the literature in order to highlight the different performance of the two shock-modeling practices.

RESULTS

A sample test-case that will be analyzed in the full paper consists in the oblique shock reflection on a flat plate, which was experimentally studied by Degrez et al. in [5]. Figures 1 and 2 show the density field computed using both the S-C and S-F approaches on nearly identical unstructured triangular grids; in particular, the S-F simulation is of an hybrid type, whereby only the strongest shocks are fitted and the remaining ones are captured. The comparison between the S-C simulation and the hybrid, S-F one clearly shows the advantages of the latter in terms of solution quality, particularly in the area where the SBLI takes place. Observe, in particular, that the captured shocks span several grid elements and are therefore characterized by a finite thickness, the size of which is comparable to the size of the recirculation region. In order to improve the quality of the S-C solution a much finer grid would be required, thus incurring in a higher computational cost.

More details about this simulation and other test-cases (e.g. transonic airfoil, hypersonic compression corner) will be discussed and analyzed in the full paper.

*Corresponding author. E-mail: alessia.assonitis@uniroma1.it.

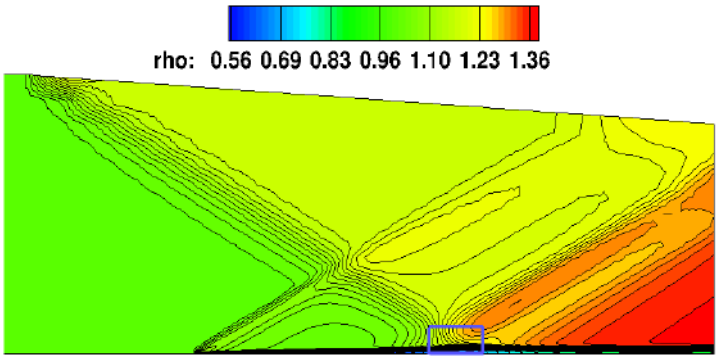

(a) Full computational domain.

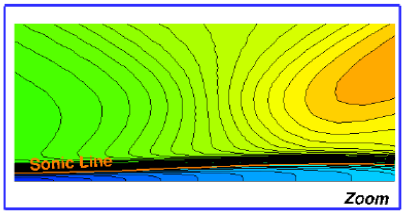

(b) Enlargement of the SBLI region.

Figure 1: Density iso-contour lines computed using the S-C technique

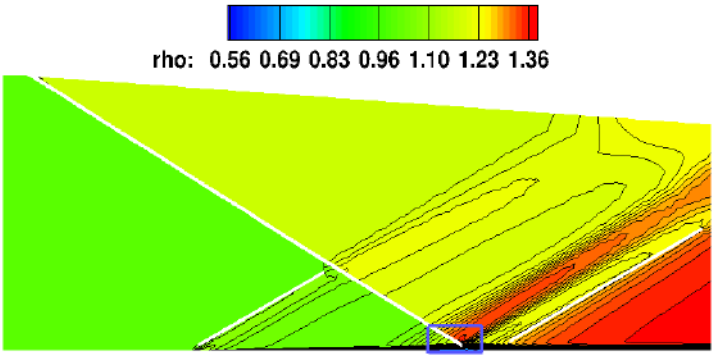

(a) Full computational domain.

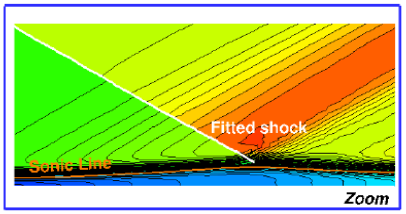

(b) Enlargement of the SBLI region.

Figure 2: Density iso-contour lines computed using the S-F technique; the fitted shocks are marked using solid white lines.

References

[1] Quirk J. J. A contribution to the great Riemann solver debate. *International Journal for Numerical Methods in Fluids Volume 18 issue 6* ,1994.

[2] Moretti G., Abbett M., A time-dependent computational method for blunt body flows, *AIAA Journal*, 2136–2141, 1966

[3] Paciorri R., Onofri M. Shock Fitting: classical technique, recent developments and memoirs of Gino Moretti. Springer International Publishing, 2017.

[4] Paciorri R., Bonfiglioli A. Shock interaction computations on unstructured, two-dimensional grids using a shock-fitting technique, *Journal of Computational Physics*, **230**(8),3155-3177, 2011.

[5] Degrez, G., Boccadoro C.H. and Wendt, J.F., The interaction of an oblique shock wave with a laminar boundary layer revisited. An experimental and numerical study, *J. Fluid Mech.* (1987) **177**:247-263.

TURBULENCE SUPPRESSION VIA COMPLIANT LUBRICATING LAYER

Alessandro Monti*[1] and Marco Edoardo Rosti[1]
[1] Okinawa Institute of Science and Technology Graduate University, Onna, Kunigami, Okinawa, Japan

Summary We study the effect of a lubrication layer on a turbulent channel flow at nominal $Re_\tau = 300$, with two immiscible, homo-viscous flows separated by a thin interface. The problem at hand is tackled by means of direct numerical simulations and the multiphase nature of the flow is accounted through the volume of fluid method. The analysis is performed for several heights of the lubricating layer and multiple interface surface tensions, the latter governed by the Weber number We. We show that, in the selected parameters subset, the lubricating layer completely or partially laminarizes, bringing drag reduction benefits. A satisfactory explanation of the turbulence suppression mechanisms will be provided.

INTRODUCTION

The benefits of lubricating high-viscosity oil pipelines with water for increasing transport-efficiency are well-known and date back to the beginning of the 20th century [1]. The technology is based on the balance, in internal flows, between the pressure gradient needed to pump the liquid and the shear-stress at wall. When a centripetal acceleration is applied to the multiphase liquid, the water, having lower viscosity than oil, migrates towards the high-shear regions (i.e. the wall). In this way, the balance above reduces in effectively pumping water instead of crude, thus reducing the energy needed to transport the liquid. These flows are known as core-annular flows and the drag-reduction mechanisms is viscosity-driven [2]. Since the seminal work by Isaacs and Speeds [1], the topic has been heavily studied due to the critical impact that petroleum industry has had in the modern society. Comprehensive overviews on the topic are provided by Joseph *et al.* [2] and, more recently, by Ghosh *et al.* [3].

While the viscosity effects on the drag reduction mechanisms are well understood, the roles of the surface tension and of the size of the lubricating layer still lack a complete explanation. A first attempt to clarify the role of the surface tension has been carried out by Roccon *et al.* [4]. The authors analysed a turbulent channel flow with a thin lubricating layer ($\delta/H = 0.15$, being H the half-height of the channel) having the same viscosity of the carrier fluid. The analysis was tackled through direct numerical simulations. The work shows that the surface tension alone can bring drag reduction with higher savings than bi-viscous flows. The homo-viscosity lubricating layer relaminarises, with the surface tension suppressing the turbulence self-sustained mechanisms of the wall-cycle [4, 5]. This drag reduction mechanism (surface-tension-driven) has been characterised and distinguished by the typical viscosity-driven drag reduction [1, 4].

Inspired by this promising work, our study aims to unravel the mechanisms of the turbulence suppression. We further increase the parameter set tackled by acting on the size of the lubricating layer. The idea is to decouple the turbulence mechanisms found close to the wall and in the logarithmic region, in the fashion of a scales-separation effect seen in high-Reynolds number flows [6]. The size of the lubricating region, therefore, will span from the edge of the buffer layer to the core of the logarithmic region. Finally, the elasticity of the separating layer will also be modified to investigate the role of the surface tension.

This work aims to fullfil the gap in the literature from the fluid-mechanics point of view, by analysing the turbulence break-down mechanisms.

METHODOLOGY

We consider the flow of two incompressible Newtonian fluids, separated by an interface, in a turbulent channel flow at $Re_\tau = 300$. The two-fluid motion is governed by the incompressible Navier-Stokes equations and the interactions between the two fluids are tackled by enforcing the continuity of the velocity field and of the traction force at the interface,

$$u_i^{f1} = u_i^{f2} \quad \text{and} \quad \sigma_{ij}^{f1} n_j = \sigma_{ij}^{f2} + \sigma\kappa n_i \tag{1}$$

where the superscripts $f1$ and $f2$ indicate the two phases, σ_{ij} denotes the Cauchy stress tensor, n_i the normal vector at the interface, κ the interface curvature, and σ the uniform surface tension. The two-phase interaction is accounted by applying the volume of fluid method [7], where the extrema of an indicator function, $H \in [0, 1]$, identify the fluid phases. The function H, here, is reconstructed via the MTHINC method [7]. The indicator function is then updated through the transport equation,

$$\frac{\partial \phi}{\partial t} + \frac{\partial u_i H}{\partial x_i} = \phi \frac{\partial u_i}{\partial x_i}, \tag{2}$$

being u_i the local fluid velocity and ϕ the cell-average value of H. Once equation (2) is solved, the momentum equation can be rewritten with the one-continuum formulation [8],

$$\frac{\partial u_i}{\partial t} + \frac{\partial u_i u_j}{\partial x_j} = \frac{1}{\rho}\left(\frac{\sigma_{ij}}{\partial x_j} + f_i\right), \tag{3}$$

*Corresponding author. E-mail: ictam2020@aimgroup.eu.

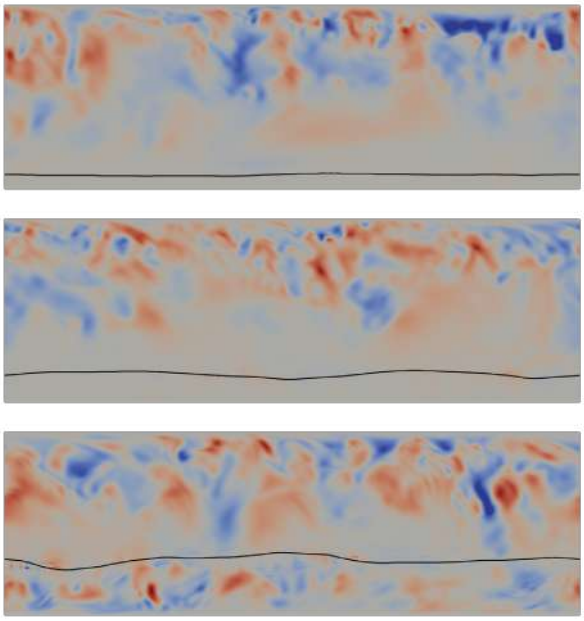

Figure 1: Contours of the wall-normal velocity normalised with the nominal friction velocity, u_τ, that gives $Re_\tau = 300$. The Weber number considered is $We_\tau = 0.5$. The x axis represents the streamwise direction, while the y axis the wall-normal one. Top panel: $\delta/H = 0.15$; Central panel: $\delta/H = 0.3$; Bottom panel: $\delta/H = 0.60$.

where ρ is the density, $f_i = \sigma\kappa n_i \delta$ (being δ the bell function used to single out the interface region) and $\sigma_{ij} = -p\delta_{ij} + 2\mu D_{ij}$ is the Newtonian stress, indicating p the pressure, δ_{ij} the Kronecker delta, μ the dynamic viscosity and D_{ij} the strain rate tensor, respectively. The two-phase fluid properties are accounted with a linear interpolation,

$$x = (1 - \phi)\, x^{f1} + \phi x^{f2} \tag{4}$$

where the function x can be replaced by ρ, μ and σ_{ij}. Finally, the Navier-Stokes equations with the modified momentum equation (3) are solved via a fractional-step method. Furher details of the methodology with the validation can be found in [9]

PRELIMINARY RESULTS

As the study is still ongoing, we present here some preliminary results. We used as initial condition a turbulent channel flow at $Re_\tau = 300$, in a $2\pi H \times 2H \times \pi H$ box, where H is the half-channel height, with periodic boundary conditions in the streamwise and spanwise directions, while a no-slip condition is applied at the walls. We then applied the volume of fluid method by placing an initially parallel-to-the-wall interface at $\delta/H = [0.15, 0.3, 0.6, 1]$, setting the surface tension by tuning the Weber number, $We_\tau = \rho u_\tau^2 H/\sigma = [0.5, 1, 1.5]$. Figure 1 shows that, for $We_\tau = 0.5$, the layer below the interface laminarises for the case $\delta/H = [0.15, 0.3]$, while partially laminarises when $\delta/H = 0.6$, i.e. when then interface is placed in the core of the logarithmic region, at $y^+ = 180$. The mechanisms of the turbulence break-down still need to be further investigated but the preliminary results are promising.

References

[1] J.D. Isaacs, and B. Speeds. Method of piping fluids. *US Patent*, 1904.
[2] D.D. Joseph, R. Bay, R. Chen, K.P. Renardy, and Y. Yuriko. Core-annular flows. *Annual Review of Fluid Mechanics*, 29(1):65–90, 1997.
[3] S. Ghosh, T.K. Mandal, G. Das, and P.K. Das. Core-annular flows. *Renewable and Sustainable Energy Reviews*, 13(8):1957–1965, 2009.
[4] A. Roccon, F. Zonta, and A. Soldati. Turbulent drag reduction by compliant lubricating layer. *Journal of Fluid Mechanics*, 863, 2019.
[5] J. Jiménez, and A. Pinelli. The autonomos cycle of near-wall turbulence. *Journal of Fluid Mechanics*, 389:335–359, 1999.
[6] N. Hutchins, and I. Marusic. Evidence of very long meandering features in the logarithmic region of turbulent boundary layers. *Journal of Fluid Mechanics*, 507:1–28,2007
[7] S. Ii, K. Sugiyama, S. Takeuchi, S. Takagi, Y. Matsumoto, and F. Xiao. An interface capturing method with a continuous function: the THINC method with multi-dimensional reconstruction. *Journal of Computational Physics*, 231(5):2328–2358, 2012.
[8] G. Tryggvason, M. Sussman, and M.Y. Hussaini. Immersed boundary methods for fluid interfaces. *Computational Methods for Multiphase Flow*, 37:239–261, 2007.
[9] M.E. Rosti, F. De Vita, and L. Brandt. Numerical simulations of emulsions in sheat flows. *Acta Numerica*, 230(2):667–682, 2019.

A RIGID BODY TRANSLATING IN A BOUNDARY LAYER

Ellen Jolley*[1], Frank T. Smith[1]
[1] Department of Mathematics, University College London, Gower Street, London, WC1E 6BT

Summary The study considers a slender, heavy body moving with streamwise velocity in a boundary layer. The application in mind is aircraft icing, in which small ice particles may adhere to the surface of an aircraft and interfere with its aerodynamics. Some such particles are small enough to enter the boundary layer of the aircraft, which results in substantially different dynamics from those outside the boundary layer due to the presence of incoming vorticity. A wide range of interesting solutions exist including 'crashes' (eventual collision with the wall), 'fly away' (escape to infinity), and 'bouncing' (repeated excursions far from the wall but with eventual return).

INTRODUCTION

The problem here is to determine the long term behaviour of a rigid body which moves due to its dynamic interaction with the surrounding fluid. This problem is of significant interest to industry due to its relevance to aircraft icing, in which small ice particles can adhere to aircraft wings, engines, or fuselages and deform the aerodynamic shape in such a way as to disrupt flight, in worst cases resulting in serious accidents [1]. In this work, we are considering a boundary layer setting and hence vorticity is present, but comparison can be made with the similar problems considered in [2, 3] which are both vorticity-free.

The flow is modelled as two-dimensional and incompressible, and we work in the streamwise rest frame of the body. The incoming boundary layer flow is first approximated as a linear profile, i.e. with constant incoming vorticity, which approximates the near-wall boundary layer flow. The body is small in both dimensions but is thin, so that its width (comparable to the boundary layer thickness) is much less than its length. Its angle of incidence is assumed to be small so that it is nearly aligned with the oncoming flow profile. The Reynolds numbers and Froude numbers of interest are large and hence the relevant force governing the body motion is the pressure force. The small vertical scale of the problem yields that pressure has no vertical dependency, and hence the pressure above the body is identified with the free-stream pressure to be zero. Hence the pressure beneath the body determines its motion. The boundary conditions consist of the kinematic conditions at the wall and the underbody surface, as well as the Kutta condition insisting on continuity of pressure at the trailing edge. The modelling assumption that the body density is significantly greater than the fluid density (appropriate for ice in air) yields that the flow is quasi-steady on the time scale of body motion, which allows significant analytic progress to be made.

RESULTS AND DISCUSSION

By making use of volume flux conservation and Bernoulli's principle, the velocity distribution and pressure can be determined in terms of the underbody curve for the entire flow region under the body. This reduces the system to a pair of non-linear integro-ODEs for the body height and angle (with height measured from its centre of mass, and its angle being the angle its chord line makes with the positive x-axis), which can be solved numerically to yield a wide-range of solutions, including 'crash' solutions (eventual collision with the wall), 'fly away' (escape to infinity), and 'bouncing' (repeated excursions far from the wall but with eventual return). The outcome depends sensitively on initial conditions as well as the incoming flow and body shape, but one predictor for whether a body will crash or not is its initial angle (positive angle making the body more inclined to a crash and negative angle inclining the body to fly away).

Crash solutions

Figure 1 shows the numerical results in a crash scenario, i.e. finite-time collision with the wall. Asymptotic analysis of the governing equations as the underbody curve approaches contact with the wall predicts that the height and angle are $O(T_0 - T)^{4/5}$,3where T is the scaled time variable and T_0 is the time of the crash. Since this predicts infinite velocity in the limit of the crash, consideration of a second time stage is required. In this second time stage, there is a small region of extremely high pressure surrounding the crash point which now forms the dominant component of the force on the body. The results, shown in Figure 2, yield constant velocity in the limit of the crash. This second stage result of constant velocity is in line with the findings of [2].

Fly away and bouncing solutions

A second category of solutions exists for which the body never collides with the wall. This can manifest as escape to infinity ('fly away') or as repeated excursions far from the wall with eventual return (termed 'bouncing', but there is no collision). In all cases, the body angle oscillates and all three can be understood by the same asymptotic regime in which the height is large and depends on a 'long' time variable while the angle remains of order unity and varies on 'short' time. This then yields a differential equation which can be solved to find the limit cycle for the body angle and predicts a parabolic solution for height with leading coefficient depending on the angle limit cycle. If this leading coefficient is positive, it leads to a parabolic height consistent with fly away solutions (Figure 3). If it is zero, we then consider a next-

*Corresponding author. E-mail: ellen.jolley.18@ucl.ac.uk

order adjustment to the height which adds an additional term to the resulting equations, accounting for the 'bouncing' behaviour, which consists of parabolic excursions with negative leading coefficient, followed by a region where the new term is most important causing a 'rebound' (Figure 4). There is a third type of solution not discussed here for which neither height nor angle depend on long time and both enter limit cycles, hence the body never collides with nor ventures far from the wall. All of these solutions with oscillating body angle are unique to flows with incoming vorticity, and thus are not found in [3] which considers a similar problem without incoming vorticity, due to a region of reverse flow occurring at the leading edge in flows with vorticity affecting the pressure distribution.

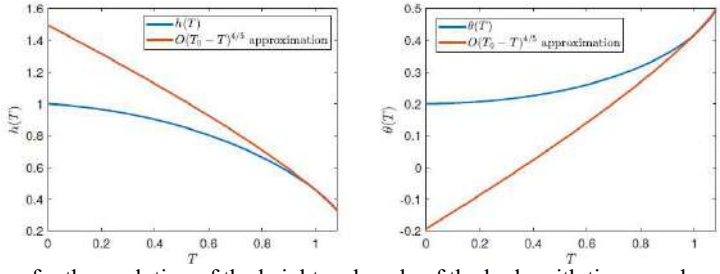

Figure 1. Numerical solutions for the evolution of the height and angle of the body with time are shown in blue and the asymptotic $(T_0 - T)^{4/5}$ approximation in red. The initial angle was positive and the body had initial downwards velocity.

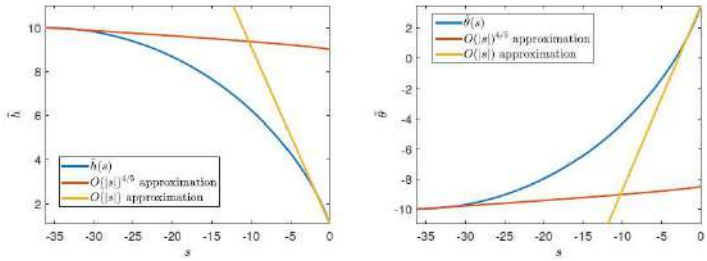

Figure 2. Numerical solutions for the time evolution of the re-scaled height and angle of the body are plotted against a re-scaled time variable in blue. The curve in red shows that the solution matches with the $(T_0 - T)^{4/5}$ approximation far from the wall, and yellow shows the linear velocity in the limit.

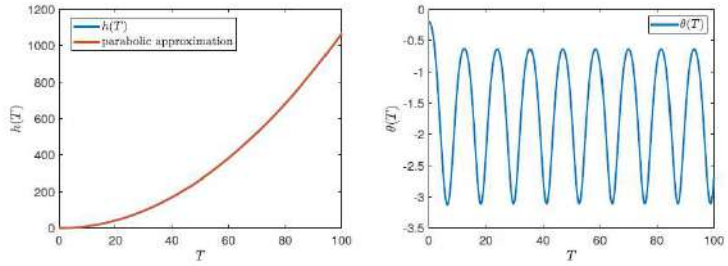

Figure 3. Numerical solutions for the evolution of body height and angle with time in a fly away case are shown in blue. The initial angle was negative and the initial velocity was zero. The curve for height overlaps closely with the parabolic approximation shown in red.

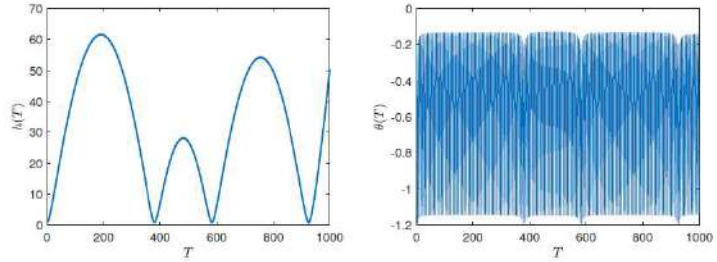

Figure 4. Numerical solutions for the evolution of body height and angle in a 'bouncing' case. Initial conditions were the same as in Figure 3 but with flow vorticity increased. Note here time ranges from 0 to 1000 rather than 0 to 100 as in Figure 3.

References

[1] Gent, R. W., Dart, N. P. & Cansdale, J. T. 2000 Aircraft icing. Phil. Trans. Roy. Soc. A **358**, 2873–2911.
[2] Smith, F. T. & Wilson, P. L. 2011 Fluid-body interactions: clashing, skimming, bouncing. Phil. Trans. Roy. Soc. A **369**, 3007–3024.
[3] Balta, S. & Smith, F. T. 2018 Fluid flow lifting a body from a solid surface. Proc. Roy. Soc. A **474**, 20180286.

FORCED IGNITION OF BLUFF-BODY FLAME IN NITROGEN DILUTING COFLOW

Qiong Lan[1], Jian Zhang *[2], and Yangwei Liu[1]
[1] National Key laboratory of Science and Technology on Aero-Engine Aero-Thermodynamics, School of Energy and Power Engineering, Beihang University, Beijing, 100191, China
[2] Institute for Aero Engine, Tsinghua University, Beijing, 100084, China

Summary The ignition process of non-premixed bluff-body flame in nitrogen diluting coflow has been performed using large-eddy simulations (LES) combined with the flamelet/progress variable approach. In the case of air-diluted coflow, the air was diluted by mixing nitrogen to keep the coflow momentum mostly identical to the case of air coflow. Therefore, We defined a $Damköhler$ (Da) number to quantify the effect of chemistry on the ignition sequence. Da number for the case of air coflow is about two times of the case of air-diluted coflow. Since the flow recirculated, the case of air coflow was easier and faster to successful ignition. And for the case of air-diluted coflow, the ignition source extinguished firstly, then a process similar to auto-ignition emerged, which demonstrated by formaldehyde (CH2O) enriched and arising of hydroxyl radical (OH) followed up.

INTRODUCTION

High efficiency and low pollutant emissions combustion technology has always been concerned in recent years. In many combustion facilities, exhaust gas recirculation (EGR) or flue gas recirculation (FGR) is often used to preheat and dilute jet reactants, which can improve the combustion efficiency and reduce the peak temperature of reactant zone and thus NO_x. Similar with this, moderate or intense low-oxygen dilution (MILD) combustion or named as flameless combustion (FLOX), highly preheated air combustion (HPAC), high temperature air combustion(HiTAC) or diluted combustion have been developed. Owing to different research organizations describe the characteristics of those technologies and emphasize differently, those technologies not fully identical, while they all operates on the reactant dilutions or high recirculation rates to enhance the uniform temperature distribution.

Bluff-body is often as a flame stabilizer resettled in pilot stage, especially in non-premixed combustor. As one of the target burner that Sydney bluff-body burner has been widely investigated. Large vortex structure in recirculation zone enhances the turbulent and mixing level to keep flame stable in bluff body wakes. Reactants dilution may directly influence the transport process of mixture and chemical mechanism. An intrinsic problem with dilution flame, especially for air dilution flame, is the ignition of fuel-air mixtures. The variation of chemical reaction composition may lead ignition difficult in dilution combustion.

This paper is mainly focus on the effect of diluting coflow for forced ignition in non-premixed bluff-body flames. With entire time sequence of force ignition for both of air-diluted coflow flame and air coflow flame at different ignition locations, we aimed to study the varying ignition regimes of bluff body in diluted environment.

MATHEMATICAL MODEL

The present simulations use Large eddy simulation (LES) combine with Flamelet progress variable (FPV) approach to solve turbulent reactive flows. The governing equations after Favre-filtered can be written as follows:

$$\tilde{D}_t\bar{\rho} = -\bar{\rho}\nabla\cdot\tilde{\mathbf{u}} \quad (1)$$

$$\bar{\rho}\tilde{D}_t\tilde{\mathbf{u}} = -\nabla\bar{p}+\nabla\cdot\bar{\underline{\underline{\sigma}}}+\nabla\cdot\bar{\underline{\underline{\sigma}}}^{res}+\bar{\rho}\mathbf{g} \quad (2)$$

$$\bar{\rho}\tilde{D}_t\tilde{Z} = -\nabla(\bar{\rho}\tilde{\alpha}\nabla\tilde{Z})+\nabla\cdot\bar{\tau}_Z^{res} \quad (3)$$

$$\bar{\rho}\tilde{D}_t\tilde{C} = -\nabla(\bar{\rho}\tilde{\alpha}\nabla\tilde{C})+\nabla\cdot\bar{\tau}_C^{res}+\bar{\rho}\tilde{\dot{\omega}}_C \quad (4)$$

$$\bar{\underline{\underline{\sigma}}} = 2\bar{\rho}\tilde{\nu}(\tilde{\underline{\underline{S}}}-\frac{1}{3}(\nabla\cdot\tilde{\mathbf{u}})\underline{\underline{I}}) \quad (5)$$

$$\bar{\underline{\underline{\sigma}}}^{res} = \bar{\rho}\tilde{\mathbf{u}}\tilde{\mathbf{u}}-\bar{\rho}\widetilde{\mathbf{u}\mathbf{u}} \quad (6)$$

$$\bar{\tau}_\psi^{res} = \bar{\rho}\tilde{\mathbf{u}}\tilde{\psi}-\bar{\rho}\widetilde{\mathbf{u}\psi} \quad (7)$$

In these equations, the superscript and represent Favre- and Reynolds-filter quantity, respectively. The subscripts $=$ represents tenor; substantial derivative $D_t=\partial_t+\mathbf{u}\cdot\nabla$; $\mathbf{u}$, $\mathbf{g}$, p, ρ, α represent velocity vector, gravity vector, pressure, density and molecular diffusivity, respectively. Mixture fraction Z and progress variable C are both scalars, ψ is generic scalar variable; In the Eq. (5), σ is viscous stress, ν is kinematic viscosity, S and I represent rate-of-strain tensor and identity matrix, respectively. Eqs. (6) and (7) are the residual stress tensor and residual scalar flux, respectively, where the superscript res represents subgrid residual quantity. The unclosed terms in the Favre-filtered equations are solved by a dynamic approach.

*Corresponding author. E-mail: zhang-jian@tsinghua.edu.cn.

	HM1e	N_2-Diluting
$(Y_{O_2\text{-}coflow})$	23%	20%
$(Y_{N_2\text{-}coflow})$	77%	80%
u_{coflow}[m/s]	34.6	34.6
u_{jet}[m/s]	108	108

Table 1: Simulation parameters

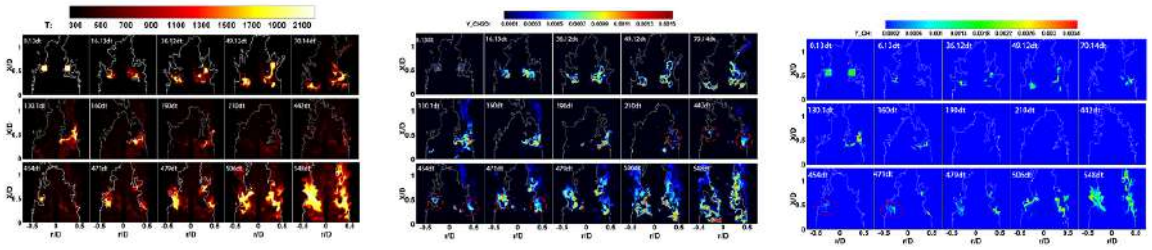

Figure 1: The instantaneous variation sequence of T, CH_2O, and OH for case of air-diluted coflow in the process of forced ignition.

COMPUTATIONAL SETUP

Numerical simulation was based on the Sydney bluff-body burner which consists of a cylindrical bluff-body with an orifice and is centered in a wind tunnel that supports a co-flowing air stream. The bluff-body diameter is $D = D_b = 50mm$ and the fuel jet diameter is $D_j = 3.6mm$. The central nozzle ejects a turbulent fuel jet at $Re = 15800$ which is composed of methane and hydrogen (1:1 by volume) with a stoichiometric mixture fraction $Z_{st} = 0.05$. U_e and U_j represent the fuel jet velocity and the external ambient coflow velocity, respectively.

The cases of simulation were listed in Table. 1. The HM1e flame is just the Sydney bluff-body HM1e flame. To compare with it, a nitrogen diluting coflow case was introduced in here. In this case, the nitrogen was used to dilute coflow air, and the mass fraction of oxygen was diluted from 23% to 20%, which led a different reacting process. Besides, the inlet velocities of fuel jet and coflow were also kept unchanged for both cases. Since the nitrogen has comparable density as air, the flow structures before flame established in both cases would be fairly similar, then we could focus on the role of the chemistry in flame ignition.

Before forced ignition source was placed, the flow of reactants was reached to a statistical stationary state without chemical reaction, which took dozens of flow-through-time in the computation. We called this state a cold flow. The forced ignition source was filled into a small and axisymmetric ring-shaped region in cold flow field. In that region, forced ignition source was numerically represented by adiabatic flame solution of steady flamelet equation.

RESULTS AND DISCUSSIONS

The burning performance parameters of bluff-body flames in air-diluted coflow and air coflow are obtained from the FPV approach. We introduced a $Damköhler$ (Da) number which is a dimensionless number represent the ratio of flow time to chemical reaction characteristic time to quantity the effect of chemistry on ignition process. It can be expressed as follows:

$$D_a = \frac{\tau_{Flow}}{\tau_{Chemistry}} = \frac{D_{ref}}{\Delta U}\frac{\dot{\omega}^*_{C,st}}{C^*_{st}} \tag{8}$$

Da number can directly quantity the chemical reaction rate. Larger Da means faster chemical reaction and easier successful ignition. The reduction of the Da number will be harmful for ignition, may result a failure of the ignition.

CONCLUSIONS

The forced ignition of non-premixed bluff-body flame in air coflow and nitrogen diluting coflow has been performed. The variation of coflow compositions nearly have almost no impact onflow structure, and the difference of ignition mainly caused by chemistry. With the nitrogen diluting coflow, Da number is about a half of the case of air coflow, ignition is relatively difficult in this condition. Corresponding to this, the ignition of case air-diluted coflow which putting ignition source at the outer edge of recirculation zone is failure. Coflow dilution led the ignition difficult and slower. A suitable ignition source position is vital for ignition. The flow recirculated can facilitate the ignition source propagated towards bluff-body and easier to successful ignition. And for the case of air-diluted coflow, stable flame also finally generated in ignition source put inside of the recirculation zone, while flame extinguished firstly, and then a process similarly auto-ignition appeared in this coflow environment.

CELLULAR FLAME DEFORMATION BY THE PASSAGE OF A SHOCK: REACTIVE RYCHTMYER-MESHKOV INSTABILITY

Hongxia Yang[1,2] and Matei I. Radulescu*[1]
[1] Department of Mechanical Engineering, University of Ottawa, Ottawa, Canada
[2] Fire & Explosion Protection Laboratory, Northeastern University, Shenyang, China

Summary We study experimentally, numerically and theoretically the head-on interaction of the shock with a cellular flame. We resolve the dynamics into four distinct stages. At times significantly less than the characteristic flame time, the flame front deforms non-linearly as an inert interface due to the Ricthmyer-Meshkov(RM) instability. At times comparable to the flame time, dilatation due to chemical energy release amplifies the growth rate of RM instability. This stage is abruptly terminated by the transverse burnout of the resulting flame funnels, followed by a longer front re-adjustment to a new cellular flame evolving on the cellular time scale of the flame. The flame evolution model obtained permits to predict the evolution of the flame geometry and burning rate for arbitrary shock strength and flame properties (burning velocity and expansion ratio).

INTRODUCTION

The interaction of shocks with flames is a fundamental problem of reactive compressible flows with applications to flame acceleration and flame control in propulsion applications. State of the art Large-Eddy-Simulations cannot descend to the scales of the flame, hence the flame enhancement by the interaction with the shock has to be modelled. In the present study, we address this fundamental problem of head-on interaction of a shock with a cellularly unstable flame experimentally, numerically and theoretically. We study the evolution of the flame surface, under the impulsive action of the shock wave leading to Ricthmyer-Meshkov(RM) instability. Numerical simulations are conducted to extend the observational time limited in the experiments.

FLAME EVOLUTION

In the experiments, a planar flame was initiated using a long tungsten wire inside a rectangular Hele-Shaw cell [1]. Through hydrodynamic instabilities, the flame acquired a cellular shape, as shown in Fig. 1a. A shock was generated at the other end of the channel, and it interacted with the flame head-on. Fig. 1a shows the evolution of the flame after the shock passage. The flame cusps reverse under the impulsive motion of the RM instability. In the experiments, the subsequent flame evolution is not available, since the shock reflects from the end wall, and re-interacts with the flame.

To extend the study of the flame evolution, we have conducted two-dimensional direct numerical simulations using a single Arrhenius model calibrated to recover the correct flame speed and gas expansion ratio. Fig. 1b provides the evolution of the flame obtained numerically, which was found in excellent agreement with experiment. Following the passage of the shock, the flame inverts and long funnels are created. These burn out after approximately 1 flame time t_f, defined as the laminar flame thickness divided by the laminar flame speed. The subsequent evolution is a re-distribution of the flame frontal curvature as the flame recovers its initial structure.

FLAME EVOLUTION STAGES

Figure 2 shows the evolution of the flame length obtained experimentally and numerically and the resulting burning rate. The evolution of the flame amplitude shows that there are four distinct stages after the reversion of the interface. The first stage can be recognized as the inert evolution of the interface, at times significantly less that the characteristic flame time t_f. The reactive and inert simulations are identical and in excellent agreement with experiments. During this stage, the evolution of the flame shape is well approximated by the non-linear growth rate of the Richtmyer-Meshkov instability in inert flow given by Mikaelian [2]:

$$\eta'_{Mik} = \frac{\eta'_0}{1 + 3\eta_0^+ kt\frac{(1+A_t)}{(3+A_t)}}, \tag{1}$$

where $\eta'_0 = \frac{1}{2}(\eta_0^- + \eta_0^+)[u]kA_t$ is the amplitude growth rate in the linear stage [3], $[u]$ is the velocity jump for the interface with the passage of the shock wave, η_0^- and η_0^+ are the amplitude before and immediately after the shock passage, and $A_t = {}^{(\rho_b-\rho_u)}/_{(\rho_b+\rho_u)}$ the Atwood number after the interaction, ρ_u and ρ_b are the unburned and burned gas density.

At times comparable to the flame time, the disturbed flame amplitude surpasses the inert model's prediction. On these time scales, energy release is no longer negligible. A correction to the inert non-linear growth rate model is to account for the volumetric expansion of the material crossing the flame, which lengthens the flame and increases its surface area .

*Corresponding author. E-mail: matei@uottawa.ca

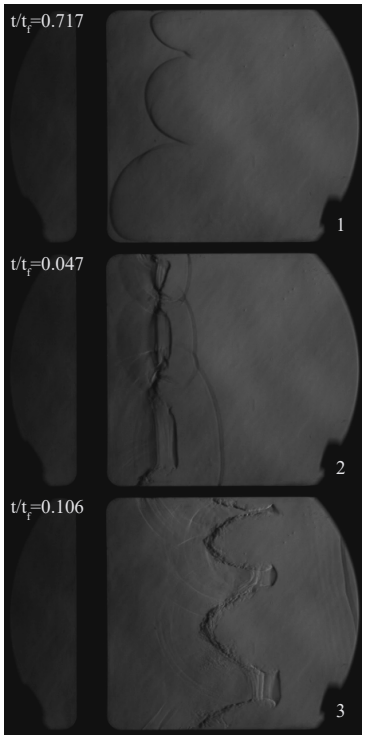

(a) Schlieren image sequence of the interaction. Time 0 corresponds to the beginning of the interaction.

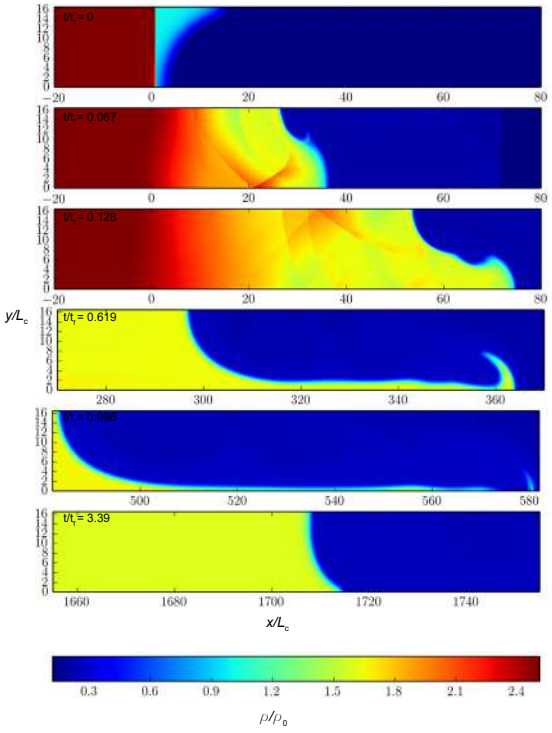

(b) Density profiles illustrating the flame evolution subsequent to the interaction. L_c refers to the characteristic length scale that gives the measure of the pre-heat zone thickness in the steady flame.

Figure 1: Experimental and simulation results of the interaction of a M=1.9 incident shock wave with stoichiometric hydrogen-air flame.

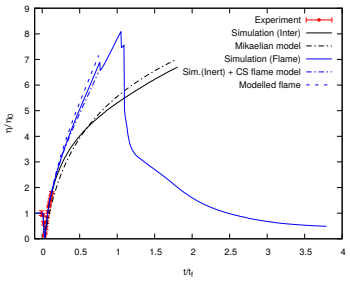

(a) Comparison of the time evolution for the experiment and the simulation of the reactive and non-reactive interaction.

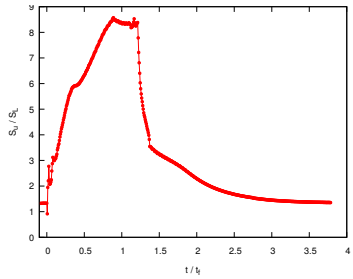

(b) Time evolution of the burning velocity for the simulation.

Figure 2: Comparison of the interface amplitude as a function of time for the experiment and the simulation of the reactive and non-reactive interaction.

The growth rate of the flame length (and surface area) depends on the surface of the flame itself, yielding an exponential feedback. The growth rate in this second stage becomes:

$$\eta'_f = \eta'_{MIK} + \frac{2\rho_u A_F S_u}{\rho_b H}, \tag{2}$$

where A_F is the flame area, S_u is the laminar burning velocity, H is the channel width. We take $A_F \simeq \eta$.

The non-linear reactively enhanced growth of the flame terminates when the funnels created burn out by the transverse reaction fronts. This occurs on a time scale associated with the flame's displacement velocity and the transverse length scale of the cellular flame, $\frac{\rho_b H}{\rho_u S_u}$, which is close to the flame time itself t_f. The subsequent flame relaxation to a new cellular structure occurs on this same time scale. The model provides a simple way to estimate the flame burning rate increase upon passage of a shock and duration of this event.

References

[1] H. Yang, M. I. Radulescu, ,*arXiv:1911.05552* (2019).
[2] K. O. Mikaelian, *Physical Review E* **67**, 026319 (2003).
[3] K. Meyer, P. Blewett, *The Physics of Fluids* **15**, 753 (1972).

DETAILED MECHANISM ON FLOW PATTERN SWITCHING UNDER THERMOACOUSTIC INSTABILITY FOR LOW-SWIRL H2 JET FLAMES

Takeshi Shoji*[1], Shigeru Tachibana[1], Terukazu Suzuki [2], Yoshihiro Nakazumi[2], and Takeshi Yokomori[2]
[1] Aeronautical Technology Directorate, Japan Aerospace Exploration Agency, Tokyo, Japan
[2] Department of Mechanical Engineering, Keio University, Kanagawa, Japan

Summary This experimental study extensively explores newly observed flow pattern switching between divergent and convergent flows under thermoacoustic instability (TI) for lean-premixed H_2 turbulent jet flames in a low-swirl combustor (LSC) via time-resolved optical diagnostics. Under stable operation in the absence of TI, the mean radial profile of axial velocity at the injector exit contains double peaks surrounding a low velocity region, indicative of divergent flow typical in LSCs. Once TI occurs at a dominant frequency of 402 Hz, an atypical top hat-like axial velocity profile, corresponding to convergent flow, is observed. More interestingly, switching between divergent and convergent flows occurs during each TI cycle period. This unique switching is caused by the interaction between the jet's shear layer and large-scale vortex-induced radial flow toward the combustor axis.

BACKGROUND AND CONTEXT OF PRESENT STUDY

Thermoacoustic instabilities (TIs) have been a primary technical challenge in the development of low-emission swirl-stabilized combustors[1]. Recently, low-swirl combustors[2] (LSC) have begun to be used to explore TIs in order to establish a fundamental understanding of flame-turbulence interactions inside gas turbine combustors[3,4]. A fundamental feature in LSCs is a divergent flow, the so-called central divergence zone (CDZ), without any inner recirculation zone, which is created by the combination of an unswirled central flow and a surrounding swirled flow. In the CDZ, a freely propagating flame is aerodynamically stabilized at a location where the local velocity equals the burning velocity.

Earlier studies[3,4] on TIs inside LSCs showed that TIs are caused by the delayed ignition of unburned mixtures trapped inside ring vortices shed from the injector rim into the external shear layer. This delayed ignition leads to in-phase thermoacoustic coupling satisfying Rayleigh's criterion[5], corresponding to the growth of TI, and induces flapping flame motion in the shear layer while, on average, the flame behaves similarly to a lifted bowl shaped CH_4 flame and is attached to the injector rim in the case of a 0.9 H_2/0.1CH_4 flame[3,4]. Detailed studies by Therkelsen et al.[3] also show that axial stretch rate, essentially the spatial decay rate of axial velocity along the centreline, is always negative even under TI because of the presence of the typical divergent flow in the LSC flowfield. However, more recent studies by our group[6] have introduced a new pattern of flame/flow dynamics for a low-swirl H_2 jet flame under TI, involving a drastic flow pattern switching between the typical divergent flow and an atypical convergent flow during a TI cycle.

Our present study conducts an in-depth experimental investigation into the mechanism of the flow pattern switching that occurs under TI for a lean-premixed low-swirl H_2 jet flame utilizing extensive time-resolved optical diagnostics.

EXPERIMENTAL APPROACH AND SAMPLE RESULTS

Experiments are conducted in an LSC with a swirl number of 0.39 and an injector diameter of D = 35 mm, using simultaneous time-resolved 200 kHz pressure fluctuation measurements, 10 kHz OH* chemiluminescence imaging, and 40 kHz PIV measurements with an Nd:YAG laser (EdgeWave GX600-2-L). Details of the methods are as in our prior studies[6]. The spatial resolutions of the optical diagnostics are higher than previously, enabling more detailed investigations of flame/flow dynamics. The bulk velocity of mixtures of H_2 and air, with seeding of tracers, is initially set at V_m = 15 m/s, and the fuel flow rate is increased linearly over 5 s while maintaining a constant air flow rate. This achieves a gradual increase in the equivalence ratio from 0.25 to 0.33, and thus transition from stable to unstable LSC operation.

Representative results of time-resolved measurements during transition are shown in Figure 1. Figure 1a depicts time-series pressure fluctuations p' during a time interval of t = 0–5 s. The amplitude of p' clearly increases with t, or equivalently ϕ, and reaches its maximum value; the system evolves into a limit cycle. Note that the dominant frequency of the limit cycle oscillation f_{peak} is 402 Hz in the present study.

Figure 1b shows radial profiles of mean axial velocity V_z normalized by V_m which were extracted near the injector exit at z = 7 mm during t = 0–0.5 s (stable operation) and t = 4.5–5.0 s (limit cycle oscillation). Under stable operation, a low axial velocity region (around $r/D \sim 0$) induced by an unswirled flow is surrounded by double velocity peaks at $r/D \sim$ 3.5, which is a typical divergent flow profile[7,8]. Interestingly, once TI occurs during t = 4.5–5.0 s, an atypical top hat-like velocity profile is observed, suggesting a convergent flow. This unique trend was first observed in our prior studies[6].

Figure 1c presents normalized axial velocity fluctuations V'_{zc} at (r, z) = (0, 7) mm during t = 4.5–5.0 s with phase-averaging based on f_{peak}. A reference pressure fluctuation signal at the same frequency is also shown. Remarkably, there is a significantly large peak-to-peak velocity-oscillation amplitude of approximately 80% of the bulk velocity V_m. Such a large velocity oscillation can be realized without blow-off only by flames with fairly high burning velocity, e.g., an H_2 flame in the present study. The phase difference between the velocity and pressure oscillations is approximately 120°.

To characterize the flow pattern switching occurring under TI, phase-averaged radial profiles of axial velocity at z = 7 mm during t = 4.5–5.0 s are shown in fig. 1d. These phase instances correspond to those in fig. 1c; i.e., phase-averaging

*Corresponding author. E-mail: shoji.takeshi@jaxa.jp.

is applied with a phase resolution of 15° but results are plotted at every 60°. Phase-averaged velocity vectors superimposed on Abel-deconvoluted OH* chemiluminescence images are also shown in figs. 1e to 1j at corresponding phases to fig. 1d. From $\theta = 60^\circ$ to 120°, when the mean axial velocity increases and reaches its maximum, an origin of a large-scale vortex is generated (white circle in fig. 1f). This vortex is likely induced in the shear layer with a relatively large velocity gradient, as confirmed in fig. 1d. At $\theta = 180^\circ$ in fig. 1g, a radially wide flame region observed at $z/D \sim 1.1$ begins to disappear due to the termination of chemical reactions, and a new flame region is ignited at $z/D \sim 0.6$. Concurrently, the large-scale vortex following the ignited flame region convects downstream. At later phase instances (θ = 240°–360°) the vortex induces a strong radial flow in the negative r direction (white square in fig. 1h), which causes interaction between the vortex-induced flow and the jet's shear layer located at $r/D \sim 0.3$–0.4. Because such interaction leads to strong positive axial velocity along the shear layer, typical LSC-like axial velocity profiles are created at $\theta = 300^\circ$. Finally, the vortex-induced flow is more entrained into the jet toward the burner axis after a certain time delay, resulting in the flow pattern switching back to top hat-like velocity profiles at later phase instances θ = 360°–60°. Therefore, the formation of the unique convergent flow under TI is attributed to the entrainment of the vortex-induced flow which constricts the central flow region toward the burner axis. It is also worth noting that the location of the vortex visualized by velocity vector fields remarkably coincides with that of vortical flame structures situated beneath the radially flat flame region.

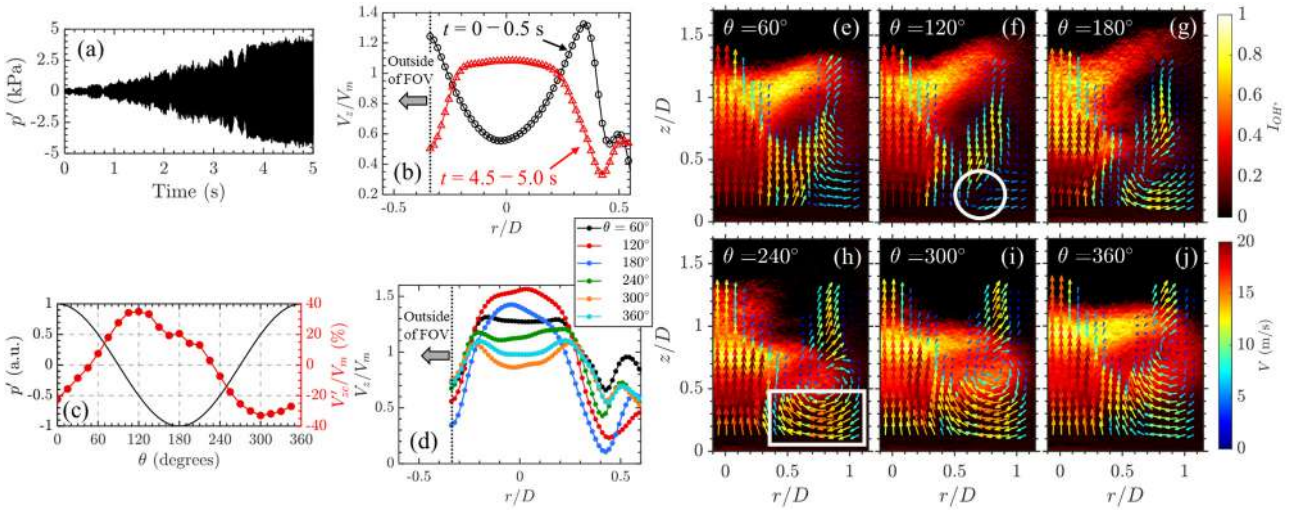

Figure 1. (a) Time-series pressure fluctuations p'. (b) Radial profiles of mean axial velocity V_z normalized by initial bulk mixture velocity (V_m = 15 m/s) taken at z = 7 mm during t = 0–0.5 s (stable operation) and t = 4.5–5.0 s (TI). Gray arrows represent the region outside the experiment field of view. (c) Reference pressure fluctuation signal at a dominant frequency of TI of 40 Hz (left ordinate axis) and phase-averaged normalized axial velocity fluctuations V'_{zc} at (r, z) = (0, 7) mm. Both plots are calculated during t = 4.5–5.0 s. (d) Phase-averaged normalized radial profiles of mean axial velocity V_z/V_m during t = 4.5–5.0 s. (e-j) Phase-averaged Abel-deconvoluted OH* chemiluminescence images with velocity vectors during t = 4.5–5.0 s. Color bar on top row shows normalized OH* chemiluminescent intensity using global maximum intensity, bottom row color bar shows velocity vector magnitude. Portions of velocity vectors corrupted by laser reflections from quartz duct are omitted.

The discussion above unveils the detailed mechanism of flow pattern switching under TI for a low-swirl H_2 jet flame. Nevertheless, as was also concluded in previous studies[3,4,6], further explorations in thermoacoustic coupling between unsteady heat release and pressure oscillations, stretch rate estimation to quantitatively characterize the flow pattern switching, and modal decomposition analyses to study relations between the switching and coherent flame/flow structures are needed for more in-depth clarification of this unique mechanism, as also presented in this study.

References

[1] Putnum A. A. Combustion-driven Oscillations in Industry. Elsevier Science Ltd., 1971.

[2] Chan C. K., Lau K. S., Chin W. K., Cheng R. K. Freely Propagating Open Premixed Turbulent Flames Stabilized by Swirl. *Proc. Combust. Inst.* **24**: 511-518, 1992.

[3] Therkelsen P. L., Portillo J. E., Littlejohn D., Martin S. M., Cheng R. K. Self-induced Unstable Behaviors of CH_4 and H_2/CH_4 Flames in a Model Combustor with a Low-swirl Injector. *Combust. Flame* **160**: 307-321, 2013.

[4] Renaud A., Yokomori T., Tachibana S. Study of a Thermo-acoustic Instability Triggering in a Low-swirl Burner Using Simultaneous Time-resolved Acetone and OH-PLIF. *Proc. Combust. Inst.* **37**: 2627-2633, 2019.

[5] Rayleigh J. The Explanation of Certain Acoustical Phenomena. *Nature* **18**: 319-321, 1878.

[6] Shoji T., Tachibana S., Suzuki T., Nakazumi Y., Yokomori T. A New Pattern of Flame/Flow Dynamics for Lean-premixed Low-swirl Hydrogen Turbulent Jet Flames Under Thermoacoustic Instability. Manuscript submitted for publication.

[7] Cheng R. K., Littlejohn D., Strakey P., Sidwell T. Laboratory Investigations of Low-swirl Injectors with H_2 and CH_4 at gas turbine conditions. *Proc. Combust. Inst.* **32**: 3001-3009, 2009.

[8] Littlejohn D., Cheng R. K., Noble D. R., Lieuwen T. Laboratory Investigations of Low-swirl Injectors Operating with Syngases. *J. Eng. Gas Turb. Power* **132**: 011502 1-8, 2010.

FORMATION OF ISOLATED FLAME CELLS PROPAGATING ACROSS ULTRA LEAN HYDROGEN MIXTURES IN NARROW GAPS

Fernando Veiga-LÓpez[1], Daniel Martínez-Ruiz[2], Mikhail Kuznetsov[3], Eduardo Fernández-Tarrazo[1], and Mario Sánchez-Sanz*[1]
[1] Department of Fluid and Thermal Engineering, Universidad Carlos III, Madrid, Spain
[2] ETSIAE, Universidad Politécnica de Madrid, Madrid, Spain
[3] Institut für Kern- un Energietechnick, Karlsruhe Institut für Technologie, 76344, Eggenstein-Leopoldshafen, Deutschland.

Summary Very lean hydrogen flames were thought to quench in narrow confined geometries. However, flames with very low fuel concentration undergo an isolated critically-sustained propagation in narrow gaps: H_2-air flames can overcome large heat losses and very lean conditions by breaking the reaction surface into isolated flame cells that locally enrich the mixture through differential diffusion over a curved front. These kernels travel steadily in straight lines or split cyclically in various unexpected patterns.

EXPERIMENTAL AND NUMERICAL CONFIGURATIONS

Morphology, stability and safety issues of ultra-lean confined hydrogen-air flames are studied in an experimental setup [2] in which two parallel flat plates, disposed vertically, are separated a small distance apart forming a narrow channel of height h. The reaction front is tracked using Schlieren techniques and high-speed imaging, with the path followed by the flames outlined by the trailing condensed water streaks formed just behind them [1] (Fig. 1). In addition, an in-house finite-element code has been used to analyze the processes [3]. Since the flow is laminar and the flame thickness $\delta_T \sim (0.5 - 1)$ mm is comparable to the gap size h, the propagation problem of the flame can be treated as quasi two-dimensional, considerably simplifying the simulations of lean hydrogen-air flames (Fig. 2).

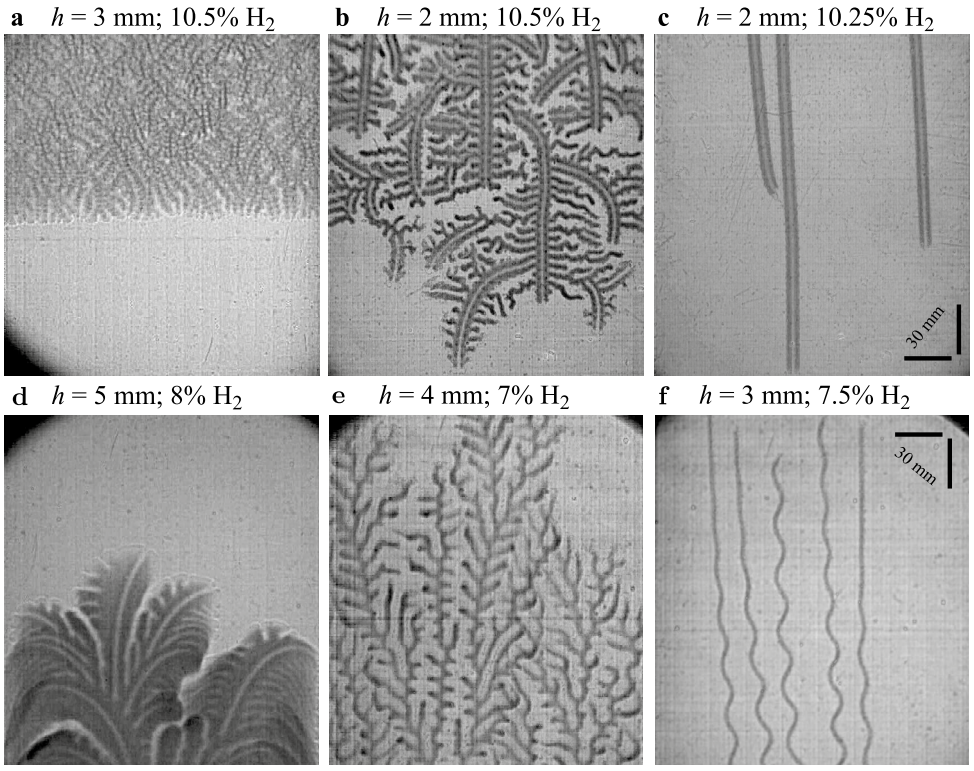

Figure 1: Different propagation modes of hydrogen flames. Downward propagation, **a** continuous flame front, **b** splitting cells and **c** several two-headed isolated steady flame cells. Upward propagation , **d** continuous flame front, **e** fractal-like propagation mode and **f** several one-headed isolated steady cells.

For sufficiently large values of h, the high mass diffusivity of hydrogen outlines a reactive front characterized by the formation of small wrinkles through thermodiffusive instabilities (Fig. 1**a** and **d**). In gaps narrower than $h < 6$ mm, the expected continuous flame front breaks into a set of small flame cells separated by cold, unburned gas, unveiling two

*Corresponding author. E-mail: ictam2020@aimgroup.eu.

regimes that only emerge in flames with low enough hydrogen concentration. In the first one, the flame front breaks into several unstable flame cells (Fig. 1**b** and **e**) that split continuously and propagate leaving a path that conforms a pattern that reminds of ferns and tree leaves. In the second regime, the flame front breaks into a few isolated stable flame cells (Fig. 1**c** and **e**) that move steadily delineating an almost straight trajectory that reminds of the fingering patterns found during smoldering combustion of thin solid materials [7].

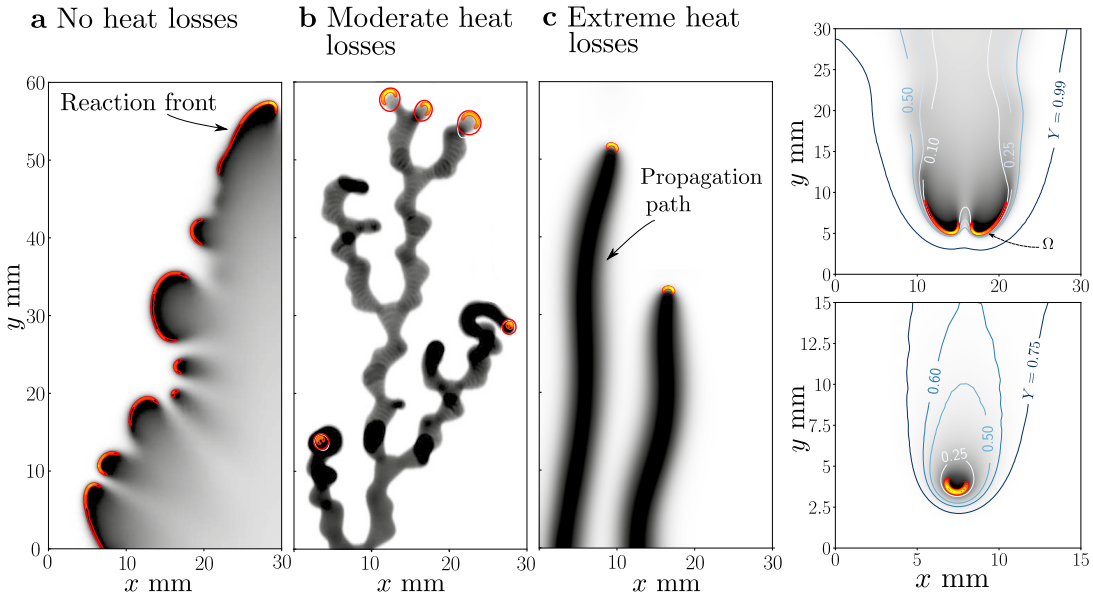

Figure 2: Numerical solutions of lean flames for increasing values of the heat-loss parameter, turning the propagation from a continuous front solution to splitting and isolated regimes. Inset detail of one and two-headed cells.

From the experimental results it is unclear both how the flame cells are formed and why hydrogen flames withstand more adverse conditions than heavier hydrocarbon fuels [6]. To investigate the causes that lead to the new propagation regimes identified experimentally, we modeled the propagation of the H_2-air flame including heat losses at the walls in an integrated averaged formulation in the transverse coordinate z. The aforementioned computations (Fig. 2) identified the intense heat losses at the walls and the high mass diffusivity of the fuel as the two main mechanisms controlling the emergence of the newly-discovered propagation modes

CONCLUSIONS

The discovery of the propagation regimes described above opens new research lines regarding near-limit hydrogen combustion in narrow geometries. Based on the experimental and numerical results and in the mathematical modelling of the problem, we appoint the conductive heat losses to the surrounding walls and the high diffusivity of hydrogen flames as the two physical mechanisms governing the onset of the two propagation regimes reported here. As the use of hydrogen in the near future is expected to increase [5, 4], we anticipate a raising concern about the safety of hydrogen-powered devices [2] that will motivate the exploration of interactions between different phenomena that may unveil unknown flame behaviours relevant in the development of safety measures.

References

[1] B. Bregeon, A. S. Gordon, and F. A. Williams. Near-limit downward propagation of hydrogen and methane flames in oxygen nitrogen mixtures. *Combustion and Flame*, 33:33–45, 1978.

[2] M. Kuznetsov and J. Grune. Experiments on combustion regimes for hydrogen/air mixtures in a thin layer geometry. *International Journal of Hydrogen Energy*, 44(17):8727–8742, 2019.

[3] D. Martínez-Ruiz, F. Veiga-López, D. Fernández-Galisteo, V. N. Kurdyumov, and M. Sánchez-Sanz. The role of conductive heat losses on the formation of isolated flame cells in hele-shaw chambers. *Combustion and Flame*, 209:187–199, 2019.

[4] A. L. Sánchez and F. A. Williams. Recent advances in understanding of flammability characteristics of hydrogen. *Progress in Energy and Combustion Science*, 41:1–55, 2014.

[5] I. Staffell, D. Scamman, A. V. Abad, P. Balcombe, P. E. Dodds, P. Ekins, N. Shah, and K. R. Ward. The role of hydrogen and fuel cells in the global energy system. *Energy & Environmental Science*, 12(2):463–491, 2019.

[6] F. Veiga-López, D. Martínez-Ruiz, E. Fernández-Tarrazo, and M. Sánchez-Sanz. Experimental analysis of oscillatory premixed flames in a hele-shaw cell propagating towards a closed end. *Combustion and Flame*, 201:1–11, 2019.

[7] O. Zik, Z. Olami, and E. Moses. Fingering instability in combustion. *Physical review letters*, 81(18):3868, 1998.

MAXIMALLY AMPLIFIED PERTURBATIONS IN A LAMINAR PREMIXED FLAME, OBTAINED BY LINEAR ANALYSIS

Chuhan Wang *[1], Thomas Ludwig Kaiser[2], Lutz Lesshafft[1], and Kilian Oberleithner[2]
[1] Laboratoire d'Hydrodynamique, CNRS / Ecole Polytechnique / Institut Polytechnique de Paris, Palaiseau,France
[2] Laboratory for Flow Instabilities and Dynamics, Technische Universit at Berlin, Berlin, Germany

Summary The instability of flames, which leads to strong heat and pressure fluctuations in combustion chambers, still represents a major challenge for optimising combustion efficiency. We seek to identify the optimal perturbations, which are maximally amplified in a 2D laminar premixed slot flame, in order to describe the physical amplification mechanisms and find strategies for their control. The optimal velocity forcing and associated flow response are computed in a global framework, where both spatial dimensions are resolved. These optimal structures exhibit the signature of the "Orr mechanism", which amplifies perturbations through sheared convection.

GLOBAL INSTABILITY ANALYSIS OF LAMINAR FLAMES

The objective of our study is to investigate the amplification of small perturbations in a laminar slot flame through global linear analysis. While the unstable flame behaviours are observed and described in various flame configurations, the precise mechanisms of this process remain little explored, and quantitative modelling via linear tools has not yet made its way into the mainstream of flame research. In closely related fields, like shear flows and thermal convection, so-called global linear analysis tools have been widely applied with great success; be it in the context of self-excited non-parallel flow systems like cylinder wakes [1], externally driven systems like laminar jets [2], or even coherent structures in turbulent jets [3].

The applicability of global linear analysis to flame dynamics has indeed been demonstrated in several recent studies, either for the description of self-excited oscillations [4, 5, 6] or for the amplification of external excitation [6, 7, 8]. In both contexts, the linear flame transfer function (FTF) plays a crucial role, and the most recent studies indicate that the FTF can successfully be obtained through linear tools in a global framework. Such a framework must account for the strong non-parallelism of the flow, for chemical reaction, and for the coupling of acoustic and vortical perturbations. The chemistry modelling in particular presents a challenge in current calculations.

SCOPE AND METHODOLOGY

We present a linear analysis of the coupled multi-physics dynamics in a laminar slot flame that is fully resolved in two spatial dimensions. In the framework of *resolvent analysis* [2, 3, 8], we identify the specific type of "optimal" perturbation that is maximally amplified and thus leads to the strongest oscillation in the flame.

The premixed air-methane flame, fully attached to the outlet of a slot, at $Re = 728$ is simulated using the AVBP code from CERFACS. Here, the compressible Navier-Stokes equations for reacting flow are resolved, such that the coupling between flow dynamics, chemical reaction and species transport are included. The flame in this configuration is stable, and its steady velocity and species fields, which serve as a base state in our analysis, are shown in figures 1(a,b).

A *linearised* flame solver, based on the compressible reactive Navier-Stokes equations, is formulated and then discretised by a continuous Galerkin finite-element method on an unstructured mesh. Reaction is modelled with a two-step reduced analytical chemistry scheme involving five species. Computation of FTFs via this linearised solver allows to validate our system of equations against the nonlinear reference solver. The computation of optimal forcing, and its associated linear flame response, involves a singular value decomposition of the linear resolvent operator. For a given definition of an energy norm, the optimal *energy gain* between input and output is obtained as a function of excitation frequency.

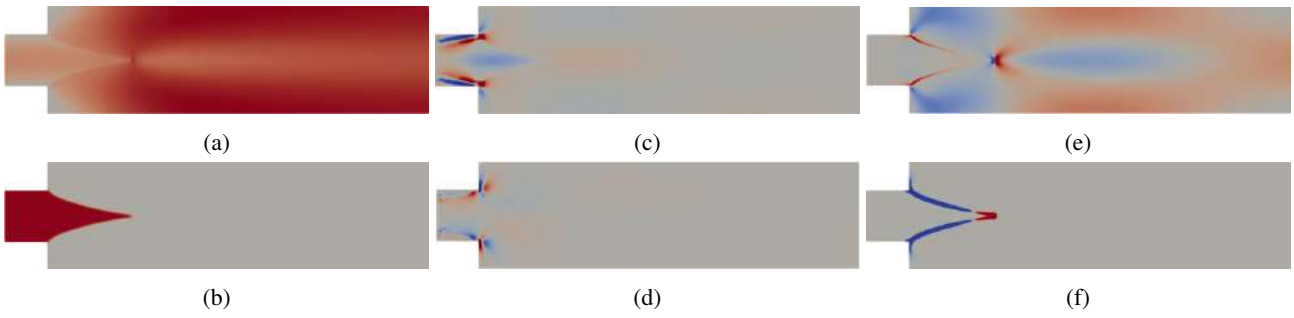

Figure 1: The laminar slot flame. Unperturbed steady state: (a) horizontal velocity; (b) CH_4. Optimal forcing: (c) horizontal velocity; (d) vertical velocity. Associated flame response: (e) horizontal velocity; (f) CH_4.

*Corresponding author. E-mail: cwang@ladhyx.polytechnique.fr

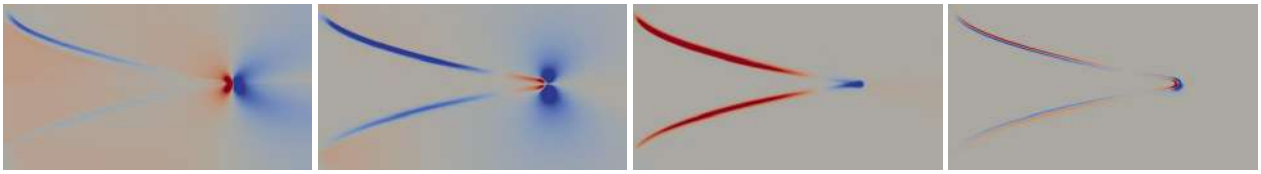

(a) (b) (c) (d)

Figure 2: Flame response obtained via nonlinear simulation (upper half) and via linear analysis (lower half) : (a) horizontal velocity; (b) vertical velocity; (c) density; (d) heat release.

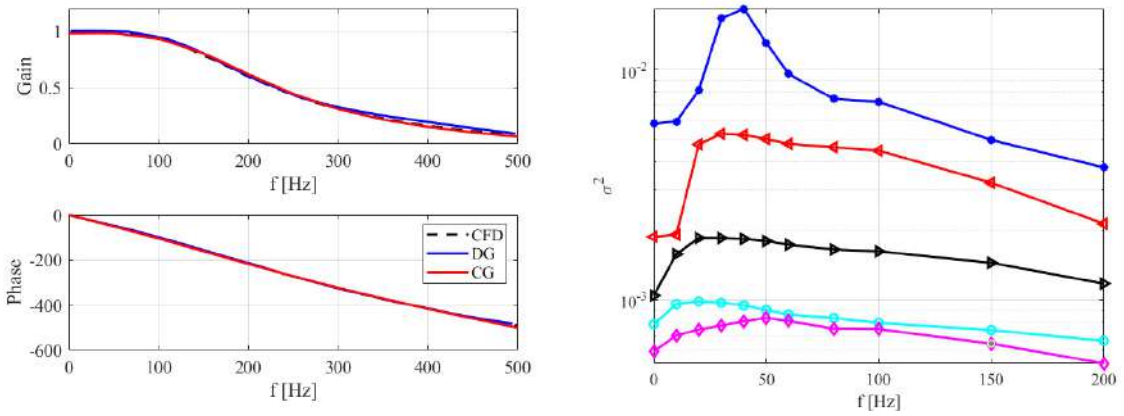

(a) (b)

Figure 3: (a) Validation of flame transfer function in reference case [6]. CFD: nonlinear calculation; DG: discontinuous Galerkin method; CG: continuous Galerkin method. CFD and DG data are retrieved from [6]. CG is the result from the present work. (b) Resolvent analysis of the target flame case. Optimal gain as a function of frequency. The five leading gain curves are presented.

CURRENT RESULTS

The linearised solver is first validated for the reference case of a premixed laminar flame with one-step global reaction [6], against nonlinear unsteady simulations. The FTF obtained via our linearised solver is presented in figure 3(a), in excellent agreement with that identified from nonlinear simulations. We then investigate the target flame case with two-step reaction, simulated with the AVBP code. The shape of the linear flame response to inflow forcing obtained in this way matches the result of nonlinear simulations, shown in figure 2.

Optimal forcing structures, in the sense of maximal amplification of kinetic fluctuation energy, at a frequency $f = 30$Hz, are shown in figures 1(c,d), alongside the linear flame response (figures 1e,f). In the spatial distribution of *optimal forcing*, tilted vortical structures are found in the slot boundary layer. These structures are indicative of the "Orr mechanism", which amplifies perturbations through sheared convection. The shape of the *flame response* to this forcing resembles that to inflow forcing in figure 2. The curves of gain in kinetic energy between input and output are shown in figure 3, which allows to identify the receptivity of the system at low frequencies.

References

[1] Sipp D., Lebedev A. Global stability of base and mean flows: a general approach and its applications to cylinder and open cavity flows. *J. Fluid Mech.* **593**: 333-358, 2007.

[2] Garnaud X., Lesshafft L., Schmid P.J., Huerre P. The preferred mode of incompressible jets: linear frequency response analysis. *J. Fluid Mech.* **716**: 189-202, 2013.

[3] Lesshafft L., Semeraro O., Jaunet V., Cavalieri A. V., Jordan, P. Resolvent-based modeling of coherent wave packets in a turbulent jet. *Phys. Rev. Fluids*, **4**(6): 063901, 2019.

[4] Oberleithner K., Stöhr M., Im S. H., Arndt C. M., Steinberg A. M. Large eddy simulation of combustion instabilities in a lean partially premixed swirled flame. *Combust. Flame* **162**(8): 3100-3114, 2015.

[5] Qadri U. A., Chandler G. J., Juniper M. P. Self-sustained hydrodynamic oscillations in lifted jet diffusion flames: origin and control. *J. Fluid Mech.* **775**: 201-222, 2015.

[6] Avdonin A., Meindl M., Polifke W. Thermoacoustic analysis of a laminar premixed flame using a linearized reactive flow solver. *Proc. Combust. Inst.* **37**(4): 5307-5314, 2019.

[7] Blanchard M., Schuller T., Sipp D., Schmid P.J. Response analysis of a laminar premixed M-flame to flow perturbations using a linearized compressible Navier-Stokes solver. *Phys. Fluids* **27**: 043602, 2015.

[8] Kaiser T. L., Lesshafft L., Oberleithner K. Prediction of the Flow Response of a Turbulent Flame to Acoustic Pertubations Based on Mean Flow Resolvent Analysis. *J. Eng. Gas Turbine Power* **141**(11): 111021, 2019.

COMBUSTION OF A PLANE HYDROGEN MICROJET AT SUBSONIC AND SUPERSONIC SPEEDS

Victor V. Kozlov[1]*, Maria V. Litvinenko[1], Yury A. Litvinenko[1], Andrey G. Shmakov[2]
[1] Khristianovich Institute of Theoretical and Applied Mechanics, Siberian Branch, Russian Academy of Sciences, Novosibirsk, Russia
[2] Voevodsky Institute of Chemical Kinetics and Combustion, Siberian Branch, Russian Academy of Sciences, Novosibirsk, Russia

Summary In this report, we presented the results of experimental studies of the diffusion combustion of a plain hydrogen microjet flowing from a slit micronozzle at subsonic and supersonic speeds. For the first time, four scenarios of diffusion combustion of a plain hydrogen microjet including supersonic combustion in the presence of supersonic cells in both air and hydrogen are presented. The stabilization of the subsonic combustion of a hydrogen microjet was established to be due to the presence of a "flame constriction region," while the stabilization of the supersonic combustion of a microjet was found to be associated with the presence of supersonic cells. The observed hysteresis of diffusion combustion of a plain hydrogen microjet depends on both the method of igniting the microjet (near or far from the nozzle exit) and the direction of change in the rate of its outflow.

INTRODUCTION

Experimental studies of the diffusion combustion of a circular hydrogen microjet [1–4] showed various scenarios for combustion proceeding depending on the increase in the microjet velocity at exit diameters ranging from 0.25 to 1 mm. The following scenarios of diffusion combustion of a circular hydrogen microjet were found: (1) combustion of a pure laminar microjet with a long-range laminar flame ($U0 \le 150$ m/s), (2) the occurrence of a spherical "flame constriction region" (FCR) with the presence of a laminar microjet and laminar flame with turbulization of a microjet and flame when a laminar microjet overcomes a narrow region of a gas density gradient ($U0 > 150$ m/s), (3) detachment of the turbulent flame from the FCR ($U0 > 200$ m/s), and (4) ceasing the combustion of the turbulent section of the microjet while maintaining the combustion in the FCR (moreover, in this situation, the combustion in the FCR is maintained up to the transonic speeds of its outflow, while there is such a phenomenon as "nozzle choking" [4–6] ($U0 > 331$ m/s); and (5) ceasing the combustion of a microjet ($U0 \approx 331$ m/s). It should be noted that "nozzle choking" occurred when the flow rate of the hydrogen microjet was close to the speed of sound in air ($U0 \approx 331$ m/s). In this case, the stabilization of the combustion of both a circular microjet [1–6] and a plain microjet [7] was provided by the presence of the FCR and the existence of combustion in it. However, we were unable to reach supersonic diffusion combustion of a hydrogen microjet due to "choking of the nozzle" by the FCR that heated the micronozzle exit and prevented the flame from cutting it off. One of the characteristics of supersonic combustion of a jet stream, along with a number of others, is the presence of supersonic cells in both the jet and the flame, but in a situation of flame detachment from the nozzle exit. This was demonstrated in detail when a circular hydrogen microjet was ignited far from the nozzle exit [8]. In this situation, it was possible to observe the presence of supersonic cells in the jet, as well as the flame separated from the nozzle exit. This study is aimed to study experimentally the features of the diffusion combustion of a plain hydrogen microjet flowing from a slit micronozzle and to determine various scenarios for this process depending on the rate of the microjet outflow. Special attention will be paid to the study of the characteristics of the microjet development at supersonic (relative to air at $U0 = 331$ m/s and hydrogen at $U0 = 1284$ m/s) speed of its flow and in the presence of supersonic cells. It should be noted that the study of the characteristics of the diffusion combustion of a plain microjet at supersonic speed will be carried out for the first time since, so far, hydrogen combustion has mainly been studied in circular microjets.

RESULTS AND DISCUSSION

Diffusion Combustion of a Plain Hydrogen Microjet (**Scenario no. 1**). Figure 1 shows the scheme of the experiment and the shadow pattern of the diffusion combustion of a plain hydrogen microjet at the rate of its outflow $U0 \le 150$ m/s.

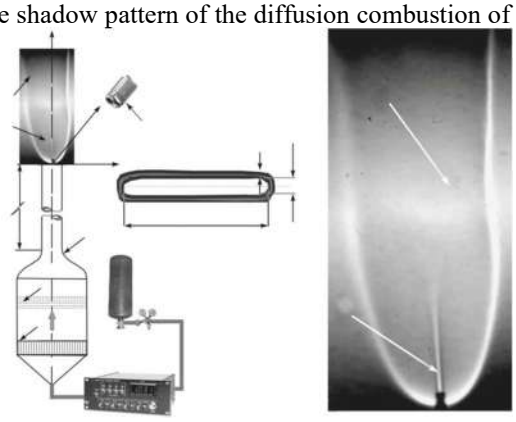

Figure 1.

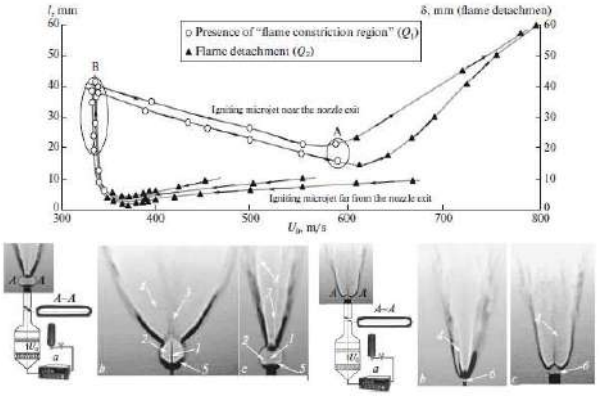

Figure 2.

---

*Corresponding author. E-mail: kozlov@ita.nsc.ru

A detailed description of the equipment used in the experiments and the research routine are presented in [11]. As seen in Fig. 1, II, the shadow pattern demonstrates the laminar combustion of a plain hydrogen microjet at the speed of its outflow $U_0 \leq 150$ m/s and in the presence of the laminar.

Scenario no. 2. At an increase in the flow rate of the microjet, it is possible to observe the emergence of the FCR, the combustion in which occurs up to the transonic velocity of the microjet outflow, but ultimately leads to "micronozzle choking" due to heating of the nozzle exit by the FCR. The range of outflow rates of a hydrogen microjet in the presence of the FCR depends on the method of its ignition: near or far from the nozzle exit. In this case, so-called hysteresis, which is clearly visible in Fig. 2, can be observed. Hysteresis of the development and disappearance of the FCR depending on the method of igniting a plain hydrogen microjet (far/close to the nozzle exit) and at a decrease or increase in its outflow rate. Based on the research results presented in [9], Fig. 2 shows a graph of development and disappearance of the FCR depending on the ignition method (near/far from the nozzle section), as well as the increase/decrease of the outflow rate of a plain hydrogen microjet. The graph clearly shows the presence of hysteresis in this process. When a microjet is ignited near the nozzle exit, the FCR heating the nozzle exit makes it possible for this region to exist until it disappears with flame detachment at a sufficiently high velocity of the microjet ($U_0 \approx 590$ m/s). However, when the microjet flow rate decreases, swapping the flame detachment for its attachment with the FCR appearance occurs at $U_0 \approx 333$ m/s. This correlates with the situation observed while igniting the hydrogen microjet far from the nozzle exit. Thus, in this case, you can observe the hysteresis cycle. Half-cycle A: the presence of the FCR, its disappearance, and flame detachment upon igniting the microjet near the nozzle exit and the increase of its outflow rate (position A). Half-cycle B: swapping the flame detachment for its attachment and the FCR appearance at a decrease in the outflow rate of the microjet while igniting it far from the nozzle exit (position B). It should also be noted that the flame detachment from the nozzle exit and the FCR disappearance, which prevent heating of the micronozzle exit and, therefore, "micronozzle choking," create conditions for the combustion of the hydrogen microjet to reach supersonic speeds.

Scenario no. 3. Supersonic combustion of a plain micro jet of hydrogen in the presence of supersonic cells relative to the speed of sound in air (331 m/s). The classical pattern of the subsonic combustion of a hydrogen microjet, in particular a plain microjet (a) studied in detail in [7]. Moreover, supersonic cells characteristic of supersonic combustion (relative to the speed of sound in air) of the circular hydrogen microjet studied in [10] can be observed in this situation.

Scenario no. 4. Supersonic combustion of a plain micro jet of hydrogen in the presence of supersonic cells relative to the speed of sound in hydrogen (1284 m/s). Figure 3 shows the shadow patterns of the diffusion combustion of a hydrogen microjet flowing from a plain micronozzle at an outflow rate of $U_0 \approx 1484$ m/s and a view of the narrow (I) and wide (II) sides of the micronozzle (a) without and (b) with combustion.

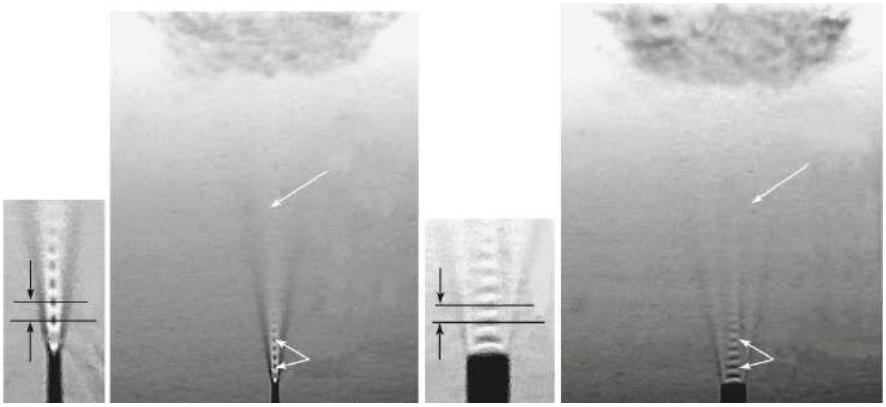

Figure 3.

ACKNOWLEDGMENTS

This work was supported by the Russian Scientific Foundation, project no. 16-19-10330.

REFERENCES

[1] Shmakov A. G., Grek G. R., Kozlov V. V., Korobeinichev O. P., and Litvinenko Yu. A., Vestnik NGU. Seriya: Fizika 10 (2), 27 (2015).
[2] Grek G. R., Katasonov M. M., Kozlov G. V., and Litvinenko M. V., Vestnik NGU. Seriya: Fizika 10 (2), 42 (2015).
[3] Kozlov V. V., Grek G. R., Korobeinichev O. P., Litvinenko Yu. A., and Shmakov A. G., Dokl. Akad. Nauk 470 (2), 166 (2016).
[4] Shmakov A. G.,. Grek G. R, Kozlov V. V., Kozlov G. V., and Litvinenko Yu. A., Sib. Fiz. Zh. 12 (2), 28 (2017).
[5] Kozlov V.V., Grek G.R, Kozlov G.V., Litvinenko Y.A., Shmakov A.G., Int. J. Hydrogen Energy 44 (1), 457 (2019).
[6] Kozlov V. V., Shmakov A. G., Grek G. R., Kozlov G. V., and Litvinenko Yu. A., Dokl. Akad. Nauk 480 (1), 34 (2018).
[7] Litvinenko Yu. A, Grek G. R., Kozlov V. V., Korobeinichev O. P., Shmakov A. G. Vestnik NGU. Seriya: Fizika 10 (2), 52 (2015).
[8] Kozlov V. V., Grek G. R., Kozlov G. V., Litvinenko Yu. A., and. Shmakov A. G, Sib. Fiz. Zh. 12 (3), 62 (2017).
[9] Kozlov V. V., Grek G. R., Litvinenko Yu. A., Shmakov A. G., and Vikhorev V. V., Sib. Fiz. Zh. 13 (2), 23 (2018).
[10] Kozlov V. V., Grek G. R., Litvinenko M. V., Litvinenko Yu. A., and Shmakov A. G., Sib. Fiz. Zh. 12 (2), 46 (2017).
[11] Annushkin Yu. M., Diffusion Combustion of Gaseous Fuels in an Unlimited Space (Trudy TsIAM, Moscow) 857, 1 (1979) [in Russian].

EVALUATION OF NANOPARTICLE POPULATION BALANCE MODELS IN FLAME SPRAY PYROLYSIS

Sebastian Klukas *[1], Marcus Giglmaier[1], and Nikolaus A. Adams[1]
[1] Chair of Fluid Mechanics and Aerodynamics, Technical University of Munich

Summary Flame spray pyrolysis (FSP) is a promising and innovative technique to fabricate versatile functional nanomaterials. Its inherent benefits include cost efficiency, a predicted scaling capability and an extensive range of applicable precursor solutions as well as an accordingly broad range of produced nanoparticles. The study at hand focuses on the formation of maghemite iron oxide nanoparticles (γ-Fe_2O_3) by application of low-cost nitrate-based precursors. The featured numerical method is able to incorporate multicomponent droplet evaporation, thermal decompositions, gaseous combustion as well as particle formation and growth. Three classes of nanoparticle population balance models (PBM) are employed and evaluated. Results show a similar spatial particle spreading for all applied models while deviations in particle size distribution become apparent.

INTRODUCTION

In general, FSP [1] can be divided into five physical subprocesses: primary and secondary spray atomization, precursor reaction, droplet evaporation, gaseous combustion as well as nanoparticle formation, coagulation and growth. These are schematically displayed in figure 1 and are, with the exception of primary atomization, reflected in the current numerical study. The FSP process is initiated by injection of a liquid fuel precursor solution. Since it is coaxially entrained by a fast gaseous flow, the emerging liquid jet is rapidly atomized into small droplets. These subsequently evaporate into a combustible gas mixture while simultaneously undergoing thermal precursor decomposition. A pilot flame and gaseous coflow provide the necessary thermal flow conditions for ignition and steady operation. The prevalent fluid properties at each inlet stream is summarized in table 1. The featured FSP burner corresponds to the laboratory scale "SpraySyn" burner as it is investigated by the German research foundation's priority program DFG-SPP 1980 [2].

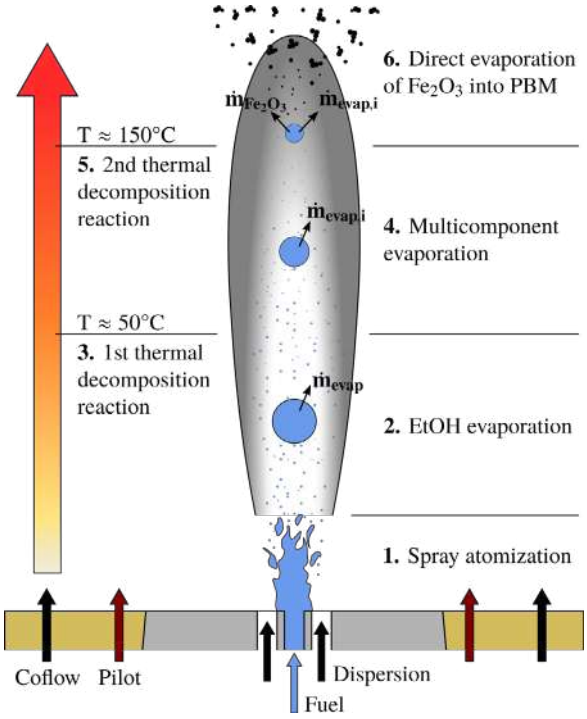

Figure 1: Schematic of the "SpraySyn" FSP burner.

Table 1: Applied inlet conditions.

	Fuel	Dispersion	Pilot	Coflow
Y_i [-]	EtOH + Precursor	O_2	CH_4 + O_2	O_2
$\overline{U}$ [m/s]	0.265	120.6	2.37	0.74
Re [-]	78	6262	1067	1530

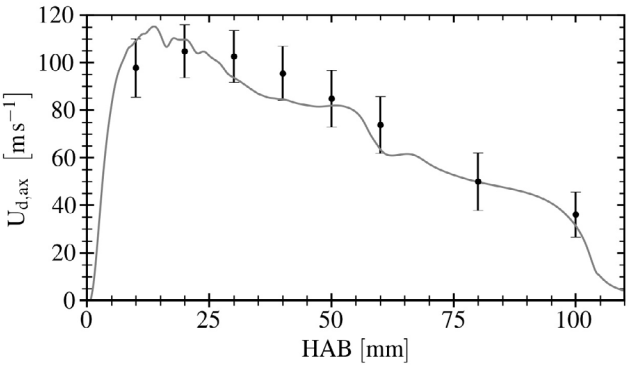

Figure 2: Instantaneous velocity compared to PDA data [2].

NUMERICAL METHOD

The challenge for the numerical method is to incorporate the considered FSP subprocesses while capturing their coupling and related time scales. In general, the reacting multiphase flow is resolved by an Eulerian-Lagrangian approach. Four-way coupling is achieved by transient source term adaptation as well as droplet breakup and collision models. Gas phase reactions are resolved by the steady laminar flamelet model (SLFM) utilizing one-dimensional non-premixed counterflow diffusion flames for thermochemical lookup table generation. The OpenFOAM software libraries are employed to solve the Reynolds-Averaged Navier-Stokes (RANS) equations.

A detailed analysis of FSP requires special attention to the liquid phase evolution. Firstly, multicomponent evaporation

*Corresponding author. E-mail: sebastian.klukas@tum.de

is prevalent since the droplets contain two or more species. Thus, the multi-species variant of the Abramzon-Sirignano model is incorporated into the solver [3]. To be consistent with the flamelet approach the evaporating species water and nitric acid are taken into account by additional species conservation equations. Therefore, both are considered to be neither fuel nor oxidizer and do not participate in any gaseous reaction. Secondly, thermal precursor decomposition is included in the Lagrangian phase and assessed by the following two-step chemical reaction of ferric nitrate [4]:

$$\mathrm{Fe(NO_3)_3 \cdot 9H_2O} \longrightarrow \mathrm{FeOH(NO_3)_2 \cdot 2H_2O + HNO_3 + 6H_2O}$$

$$\mathrm{2FeOH(NO_3)_2 \cdot 2H_2O} \longrightarrow \mathrm{Fe_2O_3 + 4HNO_3 + 3H_2O}$$

Due to their minute vapor pressure, the nucleating $\mathrm{Fe_2O_3}$ nanoparticles are assumed to evaporate instantly into the gas phase. Intermediate iron species are considered to not participate in any phase change processes. To account for the vast amount of nanoscale particles, their number concentration is conserved by PBM. The objective of this study is to assesses the performance of three different types of such models and evaluate their capability of predicting nanoparticle formation within the complex FSP process. The applied PBM are: A straightforward bimodal monodisperse model based on additional scalars for particle volume and concentration, a sectional model featuring a fixed number of particle classes in direct correlation to the number of particle molecules and a bimodal polydisperse model, which derives a particle size distribution by the method of moments.

RESULTS

Validation of the implemented numerical method is performed by comparison to experimental PDA measurements [2]. The corresponding axial profiles of droplet velocity are displayed in figure 2. The demonstrated agreement is repeated in a similar fashion for mean diameter, mean velocity as well as for radial profiles of these quantities. The results illustrate an increasing discrepancy between numerics and experiment with greater distance to the symmetry axis. Exemplary results for the bimodal monodisperse PBM are depicted in figure 3. A detailed comparison to models which take the particle size distribution into account is carried out.

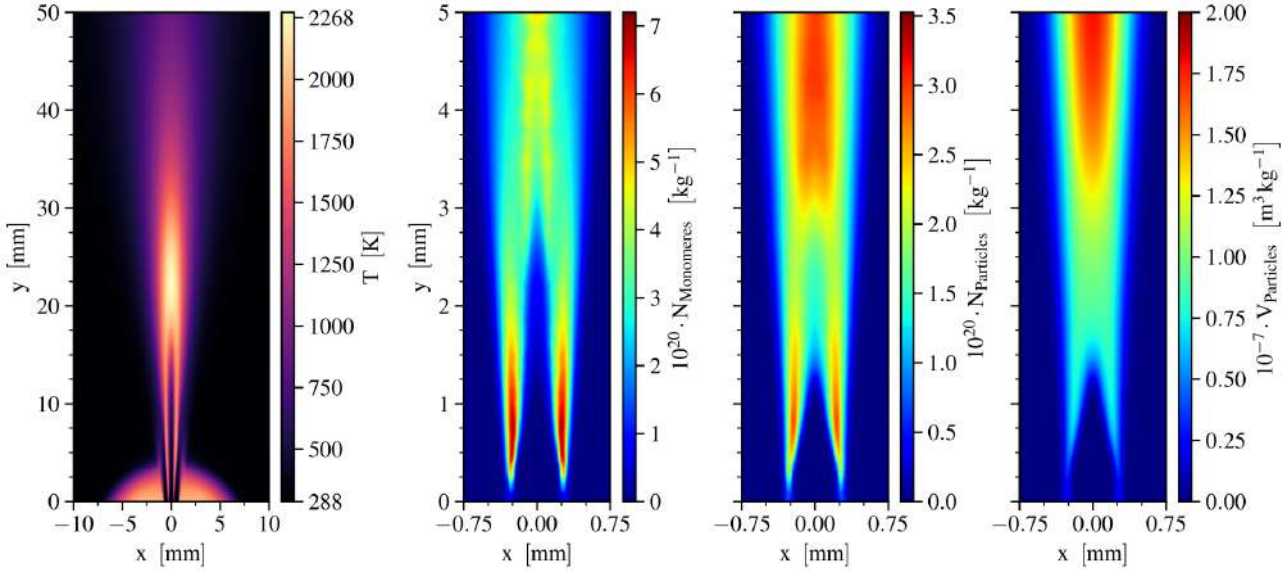

Figure 3: Results for the bimodal monodisperse particle model. Temperature, monomere and particle distributions are displayed.

CONCLUSIONS

The realized numerical method shows great promise to reflect the physical processes of nanoparticle formation in FSP in an efficient and accurate manner. Initial results for a bimodal monodisperese particle model are presented. A detailed comparison between three distinct PBM as well as a detailed experimental validation will be presented at the conference.

References

[1] Teoh W. Y., Amal R., Maedler L. Flame spray pyrolysis: An enabling technology for nanoparticles design and fabrication. *Nanoscale* **2**: 1324-1347, 2010.

[2] Schneider F., Suleiman S., Wlokas I., Dreier T., Wiggers H., Schulz C. The SpraySyn standard burner enabling coordinated research on material synthesis in spray flames. 29. Deutscher Flammentag, 2019

[3] Abramzon B., Sirignano W.A. Droplet vaporization model for spray combustion calculation. *International Journal of Heat and Mass Transfer* **32**: 1605-1618, 1989.

[4] Thermal decomposition mechanism of iron(III) nitrate and characterization of intermediate products by the technique of computerized modeling. *Journal of Thermal Analysis and Calorimetry* **115**: 145-151, 2014.

IMPACT OF HEAT LOSSES ON FREELY PROPAGATING PREMIXED FLAMES IN NARROW CHANNELS: FROM NON-SYMMETRIC TO SYMMETRIC FLAME SHAPES

Carmen Jiménez*[1], Anne Dejoan[1], Daniel Martínez-Ruiz[2], Victor Muntean[2], Mario Sánchez-Sanz[3], and Vadim N. Kurdyumov[1]
[1] Center for Research in Energy, Environment and Technology (CIEMAT), Madrid, Spain
[2] E.T.S.I.A.E., Universidad Politécnica de Madrid, Madrid, Spain
[3] Fluid Mechanics Group, Universidad Carlos III de Madrid, Leganés, Spain

Summary. The influence of heat losses on the structure of premixed flames freely propagating in narrow channels is investigated. It is shown that the flame shape depends on the channel width, the reactants mean flow rate and the heat losses. For very narrow channels only symmetric flames, with either mushroom or tulip shapes, are formed at any intensity of heat losses. For wider channels the flames are non-symmetric for adiabatic walls or for small heat losses, and become symmetric as heat losses increase.

We study by numerical simulations the effect of heat losses on the structure of premixed flames freely propagating in narrow channels of planar and circular cross sections, using kinetics of the Arrhenius type and assuming constant transport properties and unit Lewis number (see [1] for further details on the formulation). It is shown that in fairly narrow channels only symmetric flames are formed at any intensity of heat losses. The response curve (flame velocity versus heat losses) takes in this case a typical C-shaped form, as shown in Fig. 1 for a=5, where a is the channel width h scaled with the flame thermal thickness δ_T: there is a maximum critical value of the heat loss intensity above which flame propagation is impossible. This value depends also on the intensity of the mass flow rate in the channel m (Fig.1 corresponds to m=0).

The structure of the flame changes noticeably in wider channels. In these cases the flame results to be non-symmetric when heat losses are sufficiently small (or zero). Nevertheless it was found that with a gradual increase in heat losses the flame shape becomes symmetric again. This can be appreciated in Fig.1 for the cases with $a > 5$, and in Fig. 2 for a =10. As expected, for sufficiently wide channels (e.g. the case a=15 in Fig.1), flame extinction does not occur, not even for very large values of the heat losses parameter, which would correspond to isothermal (cold) walls. It is important to note that the critical quenching width depends on the intensity of the gas mass flow rate, and that near this critical value the flame remains symmetric. The detected symmetry of the flames near the critical value can facilitate the calculation of the critical extinction parameters, of importance for practical applications. We also want to note the appearance of multiplicity of steady-state regimes when flames with symmetric and non-symmetric shapes can coexist.

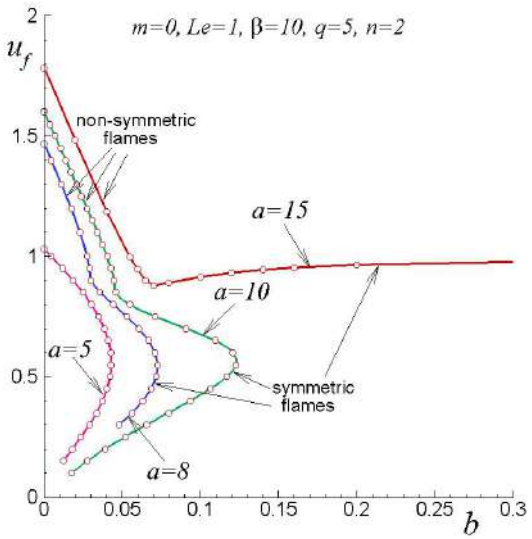

Figure 1. Computed flame velocity u_f (with respect to the wall and scaled with the laminar planar flame speed), calculated as a function of the heat-loss intensity $b = \frac{\lambda_w \delta_T}{\lambda_g h_w}$, with λ_w and λ_g the wall and gas thermal conductivities, δ_T the flame thickness and h_w the wall thickness in planar channels with reactants mass flow rate m=0.

*Corresponding author. E-mail: carmen.jimenez@ciemat.es

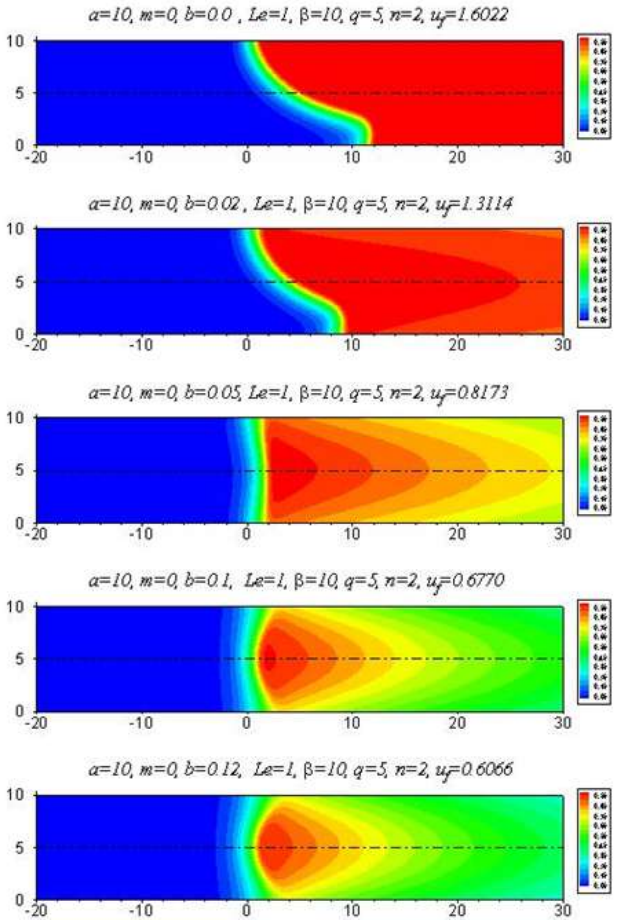

Figure 2. Structure of flames (colour isotherms) with increasing heat-loss intensity b calculated for a planar channel with width $a=10$ and reactants mass flow rate $m=0$.

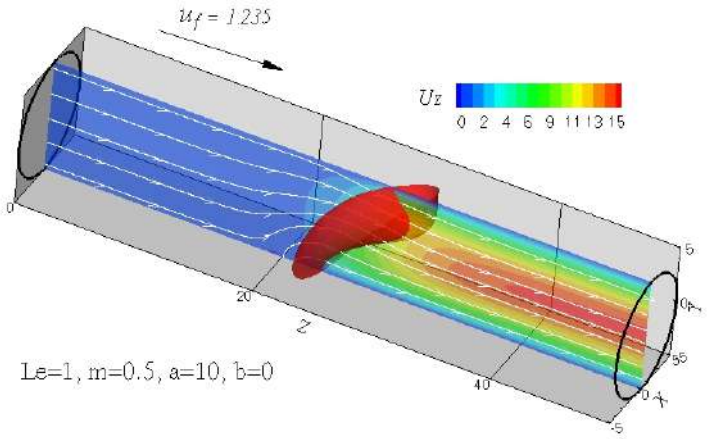

Figure 3. An example of a 3D non-symmetric flame in a channel of circular cross section.

CONCLUSIONS

We study in this paper the influence of heat losses in the flame shape and the quenching width when Le=1 flames propagate freely in narrow channels. These results may be useful for the design of micro combustion devices, and for safety issues in combustion systems, given that the flame propagation speed is closely related with its shape and surface.

References

[1] Dejoan A., Jiménez C., Kurdyumov V.N., *Combust. Flame* **209**: 430–440, 2019.

STUDY OF THE DIRECT INITIATION OF SPHERICAL DETONATIONS

Paul Clavin *[1], Raúl Hernández Sánchez[1], and Bruno Denet[1]
[1] Aix Marseille Univ, CNRS, Centrale Marseille, IRPHE, Marseille, France

Summary An analysis of the direct initiation of gaseous detonations in spherical geometry is presented, for a Mach number close to unity (small heat release). In this limit, the evolution is described by a Burgers equation, modified by a reaction and a curvature term. The solutions of this equation are presented in a pulsating detonation case.

INTRODUCTION

The direct initiation of a spherical detonation has attracted a lot of attention, starting with the suggestion of Zeldovich that a successful initiation requires that the time to reach the Chapman Jouguet (CJ) velocity is larger than the reaction time. This criterion leads to a critical radius of the order of the detonation thickness of the planar CJ detonation. It was shown experimentally that this critical radius is much too small. A quasi-steady analysis by He and Clavin [1] (see also [2]), using a square wave model, showed that the curvature of the detonation leads to a turning point representative of a curvature-induced quenching; the spherical CJ velocity has a C-shaped curve (see Figure 1) and the quasi-steady solutions exist above a critical radius much larger than the detonation thickness. However the quasi-steady approximation is not fully satisfactory and cannot reproduce the behavior of DNS trajectories, especially near criticality [1],[2],[3]. A theoretical model with an inner structure more realistic than the square wave model, will be used to assess the role of the unsteady effects, in the case of successful initiations or failures.

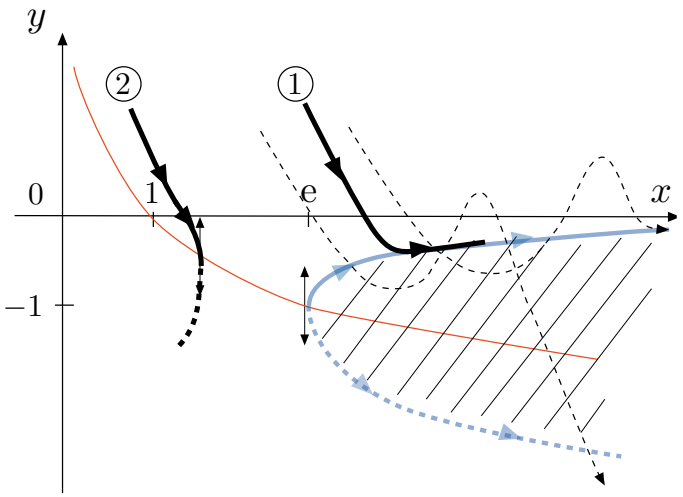

Figure 1: Sketch of the trajectories, x is proportional to the radius, y is proportional to the difference between the detonation velocity and the plane CJ velocity. Dotted lines represent schematically unsteady trajectories obtained by DNS. Solid lines are the quasi-steady trajectories.

MODEL AND RESULTS

In the limit of a small heat release, the full Euler equations reduce to a Burgers equation, modified by a reaction term and curvature term [5, 6]. This inner detonation structure has to be matched to a rarefaction wave. Sufficiently close to the Chapman-Jouguet solution, this Burgers equation can also be transformed in an integral equation [5], of the type recently used in the plane case by the authors in [7].

We present here solutions of the reactive Burgers equation with curvature [6]. For a small heat release, this equation can be written:

$$\frac{\partial \mu}{\partial \tau} + \left(\mu - \frac{y}{b}\right)\frac{\partial \mu}{\partial \xi} = \frac{1}{2}\omega(\xi, y(\tau)) - \frac{(1+\mu)}{\tilde{r}_f(\tau)}, \tag{1}$$

$$\xi = 0: \quad \mu = 1 + 2y(\tau)/b. \tag{2}$$

where μ is a reduced flow velocity in the laboratory frame, ω is the reaction term, the last term in the right hand side of (1) is a curvature term. Using the boundary condition at the shock (2), the reduced detonation velocity y can be obtained ($y = 0$ corresponds to the Chapman Jouguet velocity). An example of numerical integrations of this equation for different initial radii is shown in Figure 2.

*Corresponding author. E-mail: paul.clavin@univ-amu.fr

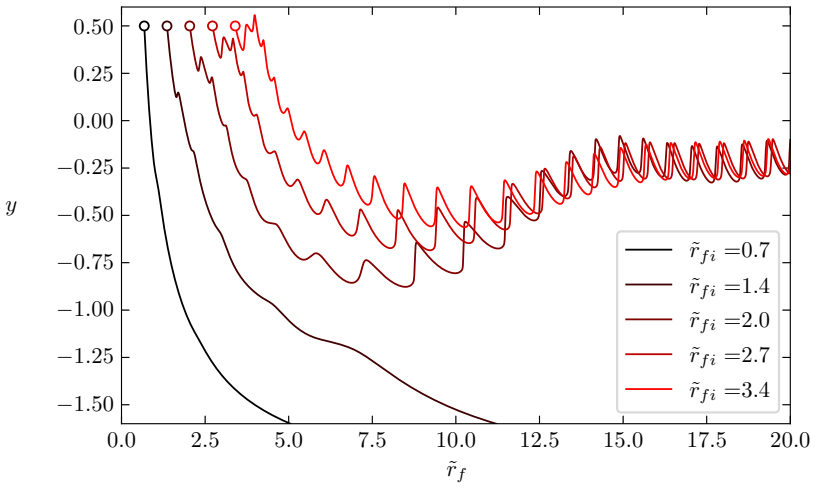

Figure 2: Examples of numerical integration of the reactive Burgers equation for a weakly unstable detonation $b = 2$. The failure occurs for initial radius small enough $\tilde{r}_{fi} < 1.5$ because of chemical-kinetics quenching.

CONCLUSIONS

For detonations close to the CJ velocity, it has been possible to simplify the full system of equations describing the spherical detonation to get a Burgers equation with reaction and curvature terms. Concerning the trajectories of the lead shock in direct initiation, the limit of small heat release is in qualitative agreement with direct numerical simulations, except for the overshoot during the re-acceleration phase which is sometimes observed in DNS.

Acknowledgements: We thank Prof. Amable Liñan for stimulating discussions. This work was supported by the French National Research Agency under agreement ANR-18-CE05-0030,

References

[1] He L., Clavin P. On the direct initiation of gaseous detonations by an energy source. *J. Fluid. Mech* **2**77: 227-248, 1994.
[2] He L. Theoretical determination of the critical conditions for the direct initiation of detonations in hydrogen-oxygen mixtures. *Combust. Flame* **1**04: 401-418, 1996.
[3] Eckett C.A., Quirk, J.J. Shepherd J.E. The role of unsteadiness in direct initiation of gaseous detonations. *J. Fluid. Mech.* **4**21: 147-183, 2000.
[4] Liñan A., Kurdyumov V., Sanchez A.L. Initiation of reactive blast waves by external energy source. *Comptes Rendus Mécanique* **3**40: 829-844, 2012.
[5] Clavin P., Denet B. Analytical study of the direct initiation of gaseous detonations for small heat release. *J. Fluid. Mech.* **8**97: A30, 2020.
[6] Clavin P., Hernández Sánchez R., Denet B. Asymptotic analysis of the critical dynamics of spherical gaseous detonations.. *J. Fluid. Mech.* submitted October 2020.
[7] Clavin P., Denet B. Decay of plane detonation waves to the self-propagating Chapman-Jouguet regime. *J. Fluid. Mech.* **8**45: 170-202, 2018.

TAYLOR DIPSERSION AND THE FLAME THERMODIFFUSIVE INSTABILITY

Joel Daou *
Department of Mathematics, University of Manchester, Manchester, UK

Summary We investigate the effect of Taylor dispersion on the thermo-diffusive instability of flames. This is a physically interesting and analytically tractable problem within a relatively unexplored class of problems pertaining to the interaction between Taylor dispersion (or flow-enhanced diffusion) and Turing-like instabilities in reaction-difusion systems. The analysis is carried out in the Hele-Shaw burner configuration and adopts a constant density approximation. Depth-averaged equations are first obtained which incorporate Taylor dispersion and show that diffusion is effectively anisotropic. A linear stability analysis of travelling wave solutions leads to a simple dispersion relation which allows stability-bifurcation diagrams to be drawn in the parameters space.

INTRODUCTION

There are two major intrinsic flame instabilities in premixed combustion. The first, known as the Darrieus-Landau or hydrodynamic instability, is the instability of an interface propagating towards a less dense medium [1]. The second instability, known as the thermo-diffusive instability [2], occurs in fuel-lean mixtures where the thermal diffusivity D_T and the fuel diffusion coefficient D_F are such that their ratio, the Lewis number $\boxed{\mathrm{Le} \equiv D_T/D_F}$, is sufficiently away from unity. The thermo-diffusive instability may be identified as a Turing-like instability [3] since it requires, as in the case of Turing instability in a reaction-diffusion system [4], two diffusive processes to have differing diffusion coefficients. Strictly speaking, however, the Turing and thermo-diffusive instabilities are quite different, not least because the former pertains to a spatially homogeneous steady state, while the latter to a travelling wave.

The rich topic of flame instabilities has been the subject of dedicated reviews e.g. [3, 5, 6]. A main objective of this paper is to complement the literature by addressing unexplored aspects of flame instability using an extension of our approach based on the *thick flame asymptotic limit* described in [7, 8]. The specific novel problem to be addressed in this paper is ***the influence of Taylor dispersion on the thermo-diffusive instability***, which is an interesting subproblem of the more general problem of ***flame instabilities in a Hele-Shaw cell under forced convection***. In fact, the Hele-Shaw configuration is ideal for investigating the instabilities of flames [9], at least in theoretical and numerical studies where heat-losses and density variations, which are difficult to ignore in practice, may be switched off or on, depending on our focus. Recent experiments on flames in Hele-Shaw cells have been conducted at the University of Aix-Marseille [10] and at the University of Southern California [11].

THEORETICAL RESULTS

As a configuration for the investigation we shall adopt that of the Marseilles experiment which is sketched in Figure 1 showing a flame propagating downwards. As described in [10], the burner's operation is briefly as follows. By opening the inlet valve at the bottom, a reactive mixture flows upwards to fill the cell and is ignited at the top of the burner where a flame parallel to the horizontal x-direction is formed and remains anchored thanks to a flow velocity exceeding on average the flame speed U_L. Closing the valve, the flow is stopped and the downwards flame propagation is recorded. It is important to point out that the effect of the flow, or forced convection, on the propagation and stability of the flame has not been addressed. Although this seems to be a simple ingredient to incorporate, it has a profound influence. Specifically, by considering flame propagation against a vertical flow, say given in the unburnt-gas by $\mathbf{u} = u_0(1 - y^2/a^2)\hat{\mathbf{z}}$ where a is the channel half-width and $\hat{\mathbf{z}}$ a unit vector in the z-direction, it is possible to investigate theoretically the effect of Taylor dispersion [12, 13] on flame propagation and stability. Indeed, Taylor dispersion modifies the effective diffusion coefficients of heat and mass in the flow direction (z-direction), which modifies the effective Lewis number $\mathrm{Le}_{\mathrm{eff}}$. In fact, the results of our publication [8] indicate that $\boxed{\dfrac{\mathrm{Le}_{\mathrm{eff}}}{\mathrm{Le}} = \dfrac{1+\gamma(1-\alpha)^2\mathrm{Pe}^2}{1+\gamma(1-\alpha)^2\mathrm{Pe}^2\mathrm{Le}^2}}$, where $\mathrm{Pe} = au_0/D_T$ is the Peclet number, $\gamma = 8/945$ a numerical coefficient, and α the gas expansion parameter defined in terms of the unburnt gas and burnt gas densities ρ_u and ρ_b by $\alpha = 1 - \rho_b/\rho_u$. The formula shows that $\mathrm{Le}_{\mathrm{eff}} \sim \mathrm{Le}$ as $\mathrm{Pe} \to 0$ and $\mathrm{Le}_{\mathrm{eff}} \sim \mathrm{Le}^{-1}$ as $\mathrm{Pe} \to \infty$. This suggests that Taylor dispersion may have significant influence, worth exploring, on the thermo-diffusive instability which critically depends on $\mathrm{Le}_{\mathrm{eff}}$. This is a highly original investigation which is best initiated by adopting first

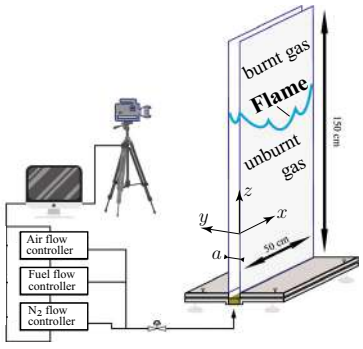

Figure 1: Hele-Shaw burner, adapted from [10]

*Corresponding author. E-mail: joel.daou@manchester.ac.uk.

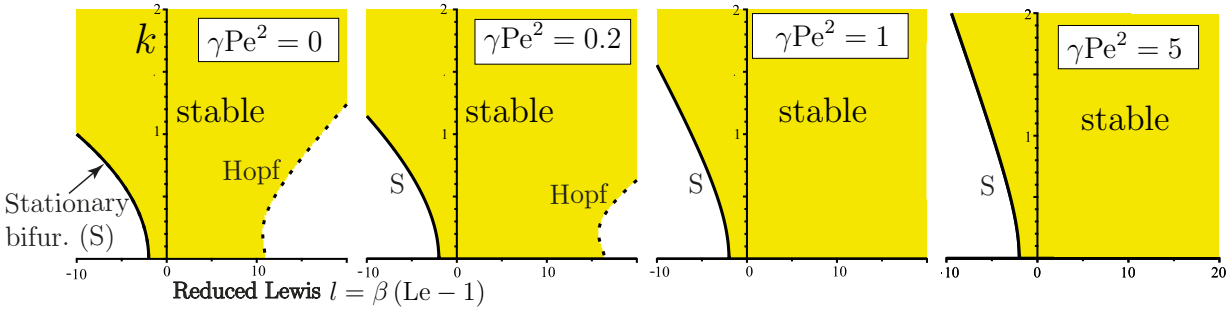

Figure 2: Stability region and bifurcations in the l-k plane for selected values of the parameter $\gamma \mathrm{Pe}^2$; l is the reduced Lewis number and k is the perturbation wave number.

the constant density approximation ($\alpha = 0$) and addressing the stability of a planar flame (parallel to the x-axis) propagating downwards against the flow. The problem has however a crucial complication: enhanced diffusion, which leads to the formula for $\mathrm{Le}_{\mathrm{eff}}$ above, is applicable in the longitudinal z-direction; in the transverse x-direction diffusion is unaffected by the flow. Therefore, the stability problem in the x-z plane (obtained by y-averaging the governing equations), is one involving ***anisotropic diffusion***. Accordingly, the classical approach of tackling the problem, using familiar jump conditions applicable at inner reaction layers needs significant revision. This revision and related aspects are addressed in this work. The main outcome is the derivation of a dispersion relation describing the linear stability of the flame to perturbations proportional to $\exp(ikx + st)$ with wave number k and growth rate s. The dispersion relation is found to be given by

$$2\Gamma^2(\Gamma - 1) + \frac{l}{1 + \gamma \mathrm{Pe}^2}\left[(\Gamma - 1 - 2s)(1 - \gamma \mathrm{Pe}^2) + 4\gamma \mathrm{Pe}^2 k^2\right] = 0\,,$$

where $l = \beta(\mathrm{Le} - 1)$ is the so-called reduced Lewis number involving the Zeldovich number β and $\Gamma = \sqrt{1 + 4s + 4k^2}$.

.

CONCLUDING REMARKS

We note that the dispersion relation incoroprates the effect of Taylor dispersion and the resulting anisotropy of diffusion. A sample of the results implied by the dispersion relation are illustrated in figure 2 for selected values of the parameter $\gamma \mathrm{Pe}^2$. When $\gamma \mathrm{Pe}^2 = 0$ we recover the classical results with a stationary bifurcation curve for small values of l and a Hopf bifurcation curve for larger values. As $\gamma \mathrm{Pe}^2$ is increased the Hopf bifurcation curve is displaced to the right and disappears for $\gamma \mathrm{Pe}^2 > 1$. Thus a sufficiently strong flow impedes the oscillatory flame instability. Also, the size of the stability domain in the left half-plane (delimited from the left by the stationary bifurcation curve) is reduced by an increase in $\gamma \mathrm{Pe}^2$ which indicates that the flow may somewhat promote the cellular instability. In any case, the results demonstrate the ability of Taylor dispersion to significantly affect Turing-like instabilities.

References

[1] Landau L.D. On the theory of slow combustion. *Acta Physicochim (USSR)*, **19**: 77-85, 1944.
[2] Markstein G.H. Cell structure of propane flames burning in tubes. *The Journal of Chemical Physics*, **17(4)**: 428-429, 1949.
[3] Buckmaster J. The structure and stability of laminar flames. *Annual review of fluid mechanics*, **25(1)**: 21-53, 1993.
[4] Turing A.M. The chemical basis of morphogenesis *Phil. Trans. R. Soc. B*, **237**: 37-47, 1952.
[5] Sivashinsky G.I. Instabilities, pattern formation, and turbulence in flames. *Annual Review of Fluid Mechanics*, **15(1)**: 179-199, 1983.
[6] Matalon M. Intrinsic flame instabilities in premixed and nonpremixed combustion. *Annu. Rev. Fluid Mech.*, **39**: 163-191, 2007.
[7] Daou J., Dold J., and Matalon M. The thick flame asymptotic limit and Damköhler's hypothesis. *Combustion Th. and Model.*, **6(1)**: 141-153, 2002.
[8] Daou J., Pearce P., and Al-Malki F. Taylor dispersion in premixed combustion: Questions from turbulent combustion answered for laminar flames. *Physical Review Fluids* **3(2)**: 023201, 2018.
[9] Joulin G. and Sivashinsky G. Influence of momentum and heat losses on the large-scale stability of quasi-2D premixed flames. *Combustion Science and Technology*, **98 (1-3)**:11-23, 1994.
[10] Sarraf E., Almarcha C., Quinard J., Radisson B. and Denet B. Quantitative analysis of flame instabilities in a hele-shaw burner. *Flow, Turbulence and Combustion*:1-18, 2018.
[11] Galisteo D., Kurdyumov V. , and Ronney P. Analysis of premixed flame propagation between two closely-spaced parallel plates. *Combustion and Flame*, **190**: 133-145, 2018.
[12] Taylor G. Dispersion of soluble matter in solvent flowing slowly through a tube. *Proc. Royal Soc. of London A*, **219**: 186-203, 1953.
[13] Pearce P. and Daou J. Taylor dispersion and thermal expansion effects on flame propagation in a narrow channel. *Journal of Fluid Mechanics*, **754**: 161-183, 2014.

VIBRATION INSTABILTY OF PREMIXED FLAMES

Christophe Almarcha *[1] and Basile Radisson[1]
[1] Aix Marseille Univ., CNRS, Centrale Marseille, IRPHE, Marseille, France

Summary We present a new combustion instability that arises when a premixed flame is propagating in a Hele-Shaw burner. In such a configuration, the wall deformations of the burner are strongly coupled to the flame shape and heat release. We demonstrate that it is possible to take advantage of this coupling for either triggering oscillatory instabilities or for studying the response of premixed flames to oscillating flows.

INTRODUCTION

A premixed flame propagating freely in a burner eventually induces pressure and flow oscillatory instabilities. Usually these two are selected by the acoustic modes of the burner. A canonical experiment was performed in a vertical tube, open at the top and closed at the bottom[1] and exhibited two parametric instabilities. A first one flattening the flame shape and a more intense second one inducing wrinkles on the flame shape. The frequency of the oscillations corresponds to a fundamental acoustic frequency of the burner, with the height of the tube corresponding to a quarter wavelength of the acoustic mode. Recent experiments of premixed flames propagating in Hele-Shaw burners have exhibited either similar [2, 3] behaviors or a totally different one: As remarked by [4], the oscillations appearing in their experiment are not corresponding to the fundamental acoustic mode, indicating that the coupling with the burner seems to be different. We demonstrate here that it is possible to trigger oscillating instabilities in a wide range of frequency by playing with the burner wall thickness, material and dimensions. We show that the new combustion instability results from the coupling between the flame and the vibration modes of the walls. The sensitivity to instability of propane-air mixtures and methane-air mixtures are tested. Finally we use the new vibro-acoustic coupling exhibited for studying the flame response to forced flow oscillations.

INSTABILITY

The vertical Hele-Shaw cell used here is 1500mm high, 500mm large, and the gap between the walls is $5mm$. It is open at the top and closed at the bottom where the supply line is situated. The walls of the Hele-Shaw burner are either of glass or of PMMA. The thickness is varied between 2mm and 19mm in order to explore a wide range of bending stiffness [5]. Thanks to mass flow controllers, the desired mixture is injected in the cell. When the upward flow inside the cell is stopped, a premixed flame can propagate inside [6]. Electret microphones are distributed inside the burner and record the pressure fluctuations. As reported on Fig.1, a lean premixed methane-air flame propagatin in a Hele-Shaw burner with a $8mm$ thick PMMA wall is unstable and exhibits a $8.5Hz$ pressure oscillation. Such a frequency cannot be related to an acoustic mode. The acoustic wavelength would be around $40m$ wich is much bigger than the burner size. When playing with the material and the thickness of the burner walls, and keeping the other dimensions constant, the range of the instability frequency appears between $5Hz$ and $200Hz$. We demonstrate that the bending stiffness of the burner walls is controlling the instability frequency.

VIBRATION RESONANCE OF THE BURNER

The coupling between the flame and the walls vibration, that is necessary for the emergence of the instability described in the preceding section, can be used to study the response of a premixed flame to imposed flow oscillations. In particular, the thresholds of primary and secondary acoustic instabilities can be examined when forcing a wall with an electromagnetic shaker. In that case, the flow oscillations inside the burner are imposed by the vibration eigenmodes of the walls. An example of the velocity induced by the first four eigenmodes of the plates in reported on Fig. 2. On the same figure, the modifications of the flame shape when it crosses nodes or antinodes is also reported. Such spatiotemporal diagrams can be used to study the thresholds of destabilization and restabilization of premixed flames. In particular, the dependance of the Markstein number on the oscillating frequency can be investigated.

CONCLUSIONS

We studied the emergence of a new kind of combustion instability where the coupling between the flame and the vibrations of the burner walls appears to be of prime importance. We demonstrate that contrary to the classical acoustic combustion instability, the frequency and mode shape of the oscillatory instability in Hele-Shaw cells can be ruled by the bending stiffness of the burner walls. As a consequence, oscillatory instabilities with frequencies as low as $8.5Hz$ have been obtained in this metric-size burner. Such finding may be of prime importance when studying burner with such geometries.

*Corresponding author. E-mail: chirstophe.almarcha@univ-amu.fr

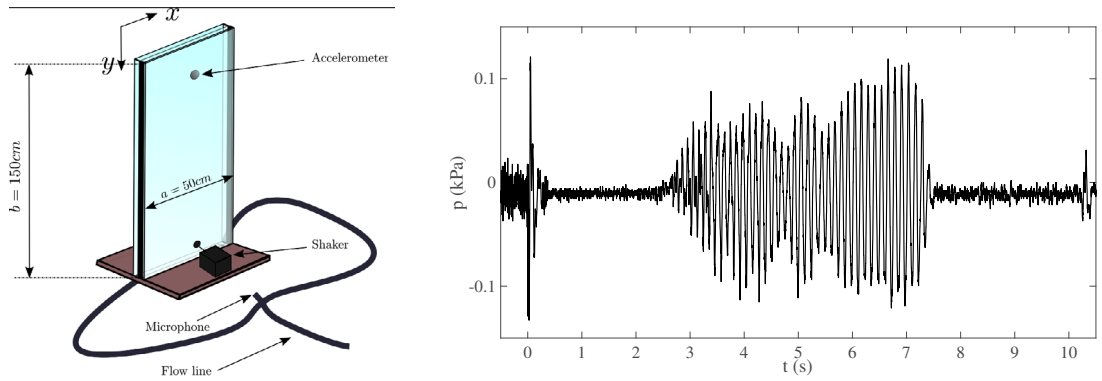

Figure 1: (left) Experimental apparatus: Hele-Shaw burner consisting of two plates separated by a $5mm$ gap. Microphones are introduced in the cell and in the flow line. (right) Oscillatory instability of a premixed methane-air flame (equivalence ratio 0.75) propagating in the burner. At $t = 0$ the upward flow is stopped and the flame is then ignited at the top. Rapidly, a 8.5Hz pressure oscillation emerges and vanishes before the flame reaches the bottom of the burner at $t = 10.5s$.

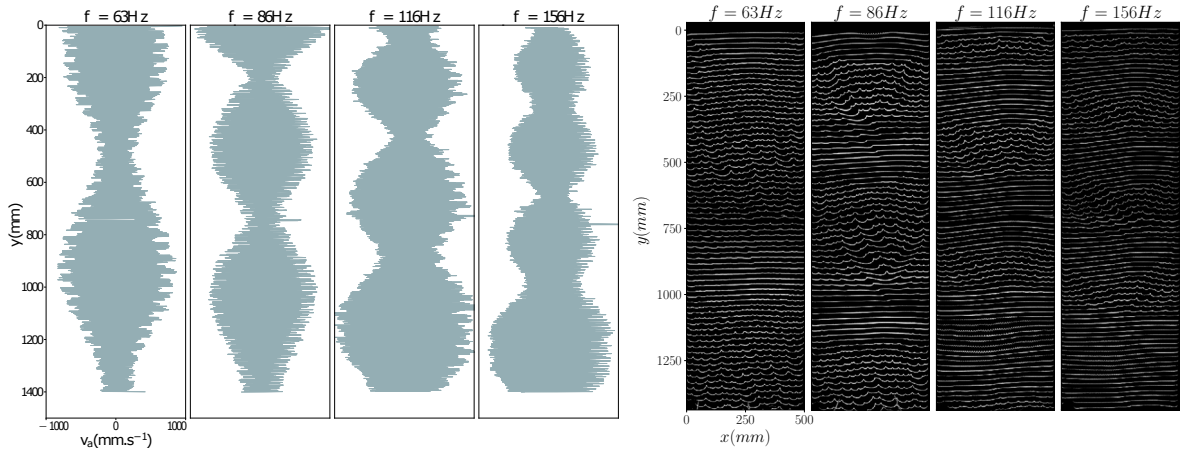

Figure 2: Flame propagation when the plate is vibrated for the first four resonant frequencies. The front undergoes periodic restabilization/destabilization during its propagation. The restabilization (respectively destabilization) zone corresponds to the antinodes (respectively nodes) of the forced plate modes.

AKNOWLEDGMENTS

We thank Daniel Mazzoni for fruitful discussions, 'Agence Nationale de la Recherche' for funding of the ANR 'PDF' ANR-14-CE05-0006, the Excellence Initiative of Aix-Marseille University - A*MIDEX, and Labex MEC, for funding.

References

[1] Searby G., Rochwerger D. A, parametric acoustic instability in premixed flames. *J. Fluid Mech.* **231**: 529-543, 1991.

[2] Veiga-Lopez F., Martinez-Ruiz D., Fernandez-Tarrazo E., Sanchez-Sanz M., Premixed-flame oscillations in narrow channels. *Phys. Rev. Fluids* **4**: 100503, 2019.

[3] Martinez-Ruiz D., Veiga-Lopez F., Sanchez-Sanz M., Experimental analysis of oscillatory premixed flames in a Hele-Shaw cell propagating towards a closed end. *Combustion and Flame* **201**: 1-11, 2019.

[4] Alexeev M. M., Semenov O. Y., Yakush S. E., Experimental study on cellular premixed propane flames in a narrow gap between parallel plates. *Combustion Science and Technology*, **191(7)**, 1256-1275, 2019.

[5] Radisson B., Piketty-Moine J., Almarcha C., Coupling of vibro-acoustic waves with premixed flame. *Phys. Rev. Fluids*, **4(12)**, 121201, 2019.

[6] Al Sarraf E., Instabilités de flammes de prémélange en cellule de Hele-Shaw, PhD Thesis, *Aix-Marseille Univ.*, 2017

EARLY DETECTION OF THERMOACOUSTIC COMBUSTION OSCILLATIONS IN A MULTI-SECTOR STAGED COMBUSTOR FOR AERO ENGINES USING MACHINE LEARNING

Yuhei Shinchi[1], Sena Kishiya*[1],Chinami Aoki[1], Naohiro Takeda[1] , Hiroshi Gotoda [1], Takeshi Shoji [2], and Seiji Yoshida [2]
[1] Department of Mechanical Engineering, Tokyo University of Science, 6-3-1 Niijuku, Katsushika-ku, Tokyo, 128-8585, Japan
[2] Japan Aerospace Exploration Agency, 7-44-1 Jindaiji-Higashimachi, Chofu-shi, Tokyo, 182-8522, Japan

Summary : We conduct an experimental study on an early detection of combustion oscillations in a multi-sector staged combustor using a new methodology combining dynamical systems theory and machine learning. The determinism of recurrence plots and the joint dimensional vicinity are useful measures for capturing a transition to well-developed combustion oscillations. The feature space obtained by a support vector machine has potential use for detecting a precursor of combustion oscillations.

Thermoacoustic combustion oscillations as a result of various mechanisms of nonlinear coupling of acoustic waves to heat-release rate fluctuations lead to serious structural damage in practical combustors. Detection methodologies for thermoacoustic combustion oscillations and the characterization of a rich variety of dynamic behavior have become of much interest in the fields of combustion physics and related branches of nonlinear science. Time series analyses inspired by symbolic dynamics [1] and complex networks [2, 3] have been adopted as promising detectors of combustion oscillations for various types of confined turbulent combustors. Machine learning inspired by information processing in the brain has widespread applications in technologies covering all scientific disciplines. Gotoda and co-workers [4, 5] have recently shown the applicability of methodologies combining complex networks, statistical complexity, and machine learning for an early detection of combustion oscillations. Our main interest in this study is to examine if machine learning is valid for detecting a precursor of combustion oscillations in an aircraft engine model combustor. In this study, we propose a new methodology that integrates dynamical systems, symbolic dynamics, and machine learning for detecting a precursor of combustion oscillations in a multi-sector staged combustor.

The multi-sector combustor, which was developed by JAXA green engine technology program, mainly consists of three lean staged fuel nozzles (LSF) and three emission control fuel nozzle (ECF) [6]. LSF has a pilot fuel injector for diffusion combustion at the center of the fuel nozzle and a main fuel–air mixer for lean premixed combustion around the pilot. All the experiments are conducted using the high-pressure and high-temperature combustion test facility at JAXA. The pressure fluctuations p' are measured by a pressure transducer. The sampling frequency of p' is set to 50 kHz.

As shown in Eqs. (1)-(3), we use a new index [7], namely, the joint dimensional vicinity J, to capture a precursor of combustion oscillations. It considers the correlation entropy [8] and the joint recurrence plots [9]. Note that ${R_R}^D$ represents the density of recurrence plots and J ranges from 0 to 1. We adopt a support vector machine as one of the machine learning technologies for J and the determinism D_E [9] in recurrence plots. The details of the support vector machine are described in Refs. [4] and [5].

$$J = \frac{S - {R_R}^D}{1 - {R_R}^D} \tag{1}$$

$$S = \frac{\frac{1}{\left(N_{sp} - 1\right)^2} \sum_{i=1}^{Nsp-1} \mathbf{JR}_{ij}^{D,D+1}}{{R_R}^D} \tag{2}$$

$${R_R}^D = \frac{1}{N^2} \sum_{i,j=1}^{N} \mathbf{R}_{i,j}^{D} \tag{3}$$

Figure 1 shows the relationship between J and D_E in terms of the amount of main fuel w_{fm}. The location of (J, D_E) moves from left to right on the J-D_E plane with an increase in w_{fm}, forming a parabolic-like shape. This indicates that the two-dimensional plane consisting of the determinism in recurrence plots and the joint dimensional vicinity can capture a transition from stable combustion state to well-developed combustion oscillations which occurs with increasing the amount of main fuel, while maintaining the amount of pilot fuel. Figure 2 (A) shows the feature space consisting of J and D_E obtained by a support vector machine. The combustion state is clearly classified into three regions on the feature space: stable combustion state (blue), combustion oscillations (red), and the transition from stable combustion state to combustion oscillations (yellow). We here increase w_{fm} over about 10 seconds so as to induce combustion oscillations (see Fig. 2(B)). The black plots are drawn on the feature space with increasing time. The combustion state changes back and forth between stable combustion state and the transition state at around 16 s $\leqslant t \leqslant$ 19 s, and well-developed combustion oscillations finally appear at approximately t = 20 s. This clearly shows that the feature space obtained by the

support vector machine allows us to detect a precursor of combustion oscillations. We will present additional results in the poster session.

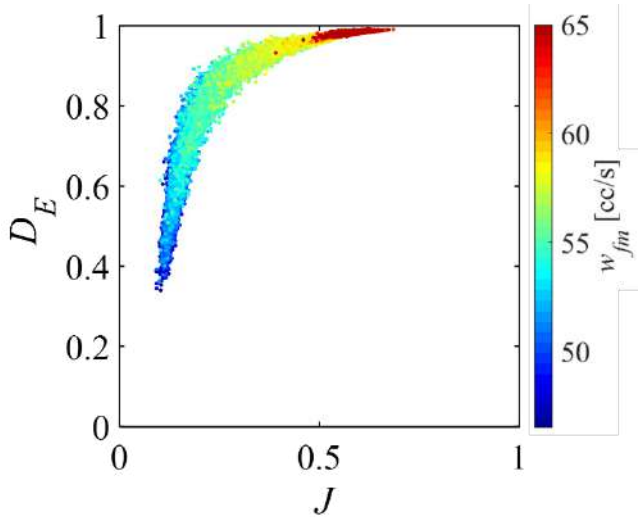

Fig. 1 Relation between J and D_E plane.

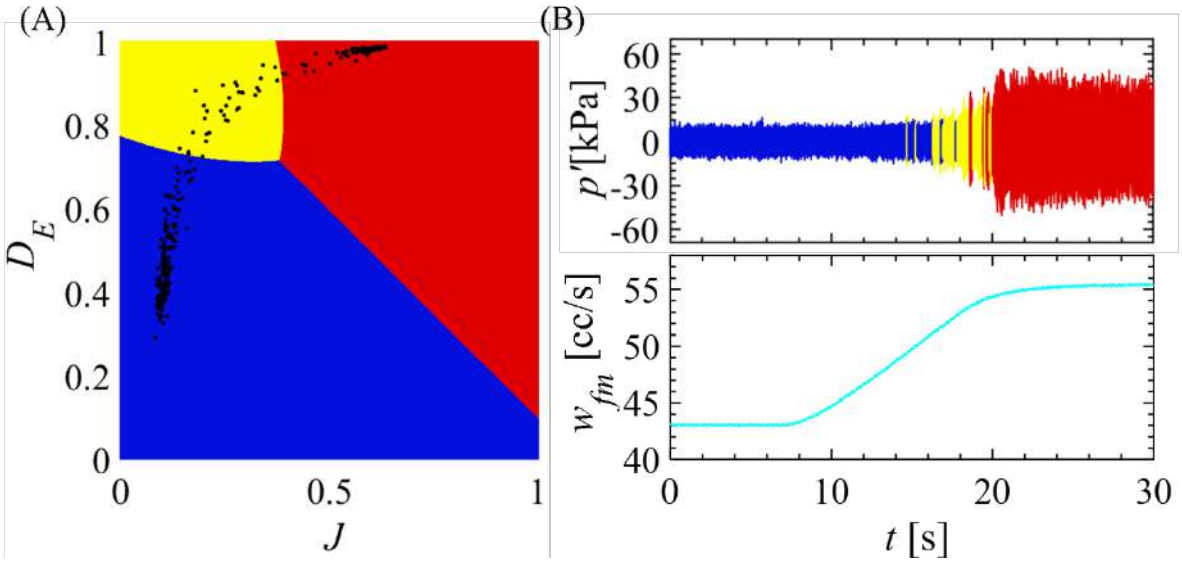

Fig. 2 (A) Feature space consisting of the joint dimensional vicinity J and the determinism D_E obtained by a support vector machine. (B) Time variations in pressure fluctuations p' with increasing the amount of main fuel w_{fm}.

References

[1] H. Kobayashi, H. Gotoda, S. Tachibana, and S. Yoshida, Detection of frequency-mode-shift during thermoacoustic combustion oscillations in a staged aircraft engine model combustor, *J. Appl. Phys.* 122, 224904 (2017).

[2] M. Murugesan and R. I. Sujith, Detecting the onset of an impending thermoacoustic instability using complex networks, *J. Propuls. Power.* 32, 707-712 (2016).

[3] S. Murayama, H. Kinugawa, I. T. Tokuda, and H. Gotoda, Characterization and detection of thermoacoustic combustion oscillations based on statistical complexity and complex-network theory, *Phys. Rev. E.* 97, 022223 (2018).

[4] T. Kobayashi, S. Murayama, T. Hachijo, and H. Gotoda, Early Detection of Thermoacoustic Combustion Instability Using a Methodology Combining Complex Networks and Machine Learning, *Phys. Rev. Appl.* 11, 064034 (2019).

[5] T. Hachijo, S. Masuda, T. Kurosaka, and H. Gotoda, Early detection of thermoacoustic combustion oscillations using a methodology combining statistical complexity and machine learning, *Chaos* 29, 103123 (2019).

[6] T. Yamamoto, K. Shimodaira, Y. Kurosawa, and S. Yoshida, Evaluation of lean axially staged combustion by multi-sector combustor tests under LTO cycle conditions of a small aircraft engine, *Proceedings of ASME Turbo Expo 2013.* GT2013-95496 (2013).

[7] Y. Shinchi, H. Gotoda, T. Shoji, N. Takeda, and S. Yoshida, Detection methodology of thermoacoustic combustion oscillations based on a recurrence-based approach, (in preparetion).

[8] M. Costa, A. L. Goldberger, and C. K. Peng, Multiscale entropy analysis of biological signals, *Phys. Rev. E.* 71, 021906 (2005).

[9] N. Marwan, M. C. Romano, T. Thiel, and J. Kurths, Recurrence plots for the analysis of complex systems, *Physical Reports* 438, 237 (2007).

*Corresponding author. E-mail: 4517044@ed.tus.ac.jp

COMBUSTION OF A ROUND HYDROGEN MICROJET IN A CO-FLOW

Iurii A. Litvinenko[1], Genrich R. Grek[1], Victor V. Kozlov [1], Maria V. Litvinenko[1], Alexander S. Tambovtsev[1] and Andrey G. Schmakov [2]
[1] *Khristianovich Institute of Theoretical and Applied Mechanics, Siberian Branch, Russian Academy of Sciences, Novosibirsk, Russia*
[2] *Voevodsky Institute of Chemical Kinetics and Combustion, Siberian Branch, Russian Academy of Sciences, Novosibirsk, Russia*

Summary Experimental data on the diffusion combustion of round hydrogen microjet in coaxial co-flows are presented. The effects on combustion of the co-current of air and that of air premixed with nanopowder of TiO_2 are of interest. The hydrogen jet flows from a round micronozzle which is surrounded by a coaxial slit to produce the co-flow. In a subsonic range, the so-called "bottleneck-flame" region is generated close to the nozzle exit, while in high-speed conditions the flame separates from the nozzle. At increasing velocity of both the hydrogen microjet and the co-flow, the "bottleneck-flame" region is still found and the combustion becomes more intense. The "bottleneck-flame" region is suppressed at the microjet velocity approaching transonic values.

INTRODUCTION

Stabilization of the diffusion combustion process is an important problem, especially when using miniature burner devices. An increase of the flow rate at maintaining the diffusion combustion process is possible up to certain values. The rate of separation of the diffusion flame, for example, hydrogen is two orders of magnitude higher, while the flame temperature reaches 1600-1800C. Such conditions can be used for hardening or spraying nanoparticles. In this case, particles can be entered through a coaxial nozzle. Co-current oxidizing jet can also stabilize the burner at high hydrocarbon gas flow rates.

EXPERIMENTAL SETUP

The Experimental set-up is shown in Fig. 1. To generate a burning microjet, the nozzle section of the test facility was supplied with hydrogen from a vessel at 100atm. pressure; a co-current air flow emanated from a coaxial slit through injection of compressed air as is shown in Figure 1. In conditions of the co-current air flow seeded with nanoparticles, micronozzle with round coaxial slit and centre hole was used. Hydrogen was supplied to the central hole and a co-current with TiO_2 particles to the coaxial gap.

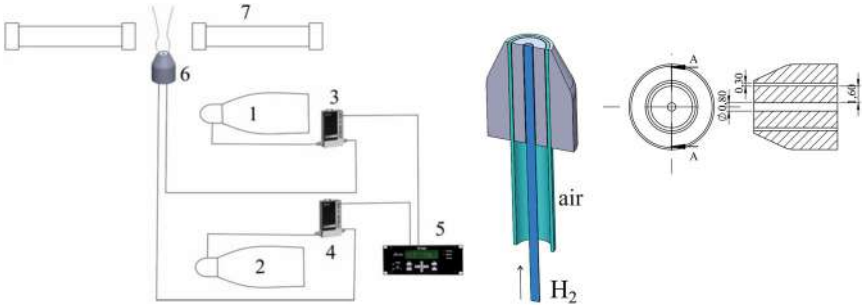

Figure.1. Experimental sketch: 1- hydrogen, 2 – air flow, 3, 4 – flow-meter valve, 5 – flow-meter controller, 6 – nozzle section, 7 – Schlieren device; cross-section of the nozzle is shown on the right

Diffusion combustion of the hydrogen microjet, occurring with and without the concurrent flow, was recorded by a digital camera and examined at acquisition of its shadow images using a Schlieren method and a digital camera providing a resolution of 24 Mpix. The volume flow rate Q (sm^3/s) was controlled by precision flow meters from MKS Instruments (USA) with an accuracy of 0.7 %. Microjet velocity was calculated as $U = Q/S$ where S stands for the cross section of the round nozzle of hydrogen microjet or that of the coaxial slit generating the concurrent flow. Note that the above formula is not appropriate in supersonic conditions as far as it does not take into account a set of parameters, particularly, gas compressibility.

RESULTS

Combustion of round hydrogen microjet in a co-current air flow in subsonic conditions

Shadow images of the microjet combustion at variation of the hydrogen velocity (U_1, m/s) and of the coaxial air microjet (U_2, m/s) are presented in Figure 2. At increasing velocity of the co-current air flow, the "bottleneck-flame" region shrinks similarly to that at acceleration of the hydrogen microjet which was observed in Refs. [1-5]. One can see in Figure 2 (a-d) that the turbulent combustion is intensified downstream of the "bottleneck-flame" region at the speed

[1] Corresponding author. E-mail: litur@itam.nsc.ru

of axial air jet getting higher. The main features of subsonic diffusion combustion of a hydrogen microjet surrounded by a co-current air jet are similar to those we observed earlier in hydrogen microjets [1-5].

Combustion of round hydrogen microjet in the co-current flow of air with nanopowder in subsonic conditions

Shadow images of the diffusion combustion of round hydrogen microjet without concurrent air jet and with are presented in Figure 2 (e-f). In a case of co-current air jet with nanopowder (see figure 2f), picture illustrates the interaction of both jets at their combustion visualized by radiation.

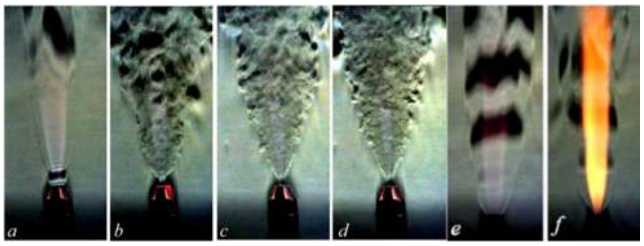

Figure 2. Shadow images of the hydrogen combustion modulated by the coaxial air jet at U_1 = 204 m/s and at variation of U_2 (m/s) as 0 (*a*), 9 (*b*), 18 (*c*), 26 (*d*); and without of coaxial jet U_1= 158m/s (*e*) and with U_1=158 m/s, U_2= 37.5 m/s (*f*)

CONCLUSION

Two options were considered including the concurrent flow of air and that of air seeded with nanoparticles. In the first case, the flame configuration is distinguished by the origination of "bottleneck-flame region" close to the nozzle exit. At variation of flow velocity, the spherically-shaped "bottleneck-flame region" turns into a cylindrical one. In conditions of supersonic combustion, the supersonic cells are generated both in the lifted hydrogen microjet and in the concurrent air flow.

In the other case of concurrent air flow premixed with nanopowder, the experimental data are also obtained at subsonic and transonic flow velocities. It was founded, that the scenarios of diffusion combustion in conditions of the concurrent flow are similar to those of the isolated hydrogen microjet. The origination of "bottleneck-flame" region at the nozzle exit is observed as well as the flame lift-off at increasing velocity of hydrogen. At the regime of "bottleneck-flame" region, the flame becomes deformed both in the center of microjet and in the concurrent flow. As it seen in figure 2f, the nanoparticles emanating from the coaxial slit are heated most of all in central area of hydrogen flow.

ACKNOWLEDGMENTS

This work was supported by the Russian Scientific Foundation, project no. 16-19-10330

References

[1] Shmakov A. G., Grek G. R., Kozlov V. V., Korobeinichev O. P. and Litvinenko Yu. A. 2015 *Vestnik NSU Series: Physics* **10** 27-41
[2] Litvinenko Yu. A., Grek G. R., Kozlov V. V., Korobeinichev O. P. and Shmakov A. G. 2015 *Vestnik NSU Series: Physics* **10** 52-66
[3] Grek G. R., Katasonov M. M., Kozlov V. V. and Litvinenko Yu.A. 2015 *Vestnik NSU Series: Physics* **10** 42-51
[4] Kozlov V. V., Grek G. R., Korobeinichev O. P., Litvinenko Yu. A. and Shmakov A. G. 2016 *Doklady Physics* **61** 457-62
[5] Shmakov A. G., Grek G. R., Kozlov V. V., Kozlov G. V. and Litvinenko Yu. A. 0120616 6 28-45

NUMERICAL RESEARCH ON DETONATION INITIATION FOR LOW-VOLATILITY LIQUID FUEL

Xiongbin Jia, Ningbo Zhao *,Xiao Liu, and Shizheng Liu
College of Power and Energy Engineering, Harbin Engineering University, Harbin, 150001, China

Summary Numerical analysis has been performed to characterize the detonation initiation for low-volatility liquid fuel with small diameter. Comparative analysis versus equivalent gaseous mixtures points out that the evaporation content of liquid fuel ahead of the flame plays a critical role at flame acceleration stage. Furthermore, detailed discussion on the flow field shows that several local detonations contribute a lot to the final stage of detonation transition. Results in present study provide theoretical guidance and explanation for future experiments.

INTRODUCTION

Tons of paper has been published to investigate the detonation initiation in gaseous system by theoretical, numerical and experimental methods in the past decades. However, the study of liquid-fueled detonation, which is believed more attractive for applications due to its high energy density per volume and easy storage, is still in its infancy due to the fact that the governing parameters of two-phase mixtures are far more than that of gaseous mixtures. In fact, apart from the chemical composition and initial pressure and temperature of the mixtures, particle parameters (e.g. particle size, shape and distribution) and complex multiple-phiysical processes including atomization, droplet breakup, partial vaporization before fuel burning are all important factors effecting the chracteristics of liquid-fueled detonation. Therefore, systematic study on liquid-fueled detonation only takes place in about 1950s. Since then, many pioneering researches have made unremarkable breakthroughs in two-phase detonation field [1].

It is now generally accepted that the detonation for high-volatile liquid fuel is premily similar to the hehavior in the equivalent gaseous system when the fuel droplet size is fine enough (smaller than 10μm). However, large-scale droplets will bring about large cell size and long reaction zone. On the one hand, large droplets inevitably increase the difficulty in initiation since the critical initiation energy increase proportionally to the third power of the cell width [2]; on the orther hand, long reaction zone may lead to detonation failure due to heat losses to the wall and incomplete combustion. Majority of previous researches focus on the characteristics of self-sustaining detonation wave, however, the liquid fueled detonation initiation mechanism still remains unclear, especially for low-volatility fuel.

Present numerical study aims to characterize the low volatility liquid-fueled detonation initiation. Perticularly, influencing factor of flame acceleration is researched and detonation transition process is analyzed in detail.

MODEL INTRODUCTION

1.5m long and 0.04m width obstructed channel with a blockage ratio of 0.35 filled with stoichoimetric gaseous air and liquid decane droplets are calculated by Eulerian and Lagrangian approach on the FLUENT platform under initial condition of 300K and 0.1Mpa. Assume that the droplets are all 20μm diameters and evenly distributed in the channel, and the initial laminar flame is ignited by a low energy input. In addition, one-step reduced reaction kinetic mode is used to predict the combustion, RANS based *k-ω* shear-stress transition model is employed to solve the turbulent flow. Especially, low speed flow is treated by PISO solver. The outlet boundary is set as pressure-outlet of 0.1MPa, and the remaining boundaries are adiabatic and no-slip boundary condition.

RESULTS ANALYSIS

Figure 1 shows the comparison of the time-dependent pressure variations of the monitoring point between the experiment [3] and present simulation with liquid fuel of n-heptanes due to the easily experimental availability. It can be seen that the deviation of pressure peak does not exceed 8.5%, validating the feasibility of current numerical strategy.

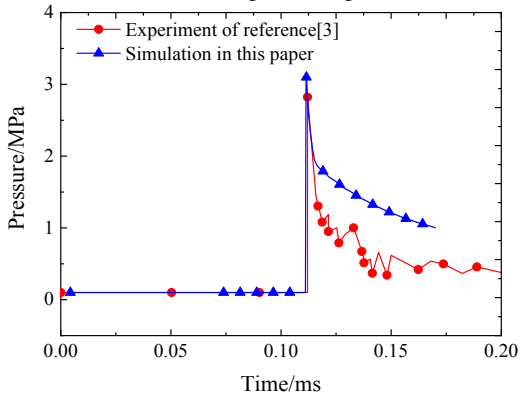

Figure 1. Comparison between experiment and simulation

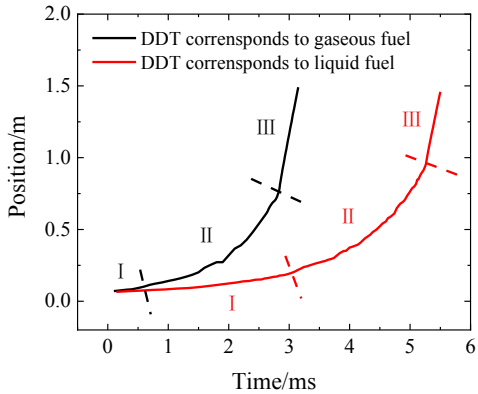

Figure 2. Time-dependent position variations of flame tip

*Corresponding author. E-mail: zhaoningboheu@126.com.

Figure 2 shows the position variations of the leading edge of flame with time of gaseous versus liquid decane system in the whole detonation initiation process, which can be divided into three stage consisting of (Ⅰ) liner flame development, (Ⅱ) exponential flame growth and (Ⅲ) stable detonation propagation stages according to the flame characteristics. Obviously, the biggest difference between two systems mainly comes from the first stage, where flame acceleration in liquid-fueled system looks much lower, and the exploration of the reason will be presented in Fig. 3.
Three frames in Fig. 3 represent the typical flame shapes (white line) with the corresponding n-decane vapor content in different stages as marked in Fig. 2, O_i represents the ith obstacle. Although the flame has been stretched into a turbulent state at the first stage, the majority of the n-decane vapor accumulates tightly around the flame surface, indicating that energy released from combustion are mainly used to break and heat the fuel droplets, which consequently restricts the flame development. On the contrary, plenty fuel droplets have been converted into vapor ahead of the flame under the action of strong shocks at the second stage, making the flame acceleration much analogous to that in the gas-phase system. Especially, the higher mass fraction of fuel vapor near the flame tip means a better compression of the evaporative mixtures, which could create larger energy density to greatly promote the exponential flame development. In the last stage, although there is almost no evaporative fuel before detonation wave since no shocks sweep over, detonation wave is strong enough to convert the droplet into vapor and simultaneously ignite it in an extremely short time.

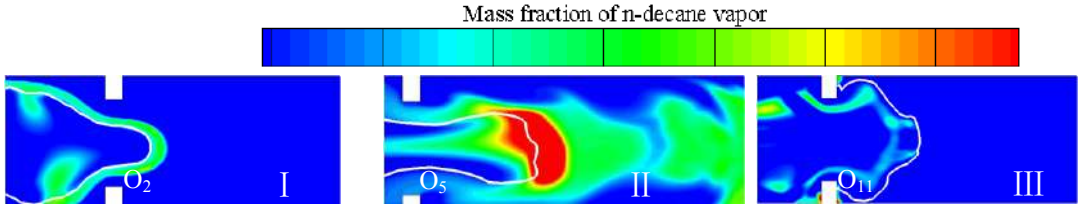

Figure 3. Mass fraction of evaporative n-decane

Figure 4 shows the typical process of liquid-fueled detonation transition. At 5232μs, the strong leading shock waves focus at the corner of the lower obstacle, triggering a local detonation (LD_1). This LD_1 quickly quenches when propagating at the narrow gap between the obstacle and oncoming flame due to insufficient fresh reactants supply, nonetheless, the flame is significantly enhanced. Similar, another local detonation (LD_2) appears at the corner of the upper obstacle and quenches just like LD1, see 5240μs. At 5260μs, the interaction of the flame and wall contributes to the formation of the LD_3. Unlike the former two, LD_3 quickly merges into the main flame, consequently, triggering an overdriven detonation coupled by leading shock and flame near the tenth obstacle at 5276μs, consistent with the classical Zeldovich gradient mechanism [4]. The OD, on the one hand, travels into the products as a retonation and decays into deflagration gradually; on the other hand, propagates forwards the reactants and attenuates into CJ detonation wave with a structure of triple-waves intersection including incident wave, Mach stem and transverse wave, see 5300μs.

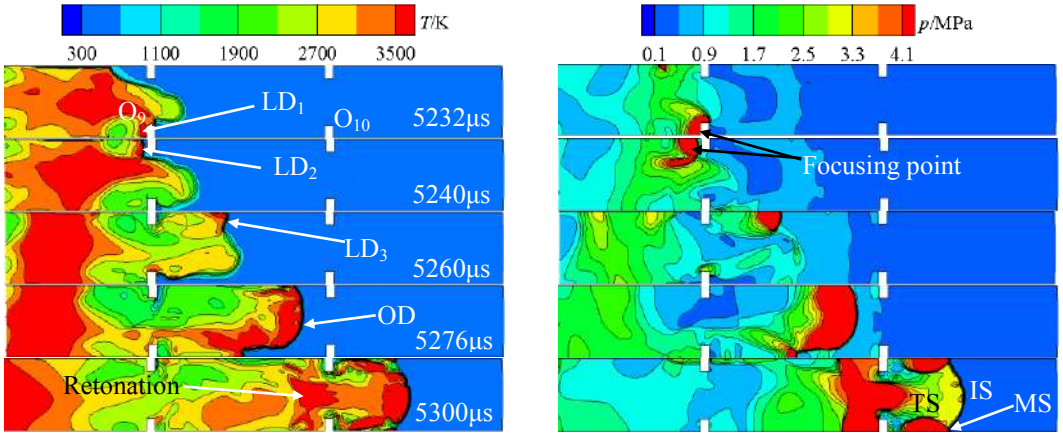

Figure 4. Flow field variations in detonation transition process

CONCLUTION

Detonation initiation for low-volatility liquid fuel is chracterized by numerical simulation in present study. Results show that the evaporation content of liquid fuel ahead of the flame plays a key role at flame acceleration stage and several local detonations contribute a lot to the final stage of detonation transition.

References

[1] Kailasanath K. Liquid-Fueled Detonations in Tubes. *J PROPUL POWER*. **22:** 1261-1268. 2006.
[2] Kaneshige M., and Shepherd J.E. Detonation Database, GALCIT Technical Report FM 1997.
[3] Jiang. T., Weng C.S. One-Dimension Euler-Lagrange Model and Simulation of Gas-Droplets Two Phase Detonation [J]. *COMPUT S* 2012.
[4] Zeldovich Y. B., Librovich V. B., Makhviladze G. M., and Sivashinskii G. I. On the Onset of Detonation in a Nonuniformly Heated Gas. *J. Appl. Mech. Tech. Phys.*, **11**: 264–270. 1970.

REALIZATION OF THE FILTERED TURBULENT FLAMELET MODEL ON DIFFUSION FLAME

Chi Zhang[1], Lipo Wang *[1], Jian Zhang[2], and Qun Hu[1]
[1] UM-SJTU Joint Institute, Shanghai Jiao Tong University, Shanghai, China
[2] Institute for Aero Engine, Tsinghua University, Beijing, China

Summary The interaction between flame and turbulence keep raising the challenges to the understanding of flame dynamics and performing simulations. In this project, a noval filtered flamelet model is proposed and examined in the framework of large eddy simulations (LES). The general methods of the simulation are developed, including the properties of the filtered flame equations and a four-dimensional flamelet tabulation, that incorporated with the LES subgrid models. Simulations are performed to justify the applicability of the modeling. Because of the involved flame model parameters can be directly calculated at the filter grid size level, and also crosspond to the solutions of the one-dimensional filtered governing equations, this model has the characteristic to reduce the unfounded uncertainty of the diffusion flame.

INTRODUCTION

In studying the structure of the filtered non-premixed turbulent flame at different filtering scale levels, Wang [1] derived a so-called filtered turbulent flamelet equation, where the differential relation between the filtered species mass fractions and the filtered mixture fraction is built. The objective of the current project is to develop and validate a new modeling idea based on the turbulent flamelet equation. First, the theoretical part is elaborated. Then the filtered flame structured is resolved and analyzed for the flamelet tabulation. Based on these setup, a turbulent jet flame is numerically investigated and preliminary results are presented.

FILTERED FLAMELET TABULATION

The governing equation for the filtered mixture fraction $\widetilde{Z}$ expressed:

$$\frac{\partial \bar{\rho}\widetilde{Z}}{\partial t}+\nabla\cdot(\bar{\rho}\widetilde{Z}\widetilde{\vec{u}})=\nabla\cdot[\bar{\rho}(D+D_T)\nabla\widetilde{Z}]=\nabla\cdot[\bar{\rho}\mathfrak{D}_T\nabla\widetilde{Z}], \tag{1}$$

and for the filtered species concentration $\widetilde{Y}_i$.

$$\frac{\partial \bar{\rho}\widetilde{Y}_i}{\partial t}+\nabla\cdot(\bar{\rho}\widetilde{Y}_i\widetilde{\vec{u}})=\nabla\cdot[\bar{\rho}(D_i+D_{T,i})\nabla\widetilde{Y}_i]+\overline{\omega_i}=\nabla\cdot[\bar{\rho}\mathfrak{D}_{T,i}\nabla\widetilde{Y}_i]+\overline{\omega_i} \tag{2}$$

Here $\bar{\cdot}$ and $\widetilde{\cdot}$ denote the filtered and density-weighted filtered quantities, respectively. Similar as the laminar flamelet, the turbulent scalar dissipation χ is defined as

$$\chi=2D_T\left(\frac{\partial\widetilde{Z}}{\partial n}\right)^2 \tag{3}$$

The one-dimensional counter flame structure is solved via Cantera [2] in physical space for the flamelet tabulation. Specifically, the fuel stream consists of methane and hydrogen with 1:1 volume ratio and the air stream functions as the oxidizer. The one-dimensional form of Eq. (1) and Eq. (2) together with the temperature equation

$$\bar{\rho}\frac{\partial\widetilde{T}}{\partial t}+\bar{\rho}\widetilde{u}\frac{\partial\widetilde{T}}{\partial x}=\frac{\partial}{\partial x}[\bar{\rho}(D+D_t)\frac{\partial\widetilde{T}}{\partial x}]-\sum_i W_i\widetilde{\omega}_i h_i \tag{4}$$

are numerically solved. The GRI-Mech 3.0 detailed mechanism is used as the chemical sources for the temperature and species equations. Specifically, the numerical procedure for the tabulation consists of the following steps.

1. For the counter flow flame with a preset strain rate a, first calculate the solution vector, from which the filtered source terms can be obtained at any filter length σ.
2. For a particular combination of the sub-filter diffusivity D_t and the filter length σ, calculate the coefficients of each term, e.g. $\widetilde{\rho}$, $\widetilde{\rho u}$, of the filtered temperature, mixture fraction and species equations. The mixture fraction can also be calculated from the species concentration using the Bilger formula.
3. Solve the linear system to obtain the filtered temperature $\widetilde{T}$, filtered species concentration $\widetilde{Y}_i$ and filtered mixture fraction $\widetilde{Z}$ at each grid point.
4. Loop over all preset D_t , σ and all possible a. (corresponding to maximum temperature T_{max} from 1750K to 2250K) and restore the solutions of all the cases in the physical space.

*Corresponding author. E-mail: Lipo.Wang@sjtu.edu.cn

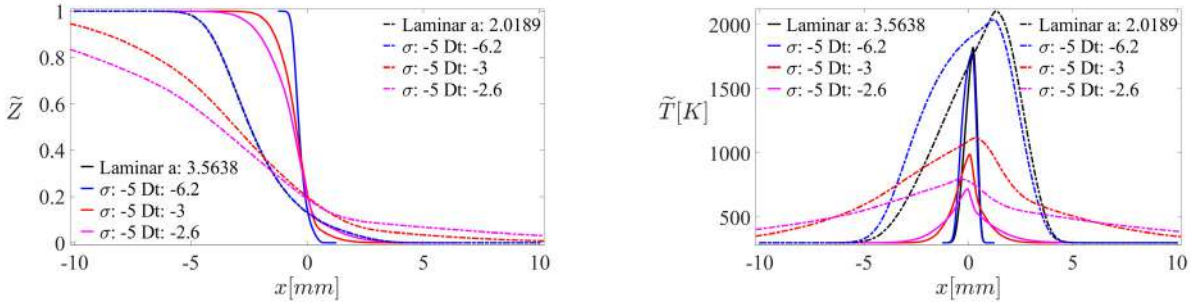

Figure 1: The effects of D_t on the filtered mixture faction $\tilde{Z}$ and the filtered flame temperature $\tilde{T}$ at different strain rate a. Here the values of D_t, σ and a are expressed in the base-10 logarithmic scale.

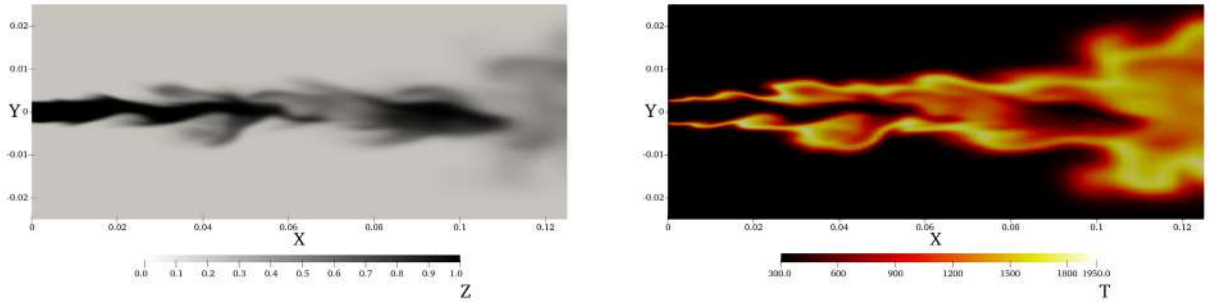

Figure 2: Contours of the calculated species fields: mixture faction $\tilde{Z}$ and the temperature temperature $\tilde{T}$

Once done, the flame solution will then be mapped into the lower dimensional space with the following involved parameters: the filtered mixture fraction $\tilde{Z}$, turbulent scalar dissipatoin χ, D_t and σ. In the post-processing code:
1. Calculate the turbulent scalar dissipation χ according to Eq. (3) at each point.
2. Mapping the filtered temperature $\widetilde{T}$, filtered species concentration $\widetilde{Y}_i$ and filtered density $\widetilde{\rho}$ to the four-dimensional look-up table.
3. The extremely large and small χ cases can be extrapolated from the existing solutions to fill up the flamelet table.

Figure 1 shows the filtered mixture faction and the temperature profile in the one-dimensional space. It can be seen that D_t have strong influences to the results. Overall, D_t and σ lead to the similar changes of the temperature profile. For a given strain rate, when D_t increases, the flame zones becomes thicker with the lower maximum temperature.

SIMULATION AND CONCLUSIONS

An open-source, finite-volume based OpenFOAM framework is used for the demonstrate simulation of a hot-jet. The pressure-based combustion solver *rhoReactingFoam* is chosen as the baseline code. This solver applies the hybrid algorithm, PIMPLE, for the pressure-velocity coupling. The density is directly calculated from the ideal gas state equation. We modified the code that the mixture fraction equation was implemented, and the species and energy equations were replaced by the lookup method described above. To perform the large eddy simulation, the subgrid stresses are closed by the standard k-equation subgrid-scale model [3]. The preliminary results are showed in Figure 2, which justify the promising potential for further improvements in turbulent combustion modeling and simulation. More quantitative and statisitical results, also the comparisons with the experiments, will be presented at the time of meeting.

This project aims to demonstrate the possibility of the numerical realization of the turbulent filtered flamelet model proposed by [1]. In the framework of large eddy simulations (LES), the general principles of the simulation have been developed. From the solutions of the filtered flame equation in the physical space, a four-dimensional flamelet tabulation was constructed and incorporated with the LES sub-grid models. The method was successfully implmented in the OpenFOAM framework, and stable results were obtained.

References

[1] Lipo Wang. Analysis of the filtered non-premixed turbulent flame. *Combustion and Flame*, 175:259–269, 2017.
[2] David G. Goodwin, Raymond L. Speth, Harry K. Moffat, and Bryan W. Weber. Cantera: An object-oriented software toolkit for chemical kinetics, thermodynamics, and transport processes. page https://www.cantera.org, 2018.
[3] Akira Yoshizawa and Kiyosi Horiuti. A statistically-derived subgrid-scale kinetic energy model for the large-eddy simulation of turbulent flows. *Journal of the Physical Society of Japan*, 54:2843–2839, 1985.

AN OPTIMIZATION ALGORITHM FOR OBTAINING GLOBAL KINETICS PARAMETERS BY USING FLAME DATA FROM SIMPLIFIED KINETICS

S M Ali *[1] and S Debnath[2]
[1] Department of Aerospace Engineering, Indian Institute of Technology, Madras, India
[2] Group Digital Transformation Office, Vedanta Limited, India

Summary The current work proposes an optimization algorithm for obtaining global kinetics parameters by performing a linear regression analysis on the flame data obtained from simplified kinetics. A two-step methane global kinetic model (DG) is optimized using this algorithm to demonstrate its applicability. A two-step methane global model (DG) is optimized using this algorithm for non-premixed flames data obtained from the simplified kinetic model (SALVI). The results showed that the optimized DG model (DG-Opt) has accurately captured the overall CH_4 and CO overall reaction rates in comparison to the simplified SALVI model.

BACKGROUND

Detailed or simplified kinetic mechanisms are developed to capture all the elementary processes and generally capable of capturing characteristics of both premixed and non-premixed flames. But, due to large number of species and reactions involved in their development, the direct use of these mechanisms in practical combustors is computationally expensive. On the other hand, global kinetic models are target-specific involving only few reactions and species, hence, require lesser computational time in comparison to detailed/simplified kinetics. This work focuses on the development of the optimization approach for obtaining global kinetic parameters by using flame data from simplified kinetics.

Figures 1a and 1b show the comparison CH_4 and CO overall reaction rates from DG global (Dryer & Glassman, 1973) and SALVI simplified (Slavinskaya et al., 2008) kinetic models near extinction of $50CH_450N_2$-air non-premixed flames. The data clearly show that the reaction rates of CH_4 and CO are not accurately captured from the two-step global kinetic model (DG). Hence, the DG model (Rxn1- $CH_4+O_2 \rightarrow CO+2H_2O$ & Rxn2- $CO+0.5O_2 \rightarrow CO_2$) has scope for optimization. The next sections describes the optimization process.

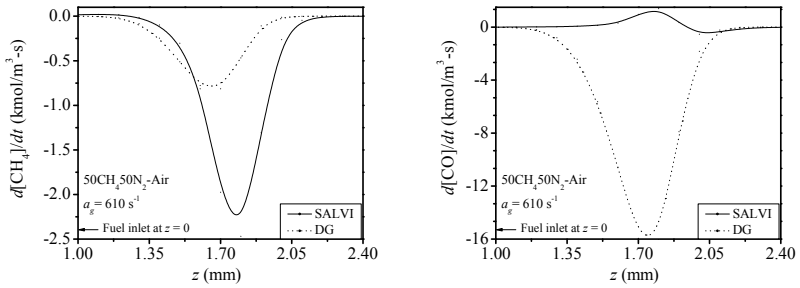

(a) CH_4 reaction rate (b) CO reaction rate

Figure 1: Comparison pf CH_4 and CO overall reaction rates from global (DG) and simplified (SALVI) kinetic model near extinction

OPTIMIZATION ALGORITHM

Figure 2 shows the flowchart for the algorithm used to perform optimization of global kinetic parameters. The concentration, temperature and reaction rates data in the flame region obtained from simplified kinetics are used to train a linear fit model for global kinetics. For model optimization, the initialized global parameters are varied to obtain an error matrix. The minimum root mean square error (RMSE) and maximum R-square (R2) is located to obtain the optimized parameters. These initial optimized models (R2 or RMSE) are improved further by removing outliers beyond 95 % prediction interval. To test the applicability, a two-step global methane kinetic model is optimized using this algorithm The subsequent section shows results of this optimization.

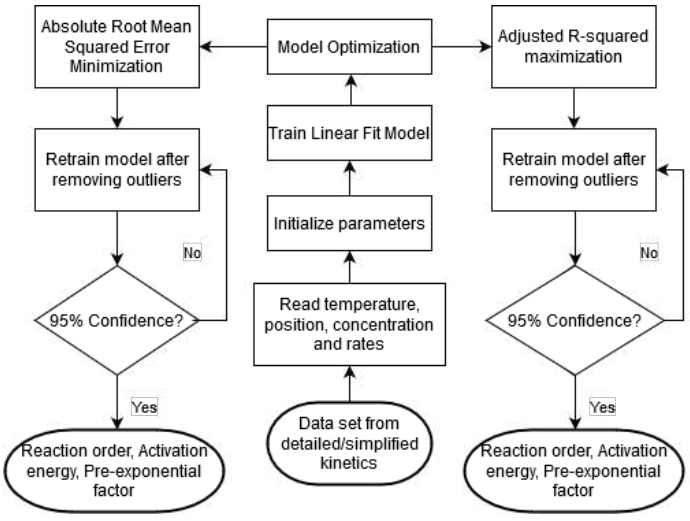

Figure 2: Flowchart for the optimization algorithm

*Corresponding author. E-mail: smughees.ali@gmail.com

RESULTS AND DISCUSSION

Figures 3a and 3b show the comparison of CH_4 and CO overall reaction rates from unoptimized (DG) and optimized (DG-Opt) with simplified (SALVI) kinetic model near extinction of CH_4-air non-premixed flame. The data show that consumption reaction rates for CH_4 and CO are accurately captured by the optimized kinetic model (DG-Opt).

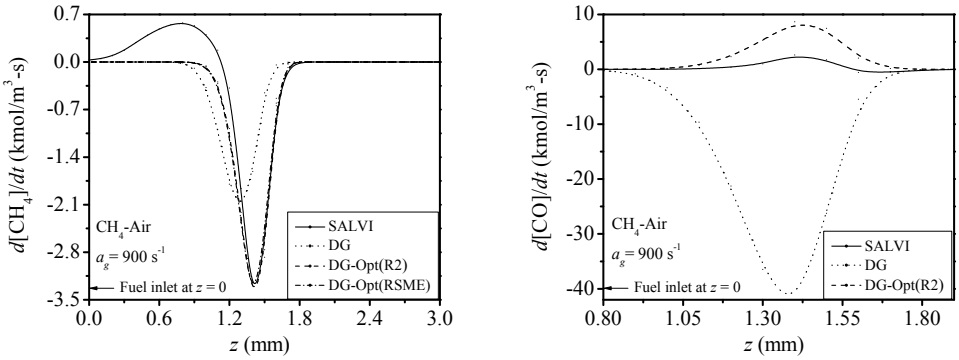

(a) CH_4 reaction rate (b) CO reaction rate

Figure 3: Comparison of CH_4 and CO overall reaction rates from unoptimized (DG) and optimized (DG-Opt) with simplified (SALVI) kinetic model near extinction of $100CH_4$-air non-premixed flame

The data from the simplified kinetics model (SALVI) show production of CH_4 on the fuel-rich side of the flame. This might be due to reverse CH_4 reaction accelerated by diffusion of radicals from the stoichiometric flame region. As the DG-Opt model is developed to capture only the forward reaction rates, its results deviate from the simplified kinetics (SALVI) in fuel rich region. But, the forward rates are accurately captured. For CO reactions, DG-Opt model has accurately capture the reaction rate trends for simplified model. The global parameters of the optimized model are compiled in the Table 1.

Table 1: Global kinetic rate parameters and reaction order for the optimized kinetic model (DG-Opt)

Model	A	n	E_a	Reaction order	A	n	E_a	Reaction order
	R2				RMSE			
$CH_4 + O_2 \rightarrow 2H_2O + CO$	$10^{14.91\pm0.33}$	0	269715±10627	$[CH_4]^{0.2}[O_2]^{1.6}$	$10^{11.81\pm0.36}$	0	253641±11320	$[CH_4]^{0.1}[O_2]^{1.0}$
$CO + 0.5O_2 \rightarrow CO_2$	$10^{11.93\pm0.29}$	0	230502±9091	$[CO]^{0.1}[O_2]^{1.1}[H_2O]^{0.1}$	$10^{10.48\pm0.33}$	1	219212±10444	$[CO]^{0.1}[O_2]^{0.8}[H_2O]^{0.1}$

Units in J, kmol, m^3, s and K.

CONCLUSIONS

The comparison of the global (DG) kinetic model with simplified (SALVI) kinetic model has shown that DG does not accurately capture the rates of CH_4 and CO oxidation. This is due to the use of specific conditions (T ~1100-1400 K; ϕ ~0.05-0.5) for construction of DG model from Plug Flow Reactor (PFR) data. In the case of non-premixed flame, the conditions for fuel oxidation are different from PFR. Hence, the DG model optimized using the data generated from the simplified model under non-premixed flames conditions improved the predictions. This conclusion related to non-premixed flames is also supported by the recent studies of Ali and Varunkumar (2019,2020). The accurate reaction rates prediction from the DG-Opt model has demonstrated the effectiveness of the proposed optimization algorithm. Future work involves the use of this algorithm for obtaining global parameters for other fuel-oxidizer combinations.

References

[1] Dryer F. and I Glassman. High-temperature oxidation of CO and CH_4, *Symposium (International) on combustion,* **14(1)**: 987-1003, 1963.

[2] Slavinskaya, N., M. Braun-Unkhoff, and P. Frank. Reduced reaction mechanism for methane and syngas combustion in gas, *Journal of engineering for gas turbines and power,* **130(2)**: 021504, 2008.

[3] Ali, S M.,Varunkumar, S. Preliminary results on syngas kinetic mechanism optimization using the new Opt-D* algorithm, *11^{th} international conference on chemical kinetics*, (2019).

[4] Ali, S M., Varunkumar, S. A three-step global kinetic mechanism for predicting extinction strain rate of syngas-air non-premixed flames, *Combustion Science and Technology,* (accepted).

COMBINED PHYSICS AND DATA-DRIVEN MODAL DECOMPOSITION OF COMPLEX COMPRESSIBLE FLOWFIELDS

Datta V. Gaitonde *[1] and S. Unnikrishnan[2]
[1] Mechanical and Aerospace Engineering, The Ohio State University, Columbus, OH
[2] Aero-Propulsion, Mechatronics and Energy, Florida State University, Tallahassee, FL

Summary High-fidelity simulations can provide all pertinent details of compressible turbulent fluctuations in complex flowfields. However, comprehending the driving physics remains a major challenge, and motivates the development and implementation of new innovative analysis techniques. Here, we summarize a powerful methodology that integrates physics-based and data-driven decompositions. The former, performed with Doak's method, yields an exact splitting of a carefully chosen vector fluctuation quantity into its hydrodynamic, acoustic and thermal components. In addition to extracting insights into driving mechanisms, these components are also superior inputs to data-driven techniques such as Dynamic Mode Decomposition and Spectral Proper Orthogonal Decomposition. 3-D results on jet noise and hypersonic transition databases illustrate the power of this combined approach.

DECOMPOSITION OF COMPRESSIBLE FLUCTUATIONS

The analysis of turbulent fluctuations has typically taken recourse to data-driven statistical techniques, which include different types of space-time correlations and modal decompositions such as variants of Dynamic Mode Decomposition (DMD) and Proper Orthogonal Decomposition (POD), all of which are agnostic of the underlying physics. The variables subjected to such approaches are often the primitive variables, or combinations of their local derivatives. Physics insights are then extracted in the context of larger scale dynamics such as different types of instabilities or energy transfer mechanisms. The results are often interpreted in a physics-based, or fluid-thermodynamic (FT), framework that has its origin in Kovásznay's decomposition [1] comprised of hydrodynamic (H), acoustic (A) and thermal (T) content and their interactions with each other.

Though conceptually powerful, the direct use of Kovásznay's method has been constrained by the difficulty in extension to non-linear fluctuations or non-uniform mean flows. The method of Doak [2] lifts these constraints using a very different approach applicable to any turbulent flow. The key distinction is that whereas Kovásznay's method associates a particular variable with each FT component (fluctuating vorticity ω' with H, pressure p' with A and entropy s' with T), Doak's method decomposes a single, carefully selected variable consistently and exactly into its three FT components, where H is rotational (solenoidal), A is irrotational-isentropic and T is irrotational-isobaric. The decomposed variable is the vector "momentum density", $\rho(\boldsymbol{x},t)\boldsymbol{u}(\boldsymbol{x},t)$, chosen because the continuity equation is naturally linear in this composite variable. This avoids the difficulty arising from associating p' solely with A, since p' also has H content. Doak's procedure then splits $(\rho\boldsymbol{u})' = (\rho\boldsymbol{u})'_H + (\rho\boldsymbol{u})'_T + (\rho\boldsymbol{u})'_A$. This requires the solution of Poisson equations; for example, $(\rho\boldsymbol{u})'_A = -\bigtriangledown\psi'_A$ where ψ'_A is obtained from $\bigtriangledown^2\psi'_A = \frac{1}{c^2}\frac{\partial p'}{\partial t}$. Computational implementation details for Large Eddy Simulation (LES) databases, with boundary treatments, are discussed in [3]. A second crucial aspect of Doak's formulation follows from its foundation in the full Navier-Stokes equations: specifically, in the non-linear turbulent region of any flow, the sources/sinks in the three FT components due to the fluctuating Lamb vector, viscous and entropic interactions can be explicitly delineated through the budget of the total fluctuating enthalpy, TFE $= (h + 0.5\boldsymbol{u}\cdot\boldsymbol{u})'$. This provides insight into various causal mechanisms, including intermittency, that can be obscured with typical statistical techniques.

Although the exact FT decomposition provides a powerful new method to analyze compressible fluctuations, substantial additional advantages accrue from applying data-driven techniques such as DMD or POD to the FT variables, as opposed to directly obtained variables such as p' or ω'. This is now illustrated in two problems, jet noise and hypersonic transition, where a Kovásznay-type viewpoint arises naturally and illustrates the dynamics in a very revealing fashion.

RESULTS

Jet noise: The following LES-based results are representative of jets at subsonic as well as supersonic Mach numbers. Figure 1(a) shows the multi-scale nature of the turbulence in typical turbulent jets, together with the radiation field (variables plotted and conditions are noted in the figure). Even though the acoustic energy is only a small fraction of the overall energy, its dynamics are crucial because of their relatively large impact on humans and structures. Representative $A_x = (\rho u)'_A$ and pressure (p') iso-levels are shown in (b); the key point to note is the compact and highly-organized wavepacket nature of the former, which should be representable with a low-ranked model. Indeed, the spectral POD decomposition of A_x in (c) confirms this postulate: the first three modes contain $\sim 75\%$ of the energy for A_x, but only $\sim 45\%$ for p'. This has profound consequences on the advantages of using A_x instead of p', two of which are shown. First, the sources to ψ'_A (performed through a TFE analysis) are restricted to $r \leq 1D$ from the jet axis. Thus, using A_x at a surface as close as $r = 1.5D$ as input to a simple wave-propagator provides an excellent prediction of the farfield noise: in this region of no significant acoustic energy production, it can be shown that ψ'_A and p' satisfy a simple scaling relationship. This close propagator surface placement is a major accuracy and efficiency benefit to LES, since it facilitates

*Corresponding author. E-mail: gaitonde.3@osu.edu

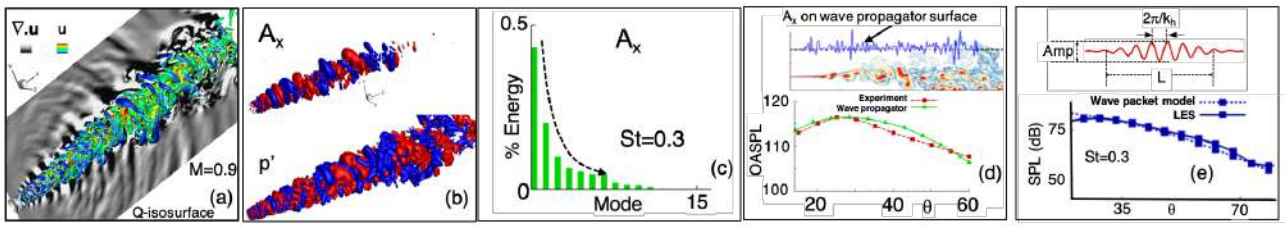

Figure 1: Combined FT and SPOD for superior far field and wavepacket modeling

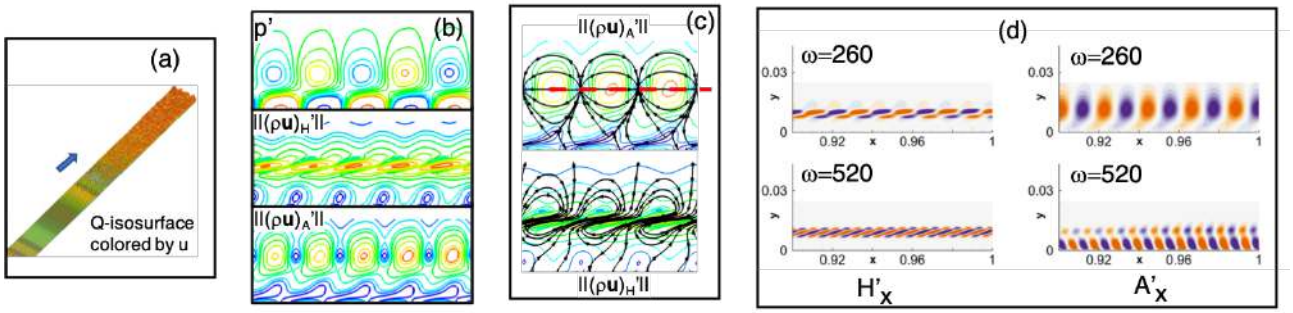

Figure 2: Combined FT and DMD for hypersonic transition

a substantial reduction to the simulation domain. Second, the fact that unlike p', ψ'_A is free from hydrodynamic content greatly improves its utility in developing wavepacket models. (e) shows how parameters such as k_h, Amplitude (Amp) and L, when extracted from A_x provide accurate noise prediction even for subsonic flows, where the use of p' requires empirical adjustment.

Hypersonic transition and breakdown: The second (or Mack) mode that emerges in hypersonic transition is especially suited for analysis with FT decomposition because of the crucial importance of acoustic energy [4], and here too, sequential application of physics-based and data-driven techniques provides a richer perspective. Figure 2(a) shows a qualitative picture of the breakdown, starting from regular imposed perturbations that grow linearly and induce transition and breakdown. (b) shows the crucial distinctions between the primitive and FT variables using the p', $||\,(\rho\boldsymbol{u})'_H\,||$ and $||\,(\rho\boldsymbol{u})'_A\,||$ fields. As in the jet case, there is only a superficial similarity between p' and A, especially in the crucial near-wall region. Their respective flux lines in (c) show that the A field exhibits trapped behavior between the critical layer and the wall, but the H field does not. Further quantitative analysis shows that although A is much smaller than H or T, its rate of amplification dominates 2nd mode growth – this crucial feature is masked by traditional variables. Furthermore, since T is also a trapped component[5], the 2nd mode is very sensitive to small changes in temperature or wall heating. This has consequences on control: the acoustic component can be used to guide actuator development. The exact nature of the FT decomposition makes it amenable for application in the non-linear breakdown region downstream as well. Here, the appearance of harmonics can be described by performing (data-driven) DMD on the individual FT fields. The results, (d), show clearly that the first superharmonic of $H_x = (\rho u)'_H$ has spatial support near the critical layer, while that for A_x appears near the wall. When combined with the more rapid growth of the latter, the evidence clearly suggests that the near-wall dynamics is more crucial than that near the critical layer.

CONCLUSIONS

There is considerable benefit to analyzing high-fidelity compressible turbulent simulations by first decomposing fluctuations into their acoustic, hydrodynamic and thermal components, and then subjecting these to data-driven statistical techniques. The form of the Navier-Stokes equation allows for a precise decomposition of $\rho\boldsymbol{u}$ (but not any arbitrary variable) in this fashion, and also provides means, through total fluctuating enthalpy budgets, to gain insight into sources and sinks of FT components. Results from two complex 3-D problems illustrate these benefits in combination with SPOD and DMD. The jet noise data was provided courtesy of G. Brés (Cascade Technologies).

References

[1] Kovásznay, L. S. G. *J. Aeronaut. Sci.* **20**: 657–682, 1953.
[2] Doak, P. E. *J. Sound Vib.*, **131**: 67–90, 1989.
[3] Unnikrishnan, S. and Gaitonde, D. *J. Fluid Mech.*. **800**: 387-432, 2016.
[4] Fedorov, A. V. *Annu. Rev. Fluid Mech.*, **43**: 79-95, 2011.
[5] Unnikrishnan, S. and Gaitonde, D. *J. Fluid Mech.*. **868**: 611-647, 2019.

FLOW MECHANICS OF DUAL-PULSE LASER-INDUCED BREAKDOWNS AND EFFECT ON IGNITION

Jonathan M. Wang *[1] and Jonathan B. Freund[1,2]
[1] Department of Mechanical Science and Engineering, University of Illinois at Urbana–Champaign, USA
[2] Department of Aerospace Engineering, University of Illinois at Urbana–Champaign, USA

Summary A focused laser can cause optical breakdown of gas into a nearly opaque plasma that efficiently absorbs subsequent laser energy. The rapid heating produces a blast wave and intricate hydrodynamic interactions that depend on the distribution of deposited energy. How subtle alterations in the hot-spot shape lead to pronounced changes in the later hydrodynamics, how multiple depositions interact to augment vorticity generating mechanisms, and how these flow characteristics ultimately mediate ignition of a combustible mixture are all investigated.

INTRODUCTION

Laser-induced breakdown offers an attractive approach for ignition systems because it provides a versatile means of depositing both energy and radical species [3]. The energy deposition drives complex local flow, which can couple with the ignition process. For some conditions gas is ejected from the focal region [1, 2], which distributes energy, creates strains on nascent flames, and increases the kernel surface area. Multiple such breakdowns can enhance ignition probability [5, 6]; the fluid mechanics underlying this are investigated.

Detailed simulations are used to analyze the post-breakdown flow, particularly the mechanisms of vorticity generation, for both single and dual-pulse cases. A secondary pulse can be used to access a broad range of hydrodynamic responses by exploiting energy otherwise lost in the shock and accentuating asymmetries associated with single-pulse ejections. The burning rate of the flame kernel in a lean H_2–O_2 mixture can be increased by controlling configuration parameters.

METHODS

The axisymmetric Navier–Stokes equations, initialized with a kernel length $L = 2\,\mathrm{mm}$, ambient speed of sound a_∞, density ρ_∞, and viscosity μ, are solved with high-order methods for a perfect gas with constant transport properties, specific heat ratio $\gamma = 1.4$, and Reynolds number $\mathrm{Re} \equiv \rho_\infty a_\infty / \mu = 4.4 \cdot 10^4$ corresponding to air at $p_\infty = 1\,\mathrm{atm}$ and $T_\infty = 298\,\mathrm{K}$. These modeling choices void complexity of the true plasma characteristics yet are sufficient to reproduce key flow features for single-pulse breakdowns [4].

RESULTS

With its kinetic energy only a small fraction of the total deposited energy, the breakdown-induced flow can be sensitive to even small alterations in the early-time kernel geometry, particularly asymmetries during the kernel's rapid expansion [4]. The dynamics of the resultant vorticity, generated baroclinically by this expansion, determine the ultimate ejection pattern, which varies markedly with subtle changes to the kernel and in some cases reverses direction.

The flow is significantly altered by a nearby secondary kernel, as shown in figure 1. This small simultaneous deposition produces low-density gas that promotes the expansion of the primary kernel, leading to generation of positive vorticity that suppresses the ejection otherwise produced by the primary kernel alone.

A time delay τ and spatial offset d broadens the range of hydrodynamic responses (figure 2). These follow from three effects: (1) passage of kernel II's shock through kernel I, (2) biased expansion of kernel II near kernel I, and (3) evolution of kernel II in the post-shock rarefaction of kernel I. The second effect is shown in figure 3 for the figure 2(d) case. The leftward protrusion of kernel II near $r = 0$, an artifact of its expansion towards the low-density remnants of kernel I, leads to pronounced flow into the narrowed inter-kernel gap. The flow diverges at a stagnation point in this dense fluid (figure 3b), and the ensuing rightward flow near $r = 0$ (figure 3c), absent in the single-pulse case, opposes the concurrent leftward flow in kernel II. This effect leads to kernel II's suppressed ejection in figure 2(d) as well as the ejections in opposite directions in figure 2(c).

These effects occur in tandem with baroclinic generation of vorticity that would produce a leftward ejection for a single pulse [4]. The curious $d \lessgtr 0$ asymmetry can be traced to the kernels' own asymmetry: the leftward ejection of kernel I is augmented by kernel II's shock for $d > 0$ and suppressed for $d < 0$, while that of kernel II is augmented by the post-shock rarefaction of kernel I for $d > 0$ and suppressed for $d < 0$.

In corresponding simulations of ignition in a lean H_2–O_2 mixture (not shown), the figure 2(c) configuration produces H_2O 47% faster than that of figure 2(a) and 2.2 times faster than a single pulse of equal energy, due to the broad distribution of hot gas.

*Corresponding author. E-mail: jmwang2@illinois.edu

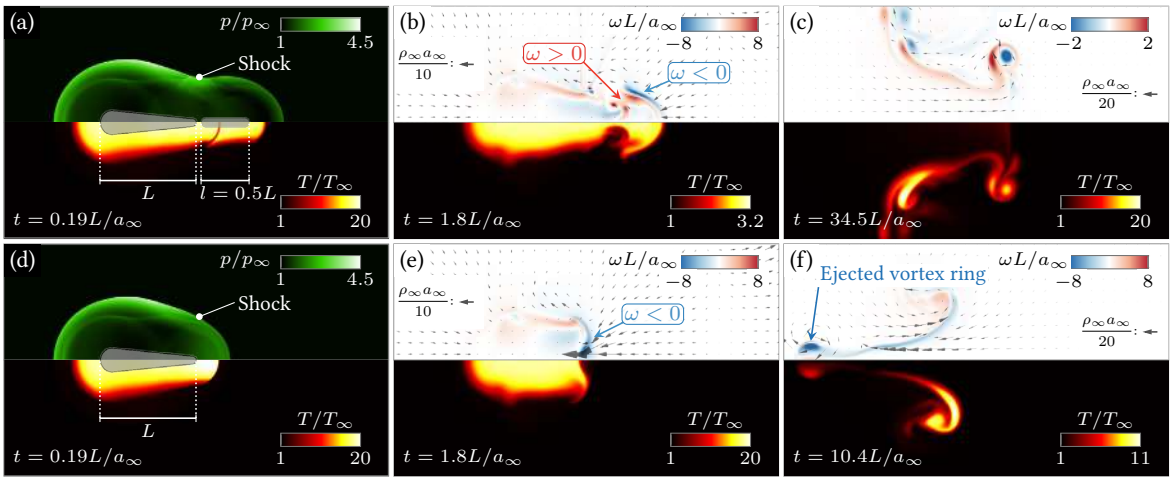

Figure 1: Flow produced by (a–c) dual pulses and (d–f) a single pulse. Vectors represent $\rho\vec{u}$ and $\omega = \partial u_r/\partial x - \partial u_x/\partial r$. Initial kernels are shown in grey.

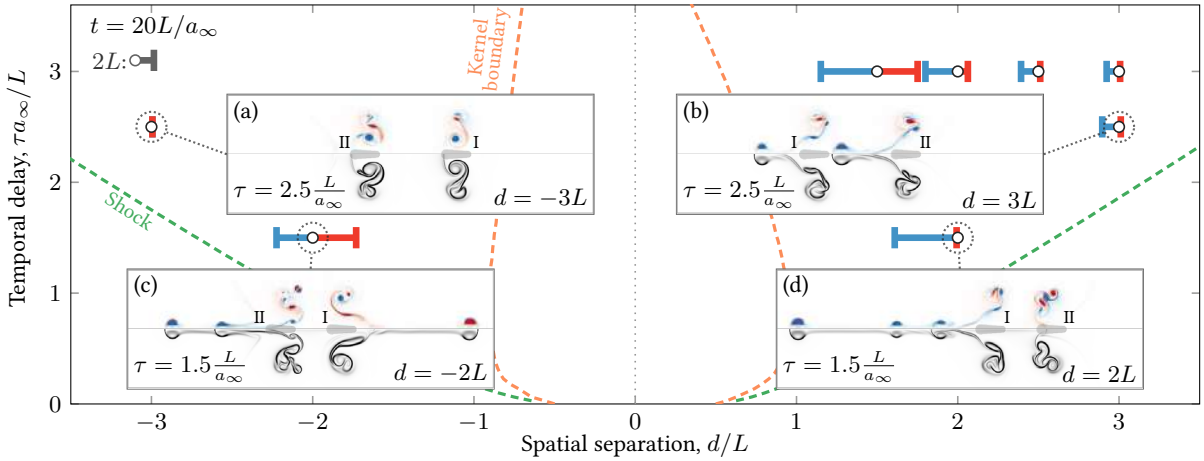

Figure 2: Flow pattern at $t = 20L/a_\infty$, visualized by ω and $|\nabla\rho|$. At each (d, τ), the lines represent the axial transport of hot gas: the blue (red) line corresponds to the leftmost (rightmost) location of $T > 2T_\infty$ gas relative to the left (right) kernel's initial position, shown in grey. The x–t trajectory of the $r = 0$ axial extents of the kernel boundary and shock for a single pulse are plotted for reference.

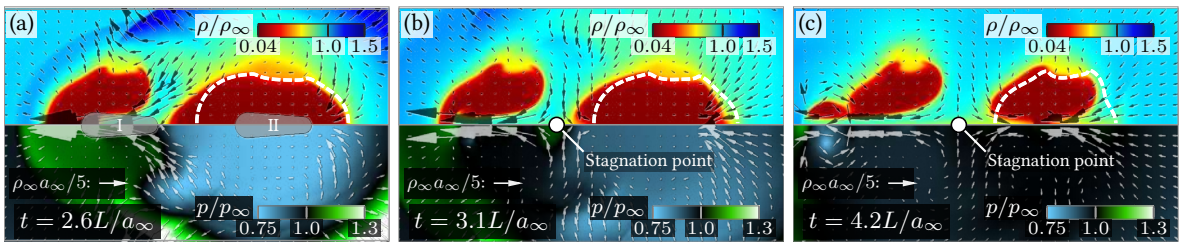

Figure 3: Flow at times (a) $2.6L/a_\infty$, (b) $3.1L/a_\infty$, and (c) $4.2L/a_\infty$ for $d = 2L$, $\tau = 1.5L/a_\infty$. The $\rho = 0.3\rho_\infty$ contour for the corresponding single-pulse case is indicated by the dashed white line. Vectors indicate $\rho\vec{u}$.

This material is based in part upon work supported by the Department of Energy, National Nuclear Security Administration, under Award Number DE-NA0002374.

References

[1] N. G. Glumac, G. S. Elliott, and M. Boguszko. Temporal and spatial evolution of a laser spark in air. *AIAA J.*, 43(9):1984–1994, 2005. doi: 10.2514/1.14886.

[2] S. S. Harilal, B. E. Brumfield, and M. C. Phillips. Lifecycle of laser-produced air sparks. *Phys. Plasmas*, 22(6):063301, 2015. doi: 10.1063/1.4922076.

[3] T. X. Phuoc. Laser-induced spark ignition fundamental and applications. *Optics and Lasers in Engineering*, 44(5):351–397, 2006. doi: 10.1016/j.optlaseng.2005.03.008.

[4] J. M. Wang, D. A. Buchta, and J. B. Freund. Hydrodynamic ejection caused by laser-induced optical breakdown. *To appear in J. of Fluid Mech.*, 2020.

[5] L. Wermer, J. K. Lefkowitz, T. Ombrello, and S.-K. Im. Ignition enhancement by dual-pulse laser-induced spark ignition in a lean premixed methane-air flow. *Proc. of the Combust. Inst.*, 37(4):5605–5612, 2019. doi: 10.1016/j.proci.2018.06.025.

[6] H. Zhao, N. Zhao, T. Zhang, S. Wu, G. Ma, C. Yan, and Y. Ju. Studies of multi-channel spark ignition of lean n-pentane/air mixtures in a spherical chamber. *Combust. Flame*, 212:337–344, 2020.

ROLE OF THE RECIRCULATION BUBBLE DYNAMICS ON THE UNSTEADINESS OF THE SHOCK WAVE BOUNDARY LAYER INTERACTION.

Ismaïl Ben Hassan Saïdi *[1], Christian Tenaud †[1], and Guillaume Fournier[2]
[1] Université Paris-Saclay, CNRS, LIMSI, 91400, Orsay, France.
[2] Université Paris-Saclay, Univ Evry, LMEE, 91020, Evry, France.

Summary The aim of the present work is to contribute to a better understanding of the physical mechanism causing the low frequency oscillations of the Shock Wave Boundary-Layer Interaction (SWBLI) by analyzing data from highly resolved unsteady numerical simulations. Results show that the low frequency reflected shock-wave motion is mainly driven by the low frequency breathing of the separation bubble that comes from a modulation of the successive enlargements and shrinkages of the separated zone (medium frequency flapping of the shear-layer); the oscillations of the reflected shocks foot being in phase with the motion of the separation point.

INTRODUCTION

The Shock-Wave Boundary-Layer Interaction (SWBLI) is a recurrent physical phenomenon present in aeronautical and space systems. If the shock wave is strong enough, the subsequent adverse pressure gradient can lead to a separation of the boundary layer. A separation bubble is then created surrounded by a complex system of shock waves. The highly 3-D separation bubble leads to a steep increase of the drag force, heat fluxes and pressure fluctuations at the wall. Previous studies have additionally shown that the recirculation bubble as well as the reflected shock wave are subjected to a low frequency streamwise motion called the unsteadiness of the SWBLI. This unsteadiness subjects structures to oscillating loads that can damage their integrity, justifying the importance of a careful study of SWBLIs and particularly its low frequency unsteadiness.

Even if this phenomenon is well known, the mechanism leading to the SWBLI unsteadiness is still not well understood. Mainly two kind of mechanisms have been referred to in order to explain the existence of the SWBLI unsteadiness [1]. The first one consists in an excitation of the SWBLI by the large scales of the incoming turbulent boundary layer. The second one is provoke by the dynamics of the recirculation zone that drives the unsteadiness of the whole SWBLI system. Despite arguments in favor of each mechanism, no definitive explanation have been yet provided. The aim of the present work is then to perform well resolved DNS of SWBLIs and analyze results in order to contribute to a better understanding of the SWBLI unsteadiness and the physical mechanism causing these low frequency oscillations. To this end, the canonical configuration of an oblique shock wave impinging a boundary layer developing on a flat plate is considered.

NUMERICAL APPROACH

The Navier-Stokes equations are solved by using a high order finite volume approach on cartesian meshes. The Euler part is discretized by means of a high-order one-step Monotonicity Preserving scheme, namely the OSMP7 scheme [2], based on a Lax-Wendroff approach, which ensures a 7th-order accuracy in both time and space in the regular regions. Monotonicity-Preserving (MP) constraints, first developed by Suresh and Huynh [3] and further extended in [2], are applied; they locally relax the TVD constraints near extrema. The resulting OSMP7 scheme recovers the 7th-order accuracy in both time and space everywhere, except near discontinuities where the scheme is Monotonicity-Preserving. Besides, the discretization of the diffusive fluxes is obtained by means of a classical centered 2nd-order scheme. These numerical schemes are implemented in the in-house parallel (MPI) Finite Volume DNS solver (code CHORUS) that has been developed at LIMSI-CNRS. This numerical tool has intensively been validated on the simulation of high Reynolds number turbulent and shocked flows [5]. Results demonstrate the correct accuracy of the numerical approach to predict turbulent features and the great efficiency of the MP procedure to capture discontinuities without spoiling the solution at an almost negligible additional cost (at most 2.5 %).

RESULTS ON SWBLI CONFIGURATIONS

In order to better understand the mechanisms leading to the unsteadiness of the SWBLI, it has been chosen to first perform a SWBLI simulation suppressing one of the two suspected mechanisms leading to the unsteadiness. By simulating the interaction between a *laminar* boundary layer and an incident oblique shock wave, the suspected influence of the large scale turbulent structures within the incoming boundary layer on the SWBLI unsteadiness has been suppressed. The only remaining suspected cause of the unsteadiness would be the dynamics of the separation bubble.

Shock-Wave Laminar Boundary-Layer Interaction:

We first chose to simulate a 3-D test-case similar to the one designed by Degrez *et al.* [4] ($M_\infty = 2.15$; $Re_{x_{sh}} = 10^5$) with however a higher shock angle ($\sigma = 33.8°$) to recover an unsteady behavior of the recirculation bubble that exhibits 3-D flow patterns. Results (Fig. 1-left) have shown that the separation point of the recirculation bubble and the foot of the reflected shock wave have a fixed location along time. This result shows that, in this configuration, the SWBLI unsteadiness has not been observed. Analyses of the dynamics of the recirculation bubble has been performed. Two

*Present address: DynFluid, Arts & Métiers ParisTech, 151 Bd de l'Hôpital, 75013 Paris, France
†Corresponding author. E-mail: Christian.Tenaud@limsi.fr

regions have been identified in the recirculation bubble: the first part of the separation, upstream of the incident shock wave impingement and the second part downstream of the impingement. Although SWBLI unsteadiness has not been observed (no motion of the reflected shock wave), the characteristic low frequency of the SWBLI unsteadiness has however been recorded that characterizes the dynamics of the whole recirculation bubble: low frequency breathing ($St_L \simeq 0.03 - 0.04$) of the recirculation bubble and medium frequency flapping ($St_L \simeq 0.12 - 0.15$) of the shear layer in whole of the bubble, in addition to higher frequencies ($St_L \simeq 0.5 - 0.6$) characterizing the vortex shedding from the shear layer in the second part of the recirculation bubble. In particular, the reattachment location is sensitive to the instabilities of the recirculation bubble, namely the breathing, the flapping and the Kelvin-Helmholtz frequencies. Even though present in the first part, the low frequency activity is not intense enough to provoke the oscillations of the separation point and the subsequent oscillations of the reflected shock foot.

Shock-Wave Turbulent Boundary-Layer Interaction:

In order to reproduce and analyze the SWBLI unsteadiness, the simulation of the interaction between a incident shock wave and a *turbulent* boundary layer has secondly been undertaken (Fig. 1-right). In this context, the accurate simulation of a turbulent compressible incoming boundary layer is of great importance. A Synthetic Eddy Method (SEM) (Jarrin et al. [2006]) that we adapted to compressible flows, has efficiently been employed at the inlet boundary to generate a fully developed flat plate turbulent boundary layer ($M_\infty = 2.33$; $Re_\theta = 2539$) upstream of the impingement of the oblique shock-wave without a prohibitive additional computational cost. In the turbulent case, the SWBLI unsteadiness has clearly been recorded. The frequencies characterizing motion of the reattachment point are characteristic of the low ($St_L \simeq 0.03 - 0.04$) and medium frequency flapping ($St_L \simeq 0.12 - 0.15$) of the separation zone, while the frequencies of the separation point are characteristic of the low frequency flapping of the separation zone. Besides, the foot of the reflected shock wave oscillates in phase with the separation point. Motions of separation and reattachment points are mainly in opposite phase indicating successive enlargements and shrinkages of the recirculation bubble; the shrinkage phase being associated with a shedding of a large amount of fluid from the separated zone to downstream. This medium frequency flapping have been shown to be irregular in time; the maximum size of the recirculation bubble being submitted to discrepancies between successive cycles. This behavior of the separation bubble is responsible for the low frequency temporal modulation of the amplitude of the separation and reattachment points and thus to the low frequency breathing of the separation bubble.

CONCLUSION

We here show that the reflected shock-wave is passive and the SWBLI unsteadiness is related to the low frequency breathing of the recirculation bubble (and not the large scales of the incoming turbulent boundary layer); the oscillations of the reflected shocks foot being in phase with the motion of the separation point. This low frequency activity of the recirculation bubble also seems to be at play in the laminar case. Although in the laminar case the behavior in the second part of the recirculation bubble is the same as in the turbulent case, the low frequency activity in the laminar regime is counter-currently damped towards the first part of the bubble as the length of the bubble is much greater than in the turbulent case. It is then not intense enough to excite, in the first part of the bubble, the separation point and the subsequent oscillations of the reflected shock foot.

Figure 1: Q criterion colored by the magnitude of the longitudinal velocity. Shock waves are highlighted by isosurfaces of $\nabla \cdot \mathbf{u}$: laminar case on the left, turbulent case on the right.

References

[1] Délery, J. and Dussauge, J.-P. *Some physical aspects of shock wave/boundary layer interactions.* Shock waves, **19**(6): 453, 2009.

[2] Daru, V. and Tenaud, C. *High order one-step monotonicity-preserving schemes for unsteady compressible flow calculations.* Journal of Computational Physics, **193**(2): 563–594, 2004.

[3] Suresh, A. and Huynh, H.T. *Accurate monotonicity-preserving scheme with Runge-Kutta time stepping.* Journal of Computational Physics, **136**(1): 83–99, 1997.

[4] Degrez, G.; Boccadoro, C. H. and Wendt, J. F. *The interaction of an oblique shock wave with a laminar boundary layer revisited. An experimental and numerical study.* Journal of fluid mechanics, **177**(13), 247–263, 1987.

[5] Ben Hassan Saidi, I.; Tenaud, C.; and Fournier, G. *Solving three dimensional turbulent compressible flows using a high order One Step Monotony Preserving scheme.* 10th International Conference on Computational Fluid Dynamics (ICCFD 2018), Barcelone, Spain, 2018.

NOISE REDUCTION AND SHOCK LEAKAGE IN BEVELLED PLANAR JETS

De-Jun Sun *[1], Chuang-Chao Ye [1], Peng-Jun-Yi Zhang [1], and Zhen-Hua Wan[1]
[1] Department of Modern Mechanics, University of Science and Technology of China, Hefei 230027, China

Summary Rectangular supersonic jets exist widely in propulsion system of modern and new design concept aircrafts, due to their advantages in design simplicity, thrust-vectoring capabilities and flexibility with integration into the frame of aircraft. However, in underexpanded supersonic jets, the upstream travelling waves referred to as screech tones can cause structural fatigue failure of nozzle. In this work, high fidelity numerical simulations are employed to investigate the effects of asymmetric lips of nozzle on shock screech. The simulation results present the phenomenon of shock leakage [1]. Compared to the symmetric planar jet, the asymmetric lips change the shock structures and intensity of shear layer oscillations. The noise level of screech decreases with increasing the length difference of two lips, and the maximum 7 dB drop is found when this difference reaches the hight of the nozzle. Dynamic mode decomposition (DMD) is further utilized to analysis the jet oscillations. DMD results show that the asymmetric nozzle mainly suppresses the most energetic DMD mode, corresponding to the dominant frequency of shock screech. In short, the oscillations of shear layer and shock leakage are suppressed when the nozzle is bevelled. The study can be used as a reference for the supersonic thrust-vectoring engine design and control of high level screech noise.

NUMERICAL METHODS AND CONFIGURATIONS

The flow development of the underexpanded jet with fully expanded jet Mach number $M_j = 1.55$ is investigated by high fidelity numerical simulations. The in-house solver HiResX is used to perform all the simulations, which solves compressible Navier-Stokes equations with the fifth order HWCNS scheme on a curvilinear coordinate system. Figure 1 shows the model of bevelled planar jets, and three models with L/H=0, 0.5 and 1.0 are studied. A similar configuration can also be found in the work of Berland *et al.* [2]. The total numbers of grid point of the computational domains are around 67.7 million, and a finer grid of symmetric nozzle model with 90 million grid points is used for convergence test. For all cases, the solutions of 250 non-dimensional time units are stored for statistics after the jets are fully developed. Two probes $P^{\pm}$ are set at the points outside of the plates $y = \pm 0.85H$ and $0.4H$ away from the planar leading edge, as shown in Figure 1.

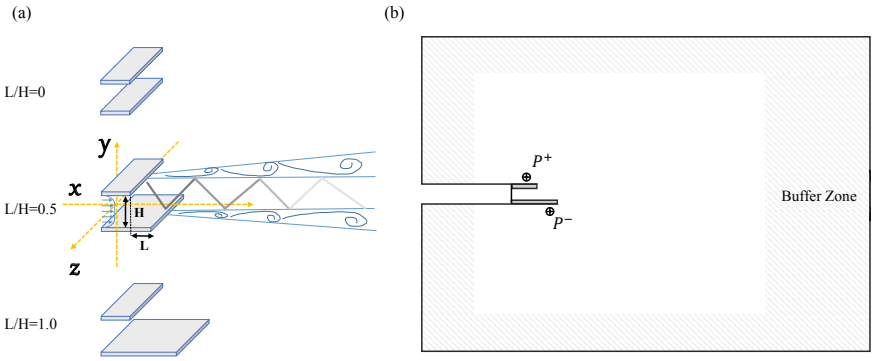

Figure 1: Schematics of the configurations of supersonic planar jets (a) and the set-up of computational domain (b).

RESULTS

Figure 2 shows the numerical schlieren with spanwise vorticity in the spanwsie middle plane. It is clear that the asymmetric nozzles change the shock structure significantly. The mainstream direction of bevelled jets bias to the side of shorter planar, with 6.2° and 9° declination in Cases L/H=0.5 and L/H=1.0, respectively. Mach waves and shock screeches are detected. Present results indicate that the screech waves may come from shock leakage near the saddle point of vorticity in the shear layer.

Compared to symmetric nozzle, bevelled nozzles decrease the shock intensity and weaken the oscillation of shear layers. Table 1 shows the overall sound pressure level (OASPL) at the probes. It is found that the OASPLs are decreased in Cases L/H=0.5 and L/H=1.0, respectively. Dynamic mode decomposition (DMD) is performed,

*Corresponding author. E-mail: dsun@ustc.edu.cn.

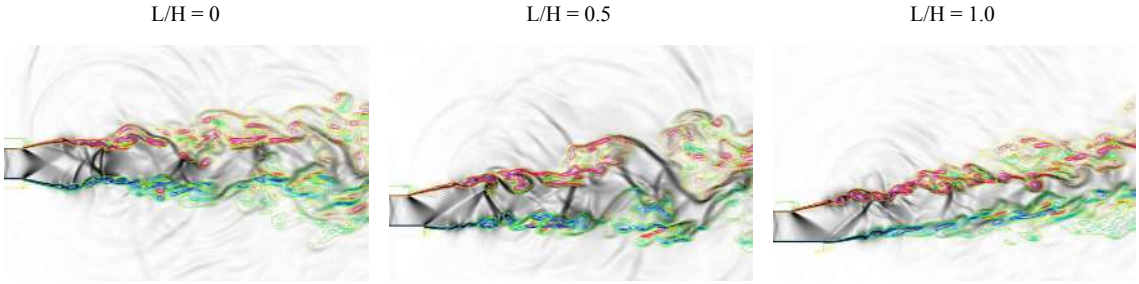

Figure 2: Numerical schlieren with spanwise vorticity in the spanwsie middle plane.

which further reveals that the bevelled nozzles suppress the first DMD mode efficiently. The frequency of the first DMD mode is corresponding to the dominant frequency of shock screech. Moreover, the power spectra density (PSD) of pressure fluctuations at probes P^+ and P^- is shown in Figure 3, the PSD is dominated by the frequency of shock screech f_s and its harmonic frequencies in the Cases L/H=0.0 and L/H=0.5. The high frequency noise in the lower plate is lower than the upper plate, especially for Case L/H=1.0, because the shock and turbulence interactions are stronger.

	$L/H=0$	$L/H=0.5$	$L/H=1.0$
Dominant St (P^+/P^-)	0.0945/0.0945	0.0925/0.0925	0.0984/0.0984
1^{st} DMD mode St	0.0946	0.0925	0.0986
OASPL/dB (P^+/P^-)	161.5/161.5	160.4/160.4	154.5/155.2
Deflection angle	0°	6.2°	9°

Table 1: Comparison of bevelled jets and symmetric jet

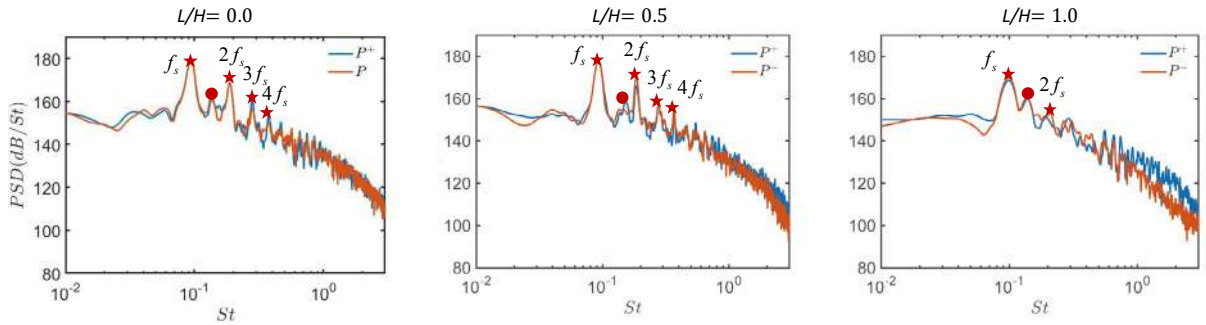

Figure 3: Power spectra density of the pressure fluctuations for probes P^+ and P^- as a function of the Strouhal number $St = fh/U_j$.

CONCLUSIONS

The effect of asymmetric nozzles for supersonic planar jets on screech is investigated with high-fidelity numerical simulations. The bevelled nozzles present the potential of thrust-vectoring. The phenomenon of shock leakage can be found in present jets. The numerical results show that the amplitudes of screech tones are also weakened with bevelled nozzles.

References

[1] Suzuki T, Lele S K. Shock leakage through an unsteady vortex-laden mixing layer: application to jet screech[J]. Journal of Fluid Mechanics, 2003, 490: 139-167.

[2] Berland J, Bogey C, Bailly C. Numerical study of screech generation in a planar supersonic jet[J]. Physics of fluids, 2007, 19(7): 075105.

ON THE CAUSALITY OF THE SHOCK-WAVE/TURBULENT BOUNDARY-LAYER INTERACTION

Kenzo Sasaki *[1], André V. G. Cavalieri[1], Diogo Camello Barros[2], and Lionel Larchevêque[2]
[1] Instituto TecnolÓgico de Aeronáutica (ITA), Aerodynamics Department, São José dos Campos, Brazil
[2] Aix Marseille Université, CNRS, IUSTI, Marseille, France

Summary The present work aims to investigate the unsteady behaviour of an impinging oblique shock wave and its interaction with a Mach 2 turbulent boundary layer by exploiting the large-eddy simulation (LES) data presented in Jiang *et al.* 2017 [1]. The main objective is to identify the mechanisms at the origin of the low-frequency unsteadiness within the interaction zone. Our approach consists in isolating the quasi two-dimensional dynamics by performing a spanwise averaging of the pressure and velocity fields. Then, data-driven methods such as single/multiple-input transfer functions, the Hilbert transform and the spectral proper orthogonal decomposition (SPOD) are applied to the resulting flow field. Preliminary results indicate that a feedback mechanism between downstream propagation of fluctuations within the mixing layer and upstream acoustic disturbances corresponds to the driving mechanism for such phenomenon, complementing previous studies for this configuration.

INTRODUCTION

Shock wave/turbulent boundary layer interaction (STBLI) is of great relevance for the aerospace industry, as it is present in a large number of practical external and internal flow problems such as in airfoil design, turbomachinery, overexpanded nozzles and supersonic inlets [2]. When interacting with a wall, an impinging shock gives rise to an adverse pressure gradient in the boundary layer responsible for flow separation. The resulting separation bubble produces an expansion fan, followed by reattachment compression waves, associated to a highly unsteady reflected shock [3].

The frequency associated to reflected shock dynamics is known to be several orders of magnitude lower than the characteristic frequencies of the incoming turbulent boundary layer, and the driving mechanism of such motion remains unclear. Some works try to relate the shock motion to the upstream turbulent boundary layer [4], while other authors argue that this flow unsteadiness is intrinsically associated to the flow dynamics downstream of the shock [5]. The objective of the current work is to shed further light on this mechanism.

PRELIMINARY RESULTS

The flow field under study is a Mach 2 plane-shock interaction, with a low-frequency characteristic Strouhal number $St \sim 0.03$ for the shock motion and $St \sim \mathcal{O}(1)$ for the turbulent boundary layer. Quantities are nondimensionalized using the interaction length and speed of sound. The origin of the streamwise coordinate system is placed at the averaged shock location on the wall. Figure 1 presents the mean streamwise velocity and its premultiplied spectrum at the shock foot.

Our goal here is to use frequency and time-domain, single and multiple-input transfer functions, which are built from the application of system identification methods directly to LES data. This method has been successfully applied for modeling the dynamics of a turbulent boundary layer [6]. These models are built directly from temporal data, and enable considerable flexibility in terms of input and output definitions. Furthermore, they allow us to extract physical information regarding the system, such as the causality relationship between quantities.

Figure 2 presents an example of the application of the method for this problem; the output position was defined as the average position of the shock foot and the input position was varied along the wall-normal and streamwise directions.

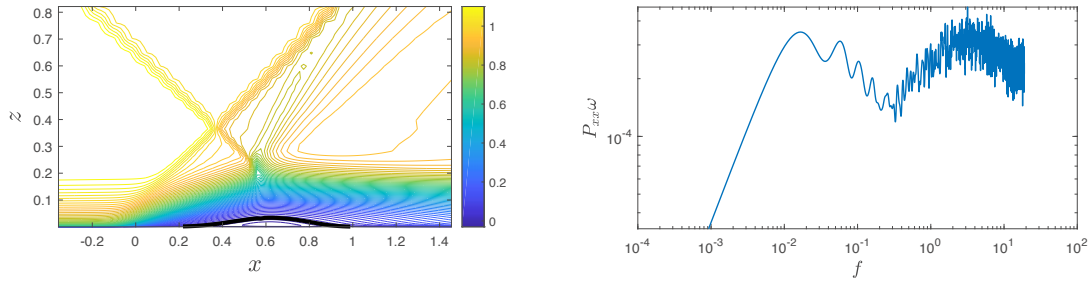

(a) Mean flow (b) Premultiplied spectra

Figure 1: (a) Mean streamwise velocity component depicting incident, reflected shock and recirculation bubble (solid black line) (b) Premultiplied spectra for the streamwise velocity fluctuation in the average shock location.

*Corresponding author. E-mail: kenzo@ita.br.

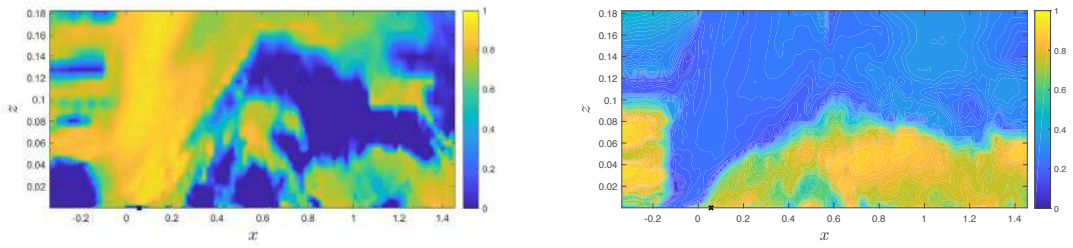

(a) Correlations (b) Causality (P) parameter

Figure 2: (a) Correlations between prediction and LES data (b) P-parameter for evaluation of the causality of the output data.

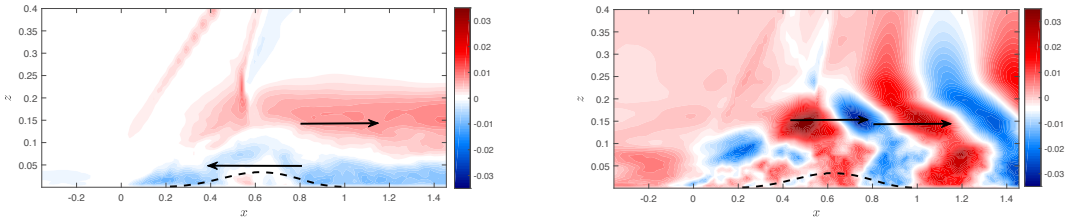

(a) SPOD for $St = 0.02$ (b) SPOD for $St = 1.0$

Figure 3: SPOD modes for the streamwise velocity fluctuations at a frequency corresponding to the shock motion and the turbulence scales; the arrows depict the approximate direction of propagation of the fluctuation.

The streamwise velocity fluctuation was considered as the measured quantity and a spanwise averaging was performed to isolate the quasi 2D dynamics. The fluctuations were also low-pass filtered to isolate the shock motion. The index (P) computed via the Hilbert transform was defined to quantify the causal relationship between input/output quantities. $P = 1$ indicates that the defined input is driving the output behaviour in a perfectly causal manner. The results of figure 2, with high correlations near the reattachment point $(x, y) = (1, 0)$ and nearly perfect causality, indicate that downstream fluctuations are driving the low-frequency behaviour of the shock and permit an accurate prediction of its motion.

To further understand the effects at play here, spectral proper orthogonal decomposition (SPOD) modes were computed at the shock frequency and at the frequency corresponding to the turbulent scales. SPOD modes are used to isolate the most energetic structures at a given frequency and have been used in other works to extract information about the flow for modeling and control applications. These results are presented in figure 3. An evaluation of the phase together with the flow animation indicate an upstream traveling motion for the low-frequencies which is complementary to the results of the transfer function analysis and previous studies [5].

CONCLUSIONS & PERSPECTIVES

The preliminary analysis performed here highlights the presence of a feedback mechanism which appears to drive the low-frequency shock oscillations. For the final version of this work, we plan to extend the transfer function (including the case with more input quantities) and SPOD analysis along with a theoretical evaluation via linear stability theory. More details regarding the implementation of these tools will be considered along with a more complete overview of STBLI configuration.

References

[1] Jiang T, Schreyer A. M., Larchevêque L., Piponniau S., Dupont P. Velocity Spectrum Estimation in Shock-Wave/Turbulent Boundary-Layer Interaction. *AIAA Journal.* **Aug 11**:3486-3498, 2017.

[2] Clemens NT, Narayanaswamy V. Low-frequency unsteadiness of shock wave/turbulent boundary layer interactions. *Annual Review of Fluid Mechanics.* **Jan 3**;46:469-92, 2014.

[3] Touber E., Sandham N. D. Large-eddy simulation of low-frequency unsteadiness in a turbulent shock-induced separation bubble. *Theoretical and Computational Fluid Dynamics.* **Jun 1 23(2)**:79-107, 2009.

[4] Plotkin K. J. Shock wave oscillation driven by turbulent boundary-layer fluctuations. *AIAA Journal*. **Aug 13(8)**:1036-40, 1975.

[5] Pirozzoli S., Grasso F. Direct numerical simulation of impinging shock wave/turbulent boundary layer interaction at $M = 2.25$. *Physics of Fluids.* **Jun 30 18(6)**: 065113, 2006.

[6] Sasaki K., Vinuesa R., Cavalieri A. V., Schlatter P., Henningson D. S. Transfer functions for flow predictions in wall-bounded turbulence. *Journal of Fluid Mechanics.* **Apr 864**:708-45, 2019.

A LATTICE BOLTZMANN FRAMEWORK FOR COMPRESSIBLE FLOW SIMULATIONS

Mohammad Hossein Saadat[1], Benedikt Dorschner[1], and Ilya V. Karlin *[1]
[1] Department of Mechanical and Process Engineering, ETH Zurich, 8092 Zurich, Switzerland

Summary We propose a numerical framework based on the lattice Boltzmann method (LBM) for simulation of compressible flows up to moderately supersonic regime. The framework is based on a compressible LB model which retains the simplicity and efficiency of the standard lattices, and is solved on irregular unstructured meshes. The promising results of the proposed algorithm pave the way for numerical simulations of realistic engineering problems.

INTRODUCTION

The development of accurate and efficient numerical schemes for the simulation of compressible fluid flows remains an active research field due to its importance in many engineering applications. The presence of shock waves in compressible flows adds another level of complexity to the computations, as this requires the scheme to not only be able to accurately resolve the small scale structures of the flow, but also to have enough dissipation to remain stable at shock jumps and avoid the Gibbs oscillations. The lattice Boltzmann method (LBM) as a kinetic theory approach to computational fluid dynamics (CFD) is now a well-established tool for the simulation of complex fluid flows. In the LBM, populations $f_i(\boldsymbol{x}, t)$ associated with a set of discrete velocities $\boldsymbol{c}_i, i = 0, ..., Q-1$, are designed to recover the target equations of continuum mechanics in the hydrodynamic limit. The evolution of populations is based on simple rules of propagation along the discrete velocities, and relaxation to a local equilibrium. This makes the LBM a simple and efficient alternative for conventional CFD solvers and an attractive candidate for simulation of flows in realistic applications.

It is, however, well known that most LB models using the standard lattices ($D2Q9$ in two dimensions and $D3Q27$ in three dimensions, where $DdQn$ model refers to d dimension model with n discrete velocities), are limited to low-speed incompressible applications up to Mach number $Ma < 0.3$, as they suffer from a limited Galilean invariance and lack of isotropy at high-speed flows. The reason is that the number of discrete velocities of the standard lattices is too low to reproduce all of the symmetries required for obtaining the full compressible Navier-Stokes-Fourier (NSF) equations. While increasing the number of discrete velocities (high-order lattice) is a systematic way to go beyond incompressible regime and simulate high-speed compressible flows, it comes at the price of drastically increasing the computational costs, which eventually makes large scale simulations unfeasible.

The present study addresses these issues with the aim of developing a compressible LB framework, while retaining the simplicity and efficiency of the standard lattices. Such a LB model would enable high fidelity simulations of fundamental and engineering applications in the compressible regime.

KINETIC MODEL DEVELOPMENT

The main idea of developing a compressible LB model on standard lattices is to employ a two-population model (one population f_i responsible for the mass and momentum conservation, and the other one g_i for the energy conservation) and introduce correction terms into the kinetic equations to eliminate the spurious terms in the momentum and energy equations resulting from the above mentioned constraints of the standard lattices. The kinetic equations can, therefore, be written in the conventional propagation-collision form as follows [1]

$$f_i(\boldsymbol{x}, t) - f_i(\boldsymbol{x} - \boldsymbol{c}_i\delta t, t - \delta t) = \Omega_{f,i} + \delta t\phi_i, \tag{1}$$

$$g_i(\boldsymbol{x}, t) - g_i(\boldsymbol{x} - \boldsymbol{c}_i\delta t, t - \delta t) = \Omega_{g,i}, \tag{2}$$

where f_i and g_i are populations of discrete velocities c_i at point $\boldsymbol{x}$ and time t, $\Omega_{f,i}$ and $\Omega_{g,i}$ are collision terms and ϕ_i are correction terms. The derivation of correction terms ϕ_i is based on the Chapman-Enskog analysis of the kinetic equations (1) and (2) (see [1] for the full derivation).

NUMERICAL METHOD

The numerical implementation involves propagation along the discrete velocities and local collision (see Eqs. (1), (2)). Here, we perform propagation on unstructured irregular mesh. This allows us to employ body conforming meshes, which give more flexibility in handling complex geometries and are more efficient in capturing small scale structures of the flow near the wall. The computational domain is therefore discretized into an irregular mesh. Then, in order to perform propagation step at each grid node, populations at its corresponding departure point $\boldsymbol{x} - \delta t\boldsymbol{c}_i$ are reconstructed using the second-order accurate finite-element interpolation scheme [2]. After propagation, the post-collision populations are computed. The Grad approximation is used for implementing the wall boundary conditions [3].

*Corresponding author. E-mail: karlin@lav.mavt.ethz.ch

RESULTS AND DISCUSSION

The proposed compressible LB model gives a unified flow solver which covers from subsonic to moderately supersonic regime with shock waves, while still using the simple $D2Q9$ lattice model. Figure 1-a shows the results of supersonic flow over NACA0012 airfoil at $Ma = 1.5$ and $Re = 10000$. It is observed that the present model can accurately simulate problems which were only possible before by employing high-order lattice ($D2Q49$).

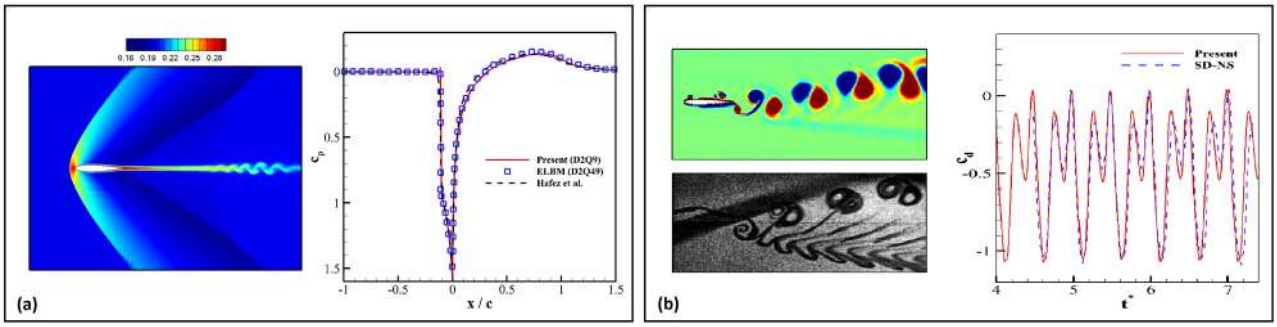

Figure 1: Flow over NACA0012 airfoil: (a) supersonic flow over airfoil, temperature contour (left) and the distribution of pressure coefficient over airfoil surface (right), (b) compressible flow over plunging airfoil, vorticity contour in comparison with the experimental results reported by [5] (left) and the time evolution of drag coefficient in comparison with numerical results of [4] (right).

An extension to a moving mesh approach makes the present model a suitable candidate for simulation of flows with deformable moving bodies and fluid-solid interaction (FSI) applications. This is achieved by employing the so-called arbitrary Lagrangian-Eulerian (ALE) technique. The preliminary results of compressible flow over an airfoil undergoing sinusoidal plunging motion are shown in Fig. 1-b. The comparison with the numerical [4] and experimental [5] results, show excellent agreement.

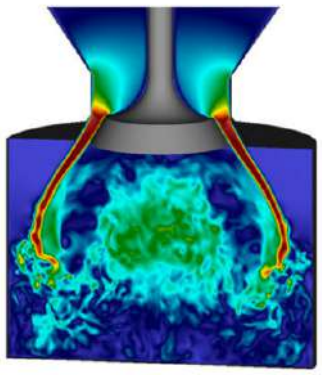

Figure 2: Simulation of valve-moving piston setup [6].

The promising results of the proposed model open interesting prospects toward the numerical simulation of engineering problems with realistic complexity such as flow in internal combustion engine (Fig. 2), compressible turbulence and shock turbulence interaction.

References

[1] Saadat MH, Bösch F, Karlin IV. Lattice Boltzmann model for compressible flows on standard lattices: Variable Prandtl number and adiabatic exponent. *Physical Review E*. 2019, 99(1):013306.

[2] Krämer A, Küllmer K, Reith D, Joppich W, Foysi H. Semi-Lagrangian off-lattice Boltzmann method for weakly compressible flows. *Physical Review E*. 2017, 95(2):023305.

[3] Dorschner B, Chikatamarla SS, Bösch F, Karlin IV. Grad's approximation for moving and stationary walls in entropic lattice Boltzmann simulations. *Journal of Computational Physics*. 2015, 295:340-54.

[4] Liang C, Ou K, Premasuthan S, Jameson A, Wang ZJ. High-order accurate simulations of unsteady flow past plunging and pitching airfoils. *Computers & Fluids*. 2011, 40(1):236-48.

[5] Jones KD, Dohring CM, Platzer MF. Experimental and computational investigation of the Knoller-Betz effect. *AIAA journal*. 1998, 36(7):1240-6.

[6] Dorschner B, Bösch F, Chikatamarla SS, Boulouchos K, Karlin IV. Entropic multi-relaxation time lattice Boltzmann model for complex flows. *Journal of Fluid Mechanics*. 2016, 801:623-51.

THE INTERACTION OF A TURBULENT CYLINDER WAKE WITH AN OBLIQUE SHOCK WAVE

Sean McCreton*[1], Manuj Awasthi[1], Danielle Moreau [1] and Con Doolan[1]
[1] School of Mechanical and Manufacturing Engineering, The University of New South Wales, Sydney, Australia

The interaction of the turbulent wake of a cylinder with an oblique shock wave is explored using high-speed schlieren imaging. Cylinders are placed in a Mach 3 flow at Reynolds numbers of 0.6 and 0.75 × 10^6 to produce turbulent wakes that pass through oblique shock waves of varying strengths. Spectral Proper Orthogonal Decomposition (SPOD) of the schlieren light intensity fluctuations reveals that the turbulent structures in the wake are modified as they pass through the shock wave. The final manuscript will present additional experimental results to further characterise the wake-shock interaction as well as a comparison to theoretical models and other studies.

Introduction

The interaction of turbulent flow with a shock wave is a complex physical problem with significant implications for high-speed flow applications. The behaviour of this phenomena and its impact on the mean flow and turbulence characteristics are of great importance in understanding the aeroacoustic loading within a supersonic combustion ramjet (scramjet). Many studies explore the behaviour of shock turbulence interaction, presenting theoretical [1]–[3], experimental [4], [5] and numerical [6], [7] results.

Linear Interaction Analysis (LIA), first proposed by Kovasznay [8], is commonly used to predict turbulence characteristics downstream of shock turbulence interaction by linearising and decomposing upstream turbulence into small and simple waves. Ribner [1], [2] and Moore [3] applied the technique to plane waves interacting with normal shock waves, reconstructing the downstream waves to produce the desired downstream turbulence quantities. When compared to LIA predictions, experimental and numerical simulations produce widely varied results. Agui et al. [4] and Braun et al. [6] observed a similar disagreement to the predicted amplification in turbulence at higher shock Mach numbers, while Barre et al. [5] and Ryu and Livescu [7] observed amplifications similar to those predicted by LIA.

Based on previous work, we have a good understanding of how homogeneous and isotropic turbulence interacts with a shock wave, but few studies explore non-homogeneous or anisotropic cases. Hence, this study aims to investigate the interaction of a highly turbulent cylinder wake with an oblique shock wave and compare the turbulent characteristics downstream of a shock wave to LIA predictions as well as experimental and computational work.

Experimental Setup

Measurements have been performed in UNSW's Mach 3 wind tunnel, a blowdown facility that produces up to 20 seconds of sustained supersonic flow [9]. A 2-dimensional converging diverging nozzle accelerates the flow to Mach 3 into a rectangular test-section with a cross-section measuring 142.6 × 101.6 mm and length of 700 mm. Stagnation pressures range between 450 kPa and 650 kPa and stagnation temperatures range between 278 K and 300 K, producing Reynolds numbers ranging from 40-50 × 10^6 m^{-1}.

The experimental figure is shown in Figure 1. Aluminium cylinders with diameters (d) of 12 mm and 15 mm were installed across the width of the tunnel (101.6 mm) at half the height of the test-section. The test Reynolds numbers based on these diameters are 0.6 and 0.75 × 10^6 respectively. A 10° wedge was installed on the floor of the tunnel to generate an oblique shock wave which crossed the turbulent cylinder wake 2.5 to 4.5 diameters downstream of the cylinder. A schlieren system in a typical z-type arrangement was used to observe the wake-shock interaction through a set of BK-7 viewing windows with their upstream edge positioned 10.5mm downstream of the centre of the cylinder. Schlieren images were recorded at 50,000 and 100,000 frames per second (fps) in monochrome using a Memrecam HX-7s high-speed camera.

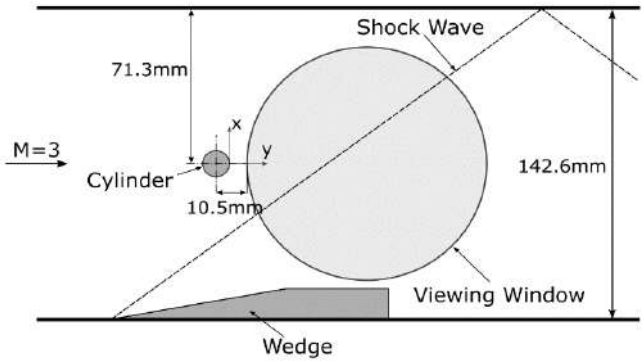

Figure 1. Schematic of the experimental setup

*Corresponding author. E-mail: s.mccreton@unsw.edu.au.

Results

The pixel intensities of the schlieren images are used to analyse the flow by calculating the power spectral density and performing dynamic mode decomposition and SPOD using code adapted from Towne et al. [9]. The mean and variance of the pixel intensities for the 12 mm cylinder with 10° wedge can be seen in Figure 2 (coloured to assist with visualisation), with edge detection shown by black lines indicating sharp gradients with key flow features identified. Figure 3 displays the results for the first SPOD mode, including spectral energy (a) and resulting pixel modal energies for subsets of the imaging region (b-c). For the first time, we can observe the interaction of a highly turbulent cylinder wake with a shock wave and the modification to turbulence characteristics downstream of the shock.

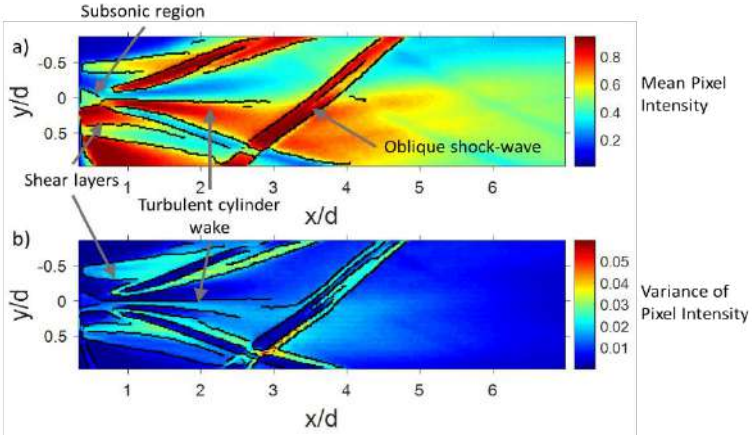

Figure 2. Schlieren images of cylinder wake-shock interaction.
a) mean pixel intensity, b) pixel intensity variance

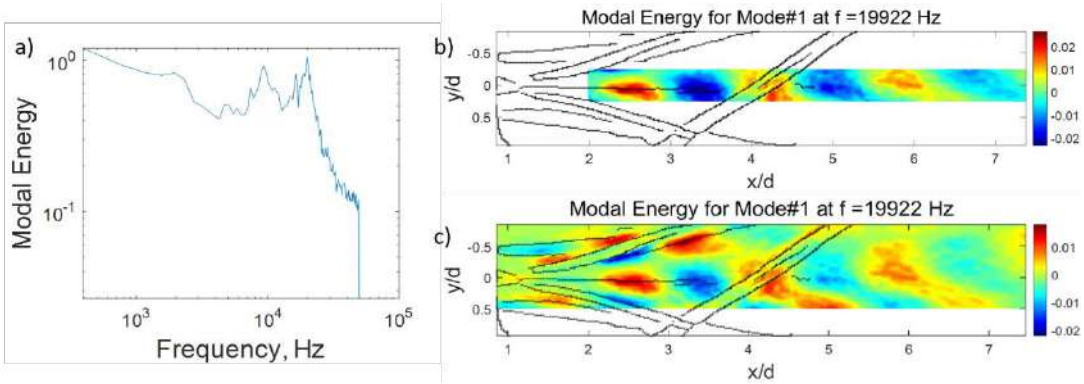

Figure 3. First SPOD mode for cylinder wake-shock interaction: a) spectral energy, b) and c) SPOD modes at 19.2 kHz for reduced domains

CONCLUSIONS

This study observes the interaction of a highly turbulent cylinder wake with an oblique shock wave in a Mach 3 wind tunnel using high-speed schlieren imaging. Numerous post-processing techniques are applied to analyse the fluctuating schlieren light intensities in the viewing region to analyse the behaviour of the wake-shock interaction. The full paper will present further experimental cases and characteristics of the turbulence modification through the shock wave to compare to LIA predictions and other experimental and computational work.

References

[1] H. S. Ribner, "Convection of a pattern of vorticity through a shock wave," 1954.
[2] H. S. Ribner, "Shock-turbulence interaction and the generation of noise," 1954.
[3] F. K. Moore, "Unsteady oblique interaction of a shock wave with a plane disturbance," 1953.
[4] J. H. Agui, G. Briassulis, and Y. Andreopoulos, "Studies of interactions of a propagating shock wave with decaying grid turbulence: Velocity and vorticity fields," *J. Fluid Mech.*, vol. 524, pp. 143–195, 2005.
[5] S. Barre, D. Alem, and J. P. Bonnet, "Experimental study of a normal shock/homogeneous turbulence interaction," *AIAA J.*, vol. 34, no. 5, pp. 968–974, 1996.
[6] N. O. Braun, D. I. Pullin, and D. I. Meiron, "Large eddy simulation investigation of the canonical shock-turbulence interaction," *J. Fluid Mech.*, vol. 858, pp. 500–535, 2019.
[7] J. Ryu and D. Livescu, "Turbulence structure behind the shock in canonical shock-vortical turbulence interaction," *J. Fluid Mech.*, vol. 756, pp. 1–13, 2014.
[8] S. G. Kovasznay, Leslie, "Turbulence in Supersonic Flow," *J. Aeronaut. Sci.*, vol. 20, no. 10, pp. 657–674, Oct. 1953.
[9] A. Towne, O. T. Schmidt, and T. Colonius, "Spectral proper orthogonal decomposition and its relationship to dynamic mode decomposition and resolvent analysis," *J. Fluid Mech.*, vol. 847, pp. 821–867, 2018.

AN ACCURATE NUMERICAL SCHEME TO SOLVE COMPRESSIBLE MULTISPECIES REACTING FLOW

Luc Lecointre *[1,2,3], Etienne Studer[1], Serguey Kudriakov[1], Ronan Vicquelin[2], and Christian Tenaud[3]
[1] Université Paris Saclay, CEA, Service de Thermo-hydraulique et de mécanique des fluides, 91191, Gif sur Yvette, France
[2] Université Paris Saclay, CNRS, CentraleSupélec, Laboratoire EM2C, 91190, Gif-sur-Yvette, France
[3] Université Paris Saclay, CNRS, LIMSI, 91400, Orsay, France

Summary We propose a numerical scheme for an accurate resolution of equilibrium compressible multispecies flows. This scheme minimises numerical diffusion and is robust enough to capture discontinuities and interfaces. It can be used for configurations where we observe interactions between shock wave and turbulence with important variation of temperature like in atmospheric reentry problem or in detonation phenomenon. To solve Euler equations, we extend the Roe's approximate Riemann solver to multispecies flows and use a Lax Wendroff approach to obtain high order one-step scheme coupled to a monotonicity preserving criterion to capture discontinuities. A splitting operator is used to compute viscous and reactive part of the Navier-Stokes equations. Moreover, we apply an adaptive grid refinement technique to refine the mesh at characteristic local scales to be fully resolved numerically.

DESCRIPTION OF THE NUMERICAL SCHEME

The simulation of severe flow conditions, such as unsteady reactive supersonic flows, requires robust accurate numerical methods. They have to deal with multi-scale phenomena, their numerical diffusion must be limited and they have to be robust enough to capture dicontinuities and interfaces such as shock-wave, contact discontinuity or flame front. They also have to combine complex chemical kinetics with physical process and then be able to treat large variations of temperature and density.

We developed here a high order scheme to solve the Navier-Stokes equations for compressible reacting multispecies flow. We describe in the following the different steps to extend the Roe's approximate Riemann solver to a robust high order scheme in order to solve the Euler part of the equations for multispecies flow with temperature dependant heat capacities. Then we present the implementation of the viscous and the reactive part and the adaptive grid refinement techniques.

Extended Roe Solver for Multispecies flow

The Roe's approximate Riemann solver is used to deal with equilibrium gases with temperature dependant heat capacities. It involves the definition of a Roe average state described by a series of thermodynamic variables. In particular, some pressure derivatives allow to compute the sound speed $\tilde{c}_s$ at the average state. Contrary to the perfect gas case, this Roe average state is not uniquely defined. The properties of the Roe solver [1] impose relations between the thermodynamic variables of the average state but are not sufficient to uniquely define all of them. Some approximations must also be made such as realised by VINOKUR and MONTAGNÉ in [2]. A comparison of different formulations to compute these thermodynamic variables can be found in [3], but the authors did not conclude on the superiority of any method.

We extend the existing approximate Riemann solver to a N-species flow by defining the corresponding Jacobian matrix and Roe average state. We compute the approximation of the Roe average state by an analogous approach to the monospecies case in particulary by using projection of the N approximated pressure derivatives variables on the N-1-subspace defined by the mass conservation condition.

In addition to the Roe solver we use an adapted Lax Wendroff approach to obtain a high order one-step scheme coupled with a monotonicity-preserving (MP) criterion to accurately capture discontinuities such as described in [4] for the perfect gas case. We succeeded to express the high order final numerical flux for the multispecies flow with only $\tilde{c}_s$ as unknown parameter. The use of this single parameter in the expression of the high order terms and in the flux limiter criterion allow to get a robust scheme and discriminate more precisely than in [3] the approximations of the Roe average state.

Resolution of the Navier Stokes equations

To solve the Navier Stokes equations, we use a 2nd-order Strang splitting scheme to complete Euler equations with viscous and reactive part [5]. The viscous part, which also take into account the diffusion of the species, is solved using a 2nd-order Runge-Kutta time integration coupled with a 2nd-order centered scheme. In order to deal with multiscale phenomena and not to limit the time step with the stiff reaction term, the reactive part is treated with a Radau5 implicit scheme.

*Corresponding author. E-mail: luc.lecointre@limsi.fr

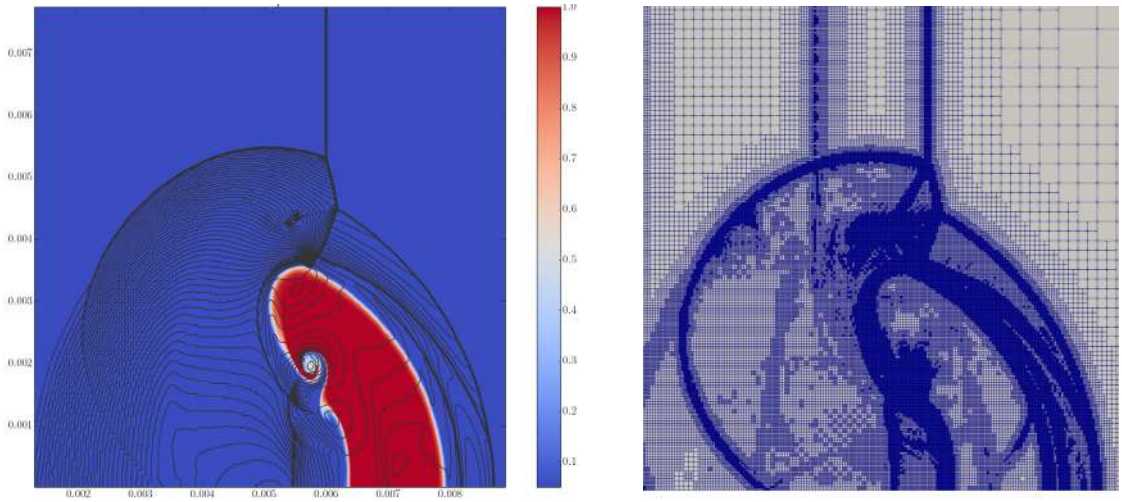

Figure 1: Interaction between a shock at Mach 2 and a hydrogen bubble according to the test case presented in [8] after $4\mu s$. Pressure isolines and hydrogen mass fraction isocontours (left) and corresponding refined mesh (right)

Grid refinement

For several configurations, in particular problems involving detonations problems, characteristic time and space scales span over several orders of magnitude, typically between the size of the system and the flame thickness. In order to solve the relevant scales and save CPU time and memory usage, we use an adaptive multiresolution procedure described in [6] to refine the mesh by using a graded tree data structure that evolve in time. Through an error estimate, a threshold parameter ϵ drives the efficiency of the grid refinement and limits local loss of accuracy.

NUMERICAL RESULTS

We illustrate our method with 1D and 2D academic test cases by using the above presented high order extension of the Roe solver for multispecies flows. For the well documented test cases with shock-bubble interations in gas-gas flows, the quality and the accuracy of our prediction of pressure and temperature improve the capture of the shock bubble interaction phenomena (see fig. 1). In particular, the instabilities around the bubble are better capture than in [7] for the same grid level. The different approximations for the Roe average state are evaluated with the high order scheme and show the best results with the VINOKUR-MONTAGNÉ's method [2].

We will also propose reactive configurations, we are planning to present at the Congress the result of a 2D premixed flame propagation in hydrogen explosions with a fifth order numerical scheme with the test case presented in [9].

CONCLUSIONS

We developed a high order scheme using an extension of the Roe solver for multispecies flow associated with a splitting scheme to treat viscous part and complex chemistry. This numerical scheme is able to accurately capture compressible phenomena inside a multispecies flow and account for configurations as detonation or atmospheric reentry problem. We finally apply adaptive grid refinement to compute the flow with a significant CPU time reduction without loss of accuracy. The numerical applications demonstrate the abilities of this new scheme in transonic and supersonic multispecies flow.

References

[1] Roe P.L. Approximate Riemann Solvers, Parameter vectors, and Difference Schemes. *J. of Computational Physics*, **43**:357 - 372, 1981
[2] Vinokur M., Montagné J. L. Generalized Flux-Vector Splitting and Roe Average for an Equilibrium Real Gas. *J. of Computational Physics*, **89**:276 - 300, 1990
[3] Mottura L., Vigevano L., Zaccanti, M. An Evaluation of Roe's Scheme Generalizations for Equilibrium Real Gas Flows. *J. of Computational Physics* **138**: 354-399, 1997.
[4] Daru V., Tenaud C. High Order One-Step Monotonicity Preserving Schemes ofr Unsteady Compressible Flow Calculations. *J. of Computational Physics*, **193**:563 - 594, 2004
[5] Duarte M. P., Adaptive Numerical Methods in Time and Space for the Simulation of Multi-Scale Reaction Fronts. *PhD Thesis*, Ecole Centrale Paris, 2011
[6] Tenaud C., Roussel O., Bentaleb L. Unsteady Compressible Flow Computations using an Adaptive Multiresolution Technique coupled with a High-Order one-step Capturing Scheme. *Computers & Fluids*, **120**:111 - 125, 2015
[7] Denner F., van Wachem B. G. M. Numerical modelling of shock-bubble interactions using a pressure-based algorithm without Riemann solvers. *Experimental and Computational Multiphase Flow*, **1:4**:271 - 285, 2019
[8] Billet G., Giovangigli V., de Gassowski G. Impact of Volume Viscosity on a Shock-Hydrogen-Bubble Interaction. *Combustion Theory and Modelling*, **12:2**:221 - 248, 2008
[9] Xiao H., Duan Q., Sun J. Premixed flame propagation in hydrogen explosions. *Renewable and Sustainable Energy Reviews*, **81**:1988 - 2001, 2018

EMERGENCE OF INTERMITTENCY AND ASYMPTOTIC STATES IN SOLENOIDALLY FORCED COMPRESSIBLE TURBULENCE

Sualeh Khurshid *[1] and Diego Donzis[1]
[1] Department of Aerospace Engineering, Texas A&M University, Texas, USA

Summary We use a large database of highly resolved direct numerical simulations of compressible isotropic turbulence to show that intermittency in the solenoidal field is well represented by scaling laws predicted for incompressible turbulence. We also show that similar to incompressible turbulence, the solenoidal field transitions from Gaussian statistics to anomalous asymptotic scaling at $R_\lambda \approx 10$, much lower than needed for establishing an inertial range. We also show that compressibility can affect the transition Reynolds number.

INTRODUCTION AND MOTIVATION

The notion of small scale universality, in some quanititave sense, has been the been the staple of turbulence theory and modelling approaches. A universal behavior is often predicted for an asymptotic relevant parameter, for example Reynolds number (R_λ), Schmidt number, Mach number. A quantitative measure of the asymptotic parameter value is, however, often missing in the description. It is therefore difficult to assess the validity of the asymptotic state predictions, if one exists, or departures from it when the asymptotic parameter value is ambiguous. Therefore, developing a quantitative understanding of asymptotic states is of obvious fundamental importance but has implications for important engineering problems. For example, computational design techniques such as large eddy simulations (LES) are based on the existence of this asymptotic universal state. Recently [1] it was shown that incompressible turbulence transitions from a low R_λ state to a universal so-called anomalous asymptotic scaling regime at $R_\lambda \approx 10$, much lower than previously believed. The universal behavior in the velocity field, for example, previously had largely been attributed to the establishment of an inertial range, which emerges only at R_λ at least an order magnitude larger than this transition R_λ. However, it was shown that scaling in the inertial range itself could be predicted from the scaling and transition of velocity gradients at $R_\lambda \sim O(10)$. This suggests that universal behavior observed in incompressible turbulent flows and features of fully developed turbulence are not a consequence of inertial range dynamics or available only at extremely large values of Reynolds number.

Flows in a wide range of natural and engineering applications, for example astrophysics, reacting flows and high speed flight, are compressible. The presence of a coupled velocity and thermodynamic field leads to more complicated physics and a wider range of parameter space than just the Reynolds number. It is therefore important to explore and characterize universal features and their emergence in compressible turbulence. In this paper, we show that compressible turbulence, analogous to incompressible flows, exhibits a transition from a low-R_λ state to fully developed turbulence and that this transition is altered by compressible motions, characterized here by the turbulent Mach number (M_t).

INTERMITTENCY AND UNIVERSAL SCALING

A well known characteristic of fully developed turbulence is presence of strongly localized large fluctuations in instantaneous quantities such as velocity gradients, enstrophy (Ω) and dissipation (ϵ). The large fluctuations lead to departures of scaling predictions for higher order moments based on Kolmogorov's 1941 theory (K41). This so-called anomalous scaling due to intermittency has historically been seen as a high-R_λ feature. It has recently been suggested that anomalous scaling, observed as an algebraic growth of velocity gradients and dissipation with Reynolds number, is achieved at $R_\lambda \sim O(10)$ [1, 2, 3, 4]. A schematic of the underlying formalism is shown in Fig. 1a. At low-R_λ the velocity gradients $(M_p = \langle(\partial u/\partial x)^p\rangle/\langle(\partial u/\partial x)^2\rangle^{p/2})$ exhibit Gaussian statistics $(Y_{2p} = (2p-1)!!)$ As R_λ increases, perturbations in the field become unstable beyond a critical Reynolds number (resembling a Landau transition) and grow such that the statistics obey algebraic scaling laws with respect to R_λ. Higher order moments transition at lower Reynolds numbers than lower order moments. Therefore, the most extreme events show signatures of fully developed turbulence earlier in R_λ. All the transitions for velocity gradients are complete at $R_\lambda \sim 10$ and the flow can then be considered fully turbulent. If the transition Reynolds is known, the scaling exponents (ρ_{2n}) can be predicted by matching the asymptotic states: Gaussian at low R_λ and algebraic scaling at high R_λ [2]. These allow for accurate calculations of scaling exponents of velocity structure functions as well.

Intermittency in compressible turbulence is modified by fluctuations in thermodynamic variables which can be strongly coupled with the velocity field [5] giving rise to new phenomena. For example, it has been suggested that the most dissipative structures in compressible turbulence concentrate in sheets instead of filaments as in incompressible turbulence [6]. In addition, small localized shocks in dilatational components, termed shocklets, alter intermittent behavior. This seems to be confined to the dilatational component of velocity as structure functions of the solenoidal velocity have been shown to scale similar to incompressible counterparts with small compressibility effects [8]. Therefore, one can expect

*Corresponding author. E-mail: sualeh@tamu.edu

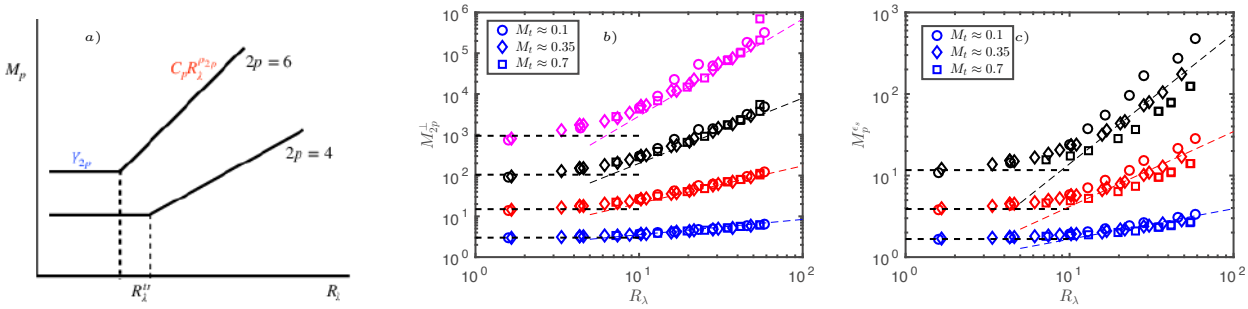

Figure 1: a) A schematic showing transition of velocity gradients from a low-R_λ Gaussian state to high-R_λ anomalous scaling. Moments of (b) transverse velocity gradients ($2p = 4, 6, 8, 10$) and (c) solenoidal dissipation ($p = 2, 3, 4$) for different M_t.

the incompressible analysis of Yakhot & Donzis [1] to apply to solenoidal variables. In Fig. 1b we plot the normalized moments of transverse velocity gradient $(\partial u/\partial y)$ at three different turbulent Mach numbers from solenoidally forced isotropic turbulence simulations. The numerical scheme is 10-th order compact in space with RK3 discretization in time. The small scale resolution (Δx) is between 1 and 2 times the mean Kolmogorov scale with a CFL of 0.3. We observe behavior similar to incompressible turbulence. At low-R_λ, the velocity gradient statistics are Gaussian (horizontal dashed lines) with a transition to anomalous scaling beyond $R_\lambda \sim 10$. The dashed scaling lines correspond to analytical results computed by Yakhot & Donzis for incompressible turbulence [2]. The excellent agreement of the data at all M_t with these predictions shows that the solenoidal velocity field in compressible turbulence indeed obeys the same scaling as incompressible turbulence with no discernible compressibility effects. Further, similar to incompressible turbulence, the asymptotic scaling is achieved in flows with no inertial range and is an emergent phenomenon from a transition. We also show the moments of solenoidal dissipation ($\epsilon_s = \mu\omega_i\omega_i$, $M_p^{\epsilon_s} = \langle\epsilon_s^p\rangle/\langle\epsilon_s\rangle^p$) in Fig. 1c for $p = 2, 3, 4$. Moments of solenoidal dissipation are related to the moments of velocity gradients as $\langle\epsilon_s^p\rangle \sim \langle(\partial u/\partial y)^{2p}\rangle$. Solenoidal dissipation then is composed of three velocity gradients, each of which exhibit Gaussian statistics at low-R_λ. The solenoidal dissipation field then should exhibit χ^2 statistics with 3 degrees of freedom if components area in fact independent. This is what we observe at low R_λ in Fig. 1c, where χ_3^2 moments are plotted as dashed horizontal lines and agree well with DNS data. Beyond $R_\lambda \sim 10$, the solenoidal dissipation moments grow algebraically and agree well with scaling observed and predicted for incompressible turbulence (dashed colored lines). However, here we see a monotonic decrease in moments with increase in turbulent Mach number. The decrease in intermittency in solenoidal dissipation field is consistent with the literature [7, 6]. This is also consistent with the assumption that dissipation intermittency within highly compressible flows occurs in sheet like structures rather than filaments. The scaling with respect to R_λ appears to be preserved even at higher M_t. The weakened moments appear to be a consequence of delayed transition with respect to R_λ at higher M_t

CONCLUSIONS

We use high-resolution direct numerical simulations of compressible isotropic turbulence to study the emergence of intermittency in transverse velocity gradients and solenoidal dissipation. We show that at low-R_λ, velocity gradients obey Gaussian statistics and transition to an anomalous scaling when R_λ increases beyond $O(10)$. The gradients do not have a statistically significant trend with respect to turbulent Mach number. We also show that moments of solenoidal dissipation obey scaling laws similar to incompressible turbulence with respect to the Reynolds number. The magnitude of the moments decreases with an increase in turbulent mach number or, equivalently, the compressibility of the flow. Anomalous scaling is observed at a much lower R_λ than is needed for the development of an inertial range. The observed scaling of the velocity gradients implies the scaling of inertial range structure functions for the solenoidal field is the same as their incompressible counterpart, as reported previously in the literature from high-R_λ simulations. We show these exponents can be computed from much lower-R_λ data than is needed for establishing a wide enough inertial range to measure the exponents reliably. Therefore, information about high-R_λ turbulence is already present at low R_λ and can be studied using highly-resoled low-R_λ simulations. Our data also suggest that the transition to fully developed turbulence with respect to Reynolds number in compressible flows can be delayed with an increase in turbulent Mach number.

References

[1] V. Yakhot, D. A. Donzis. *Phys. Rev. Lett.* **1119** 044501 2017
[2] V. Yakhot, D. A. Donzis. *Physica D* **384-385** 2018
[3] J. Schumacher, J. D. Scheel, D. Krasnov, D. A. Donzis, V. Yakhot and K. R. Sreenivasan. *Proc. Natl. Acad. Sci.* 2014
[4] J. Schumacher, A. Pandey, V. Yalhot, K. R. Sreenivasan. *Phys. Rev. E* **98-3** 2018
[5] D. A. Donzis, S. Jagannathan. *J. Fluid Mech.* **733** 221-244 2013
[6] S. Boldyrev, A. Nordlund, P. Padoan. **573** 678 2002
[7] S. Jagannathan, D. A. Donzis. *J. Fluid Mech.* **789** 669-707 2016
[8] J. Wang, T. Gotoh, T. Watanabe. *Phys. Rev. Fluids* **2** 053401 2017.

EXPERIMENTAL INVESTIGATION OF A FLOW THROUGH A LINEAR TURBINE CASCADE

Idalia Jagodzińska *[1], Bartosz Olszański[1], Konrad Gumowski[1], and Sławomir Kubacki[1]
[1] Warsaw University of Technology, Faculty of Power and Aeronautical Engineering, Institute of Aeronautics and Applied Mechanics, Nowowiejska 24, 00-665, Warsaw, Poland

Summary The paper discusses experimental investigation of flow through a linear transonic Low Pressure Turbine cascade in VKI LS-59 arrangement using the Particle Image Velocimetry technique. Experiments are performed for chord Reynolds number of $Re_{c2} = 6,87 \cdot 10^5$, isentropic Mach numbers at cascade outlet of $M_{2is} = 0,777$ and $M_{2is} = 0,975$, and the freestream turbulence level, $Tu = 2.5\%$. The analysis of the boundary layer transition in transonic flow regimes, shock wave - boundary layer interaction (SWBLI), shock-induced separation and the turbulence generation in wake behind the blade is performed. The obtained flow field data allow to evaluate the standard $k - \omega$ model by Wilcox (2008) and the algebraic transition model by Kubacki and Dick (2016). The aim was to verify, if the database is well suited for testing and development of the RANS-based techniques.

OVERVIEW

Next to a research on transonic flow over a flat plate or airfoil, the eligible test case is the flow in turbomachinery blading in transonic regime, which often encourages the fundamental phenomena like laminar-to-turbulent transition, shock wave-boundary layer interaction and shock-induced separation. For years, the Computational Fluid Dynamics (CFD) techniques, in most industrial applications, have been treated as fully-turbulent approaches thus neglected the details of flow coming from laminar and transitional boundary layers. The new transition models can be adjusted to turbomachinery flows. It provokes to their evaluation with the experimental results acquired with expanded set of the measurement techniques.

The interaction of the shock wave with the boundary layer in transonic flow regimes is mostly investigated for flat plates or airfoils. A comprehensive description of the shock wave turbulent boundary layer interaction has been done by Delery and Marvin [2]. The up-to-date review of SWBLI phenomenon has been also done by Babinsky and Holger [1]. In the transonic blade cascade the shocks generated at the blade trailing edge propagate downstream and impact the BL on the adjacent blades. Moreover, the flow over the turbine blades experiences a strong streamwise curvature making the transition prediction very challenging task. The shock wave may directly induce the BL separation. Alternatively, it may also lead to BL thickening, enhancement of the adverse-pressure-gradient (APG) effect and BL separation near to the blade trailing edge. The velocity field measurements in the wake of the blades with classical measurement techniques such as wake traverse probes as well as the blade surface pressure measurements have been done by Kiock et al. [3]. A comparison of experimental data with numerical results, obtained with various turbulence and transition models (see [4]), calls for improvement of the RANS-based approaches. The present work aims at providing the database for validation/development of the RANS-based techniques. For that purpose, the pressure measurements on blade surface were performed, and the flow characteristics in the wake region behind the blade were analysed using the non-intrusive PIV method.

EXPERIMENTAL APPARATUS AND MEASURING TECHNIQUES

The experiments have been done in the open circuit intermittent, in-draft (suction) type wind tunnel. The model of the low-pressure turbine (LPT) linear cascade, consisting of 8 blades in VKI LS-59 arrangement, was placed in the wind tunnel test section. The flow two-dimensionality was ensured. The Reynolds numbers were between $Re_{c1} = 2,59 \cdot 10^5$ upstream from the cascade up to $Re_{c2} = 6,87 \cdot 10^5$ downstream the cascade. The inlet and outlet conditions, in terms of the static pressure, static temperature, inlet turbulence level were provided. The air humidity was controlled. The pressure measurements on the blade surface were done for the pressure tappings in the mid-span plane of the blade. The PIV was performed using the Nd:YAG 200mJ Litron laser and LaVision DaVis software. The laser sheet covers the downstream region of the cascade including rear part of the blades suction side.

RESULTS

The surface Mach number distribution was compared with the data obtained in four European wind tunnels [3] for comparable outlet flow conditions, $Ma_{2is} = 0,803$ and $Ma_{2is} = 0,996$. The obtained data were also compared with numerical results obtained with the fully-turbulent model by Wilcox (2008), and with the algebraic transition model by Kubacki and Dick (2016b). For the subsonic case both models show a good agreement with experiments. For the transonic case the shock wave boundary layer interaction is visible at streamwise distance $x/c = 0.6$ (c is the blade chord). The main difference between the models is visible in the rear part of the blade (results not shown). The algebraic transition

*Corresponding author. E-mail: idalia.jagodzinska@meil.pw.edu.pl.

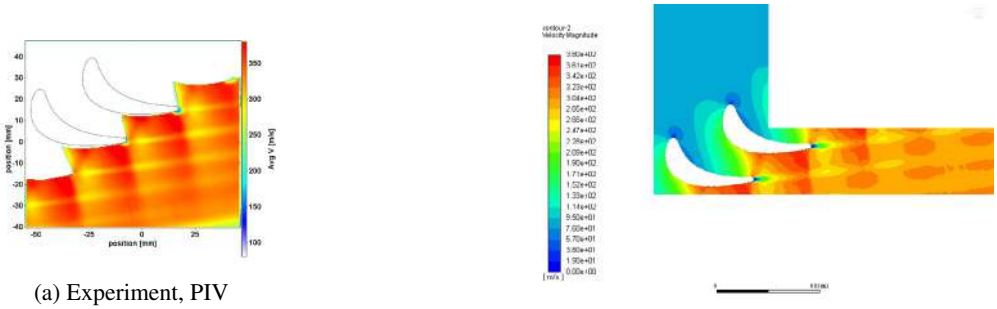

(a) Experiment, PIV

(b) CFD, algebraic transition model

Figure 1: Contour plots of velocity magnitude for $M_{2is} = 0,975$. The flow is directed from the top to to the right. The interplay of a wake with a shock wave is visible in both PIV and CFD.

(a)

(b)

Figure 2: Mean velocity magnitude (a) and turbulent kinetic energy (b) profiles at $x/c_{ax} = 1.2$ for $M_{2is} = 0,975$.

model shows a better correspondence between measured and predicted Mach number distribution in vicinity of the blade trailing edge. The fully-turbulent $k - \omega$ model produces a thicker turbulent boundary layer, which result in a too abrupt change on the surface Mach number distribution in the vicinity of the shock wave.

The Particle Image Velocimetry measurements of the mean and fluctuating velocity components for two flow conditions, $Ma_{2is} = 0,777$ and $Ma_{2is} = 0,975$, were performed. In subsonic case, $Ma_{2is} = 0,777$, a good correspondence between measured and predicted mean velocity profiles was reported (results not shown). In transonic case, $Ma_{2is} = 0,975$ (see Figures 1 and 2), somewhat lower mean velocity is reproduced in simulation, compared to measurement, at $1,2c_{ax}$ (c_{ax} is the axial chord) downstream the cascade (Fig. 2, left). Much higher differences are reported between predicted, using the standard $k-\omega$ model, and the measured turbulent kinetic energy profiles (Fig. 2, right). The algebraic model shows better correspondence with measurements. This is due to a stronger turbulent kinetic energy production in the separated boundary layer on the blade surface, compared to the production observed with the fully-turbulent approach (without the boundary layer separation). Both models show higher differences farther away from the blade trailing edge (results not showed). This shows that further closure models is necessary. Thus, the obtained experimental results can serve as database for improvement of modelling techniques.

CONCLUSIONS

By the SWBLI existance the turbomachinery transonic flow is intricate for experimental investigation. The use of PIV technique allows for verification of flow characteristics in wake behind the blades. The RANS models show deficiencies in capturing the mean and fluctuating velocity characteristics in the transonic flow regime. The differences are due to a too weak mixing reproduced with RANS in the wake region behind the blade.

References

[1] Babinsky H., J. K. Harvey, Shock Wave- Boundary-Layer Interactions, Cambridge University Press, 2011.
[2] Delery J., Marvin, Turbulent Shock-Wave/ Boundary-Layer Interaction, *AGARDograph* ***280***, 1986.
[3] Kiock R., Lehthaus F., Baines N., Sieverding C. The Transonic Flow Through a Plane Turbine Cascade as Measured in Four European Wind Tunnels, ASME Beijing International Gas Turbine Symposium and Exposition, 1985.
[4] Michelassi V., Rodi W. Experimental and Numerical Investigation of Boundary-Layer and Wake Development in a Transonic Turbine Cascade. *Aerospace Science and Technology* **2**: 191-204, 1998.
[5] Sandberg R., Michelassi V., Pichler R., Chen L., Johnstone R. Compressible Direct Numerical Simulation of Low-Pressure Turbines - Part I: Methodology. *Journal of Turbomachinery* **137(5)**, 2015.

CHARACTERIZATION OF THE SHEAR LAYER IN SEPARATED SHOCK/TURBULENT BOUNDARY LAYER INTERACTIONS

Clara M. Helm[1] and M. Pino Martín *[1]
[1] Department of Aerospace Engineering, University of Maryland, College Park, MD 20742, USA

Summary We present a thorough characterization of the shear layer that exists in large eddy simulation data of three separated, compression ramp-generated shock/turbulent boundary layer interactions. Flow conditions include freestream Mach numbers of 2.9, 7.2, and 9.1 producing shear layers with convective Mach numbers of 1.0, 1.9, and 2.0 respectively. We will show that these shear layers share many properties with canonical compressible mixing layers. For example, in each shear layer is found a region where the mean profiles can be scaled to collapse to an approximate similarity profile. Peak turbulence quantities are consistent with compressible mixing layer theory. The conservative and dissipative turbulence energy exchange mechanisms are consistent with those found in canonical mixing layers, and the spreading rate and turbulence anisotropy both decrease with increasing M_c. The signature and structure of the large shear layer vortices will also be presented including a direct measurement of the vortex convection velocity.

BACKGROUND

The mixing layer is one of the most fundamental shear flows in the study of compressible turbulence. Despite its conceptual simplicity, the compressible mixing layer exhibits certain properties that are difficult to explain physically resulting in an inability to develop precise scaling laws and robust models. One of the most documented features of the compressible mixing layer is a significant decrease in spreading rate with increased compressibility (Among many references see [1, 2, 3, 4].), however, the cause of this decrease is still not entirely understood. Complicating our understanding further is the fact that compressibility can significantly alter the development and dynamics of the Kelvin-Helmholtz vortices, causing them to become more three-dimensional and less coherent with increasing convective M_c (Among many references see [5, 6]). A major obstacle in the study of compressible mixing layers is the lack of reliable and detailed data, particularly for turbulence statistics, at elevated convective Mach number ($M_c > 1$).

OVERVIEW OF RESULTS

High convective Mach number conditions occur naturally in the Shock/Turbulent Boundary Layer Interaction (STBLI) shear layer. In this research we employ our Large Eddy Simulation (LES) database of compression ramp-generated STBLI to analyze for the first time the properties of mixing layers in hypersonic separated flow including free-stream Mach number ranging from 3 to 10 and convective Mach number from 1 to 2. All three flows are of a flat plate boundary layer over a two-dimensional wedge and are assumed to be homogeneous in the spanwise direction. All three flows are fully separated in the mean producing counter-current shear layers. Details of the database are listed in Table 1 where M_e is freestream Mach number, δ is boundary layer thickness, ϕ is the ramp angle, Re_θ is Reynolds number based on momentum thickness, Re_τ is the friction Reynolds number, and L_{sep} is the mean separation length. Grid outer dimensions in streamwise, spanwise, and wall-normal directions are listed as L_x, L_y, and L_z respectively. Also included in Table 1 is the convective Mach number $M_c = (U_1 - U_2)/(a_1 + a_2)$ where U is streamwise velocity and a the local speed of sound. The subscript 1 refers to the high-speed side of the shear layer and 2 the low-speed side. For further details on the LES method and its application to hypersonic STBLI flows, please see Helm & Martin [7] and the references within.

In Figure 1, the time- and spanwise-averaged mean turbulent kinetic energy (TKE $= \rho u_i' u_i' / 2U_e^2$) field in the M10 ramp flow highlights the region of shear behind the shock front (black line) and above the separation bubble (magenta line). A coordinate system labeled (x', z') is selected to define the similarity variable $\zeta = z'/x'$. The dashed lines in the contour plot of Figure 1 indicate the range in x' for which ζ collapses the mean flow to the profiles shown to the right. The spreading rate, convective Mach number, and peak turbulence levels can be determined from these collapsed profiles. We will show that the trends we observe are consistent with existing compressible mixing layer theory. Turbulent kinetic energy and Reynolds stress budgets show that STBLI shear layers have a much greater streamwise turbulence production rate than is observed in compressible mixing layer data, however, both the transfer of turbulence energy by the pressure-strain and the energy drain by viscosity show similar behavior to canonical mixing layer data at matching M_c (Figure 2).

Case	M_e	ϕ	δ (mm)	$(L_x \times L_y \times L_z)/\delta$	Re_θ	Re_τ	L_{sep}/δ	M_c
M3	2.92	24^o	7.0	$14 \times 4 \times 4.5$	3220	360	3.4	1.03
M7	7.17	33^o	5.0	$22.5 \times 10 \times 8$	3720	210	5.6	1.89
M10	9.05	34^o	18.0	$19.6 \times 10 \times 7$	8280	520	3.6	1.99

Table 1: LES Database Summary

*Corresponding author. E-mail: mpmartin@umd.edu

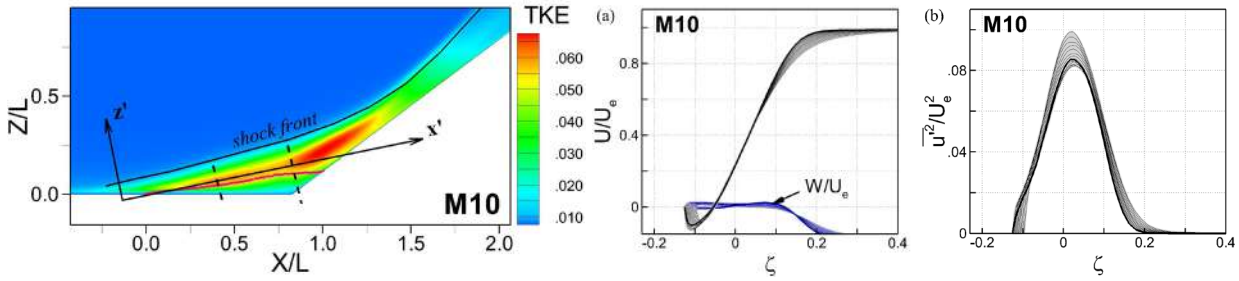

Figure 1: Shear layer similarity in Mach 10 flow.

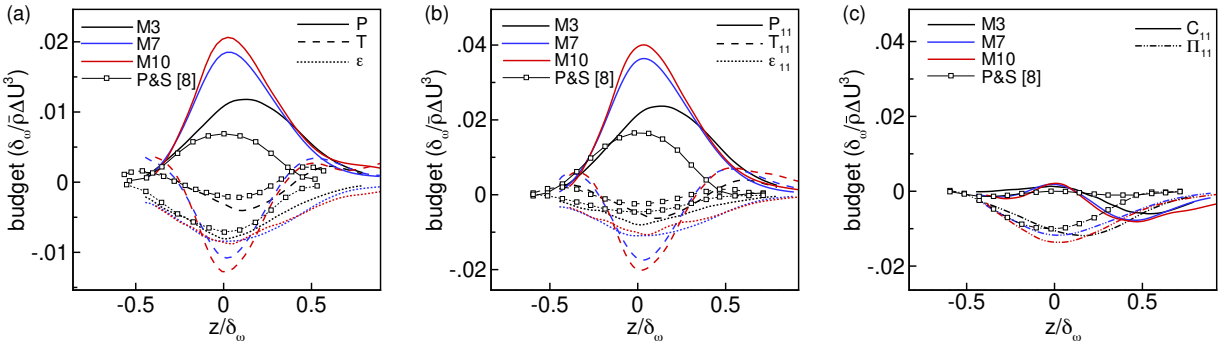

Figure 2: TKE (a) and streamwise Reynolds stress (b-c) budgets compared to data of Pantano & Sarkar[8].

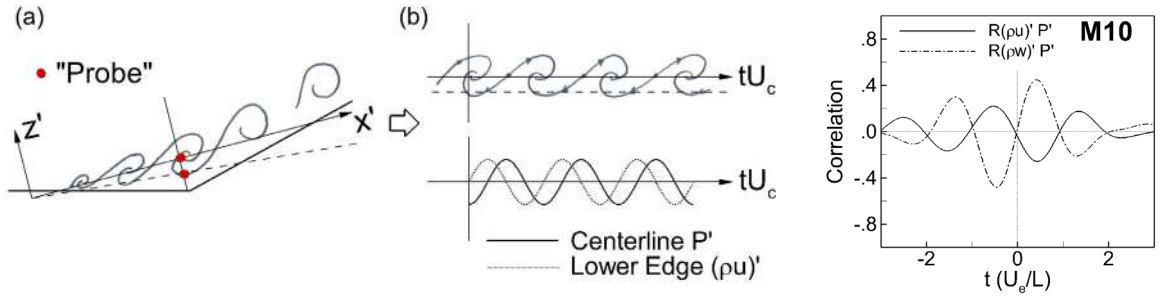

Figure 3: Conditionally averaged vortex time signature in Mach 10 flow.

As a result, the spreading rate and turbulence anisotropy decrease with increasing M_c. We will also show the averaged signature of the large shear layer vortices can be determined by taking time signals from within the similarity region and transforming them to spatial "frozen" vortices using Taylor's hypothesis as drawn schematically in Figure 3. We developed a sophisticated method of filtering and conditionally averaging the time signals to produce clean signatures of the mixing layer vortices (Figure 3), and which also allows us to accurately measure the convection velocity, a quantity that is essential for accurate interpretation of the theoretical comparison.

References

[1] Birch S. F. & Eggers J. M. 1973 Free turbulent shear flows. *NASA Report No. SP-321*.
[2] Dimotakis, D. E. 1991 Turbulent free shear layer mixing and combustion. In *Prog. in Astronautics and Aeronautics* (ed. Murthy & Curran), vol 137 AIAA.
[3] Lele, S. K. 1994 Compressibility effects on turbulence. *Ann. Rev. of Fluid Mech.*, **26**.
[4] Smits, A. J. & Dussauge, J. P. 2006 Turbulent shear layers in supersonic flow. Springer.
[5] Samimy, M., Reeder, M. F. & Elliott, G. S. 1992 Compressibility effects on large structures in free shear flows. *Phy. of Fluids A* **4** (6).
[6] Rossmann, T., Mungal, M. G. & Hanson, R. K. 2002 Evolution and growth of large-scale structures in high compressibility mixing layers. *J. of Turb.* **3**.
[7] Helm, C. M. & Martín, M. P. 2017 Görtler-like vortices in the LES Data of a Mach 7 STBLI. *AIAA Paper No. 2017-0762*.
[8] Pantano, C. & Sarkar, S. 2002 A study of compressibility effects in high-speed turbulent shear layer using direct numerical simulation. *J. Fluid Mech.* **451**.

IS THERE UNIVERSALITY IN COMPRESSIBLE TURBULENCE?

Diego Donzis *[1]
[1] Department of Aerospace Engineering, Texas A&M University, College Station, USA

Summary Compressible turbulence presents a much richer behavior that its incompressible counterpart. While universal scaling laws have been widely and successfully utilized to understand the latter, much less is known about the former. Here we argue that the lack of universal laws and disagreements across flows found in the literature, can be reconcile when the set of governing parameters is supplemented with a non-dimensional variable based on dilatational motions. Using specific analytical limits of the governing equations, we identify the correct governing parameters, show that they can indeed collapse all data in the literature, and provide a framework for further understanding and more realistic physics-based turbulence models.

INTRODUCTION AND MOTIVATION

Most flows in natural and engineered systems are turbulent exhibiting fluctuations in all hydrodynamic and thermodynamic variables which describe the state of the fluid and flow. In a number of situations one can assume the fluid to be incompressible which implies constant density fields and fluid elements that preserve their volume. This results in a great simplification of the problem as hydrodynamics decouples from thermodynamics reducing greatly the complexity of the problem. However, this is not the case in the general case which includes astrophysical phenomena, aerodynamics, reacting flows, and geophysical phenomena, among many others. In such flows hydrodynamics is coupled with thermodynamics leading to much more complex spatio-temporal behavior and a much larger parameter space than in incompressible flows. Thus it is not surprising that much less is known about the former.

Universal scaling laws have been of great value to the fundamental understanding and practical description of a number of physical phenomena including incompressible turbulence. Universal scaling laws for incompressible turbulence have been at the center of our understanding of these flows [1, 2] which are typically cast in terms of the single non-dimensional parameter, namely the Reynolds number. A widely used definition of this parameter is based on the so-called Taylor microscale λ which can be written as $R_\lambda = \langle\rho\rangle u_{rms}\lambda/\mu$ where $\langle\rho\rangle$ is the (constant) density, u_{rms} is the root-mean-square velocity, and μ is the (constant) dynamic viscosity. Universal scaling laws are important because it allows us to characterize the behavior of a system not only at different conditions (Reynolds numbers), but perhaps more importantly, across different flows and at different conditions. This is central element in turbulence modeling.

Universality in the case of compressible turbulence, on the other hand, has been more elusive, in part, due to the lack of a set of parameters that can define the state of the flow uniquely for a range of conditions. Typically, the degree of compressibility is measured by the turbulent Mach number $M_t = \langle|\mathbf{u}|\rangle/c$ where $\mathbf{u}$ is the velocity vector, c the mean speed of sound and angular brackets are a suitably defined average. Significant work has been devoted to find universal scaling laws in terms of M_t to characterize compressibility effects. However, as we show here, data from well-resolved simulations as well as specific theoretical limits of the governing equations show that this is fundamentally flawed, explaining thus the disagreement between data and the limited success in finding theoretically sound models of wide applicability.

We argue that this is due to an incomplete set of parameters to characterize the state of the flow. Furthermore, using specific asymptotic limits we show that universal scaling laws are indeed observed when the parameter space is extended to include internally generated dilatational motions regardless of the mechanisms used to drive turbulent fluctuations [3]. We support our results with a massive database of highly-resolved direct numerical simulations (DNS), along with all data available in the literature.

SIMILARITY SCALING AND GOVERNING PARAMETERS

In incompressible flows, one can use a characteristic length and velocity ($\mathcal{L}$ and $\mathcal{U}$, respectively) to normalize the governing equations. This leads to a single non-dimensional parameter, the Reynolds number, $R_\mathcal{L} = \rho\mathcal{U}\mathcal{L}/\mu$. A central theme in understanding, characterizing and modeling turbulence has been the scaling of a large number of statistics on the Reynolds number, typically the Taylor Reynolds number for convenience [1, 2]. As noted above this has been complemented with M_t as a measure of compressibility to describe fully the statistical state of the flow [4, 5]. The limitations of this approach can be readily seen in Fig. 1(left, top) where we show the normalized pressure rms for a very large database of isotropic flows with a range of forcing schemes as well as homogeneous shear layers. The present simulations and the studies from the literature are described in more detail in [3]. There is clearly no collapse of the data showing the inadequacy of M_t to scale pressure fluctuations. However, if one considers the limiting behaviors at low and high compressibility levels for which well known theoretical results can be established one can find $p^2_{rms}/\langle p\rangle^2/(M_d\gamma)^2 \approx A^2\mathcal{D}^{-2} + 1$. where $\mathcal{D} = \delta\sqrt{\delta^2+1}/M_t$, $M_d = M_t\delta/\sqrt{\delta^2+1}$, and A is a constant of $\mathcal{O}(1)$ which may depend weakly on the flow geometry. In this formulation, we see a new parameter $\delta \equiv u_{d,rms}/u_{s,rms}$ ($u_{d,rms}$ and $u_{s,rms}$ are the rms of

*Corresponding author. E-mail: donzis@tamu.edu

the dilatational and solenoidal components in a Helmholtz decomposition of $\mathbf{u}$) emerge naturally with M_t, as the proper similarity variables to describe the state of turbulence. Indeed, in Fig. 1(left, bottom) we see an excellent collapse of all the data (including isotropic and shear flows) defining two regimes: the low-compressibility regime at $\mathcal{D} \lesssim 0.5$ where pressure behaves as in incompressible turbulence and a high-compressibility regime with $\mathcal{D} \gtrsim 0.5$ where pressure attains equipartition with $\mathbf{u}_d$ [6].

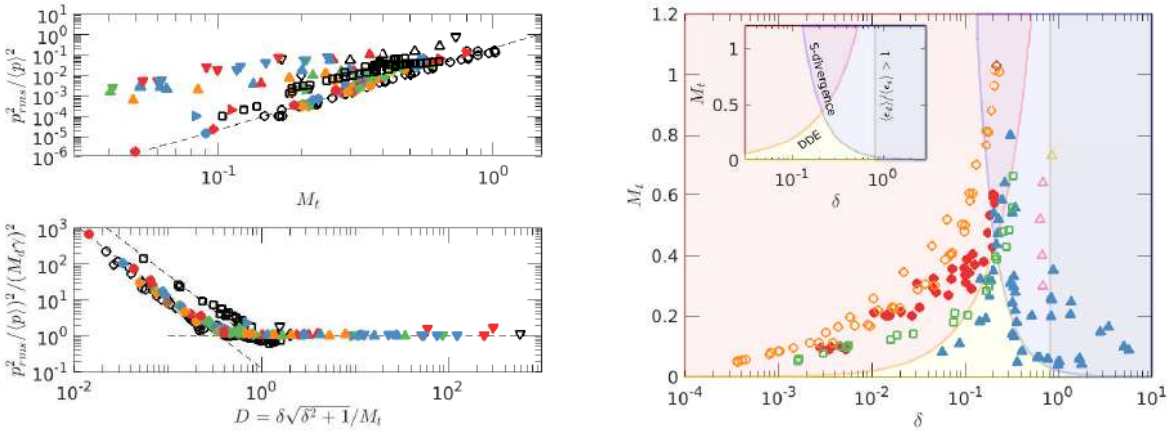

Figure 1: Left: Scaling of pressure variance in terms of M_t (top) and the new scaling parameter $D = \delta\sqrt{\delta^2+1}/M_t$ (bottom) from our DNS database [3] (symbols in colors) and the literature (black symbols) which includes isotropic flows as well as shear layers Right: database of simulations in the δ-M_t plane with different regimes (DDE: dilatationally-dominated equipartition; S-divergence: departure of velocity skewness gradient from well-known incompressible value; $\langle \epsilon_d \rangle / \langle \epsilon_s \rangle > 1$: region where dilatational dissipation dominates) in colors. (adapted from [3]).

Similar observation can be made about the so-called dilatational dissipation $\langle \epsilon_d \rangle \equiv \langle \mu (\nabla \cdot \mathbf{u})^2 \rangle$ which has been studied in a number of flows as it is critical to the general dynamics of the flow, especially its dilatational motions. A number of models have been proposed of the form $\langle \epsilon_d \rangle / \langle \epsilon_s \rangle \sim M_t^\alpha$ where $\langle \epsilon_s \rangle = \langle \mu |\boldsymbol{\omega}|^2 \rangle$ is the solenoidal dissipation, and α takes different values depending on model adopted and the difference assumptions [6]. Here we also show that this form cannot describe adequately the available data but we show that δ can. Another example of the inability of M_t to collapse the data but the success of the combination of M_t and δ, is the skewness of velocity gradients, a measure of the non-linearity in the flow and the production of vortical motions. The conclusion from these observations based on a large number of studies, is that universality does seem to emerge in compressible turbulence but only when an additional parameter including dilatational motions is included.

THE BROAD PICTURE

Universal scaling laws provide a basis for characterization, deeper understanding and modeling of complex physical phenomena. While tremendous advances in incompressible turbulence have been built on this basis, universal scaling laws for compressible turbulence have been much more elusive. We argue here that a main reason for this state of affairs is the incorrect identification of non-dimensional groups to characterize completely the statistical state of the turbulence. By including a new parameter $\delta = u_{d,rms}/u_{s,rms}$, we show that it is possible to collapse all data available for isotropic and homogeneous shear flows. Thus, we argue that the state of the turbulence ought to be identified in a δ-M_t plane as shown in Fig. 1(right). Depending the specific values of M_t and δ turbulence may exhibit fundamentally different behaviors as depicted with the different shaded regions [3]. This clearly highlights the reason why M_t alone is insufficient to characterize these flows, even in isotropic setups. The analysis also provides evidence for an ultimate regime at high Mach numbers, based on statistical mechanics and renormalization group, that leads to equipartition between solenoidal and dilatational components of the velocity field. Overall, this work provides a new view on how to seek universality in compressible turbulence, leading to new venues for better models and deeper understanding.

References

[1] A. S. Monin and A. M. Yaglom. *Statistical Fluid Mechanics, Vol. II*. MIT Press, 1975.
[2] U. Frisch. *Turbulence*. Cambridge University Press, 1995.
[3] D. A. Donzis and J. P. John. Universality and scaling in compressible turbulence. *arXiv*, (1907.07871), 2019.
[4] S. K. Lele. Compressibility effects on turbulence. *Annu. Rev. Fluid Mech.*, 26:211–254, 1994.
[5] T. B. Gatski and J-P. Bonnet. *Compressibility, turbulence and high speed flow*. Elsevier, second edition, 2013.
[6] P. Sagaut and C. Cambon. *Homogeneous Turbulence Dynamics*. Cambridge University Press, Cambridge, 2008.

IMPACT OF FREESTREAM TUNNEL NOISE ON THE MACH 6 FLOWINTERACTING WITH A 35 DEGREE COMPRESSION RAMP

Fabian Dettenrieder, Bryson Sullivan, and Daniel J. Bodony *
Department of Aerospace Engineering, University of Illinois, Urbana, Illinois, U.S.A.

Summary Conventional blow down wind tunnels generate acoustic fields from their boundary layers that impinge on the test article. At supersonic speeds, the model's bow shock distorts the sound and generates vortical and entropy waves that also impact the model. These disturbances affect the model's boundary layers and alter their transition and separation, subsequently affecting global properties of the flowfield. We study this process for a Mach 6 flow approaching a 35 degree compression ramp mounted on a flat plate with a sharp leading edge using direct numerical simulation. The conditions and model geometry match experiments conducted in the NASA Langley 20-inch Mach 6 tunnel. The incoming sound field is constructed from tunnel characterization data and included in the DNS. Comparisons of the flat plate–compression ramp flows are made between the quiet and sound-laden freestreams.

INTRODUCTION

High-speed flight is characterized, in part, by the dynamic interaction of the flow field around the inner and outer mold lines of the vehicle with the surface material and its underlying structure. Deflected vehicle control surfaces are especially prone to fluid-thermal-structure interaction (FTSI) and motivate the problem considered here (left panel of Fig. 1). Studying the FTSI of a deflected control surface with a high-speed flow is an important component of ensuring that engineering models used for vehicle design are sufficiently accurate so that vehicle integrity can be assured without the weight increase of over-design.

An ongoing, joint computational-experimental investigation between the authors and Professor Stuart Laurence (University of Maryland) is examining the shock wave–boundary layer interaction (SWBLI) of a Mach 6 flow approaching a 35 degree ramp fitted with a compliant insert, as shown in the right panel of Fig. 1. The experiments are being conducted in the NASA Langley Research Center 20-inch Mach 6 conventional blow down tunnel (see insert of Fig. 1). The 35 degree compression ramp is mounted on a 280 mm wide by 711 mm long flat plate with a sharp leading edge and exposed to the Mach 6 flow for approximately 5 seconds. Low- and high unit (per meter) Reynolds numbers of 6.6×10^6 and 23.6×10^6 were tested, resulting in ramp-approaching boundary layers that were transitional or turbulent, respectively. No measurements are available to document the boundary layer development along the flat plate. The freestream static pressure, temperature, and density values are 1,990 Pa, 63 K, and 0.11 kg/m^3. The tunnel stagnation temperature is approximately 516 K. More details can be found in [1].

The NASA LaRC 20-inch Mach 6 tunnel is conventional in the sense that tunnel wall boundary layers are turbulent and generate noise. It is well known in boundary layer transition studies that tunnel noise lowers the Reynolds number at which turbulence is observed. It is less well known how tunnel noise alters the details of the compression ramp SWBLI flow of interest and, more importantly, how it impacts validating computational models against the experimental data. The objective of this work is to evaluate the impact of tunnel noise on the details of the ramp SWBLI and, ultimately, how it affects the dynamic response of a compliant panel fitted on the ramp.

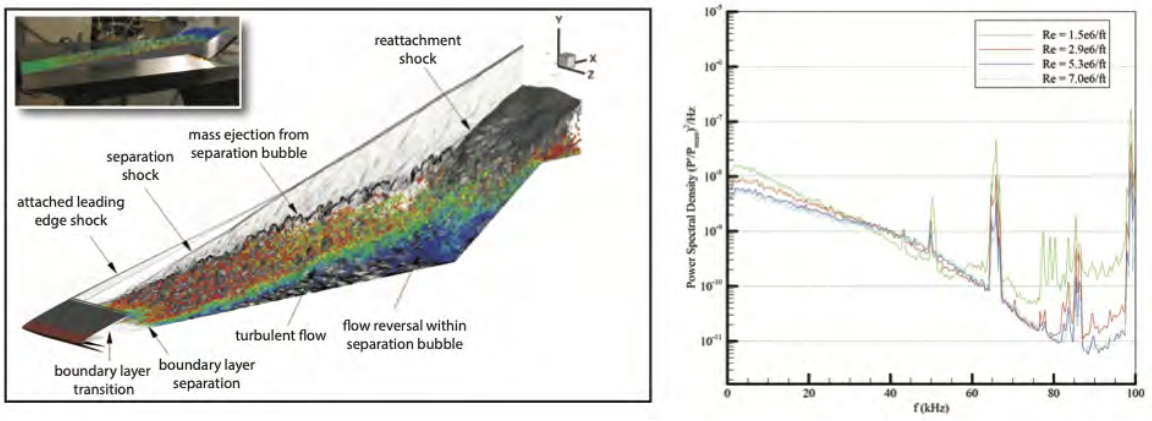

Figure 1: Left figure: Quiet freestream DNS of Mach 6 flow impinging on a compliant and deflected control surface with corresponding experimental validation (inset). Right figure: tunnel noise power spectral density (from [2]).

*Corresponding author. E-mail: bodony@illinois.edu

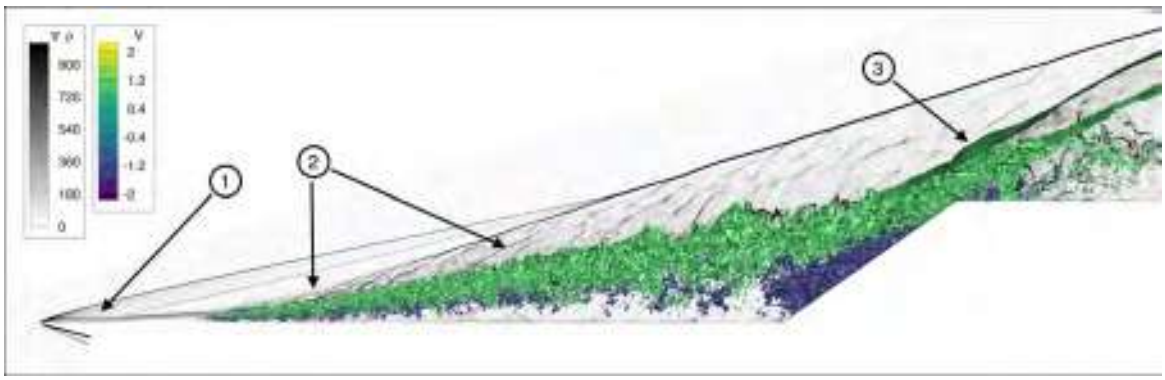

Figure 2: Quiet freestream DNS density gradient magnitude and iso-contours of wall-normal velocity showing (1) laminar boundary layer, (2) Mach waves radiated into the farfield, and (3) shocklets forming along the reattachment shock.

RESULTS

Two DNS of the flat plate–compression ramp model are used to examine how the tunnel freestream sound impacts the SWBLI described in the Introduction. The equations of continuity, momentum, and total energy for a compressible, viscous, perfect gas in curvilinear coordinates are solved using a high-order WENO spatial scheme and fourth order Runge-Kutta for time advancement. MPI and OpenMP are used for parallelization, and parallel HDF5 is used for input/output. The ghost cell approach is used for all computational boundaries. All solid surfaces are modeled as no-slip, isothermal walls with 300 K as the fixed temperature. The higher unit Reynolds number condition was studied. The simulations start from a uniform Mach 6 flow and are allowed to reach steady state. The simulation domain encompasses the entire flat plate, starting upstream of the leading edge, the compression ramp, and a portion of the region downstream of the ramp. The spanwise width of the domain is 60 mm and assumed to be periodic. The grid size is $5900 \times 500 \times 1080$ in the streamwise, wall normal, and spanwise directions. A grid convergence study (not shown) has confirmed robustness of the quantities of interest to further grid size increases.

DNS with a quiet freestream

A side-view of the DNS with a quiet freestream is shown in Fig. 2. The boundary layer is laminar just downstream of the leading edge and experiences laminar separation within 10% of the flat panel length. The separated boundary layer quickly transitions to turbulence and becomes an extensive shear layer that impinges the ramp more than half way up from the corner and forms the upper boundary of a large separation zone. The size of the separation bubble and location of the shear layer impact on the ramp exceed those found in the experimental data [1].

DNS with a sound-laden freestream

Rufer & Berridge [2] conducted a freestream noise survey of the NASA LaRC 20-inch Mach 6 tunnel using PCB and Kulite transducers. A sample power spectral density is shown in Fig. 1 for four different Reynolds numbers. At the highest unit Reynolds number, the incident pressure fluctuation root mean square is 1% of the freestream pressure.

The highest Reynolds number spectrum from Fig. 1 was used to estimate the freestream sound field. Several assumptions were necessary, including: (1) the rectangular tunnel walls contributed equally to the radiated sound from the turbulent boundary layers as measured by the probes, (2) the probes measured the post-shock pressure fluctuations, (3) the probe tip shock was normal to the freestream, (4) the phase of the sound field was random, and (5) the freestream sound was planar. Assumptions (1)–(5) can be used to estimate the freestream sound $p'(\vec{x},t)$, $\vec{u}'(\vec{x},t)$ and $\rho'(\vec{x},t)$ which must be added to the otherwise constant freestream pressure p_∞, velocity U_∞, and density ρ_∞. The DNS with the incident sound will be presented and compared with the quiet DNS results.

ACKNOWLEDGEMENTS

This material is based upon work supported by the Air Force Office of Scientific Research under award number FA9550-18-1-0035. Computational resources were provided through NSF XSEDE Stampede2 and Frontera clusters (TG-CTS090004) at the Texas Advanced Computing Center (TACC).

References

[1] T. Whalen, R. E. Kennedy, S. J. Laurence, B. Sullivan, D. J. Bodony, and G. Buck. Unsteady surface and flowfield measurements in ramp-induced turbulent and transitional shock-wave boundary-layer interactions at Mach 6. AIAA Paper 2019-1127, Presented at the 2019 AIAA SciTech Meeting and Exhibit, San Diego, CA, January 2019.

[2] S. J. Rufer and D. C. Berridge. Pressure fluctuation measurements in the nasa langley 20-inch mach 6 wind tunnel. AIAA Paper 2012-3262, Presented at the 42nd AIAA Fluid Dynamics Conference and Exhibit, 25–28 June 2012, New Orleans, LA, June 2012.

SCALING OF DECAYING TURBULENT KINETIC ENERGY IN COMPRESSIBLE TURBULENT MIXING

Eunhye An[1] and Eric Johnsen *[1]
[1] Department of Mechanical Engineering, University of Michigan, Ann Arbor, USA

Classical Kolmogorov theory is restricted to incompressible and homogeneous flow of a single fluid. However, compressible turbulent mixing involves compressibility effects and inhomogeneities, for which the classical theory is not directly applicable. In this work, we present a scaling for the rate of decay of turbulent kinetic energy in compressible turbulent mixing, in which an inhomogeneity in turbulent intensity gradients is imposed. We explain the compressible turbulent mixing at the interface by considering dilatation of turbulent kinetic energy in turbulent energy balance equation. This scaling law is compared with DNS results, with good agreement.

INTRODUCTION

Kolmogorov theory applies to incompressible, homogeneous flows of a single fluid. However, for compressible, inhomogeneous flows of multi-material fluids, the turbulence phenomenology is less well understood. Such situations can be found in engineering and nature. Turbulent mixing at gradients in turbulent intensity plays an important role in a variety of oceanic, atmospheric and astrophysical flows. For example, in the oceans, intensity gradients originate from wind along the surface or internal-wave breaking where energy cascades into smaller scales, thus leading to turbulent mixing. Additionally, in astrophysics, the turbulence in the interstellar medium (ISM) is compressible [1], with mixing between hotter and cooler regions. To understand these phenomena, it is essential to investigate the mechanism of turbulent mixing under different conditions and determine the parameters controlling the turbulent mixing process.

Previous studies of multi-component and/or compressible turbulent mixing have been carried out. Tordella and Iovieno [2] investigated the effects of difference in spectral energy with integral length scale gradients in incompressible turbulent mixing and observed both self-similarity and intermittency. Movahed and Johnsen [3] considered fluids with different densities, but the same kinematic viscosities, to understand the role of density gradients alone. However, the effect of other variables such as turbulent kinetic energy (TKE) intensity and the scaling of the mixing region growth have not been explored in detail. In this study, we introduce a scaling for the rate of decaying TKE and the mixing region growth in turbulent mixing between turbulent flows of different initial intensities.

NUMERICAL SETUP

Direct Numerical Simulation (DNS) of the compressible Navier-Stokes equations are performed for a binary system of ideal gases. The discretization scheme is based on explicit sixth-order central differences and fourth-order Runge-Kutta time marching. To simulate decaying turbulence more efficiently, a new initialization procedure was developed [4], in which a surrogate simulation is started and rescaled appropriately to the desired initial conditions. The corresponding initial velocity fields consist of fully developed turbulence initiated from a Batchelor spectrum with desired properties from the beginning.

We juxtapose two cubes where turbulent diffusion occurs at the interface and used the same fluid with different turbulent intensities. The root-mean-square velocity and the corresponding Reynolds number are varied, but all other variables such as density, viscosity, and Taylor micro-scale, are kept the same. Zero-gradient and periodic boundary conditions are applied in the inhomogeneous and spanwise directions, respectively.

SCALING

Under no forcing, the volume averaged TKE decays only by dissipation.

$$\frac{dk}{dt} = -\varepsilon \qquad (1)$$

When equation (1) is scaled by a single, constant eddy turnover time, τ, which is defined as Taylor micro-scale over the root-mean-square velocity, the TKE is shown to decay exponentially. When comparing results for a single fluid in a periodic domain for different time scales and Reynolds numbers, the TKE still exhibits exponential decay with the same exponent. However, for inhomogeneous flow like turbulent mixing, the relationship between the rate of TKE decay and dissipation is more complicated.

To address this issue, we start by considering the energy transfer term, $\frac{\partial u_i u_i u_j}{\partial x_j}$ [5] and decompose it in non-conservative form with two terms: dilatation and advection of TKE. In compressible flow, the dilatation of TKE is expected to be much larger than the advection term, so we take only the dilatational term into account. Integrating the resulting equation, a conservation law for TKE is obtained as follows, in which TKE is defined as exponential function whose argument has two terms:

*Corresponding author. E-mail: ejohnsen@umich.edu

$$k/k_0 = exp\left[-\left(c_1\, t/\tau + c_2 \int \sqrt{\Delta} dt\right)\right] \qquad (2)$$

RESULTS

For inhomogeneous flow, energy transfer at the interface is important. To understand the mixing behavior, we divide the volume into three regions: the mixing region and the regions left/right of the mixing region (referred as region 1 and region 2 below). Then, total TKE can be predicted as the sum of TKE, possibly with different coefficients in each region:

$$\langle k \rangle_{total} = a_1 \langle k \rangle_1 + a_m \langle k \rangle_{mix} + a_2 \langle k \rangle_2 \qquad (3)$$

Time scales are also likely different in each region due to the different root-mean-square velocities. The TKE averaged in region 1, in the mixing region, and in region 2 with respect to time scaled according to the different regions are presented in Figure 1. All cases with different intensity ratios have the same decay rate, while the TKE scaled only by a single, eddy turnover time decay with different rates. In regions 1 and 2, it is necessary to consider the dilatational time corresponding to this scaling. However, in the mixing region, the TKE decays only with eddy turnover time. This behavior occurs because compressibility (e.g., acoustic waves) has little effect on mixing region and only large-scale eddies are responsible for mixing. Furthermore, coefficients a_1, a_m, and a_2 in eq (3) can be determined by the mixing region extent. The mixing region is captured by the mass fraction of scalar [6]. We found that the mixing region grows as a power-law with an exponent close to 0.4. Also, the left and the right interfaces evolve with the same exponent. Thus, all coefficients in eq (3) are defined as power-law relations. As a result, a final formation of decaying TKE is obtained as follows:

$$\langle k \rangle_{total} = \sum_{n=1,m,2} a_n \langle k \rangle_n \qquad (4)$$

$$a_n \langle k \rangle_n = f(\Delta, u_{rms}, h_0, t) = \begin{bmatrix} \left(\frac{1}{2} - \frac{h_L}{L_t}\right) k_{r1,0} exp\left[-\frac{c_\varepsilon}{\pi}\left(\frac{t \cdot u_{rms1,0}}{\lambda_0} + \frac{1}{(2\pi)^2}\int \sqrt{\Delta^2} dt\right)\right] \\ \left(\frac{h}{L_t}\right) k_{m,0} exp\left[-\frac{c_\varepsilon}{\pi}\left(\frac{t \cdot u_{rmsm,0}}{\lambda_0}\right)\right] \\ \left(\frac{1}{2} - \frac{h_R}{L_t}\right) k_{r2,0} exp\left[-\frac{c_\varepsilon}{\pi}\left(\frac{t \cdot u_{rms2,0}}{\lambda_0} + \frac{1}{(2\pi)^2}\int \sqrt{\Delta^2} dt\right)\right] \end{bmatrix}$$

where Δ is the dilatation, c_ε the dissipation quantity, and h the mixing region width. Results from DNS and the scaling agree well. Our scaling thus predicts the decay of TKE as well as turbulent mixing with turbulent intensity gradients.

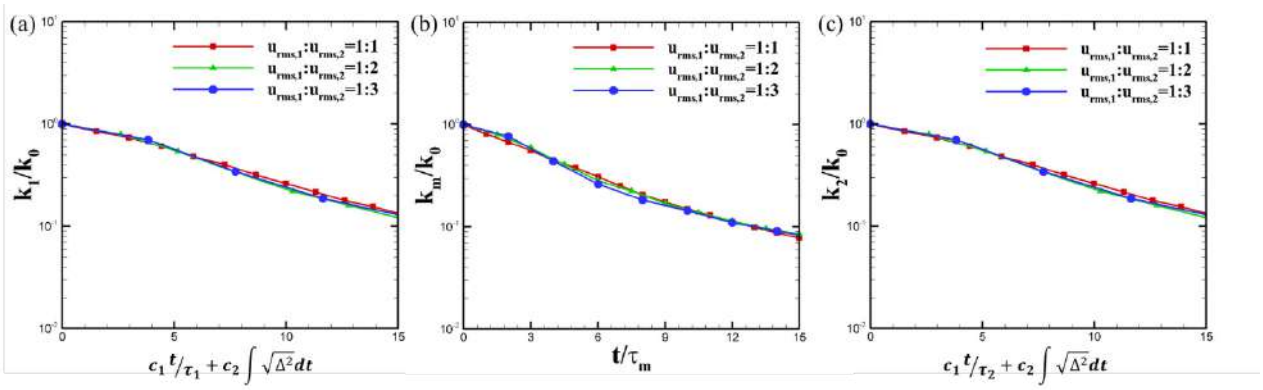

Figure 1. Turbulent kinetic energy averaged in (a) the left side, (b) mixing region and (c) the right side based on the mixing region as a function of the scaled time scale.

CONCLUSIONS

We present a scaling for the mixing region growth and TKE decay in compressible and inhomogeneous turbulent flow. Due to the inhomogeneity, the energy flux through interface plays a significant role in the compressible transport of TKE. Total TKE can be divided into the sum of TKE from the different regions separated by mixing region interfaces. The TKE decay agrees well with the proposed scaling. In the future, coefficients of the scaling will be parameterized and the formation of mixing region growth and decaying TKE completed.

References

[1] Begelman, M. C. and Fabian, A. C. Turbulent Mixing Layers in the Interstellar and Intracluster Medium. *Royal Astr. Soc*. **244**:26-29, 1990.
[2] Tordella, D. and Iovieno, M. Numerical Experiments on the Intermediate Asymptotics of Shear-Free Turbulent Transport and Diffusion. *J. Fluid Mech*. **549**: 429-441, 2006.
[3] Movahed P. and Johnsen E. The Mixing Region in Freely Decaying Variable-Density Turbulence. *J. Fluid Mech*. **772**: 386-426, 2015.
[4] An E and Johnsen E. Initialization of Decaying Turbulence to Study Turbulent/Non-Turbulent Interfaces. *71st Ann. Meeting of APS DFD*. **63**:13, 2018.
[5] Barrenblatt et al. Evolution of a Turbulent Burst. *Inzhenerno-Fizicheskii Zh*. 53:733-740, 1987.
[6] Cook A. W. and Dimotakis P. E. Transition Stages of Rayleigh-Taylor Instability between Miscible Fluids. *J. Fluid Mech*. 443:69-99, 2001.

SHOCK-LIKE STRUCTURES IN A SONIC VENTURI NOZZLE

B. Zebrowski *[1], P. Jordan[1], V. Jaunet[1], G. Lehnasch[1], R. Maury[2], and M. A. Lambert[2]
[1] Département Fluides, Thermique et Combustion, Institut Pprime - CNRS - Université de Poitiers - ENSMA, 86962 Chasseneuil-du-Poitou, France
[2] CESAME-EXADEBIT, 86000 Poitiers, France

Summary A duct acoustic analysis is performed in the cylindrical throat of a sonic venturi nozzle, in order to understand shock-like structures observed in numerical simulations. The cylindrical throat is considered as an infinitely extended hard-walled duct, in which the flow is circulating at critical condition (Mach around 1). The analysis shows that a simple analytic model, depending only on the Mach number, is able to capture the periodic flow pattern observed in the simulations.

INTRODUCTION

Critical flow venturi nozzles are devices widely used for gas flow-rate measurement. From one-dimensional Euler equations, it is straightforward to show that the mass flow-rate only depends on the stagnation quantities of the incoming flow, the nozzle critical section and the gas thermodynamic properties. These devices are defined by international standard ISO9300 [1], which includes an empirical correction factor, the discharge coefficient C_d, that account for viscous and three-dimensional effects.

A recent investigation of cylindrical-throat Venturi nozzles has highlighted a flow topology in the cylindrical section of the venturi nozzle, in which a periodic flow pattern appears (Figure 1b) [2] .

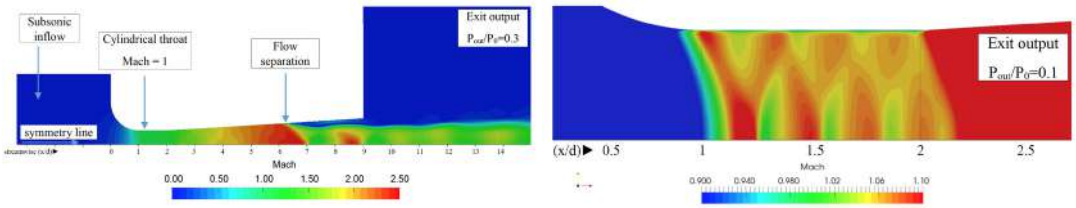

(a) Overview (b) Throat region

Figure 1: Mach contour obtained via RANS simulation of ISO9300 standard cylindrical-throat Venturi nozzles. Throat diameter 10mm.

The present work is motivated by the understanding of the origin and the modeling of this flow pattern. Indeed, the successive compression/expansion of the flow may result in a specific behavior of the boundary layer growth, that may need to be accounted for in the modeling of the nozzle discharge coefficient C_d.

METHODOLOGY

The problem is considered using a duct-acoustics model. The configuration considered involves an inviscid, isentropic plug flow in an infinitely extended hard-walled cylindrical duct flow. Using the Reynolds decomposition and assuming that the pressure fluctuation can be described by a normal mode-ansatz

$$p'(x,r,\theta,t) = \hat{p}(r)e^{i(kx+m\theta-\omega t)}, \tag{1}$$

the linearized Euler equations around the base flow reduce to one equation for the pressure fluctuation [3] :

$$\hat{p}'' + \frac{1}{r}\hat{p}' + \left((\omega - Mk)^2 - k^2 - \frac{m^2}{r^2}\right)\hat{p} = 0, \tag{2}$$

where k is the wave number, m the azimuthal wave number, ω the frequency, r the dimensionless duct radius and M the Mach number in the throat. Solution to Equation (2) can be written in form of Bessel functions $\hat{p} = J_m(r\alpha)$, where $\alpha^2 = (\omega - Mk)^2 - k^2$ is the dispersion relation.

The flow pattern observed is assumed independent of time, we thus consider $\omega = 0$. The azimuthal wave number chosen for the study is $m = 0$. Introducing the wave length $\lambda = \frac{2\pi}{k}$ in the dispersion relation gives :

*Corresponding author. E-mail: bruno.zebrowski@ensma.fr.

$$\lambda_n = \frac{2\pi\sqrt{(M^2-1)}}{\alpha_n} \tag{3}$$

where values of α_n are found by imposing a Neumann boundary condition at the duct wall $\frac{\partial p}{\partial r}\Big|_{r=1} = J_0'(\alpha_n) = 0$, with n being the n$^{\text{th}}$ root of J_0'. Equation (3) is also known as Prandtl-Pack [4] shock cell model, which was first introduced to describe shock cells wave-length in jets. The difference is that, in the jet, a different pressure boundary condition is imposed to solve Equation (2).

RESULTS

A modelled flow field is obtained by superposing a uniform flow field, at the mean Mach number (averaged along the cylindrical throat region) of the simulated flow, and a the normal mode ansatz (1) for k at $n = 1$ and arbitrary amplitude. A comparison between the modelled flow field and the simulated one is given in Figure 2a.

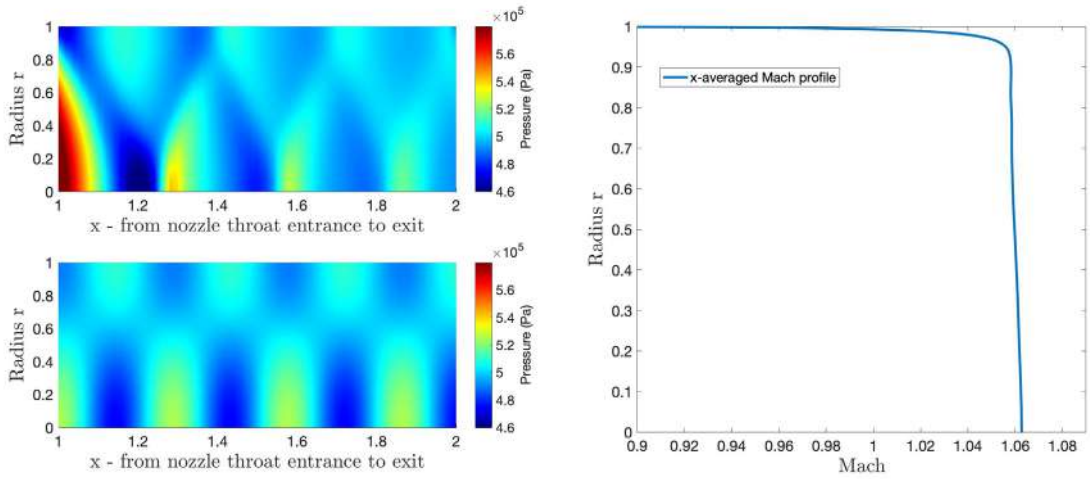

(a) (b)

Figure 2: (a) Pressure in the cylindrical throat region. Top : RANS simulation (NPR = 10) - Bottom : first mode from duct-acoustics model for M = 1.06 (b) x-averaged Mach profile from RANS simulation in the throat region

As the flow pattern can only appear if the Mach number of the base flow is supersonic, this implies that the flow computed by the RANS simulation in the throat region is not sonic as we expect but slightly supersonic. This is illustrated in Figure 2b, where the spatially averaged Mach profile inside the throat is plotted. The Mach number is greater than 1.0 in the region of uniform flow, which is the result of the small inlet radius of curvature. Similar analysis has been done for several nozzle pressure ratio ($\frac{P_{in}}{P_0}$), the same conclusion is drawn from these results.

CONCLUSIONS

A duct acoustics analysis has been used to describe shock-cell patterns observed in RANS simulations of the ISO9300 standard cylindrical throat venturi nozzle. The results show good agreement between duct acoustics model and the RANS simulations. This information will be useful for the improvement of models of the discharge coefficient of cylindrical venturi nozzles.

References

[1] ISO 9300. Measurement of gas flow by means of critical flow Venturi nozzles. (2005).
[2] Lambert M. A., Maury R., Valière J.-C., Foucault E. and Lehnasch G. Experimental and numerical investigations on the shape and roughness of cylindrical critical flow venturi nozzles (CFVN), *19th International Congress of Metrology*, 17003, Paris, 2019
[3] Rienstra S. Fundamentals of Duct Acoustics. *Technische Universiteit Eindhoven*, 2015, Page 3 - 26.
[4] Pack D. C. A note on Prandtl's formula for the wave-length of a supersonic gas jet *The Quarterly Journal of Mechanics and Applied Mathematics*, Volume 3, Issue 2, 1950, Pages 173 - 181.

CHARACTERISTICS OF ENTROPY LAYER FOR CONES AND CYLINDERS IN SUPERSONIC FLOWS

WANG Gang*, Xie Zhu-xuan, Yang Yan-guang
China Aerodynamics Research and Development Center, Mianyang 621000, China

Abstract: An analytic method is presented to study the distribution of vorticity downstream the shock wave and the characteristics of the entropy layer for various cones and cylinders in supersonic flows. The relations of shock-shape, the distribution character of various parameters within the shock layer, and the entropy increment were combined to obtain the characteristics of vorticity and the entropy gradient. Numerical simulation are performed at the Mach number of 3, 5 and 10. The results indicate that the distribution of entropy and vorticity is connected with shock shape directly. Due to the differences of the shape of shock, the vorticity and the extreme value of entropy gradient for blunt-nosed cylinders are both larger than the cases for flat cylinders. As the shock-shape of flat-nosed cylinders is more liable to be affected than blunt-nosed cylinders with increasing Mach number, the position of the extreme value moves to the surface as the Mach number increases for flat-nosed cylinders, while it remains the identical value for blunt-nosed cylinders. The vorticity is regarded as the criterion of the edge of entropy layer in the normal direction, and two methods are proposed and discussed to estimate the edge.

Keywords: Entropy layer; Vorticity distribution; Supersonic flows; Blunt-nosed cylinder.

Methods

Entropy gradient as the streamlines just flow across the shock wave:

$$\frac{\mathrm{d}s}{\mathrm{d}\bar{y}} = f(M_\infty, \overline{R_c}, \bar{y}, \beta) \tag{1}$$

$\mathrm{d}s/\mathrm{d}\bar{y}$ is relatively complicated which may occupy the space, but it is not difficult to illustrate the expression. In particular, for a calorically perfect gas within the shock layer, the specific heats at constant pressure c_p is constant as

$$c_\mathrm{p} = \frac{\gamma}{\gamma - 1} R_\mathrm{con} \tag{2}$$

Then, Eq.(1) is to be written as

$$\frac{\mathrm{d}s}{\mathrm{d}\bar{y}} = -\frac{4\gamma \overline{R_\mathrm{c}}^2 R_\mathrm{con} cos^4\theta}{\sin^2\theta} \frac{(M_\infty^2 \sin^2\theta - 1)^2}{(2\gamma M_\infty^2 \sin^2\theta - \gamma + 1)[(\gamma - 1)M_\infty^2 \sin^2\theta + 2]} \tag{3}$$

Entropy distribution behind the shock wave

$$\delta s = s - s_\infty = \int c_\mathrm{p} \frac{\mathrm{d}T}{T} - R_\mathrm{con} ln \frac{p}{p_\infty} \tag{4}$$

s is the entropy at a given temperature T and pressure p, and s_∞ is the entropy of incoming flow.

The entropy layer introduces a large amount of rotationality into inviscid flows over bodies, as can be quantitatively obtained from Crocco's theorem, which could be written as follows

$$\frac{\partial \vec{u}}{\partial t} - T\nabla s + \vec{w} \times \vec{u} + \nabla h_0 = 0 \tag{5}$$

In Eq.(5), $\vec{u}$ is the local velocity vector along the streamline; h_0 is the total enthalpy. For steady and adiabatic flows, h_0 is constant, and hence $\nabla h_0 = 0$. The vorticity $\vec{w}$ is related to the entropy gradient ∇s normal to a streamline

$$T\nabla s = \vec{w} \times \vec{u} \tag{6}$$

In Eq.(6), $\nabla s = \frac{\mathrm{d}s}{\mathrm{d}n}\vec{n}$, in which $\vec{n}$ is perpendicular to the local surface, hence

$$\frac{\mathrm{d}s}{\mathrm{d}n} = \frac{1}{\cos\alpha}\frac{\mathrm{d}s}{\mathrm{d}\bar{y}} \tag{7}$$

Results

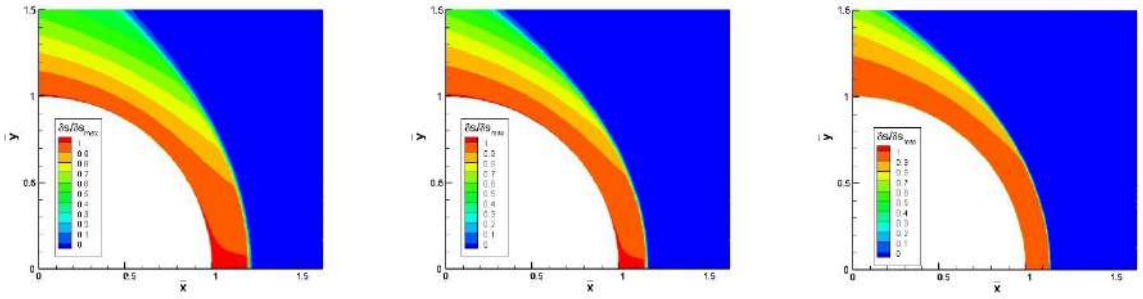

Fig.1 Entropy increase $\delta s/\delta s_{max}$ for blunt-nosed cylinders (Left:$M_\infty = 3$;Middle:$M_\infty = 5$;Right:$M_\infty = 10$)

*Corresponding author. E-mail: wanggang@cardc.cn

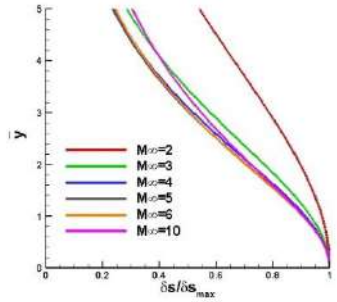

Fig.2 Entropy increase of flat-nose cylinders

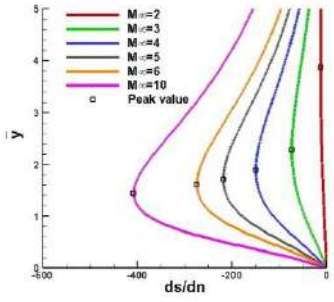

Fig.3 Distribution of ds/dn for flat-nose cylinders

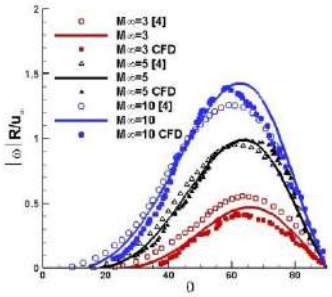

Fig. 4 Distribution of $\overline{|\omega|}$ for blunt-nosed cylinders

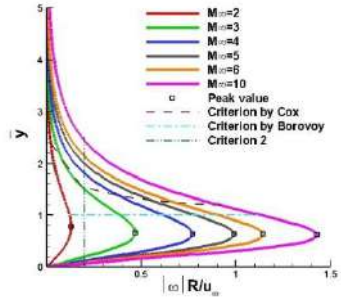

Fig.5 Distribution of $\overline{|\omega|}$ for blunt-nosed cylinders (For criteria proposed by Cox and Borovoy, regarding the $\bar{y} = 0$ as one edge of entropy layer, and the other edge is shown in the Figure)

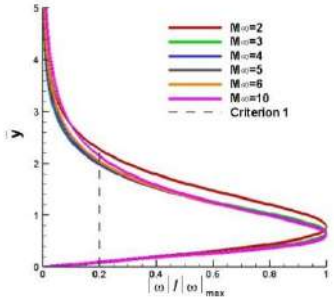

Fig.6 Distribution of $|\omega|/|\omega|_{max}$ for blunt-nosed cylinder

Conclusion

An method for estimating the distribution of entropy and vorticity for blunt-nosed cones and flat-nosed cylinders has been developed. The distribution of entropy increase, entropy gradient, and the vorticity are all related to the shape of shock waves directly. As the shock-shape of flat-nosed cylinders is more liable to be influenced than blunt-nosed cylinders with increasing Mach number, the position of the extremum moves to the surface as the Mach number increases for flat-nosed cylinders, while it nearly remains the identical value for blunt-nosed cylinders. Two hypotheses to define the edge of the entropy layer in the normal direction are proposed and the results have been discussed in detail. Although the method for defining the edge of the entropy layer is still open, it should be on the basis of the distribution of vorticity. What is more, the distribution of the entropy gradient and also the distribution of vorticity decreases slightly as the cone angle increases.

References

[1] Anderson, J.D., Hypersonic and High-Temperature Gas Dynamics2006, Virginia: American Institute of Aeronautics and Astronautics,Inc. 375-395.
[2] Hirschel, E.H., Basics of Aerothermodynamics2005, Zorneding, Germany: Springer. 169-170.
[3] Holden, M.S., Leading Edge Bluntness and Boundary Layer Displacement Effects on Attached and separated Laminar Boundary Layers in a Compression Corner, in AIAA 6th Aerospace Sciences Meetings1968: Now York.
[4] M.S.Holden, Boundary-layer displacement effects and Leading-edge bluntness on attached and separated laminar boundary layers in a compression corner:experimental study. AIAA, 1971. 9(1):p.84-93.
[5] Y.Borovoy, V., et al., Two-Dimensional Interaction of the Oblique Shock Wave with the Boundary and High-Entropy Layers of the Blunt Plate, in 49th AIAA Aerospace Sciences Meeting including the New Horizons forum and Aerospace Exposition2011, AIAA: Orlando, Florida.
[6] Egorov, I.V., Shock Wave Boundary Layer Interaction on Sharp and Blunt Flat Plate. Physics of Gases-Theory and Applications, 2014. 9(4).
[7] Billig, F.S., Shockwave shapes around spherical and cylindrical nosed bodies. Journal of Spacecraft and Rockets, 1967. 4(6): p. 822-823.

NUMERICAL INVESTIGATIONS OF HIGH MACH NUMBER SHOCK / VORTEX INTERACTION

Wang Conglei
HONGGUANG AIRBORNE EQUIPMENT CO., LTD., Nanjing, China

Summary The effect of shock Mach number from 1.2 to 3.0, on the interaction between shock wave and vortex has been numerically investigated using seventh order weighted essentially non-oscillation finite difference scheme. Because of the increasing of the shock wave strength, the higher Mach number shock interacted with vortex produces larger local supersonic area and more shear layers. Results show that the counter rotating vortex moving downward after interacted with shock. When shock Mach number increases enough, there is a new vortex generated by the escaped shock appeared up to the original vortex core and disappeared at last. Furthermore, double two-layer Lamb vector divergence structures exist in the higher shock Mach number cases and only one in the lower Mach number cases, which indicate shear layers appear in these positions.

The interaction between shock and turbulence is an important phenomenon in supersonic flow, and the interaction between shock and vortex is an important part of the interaction between shock and turbulence, which exists widely in high-speed compressible flows. The aerospace field has a wide range of application backgrounds, such as applications such as supersonic engines, supersonic aircraft and rapid inflation of inflatable structures. To date, a wide range of experimental studies [1,2], theoretical analysis [3,4], and numerical simulations [5,6] have been carried out for the problem of shock wave and vortex interaction. The related research on the mechanism of shock wave and vortex train and the interaction between shock wave and strong vortex [7,8]. Although there have been many studies on the interaction between shock waves and vortices, little attention has been paid to the interaction between high Mach number shock waves and strong vortices. The flying Mach number is mostly greater than 2.0. Therefore, in this paper, the interaction between shocks with Mach number 1.2-3.0 and strong vortex with Mach number 1.2 is studied and analysed. The changes of the strong vortex structure under the action of shocks with different Mach numbers are demonstrated. The motion and deformation of vortex and the change of vorticity under shock are researched and analysed, and the important influence of shock intensity on vorticity generation and transportation is revealed. Furthermore, the flow mechanism of vortex motion and deformation under shock of different Mach numbers is discussed.

Mathematical formulation and numerical method

Euler equation in conservative form can be expressed as:

$$\frac{\partial \boldsymbol{Q}}{\partial t}+\frac{\partial \boldsymbol{F}}{\partial x}+\frac{\partial \boldsymbol{G}}{\partial y}-\frac{1}{Re}\left(\frac{\partial \boldsymbol{F}_v}{\partial x}+\frac{\partial \boldsymbol{G}_v}{\partial y}\right)=0 \tag{1}$$

Where, $\boldsymbol{Q}$ is the conservation variables. $\boldsymbol{F},\boldsymbol{G},\boldsymbol{F}_v,\boldsymbol{G}_v$ are conservation fluxes. Re is the Reynolds number. x and y are the coordinates. t is time. These equations are numerically solved by a seventh-order weighted essentially non-oscillatory scheme for the convective terms and sixth-order central difference scheme for the viscous terms. The temporal integration is performed using a fourth-order Runge-Kutta algorithm.

Results and discussion

In this section, computational results for the cases including both the subsonic vortex case and supersonic vortex case are presented. The shock structure and its relation with the shock and vortex strengths are discussed.

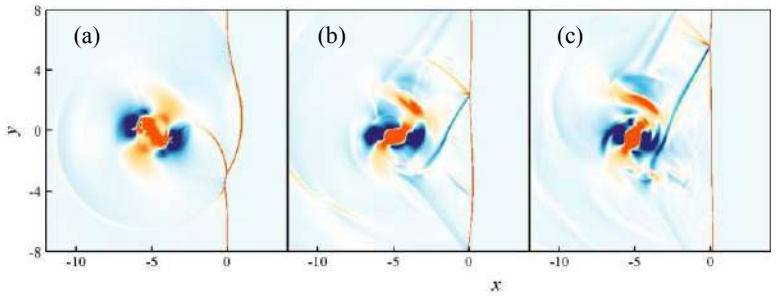

Fig. 1 Vortical structures by iso contours of the Q-criterion in different cases

To exhibit the coherent structures in the flow field, Fig. 1 shows instantaneous snapshots of the flow field depicted by iso-surface of the Q criterion. The deformation of the vortex structure is smaller than that under high Mach number shock conditions. As shown in Fig. 2, with the increase of the Mach number of the shock wave, the vorticity increases when passing through the shock wave is larger, and the vortex amount decreases after leaving the shock wave. Comparing the interaction of shocks and vortices with different Mach numbers, when the shock Mach number is less than 1.6, there are two double-layered structures connecting the vortex and shock above the vortex center. When the shock Mach number is higher than 1.6, a three-layer structure connecting the lower edge of the vortex and the shock appears, indicating that,

the momentum transport mechanism is obviously different from the momentum transport mechanism under the condition of shock wave of small Mach number. It can be found that the vorticity transport mechanism changed significantly when the shock Mach number was greater than 1.6. As shown in Fig. 5, that under the action of low and medium Mach number shocks, only one shear layer appears here. Under the action of shock waves with Mach number greater than 1.6, multiple shear layers appear here.

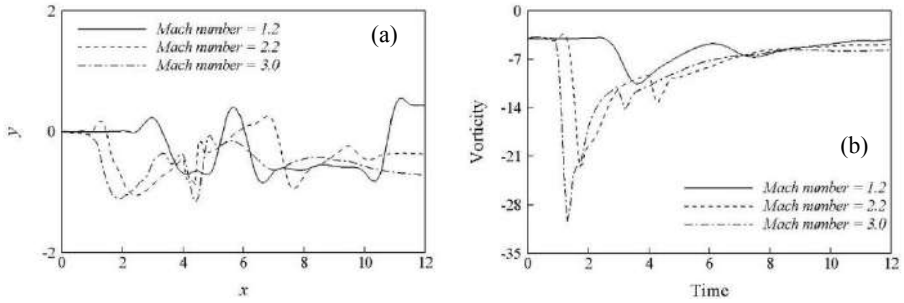

Fig. 2 Trajectory of vortex core and vorticity variation

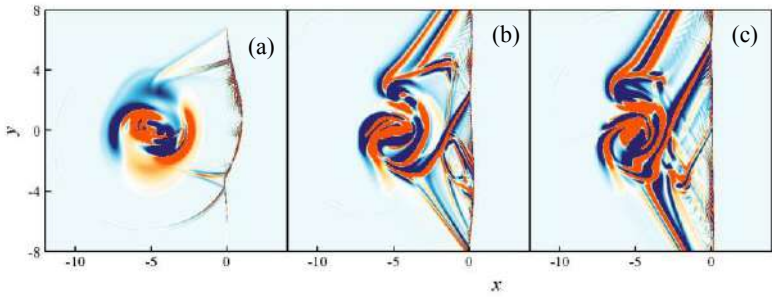

Fig. 3 Variables distribution of flow field in different cases at dimensionless time 0.25

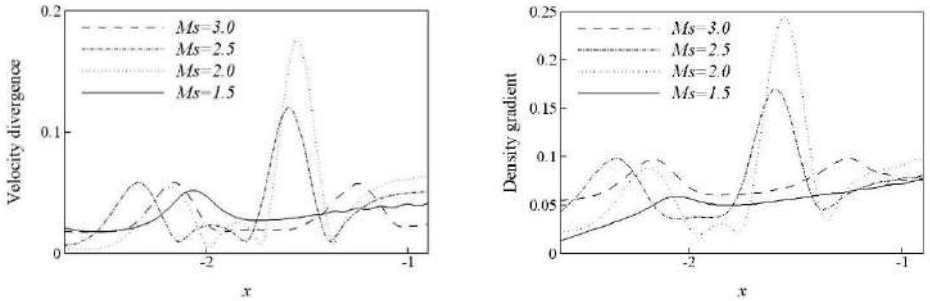

Fig. 5 Velocity divergence and density gradient distribution

CONCLUSIONS

In this paper, a direct numerical simulation method based on the 7th-order WENO algorithm based on eigen decomposition is used to study the interaction between shocks with different Mach numbers and vortices. The flow field appears significantly different from the flow structure under the condition of the interaction between the low Mach number shock and the vortex. Increasing the shock Mach number will increase the vortex core oscillation and increase the vorticity dissipation. When the shock Mach is higher than 1.6, after the vortex interacts with the shock wave, a small vortex will be induced due to the generated shock wave different from the shock condition of the low Mach number shock wave. And in the process of high Mach number shock and vortex, a three-layer structure of Lamb vector divergence and vorticity will appear.

References

[1] Dosanjh, D.S. and Weeks, T.M. (1965). Interaction of a starting vortex as well as a vortex street with a traveling shock wave. AIAA J. 3, 216-223
[2] Naumann, A. and Hermanns, E. (1973). On the interaction between a shock wave and a vortex field. AGARD CP-131, 23.1-23.10.
[3] Ribner, H. S. (1959), The sound generated by interaction of a single vortex with a shock wave. University of Toronto, Institute os aerospace studies. UTIA Rept. 61.
[4] Ribner, H. S. (1985). Cylinder sound wave generated by shock-vortex interaction. AIAA J. 23, 1708-1715.
[5] Ellzey, J.L. and Henneke, M.R. (2000). The acoustic wave from a shock-vortex interaction: comparison between theory and computation. Fluid Dyn. Res. 27, 53-64.
[6] Shuhai Zhang,Yong-Tao Zhang, Chi-Wang Shu (2005). multistage interaction of a shock and a strong vortex, Physics of Fluids, 17,116101.
[7] Barbosa, F. J. and Skews, B. W. (2001). Shock wave interaction with a spiral vortex. Phys. Fluids 13, 3049.
[8] Inoue, O., Takahashi, T. and Hatakeyama, N. (2002). Separation of reflected shock waves due to secondary interaction with vortices: Another mechanism of sound generation. Phys. Fluids 14, 3733-3744.

ENTROPY GROWTH IN VISCOUS BINARY MIXTURE SHOCK WAVE

Damir Madjarević[1] and Srboljub Simić *[2]
[1] Department of Mechanics, Faculty of Technical Sciences, University of Novi Sad, Novi Sad, Serbia
[2] Department of Mathematics and Informatics, Faculty of Sciences, University of Novi Sad, Novi Sad, Serbia

Summary Entropy growth across the shock wave appears as jump when the shock waves are modelled as singular surfaces. When the dissipation is included in the model, jumps of field variables are smoothed out into a continuous shock structure. However, in contrast with expectations, classical Navier-Stokes-Fourier model of gas dynamics exhibits non-monotonic growth of entropy density along the shock profile. The present study investigates the entropy growth in a dissipative model of binary mixture. It shows that internal viscous and thermal dissipation within constituents is insufficient to keep monotonic growth of entropy density, as it was in a single-component gas, but has to be further enhanced.

INTRODUCTION

Shock waves in classical gas dynamics are regarded as propagating singular surfaces on which jumps of the field variables occur. They are related to the speed of propagation of the shock wave through Rankine-Hugoniot relations—localized consequences of the governing conservation laws. It is well-known that Rankine-Hugoniot relations admit multiple solutions for the same value of the shock speed in supersonic, as well as in subsonic regime. Under these circumstances one must have an additional selection rule that distinguishes physically admissible solutions from the ones that are not. The entropy growth condition is one of the accepted criteria that selects supersonic jumps as admissible ones.

When the dissipation is included in the model, e.g. viscous dissipation of Navier-Stokes kind and thermal dissipation of Fourier kind, the jumps of field variables are smoothed out and transformed into a continuous shock structure (shock profile) asymptotically connecting the equilibrium states determined by the Rankine-Hugoniot relations. It is then expected that smoothed entropy profile grows monotonically along the shock structure. However, in contrast with expectations, classical Navier-Stokes-Fourier (NSF) model of gas dynamics exhibits non-monotonic growth of entropy density along the shock profile [1]. This result had been proved to be consistent with the basic modelling assumptions of classical irreversible thermodynamics [2].

Recent studies of the aforementioned unexpected behaviour suggested a possible resolution to the problem [3]. Instead of using the classical equilibrium entropy density, compatible with classical assumption of local thermodynamic equilibrium, it is proposed to exploit the kinetic entropy (as suggested in the kinetic theory of monatomic gases) and to determine its approximate macroscopic form using Grad's approximation and NSF constitutive relations. Such an entropy density increases monotonically along the shock profile.

This study is a part of the ongoing project in which we analyze the entropy growth across the shock wave for different dissipative models of gas dynamics. So far, it was shown [4] that in the multi-velocity and multi-temperature mixture of Euler fluids, a properly defined entropy grows monotonically. The purpose of this study is to extend the model with internal viscous and thermal dissipation and analyze the entropy growth across the shock wave

THE MODEL OF THE MIXTURE

The multi-temperature model of the mixture is built up within the framework of Rational Extended Thermodynamics [5] and consists of balance laws of mass, momentum and energy for each constituent. The state variables of the $n-$component mixture are the density ρ_α, the velocity $\mathbf{v}_\alpha$ and the temperature T_α of each constituent, $\alpha = 1, \ldots, n$. It will be assumed that constituents are not chemically reacting, so that mass of each constituent is conserved. The balance laws of momentum and energy contain the source terms that describe the mutual interaction between the constituents, i.e. exchange of momentum and energy. They present the source of dissipation, and determine the entropy production rate in the case of Euler fluids. Such a system is hyperbolic in the whole state space.

Concerning the model, few remarks are in order [6]: (a) closure of the model is achieved by the application of the entropy principle and Liu's procedure; (b) no prior assumption about local equilibrium was made; (c) entropy density of the mixture is sum of the partial entropy densities, $\rho S = \sum_\alpha \rho_\alpha S_\alpha$; (d) partial specific entropies satisfy partial Gibbs' relations (for constituents), $T_\alpha \mathrm{d}S_\alpha = \mathrm{d}\varepsilon_\alpha + p_\alpha \mathrm{d}(1/\rho_\alpha)$.

This model, even when restricted to Euler fluids, is capable of capturing highly non-equilibrium behaviour through the constituent-related velocity and temperature state variables. In previous studies [7] it was shown that shock structure in binary mixture of Euler fluids exhibits the behaviour that is qualitatively in agreement with the results of kinetic theory of mixtures: in the case of insufficient energy exchange between the constituents, there appears a temperature overshoot of the heavier constituent. Recent study [4], concerned with the entropy growth and entropy production rate in binary mixture shock waves, revealed that mixture entropy density grows monotonically across the shock wave, whereas entropy densities of the constituents may have non-monotonic profiles.

*Corresponding author. E-mail: ssimic@uns.ac.rs.

In this study we enhance the model of binary multi-temperature mixture by taking into account internal viscous and thermal dissipation, and analyze the entropy growth across the plane shock wave. Constitutive relations for viscous stresses and heat fluxes are taken in the classical NSF form for each constituent [8]. The entropy density is also enhanced in the spirit of [3], starting from generalized Grad's velocity distribution for mixtures and incorporating non-equilibrium terms—viscous stresses σ_α and heat fluxes q_α [9]:

$$\rho S = (\rho S)_{\mathrm{Eul}} - \sum_\alpha \left(\frac{3}{8 p_\alpha T_\alpha} \sigma_\alpha^2 + \frac{\rho_\alpha}{5 p_\alpha^2 T_\alpha} q_\alpha^2 \right), \tag{1}$$

where $(\rho S)_{\mathrm{Eul}}$ is the entropy density for mixture of Euler fluids.

PRELIMINARY RESULTS AND DISCUSSION

Shock profiles are numerically computed assuming the travelling wave profile, reducing the model to a system of ordinary differential equations. The solutions asymptotically connect upstream and downstream equilibrium states, related through Rankine-Hugoniot equations for the mixture.

Numerical computations are performed for two particular cases, that differ in the values of upstream Mach number—$M_0 = 1.3$ (Figure 1, graphs (a) and (b)) and $M_0 = 1.6$ (Figure 1, graphs (c) and (d))—while the equilibrium mass concentration of the lighter constituent $c_0 = 0.25$, and the mass ratio of the constituents $\mu = 0.1$, are the same. On graphs (a) and (c), T_1 and T_2 are the dimensionless temperatures of lighter and heavier constituent, respectively, while T is the average dimensionless temperature. For the purpose of comparison, the profiles are presented both for inviscid (mixture of Euler fluids, curves indicated by 1) and for viscous case (curves indicated by 1). In the inviscid case, the entropy density for the mixture of Euler fluids increases monotonically. However, in the viscous case both Eulerian and non-equilibrium entropy density (1), based upon Grad's distribution, have non-monotonic profiles.

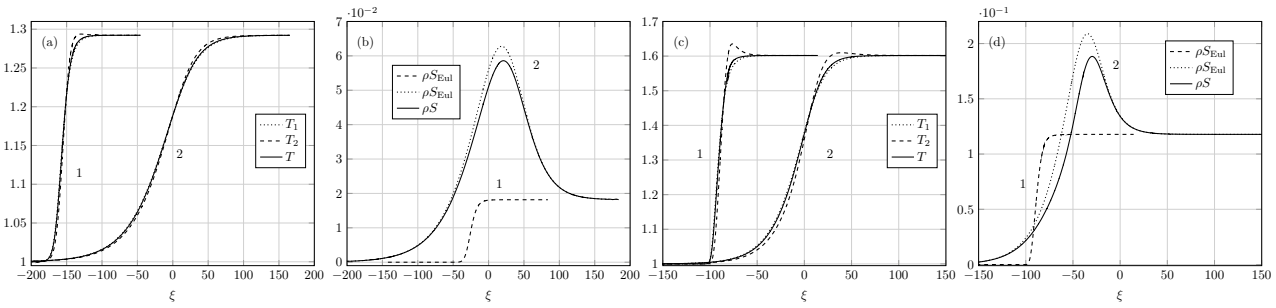

Figure 1: (a) Temperature profiles for inviscid (1) and viscous (2) case, $M_0 = 1.3$; (b) Entropy density profiles for inviscid (1) and viscous (2) case, $M_0 = 1.3$; (c) Temperature profiles for inviscid (1) and viscous (2) case, $M_0 = 1.6$; (d) Entropy density profiles for inviscid (1) and viscous (2) case, $M_0 = 1.6$.

The results of this study show that internal dissipation is insufficient to bring monotonicity to the entropy density within the shock structure, although such a simple extension of the model showed remarkable agreement with the profiles of state variables obtained by the kinetic theory of mixtures [10]. They also suggest that the method proposed in [3] cannot be extended by an *ad-hoc* procedure to mixtures, although it is physically motivated. Instead, it has to be put into broader context that will take into account mutual influences of the constituents on the partial fluxes of momenta and energy. This delineates the framework of our ongoing research.

References

[1] Morduchow M., Libby, P.A. On distribution of entropy through a shock wave, *J. Mécanique*, **4**(2): 191, 1965.
[2] Serrin J., Whang Y.C. On the Entropy Change Through a Shock Layer, *Journal of the Aerospace Sciences*, **28**(12): 990–991, 1961.
[3] Margolin L.G., Reisner J.M., Jordan P.M. Entropy in self-similar shock profiles, *Int. J. Non-Linear Mechanics*, **95**: 333–346, 2017.
[4] Madjarević D., Simić S. Entropy growth and entropy production rate in binary mixture shock waves, *Phys. Rev. E*, **100**: 023119, 2019.
[5] Müller I., Ruggeri T. Rational Extended Thermodynamics, Springer-Verlag, New York 1998.
[6] Ruggeri T., Simić S. On the hyperbolic system of a mixture of Eulerian fluids: a comparison between single-and multi-temperature models, *Mathematical Methods in the Applied Sciences*, **30**(7): 827–849, 2007.
[7] Madjarević D., Ruggeri T., Simić S. Shock structure and temperature overshoot in macroscopic multi-temperature model of mixtures, *Physics of Fluids*, **26**(10): 106102, 2014.
[8] Madjarević D. Shock Structure and Temperature Overshoot in Macroscopic Multi-temperature Model of Binary Mixtures, *in* From Particle Systems to Partial Differential Equations II, Goncalves P., Soares A.J. (Eds.), Springer, 2015.
[9] Bisi M., Groppi M., Spiga G. Grad's distribution functions in the kinetic equations for a chemical reaction, *Continuum Mech. Thermodyn.*, **14**: 207–222, 2002.
[10] Madjarević D. Shock structure for macroscopic multi-temperature model of binary mixtures: comparison with kinetic models, *PAMM – Proc. Appl. Math. Mech.*, **15**, 403–404, 2015.

LES OF H2/N2 TRANSCRITICAL COAXIAL INJECTION

Raffaele Olmeda *[1] and Christian Stemmer[1]
[1] Lehrstuhl für Aerodynamik und Strömungsmechanik, Technische Universität München , Boltzmannstr. 15, 85748 Garching b. München

Summary In modern rocket engine applications, propellant and oxidizer are injected in the combustion chamber at high pressures and low temperatures often close to their critical conditions. The prediction of the flow thermodynamic behaviour close to the injector plate is challenging due to the difficulties associated to produce reliable experiments and simulations for these scenarios. In particular, when the oxidizer enters the combustion chamber in a subcritical state, two-phase thermodynamic states must be taken into account. In the present work 3D LES simulations will be carried out to study the coaxial injection of gaseous hydrogen and subcritical nitrogen. The focus of the work will be on the density evolution of the flow in direction parallel and perpendicular to the injection. The influence of two-phase thermodynamic on the flow behaviour will be evaluated.

INTRODUCTION

To run CFD simulations of transcritical injection, several challanges need to be tackled. Since propellant and oxydizer are close to the critical point, Van der Waals forces become relevant and a real-gas Equation of State is necessary. Furthermore, the schemes used to numerically solve the governing equations must be robust enough to compute the huge gradients typical for the region close to the critical point. In particular, the pressure coefficient shows a peak along the pseudo-boiling line that exponentially increases the thermal fluxes in the shear layer between the two substances. Moreover, during the simulation the hypothesis of equilibrium of the mixture may not hold anymore in some points. In this case, a two-phase thermodynamic state must be considered, risking otherwise to misrepresent the density development right after the injector. LES simulations of a two-species jet are performed in order to study the behaviour of transcritical mixing. The computations are carried out in the attempt to correctly represent the shape of the jet and the density evolution downstream of the injector.

SETUP

The case analysed is described by Oschwald [1] (see Fig. 1). A reservoire initially contains nitrogen at 4 MP and 298 K. Nitrogen and hydrogen are injected through a coaxial injector. In the inner element, nitrogen is injected at 118 K, below its pseudo-boiling point. Hydrogen is injected from the external anulus at 270 K. The evolution of the jet has been studied experimentally by means of 2D-Raman density measurements. The choice of N2 and H2 attempts to recreate the condition of an operating rocket engine. O2 has been substituted with N2, which is close in atomic weight, to avoid chemical reactions and focus on the aspect of transcritical mixing. Preliminary simulations are run with a splitter plate setup. A 2D mesh is expanded in the third cartesian direction with a periodic boundary condition. In a second phase, simulations are performed in a full 3D domain.

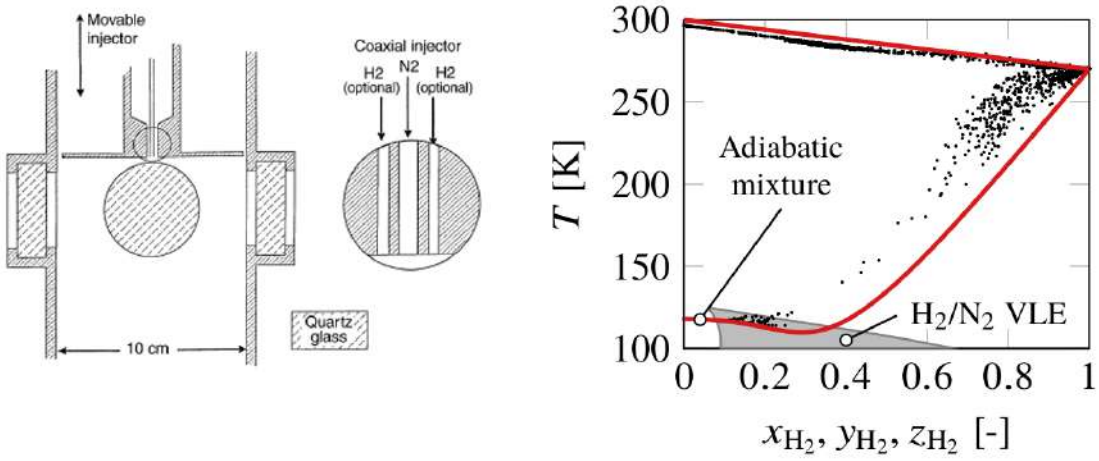

Figure 1: Experimental setup of Oschwald (left) and scatter plot of molar fraction/temperature for the mixture (right).

*Corresponding author. E-mail: raffaele.olmeda@tum.de.

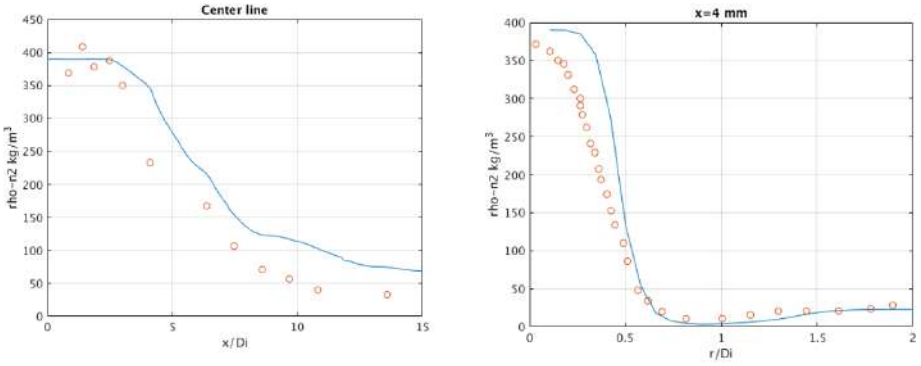

Figure 2: Nitrogen partial density profile along the central injector line (left) and in radial direction for x= 4 mm (right).

NUMERICAL METHODS

LES simulations are performed with the software CATUM [2], an in-house code developed in the Chair of Aerodynamic of the Technical University of Munich. It solves a finite volume form of the Navier-Stokes equations. A second-order scheme is used for the diffusive fluxes. Central difference or upwind are used for the convective fluxes depending on the local stability of the flow. The Peng-Robinson cubic equation of state is used to represent real-gas thermodynamics. It has been tested against the Soave Redlich Kwon EoS and proven to be superior for this test case. Since nitrogen is injected at a subcritical state, a two-phase subroutine is also necessary. As can be seen in Fig. 1, the scatter plot of of mass fraction versus temperature shows points in the two-phase region of the diagram. A Vapor-Liquid Equilibrium (VLE) method is adopted in order to correctly compute the points in this region.

PRELIMINARY RESULTS

Simulations have already been carried out with the mesh of the splitter setup. The results obtained have been compared with the experimental data and can be seen in Fig. 2. For the profile of nitrogen partial density in longitudinal direction, very good accuracy has already been obtained close to the injector. Going further downstream, there is a divergence from the experimental data which is expected to diminish increasing the mesh resolution and using the full 3D setup. For the profile in the radial direction instead, excellent accordance is found for $r/D > 0.5$. Close to the center of the injector the results are less precise. Is believed the error is caused from a delayed mixing of inner nitrogen core with the outer hydrogen layer. Also in this case, the results are expected to improve with a mesh convergence study and full 3D representation, which will compute correctly the turbulent fluctuations of the jet, accelerating the mixing.

References

[1] Oschwald, A. and Schick, M. and Klar, M. and Mayer, M. Investigation of Coaxial LN2/GH2-Injection at supercritical Presuure by spontaneous Raman Scattering. *35th AIAA/ASME/SAE/ASEE Joint Propulsion Conference and Exhibit.* Los Angeles, California, 1999

[2] Egerer, C. P. and Schmidt, S. J. and Hickel, S. and Adams, N.A. Efficient implicit LES method for the simulation of turbulent cavitating flows. *Journal of Computational Physics.* **316**: 453-469, 2016

SELF-INDUCED OSCILLATIONS OF THE SHOCK STRUCTURES IN A HYPERSONIC FLOW OVER DOUBLE WEDGE

Gaurav Kumar and Ashoke De *
Department of Aerospace Engineering, Indian Institute of Technology, Kanpur, UP, India - 208016

Summary This study investigates the presence of self-induced oscillations of shock structure in a hypersonic flow over a double wedge. Previously, this flow configuration has been numerically studied for inviscid flow with variations such as inflow Mach number (M_∞), wedge angles and wedge lengths. The current work seeks out to investigate this unsteady viscous self-induced periodic oscillations of shock structure in a low enthalpy, M_∞=7 viscous flow over a double wedge which has a fore wedge angle of 30°. A numerical error controlled fluid solver is used to investigate the double wedge flow. The current findings are in accordance with the previously published results for these parameters as the flow structures do not settle down to a steady-state in the long term. However, a more resolved study has revealed a broader bandwidth of frequency associated with the higher harmonics.

INTRODUCTION

Due to shock-shock and shock-boundary layer interaction, an enormous amount of mechanical and thermal load can be generated in hypersonic flows over surfaces containing corners which is dangerous for the structural integrity of the vehicle. Such configurations are ubiquitous in various internal as well as external flows such as control surfaces of aircraft and rockets and scramjet intakes. A comprehensive study of such shock-shock interactions for inviscid diatomic perfect gas ($\gamma = 1.4$) over double wedge at Mach number(M_∞)=9, fore to aft wedge length ratio(L_1/L_2)=1, fore angle of the wedge(θ_1) =15° and a varying range of second wedge angle(θ_2) is available in ref.[1]. The study shows the transition of shock-shock interaction type from type VI → V → IV → IVr as θ_2 increases from 35° to 60°. The study reveals a many-fold increase in pressure load as the type of shock interaction varies. In ref.[2], the same configuration is shown to exhibit a self-induced oscillation of the shock system in a range of $42 < \theta_2 < 43$ where L_1/L_2=2 is used. A high resolution numerical study was performed in ref.[3], where $M_\infty = 7$ and 9 was simulated over a double wedge with $\theta_1 = 15°$ and L_1/L_2=2. They have considered the variation of γ with temperature, but the flow was still assumed to be inviscid. A difference in θ_2 was observed compared to ref.[2] where self-induced oscillations occur, and it was demonstrated that the difference was due to the difference of gas model used and not due to the numerical resolutions or schemes. A viscous dissipation was expected to damp down such oscillations due to change in flow topology, but no detailed viscous computations were carried out due to numerical difficulties.

In ref.[4], a fully viscous computation was performed on double wedge configuration at M_∞=7, θ_1=30°, L_1/L_2=2 and $45° < \theta_2 < 60°$ with temperature-dependent gas model. This simulation was in accordance with the experimental setup in ref.[5] and a good agreement of thermal loading on the wedges was obtained. A long-time transient simulation had revealed the presence of time-periodic shock configuration in the range of $\theta_2 > 47°$. For the computations performed in ref.[4], a density-based compressible flow solver called *rhoCentralFoam*[6] was used in OpenFOAM[7] framework which is second-order accurate in space and first-order accurate in time. Also, it has been observed that rhoCentralFoam produces oscillatory solutions for not very small CFL number (>0.2). Due to this, a new improved *rhoCentralFoam* solver called *kanpurCentralFoam* (so named because code developed at IIT Kanpur) is developed which has eliminated such instability up to CFL=1.0. This solver uses a third-order TVD Runge-Kutta time integration method with the spatial discretization of *rhoCentralFoam*. Also, an improved operator-splitting method has been utilized here instead of the sequential operator-splitting method used in *rhoCentralFoam*, which further adds to the stability of the solution. Numerical methods used are briefly summarized in the next section.

NUMERICAL METHODS

The conservation equations for mass, momentum, and energy for a fluid control volume $d\Omega$ enclosed by surface $\partial\Omega$ is given by eq. (1), where $\vec{W} = [\rho \quad \rho\vec{u} \quad \rho E]^T$ represents mass density, linear momentum and total energy of the control volume. Here, $\vec{F_c}$ and $\vec{F_\nu}$ are convective flux and diffusive flux, respectively. A thermally perfect gas relation, $p = \rho RT$ is used for state equation. The calorical properties of the gas is assumed to be temperature dependent and the variation with temperature is accounted using JANAF tables[8]. The Sutherland relation is used to account for the variation of diffusion parameters (μ and κ).

$$\frac{\partial}{\partial t}\int_\Omega \vec{W} d\Omega + \oint_{\partial\Omega} (\vec{F_c} - \vec{F_\nu}) dS = 0 \tag{1}$$

*Corresponding author. E-mail: ashoke@iitk.ac.in.

RESULTS

The new solver developed has been validated extensively for a wide range of flow conditions to demonstrate good time accuracy, dispersion and dissipation properties. But, for the brevity of the paper only simulation of double wedge configuration of ref.[4] at $M_\infty = 7$, $L_1 = 50.8$ mm, $\theta_1 = 30^\circ$ and $\theta_2 = 55^\circ$ is shown here. The domain is chosen in accordance with ref.[4, 5]. For removing any obstruction created by the outlet boundaries, the top boundary is placed at a distance of $1.5L_1$ above the wedge, and the right outflow boundary at $0.75L_1$ and a non-reflecting boundary condition is applied. A fixed velocity, pressure and temperature condition is provided at the inlet as used in ref. [4, 5]. A no-slip isothermal wall boundary condition is applied at both the wedge surfaces with wall temperature ($T_w = 300$K). A high resolution structured grid is finalized based on systematic grid comparison study with first cell size normal to the wall (Δy_w) $= 5\ \mu m$ and cells near shock-shock interaction region (Δ) $= 0.127$ mm. The simulations are run at a CFL no. 1.0 ($\Delta t \approx 2$ ns) for 20 ms, which is much longer than the experimental time and long enough after the flow becomes periodic.

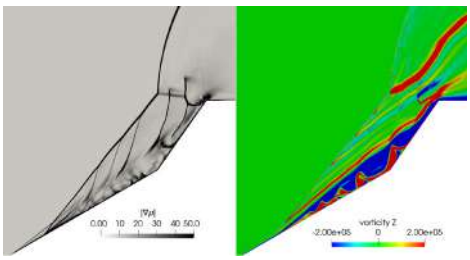

(a) Density gradient and span-wise vorticity contours at t=11.8 ms

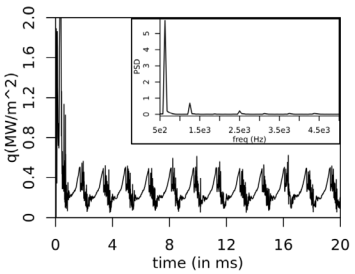

(b) Time history and PSD of wall heat flux (Middle of 2^{nd} wedge)

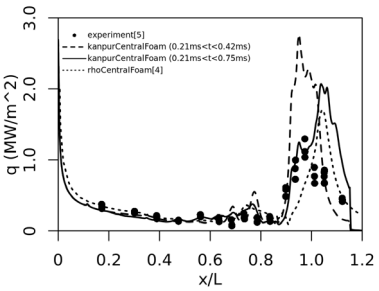

(c) Averaged wall heat flux

Figure 1: Computed results of double wedge flow, $M_\infty = 7$, $\theta_1 = 30^\circ$, $\theta_2 = 55^\circ$.

Figure 1 shows the simulated results for the above case. In fig. 1a, density gradient and span-wise vorticity field are plotted for t = 11.8 ms where all the shock interaction pattern can be seen along with a large separation region at the wedge corner. A seven shock structure is formed at the end of the second wedge. However, the overall shock structure is deformed and transient due to the interaction with shocklets originating from the separation region. Fig. 1b shows the unsteady wall heat flux at the middle of the 2^{nd} wedge surface, which becomes periodic after 1 ms and has been visually observed through flow contours as well. Due to the higher-order time integration method used, high-frequency oscillations are also resolved. Fig. 1c shows the variation of average wall heat flux along the wedge surfaces, and it has been compared with the experimental results of ref.[5] and numerical results of ref.[4]. A good match with the experimental data is observed except at the location of the peak value of wall heat flux. The location of the peak from ref.[4] is also seen to have mismatch compared to the experiment[5]. This is due to the difference in the time window for averaging, which cannot be matched with the experiment as the flow does not become steady with time and experiments were conducted for a small time window.

CONCLUSIONS

A new solver developed in OpenFOAM framework called *kanpurCentralFoam* is designed to be stable and accurate for an application in hypersonic flow calculations. It is capable of providing more accurate results to its predecessor *rhoCentralFoam*. An accurate simulation carried out in this study reveals the presence of time-periodic self-induced shock oscillation as predicted earlier. A high order time integration method has revealed a larger band of frequency near the impingement point, which was lost in the previous numerical studies.

References

[1] Olejniczak J., Wright M.J., Candler G.V. Numerical study of inviscid shock interactions on double-wedge geometries. J. Fluid Mech. 352: 1-25, 1997.
[2] Ben-Dor G., Vasilev E.I., Elperin T., Zenovich A.V. Self-induced oscillations in the shock wave flow pattern formed in a stationary supersonic flow over a double wedge. Phys. Fluids. 15(12): L85-8, 2003.
[3] Hu Z.M., Myong R.S., Wang C., Cho T.H., Jiang Z.L. Numerical study of the oscillations induced by shock/shock interaction in hypersonic double-wedge flows. Shock Waves. 18(1): 41, 2008.
[4] Durna A.S., Celik B. Time-periodic shock interaction mechanisms over double wedges at Mach 7. Shock Waves. 29(3): 381-99, 2019.
[5] Swantek A. The role of aerothermochemistry in double cone and double wedge flows. PhD Thesis, UIUC Aerospace. Eng. Dept., IL., 2012.
[6] Greenshields C.J., Weller H.G., Gasparini L., Reese J.M. Implementation of semi-discrete, non-staggered central schemes in a colocated, polyhedral, finite volume framework, for high-speed viscous flows. INT. J. NUMER. METH. FL. 63(1): 1-21, 2010.
[7] Greenshields C.J. Openfoam user guide. OpenFOAM Foundation Ltd, version. 3(1): e2888, 2015.
[8] Chase M.W., Tables NJ. Chem. Soc. and Am. Inst. of Physics, Washington, DC, USA, 1998.

EFFECT OF SURFACE CONDITION ON OBLIQUE SHOCK REFLECTION

Susumu Kobayashi[1] and Takashi Adachi [1]
[1] Department of Mechanical Engineering, Saitama Institute of Technology, Saitama, Japan

Summary To investigate the effect of surface condition (permeability and surface roughness), a series of experiment using a shock tube has been performed. We used a sintered metal plate as porous material. To compare the effect of permeability and that of surface roughness, we also carried out the experiment using wedge models with surface roughness. The incident shock Mach number was 1.30 and the reflecting wedge angle was 36 deg. The results for surface roughness of #240 are almost the same with those for smooth surface, and dynamic transition was not apparent. However, as to the results for surface roughness #30, dynamic transition was observed. In the case of reflection over a sintered metal plate, it was demonstrated that the effect of permeability was added to that of surface roughness.

INTRODUCTION

When a plane shock wave impinges on a plane solid slope, oblique shock reflection phenomenon occurs. The reflection configuration is roughly classified into two, i.e., regular reflection (RR) and Mach reflection (MR). Regular reflection is composed of two shock waves, the incident shock wave and the reflected shock wave. Mach reflection is composed of three shock waves, the incident shock wave, the reflected shock wave and the Mach stem. These three shocks have an intersection called triple point. From the triple point, there appears a slipstream (velocity discontinuity).

In the analysis of the phenomenon, von Neumann presumed 2-D steady inviscid non-heat-conducting uniform flow divided by discontinuities (shock waves and a slipstream). To make the system steady, he took the coordinate system with respect to some reference point. In the case of RR, a reflection point, where the incident shock touches the slope, is taken as the reference point, and his theory is called two-shock theory, since only two shock waves are concerned. While, in the case of MR, the triple point is taken as the reference point, and the theory is called three-shock theory since three shock waves are involved.

After von Neumann's theoretical study, oblique shock reflection phenomena have been investigated so much both numerically and experimentally. In the absence of viscosity and heat-conductivity (transport properties), the system of the phenomenon involves no characteristic length, and so it is considered to be self-similar. As a result, the reflection configuration does not change during the propagation of incident shock wave. For a fixed incident shock Mach number M_i, there exists some slope angle θ_{tr} which borders RR and MR, and below this angle the reflection is MR and above this angle RR. This angle is called transition wedge angle [1].

The authors' past research revealed that for the wedge angle θ_w slightly below θ_{tr}, transition from RR to MR occurs during the incident shock propagation [2]. This is evidently the case when the self-similarity does not hold. This means that the transport properties of fluid play an important role. In fact, the oblique shock reflection under low-pressure atmosphere exhibits this phenomenon [3]. This is because the effect of viscosity is enhanced when the pressure is low (high kinematic viscosity).

In the present paper, the authors' interest lies in the effect of surface condition over the dynamic transition. In von Neumann's two-shock theory, he assumed that the velocity behind the reflected wave is parallel to the reflection surface. This is reasonable when the slope material is not a deformable material. However, when the material is porous, the fluid can pass through it, and thus the velocity component perpendicular to the surface is allowed. We utilized a sintered metal (bronze) plate as reflection surface. Porous material has intrinsically surface roughness, and it was proved by our past experiment that the surface roughness acts to delay the dynamic transition [4]. We also performed experiments with models with surface roughness, and compared the results to investigate the effect of permeability.

EXPERIMENTS

A series of experiment has been performed using a shock tube in our institute. Wedge models are made of brass and their surface were polished with #2000 sandpapers. For the porous plate, a C-shaped attachment was prepared to observe transmitted wave behaviour as a bi-product of the present investigation. The thickness of the sintered plate was 9 mm and its length was about 62 mm. The sintered metal was made of bronze spherical particles whose diameter ranges roughly from 500 μm to 710 μm, and the surface roughness corresponds to #30 sandpaper. The porosity ranges from 25 to 43%. To compare the effect of permeability with that of surface roughness, we prepared wedge models with surface roughness by pasting a sheet of sandpaper (#240 and #30). The incident shock Mach number M_i was 1.30, meaning that all the utilized data is in the range of $1.295 \leq M_i < 1.305$. The reflecting wedge angle θ_w was 36°.

Wave configuration was visualized by shadowgraphy. Light source was a xenon flash lamp with the pulse width of 180 ns. Two pressure gauges (300 mm apart) are installed ahead of the test section to estimate the incident shock Mach number. The output from the gauge nearer the test section triggers the light source via a delay circuit. By regulating the delay timer, we can obtain images at various instant. In measurement, the origin O is taken as the tip of reflection surface, and along the surface the ξ-axis is taken and the η-axis is taken perpendicular to it. Location (ξ, η) of reflection point P and triple point T was measured by using a profile projector (V-12, Nikon) from negative films. Both points are defined by the intersection of the high-pressure edge of the visualized incident shock and the low-pressure edge of the reflected wave. Accordingly, due to the thickness of visualized wave front, η can be positive even if reflection is regular.

RESULTS

Figure 1 compares the visualized wave configuration for rough surface (#240) and sintered bronze plate at about the same distance of the triple point from the tip. Both reflections are Mach type, and the Mach stem height is larger for rough surface. In Fig. 1 (b), a transmitted wave through the sintered bronze plate can be barely observed in a cavity. This wave is a weak compression wave and propagates at sound speed.

Figure 2 (a) compares the effect of surface roughness over the location of reflection point (RR) and triple point (MR). In the case of surface roughness #240, the trajectory almost overlaps that for smooth surface (#2000). Although the surface roughness of #240 (roughness height about 0.1 mm) exceeds hydraulically smooth condition (0.0517 mm) [5], it does not seem to be effective in this case. On the contrary, the surface roughness of #30 is more effective than #240. Figure 2 (b) compares the effect of surface roughness and permeability. Compared with rough surface (#30), in the case of sintered bronze, the height of reflection point P stays about 0.4 mm at $0 < \xi < 40$ mm. Hereafter, the transition to MR occurs, but the slipstream is obscured by wavelets from the surface. Figure 2 (b) shows also that the effect of permeability is added to that of surface roughness in the case of porous surface.

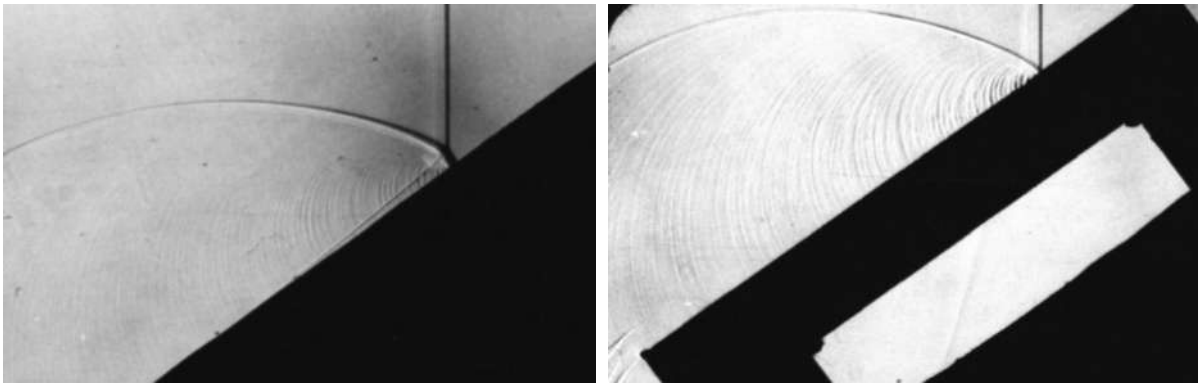

(a) Reflection over a rough surface (#240, $\xi = 50.5$ mm), (b) Reflection over a sintered bronze plate ($\xi = 47.6$ mm)

Figure 1. Comparison of visualized wave configuration ($M_i = 1.30$, $\theta_w = 36^\circ$).

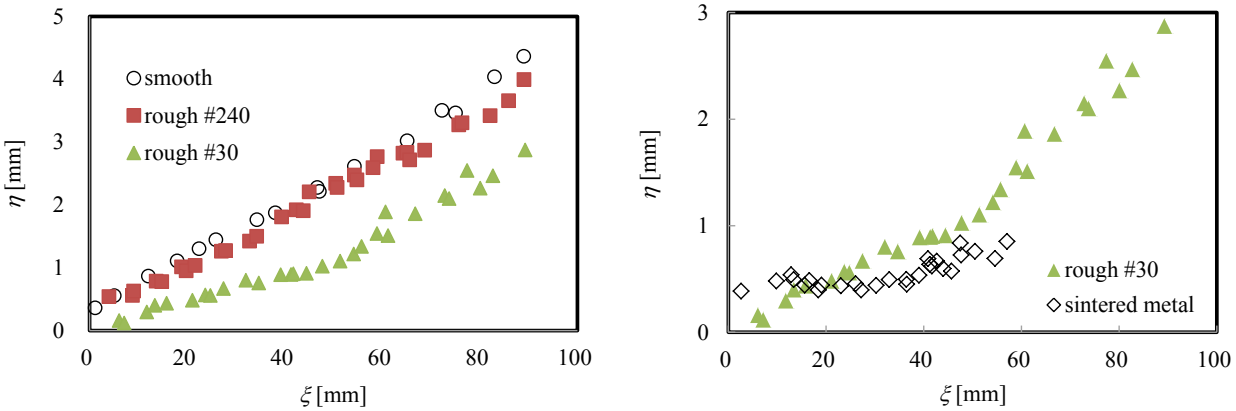

(a) Comparison of roughness, (b) Effect of permeability

Figure 2. Comparison of triple-point location ($M_i = 1.30$, $\theta_w = 36^\circ$).

CONCLUSIONS

To investigate the effect of surface condition (roughness and permeability), a series of shock tube experiment has been carried out using a sintered bronze plate. Surface roughness of #240 is not so effective as that of #30. The surface roughness surely delays the dynamic transition to MR. In the case of sintered bronze plate, it was demonstrated that the effect of permeability is added to that of surface roughness.

References

[1] Ben-Dor G. Shock Wave Reflection Phenomena, second ed. Springer, Berlin 2007.

[2] Kobayashi S., Adachi T., Suzuki T. On the Unsteady Transition Phenomenon of Weak Shock Waves. *Theoret. Appl. Mech.* **49**: 271-278, 2000.

[3] Itabashi S., Henderson L.F., Crutchfield W.Y., Takayama K. Effects of Viscous and Thermal Dissipation on the Eruption of Mach Reflection on Rigid Steel Ramps. Proc. ISSW 21, vol. 2: 887-891, 1998.

[4] Kobayashi S., Adachi T., Debatin K., Schenkel T., Oertel H. Non-self-similar Development of a Reflected Wave of Mach Reflection over a Rough Surface. in *Trends in Applications of Mathematics to Mechanics* (ed. Y. Wang and K. Hutter). 173-182, Shaker, Aachen 2005.

[5] Ben-Dor G, Mazor G., Takayama K., Igra O. Influence of Surface Roughness on the Transition from Regular to Mach Reflection in Pseudo-steady Flows. *J. Fluid Mech.* **176**: 333-356, 1987.

PREDICTION OF THE COMPRESSION WAVE PROPAGATING ALONG A HIGH-SPEED RAILWAY TUNNEL

Rohit Sankaran Iyer[1], Tae Ho Kim[1] and Heuy Dong Kim *[1]
[1] Department of Mechanical Engineering, Andong National University, Andong, Korea Republic.

Summary High-speed train ingress in a railway tunnel generates a high-pressure compression wave due to the piston effect. This compression wave propagates along the tunnel at the local speed of sound. Tunnel wall friction and blockage ratio are a key part in determining the magnitude of a compression wave during the propagation process. In this study, a 3-D computational fluid dynamics (CFD) analysis has been undertaken in order to understand the effect of steady and unsteady friction parameters on a propagating compression wave. Compressible, Euler equations with friction source terms were solved on five different blockage ratio cases (0.1, 0.2, 0.25, 0.3 and 0.4). With the increment in steady friction factor, the attenuation rate of the compression wave in propagation is affected substantially, while the unsteady friction factor has a significant effect on the distortion rate.

BACKGROUND

A distinct compression wave starts to develop near the entrance section as a high-speed enters a tunnel. According to Aero-acoustic theory [1], the train speed and blockage ratio play a major role in determining the magnitude of this entry compression wave. Thereafter, this compression wave propagates along the tunnel at the local speed of sound and eventually emits from the exit as a micro-pressure wave (MPW). It is conjectured from previous studies [2-6] that compression wave propagating along the tunnel could either steepen due to the dominance of non-linear effect over viscous dissipation or could attenuate and spread due to viscous dissipation being dominant in certain cases. In reality, both these effects collaboratively play a major role in deciding the fate of a propagating compression wave. Amongst many other parameters, the major factors that have known to considerably affect the attenuation and distortion of the propagating compression wave are tunnel wall skin friction and blockage ratio. Since Zielke's [3] introduction of the frequency dependent friction in unsteady flows, the unsteady friction term has been incorporated in many compression wave propagation studies [4-6] along with the applicable governing equations. In the past, Matsuo et al. [5] used one-dimensional Euler equations augmented with friction source terms to study on slab track tunnels and concluded that with increasing train speed, the compression waveform tends to become steeper. Also, a one-dimensional study using Fukuda et al.'s [2] model to estimate the effect of friction terms on propagating wave in tunnels with acoustic absorbers was studied by Stefan Adami et al. [6]. Although till date there have been few analytical studies using one dimensional Euler equations with friction terms augmented into it, but a 3-D CFD study on the effects of steady and unsteady friction parameter has not been performed. Hence, a 3-D computational study using Euler equations with friction source terms have been used here to perform simulations on five different blockage ratio cases 0.1,0.2,0.25,0.3 and 0.4. At different blockage ratios, using two different values of λ_s the distinctive effects of both the friction terms have been explored on the propagating compression wave.

METHODOLOGY

Assuming ideal gas behaviour with fluid friction on wall, the Euler equations that are used to carry out the current CFD simulations can be written as follows:

$$\frac{\partial U}{\partial t} + \frac{\partial F}{\partial n} + S = 0$$

$$U = \begin{pmatrix} \rho \\ \rho u \\ e \end{pmatrix} \quad F = \begin{pmatrix} \rho u \\ p + \rho u^2 \\ (e+p)u \end{pmatrix} \quad S = \begin{pmatrix} 0 \\ f \\ 0 \end{pmatrix}$$

$$f = f_s + f_{us}$$

where 'n' is the normal vector(for 2-D; n=x, y), t being time, ρ density of fluid, u is the fluid velocity, p pressure, e being internal energy and 'f' is the source term which is the summation of steady and unsteady friction parameters. The fluid friction term f_s and f_{us} could be written as follows, stated in [2]:

$$f_s = \frac{\boldsymbol{\lambda_s}.\rho(u+c)^2}{2d_h}$$

$$f_{us} = \boldsymbol{\varepsilon_{us}}.\int_0^t W(\tau).\frac{\partial u}{\partial \tau}.d\tau$$

Where $W(\tau)$ is the weighting function as stated in [3]:

*Corresponding author. E-mail: kimhd@anu.ac.kr

$$W(\tau) = 3e^{-26.37\tau} + e^{-70.85\tau} + e^{-135.02\tau} + e^{-218.92\tau} + e^{-322.55\tau} + e^{-445.93\tau} + e^{-589.04\tau}$$

'λ_s' and 'ε_{us}' are the steady and unsteady friction factors as mentioned above.

RESULTS AND DISCUSSION

For a 'λ_s' value of 0.5 and 0.9 and 'ε_{us}' values of 10, the attenuation and distortion rate for blockage ratios varying from 0.1 to 0.4 has been shown in Fig.1(a) to Fig.1(d).

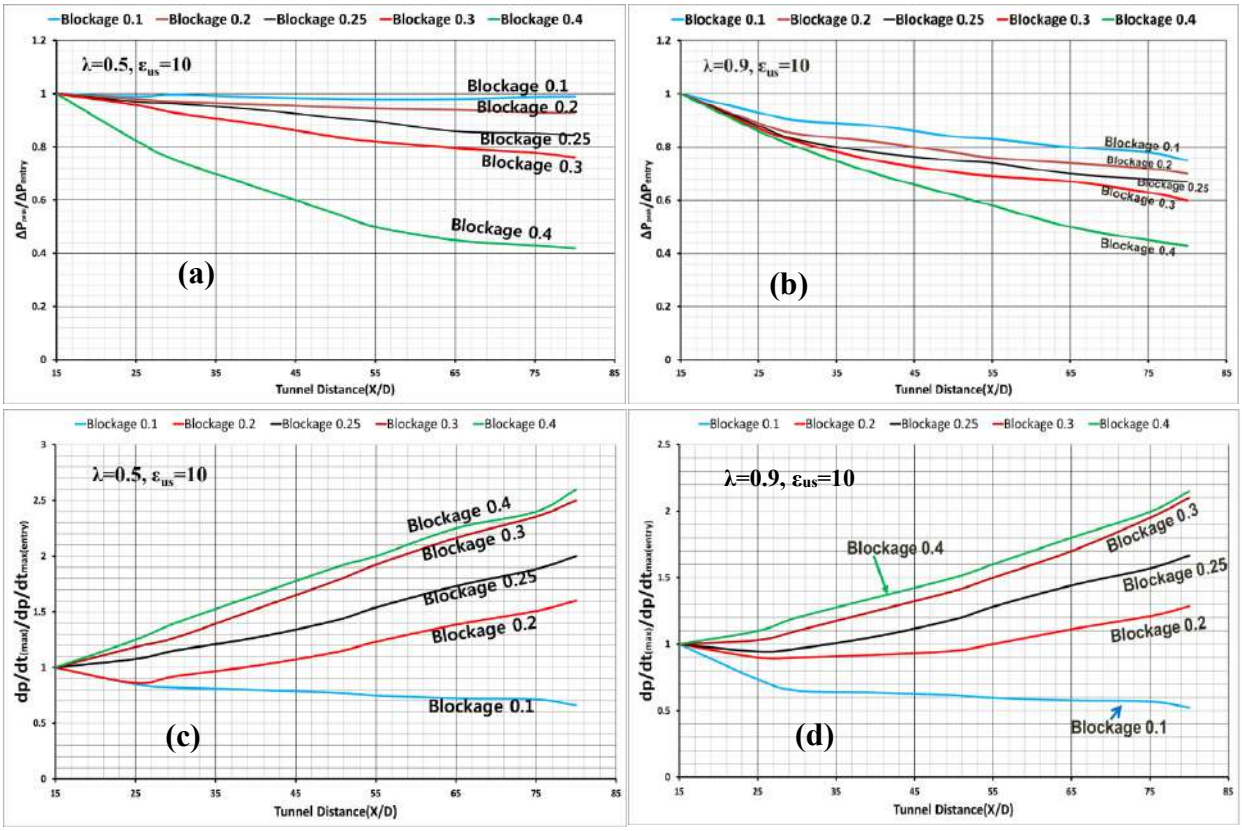

Figure 1(a): Attenuation of compression wave in tunnel for λ_s=0.5 and ε_{us}=10; (b): Attenuation rate for λ_s=0.5 and ε_{us}=10; (c): Distortion rate of compression wave λ_s=0.5 and ε_{us}=10; (d): Distortion rate of compression wave λ_s=0.9 and ε_{us}=10.

The effect of wall steady friction factor λ_s has been predominantly found more significant on the attenuation rate of compression wave for high blockage ratios and has negligible effect as the λ_s value was changed from 0.5 to 0.9 on the distortion rate. This could be attributed to the increase in wall shear forces inside the tunnel thereby reducing the strength of the compression wave as it propagates along the tunnel.

CONCLUSIONS

From the current numerical results, it could be inferred that the strength of the compression wave tends to be decreased as the steady friction factor is increased from 0.5 to 0.9.

References

[1] Hara T. Aerodynamics Force Acting on a High Speed Train at Tunnel Entrance, Bulletin of Japan Soc. Mech. Eng., Vol.4, 15, 1961.
[2] Fukuda T., Ozawa S., Iida M., Takasaki T. and Wakabayashi Y. Distortion of Compression Wave Propagating through Very Long Tunnel with Slab Tracks, JSME International journal- B,49-4, 2006.
[3] Zielke W. Frequency-Dependent Friction in Transient Pipe Flow, Trans. ASME: J.Basic Eng., 90(1):109-115, 1968.
[4] Nakao S., Aoki T., Yasunobu T. and Matsuo K. A study on Transition from a Compression Wave to a Shock Wave in a High-speed Train Tunnel, Theoretical and Applied Mechanics Japan, 50, 359-364, 2001.
[5] Matsuo K., Aoki T., Kashimura H., Mashimo S, Nakao S. Numerical study of Attenuation and Distortion of a Compression Wave Propagating in a High-speed Railway Tunnel, Trans. Built Env., Vol.18, 1996.
[6] Adami S. and Hans-Jakob Kaltenbach. Sensitivity of the Wave-Steepening in Railway Tunnels with Respect to the Friction Model, BBAA VI Int'l. Colloquium: Bluff Bodies Aerodyn. & Appl., 2008.

EFFECT OF FUEL MASS FRACTION HETEROGENEITY ON THE DETONATION PROPAGATION SPEED

Alberto Cuadra-Lara, César Huete *, and Marcos Vera
Grupo de Mecánica de Fluidos, Universidad Carlos III de Madrid, Leganés, Spain

Summary We present the asymptotic linear theory describing the propagation of a planar detonation front through a heterogeneous mixture of reactive gases consisting of random fluctuations in the fuel mass fraction. The study begins with the derivation of the transfer functions that relate the upstream fuel-mass-fraction inhomogeneities with the burnt-gas perturbation variables via normal-mode analysis. The results are then used in a Fourier analysis of the detonation interaction with two- and three-dimensional isotropic heterogeneous fields to provide integral formulae for the turbulent kinetic energy, sonic energy and averaged vorticity and entropy production rates. Second-order corrections for the averaged Rankine-Hugoniot conditions are provided, along with analytical expressions for the deviation of the detonation propagation velocity with respect to that of the equivalent homogeneous mixture. Upstream inhomogeneities are found to speed up the detonation front, with a velocity amplification factor that depends on the properties of the fuel-air equivalence ratio, which translates into variations of the density and the heat release with the fuel mass fraction.

INTRODUCTION

Detonation waves have been explored extensively for propulsion applications given their theoretical advantage over deflagrative pre-mixed combustion. For instance, rotating detonation engines, which do not operate under the Brayton Cycle, benefit from the additional work extraction from the cycle and a decrease in the physical size of the combustor [1]. However, many challenges must be surmounted before detonation-based engines could be presented as a competitive alternative. Some hurdles include the incomplete fuel-air mixing at the molecular level, the stability of the detonation, and the strong noise generated by the system even in highly idealized configurations [2]. It has been found that upstream heterogeneities play a pivotal role in the detonation dynamics [3, 4].

The interaction of a strong detonation with inhomogeneous entropic and vortical fields have been analyzed in previous works [5, 6]. The motivation was there to improve descriptions of the influences of compressible turbulence on detonation propagation and, in particular, to determine how passage of a planar detonation modifies the turbulence. By employing the same mathematical description as in the pioneering work of Ribner [7] and the analysis of Jackson *et al.* [8], this work [9] complements these fundamental studies by placing the focus on the mixture imperfections, which adds another type of convective perturbation associated to the mixture equivalence ratio, *i.e.*, local heat of combustion of the mixture. The linear-interaction analysis predicts a second-order propagation velocity augmentation for weakly overdriven detonations independently of the type of perturbations generated by the equivalence ratio fluctuations, *i.e.*, positive or negative perturbations in the upstream density and/or heat of combustion fields. For strongly overdriven detonations, a weak deficit in the propagation speed is found only when upstream perturbations in the equivalence ratio are dominated by heat release perturbations.

PROBLEM DESCRIPTION

It is considered a planar detonation front that propagates through a heterogeneous gaseous mixture, as depicted in Fig. 1(a). It is assumed that the deviation of the local fuel mass fraction Y_u with respect to its mean value $\langle Y_u \rangle$ is sufficiently small for linear theory to be applicable, namely, $|\delta Y_u| = |Y_u - \langle Y_u \rangle| \ll 1$. Assuming that there is no privileged direction in the upstream flow, the spectrum of the fuel mass fraction perturbation $\delta Y_u(k)$ is taken to be homogeneous and isotropic. The function k refers to the wave number amplitude characterizing the size of the fuel mass fraction deviations.

Anticipating that the heterogeneous mixture is dominantly static, isobaric and isothermal, the variations of the fuel mass fraction are solely associated to density and heat of combustion changes. Taking a generic air-fuel mixture, for fuels heavier than air positive values of δY_u are associated to positive deviations of density in the upstream flow $\delta \rho_u$, and vice-versa. By knowing that the maximum of the heat release of a given mixture occurs in slightly richer conditions, the sign of the heat release deviations respect to the mean values can be also anticipated. Therefore, positive values of δY_u leads to negative deviations of the heat release δq_u in sufficiently rich environments, while the contrary applies in lean mixtures. Figure 1(b) shows the variation of density and heat release with the fuel mass fraction for different gases. The small parameter δY_u is employed to write the perturbed density and potential heat of combustion fields

$$\rho_u = \langle \rho_u \rangle + \delta \rho_u = \langle \rho_u \rangle (1 + \delta Y_u W) \quad \text{and} \quad q_u = \langle q_u \rangle + \delta q_u = \langle q_u \rangle (1 + \delta Y_u H), \tag{1}$$

where the parameters W and H relate to the local slope of the $\rho_u - Y_u$ curve and the $q_u - Y_u$ curve, respectively. Accurate values of q_u can be obtained with either numerical codes or experimental data.

For sufficiently weak perturbations, the heterogeneous mixture can be approximated with the linear superposition of independent modes, each of them being characterized by the wavenumber $\vec{k}$, so that $\delta Y_u(\vec{x}_l) = \epsilon(k) e^{\mathrm{i}\vec{k}\cdot\vec{x}_l}$, where $\vec{x}_l$ is the

*Corresponding author. E-mail: chuete@ing.uc3m.es

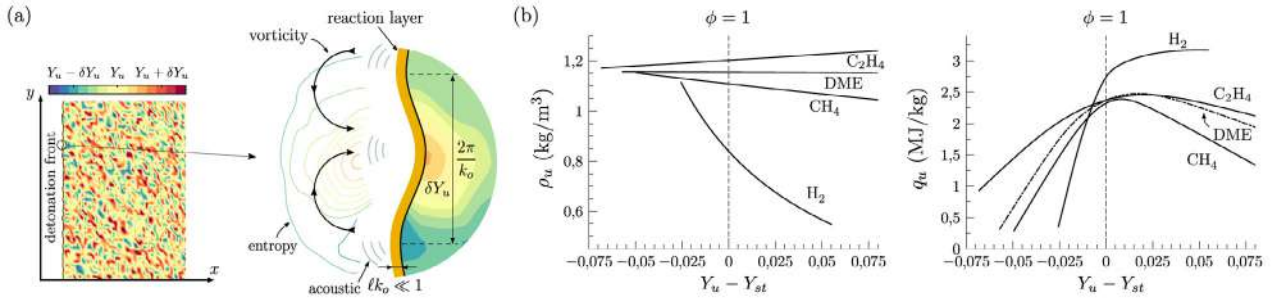

Figure 1: (a) Sketch of the corrugated detonation front through a heterogeneous gaseous mixture, where $|\delta Y_u| = |Y_u - \langle Y_u \rangle| \ll 1$. The detonation length ℓ is assumed to be much smaller than the characteristic upstream length k_o^{-1}. (b) Variation of density and heat release with the fuel mass fraction for representative fuel-air mixtures. The dashed line represents the stoichiometric condition given by $Y_u = Y_{st}(\phi = 1)$ Computations are given for hydrogen, methane, ethylene and dimethyl ether (DME) at 300 K and 10^5 Pa in fresh conditions. See Ref.[9] for further details.

vector defining the position in a reference frame comoving with upstream flow and $\epsilon(k)$ represents the amplitude of the perturbation for a given wavenumber vector amplitude $\vec{k}$.

For the interaction with a single-frequency perturbation field, the long-time amplitude of the perturbations can be written in terms of the characteristic oscillation frequency of the detonation front. Neutral conditions associated with the absence of pressure perturbations at the oscillating detonation or fully planar propagating detonations occur for distinguished conditions of reactive mixture associated to the density and heat release variations, W and H, respectively. Fourier superposition for two- and three-dimensional isotropic fields is used to obtain integral formulae for the amplification of the kinetic energy, enstrophy, and density fluctuations in the burnt gas. The effects of the propagation Mach number, overdrive, and mixture properties through W and H are identified, and the later plays a key role in the intensity of the turbulence generation. Regarding the type of upstream mixture, density perturbations dominate the turbulence generation for moderate-to-high overdrives, while heat release variations become relevant for weak overdrives. As a direct result, heat-release variations make the acoustic contribution the same order as the rotational and entropic perturbations. Aside from the fact that viscosity and molecular diffusion are not accounted for in the model, in which case the spectra would become time-dependent functions after the passage of the detonation, the small-scale regime must be taken with caution as the thin-detonation hypothesis may not be fulfilled. Properties of the turbulent flow behind the detonation front predicted by the linear interaction theory should be further extended to include the effects of finite reaction lengths.

CONCLUSIONS

This work aims to shed further light, from a theoretical framework, on the hydrodynamical aspects that contribute to the modification of detonation velocity when it propagates through a non-uniform mixture of reactive gases. The linear analysis shows how a non-uniform fresh mixture that exhibits weak fuel mass fraction deviations perturbs the detonation front surface, thereby creating additional disturbances in the burnt gas. The deposition of rotational/acoustic velocity perturbations in the downstream flow along with the amplification of the entropic fluctuations comes with a price in the overall RH relations. In particular, changes are expected in the jump conditions given the averaged downstream magnitudes with respect to the case of uniform mixtures with the same averaged upstream properties. As a direct consequence, the averaged propagation speed of the detonation wave will also be affected, as previously noted for inert shocks [10]. The second-order correction to the propagation speed is determined by the type of turbulence generated downstream. For overdriven detonations, the downstream acoustic contribution plays a subdominant role in favour of rotational-entropic disturbances, while the contrary applies for weakly overdriven detonations, for which the effect of upstream heat-release variations is of utmost importance.

References

[1] Huff, R., et al. J. Exit Condition Measurements of a Radial Rotating Detonation Engine Bleed Air Turbine. AIAA Scitech Forum (2019).
[2] Kailasanath, K. Review of propulsion applications of detonation waves. AIAA J. 38.9 (2000): 1698-1708.
[3] Kessler, D., et al. Oran. Gas-phase detonation propagation in mixture composition gradients. Philos. Trans. R. Soc. A 370.1960 (2012): 567-596.
[4] Prakash, S., et al. Analysis of the detonation wave structure in a linearized rotating detonation engine. AIAA J. (2019): 1-15.
[5] Huete, C., et al. Theory of interactions of thin strong detonations with turbulent gases. Phys. Fluids 25.7 (2013): 076105.
[6] Huete, C., et al. Interaction of a planar reacting shock wave with an isotropic turbulent vorticity field. Phys. Rev. E 96.5 (2017): 053104.
[7] Ribner, H. S. Shock-turbulence interaction and the generation of noise. No. NASA-L-1233 Report (1955).
[8] Jackson, T. L., M. Y. Hussaini, and H. S. Ribner. Interaction of turbulence with a detonation wave. Phys. Fluids A 5.3 (1993): 745-749.
[9] Cuadra, A., Huete, C. and Vera, M. Effect of equivalence ratio fluctuations on planar detonation discontinuities. J. Fluid Mech., 903, A30 (2020).
[10] Velikovich, A.L. Huete, C, and Wouchuk, J.G. Effect of shock-generated turbulence on the hugoniot jump conditions. Phys. Rev. E, 85, 016301 (2012).

EXAMINING THE THERMAL BOUNDARY LAYER IN TRANSCRITICAL TURBULENT CHANNEL FLOWS

Jack Guo *[1] and Matthias Ihme[1]
[1] Department of Mechanical Engineering, Stanford University, Stanford, California, USA

Summary Flows at supercritical conditions play an important role for practical applications including chemical processing, propulsion, and geophysical flows. These applications motivate the study of wall-bounded variable-density turbulent heat transfer. We investigate a series of transcritical turbulent channels with density ratios up to $O(10)$. The density ratio is controlled by imposing a temperature gradient between the hot and cold walls of the channels. Analysis of the boundary layer structure shows that the temperature law of the wall is clearly visible with noticeable differences between the hot and cold walls. When compared to other methods, semi-local scaling performs best when matched with existing correlations.

INTRODUCTION AND MOTIVATION

At pressures above the critical point, a "supercritical pseudotransition" is observed as the fluid transitions between liquid-like and gas-like states despite the absence of a classical phase transition. Macroscopically, this pseudotransition is characterized by a distinct peak in specific heat capacity and by sharp gradients in density, thermal conductivity, and dynamic viscosity. These characteristics contribute to well-documented difficulties in accurately describing the thermodynamic state [1]. Neither current experimental techniques nor engineering simulation tools adequately perform in turbulent flows at transcritical conditions, specifically suffering from insufficient characterization of the near-wall turbulent heat transfer dynamics [1, 2]. Thus, direct numerical simulations have been employed for studying this flow regime.

In variable-density wall-bounded flows, a majority of previous work focuses on viscous boundary layer structure with results including the law of the wall, similarity scaling via wall-units and semi-local units, the van Driest transformation, and the Trettel-Larsson transformation [1, 3]. In this study, we turn our attention to thermally-derived statistics, specifically the temperature law of the wall as a thermal analogy of the celebrated velocity law of the wall. When appropriately scaled, the mean temperature differential, $\overline{\theta} = \overline{(T - T_w)}$, follows a linear profile with respect to the wall-normal distance y in the near-wall regime in the thermal sublayer and a logarithmic dependence on the wall-normal distance further away in the logarithmic layer. The temperature law of the wall was proposed as an algebraic correlation by Kader [4] – hereafter, we denote this Kader temperature law of the wall as KLOW. While there has since been significant analysis in the constant-property regime [5], the variable-property regime has received limited investigation and is confined to small density ratios of $O(1)$ and to simplified thermodynamics. Lee *et al.* [6] numerically investigated an incompressible turbulent boundary layer with temperature-dependent viscosity; they modify KLOW by specifying a constant value for the slope in the logarithmic layer. Patel, Boersma & Pecnik [7] later analyze variable-density turbulent channels with imposed constitutive relations for density, viscosity, and thermal conductivity as a function of temperature but with constant specific heat. They found that using a van Driest-transformed temperature profile results in improved matching with KLOW, while the Lee *et al.* modification has mixed success and fails to consider effects of property variations in the logarithmic layer. To address inadequacies in analysis completed thus far, we perform DNS calculations of transcritical turbulent channels with 1) a fully-compressible formulation, 2) thermodynamic variables specified as functions of two independent, intensive properties, and 3) density variations of up to $O(10)$.

METHODS AND APPROACHES

For the computational domain, we use a streamwise- and spanwise-periodic plane channel with isothermal and no-slip wall boundary conditions. The working fluid is molecular nitrogen (N_2) with critical pressure $p_c = 3.3958$ MPa, critical temperature $T_c = 126.19$ K, and critical density $\rho_c = 312.31\ kg/m^3$. The working fluid is set at a bulk pressure of $p_0 = \int pdV / \int dV = 3.87$ MPa, corresponding to a reduced pressure of $p_r = p_0/p_c = 1.14$. Other details of the setup are found in [1]; the only modification to the setup was to the value of the hot wall temperature boundary condition.

Our calculation uses the finite-volume compressible code CharLES$^{\text{X}}$, with an additional entropy-stable double-flux model [8] specifically designed for transcritical flows. For further details for the solver and for documentation of its previous use in turbulent flow calculations, refer to [1] and the references therein.

RESULTS

Figures 1 and 2 illustrate the mean reduced temperature and mean reduced density, respectively, averaged across homogeneous directions and in time. Four cases are presented, constructed by modifying the hot wall temperature, while the cold wall temperature is kept constant at $T_{w1} = 100$ K for all cases. A broad range of density ratios is considered; the cases with hot wall temperature $T_{w2} = \{125, 140, 190, 300\}$ K correspond to density ratios of $\overline{\rho}_{hot}/\overline{\rho}_{min} = \{1.63, 5.26, 10.10, 17.84\}$, respectively.

*Corresponding author. E-mail: jguo96@stanford.edu

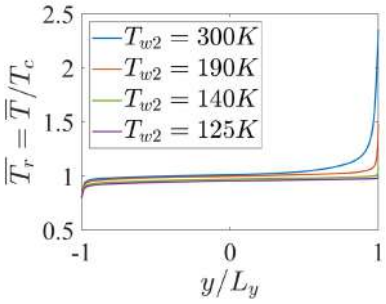

Figure 1: Mean reduced temperature profiles, plotted against channel width.

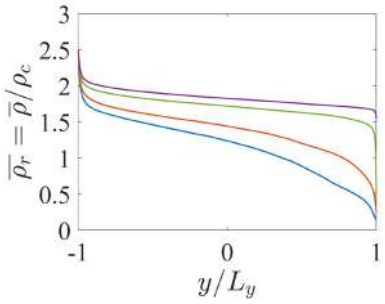

Figure 2: Mean reduced density profiles, plotted against channel width.

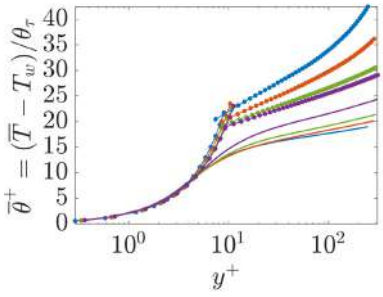

Figure 3: $\overline{\theta}^+$ profiles for cold wall; KLOW shown in lines with filled circles.

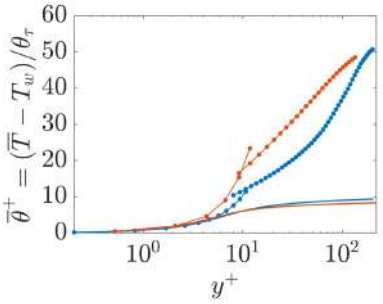

Figure 4: $\overline{\theta}^+$ profiles for hot wall; see Figure 3 for plot legend.

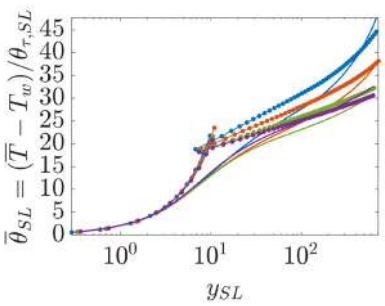

Figure 5: Semi-locally-scaled mean temperature differential profiles at cold wall.

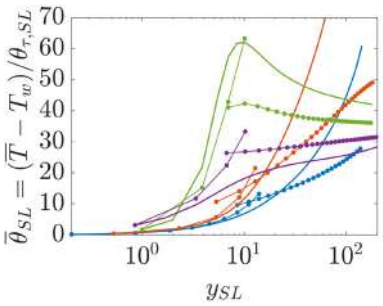

Figure 6: Semi-locally-scaled mean temperature differential profiles at hot wall.

Figures 3 and 4 show the mean temperature differential profiles along with KLOW for the cold and hot wall cases, respectively. Here, the friction temperature used for normalization is defined as $\theta_\tau = q_w/\left(\rho_w c_{p,w} u_\tau\right)$, where q_w is the heat flux at the wall. As done in [6] and [7], the constant Prandtl number in the original KLOW is replaced by a local averaged Prandtl number, $Pr(y)$. We see that as $\Delta T = T_{w,2} - T_{w,1}$ decreases, the agreement for the cold wall improves, while the performance of KLOW at the hot wall is unsatisfactory. Figure 4 includes only two of the cases to simplify visualization; as ΔT decreases, KLOW actually increases in magnitude and performs worse compared with the DNS profiles. Comparison with the Lee correlation [6] and transformation via a van-Driest integral $\int_0^{\overline{\theta}/\theta_\tau} \sqrt{\overline{\rho}/\rho_w} d(\overline{\theta}/\theta_\tau)$ as done in [7] are not shown here since neither provided noticeable improvement. Instead, significant improvement is made when both y and θ are normalized by local quantities, with $\overline{\rho}(y), \overline{\mu}(y)$ and $\overline{c_p}(y)$ being used to obtain semi-local coordinate y_{SL} and semi-locally-scaled temperature differential $\overline{\theta}_{SL}$. Results for the cold and hot walls are shown in Figures 5 and 6, respectively. Interestingly, the complex interaction of variable properties causes the semi-locally-scaled $\overline{\theta}$ to no longer exhibit a logarithmic profile in certain cases, a phenomenon requiring future investigation.

CONCLUSIONS

We have provided results of a DNS calculation of transcritical turbulent channels with density ratios up to $O(10)$, along with analysis of the thermal boundary layer structure. Current correlations for the mean temperature differential are matched poorly using existing scalings because the effects of thermodynamic gradients are not fully accounted for. However, use of semi-local scaling yields significant improvement by more fully capturing the local flow behavior.

References

[1] Ma, P. C., Yang, X. I. A., Ihme, M. Crossing the Widom-line–Supercritical pseudo-boiling. *Phys. Rev. Fluids* **3(3)**: 034609, 2018.
[2] Yoo J. Y. The turbulent flows of supercritical fluids with heat transfer. *Ann. Rev. Fluid Mech.* **45**: 495-525, 2013.
[3] Trettel, A., Larsson, J., Mean velocity scaling for compressible wall turbulence with heat transfer. *Phys. Fluids* **28(2)**: 026102, 2016.
[4] Kader, B. A. Temperature and concentration profiles in fully-turbulent boundary layers. *Int. J. Heat Mass Tran.* **24(9)**: 1541-1544, 1981.
[5] Abe, H., Antonia, R. A., Relationship between the heat transfer law and the scalar dissipation function in a turbulent channel flow. *J. Fluid Mech.* **830**: 300-325, 2017.
[6] Lee, J. Jung, S. Y., Sung, H. J., Zaki, T. A. Turbulent thermal boundary layers with temperature-dependent viscosity *Int. J. Heat Mass Tran.* **49**: 43-52, 2014.
[7] Patel, A., Boersma, B. J., Pecnik, R., Scalar statistics in variable property turbulent channel flows. *Phys. Rev. Fluids* **2(8)**: 084604, 2017.
[8] Ma, P. C., Lv, Y., Ihme, M. An entropy-stable hybrid scheme for simulations of transcritical real-fluid flows. *J. Comput. Phys.* **340**: 330-357, 2017.

STUDY OF TURBULENT KINETIC EQUATION IN CONVERGING SPHERICAL SHOCK-TURBULENCE INTERACTION

Chen Boxuan[1], Fu Song *[1], and Yan Bowen[1]
[1] Department of Engineering Mechanics, Tsinghua University, Beijing, China

Summary Simulations of interaction between converging spherical shock wave and compressible isotropic turbulence are carried out. Mean fields of these flow are showed in this paper. Turbulent kinetic energy equation is used to study these flow. The turbulent kinetic energy of these flow is not fit standard k-ε turbulent model. Reynold stress is better to use realizable k-ε model, not Boussinesq eddy viscosity model. Terms in turbulent kinetic energy equation related to viscosity, like dissipation, is not important in these flow. Terms in turbulent kinetic energy equation related to pressure, like pressure-dilatation and pressure-diffusion, is important in these flow.

SHOCK-TURBULENCE INTERACTION

The flow is solved by BGK method. This method is based on kinetic molecular theory.

The calculate domain is a block in 3 dimension with side length 2π. In this region, there is isotropic compressible turbulence flow. To avoid the reflect of shock, there is a buffer area outside. Due to the study of Ankit Bhagatwala and Sanjiva K. Lele, it is enough to simulate these flow on 256^3 grids.

The isotropic compressible turbulence is generated using the result of isotropic compressible decay turbulence. It lets the isotropic compressible turbulence develop to a state where the nonlinear energy transfer mechanism is fully active. The methodology to calculate isotropic compressible decay turbulence is proposed by Ristorcelli and Blaisdell. The Taylor scale Reynolds number of the flow Re_λ is 45, and the turbulent Mach number M_t is 0.4.

The converging shock is launched by a spherical interface. There is low density and low pressure inside while high density and high pressure outside. In typical shock tube problem, there will be shock wave, expansion wave and contact surface. However, the contact surface should be avoided so the ratio of density and pressure is determined only by the Mach number M_s of the shock. This paper shows the result of the case which Mach number M_s equals 2.4.

Vorticity field can show the turbulence clearly, and dilatation field can show the shock clearly. Figure 1 gives the vorticity result where the black line is the shock wave displayed by dilatation. The vorticity structure outside the shock is smaller than the vorticity inside the shock. This is because of the compression of the shock. Shock provides anisotropic in radius direction to turbulence flow. Due to the turbulence, the fluctuating shock can be seen as a spherical shock and many "shocklets" integrated together. The "shocklets" are much stronger than usual. It explains why the turbulent kinetic equation in this flow is different with purely turbulence.

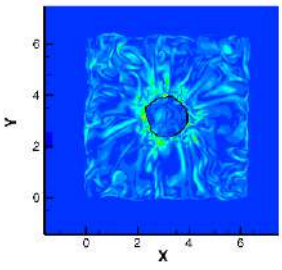

Figure 1. Vorticity field of turbulence, and black line show the shock.

The flow is spherically symmetric so the mean field can be written as a function of radius r. The data values within a shell were averaged and this gave the mean field of the flow. Turbulent kinetic equation is calculated in this way.

TURBULENT KINETIC EQUATION

Turbulent kinetic equation assumes the following form:

$$\bar{\rho}\frac{DK}{Dt} = -\overline{\rho u_m'' u_n''}\frac{\partial \widetilde{u_m}}{\partial x_n} + \frac{\partial}{\partial x_n}\left(\overline{t_{mn}'' u_m''} - \overline{\rho u_n''\frac{1}{2}u_m'' u_m''} - \overline{p' u_n''}\right) + \overline{u_m''}\left(\frac{\partial \widetilde{t_{mn}}}{\partial x_n} - \frac{\partial \bar{p}}{\partial x_m}\right) + \overline{p'\frac{\partial u_m''}{\partial x_m}} - \overline{t_{mn}''\frac{\partial u_m''}{\partial x_n}}$$

where t_{mn} is viscosity stress, and the right hand side of equation is production, diffusion, mass-flux, pressure-dilatation and dissipation.

Turbulent kinetic equation provides Reynolds stress. Production term in turbulent kinetic equation also needs Reynolds stress to calculate. Using Boussinesq approximation to calculate Reynolds stress would have unrealistic results: Reynolds stress may be negative or too big. The way to avoid it is to use realizable k-ε(RKE) eddy viscosity model. Figure 2(a) shows the results of Reynolds stress calculate by simulation and RKE model. Figure 2(b) shows the results of production in turbulent kinetic equation calculate by simulation and RKE model.

*Corresponding author. E-mail: fs-dem@mail.tsinghua.edu.cn.

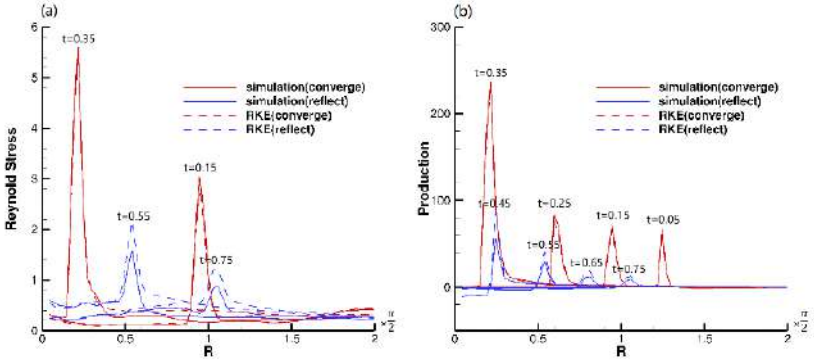

Figure 2. Reynold stress (a) and production term (b) calculate by simulation and RKE model.

The part in brackets of diffusion term is what we care about. Molecular diffusion $\overline{t''_{mn}u''_m}$ is too small so it doesn't need study in this case. Pressure diffusion $-\overline{p'u''_n}3$is bigger than turbulent diffusion $-\overline{\rho u''_n \frac{1}{2}u''_m u''_m}$, while pressure diffusion $-\overline{p'u''_n}3$ is usually neglected under normal conditions. There was a relation we found which can be approximated as:

$$-\overline{p'u''_n} \sim \nu_t \frac{\partial \bar{p}}{\partial x_n}$$

Figure 3(a) shows this.

Pressure-dilatation $\overline{p'\frac{\partial u''_m}{\partial x_m}}$ can be simplified by adding $\frac{\partial}{\partial x_m}(-\overline{p'u''_m})$. It gives $-\frac{\partial}{\partial x_m}\overline{p'u''_m} + \overline{p'\frac{\partial u''_m}{\partial x_m}} = -\overline{u''_m \frac{\partial p'}{\partial x_m}}$. There was a relation we found which can be approximated as:

$$-\overline{u''_m \frac{\partial p'}{\partial x_m}} \sim \nu_t \Delta \bar{p}$$

where Δ is Laplace operator. Figure 3(b) shows this.

For mass-flux $\overline{u''_m}\left(\frac{\partial \bar{t}_{mn}}{\partial x_n} - \frac{\partial \bar{p}}{\partial x_m}\right)$, viscosity work $\overline{u''_m \frac{\partial \widetilde{t_{mn}}}{\partial x_n}}$ is very small so we only consider pressure work $-\overline{u''_m}\frac{\partial \bar{p}}{\partial x_m}$. Zeman and Ristorcelli have found a relation between $\overline{u''_m}$ and mean flow, so $-\overline{u''_m}\frac{\partial \bar{p}}{\partial x_m}$ can be approximated as:

$$-\overline{u''_m}\frac{\partial \bar{p}}{\partial x_m} \sim -\frac{\nu_t}{\bar{\rho}}\frac{\partial \bar{\rho}}{\partial x_m}\frac{\partial \bar{p}}{\partial x_m}$$

Figure 3(c) shows this.

For all of the above, coefficients are relate to M_t and M_s, and it needs further study.

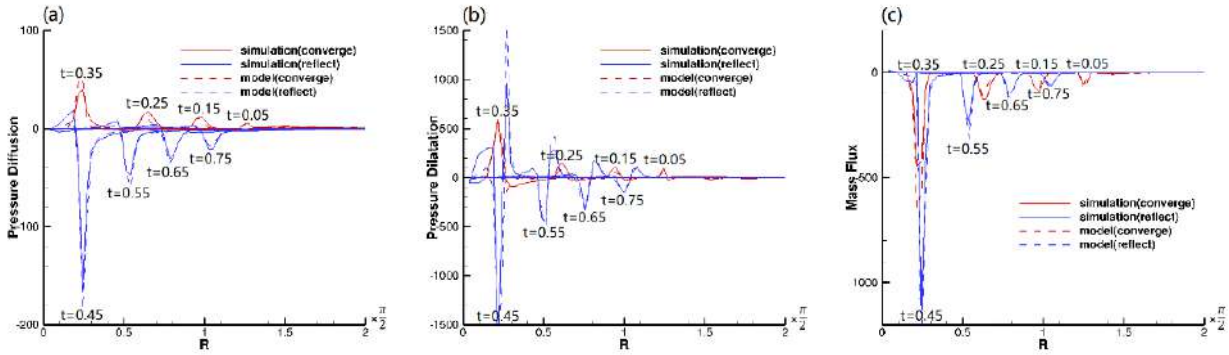

Figure 3. Pressure diffusion term (a), pressure dilatation term (b) and mass flux term (c) calculate by simulation and model.

References

[1] Bhagatwala A., Lele S.K. Interaction of a converging spherical shock wave with isotropic turbulence. *Physics of Fluids*. **24(8)**:85-102, 2012.
[2] Ristorcelli J.R., Blaisdell G.A. Consistent initial conditions for the DNS of compressible turbulence. *Physics of Fluids*. **9(1)**:4, 1997.
[3] D.C. Wilcox. Turbulence Modeling for CFD. DCW Industries, Inc. California 2006.
[4] Shih T.H., Liou W.W., Shabbir A., et al. A New k-ε Eddy Viscosity Model for High Reynolds Number Turbulent Flows. *Computers & Fluids*. **24(3)**:227-238, 1995.

EFFECT OF CO-FLOW ON COUNTER ROTATING VORTEX RING FORMATION IN A MODERATELY UNDER-EXPANDED JET

Haroon Ahmad[1], Nadeem Hasan[2], and Sajeev Sanghi [1]
[1] Department of Applied Mechanics, Indian Institute of Technology, Hauz Khas, New-Delhi, India
[2] Department of Mechanical Engineering, Aligarh Muslim University, Aligarh, U.P., India

Summary Axisymmetric *DNS* is done for a moderately under-expanded jet at exit-Reynolds number $Re_j = 5 \times 10^4$, exit-Mach number $M_j = 1.5$ and pressure ratio $p_j/p_a = 1.5$, respectively. The effect of co-flow ratio (V_a/V_j) at three different magnitudes, *i.e.* $V_a/V_j = 0$, 0.15 & 0.3, is explored. The increase in co-flow ratio suppresses the formation of counter rotating vortex ring (*CRVR*). The *CRVR* formation occurs earlier in time with increasing V_a/V_j.

INTRODUCTION & METHODOLOGY

A counter rotating vortex ring (*CRVR*) having circulation opposite to that of the primary vortex ring (*PVR*), is formed on the *PVR* periphery in the under-expanded jets [1]. The main cause behind the *CRVR* formation is the rolling-up of the slip-streams emanating from the triple points of Mach-reflection between oblique intercepting shocks and embedded shock, respectively [1]. This rolling up has been attributed to the effect of Kelvin-Helmholtz instability [1]. The *velocity ratio* or *co-flow ratio* ($\frac{V_a}{V_j}$) is the ratio of the ambient fluid speed (V_a) to the jet fluid speed the nozzle exit (V_j). Lovaraju & Rathakrishnan [2] experimentally studied the effect of co-flow on subsonic, correctly-expanded and under-expanded jets. They observed that co-flow retarded the mixing which caused potential core elongation.

An initially axisymmetric and laminar jet of calorically and thermally perfect gas, issuing from a circular nozzle/orifice is considered. The compressible Navier-Stokes equations are formulated in the cylindrical-polar coordinate system that causes an inherent polar-coordinate singularity in the governing equations. This is handled by introducing a new user-defined coordinate system ($\tilde{r}$,$\tilde{\theta}$) in place of (r,θ). The concept has been adapted from Mohseni & Colonius [3]. The domain varies from $(-R, R)$ and $(0, \pi)$ in $\tilde{r}$, $\tilde{\theta}$ coordinates. For non-dimensionalisation, $U_j - U_a$ is the velocity scale, jet-diameter (D_j) is the length scale, ambient temperature and ambient density as the scales for temperature and density, respectively. The axisymmetric form of the compressible Navier-Stokes equations in the new user-defined coordinate system has been solved using the modified version of the *PVUM+* scheme proposed by Hasan et al. [4]. The algebraic Euler characteristic boundary conditions are used [5]. Hat shaped velocity profile for axial-velocity at the nozzle-exit has been used as the initial condition. Initially, density & temperature are fixed at their respective ambient values. The domain spans upto $27D$ longitudinally and it radially spans about $\pm 10D$. The jet emanates from the nozzle whose opening lies just behind the domain face and its dimension ranges from $-0.5 \leq \tilde{r} \leq 0.5$ (see Fig. 1).

RESULTS

Axisymmetric *DNS* simulations were performed for three different co-flow ratios *i.e.* $V_a/V_j = 0$, 0.15 & 0.3 for a starting under-expanded jet at exit-Reynolds number $Re_j = 5 \times 10^4$, exit-Mach number $M_j = 1.5$ and pressure ratio $p_j/p_a = 1.5$, respectively. Figure 1 shows the instantaneous numerical-schlieren snapshots for these jets at different V_a/V_j. With increasing V_a/V_j, Mach reflection occurs earlier in time and its life-span also reduces due to relatively faster propagation of *PVR*. At high co-flow ratio magnitude *i.e.* $V_a/V_j = 0.3$, Mach reflection becomes quite weak due to which the slip-streams cease to emanate in absence of triple-points. Figure 1 also shows that with increasing V_a/V_j, the formation of *CRVR* also occurs earlier in time but about 15% increase in V_a/V_j results in a single *CRVR* pair in contrast to multiple *CRVR*s formed in absence of any co-flow. This shows that increasing V_a/V_j results in the suppression of *K-H instability* that rolls up the slip-stream in form of a *CRVR*. Again, at $V_a/V_j = 0.3$ there is no *CRVR* formation due to the absence of proper Mach reflection. In agreement with [2], it is seen that increasing V_a/V_j elongates the developing inviscid core of the starting jet while, the radial elongation of the *PVR* reduces due to the reduced entrainment of the ambient fluid into the *PVR*. With increasing V_a/V_j, the onset of instability inside the *PVR* and the shock-shear layer-vortex interaction occur earlier in time. But the life-span of hock-shear layer-vortex interaction gets reduced.

References

[1] Dora, C. L., Murugan, T., De, S., & Das, D. 2014 Role of slipstream instability in formation of counter-rotating vortex rings ahead of a compressible vortex ring. *J. Fluid Mech.*, **753**, 29-48.
[2] Lovaraju, P., and Rathakrishnan, E., 2011 Experimental studies on co-flowing subsonic and sonic jets. *Flow Turbulence Combust.* **87**, 115-132.
[3] Mohseni, K., and Colonius. T., 2000 Numerical treatment of polar coordinate singularities. *J. Comput. Phys.*, **157**, 787-795.
[4] Hasan, N., Khan, S., M., and Shameem, F. 2015 A new flux-based scheme for compressible flows. *Comp. & Fluids* **119**, 58-86.
[5] Arif, R., M., and Hasan, N. 2019 Performance of characteristic numerical boundary conditions for mixed convective flows past a heated square cylinder using a non-Boussinesq approach. *Numerical Heat Transfer, Part A: Applications* **76**, 4, 254280.

*Corresponding author. E-mail: sanghi@am.iitd.ac.in

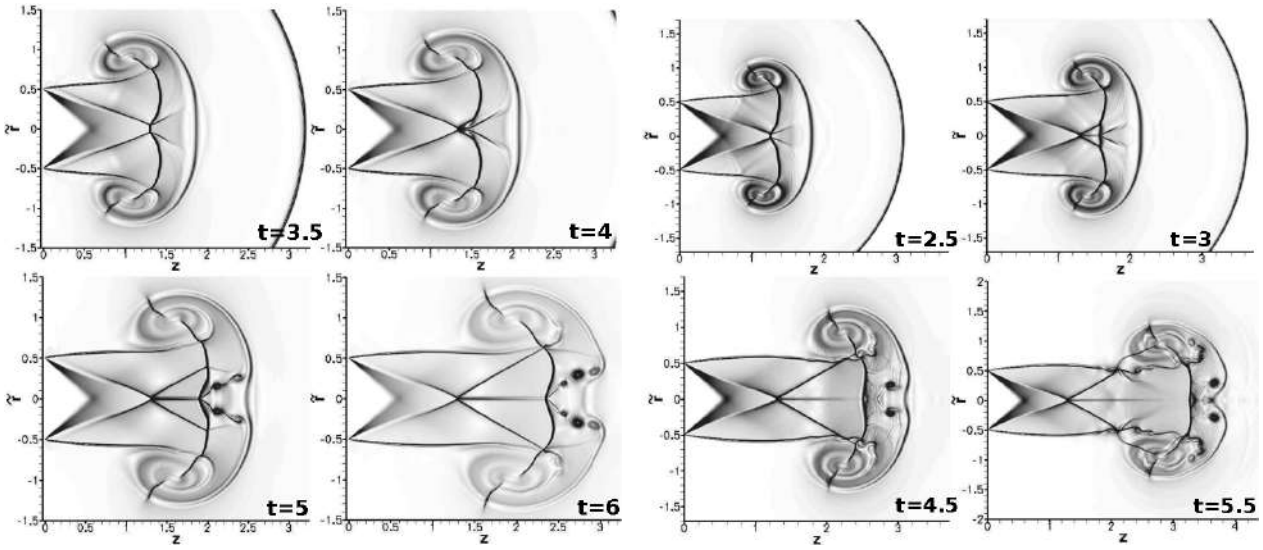

(a) (b)

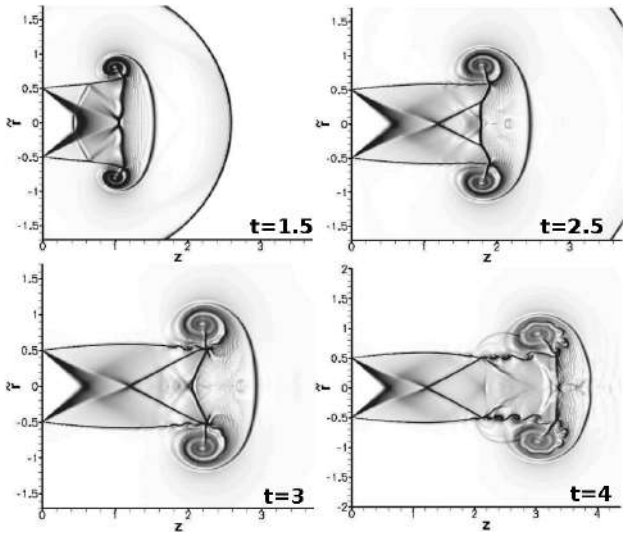

(c)

Figure 1: Instantaneous numerical schlieren $|\nabla\rho|$ contours showing CRVR formation in an under-expanded jet at $Re_j =$

STABILITY OF EXPANDING ACCRETION SHOCKS IN REACTIVE MEDIA

César Huete*[1], Andrés Calvo[1], Daniel Martínez-Ruiz[2], and Alexander L. Velilkovich[3]
[1] Grupo de Mecánica de Fluidos, Universidad Carlos III de Madrid, Leganés, Spain
[2] ETSIAE, Universidad Politécnica de Madrid, Madrid, Spain
[3] Plasma Physics Division, Naval Research Laboratory, Washington, DC 20375, USA

Summary Stagnation of a cold material streaming to the center or axis of symmetry via an expanding accretion shock wave is a phenomenon of paramount importance in high-energy-density physics. The examples range from plasma flows in x-ray-generating Z pinches, impact ignition in Inertial Confinement Fusion, and core-collapse supernovae in astrophysics. We present a theoretical analysis for the case of stagnation that does not involve a rarefaction wave behind the expanding shock front. The dispersion equation that determines the eigenvalues of the problem and the explicit formulas for the eigenfunction profiles corresponding to these eigenvalues are presented for strong shock waves propagating in reactive media. Non-adiabatic transformations as dissociation, ionization and global chemical reaction are analyzed. The boundaries of stability are explicitly determined.

INTRODUCTION

In the high-energy-density context, non-adiabatic shocks can develop in a wide range of phenomena, including thermonuclear detonations formed in thermonuclear supernovae. Further examples can be found in the so-called core-collapse supernovae (CCSNe), a type of supernovae powered by stellar core collapse. The shock wave evolves through a phase of accretion shock, in which it becomes endothermic due to the nuclear dissociation process taking place across the shock. A distinctive common feature of these two fronts is that energy variations (either exothermic and endothermic) may likely depend on thermodynamical absolute values, and thus on the shock intensity. A clear example is found in the energy lost by radiation in the so-called radiative shocks. Under the ICF/HEDP experimental conditions [1, 2], the mechanism of plasma stagnation via the expanding shock is roughly similar, although the gravity does not play a significant role.

To study the stability of the expanding shock, a linear perturbation analysis is carried out [3], which is applicable under the following assumptions [4]: the non-adiabatic transformations of the fluid particles occur in a very thin layer right behind the shock for the whole supersonic front to be considered a fluid discontinuity. Besides, pressure, density and temperature are related through the perfect gas equation of state in the perturbation variables in the equilibrium states. The name non-adiabatic comprises any type of energy gain or loss across the shock, *e.g.,* reactive, dissociating, radiating or ionizing, along with the associated molecule structure changes.

PROBLEM DESCRIPTION

The initial conditions for the Noh problem are $\rho_1(r, t = 0) = \rho_0$, $p_1(r, t = 0) = p_0$ and $\boldsymbol{v}_1(r, t = 0) = -v_0\boldsymbol{e}_r$, where ρ_0 and p_0 are the initial density and pressure, and $v_0 > 0$ is the uniform initial radial velocity, and $\boldsymbol{e}_r$ is a unit vector in the positive radial direction. The subscript 1 refers to variable conditions in the whole domain ahead of the shock front while the subscript 0 to the initial conditions. The evolution of the upstream flow can be derived by employing the self-similar coordinate $\xi = r/(v_0 t)$. The singularity is resolved by the expanding shock that moves at constant speed $\dot{r}_s$ emerges at $t > 0^+$ and puts the downstream flow at rest. The linear, small-amplitude stability analysis covers the general case of 3D perturbations of the classic Noh solution for spherical geometry, with small-amplitude distortion of the expanding shock front proportional to the spherical harmonic, $Y_l^m(\theta, \phi)$ and the particular filamentation 2D perturbation $\sim \exp(im\theta)$ for cylindrical geometry. For the above two cases, our perturbation problem is solved analytically, resulting in an explicit dispersion equation for the eigenvalues determining the time evolution of the solutions, as well as explicit formulas for the corresponding eigenfunctions.

For a spherical geometry, the perturbed shock front position is written in terms of spherical harmonics, *i.e.*,

$$\frac{r_s(\theta, \phi, t)}{\dot{r}_s t} - 1 = \epsilon \sum_{l,m} \left(\frac{t}{t_0}\right)^{\sigma} Y_l^m(\theta, \phi), \tag{1}$$

where $\dot{r}_s t$ corresponds to the unperturbed radial position of the shock. The term proportional to the small-amplitude parameter ϵ includes $Y_l^m(\theta, \phi) = P_l^m(\cos\theta)e^{im\phi}$, where P_l^m is the associated (generalized) Legendre function and l and $m \leq l$ correspond to the integer mode numbers. The deviation from the unperturbed position $\delta r_s = r_s - \dot{r}_s t$ depends on time as well as the polar $\theta \in [0, \pi]$ and azimuthal $\phi \in [0, 2\pi]$ angles, see scheme in Fig.1. The lack of scales dictates the power-law dependence $(t/t_0)^{\sigma}$, where the t_0 is an arbitrary temporal parameter used to provide of dimensional consistency. The eigenvalue $\sigma = \sigma_{\mathrm{R}} + i\sigma_{\mathrm{I}}$ is a complex parameter to be determined and whose properties describe the shock dynamics: the oscillation frequency will be dictated by the value of σ_{I} while the real part will determine if the shock is stable ($\sigma_{\mathrm{R}} \leq 0$) or unstable ($\sigma_{\mathrm{R}} > 0$).

*Corresponding author. E-mail: chuete@ing.uc3m.es

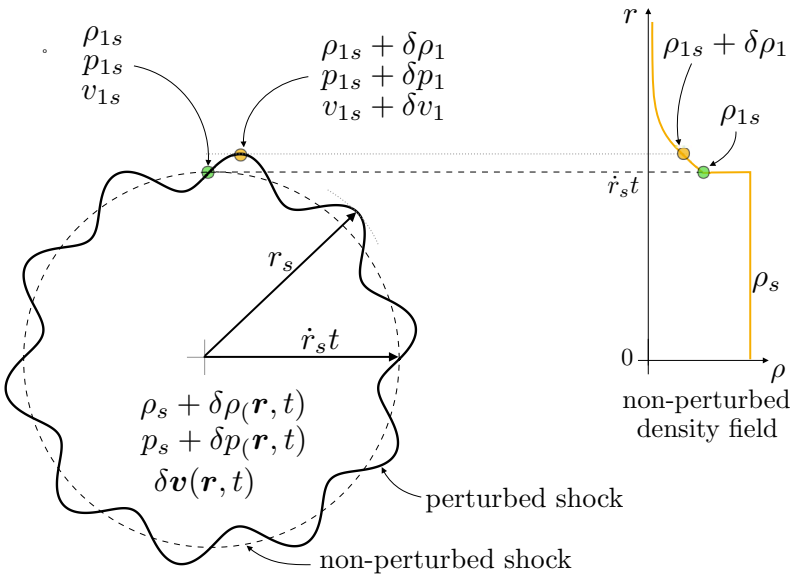

Figure 1: Sketch of the perturbed shock moving through the non-uniform upstream flow. Representation for the cylindrical geometry with $m = 10$.

The problem formulation includes the perturbation of the flow variables downstream in term of the corresponding eigenfunctions and the eigenvalue σ. The inviscid Euler equations are solved with the aid of the linearized Rankine-Hugoniot equations, which finally render the dispersion relationship

$$\begin{aligned}&\{(\sigma+\nu-1)\left[\mathcal{R}_s(\nu-1)-\sigma-\nu\right]+\mathcal{R}_s j(j+\nu-2)\}(1+h)F_{1s}^{+}\\&+\left[2(\sigma+\nu)-\mathcal{R}_s(\nu-1)\left(1+h_1\right)\right](\sigma+\nu+j-1)F_{1s}^{-}=0\end{aligned}\tag{2}$$

that determines the eigenvalue σ as a function of the geometry factor ν, the mode number j, the mass compression ratio $\mathcal{R}_s$, and the functions h and h_1. The factor h is recognized as the D'yakov-Kontorovich parameter that measures the slope of the Rankine-Hugoniot curve relative to the Rayleigh–Mickelson line. The parameter h_1 is an independent coefficient accounting for the influence in the post-shock values due to the change of pre-shock properties. The functions F_{1s}^{+} and F_{1s}^{-} refer to the hypergeometric functions evaluated at the shock front that can be defined conjointly as

$$F_{1s}^{\pm}={}_2F_1\left(\frac{j-\sigma}{2},\frac{j\pm1-\sigma}{2};j+\frac{\nu}{2};\eta^2=\mathcal{M}_s^2\right),\tag{3}$$

where $\mathcal{M}_s$ is the post-shock Mach number. As discussed in [3], there exits a infinite set of complex eigenvalues for any mode number j, which are the mathematical manifestation of the acoustic reverberations between the shock and geometrical center. Each of those exhibit a different temporal power-law decay, when stable.

CONCLUSIONS

The linear stability analysis of the expanding accretion non-adiabatic shock is performed, on condition that reactive processes occur in a negligible thickness layer behind the shock. The model, that allows the inclusion of any phenomenon that may alter the energy balance across the shock, is applied to different contexts of interest in high-energy-density physics, as they are ionization, dissociation, and global exothermic reactions. The boundaries of stability are explicitly determined. Numerical simulations are carried out to include non-linear interactions and finite-length effect contributions.

References

[1] Azechi,T. et al. Experimental evidence of impact ignition: 100-fold increase of neutron yield by impactor collision. Phys. Rev. Lett. 102, 235002 (2009).
[2] Maron, Y. et al. Pressure and Energy Balance of Stagnating Plasmas in Z-Pinch Experiments: Implications to Current Flow at Stagnation. Phys. Rev. Lett. 111, 035001 (2013).
[3] Velikovich, A.L. et al. Stability of stagnation via an expanding accretion shock wave. Phys. Plasmas, 23, 052706 (2016).
[4] Huete, C., Cobos-Campos, F., Abdikamalov, E. and Bouquet, E. Phys. Rev. Fluids, accepted (2020).

BISTABILITY AND SEPARATION HYSTERESIS OF SHOCK WAVE BOUNDARY LAYER INTERACTION

Yan-Chao Hu*[1], Wen-Feng Zhou [1], Yan-Guang Yang [2], Zhi-Gong Tang [2], and Zhao-Hu Qin [3]
[1] Hypervelocity Aerodynamics Institute, China Aerodynamics Research and Development Centre, Mianyang, China
[2] China Aerodynamics Research and Development Centre, Mianyang, China
[3] State Key Laboratory for Turbulence and Complex Systems, College of Engineering, Peking University, Beijing, China

Summary The bistability and separation hysteresis of shock wave boundary layer interaction flows are observed and investigated numerically, using curved compression ramp geometrical configuration. The occurrence of this new phenomenon indicates that the boundary layer's state (attachment/separation) depends on its evolutionary history even for the same free-stream and boundary conditions. Specifically, beginning with an attachment state, the boundary layer remains attached as the angle of attack (AOA) increases slowly and suddenly separates once AOA reaches a marginal angle. However, if AOA is decreased back from this angle, the boundary layer will not attach and remain separated until AOA reaches a small enough angle. The mechanism of the separation hysteresis is expounded using three characteristic adverse pressure gradients.

INTRODUCTION

Hysteresis is a general property of multistable systems manifested as the dependence of a system on its evolutionary history, which is ubiquitous in aerospace flow systems, such as aerodynamic hysteresis (subsonic external flow hysteresis) [1], and shock wave reflection hysteresis (supersonic internal flow hysteresis) [2,3]. However, for supersonic external flows, as far as we know, even though hysteresis phenomenon has been proposed theoretically [4], it has not yet been observed experimentally or numerically. In this paper, we report the separation hysteresis in curved compression ramp flows (SHCCR) induced by AOA-variation, which is observed for the first time. The features of CCR flows with the laminar boundary layer are presented, and the mechanism of SHCCR is discussed.

BISTABILITY OF CURVED COMPRESSION RAMP FLOW

The bistability of curved compression ramp flow is studied thorough three dimensional Direct numerical simulations (DNS) []. As shown in figure 1, the streamwise and spanwise regions are $-82mm \leq x \leq 107.2mm$ and $0mm \leq z \leq 40mm$, respectively. The turning angle is $\phi = 18°$. The curvature radius of the concave region is $R = L/\tan(\phi/2)$, where $L = 25mm$ is the distance from the original point of the curved wall to $(0,0)$. The free-stream Mach number is fixed at 6.0 and other flow parameters are consistent with our previous work [6]. The incoming boundary layers are both laminar on the flat plate and will become turbulent downstream. It can be seen that there are two different flow states, (a) attachment and (b) separation, for the same free-stream and boundary conditions, and both simulations of these two states are convergent. The reason of the existence of the bistability is as follows. When L is large, the adverse pressure gradient (APG) is small and the flow tend to be attaching. If L is small enough, the flow should separate induced by strong APG. For an appropriate L, the flow may be attached or separated, which is determined by the evolution process.

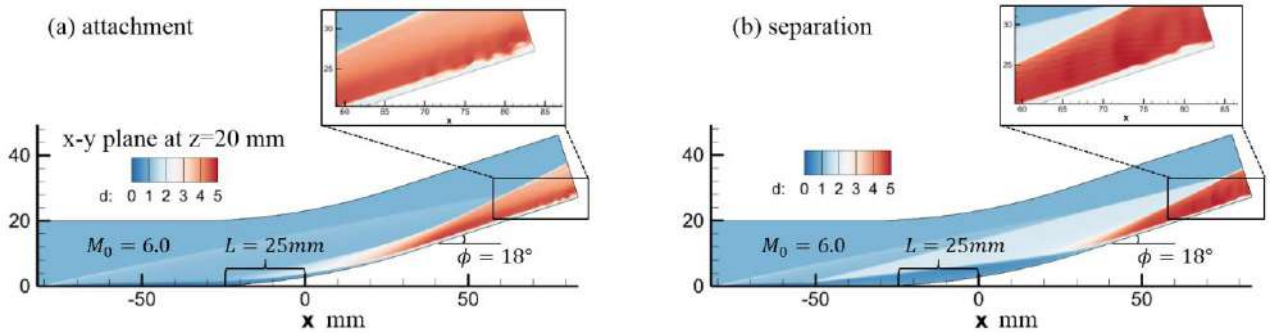

Figure 1. bistablitiy of the curved compression ramp flow.

SEPARATION HYSTERESIS OF CURVED COMPRESSION RAMP FLOW

The separation hysteresis is expected to occur by tunning the AOA. As shown in figure 2, the simulation begins with $\alpha = 0°$ corresponding to an attachment state (state 1). As AOA increases $\alpha = 21°$ in state 4), the attachment state is maintained. However, when AOA is large enough ($21° < \alpha < 22°$), the separation arises suddenly. Since the flow in the separation bubble is subsonic at a low speed, we can distinguish the separation state with an obvious blue area representing M < 1 on the curved wall. If AOA decreases gradually from $\alpha = 22°$ (state 3) back to $\alpha = 0°$ (state 5), the separation state persists ($\alpha = 21°$ in state 4). Note that for the same free-stream conditions (states 1 and 5, 2 and 4), there are two

*Corresponding author. E-mail: yanchaohu@pku.edu.cn

steady states (attachment and separation). Furthermore, if we decrease AOA from $\alpha = 0°$ (state 5) to $\alpha = -4°$ (state 6), the leading edge shock transits to an expansion fan, and the separation region becomes smaller. As AOA continues to decrease, the separation shrinks gradually and the boundary layer attaches again when $-5° < \alpha < -4°$. Finally, as AOA increases from $-5°$ back to $0°$, the flow maintains the attachment state (states 7 and 8). The process from state 1 to state 8 constitutes a new flow hysteresis phenomenon, i.e., SHCCR induced by AOA-variation.

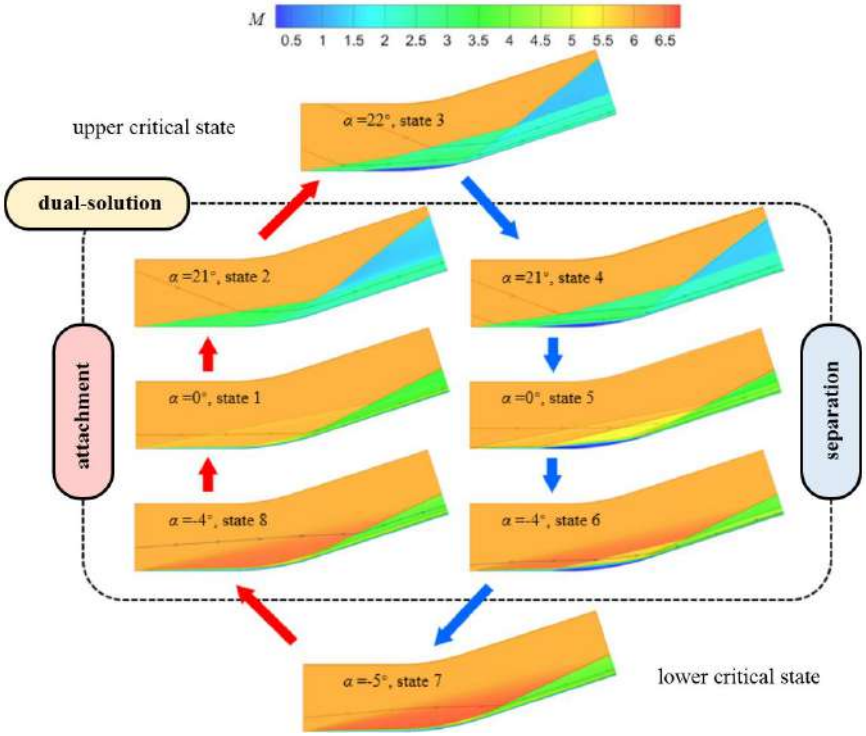

Figure 2. Separation hysteresis of the curved compression ramp flow.

THE MECHANISM OF SEPARATION HYSTERESIS

Here, the relative magnitude of APG induced by separation and curved wall should be further emphasized. We denote the resistance of the boundary layer to APG as I_b, and the maximum APG induced by the curved wall in attachment states as I_{cw}. If the boundary layer cannot resist the APG induced by the curved wall, i.e., $I_b < I_{cw}$, a separation bubble will occur and form a "virtual ramp" inducing a stronger APG, whose maximum value is denoted as I_{sb}. Generally, as mentioned above, near the separation point, APG induced by the virtual ramp ($R \to 0$) is larger than that induced by the curved wall, i.e., $I_{sb} > I_{cw}$. Therefore, the boundary layer must be attached when $I_b > I_{sb}$. However, by changing the inflow or boundary conditions (such as tunning the AOA), I_b may locate in $[I_{cw}, I_{sb}]$, where both attachment and separation are theoretically possible. In this region ($I_{cw} < I_b < I_{sb}$), a separation hysteresis could occur induced by the variation of some flow parameter, which is just the new phenomenon we have discussed above.

CONCLUSIONS

In this paper, SHCCR induced by AOA-variation is observed numerically. Starting from an attachment state, the boundary layer keeps attaching with increasing AOA and suddenly separates when the AOA reaches the upper marginal angle, with the separation bubble covering the curved ramp and forming a virtual ramp. While AOA decreases back gradually, the separation bubble seems to be frozen and the boundary layer will not attach until AOA is small enough. The mechanism of the separation hysteresis is expounded.

References

[1] Yang, Zifeng, Hirofumi Igarashi, Mathew Martin, and Hui Hu. "An Experimental Investigation on Aerodynamic Hysteresis of a Low-Reynolds Number Airfoil." 46th AIAA Aerospace Sciences Meeting and Exhibit, 2008.

[2] Ben-Dor, G, M Ivanov, E.I Vasilev, and T Elperin. "Hysteresis Processes in the Regular Reflection and Mach Reflection Transition in Steady Flows." Progress in Aerospace Sciences, vol. 38, no. 4, 2002, pp. 347–387.

[3] Hu, Yan-Chao, Zhi-Gong Tang, Yan-Guang Yang, Wen-Feng Zhou, and Zhao-Hu Qin. "Origin of Hysteresis in Shock Wave Reflection." ArXiv Preprint ArXiv:2005.07905, 2020.

[4] Zametaev, V. B. "Existence and Nonuniqueness of Local Separation Zones in Viscous Jets." Fluid Dynamics, vol. 21, no. 1, 1986, pp. 31–38.

[5] Hu, Yan-Chao, Bi Wei-Tao, Li Shi-Yao, and She Zhen-Su. 2017. "β -Distribution for Reynolds Stress and Turbulent Heat Flux in Relaxation Turbulent Boundary Layer of Compression Ramp." Science China-Physics Mechanics & Astronomy, vol. 60, no. 12, 2017, p. 124711.

[6] Hu, Yan-Chao, Wen-Feng Zhou, Gang Wang, Yan-Guang Yang, and Zhi-Gong Tang. "Bistable States and Separation Hysteresis in Curved Compression Ramp Flows." Physics of Fluids, vol. 32, no. 11, 2020, p. 113601.

SELF-SUSTAINED BIPHASIC CATALYTIC PARTICLE TURBULENCE

Ziqi Wang[1], Varghese Mathai[2], and Chao Sun *[1]
[1] Center for Combustion Energy, Key Laboratory for Thermal Science and Power Engineering of Ministry of Education, Department of Energy and Power Engineering, Tsinghua University, 100084 Beijing, China
[2] School of Engineering, Brown University, Providence, Rhode Island, 02912, USA

Summary Turbulence is known for its ability to vigorously mix fluid and transport heat. While over a century of research for enhancing heat transport, few have exceeded the inherent limits posed by turbulent-mixing. Here we have conceptualized a kind of "active particle" turbulence machine: we find that by adding a minute concentration ($\phi_v \sim 1\%$) of a heavy liquid (hydrofluoroether) to a water-based turbulent convection system, remarkably, high efficient biphasic dynamics is born, which supersedes turbulent heat transport by up to 500%. The system is unique in that it operates on a self-sustained dynamically equilibrated cycle of a "catalyst-like" species, and exploits several heat-carrier agents including pseudo-turbulence, latent heat and bidirectional wake capture. We find that the heat transfer enhancement is dominated by the kinematics of the active elements and their induced-agitation [1]. The present finding opens the door towards the establishment of tunable, ultra-high efficiency heat transfer/mixing systems.

INTRODUCTION

In the global context of energy exchange, thermal turbulence holds a central place as a major driver in many natural and industrial processes [2]. The primary heat transporters of thermal turbulence are the "plumes" (a form of coherent turbulent structure), and they form an essential component in ocean currents, atmospheric and mantle convection, volcanic eruptions, bio-chemical and combustion reactions, as well as in the sustenance of thermonuclear phenomena in the sun, the stars, and other galactic powerhouses[3]. A remarkable property of these coherent plume structures is their ability to mix initially distinct constituents across multi-decadal length and time scales, yielding extremely efficient (super-diffusive) transport of scalars[4], which are typically orders of magnitude faster than those achievable by molecular diffusion alone. The same characteristics of the plumes have become to be exploited in design of efficient heat exchangers and mixing networks. From a fundamental perspective, a central question for any heating or cooling device is to establish a robust relationship between an applied temperature difference and the corresponding heat flux[3]. The vast majority of recent explorations for marginal to moderate heat flux enhancements underlines the need for fundamentally new concepts of heat transport in closed-system heat exchangers.

EXPERIMENTS

We begin with a classical (water-based) thermal convection system (aspect ratio 0.5, with a heated bottom plate ($T_b \approx 35°C$) and a cooled top plate ($T_t \approx 5°C$) at atmospheric pressure p_0. To this, we introduce a minute fraction ($\phi_v \sim 1\%$) of a low conductivity liquid (hydrofluoroether (HFE-7000)), through which a highly efficient active particle turbulence is born (Fig. 1(a). The active species enters a dynamic boiling condensation cycle, thereby creating self-sustained biphasic catalytic heat-carrier elements (see insets (b)-(d)) and supplanting the plumes (classical coherent structures) of thermal turbulence (insets (e)-(f)).

RESULTS

The collective dynamics of the vapor-liquid elements gives rise to even stronger coherent structures than in thermal turbulence. We report heat flux enhancements of up to 500% (green-shaded half of Fig. 1(g)). When the bottom plate temperature T_b is raised above a critical value T_{cr}, the heat transfer (Nu/Nu_0) increases almost linearly (Fig. 1(g)), where Nu_0 is the heat exchange possible due to convective turbulence alone. This occurs as a consequence of increased activity of the biphasic particles (see insets Fig. 1(b)-(d)). Remarkably, the five fold enhancement in heat flux is attained with only a 1.3% (by volume) activity of the biphasic species (inset to Fig. 1(g)). The HFE-7000 liquid boils to form vapor bubbles and the vapor bubbles will detach from the bottom plate and rise; at the meantime of rising through the bulk of the cell the vapor will condense into liquid; so the bubbles become biphasic with more and more liquid fraction, and consequently more and more heavier until they reach the top plate, where they condense totally into liquid droplets. The liquid droplets will fall and return the bottom plate. These processes are self-sustained. The biphasic particles appear from the bottom plate with a lower density (positive buoyancy) as compared to water, and after releasing heat in the bulk and near the top plate, they increase their overall density (gain negative buoyancy) and move downward to recover their initial state. Thus the role of the biphasic species to the thermal convection system holds a close analogy to that of a "catalyst". We also investigate the detailed mechanism of drastic heat transfer enhancement the active biphasic particles. The effective heat transfer gain (up to 500%) of biphasic turbulence is believed to result from the combined contributions of (a) the kinematics of the active particles (see the blue shaded part in Fig. 2), and (b) their induced liquid agitation (see the blue shaded part in Fig. 2).

*Corresponding author. E-mail: chaosun@tsinghua.edu.cn

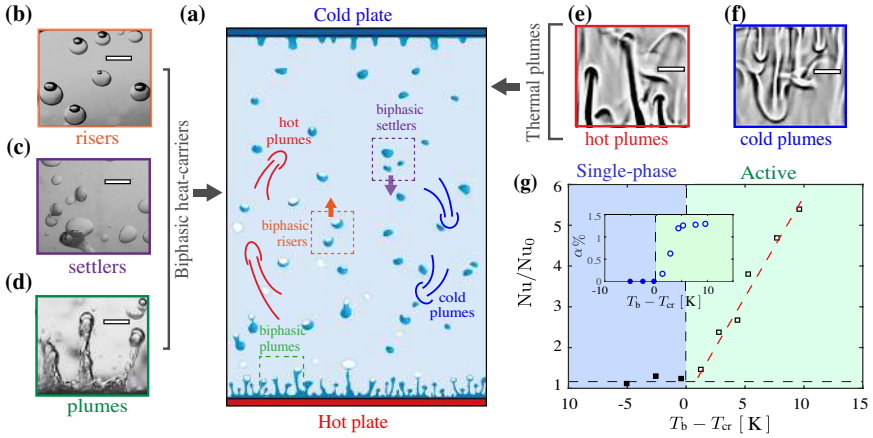

Figure 1: (a) Schematic of a classical thermal turbulence setup with water as working liquid, and augmented by $\sim 1\%$ volume of active species: HFE-7000. Insets (b)-(d) show novel heat carriers of the system: (b) biphasic risers, (c) settlers, and (d) plumes. Insets (e)-(f) show shadowgraphy images of the classical heat transporters of thermal turbulence, namely (e) hot and (f) cold thermal plumes. Inset scale bars: 6 mm. (g) Heat flux enhancement expressed as the ratio of Nusselt numbers $\mathrm{Nu}/\mathrm{Nu}_0$ vs temperature difference $T_b - T_{cr}$. Here Nu is the Nusselt number of the current system, Nu_0 is the Nusselt number of classical thermal turbulence, T_b is the bottom plate temperature, and T_{cr} is the boiling point of HFE-7000 liquid above which the dynamic evaporation-condensation cycles begin. Inset shows the vapor phase of the biphasic species volume fraction α.

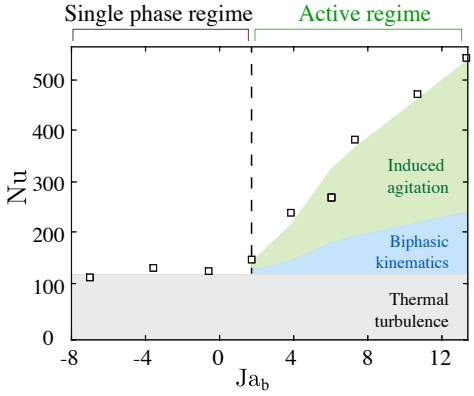

Figure 2: Nusselt number for increasing Jakob number Ja_b. The shaded areas show different contributions to the total heat transfer enhancement, namely thermal turbulence (gray), biphasic particle kinematics (blue) and induced liquid agitation (green).

CONCLUSIONS

In summary, we have created an efficient class of active biphasic thermal turbulence by the addition of a minute quantity ($\sim 1\%$) of a low boiling point liquid, which provides sustained heat transport enhancements (by up to 500%) that well-surpasses the limits achievable by classical thermal turbulence. The drastic enhancement is found to be the kinematics of the active particles and their induced liquid agitation. The biphasic particle system attains this state through minimal operational modifications to the existing thermal turbulence system, which may revolutionize future industrial designs. Remarkably, the system shows regimes of linear scalings of heat exchange with temperature change (for independent changes in bottom and top plate temperatures), and for aspect ratio changes, suggesting robust predictability and heat transfer control in both heating and cooling applications. The biphasic transport here is efficient, self-sustained and dynamically equilibrated, and requires minimal operational modifications to existing closed-system heat exchangers. Furthermore, the biphasic species (HFE-7000) is non-corrosive, non-flammable, and non-ozone depleting (ODP 0), and hence holds promise as a safe and highly effective "catalyst-like" additive in contemporary clinical, biochemical, and nuclear engineering settings.

References

[1] Z. Wang, V. Mathai, C. Sun, *Self-sustained biphasic catalytic particle turbulence*, Nat. Communi. **10**, 3333 (2019).
[2] G. Falkovich, K. Gawedzki, and M. Vergassola, *Particles and fields in fluid turbulence*, Rev. Mod. Phys. **73**, 913 (2001).
[3] G. Ahlers, S. Grossmann, and D. Lohse, *Heat transfer and large scale dynamics in turbulent Rayleigh-Bénard convection*, Rev. Mod. Phys. **81**, 503–537 (2009).
[4] H. Xia, D. Byrne, G. Falkovich, and M. Shats, *Upscale energy transfer in thick turbulent fluid layers*, Nat. Phys. **7**, 321–324 (2011).

RAYLEIGH–BÉNARD CONVECTION IN CYLINDRICAL CONTAINERS WITH RING-SHAPED ROUGHNESS OF THE PLATES

Mohammad Emran and Olga Shishkina *[1]
[1] Max Planck Institute for Dynamics and Self-Organization, Am Fassberg 17, 37077 Göttingen, Germany

Summary We investigate the influence of the regular roughness of the heated and cooled plates on the mean heat transport in a cylindrical Rayleigh–Bénard convection (RBC) cell of the aspect ratio one, by means of three-dimensional direct numerical simulations (DNS; totally 115 different cases). The roughness is introduced by a set of isothermal obstacles, which are attached to both plates and have a form of concentric rings of the same width. The considered Prandtl number is $\mathrm{Pr} = 1$, the Rayleigh number Ra varies from 10^6 to 10^8, the number of the rings on each plate is up to 10, the height of the rings is varied from 3% to 80% of the cylinder radius and the gap between the rings is varied from 3% to 37.6% of the cell radius. Our DNS show that by small Ra and wide roughness rings, a small reduction of the mean heat transport (the Nusselt number Nu) is possible, but in general, the presence of the heated and cooled obstacles leads to an increase of Nu, compared to the case of classical RBC with smooth plates. For very tall obstacle rings and sufficiently wide gaps between them, the effective mean heat flux can be several times larger than in the smooth case. For any prescribed roughness geometry, the scaling exponent in the Nu vs. Ra scaling first increases with growing Ra, up to approximately 0.5, but then smoothly decreases back towards the exponent in the no-obstacle case.

INTRODUCTION

In classical RBC [1] the heating and cooling plates are assumed to be smooth, while in most applications this assumption is not fulfilled. Roughness of the plates or the presence of the heated and cooled obstacles, which are attached to the corresponding plates, can influence significantly the mean heat and momentum transport in the system, which are represented by the Nusselt number Nu and Reynolds number Re, respectively. Moreover, the scaling relations of Nu and Re on the main input parameters of the system, which are the Rayleigh number Ra and Prandtl number Pr, are also affected by the wall roughness. Thus, it was reported that, compared to the case of smooth plates, the exponent γ in the scaling relation $\mathrm{Nu} \sim \mathrm{Ra}^{\gamma}$ can be larger (e.g., [5, 7, 13]) and/or the pre-factor in this relation can be increased (e.g., [6, 9]). For moderate Ra up to 10^8, 3D DNS [12] in a cubical container with a fixed rectangular roughness showed that γ first increases with growing Ra, but then saturates back to the smooth-wall value. Similar results were obtained in 2D DNS [14], for a broad Pr-range and Ra up to 10^{10}. 2D simulations based on the immersed boundary method (IBM) [16] for Ra up to 10^{12} showed that at $\mathrm{Ra} \approx 3 \times 10^9$ there is a transition from one scaling regime with $\gamma \approx 1/2$ for smaller Ra to another regime with $\gamma \approx 1/3$ for larger Ra. Therefore the regime with $\gamma \approx 1/2$ can be interpreted neither as the ultimate regime for extremely high Ra nor as a transition to it, but rather as an intermediate regime triggered by the regular roughness. Similar results were obtained also in experiments [8]. In [2], it was obtained experimentally that γ increases for non-regular (power-law distributed) roughness, while for regular (periodic) roughness it is unaffected. This supported a theoretical model [11] that proposes a relation between the increase of γ and the surface's fractal dimension, for the case when the spectrum of the typical roughness length scales is sufficiently broad.

To address the question, whether the number of the roughness scales influences the Ra-range with increased γ, in [17] the effect of the multi-scale roughness in 2D IBM simulations, for Ra up to 10^{12}, was studied. A sinusoidally shaped roughness, represented by 3 different length scales, lead to the enhanced heat transport with $\gamma \approx 1/2$, which was observed for more than 3 decades of Ra. Note that for a single-scale roughness, this regime was restricted to only one and half decades of Ra [16]. Therefore, the more roughness scales means the broader Ra-range, where the increased γ can be observed. With an infinite spectrum of the roughness length scales, such that for any distance to the plate there exists a roughness scale which is smaller than this distance, one can anticipate a scaling regime with an increased γ that extends to extremely large Ra and thus is indistinguishable from the ultimate regime.

One should mention also that the plate roughness can not only increase but also can decrease Nu. This was obtained first in 2D DNS [10] and then confirmed in [15] and [4]. The reduction of Nu happens when the fluid stagnates in the gaps between the roughness elements and this leads in general to thicker thermal boundary layers (BLs) and smaller overall heat transport in the system, compared to the case of the smooth plates. The effect of Nu reduction happens at small roughness heights and this critical roughness height decreases very rapidly with growing Ra [15].

RESULTS

In this study we investigate the effect of the regularly distributed isothermal roughness obstacles in a cylindrical domain of the aspect ratio 1, which are attached to the heated bottom and cooled top plates and have the temperatures of the corresponding plates. The effect of the plate roughness is not modelled but instead, 3D DNS, using a direct Poisson solver, are conducted for Ra from 10^6 to 10^8, $\mathrm{Pr} = 1$ and various types of the concentric ring-shaped obstacles – on total 115 different cases [3]. The choice of the geometry is motivated mainly by the following reason: In cylindrical domains

*Corresponding author. E-mail: Olga.Shishkina@ds.mpg.de

with ring-shaped roughness elements, the turbulent wind, or the large-scale circulation (LSC) that develops in RBC cells for sufficiently large Ra, unavoidably goes across the roughness elements, independently from the LSC orientation. The full system of the governing equations under Oberbeck–Boussinesq approximation is considered. The effective quantities $\mathrm{Ra}_{\mathrm{eff}}$, $\mathrm{Re}_{\mathrm{eff}}$, $\mathrm{Nu}_{\mathrm{eff}}$ are based on the effective cell height H_{eff} which is determined by the fluid volume (the cylinder volume minus the volume of all obstacles) divided by the area of the horizontal cross-section of the cylinder.

The obtained results show that in the most cases the regular roughness leads to an increase of Nu. Only for small Ra and relatively small gaps between the obstacles, a reduction of Nu is possible, compared to the smooth-plate case, which, therefore, becomes irrelevant for high Ra. Our DNS confirm that the effect of the roughness comes out when the obstacle height is larger than the thickness of the thermal BL. In this case, the width of the gaps between the obstacles (a) and obstacle height (h) become important: for large gaps and tall obstacles, the mean heat flow can increase by several times, compared to the smooth-plate case. When the cavities between the obstacles are only partly washed out by the convective flow, the scaling exponent γ can increase up to $\approx 1/2$, but with further increase of Ra, the exponent slowly decreases and tends to that in the smooth-plate case. Larger number of the ring-shaped obstacles of sufficiently large heights and gaps between them, usually means a stronger heat transport in the system, since the additional heat flux in that case is proportional to the additional covering area of the heated/cooled surfaces.

Interesting funding is also that the destruction, or a complete re-organisation of a single-big-roll LSC, which is usually observed in classical RBC with smooth plates, can also lead to an increase of the global heat transport. Thus, by extremely tall obstacles, for a sufficiently large gaps between them, the LSC is transformed into a set of smaller rolls, each of which is located in a gap between two neighbouring obstacles of the same temperature and extends from the very bottom to the very top of the cell. This is similar to the phenomenon of Nu increase in classical RBC, affected by the cell confinement.

For any Ra, there exists an optimal configuration of the ring-shaped obstacles that provides the maximal Nu. Deeper investigation of this problem and also the dependence of the optimal configuration on Pr needs to be addressed in the future studies. From our present study, however, for $\mathrm{Pr} = 1$ and cylindrical container of the aspect ratio one, we can conclude the following. For a fixed effective Rayleigh number, $\mathrm{Ra}_{\mathrm{eff}}$, an increase of $\mathrm{Nu}_{\mathrm{eff}}$ due to the roughness can be obtained if both, the gap between the roughness elements, a, and the roughness height, h, are larger than the thicknesses of the thermal BL, δ_θ, in the smooth-plate case. An increase of the gap in the interval up to $a_{\mathrm{cr}} \approx 4\delta_\theta$, leads to a significant increase of the effective Nusselt number, $\mathrm{Nu}_{\mathrm{eff}}$. Further increase of a does not influence much the value of $\mathrm{Nu}_{\mathrm{eff}}$. Furthermore, for $a > \delta_\theta$, and $h > \delta_\theta$, the mean heat flux increases almost linearly with the roughness elements height, or with the additional area of the heated/cooled surfaces. Thus, the largest heat transport in the system is anticipated for thin and extremely tall roughness elements, where the gap between them equals $a = a_{\mathrm{cr}}$.

Acknowlegements. This work was supported by the Deutsche Forschungsgemeinschaft (DFG) under the grant Sh405/3. The authors acknowledge the Leibniz Supercomputing Centre (LRZ) for providing computing time.

References

[1] G. Ahlers, S. Grossmann, and D. Lohse. Heat transfer and large scale dynamics in turbulent Rayleigh–Bénard convection. *Rev. Mod. Phys.*, 81:503–537, 2009.
[2] S. Ciliberto and C. Laroche. Random roughness of boundary increases the turbulent scaling exponents. *Phys. Rev. Lett.*, 82:3998–4001, 1999.
[3] M. S. Emran and O. Shishkina. Natural convection in cylindrical containers with isothermal ring-shaped obstacles. *J. Fluid Mech.*, 882:A3, 2020.
[4] N. Foroozani, J. J. Niemela, V. Armenio, and K. R. Sreenivasan. Turbulent convection and large scale circulation in a cube with rough horizontal surfaces. *Phys. Rev. E*, 99:033116, 2019.
[5] H. Jiang, X. Zhu, V. Mathai, R. Verzicco, D. Lohse, and C. Sun. Controlling heat transport and flow structures in thermal turbulence using ratchet surfaces. *Phys. Rev. Lett.*, 120:044501, 2018.
[6] P. Joshi, H. Rajaei, R. P. J. Kunnen, and H. J. H. Clercx. Heat transfer in rotating Rayleigh–Bénard convection with rough plates. *J. Fluid Mech.*, 830:R3, 2017.
[7] O. Liot, J. Salort, R. Kaiser, R. du Puits, and F. Chillá. Boundary layer structure in a rough Rayleigh–Bénard cell filled with air. *J. Fluid Mech.*, 786:275–293, 2016.
[8] E. Rusaouën, O. Liot, B. Castaing, J. Salort, and F. Chillà. Thermal transfer in Rayleigh–Bénard cell with smooth or rough boundaries. *J. Fluid Mech.*, 837:443–460, 2018.
[9] Y. Shen, K.-Q. Xia, and P. Tong. Turbulent convection over rough surfaces. *Phys. Rev. Lett.*, 76:908–911, 1996.
[10] O. Shishkina and C. Wagner. Modelling the influence of wall roughness on heat transfer in thermal convection. *J. Fluid Mech.*, 686:568–582, 2011.
[11] E. Villermaux. Transfer at rough sheared interfaces. *Phys. Rev. Lett.*, 81:4859–4862, 1998.
[12] S. Wagner and O. Shishkina. Heat flux enhancement by regular surface roughness in turbulent thermal convection. *J. Fluid Mech.*, 763:109–135, 2015.
[13] Y.-C. Xie and K.-Q. Xia. Turbulent thermal convection over rough plates with varying roughness geometries. *J. Fluid Mech.*, 825:573–599, 2017.
[14] B.-L. Xu, Q. Wang, Z.-H. Wan, R. Yan, and D.-J. Sun. Heat transport enhancement and scaling law transition in two-dimensional Rayleigh–Bénard convection with rectangular-type roughness. *Int. J. Heat Mass Transfer*, 121:872–883, 2018.
[15] Y.-Z. Zhang, C. Sun, Y. Bao, and Q. Zhou. How surface roughness reduces heat transport for small roughness heights in turbulent Rayleigh–Bénard convection. *J. Fluid Mech.*, 836:R2, 2018.
[16] X. Zhu, R. Stevens, R. Verzicco, and D. Lohse. Roughness-facilitated local 1/2 scaling does not imply the onset of the ultimate regime of thermal convection. *Phys. Rev. Lett.*, 119:154501, 2017.
[17] X. Zhu, R. J. A. M. Stevens, O. Shishkina, R. Verzicco, and D. Lohse. $Nu \sim Ra^{1/2}$ scaling enabled by multiscale wall roughness in Rayleigh–Bénard turbulence. *J. Fluid Mech.*, 869:R4, 2019.

DOUBLE-DIFFUSIVE CONVECTION IN SEDIMENT-LADEN FLOWS

R. Ouillon[1], P. Garaud[2], A. Alsinan[1], J.F. Reali[2], P. Edel[1]& E. Meiburg[1]
[1] Department of Mechanical Engineering, UC Santa Barbara, Santa Barbara, CA, USA
[2] Department of Applied Mathematics and Statistics, UC Santa Cruz, Santa Cruz, CA, USA

Summary We employ linear stability analysis as well as DNS simulations to investigate double diffusion when the unstably stratified scalar contributing to the density field settles with respect to the fluid. The linear stability analysis identifies a new, settling-driven instability mode that competes with the traditional double-diffusive mode. DNS simulations demonstrate the formation of layers in regions of parameter space where they do not occur for non-sedimentary systems. In a different regime, DNS simulations demonstrate the formation of gravity waves in regions of parameter space where they do not occur for non-sedimentary systems. A mean-field analysis clarifies the role of settling on both γ- and collective instability mechanisms.

INTRODUCTION

Stably stratified fluids whose density is a function of two scalar fields can give rise to double-diffusive instabilities, provided these two scalars diffuse at different rates and one of them is unstably stratified while the other one is not. An important example concerns the world's oceans, as heat diffuses about one hundred times more rapidly than salt. When warm, salty water overlies cooler, fresher water, so that the more slowly diffusing scalar is unstably stratified, we commonly observe an exponentially growing instability called salt fingering. By contrast, if the cold and fresh water is on top, the evolving instability is oscillatory in nature. In both cases, the resulting instability can contribute significantly to vertical transport. Other environments in which double-diffusion plays an important role include magmas, metals and stellar interiors. A comprehensive review of the field is given in the beautiful, recent book by Radko (2013).

In the present work, we aim to understand how the traditional picture of double-diffusion is modified if the unstably stratified scalar is a particulate phase with a Stokes settling velocity. A number of laboratory flow visualization experiments demonstrate that thermal or compositional density gradients can dramatically alter the effective settling velocity of the particles by driving double-diffusive instabilities or settling-driven convection. We provide a detailed quantitative understanding of double-diffusive instabilities involving a sediment phase, with implications for a wide range of processes, among them the outflow of sediment from buoyant river plumes into colder lakes or the saline ocean, the dynamics of certain classes of clouds, as well as ecological, astrophysical and engineering applications.

BASIC INSTABILITY MECHANISM

We conduct a linear stability analysis for a base state with constant gradients of temperature (or salt) and sediments. We find that the settling velocity generates a phase shift between the perturbation fields of the two scalars, which gives rise to a novel, settling-driven instability mode. This instability mechanism favors the growth of waves that are inclined with respect to the horizontal. It is active for all density and diffusivity ratios, including cases in which the two scalars diffuse at identical rates. If the scalars have unequal diffusivities, the new settling-driven instability mode competes with the elevator modes of the classical double-diffusive fingering instability. We present detailed linear stability results as a function of the governing dimensionless parameters, including cases involving lateral gradients of the base state density fields that result in predominantly horizontal intrusion instabilities (figure 1).

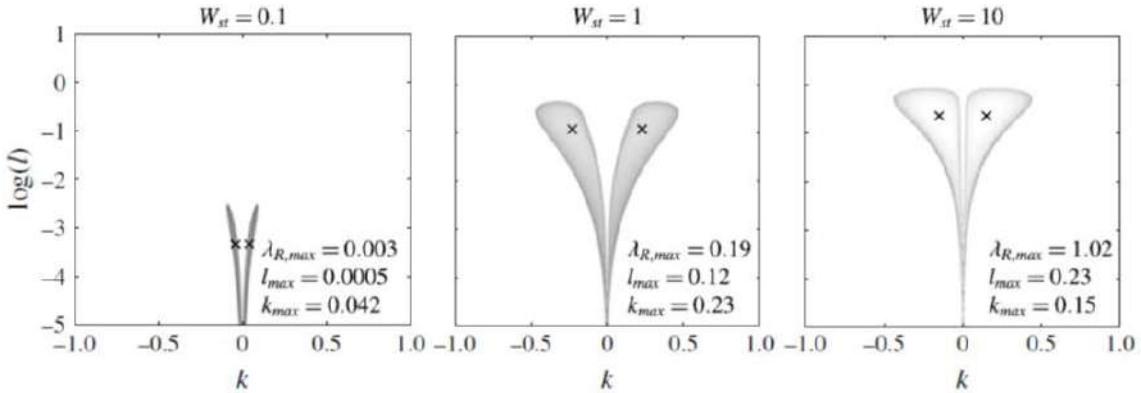

Figure 1. Linear stability results: maximum real part of the growth rate, as a function of the vertical (k) and horizontal (l) wavenumbers, for three different values of the settling velocity (from Alsinan et al. 2017).

LAYER FORMATION

Highly resolved two- and three-dimensional DNS results of the above systems serve to illustrate the nonlinear competition of the various instabilities in different parameter regimes. In particular, we find evidence for layer formation in sedimentary fingering convection in regions of parameter space where it does not occur for non-sedimentary systems (Reali et al. 2017, figure 2). This is due to two complementary effects. Sedimentation affects the turbulent fluxes and broadens the region of parameter space unstable to the γ-instability (Radko 2003) to include systems at larger density ratios. It also gives rise to a new layering instability that exists in γ-stable regimes. The former is likely quite ubiquitous in geophysical systems for sufficiently large settling velocities, while the latter probably grows too slowly to be relevant, at least in the context of sediments in water. Similarly, we also find that sedimentation broadens the range of parameter space where the basic instability gives rise to the spontaneous excitation of large-scale gravity waves (Ouillon et al. 2020), for the same two complementary reasons: the modification of the turbulent fluxes renders the flow unstable to the traditional collective instability (Stern 1969, Traxler et al. 2011), while settling gives rise to a new pathway towards instability. We finally note that layers induced by the γ-instability can form in the absence of gravity waves, further validating Radko's theory of layering (Radko 2003).

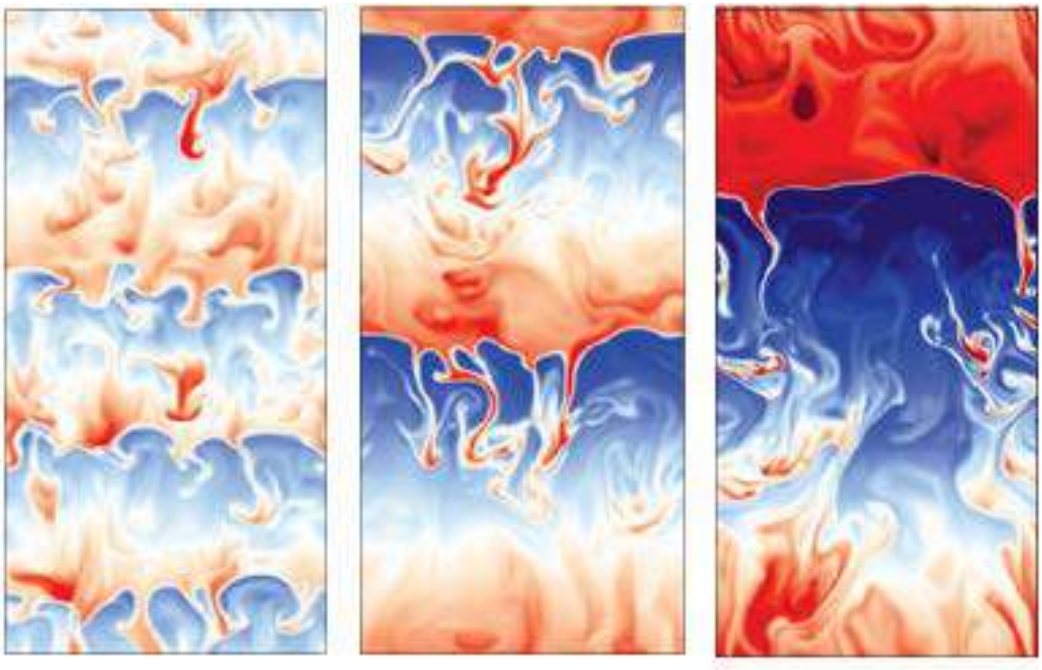

Figure 2. DNS simulation of layer formation in double-diffusive sedimentation (from Reali et al. 2017).

References

[1] Radko, T. 2013 Double-diffusive Convection. Cambridge University Press.
[2] Alsinan, A., Meiburg, E. and Garaud, P. 2017 A settling-driven instability in two-component, stably stratified flow. J. Fluid Mech. 816, 243-267.
[3] Reali, J.F., Garaud, P., Alsinan, A. and Meiburg, E. 2017 Layer formation in sedimentary fingering convection. J. Fluid Mech. 816, 268-305.
[4] Radko, T. 2003 A mechanism for layer formation in a double-diffusive fluid. J. Fluid Mech. 497, 365-380.
[5] Ouillon, R., Garaud, P., Edel, P. and Meiburg, E. 2020 Settling-driven large-scale instabilities in double-diffusive convection, in preparation.
[6] Stern, M.E. 1969 Collective instability of salt fingers. J. Fluid Mech. 35, 209-218.
[7] Traxler, A., Stellmach, S., Garaud, P., Radko, T. & Brummel, N. 2011 Dynamics of fingering convection. Part 1. Small-scale fluxes and large-scale instabilities. J. Fluid Mech. 677, 530–553.

CONVECTIVELY-TRIGGERED MIXING OF A SHEARED INTERNAL WAVE

C. J. Howland[1], J. R. Taylor[1], and C. P. Caulfield [2]
[1] DAMTP, University of Cambridge, Cambridge, UK
[2] DAMTP & BP Institute, University of Cambridge, Cambridge, UK

Summary We use direct numerical simulations to investigate the turbulent mixing that arises due to the interaction of a sinusoidal shear flow and an internal gravity wave. Although the flow is in principle susceptible to shear instabilities, quasi-exponential growth of perturbations is only observed when the flow becomes sufficiently statically unstable, in the sense that a locally-defined Rayleigh number exceeds a critical value. This dynamical behaviour has significant implications for the ensuing irreversible mixing.

INTRODUCTION

Turbulent mixing exerts a vital influence on the transport of tracers such as heat, carbon and nutrients throughout the ocean. This mixing is especially important in the thermocline, where strong stratification inhibits vertical transport and turbulence can enhance diapycnal mixing (across density surfaces). Due to the strong stratification, turbulence in the thermocline is highly intermittent in both space and time, with sporadic, highly energetic 'mixing events' commonly attributed to the breaking of internal waves.

Near-inertial internal waves, whose dynamics are controlled by the Earth's rotation, introduce vertical shear and can break at sufficiently large amplitude through shear instabilities. By contrast, higher frequency internal gravity waves introduce vertical motion and strain into the density field, which can lead to breaking via a combination of shear and convectively-driven instabilities. Observations in the thermocline [1] reveal that local overturns in density profiles, associated with mixing, can be produced in regions where both shear and wave-induced strain contribute significantly to the flow dynamics.

Understanding how the interaction of internal gravity waves and near-inertial shear leads to turbulent mixing is thus vital in constraining diapycnal fluxes in the ocean interior. This study aims to identify whether turbulence is primarily induced by shear-driven instabilities or convectively-driven instabilities in such flows and pinpoint how these instabilities depend on the relative amplitude of the gravity waves compared to the shear. We also aim to quantify mixing, appropriately defined as the irreversible transfer of available potential energy to background potential energy, in these flows and test how well simple parameterisations can describe their energetics.

METHOD

Motivated by the observations of [1] in the ocean thermocline, we consider an initial value problem where the shear flow $\overline{u} = \sin(z)$, with a minimum gradient Richardson number of 1, is superimposed on a finite-amplitude internal gravity wave with wave vector $\mathbf{k} = (1/4, 0, 3)$. We perform the simulations in a triply-periodic domain at Reynolds numbers of 5000 and 8000, and vary the initial wave steepness s to investigate the relevant breaking mechanisms in different flow scenarios. The equations of motion are solved subject to the Boussinesq approximation and a uniform background stratification.

We extend the definitions of available potential energy from [2] and [3] for use in our triply-periodic computational domain, and compare the 'true' rate of irreversible turbulent mixing

$$\phi_d = \frac{Ri_0}{RePr} \left\langle \frac{\partial z_*}{\partial \theta} |\nabla \theta|^2 \right\rangle, \tag{1}$$

to the dissipation rate of scalar variance χ commonly used to infer mixing rates in stratified turbulence.

RESULTS

The initial dynamics of all our numerical simulations involve the shear flow distorting the internal wave in a similar fashion to how waves are refracted in weakly nonlinear ray tracing calculations. Perturbation length scales increase in regions associated with positive shear, whereas in regions of negative shear these scales decrease. For the larger values of initial wave steepness (e.g. $s = 1$) this quickly leads to regions with statically unstable density profiles, and a build-up of available potential energy. As shown in figure 1a, convective plumes develop locally in the region of negative shear (close to $z = \pi$), introducing spanwise variation to the initially two-dimensional flow. Only at later times do local shear instabilities develop, leading to the 'trains' of turbulent billow structures seen in figure 1b.

The energy associated with the spanwise velocity component grows exponentially in every simulation once a local Rayleigh number of $Ra = O(1000)$ exists somewhere in the domain, as seen from the orange curves (and dashed lines) in

*Corresponding author. E-mail: cpc12@cam.ac.uk

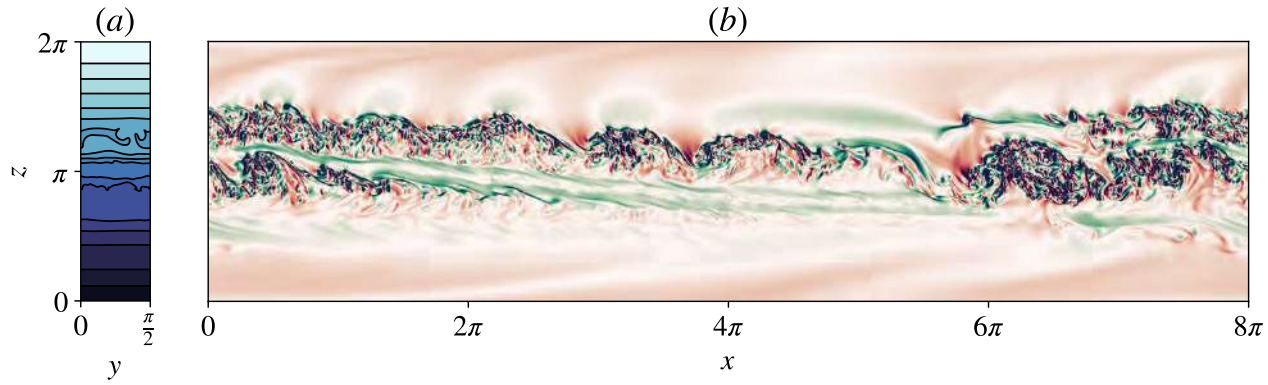

Figure 1: (a) Snapshot of density field contours in a spanwise-vertical plane at time $Nt = 26$. (b) Snapshot of the spanwise vorticity component in a streamwise-vertical plane at time $Nt = 32$. Both snapshots are taken from the simulation with initial wave steepness $s = 1$ at $Re = 5000$.

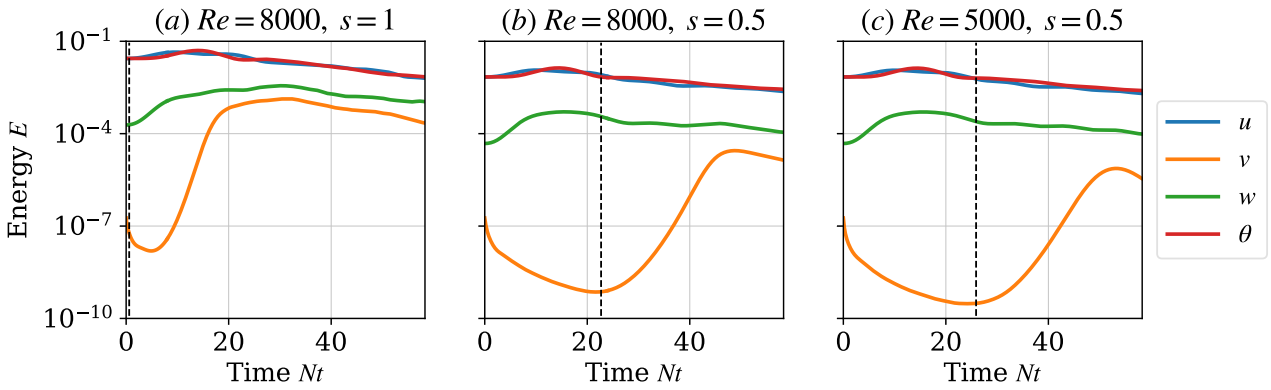

Figure 2: Time series of the perturbation energy associated with individual components of velocity $\mathbf{u}$ and the scalar field θ, plotted on a logarithmic scale. Dashed lines mark the first time when the maximum local $Ra \geq 2000$.

figure 2. We can deduce that a linear convective instability plays the key role in the early development of three-dimensional motion in these flows. Figure 2 also shows that the onset time of this exponential growth depends strongly on the initial wave steepness s, but not so much on the Reynolds number of the flow. The difference in the peak values of the spanwise energy in figures 2b and 2c highlights that smaller Re does however affect the nonlinear saturation of the instability.

As well as providing the apparently dominant mechanism for the generation of small scales, this local convection significantly modifies the density profile on which the turbulent structures seen in figure 1b develop. Locally this leads to strong variations in the correlations between the viscous dissipation rate ε and the irreversible mixing rate ϕ_d. Highly turbulent regions associated with high values of ε coincide with regions of both weak stratification and strong stratification, leading to extreme variations in the local instantaneous mixing efficiency. The ensuing changes in the local mixing rates may furthermore lead to significant changes in the inferred values of both the global mixing efficiency and the total diapycnal flux associated with these wave breaking events, demonstrating the central importance of convection, even in (apparently) statically stable shear-driven flows.

References

[1] Alford M. H., Pinkel R. Observations of overturning in the thermocline: The context of ocean mixing. *J. Phys. Oceanogr.* **30**(5):805-832, 2000.

[2] Winters K. B., Lombard, P. N., Riley J. J., D'Asaro E. A. Available potential-energy and mixing in density-stratified fluids. *J. Fluid Mech.* **289**:115-128, 1995.

[3] Scotti A., White B. Diagnosing mixing in stratified turbulent flows with a locally defined available potential energy. *J. Fluid Mech.* **740**:114-135, 2014.

REDUCED FLOW REVERSALS IN TURBULENT RAYLEIGH-BÉNARD CONVECTION IN THE ABSENCE OF CORNER VORTICES

Heng-Dong Xi *[1], Xin Chen[1], and Dong-Pu Wang[1]
[1] School of aeronautics, Northwestern Polytechnical University, Xi'an, China

Summary We report a comparative experimental study of the reversal of the large-scale circulation in turbulent Rayleigh-Bénard convection in quasi-two dimensional (2D) cell with and without corner vortices. It is found that the reversal frequency (f) is greatly reduced in the corner-less cell. The reduction of the reversal frequency is more significant, in terms of both the amplitude and the scaling exponent, in the high Ra regime. Our results reveal that the role of corner vortices is to destabilize the main vortex thus increase the reversal frequency, especially in the high Ra regime. In addition, we classified the reversals into main-vortex-led (MVL) and corner-vortex-led (CVL). The frequency of MVL reversal in normal cell is found in excellent agreement with the frequency of reversals in corner-less cell where all the reversals should be MVL.

INTRODUCTION

Thermal convection is ubiquitous in nature and many engineering applications. Rayleigh-Bénard convection (RBC) is a model system for the study of the thermal convection problem [1-4]. In RBC, a well known coherent flow structure called large-scale circulation (LSC) had been studied extensively for last two decades. A fascinating feature of the LSC is the spontaneous and random reversal of its flow direction. The reversal of the LSC is of general interest for its putative connection to similar reversals in the atmosphere, and in the outer core of the earth. In the studies of the reversal of the LSC very often the (quasi-) two-dimensional (2D) rectangular convection cells are used and in such (quasi-) 2D geometry, the LSC consists of a big main vortex of a tilted-ellipse shape and two small corner vortices diagonally opposite to each other. It was found that the reversal of the LSC is accomplished as following: the corner vortices grow both in size and amplitude, squeeze and eventually break up the main vortex, then connect to each other to form a new big single-roll vortex again, but with a reversed circulating direction [5]. In this picture the corner vortices play a crucial role in the reversal process. However, it was recently found in a vertical thin circular cell where the corner vortices are absent that the reversal of the LSC could still occur [6]. It was also found that the scaling of the reversal frequency on Ra is controlled by the stability of main vortex [7]. To unlock the intricate dynamics behind these seemingly contradictory results a comparative study of the reversals in cells with and without the corner vortices becomes essential.

In this paper we report a comparative experimental study of the reversals of the LSC in a corner-less and a normal convection cell. It is found that in the corner-less cell the reversal of LSC still happens, and the reversal frequency decreases with Ra, and is divided into slow and fast decrease regimes. The transition of the reversal frequency in this corner-less cell is very similar to that in the normal cell, while the reversal frequency in the corner-less cell is greatly reduced. The reduction of the reversal frequency is more significant, in terms of both the amplitude and the scaling exponent, in the high Ra regime. Our results reveal, for the first time, the quantitative role of the corner vortices in the occurrence of the reversals of the LSC.

RESULTS AND DISCUSSION

We first compare the flow topology in the normal and the corner-less cells. The upper-right and lower-left insets of Figure 1 show the time averaged velocity field captured in the normal and the corner-less cells at similar Ra (7.94×10^8 and 7.56×10^8 respectively) for $Pr = 7.0$, and during the 2 hours average time, no reversal occurs. From the two velocity maps, one can see that the typical flow pattern in the normal cell, *i.e.* a main vortex in the shape of tilted ellipse and two small corner vortices sitting at the up-left and down-right corners. For the corner-less cell the flow pattern is totally different, due to the existence of the screens the main vortex feels no corners, thus it is in a circular shape. The fluid in the corner is trapped by the screen, forms a fixed-size small vortex at each corner. And those four fixed-size small vortices are restricted by the screens thus have no direct interaction with the main vortex. With the addition of the four screens a LSC without (the effects of) the corner vortices is indeed achieved.

We then examine the reversal frequency f in the normal cell and corner-less cell where f is defined as the averaged number of reversal events per second. In Figure 1, the measured reversal frequency f as a function of Ra for both corner-less and normal cell are plotted. As shown in the figure, similar to the normal cell case [7], it is found that in the corner-less cell the reversal frequency exhibits a slow decrease followed by a fast decrease with increasing Rayleigh number Ra, separated by a transitional Ra ($Ra_{t,r}$). Besides, the data from the corner-less cell also falls on the top of each other with two distinct scaling regimes being $f \cdot t_E \sim Ra^{-1.53\pm0.12}$ and $f \cdot t_E \sim Ra^{-5.05\pm0.18}$. The existence of the transition for both cases, with and without the corner vortices, confirms that the transition is originated from the stability of the main vortex [7].

*Corresponding author. E-mail: hengdongxi@nwpu.edu.cn

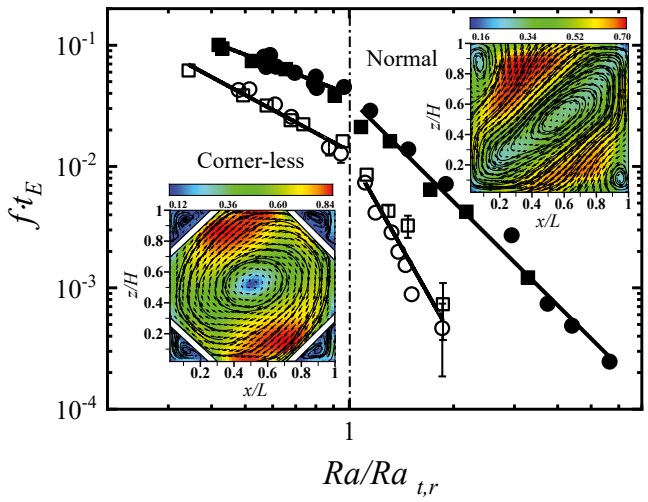

Figure 1: Flow reversal frequency f (normalized by $1/t_E$) as a function of Ra (normalized by transitional Ra ($Ra_{t,r}$)) for $Pr = 5.7$ (circles) and $Pr = 7.0$ (squares), where t_E is the turnover time of the LSC. The solid and open symbols are the data measured from normal cell and corner-less cell respectively. The solid lines are the power-law fits to the data. The two insets are the long time averaged PIV velocity maps with streamlines measured from the normal cell at $Ra = 7.94 \times 10^8$ (upper right) and the corner-less cell at $Ra = 7.56 \times 10^8$ (lower left), both at $Pr = 7.0$. The velocity is coded with both colour and vector length in units of cm/s.

Compared to that in the normal cell, f in the corner-less cell is greatly reduced. Moreover, one can see that the slope in $Ra < Ra_{t,r}$ regime does not change as much as that in $Ra > Ra_{t,r}$ regime. The reason is understandable: when $Ra < Ra_{t,r}$ the LSC is in the abnormal-single-roll-state (ASRS) where the interior of the main vortex is already broken into two small vortices [7], thus is very unstable, the reversal is mainly induced by the instability of the main vortex, the corner-vortex does not play a significant role. Thus when the corner-vortices are eliminated, the decay rate of the reversal frequency does not change much. While when $Ra > Ra_{t,r}$ the flow is in the single-roll-state (SRS), the main vortex is very stable and it is very hard for the reversal to occur if there are no corner vortices to drain energy from, and weaken and break the main vortex. In this regime the corner vortices are significant to the occurrence of the reversal, thus once the corner-vortices are eliminated, the reversal frequency is greatly reduced. Our results reveal that although the corner vortices are not necessary for the reversal, the presence of the corner vortices greatly increase the reversal frequency through destabilizing the main vortex, especially in the high Ra regime.

We are grateful to stimulating discussions with Detlef Lohse, Ke-Qing Xia and Jun Zhang, and the support by the NNSF of China (Grant Nos.11772259, and U1613227), the “111 Project” of China (B17037) and the Fundamental Research Funds for the Central Universities of China (No.3102019PJ002).

References

[1] Ahlers, G., Grossmann, S. and Lohse, D: Heat transfer and large scale dynamics in turbulent Rayleigh-Bénard convection. *Rev. Mod. Phys.* **81**, 503, 2009.
[2] Lohse, D. Xia, K.-Q: Small-scale properties of turbulent Rayleigh-Bénard convection. *Annu. Rev. Fluid Mech* **42**, 335-364, 2010.
[3] Chilla, F. Schumacher, J: New perspectives in turbulent Rayleigh-Bénard convection. *Eur. Phys. J. E* **35**, 58, 2012.
[4] Xia, K.-Q: Current trends and future directions in turbulent thermal convection. *Theor.Appl. Mech. Lett.* **3**, 052001, 2013.
[5] Sugiyama, K., et al.: Flow reversals in thermally driven turbulence. *Phy. Rev. Lett.* **105**, 034503, 2010.
[6] Wang, Y., Lai, P.-Y., Song, H. and Tong P.: Mechanism of large-scale flow reversals in turbulent thermal convection. *Sci. Adv.* **4**, eaat7480, 2018.
[7] Chen, X., Huang, S.-D, Xia, K.-Q and Xi, H.-D: Emergence of substructures inside the large-scale circulation induces transition in flow reversals in turbulent thermal convection. *J. Fluid Mech.* **877**, R1, 2019.

WEAK FORMULATION AND SCALING PROPERTIES OF ENERGY FLUXES IN THREE-DIMENSIONAL NUMERICAL TURBULENT RAYLEIGH-B NARD CONVECTION

Valentina Valori[1,2], Alessio Innocenti[3], Bérengère Dubrulle[1], and Sergio Chibbaro *[3]
[1] SPEC, CEA, CNRS, Université Paris-Saclay, CEA Saclay, F-91191 Gif-sur-Yvette Cedex, France
[2] Present address: Institut für Thermo und Fluiddynamik, Technische Universität Ilmenau, Postfach 100565, D-98684 Ilmenau, Germany
[3] Sorbonne Université, CNRS, UMR 7190, Institut Jean Le Rond d'Alembert, F-75005 Paris, France

Summary We apply the weak formalism on the Boussinesq equations, to characterize scaling properties of the mean and the standard deviation of the potential, kinetic and viscous energy flux in very well-resolved numerical simulations. We investigate the scale-by-scale averaged terms of the weak equations, which are a generalization of the Kármán-Howarth-Monin and Yaglom equations. We have not found the classical Bolgiano-Oboukhov (BO) picture, but evidence of a mixture of BO and Kolmogorov scalings. All the energy fluxes are compatible with a BO local Hölder exponent for the temperature and a Kolmogorov 41 for the velocity. This behaviour may be related to anisotropy and to the strong heterogeneity of the convective flow, reflected in the wide distribution of BO local scales. We then investigate the properties of extremes events finding a way to characterise plumes in the core of the flow.

INTRODUCTION

According to the prediction based on a generalization of the Kolmogorov theory for turbulent fluids, first suggested for stably stratified flows (2; 7), the velocity and temperature increments scale like $\delta u_\ell \sim \ell^{1/5}$, $\delta T_\ell \sim \ell^{3/5}$ above the BO length, L_{BO}, resulting in a constant flux of potential energy towards small scale. In contrast, for scale $\ell < L_{BO}$, the kinetic energy flux is constant, so that $\delta u_\ell \sim \ell^{1/3}$. Unfortunately, several issues make difficult the measurement of the BO scaling in a closed domain (6). In particular, L_{BO} has been found to be globally of the order of the entire volume of the box, and the anisotropy could make also ambiguous to discern between the BO scaling and other shear-scaling (1). Moreover, the similarity argument does not take into account intermittency effect, produced by large fluctuations of velocity gradients or temperature gradients. Indeed, it is well known that both velocity and temperature are highly intermittent random fields, and therefore local dynamics or local energy exchange may be subject to intense fluctuations and strong inhomogeneity. The purpose of the present work is to put forward an approach capable to capture the full complexity of local energy fluxes and exchanges.

METHODS

We have carried out a very high-resolved DNS analysis of the small-scale properties of turbulent Rayleigh-Bénard convection in a cubic cell at $Pr = 1$. The unusually accurate resolution allows to go well below the Kolmogorov length. We have used two simulations at $Ra = 10^7$ and $Ra = 10^8$.
To compute the local inter-scale energy transfer and viscous dissipation in numerical data, we use the weak solution formulation generalization of the Kármán-Howarth-Monin equation (3). We present the local energy budget of Boussinesq equations, which relies on weak formulation of the equations (4) and has been derived in a recent work (5) for the case of stable-stratified flows. The local budget involves filtered or coarse-grained observable $\widetilde{o}_\ell$ defined as $\widetilde{o}_\ell(x,t) \equiv \int d^d r G_\ell(r) o(x+r,t)$, where the subscript ℓ refers to the scale dependence introduced by the filtering.

RESULTS

We have not found evidence of a standard BO scaling, which would mean $h_u = 3/5$, $h_T = 1/5$. Instead, our numerical experiment points out that only the temperature follows this BO scaling, so that buoyancy effects are found to be dominant on the temperature variance budget at small scales. Yet the velocity follows the Kolmogorov 41 scaling $h_u = 1/3$, at least in the available range of scales.

We will present also some results about instantaneous fluctuating budgets to highlight the link between plumes and extreme events in the flow. In figure 1, we show an example of instantaneous extreme event of inertial energy dissipation at $Ra = 10^8$ (left plot), and its corresponding temperature field (right plot). A clear connection between the two fields is visible.

*Corresponding author. E-mail: chibbaro@ida.upmc.fr.

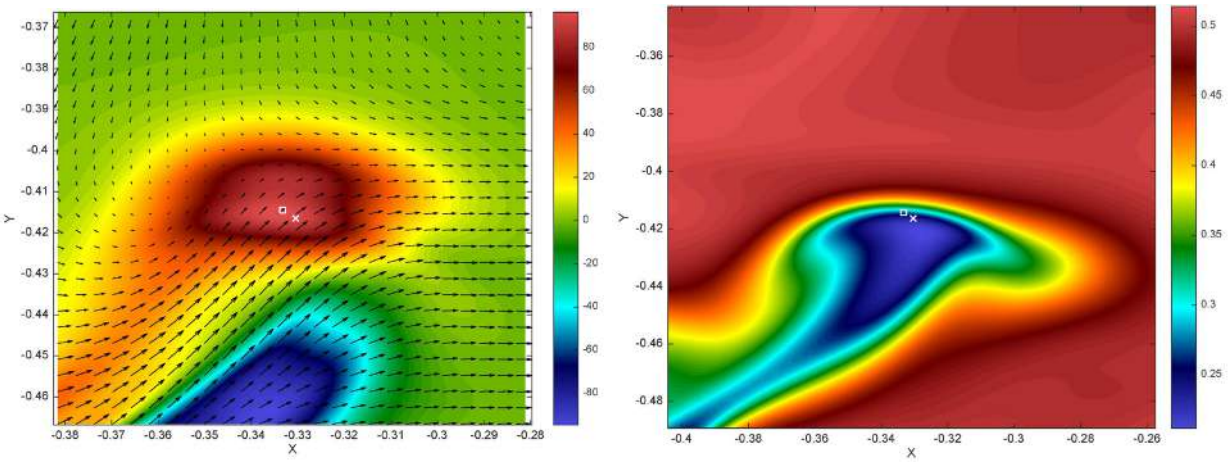

Figure 1: Instantaneous extreme event of inertial energy dissipation (left), and corresponding temperature field (right plot) at $Ra = 10^8$. The snapshots are plotted on an horizontal slice at half height of the cell.

CONCLUSIONS

From the analysis of the scale by scale averaged terms of the weak form of the Karman-Howarth-Monin equations we have observed a mixture of BO scaling for the temperature and Kolmogorov scaling for the velocity. Such peculiar behavior can be explained by removing the isotropic condition, and consider that the horizontal velocity increments and the vertical velocity increment scale with a different exponent, respectively h_u^H and h_u^V. In such a case, it is easy to see that the scaling exponent $\mathcal{D}$, $\mathcal{D}^T$, $\mathcal{D}^\nu$, $\mathcal{D}^\kappa$ will be respectively $\min(3h_u^H - 1, 3h_u^V - 1)$, $\min(h_u^H + 2h_T, h_u^V + 2h_T)$, $\min(2h_u^H - 2, 2h_u^V - 2)$, $2h_T - 2$. If we take $h_u^H = 1/3$, $h_u^V = 3/5$ and $h_T = 1/5$, we thus get the theoretical results.

ACKNOWLEDGMENT

This work has been supported by the ANR EXPLOIT, grant agreement no. ANR-16-CE06-0006-01. We acknowledge PRACE for awarding us access to Marconi at CINECA, Italy under the grant n^0 2018184426.

References

[1] Biferale, L. & Procaccia, I. Anisotropy in turbulent flows and in turbulent transport. Physics Reports 414 (2-3), 43–164, 2005.

[2] Bolgiano, Jr. R. Turbulent spectra in a stably stratified atmosphere. Journal of Geophysical Research 64 (12), 2226–2229, 1959.

[3] Dubrulle, B. Beyond Kolmogorov cascades. Journal of Fluid Mechanics 867, P1, 2019.

[4] Duchon, J. & Robert, R., Inertial energy dissipation for weak solutions of incompressible Euler and Navier-Stokes equations. Nonlinearity 13 (1), 249, 2000.

[5] Faranda, D., Lembo, V., Iyer, M., Kuzzay, D., Chibbaro, S., Daviaud, F. & Dubrulle, B. Computation and characterization of local subfilter-scale energy transfers in atmospheric flows. Journal of the Atmospheric Sciences 75 (7), 2175–2186, 2018.

[6] Lohse, D. & Xia, K.-Q. Small-scale properties of turbulent Rayleigh-Bénard convection. Annual Review of Fluid Mechanics 42, 2010.

[7] Oboukhov, A. Effect of Archimedean forces on the structure of the temperature field in a turbulent flow. Dokl. Akad. Nauk SSSR 125 (6), 1246–1248, 1959.

SECONDARY FLOW AND HEAT TRANSFER IN TURBULENT FLOW OVER STREAMWISE RIDGES

Alexander Stroh*[1], Kay Schäfer[1], Pourya Forooghi[2], and Bettina Frohnapfel[1]
[1] Institute of Fluid Mechanics, Karlsruhe Institute of Technology, Karlsruhe, Germany
[2] Department of Engineering, Aarhus University, Aarhus, Denmark

Summary Surface structuring in form of streamwise-aligned triangular ridges is investigated in the framework of a fully developed turbulent channel flow with constant wall temperatures of different values prescribed on the upper and lower walls at $\mathrm{Re}_b = 18000$. Two arrangements of the ridges on both channel walls are considered – a symmetrical arrangement and a staggered arrangement with a spanwise shift of the upper wall structure by a half ridge-to-ridge separation. The ridges generate a strong large-scale secondary motion and hence enhance momentum and heat transfer in the channel by approximately 30% relatively to the smooth channel. In spite of the fact that both arrangements translate into very similar global flow properties, the composition of skin friction coefficient and Stanton number significantly differs. The componental split-up of the friction coefficient reveals that the enhancement of momentum transfer mainly originates from the dispersive component linked to the secondary flows. For the Stanton number, however, the enhancement arises not only from the dispersive component, but also from a strong modification of the turbulent flow properties.

INTRODUCTION

Secondary flows of Prantl's second kind are known to be generated in turbulent boundary layer flows subjected to a spanwise inhomogeneity of the near-wall flow field [1]. The spanwise inhomogeneity alters local turbulent properties of the flow and introduces distinct gradients into the Reynolds stress distribution, which eventually manifests in the presence of large-scale vortex pairs occupying the entire boundary layer thickness and can significantly modify the mean velocity profile.The presence of secondary flow translates into an enhancement of momentum and heat transfer, which is of great interest from atmospherical, geological and technical point of view [2]. In technical applications, the spanwise inhomogeneity of the near-wall flow field can be introduced by various means of intentional surface structuring or unintentional local surface roughening through e.g. erosion or deposition during device operation. The present contribution presents a detailed analysis of the secondary flow generated in a channel with streamwise ridges and the related heat transfer.

METHODOLOGY

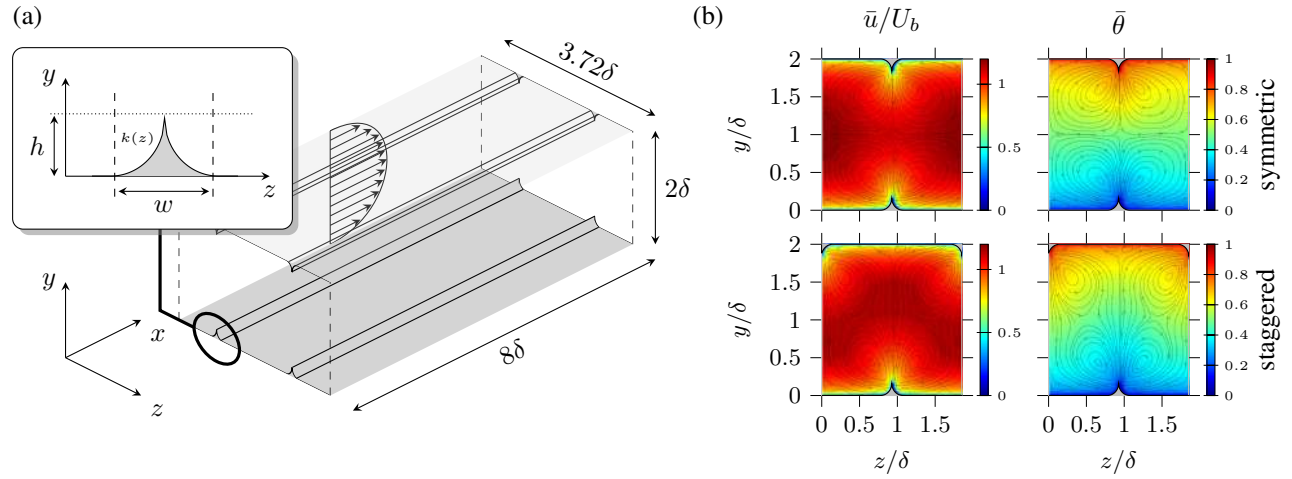

Figure 1: (a) Schematic of the simulation domain with ridge geometry and (b) mean velocity and temperature fields overlayed with secondary motion patterns for symmetric and staggered arrangement. [3]

The analysis is carried out using flow fields produced by a direct numerical simulation (DNS) in a fully developed turbulent channel flow driven at a constant flow rate (CFR) fixed to $Re_b = 2U_b\delta/\nu = 18000$ for all considered simulations. Periodic boundary conditions are applied for velocity field in the streamwise and spanwise directions, while the wall-normal extension of the domain is bounded by no-slip boundary conditions at the lower and upper domain wall ($y = 0, 2\delta$). Temperature is treated as a passive scalar with periodic boundary conditions applied for the thermal field in x- and z-directions, while a constant temperature on lower and upper wall is applied (T_l and T_u). This results in a fixed heat flux in the wall-normal direction. The Prandtl number is chosen to be Pr = 0.71, assuming air as the working fluid. The schematic of the numerical domain is depicted in Figure 1(a). The domain is discretized with $768 \times 385 \times 384$ grid nodes.

The wall structuring is modeled by an immersed boundary method (IBM) through introduction of external volume force field to the Navier-Stokes equations [4]. The surface geometry of a streamwise-elongated triangular ridge is formed by two converging arcs with $r = 0.16\delta$ resulting in a height distribution $k(z)$ (see Figure 1 a). The elevated structures are placed on both channel walls in symmetric or staggered arrangement, where the structures on the upper wall are shifted in spanwise direction by half the element separation. The spanwise spacing between the ridges is given by $S = 1.86\delta$.

*Corresponding author. E-mail: stroh@kit.edu.

case	U_b^+	Re_τ	Nu	C_f	C_f^L	C_f^T	C_f^D	C_f^F	St	St^L	St^T	St^D	St^F	$\cdot 10^3$
smooth	18.17	495.6	79.9	6.06	0.67	5.38	-	-	3.13	0.21	2.90	-	-	
symmetric	15.67	574.2	103.6	8.14	0.67	5.01	1.93	0.48	4.05	0.20	3.26	0.48	0.11	
staggered	15.60	577.0	104.4	8.23	0.67	4.77	2.25	0.50	4.11	0.20	2.91	0.88	0.11	

Table 1: Integral flow properties and decomposition of the skin friction coefficient and Stanton number.

RESULTS

The topology of the secondary flow, its influence on the streamwise mean velocity distribution and the related temperature distribution are shown in Figure 1(b) for the two considered configurations. Table 1 summarizes the integral properties of the three considered flow configurations. An increase of skin friction coefficient by 34% and 36% and an enhancement of Stanton number by 29% and 31% are estimated for the symmetrical and staggered arrangement in comparison to the smooth case, respectively. In spite of the fact that the two different arrangements yield very similar global behavior in terms of friction coefficient and Stanton number, the composition of these flow properties differs significantly. The triple decomposition [5] and FIK-identity split-up [6] (see Table 1) with laminar part ($\cdot^L$), a turbulent fluctuation part ($\cdot^T$), a dispersive fluctuation part ($\cdot^D$) and an IBM-related contribution ($\cdot^F$) for skin friction coefficient, $C_f = C_f^L + C_f^T + C_f^D + C_f^F$ and Stanton number, $\mathrm{St} = \mathrm{St}^L + \mathrm{St}^T + \mathrm{St}^D + \mathrm{St}^F$, reveal the fact that the augmentation of skin friction coefficient is governed by the additional dispersive component originating from the generated secondary motion. The dispersive component is more dominant in the staggered arrangement. As for the Stanton number, it is evident that its augmentation also emerges mainly from the dispersive contribution in the staggered arrangement. The symmetric arrangement demonstrates a weaker dispersive contribution in combination with a significant enhancement of the turbulent contribution in the outer flow region. The wall-normal distribution of the individual contributions to C_f and St are shown in Figure 2(a) and (b), respectively. The figure reveals that the local componential contribution is linked to the secondary flow topology. In the staggered arrangement the secondary flow is allowed to expand more freely into the opposite channel half, while in the symmetric arrangement the wall-normal jets on the ridge-tips oppose each other and confine the topology of the secondary motion (see Figure 1,b). This translates into the enhancement of turbulent heat flux for the symmetric case, while only a slight enhancement can be observed close to the centerline of the channel in staggered arrangement.

CONCLUSION

A DNS study of a turbulent fully-developed flow over structured surfaces in two configurations (symmetric and staggered arrangement) is performed and compared to the smooth channel case. We find that the introduction of the ridges results in a generation of strong large-scale secondary motion with a local magnitude up to $6.6\%U_b$. The presence of secondary motion significantly affects momentum and heat transfer properties of the flow. In spite of the fact that the two different arrangements yield very similar global behavior in terms of friction coefficient and Stanton number, the composition of these flow properties differs significantly. The results suggest that both dispersive and turbulent contributions are mutually affected by the secondary flow topology, which are in turn controlled by the arrangement of the surface structures. This indicates the possibility to manipulate the mechanisms involved in momentum and heat transfer by varying the surface structure. The study also confirms an alteration of turbulent properties away from the wall through generation of large-scale secondary motions introduced by wall structuring.

References

[1] P. Bradshaw. Turbulent secondary flows. *Annu. Rev. Fluid Mech.*, 19(1):53–74, 1987.
[2] Z.-Q. Wang and N.-S. Cheng. Time-mean structure of secondary flows in open channel with longitudinal bedforms. *Adv. Water Resour.*, 29(11):1634–1649, 2006.
[3] A. Stroh, K. Schäfer, P. Forooghi, and B. Frohnapfel. Secondary flow and heat transfer in turbulent flow over streamwise ridges. *Int. J. Heat Fluid Fl.*, 81:108518, 2020.
[4] D. Goldstein, R. Handler, and L. Sirovich. Modeling a no-slip flow boundary with an external force field. *J. Comput. Phys.*, 105(2):354–366, 1993.
[5] W. Reynolds and A. Hussain. The mechanics of an organized wave in turbulent shear flow. Part 3. Theoretical models and comparisons with experiments. *J. Fluid Mech.*, 54(2):263–288, 1972.
[6] K. Fukagata, K. Iwamoto, and N. Kasagi. Contribution of Reynolds stress distribution to the skin friction in wall-bounded flows. *Phys. Fluids*, 14:L73–L76, 2002.

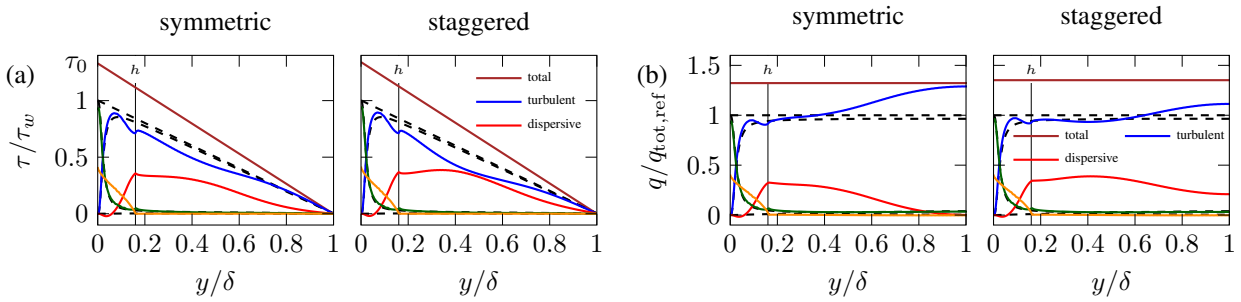

Figure 2: Decomposition of the total wall shear stress and heat flux. Dashed lines mark smooth wall reference [3].

TOWARDS THE DIRECT NUMERICAL SIMULATION OF THE ULTIMATE REGIME OF RAYLEIGH–BÉNARD CONVECTION

Richard J.A.M. Stevens *[1], Roberto Verzicco [1,2,3], and Detlef Lohse[1,4]

[1] Physics of Fluids Group, Max Planck Center for Complex Fluid Dynamics, J. M. Burgers Center for Fluid Dynamics and MESA+ Research Institute, Department of Science and Technology, University of Twente, P.O. Box 217, 7500 AE Enschede, The Netherlands

[2] Dipartimento di Ingegneria Industriale, University of Rome "Tor Vergata", Via del Politecnico 1, Roma 00133, Italy

[3] Gran Sasso Science Institute - Viale F. Crispi, 7 67100 L'Aquila, Italy

[4] Max Planck Institute for Dynamics and Self-Organization, Am Fassberg 17, 37077 Göttingen, Germany

Summary We present our efforts on the development of direct numerical simulations of Rayleigh-Bénard convection towards the ultimate regime. In particular, we present new simulation results for simulation up to $Ra = 10^{13}$ and $Pr = 0.7$ in a $\Gamma = 1/2$ cell. A one-to-one comparison with the Göttingen measurements shows excellent agreement between experiments and simulations, both for the overall heat transfer and measurements of local flow quantities. The Göttingen measurements reveal that the transition to the ultimate regime takes place around $Ra \approx 2 \times 10^{13}$, so our simulations are close to reaching this. Furthermore, results for $Ra = 10^{14}$, $Pr = 0.7$ in a $\Gamma = 0.23$ cell will be discussed. These simulations are in good agreement with measurements by Roche et al., New J. Phys. 12, 085014 (2010).

INTRODUCTION

Rayleigh-Bénard (RB) convection, the flow in a box heated from below and cooled from above, is the model system used to study thermal convection. The main control parameters are the Prandtl number $Pr = \nu/\kappa$, the ratio of viscosity to diffusivity, and the Ra number $Ra = \beta g \Delta L^3/\kappa\nu$, which measures the strength of thermal driving. Here, β is the thermal expansion coefficient, g the gravitational acceleration, Δ the temperature difference between two plates, and L the height of the sample. Both in experiments and simulations of RB convection, it is a major challenge to reach the ultimate regime in which the boundary layers transition from laminar to turbulent [1]. Figure 1a shows that for not too high Ra, i.e. $Ra = 5 \times 10^{11}$, all experiments and simulations on the heat transport agree very well. For higher Ra, in the ultimate regime, the scaling exponent γ in the relation $Nu \sim Ra^{\gamma}$, where Nusselt Nu is the dimensionless heat transport, increases. This figure also shows that there are two facilities (in Grenoble), which show an increased Nusselt number already around $Ra = 5 \times 10^{11}$, while other experiments (in Göttingen) [2] show this transitions around $Ra \approx 2 \times 10^{13}$. The observation of the ultimate regime in the Göttingen experiments are in agreement with the unifying theory for thermal convection [3], according to which the ultimate regime should set in when the shear Reynolds numbers at the boundaries is sufficiently high. There is no clear explanation for the mentioned disagreement. However, it is conjectured that unavoidable variations of the Pr number, finite conductivity of the horizontal plates and sidewall, non-Oberbeck-Boussinesq effects, i.e., the dependence of the fluid properties on the temperature, and even wall roughness and temperature conditions outside the cell might play a role. So far, the highest Ra obtained in direct numerical simulations is $Ra = 2 \times 10^{12}$ for aspect ratio $\Gamma = 0.5$ [4].

MAIN RESULTS

A major challenge in obtaining a high Ra number in direct numerical simulations is the required grid resolution to resolve all physical flow scales. An estimate of the computational resources needed for direct numerical simulation of turbulent RB convection is obtained by evaluating the number of nodes that is required. The basic assumption is that the flow can be divided into bulk and boundary layer regions, the former discretized by a mesh of the same size as the smallest between the Kolmogorov and Batchelor scales and the latter with the resolution criteria suggested by [5]. We further assume that the rectangular box has a size $W \times W \times L$ discretized in Cartesian coordinates, while the cylinder has a diameter D and a height L discretized in cylindrical coordinates. For the ease of discussion, we will restrict to $Pr = 1$, keeping in mind that as the Prandtl number deviates substantially from unity. The simulation becomes more demanding either because the velocity field develops finer scales than the temperature ($Pr \ll 1$) or vice versa ($Pr \gg 1$). For the mean Kolmogorov scale η we can easily write $\eta/L \approx (RaNu)^{1/4}$ that with a fit $Nu = ARa^{\beta}$ ($A \simeq 0.05$ and $\beta = 1/3$ from the high end of Ra in figure 1) yields a number of nodes per unit length in the bulk $N_{bu} = 0.473Ra^{1/3}$. For the resolution of each boundary layer we rely on the correlation derived by [5] which suggest a number of nodes $N_{bl} \approx 0.35Ra^{0.15}$. Within these figures, the total number of nodes for the rectangular domain reads $N_{Car} = \Gamma^2(0.105Ra + 0.156Ra^{0.816})$. For the cylindrical case this gives $N_{Cyl} = 0.5\pi\Gamma^2(0.105Ra + 0.156Ra^{0.816}) + \pi\Gamma(0.223Ra^{0.816} + 0.116Ra^{0.633})$. Dissipation spectra of turbulence [6] show a peak of around 10η, which implies that also a mesh of size 1.5–2η is sufficient to resolve

*Corresponding author. E-mail: r.j.a.m.stevens@utwente.nl.

most of the dissipation. In agreement with this view, numerical experiments show the simulation results convergence when we use about $1/8$ of the number of grid points given by the above estimates [8].

We will present a comparison between the Göttingen experiments and direct numerical simulations up to $Ra = 10^{13}$ [7, 9]. We find perfect agreement between experiments and simulations, both for the heat transfer, see figure 1a, and for the mean and temperature variance profiles close to the sidewall, see figure 1b and figure 1c. In addition, we discuss simulations for $\Gamma = 0.23$ up to $Ra = 10^{14}$, which are performed on grids with almost 100×10^9 nodes. The preliminary results from these simulations are in good agreement with measurements by Roche et al. [10].

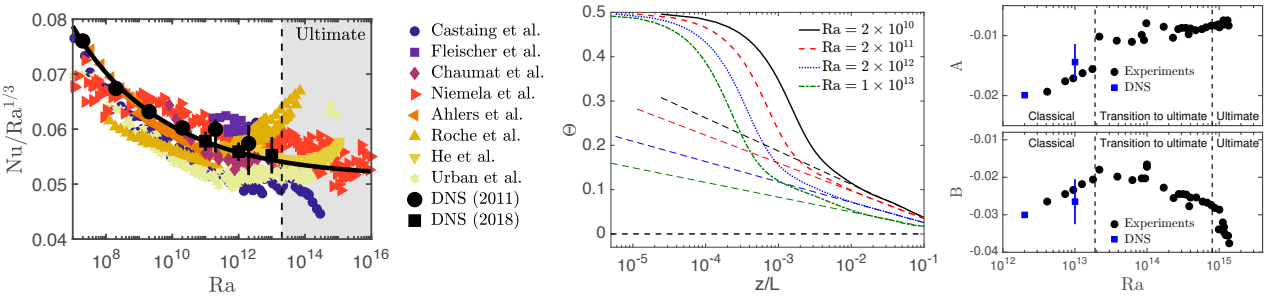

Figure 1: (a) Nu versus Ra for various experiments and simulations; detailed reference information can be found in Ref. [11]. (b) Logarithmic temperature profiles as function of height close to the sidewall at $(R - r)/L = 0.0045$ measured in the simulations. Panel (c) shows that excellent agreement is obtained for the coefficients A and B of the observed logarithmic temperature profiles $\Theta(z) = A \ln z/L + B$ shown in panel b, see Ref. [2]. The data for $Ra = 10^{13}$ is preliminary analysis of a simulation with $Pr = 0.7$ in a $\Gamma = 0.5$ cell performed on a computational grid with $6144 \times 1536 \times 6144$ nodes in the azimuthal, radial, and axial direction, respectively.

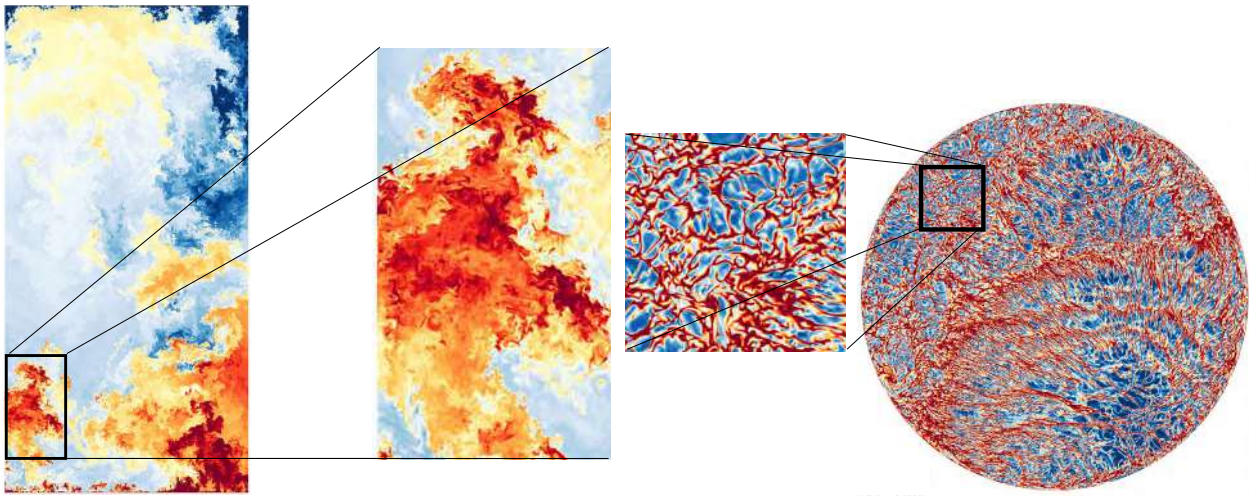

Figure 2: (left) Visualization of RB convection in a $\Gamma = 1/2$ cell at $Ra = 10^{13}$ for $Pr = 0.7$, which is close to the onset of the ultimate regime in corresponding measurements performed in Göttingen. (right) Snapshots of the temperature field at boundary layer height just above the hot bottom plate, which is at about 0.02% of the domain height of the cylinder.

References

[1] G. Ahlers, S. Grossmann, and D. Lohse. Heat transfer and large scale dynamics in turbulent Rayleigh-Bénard convection. *Rev. Mod. Phys.*, 81:503–537, 2009.

[2] G. Ahlers, E. Bodenschatz, D. Funfschilling, S. Grossmann, X. He, D. Lohse, R. J. A. M. Stevens, and R. Verzicco. Logarithmic temperature profiles in turbulent Rayleigh-Bénard convection. *Phys. Rev. Lett.*, 109:114501, 2012.

[3] S. Grossmann and D. Lohse. Scaling in thermal convection: A unifying view. *J. Fluid Mech.*, 407:27–56, 2000.

[4] R. J. A. M. Stevens, D. Lohse, and R. Verzicco. Prandtl and Rayleigh number dependence of heat transport in high Rayleigh number thermal convection. *J. Fluid Mech.*, 688:31–43, 2011.

[5] O. Shishkina, R. J. A. M. Stevens, S. Grossmann, and D. Lohse. Boundary layer structure in turbulent thermal convection and its consequences for the required numerical resolution. *New J. Phys.*, 12:075022, 2010.

[6] S. B. Pope. *Turbulent Flow*. Cambridge University Press, Cambridge, 2000.

[7] X. He, D. Funfschilling, H. Nobach, E. Bodenschatz, and G. Ahlers. Transition to the ultimate state of turbulent Rayleigh-Bénard convection. *Phys. Rev. Lett.*, 108:024502, 2012.

[8] R. J. A. M. Stevens, D. Lohse, R. Verzicco, Towards DNS of the Ultimate Regime of Rayleigh-Bénard Convection. *submitted to ERCOFTAC workshop direct and large eddy simulation (DLES) 12*, 2020

[9] G. Ahlers, E. Bodenschatz, and X. He. Ultimate-state transition of turbulent Rayleigh-Bénard convection. *Phys. Rev. Fluids*, 2:054603, 2017.

[10] P. E. Roche, G. Gauthier, R. Kaiser, and J. Salort. On the triggering of the ultimate regime of convection. *New J. Phys.*, 12:085014, 2010.

[11] R. J. A. M. Stevens, E. P. van der Poel, S. Grossmann, and D. Lohse. The unifying theory of scaling in thermal convection: The updated prefactors. *J. Fluid Mech.*, 730:295–308, 2013.

ROTATING RAYLEIGH-BENARD CONVECTION WITH A MELTING BOUNDARY

S. Ravichandran *[1] and J. S. Wettlaufer [1,2]
[1] Nordita, KTH Royal Institute of Technology and Stockholm University, Stockholm, Sweden
[2] Yale University, New Haven, Connecticut, USA

Summary We study numerically the convection of fluid heated from below in a rotating container when the solid upper boundary can melt. The solid is composed of the same (pure) substance as the liquid. We examine the morphology of the phase boundary as a function of the Rayleigh, Rossby, Prandtl and Stefan numbers. In particular, we report here the influence of the Prandtl number. The effects are mediated through the columnar vortex state, typical of rotating Rayleigh-Benard convection. For the Rayleigh number $\mathcal{O}\left(10^7\right)$ considered here, columnar vortices with larger vertical velocities form for higher Prandtl numbers. Since these columnar vortices carry hot fluid from the heated boundary, the solid boundary melts in a pattern reflecting the size and number of columnar vortices.

INTRODUCTION

Rotating convecting systems that involve solidification or melting are common in astrophysical and geophysical fluid dynamics. Here, we study the dynamics of a single-component system with solid and liquid phases heated from below. Initially the lower half of the container is molten, and the upper half is solid. The vertical motion due to thermal buoyancy brings the heat necessary for phase change to the upper boundary. Thus, the Stefan problem associated with the melting of the solid and the movement of the solid-liquid interface has to be solved, in addition to that of fluid convection. The morphology of the melting solid is a result of the nonlinear interactions between convection and melting at the solid-liquid interface.

SETUP

The rigid container is of size $L \times L \times (A \times L)$, with gravity g along the $-z$ direction, and rotating about the $+z$ axis with an angular velocity Ω. The aspect ratio is taken to be $A = 0.5$ here. We assume that the solid and liquid have the same density ρ and heat capacity C_p, with possibly different thermal diffusivities κ_s and κ_l. The latent heat of fusion is λ. The lower boundary is hotter than the melting temperature T_m by an amount ΔT which is also taken to be the scale of temperature differences. The enthalpy H and the temperature T are nondimensionalised in terms of these quantities, giving

$$\phi = \frac{H - H_0}{C_p \Delta T}, \tag{1}$$

$$\theta = \frac{T - T_m}{C_p \Delta T}, \tag{2}$$

$$\tag{3}$$

where H_0 is the enthalpy of the solid at T_m. The equation of state relating θ to ϕ is

$$\theta = \begin{cases} \phi & \text{solid} \\ \phi - St^{-1} & \text{liquid,} \end{cases} \tag{4}$$

where $St = C_p \Delta T / \lambda$ is the Stefan number.

The length scale is the dimension of the container L, and the buoyancy velocity $U_b = (g\alpha \Delta T L)^{1/2}$ is the velocity scale (α is the coefficient of thermal expansion). Using these scales, the equations governing the motion can be nondimensionalised and become

$$\frac{D\mathbf{u}}{Dt} = -\frac{\nabla p}{\rho} + \frac{1}{Re}\nabla^2 \mathbf{u} + \mathbf{e}_z \theta - 2Ro^{-1}\mathbf{e}_z \times \mathbf{u}, \tag{5}$$

$$\nabla \cdot \mathbf{u} = 0 \tag{6}$$

$$\frac{D\phi}{Dt} = \frac{1}{RePr}\nabla \cdot (\hat{\kappa} \nabla \theta), \tag{7}$$

where $Re = U_b L/\nu$ is the Reynolds number, $Pr = \nu/\kappa_l$ is the Prandtl number, $Ro = U_b/(\Omega L)$ is the Rossby number, and $\hat{\kappa} = \kappa/\kappa_l$ is the ratio of local thermal diffusivity to the diffusivity in the liquid.. The Rayleigh number $Ra = Re^2 Pr/A^3$. In the solid, $\mathbf{u} = 0$ in equations (5-7).

*Corresponding author. E-mail: ravichandran@su.se

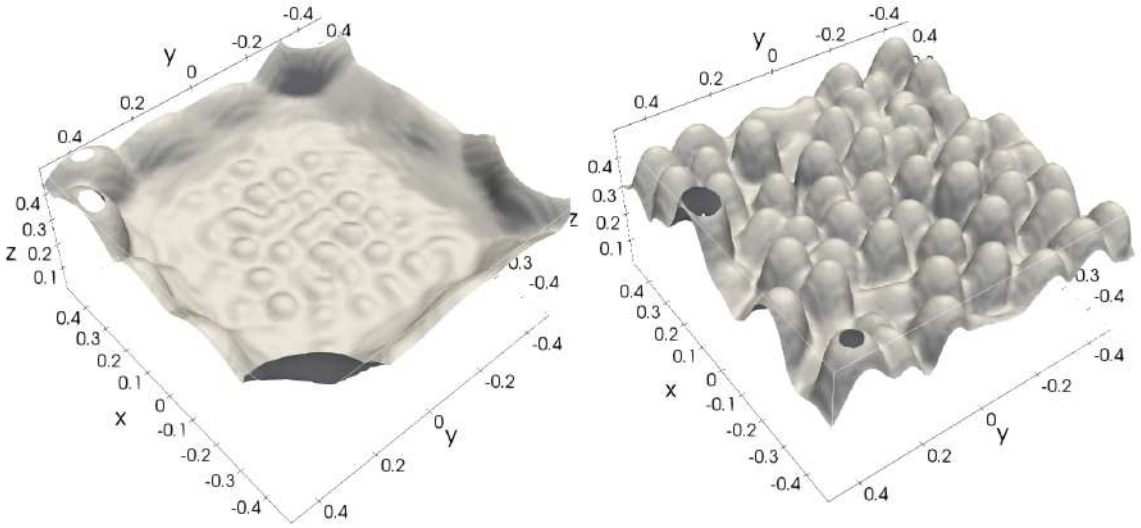

Figure 1: The solid-liquid interface at $t = 120$ for cases with $Pr = 1$ (left) and $Pr = 5$ (right). In the former, the flow is predominantly a peripheral streaming flow, with the result that more melting occurs around the periphery than near the axis. In stark contrast, for $Pr = 5$, the resultant melting forms inverted lobes, with the characteristic number and size of the columnar vortices for the given parameters reflected in the morphology of the interface. The solid-liquid interface shown is the iso-surface $\chi = 0.5$ (Eq. 8).

At $t = 0$, the bottom half of the domain is liquid, with enthalpy $\phi = St^{-1}$; the top half has enthalpy $\phi = 0$. The upper and lower boundaries are held at temperatures $\theta = -p$ and $\theta = 1$ respectively (p is a small number, taken to be $p = 0$ here). The lateral boundaries are insulating, no-slip walls. No-slip conditions are also applied at the solid-liquid interface, which is of an arbitrary shape and has a temperature $\theta = 0$. The lower wall has a constant temperature and free-slip.

Equations 5 - 7 are solved using a finite volume solver. The enthalpy method [1] is used to track the moving interface. The requisite velocity conditions in the resulting arbitrarily shaped solid region are applied using the volume-penalisation method [2] wherein the solid is modelled as a porous medium with vanishing porosity. This amounts to adding a term $-\frac{\chi}{\eta}\mathbf{u}$ to the right hand side of equation (5), where $\eta \ll 1$ is the penalisation parameter and χ is a phase-field identifying the solid region. χ can be related to the enthalpy ϕ as

$$\chi = 1 - \max\left(0, \min\left(1, St\phi\right)\right). \tag{8}$$

RESULTS

We present results for the case $St = 1$, with $Re = 5000$, $Ro = 0.2$ and two Prandtl numbers $Pr = 1$ and $Pr = 5$, with $\hat{\kappa} = 1$ for simplicity. The initial conditions are such that the entire system is at $\theta = 0$. The flow, we note, is in the rapidly rotating regime. For the parameters considered, the flow takes the form of columnar vortices spanning the entire liquid height for $Pr = 5$. For $Pr = 1$, on the other hand, a peripheral cyclonic streaming flow of alternating up- and downwelling regions results. These structures impinge on the solid in the upper half of the container, where the heat transported by them melts the solid in patterns reflecting the characteristics of the flow. Figure 1 shows the resultant solid-liquid interface at $t = 120$. When columnar vortices are present, the solid melts in an array of inverted lobes, the number of which corresponds to the number of columnar vortices.

CONCLUSIONS

The Stefan problem in a rotating convecting system has been studied using the enthalpy method, with the solid region simulated using a volume-penalisation method. This combination of numerical methods is straightforward to incorporate into an existing numerical solver. The influence of the Prandtl number on the characteristics of the flow, and thence on the melting of the solid, is demonstrated. The roles of the Rayleigh, Rossby and Stefan numbers, and the influence of other boundary conditions are explored in detail in a publication currently under review ([3]).

References

[1] V. Voller and M. Cross. Accurate solutions of moving boundary problems using the enthalpy method. *Int. J. Heat Mass Transf.*, 24(3):545–556, 1981.

[2] Nicholas K-R Kevlahan and Jean-Michel Ghidaglia. Computation of turbulent flow past an array of cylinders using a spectral method with brinkman penalization. *European Journal of Mechanics-B/Fluids*, 20(3):333–350, 2001.

[3] S. Ravichandran and J. S. Wettlaufer. Melting driven by rotating Rayleigh-Bénard convection (preprint). *arXiv:2007.12751*, 2020.

ULTIMATE HEAT TRANSFER IN 'WALL-BOUNDED' CONVECTIVE TURBULENCE

Shingo Motoki *[1], Kouki Kawano[1], Masaki Shimizu[1], and Genta Kawahara[1]
[1] Graduate School of Engineering Science, Osaka University, Toyonaka, Osaka, Japan

Summary Direct numerical simulations have been performed for turbulent thermal convection between two horizontal no-slip, permeable plates with the distance H and the temperature difference ΔT. On the no-slip plate surfaces $z = 0, H$ the wall-normal transpiration velocity is assumed to be proportional to the local pressure fluctuation, i.e., $w = -\beta p'/\rho, +\beta p'/\rho$ (Jiménez *et al.* 2001). The permeability parameter is fixed at $\beta(g\alpha\Delta T H)^{1/2} = 3$, and the Prandtl number is set to unity, where $(g\alpha\Delta T H)^{1/2}$ represents the buoyancy-induced terminal velocity. At lower Rayleigh number Ra, the Nusselt number Nu scales with Ra as $Nu \sim Ra^{1/3}$, as commonly observed in turbulent Rayleigh–Bénard convection. At higher Ra, on the other hand, the ultimate scaling $Nu \sim Ra^{1/2}$ is observed. We shall discuss the reason why the ultimate scaling can be achieved in this 'wall-bounded' system.

INTRODUCTION

Rayleigh–Bénard convection is one of the most canonical turbulent flows. It is thermal convection driven by buoyancy, and dimensionless parameters in this system are the Rayleigh number Ra and the Prandtl number Pr. At low Ra wall-to-wall heat flux is given by thermal conduction. When Ra is increased, thermal convection arises and eventually convective turbulence appears to drastically enhance the heat flux. The dimensionless wall-to-wall heat flux normalized with the thermal conduction heat flux is the Nusselt number Nu. A large number of experiments and numerical simulations have been performed, and the scaling law $Nu \sim Ra^{0.31}$ have been commonly observed at $Ra \sim 10^8 - 10^{11}$ (see e.g. He *et al.* 2012). Grossmann & Lohse (2000) have proposed the scaling theory of Nu with Ra and Pr. Their theory gives us the scaling $Nu \sim Ra^{1/3}$ in the high-Ra range $Ra \sim 10^8 - 10^{14}$ for $Pr \sim 1$.

It has long been anticipated that at extremely high Ra, both thermal and kinetic energy dissipation ϵ are dominated by the bulk region rather than the thermal and kinetic boundary layers, leading to the so-called ultimate scaling $Nu \sim Ra^{1/2}$ (Kraichnan 1962; Grossmann & Lohse 2000). However, the ultimate scaling has not been observed even at very high Ra as yet. Even in convective turbulence with surface roughness, it is still an open question whether or not the ultimate scaling can be achieved (Zhu *et al.* 2017, 2019).

In this study we investigate turbulent thermal convection between horizontal no-slip, permeable plates heated from below and cooled from above by numerically solving the Boussinesq equation (Kawano *et al.* 2020). We have found that wall permeability brings about the ultimate scaling $Nu \sim Ra^{1/2}$.

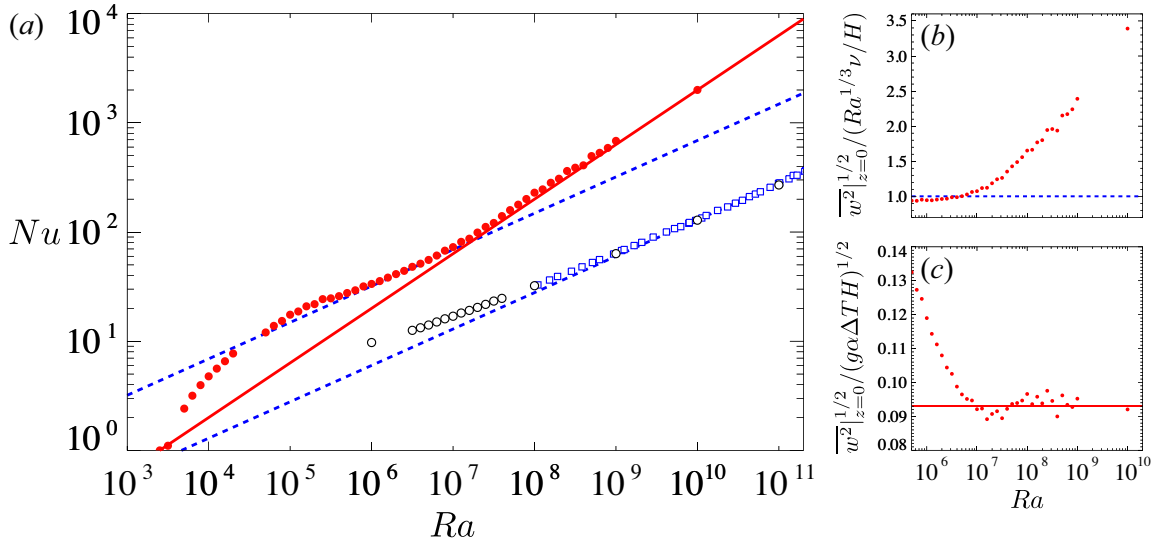

Figure 1: (*a*) Nusselt number Nu as a function of the Rayleigh number Ra. (*b,c*) Root-mean-square vertical velocity at the wall normalized by (*b*) $Ra^{1/3}\nu/H$ and (*c*) $(g\alpha\Delta T H)^{1/2}$. The closed red circles and the open black circles respectively represent the permeable case $\beta(g\alpha\Delta T H)^{1/2} = 3$ and the impermeable case $\beta(g\alpha\Delta T H)^{1/2} = 0$ for the Prandtl number $Pr = 1$. The blue open squares indicate experimental turbulent data from Niemela & Sreenivasan 2006 (cylindrical container). The solid red line and the dashed blue line stand for the scalings $Nu \sim Ra^{1/2}$ and $Nu \sim Ra^{1/3}$, respectively.

*E-mail: motoki@me.es.osaka-u.ac.jp

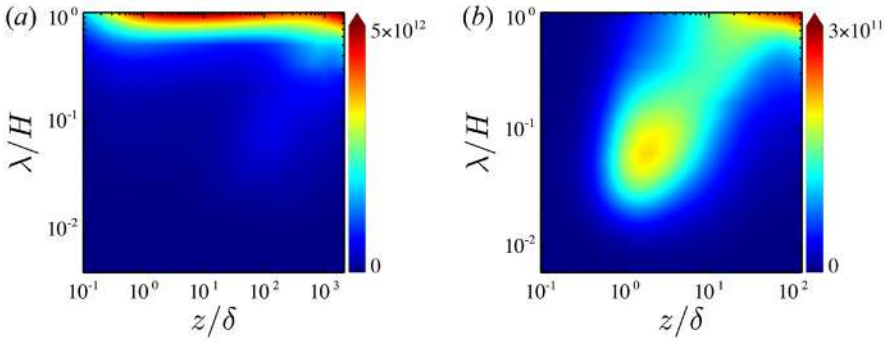

Figure 2: Premultiplied spectra of buoyancy power $g\alpha Tw$ as a function of the horizontal wavelength λ and the distance to the lower wall z in (a) the permeable case $\beta(g\alpha\Delta TH)^{1/2} = 3$ and (b) the impermeable case $\beta(g\alpha\Delta TH)^{1/2} = 0$ at $Ra = 10^{10}$ for $Pr = 1$. $\delta = \Delta T/\mathrm{d}\overline{T}/\mathrm{d}z|_{z=0}$ represents the thermal conduction length.

SCALING OF THE NUSSELT NUMBER WITH THE RAYLEIGH NUMBER

We perform direct numerical simulations for convective turbulence between the horizontal plates with the distance H and the temperature difference ΔT using a Fourier–Chebyshev spectral method. The no-slip, permeable conditions, $u = v = 0$ and $w = -\beta p'/\rho$, $+\beta p'/\rho$ (Jiménez *et al.* 2001), are imposed on the plate surfaces $z = 0$, H. The permeability parameter is fixed at $\beta(g\alpha\Delta TH)^{1/2} = 0$ (impermeable case), 3 (permeable case), where $(g\alpha\Delta TH)^{1/2}$ denotes the buoyancy-induced terminal velocity. The Prandtl number is set to unity, and both horizontal periods, L_x and L_y, are taken to be H.

Figure 1(a) shows the Nusselt number Nu as a function of the Rayleigh number $Ra = g\alpha\Delta TH^3/(\nu\kappa)$. In the impermeable case $\beta(g\alpha\Delta TH)^{1/2} = 0$, at high $Ra \sim 10^8 - 10^{10}$ the Nusselt number can be seen to scale with the Rayleigh number as $Nu \sim Ra^{1/3}$, nearly consistent with the well-known turbulent scaling law $Nu \sim Ra^{0.31}$ (see e.g. He *et al.* 2012). In the permeable case $\beta(g\alpha\Delta TH)^{1/2} = 3$, on the other hand, the ultimate scaling $Nu \sim Ra^{1/2}$ can be observed undoubtedly at higher $Ra = 10^8 - 10^{10}$, whereas the ordinary scaling $Nu \sim Ra^{1/3}$ is confirmed at lower $Ra \sim 10^6$. It is worthy of note that the scaling property of Nu critically changes at $Ra \sim 10^7$ from $Nu \sim Ra^{1/3}$ to $Nu \sim Ra^{1/2}$ with increasing Ra. Even in the permeable case, at lower $Ra \sim 10^6$ we have not observed significant wall-normal transpiration velocity (figure 1b) in the near-wall region, implying that the ultimate scaling cannot be achieved.

DISCUSSION ON ULTIMATE SCALING

Premultiplied spectra of buoyancy power $g\alpha Tw$ are shown in figure 2 as a function of the horizontal wavelength λ and the distance to the lower wall z in the permeable case $\beta(g\alpha\Delta TH)^{1/2} = 3$ and the impermeable case $\beta(g\alpha\Delta TH)^{1/2} = 0$ at $Ra = 10^{10}$ for which the ultimate scaling has been observed in the permeable case (see figure 1a). In the impermeable case the significant buoyancy power can be seen for small-horizontal-scale motion, i.e. near-wall plumes, in the vicinity of the wall $z/\delta \sim 10^0$. In the permeable case, on the other hand, even in the the vicinity of the wall $z/\delta \sim 10^0$ the large-horizontal-scale motion can be induced by buoyancy.

Let us discuss this remarkable difference in the near-wall length scale between the permeable and the impermeable case, leading to difference in the Nu scaling. In the permeable case at higher $Ra \sim 10^8 - 10^{10}$ significant wall-normal transpiration velocity is induced even in the near-wall region (figure 1c). Therefore, although the thermal conduction layer still exists on the wall, there is no near-wall layer of the wall-normal (vertical) velocity in the higher-Ra permeable case, suggesting that there would not appear small-scale vertical motion in the near-wall region where the effects of the viscosity on the vertical velocity is negligible. The vertical motion should exhibit the length scale comparable with H anywhere, and thus the balance between the dominant buoyancy and inertial terms in the vertical Boussinesq equation gives us the velocity scale of the order of the buoyancy-induced terminal velocity $(g\alpha\Delta TH)^{1/2}$. Then the energy budget equation, including pressure power on the permeable plates (being an energy sink and comparable with ϵ), provides us with the Taylor's dissipation law $\epsilon \sim (g\alpha\Delta TH)^{3/2}/H$ as well as the ultimate scaling $Nu \sim Ra^{1/2}$ in the higher-Ra permeable case.

References

[1] He X., Funfschilling, D., Nobach, H., Bodenschatz, E., Ahlers, G. *Phys. Rev. Lett.* **108**: 024502, 2012.
[2] Grossmann S., Lohse, D. *J. Fluid Mech.* **407**: 27–56, 2000.
[3] Kraichnan R. H. *Phys. Fluids* **5**: 1374–1389, 1962.
[4] Zhu X., Stevens R. J. A. M., Verzicco R., Lohse D. *Phys. Rev. Lett.* **119**: 154501, 2017.
[5] Zhu X., Stevens R. J. A. M., Shishkina O., Verzicco R., Lohse D. *J. Fluid Mech.* **869**: R4, 2019.
[6] Jiménez J., Uhlmann M., Pinelli A., Kawahara G. *J. Fluid Mech.* **442**: 89–117, 2001.
[7] Kawano K., Motoki S., Shimizu M., Kawahara G. *J. Fluid Mech.* in press, 2020.
[8] Niemela J. J., Sreenivasan K. R. *J. Fluid Mech.* **557**: 411–422, 2006.

O0106166 - FM05 - Convection - Oral

FROM RAYLEIGH-BÉNARD CONVECTION TO POROUS-MEDIA CONVECTION: HOW POROSITY AFFECTS HEAT TRANSFER AND FLOW STRUCTURE

Detlef Lohse *[1], Shuang Liu[2], Lin-Feng Jiang[2], Kai Leong Chong[1], Xiao-Jue Zhu[1], Zhen-Hua Wan[3], Roberto Verzicco[4], Richard J. A. M. Stevens[1], and Chao Sun[2]

[1] Physics of Fluids Group & Max Planck Center, Univ. of Twente, PO Box 217, 7500AE Enschede, Netherlands

[2] Center for Combustion Energy, Key Laboratory for Thermal Science & Power Engineering, Dept. of Energy & Power Engineering, Tsinghua Univ., Beijing 100084, China

[3] Dept. of Modern Mechanics, Univ. of Science and Technology of China, Hefei, Anhui 230027, China

[4] Dept. of Engineering, Univ. of Rome 'Tor Vergata', Via del Politecnico [1], 00133 Roma, Italy

Summary Numerical simulations for 2D Rayleigh-Bénard convection with regular obstacles with varying density, mimicking different porosity ϕ, are performed, in order to reveal the transition from the traditional RB convection to Darcy-type porous-media convection. The heat transfer $Nu(\phi)$ is surprisingly found to vary non-monotonously: With decreasing ϕ, it first increases, before it decreases for ϕ approaching 0. The non-monotonous behavior originates from two competing effects of the porous structure on the heat transfer, which we identify, based on both global and local analysis of the flow: On the one hand, the flow coherence is enhanced in the porous media, which is beneficial for the heat transfer. On the other hand, the convection is slowed down by the enhanced resistance due to the porous structure, leading to heat transfer reduction.

INTRODUCTION

One of the paradigms for thermal convection studies is Rayleigh-Bénard (RB) convection, i.e., convection in a box heated from below and cooled from above, and it has been studied extensively over the last decades [1–3]. Also the related problem of convection in a fluid-saturated porous medium has received increasing attention, owing to its importance in a wide range of natural and industrial processes, such as geothermal energy recovery and geological sequestration of carbon dioxide [4, 5]. When a porous medium is present in a convection cell, the convection is blocked and the flow is stabilized. The strength of the stabilizing effect can be quantified by the porosity ϕ. On first sight the stabilizing effect is stronger for more blockage, i.e., for smaller porosity ϕ. In thermal convection, however, in general the interplay between stabilizing and driving forces can result in surprising effects. Chong *et al.* [6] found that for thermally driven flows stabilized in various ways the appropriate strength of the stabilizing force can lead to significant heat transfer *enhancement* due to increased flow coherence, in particular, revealing an universal mechanism of the turbulent transport enhancement in the presence of stabilizing forces. Obviously, when the stabilizing force gets even stronger, the flow motion is eventually suppressed, leading to heat transfer reduction. Consequently, the heat transport varies non-monotonously with the strength of the stabilizing force.

The objective of this study is to find out whether such a non-monotonic behavior also exists for thermally driven flow stabilized by porosity, i.e., to find out whether the (dimensionless) heat transfer $Nu(\phi)$ is non-monotonic, to clarify the connection of this system to other stabilizing-destabilizing flows, and to understand the local flow structure. Surprisingly, although both the traditional RB convection without the porous structure and the Darcy-type porous-media convection have been studied extensively, hardly any studies have been done to reveal the physics of the transition process between these two extreme cases.

METHOD

We perform a numerical study of a representative porous medium model, namely two-dimensional (2D) RB convection in regular porous media. Circular, solid obstacles with diameter l are spaced uniformly on a square lattice. In such a pore-scale model, the detailed flow in the pores is resolved and the interaction between the porous medium and various flow structures of convection is faithfully captured, which are essential to connect the macroscopic properties with the microscale mechanisms. As Prandtl number, we take $Pr = 4.3$ for water.

RESULTS AND DISCUSSION

Figure 1a shows the effect of the porosity ϕ on the (dimensionless) heat transfer Nu for $Ra = 10^7$ and 10^8. It is observed that $Nu(\phi)$ varies non-monotonously as ϕ is decreased from 1 (full porosity, so no obstacles included). First, when ϕ is slightly decreased, the heat transfer is enhanced, and then when ϕ is sufficiently small, it is reduced as compared to the $\phi = 1$ case. Correspondingly, there is an optimum porosity for the heat transfer, which dependents on Ra. The non-monotonic behavior of $Nu(\phi)$ is indeed reminiscent of the influence of other stabilizing forces on turbulent transport through coherent structure manipulation [6]. The reason for the non-monotonic behavior is that the obstacle array has two

*Corresponding author. E-mail: d.lohse@utwente.nl

Thematic Session FM

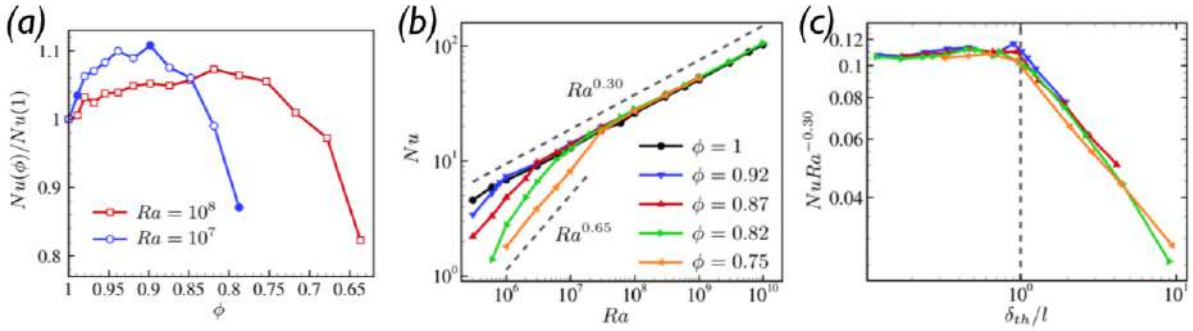

Figure 1: Global transport quantities: (a) $Nu(\phi)$ for two different Rayleigh numbers Ra, (b) $Nu(Ra)$ for different porosities ϕ, (c) The compensated Nusselt number $Nu/Ra^{0.30}$ vs the thermal boundary layer thickness δ_{th} (in terms of the obstacle diameter l) shows universal behavior.

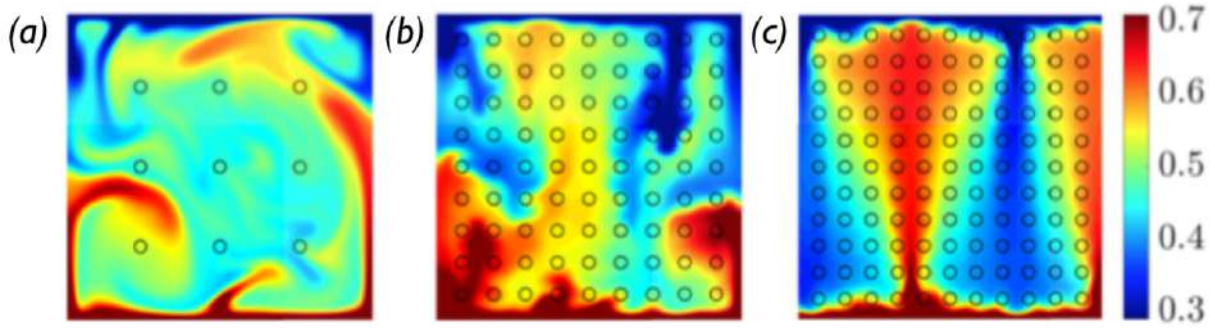

Figure 2: Local flow properties: Snapshots of the instantaneous temperature field at $Ra = 10^7$ and different porosities ϕ, corresponding to the three filled symbols in figure 1a. (a) $\phi = 0.99$, (b) $\phi = 0.90$, (c) $\phi = 0.85$.

competing effects on the heat transfer. On the one hand, the flow becomes more coherent with the correlation between temperature fluctuation and vertical velocity being enhanced, leading to heat transfer enhancement. On the other hand, the convection strength is reduced due the impedance of the obstacle array, leading to heat transfer reduction. This interpretation is supported by the local snapshot of the flow (figure 2).

The influence of porosity on flow properties depends on Ra, and two different heat transfer regimes are observed at fixed ϕ, see figure 1b. In the small-Ra regime where viscosity dominates, Nu is decreased as compared to the $\phi = 1$ case with a steep effective power law $Nu \sim Ra^{0.65}$, while in the large-Ra regime Nu is increased as compared to $\phi = 1$ with the classical power law $Nu \sim Ra^{0.30}$. The scaling crossover occurs when the thickness δ_{th} of the thermal boundary layer δ_{th} is comparable to the pore scale l – implying an universal curve $Nu(\phi)$ vs δ_{th}/l, see figure 1c. In both scaling regimes the $Nu(Ra)$ dependence can be estimated in the spirit of the unifying theory of refs. [7], in which the energy dissipation rate and the thermal dissipation rate and their distributions between bulk and boundary layer play the central role.

OUTLOOK

Presently, we have restricted us to the heat transfer and flow structure of 2D RB convection in regular rectangular porous media. In the future, we will extend the study to the 3D case, to allow for a one-to-one comparison to experiment, and to different regular and disordered obstacle arrangements.

References

[1] G. Ahlers, S. Grossmann, and D. Lohse, *Heat transfer and large scale dynamics in turbulent Rayleigh–Bénard convection*, Rev. Mod. Phys. **81**, 503 (2009).
[2] D. Lohse and K.-Q. Xia, *Small-scale properties of turbulent Rayleigh–Bénard convection*, Annu. Rev. Fluid Mech. **42**, 335 (2010).
[3] F. Chillà and J. Schumacher, *New perspectives in turbulent Rayleigh–Bénard convection*, Eur. Phys. J. E **35**, 58 (2012).
[4] F. M. Orr, *Onshore geologic storage of CO_2*, Science **325**, 1656 (2009).
[5] H. E. Huppert and J. A. Neufeld, *The fluid mechanics of carbon dioxide sequestration*, Annu. Rev. Fluid Mech. **46**, 255 (2014).
[6] K. L. Chong, Y.-T. Yang, S.-D. Huang, J.-Q. Zhong, R. J. A. M. Stevens, R. Verzicco, D. Lohse, and K.-Q. Xia, *Confined Rayleigh–Bénard, rotating Rayleigh–Bénard, and double diffusive convection: A unifying view on turbulent transport enhancement through coherent structure manipulation*, Phys. Rev. Lett. **119**, 064501 (2017).
[7] S. Grossmann and D. Lohse, *Thermal convection for large Prandtl numbers*, Phys. Rev. Lett. **86**, 3316 (2001); Phys. Fluids **16**, 4462 (2004).

TURBULENT ROTATING CONVECTION TO THE EXTREME

Matteo Madonia[1], Andrés Aguirre Guzmán[1], Jonathan Cheng[2], Herman Clercx[1], and Rudie Kunnen *[1]
[1] Fluids and Flows group, Department of Applied Physics, Eindhoven University of Technology, Eindhoven, The Netherlands
[2] MixingLab, Department of Mechanical Engineering, University of Rochester, Rochester, NY, USA

Summary We study turbulent rotating convection in the so-called geostrophic regime; a state where rotation strongly shapes the flow but buoyant forcing is strong enough to enforce vigorous turbulence. The geostrophic regime is believed to be descriptive of geophysical and astrophysical flows. We report heat transfer and flow measurements from dedicated large-scale experiments of geostrophically constrained convection, a unique foray into this scarcely accessed but eminently relevant flow regime.

Introduction

Planetary-scale buoyancy-driven flows abound in nature, where the interplay between buoyant forcing and the rotation of the celestial body is decisive in the shaping of these flows. We study this interplay in a model system: rotating Rayleigh–Bénard convection (RRBC), the flow between two rotating horizontal plates driven by heating from below and cooling from above. The strength of the thermal forcing is quantified by the Rayleigh number $Ra = g\alpha\Delta T H^3/\nu\kappa$, where g is the gravitational acceleration, H the vertical separation of the plates and ΔT the applied temperature difference, and α, ν and κ are the thermal expansion coefficient, kinematic viscosity and thermal diffusivity of the fluid, respectively. The Prandtl number $\sigma = \nu/\kappa$ characterizes the fluid. Finally, to quantify rotation we use the Ekman number $E = \nu/2\Omega H^2$ with Ω the rotation rate.

Due to the sheer size of natural flows, we are faced with extreme parameter values: the Rayleigh number, with its cubic dependence on size, can take large values $Ra \sim 10^{20} - 10^{25}$, while the Ekman number, scaling as H^{-2}, is small, $E \sim 10^{-15} - 10^{-12}$. The flow behaviour at these extreme parameters is considerably different from that at moderate parameter values; the so-called geostrophic regime of rotating convection, named after the dominant geostrophic balance of pressure gradient and Coriolis force, is expected to be descriptive of these natural flows. However, to study this regime in a laboratory setting, to get to extreme parameter values, poses quite some challenges.

Figure 1: TROCONVEX at 4 m height.

TROCONVEX: a unique laboratory setup

It is clear that the height H of the convection volume is a crucial parameter for reaching extreme values for Ra and E [1]. This is the starting point of the design of TROCONVEX (Turbulent ROtating CONVection to the EXtreme), a 4 m tall cylindrical vessel for the study of RRBC in water (figure 1). A convenient coincidence is that strong rotational constraint (small E) reduces the typical horizontal scale considerably; it follows the length scale of convective onset $L_C \sim E^{1/3}$ [2, 3]. That is why our slender container (diameter 0.39 m) still captures at least ten horizontal length scales L_C. The cylinder consists of four sections, so that we can also use smaller H when desired. The setup can perform heat transfer measurements and is equipped with active thermal insulation on bottom and sidewall, where temperature-regulated heat shields prevent losses. Additionally, thermistors at several vertical positions in the sidewall can be used for diagnostics.

Results: flow structure and heat transfer

To check the feasibility of replicating the various flow features expected in the geostrophic regime based on asymptotically reduced models [2], we have visualised the flow with rheoscopic fluid extracted from shaving cream [4]. Figure 2 displays some examples, where we indeed find the expected flow features of (rotating) convection. The various degrees of axial organisation at different ratios of buoyancy and rotation is striking: starting from a strong vertical coherence as rotation dominates (columns; fig. 2c), as the thermal forcing is increased, columns turn into plumes with some wavy vertical variation (fig. 2d); then on to geostrophic turbulence (fig. 2e) where small-scale coherence is mostly lost and a fluctuating bulk is observed; finally on to rotationally-influenced turbulence (fig. 2f) where buoyancy is strong enough to mostly overcome the restrictions imposed by rotation.

These visualisations can be used in the interpretation of the heat transfer data, compiled in figure 3 (left panel). We report the Nusselt number $Nu = qH/k\Delta T$, where q is the heat flux density and k the thermal conductivity of the fluid, the total heat flux normalised by the conductive flux. From convective onset, we find a series of scaling ranges with different slopes [1], approaching the nonrotating heat transfer at higher Ra as expected when buoyancy dominates over rotation.

*Corresponding author. E-mail: r.p.j.kunnen@tue.nl

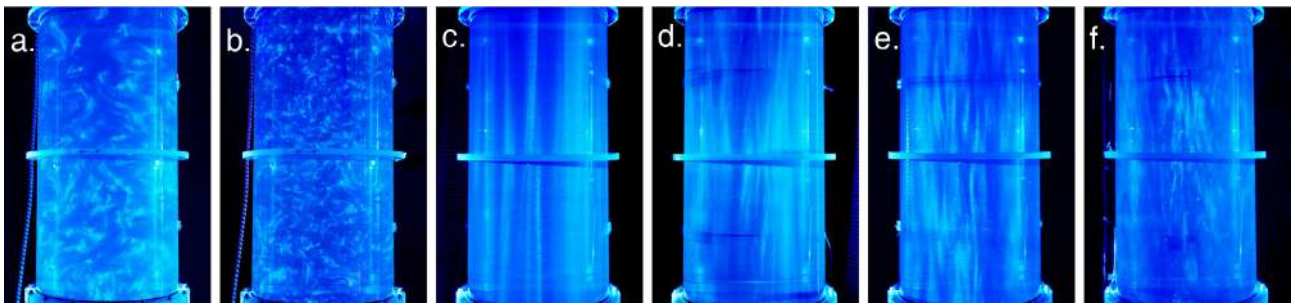

Figure 2: Visualisations of (rotating) convection. Nonrotating convection at (a) $Ra = 1.4 \times 10^{11}$, (b) $Ra = 2.2 \times 10^{12}$. Rotating convection at $E = 5 \times 10^{8}$ and (c) $Ra = 9.6 \times 10^{10}$ (convective Taylor columns), (d) $Ra = 8.6 \times 10^{11}$ (plumes), (e) $Ra = 1.6 \times 10^{12}$ (geostrophic turbulence), (f) $Ra = 3.3 \times 10^{12}$ (rotationally-influenced turbulence).

However, regime boundaries (dotted and dashed vertical lines) are not quite conclusively identified by considering only the heat transfer.

That is why we turn to the sidewall temperature statistics. The vertical profile of temperature $\overline{T}(z)$ displays a mean bulk gradient in RRBC [2], in contrast to the vanishing slope of nonrotating convection. We determine the mid-height temperature gradient $-\partial_z \overline{T}|_{z=0.5}$ and plot it in figure 3 (right panel) for the measurements at $E = 3 \times 10^{-7}$ (other E omitted for clarity). A clear, non-monotic dependence on Ra can be observed, where the scaling inversions do align nicely with predicted transitions between flow states. We thus have a potent diagnostic for the delineation of the flow phenomenology that is more pronounced than just the heat transfer.

Conclusion and outlook

TROCONVEX is a dedicated experimental tool to map the convective heat transfer and the corresponding flow structures in the geostrophic regime of RRBC in detail. There is solid agreement between experiments and accompanying direct numerical simulations; however, the latter can only probe the flow at reduced parameter values. For exploration of the flow statistics in geostrophic convection the experimental approach is more feasible. That is why we are currently implementing a transparent section for extension to stereo-particle image velocimetry, to get quantitative flow data. The first results will be presented at this conference.

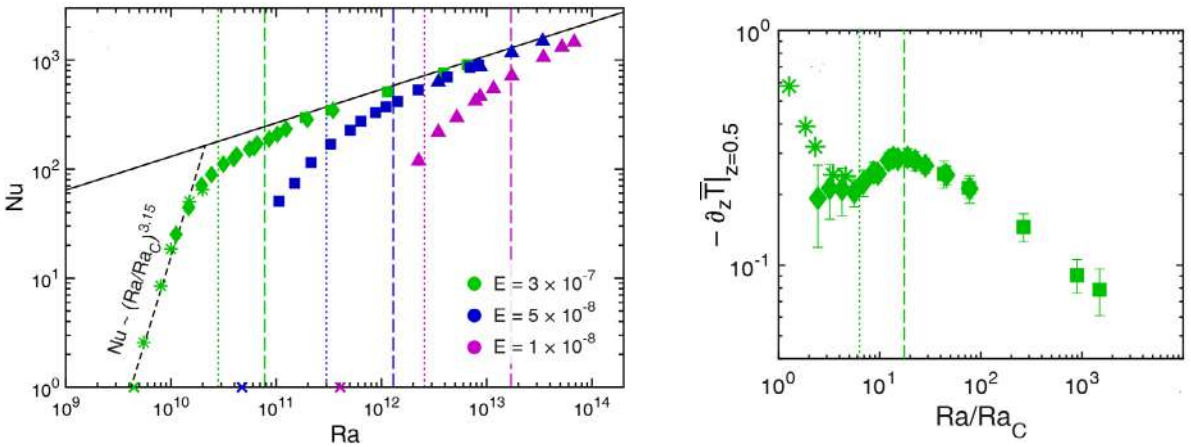

Figure 3: Left panel: Heat transfer data from TROCONVEX. Symbol shape indicates tank height H: 0.8 m (diamonds), 2 m (squares), 4 m (triangles). Asterisks are results from accompanying direct numerical simulations. Crosses indicate the critical Ra_C for onset of convection [3]. The solid line in the left panel is the best-fit trend $Nu = 0.11 Ra^{0.308}$ to our datapoints for nonrotating convection (not shown here); dotted lines indicate the predicted transition from columns to plumes, vertial dashed lines the predicted transition from geostrophic to rotationally-influenced turbulence. Right panel: corresponding measurements of the mid-height temperature gradient at $E = 3 \times 10^{-7}$.

References

[1] Cheng J. S., Aurnou J. M., Julien K., Kunnen R. P. J. A heuristic framework for next-generation models of geostrophic convective turbulence. *Geophys. Astrophys. Fluid Dyn.* **112**: 277–300, 2018.

[2] Sprague M., Julien K., Knobloch E., Werne J. Numerical simulation of an asymptotically reduced system for rotationally constrained convection. *J. Fluid Mech.* **551**: 141–174, 2006.

[3] Chandrasekhar S. Hydrodynamic and Hydromagnetic Stability. Oxford University Press 1961.

[4] Borrero-Echeverry D., Crowley C. J., Riddick T. P. Rheoscopic fluids in a post-Kalliroscope world. *Phys. Fluids* **30**: 087103, 2018.

CONTROL OF THE VERTICAL SPEED OF BUOYANCY-DRIVEN FINGERS BY DIFFERENTIAL DIFFUSION EFFECTS

S. S. Gopalakrishnan [1], B. Knaepen[1], and A. De Wit *[1]
[1] Université libre de Bruxelles (ULB), CP231, 1050 Brussels, Belgium

Summary A miscible horizontal interface separating two solutions of different solutes in the gravity field can deform into convective finger-like structures due to buoyancy-driven instabilities like the classical Rayleigh–Taylor (RT) instability or the double-diffusive (DD) and diffusive-layer-convection (DLC) instabilities, triggered by differential diffusion of the solutes in the solutions. We show that, in two-species stratifications, the vertical speed of the fingers induced by these various instabilities scale as the dynamic density jump triggered by differential diffusion effects.

FINGERING IN PRESENCE OF DIFFERENTIAL DIFFUSION

In the gravity field, a stratification between two solutions of different compositions can become unstable because of various buoyancy-driven instabilities. The Rayleigh–Taylor (RT) instability develops at the interface when a denser solution overlies a less dense one in the gravitational field deforming it into finger-like structures [1]. When a less dense solution overlies a denser one, differential diffusion effects can destabilize the miscible interface if at least two different solutes contribute to change the density. When the denser lower solution contains a solute diffusing faster than the solute in the upper less dense zone, a double-diffusive (DD) instability can induce a fingered deformation of the interface [1]. Such a double-diffusive instability has been extensively studied in the context of salt fingers that form in oceans where thermohaline convection is triggered by the differential diffusion of salt and heat. When the solute in the upper solution is the one that diffuses faster, an unstable scenario arises due to the formation of an accumulation zone below the interface and a depletion zone above it. The formation of a locally unstable density stratification on either sides of the interface drives locally convective motions that propagate independently through the solutions. This instability mechanism is referred to as diffusive-layer convection (DLC) [1].

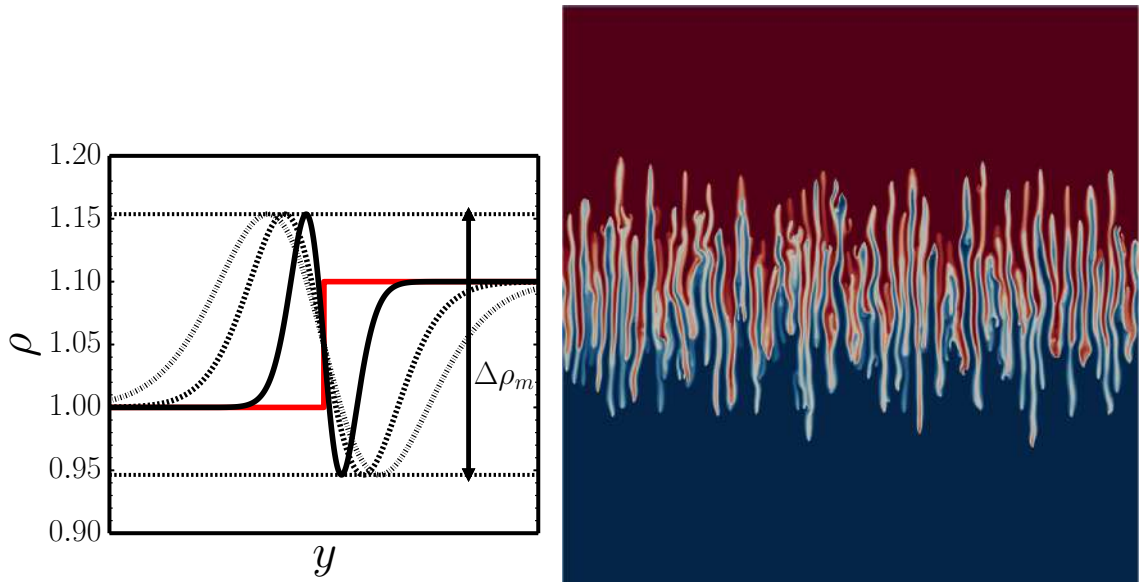

Figure 1: (Left) In presence of differential diffusion, the density profile becomes non-monotonic and features a dynamic density jump $\Delta\rho_m$ that can be larger than the initial density difference $\Delta\rho_0$ (here in red) between the two solutions. (Right) Rayleigh-Taylor fingering in presence of differential diffusion. The vertical speed of the fingers scales linearly with $\Delta\rho_m$.

We show numerically that, in presence of differential diffusion, a non-monotonic density profile can develop for these various instabilities, in which the dynamic density jump $\Delta\rho_m$ between the two extrema can be larger than the initial density difference $\Delta\rho_0$ between the two solutions (Fig.1). When buoyancy-driven fingers develop due to RT, DD or DLC modes, the vertical speed of the fingers observed (see Fig.1 for an example of RT [2]) is found to scale linearly with $\Delta\rho_m$ when $\Delta\rho_m > \Delta\rho_0$ (Fig.2). We classify the various scalings in the parameter space spanned by the two parameters of the problem: the buoyancy ratio R which is related to the ratio of the densities of the two solutions and δ the ratio of diffusion coefficients of the two solutes involved [3].

*Corresponding author. E-mail: adewit@ulb.ac.be

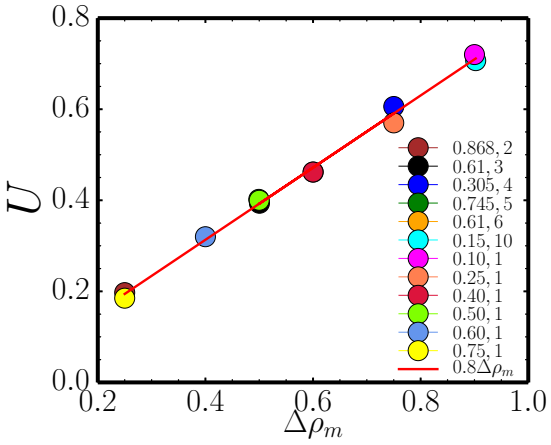

Figure 2: The vertical speed U of the fingers scales as the dynamic density jump $\Delta\rho_m$ for different couple of (R, δ) values.

CONCLUSIONS

In two-species stratifications, the fact that the two different solutes influencing density diffuse at different rates can induce non-monotonic density profiles. If the adverse dynamic density jump $\Delta\rho_m$ developing in this case is larger than the initial density difference $\Delta\rho_0$ between the two solutions, the vertical speed of the fingers scales linearly with $\Delta\rho_m$. This paves the way to differential diffusion control of the mixing between two solutions by a careful choice of the solutes at hand [3].

References

[1] Trevelyan P.M.J., Almarcha C., De Wit A., Buoyancy-driven instabilities of miscible two-layer stratifications in porous media and Hele-Shaw cells. *J. Fluid Mech.* **670**: 38-65, 2011.

[2] Gopalakrishnan S.S., Carballido-Landeira J., Knaepen B., De Wit A. Control of Rayleigh-Taylor instability onset time and convective velocity by differential diffusion effects. *Phys. Rev. E* **98**: 011101(R), 2018.

[3] Gopalakrishnan S.S., Knaepen B., De Wit A. On scalings of the rate of advancement of buoyancy-driven fingers. *J. Fluid Mech.* Submitted.

BI-DIMENSIONAL SOLUTAL PLUME GENERATED FROM AN EXTENDED SOURCE

Niloy De *[1], Patrice Meunier[2], Yves Méheust[3], and François Nadal[1]
[1] Wolfson school of Mechanical and Electrical Engineering, Loughborough University, Loughborough, UK
[2] IRPHE, CNRS, Aix-Marseille University, France
[3] Laboratoire GéoScience, Université de Rennes, France

Summary Experiments and numerical calculations are performed to study the dynamics of a single 2D plume generated from an extended source. A water-filled Hele-Shaw cell is placed vertically in a pressure chamber and pressurized with carbon dioxide. The CO_2-enriched layer that builds underneath the surface destabilizes into a plume that pours down to the bottom of the cell. At moderate Rayleigh numbers, the transverse concentration profile is reasonably fitted by a function of the form $c(x) = A[\cosh(x/l)]^2$, where both the amplitude A and the width l are functions of the altitude. The scaling laws observed in the numerical simulations for the dimensionless plume width l and vertical velocity w are close to the theoretical scaling laws obtained from mass conservation: $l \sim Ra^{1/2}$ and $w \sim 1$ for $Ra < Da^{-1}$; $l \sim Ra^{3/4}Da^{1/4}$ and $w \sim (RaDa)^{1/2}$ for $Ra > Da^{-1}$.

INTRODUCTION

In the current context of global warming, the mitigation of greenhouse gas emission is the utmost concern. In this context, geological storage of carbon dioxide (CO_2) appears a promising solution. Upon injection, supercritical CO_2 rises up to the top caprock and immediately starts dissolving at the water/brine interface, leading to a CO_2-enriched layer of brine that happens to be heavier that the underlying pure brine. After a diffusion stage, this (gravitationally) unstable configuration triggers a gravitational instability where convective plumes are generated and pour downwards to the bottom of the aquifer. In such a convective regime, the dissolution rate of CO_2- that is the efficiency of the CO_2-trapping - is greatly enhanced.

At the laboratory scale, such gravitational instability can be reproduced by means of CO_2-pressurized Hele-Shaw cells [2] and visualized with pH -sensitive color indicators - since CO_2-dissolution increases the acidity of aqueous solutions. Amongst all the available pH indicators, Bromocresol purple (BP) has a pH range between 6.8 and 4.8, which is suitable for changes in pH induced by moderate partial pressures of carbon dioxide. A theory based procedure is then used to convert the pH -map into a CO_2-concentration field. In the present work, we have used BP to experimentally study the dynamics of a single plume in a Hele-Shaw cell generated from an laterally extended source. We have explored the plume dynamics for a partial pressure of CO_2 ranging from 0.5 to 5 bar, and a source size lying in the range $2 \rightarrow 8$ mm. 2D numerical calculations have been performed to complement the experimental results and confirm the scaling laws predicted by mass conservation considerations over a wide range of Rayleigh and Darcy numbers.

EXPERIMENTAL CONFIGURATION AND METHOD

Mechanical and optical set up

The experimental set up consist of a Hele-Shaw cell filled with the solution of pH indicator (BP) and placed at the centre of a pressure chamber initially filled with nitrogen. The chamber is connected to a CO_2-filled reservoir by a ball valve

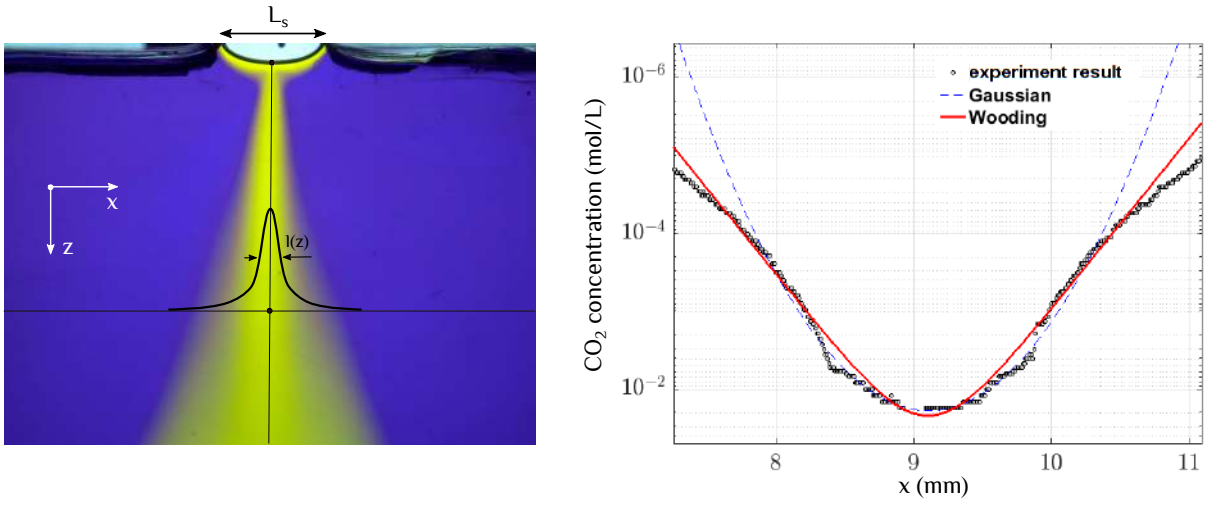

Figure 1: Left: raw picture of the CO_2-plume generated by an extended source visualized by means of bromocresol purple (partial pressure of $CO_2$is $P_{CO_2} = 4$ bar, $L_s = 8$ mm and Hele-Shaw cell thickness is 1 mm) ; Right: transverse concentration profile inferred from the RGB map at an altitude $z = 25$ mm.

*Corresponding author. E-mail: N.De@lboro.ac.uk

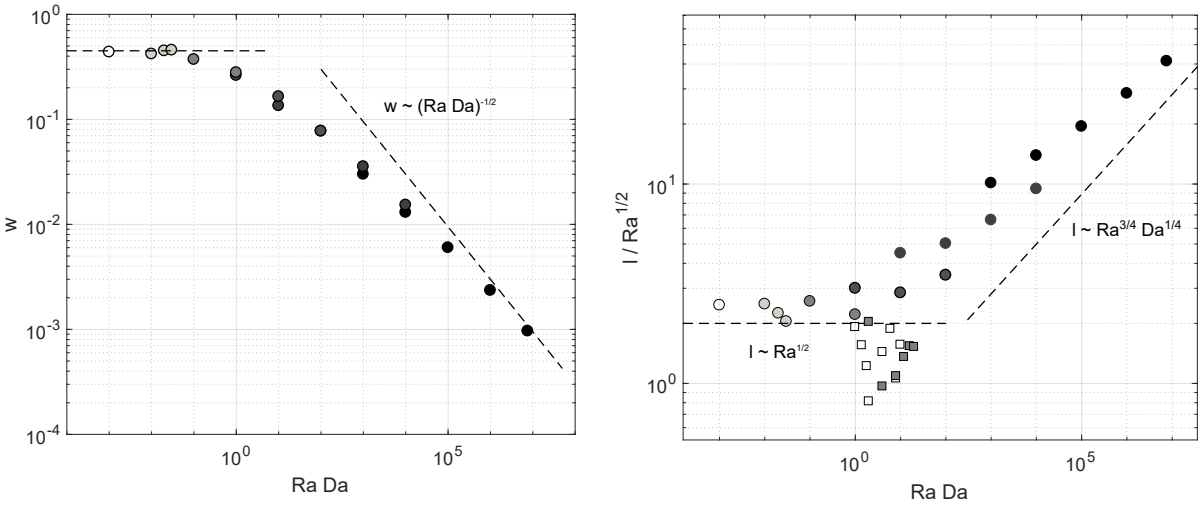

Figure 2: Left: dimensionless vertical velocity w measured at the plume neck (where the plume width l is minimum) as a function of the dimensionless parameter $Ra\,Da$; Right: dimensionless plume width l (multiplied by the square root of the Rayleigh number) as a function of $RaDa$. Numerical and experimental results are plotted in with circles and squares respectiveley.

(the chamber-reservoir combination was required to perform experiments isothermally at the highest pressures) which, once opened ensured a mixing time which is much smaller than the growth time of the onset time of the gravitational plume. A single plume is then generated by partially blocking the open surface of the Hele-Shaw cell in order to obtain an extended source (dissolution interface) of lateral size L_s (see Fig.1).

Governing Equations and non-dimensional parameters

The dimensionless forms of the Navier-Stokes and advection-diffusion equation used in the numerical calculations can be written as follow [2]

$$\frac{1}{Sc}\left[\frac{\partial \boldsymbol{u}}{\partial t}+(\boldsymbol{u}\cdot\boldsymbol{\nabla})\boldsymbol{u}\right]=-\boldsymbol{\nabla}p+\boldsymbol{\nabla}^2\boldsymbol{u}-\frac{1}{DaRa^2}c\,\boldsymbol{z},\quad\text{and}\quad\frac{\partial c}{\partial t}+(\boldsymbol{u}\cdot\boldsymbol{\nabla})\,c=\boldsymbol{\nabla}^2 c, \tag{1}$$

where $\boldsymbol{u}$, p and c are the velocity, pressure and CO_2-concentration fields. The Rayleigh, Darcy and Schmidt numbers are defined as $Ra=\Delta\rho g\kappa L_s/\mu D$ and $Da=\kappa/L_s^2$ and $Sc=\rho\,D/\mu$. In the expressions of the dimensionless groups, κ, μ, ρ, and D denote the permeability of the Hele-Shaw cell, the viscosity and density of the solution and the diffusivity of the carbon dioxide. The density difference to pure water at saturation CO_2-concentration is referred to as $\Delta\rho$.

RESULTS AND PRELIMINARY CONCLUSIONS

Far from the source, the transverse profile of concentration in the plume is reasonably rendered by a function of the form $c(x)=A\,[\cosh(x/l)]^2$ (Wooding's solution [1]) - as expected as long as the extended nature of the source can be ignored - where both the plume width l and the maximum amplitude of the concentration profile are functions of the altitude z that are connected by mass conservation. The numerical results are in fairly good agreement with the scaling law coming from the mass flux conservation at the neck of the plume (balance between lateral and vertical mass fluxes). The width of the concentration transverse profile (measured at the plume neck) is proportional to the square root of the Rayleigh number ($l\sim Ra^{1/2}$) at low Rayleigh numbers ($Ra<Da^{-1}$) and scales as $Ra^{3/4}Da^{1/4}$ at large Rayleigh numbers ($Ra>Da^{-1}$). The vertical velocity w plateaus at low Rayleigh numbers and scales as $(Ra\,Da)^{-1/2}$ at large Rayleigh numbers. In the quite narrow range of parameters where experiments can be performed (one order of magnitude in $Ra\,Da$), the experimental results are currently overestimated by almost a factor 2 by the numerical calculations. This could be due to the effect of the meniscus in the experimental configuration, which accelerates the flow and consequently reduces the plume width (see Fig.2).

References

[1] Wooding R. A. Convection in a saturated porous medium at large Rayleigh number or Peclet number. *J. Fluid Mech.* **15**: 527–544, 1963.
[2] Vreme A., Nadal F., Pouligny B., Jeandet P., Liger-Belair G., Meunier P. Gravitational instability due to the dissolution of carbon dioxide in a Hele-Shaw cell. *Phys. Rev. Fluids* **1**: 64301, 2016.

BOUNDARY LAYER PROFILES AND HEAT TRANSPORT IN TURBULENT RAYLEIGH-BE NARD CONVECTION: A THEORETICAL STUDY

Emily S.C. Ching *[1], N.C. Tai[1], Lukas Zwirner[2], and Olga Shishkina[2]
[1] Department of Physics, The Chinese University of Hong Kong, Shatin, Hong Kong
[2] Max Planck Institute for Dynamics and Self-Organization, Am Fassberg 17, 37077 Göttingen, Germany

Summary In turbulent Rayleigh-Bénard convection, the boundary layers are unsteady with fluctuations, the time-averaged large-scale circulating velocity vanishes far away from the top and bottom plates, and the motion arises from buoyancy. We have derived the full set of boundary layer equations for both the temperature and velocity fields from the Boussinesq equations for a quasi-two-dimensional flow above a heated plate, taking into account all the above effects. By solving these boundary layer equations, we obtain theoretical results for the time-averaged temperature and velocity boundary layer profiles and the Nusselt number which measures the heat transport.

INTRODUCTION

For a container with a given geometry, the dynamics of Rayleigh–Bénard convection (RBC) system is determined by two dimensionless parameters, the Rayleigh number $\mathrm{Ra} = \alpha g \Delta L^3/(\kappa\nu)$ and the Prandtl number $\mathrm{Pr} = \nu/\kappa$, where α denotes the isobaric thermal expansion coefficient, ν the kinematic viscosity and κ the thermal diffusivity of the fluid, g the acceleration due to gravity, Δ the temperature difference between the bottom and top plates, and L the height of the container. In turbulent RBC, boundary layers (BLs) develop and play a crucial role in turbulent transport. The BLs are unsteady with fluctuations, the time-averaged velocity along the direction of the large-scale circulation vanishes far away from the plates, and the motion of the fluid is not forced but arises from buoyancy. We have recently derived the full set of BL equations for both the temperature and velocity fields for general Pr from the quasi-2D Boussinesq equations, accounting for all these physical effects [1, 2], which have not been successfully incorporated in any prior existing BL theory. Solving these BL equations, we obtain theoretical results for the time-averaged temperature and velocity BL profiles and the Nusselt number (Nu).

THEORY

We consider a quasi-2D fluid flow above a semi-infinite horizontal heated plate in RBC. The velocity field is $\mathbf{u}(x,z,t) \equiv u(x,z,t)\,\hat{x} + v(x,z,t)\,\hat{z}$ with the vertical direction $\hat{z}$ and the horizontal direction $\hat{x}$ and the temperature field is $T(x,z,t)$. The governing Boussinesq equations are the continuity equation $\nabla\cdot\mathbf{u} = 0$ and

$$\partial_t \mathbf{u} + \mathbf{u}\cdot\nabla\mathbf{u} = -\nabla p/\rho + \nu\nabla^2\mathbf{u} + \alpha g(T - T_h)\hat{z}, \quad (1)$$

$$\partial_t T + \mathbf{u}\cdot\nabla T = \kappa\nabla^2 T, \quad (2)$$

where $p(x,z,t)$ is the hydrodynamic pressure, ρ the density, and T_h is the temperature of the heated plate situated at $z = 0$. We perform the Reynolds decomposition: $u = U + u'$, $v = V + v'$, $T_h - T = \Theta + \theta'$ and $p = P + p'$, average (1) and (2) over time and define the space-dependent eddy viscosity $\nu_t(x,z)$ and eddy thermal diffusivity $\kappa_t(x,z)$ by $\langle u'v'\rangle_t \equiv -\nu_t\partial_z U$ and $\langle v'\theta'\rangle_t \equiv -\kappa_t\partial_z\Theta$ to obtain

$$U\partial_x U + (V - \partial_z\nu_t)\partial_z U = (\nu + \nu_t)\partial_z^2 U - \mathcal{H}_B\rho^{-1}\partial_x P, \quad (3)$$

$$U\partial_x\Theta + (V - \partial_z\kappa_t)\partial_z\Theta = (\kappa + \kappa_t)\partial_z^2\Theta. \quad (4)$$

We have taken the BL approximation that partial derivatives of flow quantities along the plate are much smaller than those away from the plate and assumed that the convection-diffusion terms in the vertical direction are negligible compared to the buoyancy term, which is then balanced by the pressure gradient. This balance implies $P \sim B\rho U^2$ with $B \equiv \mathrm{Ra}/(2\mathrm{PrRe}^{5/2})$ where Re is the Reynolds number that measures the time-averaged velocity of the large-scale circulation. Thus the problem is divided into two classes: (1) $\mathcal{H}_B = 1$ when B is at least of order 1 such that the horizontal pressure gradient $\partial_x P$ plays a direct role and (2) $\mathcal{H}_B = 0$ where $B \ll 1$ such that $\partial_x P$ is negligible and buoyancy effect is manifested indirectly via the velocity boundary condition. We introduce the stream function Ψ with $U = \partial_z\Psi$ and $V = -\partial_x\Psi$ and define the similarity variable $\xi \equiv \mathrm{Pr}^a\mathrm{Ra}^b(z/L)(x/L)^c$, the dimensionless functions $\psi(\xi)$, $F(\xi)$ and $\theta(\xi)$ by $\Psi \equiv \mathrm{Pr}^a\mathrm{Ra}^b\nu(x/L)^{c+1}\psi(\xi)$, $P \equiv \mathrm{Pr}^{-(1+a)}\mathrm{Ra}^{1-b}(\rho\nu^2/2L^2)(x/L)^{-c}F(\xi)$, $\Theta \equiv (\Delta/2)\theta(\xi)$. Using ideas of Prandtl's mixing length model, we propose a closure model extending our previous idea [3] $\nu_t/\nu \approx k_1 G$ and $\kappa_t/\kappa \approx k_2 G$, where $G \equiv \int_0^\xi \psi(p)dp$ and k_1, k_2 are positive constants, to account for fluctuations. We look for nontrivial similarity solution and further require the equations to be independent of Ra. This gives $b = -a = 1/5$, $c = -2/5$ for $\mathcal{H}_B = 1$ and $c = -3/4 + k_1/8$ with $0 \le k_1 < 2$ for $\mathcal{H}_B = 0$. We define the velocity BL thickness $\delta(x)$ as the distance at

*Corresponding author. E-mail: ching@phy.cuhk.edu.hk

which $U(x,z)$ attains its maximum value and show that $\delta(x)$ is approximately inversely proportional to $\sqrt{\mathrm{Re}}$ albeit with a different x-dependence from that of the Prandtl-Blasius theory: $\delta(x)/L = [\psi_\xi(\xi_m)/2(c+1)\mathrm{Re}]^{1/2}\xi_m(x/L)^{-c}$, where ψ attains its maximum value at $\xi = \xi_m$. The full set of BL equations for $\psi = G_\xi$ and $\theta = -F_\xi$ are obtained:

$$\mathcal{H}_B = 1: \quad 5(1+k_1G)G_{\xi\xi\xi\xi} + (5k_1+3)G_\xi G_{\xi\xi\xi}] - (G_{\xi\xi})^2 - F + \xi F_\xi = 0 \tag{5}$$

$$5(1+k_2G)F_{\xi\xi\xi} + (3\mathrm{Pr}+5k_2)G_\xi F_{\xi\xi} = 0 \tag{6}$$

$$\mathcal{H}_B = 0: \quad 8(1+k_1G)G_{\xi\xi\xi\xi} + (2+9k_1)G_\xi G_{\xi\xi\xi} + 2(2-k_1)(G_{\xi\xi})^2 = 0 \tag{7}$$

$$8(1+k_2G)\theta_{\xi\xi} + [\mathrm{Pr}(2+k_1)+8k_2]G_\xi\theta_\xi = 0 \tag{8}$$

The boundary conditions are $G(0) = G_\xi(0) = G_{\xi\xi}(0) = 0$, $G_{\xi\xi}(\infty) = G_{\xi\xi\xi}(\infty) = 0$, $\theta(0) = 0$ and $\theta(\infty) = 1$. Hence solving these BL equations, we obtain the time-averaged temperature and velocity BL profiles, $\theta(\xi)$ and $\psi_\xi(\xi)/\psi_\xi(\xi_m)$. We have shown that the normalized time-averaged temperature BL profiles at high Pr ($\mathrm{Pr} = 4.38$ and $\mathrm{Pr} = 2547.9$) [2] and the time-averaged temperature and velocity BL profiles at low Pr ($\mathrm{Pr} = 0.1$) [1] obtained in direct numerical simulation (DNS) are well described by our theoretical results. We can further obtain theoretical results for Nu and Re:

$$\mathcal{H}_B = 1: \quad \mathrm{Nu} = \frac{5}{6}\theta_\xi(0)\mathrm{Pr}^{-1/5}\mathrm{Ra}^{1/5}; \qquad \mathrm{Re} = \frac{5}{6}\psi_\xi(\xi_m)\mathrm{Pr}^{-2/5}\mathrm{Ra}^{2/5}, \tag{9}$$

$$\mathcal{H}_B = 0: \quad \mathrm{Nu} = \frac{2}{\sqrt{2+k_1}}\frac{\theta_\xi(0)}{\sqrt{\psi_\xi(\xi_m)}}\mathrm{Re}^{1/2}. \tag{10}$$

Data obtained from DNS show that B decreases as Pr decreases at fixed Ra, and decreases as Ra increases at fixed Pr [1]. Thus the class $\mathcal{H}_B = 0$ is expected to be reached at a sufficiently high Pr for a fluid with any given Pr. For the class $\mathcal{H}_B = 0$, using the BL equations (7) and (8), we derive analytical results for ξ_m, $\psi_\xi(\xi_m)$ and $\theta_\xi(0)$ and, as a result, obtain the dependence of Nu on Re and Pr in the high-Pr [$\mathrm{Pr} \gg 1$ and $\mathrm{Pr}(2+k_1)/(8k_2) \gg 1$ with $B \ll 1$] and low-Pr ($\mathrm{Pr} \ll 1$) limits:

$$\mathrm{Nu} = F_1(k_1)\mathrm{Re}^{1/2}\mathrm{Pr}^{1/3} = \frac{3^{1/2}}{2^{2/3}\Gamma(1/3)}\left(\frac{2-k_1}{2+k_1}\right)^{\frac{1}{6}}\left[1+\frac{(7k_1-2)}{4(2-k_1)}\right]^{\frac{2+k_1}{2(7k_1-2)}}\mathrm{Re}^{1/2}\mathrm{Pr}^{1/3} \text{ (high-Pr limit)}, \tag{11}$$

$$\mathrm{Nu} \to \frac{1}{\sqrt{\pi}}\mathrm{Re}^{1/2}\mathrm{Pr}^{1/2} \quad \text{(low-Pr limit)}. \tag{12}$$

These results reveal a close resemblance of the scaling dependencies of Nu in turbulent RBC and in steady forced convection where temperature is passive as described by the Prandtl-Blasius-Polhausen (PBP) theory. This surprising finding is nontrivial as the velocity BL equations in the two theories are different and fluctuations play a significant role in turbulent RBC. DNS results in a cylindrical container of the diameter-to-height aspect ratio 1 for $10^4 \le \mathrm{Ra} \le 10^{10}$ and $0.005 \le \mathrm{Pr} \le 300$ show that $\mathrm{NuRe}^{-1/2}$ scales as $\mathrm{Pr}^{1/2}$ when Pr is small ($\mathrm{Pr} < 1$) and as $\mathrm{Pr}^{1/3}$ when Pr is large ($30 < \mathrm{Pr} < 100$) provided $B < 1$, which are in good agreement with the theoretical results.

CONCLUSIONS

We have derived the full set of BL equations for both the velocity and temperature fields in turbulent RBC from the quasi-2D Boussinesq equations. Our theory takes into account various physical effects that were not included in existing BL theories. By solving the BL equations, we have obtained theoretical results for the time-averaged velocity and temperature BL profiles and Nu. In the regime $\mathcal{H}_B = 0$ which is expected to be reached at sufficiently high Ra, we have found a close resemblance of the scaling dependencies of Nu on Re and Pr in turbulent RBC and in steady forced convection where temperature is passive as described by the PBP theory.

ACKNOWLEGEMENT

ESCC and NCT acknowledge support by the Hong Kong Research Grants Council under Grant No. CUHK-14302419. OS and LZ acknowledge the support of the Deutsche Forschungsgemeinschaft (DFG) under grant Sh405/7 (Priority Programme SPP1881 "Turbulent superstructures") and thank the Leibniz Supercomputing Centre (LRZ) for providing computing time.

References

[1] Ching E. S. C., Leung H. S., Zwirner L., Shishkina O. Velocity and thermal boundary layer equations for turbulent Rayleigh-Bénard convection. *Phys. Rev. Research* **1**: 033037, 2019.

[2] Shishkina O., Horn S., Wagner S., Ching E. S. C. Thermal Boundary Layer Equation for Turbulent Rayleigh-Bénard Convection, *Phys. Rev. Lett.* **114**: 114302, 2015.

[3] Shishkina O., Horn S., Emran M. S., Ching E. S. C. Mean temperature profiles in turbulent thermal convection, *Phys. Rev. Fluids* **2**: 113502, 2017.

STATISTICAL PROPERTIES OF THERMAL PLUMES IN TURBULENT RAYLEIGH-BENARD CONVECTION WITH A ROUGH PLATE

Mebarek Belkadi[1,2], Anne Sergent *[1,3], Yann Fraigneau[1], and Bérengère Podvin[1]
[1] Université Paris-Saclay, CNRS, LIMSI, Orsay, France
[2] Laboratory of Turbomachinery, Ecole Militaire Polytechnique, Algiers, Algeria
[3] Sorbonne Université, Faculté des Sciences et Ingénierie, UFR d'Ingénierie, Paris, France

Summary A comparative study of the plume dynamics near the rough and smooth horizontal plates of a water-filled asymmetric Rayleigh-Bénard cell is presented. Direct numerical simulations are performed over a large range of Rayleigh numbers (from 10^5 to 10^{10}) in order to cover the three heat transfer regimes. Several techniques of plume feature description are used to highlight how roughness changes the dynamics of plume emission and the energetic content of plumes.

MOTIVATION

In a real thermal system, the underlying surfaces involve specific topographies or small-scale roughness which have a significant impact on the heat transfer. Particularly, in the case of turbulent convection, the addition of wall roughness results in a global heat transfer enhancement and in some cases, in an increase of the exponent of the heat transfer scaling law ($Nu \sim Ra^{\beta}$, Nu Nusselt number, Ra Rayleigh number) [1, 2]. It is commonly admitted that the heat transfer enhancement originates from an intensification of the thermal plume emission at the tips of roughness elements [3].

In classic turbulent Rayleigh-Bénard convection, previous studies have shown the role of thermal plumes in the heat transport within the cavity [4]. Several techniques of plumes description have been proposed to characterize plumes in terms of geometry, number, intensity or velocity. They can be based on the post-processing of a temperature field determined from thermochromic liquid crystal microspheres [5], on the identification of temperature threshold in numerical snapshots [6], on the analysis of cliff-ramp structures in local time series [7], or on shadowgraph treatment [8].

In the present numerical study, we consider convection over a regularly roughened plate in a Rayleigh-Bénard cell. The three successive heat transfer regimes, previously observed in this kind of configuration (see for example [1]), are modelled from inactive roughness (regime I) to a regime (called III) where the relative heat transfer increase is larger than the relative surface increase induced by roughness addition. The objective of this work is to identify how roughness changes the plume features and their dynamics, depending on the regime.

NUMERICAL SET-UP

We study the fluid flow occurring in an asymmetric 3D Rayleigh-Bénard rectangular cell filled with water. The cell is heated from below by an isothermal rough plate, modeled by a set of square-based obstacles as sketched on figure 1. Sizes of the roughness elements share some common geometric features with the Lyon's experiments [9, 2] such as aspect ratios or distribution, but we retain a larger roughness height ($H_r/H = 0.03$, H cavity height) in order to trigger the first transition between the heat transfer regimes I and II to a lower Ra.

The Navier-Stokes equations are solved under the Boussinesq approximation. The parallel numerical solver (SUNFLUIDH code) uses a finite volume discretization on staggered grids. The time marching is treated by a semi-implicit scheme combined with a prediction - correction scheme for the velocity - pressure coupling, with a global second-order accuracy. The code has been validated for the classic turbulent Rayleigh-Bénard convection by comparison with the DNS data [10]. Numerical simulations are performed for a large range of Rayleigh numbers in order to cover the three heat transfer regimes ($10^5 \leq Ra \leq 10^{10}$). We use meshes from $1.3 \cdot 10^6$ to $5 \cdot 10^8$ cells in order to ensure a sufficient space resolution. The computational domain is decomposed into 256 to 2048 subdomains depending on the considered Ra number. The convergence in space and time has been *a posteriori* checked by testing the convergence of several formulations of the time-averaged Nusselt number.

*Corresponding author. E-mail: anne.sergent@limsi.fr

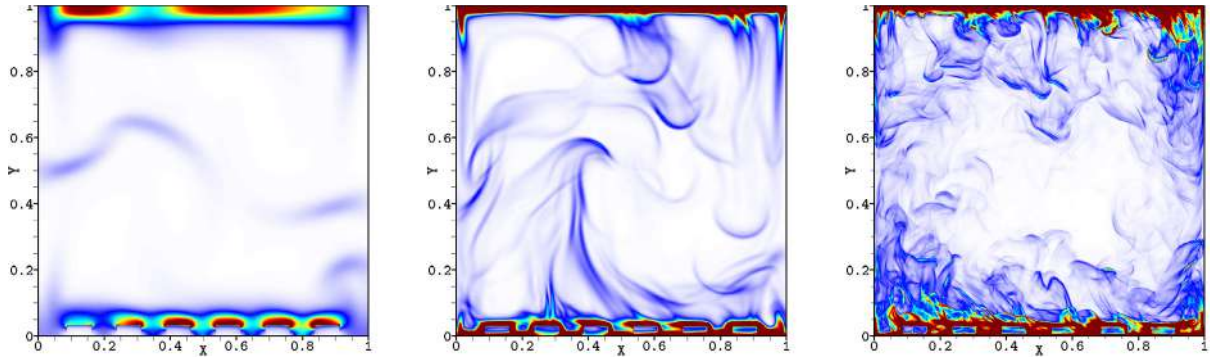

Figure 1: Instantaneous flow vizualisation at $Ra = 10^6$, $5 \cdot 10^7$ and $2 \cdot 10^9$, respectively belonging to regimes I, II and III. Colour indicates the thermal dissipation field.

RESULTS

Taking advantage of the cavity asymmetry, we conduct a comparative study of the plume dynamics near the rough and smooth horizontal plates within the same Rayleigh-Bénard cavity for the three regimes of heat transfer.

First, we consider more specifically three particular Ra numbers, each belonging to a different regime (figure 1). The time monitoring of a set of probes recording temperature or vertical velocity, and located near the rough and smooth plates, shows how roughness alters the statistical properties of thermal plumes. In agreement with the experiments (see for example [3, 4, 9]), intense temperature fluctuations are observed more frequently near the rough plate than near the smooth plate, especially in the intermediate regime II. Concurrently, the largest vertical velocity fluctuations are found near the smooth plate rather than around the rough one. In addition, instantaneous characteristics of thermal plumes such as amplitude (in terms of local increment) or width (equivalent to a transit time) can also be calculated from the time series, following the [7] methodology. As expected, log normal distributions are generally recognized in the PDFs of the plume features. However, a noticeable change is observed in regime II, with a more frequent detachment of high energy plumes close to the rough plate, both in terms of potential and kinetic energy.

Finally, we make use of space-time diagrams [8] to quantify the spatio-temporal dynamics of the thermal plumes. An increase of the plume number with Ra is observed on both sides of the cavity for all regimes. Although a similar plume distribution near the smooth and rough plates is found in regime I and III, we show that a strong asymmetry between the two horizontal plates is established in regime II with a significant increase of the number of plumes close to the roughness. Moreover, we note in this regime the presence of highly dissipative structures not only near roughness but also within the bulk of the cavity (as seen on figure 1).

ACKNOWLEDGMENTS

This work was granted access to the HPC resources of GENCI-IDRIS under allocation 2a0326 made by GENCI. This work has benefited from the financial support of the INSIS CNRS (PEPS Energie 2018 CORINThe).

References

[1] Xie Y.-C., Xia K.-Q. Turbulent thermal convection over rough plates with varying roughness geometries. *J. Fluid Mech.* **825**:573–599, 2017.

[2] Rusaouën E., Liot O. , Castaing B., Salort J., Chillà F. Thermal transfer in Rayleigh-Bénard cell with smooth or rough boundaries. *J. Fluid Mech.* **837**:443–460, 2018.

[3] Du Y.-B., Tong P. Turbulent thermal convection in a cell with ordered rough boundaries. *J. Fluid Mech.* **407**:57–84, 2000.

[4] Shang X.-D., Qiu X.-L., Tong P., Xia K.-Q. Measured local heat transport in turbulent Rayleigh-Bénard convection. *Phys. Rev. Lett.* **90**:074501, 2003.

[5] Zhou Q., Sun C., Xia K.Q. Morphological evolution of thermal plumes in turbulent Rayleigh-Bénard convection. *Phys. Rev. Lett.* **98**:074501, 2007.

[6] Shishkina O., Wagner C. Analysis of sheet-like thermal plumes in turbulent Rayleigh-Bénard convection. *J. Fluid Mech.* **599**:383–404, 2008.

[7] Zhou S.-Q., Xie Y.-C., Sun C., Xia K.-Q. Statistical characterization of thermal plumes in turbulent thermal convection. *Phys. Rev. Fluids*, **1**:054301, 2016.

[8] Belkadi M., Guislain L., Sergent A., Podvin B., Chillà F., Salort J. Experimental and numerical shadowgraph in turbulent Rayleigh-Bénard convection with a rough boundary: investigation of plumes. *submitted*, 2019.

[9] Liot O., Ehlinger Q., Rusaouën E., Coudarchet T., Salort J., Chillà F. Velocity fluctuations and boundary layer structure in a rough Rayleigh-Bénard cell filled with water. *Phys. Rev. Fluids*, **2**:044605, 2017.

[10] Kaczorowski M., Chong K.-L., Xia K.-Q. Turbulent flow in the bulk of Rayleigh-Bénard convection: aspect-ratio dependence of the small-scale properties. *J. Fluid Mech*, **747**:73–102, 2014.

STATISTICAL CHARACTERISTICS OF THERMALS IN CONVECTIVE ATMOSPHERIC BOUNDARY LAYER

Natalia Vazaeva *[1,2], Otto Chkhetiani[1], Michael Kurgansky[1], Margarita Kallistratova[1], Vasiliy Lyulyukin[1], Daria Zaytseva[1]
[1] Obukhov Institute of Atmospheric Physics, Russian Academy of Sciences, Moscow, Russia
[2] Bauman Moscow State Technical University, Moscow, Russia

Summary In recent decades great interest has been expressed in thermal convection structures (TCS), also called thermals, in the atmospheric boundary layer (ABL) and its characteristic manifestations. The new method of acoustic sounding data treatment for detecting these structures has been obtained. The structures have been measured under different wind and temperature conditions over arid-steppe zones of Rostov region and of the Caspian lowland in the eastern part of Kalmykia Republic, Russia in summer time of years 2007, 2016, 2018, 2019. The duration of over-limit vertical velocity, the maximum velocity in this interval and the horizontal scale have been calculated. The statistical distribution was proved to be close to Rayleigh distribution.

INTRODUCTION

In studying thermal convection structures (TCS) in the atmospheric boundary layer (ABL) a large number of theoretical physico-mathematical models have been created. However, numerical solution of the thermohydrodynamics equations are difficult for calculating, analysis and understanding the results. Exact analytic solutions are found only in some case studies. Consequently, the statistic methods retain its relevance and significance and continue to develop [Petenko I. and Bezverkhnii V., 1999; Petenko I. and Shurygin E., 1999]. In addition, it should be pointed out that the Maxwell distribution for ensemble of the TCS was received in the paper [Vulfson A. and Borodin O., 2018].

EXPERIMENTAL DATA

TCS and their characteristic manifestations in the ABL were investigated using acoustic sounding. The multiple-frequency Doppler sodars LATAN-3M [Kouznetsov R, 2009] with a vertical resolution of 20 and 10 m, a pulse emission interval of 5 and 3 s, an altitude range of 600 and 350 m and a basic carrier frequency of 2 kHz and 4 kHz had measured the profiles of the wind velocity components. These profiles were used for calculating the scale of TCS. Experimental data were being obtained during the field campaigns organized by the A.M. Obukhov Institute of Atmospheric Physics RAS over semi-arid zones of the Caspian lowland in the eastern part of Kalmykia Republic, Russia, and in Rostov region, Russia in summer time of years 2007, 2016, 2018, 2019. The structures were investigated under weak wind conditions. The convection was well-developed during all these case studies.

RESULTS AND DISCUSSION

An original method of the acoustic sounding data treatment for extracting TCS has been developed. The episodes of the vertical velocities above limit values at which TCS aroused hypothetically were considered. A moving rectangular filter was used for averaging the original data of the horizontal and vertical wind-velocity components. The duration of vertical velocity excess over the threshold, the maximum velocity within this interval and the horizontal scale were calculated. It is assumed that TCS move forward during any relatively small time step with some averaged velocity (Taylor's hypothesis). This time step has been taken empirically and amounted to 10 minutes. In this case, the spatial distribution of velocity field and its time variations have been adequately reproduced. As the threshold, a few alternatives were used: 0.3 m/s, 0.6 m/s and 1.2 m/s.

The statistical distribution of calculated characteristics was close to Rayleigh distribution [Kurgansky M., 2000] (see example for 23d of July, 2016, in Figure 1):

$$\rho(U) = \frac{2U}{{U_0}^2}\exp\left(\frac{{U_m}^2-U^2}{{U_0}^2}\right),$$

where ${U_0}^2 = \left[\langle U^2\rangle - {U_m}^2\right]$, $\langle U^2\rangle$ is the mean-square vertical velocity of TCS, and U_m – the threshold for vertical velocity.

*Corresponding author. E-mail: vazaevanv@ifaran.ru.

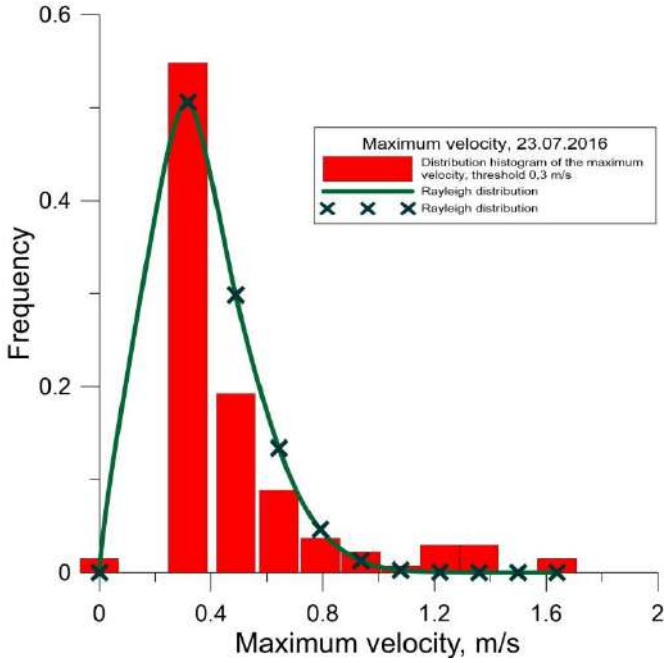

Figure 1. Distribution histogram of the maximum vertical velocity, and Rayleigh distribution, Kalmykia, 23d July, 2016.

This fact can be implemented in the parameterization, forecast of TCS, and can facilitate the understanding of the processes in the so-called "grey-zone" of numerical simulation. Note that Rayleigh distribution is universe and can be applied, for example, to the statistics of the intense moist convective vortices and also of the height of the ocean waves.

ACKNOWLEGMENTS

This work was supported by Russian Foundation for Basic Research (projects No. 19-05-50110, No. 19-05-01008), and by fundamental research program of Russian Academy of Science (program No. 1).

References

[1] Kurgansky M. Statistical distribution of intense humid convective spiral vortices in the atmosphere. *Doklady Akademii Nauk.* **371**(2): 240-242, 2000.
[2] Kouznetsov R The multiple-frequency sodar with heigh temporal resolution. Meteorol. Z., **18**(2):169-173, 2009.
[3] Petenko I. and Bezverkhnii V. Temporal Scales of Convective Coherent Structures Derived from Sodar Data. *Meteorol. Atmos. Phys.* **71**: 105-116, 1999.
[4] Petenko I. and Shurygin E. A two-regime model for the probability density function of the temperature structure parameter in the convective boundary layer. *Bound.-Layer Meteor*. **93**: 381–394, 1999.
[5] Vulfson A. and Borodin O. Brownian ensemble of random-radius buoyancy vortices and Maxwell velocity distribution in a turbulent convective mixed-layer. *Physics of Fluids*. Sep 12. **30**(9): 095103, 2018.

STRAIN RATE SIGNATURES OF PLUMES IN RAYLEIGH BE NARD CONVECTION

Prafulla P. Shevkar *[1], R. Vishnu[2], Sanal K. Mohanan[1], and Baburaj A. Puthenveettil[1]
[1] Department of Applied Mechanics, Indian Institute of Technology Madras, Chennai, India
[2] Department of Aerospace Engineering, Indian Institute of Technology Madras, Chennai, India

Summary We present a new criteria to detect thermal plumes from the velocity field in a horizontal plane that pass from the local boundary layer to the plume close to the hot plate in turbulent Rayleigh Bénard convection. Based on the characteristics of deformation of fluid elements, we propose that the negative dominant eigenvalues of the 2D strain rate picks up the thermal plume regions. We also show that the areas identified by this criteria match the areas identified by the horizontal divergence criteria $\bar{\nabla}_H.\bar{u} < 0$ proposed by Vipin and Puthenveettil [4].

Thermal plumes play major role in transporting heat [1, 7] from the hot plate in turbulent Rayleigh Bénard convection (RBC), and hence, detecting them and understanding their dynamics is important to understand the phenomenology of RBC. There are several temperature based criteria [2, 6] to identify thermal plumes. However detecting plumes from the velocity field near the hot plate is hard since their velocity or strain signatures are not known. Such detection, in addition to being important experimentally, since velocity fields are easily available from PIV, also give insights into the kinematics of plumes in RBC. In this paper, we arrive at a criteria to identify thermal plumes near the hot plate using the eigenvalues of the 2D strain rate tensor S in a plane close to the hot plate.

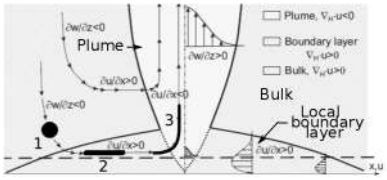

Figure 1: Schematic of the deformation of a fluid element near the hot plate in RBC.

Cases	λ_1	λ_2	$\lvert\lambda_1/\lambda_2\rvert$	$\nabla_H.\bar{u}$	Region
1	+	+	> 1	> 0	non-plume
2	+	-	> 1	> 0	non-plume
3	+	-	< 1	< 0	plume
4	-	-	< 1	< 0	plume

Table 1: Possible values of eigenvalues at each point and the region corresponding to those points.

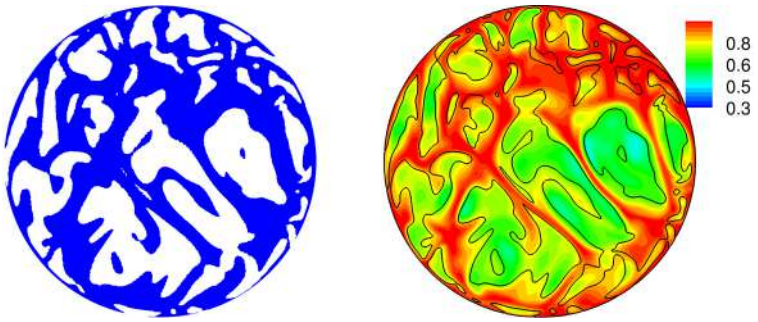

(a) (b)

Figure 2: (a), Dominant negative eigenvalues of S in a horizontal plane at a height of $0.006H$ from the hot surface and; (b), T overlaid with the $w = 0$ contour line at $Ra = 2 \times 10^8$ and $Pr = 1$, both obtained computationally.

Eigenvalues of the two dimensional strain rate tensor S, due to the 2 horizontal components of velocity in a plane, describe the deformation charcteristics of fluid elements in the form of extension or compression strains occurring at a points in the plane [3]. These eigenvalues at a point take positive or negative signs, corresponding to the extension and compression strains along the principal axes, with the associated eigenvectors giving the lines of action of the elemental deformations at that point. Figure 1 shows a schematic of the change in shape of a spherical fluid element at three different positions along it's path near the hot plate in RBC. The spherical fluid element is initially in the bulk (location 1) which then moves into the boundary layer (location 2), and finally becomes a part of the plume (location 3) [7]. Inside the boundary layer, due to the horizontal shear forces present, the fluid element undergoes predominantly horizontal stretching, implying that the extensional strain dominates in the horizontal direction within the boundary layer; the dominant eigenvalue of S in a horizontal plane is then expected to take a positive sign at location 2. As the fluid element reaches location 3, inside the plume, it gets further stretched in the vertical direction. The extensional strain then dominates in the vertical direction inside the plume resulting in a compressive strain in the horizontal direction to conserve mass. The dominant eigenvalue of S is then expected to take negative signs within plumes. Such a displacement and deformation of a fluid volume can be inferred from the visualization experiments in a vertical plane using passive markers [5].

*Corresponding author. E-mail: prafulla145@gmail.com

We construct an instantaneous S at every spatial point in a horizontal plane close to the hot plate from experimental and computational data. The ordered eigenvalues λ_1 and λ_2 of S at each point so that $\lambda_1 > \lambda_2$, which provide the local principal strain rates, are calculated from,

$$\lambda_{1,2} = \frac{1}{2}\left(u_x + v_y \pm \sqrt{(u_x - v_y)^2 + (u_y + v_x)^2}\right) \tag{1}$$

where, u and v are the velocities in the x and y directions and subscripts x and y denote the derivatives in these directions. The dominant eigenvalue at a point is λ_1, if $|\lambda_1/\lambda_2| > 1$ and is λ_2, if $|\lambda_1/\lambda_2| < 1$. Figure 2(a) shows the dominant negative eigenvalues calculated numerically in a plane close to the hot plate in RBC; figure 2(b) shows the corresponding dimensionless temperature field T overlaid with the vertical velocity $w = 0$ contour line. $T = (\theta - \theta_c)/(\theta_h - \theta_c)$ where, θ is dimensional temperature and subscripts c and h denotes the cold and hot plate temperatures. From figures 2(a) and 2(b), it is clear that the regions with negative dominant eigenvalues are the regions in which w is positive and T is mostly > 0.75, making these regions most likely to be the thermal plumes [2]. Thus, we expect that, close to the hot plate in RBC, regions with negative dominant λ's are the thermal plumes while the remaining regions are the boundary layers.

Figure 3(a) shows the distribution of the dominant eigenvalues and the corresponding eigenvectors calculated from the velocity field obtained by PIV in a convection cell from a central 84.10×73.76 mm^2 region near the hot surface in a horizontal plane within the Prandtl-Blasius and the natural convection boundary layer thicknesses. The negative dominant eigenvalues fall in the plume region with the eigenvectors being normal to the plumes in regions with weak shear (mainly seen at low Ra), while in the shear dominant regions, the eigenvectors are likely to be inclined at a small angle to the plumes. Vipin and Puthenveettil [4] proposed a velocity based criteria to identify thermal plumes, the criteria identifies negative horizontal divergence ($\bar{\nabla}_H.\bar{u} < 0$) regions as plumes; this criteria was used by Shevkar et al. [3] to find the scaling of mean plume spacing with shear in RBC. Since $u_x + v_y = \bar{\nabla}_H.\bar{u}$ in (1), regions with negative values of $\bar{\nabla}_H.\bar{u}$ are also the regions with the negative dominant eigenvalues. Hence, regions with negative $\bar{\nabla}_H.\bar{u}$ shown in figure 3(b), match with the regions of negative dominant eigenvalues of S, shown in figure 3(a). Table 1 summarises the various combinations of λ, and their occurrence in plume and non-plume regions, close to the hot plate in RBC. Case 1, with both positive eigenvalues, corresponds to the local impingement regions on the hot plate, where fluid elements get stretched in all the horizontal directions.

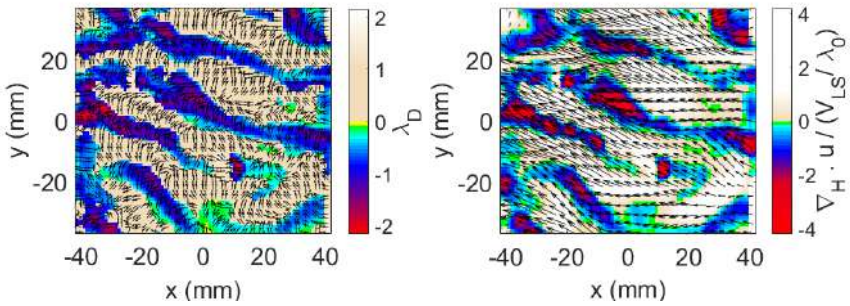

Figure 3: (a), Dominant eigenvalues of the 2D strain rate tensor S, overlaid over the corresponding eigenvectors in a horizontal plane at a height of 1.3 mm from the hot plate calculated from PIV and; (b), the corresponding dimensionless horizontal divergence field, overlaid over the horizontal velocity vector field at $Ra = 1.2 \times 10^9$ and $Pr = 5.09$.

In conclusion, in a horizontal plane close to the hot plate, regions with negative dominant eigenvalues of S, i.e. $|\lambda_1/\lambda_2| < 1$ where, λ's are ordered eigenvalues pick up plume regions, on which also fall the negative $\bar{\nabla}_H.\bar{u} < 0$ regions [4]. Regions identified by this criteria as thermal plumes consist mostly larger temperatures than background regions and positive values of w; they are also line like, similar to the plumes on the hot plate[1]. Hence we conclude that in a horizontal plane in the plume regions, the compressive strain dominates the extensional strain.

References

[1] Puthenveettil, B. A. and Arakeri, J. H, Plume Structure in High-Rayleigh-Number Convection, *J. Fluid Mech.*, **542**: 217-250, 2005.
[2] Schumacher, J., Lagrangian Studies in Convective Turbulence, *Phys. Rev. E*, **79**: 056301, 2009.
[3] Shevkar, P. P., Gunasegarane, G. S., Mohanan, S. K. and Puthenveettil, B.A., Effect of Shear on Coherent Structures in Turbulent Convection, *Phys. Rev. Fluids.*, **4**: 043502, 2019.
[4] Vipin, K. and Puthenveettil, B. A., Identification of Coherent Structures on the Horizontal Plate in Turbulent Convection, ExHFT-8, Lisbon, 2013.
[5] Weijermars R., New Laboratory Method for Analyzing Deformation and Dispacement in Creeping Fluid: Example from Stokes Flow and a Thermal Plume, *J. Geophys. Res.* **93**: 2179-2190, 1988.
[6] Gastine, T., Wicht, J. and Aurnou, J. M., Turbulent Rayleigh-Bénard convection in Spherical Shells, *J. Fluid Mech.*, **778**: 721-764, 2015.
[7] Puthenveettil B. A., Investigations on High Rayleigh Number Turbulent Free Convection, *PhD Thesis*, IISc Bangalore, Bangalore, 2004.

EFFECT OF THERMAL RADIATION ON HEAT TRANSFER EFFICIENCY IN TURBULENT RAYLEIGH-B NARD CONVECTION

Pavel Urban[1]*, Tomáš Králík[1], Pavel Haznelka[1], Věra Musilová[1], Tomáš Věžník[1], David Schmoranzer[2], and Ladislav Skrbek[2]
[1] The Czech Academy of Sciences, Institute of Scientific Instruments, Královopolsk 147, Brno, Czech Republic
[2] Faculty of Mathematics and Physics, Charles University, Ke Karlovu 3, Prague, Czech Republic

Summary We examine the effect of thermal radiation and its influence on the measured efficiency of convective heat transport in Rayleigh-Bénard convection (RBC) experiments performed at room and cryogenic temperatures. We present a detailed analysis of conventional far-field radiative heat transport occurring in selected, well-documented, RBC experiments with transparent gaseous working fluids. Our findings reveal that while the effect of thermal radiation across transparent fluids is negligibly small at cryogenic temperatures, it generally cannot be neglected in large-scale high Rayleigh number experiments performed at room temperatures without further analysis. Additionally, we discuss experiments with radiatively participating (absorbing thermal radiation) working fluids and show that their analysis needs special attention.

Rayleigh-Bénard Convection (RBC) is a physical model used for study of thermally-generated convection between two infinite parallel horizontal plates mutually displaced by distance L. The convective flow is generated by the temperature difference ΔT between the bottom hot plate (T_b) and the top cold plate (T_t). RBC in the Oberbeck-Boussinesq working fluid is fully characterized by two dimensionless control parameters expressing physical similarity of the convective flow: the Rayleigh number, $Ra = (g\alpha\Delta TL^3)/\nu\kappa$, and the Prandtl number, $Pr = \nu/\kappa$, where g, α, ν and κ denote respectively the acceleration due to gravity, isobaric thermal expansion coefficient, kinematic viscosity, and thermal diffusivity. The aspect ratio $\Gamma = D/L$ is the third dimensionless parameter characterising RBC, when the experiment is conducted in a vertical cylindrical cell with the diameter D.

The basic problem in RBC study is to find the efficiency of heat transfer, which is defined by the dimensionless Nusselt number, Nu, via $Nu = Nu(Ra; Pr; \Gamma)$ scaling. The classical theories [1] predict scaling law of $Nu \sim Ra^{1/3}$ under the assumption that the heat transfer in turbulent RBC is controlled by the heat conduction of marginally stable thermal boundary layers, although the bulk between them is turbulent. In this model, the convective heat transport does not depend on the height L and all of the temperature difference ΔT is spread over the top and bottom boundary layers with thickness $l = L/(2Nu)$, which are thin in comparison with L in turbulent RBC.

Standard interpretation of RBC experiments does not consider heat transfer via thermal radiation. At room temperature, the effect of radiation can be significant, as the heat flux by thermal radiation increases with the fourth power of absolute temperature T. To assess the role of thermal radiation in RBC, we have analysed selected experiments performed in cylindrical cells of various aspect ratio Γ with gaseous working fluids at room (helium, nitrogen and sulphur hexafluoride) and cryogenic temperatures (helium) [2]. For fully transparent working fluids, we show that in some turbulent high Ra experiments the radiative heat transfer ought to be taken into account, as it affects the Nu numbers and also appreciably changes $Nu(Ra)$ scaling relation. Since the thermal radiation does not directly affect the working fluid in this case, the measured value of Nu may be simply corrected by adjusting the value of the convective heat flux [2].

On the other hand, in the case of radiatively participating fluids, radiation is absorbed in the fluid at least partly and can affect the convective flow significantly. For example, in room temperature experiments on heat transfer efficiency with CO_2 [3], the delayed onset of convection and decrease in Nu number by 20 % at Ra up to 10^4 (in comparison with transparent air) were observed. The authors attributed both these observations to the stabilizing effect of the gas thermal radiation on RBC [3]. Influence of radiation on the character of the $Nu(Ra)$ dependence was also demonstrated in water experiments [4]. The working fluid was homogeneous mixture of water with a tuneable density of dye for absorption of visible light incoming from an external source below the transparent bottom plate. Tuning the dye density varied depth of penetration of radiation from the boundary layer to the turbulent bulk. When the radiation was absorbed in the region of the boundary layer close to the bottom plate, similarly as in standard RBC, 1/3 $Nu(Ra)$ scaling law was observed (Ra up to 10^9). On the other hand, when also the turbulent bulk was heated, a steeper 1/2 scaling law was observed, signifying a more efficient heat transport (Ra up to 10^8).

A natural question is, how the Nu number can be affected by thermal radiation in room temperature experiments when a radiatively participating fluid is used, specifically at very high Ra number experiments with water (Ra up to 10^{12}) and SF_6 gas (Ra up to 10^{15}). The radiative part of heat transfer in this case cannot be simply corrected as in the case of transparent fluids. We have used spectral absorption coefficients [5, 6] for these two fluids and calculated absorption of the thermal radiation emitted by the bottom plate with temperature $T_b = 293$ K over the 1 m thick layers of SF_6 (Figure 1) and water (Figure 2). The absorption was calculated for two values of density of SF6 (6 kg/m3 and 160 kg/m3), corresponding to atmospheric pressure and elevated pressure of 20 bar realized in the Göttingen experiments [7]. The distance z of 1 m corresponds to the height of the RBC cell, while the boundary layer thickness z is of the order 1 mm and less. For both atmospheric and elevated pressure, most of radiation power emitted by the bottom plate is absorbed in the gas outside the boundary layer. The absorption was calculated for the forward and omnidirectional thermal radiation from the bottom plate. Thermal radiation of the gas was omitted in this calculation. In Göttingen SF_6 experiment [7] the transferred heat flux varied from ~4 W/m^2 to ~500 W/m^2 at Ra numbers from ~10^{11} to 10^{14}. For example, the bottom plate

with emissivity $e = 0.05$ at $T_b = 295$ K emits a heat flux of 22 W/m^2 which is especially significant at lower *Ra* numbers with respect to the measured transferred heat flux.

Regarding absorption in water, all the heat emitted by the bottom plate is absorbed within very thin layer with $z < 10^{-4}$ m, in stark contrast to SF6.

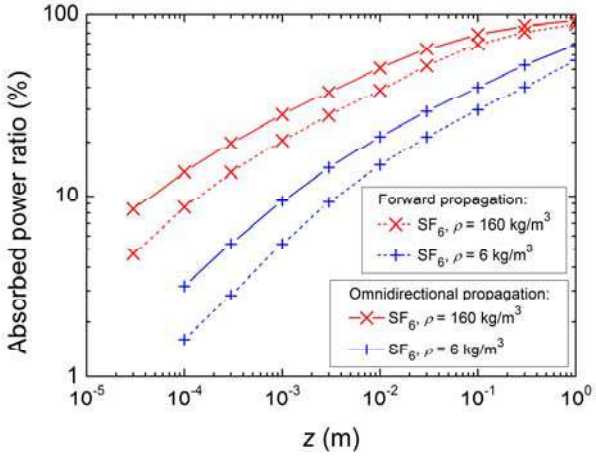

Figure 1. Radiative power absorbed in SF_6 gas layer (ratio with respect to the heat power emitted by the bottom plate with temperature $T_b = 295$ K) plotted versus distance z from the emitting plate. Densities 6 kg/m^3 and 160 kg/m^3 of SF_6 gas correspond to atmospheric pressure and elevated pressure of 20 bar realised in the Göttingen experiments [7].

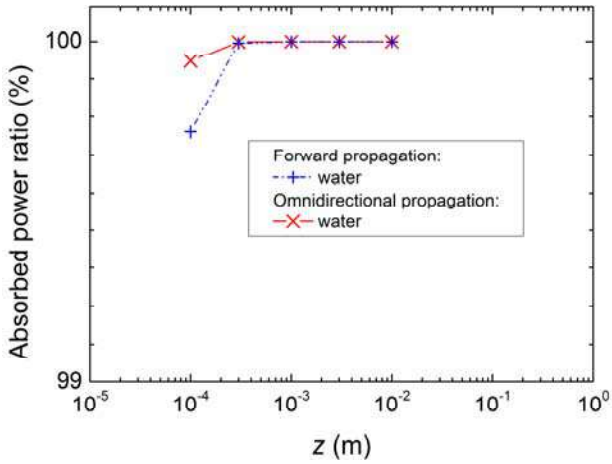

Figure 2. Radiative power absorbed in water layer (ratio with respect to the heat power emitted by the bottom plate with temperature $T_b = 295$ K) plotted versus distance z from the emitting plate.

In conclusion, for fully transparent working fluids at room temperature, we show that the radiative heat transfer could affect the *Nu* number appreciably and can be corrected. Experiments utilizing fluids absorbing thermal radiation require special care and thermal radiation as well as its absorption inside the RBC cell ought to be taken into account. On the contrary, in the cryogenic experiments (at temperatures of a few K) with gaseous or liquid helium, the radiative heat transport contributes to the total heat transport through the cell by a negligibly small amount [2].

We thank M. Macek for stimulating discussions. The support of Czech Science Foundation under GA ČR 20-00918S is acknowledged.

References

[1] Priestley C. H. B., Turbulent Transfer in the Lower Atmosphere (University of Chicago Press, Chicago, 1959). Malkus M. V. R., Proc. R. Soc. London, Ser. A 225, 196 (1954).

[2] Urban P., Králík T., Hanzelka P., Musilová V., Věžník T., Schmoranzer D., Skrbek L. Thermal Radiation in Rayleigh-Bénard Convection Experiments. *Physical Review E*, 2020 (under review).

[3] Hutchison, J. E. & Richards, R. F. 1999 Effect of nongray gas radiation on thermal stability in carbon dioxide. *J. Thermophysics and Heat Transfer* 13, 25–32.

[4] Lepot S., Aumaïtre S., Gallet B., Radiative heating achieves the ultimate regime of thermal convection. *Proc. Nat. Acad. Sci. USA* 115, 8937, 2018.

[5] Rothman, L. et al. The HITRAN 2008 molecular spectroscopic database. *J. Quant. Spectrosc. Radiat. Transfer* 110, 533 – 572, 2009.

[6] Chapados, C., Birnbaum, G., Infrared absorption of SF6 from 32 to 3000 cm−1 in the gaseous and liquid states. *J. Mol. Spectrosc.* 132, 323 – 351, 1988.

[7] He, X., Funfschilling, D., Bodenschatz, E. & Ahlers, G. Heat transport by turbulent Rayleigh-Bénard convection for Pr ≃ 0.8 and $4\times10^{11} \leq$ Ra $\leq 2\times10^{14}$: ultimate-state transition for aspect ratio Γ = 1.00. *New J. Phys.* 14, 063030, 2012.

SINE-HELICOIDAL CHANNEL FLOWS TO IMPROVE MIXING AND HEAT TRANSFER

Abbas Aldor[1,2], Kamal El Omari[1,3], Charbel Habchi[2], Yann Moguen[1], Pierre-Henri Cocquet[3,1], and Yves Le Guer *[1]
[1] Université de Pau et des Pays de l'Adour, E2S UPPA, SIAME, Pau, France
[2] Notre Dame University–Louaize, Thermofluids Research Group, Zouk Mosbeh, Lebanon
[3] Université de La Réeunion, Laboratoire PIMENT, Le Tampon, France

Summary We present an innovative sine-helicoidal channel geometry which allows, due to the alternation of centrifugal forces, the perturbation of the Dean cells, and consecutively the obtention of chaotic advection. Numerical investigations have been carried out to study the laminar flow patterns in the sine-helicoidal channel. Its thermal efficiency is compared to the one given by a classical helicoidal channel for a thermal Dirichlet boundary condition. Results showed that the sine-helicoidal geometry improves the mixing and heat transfer significantly. One might thus envision the use of such device for applications in which the lack of mixing is a limiting factor.

INTRODUCTION

Flows in curved channels are often used for many industrial operations: heat transfer, chemical reaction, filtration, separation, dispersion, etc. (1). The particularity of the flow in a curved channel is to develop, due to the centrifugal force and to the viscous drag along the walls, two symmetrical vortex cells in the flow cross section. This leads to helicoidal Lagrangian trajectories. The flow is characterized by the dimensionless Dean number ($\mathrm{Dn} = \mathrm{Re}\sqrt{a/R}$ where Re is the Reynolds number and a characteristic length of the cross-section). These Dean cells appear from $\mathrm{Dn} \simeq 0$ until large values of Dn where they subsist as coherent structures in the turbulent flow. Their intensity will be stronger if the radius of curvature R is smaller (*i.e.* stronger curvature k). If the length of the curved channel is increased, it is necessary to give it a certain torsion. We then obtain a helicoidal channel. Dean's vortex cells are slightly modified by this channel torsion, the plane of curvature separating the two vortices is just rotated to match the torsion angle. The particle trajectories are always toroidal and there is no fluid exchange between the two vortex regions. However, if we twist two consecutive portions of toroidal channel, we can break the flow symmetry and obtain complex trajectories of so-called chaotic advection. This chaotic advection flow within twisted channels was first numerically evidenced by Jones *et al.* in 1989 (2) and experimental confirmation given by Le Guer and Peerhossaini in 1991 (3). Numerous studies have then proven the effectiveness of this geometry with twisted curved channels to improve mixing, heat and mass transfer and reactive transfer. In the following sections we present an original geometry of channel arranged in a sine-helicoidal shape and some numerical results of flow patterns and heat transfer efficiencies compared to those given by the flow in a helicoidal channel.

GEOMETRY AND PARAMETERIZATION

The wavy square channel is parametrized by a sine-helicoidal smooth analytical curve winding around a circular cylinder. The two geometries are shown in Fig. 1 (a). The two channels have the same length. They are equipped with identical straight sections at inlet and outlet. The difference between the two channels is how the curvature is organized around the cylinder. The curvature of the sine-helicoidal channel periodically changes while revolving around the cylinder surface (of radius R) through two opposite curvature extrema (up and down). The radius of curvature of the helicoid is unique and equal to the one of the cylinder (*i.e.* $R_h = R$) when the radius of curvature of the sinusoid R_s is variable and can be obtained by considering the sinusoid flattened on a (X, Y) plane (the flattened cylinder surface):

$$Y(X) = cR\sin\left(bX\frac{2\pi}{L}\right) + pX\ , \tag{1}$$

with $L = 2\pi R$, R the radius of the helicoid, p the vertical step, c a coefficient, $c\,R$ the amplitude of the sinusoid, and b the number of sinusoids per revolution. The relationship between the two radii of curvature depends strongly on the choice of the number of sinusoids per revolution b (quadratic dependence) and the coefficient of the amplitude of the sinusoid c. We introduce two Dean numbers, the first one is related to R_h, the curvature of the cylinder $\mathrm{Dn}_h = \mathrm{Re}\sqrt{a/R_h}$ and the second one is related to R_s, the curvature of the sinusoid $\mathrm{Dn}_s = \mathrm{Re}\sqrt{a/R_s}$ with the Reynolds number $\mathrm{Re} = Ua/\nu$. We can therefore show that $\mathrm{Dn}_h = \mathrm{Re}\sqrt{a/(b^2c\,R_s)} = \mathrm{Dn}_s/(b\sqrt{c})$.

*Corresponding author. E-mail: yves.leguer@univ-pau.fr

RESULTS

The fluid is Newtonian. The flow is steady, incompressible and laminar. The fluid temperature at the wall is chosen with a certain deviation from the fluid temperature at the inlet. The Prandtl number is close to that of water, $\mathrm{Pr} = 10$. The helicoidal and the sine-helicoidal channel lengths are identical. Both mesh sizes are also approximately the same, with 3×10^6 cells. In Fig. 1 (b) are shown the results for $\mathrm{Re} = 400$ for a fluid with a Prandtl number $\mathrm{Pr} = 10$. It is observed that the flow reaches rapidly ($\theta \approx \pi/2$ from the inlet channel) a hydrodynamically fully developed state in the case of the helicoidal configuration. Correlatively, the thermal field reaches a thermally fully developed state, but with a longer length (not shown here). This is not the case for the sine-helicoidal configuration for which the velocity field exhibits a strong periodic modulation along the channel, which results in the creation of a thermal strange eigenmode pattern for the thermal field observed at periodic locations along the channel (4). The results shown in the figure clearly evidence that the sine-helicoidal geometry offers an additional degree of freedom allowing a modulation of the velocity field that makes the fluid mixing more efficient.

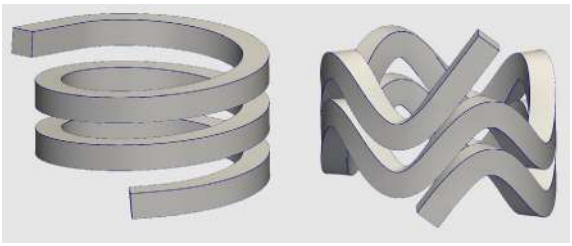

(a)

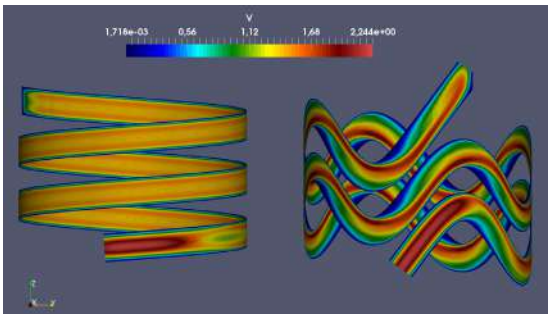

(b)

Figure 1: (a) The helicoidal and sine-helicoidal channel geometries and (b) Module of the velocity field in a cylindrical slice coinciding with the curved plane passing through the middle of the channel section with the Reynolds number $\mathrm{Re} = 400$.

In order to evaluate the heat transfer performance for the two flows, three different mixing indicators are considered, which can be monitored throughout the evolution of the fluid in the channels: mean temperature T_m of the fluid, which represents the energy extracted from the walls, the coefficient of variation CoV of the fluid temperature, which accounts for the level of homogenization of the scalar temperature inside a cross-section and finally the overall Nusselt number which characterizes the parietal heat transfer along the channels. With $\mathrm{Re} = 400$ ($\mathrm{Dn}_h \simeq 253$ and $\mathrm{Dn}_s \simeq 506$) and a constant wall temperature, the sine-helicoidal channel configuration gives always better results in terms of the mean temperature T_m (increase) and its homogenization in the cross section (decrease of CoV) and also for the parietal Nusselt number (increase of 18%). The results are given in table 1.

Table 1: Mean temperature T_m on the cross-section and its coefficient of variation CoV for the helicoidal and sine-helicoidal flows after a quarter turn in the channel ($\theta = \pi/2$). The overall parietal Nusselt number is also given.

Geometry	T_m	CoV	Nu
Helicoidal	0.33	0.958	5.11
Sine-helicoidal	0.364	0.681	6.03
Relative enhancement (%)	10	29	18

We have also conducted a parametric study in order to found the optimal Reynolds number for which the geometry considered here is the most efficient for thermal mixing.

CONCLUSION

The potentiality of the sine-helicoidal flow has been proven to enhance thermal mixing by chaotic advection. This mathematically parameterizable geometry offers potential for the search of optimal geometries for the design of innovative and highly efficient mixers, heat exchangers and reactors.

References

[1] Vashisth S., Kumar V. and Nigam K.D.P. A review on the potential applications of curved geometries in process industry. *Ind. Eng. Chem. Res.* **47(10)**: 3291-3337, 2008.

[2] Jones S. W., Thomas O.M. and Aref H. Chaotic advection by laminar flow in a twisted pipe. *J. Fluid Mech.* **209**: 335-357, 1989.

[3] Le Guer Y. and Peerhossaini H. Order breaking in Dean flow. *Phys. Fluids* **3 (5)**: 1029-1032, 1991.

[4] El Omari K. and Le Guer Y. Alternate rotating walls for thermal chaotic mixing. *Int. J. Heat Mass Trans.* **53**: 123-134, 2010.

STABILITY OF MIXED BAROCLINIC CONVECTION IN A NEARLY SEMI-CYLINDRICAL CAVITY

Abhishek Kumar *[1] and Alban Pothérat[1]
[1] Centre for Fluid and Complex Systems, Coventry University, Coventry CV1 5FB, United Kingdom

Summary In this work, we are seeking the critical conditions for the oscillatory instability that arises in a nearly semi-cylindrical cavity fed in with hot fluid at the upper boundary, bounded by a cold, porous semi-circular boundary at the bottom, and infinitely extended in the third direction. In this geometry, the flow is driven by an unusual type of mixed convection, which is the combination of the buoyancy indirectly caused by the shape of the boundaries and the through-flow. Linear stability analysis and direct numerical simulations are performed, using the spectral element method to identify observable states. Our analysis reveals that the unstable modes are three-dimensional. They show oscillatory or non-oscillatory behaviour depending upon the strength of through-flow. The nature of the bifurcation is determined through Stuart–Landau analysis.

We study the convective patterns that arise in cavities with curved isothermal boundaries and permeated by a through-flow (see Fig. 1(a)). This generic configuration is representative of numerous problems where solid materials are melted, for instance, metallurgical casting processes [1]. In this configuration, despite the stable stratification, the pressure gradient and the temperature gradient form an angle, which is maximum near the upper corners. This results in a buoyancy force that cannot be opposed by pressure and leads to a baroclinic imbalance, which drives the base flow [2].

The non-dimensional equations governing stratified flows under Boussinesq approximation are

$$\frac{\partial \mathbf{u}}{\partial t} + (\mathbf{u}\cdot\nabla)\mathbf{u} + \nabla p = RaPrT\mathbf{e}_y + Pr\nabla^2\mathbf{u}, \quad (1)$$

$$\frac{\partial T}{\partial t} + (\mathbf{u}\cdot\nabla)T = \nabla^2 T, \quad (2)$$

$$\nabla\cdot\mathbf{u} = 0, \quad (3)$$

where $\mathbf{u}$ is the velocity field, p the pressure field, t is the time, and T is the temperature field. The flow is characterised by three non-dimensional parameters, the Rayleigh number Ra (which is the ratio of buoyancy force to dissipative force), the Prandtl number Pr (which is the ratio of kinematic viscosity to thermal diffusivity), and the Reynolds number Re based on the dimensional feeding velocity u_0. In all simulations, we fixed Pr to 0.02, a value typical of liquid metals in continuous casting processes. Equations (1)-(3) are solved using the spectral element method. We impose a free-slip and a no-slip boundary conditions for the velocity field at the upper free surface and at the front wall respectively. For the temperature field, we impose a conducting boundary condition at both the upper free surface and at the front wall. We apply a no-slip boundary condition for the velocity field and an insulating boundary condition for the temperature field at the right and left side- walls. To satisfy the uniform inflow and outflow, we set vertical velocity to $-u_0$ at the upper free surface and the front wall.

We perform three different types of numerical computations using the open source-code NEKTAR++ [3]. First, we obtain a two-dimensional steady base flow using direct numerical simulation (DNS). Second, we perform linear stability analysis (LSA) of three-dimensional perturbations on the two-dimensional base flow by solving the linearised governing equations (see [2] for details). Third, three-dimensional (3D) DNS are performed in weakly sub- and supercritical regimes

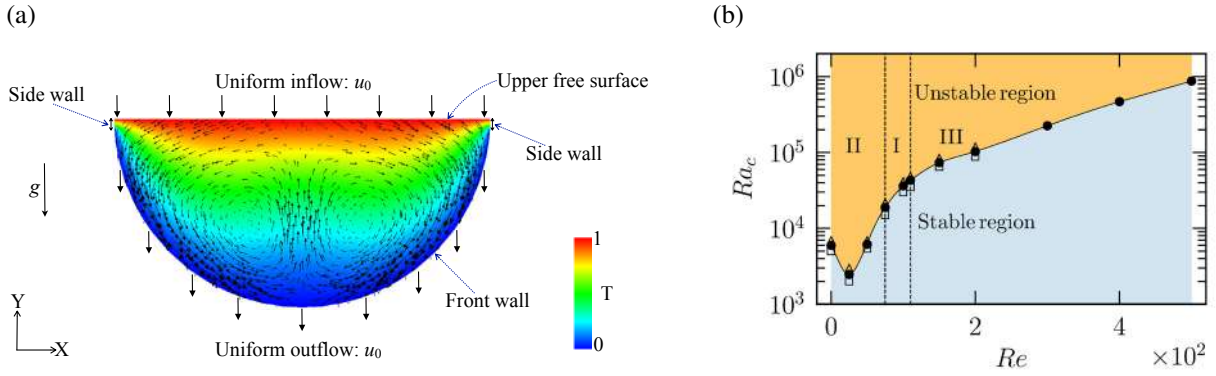

Figure 1: (a) Two-dimensional base flow at $Pr = 0.02$. $Ra = 10^4$, and $Re = 50$. Colours represent the temperature field and arrows represent the velocity vector $\mathbf{u}$. (b) Critical Rayleigh number Ra_c as a function of Re. Blue (orange) regions below (above) the curve represents flow regimes that are linearly stable (unstable) to two or three-dimensional perturbations.

(a) LSA (b) DNS

Figure 2: For $Re = 0$ and $Ra = 7 \times 10^3$: (a) Vorticity perturbation along the homogeneous direction. Out-of-plane vorticity component ζ_z' computed from the linear stability analysis (LSA) at $z = 0$ plane for $k = 6$; (b) ζ_z' computed from the direct numerical simulation (DNS) in the $z = 0$ plane.

to assess the relevance of the linear stability results and to find the nature of the bifurcation by computing the parameters of the Stuart–Landau model [4].

The two-dimensional (2D) base flow is driven by baroclinic imbalance and produces two counter-rotating rolls (see Fig. 1(a) for example). This 2D base flow becomes linearly unstable to three different types of mode, depending on Re at a sufficiently high Rayleigh number. Fig. 1(b) displays the estimate of the critical Rayleigh number Ra_c, at which this transition occurs for a stable state to an unstable state, as a function of Re. When Re is increased from 0, the critical Rayleigh number $Ra_c(Re)$ initially decreases up to $Re = 25$ and then increases. Thus the through-flow has a stabilising influence as soon as the Reynolds number Re exceeds 25. Figure 2 shows the vorticity distributions in a weakly supercritical case for $Re = 0$ and $Ra = 7 \times 10^3$. The snapshots of the topologies of the perturbation from LSA and DNS are presented Fig. 2(a) and Fig. 2(b) respectively, and they match very well. We also find an excellent agreement in the estimate of the growthrate, frequency and the dominant wavenumber between LSA and DNS. Thus the 3D DNS confirm the relevance of the linear stability analysis.

In this study, we observe that the base flow is susceptible to three distinct types of infinitesimal perturbations. For $Re \leq 75$ the most unstable mode corresponds to Branch II as obtained from the linear stability analysis. The three-dimensional DNS show that the most unstable mode is a wave travelling in the $\mathbf{e}_z$ direction. DNS for $100 \leq Re \leq 110$ shows that the instability sets in as a standing oscillation (type I mode), while for $Re \leq 150$ the most unstable mode is non-oscillatory and corresponds to Branch III. Further, from the 3D DNS data, we determined the nature of the bifurcations points through Stuart–Landau analysis for completeness. DNS data revealed that the nature of the bifurcation associated to the three modes varies too. Modes corresponding the branch II and III shows *supercritical* bifurcation, whereas the onset of mode I is *subcritical*.

References

[1] Flood, S. C. & Davidson, P. A. Natural convection in aluminium direct chill cast ingot. *Materials Science and Technology* **10(8)**: 741–752, 1994.

[2] Kumar, A. & Pothérat, A. Mixed baroclinic convection in a cavity. *J. Fluid Mech.* in press, (ArXiv reprint arXiv:1912.00093) 2019.

[3] Cantwell, C. D., Moxey, D., Comerford, A., Bolis, A., Rocco, G., Mengaldo, G., Grazia, D. D., Yakovlev, S., Lombard, J. E., Ekelschot, D., Jordi, B., Xu, H., Mohamied, Y., Eskilsson, C., Nelson, B., Vos, P., Biotto, C., Kirby, R. M. & Sherwin, S. J. Nektar++: An open-source spectral/hp element framework. *Comput. Phys. Commun*, **192**, 205–219, 2015.

[4] Sheard, G. J., Thompson, M. C. & Hourigan, K. From spheres to circular cylinders:non-axisymmetric transitions in the flow past rings *J. Fluid Mech.* **506**, 45–78, 2004.

*Corresponding author. E-mail:ac7600@coventry.ac.uk

EFFECT OF ROTATION ON THERMAL VIBRATIONAL CONVECTION IN HORIZONTAL PLANE LAYER

Victor Kozlov*[1], Kirill Rysin[1], Aleksei Vjatkin[1]
[1]Laboratory of vibrational hydromechanics, Perm State Humanitarian Pedagogical University, Perm, Russia

Summary. We study the thermal vibrational convection of liquid in a rotating horizontal plane layer with isothermal boundaries of different temperatures. Vibrational convection is excited by circular cavity vibrations in the horizontal plane under the stable fluid stratification in the gravity - the layer is heated from above. In the absence of rotation, vibrational convection manifests itself in the form of two-dimensional rolls upon reaching the threshold value of the vibrational parameter. Under rotation, the vibroconvective patterns take the form of cells. With growth of the dimensionless rotation rate, the critical value of the vibrational parameter increases and the size of the vibroconvective cells decreases. The results are analyzed in the space of governing dimensionless parameters, the vibrational and gravitational Rayleigh numbers and dimensionless rotation rate.

EXPERIMENTAL METHODICS AND RESULTS

Thermal vibrational convection is an averaged convection of a non-isothermal fluid excited by the oscillating force fields, for example, the inertial force field in a vibrating cavity [1]. Rotation has a significant effect on vibrational thermal convection, since the Coriolis force affects not only the averaged flows, but also directly acts on the oscillating component of the velocity – the generator of vibrational convection [2]. A special case is represented by force field rotating in the reference frame of the cavity. It could be excited by circular vibrations of the cavity, or by external static fields (in the case of the cavity rotation). Not speaking about the weightlessness conditions, the circular vibrations can cause intense averaged thermal convection even under the conditions of a strong stabilizing effect of other convective mechanisms, for example, in a flat layer heated from above [3].

The objective of this work is to study the effect of rotation on the excitation threshold of vibrational thermal convection in a horizontal plane layer. To exclude the gravitational mechanism of convection, the layer is heated from above, at this the gravitational force plays an exclusively stabilizing role.

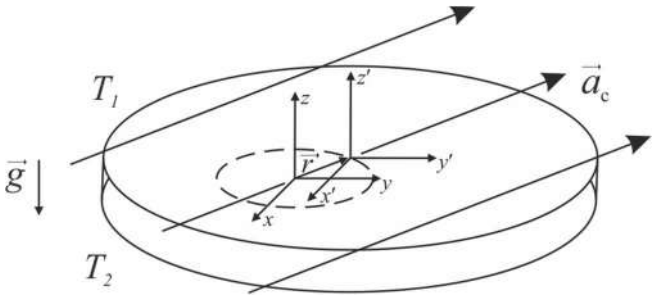

Figure 1. The problem statement

In this case, the thermal vibrational convection is determined by the following dimensionless parameters: the Prandtl number $Pr = \nu/\chi$, the vibrational parameter $R_v = \left(b\Omega_v\beta\Theta h\right)^2/2\nu\chi$, gravitational Rayleigh number $Ra = g\beta\Theta h^3/\nu\chi$ and dimensionless rotation rate $\omega \equiv \Omega h^2/\nu$. Here b and Ω_v – are the amplitude and the radian frequency of circular cavity vibration, which excite the rotating inertial force field $\vec{a}_c$ (Figure 1), Ω – cavity rotation rate, Θ and h – temperature difference and layer thickness, β,χ,ν – coefficients of volume expansion, thermal diffusivity, and kinematic viscosity of fluid. In the experiments the rotation rate was relatively low $\Omega << \Omega_v$.

The experimental procedure is as follows. For a given temperature difference Θ and rotation rate Ω, the frequency of circular vibrations at definite amplitude b monotonically increases. At this, the heat transfer through the layer is measured and the structure of convective flows is studied. For this purpose, the photochromic film is pasted on the lower cold boundary of the working layer, whose color varies depending on temperature. The temperature of the upper boundary of the layer is set by a transparent heat exchanger through which the photographic recording of convective flows is carried out.

The experiments show that with an increase of intensity of the layer vibration, the regular convective structures develop in a threshold way (Fig. 2), which is accompanied by a significant increase in the heat flux. The rotation has a stabilizing effect on the threshold of excitation of vibrational convection.

*Corresponding author. E-mail: kozlov@pspu.ru

The threshold of convective stability increases with a dimensionless frequency (Fig. 3); at various values of Ra the points are consistent with each other. Here R_v^* is the stability threshold at a given Ra in the absence of rotation.

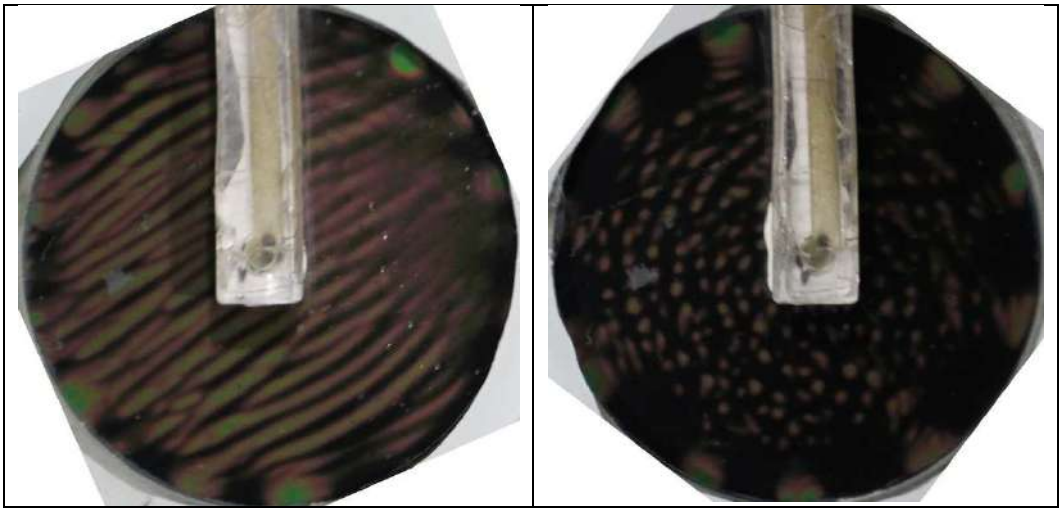

Figure 2. Photos of vibroconvective structures in the supercritical region, $Ra = -1.11 \cdot 10^5$, $R_v = 2.03 \cdot 10^5$: left – in the absence of rotation; right – under rotation, $\omega = 20.2$

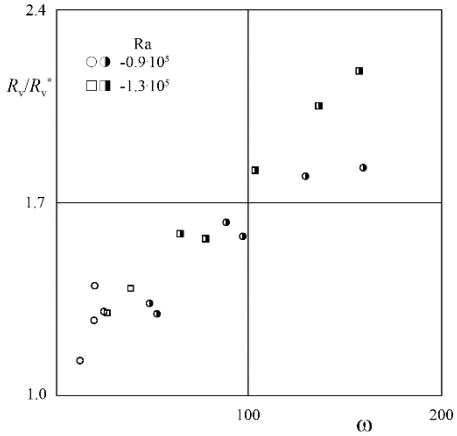

Figure 3. The threshold of vibrational convection excitation at various values of the gravitational Rayleigh number versus the dimensionless rotation rate

CONCLUSIONS

The vibrational thermal convection in a horizontal plane layer rotating around a vertical axis is experimentally investigated. The convection is excited by a high-frequency circular oscillations of the cavity in the horizontal plane. The fluid is stably stratified in the field of gravity – the layer is heated from above. It is found that in the absence of rotation the vibrational convection appears in the form of two-dimensional rolls, the excitation threshold is in good agreement with the theoretical expectation. Experiments demonstrate that under rotation the vibroconvective patterns have the form of cells. With increase of the dimensionless rotation rate, the critical value of the vibrational parameter (at a definite Rayleigh number) grows, and the size of the vibroconvective cells decreases. The effect of rotation on the thermo-vibrational convective mechanism is similar to the effect of rotation on natural convection in a horizontal plane layer.

ACKNOWLEDGEMENT

The work is supported by the Russian Science Foundation (project 18-71-10053).

References

[1] Gershuni G.Z., Lyubimov D.V., Thermal Vibrational Convection. Wiley, NY 1998.
[2] Kozlov V.G. Thermal Vibrational Convection in Rotating Cavities. *J. Fluid Dynamics* **39**: 3–11, 2004.
[3] Kozlov V.G., Rysin K.Y., Vjatkin A.A. Vibroconvective Stability of Liquid in Horizontal Plane Layer Subject to Circular Translational Vibrations. *J. Microgravity Sci. Technol.* 2019.

STOCHASTIC MODELING OF TRANSIENT BOUNDARY LAYERS IN HIGH-RAYLEIGH-NUMBER THERMAL CONVECTION

Marten Klein*[1], Alan R. Kerstein[2], and Heiko Schmidt[1]
[1] Department of Numerical Fluid and Gas Dynamics, Brandenburg University of Technology (BTU Cottbus-Senftenberg, Cottbus, Germany
[2] Consultant, Danville, California, U.S.A.

Summary One-dimensional turbulence (ODT) modeling is used to investigate the boundary layer in high-Rayleigh-number thermal convection for a notionally infinite horizontal layer of fluid. The model formulation distinguishes between turbulent advection, which is modeled by a stochastic process, and deterministic molecular diffusion to capture relevant vertical transport processes (including counter-gradient fluxes). For this study, statistical homogenization is applied to the two horizontal dimensions so that we use ODT as stand-alone tool. We show that the model yields mean and fluctuation temperature profiles that are in several respects consistent with available reference data. Furthermore, the profile of a surrogate for the fluctuation velocity is reminiscent of canonical wall turbulence.

INTRODUCTION

Turbulent thermal convection manifests itself by irregular fluid motions on a range of scales, which are the results of a nonlinear interplay of buoyancy, inertial, and viscous forces as well as thermal diffusion. The fluid-surface coupling is achieved by shallow boundary layers so that it is mandatory to accurately capture their dynamical properties in numerical simulations if one wishes to quantitatively predict, for instance, the heat transfer or the induced flow velocities. For typical control parameters found in applications, the resolution requirements are far too high as direct numerical simulation (DNS) would be possible in the foreseeable future (e.g. [1]). Unfortunately, widely used and economical gradient-diffusion closures for modeling the sub-filter scale dynamics will not be sufficient to be predictive (e.g. [2]). We address this dilemma by utilizing the stochastic one-dimensional turbulence (ODT) model [3] for the simulation of nonstationary boundary layers in thermal convection problems. The objective is to investigate the turbulent boundary layer properties up to very high Rayleigh numbers with a physics-based but feasible numerical model.

In the following we, first, describe the flow configuration and model application. After that, we present some key results for the temperature and velocity statistics including a surrogate analysis. Finally, we close with our main conclusions and an outlook to what will be presented at the conference.

OVERVIEW OF THE FLOW CONFIGURATION AND MODEL FORMULATION

Figure 1(a) shows a sketch of the canonical Rayleigh–Bénard set-up investigated together with the ODT computational domain (ODT line). A Boussinesq fluid is confined between two smooth horizontal isothermal no-slip walls that are located at $z = 0$ and $z = L$. The heated and cooled walls have prescribed temperatures T_{hw} and T_{cw}, respectively, with constant difference $\Delta T = T_{\mathrm{hw}} - T_{\mathrm{cw}}$. The flow properties are governed by the Rayleigh number, $Ra = g\,\beta\,\Delta T\,L^3/(\nu\kappa)$, and Prandtl number $Pr = \nu/\kappa$, where g is the background gravity and β, κ, ν denote the fluid's thermal expansion coefficient, thermal diffusivity, and kinematic viscosity, respectively.

Figure 1(b) shows statistically representative vertical profiles of the temperature, $T(z,t)$, and a horizontal velocity component, $u(z,t)$ (inset). Deterministic molecular diffusion is directly resolved along the ODT line whereas the effects of turbulent advection are modeled by a stochastic process. The computational domain is thus a single vertical line along which flow profiles are evolved in time as described in [3, 4, 5, 6]. In contrast to the original model formulation [3, 4], we incorporate the vector velocity, $\boldsymbol{u} = (u, v, w)^{\mathrm{T}}$ as in [5, 6].

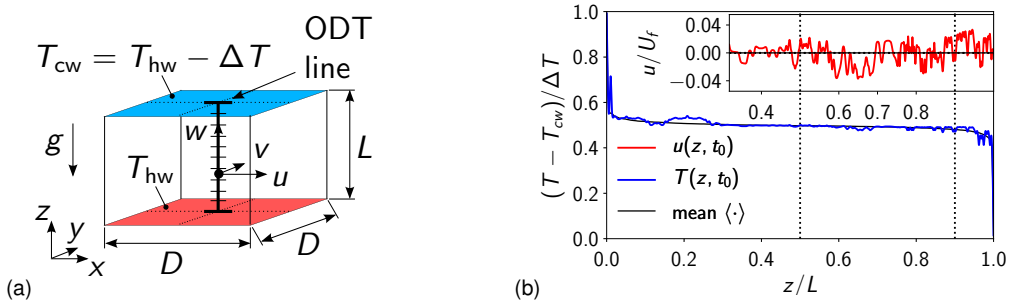

Figure 1: (a) Sketch of the Rayleigh–Bénard configuration investigated. Here, the vertical spacing, L, is fixed, whereas the horizontal dimension, D, is taken to infinity ($D \to \infty$). A stochastic ODT simulation aims to capture the nonstationary vertical transport and is carried out on a one-dimensional computational domain (ODT line). (b) Representative instantaneous and time-averaged vertical profiles of the temperature, T, and a horizontal velocity component, u, for $Ra = 10^{10}$, $Pr = 0.7$ (air). The velocity reference scale is the free-fall velocity, $U_f = \sqrt{g\,\beta\,\Delta T\,L}$.

*Corresponding author. E-mail: marten.klein@b-tu.de.

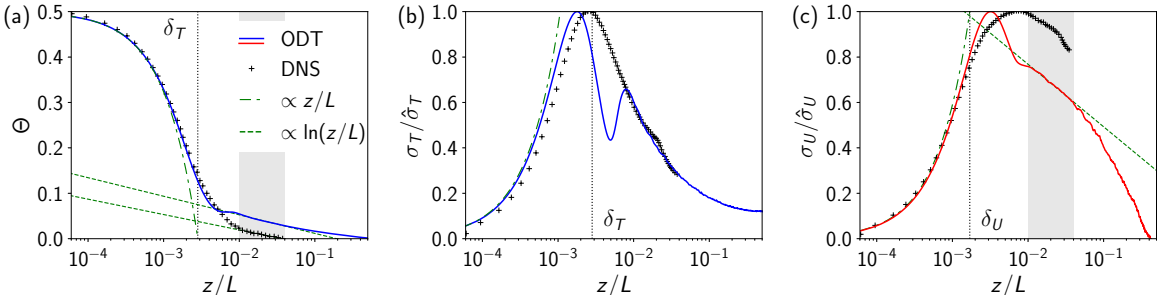

Figure 2: Boundary layer profiles over the heated wall for $Ra = 3 \times 10^{10}$ and $Pr = 0.7$ from ODT together with reference DNS data from [7] for the axis of a cylindrical set-up of aspect ratio one. (a) Normalized mean temperature, Θ; (b) normalized standard deviation of the fluctuation temperature, $\sigma_T/\hat{\sigma}_T$; and (c) normalized standard deviation of the fluctuation horizontal velocity, $\sigma_U/\hat{\sigma}_U$. The cap $\hat{(\cdot)}$ denotes the maximum value. In ODT, a 'mean boundary-layer downstream velocity', $\langle u_\mathrm{d} \rangle$, is used as a surrogate for the fluctuation velocity, σ_U, that is, we take $\langle u_\mathrm{d} \rangle \sim \sigma_U$. Linear and logarithmic regions, as well as the thermal, δ_T, and viscous, δ_U, boundary-layer thicknesses (slope method) are indicated. Logarithmic profiles have been fitted across $10^{-2} \leq z/L \leq 4 \times 10^{-2}$ (shaded region).

KEY RESULTS

Figure 2(a) shows the normalized mean temperature, $\Theta = (\langle T \rangle - T_\mathrm{b})/\Delta T$, where $T_\mathrm{b} = (T_\mathrm{hw} + T_\mathrm{cw})/2$ is the bulk temperature and $\langle \cdot \rangle$ a conventional temporal average. ODT reproduces the near-wall structure, but Θ departs from the reference data towards the bulk. It is remarkable that the present ODT results suggest the onset of a logarithmic region, $\Theta(z) = A \ln(z/L) + B$, which is in general consistent with [8]. The ODT solution exhibits approximately the same prefactor, A, as the reference data but a larger additive constant, B, due to the earlier departure from the sublayer.

Next, figure 2(b) shows profiles of the standard deviation of the fluctuation temperature, $\sigma_T = \sqrt{\langle T^2 \rangle - \langle T \rangle^2}$. Reasonable agreement between ODT and the reference data is observed close to and far from the wall. However, an unphysical bimodal structure can be discerned around $z \approx \delta_T$, which is precisely where Θ departs from the linear sublayer. This structure is presumably of the same origin as a similar one in the ODT fluctuation velocity observed in turbulent channels [5]. Here, the responsible modeling error manifests itself primarily in the driving Boussinesq temperature.

At last, we consider a surrogate analysis for the fluctuation velocity since ODT exhibits zero-mean velocity (see figure 1(b)). This differs from available reference data, which exhibits a large-scale circulation (e.g. [7]). We therefore consider a synthetic 'boundary-layer downstream velocity', $u_\mathrm{d}(z,t) = \boldsymbol{u}(z,t) \cdot \boldsymbol{e}_\mathrm{d}(t) \geq 0$, which is a projection of the vector velocity, $\boldsymbol{u}$, on an instantaneous 'boundary-layer downstream direction', $\boldsymbol{e}_\mathrm{d} = [\boldsymbol{e}_x(\partial_z u)_\mathrm{hw} + \boldsymbol{e}_y(\partial_z v)_\mathrm{hw}]/[(\partial_z u)^2_\mathrm{hw} + (\partial_z v)^2_\mathrm{hw}]^{1/2}$. The temporal mean, $\langle u_\mathrm{d} \rangle$, of instantaneous positive semi-definite $u_\mathrm{d}(z,t)$ profiles is used as surrogate for the positive semi-definite horizontal fluctuation velocity, $\sigma_U = \sqrt{\langle U^2 \rangle - \langle U \rangle^2}$, where $U = \sqrt{u^2 + v^2}|_\mathrm{axis}$ is evaluated at the axis of a cylindrical set-up [7]. Figure 2(c) shows profiles of the reference horizontal fluctuation velocity, σ_U, in comparison to the ODT surrogate, $\langle u_\mathrm{d} \rangle$. There is good qualitative agreement between both quantities and there is no bimodal structure in $\langle u_\mathrm{d} \rangle$ obtained by ODT. Furthermore, the profile of $\langle u_\mathrm{d} \rangle$ is reminiscent of the streamwise fluctuation velocity in canonical wall turbulence (e.g. [9]). Note that the profile seems to exhibit the onset of a logarithmic region but the vertical extend is small which suggests further analysis at higher Ra numbers.

CONCLUDING REMARKS AND OUTLOOK

The capabilities for economical but also reasonably accurate and robust modeling of transient boundary layers in turbulent thermal convection have been addressed by utilizing the stochastic one-dimensional turbulence (ODT) model. We have shown that point-wise temperature and velocity statistics (at least up to second order) exhibit reasonable agreement with available reference data. We have furthermore suggested a 'boundary-layer downstream velocity' surrogate for the fluctuation velocity. Vertical profiles of this surrogate are reminiscent of the streamwise fluctuation velocity in wall turbulence which is currently further investigated.

In the talk, we will outline the model formulation. After that, we will discuss the boundary-layer properties. At last, we will address the Ra number dependence and scaling properties by making use of the model's predictive capabilities.

References

[1] Schumacher J., Bandaru V., Pandey A., Scheel J. D. *Phys. Rev. Fluids* **1**: 084402, 2016.
[2] Deardorff J. W. *J. Atmos. Sci.* **23**: 503-506, 1966.
[3] Kerstein A. R. *J. Fluid Mech.* **392**: 277-334, 1999.
[4] Wunsch S., Kerstein A. R. *J. Fluid Mech.* **528**: 173-205, 2005.
[5] Lignell D. O., Kerstein A. R., Sun G., Monson E. I. *Theor. Comp. Fluid Dyn.* **27**(3): 273-295, 2013.
[6] Gonzalez-Juez E. D., Kerstein A. R., Lignell D. O. *Geophys. Astro. Fluid Dyn.* **107**(5): 506-525, 2013.
[7] Li L., Shi N., du Puits R., Resagk C., Schumacher J., Thess A. *Phys. Rev. E* **86**: 026315, 2012.
[8] Ahlers G., Bodenschatz E., Funfschilling D., Grossmann S., He X., Lohse D., Stevens R. J. A. M., Verzicco R. *Phys. Rev. Lett.* **109**: 114501, 2012.
[9] Marusic I., Kunkel G. J. *Phys. Fluids* **15**: 2461-2464, 2003.

EXPERIMENTS ON FLOWS IN A CHANNEL WITH SURFACE CORRUGATION AND PERIODIC HEATING

Ayumu Inasawa*[1], Kanato Hara[1], and Jerzy M. Floryan [2]
[1] Department of Aeronautics and Astronautics, Tokyo Metropolitan University, Hino, Tokyo, Japan
[2] Department of Mechanical and Materials Engineering, University of Western Ontario, London, ON, Canada

Summary Flows in a channel with surface corrugations and periodic heating were examined experimentally to demonstrate the formation of the thermal drift phenomenon. The lower wall had a sinusoidal surface corrugation with an amplitude of 10% of the channel half-width and a non-dimensional wavenumber of 1. This wall was exposed to periodic heating with the same wave number. The heating and groove patterns were misaligned with a phase difference of $\pm\pi/2$. The upper smooth wall was kept isothermal with its temperature equal to the mean temperature of the lower wall. The results show that a pair of counter-rotating stationary rolls created by the periodic heating lead to the formation of a net horizontal flow whose direction is dictated by the phase difference. The volumetric flow rate carried by this flow increases monotonically with the heating intensity.

INTRODUCTION

Thermal convection is a canonical problem in fluid dynamics. In general, convection is driven either by vertical temperature gradients, assuming that the critical stability conditions are met, or by horizontal temperature gradients, which lead to horizontal density variations and convection regardless of the magnitude of these gradients. A representative example of the former is the classical Rayleigh-Bénard (RB) convection, and an example of the latter is horizontal convection [1]. Recent theoretical analyses of RB convection at subcritical Rayleigh numbers have revealed that stationary convection is possible between isothermal walls with geometrical surface irregularities [2]. A systematic way to create horizontal convection involves the use of spatially patterned heating [3], which generates stationary buoyancy-driven rolls over a wide range of Rayleigh numbers, offering the potential for the development of novel drag-reducing methodologies [3-4]. Additional flow phenomena were predicted analytically when either a proper combination of patterns of heating were used at the upper and lower walls [5] or a combination of surface corrugation and patterned heating were employed [6], both of which were able either to create net horizontal forces between the bounding walls or to induce net horizontal flow. This effect is referred to as thermal drift [5-6]. A significant advantage of using patterned heating for flow control is that it does not require placing mechanical devices in the flow. Although the characteristics of such flows were determined analytically, no experimental observations are available to confirm their existence. In the present study, flows in a channel with periodic surface corrugations and periodic heating are examined experimentally to confirm the existence of net horizontal flows driven by the thermal drift effect. This problem can be viewed as a pattern interaction problem with the global flow created through an interaction between the properly placed heating and topography patterns.

EXPERIMENTAL SETUP

The experiment was conducted in a horizontal rectangular open conduit whose width, height and length were 400mm, 20mm (=2h) and 749mm, respectively, giving an aspect ratio (the ratio of width to height) of 20 (Fig. 1a). The lower wall with a sinusoidal surface corrugation with amplitude of 0.1h was heated periodically by supplying hot/cold water to the embedded aluminium pipes (see Fig. 1b), while the upper smooth wall was kept isothermal at T_0=293K, by supplying water with a fixed temperature to embedded pipes. The spatial distribution of the grooves and the heating were characterized by the same wavelength of λ=62.8mm, giving a non-dimensional wavenumber of $\alpha=2\pi h/\lambda = 1$. The phase difference between the heating and corrugation patterns could be changed from $\Omega = +\pi/2$ to $\Omega = -\pi/2$. The periodic Rayleigh number Ra_p measuring the intensity of the periodic heating was defined as $Ra_p=g\beta h^3\Delta T_p/(\nu\kappa)$, where ΔT_p denotes the peak-to-peak amplitude of the absolute temperature along the lower wall, g stands for the gravitational acceleration, β is the thermal expansion coefficient and κ denotes thermal diffusivity. The experiments were carried out for Ra_p=750-3000. Properties of the fluid (air) at the upper wall temperature were used as the reference quantities. Special plates were installed at the exits of the conduit to eliminate thermal plumes. A particle image velocimetry (PIV) system (Dantec) consisting of a double-pulsed Nd:Yag laser and a CCD camera of 2048 × 2048 pixels was used to obtain instantaneous velocity fields. The surface temperature was measured using a combination of thermography and thermocouples.

RESULTS

Figures 2(a) and (b) display the time-averaged flow field expressed in terms of a map of the horizontal velocity U and streamlines for Ra_p=1500. In the case of $\Omega=\pi/2$, shown in Fig. 2(a), pairs of counter-rotating stationary rolls whose upward and downward motions occur above the hot spots ($x/h \approx 39, 45$) and cold spots ($x/h \approx 36, 42$), respectively, were formed and aligned periodically in x. The upward motion was much stronger than the downward motion, resulting in the centers of the rolls being attracted to the upwash zone. A stream tube meandering between the convection rolls and carrying net horizontal mass flow is clearly visible. The direction of flow in this stream tube is such that the fluid passing above the

*Corresponding author. E-mail: ainasawa@tmu.ac.jp

hot spots moves upwards while it is directed downwards above the cold spots on the corrugated surface. The flow direction is reversed when the phase difference between the heating and the grooves is shifted by π, as shown in Fig. 2(b). Figure 3 illustrates the Rayleigh number dependency of the volumetric flow rate of the net horizontal flow, calculated by integrating the horizontal velocity profile at the corrugation peak (x/h=37.7). It can be seen that the flow rate increases monotonically with the heating intensity up to Ra_p=3000 regardless of the phase difference between the heating and corrugation patterns, indicating that a proper combination of corrugation and heating patterns can drive net flow in either of the horizontal directions.

CONCLUSIONS AND OUTLOOK

Flows in a channel with surface corrugations and periodic heating were examined experimentally. The results show that periodic heating creates pairs of counter-rotating stationary rolls which generate a net horizontal flow, thus confirming the existence of the theoretically predicted thermal drift. The direction of the net horizontal flow is reversed when the phase of the heating is shifted by π with respect to the corrugation. The volumetric flow rate carried by this flow is found to increase monotonically with the heating intensity. In the presentation, properties of the flow fields will be discussed and compared with the theoretical predictions.

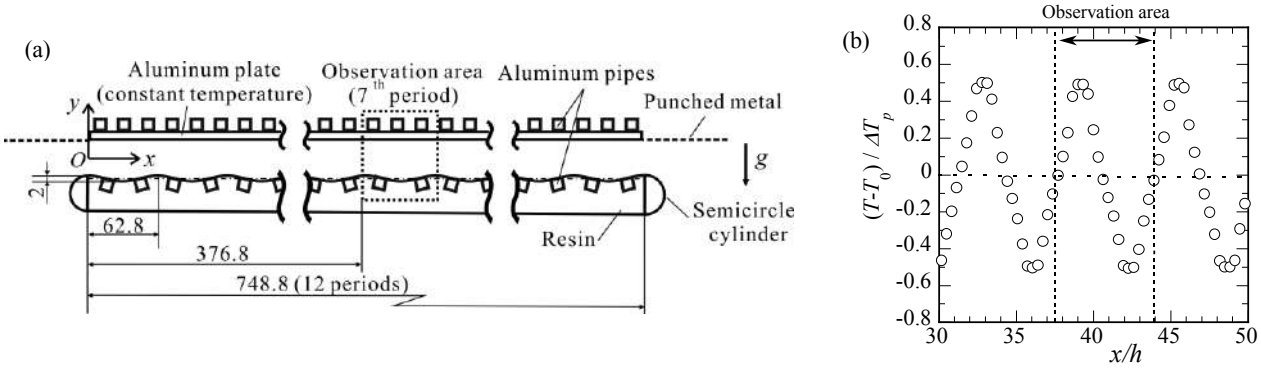

Figure 1. (a) Experimental setup (dimensions in mm) and (b) variation of the bottom surface temperature (Ra_p=1500, Ω=π/2).

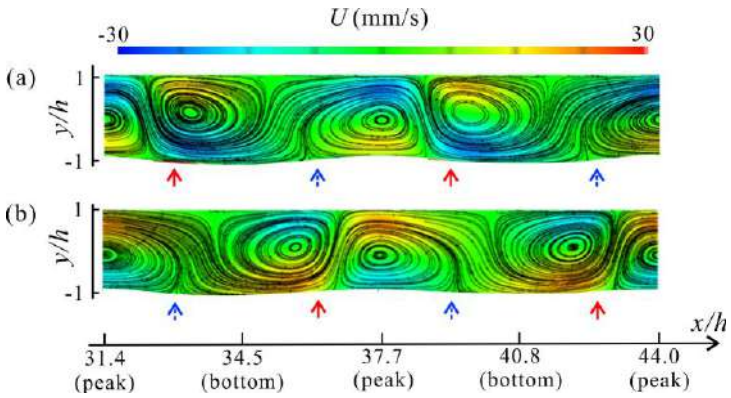

Figure 2. Flow patterns created by convection for Ra_p=1500. The red /blue arrows identify locations of the hot/cold spots at the lower wall. (a) Ω=π/2, (b) Ω=-π/2. Locations of the corrugation peaks/bottoms are marked at the bottom of the figure.

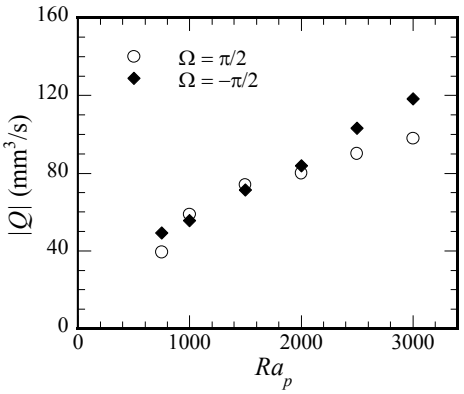

Figure 3. Variations of the volumetric flow rate Q created by the thermal drift as a function of Ra_p.

References

[1] Hughes, G.O., and Griffiths, R.W. Horizontal convection. *Annu. Rev. Fluid Mech.* **40**: 185–208, 2008. ,
[2] Hossain, M.Z., and Floryan, J.M. Instabilities of natural convection in a periodically heated layer. *J. Fluid Mech.* **733**: 33-67, 2013.
[3] Hossain, M.Z., Floryan, D., and Floryan, J.M. Drag reduction due to spatial thermal modulations, *J. Fluid Mech.* **713**: 398-419, 2012.
[4] Inasawa, A., Taneda, K., and Floryan, J.M. Experiments on flows in channels with spatially distributed heating, *J. Fluid Mech.* **872**: 177-197, 2019.
[5] Hossain, M., and Floryan, J.M. Natural convection in a horizontal fluid layer periodically heated from above and below, *Phys. Rev. E.* **92**: 02301, 2015.
[6] Abtahi, A., and Floryan, J.M. Natural convection and thermal drift, *J. Fluid Mech.* **826**: 553-582, 2017.

DENDRITE PREVENTION IN BATERRIES USING FLOW

Oles Dubrovski[1] and Ofer Manor *[2]
[1] Department of Mathematics, Technion – Israel Institute of Technology, Haifa, Israel
[2] Department of Chemical Engineering, Technion – Israel Institute of Technology, Haifa, Israel

Summary: We study the inhibiting effect of flow on dendritic growth. Our system is a flow battery chamber recharging an entering electrolyte with concentration C_{Li} and at velocity U_0. The reaction takes place at the cathode, where an initial sinusoidal distribution of dendrites is present. A concentration boundary layer develops at the surface of the cathode. We solve asymptotically the governing equations, coupled with the limiting current boundary condition. Our results indicate a smoothing effect that the flow has on the flux of ions to the dendrites, which inhibits dendritic growth.

INTRODUCTION

Dendrites pose a significant safety concern for commercial batteries. Vast research is taking place today to prevent the formation of dendrites and especially to render Lithium-metal batteries chargeable. Usually, the focus is on using new materials for electrodes and adopting new kinds of electrolytes [1,2]. Theoretical studies have been considering only the surface tension and deformation stresses in the solid cathode as growth-inhibiting mechanisms [3,4,5]. However, it has been known for a long time that flow in electrochemical cells may inhibit the growth of dendrites [6,7]. We develop a theoretical model for the description of dendritic growth under the influence of flow in a concentration boundary layer, where we employ the limiting current conditions to account for the ion mass flux between the electrodes in the electrochemical cell.

THEORY

The system configuration is given in Figure 1. We consider a recharge process of a flow battery. An electrolyte containing lithium ions with concentration C_{Li} enters at velocity U_0 into a battery chamber containing an anode and a cathode. On the cathode lithium ions deposit according to the limiting current conditions. The punctured line indicates a sinusoidal deformation of the cathode characterized by the wavenumber k due to an initial presence of dendrites along the surface. The Reynolds number is small, and the Peclet number is large. Therefore a concentration boundary layer develops at the surface of the cathode with the leading-edge region at the forefront. Our model includes an asymptotic analysis of the ion concentration in the bulk electrolyte, the leading edge of the electrode, and the boundary layer regions.

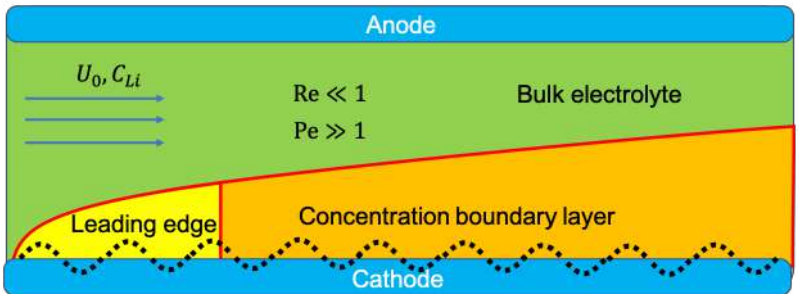

Figure 1. **Dendritic growth in a flow battery system configuration.** The electrolyte enters the chamber with concentration C_{Li} and at velocity U_0. A leading edge and concentration boundary layer regions develop at the surface of the reacting cathode. The initial sinusoidal dendrite distribution on the cathode is depicted by the dashed line.

RESULTS AND CONCLUSIONS

The initial presence of the dendrites serves as a hotspot for the depositing lithium ions, which without any inhibiting mechanism, will grow indefinitely. Our results indicate that the flow has a smoothing effect on the lithium-ion flux distribution along the cathode, essentially canceling the dendritic growth hotspots at large enough k. The smoothing effect originates from the advective transport of ions in the electrolyte.

*Corresponding author. E-mail: manoro@technion.ac.il

References

[1] Wang X., Zeng W., Hong L., Xu W., Yang H., Wang F., Duan H., Tang M., Jiang H.
Stress-driven lithium dendrite growth mechanism and dendrite mitigation by electroplating on soft substrates. Nature Energy **3**: 227-235, 2003.

[2] Barai P., Higa K., Srinivasan V.. Lithium dendrite growth mechanisms in polymer electrolytes and prevention strategies
Phys.Chem.Chem.Phys **19**: 20493-20505, 2017.

[3] Monroe C., Newman J. Dendrite Growth in Lithium/Polymer Systems. *J. Elec. Soc.***150**: A1377-A1384, 2003.

[4] Monroe C., Newman J. The Impact of Elastic Deformation on Deposition Kinetics at Lithium/Polymer Interfaces. *J. Elec. Soc.* **152**: A396-A404, 2005.

[5] Sundstrom L.G., Bark F.H. On Morphological Instability During Electrodeposition with a Stagnant Binary Electrolyte.
Electrochimica Acta. **5**: 599-614, 1995.

[6] Jorne J., Lii Y-J, Yee K.E. Suppression of dendrites and roughness during electrodeposition by impinging flow. J. Elec. Soc. **134**: 1399-1402, 1987.

[7] Zhang W., Stone H.A., Sherwood J.D. Mass transfer at a microelectrode in channel flow J. Phys. Chem. **100**: 9462-9464, 1996.

CONVECTION AND ELECTROVORTEX FLOW IN LIQUID METAL BATTERIES

Jonathan S. Cheng *[1], Ibrahim Mohammed[1], Gerrit M. Horstmann[2], and Douglas H. Kelley[1]
[1] Department of Mechanical Engineering, University of Rochester, Rochester, USA
[2] Helmholtz-Zentrum Dresden-Rossendorf, Dresden, Germany

Summary We study thermal convection and electrovortex flow (EVF) in series of liquid gallium laboratory experiments. These two forces notably interact in liquid metal batteries (LMBs), a promising technology suited for grid-scale energy storage: convection occurs due to the presence of internal heating while EVF is driven by diverging current densities. Though these forces have potential to both help and hinder the batteries' operation, flow structures and scaling properties in this context remain largely unknown. To this end, we present a suite of velocity measurements which reveal the dominant flow modes and typical flow speeds over broad ranges of convective forcing, EVF forcing, and container shape. These data are compared to predictions from both the EVF and convection literature.

Introduction

As renewable energy sources such as wind and solar power become increasingly relevant, so too do the unique challenges associated with their implementation. Some of these sources are intermittent and unpredictable, and therefore require our electrical grids to be capable of storing large amounts of energy. A variety of technologies are in development to address this challenge. Among them, liquid metal batteries (LMBs) – galvanic cells where the cathode, anode, and electrolyte material are each composed of a different fluid (Fig. 1a) – stand out due to their potential to be remarkably cost-effective.

The LMB system is inherently stably stratified, with density gradients naturally separating each fluid layer. However, the combination of heat production and electromagnetic forces caused by the flow of ions ensures that vigorous flows manifest [4]. Two of the most prominent flows that occur within a single layer of an LMB are thermal convection and electrovortex flow (EVF). Convection is caused by heating of the electrolyte layer during operation, which creates significant adverse temperature gradients. EVF emerges when a divergent current density interacts with its own induced magnetic field [2], and occurs in liquid metal battery setups due to the size difference between positive and negative current collectors.

These flows have a host of effects on the viability of an LMB, from enhancing mixing within the cathode or anode layer (leading to even greater efficiency), to disrupting the middle electrolyte layer (leading to direct contact between cathode and anode material and failure of the battery). However, while significant literatures exist for each effect independently, their interaction within the LMB context remains largely unexplored. In this study, we tackle this issue using a large experimental survey of convection and EVF interactions, in a broad range of forcings and geometries relevant to liquid metal batteries.

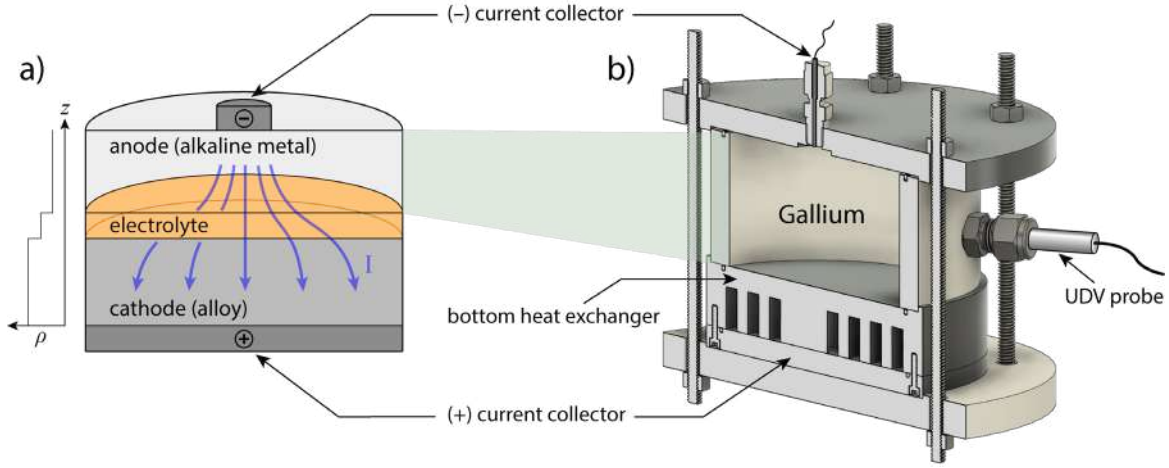

Figure 1: a) Diagram of a liquid metal battery cell modified from [4], showing the current density during the discharge process, and b) Cross section view of the design drawing of the experimental setup. Current collectors connect to a power supply and induce EVF while heat exchangers connect to thermal baths to induce convection. The top heat exchanger (not pictured) is a double wound copper spiral attached above the gallium layer.

*Corresponding author. E-mail: j.s.cheng@rochester.edu.

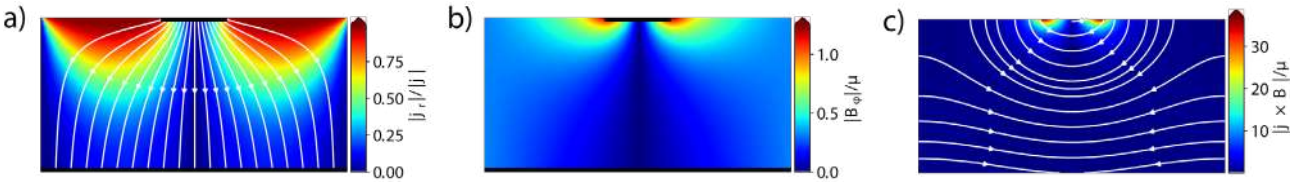

Figure 2: Analytic solutions for a) the current density, b) the magnetic field, and c) the Lorentz force distribution for an aspect ratio $\Gamma = 2$ layer.

Experiment

The experimental apparatus (Fig. 1b) is a closed cylindrical cell of fixed diameter $D = 12$ cm and interchangeable heights ranging from $H = 3$ cm (aspect ratio $\Gamma = D/H = 4$) to $H = 12$ cm ($\Gamma = 1$). Previous studies and linear theory predict that the onset modes for both EVF and convection are dependent on container shape, a somewhat free parameter in LMBs. The working fluid is liquid gallium, which has physical properties resembling LMB materials but melts near room temperature. We induce convection with cold and hot heat exchangers attached to the top and bottom boundaries of the cell, respectively. We induce EVF by passing an axisymmetric vertical current through the system; the top current collector is much narrower than the bottom, leading to a strong divergence in the current density. The flexibility of this setup allows us to access broad ranges of the governing parameters: the Rayleigh number Ra, describing the strength of convective forcing, reaches values as high as $\sim 10^7$ in our device. The EVF parameter S, likewise describing the EVF forcing, reaches values as high as $\sim 10^5$. In addition, we are able to impart a stabilizing temperature gradient to the system. This occurs in the cathode of the LMB during operation, and the combination of stable density stratification and EVF is an important phenomenon that has not been previously addressed.

Data are acquired using several ultrasonic doppler velocimetry probes positioned at different locations in the sidewall and ceiling of the cell. The probes measure flow velocities along the line of the emitted beam, in the direction of said beam. By examining measurements from multiple probes, flow structures can be deduced.

Phase diagram

We present our velocity data in the form of phase diagrams describing the transitions between different dominant flow structures and velocity scalings, as the experiment scans over ranges of convective forcing (Ra), EVF (S), and aspect ratio (Γ). Linear theory is used to predict the onset modes of EVF in different tank dimensions (see Fig. 2). Combining this with previous theoretical arguments and experimental/numerical results, an array of predictions for exclusively convection or exclusively EVF are plotted in the (Ra, S, Γ) phase space. The predictions serve as a benchmark for our experiments.

In most cylindrical geometries, convection leads to a poloidal, torus-shaped roll with the upward flow at the central axis. EVF is predicted to produce a similar structure, but with downward flow at the central axis instead. In the presence of an external B-field (very likely to be present in practical LMB arrays), EVF manifests as a container-scale horizontal swirling flow beyond some S. These different modes inevitably interfere with each other depending on the degree of each forcing, leading to changes in their onset values, velocities and overall structure in time and space. The analysis of [3], though in a different geometry and applied to vacuum arc remelting, predicts the crossover between convection-dominated and EVF-dominated flows. Ashour *et al.* [1] make a similar but more reduced prediction in the cylindrical geometry, and both analyses are incorporated in the phase diagram for comparison with experimental results.

Conclusion

We employ a novel experimental device to explore the flow regimes driven by convection and EVF in liquid gallium, laying the groundwork for future LMB design. Velocities measured via ultrasonic doppler velocimetry are used to produce a phase diagram which predicts the types of flows that emerge from convection and EVF for a given LMB setup. In an actual three-layer system, these flows will have a significant effect on the efficiency and viability of the battery.

References

[1] Rakan F Ashour, Douglas H Kelley, Alejandro Salas, Marco Starace, Norbert Weber, and Tom Weier. Competing forces in liquid metal electrodes and batteries. *J. Power Sources*, 378:301–310, 2018.

[2] V Bojarevičs, Ya Freibergs, E I Shilova, and E V Shcherbinin. *Electrically Induced Vortical Flows*. Kluwer Academic Publishers, Dordrecht, The Netherlands, 1989.

[3] P. A. Davidson. *An Introduction to Magnetohydrodynamics*. Cambridge Texts in Applied Mathematics, first edition, 2001.

[4] Douglas H Kelley and Tom Weier. Fluid mechanics of liquid metal batteries. *Appl. Mech. Rev.*, 70(2):020801, 2018.

LINEAR STABILITY OF MIXED CONVECTION UNDER SORET AND VISCOUS HEATING EFFECTS

K. Ali amar *, S. C. Hirata, and M. N. Ouarzazi
Univ. Lille, EA 7512 - Unité de Mécanique de Lille - Joseph Boussinesq (UML), F-59000 Lille, France

Summary The aim of this work is to investigate analytically and numerically the Soret effect on the linear stability of mixed convection due to viscous dissipation in a horizontal channel of infinite lateral extention filled with a binary fluid mixture. No external temperature difference is imposed on the layer. Thus, the sole cause of thermal instability is the flow rate, through the volumetric heating induced by the viscous dissipation. A linear stability analysis suggests that the most unstable perturbations are in the form of longitudinal rolls. Positive as well as negative separation ratios are analyzed which revealed that for $\psi > 0$ the system undergoes a "Pitchfork" bifurcation, while for $\psi < 0$ the system loses its stability via a "Hopf" bifurcation. Afterwards, the thresholds for the appearance of the monocellular flow are derived analytically using the parallel flow approximation.

INTRODUCTION

In shear flows, the heat generated by viscous friction between adjacent fluid layers may produce a local temperature increase, which can lead to unstable temperature gradients within the fluid. In the last decades, a series of papers proved that viscous heating (or viscous dissipation) effects should not be neglected when considering the stability of shear flows of highly viscous fluids [1].

The aim of the present paper is to extend the linear analysis of Barletta et al. [2] to the case of a binary fluid. As it is well-known, a temperature gradient applied to a binary fluid mixture induces a mass fraction gradient. This phenomenon is known as thermodiffusion, or the Soret effect. We recall that the Soret separation ratio ψ, being proportional to the strength of the Soret effect, can be either positive or negative. In the case of a positive ψ, the lighter component of the fluid mixture is driven into the direction of higher temperatures, thus further enhancing the density gradient. For negative ψ, the opposite situation occurs.

In this work, we investigate the linear stability of the Poiseuille flow of binary fluids by taking into account the effects of viscous heating and thermodiffusion. As in [2, 3], no external temperature difference is prescribed over the layer: the upper boundary is considered isothermal and the lower one is adiabatic. Positive as well as negative separation ratios are analyzed. Differently from [4], in our case the Squire transformation cannot be used. Therefore, the full three-dimensional linear eigenvalue problem is solved in order to determine the thresholds for the onset of the different convective structures (transverse, oblique, or longitudinal modes).

RESULTS AND DISCUSSION

A linear stability analysis has been carried out by solving numerically the eigenvalue problem for arbitrarily oriented convection rolls. The influence of the Prandtl number, Pr, the Lewis number, Le, and the inclination angle of the rolls, ϕ, on the neutral stability condition have been investigated. The neutral stability curves have been represented by tracing the functional dependence of $\Lambda = GePe^2$ on the wave number k of the normal-mode disturbance, where the Péclet Pe and Gebhart Ge numbers can be seen as measures of the main flow intensity and viscous dissipation effects, respectively. The most relevant results obtained are described in the following.

(i) The minimum of the neutral stability curve $\Lambda(k)$, i.e. the critical point (k_c, Λ_c), is at its lowest when the inclination angle of the wave-like disturbance roll is $\phi = \dfrac{\pi}{2}$, as can be seen in figure 1. This means that the most unstable disturbances are the longitudinal rolls and justifies the use of Λ as an appropriate parameter for describing the transition to the instability;

(ii) Frames (a)–(c) of figure 2 shows the critical values of Λ_c, k_c and ω_c for the onset of longitudinal rolls versus the separation ratio ψ . The behaviour displayed in figure 2 reveals that for positive separation ratios, we observe the appearance of a stationary convective structure characterized by a zero frequency $\omega = 0$. The critical wave number vanishes when ψ exceeds a particular value ψ_{mono}, thereby indicating that the primary instability is structured in the form of a single-cell flow (monocellular flow). For negative separation ratios, the flow crosses a new bifurcation threshold called Hopf bifurcation at ψ^*, i.e. the codimension-2 bifurcation point where two modes becomes simultaniously convectively unstable, constituting a new convective state macroscopically different from the previous one, in the form of oscillating rolls with finite amplitudes and smaller wavelengths to increase the evacuation of the inherent heat of the system;

(iii) By using the parallel flow approximation along the y-direction for $\psi > \psi_{mono}$, the critical value of the onset of convection is readily obtained as $\Lambda_c = \dfrac{120}{Le\ \psi}$.

Finally, based on the obtained results we propose a protocol to estimate the Soret coefficient.

*K. Ali amar. E-mail: katia.ali-amar@univ-lille.fr.

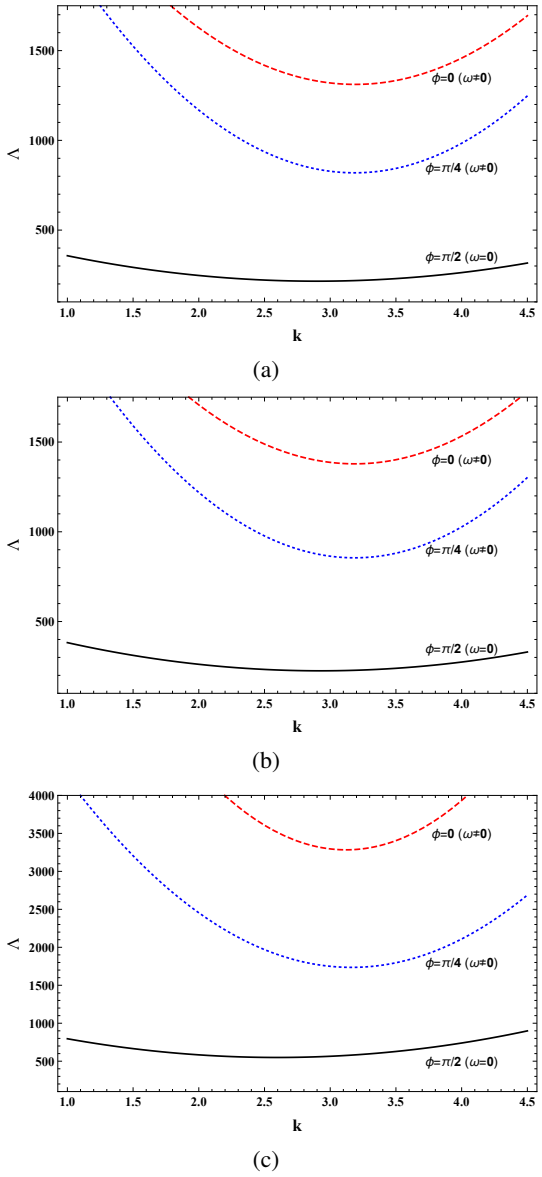

Figure 1: Neutral stability curves $\Lambda = \Lambda(k)$ at $Le = 1$ and $Pr = 50$ for $\psi = 0.01$ (a), $\psi = -0.01$ (b) and $\psi = -0.3$ (c).

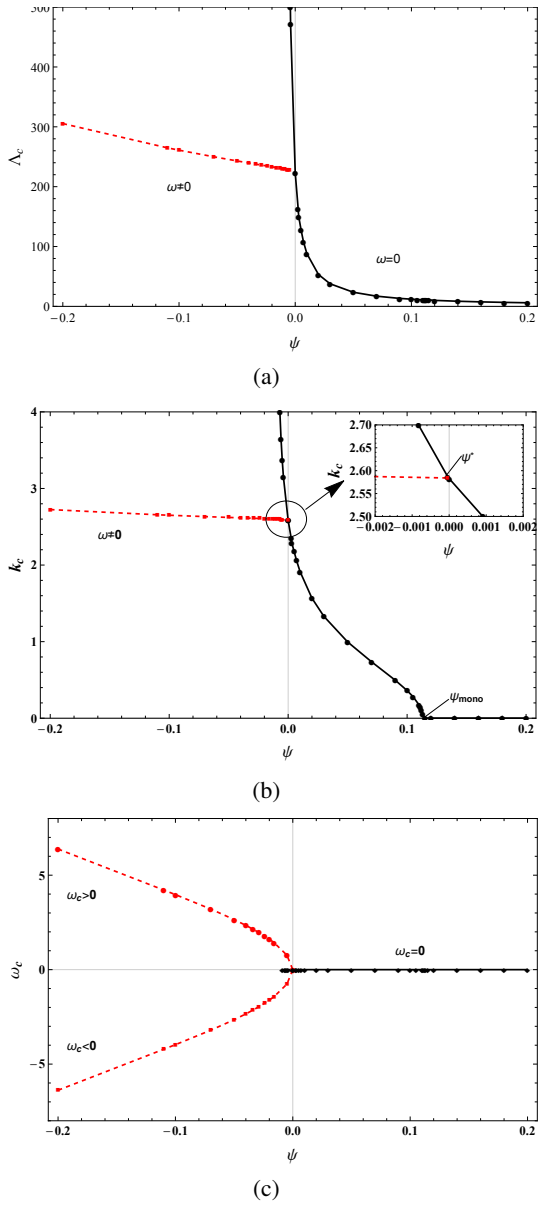

Figure 2: Critical value of Λ_c (a), k_c (b) and ω_c (c) versus ψ for $Le = 100$ and $Pr = 10$, relative to the onset of longitudinal rolls: stationary mode $\omega = 0$ (solid line), oscillatory mode $\omega \neq 0$ (dashed line).

References

[1] Barletta A. On the thermal instability induced by viscous dissipation. *International Journal of Thermal Sciences* **88**: 238-247, 2015.

[2] Barletta A., Celli M., and Nield D.A. On the onset of dissipation thermal instability for the Poiseuille flow of a highly viscous fluid in a horizontal channel. *Journal of Fluid Mechanics* **681**: 499-514, 2011.

[3] Requilé Y., Hirata S., Ouarzazi M. N., and Barletta A. Weakly nonlinear analysis of viscous dissipation thermal instability in plan Poiseuille and Couette flows. *Journal of Fluid Mechanics* **886**: A26, 2020.

[4] Hu J., Ben Hadid H., and Henry D. Linear stability analysis of Poiseuille-Rayleigh-Benard flows in binary fluids with Soret effect. *Physics of Fluids* **19**: 1-17, 2007.

OBLIQUE IMPINGING JET MECHANISM IN TURBULENT RAYLEIGH-B ENARD CONVECTION

Wen-Feng Zhou*[1,2], Jun Chen[2], Yan-Chao Hu[1], and Yan-Guang Yang[3]
[1] Hypervelocity Aerodynamics Institute, China Aerodynamics Research and Development Centre, Mianyang, China
[2] State Key Laboratory for Turbulence and Complex Systems, College of Engineering, Peking University, Beijing, China
[3] China Aerodynamics Research and Development Centre, Mianyang, China

Summary The oblique impinging jet (OIJ) Mechanism is found to play a key role in heat transfer near the plate in Rayleigh-Bénard (RB) convection. The OIJ is induced by the large scale circulation impinging onto the horizontal plate, and then develops into a wall jet. The OIJ demonstrates the conservation in space and similarity for various Rayleigh (Ra) numbers. The local heat transfer Nu distribution $Nu_{loc} = Nu_m exp[-(x - x_{rea})/(L_x - x_{rea})]$ is derived theoretically by similarity analysis of wall jet equation, where x_{rea} is the location of reattachment, L_x is the length of the cell and Nu_m is the local Nu at reattachment point obtained through an impinging-jet-based model. Both the scaling and distribution of Nu_loc agree with the DNS. The same heat transfer scaling for both the impinging region and the cell reveals that the OIJ dominates the near wall flow at moderate Ra.

INTRODUCTION

Enormous phenomenon in nature such as convection in the earth's mantle, cloud formation, and large-scale circulation (LSC) in the ocean are mainly driven by the convection. A fluid in a confinement heated from the bottom at high temperature and cooled from the top is popularly known as the Rayleigh-Bénard (RB) convection [1, 2]. The heat transport in a confinement of width L_x and height L_z filled with a fluid is often determined by three dimensionless parameters, namely, the Rayleigh number $Ra = g\beta\Delta T L_z^3/(\nu\kappa)$, the Prandtl number $Pr = \nu/\kappa$, and the aspect ratio $\Gamma_x = L_x/L_z$. Here, ΔT is the temperature difference between the top and bottom plates, g the acceleration due to gravity, β the thermal expansion coefficient, ν the kinematic viscosity, and κ the thermal diffusivity, L_y the depth of the container, respectively.

The heat and momentum transfer ability related to those three parameter is the most important issue in this system. Much attention is pay on the property of the boundary-layer like flow near the wall. It has been found that a local Nu (defined as $Nu_{loc} = \frac{\partial T/\partial z}{\kappa\Delta/L_z}$) reaches the maximum in the region between LSC and corner-roll (CR) and drops along the streamwise direction [3], which seems to be counter-intuitive with the view of BL development. The mechanism of heat transfer inspired us to understand the flow and heat transport influenced by LSC and CR.

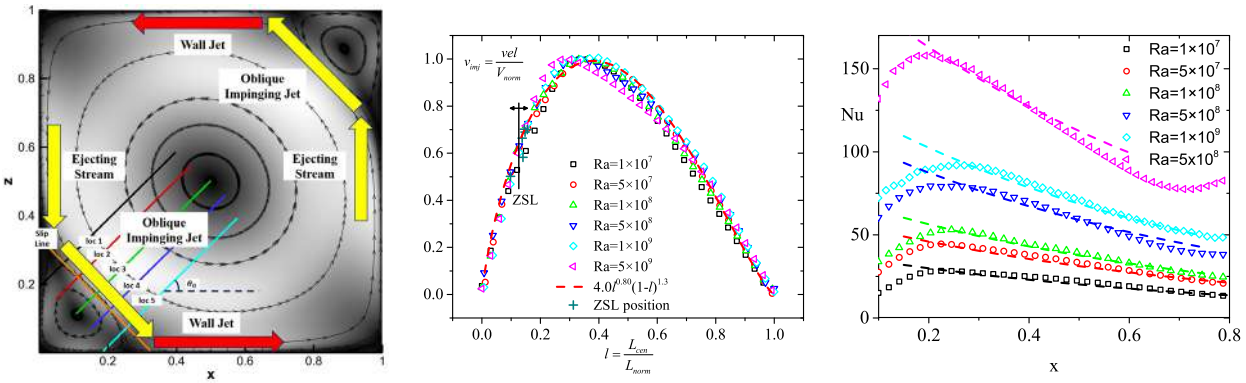

(a) (b) (c)

Figure 1: (a)The distribution of average velocity on xz-plane at $\mathrm{Ra} = 1 \times 10^8$; (b) Normalized velocity distributions of different Ra along the line from CR center to LSC center; (c)Nu distribution from DNS and theoritical work.

OBLIQUE IMPINGING JET PROCESS

Our study is based on the DNS data in a slim rectangular box with the spanwise aspect ratio $\Gamma_y = L_y/L_z = 1/6$ and $\Gamma_x = 1$ [3, 4]. Ra ranges from 10^7 to 5×10^9 and $Pr = 0.7$. The LSC motion near CR and along the horizontal plate is analogy with the oblique impinging jet [5] and corresponding attaching wall jet. The magnitude of time-spanwise average velocity $vel = \sqrt{U^2 + W^2}$ on xz-plane is shown in Fig.1(a). The OIJ corresponds to separated down/up stream of LSC, which originates from the deflected flow in the plume-emission region. This stream goes along with the shear layer of CR and impinges onto the bottom/top plate, then reattaches. The OIJ induced by LSC transports more momentum to the near-wall region and correspondingly carries more heat flux from the plate than the downstream shear flow. After impinging, the flow reattaches and develops on the horizontal plate, which corresponds to a WJ.

*Corresponding author. E-mail: wenfeng_zhou@pku.edu.cn

The streamwise and Ra similarity properties are found in the OIJ. The velocity magnitude profile of OIJ at different positions on the zero streamline (ZSL) separating the corner-roll and LSC (e.g., $loc1$ to $loc5$ in Fig.1(a)) collapse together, indicating streamwise similarity and a good conservation of the 'jet' like flow without obvious diffusion behavior. For Ra similarity, we show the normalized vel profile with different Ras in Fig.1(b). vel are scaled by the maximum magnitude V_m, and the length are scaled by the distance of two centers L_c : $v_{imj} = \frac{vel}{V_m}, l = \frac{l_{cr}}{L_c}$, where l_{cr} is the distance to the CR's center, L_c is the length of center of CR to the center of LSC. vel profiles collapse together, demonstrating a Ra-similarity of OIJ process, and can be empirically described by a beta function $v_{imj} = 4.0l^{0.80}(1-l)^{1.30}$.

As the normalized vel distributions collapse, V_m and L_c should be appropriate scales to characterize the OIJ process. Re_{vimj}, defined by the above two scales with viscosity ν fulfill the Ra scaling $Re_{vimj} = \frac{V_m L_c}{\nu} \sim Ra^{0.50}$.This scaling is consistent with the previous Re-scaling [6] defined by large-scale motion and scale indicating that the OIJ is mainly dominated by wind of LSC, as a result of interaction process between LSC and CR.

NUSSELT DISTRIBUTION IN THE IMPINGING REGION

The distribution of the heat transport on the plate is well described by

$$Nu_{loc} = Nu_m e^{-(x-x_{rea})/(L_x-x_{rea})}, \tag{1}$$

where Nu_m is the local Nusselt number at the reattachment point, x_{rea} is the location of the reattachment point. The above correlation fits the present data for the WJ region to within 15% as shown in Figure 1(c). The exponential decay in x direction near the reattachment points is compatible with the similarity analysis of Navier-Stokes equations by Cantwell [7] and Shishkina *et al.*[8]. This formula is similar to the empirical formula proposed by Goldstein *et al.*in the study of OIJ [5].

The perspective of OIJ makes it possible to understand the Nu_{loc} distribution. Fig.1(c) shows that Nu decreases in the wind direction, which seems to conflict with the view of traditional forced convection BL flow. For BL, the heat flux correlate to the shear positively. As the flow develops, the shearing is strengthened thus Nu_{loc} increases. However, for the WJ induced by OIJ, the high heat transfer induced by impinging concentrates on the reattachment point, which dominates heat transfer more than the shear.

Equation (1) shows that the heat transfer for different Ra is characterized by the stagnation heat transfer Nu_m. The relation between $\mathrm{Nu_m}$ and Ra number is derived by using scale analysis of the temperature equation for OIJ: $\mathcal{U}\Delta/\mathcal{L}_x \sim \kappa\Delta/\mathcal{L}_z^2$. The right side of the above equation is the diffusion term with the scale of thermal BL: $\mathcal{L}_z \sim \lambda_\theta$. The left side of the equation is convection term. The velocity in this term is the characteristic velocity of OIJ, which is the same scale as the bulk velocity of LSC; the length scale is similar to the scale of CR. Based on this fact, we have

$$Nu = \frac{L_z}{2\lambda_\theta} \sim \frac{1}{\sqrt{2}} \mathrm{Re}_{\mathrm{lsc}}^{1/2} \mathrm{Pr}^{1/2} (r_{\mathrm{cr}}/L_z)^{-1/2} \sim \mathrm{Ra}^{0.2925} \tag{2}$$

The LSC Reynolds number $\mathrm{Re_{lsc}}$ can be estimated as Re_{vimj} and have $\mathrm{Re_{lsc}} \sim \mathrm{Ra}^{0.50}$. One the other hand, $r_{\mathrm{cr}}/L_z \sim \mathrm{Ra}^{-0.085}$ is provided in Ref.[4]. It is noted that the relation between Nu and Re with regards to the scale of CR gives an effective exponent 0.585 larger than 0.5 , but smaller than the impinging jet (0.7) [5] and that of TBL (0.8). This indicates that within the range of the Rayleigh number in this work, the impinging jet is under developing.

CONCLUSION

In this paper, an oblique impinging jet (OIJ) process is proposed to analyze to momentum and heat transfer in Rayleigh-Bénard convection. The OIJ originates from the plume-emission region and contains abundant cold/warm fluid and carried by LSC. When the impinging occurs, the well-mixing enhances the heat transfer, leading to a local heat maximum. This OIJ process and the corresponding wall jet (WJ) process impact a quite large region in RB cell. Nu_{loc} decay exponentially in x-direction while the maximum Nu fulfill $Nu_m \sim Ra^{0.2925}$ is derived from the impinging jet model and consistent with the DNS result. A close Nu scaling of wall jet heat transport (0.2925) and the global Nu (scaling exponent 0.30) reveals that the OIJ mechanism provides a new angle of view to understand the local inhomogeneous heat transport and has important relevance to global heat transport.

We thank Zhen-Su She for helpful comments and suggestions. This work is supported by National Nature Science (China) Fund 11452002, 11521091, and 11372362, and by MOST (China) 973 project 2009CB724100.

References

[1] Leo P. Kadanoff. Turbulent heat flow: Structures and scaling. *Physics Today*, 54(8):34, 2001.
[2] Siegfried Grossmann and Detlef Lohse. Scaling in thermal convection: a unifying theory. *Journal of Fluid Mechanics*, 407:27–56, 2000.
[3] Hong-Yue Zou, Wen-Feng Zhou, Xi Chen, Yun Bao, Jun Chen, and Zhen-Su She. Boundary layer structure in turbulent Rayleigh–Bénard convection in a slim box. *Acta Mechanica Sinica*, 35(4):713–728, aug 2019.
[4] Wen Feng Zhou and Jun Chen. Letter: Similarity model for corner roll in turbulent Rayleigh-Bénard convection. *Physics of Fluids*, 30(11):111705, nov 2018.
[5] R. J. Goldstein and M. E. Franchett. Heat transfer from a flat surface to an oblique impinging jet. *Journal of Heat Transfer*, 110(1):84–90, feb 1988.
[6] Chao Sun and Ke-Qing Xia. Scaling of the reynolds number in turbulent thermal convection. *Physical Review E*, 72(6):067302, 2005.
[7] BJ Cantwell and TH Moulden. *Introduction to Symmetry Analysis*. 2002.
[8] Olga Shishkina, Susanne Horn, Sebastian Wagner, and Emily S. C. Ching. Thermal boundary layer equation for turbulent rayleigh-benard convection. *Physical Review Letters*, 114(11):114302–114302, 2015.

ON THE EFFECTIVE HORIZONTAL BUOYANCY IN TURBULENT THERMAL CONVECTION

Lu Zhang[1,2], Guang-Yu Ding[1,2], and Ke-Qing Xia [1,2]
[1] SUSTech Center for Complex Flows and Soft Matter Research and Department of Mechanics and Aerospace Engineering, Southern University of Science and Technology, Shenzhen, 518055, China
[2] Department of Physics, The Chinese University of Hong Kong, Shatin, Hong Kong, China

Summary A misalignment between the global temperature gradient and the gravity in thermal convection will produce an effective horizontal buoyancy. It breaks the reflection symmetry of the system and results in an overall horizontal heat transfer. Experimentally, a condition of increasing horizontal Rayleigh number (Ra_H) under fixed vertical Rayleigh number (Ra_V) is achieved by tilting the convection cell and simultaneously increasing the imposed temperature difference. We find that, with increasing buoyancy ratio ($\Lambda = Ra_H/Ra_V$), the overall heat transfer features a monotonic increase of the vertical component (Nu_V) as well as an increase in the horizontal component (Nu_H). The effect of Prandtl number (Pr) is also studied numerically. Finally, we extend the Grossmann-Lohse theory to the present case, the result of which is successful in predicting $Nu_V(Ra_V, \Lambda, Pr)$.

INTRODUCTION

Thermal convection is of crucial importance for understanding many thermally-driven fluid flows in nature, for example, ocean circulation, mantle convection and convections in celestial bodies. In certain circumstances involving convective flows, either the imposed temperature gradient has a non-parallel component with respect to the gravity or the gravitational field itself is altered, resulting in an effective horizontal buoyancy with respect to the temperature gradient which makes the problem even more complicated. For example, mantle convection near the subduction zone, convection in binary star systems and atmospheric circulation with wide latitude scales. A simple implementation of the effective horizontal buoyancy is to tilt the regular Rayleigh-Bénard convection (RBC) setup by an angle β.

To explore the effect of horizontal buoyancy separately, unlike in most previous studies of tilted RBC [1, 2, 3], we use $\tau = \sqrt{H/(\alpha \Delta g \cos\beta)}$ as the typical time scale (the free fall time for a fluid parcel to travel from the top plate to the bottom plate when the cell is tilted by an angle β), instead of $\tau = \sqrt{H/(\alpha \Delta g)}$ (the conventional free fall time), together with the cell height H, the temperature difference between the two plates Δ, to normalize the governing equations, which yields:

$$\frac{\partial \tilde{\boldsymbol{u}}}{\partial \tilde{t}} + \tilde{\boldsymbol{u}} \cdot \nabla \tilde{\boldsymbol{u}} = -\nabla \tilde{p} + \sqrt{\frac{Pr}{Ra_V}} \nabla^2 \tilde{\boldsymbol{u}} + \tilde{T}\hat{\boldsymbol{z}} + \frac{Ra_H}{Ra_V}\tilde{T}\hat{\boldsymbol{x}}, \tag{1}$$

where $Ra_V = \alpha g \cos\beta \Delta H^3/(\nu\kappa)$ is the vertical Rayleigh number, $Ra_H = \alpha g \sin\beta \Delta H^3/(\nu\kappa)$ is the horizontal Rayleigh number and $Pr = \nu/\kappa$ is the Prandtl number. For simplicity, we define $\Lambda = Ra_H/Ra_V = \tan\beta$ as the buoyancy ratio. In this study, we fix the vertical thermal driving strength while varying the effective horizontal buoyancy over the vertical one (see figure 1). Experimentally, this is achieved by tilting the convection cell with respect to the gravity by an angle β and simultaneously raise the temperature difference Δ across the conducting plates accordingly.

For classical RBC, the governing equations satisfy the K_x reflection symmetry ($u_x \to -u_x, x \to -x$). In other words, if (T, u_x, u_y, u_z) is a solution, so is $(T', u_x', u_y', u_z')(x, y, z) = K_x(T, u_x, u_y, u_z)(x, y, z) = (T, -u_x, u_y, u_z)(-x, y, z)$. However, the presence of an effective horizontal buoyancy (i.e. the last term on the r.h.s. of Eq. 1) breaks the K_x symmetry, which results in a global horizontal Nusselt number:

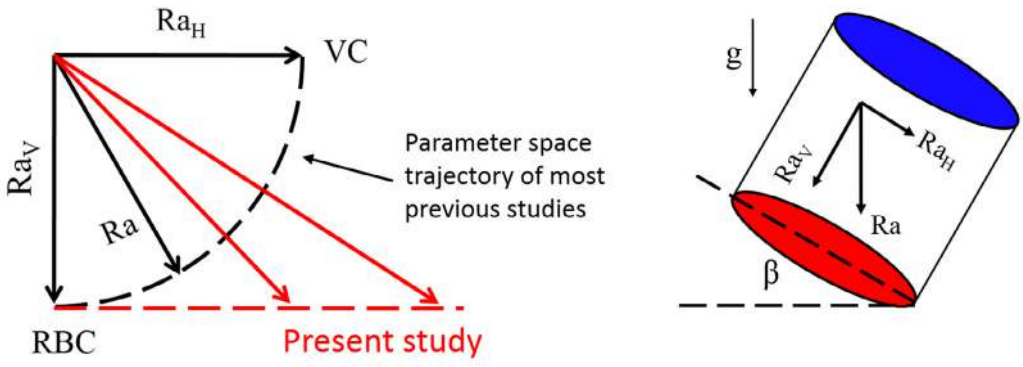

Figure 1: Comparison between the parameter space trajectory explored in the present study (red dashed line) and that by simply tilting the cell (black dashed curve, which is the case in most of the previous studies). Ra_V is the vertical Rayleigh number and Ra_H is the horizontal Rayleigh number. Here RBC stands for 'leveled' Rayleigh–Bénard convection, and VC stands for vertical convection.

*Corresponding author. E-mail: xiakq@sustech.edu.cn.

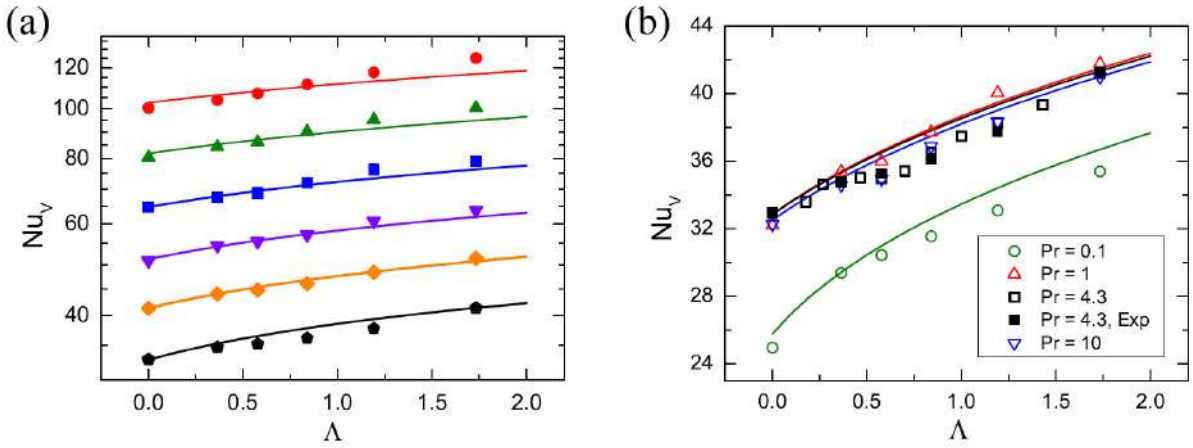

Figure 2: Vertical Nusselt number as function of the buoyancy ratio. Solid symbols are the experimental data, open symbols are the DNS data, and the solid lines show the predictions of the generalized theory. (a) From top to bottom, $Ra_V = 4.6 \times 10^9$, 2.2×10^9, 1.0×10^9, 4.6×10^8, 2.2×10^8, 1.0×10^8. The Prandtl number is fixed at $Pr = 4.3$. (b) $Nu_V - \Lambda$ for different Prandtl numbers, the vertical Rayleigh number is fixed at $Ra_V = 10^8$.

$$Nu_H = \frac{1}{V}\left(\int_{z=0} x\frac{\partial T}{\partial z}dS - \int_{z=H} x\frac{\partial T}{\partial z}dS\right)/(\Delta/H). \tag{2}$$

The horizontal Nusselt number, together with the vertical Nusselt number (Nu_V) and the Reynolds number (Re), are the three response parameters of the system. In leveled RBC, the horizontal Nusselt is always zero and can be viewed as a conservative quantity corresponding to the K_x symmetry.

RESULTS

Figure 2 shows the vertical Nusselt number as function of the buoyancy ratio for (a) different vertical Rayleigh number and (b) different Prandtl numbers. Solid symbols are the experiment data and open symbols are from DNS. It is seen that for fixed vertical Rayleigh number, the vertical heat transfer increase monotonically with the buoyancy ratio, and the relative increase in Nu_V is insensitive to the change in Ra_V for $Pr = 4.3$. The Prandtl number dependence seems more complicated, the enhancement in Nu_V is larger for low Prandtl number. On the other hand, for fixed buoyancy ratio Λ, the highest vertical Nusselt occurs around $Pr = 1$, further increase in Prandtl results in a small reduction of Nu_V.

To explain the intricate $Nu_V(Ra_V, \Lambda, Pr)$ behavior in Figure 2, we developed a generalized Grossmann-Lohse theory [4]. The central idea of the generalized theory is to write the contribution from horizontal Nusselt number in the exact relation for the balance between viscous dissipation and global transfer, i.e., the second term on the r.h.s of:

$$\epsilon_u = \frac{\nu^3}{H^4}Ra_V Pr^{-2}(Nu_V - 1) + \frac{\nu^3}{H^4}\Lambda Ra_V Pr^{-2}\left(Nu_H + \langle\frac{\partial\tilde{T}}{\partial\tilde{x}}\rangle_V\right), \tag{3}$$

as a smooth function connecting two limiting cases with extreme high and low Prandtl numbers:

$$c_5\frac{\Lambda Ra_V Pr^{-1}Re}{4Nu_V}f(6aNu_V Re^{-1/2}), \tag{4}$$

where $f(x) = (1+x^4)^{-1/4}$ and c_5 is a constant determined using the experimental data. The predictions of the generalized theory are plotted in Figure 2 as solid lines, which not only captures the general feature of the buoyancy ratio dependence, but also the intricate Pr effect.

We gratefully acknowledge the support of SUSTech Startup Fund and the Center for Computational Science and Engineering of Southern University of Science and Technology, and by the Research Grants Council of Hong Kong SAR (No. CUHK14302317).

References

[1] Weiss S., Ahlers, G. Effect of tilting on turbulent convection: cylindrical samples with aspect ratio $\Gamma = 0.5$. *J. Fluid Mech.* **715**, 314-334.
[2] Shishkina O., Horn S. Thermal convection in inclined cylindrical containers. *J. Fluid Mech.* **790**: R3, 2016.
[3] Teimurazov A., Frick P. Thermal convection of liquid metal in a long inclined cylinder. *Phys. Rev. Fluids* **2**: 11, 2017.
[4] Grossmann S., Lohse D. Scaling in thermal convection: a unifying theory. *J. Fluid Mech.* **407**: 27-56, 2000.

TERMINAL EXTENSIONAL VISCOSITY OF DILUTE POLYMER SOLUTION USING CABER-DOS SYSTEM

Daiki Yamada[1], Andres Franco-Gomez[1] and Yoshiyuki Tagawa *[1]
[1] Department of Mechanical Systems Engineering, Tokyo University of Agriculture and Technology, Tokyo, Japan

Summary Understanding the behaviour of extending polymer fluids is of great importance for various applications such as inkjet printing and microfluidic devices. Imaging of ultra-high spatial resolution (0.5 μm/pixel) enable us to observe a behaviour of a viscoelastic fluid before pinch-off. The results using Capillary Breakup Extensional Rheometer Dripping onto Substrate (CaBER-DoS) show that the extensional viscosity is almost constant in high Hencky strain region. After showing a terminal extensional viscosity, a very thin liquid thread becomes unstable due to the effect of surface tension and forms a beads-on-a-string and pinch-off.

INTRODUCTION

Liquid jets are applied to printing technologies such as inkjet printers. In inkjet printers, a small amount of polymer is added to the ink. This method minimizes the formation of satellites and secondary droplets, which is essential for print quality. Fluids containing polymers have viscoelastic properties and a significantly increased resistance to elongational flow. When the polymer fluid stretches in a uniaxial-like extensional flow, the fluid forms a thread, leading to the delay of the thread breakup. The thread thinning dynamics is a very important research topic for controlling the volume of the liquid.

In recent years, Capillary Breakup Extensional Rheometer Dripping onto Substrate (CaBER-DoS) has been reported as a new method for stretching rheological measurement [1][2]. Sur *et al.* [2] observed the thread thinning dynamics of viscoelastic fluid using CaBER-DoS system and reported that the temporal evolution of necking radius, which is the representative length of the liquid thread, agree with the exponential decay model. In contrast, before pinch-off, the model does not agree with the result.

In this paper, the O (10^1) μm of liquid thread is measured with an improved spatial resolution of the camera. The results suggest that the polymer reaches the extensibility limit before pinch-off, and there is a transition from elastic to viscous dominance.

METHOD

Figure 1(a) shows the experimental setup. The liquid flows from the nozzle tip (Nozzle diameter and radius $D_0 = 2R_0 = 1.27$ mm) and dropped onto a glass substrate (S2112, Matsunami, spreading parameter $S < 0$) placed under the nozzle at distance H from the substrate, with the aspect ratio (H / D_0) is around 3. As soon as the dripping fluid touches the substrate, the contact area increases, and a liquid bridge is formed between the substrate and the nozzle. We use two fast cameras (Photron, FASTCAM SA-X), one is to secure a shooting area that can capture the entire thread (spatial resolution is 3 μm/pixel), and the other is to capture liquid threads of O (10^1) μm under shooting conditions with improved spatial resolution (spatial resolution is 0.5 μm/pixel). In this experiment, semi-dilute polymer solutions of polyacrylamide (PAM) solutions are prepared in a mixture of glycerin / water (70 / 30 %).

RESULT AND DISCUSSION

The continuous images obtained by the experiment are shown in Figure 1 (b, c). The liquid becomes thinner with time maintaining a cylindrical shape, and from Figure 1 (c), in a very thin liquid thread, (iii) an instability due to slight disturbance at the liquid thread interface propagates by the effect of surface tension, (iv) forming beads-on-a-string [3] and (v) pinch-off.

The necking process is captured by estimating the minimum length R of the liquid thread using Matlab image analysis. The figure shows the necking radius R as a function of time t. The model of viscoelastic fluid is FENE-P dumbbell model [4]. The necking radius decays exponentially with time due to the balance between capillary force and elasticity of the polymer chains (Elasto-capillary regime, EC regime), expressed by

$$\frac{R}{R_0} \approx \left(\frac{GR_0}{2\sigma}\right)^{\frac{1}{3}} \exp\left(-\frac{t}{3\lambda}\right),$$

where G is the elastic modulus of the fluid, σ is the surface tension, and λ is the extension relaxation time. The dashed line in the figure represents the theoretical line fitted by measuring the physical properties of the solution. The strain rate under the condition of extensional flow expressed by,

$$\dot{\varepsilon} = -2\frac{d\ln R}{dt} = -\frac{2}{R}\frac{dR}{dt},$$

*Corresponding author. E-mail: tagawayo@cc.tuat.ac.jp

where dR/dt is the rate of change of the necking radius. In the EC regime, the Weissenberg number, which is a dimensionless number that compares elastic to viscous force in a flow, is constant ($Wi = \lambda\dot{\varepsilon} = 2/3$). The calculated relaxation time of the three solutions are 190 ms (0.4 wt%), 394 ms (0.6 wt%), and 494 ms (0.8 wt%), respectively. The results show that the necking radius before pinch-off does not match the line of the EC model.

To understand the behaviour, it is necessary to consider extensional viscosity and Hencky strain. Extensional viscosity is characterized as the resistance to the extensional flow, while Hencky strain is the integral of the strain rate with respect to time t.

$$\eta_E = \frac{\sigma}{\dot{\varepsilon}R} = \frac{\sigma}{-2dR/dt}, \qquad \varepsilon = 2\ln\frac{R_0}{R},$$

Figure 2 (b) shows the extensional viscosity as a function of Hencky strain. The extensional viscosity of the three liquids increases with increasing Hencky strain, except in the high Hencky strain region ($\varepsilon \geq 3$), it tends to an asymptotic value. Under the extensional flow, the randomly arranged polymer chains begin to orient in the stretching direction. In the EC regime, this phenomenon becomes prominent and dominant the liquid thread thinning. However, polymer chains have finite extensibility. In the high strain region, the polymer chain exceeds the finite extensibility, necking like a Newtonian behavior. Finally, a very thin liquid thread becomes unstable due to the effect of surface tension induced by a slight disturbance and forms a beads-on-a-string and pinch-off.

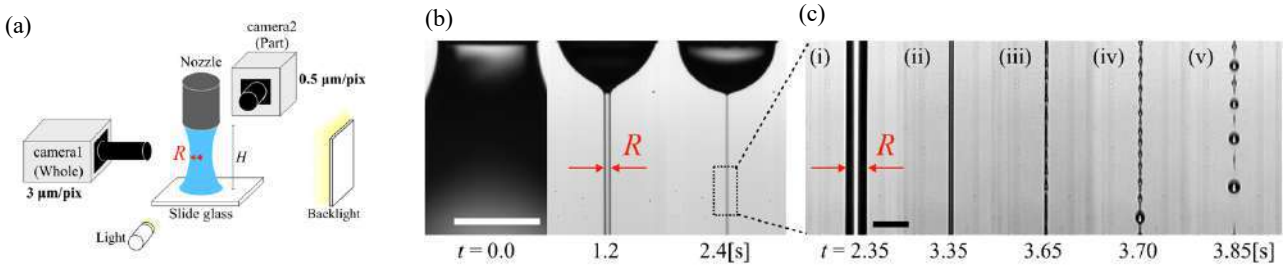

Figure 1 (a) Schematic view of an experimental setup. (b) Continuous images of the thread (0.6 %PAM solution in glycerin/water (70/30 %)) filmed by camera 1(Whole). The white bar is 1 mm. (c) Detail images of the thread filmed by camera 2(Part). The black bar is 50 μm.

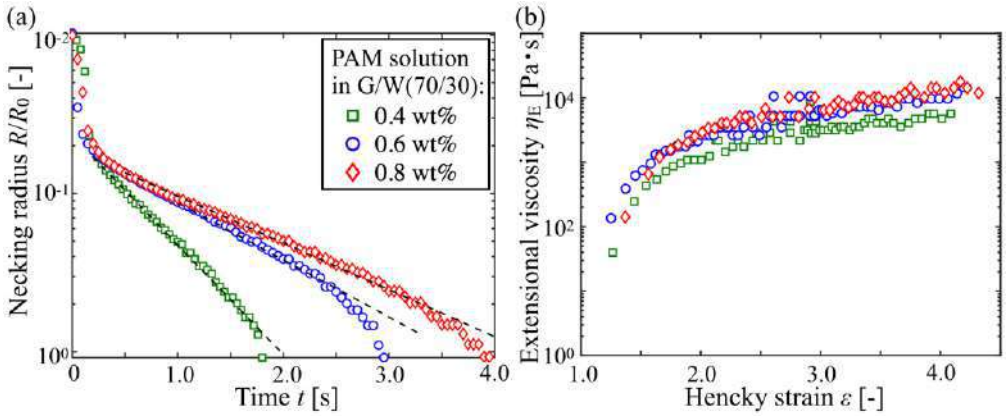

Figure 2 (a) Dimensionless necking radius R/R_0 as a function of time t analysed by the image filmed by camera 1(Whole). The dashed lines show the fitted region that can be described by the equation shown and corresponds to constant strain rate region. (b) Extensional viscosity η_E as a function of hencky strain ε. The plot of $\varepsilon \leq 3$ was calculated from the image of camera 1(Whole), and $\varepsilon \geq 3$ was calculated from the image of camera 2 (from (i) to (ii) in Figure 1. (c)).

CONCLUSIONS

In this paper, the thread thinning dynamics is experimentally investigated using CaBER-DoS. The spatial resolution of images is improved to film the thread of O (10^1) μm. The results suggest that the polymer fluid, which normally should be elastic, necks like the behavior of a Newtonian fluid before pinch-off. A very thin liquid thread becomes unstable due to the effect of surface tension induced by a slight disturbance and forms a beads-on-a-string and pinch-off.

References

[1] Dinic. J., Jimenez. L. N., and Sharma. V. *Lab Chip.* **17**: 460-473, 2017.
[2] Sur. S., and Rothstein. J. *J. Rheol.* **62**: 1245-1259, 2018.
[3] Monica. S. N., Yeh. R. O., and McKinley. G. *J. Non-Newtonian Fluid Mech.* **137**: 137-148, 2006.
[4] Wagner. C., Bourouiba. J., and McKinley. G. *J. Non-Newtonian Fluid Mech.* **218**: 53-61, 2015.

DROP FRAGMENTATION BY LASER-PULSE IMPACT

Alexander L. Klein[1], Dmitry Kurilovich[2], Henri Lhuissier[3], Oscar O. Versolato[2], Detlef Lohse[1], Emmanuel Villermaux[3,4], and Hanneke Gelderblom *[5]
[1] Physics of Fluids, Department of Science and Technology, University of Twente, Enschede, The Netherlands
[2] Advanced Research Center for Nanolithography (ARCNL), Amsterdam, The Netherlands
[3] Aix-Marseille Université, Marseille, France
[4] Institut Universitaire de France, Paris, France
[5] Department of Applied Physics, Eindhoven University of Technology, Eindhoven, The Netherlands

Summary The impact of a laser pulse onto an opaque liquid drop induces a violent fluid-dynamic response: due to plasma formation and local boiling the drop gets propelled forward and deforms into a thin, radially expanding sheet. This sheet destabilizes through the expulsion of radial ligaments and the nucleation of holes, and eventually breaks up into tiny fragments. We reveal the dynamics of these processes via high-speed and stroboscopic imaging complemented with analytical modelling. By combining experimental data from two vastly different liquid systems, we show how the early-time laser-matter interaction controls the late-time fragmentation.

INTRODUCTION

The impact of a nanosecond laser-pulse onto a free-falling opaque liquid drop induces a strong deformation and eventually fragmentation of the liquid [1, 2]. As shown in Figure 1, the laser impact causes the spherical drop to deform into a thin sheet that destabilizes into a fine web of ligaments and smaller droplets. Control of the fragmentation of liquid tin drops upon laser impact is of direct importance to extreme ultraviolet light sources used in nanolithography [1, 4]. Drop fragmentation upon impact onto a solid object has been widely studied. While there are some similarities between these cases and laser-impacted drops, there are also strong differences due the the fundamentally different impact mechanisms involved [5]. Hence, how a drop fragments as the result of a laser impact is still an open question.

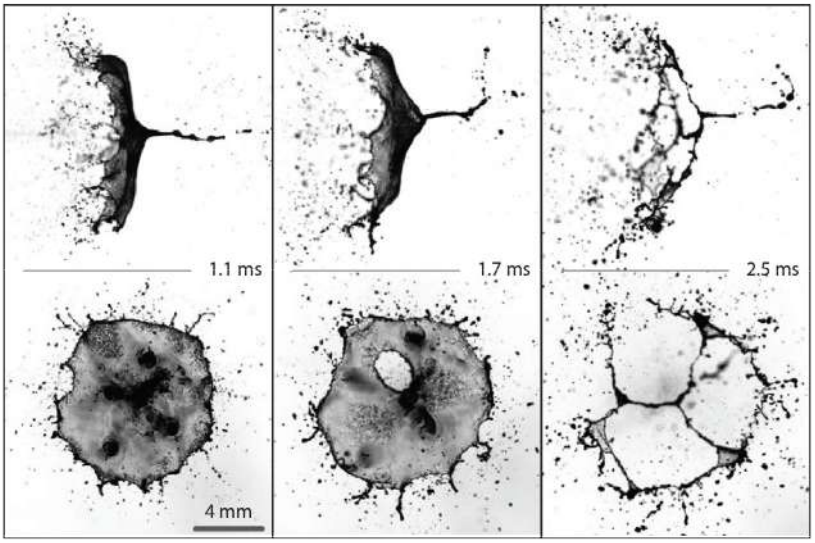

Figure 1: Deformation and fragmentation of a dyed solvent drop at different times after the impact of a nanosecond laser pulse, in side-view (top row, laser pulse coming from the left) and back-view (bottom row, laser pulse pointing into the paper). The initially spherical 0.9-mm sized drop deforms into a thin sheet bordered by a rim. This rim destabilizes through the radial expulsion of ligaments, which subsequently break up into droplets. On the expanding sheet corrugations appear that eventually pierce holes close to the rim (at t = 1.1 ms), and close to the centre of the sheet (t = 1.7 ms). A final web of ligaments is shown for t=2.5 ms. Taken from [2].

*Corresponding author. E-mail: h.gelderblom@tue.nl

METHODOLOGY

We study laser-induced fragmentation experimentally using two different liquid systems: millimeter-sized dyed solvent (methyl-ethyl-ketone) drops and micrometer-sized liquid tin drops. The combination of the two systems allow us to explore a broad range of parameters and study the effect of differences in the laser-matter interaction: the solvent drops are propelled by rapid vaporization, while the tin drops are driven by plasma-recoil.

The response of the drops to a 10-ns Nd:YAG laser pulse is recorded by stroboscopic imaging in side- and back-view (Figure 1). Details of the experimental setups are described in [3] for the solvent drops and [4] for the tin drops. Experimental observations are complemented by an analytical model for the deformation of the drop into an expanding sheet [5, 2], as well as a theoretical analysis of the fluid dynamic instabilities at play [2].

RESULTS

In both the solvent and the tin drops, two types of breakup contribute to the fragmentation, as shown in Figure 1: the radial expulsion of ligaments from the rim of the sheet formed by the expanding drop and the nucleation of holes on the thin sheet itself. We identify two Rayleigh-Taylor instabilities that are triggered by accelerations of the drop in two orthogonal planes as the cause of these breakups. We present theoretical models predicting the growth rate and preferred wavelength of the instabilities, which are in agreement with our experimental observations.

On top of the random nature of these instabilities, the laser-induced hole nucleation shows strong deterministic features, as illustrated in Figure 2. These features result from variations in the sheet thickness caused by the global drop deformation dynamics and the laser-beam profile. The random hole nucleation caused by the instability therefore gets convoluted by a deterministic thickness profile. The resulting web of ligaments shows a complex distribution in ligament thickness. At least five different processing leading to ligamentation are identified, which give rise to a broad drop-size distribution.

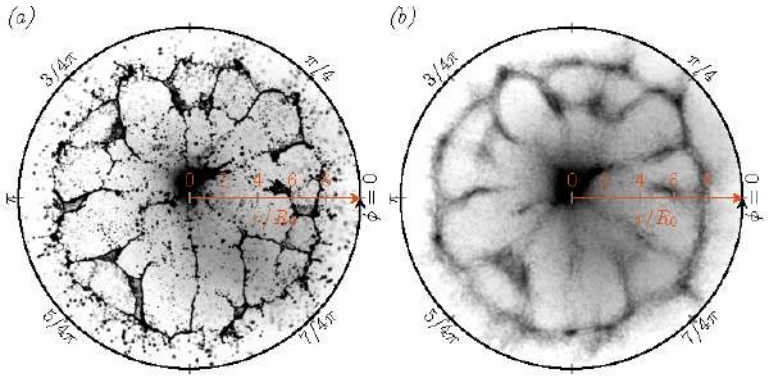

Figure 2: (a) Back-view of a web of ligaments formed by the fragmentation of a solvent drop. (b) Image overlay of 31 different experiments recorded under the same conditions as in (a), revealing the highly deterministic nature of the final web of ligaments. Taken from [2].

CONCLUSIONS

We studied the fragmentation of a drop that is propelled by a laser-induced phase change. Two liquid systems have been considered, which differ not only in length scale but also in propulsion mechanism: millimetre-sized vapour-driven drops of dyed solvent and micron-sized plasma-driven tin drops. In both systems, two types of Rayleigh-Taylor instabilities induced by the rapid acceleration of the drop have been identified, which cause the formation of ligaments that eventually break into droplets. The final web of ligaments and spray of droplets result from a subtle interplay between these instabilities and deterministic fluctuations in the sheet thickness caused by the laser-beam profile and drop dynamics.

References

[1] Klein A. L., Bouwhuis W., Visser C. W., Lhuissier H., Sun C., Snoeijer J. H., Villermaux E., Lohse D. and Gelderblom H. Drop shaping by laser-pulse impact. *Phys. Rev. Applied* **3** (4): 044018, 2015.

[2] Klein A. L., Kurilovich D., Lhuissier H., Versolato O. O., Lohse D., Villermaux E., and Gelderblom H. Drop fragmentation by laser-pulse impact. *arXiV* 1910.02522, 2020.

[3] Klein A. L., Lohse D., Versluis M. and Gelderblom H. Apparatus to control and visualize the impact of a high-energy laser pulse on a liquid target. *Rev.Sci. Instrum.* **88**: 095102, 2017.

[4] Kurilovich D., Klein A. L., Torretti F., Lassise A., Hoekstra R., Ubachs W., Gelderblom H. and Versolato O. O. Plasma propulsion of a metallic microdroplet and its deformation upon laser impact. *Phys. Rev. Appl.* **6** (1): 014018, 2016.

[5] Gelderblom H., Lhuissier H., Klein A.L., Bouwhuis W., Lohse D., Villermaux E., and Snoeijer J. H. Drop deformation by laser-pulse impact. *J. Fluid Mech.* **794** 676-699, 2016.

EFFECTS OF INJECTION ANGLE ON LIQUID JET PRIMARY ATOMIZATION IN SUPERSONIC CROSSFLOW

Feng Xiao[1], Chi-Bing Shen *[1], Yi-Heng Tong[2], Sen Lin[1], and Shao-Kang Peng[1]
[1] Science and Technology on Scramjet Laboratory, National University of Defense Technology, Changsha, 410073, China
[2] Department of Aerospace Science and Technology, Space Engineering University, Beijing, 101416, China

Summary In this paper, the primary atomization process of the liquid jet injected into supersonic flow from the flat wall at different angles are simulated using an interface tracking method. The simulated liquid jet injected at different angles demonstrate substantially different primary atomization morphology and shock structures. The growth of liquid jet penetration as injection angles increases is correctly predicted by the present two-phase flow solver in comparison with the experimental measurements. The liquid jet injected at the angle of 120° produces a more efficient atomization process, which can promote the mixing between the liquid fuel and the supersonic air flow in a Scramjet engine.

INTRODUCTION

In order to achieve reliable engine starting and high combustion efficiency in a liquid-fueled supersonic combustion ramjet (Scramjet) engine, the liquid fuel jet must atomize efficiently in the supersonic air flow for sufficient fuel/air mixing. Since the fuel is typically injected into the supersonic air flow from the wall in the combustion chamber, extensive experimental studies of liquid jet atomization in supersonic gas crossflow have been carried out. However, the majority of these studies focus on the atomization of liquid jet injected perpendicularly into the air flow, and the atomization of liquid jet injected in other angles has been rarely investigated though the angled fuel injection could improve the atomization performance. Further understanding of the injection angle effects on liquid jet primary breakup is desired, and this subject is investigated here using both numerical and experimental methods.

NUMERICAL METHODS

In the developed two-phase flow solver, a coupled Level set and Volume of Fluid method (CLSVOF) method is implemented to capture the liquid/gas interface. The liquid flow is solved by an incompressible flow solver using a finite volume method while the gas flow is solved by a compressible flow solver using a finite difference method. The coupling of the gas flow solver and the liquid flow solver is achieved by specifying boundary conditions for each other at the interface. Specifically, the gas variables are used to provide pressure boundary conditions for the liquid flow solver; the liquid variables are used to provide velocity boundary conditions for the gas flow solver (see [**?**] for details).

RESULTS

The experiments were carried out, and High-Speed schlieren photography was used. Fig. 1 shows the photos of the liquid jet primary atomization in a Mach 1.86 air crossflow at three different injection angles: $\alpha = 60°$, $\alpha = 90°$, and $\alpha = 120°$.

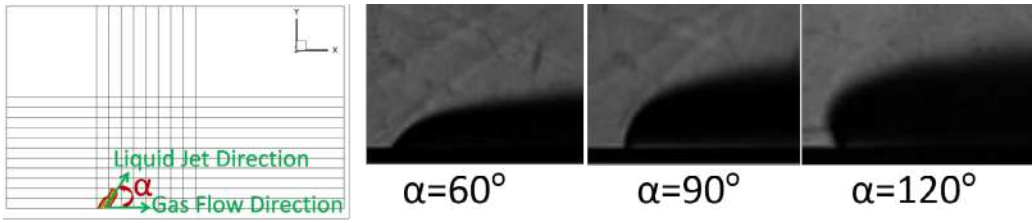

Figure 1: Schlieren photos of liquid jet primary atomization in supersonic air crossflow at different injection angles

In the simulated test cases, the liquid jet diameter D is $0.2mm$. Liquid jet velocity V_L and freestream air velocity U_G are $23.24m/s$ and $517.6m/s$ respectively. The Mach number of the air flow is 2. Figure 2 presents instantaneous primary atomization morphology of liquid jet in the supersonic crossflow at the three different injection angles. Significant differences in liquid column breakup morphology at different injection angles are observed. At $\alpha = 60°$ and $\alpha = 90°$, the predicted liquid column first moves in the liquid injection direction, and then bends in the gas crossflow direction. When the liquid jet is injected at an angle of 120°, the liquid column first moves upstream; as the liquid velocity component in

*Corresponding author. E-mail: 285403264@qq.com

the direction opposite to the crossflow reduces to 0 due to drag forces from the gas, the liquid column reaches the utmost upstream position, and then the liquid column starts to bend in the crossflow direction. These predicted liquid column behaviours are consistent with schlieren photos in Fig. 1 at all three injection angles. It is demonstrated in Figs. 2 that the liquid jet disintegrates more progressively as α increases. When the injection angle is $120°$, the liquid ligaments and droplets arising from liquid jet primary atomization are generally smaller than those at $\alpha = 60°$ and $\alpha = 90°$. And the resulting liquid structures are observed to scatter more widely in the vertical (y) and spanwise (z) directions at $\alpha = 120°$, indicating that liquid fuel inject at the angle of $120°$ is likely to result in more efficient mixing between the fuel and the supersonic air crossflow than at the two smaller injection angles. The contours of the nondimensionalized pressure $P^* = P/(\rho_G U_G^2)$ in slice z=0 are also included in Figs. 2 to show the shocks. When the liquid is injected at an angle of $60°$, an oblique shock is formed in front of the liquid jet. As the injection angle grows, the angle of the predicted shock ahead of the liquid jet increases, and a strong normal shock is formed at $\alpha = 120°$. These agree well with the experimental observation of the shock structures illustrated in Fig. 1.

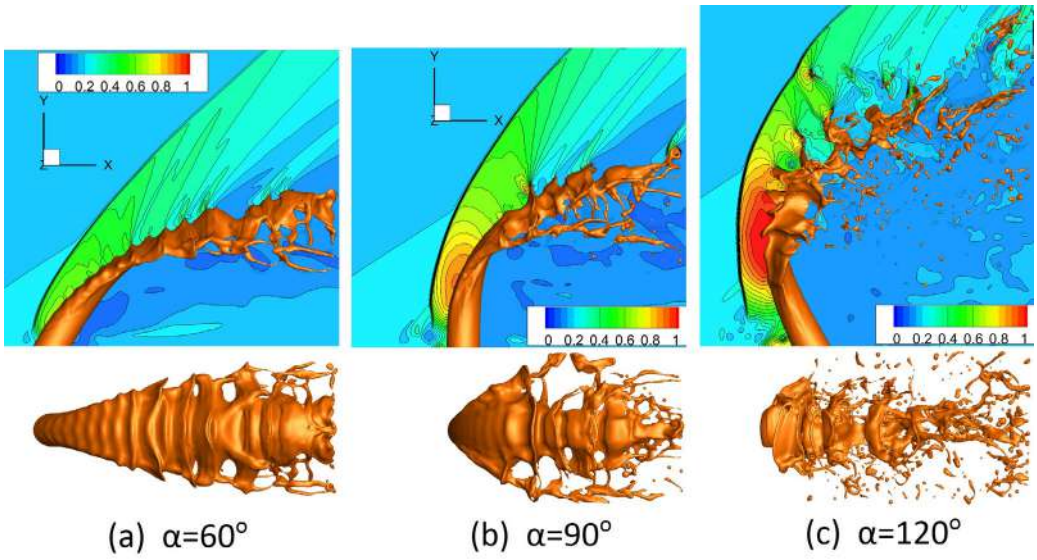

Figure 2: Primary atomization morphology of liquid jet in the Mach 2 crossflow at $\alpha = 60°$ from a front view (upper figure) and top view (lower figure) with P^* contours in slice z=0

The liquid jet penetration in supersonic gas crossflow predicted by simulations at different injection angles are measured and compared with the experimental measurements in Fig. 3. The liquid jet penetration predicted on Grid A and Grid B differs slightly by 5%, implying that the liquid column deformation and breakup can be properly resolved on the current grid resolution. The liquid jet penetration at the injection angles of $60°$ and $120°$ agrees well with the experimental measurements while the liquid jet penetration at the injection angle of $90°$ is slightly underestimated. The tendency that the liquid jet penetration increases as the injection angle grows is well reproduced by the current two-phase flow simulation methodology.

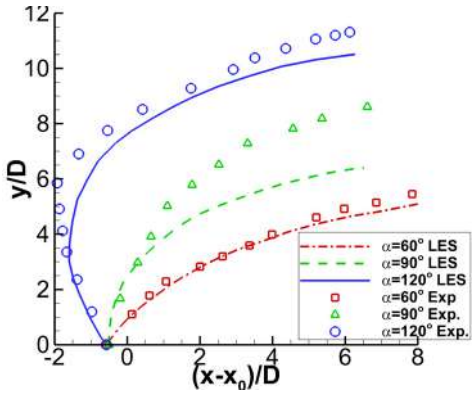

Figure 3: Liquid jet penetration in supersonic crossflow at different injection angles

References

[1] Xiao F., Wang Z., Sun M., Liang J., Liu N., *Int. J. Multiphase Flow* **87**:229-240, 2016.

BUBBLE TYPES EJECTED FROM COAXIAL NOZZLES

Ewout Zuiderduin[1], Bart van der Vaart[1], Stefano Coco[1], Kees Venner[1], and Claas Willem Visser *[1]
[1] Department of Thermal and Fluid Engineering, Faculty of Engineering Technology, University of Twente

Summary Gas bubbles ejected from core-shell nozzles were recently applied as building blocks for tailored polymer foams (Visser et al., Adv. Mater. 31(46), 2019). Here we study the bubble ejection regime as a function of the liquid flow, the gas pressure, and the nozzle geometry. Different ejection regimes including jetting, monodisperse bubbles, bidisperse bubbles, and spraying are reproduced and classified. Their incidence could be reasonably collapsed on a single master graph, providing engineers a tool for predictive design of core-shell nozzles.

Ejecting a gas and a liquid from a core-shell nozzle into ambient air or gas results in rapid production of gas-filled bubbles. These "flying bubbles" have been fabricated with shells of water [1], tin [1], copper [2], gold [2], and polymers [2]–[4], and find application in laser target generation[5] and fabrication of scaffolds in tissue engineering[3]. Recently, we used this method for "*direct bubble writing*", in which the resulting bubbles are stacked into 3D-printed polymer foams with locally controlled gradients in the cell size and cell interconnectivity [4]. Here, the foam's cell size, cell size distribution, and density directly result from the ejected bubble size, their consistency, and the relative thickness of the liquid shell, respectively. Therefore, understanding and predicting the ejection regime of gas-filled bubbles from core-shell nozzles is essential for fabrication of foams with new ink formulations or nozzle geometries.

It is well-known that the ejection of bubbles into air can occur in different regimes that depend on the liquid flow rate and gas pressure applied to the core-shell nozzle[3], [6]–[10]. Figure 1 shows the nozzle design (a-c) as well as the observed regimes, including pure-liquid dripping (d) or jetting (f), the formation of a large blob of bubbles at the nozzle (e), various coherent bubble ejection regimes (g-i), and ejection of less-controlled sprays (j). In our recent work[4] we hypothesized that the Weber number $\mathrm{We} = \rho D V^2/\sigma > 1$ is a prerequisite for ejection in the form of a coherent stream (Figure 1f-j). Here, $\rho, \sigma, D,$ and V denote the liquid's density and surface tension, the outer nozzle diameter, and the estimated ejection velocity $V = Q/(1/4\pi D^2)$, respectively. Furthermore we assumed that gas is only entrained (Figure 1e,g-j) if the gas pressure exceeds the sum of the liquid-induced, inertial, viscous, and capillary pressures at the inner nozzle tip: $P_{tot} = P_I + P_\mu + P_\sigma$; for details we refer to [4]. This abstract provides first results of systematic tests of these hypotheses.

Here, we designed and 3D-printed core-shell nozzles with inner diameters $0.6\mathrm{m} < D_i < 1.5\mathrm{mm}$, outer diameters $0.6\mathrm{m} < D < 1.5\mathrm{mm}$, and heights $1\mathrm{mm} < H < 1.4\mathrm{mm}$, as shown in Figure 1a-c. Subsequently, gas (air) and liquid (water with 0.4% Tween-80 surfactant) were fed to the shell and the core of the nozzle, respectively. The liquid flow rate was controlled with metal syringes that were driven a syringe pump, whereas a pressure controller was used to set the gas pressure.

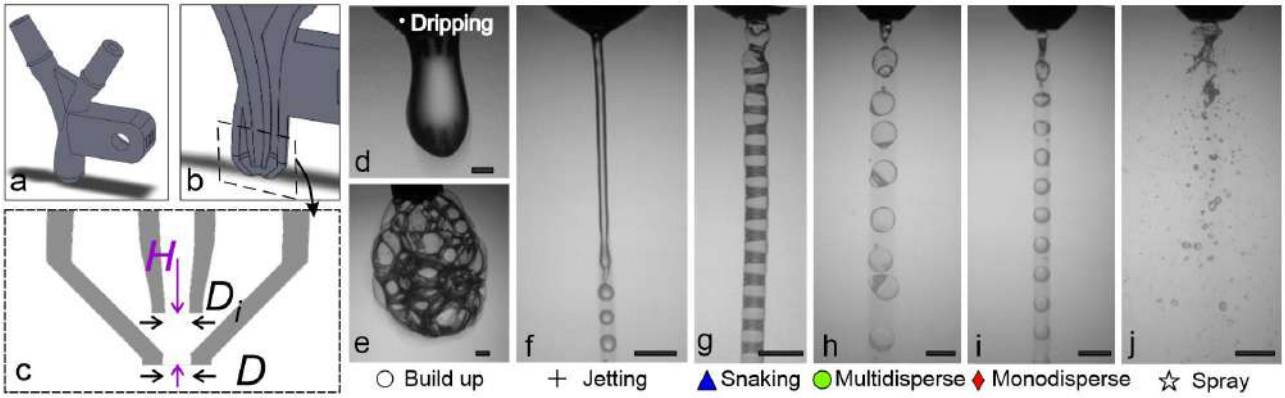

Figure 1: Ejection regimes from core-shell nozzles. (a) Visualized 3D model of the nozzle. (b) Cross section of the nozzle tip. (c) Schematic cross section, indicating geometrical control parameters. (d-j) Ejection regimes in the dripping mode (d), Build-up (e), pure-liquid jetting (f), snaking (g), bidisperse bubble ejection (h), monodisperse bubble ejection (i), and spraying (j).

The resulting ejection regimes are shown and named in figure 1d-j. Each regime is plotted as a function of the liquid flow rate and the gas pressure in figure 2. For the dripping regimes observed at low flow rates $Q \leq 12\mathrm{ml/min}$ without (d) and with (e) gas ejection, gravity eventually pulls the droplet from the nozzle. At higher flow rates, pure-liquid jetting is observed up to a certain threshold gas pressure, for which air-containing regimes (figure 1g-i) are observed. This threshold increases with increasing flow rates. The red line displays the predicted threshold for gas entrainment $P = P_{tot}$ [4]. Here, both viscous pressure build-up in the nozzle and the inertial pressure exerted by the liquid are overcome by the gas pressure.

To test this prediction over a wider range of the control parameters, in Figure 3 we plot the ejection regime data for 16 nozzle geometries as a function of the dimensionless pressure P/P_{tot} and the dimensionless flow rate (the Weber number). A reasonable collapse is observed. At $\mathrm{We} \approx 4$, the transition from pure-liquid dripping to jetting is consistently

*Corresponding author. E-mail: **c.visser@utwente.nl**.

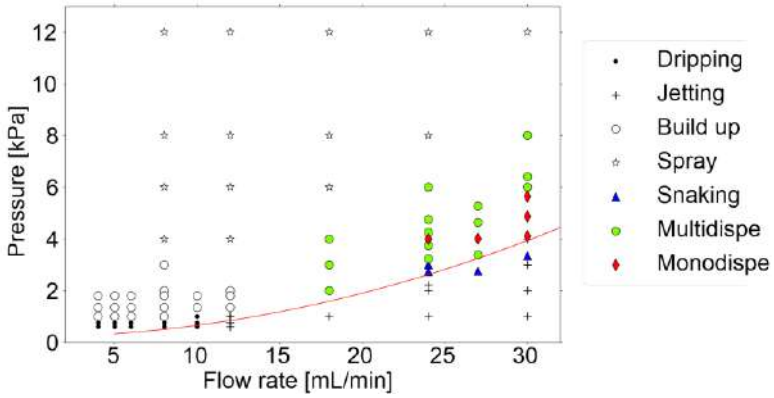

Figure 2: Ejection regimes as a function of the gas pressure and the liquid flow rate. The solid line indicates $P = 0.8P_{tot}$, which corresponds reasonably well with the transition from pure-liquid to gas-containing ejection regimes.

observed, as expected [11]. The equivalent transition from gas-containing dripping droplets to coherent trains of bubbles occurs at higher Weber number for $P \approx P_{tot}$, possibly because multiple thin liquid-gas interfaces can "stick" to the nozzle surface which will increase their adhesion. However, details of this transition remain to be investigated. Furthermore, we observe controlled bubble ejection (the most useful window for applications, indicated by coloured markers) only in a window between pure-liquid ejection at low pressures and spraying at high pressures. This window narrows for increased flow rates, where the most interesting domain (monodisperse bubbling) is observed. The mechanisms behind the regime transitions, as well as design changes to broaden the useful range of control parameters, will be subject of future studies.

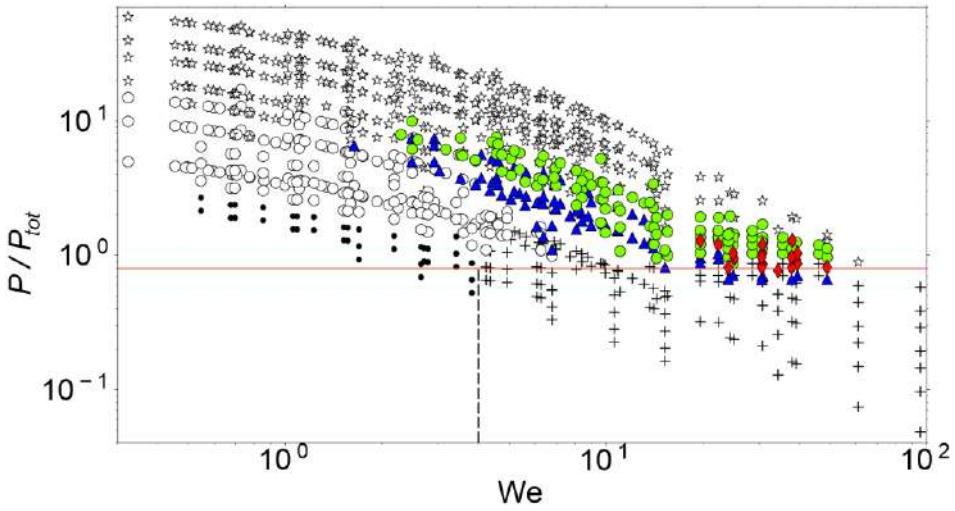

Figure 3: Ejection regimes as a function of the normalized pressure and the Weber number. The red line indicates $P = 0.8P_{tot}$; the vertical dashed lined indicate the expected and observed transition from jetting to dripping at We = 4.

In conclusion, various ejection regimes from core-shell nozzles were observed. Their incidence was quantitively measured as a function of the liquid flow rate and the gas pressure. Non-dimensionalizing these parameters revealed that controlled bubble ejection is expected in a narrow regime within $3 < \mathrm{We} < 50$, and $0.7 < P/P_{tot} < 7$. This result may already benefit predictive (rather than trial-and-error) nozzle designs. In the future, we aim to improve our understanding of the observed transitions and to widen the operation window for direct bubble writing [4].

References

[1] J. M. Kendall, M. C. Lee, and T. G. Wang, *J. Vac. Sci. Technol.*, vol. 20, no. 4, pp. 1091–1093, 1982.
[2] C. D. Hendricks, "Liquid drop technique for generation of organic glass and metal shells," 1981, pp. 124–128.
[3] K. Y. Chung, N. C. Mishra, C. C. Wang, F. H. Lin, and K. H. Lin, *Biomicrofluidics*, vol. 3, no. 2, 2009.
[4] C. W. Visser, D. N. Amato, J. Mueller, and J. A. Lewis, "Architected Polymer Foams via Direct Bubble Writing," *Adv. Mater.*, p. 1904668, Sep. 2019.
[5] R. J. Calliger, R. J. Turnbull, and C. D. Hendricks, *Rev. Sci. Instrum.*, vol. 48, no. 7, pp. 846–851, 1977.
[6] T. V. Vu, H. Takakura, J. C. Wells, and T. Minemoto, "Breakup modes of a laminar hollow water jet," *J. Vis.*, vol. 14, no. 4, pp. 307–309, 2011.
[7] J. M. Kendall, *Phys. Fluids*, vol. 29, no. 7, Jul. 1986, pp. 2086–2094, 1986.
[8] C. P. Lee and T. G. Wang, *Phys. Fluids*, vol. 29, no. 7, Jul. 1986, pp. 2076–2085, 1986.
[9] A. M. Gañán-Calvo and J. M. Gordillo, *Phys. Rev. Lett.*, vol. 87, no. 27, p. 274501, 2001.
[10] P. Garstecki, I. Gitlin, W. Diluzio, G. M. Whitesides, E. Kumacheva, and H. A. Stone, "Formation of monodisperse bubbles in a microfluidic flow-focusing device," *Appl. Phys. Lett.*, vol. 85, no. 13, pp. 2649–2651, 2004.
[11] C. Clanet and J. C. Lasheras, "Transition from dripping to jetting," *J. Fluid Mech.*, vol. 383, pp. 307–326, Mar. 1999.

ABSORPTION OF A LIQUID DROP BY SWELLING FIBERS

Pierre Van de Velde[1], Suzie Protière [2] , and Camille Duprat *[1]
[1] LadHyX, Ecole polytechnique, Palaiseau, France
[2] Institut Jean le Rond d'Alembert, Sorbonne Université, Paris, France

Summary The present work describes the imbibition dynamics of a drop placed on one or multiple swelling fibers. Several timescales are observed during the absorption of a drop on a single fiber. The drop and fiber geometries are described experimentally and help rationalizing the imbibition dynamics. When placed on two parallel fibers, a drop is able to deform the fibers leading to the transition from a bridge to a collapsed state. This swelling induced transition can drastically reduce the absorption time.

INTRODUCTION

Many examples of drops interacting with fibers can be found both in nature and industry, from wet dog hair or bird feathers to drying or coloring of fabrics or the fabrication of paper. The dynamics of drops on fibers can be counterintuitive. For example, a wetting drop placed on a cone will spontaneously move towards the region of higher curvature and thus away from the tip [1]. Placed on an array of elastic fibers, the drop exerts a capillary force on the fibers that can cause large deformations of the fibers, drop motion and a significant change in droplet shape [2]. On a larger scale, localized wetting and swelling of a fibrous material such as paper may cause large macroscopic deformations [3]. Understanding the swelling behavior of individual fibers is crucial to predict the mechanical response of larger fibrous networks.

In the present work, we aim at predicting the time taken by a fibrous medium to absorb a given volume of fluid. We thus study the dynamics of a drop placed on one or several deformable fibers in the presence of swelling. We find that the geometry of the drop plays an important role on the observed imbibition and wetting dynamics. We link the drop geometry to the observed dynamics by examining the drop shape on non-swelling fibers.

EXPERIMENTAL SETUP

Elastomer PVS (polyvinylsiloxane, Zhermack Elite double 32) fibers of various radii (r_{fiber} from 200 to 500µm) are molded and clamped at their ends. A drop of silicon oil (viscosity of 2 cPa.s) is deposited of the fiber using a micropipette. The shape of the drop is then followed in time using two digital cameras placed above and in front of the fiber respectively. Images are analyzed with a custom image treatment code.

DROPS PLACED ON A SINGLE FIBER

We first investigate the case of a single drop placed on a swelling fiber. Figure 1 presents the evolution of the droplet height with time for different initial volumes. We observe three different regimes with different timescales.

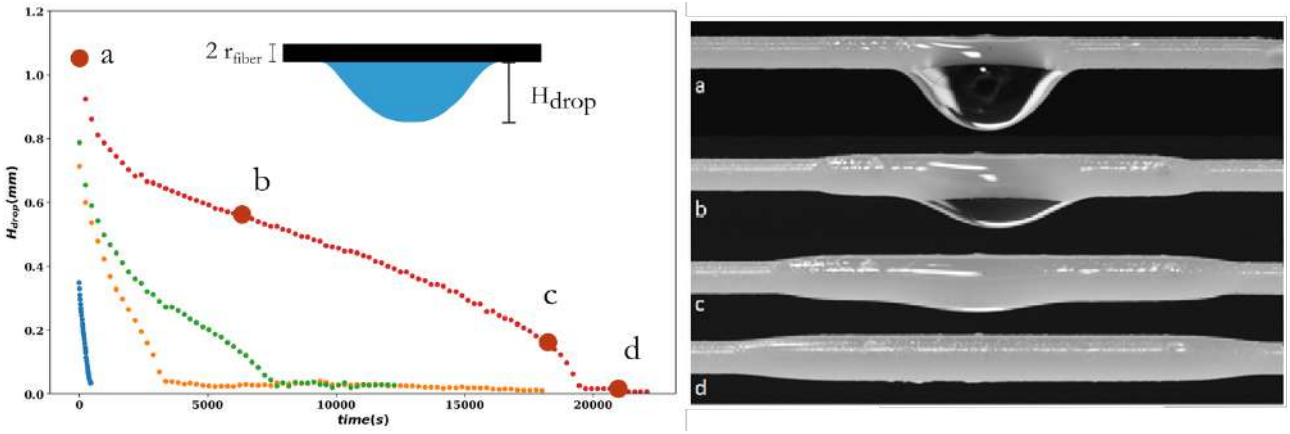

Figure 1 Experimental evolution of the drop height H_{drop} with time (silicon oil with 2 cPa viscosity) on a PVS fiber (radius = 250 µm) during the swelling process.

In the first regime (a), we observe a fast initial imbibition with a characteristic time (t_{swell}) that does not depend on the initial volume. This corresponds to the time needed for the fluid to diffuse from the drop towards the center of the fiber in the radial direction. Additional experiments with completely immersed fibers confirm that this time depends only on the initial fiber radius. In a second regime (b-c), when the maximum swollen radius is reached, the drop rests on

*Corresponding author. E-mail: camille.duprat@ladhyx.polytechnique.fr

a saturated zone of the fiber leading to a deceleration of the imbibition governed by diffusion in the axial direction. This regime is only observed for volumes large enough to reach local saturation at the position of the drop. In the third regime (c-d), once most of the drop is absorbed within the fiber, the remaining drop volume is sufficiently small for it to roll up and spread around the fiber leading to a reacceleration of the absorption of all the liquid by the fiber. Here the geometries of the drop and the fiber play a crucial role in the imbibition dynamics at all stages.

We thus study the shape of the drop on non-swelling nylon fibers for various radii and explain the origin of the different regimes shown before. The minimal volume necessary for the appearance of the second regime can be directly estimated from the drop geometry on the fiber.

DROPS PLACED ON TWO PARALLEL FIBERS

We now investigate the swelling of two fibers when a drop is placed between them. We focus on two parallel stretched fibers. When placed between two parallel and elastic fibers, a drop can either stay compact and bridge the fibers or spread over a long distance, sticking the two fibers together (zipped state) [4]. The spacing between the fibers and the resulting drop geometry play a crucial role in determining if the zipped state can be reached. In the case of swelling PVS fibers, the drop modifies the geometry locally and is under specific conditions able to bring the fibers closer together, leading to a spontaneous zipping of the fibers (i.e. they come in contact as they collapse) as shown in Figure 2. The zipping can drastically decrease the total absorption time of a given volume compared to the case of a single fiber, since the spreading of the drop at the zipping transition allows it to be absorbed in a much larger region of the fiber without saturating the fiber locally.

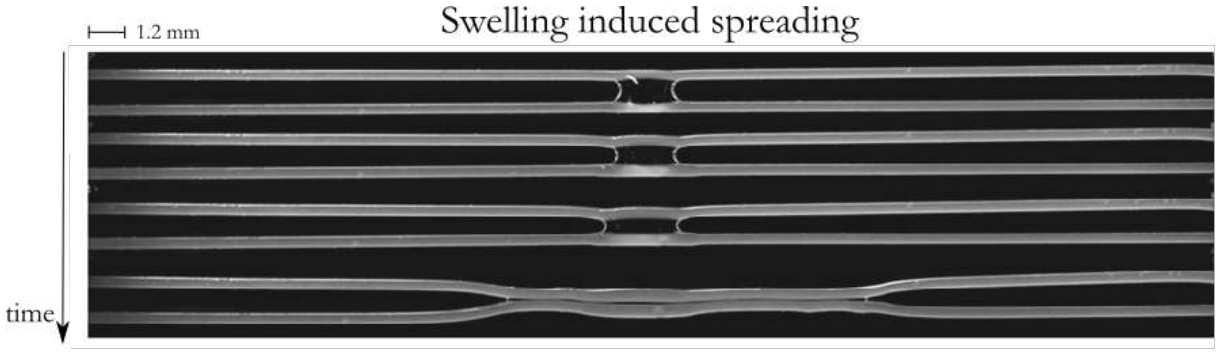

Figure 1 Evolution of a drop placed between two parallel streched PVS fibers. The drop swells the fibers locally bringing them close enough to cause the zipping transition. (2 min between pictures)

We investigate the parameters determining the zipping transition and link them to the swelling of a single fiber. We construct a phase diagram to identify the different possible morphologies after swelling. From experiments on this model system, we can start rationalizing the effect of swelling during the imbibition of fibrous networks.

References

[1] É. Lorenceau and D. Quéré, “Drops on a conical wire,” *J. Fluid Mech.*, vol. 510, no. 510, pp. 29–45, 2004.
[2] C. Duprat, S. Protière, A. Y. Beebe, and H. A. Stone, “Wetting of flexible fibre arrays,” *Nature*, vol. 482, no. 7386, pp. 510–513, 2012.
[3] E. Reyssat and L. Mahadevan, “How wet paper curls,” *Epl,*, vol. 93, no. 5, p. 54001, Mar. 2011.
[4] C. Duprat and S. Protiere, “Capillary stretching of fibers,” *Epl*, vol. 111, no. 5, pp. 1–5, 2015.

SURFACTANT-LADEN DROPLETS ON SUPERHYDROPHOBIC SURFACES

Ahmed Aldhaleai, Peichun Amy Tsai *

Summary We experimentally and theoretically examine the influence of a double chain cationic surfactant, didodecyldimethylammonium bromide (DDAB), on the wetting states and contact angles on superhydrophobic (SH) surfaces made of regular hydrophobic microstructures. We use two types of hydrophobic micro-patterns of different surface roughness r and packing fraction ϕ and vary nine surfactant concentrations (C_S) in the experiments. At low C_S, some of the droplets are in a gas-trapping, Cassie-Baxter (CB) state on the high-roughness microstructures, whereas some droplets are in a completely wetting Wenzel (W) state on the low-roughness microtextures. We found that the contact angle of CB drops can be well predicted using a thermodynamic model considering surfactant adsorption at the liquid-vapor (LV) and solid-liquid (SL) interfaces. At high C_S, however, all drops wetting on W mode. Based on a Gibbsian thermodynamic analysis, we find that for the two types of superhydrophobic surfaces used, Wenzel state has a lowest thermodynamic energy and thus is more favorable theoretically. The CB state, however, is metastable at low C_S due to a thermodynamic energy barrier and becomes more stable on the SH microtextures with greater ϕ and r, in an agreement with our experimental observations.

INTRODUCTION

The wetting and spreading characteristics of pure liquids on solid surfaces is of significant interest in several engineering and industrial applications, including droplet-based microfluidics, coating, inkjet or electrohydrodynamic jet printing, and membranes technology, especially for oil-water separation. In particular, droplet wetting on low-energy surfaces as so-called ultrahydrophobic or superhydrophobic (SH) surfaces with water contact angle (CA) ($\theta \geq 150°$) and small contact angle hysteresis (CAH) has received a great interest due to their promising applications for friction control, anti-icing, anti-fouling, self-cleaning, and improving corrosion resistance. Such SH surfaces allow the drop to sit on the top of the surface textures with air trapped underneath with a partial gas-liquid interface, as the so-called Cassie-Baxter (CB) or "Fakir" wetting state. The presence of a gas layer minimizes the interfacial energy by reducing the contact between the liquid and solid-surface area, thereby making the CB state is more favorable. However, the long-term stability of the preferred CB state on SH surfaces is still challenging and can be lost through an irreversible wetting transition to Wenzel (W) state, where the liquid fills in the surface cavities. To date, the wetting properties of SH surfaces have been extensively investigated, but mostly limited to pure liquids. Amphiphilic aqueous surfactant solutions, on the other hand, were investigated to a less extent, and there are only few experimental studies reported CB-W transition of surfactant-laden drops on SH surfaces. Here we investigate experimentally and theoretically how a cationic surfactant and its concentration (C_S) change the contact angle (CA) and wetting state of droplet on ulatra-hydrophobic microstructures of different solid-fraction (ϕ) and surface roughness (r). Systematic measurements were conducted to record both CA and wetting state for nine DDAB surfactant concentration solutions. We fit our experimental results to a thermodynamic model based on surfactant adsorption at interfaces to examine C_S-dependent CA. Using Gibbsian thermodynamic analysis, we also elucidate theoretically the probability and the stability of the experimentally observed CB state at low C_S.

RESULTS AND DISCUSSION

C_S-dependent contact angles

Fig. 1 shows the experimental and predicted results for the C_S-dependent CAs of CB and W drops on S1 (◆) and S2 surfaces for the last 10 s recording period. For the CB wetting state, there is a good agreement between our experimental data (filled symbols) and the predictions (solid lines) of the C_S-dependent CAs of CB drops, and the prediction is match better our measurement on S2. This may attributed to the smaller solid fraction (lower ϕ) and hence less pinning of the contact line. Both measured and predicted CB CAs on S2 (lower ϕ) are greater compared to S1 (higher ϕ) due to a greater liquid-air contact with smaller ϕ. However, the poorly predicted C_S-dependent CAs of modified W equation can be assisted through the use of newly modified W models that incorporate the pinning effect for W drops.

Free energy analysis for the stability and metastability of the wetting states

To explain the occurrence of different wetting states depending on the C_S on the different microstructures, we carried out an analysis starting from the Gibbsian thermodynamics (1; 2), following the recent published work by Shardt(**?**), and analytically solved the free energy (E) of our composite system of DDAB-laden surfactant droplets sitting on each microstrucuted surface. The derived free energy equation, $E - E_0$, with respect to the assumed reference state has the form of Shardt et al.(3) free energy:$E - E_0 = \gamma_{LV}\pi R^2(2 - 3\cos\theta + \cos^3\theta) - 4\pi\gamma_{LV}R_0^2$, where E_0 is the reference free energy, defined as the free energy of a spherical drop with no SL contact; R is the spherical cap radius of curvature; R_0 is the initial radius of a spherical drop of 10 μl; $\cos\theta = f\cos\theta_Y(C_S) - f_1$. Here, f is the ratio of the SL surface area (pillar-top area) to the total (SL and LV) areas and f_1 is the ratio of the LV interfatial area to the total projected area beneath the drop. Fig.2c shows that there is a free energy barrier between the CB and W states, $E_{max} - E_{CB} > 0$, for C_S from 0 to ~ 0.25 on

*Corresponding author. E-mail: peichun.amy.tsai@ualberta.ca.

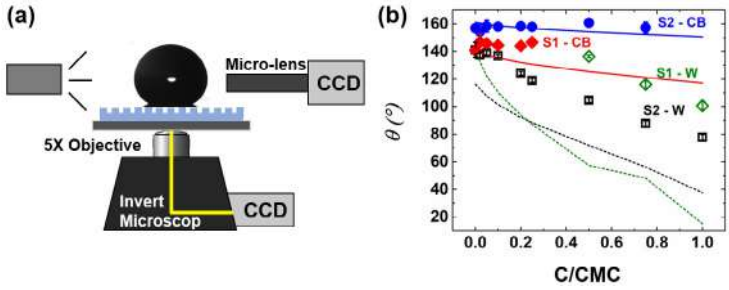

Figure 1: (a) Schematics of experimental setup, and (b) measured and predicted contact angles for DDAB droplets at concentrations between 0 and 1 CMC on two SH microstructures, high-r S1 (◆,◇) and low-r S2 (●,□) in a Cassie-Baxter (CB) (◆,●) and a Wenzel (W) (◇,□) wetting state during the last 10 secs in a time period of 100 s. The error bars represent the standard deviations of ten drops. Theoretical prediction of the CB and W contact angles considering surfactant adsorption, are also plotted for S1 (—,- - -) and S2 (—,- - -), respectively.

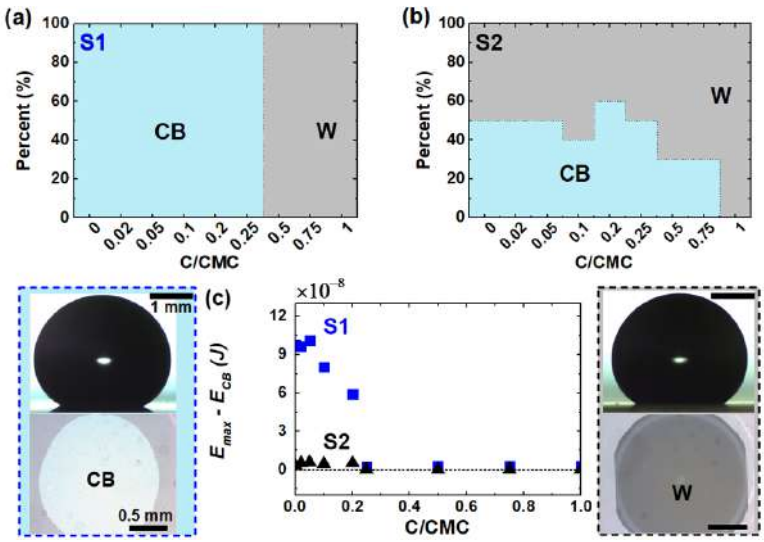

Figure 2: Percentage of experimental droplets in a Cassie-Baxter (CB) and Wenzel (W) states vs. surfactant concentration for (a) S1 and (b) S2, based on an average of 10 independent droplets at each DDAB surfactant concentration (C_S). (c) The free energy barrier, $E_{max} - E_{CB}$, as a function of C_S for S1 (■) and S2 (▲). Side and bottom-view snapshots showed a Stable CB (Left) and Stable W (Right) drops.

both surfaces S1 and S2. By comparing the calculated free energy barrier on S1 (higher ϕ and r; ■) with the percentage of CB drops experimentally observed as a function of C_S, the CB state was observed for droplets with ≤ 0.25. This can be attributed to the presence of high energy barrier at these concentrations. Either CB state for C_S from 0 to 0.75 CMC before the transition occurs at 1 CMC or W state was observed for all C_S on S2 (lower ϕ and r; ▲) due to the lower energy barrier than that of S1. On both surfaces, at high C_S, W state was more frequently observed.

In conclusion, we experimentally measured the contact angles and wetting states of DDAB surfactant-laden drops for nine different concentrations on two superhydrophobic microstructured surfaces of different packing-fraction (ϕ) and surface roughness (r). A model considering surfactant adsorption at the LV and SL interfaces has been derived and compared to the experimental data of the contact angles and wetting states of the surfactant drops on the superhydrophobic microtextures. The experiments and the theoretical predictions of the CB contact angles were in a good agreement. We further consider thermodynamic surface energies to predict the stability or metastability of the wetting states depending on C_S. We found that the Wenzel state is thermodynamically favorable for both surfaces at all DDAB concentrations, but there is a free energy barrier between the CB and W states for $C_S \leq 0.25$ for our SH surfaces. This thermodynamic analysis implies that the CB state is metastable at these concentrations and, moreover, this metastable CB state becomes more stable on surfaces with greater ϕ and r.

References

[1] J. W. Gibbs, Am. J. Sci. 441 (1878); C. Ward, E. J. Levart, Appl. Phys. 56, 491 (1984).
[2] J. A. Elliott, O. Voitcu, Can. J. Chem. Eng. 85, 692 (2007); F. Eslami, J. A. Elliott, J. Phys. Chem. B. 115, 10646 (2011); W. Gong, Y. Zu, S. Chen, Y. Yan, Sci. Bull. 62, 136 (2017).
[3] N. Shardt, M. B. Bigdeli, J.A. Elliott, P.A. Tsai, Phys. Chem. Lett. 10, 7510 (2019).

MEAN FLOWREVERSAL IN VIBRATED SESSILE DROPS

Dong Luo, Binxu Wang, and Jianjun Tao *
SKLTCS, CAPT, Department of Mechanics and Engineering Science, College of Engineering, Peking University, Beijing, 100871, P. R. China

Summary Three-dimensional simulations of vibrated sessile drops with pinned contact lines are carried out, and a flow reversal phenomenon is revealed: the direction of the mean flow around the drop axis can be reversed by changing the exerted vibration frequency or acceleration amplitude. The regions for the upward and the downward axis mean flows in the vibration frequency-amplitude space are distinguished from each other by systematic simulations for both the hydrophilic and the hydrophobic cases. Based on a dynamic model, the analytical relation among the vibration frequency, the acceleration amplitude, and the resonance frequency is derived for the marginal states between the upward and the downward mean-flow regions and is confirmed by the numerical simulations, indicating that the reversal phenomenon is intrinsically determined by the oscillating kinetic energy.

INTRODUCTION

The dynamic behavior of an oscillating drop is of great importance for the crystal growth, spray coating, condensation, microfluidic mixing, and atomization processes. Under the assumption of zero gravity, the dynamics of an oscillating unsupported inviscid drop was studied by Rayleigh [1]. Because of the nonlinear effect, an internal mean flow may be generated by periodic oscillations. At low oscillating frequencies (less than 1kHz), a downward mean flow along the symmetry axis was observed experimentally and numerically by tracing tracer particles and was explained in terms of Stokes drift driven by capillary waves originated from the oscillating contact line [2, 3]. On the contrary, an upward mean flow starting from the bottom center of a droplet along the symmetric axis was reported in other experiments, where the sessile water droplets were vibrated by the oscillating hydrophobic substrates and the contact lines either oscillated [4, 5] or were not oscillatory [6]. Therefore, the factors determining the direction of the axis mean flows need to be clarified.

METHODS AND RESULTS

We consider a sessile water drop of density $\rho_1 = 1000\, kg \cdot m^{-3}$ and viscosity $\mu_1 = 10^{-3}\, Pa \cdot s$ with a pinned circular contact line on a vibrated flat support in the ambient gas of density $\rho_2 = 1.25\, kg \cdot m^{-3}$ and viscosity $\mu_2 = 10^{-5}\, Pa \cdot s$ as shown in Fig. 1. The x and z coordinates are fixed on the support surface and the vibration corresponds to an oscillating body force in the vertical direction $a = Asin(2\pi ft)$, where A is the acceleration amplitude, and f is the vibration frequency. In the simulations, the surface tension coefficient is $72mN/m$ and Volume of Fluid (VOF) method is applied to catch the interface. The computational domain (L_x, L_y, L_z), the drop's volume V, and the drop's bottom radius R are $(6mm, 3mm, 6mm)$, $20\mu l$, and $2.5mm$ for the hydrophilic substrate, and $(6mm, 3mm, 6mm)$, $5\mu l$, and $1.138mm$ for the hydrophobic substrate, respectively. It was found that different vibration frequencies lead to different oscillating (m, n) modes, where n is the azimuthal wave number and $(m - n)/2 + 1$ is the number of layers of polar wave peaks or troughs observable from the side views. We have checked that the oscillating modes obtained with the uniform mesh (n_x, n_y, n_z)=(128,64,128) at different frequencies are consistent with the experimental observations [7].

In the following simulations, we focus on the oscillating $(2, 0)$ mode, an axisymmetric mode, and hence its mean flow is shown in the meridian plane. The mean flow has a dominating inner vortex ring, which is responsible for the position of the saddle point (the blue point in Fig. 1) and corresponds to an upward or downward drift flow along the drop axis. More importantly, a flow reversal phenomenon is found, i.e. the direction of the dominating mean flow along the axis may be changed by varying either the acceleration amplitude (Fig. 1) or the frequency of the vibration. The regions for the upward (red delta) and the downward (green gradient) axis mean flows in the $f - A$ space are determined numerically and are shown in Fig. 2(a) for the hydrophilic and in Fig. 2(b) for the hydrophobic substrates, respectively.

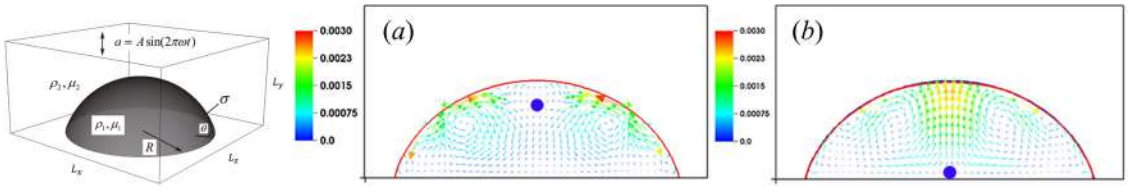

Figure 1: Computation configuration and the mean flows of the oscillating mode (2,0) at $(a) f = 80Hz,\ A = 5m/s^2$ and $(b) f = 80Hz,\ A = 15m/s^2$. The color indicates the velocity amplitude.

*Corresponding author. E-mail: jjtao@pku.edu.cn

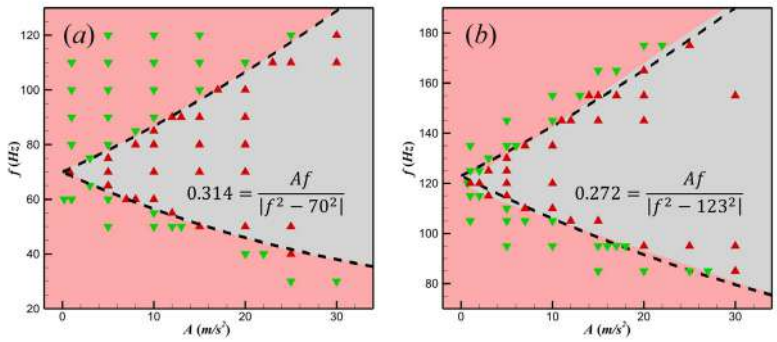

Figure 2: The direction of the axis mean flow in the $f - A$ space for (a) the hydrophilic and (b)the hydrophobic cases, where the static contact angles are $70°$ and $115°$, respectively. The symbols indicate the numerical results, and the black dashed lines represent the reversal boundaries defined by the dynamic model.

The reversal mechanism is explained as follows. The vibrated drop surface has two layers in the vertical direction for mode (2,0). The top point of the drop has largest oscillation amplitude and hence the top layer causes an upward axis mean flow according to the nonlinear theory for the standing water wave [8], while the influence of the bottom layer on the axis mean flow is mainly determined by the downward or inward flow near the node circle. When the vibration becomes stronger, e.g. the vibrational acceleration amplitude increases from $5m/s^2$ to $15m/s^2$ as shown in Fig. 1, the oscillation at the drop top is more enhanced than the bottom layer and hence the top layer's effect becomes dominant. Consequently, there should be a kinetic energy threshold, above which the downward axis mean flow turns to be upward. It is known that drops have their intrinsic oscillating frequency f_0 [1], and the resonance occurs when the vibrated frequency $f = f_0$. Based on the Navier-Stokes equations, a dynamic model is built and the total kinetic energy is derived to be proportional to $\frac{\rho_1 V(Af)^2}{(f^2-f_0^2)^2}$. Therefore, we may assume that the energy threshold for the mean flow reversal as $E_c = \frac{C_0\rho_1 V(Af)^2}{(f^2-f_0^2)^2}$, where C_0 is a coefficient, or at the reversal boundary in the $f - A$ space we have

$$\frac{Af}{|f^2 - f_0^2|} = \sqrt{\frac{E_c}{C_0\rho_1 V}} = C. \tag{1}$$

The intrinsic frequencies f_0 for the present hydrophilic and hydrophobic cases are 70 Hz and 123Hz, respectively. It is shown in Fig. 2 that when $C = 0.314m/s$ and $0.272m/s$, the reversal boundaries predicted by the dynamic model agree with the numerical simulations very well.

CONCLUSIONS

In this paper, the flow fields of vibrated sessile drops are simulated numerically with the VOF method, and it is found that the axis mean flow may change its direction with the increase or decrease of the vibration frequency and the acceleration amplitude. The mean-flow reversal results directly from the competition between the nonlinear upward axis mean flow caused by the standing wave at the upper layer and the downward axis drift flow related to the bottom layer. A dynamic model is proposed to define the kinetic energy threshold for the mean flow reversal, whose dependencies on the vibration frequency and the acceleration amplitude are shown in Eq. (1) and are confirmed quantitatively by the numerical simulations for both the hydrophilic and the hydrophobic cases.

References

[1] Rayleigh L. On the capillary phenomena of jets. *Proc. R. Soc. Lond.* **29**: 71-97, 1879.
[2] Mugele F., Staicu A., Bakker R., van den Ende D. Capillary Stokes drift: a new driving mechanism for mixing in AC-electrowetting. *Lab Chip*, **11**: 2011-2016, 2011.
[3] Oh J. M., Legendre D., Muggle F. Shaken not stirred On internal flow patterns in oscillating sessile drops. *Eur. Phys. Let.*, **98**: 34003, 2012.
[4] Kim H., Lim H. C. Mode pattern of internal flow in a water droplet on a vibrating hydrophobic surface. *J. Phys. Chem. B*, **119**: 6740-6746, 2015.
[5] Park C. S., Kim H., Lim H. C. Study of internal flow and evaporation characteristics inside a water droplet on a vertically vibrating hydrophobic surface. *Exp. Therm. Fluids Sci.*, **78**: 112-123, 2016.
[6] Sanyal A., Basu S. Evolution of internal flows in mechanically oscillating sessile droplets undergoing evaporation. *Chem. Eng. Sci.*, **163**: 179-188, 2017.
[7] Chang C. T., Bostwick J. B., Steen P. H., Daniel S. Substrate constraint modifies the Rayleigh spectrum of vibrating sessile drops. *Phys. Rev. E*, **88**: 023015, 2013.
[8] Longuet-Higgins M. S. Mass transport in water waves. *Philos. T. R. SOC. A*, **245**: 535-581, 1953.

ON THE BEHAVIOR OF MICROBUBBLE CLUSTERS IN ULTRASOUND FIELD

Hironobu Matsuzaki[1], Yunqiao Liu[2], Kazuyasu Sugiyama[3] and Shu Takagi*[1]
[1] Department of Mechanical Engineering, The University of Tokyo, Tokyo, Japan
[2] Department of Engineering Mechanics, Shanghai Jiao Tong University, Shanghai, China
[3] Department of Mechanical Science and Bioengineering, Osaka University, Osaka, Japan

Summary In the present study, the behaviour of microbubble clusters is analysed under the presence of ultrasound field. From the experimental observation, it is shown that there exists the maximum size of microbubble clusters which can be captured in the focal region of focused ultrasound. This maximum size depends on the ultrasound frequency and the behaviour of bubble cluster is qualitatively well-predicted by introducing the classical theory for resonant frequency of bubble-clusters (Omta (1987)[1]). The present experimental results show quantitatively some deviation from this theory. Here, we discuss the effect of bubble number density and surface-coated shell characteristics on the bubble cluster behaviour.

INTRODUCTION

Microbubbles of a few μm diameter have been clinically used as contrast agents for ultrasound imaging. They are also expected to be used for the drug delivery system (DDS). In case of DDS, a vesicle containing microbubbles can be used to deliver the drag under the ultrasound irradiation to control the location and break-up the vesicle for the release of drag at the target region. These techniques can be further utilized to bring some chemical reaction at some specific timing and the location. For these purposes, manipulation of microbubble using ultrasound field is an important research target to investigate. For the manipulation of microbubbles, Bjerknes force [2] is utilized. Especially, primary Bjerknes force is often used to manipulate the bubble positions. Primary Bjerknes force F_{B1} is expressed using time-dependent bubble volume $V(t)$ and pressure $P(r,t)$ as $F_{B1} = -\langle V(t)\nabla P(r,t)\rangle$. Due to this force, small bubbles which have the natural frequency higher than the imposed ultrasound frequency stay at the anti-node, and large bubbles of lower natural frequency stay at the node in standing wave. This effect is also observable in the focused ultrasound experiment. In the case of the focused ultrasound, focal region becomes anti-node and small microbubbles are attracted in the focal region, forming bubble clusters. Here in the present study, this phenomenon is analyzed in detail.

METHODS

Schematic figure of experimental setup is shown in Fig.1. The ultrasound transducer is set at the top. The focused ultrasound is irradiated toward the bottom of container filled with polyacrylamide gel, where the water with microbubbles are confined in the small volume around the bottom of the gel to avoid the effect of acoustic streaming. Focal region of the ultrasound appears in this small confined region filled with water and the microbubbles are moving toward this region. Ultrasound frequency is varied from 0.3MHz to 5.5MHz. Bubble cluster formation is observed from the bottom using inverted microscope (TE2000-E, Nikon Corp.) with high speed camera(MotionPro X3, IDT Inc.). Observed bubble clusters are shown in Fig.2.

In addition to the above experiment, we also conducted theoretical estimation for bubble cluster formation, using the technique developed by Ref. [3], [4] and [5]. Takahira et al.[3] used multipole expansion technique to analyse the multi-bubble interaction problems and Ilinskii et al. [4] introduced Lagrangian and Hamiltonian mechanics in the similar problem and Liu et al. [5] extended Takahira's method by introducing Toroidal-Poloidal field theory for hyperelastic membrane model of the surface-coated microbubbles. Here, we combine these techniques to analyse the natural frequency of a surface-coated-bubble cluster.

RESULTS AND DISCUSSION

From the Omta's theory[2], the following relation is hold for the natural frequency of bubble cloud and its size under the assumption of dilute bubble concentration with potential flow theory, denoting α :volume fraction of bubble and γ :effective polytropic index.

$$\frac{D_c}{D_b} = \frac{2\alpha^{\frac{1}{6}}}{\pi}\sqrt{\frac{3}{\gamma}}\left(\frac{\omega_c}{\omega_b}\right)^{-1}$$, where D_c and D_b are the diameter of the bubble cloud and each bubble, ω_c and ω_b are the natural frequency of them, respectively.

*Corresponding author. E-mail: takagi@mech.t.u-tokyo.ac.jp

This relation indicates that the natural frequency of bubble cloud is inversely proportional to the diameter of bubble cloud, if the same size mono-dispersed bubbles are used in experiment. In the present experiment, bubbles are attracted toward the focal point of focused ultrasound and start forming the bubble cluster. The bubble cluster becomes larger and larger by taking more microbubbles in it. This process continues gradually until the bubble cluster suddenly disappear from the focal point. This phenomena can be explained by the primary Bjerknes force theory and the natural frequency of bubble cloud (cluster). That is, growth of a bubble cluster size gives the reduction of natural frequency of bubble cluster and the focal point becomes unstable region beyond a certain critical size of bubble cluster, when the natural frequency of a bubble cloud becomes lower than the imposed ultrasound frequency. This critical size cluster is expected to have the natural frequency which is the same as the imposed ultrasound frequency. The experimental results are shown in Fig. 3. It is shown that there is a simple well-correlated tendency and that the cluster diameter when they escape from the focal point is roughly inversely proportional to the imposed ultrasound frequency.

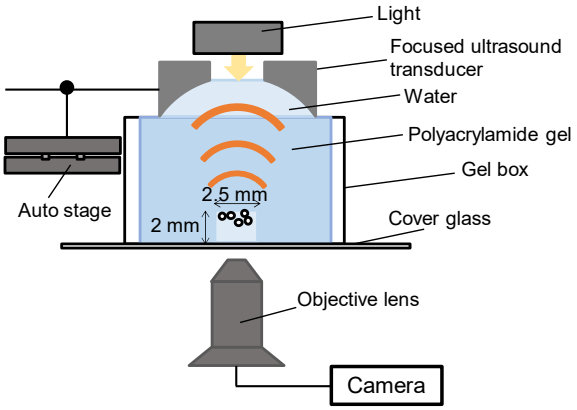

Figure 1. Experimental setup for bubble cluster observation

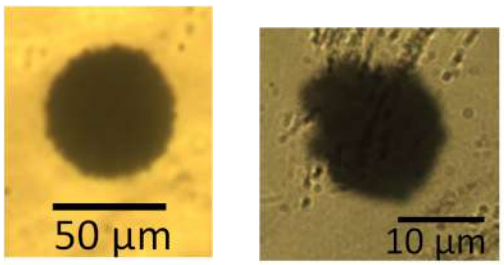

(a) 0.4 MHz (b) 2 MHz
Figure 2. Photos of captured bubble clusters (Captured by (a) 0.4MHz Ultrasound, (b) 2 MHz)

CONCLUSIONS

The maximum size of bubble clusters captured by focused ultrasound was investigated. Given the imposed ultrasound frequency, microbubbles accumulate in the focal region of focused ultrasound and forming a bubble cluster. This bubble cluster continues growing until it reaches the maximum size, beyond which the cluster escapes from the focal region. This maximum size is explained using the theories of the Bjerknes force[2] and resonant frequency of bubble cloud[1] and the behaviour is well-predicted qualitatively. Compared with the prediction by Omta's theory, surface-coated-microbubble clusters captured by focused ultrasound shows quantitatively different behaviours. The present bubble clusters behave to have larger natural frequency than the theoretical prediction for the same size free-surface-bubble cloud.

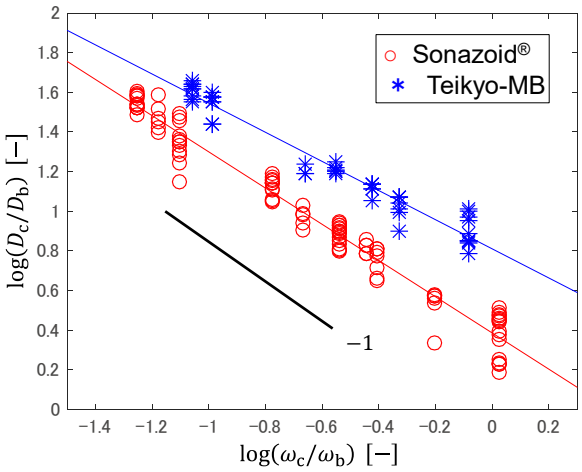

Figure 3. Dependence of the maximum cluster size on focused ultrasound frequency

Acknowledgement

Teikyo-Microbubbles are supplied by Profs. Maruyama and Suzuki lab, the microbubble DDS group in Teikyo University.

References

[1] Omta, R., Oscillations of a cloud of bubbles of small and not so small amplitude. *J. Acoust. Soc. of Am.*, **82**(3): 1018-1033, 1987.
[2] Bjerknes V. F. K., Fields of Force, Columbia University Press, NY 1906.
[3] Takahira, H., Akamatsu, T., & Fujikawa, S., Dynamics of a cluster of bubbles in a liquid: Theoretical analysis. *JSME International Journal Series B* Fluids and Thermal Engineering, 37(2), 297-305, 1994.
[4] Ilinskii, Y. A., Hamilton, M. F., & Zabolotskaya, E. A., Bubble interaction dynamics in Lagrangian and Hamiltonian mechanics. *J. Acoust. Soc. of Am.*, 121(2), 786-795, 2007.
[5] Liu, Y., Sugiyama, K., & Takagi, S. On the interaction of two encapsulated bubbles in an ultrasound field. *J. Fluid Mech.*, 804, 58-89, 2016.

THERMALLY-DRIVEN BUBBLE OSCILLATION IN AN IMPACTING DROP

Masaki Kato, Takahiro Okabe and Minori Shirota*[1]
Graduate School of Science and Technology, Hirosaki University, Hirosaki, Japan

Summary We experimentally observed a unique circular subcooled boiling for the first time in an impacting water drop on a heated solid surface: bubbles at the front of the circular boiling region perform violent volume oscillations which helps to rapidly enlarge the boiling area in the spreading drop. Observation through a high-speed camera revealed that the collapse of the bubble was closely related to the dry-out of the microlayer formed in between the bubble and the solid. After the analysis with a spherical bubble growth model, we clarified that the evaporation of microlayer and the condensation on the subcooled liquid play important roles to determine the bubble dynamics.

INTRODUCTION

Spray cooling is a promising heat reduction technology for further development in high-performance electro devices such as microchips. Such a high cooling heat flux as 1000 W/cm^2 can be achieved with spray cooling probably due to the bubble dynamics in impacting drops on heated solids. The importance of bubble motion in pool boiling has been widely studied. However, bubble dynamics, mainly driven by phase change, in an impacting drop is yet to be investigated.

The characteristics of the boiling in an impacting drop can be summarized as follows: while bubbles nucleate and grow on the heated solid surface the bulk liquid above the solid is kept cold during the impacting process of typically several milli-seconds. The situation causes a high temperature gradient in the thermal boundary layer in the liquid surrounding the bubble. Under certain conditions, the high temperature gradient might cause subcooled boiling with violent bubble collapses, which has been well studied in pool boiling triggered with MEMS technology [1].

In the present study we focus on subcooled boiling in impacting drops of water. By employing a high-speed imaging technique, we explore the bubble dynamics in both the drop-size and the bubble-size scales. We also construct a theoretical model for thermally driven bubble oscillation in a thermal boundary layer with the development of the microlayer in between a bubble and a heated solid.

EXPERIMENTAL METHOD AND THEORETICAL MODELLING

Room temperature water drops were gently released from a needle to a sapphire plate heated at about 170 °C. The transparent sapphire plate enabled us to observe bubble formation process from below through a mirror using a high-speed camera (Photron SA-Z or Shimadzu HPV-X2 with frame rate up to 500 000 fps) with an LED backlight.

We constructed a theoretical model for the bubble growth and shrink in an impacting drop on a heated wall; the overview of the model is shown in Fig. 1. The bubble was assumed to be a spherical cap whose time change in radius followed Rayleigh-Plesset equation [2]. The bubble started to grow several milli-seconds after the drop contacted the wall. The surrounding liquid of the bubble therefore had a temperature gradient in the direction normal to the solid. In such thermal boundary layer, heat Q_l conducted through the bubble surface in both directions, i.e., toward the bubble from a superheated region and toward the surrounding liquid in subcooled region.

In the modelling, we also examined the effect of microlayer evaporation on the bubble growth. Here we assumed the heat conduction through the microlayer Q_{ml} was determined by Fourier's law. We also took into account the enthalpy

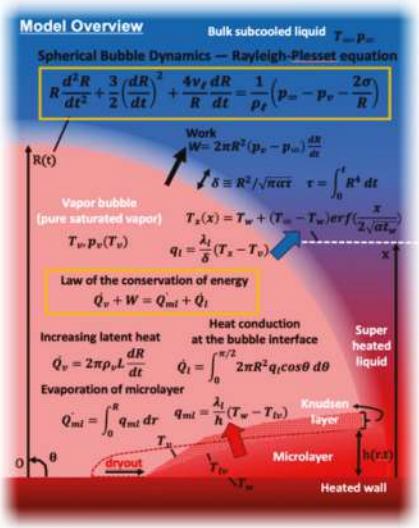

Fig. 1 Overview of bubble growth model.

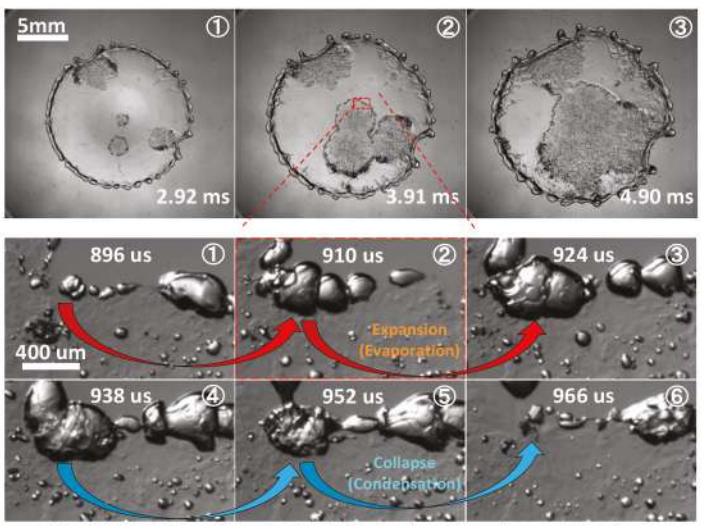

Fig. 2 Circular subcooled boiling region in an impacting drop.

*Corresponding author. E-mail: mshirota@hirosaki-u.ac.jp

change of vapor inside the bubble due to the evaporation and condensation on the bubble surface Q_v. The conservation of energy therefore reads $Q_v + W = Q_{ml} + Q_l$.

RESULTS AND DISCUSSION

Typical images of subcooled boiling in an impacting drop is shown in Fig. 2. We see from this figure that at about 3 ms after the contact of the drop with the heated solid four circular boiling regions started to grow and fully covered the spreading drop in about 4 ms. A close observation of the circular boiling region revealed that bubbles continued violent expansion and collapse at the front while inside the circle the bubble motions were very gentle.

The circular boiling region originated from a single bubble collapse which is clearly shown in Fig. 3. In this figure, the boundary between a microlayer and a dry-out region can be observed with backlighting as the boundary has a large difference in refractive index and the curvature. We can also observe the formation of a droplet ring from the residue of the microlayer. We also revealed from the observations that bubbles collapse soon after the microlayer was dried out. Interestingly, if we increased the initial drop temperature, the violent bubble oscillation disappeared. Therefore, we conclude the bubble growth is mainly driven by the heat supply from microlayer. The shrink should be then occurred when the heat release to the subcooled surrounding liquid exceeds the heat supply.

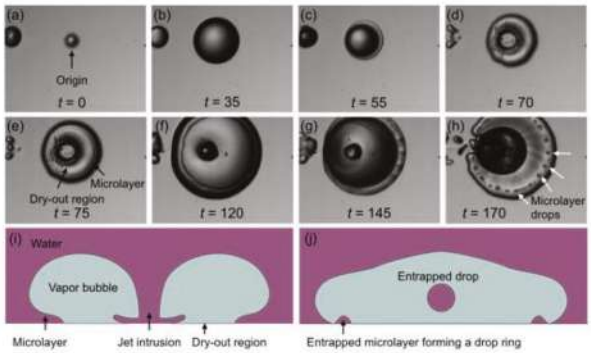

Fig.3 Images of the onset of circular boiling region (a-h) and schematic drawings showing the formation of microlayer (i) and microlayer drop ring (j).

In order to evaluate the validity of our model and to investigate the effect of microlayer and the temperature distribution in the thermal boundary layer developed on the heated solid, we first compare in Fig. 4 our experimental results on the time change in bubble radius with that of model predictions without microlayer for different drop temperatures T_∞. Note here that we used the same initial conditions for all the model predictions. Figure 4 clearly shows that without the microlayer the bubble cannot grow enough with the experimental condition, i.e., the initial drop temperature $T_\infty = 25$ °C.

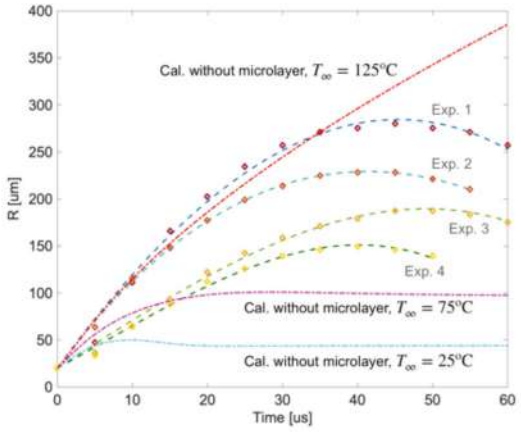

Fig.4 Comparison on the bubble radius between experimental value and model prediction without microlayer.

We therefore conclude that both the microlayer and the thermal boundary layer play crucial roles in the evolution of subcooled boiling in an impacting drop. To investigate the contributions more specifically, we look into the energy budget to confirm the assumption in our model, i.e., bubble starts to shrink when the microlayer is dried out and the heat release to the surrounding subcooled liquid exceeds the heat supply. To proceed the analysis, we have to know $Q_{ml}(t)$ for given $R(t)$. The difficulty in this problem arises from the fact that to apply the Fourier's law for the heat conduction in microlayer we have to specify the temperature at the interface between the Kunudsen layer and the bulk vapor, T_{lv}, see Fig. 1. In the present analysis, ewe adopted a kinetic boundary condition [3] to obtain T_{lv}.

By giving experimentally obtained $R(t)$ and its derivatives, we evaluated the energy budget as shown in Fig. 5. We find in this figure that in case of $T_\infty = 25$ °C, $dQ_{ml} \approx W + dQ_v - dQ_l$. This evidence confirms that our assumption in the modeling does not lose the essence of the physics regardless of its simplicity.

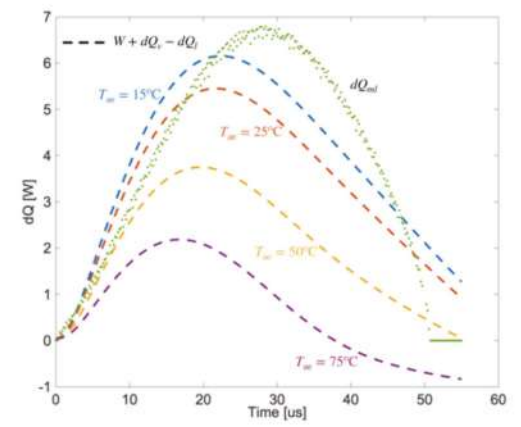

Fig.5 Energy budget estimated by the model prediction with experimentally obtained bubble radius $R(t)$ and its derivatives.

References

[1] Koizumi Y., Shoji M., Monde M., Takata Y. and Nagai N. Boiling: Research and Advances., Elsevier, 2017.

[2] Plesset M. S. and Zwick S. A. The growth of vapor bubbles in superheated liquids, *J. Appl. Phys.* **25**, 493—500, 1954.

[3] Kon M., Kobayashi K. and Watanabe M. Kinetic boundary condition in vapor-liquid two-phase system during unsteady net evaporation/condensation, *Eur. J. Mech. B/Fluids* **64**, 81-92, 2017.

RAYDROP : A UNIVERSAL DROPLET GENERATOR BASED ON A NON-EMBEDDED "CO-FLOW-FOCUSING"

Adrien Dewandre[1], Javier Rivero-Rodriguez[1], Youen Vitry[1], Benjamin Sobac[1], and Benoit Scheid*[1]
[1] TIPs Lab, Université libre de Bruxelles, Brussels, Belgium

Summary We present a new configuration based on the alignment of two capillaries immersed in a pressurized chamber containing a continuous phase. The dispersed phase exits one of the capillary through a 3D-printed nozzle, placed in front of the extraction capillary for collecting the droplets. This non-embedded and co-flowing implementation of an axisymmetric flow-focusing is referred to as the Raydrop device. Experimental results demonstrate the universality of the Raydrop in terms of the variety of fluids that can be emulsified, as well as the range of droplet radii that can be obtained, without neither the need of surfactant nor coating. Numerical computations of the Navier-Stokes equations based on the quasi-steadiness assumption are shown to correctly predict the droplet radius in the dripping regime, as well as the dripping-jetting transition, when varying the geometrical and fluid parameters.

THE RAYDROP DEVICE

Most commercial microfluidics droplet generators rely on the planar flow-focusing configuration implemented in polymer or glass chips. The planar geometry, however, suffers from many limitations and drawbacks, such as the need of specific coatings or the use of dedicated surfactants, depending on the fluids in play. On the contrary, and thanks to their axisymmetric geometry, glass capillary-based droplet generators are a priori not fluid-dependent. Nevertheless, they have never reached the market because their assembly requires art-dependent and not scalable fabrication techniques.

The device presented in this paper relies on the alignment of two glass capillaries inside a pressurized chamber, forcing by flow-focusing the tip-streaming regime as presented by Evangelio *et al.* [1]. A 3D-printed micro-nozzle is additionally connected at the tip of the injection capillary (see Fig. 1(d)), enforcing the dripping of small droplets as in embedded axisymmetric co-flow (see Utada *et al.* [2]). Therefore, our non-embedded design presents both the characteristics of

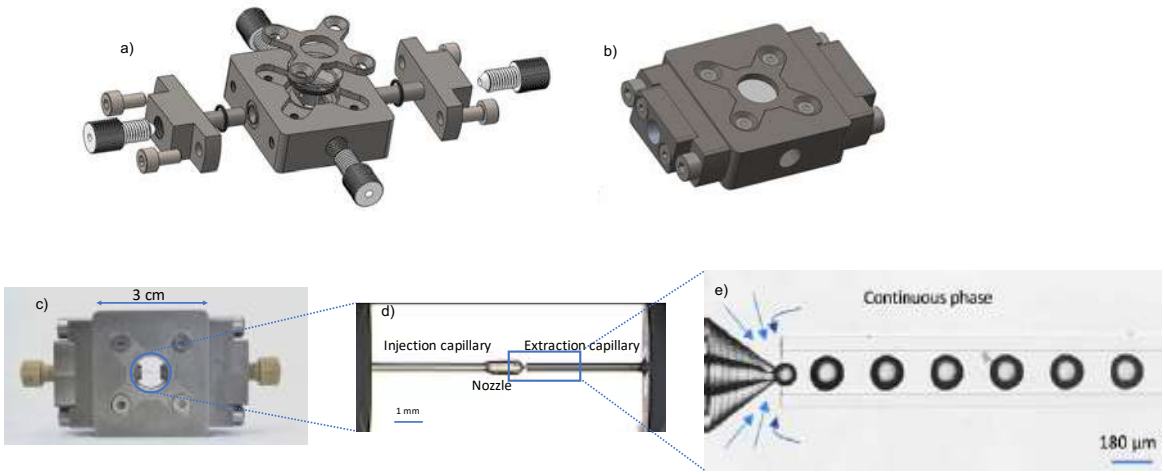

Figure 1: (a) Exploded view and (b) assembled view of the Raydrop. (c) The Raydrop with the injection and extraction glass capillaries. (d) Zoom through the top window of the two capillaries aligned in the chamber filled with the continuous phase. (e) Zoom on the droplet generation area. The 3D-printed nozzle connected to the injection capillary carries the dispersed phase while the extraction capillary collects droplets of the dispersed phase entrained by the continuous phase. At the entrance of the extraction capillary, the continuous phase is dramatically accelerated because of the change of section and squeezes the dispersed phase, resulting in the droplets formation.

a co-flow (axisymmetric geometry) and a flow-focusing (dramatic local accelerations of the continuous phase), and is thereby called non-embedded "co-flow-focusing". The technological breakthrough of this design is two-folds. Firstly, it enables high-throughput generation of mono-disperse droplets, intrinsic to the dripping regime, for a wide variety of fluids, thanks to the fact that the continuous phase is not confined before entering the extraction capillary, allowing for flushing very viscous continuous phases. Secondly, it takes benefit of specific fabrication techniques and materials compatible with a large-scale production of the device, while ensuring a very precise and reproducible alignment of the two capillaries in the chamber. Additionally, the device is made plug-and-play thanks to the standard connections and the possibility to easily assemble and disassemble all parts for cleaning.

EXPERIMENTAL AND NUMERICAL RESULTS

Excellent agreement between droplet radius measured experimentally and predicted by transient modeling, as shown in Fig. 2, confirms that the droplet generation essentially depends on the geometrical parameters as well as on the flow-rate of the continuous phase, and shows little sensitivity to the flow rate of the dispersed phase. This little sensitivity

*Corresponding author. E-mail: bscheid@ulb.ac.be

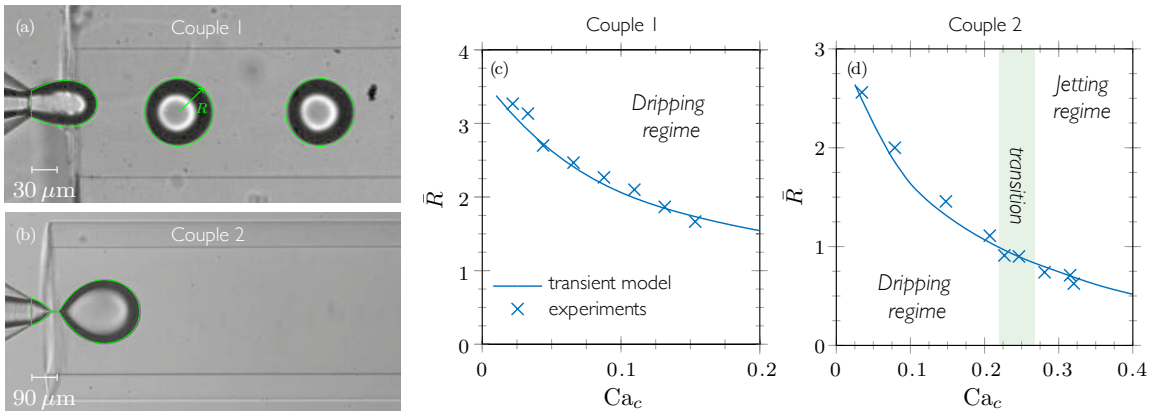

Figure 2: (a-b) Comparison between transient simulations (green lines) and experimental pictures for the formation of water drops in mineral oil for two geometries referred to "Couple" 1 and 2; (c-d) comparisons of dimensionless droplet radius for various values of the capillary number of the continuous phase, Ca_c. The shaded area in (d) shows the experimental dripping-jetting transition.

allows to consider a quasi-static (QS) model for which the dispersed flow rate tends to zero, recovering a system very analog to the pendent droplet, provided the gravity force is replaced by viscous forces. And as in the pendent droplet problem, the dripping mechanism can be associated to the bifurcation point in terms of droplet volume for which viscous forces are not balanced anymore by surface tension forces. This bifurcation point depends on the capillary number of the continuous phase Ca_c and it is shown to disappear at a transition Ca_c^* above which force equilibrium remains possible, which then corresponds to the jetting mode in the quasi-static limit, precursor of the tip-streaming regime. Figure 3 shows the dripping-jetting transition as predicted in the quasi-static limit in function of the viscosity ratio λ between the dispersed and the continuous phase. The influence of inertia has also been studied, as quantified by the Laplace number

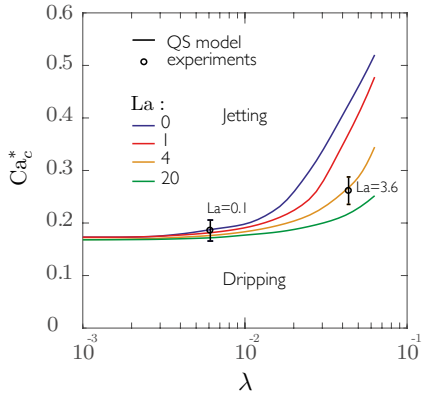

Figure 3: Influence of λ on the dripping-jetting transition at Ca_c^* in the quasi-static dripping regime for different values of the Laplace number La gauging the role of inertia. The geometry of "couple" 2 has been used. The point for $La = 3.6$ corresponds to the experimental transition identified in Fig. 2(d) and show an excellent agreement.

La (which corresponds to the Reynolds number defined with the capillary-viscous velocity). We found that, thought the drop size prediction is essentially independent on inertia, the prediction of the dripping-jetting transition does. Actually, it enhances the dripping-jetting transition, i.e. Ca_c^* decreases with increasing La for a fixed λ, and this enhancement is more pronounced as λ increases. On the contrary, inertia plays almost no role in the inviscid limit, i.e. for $\lambda \to 0$.

CONCLUSIONS

The present paper shows the ability of the Raydrop device to produce droplets with diameters in the range from 20 to 400 μm and with various fluids (water, oil, organic solvent, polymer resin, air). The monodispersity ensured by the dripping regime, the robustness of the fabrication technique, the universality of the axisymmetric configuration, and the optimization capabilities from the numerical modeling relying on the quasi-static assumption, confer to the Raydrop device a very high potential in the race towards high-throughput droplet generation processes through parallelization.

References

[1] A. Evangelio, F. Campo-Corts, and J. M. Gordillo. Simple and double microemulsions via the capillary breakup of highly stretched liquid jets. *Journal of Fluid Mechanics*, 804:550–577, 2016.

[2] A. S. Utada, E. Lorenceau, D. R. Link, P. D. Kaplan, H. A. Stone, and D. A. Weitz. Monodisperse Double Emulsions Generated from a Microcapillary Device. *Science*, 308(5721):537–541, 2005.

EFFECT OF SUBSTRATE STIFFNESS ON THE MAGNETOWETTING DYNAMICS OF SESSILE FERROFLUID DROPLETS

Bhaskarjyoti Sarma *, Dipankar N. Basu, and Amaresh Dalal
Department of Mechanical Engineering, Indian Institute of Technology Guwahati, Assam, India-781039

Summary Magnetic field mediated wetting of paramagnetic sessile droplets has been studied extensively. However, the wetting dynamics and shape evolution of a ferrofluid droplet are substantially altered by the substrate compliance, as elucidated in the present experimental study. For example, the rigid surfaces offer less resistance to the droplet contact-line motion, while the softest substrate pins the contact line. Next, we find that both wetting time and the wettability increases with the decrease in the stiffness of the underlying substrate. Further, the non-uniform magnetic field was able to split the parent droplet into a secondary droplet, which size increases with the increasing softness of the substrate. The study is fundamentally essential for paving building blocks for futuristic applications involving elasto-magnetocapillary interactions.

INTRODUCTION

The wetting nature of ferrofluid droplets in a uniform or non-uniform magnetic field has received considerable attention in the last few decades owing to its unmatched applicability in many industrial processes, which involves mechanical sealing and acoustics [1], tissue engineering [2], magnetic self- assembly [3], etc. to name a few. Apart from these dynamical systems, the static deformation of a paramagnetic droplet has also been one of the prime subjects of investigations in the recent past [4,5]. Interestingly, the aforementioned static magnetowetting studies haven't taken the stiffness and wettability of the underlying substrate into account.

Here, we experimentally elucidate the wetting dynamics of ferrofluid (FF)droplets on substrates of different stiffness and wettability. Our prime intention is to co-relate the change in apparent dynamic contact angle and the motion of the air-liquid-solid three-phase contact line to the substrate compliance. We believe this study will shed light on the previously unexplored magneto-elastocapillary regime, a potential host for cutting edge applications in the future.

EXPERIMENTAL DETAILS

Figure 1*a* shows the schematic of the experimental set-up for this study, wherein a ferrofluid (EMG 408, Ferrotec, USA) droplet is dispensed atop a solid substrate with the help of a micropipette and subsequently a permanent magnet (Rectangular rare earth neodymium magnets (N52); dimensions: 10 mm $\times$ 20 mm $\times$ 2 mm) is placed atop the droplet to create a non-uniform magnetic field in the vertical (z-axis) direction (refer to figure 1*b*). The solid substrates are chosen to get a range of substrates stiffness, including rigid glass substrate to thin PDMS film-coated glass substrates. We mix PDMS (polydimethylsiloxane, Sylgard 184) and cross-linker (both purchased from Dow Corning, Wiesbaden, Germany) in three different ratios, namely 10:1, 30:1 and 50:1 resulting in substrates with elastic modulus, E = 1.5, 0.06, and 0.02 respectively. The thickness of the aforementioned PDMS coated surfaces ranges from 2 to 4 μm, while the surface roughness is approximately 2 $\pm$ 0.3 nm. The magnet is attached to a vertically movable frame, thereby facilitating the generation of a desired magnetic field. Here we have experimentally investigated the spatiotemporal evolution of a 3 μL FF droplet when the magnet is placed above at a distance, H = 4.71 mm (measured from the surface of the substrate), resulting in a magnetic field, B_z = 450 mT.

We have employed a continuous videography method after evaluating the temporal scale of deformations. The videos are recorded with a Sony camcorder at a rate of 25 frames per second, while the background is illuminated with a white LED light giving a sharp contrast to the snapshots recovered. The image analysis is done by ImageJ [6] software.

RESULTS AND DISCUSSIONS

In this study we evaluate the temporal variations in droplet dynamic contact angle, (θ_d or θ_d^*) and contact radius (r_d or r_d^*), as a measure of the deformation of the FF droplet in the presence of a magnetic non-uniform magnetic field in axial direction. Figure 2(*a-i*) exhibits a brief overview of the droplet deformation process in the magnetic environment. Briefly, the initially hemispherical droplet (t =0) experiences a pull in the vertical portion, resulting in elongation of the apex as well as the movement of the contact line along the surface. The droplet after reaching its maximum elongation splits into two parts as soon as magnetic force overcomes the surface tension force as seen in the final snapshot.

As the droplet elongates the θ_d (or θ_d^*) and r_d (or r_d^*) is also modified depending upon the stiffness of the underlying substrate as shown in figure 2(*j-k*). Here we have non-dimensionalized the time with the splitting time (t_s), defined as the time period from t = 0 to the instant of droplet splitting and the r_d and θ_d with their initial equilibrium values. It can be discerned that the contact line gradually decreases from its maximum to a lower value until the droplet is fragmented except for a rigid glass surface. For the rigid glass surface, the contact angle initially decreases to a lower value, beyond

*Corresponding author. E-mail: bhaskar.sarma25@gmail.com

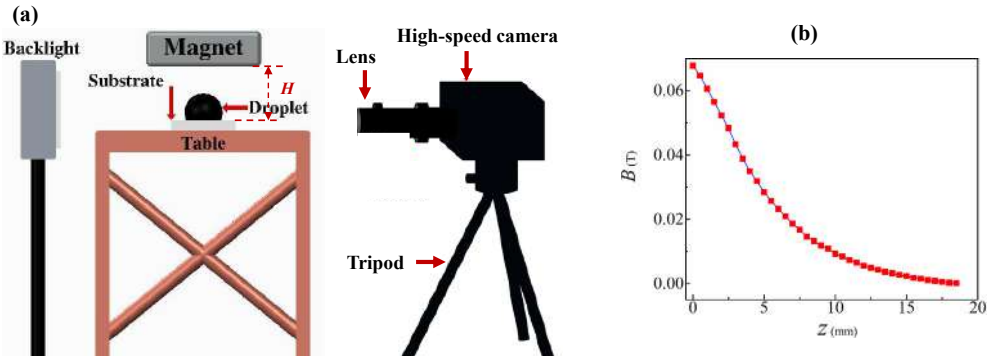

Figure 1: (a) Schematic of the experimental set-up. (b)Magnetic flux density (B) as a function of the vertical gap (H) between the magnet and the bottom substrate.

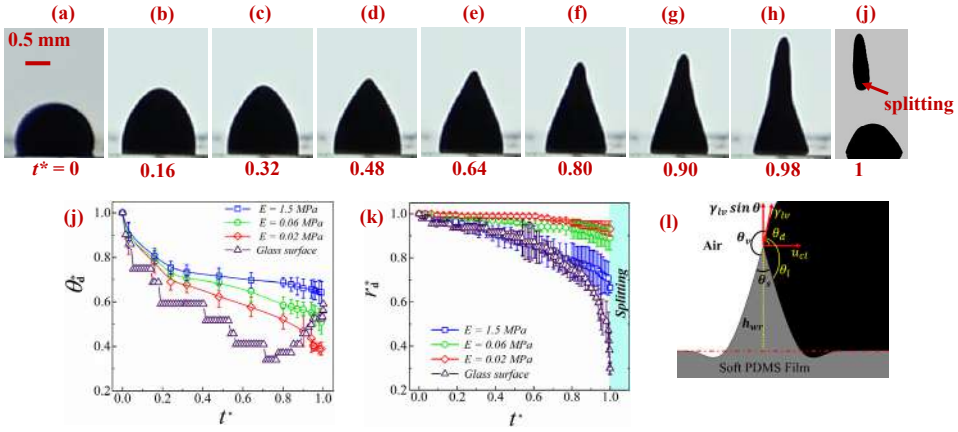

Figure 2: (a)-(i) Shape evolution of a FF droplet on a 10:1 PDMS surface. (j) and (k) variations in θ_d^* and r_d^* with time for all the substrates of this study. (l) schematic of wetting ridge formation on soft substrate (30:1 and 50:1 PDMS surface).

which it increases. In contrast, the contact radius, r_d^*, decreases approximately by 80 % for the rigid glass surface, whereas for the soft viscoelastic surfaces, the radius nearly remains constant for the whole deformation cycle. For example, for the softest PDMS surface (50:1), the change in radius is approximately 4 % till the instant of breakup of the droplet.

The anomalous behavior of the θ_d^* on a glass surface can be attributed to the higher wettability of the water-based FF on the former. While a spherical cap approximation can approximate the droplet on the PDMS based hydrophobic surfaces, the droplet takes the shape of the elliptical lens on the glass surface before the application of the magnetic field. Further, the near pinning behaviour of the contact radius on the soft substrate can be attributed to the formation of wetting ridges at the contact line [7]. The softer the substrate, the larger the wetting ridge and hence higher the pinning. Due to the absence of pinning the contact radius can move freely on a rigid surface like glass during magnetowetting. Furthermore, the secondary droplet size also depends on substrate stiffness which couldn't be shown due to page limitation.

CONCLUSIONS

A sessile FF droplet experiences sever deformation leading to the splitting in a non-uniform magnetic filed. The change in contact angle and radius during deformation depends strongly on softness of the underlying substrate. Soft substrates favours formation of large wetting ridge and promotes pinning of the contact line.

References

[1] Raj, K., Moskowitz, B., Casciari, R. Advances in Ferrofluid Technology. *J. Magn. Magn. Mater.* **149**:174–180, 1995.
[2] Timonen, J. V., Latikka, M., Leibler, L., Ras, R. H., Ikkala, O. Switchable Static and Dynamic Self-assembly of Magnetic Droplets on Superhydrophobic Surfaces. *Science* **341**:253-257, 2013.
[3] Huang, G., Li, M., Yang, Q., Li, Y., Liu, H., Yang, H., Xu, F. Magnetically Actuated Droplet Manipulation and its Potential Biomedical Applications. *ACS Appl. Mater. Interfaces*, **9**:1155-1166, 2017.
[4] Nguyen, N. T., Zhu, G., Chua, Y. C., Phan, V. N., Tan, S. H. Magnetowetting and Sliding Motion of a Sessile Ferrofluid Droplet in the Presence of a Permanent Magnet. *Langmuir*, **26**:12553-12559, 2010.
[5] Banerjee, U., Sen, A. K. Shape Evolution and Splitting of Ferrofluid Droplets on a Hydrophobic Surface in the Presence of a Magnetic Field. *Soft Matter*, **14**:2915-2922, 2018.
[6] Schneider, C. A., Rasband, W. S., Eliceiri, K. W. NIH Image to ImageJ: 25 Years of Image Analysis. *Nat. Methods*, **9**:671, 2012.
[7] Sarma, B., Shahapure, V., Dalal, A., Basu, D. N. Magnetowetting dynamics of sessile ferrofluid drops on soft surfaces. *Soft Matter*.

ASYMMETRIC BUBBLE PINCH-OFF IN TURBULENCE

Daniel J. Ruth[1], Wouter Mostert[1], Stephane Perrard[1,2], and Luc Deike *[1]
[1] Department of Mechanical and Aerospace Engineering, Princeton University, Princeton, United States
[2] Departement de Physique, Ecole Normale Superieure, PSL (Paris Sorbonne Lettres) Research University, Paris, France

Summary We study the pinch-off of a bubble surrounded by a turbulent flow, in which the turbulence initially deforms the bubble and sets a complex bubble shape that prescribes the dynamics of the inertial collapse. The mean power-law behavior remains similar to that expected for an axisymmetric bubble in a quiescent fluid, but the turbulent deformations introduce shape asymmetries which persist through the collapse [1]. Specifically, the bubble's size relative to the scale at which turbulence is balanced by surface tension controls the appearance of a kink-like structure in the neck. Here, we analyze the spatial asymmetries in the neck collapse by contrasting the motions of four separate points on the neck, each imaged with a high-speed camera, with the mean collapse dynamics, finding greater variability than would be inferred by just considering the mean behavior.

BACKGROUND

In recent decades, much theoretical and experimental effort has been put into understanding the process by which an axisymmetric bubble or droplet splits into multiple "child" pieces. The final part of this process involves the "pinch-off" of the neck of fluid separating the two lobes by the surrounding fluid. During this phase, the mean radius of the neck $\overline{r}$ shrinks as a power law collapse $\overline{r} \sim (t_0 - t)^\alpha$, where t_0 is the pinch-off time and α is the similarity exponent. When dominated by the inertia of the continuous phase (as is the case for an air bubble breaking apart under water), α is a slowly-varying exponent approaching $1/2$ [2]. In industrial and environmental processes in which bubbles break apart, though, surrounding turbulence will prevent the bubble's initial condition from being axisymmetric, instead introducing a deformed initial condition for the pinch-off. We aim to describe bubble pinch-off in these realistic conditions in which multi-scale perturbations are present.

TURBULENT DEFORMATIONS AND FREEZING

In this study, we investigate the pinch-off of a bubble underwater that is surrounded by a homogeneous and isotropic turbulent flow in the continuous phase. The turbulence deforming the bubble is characterized by its energy dissipation rate ϵ, while the surface tension σ of the air-water interface acts to minimize the surface area of the bubble. With these parameters and the water density ρ, we can construct the Hinze length scale $d_\mathrm{H} = (\sigma/\rho)^{3/5}\epsilon^{-2/5}/2$, which is the length scale at which turbulent stresses are balanced by surface tension [3]. When the bubble, whose size is comparable to the diameter of the needle through which it is injected d_n, is much smaller than d_H, surface tension is able to counteract the turbulent stresses, and the bubble shape is not significantly deformed compared to the quiescent case. When $d_\mathrm{n} > d_\mathrm{H}$, however, the turbulent stresses dominate, and the bubble is significantly deformed by the turbulence as the neck pinches off.

With a power-law collapse given by $\overline{r} = r_\tau[(t_0 - t)/\tau]^\alpha \equiv c(t_0 - t)^\alpha$, where the neck has a radius r_τ at a time τ before pinch-off, the relative speed of two opposing points on the neck is $2\overline{v}_\mathrm{col} = 2\alpha c(t_0 - t)^{\alpha-1}$. Expressed as a function of the mean neck size, $2\overline{v}_\mathrm{col} = 2\alpha c^{1/\alpha}\overline{r}^{1-1/\alpha}$. This permits a comparison to the typical velocity difference between two points separated by a distance $2\overline{r}$ in the turbulence, which is $v_\mathrm{turb} = 2^{5/6}(\epsilon\overline{r})^{1/3}$ in the inertial subrange of the turbulence. The ratio of the two speeds is $2v_\mathrm{col}/v_\mathrm{turb} = \alpha c^{1/\alpha}\epsilon^{-1/3}\overline{r}^{2/3-1/\alpha}/2^{1/3}$. So long as $\alpha < 3/2$, the collapse rate becomes much greater than the local turbulent velocity scale once $\overline{r}$ shrinks beyond

$$r_\mathrm{freeze} = \left(2^{1/6}\epsilon^{1/3}c^{-1/\alpha}\alpha^{-1}\right)^{3\alpha/(2\alpha-3)},$$

so for $\overline{r} \ll r_\mathrm{freeze}$ we expect an inertial collapse controlled by the initial and boundary conditions set by the turbulent field, no longer with any direct interaction between turbulent eddies and the shrinking neck. In a recent paper [1], we showed that on average, the neck collapse in such a scenario does follow the $\alpha \approx 1/2$ behavior characteristic of an inertial collapse. On a case-by-case basis, however, we observed rich dynamics in the form of neck shape modulations and deformation-induced "kinking" of the fluid neck, which are attributed to the turbulent stresses overcoming the bubble's restoring surface tension to deform the initial shape of the bubble. As $d_\mathrm{n}/d_\mathrm{H}$ increases, a kink is more likely to occur during the collapse, and it is more likely to happen earlier on, when the neck width is larger [1]. Prior to any kink, though, the neck collapse can still exhibit asymmetries while the azimuthal-averaged dynamics suggest an inertial collapse, a result of collapse having memory of its initial conditions [4]. Here, we expand on those results by investigating further the azimuthal asymmetries induced by the turbulence.

*Corresponding author. E-mail: ldeike@princeton.edu.

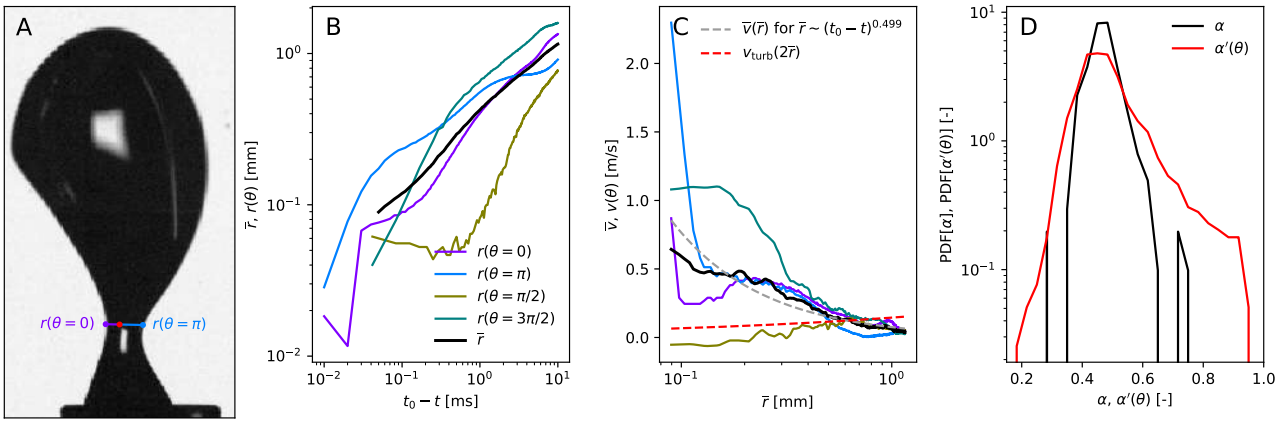

Figure 1: The pinch-off of a bubble rising into a turbulent field. (A) The bubble at $0.5\,\mathrm{ms}$ before pinch-off. Lines showing two of the four measured points on the neck $r(\theta)$ are shown in purple and blue, each measured from the pinch-off point, shown in red. (B) The distances between the pinch-off point and four imaged points on the neck $r(\theta)$, as well as the average neck size $\overline{r}$. (C) The collapse rate of the four sides of the neck $v(\theta,t) = -\partial r(\theta,t)/\partial t$, showing that the four sides of the neck collapse with different behavior. The mean collapse rate $\overline{v}$ and a power-law fit to it with $\alpha = 0.499$ are shown as the solid black and dashed gray lines, respectively. The dashed red line shows the turbulent velocity scale $v_{\mathrm{turb}} = 2^{5/6}(\epsilon\overline{r})^{1/3}$, which becomes much slower than the collapse velocities once the neck is very small. (D) The distribution of scaling exponents fit to the mean collapse curves from ~ 300 experiments, in black, and that of the exponents fit to the collapses of each of the four points measured on the neck, in red.

RESULTS AND DISCUSSION

Experimentally, we use two high-speed cameras viewing an air bubble rising from a needle into a turbulent water flow from 90° angles to track the collapse of the four resolved points on the neck (that is, the left and right side of the neck in each orthogonal view). This gives $r(\theta,t)$ for $\theta = 0, \pi/2, \pi$, and $3\pi/2$, where θ is the azimuthal angle around the neck cross-section, and each curve $r(\theta,t)$ measures the distance between the bubble interface and the eventual pinch-off point.

One of the two cameras' views is shown, along with the two distances corresponding to $r(\theta = 0)$ and $r(\theta = \pi)$, in Figure 1 a). The four collapse curves are shown along with the average collapse $\overline{r}$ in b), and the corresponding collapse velocities of the four points are shown in c) as a function of the mean neck size $\overline{r}$. The mean collapse rate is compared with a power-law collapse $\overline{v}_{\mathrm{col}} = a\overline{r}^{1-1/\alpha}$, with α and a fit to the data shown as the dashed gray line. Finding α in this manner, as opposed to with a fit to $\overline{r} \sim (t_0 - t)^{\alpha}$, alleviates the issue caused by the kink appearance modifying the pinch-off time. It is apparent that the close agreement between the experimentally-measured $\overline{v}$ curve, for which $\alpha = 0.499$, and that predicted for an inertial collapse, $\alpha \approx 1/2$, masks the complexities of the neck's collapse, which are evidenced by the differently-behaved $r(\theta,t)$ and $v(\theta,\overline{r})$ curves. Finally, the characteristic turbulent velocity over the neck scale, $v_{\mathrm{turb}}(2\overline{r}) = 2^{5/6}(\epsilon\overline{r})^{1/3}$, is shown as the dashed red line in Figure 1 c), showing that it is only comparable to the collapse velocities when the neck is relatively large.

For the ~ 300 cases of bubbles pinching off in turbulence with $0.27 \leq d_{\mathrm{n}}/d_{\mathrm{H}} \leq 1.63$ initially presented in ref. [1], we now perform the power-law fit to obtain the scaling exponent α describing the mean collapse for each case. Additionally, we fit $v(\theta) \sim \overline{r}^{1-1/\alpha'(\theta)}$ to find the power-law exponent $\alpha'(\theta)$ describing the motion of each of the four imaged points on the neck in each case. The distributions of α and α' are given in Figure 1 d). Each is centered near $1/2$, but there is a much wider variability in the local exponent $\alpha'(\theta)$ than the mean exponent α. Results from all cases with turbulence are included in this plot, but binning the results by $d_{\mathrm{n}}/d_{\mathrm{H}}$ reveals that the spread of $\alpha'(\theta)$ increases with increasing turbulence.

These results complement recent findings [1] by introducing a new metric, the local collapse exponent $\alpha'(\theta)$, as a measure of the local collapse dynamics. The wide distribution of $\alpha'(\theta)$ provides further evidence that while the mean dynamics of bubble collapse in turbulence may resemble the scaling expected for symmetric collapse in a quiescent fluid, the turbulence-induced deformations to the bubble's initial shape yield changes to the entirety of the collapse, even beyond the finite scales of the turbulence.

References

[1] Ruth, D. J., Mostert, W., Perrard, S., & Deike, L. (2019). Bubble pinch-off in turbulence. *Proceedings of the National Academy of Sciences*, 116(51), 25412-25417.

[2] Eggers, J., Fontelos, M. A., Leppinen, D., & Snoeijer, J. H. (2007). Theory of the collapsing axisymmetric cavity. *Physical review letters*, 98(9), 094502.

[3] Hinze, J. O. (1955). Fundamentals of the hydrodynamic mechanism of splitting in dispersion processes. *AIChE Journal*, 1(3), 289-295.

[4] Schmidt, L. E., Keim, N. C., Zhang, W. W., & Nagel, S. R. (2009). Memory-encoding vibrations in a disconnecting air bubble. *Nature physics*, 5(5), 343.

A UNIFIED EULERIAN MULTIPHASE FRAMEWORK FOR FLUID-STRUCTURE INTERACTION PROBLEMS INCLUDING CAVITATION

Mauro Rodriguez *[1], Spencer Bryngelson[1], Shunxiang Cao[1], and Tim Colonius[1]
[1] Division of Engineering and Applied Science, Department of Mechanical and Civil Engineering, California Institute of Technology, Pasadena, California, USA

Summary Understanding the impact load mechanisms from cavitation bubbles and shocks emitted by their collapse in and near solid deformable media is important for engineering and biomedical applications. In such flows, transient pressure fluctuations can lead to a cloud of small vapor bubbles near the solid object. A unified Eulerian framework for fluid-structure interaction problems including cavitation is developed to incorporate numerically unresolved and resolved bubbles and the solid material elasticity. The numerical model uses interface-capturing techniques for the fluid-structure coupling with phase change. The method is based on a high-order accurate weighted essentially non-oscillatory shock and interface capturing scheme. Studies of single bubble and cloud dynamics near a solid/compliant structure relevant to therapeutic ultrasound applications are presented.

INTRODUCTION

Understanding the bubble dynamics in or near compliant or hard matter is important for engineering and biomedical applications, particularly in the context of cavitation-induced damage. Biomedical applications include therapeutic ultrasound tools with ultrasound waves of amplitudes and frequencies ranging from -25 to 100 MPa and 100 kHz to MHz, respectively, to treat pathogenic tissues (soft) and stones (hard). Two examples of these tools are extracorporeal shockwave and burst wave lithotripsy, therapeutic ultrasound treatments using 4 to 40 MPa peak positive and -25 MPa peak negative pressure amplitudes and 100 kHz to MHz frequencies ultrasound waves, respectively, to break urinary stones (e.g., kidney and gall bladder stones). In burst wave lithotripsy, an array of ultrasound transducers emit focused ultrasounds waves that effectively fractionate larger stones due to the incident wave reflecting off the distal side of the stone switching sign and focusing to a maximum tensile stress. The negative pressure in the wave may lead to the generation of bubbles near the surface of the stone. The gas bubbles then respond to the burst wave by oscillating in volume, coalesce and forming larger bubbles, and/or collapse emitting shocks into the surroundings. The small stones have been shown to be most effective at eroding the stone.

To study these fluid-structure interaction problems, the challenge is to numerically simulate: (i) growth and coalescence of small bubbles in the bubble cloud to larger, resolvable bubbles and (ii) wave dynamics in the fluid(s) and nearby solid. During the oscillations, vapor can condense, gases can dissolve into the liquid, and vice versa across the bubble interface and affect the bubble dynamics. Unlike resolving a single bubble, resolving a population of bubbles in the bubble cloud is computationally unfeasible. These flows are typically modeled using a sub-grid model in an Eulerian framework [3, 4]. However, it is not well understood how to appropriately transition from a region in a bubble cloud where the unresolved (sub-grid) bubbles are sufficiently large to be resolved. Unlike the gas bubbles and surrounding liquid that lend themselves to an Eulerian framework, the nearby solid undergoes infinitely small to finite deformations that are well-suited to be captured in a Lagrangian framework. However, algorithmic complexity increases significantly with two separate solvers and coupling between them. Of the two current Eulerian approaches (i.e., hyperelastic (Godunov-based) and hypoelastic (conventional)) used to study wave dynamics and deformations in solids [2], the hypoelastic approach's algorithm is well-suited to incorporate elasticity to existing multiphase/multi-component numerical solvers [5]. Thus, we leverage the Eulerian numerical framework in the open-source Multi-component Flow Code (MFC) [1, 3, 8] in conjunction with (i) the heat and mass transfer relaxation approaches of [6, 7] and (ii) the hypoelastic numerical model of [5] to develop a numerical model and framework to solve multi-component fluid-structure interaction problems including multi-scale cavitation ranging from resolved singular bubbles to unresolved bubbles in a bubble cloud.

NUMERICAL MODEL AND METHODS

The open-source MFC solver, an Eulerian numerical shock- and interface-capturing method, is used to develop a unified numerical solver to solve 3D fluid-structure interaction problems with multi-scale cavitation. The solution is evolved in time using Runga-Kutta schemes. Approximate Riemann solvers (e.g., Harten-van Leer-Lax and contact, HLLC) in conjunction with a high-order accurate weighted essentially non-oscillatory schemes are used for upwinding the solution [1]. Bubble cloud model is an Eulerian-Eulerian sub-grid model [3] that resolves the cavitation bubble dynamics directly or models them via phase averaging, depending upon the characteristic length sizes and bubble number. The 6-equation numerical model of [6, 7] and associated relaxation procedures are solved to include heat and mass transfer (including phase change) at the material interfaces. As proposed by [5], evolution equations of the elastic contribution of the Cauchy stress tensor are solved to incorporate elasticity for material solid in the Eulerian numerical framework.

*Corresponding author. E-mail: mrdz@caltech.edu.

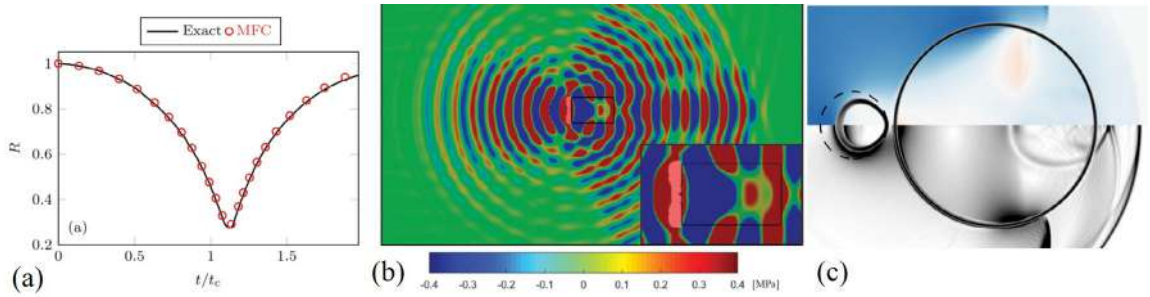

Figure 1: Cavitation bubble dynamics simulations: (a) validation of MFC with a resolved single spherical bubble collapse dynamics [8]; (b) pressure contours of MFC simulation of burst wave lithotripsy wave interacting with a cavitation cloud near a kidney stone (simulated as a stiff liquid) [4]; (c) Contours of pressure (top) and numerical Schlieren (bottom) of a single gas bubble collapsing near a spherical kidney stone using the hypoelastic approach of [5].

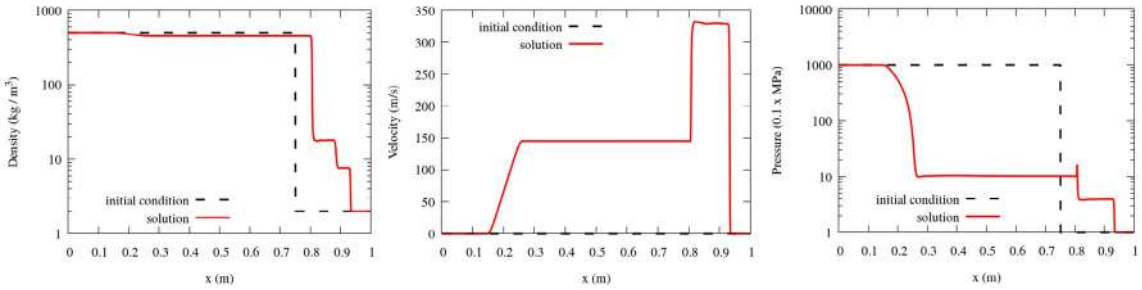

Figure 2: Dodecane liquid-vapor shock tube with mass transfer solved with MFC. The initial (black line) and numerical solution (red line) at $t = 400$ μs are shown.

RESULTS

A unified Eulerian numerical model and multiphase/multi-component framework for fluid-structure problems involving multi-scale cavitation has been developed using MFC. Figure 1 shows cavitation bubble dynamics simulations, the first two subfigures by MFC and third by the similar numerical framework of [5]. MFC has been validated for resolved, single spherical bubble dynamics (growth and collapse) with comparison to the numerical solution of the Keller-Miksis equation (see Fig. 1a) [8]. Numerical simulations of focused, burst wave lithotripsy experiments interacting with a bubble cloud at the surface of a cylindrical model kidney stone (represented by a stiff liquid) have been conducted in MFC to study the wave dynamics and damage mechanisms in the stone (see Fig. 1b) [4]. The numerical multiphase interface- and shock-capturing hypoelastic model of [5] and similar to MFC has been used to study the shock-induced single bubble collapse near a model spherical kidney stone (see Fig. 1c). The figure shows the transmission and internal reflection of the incident shock inside of the stone generating a focused region of tension (highlighted in red) inside of the stone as the bubble begins to collapse. Figure 2 shows the result of the dodecane liquid-vapor shock tube problem with mass transfer solved with MFC. The initial and numerical solutions at $t = 400$ μs are shown. A similar numerical solution of the density, showing the rarefaction, evaporation, contact and shock waves, velocity and pressure is also obtained by [7]. In addition to validation results, numerical simulations of fluid-structure problems involving the growth and collapse of a single bubble and/or bubble clouds with gas and vapor, undergoing phase change, in a liquid near a compliant or hard solid to understand the bubble and wave dynamics and associated damage mechanisms are also presented.

References

[1] Coralic, V., & Colonius, T., Finite-volume WENO scheme for viscous compressible multicomponent flows. J. Comp. Physics, **274**, 95–121, 2014.
[2] Gavrilyuk, S. L., Favrie, N., & Saurel, R. Modelling wave dynamics of compressible elastic materials. J. Comp. Physics, **227**, 2941–2969, 2008.
[3] Maeda, K., & Colonius, T., Eulerian–Lagrangian method for simulation of cloud cavitation. J. Comp. Physics, **371**, 994–1017, 2018.
[4] Maeda, K., Maxwell, A. D., Colonius, T., Kreider, W., & Bailey, M. R., Energy shielding by cavitation bubble clouds in burst wave lithotripsy. J. Acoustical Society of America, **144**, 2952–2961, 2018.
[5] Rodriguez, M., & Johnsen, E., A high-order accurate five-equations compressible multiphase approach for viscoelastic fluids and solids with relaxation and elasticity. J. Comp. Physics, **379**, 70–90, 2019.
[6] Pelanti, M., & Shyue, K. M., A mixture-energy-consistent six-equation two-phase numerical model for fluids with interfaces, cavitation and evaporation waves. J. Comp. Physics, **259**, 331–357, 2014.
[7] Saurel, R., Petitpas, F., & Abgrall, R. Modelling phase transition in metastable liquids: application to cavitating and flashing flows. J. Fluid Mech., **607**, 313–350, 2008.
[8] Schmidmayer, K., Bryngelson, S. H., & Colonius, T., An assessment of multicomponent flow models and interface capturing schemes for spherical bubble dynamics. J. Comp. Physics, **228**, 2019.

BUBBLE BREAK-UP STATISTICS IN AN HOMOGENEOUS AND ISOTROPIC TURBULENT BACKGROUND

Aliénor Rivière *[1,2], Wouter Mostert[2], Stéphane Perrard[1,2], and Luc Deike[2,3]
[1] Département de Physique, ENS, PSL Université, CNRS, 24 rue Lhomond, 75005 Paris.
[2] Department of Mechanical and Aerospace Engineering, Princeton University, Princeton, USA
[3] Princeton University, Mechanical and Aerospace engineering, Princeton, USA

Summary We study the break-up of a gas bubble in a much denser turbulent flow, a crucial problem for bubble mediated gas transfer at the ocean-atmosphere interface, by performing ensembles of direct numerical simulations (DNS). We investigate the effect of the Weber number, We, defined as the ratio of turbulent and surface tension forces, on the bubble life time, the number of children and their size distribution. We confirm that life time is given by the eddy turnover time at its scale, with a much broader distribution in the vicinity of the critical We below which bubbles are stable. The number of children increases with We along with a wider distribution of radius. We propose a scaling law for the children number as a function of the mother We and the time elapsed since the mother break-up. We adapt a model for the size distribution, valid for binary break-up and all investigated We.

INTRODUCTION

The description of bubbles generated by breaking waves is of strong interest in the understanding of the interactions between the atmosphere and oceans [1], bubbles having a dramatic effect on gas transfer [2]. The smallest bubbles tend to dissolve in water whereas larger ones rise to the surface and collapse. The bursting of bubbles at the surface produces sea spray aerosols, that can be transported in the atmosphere and evaporate, playing a role in the thermodynamics of the atmosphere. As a consequence, improving the accuracy of climate models requires a better description of air entrainment and bubble statistics under breaking waves and a better understanding of the dynamics of bubbles in a turbulent flow. Moreover, bubbles in turbulence appear in other contexts, such as by air entrainment by ships and submarines, and they have practical implications in petroleum engineering for transportation in pipe flows [3].

The size distribution of bubbles under a breaking wave has been studied both experimentally [4] and numerically [5] and a model for the size distribution has been developed [6] for bubbles above a critical scale, the Hinze scale, which balances surface tension and deformation induced by turbulence. However, for bubbles below this critical scale, the statistics remains poorly characterized and the formation mechanisms are still to be determined [5]. The critical Hinze scale is equivalent to a critical Weber number, of order unity, W_{e_c}, and reads $d_H = C_\epsilon^{2/5}\epsilon^{-2/5}\sigma^{3/5}\rho^{-3/5}$, where ϵ is the turbulent dissipation rate, ρ the density of the liquid, σ the surface tension and $C_\epsilon \approx 2$ is a numerical coefficient. For bubbles initially close to the Hinze scale, binary break-up has been described and various models have been proposed for the size of the child bubble and the break-up time [7]. However, for Weber numbers far from the critical conditions, little quantitative information is available. In this study, we explore the physics of bubble break-up at various Weber numbers, and describe the resulting size distribution.

ENSEMBLE OF STATIONARY STATE SIMULATIONS AT VARIOUS WEBER NUMBER

We perform direct numerical simulation (DNS) of the two-phase, three-dimensional, incompressible Navier-Stokes equations with surface tension. We use the free software Basilisk, which is based on an spatial adaptive quad/octree grid allowing to save computational time while resolving the different length scales of the problem, combined with a geometric volume-of-fluid reconstruction of the interface [8]. As discussed in the recent review of Elghobashi [3], direct numerical simulations of two-phase turbulent flow are challenging, and so far bubble breakup in turbulence has only been studied using diffusive interface techniques.

The simulations are performed in a two-step process. First, we perform a precursor simulation and create an homogeneous and isotropic turbulent flow in a cubic box using forcing in real space as proposed by Rosales and Meneveau [9], and obtain a statistically stationary state, characterized by the Reynolds number Re_λ. Second, a bubble is injected in the box at a given time and we follow the bubble deformation and break-ups, the initial bubble being characterized by the Weber number W_e. Figure 1 shows a sequence of snapshot extracted from a numerical simulation performed at $Re_\lambda = 37$ and $W_e = 2$ in which two successives binary break-ups occur. We observe that the same numerical parameters but different instantaneous flow states lead to a variable bubble number and child size distribution, due to the chaotic nature of the velocity and pressure fluctuations. To account for the sensitivity to the initial conditions we follow a statistical approach, and perform an ensemble of simulations (between 20 to 40) for each set of parameters by considering different times in the precursor. Each simulation runs until a stationary state in terms of number of bubbles is reached: all child bubbles that could break have broken. We perform ensembles at $Re_\lambda = 37$ spanning various Weber numbers, $W_e \in \{2, 5, 10, 15\}$ and investigate sensitivity to Reynolds number with two more ensembles at $Re_\lambda = 76$ and $W_e \in \{2, 5\}$. The values of Reynolds number reached are typical of what is accessible in two-phase simulations of turbulent flow [3]. Mesh size

*Corresponding author. E-mail: alienor.riviere@ens.fr.

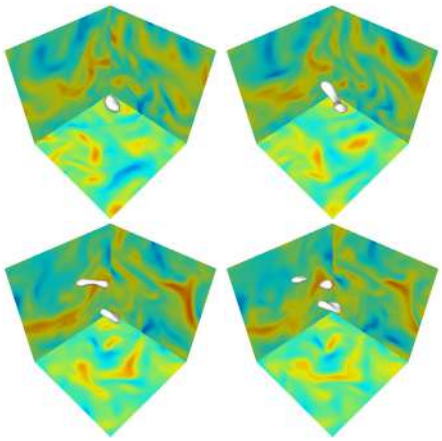

Figure 1: Snapshots of bubble break-up in turbulence from DNS of the two-phase Navier-Stokes equations using the solver Basilisk. Each background plane shows one component of the velocity. Bubbles interfaces are represented in white. Parameters are $R_{e_\lambda} = 37$ and $W_e = 2$. We observe two successive binary breakups leading to the creation of three child bubbles.

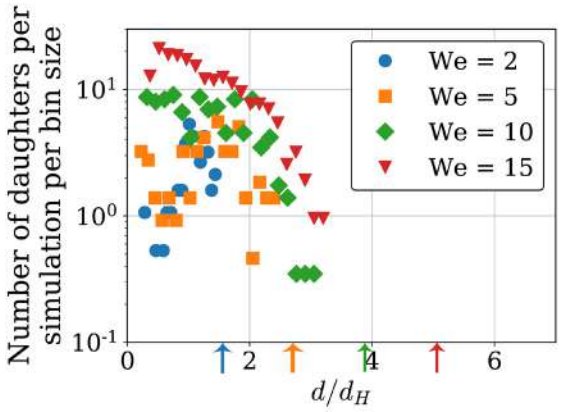

Figure 2: Child bubble size distribution for various initial Weber number for $R_{e_\lambda} = 37$, the diameter is made dimensionless by using the Hinze lengthscale d_H. The arrows represent the initial injection sizes for each ensemble. More bubbles of smaller sizes compared to the injection size are created when We increases.

convergence tests, as well as sensitivity tests to the adaptive mesh refinement criteria have been performed to ensure the physical accuracy of the results.

From this extensive data set, we analyze the final size distribution of child bubbles after multiple break-up events as a function of the initial Weber number. At low initial Weber number, $W_e = 2$ close from the critical Weber number, the majority of the break-ups are binary, with two child bubbles of similar sizes, just below the Hinze scale, as shown by the final averaged size distribution in fig. 2. This corresponds to a classic break-up scenario close to critical conditions, and described in previous studies [7]. At higher initial Weber number, $W_e > 10$, more bubbles are formed, with a broader distribution of sizes, with bubbles up to an order of magnitude smaller than the initial bubble, as shown in fig. 2.

Next, we analyze each break-up individually and characterize the life time of the bubbles as well as the number of bubbles being formed in a given time, for various instantaneous mother Weber numbers We^M. The life time of bubbles depends primarily on their Weber number and scales with t_c the eddy turnover time at the scale of the initial bubble, with the distribution of life times broadening for Weber number close to critical conditions. As multiple break-up events occur, we characterize the average number of bubbles, $\bar{N}$, created during a given observation time after the first break-up Δt, the first break-up defining the mother Weber number W_e^M. We obtain an empirical functional form $\bar{N} = f(W_e^M, \Delta t)$ which describe the entire range of Weber numbers that we explore and a duration time in the range $\Delta t \in [0, 9t_c]$. Finally we characterize the child bubble distribution when considering every break-up independently, depending on the Weber number of the mother, W_e^M, by modifying existing models in the literature [7]; which accounts for binary break-up and is valid at all Weber number.

In this work we have quantified how bubble break-up in turbulence is controlled by the relative strength between the turbulent fluctuations and the bubble cohesion due to surface tension. We have described both the statistical and the dynamical properties through the analysis of the bubble life time, the children size distribution at infinite and short times, and the number of child bubbles. This work paves the way for further theoretical description of bubble break-up in turbulence.

References

[1] Ralph F Keeling. On the role of large bubbles in air-sea gas exchange and supersaturation in the ocean. *Journal of Marine Research*, 51(2):237–271, 1993.

[2] L. Deike and W. K. Melville. Gas transfer by breaking waves. *Geophysical Research Letters*, 45(19):10,482–10,492, 2018.

[3] S. Elghobashi. Direct numerical simulation of turbulent flows laden with droplets or bubbles. *Annual Review of Fluid Mechanics*, 51(1):217–244, 2019.

[4] G. B. Deane and M. D. Stokes. Scale dependence of bubble creation mechanisms in breaking waves. *Nature*, 418:839–844, August 2002.

[5] L. Deike, W. K. Melville, and S. Popinet. Air entrainment and bubble statistics in breaking waves. *Journal of Fluid Mechanics*, 801:91129, 2016.

[6] C. Garrett, M. Li, and D. Farmer. The connection between bubble size spectra and energy dissipation rates in the upper ocean. *Journal of physical oceanography*, 30(9):2163–2171, 2000.

[7] C. Martínez-Bazán, J. Rodríguez-Rodríguez, G. B. Deane, J.L. Montaes, and J. C. Lasheras. Considerations on bubble fragmentation models. *Journal of Fluid Mechanics*, 661:159–177, June 2010.

[8] S. Popinet. An accurate adaptive solver for surface-tension-driven interfacial flows. *Journal of Computational Physics*, 228:58385866, 2009.

[9] C. Rosales and C. Meneveau. Linear forcing in numerical simulations of isotropic turbulence: Physical space implementations and convergence properties. *Physics of Fluids*, 17(9):095106, 2005.

FORCES ON CAPILLARY DISKS

Giuseppe Pucci[1,2], Ian Ho[1], and Daniel M. Harris[1]
[1] Brown University, School of Engineering, 184 Hope St., Providence (RI), United States
[2] Univ Rennes, CNRS, IPR (Institut de Physique de Rennes) - UMR 6251, F-35000 Rennes, France

Summary We consider centimetric disks that float at the water-air interface as a result of the equilibrium between the disk's weight, the hydrostatic force and the surface tension force. We first show that the water surface reaction can be approximated by a linear spring force if the disk radius is much larger than the capillary length. We then overview recent experimental and theoretical work on the frictional force experienced by a disk in motion and the capillary attraction force between two disks, and show that these forces are adequately captured by relatively simple analyses.

INTRODUCTION

A solid body can be supported at the water-air interface by virtue of the equilibrium between its weight $m\vec{g}$, surface tension force $\vec{F}_\sigma$ and hydrostatic force $\vec{F}_h$ (fig.1(a)) [1]. Here we consider cylindrical disks with radius R that deform the underlying interface by a displacement δ. The interface is pinned to the bottom perimeter of the disks.
We report our recent work on three forces experienced by these capillary disks: the vertical force that results from hydrostatic pressure and surface tension; the horizontal friction force experienced by a disk in sliding motion [2]; the horizontal attractive capillary force between two disks [3].

VERTICAL FORCE AS A LINEAR SPRING

The vertical force balance [4] on a disk yields

$$mg = \pi R^2 \rho g \delta + 2\pi R \sigma \sin\theta. \tag{1}$$

where σ is the surface tension, ρ the liquid density and θ the angle formed by the interface with the disk contour. The relevant length scale in this problem is the capillary length $l_c = \sqrt{\sigma/\rho g}$, which for water at room temperature is $l_c \approx 2.7$ mm. Assuming $\delta \ll l_c$ and $R \gg l_c$ one can show that the liquid profile is described to leading order by $u(r) = -\delta\, \mathrm{e}^{-(r-R)/l_c}$ [5], which yields $(\mathrm{d}u/\mathrm{d}r)_{r=R} = \delta/l_c = \tan\theta \approx \sin\theta \approx \theta$. As a result, equation 1 can be rewritten as $mg = k\delta$, which highlights the fact that the combination of hydrostatic and surface tension forces in equation 1 act as a linear spring with effective spring constant

$$k = \pi\sigma(Bo + 2\sqrt{Bo}), \tag{2}$$

where $Bo = \rho g R^2/\sigma = (R/l_c)^2$ is the Bond number. We compare our approximation to numerical solutions of the non-linear Young-Laplace equation (fig. 1(b)). Our result remains a very good approximation even for $\delta \sim l_c$, provided that $R \gg l_c$, thus extending the regime of validity of the linear spring constant in equation 2.

HORIZONTAL FRICTION FORCE

A disk sliding on the water-air interface (*slider*) experiences a friction force that is principally dominated by skin friction [2] (fig.1(c)). Skin friction results from the viscous boundary layer that forms underneath the disk. Interestingly, an analytical expression of this friction force can be obtained when the boundary layer can be considered as quasi-static. This occurs when the typical time scale for the boundary layer to develop [6] $t_{BL} = R/v$ is small compared to the typical time scale of acceleration (or deceleration) of the disk $t_D = m/\rho\sqrt{\nu v R^3}$, where v is the instantaneous body speed and ν the liquid kinematic viscosity. t_{BL} is obtained by balancing fluid inertia and viscous stress and t_D by balancing the disk's inertia and viscous stress. The ratio t_{BL}/t_D yields the dimensionless *sliding number*

$$S_l = \frac{\rho}{m}\sqrt{\frac{R^5\nu}{v}}, \tag{3}$$

which can also be obtained as the ratio between fluid inertia and body inertia. When $S_l \ll 1$ the boundary layer is quasi-static and the Blasius boundary layer theory [7] can be applied, yielding an expression for the friction force

$$F_D = \alpha\rho\sqrt{\nu}R^{3/2}v^{3/2}, \tag{4}$$

where $\alpha = 1.64$. In figure 1(d) we show a number of experimental data sets collapsed by this analysis.

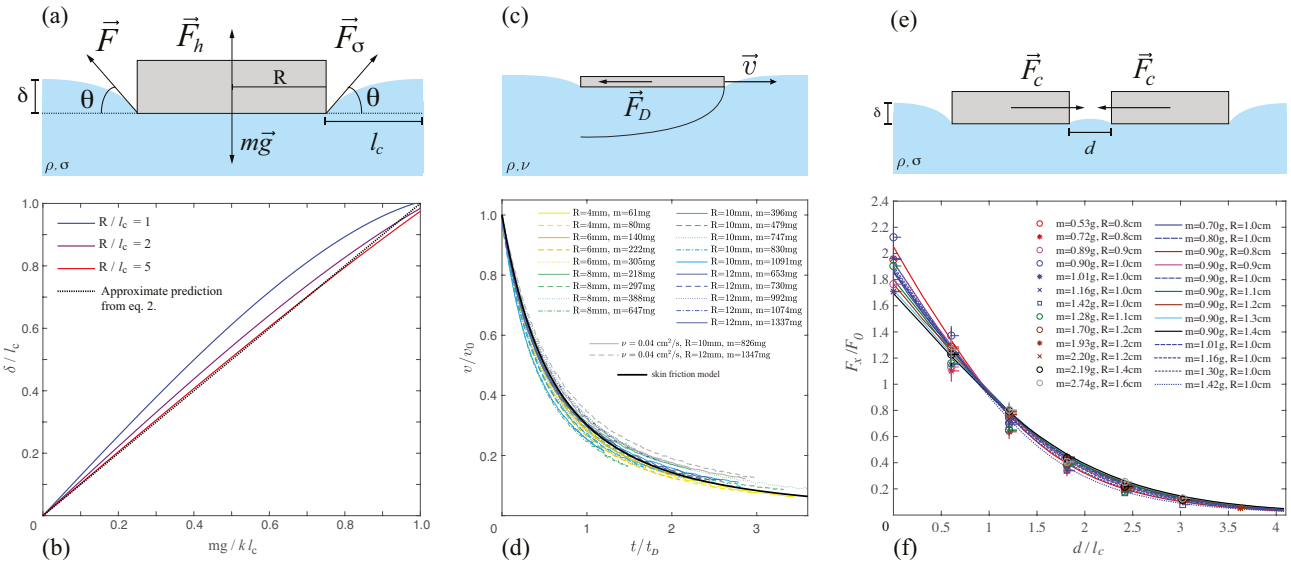

Figure 1: (a) Side view schematic of a disk resting on a water-air interface. (b) Comparison of numerical solutions of the Young-Laplace equation (continuous lines) to the prediction obtained in the limit $\delta \ll l_c$ and $R \gg l_c$ (dotted line). (c) Side view schematic of a sliding disk and the boundary layer in the underlying fluid (not to scale). (d) Collapse of deceleration data. The black line is $v(t)/v_0 = 1/(1+\alpha t/t_D)^2$ as derived from the quasi-static boundary layer theory. (e) Side view schematic of the capillary attraction between two disks. (f) Collapse of data of the capillary attraction force. In all figures, R is the disk(s) radius, m the mass and ν the liquid kinematic viscosity. Unless otherwise specified, $\nu = 0.01$ cm^2/s.

HORIZONTAL CAPILLARY FORCE

We now consider the interaction force between two disks resting at the water-air interface [3] (fig.1(e)). It is well known that two particles trapped at a fluid interface may interact due to the deformation they induce on the free surface [8], but only a few direct measurements of the capillary attraction force between macroscopic floating bodies have been reported [9]. We performed direct measurements of the force between centimetric disks floating at an air-water interface. We developed a custom experimental setup which uses a magnetic force to balance the capillary attraction force and characterised how the attraction force depends on the disk mass, diameter and relative spacing. Experimental results are captured by numerical simulations that take into account the disk's vertical displacement and spontaneous inward tilt, highlighting the significance of the latter. Moreover, a relatively simple scaling analysis can be developed assuming small deformations $\delta \ll l_c$, large disk size $R \gg l_c$ and nearby disks $d \ll l_c$, where d is the distance between the disks (fig.1(e)). In these limits, the hydrostatic component of the attractive force is small relative to the contribution from surface tension, and the capillary attraction scales with

$$F_0 = \sigma \frac{\delta^2 R^{1/2}}{l_c^{3/2}}, \tag{5}$$

where δ can be derived from eq. 1. In figure 1(f) we show a number of experimental and numerical data sets collapsed by this scaling analysis.

CONCLUSIONS

We have summarised recent comprehensive work on the vertical, horizontal, and interaction forces experienced by capillary disks at the water-air interface. Quantifying the forces these bodies experience is relevant to the understanding of the motion of living organisms at the water-air interface [10] and may inform the design of aerial-aquatic microrobots for environmental exploration and monitoring [11].

References

[1] Vella D. Floating Versus Sinking. *Annu. Rev. Fluid Mech.* **999**: 991-996, 1999.
[2] Pucci G., Ho I. and Harris D. M. Friction on water sliders. *Sci. Rep.* **9**: 4095, 2019.
[3] Ho I., Pucci G. and Harris D. M. Direct measurement of capillary attraction between floating disks. *Phys. Rev. Lett.* **123** (25): 254502, 2019.
[4] Keller J. B. Surface tension force on a partly submerged body. *Phys. Fluids* **10** (11): 3009-3010, 1998.
[5] De Gennes P.-G., Brochard-Wyart F. and Quéré D. Capillarity and wetting phenomena: drops, bubbles, pearls and waves. Springer Science, 2013.
[6] Hall M. G. The boundary layer over an impulsively started flat plate. *Proc. R. Soc. Lond. A* **310**: 401-414, 1969.
[7] Kundu P. K., Dowling D. R., Tryggvason G. and Cohen I. M. Fluid mechanics. Academic Press, 2015.
[8] Vella D. and Mahadevan L.. The cheerios effect. *Am. J. Phys.* **73** (9): 817-825, 2005.
[9] Mansfield E. H., Sepangi H. R. and Eastwood E. A. Equilibrium and mutual attraction or repulsion of objects supported by surface tension. *Phil. Trans. R. Soc. Lond. A* **355**: 869-919, 1997.
[10] Bush J. W. M. and Hu D. L. Walking on water: biolocomotion at the interface. *Annu. Rev. Fluid Mech.* **38**: 339–369, 2006.
[11] Y. Chen *et al.* Controllable water surface to underwater transition through electrowetting in a hybrid terrestrial-aquatic microrobot. *Nat. Commun.* **9**: 2495, 2018.

NUMERICAL STUDY OF DROP BOUNCING ON A FLUID-FLUID INTERFACE

Jean-Lou Pierson[1]
[1] IFP Energies Nouvelles, Rond-point de l'echangeur de Solaize, 69360 Solaize, France

Summary We investigate numerically the motion of an axisymmetric drop toward a fluid-fluid interface. This free boundary problem is solved by a Volume of Fluid method. Thanks to an Adaptative Mesh Refinement technique the thin film located between the drop and the interface can be resolved. Particular attention is given on the influence of each dimensionless parameters driving the problem dynamics. When viscous and inertia effects have comparable orders of magnitude the drop velocity decreases monotonously to zero as it approaches the interface. When inertia effects are larger than viscous effects a strikingly different behaviour is observed : the drop bounces back from the fluid-fluid interface. We identify the underlying mechanisms necessary for bouncing and discuss them in connection with several other canonical situations such as the bouncing of a solid sphere or a drop on a wall.

INTRODUCTION

In the chemical industry, fluid-fluid separators are frequently used to separate a dispersed phase from a surrounding fluid. Different kinds of processes exist such as hydrocyclone, flotation and gravity separator. For the latter the main separation mechanism is the buoyancy force due to the density difference between the two phases. The speed at which the drops can rise and coalesce is often a key factor in the efficiency of such a process. The aim of the present study is to investigate the rise of an axisymmetric droplet toward a fluid-fluid interface as an idealisation of the full process.

Many researchers have focused on the film drainage problem when the film present between the drop and the interface becomes sufficiently thin to allows a lubrication type analysis (see for instance [1] for a review). Very few papers have investigated the full dynamics of the drop when it is released far form the interface. Chi & Leal [2] have performed a numerical investigation of a drop rising towards a fluid interface in the Stokes regime. They showed that the decrease of the film thickness is dramatically affected by the viscosity ratio. Mohamed-Kassim & Longmire [6] have investigated experimentally the impact of a drop on a fluid-fluid interface in inertial regimes. They showed that the drop can bounce at the interface. To better understand the characteristic mechanisms leading to bouncing, we carry out an extensive numerical investigation of this problem.

NUMERICAL METHODOLOGY AND PROBLEM DEFINITION

Computations are carried out by solving the full Navier-Stokes equations using the Volume of Fluid approach implemented in the Basilisk code [7] (see also basilisk.fr). The corresponding finite-volume spatial discretization schemes make use of a graded quadtree partitioning. An Adaptative Mesh Refinement technique is used to accurately catch the dynamics of the thin film. This technique enables us to accurately describe the film up to the minimal thickness of $5 \times 10^{-3} D$ where D is the initial drop diameter. The simulations are stopped once this criterion is reached.

The problem is governed by 4 dimensionless parameters : the Archimedes number (Ar) which can be seen as Reynolds number based on gravitational velocity, the Bond number (Bo), which compares buoyancy and surface tension forces, the viscosity ratio (λ) and the density (ζ) ratio. The Archimedes number is varied by 1 order of magnitude, the Bond number and viscosity ratio by 3 orders and the density ratio is fixed to 0.9. Depending on the value of these parameters, a variety of flow regimes, rising velocity, decrease of the film thickness and bouncing are observed. In this talk we shall focus on the main mechanisms governing the appearance of the bouncing regime.

BOUNCING MECHANISMS

Figure 1 (a) reveals the strong dependence of the terminal velocity (which can be observed for $z/D \leq -2$) on the viscosity ratio when $Ar = 4$. For the range of Bond numbers presented in figure 1 (a), the terminal velocity is almost insensitive to the Bond number. When $Ar = 40$ (figure 1 (b)) a much stronger dependence of the steady velocity on the Bond number is observed. The most striking difference bewteen figure (a) and (b) is the presence of bouncing (negative velocity) when the drop reaches the interface for $Ar = 40$. Why is the rebound promoted by larger inertia effect ? The explanation lies in the value of the Stokes number which characterizes the particle inertia relative to viscous force, and scales as ζAr. This compares well to the bouncing of a solid sphere on a wall [3]: when the Stokes number is smaller than a critical value, viscous effect dissipates all the surface energy stored by the small deformation of the particle and as a results it does not bounce.

During the bouncing of a drop at high Bond number important deformations, of both the drop and the interface are observed (figure 2). By comparing figure 2 (a) and (b) it appears that the shape of the drop does not change much when the drop approach the interface, whereas the interface undergoes more pronounced deformations. As first shown by [6], the interface deformation appears sooner than drop deformation because surface tension effect are larger within the drop. In figure 2 (c), the drop takes a hemi-spherical shape while the interface follows closely the drop shape. The drop upper

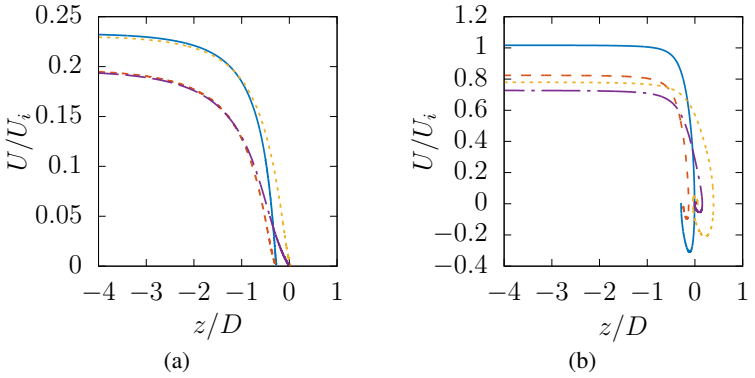

Figure 1: Rising velocity as function of the drop position with respect to the initial position of the horizontal interface. — $\{Bo = 1, \lambda = 1\}$, – – $\{Bo = 1, \lambda = 10\}$, -- $\{Bo = 10, \lambda = 1\}$, –·– $\{Bo = 10, \lambda = 10\}$. (a) $Ar = 4$, (b) $Ar = 40$.

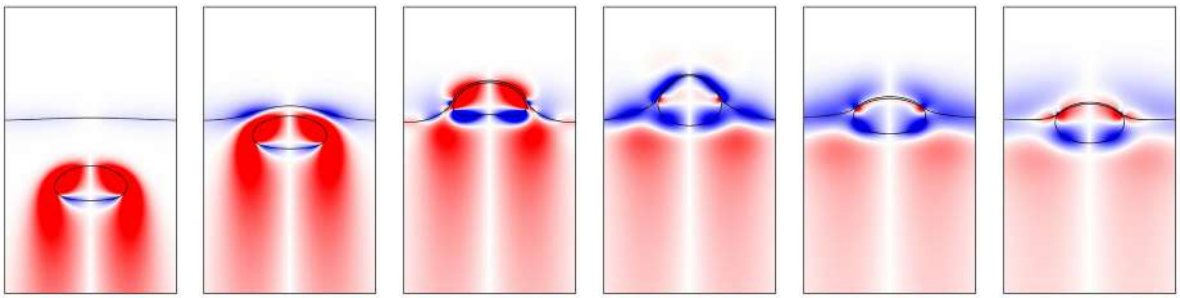

Figure 2: Drop rising toward a fluid-fluid interface, $Ar = 40$, $Bo = 10$, $\lambda = 1$. The time interval between each frame is $t = 1.2t_i$ where t_i is the inertial time scale. Colors refer to the magnitude and sign of the azimuthal vorticity.

part keeps an upward velocity as evidenced by the positive (red) vorticity contours. Due to this velocity the maximum height reached by the drop is increased in figure 2 (d). The drop is surrounded by negative vorticity contours which means that the drop and the interface undergo a downward motion. This bouncing behaviour has two possible candidates : the first one is based on the surface energy due to the deformation of the drop as evidenced by [5] when studying a drop bouncing on a wall. However in the present configuration this is not a convincing explanation since the surface tension force is negligible ($Bo = 10$). The privileged explanatation relies on the downward oriented buoyancy force, induced by the interface deformation, which acts on the drop [4].

CONCLUSION

A computational investigation of the rise of a drop toward a horizontal fluid-fluid interface allowed us to identify the key ingredients for bouncing. In particular, when the Stokes number associated with the drop is of order 1 the drop velocity decreases monotonously to zero, while for larger value of the Stokes number bouncing of the drop is observed. For high Bond and high Archimedes numbers the deformation of both the interface and the drop are important during the impact. We showed that the bouncing in this regime is mainly explained by the interface deformation.

References

[1] A. Chesters. The modelling of coalescence processes in fluid-liquid dispersions: a review of current understanding. *Chemical Engineering Research and Design*, 69(A4):259–270, 1991.

[2] B. Chi and L. Leal. A theoretical study of the motion of a viscous drop toward a fluid interface at low reynolds number. *Journal of Fluid Mechanics*, 201:123–146, 1989.

[3] P. Gondret, E. Hallouin, M. Lance, and L. Petit. Experiments on the motion of a solid sphere toward a wall: From viscous dissipation to elastohydrodynamic bouncing. *Physics of Fluids*, 11(9):2803–2805, 1999.

[4] J. B. Keller. Surface tension force on a partly submerged body. *Physics of Fluids*, 10:3009–3010, 1998.

[5] D. Legendre, C. Daniel, and P. Guiraud. Experimental study of a drop bouncing on a wall in a liquid. *Physics of Fluids*, 17(9):097105, 2005.

[6] Z. Mohamed-Kassim and E. K. Longmire. Drop impact on a liquid–liquid interface. *Physics of Fluids*, 15(11):3263–3273, 2003.

[7] S. Popinet. An accurate adaptive solver for surface-tension-driven interfacial flows. *Journal of Computational Physics*, 228(16):5838–5866, 2009.

A DROP DOES NOT FALL IN A STRAIGHT LINE: A RATIONALE FOR THE WIDTH OF STALAGMITES

J. Parmentier *[1], S. Lejeune[1], M. Maréchal[2], F. Bourges[3], D. Genty[4], V. Terrapon[1], J.-C. Maréchal[2], and T. Gilet[1]
[1] Department of Aerospace and Mechanics, University of Liège, Liège, Belgium
[2] BRGM, University of Montpellier, Montpellier, France
[3] Géologie-Environnement-Conseil, Saint-Girons, France
[4] EPOC, University of Bordeaux, Bordeaux, France

Summary Drops loaded in calcium ions detach from stalactites and impact the underlying stalagmites, thereby allowing these latter to grow through calcite precipitation. Nevertheless, little is known about the influence of the drop free fall and splash dynamics on stalagmite shape and width. Through high-speed imaging of impacting drops on stalagmites from several caves, we observed that the impact point position of the drops is scattered, sometimes over several centimetres. We show that this dispersal has no external cause and must, therefore, be self-induced. Using a Langevin-like equation, to describe the free fall in response to gravity and aerodynamic forces, we then propose a prediction of the impact point dispersal as a function of the falling height travelled by the drops. We finally show that measured stalagmite widths are correlated to the impact point dispersal of the drop.

INTRODUCTION

Beyond their outstanding beauty, stalagmites help to understand past climate and hydrology. Measuring e.g. the size variations of the annual laminae seen in vertical cross sections of stalagmites give information on the precipitation history in regions where ice or sediment cores cannot be used [1]. While the chemical reactions underlying the slow growth of the stalagmites is fairly well understood, little is known about the fluid dynamics at play during their formation. The calcite is brought by drops detaching from the stalactite. The drops fall and impact a very thin film of water that covers the stalagmite. For most stalagmites, the drop velocity is sufficient to generate a splash, with the formation of a corona and secondary droplets (Figure 1).

In previous models of stalagmite growth, it was commonly accepted that drops fall on a straight vertical line from the stalactite, thereby feeding the stalagmite film from one central point [2]. However, our high-speed movies revealed that the impact points of drops originating from a single stalactite are scattered, sometimes over several centimeters (Figure 2).

MATERIALS AND METHODS

We have taken high-speed movies of drops splashing on a wide variety of stalagmites as well as still pictures of stalagmites only, in seven different caves of the south of France. The radius, velocity and impact point of the drop, along with the radius of the spreading lamella formed at impact and the stalagmite width, were measured by image processing. Additional data were also taken in a more controlled lab setting, for a drop radius similar to that encountered in natural conditions.

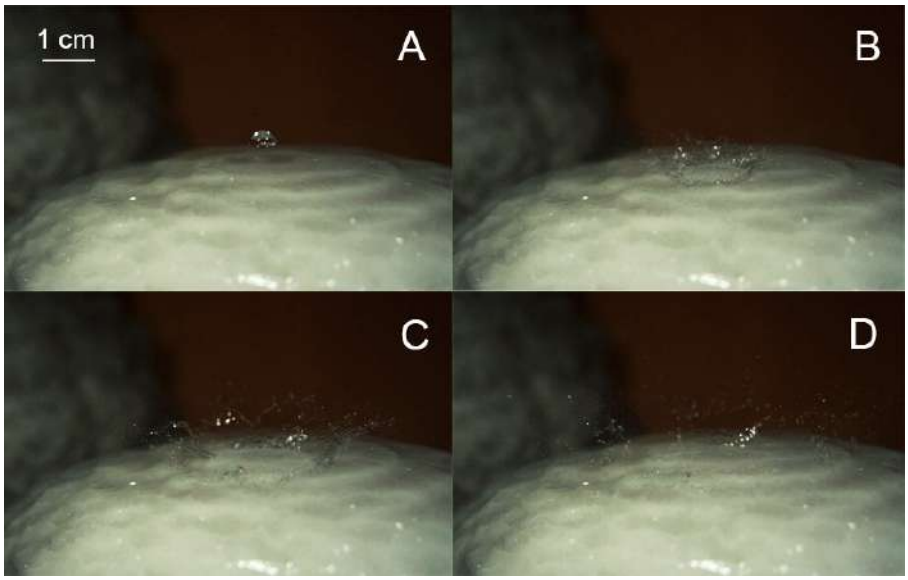

Figure 1: (A-D) Time sequence of the impact of a drop on a stalagmite (Orgnac cave, South of France), with lamella spreading and crown formation. All frames A-D are separated by 1.9 ms. (A) The drop of radius 2.61 mm at most 625 μs before the impact. (B) Formation of the crown at least 625 μs after the drop crushed on the stalagmite. (C) Spreading of the lamella in the water residual film and ejection of secondary droplets. (D) Fragmentation of the crown. The lamella has reached the stationary value $r = 2.3$ cm, around 7 ms after the initial impact.

*Corresponding author. E-mail: jparmentier@uliege.be.

RESULTS

Our measurements show that drops falling from the ceiling of caves all have the same radius and that the size of the fluid lamella formed by their impact on the stalagmite is weakly dependent on the drop velocity. On the other hand, drops falling from higher ceilings are faster and more dispersed. We postulate that drops do not fall straight, but rather follow a wavy trajectory owing to their aerodynamic interaction with the surrounding air. This hypothesis does not come out of the blue; the same phenomenon is also observed in a controlled lab environment, where the falling drops are protected from parasitic air currents. Furthermore, the airflow measured in caves could only cause a deviation of a few millimeters at most.

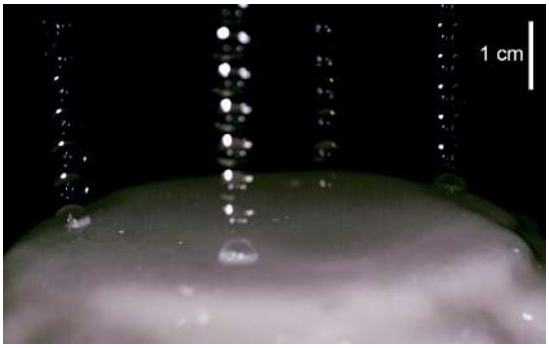

Figure 2: Drops coming from the same stalactite fall in different locations on the stalagmite below (Orgnac cave, South of France). This image was obtained by superimposing frames showing the trajectories followed by four drops landing on this stalagmite. For each drop the frames are separated by 625 μs, from the moment the drop appears in the field of view, up to right before impact.

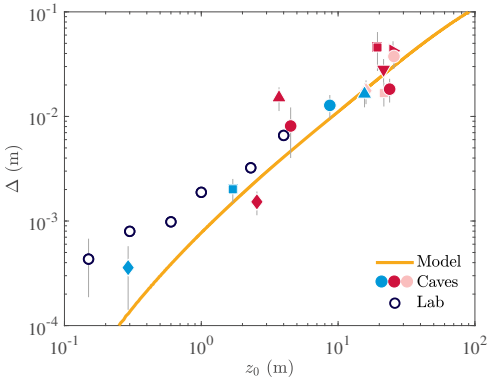

Figure 3: Standard deviation Δ of impact point position as a function of the falling height z_0. The solid curve is obtained by solving numerically the recurrence relations obtained for the drop position and velocity. Hollow symbols correspond to data from a lab setting, and solid symbols to in situ measurements, both obtained with high-speed videos. (Credit: The Royal Society 2019 [3])

The aerodynamic force acting on a drop considered spherical, can be formulated as follows:

$$\mathbf{F} = -C_d \frac{\rho_a S \left|\dot{\mathbf{X}}\right|}{2} \dot{\mathbf{X}} - C_l \frac{\rho_a S \left|\dot{\mathbf{X}}\right|}{2} \mathbf{e}_r \times \dot{\mathbf{X}} \tag{1}$$

where ρ_a is the air density, S is the cross-sectional area of the drop perpendicular to its motion, $\mathbf{e}_r$ is a unit vector of random direction in the plane perpendicular to the velocity vector of the drop, $\dot{\mathbf{X}}$, and C_D and C_L are the drag and lift coefficients, respectively. The first contribution of this force, the drag, is responsible for the saturation velocity reached by drops falling from very high ceilings ($z_0 > 20$ m). The second term of the equation represents a lift force which originates from the wake of the drop. Above a Reynolds value of around 212, which is still laminar though, the break of symmetry in the wake of the drop induces the shedding of randomly oriented vortices at a frequency increasing with the drop velocity. It is assumed that each of these vortices pushes the drop in a direction opposed to that of its emission, therefore deviating the drop from its original position and creating a random walk-like trajectory.

Integrating the horizontal projection of Newton's equation over one vortex shedding period yields two discrete equations for the position and velocity of the drop. An ensemble average over many falling successive drops allows to estimate the horizontal dispersal as a function of the falling height of the drop (comparison with lab and cave measurements in Figure 3).

The width of several dozens of stalagmites is finally related to the size reached by the liquid lamella formed at impact and to the impact point dispersal. For small falling heights, the stalagmite width is mostly set by the maximum spreading of the lamella, while for large falling heights, the stalagmite radius increases proportionally to the impact point dispersal.

CONCLUSION

We show that there is a strong positive correlation between the falling height, the impact point dispersal and the stalagmite width. We propose a theoretical model of the fall of the drop that includes aerodynamic forces. Owing to some lift of random direction that represents the effect of vortex shedding, the drop experiences a random walk, and its impact point on the stalagmite is scattered.

References

[1] Baker A., Mattey D. and Baldini J. Reconstructing modern stalagmite growth from cave monitoring, local meteorology, and experimental measurements of dripwater films. *Earth Planet. Sc. Lett.* **392**: 239-249, 2014.
[2] Dreybrodt W. Processes in Karst Systems. Springer, Berlin 1988.
[3] Parmentier J., Lejeune S., Maréchal M., Bourges F., Genty D., Terrapon V., Maréchal J.-C., Gilet T. A drop does not fall in a straight line: a rationale for the width of stalagmites. *Proc. R. Soc. A* **475**: 239-249, 2014.

COLLIDING MERGING OF BINARY IMMISCIBLE DROPLETS

Chu-Po Huang[1], and Kuo-Long Pan *[1]
[1] Department of Mechanical Engineering, National Taiwan University, Taipei, Taiwan, R.O.C.

Summary Two types of merging between immiscible drops in collision are studied. Depending on the interfacial tensions among the three media, including air and two liquids at equilibrium with negligible motions, partial and complete engulfing between the drops can be identified. With impact inertia, it may yield adhesive merging, where two drops adhere to each other, or encapsulation, where the softer drop engulfs the harder one. Based on two parameters, a Weber number and an impact parameter, we have created a regime diagram that indicates the parametric conditions of various outcomes. While the contact result between two drops at rest can be analyzed by a free-energy approach, those with substantial motions need to consider the impact energy. Via an analysis based on the conservation of energy, a model is built to predict the critical Weber number of transition between two regimes of merging.

INTRODUCTION

There has been considerable research aiming to understand the fundamentals of binary droplet collisions. Depending on the collision Weber number (We) and the impact parameter (B), which characterize, respectively, the ratio of impact inertia to surface tension and the relative directions of the colliding drops, two identical droplets may coalesce permanently, rebound, coalesce temporarily followed by creation of satellite droplets, or coalesce temporarily followed by rotational/stretching separation when the impact trajectories of the drops are sufficiently off-centered.

Previous studies have been mostly concerned with identical liquids and thus show a symmetric pattern of two identical drops during head-on impact. An intriguing topic of considerable relevance, but much less considered, is the collision between droplets of diverse properties [1], particularly when they are immiscible. Specifically, it was found in [2] that a droplet can merge (macroscopically) with another droplet made of immiscible liquid, instead of bouncing as would be expected. This suggests a different form of coalescence which is distinct from the general one caused by miscibility at a microscale level. Depending on various factors to be explored, the 'soft' drop with lower surface tension may attach to the hard drop with higher surface tension, with the interior liquid either exposed non-uniformly to the surroundings, or totally encapsulated, as shown in Fig. 1. To realize the behaviors and transformation, the key factors such as the effects of fluid material properties (disparities in surface tension and viscosity, molecular formulation), the geometrical conditions of the drops (size and volume ratio) and kinematic conditions (impact inertia and colliding path orientation) are studied to understand anisotropic droplet collisions.

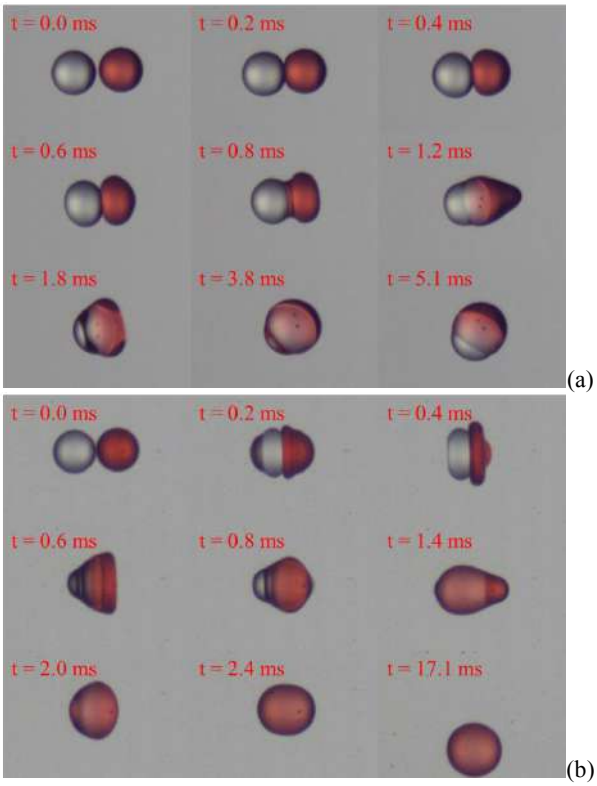

Figure 1. Collisions between a water droplet and another made of (a) heptadecane showing adhesive merging and (b) hexadecane showing encapsulation.

EXPERIMENTAL SETUP

The experimental setup was similar to that described in [3]. Two identical droplets were generated by nozzles that were triggered by the vibration of piezoelectric plates. They were made to impinge onto each other with adjusted angles of the colliding path. Time-resolved images were either taken through stroboscopy synchronized with the droplet generation circuit or recorded by a high-speed CMOS digital camera, which supported a maximum resolution of 512×512 pixels with 5100 frames per second (fps). The shutter of the high-speed camera was synchronized with a LED lamp that can support the shortest duration of 1 μs, so as to capture images with sufficiently small exposure and adequate light intensity while avoiding slurring due to background scattering.

RESULTS AND DISCUSSION

In this work, the regime diagrams for the impact between two immiscible droplets have been obtained for the first time. For the conditions at low or moderate We, the collision outcomes basically follow that of static cases which can be predicted by using the free-energy analysis [4]. For the impact of two drops made of immiscible liquids, based on the

*Corresponding author. E-mail: panpeter@ntu.edu.tw.

interfacial tensions between each pair of the three phases, the contact outcome of immiscible drops follows the minimization of free energy at equilibrium, as indicated by Fig. 2.5. Here the spreading parameters are defined as

$$S_1 = \sigma_{23} - (\sigma_{12} + \sigma_{13}),\ S_2 = \sigma_{13} - (\sigma_{23} + \sigma_{12}),\ S_3 = \sigma_{12} - (\sigma_{13} + \sigma_{23}).$$

While not shown herein, in the situations of weak impact inertia, the experimental results basically agree with that predicted for the static cases in terms of equilibrium evaluation, whereas some variations shall be concerned, such as evaporation of volatile liquids which would change surface tension due to ambient conditions like temperature or Marangoni effects due to spatial gradients of surface tension, particularly when the predicted values are near the thresholds. This gives a demonstration for extension and application following similar tracks of droplet interaction such as synthesis of biological materials or medicines. On the other hand, one of the motives for this research is to understand why most studies have reported encapsulation but not adhesive coalescence [5]. Indeed, by using the present approach, it is found that while adhesive coalescence is expected to occur at static situation, with substantial impact inertia, insertive motion can be created and lead to encapsulation spanning for a noticeable range of Weber number as seen in Fig. 2.

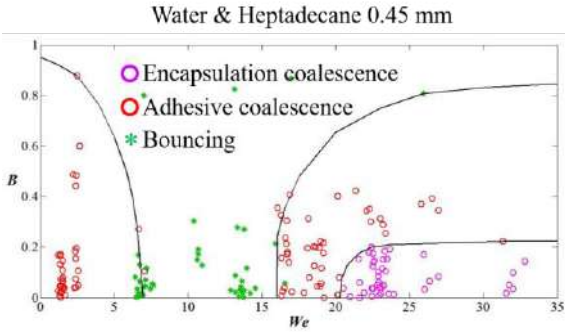

Figure 2. Regime diagram of H_2O-$C_{17}H_{36}$ collision in terms of *We* and *B*.

To predict the parametric conditions of transition from adhesive coalescence to encapsulation with increasing inertia relative to surface tension, we have derived a criterion based on the conservation of energy.

$$\frac{1}{2} * (\rho_1 + \rho_2) * \frac{1}{6}\pi D^3 \left(\frac{1}{2}U\right)^2 + \pi D^2 * (\sigma_1 + \sigma_2) = \pi D^2 * \left(2^{\frac{2}{3}} * \sigma_2 + \sigma_3\right) + \mu * \frac{U^2}{D^2} * \pi D^3 * Z * t$$

This is further reduced to $A \times \sigma_2 D^2 + C \times \rho_2 U^2 D^3 = Z \times G \times \mu_2 D U^2 \times \tau$, where *A*, *C*, and *G* are the coefficients to be fit for surface energy, kinetic energy, and viscous dissipation, respectively. They express $(\sigma^* + 1) - \left(2^{\frac{2}{3}} + \sigma_3/\sigma_2\right)$, $(\rho^* + 1)/48$, and $(\mu^* + 1)$, respectively, where $\sigma^* = \sigma_1/\sigma_2$, $\rho^* = \rho_1/\rho_2$, and $\mu^* = \mu_1/\mu_2$. By using the modified characteristic time of oscillation: $\tau = \frac{\pi}{4}\sqrt{\frac{2\rho_1 D^3}{\sigma_1}}$, the relation between *We* and *Oh* which indicates the transformation boundary can be obtained as:

$$We = 1/\left(\frac{Z}{A} \times G \times Oh \times \frac{\pi}{4} \times \sqrt{\frac{2\rho^*}{\sigma^*}} - \frac{C}{A}\right),$$

where $We = \frac{\rho_2 D U^2}{\sigma_2}$ and $Oh = \frac{\mu_2}{\sqrt{\sigma_2 \rho_2 D}}$. This transition from adhesive coalescence to encapsulation with increasing *We* only occurs for fluids that allow for formation of partial encapsulation, thus being observed in the present experiments of water-hexadecane and water-heptadecane. In a comparison, it is seen in Fig. 3 that the theoretical model basically predicts the experimental results. Furthermore, the experimental results of [2] that show encapsulation are indeed located in the area above the theoretical curve. More data and refinement would be investigated to improve the model.

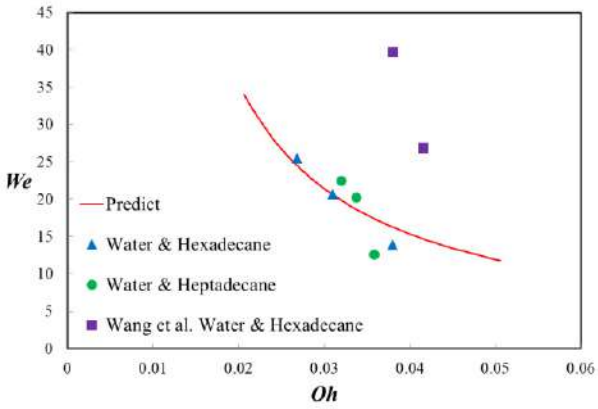

Figure 3. The transition boundary between adhesive coalescence and encapsulation given by the model and experimental results.

CONCLUSIONS

Regime diagrams are obtained by using techniques for generating controlled droplets with high accuracy in binary droplet collision of immiscible liquids. Two types of coalescence, adhesive and encapsulation, are analyzed by using a free energy analysis for near equilibrium configuration. Impact dynamics can change adhesive coalescence to encapsulation, but not the other way around. A phenomenological model is built to identify the transitional trend. While the consequences of tested liquids mostly follow the analysis, some need delicate concerns due to property variations such as surface tension/temperature (water-hexadecane) and surfactant/Marangoni effect (water-octanol).

References

[1] Wang C. H., Pan K. L., Fu S. Y., Huang W. C., Yang J. Y., An Experimental Investigation on The Coalescent Behaviors of Colliding Droplets," *J. Mech.* **23**, 415, 2007.

[2] Wang, C. H., Lin, C. Z., Hung, W. G., Huang, W. C., Law, C. K. On The Burning Characteristics of Collision-Generated Water/Hexadecane Droplets. *Combust. Sci. Tech.* **176** (1): 71-93, 2004.

[3] Pan K. L., Chou P. C., and Tseng Y. J. Binary Droplet Collision at High Weber Number. *Phys. Rev. E* **80**: 036301, 2009.

[4] Torza S., Mason, S. G. Coalescence of Two Immiscible Liquid Drops. *Science* **163** (3869): 813-814, 1969.

[5] Planchette C., Lorenceau, E., Brenn, G. The Onset of Fragmentation in Binary Liquid Drop Collisions. *J. Fluid. Mech.* **702**: 5-25, 2012.

DROPLET GENERATION IN ENSEMBLES OF RANDOMLY CORRUGATED LIGAMENTS

Sagar Pal *, Marco Crialesi-Esposito, Daniel Fuster, and Stéphane Zaleski
Institut Jean le Rond d'Alembert, Sorbonne Université and CNRS, Paris, France

Summary This study focuses on a description of droplet sizes, created as a result of capillary-induced breakup of ligaments. Direct numerical simulations of air-water systems are employed by solving the two-phase Navier-Stokes equations with surface tension. The breakup of individual ligaments are triggered by initial surface corrugations, the subsequent evolution of which is governed by deterministic dynamics. Stochasticity is introduced in the mix by conducting an ensemble of numerical simulations of slender corrugated ligaments, each realization corresponding to a random but unique initial configuration. Probability density functions of the droplet sizes are computed using different ensemble sizes. These results combining the effects of stochasticity with the capillarity-driven non-linear dynamics facilitate our understanding of the nature of drop size distributions encountered in realistic and complex fluid fragmentation scenarios.

INTRODUCTION & METHODOLOGY

Ligaments constitute the penultimate stage in the complex sequence of capillary-driven topological changes that are typical of liquid fragmentation processes, finally resulting in the generation of polydisperse collections of drops. There are several hypotheses in existing literature [1] that attempt to explain the physical mechanisms responsible for the selection of droplet size. A popular model [2] asserts that the polydispersity in the droplet sizes is strongly correlated to the corrugations initially present in the ligaments from which the drops originate. But so far, neither experimental nor numerical studies have been conducted with the aim of improving our understanding of how droplet size distributions are influenced by the corrugation-coalescence driven mechanism. In the present study, we have developed a numerical experiment that grants us precise control over both quantitative and qualitative aspects of such random corrugations, and its subsequent influence on the resulting droplet sizes. We perform direct numerical simulations of the two-phase Navier-Stokes equations under the incompressible framework. Material properties correspond to that of air-water systems at 20 degrees Celsius. Simulations are carried out in the axi-symmetric framework, therefore excluding the existence of azimuthal modes with respect to the central axis of the ligament. The ligaments are initially at rest, but rapidly destabilize and evolve into droplets due to the initial surface corrugation (large potential energies). We perform many such realizations, each corresponding to a slender ligament with random surface corrugations, simultaneously ensuring that the random profile is unique to that particular realization. Finally, we provide a statistical description of the droplet size distributions using different ensemble sizes. A detailed exposition of the key aspects of our methodology are discussed ahead.

Numerical Method

We use the open-source toolbox Basilisk [6], which couples finite-volume discretization on octree meshes to solve the two-phase Navier-Stokes equations. The one-fluid formulation with variable density and viscosity is adopted, where the interfacial description and transport is carried out under the Volume-of-Fluid framework coupled with hight function based interface curvature modeling. The solver utilizes a robust and accurate implementation of the surface tension force distribution across the interface, which has been extensively validated in existing literature. More details regarding the numerical schemes involved can be found in Popinet (2009) [5] .

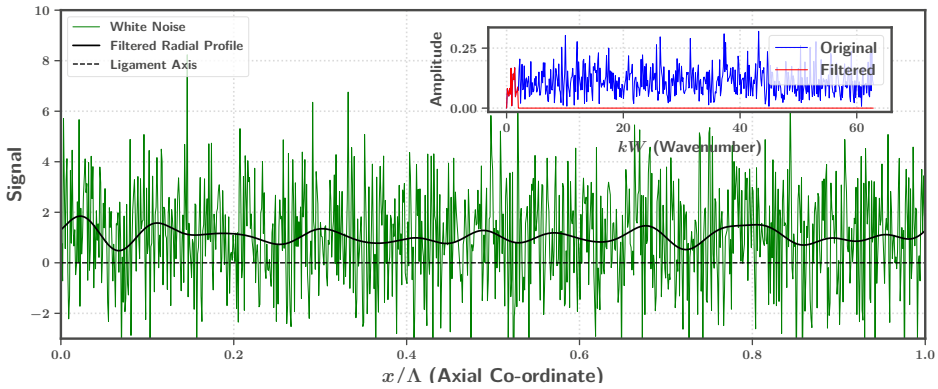

Figure 1: Axial profile of the ligament radius for one spatial period. Inset : Spectral densities of the original and filtered signals.

Surface Corrugation

We consider infinitely long ligaments having zero initial kinetic energy, with spatial periodicity along the axis. A robust random (white) noise generation [4] algorithm is treated by a low-pass filter in order to obtain the shape of the radial profile along the axis of the ligament (fig. 1). The radial profile corresponding to an individual ligament simulation is uniquely determined by the value of the seed used as input for our random noise generator, therefore we are able to ensure that none of the ligaments in our ensembles are identical by simply using unique seeds for each realization. The amplitude of the surface corrugations are controlled by the dispersion of the initial white noise signal. The volume of the corrugated ligament per unit spatial period is controlled by our choice of ligament aspect-ratio.

*Corresponding author. E-mail: sagar.pal@dalembert.upmc.fr

Parameter Space

The ensemble is generated by a fixed cut-off wavenumber (normalized by ligament width), a fixed amplitude of the corrugations (normalized by ligament radius), a fixed aspect-ratio of the ligament and the time at which the drops are counted (rescaled by capillary time-scale) denoted by K , ϵ , Λ and T respectively. The aspect-ratio is the length of one spatial period divided by mean width of the initial ligament. In addition, we use Ohnesorge (Oh) number based on the heavier fluid to characterize our ensembles, with $We = 0$ due to the absence of initial kinetic energy. To summarize, the ensemble is completely determined by a point in the parameter space defined as $\Phi \equiv (Oh, K, \epsilon, \Lambda, T)$.

RESULTS & CONCLUSIONS

We present the statistical distributions of droplet sizes and volumes in fig. 2 , which originate from ligament ensembles characterized by $\Phi_0 \equiv \left(Oh = 10^{-2}, K = 2\pi, \epsilon = 0.50, \Lambda = 50, T = 30.0\right)$. The choice of Oh number correlates to millimeter length-scale in air-water systems. The Gaussian and Log-Normal curves are not *fitted* to the histograms, instead, they are determined using the mean and variance of the original data sets. The gamma distributions are defined as proposed in Villermaux et al. [2], are subsequently plotted using values of 'n' corresponding to the best fits to the histograms.

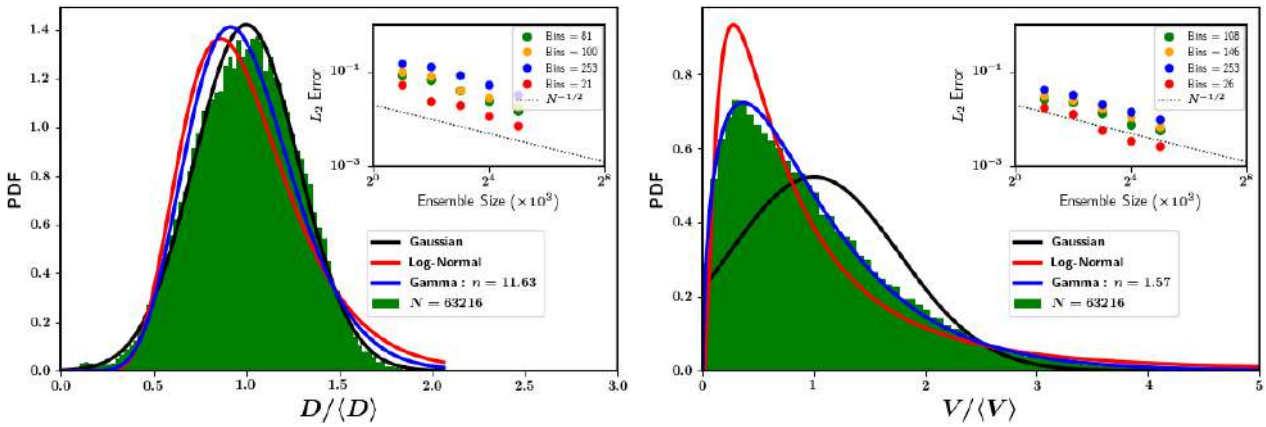

(a) Normalized Diameter

(b) Normalized Volume

Figure 2: Probability Density Functions. Inset: Error convergence with respect to ensemble sizes.

The droplet diameters are most accurately described by a normal distribution, and droplet volumes best described by gamma distributions. Several binning criteria were used to determine the optimal bin-width. Additionally, the numerical experiments were repeated for several different ensemble sizes, with the largest ensemble containing approximately $64,000$ droplets. We observe that the characteristic shapes of the distributions and corresponding fits to the data are independent of both the binning criteria as well as ensemble sizes (not shown). We compute the error of the PDFs for different ensemble sizes, relative to the largest ensemble. A $N^{-1/2}$ scaling is observed (fig. 2 inset), strongly suggesting the absence of any hidden correlations in our numerical experiments. In our ensemble, mean droplet size is rescaled with respect to the initial ligament diameter resulting in $\langle D\rangle/W \approx 3.14$. Considering the fastest growing wavelength of the inviscid Rayleigh-Plateau instability [3], the droplet size corresponds to $\langle D\rangle/W \approx 1.89$, which is significantly different from the value observed in our experiments (where a considerable number of coalescence events give rise to larger drops). Therefore, the evidence suggests that the dynamics of the ligament breakup for our ensemble Φ_0 are not described by dominance of the fastest growing Rayleigh-Plateau modes, instead they involve more complex non-linear interactions amongst the different capillary waves propagating along the ligament, and the subsequent aggregation phenomena post breakup.

In conclusion, we are able to conduct precise and controlled numerical experiments that provide us with reliable and reproducible droplet statistics. The numerical experiment can be repeated to generate ensembles corresponding to different points in our parameter space Φ, therefore resulting in different size distributions. The combination of such distributions characterized by different points in the parameter space could lead to more complicated and asymmetric probability distributions, thereby providing an alternate interpretation to the skewness observed in the drop size distributions typical of more complex fragmentation/atomization processes.

References

[1] Villermaux E. Fragmentation. *Annu. Rev. Fluid Mech.* **39**: 419-446, 2007.
[2] Villermaux E., Marmottant PH., Duplat J. Ligament-mediated spray formation. *Phys. Rev. Lett.* **92**: 074501, 2004.
[3] Rayleigh L. J. On the instability of jets. *Proc. R. Soc. Lond. A* **s1-10**: 4-13, 1878.
[4] Matsumoto M., Nishimura T. Mersenne twister: a 623-dimensionally equidistributed uniform pseudo-random number generator. *ACM Trans. Model. Comput. Simul.* **8(1)**: 3-30, 1998.
[5] Popinet S. An accurate adaptive solver for surface-tension-driven interfacial flows. *J. Comput. Phys.* **s1-10**: 4-13, 2009.
[6] Popinet, S. Basilisk, a Free-Software program for the solution of partial differential equations on adaptive Cartesian meshes (2018). **http://basilisk.fr**.

SLIDING DROPLETS: ROLE OF SUBSTRATE SOFTNESS

Mathieu Oléron[1], Matthieu Roché *[1], Julien Dervaux[1], and Laurent Limat[1]
[1] Laboratoire Matière et Systèmes Complexes, Université de Paris - CNRS UMR 7057, Paris, France

Summary Dew collectors rely on the cooling of its surface below atmospheric dew point and allows to harvest water in dry regions. These devices can be optimized in terms of dew nucleation rate and water extraction. The former can be improved by coating the surface of the collector with a polymer layer. However, this coating introduces viscoelastic effects that may be detrimental to water extraction that usually occurs by letting water droplets slide down the surface of the collector. Here, we investigate systematically how droplets slide on a viscoelastic substrate. We show that droplet shape depends on the viscoelasticity of the polymeric layer, and that the presence of the soft coating also alters the transition to an unstable shape of the droplet resulting in the deposition of satellite droplets.

INTRODUCTION

Climate change threatens global water resources, and water scarcity may become a major issue. Scientists and engineers have already proposed candidate solutions to tackle this problem, such as dew collection.

Dew collectors rely on the cooling of a solid surface below the atmospheric dew point. Under this condition, water vapor present in the atmosphere condenses on the surface and can then be collected, by tilting the surface to trigger flow for example. A collector with the highest up-time possible is desirable. To this end, both dew formation and water extraction must be optimized. The first aspect can be improved using polymeric coatings[1]. Optimization of water extraction must circumvent flow instabilities such as pearling[2–4]. The study of this latter problem for droplets on silicon wafers showed that the relevant non-dimensionalized numbers are the capillary number and the Bond number that compare capillary stresses to viscous and gravitational stresses respectively:

$$Ca = \frac{\eta U}{\gamma}, \qquad Bo = \frac{\rho g R^2}{\gamma}, \tag{1}$$

where η is the dynamic viscosity, ρ the density, γ the surface tension, R the radius, U the velocity of the drop and g gravity. When both Ca and Bo are fixed, the shape of the drop is determined. Moreover, droplets reaching capillary numbers $Ca > Ca_c$ experience the pearling instability.

The coating of a surface with a polymer layer increases the nucleation rate[1]. However, these layers are often viscoelastic. When the droplet moves, the substrate dissipates energy, possibly at a larger rate than the liquid that spreads on its surface. As a result, the motion of droplets is slowed down at the surface of elastomers[5]: water extraction is then hindered. These issues may be circumvented by controlling the properties of the coating, such as its formulation or its thickness[6]. However, few studies have investigated droplets sliding on soft substrates[7;8] and a lot of questions remain.

The purpose of this contribution is to report the results of a systematic study of droplets sliding on solid-supported elastomeric layers. We discuss the dependence of the shape of a sliding droplet on the properties of the substrate. We also investigate the modifications to the pearling instability induced by the viscoelastic substrates over a large range of elastic moduli.

EXPERIMENTAL SETUP AND OBSERVATIONS

We deposit a droplet of glycerol on a horizontal piece of glass-supported 5-mm thick silicone elastomer layer. Its shear modulus μ ranges continuously from 1 kPa up to 1 MPa. At time $t = 0$, we tilt the substrate and the liquid starts its downward motion. A camera records a top view of the motion (Fig. 1a), and a LED panel lights the drop from below. As glycerol can absorb atmospheric water, its viscosity η_g may change over time, an issue we account for by measuring η_g with a capillary viscosimeter at the same time the experiment runs. The droplet volume is carefully controlled, in the range $20 \leq V \leq 40$ µL. Inclination angles are set in the range $0 \leq \theta \leq 90$ °. We have good control over Ca and Bo.

Photographs displayed in figure 1b illustrate the shape adopted by the droplet when the shear modulus μ of the sloping plane varies from 1 kPa to 1 MPa, for identical Ca and Bo. We notice a clear difference between the soft and the rigid cases. The softer the substrate is, the more the drop elongates. The drop on the softer substrate also exhibits a rivulet at its back. The comparison of these two experiments indicates that the shape of the droplet running downhill is also controlled by the mechanical properties of the substrate.

We have observed that the pearling instability still occurs above a threshold capillary number. Figure 1c illustrates this phenomenon for a 30 µL drop on a $\mu = 1$ kPa substrate. As the drop slides, it elongates more and more in the flow direction and forms a rear that eventually splits in smaller droplets. The threshold capillary number Ca_c above which we observe the pearling instabilty in our experiments using this soft substrate was $Ca_c \simeq 0.03$. This threshold is larger than that reported for a silicon substrate by Peters *et al.*[3], $Ca_c \simeq 0.007$.

*Corresponding author. E-mail: matthieu.roche@univ-paris-diderot.fr

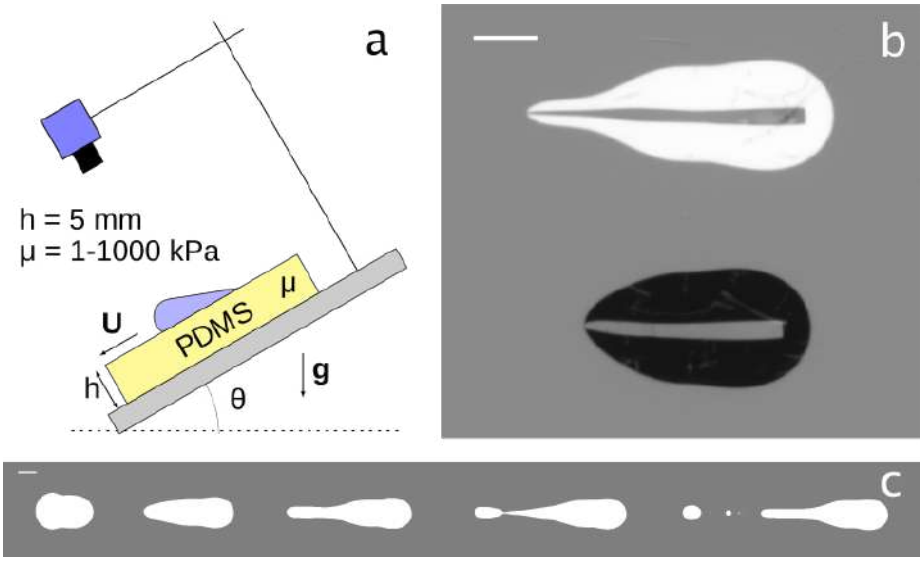

Figure 1: (a) Sketch of our experimental setup. (b) Shape of a glycerol droplets sliding onto two different silicon subtrates. In both pictures, the background has been removed and intensities have been enhanced. The gray stripe inside each drop corresponds to the image of a rectangular filter put upon our light source. Shear modulus μ is equal to 1 kPa (respectively 1 MPa) in the case of the white (respectively black) droplet. $Ca = 0.026$ and $Bo = 0.64$ for both pictures. Scale bar: 2 mm. (c) Pearling instability: binary snapshots of a droplet taken at respectively $t = 0, 2, 7, 10, 10.2$ s, that illustrate the process. $\mu = 1$ kPa, $\theta = 70°$, $V = 30\,\mu$L.

CONCLUSIONS AND PERSPECTIVES

On-going work is carried out at the time of abstract submission to characterize these observations thoroughly. In particular, we study the dependence of droplet shape on the ratio between dissipation in the fluid and in the substrate as well as on the viscoelastic properties of the substrate. We also plan to explore the relationship between the threshold of the pearling instability (*i.e.* Ca_c) and the viscoelasticity of the substrate. We have also identified a dependence of our observations on droplet size. We are looking forward to present and discuss our work during the forthcoming International Congress of Theoretical and Applied Mechanics (ICTAM 2020) in Milan.

References

[1] M. Sokuler *et al.*, The softer the better: fast condensation on soft surfaces, *Langmuir* **26**, 1544, 2010.
[2] T. Podgorski, J.-M. Flesselles and L. Limat. Corners, cusps, and pearls in running drops. *Phys. Rev. Lett.* **87**, 036102, 2001.
[3] I. Peters *et al.*, Coexistence of two singularities in dewetting flows: Regularizing the corner tip. *Phys. Rev. Lett.*, **103**, 114501, 2009.
[4] E. Rio, A. Daerr, B. Andreotti and L. Limat. Boundary conditions in the vicinity of a dynamic contact line: experimental investigation of viscous drops sliding down an inclined plane. *Phys. Rev. Lett.* **94**, 024503, 2005.
[5] A. Carré and M. Shanahan. Viscoelastic braking of a running drop. *Langmuir* **17**, 10, 2982, 2001.
[6] M. Zhao *et al.*, Geometrical control of dissipation during the spreading of liquids on soft solids. *Proc. Natl. Acad. Sci. USA* **115**, 1748, 2018.
[7] S. Karpitschka *et al.*, Liquid drops attract or repel by the inverted Cheerios effect, *Proc. Natl. Acad. Sci. USA* **113**, 7403, 2016.
[8] A. Hourlier-Fargette *et al.*, Role of uncrosslinked chains in droplets dynamics on silicone elastomers. *Soft Matter*, **13**, 3484, 2017.

DROPLET DYNAMICS ON CHEMICALLY HETEROGENEOUS SUBSTRATES WITH MASS TRANSFER

Danny Groves[1] and Nikos Savva*[2]
[1] School of Mathematics, Cardiff University, Cardiff, United Kingdom
[2] Computation-based Science and Technology Research Center, The Cyprus Institute, Nicosia, Cyprus

Summary We consider the dynamics of thin viscous droplets on chemically heterogeneous surfaces moving under the combined effects of slip, mass transfer and capillarity. The equation governing the long-wave dynamics of the droplet thickness is treated with matched asymptotics to obtain a lower-dimensional system of differential equations for the evolution of the contact line, by assuming that the droplet evolves quasi-statically in the limit of slow mass transfer rates and vanishingly small slip lengths. We also propose a hybrid scheme which couples the results of the asymptotic analysis with the boundary integral method. We demonstrate with a number of representative cases that the reduced system agrees excellently, within its domain of applicability, with simulations performed with the full model, highlighting also a number of interesting features of the underlying dynamics.

MOTIVATION

Moving droplets on surfaces is ubiquitous in the natural world, which also finds application in a broad spectrum of technologies [1]. Yet, their study is inherently complex and many of these applications are based on empirical models derived from experiments. This complexity stems from the multi-scale nature of the phenomenon, from forces that manifest themselves at the macro-scale, such as gravity and capillarity, to the micro-scale effects close to the droplet front. Although impressive progress in contact line phenomena and the broader field of wetting hydrodynamics has been made in recent decades [1, 2], there are several open questions that still remain, including the poorly understood contact line dynamics on surfaces with heterogeneities.

Interesting dynamics also emerge when a droplet is subjected to change in its mass which may occur due to a variety of mechanisms, including, e.g., liquid imbibition through a permeable substrate, pumping liquid into the droplet or evaporation. During mass transfer, two distinct modes or a combination thereof are reported primarily in the context of evaporative dynamics, namely the *constant-radius mode*, during which the contact line appears to be pinned, and the *constant-angle mode*, i.e. when the radius evolves such that the apparent contact angle remains constant [3].

MODEL AND ANALYTICAL METHODOLOGY

In the present study, we consider a thin droplet of variable mass spreading over a horizontal and chemically heterogeneous surface. We assume small slopes everywhere, strong surface tension effects and negligible inertia, which allows us to invoke the long-wave approximation. Hence, the small-slopes expansion of the Stokes equations yields a partial differential equation for the evolution of the droplet thickness $h(\boldsymbol{x},t)$ at position $\boldsymbol{x}$ and time t, namely

$$h_t + \frac{\sigma}{3\mu}\boldsymbol{\nabla}\left[h(h^2+3\lambda^2)\boldsymbol{\nabla}\nabla^2 h\right] = \frac{q}{\rho}. \tag{1a}$$

Here, μ, ρ and σ are the fluid's viscosity, density and surface tension, respectively, λ is the slip length used to alleviate the stress singularity of the moving contact line [2], and $q(\boldsymbol{x},t)$ models the mass flux. This corresponds to a free-boundary problem, where the contact line at $\boldsymbol{x}=\boldsymbol{c}$ must be determined as part of the solution. Equation (1a) is thus complemented with the appropriate boundary conditions at $\boldsymbol{x}=\boldsymbol{c}$, namely

$$h=0, \quad h_\nu = \theta \quad \text{and} \quad \left(\boldsymbol{c}_t - \frac{\sigma\lambda^2}{\mu}\boldsymbol{\nabla}\nabla^2 h\right)\cdot\boldsymbol{\nu} = \frac{q}{\rho\theta}, \tag{1b,c,d}$$

where $\boldsymbol{\nu}$ is the unit outward normal to the contact line and $\theta(\boldsymbol{x})$ prescribes the heterogeneity of the substrate through a spatially varying contact angle. Conditions (1b) and (1c) are the usual conditions applied to contact line problems with sharp interfaces, whereas (1d) is of kinematic type and is directly derivable from a local expansion of (1a) about $\boldsymbol{x}=\boldsymbol{c}$.

Through a systematic asymptotic analysis, which has been previously utilized for three-dimensional droplets of constant mass [4], we derive a new coupled system of evolution equations that governs the Fourier coefficients of the contact line, $c_m(t)$, cast in the form

$$\vartheta^3 - \theta^3 = \frac{9\mu}{\sigma}\sum_m \left(\dot{c}_m(t)\ln\frac{\ell_m(t)}{\lambda} + v_m(t)\right)\mathrm{e}^{\mathrm{i}m\phi}. \tag{2}$$

Here the dot denotes differentiation with respect to t, ϑ is the apparent contact angle, $\ell_m(t)$ is a macroscopic lengthscale and $v_m(t)$ captures the velocity corrections due to changes in the droplet mass. Equation (2) is reminiscent of a Cox–Voinov-type law [1], which is augmented to take into account mass transfer effects. It is obtained by matching asymptotically the bulk dynamics with the flow in the vicinity of the contact line, by assuming vanishingly small values of λ, slow dynamics and nearly circular contact lines.

*Corresponding author. E-mail: n.savva@cyi.ac.cy

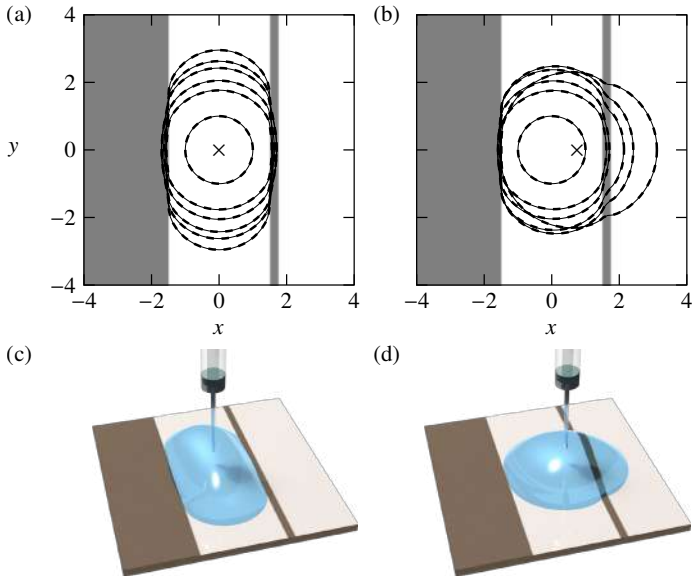

Figure 1: A droplet with liquid injection at two different locations spreading over a chemically heterogeneous substrate (darker shades denote lower wettability regions, i.e. higher contact angles). In (a) and (b) solid curves correspond to contact line profiles at different times as predicted by solutions to (1), whereas dashed curves show the corresponding predictions of (2) with the hybrid approach. The symbols × mark the points of injection. Panels (c) and (d) show renderings of the final droplet shapes in (a) and (b), respectively.

NUMERICAL METHODS AND RESULTS

Numerical experiments are performed to assess how well the predictions of (2) compare with those of full problem, (1). The full problem, which becomes increasingly stiff as λ approaches realistically small values, is solved using a pseudospectral collocation scheme for the spatial discretization and the method of lines for time-stepping. It is seen that the two approaches compare generally favorably and, importantly, simulations with (2) require minimal computational resources compared to those required for the full problem.

Also explored is the development of a hybrid method which improves the agreement with the full model, by leveraging the merits of the lower-order model, (2), but with the inclusion of a small computational overhead. This approach is based on the boundary integral method which allows us to more accurately determine the apparent contact angle ϑ in (2) for a given contact line shape, which then improves the accuracy of the predicted dynamics for $c_m(t)$.

Simulations of a number of representative cases are able to uncover experimentally observed phenomena, such as pinning, stick-slip, and hysteresis-type effects, as well as present convincing numerical evidence that suggests that the reduced and especially the hybrid model can replace the full model within its domain of validity. In this manner, we are able to mitigate considerably the high computing costs required to fully resolve the dynamics across the disparate lengthscales that are present in the system.

Such an example is shown in figure 1, where a localized liquid flux is introduced at two different positions of the free surface of the droplet as it spreads on a substrate decorated with regions of lower wettability. In one case, the droplet becomes elongated and remains trapped between the lower wettability barriers, whereas by shifting slightly the position of the localized flux the droplet is able to move across the rightmost barrier.

CONCLUDING REMARKS

This study shows how the systematic framework presented in [4] can be extended to account for the combined effects of chemical heterogeneities and mass transfer. It is important to highlight that the hybrid theoretical model is able to capture excellently the underlying dynamics, even in cases where the droplet undergoes stronger deformations than those assumed for the analysis to hold (see figure 1), thus offering a compelling alternative approach to full model simulations. Further analysis and extensions to (2) to tackle other complexities will be the subjects of future investigations.

Acknowledgments: DG acknowledges support from the Engineering and Physical Sciences Research Council of the UK through Grant No EP/P505453/1; NS acknowledges support from the European Union's Horizon 2020 research and innovation programme under grant agreement No 810660.

References

[1] Bonn D., Eggers J., Indekeu J., Meunier J., Rolley, E. Wetting and spreading. *Rev. Mod. Phys.* **81**: 739–805, 2009.
[2] Snoeijer J.H., Andreotti B. Moving Contact Lines: Scales, Regimes, and Dynamical Transitions. *Annu. Rev. Fluid Mech.* **45**: 269–292, 2013.
[3] Stauber J.M., Wilson S.K., Duffy B.R., Sefiane K. On the Lifetimes of Evaporating Droplets. *J. Fluid Mech.* **744**: R2, 2014.
[4] Savva N., Groves D., Kalliadasis S. Droplets on Chemically Heterogeneous Substrates. *J. Fluid Mech.* **859**: 321-361, 2019.

THINNING OF FLUID INTERFACES UNDER DOMINANT SURFACE DISSIPATION

Alejandro Martínez-Calvo *[1] and Alejandro Sevilla †[1]
[1] Grupo de Mecánica de Fluidos, Universidad Carlos III de Madrid, Leganés, Spain

Summary We report theoretical and numerical evidence of universality in the thinning of fluid interfaces at high superficial concentration of surfactants. These saturated interfaces are shown to exhibit an asymptotic balance of surface dissipation with surface tension at small scales, yielding an exponential thinning with an e-fold time that only depends on the surface shear and dilatational viscosities.

INTRODUCTION

The presence of surfactants at fluid interfaces plays an important role in many physical systems of great relevance in biology, medicine and different technological contexts [1, 2, 3]. The rich complexity of bulk and surface interactions hinder both, the precise measurements of the material properties associated with adsorbed surfactant layers, as well as the derivation of appropriate continuum models [2]. These surface material parameters are the surface tension coefficient σ, and the surface shear and dilatational viscosities, μ_s and κ_s respectively, which depend on the temperature and on the superficial concentration of surfactant. An interesting limit to explore is that of high surfactant concentrations, where the interface is said to be saturated, in that the Marangoni stresses are negligible, and the surface viscosities take constant values if the surface rate-of-strain is small enough [4, 5]. This particular limit can be achieved by means of a fluid that acts as a surfactant reservoir able to replenish the interface when the surfactant is depleted by advection. Under these conditions, here we report strong numerical and theoretical evidence suggesting the realizability of a new asymptotic regime where surface dissipation balances surface tension, thereby precluding the appearance of a finite-time singularity associated with capillary drainage. In particular, we consider the thinning of an axisymmetric liquid thread of initial radius R_0 due to capillary drainage. Provided that the local radius satisfies $R(t) \ll \mu_s/\mu$, it can be anticipated that $\sigma/R^2 \sim \mu_s \dot{R}/R^3$, where $\dot{R} = \mathrm{d}R/\mathrm{d}t$ is the radial velocity of the filament, and thus $R(t) \propto \exp(-t/t_c)$, where $t_c = \mu_s/\sigma$ is the *surface-visco-capillary time*, which depends only on material parameters [6].

For a Newtonian interface, the most widely used approximation for the surface stress tensor is the Boussinesq–Scriven (B-S) constitutive equation, which is the surface analogue of the Navier–Poisson law, and that reads

$$\boldsymbol{T}_s = \left[1 + \frac{\Theta - 1}{\Theta + 3}(\boldsymbol{\nabla}_s \cdot \boldsymbol{u}_s)\right] \boldsymbol{I}_s + \frac{1}{\Theta + 3}\left[(\boldsymbol{\nabla}_s \boldsymbol{u}_s) \cdot \boldsymbol{I}_s + \boldsymbol{I}_s \cdot (\boldsymbol{\nabla}_s \boldsymbol{u}_s)^{\mathrm{T}}\right], \tag{1}$$

in dimensionless form, where $\boldsymbol{u}_s$ is the fluid velocity at the interface $\partial\mathcal{V}$, $\boldsymbol{\nabla}_s = \boldsymbol{I}_s \cdot \boldsymbol{\nabla}$ is the surface nabla operator, $\boldsymbol{I}_s = \boldsymbol{I} - \boldsymbol{nn}$ is the surface projection tensor, $\boldsymbol{n}$ being the unit normal vector to the interface (see Fig. 1), and $\Theta = \kappa_s/\mu_s$ is the dilatational-to-shear surface viscosity ratio. Note that (1) has been scaled taking R_0 as the characteristic length scale and the surface visco-capillary velocity $\sigma R_0/(3\mu_s + \kappa_s)$ as characteristic velocity scale.

THINNING OF AXISYMMETRIC THREADS: NUMERICAL SIMULATIONS AND LOCAL ANALYSIS

We numerically integrated the Stokes equations for three different configurations involving the capillary drainage of axisymmetric liquid threads, making use of the B-S constitutive law to implement the surface stress balance. In particular, we studied: (I) a spatially periodic thread in the absence of gravity and immersed in a passive ambient. (II) A liquid bridge of length L/R_0, also immersed in a passive ambient, but vertically oriented with gravity with an associated Bond number $Bo = \rho g R^2/\sigma$. And (III) a spatially periodic thread inside an unbounded liquid bath in the absence of gravity, but with a finite value of outer-to-inner viscosity ratio N_μ. Figure 1 shows several snapshots for the three cases. In panels (a), (e) and (i) the computational domain is indicated with dashed lines, and in panel (d) the inset shows the local structure of the flow around the symmetry plane, displaying an elongated thread connecting the two main drops in case I.

Motivated by the interfacial evolution displayed in figure 1, we developed a simple local theory to explain the numerically observed exponential thinning regime. The local shape of the thread is assumed cylindrical, $r = R(t)$, with an inner velocity field $\boldsymbol{u}(r, z, t) = -2z\dot{R}/R\boldsymbol{e}_z + r\dot{R}/R\boldsymbol{e}_r$, and with a pressure jump $p(t) - \hat{p}(t)$ that depends only on time. Under these conditions, the surface stress tensor (1) simplifies to

$$\mathsf{T}_s^{zz} = 1 - \frac{\dot{R}}{R}, \quad \text{and} \quad \mathsf{T}_s^{\theta\theta} = 1 + \frac{3 - \Theta}{3 + \Theta}\frac{\dot{R}}{R}. \tag{2}$$

In the limit $N_\mu \ll 1$ and for times $t \gg 1$, the surface stress balance $(\hat{\boldsymbol{T}} - \boldsymbol{T}) \cdot \boldsymbol{n} + \boldsymbol{\nabla}_s \cdot \boldsymbol{T}_s = \boldsymbol{0}$ yields

$$\dot{R} = -F(\Theta)\, R, \quad \text{where} \quad F(\Theta) = \frac{3 + \Theta}{3 - \Theta}\left[1 - \lim_{t\to\infty}(p_s - \hat{p}_s)R\right], \tag{3}$$

*e-mail: amcalvo@ing.uc3m.es
†e-mail: asevilla@ing.uc3m.es

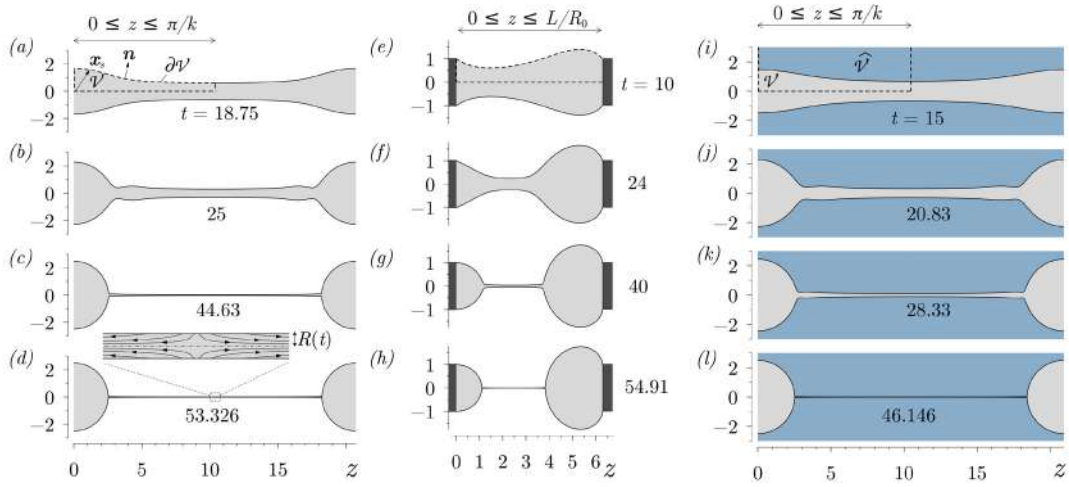

Figure 1: Snapshots of the liquid column obtained from the numerical simulations. (a)–(d) Case I with $Bq = 3.4$, $\Theta = 1$ and $k = 0.303$. (e)–(h) Case II with $Bq = 0.1$, $\Theta = 2$, $L/R_0 = 2\pi$ and $Bo = 0.3$. (i)–(l) Case III with $Bq = 2$, $\Theta = 3$, $N_\mu = 10^{-3}$ and $k = 0.3$.

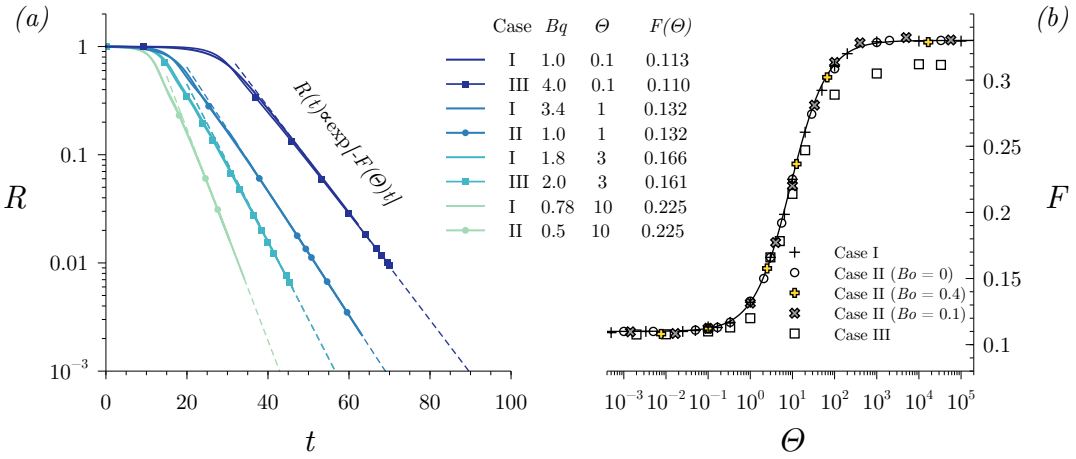

Figure 2: (a) The minimum thread radius $R(t)$ for different conditions specified in the legend. (b) The universal function $F(\Theta)$.

represented for the three cases in Fig. 2(b) together with the approximation

$$F(\Theta) \approx F_{-\infty} + \frac{F_\infty - F_{-\infty}}{2}\left\{1 + \tanh\left[\frac{1}{2}\log\left(\frac{\Theta}{9}\right)\right]\right\}, \tag{4}$$

with $F_{-\infty} = 0.11$ and $F_\infty = 0.33$, which provides a good fit to the numerical results. The solution of (3) is $R(t) \propto \exp\left[-F(\Theta)\, t\right]$, in close agreement with all the numerical results represented in figure 2(a).

DISCUSSION

The present study calls out for a careful experimental campaign to test the new asymptotic regime reported herein. Besides their fundamental hydrodynamic interest, our results pave the way to develop a new non-intrusive measurement technique for the surface viscosity coefficients. Moreover, our findings should be extended to other relevant interfacial thinning configurations involving high concentrations of surfactants, like Plateau borders and films pulled out from a bath, large-amplitude oscillations of surfactant-laden droplets and bubbles, or the retraction of sheets and filaments.

References

[1] G. G. Fuller and J. Vermant, *Annu. Rev. Chem. Bio. Eng.* **3**, 519, 2012.
[2] N. Jaensson and J. Vermant, *Curr. Opin. Colloid Interface Sci.* **37**, 136, 2018.
[3] D. Langevin, *Annu. Rev. Fluid Mech.* **46**, 47 2014.
[4] B. Scheid, J. Delacotte, B. Dollet, E. Rio, F. Restagno, E. A. van Nierop, I. Cantat, D. Langevin, and H. A. Stone, *EPL* **90**, 24002, 2010.
[5] B. Scheid, S. Dorbolo, L. R. Arriaga, and E. Rio, *Phys. Rev. Lett.* **109**, 264502, 2012.
[6] A. Martínez-Calvo and A. Sevilla, *J. Fluid Mech.* **846**, 877, 2018.

THE FATE OF A PAIR OF DEFORMABLE BUBBLES RISING IN LINE

Jacques Magnaudet *[1], Jie Zhang[2], and Mingjiu Ni[3,2]
[1] Institut de Mécanique des Fluides de Toulouse, Université de Toulouse, CNRS, INPT, UPS, Toulouse, France
[2] State Key Laboratory for Strength and Vibration of Mechanical Structures, School of Aerospace, Xian Jiaotong University, Shaanxi 710049, China
[3] School of Engineering Science, University of Chinese Academy of Sciences, Beijing 101408, China

Summary The three-dimensional dynamics of a pair of deformable rising bubbles released in line is investigated by means of direct numerical simulation. A wide parameter range is explored, covering situations corresponding to moderate-to-large Reynolds number and low-to-moderate deformation. Four different interaction scenarios are identified, namely the drafting-kissing-tumbling process already known with rigid particles, a sideways shift of the trailing bubble leaving the leading bubble path almost unaffected, a twin path instability of the bubble pair, and a gradual approach process ending with coalescence. The mechanisms at the root of the escape of the trailing bubble from the wake of the leading one are analyzed, highlighting the specificities of bubbles as compared to rigid particles.

Buoyancy-driven bubbly flows are ubiquitous in geophysics and engineering and offer remarkable dynamics and mixing properties. The chief difficulty in the modeling of such flows stands in the subtle couplings existing between the light deformable dispersed bodies and the surrounding liquid. A fundamental building block in the prediction of the mesoscale structure of these flows lies in the understanding of pair interactions between two neighboring bubbles. Even this canonical situation involves complex and rich dynamics, as many parameters are involved. In particular, the angle between the line joining the centroids of the two bubbles and the vertical plays a crucial role, making the in-line and side-by-side configurations behave very differently. In the in-line geometry, early approaches grounded on potential flow theory [1] predict that two spherical bubbles always repel each other. In contrast, the solution of the full Navier-Stokes equations [2], or the potential flow approach supplemented by a wake model [3], predict an equilibrium distance, owing to the sheltering effect induced on the trailing bubble by the wake of the leading one. In contrast, experimental observations in water [4] reveal that no equilibrium separation distance is reached with sub-millimeter size bubbles, presumably contaminated by surfactants, which always collide and coalesce. Recent experiments [5] uncover much more complex scenarios, including four types of interaction: separation, approach, coalescence and overtaking.

In the present work, we employ three-dimensional direct numerical simulation to examine the fate of two deformable rising bubbles initially released in line in the regime of moderate-to-large Reynolds numbers. We make use of the open source code *Basilisk* [6], taking advantage of the potentialities offered by the adaptive mesh refinement technique to explore subtle mechanisms that find their root at or nearby the fluid-bubble interface, among which those related to vorticity generation and small-scale deformation. When two bubbles are very close to colliding or coalescing, the grid resolution allows us to capture the fluid flow within the film standing between them down to a minimum thickness e_m less than 1% of the bubble radius, which gives an idea of the range of scales resolved in the present approach.
Considering that the two bubbles have the same initial radius a and that the density ρ and viscosity μ of the surrounding liquid are much larger than those of the gas filling the bubbles, the problem under consideration depends on three characteristic parameters, namely the initial dimensionless separation S between the bubble centers, the so-called Galilei number $Ga = V_g a/\nu$ which is a Reynolds number based on the gravitational velocity scale $V_g = (ga)^{1/2}$, and the Bond number $Bo = \rho g a^2/\gamma$, where γ is the surface tension. We explore the range $0.02 \leq Bo \leq 2$, $10 \leq Ga \lesssim 10^2$, which yields Reynolds numbers based on the actual rise velocity from 15 to 10^3, approximately. Having frozen the initial separation to some units ($S = 8$ in what follows), four typical evolutions are observed, depending on Ga and Bo (Figure 1).

When Ga is of $\mathcal{O}(10)$ and the Bond number is lower than a critical value $Bo_c(Ga)$ (with Bo_c typically ≈ 0.3 for $Ga < 50$, then decreasing gradually to less than 0.1 for $Ga = 10^2$), the system follows the drafting-kissing-tumbling (DKT) scenario (Figure 2) already known for rigid spheres [7]. In the final configuration, the two bubbles rise side-by-side along two quasi-vertical lines, the positions of which are almost symmetric with respect to the initial vertical path. For larger Ga, and Bo still less than $Bo_c(Ga)$, a sharp lateral escape of the trailing bubble is observed, while the path of the leading bubble is left virtually unaltered, which defines an asymmetric side escape regime. In these first two regimes, the paths remain planar throughout the rise of the two bubbles. For larger Bond numbers, the two bubbles first rise in straight line, or, for large enough Ga, follow zigzagging or spiraling paths. At some point, they get very close to each other and the film of liquid that still separates them is continuously squeezed and becomes eventually thinner than e_m, which corresponds to the early stages of coalescence. However, for $Ga \gtrsim 30$ (i.e. Reynolds numbers larger than ≈ 250), the former scenario is only observed beyond a second critical threshold $Bo_{c2} > Bo_c$, with $Bo_{c2}(Ga) \approx 0.4 - 0.5$. In the intermediate range $Bo_c(Ga) \leq Bo \leq Bo_{c2}(Ga)$, the two bubbles exhibit approximate oblate spheroidal shapes with an aspect ratio $2.1 \leq \chi \leq 2.8$, and their path would be unstable, were they rising alone [8]. This is why a twin path instability sets in, in which the motion of both bubbles soon exhibits large lateral oscillations. The corresponding paths are still planar for moderate Ga, corresponding to pure zigzagging trajectories, but exhibit a significant three-dimensionality, especially regarding the trailing bubble, when Ga is large enough.

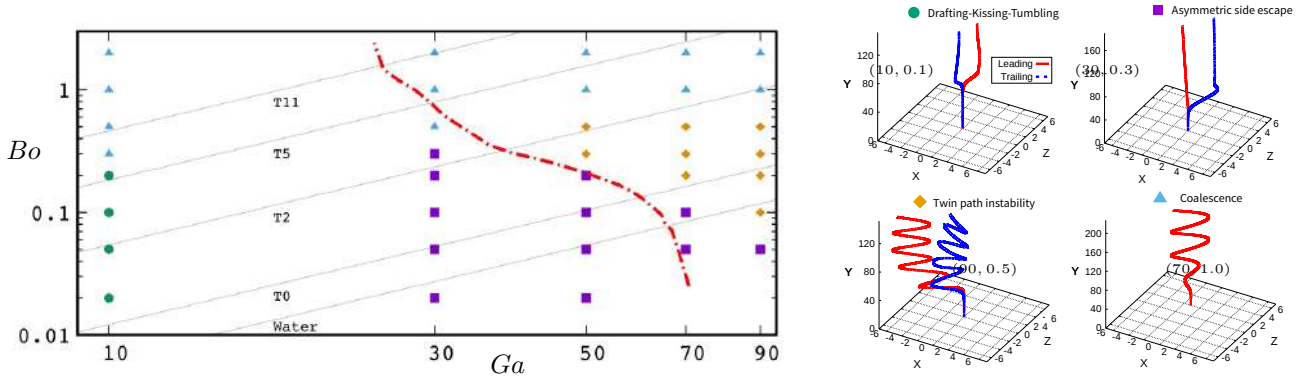

(a) (b)

Figure 1: (a): Regime map showing the subdomains within which each specific interaction scenario is observed. Bullets: drafting-kissing-tumbling, squares: asymmetric side escape, diamonds: twin path instability, triangles: coalescence. (b) Path of selected bubble pairs displaying each of the four scenarios; the corresponding (Ga, Bo) is specified in each panel. Dash-dotted line in (a): approximate neutral curve for the path instability of an isolated bubble [8]; thin solid lines: iso-Mo lines (with $Mo = Bo^3/Ga^4 = g\mu^4/\rho\gamma^3$) corresponding to different liquids, from pure water at the bottom to T11 silicone oil ≈ 10 times more viscous than water at the top.

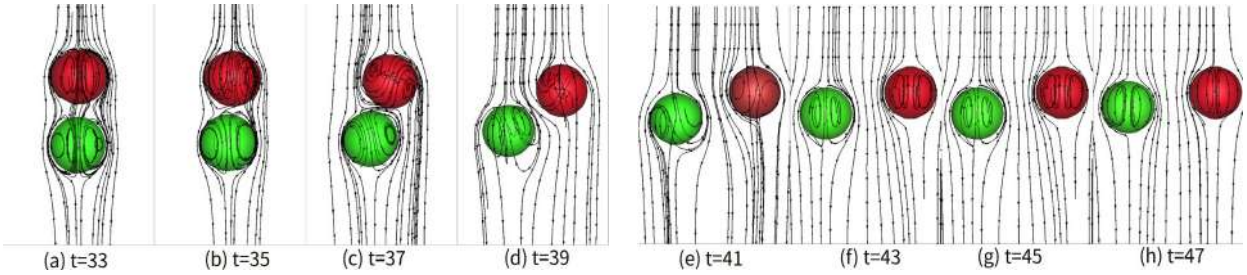

Figure 2: The DKT scenario for a bubble pair with $(Ga = 10, Bo = 0.1)$. Streamlines are plotted in the reference frame of the leading bubble. Time is normalized with the gravitational scale, $(a/g)^{1/2}$.

In all but one (coalescence) of the above scenarios, the mechanism that extracts the trailing bubble from the wake of the leading one plays a key role. It has long be recognized [1] that, as soon as some infinitesimal disturbance shifts the centroid of the trailing bubble from the axis of the leading-bubble wake, the generation of streamwise vorticity past the former results in a sideways force making the in-line configuration unstable. The same mechanism holds for pairs of rigid particles. However, compared to this case, the non-axisymmetric evolutions observed with bubbles take place in a significantly different context. The key difference stands in the weakness of boundary layer effects past clean bubbles, owing to the shear-free condition obeyed by the outer flow at their surface. A direct consequence of this much weaker near-interface vorticity is that, compared to a rigid particle with a similar shape, a much larger lift force is exerted on the trailing bubble for a given lateral deviation from the wake axis, i.e. a given upstream shear. This mechanism is responsible for the vigorous horizontal motions revealed by present simulations.

The vorticity distribution about each bubble is also at the root of the striking difference between the almost symmetric DKT evolution observed for $Ga = \mathcal{O}(10)$ and the asymmetric side escape regime that takes place at higher Ga. Indeed, viscous effects make vorticity significantly diffuse past each bubble for low-to-moderate Ga, and the corresponding vortex dipole results in a fairly long-range repulsive transverse interaction once the bubble pair gets close to the side-by-side configuration. In contrast, the near-bubble vorticity fields are confined to thin boundary layers when Ga is larger, so that they do not interact significantly, leaving the transverse force controlled by the attractive short-range interaction induced by the pressure minimum in between the two bubbles [9]. For short separation distances, the transverse force is strong in the former case, so that it is able to move the formerly leading bubble sideways, which tends to preserve symmetrical lateral offsets of bubble paths after the tumbling stage. Comparatively, the attractive interaction at higher Ga is much weaker, leaving the asymmetry reached at the end of this stage almost unaffected.

References

[1] Harper J. F. *J. Fluid Mech.* **41**: 751-758, 1970.
[2] Yuan H. and Prosperetti A. *J. Fluid Mech.* **278**: 325-349, 1974.
[3] Harper J. F. *J. Fluid Mech.* **351**: 289-300, 1997.
[4] Katz J .and Meneveau C. *Int. J. Multiphase Flow* **22**: 239-258, 1996.
[5] Kusuno H. and Sanada T. *Multiphase Sci. Technol.* **27**: 51-66, 2015.
[6] Popinet S. *J. Comput. Phys.* **302**: 336-358, 2015.
[7] Fortes A. S., Joseph D. D. and Lundgren T. S. *J. Fluid Mech.* **177**: 467-483, 1987.
[8] Cano-Lozano J. C., Martinez-Bazan C., Magnaudet J. and Tchoufag J. *Phys. Rev. Fluids* **1**: 053604, 2016.
[9] Legendre D., Magnaudet J. and Mougin G. *J. Fluid Mech.* **497**: 133-166, 2003.

*Corresponding author. E-mail: jmagnaud@imft.fr

THREE-DIMENSIONAL DIFFUSE-INTERFACE IMMERSED-BOUNDARY METHOD FOR FLUID-STRUCTURE INTERACTION WITH DYNAMIC WETTING

Hailong Li[1], Hang Ding *[1], and Hao-Ran Liu[1]
[1] Department of Modern Mechanics, University of Science and Technology of China, Hefei, China

Summary We propose a three-dimensional (3D) diffuse-interface immersed-boundary method to simulate fluid-structure interaction involving multiphase flows and dynamics wetting. In this work, the immersed boundary method is used to accurately enforce the no-slip boundary condition at the solid surface, and a three-component diffuse-interface model is implemented to capture the interfaces. A hybrid capillary force model is proposed to compute the surface tension force that the interface applies to the solid object at the contact line. The stability and accuracy of the method are validated against experimental results for a variety of 3D test cases, including the impact of a droplet on the column surface, the sinking of a superhydrophobic solid sphere from the water surface and the collision between a heavy droplet and a flying mosquito. The numerical results agree well with the experimental data.

INTRODUCTION

Fluid-structure interaction in the presence of a fluid-fluid interface is ubiquitously seen in our lives, and some may stimulate our curiosity. For example, one may be interested in the answer to the questions like why can water striders run on the water surface or will a mosquito survive raindrop collisions. To gain a full understanding of the physics underlying these flow problems, one may have to resort to direct numerical simulation. However, it is quite a challenging job. Firstly, it encounters the difficulty in resolving the stress singularity at moving contact lines (MCLs), due to its incompatibility with the no-slip condition in the continuum mechanics. A recent review of MCL models in numerical simulations can be found in [1]. Secondly, the applications in practice are normally involved with complex substrates, which brings additional difficulties into the simulation of flows with MCLs, especially in 3D simulation. On the other hand, dynamic wetting plays an important role in the interaction between the fluid-fluid and moving objects at a scale smaller than the capillary length. In this work, we propose a 3D diffuse-interface immersed-boundary method to simulate fluid-structure interaction involving dynamics wetting. In this method, a three-component diffuse-interface model is used to model the interface evolution, since it is able to deal with the multi-phase flow with large density ratios [2]. An immersed boundary method is used to model the fluid-structure interaction, because of its flexibility and efficiency in dealing with moving boundary problems. Finally, a characteristic MCL model, which can accurately meet the wetting condition on the complex geometric solid surface, is extended to the 3D flow problems. The stability and accuracy of the method are validated against experimental results for a variety of 3D test cases, including the impact of a droplet on the column surface, the sinking of a superhydrophobic solid sphere from the water surface and the collision between a heavy droplet and a flying mosquito.

NUMERICAL METHODS

We investigate here 3D flows of two incompressible fluids interacting with moving rigid objects. The fluid motion is governed by 3D incompressible Navier-Stokes equations, of which a dimensionless form can be written as

$$\rho(\frac{\partial \mathbf{u}}{\partial t} + \mathbf{u}\cdot\nabla\mathbf{u}) = -\nabla p + \frac{1}{Re}\nabla\cdot[\mu(\nabla\mathbf{u}+\nabla\mathbf{u}^T)] + \frac{\mathbf{f}_s}{We} + \frac{\rho}{Fr}\mathbf{k} + \mathbf{f}_{IB}, \qquad \nabla\cdot\mathbf{u} = 0, \tag{1}$$

where $\mathbf{f}_s$ denotes the surface tension at the interface region that separates the two immiscible fluids, and $\mathbf{f}_{IB}$ represents the force acted by the solid objects on the surrounding fluids.

The three-component is denoted by volume fraction C and the mathematically sharp interface is modeled by a diffuse interface. In this model, the evolution of the gas-liquid interface is described by the volume fraction of the liquid C_L, which is governed by the Cahn-Hillard equation,

$$\frac{\partial C_L}{\partial t} + \nabla\cdot(\mathbf{u}C_L) = \frac{1}{Pe}\nabla^2\psi, \tag{2}$$

where Pe is the Péclet number and ψ is the chemical potential.

The interface of solid objects is represented by the volume fraction of solid C_S, which is updated by a signed distance function according to the centroid location and the rotation angle of the rigid solid object.

To estimate the effect of solid objects on surrounding fluid flow, an immersed boundary method [3] is used here to enforce the no-slip boundary condition at the solid surface. In this method, the solid objects are represented by a set of Lagrangian points and flows are solved on the Cartesian Eulerian points.

*Corresponding author. E-mail: hding@ustc.edu.cn.

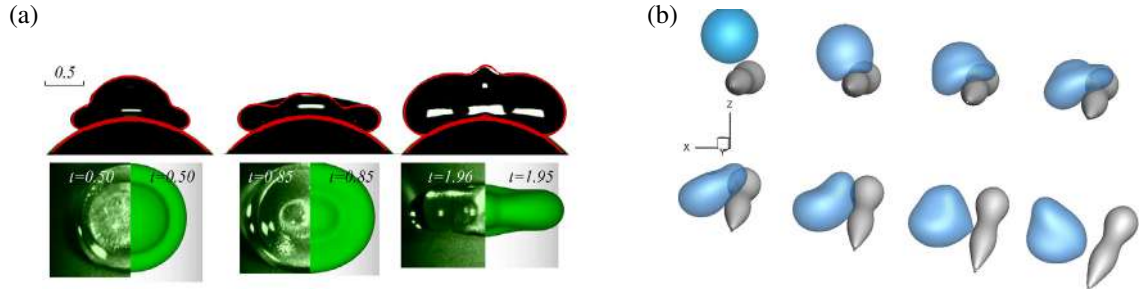

Figure 1: (a). Selected snapshots showing the time evolution of a droplet impact on a concave cylindrical solid surface at different times ($t = 0.54, 0.85, 1.95$), which is in the spreading stage, the largest spreading stage and the retracting stage respectively. The top panel corresponds to the cross-section view parallel to the azimuthal direction, in which the background parts are from the experiment, and the solid red lines are from the numerical result. The bottom panel is the plan view from above the drop, in which the left parts are from the experiment and the left parts are from the numerical result. (b). Time evolution of the collision between the raindrop and flying mosquito at $t = 0,\ 0.54,\ 1.08,\ 1.62,\ 2.16,\ 2.7,\ 3.24,\ 3.78$ from left to right from up to bottom with $Re = 1000$, $We = 10$, $\theta = 140^{\circ}$ and the mass ratio of the mosquito to the droplet is 0.067.

The motion of rigid objects in fluids can be described by its translation velocity and rotation velocity. In this work, the six-degree freedom equations of rigid body motion are solved. The forces exerted on the solid object consists of capillary force, hydrodynamic force and gravity force. Capillary force $\mathbf{f}_{cap}$ is caused by capillary phenomena which occurs at the three-phase contact line. In this model, to deal with complex geometrical solid, the solid surface is divided into lagrangian patches that cover the entire solid surface and a simple projection is used to transfer the integration formula to the solid surface. We prove that it is equivalent to integrate the following equation on the solid surface,

$$\mathbf{f}_{cap} = \frac{3\sqrt{2}}{We\ Cn} \int_{CL} \int_{-\infty}^{+\infty} C_L^2 (1 - C_L)^2 \mathbf{t}\ d\xi_n d\xi_\tau, \tag{3}$$

where Cn is the thickness of diffuse interface, ξ_n and ξ_τ are infinitesimal length along the normal and tangent direction of the contact line, respectively.

RESULTS AND DISCUSSIONS

The dynamics of a water drop impacting onto a cylinder was recently investigated experimentally by Liu et al. [4]. We attempt to numerically reproduce the experimental observations using the present method and make a direct comparison with the experimental data, see Fig. 1 (a). The flow parameters are chosen to be the same as the experimental setup. We also present a model of mosquito body and simulate the dynamic process of the collision between a raindrop and the mosquito, see Fig. 1 (b). The numerical results show that the mosquitoes more likely survive from the collision with raindrops by virtue of their low mass and superhydrophobicity.

CONCLUSIONS

A three-dimensional diffuse-interface immersed boundary method has been proposed to simulate the interaction between fluid-fluid and moving complex geometric solid. The 3D characteristic MCL model is used to satisfy the wetting conditions at the solid surface with arbitrary shape, where the normal directions of the solid and liquid surface are carefully handled and the contact angle hysteresis is also considered. A hybrid capillary model is used to compute capillary force acting on the structure to keep the conservation of momentum. The performance of the approach has been tested by a variety of test cases. The numerical tests show that the approach can produce converged results with mesh refinement and show good agreement with experimental results.

References

[1] Sui, Yi and Ding, Hang and Spelt, Peter D. M. Numerical Simulations of Flows with Moving Contact Lines *Annual Review of Fluid Mechanics* **46**: 97-119, 2014.

[2] Ding, Hang and Spelt, Peter D. M. and Shu, Chang. Diffuse interface model for incompressible two-phase flows with large density ratios *Journal of Computational Physics* **226**: 2078-2095, 2007.

[3] Liu, Hao-Ran and Gao, Peng and Ding, Hang. Fluid-structure interaction involving dynamic wetting: 2D modeling and simulations *Journal of Computational Physics* **348**: 45-65, 2017.

[4] Liu, Yahua and Andrew, Matthew and Li, Jing and Yeomans, Julia M and Wang, Zuankai Symmetry breaking in drop bouncing on curved surfaces *Nature communications* **6**: 10034, 2015.

DIRECT MEASUREMENT OF TIME-DEPENDENT EVAPORATIVE FLUX AND DIFFUSED VAPOR CLOUD OF EVAPORATING DROPLETS

Gilgu Lee[1] and Hyoungsoo Kim[1]
[1] Department of Mechanical Engineering, Korea Advanced Institute of Science and Technology, Daejeon, Korea

Summary: It is well-known that an evaporative flux of a droplet placed on the substrate is mainly dependent on the location and the contact angle while the vapor of the liquid across the liquid-gas interface continuously is evaporated in time. The evaporation mechanism is driven by diffusion and it is assumed to be steady. In this study, we directly visualize the evaporative flux of an evaporating droplet using a Mach-Zehnder interferometry method to explore the unsteady effect and the density effect of the evaporation. Based on the current measurement technique, we measure the time- and space-dependent evaporative flux by varying the molecular weight of the volatile liquid component and the gravitational effect, which would be important to understand and control a final deposition pattern of the evaporated droplet.

INTRODUCTION

A particle-laden droplet leaves a coffee ring pattern due to the inhomogeneous evaporation rate at the liquid surface. The non-uniformity of the dried pattern is crucial in various areas such as inkjet printing and bio-industry [1, 2]. To understand the particle deposition mechanism, most of these studies mainly tried to observe the flow pattern inside droplets and the movement of the suspended particles, which are directly related to the deposition of the particles. To date, it has been rarely investigated to measure the time-dependent signals including diffused vapor cloud and evaporative flux due to the difficulty of the gas visualization experiments. Alternatively, to see the effect of the diffused liquid components on the evaporation, some studies performed the experiment in a liquid-liquid system, which showed that the induced convection effect alters the evaporation rate [3, 4]. In this study, we question effects of the time-dependent evaporative flux and the diffused vapor cloud on the evaporation. To investigate this, we use the Mach-Zehnder interferometry method to visualize the diffused vapor cloud in time. By using several liquids having different vapor pressures and molecular weights, we systematically and quantitatively compare the evaporation rate in time and space. Furthermore, to see the effect of the gravitational effect, we change the angle of the substrate.

VISUALIZATION OF EVAPORATION OF DROPLET USING INTERFEROMETRIC INSTRUMENT

Laser spatial interference technology was applied to evaporating droplets for the visualization of the diffused vapor. The optical instrument is based on the Mach-Zehnder Interferometer (Figure 1(a)). The first beam splitter is divided into the reference light and measurement light. The measurement light passes through the evaporating droplets, and the reference light passes through the air. The transmitted light is interfered at the last beam splitter, which is recorded by the camera. In the absence of an evaporating droplet, the interfered signal shows a straight (undistorted) fringe pattern (see Figure 1(b)) because two lights are identical. However, if there is an evaporating droplet, the fringe pattern is distorted because refractive indices are different in the reference light and measurement light (see Figure 1(c)). The recorded fringe pattern is transformed into a phase distribution map by the Fourier transform profilometry method [5]. The extracted phase results are converted by the inverse Abel transformation that transforms the projection to the inverse projection for estimating the mole fraction outside the droplet [6]. The local evaporation rate of the droplet is obtained based on the converted mole fraction.

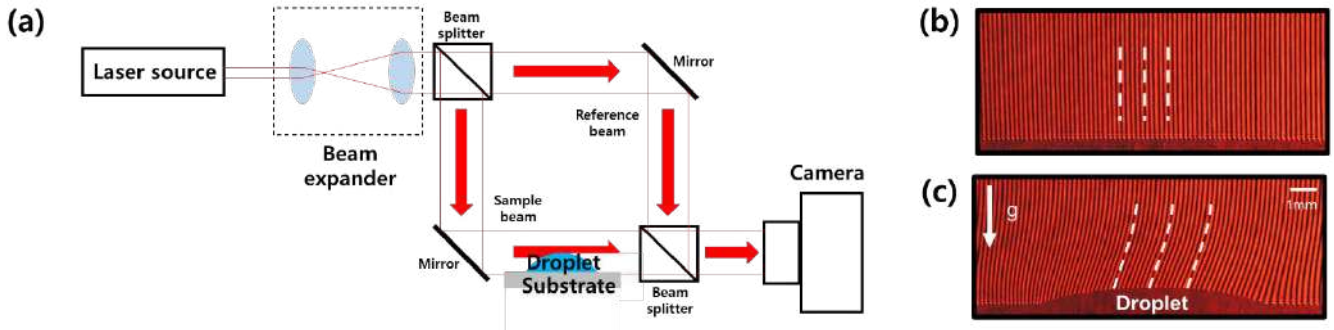

Figure 1. (a) Schematic of the experimental setup of Mach-Zehnder interferometer (b) Undistorted stripe pattern (c) Distorted stripe pattern due to an evaporating droplet.

We measure that a non-uniform evaporation rate along the droplet surface in time. From the measurement result, at the droplet edge, we observe that there is a maximum evaporative flux, which confirms that Deegan's evaporation model is correct [4, 7]. Additionally, we present that the distribution of mole fractions around the droplets is not uniform during evaporation (Figure 2). Figure 2 shows that the distribution of the diffused vapor cloud tends to spread laterally when the droplet is placed on the substrate (Figure 2(a)) while the vertical plume shape of the vapor distribution is measured when the droplet is suspended under the substrate (Figure 2(b)). Based on this observation, we address that the evaporated molecules could change the vapor concentration along the interface of the evaporating droplet, which changes the evaporative flux, as shown the vector arrows in Figure 2. We observe that the evaporative flux is different depending on the orientation of the droplet position. Furthermore, we test the same experiments by varying the molar mass of the liquid. We will compare and discuss the effect of the molar mass on the evaporative flux.

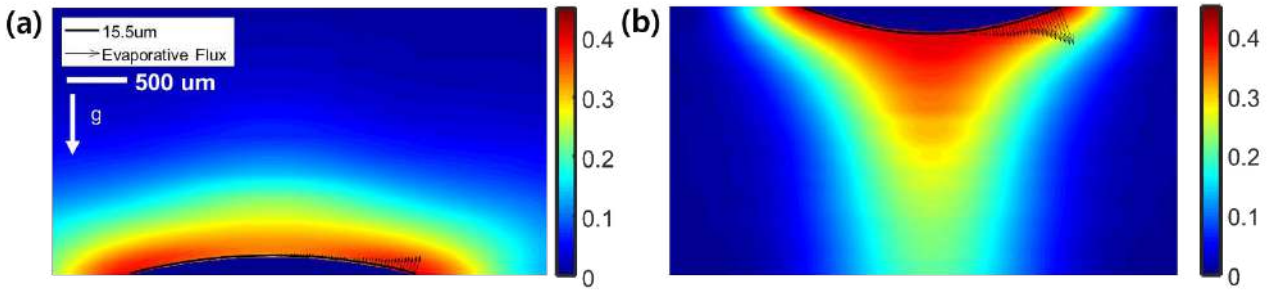

Figure 2. Mole fraction map (color map) and evaporative flux (vectors) of volatile liquid droplet (a) on the substrate and (b) under the substrate.

CONCLUSIONS

We successfully measure the vapor distribution of the evaporating droplet from Mach Zehnder interferometer by varying a molecular weight of liquids and the droplet position. For the first time, we observe that the distribution of the evaporated vapors is not constant in time and space during the evaporation, and also the distribution is significantly different if the droplet is placed on a different position. We expect that this vapor visualization result could provide some insights to understand and control the final dried mark after printing and coating process. Furthermore, the vapor distribution measurement could help to optimize the flow controller and mixer by using vapor-driven solutal Marangoni effect [8-9].

References

[1] Nayak L., Mohanty S., Nayak S. K., Ramadoss A., A review on inkjet printing of nanoparticle inks for flexible electronics. *J. Mater. Chem. C* **7**:8771, 2019

[2] Dugas V., Broutin J. Souteyrand E., Droplet evaporation study applied to DNA chip manufacturing, *Langmuir* **21**(20): 9130-9136, 2005.

[3] Dietrich E., Wildeman S., Visser C. W., Hofuis K., Kooij E. S., Zandvliet H. J. W., Lohse D., Role of natural convection in the dissolution of sessile droplets, *J. Fluid Mech.* **794**: 45-67, 2016.

[4] Dehaeck S., Rednikov A., Colinet P., Vapor-based interferometric measurement of local evaporation rate and interfacial temperature of evaporating droplets, *Langmuir* **30**(8):2002-2008, 2014.

[5] Takeda M., Mutoh K., Fourier transform profilometry for the automatic measurement of 3-D object shapes, *Appl. Optics* **22**(24):3977-3982, 1983.

[6] Fagrich M. E., Chehouani H, A simple Abel inversion method of interferometric data for temperature measurement in axisymmetric medium, *Opt. Lasers Eng.* **50**(3): 336-344, 2012.

[7] Deegan R. D., Bakajin O., Dupont T. F., Huber G., Nagel S. R., Witten T. A., Capillary flow as the cause of ring stains from dried liquid drops, *Nature* **389**: 827-829, 1997.

[8] Park J., Ryu J., Sung H.J., Kim H., Control of solutal Marangoni-driven vortical flows and enhancement of mixing efficiency, *J. Colloid Interface Sci* **561**(1):408-415, 2020.

[9] Ryu J., Kim J., Park J., Kim H, Analysis of vapor-driven solutal Marangoni flow inside a sessile droplet, under review.

LEVEL-SET SIMULATIONS OF SHEARED 2D FOAMS

Y. Mezache[1], M. Le Merrer *[1], F. Detcheverry[1], P.D.M. Spelt[2], and A.-L. Biance[1]
[1] Université de Lyon, Université Claude Bernard Lyon 1, CNRS, Institut Lumière Matière, F-69622, Villeurbanne, France
[2] Laboratoire de Me canique des Fluides et d'Acoustique, UMR CNRS 5509, Universite de Lyon, 69134 Ecully, France

Summary Liquid foams are dispersions of gas bubbles in a soapy liquid matrix. They are also yield-stress fluids, intermediate between solids and liquids, used in various applications for their large specific area, light weight, and insulating properties. In particular, their stability and rheology strongly depend on the type of surfactants used to generate them. To link these macroscopic properties to the microscopic dynamics at the bubble and surfactant scale, we investigate bubble rearrangements, called T1 events, under shear through numerical simulations. We use a two-phase flow level-set method adapted to include surfactant dynamics (Titta et al., Journal of Fluid Mechanics, 2018) and investigate the role of the adsorption depth, a measure of surfactant distribution between the bulk and surface, on surfactant transport and dissipation due to viscous and surface (Marangoni) effects.

INTRODUCTION

Liquid foams are yield stress fluids, as well as ephemeral structures. However, both their rheology and their stability highly depend on the type of surfactants used to generate them [1]. In order to understand the mechanical behavior of foams at the macroscopic scale, we thus investigate the elementary process of foam flow, named bubble rearrangements or T1 events, sketched in figure 1a. These bubble rearrangements are also known to trigger foam collapse [2].

In order to capture the complex coupling between the flow and surfactant dynamics, we use a two-phase flow level-set method that has been adapted to include surfactant dynamics, namely bulk diffusion and bulk/surface exchanges (adsorption/desorption) [3]. The simulation geometry is summarized in figure 1b. It consists in an initial hexagonal arrangement of 2D hemispherical bubbles attached to upper and lower impermeable walls, with a distance of $\frac{2H}{\sqrt{3}}$ between nearest bubble centers. A shear flow is imposed by the velocity $\pm U$ at the walls. Periodic boundary conditions are imposed at the inlet and outlet of the flow. The simulations account for both the flow dynamics through Navier-Stokes equations, as well as the surfactant dynamics, driven by diffusion, adsorption/desorption and advection. Both bulk and surface surfactant concentrations, called F and f, are tracked. The surfactant dynamics feed back onto the flow through Marangoni stresses induced by surfactant inhomogeneities. More details on the physical equations and the numerical implementation can be found in [3].

In this work, we investigate in more detail the role of the so-called adsorption depth $h = f_e/(HF_e)$, i.e. the ratio of the equilibrium surfactant concentration at the interface and in the bulk, here normalized by the domain size. This quantity is a measure of availability for exchange of surfactant in the neighborhood of interfaces. Another key dimensionless quantity is the Péclet number $Pe = UH/D$ which compares advective and (bulk) diffusive mechanisms of surfactant transport.

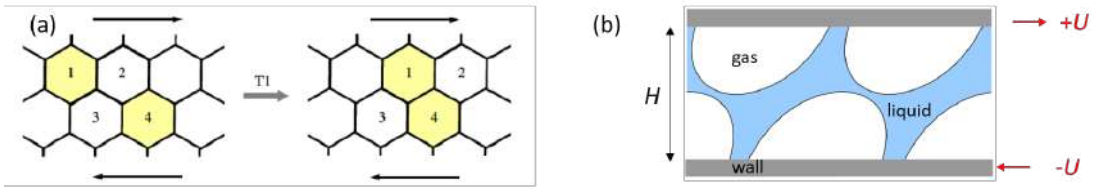

Figure 1: (a) Example of topological rearrangement of type 1 (T1 event). (b) Geometry of sheared bubbles and notations.

SURFACTANT REPARTITION

Before the flow starts, surfactant concentration is homogeneously distributed, both in the liquid and its surface, and at thermodynamic equilibrium ($F/F_e = f/f_e = 1$). After the walls are set into motion, bubbles become stretched in film regions where interfaces slip past each other, and are compressed near Plateau borders where opposite interfaces move either towards or away from each other. This results in zones on the interface that are either depleted or enriched in surfactants (see interfacial surfactant distributions, insets of figure 2), and leads to surfactant adsorption/desorption and bulk surfactant inhomogeneities. Figure 2 shows the surfactant concentrations both in liquid bulk (F) and on the surface (f) during T1 rearrangements at $Pe = 100$. Simultaneous snapshots are shown for two simulations with $h = 1$ (figure 2a) and $h = 0.01$ (figure 2b). Much more heterogeneous concentration distributions (hence stronger Marangoni stresses), both in bulk and on the interface, are observed for $h = 1$ than for $h = 0.01$.

*Corresponding author. E-mail: marie.le-merrer@univ-lyon1.fr.

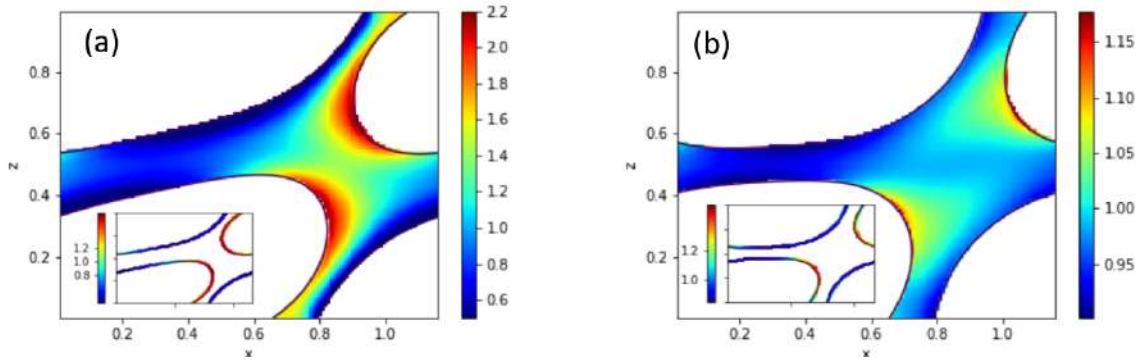

Figure 2: Bulk concentration F (in the liquid) during T1 event for (a) $h = 1$ and (b) $h = 0.01$. Top and bottom bubbles, in white, are moving to the right and left, respectively. Inset: Concentration f along the bubble surface. Bulk and surface concentrations are normalized by their equilibrium values F_e and f_e, respectively.

MECHANICAL RESPONSE

Reaction forces at the walls are computed as the sum of capillary forces at contact lines and the viscous drag forces from the gas and liquid [3]. From this, we calculate the total injected power for steady wall shear P_{inj}, whose temporal evolution is shown in figure 3a. We also compute the total rate of viscous dissipation in the bulk D_v. Figure 3a shows that both P_{inj} and D_v reach a steady state after approximately one bubble rearrangement. Once in steady state, we can therefore extract their time average $\langle P_{inj} \rangle$ and $\langle D_v \rangle$ (dashed lines in figure 3a), reported in figure 3b as a function of the adsorption depth h for two different Péclet numbers. For both $Pe = 1$ and 100, we observe that the total injected power $\langle P_{inj} \rangle$ increases with the adsorption depth. Finally, we also see that the power delivered to the plates is not entirely dissipated by the bulk viscosity : $\langle P_{inj} \rangle > \langle D_v \rangle$. This is because part of the energy supplied by the moving plates must do work at the interfaces, and is associated with an effective surface dissipation due to surfactant diffusion and adsorption/desorption, noted : $\langle D_s \rangle \equiv \langle P_{inj} \rangle - \langle D_v \rangle$ [3]. As h increases, the dissipation increase is mostly due to viscosity at $Pe = 100$ (stronger Marangoni stresses), while it is surface dissipation which increases at $Pe = 1$.

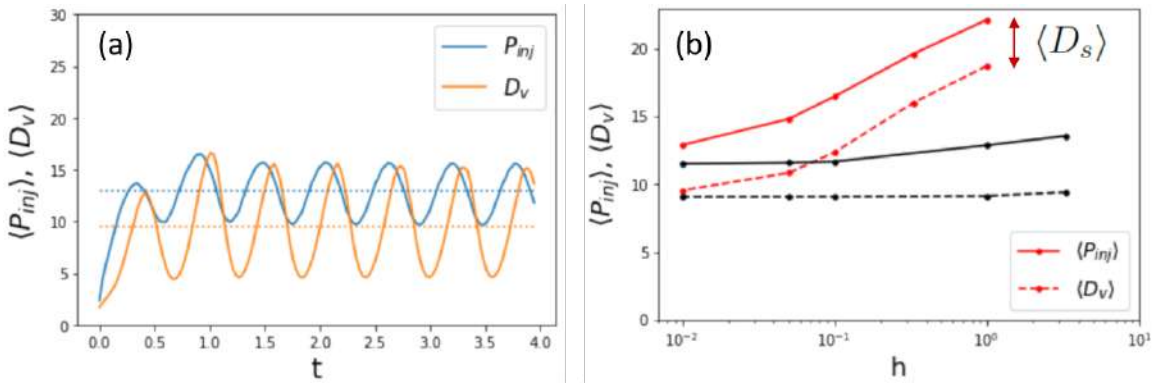

Figure 3: (a) Injected power P_{inj} and viscous dissipation D_v as a function of time t for $Pe = 100$ and $h = 0.01$. (b) Time-averaged injected power $\langle P_{inj} \rangle$ and viscous dissipation $\langle D_v \rangle$ as a function of h for $Pe = 100$ (red) and $Pe = 1$ (black). The difference between the two values correspond to effective surface dissipation $\langle D_s \rangle$.

CONCLUSION

We have shown that variations in adsorption depth result in more heterogeneous surfactant distributions in sheared layers of bubbles. This results in larger forces, which are due to dissipation both in bulk and on the interface. Our results will be compared to a classical model for interfacial dissipation in a simpler geometry [4].

References

[1] I. Cantat, S. Cohen-Addad, F. Elias, F. Graner, R. Höhler, O. Pitois, F. Rouyer, and A. Saint-Jalmes. *Les mousses : structure et dynamique*. Belin, 2010.

[2] A.-L. Biance, A. Delbos, and O. Pitois. *Phys. Rev. Lett.*, 106(6):068301, February 2011.

[3] A. Titta, M. Le Merrer, F. Detcheverry, P. D. M. Spelt, and A.-L. Biance. *Journal of Fluid Mechanics*, 838:222–247, 2018.

[4] J. Lucassen and M. Van den Tempel. *Chemical Engineering Science*, 27:pages 1283–1291, 1972.

NUMERICAL SIMULATIONS OF EVAPORATING SESSILE DROPLETS

Cecile Lalanne *[1], Florence Lequien[1], and Jose-Maria Fullana[2]
[1] Den-Service de la Corrosion et du Comportement des Materiaux dans leur Environnement (SCCME) CEA, Universite Paris-Saclay, F-91191 Gif-sur-Yvette, France
[2] Sorbonne Universite, CNRS, UMR 7190, Institut Jean Le Rond dAlembert, Paris, France

Summary The evaporation dynamics of saline sessile droplets has a strong influence on the corrosion phenomenon under the drop. In order to complete some experimental studies conducted a few years ago, numerical simulations with a two-phase solver, Basilisk are performed. A validation of the model is done considering a pure water droplet following an unpinned of evaporation.

INTRODUCTION

In a marine environment, the sea spray carries small saline droplets coming from the ocean. Those droplets contains chlorides which are an aggressive polluant. The sea spray will deposit droplets on surroundings infrastructures such as buildings or industrial equipment: a drop resting on a surface is called a sessile droplet (Figure 1). In this configuration, the chlorides ions inside the saline sessile droplet are in contact with the material surface. They will etch locally the surface below the droplet and induce atmospheric corrosion phenomenon, such as pitting corrosion (Figure 1). The day/night cycles induce a variation of atmospheric conditions like humidity and temperature creating a repetition of evaporation and condensation phases for the sessile droplets: it increases the corrosion phenomena [2]. After the complete evaporation of the droplet, a salt deposit stays on the surface. The deposit pattern is the consequence of complex flows inside the drop during evaporation and is linked to the location of the corrosion.

(a) (b)

Figure 1: (a) Sessile droplet and (b) example of pitting corrosion.

The aim is to use numerical simulation in order to understand the corrosion induced by saline sessile droplets evaporation. First, pure water droplets are studied to validate the numerical model. Then, saline droplets will be considered.

DYNAMIC OF EVAPORATION

The evaporation of a sessile droplet involves various evaporation modes [1] which may succeed one another (Figure 2). Typical mode is called the constant radius mode or pinned mode: the radius of the drop remains constant whereas the contact angle decreases. This mode appear for particule laden droplets, surfaces with rought surfaces, or droplets wih an initial contact angle below 90 $^\circ$. The pinned mode allows to explain the coffee-ring effect [1]. A second well-known mode called the constant contact angle mode or unpinned mode usually appears, characterized by a constant contact angle whereas the contact line is moving as the radius decreases. The constant radius mode is frequently used to describe evaporation of a pure liquid droplet on a smooth surface: this mode is only academic and we will use it for the first study case of this work. Finally, when the droplet is really small, it becomes quite complicated to determine the exact evaporation behaviour. This last phase is described as a combination of the two first modes : the radius and the contact angle are varying simultaneously, as a stick and slide mode. The stick and slide mode is usually quite short, therefore it is neglected.

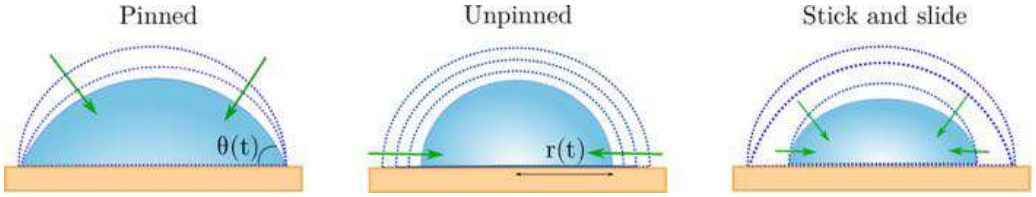

Figure 2: Evaporation modes for a sessile droplet.

We consider a 2D pure diffusive model. The vapor concentration gradient around the sessile droplet drives the evaporation. For sessile droplets with a contact angle θ different than 90 $^\circ$, the evaporation flux across the interface is non-uniform: the flux is stronger near the triple contact line than at the top of the drop (Figure3). Then, a capillary flow inside the droplet compensates this non-uniformity and ensures that the droplet keeps its spherical-cap shape.

*Corresponding author. E-mail: cecile.lalanne@dalembert.upmc.fr

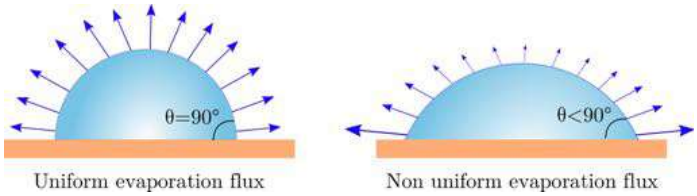

Figure 3: Evaporation flux along the interface for a sessile droplet, depending on the contact angle.

NUMERICAL MODEL

The numerical solver used is Basilisk, a free software, developped at Jean Le Rond DAlembert Institute by Stephane Popinet [3]. It implements numerical methods of finite volume for the Navier-Stokes equations and uses a VOF method to follow the gas-liquid interface with an adaptative mesh. Basilisk is written in C language and allows to simulate a wide range of incompressible flows.

EVAPORATION OF A PURE WATER SESSILE DROPLET

The case we propose is the evaporation of a pure water sessile droplet, evaporating according to an unpinned mode. The simulations have been done with different contact angles. The results (Figure 4) are in good agreement with the experimental results of [4]: when the contact angle decreases, the evaporation rate is higher. Indeed, the radius decreases faster in time for small contact angles. More results about the evaporation flux along the interface of the droplet and about the flows inside the droplet will be presented.

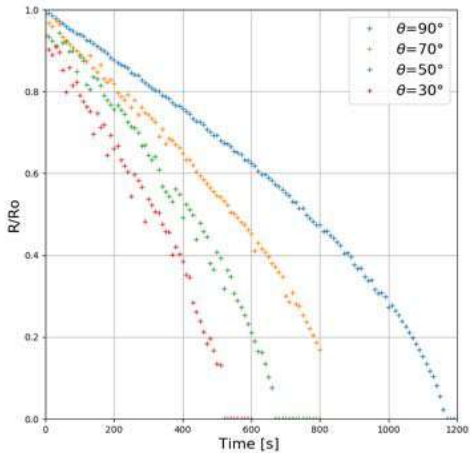

Figure 4: Evolution of the drop radius in time, depending on the contact angle.

CONCLUSIONS AND PERSPECTIVES

The study of a pure water droplet validates our numerical model. A new tracer field for the salt concentration has to be added in order to simulate saline sessile droplet. Coupling Marangoni effects with salt concentration dynamics is an interesting issue we are working on.

References

[1] Amirhossein Amini and G. M. Homsy. Evaporation of liquid droplets on solid sub- strates. I. Flat substrate with pinned or moving contact line. Physical Review Fluids, 2(4), April 2017.

[2] Robert D. Deegan, Olgica Bakajin, Todd F. Dupont, Greb Huber, Sidney R. Nagel, and Thomas A. Witten. Capillary flow as the cause of ring stains from dried liquid drops. Nature, 389(6653):827829, October 1997.

[3] Stephane Popinet. Gerris: a tree-based adaptive solver for the incompressible Euler equations in complex geometries. Journal of Computational Physics, 190(2):572600, September 2003.

[4] Virginie Soulie. Sessile droplets of salt solutions on inert and metallic surfaces : influence of salt concentration gradients on evaporation and corrosion behaviour. PhD thesis, Montpellier, 2015.

ENERGY BUDGETS IN BUBBLE COLLAPSE NEAR A RIGID SURFACE

Minki Kim, Shahaboddin Alahyari Beig, and Eric Johnsen
University of Michigan-Ann Arbor, Department of Mechanical Engineering, Michigan, USA

Summary Damage produced by collapsing cavitation bubbles depends on shock waves produced upon collapse. Additionally, the strength of these shock waves depends on the energy concentration during collapse, which itself is affected by the bubble dynamics. Thus, a better understanding of the underlying physics governing the bubble dynamics is essential to comprehend the damage mechanisms. This study investigates energy transfer pathways and energy concentration during the collapse of a cavitation bubble. Rayleigh−Plesset−type equations and the Boundary Integral Method are used to simulate spherical and non-spherical collapse of a bubble in incompressible and compressible liquids. Each energy partition (e.g., potential, kinetic and acoustic energy) is theoretically defined to compute the component of energy of the bubble and liquid, respectively.

INTRODUCTION

Cavitation occurs due to local pressure reductions in a liquid, leading to the formation of vapor bubbles [1]. When subjected to high pressure regions, the cavitation bubbles undergo a rapid compression that concentrate energy into a small volume, followed by the generation of a pressure wave propagating radially outward, which is capable of damaging its surroundings. In the vicinity of a solid boundary, the collapse becomes asymmetrical, as is evidenced by the formation of a high-speed liquid jet piercing the bubble. The impact of the jet upon the opposite side of the bubble or directly onto the solid boundary generates a shock, which subsequently creates high pressure, temperature, and stress region along the surface as it interacts with the boundary [2]. A better understanding of underlying physics governing bubble dynamics is essential to comprehend structural damage mechanisms, and potentially control/mitigate the erosion.

During the collapse of a cavitation bubble near a solid wall, the initial potential energy of the system is transferred into different modes: kinetic energy of the system, internal energy of the gas and the liquid, and energy radiated away through acoustic radiation. Understanding the energy transfer pathways between different modes helps to determine the origin of the pressure, temperature and shear stresses along the wall. Such quantities are of great importance when investigating cavitation erosion. We carry out numerical simulations of spherical and non-spherical collapse of a single bubble to identify the energy transfer pathways, quantify the energy concentration efficiency, and estimate the pressures and temperatures thereby produced.

METHODS AND PROBLEM SETUP

The efficiency of energy concentration and strength of the emitted pressure waves are expected to depend on the energy transfer between the bubble and the surrounding liquid. Here, the liquid compressibility is hypothesized to play a key role in the energy transfer. To examine the role of compressibility in the context of collapse of a single gas bubble near a rigid wall, we consider two problems: collapse in (a) incompressible, and (b) compressible liquids. Spherical collapse is described using the Rayleigh–Plesset [1] and Keller–Miksis [3, 4] equations. For non-spherical collapse, the mass and momentum equations are solved using the Boundary Integral Method (BIM) [5]. Additionally, we improve the BIM by taking the effects of liquid compressibility into account. This enables us to simulate the inertial collapse of individual bubbles at a higher driving pressure, where liquid compressibility can no longer be ignored. The problem is initialized by considering a bubble at its maximum volume, filled with a non-condensible gas. The collapse is driven by the difference in pressure inside and outside the bubble.

ENERGY PARTITION IN COLLAPSE OF A BUBBLE

Energy in the liquid-bubble system consists of potential (internal), kinetic and acoustic energy. The potential energy of the liquid is the energy stored in the liquid by the pressure at the far field, p_∞ with respect to the state of zero potential energy. It is defined as

$$E_{L,pot} = p_\infty V_B, \tag{1}$$

where V_B is the bubble volume. Another type of the energy in the liquid is the kinetic energy. The kinetic energy of the liquid is the kinetic energy of the fluid particles in the flow, which can be calculated by integrating the local kinetic energy along the boundary of the liquid domain,

$$E_{L,kin} = \frac{1}{2} \oint_{S_B+S_\infty} \phi \frac{\partial \phi}{\partial n} dS, \tag{2}$$

where ϕ is the velocity potential, S_B and S_∞ is the inner and outer boundary of the domain. For the spherical bubble, Eq. 2 reduces to $3/2\left(4\pi\rho_\infty R^3/3\right)\dot{R}^2$, where ρ_∞ is the reference density of the liquid, R is the bubble radius, and $\dot{R}$ is the

*Corresponding author. E-mail: ejohnsen@umich.edu.

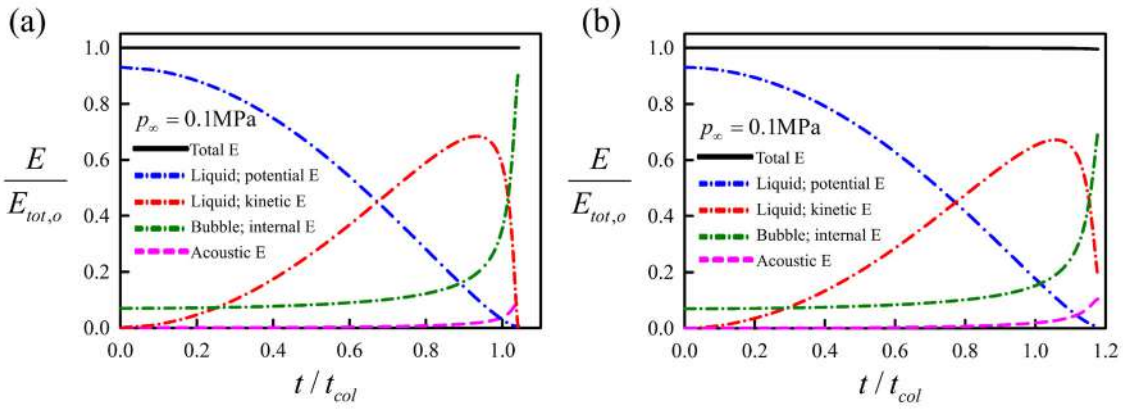

Figure 1: Time evolution of the different modes of energy in (a) spherical and (b) non-spherical collapse of a bubble with p_∞ = 0.1MPa. The total energy (black line), liquid potential (blue line) and kinetic (red line) energy, bubble internal energy (green line) and acoustic energy (pink line) are shown.

bubble wall velocity. The internal energy of the bubble is the sum of the energy of the gas particles in the bubble and can be obtained using the equation of state,

$$E_{B,int} = \frac{p_B V_B}{k-1}, \tag{3}$$

where p_B is the pressure inside a bubble, and k is the specific heat ratio of the gas. Since the bubble is homobaric and follows a polytropic relation, the kinetic energy of the bubble is always zero. The energy of the acoustic waves radiated away from the bubble to the far-field is [5]

$$E_{ac} = \int_0^t -\frac{1}{4\pi}\frac{\rho_\infty}{c_\infty}\dot{V}_B\ddot{V}_B dt, \tag{4}$$

where c_∞ is the reference sound speed in the liquid.

RESULTS AND DISCUSSIONS

Figure 1 shows the time evolution of the different modes of energy in both spherical and non-spherical collapse, both liquid and bubble energy are potential at $t = 0$. During the collapse, this potential energy of the liquid is transferred to internal energy of the bubble and kinetic energy of the surrounding liquid. This latter reaches a maximum value prior to the collapse. Thereafter, the liquid kinetic energy starts to decrease when the bubble reaches the maximum velocity. Differences between the spherical and non-spherical collapse are mainly observed at the final stage of the collapse. When the bubble collapses spherically, the pressure increase inside the bubble decelerates the bubble wall to a full stop at collapse, such that the kinetic energy of the liquid becomes zero. However, in the non-spherical collapse, a re-entrant jet develops and penetrates the bubble. The collapse becomes highly non-spherical when the jet hits the opposite side of the bubble wall. Due to the formation of the liquid jet, a significant portion of the initial potential energy is transferred into the kinetic energy of the surrounding liquid, thus impeding the energy concentration into the bubble potential energy. In both spherical and non-spherical cases, due to liquid compressibility, a substantial portion of the initial potential energy is radiated away from the bubble through acoustic radiation.

CONCLUSIONS

In this study, we investigate the energy transfer pathways into different modes of energy (potential, kinetic, acoustic) during the spherical and non-spherical collapse of a single gas bubble. In the presentation, we will further examine more about non-spherical collapse. For which the initial stand-off distance of the bubble is an important factor determining the efficiency of energy concentration. Thus, energy partition at the final collapse will be compared as the initial stand-off distance varies.

References

[1] Brennen, C.E. Cavitation and Bubble Dynamics. Oxford University Press, 1995.
[2] Kim, K.H., Chahine, G., Franc, J.P. and Karimi, A. Advanced Experimental and Numerical Techniques for Cavitation Erosion Prediction. Springer, 2014.
[3] Keller, J.B. and Miksis, M. Bubble Oscillations of Large Amplitude. *J. Acoust. Soc. Am.* **68**, 628-633, 1980.
[4] Prosperetti, A. and Lezzi, A. Bubble Dynamics in a Compressible Liquid. Part 1. First-Order Theory. *J. Fluid. Mech.* **168**, 457-478, 1986.
[5] Wang, Q. Multi-oscillations of a Bubble in a Compressible Liquid near a Rigid Boundary. *J. Fluid. Mech.* **745**, 509-536, 2014.

CONTACT LINE DISSIPATION FILTERS DROPLET IMPACT ENERGY

Vanessa R Kern[1] and Paul H Steen *[1]
[1] Department of Chemical and Biomolecular Engineering, Cornell University, Ithaca, New York

Summary The dynamics of 2-15μL water droplets vertically impacting rigid hydrophobic and hydrophilic substrates at $Re = 0 - 800$ and $We < 16$ are recorded at a frame rate of at least 5000 fps and post-processed in MATLAB using sub-pixel edge detection techniques [1]. The partitioning of the droplet's energy between contact line dissipation and vibrational energy is studied in a continuum mechanics framework [3]. It is found that contact line dissipation acts as a filter, filtering out the spreading energy to leave the post contact-line-pinning energy. That is, the post contact-line-pinning energy is shown to be invariant to the impact energy. A method for predicting this partitioning is presented. The partitioned pinning energy depends only on the pinning contact angle (α_P), equilibrium contact angle ($\overline{\alpha}$) and the contact angle hysteresis ($2\Delta\alpha_A$).

EXPERIMENTAL OVERVIEW

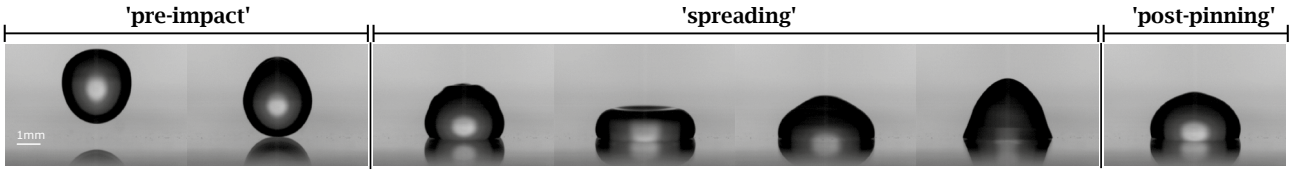

Figure 1: A 13.8 μL water droplet impacting a fluorosilanated glass surface. Time increases left to right. The impacting event can be divided into 3 stages: 'pre-impact', 'spreading', and 'post-pinning'. Each stage has an associated energy contribution.

Water is pumped from a beaker using a Ramé-Hart auto-dispensing system through a syringe tip at a rate of 1.0 μL/s. The droplet is allowed to break from the syringe tip due to gravity and fall onto a homogeneous chemically prepared surface. The impacting event and subsequent dynamics are recorded with a frame rate of at least 5000 fps using a Redlake MotionXtra HG-XL high-speed camera. See Figure 1 for typical experimental images. Multiple syringe tips of gauges 22-30 are used to control the droplet's volume to ±0.1μL. The droplet's 'pre-impact' kinetic energy, K_0, is controlled by varying the fall height. Various surface and liquid combinations are tested to explore a variety of equilibrium contact angles, $69° \leq \overline{\alpha} \leq 105°$, (half) contact angle hysteresis $\Delta\alpha_A = \alpha_A - \overline{\alpha}$, $8° \leq \Delta\alpha_A \leq 22°$, surface tensions, $0.048 \leq \sigma \leq 0.073$ N/m, and viscosities, $1 \leq \mu \leq 20$ cP. Surfaces are characterized using a Ramé-Hart goniometer. Experimental We and Re for each surface/liquid combination are chosen to span a range of K_0, limited to avoid energetic regimes where partial rebound and/or droplet ejection events occur.

DISCUSSION

We will frame our discussion about droplet impact around equation (2.7) from [3], with modified notation:

$$\frac{\mathrm{d}}{\mathrm{d}t}\left(K+\mathcal{A}\right) = -\int_V tr\left(T\cdot D\right)\mathrm{d}V + \int_{\Gamma_{ls}} u\cdot T\cdot n_1 \mathrm{d}s + \sigma\oint_\gamma U\left(\cos\left(\overline{\alpha}+\Delta\alpha\right)-\cos\overline{\alpha}\right)\mathrm{d}l \tag{1}$$

where $\Delta\alpha \equiv \alpha - \bar{\alpha}$ and α is the actual (dynamic) contact angle. The kinetic and surface energies are defined as,

$$K \equiv \frac{1}{2}\int_V \rho u^2 \mathrm{d}V, \quad \mathcal{A} \equiv \sigma_{lg}(A_{lg} - \cos\overline{\alpha}A_{ls}) \tag{2a, b}$$

where subscripts sg, lg and ls denote solid-gas, liquid-gas and liquid-solid interfaces, respectively, and where the surface energy assumes $\sigma_{sg} \approx 0$. The notation is standard.

For normal impact onto a homogeneous surface, we assume that the contact line spreads with radial symmetry, $R(t)$, that is, with a circular shape. We also assume the fluid is inviscid, $\mu << 1$, and incompressible, $\nabla\cdot\boldsymbol{v} = 0$. Together these assumptions allow us to neglect the first two terms on the right hand side of (1), which leaves after integration,

$$\{K+\mathcal{A}\}_0 - \{K+\mathcal{A}\}_p = -\sigma\int_0^{t_s} 2\pi R\dot{R}\left(\cos\left(\overline{\alpha}+\Delta\alpha\right)-\cos\overline{\alpha}\right)\mathrm{d}t. \tag{3}$$

Here, $\{K+\mathcal{A}\}_0$ denotes the droplet's 'pre-impact' energy and $\{K+\mathcal{A}\}_p$ the droplet's 'post-pinning' energy. The right hand side represents the energy dissipated at the contact line (CL) during the 'spreading' stage, where t_s is the duration of the 'spreading' stage, R the radius of the CL, $\dot{R}$ the speed of the CL and $\Delta\alpha$ the deviation of the instantaneous contact

*Corresponding author. E-mail: phs7@cornell.edu.

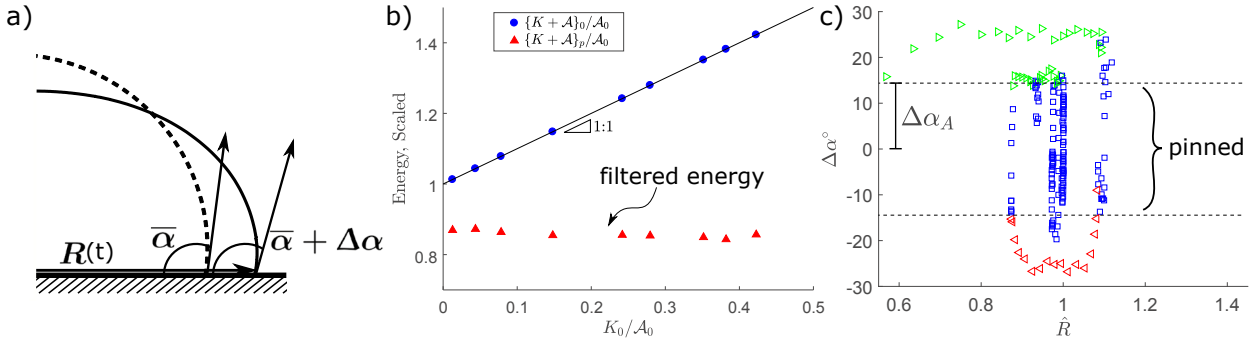

Figure 2: Post droplet impact filtering of impact energy: (*a*) Definition sketch for radial advancing/receding of CL, showing deviation contact angle $\Delta\alpha$, relative to angle $\overline{\alpha}$ measured at rest shape (dashed), at instantaneous spreading radius $R(t)$; (*b*) The 'pre-impact' energy (solid circles) and the 'post-pinning' energy (solid triangles) plotted vs the 'pre-impact' energy for a water droplet impacting a fluorosilanated surface. All energies are scaled by the droplet's 'pre-impact' surface energy; (*c*) $\Delta\alpha$ plotted against $\hat{R}$ for a droplet of water impacting a fluorosilanated surface with an impact kinetic to surface energy ratio, $K_0/\mathcal{A}_0$, of 0.33. Time moves clockwise. ▷ represents an advancing contact line, ◁ a receding contact line and □ a pinned contact line. Advancing/receding occurs when $|\Delta\alpha| > \Delta\alpha_A$. The radius of the droplet's footprint, $\hat{R}$, is scaled by the droplet's equilibrium footprint radius. $\Delta\alpha$ is measured using the goniometer software DropImgAdv and $\hat{R}$ is measured from images in MATLAB using subpixel edge detection techniques [1].

angle from the equilibrium contact angle, $\overline{\alpha}$. Eqn. (3) implies that the only form of dissipation in the system is from the work done by the contact line as it moves along the surface, consistent with [4,5].

In order to quantify $\{K+\mathcal{A}\}_p$, the 'post-pinning' energy, we use sub-pixel edge detection techniques from [1] in MATLAB to track the deflection of the droplet's lg interface. We then decompose the motion of this interface into modal contributions from [2] and calculate the interfacial energy. This calculation is validated by measuring the surface energy directly from the experimental images. The 'pre-impact' kinetic energy, $\{K+\mathcal{A}\}_0$, is calculated by measuring the droplet's fall height, and validated by measuring the impacting velocity from the experimental images. We assume the droplet is spherical prior to impact. Fig. 2 (b) summarizes these findings, showing the invariance of the 'pre-impact' energy to the 'post-pinning' energy.

In order to quantify the 'spreading' energy, the position of the contact line, R, is tracked in time in MATLAB using subpixel edge detection techniques from [1], and the deviation of the contact angle from $\overline{\alpha}$, denoted $\Delta\alpha$, is calculated using the software DropImgAdv. These values are then used to calculate the right hand side of eqn. (3). Typical plots generated during this calculation are shown in Fig. 2 (c). After impact, the droplet's contact line oscillates about its equilibrium value, dissipating energy. If subject to a forced vibration from below, a plot such as Fig. 2 (c) would form a closed loop [4]. In summary, for low $K_0/\mathcal{A}_0$, it is found that eqn. (3) holds.

Lastly, by manipulating equation (3), we arrive at a prediction for the 'post-pinning' energy,

$$\frac{\{K+\mathcal{A}\}_p}{\mathcal{A}_0} = 1 - f(\alpha_P)\left(\cos\overline{\alpha} - \cos\left(\overline{\alpha} + \Delta\alpha_A\right)\right), \tag{4}$$

where $f(\alpha_P)$ represents the geometry of the pinned drop and is explicitly known.

CONCLUSIONS

The dynamics of 2-15μL water droplets vertically impacting chemically modified rigid substrates are studied. It is experimentally determined that droplets vibrate post impact with frequencies and shapes of the pinned $l = 0$ modes detailed in [2]. A discussion of the partitioning of a droplet's energy between 'spreading' and 'post-pinning' is presented and framed using theory from [3]. It is shown experimentally that a droplet's 'post pinning' energy, $\{K+\mathcal{A}\}_p$, is approximately invariant to its 'pre-impact' energy, with the remainder going to contact line dissipation. It is also shown that, for low $K_0/\mathcal{A}_0$, eqn. (3) holds. Lastly, a method for predicting the filtered energy $\{K+\mathcal{A}\}_p/\mathcal{A}_0$ is presented. The filtering depends only on $f(\alpha_P)$, $\overline{\alpha}$ and $\Delta\alpha_A$. The difference between the 'pre-impact' and 'post-pinning' energies represent the energy available for advancing/receding CL motion.

References

[1] Trujillo-Pino, A., et. al. Accurate subpixel edge location based on partial area effect. *Image and Vision Computing*. **31**: 72-90, 2013.
[2] Bostwick J. B., Steen P. H. Dynamics of sessile drops. Part 1. Inviscid theory. *Journal of Fluid Mechanics*. **760**: 5-38, 2014.
[3] Dussan V., E. B., Davis, S. H. Stability in systems with moving contact lines. *Journal of Fluid Mechanics*. **173**: 115-130, 1986.
[4] Xia, Y. and Steen, P.H. Moving contact-line mobility measured. *Journal of Fluid Mechanics*. **841**: 767-783, 2018.
[5] Carlson, A., Bellani, G., and Amberg, G. Contact line dissipation in short-time dynamic wetting. *Europhysics Letters*. **97.4**: 44004, 2012.

MULTILAYER VOLUME-OF-FLUID FOR COALESCENCE PREVENTION WITH APPLICATION TO A FOAMING WATERFALL

Petr Karnakov[1], Sergey Litvinov[1], and Petros Koumoutsakos*[1]
[1] Computational Science and Engineering Laboratory, ETH Zurich, Switzerland

Summary We present a new algorithm for simulating multiphase flows with bubbles and drops that do not coalesce. The algorithm is more efficient than the standard multi-marker volume-of-fluid method since the number of required fields does not depend on the number of bubbles. Together with a novel particle method for curvature estimation, this allows us to solve problems with large clusters of small bubbles on a uniform mesh. The capabilities of our method and its high performance implementation are demonstrated on simulations of constrained mean curvature flow, drop impact on a liquid-liquid interface and a foaming waterfall. The implementation is open source (`https://github.com/cselab/aphros`).

INTRODUCTION

Many processes in nature and industry involve multiphase flows where bubbles and drops do not coalesce but instead collide or form clusters. Examples include crowns of foam on sea water [1], viscous suspensions, and turbulent bubbly flows in chemical reactors. Coalescence is prevented by surfactants, viscous forces and the Marangoni effect. Numerical simulations of such flows are challenging since they resolve only finite length scales, while the liquid film between bubbles can be arbitrarily thin. Front-capturing methods, such as the volume-of-fluid or level-set methods, cannot describe multiple interfaces in one computational cell, so bubbles always coalesce at shorter distances. To prevent coalescence, the multi-marker volume-of-fluid method [2] introduces a separate volume fraction field for each bubble, which is expensive for systems with many bubbles. The Voronoi implicit interface method [3] uses a single level-set function but has a super-linear complexity and requires a band of cells near the interface which puts limits on the minimal resolution.

NUMERICAL ALGORITHM

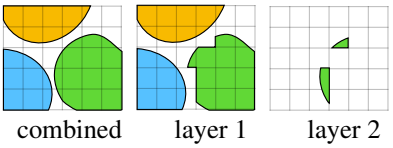

Figure 1: Multiple layers with color functions. Combined field can describe overlapping interfaces, while each layer has at most one bubble per cell.

We propose an algorithm that is equivalent to the multi-marker volume-of-fluid method [2] and uses standard routines of the volume-of-fluid method, but its cost does not depend on the number of bubbles. Our algorithm represents many bubbles with only few fields, referred to as *layers*, and employs *color functions* to distinguish between bubbles. To perform a stencil operation, we combine values from cells of the same color. We apply the algorithm to incompressible multiphase flows with surface tension using a projection-based method for the Navier-Stokes equations and a novel particle method [4] for curvature estimation. The high performance implementation of our solver is based on the Cubism library [5] and shows good scaling of 80% up to 2000 compute nodes of Piz Daint supercomputer. The open source implementation, documentation, examples of simulation setups and visualizations are available at `https://github.com/cselab/aphros` [7].

APPLICATIONS

Constrained mean curvature flow

In the limiting case of no inertia, the equations of fluid flow with surface tension simplify to one expression for the velocity field

$$\boldsymbol{u} = \sum_{l=1}^{L} \kappa_l \nabla \alpha_l - \nabla p,$$

where κ_l and α_l are the mean curvature and the volume fraction field on layer l, the number of layers $L = 4$ and the scalar field $p(\boldsymbol{x}, t)$ is found from the Poisson equation $\nabla^2 p = 0$ to make the velocity field divergence-free. We adopt the initial conditions from [3] which are defined as a Voronoi diagram of a randomly chosen set of 100 points. Zero Neumann boundary conditions are imposed for the volume fraction fields. Initially, the interfaces are straight and form junctions at various angles. The flow minimizes the area (length) of the interfaces such that the angles at triple junctions approach 120°. As seen from Figure 2, our method produces results similar to that of the Voronoi implicit interface method (VIIM) [3]. Both methods operate on a mesh of 256^2 cells. Unlike VIIM, our algorithm has linear complexity to the number of cells and uses standard routines of the volume-of-fluid method.

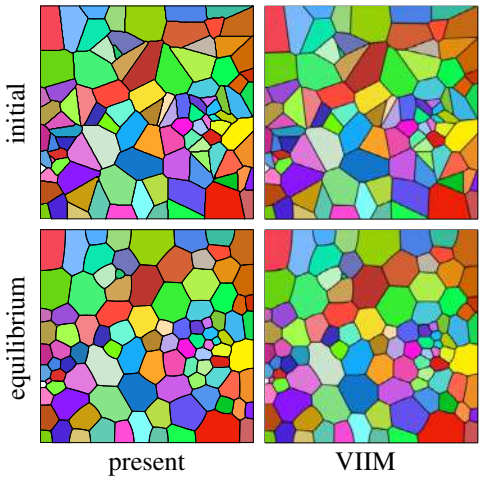

Figure 2: Constrained mean curvature flow. Our method (left) produces results similar to that of the Voronoi implicit interface method [3] (right). Interfaces at triple junctions form 120° angles.

*Corresponding author. E-mail: petros@ethz.ch

Drop impact on liquid-liquid interface

The second test validates the model on the case of the gravity-driven impact of a liquid drop onto a liquid-liquid interface. The problem is solved in a rectangular domain with a height of 10 cm on a mesh containing $160\times320\times160$ cells with no-slip walls in the vertical direction and periodic conditions in the other directions. Parameters of the problem are taken from numerical study [2] based on experiment [6] (Combination 1): density $\rho_1 = 949$ and $\rho_2 = 1128$ kg/m^3, viscosity $\mu_1 = 0.019$ and $\mu_2 = 0.0063$ Pa $\cdot$ s, gravitational acceleration $g = 9.8$ m/s^2 and surface tension coefficient $\sigma = 0.029$ N/m. They correspond to a water+glycerin drop falling in silicon oil. A spherical drop of a radius 5.1 mm is initially placed at a distance of 67 mm between its center and the interface. The drop rests on the interface without coalescence due to high viscosity of the liquids. Slices of the interfaces are shown in Figure 3 compared to numerical [2] and experimental data [6]. Our algorithm produces the same results as the multi-marker volume-of-fluid method method [2], but it is more efficient for systems with many bubbles or drops.

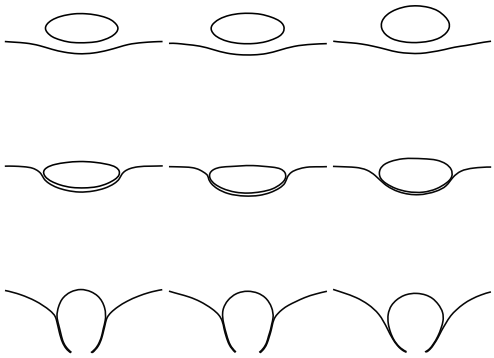

Figure 3: Drop impact on liquid-liquid interface. Our method (left) produces the same results as the multi-marker volume-of-fluid method [6] (center), but it is more computationally efficient for systems with many bubbles or drops. Both methods agree well with experimental data [6] (right).

Foaming waterfall

This application combines various physical processes such as air entrainment, bubble breakup in turbulent flows and generation of foam. The problem is solved in a rectangular domain with a height of 10 cm on a mesh containing $768 \times 384 \times 384$ cells. The initial velocity is zero, and the volume fraction represents the water surface in the middle of the domain. The boundary conditions are periodic in the depth direction and the other boundaries are free-slip walls. Parameters of the problem are density $\rho_1 = 1000$ and $\rho_2 = 10$ kg/m^3, viscosity $\mu_1 = 10^{-3}$ and $\mu_2 = 10^{-5}$ Pa $\cdot$ s, gravitational acceleration $g = 9.8$ m/s^2 and surface tension coefficient $\sigma = 0.072$ N/m. The thickness of the waterfall is 5 mm and the inlet velocity is 1.5 m/s. The sheet of water impacts the surface and causes air entrainment. This generates bubbles that rise and cluster up on the surface. Figure 4 shows a snapshot of the interface and a horizontal cross section through the cluster of bubbles. At this time, the total number of bubbles in the liquid is about 25'000. The cluster of bubbles shows characteristic features of foam: thin membranes separating neighboring bubbles (lamellae) and junctions of multiple membranes (Plateau borders). This case demonstrates that our method of coalescence prevention can describe the formation of clusters with thousands of bubbles.

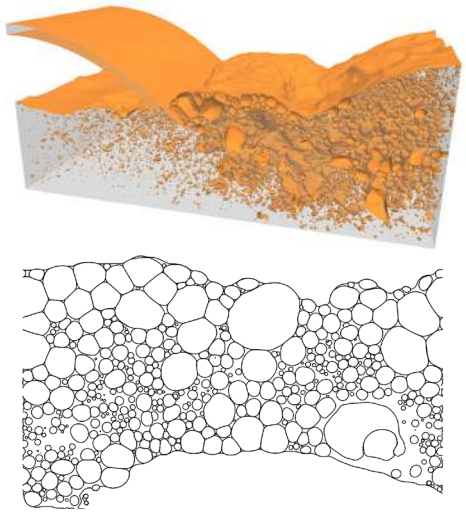

Figure 4: Foaming waterfall. Snapshot of the interface (top) and a horizontal cross section through the cluster of foam (bottom).

CONCLUSIONS

We have presented a new algorithm for simulating multiphase flows with non-coalescing bubbles or drops. Our algorithm produces the same results as the standard multi-marker volume-of-fluid method, but it is more computationally efficient since the number of fields required to represent overlapping interfaces does not depend on the number of bubbles in the simulation. Unlike the Voronoi implicit interface method, it has linear complexity to the number of cells, uses standard routines of the volume-of-fluid method and does not require a band of a few cells between the interfaces. The case of foaming waterfall demonstrates that our method can describe the formation of clusters of foam.

References

[1] Karnakov P., Litvinov S. Favre J.M. and Koumoutsakos P., 2019. Breaking waves: to foam or not to foam? *APS Gallery of Fluid Motion* https://doi.org/10.1103/APS.DFD.2019.GFM.V0018
[2] Coyajee, E. and Boersma, B.J., 2009. Numerical simulation of drop impact on a liquid–liquid interface with a multiple marker front-capturing method. *Journal of Computational Physics*, 228(12), pp.4444-4467.
[3] Saye, R.I. and Sethian, J.A., 2011. The Voronoi implicit interface method for computing multiphase physics. *Proceedings of the National Academy of Sciences*, 108(49), pp.19498-19503.
[4] Karnakov P., Litvinov S. and Koumoutsakos P., 2020. A hybrid particle volume-of-fluid method for curvature estimation in multiphase flows *International Journal of Multiphase Flow*, 125, p.103209
[5] Wermelinger, F., Rasthofer, U., Hadjidoukas, P.E. and Koumoutsakos, P., 2018. Petascale simulations of compressible flows with interfaces. *Journal of Computational Science*, 26, pp.217-225.
[6] Mohamed-Kassim, Z. and Longmire, E.K., 2003. Drop impact on a liquid–liquid interface. *Physics of Fluids*, 15(11), pp.3263-3273.
[7] Aphros: Finite volume solver for incompressible multiphase flows with surface tension (https://github.com/cselab/aphros).

PATTERN FORMATION DURING THE IMPACT OF A PARTIALLY FROZEN DROPLET ON AN UNDERCOOLED SURFACE

Pallav Kant *[1], Henrik Müller-Groeling[2], and Detlef Lohse[1,3]
[1] Physics of Fluids Group, Max Planck Center Twente for Complex Fluid Dynamics, University of Twente, 7500 AE Enschede, The Netherlands
[2] Department of Physics and Astronomy, University of Heidelberg, Germany
[3] Max Planck Institute for Dynamics and Self-Organization, 37077 Göttingen, Germany

Summary Impact of a droplet on an undercooled solid surface instigates several physical processes simultaneously. The involved processes are further complicated when the impacting droplet is partially frozen. Here, we experimentally probe the complex interplay between droplet scale motion and phase transition effects during the impact of a binary droplet on an undercooled surface which partially freezes in flight due to the evaporative cooling of the volatile component. We adapt the TIR (Total-Internal-Reflection) optical technique to visualize the nucleation and growth of the solidified phase while the droplet spreads on the surface. Our experiments reveal that when a partially frozen droplet impacts onto an undercooled surface, the presence of crystals near the advancing contact line locally increases the effective viscosity and results in classical viscous fingering.

INTRODUCTION

Freezing or solidification of impacting droplets is omnipresent in nature and technology, be it a rain droplet falling on a supercooled surface, be it in inkjet printing where often molten wax is used, be it in added manufacturing or in metal production processes or in extreme ultraviolet lithography (EUV) for the chip production where molten tin is used to generate the EUV radiation. For many of these industrial applications, a detailed understanding of the solidification process is essential. Whereas a large number of studies have investigated the corresponding interface deformations and the spreading of a droplet after it impinges onto an undercooled surface [1], the *kinetics* of phase transition within the impacting droplet has been addressed only in a few [2]. Moreover, the literature on this topic has been limited to the idealised scenarios where a liquid droplet solidifies post its impact on an undercooled surface, whilst, in nature and in industry complex scenarios arise due to the impact of partially frozen droplets.

In the present work, we adapt the total-internal-reflection (TIR) technique to visualise the phase transition in the vicinity of the liquid-substrate interface after a droplet impacts onto an undercooled transparent surface. This unique technique allows temporally and spatially resolved insight into the nucleation events and crystal growth occurring next to the cold surface on an evanescent length scale ($\sim$ 100 nm), which is otherwise inaccessible through any other optical technique. Through this technique, we are able to reveal the complex interplay between drop-scale fluid motion within droplet and crystal growth that results in morphologies analogous to patterns observed in classical displacement flows.

EXPERIMENTAL METHODS

A schematic diagram of the experimental setup is shown in Fig. 3. In each experiment, a pendant drop of 80:20 binary mixture of hexadecane (99%, Sigma-Aldrich) and diethyl ether (Sigma-Aldrich) was released from the tip of a needle. Both liquids are optically transparent at room temperature and completely miscible. Hexadecane has a high melting point $T_\mathrm{m} = 18°\mathrm{C}$ and is non-volatile at room temperature. Whereas diethyl ether has low boiling point $T_\mathrm{b} = 36°\mathrm{C}$ and is extremely volatile at room temperature. Thus, the evaporation of volatile diethyl ether from a binary droplet hanging from the needle results in the preferential freezing of hexadecane. Thus, in each experiment the pendant droplets while hanging from the needle tip froze from the outside in and the impacting droplet was covered in a frozen shell. The impact event was recorded in side-view as backlit shadow-graphs and in bottom-view *via* the total-internal-reflection technique. The solidified phase appears as a gray-shaded region in the TIR imaging. The impact velocity and shape/size of the droplet at the time of impact were measured from side-view images recorded with a high-speed camera (Photron Mini) at 10000-14000 fps with a macro lens. Bottom view observations (*via* TIR) were recorded using a high-speed camera (Photron Fastcam, NOVA) connected to a long-distance microscope (Navitar 12x Telecentric zoom system) at 80,000 fps.

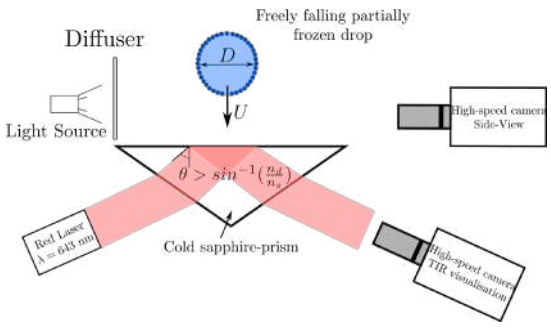

Figure 1: Schematic diagram of the experimental setup employing total-internal-reflection technique to visualise the freezing behaviour of an impacting droplet on undercooled surface.

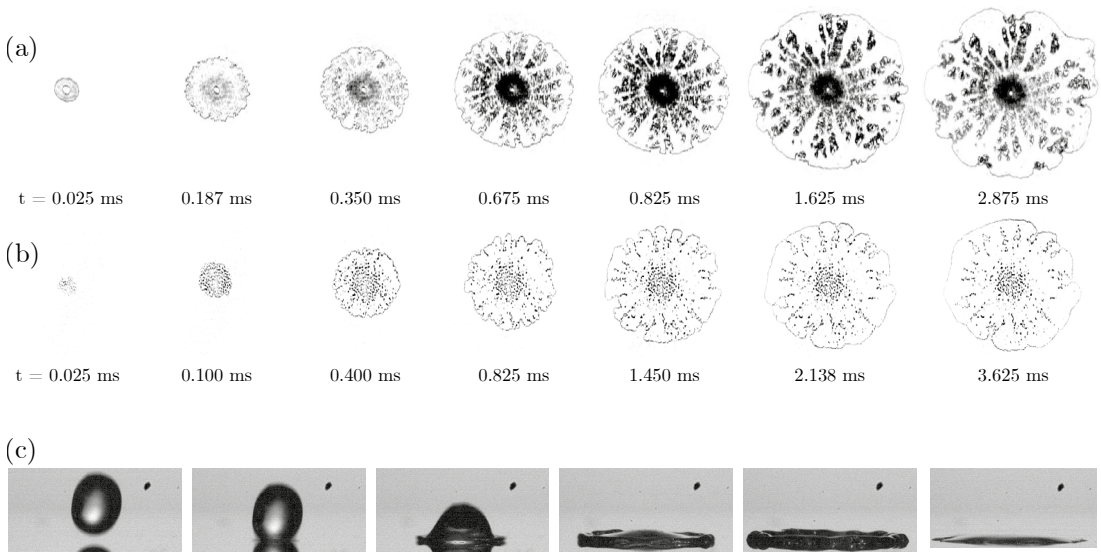

Figure 2: Sequences of experimental snapshots highlighting the outcomes of impact of (a) partially frozen binary droplet on an undercooled surfaces maintained at $\Delta T = T_m - T_s = 9\,\mathrm{K}$ and (b) liquid marble. In both cases the impact velocity of the droplet is $U = 2.8$ m/s. (c) Typical interface deformations associated with the impact of a partially frozen droplet.

RESULTS

Sequence of snapshots in Fig. 2a show the evolution of the footprint of an impacting partially frozen droplet while is spreads on a flat surface at $\Delta T = T_m - T_{substrate} = 9\mathrm{K}$. The Reynolds number $Re = \rho DU/\mu$ associated with the impact is 1150. Typical deformations of the partially frozen droplet, recorded from side-view are shown in the sequence Fig. 2c.

Immediately after the droplet makes contact with the substrate two concentric rings appear in the TIR images; see the first panel of the sequence in Fig. 2a. The outer ring corresponds to the contact line of the droplet that continues to move radially outwards. The inner ring highlights the footprint of the bubble entrapped underneath the droplet interface. In time, we notice that the footprint of the impacting partially frozen droplet evolves in a non-circular fashion, perturbations at the contact line are clearly visible in the images. The solidification first initiates at the center as a cloud of crystallites appears in the middle of the wetted area. Further, the solidified area evolves into growing finger-like patterns as the droplet continues to spread outwards in a non regular fashion. We believe that the growth of solidified phase in this particular fashion is directly related to the presence of crystallites at the droplet interface during spreading. To confirm our hypothesis we performed impact experiments with liquid marbles; see sequence of snapshots in Fig. 2b. In both cases we observe non-regular advancing motion of contact as well as growth of finger-like structure. Furthermore, we noticed that the overall solidification patterns are greatly affected by the impact velocity. The finger-like patterns become increasingly disconnected from the central frozen area with increasing impact velocity; see Fig. 3.

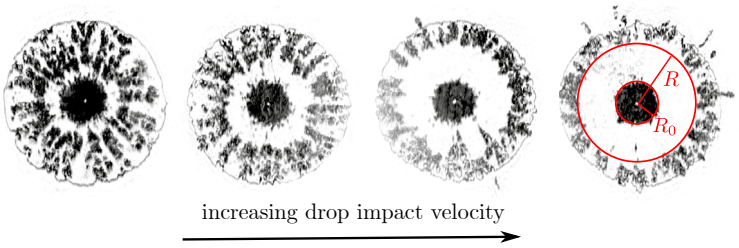

Figure 3: Appearance of the white annular region around the location of impact at high impact velocities.

CONCLUSION

We have shown that the impact of a partially frozen droplet on an undercooled surface results in the formation of growing finger-like patterns. The ongoing investigations explore the parameter space under what exact conditions this instability occurs.

References

[1] Bennett, T. and Poulikakos, D. "Splat-quench solidification: estimating the maximum spreading of a droplet impacting a solid surface". *J. Mater. Sci.* **28**: 963-970, 1993.

[2] Kant, P., Koldeweij, R., Harth, K., van Limbeek, M. and Lohse, D. "Fast-freezing kinetics inside a droplet impacting on a cold surface". *PNAS*, To appear, 2020.

*Corresponding author. E-mail: p.kant@utwente.nl.

THE EFFECT OF GEOMETRIC PERTURBATIONS ON A STATIC MENISCUS

Eleanor C. Johnstone *[1], Andrew L. Hazel[1], and Oliver E. Jensen[1]
[1] Department of Mathematics, University of Manchester, Manchester, U.K.

Summary We present results for the shape of a static air-liquid meniscus in a rectangular channel with geometric perturbations imposed on the walls. The sensitivity of the meniscus shape to small perturbations is examined in a linearised system. We show that perturbations which change the volume of the system induce long-range responses in the meniscus shape and non-monotonic displacement of the contact line. These experimentally-testable results show that static menisci can be strongly influenced by small occlusions in a channel.

INTRODUCTION

Numerous wetting and coating processes take place within physical domains in which there are small geometric imperfections that can have a profound influence on the dynamics ([1], [2]). Working in a Hele-Shaw geometry, we show here how capillary effects alone allow geometric perturbations to have a long-range impact on static interface shapes.

STATEMENT OF PROBLEM

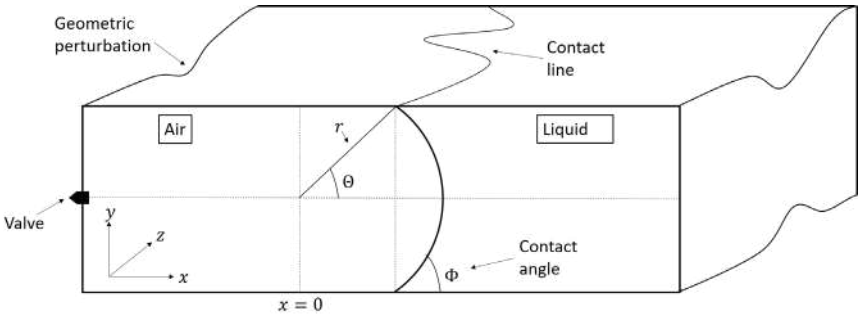

Figure 1: A static meniscus in a rectangular channel with geometric perturbations to the upper and lower walls.

We consider a static air-liquid meniscus in a rectangular channel with non-dimensional size $2L$, 2 and $2W$ in the x, y and z directions respectively; see figure 1. The upper and lower walls of the channel have geometric perturbations, $\epsilon\beta_U(z)$ and $\epsilon\beta_L(z)$ respectively, which are small relative to the height of the channel (so $\epsilon \ll 1$). In practice, these perturbations could be implemented by etching the channel walls with a needle to create a groove, or adding a strip of paint to create a ridge. We assume that the meniscus meets the channel walls with fixed contact angle ϕ. In order to remove translational invariance, we also impose that the volume of fluid in the channel is fixed. Subject to these physical constraints, the problem is then to find the surface of mean curvature for a given channel geometry, given by the Young–Laplace equation.

We assume that the perturbation to the interface shape and contact line displacement are also $O(\epsilon)$. We perturb around the base state in which the meniscus is the arc of a cylinder with radius $R = \sec(\phi)$. Adopting cylindrical polar coordinates (r, θ, z) about an axis lying in the mid-plane of the channel (see figure 1), we can write the interface location as $r = R+\epsilon f(z, \theta)$ and $\theta \in [-(\pi/2) + \phi + \theta_L(z), (\pi/2) - \phi + \theta_U(z)]$. Together with the physical constraints described above, the Young-Laplace equation for the perturbation to the interface shape then becomes the Helmholtz equation

$$\frac{1}{R^2} f + \frac{1}{R^2} f_{\theta\theta} + f_{zz} = -p, \tag{1}$$

with p the pressure difference across the meniscus. The boundary conditions on the upper and lower walls remain that the contact angle is fixed to be ϕ and we also impose the condition that the meniscus meets the side walls normally. The problem is closed with a condition on the volume of fluid in the channel:

$$\int_{-W}^{W} \int_{-\frac{\pi}{2}+\phi}^{\frac{\pi}{2}-\phi} f(z, \theta)\, \mathrm{d}\theta\, \mathrm{d}z \propto \int_{-W}^{W} [\beta_U(z) - \beta_L(z)]\, \mathrm{d}z. \tag{2}$$

The volume constraint allows two specific configurations: a volume-preserving configuration with $\beta_U(z) = \beta_L(z) = B(z)$ (mirror anti-symmetric), and a volume-changing configuration with $\beta_L(z) = -\beta_U(z) = B(z)$ (mirror symmetric). Self-adjointness of the Helmholtz equation (1) shows that the pressure difference at the meniscus has the same dependence

*Corresponding author. E-mail: eleanor.johnstone@manchester.ac.uk

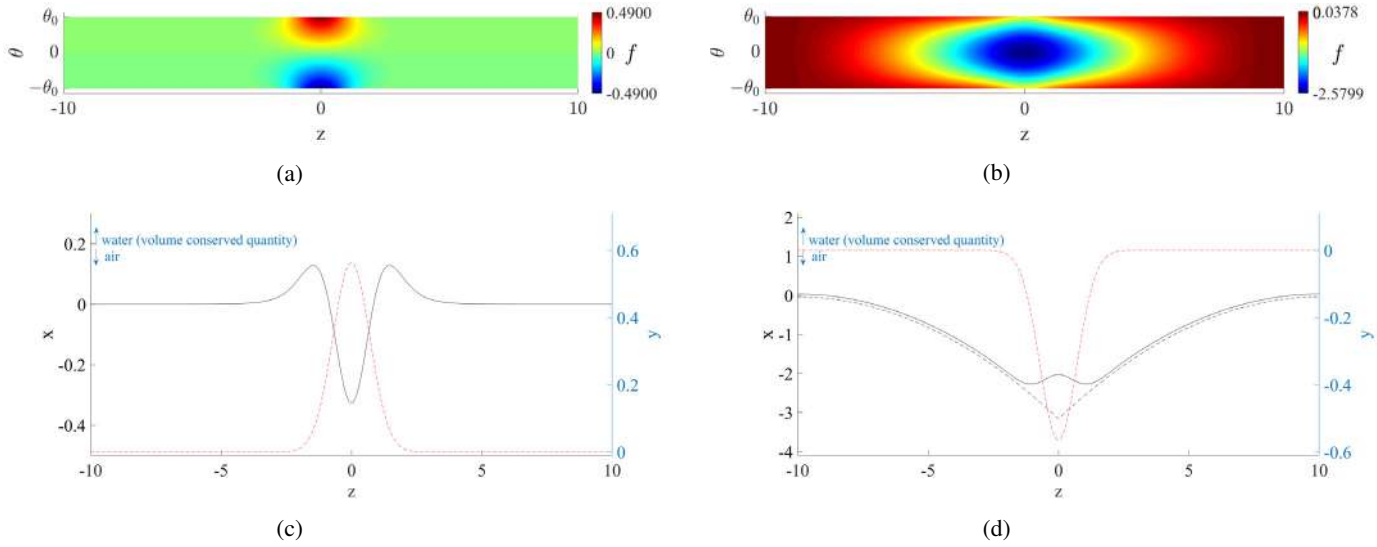

Figure 2: Results for a channel with half-width $W = 10$, half-length $L = 20$ and contact angle $\phi = \pi/16$. (a)-(b): the change in meniscus shape $f(z, \theta)$. (c)-(d): the upper wall contact line displacement $x = f(z, \pi/2 - \phi)\sin(\phi) - f_\theta(z, \pi/2 - \phi)\cos(\phi)$ (black line), and the geometric perturbations $y = \beta_U(z)$ (red dashes). (a), (c): volume-preserving configuration; (b)-(d): volume-changing configuration. The black dashed line in (d) is the far-field approximation (3).

on the boundary data; $p \propto W^{-1}\int_{-W}^{W}[\beta_U(z) - \beta_L(z)]\,\mathrm{d}z$. In particular, for volume-preserving perturbations, no pressure difference at the meniscus is induced and the Helmholtz equation is unforced.

For zero contact angle $\phi = 0$ the problem remains the same, however an expansion to powers of $O(\epsilon^2)$ is needed to obtain the boundary conditions as a degeneracy appears when the meniscus meets the walls tangentially.

RESULTS

We assume that the geometric perturbations to the channel take the form of a Gaussian distribution. The problem (1)-(2) is most easily solved analytically via separation of variables. In the volume-preserving case (figure 2a), the meniscus protrudes into the air at the groove on the upper wall, and recedes at the ridge on the upper wall. Here the response is localised around the perturbation. However in the volume-changing case (figure 2b), the narrow ridges on the upper and lower walls induce a long-range response in the shape of the meniscus, which bulges into the air across the entire width of the channel.

The contact line displacement (2c) is not monotonic for positive z, despite the perturbation being monotonic for $z > 0$. For the volume-preserving configuration there is no contact line displacement for large z; however, for the volume-changing configuration the local perturbation induces a displacement of the contact line which, for a fixed contact angle, depends on the volume of the perturbations.For zero contact angle the functional behaviour in the far-field is given by

$$f(z, \theta) \approx p + \frac{2p}{\pi}\left[(W - |z|)^2\cos(\theta) - \theta\sin(\theta)\right], \tag{3}$$

as shown in figure 2d. Thus since the dependence is quadratic in W, and the induced pressure is $O(W^{-1})$, small perturbations in channels of large width can induce very large contact line displacement.

CONCLUSIONS

We have demonstrated that small narrow occlusions in a rectangular channel can induce significant long-range responses in a static meniscus, including non-monotonic contact line displacement. These results could be observed experimentally. We highlight the sensitivity of this surface-tension dominated system to small disturbances, particularly those which change the volume of the system.

References

[1] Franco-Gómez A., Thompson A. B., Hazel A. L., Juel A. Sensitivity of Saffman-Taylor fingers to channel-depth perturbations. *J. Fluid Mech.* **794**: 343-368, 2016.

[2] Xu, F., Jensen O. E. Trapping and displacement of liquid collars and plugs in rough-walled tubes. *Phys. Rev. Fluids* **2**: 094004, 2017.

VISCOUS BOUNCING DROPS

Aditya Jha[1,2], Pierre Chantelot[1,2], and David Quéré[1,2]
[1] PMMH, ESPCI Paris, 75005 Paris, France
[2] LadHyX, Ecole polytechnique, 91128 Palaiseau, France

Summary By definition, a water-repellent material is a material on which water drops bounce after an impact, an effect arising from the non-wetting properties of the substrate but also from the low viscosity of water. In this project, we impact increasingly viscous drops to test their bouncing capability. Our findings exhibit the bouncing of highly viscous drops (typically 100 times more viscous than water) with nearly an unchanged contact time but reduced energy post rebound.

INTRODUCTION

In an earlier work done by Richard *et. al.* [1], it was shown that water drops impacting a super-hydrophobic surface can undergo bouncing with an extremely small loss of energy. This was measured in terms of coefficient of restitution ε, the ratio of velocity of the drop post impact to the velocity before impact, which can be as high as 0.9 for water. Furthermore, it was realized that the time τ_0 spent by the drop in contact with the surface is independent of the impact velocity of the drop. It results from a balance between inertia and surface tension, and thus, scales as $\tau_0 \propto \sqrt{\rho R^3/\gamma}$. Here, ρ represents the density of the drop, R is the drop radius while γ is the surface tension. To further venture into the details of the impact phase, Laan *et. al.* [3] studied the effect of viscosity on the spreading which they quantified in terms of an associated impact number. Complementary research by Bartolo *et. al.* [4] looked at the transition of the retraction velocity from an inertial regime to a viscous regime where the Ohnesorge number was found to decide the switch-over velocity. In this experimental study, we investigate the effect of increasing the viscosity of the impacting drop of radius $R = 1$ mm using water-glycerol mixtures.

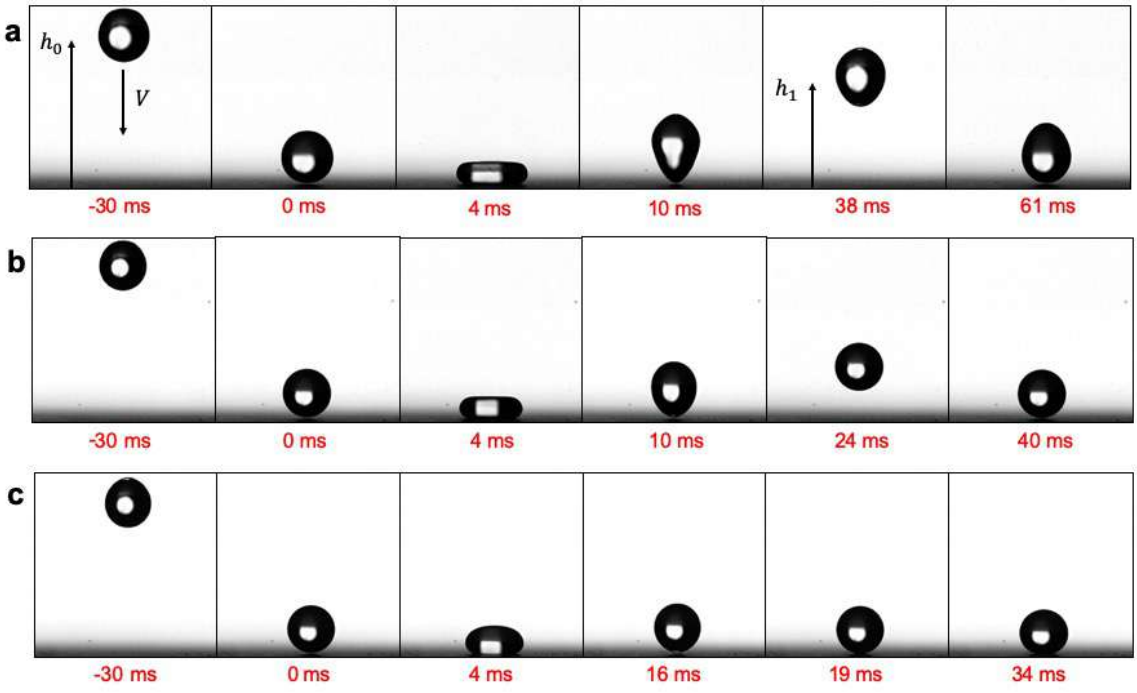

Figure 1: Impact on a super-hydrophobic surface of (a) A water drop (η = 1 mPa.s), (b) A water-glycerol drop (η = 80 mPa.s) and (c)A more viscous water-glycerol drop (η = 200 mPa.s). The radius and velocity remain the same (R =1 mm and V = 0.3 m/s)

Figure 1a shows the behavior of a millimetric water drop impacting and bouncing on a super-hydrophobic surface. Remarkably we see that at 80 times the viscosity of water, bouncing still persists henceforth, extending the phenomenon of bouncing drops to higher viscosity. On a closer inspection, it can be seen that the contact time τ_0 remains nearly the same for both the cases at 10 ms while there is a significant reduction in the take-off energy of the viscous drop exhibited by its reduced maximum height h_1 achieved after impact. Further increasing the viscosity to 200 mPa.s eventually suppresses the rebound thus, defining the limiting bouncing viscosity of this family of drops.

CONCLUSION

In previous studies, the phenomenon of bouncing of a drop has been modeled using a spring-mass system where the stiffness of the spring scales as the surface tension of the drop γ. To take into account the effect of bulk viscosity, we add a damper to the same system whose damping coefficient scales as ηR. Upon simplifying this scaling model, we obtain the limiting bouncing viscosity as function of the Ohnesorge number $Oh = \eta/\sqrt{\rho R \gamma}$. A linearised version of the same equations helps us to understand the slow variation in contact time with increasing viscosity and the variation of coefficient of restitution as well.

References

[1] D. Richard and D. Quere, Europhysics Letters **50**, 769-775 (2000)
[2] D. Richard, C. Clanet and D. Quere, Nature **417**, 811-811 (2002)
[3] N. Laan, K.G. Bruin, D. Bartolo, C. Josserand and D. Bonn, Physical Review Applied **2**, 1-7 (2014)
[4] D. Bartolo, C. Josserand and D. Bonn, Journal of Fluid Mechanics **545**, 329-338 (2005)

STATE- AND RATE-DEPENDENT CONTACT LINE DYNAMICS OVER AN AGING SOFT SURFACE

Dongshi Guan*[1], Elisabeth Charlaix[3], and Penger Tong[2]
[1] State Key Laboratory of Nonlinear Mechanics, Institute of Mechanics, Chinese Academy of Sciences, Beijing 100190, China
[2] Department of Physics, Hong Kong University of Science and Technology, Kowloon, Hong Kong, China
[3] Laboratoire Interdisciplinaire de Physique, CNRS,Universite Grenoble Alpes, Grenoble F-38000, France

Summary The pinning-depinning of an interface is a common phenomenon in nature. Earthquakes on faults and friction between two solid surfaces in contact are two outstanding examples of such pinning-depinning events, which often exhibit a state-dependent increase of pinning strength owing to the contact aging. Here we report systematic measurements of pinning-depinning dynamics at a moving contact line (CL) between a liquid-air interface and a soft solid surface. It is the first time that the state- and rate-dependent pinning-depinning dynamics are observed for a moving CL on an aging soft surface. This work represents a breakthrough in understanding the microscopic origin of the state- and rate-dependent CL dynamics. It should be of broad interest to researchers in the interdisciplinary field of fluid dynamics, soft matter physics, mechanics and solid friction.

INTRODUCTION

While liquid interfaces between two (immiscible) fluids are common in nature and industry, our understanding of their motion over a solid surface is often challenged by the pinning and depinning of the three-phase contact line (CL) between the liquid interface and solid surface due to the physical roughness and/or chemical inhomogeneity on the solid surface. The CL pinning causes the contact angle θ between the liquid and solid surfaces to display some hysteresis. Although considerable progress has been made recently in controlling the wettability of various textured solid surfaces, one still has a poor understanding of contact angle hysteresis on many ambient solid surfaces of practical interest.

The situation becomes more complicated when the solid substrate is made of soft materials, such as elastomers and polymer gels, which deform under the pulling of the capillary force and develop a "wetting ridge" below the CL. The ridge height h is determined by the balance between the normal component of the capillary force $\gamma\sin\theta$ and elastic deformation force Eh, i.e., $h \approx l_s\sin(\theta)$, where $l_s = \gamma/E$ is an elasto-capillary length with γ being the liquid surface tension and E the Young's modulus of the substrate. For a water droplet ($\gamma \approx 72$ mN/m) on a glass substrate ($E \approx 70$ GPa), we have $h \approx 10^{-12}$ m, which is negligibly small. If the glass substrate is replaced by a soft polymer with $E \approx 100$ kPa, we have $h \approx 1$ μm, which will have a great impact on many micro-fluidic and nanotechnology applications. While considerable progress has been made recently in studying the asymptotic shape and development of the wetting ridge, our current understanding of the contact angle hysteresis and CL pinning-depinning dynamics over a deformable surface is still limited, as the (moving) CL, in this case, encounters a slow time-varying (aging) defect landscape.

Here, we report direct atomic-force-microscope measurements of capillary force hysteresis (CFH) of a circular contact line (CL) formed on a long glass fiber [1-4], which is coated with a thin layer of soft polymer film and intersects a water-air interface, as shown in Fig. 1. The measured CFH shows a distinct overshoot for the depinning of a static CL, and the overshoot amplitude grows logarithmically with both the hold time τ and fiber speed V. A unified model based on the slow growth of a wetting ridge and force-assisted barrier crossing is developed to explain the observed time- (or state-) and speed- (or rate-) dependent CL depinning dynamics over an aging soft surface.

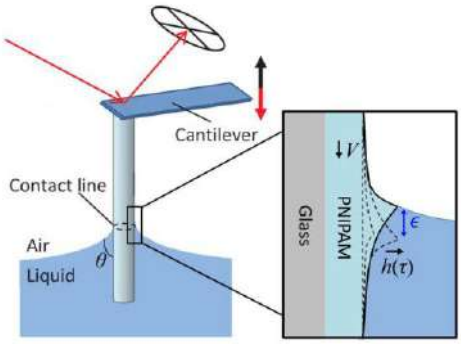

Figure 1. Sketch of the AFM-based capillary force apparatus at a liquid-air interface. "The long needle" AFM involves a vertical glass fiber of diameter d in the range 1-3 μm and length 150-300 μm, which is glued onto the front end of a rectangular cantilever beam. The surface of the glass fiber is coated with a thin layer of soft polymer film (PNIPAM). Inset indicates a slow growing wetting ridge (dashed lines) of height h(t) formed beneath the three-phase CL. The solid line indicates the tangential displacement ε of the wetting ridge resulting from the CL pulling when the fiber moves downward.

*Corresponding author. E-mail: dsguan@imech.ac.cn.

RESULTS and DISCUSSIONS

In the experiment, we use a recently developed "long-needle" atomic force microscope (AFM) to directly measure the capillary force acting on a CL [1-4]. As shown in Fig. 1, the long needle is made of a thin glass fiber coated by a layer of PNIPAM of thickness ~60 nm and is immersed through a liquid-air interface, at which a circular CL is formed on the fiber surface. The long-needle AFM can accurately measure the capillary force, $f_i(s)= -\pi d\gamma\cos\theta_i(s)$, as a function of fiber traveling distance s in the advancing (fiber moves downward, i=a) and receding (fiber moves upward, i=r) directions.

Figure 2 shows the typical CFH loops obtained when the PNIPAM-coated fiber is first pushed downward (advancing, →) and then is pulled upward (receding, ←) through a water-air interface at a constant speed V. Before the fiber starts to move downward, it was partially immersed in the water and was held stationary for a hold time τ. When the fiber advances, the pinned interface is stretched, causing a sharp linear increase in f with the distance travelled s, as shown by a straight line on the left side of the loop. When the restoring force becomes larger than a critical value, $(f_a)_c$, the CL depins with an abrupt decrease in f and then begins a steady stick-and-slip motion with the measured f fluctuating around a mean value f_a in the force curve. It is seen that the overshoot value, $(f_a)_c$- f_a, increases logarithmically with the hold time τ. Similar logarithmic time dependence was also observed for the static fiction between two solid surfaces made of rocks, polymers and other materials. This aging effect was attributed to the slow creeping and/or interfacial strengthening of the asperities in the contact area under the normal stress applied to the solid surfaces. In our case, the overshoot of the depinning force for a static CL, as shown in Fig. 2, is caused by the wetting ridge formed under the pulling of the normal component of the capillary force. This wetting ridge, on which the CL is anchored, acts as a physical barrier that hinders the CL motion.

By taking both the aging effect of the wetting ridge and thermal activation effect of the force-assisted barrier crossing into account, we develop a theoretical model to quantitatively describe the CL depinning force per unit length,

$$\Delta F(\tau,V)= \Delta F_0+ A\ln(1+\tau/\tau_0)+B\ln(1+V/V_0), \quad (1)$$

where ΔF_0 is the residual CFH, which is independent of τ and V. The second and third terms on the right hand side are, respectively, the state- and rate-dependent parts of the CFH. The model describes the experimental data very well, and details will be presented in our recent work [4].

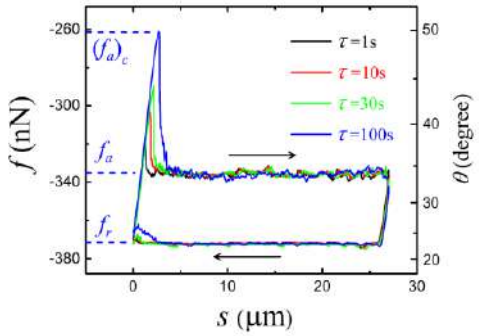

Figure 2. Variations of the measured capillary force f and corresponding contact angle θ when the glass fiber is first pushed downward (advancing, →) and then is pulled upward (receding, ←) through a water-air interface. The measurements are made at a fixed fiber speed V=10 μm/s at room temperature for different hold times: τ =1 s (black), 10 s (red), 30 s (green) and 100 s (blue).

CONCLUSIONS

The above results thus demonstrate that the aging effect of the wetting ridge causes the depinning force to exhibit a logarithmic time dependence for a static CL and speed-weakening for a moving CL. Our experimental findings thus demonstrate a unique microscopic mechanism underpinning the state- and rate-dependent pinning-depinning dynamics, which has many important applications in micro-fluidics and nano-technology. Furthermore, it has important implications to a common class of problems involving depinning dynamics in a defect/roughness landscape, such as friction of solid interfaces.

References

[1] Asymmetric and speed-dependent capillary force hysteresis and relaxation of a suddenly stopped moving contact line, Dongshi Guan, Yong Jian Wang, Elisabeth Charlaix and Penger Tong, **Physical Review Letters** 116, 066102 (2016).

[2] Simultaneous observation of asymmetric speed-dependent capillary force hysteresis and slow relaxation of a suddenly stopped moving contact line, Dongshi Guan, Yong Jian Wang, Elisabeth Charlaix and Penger Tong, **Physical Review E** 94, 042802 (2016).

[3] Noncontact viscoelastic imaging of living cells using a long-needle atomic force microscope with duel-frequency modulation, Dongshi Guan, Elisabeth Charlaix, Robert Z. Qi, and Penger Tong, **Physical Review Applied** 8, 044010 (2017) (Editor's Suggestion, Featured in Physics).

[4] State- and rate-dependent contact line dynamics over an aging soft surface," Dongshi Guan, Elisabeth Charlaix and Penger Tong, **Physical Review Letters** (under review).

NUMERICAL INVESTIGATION OF VORTICITY GENERATION MECHANISMS IN MULTIPHASE FLOWS

Daniel Fuster *[1] and Maurice Rossi y[1]
[1] Sorbonne Université, Centre National de la Recherche Scientifique, UMR 7190, Institut Jean Le Rond D'Alembert, F-75005 Paris, France

Summary This work investigates the influence of density ratio and surface tension on vorticity production at relatively high Reynolds numbers. For Weber numbers below 10, the interface response is essentially controlled by surface tension. In that instance, no rollup occurs and the dynamics is only slightly influenced by the Reynolds number. For very large Weber numbers, density ratio plays a critical role on the generation of small structures coming from the destabilization of the vorticity layers generated by the interface. These structures are much Reynolds number dependent. Between these two scenarii, an intermediate regime exists where the interface is significantly affected by the vorticity layer generated but the Reynolds number plays only a minor role. The range of Weber numbers for which this intermediate regime is observed strongly depends on the density ratio.

INTRODUCTION

The presence of an interface between two immiscible fluids is known to act as a source of vorticity that generates thin vorticity layers significantly impacting the interface dynamical response. The generation of vorticity due to the presence of an interface has been theoretically discussed by [1, 2, 3]. In two-dimensional flows the evolution of the circulation Γ of a closed curve $\mathbf{C}$ which crosses an interface S_{int} separating two phases is given by

$$\frac{d}{dt}\Gamma = -\oint_{\mathbf{C}} [\nu\, \boldsymbol{\nabla} \times \boldsymbol{\omega}] \cdot \boldsymbol{t}\, \mathrm{d}\ell + \int_{I_f} S_\omega ds, \tag{1}$$

where the curve I_f is located on the interface S_{int} and connects the two intersections of curve $\mathbf{C}$ with the interface. The first integral is a classical diffusion term and the second integral corresponds to the vorticity sources located at the interface S_{int}. If the surface tension coefficient is denoted as σ and both fluids have the same dynamical viscosity μ, quantity S_ω then becomes

$$S_\omega = -\frac{1}{\rho_m}\frac{\partial(\sigma\kappa)}{\partial s} + [[\frac{1}{\rho}]]\frac{\partial p_m}{\partial s} \tag{2}$$

where $[\![Q]\!] \equiv Q_1 - Q_2$ represents the jump of quantity Q between phases 1 and 2, $\frac{2}{\rho_m} \equiv \frac{1}{\rho_1} + \frac{1}{\rho_2}$, $p_m \equiv \frac{p_1+p_2}{2}$ This equation displays the importance of density differences and surface tension forces on the production of vorticity across the interface. How the vorticity generated impacts the evolution of the interface in non-linear regimes is the topic of this presentation.

NUMERICAL RESULTS

In this work we use the Gerris Flow Solver [4] to investigate the consequences of vorticity generation in the dynamics of the interface throughout simplified problem examples. This software is well suited for the simulation of multiphase flows due to its accurate and robust methods for surface tension and the AMR capabilities, that allow us to well resolve the boundary layers around it.

We start investigating the interaction of a planar interface with a Lamb-Oseen vortex with circulation Γ_0 that is initially placed in the light fluid at distance d_0 from the interface. If the vortex core size is small compared to d_0, the solution of this problem essentially depends on the three dimensionless quantities

$$r_\rho \equiv \frac{\rho_2}{\rho_1}, \quad Re \equiv \frac{\frac{\rho_1+\rho_2}{2}\Gamma_0}{2\pi\mu}, \quad \text{and} \quad We \equiv \frac{\frac{\rho_1+\rho_2}{2}\Gamma_0^2}{(2\pi)^2 d_0 \sigma}. \tag{3}$$

When $r_\rho = 1$ and no surface tension is present the interface acts like a passive tracer that rolls-up creating a spiral where the curvature at the tip increases as $\kappa \sim t^3$. When $r_\rho = 1$ but in the presence of surface tension forces, the vorticity production is approximately symmetric but of opposite sign at both sides of the tip where no vorticity production occurs. Like in the classical Taylor-Culick problem the tip retracts and a rim appears (Figure 1a), the importance of this effect increasing as the Weber number is decreased. For $We < 10 \approx We_c^I$ it is no longer possible to define a rim and surface tension forces just prevent any interface roll up. In Figure 1a we can appreciate the emission of a vorticity sheet that is emitted from the rim when $We > We_c^I$ where, as we can see, the Reynolds number does not alter significantly the interface shape.

*E-mail: fuster@dalembert.upmc.fr
†E-mail: maurice.rossi@upmc.fr

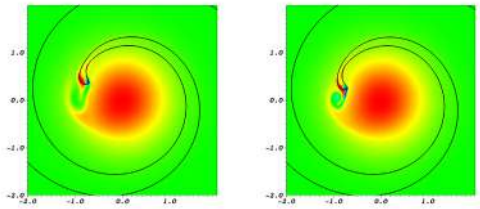

(a) Influence of Reynolds for $r_\rho = 1$ and $We = 10^3$. Zoomed view of the vorticity field and interface at time $t = 15$. $Re = 10^3$ (left) and 10^4 (right).

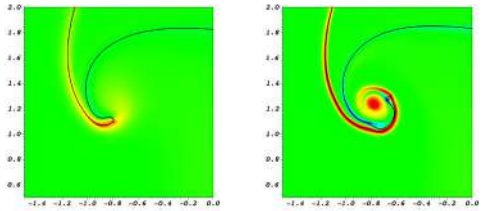

(b) Influence of Reynolds for $r_\rho = 5$ and $We = 10^3$. Zoomed view of the vorticity field and interface at time $t = 4$. $Re = 10^3$ (left) and 10^4 (right).

The baroclinic vorticity production and its influence on the dynamic response of the interface is significantly different than in the case of surface tension. Unlike the previous case, it can be shown that at short times the vorticity production is possitive and does not change sign at the ligament tip. The vorticity generated at the interface detaches from the tip rolling in the light fluid and, if the Weber number is sufficiently large, the vortex generated stretches the interface creating very small structures (Figure 1b), this phenomenon being extremely sensitive to the Reynolds number.

Numerical experiments reveal that when $r_\rho > 1$ and surface tension is present it is possible to define a critical Weber number, We_c^{II}, below which surface tension effects become dominant over density differences. In this regime the interface rolls up but the structures formed at the ligament tip are stabilized by surface tension forces, the Reynolds number not playing a significant role on the interface structures observed. This transition is shown to essentially depend on the density ratio, which ultimately controls the baroclinic vorticity production: the smaller the density ratio, the larger the value of We_c^{II} is.

During the presentation of this work, a detailed study of this particular problem is displayed. We will also show that these two critical Weber numbers also appear in a variety of other problems involving the non-linear response of interfaces.

References

[1] Wu J.Z. A theory of three-dimensional interfacial vorticity dynamics. *Phys. Fluids* **7(10)**: 2375-2395, 1995.
[2] Lundgren T., Koumoutsakos P. On the generation of vorticity at a free surface. *J. Fluid Mech.* **382**: 351-366, 1999.
[3] Brøns M., Thompson M.C., Leweke T., and Hourigan K. Vorticity generation and conservation for two-dimensional interfaces and boundaries. *J. Fluid Mech.* **758**: 63-93, 2014.
[4] Popinet S. An accurate adaptive solver for surface-tension-driven interfacial flows. *J. Comp. Phys.* **228**: 5838-5866, 2009.

DYNAMICS OF VAPOR-GAS BUBBLES NEAR RIGID SURFACES IMMERSED IN A LIQUID UNDER ULTRASONIC TREATMENT

Tatyana Lyubimova[1,2], Oskar Fattalov *[1], Konstantin Rybkin [1]
[1] Perm State University 614990, Perm, Bukirev Street 15, Russia
[2] Institute of Continuous Media Mechanics UB RAS, 614013, Perm, Acad. Korolev Street 1, Russia

Summary. In this work, the dynamics of vapor-gas bubbles near rigid surfaces of different hydrophobicity immersed in a liquid under the action of ultrasound (US) is investigated. The experiments have shown a significant effect of surface properties on bubble dynamics. In the case of hydrophilic surface, inertial bubbles formed in a liquid under the action of ultrasound are subjected to the drift near and on the rigid surface and most of them rise when the ultrasound is switched off. For hydrophobic surface, stable attachment of the vapor-gas bubbles to the rigid surface is observed, the bubbles form linear chains (clusters) of bubbles which grow with time and remain attached to the rigid surface when the ultrasound is switched off.

INTRODUCTION

The dynamics of the cavitation bubbles arising in a liquid under the action of ultrasound depends on various factors, either the collapse of the bubbles or their coalescence and the long-term existence of relatively large bubbles both in the volume of the liquid and near rigid surfaces can be observed [1, 2]. The interaction of cavitation bubbles with rigid surfaces is also a subject of discussions [3]. The collapse of the bubbles creates the local extreme pressures and temperatures, as well as shock waves in a liquid, which have significant effect on the surface. This effect can be used as a tool for the formation of new surfaces and nanostructured materials with a very high potential for application, but so far many aspects of this issue have not been fully disclosed.

Ultrasound can also increase the probability of the collision of bubble and particle due to the average forces arising under the action of acoustic field, in particular, the Bjerknes primary force [4] and average vibrational force [5]. In [6], the dynamics of two bubbles is discussed, when the action of the secondary Bjerknes force promotes the movement of the bubbles towards each other. As a result of rapprochement, under certain parameters, their coalescence occurs. The solution of the Rayleigh-Plesset equation involves changing the diameter of the bubble in the liquid under the action of ultrasound with time, as a result, low pressure areas are formed around the oscillating bubble, which helps to keep the bubble near a rigid surface, in this case the secondary Bjerknes force acts on the bubble. As a result, the discharged region around the pulsating bubble involves other bubbles, which contributes to their coalescence. To achieve the resonant frequency of bubble pulsations, it is necessary that the coalescence effect of the bubbles allows them to grow to resonance sizes, which was observed in the experiments. All of the above effects can contribute to the attachment and retention of bubbles near rigid surface.

EXPERIMENTAL METHOD

The source of ultrasound was a metal disk placed at the bottom of the cavity such that the center of the emitter coincided with the center of the bottom of the cavity. It was connected to an ultrasonic source with a frequency f = 40 kHz.

Using the photographs taken in the experiments, we analyzed the temporal evolution of the area of rigid surface covered with the bubbles under the action of ultrasound and after its turning off. The dynamics of individual bubbles near rigid surfaces with different properties was also studied. Deionized and degassed water was used in experiments. Rigid plates were made of amorphous quartz (contact angle 1^0), organic glass (contact angle 51^0) and teflon (contact angle 118^0). New plate was taken for each new experiment, then the surface was cleaned with alcohol, and its washing with distilled water was performed. This was needed because the ultrasound is potentially capable of changing the degree of hydrophobicity of the surfaces of rigid plates immersed in a liquid. After immersion of the rigid plates in the liquid, the ultrasonic emitter was switched on and camera shooting began. Experiments continued for some time after the ultrasound was turned off to study the effect of detachment of bubbles from the surface.

RESULTS

In all series of the experiment, the hydrophobicity of the surface facilitated the attachment of the bubbles to it. The diameter of the attached bubbles continuously increased during the entire time of ultrasonic irradiation due to coalescence with bubbles arising due to acoustic cavitation. At the moment of switching off the ultrasound, the bubbles remained attached to the hydrophobic surface and did not rise, since the surface forces exceeded the force of Archimedes. After turning off the ultrasound, the bubbles oscillating near the surface were rising (Figure 1).

*Correponding author. E-mail: fattalov@mail.ru

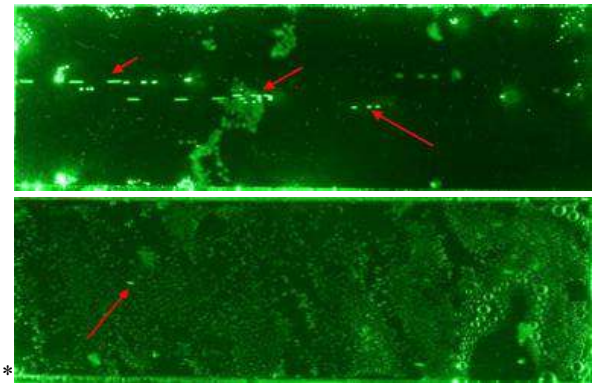

Figure 1. Above – the tracks of bubbles rising near the quartz plate. Almost all the bubbles leave the quartz plate at the time of ultrasound switching off. Below - the teflon surface at the time of switching off the ultrasound. Tracks of single rising bubbles are observed. Gravity is directed to the right.

The dynamics of vapor-gas bubbles on the hydrophilic surface of quartz differ qualitatively from the dynamics of bubbles on the hydrophobic surface of teflon (Figure 2). In this case, single bubbles, formed in the antinode regions of the acoustic wave, oscillate until the ultrasound is switched off. Obviously, in this case, the strength of Archimedes did not exceed the sum of the primary and secondary forces of Bjerknes [5], which allows the bubble to stay near the surface for a long time. It should be noted that the bubbles are aligned in the direction of ultrasound propagation.

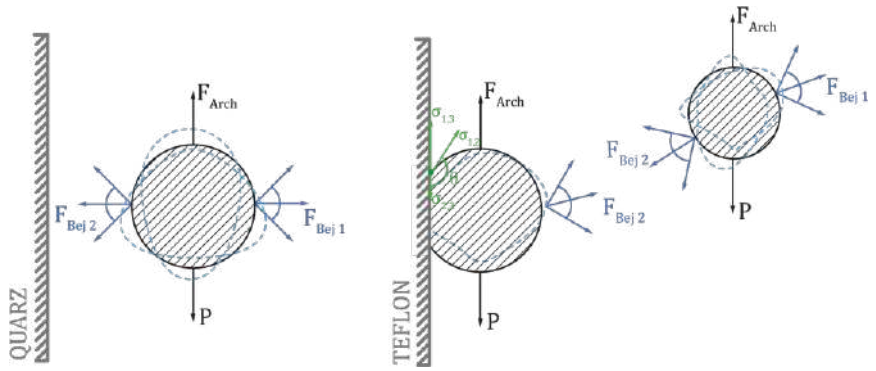

Figure 2. In the case of quartz, the bubble oscillates near the surface. A typical diagram is presented on the right, when a gas-vapor bubble is attached to the surface of teflon and is held on it due to the predominance of surface forces. The second bubble, due to the secondary Bjerknes force, drifts towards the attached bubble.

CONCLUSIONS

Thus, as follows from the experimental observations, in a distilled water under the action of ultrasonic waves near the hydrophilic surface of quartz, inertial oscillating bubbles are formed, most of which rise when the ultrasound is switched off. On the hydrophobic surface, the vapor-gas bubbles form linear chains (clusters) of bubbles that grow with time under the action of ultrasound, the chains are oriented orthogonally to the direction of ultrasound propagation and remain attached to the rigid surface when ultrasound is switched of.

ACKNOWLEDGEMENTS

The study was supported by Russian Foundation for Basic Research (grant 19-31-90138) and Government of Perm Krai (Program for the support of Scientific Schools of Perm Krai, grant C-26/788).

References

[1] Bremond, N., Arora, M., Ohl, C. D., & Lohse, D. Controlled multibubble surface cavitation. Physical review letters, **96(22)**, 224501., 2006.
[2] Rybkin, K. A., Bratukhin, Y. K., Lyubimova, T. P., Fatallov, O., & Filippov, L. Experimental study of formation and dynamics of cavitation bubbles and acoustic flows in NaCl, KCl water solutions. Journal of Physics: Conference Series, V. 879, No. 1, p. 012026. 2017.
[3] Bremond, N., Arora, M., Dammer, S. M., & Lohse, D. Interaction of cavitation bubbles on a wall. Physics of fluids, **18(12)**, 121505.
[4] Cui, Z., Li, Y., Ge, Y., & Fan, L. Bubble modulation using acoustic standing waves in a bubbling system. Chemical engineering science, **60(22)**, 5971-5981, 2005.
[5] Lyubimov D.V., Klimenko L.S., Lyubimova T.P., Filippov L.O. The interaction of a rising bubble and a particle in oscillating fluid / Journal of Fluid Mechanics, Vol. 807, P. 205–220, 2016.
[6] Ida, M. Alternative interpretation of the sign reversal of secondary Bjerknes force acting between two pulsating gas bubbles. Physical Review E, **67(5)**, 056617, 2003.

DRAINAGE SPEEDUP OF A DROP ON A SMOOTH SURFACE

Laurent Duchemin *[1] and Christophe Josserand[2]
[1] PMMH, CNRS, ESPCI Paris, Université PSL, Sorbonne Université, Université de Paris, F-75005, Paris, France
[2] LadHyx, Ecole Polytechnique, Palaiseau, France

Summary The present study aims at understanding the drainage dynamics of the thin air film squeezed between a millimetric droplet and a solid or liquid surface. Solving coupled lubrication equations and analyzing the dominant terms in the solid and liquid-film cases, we explain why the drainage is much faster in the liquid-film case, leading to a shorter coalescence time, as observed in recent experiments.

The thin film drainage until rupture is a widely studied fluid dynamics issue [1], relevant to numerous applications, like the ageing of foams [2], dimple formation and bubble entrapment [3, 4], drop coalescence [1, 5], the surprising non-coalescence of a droplet with a bath [6, 7, 8]. Among the open questions is the time it takes for a free thin film to rupture [9] and the relevant mechanisms at play : usual suspects are thermal fluctuations, Marangoni currents... In the case of gas film drainage, a potential mechanism for the dynamics of drainage is the presence of body forces, like gravity, driving the surrounding liquid [10, 11].

Recently, an experimental investigation of the coalescence of a millimetric drop gently deposited on a thin viscous film [12] has revealed unexpected drainage dynamics. The present study aims at understanding the drainage dynamics of the thin air film squeezed between a millimetric drop and a solid or liquid surface. We solve numerically the coupled lubrication equations for the three layers shown in figure 1 : the bottom part of the liquid droplet, that we suppose inviscid (3), the thin air film (2) and the liquid film underneath (1). The three dimensionless numbers, assuming negligeable inertia, are the Bond number and the Stokes numbers related to regions (1) and (2) :

$$\mathrm{Bo} = \frac{\rho_3 g R^2}{\gamma}, \quad \mathrm{St}_1 = \frac{\eta_1}{\rho_3 R\sqrt{gR}}, \quad \mathrm{St}_2 = \frac{\eta_2}{\rho_3 R\sqrt{gR}}, \tag{1}$$

where R is the radial distance where the slope of the sessile top drop is equal to one, η_1 and η_2 are the dynamic viscosities of the liquid and gas films respectively, γ is surface tension, and g is gravity.

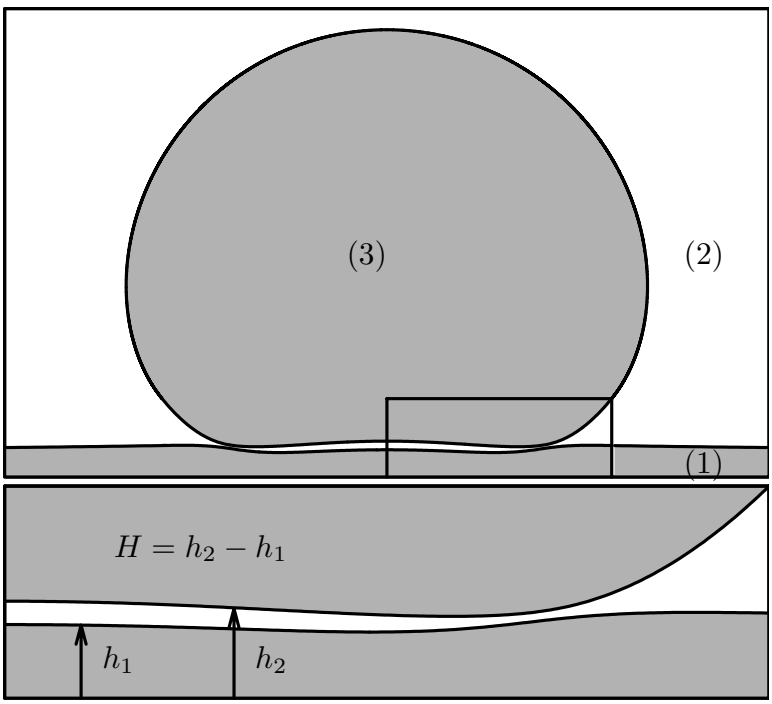

Figure 1: Sketch of a droplet lying on a thin liquid film.

In this study, we focus our attention on the influence of St_1 on the drainage of the air film. Solving the lubrication equations in the liquid-film case ($\mathrm{St}_1 \simeq 0.6$, which corresponds approximately to the experiments described in [12]) and solid-film case ($\mathrm{St}_1 \to \infty$), we obtain two very different drainage dynamics, as seen in figure 2. After the dimple is

*Corresponding author. E-mail: laurent.duchemin@espci.fr

formed, at short time, it is going to drain much faster in the case of a liquid film underneath. This fact is closely related to the continuity of tangential velocity across interface $1/2$: in the solid case, this velocity is zero, whereas it is finite in the case of a liquid film. Then, viscous dissipation in the gas film at the tip of the dimple (where the air gap $H = h_2 - h_1$ is minimal) slows down the dimple drainage, in comparison with the liquid film case.

In the solid-film case, analyzing the lubrication equations in terms of dominant balance of the different terms, we obtain the following long-time behaviour, already obtained for instance by [10] :

$$H_0 \sim t^{-1/4}, \quad H_{\min} \sim t^{-1/2}, \quad \ell \sim t^{-1/4}, \tag{2}$$

where H_0 is the dimple height on the axis of symmetry, H_{min} is the minimum air gap thickness and ℓ the radial size of the region where H is minimal. These scalings are confirmed by the numerical solution, as seen in figure 2, where the solid curves correspond to the solid-film case ($\mathrm{St}_1 \to \infty$).

In the liquid-film case, the dimple deflation obeys a very different dynamics, because viscous dissipation is highly reduced. We theoretically obtain the following different scalings for H_0, H_{min} and ℓ :

$$H_0 \sim t^{-2/3}, \quad H_{\min} \sim t^{-2/3}, \quad \ell \sim t^{-1/3}. \tag{3}$$

These scalings are alos confirmed by numerical simulations, as seen in figure 2. The agreement, although very good, is not perfect because the dominant balance is only an approximation in this case.

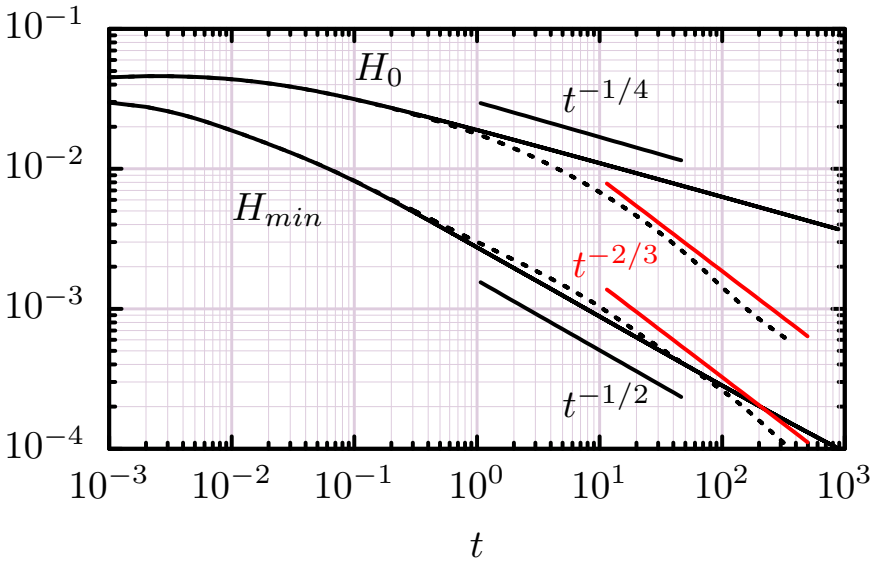

Figure 2: Height of the dimple H_0 and minimum height $H_{\min}$ as a function of time in the case of a liquid film ($\mathrm{St}_1 = 0.6$, solid curves) and a solid film ($\mathrm{St}_1 \to \infty$, dashed curves).

References

[1] Derek YC Chan, Evert Klaseboer, and Rogerio Manica. Film drainage and coalescence between deformable drops and bubbles. *Soft Matter*, 7(6):2235–2264, 2011.

[2] CJW Breward and PD Howell. The drainage of a foam lamella. *Journal of Fluid Mechanics*, 458:379–406, 2002.

[3] S Hartland, B Yang, and SAK Jeelani. Dimple formation in the thin film beneath a drop or bubble approaching a plane surface. *Chemical engineering science*, 49(9):1313–1322, 1994.

[4] Stanley Hartland and John D Robinson. A model for an axisymmetric dimpled draining film. *Journal of Colloid and Interface Science*, 60(1):72–81, 1977.

[5] AF Jones and SDR Wilson. The film drainage problem in droplet coalescence. *Journal of Fluid Mechanics*, 87(2):263–288, 1978.

[6] Y Amarouchene, G Cristobal, and H Kellay. Noncoalescing drops. *Physical Review Letters*, 87(20):206104, 2001.

[7] Yves Couder, E Fort, C-H Gautier, and A Boudaoud. From bouncing to floating: noncoalescence of drops on a fluid bath. *Physical review letters*, 94(17):177801, 2005.

[8] Yves Couder and Emmanuel Fort. Single-particle diffraction and interference at a macroscopic scale. *Phys. Rev. Lett.*, 97:154101, Oct 2006.

[9] Henri Lhuissier and Emmanuel Villermaux. Bursting bubble aerosols. *Journal of Fluid Mechanics*, 696:5–44, 2012.

[10] Stergios G Yiantsios and Robert H Davis. On the buoyancy-driven motion of a drop towards a rigid surface or a deformable interface. *Journal of Fluid Mechanics*, 217:547–573, 1990.

[11] Stergios G Yiantsios and Robert H Davis. Close approach and deformation of two viscous drops due to gravity and van der waals forces. *Journal of colloid and interface science*, 144(2):412–433, 1991.

[12] Hau Yung Lo, Yuan Liu, and Lei Xu. Mechanism of contact between a droplet and an atomically smooth substrate. *Physical Review X*, 7(2):21036, 2017.

COMPETING MARANGONI AND RAYLEIGH CONVECTION IN EVAPORATING BINARY DROPLETS

Christian Diddens *[1,2], Yaxing Li[1], and Detlef Lohse[1,3]
[1] Physics of Fluids group, Department of Science and Technology, Max Planck Center for Complex Fluid Dynamics and J. M. Burgers Centre for Fluid Dynamics, University of Twente, Enschede, The Netherlands
[2] Department of Mechanical Engineering, Eindhoven University of Technology, Eindhoven, The Netherlands
[3] Max Planck Institute for Dynamics and Self-Organization, Göttingen, Germany

Summary For a small sessile or pending droplet it is generally assumed that gravity does not play any role once the Bond number is small. This argument has also been used for evaporating binary droplets, where preferential evaporation can induce composition gradients and hence Marangoni flow and natural convection can emerge. Recent studies have revealed that gravity can indeed be the dominant driving mechanism for the flow inside small evaporating binary droplets [1, 2]. Here, we derive and validate a quasi-stationary model for the flow inside evaporating binary sessile and pendant droplets, which successfully allows to predict the prevalence and the intriguing interaction of Rayleigh and/or Marangoni convection on the basis of a phase diagram for the flow field expressed in terms of the Rayleigh and Marangoni numbers.

MOTIVATION

In applications based on droplet evaporation, e.g. inkjet printing, it is crucial to overcome the coffee-stain effect, i.e. the preferential deposition of solute particles near the rim of the droplet due to a persistent capillary outward flow towards the pinned contact line. By using binary droplets, one can utilize the preferential evaporation of the more volatile component to induce compositional gradients inside the droplet. These gradients can in turn drive recirculating flow, namely Marangoni flow, driven by the composition-dependent surface tension, and natural convection due to density differences of the components. In recent studies it has been shown that natural convection can even dominate in sub-millimeter-sized droplets [1, 2], although de Bond number is small. This observation demands a detailed analysis of the possible flow patterns and the interplay of Rayleigh and Marangoni convection in evaporating binary droplets.

QUASI-STATIONARY MODEL

Based on the observations from full simulations and experiments, the recirculating flow inside the droplet due to Marangoni/Rayleigh convection is usually much faster than the movement of the liquid-gas interface due to evaporation. When the flow is regular, i.e. not chaotic, this observation allows for a quasi-stationary treatment of the flow and composition distribution in the evaporating droplet at each instant during the drying process. By expanding the composition-dependent surface tension and density via a first order Taylor expansion around the instantaneous average composition of the droplet, the problem can be nondimensionalized and three control parameters can be extracted, namely the Marangoni number Ma, the Rayleigh number Ra and the contact angle θ.

PHASE DIAGRAM OF THE FLOW IN BINARY DROPLETS

By doing a numerical parameter study with respect of these three dimensionless parameters, the phase space of the flow and composition distribution in binary droplets can be investigated. We reveal in total five different regimes, which are depicted in Fig. 1. Here, the blue fluid is more volatile, has the higher surface tension but a lower density than the red fluid (e.g. blue: water, red: glycerol). When Ma is large and $|\mathrm{Ra}|$ is small, the Marangoni effect (black stream lines) dictates the flow direction in the droplet (regime *Ma dom.*). Vice versa, in absence of a considerable surface tension difference, natural convection can determine the flow direction (white stream lines, regime *Ra dom.*). If both effects are present, but support opposite flow directions, one gets natural convection in the bulk and a counter-rotating Marangoni vortex in the vicinity of the interface (*Ma vs. Ra*). By reversing the direction of gravity, Ra can become negative. Then, both effects support flow in the same direction (*Ma & Ra same dir.*). If the driving of both mechanisms are sufficiently strong, however, the quick natural convection in the bulk deforms the internal composition field so that it results in altered replenishing diffusive fluxes of the blue liquid close to the apex and the contact line. This eventually leads to a reversal of the interfacial composition gradient and in turn to an emergence of a counter-rotating Marangoni-vortex close to the interface (*Ra reverses Ma*). For negative Marangoni numbers, chaotic flow can be expected due to the Marangoni instability. The entire phase diagram is also a function of the contact angle θ and approximately flips upside down when moving from $\theta < 90°$ to $\theta > 90°$.

*Corresponding author. E-mail: c.diddens@utwente.nl.

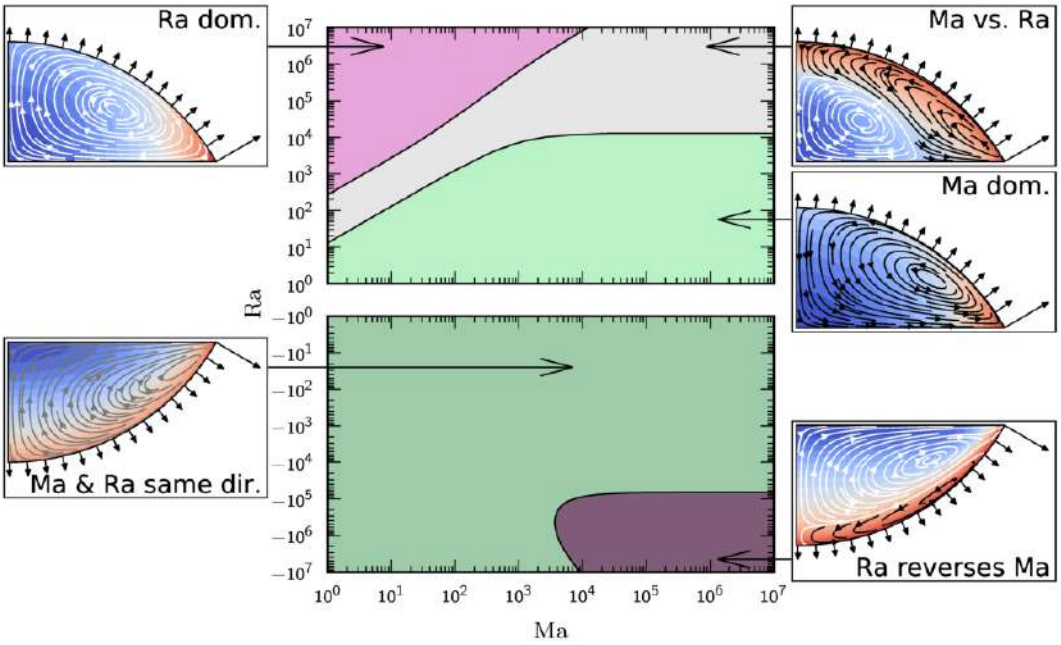

Figure 1: Phase diagram of the different flow scenarios in an evaporating binary droplet with a contact angle of $\theta = 60°$ depending on the Rayleigh and Marangoni numbers.

VALIDATION OF THE QUASI-STATIONARY MODEL

We have compared the result of a full simulation of an evaporating glycerol-water droplet with the prediction of the quasi-stationary model at different instants. By extracting the volume, the contact angle and the average droplet composition from the full simulation at a particular instant, one can directly calculate the corresponding Rayleigh and Marangoni number and use the phase diagram of the quasi-stationary model to predict the flow inside the droplet. The validity of this prediction can be seen in Fig. 2, where the result of the full temporal simulation is compared with the redimensionalized result of the quasi-stationary model, revealing very good agreement in terms of the composition distribution and the velocity field. It is noteworthy that the composition difference entering the Rayleigh and Marangoni numbers is not required to be extracted from the full simulation. Instead, it is calculated by considering the volatilites of both components only. This feature allows to use the phase diagram also for the prediction of experiments on binary droplets, where composition differences inside the droplet are hard to quantify directly. We therefore also validated the quasi-stationary theory with experiments on different binary droplets with different volumes and contact angles, again confirming the predictive power of the quasi-stationary model.

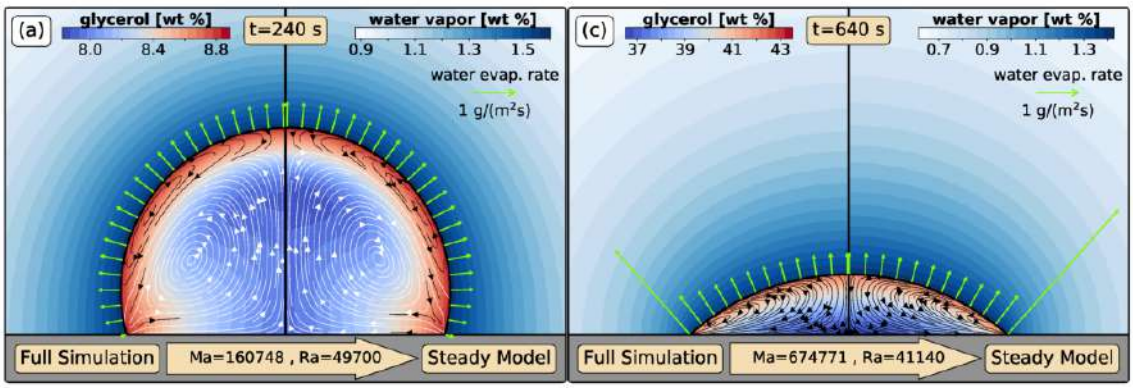

Figure 2: Comparison of a full simulation of a binary glycerol-water droplet (left half) with the redimensionalized prediction by the quasi-stationary model (right half) at different instants. Obviously, the entire flow and composition field is well predicted by the quasi-stationary model, which just requires the contact angle and the Rayleigh and Marangoni numbers as parameters.

References

[1] Edwards A. M. J., Atkinson P. S., Cheung C. S., Liang H., Fairhurst D. J., Ouali F. F. Density-Driven Flows in Evaporating Binary Liquid Droplets, *Phys. Rev. Lett.* **121**, 184501, 2018.

[2] Li Y., Diddens C., Lv P. Wijshoff H. Versluis M., Lohse D. Gravitational Effect in Evaporating Binary Microdroplets, *Phys. Rev. Lett.* **122**, 114501, 2019.

SPHERICAL OSCILLATIONS OF ENCAPSULATED MICROBUBBLES: A GENERAL MODEL

Georges Chabouh[1], Benjamin Dollet[1], Catherine Quillet[1], and Gwennou Coupier *[1]
[1] Université Grenoble Alpes, CNRS, LIPhy, F-38000 Grenoble, France

Summary We introduce a model that describes spherical oscillations of encapsulated microbubbles in an unbounded surrounding fluid. A Rayleigh-Plesset-like equation is derived by coupling the Navier-Stokes equation that describes fluid dynamics with the Navier equation that describes solid dynamics via the internal/external boundary conditions. While previous models were restricted to incompressible isotropic shells, the solid shell is modeled here as a compressible viscoelastic isotropic material, then generalised to an anisotropic material. The exact value of the resonance frequency is calculated analytically and the damping constant is computed in the approximation of weak damping. A correction of the widely used Church model for incompressible shells is evidenced, and the effects of shell compressibility and anisotropy are discussed.

INTRODUCTION

Ultrasound contrast agents (UCAs) consist of a gas core surrounded by a stabilizing shell made of various materials, including polymers, lipids, and proteins. After the famous Rayleigh-Plesset equation [1] describing the oscillations of a bubble, several models were developed to describe spherical oscillations of UCAs by adding ad-hoc viscoelastic constants to account for the presence of the encapsulating shell [2], or by modeling the shell as a 3D homogeneous, incompressible, isotropic material, that is described by the Kelvin-Voigt model [3, 4]. Previous works on UCAs focused on incompressible shells [3, 4, 5, 6]. Our model generalises the existing descriptions by accounting for the effect of compressibility and anisotropy of the encapsulating solid shell.

BASIC EQUATIONS

We consider an encapsulated gas bubble immersed in an incompressible fluid with a density ρ_f and a shear viscosity μ_f. The bubble shell is modeled as a visco-elastic solid of initial internal and external radius R_{10} and R_{20} respectively. From the conservation of radial momentum, the internal and external boundary conditions write:

$$-P_G(t) = \sigma^{el}_{rr,1} + \sigma^{visc}_{rr,1} - \frac{2\gamma_1}{R_1}, \qquad \sigma^{el}_{rr,2} + \sigma^{visc}_{rr,2} = -P_{f,2} + S^f_{rr,2} - \frac{2\gamma_2}{R_2}, \tag{1}$$

where γ_1 and γ_2 are the surface tensions and $P_G(t)$ is the pressure of the gas inside the bubble. We assume the gas obeys a polytropic law, such that $P_G(t) = P_{G_0}(\frac{R_{10}}{R_1})^{3\kappa}$, where P_{G_0} is the equilibrium gas pressure and κ is the polytropic exponent of the gas. In the external fluid, P_f denotes for the pressure and S^f for the viscous stress. In the shell, $\sigma^{el}_{rr,i}$ and $\sigma^{visc}_{rr,i}$ account for the elastic and viscous stresses respectively.

The elasticity of the material is characterized by the 3D shear modulus G' and the 3D compression modulus K', while the viscosity of the material is characterized by the shear viscosity μ_G and the compression viscosity μ_K.

We consider the fluid mechanics as being described by the Navier-Stokes equation while the viscoelastic behavior of the shell is described by the Kelvin-Voigt model. We assume that in the shell elastic waves propagate at infinite velocity due to the huge ratio between the expected wavelength and the typical shell thickness. This allows to easily calculate the stresses inside the shell. We obtain a Rayleigh-Plesset-like equation:

$$\begin{aligned}\rho_f\left(R_2\ddot{R}_2 + \tfrac{3}{2}\dot{R}_2^{\,2}\right) = &-P_0 - P_{ac}(t) - 2\tfrac{\gamma_2}{R_2} - 4\mu_f\tfrac{\dot{R}_2}{R_2} + \left(P_G - 2\tfrac{\gamma_1}{R_1}\right)\left[1 - \left(\tfrac{4G'}{3K'+4G'}\right)\left(\tfrac{R_2^3-R_1^3}{R_2^3}\right)\right] \\ &-4G'\left(\tfrac{3K'}{3K'+4G'}\right)\left(\tfrac{R_2^3-R_1^3}{R_2^3}\right)\left(\tfrac{R_1-R_{1e}}{R_1}\right) + 4\tfrac{\dot{R}_2}{R_2}\left[\mu_G\left(1 - \tfrac{4G'}{3K'+4G'}\right) - \tfrac{3}{4}\mu_K\left(\tfrac{4G'}{3K'+4G'}\right)\right] \\ &-4\tfrac{\dot{R}_1}{R_1}\left[\mu_G\left(1 - \tfrac{4G'}{3K'+4G'}\right) - \tfrac{3}{4}\mu_K\left(\tfrac{4G'}{3K'+4G'}\right)\tfrac{R_1^3}{R_2^3}\right]\end{aligned} \tag{2}$$

RESULTS

Assuming a small perturbation around the equilibrium radii, the undamped resonance frequency is found:

$$\begin{aligned}\omega_0^2 = &\left\{\left(3\kappa P_{G0} - \tfrac{2\gamma_1}{R_{10}}\right)\left(1 - \tfrac{4G'}{3K'+4G'}\tfrac{R_{20}^3-R_{10}^3}{R_{20}^3}\right) + 4G'\left(\tfrac{3K'(R_{20}^3-R_{10}^3)}{(3K'+4G')R_{20}^3}\right)\right\} \\ &\times\left\{\rho_f R_{20}^2\tfrac{\left(3\kappa P_{G0} - \frac{2\gamma_1}{R_{10}}\right)(R_{20}^3-R_{10}^3)+4G'R_{20}^3+3K'R_{10}^3}{(4G'+3K')R_{20}^3}\right\}^{-1} - \tfrac{2\gamma_2}{\rho_f R_{20}^3}\end{aligned} \tag{3}$$

*Corresponding author. E-mail: gwennou.coupier@univ-grenoble-alpes.fr

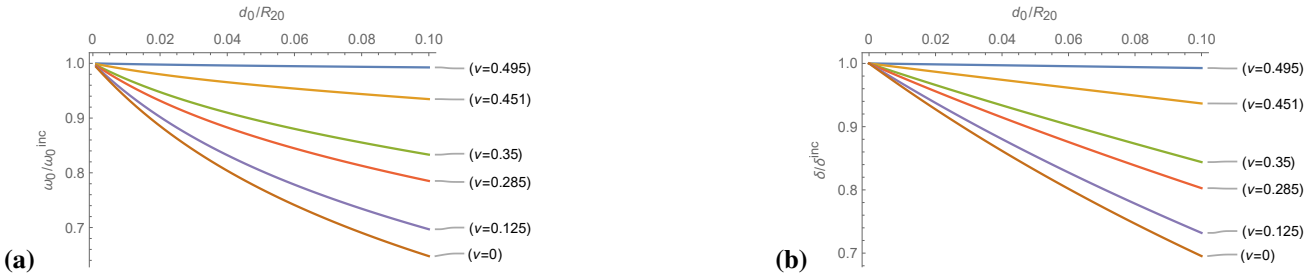

Figure 1: **(a)** Ratio of the undamped resonance frequencies ω_0/ω_0^{inc} and **(b)** Ratio of the damping constants δ/δ^{inc}, where $\omega_0^{inc} = \omega_0(K' = \infty)$ and $\delta^{inc} = \delta(K' = \infty)$ as a function of equilibrium external bubble radius. $G' = 88.8$ MPa is fixed and the pressure at rest in the shell is the atmospheric pressure. We varied K' as $100G', 10G', 3G', 2G', G'$ and $\frac{2}{3}G'$ and the corresponding Poisson ratio $\nu = (3K' - 2G')/(6K' + 2G')$ is shown on each curve.

Figure 2: **(a)** Ratio of the damping constants δ/δ^{inc}, with $\delta^{inc} = \delta(K' = \infty)$, for $\mu_K = 0.7\mu_G$ and **(b)** undamped resonance frequency ω_0^T/ω_0 for different ratio between the orthoradial and radial Young moduli. Poisson coefficients are set to 0.3.

The last term in the above expression is the classical contribution of the surface tension of the outer surface, which acts against an effective mass of fluid whose scale is given by the shell size. All elastic contributions are divided by a mass term, the first term by the external mass term $\rho_f R_{20}^2$ and the second one by the internal mass term which is corrected due to the shell deformation. The Rayleigh-Plesset expression for a free bubble [1] is recovered here with in the above equation taken in the limit of vanishing shell volume ($R_{10} \to R_{20}$), which is not the case for the work done in [3] for incompressible shell.

We discuss how the frequency is modified when the material is compressible. First, when considering as a basis the reference configuration, denoted $\mathcal{R}$, which is considered in [3]: $d_0 = 15$ nm, $P_{G_0} = 101.3$ kPa, $\rho_f = 1000$ kg/m^3, $\rho_S = 1100$ kg/m^3, $\mu_f = 0.001$ Pa.s, $G' = 88.8$ MPa, $\gamma_1 = 0.04$ N/m, $\gamma_2 = 0.005$ N/m and $\kappa = 7/5$. For such a shell whose external radius lies in the range $1 - 10\,\mu$m, we find that $0.99 < \omega_0^{inc}/\omega_0^{Ch} < 1$, which indicates that while our model has led us to neglect the inertia of the shell, this assumption will modify the final result by a negligible amount. Note that in this example, since $\gamma_i/R_{i0} \ll G'$, the inaccuracy that we exhibited in the [3] model has no quantitative consequence.

Compressibility introduces a dependency of the frequency on the shell radius that is more complex than in the incompressible case, where $\omega_0 \propto 1/R_{20}$ in the thin shell limit. It reduces the resonance frequency, all the more that the relative thickness d_0/R_{20} increases, the Poisson ratio decreases, and the shear modulus increases as seen in Fig. 1, the ratio ω_0/ω_0^{inc} is calculated for different values of G' and K', that are set relatively to $\tilde{P} = P_{G_0} - \frac{2\gamma_1}{3\kappa R_{10}}$ by setting $\gamma_2 = 0$ since its contribution is purely additive. In particular, when the bubble radius decreases at fixed thickness, this effect of compressibility will become relatively more important.

Interestingly, the effect of compressibility on the damping is independent from the choice of the model for the viscous Poisson ratio as seen in Figs. (1**(b)** where $\nu_{el} = \nu_{vis}$ and 2**(a)** where $\mu_K = 0.7\mu_G$). Finally, anisotropy can lead to large variations of the resonance frequency (Fig. 2 **(b)**). Our study provides a necessary tool in the interpretation of UCAs' behavior, crucial to extract shell parameters and to compare quantitatively with effective values.

References

[1] Plesset, M. S. and Prosperetti, A. Bubble dynamics and cavitation. Ann. Rev. Fluid Mech., 1, 145–185, 1977.
[2] De Jong, N. Cornet, R. and Lancee, CT. Higher harmonics of vibrating gas-filled microspheres. Part one: simulations. Ultrasonics, 6, 447-453,1994.
[3] Church C. The effects of an elastic solid surface layer on the radial pulsations of gas bubbles. JASA,3,1510–1521, 1995.
[4] Hoff, L. Sontum, P. C. and Hovem, J. M. Oscillations of polymeric microbubbles: Effect of the encapsulating shell. JASA,4,2272–2280,2000.
[5] Sarkar, K. Shi, W. T. Chatterjee, D. and Forsberg, F. Characterization of ultrasound contrast microbubbles using in vitro experiments and viscous and viscoelastic interface models for encapsulation. JASA,1,539–550,2005.
[6] Marmottant, P. Van Der Meer, S. Emmer, M. Versluis, M. De Jong, N. Hilgenfeldt, S. Lohse, D. A model for large amplitude oscillations of coated bubbles accounting for buckling and rupture. JASA,6,3499–35005,2005.

FLUCTUATION INDUCED HETEROGENEOUS VAPOR BUBBLE NUCLEATION

Mirko Gallo[1], Francesco Magaletti[2], and Carlo Massimo Casciola[1]
[1] Dipartimento di Ingegneria Meccanica e Aerospaziale, Università di Roma La Sapienza, Italy
[2] School of Computing, Engineering and Mathematics, University of Brighton, UK

Summary In many cases heterogeneous nucleation is the effective mechanism for phase transition. Solid walls and impurities act as a catalyst for the formation of a new phase by reducing the activation energy needed for phase change. Formation of vapor bubbles close to solid, ideally flat walls is addressed here by exploiting a mesoscale description that couples a diffuse interface modeling of the two-phase liquid-vapor system with Fluctuating Hydrodynamics, extending previous work by the authors on homogeneous nucleation. This methodology provides access to the complete bubble dynamics, from inception to the long-time macroscopic expansion, on time and spatial scales unaffordable by standard techniques for nucleation, such as Molecular Dynamics. Individual bubbles are analyzed demonstrating substantial bubble–bubble interactions.

INTRODUCTION

Fluctuations are crucial for nucleation, the incipit of phase transitions in metastable systems like, e.g., in cavitation, boiling, freezing rain and crystal formation. These activated processes require an energy to overcome the free energy barriers that may be quite high, e.g. tensile strength on the order of $1\,\mathrm{kbar}$ is observed in water. Nevertheless bubble formation is a common experience whenever impurities, dissolved gas and solid walls are present with nucleation enhancement depending on the wetting properties of the system.

Purpose of the talk is illustrating a new model the authors have been developing in recent years which is meant to allow describing the process from nucleation onset to the fully non-linear, inertia dominated stage of bubble dynamics where the model recovers the traditional Navier-Stokes equations. The framework is the diffuse interface model which has been traditionally used to describe immiscible fluids [4]. The authors extended the approach to a fully thermodynamic consistent model for liquid-vapor systems shown able to account for the fully non-linear dynamics that occurs, e.g., in the collapse of a vapor cavity in free space [5] and at solid walls [6].

PHYSICAL MODELING

Thermal fluctuations have been included in the continuum (mesoscale) model demonstrating its ability to describe vapor cavity nucleation in a way which is consistent with statistical mechanics and thermodynamics [7]. Successively [8] the dynamics of a single bubble, from fluctuation induced nucleation to non-linear bubble oscillations *à la* Raileigh-Plesset was addressed in detail [8]. Fluctuation are treated by extending to capillary systems Landau and Lifshitz's pioneering intuition [1] that led to what is presently known as *Fluctuating Hydrodynamics*, see [3] for a beautiful paper on the subject. In a nutshell, the idea is to include a stochastic term in the Capillary-(Van der Waals)-Navier-Stokes equation, where a distributed capillary force accounts for surface tension and a suitable equation of state describes the thermodynamics of the two phase flow [7]. The procedure turns the relevant PDEs into a stochastic system of partial differential equations (SPDEs) where a Weiner process (white noise) of suitable intensity induces thermal fluctuations. The noise intensity is determined through a *Fluctuation-Dissipation Balance* (FDB) that ensures the system reproduces the equilibrium correlations of the fluctuating field, as determined by the field probability distribution functional expressed in terms of entropy fluctuations, Einstein 1910 [2].

The novel advancement over the state of the art in the field to be discussed here concerns the extension of our recent theoretical model and related numerical solution techniques to heterogeneous nucleation at solid boundaries of different wettability (heterogeneous nucleation). The SPDEs, discussed at length in a, as yet, unpublished paper [9],

$$\begin{aligned}
\frac{\partial \rho}{\partial t} + \nabla \cdot (\rho \mathbf{v}) &= 0\,, \\
\frac{\partial \rho \mathbf{v}}{\partial t} + \nabla \cdot (\rho \mathbf{v} \otimes \mathbf{v}) &= \nabla \cdot \boldsymbol{\Sigma} + \mathbf{f}_{\boldsymbol{\Sigma}}\,, \\
\frac{\partial E}{\partial t} + \nabla \cdot (\mathbf{v} E) &= \nabla \cdot (\mathbf{v} \cdot \boldsymbol{\Sigma} - \mathbf{q}) + \mathbf{v} \cdot \mathbf{f}_{\boldsymbol{\Sigma}} + f_q\,,
\end{aligned}$$

describe mass (ρ), momentum ($\rho\mathbf{v}$) and (total) energy E density dynamics, with $\mathbf{f}_{\boldsymbol{\Sigma}}$ and f_q the vector and scalar noise processes respectively associated with momentum and energy fluctuations. Both are in divergence form, as directly follows from the FDB and is physically intuitive since momentum and energy are conserved (at the same rate, mass density is not allowed to fluctuate). The new aspects to be discussed concern the inclusion in the system free energy functional of the surface term f_w that accounts for the (hydrophobic/hydrophilic) interaction with the solid wall

$$F\left[\rho, \theta\right] = \int_V f\left(\rho, \nabla\rho, \theta\right)\, dV + \oint_{\partial V} f_w\left(\rho, \theta\right)\, dS\,.$$

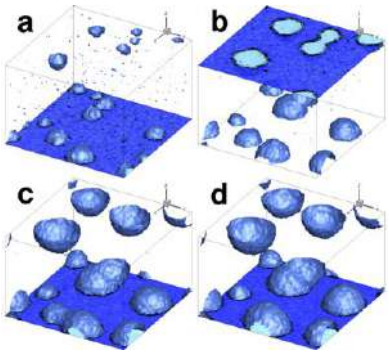

Figure 1: Nucleation on two planar parallel surfaces. For purpose of comparison with literature, the selected fluid is made of Lennard-Jones particles (see [10] for the equation of state derived from molecular dynamics simulations). Dimensionless units are used throughout, based on the following parameters: $\sigma = 3.4 \times 10^{-10}$ m, $\epsilon = 1.65 \times 10^{-21}$ J, $m = 6.63 \times 10^{-26}$ Kg. The liquid density is $\rho_L = 0.48$ (800 Kg/m^3) and the contact angle on both surfaces is $\phi = \pi/2$. The different frames refer to time $t = 90000$, $t = 165000$, $t = 235000$, $t = 258000$ (dimensionless time t = 100000 corresponds to 2.15 μs). Figure adapted form [9].

RESULTS AND CONCLUSIONS

A few snapshots of the system configurations along the nucleation process on two planar, parallel solid walls are illustrated in Fig. 1, [9]. The simulations are run for a Lennard-Jones fluid, i.e. a fluid consisting of Lennard-Jones particles at atomistic level [10], see the caption of the figure for a few more details. The bubbles form right at the wall for this specific case where the equilibrium contact angle is 90°. The dynamics is quite rich, with the bubble undergoing coalescence while they grow one close to the other, see the time history of bubble volumes in the leftmost panel of Figure 2 which also reports on temperature (it should be stressed that the system *is not* isothermal, as appropriate here) and pressure inside the bubbles (middle and rightmost panel). Based in these results, the talk will illustrate the theory behind the model and discuss with several examples the effect of wall wettability on nucleation rate and ensuing bubble dynamics.

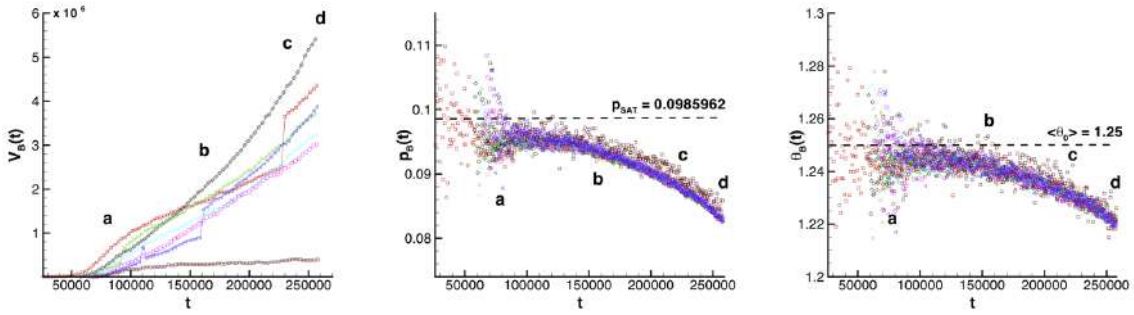

Figure 2: Left panel: Bubble volume evolution.Volume jumps correspond to coalescence events. Middle and right panels: Bubble temperature and, respectively, pressure scatter plot along nucleation (the average field temperature is $\langle\theta_0\rangle = 1.25$ (149 K), the saturation pressure is $p_{SAT} = 0.098$ (4, 1 MPa). In all frames a, b, c, d refer to the configurations shown in Fig. 1. Figure adapted form [9].

References

[1] Landau L.D., Lifshitz E.M. Statistical physics, vol. 5. *Course of theoretical physics*, 1980.

[2] Einstein A. Theorie der Opaleszenz von homogenen Flüssigkeiten und Flüssigkeitsgemischen in der Nähe des kritischen Zustandes. *Annalen der Physik* **338**:16, 1275–1298, 1910.

[3] Fox R., Uhlenbeck G.E. Contributions to Non-Equilibrium Thermodynamics. I. Theory of Hydrodynamical Fluctuations. *Physics of Fluids* **13**: 8 1893–1902, 1970.

[4] Magaletti F.,Picano F., Chinappi M., Marino L., Casciola C.M. The sharp-interface limit of the Cahn–Hilliard/Navier–Stokes model for binary fluids, *Journal of Fluid Mechanics* **714**: 95–126, 2013.

[5] Magaletti F., Gallo M., Marino L., Casciola C.M. Shock Wave Formation in the Collapse of a Vapor Nanobubble *Physical Review Letters* **114**:6, 064501, 2015.

[6] Magaletti F., Gallo M., Marino L., Casciola C.M. Shock-induced collapse of a vapor nanobubble near solid boundaries. *International Journal of Multiphase Flow* **84**: 34-45, 2016.

[7] Gallo M., Magaletti F., Casciola C.M. Thermally activated vapor bubble nucleation: The Landau-Lifshitz–Van der Waals approach. *Phys. Rev. Fluids* **3**:5-053604, 2018.

[8] Gallo M., Magaletti F., Cocco D., Casciola C.M. Nucleation and growth dynamics of vapour bubbles. *Journal of Fluid Mechanics* **883**, 2020.

[9] Gallo M., Magaletti F., Casciola C.M. A mesoscale model for heterogeneous vapor bubble nucleation dynamics. Submitted 2020.

[10] Johnson J.K., Zollweg J.A., Gubbins K.E. The Lennard-Jones equation of state revisited. *Molecular Physics* **78**:3 591–618,1993.

CLOSURE OF PHASE-AVERAGED BUBBLY, CAVITATING FLOW MODELS

Spencer H. Bryngelson*[1] and Tim Colonius[1]
[1] Division of Engineering and Applied Science, California Institute of Technology, Pasadena, California

Summary Phase-averaged bubbly flow models are closed by high-order statistical moments of the disperse bubble dynamics. Evaluating these moments in a simulation environment is computationally expensive because the integrands are highly oscillatory. The cost of this closure is demonstrated for an ensemble-averaged bubbly flow model. A machine-learning-based method for accelerating the moment evaluation is formulated.

INTRODUCTION

Bubble cloud dynamics play a central role in phenomena ranging from blast trauma injury[1] to kidney stone pulverization.[2] When the size distributions of bubble nuclei are broad, the average response of the bubbles to pressure fluctuations damps and disperses.[3] Bubbly flow models must account for such size distributions if they are to represent the dynamics of realistic bubbly flows.

PHASE-AVERAGING

Phase-averaged computational methods can represent the interaction between polydisperse bubble clouds and the flow that stimulates them. Current methods utilize either ensemble- or volume-averaging. Volume-averaging,[4] shown in figure 1 (left), represents bubbles as Lagrangian features that advect and evolve according to an assumed bubble dynamics model (e.g. Rayleigh–Plesset). The bubble population, sampled from an equilibrium bubble radius distribution, couples to the suspending liquid via a volumetric smoothing operator. Figure 1 (right) shows ensemble averaging.[5] It represents the bubble population as an evolving probability distribution, again according to a bubble dynamics model, in the equilibrium bubble size space on the Eulerian grid. The bubble population moments couple to the mixture-averaged flow equations and advect via a transport equation.

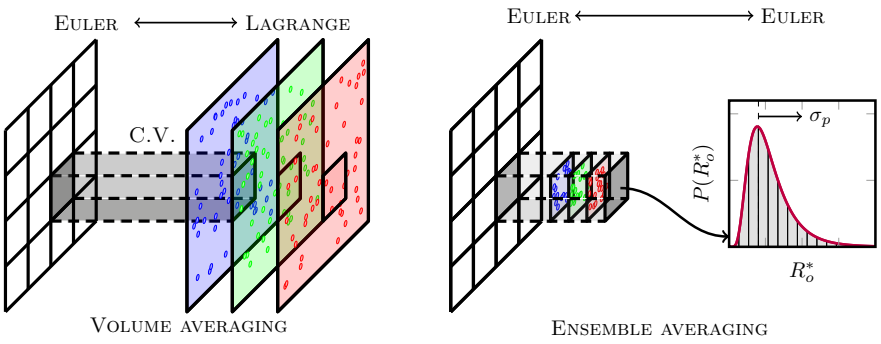

Figure 1: Schematic illustration of phase averaged methods.

Ensemble averaging is computationally cheaper than volume averaging when the bubble population is not significantly polydisperse.[6] However, ensemble averaging methods often approximate the required moments via classes methods. These methods bin and evolve the underlying probability density function. While simple, this approach is computational expensive for broad bubble size distributions. Our goal is to accelerate ensemble-averaged methods for polydisperse cases via a moment-based method.

CLOSURE VIA MOMENT METHODS

Statistical moments often more efficiently represent distributions than bins. Evolution of such moments follow from a population balance equation. This technique has been used to model polydisperse bubbly flows, though has not been applied to cavitating bubble populations, which undergo large volume changes. The moment evolution equations are not a function of only lower order moments when the bubble dynamics are nonlinear. Quadrature-based moment methods[7] can address this issue, though computing high-order moments with them is expensive. Instead, we use a Gaussian closure method. For this, a specific moments $\{l, m\}$ is

$$\mu_{lm} = \int R^l \dot{R}^m P(\vec{\mathbf{x}}, \vec{\boldsymbol{\theta}}) \, \mathrm{d}\vec{\mathbf{x}} \tag{1}$$

*Corresponding author. E-mail: spencer@caltech.edu.

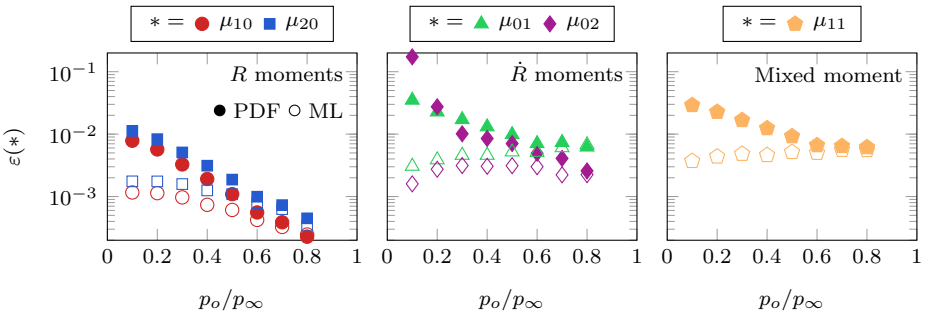

Figure 2: First- and second-order moment model errors. PDF and ML correspond to the Gaussian closure and neural network augmented methods, respectively.

where $\vec{\mathbf{x}} \equiv \{R, \dot{R}\}$ are the internal coordinates and $\vec{\boldsymbol{\theta}}$ are the shape parameters of the probability density function P (e.g. the means and variances). The moment system evolves as

$$\frac{\partial \mu_{lm}}{\partial t} = l\mu_{l-1,m+1} + m \int \ddot{R}(\vec{\mathbf{x}}) R^l \dot{R}^{m-1} P(\vec{\mathbf{x}}, \vec{\boldsymbol{\theta}}) \, \mathrm{d}\vec{\mathbf{x}}. \tag{2}$$

The integral term of (2) is closed by assuming P is a bivariate Gaussian density function and that the Rayleigh–Plesset equation represents the bubble dynamics $\ddot{R}$ with driving pressure ratio p_o/p_∞. The moment system (2) is five dimensional because P has only two shape parameters. This is significantly smaller than the hundreds of bins that significantly polydisperse populations require.[6]

Figure 2 shows that the model error ε is small for all moments when the driving pressure ratio approaches unity. This is because the dynamics are linear in this limit and the Gaussian closure is exact. However, for lower pressure ratios the bubble dynamics are more violent and model errors are significant (figure 2 PDF, filled symbols). This model deficiency results from high-order moment development, which Gaussian closure does not represent. To treat this issue, we train a long short-term memory (LSTM) recurrent neural network (RNN) to augment the low-order moment evolution equation (2). Figure 2 (ML) shows that this significantly decreases the model error for validation cases at low pressure ratios.

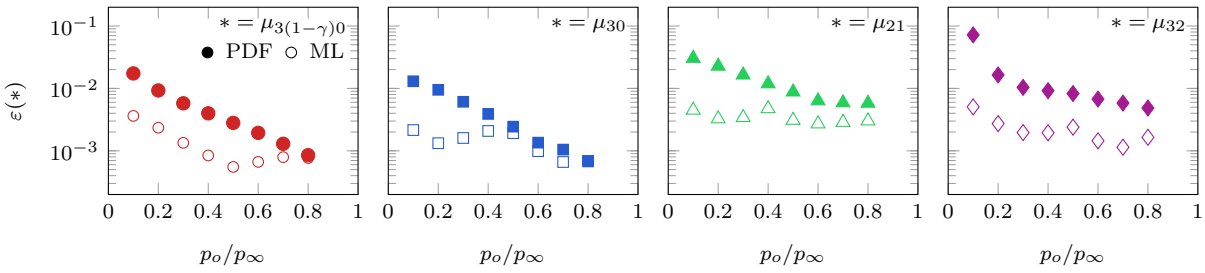

Figure 3: Model errors for the phase-averaged-model required moments.

Ensemble-averaged models require four high-order moments of the evolving population. Assuming Gaussian closure for P is sufficient to evaluate these, though figure 3 (PDF) shows that this again results in significant errors for low pressure ratios, even if the low-order moments are accurate. This is because the statistics are non-Gaussian in this regime. To treat this, we train another LSTM RNN to correct these moments. Figure 3 shows that this again significantly reduces the model errors, particularly for low pressure ratios.

This work was supported in part by the US Office of Naval Research under grant number N0014-17-1-2676.

References

[1] K. Laksari, S. Assari, B. Seibold, K. Sadeghipour and K. Darvish, "Computational simulation of the mechanical response of brain tissue under blast loading," Biomech. Model. Mechanobiol. **14**, 459 (2015).
[2] Y. A. Pishchalnikov, O. A. Sapozhnikov, M. R. Bailey, J. C. Williams, R. O. Cleveland, T. Colonius, L. A. Crum, A. P. Evan and J. A. McAteer, "Cavitation bubble cluster activity in the breakage of kidney stones by lithotripter shockwaves," J. Endourol. **17**, 435 (2003).
[3] P. Smereka, "A Vlasov equation for pressure wave propagation in bubbly fluids," J. Fluid Mech. **454**, 287 (2002).
[4] L. V. Wijngaarden, "On the equations of motion for mixtures of liquid and gas bubbles," J. Fluid Mech. **33**, 465 (1968).
[5] D. Z. Zhang and A. Prosperetti, "Ensemble phase-averaged equations for bubbly flows," Phys. Fluids **6** (1994).
[6] S. H. Bryngelson, K. Schmidmayer and T. Colonius, "A quantitative comparison of phase-averaged models for bubbly, cavitating flows," Int. J. Mult. Flow **115**, 137 (2019).
[7] D. L. Marchisio and R. O. Fox, "Solution of population balance equations using the direct quadrature method of moments," J. Aerosol Sci. **36**, 43 (2005).

SLUG FLOW DYNAMICS WITHIN CAPILLARY TUBES IN THE PRESENCE OF SURFACTANTS

Assen Batchvarov *[1], Mirco Magnini[2], Lyes Kahouadji[1], Ricardo Constante-Amores[1], and Omar K. Matar[1]
[1] Department of Chemical Engineering, Imperial College London, London, UK
[2] Department of Mechanical Engineering, Nottingham University, Nottingham, UK

Summary The effect of surfactants on the tail dynamics of bubbles propagating through capillary tubes is accessed through an extensive three-dimensional numerical study using a hybrid front-tracking/level-set method originally developed by Shin *et al.* [1]. High Reynolds number flows are shown to result in complex undulation structures at the tails [2] of capillary bubbles. The particular effect of a wide range of surfactant properties including diffusivity, elasticity, and solubility, is investigated, focussing in particular on the interfacial shape of the bubble tail.

INTRODUCTION

The dynamics of bubbles propagating through capillary tubes are of great industrial importance due to their occurrence in applications such as electronic cooling systems, enhanced oil recovery, and coating processes. The scientific foundation of the problem was laid out through the initial experimental work of Taylor [3], who showed that the wall film thickness, h_0/R, reaches an asymptotic value of approximately $1/3$ when $Ca \to 2$. Using lubrication theory, Bretherton [5] showed that this thickness in the limits of $Re \ll 1$ and $Ca \ll 1$ scales as $h_0/R \sim Ca^{2/3}$. In both cases the effect of surface active agents (e.g. surfactants) was not considered. The effect of surfactants was later studied by Ratulowski and Chang [4] and more recently by Olgac and Moradoglu [6]. Both works considered bubble dynamics in the limits of $Re \ll 1$ and $Ca \ll 1$ and found that the presence of surfactants has a liquid film thickening effect. When inertia is present in these flows, the dynamics of the rear bubble menisci exhibit undulations. Recent work by Magnini *et al.* [2] used both lubrication theory and computational fluid dynamics approaches to systematically study the effect of Re on tail dynamics and showed that increasing inertia decreases monotonically the wavelengths of the tail undulations and increases their amplitude. The present work aims to perform a comprehensive computational study of the effect of surfactants on dynamics of gas bubbles in the presence of inertia ($Re \gg 1$).

FORMULATION AND PROBLEM STATEMENT

To study the effect of surfactants on the dynamics of bubbles propagating through capillary tubes we employ a Level Contour Reconstruction Method (LCRM) CFD technique. Using this hybrid front-tracking level-set code developed by Shin *et al.* [1], we solve the two-phase incompressible mass and momentum equations for two Newtonian fluids, with surface tension, neglecting gravity. The two fluids are chosen as air and water, where the density and viscosity ratios represented by ρ_l/ρ_b and μ_l/μ_b, respectively, where ρ_l and ρ_b are the density of the liquid and gas, and μ_l and μ_b denote the viscosity of the liquid and gas, respectively. In addition to the continuity and momentum equations, we solve convective-diffusion transport equations for the interfacial and bulk surfactant species. The following non-dimensional groups can be obtained by using the channel diameter D and average liquid velocity U_l as length and velocity scales, respectively:

$$Re_l = \frac{\rho_l U_l D}{\mu_l},\ Ca_l = \frac{\mu_l U_l}{\sigma_s},\ Pe_c = \frac{U_l D}{D_c},\ Pe_s = \frac{U_l D}{D_s}, \beta_s = \frac{RT\Gamma_\infty}{\sigma_s},\ Bi = \frac{k_d D}{U_l},\ Da = \frac{\Gamma_\infty}{DC_\infty},\ k = \frac{k_a C_\infty}{k_d}, \quad (1)$$

where D_c and D_s are the diffusion coefficients in the bulk and at the interface, σ_s denotes the surface tension of 'clean' interface, R is the ideal gas constant, T is temperature, and $\beta_s = RT\Gamma_\infty/\sigma_s$ is defined as the the elasticity number. k_a and k_d are the adsorption and desorption coefficients, respectively, C_∞ is the concentration of surfactant in the bulk, and Γ_∞ is the saturated interfacial surfactant concentration. Here, Re_l and Ca_l are the liquid Capillary and Reynolds numbers, respectively. The competition between convection and diffusion for the surfactant species is represented by bulk and interfacial Peclet numbers, Pe_c and Pe_s, respectively. Other surfactant-related parameters are elasticity, β_s, Biot number, Bi, Damkohler number, Da, and the adsoprtion depth, k. In addition to the governing surfactant parameters, the present work analyzes the effect of Marangoni stresses on the flow dynamics, $\tau_m = d\sigma/ds$, which have been non-dimensionalised with the viscous stress, $\tau_{vis} = \mu_l U_l/D$, resulting in the definition of the Marangoni number, $Ma = \tau_m/\tau_{vis}$. The local surface tension is defined by a Langmuir adsorption equation of state, $\sigma = \sigma_s \left[1 + \beta_s ln\left(1 - \frac{\Gamma}{\Gamma_\infty}\right)\right]$, where Γ is the local interfacial surfactant concentration.

The three-dimensional computational domain consists of a cylindrical channel of diameter D. The bubble is initially located at the beginning of the channel and its shape is initialised using a cylindrical body and two spherical caps at the front and back. The length of the bubble for the baseline case is $L_b = 5D$, although this will be varied when studying the impact of the bubble length on the flow dynamics. The flow is initiated by imposing a fully-developed parabolic velocity profile at the inlet. A no-slip boundary condition is imposed on the channel wall. The channel length is set to be sufficiently long to allow the bubble to achieve a steady-state motion (e.g. $L_x = 27.8D$).

*Corresponding author. E-mail: aab12@ic.ac.uk

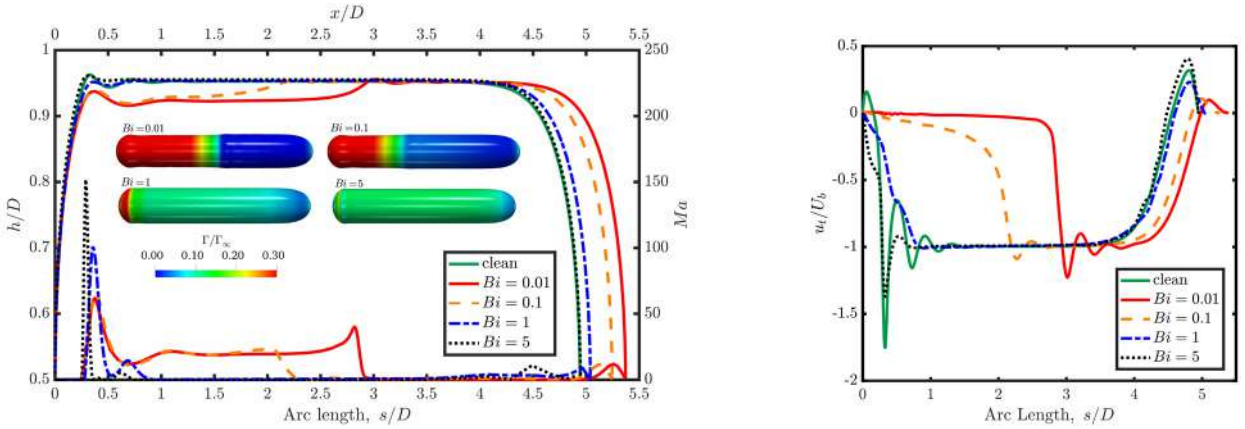

(a) (b)

Figure 1: Effect of varying surfactant solubility through Bi, where other surfactant parameters are kept constant: $Re_l = 443$, $Ca_l = 0.0089$ $Pe_c = Pe_s = 100$, $Da = 1$, $k = 1$, $\beta_s = 0.5$. (a) Spatial variation of the interfacial shape of 'clean' and 'surfactant' bubbles and Ma distribution along the bubble arc length; 3D bubble shapes and interfacial surfactant distribution shown inside the panel; (b) Streamwise tangential velocity at the bubble interface in a reference frame moving with the speed of the bubble tip, plotted as a function of the bubble arc length.

RESULTS

We perform an extensive parametric study of the key non-dimensional groups identified in the previous section. A sample result set is given by Fig. 1, where we show the effect of varying surfactant solubility on the bubble dynamics; the addition of surfactants alters the local surface tension. As the bubble propagates through the channel, surfactants accumulate at the back of the bubble, where they generate surface tension gradients and hence Marangoni stresses, which as seen in Fig. 1, are effective in stabilising the bubble dynamics and suppressing the bubble tail undulations otherwise observed in the surfactant-free case. The highly soluble surfactant, $Bi = 5$, produces the highest concentration gradient at the bubble tail, which results in the highest Marangoni stress. As surfactant solubility is decreased, the effective magnitude of the Marangoni stresses is reduced, however, the overall affected area increases as surfactants are unable to evacuate the interface as quickly and diffusion promotes their movement towards the bubble front. As a result, at moderate solubility, $Bi = 1$, the Marangoni stresses generated at the bubble tail pushes the liquid film inwards. This effect becomes more pronounced for $Bi = 0.1$, where a sudden increase of the film thickness near the bubble tail is apparent in Fig. 1a; this is due to the bubble interface behaving as a rigid wall and imposing a no-slip condition to the flow, as suggested by the u_t decreasing locally to zero, see Fig. 1b. In the the lowest solubility case, $Bi = 0.01$, surfactants are unable to evacuate the interface. The resultant uniform Marangoni stress acts to generate a thicker film region at the back end of the bubble. The film becomes completely rigid in the thicker film region as seen in Fig. 1b, whereas at the front of the bubble surfactants are largely absent and the interface exhibits similar behaviour to that observed for the surfactant-free case.

CONCLUSIONS

This work focuses on investigating the effect of surfactant species on capillary bubble tail dynamics, by employing high-accuracy numerical simulations. In the sample result set presented, we see that by lowering the surfactant solubility, surfactant species are convected towards the bubble tail, where they result in local surface tension gradients. The resultant Marangoni stresses act to rigidify the bubble tail and suppress bubble undulations. In the lowest solubility case, a uniform Marangoni force is generated at the bubble rear end. This induces a no-slip condition on the bubble interface, which is triggers a sharp thicknening of the liquid film in the proximity of the bubble tail.

References

[1] Shin S., Chergui J. C, Juric D., Kahouadji L., Matar O. K., and Craster R. V. A hybrid interface tracking–level set technique for multiphase flow with soluble surfactant.*Journal of Computational Physics.* **359**: 409–435, 2018.

[2] Magnini M., Ferrari A., Thome J. R., and Stone H. A. Undulations on the surface of elongated bubbles in confined gas-liquid flows. *Physical Review Fluids.* **2**: 1–21, 2017.

[3] Taylor G. I. Deposition of a viscous fluid on a plane surface. *Journal of Fluid Mechanics.* **9**: 218–224, 1960.

[4] Ratulowski J. and Chang H. C. Marangoni effects of trace impurities on the motion of long gas bubbles in capillaries.*Journal of Fluid Mechanics.* **210**: 303–328, 1990.

[5] Bretherton F. P. The motion of long bubbles in tubes. *Journal of Fluid Mechanics.* **10**: 166–188, 1961.

[6] Olgac U. and Muradoglu M. Effects of surfactant on liquid film thickness in the Bretherton problem. *International Journal of Multiphase Flow.* **48**: 58-70, 2013.

DYNAMICS OF H2 BUBBLES GROWING AT MICROELECTRODES

Aleksandr Bashkatov*[1], Syed Sahil Hossain[1], Xuegeng Yang[1], Gerd Mutschke[1], and Kerstin Eckert[1,2]
[1] Institute of Fluid Dynamics, Helmholtz-Zentrum Dresden-Rossendorf, Dresden, Germany
[2] Institute of Process Engineering and Environmental Technology, Technische Universität Dresden, Dresden, Germany

Summary Recently a new phenomenon of long-lasting position oscillations of hydrogen gas bubbles produced via electrolysis at horizontally installed microelectrodes has been found. The bubbles grow until their detachment when buoyancy exceeds the retarding forces. The phenomenon itself consists in multiple bubble returns to the electrode. It was found that the mother bubble sits on and is fed by a carpet of small bubbles. The dynamics of the growing bubble was systematically studied and found to be strongly dependent on the cathodic potential and electrolyte concentration. A new insight into the multifaceted and complex process has been established. Regions of different bubble dynamics regimes are summarized in a diagram.

The growth of hydrogen bubbles in water electrolysis is a particularly interesting problem of high practical relevance due to the prominent role of hydrogen in energy storage via power-to-gas processes. However, alkaline water electrolysis is suffering from inadequate efficiency. Major reasons are the blockage of the active electrode area and the increase the ohmic resistance of the electrolyte by the gas bubbles produced. A deeper understanding of the mechanism of hydrogen bubble evolution therefore may provide additional opportunities to control and enhance the process. Microelectrodes are the method of choice [1] to study localized phenomena at H_2 bubbles in detail since they provide a low number of nucleation sites and the possibility to grow relatively large bubbles.

The dynamics of single hydrogen bubbles produced via electrolysis at microelectrode was systematically studied at different cathodic potentials and electrolyte concentration. The hydrogen gas bubbles were generated at a $\varnothing 100$ μm Pt microelectrode installed horizontally in electrolytic cell filled with sulfuric acid of 0.1...1 mol/L concentration, using a three-electrode setup. A mercury/mercurous sulfate electrode (MSE, 0.65 V vs SHE) and a Pt wire ($\varnothing 1$ mm) served as the reference electrode and anode, respectively [1]. High-speed microscopic shadowgraphy at 1000 frames per second and a spatial resolution of up to 820 pix/mm coupled to measurements of the electric current in potentiostatic mode (-2...-10 V) led to observation of three different bubble evolution regimes, including novel dynamic phenomenon covering the transition from monotonic to oscillatory growth reported in [2].

In Figure 1(a) a scheme of a slightly deformed spherical bubble, sitting on the Pt electrode, and the carpet of microbubbles beneath, with their relevant geometric parameters is shown, where H — bubble height, W — bubble width, ε — bubble elongation reflecting its deformation, δ — thickness of the carpet and **j** — current lines directed from anode to cathode. Significant differences have been found in the bubble evolution behavior depending on the potential and electrolyte concentration.

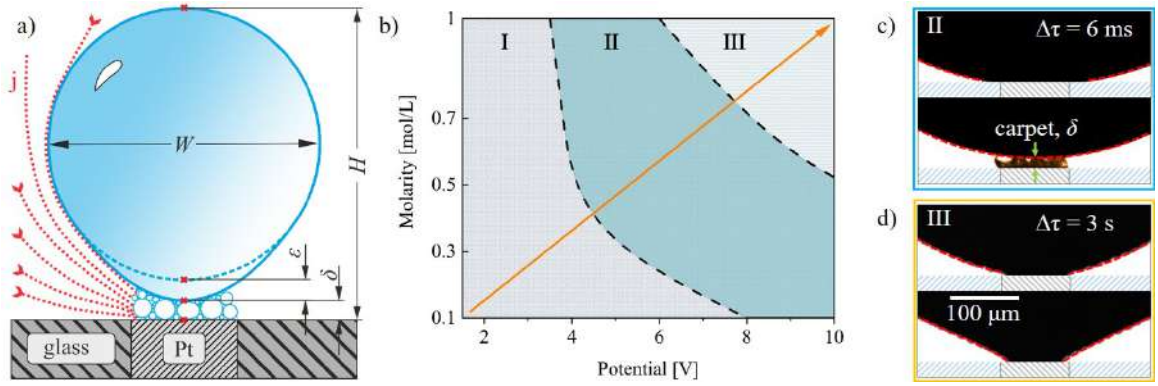

Figure 1: (a) Scheme of slightly deformed spherical bubble sitting on the Pt electrode and the carpet of microbubbles beneath (reprinted from [2]). (b) Diagram representing three distinct regions of the bubble evolution. (c) Bubble at its lowest and highest position in an oscillation phase, at -5 V and 0.5 mol/L, $\triangle\tau$ = 6 ms. (d) Representation of the bubble shape deformation at two distinct moments of time, at -10 V and 1 mol/L, $\triangle\tau$ = 3 s.

Fig. 1(b) visualizes three different bubble growth regimes I, II, III depending on potential and electrolyte concentration which are described in detail in following. The orange colored arrow shows the direction from lower to higher concentration/potential. This increment along the arrow leads to higher retarding forces acting downward, like Marangoni force F_M [3, 4, 5], electric force F_e [2] and a dynamic force F_d due to faster gas generation and hence bubble-carpet interaction. This step-by-step leads to a reduction of carpet thickness, to the appearance of instabilities like bubble position oscillations, and to shape deformations. The transition between the different regimes is smooth. Depending on the

*Corresponding author. E-mail: a.bashkatov@hzdr.de

magnitude of the retarding forces that hold the bubble at the electrode and hence their contribution to the force balance, the bubbles grow in different ways and detach at different diameter and lifetime [1].

In the first 'I' region of Fig. 1(b) the bubble follows smooth and conventional evolution characterized by the growth law, $R \propto t^{1/3}$, as reported in [1]. Furthermore, a permanent existence of a carpet of microbubbles below the main bubble is detected as shown on Fig. 1(a). The evolution in that case proceeds mainly by coalescence with the carpet permanently feeding the main bubble. Depending on the potential/concentration the visible carpet might already exist shortly after formation of a single bubble at the electrode or might appear later as the bubble moves slowly away from the electrode. As the bubble increases in volume, it tends to move upward to detach. However, the distance dependent electric force revealed in [2] increases, and the bubble continues to levitate above the electrode, thereby adsorbing small bubbles from the carpet. At some point, the bubble detaches, as the derivative of F_e becomes negative, while the buoyancy F_b rises. However, at such potential/concentration the increment in the electric force is not sufficient to bring the bubble back to the electrode and hence trigger the oscillations characteristic of the second 'II' region.

The second 'II' region represents the bubble evolution regime during which in time the transition from monotonic to oscillatory growth is observed. The oscillatory phenomenon consists in periodic upward and downward movements of the bubble. Here, the bubble grows and slowly moves upward, while the carpet thickness δ increases. It reshapes the geometry of the current lines **j** directed from anode to cathode affecting the electric force that brings the bubble back to the electrode. In [2] it was shown numerically that the electric force increases together with the carpet thickness until its critical value of around δ_{crit} = 20...30 μm at which the bubble detaches. The oscillation amplitude (and carpet thickness) rises during the oscillations until this critical value δ_{crit}. With concentration decrease, the oscillations regime shown in Fig. 1(b) is shifted towards higher potentials, meaning that the reduction in magnitude of the retarding forces with concentration decrease might be compensated by the potential increment. The images in Figure 1(c) represent bubble positions at two distinct moments of time within one upward-downward phase with $\triangle\tau$ = 6 ms. The first image is the lowest position of the bubble, while the second is the highest, where the carpet can be clearly seen.

The third 'III' region represents the evolution under relatively high potential, providing 'naturally' high retarding forces. By holding the bubble at the electrode, any oscillations and any visible carpet along the whole evolution are suppressed. The bubble sits at the electrode and grows monotonously, mainly by diffusion, whereby progressive shape deformations become visible. Although the F_e is already high at these conditions, the shape deformation additionally contributes to a longer lifetime. The images in Figure 1(d) represent bubble shapes at two distinct moments of time with $\triangle\tau$ = 3 s, while the second image is recorded shortly before detachment.

In summary, depending on voltage and electrolyte concentration, three different bubble evolution scenarios were identified. The magnitude of retarding forces (incl. F_e) governed by the potential/concentration is responsible for the carpet existence and its thickness, positions oscillations and shape deformations of the bubble. The transition from the conventional evolution path to oscillations and to shape deformations is smooth and additionally dependent on the electrode preparation. The impact of the carpet-bubble interaction needs to be taken into account and to be analyzed in a future research, as suggested in [6].

This project is supported by the German Space Agency (DLR) with funds provided by the Federal Ministry of Economics and Technology (BMWi) due to an enactment of the German Bundestag under Grant No. DLR 50WM1758 (project MADAGAS).

References

[1] Yang X. et al. Dynamics of single hydrogen bubbles at a platinum microelectrode. *Langmuir* **31**: 8184–8193, 2015.
[2] Bashkatov A. et al. Oscillating Hydrogen Bubbles at Pt Microelectrodes. *Phys. Rev. Lett.* **123**: 214503, 2019.
[3] Massing J. et al. Thermocapillary convection during hydrogen evolution at microelectrodes. *Electrochimica Acta* **297**: 929–940, 2019.
[4] Hossain S.S. et al. The thermocapillary effect on gas bubbles growing on electrodes of different sizes. *Electrochimica Acta* **353**: 136461, 2020.
[5] Yang X. et al. Marangoni convection at electrogenerated hydrogen bubbles. *Physical Chemistry Chemical Physics* **20**: 11542–11548, 2018.
[6] Zhou J. et al. A modified bubble dynamics model for predicting bubble departure diameter on micro-pin-finned surfaces under microgravity. *Applied Thermal Engineering* **132**: 450–462, 2018.

BUOYANCY-DRIVEN BUBBLE MOTION IN A CONSTRICTED TUBE

Zhicheng Zhu[1], Haoran Liu*[1], and Hang Ding[1]
[1] Department of Modern Mechanics, University of Science and Technology of China, Hefei, China

Summary We numerically investigate the dynamics of bubble rising in a constricted tube. The bubble is released from the bottom of a tube, and rises up due to buoyancy. However, a throat in the constricted tube may hinder the bubble motion, possibly leading to the bubble entrapment. To investigate at what conditions that the bubble would pass through or be entrapped at the throat, a diffuse-interface immersed-boundary method is used to simulate this dynamic process. We found that the fate of the bubble is determined by the bubble deformation, buoyancy force, surface tension and the tube geometry. A scaling law is proposed to predict the boundary that separates the two regimes. The theoretical prediction is in good agreement with our numerical results.

INTRODUCTION

Bubble motion in a tube with complex geometries is relevant to a wide range of industrial processes in food, petroleum and energy. Previous studies focused on the deformation and vibration of bubbles in a tube. Hemmat & Borhan (1996) experimentally observed the periodic deformation of drops and bubbles in a constricted tube. Later, Legendre et al. (2005) proposed a mass-spring system model to describe the periodic bubble deformation. Zenit (2009) found that the viscous effect is effectively equivalent to a damper with a fixed coefficient, and then extended the mass-spring model by including the viscous effect. In our work, we consider the axisymmetric flow of a buoyancy-driven bubble in a vertical constricted tube as shown in Figure 1(a), in which the curved solid wall in the middle assumes an arc shape. The bubble with a density ratio of 0.001 to the surrounded liquid is released from the bottom of the tube at the very beginning. Due to the buoyance force, the bubble ascends with time until reaching the throat of the constricted tube, which may hinder the bubble motion, possibly leading to the bubble entrapment. To investigate at what conditions that the bubble would pass through or be entrapped at the throat, a diffuse-interface immersed-boundary method is used to simulate this dynamic process.

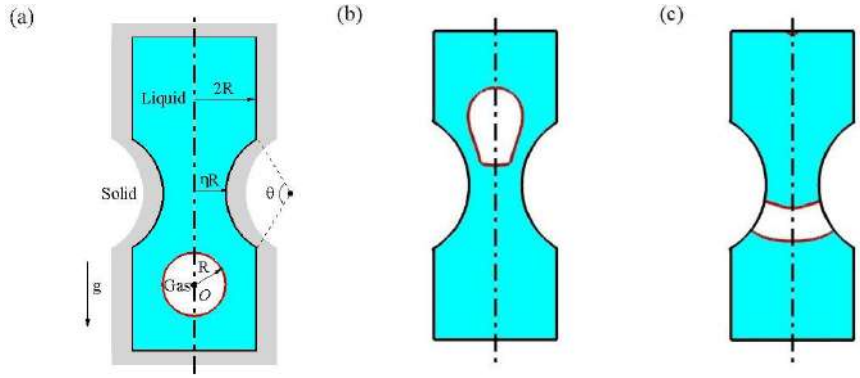

Figure 1. A sketch of a bubble floating in constricted tube. (a) Setup of numerical simulations. Initial bubble radius is denoted by R and the tube throat radius is ηR. (b) Passing model and (c) entrapment model.

NUMERICAL AND THEORETICAL METHODS

The bubble motion in the constricted tube is simulated by using an axisymmetric diffuse-interface immersed-boundary method (Liu & Ding, 2015). It allows us to simulate incompressible multiphase flows involving moving contact lines on the rigid objects of irregular shape with large density and viscosity ratios. The liquid-gas interface is represented by the volume fraction of the liquid, C_L, the evolution of which is governed by the Cahn-Hilliard equation

$$\frac{\partial C_L}{\partial t} + \nabla\cdot(\mathbf{u}C_L) = \frac{1}{Pe}\nabla^2\psi$$

where $\mathbf{u}$ stands for the flow velocity, and the chemical potential ψ is defined as

$$\psi = C_L^3 - 1.5C_L^2 + 0.5C_L - C_L C_S(1 - C_L - C_S) - Cn^2\nabla^2 C_L,$$

and Cn is the thickness of diffuse interface. The motion of fluids is governed by the Navier-Stokes equations,

$$\rho\frac{\partial \mathbf{u}}{\partial x} + \mathbf{u}\cdot\nabla\mathbf{u} = -\nabla p + \frac{1}{Re}\nabla[\mu(\nabla\mathbf{u} + \nabla\mathbf{u}^T)] + \frac{\mathbf{f_s}}{We} - \frac{\rho}{Fr}\mathbf{j} + \mathbf{f}_{IB}$$
$$\nabla\cdot\mathbf{u} = 0,$$

where $\mathbf{f}_s$ donates the surface tension force and $\mathbf{j}$ is the vertical direction. $\mathbf{f}_{IB}$ represents the additional force arising from the immersed boundary method.

*Corresponding author. E-mail: liuhr@ustc.edu.cn, now at Physics of Fluids Group, University of Twente, The Netherlands

The fluid properties of bubble and fluid are used to define the dimensionless group: Reynolds number $Re = \rho UR/\mu$, Weber number $We = \rho U^2 R/\sigma$, Froude number $Fr = U^2/gR$, and Bond number $Bo = \rho g R^2/\sigma$. Here, ρ, μ and σ denote the density, viscosity and surface tension of the fluid respectively.

RESULTS AND DISCUSSIONS

The numerical results confirm that the bubble either passes through or is trapped at the tube throat. We find that when the bubble is smaller than the size of throat, it is just slightly elongated and passes through the throat with ease, namely passing mode (see Figure 1b). On the other hand, a bigger bubble could be captured by the throat, and subsequently contact lines are generated and pinned at the side wall, namely entrapment mode (see Figure 1c). In this case, the buoyancy force is not so strong enough as to break up the bubble, mainly because of the limited size of the throat. As a result, the bubble rests at the throat and the flow vanishes gradually due to viscosity. Figure 2 shows the phase diagram of bubble released from or captured at the constricted tube with respect to η versus Bond number. We can see that the boundaries separating two flow regimes have different trends for small and large bubbles. We use a mass-spring model (Legendre et al., 2005) to analyse the bubble vibration, and also take account of the bubble dynamics near the tube throat. We find that the difference in trends is mainly due to the competition between buoyancy and surface tension forces. A scaling law is proposed to predict the boundary that separates the two regimes. The theoretical prediction is in good agreement with our numerical results. as shown in Figure 2.

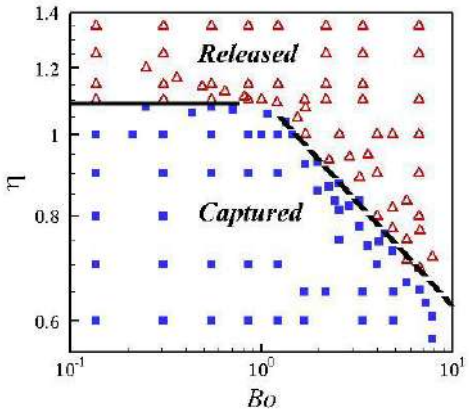

Figure 2. Phase diagram of a bubble floating in constricted tube with respect to η and Bo, including the regimes of released (△) and captured (■). the lines are theoretical predictions for the transition of regimes.

CONCLUSIONS

We numerically simulated the motion of a buoyancy-driven bubble in a constricted tube by using a diffused-interface immersed-boundary method. The effects of bubble-to-orifice ratio η and the Bond number on the dynamics and mode of the bubble have been investigated. Scaling laws are proposed to predict the boundary between passing and entrapment modes. Good agreements between our theoretical predictions and numerical results are achieved.

References

[1] Hemmat, M. & Borhan, A. 1996 Buoyancy-driven motion of drops and bubbles in a periodically constricted capillary. Chem. Engng. Commun. **148-150**, 363-384.
[2] Legendre, D., Daniel, C. & Guiraud, P. 2005 Experimental study of a drop bouncing on a wall in a liquid. Phys. Fluids **17 (9),** 097105.
[3] Zenit, R. & Legendre, D. 2009 The coefficient of restitution for air bubbles colliding against solid walls in viscous liquids. Phys. Fluids **21 (8),** 083306.
[4] Liu, H. R. & Ding, H. 2015 A diffuse-interface immersed-boundary method for two-dimensional simulation of flows with moving contact lines on curved substrates. J. Comput. Phys. **294 ,** 484–502.

MICROFLUIDIC DEVICE FOR TESTING STRING-METHOD PREDICTIONS OF GAS BUBBLE NUCLEATION

Andy Ylitalo[1], Huikuan Chao[1,2], Thomas C. Fitzgibbons[2], Weijun Zhou[2], Zhen-Gang Wang[1], Julie A. Kornfield*[1]
[1] Division of Chemistry and Chemical Engineering, California Institute of Technology, Pasadena, CA, USA
[2] Dow Inc., Lake Jackson, TX, USA

Summary Gas bubble nucleation is a fundamental phenomenon both throughout the natural sciences and in the production of foams for lightweight, functional materials. Experimental challenges of measuring the kinetics of this rapid, multiscale process pose a roadblock for theoretical modelling of bubbles and foams. Using microfluidic hydrodynamic focusing developed for measurement of protein and chemical kinetics, we built a microfluidic cell to probe gas bubble nucleation of CO_2 in polyol at controlled pressure with millisecond resolution over acquisition times sufficient for optical, IR, and X-ray measurements. Our preliminary validation of a string-method model demonstrates the utility of this device to explore untested predictions of low-barrier nucleation.

CHALLENGES OF MEASURING BUBBLE NUCLEATION KINETICS

The nucleation of gas bubbles is a phenomenon significant as much for its role in the production of foamed materials as for its ubiquity throughout the natural sciences. Substantial progress has been made in the modelling and measuring of bubble nucleation along surfaces[1]; however, nucleation in the liquid bulk, by which most of a foam's cells are born, has proven to be more difficult to study.

Gas bubble nucleation occurs when a reduction in pressure (and/or an increase in temperature) instigates the supersaturation of gas in the liquid—the popping of a cork from a champagne bottle, for example. On the order of milliseconds, nucleated bubbles grow several orders of magnitude—nanometers to micrometers—so locating and capturing a bubble nucleation event is challenging. Gentle rubbing of a surface can reproducibly localize nucleation to allow for high-resolution imaging. Unlike nucleation on surfaces, nucleation events in the bulk are random in space as well as in time, precluding reliable localization of nuclei in experiments. Consequently, theoretical understanding of bulk bubble nucleation has outpaced experimental validation, leaving exciting predictions like the nucleation of a CO_2-rich liquid in PMMA and PS unexplored[2]. Moreover, this problem hinders our understanding of foaming, as Di Maio and Kiran recently found that the "current lack of [nucleation]'s full understanding presents the main actual limitation to modelling the foaming process."[3]

A Solution: Microfluidic Hydrodynamic Focusing

The development of microfluidic hydrodynamic focusing has overcome the challenge of probing fast, random kinetic phenomena, from protein folding[4] to chemical kinetics[5]. In this technique, an outer sheath stream flows around a thin inner stream, shielding the inner stream from the effects of the walls. The inner stream is thin enough that, although the microscopic dimensions ensure laminar flow, the two solutions quickly mix through diffusion and initiate a configurational or chemical change. Subsequent points along the flow thus correspond to chronological moments in the kinetic process, effectively mapping the kinetic timeline along the length of the flow. As a result, long acquisitions required for techniques like X-ray scattering are possible while still achieving millisecond resolution of the kinetics.[4]

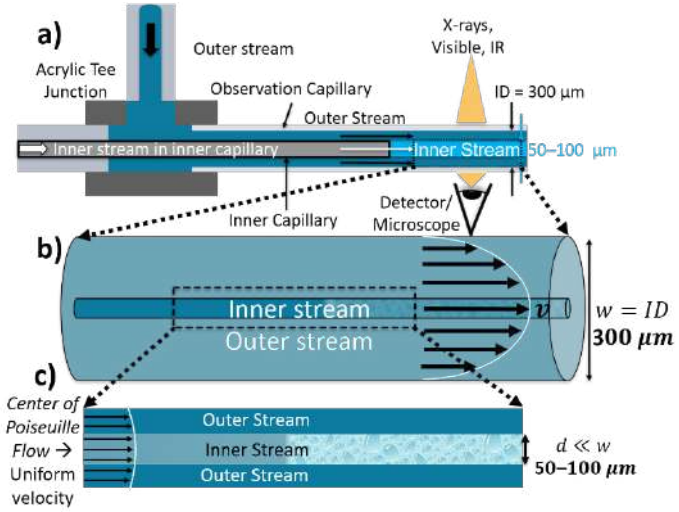

Figure 1. a) Tee-junction flow-focusing device design. The inner stream flows through a thin inner capillary into the observation capillary while the outer stream surrounds the inner capillary to produce sheath flow. The observation capillary can be probed with IR, light, and X-rays. b) Zoomed-in view of the Poiseuille flow field of sheath flow. Bubbles nucleate partway down the channel. c) Zoomed-in view of the laminar, uniform velocity field of the inner stream.

*Corresponding author. Email: jak@cheme.caltech.edu

We adapted microfluidic hydrodynamic-focusing devices[4,6] to probe bulk gas bubble nucleation under large, controlled pressure drops (see Fig. 1). We built the device to withstand over 100 bar (10 MPa), which is relevant for industrial foaming and supercritical CO_2 and allows us to explore the unique qualitative behaviour of supercritical foaming[3]. Previous high-pressure microfluidic devices have studied reaction kinetics[5], but we believe that our device is the first to be used to study bubble nucleation. Because the sheath-dominated flow will obey Poiseuille flow, the pressure will drop linearly along the length of the channel, allowing for controlled studies of supersaturation effects. With a thin enough inner stream, the velocity will also be uniform, ensuring a precise correspondence among time, pressure, and distance. By keeping the pressure well above the saturation pressure until the flow enters the observation capillary, we also prevent the effects of the walls leading up to the capillary. We have so far measured nucleation with high-speed optical microscopy, but the design can probed with X-ray scattering, thermography, and FTIR.

RESULTS

To guide our measurements of bubble nucleation, we developed a theoretical model of the nucleation barrier using the string method applied to density functional theory (DFT) with a perturbed-chain statistical associating fluid theory (PC-SAFT) equation of state for the system, as in Xu *et al*.[2] Model parameters were fit and validated with data collected using Di Maio's gravimetry-axisymmetric drop-shape analysis[7]. The model indicates several interesting parameter spaces that yield drastic reductions in the nucleation barrier for us to explore with our microfluidic device.

Experimentally, we have used our device to observe bubble formation and growth with high-speed microscopy as pressure decreases along the channel. Example high-speed micrographs along the length of the capillary are shown in Fig. 2. In these micrographs, we see an onset of bubble nucleation between 48 and 78 mm (roughly 50 and 20 bar) Additionally, we see that the number of bubbles dramatically increases after this onset corresponding with decreasing pressure, a quantity we measure with custom image-processing software. We present a comparison of bubble population with theoretical predictions of the bubble nucleation barrier and explore the possibility of low-barrier CO_2-rich liquid nucleation[2]. We will also present a comparison between measurements of bubble growth and predictions based on a modified Epstein-Plesset model, as well as a discussion of coalescence, as shown in Fig. 2.

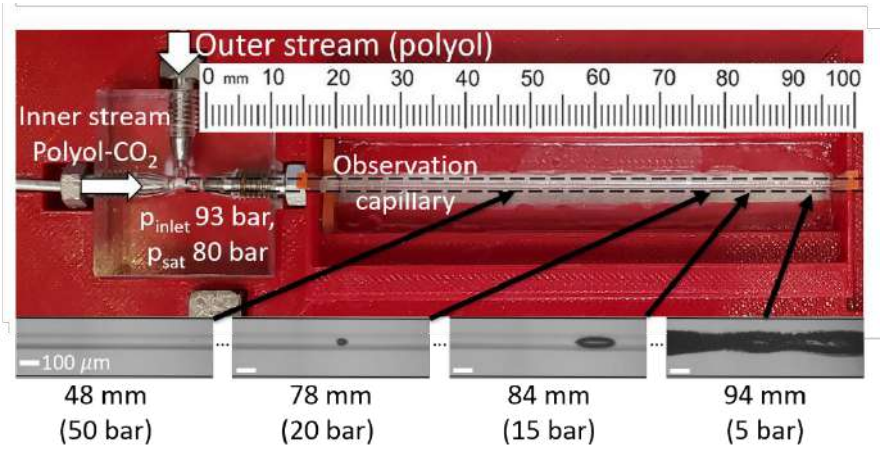

Figure 2. Top: microfluidic flow-focusing device in a 3D-printed mount with polyol-CO_2 saturated at 80 bar (8.0 MPa) entering the observation capillary (quartz) at 93 bar (9.3 MPa), ensheathed in pure polyol. The ruler above indicates the distance along the observation capillary (mm). Bottom: High-speed micrographs along the observation capillary show the inner walls of the capillary outlined in black with the inner stream in the centre. The outer stream of pure polyol separates the inner stream from the capillary walls. Bubbles nucleate, grow, and coalesce into a foam as the pressure in the capillary decreases.

We presented a novel microfluidic flow-focusing device constructed for probing bulk gas bubble nucleation of CO_2 in polyol to explore untested theoretical predictions and enhance understanding of polymer foaming. The device was based on microfluidic principles that effectively map the chronology of fast kinetic processes like bubble nucleation along the length of the channel in a stream of fluid insulated from the inner walls of the device. We adapted these principles for supercritical pressures (100 bar, 10 MPa) and suitability for optical microscopy, X-ray scattering, thermography, and FTIR. Preliminary high-speed micrographs are consistent with our theoretical predictions, holding promise for the exploration of untested theoretical predictions, such as CO_2-rich liquid nucleation predicted in the literature[2].

Acknowledgement Funding for this project was provided by the Dow Inc. UPI program and the NSF GRFP.

References

[1] S. Wildeman, H. Lhuissier, C. Sun, D. Lohse, and A. Prosperetti, Proc. Natl. Acad. Sci. U. S. A. **111**, 10089 (2014).
[2] X. Xu, D.E. Cristancho, S. Costeux, and Z.-G. Wang, Soft Matter **9**, 9675 (2013).
[3] E. Di Maio and E. Kiran, J. Supercrit. Fluids **134**, 157 (2018).
[4] L. Pollack, M.W. Tate, N.C. Darnton, J.B. Knight, S.M. Gruner, W.A. Eaton, and R.H. Austin, Biophysics (Oxf). **96**, 10115 (1999).
[5] H. Chen-Jolly, P. Guillot, and E. Mignard, Chem. Eng. J. **334**, 389 (2018).
[6] T. Hessberger, L.B. Braun, F. Henrich, C. Müller, F. Gießelmann, C. Serra, and R. Zentel, J. Mater. Chem. C **4**, 8778 (2016).
[7] M. Giovanna Pastore Carbone, E. Di Maio, S. Iannace, and G. Mensitieri, Polym. Test. **30**, 303 (2011).

DYNAMIC TRANSITION APPROACHING JETTING SINGULARITY DURING THE COLLAPSE OF DROP-IMPACT CRATERS

Zi Qiang Yang *[1], Yuan Si Tian [1], and S. T. Thoroddsen [1]
[1] Division of Physical Science and Engineering, King Abdullah University of Science and Technology (KAUST), Thuwal, Saudi Arabia

Summary Understanding the dynamical transition from capillary-driven to pure inertial focusing is important to revealing the mechanism underlying the most singular micro-jetting produced from drop-impact craters. Herein we study dimple dynamics from the collapse of these craters when the drop is of a different immiscible liquid than the pool. The parameter space is considerably more complex than for identical liquids, revealing intricate compound-dimple shapes. In contrast to the universal capillary-inertial drop pinch-off regime, where the neck radius scales as $R \sim t^{2/3}$, a purely inertial collapse of the air-dimple portrays $R \sim t^{1/2}$ and is sensitive to initial and boundary conditions. Capillary waves can therefore mold the dimple into different collapse shapes. We observe a clear cross-over in the nature of the dynamics from capillary-inertial to purely inertial immediately before the pinch-off. Notably, for singular jetting the cross-over time occurs much earlier, irrespective of the Weber number.

INTRODUCTION

Singularities occur in various branches of physics and mechanics, from the gravitational collapse of black holes to the necking pinch-off of a pendent drop dripping from a faucet. What makes singularities a particularly attractive "laboratories" is the rapid time-scale and small length-scales which expose the key force balance which governs the dynamics. In fluid mechanics the pinch-off of a fluid cylinder is the most iconic example of a singularity, which has been extensively studied over the last three decades. There is a remarkable difference between the pinch-off of a drop from a nozzle vs that of a bubble. For the drop the necking evolves in a self-similar manner, forming conical shape with capillary-inertial scaling of the necking radius, i.e. $R \sim t^{2/3}$ [1]. On the other hand, the pinch-off of a bubble follows a purely inertial dynamics, where $R \sim t^{1/2}$ [2, 3, 4]. Despite a rather modest difference in the two exponent values, the fact that the inertia is inside the neck for the drop, while it is outside of the air-cylinder for the bubble, changes profoundly the dynamical nature of the pinch-off. For the purely inertia collapse the surface tension becomes irrelevant and the dynamics show strong dependence on the initial or boundary conditions. This memory of the boundaries has been best demonstrated for a bubble pinching off from a nozzle with an elliptic cross-section [5, 6].

Herein, we focus on the jetting from the rebounding of a drop-impact-produced crater. The finest and most *singular jets* emerge when a dimple forms at the bottom of the crater and collapses without pinching of a bottom bubble. The final stage of collapse follows pure inertial scaling [7].

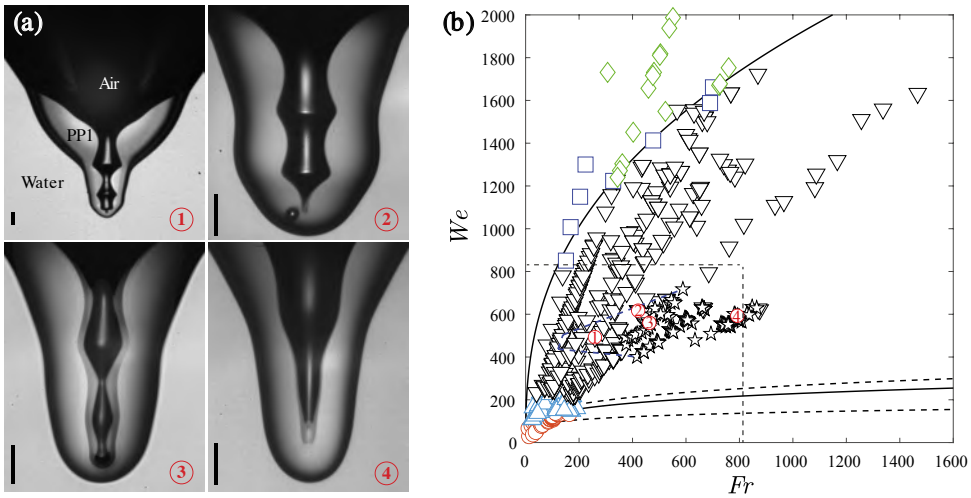

Figure 1: (a) Typical dimple shapes for different impact conditions in the multi-dimple regime corresponding to the circled red numbers in (b). Multi-pinch-offs dimple: ① D = 1.16 mm, U = 1.7 m/s, Fr = 259, We = 493; ② D = 1.02 mm, U = 2.1 m/s, Fr = 421, We = 617; ③ D = 0.93 mm, U = 2.05 m/s, Fr = 463, We = 560 and singular telescopic dimple: ④ D = 0.73 mm, U = 2.38 m/s, Fr = 792, We = 593. The scale bars are 100 μm long. (b) Characterization of the dimples and jets in *Fr-We* space for drop impacts of immiscible liquids. The two dash curves are the bounds of the regular bubble entrapment measured by [8, 9], for identical liquids. The two solid curves mark the bubble entrapment region based on our study. The symbols correspond to different dimple shapes: (○) no pinch-off shallow dimple; (△) dimple pinch-off with bubble going out with jet; (▽) tiny bubble pinched off near secondary critical pinch-off; (☆) singular telescopic dimple; (▽) pinched-off bubble entrapped in PP1 drop; (□) liquid column break-up without dimple pinch-off; (◇) water entrapped in PP1 drop without pinch-off. The dashed cyan lines mark the region of multi-dimples.

*Corresponding author. E-mail: ziqiang.yang@kaust.edu.sa

EXPERIMENTAL SETUP: We use different immiscible liquids: The pool is purified water, while the drop consists of PP1 (Perfluorohexane, C_6F_{14}). PP1 is 1.71 times heavier than water and has very low surface tension σ_d = 11.9 mN/m. The interfacial tension between the two liquids is 48 mN/m. The range of drop sizes is D = 0.6 - 2.0 mm. By changing drop release-height we get impact velocities U from 0.1 to 3.9 m/s. The corresponding range of Reynolds, Weber and Froude numbers, based on drop properties are: $Re = \rho_d DU/\mu_d = 374 - 10,200$; $We = \rho_d DU^2/\sigma_d = 10 - 2,000$; $Fr = U^2/(gD) = 10 - 1,500$; where g is gravity acceleration, ρ_d and μ_d are drop density and dynamic viscosity.

RESULTS AND DISCUSSIONS

The impact produces a hemispheric crater into the free surface of the pool, with the PP1 drop liquid forming a thin continuous layer coating it. The subsequent rebound can form a bottom dimple whose collapse produces singular jets [7, 8]. The free surface of this dimple therefore remains between air and the PP1 drop liquid. Figure 1 highlights the regime where a dimple forms during its collapse. This occurs at much larger values of We (based on drop properties), than for the classical regime (dashed lines) where the dimple entraps a bubble for identical liquids in both drop and pool [9]. Figure 1(a) shows a prominent new feature of the dimples, i.e. capillary waves travelling down towards their tips, which can lead to multiple pinch-offs. The thinnest and fastest jets emerge when no bubble in pinched off [7].

What is the role of capillary waves in setting up the dimple for the inertial focusing? For the singular jets from bursting bubbles or super-critical surface waves, the dimple dynamics have until recently been formulated in the self-similar capillary-inertial formalism [10, 11], while the final cylindrical collapse has been shown to follow pure inertial focusing [7, 12]. One can therefore expect a dynamical transition in the vicinity of the final jet formation. In Figure 2 we track the radius of pinch-off neck for a typical dimple, shown in the inset. There is a clear cross-over in the nature of the dynamics from capillary-inertial $R \sim t^{2/3}$ to purely inertial with $R \sim t^{0.55}$ [3, 7] at $t_c \simeq 65$ μs before pinch-off, as marked by the arrow. Figure 2(b) shows that the cross-over time scales with the impact time $t_c \simeq 0.235 R_d/U$ for the pinch-off cases. On the other hand, for singular jetting the cross-over time occurs much earlier, irrespective of We.

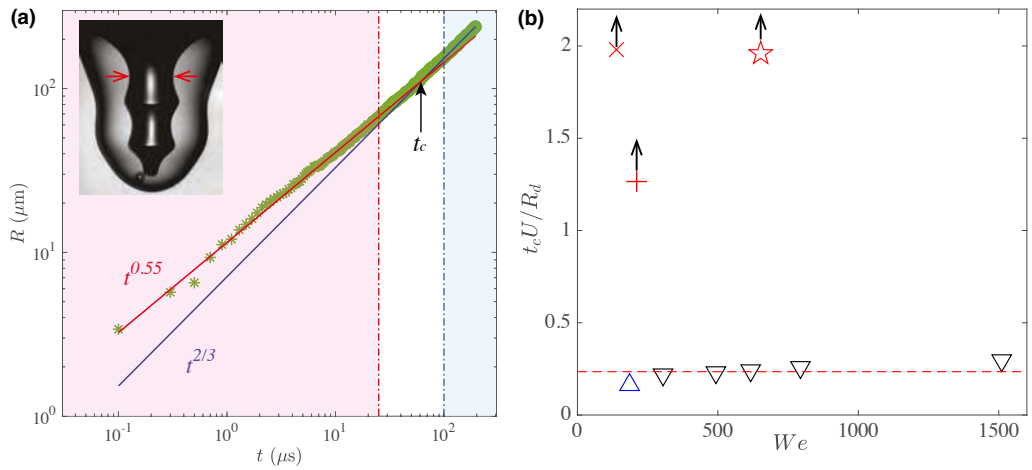

Figure 2: (a) Logarithmic scaling of the dimple radius vs time before pinch-off. There is a transition of power-law exponents from 2/3 to 0.55 closest to the pinch-off. The background shading marks the validity of each, with the arrow indicating the approximate cross-over time t_c. The data is taken from two video clips spanning time-scales from 100 ns to 200 μs before pinch-off. (b) It shows how t_c normalized by the impact time D/U changes with We, for dimple pinch-off (△ & ▽) and singular jets (×, + & ☆). The vertical arrows indicate these are lower bounds, as for these cases the dynamics remain inertial for the entire video clip.

References

[1] Day R. F., Hinch E. J. & Lister J. R., Self-similar cap-illary pinchoff of an inviscid fluid. *Phys. Rev. Lett.*, **80**, 704 (1998).
[2] Burton, J. C., Waldrep, R. & Taborek, P. *Phys. Rev. Lett.*, **94**, 184502 (2005).
[3] Eggers J., Fontelos M. A.,Leppinen D. & Snoeijer J. H. , Theory of the collapsing axisymmetric cavity. *Phys. Rev. Lett.*, **98**, 094502 (2007).
[4] Thoroddsen S. T., Etoh T. G. & Takehara K., Experiments on bubble pinch-off. *Phys. Fluids*, **19**, 042101 (2007).
[5] Schmidt L. E., Keim N. C., Zhang W. W. & Nagel S. R. Memory-encoding vibrations in a disconnecting air bubble *Nat. Phys.*, **5**, 343 (2009).
[6] Lai L., Curvature singularity in the asymmetric breakup of an underwater air bubble. *Phys. Fluids*, **24**, 102106 (2012).
[7] Thoroddsen S. T., Takehara, K., Nguyen, H. & Etoh T. G., Singular jets during the collapse of drop-impact craters. *J. Fluid Mech.*, **848**, **R3** (2018).
[8] Pumphrey H. C. & Elmore P. A., The entrainment of bubbles by drop impacts. *J. Fluid Mech.*, **220**, 539 (1990).
[9] Prosperetti, A. & Oguz, H. N. The impact of drops on liquid surfaces and the underwater noise of rain. *Annu. Rev. Fluid Mech.*, **25**, 577 (1993).
[10] Deike, L. *et al.*, Dynamics of jets produced by bursting bubble. *Phys. Rev. Fluids*, **3**, 013603 (2018).
[11] Zeff B. W. *et al.*, Singularity dynamics in curvature collapse and jet eruption on a fluid surface. *Nature*, **403**, 401 (2000).
[12] Gordillo J. M. & Rodríguez-Rodríguez J., Capillary waves control the ejection of bubble bursting jets. *J. Fluid Mech.*, **867**, 556 (2019).

PRESSURE AMPLIFICATION INDUCED BY MULTIPLE CAVITIES COLLAPSE ALONG HIGH-SPEED DROPLET IMPACT INSIDE A TUBE

Wangxia Wu[1], Qingquan Liu *[1], and Bing Wang y[2]
[1] School of Aerospace Engineering, Beijing Institute of Technology, Beijing, China
[2] School of Aerospace Engineering, Tsinghua University, Beijing, China

Summary This paper performs a numerical study of the droplet impact inside a solid tube with the initial speed of 300 m/s. The comparison of impingement is conducted between the dense droplet and the droplet embedded with different arrangement of cavity lines. The results show that the focus shock wave is generated once the droplet impacts on the bottom of the tube which may focus inside the droplet. For the cases of the droplet initial embedded with the cavities, the focus shock wave might induce the cavities collapse, and the transient highest pressure value is observably amplified. It indicates that through the properly arrangement of the cavities the transient highest pressure value can be further amplified.

INTRODUCTION

The high-speed droplet impingement problem especially the extremely high pressure during this procedure has aroused widely attentions nowadays. Once a high-speed droplet impacts on the solid structure, the confined water-hammer shock wave may generate inside the droplet [1]. Also, the shock waves may induce the evolution of cavities inside the droplet, which may induce transient local high pressure [2, 3].

During the high-speed impingement procedure, the local maximum pressure is an important parameter which is closely concerned in engineering applications, for example the generation of high pressure in a particular region can be applied to increase the success of generating inertial confinement fusion [1]. Some researchers pointed out that stronger shock wave may generate when the shape of the target surface conforms with the droplets interface [4]. Besides, previous investigations of the planar shock wave inducing cavities collapse in an open liquid area found that through a reasonable distribution of some cavities can further amplification the maximum pressure value during the cavity collapse [5].

In the present work, a high-speed droplet impact in the tube shape solid which conforms well with the droplets interface is considered. The evolution properties of the water-hammer shock wave is numerical studied by the case of the dense droplet impingement. Moreover, several cases of the droplets embedded with different distributions of cavities are numerically simulated in detail to understand the pressure amplified mechanism during cavity collapse.

PHYSICAL CONFIGURATION & NUMERICAL METHOD

In this work, the droplet with the initial speed of V_0 (= 300 m/s) and the initial diameter of D_0 (= 5 mm) is considered. And the impacted subject is a solid tube with the bottom shape that conforms well with the droplets interface, as shown in figure 1. For the cases that some air cavities are initially embedded, the diameter of all the cavities are 0.04 D_0. The cavities arrange in line and the distance between the center of each of two cavities are all 0.1 D_0. Several configurations are considered in the present work, including the case (I) for dense droplet, and the case (II), (III) and (IV) being corresponded to the droplet embedded with one, two and three cavity lines, as shown in figure 1. In this study, the simulations for all cases begins with the instant that the droplet just interacts with the tube.

The multi-components Eulerian compressible two-phase fluid model is applied to simulated the present problem. The numerical fluxes are obtained by employing a Godunov-Type HLLC approximate Riemann solver coupled with the 5^{th} order WENO scheme. The immersed boundary method is utilized for the solid tube surface, and the top boundary condition is non-reflected boundary condition. The detailed introduce of the numerical setup can be referred to our previous works [2, 3].

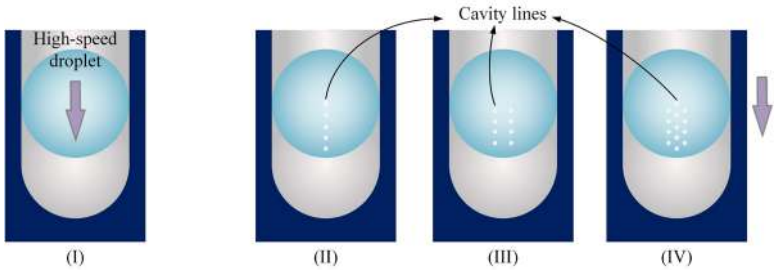

Figure 1: The schematic diagrams of different configurations of high-speed droplet impact inside a tube.

*Corresponding author. E-mail: liuqq@bit.edu.cn.
†Corresponding author. E-mail: wbing@tsinghua.edu.cn.

RESULTS & DISCUSSIONS

Firstly, in order to understand the properties of the confined water-hammer shock wave during the impinging procedure, the dense droplet impingement problem is investigated, the corresponding numerical result is given in figure 2(a-1) $\sim$ figure 2(f-1). As shown in figure 2(b-1), once the droplet impacts on the bottom of the tube which just conforms well to the droplet itself, a concave shape shock wave is generated, which shows a trend of focus propagation. Therefore, this focus propagation water-hammer shock wave is called as focus shock wave in this work. Since the initial curvature of the shock front is the same as the droplets interface, the shock wave focus at the instant when it propagates to the center point of the droplet, and the highest pressure value is generated, as show in figure 2(e-1).

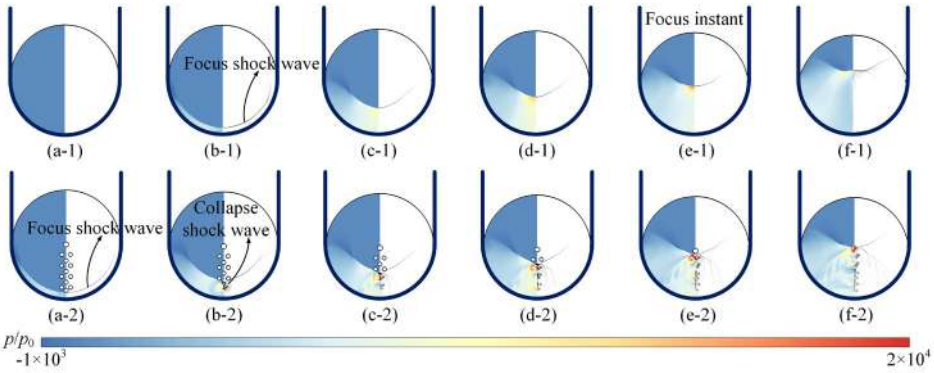

Figure 2: Evolution procedures of different configurations of droplet impingement inside a tube.

As shown in figure 2(a-2) $\sim$ figure 2(f-2), for the cases of the droplet initial embedded with some cavities inside, the focus shock wave might induce the cavities collapse. The collapse shock waves are generated during the cavities collapse process, which induce local high pressure. And the transient highest pressure value is observably larger than the highest pressure value in the dense case.

Figure 3 shows the maximum pressure distributions of different cases during the high-speed impingement. It shows that the maximum pressure values are amplified by multiple cavities collapse. The figure 2(b-2) to figure 2(f-2) are corresponded to several pick pressure value instants in figure 3, respectively. These pick pressure values are all induced by the collapse shock waves interaction, which are generated from the collapse of the cavities of left and right line. Therefore, through the properly arrangement of the cavities, the transient highest pressure value can be further amplified. In the present case, the highest transient pressure value can reach about 11 GPa.

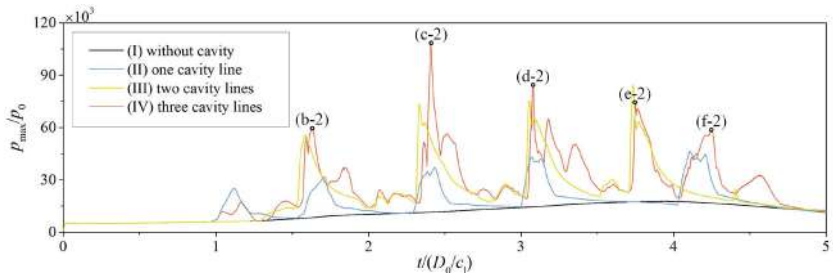

Figure 3: The maximum pressure distributions of different cases during the high-speed impingement.

CONCLUSIONS

The high-speed droplet impact inside a solid tube is then numerically investigated. Once the impaction happens, the focus propagation shock wave is generated since the bottom of the tube conforms well with the droplets interface. When the case initial embedded with the cavities, the highest pressure value induced from cavity collapse is observably amplified. Moreover, the properly arrangement of the cavities can further amplify the transient highest pressure value during the cavities collapse.

References

[1] Ventikos Y., Hawker N. High velocity droplet impacts. *U.S. Patent.* 9,704,603, 2017.
[2] Wu W., Xiang G., Wang B. On high-speed impingement of cylindrical droplets upon solid wall considering cavitation effects. *J. Fluid Mech.* **857**: 851-877, 2018.
[3] Wu W., Wang B., Xiang G. Impingement of high-speed cylindrical droplets embedded with an air/vapour cavity on a rigid wall: numerical analysis. *J. Fluid Mech.* **864**: 1058-1087, 2019.
[4] Burson-Thomas C. B., Wellman R., Harvey T. J., Wood R. J. K. Importance of Surface Curvature in Modeling Droplet Impingement on Fan Blades. *J. Eng. Gas Turbines Power.* **141(3)**: 031005, 2019.
[5] Betney M. R., Tully B., Hawker N. A., Ventikos Y. Computational modelling of the interaction of shock waves with multiple gas-filled bubbles in a liquid. *Phys. Fluids.* **27(3)**: 036101, 2015.

NUMERICAL STUDY ON THE INTERFACE-DYNAMICS OF AN ANNULAR BUOYANT JET: EFFECT OF INJECTION VELOCITY

Kuntal Patel *[1]
[1] Department of Mechanical Engineering, Indian Institute of Technology Bombay, Mumbai, India

Summary Two-dimensional axisymmetric numerical experiments have been carried out to investigate the dynamics of an annular buoyant jet, made-up of 70% paraffin oil and 30% heptane, rising in stagnant water. A ghost-fluid method based sharp-interface level-set method [1] is used in present numerical simulations to accurately capture the lower-dimensional fluid-fluid interface. Three distinct states of the oil-water system are observed: (1) translation of planar oil-water interface in the axial direction (2) oscillating water-column assisted flotation of a water droplet and (3) formation and breakup of compound droplets; corresponding to the average injection velocity of 0.05, 0.15 and 0.25 m/s, respectively.

INTRODUCTION

Fluid flows involving a single jet or multiple jets exhibit very rich interface dynamics and have practical relevance to many real-time applications. There are several types of fluid flow configurations that involve jet. For example, injection of lighter fluid into a heavier fluid against the gravity [2], simultaneous injection of two different immiscible liquids in a co-flowing fluid [3, 4], etc. In the present work, the configuration corresponding to an annular buoyant jet is considered and the influence of the injection velocity V_i on the interface dynamics is studied numerically.

PROBLEM SET-UP AND CODE VERIFICATION

Computational domain for the present problem along with the boundary conditions is shown in Figure 1(a). In order to simulate this problem, the ghost-fluid method based sharp-interface level set method (SI-LSM) is employed. Details on the implementation of present SI-LSM based multi-phase flow solver can be found in [1]. Grid sensitivity study is done for the case of the annular jet with V_i=0.05 m/s. Based on the results of the grid sensitivity test a grid size of 50 x 800 is adopted for the present simulations. Validation of present numerical methodology is carried out using the problem of jet break-up from Lakdawala et al. [2]. The temporal variation of a jet length obtained from the present simulation is then compared with that reported in [2]. A good agreement is obtained for the same (shown in Figure 1(b)).

RESULTS AND DISCUSSION

Results obtained from the computer simulations reveal that the present two-fluid system exhibit three different types of behavior upon injecting an annular jet. The behavior of the system depends on the average injection velocity (V_i) of an annular jet. Different types of system behavior includes (1) translation of planar oil-water interface in the axial direction (for V_i=0.05 m/s, see Figure 2(a)) (2) oscillating water-column assisted flotation of a water droplet (for V_i=0.15 m/s, see Figure 2(b)) and (3) formation and breakup of compound droplets (for V_i=0.25 m/s, see Figure 2(c)). For the injection velocity of 0.05 m/s, annular jet merges at the center and later oil-water interface becomes planar. Which then translates in the positive axial direction. Eventually, water gets replaced by the oil in the entire domain except at the bottom of the domain. On increasing the value of V_i, interface dynamics shifts from more ordered (for V_i=0.05 m/s) to the chaotic (for V_i=0.15 m/s) one. Chaotic behavior for V_i=0.25 m/s involves the frequent generation and collapse of the compound droplets of varying sizes. The case with the intermediate injection velocity of V_i=0.15 m/s shows transitional behavior — connecting ordered and chaotic state. In this case too, later on, the oil-water interface becomes planar. However, there exists an entrained water droplet at the center and a water film near the bottom of the domain (Figure 2(b)). The water droplet at the center and the film accumulated at the bottom try to settle down. However, the inflow of the oil resists water film from doing so by pushing it in the positive axial direction and this leads to the oscillations of water film (see Figure 3). Moreover, these oscillations of the water film push the water droplet in the positive axial direction and keep it floating. Sequences of the oscillation of the water film and the floating droplet along with the axial velocity distribution are depicted in Figure 3. Further investigation on the influence of the fluid-properties and wall roughness on the interface dynamics is currently under progress.

ACKNOWLEDGEMENT

The author would like to thank Dr. Absar Lakdawala for introducing him to the topic of jet dynamics. Numerical solver used in the present work is the outcome of CFD code development by Prof. Atul Sharma and co-members at CFD Lab (F29) - IIT Bombay. Computational facility provided by CFD Lab (F29) is gratefully acknowledged.

*Corresponding author. E-mail: kuntalhpatel757@gmail.com. Present Institution: Institut für Theoretische Physik, TU Berlin, Germany.

References

[1] Shaikh J., Bhardwaj R., Sharma A. On comparison of the sharp-interface and diffuse-interface level set methods for 2D capillary or/and gravity induced flows. *Chem. Eng. Sci.* **176**: 77-95, 2018.

[2] Lakdawala A., Gada V. H., Sharma A. A dual grid level set method based study of interface-dynamics for a liquid jet injected upwards into another liquid. *Int. J. of Multiphase Flow* **59**: 206-220, 2014.

[3] Truong V. Vu, Homma S., Tryggvason G., Wells J. C., Takakura H. Computations of breakup modes in laminar compound liquid jets in a coflowing fluid. *Int. J. of Multiphase Flow* **49**: 58-69, 2013.

[4] Odier N., Balarac G.,Corre C. Numerical analysis of the flapping mechanism for a two-phase coaxial jet. *Int. J. of Multiphase Flow* **106**: 164-178, 2018.

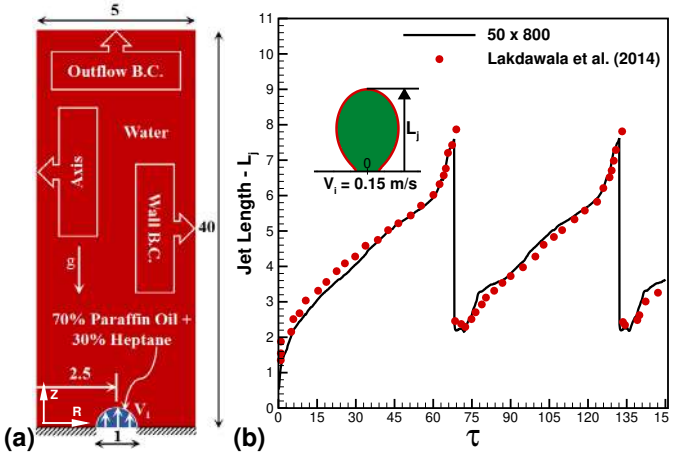

Figure 1: (a) Computational setup for the present problem on the annular buoyant jet (b) Validation of present sharp-interface level-set method based two-phase flow solver with the numerical results of Lakdawala et al. [2] for the problem on jet breakup with a two-fluid system similar to that studied in present work.

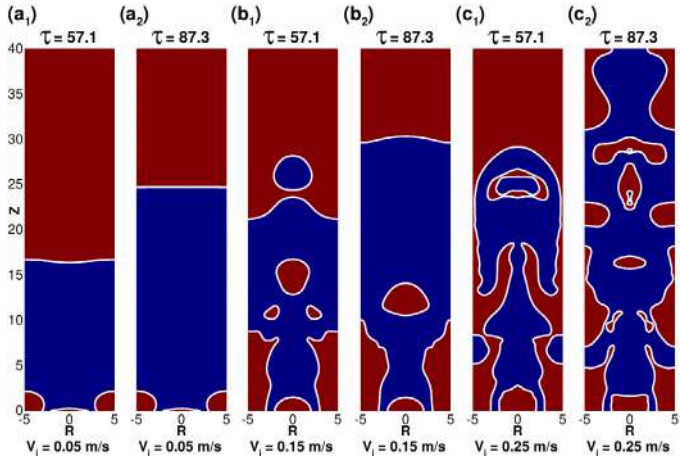

Figure 2: Influence of the average jet injection velocity on the evolution of the fluid-fluid interface.

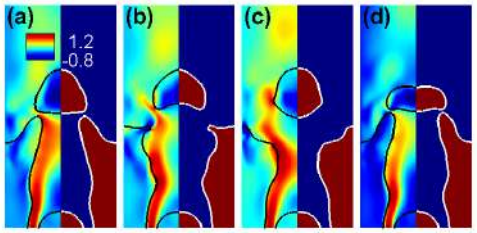

Figure 3: Time-wise variation of the axial velocity (left) and the interface separating two phases (right) for the average jet injection velocity of 0.15 m/s — indicating the phenomenon of a floating droplet.

SURFACE TENSION-DRIVEN FORMATION OF MINERAL CAPSULE USING WATER-IN-OIL EMULSION

Kwangseok Park[1] and Hyoungsoo Kim*[1]
[1] Department of Mechanical Engineering, KAIST, Daejeon, South Korea

Summary We demonstrated a facile fabrication of a mineral capsule made through solvent diffusion from a salt-saturated water-in-oil emulsion. If the initial emulsion is smaller than a capillary length, the surface tension is predominant. In this case, we observe that two-dimensional crystallites of the monoclinic salt enclose the emulsion interface, and a spherical shell is made. We investigate the capsule using scanning electron microscopy to see the shape and to measure the size. We suggest a theoretical model to estimate the shell thickness based on an assumption of a thin-walled spherical vessel where the capillarity is dominant. In this talk, from the comparison between the elasto-capillary length and the crystal size, we explain how the self-assembled spherical shell spontaneously forms.

To control the release of the core material or to set apart from the external material, microencapsulation is needed. These days, not only microscale but also nanoscale capsules can be formed through microencapsulation. Polymers have been usually selected as a capsule material due to their biocompatibility and biodegradability.[1] However, the existing microencapsulation methods using polymeric shell (e.g. nanoprecipitation, polymer coating, emulsion coacervation, and layer-by-layer method) have inevitable complexity in the process since they include multiple steps in the fabrication.[2] The process may require either mechanical or ultrasonic agitation to decrease the capsule size.[3] In this sense, for the main process, polymerization must need adjustment of systematic properties such as temperature, pressure, and pH.[4]

To avoid the abovementioned complexity, here, we introduce a novel method that the capsules are fabricated by minerals encapsulating a hydrophilic core through solvent diffusion of a water-in-oil (W/O) emulsion. Here, we use calcium propionate (CaPr) and silicone oil for the capsule material and the oil phase of the emulsion, respectively. The selected mineral CaPr has a monoclinic crystal structure exhibiting plate-like crystallites, and the crystal will grow at the liquid-liquid interface where it will reach to the critical condition for the crystallization due to the diffusion. To test this idea for the experiments, we prepare a CaPr-saturated aqueous solution in the oil, and the emulsion is kept at room temperature and atmosphere. The encapsulation process is sketched in Fig. 1(a) and the obtained capsule shape is taken by SEM as shown in Fig. 1(b).

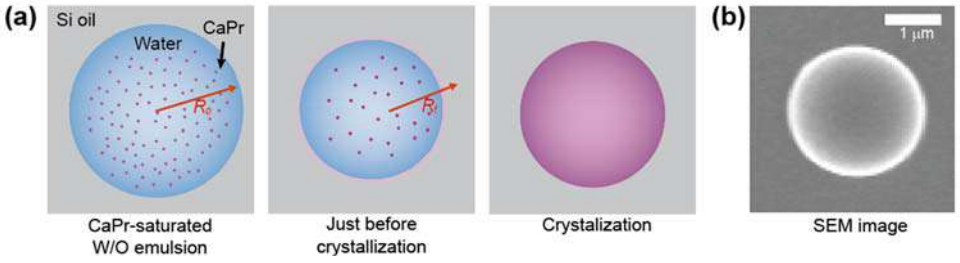

Figure 1. Illustration of fabrication of the process of the CaPr spherical shells via solvent diffusion. (a) Schematics of a W/O emulsion for initial state and after crystallization. (b) SEM image of the CaPr capsule.

We observe that the crystal grew in a different way depending on the initial emulsion size. When the initial size is sufficiently small, capillarity driven by Laplace pressure could help the crystallized CaPr bent and the crystal covers the liquid-liquid interface. If the emulsion size is too large, the crystal will grow out of the emulsion interface. In case of the dominant capillary effect, the bent crystallites can enclose the whole emulsion interface, thereby forming the spherical mineral shell of CaPr (see Fig. 1(b)).

We observe that the crystallized CaPr capsules using scanning electron microscopy. The capsules have a relatively smooth surface and the measured size of the capsules is in the range of O(100 nm) to O(1-10 μm). We expose an electron beam with an acceleration voltage up to 10 kV for a few minutes (1-3 minutes) to check whether the capsule is a rigid sphere or a spherical shell. When the capsules are enough irradiated by the electron beam, the plastic deformation occurs as shown in Fig.2. Presumably, such remarkable deformation may not occur with a rigid sphere, and it can be inferred that the spherical CaPr capsules produced by the current method are shells.

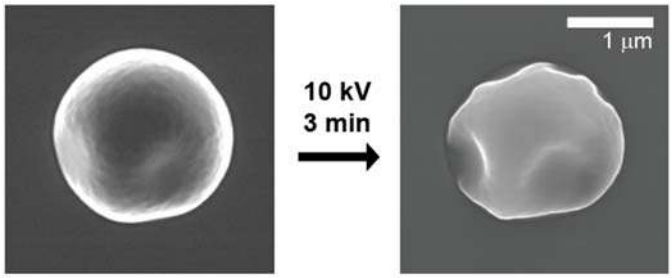

Figure 2. Exposure of 10 kV, 10 μA electron beam to the CaPr capsule with the diameter of 2.55 μm.

To understand the mechanism how the salt capsule made, we develop a theoretical model considering the mineral shell as a thin-walled vessel where the Laplace pressure acts as the internal pressure, and then based on the model, we estimate the shell thickness. In the model, we assume that the Laplace pressure is balanced with the shell stress. With the stress-strain relation and the size change of the emulsion, we calculate the shell thickness and elasto-capillary length. For the case where the W/O emulsion size decreased from the initial 10 μm to 1 μm, the shell thickness and elasto-capillary length are estimated 52 nm and 927 nm, respectively. Since the characteristic length of the emulsion is larger than the elasto-capillary length, the crystal near the emulsion interface can grow larger than the elasto-capillary length, which means the gained energy at the surface is larger than the stored bending energy. Therefore, it can be expected that the bending of the CaPr crystallites is highly spontaneous, and the size of bending element, which can be a single crystallite or several crystallites, is approximately $O(100\ \text{nm})$.

References

[1] Qian K. *et al.*, Biodegradable double nanocapsule as a novel multifunctional carrier for drug delivery and cell imaging, *Int. J. Nanomed.* **10**: 4149, 2015.
[2] Mora-Huertas C.E. *et al.*, Polymer-based nanocapsules for drug delivery, *Int. J. Pharm.* **385**: 113-142, 2010.
[3] Shakeri-Zadeh A. *et al.*, Synergistic effects of magnetic drug targeting using a newly developed nanocapsule and tumor irradiation by ultrasound on CT26 tumors in BALB/c mice. *J. Mater. Chem. B* **3**: 1879-1887, 2015.
[4] Brum A.A.S. *et al.*, Lutein-loaded lipid-core nanocapsules: Physicochemical characterization and stability evaluation. *Colloids Surf. A* **522**: 477-484, 2017.

THE THERMOCAPILLARY EFFECT AT GAS BUBBLES GROWING DURING ELECTROLYSIS

S. Sahil Hossain[1], Gerd Mutschke *[1], Aleksandr Bashkatov[1], and Kerstin Eckert[1,2]
[1] Institute of Fluid Dynamics, Helmholtz-Zentrum Dresden-Rossendorf, Bautzner Landstrasse 400, Dresden, 01328 Germany
[2] Institute of Process Engineering and Environmental Technology, Technische Universit at Dresden, Dresden, 01062 Germany

Summary Capillary flow at electrogenerated gas bubbles growing on microelectrodes was unveiled only recently [1]. The primary origin was later attributed to thermocapillarity caused by the inhomogeneous distribution of the electric current density near the bubble foot which results in temperature gradients along the bubble interface [2]. The present paper carries out a systematic numerical investigation of the thermocapillary effect at various operating conditions of the electrolysis, thereby especially considering electrodes of different sizes. A detailed understanding of the thermocapillary flow pattern at microelectrodes is provided. Two vortices are generated, the size and location of which changes when the size of the electrode is increased from small to large with respect to the bubble size. The resulting force on the bubble simultaneously changes from retarding towards supporting the bubble departure. Estimations of the contribution of the Marangoni force to the static force balance at different operating conditions including industrially relevant current densities are given.

Green hydrogen produced by electrolysis powered by regenerative energy sources appears attractive for energy storage and for producing green fuels. A deeper understanding of the dynamics of the growing gas bubbles may allow for improving the efficiency of industrial electrolysis processes.

The existence of thermocapillary flow at the interface of gas bubbles generated by water electrolysis was proven only recently [1, 2]. The resulting force on the bubble is known to affect the bubble dynamics and to retard the departure of the gas bubbles. More recent research in our group includes the effect of an electrostatic force on the static force balance of the bubble and is able to explain oscillatory bubble phenomena [3].

In this study we perform a detailed quantitative characterization of the thermofluidic behaviour of the aqueous electrolyte in the vicinity of the gas bubble. Besides investigating different operating conditions, we systematically extend the analysis of the thermocapillary effect on the bubble from microelectrodes to larger and eventually planar macroelectrodes [4]. In the simulations performed, a coupled system of equations for electric potential, fluid flow and heat transfer is solved using the finite element software COMSOL Multiphysics. The surface tension of the bubble interface is taken to be linearly dependent on temperature.

As sketched in Fig. 1, varying the size of the electrode from small to large with respect to the bubble size leads to a dislocation of the temperature hotspot which is caused by inhomogeneous Ohmic heating. This results in a modification of the size and the position of the two vortices driven by the thermocapillary stress at the bubble interface. Simultaneously, the direction of the Marangoni force on the bubble is found to change from downward to upward. More details will be presented in the talk. Furthermore, the influence of the current density on the thermocapillary effect will be elucidated, and quantitative estimations of the Marangoni force on the bubble with respect to buoyancy will be given [4].

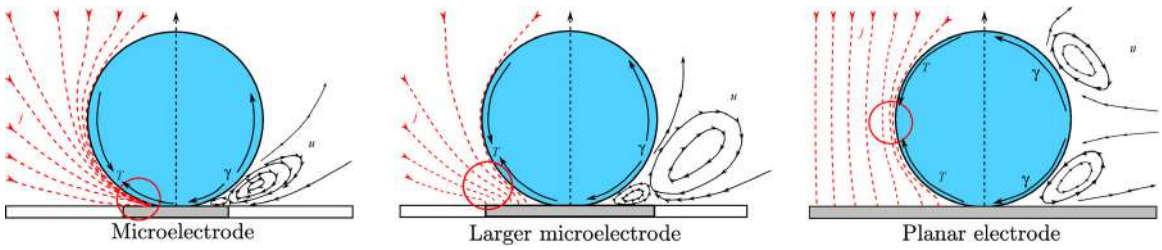

Figure 1: Sketch comparing the current distribution, the position of the temperature maxima and the thermocapillary flow as the electrode size is varied.

References

[1] X. Yang et al. Marangoni convection at electrogenerated hydrogen bubbles. *Phys. Chem. Chem. Phys.* **20** (2018) 11542 - 11548.
[2] J. Massing et al. Thermocapillary convection during hydrogen evolution at microelectrodes. *Electrochim. Acta* **297** (2019), 929 - 940.
[3] A. Bashkatov et al., Oscillating hydrogen bubbles at Pt microelectrodes. *Phys. Rev. Lett.* **123** (2019) 214503.
[4] S. Hossain et al., The thermocapillary effect on gas bubbles growing on electrodes of different sizes. *Electrochim. Acta* **353** (2020), 136461.

*Corresponding author. E-mail: g.mutschke@hzdr.de

BUBBLE DIAMETER DISTRIBUTION IN VERTICAL LIQUID CROSS FLOWS

L.A.O. Guerra[1], J.B.R. Loureiro *[1], and A.P. Silva Freire[1]
[1] Interdisciplinary Center for Fluid Dynamics (NIDF), Universidade Federal do Rio de Janeiro, Rio de Janeiro, Brazil

Summary The flow dynamics of gas injected into a liquid cross flow in a vertical pipe is discussed for three distinct injection angles (-45^o, 0^o, 45^o), two orifice diameters (2 and 5 mm), with air and water flow rates varying respectively in the intervals 7.8 to 25.8 lmin^{-1} and 2 to 5 m^{3}h^{-1}. Global and local measurements provide data on the bubble diameter distribution, shapes of bubble, air jet deflection angle, liquid mean velocity profiles and pressure distributions.

INTRODUCTION

To make sure that producing oil wells are capable of mounting enough energy to sustain the desired production during the prospect of their entire economic life, gas and water are normally injected into depleting reservoirs for pressure increase. Additionally, complementary techniques are used to ensure that further necessary energy is transferred downhole. Gas-lift systems resort to the injection of high-pressure gas into the flow column to decrease the hydrostatic weight, hence providing adequate pressure loads for the desired flow rates.

In view of their simplicity, reliability and flexibility, gas-lift systems are extensively used in industry. Their design selection, however, is not straightforward. Several considerations including economical, technological, geographical and environmental aspects must be considered for the best possible choice. Despite the great advantages of these systems – handling of large volumes of solid particles; wide operational range; easy servicing – one severe problem is the small tubing diameters and pumping systems that they are allowed to use, and, consequently, the resulting small flow rates that they deliver.

Optimization of the gas injector is thus a crucial aspect of any successful air-lift system. Optimum designs depend on both (i) the geometric design of the injector (radial, axial, dual, swirl, distributed) and (ii) the injection method (continuous, periodic, pulsatile) (Ahmed W. H. et al. (2016)).

The purpose of the present work is to study the effects of the injection angle on the effectiveness of gas-lift systems. Two different injectors with internal diameters of 2 and 5 mm are tested for three injection angles (-45^o, 0^o, 45^o) and air and water flow rates between respectively 7.8 to 25.8 lmin^{-1} and 2 to 5 m^{3}h^{-1}. Particle Image Velocimetry and Shadow Sizing are used to provide data on flow patterns, including bubble equivalent diameter and velocity distributions and water velocity profiles. Data on pressure losses (hydrostatic, friction, turbulent agitation, acceleration) are also presented.

The work concludes that orthogonal injection (0^o) provides the most beneficial effects.

EXPERIMENT

The test loop consists of a plexiglas vertical pipe (44 mm in diameter and 10 m in length) with air and water charge and discharge systems. Four pneumatic, quick closing, hold up valves are used to determine the hydrostatic pressures. The local measurements resorted to Shadow Sizing (SS) and Particle Image Velocimetry (PIV). A transparent box filled with water was used to eliminate optical distortions. The experimental flow conditions are shown in Table 1.

Orifice Diameter (mm)	Injection Angles (^{o})	Q_g (lmin^{-1})	Q_l (m^{3}h^{-1})
2	-45, 0, 45	7.8, 9.5, 17.4, 26.8, 35.8	2, 3, 4, 5
5	-45, 0, 45	9.5, 35.8	3, 4, 5

Table 1: Experimental flow conditions.

The general flow patterns for the three injection angles are shown in Figs. 1 and 2. The figures suggest (and the measurements confirm) that for *low* gas flow rates the co-current injection angles results in the *highest* frequency of small diameter bubbles. For *high* gas flow rates, the situation is the opposite, the orthogonal and counter-current injection results is distributions with a *higher* number of smaller bubbles. In particular, the orthogonal configuration resulted in distributions with the *highest* number of small bubbles.

Typical bubble diameter distributions are shown in Fig. 3. Mean velocity profiles are shown in Fig. 4. Data on the shape distribution of bubbles, the deflection angle of the gas jet, and pressure distributions were also obtained.

The pressure gradient in a vertical pipe as a result of gas injection in a liquid flow can be split into four contributions due to gravity, wall friction, turbulent agitation and fluid acceleration (Guet and Ooms (2006)). The holdup valves allowed the contribution of the gravity term to the pressure drop be separated from the other three terms. This distinction is important because, although all terms are affected by the direction of gas injection, the gravitational term is always

*Corresponding author. E-mail: jbrloureiro@mecanica.coppe.ufrj.br.

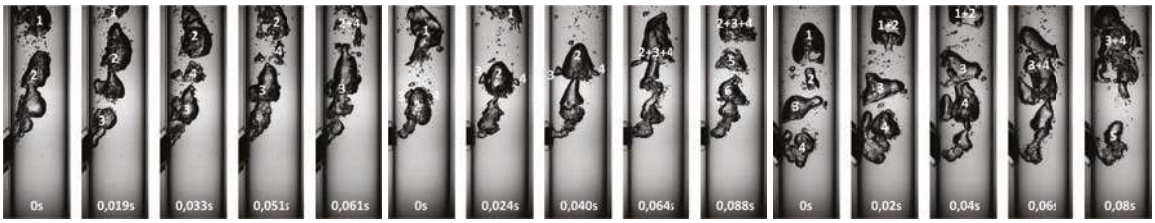

Figure 1: Flow pattern for co-current flow (frames 1-5), orthogonal flow (frames 6-10) and counter-current flow (frames 11-15). Q_l = 2 m^3h^{-1}, Q_g = 9.5 $lmin^{-1}$; d = 2 mm.

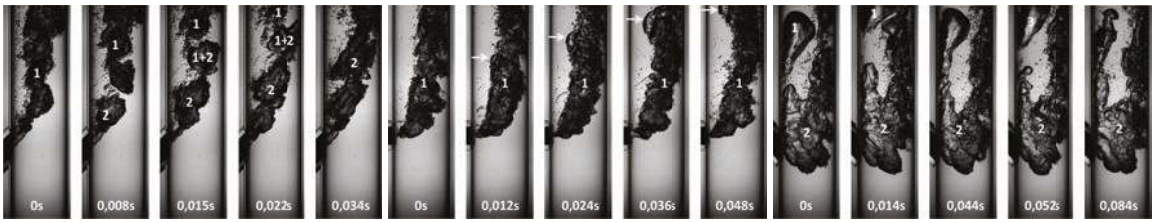

Figure 2: Flow pattern for co-current flow (frames 1-5), orthogonal flow (frames 6-10) and counter-current flow (frames 11-15). Q_l = 5 m^3h^{-1}, Q_g = 35.8 $lmin^{-1}$; d = 2 mm.

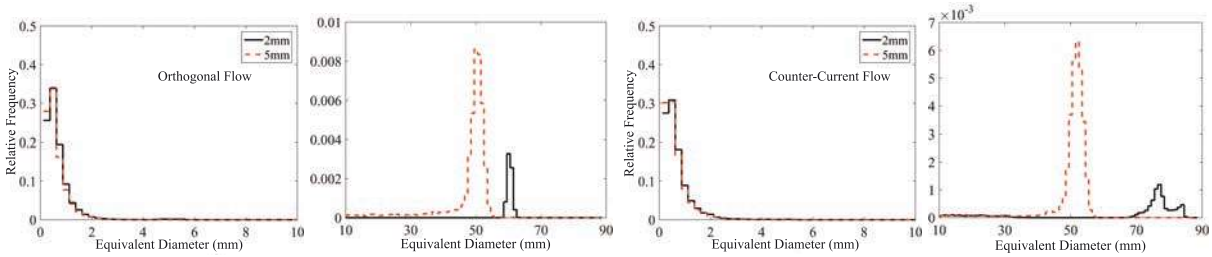

Figure 3: Typical bubble diameter distributions. Orthogonal (two figures on the left) and counter-current (two figures on the right) flows with d = 2, 5 mm and Q_l = 5 m^3h^{-1}, Q_g = 35.8 $lmin^{-1}$.

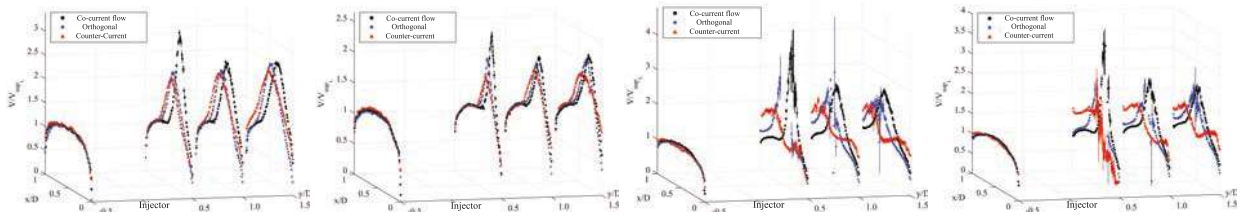

Figure 4: Water mean velocity profiles. (a) Q_l = 2 m^3h^{-1}, Q_g = 7.8 $lmin^{-1}$; (b) Q_l = 3 m^3h^{-1}, Q_g = 7.8 $lmin^{-1}$; (c) Q_l = 4 m^3h^{-1}, Q_g = 26.8 $lmin^{-1}$; (d) Q_l = 5 m^3h^{-1}, Q_g = 26.8 $lmin^{-1}$.

reduced with the increase in gas injection. On the other hand, all other three terms increase with the increase in gas flow rate. This could raise doubts as whether particular gas injection rates would result in combined losses provoked by the last three terms that may *locally* balance the beneficial effect obtained with a reduction of the gravitational term. One observed evident result is that as Q_g increases for a given Q_l the value of ΔP_g decreases (gravitational pressure). One second observed evident result is that as α increases from the negative angle (-45^o) to the positive angle (45^o), the pressure difference increases. This trend is particularly notable for the high injection rates, over 2 m^3h^{-1}. For the low injection rates (below 1.3 m^3h^{-1}), a reduction in ΔP_g is also noticed but much less pronounced. The combined effects of all pressure drop terms was also assessed. The data shows that the beneficial (gravity) and detrimental effects (friction, turbulent agitation and acceleration) tend to cancel each other out yielding equivalent results. In fact, for the highest gas injection rate, it is clear that the upstream injection furnishes the highest pressure losses. However, the differences are small. Over the whole range of tested conditions, the injection in all three directions furnished almost the same total pressure drop.

References

[1] Ahmed W. H., Aman A. M., Badr H. M., and Al-Qutub, A M. Air injection methods: The key to a better performance of airlift pumps. *Exp. Thermal Fluid Sci.* **70**:354365, 2016.

[2] Guet S., Ooms, G. Fluid mechanical aspects of the gas-lift technique. *Annu. Rev. Fluid Mech.* **38**:225249, 2006.

HIGHLY VISCOUS LIQUID MICROJET FOR ON-DEMAND AUTOMOBILE PAINTING

Kyota Kamamoto[1], Hajime Onuki[1], and Yoshiyuki Tagawa*[1]
[1] Department of Mechanical systems Engineering, Tokyo University of Agriculture and Technology, Tokyo, Japan

Summary The highly viscous liquid jet generator has been developed since the ejection of highly viscous liquid is required. This study introduces a novel device for practical use and the jet velocity of the novel device is investigated. The result shows that the experimental data agrees with the pressure-impulse model when the length ratio is small while it deviates from the model when the length ratio is large. In this research, a new jet-velocity model considering pressure-impulse and mass conservation is proposed. This new model agrees with all experimental data. Furthermore, the data of increment ratio of jet velocity β shows a good agreement with the previous research.

INTRODCUTION

Spray coating is an important process in automobile painting among others. However, it is inefficient and harmful because the spray method needs the use of organic solvent to reduce the paint viscosity [1][2]. One of the solutions to these problems is to eject highly viscous liquid as a microjet. Onuki *et al.,* developed a viscous microjet generator induced by impulsive force [3]. The jet velocity of this device can be computed with pressure-impulse model. It is expected that the painting process will become automated and work environment will be improved.

However, this highly viscous liquid jet generator [3] has problems such as the contact of jet with the inner wall of the injection pipe since there is a nontrivial distance between the meniscus and the nozzle exit (Figure 1 (a)). In this study, a novel device is proposed for practical use (Figure 1 (b)). There is no contact between the jet and the inner wall because the injection pipe of the novel device is short. The jet velocity of the novel device is investigated. The purpose of this study is to clarify the jet behavior of the novel device experimentally. Experiments are conducted with the novel device and the relationship between the length ratio and the velocity ratio is investigated. Finally, the validity of the model is reported.

EXPERIMENTAL SETUP

The experimental setup is shown in Figure 1 (b). The glass syringe filled with silicone oil (viscosity ν = 1, 10, 100 mm^2/s) is dropped freely and collides with a metal plate to generate a jet. The jet velocity V_{jet} and the falling velocity of the syringe U_0 is calculated from the displacement of the jet tip and syringe tip, respectively. A high-speed camera (FASTCAM SA-X) and a light source (LLUB White Led Backlight) are used for shooting. The frame rate is 30,000 fps. The experiments are conducted in the range of 0.23 m/s $<U_0<$1.27 m/s and $3 < l_{top} / l_{bottom}<145$, where l_{top} is the height of the liquid in the barrel, and l_{bottom} is the height of liquid in the nozzle.

RESULTS AND MODEL

The jet velocity is computed by using pressure-impulse approach [3][4]. The velocity ratio V_{jet} / U_0 was previously expressed as

$$\frac{V_{jet}}{U_0} = \beta \frac{l_{top}}{l_{bottom}} \tag{1}$$

where β is the increment ratio of jet velocity, l_{top} / l_{bottom} is the length ratio, and U_0 is the initial velocity. Figure 2 shows the relationship between the length ratio and the velocity ratio. The vertical axis shows the velocity ratio V_{jet} / U_0, and the horizontal axis shows the length ratio l_{top} / l_{bottom}.The experimental data agrees well with equation (1) when the length ratio is small ($l_{top} / l_{bottom} <10$) while it deviates from the model when the length ratio is large ($10 < l_{top} / l_{bottom}$). To consider the reason for the deviation, numerical simulation of the novel device is conducted. The boundary conditions applied are velocity U = 1.0 m/s at the base of the barrel (Figure 3 (a), green line) and the pressure p = 0 at the gas-liquid interface and the top of the barrel (Figure 3 (a), yellow line). The flow field is calculated in no inflow and outflow by using the potential flow. Figure 3(a) shows the potential flow field of the novel device immediately after the impact. According to Figure 3 (a), the position of the stagnation point is higher than the position calculated with equation (1). The influence of stagnation point shift l_s becomes large when l_{bottom} is small (Equation (3)). This is the reason why the result deviated from the previous pressure-impulse model (equation (1)).

To take the stagnation point shift into the consideration, a new model using the law of mass conservation is proposed. The law of mass conservation of the novel device is expressed as

$$\pi r^2 U' = 2\pi r l_s U_0 \tag{2}$$

where the flow velocity in the nozzle is U', stagnation point shift is l_s, the nozzle radius is r, and the magnitude of the fluid inflow U_{in} is estimated as the initial velocity U_0 (Figure 3 (b)). Also, the jet velocity considering l_s is expressed by equation (3) using pressure-impulse approach (Figure 1 (b)).

$$V_{jet} = \beta \left(\frac{l_{top} - l_s}{l_{bottom} - l_s} \right) U_0 \tag{3}$$

*Corresponding author. E-mail: tagawayo@cc.tuat.ac.jp

By using equations (2) and (3), a new model of the velocity ratio of the novel device can be derived. The new model equation is shown below.

$$\frac{V_{jet}}{U_0} = \beta \frac{-(2l_{bottom}+r)+\sqrt{(2l_{bottom}+r)^2+8rl_{top}}}{2r} \quad (4)$$

The velocity ratio of the new model is affected greatly by the absolute value of l_{top}, l_{bottom} and r, instead of the length ratio l_{top} / l_{bottom} which greatly affects the previous model.

The new model is applicable even when the length ratio is large, which cannot be described with the previous model. Previous research [3] shows that the results under different conditions can be unified by using Reynolds number $Re = U'r / \nu$ and the increment ratio of jet velocity β. In order to verify the validity of the new model, the experimental data using the new model are compared with the data from previous research (Figure 4). The horizontal axis shows Reynolds number Re, while the vertical axis shows increment ratio of jet velocity β. Figure 4 confirms that the results of the previous research and this result are in good agreement. The results show that the jet velocity in the novel device can be accurately described by using the new model (Equation (4)).

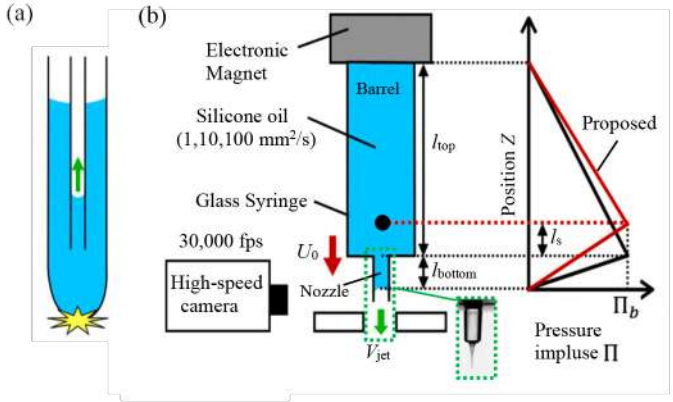

Figure 1 (a)Schematic view of current device. (b) Schematic view of novel device(left) and Π-Z diagram of novel device (right). Pressure-impulse gradient changes due to stagnation point shift.

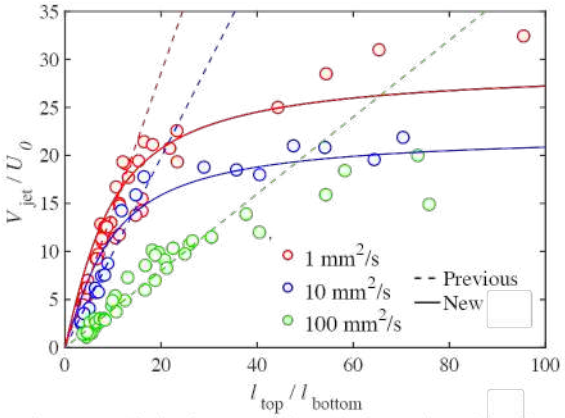

Figure 2 Relation between the velocity ratio and the length ratio. The circles are the experimental data. Dotted line shows previous model and solid line shows new model.

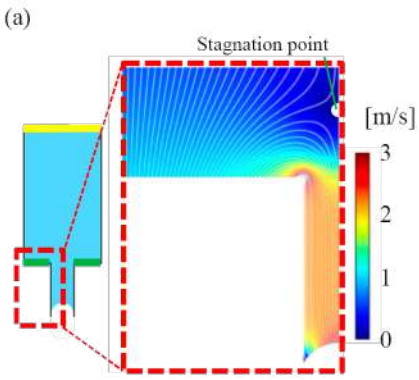

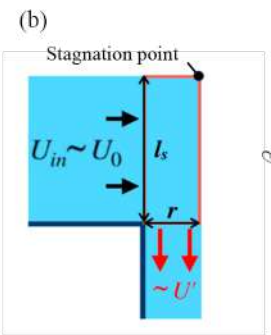

Figure 3 (a) Flow fields in the liquid of novel device and streamline by using potential flow. (b) Physical model of novel device based on a mass conservation.

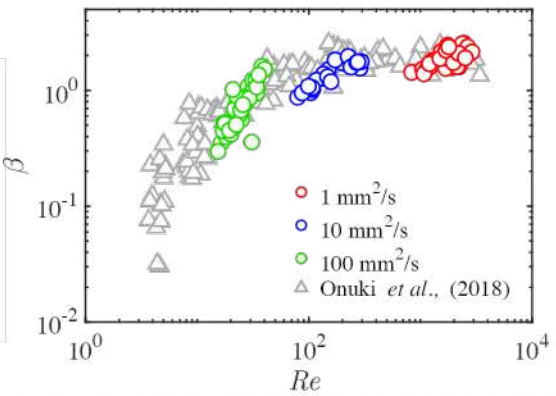

Figure 4 Increment ratio of jet velocity β (= V_{jet}/U') vs Reynolds number Re. The circle are experimental results and the triangles are previous research data.

CONCLUSIONS

In this paper, the jet velocity of the novel device was investigated for the development of the highly viscous liquid jet generator. From the experimental results, it was found that the model using only the pressure-impulse cannot accurately describe the jet velocity of the novel device. Therefore, a new model that considered shift of the stagnation point was proposed. Remarkably, the new model describes the case where the distance ratio was large, which cannot be described by the previous pressure-impulse model. By applying this new model, the results obtained agreed well with previous research. This had proven the validity of the new model.

References

[1] Streitberger H.J., Dossel K.F. Automotive Paints and Coatings. Wiley-VCH Verlag GmbH & Co. KGaA. 2008.
[2] Akafuah N.K., Poozesh S., Salaimeh A., Patrick G., Lawler K., and Saito K. Evolution of the Automotive Body Coating Process - A Review. *Coatings*. **6**: 24, 2016.
[3] Onuki H., Yuto O., and Yoshiyuki T., Microjet Generator for Highly Viscous Fluid. *Phys. Rev. Appl.* **9**: 014035, 2018.
[4] Antkowiak A., Bremond N., Dizes S.L., and Villermaux E. Short-term dynamics of a density interface following an impact. *J. Fluid Mech.* **577**: 241-250, 2007.

NUMERICAL ANALYSIS OF HIGH WEBER-NUMBER INTERFACE DEFORMATION

Jakob W. J. Kaiser *[1], Josef M. Winter[1], Stefan Adami[1], and Nikolaus A. Adams[1]
[1] Department of Mechanical Engineering, Technical University of Munich, Garching, Germany

Summary We investigate the interface deformation of a water column in an ambient flow field at high Weber number by high-resolution numerical simulation. We discretize the compressible Navier-Stokes equations with a finite volume approach, and apply a level-set based sharp-interface method with conservative interface-exchange terms to model the interaction of the two fluids. Our simulation results reproduce the flattening of the cylinder and the sheet-stripping at the droplet equator, which are characteristic for this breakup mode. Unsteady vortex shedding results in the local formation of recirculation zones, which contribute to the ongoing sheet-stripping. Resolving interface waves at the very early stages is paramount to reproduce a hat-like structure on the upstream side of the cylinder which is found in experimental investigations of this breakup mode.

MOTIVATION

The breakup of a spherical liquid drop into smaller fragments is of fundamental importance for many technological applications, ranging from internal liquid-fuel combustion engines to manufacturing of medical drugs and splatter of rain drops on supersonic aircrafts. The initial deformation of the drop is driven by a relative velocity to the ambient flow field, which may further lead to the breakup of the drop. The characteristics of the breakup process and, consequently, the final droplet size are determined by the relation of inertial forces, viscous forces, and capillary forces acting on the drop. Thus, accurate process control requires comprehensive understanding of the underlying physical breakup mechanisms.

The breakup process is classified by two dimensionless numbers: the Weber and the Ohnesorge number, which describe the ratio of inertial to capillary forces and the ratio of viscous to capillary forces, respectively. For high Weber numbers, the Shear-Induced Entrainment (SIE) is the dominating instability mode, which exhibits a stripping of liquid material from the "edge" of the drop [7]. Systematic experimental and numerical investigations have been performed to improve the understanding of the breakup process [1, 7]. Many numerical studies focus on two-dimensional setups for efficiency reasons, since from experimental investigations it has been found that the breakup modes of two-dimensional water columns and three-dimensional spherical drops in crossflow are phenomenologically equivalent [1].

In this work, we perform high-resolution numerical simulations of liquid-column breakup in the SIE regime. Based on the setup of Igra and Takayama [3], the focus of our investigation is on the interplay of the interface deformation and the surrounding flow field. We apply a finite-volume approach with flux reconstruction based on low-dissipative WENO schemes to accurately represent small-scale flow structures. and a level-set based sharp interface method to represent the liquid-gas phase interface with conservative interface-exchange terms. High computational efficiency is enabled by a block-structured wavelet-based multiresolution scheme with adaptive local timestepping [4].

METHODOLOGY

The problem is governed by the compressible Navier-Stokes equations including surface tension

$$\frac{\partial}{\partial t}\begin{pmatrix}\rho\\ \rho\mathbf{u}\\ E\end{pmatrix}+\nabla^T\cdot\begin{pmatrix}\mathbf{u}\rho\\ \rho\mathbf{u}\otimes\mathbf{u}+p\mathbf{I}\\ \mathbf{u}(E+p)\end{pmatrix}+\nabla^T\cdot\begin{pmatrix}0\\ \mathbf{T}\\ \mathbf{T}\cdot\mathbf{u}\end{pmatrix}=\begin{pmatrix}0\\ \kappa\sigma\mathbf{n}_\Gamma\\ \kappa\sigma\mathbf{n}_\Gamma\cdot\mathbf{u}\end{pmatrix} \tag{1}$$

where ρ denotes the density, t the time, $\mathbf{u}$ the velocity vector, p the pressure, $\mathbf{I}$ the identity matrix, $\mathbf{T}$ the Cauchy stress tensor, κ the surface curvature, $\mathbf{n}_\Gamma$ the surface normal unit vector, and E the total energy, composed of the internal energy (ρe) and the kinetic energy ($1/2\rho\mathbf{u}\cdot\mathbf{u}$). The system of equations is closed by the stiffened equation-of-state

$$p=(\gamma-1)\rho e-\gamma p_\infty\,, \tag{2}$$

with the ratio of specific heats γ and the background pressure p_∞. Note that we use this equation of state for both fluids, air ($\gamma=1.4$, $p_\infty=0$) and water ($\gamma=6.12$, $p_\infty=3.43\times10^8$ Pa) .

The governing equations (1) are discretized by a finite-volume approach on Cartesian square cells in the domain Ω, which is divided into two subdomains Ω_l (liquid phase) and Ω_g (gaseous phase) by a time-evolving interface Γ. Convective fluxes at cell faces are approximated by the fifth-order WENO (Weighted Essentially Non-Oscillatory) scheme applied on characteristic fluxes, split by the global Lax-Friedrich (GLF) scheme. Viscous fluxes are discretized with a fourth-order central scheme. For temporal discretization, we use a strongly stable third-order Runge-Kutta scheme. The maximum admissible timestep size is determined from a Courant-Friedrichs-Lewy (CFL) stability criterion considering the maximum wave speed, viscous diffusion, and propagation of capillary waves at the interface. In all simulations, we use CFL$=0.5$

*Corresponding author. E-mail: jakob.kaiser@tum.de.

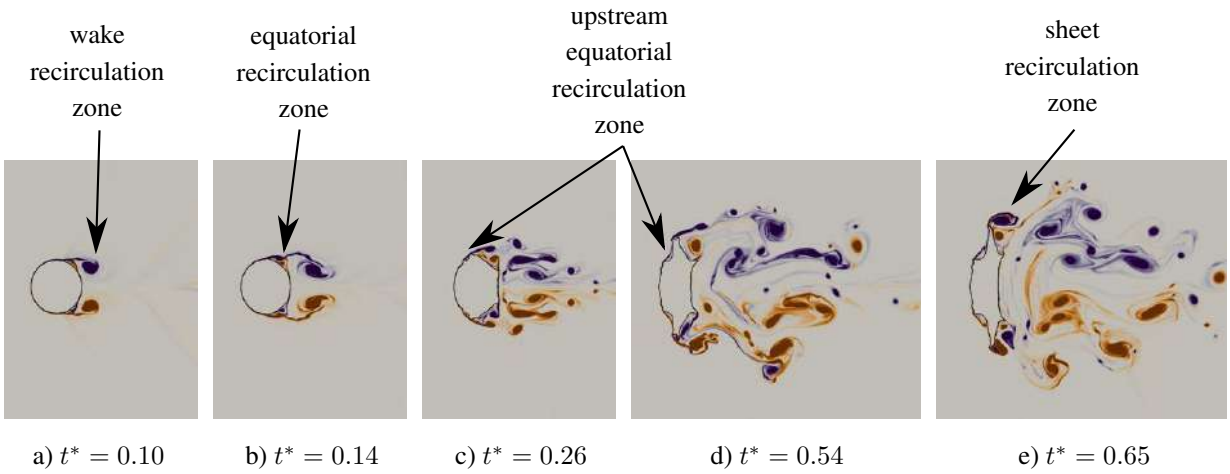

Figure 1: Positive (orange) and negative (purple) z-vorticity streams that interact and form multiple recirculation zones at various instants.

The level-set function ϕ represents the phase interface as the zero-crossing of a multi-dimensional continuous function. The absolute value of ϕ describes the normal signed distance of the cell center $\mathbf{x}$ to the interface Γ. The level set is evolved in time with the advection equation

$$\frac{\partial \phi}{\partial t} + u_\Gamma \mathbf{n}_\Gamma \cdot \nabla \phi = 0\,. \tag{3}$$

The interaction of the two fluids is solved based on the conservative interface-interaction model of Hu et al. [2] with the extension for viscous and capillary forces of Luo et al. [5]. First, the interface velocity u_Γ and the interface pressures $p_{\Gamma,l}$ and $p_{\Gamma,g}$ are obtained from a linearized two-material Riemann solver. Second, momentum and energy exchange across the interface are modeled for each phase by explicit exchange terms, see Luo et al. [5].

PRELIMINARY RESULTS

We simulate the interaction of a shock-wave ($Ma_S = 1.47$) with a water cylinder ($D_0 = 4.8\,\mathrm{mm}$) at $t = 0$. The effective resolution is 200 cells per initial cylinder diameter. Pre-shock air and water are at rest at standard conditions ($\rho_g = 1.20\,\mathrm{kg/m^3}$, $\rho_l = 1000.0\,\mathrm{kg/m^3}$, $p_g = p_l = 1.0\,\mathrm{atm}$).

Fig. 1 shows the $z-$vorticity in the vicinity of the water-column at different instants after shock passage. Note that we normalize the ouptut time following $t^* = t \cdot \sqrt{(\rho_g u_g^2) \,/\, (\rho_l D_0^2)}$. Unsteady vortex shedding after the shock passage results in the formation of a recirculation zone in the wake of the cylinder ($t^* = 0.10$). This vortex stream that is shed at the cylinder equator is diverted at the downstream stagnation point of the cylinder. It interacts with the vorticity stream near the cylinder equator, which leads to the formation of a recirculation zone at the cylinder equator ($t^* = 0.14$). These results agree well with Meng and Colonius [6], who found that the equatorial recirculation zone plays an important role in the sheet-stripping process. Furthermore, our high-resolution simulations show that additional recirculation zones form along the interface, which can be related to local unsteady vortex shedding at the deforming interface. Interface disturbances upstream of the cylinder equator are linked to the formation of a recirculation zone on the upstream side of the cylinder near the equator ($t^* = 0.26$). This recirculation zone is located at later time instants at the transition of a hat-like structure that forms on the upstream side of the cylinder to the water filament ($t^* = 0.54$). Another recirculation zone forms at the tip of the water sheet due to the interaction of multiple vortices in this area, and contributes to the flapping of the sheet in the wake of the cylinder ($t^* = 0.65$).

Our preliminary results underline the close relation of local flow disturbances and sheet-stripping for the breakup in the SIE regime. More detailed analyses of the flow field and interface-deformation dynamics, the hat formation, as well as comparison to experimental data will be presented at the conference.

References

[1] Guildenbecher D. R., Lopez-Rivera C., Sojka, P. E. Secondary Atomization. *Exp. Fluids* **46**: 2009.
[2] Hu X. Y., Khoo B. C., Adams N. A., Huang F. K. A conservative interface method for compressible flows. *J. Comput. Phys.* **219**: 2006.
[3] Igra D., Takayama K. Investigation of aerodynamic breakup of a cylindrical water droplet. *At. Sprays* **11**: 2001.
[4] Kaiser J. W. J., Hoppe N., Adami S., Adams N. A. An adaptive local time-stepping scheme for multiresolution simulations of hyperbolic conservation laws. *J. Comput. Phys. X* **4**: 2019.
[5] Luo J., Hu X., Adams N. A. A conservative sharp interface method for incompressible multiphase flows. *J. Comput. Phys.* **284**: 2015.
[6] Meng J. C., Colonius T. Numerical simulations of the early stages of high-speed droplet breakup. *Shock Waves* **25**: 2015.
[7] Theofanous T., Mitkin V. V., Ng C. L., Chang C. H., Deng X., Sushchikh S. The physics of aerobreakup. Part II. Viscous Liquids. *Phys. Fluids* **24**: 2012.

AEROBREAKUP OF LIQUID METAL DROPLETS WITH OXIDE SKINS

Thomas Hopfes*[1], Zhaoguang Wang[1], Julia Petersen[1], Marcus Giglmaier[1] and Nikolaus A. Adams[1]
[1] Chair of Aerodynamics and Fluid Mechanics, Technical University of Munich, Munich, Germany

Summary This short paper presents experimental results of liquid metal droplet breakup using Galinstan in a shock-induced gas flow. A representative image sequence shows a breakup similar to the multimode regime classified for regular liquids, despite the formation of an oxide skin at the metal surface. Further work will investigate the influence of this oxide skin on the breakup under different flow conditions.

INTRODUCTION

The characterization of atomization processes of liquid metals is a relevant field of research for many industrial applications such as metal powder production, thermal spray deposition and liquid metal cooling systems, as well as in model validation and basic research [1]. As part of the atomization process, secondary atomization describes a drop that is exposed to a disrupting liquid or gas flow and undergoes deformation and fragmentation. Most experiments on this topic are carried out with ordinary Newtonian liquids such as water (see [2] for a detailed review), while others focus on more complex liquids like non-Newtonian polymer solutions (e.g. [3]). In comparison to those fluids, liquid metals provide significantly different properties such as higher ranges of density and surface tension [1], and very different features like the creation of an oxide layer [4] or partial solidification and crust building during the cooldown [5]. These effects are expected to lead to differences in the resulting deformation and breakup behavior.

Reference work on the breakup of liquid metal droplets is often carried out in liquid-liquid systems. For example, Patel and Theofanous [6] investigate the fragmentation of mercury, gallium and acetylene tetrabromide drops in water accelerated by a shock wave in a hydrodynamic shock tube. Ciccarelli and Frost [7] also study molten metal droplets in an ambient flow of water. They differentiate between cold drops that break up due to stripping by the relative flow, and hot drops where the growth and collapse of vapor bubbles dominate the fragmentation. Validating against both these works, Thakre and Ma [5] present numerical investigations and highlight various deformation patterns that lead to a significant increase in surface area. Due to their interest in iron sedimentation, Wacheul et al. [8] study the fragmentation dynamics of liquid gallium. They identify a variety of stable shapes for liquid metal drops and complex dynamics within a cloud of fragments.

Liquid metal breakup in gas has been studied recently in experiments and corresponding simulations. Chen et al. [1] study the aerobreakup of a Galinstan liquid metal column in an air flow induced by a shock wave for moderate Weber numbers. They note a strong similarity to the breakup morphologies in water, but also highlight key differences. Notably, the onset of breakup occurs earlier in non-dimensional time for Galinstan, while also appearing more violently. Further, local bag formation and breakup occurs in a different form. Complementing work by Arienti et al. [9] further details that surface oxides resist deformation and thus lead to irregular shapes of fragments.

However, detailed studies of aerobreakup of liquid metals in gas are rare, and we want to provide further insight by examining this topic and presenting results of the breakup of a single Galinstan droplet in a shock-induced flow.

EXPERIMENTAL FACILITY

A schematic of the shock tube, used for the experiments, is shown in Figure 1. The tube has an overall length of 24 m, an inner diameter of 290 mm and consists of three main parts: the driver, the driven and the test section. Driver and driven sections are initially separated by a diaphragm and the initial pressure values in each section define the flow conditions for the experiments. After the diaphragm ruptures, a shock wave propagates into the driven section and induces a gas flow towards the test section.

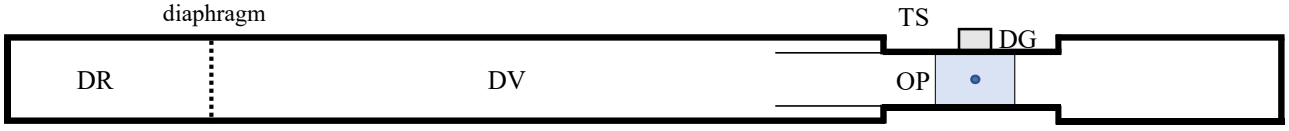

Figure 1. Sketch of the shock tube with driver section (DR), driven section (DV), test section (TS), droplet generator (DG), and optical system at the window with Z-type schlieren and camera (OP).

As part of the test section, a droplet generator produces millimeter-sized Galinstan droplets. Galinstan is a commercially-available liquid metal alloy of gallium, indium, and tin with a very low melting point well below 0°C and nontoxic characteristics [10]. Shortly after the droplet is produced, the shock wave passes the test section and the droplet is exposed to the flow. The resulting deformation and breakup are recorded with a Shimadzu HyperVision HPV-X ultra-high-speed camera with a resolution of 400x250 pixels at up to 5 million frames per second. Simultaneously, PCB Piezotronics ICP® fast-response pressure sensors monitor and record the pressure at a frequency of 1 MHz per channel.

*Corresponding author. E-mail: thomas.hopfes@tum.de

RESULTS

First experiments were conducted using Galinstan as the working fluid and air as surrounding medium. A corresponding image sequence is presented in Figure 2, with the time normalized by the characteristic transport time after Ranger and Nicholls [11]. First images show a string-like appendix on the droplet that results when the drop detaches from the needle of the droplet generator and immediately oxidizes at the surface. This elastic oxide skin prevents a spherical shape, and can also influence the breakup behavior [1]. After the impact of the incident shock, the appendix at the top of the droplet is bent and stretched along the flow direction and breaks into discrete fragments under the effect of Rayleigh-Pletaue instabilities. The main body experiences a pronounced flattening at the windward surface, with a thin sheet developping around the periphery (T = 0.4-0.6). Bags form along the sheet, inflate, and rupture quickly with a splash-like outwards movement that ejects secondary particles (compare the bottom of the drop for T = 0.6-0.8). This process is very similar to what Chen et al. [1] observe in their work. Fragmentation persists continuously and is driven by the repeated inflation and breakup of local bags, as well as by the stripping of fragments from the periphery. This behavior as well as the Weber number of We = 80 match well with the multimode breakup regime defined in the literature [2].

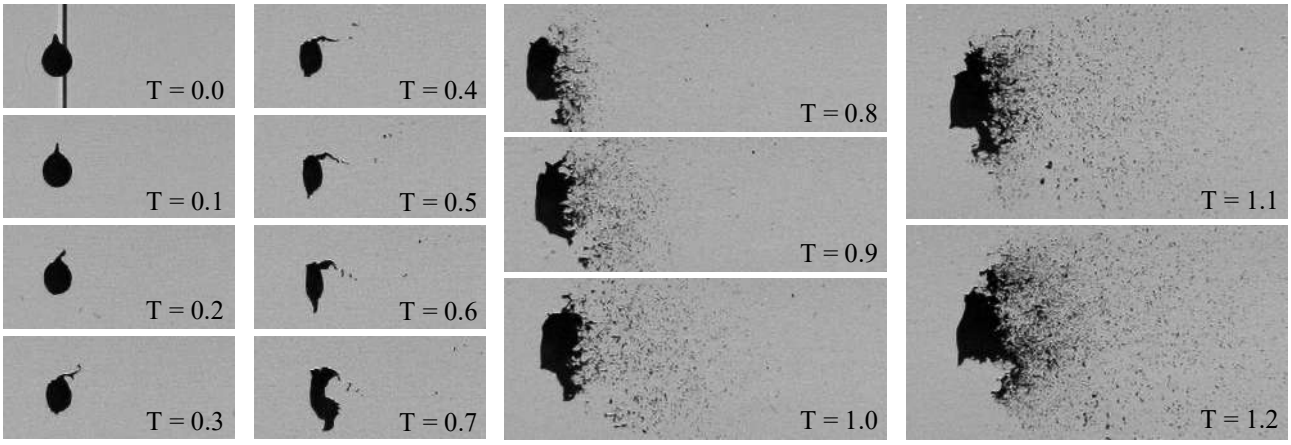

Figure 2. Breakup of Galinstan droplet of initial equivalent diameter d_0 = 3.21 mm for We = 80; The frames show time moments that range from T = 0 (top left) to T = 1.2 (bottom right). The air flow goes from left to right.

CONCLUSION AND OUTLOOK

This short paper presents results of liquid metal droplet breakup in an air flow. High speed photography shows that the oxide skin generated when the liquid is exposed to air influences the initial shape, but also that the breakup in general can be classified in accordance to previous work on regular liquids. To study this classification in more detail, we will conduct experiments at various Weber numbers. In addition, experiments will be carried out with pure nitrogen as the gas in the driven section of the shock tube. This prevents the formation of the oxide skin and allows a direct analysis of the role of the oxide skin and its influence on the breakup. Additional images, videos and a detailed analysis will be presented at the conference.

Acknowledgements

The authors acknowledge funding by the European Research Council (ERC) under the European Union's Horizon 2020 research and innovation program (grant agreement No. 667483).

References

[1] Y. Chen, J. L. Wagner, P. A. Farias, E. P. DeMauro, and D. R. Guildenbecher, "Galinstan liquid metal breakup and droplet formation in a shock-induced cross-flow," *Int. J. Multiph. Flow*, vol. 106, no. 505, pp. 147–163, 2018.
[2] D. R. Guildenbecher, C. López-Rivera, and P. E. Sojka, "Secondary atomization," *Exp. Fluids*, vol. 46, no. 3, pp. 371–402, Mar. 2009.
[3] T. G. Theofanous, V. V. Mitkin, and C. L. Ng, "The physics of aerobreakup. III. Viscoelastic liquids," *Phys. Fluids*, vol. 25, no. 3, 2013.
[4] P. Yim, "The Role of Surface Oxidation in the Break-Up of Laminar Liquid Metal Jets," 1996.
[5] S. Thakre and W. Ma, "3D simulations of the hydrodynamic deformation of melt droplets in a water pool," *Ann. Nucl. Energy*, vol. 75, pp. 123–131, 2015.
[6] P. D. Patel and T. G. Theofanous, "Hydrodynamic fragmentation of drops," *J. Fluid Mech.*, vol. 103, pp. 207–223, 1981.
[7] G. Ciccarelli and D. L. Frost, "Fragmentation mechanisms based on single drop steam explosion experiments using flash X-ray radiography," *Nucl. Eng. Des.*, vol. 146, no. 1–3, pp. 109–132, 1994.
[8] J.-B. Wacheul, M. Le Bars, J. Monteux, and J. M. Aurnou, "Laboratory experiments on the breakup of liquid metal diapirs," *Earth Planet. Sci. Lett.*, vol. 403, pp. 236–245, Oct. 2014.
[9] M. Arienti *et al.*, "Comparison of simulation and experiments for multimode aerodynamic breakup of a liquid metal column in a shock-induced cross-flow," *Phys. Fluids*, vol. 31, no. 8, p. 082110, Aug. 2019.
[10] T. Liu, P. Sen, and C. J. Kim, "Characterization of liquid-metal Galinstan® for droplet applications," *Proc. IEEE Int. Conf. Micro Electro Mech. Syst.*, pp. 560–563, 2010.
[11] A. A. Ranger and J. A. Nicholls, "Aerodynamic shattering of liquid drops.," *AIAA J.*, vol. 7, no. 2, pp. 285–290, 1969.

NUMERICAL STUDY OF PLANAR SHOCK INTERACTING WITH CYLINDRICAL WATER COLUMN CONSIDERING CAVITATION EFFECTS

Zhan Gao[1] and Bing Wang *[1]
[1] School of Aerospace Engineering, Tsinghua University, Beijing, China

Summary The droplet-shock interaction process contributes to the atomization in scramjets. The understanding of cavitation occurring in the shock interacted droplet has been limited yet. This study numerically simulates such interaction process. Compared with previous experiments, the detailed analysis of the wave evolution in the water column reveals that the reflected expansion waves focus near the downstream interface, create the local negative pressures, and trigger the cavitation thereafter. The theoretical derivation shows that the cavitation location depends exclusively on the critical incidence angle of the shock, at which a free precursor shock arises in the refraction pattern. The predicted cavitation location agrees with the numerical results. Planar shocks with different Mach numbers are simulated, and the corresponding cavity collapse pressure are compared.

INTRODUCTION, METHODOLOGY AND VALIDATION

The interaction of a planar shock with a droplet experiences a complex physical process, which can be found in the liquid jet atomization in scramjets. Recent experiments on the planar shock interacting with the cylindrical water column have suggested that cavitation is triggered due to the negative pressures created by focusing of the reflected expansion waves (REW)[1]. However, the physical mechanism of the focusing of the REW is still unclear, and the exact location of cavitation remains unclear. Therefore, the objective of this study is to shed light on the aforementioned problems by numerical simulation and theoretical analysis.

The governing equations consist of Euler equations and scalar transportation equations for the volume of fraction. The thermodynamic state of the fluid is described by the stiffened gas equation of state (SG-EOS). The finite volume method is used to discretize the governing equations. The weighted essentially non-oscillatory (WENO) scheme is applied for the spatial reconstructions to the primitive variables. A Godunov-type Harten-Lax-van Leer Contact (HLLC) approximate Riemann solver is employed to solve the numerical flux at the edges of the cells. A third-order total variation diminishing (TVD) Runge-Kutta scheme is utilized for time marching. The phase transition is implemented referring to Wu *et al.*[3]. Previous experiments suggest that for tap water, the cavitation threshold is around -1 bar. In the shock/droplet interaction, the tap water is compressed by the transmitted shock, and its cavitation threshold is changed[2]. Thus the exact cavitation threshold in experiments[1] is hard to determine, and this study adopts -1 bar as cavitation threshold for convenience.

Figure 1 shows the simulation results compared with the experiments by Sembian *et al.*[1]. In simulation, the Mach number of the incident shock is $Ms = 2.4$ and the water column radius is $r_0 = 4$ mm. The wave structures in the simulation are consistent with those in experiments. The REW passed through cavitation zones in simulation are weaker than that in experiments, because with the -1 bar cavitation threshold cavitation is triggered more easily and absorbs more energies of the waves. The collapse of cavitation bubble generates strong shock waves, which can also contribute to the droplet breakup.

RESULTS AND DISCUSSION

The ray analysis[3] is utilized to analyse the propagation of the transmitted shock wave in the water column, and the detailed analysis will be presented in the full paper, due to limited space here. The incident shock moves and interacts with the air-water interface, and it is reflected back to the air and refracted into the droplet. The refraction wave moves faster than the incident shock because of the difference of fluid impedance. Due to the curvature of the droplet surface, the incident, the reflected and the refracted shock waves connect at the interacting point on the droplet surface in the early stage of interacting. This point is also called as triple-wave point. However, once the triple-wave point reaches a critical one, for instance at critical point C in Figure 1(b), the refraction pattern will change and the refracted shock wave will propagate freely in the droplet, which is called as the free precursor shock (FPS). The reflection of the FPS at the interface will occur, and the REW will generate a local minimum pressure region denoted by F in Figure 1(a). The ray analysis shows that, as the FPS propagates forward, F goes along the envelope line of the firstly reflected rays of that emitted from the critical point C, illustrated as the thick blue line in Figure 2(b). The envelope line intersects with the axial line at $\mathrm{F_e}$, and the two F on both sides of the axial line will finally focus at $\mathrm{F_e}$, causing much lower pressures and cavitation thereafter. The location of the focusing point $\overline{\mathrm{AF_e}} = \min(R\sin(\alpha)/\sin(3\alpha - \beta_c))|\alpha \in [\beta_c/2, (\pi - \beta_c)/4]$, where R is the droplet radius, α is the intersection angle between OC and emitted rays, β_c is the intersection angle between the incident shock and the air-water interface when the FPS arises. β_c is around $37°$ when the incident shock Mach number is 2.4, estimated from simulation[4]. Thus the conclusion is that $\overline{\mathrm{AF_e}} = 1.6R$ when $Ms = 2.4$, which agrees well with the present numerical simulation. The effects of the intensity of incident shock on the cavitation occurrence will also be discussed in detail in the full paper.

*Corresponding author. E-mail: wbing@tsinghua.edu.cn.

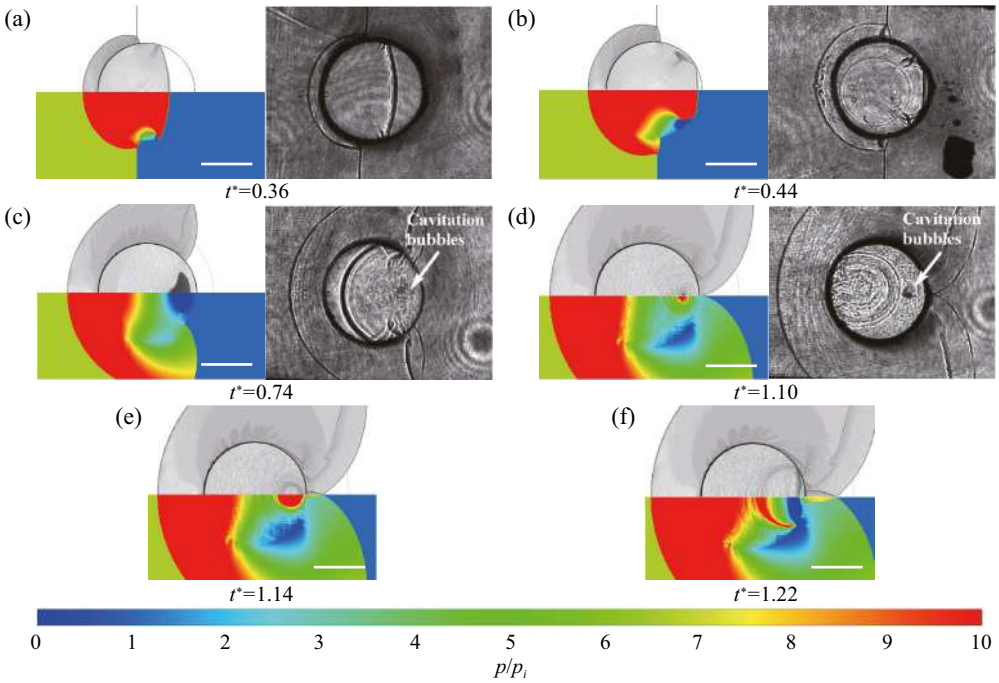

Figure 1: Numerical schlieren contours (top) and pressure contours (bottom) at different non-dimensional simulation times t^* for shock Mach number $Ms = 2.4$. Also shown on the right side of (a-d) are the results from Sembian *et al.*[1]. The pressures are normalized by the initial ambient pressure $p_i = 1$ bar. The length of the scale bar is 4 mm.

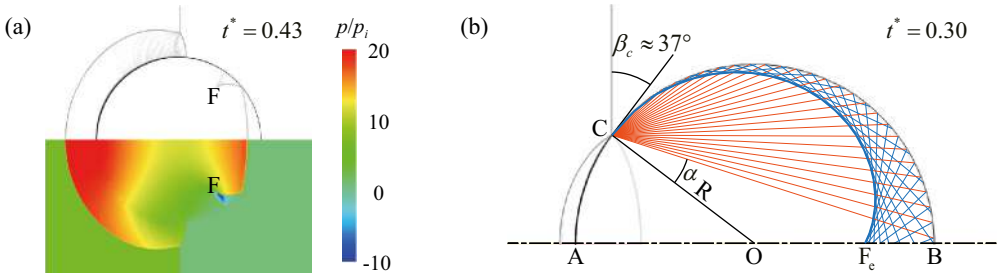

Figure 2: Analysis of focusing of REW. (a) Numerical schlieren contours (top) and pressure contours (bottom) at non-dimensional time $t^* = 0.43$ for $Ms = 2.4$. F denotes the local minimum pressure region generated by REW. (b) Numerical schlieren contours at $t^* = 0.30$ for $Ms = 2.4$ and the illustration of rays (orange) emitted from the critical point C. The blue lines are the firstly reflected rays, and their envelope line (thick blue lines) indicate the locus of F.

CONCLUSIONS

This study numerically simulated the planar shock/water column interaction, in which the agreement between the simulation results and experimental visualization was presented. A detailed analysis is conducted for the evolution of the wave structures inside the water column, especially the focusing of the REW of the FPS. The focusing position, where the cavitation occurs, is derived theoretically, and compared to the present numerical results. The cavitation position in the shocked droplet is dependent on the critical incident angle, at which the refraction pattern of the incident shock changes and the FPS arises. The critical angle is determined by the incident shock intensity and impedance of the fluids, if the droplet is interacted with the planar shock wave. The collapsing pressures of cavitation are compared with different incident shock Mach numbers, showing that it increases drastically with shock Mach number.

References

[1] Sembian S., Liverts M., Tillmark N., Apazidis N. Plane Shock Wave Interaction With a Cylindrical Water Column. *Phys. Fluids* **28**, 2016.
[2] Andersen A., Morch K. Cavitation Nuclei in Water Exposed to Transient Pressures. *J. Fluid Mech.* **771**, 2015.
[3] Wu W. X., Xiang G. M., Wang B. On High-Speed Impingement of Cylindrical Droplets Upon Solid Wall Considering Cavitation Effects. *J. Fluid Mech.* **857**: 851-877, 2019.
[4] Nourgaliev R. R., Sushchikh S. Y., Dinh T. N., Theofanous T. G. Shock Wave Refraction Patterns at Interfaces. *Int. J. Multiph. Flow* **31**: 969-995, 2005.

A DROP IN A NONLINEAR EXTENSIONAL FLOW

Moshe Favelukis *
Department of Chemical Engineering, Shenkar College, Ramat-Gan, Israel

Summary The deformation and breakup of a drop in a nonlinear extensional creeping flow is the subject of this theoretical report. The problem is governed by the capillary number (Ca), the viscosity ratio (λ), and the nonlinear intensity of the flow (E). The flow outside the drop is different than the linear case ($E = 0$), suggesting closed circulations ($E > 0$) and separating surfaces ($E < 0$). The flow inside the drop predicts that when $E < -3/7$, the number of internal circulations is doubled. When the extensional flow is linear, we have prolate spheroidal drops for uniaxial flow ($Ca > 0$) and oblate spheroidal drops for biaxial flow ($Ca < 0$). For the same Ca, drops with $E > 0$ are more elongated than $E = 0$, and drops with $E < 0$ are less elongated than $E = 0$. Compared to the linear case, $E > 0$ tends to facilitate drop breakup, while $E < 0$ makes the breakup of the drop more difficult.

INTRODUCTION

Many industrial products appear as foams or emulsions in which gas bubbles or liquid droplets are embedded in a liquid. These two-phase systems are often processed in mixing devices generating shear, extensional, or other complicated flows. While the majority of the studies simulate these processes with linear flows, very little is dedicated to nonlinear flows which can describe better (than the linear flow) the flow produced in industrial rotating equipment.

When a drop of one fluid is embedded in another fluid undergoing a linear flow such as simple shear or simple extensional flow, it will deform, and if the strength of the flow exceeds some critical value, it may even break. For incompressible Newtonian fluids under creeping flow conditions, the problem, is governed by the capillary number (Ca) and the viscosity ratio (λ). The deformation of the drop spans a wide domain, from a slightly perturbed sphere up to a slender body. This report is dedicated to the small deformation regime only, obtain at $|Ca| << 1$. A summary of this fundamental topic having many industrial applications can be found in the reviews of Rallison [1] and Stone [2].

Sherwood [3] suggested an axisymmetric nonlinear extensional creeping flow in his slender drop studies. A pointed drop in a two-dimensional nonlinear extensional creeping flow was considered by Antanovskii [4], which argued that the flow field produced in Taylor's four-roller apparatus is better described by a nonlinear flow rather than the linear one. Recently, the nonlinear theory was expanded by Favelukis [5]-[6], in order to cover the small deformation regime as well, where new and exiting deformation and breakup patterns, when compared to the linear case, were found. Thus, it is the purpose of this theoretical report to review the recent findings in [5]-[6] as well as to present new results on the subject of deformation and breakup of a drop in a nonlinear extensional creeping flow at small capillary numbers.

THE GOVERNING EQUATIONS

Figure 1 shows a spherical drop (radius a) positioned at the origin of a cylindrical coordinate system. Far away from the drop, the fluid is subjected to an axisymmetric nonlinear extensional flow, suggested by Sherwood [3] and given by: $v_\rho = -(A\rho + 3B\rho z^2)/2$ and $v_z = Az + Bz^3$. Here A and B can obtain positive or negative values. When $B = 0$, the linear extensional flow is recovered, and we distinguish between uniaxial ($A > 0$) and biaxial ($A < 0$) extensional flows.

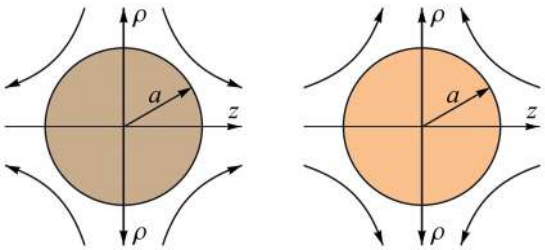

Figure 1. A drop in an extensional flow. Left: uniaxial; right: biaxial.

Let the two fluids be incompressible, Newtonian and under creeping flow conditions. The problem, which is described by the Stokes equations, is governed by three dimensionless parameters: the capillary number $Ca = \mu Aa/\sigma$, the viscosity ratio $\lambda = \mu_{in}/\mu$, and the nonlinear intensity of the flow $E = Ba^2/A$. Here μ_{in} and μ are the internal and external viscosities respectively, and σ is the surface tension.

A general analytical solution to the Stokes equations for any type of axisymmetric flow in spherical coordinates can be found in Leal [7]. The usual boundary conditions suggests: (1) Far from the drop, the undisturbed motion must be recovered; (2) zero normal velocities of the two phases at the interface; (3) equal tangential velocities of the two phases at the interface; (4) equal tangential stresses of the two phases at the interface; and (5) finite velocities and stresses at the origin. The above conditions are sufficient to obtain the $O(Ca^0)$ (spherical) solution, same for uniaxial and biaxial flows, which is then substituted into the normal stress balance in order to obtain the $O(Ca^1)$ deformed shape.

*Corresponding author. E-mail: favelukis@gmail.com

RESULTS AND DISCUSSION

Figure 2 describes streamlines of the $O(Ca^0)$ disturbed motion, for a drop with $\lambda = 1$, as a function of the nonlinear intensity of the flow (E). The first quarter describes the linear case ($E = 0$). When $E > 0$ and as E increases, the flow rate also increases, and above some critical value of E, an external closed circulation is developed near the spherical polar angle $\theta = \pi/2$. This critical E is a function of λ, and as λ increases the critical E decreases. For a bubble or an inviscid drop ($\lambda = 0$) no circulation is possible, for a drop with $\lambda = 1$, $E = 7.03$, and for a solid particle ($\lambda = \infty$), $E = 5/4 = 1.25$. When $E < 0$, a separating surface is created, and as $|E|$ increases, or the flow becomes more nonlinear, the surface moves from $z = \pm\infty$ towards $z = 0$. If $E < -3/7 = -0.429$ (independent of λ), the number of internal circulations is doubled.

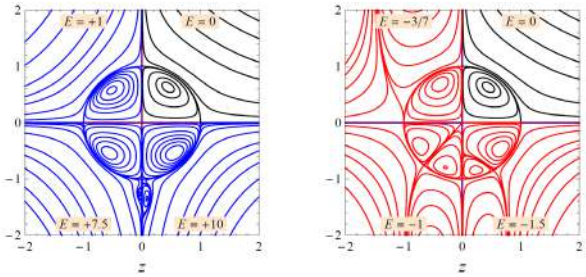

Figure 2. Disturbed streamlines for a drop with $\lambda = 1$. Left: $E \geq 0$; right: $E \leq 0$.

The deformation of a drop with $\lambda = 1$ at $Ca = \pm 0.2$, as a function of the nonlinear intensity of the flow (E), is presented in Figure 3. When the extensional flow is linear ($E = 0$), the literature suggests prolate spheroidal drops for uniaxial flow ($Ca > 0$) and oblate spheroidal drops for the biaxial flow ($Ca < 0$). For the same $|Ca|$, and compared to the linear case, higher deformed drops are obtain if $E > 0$, and lower deformed drops when $E < 0$.

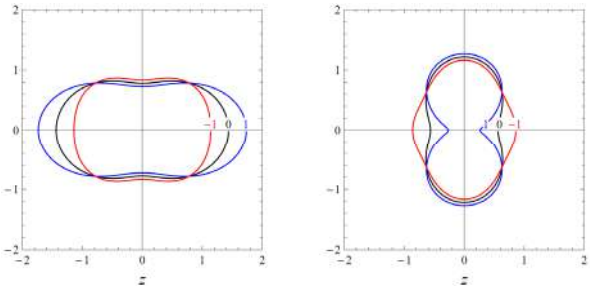

Figure 3. Deformation of a drop with $\lambda = 1$ and $Ca = \pm 0.2$, for different values of E. Left: uniaxial ($Ca > 0$); right: biaxial ($Ca < 0$).

For most cases, the breakup mechanism is by centre pinching ($\theta = \pi/2$ for uniaxial, and $\theta = 0$ and $\theta = \pi$ for biaxial). According to Favelukis [5], $E > 0$ tends to facilitate drop breakup while $E < 0$ makes the breakup more difficult. When $E < -3/7$, the separating surface touches the surface of the drop, which experiences both uniaxial and biaxial flows simultaneously. This weird situation, described in Figure 4, for a drop with $\lambda = 1$ and $E = -2$, for different capillary numbers (Ca), suggests a pinching mechanism progressing from two directions as well as other peculiar shapes.

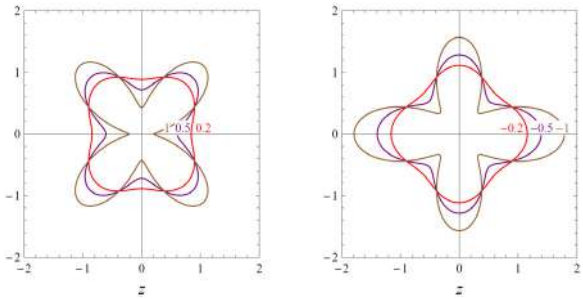

Figure 4. Deformation of a drop with $\lambda = 1$ and $E = -2$, for different values of Ca. Left: uniaxial ($Ca > 0$); right: biaxial ($Ca < 0$).

References

[1] Rallison J.M. The Deformation of Small Viscous Drops and Bubbles in Shear Flows. *Annu. Rev. Fluid Mech.* **16:** 45-66, 1984.
[2] Stone H.A. Dynamics of Drop Deformation and Breakup in Viscous Fluids. *Annu. Rev. Fluid Mech.* **26:** 65-102, 1994.
[3] Sherwood J.D. Tip Streaming from Slender Drops in a Nonlinear Extensional flow. *J. Fluid Mech.* **144:** 281-295, 1984.
[4] Antanovskii L.K. Formation of a Pointed Drop in Taylor's Four-Roller Mill. *J. Fluid Mech.* **327:** 325-341, 1996.
[5] Favelukis M. A Drop in Uniaxial and Biaxial Nonlinear Extensional Flows. *Phys. Fluids.* **29:** 087102, 2017.
[6] Favelukis M. Mass Transfer Around Bubbles, Drops, and Particles in Uniaxial and Biaxial Nonlinear Extensional Flows. *AIChE J.* **65:** 398-408, 2019.
[7] Leal L.G. Advanced Transport Phenomena. Cambridge University Press, 2007.

DYNAMICS OF A BUBBLE RISING IN A VISCOELASTIC LIQUID COLUMN

Pınar Eribol * [1], Arda İnanç [2], M. Naci İnci[2], and A. Kerem Uğuz[1]
[1] Department of Chemical Engineering, Boğaziçi University, Istanbul, Turkey
[2] Physics Department, Boğaziçi University, Istanbul, Turkey

Summary The motion of gas bubbles in non-Newtonian liquids is important for many industrial processes including bubble columns, fermentation, and plastic foam processing. When a gas bubble rises in a viscoelastic liquid, a negative-wake is formed at the tailing end of the bubble and results into important changes at some critical bubble volume. The aim of this study is to find the changes in the velocity, the volume and the shape of the bubble; and the stress around it while establishing a correlation between these elements. For this purpose, the stress will be quantified through a non-invasive optical method called birefringence. The light around a bubble rising in a viscoelastic birefringent liquid will be photographed and employing the stress-optics law, the stress field around the bubble will be determined for various parameters.

Keywords: Stress, viscoleasticity, rising bubble, birefringence

INTRODUCTION

The motion of a bubble rising in a viscoelastic fluid is an important field of study for the purpose of industrial uses. This study becomes interesting due to some factors i.e. the presence of a negative wake at the trailing tip of the bubble, the change in the bubble shape and the jump in the velocity [1-3].

EXPERIMENTAL SETUP & METHODS

A schematic diagram of the experimental setup used in this study is shown in Fig.1. The experimental setup consists of a liquid column, a laser, a polarizer, an analyzer and 3 cameras (camera 1 is for birefringence; and camera 2 and 3 are for volume and velocity measurements, respectively). A glass liquid column with dimensions of 12 cm x 12 cm x 50 cm; and it was made certain that the wall effect on the rising bubble is eliminated with the dimensions preferred. In the experiments, the light emitted by the laser is polarized through the polarizer and then the analyzer repolarizes the light after it passes through the sample medium. When there is a bubble rising through the column, this creates a stress field in the polymeric liquid around the bubble. The birefringent property of the liquid arises when a stress field occurs; and it is captured on the camera as bright fields whereas there is no stress at dark fields.Polyacrylamide (PAAm SH) solutions were prepared with different weight percentages. A fixed weight percentage (1 wt%) of hydroxypropylcellulose (HPC) which is liquid crystalline liquid that is highly birefringent; is added in every PAAm SH solution as PAAm SH does not show enough birefringent property alone (Fig.1b). The solutions are characterized as highly viscoelastic by rheological analysis. The birefringence is calculated through stress optical law (Eq. 1-2). I_o, $I(\theta)$, θ, δ, Δn, χ, h and λ are the intensity of the laser beam, transmitted intensity, the angle between polarizer and analyzer, retardance, birefringence, stretching angle of the polymer, the thickness of the sample medium and wavelength of the laser beam, respectively. The edge detection was performed using Otsu Method on Matlab Image Processesing Toolbox for birefringence, volume and velocity measurements.The bubble volume is calculated through the equivalent diameter, D.

$$I(\theta) + I(\theta + 45) = I_o \sin^2\left(\frac{\delta}{2}\right) = I_o \sin^2\left(\frac{\frac{2\pi h}{\lambda}\Delta n}{2}\right) \tag{1}$$

$$\frac{I(\theta)}{I(\theta + 45)} = \tan^2(2\chi) \tag{2}$$

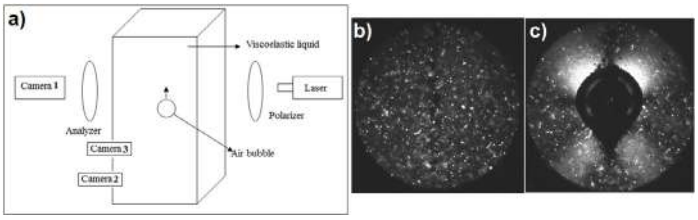

Figure 1: The sketch of the experimental setup (a),the captured image of the birefringence experiment in the absence (b) and presence (c) of a stress field.

*Corresponding author. E-mail: pinareribol@gmail.com.

RESULTS AND DISCUSSION

The results show that there are critical bubble volumes at which the sudden increase in the rise velocity occurs (from Fig. 2a to 2b and from Fig. 2c to 2d). As the bubble rises throughout the column, the viscous and the viscoelastic stresses start having an effect on the bubble; and the bubble shape can change from prolate to cusp-like shape. There is no significant change in the shape of the bubble at the critical point.

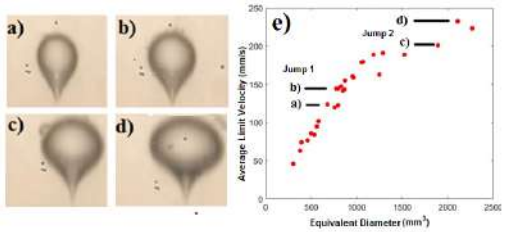

Figure 2: Jumps ocurred from a to b and c to d.

The stress that arises around the bubble is visualized using the birefringence method. The analyzed images displays that the stress around the bubbles increases with the increasing bubble size; and there is a critical bubble volume where no birefringence is observed below it (Fig. 3). The visualized stress is quantified using the stress-optical law (Eqs. 1-2) in terms of retardance, δ and birefringence, Δn. The change in the PAAm concentration alters the viscoelasticity of the solution causing into a change in the formed negative wake. The results indicate that this negative wake is not observed below a critical polymer concentration value. Even when there exists a stress at the tail due to the negative wake, it is relatively much smaller for the lower polymer concentration (Fig. 4a) compared to the higher one (Fig. 4b).

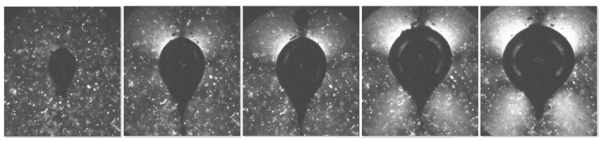

Figure 3: Birefringence observed for increasing volume of bubbles.

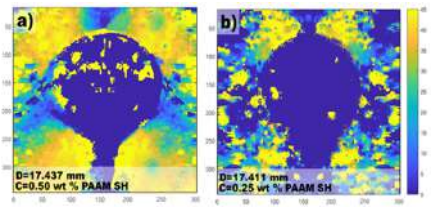

Figure 4: Stretching angle, χ of a bubble (D$\simeq$17.4 mm) at different PAAM SH concentrations a) 0.5 and b) 0.25 wt % .

CONCLUSION

In this study, the light around a bubble rising in a viscoelastic birefringent liquid will be photographed and employing the stress-optics law, the stress field around the bubble will bedetermined for various parameter. The ultimate aim is to find the correlation between velocity, volume and shape of the bubble; and the stress around it.

ACKNOWLEDGEMENT

The authors would like to acknowledge the financial support provided by TUBITAK through Project No 118M601.

References

[1] Funfschilling, D. and Li, H. Z. Flow of non-Newtonian fluids around bubbles: PIV measurements and birefringence visualisation. *Chem Eng. Sci* **56**: 1137-1141, 2001.

[2] Pillapakkam, S. B., Singh, P., Blackmore, D. and Aubry, N. Transient and steady state of a rising bubble in a viscoelastic fluid. *J. Fluid Mech.* **589**: 215–252, 2007.

[3] Ohta, M., Hieda, Y., Tokui, N. and Iwata, S. The motion of a bubble rising through viscoelastic polymeric liquids. *JSMET* **81**: 14-00612, 2015.

5 MICRON NARROW BAND ULTRASONIC MIST MAKER

Maryam Ebrahimiazar, Parsia Mohammadshahi, and Nasser Ashgriz
Department of Mechanical and Industrial Engineering, University of Toronto, Toronto, Canada

Summary In the present experiments the ultrasonic atomization of a 2 mm dripping droplet at 2.5 MHz and 40 V was studied. The results show that the size of the generated droplets strongly depends on the size of the liquid on the surface of the piezoceramic. Larger parent drops (~2 mm) generate both large and small droplets. To generate 4-7 micron droplets only, the size of the parent drop should be few hundred microns. Moreover, a new model based on acoustic radiation pressure has been suggested for predicting the size of the generated droplets.

INTRODUCTION

Ultrasonic atomization has numerous applications such as in drug delivery systems, surface coating, ink-jet printing, and mass spectrometry. Ultrasonic nebulizers are advantageous over pneumatic nebulizers in that they can generate droplets in the order of 3-5 microns in diameter. Although there is no general agreement in literature regarding the physical mechanism responsible for the ultrasonic atomization, capillary waves formation has been considered to be the main mechanism. Capillary waves are believed to grow on the liquid surface and eject small droplets from the wave crests. Lang used the Kelvin equation for the critical capillary wavelength and found that the median diameter, D_p, of the generated aerosol can be predicted by

$$D_p = C\lambda_{cr} = C\left(\frac{8\pi\sigma}{\rho f^2}\right)^{1/3} \qquad \text{Eq. 1}$$

where λ_{cr} is the critical wavelength, σ is the surface tension coefficient, ρ is the liquid density, and f is the sound forcing frequency. For sub-MHz ranges, C has been empirically determined to be 0.34.
All the previous ultrasonic nebulizers generate droplets between 2 to 20 microns. The objective of the present study is to design an ultrasonic nebulizer to generate 5-7 micron droplets only.

EXPERIMENTAL SETUP

A commercially available mist-maker piezoceramic with resonance frequency of 2.5 MHz, diameter of 16 mm, and thickness of 1 mm was excited at 2.5 MHz and 40 V. A capillary needle with inner diameter of 0.15 mm was positioned vertically atop of the piezoceramic and was used to generate a 2 mm dripping droplet. Both high-speed and conventional cameras were used for visualization.

RESULTS AND DISCUSSION

Description of Temporal Evolution of the Dripping Droplet

The general sequence of the single ethyl-alcohol droplet impacting on the surface of a piezoceramic operating at 2.5 MHz are shown in Fig. 1. The snapshots presented in these figures are from the conventional camera and selected from different sets of experiments with their time intervals being randomly selected. Fig. 1-a shows the initial impact of a droplet on the surface of the piezoceramic. The image is similar to the droplet impact on a non-vibrating surface, indicating that the acoustic field has not yet affected the droplet dynamics. The interaction between the ultrasonic waves and the droplet causes the initial impacting droplet to deform into a fountain, on the surface of which capillary waves are observed (see Fig. 1-b, and 1-c). The deformed parent droplet into the shape of fountain soon becomes unstable and collapses into large child droplets, forming a thick liquid layer on the surface of the piezoceramic (see figure 1-d), which starts to be atomized and generates both large (100 microns) and fine (4-7 microns) drops. Large droplets of about 100 microns in diameter are formed when intermittent jets breakup directly from the surface of the thick liquid layer on the piezoceramic. The jets elongate, thin out, and eventually break due to capillary pinch off, as shown in Fig. 1-d, and 1-e. Fig. 1-f, 1-g and 1-h show the breakup of few hundred-micron leftover droplets which leads to the formation of fine drops, with diameter in the range of 4-7 microns. No large drop formation is observed in this stage of atomization. The main conclusion from this observation is that ultrasonic atomization and the size of the generated droplets are strongly dependent on the size of the liquid on the surface. Thus, in order to have a continuous formation of fine (4-7 microns) mist, it is essential to continuously introduce a few hundred-micron (200-500 micron) droplet on the surface of the piezoceramic, which is the leading idea for designing and developing a narrow band fine ultrasonic mist generator.

Design and Develop a Narrow Band 5 Micron Ultrasonic Mist Generator

As the results show, continuous introduction of a 200-500 micron droplet on the surface can generate a stream of 4-7 micron mist. To do so, a capillary needle with diameter of 0.15 mm is used for continuous liquid introduction (see Fig. 2-a). As soon as the few hundred-micron droplet is introduced on the surface, atomization starts, and fine mist is generated. The picture presented in Fig. 2-b shows the continuous formation of 4-7 micron mist from the tip of the needle. The newly

designed ultrasonic mist generator is advantageous over the existing ultrasonic nebulizers in that it generates narrow band 4-7 micron mist, and that no liquid is accumulated on the surface of the piezoceramic.

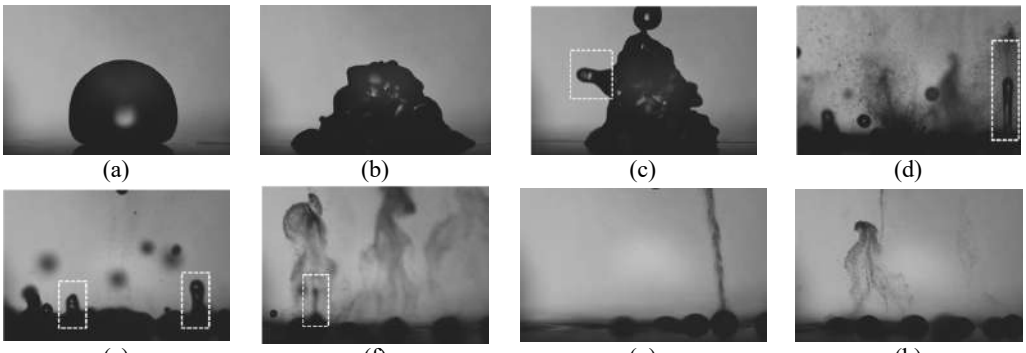

Figure 1-Temporal evolution of a 2mm dripping ethyl-alcohol droplet on the surface of a piezoceramic vibrating at 2.5 MHz: (a) Initial impact; (b,c) Fountain formation; (d,e) Fountain breakup and formation of a thick liquid layer on the surface; (f,g,h) Ultrasonic atomization of left-over sessile drops. Field of view is 3.5 mm×2.5 mm

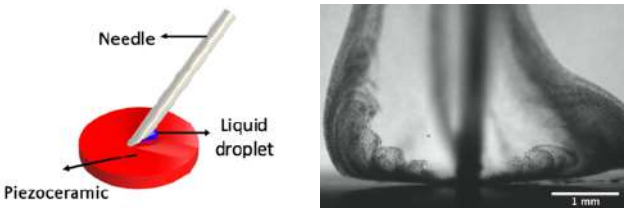

Figure 2- Continuous ultrasonic mist generation

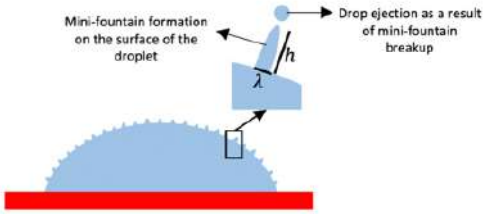

Figure 3- Mini-fountain formation on the liquid's surface and droplet ejection from the surface

Size Distribution Prediction Based on Acoustic Radiation Pressure

When ultrasonic wave reaches the surface of the droplet, due to the mismatch in the acoustic impedance of the liquid and the air, the sound wave reflects back to the droplet. Repeated impact and reflection of the wave on the liquid-air interface results in a steady stress on the droplet, leading to droplet deformation and atomization. Acoustic radiation pressure inside the droplet can be calculated from

$$p_r = p_0 \left(\frac{1}{1 + \frac{\partial \zeta}{\partial z}} \right)^{\gamma} \qquad \text{Eq. 2}$$

in which p_0 is the pressure inside the droplet at rest, ζ is the particle displacement inside the droplet, and γ is the nonlinearity coefficient for the liquid. It is assumed that in ultrasonic atomization, mini-fountains with base diameter of λ_{cr} are formed on the surface of the parent droplet (see Fig. 3), which their height, h can be calculated from pressure balance:

$$p_{in} = p_{ref} - \rho g z + p_r \qquad \text{Eq. 3}$$

where p_{ref} is the reference pressure, and p_{in} is the pressure inside the droplet that can be calculated from Laplace equation. The breakup of each of these mini-fountains will generate a droplet, the size of which can be calculated using mass balance: $\pi \lambda^2 h/4 = \pi D_p^3/6$. Using Eq. 3, the size of the generated droplet is predicted to be 4 micron which is comparable with the results from Malvern laser diffractometer.

CONCLUSIONS

The experimental results show that although all the commercially available ultrasonic nebulizers generate both large and small droplets, it is possible to develop an ultrasonic nebulizer generating 4-7 micron droplets only. This can be done by keeping the size of the parent drop on the surface of the piezoceramic around 200 microns. Additionally, due to acoustic radiation pressure, mini-fountains are formed on the surface of the droplet. Assuming that mini-fountains have a base diameter of λ_{cr}, their height can be calculated by doing a pressure balance at the tip of the fountains. Then, using mass balance, the size of the generated droplets is predicted to be 4 microns.

MHT-X: EFFICIENT MULTIPLE HYPOTHESIS TRACKING FOR MULTIPHASE FLOW ANALYSIS

Peteris Zvejnieks[1], Mihails Birjukovs*[1], Martins Klevs[1], and Andris Jakovics[1]
[1] Institute of Numerical Modelling, University of Latvia, UL, Jelgavas iela 3, LV-1004, Riga, Latvia

Summary An efficient and versatile implementation of offline multiple hypothesis tracking using Algorithm X for optimization has been developed using Pyhthon. The code is intended for scientific applications that do not require online processing. Directed graph framework is used and multiple scans with progressively increasing time window width are used for construction of maximum likelihood trajectories. The current version was developed for applications in multiphase hydrodynamics, e.g. bubble and particle tracking, and is capable of resolving object motion, merges and splits. Feasible object associations and trajectory graph edge likelihoods are determined using weak mass and momentum conservation laws translated to statistical functions for object properties. The code can handle n-dimensional motion with arbitrarily many tracked object properties and is easily extendable beyond the present application. The code is open-source and is in active development.

INTRODUCTION

Multiple Hypotheses Tracking (MHT) is classically considered to be the most reliable method for finding the optimal solution for data association problems [1, 2]. However, is often avoided for real-time (online) applications due to its computational complexity. In this paper, the MHT association search problem is formulated as an exact cover problem within a directed graph framework, which is then solved using *Algorithm-X* (Knuth's algorithm) [3], dramatically reducing complexity of covering the entire search-space of viable solutions. This solution was developed for the analysis of multiphase hydrodynamic systems. In our case, there are several problems of interest: dynamic optical, X-ray and neutron imaging of argon bubble flow in liquid gallium or galinstan; neutron imaging of gadolinium oxide particle flow in liquid gallium; bubble flow simulations using the volume of fluid method [4]. The objective is to trace objects (bubbles/particles segmented beforehand) in time, reconstructing trajectories, resolving interactions (i.e. bubble coalescence and particle adhesion) and performing velocimetry. The output can then be used, for instance, for an in-depth analysis of bubble/particle collective dynamics, comparison of simulation and experiment data, etc. The code was also designed to be able to account for significant shape oscillations for objects that are typical in the above applications. The offline implementation is dictated by scientific use, where real time data interpretation is not required, but rather reliable solutions are expected for potentially very large scale problems within acceptable time intervals. The main framework of our code is universal and can be readily adapted to any type of offline tracking problem beyond the tracing examples showcased herein.

METHODOLOGY AND FIRST RESULTS

For offline tracking, a complete set of measurements for object detection events is required as input. We propose to construct a directed graph with objects as nodes storing object properties, and store association likelihoods between objects on graph edges (edge direction aligned with the arrow of time). This input representation was chosen because of its intuitive interpretation, making it conceptually easier to implement and customize for any application. This MHT implementation, herein referred to as MHT-X, consists of several core parts used to solve for the likeliest set of edges (equivalently, trajectories). This modularity further facilitates adaptability to various problems. In addition to object nodes, two auxiliary *Entry* and *Exit* nodes (*special nodes*) are introduced to handle trajectory endpoints. With the *a priori* knowledge that objects detected in the first and last frames are, respectively, start- and endpoints of trajectories, a starting graph configuration (edges and likelihoods) is initialized. Then the tracing problem is solved in the following steps. First, edges with likelihood below threshold are deleted from the initial graph. Then the main component of the algorithm, graph sweep, is started: a time window is defined that is $Deltat$ time steps wide which is translated trough the graph in time. At every time step (t) associations are attempted within the window: the algorithm searches for trajectories without continuation within $[t; t + \Delta t)$ and for trajectories without origins within $(t; t + \Delta t]$. It is then attempted to associate these trajectories using the *pairwise association conditions* and *combination constraints*. Each of the feasible associations are then evaluated using *statistical functions* (in this case based on trajectory compliance with mass and momentum conservation), yielding their likelihoods. Finally, the association configuration with the highest global likelihood is found. Classically this is a $\mathcal{O}(n) = 2^n$ complexity problem where n is the number of considered associations. To sidestep this, we propose to formulate association optimization as an exact cover problem and solving it using Algorithm X, reducing complexity to $\mathcal{O}(n) = n \log n$ (best case). Complexity is reduced further by clustering associations into disjoint sets before formulating and solving the exact cover problem. After obtaining a solution for each window step, only

*mihails.birjukovs@lu.lv

the associations impossible to form in the next time step are added to the graph. Once the first graph sweep is complete and every node has an inbound and outbound edge(-s), a time window with increased Δt is reinitialized and the graph sweep is started over. This is repeated for increasing Δt to resolve associations over longer ranges, which provides robustness against failed/false object detections. The process stops at a final solution once maximum Δt is reached. The application of MHT-X to simulation and experiment data is illustrated in Figures 1 and 2.

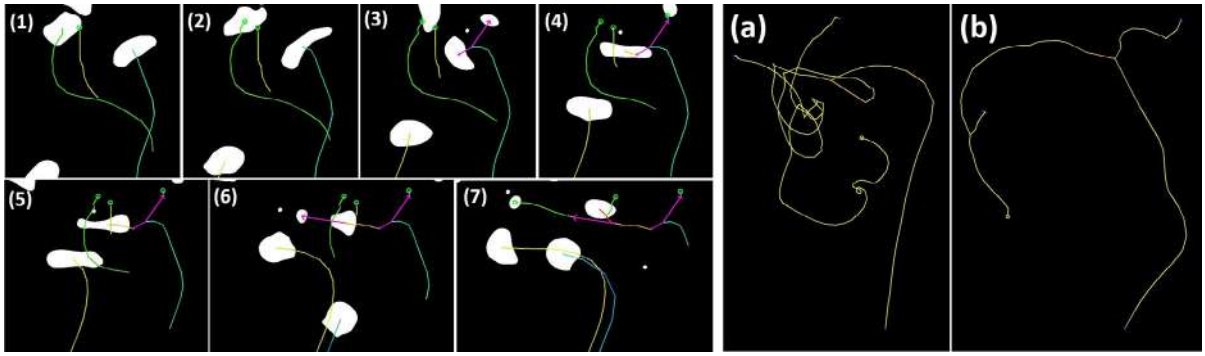

Figure 1: (1-7) Several nearby bubble trajectories and splitting events resolved over sequential frames from simulation data, and (a,b) examples of characteristic trajectory families.

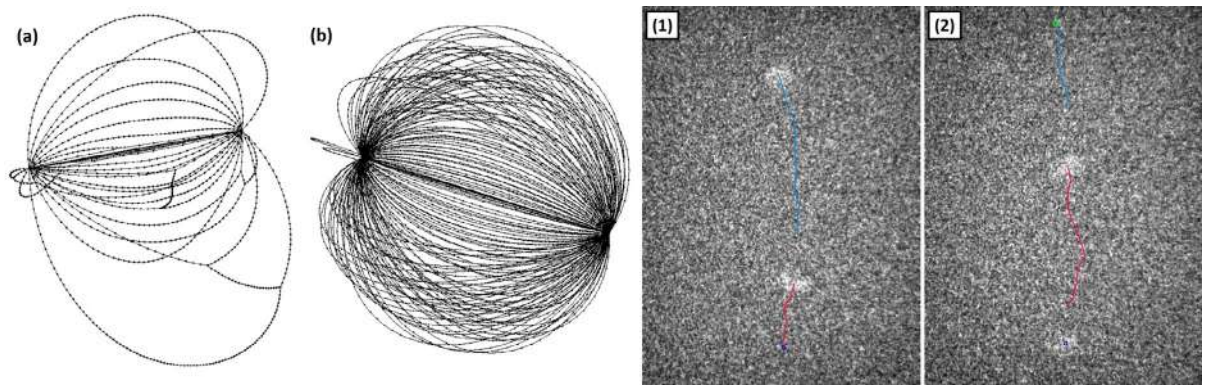

Figure 2: Example solution graphs (trajectories) for bubble flow (a) simulation and (b) neutron radiography frames, and (1,2) - example neutron radiography images with traced bubbles (bright spots).

ACKNOWLEDGMENTS

This research is a part of the ERDF project "Development of numerical modelling approaches to study complex multiphysical interactions in electromagnetic liquid metal technologies" (No. 1.1.1.1/18/A/108). Neutron images were acquired at the Swiss spallation neutron source SINQ, Paul Scherrer Institute (PSI). The authors are grateful to Pavel Trtik (PSI) and Jan Hovind (PSI) for assistance in the neutron radiography experiments.

REFERENCES

[1] "Multiple Target Tracking and Identity Linking Under Split, Merge and Occlusion of Targets and Observations". In: *Proceedings of the 1st International Conference on Pattern Recognition Applications and Methods*. SciTePress - Science, 2012, pp. 15–24. ISBN: 978-989-8425-98-0 978-989-8425-99-7. DOI: 10.5220/0003710600150024.

[2] C. Kim et al. "Multiple Hypothesis Tracking Revisited". In: *2015 IEEE International Conference on Computer Vision (ICCV)*. 2015, pp. 4696–4704. DOI: 10.1109/ICCV.2015.533.

[3] Donald E. Knuth. "Dancing links". In: *arXiv:cs/0011047* (Nov. 14, 2000). arXiv: cs/0011047. (Visited on 11/29/2020).

[4] Mihails Birjukovs et al. "Phase boundary dynamics of bubble flow in a thick liquid metal layer under an applied magnetic field". In: *Physical Review Fluids* 5.6 (June 18, 2020), p. 061601. DOI: 10.1103/PhysRevFluids.5.061601.

SEA SPRAY AT HIGH WINDS: MECHANISMS OF PRODUCTION AND ROLE IN HEAT TRANSFER AND SURFACE DRAG

Yu. Troitskaya[1], D. Sergeev[1], O. Ermakova[1], M. Vdovin[1], D. Kozlov[1], S. Zilitinkevich[2], and O. Druzhinin[1]
[1] Institute of Applied Physics, Nizhny Novgorod, Russia,
[2] Finnish Meteorological Institute, Helsinki, Finland

Summary The record strengths of recent hurricanes have highlighted needs for improving forecasts of tropical cyclone intensities most sensitive to models of the air-sea interaction. Especially challenging is the nature of sea-spray supposed to strongly affecting the momentum- and energy- air-sea fluxes at strong winds. Even the spray-generation mechanisms in extreme winds remained undetermined. Basing on high-speed video here we identify it as the bag-breakup mode of fragmentation of liquid in gaseous flows known in a different context. From the general principles of statistical physics we develop statistics of the "bag-breakup" events, estimated the production rate of spray and showed, that at extreme winds "bag-breakup" is the dominant mechanism of sea spray production. This findings form a new basis for modeling the sea-spray and air-sea exchange at hurricane wind.

INTRODUCTION

Air-sea interaction at extreme winds is of special interest now in connection with the problem of the sea surface drag reduction at the wind speed exceeding 30-35 m/s. This phenomenon predicted in [1] and confirmed by a number of field [2] and laboratory [3] experiments still waits its physical explanation. Several papers attributed the drag reduction to spume droplets - spray tearing off the crests of breaking waves (e.g., [4,5]). The fluxes associated with the spray are determined by the rate of droplet production at the surface quantified by the sea spray generation function (SGF), defined as the number of spray particles of radius r produced from the unit area of water surface in unit time. However, the mechanism of spume droplets' formation is unknown and empirical estimates of SGF varied over six orders of magnitude [6]; therefore, the production rate of large sea spray droplets is not adequately described and there are significant uncertainties in estimations of exchange processes in hurricanes. Herewith, it is unknown what is air-sea interface and how water is fragmented to spray at hurricane wind.

Using high-speed video, we observed mechanisms of production of spume droplets at strong winds by high-speed video filming, investigated statistics and compared their efficiency [7,8]. Experiments showed, that the generation of the spume droplets near the wave crest is caused by the following events: bursting of submerged bubbles, generation and breakup of "projections" and "bag breakup". Statistical analysis of results of these experiments showed that at hurricane winds the main mechanism of spray production is attributed to "bag-breakup" (Figure 1). On the base of general principles of statistical physics (model of a canonical ensemble) we developed statistics of the "bag-breakup" events: their number and statistical distribution of geometrical parameters depending on wind speed. The size distribution function of bags is lognormal and prescribed by the wind velocity.

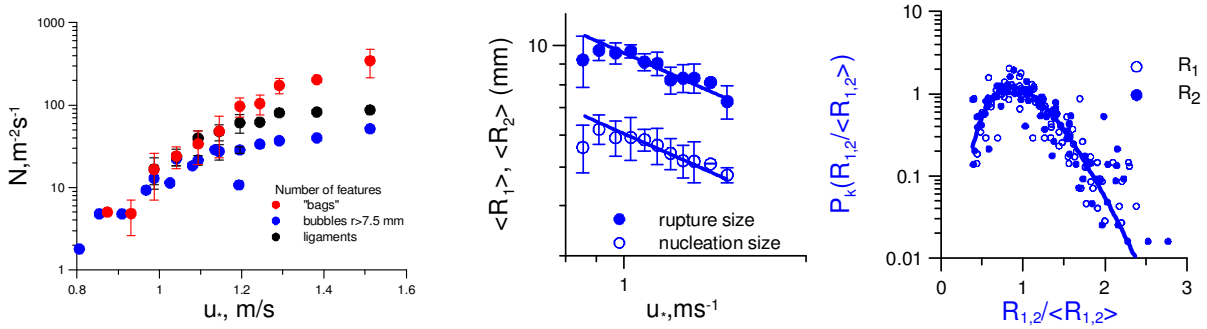

Figure 1. The specific number of events (per unit time per unit area) responsible for generation of spume droplets versus friction velocity (left), average sizes, velocities and lifetimes of "bags" via wind friction velocity (middle) , size distribution of "bags"**(right)**

SPRAY GENERATION FUNCTION

However due to a lack of experimental data, the SGF was constructed with the use of a number of assumptions. In particular, available data on the fragmentation of similar objects were used to estimate the parameters of droplets generated by the "bag-breakup" fragmentation events, namely droplets in gaseous flow or bursting bubbles. To study the peculiarities of the "bag-breakup" fragmentation process at air-water interface, the special experiment was conducted, in which the generation of droplet from a single isolated bag-breakup event was investigated and differences from the fragmentation of droplets and bursting bubbles were identified.

As it was found earlier in [7,8], the "bags" generate spray in two ways:1. Rupturing the film of inflated bag (film spray); 2. Fragmentation of the rim stayed after the bag's rupture (rim spray).

The canopy droplets were generated due to the same mechanism as the fragmentation of the bursting bubbles enclosed in [9] (Figure 1). The spray are generated by the fragmentation of the thin rim around the hole in the canopy due to the Rayleigh-Taylor (R-T) instability due to centrifugal acceleration, but there are differences:

1. The film thickness of a canopy is not constant, but it is the random value with lognormal distribution
2. In contrast to the film of the busting bubble, the thickness of the canopy does not depend on its radius. It is the random value with the average is prescribed by the wind speed ~U^{-2}. This difference can be explained by difference in the mechanisms of the film rupture in these two cases. The mechanism of the bubble rupture is thinning due to

convection in the film. In the case of the bag-breakup the film ruptures presumably due to the Kelvin-Helmholtz instability under the action of the wind. The dependence on the wind speed points this out.

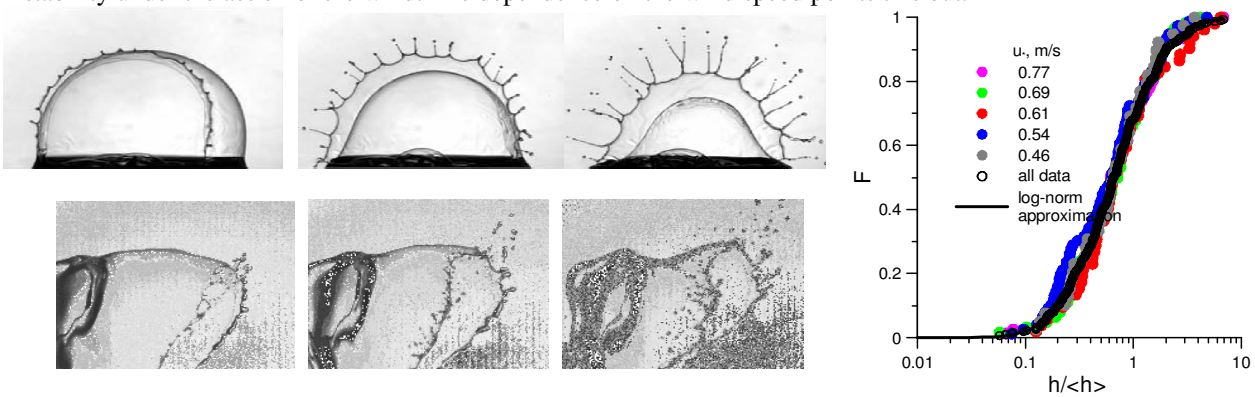

Figure 2. Fragmentation of the bursting bubble from [9] (top) and fragmentation of the canopy of the bag (bottom). Cumulative distribution of the film thiclness.

The size spectrum of the spray from bursting of one canopy of the bag as the convolution of the distribution of the film thicknesses and distribution of the droplets from the film of a certain thickness.

The formation of drops from the rim occurs through two mechanisms. Before the rupture of the canopy, the R-T instability develops at the rear edge of the bag, which results in the formation of a small number of large droplets (type 1). Then, after breaking the canopy, the remaining rim is fragmented to form smaller droplets (type 2) (Figure.2). Given the presence of two mechanisms of formation of droplets, we consider the above groups of droplets separately and examine their statistical patterns and constructed the size spectrum of the rim droplets from one bag as the composition of two lognormal distributions with parameters prescribed by the Weber number of the "bag". Based on this experiment, the distribution function of droplets from one "bag-breakup" event was built.

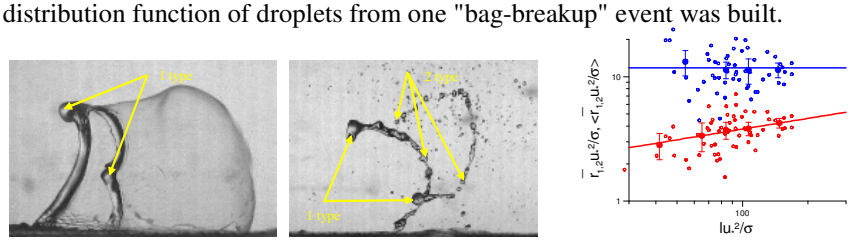

Figure 3. Droplet formation during fragmentation of the rim. Sizes of droplets of the 1-st type (blue) and 2-ng type (red).

The bag-breakup spray generation function is the convolution of the size spectra of bags with the size spectra of droplets produced by a sole bag. An important question is transferring this lab results to field conditions. The main difference between field and laboratory conditions is fetch. To adapt the results of the laboratory measurements of the statistics of the spray generating phenomena to field conditions, we used the so-called "Whitecap Method". It uses the laboratory data on spray generating phenomena normalized by the area of whitecaps and the field data on statistics of whitecaps. Using the proposed SGF, estimates are given for the air-sea fluxes of momentum, sensible and latent heat, and enthalpy.

CONCLUSIONS

We studied the peculiarities of the sea spray production at the stormy winds. The dominant mechanism of generation of spume droplets is shown to be the “bag-breakup” fragmentation. Basing on laboratory experiments with the high-speed video-filming, the SGF for the “bag-breakup” is suggested. The suggested SGF is used for estimates of the spray-mediated momentum and enthalpy fluxes. The estimates showed, that the microphysical processes are essential for intensification of the storms.

Acknowledgements. This work has been supported by the Russian Science Foundation (project 19-17-00209)

References

[1] Emanuel, K. A., 1995: Sensitivity of tropical cyclones to surface exchange coefficients.....J. Atmos. Sci., 52, 3969–3976
[2] Powell, M. D., P. J. Vickery, and T. A. Reinhold, 2003: Reduced drag coefficient for high wind speeds in tropical cyclones. Nature, 422, 279–283
[3] Donelan, M. A., et al (2004), On the limiting aerodynamic roughness of the ocean in very strong winds, Geophys. Res. Lett., 31, L18306
[4] Kudryavtsev, V.N. and V.K. Makin, 2011: Impact of ocean spray ... Boundary-Layer Meteorology, 140, 383–410
[5] Andreas, E. L., 2004: Spray stress revisited. J. Phys. Oceanogr., 34, 1429–1440.
[6] Andreas, E. L., 2002: A review of the sea spray generation function for the open ocean. Atm.-Ocean Interactions, , W. Perrie, Ed., WIT Press, 1–46
[7] Troitskaya Y., et al, 2017: Bag-breakup fragmentation as the dominant mechanism of sea-spray production in high winds. Sci. Rep., 7, 1614
[8] Troitskaya, Y., et al, 2018: “Bag-breakup” spume droplet generation mechanism at hurricane wind. Part I. Spray generation function.
[9] Lhuissier, H., and E. Villermaux, 2012: Bursting bubble aerosols. J. Fluid Mech., 696, 5–44

DROPLET DIAMETERS AND FLOW RATES IN SPRAYS AND AEROSOLS WITH SUBMICRON DROPLETS

Maksim Mezhericher*[1] and Howard A. Stone[1]
[1] Department of Mechanical and Aerospace Engineering, Princeton University, Princeton, USA

Summary In our recent work we demonstrated a novel liquid atomization process generating micro-sprays and aerosols of submicron-diameter droplets for pure solvents, suspensions and solutions. The process is based on disintegration by gas jets of thin liquid films formed as bubbles on a liquid surface. Here we show that the diameters and flow rates of the produced droplets are governed by the interplay of process timescales including capillary Rayleigh breakup, liquid viscosity and gas jet pressure. Those timescale ratios can be converted into the ratios of specific energies and into the ratios of specific energy rates, provided by the gas jets and dissipated by the atomized liquid. We introduce atomization diagrams as new graphic tool for theoretical determination of the diameters and flow rates of generated droplets, and demonstrate good agreement of our calculations with experiments.

INTRODUCTION

In our previous articles [1,2] we demonstrated a novel liquid atomization process generating micro-sprays and aerosols of submicron-diameter droplets for pure solvents, suspensions and solutions with wide ranges of viscosity and surface tension. The process is based on gas jetting on thin liquid films formed as bubbles on a liquid surface (see Fig. 1a). The research question addressed in this study is development of theoretical description for prediction of droplet diameters and flow rates produced by the new process for various liquids.

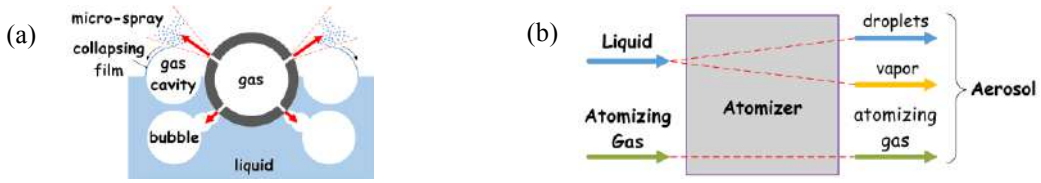

Figure 1. (a) Schematic of liquid atomization process, (b) Control volume for thermodynamic analysis.

MATERIAL AND METHODS

The developed liquid atomization process is analyzed by applying the law of mass conservation and the First Law of Thermodynamics for the control volume shown in Fig. 1b. Assuming steady-state flow for continuous adiabatic process at room temperature, neglecting the changes in potential energy of both fluids, evaporation and the change in liquid kinetic energy, assuming complete ideal expansion of the gas jet, and disregarding drag, we get:

$$e_{\Delta p} = e_c + e_v \,, \tag{1}$$

where $e_{\Delta p}$, e_c and e_v are respectively specific energies supplied by the gas pressure and dissipated by the surface tension and viscosity of atomized liquid. In our previous work [2], using the theory of dimensional analysis, we established that two dimensionless groups $\mathrm{La}_d = \rho_l \gamma_l d / \mu_l^2$ and $\mathrm{N}_d = \Delta p_{gj} d / \gamma_l$ are playing the central role for droplet diameters. Here ρ_l, γ_l, μ_l are density, surface tension and dynamic viscosity of the liquid, $\Delta p_{gj} = p_g - p_\infty$ is pressure drop over the nozzle producing gas jet, and d is droplet diameter. Using the characteristic time scales of the physical phenomena into the liquid atomization, including supplied energy of the gas jet $\tau_{\Delta p}$ $\left(\rho_l l_c^2 / \Delta p_{gj}\right)^{1/2}$, and capillary Rayleigh breakup τ_c $\left(\rho_l l_c^3 / \gamma_l\right)^{1/2}$ and viscous dissipation τ_v $\rho_l l_c^2 / \mu_l$ in the liquid, with approximation $l_c = d$ for all the phenomena, the respective dimensionless groups can be expressed as the ratios of the timescales, La_d τ_v^2 / τ_c^2 and N_d $\tau_c^2 / \tau_{\Delta p}^2$. On the other hand, the energy scales and times scales are connected, $e_{\Delta p}$ $l_c^2 / \tau_{\Delta p}^2$, e_c l_c^2 / τ_c^2 and e_v l_c^2 / τ_v^2, and we again assume $l_c = d$. Therefore, La_d e_c / e_v and N_d $e_{\Delta p} / e_c$, or $\mathrm{La}_d = k_1 e_c / e_v$ and $\mathrm{N}_d = k_2 e_{\Delta p} / e_c$, where k_1 and k_2 are proportionality coefficients. Substituting the two latter expressions into Eq. (1), we get:

$$\mathrm{N}_d = k_1 + k_1 k_2 \, \mathrm{La}_d^{-1} \,. \tag{2}$$

The obtained equation connects between the specific energies provided by the gas jets and dissipated by the atomized liquid in nondimensional form and determines the diameters of the produced droplets.

The balance of specific energy rates in the atomization can be obtained by taking the time derivative of Eq. (1):

*Corresponding author. E-mail: maksymm@princeton.edu.

$$\varepsilon_{\Delta p} = \varepsilon_c + \varepsilon_v \,. \tag{3}$$

Employing the dimensionless analysis and algebraic manipulations similar to those performed above for droplet diameters, two dimensionless numbers $\mathrm{N}_{l,cv} = \rho_l^2 \gamma_l d^3 n_d / \mu_l^3$ and $\mathrm{N}_{l,pc} = \Delta p_{gj}^{3/2} / \left(\gamma_l \rho_l^{1/2} n_d \right)$ playing the central role for droplet flow rates are established, where n_d is droplet production rate. Correspondingly, $\mathrm{N}_{l,cv}$ $\varepsilon_c / \varepsilon_v = k_3 \varepsilon_c / \varepsilon_v$ and $\mathrm{N}_{l,pc}$ $\varepsilon_{\Delta p} / \varepsilon_c = k_4 \, \varepsilon_{\Delta p} / \varepsilon_c$, where k_3 and k_4 are proportionality coefficients. Substituting into Eq. (3), we get:

$$\mathrm{N}_{l,pc} = k_3 + k_3 k_4 \, \mathrm{N}_{l,cv}^{-1} \,. \tag{4}$$

The obtained equation connects between the rates of specific energies provided by the gas jets and dissipated by the atomized liquid in nondimensional form and determines the flow rates of the produced droplets.

RESULTS AND DISCUSSION

The atomization diagrams for diameters and flow rates of water droplets are given in Fig. 2. The droplet diameter and gas jet pressure were varied in Fig. 2a, and the droplet production rate and droplet diameter were varied at $\Delta p_{gj} = 2.5$ bar in Fig. 2b. The central lines of atomization region on the diagrams were obtained from Eqs. (2) and (4), assuming the proportionality coefficients to be order of unity. The lower and upper boundaries of the atomization region are calculated by assuming tenfold difference of the dimensionless numbers N_d (Fig. 2a) and $\mathrm{N}_{l,pc}$ (Fig. 2b) with respect to those of the corresponding central lines $\mathrm{N}_d^* = 1 + \mathrm{La}_d^{-1}$ and $\mathrm{N}_{l,pc}^* = 1 + \mathrm{N}_{l,cv}^{-1}$. From Fig. 2a for $\Delta p_{gj} = 2.5$ bar, we can calculate that the atomization process is expected to generate droplets with diameters in the range 40 nm – 3 μm, and mean droplet diameter ~300 nm. In our experimental studies [1], the arithmetic mean diameter was ~250 nm and the upper boundary of the obtained number based droplet size distribution was ~3 μm, whereas the lowest measured droplet diameter was set by the measuring range 100 nm – 900 μm of the utilized laser scattering device. For the calculated mean diameter of 300 nm, Fig. 2b reads 10^8 drop/s, while the experiment [1] measured 10^7 drop/s. This difference can be attributed to a theoretical assumption of a continuous atomization process, while in fact there is a periodic disintegration by a gas jet of bubbles rising to the liquid surface (Fig. 1). The calculations for other liquids (not shown here), including gasoline, diesel and solutions of sodium alginate, also demonstrated a good agreement between the theory and experiment. Finally, it is worth noting that for the region of $\mathrm{La}_d \geq 1$ in Fig. 2a, the distribution of droplet diameters in the atomization region follows a log-normal law, which is widely observed in technical and natural liquid atomization processes [3].

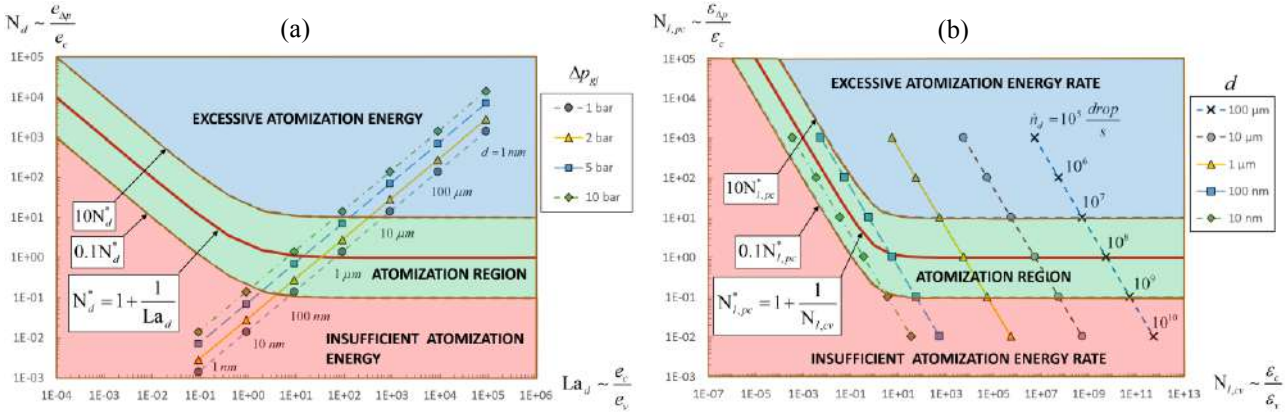

Figure 2. Atomization diagrams for diameters (a) and flow rates (b) of water droplets.

CONCLUSIONS

In this work we demonstrated new theoretical approach to determine droplet diameters and flow rates in sprays and aerosols using atomization diagrams. The approach is based on the first principles of conservation of mass, energy, and energy rates. The comparison between theoretically predicted and measured droplet diameters and droplet flow rates demonstrated a good agreement for new liquid atomization process generating micro-sprays and aerosols of submicron-diameter droplets.

References

[1] Mezhericher M., Ladizhensky I., Etlin I. Atomization of Liquids by Disintegrating Thin Liquid Films Using Gas Jets. *Int. J. Mult. Flow*. **88:** 99-115, 2017.

[2] Mezhericher M., Razorenov N., Mazor G., Ju Y., Stone H.A., Submicron Aerosols of Liquid Fuels: Method of Production, Experimental Characterization and a Semi-Empirical Model. *App. Energy*. **235**:1651–1663, 1999.

[3] Ashgriz N. (ed.). Handbook of Atomization and Sprays: Theory and Applications. Springer, NY 2011.

SPONTANEOUS DYNAMICS OF LEIDENFROST DROPS

Rodolfo Brandão * [1] and Ory Schnitzer[1]
[1] Department of Mathematics, Imperial College London, SW7 2AZ London, UK

Summary Recent experiments have revealed that Leidenfrost drops (levitated by their vapor above a hot surface) undergo "symmetry breaking", leading to spontaneous rolling motion in the absence of external gradients/asymmetries. We present a simplified two-dimensional dynamical model of a Leidenfrost drop that predicts an instability of the symmetric Leidenfrost drop, symmetry breaking and spontaneous motion, in compelling qualitative agreement with the experiments. The key enabling mechanism is shown to be the nonlinear coupling between the internal flow of the liquid and the lubricating flow in the vapor thin-film.

INTRODUCTION

A liquid deposited above a sufficiently hot substrate can generate a thin layer of insulating vapour — a phenomenon known as the Leidenfrost effect. This vapour layer prevents direct contact between the liquid and the substrate, thus considerably slowing down the evaporation process.

Particular attention has been devoted to Leidenfrost drops, namely slowly-evaporating drops in the Leidenfrost state. These drops levitate above their own vapor and experience very low friction, attributes that hold promise in various microfluidic applications. Due to the combination of hydrodynamic, thermal and capillary effects, Leidenfrost drops exhibit very rich dynamics, including oscillations, bouncing and directed propulsion using textured surfaces [1].

Recent experiments have revealed that Leidenfrost drops above a flat surface can also generate their own dynamics from a symmetry-breaking mechanism [2]. In detail, a rotational flow can be spontaneously established within an immobilized drop; the rotation induces an asymmetry at the drop base and, when the drop is released, it begins to move at an acceleration approximately equal to the "characteristic slope" of the asymmetry times the gravitational acceleration g, akin to a drop rolling down a virtual inclined plane. The symmetry breaking only occurs for drops smaller than the capillary length $l_c = \sqrt{\gamma/\bar{\rho}g}$, wherein $\bar{\rho}$ is the drop density and γ is the surface tension, but not arbitrarily small, and the range of unstable drop radii depends on the substrate temperature. These discoveries received significant attention, as they may help to explain the exceptional mobility of Leidenfrost drops and open new avenues of practical exploitation.

We theoretically investigate the mechanics enabling symmetry-breaking spontaneous dynamics of Leidenfrost drops based on a simplified two-dimensional model [3]. Our model consists of the equations of motion of the drop with the torques and forces calculated from an instantaneous lubrication model of the vapor thin film.

MODEL

We consider a liquid drop (area πR^2, density $\bar{\rho}$, viscosity $\bar{\mu}$) levitated by its vapor (thermal conductivity k, density ρ, viscosity μ) above a superheated flat surface of temperature ΔT relative to the drop. We shall focus exclusively on the limit $B \ll 1$, where $B = (R/l_c)^2$ is the Bond number. In that case, the drop interface is approximately a circle except close to a small $O(BR)$ "flat spot" at the bottom of the drop. Furthermore, the internal flow in the drop is a superposition of a rigid-body translation, at velocity $\mathcal{U}(t)\hat{\mathbf{e}}_x$, and and rigid-body rotation, at angular velocity $\Omega(t)\hat{\mathbf{e}}_y$ (see Figure 1) [3].

Vapor thin-film

The vapor thickness profile $h(x,t)$ and the vapor pressure $p(x,t)$ are governed by the thin-film equations,

$$\frac{\partial}{\partial x}\left(\frac{h^3}{12\mu}\frac{\partial p}{\partial x}\right) + \frac{\mathcal{U}+\Omega R}{2}\frac{\partial h}{\partial x} = -\frac{\lambda}{h}, \quad p = \frac{\gamma}{R} - \gamma\frac{\partial^2 h}{\partial x^2}, \tag{1}$$

where $\lambda = k\Delta T/\rho l$, l being the latent heat of evaporation. At large distances, $p \to 0$ and the profile h matches that of a non-wetting drop on a horizontal plane,

$$h \sim \frac{1}{2R}\left(x \mp \frac{\pi BR}{2}\right)^2 + h_\pm + o(1) \quad \text{as} \quad x \to \pm\infty. \tag{2}$$

Equations of motion

The drop flows like a rigid body. The linear and angular momentum equations are, respectively,

$$m\frac{d\mathcal{U}}{dt} = \mathcal{P} - \mathcal{F}, \quad I\frac{d\Omega}{dt} = \mathcal{T} - R\mathcal{P} + R\mathcal{F}, \tag{3}$$

where $m = \pi\bar{\rho}R^2$ and $I = mR^2/2$ are respectively the mass and moment of inertia of the drop. The forces and torques appearing in (3) are calculated from the lubrication model for the vapor film and given by

$$\mathcal{P} = \frac{1}{2}\alpha mg, \quad \mathcal{T} = \alpha mgR, \quad \mathcal{F} = \mu(\mathcal{U}-\Omega R)\int_{-\infty}^{\infty}\frac{dx}{h}, \tag{4}$$

where $\alpha = (h^- - h^+)/\pi BR$ is the characteristic slope of the drop base.

*Corresponding author. E-mail: r.brandao18@imperial.ac.uk.

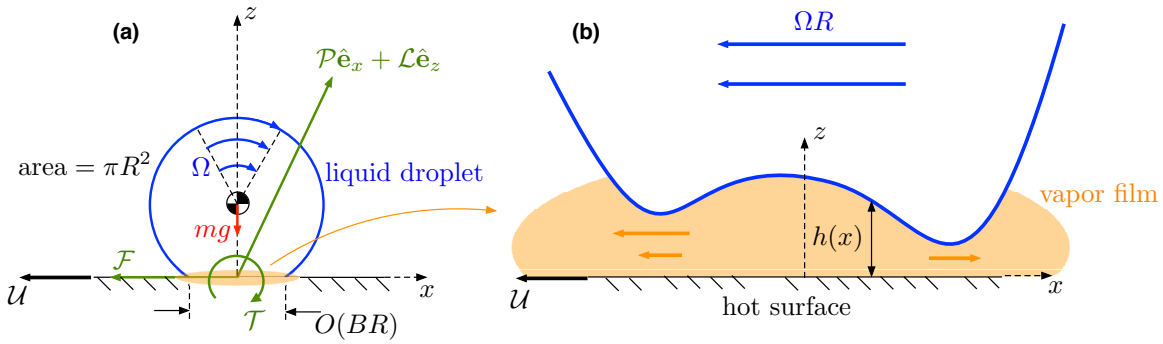

Figure 1: Sketch of a two-dimensional near-circular Leidenfrost drop in a comoving frame. (a) Drop-scale dynamics. (b) Lubrication region.

RESULTS

Free drops

Let us first consider a Leidenfrost drop which is free to move until it reaches a steady state. Fixed points of the dynamical system (3) satisfy the "force-free" condition $\mathcal{P} = \mathcal{T} = \mathcal{F} = 0$. Equivalently, fixed points satisfy the conditions $\alpha = 0$ and $\mathcal{U} = \Omega R$ ("pure-rolling").

Due to the symmetry of the dynamical system, there is always the trivial fixed point $(\mathcal{U}, \Omega) = (0, 0)$ which corresponds to the usual stationary-symmetric state of a Leidenfrost drop [1]. The symmetric state, however, is stable only for $R < R_1 \approx 3.2(\mu\lambda\gamma^5/\bar{\rho}^6 g^6)^{1/13}$. For $R > R_1$, α exhibits two non-trivial zeros corresponding to stable left- and right-going pure-rolling steady states, which bifurcate at $R = R_1$ from the trivial zero.

Initially immobilized drops

The constant-acceleration motion observed in the experiments [2] suggests that the system is not in a steady "pure-rolling" state. Moreover, the experimental data also suggests an inertial time scale much larger than the observation time, which indicates that the experiments are restricted to early stages of the dynamics. To model the initial dynamics of the drop, we note that each experiment in [2] consists of two stages. In the first stage, the drop is immobilized, by a needle, and a steady rotational flow builds within the drop. In the second stage, the drop is released and is free to move for a short duration of time relative to the inertial time scale.

When the drop is immobilized, its dynamics is governed solely by the angular momentum equation in (3) with the forces calculated from (4) with $\mathcal{U} = 0$. Fixed points of this reduced system satisfy $\mathcal{P} - \mathcal{F} = \mathcal{T}/R$, representing the zero-net-torque condition for an immobilized drop. Analogously to the free-drop case, the symmetric state $\Omega = 0$ is stable only for $R < R_2 \approx 6.3(\mu\lambda\gamma^5/\bar{\rho}^6 g^6)^{1/13}$. For $R > R_2$, there are stable steady states of angular velocity $\Omega = \Omega^*$.

Now assume that an immobilized drop rotating at the stationary angular velocity $\Omega = \Omega^*$ is released at $t = 0$. From (3) and (4), the drop starts to move with acceleration

$$\frac{d\mathcal{U}}{dt} = \alpha g. \tag{5}$$

This expression agrees with that observed in the three-dimensional experiments [2].

Further agreement between theory and experiment can be verified by analyzing the dependency of the drop acceleration with the physical parameters. Our model predicts that the acceleration has a maximum as R is varied with all other parameters held fixed. Furthermore, as the temperature difference ΔT is increased, the position of the maximum shifts to a larger radius and the magnitude of the maximal acceleration increases. These trends are in good qualitative agreement with the experiments [2].

References

[1] D. Quéré. Leidenfrost dynamics. *Annu. Rev. Fluid Mech*, **45**, 197-215, 2013
[2] A. Bouillant *et al.*. Leidenfrost wheels. *Nat. Phys.*, **14**, 1-6, 2018
[3] R. Brandão, and O. Schnitzer. Spontaneous dynamics of two-dimensional Leidenfrost wheels. *Phys. Rev. Fluids*, **5**, 091601, 2020

X-RAY IMAGING OF BUBBLE FLOW IN LIQUID METAL: SHAPE DYNAMICS UNDER CONFINEMENT

Mihails Birjukovs*[1], Tobias Lappan †[2], Natalia Shevchenko[2], Olga Keplinger[2], Sven Eckert[2], and Andris Jakovics[1]
[1] Institute of Numerical Modelling, University of Latvia, UL, Jelgavas iela 3, LV-1004, Riga, Latvia
[2] Helmholtz-Zentrum Dresden-Rossendorf, HZDR, Bautzner Landstrasse 400, 01328 Dresden, Germany

Summary Argon bubbles injected into thin vessels filled with galinstan are imaged using X-ray radiography. Confinement results in significant bubble deformations and shape variations, agglomeration, as well as intensified merging and breakup. We have developed a shape analysis algorithm suitable for arbitrary bubble shapes. Here it is used to quantify the effects of flow confinement and varying gas flow rate, and to study the physics of breakup and merging in detail. We demonstrate a clear influence of flow rate and container thickness on various bubble characteristics derived from the shape analysis and explain the physical origins thereof, providing insights into collective bubble dynamics and further validating X-ray radiography as a reliable method for analysis of optically opaque gas/liquid systems. The results of this study are relevant to theoretical and applied magnetohydrodynamics.

INTRODUCTION

Bubble flow in liquid metal has several applications, e.g. in metallurgical processes, such as metal stirring, purification and homogenization, and in liquid metal-based chemical reactors [1]. However, bubble flow exhibits complex collective dynamics, therefore appropriate experimental methods are necessary to study the underlying physics in hopes of optimizing industrial processes. One usually experiments with downscaled (via similarity criteria) systems of interest and using low melting point model liquids and inert gases [1]. One of the prospective contactless methods for bubble flow analysis is the high frame rate dynamic X-ray transmission radiography (XTR), which has been successfully validated both experimentally [2] and *in silico* [3]. XTR allows direct observations of gas/liquid phase boundaries, enabling in-detail analysis of bubble shape dynamics and collective behaviour. Bubble breakup [4], coalescence [5] and agglomeration are of special interest, but thus far XTR studies have been limited to qualitative analysis due to challenges related to image processing [4, 5]. Here we present our image processing approach and bubble shape analysis method. Applicable to most types of bubble shapes, these tools are employed to study the effects of flow confinement on bubble collective dynamics.

METHODOLOGY AND PRELIMINARY RESULTS

Previously bubble coalescence and breakup were studied in systems with 12 mm liquid metal thickness using XTR [4, 5]. Here, we turn to much more confined systems with 3- and 6 mm thickness, imaged with gas flow rates 50 - 250 and 50 - 685 cm^3/min, respectively. Injecting large gas volume into flat containers promotes stronger bubble flattening and deformations and intensifies bubble collisions, agglomeration, breakup and coalescence (Figure 1) due to partial container obstruction by ascending bubbles. Using an XTR setup similar to the one in [5], we observe a wide range of different bubble shapes. Their detection and description requires a special approach. Additionally, due to agglomeration, one must accurately resolve thin metal films between bubbles (Figure 1).

To do this, we use uncompressed high resolution images and the following processing steps. Local adaptive binarization followed by a self-snakes filter and single threshold Otsu binarization, after which morphological closing and Canny edge detection are applied. Logical filters remove image artefacts and bubble contours are extracted (Figure 2), allowing to resolve collisions, breakup and collective ascension. Our shape analysis algorithm then finds bubble centroids and computes bubble center lines (BCL) as maximum length curves from the minimum spanning tree of the Voronoi mesh nodes computed from bubble boundary mesh nodes and using the derived boundary curvature distribution (Figure 3). This, in turn, enables one to compute bubble thickness profile over BCL arc length, BCL curvature, length, etc., accounting for bubble shape irregularity and yielding insight into how bubbles split or merge (Figures 3d, 3e). One may also construct a chord connecting the BCL endpoints – the ratio of the chord length to that of the BCL is a measure of bubble ellipticity; the distance profiles between chord and BCL nearest points and integrals thereof over the BCL characterize the degree of bubble bending and irregularity (Figures 3a, 3b, 3c). Chord orientation, for small instantaneous bubble deformations, informs one of rotational motion. In addition, one may derive thickness profiles for metal films separating agglomerated bubbles to study their interactions. All of this (and more) quantifies the effects of

*mihails.birjukovs@lu.lv
†t.lappan@hzdr.de

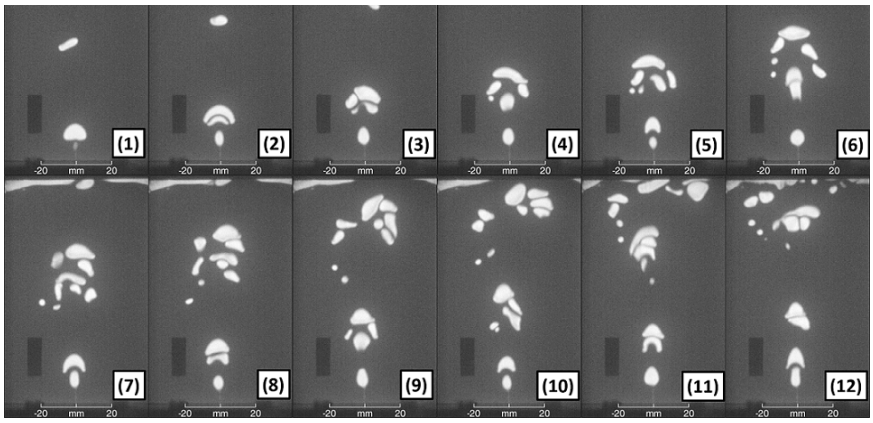

Figure 1: XTR images of argon bubbles in a 3 *mm* pool of galinstan. Numbers indicate the order of frames.

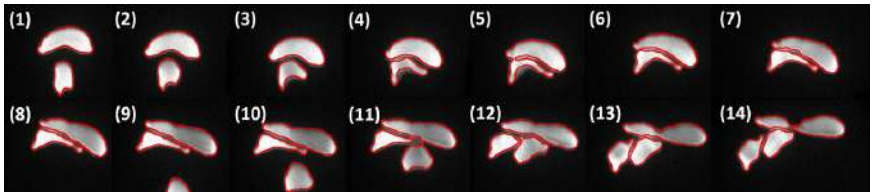

Figure 2: Bubble shapes resolved by our image processing pipeline. Numbers indicate the order of frames.

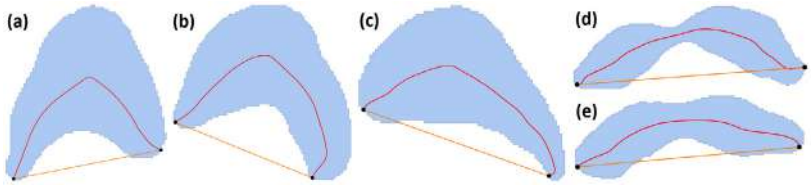

Figure 3: Bubble center lines (red) and principal chord lines (orange) derived using our shape analysis tool. Bubble shapes are represented by light blue areas.

varying flow rate or the degree of bubble confinement. In addition, high XTR frame rate (150 frames per second) allows us to obtain bubble velocity via simple linear velocimetry. Combined with derived shape parameters, analysis of bubble trajectories and envelopes thereof (computed using the statistics-sensitive non-linear iterative peak-clipping (SNIP) algorithm) we are able to construct various correlation curves which should help interpret bubble flow physics.

The approach presented herein is of high interest for subsequent studies of how applying different configurations of magnetic field (not necessarily static) affects bubble/bubble and bubble/flow interactions in liquid metal under geometric confinement because many aspects of these phenomena are currently unclear. Further work will allow us to establish relevant correlations of bubble/flow characteristics and infer physical mechanisms that govern bubble dynamics. Our shape analysis method is also easily applicable to neutron transmission radiography of gas/liquid metal systems [6, 7], but also beyond.

References

[1] Eckert S., Gerbeth G., Raebiger D., Willers B., Zhang C. Experimental Modelling Using Low Melting Point Metallic Melts: Relevance for Metallurgical Engineering. *Steel Res. Int.* **78**: 419-425, 2007.

[2] Keplinger O., Shevchenko N., Eckert S. Validation of X-ray Radiography for Characterization of Gas Bubbles in Liquid Metals. *IOP Conf. Ser. Mater. Sci. Eng.* **228**: 012009, 2017.

[3] Krull B., Strumpf E., Keplinger O., Shevchenko N., Fröhlich J., Eckert S., Gerbeth G. Combined Experimental and Numerical Analysis of a Bubbly Liquid Metal Flow. *IOP Conf. Ser. Mater. Sci. Eng.* **228**: 012006, 2017.

[4] Keplinger O., Shevchenko N., Eckert S. Experimental Investigation of Bubble Breakup in Bubble Chains Rising in a Liquid Metal. *Int. J. Multiph. Flow* **116**: 39-50, 2019.

[5] Keplinger O., Shevchenko N., Eckert S. Visualization of Bubble Coalescence in Bubble Chains Rising in a Liquid Metal. *Int. J. Multiph. Flow* **105**: 159-169, 2018.

[6] Birjukovs M., Dzelme V., Jakovics A., Thomsen K., Trtik P. Argon Bubble Flow in Liquid Gallium in External Magnetic Field. Accepted in *Int. J. Appl. Electrom.* (2019), **pending print**.

[7] Birjukovs M., Dzelme V., Jakovics A., Thomsen K., Trtik P. Phase Boundary Dynamics of Bubble Flow in Liquid Metal Under Applied Magnetic Field. **Under review** in *Phys. Rev. Lett.* (2019).

INTERNAL STRUCTURE OF FLOWS CONVEYING COARSE PARTICLES IN OPEN CHANNEL AND PRESSURIZED PIPE

Václav Matoušek[1,2]
[1] Department of Civil Engineering, Czech Technical University in Prague, Prague, Czech Republic
[2] Institute of Hydrodynamics, Czech Academy of Sciences, Prague, Czech Republic

Summary In many industrial applications (e.g. mining, dredging) or geomorphological applications (e.g. river control, stream restoration), transport of coarse solid grains in flow of water must be considered and evaluated. In order to assess the transport successfully, granular support mechanisms must be analyzed and their effect on the flow of the solid-liquid mixture quantified. Particle-laden flows carrying particles at high volume concentrations establish a layered internal structure and occur in the form of sliding-bed flows in pressurized pipes and in the form of sheet flows in open channels with mobile beds. Results and developments are discussed of our work on physical and mathematical modelling of such flows and their internal structures. The results include experimental observations from pipe- and flume set-ups in two laboratories in Prague. Furthermore, present and future activities are outlined of our research work in this field.

INTRODUCTION

In industrial slurry launders or in steep morphological streams with mobile beds, particles are transported at high concentration in flow of carrying liquid. If the transport is intense due to high shear stress applied at the top of the mobile bed, then the flow carrying particles over a plane surface of the eroded bed tends to develop a layered structure across the flow depth. It is typical for such a flow that particles are non-uniformly distributed across the flow depth and a transport layer develops through which the particles are transported above the bed. The distribution of particles is mutually related with the distribution of particle velocity and both are important for an identification of an internal structure of the flow. The particle distribution affects flow resistance and hence a relationship between the flow rate and the flow depth in the open channel flow.

Settling slurry flows in pressurized pipes exhibit very similar behaviour and a comparable internal structure of the flow as sediment-laden open-channel flows. It is of interest to study the two types of particle-laden flow in parallel and to analyse their similarities and differences.

EXPERIMENTS ON INTERNAL STRUCTURE OF PARTICLE-LADEN FLOWS

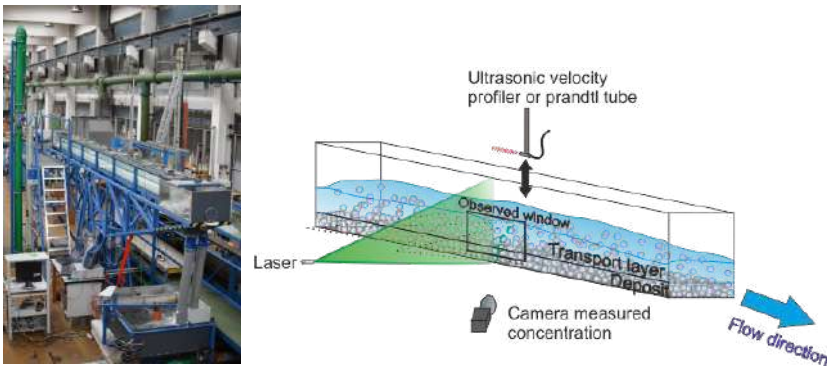

Figure 1. Sediment-transport tilting flume at Czech Technical University in Prague.

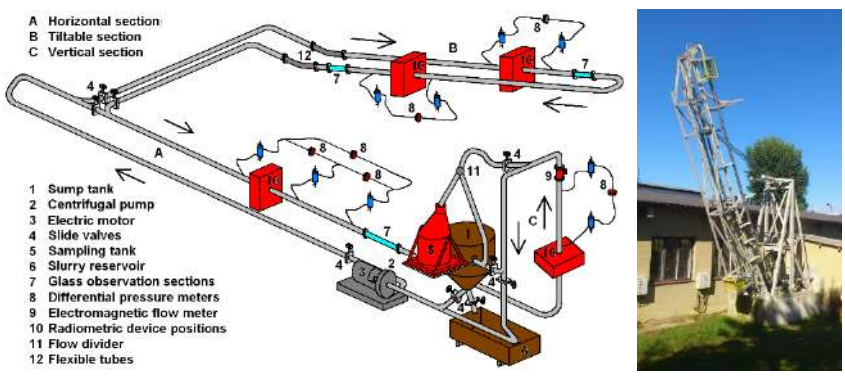

Figure 2 Slurry pipe loop at Institute of Hydrodynamics in Prague.

Our experimental works are carried out on two laboratory set-ups of very different geometries. Experiments in a recirculating tilting flume at the Water Engineering Laboratory of Czech Technical University in Prague produce distributions of flow velocity and sediment concentration along the flow depth (Figure 1) [1]. Our recent investigations focused on collisional transport and our present activities include testing of transport of combined load composed either of one fraction of sediment or of bimodal sediment. The other set-up is a slurry pipe loop (an internal diameter of the pipe is 100 mm) with an inclinable inverted U-tube at the Institute of Hydrodynamics in Prague. It allows to measure distribution of particles across the pipe cross section at various locations along the loop, including the inclinable sections (Figure 2). Our recent tests investigated an effect of a pipe inclination on the distribution of particles in flow of settling (sand-water) slurry. The experimental program continues with testing the effect of particle size distribution on settling slurry flow behavior.

OPEN-CHANNEL SEDIMENT-LADEN FLOW

Experimental information on an internal structure of sediment-laden flow from the tilting flume assists to validate simplified vertical distributions of granular velocity and concentration across the transport layer considered in our recent transport model for collisional load in sediment-laden open-channel flow [2]. The model employs constitutive relations based on the classical kinetic theory of granular flows. For given slope and depth of the flow, the model predicts the total discharge and the discharge of sediment, and the thicknesses of the water layer and of the transport layer with is frictional and collisional sub-layers. An extension of the transport model is work currently in progress and it aims on transport of combined load (combination of contact load and turbulent suspension load). The work includes an analysis of an ability of turbulent eddies to support locally grains at different locations within the transport layer [3].

PRESSURIZED-PIPE SLURRY FLOW

Recent experiments in the slurry pipe loop revealed an anomalous variation in distribution of particles in a settling slurry pipe if it was inclined to positive and negative angles (ascending and descending flows). It was shown that the anomalous behaviour affected the pressure drop in the inclined flow. Model tests revealed that this effect could be captured by our layered model for inclined settling slurry flows [4].

Our present project investigates a suitable granulometric composition of bimodal slurries with an aim to minimize energy costs of the slurry transport. The research is based on an identification and description of mechanisms governing interaction of two fractions in the bimodal slurry flow. A special attention is paid to the proportion of grain sizes and volume concentrations of individual fractions as well as to an effect of flow conditions on an optimization of design and operation of pipelines transporting heterogeneous slurries.

Furthermore, our present modelling efforts include works on a detailed description of pipe flow of fully suspended slurry, including its internal structure, using two-fluid modelling technique and its validation by experimentally determined distributions of particles in the suspension flow at different flow conditions (flow velocities and particles concentrations) [5].

CONCLUSIONS

Works are under way on mathematical and physical modelling of particle-laden flows transporting various fractions of particles in different flow geometries. Our recent results for open-channel sediment-laden flows include an analysis of a transport layer in which collisional support of the particles dominates. At present, a transport layer composed of combined load is studied and prevailing particle support mechanisms identified at local level within in the internal structure of the transport layer. In pipe slurry flows, recent investigations revealed variations in the internal structure of the settling slurry flow caused by changes in an inclination of the pipe. The present and near-future activities focus on sensitivity of the flow structure and flow behaviour on changes in a granulometric (narrow-graded versus broadly graded) composition of the transported fraction of particles.

Acknowledgment

The research has been supported by the Czech Science Foundation through the grant projects Nos. 19-18411S and 20-13142S.

References

[1] Matoušek V., Zrostlík Š., Fraccarollo L., Prati A., Larcher M. Internal Structure of Intense Collisional Bed Load Transport. *Earth Surf Process Landf*, **44**(11): 2285-2296, 2019.

[2] Matoušek V., Zrostlík Š. Collisional Transport Model for Intense Bed Load. *J Hydrol Hydromech*, **68**(1): in press, 2020.

[3] Matoušek V., Zrostlík Š. Combined Load in Open Channel: Modelling of Transport Layer at High Bed Shear. Proc. River Flow 2020, Delft, Netherlands, 2020.

[4] Matoušek V., Krupička J., Kesely M. A Layered Model for Inclined Pipe Flow of Settling Slurry. *Powder Technol*, **333**: 317-326, 2018.

[5] Messa G., Matoušek V. Analysis and Discussion of Two Fluid Modelling of Fully Suspended Slurry Flow. *Powder Technol*, **360**: 747-768, 2020.

FRONTIERS IN IMPACT EROSION MODELLING AND TESTING

Stefano Malavasi* , Gianandrea Vittorio Messa, Yongbo Wang, and Marco Negri
Department of Civil and Environmental Engineering, Politecnico di Milano, Milano, Italy

Summary The removal of material from solid surfaces due to the impingements of solid particles transported by a fluid, referred to as impact erosion, has been the subject of scientific research for long time due to the serious economic implications of this phenomenon. Owing to the fact that experiments are very costly and difficult-to-perform, since the last two decades there has been an increasingly use of numerical modelling based on Computational Fluid Dynamics (CFD) as an approach for impact erosion prediction. In this keynote, an overview of the state-of-the-art in impact erosion modelling and testing of impact erosion will be presented, with particular emphasis on the efforts made within our research group as well as on the open issues and challenges for future researchers.

Erosion is a general term denoting the removal of material from solid surfaces, which can occur in either a natural or a manmade environment and might be produced by different causes. Focus of the present keynote is a very specific type of erosion, called impact erosion, which is produced by the impingements of solid particles dragged by a carrier fluid. Researchers are intrigued by impact erosion, not only because its occurrence is a threat to the optimal design and management of engineering systems, with important economic implications, but also because of the complex multidisciplinary nature of this phenomenon, at the frontier between fluid and solid mechanics. From the solid mechanics perspective, the challenge is how to estimate the damage that a particle impinging against a surface is potentially capable to provide, which, broadly speaking, consists in establishing a functional relationship for the severity of erosion damage. Since pioneering studies [1-3], it has been agreed that erosion damage is the result of cutting wear, mainly occurring at low particle impact angles, and deformation wear, enhanced at high particle impact angles. Furthermore, it has been experimentally assessed [4,5] that the erosion damage is dependent upon the particle impact velocity, in the form of a power law with exponent generally higher than 2, and upon the particle impact angle, which plays a different role according to the mechanical behavior of the target material (brittle or ductile). Throughout the years, the functional relationship was extended by accounting for many other parameters, including material hardness, particle size and particle shape, and finally turned into empirical formulas called single-particle erosion models [6-8]. Such erosion models provide the basis for erosion prediction via Computational Fluid Dynamics (CFD), following a three-step procedure [8]. Firstly, the particle-fluid flow is calculated using an Eulerian-Lagrangian two-phase model, in which the fluid flow field is solved in an Eulerian, cell-based framework, whereas the motion of the solid phase is represented by tracking the trajectories of a certain number of computational particles. Secondly, the locations and velocities of the particles at their stage of impingement against the solid walls are stored. Thirdly, erosion models are applied to each particle-wall collision and the erosion damage is estimated. The reliability of erosion predictions does not depend only upon the accuracy of the erosion model, but also on that of the calculated particle-fluid flow field, especially close to the solid walls. This is the main challenge of impact erosion modelling from the fluid-dynamic perspective.

A number of research groups throughout the world have been and still are active in the study of impact erosion of hydraulic equipment, with different reference applications. For instance, the research carried out at the Erosion/Corrosion Research Center at the University of Tulsa, as well as in several other institutions in China and northern Europe, is focused on the erosion occurring in oil and gas production processes [8-10]. India and Switzerland have long tradition in the study of erosion in hydraulic turbines, which is a significant issue in the hydropower plants located in those areas owing to the presence of suspended sediment concentration and hard mineral particles in mountainous rivers [11,12]. Finally, it is noted that, in some applications, the removal of material brought about by the erosive action might not be an adverse effect but the key benefit. This is the case, for instance, of the abrasive slurry jet machining [13] for manufacturing processes or the sandblasting technique for cleaning operations [14].

Even our research group (FluidLab at Polimi) has put effort in providing a contribution to the field by trying to increase the reliability and accuracy of CFD-based erosion prediction, with particular interest on the impact erosion produced by liquid-solid slurry flows in industrial systems. Numerical modelling and experimental testing have been combined, the experimental data collected in two setups in the Hydraulic Laboratory of Politecnico di Milano being used to further understand the erosion process as well as to validate the CFD simulations. A preliminary achievement was the assessment of the how the various sub-models and parameters of a CFD-based erosion prediction model affect the erosion estimates, as discussed in the paper [15] referring to the benchmark case of slurry direct impact test. In addition, a significant part of our research has been aimed at developing methods to predict the impact erosion produced by flows with massive amounts of particles, which is not practically possible using the standard methodology due to the high computational cost of Eulerian-Lagrangian models. A mixed Eulerian-Eulerian / Eulerian-Lagrangian approach was first developed [16], in which the tracking of the particle trajectories was limited to the vicinity of wall boundaries, whereas the bulk flow field was solved using an Eulerian-Eulerian model. Later, the mixed Eulerian-Eulerian / Eulerian-Lagrangian was further improved by accounting for the nonlinear time evolution arising from the eroding surface changes [17]. This allowed improving the reliability of the wear estimates by overcoming another serious drawback of the existing methodology, that is, the assumption of steady-state erosion. As a distinctive character of our group, each modelling achievements have been

* Corresponding author. E-mail: stefano.malavasi@polimi.it.

immediately applied to the simulation of complex hydraulic equipment for real applications, such as flow control valves [16, 18, 19], injectors of Pelton turbines [20] and pumps used as turbines [21].

Despite the significant advancements achieved so far, there still exist many unresolved issues in the modelling of the impact erosion processes. For instance, the use of empirically derived single-particle erosion models taken from the literature is a considerable source of uncertainty, even more so when these models are applied outside their calibration conditions. Although some valuable work was done to overcome this issue by developing protocols for case-specific calibration of empirical erosion models [22], the use of physically derived erosion models, based on the laws of solid and damage mechanics, as recently explored at EPFL Lausanne [23], would provide a breakthrough in erosion modelling. Other challenges exist in the modelling of the particle-laden flow. These include, for instance, the modelling of quick particle-particle collisions and enduring inter-granular contacts, which are well known to play a significant role on the development of the wear process [24], and the modelling of the movement of the finite-size particles in the near-wall regions of the flow domain [25]. Finally, it is important to note that any activity of model development requires experimental data for validation. Big challenge is the accurate laboratory testing of impact erosion, especially in complex devices. In this regard, critical issues are the control and the accurate monitoring of the solid concentration in the system [26], and the need to avoid spurious effects related with the change in particle properties (e.g. size and shape) during the execution of the tests [27-29].

References

[1]. I. Finnie. Erosion of surfaces by solid particles. *Wear*. **3**: 87-103, 1960.
[2]. G.P. Tilly. A two stage mechanism of ductile erosion. *Wear*. **23**: 87-96, 1973.
[3]. R. Bellman Jr., A. Levy. Erosion mechanism in ductile metals. *Wear*. **70**: 1-27, 1981.
[4]. I. Finnie. Some observations on the erosion of ductile metals. *Wear*. **19**: 81-90, 1972.
[5]. G. Grant, W. Tabakoff. Erosion prediction in turbomachinery resulting from environmental solid particles. *J. Aircraft*. **12**: 471-478, 1975.
[6]. Y.I. Oka, K. Okamura, T. Yoshida. Practical estimation of erosion damage caused by solid particle impact. *Wear*. **259**: 95-109, 2005.
[7]. Y. Zhang, E.P. Reuterfors, B.S. McLaury, S.A. Shirazi, E.F. Rybiki. Comparison of computed and measured particle velocities and erosion in water and air flows. *Wear*. **263**: 330-338, 2007.
[8]. M. Parsi, K. Najmi, F. Najafifard, S. Hassani, B.S. McLaury, S.A. Shirazi. A comprehensive review of solid particle erosion modeling for oil and gas wells and pipelines applications. *J. Nat. Gas Sci. Eng.* **21**: 850-873, 2014.
[9]. G.R. Wang, F. Chu, S.Y. Tao, L. Jiang, H. Zhu. Optimization design for throttle valve of managed pressure drilling based on CFD erosion simulation and response surface methodology. *Wear* **338-339**: 114-121, 2015.
[10]. A. Forder, M. Thew, D. Harrison. A numerical investigation of solid particle erosion experienced within oilfield control valves. *Wear* **216**: 184-193, 1998.
[11]. M.K. Padhy, R.P. Saini, A review of silt erosion in hydro turbines. *Ren. Sus. Energy Rev.* **12**: 12974-1987, 2008.
[12]. D. Felix, I. Albayrak, A. Abgottspon, R.M. Boes. Hydro-abrasive erosion of hydraulic turbines caused by sediment–a century of research and development. In: *IOP Conference Series: Earth and Environmental Science* **49**: 1755-1315, 2016.
[13]. H. Nouraei, K. Kowsari, J.K. Spelt., M. Papini. Surface evolution models for abrasive slurry jet micro-machining of channels and holes in glass. *Wear*, **309**: 65-73, 2014.
[14]. A. Sansonetti, M. Mecchi, T. Poli, M. Realini. Problems in drawing up standards to evaluate effectiveness and harmfulness in cleaning operations. In: *Proceedings of Conservation Science Conference.* Milano, Italy, 2007.
[15]. G.V. Messa, S. Malavasi. The effect of sub-models and parameterizations in the simulation of abrasive jet impingement tests. *Wear*. **370-371**: 59-72, 2017.
[16]. G.V. Messa, G. Ferrarese, S. Malavasi. A mixed Euler-Euler/Euler-Lagrange approach to erosion prediction. *Wear*. **342**: 138-153, 2015.
[17]. G.V. Messa, S. Malavasi. A CFD-based method for slurry erosion prediction. *Wear*. **398**: 127-145, 2018.
[18]. G.V. Messa, Y. Wang, S. Malavasi. A discussion of the test procedure of the API 6AV1 standard based on wear prediction simulations. *Wear*. **426**: 1416-1429, 2019.
[19]. S. Malavasi, G.V. Messa, M. Negri. Prediction of erosion damage in a choke valve working in severe slurry conditions. In: *Proceedings ASME PVP 2018 Conference.* Prague, Czech Republic, 2018.
[20]. G.V. Messa, S. Mandelli, S. Malavasi. Hydro-abrasive erosion in Pelton turbine injectors: a numerical study. *Renew. Energ.* **130**: 474-488, 2019.
[21]. O. Fecarotta, G.V. Messa, F. Pugliese. Numerical assessment of the vulnerability to impact erosion of a Pump As Turbine in a Water Supply System. *J. Hydroinform.* 2020. Just Accepted.
[22]. A. Mansouri, H. Arabnejad, S.A. Shirazi, B.S. McLaury. A combined CFD/experimental methodology for erosion prediction. *Wear*. **332**: 1090-1097, 2015.
[23]. S. Leguizamon, E. Jahanbakhsh, A. Maertens, S. Alimirzazadeh, F. Avellan. A multiscale model for sediment impact erosion simulation using the finite volume particle method. *Wear*. **392**: 202-212, 2017.
[24]. T. Frosell, M. Fripp, E. Gutmark. Investigation of slurry concentration effects on solid particle erosion rate for an impinging jet. *Wear* **342-343**: 33-43, 2015.
[25]. L. Ma, C. Huang, Y. Xie, J. Jiang, K.Y. Tufa, R. Hui, Z.S. Liu. Modeling of erodent particle trajectories in slurry flow. *Wear* **334-335**: 49-55, 2015.
[26]. M. Mahdavi, S. Karimi, S.A. Shirazi, B.S. McLaury. Parametric study of erosion under high concentrated slurry: Experimental and numerical analyses. In: *Proceedings ASME FEDSM 2016 Conference*. Washington, USA, 2016.
[27]. H. M. Clark. Particle velocity and size effects in laboratory slurry erosion measurements OR…do you know what your particles are doing? *Tribol. Int.* **35**: 617-624, 2002.
[28]. V. Hadavi, C.E. Moreno, M. Papini. Numerical and experimental analysis of particle fracture during solid particle erosion, part I: modeling and experimental verification. *Wear*, **356**: 135-145, 2016.
[29]. V. Hadavi, C.E. Moreno, M. Papini. Numerical and experimental analysis of particle fracture during solid particle erosion, part I: modeling and experimental verification. *Wear*, **356**: 146-157, 2016.

A UNIFIED THEORY OF PARTICLE DYNAMICS, THERMODYNAMICS, AND RHEOLOGY OF SOFT PARTICLE GLASSES

Roger T. Bonnecaze[1], Michel Cloitre [2], and Fardin Khabaz [3]
[1] McKetta Department of Chemical Engineering, University of Texas at Austin, Austin, TX, USA
[2] Molecular, Macromolecular Chemistry, and Materials, ESPCI Paris, CNRS, PSL University, 10 Rue Vauquelin, 75005 Paris, France
[3] Departments of Chemical and Polymer Engineering, University of Akron, Akron, OH, USA

Soft particle glasses (SPGs) are concentrated suspensions of deformable particles above the jamming transition. The particles can be microgels, emulsions, core-shell micelles and polymer-coated hard spheres. SPGs exhibit both solid- and liquid-like behaviour. An important challenge is the design of SPGs as additives to impart yield stress and shear-thinning rheology for a range of applications. Here we present a unified theory to do so that connects the particle dynamics, a newly discovered thermodynamics, and the rheology of SPGs. Remarkably, it is also found how to determine multiple dynamical properties from a single dynamical measurement. For example, microrheological measurements of shear diffusivity can predict the shear stress and first and second normal stress differences.

INTRODUCTION

Soft particle glasses (SPGs) are amorphous materials composed of deformable particles jammed at volume fractions beyond close-packing where they are in contact and interact through elastic forces. They include many systems of practical interest such as concentrated emulsions, microgel pastes, micelles, or star polymer solutions. In SPGs each particle is constrained in a cage by elastic forces and cannot move over long distances unless an external stress larger than the yield stress is applied. The flow curve that relates the shear stress to the shear rate is well described by the generic Herschel-Bulkley equation [1]; the first and second normal stress differences follow similar relations. An open and important question concerns the physical origin of these empirical equations and their connection with the particle scale dynamics of SPGs.

Another important challenge is to minimize the number of experiments used to characterize SPGs. There are several important rheological properties for SPGs, such as the flow curves relating shear stress and first and second normal stress differences to shear rate. The measurement of normal stresses is particularly challenging. It is also advantageous to develop microrheological measurements of SPGs, requiring smaller samples, which can be done in parallel on many different formulations at high throughput. For example, it would be useful to determine the first and second normal stress differences from measurements of the shear stress flow curve or to determine all the shear and normal stress flow curves from measurements of the shear-induced diffusion. Interestingly, a thermodynamic theory for SPGs under shear exists. Like all thermodynamic theories, it provides a means to connect one measureable parameter to another, such as shear stress to second normal stress differences or diffusivity to shear stress.

The aim of this paper is to provide a unified theory that connects the particle dynamics and thermodynamics of SPGs to their dynamical and rheological properties. In doing so, the interconnection among these properties is illuminated. Finally, while the theory is presented for SPGs, we discuss how it can be used for other colloidal systems.

METHODOLOGY

The details of the model and the simulation method have been presented in previous studies [1]. Briefly, the important features are the following. Soft particle glasses are modeled as suspensions of N non-Brownian elastic particles in a solvent with a viscosity, which are jammed in a cubic simulation box at volume fractions larger than the random close-packing of hard spheres (Fig. 1). $N = 1000$ in most of the simulations reported in this work and we checked that the results are not affected by finite size effects. Suspensions with an average radius of unity, polydispersity index of 0.2, and volume fractions of 0.7, 0.8 and 0.9 are studied. The value of the polydispersity agrees with that currently found in experiments, and it prevents crystallization at high shear rates [2]. Because the particles are compressed, they have a polyhedral shape with flat facets at contact instead of their initial spherical shape. We have shown that these elastic contacts are central to the rheological properties of SPGs [1,2]. The excess entropy is computed using the two-body approximation [3].

RESULTS

The steady-state dimensionless shear stress σ/σ_y and first and second normal stress differences N_1/σ_y and $-N_2/\sigma_y$ is plotted against the dimensionless shear rate $\dot{\gamma}\eta_s/G_0$ in Fig. 1. Suspensions show a yield behavior at very low shear rates, and then by increasing the shear rate they start flowing. Note that σ_y is the shear yield stress and G_0 is the low frequency shear modulus. The particle dynamics can also be measured for similar situations. Fig. 2 presents the shear diffusivity as a function of the shear rate and the excess entropy of the system. In fact a thermodynamic relationship is shown to exist between the shear and normal stresses and the excess entropy. Thus, we show these dynamical properties fall onto a

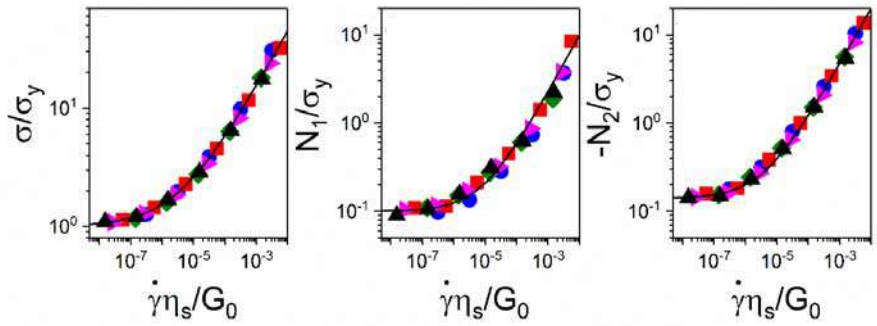

Fig. 1. Shear stress and first and second normal stress differences versus shear rate.

master curve of the shear stress normalized by the yield stress. In Fig. 3a the diffusion coefficient is plotted as a function of the shear stress. The diffusion coefficients of SPGs increase with the applied shear stress and show a universal behavior. Furthermore, the first and second normal stress coefficients, $\Psi_1(G_0/\eta_s)^2$ and $-\Psi_2(G_0/\eta_s)^2$, plotted against the shear stress in Fig. 3b and Fig. 3c also show the collapse onto a master curve. Note that $\psi_1 = N_1/\dot{\gamma}^2$ and $\psi_2 = N_2/\dot{\gamma}^2$, respectively. Thus, from the measurement of the shear stress flow curve, the shear diffusivity and the two normal stresses can be determined. Remarkably, the measurement of any one of the four dynamical properties (i.e., diffusivity, shear stress or viscosity, and first and second normal stress coefficients) allows one to determine the other three.

CONCLUSIONS

We show that the particle dynamics, in the form of shear-induced diffusion, is related to the excess entropy of SPGs. In addition rheological properties of the SPGs are also related to the excess entropy and other thermodynamic descriptors. From this, one interrelate shear-induced diffusion, shear stress and first and second normal stress differences.

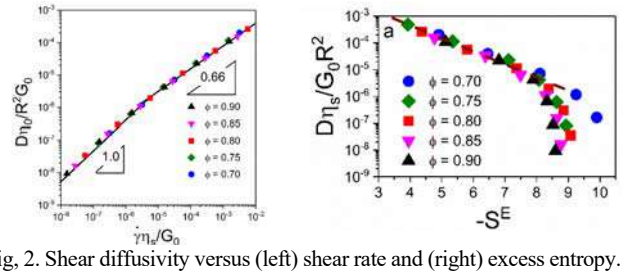

Fig, 2. Shear diffusivity versus (left) shear rate and (right) excess entropy.

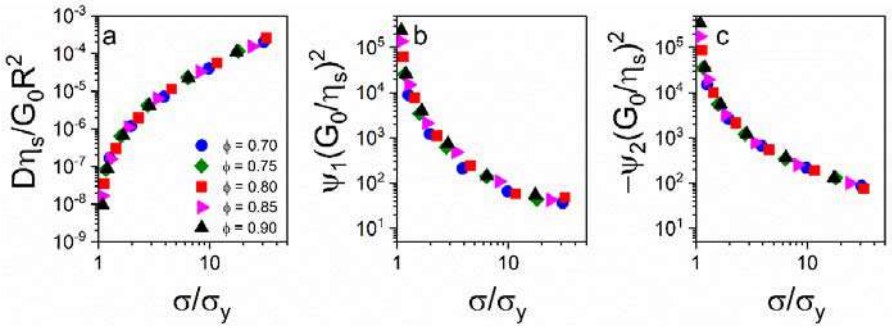

Fig 3. (a) Diffusion coefficient, (b) first normal stress function, and (c) second normal stress difference function versus shear stress obtained for SPGs with different volume fractions.

References

[1] Seth, J.R., L. Mohan, C. Locatelli-Champagne, M. Cloitre, and R.T. Bonnecaze, *A Micromechanical Model to Predict the Flow of Soft Particle Glasses.* Nat. Mater., 2011. **10**(11): p. 838-843.

[2] Khabaz, F., T. Liu, M. Cloitre, and R.T. Bonnecaze, *Shear-Induced Ordering and Crystallization of Jammed Suspensions of Soft Particles Glasses.* Phys. Rev. Fluids, 2017. **2**(9): p. 093301.

[3] Baranyai, A. and D.J. Evans, *Direct Entropy Calculation from Computer Simulation of Liquids.* Physical Review A, 1989. **40**(7): p. 3817.

YIELDING AND FLOW INHOMOGENEITIES IN SOFT SOLIDS

Emanuela Del Gado * [1]
[1] Department of Physics and Institute for Soft Matter Synthesis and Metrology, Georgetown University, Washington DC, USA.

Summary Soft condensed matter (proteins, colloids or polymers) easily form gels or other amorphous soft solids, where rigidity emerges in diverse structures with a variety of mechanical features. Examples include glass, cement, compacted sand, and even yogurt or chocolate mousse. Through the interplay between their microstructure with an imposed deformation, these materials can be stretched, flow, squeezed or fractured. Controlling and being able to design such processes is of paramount importance in a number of technologies, such soft inks for 3D printing technologies or self-healing materials for soft robotics. I will give an overview of our work on yielding of soft materials, in particular focusing on particle gels and jammed emulsions, where a major challenge is the emergence of persistent flow inhomogeneities.

INTRODUCTION

Soft solids such as densely packed emulsions or dilute particle gels yield and eventually flow under an imposed shear deformation, a feature important for materials from wet cement to food, paint or pharmaceutical products. Controlling the flow properties upon yielding is tough, since the evolution towards the steady-state is often accompanied by strong spatial inhomogeneities, where only part of the material flows while the rest stays jammed. Such phenomenon is called shear banding and has been known for many decades to geologists and engineers, but the question of what favors the stress accumulation and the persistence of flow inhomogeneities upon yielding is fundamentally unanswered.

A consistent theoretical description of the fundamental physical mechanisms that control yielding in such materials is challenging and is a topic of intense debate. Flow induced structuring or ordering transitions may underlie the development of bands flowing at different rates in various complex fluids, and may be affected by effective interactions between molecules, particles or droplets. For soft glassy solids, the flow inhomogeneities delaying the fluidization are thought to emerge from the relaxation of stress heterogeneities elastically stored in the material during the stress overshoot.

MODELS, NUMERICAL SIMULATIONS AND RESULTS

We have designed 3D numerical simulations of soft spheres models, with size polidispersity and in athermal conditions, and of soft dilute particle gels, which are more sensitive to thermal fluctuations. In the simulations, we consider different types of drag coefficients and compare the results obtained using Lees-Edwards periodic boundary conditions with the case in which the same model solid is confined between two walls. We find that the presence of a stress-overshoot and of transient shear banding for large enough samples are a robust feature for overdamped systems. We have characterized the linear response of the material initially subjected to oscillatory rheology and then investigated the yielding behavior of samples of different sizes and aged in different ways. We have also performed an investigation of the microscopic structure, the local packing, the local velocity profile as well as stress and strain localization. We combine these studies with quantitative analysis of the evolution of the shear banding into the steady state flow of the material.

CONCLUSIONS

Understanding the emergence and persistence of flow inhomogeneities in soft amorphous solids requires investigating the stress heterogeneities frozen-in during the material solidification and depending on the material history. Stress localization that preceeds the onset of flow inhmogeneities can be traced back to microstructural features that can be different for different materials, but common underpinnings can be identified in the local and global microscopic mechanical constraints developed in the microstructure at rest and under flow.

*Corresponding author. E-mail: ed610@georgetown.edu.

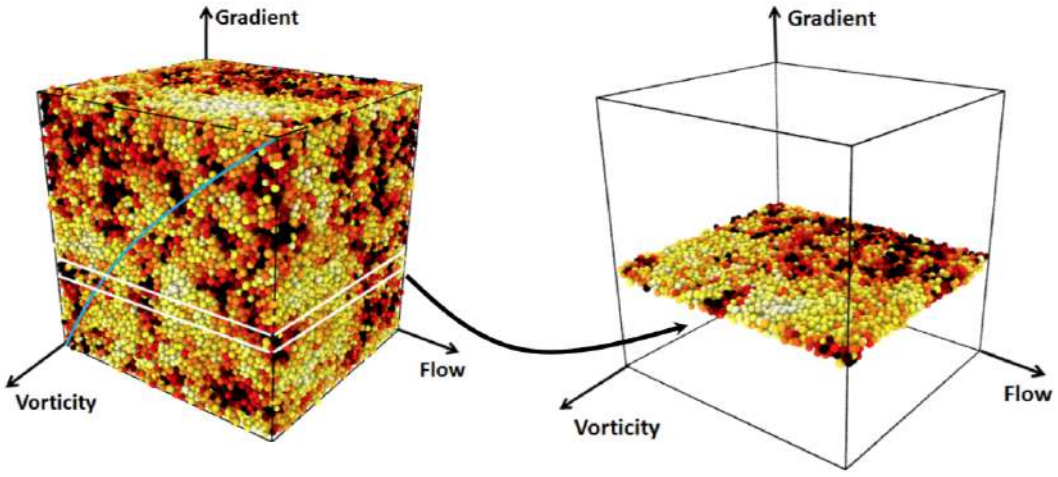

Figure 1: Schematics of the numerical simulations for jammed emulsions, with the jammed material being sheared and the local velocity profile being reconstructed in the numerical analysis.

CONTRIBUTIONS OF TURBOPHORETIC AND DIFFUSIVE FLUXES TO PARTICLE TRANSPORT IN A TURBULENT SMOOTHWALL PIPE

Tony Zahtila * , Leon Chan, Andrew Ooi, and Jimmy Philip
Department of Mechanical Engineering, The University of Melbourne, Victoria, Australia

Summary In order to understand the wall-ward motion of particles in a turbulent pipe flow, we carry out direct numerical simulations of particles with different Stokes number and model the evolution of particle concentration via a 1D advection-diffusion equation. Employing the DNS data, wall-directed particle number flux that is inhomogeneous in the wall-normal direction is decomposed into a convective turbophoretic flux and a flux due to turbulent diffusivity. Diffusivities for both turbophoretic and diffusive components that are functions of radial distances are employed in an advection-diffusion equation to estimate the particle migration with time, the solution of which is then compared with the DNS particle concertation evolution, and we obtain reasonable agreements. Our findings provide further support to the modelling of particle migration based on the Reynolds averaged equations [1].

INTRODUCTION

The accumulation of particles at solid walls in turbulent pipe flows, where the particle distribution was uniform at the beginning, is a well-known phenomena, arising as a result of the interaction between particle inertia and fluid turbulence. A considerable amount of experimental data [2] in vertical tubes and channels exist which measure particle deposition to surfaces. For $St^+ < 1$, particles only slowly deposit and persist in an even distribution from wall to centreline, however, this quite small deposition increases by orders of magnitude when the dimensionless particle relaxation time increases from $St^+ = 1$ to $St^+ = 10$. Here, $St^+ = \tau/(\nu/u_\tau^2)$, where τ is the Stokes particle relaxation time and superscript $+$ indicates viscous normalization with ν and u_τ, the kinematic viscosity and friction velocity in turbulent wall flows. Beyond $St^+ = 30$, there is a moderate decrease observed in deposition, as these particles' inertia is now sufficient to pass through eddies. More recently, direct numerical simulation of particles in channels [3] showed near-wall concentration peaks over a thousand times the centreline concentration for populations of $St^+ = 10, 50$ and 100.

Prediction of concentration profiles for particles suspended in gas is sought after for efficient delivery of aerosol medications, development of particle based solar receivers and is widely relevant in chemical processing, where quality of the final product often requires particle removal. Recently, particle wall-normal velocity variance determined from DNS carried out in a turbulent channel flow was found to be sufficient to predict steady-state concentration profiles [4]. They show that the dominant effect for heavy particles was turbophoresis, and for lighter particles an additional biased sampling term is required. The present analysis, however, seeks to determine whether it is possible to predict the instantaneous wall-directed flux profile, which evolves as concentration gradients form due to local depletion and accumulation of particles. Knowledge of this instantaneous flux profile would allow for the fast computation of particle concentration profiles as they evolve in time.

NUMERICAL SIMULATIONS AND MODEL DEVELOPMENT

In this study, the Euler-Lagrangian method is used to conduct particle laden point-particle direct numerical simulations (PP-DNS). The fluid is represented by the incompressible Navier-Stokes equations which were solved using the finite volume method. Particles in the simulation were individually represented as points, with particle acceleration computed from the particle relaxation time, as well as, the slip velocity between the particle velocity and the sampled fluid velocity, is represented using the Stokes' drag. Simulations were conducted of a turbulent friction Reynolds number, $Re_\tau = (u_\tau R)/\nu = 180$ pipe flow, with R the pipe radius, laden with four sets of inertial particles with relaxation times, $St^+ = 0.1, 1, 10$ and 100. Each particle set was represented by two million one-way couples particles which collide fully elastically with walls.

Towards the development of a 1D model for the particle concentration ($C*$, where $*$ represents normalisation by the bulk concentration), we calculate particle fluxes as particles cross imaginary surfaces with wall normal spacing of $\Delta y^+ = 4.5$ (as depicted in Figure 1). They are counted across eight hundred snapshots in time and at each snapshot, the local particle concentration and gradient is known. Profiles for turbophoretic and diffusive flux are thus determined from the DNS data. Features of the turbophoretic profile are a monotonic increase from wall to approximately $y^+ = 30$, and then, a monotonic decrease thereafter to the centreline. Broadly, this profile can be interpreted as the mean radial velocity of the particle. The diffusive profile, increasing sharply until approximately $y^+ = 60$ and thereafter moderately decreases, is thought to correspond to the particle radial turbulent fluctuations. These profiles, in part, validate a previously suggested Eulerian description [1] that explained the different deposition regimes across particle sizes, obtained through Reynolds averaging of the particle mass and momentum equations.

*Corresponding author. E-mail: tzahtila@student.unimelb.edu.au.

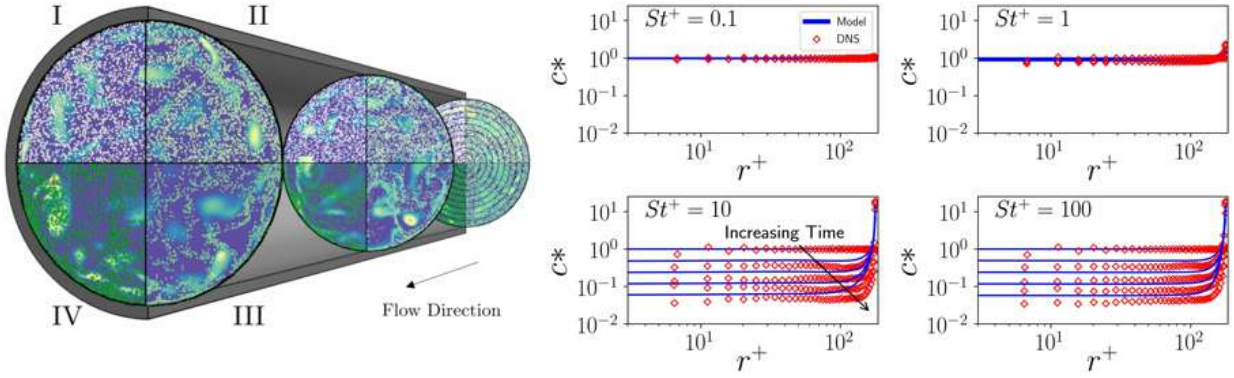

Figure 1: (Left) Visualization of streamwise vorticity and four particle populations ($St^+ = 0.1, 1, 10, 100$), corresponding to quadrants I - IV respectively, at three subsequent snapshots in time, $t^+ = 0, t^+ = 180$ and $t^+ = 360$. Particles are injected uniformly into a fully developed turbulent pipe and the dark rings in the right-most slice represent the imaginary surfaces across which particle fluxes are counted. (Right) Comparison of predicted particle concentration profiles ($C*$) with the DNS obtained results for 5 instances in time, $t^+ = 0$, $t^+ = 900, t = 1800, t^+ = 2700$ and $t^+ = 3600$.

RESULTS

With empirically determined turbophoretic and diffusive profiles, an unsteady one-dimensional advection-diffusion equation is formulated. The equation is solved in finite volume form, in order to impose realistic boundary conditions of no-flux at the wall so that particle number is conserved exactly. The solution is calculated for the same length of time as the DNS, and with the same initially uniform concentration profile as in DNS. The evolution of the particle concentration profiles show fair agreement with those obtained from DNS, and are shown in Figure 2 (with near wall peak concentration within 10% error). As concentration profiles change with time, the separate and evolving contributions of turbulent diffusivity and turbophoresis reveal that increasingly sharp near-wall gradients increasingly oppose the wall-directed convective tendency.

Mechanistically, we observe that low relaxation time particles ($St^+ = 0.1$) sample stream-wise turbulent events in the viscous region ($y^+ < 5$) without bias, however, organisation into streaks is apparent for the remaining cases. Further, sampling of stream-wise vorticity reveals that distinct regimes occur in the segregation of particles (cf. Figure 1). Low relaxation time particles ($St^+ = 0.1$) evenly sample regions of high/low stream-wise vorticity, however there is increasing curvature-fleeing observed across ($St^+ = 1, 10$); and finally, the highest relaxation time particles exhibit segregation but not necessarily with the instantaneously sampled vorticity, suggesting their inertia is significant enough to filter fluid motions. Particle-turbulence interaction has previously been studied in terms of the coherent motions of turbulence, particles able to trace the flow have wall-ward motion that is strongly correlated with the coherent sweeps and ejections of turbulence [5], an effect that becomes complicated with increasing particle inertia. We observe, for instance, $St^+ = 0.1$ particles at $y^+ = 30$ sampling a strong Q2 ejection fluid event yield 99% probability that particle velocity is directed away from the wall, however, this statistic decreases to 70% probability of wall-fleeing for $St^+ = 100$ particles, revealing a decrease in efficiency of the turbulent fluid mechanism to transport particles away from walls.

SUMMARY

In summary, we directly evaluate the turbophoretic and diffusive flux from the DNS of a turbulent pipe flow, and employ these fluxes in a 1D advection-diffusion equation for particle concentration. This model shows reasonable agreement with DNS data. This also gives credence to the Reynolds averaging procedure used in the literature, which can predict the experimentally and numerically observed results for the wall-normal transport of particles. Current work is further aimed at pinpointing the 3D mechanisms in wall turbulence that contribute to the tendency for particles to migrate towards, in particular, quantifying particle-eddy interaction and momentum transport mechanisms as particles increase in inertia.

References

[1] Guha, A. A unified Eulerian theory of turbulent deposition to smooth and rough surfaces. *J. Aerosol Sci* 28.8: 1517-1537,1997.
[2] Liu, B., and Agarwal, J., Experimental observation of aerosol deposition in turbulent flow. *J. Aerosol Sci* 5.2 (1974): 145-155.
[3] Sardina, G., Schlatter, P., Brandt, L., Picano,F. Wall accumulation and spatial localization in particle-laden wall flows. *J. Fluid Mech* 699 (2012): 50-78.
[4] Johnson, P., Bassenne, M., and Moin, P. "Turbophoresis of small inertial particles: theoretical considerations and application to wall-modelled large-eddy simulations." *J. Fluid Mech* 883 (2020).
[5] Marchioli, C., and Soldati, A. "Mechanisms for particle transfer and segregation in a turbulent boundary layer." *J. Fluid Mech* 468 (2002).

INERTIAL FOCUSING OF SPHERICAL PARTICLES SUSPENDED IN SQUARE CHANNEL FLOWS

Masako Sugihara-Seki[1, 2], and Hiroshi Yamashita [1]
[1] Department of Pure and Applied Physics, Kansai University, Osaka, Jana
[2] Graduate School of Engineering Science, Osaka University, Osaka, Japan

Summary The inertial migration of spherical particles suspended in square channel flows was investigated experimentally and numerically to obtain the particle focusing positions in the downstream cross-section of the channel. The particle focusing patterns were found to be classified into four types for the ratio of the particle diameter to channel width ~ 0.1; in the regime of the lowest Reynolds numbers, particles were focused on the centre of channel faces (channel face equilibrium position (EP)); in the second and third regimes, additional focusing points were located on intermediate positions symmetric relative to the diagonal (intermediate EP) and on the diagonal near the corners (channel corner EP); in the last regime, they were focused on the channel face EPs and the channel corner EPs. The transitions between neighbouring regimes were described in terms of the bifurcation of EPs.

INTRODUCTION

It has been long known that spherical particles suspended in circular tube flows cross streamlines towards an annulus of 0.6 times the tube radius at low Reynolds numbers (Re) [1]. This focusing phenomenon, referred to as the Segre-Silberberg effect, originates from the inertial effect and has recently gained considerable attention in the field of microfluidics due to the broad range of applications, such as in the separation and filtration of particles and biological cells [2, 3]. In microfluidics, channels of rectangular cross-sections, rather than circular cross-sections, are commonly used. Particles suspended in rectangular channel flows were focused on several discrete points in downstream cross-sections. In particular, spherical particles in square channel flows were observed to approach four points at the centre of channel faces at low Re (<100) [3]. The focusing points and their number in the cross-section vary depending on Re and the ratio of the particle diameter to channel width (size ratio) [4]. In the present study, we investigated experimentally and numerically the variation of the focusing points of neutrally buoyant spherical particles suspended in the square channel flow in the wider range of Re for various size ratios.

METHODS

Experimental methods

Details of the experimental method were described elsewhere [5, 6]. Briefly, polystyrene spherical particles with several ten μm in diameter and 1.05×10^3 kg/m^3 in density were suspended in a glycerol-water solution at a volume fraction of ~10^{-2} %. This suspension was made to flow through a horizontally placed borosilicate square tube of several hundred μm in width by use of a syringe pump. The tube cross-section about 2–3mm upstream of the outlet was observed from the downstream side using a high-speed camera equipped with a long working distance objective. The obtained images were analysed with the public domain software ImageJ to yield the positions of the particle centre in the tube cross-section.

Numerical methods

In the numerical simulation, we considered the motion of a single rigid spherical particle suspended in a pressure-driven flow of a Newtonian fluid through a square channel. The particle was assumed to be neutrally buoyant. The computational method was presented previously [7, 8]. Briefly, we adopted the immersed boundary method for multiphase flows proposed by Kajishima et al. [9]. Using a periodic boundary condition in the main flow direction, we obtained the flow field by a fractional step method, and evaluated the lateral velocity of the particle or the lateral force exerted on the particle.

RESULTS AND DISCUSSION

Figure 2 shows representative examples of the experimental results for the particle distribution over the channel cross-section at various Re for $d/D = 0.125$ and $L/D = 750$, where d, D and L represent the particle diameter, channel width and channel length, respectively. The positions of at least 350 particles were detected in the cross-section and their centre positions are represented by dots in each figure. Figures 2(a) – (d) show four types of the particle focusing pattern. Their Re regimes are called regime A, B, C and D, respectively. Figure 2 indicates the presence of three types of equilibrium positions (EPs): channel face EPs located at the centre of channel faces, channel corner EPs located on the diagonal near the channel corners, and intermediate EPs located at intermediate positions symmetric with respect to the diagonal. In regime A, the particle focusing positions are channel face EPs (figure 2(a)); in regime B, intermediate EPs are added as the focusing position (figure 2(b)); in regime C, channel corner EPs are added (figure 2(c)); in regime D, particles are focused on the channel face EPs and the channel corner EPs (figure 2(d)).

The present numerical computation confirmed these particle focusing patterns. Figure 3 represents the azimuthal angle of EPs, θ_e, in the first quadrant of the cross-section obtained numerically. The horizontal lines at $\theta_e = 0$ and $\pi/2$ represent

the channel face EPs, the horizontal line at $\theta_e = \pi/4$ represents the channel corner EPs, and the other lines represent the intermediate EPs. Solid lines indicate stable EPs, and dotted lines indicate saddle EPs. Note that the centre of the cross-section is an EP, but it is always unstable.

Figure 3 shows that there are three critical Re, i.e., Re_{c1}, Re_{c2}, and Re_{c3}, between regimes A and B, B and C, and C and D, respectively. At $Re = Re_{c1}$, a pair of saddle and stable intermediate EPs (IME_1, IME_2) emerge, corresponding to a saddle-node bifurcation. At $Re = Re_{c2}$, the channel corner EP is changed to be stable accompanying the emergence of saddle intermediate EPs (IME_3), corresponding to a pitchfork bifurcation. At $Re = Re_{c3}$, IME_2 and IME_3 merge and disappear, corresponding to a saddle-node bifurcation. The positions of EPs obtained experimentally and numerically nearly agreed with each other. The critical Re values were comparable, but the values obtained numerically were slightly lower than those obtained experimentally in the case of $d/D = 0.125$.

For larger size ratios, another type of the focusing pattern was observed such that the particles were focused on the channel corner EPs at low Re. For even larger size ratios, we found a direct transition between regime A and regime D, i.e., disappearance of regimes B and C. These variations of the particle focusing pattern can be summarized in the wide range of Re for various ratios of the particle diameter to channel width.

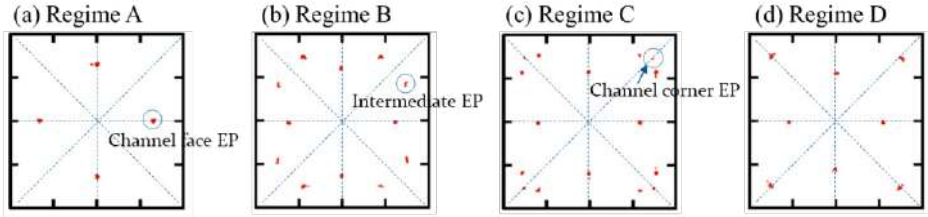

Figure 2. Typical particle focusing pattern in each regime obtained in experiments at Re = (a) 100, (b) 300, (c) 350, and (d) 450, for $d/D = 0.125$ and $L/D = 750$.

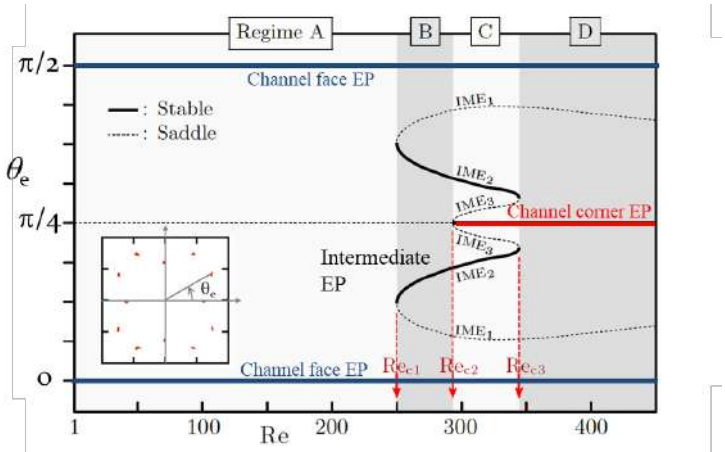

Figure 3. Azimuthal angle of equilibrium positions for spherical particles in square channel flows obtained numerically ($d/D = 0.125$).

CONCLUSIONS

The inertial migration of spherical particles suspended in square channel flows was investigated experimentally and numerically. The particle focusing patterns in the channel cross-section were described as a function of Re and size ratio.

References

[1] Segre G., Silberberg, A. Radial particle displacements in Poiseuille flow of suspensions. *Nature* **189**, 209, 1961.

[2] Di Carlo D., Irimia, D., Tompkins, R.G., Toner M. Continuous inertial focusing, ordering, and separation of particles in microchannels. *Proc. Natl. Acad. Sci.* **104**, 18892, 2007.

[3] Bhagat A.A.S., Kuntaegowdanahalli S.S., Papautsky I. Enhanced particle filtration in straight microchannels using shear-modulated inertial migration. *Phys. Fluids* **20**, 101702, 2008.

[4] Miura K., Itano T., Sugihara-Seki M. Inertial migration of neutrally buoyant spheres in a pressure-driven flow through square channels, *J. Fluid Mech.* **749**, 320, 2014.

[5] Shichi H., Yamashita H., Seki J., Itano T., Sugihara-Seki M. Inertial migration regimes of spherical particles suspended in square tube flows. *Phys. Rev. Fluids* **2**, 044201, 2017.

[6] Nakayama S., Yamashita H., Yabu T., Itano T., Sugihara-Seki M. Three regimes of inertial focusing for spherical particles suspended in circular tube flows. *J. Fluid Mech.* **871**, 952, 2019.

[7] Nakagawa N., Yabu T., Otomo R., Kase A., Makino M., Itano T., Sugihara-Seki M. Inertial migration of a spherical particle in laminar square channel flows from low to high Reynolds numbers. *J. Fluid Mech.* **779**, 776, 2015.

[8] Yamashita H., Itano, T., Sugihara-Seki M. Bifurcation phenomena on the inertial focusing of a neutrally buoyant spherical particle suspended in square duct flows. *Phys. Rev. Fluids* **4**, 124307, 2019.

[9] Kajishima T., Takiguchi S., Hamasaki H., Miyake Y. Turbulence structure of particle-laden flow in a vertical plane channel due to vortex shedding. *JSME Intl J.* **B44**, 526, 2001.

SPREADING OF GRANULAR SUSPENSIONS: SCALE-DEPENDENT DISSIPATION

Menghua Zhao[1], Alice Pelosse[1], Matthieu Oléron[1], Laurent Limat[1], Elisabeth Guazzelli[1], and Matthieu Roché[1]
[1] *Laboratoire Matière et Systèmes Complexes, Université de Paris, CNRS UMR 7057, Paris, France*

Summary We report the results of an investigation of the spreading of granular suspensions on the surface of a solid. We find that the apparent viscosity of these Newtonian bulk suspensions extracted from the characterization of the motion of the line of contact between the suspension, the solid and the atmosphere depends on the size of the particle. This observation is in contrast to the particle-size independence of the apparent bulk viscosity. We show that particles are repelled from the immediate vicinity of the contact line. We discuss the insights that models of spreading flows of suspensions relying on a purely geometric exclusion of the particles close to the contact line provide.

INTRODUCTION

Granular suspensions are obtained by dispersing solid particles with diameters $d_p >> 1$ µm in a suspending liquid. Examples of these complex fluids include concrete and mortar, mud, blood and landslides. The study of the mechanics of these materials is still a very active field, and scientists have now a good understanding of the relation between the flow of these liquids and their formulation. For example, rigid particles dispersed at high volume fractions in Newtonian suspending liquids and experiencing hard-core repulsion only form suspensions that are Newtonian in the bulk [1].

Most models of these materials assume that they behave as an effective medium. This assumption breaks down when the characteristic size $\mathscr{L}$ of the flow becomes comparable to d_p. In this case, much less is known. The viscosity of even dilute suspensions increases as the confinement ratio $\beta = \mathscr{L}/d_p$ decreases [2], and oscillates when $\beta \sim 1$ [3].

Corner flows such as that occuring during the spreading of a droplet on a solid surface in a surrounding atmosphere are examples of flows where $\beta \to 0$. In these flows, the liquid/fluid interface makes an angle θ_{app} with the solid/liquid interface at the contact between the three phases (Fig. 1). For a liquid of viscsotiy η and surface tension γ, the value of θ_{app} is related to the ratio of the capillary stress and the viscous stress, *i.e.* the capillary number $Ca = \eta U_{CL}/\gamma$, by the Cox-Voinov equation [4]:

$$\frac{\theta_{app}^3}{9} = \frac{\theta_m^3}{9} + Ca \ln\left(\frac{x}{\ell}\right) \tag{1}$$

where θ_m is a microscopic contact angle, x is the distance from the contact line at which θ_{app} is measured and ℓ is a microscopic length scale introduced to circumvent stress divergence at the contact line. Here, we show that the apparent viscosity of model neutrally-buoyant suspensions extracted from spreading experiments depends on particle size d_p, in contrast to their bulk apparent viscosity. We bring evidence that this observation results from the existence of a particle-depleted region in the vicinity of the triple-phase contact zone. We discuss the validity of a geometric origin for the observations and indicate perspectives.

MATERIALS AND METHODS

We use polyethylene glycol-ran-propylene glycol monobutyl ether (PEG-ran-PPG ME, Sigma Aldrich, density $\rho_0 = 1056\,\mathrm{kg\,m^{-3}}$, surface tension $\gamma_0 = 35\,\mathrm{mN\,m^{-1}}$) as the suspending fluid. We account for the temperature dependence of its viscosity in the analysis of the data. We use polystyrene beads (Microbeads Dynoseeds TS, average particle diameter $10 \leq d_p \leq 550$ µm, density $\rho_p = 1050\,\mathrm{kg\,m^{-3}}$), carefully dispersed in PEG-ran-PPG ME in a beaker to obtain homogeneous neutrally-buoyant suspensions having volume fractions varying in the range $20 \leq \phi \leq 40\%$. The surface tension of these mixtures is equal to that of PEG-ran-PPG ME [5] and their rheology is well documented [5–8].

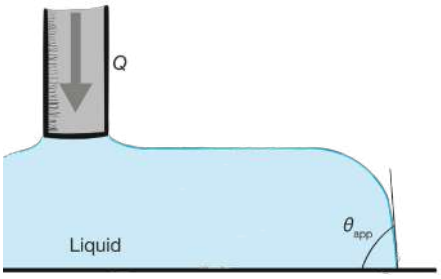

Figure 1: Sketch of the experimental set-up.

We release droplets of suspensions on the surface of a silicon wafer using a steel needle (Vita Needles, inner diameter $d_i = 4.58$ mm) connected to a syringe pump (Harvard Apparatus PHD ULTRA) (Fig. 1). The surface of the wafer is cleaned with acetone, ethanol, and water prior to each experiment using a clean-room cloth. We track the axisymmetry of spreading drops and make sure thant contact angles are measured in this regime. Movies of the side-view spreading of the drop are captured with a digital camera. Contact angles are measured using FiJi. We also record top-view movies to characterize the suspension behavior close to the contact line.

OBSERVATIONS

The apparent shear viscosity η_s of the suspensions we use is proportional to that of the suspending liquid η_0:

$$\eta_s = f(\phi, \phi_c)\eta_0 \tag{2}$$

with $f(\phi, \phi_c) = \left(1 + \frac{5\phi}{4(1-\phi/\phi_c)}\right)^2$ an empirical prefactor, following Eilers' definition [1].Thus, we propose to compare measurements of the apparent contact angle θ_{app} for suspensions with those for the suspending liquid. Following Eq. 2, and plotting data against the capillary number defined on the properties of PEG-ran-PPG ME, we expect to observe parallel $(Ca, \theta_{app}^3/9)$ curves, distinguished by a shift that should account for Eilers' prefactor. Figure 2a and b shows that experiments do not confirm this expectation. We obtain cirves that are indeed parallel to that of the suspending liquid, but their shift depends on particle size.

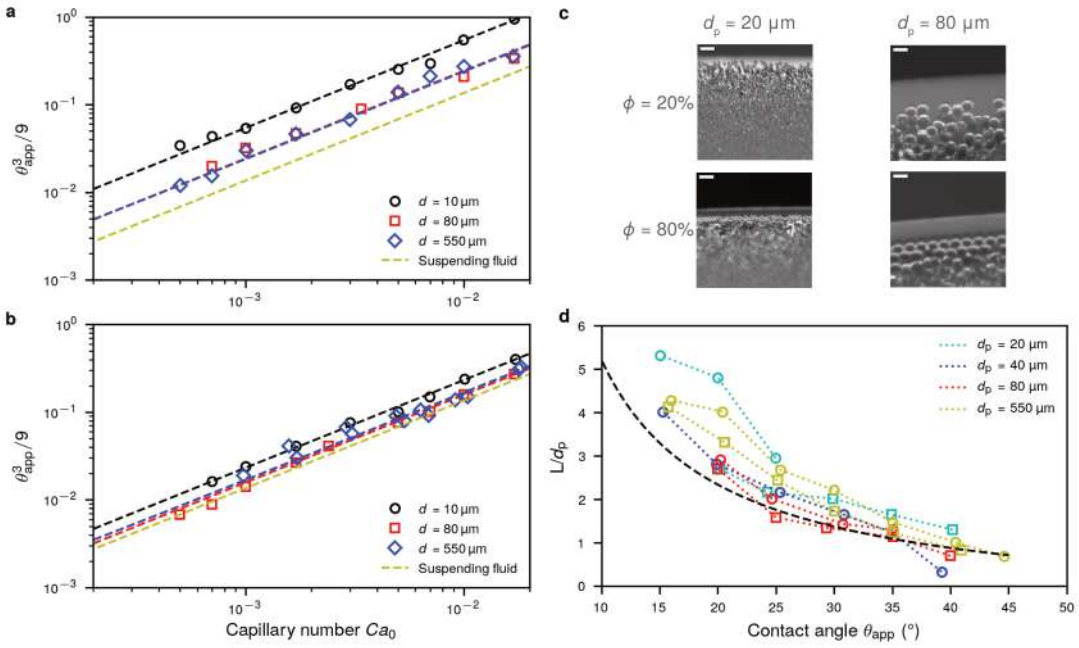

Figure 2: Dependence of the apparent dynamic contact angle θ_{app} on the capillary number Ca_0 of the experiment defined with the properties of the suspending liquid for (a) $\phi = 40\%$ and (b) $\phi = 20\,\%$. (c) Close-up top views of the region around the moving contact line showing the particles and the depeleted region. (d) Size of the depleted region L scaled by particle diameter as a function of the apparent contact angle. Dashed line: geometric predicition.

A look at the moving contact line from the top shows that the region in the immediate vicinity of the triple-contact region is depleted in particles (Fig. 2c). The extent L of this depleted region is a function of d_p (Fig. 2c). However, it seems that geometry may not be enough to explain the apparent viscsosity that we measure.

We are currently working on modelling this problem and discussing the extent to which a simple geometric approach is successful.

CONCLUSIONS

The study of the spreading of Newtonian granular suspensions has received little attention until now. However, simple experiments show that these liquids spread in an unconventional fashion, with a viscosity that is dependent on the size of the particles. These results lead to interesting questions related to the importance of confinement in the flow of suspensions, how bidisperse systems behave, how the shape of the interface evolves spatially, and finally how spreading occurs.

References

[1] É. Guazzelli and O. Pouliquen, J. Fluid Mech. **852** (2018).
[2] P. Peyla and C. Verdier, EPL **94**, 44001 (2011).
[3] W. Fornari, L. Brandt, P. Chaudhuri, C. U. Lopez, D. Mitra, and F. Picano, Phys. Rev. Lett. **116**, 018301 (2016).
[4] D. Bonn, J. Eggers, J. Indekeu, J. Meunier, and E. Rolley, Rev Mod Phys **81**, 739 (2009).
[5] É. Couturier, F. Boyer, O. Pouliquen, and É. Guazzelli, J Fluid Mech **686**, 26 (2011).
[6] F. Boyer, O. Pouliquen, and É. Guazzelli, J Fluid Mech **686**, 5 (2011).
[7] F. Boyer, É. Guazzelli, and O. Pouliquen, Phys Rev Lett **107**, 188301 (2011).
[8] J. Château, É. Guazzelli, and H. Lhuissier, J. Fluid Mech. **852**, 178 (2018).

THERMOKINETIC MODEL FOR COMPRESSIBLE MULTIPHASE FLOWS

Ehsan Reyhanian, Benedikt Dorschner, and Ilya Karlin*
Department of Mechanical and Process Engineering, ETH Zurich, 8092 Zurich, Switzerland

Summary We propose a novel kinetic theory to simulate compressible multiphase flows. The model is thermodynamically consistent and thus inherently able to capture the real gas effects. In combination with complete Galilean invariance through adaptively created particles, our model removes the typical restrictions of conventional kinetic methods, such as the lattice Boltzmann method. Owing to full energy conservation, simulations of compressible-multiphase flows are presented for the first time within this framework. Different benchmarks associated with real-gas thermodynamics illustrate the large range of compressible-multiphase problems this model can handle.

INTRODUCTION

The lattice Boltzmann method (LBM) is a kinetic-based approach for the simulation of hydrodynamic phenomena with applications ranging from turbulence to micro and multiphase flows. The fully discretized kinetic equations evolve particle distribution functions (populations) $f_i(\boldsymbol{x}, t)$, associated with a set of discrete velocities $\boldsymbol{c}_i$ according to a simple stream-and-collide algorithm and recovers the Navier-Stokes equation in the hydrodynamic limit. Efficiency of LBM and its ability of dealing with various types of flow and complex geometries have drawn considerable attention.

While various LBM formulations have been proposed for real gases, it is most common to include non-ideal gas as well as capillary effects by an additional force term in the Boltzmann equation. However, validity of conventional LBM is restricted to low Mach numbers or isothermal incompressible flows. Thus, developing an energy-conserving scheme to model high-speed real-gas flows has remained an unresolved issue within the LBM framework.

Recently, the so-called "Particles on Demand for Kinetic Theory" or "PonD" [1] has been introduced, which removes these limitations by defining adaptive sets of microscopic velocities. In PonD, the conventional discrete velocities $\boldsymbol{c}_i$ are regarded as relative velocities with respect to local reference of frame $\boldsymbol{u}, \theta$, where $\boldsymbol{u}$ is the local velocity of the fluid and θ is the temperature, reduced by the lattice temperature, a quantity known for any lattice. The most important consequence of this definition is that the local equilibrium eliminates the Galilean invariance errors and takes a simple yet exact form $f_i^{eq} = \rho W_i$, where weights W_i are constants defined for every set of discrete speeds. This is in contrast to LBM, where a truncated polynomial of the equilibrium distribution function around zero velocity and the lattice temperature is used.

Similarly, we propose to define the velocity sets such that the real gas effects are taken into account. The thermodynamic consistency of the proposed scheme allows us to span a wide range of real-gas phenomena such as super-critical flows, throttling, phase segregation and shock-interface interaction. The relative simplicity of the model and its ability to model the interfacial and phase thermodynamics such as phase-separation and surface tension, make it a promising method compared to its counterparts in the field of fluid dynamics. We start by defining the following particle velocities:

$$\boldsymbol{v}_i = \sqrt{\frac{p}{\rho T_L}}\boldsymbol{c_i} + \boldsymbol{u}, \tag{1}$$

where p is the thermodynamic pressure equation of state (EoS), ρ is density and T_L is the the lattice temperature. Equation (1) thus constructs particles, which are moving relative to the reference frame $\lambda = \{\boldsymbol{u}, \theta\}$ where $\theta = \dfrac{p}{\rho T_L}$. The immediate outcome of this definition is that the ideal gas pressure in the stress tensor is now replaced by the real gas pressure.

The evolution of the flow field is governed by the kinetic equations for the two sets of populations, f_i and g_i. The former maintains the density and momentum, while the latter is adopted to conserve energy. Local conservation of density, momentum and total energy can be evaluated as $\{\rho, \rho\boldsymbol{u}, 2\rho E\} = \sum_{i=1}^{Q}\{f_i, f_i\boldsymbol{v}_i, g_i\} = \sum_{i=1}^{Q}\{f_i^{eq}, f_i^{eq}\boldsymbol{v}_i, g_i^{eq}\}$ where Q is the number of discrete velocities. The populations are evolved in time and space in two steps: First, the semi-Lagrangian advection is performed, where the populations at off-lattice points are streamed along the characteristic $\boldsymbol{x} - \boldsymbol{v}_i\delta t$ to the point $(\boldsymbol{x}, t)$, where δt is the time step [1]. Second step is the collision and we use the classical BGK approximation. While the method applies to a generic EoS, we have adopted the van der Waals EoS in the results presented below.

RESULTS AND DISCUSSION

In this contribution, we shall demonstrate a wide range of thermodynamics that can be addressed with such a generic approach. Exemplarily, we show two benchmarks below.

*Corresponding author. E-mail: karlin@lav.mavt.ethz.ch.

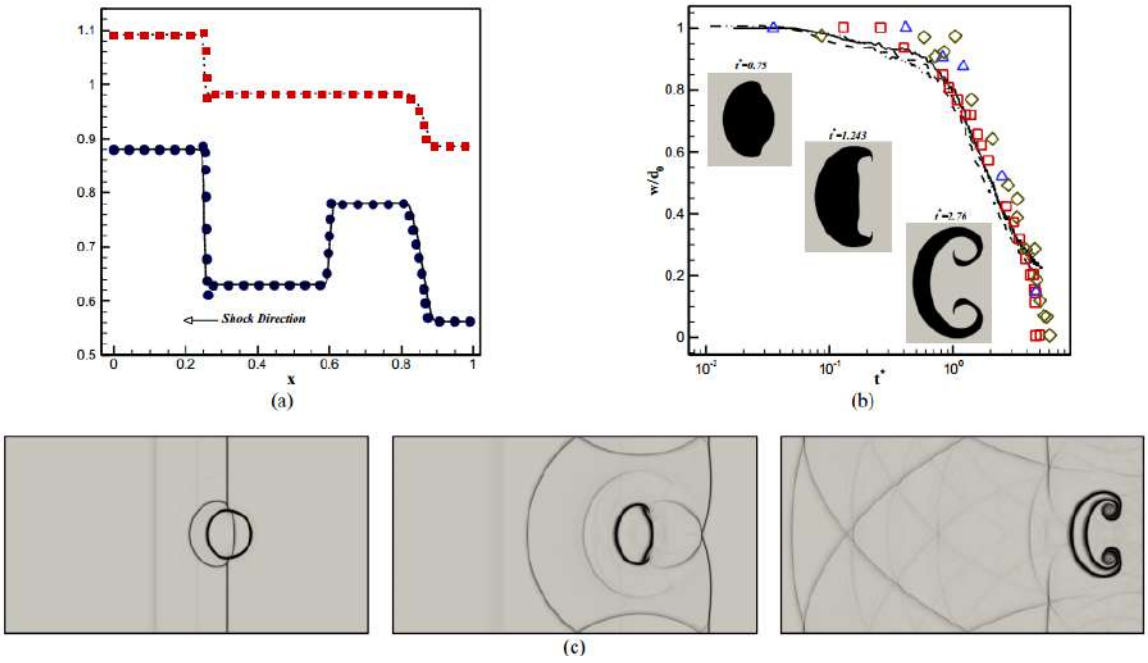

Figure 1: (a) Simulation of an anomalous shock in the van der Waals fluid, $\delta = 1/C_v = 0.0125$. Initial conditions: $(p_{\mathrm{L}}, \rho_{\mathrm{L}}) = (1.09, 0.879)$, $(p_{\mathrm{R}}, \rho_{\mathrm{R}}) = (0.885, 0.562)$ were applied to the left and right part of the tube. The snapshot is taken at time $t^* = (t/L)\sqrt{p_{\mathrm{cr}}/\rho_{\mathrm{cr}}} = 0.45$, where L is the length of the domain. Line: Density [2], dashed: Pressure [2], symbols: Present. (b) 2D droplet center-line width evolution during reduced time $t^* = t(u_g/d_0)\sqrt{\rho_{\mathrm{g}}/\rho_{\mathrm{l}}}(\varsigma_l/\varsigma_g)$; $\varsigma_{l,g}$ is the speed of sound in the liquid and the post-shock gas, $\rho_{l,g}$ are corresponding densities, d_0 is the initial diameter of the liquid column and u_g is the flow speed upstream. Lines: Present scheme, solid line: $M_s = 1.18$, long dashed: $M_s = 1.33$, dashed: $M_s = 1.47$. Symbol: Experiment [3], square: $M_s = 1.18$, delta: $M_s = 1.30$, diamond: $M_s = 1.47$. (c) Schlieren images of the interaction of a shock wave at $\mathrm{Ma} = 1.47$ and a droplet at different times using the present scheme. From left to right: $t^* = 0.298$, $t^* = 0.879$, $t^* = 2.413$.

Anomalous shock: Only compression shocks and rarefaction waves are observed during the simulation of the shock-tube test in an ideal-gas. On the other hand, in the real-gas framework, it has been noted that there exist a region near the vapor saturation line where an anomalous behaviour may be observed in terms of the existence of a rarefaction shock [2]. The fluids that can show such a behaviour are known as BZT (Bethe, Zel'dovich and Thompson) fluids [4]. This anomalous behaviour which is classified as "Nonclassical Gas Dynamics" is characterized by the fundamental derivative defined as $\Gamma = v^3/2c^2(\partial^2 p/\partial v^2)_s$ where c is the speed of sound. For fluids with complex molecules, nonclassic behaviour occurs when $\Gamma < 0$ or when the $\Gamma = 0$ boundary is passed during the evolution of the flow [2]. Note that rarefaction shocks are not admissible in ideal-gases since the fundamental derivative is always positive, i.e., $\Gamma = \frac{1+\gamma}{2} > 0$ where $\gamma = C_p/C_v$ is the adiabatic exponent. The rarefaction shock is clearly visible in Figure 1.a, traveling to the high-pressure side of the tube.

Shock water-column interaction: The interaction of a water column with a planar shock wave and the subsequent deformation of the water column are investigated using the proposed scheme. To this end, a planar shock wave was generated, which separates the post-shock part and the saturated vapor. The droplet resides in the downstream of the shock, where it is initially in equilibrium with its own vapor at the temperature $T/T_{cr} = 0.9$. Simulations were conducted at three different Mach numbers, namely $M_s = 1.18$, $M_s = 1.33$ and $M_s = 1.47$. The time when the shock front reaches to the upstream interface of the droplet was assigned as $t = 0$. The width of the water-column during time has been measured and compared to experimental results in Figure1.b, which shows an excellent agreement. In addition, Schlieren images of water-column at three different times are presented in figure 1.c.

References

[1] B. Dorschner, F. Bösch, and I. V. Karlin. "Particles on Demand for Kinetic Theory". In: *Phys. Rev. Lett.* 121 (13 Sept. 2018), p. 130602.

[2] ALBERTO Guardone and Luigi Vigevano. "Roe linearization for the van der Waals gas". In: *Journal of Computational Physics* 175.1 (2002), pp. 50–78.

[3] D Igra and K Takayama. "A study of shock wave loading on a cylindrical water column". In: *Report of the Institute of Fluid Science, Tohoku University* 13 (2001), pp. 19–36.

[4] Calin Zamfirescu, Alberto Guardone, and Piero Colonna. "Admissibility region for rarefaction shock waves in dense gases". In: *Journal of Fluid Mechanics* 599 (2008), pp. 363–381.

MIXING AND UNMIXING INDUCED BY SELF-PROPELLED CAMPHOR PARTICLES

Clément Gouiller[1], Florence Raynal * [2], Mickaël Bourgoin[3], Cécile Cottin-Bizonne[1], Romain Volk[3], and Christophe Ybert[1]
[1] ILM, Univ Lyon, Univ Lyon 1, CNRS, F-69622 Villeurbanne CEDEX, France
[2] LMFA, Univ Lyon, Ecole Centrale Lyon, INSA Lyon, Université Lyon 1, CNRS, F-69134 Ecully, France
[3] Laboratoire de Physique, ENS de Lyon, Univ Lyon, CNRS, 69364 Lyon CEDEX 07, France

Summary In this experimental study, we report on the mixing properties of floaters by chemical and hydrodynamical currents generated by self-propelled camphor disks swimming at the air-water interface. While mixing is very rapid at short times, the system remains partially unmixed. This intermediate state results from a competition between (i) the mixing induced by the motion of the camphor swimmers and (ii) the unmixing promoted by the chemical cloud attached to each individual self-propelled disk.

INTRODUCTION

In a recent work, we considered a simple and historical system of active self-propelled particles made of camphor disks lying at the air-water interface [1, 2]. Remarkably, the collective dynamics of such swimmers was shown to exhibit multi-scale dynamics mimicking the canonical Kolmogorov K41 fluid turbulence [3]. Here we study mixing of inert floaters initially introduced at the center of such a system, for different numbers of swimmers, and different swimmers diameters. Remarkably, a stationary state is rapidly reached, that does not correspond to a fully mixed state. We show that the origin of this stationary heterogeneous state is associated to the competition between two antagonist mechanisms of mixing and unmixing, and explain the origin of the unmixed region.

EXPERIMENTAL APPARATUS

The experimental apparatus is described in figure 1: A small quantity of inert floating particles is poured at center of a container stirred with camphor swimmers. The concentration field is recorded as a function of time.

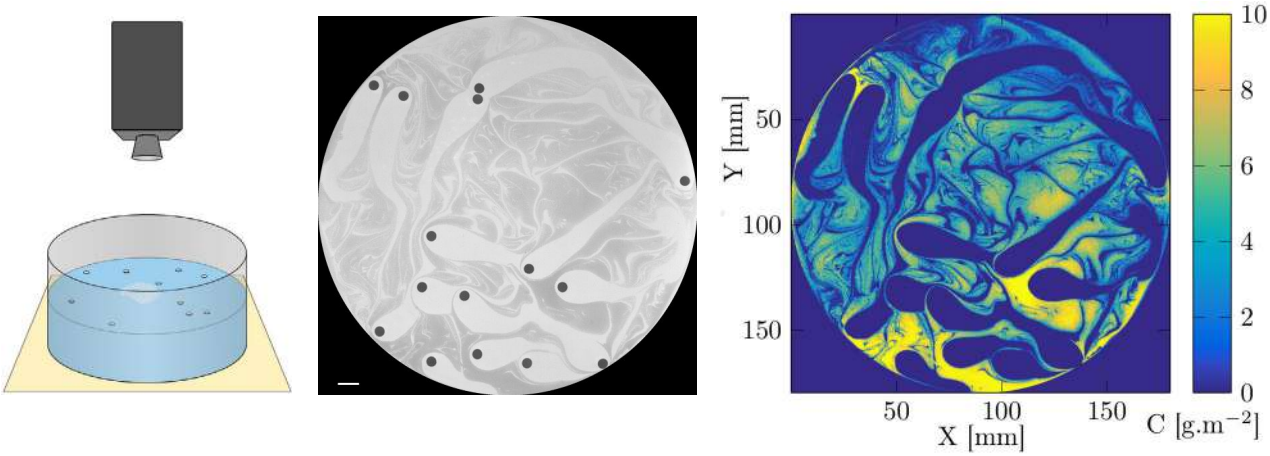

(a) (b) (c)

Figure 1: (a) Exprimental apparatus: in a glass container, we set N camphor swimmers, together wih a small quantity of micro-particles of glass at the center; (b) Typical image obtained after 10 minutes for $N = 15$ swimmers of radius 2.5 mm; (c) After calibration, corresponding concentration field.

MIXING PROPERTIES

Mixing is investigated using the standard deviation of the concentration $C_{std}(t) = \sqrt{\langle C^2 \rangle - \langle C \rangle^2}$. When the patch is poured, it gets rapidly stretched and folded by the velocity field induced by the camphor swimmers, as shown in figure 2, so that C_{std} converges rapidly towards a non zero value C^{∞}_{std}; decay is exponential at short times, which is typical of turbulent or chaotic mixing. The reason for this incomplete mixing is obviously the importance of the depletion area around each swimmer. Concentration spectra (not shown here) are also used for the characterization.

*Corresponding author. E-mail: florence.raynal@ec-lyon.fr.

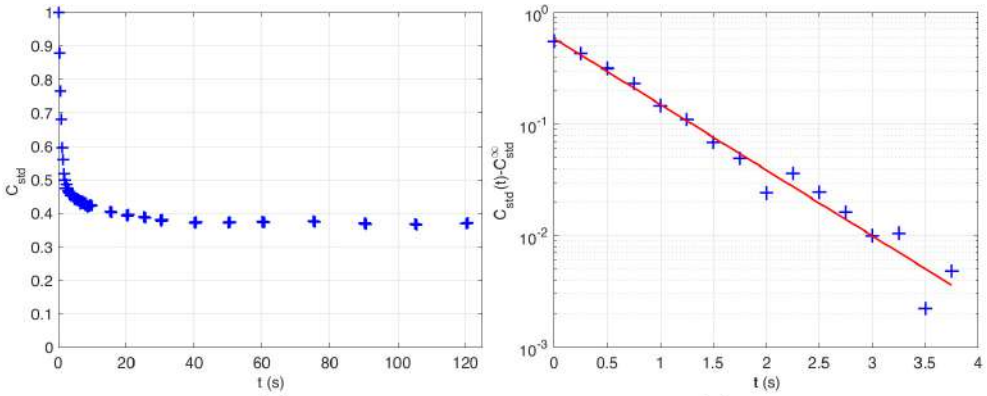

(a) (b)

Figure 2: (a) Temporal evolution of the non dimensional concentration field standard deviation $C_{std}(t) = \sqrt{\langle C^2 \rangle - \langle C \rangle^2}$ in the case of 15 swimmers. (b) Short term evolution of $C_{std} - C_{std}^{\infty}$, with C_{std}^{∞}=0.45.

WAKE OF A SWIMMER

The typical area produded by a swimmer is estimated in figure 3a for various numbers N of swimmers. The typical Reynolds number of a camphor swimmer is 50. In order to understand if the wake around the swimmer is of mechanical or chemical origin, we perform two experiments: in the first one we pull a disk without camphor at the same velocity as a swimming camphor disk : no such wake is observed. In the second experiment, a single camphor disk is forced to remain at the same location. The surface of depletion area observed, here 26 cm^2, is in very good agreement with what is observed in figure 3a for $N = 1$.

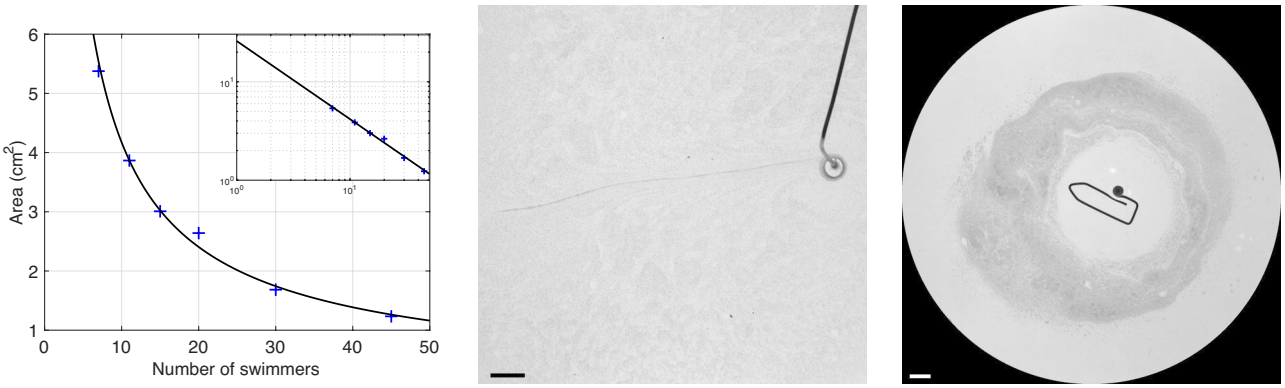

(a) (b) (c)

Figure 3: (a) Depletion area of a given wake as a function of the number of swimmers N, for camphor disks of radius 2.5 mm; (b) wake produced by a particle not filled with camphor, forced to move at the velocity of a camphor particle; (c) depletion area produced by a camphor disk forced to remain at the same location.

CONCLUSIONS

We studied an original surfacic mixing system, where the velocity field is induced by camphor swimmers actively moving at the surface of the water. Whilst the system rapidly mixes at short times, it reaches a stationary state of imperfect mixing. We proved that the wake around the swimmers, at the origin of this partial mixing, is of chemical origin.

References

[1] Nakata S., Hayashima Y., and Komoto H., Spontaneous switching of camphor motion between two chambers; *Physical Chemistry Chemical Physics* **2**, 2395-2399 (2000).

[2] Boniface D., Cottin-Bizonne C., Kervil R., Ybert C., and Detcheverry F., Self-propulsion of symmetric chemically active particles: Point-source model and experiments on camphor disks, *Phys. Rev. E* **99**, 062605 (2019).

[3] Bourgoin M., Kervil R., Cottin-Bizonne C., Raynal F., Volk, R., Ybert C., Kolmogorovian active turbulence of a sparse assembly of interacting swimmers, *submitted* (2020).

COLLISION EFFICIENCY OF PARTICLES IN A SIMPLE SHEAR FLOW - THE ROLE OF NON-CONTINUUM HYDRODYNAMIC INTERACTIONS

Pijush Patra* , Abhisek Kundu, and Anubhab Roy
Department of Applied Mechanics, Indian Institute of Technology Madras, Chennai, Tamil nadu 600036, India

Summary We calculate the collision efficiency of non-Brownian spherical particle pairs in a non-continuum gas subject to a linear shear flow. When the fluid medium is assumed to be continuum, two types of trajectories exist in a simple shear flow - open and closed. Continuum lubrication forces prevent particles from touching and collisions occur only with the inclusion of colloidal forces. In a rarefied medium, the lubrication forces are weaker than their continuum counterpart and thus allows for particle contact in finite time. The non-continuum modifications to the axisymmetric mobility functions are then obtained based on the theory of Sundararajakumar & Koch (1996) ([7]). Pair trajectories in a weakly rarefied medium are then calculated and compared with known continuum trajectories (given in Batchelor & Green 1972b ([1])). We find that near-field non-continuum interactions are responsible for the occurrence of colliding trajectories in a simple shear flow, even in the absence of colloidal forces.

INTRODUCTION

Pairwise hydrodynamic interactions in a linear flow is of direct interest in studying the rheological properties of a semi-dilute suspension, collision and coagulation of small particles dispersed in a fluid and understanding particle interactions with surfaces. When the suspending medium is treated as a continuum, lubrication forces prevent particle collisions in the pure hydrodynamic scenario. In steady straining motion, all the pair trajectories are open whereas in simple shear flow, there exists open and closed trajectories. Previous studies have obtained particle collisions due to the inclusion of inter-particle forces ([9]), interfacial mobility ([8]), deformation ([5]) and compressibility ([3]). With non-continuum lubrication, we find three types of trajectories - (1) open trajectories that arrive from infinity and depart to infinity without reaching the collision sphere, (2) collision trajectories, are the trajectories arriving from infinity and hitting on the surface of the contact sphere, or emerging from the surface of the contact sphere and going to infinity, and (3) semi-closed trajectories that starts from the surface of the contact sphere and hits back on it. The upstream interception area, which defines the area within which two widely separated particles will eventually collide is determined by a trajectory analysis which includes non-continuum hydrodynamic interactions, attractive van der Waals force and a combination of both.

THEORY

We consider a particle pair in a simple shear field of a non-continuum gas flow given by, $\mathbf{u}^{\infty}(\mathbf{x}) = (\dot{\gamma}x_2, 0, 0)$, which can also be written as $\mathbf{u}^{\infty}(\mathbf{x}) = \mathbf{E}.\mathbf{x} + \mathbf{\Omega}.\mathbf{x}$, where $\mathbf{E}$ and $\mathbf{\Omega}$ are the rate-of-strain and rate-of-rotation. Fluid motion is assumed to be sufficiently slow that satisfy the Stokes equations for creeping flow and particle inertia is neglected due to their small size. We choose a spherical coordinate system (r, θ, ϕ), with origin at the centre of sphere 1 and $\theta = 0$ being the vorticity axis (x_3). The relative velocity between the particles can be written as ([8]):

$$\begin{aligned}\mathbf{V}_{21}(\mathbf{r}) &= \mathbf{\Omega} \times \mathbf{r} + \mathbf{E}.\mathbf{r} - \left[A(s)\frac{\mathbf{rr}}{r^2} + B(s)(\mathbf{I} - \frac{\mathbf{rr}}{r^2})\right].(\mathbf{E}.\mathbf{r}) \\ &\quad - \frac{D_{21}^{(0)}}{k_B T}\left[G(s)\frac{\mathbf{rr}}{r^2} + H(s)(\mathbf{I} - \frac{\mathbf{rr}}{r^2})\right].\nabla(\Phi_{21}) \end{aligned} \tag{1}$$

The mobility functions for two hydrodynamically interacting spherical particles in a linear flow field are denoted by $A(s)$ and $B(s)$ and the Mobility functions for two spherical particles interacting hydrodynamically and moving because of a central potential between them are denoted by $G(s)$ and $H(s)$. $A(s)$ and $G(s)$ are the axisymmetric mobilities (i.e. mobility functions due to the relative motion along the line-of-centres) and $B(s)$ and $H(s)$ are asymmetric mobilities (i.e. mobility functions due to relative motion normal to the line-of-centres). All these mobilities depends on radii-ratio, $\kappa = a_2/a_1$, and non-dimensional centre-to-centre distance, $s = 2r/(a_1 + a_2)$, between the spherical particles. We used uniformly valid axisymmetric mobilities $A(s)$ and $G(s)$ recently developed by Dhanasekaran et al. ([2]). The relative diffusivity due to Brownian motion for two widely separated spherical particles is given by :

$$D_{21}^{(0)} = \frac{k_B T((1 + \kappa^{-1})}{6\pi\mu a_1} \tag{2}$$

The interparticle force potential is usually the sum of an attractive van der Waals force and a repulsive eletrical double layer force. For now, we will consider only the unretarded van der Waals force, $\Phi_{21} = \Phi_{vdW}$. If we assume pairwise additivity of the intermolecular attractions ([4, 6]) we have

$$\Phi_{vdW} = -\frac{A_H}{6}\left[\frac{8\kappa}{(s^2-4)(1+\kappa)^2} + \frac{8\kappa}{s^2(1+\kappa)^2 - 4(1-\kappa)^2} + \log\left\{\frac{(s^2-4)(1+\kappa)^2}{s^2(1+\kappa)^2 - 4(1-\kappa)^2}\right\}\right], \tag{3}$$

*Corresponding author. E-mail: pijush.bankura2011@gmail.com

where A_H is the composite Hamaker constant for the materials composing the two spheres and the surrounding fluid medium, $k_B = 1.381 \times 10^{-23} JK^{-1}$ is the Boltzmann constant and T is the absolute temperature. We define a dimensionless quantity, N_F, which measures the relative importance of ambient flow to the van der Waals attraction:

$$N_F = \frac{\frac{1}{4}a_1^2 (1+\kappa)^2 \dot{\gamma}}{A_H D_{12}^{(0)}/K_B T} = \frac{6\pi\mu a_1^3 \kappa (1+\kappa)\dot{\gamma}}{4A_H} \tag{4}$$

RESULTS AND DISCUSSION

Three velocity components obtained from equation (1) form an autonomous system of ODEs which are solved numerically using fourth-order Runge-Kutta method to find pair trajectories. The collision efficiency E_{21} is defined as the ratio of the collision rate in the presence of interactions to that in their absence. We found that the variation of collision efficiency with Knudsen number Kn (see figure 1(a)) in uniaxial compressional flow is different from that of simple shear flow. It is important to note that in case of simple shear flow depending on the radii ratio κ there exist a particular value of Kn below which there is no collision trajectories and those trajectories fundamentally behaves like continuum trajectories.

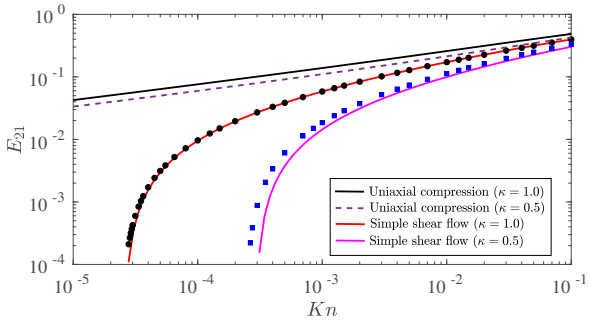

(a) Only non-continuum interactions

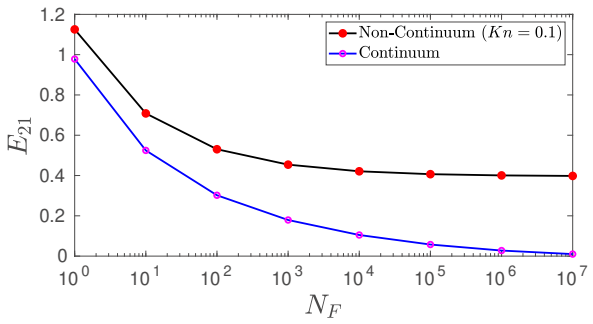

(b) Non-continuum interactions with van der Waals force

Figure 1: Collision efficiency as a function of Kn is plotted in figure (a). The black line in (a) shows the variation of collision efficiency E_{21} in uniaxial compressional flow for $\kappa = 1.0$ and the dashed violet line shows the same for $\kappa = 0.5$. The red curve in (a) indicates the variation of E_{21} with Kn in simple shear flow for $\kappa = 1.0$ when collision efficiencies are calculated analytically and the solid black dots on that line are produced from numerical calculation. The magenta color curve and solid square dots indicate the same for $\kappa = 0.5$. Collision efficiency for two equal sized spherical particles considering continuum hydrodynamic interactions and non-continuum hydrodynamic interactions at $Kn = 0.1$ are plotted in figure (b) as a function of N_F.

CONCLUSION

The present study provides a map of pair trajectories for non-continuum lubrication interactions. The non-continuum interactions results in collision trajectories and no closed trajectories unlike its continuum counterpart. These trajectory calculations will be useful in obtaining pair probability and consequently in calculating the effective viscosity of a non-continuum suspension. This study also provides the calculation of collision efficiency of small solid/liquid particles in gaseous medium in the absence of attractive colloidal forces. This will be particularly important to study droplet growth in clouds.

References

[1] G. K. Batchelor and J. T. Green. The hydrodynamic interaction of two small freely-moving spheres in a linear flow field. *Journal of Fluid Mechanics*, 56(2):375–400, 1972.

[2] J. Dhanasekaran, A. Roy, and D. L. Koch. Collision rate of bidisperse spheres settling in a compressional non-continuum gas flow. *Submitted to J. Fluid Mech.*

[3] A. Gopinath, S. B. Chen, and D. L. Koch. Lubrication flows between spherical particles colliding in a compressible non-continuum gas. *Journal of Fluid Mechanics*, 344:245–269, 1997.

[4] H. Hamaker. The london-van der waals attraction between spherical particles. *physica*, 4(10):1058–1072, 1937.

[5] M. A. Rother and R. H. Davis. The effect of slight deformation on droplet coalescence in linear flows. *Physics of Fluids*, 13(5):1178–1190, 2001.

[6] W. B. Russel, D. A. Saville, and W. R. Schowalter. *Colloidal Dispersions*. Cambridge Monographs on Mechanics. Cambridge University Press, 1989.

[7] R. R. Sundararajakumar and D. L. Koch. Non-continuum lubrication flows between particles colliding in a gas. *Journal of Fluid Mechanics*, 313:283–308, 1996.

[8] H. Wang, A. Z. Zinchenko, and R. H. Davis. The collision rate of small drops in linear flow fields. *Journal of Fluid Mechanics*, 265:161–188, 1994.

[9] G. R. Zeichner and W. R. Schowalter. Use of trajectory analysis to study stability of colloidal dispersions in flow fields. *AIChE Journal*, 23(3):243–254, 1977.

TURBULENCE IN A NETWORK OF RIGID FIBERS

Stefano Olivieri * [1], Marco E. Rosti[2], Luca Brandt[3], and Andrea Mazzino[1]
[1] DICCA, University of Genova, and INFN, Genova Section, I-16145 Genova, Italy
[2] Complex Fluids and Flows Unit, OIST, Onna-son, Okinawa 904-0495, Japan
[3] Linné Flow Centre and SeRC, KTH Mechanics, S-100 44 Stockholm, Sweden

Summary We study the effect of a network of fixed fibers on various kinds of turbulent flows, in order to provide useful insights for the analysis of particle-laden and porous media flows. To this aim, we perform direct numerical simulations using an immersed boundary method. We first consider the so-called ABC cellular flow finding that, for a sufficiently large concentration where the resulting configuration mimicks the stable solution, the effect of the network can be effectively modelled by means of a Darcy's friction term. We propose a phenomenological expression that is corroborated in the case of the Kolmogorov parallel flow and homogeneous isotropic turbulence. Moreover, we examine the overall energy distribution across the scales of motion, highlighting the presence of small-scale activity with a secondary peak in the energy spectra at a wavenumber characteristic of the network.

INTRODUCTION

The interaction between turbulent flows and fiber-like objects is an intriguing topic concerned by a large number of natural and engineering processes, such as, e.g., aerosol deposition or papermaking. Nevertheless, the understanding of how turbulence is generally modified by the presence of dispersed particles, on a fundamental basis, is still not fully clear [1]. In this work, we tackle the problem by focusing, in particular, on the case where fibers are fixed. On one hand, this can be intended as a preliminary step before considering suspensions of moving fibers. However, it also supplies an essential representation of flow within a canopy, with several features of interest in boundary-layer meteorology, such as the influence of the canopy on the transport and mixing properties [2].

PHYSICAL MODEL AND NUMERICAL METHOD

We consider a cubic domain with side $L = 2\pi$ and periodic boundary conditions. We perform direct numerical simulations (DNS) of the incompressible Navier-Stokes equations, using a finite-difference based code, for a variety of three-dimensional flows, such as homogeneous isotropic turbulence (Fig. 1a). Within this representative volume, we place an ensemble of N one-dimensional fibers (Fig. 1b). Each fiber composing the network has length c. The fiber centroids are evenly spaced placing an integer number of rods along each direction (although one case of randomly spaced fibers is also considered), while the orientation is randomly distributed. To take into account the effect by the fibers on the flow, we employ an immersed boundary (IB) method, which adds an additional localized forcing in order to enforce the no-slip condition. Specifically, we employ the numerical procedure already used for moving and flexible fibers both in laminar and turbulent flow conditions, see e.g. [3, 4].

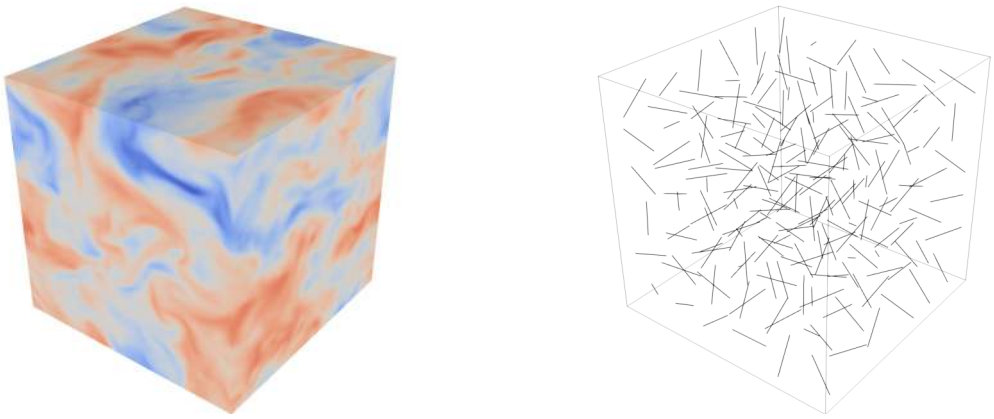

Figure 1: Left: homogeneous isotropic turbulent flow (the colormap showing one velocity component); right: network of $N = 6^3$ fibers with $c/L = (2\pi)^{-1}$ placed in the same triperiodic fluid domain.

*Corresponding author. E-mail: stefano.olivieri@edu.unige.it.

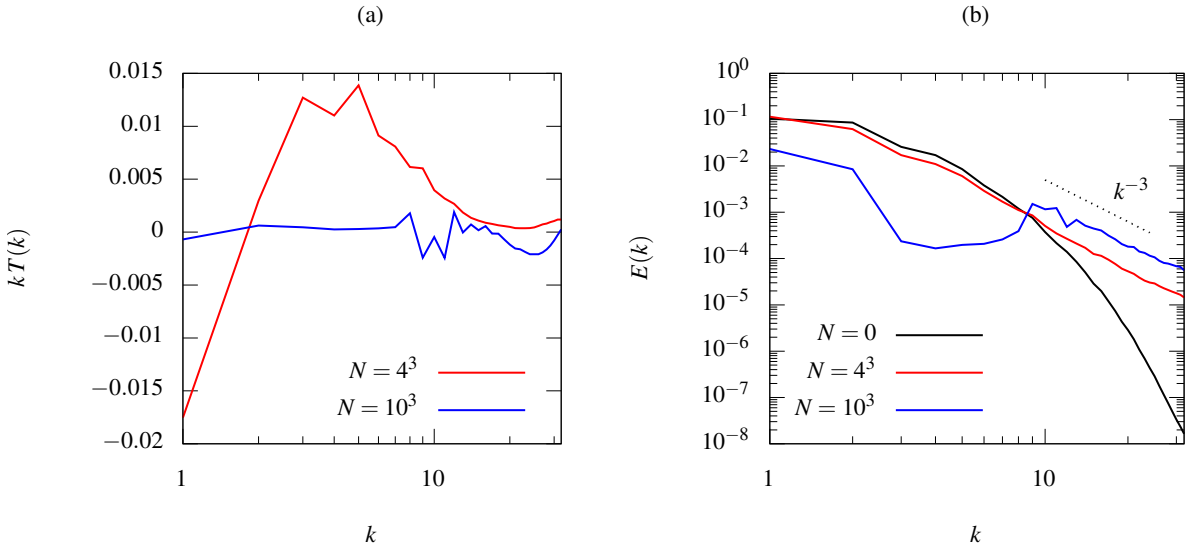

Figure 2: (a) Nonlinear terms appearing into the spectral power balance (multipled by k to improve readibility) and (b) energy spectra, from DNS of homogeneous isotropic turbulence at $Re_\lambda \approx 40$ for different fiber concentrations (black: $N = 0$, red: $N = 4^3$, blue: $N = 10^3$) with fiber length $c/L = (4\pi)^{-1}$.

RESULTS AND DISCUSSION

We first consider a steady large-scale external forcing, for which, if the Reynolds number is below a critical value, the stable Arnold-Beltrami-Childress (ABC) solution is obtained, and investigate the stabilizing effect of fixed fibers on this kind of cellular flow. For the latter, stability analyses have been carried out by several authors, and can be used as a reference to study the effect of a network of fibers. We choose an unstable and chaotic flow condition at a given $Re > Re_{\rm cr}$ and perform a parametric study by varying the number of fibers N and the fiber length c. Results show that, for sufficiently large concentrations, we recover a completely steady behavior. Two main features can be clearly observed: (i) the qualitative resemblance of the large-scale flow structure with that of the (stable) ABC flow; (ii) the presence of small-scale activity at the characteristic wavenumber $k_{\rm c} = 2\pi/(L/\sqrt[3]{N})$, corresponding to the spacing between the network fiber elements. Based on this numerical evidence, we focus on a scale-by-scale analysis and, in particular, we propose an effective large-scale description by means of a simple Darcy's friction term, i.e. $-D\mathbf{u}$, where the friction coefficient is expressed by the following phenomenological expression:

$$D = \alpha\, \nu\, n L \left(\frac{c}{L}\right)^{\frac{2}{3}}, \tag{1}$$

where ν is the kinematic fluid viscosity, $n = N/L^3$ and $\alpha \approx 7$ is a numerical factor.

Hence, we move to corroborate our prediction in the framework of different flow configurations, such as the parallel Kolmogorov flow $\mathbf{u} = (\cos y, 0, 0)$, as well as homogeneous isotropic turbulence. Moreover, we also carry out the corresponding effective simulations, replacing the IB forcing with the Darcy's term computed using Eq. (1).

Focusing on results for HIT (Fig. 2), good agreement is found between the fully-resolved cases and the corresponding effective ones, provided that the fiber concentration and/or the fluid viscosity is sufficiently high. In this condition, the nonlinear terms are substantially negligible (Fig. 2a) and our approach is fully justified. Looking at the energy spectra (Fig. 2b), one can note that the large-scale/low-wavenumber components decrease for increasing fiber concentration, while the opposite occurs for the small-scales/high-wavenumbers, for which we recover the $\sim k^{-3}$ scaling characteristic of viscosity-dominated regimes. For the case with the highest concentration, we can clearly observe the gap for intermediate wavenumbers and the secondary peak at $k = k_{\rm c}$, representing the signature of the same mechanism of energy distribution that was already identified when considering the ABC cellular flow.

Overall, our effective description appears to work well both on a qualitative and quantitative basis when applied to a variety of different flow conditions. Moreover, we underline that our findings could be relevant also for particle-laden flows where the inertia of particles plays a dominating role [5]. Finally, on-going activity is planned indeed to extend the analysis to suspensions of moving fibers.

References

[1] Sardina G., Brandt L., Boffetta G., Mazzino A. *Phys. Rev. Lett.* **121**: 224501, 2018.
[2] Finnigan J. *Annu. Rev. Fluid Mech.* **32**: 519, 2000.
[3] Banaei A. A., Rosti M. E., Brandt L. *J. Fluid Mech.* **882**: A5, 2020.
[4] Rosti M. E., Olivieri, S., Banaei A. A., Brandt L., Mazzino A. *Meccanica* https://doi.org/10.1007/s11012-019-00997-2, 2019.
[5] Saffman P. G. *J. Fluid Mech.* **13**: 120-128, 1962.

SUSPENSION SHEAR THICKENING: CONTACT FORCE NETWORKS

Omer Sedes[1], Jeffrey F. Morris * [1], Hernan Makse[1], and Bulbul Chakraborty[2]
[1] Levich Institute, CUNY City College of New York; New York, NY USA
[2] Department of Physics, Brandeis University, Waltham MA, USA

Summary The rheology of suspensions of spheres is simulated. Interparticle forces due to hydrodynamic lubrication, short-range repulsion and contact with friction are included. Strong continuous shear thickening is found at solid fractions $\phi > 0.5$ and discontinuous shear thickening for $\phi > 0.55$. Contact force networks are analyzed here, with a focus on the sub-networks of particles each mutually connected by k or more contacts to other members of this sub-network: this is a k-core. Sampling of the connected structures is performed as a function of ϕ and shear rate within the ensemble of non-equilibrium steady states. The network at small stress is formed of disconnected quasi-linear structures ($k = 1$), which grow and merge to form loops ($k = 2$) and percolating structures at sufficient stress, with the sudden appearance of a system spanning $k = 3$ component at large stress.

INTRODUCTION

Concentrated or 'dense' suspensions display strong shear thickening, a behavior that has been related to shear-induced jamming [1]. In the last several years, the influence of contact forces on shear thickening in suspensions has been studied intensively. At large solid fraction ϕ, strong continuous shear thickening (CST) or discontinuous shear thickening (DST) are observed. Both simulations [2] and theory [3] show that a relatively simple scenario in which lubricated contacts give way to frictionally contacting particles, with the rate of this transition controlled by a repulsive force such as that due to surface charge, is able to capture qualitative features seen in experiment, while experiments specifically probing the development of stress due to contact have been reported [4]. Thus the network of contact forces arises as an important microstructural variable. Here, networks determined from simulations by an established approach [2] are studied. Among several approaches [5, 6] to analyze the networks, we are motivated by prior considerations of granular systems by k-core analysis [6] to consider groups of mutually contacting particles each with k or more contacts to others in this group, forming a 'k-core.' We consider the steady states of the suspension as a function of ϕ and imposed shear rate $\dot{\gamma}$, sampling the network structure as the suspension is sheared through a large number of configurations. This provides network statistics from which we gain insight to how the network develops and is related to the shear thickening transition.

SIMULATION METHOD & RHEOLOGY

The suspension is simulated by the lubricated flow-discrete element method [2]. We study bidisperse suspensions in which the spherical particles have radii a and $1.4a$, with 50% of the particle volume contributed by particles of each size. Hydrodynamic interactions are limited to short-range lubrication forces of the form $\mathbf{F}_{ij}^{\text{lub}} = -\mathbf{R}_2 \cdot (\mathbf{u}_i - \mathbf{u}_j)$, with $\mathbf{u}$ a particle velocity. The resistance tensor $\mathbf{R}_2$ scales as $1/(\delta+h)$ for normal motion and $\log(\delta+h)$ for tangential motion, where h is the pair surface separation, and $\delta = 10^{-3}a$ cuts off the lubrication force singularity which would otherwise occur at contact, $h = 0$. Short-range pair repulsive forces, of form $F_R e^{-\kappa h}$ modeling electrostatic repulsion with Debye length $1/\kappa$, as well as a stiff elastic interaction at contact, are included. At contact, Coulomb friction is modeled, with $F_{\text{C,t}} \leq \mu F_{\text{C,n}}$ relating tangential ($F_{\text{C,t}}$) and normal ($F_{\text{C,n}}$) force components; here $\mu = 1$.

The importance of the contacts to the stress response is illustrated in a simple way by the number of frictional contacts per particle Z growing with shear rate in the upper part of figure 1, just as the relative viscosity increases strongly with shear rate, here in a dimensionless form scaled by $\dot{\gamma}_0 = F_R/(6\pi\eta_0 a^2)$. This plot shows CST for $\phi = 0.54$ and DST at $\phi > 0.55$; while not readily apparent here, it is possible to show that there an S-shape to the $\eta(\dot{\gamma})$ curves for $\phi > 0.55$ accessible under shear stress control. At $\phi = 0.55$, the suspension behavior is, to a close approximation, at the transition from CST to DST.

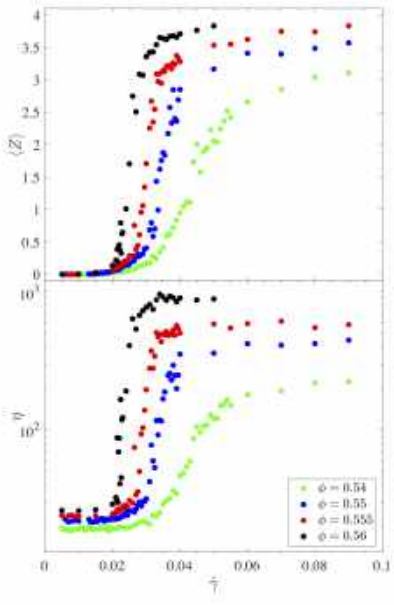

Figure 1: Bottom: relative viscosity η; top: ensemble average contacts per particle, $\langle Z \rangle$, plotted as a function of dimensionless shear rate.

FORCE NETWORK ANALYSIS

The contact number shown in figure 1 is a limited description of the contact state, so we consider the frictional contact network. Typical networks at rates just below and above strong shear thickening are illustrated in figure 2, for $\phi = 0.55$. These show links between frictionally-interacting particles.

*Corresponding author. E-mail: morris@ccny.cuny.edu .

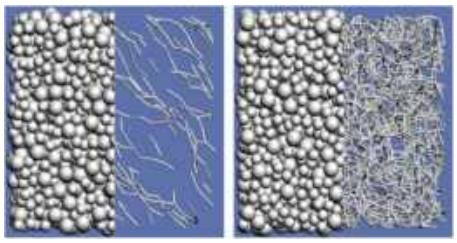

Figure 2: Particle configurations and contact force networks for $\phi = 0.55$, in the low- (left) and high-viscosity (right) states, $\dot{\gamma} \approx 0.025$ and 0.04 in figure 1.

The direction of the frictional force is not indicated. At the lower shear rate (lower viscosity), the network of contact forces is composed of quasi-linear structures along the compressive axis, while in the thickened state the networks become dense and relatively more isotropic. The frictional networks percolate in all directions, but the states are not jammed. Flow is necessary to achieve the stress to drive certain of these close interactions into contact, and thus the contact state is intrinsically linked to the flow.

At very low shear rate, the repulsive force is able to maintain surface separation between all particles. As the rate is increased, some particles are forced into contact, forming first dimers and then the quasi-linear structures of figure 2 (left side); these are $k = 1$ structures, or 1-cores; note that while most have two contacts, progressive pruning of the singly connected structures leaves again singly connected structures and this is a 1-core [6]. These 1-core structures become progressively longer and more dense in the suspension with increase of the shear rate (and consequently the stress), until in the beginning of the rapid upturn of the stress, whether in CST or DST, they begin to merge into 2-cores which percolate across the domain. With increase of the shear rate, the 2-core rapidly grows, with the mean number of contacts per particle Z rising rapidly, until a 3-core that spans the system emerges. Small non-spanning 3-cores are also found just before the system spanning structure, but these do not grow and merge; rather these appear and disappear rapidly. Z is a one-to-one function of the stress, as shown by figure 3a, and the fraction of particles within each core type is shown in figure 3b, as a function of Z.

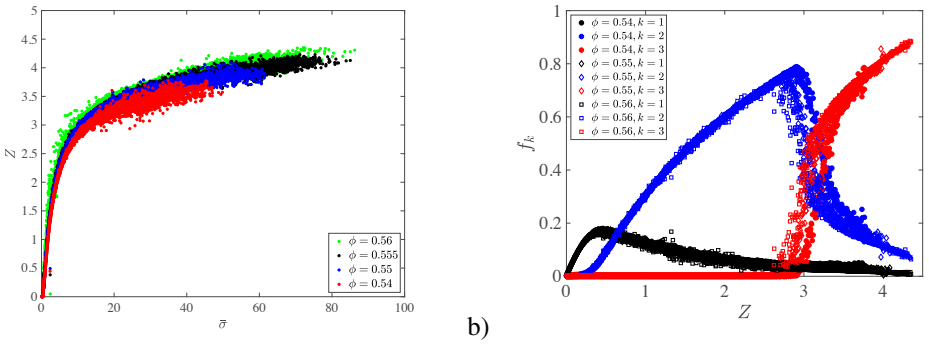

a) b)

Figure 3: a) Instantaneous average contact numbers, Z, as a function of the dimensionless shear stress, scaled by $F_R/(6\pi a^2)$; b) the fraction of total particles in each size of core as a function of Z over all shear rates simulated for $\phi = 0.54, 0.55$ and 0.56.

An analysis of the stress contributed by each core type finds that in CST, the stress is similar in all core types, with mildly stronger stress contributed by the more highly-connected structures, whereas in the DST regime, there is a very sharp increase in the stress contributed by 3-cores relative to 2-cores. This relationship between the connectivity of the structures and the stress response is indicative of the underlying basis for the mechanical behavior. It is found that when 4-cores arise, at $\phi > 0.58$, the system generally jams, but this point demands further study.

CONCLUSIONS

Shear thickening in dense suspensions is described here by a lubricated-to-frictional rheology, with the transition to the large-viscosity state at a critical level of stress related to a microscopic repulsion force. This leads to development of a frictional contact network, found from simulation to evolve with increasing stress from disconnected quasi-linear structures to loop structures and percolation, and then to a fully dense network. In the language of k-cores, this is roughly a transition from 1- to 2- to 3-cores. The stress response is directly related to the contact state, as stress increases with mean contact number Z. A signature of DST is that there is a sharp increase in stress in the 3-core structures when DST is observed whereas this increase is absent at slightly lower ϕ where CST occurs.

References

[1] Morris, J. F. Shear thickening of concentrated suspensions: recent developments and related phenomena. *Ann. Rev. Fluid Mech.* **52**, 2020.
[2] Mari, R. *et al.* Shear thickening, frictionless and frictional rheologies. *J. Rheol.***58**, 1693, 2014.
[3] Wyart, M.; Cates, M. E. Discontinuous shear thickening without inertia in dense non-Brownian suspensions. *Phys. Rev. Lett.* **112**, 098302, 2014.
[4] Lin, N. *et al.* Hydrodynamic and contact contributions to continuous shear thickening in colloidal suspensions, *Phys. Rev. Lett.* **115**, 228304, 2015.
[5] Thomas, T. *et al.* Microscopic origin of frictional rheology in dense suspensions: correlations in force space. *Phys. Rev. Lett.* **121**, 128002, 2018
[6] Morone, F. *et al.* The jamming transition is a k-core percolation transition. *Physica A* **516**, 172, 2019.

FREEZING A RIVULET

Antoine Monier * [1], Axel Huerre[2], Christophe Josserand[2], and Thomas Séon[1]
[1] Sorbonne Université, CNRS, UMR 7190, Institut Jean Le Rond d'Alembert, F-75005 Paris, France
[2] LadHyX, UMR 7646 CNRS-Ecole Polytechnique, IP Paris, 91128 Palaiseau CEDEX, France

Summary We investigate experimentally the formation of the particular ice structure obtained when a capillary trickle of water flows on a cold substrate. We show that after a few minutes the water ends up flowing on a tiny ice wall whose shape is permanent. We characterize and understand quantitatively the formation dynamics and the final thickness of this ice structure. In particular, we identify two growth regimes. First, a 1D solidification diffusive regime, where ice is building independently of the flowing water. Second, once the ice is thick enough, the heat flux in the water comes into play, breaking the 1D symmetry of the problem, and the ice ends up thickening linearly downward. The system reaches ultimately a stationary state where water continues to flow on ice without solidifying anymore. This linear pattern is explained by considering the competition between the water cooling and its convection.

INTRODUCTION

Solidification in flowing systems is a question encountered in numerous area such as geophysics, metallurgy and aeronautics. From a geophysical point of view, understanding of solidification of lava flows could help preventing the impact of volcanic eruptions on human populations [1]. The metallurgic industry is also interested in understanding the fine coupling between hydrodynamics and solidification to control the aparition of cracks during the formation of metal sheets [2]. Finally, freezing of velocity sensors during commercial flights is thought to be responsible for plane crashes. As a result, understanding the freezing process of small quantities of liquid flowing over a cold surface could help for all those topics. In this study, we will investigate experimentally and theoretically the freezing of a rivulet, obtained by flowing water on a cold solid substrate.

EXPERIMENTAL METHOD

In order to study the effect of different parameters on the shape and the dynamics of the ice structure formed while freezing a rivulet, we built a simple model experiment. We flowed water dyed with fluorescein (water layer thickness h_w) on a aluminium inclined substrate which is cooled to a given temperature, T_s, with liquid nitrogen. We recorded the evolution of the ice thickness h_i, taking advantage of the de-activation of fluorescein upon freezing (see Figure 1a). We vary experimentally the thermal parameters: the substrate and the liquid temperatures (T_s and T_in, respectively).

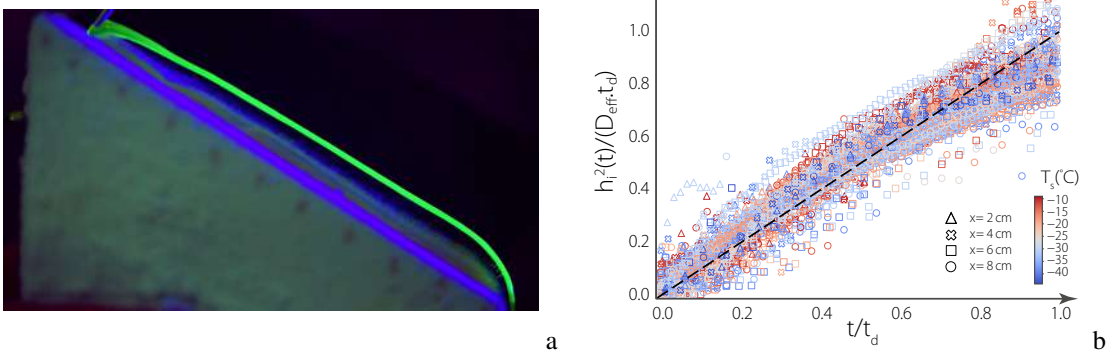

a b

Figure 1: (a) Side view of the ice structure (brown/black) with water flowing on top (green) (b) Rescaled ice thickness $h_\mathrm{i}^2(t)/(D_\mathrm{eff}t)$, $t \in [0, t_\mathrm{d}]$ as a function of the non-dimensional time t/t_d. D_eff is computed from [5] and t_d, the time where the spatially homogeneous growth ends, is experimentally determined.

INITIAL DIFFUSIVE GROWTH

When growing initially, the ice layer thickness is found to vary with the square-root of time. To understand this short time behavior of the ice layer growth, we model it by using the Stefan condition, where the latent heat produced by the ice formation results from the difference between the heat fluxes through the ice and the water. It reads here:

$$\rho_\mathrm{i}\mathcal{L}\partial_t h_\mathrm{i} = \lambda_\mathrm{i}\partial_y T\left(x, h_\mathrm{i}^-, t\right) - \lambda_\mathrm{w}\partial_y T\left(x, h_\mathrm{i}^+, t\right), \quad (1)$$

*Corresponding author. E-mail: ictam2020@aimgroup.eu.

where ρ_i is the ice density, $\lambda_{i,w}$ are the heat conductivities of the ice and water respectively, and $\mathcal{L}$ the latent heat of solidification. Initially, when $h_i \ll h_w$, the flux through the ice, which scales as $\lambda_i(T_m - T_s)/h_i$, T_m being the water melting temperature, is dominant compared to the flux through the water. This dynamics at short time corresponds to the classical one dimensional problem of the growth of an ice layer when a liquid is suddenly put in contact with a substrate at a uniform subfreezing temperature, usually known as the *classical Stefan problem* [3, 4]. In this situation, the front follows a diffusive dynamics: $h_i(t) = \sqrt{D_{eff}\, t}$, where the coefficient D_{eff} is solution of a transcendental equation that involves T_s, $\mathcal{L}$ and the ice and aluminum thermal coefficients.

In Fig. 1b, we plot the rescaled ice thickness $h_i^2(t)/(D_{eff} t_d)$, where D_{eff} is calculated using a refined model of the classical Stefan problem [5], versus the non-dimensional time t/t_d, $t \in [0, t_d]$. The graph presents the results of 31 experiments and 4 different positions along the plane, where T_s varies from -9 to -44°C and T_{in} from 8 to 35°C. All the data collapse on a line of slope 1, confirming that at short time the ice growth is only determined by the heat transfer toward the substrate without influence of the water flow.

PERMANENT REGIME

After few minutes, the ice thickness reaches a permanent regime where the water continues to flow on the ice wall previously formed. The height of the ice layer grows linearly along the plane, forming an angle β with the metallic plane.

The presence of such a permanent regime can be understood qualitatively by considering the thermal fluxes at the ice-water interface. Because the ice acts as a thermal diffusive layer between the plate and the liquid, the cooling flux - through the ice layer - diminishes as the ice layer thickens and the temperature gradient decreases. On the other hand, since the flowing water is dispensed at constant temperature on the forming ice layer, the heat flux brought to the system is constant. Consequently, an equilibrium is reached when the ice layer thickness is such that both fluxes balance.

To rationalize the peculiar structure formed by the ice, we derive and solve the temperature field in the ice layer and in the water. Coupling this to the flux continuity at the interface, we show that the ice thickness should follow the linear trend:

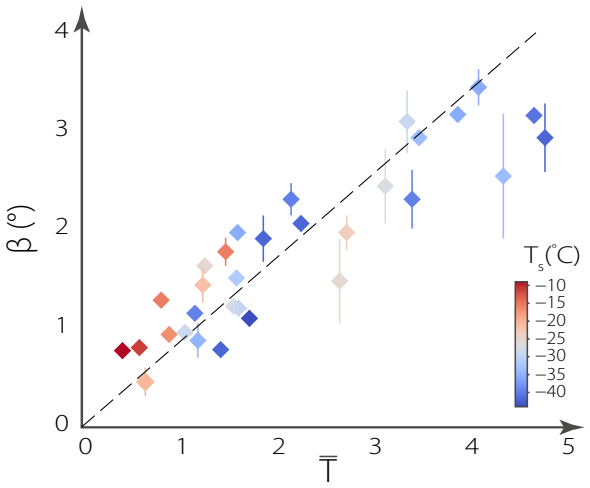

Figure 2: Slope of the ice layer β as a function of the rescaled temperature $\bar{T} = \frac{T_m - T_s}{T_{in} - T_m}$.

$$h_i(x) \sim h_w \frac{\lambda_i}{\lambda_w} \frac{T_m - T_s}{T_{in} - T_m}(1 + a\, x)\ . \tag{2}$$

This calculation predicts, in particular, that the slope of the ice structure β should vary linearly with the reduced temperature $\bar{T} = (T_m - T_s)/(T_{in} - T_m)$. Figure 2 shows precisely the experimental values of β, measured for all of our experiments with different water and substrate temperatures, as a function of $\bar{T}$. The color-code corresponds to experiments performed with different T_s. The dashed line is a linear fit of the data, showing a very good agreement with the prediction of Eq. (2).

CONCLUSIONS

Performing simple experiments and exploring both the ice shape and dynamics, we were able to probe the effect of hydrodynamics on the solidification process. After an initial diffusive growth, we observe a steady regime. It could be explained by a subtle balance between the advection of heat imposed by the water flow and the diffusion through the ice layer.

References

[1] Hardee, H. C. *J. Volcanol. Geotherm. Res.*. **3**:211-23, 1980.
[2] Cieslak, M. J. *Welding Journal*. **70**.2, 1991.
[3] Rubinstein, L.I., *The Stefan Problem*. American Mathematical Soc., 1971.
[4] Stefan, J. *Annal. der Phys.*. **278**:269-286, 1891
[5] Thiévenaz, V. et al. *J. Fluid Mech.*, **874**:756-773, 2019.

SEDIMENT TRANSPORT AND SEDIMENT DYNAMICS IN A TURBULENT OSCILLATORY BOUNDARY LAYER: RESULTS OF INTERFACE-RESOLVED SIMULATIONS

Marco Mazzuoli *[1], Paolo Blondeaux[1], and Giovanna Vittori[1]
[1] Department of Chemical, Civil and Environmental Engineering, University of Genoa, Genoa, Italy

Summary The dynamics of sediments under the action of an oscillatory flow in the intermittently turbulent regime is investigated by means of interface-resolved direct numerical simulations. The sediments are mono-sized spherical particles characterised by a diameter and a density typical of silica medium-sand grains. Moreover, the values of the other parameters are chosen to describe sediments under monochromatic sea waves propagating over a flat bed offshore from the breaker line. The simulations required formidable resources and time and reveal the mechanisms which control the interaction of the sediment particles with the turbulent vortices and the pressure gradient oscillations they induce. Limits and capability of the actual sediment transport predictors (proposed for steady flows) to estimate the bed load and the suspended load under oscillatory flows are also discussed.

BRIEF INTRODUCTION AND NUMERICAL APPROACH

The sediment transport induced by non-breaking sea waves can assume significant values because the bottom shear stress and the pressure gradient which are generated by propagating sea waves close to the bottom can mobilize large amounts of sediments. Hence, it turns out that fluid dynamics within the oscillatory boundary layer (OBL) generated close to the bottom is closely coupled with the dynamics of the sediments. The models currently used in coastal engineering applications to predict the sediment transport rate are mainly empirical and the effects associated with the rich dynamics of the OBL are often neglected or misrepresented. In an OBL characterized by the presence moving sediments, the velocity oscillations are characterised by the amplitude U_0^* and the angular frequency ω^* and the properties of the OBL are mainly controlled by two parameters, namely the Reynolds number $R_\delta = U_0^* \delta^* / \nu^*$, based on the thickness of the Stokes boundary layer $\delta^* = \sqrt{2\nu^*/\omega^*}$, and the dimensionless size of sediments d^*/δ^*, ν^* denoting the kinematic viscosity of the fluid and d^* a representative size of cohesionless sediments. The asterisk indicates dimensional quantities. For a wide range of values of R_δ and for values of d^*/δ^* typical of medium-sand, the flow is not always turbulent, but it re-laminarises in the phases of the wave-cycle around the flow reversal and at the beginning of the accelerating phases. Such behaviour characterises the so-called intermittently turbulent regime. Five direct numerical simulations (DNS) of an intermittently turbulent OBL developing over movable sediments were performed. In the DNS, sediments consist of mono-sized spheres characterised by values of the diameter d^* and the density ϱ_s^* typical of silica medium-sand grains. The Reynolds number R_δ is equal to 775, 1000 and 1500 while the dimensionless diameter d^*/δ^* is equal to 0.168, 0.335 and 0.670. Navier-Stokes and continuity equations are solved numerically by means of a finite difference approach which uses a second-order central-difference scheme to discretise the spatial derivatives and a fractional-step method to advance in time. The boundary condition at the moving fluid-solid interface is forced by using the immersed boundary method developed for particulate flows by [1]. Particle collisions are modelled with a Discrete Element Method (DEM) which comprises a linearised spring-dashpot system for normal and tangential stresses between spherical sediment grains. This approach underwent long validation and was adopted by [2, 3]. Figure 1a shows the flow and particle configuration of one of the simulations when the particles are picked-up from the bottom and suspended by turbulent vortices. [3] have recently described some of the present simulations and found that as long as particles roll, slide and saltate without going into suspension, the sediment flow rate can be fairly estimated assuming that the oscillatory flow is just a sequence of steady states, i.e. neglecting the effects of flow acceleration. This results can be justified by the fact that, for the sediment presently considered, the particle relaxation time is much smaller than the oscillation period. In the following, the approach of [4] is followed to develop a relatively simple model of bedload sediment transport which takes into account the dynamics of sediment particles during the wave cycle.

RESULTS AND ONGOING RESEARCH

The numerical simulations show that some of the empirical formulae used to quantify the bed load sediment transport can be tuned to provide a more accurate evaluation of the sediment transport rate. Let us consider the configuration of the present simulations, where sediment particles are spherical and mono-sized. The mean sediment flow rate q_s^* is equal to $\mathcal{V}^{*(p)} v_p^* n^{*(p)}$, $\mathcal{V}^{(p)}$ denoting the volume of a single particle, v_p^* being the particle velocity averaged over the computational domain above the resting bed and $n^{*(p)}$ being the number of particles per unit area that are moving. The dimensionless form of the sediment transport rate turns out to be:

$$\Phi_s = (\pi/6)\, \Psi^{1/2}\, v_p\, p \ , \tag{1}$$

Φ_s and v_p being equal to $q_s^*/(v_s^* d^*)$ and v_p^*/U_0^*, respectively, where v_s^* is equal to $\sqrt{(s-1)g^* d^*}$. Moreover $p = n^* d^{*2}$ is the probability to detect a moving particle over an area of the bed surface of extension d^{*2}. Lastly, the parameter Ψ

*Corresponding author. E-mail: marco.mazzuoli@unige.it.

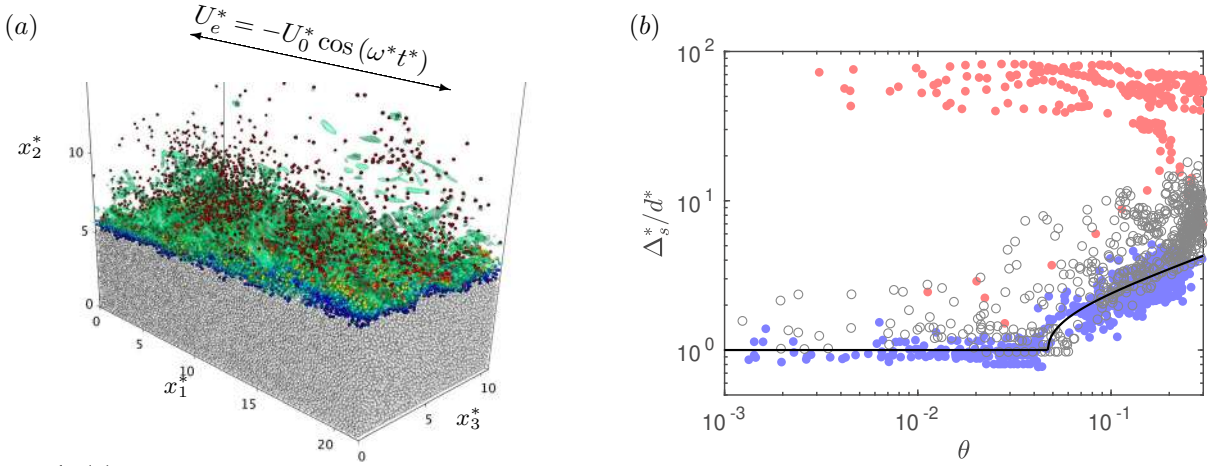

Figure 1: (a) Visualisation of the particle/flow configuration at an instant during the deceleration phases of the run at $R_\delta = 1000$ and $d^*/\delta^* = 0.168$ ($\omega^* t^* = 2.1\pi$). Gray particles are resting while moving particles are shaded by warmer colours according to their velocity. A significant amount of sediment particles is floating under the action of turbulent vortices, which are highlighted by green isosurfaces of λ_2. U_e^* denotes the fluid velocity far from the bed.(b) Values of the dimensionless thickness of the saltation layer plotted versus the Shields parameter for $R_\delta = 1000$ and $d^*/\delta^* = 0.167$ (light red), 0.335 (grey circles) and 0.670 (light blue). Solid thick line is obtained with the expression (5).

is the mobility number which is equal to U_0^{*2}/v_s^{*2}. The particle velocity is estimated on the basis of particle dynamics. The force acting on moving sediment particles results from the balance between the drag force, which is proportional to the square of the fluid velocity flowing around the particles, and the resisting force that is written as a friction force proportional to the resulting bed-normal force (gravitational and lift components) and to a friction coefficient (μ_s or μ_d for static or dynamic conditions, respectively). Assuming that the mean fluid velocity can be approximated by the product between a coefficient, α (~ 10), and the friction velocity u_τ^*, after some manipulations, the dimensionless mean particle velocity is found to be

$$v_p = \alpha \Psi^{-1/2} (\theta^{1/2} - c_1 \theta_{cr}^{1/2}) \ , \quad \text{with} \quad c_1 = \sqrt{\mu_d (c_D + \mu_s c_L)/[\mu_s (c_D + \mu_d c_L)]} \ , \tag{2}$$

where c_D and c_L denote the drag and lift coefficients, respectively, θ the Shields parameter defined as the ratio of the bottom shear stress to $\varrho^* v_s^{*2}$ and θ_{cr} the critical value of θ for the incipient motion of sediments. The values of the c_D and c_L depend on the fluid velocity and can be estimated with the empirical formulae that can be found in the literature (e.g. Schiller-Neumann formula of [5]). The value of p can be estimated by assuming that the momentum transferred from the flow to the bed is distributed in part to the resting bed, leading to inter-granular contact forces, and in part to the moving particles. The threshold of such distribution is θ_{cr}. This concept is expressed mathematically by the equation

$$p = (6/\pi)\, c_2 (\theta - \theta_{cr}) \ , \quad \text{with} \quad c_2 = (c_D + \mu_d c_L)/(\mu_d c_D) \ . \tag{3}$$

Hence, from (1), (2) and (3), estimates of the dimensionless sediment flow rate can be computed

$$\Phi_s = \alpha\, c_2 (\theta^{1/2} - c_1 \theta_{cr}^{1/2})\, (\theta - \theta_{cr}) \ , \tag{4}$$

which meets reasonably well the results obtained by means of the DNS as long as sediment particles do not go into suspension. The reliability of the model described above is strongly related to the maximum distance from the bed surface reached by particles during the wave cycle. Let us refer to this distance as *saltation layer thickness* and denote it with Δ_s^*. Figure 1b shows the values of Δ_s^* normalised by the sediment diameter for $R_\delta = 1000$. The values of Δ_s^*/d^* obtained for $d^*/\delta^* = 0.335$ and 0.670 are fairly approximated by the curve described by the equation

$$\Delta_s^*/d^* = 1 + A_b\, (\theta/\theta_{cr} - 1)^m \ , \tag{5}$$

with $A_b = 1.3$ and $m = 0.55$, which was proposed in several studies on sediment transport in steady flow conditions. However, equation (5) fails in representing the maximum height of particle trajectories for the case at $d^*/\delta^* = 0.168$ because particles are set into suspension rather than saltating. Indeed, in this run, the distance from the bed surface reached by particles is approximately one order of magnitude larger than that of saltating particles.
The interested reader can find a detailed description of further results which were obtained from the present runs in [6].

References

[1] M. Uhlmann. An immersed boundary method with direct forcing for the simulation of particulate flows. *Journal of Computational Physics*, 209(2):448 – 476, 2005.

[2] M. Mazzuoli, A. G. Kidanemariam, and M. Uhlmann. Direct numerical simulations of ripples in an oscillatory flow. *Journal of Fluid Mechanics*, 863:572–600, 2019.

[3] M. Mazzuoli, P. Blondeaux, G. Vittori, M. Uhlmann, J. Simeonov, and J. Calantoni. Interface-resolved direct numerical simulations of sediment transport in a turbulent oscillatory boundary layer. *Journal of Fluid Mechanics*, 885:A28, 2020.

[4] K. Ashida and M. Michiue. Study on hydraulic resistance and bed-load transport rate in alluvial streams. In *Proceedings of the Japan society of civil engineers*, volume 1972, pages 59–69. Japan Society of Civil Engineers, 1972.

[5] F. Takemura and J. Magnaudet. The transverse force on clean and contaminated bubbles rising near a vertical wall at moderate reynolds number. *Journal of Fluid Mechanics*, 495:235–253, 2003.

[6] Giovanna Vittori, Paolo Blondeaux, Marco Mazzuoli, Julian Simeonov, and Joseph Calantoni. Sediment transport under oscillatory flows. *International Journal of Multiphase Flow*, 133:103454, 2020.

EULERIAN-EULERIAN TWO-PHASE FLOW LARGE EDDY SIMULATION OF DILUTE SUSPENDED SOLID PARTICLES IN WATER

Antoine Mathieu* [1], Julien Chauchat[1], Cyrille Bonamy[1], Guillaume Balarac[1], and Tian-Jian Hsu[2]
[1] University of Grenoble Alpes, LEGI, G-INP, CNRS, Grenoble, France
[2] Civil and Environmental Engineering, Center for Applied Coastal Research, University of Delaware, Newark, USA

Summary Two-phase flow Large Eddy Simulation methodology is used to investigate dilute suspended load in starved-bed conditions. The objective is to better understand and model the interactions between the fluid turbulence and the particle dynamics, the so-called turbulence-particle interactions. Experimental results involving quasi neutrally buoyant sediments and natural sediments are reproduced numerically using a two-phase flow model: sedFoam implemented in the toolbox OpenFOAM. The numerical results obtained for particle-laden flows showed that the vertical profile of particle concentration for neutrally buoyant sediments is in good agreement with the experimental data while for natural sediments, concentration profile is under-estimated. The major difference between the two configurations is the particle response time while the flow turbulence is the same suggesting that the observed discrepancy is related to the Stokes number which becomes larger than unity for natural sediments.

The suspension mechanism of solid particles in a horizontal boundary layer is a fundamental but poorly understood phenomenon given the complex interactions occurring between the fluid turbulence and the particles. A wide spectrum of temporal and spatial scales are involved in the solid particles suspension making it difficult to be modeled. Up to now, the prediction of the average profile of suspended sediment concentration lacks of physical representation as it relies on empirical formulations. However, a lot of effort has been devoted to develop numerical models to improve its prediction over a broad range of flow and particles parameters. Various modeling techniques such as Eulerian-Lagrangian or Eulerian-Eulerian methodologies are available having different degrees of representation of the physical processes involved and different computational costs.

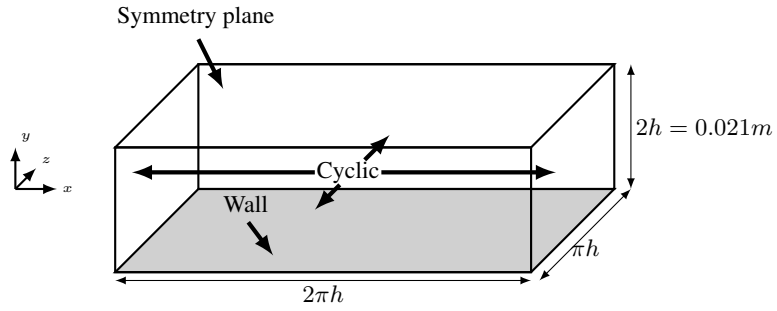

Figure 1: Sketch of the geometry and boundary conditions of the numerical domain for the configuration from Muste et al. (2005) [2].

In the Eulerian-Eulerian framework, both phases are seen as continua. Continuity and momentum equations are solved for both phases and particle-particle and fluid-particle interactions are modeled. The performances of the Eulerian-Eulerian methodology using Large Eddy Simulation (LES) formalism is yet to be demonstrated for turbulent suspension of inertial particles. In this study, the filtered Eulerian-Eulerian two-phase flow model for LES is applied to the experimental configurations from Muste et al. (2005) [2] involving non-inertial almost Neutrally Buoyant Sediments (NBS) and inertial Natural Sediment (NS). Both type of particles are finite sized ($d/\eta > 1$ with d the particle diameter and η the smallest turbulent scales or Kolmogorov scales). Both configurations are in starved bed condition. The mean volumetric concentration of sediment is equal to $\phi_{mean} = 4.6 \times 10^{-4}$.

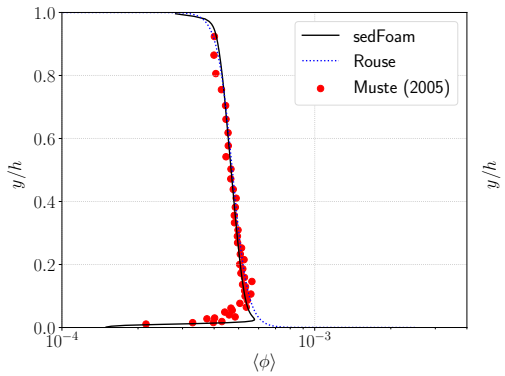

Figure 2: Concentration profiles from NBS configuration using sedFoam compared with analytical Rouse profile and experimental data from Muste et al. (2005) [2].

For both configurations, the hydrodynamic configuration is the same. The targeted friction velocity is $u_\tau = 0.042m.s^{-1}$ giving a Reynolds number based on the wall friction velocity $Re_\tau = 882$. The computational domain is a rectangular box with bi-periodic boundary conditions (figure 1). The flow is driven by a pressure gradient along the x axis in order to match the same discharge as in the experiments.

The mesh is composed of 7 920 000 cells with constant streamwise and spanwise grid resolution $\Delta x^+ = 12.6$ and $\Delta z^+ = 7.0$ in wall units ($+$ symbol with $\psi^+ = \psi u_\tau / \nu^f$). The mesh resolution is stretched along the y axis with the first grid point located at $\Delta y^+ \approx 1$ and $\Delta y^+ \approx 3$ at the top.

*Corresponding author. E-mail: antoine.mathieu@univ-grenoble-alpes.fr.

Particles having a density ratio $\rho^s/\rho^f = 1.025$ and diameter $d = 230\mu m$ are used for the NBS configuration giving a size ratio $d/\eta = 9.5$. The Stokes number for this configuration defined as the ratio between the timescale associated with the particle and the timescale associated with the Kolmogorov scale is $St = t^s/t^\eta = 0.12$ smaller than unity meaning that the particle will follow every fluid velocity fluctuations and should behave as a passive tracer.

The vertical sediment concentration profiles from the experiment and simulation are represented in figure 2 in semi-logarithmic scale. They are compared with the analytical Rouse profile with free surface correction given by expression (1) with ϕ_0 the reference concentration at the reference position y_0 and R_o the Rouse number given by $R_o = v^s_{fall}/\kappa u_\tau$ with v^s_{fall} the particles fall velocity and $\kappa = 0.41$ the von Karman constant.

$$\phi = \phi_0 \left(\frac{y_0(1 - y/h)}{y(1 - y_0/h)} \right)^{-R_o}. \tag{1}$$

Analytical and experimental concentration profiles correspond almost perfectly to the numerical data. Numerical concentration profile follows exactly the Rouse profile on the upper part of the channel. Close to the wall, the two-phase flow model quantitatively reproduces the reduction of concentration observed experimentally. The two-phase flow model is shown to accurately reproduce turbulent suspension of particles having low inertia.

Compared with the NBS configuration, only the particle to fluid density ratio changes in the NS configuration. The particle size is the same with $d/\eta = 9.5$ but the new density ratio is $\rho^s/\rho^f = 2.65$. The same hydrodynamic configuration is kept in order to isolate the influence of the particles inertia. Indeed, by increasing the density ratio, the Stokes number is increased to up to $St = 10.5$. According to Balachandar (2009) [1], the particle dynamics is primarily influenced by eddies in the inertial range of turbulence having the same timescale as the particles.

The concentration profile from simulations of the NS configuration are compared to the measurements and the analytical profile in figure 3. The standard Rouse analytical profile does not reproduce the experimental data. To fit the experiments, the Rouse number needs to be multiplied by S_c the turbulent Schmidt number characterizing the increased efficiency of inertial particles turbulent dispersion. Van Rijn (1984) [4] proposed the following empirical expression for the inverse of the Schmidt number:

$$\frac{1}{S_c} = 1 + 2 \left[\frac{v^s_{fall}}{u_\tau} \right]^2 \tag{2}$$

The concentration profile from the simulations is largely underestimated compared with both experimental data and analytical profile with or without the correction. The two-phase flow model does not seem to accurately reproduce the suspension of inertial particles. Subgrid interaction models from Ozel et al. (2013) [3] using dynamic procedures to take into account unresolved fluid-particle interactions have been tested and the turbulent dispersion of particles is still underestimated.

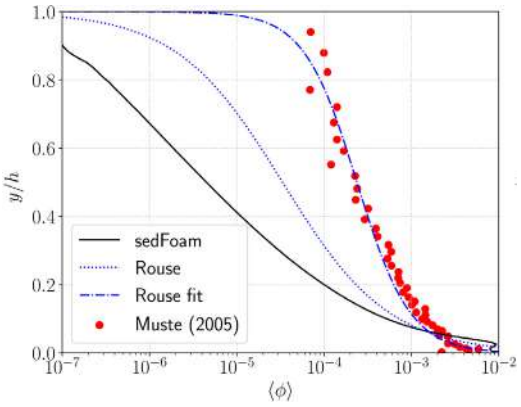

Figure 3: Concentration profiles from NS configuration using sedFoam compared with analytical Rouse profile with correction for inertial particles with $Sc = 0.48$ (Rouse fit) and without correction (Rouse) and experimental data from Muste et al. (2005) [2].

From the results presented in this paper, the Eulerian-Eulerian two-phase flow model can quantitatively reproduce velocity and concentration profiles for unidirectional channel flow laden with finite-size particles with low inertia ($St < 1$). However, when particles become inertial ($St > 1$), the two-phase flow model underestimates the turbulent diffusion and particles settle toward the bottom boundary.

It seems that some of the physics behind the turbulent suspension of inertial particles is not reproduced by the Eulerian-Eulerian two-phase flow equations. This physics is probably associated with small scale processes not resolved by the Eulerian-Eulerian approach and needs to be parameterized in order to get quantitative results. During the conference, the latest numerical results will be presented. The most recent simulations suggest that a correction for the finite size effect of the particles needs to be included in the model to recover the experimental and analytical concentration profiles.

References

[1] Balachandar, S. 2009. *A scaling analysis for point-particle approaches to turbulent multiphase flows*. International Journal of Multiphase Flow, 35:801–810.

[2] Muste, M. & Yu, K. & Fujita, I. & Ettema, R 2005. *Two-phase versus mixed-flow perspective on suspended sediment transport in turbulent channel flows.* Water Resources Research, 41(10).

[3] Ozel, A. & Fede, P. & Simonin, O. 2013. *Development of filtered Euler-Euler two-phase model for circulating fluidised bed: High resolution simulation, formulation and a priori analyses.* International Journal of Multiphase Flow, 55:43-63

[4] van Rijn, L.C. 1984. *Sediment transport, part ii: Suspended load transport.* Journal of Hydraulic Engineering, 110(11):1613–1641.

THE EFFECTS OF GEOMETRY AND REYNOLDS NUMBER ON PARTICLE-LADEN FLOW EROSION WEAR MODELLING

Felipe L. M. Reis[1], Eduardo R. David[1], Daniel A. Rodrigues[1], and Atila P. Silva Freire *[2]
[1] Interdisciplinary Center for Fluid Dynamics (NIDF/UFRJ), Federal University of Rio de Janeiro, Rio de Janeiro, Brazil
[2] Mechanical Engineering Program (PEM/COPPE/UFRJ), Federal University of Rio de Janeiro, Rio de Janeiro, Brazil

Summary Erosion caused by particle-laden flows is an important phenomenon in many industrial applications, but existing models are restricted to simple geometries. The present work compares erosion predicted by wear models described in the literature with experimental results to assess the applicability of such models for CFD simulations of complex geometries. Numerical simulations for three different Reynolds numbers are used to compare wear patterns occurring in the flows resulting from an impinging jet and a square T-junction. The work reports differences on the extent and magnitude of the damages for both configurations that can be as high as 50%.

INTRODUCTION

Particle-laden flows are a major concern to industries in many sectors. The solid particles that are transported with the flow often cause damage on key components and equipment, reducing their lifespan and reliability. Erosion prediction in those environments are, thus, critical to ensure both high operational safety levels and proper forecast of maintenance interventions and expenditures.

The main issue of erosion prediction on industrial components is that erosion is a highly-complex phenomenon and classical modelling attempts at describing the provoked damages are derived and calibrated mainly through the impinging jet configuration. The absence of a general predictive model hinders the application of most models to other geometries and conditions [1].

This work aims at assessing the applicability of erosion wear models developed for jet impingement to other types of configurations, particularly to a square T-junction (a T-junction made with square cross section pipes). The work discusses how variations in Reynolds number and the change in geometry affect the extent (and the shape profile) of the damage caused by solid particle erosion.

The square geometry for the *Tee* was chosen so as to facilitate the use of removable metal coupons for erosion testing and to reduce the warping of flow visualization techniques. There are few studies in the literature on square Tee's and, for that reason, the numerical results presented of the following sections are compared with experimental data collected at a slurry flow experiment carried out at NIDF/UFRJ.

SET-UP AND CONDITIONS

The investigation conducted in the present work was based upon numerical simulations on the open-source CFD package OpenFOAM. The meshing for both the jet and the square *Tee* geometry were generated trough the `blockMesh` tool, with proper wall refinement to achieve (y^+) values compatible to the selected turbulence model. The hydraulic diameter for both the jet and the square T-junction is D_h = 25 mm. The nozzle distance to wall is also 25 mm and, for the *Tee*, each leg measured 25 D_h.

Water was the continuous phase, with kinematic viscosity of $\nu = 1.0\times10^{-6}\mathrm{m^2s^{-1}}$. Due to numerical requirements of the Lagrangian model, the cell sizes had to be kept larger than the particle sizes in order to avoid instabilities, which led to selecting the κ-ϵ model. The fluid flow was solved using the SIMPLE algorithm and the `simpleFoam` application. The Reynolds numbers are 6.25×10^4, 1.25×10^5 and 2.50×10^5.

The discrete phase was evaluated subsequently to the continuous field. A cloud of particles was released into the domain through the `icoUncoupledKinematicParcelFoam` module with an one-way coupling condition. The solid particles are Mesh 150 carbon silicate (SiC) abrasive particles, with size distribution presented in Figure 1a, density of $\rho_p = 3200\mathrm{kgm^{-3}}$ and sphericity of $\varphi = 0.8$ for the non-spherical drag model of Haider and Levenspiel [2]. In addiction to the default tools, additional libraries were developed to include partially inelastic particle-wall collision as a function of the angle of impact (Grant and Tabakoff [3]) and to compute the erosive damage using wear models available on the literature. The wall material was modelled as AISI 304 stainless steel flat plates, with density of 7896 $\mathrm{kgm^{-3}}$, elastic modulus of 193 MP_a and Brinell Hardness of 123.

*Corresponding author. E-mail: atila@mecanica.coppe.ufrj.br

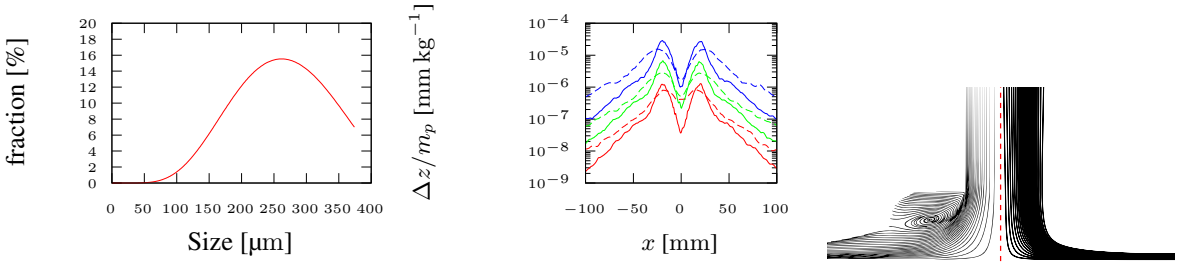

(a) Measured particle size distribution for SiC Mesh 150

(b) Eroded profile along the centreline per kilogram of introduced particles for the Jet (solid line) and 'Tee' (dashed line) geometries at Reynolds 6.25×10^4 (red), 1.25×10^5 (green) and 2.50×10^5 (blue)

(c) Comparison between streamlines for both geometries. Left: square T-junction; right: impinging free jet.

Figure 1: Particle size distribution and erosion damage results

RESULTS

The numerical results are presented in Figure 1b, where the erosion profiles for all cases are plotted according to the wear model developed by Oka and Yoshida [4].

It is observed that the damage profile for both geometries are qualitatively similar; they have a W-shaped profile that is expected for slurry flows. Their resemblance is due to the similarity of velocity fields on the centreline of the jet and on the square T-junction, which produce similar dynamic conditions for the transport of the abrasive particles and subsequent wear.

It is also observed that changes on Reynolds number and geometry have effect not only on the magnitude of the damage, but also on the extent of the wear. Reynolds number clearly have an effect on the magnitude of the damage since it is intimately associated to the particles kinetic energy on impact. However, it is the change in geometry that produces interesting results.

The width of the erosion profile is larger at the *Tee* geometry than at the impinging jet configuration. Energy dissipates with the square of distance to the centreline on the jet, whereas the dominant 2D nature of the *Tee* reduces dissipation to the viscous effect of the flow.

The peak value of damage computed for the *Tee* is approximately 50% of that found for the jet at the same Reynolds number. The recirculating regions located on the opposite walls of the stagnation region help divert the trajectories of the particles compared to the jet case, as seen on Figure 1c.

CONCLUSIONS

The present work discusses the influence of Reynolds number and geometry changes on erosion pattern for particle-laden flows. Impact velocities and angles on the square T-junction are well within the values found and calibrated on the impingement jet configuration. This allows a measure of confidence when using the wear models available in the literature. Validation of the numerical results with experiments are also discussed.

The ultimate goal is to apply and validate jet-calibrated erosion models to very complex geometries where direct experimental validation of results becomes increasingly more difficult.

ACKNOWLEDGEMENTS

The authors are thankful to ANP and Petrobras for sponsoring this research effort.

References

[1] Meng H.C. and Ludema K.C., Wear models and predictive equations: their form and content. *Wear*, **181**: 443-457, 1995.
[2] Haider A. and Levenspiel O., Drag coefficient and terminal velocity of spherical and nonspherical particles. *Powder Technol.*, **58(1)**: 63-70, 1989.
[3] Grant G. and Tabakoff W., Erosion prediction in turbomachinery resulting from environmental solid particles. *J. Aircr.*, **12(5)**: 471-478, 1975.
[4] Oka Y.I. and Yoshida T., Practical estimation of erosion damage caused by solid particle impact: Part 2: Mechanical properties of materials directly associated with erosion damage. *Wear*, **259(1-6)**: 102-109, 2005.

FLOW OF THIN FILMS OF VISCOUS FLUID OVER PARTICLE-LADEN SUBSTRATES

Katarzyna N. Kowal* [1,2], Elvinas Ribinskas[1,3], and Zhenghao Li[1,4]
[1] Department of Applied Mathematics and Theoretical Physics, University of Cambridge, Wilberforce Road, Cambridge CB3 0WA, United Kingdom
[2] Trinity College, University of Cambridge, Cambridge, CB2 1TQ, United Kingdom
[3] Christ's College, University of Cambridge, Cambridge, CB2 3BU, United Kingdom
[4] Peterhouse, University of Cambridge, Cambridge, CB2 1RD, United Kingdom

Summary Motivated by the flow of glacial ice sheets over unconsolidated subglacial sediment and the formation of subglacial bedforms, we perform a theoretical and experimental study of the transport properties of particle-laden beds sheared by an overlying thin film of viscous fluid spreading under its own weight in two dynamical regimes. In the first regime, we examine motion at the particle scale as a superposition of a number of contributors to motion, including translational and rotational motion of a single particle, as well as shear flow and parabolic flow of a thin film of viscous fluid past an obstacle. In the second regime, we examine large-scale deformational motion of deep granular beds in terms of a model of bulk erosion and deposition of particles. We also conduct a series of fluid-mechanical laboratory experiments highlighting the mechanisms of particle transport in both regimes.

INTRODUCTION

Particle-laden flows and the transport of granular material at the bed of thin films of viscous fluids spreading under gravity, or viscous gravity currents, are ubiquitous in nature and result in the formation of various geophysical features including subglacial bedforms, moraines, and grounding zone wedges, or accumulations of subglacial sediment in the grounding zones of marine ice sheets, separating freely floating ice shelves from grounded ice sheets that are in contact with the bedrock and subglacial sediment.

We consider particle transport properties in two regimes, involving (a) the viscous transport of individual particles on the small scale and (b) the erosion and deposition of deep granular beds using a bulk transport model. These are detailed in the sections, below.

VISCOUS TRANSPORT AT THE PARTICLE SCALE

The first part of the study is concerned with viscous transport of granular material at the particle scale. In particular, we consider the transport of dense particles sheared by the flow of a thin film of viscous fluid spreading under the action of gravity as depicted in the schematic of Fig. 1a. We assume that the horizontal length scale associated with the flow of the thin film of viscous fluid is much larger than its depth and use lubrication theory to model the flow.

On the particle scale, we consider the motion of a spherical particle translating and rotating in a viscous fluid of nonuniform velocity along a rough horizontal substrate. We assume that the scale of roughness, δ, is small and build upon the methodologies of [9, 7, 3] to determine the motion of the particle in terms of a superposition of four contributions following from the linearity of the Stokes equations. These contributions involve (i) the translational motion of the particle in a fluid at rest far from the substrate, (ii) the rotational motion of the particle in a fluid at rest far from the substrate, (iii) a linear shear flow past a fixed particle, and (iv) a parabolic flow past a fixed particle. The last of these contributions follows from the hydrostatic pressure distribution within the gravitationally spreading film of viscous fluid. Each of these induce a hydrodynamic force and torque on the particle, which depends additionally on the proximity of the particle to the horizontal substrate. These have been determined by [5, 6] and used to determine particle motion by [9, 7, 3] for flows of the type (i)–(iii). We build upon this approach to determine particle motion in the additional presence of a parabolic component of velocity of the type (iv), associated with the flow of viscous fluids under gravity, by using expressions for the hydrodynamic force and torque determined by [10]. We also conduct a series of analogue fluid mechanical laboratory experiments highlighting the mechanisms of particle transport and conditions for particle accumulation. The experiments spanned a range of values for the fluid viscosity, density, source flux, as well as particle size and density.

BULK EROSION AND DEPOSITION OF DEEP GRANULAR BEDS

The second part of the study is concerned with bulk erosion and deposition of a deep particulate material or granular bed. In particular, we consider the flow of a thin film of viscous fluid spreading under gravity over a deep, saturated granular medium as depicted in the schematic of Fig. 1b. Its depth varies owing to the transport of particles sheared by the flow of the viscous fluid, resulting in net particle erosion and deposition. As depicted by the schematic of Fig. 1b, the granular bed consists of an upper layer of mobile particles, sheared by the overlying flow field, and a lower layer

*Corresponding author. E-mail: k.kowal@damtp.cam.ac.uk

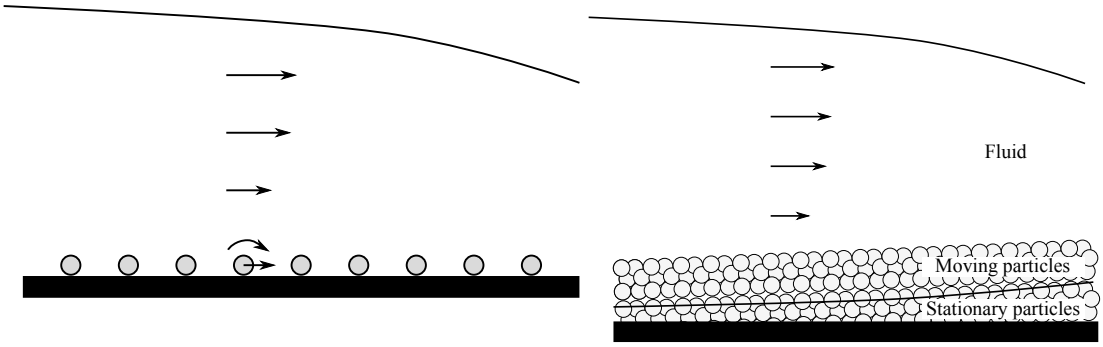

Figure 1: Schematic of the transport of particle-laden substrates at the particle scale (left) and bulk particle erosion and deposition of deep granular beds (right).

of stationary particles, unaffected by the flow. This approach contrasts with that of [8], in which subglacial material is modeled using a purely viscous rheology.

We model the flow of the viscous fluid using lubrication theory, assuming that the horizontal length scale is much larger than the film thickness. We assume that the dominant resistance to the flow of the thin film of viscous fluid is provided mainly by vertical shear stresses and that the Darcy velocity scale for the flow within the granular medium is much smaller than the velocity of the overlying viscous fluid, so that percolation through the pores is negligible. We model the erosion and deposition of particles by applying the principles developed by [4] and modified by [1, 2].

In particular, a particle is set into motion when the bottom shear stress exceeds a fraction of the apparent weight of the particle. Equivalently, this can be thought about in terms of the Shields number θ, involving the ratio of the basal shear stress to the apparent weight of the particle, which needs to exceed a threshold value in order for motion to occur. Following the theoretical development of [11, 4] and [1], we assume that the particle erosion rate is proportional to the excess shear rate above a threshold value, and that the deposition rate is proportial to the particle density per unit area, and inversely proportional to the settling time, or typical saltation time of moving particles during saltation flights. The number density of moving particles additionally depends upon the divergence of the flux of the number of moving particles, which we let to be proportional to the number density of moving particles and the mean particle velocity.

We additionally conduct a series of analogue fluid-mechanical laboratory experiments of the flow of viscous fluids over deep beds of granular material, depicting the main mechanisms of bed deformation.

CONCLUSIONS

We have performed a theoretical and experimental study of the transport of dense granular material sheared by the flow of an overlying film of viscous fluid in two dynamical regimes. We find large accumulations of granular material in regions of high basal shear stress, such as at the contact line of viscous gravity currents, which may serve as an explanation of the formation of glacial moraines and other subglacial bedforms.

We thank Mark Hallworth and the technicians of the G.K. Batchelor Laboratory for assistance in the setup of our experimental apparatus. We acknowledge financial support of the EPSRC-UROP Scheme and the L'Oréal-UNESCO UK and Ireland Fellowship For Women In Science.

References

[1] F. Charru and E. J. Hinch. Ripple formation on a particle bed sheared by a viscous liquid. Part 1. Steady flow. *J. Fluid Mech.*, 550:111–121, 2006.

[2] F. Charru and E. J. Hinch. Ripple formation on a particle bed sheared by a viscous liquid. Part 2. Oscillating flow. *J. Fluid Mech.*, 550:123–137, 2006.

[3] F. Charru, E. Larrieu, J. B. Dupont, and R. Zenit. Motion of a particle near a rough wall in a viscous shear flow. *J. Fluid Mech.*, 570:431–453, 2007.

[4] F. Charru, H. Mouilleron, and O. Eiff. Erosion and deposition of particles on a bed sheared by a viscous flow. *J. Fluid Mech.*, 519:55–80, 2004.

[5] A. J. Goldman, R. G. Cox, and H. Brenner. Slow viscous motion of a sphere parallel to a plane wall: I Motion through a quiescent fluid. *Chem. Eng. Sci.*, 22:637–651, 1967.

[6] A. J. Goldman, R. G. Cox, and H. Brenner. Slow viscous motion of a sphere parallel to a plane wall: II Couette flow. *Chem. Eng. Sci.*, 22:653–660., 1967.

[7] M. R. King and D. T. Leighton. Measurement of the inertial lift on a moving sphere in contact with a plane wall in a shear flow. *Phys. Fluids.*, 9:1248–1255, 1997.

[8] K. N. Kowal and M. G. Worster. Lubricated viscous gravity currents. *J. Fluid Mech.*, 766:626–655, 2015.

[9] G. P. Krishnan and D. T. Leighton. Inertial lift on a moving sphere in contact with a plane wall in a shear flow. *Phys. Fluids*, 7:2538–2545, 1995.

[10] S. S. Ozarkar and A. S. Sangani. A method for determining stokes flow around particles near a wall or in a thin film bounded by a wall and a gas-liquid interface. *Phys. Fluids*, 20(063301), 2008.

[11] L. C. van Rijn. Sediment transport, Part I: Bed load transport. *J. Hydraul. Engng.*, 110:1431–1456, 1984.

PARTICLE-DROPLET INTERACTION IN TURBULENT CHANNEL FLOW

Arash Hajisharifi[1], Cristian Marchioli *[1], and Alfredo Soldati[1,2]
[1] Department of Engineering and Architecture, University of Udine, Italy
[2] Institute of Fluid Mechanics and Heat Transfer, TU Wien, Austria

Summary We examine the interaction between a swarm of small (sub-Kolmogorov) inertial particles and large deformable droplets in turbulent channel flow. To simulate such solid-liquid-liquid flow, we exploit an Eulerian-Lagrangian methodology based on direct numerical simulation of turbulence, coupled with a Phase Field Model to capture the interface dynamics and Lagrangian tracking to compute particle trajectories. We quantify particle-interface interaction in a situation where the droplets have the same density and viscosity of the carrier liquid (mimicking a water-oil emulsion), and particles are one-way coupled with the carrier phase. Our results show that particles can get trapped at the interface and accumulate in the regions of highest positive curvature. Accumulation is modulated by particle inertia: low-inertia particles exhibit a stronger tendency to stay on the interface, whereas high-inertia particles can escape more easily and after shorter trapping.

INTRODUCTION

A large variety of systems involves the adsorption of solid particles to the fluid interface between droplets/bubbles and a carrier liquid. Surface tension drives particle adhesion, thus forming a layer that may change the mechanical and mass transport properties of the interface. Important industrial applications where such phenomenon occurs include scrubbing processes, in which large liquid droplets are exploited to collect dust particles; froth flotation processes, in which particle adsorption to bubbles is essential for separating minerals from the slurry. Most of three-phase computational models available in the literature have been used to study the dynamics of a single particle trapped at a planar fluid interface [1], or the surface stress tensor modification for a pendant drop covered by a monolayer of particles in the low-Reynolds-number limit [2]. Only recently, a multiscale DEM-VOF method was developed to reproduce droplet formation and interface perturbations from a single particle [3]. In this paper, we perform a DNS (Direct Numerical Simulation)-based study of a three-phase turbulent flow in which a solid phase (particles) and a liquid phase (deformable droplets) are transported by a carrier phase (fluid). Specifically, we investigate the interaction between the particles and the droplets in a channel flow configuration. We consider particles with different size to investigate such interaction at varying particle inertia.

Methodology

The computational approach is based on DNS of the Continuity, Navier-Stokes and Cahn-Hilliard equations and on the solution of a Lagrangian equation of particle motion stemming from the balance of the forces acting on the particles (drag force and surface tension force, in the present study). The flow solver is based on a pseudo-spectral method that transforms the field variables into wave space to discretize the governing equations. In the homogeneous directions, all the quantities are expressed by Fourier expansions. In the wall-normal non-homogeneous direction, they are represented by Chebychev polynomials. The time integration algorithm follows an implicit/explicit scheme. All calculations relative to Continuity, Navier-Stokes and Cahn-Hilliard equations are carried out in wave space except for the non-linear terms, which are computed in the physical space and then transformed back to wave space. Particle tracking is performed in the physical space. The particle-interface interaction is modeled by considering a capillary force related to the liquid-liquid surface tension. This capillary force is exerted on the particles when they are in close proximity to the interface, and acts to push the particles towards the interface and capture them there. In other words, the force provides a potential well that drives particle accumulation at the interface, which thus acts as particle adsorber. Such accumulation may be favored or hindered depending on the combined action of turbulence, which tends to deform continuously the interface, and particle inertia, which tends to make particles deviate from fluid streamlines. One expects the surface tension force to be dominant over the other hydrodynamic forces (in particular, drag) at low particle inertia (namely, low Stokes number), thus favouring trapping. Conversely, as particle inertia increases with respect to the surface tension force, one should expect the drag force to become more important, possibly providing a means for particles to escape from the interface.

RESULTS

In this paper we show results relative to friction Reynolds number $Re = 150$ based on the channel half height h (the channel dimensions being $4\pi h \times 2\pi h \times 2h$ in the streamwise, spanwise and wall-normal directions, respectively), Weber number $We = 0.75$ (ratio between inertial forces and surface tension), Cahn number $Ch = 0.02$ (dimensionless interface thickness), Péclet number $Pe = 50$ (ratio between diffusive timescale and convective timescale) and particle friction Stokes numbers $St = 0.1$, 0.2, 0.4 and 0.8. For sake of brevity, we will show results for the $St = 0.8$ particles only. In our framework, particle accumulation is higher (resp. lower) for the lower-inertia (resp. higher-inertia) particles. The capillary force acting on the particles depends on the surface tension and on the local curvature of the droplet interface.

*Corresponding author. E-mail: cristian.marchioli@uniud.it.

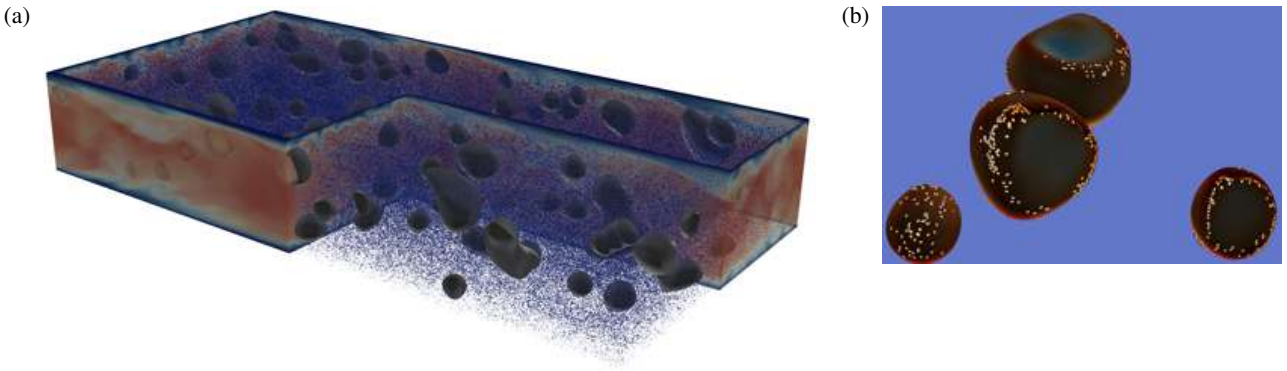

Figure 1: (a) Schematic of three-phase turbulence channel flow. (b) Droplets are rendered by colouring the interface with the local magnitude of curvature: Red areas correspond to higher-than-mean positive curvature (convex interfacial regions), blue areas correspond to the highest negative curvature (concave interfacial regions). Particles (yellow dots) appear to accumulate in regions of highest positive curvature.

The former changes with modification of surface composition and temperature, yet remains constant when these do not vary (as we assume in our simulations). Hence, the only parameter that can change the magnitude of the capillary force in our problem is the local curvature: The capillary force is stronger in regions where the curvature is higher (see Fig. 1b).

While trapped within the interface, particles tend to move towards the regions of highest positive curvature. This sampling is observed for all particle sets, and appears modulated by particle inertia. To quantify this effect, in Fig. 2 we show the Probability Density Function (PDF) of the interface curvature measured at particle position. To compute this PDF, we considered only the position that the particles occupy at the time instant in which they are leaving the interface after being trapped there. The PDF becomes negatively skewed as St increases, indicating higher probability of finding low-inertia particles in regions of strong interface convexity. Particles with higher inertia are believed to possess enough inertia to escape from the interface before reaching these region. Current work is devoted to the understanding of the physical mechanism that actually drive particle detachment from strongly-convex areas of the interface.

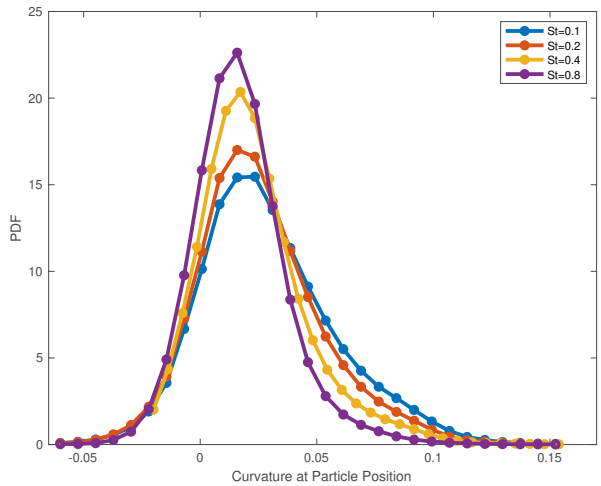

Figure 2: PDF of interface curvature at the position of the particles that are leaving the interface after trapping.

CONCLUSIONS

Our results show that inertia provides particles with a way to escape from the interface and reduce the time window over which particles interact with the interface. Low-inertia particles are found to accumulate at higher rates and are able to stay longer in close proximity of the droplet interface: Once trapped there, these particles exhibit the strongest tendency to collect in regions characterized by highly-positive values of the curvature.

References

[1] HI Mehrabian, J Harting, JH Snoeijer, Soft Matter, Vol 12 (2016), 1062
[2] C Gu, L Botto, Soft Matter, Vol 12 (2016), 705–716
[3] G Pozzetti, B Peters, Int J Multiphase Flow, Vol 9 (2018), 186-204

MECHANISM OF TURBULENCE COLLAPSE IN PARTICLE-LADEN TURBULENT CHANNEL FLOW

Partha. S. Gowami *[1], Pradeep Muramulla[1], and Viswanath Kumaran[2]
[1] Department of Chemical Engineering, Indian Institute of Technology, Bombay, India
[2] Department of Chemical Engineering, Indian Institute of Science, Bangalore, India

Summary Direct Numerical Simulation of vertical particle-laden channel flows has been investigated to study the turbulence attenuation mechanism. A discontinuous decrease in the turbulence intensity at a critical volume fraction is observed. At the critical volume fraction turbulent energy production rate decreases by an order of magnitude but the energy dissipation due to particle drag increases by a smaller extent. Consequently, there is a decrease in the total energy dissipation. In the present study, the role of cross stream particle migration on the discontinuous transition, and the disruption of spatio-temporal evolution of the stream wise coherent structures at different particle loading have been explored.

INTOUDUCTION

Particle laden turbulent flows find applications in many industrial and environmental processes. In such flows, the presence of dispersed particle phase, largely influence the dynamic properties of carrier phase. Investigation of wall bounded particle laden flows is very important as presence of wall introduces additional complexity by making the flow inhomogeneous. One of the most complex issue in the dynamics of turbulent particle-gas suspensions is to predict the effect of the particles on the gas phase turbulence, i.e whether the particles will enhance or reduce the fluid turbulence. The broad consensus is that, in the presence of large particle intensity of turbulence increases due to wake formation behind the particles and small particles reduces turbulence due to particle induced drag. In our recent article ([1]), we have extensively studied the turbulence attenuation mechanism, for wide range of volume fractions, particle Stokes number and at two different Reynolds number. For the first time it has been observed in our work that the turbulence attenuation mechanism is not continuous with increase in particle volume fraction. At a critical volume loading, a discontinuous decrease in the fluid turbulence happens with a small change in volume fraction which is of the order of 10^{-4}. We concluded that, the reason for discontinuous decay is the reduction in turbulence production, but not due to increase in particle induced dissipation. In the current work, we have investigated the effect of particle migration on reduction in turbulence production, and disruption of turbulence structures in the presence of particles.The main focus is to quantify the extent of particle migration required in the wall normal direction for disruption of turbulence production. The effect of particle volume loading on the coherent structures have also been investigated.

NUMERICAL METHODOLOGY

The pressure-driven flow of a fluid with kinematic viscosity ν in a vertical channel of width h with average velocity $\bar{u}$ is simulated using two way coupled Direct Numerical Simulations (DNS). An Eulerian-Lagrangian method has been used with point-particle approximation for the particle phase. The dimensions of the channel are $4\pi h \times h \times (2\pi h/3)$ in the flow (x), wall-normal (y) and the span-wise (z) directions. Zero velocity boundary conditions are applied at the walls , while periodic boundary conditions are applied in the flow and the span-wise directions. The pseudo spectral method is used to solve the Navier Stokes equation for fluid phase. For Re $= 3300$, $128 \times 65 \times 64$ and for Re $= 5600$, $192 \times 129 \times 160$ nodes are used in x, y, and z direction respectively. The particle velocity is solved using the Newton'laws, the force on the particles is the sum of the drag force, force due to particle-particle, particle-wall collisions and the gravity. The particles are modelled as hard spheres and perfectly elastic. In the present work while modelling the particle drag force, corrections due to 'undisturbed' velocity at the particle center the wall effect on the particle drag and lift force are considered to capture the physics accurately. The particle phase is coupled with fluid phase by adding a feedback force, which is the neagtive of the particle drag force, to the fluid grid points using projection to the nearest neighbours. The particles are randomly distributed into the unladen turbulent flow, with velocity equal to fluid velocity interpolated at particle position. When the particle-gas suspension reaches steady state, the fluid and particle statistics are averaged in the homogeneous streamwise and spanwise direction over a period of 300 $(h/\bar{u})$ integral time scale.

RESULTS

Simulations are performed to study the effect of particle volume fraction $(0 - 2 \times 10^{-3})$ on turbulence attenuation for different Stokes number $(4.7 - 380)$ for two different Reynolds number ($Re_b = 3300\&5600$). It is observed that the turbulent intensity and Reynolds stress reduces by an order of magnitude at critical volume fraction for all the stokes number investigated here. From figure 1, it can be observed that the turbulence production rate decreases drastically at this critical volume fraction, and there is an increase in rate of energy dissipation due particle drag. But this rate of increase in the energy dissipation due to particle drag does not compensate and also much smaller than the rate of decrease in

*Corresponding author. E-mail: psg@iitb.ac.in.

turbulence production. Such an observation suggests that there is a discontinuous collapse in turbulence intensity due to disruption in turbulence production mechanism but not due to continuous increase in energy dissipation due to particle drag.

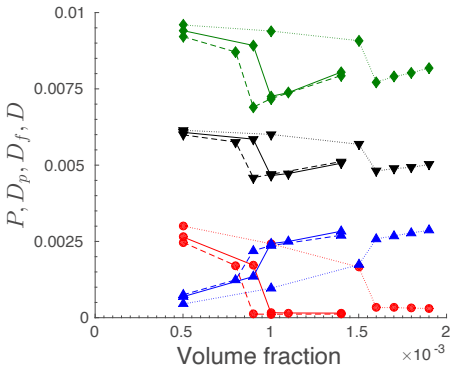

Figure 1: The scaled total rate of dissipation of energy per unit mass $D = -P + D_f + D_p$ ($\diamond$), the rate of transfer of energy per unit mass from the mean flow to the fluctuations $-P = \frac{h}{\bar{u}^3}\langle \overline{u'_x u'_y} \frac{d\bar{u}_x}{dy}$ ($\circ$), the rate of dissipation of energy due to the drag force exerted on the particles $D_p = \frac{h}{\rho \bar{u}^3 V} \sum_I \overline{\mathbf{u} \cdot \mathbf{F}_I}$($\triangle$), and the rate of dissipation of energy due to the mean shear in the fluid $D_f = \frac{\mu}{(\rho \bar{u}^3/h)} \langle \left(\frac{d\bar{u}_x}{dy} \right)^2 \rangle_s$ (∇) as a function of volume fraction for particle Stokes number 7.66 (dotted lines), 38.3 (solid lines), 114.9 (dashed lines)

We have also investigated the effect of particle migration in the wall-normal direction. To investigate this effect we have considered two zones in the channel; Zone-1 (case a), where turbulence production and fluid intensity is maximum and Zone-2 (case b), where energy dissipation due to particle drag force is maximum (figure 2a). If the same number of particles are added in the Zone-1 and Zone-2 the percentage attenuation is maximum in case (a) compared to case (b). Another thought experiment is performed by adding the particles only in one half of the channel such that the particles are allowed to migrate from one wall to a certain distance in the wall normal direction for different case studies as shown in figure 2b. The other half of the channel is not disturbed so that there is no modification in turbulence intensity or Reynolds stress. From figure 2c, it can be observed that if the particles migrate less than a critical $y+$, decay in Reynold stress does not happen.

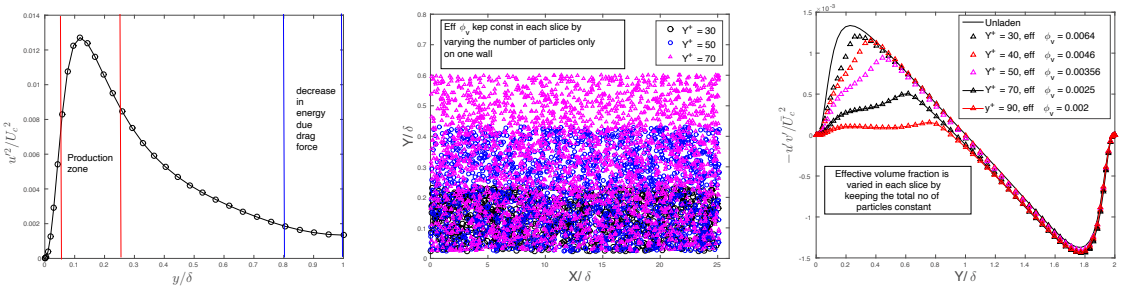

(a) Prodction and dissipation zones (b) Migration along differnet y (c) Decay in Reynolds stress

Figure 2: Effect of particle migration in wall-normal direction on turbulence intensity

CONCLUSIONS

The present findings suggest that there is a critical volume fraction for a particular stokes number where turbulence collapses discontinuously and particle migration in wall normal direction plays important role in behind the phenomena of turbulence collapse.

References

[1] Kumaran, V., Muramalla, P., Tyagi, A. and Goswami, P.S., 2018. Turbulence collapses at a threshold particle loading in a dilute particle-gas suspension. arXiv preprint arXiv:1811.06694.

INTERFACE-RESOLVED SIMULATIONS OF INERTIAL PARTICLES IN TURBULENT CHANNEL FLOW

Pedro Costa* [1], Luca Brandt[2], and Francesco Picano[3]
[1] Faculty of Industrial Engineering, Mechanical Engineering and Computer Science, University of Iceland, Hjardarhagi 2-6, 107 Reykjavik, Iceland
[2] Linné FLOW Centre and SeRC (Swedish e-Science Research Centre), Department of Engineering Mechanics, SE-100 44 Stockholm, Sweden
[3] Department of Industrial Engineering, University of Padova, Via Venezia [1], 35131 Padova, Italy

Summary We use interface-resolved direct numerical simulations to study gravity-free turbulent channel flow laden with small inertial particles with a diameter of three viscous wall-units and 100 times denser than the suspending fluid. The bulk Reynolds number is fixed so that it corresponds in the single-phase limit to a friction Reynolds number $Re_\tau \approx 180$, and three solid volume fractions are considered: 0.003%, 0.03% and 0.3%. The aim of these simulations is to study this flow in the point-particle limit, but without relying on the point-particle approximation to describe the particle dynamics. The resulting dataset is used to study the turbulence modulation by the dispersed phase, and can be used as benchmark to access the validity of one- and two-way coupling point-particle models.

INTRODUCTION

For many years, direct numerical simulations of particle-laden turbulent flows have been carried out using the point-particle approximation. This approximation assumes that the momentum exchange between the phases is well modeled by localised forces that mimic the presence of particles. Moreover, if the particle Stokes number is high enough, the equations governing the particle dynamics are often simplified to a balance between inertial and drag forces. At present, thanks to the continuous increase in computing time together with the development of efficient numerical methods, it has become possible to simulate these flows without relying on the point-particle assumption. Instead, it is now possible to directly enforce no-slip/no-penetration boundary condition on the surface of hundreds of thousands, or even millions of small spherical particles.

The present work revisits interface-resolved DNS of turbulent channel flows in the point-particle limit, without relying on modelling assumptions. We simulated three turbulent channel flow configurations with varying mass fraction. The goal is to mimic the so-called 1-way, 2-way coupling regimes [1]. The number of particles was varied from 500 to $50,000$ particles, simulated on a mesh with $12D/\Delta\ell$ grid points over the particle diameter, corresponding to 13.5 billion Eulerian grid points. The objective of the study is to develop a database for validation of point-particle models, to better quantify the borderline between coupling regimes, and to better understand the underlying mechanisms responsible for turbulence modulation in this complex flow.

NUMERICAL METHOD AND COMPUTATIONAL SETUP

The Navier-Stokes equations are solved with a second-order finite-difference method on a three-dimensional, staggered Cartesian grid, using a fast-Fourier-transform-based pressure-projection method. The solver was extended with a direct forcing immersed-boundary method (IBM) for particle-laden flows developed in [2] and the collision model for particle–particle and particle–wall interactions in [3]. Pressure-driven turbulent channel flow is simulated in a domain periodic in the streamwise and spanwise directions, with no-slip/no-penetration boundary conditions imposed at the walls. The physical and computational governing parameters are reported in table 1. We should note that the first two cases in table 1, *VD* and *D*, have been presented in [4].

RESULTS

Figure 1 (left) shows a visualization of the turbulent channel flow laden with the interface-resolved particles for the dilute case *D* (see table 1). In addition to the flow coherent structures, resmbling those of turbulent channel flow at this relatively low Reynolds number, the figure clearly shows the localized effect of each resolved particle on the flow with high-vorticity regions caused by their wakes. The overall drag, expressed in terms of a friction Reynolds number, is shown in Table 1. As discussed in [4], case *D*, with 3% bulk mass fraction of particles, shows a considerably large increase in drag, while case *VD* has negligible two-way coupling effects. This large increase for case *D* is attributed to a dense and localized layer of particles near the wall, flowing with high velocity. Interestingly, the semi-dilute case *SD*, with a mass fraction ten times larger than *D*, shows a milder increase in drag.

To better understand this milder increase in drag from case *D* to *SD*, we present the profiles of mean velocity and Reynolds stresses in the right-hand-side of figure 1. The mean velocity profile (top label of the figure) shows a significant

*Corresponding author. E-mail: pcosta@hi.is.

Case	Φ (N_p)	Ψ	Notes	Re_τ
VD	0.003% (500)	0.337%	very dilute (VD) case	180 ± 1
D	0.034% $(5\,000)$	3.367%	dilute (D) case	188 ± 1
SD	0.334% $(50\,000)$	33.67%	semi-dilute (SD) case	193 ± 1

Table 1: Computational parameters. Φ/Ψ denotes the bulk solid volume/mass fraction, and N_p the total number of particles. For all cases, the bulk Reynolds number $Re_b = 5\,600$ (i.e. unladen friction Reynolds number $Re_\tau^{sph} \approx 180$); particle size ratio $D/(2h) = 1/120$; particle-to-fluid mass density ratio $\Pi_\rho = 100$, corresponding to a particle diameter (in viscous units) $D^+ = 3$ and a Stokes number $St = 50$. The fluid domain is discretized on a regular Cartesian grid with $(L_x/N_x) \times (L_y/N_y) \times (L_z/N_z) = (6h/4320) \times (2h/1440) \times (3h/2160)$, while the particles are resolved with $D/\Delta x = 12$ grid points over the particle diameter (420 Lagrangian grid points in total). The last column reports the friction Reynolds number Re_τ extracted from the simulations.

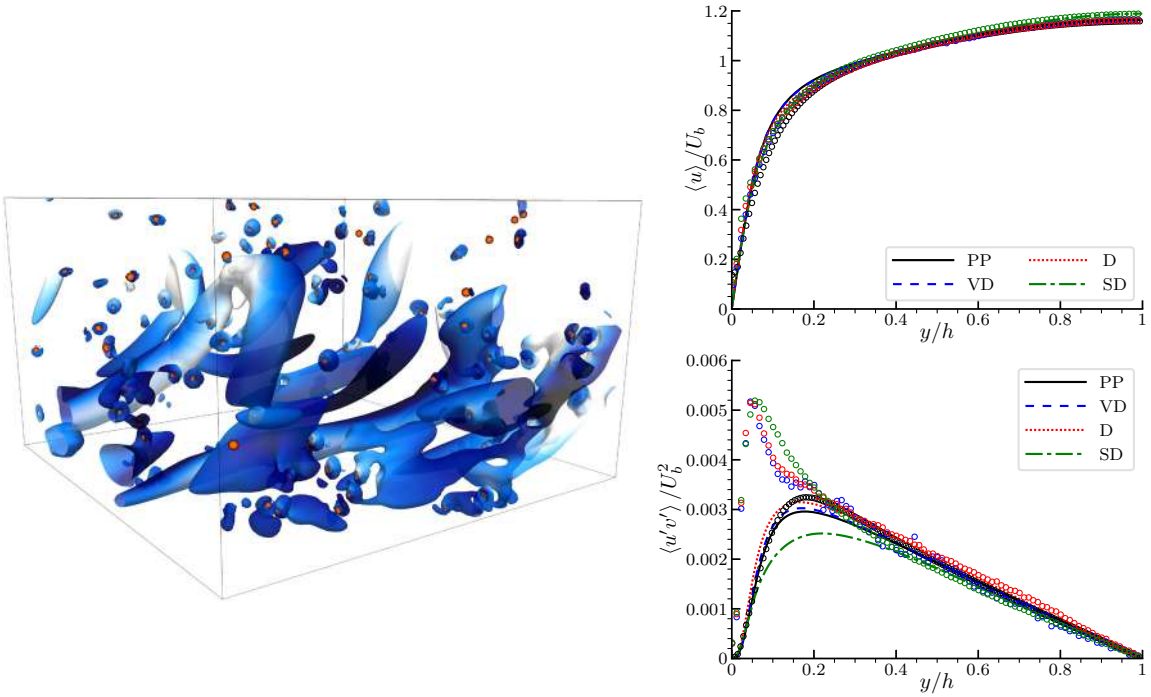

Figure 1: Left: Visualization of case *D* near the wall. Isocontours of the Q-criterion $Q = 20(U_b/h)^2$ coloured by the local wall-normal velocity (blue – low and white – high), with the particles shown in orange. Right: Profiles of mean streamwise velocity (top) and Reynolds-stresses (bottom). The profiles are normalized by the bulk velocity U_b and half channel height h. The symbols (color-matched) pertain to the solid phase velocity statistics. Case *PP*, corresponds to a one-way-coupled point-particle simulation with dynamics driven by a balance between inertial and (Schiller-Naumann) drag forces [4].

increase in centreline velocity for case *D*. This trend is opposite to what is observed in single-phase turbulent channel flow with increased friction Reynolds number, where the centreline velocity normalized by the bulk velocity decreases. This can be a first indication that, despite the increase in friction Reynolds number, some competing mechanism responsible for turbulence attenuation is mitigating the drag increase. Indeed, despite the increase in drag for case *SD*, the profile of fluid Reynolds stresses is greatly reduced (see the bottom panel on the right-hand-side of the figure 1). This suggests that, while for case *D* the flow statistics resemble those of a turbulent channel flow with increase wall friction due to the slip velocity that near-wall particles enforce on the flow, the statistics in case *SD* cannot be qualitatively explained by an effective increase in wall shear. Instead, two-way coupling effects in the bulk of the channel appear to be become non-negligible.

References

[1] S. Balachandar and J. K. Eaton. Turbulent dispersed multiphase flow. *Annu. Rev. Fluid Mech.* **42**: 111-133, 2010.

[2] W.-P. Breugem. A second-order accurate immersed boundary method for fully resolved simulations of particle-laden flows. *J. Comput. Phys.* **231(13)**: 4469-4498, 2012.

[3] P. Costa, B. Boersma, J. Westerweel and W.-P. Breugem. Collision model for fully resolved simulations of flows laden with finite-size particles. *Phys. Rev. E* **92(5)**: 053012, 2015.

[4] P. Costa, L. Brandt, F. Picano. Interface-resolved simulations of small inertial particles in turbulent channel flow. *J. Fluid. Mech* **883**: A54, 2020.

SURFACTANT-LADEN BURSTING BUBBLES

R. Constante-Amores * [1], L. Kahouadji[1], A. Batchvarov[1], S. Shin[2], J. Chergui[3], D. Juric[3], and O. K. Matar[1]
[1] Department of Chemical Engineering, Imperial College London, United Kingdom
[2] Department of Mechanical and System Design Engineering, Hongik University, Republic of Korea
[3] Laboratoire d'Informatique pour la Mécanique et les Sciences de l'Ingénieur (LIMSI), Centre National de la Recherche Scientifique (CNRS), Université Paris Saclay, France

Summary The physical mechanisms which govern the ejection of droplet in bursting bubbles have received a significant interest due to their occurrence in a multitude of natural and industrial applications. The effect of the surfactant, and associated Marangoni stresses on their dynamics have not been reported. For that reason, we perform fully three-dimensional direct numerical simulations in the presence of soluble surfactant to elucidate its effect on the bubble dynamics. The characteristics of the ejected droplets (e.g. number, sizes, velocity) are analysed and the importance of Marangoni stresses are studied.

BACKGROUND

When bubbles are resting close to a liquid-gas interface, the formation of a central jet and subsequently small droplets is observed after they burst. Those droplets play a key role in the exchange between the air and the liquid phase since they have a similar chemical composition as the liquid. The dynamics of surfactant-free bursting bubbles for the ejection of droplets have been widely documented [2-5]. However, the effect of surfactant on the dynamics of the interface is not well understood. The presence of surfactants give rise to the formation of gradients in surface tension, and hence Marangoni stresses in the plane of the interface. We present fully three-dimensional direct numerical simulations where surfactant is either soluble or insoluble.

PROBLEM FORMULATION

The numerical simulation was performed by solving the 3D, two-phase, incompressible Navier-Stokes equations with surface tension. The physical parameters of the system are the initial bubble radius R_o, the liquid density ρ, the liquid viscosity μ, the surface tension σ_s and the gravity g. The viscosity and density ratios correspond to water in air with, $\rho_a/\rho = 1.2 \times 10^{-3}$ and $\mu_a/\mu = 0.018$, where the subscript designates the air phase. The governing equations for the flow have been made dimensionless by using R_o and $t = \sqrt{\rho R_o^3/\sigma}$ as length and time scales, respectively. Therefore, the system is fully described by two dimensionaless parameters: the Ohnesorge number Oh (ratio of capillary forces to viscous forces) and the Bond number Bo (ratio of gravity to capillary forces). Here, we will use Laplace number, La and Bo to parametrise our flow:

$$La = \frac{1}{\sqrt{Oh}}, \quad La = \frac{\rho\sigma R_o}{\mu^2}, \quad Bo = \frac{\rho g R_o^2}{\sigma_s} \tag{1}$$

In our simulations, surfactant is present either on the interface and/or in the bulk, with concentration Γ and C, respectively, allowing mass transfer between the bulk and the interface. The nondimenionalisation of the surfactant transport equations (using the maximum packing concentration, Γ_∞) leads to the following dimensional parameters

$$Pe = \frac{uR_o}{D}, \quad \beta = \frac{R_o T \Gamma_\infty}{\sigma_s}, \quad x = \frac{\Gamma_{eq}}{\Gamma_\infty} = \frac{k}{1+k}, \quad k = \frac{k_a C_\infty}{k_d}, \quad Bi = \frac{k_d R_o}{u} \tag{2}$$

where Pe is the Peclet number (ratio of convective to diffusive time scales at the interface and in the bulk), β is the elasticity number (a measure of the effect of surfactant on the surface tension), x is the surface coverage, Bi is the Biot number (ratio of desorption to convective time scales) and k (ratio of adsorption to desorption time scales) is the adsorption parameter. In the previous equations, u stands for the velocity, D stands for the surfactant interfacial and bulk diffusivities, k_a and k_d stand for the kinetic constants for adsorption and desorption, respectively and C_∞ denotes the surfactant concentration in the bulk.

We use the Level Contour Reconstruction Method proposed by Shin *et al.* (2018) [6] to perform our high-fidelity numerical simulations. The interface-tracking nature of the numerical method facilitates tracking the spatio-temporal evolution of the interfacial concentration field. The numerical simulations have been validated against the work of Lai *et al.* (2018) [4] and Eggers (1997) [1] in terms of scaling arguments with respect to the length of the jet and the breakup of a liquid thread, respectively. The initial bubble shape is determined by solving the Young-Laplace equations.

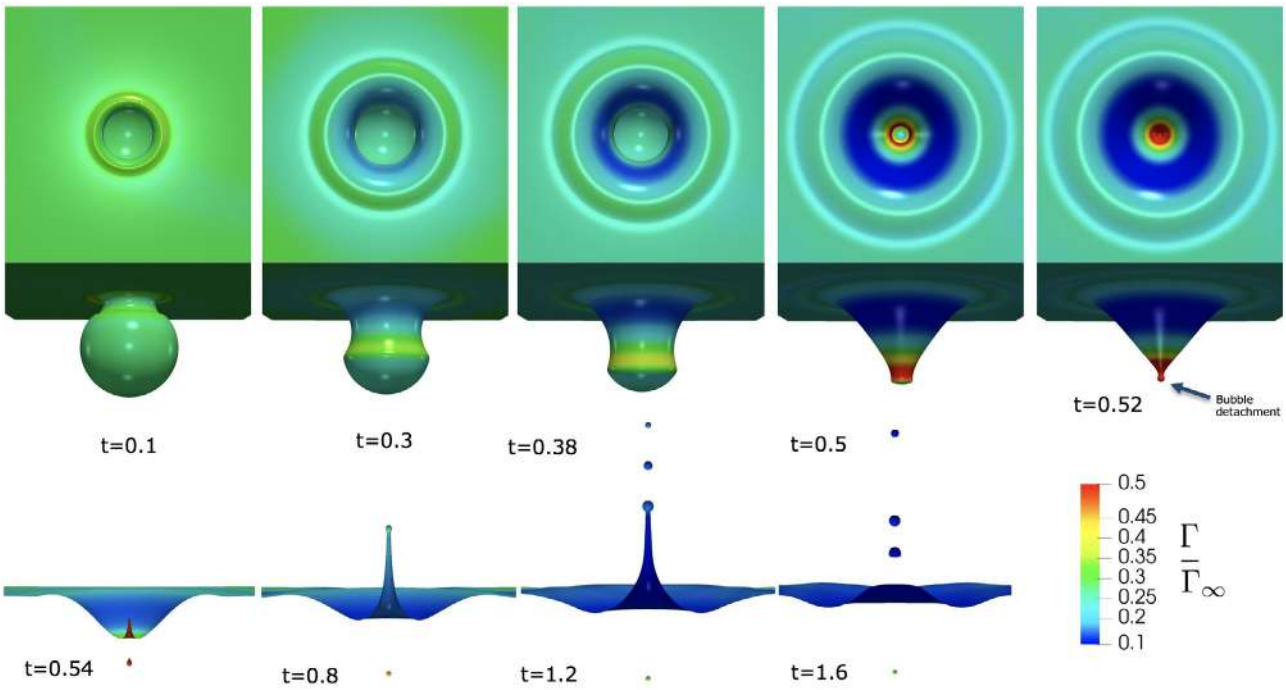

Figure 1: Spatio-temporal dynamics of bursting bubbles in the presence of soluble surfactant with $La = 2000$, $Bo = 10^{-3}$, $Pe_s = 10$, $\beta_s = 0.3$, $Bi = 2$, $x = 0.5$, and $\Gamma_o = x\Gamma_\infty/2$.

RESULTS

To simplify the initialisation of the interface we have removed the spherical cap ($r \sim 0.01R_o$) as in previous studies [3,4]. Fig. 1 shows the spatio/temporal evolution of the interface coloured by the surfactant concentration. As time increases, a higher deformation of the interface is observed, and the bubble tries to penetrate the interface. Surfactant is swept at the back of the bubble where it is accumulated, achieving its maximum surfactant concentration at the moment of the bubble detachment ($t \sim 0.52$). Fig. 1 shows the flow time scales which is in order of microsecond.

In the presence of surfactant, and due to the Marangoni-induced retardation of the dynamics as a result of flow flowing from high-concentration to low-concentration regions, the jet is shorter in length and a reduction of the number of resultant droplets is observed (as the resulting Marangoni stresses induce fluid down from the tip of the jet to the bulk). We have also observed a stronger production of vorticity close to the interface due to the presence of Marangoni stresses (not shown here).

CONCLUSIONS

The effects of surfactant, and associated Marangoni stresses on the dynamics of bursting bubbles are studied. In the sample result presented here we see the spatio-temporal evolution of the interfacial concentration where surfactant species are convected to the back of the bubble. The resultant Marangoni stress acts to retard the dynamics and a stronger production of vorticity is observed.

References

[1] Eggers J., Nonlinear dynamics and breakup of free-surface flows. *Rev. Mod. Phys.*, **69**(3), 865-930 (1997)
[2] Gordillo J. M., Rodríguez-Rodríguez J. Capillary waves control the ejection of bubble bursting jets. *J. of Fluid Mech.*, **867**, 556–571 (2019)
[3] Lai C, Y., Eggers J., Deike, L. Bubble bursting: universal cavity and jet profiles. *Phys. Rev. Lett*, **121**, 144501.
[4] Ghabache E., Antkowiak A., Josserand C., Séon, T. On the physics of fizziness: How bubble bursting controls droplets ejection. *Phys Fluids*, **26**, 121701 (2014)
[5] Zeff B. W., Kleber B., Fineberg J., Lathrop D. P. Singularity dynamics in curvature collapse and jet eruption on a fluid surface *Nature*, **403**, 401–404 (2000)
[6] Shin S., Chergui J., Juric D., Kahouadji L., Matar O. K., Craster R. V. An Interface-Tracking Technique for Multiphase Flow with Soluble Surfactant *J. Comp. Phys*, **359**, 409-435 (2018)

*Corresponding author. E-mail: crc15@imperial.ac.uk

BREAKUP OF A LIQUID COLUMN JET IN A SURROUNDING GAS FLOWING THROUGH A COAXIAL CYLINDRICAL SHEATH

Takao Yoshinaga*
Research Center for Highly-Functional Nanoparticles, Doshisha University, Kyotanabe, Kyoto, Japan

Summary In this article, breakup phenomena of a viscous liquid column jet in an inviscid stationary surrounding gas are analytically investigated, when the jet flows through a coaxial cylindrical sheath. Under a long wave approximation, axisymmetric nonlinear evolution equations of the jet and surrounding gas are derived and numerically solved under a spatially periodic boundary condition. In the nonlinear analysis, there exist three types of breakup modes: Rayleigh, first and second wind-induced modes, and their existing regions are shown in the parameter space of Weber number and sheath radius. In particular, it is found that the second wind-induced mode always appears even in a small Weber number if the coaxial cylindrical sheath is more closely placed to the jet.

INTRODUCTION

Liquid jets are of great importance in engineering and industrial applications in producing micro-drops and thin fibers, where destabilization in the former and stabilization in the latter play an important role. Such instabilities have been investigated experimentally and theoretically since Lord Rayleigh examined linear instabilities of periodic disturbances on a liquid column. It is known that, when Weber number (=inertial/surface tension) increases, some breakup mode transitions appear from Rayleigh mode to atomization mode through the first and second wind-induced modes [1]. In the Rayleigh mode the surface tension dominates and large liquid drops are produced by pinching, while in the first wind-induced mode produced drops diminish due to the reduction of the surface tension. In the second wind-induced mode, fine liquid drops are produced at the jet surface as well as at the top of the jet, while in the atomization mode fine droplets are produced near the nozzle. In these last two modes the aerodynamic instabilities are dominated. Although the Rayleigh and first wind-induced modes have been examined analytically and experimentally, the second wind-induced and atomization modes are mainly examined in experiments except for linear instabilities and numerical analyses. In this article, analytically examined is breakup of a liquid jet in a surrounding gas flowing through a coaxial cylindrical sheath. The end of this study is to analytically clarify the influence of the sheath wall on the breakup modes from the Rayleigh to the second wind-induced ones in the nonlinear regime.

FORMULATION AND LONG WAVE APPROXIMATIONS

As is shown in Fig. 1, we consider a problem of a viscous liquid jet in a surrounding gas in the (r, θ, z) cylindrical coordinate system. The jet of radius $r = h(\theta, z, t)$ flows through a coaxial cylindrical sheath of constant radius $r = H$ $(h < H)$. Denoting the jet and the surrounding gas as $j = 1$ and 2, respectively, the velocity vector $\boldsymbol{v}_j = (u_j, v_j, w_j)$, the pressures p_j are functions of r, θ, z and time t. The surface tension is denoted as σ, the densities as ρ_j and the viscosities as μ_j, where the gas viscosity is neglected $(\mu_2 = 0)$, for simplicity. The basic equations consist of the continuity and momentum equations, while the boundary conditions consist of the kinematical and dynamical conditions on the interface and vanishing normal velocity is imposed on the sheath wall.

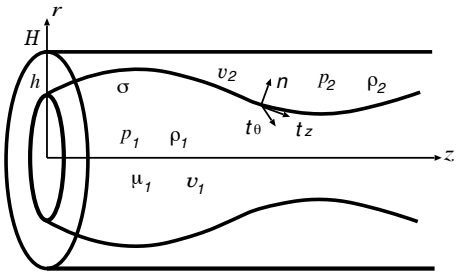

Figure 1: Schematic of a liquid jet in a surrounding gas flowing through a coaxial cylindrical sheath.

In the nonlinear analysis, we consider axisymmetric deformations of the jet, though full-three dimensional linear instabilities are examined in order to see the validity of a long wave approximation. As the long wave approximation, the following series expansions are adopted to the core jet $(0 \le r < h)$ [2]: $w_1 = w_1^{(0)} + r^2 w_1^{(2)} + \cdots$, $p_1 = p_1^{(0)} + r^2 p_1^{(2)} + \cdots$, while to the surrounding gas phase $(h < r < H)$ [3, 4]: $u_2 = u_2^{(0)} + (r-R)u_2^{(1)} + (r-R)^2 u_2^{(2)} + \cdots$, $w_2 = w_2^{(0)} + (r-R)w_2^{(1)} + (r-R)^2 w_2^{(2)} + \cdots$, $p_2 = p_2^{(0)} + (r-R)p_2^{(1)} + (r-R)^2 p_2^{(2)} + \cdots$. In the above and hereafter the radius at the mid-plane of the surrounding gas phase $R \equiv (H+h)/2$ and the thickness $b \equiv H - h$ are introduced for convenience. Then, substituting these expansions into the continuity, momentum equations and the boundary conditions and neglecting the terms of $O(h^2)$ and $O(b^2)$, we finally obtain the following time evolution equations: $\dfrac{\partial h}{\partial t} = -w_1 \dfrac{\partial h}{\partial z} - \dfrac{h}{2}\dfrac{\partial w_1}{\partial z}$, $\dfrac{\partial w_1}{\partial t} =$

*Corresponding author. Email: tyoshina@mail.doshisha.ac.jp

$$-w_1\frac{\partial w_1}{\partial z}-\frac{\partial p_1}{\partial z}+\frac{1}{\mathrm{Re}}\Big(2\frac{\partial^2 w_1}{\partial z^2}+\frac{6}{h}\frac{\partial h}{\partial z}\frac{\partial w_1}{\partial z}\Big),\quad \frac{\partial u_2}{\partial t}=-w_2\frac{\partial u_2}{\partial z}-\frac{1}{\gamma}p_2^{(1)},\quad \frac{\partial w_2}{\partial t}=-w_2\frac{\partial w_2}{\partial z}-\frac{1}{\gamma}\Big(\frac{\partial p_2^{(0)}}{\partial z}-p_2^{(1)}\frac{\partial R}{\partial z}\Big),$$

and the following simultaneous pressure equations: $\Big(A_1\frac{\partial^2}{\partial z^2}+A_2\frac{\partial}{\partial z}\Big)p_2^{(0)}+\Big(A_3\frac{\partial^2}{\partial z^2}+A_4\frac{\partial}{\partial z}+A_5\Big)p_2^{(1)}+A_6=0$, $\Big(B_1\frac{\partial^2}{\partial z^2}+B_2\frac{\partial}{\partial z}\Big)p_2^{(0)}+\Big(B_3\frac{\partial^2}{\partial z^2}+B_4\frac{\partial}{\partial z}+B_5\Big)p_2^{(1)}+B_6=0$. In the above, the coefficients of A_1 to A_6 and B_1 to B_6 are rather complicated functions of h, w_1, w_2 and u_2 and the following pressure relation is to be used: $p_1=p_2^{(0)}+p_2^{(1)}(h-R)+\frac{\kappa}{\mathrm{Wb}}-\frac{1}{\mathrm{Re}}\frac{\partial w_1}{\partial z}$. Nondimensional parameters such as Weber number $\mathrm{Wb}=\rho_1 W^2 a/\sigma$, Reynolds number $\mathrm{Re}=\rho_1 W a/\mu_1$, density ratio $\gamma=\rho_2/\rho_1$ and sheath radius H are introduced in the use of characteristic axial velocity W and jet radius a.

NUMERICAL RESULTS AND CONCLUDING REMARKS

Figure 2 shows typical breakup profiles when the above evolution and pressure equations are numerically solved for sinusoidal disturbances with initial wave number $k=k_m$ corresponding to the linear maximum growth rate. It is found in the figure that the Rayleigh modes appears in (a) by producing large drops and satellites, while the second wind-induced mode in (b) by cusp formation and fine droplets are to be produced from tip of the cusp. On the other hand, the first wind-induced mode appears in (c) by producing smaller blobs connected by threads without pinching. Figure 3 shows existing regions of these typical breakup modes in the parameter space of Wb and H. It is found for $\mathrm{Re}=\infty$ (solid lines) that the second wind-induced mode prevails always for smaller H whose boundary gradually increases with the increase of Wb. On the other hand, when H increases above the boundary, the Rayleigh mode prevails for smaller Wb, while the first wind-induced mode for larger Wb. In addition to this, the Rayleigh mode appears between the first and second wind-induced modes for $200\lesssim\mathrm{Wb}\lesssim 500$. In these existing regions, the second wind-induced mode survives for larger H as $\mathrm{Re}=100$ (broken lines), while as γ increases we can show that the first wind-induced mode appears for much smaller Wb though the second wind-induced mode is always existing in smaller H.

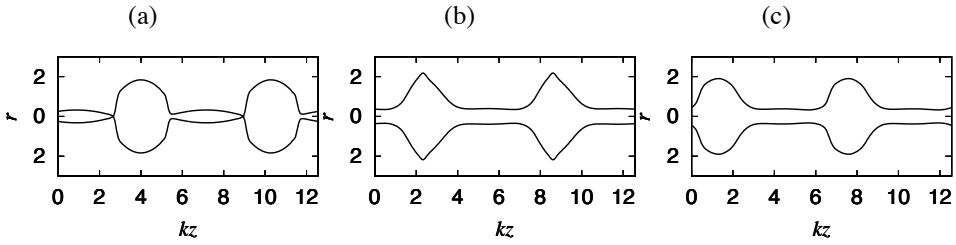

Figure 2: Breakup profiles when $\gamma=0.001$ and $\mathrm{Re}=\infty$, where $H=2$ ($k_m=0.738$) and $\mathrm{Wb}=100$ in (a), $H=2.2$ ($k_m=1.042$) and $\mathrm{Wb}=1000$ in (b) and $H=2.3$ ($k_m=1.042$) and $\mathrm{Wb}=1000$ in (c) .

It is shown in the experiments for the unbounded surrounding gas [1] that the first-wind induced mode appears when $600\lesssim\mathrm{Wb}\lesssim 6500$, while the second-wind induced mode appears when $6500\lesssim\mathrm{Wb}\lesssim 20000$. However, the present results show that the first wind-induced modes can appear for larger Wb than $200\sim500$ depending on H, while the second wind induced mode always appears when $H\lesssim 2$ even for a small Wb which is the most influence of the sheath wall. Consequently, by placing it closely to the jet, the sheath wall could be available to produce the cusp breakup from which fine droplets to be produced.

This work has been partially supported by JSPS KAKENHI Grant Number JP16K06082.

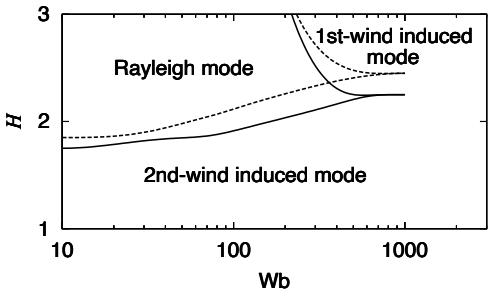

Figure 3: Regions of the Rayleigh and Taylor (1st- and 2nd-wind induced) modes in the parameter space of Wb and H, where $\gamma=0.001$ for $\mathrm{Re}=\infty$ (solid lines) and 100 (broken lines).

[1] Chigier N. and Reitz R. D. Regimes of jet breakup and breakup mechanism (*In Recent Advances in Spray Combustion: Spray Atomization and Drop Burning Phenomena* vol 1) ed K. K. Kuo *AIAA*: 109-135, 1996.

[2] Eggers J. and Villermaux E. Physics of liquid jets *Rep. Prog. Phys.*: **71**, 036601, 2008.

[3] Yoshinaga T. and Maeda M. Instability and encapsulation of a compound liquid jet *J. Fluid Sci. Tech.* **4**: 324-334, 2008.

[4] Yshinaga T. and Yamamoto K. Nonlinear instability and breakup of a viscous com@ound liquid jet *J. Fluid Sci. Tech.*: **6**: 477-486, 2011.

A COMPUTATIONAL TECHNIQUE FOR STUDYING SHOCK-INDUCED BUBBLE CAVITATION NEAR COMPLIANT SURFACES

Mohamad Aslani[1], Kourosh Shoele *[1]
[1] Department of Mechanical Engineering, Florida State University, Tallahassee, Florida, USA

Summary A cavitating bubble hitting a solid surface generates a convoluted interaction between the resultant flow field from the bubble dynamic and the sold surface. We present details of a computational technique for a compressible flow solver capable of simulating such a stiff multi-material interaction. The developed scheme uses an interface capturing technique in a control volume setting and tracks the computationally smoothed interfaces using an advection equation for the volume of the phases. In this way, fluid and solid flows are all integrated into a fully Eulerian framework which significantly improves the computational efficiency of the overall algorithm. Preliminary results show that the method is capable of simulating shock-bubble interaction with interfacial forces.

INTRODUCTION

This research is motivated by the importance of understanding the cavitating bubble-compliant surface interaction and the merging technology of cleaning biofilms based on this technique. Biological fouling activities can cause losses in heat transfer efficiency of cooling systems, mechanical blockage in fluid transport systems, and an increase in drag of marine surfaces. Multiple chemical, material, and physical approaches are proposed and utilized to fight against biofouling, but these methods come with several shortcomings. An alternative novel technique in this area is bubble cavitation (commonly known to be a devastating phenomenon). This method is an emerging technology for cleaning biofilms in different industrial and medical applications [1]. It has been used to clean up biofilm on the surface of membrane filtration in the wastewater treatment where ultrasound can significantly decrease the concentration of biofilm near membrane filters through disturbing biofilm extracellular substances without the use of any chemical cleaning reagent. It has also been leveraged in ultrasound histotripsy allowing the noninvasive break down of the tissue using the transient cavitation action of microbubbles. Given the complex procedure of bubble cavitation using compression waves, and convoluted interaction between resultant flow field from bubble dynamic and the characteristics of the biofilm, it is almost impossible to come to the conclusion of the effectiveness of this technology for the removal of marine biofilm solely from experiments. Numerical simulations of such phenomena require compressible multiphase flow simulations with special treatment for solid-fluid interfacial interactions.

Developing high-fidelity numerical techniques capable of simulating gas, liquid, and solid phases are ongoing research. The interfaces in such flows could potentially undergo rapid evolution with deformation in a three-dimensional configuration that requires efficient numerical modeling. In this study, we focus on a numerical technique to simulate compressible gases, liquids, and elastic solids using an interface capturing method [2]. The method takes into account viscous and interfacial forces to accurately model the interaction of a cavitating bubble with a deforming solid interface. The aspects of the developed techniques are briefly discussed in the next two sections.

GOVERNING EQUATIONS

Mass, momentum, and energy conservation laws in the Eulerian framework dictate the governing equations. To describe the continuous medium in the Eulerian framework, we use the backward characteristic model already discussed in [3]. This equation is used to track and evolve the gradient of the deformation in the current framework needed in the Cauchy stress tensor. Finally, an advection equation is required to track the location of interfaces. The overall scheme is written in a quasi-conservative form in order to prevent possible pressure oscillations in the interfaces (for more details see [4-5]). There are extra forces due to the capillary effects which are introduced through the continuous surface force (CSF) model. One important feature of this study is the inclusion of viscous and interfacial forces in the model.

To close the system of equations, we use a constitutive law to model gas, liquid, and solid phases. In this model, the internal energy is defined as

$$e = \underbrace{\underbrace{\frac{\kappa(s)}{\gamma-1}\left(\frac{1}{\rho}-b\right)^{1-\gamma}}_{I} - a\rho + \frac{p_\infty}{\rho}}_{II} + \overbrace{\frac{\xi}{\rho_0}(Tr(\bar{B})-3)}^{III}$$

where (I) is the van der Waals law for the gas phase, (II) is the stiffened gas equation for the liquid phase and (III) part is the neohookean elastic solid model.

NUMERICAL SCHEME

The overall numerical scheme is based on solving the approximate Riemann problem using a modified Harten–Lax–van Leer Contact (HLLC) technique and integrating the equations using a third-order TVD Runge-Kutta method. The HLLC

*Corresponding author. E-mail: kshoele@fsu.edu.

solver is modified to account for elastic solid and the pressure jump in the interface of a liquid due to the capillary effects. It should also be noted that due to the numerical diffusion introduced into the solution from the HLLC method (upwinding) the density and the volume fraction are stiffened systematically and consistently using a compressible version of the Tangent of Hyperbola for Interface Capturing (THINC) method.

PRELIMINARY RESULTS

In this section, we present the preliminary results obtained for the simulation of a bubble interacting with a shockwave. The shockwave is initiated in water (simulated as a stiffened gas) and undergoes a complex geometry change when the shockwave passes through it. This complex geometry is the result of multiple waves interacting with the bubble medium that reflects back and forth and change in the impedance of the mediums. The method is able to accurately capture all of these features as it can be seen in these simulations.

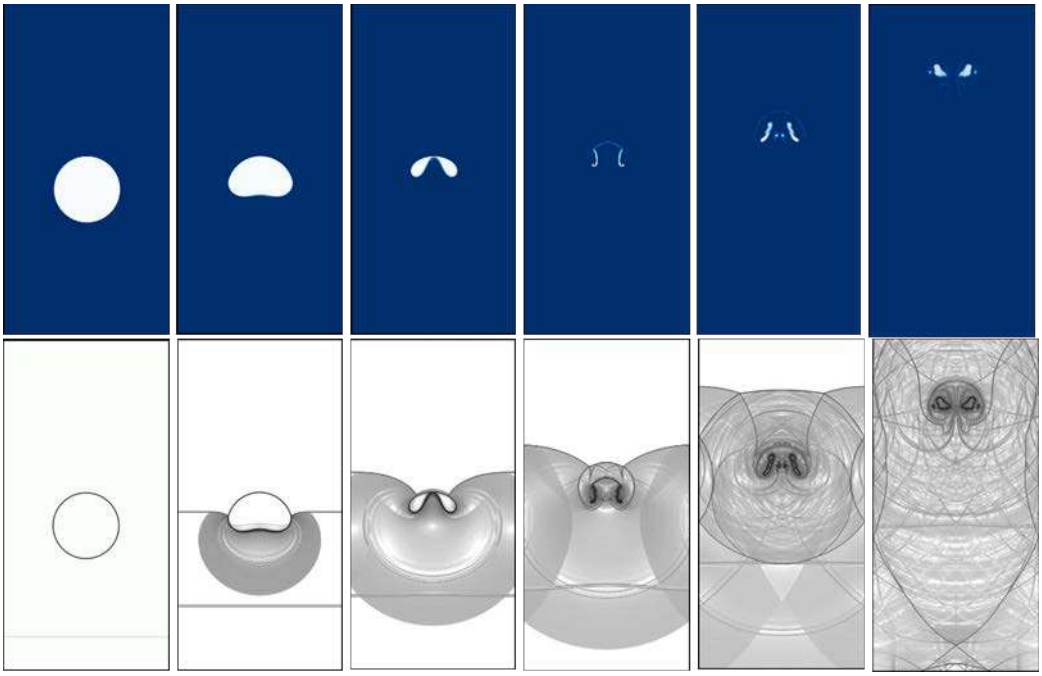

Figure 1. Preliminary results for the shock-induced cavitating bubble. The top is the phasic volume and below are the magnitude f density gradients.

CONCLUSIONS

In this abstract, we briefly discussed the development of a compressible flow solver capable of simulating gas, fluid, and solid phases consistently and accurately. The compressible Navier-Stokes equations were discretized using a finite-volume scheme and the upwind fluxes were found using a modified HLLC scheme. A constitutive law was used to account for the state variables in gas, liquid, and elastic materials. This model will be used to further study the biofilm removal techniques based on cavitating bubbles.

References

[1] Kyllönen, H. Experimental Aspects of Ultrasonically Enhanced Cross-Flow Membrane Filtration Of Industrial Wastewater. *Ultrasonics sonochemistry* **13**: 295-302, 2006

[2] Saurel, R., A Simple Method for Compressible Multifluid Flows, *SIAM J. Sci. Comput*. **21**: 1115–1145, 1999

[3] Brauer A., A Cartesian scheme for compressible multi-material model in 3D, *Journal of Computational Physics* **313**: 123-143, 2016

[4] Garrick D., A finite-volume HLLC-based scheme for compressible interfacial flows with surface tension, *Journal of Computational Physics*, **339**: 46-67, 3017

[5] Aslani, M, A localized artificial diffusivity method to simulate compressible multiphase flows using the stiffened gas equation of state, *International Journal for Numerical Methods in Fluids,* **88: 413-433,** 2018.

NUMERICAL INVESTIGATION OF THE EFFECT OF PRESSURE ON THE FLOW FIELD AND SPRAY STRUCTURE AND EVAPORATION

Ala sadooghi*[1], Maryam Shahrasebi [2], Hassan Khaleghi[1]
[1] Department of Mechanical Engineering, Tarbiat Modares University, Tehran, Iran
[2] Department of Mechanical Engineering, K.N.Toosi University of techonology, Tehran, Iran

Summary: In this paper, the effect of ambient pressure on the evaporation of the fuel Spray of droplets is numerically investigated in Eulerian-Lagrangian two-phase modeling. In the spray modeling, size distributions for the initial diameter of droplets, Break-Up of droplets, Collision phenomena, and evaporation of droplets are considered. Besides, turbulence dispersion and modulation are investigated simultaneously. Moreover, the coupling between the continuous phase and the discrete phase is 2-ways coupling. Although the evaporation of droplets in both, high and low temperatures has a direct relation with the ambient pressure, it should be noted that the higher impact is regarding high-pressure conditions. Also, the effect of the ambient pressure on the spray structure and spray tip-penetration is shown that the results show the Spray structure is thinner in high ambient pressure which comes with low penetration in the continuous phase. With respect to the continuous phase, the temperature of the gas-phase goes down during the time that the droplets evaporate and get heat from the gas phase, especially in the core of the spray that the number of droplets is more than other parts of the spray. Also, the impact of droplet's momentum on the gas-phase is shown, especially on the Z-direction which is near the attitude of injection direction and the velocity of the continuous phase is changed and increased.

Liquid and gas phase equations

In this section, first, the equations that are governed the gas-phase are introduced, and then the equations that are governed the liquid-phase, which is Lagrangian-phase, are introduced.

On the gas-phase which is the continuous phase, Navier-Stokes equations are governed. Also, the $k-\varepsilon$ turbulent model is used in this study. The general transport equation that includes ϕ and Γ can be replaced by the parameters of Table-1 for having mass, momentum, energy, turbulent kinetic energy, turbulent dissipation energy, and fuel vapor mass fraction.

$$\frac{\partial(\rho\phi\theta)}{\partial t}+\frac{\partial}{\partial r}(\rho\phi u\theta)+\frac{v}{r}\frac{\partial}{\partial \gamma}(r\rho\phi v\theta)+\frac{\partial}{\partial z}(\rho\phi w\theta)=\frac{1}{r}\frac{\partial}{\partial r}\left(\theta\Gamma_{r3}\frac{\partial\phi}{\partial r}\right)+\frac{1}{r}\frac{\partial}{\partial \gamma}\left(\theta\Gamma_{\gamma}\frac{\partial\phi}{\partial \gamma}\right)+\frac{\partial}{\partial z}\left(\theta\Gamma_{z}\frac{\partial\phi}{\partial z}\right)+S_{\phi}+S_{\phi.d}\text{3s3} \quad (1)$$

With respect to two-way coupling, there are some other source terms due to existing droplets in the domain, so they are listed below for mass, momentum and heat transfer equations:

$$S_{m.d}=-\frac{\pi}{6}\frac{\rho_d}{\delta t}\sum_k N_{dk}\{(D_{dk}^{n+1})^3-(D_{dk}^{n})^3\}3 \quad (2)$$

$$S_{u_{i_{dk}}}=-\frac{\pi}{6}\frac{\rho_d}{\delta t}\sum_k N_{dk}\{(D_{dk}^{n+1})^3u_{i_{dk}}^{n+1}-(D_{dk}^{n})^3u_{i_{dk}}^{n}\}3 \quad (3)$$

$$S_{hd}=-\frac{\pi}{6}\frac{\rho_d}{\delta t}\sum_k N_{dk}\left\{(D_{dk}^{n+1})^3\left(C_pT_{dk}\right)^{n+1}-(D_{dk}^{n})^3\left(C_pT_{dk}\right)^{n}\right\}33 \quad (4)$$

For3the3second3phase3(droplets),3equations3that3are3governed3in3the3agrangian3frame[3].3The3evaporation3model3is3developed3based3on3the3Abramzon3model3[1].33

Grid independence and validation

For3making3the3satisfy3grid,3the3grid3generated3in3polar3coordinate and then 3 different meshes, 160000,432000 and 960000, are used to study the grid independency, after that the 432000 grids satisfied the grid independency conditions. The validation results of the code are compared with Sandia Spray-A [4].

Results and Discussion

the3angle3of3injection3which3is3shown3in3figure(3)to(6)3is3153degrees3to3the3top3of3the3cylinder3The3ambient3temperature3in3the3"High3emperature"3condition3is3800k3and3the3wall3temperature3is3800k,3and.3The3ambient3temperature3of3the3"low3emperature"3condition3is3440k3and3the3wall3temperature3is3440k.3The3first3results3which3are3important3in3the3spray3are3the3total3mass3evaporation,3this3parameter3is3compared3for353different3pressure3at3low3temperature3that3is3shown3in3figure3(1)3

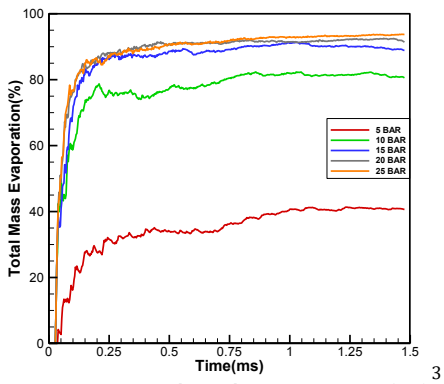

Figure313comparison3the3total3mass3evaporation3for353different3pressure3at3low3emperature.3

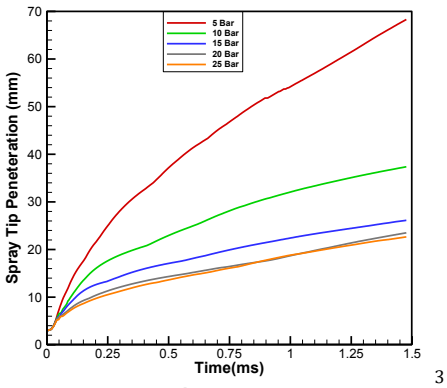

Figure223comparisons3between3spray3tip3penetration3for353different3pressure3

*Corresponding author. E-mail: ala.sadooghi@modares.ac.ir.

It is clear that the total mass evaporation of the spray increases with pressure even in low temperatures. One of the important parameters in the spray is spray tip penetration, which is really affected by pressure and decreases by pressure.

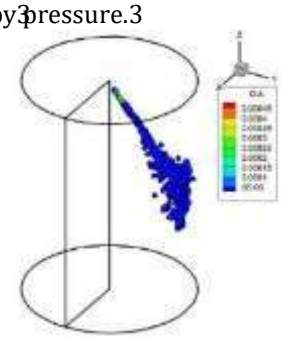

Figure 3 Isometric view of spray structure in 5 Bar, low-temperature

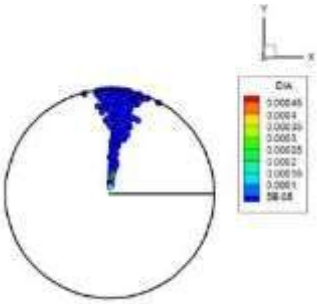

Figure 4 x-y view of spray structure in 5 Bar, low-temperature

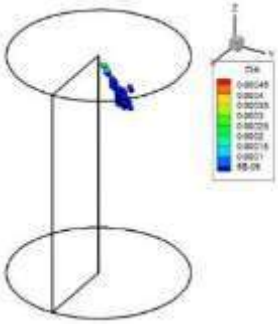

Figure 5 Isometric view of spray structure in 25 Bar, low-temperature

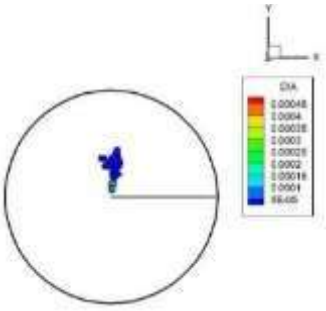

Figure 6 x-y view of spray structure in 25 Bar, low-temperature

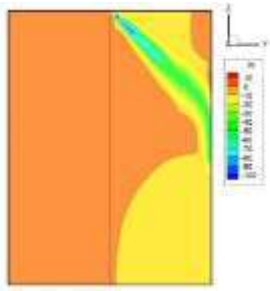

Figure 7 W velocity field of gas-phase in 5 Bar and low-temperature Condition

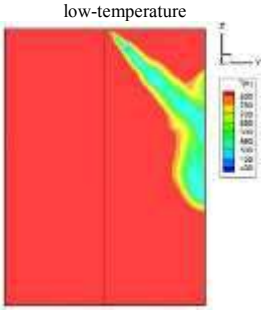

Figure 8 Temperature field of gas-phase in 5 Bar and high-temperature Condition

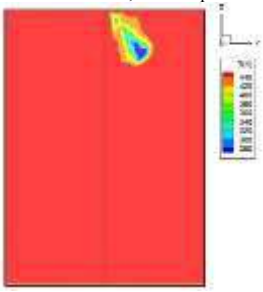

Figure 9 Temperature field of gas-phase in 25 Bar and low-temperature Condition

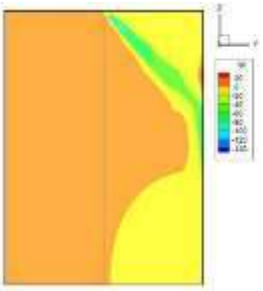

Figure 10 W velocity field of gas-phase in 5 Bar and high-temperature Condition

CONCLUSIONS

In this paper, the effect of pressure and temperature on the evaporation spray have been discussed. The effect of the liquid droplets phase is also considered to the gas-phase. The results show the effect of pressure is really important in the evaporation of spray. Also, pressure plays an important role in the diffusion of the droplets in the environments. In addition, the heat that the droplets give from the gas-phase causes a significant drop in the temperature of the gas-phase.

References

[1] Sirignano, W. A., & Abramzon, B. (1989). Droplet vaporization model for spray combustion calculations. International Journal of Heat and Mass Transfer, 32(9), 1605–1618.Icer D.F., Adams J.A. Mathematical Elements for Computer Simulation. McGraw Hill, NY 1977.

[2] Azami, M. H., & Savill, M. (2016). Modeling of spray evaporation and penetration for alternative fuels. Fuel, 180, 514–520

[3] . Khaleghi, H., Yazdanparast, S., Keshtkar, M. R., & Firouznia, Z. (2018). Development of a spread submodel for spray/wall impaction. Atomization and Sprays, 28(10), 857–873.

[4] Sandia National Laboratories. Engine Combustion Network (ECN), Accessed 8 Nov 2017;https://ecn.sandia.gov/ecn-data-search/.

GPU-BASED MODELLING OF A TWO-PHASE FLOW IN CAPILLARY NETWORKS

Sergei Prokopev*[1], Tatyana Lyubimova[1], Anatoliy Vorobev[2], Timofey Zagvozkin[1]
[1] Institute of Continuous Media Mechanics Ural Branch RAS, Perm, Russia
[2] University of Southampton, Southampton, UK,

We model the liquid/liquid displacement flow through capillary tubes using the phase-field approach[1,2]. We assume that a capillary is initially saturated with one liquid that is displaced (or washed out) by the injection of another liquid. An accurate description of such a problem requires a theoretical model that takes into account the interfacial diffusion. For solution of the latter task, one needs to trace the evolution of the shape of a liquid/liquid interface. In addition, miscible interfaces are endowed with dynamic interfacial stresses (e.g. a honey droplet immersed in tea possesses a spherical shape that can be explained by the action of surface tension effects) that also needs to be considered. We develop a new approach for modelling the behaviour of miscible liquids taking into account the effects of interfacial diffusion and dynamic surface tension. Our approach is based on the phase-field method that is applied as a physics-based model for description of heterogeneous binary mixtures. The Boussinesq approximation of the Cahn-Hilliard-Navier-Stokes equations are solved for the configuration of capillary tubes. The governing equations are numerically solved in the pressure-velocity notation, using the fractional-step (or projection) method implemented on the basis of the finite difference approach. We found that the model elaborated is capable to reproduce the classical analytical relation such as Washburn equation for the velocity on the meniscus edge or the formula for the jump of capillary pressure through the interface.

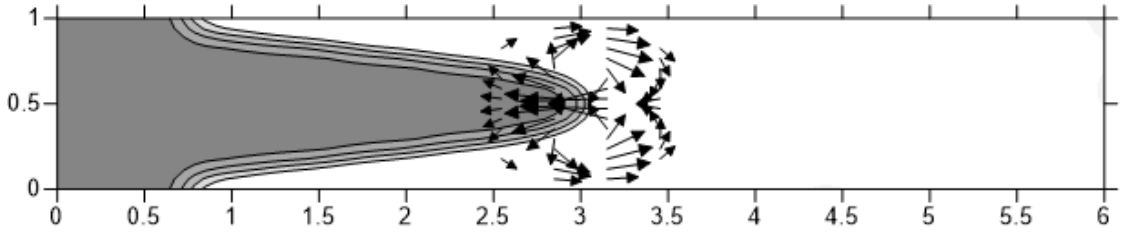

Figure 1. The fields of concentration (isolines) and deviation of the velocity from the parabolic Poiseuille profile (vectors).

Based on the theoretical and numerical model developed for a single capillary we also developed a very detailed description for the immiscible liquid/liquid displacement through a uniform network of capillaries that we use as a rough representation of a micro-volume of a porous medium. We found that, qualitatively, for all considered geometries, the liquid/liquid displacement always undergoes the same set of particular stages: (i) right after the moment of turning on the pressure difference between the ends of the matrix, the liquid/liquid menisci experience a number of capillary oscillations; the magnitude of the oscillations is controlled by the surface tension coefficient and by the Peclet number; (ii) later, the meniscus' shape is set and the piston-like propagation of the displacement front through the matrix can be observed; (iii) when the menisci reach the outlet end of the matrix (the break-through time), some volumes of the displacing liquid still remain on the walls of the matrix; so further pumping of the displacing fluid results in scratching of these remainders from the walls; (iv) finally, the steady stage is reached when the displaced fluid however still remains within some elements of the matrix, although the further pumping of the displacing liquid does not lead to any differences in distribution of the liquids within the matrix. We also showed the Peclet number defines the speed of sliding of the contact line along the walls. We demonstrate that all integral parameters (including the capillary pressure) that characterise the liquid/liquid displacement within the matrices of different sizes converge to some limiting curves, indicating that the matrix with the size less than 10x10 elements is fully sufficient to give the accurate prediction of the capillary pressure in a homogeneous porous medium.

*Corresponding author. E-mail: prokopev.s@icmm.ru.

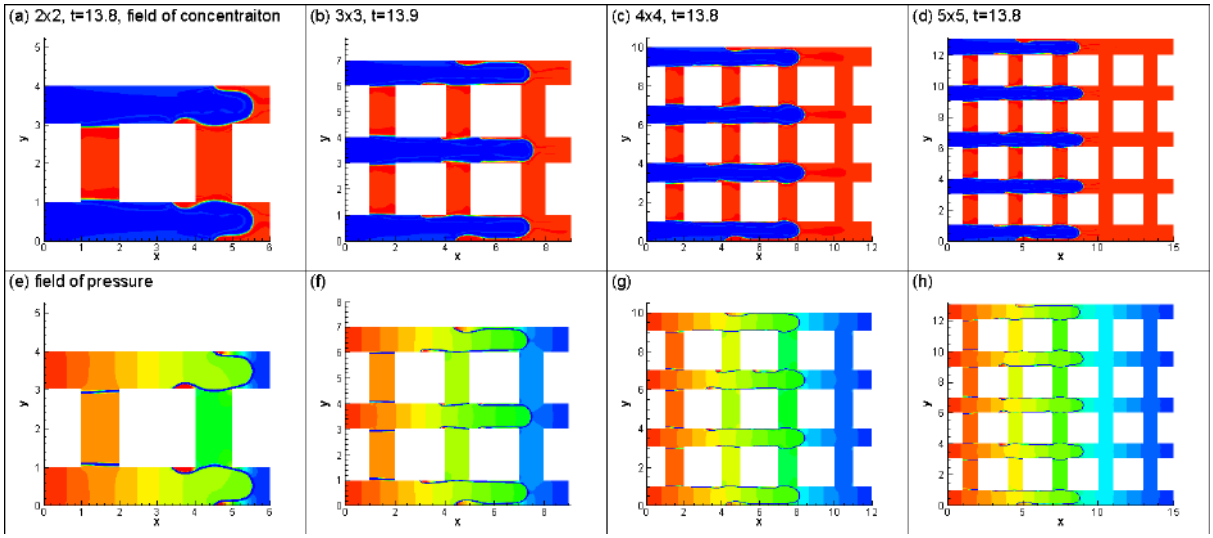

Figure 2. The piece of the matrix of capillary tube network. The example of flow, a,b,c,d are the fields of concentration, e,f,g,h are the fields of pressure

The phase-field theory demands a relatively high numerical resolution. Taking into account the extended geometry that consists of numerous capillaries we deal with significant computational challenge. To cope with all the difficulties we choose a modern effective programming approach of using graphical process units (GPUs) and CUDA toolkit. We use an explicit finite-difference scheme that is easily parallelized among GPU cores. We have written an effective rapid algorithm using CUDA C language. The performance tests demonstrated following speed-up results for some Nvidia GPU devices: GeForce GTX 1050 ~ 5 times, Tesla k40 ~ 20 times, Tesla v100 ~ 100 times. The reference computation was made with the sequential version of the same algorithms on intel i7-4770k.

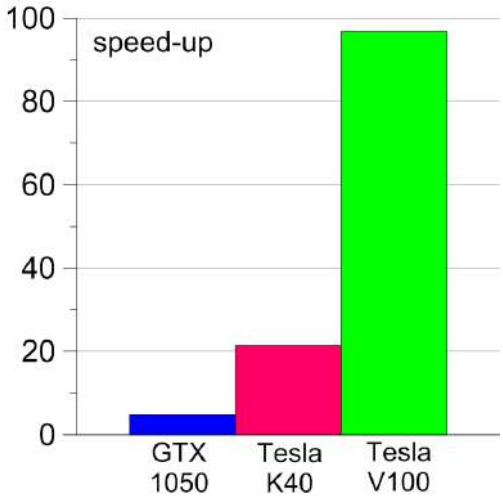

The speed-up of computations on GPU in comparison with intel i7-4770k.

Acknowledgements

The study was supported by Russian Foundation for Basic Research (grant 18-01-00782) and Government of Perm Krai (Program for the support of Scientific Schools of Perm Krai, grant C-26/788).

References

[1] S. Prokopev, A. Vorobev, T. Lyubimova, Phase-field modeling of an immiscible liquid/liquid displacement in a capillary, Physical Review E, **99(3),** 033113, 2019

[2] T. Lyubimova, A. Vorobev, S. Prokopev, Rayleigh-Taylor instability of a miscible interface in a confined domain. Physics of Fluids , **31(1)**, 014104, 2019

RANS MODELING OF FLOW STRUCTURE, TURBULENCE AND HEAT TRANSFER IN A SEPARATED DROPLET-LADEN MIST FLOW

Maksim Pakhomov*[1]
[1]Laboratory of Thermal and Gas Dynamics, Kutateladze Institute of Thermophysics, Novosibirsk, Russia

Summary The results of a numerical investigation of the effect of droplets' thermophysical properties on the flow structure, turbulence, and heat transfer in a two-phase mist flow in a backward-facing step are presented. Predictions are carried out for droplets of water, ethanol, and acetone for initial droplet diameters varying in the range d_1 = 1–100 μm. The RANS approach is used to simulate a gaseous phase, and the motion and heat transfer of a dispersed phase are computed using the two-fluid Eulerian model. Gas phase turbulence is predicted using the model of Reynolds stress transport modified for the case of particle presence. It is shown that the addition of droplets leads to a significant increase in heat transfer (up to 50% at M_{L1} = 0.05) in comparison with a single-phase separated flow. The maximal heat transfer enhancement with the use of ethanol droplets is slightly higher than the corresponding value for water droplets (by approximately 10–20%). The length of the region of intensified heat transfer is maximal for water droplets, while it is minimal for acetone droplets. The effect of heat transfer intensification and suppression of carrier gas phase turbulence is minimal for the acetone droplets.

INTRODUCTION

Two-phase droplet-laden separated flows are observed in many engineering and natural processes, such as cyclonic separation, flame stabilization in internal combustors, pneumatic transport, and many others. The effect of the thermophysical properties of three liquids (water, ethanol, and acetone) on flow structure, turbulence, and heat transfer in a droplet-laden mist flow in a sudden pipe expansion is simulated numerically using the Eulerian approach. The aim of the present paper is to numerically examine the effect of the droplets on flow and heat transfer in the mist backward-facing step flow for liquids with various values of latent heat of evaporation (water, ethanol, and acetone).

MATHEMATICAL MODEL

In the present paper, the dilute gas-droplet turbulent flow behind a backward-facing step is numerically examined. The set of steady-state Reynolds Averaged Navier-Stokes (RANS) equations for the gas phase with negligible mass forces is employed in the study. The mean flow is described by the continuity, the two-momentum equations, the energy equation and the equation of vapor diffusion into the binary gas–vapor mixture [1]. Gas phase turbulence is modeled with the use of elliptic blending second moment closure (SMC) [2] with the effect of particles on the carrier phase turbulence. Two-way coupling is achieved between dispersed and carrier phases in the mean and fluctuating transport [3]. The back effect of particles on the carrier phase turbulence (two-way coupling) is considered [1].

NUMERICAL RESULTS AND DISCUSSION

The increase in the Stokes number causes an increase in the mass concentration of droplets in the flow core region (see Fig. 1). The large droplets practically do not penetrate into the recirculation zone and the fraction value increases markedly in the central part of the duct. Initially, an increase in the Stokes number of the dispersed phase leads to an increase in the dispersed phase concentration in the separation zone. The mass fraction of droplets decreases significantly due to their absence in the region of separated flow with further rises of the Stokes number. In the near-wall region, the mass fraction of droplets is significantly less than that in the region of the flow core due to their fast evaporation (at small Stokes numbers) and their absence in this region (at large Stokes numbers).

The addition of droplets leads to a significant increase in heat transfer (up to 50% at M_{L1} = 0.05) in comparison with a single-phase separated flow. The intensification of heat transfer with the use of ethanol droplets is higher (by approximately 10–20%) than the corresponding value for water droplets (see Fig. 2). The region of two-phase flow decreases significantly and the level of turbulence suppression in the carrier phase is decreased (by up to 10–15%) due to the presence of evaporating dispersed particles. The effect of evaporation of acetone particles on the heat transfer and turbulence of the carrier gas phase is minimal.

Fig. 3 shows the turbulence kinetic energy (TKE) profiles of the gas and dispersed phases measured [4] and predicted by authors at the few stations. Distributions of turbulence energy for a single-phase flow (*1*), gas (*2*) and dispersed (*3*) phases have a qualitatively similar form. The level of turbulence in a single-phase flow (*1*) is close to the TCE level in the gas phase of a two-phase flow (*2*). The turbulent energy of droplets (*3*) is less than the corresponding value for gas (*2*). The transverse profiles of the turbulent energy of gas and droplets have a pronounced maximum located in the region of the shear layer, which is typical for experiments [4] and for our numerical data. The largest values of the TKE level for both phases are at the distance x/H = 4–5. This allows concluding that the particles penetrate to this region and interact well with the gas carrier phase. In the region of the reattachment point ($x_R/H \approx 6.2$), the value

*Corresponding author. E-mail: pakhomov@ngs.ru.

of gas turbulence decreases significantly and the kinetic energy of turbulence approaches the value for the carrier medium.

CONCLUSION

The effect of the thermophysical properties of three liquids (water, ethanol, and acetone) on dispersed phase scattering, turbulence, wall friction, and heat transfer in a droplet-laden mist flow in a backward-facing step was simulated numerically using the Eulerian approach.

The fine droplets (Stk < 1) are observed in the whole duct cross-section (flow core, shear layer and recirculation region). The largest droplets studied Stokes number (Stk > 1) do not almost penetrate into the recirculation zone and they dispersed only in the shear and recirculation zones. Gas phase turbulence in the two-phase flow attenuates by fine droplets additions (up to 15%) and an increase of these inlet parameters leads to higher reduction of the gas phase turbulent kinetic energy.

This work is supported by the Russian Science Foundation (Project No. 21-19-00162).

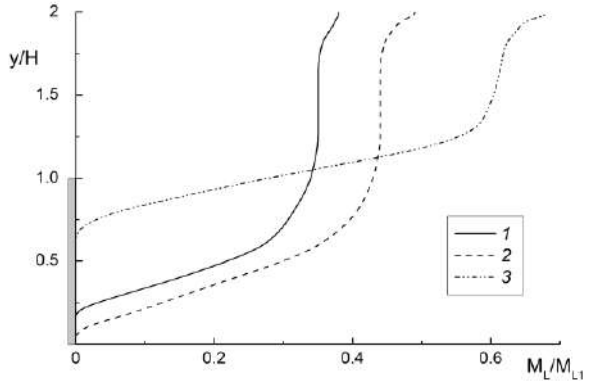

Figure 1. The transverse dictributions of droplets mass fractions in the two-phase separated flow. $x/H = 2$, $M_{L1} = 0.05$. *1* – $d_1 = 10$ μm, Stk = 0.03; *2* – 30, 0.28; *3* – 100, 2.9.

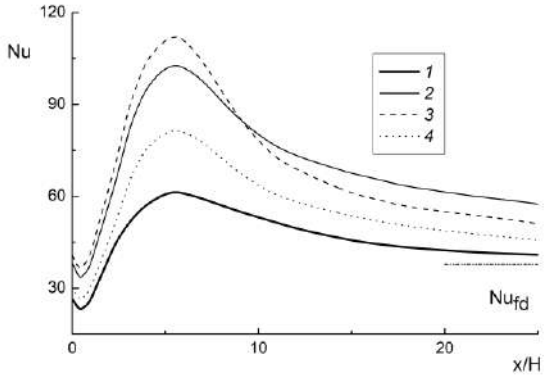

Figure 2. The effect of thermophysical properties of droplets on heat transfer in two-phase separated flow for inlet droplets diameter d_1 = 30 μm. M_{L1} = 0.05. *1* – single-phase separated flow, *2* – water, *3* – ethanol, *4* – acetone, *5* – the value of heat transfer for single-phase fully developed flow in a pipe backward-facing step.

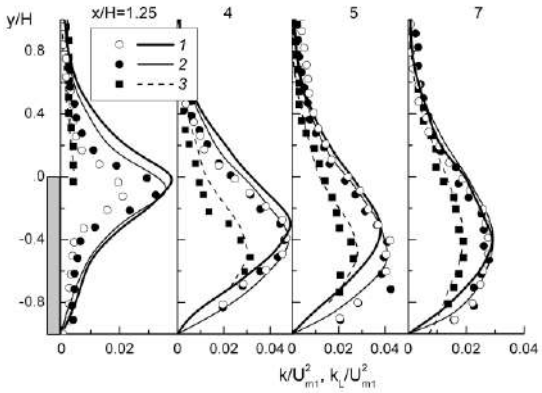

Figure 3. The profiles of turbulent kinetic energies of gas and dispersed phases. *1* – single-phase air flow, *2* – gas phase of droplet-laden mist flow, *3* – dispersed phase. d_1 = 60 μm, M_{L1} = 0.04, H = 20 mm.

References

[1] Pakhomov M. A., Terekhov V. I. Effect of Evaporating Droplets on Flow Structure and Heat Transfer in an Axisymmetrical Separated Turbulent Flow. *Int. J. Heat Mass Transfer*. **140**: 767–776, 2019.

[2] Fadai-Ghotbi A., Manceau R., Boree J. Revisiting URANS Computations of the Backward-Facing Step Flow Using Second Moment Closures. Influence of the numerics, *Flow, Turbulence and Combust.* **81**: 395–410, 2008.

[3] Zaichik L. I., Alipchenkov V. M. A Statistical Model for Predicting the Fluid Displaced/Added Mass and Displaced Heat Capacity Effects on Transport and Heat Transfer of Arbitrary-Density Particles in Turbulent Flows. *Int. J. Heat Mass Transfer* **54**: 4247–4265, 2011.

[4] Hishida K., Nagayasu T., Maeda M. Augmentation of Convective Heat Transfer by an Effective Utilization of Droplet Inertia, *Int. J. Heat Mass Transfer* **38**: 1773–1785, 1995.

SINGULARITY IN PARTICLE-LADEN FLOW

Seulgi Lee[1], Changhoon Lee *[1,2]
[1] Department of Mechanical Engineering, Yonsei University, Seoul, Republic of Korea
[2] Department of Computational Science and Engineering, Yonsei University, Republic of Korea

Summary Collision of particles suspended in turbulent flows is investigated using a new concept. Under the assumption that motion of particles with small Stokes number is smooth function of space, the velocity is uniquely determined by the position. Therefore, flow of particles exists and is examined to find the condition of collision by noticing that singularity of velocity gradient of particles occurs when collision happens. The motion of particle is derived in Eulerian approach. Using this concept, the singularity of velocity gradient for various Stokes number and gravity is investigated in a Taylor-Green vortex flow and two-dimensional turbulence.

INTROUDUCTION

Particle-laden flows are frequently observed in various environments such as indoor system, industrial problems and natures. For example, the formation of clouds and precipitation is caused by interactions between small droplets contained in atmosphere, and dust from urban pollution can lead many serious health problems. Especially, small sized particles has emerged as an important problem for people's health. Other examples of particle-laden flows for industrial areas are injection of fuel droplets in diesel engines and spray applications in many manufacturing.

However, current mathematical descriptions and comprehension of the underlying mechanisms for particle-laden flow have not been fulfilled yet. It is because that the underlying mechanism for turbulent flows causing the movement of spherical particle is not fully understood by strong nonlinearity and multi-scale nature. Furthermore, the motion of particles having another kind of nonlinearity makes additional complexity.

In order to understand the behaviour of particles suspended in turbulent flow, the interaction between particles and coherent structures needs to be investigated. However, it is quite difficult to describe the solution mathematically. Thus, we consider another approach to understand interaction between particles and background turbulence. The particle velocity can be uniquely determined by position by assuming that particle velocity is a smooth function of space. Then detailed mechanism of collision can be studied by investigating the behaviour of evolution of the particle velocity field.

METHODOLOGY

Taylor-Green vortex flow is used to performing a numerical analysis of collision of particles suspended in the background flow. The reasons of adopting Taylor-Green vortex flow are simple having an exact solution and easy to intuitively understand behaviour of suspended particles. The solutions of Taylor-Green vortex flow in two dimensional domain $[2\pi, 2\pi]$ are given by $u_1 = f(t)\cos x \sin y$ and $u_2 = -f(t)\sin x \cos y$ where $f(t) = e^{-2\nu t}$, ν is the kinematic viscosity of fluid. The exact fluid velocities are used with time.

Eulerian approach for motion of particle

The motion of particles assuming smooth function , the so-called 'flow particle' [1,2] can be derived as below

$$\frac{\partial v_i}{\partial t} + \mathrm{v_j}\frac{\partial v_i}{\partial x_j} = \frac{u_i - v_i + w_i}{\tau_p} \quad (1)$$

where v_i and u_i are particle velocity and fluid velocity and $w_\mathrm{i} = -\tau_\mathrm{p}\ \mathrm{g}$ which is terminal velocity. Here, τ_p is the particle response time. The particle dynamics are determined by the ratio of particle response time τ_p to flow time scale τ_f, namely the Stokes number $St = \tau_\mathrm{p}/\tau_\eta$.

Discretization in space is applied using a spectral method in two-dimensional periodic domain, and a third-order explicit Runge-Kutta algorithm for discretization in time is adopted. The initial particle velocities are generated as the same as a background flow.

RESULTS AND CONCLUSIONS

The motion of particles are investigated with varying Stokes numbers and gravity. Equation (1) can be used to examine the order of magnitude analysis of singularity solution [3-5]. Taking the gradient of Eq. (1) yields a solution that might blow up in finite time in the order-of-magnitude sense as below

$$\sigma(t) \sim \frac{1}{t - t_c}$$

*Corresponding author. E-mail: clee@yonsei.ac.kr.

where $\sigma = \nabla \boldsymbol{v}$ is gradient of particle velocity. This blow-up of the velocity gradient of a particle implies collision between two particles. Our numerical study of Eq. (1) clearly indicates that finite-time singularity is observed for large Stokes number, but strong gravity suppresses or delay the blow up.

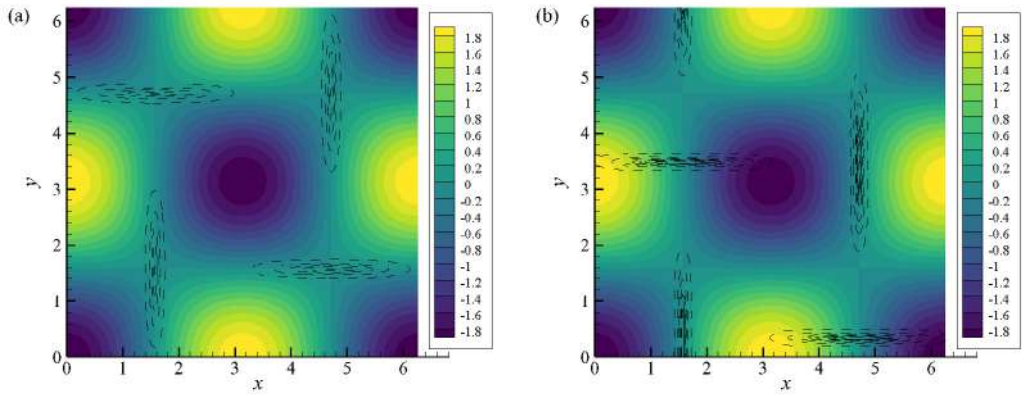

Figure 1. Plots of representing collision of particle. Coloured contour represents vorticity level of the background flow and dashed lines for divergence level of particle are denoted. (a): $\tau_p = 0.5,\ w_2 = 0$ and (b): $\tau_p = 5,\ w_2 = -5$.

Collision of particles are visually shown in Fig. 1, where contour levels represent vorticity for the background flow and dashed line means negative divergence level of particle velocity field. This kind of singularity would provide a more accurate description of the collision process through modelling by finite-time blow-up. Finally, finite-time t_c can be estimated accurately in this simulation. More detailed results will be discussed in the presentation.

References

[1] Park Y., Lee C. Gravity-driven clustering of inertial particles in turbulence. *Physical Review E* **89**: 061004(R), 2014.
[2] Fouxon I., Park Y., Harduf R., Lee C. Inhomogeneous distribution of water droplets in cloud turbulence. *Physical Review E* **92**: 033001, 2015.
[3] Beal J. T., Kato T., Majda A. Nygus G. Remarks on the breakdown of smooth solutions for the 3-D Euler Equations. *Communications in Mathematical Physics* **94**: 61, 1984.
[4] Majda A. Vorticity, Turbulence and acoustics in fluid flow. *SIAM Review* **33**: 349, 1991.
[5] Bustamante M. D., Kerr R. M. 3D Euler about a 2D symmetry plane. *Physica D* **237**: 1912, 2008.

NUMERICAL INVESTIGATION OF FILM BOILING HEAT TRANSFER ON THE HORIZONTAL SURFACE UNDER VERTICAL OSCILLATION

Young Seock An[1] and Byoung Jae Kim *[1]
[1] School of Mechanical Engineering, Chungnam Naional University, Daejeon, South Korea

Summary Film boiling is critical to nuclear safety because it directly influences the integrity of the nuclear fuel cladding in the case of accidents involving loss of coolants. The departure frequency of vapor bubbles on a fixed heating wall is in the order of a few hertz. Interestingly, this is close to that for the natural frequency of a typical pressurized water reactor building (about 4–5 Hz). Therefore, if an earthquake with low frequencies occurs, it would cause the nuclear reactor to oscillate considerably. In this scenario, the fluid in the system would undergo an oscillating body force. This study presents numerical simulations of saturated film boiling on a horizontal surface under vertical oscillation.

NUMERICAL METHOD

Figure 1 shows the simulation domain under vertical oscillation with $\ddot{\mathbf{R}} = \ddot{R}\mathbf{j} = A(2\pi f)^2 \sin(2\pi ft)\mathbf{j}$. Simulations were performed at a near critical pressure.

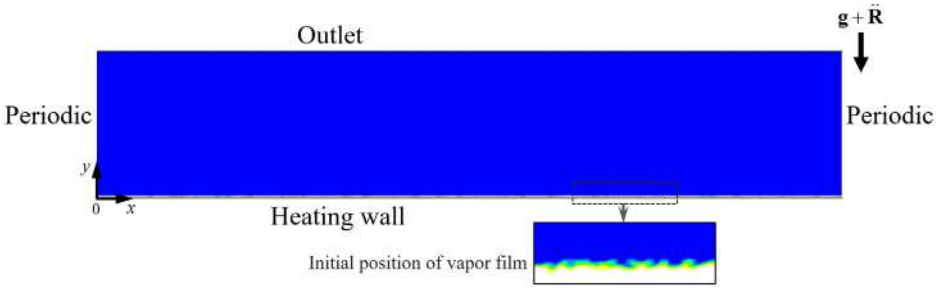

Figure 1. Simulation domain for multimode film boiling in a pool.

The CLSVOF method was used to perform simulations of incompressible two-phase flow with phase change. The mass, momentum, and energy equations are given by

$$\frac{\partial \alpha}{\partial t} + \nabla \cdot (\alpha \mathbf{u}) = \frac{\dot{m}}{\rho_v}, \tag{1}$$

$$\frac{\partial}{\partial t}(\rho \mathbf{u}) + \nabla \cdot (\rho \mathbf{u}\mathbf{u}) = -\nabla p + \nabla \cdot [\mu(\nabla \mathbf{u} + \nabla \mathbf{u}^T)] + \mathbf{F}_{st} + \rho(\mathbf{g} - \ddot{\mathbf{R}}), \tag{2}$$

$$\frac{\partial}{\partial t}(\rho h) + \nabla \cdot (\rho h \mathbf{u}) = \nabla \cdot (k \nabla T) - \dot{m} L, \tag{3}$$

where $\dot{m}$ is the vapor generation rate computed by Sun`s model [2]

$$\dot{m} = \frac{2k_v(\nabla \alpha \cdot \nabla T)}{L}. \tag{4}$$

RESULTS AND DISCUSSION

Figure 2(a) shows the effect of the oscillation frequency on the heat transfer. The oscillation amplitude is fixed at $A = 4$ mm. For low frequencies under 6 Hz, the heat transfer decreases with increasing oscillation frequency. This is caused by the interaction between the vapor bubble rise and the system oscillation. Figure 3 shows the successive snapshots of rising bubbles and the variation of the space-averaged Nusselt number with time. It is interesting to note that all vapor bubbles detach at nearly the same time (t=4.86 s). Different bubbles are separated from the vapor film at the instance when the effective gravity reaches the maximum value. A decrease in the heat transfer can be explained by Fig. 3. Compared to the stationary case, the decrease in low peaks are greater than the increase in high peaks. Moreover, the time period during which the heat transfer is maintained at low values is prolonged. Thus, the average heat transfer becomes lower than that for the stationary case. However, in the region with high frequencies (f>6.25 Hz), the average heat transfer increases with increasing frequency. This is attributed to the agitated liquid flow cased by the oscillation. The agitated liquid flow facilitates the detachment of vapor bubbles from the wall, which prevents the vapor layer from being thick.

Figure 2(b) shows the dominant frequency of the bubble detachment according to the oscillation intensity. The bubble departure frequency is not affected by the oscillation when the oscillation intensity is weak. However, the bubble departure frequency becomes nearly the same as the oscillation frequency when the oscillation intensity is strong.

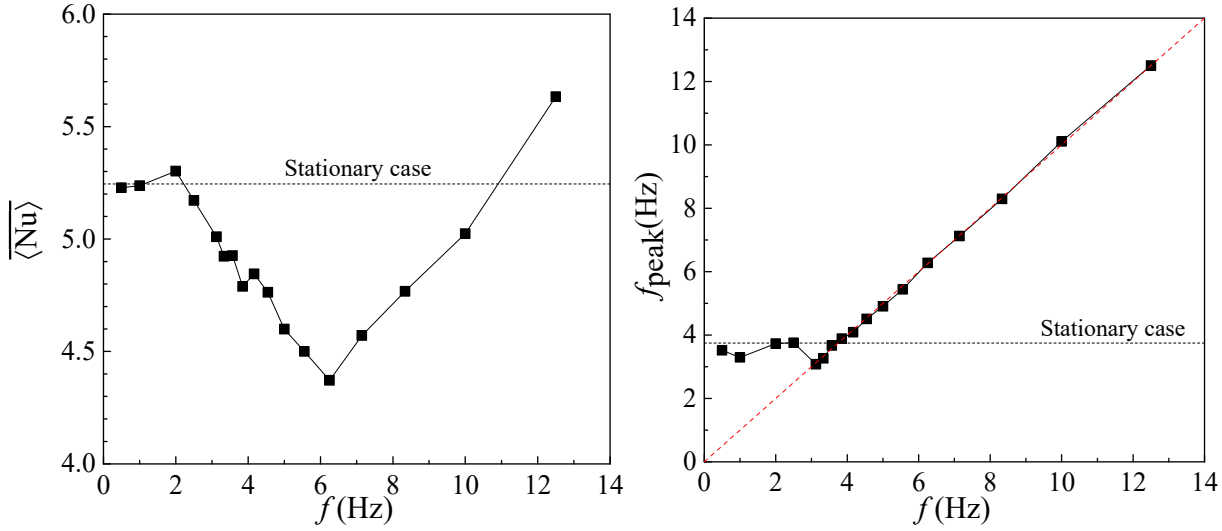

Figure 2. (a) Change in the average heat transfer according to the oscillation; (b) Dominant frequencies of heat transfer for oscillation frequencies.

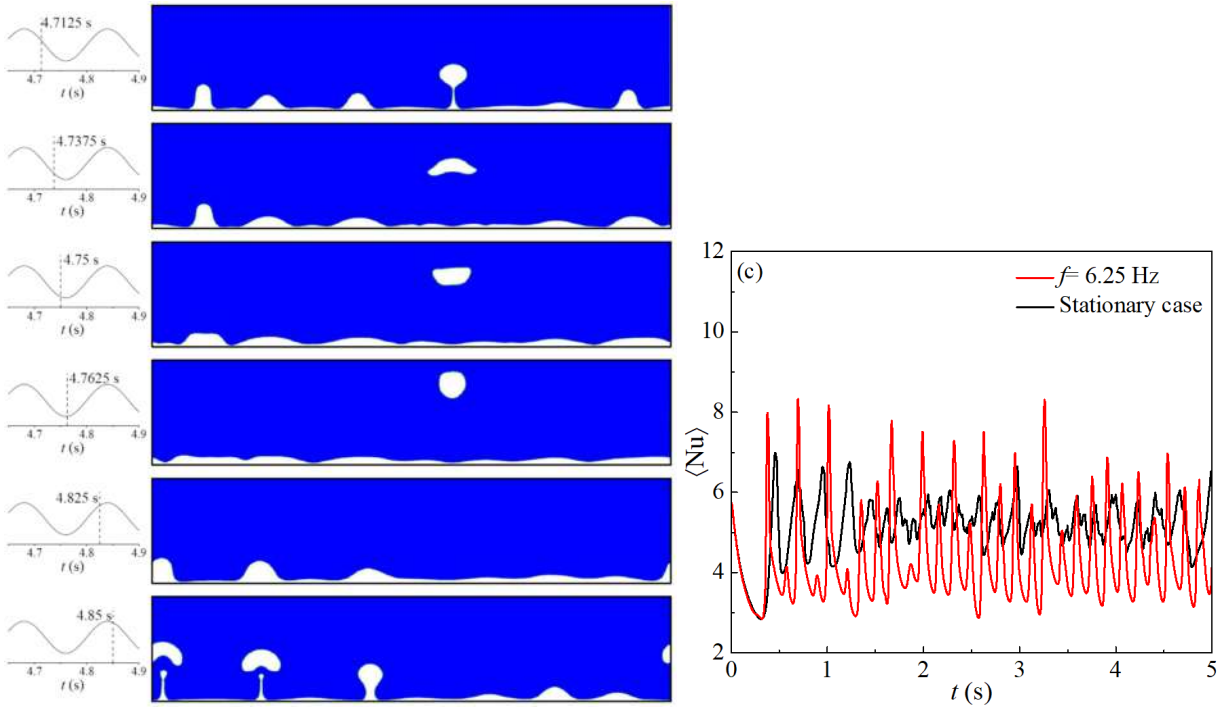

Figure 3. Result for the oscillation frequency of f=12.5 Hz: (a) Successive snapshots of rising bubbles at different time instances; (b) Variation of the space-averaged Nusselt number with time

CONCLUSIONS

The present multimode simulation showed that the system oscillation did not always increase heat transfer and that the oscillation did not alter the bubble departure frequency. From the results so far, there are the three regimes. In the first regime, as the oscillation frequency increases, the heat transfer decreases while the bubble departure frequency remains nearly the same. In the second regime, as the oscillation frequency increases, the heat transfer decreases and the bubble departure frequency becomes the same as the oscillation frequency. In the third regime, as the oscillation frequency increases, the heat transfer increases and the bubble departure frequency synchronizes with the oscillation frequency. This regime classification may not be general. Therefore, in the future, simulations and experiments at a low pressure will be conducted to confirm the heat transfer characteristics.

References

[1] D.-L. Sun, J.-L. Xu, L. Wang, Development of a vapor–liquid phase change model for volume-of-fluid method in FLUENT, Int Commun Heat Mass, 39(8) (2012) 1101-1106.

Acknowledgement

This work was supported by a National Research Foundation of Korea grant funded by the Ministry of Education (No. NRF-2020R1A2C1010460).

NUMERICAL STUDY ON THE DYNAMICS OF PERMANENT MAGNETIC PARTICLES SUSPENDED IN A CONFINED SHEAR FLOW

Tae Gon Kang *[1], Im Doo Jung[2], and Seong Jin Park [3]
[1] School of Aerospace and Mechanical Engineering, Korea Aerospace University, Goyang, Republic of Korea
[2] Korea Institute of Materials Science, Changwon, Republic of Korea
[2] Department of Mechanical Engineering, Pohang University of Science and Technology, Pohang, Republic of Korea

Summary A direct simulation method is developed to solve a particulate flow with permanent magnetic particles in an applied magnetic field. The method is based on the finite element method and a fictitious domain method, considering the magnetic and the hydrodynamic interactions among the particles. The circular (or spherical in three-dimension) particles are assumed to be magnetic particles with a constant magnetic moment and negligible susceptibility. The developed method is validated by comparting the particle motions in a shear flow with that from a particle dynamics method based on the Jeffrey model and extended forms of the Oseen-Burgers tensor. In a shear flow, the particle motion and the structure of the particles are highly influence by the ratio between the magnetic torque and the viscous torque and the ratio between the permanent magnetic moment and the strength of the applied field.

INTRODUCTION

Suspensions with permanent magnetic particles are used in a variety of applications. In magnetic powder injection molding to mass-produce small and precise magnetic components, for example, the prediction of the orientation of permanent magnetic particles during cavity filling stage is of great importance since the particle orientations govern the magnetic properties of final products [1]. In this process, particle orientation is determined by the combined effect of the viscous torque due to continuous shearing and the magnetic torque caused by the magnetic moment of the particles and the applied magnetic field. In this regard, we attempt to develop a direct simulation to solve particulate flows with permanent magnetic particles in the presence of an externally applied magnetic field. The developed method is applied to a confined shear flow to investigate the particle orientation and the formation of columnar structures, focusing on the influence of a dimensionless number, called the Mason number, on the particle motions and structure formation.

MODELING AND NUMERICAL METHODS

Since we are concerned with tiny permanent magnetic particles suspended in a highly viscous fluid, the effect of inertia can be neglected, thus the Stokes equation is solved. As for particle motions, a fictitious domain method is employed, enabling us to solve the same governing equation as that of fluid flow, which has been used to solve particulate flows with suspended paramagnetic particles [2]. The governing equations for the particulate flow are given by

$$\nabla \cdot \mathbf{u} = 0 \tag{1}$$

$$\nabla \cdot (\boldsymbol{\sigma} + \mathbf{T}_m) = \mathbf{0} \tag{2}$$

$$\boldsymbol{\sigma} = -p\mathbf{I} + 2\eta\mathbf{D} \tag{3}$$

$$\mathbf{T}_m = \mu(\mathbf{HH} - 1/2\, H^2\mathbf{I}) \tag{4}$$

where $\mathbf{u}$ is the velocity, $\boldsymbol{\sigma}$ the Cauchy stress, η the viscosity, $\mathbf{D}$ the rate-of-deformation tensor, $\mathbf{T}_m$ the Maxwell stress, μ the magnetic permeability, and $\mathbf{H}$ the magnetic field intensity. On the particle surfaces, no-slip condition is imposed as a constraint. The magnetic field in the entire domain is obtained by solving the Maxwell equations. In this study, the Maxwell equations are transformed into a governing equation for the magnetic potential ϕ, given by

$$\nabla \cdot (-\mu\nabla\phi + \mu_0\mathbf{M}) = 0 \tag{5}$$

where μ_0 is the permeability in vacuum and $\mathbf{M}$ the permanent magnetic moment in a particle domain.

The governing equations for the flow and magnetic problems are solved using the finite element method. The weak form for the flow problem is the same as that used to solve flows with suspended paramagnetic particles (See [2,3]). The weak form for the magnetic problem with magnetic particles with a permanent magnetic moment is represented by

$$\int_\Omega \mu\nabla\phi\cdot\nabla\psi\, d\Omega = \int_\Gamma \mu(\nabla\phi\cdot\mathbf{n})\, d\Gamma + \int_\Omega \mu_0\mathbf{M}\cdot\nabla\psi\, d\Omega\,, \tag{6}$$

*Corresponding author. E-mail: tgkang@kau.ac.kr

where ψ is the weighting function for the potential ϕ. The weak form (Eq. (6)), which is applied to magnetic particulate flows, is a new contribution of our study.

RESULTS

To validate the developed numerical method, we solved a single particle problem (See Fig. 1a). The rigid body motion of the particle is compared to that obtained from a particle dynamics method [4]. From Fig. 1b, one can find that both results agree with each other, but with a slight deviation. The difference is thought to be caused by the particle-wall interaction that is not taken into account in the particle dynamics method. Figure 2 shows particle motions in a confined shear flow, affected by the Mason number defined by $Mn = \eta\gamma/\mu_0 MH_0$ and $\lambda = M/H_0$. If Mn is large, the viscous effect is dominant over the magnetic effect. In addition, if λ is large, the magnetic interaction due to the magnetic moment is dominant rather than that due to the external field.

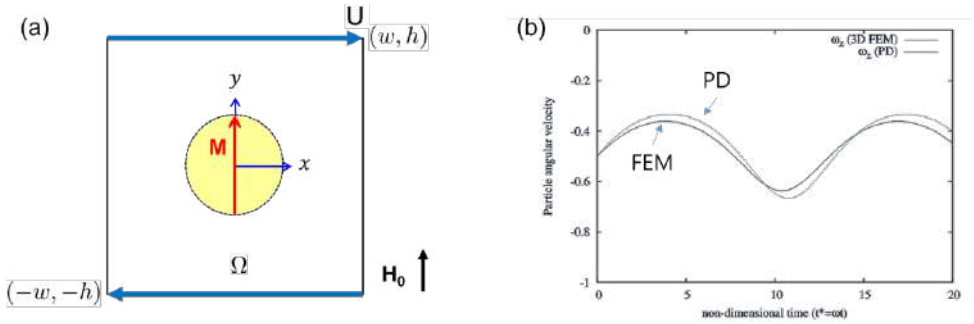

Figure 1. A single particle suspended in a shear flow in the presence of an externally applied field $\mathbf{H}_0$.

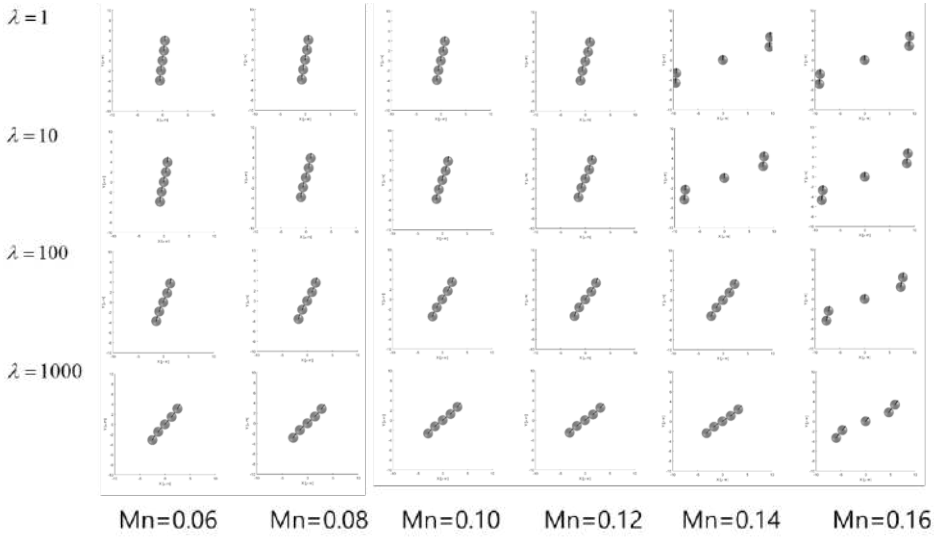

Figure 2. Particle dynamics in a shear flow affected by the Mason number (Mn) and λ.

CONCLUSIONS

We developed a direct numerical method to solve particulate flows with hard magnetic particles (with permanent magnetic moment) in the Stokes flow regime. The developed method is validated by comparing particle motions obtained from the method with those from a particle dynamics method. Particle motions in a confined shear flow are highly influenced by the Mason number and the value of λ.

References

[1] Murillo N., Gonzalez J., Guraya C. Gutierrez M. Structural and magnetic properties of sintered Sr-ferrites fabricated by powder injection molding J. Magn. Magn.Mater. **203**: 165–168, 1999.
[2] Kang T.G., Hulsen M.A., den Toonder J.M.J. Dynamics of magnetic chains in a shear flow under the influence of a uniform magnetic field. Phys. Fluids **24**: 042001, 2012.
[3] Kang T.G., Gao Y., Hulsen M.A., den Toonder J.M.J., Anderson P.D. Direct simulation of the dynamics of two spherical particles actuated magnetically in a viscous fluid, Computers & Fluids **86**: 569–581, 2013.
[4] Jung I.D., Kang T.G., Shin D.S. Park S.J. Modeling of magnetic particle orientation in magnetic powder injection molding. J. Phys. D: Appl. Phys. **51**: 115002, 2018.

PREDICTING RARE EVENTS IN STOCHASTIC RESONANCE

L. T. Giorgini * [1], S.H. Lim[1], W. Moon[1,2], and J.S. Wettlaufer[1,3]
[1] Nordita, Royal Institute of Technology and Stockholm University - Stockholm 106 91, Sweden
[2] Department of Mathematics, Stockholm University - Stockholm 106 91, Sweden
[3] Yale University - New Haven, Connecticut 06520, USA

Summary In stochastic resonance, a periodically forced Brownian particle in a double-well potential jumps between minima at rare increments, the prediction of which poses a major theoretical challenge. We used a path-integral method to find a precursor to these transitions by determining the most probable space-time path of a particle. We demonstrated the method numerically, which allows us to determine whether a state is following a stable periodic path or will experience an incipient jump. The vast range of systems that exhibit stochastic resonance behavior insures broad relevance of our framework, which allows one to extract precursor fluctuations from data.

Rare events, which frequently accompany fluctuations or phase transitions, arise in a wide range of natural and social systems, such as infectious disease outbreaks, earthquakes, stock market crashes, and many others e.g. [1]. Of particular interest are dynamical systems that have bifurcations, at which sudden transitions to distinct dynamical regimes occur [2]. Even before reaching a bifurcation, noise-induced transitions can occur with low probability [3]. In consequence, a system experiences a large-magnitude change resulting in significant positive and/or deleterious consequences. Hence, it is important to understand the mechanism leading to the occurrence of such events, and to quantify, predict and potentially control them.

The desire to predict these rare events in advance has fueled studies, to simulate [4], classify [5], analyze [6] and predict [7] their properties. Although the existence of early-warning signals for rare events has been suggested, there are few results determining reliable and robust indicators for noise-induced transitions [8]. Because most systems are inherently noisy, understanding the role of noise in inducing these transitions is critical for their quantitative prediction well in advance. We described a theory quantifying the role of noise in rare events, which underlies reliable forecast models.

We studied noise-induced transitions using a class of periodically forced low dimensional stochastic dynamical systems and we identified a novel early-warning indicator for the jumps from one stable state of the system to another. Periodically forced stochastic systems are ubiquitous in nature. For example, periodic forcing and background noise are the main ingredients of stochastic resonance [9] (see [10] for reviews), wherein the response to a weak signal is magnified by noise induced fluctuations that drive hopping from one stable state to the other in a double-well potential with two minima. Settings of relevance range from the human cardiovascular system [11] to the seasonal variability of the Earth's climate [12].

We have developed a theory to predict and study noise-induced rare events within the general framework of stochastic resonance. We have studied a periodically and noise forced system in a double-well potential that jumps between minima, but the time-scale separation of these forcings insures that the system oscillates for a long time about one of the local minima of the potential and only very rarely jumps to the other minima. The ubiquity of such transitions underlies the importance of trying to predict when they will occur.

We have used a path-integral method to determine the particular manner in which the fluctuations around the unperturbed deterministic flow must organize prior to the system jump (see Fig. 1). We characterized the optimal path using a direct comparison principle between the Langevin and Hamiltonian dynamical descriptions, allowing us to express the jump condition in terms of the accumulation of noise around the stable periodic path. In consequence, as a system approaches a rare event these fluctuations approach one of the deterministic minimizers, thereby providing a precursor for predicting a stochastic transition. We have harnessed the signature of this fluctuation behavior as an advanced indicator of a jump and have computed the probability of such rare events. The method provides a framework to examine data in a manner that facilitates predictions across a broad spectrum of stochastic systems.

For more details see [13].

References

[1] M. Ghil, P. Yiou, S. Hallegatte, B. Malamud, P. Naveau, A. Soloviev, P. Friederichs, V. Keilis- Borok, D. Kondrashov, V. Kossobokov, *et al.*. *Nonlinear Processes in Geophysics* **18**, 295 (2011).
[2] M. Scheffer, J. Bascompte, W. A. Brock, V. Brovkin, S. R. Carpenter, V. Dakos, H. Held, E. H. Van Nes, M. Rietkerk, and G. Sugihara, Nature **461**, 53 (2009).
[3] P. Hänggi, P. Talkner, and M. Borkovec, Reviews of Modern Physics **62**, 251 (1990).
[4] T. Grafke and E. Vanden-Eijnden, Chaos: An Inter- disciplinary Journal of Nonlinear Science **29**, 063118 (2019).
[5] P. Ashwin, S. Wieczorek, R. Vitolo, and P. Cox, Philosophical Transactions of the Royal Society A: Mathematical, Physical and Engineering Sciences **370**, 1166 (2012).

*Corresponding author. E-mail: ludovico.giorgini@su.se

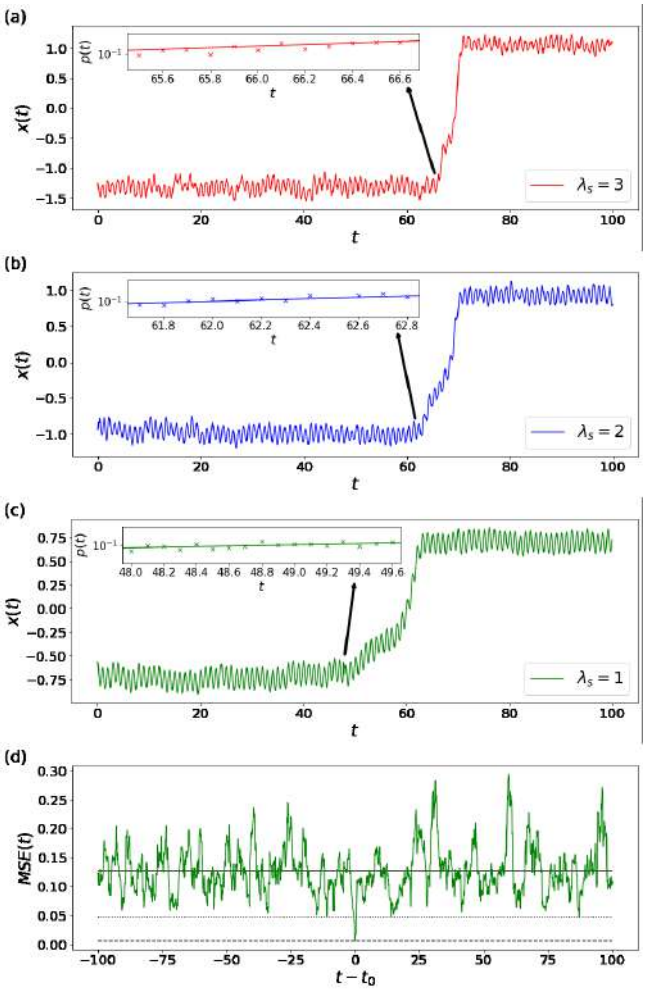

Figure 1: (a)-(c) Numerical simulations of the time evolution $x(t)$ of the system inside three different double well potentials associated with different values of the Lyapunov exponent λ_s in correspondence of a transition. On the top of each plot are reported the realization of the noise $p(t)$ immediately prior to the jump (along with the analytical prediction). (d) The mean standard error (MSE) of the noise realizations with respect to the analytical prediction, using the data from the simulation shown in (c) displayed over a larger time window. The solid line is the average MSE, the dashed line is the MSE corresponding to the values of $p(t)$ in the time window highlighted in the top left of (c) and the dotted line is the minimum value reached by the MSE if these values of $p(t)$ are removed.

[6] F. Romano and C. Kuehn, International Journal of Bifurcation and Chaos **28**, 1850103 (2018).
[7] C. Kuehn, G. Malavolta, and M. Rasmussen, Journal of Mathematical Analysis and Applications **464**, 58 (2018).
[8] Y. Chen, J. A. Gemmer, M. Silber, and A. Volken- ing, Chaos: An Interdisciplinary Journal of Nonlinear Science **29**, 043119 (2019).
[9] R. Benzi, A. Sutera, and A. Vulpiani, Journal of Physics A: Mathematical and General **14**, L453 (1981).
[10] L. Gammaitoni, P. Hänggi, P. Jung, and F. March- esoni, Reviews of Modern Physics **70**, 223 (1998).
[11] A. Stefanovska, Contemporary Physics **40**, 31 (1999).
[12] W. Moon and J. S. Wettlaufer, Scientific Reports **7**, 44228 (2017).
[13] L.T. Giorgini, S.H. Lim, W. Moon, J.H. Wettlaufer, arXiv preprint arXiv:1906.10469, (2019).

MULTIFRACTAL ANALYSIS OF GAS BUBBLE TRAJECTORIES

Jakub Augustyniak[1], Dariusz M. Perkowski[1], and Romuald Mosdorf [1]
[1] Department of Mechanics and Applied Computer Science, Faculty of Mechanical Engineering, Bialystok University of Technology, Bialystok, Poland

Summary The trajectories of gas bubbles movement generated from nozzles with an inner diameter of 1 mm, 0.38 mm, 0.34 mm and 0.32 mm respectively, and for two liquid column heights: 450 mm and 800 mm were studied. The tests were carried out for an air volume flow rate, whose value ranged from 0.00492 l / min to 0.0645 l / min. This range depended on the diameter of the nozzle and the height of the liquid column (from the periodic detachment of bubbles until the phenomenon of coalescence was observed). The results were recorded using a high speed camera, PHANTOM v1610. An image processing and analysis algorithm was developed, which using tools such as blur filters, edge filters, thresholding, identification, tracking, etc., allowed three-dimensional reconstruction of the movement trajectory of individual bubbles moving inside the bubble column. The work analyzed three-dimensional trajectories of gas bubble motion generated in a liquid filled tank with the help of multifractal analysis algorithm trying to determine the impact of changing the diameter of nozzles generating bubbles and the air delivered to the nozzle on the flow of gas bubbles in the bubble column.

INTRODUCTION

In many industrial processes such as aeration, fermentation, homogenization etc. used in the pharmaceutical, chemical, petrochemical and metallurgical industries, the knowledge of the dynamics of movement of gas bubbles in a liquid is of key importance. The efficiency of such processes depends to a large extent on many factors such as the size of the bubble (closely related to the size of the nozzle) [1-2], the frequency of subsequent departing bubbles (the effect of airflow), bubble residence time in liquid, and others: example of liquid or gas properties. In order to analyze the flow of gas bubbles in a liquid and considering all aspects affecting the nature of the process, a multifractal analysis method was developed. It is able to capture all aspects of a heterogeneous system as subsets of basic elements [3].

EXPERIMENTAL SETUP

The analysis of the trajectory of gas bubbles in liquid was carried out in two glass tanks of 300x300x1500 mm and 300x150x500 mm, respectively, filled with distilled water with a temperature equal to $T = 21 \pm 1$ ° C. Experimental tests were carried out for two liquid column heights: 450 mm and 800 mm (the construction scheme of the experimental setup is shown in Fig. 1). At the bottom of the tank, in the center of the base, a brass nozzle (No. 6, see Fig. 1) with a height of 50 mm was placed. The tests were carried out for four nozzles whose internal diameters had respectively: 1 ± 0.001 mm, 0.38 ± 0.001 mm, 0.34 ± 0.001 mm, 0.32 ± 0.001 mm. Internal diameter measurements were made on a Phenom XL scanning electron microscope.

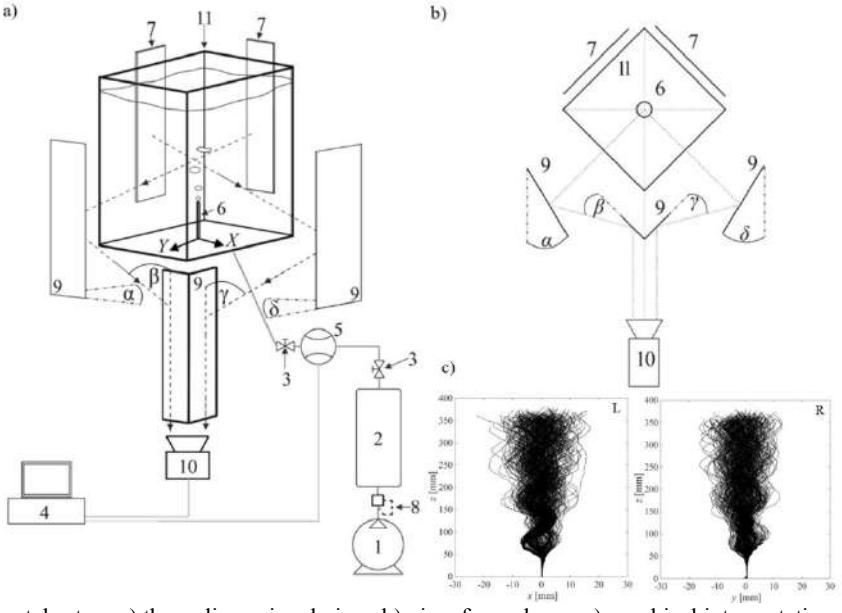

Figure 1. Experimental setup: a) three-dimensional view; b) view from above; c) graphical interpretations of bubble trajectories in both views (left-L and right-R): 1 - compressor, 2 - air tank, 3 - valves, 4 - computer, 5 - mass flow meter, 6 - brass nozzle, 7 - led panels, 8 - proportional valve, 9 - mirror system, 10 - camera, 11 - glass tank, α and δ - mirror angles, β and γ - the angle of incidence of the image reflected from the mirrors.

*Corresponding author. E-mail: j.augustyniak@pb.edu.pl.

NON-LINEAR ANALYSIS OF GAS BUBBLE TRAJECTORIES

The nature of the gas bubble path generated in the liquid, and thus its shape, depends on many factors (nozzle size, air flow, medium in which the bubble is generated, etc.). Therefore, a multifractal analysis algorithm (WTMM-Wavelet Transform Modulus Maxima method) that would be able to capture all aspects of the heterogeneous system as subsets of basic elements was introduced [4]. Authors believed that it would allow to determine and compare the degree of complexity of the system based on the range (band) of characteristic exponents in the statistical distribution. The extent of exponent changes is a measure of the complexity of the process being investigated [5]. The results of multifractal analysis are presented as a multifractal spectrum that describes the dimension of a fractal subset of function points. Figure 2 shows a typical multifractal spectrum calculated for a single time series. Analyzed time series were incremental measurements therefore they are without a trend. Such signals are easier to analyze due to the lack of accumulation of error.

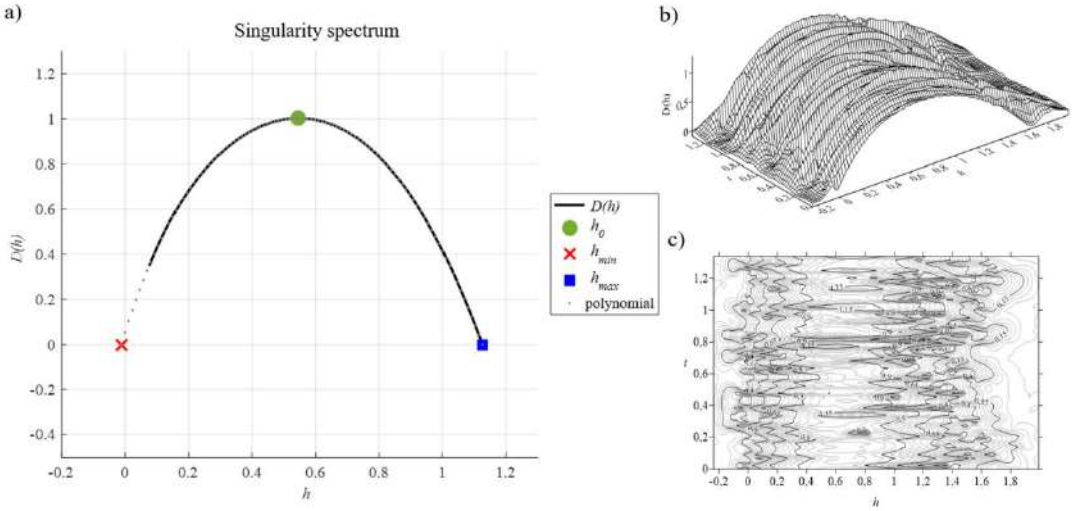

Figure 2. Multifractal spectrum: a) for a single time series for air volume flow rate q = 0.0228 l / min, nozzle inner diameter 0,38 mm and liquid column height 800 mm, b) surface created on the basis of curves characterizing multifractal spectra, c) corresponding contour view (t is a parameterless variable).

Points marked with a x characterize the process of small scale oscillations - h_{min}, where squares define large scale fluctuations of lateral bubble displacement - h_{max}. The highest point of the spectrum (marked with a circle) determines the sum of the small and large fluctuations of the bubble – h_0 (it identifies the entire process). The value of this point (local Hölder exponent) may be associated with the Hurst exponent.

CONCLUSIONS

The authors conducted a series of experiments on three-dimensional reconstruction of gas bubble trajectories with the help of a proprietary computer program. The experiments were carried out for different tank sizes, nozzle inner diameters, liquid height and air volume flow rates. The proposed method allowed to determine and compare the degree of complexity of the system on the basis of the range of occurrence of characteristic exponents in the statistical distribution, where the extent of exponent changes is a measure of the complexity of the examined process. As part of the analysis of recorded data it was established: that the dynamics of motion of gas bubbles moving in a vertical column are significantly influenced by three characteristic values: small-scale high-frequency oscillations (bubble surface deformations), large-scale low-frequency oscillations (deflection of the bubble column from the vertical axis) and Hurst exponent testifying to the behavior of self-similar bubbles; the degree of complexity of the nature of multifractal two-phase flow directly affects the predictability of individual bubble paths [6].

References

[1] Ziegenhein T., Lucas D., Observations on bubble shapes in bubble columns under different flow conditions, *Exp. Therm. Fluid Sci*., **85**, 248-256, 2017.
[2] Tomiyama A., Celata G. P., Hosokawa S., and Yoshida S., Terminal velocity of single bubbles in surface tension force dominant regime, *Int. J. Multiph. Flow*, 28,1497-1519, 2002.
[3] Mosdorf, R. Wyszkowski, T. Dąbrowski, K., Multifractal properties of large bubble paths in a single bubble column, *Archives of Thermodynamics*, **32**, 3-20, 2011.
[4] Goldberger AL, Amaral LAN, Glass L, Hausdorff JM, Ivanov PCh, Mark RG, Mietus JE, Moody GB, Peng C-K, Stanley HE. PhysioBank, PhysioToolkit, and PhysioNet: Components of a New Research Resource for Complex Physiologic Signals. Circulation **101**, 215-220, 2000.
[5] Muzy J. F., Barcy E., Arneodo A., Wavelets and multifractal formalism for singular signals: Application to turbulence data, *Phys. Rev. Lett*, **67**, 3515-3518, 1991.
[6] Augustyniak J., Perkowskie D. M., Mosdorf R., Measurement of properties of chaotic bubble paths, Int. J. Heat Mass Tran., **85**, 732-739, 2015.

FLUID PLACEMENT IN A CLOSED END PIPE WITH APPLICATIONS IN PLUG AND ABANDONMENT OF OIL AND GAS WELLS

Soheil Akbari and Seyed Mohammad Taghavi
Department of Chemical Engineering, Université Laval, Québec, QC Canada G1V 0A6

Summary The plug and abandonment (P&A) of oil and gas wells is an operation to prevent the migration of the reservoir fluids and the contamination of fresh water resources. The dumping method in the P&A operations is conducted using the placement of a heavy cement plug to replace a light in-situ fluid. In this study, we consider this method and investigate experimentally the placement of a heavy fluid to displace a light fluid, in a closed-end pipe. Both fluids are Newtonian and they have the same viscosity. The heavy fluid is imposed continuously. The experiments present five flow stages: initial jet, mixing region, slumping flow, reaching the pipe end, and turning back of the flow toward the mixing region. Considering the placement flows at different density differences, we find that by increasing the density difference, the penetration front velocity in the slumping flow stage increases.

INTRODUCTION

All oil and gas wells at some point in time must go through the plug and abandonment (P&A) processes. These processes are performed to avoid the contamination of the environment outside the well (atmosphere and water aquifers), which may happen through the leakage of reservoir fluids out the well. The wells are plugged using the cement plugs in the wellbore at specific intervals using several techniques such as the dump bailing method [1]. In this method, the cement slurry is lowered down in a well by a bailer, and the slurry is then placed on a mechanical bridge plug, as illustrated in **??**.a. During this process, the cement slurry displaces the in-situ drilling fluid in the well, ideally with minimum mixing.

The dominant fluid dynamic phenomenon in the P&A operations is the placement (or displacement) flow of two miscible fluids in the wells. In these operations, an extensive range of fluids is used, in which high density differences (up to 600 kg/m^3), and shear-thinning and yield stress rheological behavior are usually found. In order to increase the quality of the cement plug placement, it is necessary to study the key parameters of the displacement of the cement slurry and the drilling fluid. Several parameters can influence the displacement flow behavior, including the type of fluids (Newtonian or non-Newtonian fluids), the physical properties of the fluids (density and viscosity), the type of the flow geometry (pipe, annulus or channel), and the operational conditions (flow velocity and geometry inclination). Based on the aforementioned parameters involved, various kinds of displacement and mixing flows can occur, including stable and unstable flows in exchange or imposed flow configurations. Furthermore, the competition between the governing forces, such as inertia, buoyancy and viscosity, leads to the formation of different flow regimes (e.g. inertial, viscous, etc.).

The density difference produces a buoyancy force. Based on the previous experimental findings [2,3], it is expected that, when the flows are buoyant, the density difference acts to segregate the heavy and light fluids, towards the lower and upper pipe walls. The density difference is represented by the Atwood number ($At = \frac{\hat{\rho}_H - \hat{\rho}_L}{\hat{\rho}_H + \hat{\rho}_L}$) as a dimensionless number, where $\hat{\rho}_H$ and $\hat{\rho}_L$ are the densities of the heavy and light fluids, respectively. The density difference affects the buoyancy force significantly through the densimetric Froude number ($Fr = \frac{\hat{V}_0}{\sqrt{At\hat{g}\hat{D}}}$); here, $\hat{V}_0$, $\hat{g}$, and $\hat{D}$ are the mean imposed velocity, the gravitational acceleration and the hydraulic diameter, respectively. Also, another important parameter is the Reynolds number, $Re = \frac{\hat{V}_0\hat{D}}{\hat{v}}$, where $\hat{v}$ is the kinematic viscosity, defined using the mean density ($\bar{\hat{\rho}} = \frac{\hat{\rho}_H + \hat{\rho}_L}{2}$) and the common viscosity ($\hat{\mu}$) of the two fluids.

In this study, we experimentally consider the placement of a fluid injected into a closed-end pipe (through an inlet), which is representative of the flow domain in the dump bailing method; see **??**b; from a fluid mechanics point of view, this configuration has not been studied in the literature. The two fluids are Newtonian and miscible, and they have the same viscosity. We describe the placement behavior of a heavy fluid used to displace and remove a light fluid from the flow domain. We also investigate the impacts of the geometry inclination and buoyancy in this flow system.

DESCRIPTION OF THE EXPERIMENT

The experiments were conducted in a physical model made of two transparent pipes, representing the dump bailing method. The displacing (heavy) fluid was a solution of water and salt, and the displaced (light) fluid was pure water; both were Newtonian and miscible. For visualization purposes, a specific amount of ink (Fountain Pen India black ink) was added to the heavy fluid. In each experimental test, the outer pipe was initially filled with the lighter fluid. Then, the heavier fluid was injected into the pipe through the inner pipe to displace the lighter fluid. The displacing fluid was fed into the pipe by gravity from an elevated tank, to avoid some unwanted effects, such as flow disturbances. The domain of the study in the experiments, shown in **??**.b, was captured during the experiments using a camera (Basler acA2040, with 4096 grey scale levels). The recorded images were processed by ImageJ and MATLAB to analyze quantitatively the flow parameters, such as the penetration front velocity ($\hat{V}_f$) of the heavy fluid into the light fluid.

*Corresponding author. E-mail: Seyed-Mohammad.Taghavi@gch.ulaval.ca.

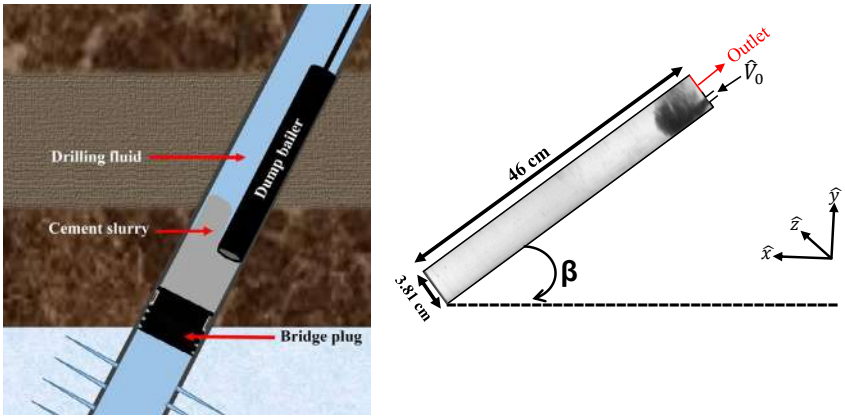

Figure 1: (a) Schematic of the dump bailing method in the P&A process. The bailer contains the cement slurry and it releases the slurry on a bridge plug, which marks the flow domain end. Then, the cement slurry displaces the in-situ drilling fluid in the well. The shape of the fluids interface is illustrative; (b) Schematic view of the domain and parameters in this study.

RESULTS AND DISCUSSIONS

We have observed in our experiments five distinct flow stages. First, the heavy fluid enters the flow domain as a jet, and then a mixing region is developed. After that, the fluid slumps under the light fluid, on the lower wall of the pipe, and moves toward the end of the pipe. The fourth stage is when the fluid front reaches the end of the pipe, and the last stage is turning back of the flow front toward the mixing region. **??**a shows the experimental snapshots of each flow stage. We have attempted to distinguish between these stages and also describe the flow behavior of each stage using dimensionless parameters. As an example, **??**b illustrates the penetration front velocity of the displacing fluid along the length of the pipe (x). This figure shows the front velocity from the beginning of the flow until reaching the pipe end. For $0 < x < 2$, the jet and mixing regions develop, and then the front velocity roughly approaches a constant value for $x > 2$, although this constant limit slightly increases for the higher inclination (β=45°). The figure also depicts that, by increasing Re/Fr (or decreasing the inclination from horizontal), the front velocity in the slumping region increases as well.

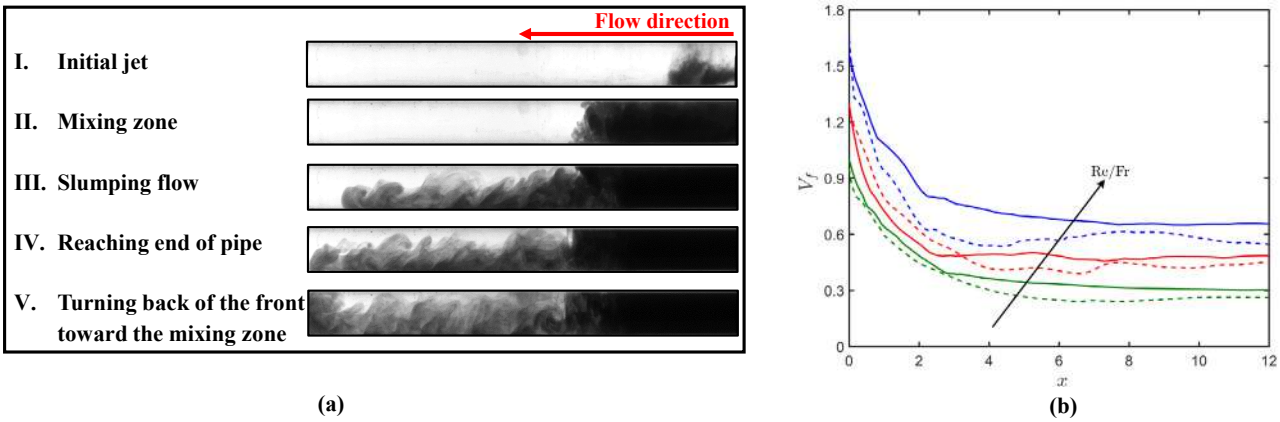

Figure 2: (a) Experimental snapshots of different flow stages observed in our experiments, (b) Dimensionless front velocity ($\hat{V}_f/\hat{V}_0$) of the heavy fluid along the length of the pipe (x= $\hat{x}$ / $\hat{D}$) from beginning of the flow till reaching the pipe end. Different line colors represent Re/Fr=736 (green), Re/Fr=1652 (red) and Re/Fr=2348 (blue). The solid lines are for β=15° and the dashed lines are for β=45°. $Re \approx 8400$ for all experiments. The solid arrow shows the increasing of Re/Fr as an eye guide.

These findings can help us to propose strategies for enhancing the placement efficiency and reducing the fluids mixing in the P&A processes. In the future, we will consider more deeply each stage of the flow and will quantify the impacts of the other hydrodynamic parameters, such as non-Newtonian fluid behavior, on this type of fluid placement.

References

[1] Nelson E. B. Well cementing. Newnes, Vol. 28, 1990.
[2] Taghavi S. M., Seon T., Wielage-Burchard K., Martinez D. M. and Frigaard I. A. Stationary residual layers in buoyant Newtonian displacement flows. *Phys. Fluids*, **23(4)**, p.044105, 2011.
[3] Seon T., Hulin J. P., Salin D., Perrin B. and Hinch E. J. Buoyant mixing of miscible fluids in tilted tubes. *Phys. Fluids*, **16(12)**. 103-106, 2004.

VELOCITY FIELD CHARACTERIZATION OF SINGLE AND TWO-PHASE FLOWS ACROSS TUBE BUNDLES BASED ON SPATIAL FILTER VELOCIMETRY TECHNIQUE

Douglas Martins Rocha*[1], Fabio Toshio Kanizawa[2], Kosuke Hayashi[3], Shigeo Hosokawa[4], Akio Tomiyama[3], and Gherhardt Ribatski[1]
[1]Heat Transfer Research Group, Department of Mechanical Engineering, São Carlos School of Engineering, University of São Paulo, São Carlos, SP, Brazil
[2]Department of Mechanical Engineering, School of Engineering, Universidade Federal Fluminense, RJ, Brazil
[3]Graduate School of Engineering, Kobe University, Kobe, Japan
[4]Faculty of Societal Safety Science, Kansai University, Osaka, Japan

Summary This paper presents experimental velocity fields obtained through Spatial Filter Velocimetry during single and two-phase flows across tube bundles. Experiments were performed in a test section made of acrylic with 20 rows of 4 tubes of 20mm O.D. mounted in a normal triangular configuration and transverse pitch per diameter ratio of 1.25. Results were obtained for liquid Reynolds numbers of 3909 and 10000, and gas Reynolds number of 77.7. The results indicate that the SFV technique provides accurate velocity data and is suitable to be applied in tube bundles, especially for two-phase flows. Moreover, the gas injection considerably increased the local mean velocities, which indicates significant differences between the flow structure of single and two-phase flows across tube bundles. Finally, the effects of the gas injection were more pronounced for the flow with reduced flow rate.

INTRODUCTION

The flow field characterization of external flows across tube bundles has significant importance for heat exchangers design. However, there are fewer studies concerning the flow field characterization of external flows across tube bundles [1], especially during two-phase flows [2]. The geometry of tube bundles precludes the use of probes close to the region of interest. Moreover, the passage of bubbles during two-phase flows and the high seeding particle concentration of PIV deteriorates the flow visibility, which hinders the application of optical velocimetry techniques. Therefore, the use of optical velocimetry techniques that provide high flow visibility, such as SFV [3, 4, 5], became a promising alternative for the flow field characterization of tube bundles.

Rocha et al. [4, 5] employed the SFV technique for the analysis of the flow field of external flows across tube bundles and obtained sufficient spatial and temporal resolution to characterize the flow turbulence and to extract pressure information from the velocity field. The results of Rocha et al. [4, 5] indicate that the SFV is a suitable technique to be applied in tube bundles.

In this context, the present study concern the flow field characterization of upward external flows across tube bundles. The experiments were conducted during single ($Re_l = 3900$; $Re_l = 10000$) and two-phase flows ($Re_l = 3900$ and $Re_g = 77.7$; $Re_l = 10000$ and $Re_g = 77.7$) to analyze the effects of the gas injection in the velocity profile. Moreover, the turbulent behavior of single and two-phase flows was analyzed.

EXPERIMENTAL PROCEDURE AND DATA ANALYSIS

The experimental apparatus designed and built at EESC-USP (São Carlos School of Engineering at the University of São Paulo) is schematically depicted in Figure 1.

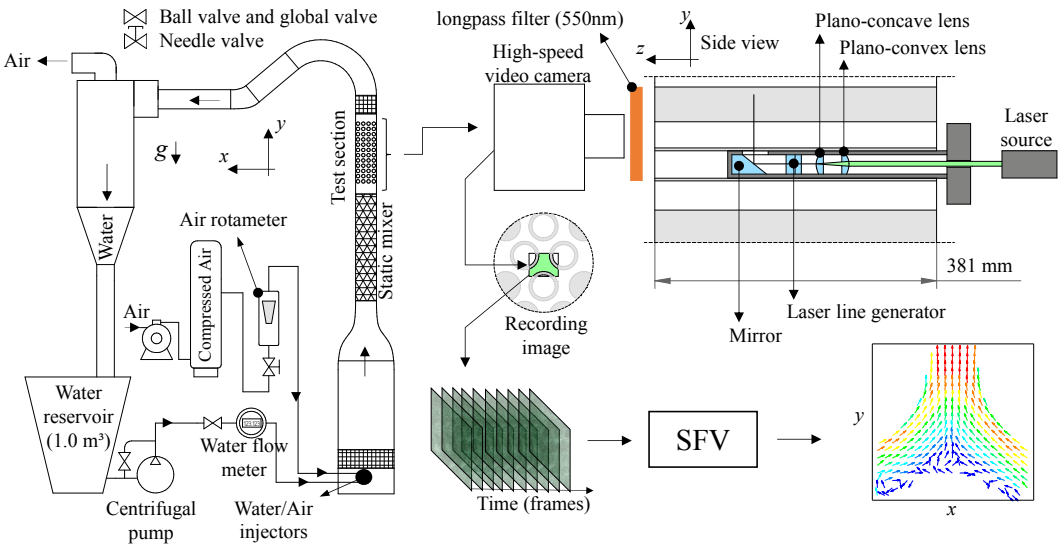

Figure 1: Experimental apparatus and data analysis for the SFV technique application.

*Corresponding author. E-mail: douglas.rocha@usp.br.

During the experiments, water was propelled by a centrifugal pump from the reservoir; then it was directed to the volumetric flow meter. The phases were injected in the bottom of the test section setup and upstream of a static mixer to promote uniform flow and distribution of the phases in the test section inlet. The test section was composed of 20 rows of 4 tubes 381 mm long, each with 20 mm O.D. mounted with a transverse pitch of 25 mm, corresponding to a pitch to diameter ratio of 1.25, in a triangular configuration. Half rods of acrylic were fixed in the lateral of even rows to avoid bypass flow through the laterals. The test section was made of acrylic providing full visual access to the flow within the tube bundle. As illustrated in Figure 1, the optical system used for the SFV application comprised a high-speed video camera (Phantom V2012), a laser source (1W, 520nm), and a setup of mirror and lenses to create a laser sheet perpendicular to the tube axis. In the case of two-phase flow experiments, fluorescent particles, and a longpass filter (cut-off wavelength: 550nm) were used to remove the light reflected on the phases interfaces from the captured images.

RESULTS AND DISCUSSION

Figure 2 shows the averaged velocity profiles obtained for single and two-phase flows with Re_l equal to 3900 and 10000. The gas injection considerably increased the averaged liquid velocities for Re_l equal to 3900. The highest velocity of the velocity field during two-phase flow is approximately 67% higher than the highest velocity of the velocity profile obtained during single-phase flow for the same liquid flow rate. For Re_l equal to 10000, the gas injection increased 35.1 % the highest local velocity obtained during single-phase flow. Therefore, the effects of the gas injection are less pronounced for the highest liquid Reynolds number because of the prevalence of inertial forces of the liquid phase. Moreover, as shown in Figure 2, the gas injection also changed the flow structure by suppressing recirculation regions. The buoyancy effects of the gas phase provided energy to the flow, which balanced the energy dissipation near the tube surface and suppressed the flow separation. Only the bubbly flow pattern was covered during the two-phase flows experiments.

Further investigation concerning the flow turbulence characterization and the velocity behavior along the time was accessed since SFV provides also the velocity variation along the time. The results indicate that the flow separation affected the turbulence strength and the turbulent shear stress. The maximum turbulent shear stress for single-phase flows occurred near the recirculation regions and reached values two times higher than the viscous shear stresses. The maximum turbulence strength in the flow direction occurred near the recirculation regions. The maximum turbulence strength transversal to the flow direction presented the same magnitude than the values observed for the main flow direction, which indicates a high flow mixing [1]. The gas injection increased the turbulence strength in the entire flow field for the two-phase flows experiments, but more effectively for the lowest liquid flow rate.

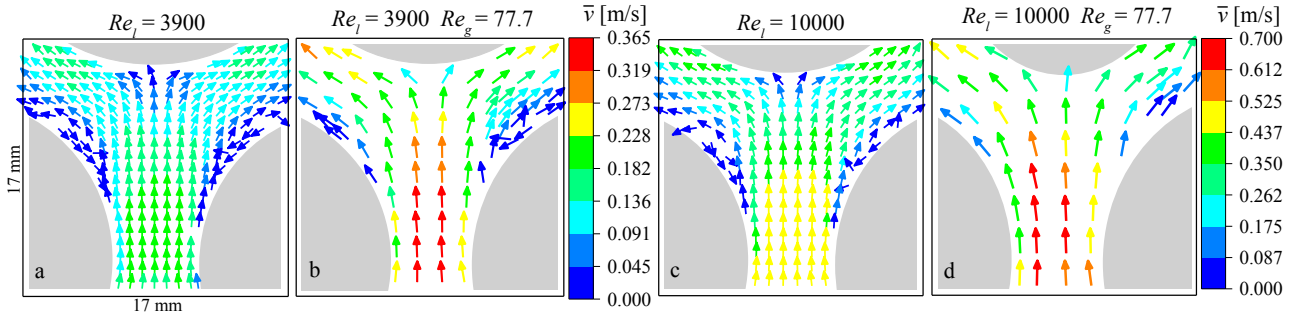

Figure 2: Experimental velocity field along the liquid phase for single (a and c) and two-phase flows (b and d).

CONCLUSIONS

The SFV technique proved to be efficient and reliable for experiments with difficult visual access, such as two-phase flows across tube bundles. The gas injection considerably increased the flow velocity, which indicates significant differences between the flow structure of single and two-phase flows across tube bundles. The passage of bubbles hindered the starting of the flow separation and increased the turbulence strength. Moreover, the effects of the gas injection were more pronounced for the flow with reduced liquid Reynolds number. The flow with the highest liquid Reynolds number possesses a higher inertial force, which mitigates the perturbation caused by the bubbles passage.

References

[1] Iwaki, C., Cheong, K.H., Monji, H. and Matsui, G. PIV measurement of the vertical cross-flow structure over tube bundles. *Experiments in Fluids*, 37(3), pp.350-363, 2004.

[2] Iwaki, C., Cheong, K.H., Monji, H. and Matsui, G. Vertical, bubbly, cross-flow characteristics over tube bundles. *Experiments in Fluids*, 39(6), p.1024, 2005.

[3] Hosokawa, S., Tomiyama, A. Spatial filter velocimetry based on time-series particle images. *Experiments in fluids*, 52(6), pp.1361-1372, 2012.

[4] Rocha, D.M., Kanizawa, F.T., Hayashi, K., Hosokawa, S., Tomiyama, A., Ribatski, G. Pressure and shear stress analysis in a normal triangular tube bundle based on experimental flow velocity field. *Journal of the Brazilian Society of Mechanical Sciences and Engineering*, 42(4),2020.

[5] Rocha, D.M., Kanizawa, F.T., Hayashi, K., Hosokawa, S., Tomiyama, A., Ribatski, G. Characterization of the Velocity Field External to a Tube Bundle Using Spatial Filter Velocimetry Based on Variable Meshing Scheme. *Flow, Turbulence and Combustion*, pp.1-25, 2020.

REDUCING UNCERTAINTY IN VELOCITY FIELD RESULTS FROM POSITRON EMISSION PARTICLE TRACKING (PEPT) MEASUREMENTS

Avshalom Offner and Jacques Vanneste *
School of Mathematics, The University of Edinburgh, Edinburgh, United Kingdom

Summary Positron Emission Particle Trackiing (PEPT) is an experimental method for visualisation of opaque fluid flow. PEPT produces time-dependent data of particle position, from which the Lagrangian velocity field is easily calculated. Here, we capitalise on the flow incompressibility to infer a divergence-free velocity field that automatically satisfies the system boundary conditions. The results demonstrate how inconsistencies in the original field are corrected, resulting in a smoother, more reliable velocity field.

INTRODUCTION

An abundance of natural and man-made phenomena involve multiphase fluid flows. Key examples include dispersion of pollutants in our atmosphere and mixing of colloids in pharmaceutical manufacturing lines, respectively. The interaction between the phases and the flow tendency to swiftly become turbulent are inherent features that overly complicate the modelling of these flows, and limit our understanding of the underlying physics that drives them. Consequently, studying such flows heavily relies on experimental research, where standard visualisation methods (e.g. PIV or PTV) are typically used to recover the velocity field of the suspended matter. However, in case either the fluid or the environment through which it flows are opaque, optical equipment cannot be used to visualise the flow. We use an alternative technique – Positron Emission Particle Trackiing (PEPT) [1, 2] – that allows for visualisation of opaque fluids or flows inside opaque equipment. In this method, particles are coated with radioactive material, resulting in back-to back photon emissions from positron-electron annihilation events. When flowing in the vicinity of a CT-scanner-like machine, photons annihilated by these particles are detected by array sensors, from which the particle time-dependent position can be recovered.

UNCERTAINTY QUANTIFICATION

As any visualisation method, the particle position recorded using PEPT bares uncertainties. However, as opposed to PIV or PTV where the sampling rate is constant and known a priori, annihilation events are inherently random, making the error in velocity calculations through finite differences difficult to estimate. Moreover, the parameters directly affecting the measurement accuracy are much harder to control, when compared with optical methods (see table 1 for a comparative summary). Inferring a reliable velocity field from data obtained using PEPT is therefore challenging; we wish to make use of the flow incompressibility to calculate a divergence-free velocity field that is the closest possible to the observed data.

Let $\underline{v} = \{v_r, v_\theta, v_z\}$ be the observed velocity field, for which

$$\underline{\nabla} \cdot \underline{v} \equiv \frac{1}{r}\frac{\partial}{\partial r}(r v_r) + \frac{1}{r}\frac{\partial v_\theta}{\partial \theta} + \frac{\partial v_z}{\partial z} \neq 0. \tag{1}$$

Averaging over θ, we define

$$\widehat{\underline{v}}\,(r,z) := \frac{1}{2\pi}\int \underline{v}\,\mathrm{d}\theta \tag{2}$$

and seek a divergence-free velocity field of the form

$$\widehat{\underline{V}} = \widehat{\underline{v}} + \underline{\nabla}\phi, \tag{3}$$

which satisfies

$$\widehat{\underline{V}} = \underset{\underline{u}:\,\underline{\nabla}\cdot\underline{u}=0}{\operatorname{argmin}} \left\|\widehat{\underline{v}} - \underline{u}\right\|^2. \tag{4}$$

	PIV/PTV	PEPT
Sampling rate	constant; controlable	non-constant; uncontrolable
Temporal resolution	adjust high-speed camera FPS	Modify particle activity (coating homogeneity and depth)
Spatial resolution	Camera pixels (known)	Sensor density in array (known; low upper barrier)

Table 1: Comparison between the criteria that set the measurement uncertainty in optical methods (PIV or PTV) and PEPT. The uncertainty in PEPT is much more difficult to quantify and the parameters with which to improve the accuracy are extremely difficult to modify (if at all).

*Corresponding author. E-mail: j.vanneste@ed.ac.uk

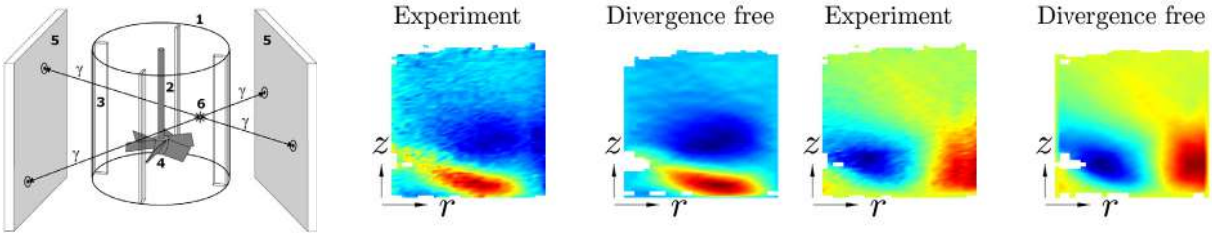

(a) System schematics (b) Radial velocity (c) Axial velocity

Figure 1: System schematics and results.

Taking a curl from (3) we obtain

$$\frac{\partial^2\psi}{\partial z^2}+\frac{\partial^2\psi}{\partial r^2}-\frac{1}{r}\frac{\partial\psi}{\partial r}=r\left(\frac{\partial\widehat{v}_r}{\partial z}-\frac{\partial\widehat{v}_z}{\partial r}\right), \tag{5}$$

where

$$\widehat{V}_r=\frac{1}{r}\frac{\partial\psi}{\partial z}\ ,\ \widehat{V}_z=-\frac{1}{r}\frac{\partial\psi}{\partial r}. \tag{6}$$

defines the stream function of the divergence-free velocity field. Equation (5) can easily be solved numerically using finite differences with no slip and no penetration boundary conditions.

We applied these calculations to a set of data from experiments conducted in a cylindrical mixing tank (see figure 1a). An impeller rotated at 490 RPM mixed 20 wt% of particles immersed in a salt solution. The velocity field inferred directly from the observed data is shown on the left of figures 1b and 1c, where a standard heat map colour scheme is applied (red – positive, blue – negative). The $r-z$ plane was discretised and the velocities were averaged over all particle passes through each element. Elements through which the number of passes was insufficient to deduce a representative average were discarded. To the right of each respective image is the corrected, divergence-free velocity that was calculated using the method described above.

At first glance, the divergence-free velocity field appears as a smoothed version of the raw data. However, the constraints imposed on the velocity field, namely satisfying the boundary conditions and (especially) conserving mass at each element, are responsible for the smoothing effect, clearing local inconsistencies and verifying that velocities decay to zero towards the tank walls.

To conclude, inferring reliable results for the velocity field – a set of data used for nearly all subsequent data-driven calculations (e.g., diffusion or mixing) – is an essential step forward in using the PEPT results to enhance our understanding of multiphase flows that can otherwise not be visualised.

References

[1] Parker, D. J., Broadbent, C. J., Fowles, P., Hawkesworth, M. R. & McNeil, P., Positron emission particle tracking - a technique for studying flow within engineering equipment, *Nuclear Instruments and Methods in Physics Research A* **326**(3): 592-607, 1993.

[2] Wildman, R. D. & Parker, D. J., Coexistence of two granular temperatures in binary vibrofluidized beds, *Physical Review Letters* **88**(6): 064301, 2002.

OPTIMAL NONLINEAR RECEPTIVITY ANALYSIS OF A FLAT-PLATE BOUNDARY LAYER

Denis Sipp[1], Georgios Rigas *[2], and Tim Colonius [3]
[1]Department of Aerodynamics, Aeroelasticity and Acoustics, ONERA, Universit Paris-Saclay, Meudon, France
[2]Department of Aeronautics, Imperial College, London, United-Kingdom
[3]Department of Mechanical and Civil Engineering, California Institute of Technology, Pasadena, CA, USA

Summary In a linear input-output analysis framework, the most amplified instabilities are typically described by considering singular vectors of the resolvent operator of the linearized Navier-Stokes equations. In this study, we extend the methodology to take into account nonlinear triadic interactions by considering a finite number of harmonics in the frequency domain using the Harmonic Balance Method. Optimal nonlinear forcing mechanisms that lead to transition and maximize the skin-friction coefficient are identified using direct-adjoint looping. We demonstrate the framework on a zero-pressure flat-plate boundary layer by considering three-dimensional perturbations triggered by a few optimal forcing modes of finite amplitude. Depending on the frequency, spanwise wavenumber, amplitude and symmetries of the perturbation, we recover all the transition stages associated with K-type and H-type transition mechanisms, oblique waves, streaks, and their breakdown. The proposed frequency-domain framework identifies the worst-case frequency disturbances for wall-bounded laminar-turbulent transition.

APPROACH

We introduce a new framework to analyse nonlinear transition scenarios in frequency space. We consider the incompressible Navier-Stokes equations

$$\partial_t u + u\cdot\nabla u = -\nabla p + \nu\Delta u + f(x,y,z,t), \qquad \nabla\cdot u = 0,$$

where $f(x,y,z,t)$ is a momentum forcing and (u,p) is the velocity-pressure field. The configuration is sketched in fig. 1: a flat-plate boundary layer develops in the streamwise x −direction, the wall-normal direction is y, and the spanwise z −direction is homogeneous. These equations are discretized in the (x,y) directions:

$$\partial_t w + Lw + \frac{1}{2}N(w,w) = Pf,$$

where $w(z,t)$ and $f(z,t)$ are now vectors representing the velocity-pressure and forcing quantities and P is a matrix that allows to select forcing components. L represents the Stokes operator and N the nonlinear convection term.

Harmonic Balance Method

The time and spanwise directions being homogeneous, we look for periodic solutions in these two directions. We therefore make the following ansatz:

$$f(z,t) = \sum_{(m,n)\neq(0,0)} e^{im\beta z + in\omega t}\hat{f}_{mn}, \qquad w(z,t) = \sum_{\substack{|m|\leq M,\\ |n|\leq N}} e^{im\beta z + in\omega t}\hat{w}_{mn},$$

where β and ω are the fundamental wavenumber and frequency, that may be chosen arbitrarily. The semi-discretized equations then yield the following coupled nonlinear equations:

$$[in\omega I + L_m + \gamma_{mn}N_0^m(\hat{w}_{00},\cdot)]\hat{w}_{mn} + \sum_{\substack{m=m_1+m_2\\ n=n_1+n_2\\ (m_1,n_1)\neq(0,0)\\ (m_2,n_2)\neq(0,0)}} N_{m_1}^{m_2}(\hat{w}_{m_1n_1},\hat{w}_{m_2n_2}) = P\hat{f}_{mn},$$

which may be recast in the following compact form:

$$R(\hat{w}) = P\hat{f}.$$

Note that P may also be used to select specific forcing components (m,n).

Nonlinear Optimization

The optimization of the forcing $\hat{f}$ is based on a gradient-based method. The objective functional is the mean-shear stress integrated over the flat-plate:

$$J(\hat{w}) = (\hat{w}_{00}-w_b)^*C^*C(\hat{w}_{00}-w_b), \qquad Cw = \int_{\text{flat plate}} \partial_y u dx.$$

This cost-functional may directly be related to the drag coefficient increase $\Delta C_D = \frac{2\nu J^{0.5}}{L}$, and accurately quantifies the transition to turbulence. Here w_b is the base-flow (the solution of the governing equations without forcing) and L is the length of the flat-plate. The gradient of the cost-functional with respect to the forcing may be obtained through a Lagrangian formulation:

$$\mathcal{L}(\hat{w},[\tilde{w},\lambda],\hat{f}) = J(\hat{w}) - \tilde{w}^*\big(R(\hat{w}) - P\hat{f}\big) - \lambda\big(\hat{f}^*Q\hat{f} - A^2\big).$$

The first term on the rhs is the objective functional, the second term represents penalization of the governing equation and the last term restricts the amplitude of the forcing to a given amplitude A (based on the scalar-product Q)

RESULTS

The considered (m,n) components for the forcing and response are shown in figure 1 (right). This setting, also called fundamental forcing, allows triggering of 2D Tollmien-Schlichting waves $(0,\pm1\omega)$, 3D streaky structures $(\pm1\beta,0)$ and oblique waves $(\pm1\beta,\pm1\omega)$. Nonlinear interactions may then generate higher-order structures, such as $(\pm2\beta,0)$ streaks or $(\pm3\beta,\pm1\omega)$ oblique waves. The result of the optimization process for $\beta = 33.3\times10^{-5}$, $\omega = 11.7\times10^{-5}$ and $A = 14.1\times10^{-5}$ (considering U_∞ and ν to nondimensionalize all quantities and the flat-plate length $L = 360000$). The result is shown in figure 2. Is is seen that the optimal forcing consists in oblique waves and the response in streaky structures that undergo sinuous instabilities. Links with linear resolvent analysis [4], oblique wave transition scenario [3], minimal seed to turbulence in the time-domain [1] or various other types of transition scenarios [2] will be discussed.

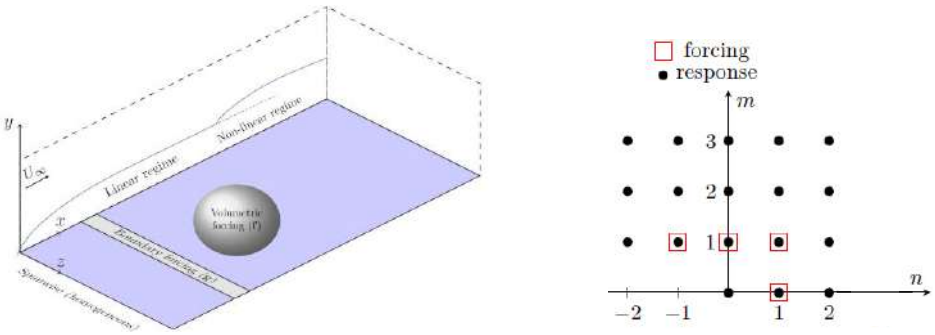

Figure 1. Left: Schematic of the zero-pressure gradient flat-plate set-up. Transition of the laminar boundary layer is triggered here only by volumetric momentum forcing (no suction/blowing). Right: components considered for forcing and response.

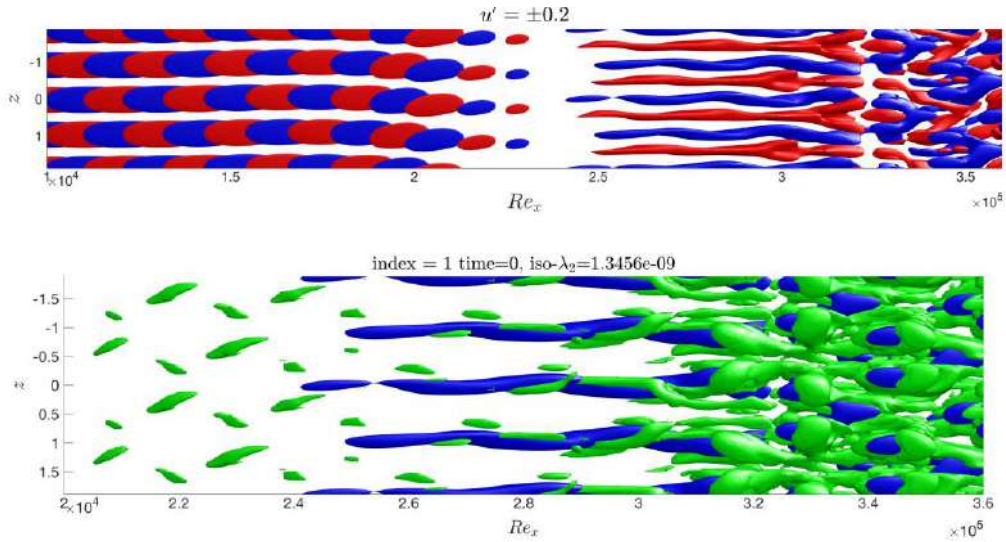

Figure 2. Optimal oblique forcing at $\beta = 33.3\times10^{-5}$ and $\omega = 11.7\times10^{-5}$ for $A = 14.1\times10^{-5}$. Iso-surfaces of streamwise forcing (upper left) and velocity perturbation (upper right) in physical space, blue negative values, red positive values. Vortical structures visualized with λ_2-criterion (green) and low-speed streaks u' (blue) (lower plot).

References

[1] Kerswell R.R. Nonlinear nonmodal stability theory. *Ann. Rev. Fluid. Mech.* **50**: 319-345, 2018.

[2] Sayadi T., Hamman C.W., Moin P. Direct numerical simulation of complete H-type and K-type transitions with implications for the dynamics of turbulent boundary layers. *J. Fluid Mech.* **724**:480-509.

[3] Schmid P.J., Henningson D.S. A new mechanism for rapid transition involving a pair of oblique waves. *Phys. Fluids. A* **4**:1986-1989.

[4] Monokrousos A., Åkervik E., Brandt L., Henningson, D. S. Global three-dimensional optimal disturbances in the Blasius boundary-layer flow using time-steppers. *J. Fluid Mech.*, **650**: 181-214.

FREE-STREAM TURBULENCE INDUCED BOUNDARY-LAYER TRANSITION IN LOW-PRESSURE TURBINES

Kristina Đurović [1], Luca De Vincentiis[1], Daniele Simoni[2], Davide Lengani[2], Jan Pralits[3], Dan S. Henningson[1], and Ardeshir Hanifi[1]
[1]Department of Engineering Mechanics, Linn e FLOW Centre, KTH Royal Institute of Technology, Stockholm, Sweden
[2]DIME, University of Genova, Genova, Italy
[3]DICCA, University of Genova, Genova, Italy

Summary The aerodynamic efficiency of turbomachinery blades is highly affected by the occurrence of laminar-turbulent transition in the boundary layer over them, as it significantly affects flow characteristics. Depending on the free-stream turbulence level, different path towards a turbulent state can be identified. The present study uses direct numerical simulation to investigate the flow behaviour of a low-pressure turbine blade. Isotropic homogeneous free-stream turbulence is prescribed at the inlet. Two levels of the free-stream turbulence intensity were investigated. We observed that, in the low-turbulence case on the suction side, the Kelvin-Helmholz instability dominated the transition process and full-span vortices were shed from the separation bubble. In the high-turbulence case transition proceeded more rapidly, where the generated streaks broke down into turbulent spots and caused bypass transition. On the pressure side, we have identified the appearance of longitudinal vortical structures. These structures are not produced by Görtler instability.

INTRODUCTION

Numerical simulations of the fluid flow have become an imperative part of the turbomachinery design process. Prediction of the onset and the extension of transitional flow regim is of great interest, since they significantly affect the drag and the lift forces. Especially, in low-pressure turbine applications, understanding of transition behaviour is of significant practical interest since the behaviour of boundary layer largely determines the overall efficiency of the low-pressure turbine. Investigation of transitional flows in a low-pressure turbine have been performed earlier, both in experimental and numerical works. Studies have shown that in the case of laminar separation of the boundary layer, velocity fluctuations are amplified along the inflection point of the velocity profile which in turn induce the formation of roll up vortices [1, 2, 3, 4]. There are recent high-fidelity computations that focus on data analysis of loss quantification. These recent works [5, 6, 7] highlighted some typical characteristics of the boundary-layer structures. However, since the flow physics is highly complex further efforts are needed to better understand it.

Here, we investigate the role of free-stream turbulence (FST) on the dominant transition mechanisms in the flow over a low-pressure turbine blade. This paper discusses the numerical setup and presents the preliminary results obtained from these direct numerical simulations.

METHODS AND RESULTS

In the present study, we use direct numerical simulation as the main tool to investigate the flow behaviour. The numerical tool used for the simulations is Nek5000 [8]. The incompressible Navier-Stokes equation together with the continuity equation subject to constant fluid properties are directly solved in the non-dimensional form. The free-stream turbulence is prescribed as a superposition of Fourier modes with a random phase shift. The amplitude of the free-stream modes is scaled using the von Kármán spectrum. Three-dimensional simulations have been performed with two levels of FST of the incoming flow ($Tu = 0.19$, and 5.2%).The simulation was designed to follow the experiments by Lengani & Simoni [9].

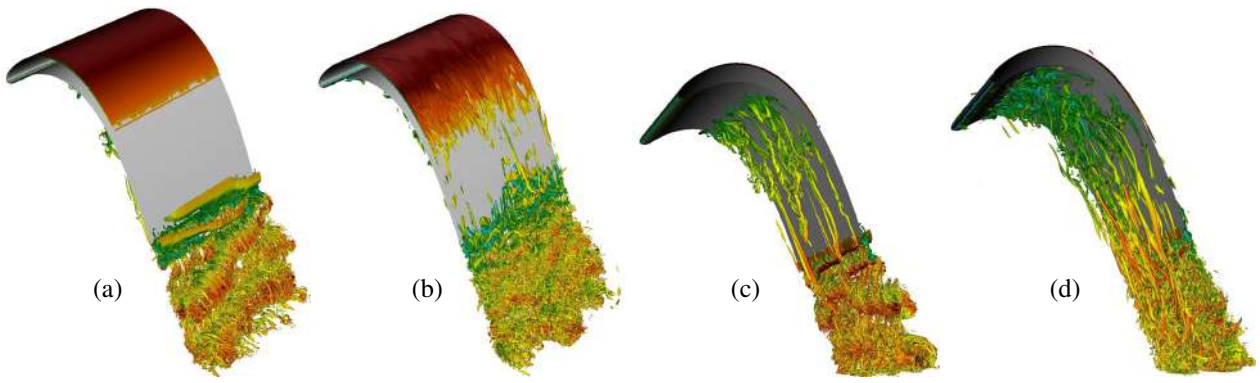

Figure 1: Visualization of instantaneous λ_2 structures on the suction side (a) for low FST case, where we see Kelvin-Helmholtz rolls; (b) for high FST case, showing developed streaks and turbulent spots; and on the pressure side (c) for low FST case; (d) for high FST case, showing longitudinal structures observed in both cases (coloured with streamwise velocity)

*Corresponding author. E-mail: kdj@mech.kth.se

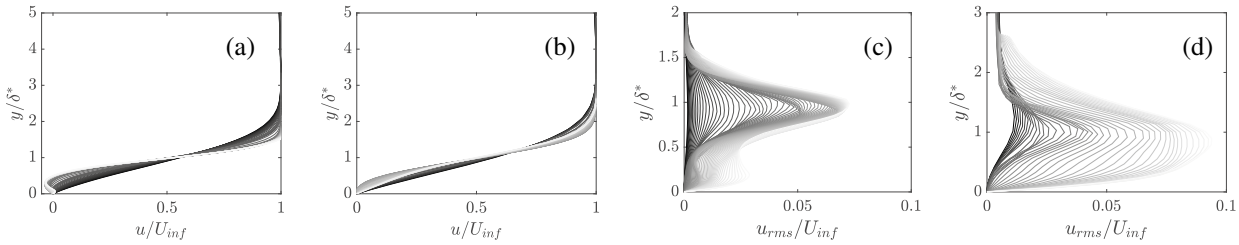

Figure 2: Distributions of normalized u_{rms} and mean velocity u by the the free stream velocity U_{inf} versus normalized wall-normal coordinate y by the displacement thickness δ^* at different streamwise locations. (a) mean velocity distribution for the low FST case; (b) mean velocity distribution for the high FST case; (c) u_{rms} distribution for the low FST case; (d) u_{rms} distribution for the high FST case. Lighter line corresponds to location further away from leading edge.

The response of the boundary layer on the suction side is visualized in Fig. 1(a) and (b). For low FST case (a), we can see structures that resemble the Kelvin-Helmholtz rolls. These rolls are observed to appear around 80 % of the chord and they are convected downstream. We can also notice the appearance of a laminar separation bubble. In the high FST case (b), the laminar part of boundary layer is dominated by distinct streamwise streaky structures. These streaks reach an amplitude of roughly 10% of freestream velocity for the high FST case before their breakdown to turbulence. Turbulent spots appear at around 90 % of the chord and the turbulent boundary layer that is formed close to the trailing edge is attached to the blade surface. Figure 1 also shows the response of the boundary layer on the pressure side to the external perturbations: in (c) for low FST case and (d) for high FST case. It is interesting to note the appearance of longitudinal vortical structures. These structures do not arise due to Görtler instability, despite that they emerge on a concave surface. In our simulations, we found that the local values of Görtler number are always below the critical one, which is in agreement with previus findings [1, 10].

The time- and span-averaged velocity profiles at different streamwise locations on the suction side of the blade are plotted in Fig. 2 (a) and (b). The profiles of mean velocity for the low FST case illustrate flow reversal in the separated region. This separation bubble does not reattach. In the high FST case, we can see that velocity profiles transition from laminar to turbulent ones and flow stays attached over the whole suction side. In Fig. 2(c) and (d), profiles of the root-mean-square (r.m.s.) values of streamwise velocity at different streamwise locations are shown. In the low FST case (c), r.m.s. fluctuations of streamwise velocity indicates that in the first half of the separation bubble the growth rate of velocity perturbation is relatively slow and profiles exhibit a second peak close to the wall. The outer peak in the shear layer grows rapidly in the second half of the bubble, because of amplification of disturbances due to Kelvin-Helmholz instability, leading to formation of large scale eddies and breakdown. Interestingly, all the profiles exhibit their maximum at the inflection point, further supporting the dominant role of the inviscid instability in the transition process in the low FST case. In the high FST case (d), peak values of u_{rms} increases in the streamwise direction, while the location of the maximum value moves slightly towards the wall.

CONCLUSIONS

We have performed direct numerical simulations of the FST-induced boundary-layer transition on a low pressure turbine blade. We observed that in the case of low FST, the Kelvin-Helmholz instability dominated the transition process on the suction side and full-span vortices were shed from the appearing separation bubble. Transition on the suction side proceeded more rapidly in the high FST case, where the generated streaks broke down into turbulent spots and caused the boundary layer transition. On the pressure side we have identified the appearance of the longitudinal vortical structures which are not produced by Görtler instability as the Görtler number in the current case is smaller than the critical value.

References

[1] Wu X., Durbin P.A. Evidence of longitudinal vortices evolved from distorted wakes in a turbine passage. *J. Fluid Mech.* **446**: 199–228, 2001.
[2] Wissink W.G., Rodi W. DNS of a Laminar Separation Bubble in the Presence of Oscillating External Flow. *Flow Turbul. and Combust.* **71**: 311-331, 2003.
[3] Hodson H.P., Howell R.J. The role of transition in high-lift low-pressure turbines for aeroengines. *Prog. Aerosp. Sci.* **41**: 419-454, 2005.
[4] Stieger R.D., Hodson H.P. The unsteady development of a turbulent wake through a downstream low-pressure turbine blade passage. *J. of Turbomach.* **127**: 388-394, 2005.
[5] Sarkar S., Voke P. Large-Eddy Simulation of Unsteady Surface Pressure Over a Low-Pressure Turbine Blade due to Interactions of Passing Wakes and Inflexional Boundary Layer. *ASME J. of Turbomach.* **128**: 221-231, 2006.
[6] Michelassi V., Chen L., Pichler R., Sandberg R. Compressible Direct Numerical Simulation of Low-Pressure Turbines—Part II: Effect of Inflow Disturbances. *J. of Turbomach.* **137**: 071005, 2014.
[7] Lengani D., Simoni D., Ubaldi M., Zunino P., Bertini F., Michelassi V. Accurate Estimation of Profile Losses and Analysis of Loss Generation Mechanisms in a Turbine Cascade. *ASME J. of Turbomach.* **139**: 121007, 2017.
[8] Fischer P.F., Lottes J. W., Kerkemeier S. G., nek5000, web site **http://www.nek5000.mcs.anl.gov**
[9] Lengani D., Simoni D. Recognition of coherent structures in the boundary layer of a low-pressure-turbine blade for different free-stream turbulence intensity levels. *Int. J. Heat. Fluid Fl.* **54**: 1-13, 2015.
[10] Hosseini S.M. On stability, transition and turbulence in three-dimensional boundary-layer flows. *PhD Thesis*, Royal Institute of Technology (KTH), Stockholm, Sweden, 2015.

TOWARDS A THEORETICAL UNDERSTANDING OF SPATIOTEMPORAL INTERMITTENCY IN WALL-BOUNDED SHEAR FLOWS

Dwight Barkley

Summary The route to turbulence in wall-bounded shear flows is reviewed with emphasis on what is known from experiments and numerical simulations. Some key open theoretical questions concerning the intermittent region are then addressed. These include the following: turbulent-laminar fronts in planar shear flows; the connection between puff splitting and the onset of weak slugs; the onset of oblique turbulent bands as a problem in pattern formation.

INTRODUCTION

Explaining the route to turbulence has been a long and tortuous journey. After years of missteps, controversies, and uncertainties, we are at last converging on a unified and fascinating picture of transition in wall-bounded shear flows such as pipes, channels, and ducts. Classically, subcritical transition (such as in a pipe), was thought to imply a discontinuous route to turbulence. We now know that this is not the case – subcritical shear flows may, and often do, exhibit continuous (second-order) transition. From this we understand how to define precise critical points for systems without linear instabilities and how to characterize the onset of turbulence in terms of non-trivial, but universal power laws, e.g. Lemoult et al. (2016); Sano & Tamai (2016); Chantry et al. (2017).

For a range of Reynolds numbers above the critical point wall-bounded shear flows are spatiotemporally intermittent with coexisting turbulent and laminar domains. See Tuckerman et al. (2020) and references therein. Eventually at higher Reynolds numbers the turbulent-laminar intermittency gives rise to fully turbulent flow, often referred to as featureless turbulence or as uniformly turbulent flow. From experiments and from direct numerical simulations of the Navier-Stokes equations we now know a great deal about the dynamics of the turbulent and laminar domains within the intermittent regime, e.g. Coles (1962); Wygnanski & Champagne (1973); Darbyshire & Mullin (1995); Prigent et al. (2002); Nishi et al. (2008); Duguet et al. (2010) However, our theoretical understanding of the structure and dynamics of turbulence within the intermittent regime remains limited.

In this talk I will briefly summarize for the non-experts some of the outstanding theoretical challenges to understanding the intermittent route to turbulence in wall-bounded shear flows. I will then discuss recent ideas on how to address some of these challenges.

TURBULENT-LAMINAR FRONTS

Understanding turbulent-laminar intermittency is largely a question of understanding fronts between turbulent and laminar flow (Coles, 1962; Pomeau, 1986; Barkley et al., 2015) and how the large-scale mean flow is dictated by turbulent structures (Barkley & Tuckerman, 2007; Duguet & Schlatter, 2013). In the case of pipe flow, geometry restricts the allowed turbulent structures to relatively simple localized patches known as puffs. In the case of planar shear flows turbulent patches take the form of oblique bands that split, fragment and change orientations resulting in a much more complex spatiotemporal situation (Chantry et al., 2017; Shimizu & Manneville, 2019). The large-scale mean flow is especially significant in this case and it especially challenging. By working in tilted computational domains (minimal band units) one can captures some, but not all of the features of turbulent-laminar intermittency in planar flows (Barkley & Tuckerman, 2005; Tuckerman et al., 2020). I will present some ideas on how to address turbulent-laminar fronts for planar flows in this setting.

PUFF SPLITTING

The onset of sustained turbulence in pipe flow is dictated by the interplay between puff decay and puff splitting (Avila et al., 2011). Neither process is fully understood, although puff decay does not present any difficulties for computations and experiments, other than resolving long time scales. There have been studies of puff splitting e.g. Shimizu et al. (2014), but on the whole the process lacks theoretical understanding. Moreover, at the upper end of the transition region in pipes, turbulence begins to expand in the form of slugs – first weak slugs and eventually strong slugs (Barkley et al., 2015). I will address possible connections between puff splitting and expansion in the form of weak slugs.

PATTERN FORMATION

It has long been recognized that the formation of oblique turbulent bands from uniform turbulence, as Reynolds number is decreased, has all the hallmarks of a pattern formation problem. See Tuckerman et al. (2020) and references therein. One can view the problem in terms of spatial dynamics in which space is map to a temporal variable and this provides a compact and appealing description of the transition. However, past (unpublished) evidence indicates that this transition does not fall into the classical Eckhaus picture. I will review and discuss this issue.

*Corresponding author. E-mail: D.Barkley@warwick.ac.uk.

References

Avila K, Moxey D, de Lozar A, Avila M, Barkley D, Hof B. 2011. The onset of turbulence in pipe flow. *Science* 333:192–196

Barkley D, Song B, Mukund V, Lemoult G, Avila M, Hof B. 2015. The rise of fully turbulent flow. *Nature* 526:550–553

Barkley D, Tuckerman LS. 2005. Computational study of turbulent laminar patterns in Couette flow. *Phys. Rev. Lett.* 94:014502

Barkley D, Tuckerman LS. 2007. Mean flow of turbulent–laminar patterns in plane Couette flow. *J. Fluid Mech.* 576:109–137

Chantry M, Tuckerman LS, Barkley D. 2017. Universal continuous transition to turbulence in a planar shear flow. *J. Fluid Mech.* 824

Coles D. 1962. Interfaces and intermittency in turbulent shear flow. *Mécanique de la Turbulence* 108:229

Darbyshire A, Mullin T. 1995. Transition to turbulence in constant-mass-flux pipe-flow. *J. Fluid Mech.* 289:83–114

Duguet Y, Schlatter P. 2013. Oblique laminar-turbulent interfaces in plane shear flows. *Phys. Rev. Lett.* 110:034502

Duguet Y, Schlatter P, Henningson DS. 2010. Formation of turbulent patterns near the onset of transition in plane Couette flow. *J. Fluid Mech.* 650:119–129

Lemoult G, Shi L, Avila K, Jalikop SV, Avila M, Hof B. 2016. Directed percolation phase transition to sustained turbulence in Couette flow. *Nat. Phys.* 12:254–258

Nishi M, Ünsal B, Durst F, Biswas G. 2008. Laminar-to-turbulent transition of pipe flows through puffs and slugs. *J. Fluid Mech.* 614:425

Pomeau Y. 1986. Front motion, metastability and subcritical bifurcations in hydrodynamics. *Physica D* 23:3–11

Prigent A, Grégoire G, Chaté H, Dauchot O, van Saarloos W. 2002. Large-scale finite-wavelength modulation within turbulent shear flows. *Phys. Rev. Lett.* 89:014501

Sano M, Tamai K. 2016. A universal transition to turbulence in channel flow. *Nat. Phys.* 12:249–253

Shimizu M, Manneville P. 2019. Bifurcations to turbulence in transitional channel flow. *Phys. Rev. Fluids* 4:113903

Shimizu M, Manneville P, Duguet Y, Kawahara G. 2014. Splitting of a turbulent puff in pipe flow. *Fluid Dynamics Research* 46:061403

Tuckerman LS, Chantry M, Barkley D. 2020. Patterns in wall-bounded shear flows. *Annual Review of Fluid Mechanics* 52:343–367

Wygnanski I, Champagne H. 1973. Transition in a pipe. part 1. the origin of puffs and slugs and flow in a turbulent slug. *J. Fluid Mech.* 59:281–335

EFFECTS OF LAYER INTERACTIONS ON THE INSTANTANEOUS STABILITY OF FINITE STOKES FLOWS

Chen Zhao[1], Zhenli Chen *[1], and Dong Li[1]
[1]School of Aeronautics, Northwestern Polytechnical University, Xi'an, China

Summary Stability analysis of Stokes flow is of practical importance, such as in flow control. In the present work, stability of finite Stokes flow, formed by two synchronizing oscillating parallel plates, is analyzed via instantaneous linear stability theory when the interactions between two Stokes layers over flat plates are considered. Effects of the distance between two plates on the stability are studied. The effects are strong when the ratio of Stokes layer thickness to the half distance between two plates is larger than 0.12. In view of the maximum instantaneous growth rate, with the decreasing of wall distance, the interactions between two Stokes layers destabilize the flow first, and then stabilize the flow. The most instantaneous unstable mode is of higher wavenumber. The flow is stable over a period when the two plates are very close. It is observed that the phase of maximum instantaneous growth rate appears earlier when two plates move closer. However, the mode which have the maximum instantaneous growth rate may not be the most unstable mode in view of the net growth over a period.

INTRODUCTION

The Stokes flow is usually viewed as a prototype to analyze the stability of unsteady flows because of its analytical velocity profiles. Linear stability of the Stokes flow can be analyzed via the Floquet method or an instantaneous linear stability theory(LST).[1] Floquet method is used to predict the net growth of a perturbation over an entire period of an oscillating base flow, whereas in the instantaneous LST, the base flow is treated as quasi-steady.[3] In instantaneous LST, Orr-Sommerfeld equation is solved at every frozen state. Even if a base flow is Floquet-stable, it can still support substantial perturbation growth during finite time of a period.[4] Thus, the instantaneous LST has advantages in analyzing the transient growth of the perturbations. The instantaneous stability of the finite Stokes flow was analyzed by Luo and Wu.[4] However, in their analysis, the two walls are so far from each other that the interactions between Stokes layers can be neglected. Thus, in the present work, the instantaneous LST is used to study the effects of wall distance on the stability of Stokes flows.

PHYSICAL MODEL AND NUMERICAL METHOD

We consider a two-dimensional viscous incompressible parallel flow bounded by two infinite parallel plates separated by a distance of $2h^*$. The finite Stokes flow is produced by the synchronizing oscillations of two plates with a velocity $U_0^*\mathrm{Cos}(\Omega t^*)$. The oscillation has a period of $T = 2\pi/\Omega$. The phase of oscillation is $\varphi = t^*/T$. The streamwise and normal directions are indicated by x and y. The Stokes layer thickness is defined as δ^* and nondimensionlized as $\delta = \delta^*/h^*$. The corresponding Reynolds number is $Re_\delta = U_0^*\delta^*/\nu$. In present research, $Re_\delta = 1560$. The infinitesimal perturbations are governed by Orr-Sommerfeld equation. The instantaneous linear stability theory is used to solve the governing equation with the given real spatial wavenumbers α to analyze the temporal stability of the flow. The temporal growth rate of perturbations is signified as ω_i. The most unstable transient mode is determined over all phases of a period.

RESULTS

To analyze the effects of Stokes layer interactions on the stability of the flow, maximum velocity and frequency of the oscillation are kept invariant. The distance between two plates is changed to formulate two Stokes layers. It is observed that the second-order derivatives of the base flow velocity to y, signified as D^2U, at the central parts between two plates

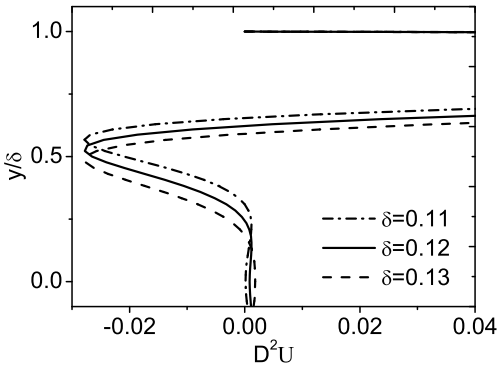

Figure 1: Second-order derivative of base flow velocity to y at the phase $\varphi = 0$.

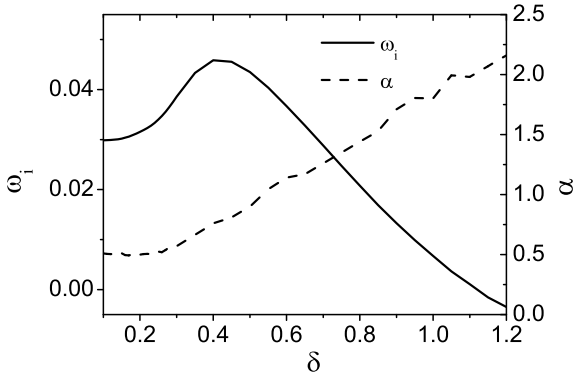

Figure 2: Maximum instantaneous growth rate and the corresponding α for the cases of different δ.

*Corresponding author. E-mail: zhenlichen@nwpu.edu.cn.

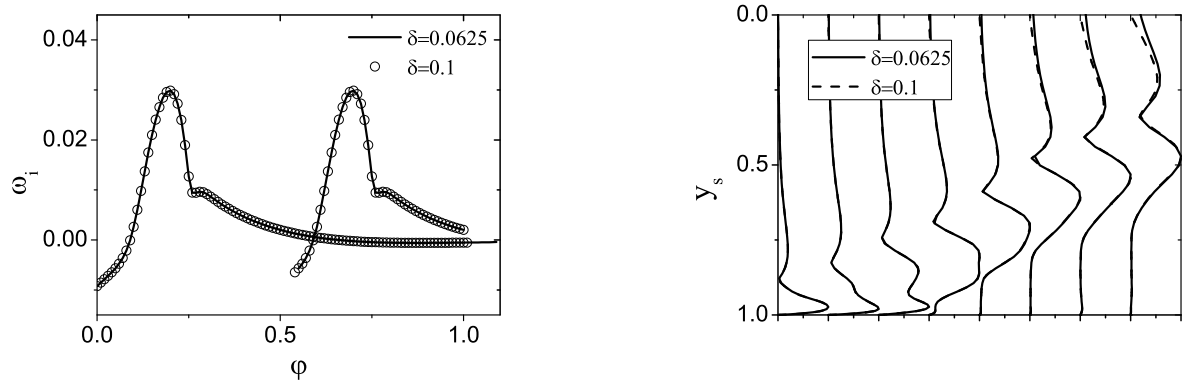

Figure 3: Instantaneous growth rates and eigenvectors varying with phase: (a) Growth rate; (b) Eigenvectors at selected phases $\varphi = 0, 0.15, 0.25, 0.35, 0.50, 0.65, 0.75, 0.85$(from left to right).

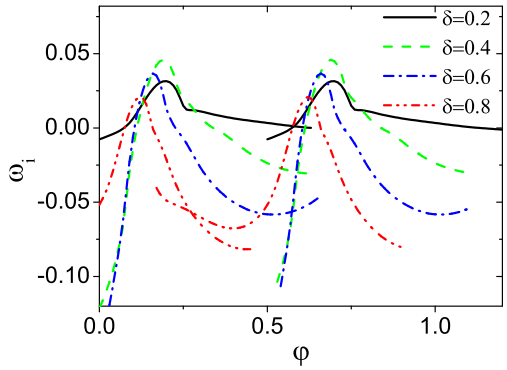

Figure 4: Instantaneous growth rates varying with phase for the cases of different δ.

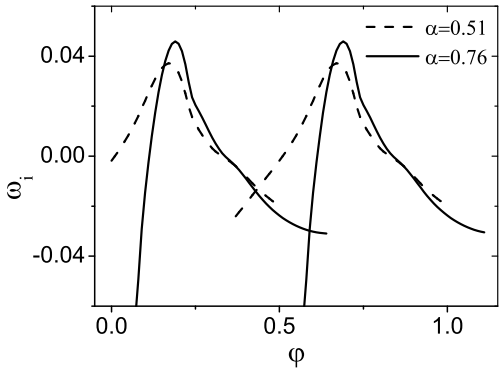

Figure 5: Instantaneous growth rates of two different modes varying with phase at $\delta = 0.4$.

depart from zero for a finite value when $\delta > 0.12$, shown in Fig.1. Thus, it is reasonable to deduce that the effects of layer interactions should be considered when $\delta > 0.12$, which is also proved in Fig.2. Maximum instantaneous growth rate at different δ and the corresponding spatial wavenumber are depicted in Fig.2. With the decrease of h^*, the interactions between the Stokes layers destabilize the flow first, and then stabilize the flow. When the two plates move to be very close, the maximum growth rate can be negative, which signifies that the flow is stable over a period. And the spatial frequency of the most instantaneous unstable mode increases with the shorter distance between two plates.

The instantaneous growth rates of the most unstable mode over a period are compared for the cases at $\delta = 0.0625$ and 0.12, shown in Fig.3(a). The results of two cases are identical, which is consistent with Fig.2. The eigenvectors of two cases at different phases are compared in Fig.3(b). It is found that the eigenvectors of two cases near the central parts between two plates are slightly different at the later time of a period. Fig.4 presents the instantaneous growth rates of the most unstable mode for the cases at $\delta = 0.2, 0.4, 0.6$ and 0.8. It shows that the phase of maximum growth rate appears earlier when the two plates move closer. The instantaneous growth rates of two different modes at $\delta = 0.4$ are depicted in Fig.5. Mode $\alpha = 0.76$ has the maximum instantaneous growth rate. However, mode $\alpha = 0.51$ grows for a longer time interval than mode $\alpha = 0.76$, which means that the mode which has the maximum instantaneous growth rate may not be the most unstable mode in view of the net growth over a period.

References

[1] Davis S. H. The stability of time-periodic flows. *Annu. Rev. Fluid Mech.* **8**, 57 1976.
[2] Hack M. J. P. and Zaki T. Modal and non-modal stability of boundary layers forced by spanwise wall oscillations. *J. Fluid Mech.* **778**, 389 2015.
[3] Zhao C., Chen Z. L. and Li D. Instantaneous linear stability of plane Poiseuille flow forced by spanwise oscillations. *Phys. Fluids.* **31**, 043608 2019.
[4] Luo J. S. and Wu X. S. On the linear instability of a finite stokes layer: Instantaneous versus Floquet modes. *Phys. Fluids.* **22**, 054106 2010.

NONLINEAR EVOLUTION AND ACOUSTIC RADIATION OF HELICAL-MODE WAVEPACKET IN THE NEAR-NOZZLE REGION OF A SUBSONIC CIRCULAR JET

Zhongyu Zhang[1] and XuesongWu *[1,2]
[1]Department of Mechanics, Tianjin University, Tianjin 300072, P.R. China
[2]Department of Mathematics, Imperial College London, London SW7 2AZ, U.K.

Summary In the near-nozzle region of a circular jet, helical modes with different azimuthal wavenumbers coexist and interact with each other. In this work, the nonlinear evolution of a wavepacket consisting of an arbitrary number of interacting helical and axisymmetric modes are investigated theoretically using high-Reynolds-number asymptotic approach. Furthermore, the acoustic radiation of such a form of disturbance is analysed on the basis of the first principles. Unlike acoustic analogy, which predesignates the sound sources in a heuristic manner, our current asymptotic approach to aeroacoustics determines the physical sound sources unambiguously by analysing the large-distance asymptote of the near-field hydrodynamic fluctuations. It is shown that interactions of subsonic modes generate a slowly modulated mean-flow distortion and emit low-frequency sound waves on the scale of the wavepacket envelope. [1]

NONLINEAR EVOLUTION: A WEAKLY NONLINEAR CRITICAL-LAYER THEORY

In the near-nozzle region, a thin shear layer develops along the lip line and its thickness δ^* is much smaller than the nozzle diameter D^*. A helical mode with azimuthal wavenumber m is weakly three-dimensional because $m/r_c \ll 1$ plays the role of the spanwise wavenumber, where $r_c = O(D^*/\delta^*)$ denotes the centre of the shear layer, normalized by δ^*. It follows that all helical modes, together with their 'side-band' components share the same critical layer since the phase speeds of these components are all close to that of the neutral mode (Long & Petersen, 1992; Strange & Crighton, 1983). In particular, when $r_c^{-1} = O(\epsilon^{1/5})$, the nonlinear inter-modal interactions and azimuthal modulation become important simultaneously when the linear growth rates reduce to $O(\epsilon^{2/5})$, where ϵ is a measure of the helical mode magnitudes (Wu, 1993). In the cylindric coordinate system (x, r, θ), the disturbance can be expressed as $A(\tau, \bar{x}, \theta)\phi(r)\mathrm{e}^{\mathrm{i}(\alpha x - \omega t)}$, where α and ω denote the axial wavenumber and frequency of the common carrier wave. Different helical modes (with the axisymmetric mode being a special case) and their side-band components are accommodated by the dependence of the amplitude function A on the azimuthal coordinate θ and the slow time variable $\tau = \epsilon^{2/5}t$. The spatial evolution is described by the slow axial variable $\bar{x} = \epsilon^{2/5}x$.

In the majority of the jet flow, the wavepacket is linear and inviscid, but nonlinear interactions take place in the critical layer, where viscosity and non-equilibrium both appear at leading order in the governing equations. Unlike an axisymmetric mode or a two-dimensional mode in a planar mixing layer, either of which has a strongly nonlinear critical layer (Zhang & Wu, 2020), a wavepacket of helical modes is governed by weakly nonlinear critical-layer dynamics; see a recent review by Wu (2019). For a laminar base flow, the non-parallelism associated with the axial spreading of the jet enters at a higher order than does the non-equilibrium with respect to τ and $\bar{x}$. This leads to the translating-critical-layer effect (Cowley, 1985; Wu & Zhuang, 2016) and influences the modulation significantly. The present theory is a composite theory including both effects of non-equilibrium and non-parallelism. By matching the solutions in the critical layer and the bulk of the jet, the amplitude evolution-modulation equation is derived, which turns out to be an integro-partial-differential type with respect to the slowly temporal and spatial variables, τ and $\bar{x}$ (Zhang & Wu, 2019). A significant feature of this equation is that the nonlinear terms are history-dependent and involve derivatives with respect to θ.

ACOUSTIC RADIATION: A FIRST-PRINCIPLE DESCRIPTION FOR ACOUSTICS

Unstable wavepackets are considered to be an important sound source, especially in the case of circular jets. The analysis of the disturbance in the main jet and critical layer allows one to investigate how such a wavepacket radiates sound on the basis of first principles, and the key and natural idea is to identify the radiating part of the disturbance by examining the large-distance asymptote of the near-field disturbance (Wu & Zhang, 2019).

The eigenfunction of a subsonic unstable wavepacket attenuates exponentially in the radial direction, and hence the wavepacket itself radiates only exponentially small sound waves. However, the nonlinear interaction of the wavepacket generates a slowly-breathing mean-flow distortion, which emits sound waves with low frequencies of $O(\epsilon^{2/5})$. Such a radiation mechanism is broadly similar to that described by Wu & Huerre (2009) for a single pair of subsonic helical modes in the developed regime of a circular jet. For the present multiple helical modes in the near-nozzle region, the main difference is that the physical emitter is no longer the leading-order mean-flow distortion, and instead it is the secondary-order mean-flow distortion that radiates the primary sound waves.

An equivalent sound source in the context of Lighthill's analogy is derived by matching with the near-field solution, and it contains the contributions from the critical layer and the bulk of the jet. The radiated acoustic field consists of azimuthal components with $m = 0, \pm 1, \ldots$, and the respective intensity is of $O[\epsilon^{(11+|m|)/5}]$. It follows that the axisymmetric sound is at leading order and the sound waves with azimuthal wavenumbers $m = \pm 1$ are the next.

*Corresponding author. E-mail: x.wu@imperial.ac.uk
[1]This investigation was supported by the Natural Science Foundation of China (NSFC grant No.11472190).

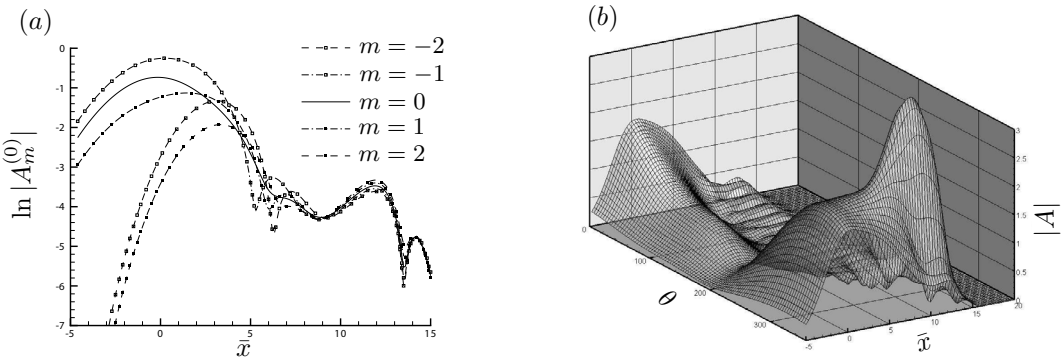

Figure 1: (a) Evolution of $A_m^{(0)}$, the amplitude of the central-frequency components of axisymmetric ($m=0$) and helical ($m=\pm1$, ±2) modes; (b) evolution of the total amplitude $|A|$ shown as a perspective plot against the streamwise and azimuthal variables, $\bar{x}$ and θ.

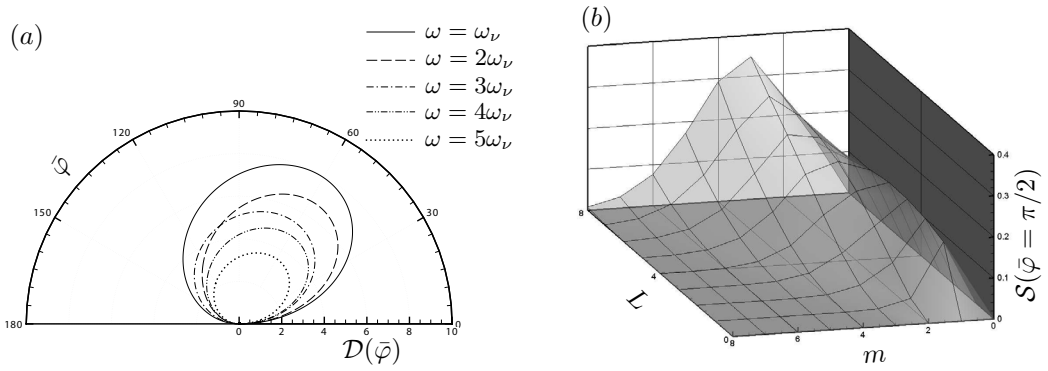

Figure 2: (a) Directivity of sound waves with azimuthal wavenumbers $|m|=1$ and frequencies $n\omega_\nu$, $n\in\mathbb{Z}^+$, where $\omega_\nu=\epsilon^{2/5}\Delta$ is the difference frequency; (b) spectrum of the sound in the direction making $\pi/2$ angle to the downstream axial direction.

MAIN RESULTS AND CONCLUSIONS

Of interest is a wavepacket consisting of helical and axisymmetric modes, each having side-band components with frequencies $\omega+n\epsilon^{1/5}\Delta$ $(n=0,\pm1,\ldots)$. In this case, the solution for the amplitude function A can be decomposed as $A(\tau,\bar{x},\theta)=\sum_{m,n}A_m^{(n)}(\bar{x})\exp\left[\mathrm{i}(m\theta-n\Delta\tau)\right]$. The nonlinear evolution depends on the modes seeded upstream. Figure $1(a)$ displays the development of $A_m^{(0)}$ when nine helical modes $(m,n),m,n=0,\pm1$ with frequencies $\omega+n\epsilon^{2/5}\Delta$, in which $\epsilon=0.09$, $\omega=1.37$ and $\Delta=0.20$ are seeded. The mutual interactions of the seeded modes excite modes $m=1,2$ (and their sideband components). All modes eventually attain nearly the same amplitudes, and attenuate under the influence of nonlinearity, Figure $1(b)$ shows a perspective plot of $|A|$ as a function of $\bar{x}$ and θ.

The helical modes and their side-band components in the wavepacket generate low-frequency components. These components attenuate only algebraically in the radial direction and evolve to acquire the character of sound waves. Figure $2(a)$ shows the directivity of the acoustic components $m=\pm1$ with frequencies $n\omega_\nu=\epsilon^{2/5}n\Delta$. Panel (b) displays the spectrum at $\pi/2$ angle to the downstream axial direction.

Further results on the nonlinear evolution and acoustic radiation will be presented at the Congress.

References

[1] Cowley, S. J. (1985) Pulsatile flow through distorted channels: Low-Strouhal-number and translating critical-layer effect. *Q. J. Mech. App. Maths.* **38**(4) 589-619.

[2] Long, T. A., Petersen, R. A. (1992) Controlled interactions in a forced axisymmetric jet. Part 1. The distortion of the mean flow. *J. Fluid Mech.* **235**: 37–55.

[3] Strange, P. J. R., Crighton D. G. (1983) Spinning modes on axisymmetric jets. Part 1. *J. Fluid Mech.* **134**: 231–245.

[4] Wu, X. (1993) Nonlinear temporal-spatial modulation of near-planar Rayleigh waves in shear flows: formation of streamwise vortices. *J. Fluid Mech.* **256**: 685-719.

[5] Wu, X. (2019) Nonlinear theories for shear-flow instabilities: physical insights and practical implications. *Annu. Rev. Fluid Mech.* **51**: 421–485.

[6] Wu, X., Huerre, P. (2009) Low-frequency sound radiated by a nonlinear modulated wavepacket of helical modes on a subsonic circular jet. *J. Fluid Mech.* **637**: 173–211.

[7] Wu, X., Zhang, Z. (2019) First-principle description of acoustic radiation of shear flows. *Phil. Trans. R. Soc. Lond. A.* **377**: 20190077.

[8] Wu, X., Zhuang, X. (2016) Nonlinear dynamics of large-scale coherent structures in turbulent free shear layers. *J. Fluid Mech.* **787**: 396–439.

[9] Zhang, Z., Wu, X. (2020) Nonlinear evolution and acoustic radiation of coherent structures in subsonic turbulent free shear layers. *J. Fluid Mech.* **884**(A10): 1–68.

[10] Zhang, Z., Wu, X. (2019) Nonlinear evolution of multiple helical modes in the near-nozzle regime of subsonic circular jets: a weakly nonlinear critical-layer theory. In: *Ninth IUTAM Symposium on Laminar-Turbulent Transition.* London, U.K..

HYPERSONIC ATTACHMENT-LINE INSTABILITIES WITH LARGE SWEEP MACH NUMBERS

Youcheng Xi*[1] and Song Fu †[1]
[1]School of Aerospace Engineering, Tsinghua University, Beijing, 100084, China

Summary Highly swept flows over a cold cylinder that give rise to large sweep Mach numbers are studied. Using local and global stability theory, an attachment-line mode is found to be is found to be dominant for the laminar-turbulent transition along the leading edge, which agrees well with experimental observations. It is obviously demonstrated that the global modes display the features of both attachment-line modes, as in sweep Hiemenz flow, and cross-flow-like modes further downstream along the surface. In contrast to incompressible flows, results from high sweep Mach number show that the leading-edge curvature has a destabilizing effect on the attachment-line mode for large span-wise wave number but a stabilizing effect for small span-wise wave number.

INTRODUCTION

The leading edge of a wing plays a very important role in boundary layer transition, especially in hypersonic region. However, the Mach number effect of compressible attachment-line instability is still not clearly understood, most prominently in the hypersonic region. Two significant problems address our interests. First, as highlighted in the series of experiments from Gaillard[1], instability mechanisms are not well understood in the high sweep Mach number region. Also, in high-speed regions, the relation between attachment-line modes and cross-flow modes is far from clear. In some cases [2], the attachment-line instabilities in the leading-edge region connected with cross-flow modes further away from the leading edge. Contrarily, these connections may disappear in some other cases as pointed by Paredes[3].

METHODOLOGY

The hypersonic flow around a swept cylinder is studied here based on relevant experimental conditions [1]. A cylinder of radius $R = 33mm$ is assumed to be of infinite length in the spanwise direction. The incoming flow impinges onto the the surface of the cylinder with a sweep angle Λ. A high fidelity base flow is obtained by solving the full Navier-Stokes equations with a high-order shock-fitting method. Both local and global stability theory are used for identification of the instabilities. And non-negligible variations of base ow with respect to x direction together with the curvature effect around the attachment line and the features of downstream region can be taken into account properly by the global stability analysis, simultaneously.

STABILITY ANALYSIS

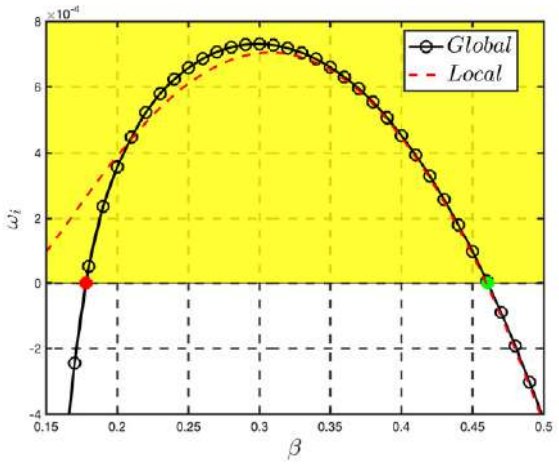

Figure 1: Dependences of ω_i on β of C3376 cases. The black line with black circles represents the results from global calculations and the red dashed line represents the results from local calculation. The red and green points represent the critical value points.

*E-mail: xiyc14@mails.tsinghua.edu.cn
†Corresponding author. E-mail: fs-dem@tsinghua.edu.cn

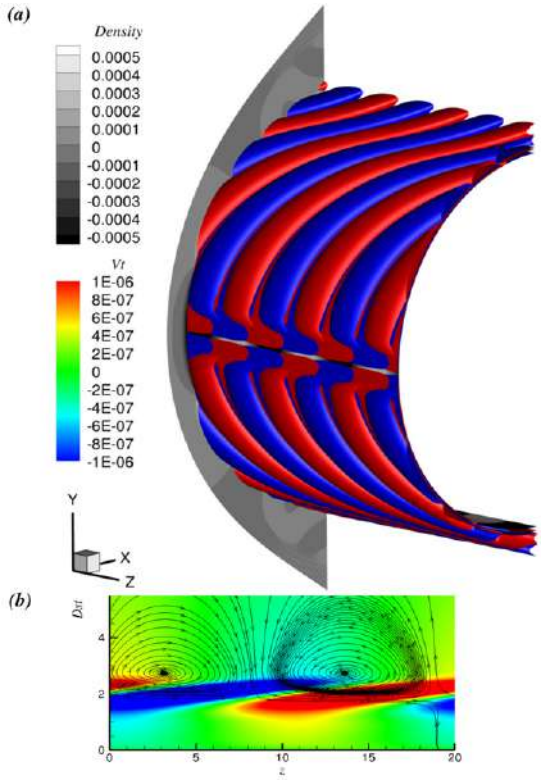

Figure 2: (a) The leading global modes of the eigenvalues $\omega = (0.25097, 0.00073146)$ is visualized by iso-surface (positive values in red, negative values in blue) of the surface tangential velocity perturbations for case C3376a, contours of the relative density perturbation are also shown at the background. (b) represents contour of the $x - z$ plane cross-cut at $y = 0.001$ for surface tangential velocity perturbation $V_t(x, y, z)$ together with the streamline over this plane.

CONCLUDING REMARKS

The analysis is performed using high fidelity realistic base flow, calculated by high-order shock fitting methods, together with the local/global stability model, which fully resolves the base flow and all the geometry information. The theoretical results match well with the experimental results. According to the global stability analysis, the leading attachment-line global mode is also found to be connected with cross-flow like modes further away from the attachment-line. As first presented by Mack[2] over an adiabatic wall surface with relative low sweep Mach number, this connection also exists over cold wall surface with corresponding high sweep Mach number.

Based on the local and global analysis, we also found that the attachment-line mode, unlike the incompressible cases, at the simulation conditions is not entirely suppressed by the leading curvature. For the cases at sweep Mach number 5.8, the growth rate of leading global mode is found a little bit larger than local calculation when the span-wise wave number β is above 0.2084 and the global growth rates are lesser than local calculations when the span-wise wave number is lower than 0.2084. This finding indicates that the leading edge curvature has double effect on the attachment-line modes which slightly destabilizes the mode for large span-wise wave numbers and stabilizes the mode for low span-wise wave numbers.

References

[1] GAILLARD, L., BENARD, E., AND ALZIARY DE ROQUEFORT, T. Smooth leading edge transition in hypersonic flow. *Experiments in Fluids 26*, 1 (1999), 169–176.

[2] MACK, C. J., SCHMID, P. J., AND SESTERHENN, J. L. Global stability of swept flow around a parabolic body: connecting attachment-line and crossflow modes. *Journal of Fluid Mechanics 611* (2008), 205–214.

[3] PAREDES, P., GOSSE, R., THEOFILIS, V., AND KIMMEL, R. Linear modal instabilities of hypersonic flow over an elliptic cone. *Journal of Fluid Mechanics 804* (2016), 442–466.

2D SELF-SUSTAINING PROCESSES IN PLANE POISEUILLE-COUETTE FLOW INVOLVING CRITICAL LAYER / BOUNDARY LAYER INTERACTION

Andrew Walton [*1] and Rishi Kumar[1]
[1]Department of Mathematics, Imperial College London, South Kensington Campus, London SW7 2AZ, UK

Summary Plane Poiseuille-Couette flow is well-known to exhibit a linear Tollmien-Schlichting-type instability provided the wall sliding speed does not exceed a critical value. Here we investigate how this instability is modified by the inclusion of finite-amplitude effects. A large Reynolds number self-sustaining structure is found which involves the interaction of two nonlinear critical layers with near-wall Stokes regions. A global property of the flow-field, involving the vorticity of the mean-flow distortion, is used to determine the amplitude of the modes which are found to exist beyond the linear cut-off. In the situation where the phasespeed is almost equal to the sliding speed, a new nonlinear structure arises involving critical layer/shear layer interaction. The numerical results from this latter interaction are found to compare well with full solutions of the Navier-Stokes equations.

INTRODUCTION

A dynamical systems approach to transition, in which equilibrium solutions of the Navier-Stokes equations play a key role in transitional and turbulent dynamics, has become increasingly popular in recent years. The relevant equilibrium solutions are those in which there is a mutual interaction between a roll flow in the cross-stream plane, a streamwise streak and a wave propagating in the streamwise direction. This interaction is fundamentally three-dimensional in nature and has no obvious two-dimensional analogue. If we wish to consider Tollmien-Schlichting (TS) instabilities, which are inherently two-dimensional, then the roll/streak/wave theories are not directly applicable, even at high Reynolds number, unless a very specific spanwise variation is imposed. In this talk we discuss self-sustaining processes that can operate in two dimensions, involving the interaction of internal critical layer dynamics with structures that arise near the boundaries. As a specific example we consider plane Poiseuille-Couette flow (PCF) which is well-known to support a TS form of instability provided the sliding speed $V < V_c \simeq 0.34$ [1]. The basic PCF can be written in the non-dimensional form

$$U_0 = 1 - y^2 + Vy, \tag{1}$$

where the channel walls are positioned at the scaled locations $y = \pm 1$ and V is the scaled wall speed. The Reynolds number R here is based on the channel half-width and the maximum velocity of the Poiseuille component of the flow.

A new investigation of the linear stability of this flow through the use of the Orr-Sommerfeld equation has revealed surprisingly intricate stability properties as the sliding speed is increased, with multiple neutral curves co-existing for $V < V_c$. In figure 1(a) we show the results of some recent computations. For $V = 0.017$, we note the existence of a stable intrusion inside the familiar neutral curve that one would expect for plane Poiseuille flow. As V is increased, this finger of stability extends to smaller R before slicing off a portion of the original neutral curve (figure 1(b)), thereby generating a second curve. Eventually however, as $V \to V_c-$, all regions of instability disappear. In this talk we will see that, by comparing Navier-Stokes solutions with a nonlinear asymptotic SSP model, such a model can accurately describe the nonlinear solutions that bifurcate from the upper neutral curve in figure 1(b).

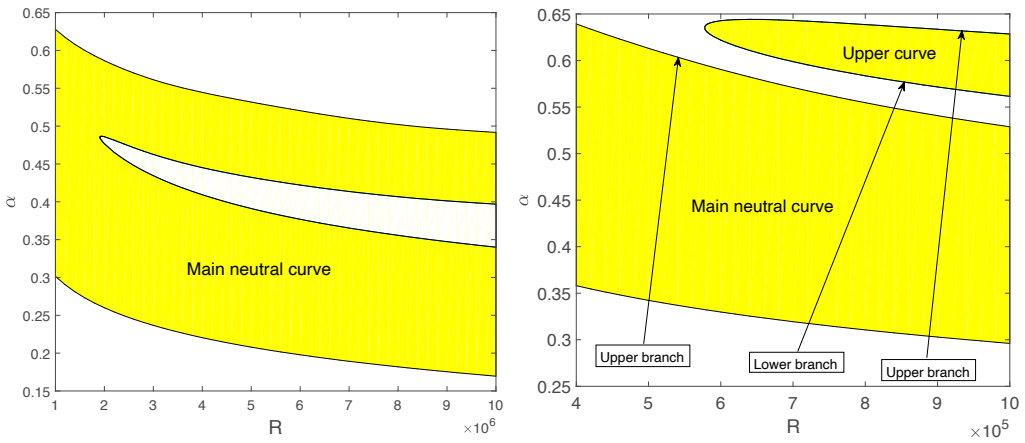

Figure 1: Linear neutral curves for PCF. (a) $V = 0.017$; (b) $V = 0.019$. Wavenumber α versus Reynolds number R. The shaded regions are unstable.

*Corresponding author. E-mail: a.walton@imperial.ac.uk

PROPERTIES OF THE SSP

Consider the quantity

$$\tau_M(y) = \frac{1}{2\pi}\frac{d}{dy}\int_0^{2\pi} (u - U_0)\, d\xi \tag{2}$$

as a measure of the vorticity associated with the mean-flow distortion brought about by nonlinear wave interaction. Here $\xi = \alpha(x - ct)$ is a travelling wave coordinate, while $u(\xi, y)$ represents the streamwise velocity of a disturbance with wavenumber α and phasespeed c. Integration of the Navier-Stokes equations reveals that τ_M assumes the same value at both walls. It follows from this that any jump in vorticity occurring across internal critical layers must be exactly balanced by an equal and opposite jump across the boundary layers that adjoin each wall. Away from these regions the flow is essentially inviscid in nature with the travelling waves satisfying a form of Rayleigh's equation. The critical layers in our theory are of strongly nonlinear type, ensuring that the regularising effects of viscosity are only encountered at high order with the singularity occurring in the Rayleigh equation effectively smoothed out by nonlinear effects via a jump condition.

FORMULATION OF THE SSP

We will consider two different interaction structures. The first consists of two internal critical layers embedded within an inviscid region, with Stokes layers adjoining each wall. The solution procedure consists of solving a Rayleigh eigenvalue problem subject to nonlinear jump conditions at the singular points: this determines c as a function of wavenumber and sliding speed. The amplitude of the modes is found by calculating the vorticity jumps across the two critical layers and two Stokes layers and setting the total jump to zero. Although the Rayleigh part of the problem is a numerical one, the jumps can all be determined analytically, leading to an explicit expression for the amplitude in terms of the wavenumber and sliding speed. Calculations show that solutions exist for sliding speeds considerably in excess of the linear cut-off. This structure is relevant to solutions which bifurcate from the upper branch of the main neutral curve in figure 1(b).

As the mode amplitude is increased, calculations show that $c \to V$ and hence the upper critical layer moves ever closer to the Stokes region. A new distinguished scaling describes how the two layers merge, forming a near-wall shear layer. In this novel structure, although a Rayleigh equation still governs the bulk of the flow, the vorticity jump across the lower Stokes layer is now a higher-order effect, leaving the amplitude dependence determined by balancing the jumps across the single critical layer and the shear layer. Again, these jumps can be computed analytically and an explicit formula for the amplitude obtained. More detail concerning these structures will be given in the talk: see also [2], [3].

COMPARISON OF ASYMPTOTIC THEORY WITH NAVIER-STOKES SOLUTIONS

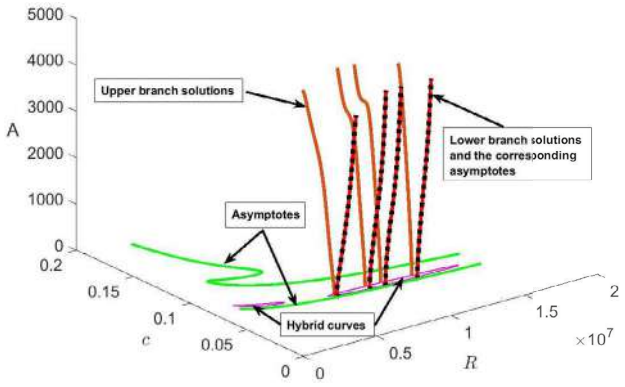

Figure 2: Solid lines: Navier-Stokes solutions at fixed R that bifurcate from the upper linear neutral curve (denoted 'hybrid curve' here). Dots: asymptotic predictions arising from the SSP theory. The sliding speed $V = 0.025$.

To test the accuracy of the asymptotic SSP at finite Reynolds number we have computed nonlinear travelling wave solutions of the full Navier-Stokes equations by a homotopy process starting from the upper curve on figure 1(b). The results, together with asymptotic predictions, are shown in figure 2. The solutions which bifurcate from the lower branch of this curve can be seen to be in excellent agreement with those arising from the asymptotic theory.

References

[1] Potter M. C. Stability of plane Poiseuille-Couette flow. *J. Fluid Mech.* **24**: 609–619, 1966.
[2] Kumar R., Walton A. G. Amplitude-dependent three-dimensional neutral modes in plane Poiseuille-Couette flow at large Reynolds number. *Q. J. Mech. Appl. Math.* **72**: 87–130, 2019.
[3] Kumar R., Walton A. G. Self-sustaining dual critical layer states in plane Poiseuille-Couette flow at large Reynolds number. *Proc R. Soc. Lond.* **A475**: 20180881, 2019.

OPTIMAL PERTURBATIONS AND GLOBAL MODES OF ABLATIONS FLOWS RELATIVE TO INERTIAL CONFINEMENT FUSION

Grégoire Varillon[*1,2], Jean-Marie Clarisse[1], Clotilde Degroote[1], and Arnaud Couairon[2]
[1]CEA, DAM, DIF, F-91297 Arpajon, France
[2]CPHT, CNRS, Ecol ePolytechnique, Institu tPolytechnique de Paris, F-91128 Palaiseau, France

Summary The first non-modal linear stability analysis of an unsteady ablation waves in the context of inertial confinement fusion is carried out. Optimal initial perturbations are computed using a direct-adjoint method obtained by applying the Lagrange multiplier technique. The non-normality of the perturbation evolution operator under the assumption of a frozen mean flow is also studied. Ablation wave perturbations are found to be prone to transient amplification at both short and intermediate final times whether for small or large perturbation wavelengths. Two distinct mechanisms of optimal growth are presently identified. These results contrast with previous results based on normal mode analysis, simulations and dedicated experiments of selected perturbation configurations, for which only large wavelengths are subject to a possible amplification whereas small wavelengths are damped.

INTRODUCTION

Inertial confinement fusion (ICF) aims at achieving controlled thermonuclear fusion by imploding spherical hollow pellets filled with light fusible nuclei [1]. These implosions occur under the action of an external irradiation flux which is tailored to induce a deflagration, or *ablation*, heat wave that thrusts inwardly the pellet outer shell, the *ablator*, chosen to be opaque to the incident irradiation. The resulting flow consists of a subsonic heat front, or *ablation front*, coinciding with the leading edge of the expansion wave of the heated material, that penetrates into the ablator, preceded by a forerunning shock wave (Fig. 1 top). Inherently unsteady, such ablation flows are compressible and highly nonuniform with a steep heat front, owing to the strong nonlinearity of the heat transport and the intense incident heating. The success of ICF depends on reaching, and maintaining for a sufficiently long time, the high temperatures and densities in the fusible payload that are necessary to ignite thermonuclear reactions.

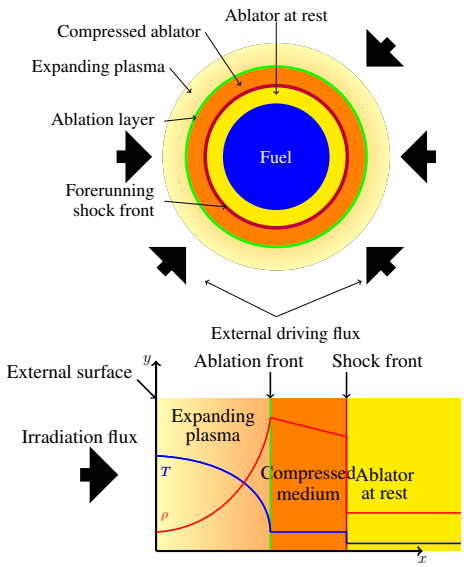

Figure 1: (top) Configuration of the early stage, so-called *shock transit phase*, of an ICF pellet implosion. Pellet sizes are of the order of one millimeter and implosion durations are in the 10–20 nanosecond range. (bottom) Structure of a planar ablation wave representative of the shock transit phase.

Hydrodynamic instabilities that develop during a pellet implosion, because they could induce burn-through of the ablator, excessive losses of symmetry, too large amounts of mixing between the heated and colder parts of the fusible, are detrimental to such a goal [1]. The understanding of hydrodynamic perturbation dynamics during such implosions is therefore of primary importance to ICF. In particular, the hydrodynamic stability of ablation fronts remains one of the most critical issues to the success of ICF [2].

NON-MODAL LINEAR STABILITY ANALYSIS

The hydrodynamic stability of ablation flows has been theoretically investigated using simplifying mean-flow assumptions that are not necessarily met in actual cases: e.g. mean-flow steadiness, low Mach-number approximation, unbounded domains, discontinuous ablation front, flow region uniformity of some sort [3]. In addition, these works have exclusively relied on the method of normal modes, focusing on the least stable eigensolutions that only yield asymptotic stability results and thus omitting possible transient growth phenomena proper to non-normal operators. Moreover, ablation flow unsteadiness induces finite durations of perturbation evolution regimes, thus logically raising the question of short-term perturbation dynamics [4]. More realistic configurations are classically investigated by means of multidimensional numerical simulations with ICF hydrodynamics codes which incorporate the most relevant physical phenomena. These "full-physics" simulations which overcome the above shortcomings, consist in computing perturbation amplifications from selected perturbed initial or boundary conditions that are considered to be the "most dangerous" for a given mean-flow configuration. Besides the computational cost of such simulations, this way of proceeding faces a major difficulty in having to deal, in actual ICF implosions, with multiple perturbation sources whose contributions remain, for some of them, unsufficiently known and controlled.

*Corresponding author. E-mail: gregoire.varillon@polytechnique.edu.

Given this context, methods of non-modal stability theory [5], being capable of identifying the most dangerous perturbations in time-dependent flows of finite durations, are not only most appropriate but also appear to be a necessity. Since the current cost of full-physics simulations forbids the implementation of such methods with existing ICF hydrocodes, we presently have recourse to a simplified modeling of unsteady ablation waves. This modeling is provided by self-similar solutions to the Euler equations with nonlinear heat conduction in slab symmetry. Some of these solutions are representative of the first stage of a pellet implosion, or *shock transit phase*, during which the fore-running shock wave is still traveling inside the ablator [6]. In particular these self-similar flows present the complete structure of an ablation wave: a leading shock front, a compressed region, an ablation layer and an expanding flow region (Fig. 1 bottom).

Optimal initial perturbations and global modes

In the present work we report on results obtained from the first non-modal stability analysis ever performed on an ablation flow relevant to ICF. Dealing with an unsteady mean flow, optimal initial perturbations (OIPs) are searched by means of direct-adjoint iterations.

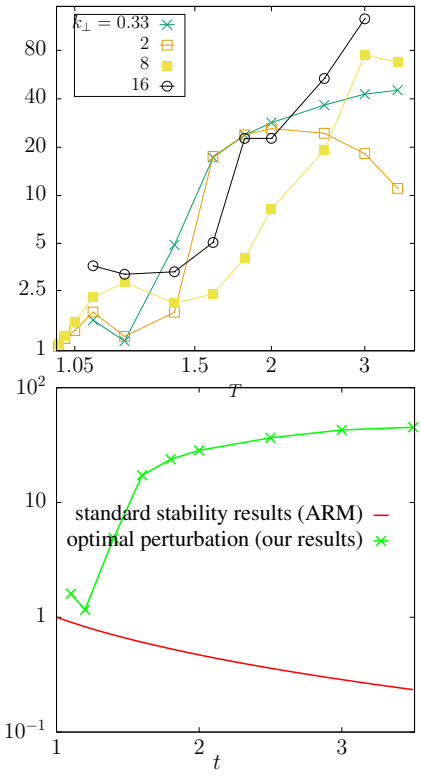

Figure 2: (top) Gain curves of perturbations norm for various transverse wavenumbers. (bottom) Amplification of perturbations norm in the case of the classical ablative Richtmyer–Meshkov instability (ARM) in red, and the amplification of the optimal initial perturbation in green.

The adjoint problem is derived from the Lagrange multipliers technique [7]. In the process, we obtain for the first time, to our knowledge, a proper formulation of a Lagrange functional in the case of an incompletely parabolic system of evolution equations with perturbed dynamical boundaries. This analysis is supplemented by a study of the non-normality of the ablation flow by means of the numerical range and global modes of the perturbation evolution operator under the assumption of a frozen mean flow. Optimal initial perturbations and global modes are characterized in terms of linear propagating waves (acoustics, entropy, vorticity).

Amplification of initial perturbations previously held to be stable

The optimization of initial perturbations exhibits short-term perturbation amplification for all transverse wavenumbers spanning the perturbation spectrum classically considered for ICF pellets and all terminal times within the duration of the shock transit phase of a pellet implosion (Fig. 2 top). These results contrast with previous results based on normal mode analysis, simulations and dedicated experiments of selected perturbation configurations, for which only large wavelengths are subject to a possible amplification whereas small wavelengths are damped. This finding points out the necessity of a non-modal analysis for ablation flows in the context of ICF. Optimal growth mechanisms are analyzed to consist in *acoustic–vorticity wave interactions* at short terminal times and *ablation layer–shock front couplings* at long terminal times. A physical analysis of OIPs shows that these strongly differ from the perturbation configuration of the ablative Richtmyer–Meshkov instability (ARM) [8] usually held as one of the most dangerous in ICF. In particular, OIPs may lead to stronger amplifications than the ARM configuration of identical wavenumber (Fig. 2 bottom).

CONCLUSIONS AND PERSPECTIVES

In the present work we have conducted the first non-modal analysis of ablation flows relevant to inertial confinement fusion. Our results show that ablation flows are prone to amplifying a wide range of perturbations and particularly that perturbation wavelengths up to now believed to be stable may actually lead to strong transient amplifications. This work illustrates the necessity of non-modal analysis in the context of ICF and paves the way to a receptivity analysis and, on the longer term, to *optimal design* of ICF pellets.

References

[1] S. Atzeni and J. Meyer-ter-Vehn. The physics of inertial fusion. Oxford University Press, Oxford, UK 2004.
[2] J. Lindl *et al*. Review of the National Ignition Campaign 2009-2012. *Phys. Plasmas* **21**, 2014.
[3] V. Bychkov *et al*. Combustion phenomena in modern physics: I. Inertial confinement fusion. *Prog. Energy Comb. Sci.* **47**, 2015.
[4] J.-M. Clarisse *et al.* Transient effects in unstable ablation fronts and mixing layers in HEDP. *Phys. Scr.* **91**, 2016.
[5] P. J. Schmid, Nonmodal stability theory. *Annu. Rev. Fluid Mech.* **39**, 2007.
[6] C. Boudesocque-Dubois *et al.* Self-similar solutions of unsteady ablation flows in inertial confinement fusion. *J. Fluid Mech.* **603**, 2008.
[7] M. D. Gunzburger. Introduction into mathematical aspect of flow control and optimization *in* Lecture Series 1997-05 on Inverse Design and Optimisation Methods. VKI Fluid Dynamics, 1997.
[8] V. N. Goncharov. Theory of the ablative Richtmyer-Meshkov instability. *Phys. Rev. Lett.* **82**, 1999.

VISCOUS EFFECT ON THE CYLINDRICAL RAYLEIGH-TAYLOR INSTABILITY

Renhao Zeng, Jianjun Tao *, and Yuanbo Sun
Department of Mechanics and Engineering Science, Peking University, Beijing, China

Summary The three-dimensional Rayleigh-Taylor instability (RTI) at the cylindrical interface between two viscous fluids is analysed without the irrotational assumption. It is revealed that the most unstable mode is three dimensional, and the corresponding azimuthal wavenumber increases step by step with the increase of the interface radius R. Depending on the scale of the amplitude of the wavenumber vector relative to 1/R, the cylindrical RTI may be close to different asymptotic cases, e.g. the semi-infinite planar viscous limit, the semi-infinite planar inviscid limit, the finite-thickness but inviscid limit, or the finite-thickness creeping-flow limit, and the growth-rate curves show different scaling laws accordingly.

INTRODUCTION

The Rayleigh-Taylor instability (RTI) may occur at the interface when the lighter fluid is accelerated into the heavier one. Chandrasekhar considered the RTI of an radially accelerated spherical interface between incompressible viscous fluids [1]. For the cylindrical interface, the effects of compressibility, geometry, and nonlinearity have been studied for inviscid fluids [2, 3]. With the irrotational assumption, where the tangential stress at the interface and the unstable vorticity field are ignored, the viscous effect was considered to study the Rayleigh-Plateau instability rather than the RTI as claimed in the paper's title [4]. Therefore, the full three-dimensional stability analysis of RTI at the cylindrical interface between viscous fluids, to the best of our knowledge, has not been carried out so far, and is the main objective of the present paper.

PHYSICAL MODEL AND RESULTS

We consider a cylindrical interface separating two incompressible, immiscible, and viscous fluids, i.e. the inner fluid 1 and the outer fluid 2. The fluids are subjected to a steady inward deceleration $\vec{g} = g\vec{e}_r$, where $g > 0$ and $\vec{e}_r$ is the unit radial direction. The outer fluid is denser than the inner, i.e. $\rho_2 > \rho_1$, and the kinematic viscosity ratio is named as $S = \gamma_2/\gamma_1$. The characteristic length, time, and pressure scales are selected as $(\nu_1^2/g)^{1/3}$, $(\nu_1/g^2)^{1/3}$, and $\rho_1(\nu_1 g)^{2/3}$, respectively, and the dimensionless linearized governing equations for the disturbing velocity $\widetilde{u}$ and pressure $\widetilde{p}$ can be obtained. The Atwood number is defined as $A_t = \frac{\rho_2-\rho_1}{\rho_2+\rho_1}$. Following the method proposed in our previous paper [5], the disturbing velocity is decomposed into an irrotational part $\widetilde{\vec{u}}_j^1$ and a viscous part $\widetilde{\vec{u}}_j^2$, and the normal mode is introduced in the form of $f(\widetilde{r},\theta,\widetilde{z}) = F(\widetilde{r})e^{i(n\theta+\widetilde{kz})+\widetilde{\sigma t}} + c.c.$, where n, $\widetilde{k}$, and $\widetilde{\sigma}$ are the azimuthal wave number, the axial wave number, and the growth rate, respectively. The initial interface lies at $R = r_0/(\nu_1^2/g)^{1/3}$, and the total wavenumber $\widetilde{k}_t$, the amplitude of the wavenumber vector, is defined as $\widetilde{k}_t = \sqrt{\widetilde{k}^2 + \frac{n^2}{R^2}}$.

It is assumed that at far field $\widetilde{\vec{u}}_2$ dies away and the boundary conditions at the axis are the same as used in [6]. After applying the continuity conditions at the interface for the velocities and the stresses, we can obtain the dispersion relation $\widetilde{\sigma} = f(n, \widetilde{k}, A_t, R, S)$. For details of the solving method we refer to the previous paper [5]. When the character wavelength is much smaller than the interface radius, or $\widetilde{k}_t \gg 1/R$, the system degenerates to the infinite plane case, and the viscous dispersion relation reduces to the same as that of Bellman *et al.* [7]. For inviscid fluids, the dispersion relations of the three-dimensional and two-dimensional cases [2, 3] can be recovered from the present relation as well.

Different from the inviscid cases studied previously, the most unstable mode of the cylindrical viscous RTI has finite azimuthal and axial wavenumbers. For interfaces of small radii R at $A_t = 0.5$ and $S = 1$, e.g. $R = 0.1$ and 1 as shown in Fig. 1, the most unstable mode is anti-symmetric in the cross section, i.e. $n = 1$. With the increase of the interface radius R, the azimuthal wavenumber of the most unstable mode increases step by step, and the corresponding axial wavenumber

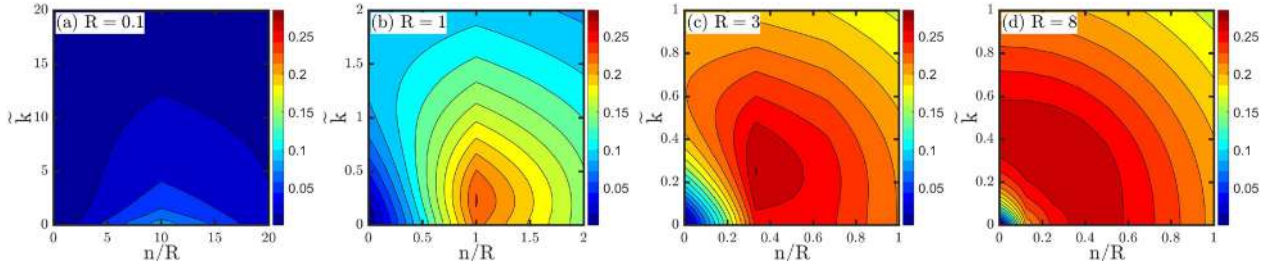

Figure 1: The isocontours of the growth rate $\widetilde{\sigma}$ in the wavenumber n-$\widetilde{k}$ space. $A_t = 0.5$ and $S = 1$.

*Corresponding author. E-mail: jjtao@pku.edu.cn

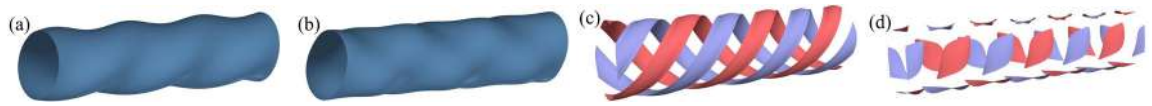

Figure 2: The interfaces and the isosurfaces of vorticity for the most unstable mode of $(R, A_t, S) = (8, 0.5, 1)$ are shown in (a)(b) and (c)(d), respectively. (a) and (c) are the results for the single mode, and (b) and (d) are the superposition of the modes with the positive and negative axial wavenumbers. Red and green isosurfaces in (c) and (d) represent the positive and negative axial component of vorticity, respectively.

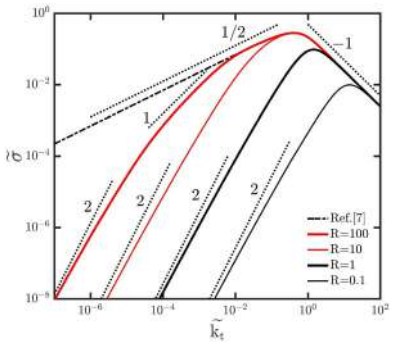

Figure 3: The growth rate $\widetilde{\sigma}$ as a function of $\widetilde{k_t}$ at different R. $A_t = 0.5, S = 1$, and $n = 0$. The result of semi-infinite planar viscous RTI is shown as the dot dash line.

increases as well at each step of the azimuthal wavenumber. When R is large enough, the growth rate is nearly isotropic and the RTI is close to the case of plane interface between semi-infinite fluids. Some examples of the unstable interface and the isosurfaces of vorticity are shown in Fig. 2. It is noted that the interface distortion is amplified in order to show the mode pattern clearly.

It is shown in Fig.3 that the growth rates for different R have different scaling laws at different wavenumber ranges. When the wavelength is much smaller than the cylindrical interface radius, or the total wavenumber is much larger than $1/R$, the curvature effect becomes weak and the cylindrical RTI is close to the plane case. For plane interface between semi-infinite viscous fluids, the approximate but analytical solution of Bellman and Pennington [7] can be expanded for large k as

$$\sigma = \nu_c k^2 + \frac{1}{2}\nu_c^{-1} k^{-2} g k A_t - \nu_c k^2 + O[(gkA_t)^2] \approx \frac{gA_t}{2}\nu_c^{-1} k^{-1}, \tag{1}$$

where the combined viscosity $\nu_c = (\mu_1 + \mu_2)/(\rho_1 + \rho_2)$. Therefore, $\widetilde{\sigma}$ scales as $\widetilde{k_t}^{-1}$ for different R at high $\widetilde{k_t}$ regime as shown in Fig. 3. In the presentation, other slopes of the growth rate shown in Fig. 3, i.e. 2, 1, 1/2, will be explained in terms of the finite-thickness and creeping flow limit, the finite-thickness but inviscid limit, and the planar and inviscid limit, respectively. In addition, the effects of the Atwood number and the viscosity ratio will be discussed as well.

CONCLUSIONS

In the previous studies on the cylindrical RTI, the viscous effect was ignored and higher wavenumber lead to higher growth rate of the unstable mode. When the viscous effect is considered, it is revealed that the most unstable mode is three-dimensional and has finite azimuthal and axial wavenumbers, which increase generally with the increase of the interface radius. When the total wavelength is much longer than the interface radius, the finite-thickness effect brought by the cylindrical geometry substantially lower the growth rate in comparison with the semi-infinite planar case as shown in Fig. 3, and causes different scaling laws at different wavenumber regimes.

References

[1] Chandrasekhar S. The character of the equilibrium of an incompressible fluid sphere of variable density and viscosity subject to radial acceleration. *Q. J. Mech. Appl. Math.* **8**: 1-21, 1955.

[2] Anuchina N. N., Volkov V. I., Eskov N. S., Ilyutina O. S., Kozyrev O. M. 2D and 3D simulation of Rayleigh-Taylor instability in cylindrical and spherical geometries. *Matem. mod* **16**: 69-86, 2004.

[3] Epstein R. On the Bell-Plesset effects: The effects of uniform compression and geometrical convergence on the classical Rayleigh-Taylor instability. *Phys. Plasmas* **11**: 5114-5124, 2004.

[4] Asthana R., Awasthi M. K., Agrawal G. S. Viscous Potential Flow Analysis of Rayleigh-Taylor Instability of Cylindrical Interface. *Appl. Mech. Mater.* **110-116**: 769-775, 2012.

[5] Sun Y. B., Tao J. J., He X. T. Unified decomposition method to study Rayleigh-Taylor instability in liquids and solids. *Phys. Rev. E* **97**: 063109, 2018.

[6] Tao J. Critical Instability and Friction Scaling of Fluid Flows through Pipes with Rough Inner Surfaces. *Phys. Rev. Lett.* **103**: 264502, 2009.

[7] Bellman R., Pennington R. H. Effects of Surface Tension and Viscosity on Taylor Instability. *Q. Appl. Math.* **12**: 151-162, 1954.

MECHANISM OF CROSSFLOW INDUCED BREAKDOWN IN A HYPERSONIC THREE- DIMENSIONAL BOUNDARY LAYER

Caihong Su*[1], and Yufeng Han[1]
[1]Lab for high-speed aerodynamics, School of Mechanical Engineering, Tianjin University, Tianjin, China

Summary The mechanism of transition induced by crossflow is investigated for a hypersonic swept flat plate boundary layer using direct numerical simulation (DNS). Results show that the nonlinear evolutions of the stationary vortex can lead to a slight increase of the wall friction coefficient. However, laminar breakdown occurs only when secondary instability modes set in. Stability characteristics of the distorted mean flow are analyzed using linear stability theory. It shows that the process of laminar breakdown can be divided into two stages. During the first stage, the infection point of the mean flow appear, and the modes with high frequency modes are unstable and amplify. Then followed by the second stage, low-frequency modes are significantly amplified so that the flow profiles are greatly modified and breaks down to turbulence.

INTRODUCTION

For a sustained hypersonic flying vehicle, an accurate prediction of boundary-layer transition is of great importance for evaluating the aerodynamic force and designing the thermal protection system. For a complex three-dimensional body, crossflow instability may arise and dominate transition. Conceptually, transition induced by crossflow instability involves the following stages [1-2]: 1) primary instability, which could manifest as either stationary or travelling vortex; 2) secondary instability following the saturation of the crossflow vortex; 3) breakdown to turbulence. Most research work focus on primary and secondary instabilities, and only a few studies are concerned with the laminar breakdown to turbulence, but mainly in low-speed regime. In the current paper, we are concerned with the mechanism of crossflow induced breakdown of a hypersonic blunt plate boundary layer. We are aiming to show that during breakdown, how the stability characteristics of the mean flow are changed, finally leading to turbulence.

METHODOLOGY AND MEAN FLOW

The flow over a swept flat plate with a circular nose is investigated, as shown in Fig. 1. The Mach number is 6, and the nose radius is 3.5cm. The temperature of the oncoming flow is 226.5K. The swept angle is 45°. The governing equations are three-dimensional Navier-Stokes equations. The reference length is taken as the nose radius. The physical quantities of oncoming flow are used to non-dimensionalize the equations except $\rho_\infty u_\infty^2$ for pressure. The Reynolds number so defined is 79100. The computations involve two steps. 1) Steady computations. First, the base flow containing the bow shock ahead of the body is computed. Then a domain behind the shock, downstream of the nose, as shown in Fig.1, is taken out to compute the evolution of the stationary vortex. 2）Unsteady computations. Secondary instability modes are introduced on the flow distorted by the stationary vortex to trigger transition. High-order difference schemes are used to discretize the governing equations. The wall is non-slip and assumed to be adiabatic.

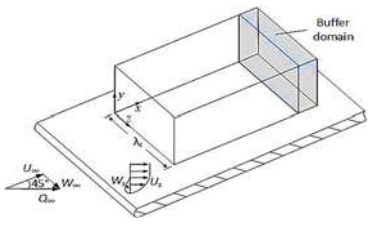

Figure 1 Computational model.

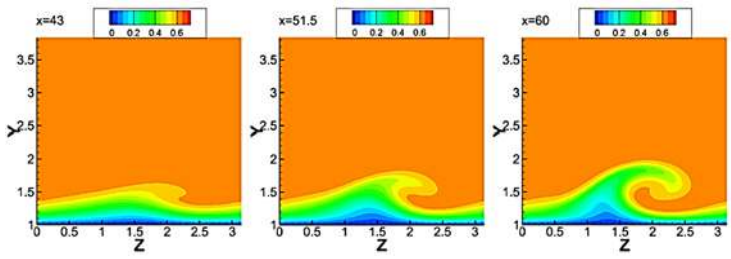

Figure 2 Contour of streamwise velocity fluctuations at different x for β=2.

RESULTS

Evolution of stationary vortex

The computation of the evolution of the stationary vortex starts at x=6 (with the origin at the center of the circular nose). Its spanwise wavenumber is taken to be β=2, and the computational domain in the spanwise direction is taken as one wavelength of the stationary vortex. As shown in Figure 2, the stationary vortex grows and saturates. It was found that the evolutions of stationary vortex with different spanwise wavenumbers are similar (not shown here).

Breakdown to turbulence

As the stationary vortex grows, the mean flow is distorted, so that it is susceptible to secondary instability. Bi-global analysis is performed for the modified mean flow at x=36 to obtain the secondary modes. Two secondary instability

*Corresponding author. E-mail: su_ch@tju.edu.cn.

modes of type z with frequencies of ω=4 and 5 are introduced simultaneously at x=36 to trigger transition. The initial amplitudes of two modes are 0.01. Figure 3 shows the iso-surface of streamwise velocity with u=0.55. Figure 4 shows the wall friction coefficient, in which the case without introducing secondary modes is also plotted for comparison. It can be seen that the stationary vortex causes a slight increase of C_f as it saturates, but the stationary vortex alone cannot trigger transition. As the introduced secondary modes amplify, breakdown occurs. It can be divided into two stages. In stage I, starting from x=46.25 to x=52.5, C_f deviates that of the laminar flow but agrees with that of the stationary vortex. Then stage II follows, where C_f continue to grow and the flow finally transitions to turbulence.

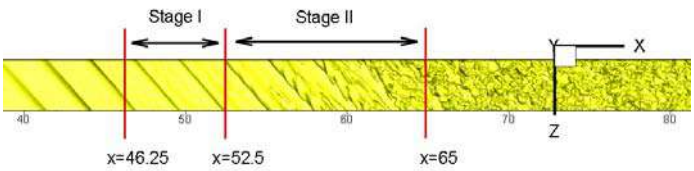

Figure 3 Iso-surface of streamwise velocity (u=0.55).

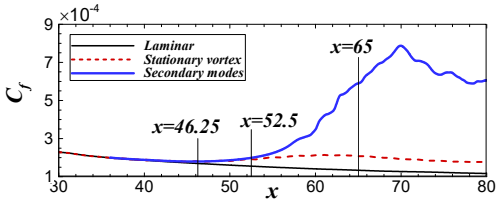

Figure 4 Wall friction coefficient.

Mechanism of breakdown

Distorted mean flow of stage I and stage II is shown in Figure 5a and 5b, respectively. In stage I, infection points appear in the upper part of the mean flow profile, which indicates a type of instability. While in stage II, the infection point weakens and meanwhile the lower part of the mean flow is modified significantly and finally evolves into a turbulent profile. Figure 6 shows the unstable region of the mean flow obtained by linear stability analysis, in which the case without introducing secondary modes is also plotted for comparison. As expected, in stage I (figure 6a-6d), for both cases, the unstable region of the mean flow enlarges, indicating more unstable modes are to amplify and in turn modify the mean flow. While in stage II, for the case of secondary modes, the modes with high frequencies gradually decay (see figure 6e) and meanwhile those with low frequencies amplify (see figure 6f). At x=62.5, multiple groups of modes appear. Finally at x=65, there is no unstable mode and the flow becomes turbulent. In contrast, for the case of stationary vortex, unstable region does not change much.The modes with low frequencies (near ω=0) are marginally unstable, and the laminar breakdown does not occur.

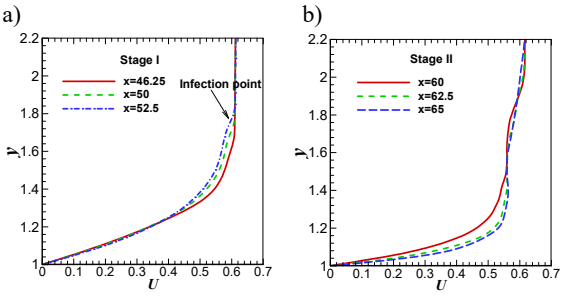

Figure 5 Distorted mean flow of a) stage I and b) stage II.

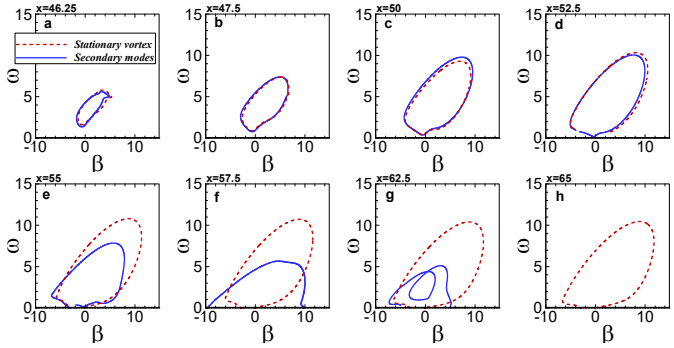

Figure 6 Unstable region of distorted mean flow.

CONCLUSIONS

The mechanism of transition induced by crossflow is investigated for a hypersonic swept flat plate boundary layer. The whole process of transition including the evolutions of stationary vortex, secondary modes and the laminar breakdown is simulated using DNS. Results show that breakdown occurs only when secondary instability modes set in and amplify. The process of breakdown involves two stages. In stage I, C_f deviates from the value of laminar flow, but agrees with that of the stationary vortex. And in stage II, C_f continues to grow and the flow breakdowns to turbulence. Stability characteristics of the mean flow show that, during stage II, the high-frequency modes decay and meanwhile the low-frequency modes become significantly unstable, and the mean flow is modified rapidly to a turbulent profile.

References

[1] Saric W. S., Reed H. L., White E B. Stability and transition of three-dimensional boundary layers. *Annual Review of Fluid Mechanics*, 2003, 35(1): 413-440.

[2] Kocian T. S., Moyes A. J., Reed H. L., et al. Hypersonic Crossflow Instability, *Journal of Spacecraft and Rocket*, 2019, 56(2): 432-446.

THE INFLUENCE OF THREE-DIMENSIONALITY ON ROSSITER MODES IN A COMPRESSIBLE OPEN CAVITY

Marlon Sproesser Mathias*[1] and Marcello A F Medeiros[1]
[1]São Carlos School of Engineering, University of São Paulo, São Carlos, São Paulo, Brazil

Summary We study the stability of a compressible flow in an open cavity. First, bi-global instability analysis was performed in a region of the parameter space where Rossiter and centrifugal modes are unstable, with the Rossiter modes substantially more unstable. Next, DNS was carried out investigating the interaction of these modes. Without the centrifugal modes the non-linear regime of the Rossiter modes has sharp spectral peaks that diverge substantially from Linear Stability Theory (LST) predictions and approach empirical predictions of Rossiter modes. In the presence of centrifugal modes, the Rossiter modes are much more broad band in spectra, but frequency and other aspects are substantially closer to LST predictions.

INTRODUCTION

Open cavities represent a canonical flow that has been extensively studied. However, the parameter space is vast and there remains several areas that require investigation. Two well-known modes of open cavity flows are the Rossiter modes and the centrifugal modes. The Rossiter mode is predominantly 2D [1], while the centrifugal mode is essentially 3D [2, 3]. These modes can co-exist, but their mutual interaction has not been studied in great detail. Here we investigate a scenario where the Rossiter modes are much more unstable and have much higher frequencies than centrifugal ones. This is a typical scenario, in particular at higher Mach [4, 5]. We carried out LST of the bi-global type to investigate the modes and performed nonlinear DNS to study their interaction. Despite the frequency and amplitude difference the centrifugal mode had a remarkable effect on the Rossiter mode dynamics.

METHODS

The study used two different tools, both developed in our research group. A DNS was used for the flow simulation, which integrates the compressible Navier-Stokes equations using a stretched Cartesian grid; a spectral-like finite differences scheme; a 4th order Runge Kutta method for time marching; and buffer-zones at the open boundaries. The LST was performed by a Jacobian-free time-stepping algorithm. More details of both methods can be found in [6].

RESULTS

The flow parameters in this study are: cavity aspect ratio $L/D = 2$, Reynolds number $Re_D = 1000$, Mach number $Ma = 0.5$, incoming boundary layer thickness $D/\theta_C = 100$. L and D are the cavity length and depth and θ_C is the boundary layer momentum thickness at the cavity leading edge.

Figure 1 exhibits the results from the linear stability analysis. The left-hand side plots show the leading (most unstable) flow modes as a function of the span-wise wave-number β, the top graph shows the real part of the eigenvalue, which corresponds to the temporal growth; and the bottom graph shows the imaginary part, which gives to the mode frequency.

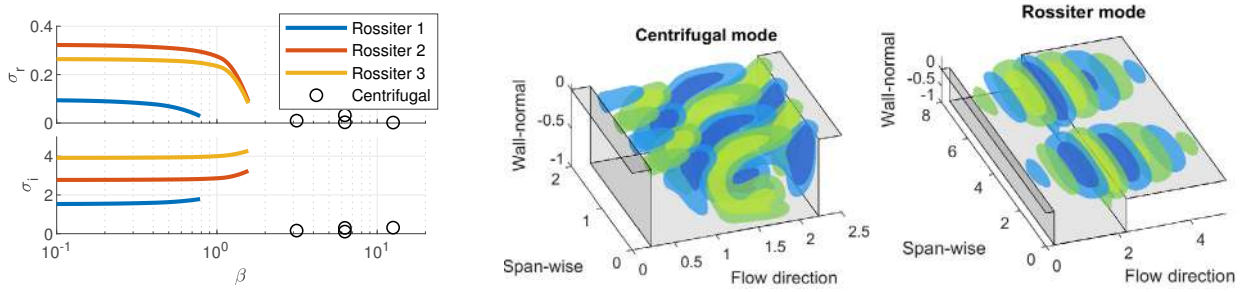

Figure 1: Linear stability results. (left) Eigenmodes as a function of β. (centre) iso-surfaces of stream-wise velocity for a centrifugal mode. (right) iso-surfaces of stream-wise velocity for a Rossiter mode

Rossiter modes are most unstable when $\beta = 0$, that is, 2D, but may also be unstable for long span-wise wavelengths, i.e. low β. Centrifugal modes are essentially 3D. In our set of parameters, they are much less unstable than the Rossiter modes, and are unstable only at values of β that are higher than the highest β for an unstable Rossiter mode. The right-hand side plots of Fig. 1 show iso-surfaces of stream-wise velocity for a centrifugal and a 3D-modulated Rossiter modes.

*Corresponding author. E-mail: marlon.mathias@usp.br.

Figure 2 (top) shows the time series of pressure at the cavity trailing edge obtained from DNS for different span-wise domains and grid refinements. Figure 2 (bottom) shows their spectra as a function of time, which was obtained by using a moving time window. In the figure, the resulting frequencies are compared with those predicted by the LST and by a Rossiter mode empirical equation [4]. LST and empirical frequency predictions are close, but distinguishable. From Fig. 1, LST predicts modes R1 to R3 to be unstable, with mode R2 as the most unstable. Accordingly, the 2D simulation shows that initially mode R2 is the dominant and exhibits the frequency predicted by LST. In the colour logarithmic scale used, when mode R2 is discernible, harmonics are also seen. Soon after, mode R2 frequency approaches the Rossiter mode empirical predictions, which are slightly lower than LST predictions. In the third and final stage, mode R1 becomes the dominant with a frequency very close the empirical prediction.

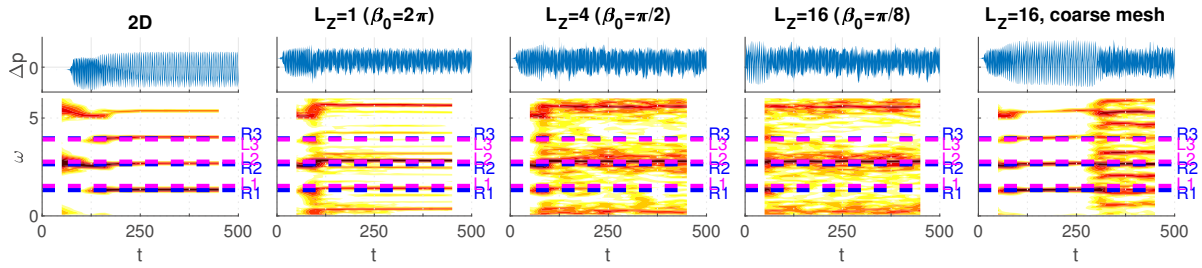

Figure 2: (top) Time series of pressure at the cavity trailing edge for various span-wise domain lengths. (bottom) Spectra as a function of time, logarithmic colour scale.

The next simulation is 3D, with a span-wise domain ($L_Z = 1$) that is large enough for one centrifugal mode, but not enough for unstable 3D Rossiter modes. In the early stages, the 3D simulation somewhat resembles the 2D one. However, they differ severely in later stages, where mode R2 remains the dominant at a frequency close to LST predictions. The 3D simulation produces a flow in which the Rossiter modes are closer to the linear theory predictions. Also consistent with LST, a centrifugal mode is observed in the spectrum, at low frequency and small amplitude.

The two largest span-wise domains tested admit many centrifugal modes and also unstable 3D Rossiter modes. Their results are essentially statistically independent on the span-wise domain. Mode R2 is dominant, the centrifugal modes are also observed, while modes R1 and R3 are not observed. The spectral peaks become much broader, but the frequency of the R2 mode is closer to the LST predictions than to the empirical ones. Once more, the 3D simulation results are fairly consistent with LST, including the frequency of the Rossiter mode and the fact that the observed mode is the most unstable according to LST. It is also observed that the spectra are much broader than in 2D or short 3D simulation.

For the last simulation the span-wise refinement was reduced such that it could not capture the centrifugal mode. The flow dynamics remain very similar to 2D simulations for a long initial period. This suggests that it is the centrifugal mode that leads to the dominance of the R2 mode. At the later stages of this simulation the results are more irregular, but we believe this is an artifact of the poor resolution.

FINAL REMARKS

Rossiter modes are essentially 2D, but 3D effects must not be disregarded. Despite being much less unstable than the Rossiter modes in our paremeter set, the centrifugal modes have a very substantial impact on the dynamics of the Rossiter modes. The final stage of the 3D non-linear simulation with sufficiently long span-wise domains are consistent with LST predictions in that the most unstable mode as predicted by LST (R2 mode) is the dominant and its frequency is closer to the LST predictions than to empirical ones. However this result is crucially dependent on the presence of centrifugal modes. In essence, it seems that LST provides good prediction, but not for the reasons expected. Tests we made for $D/\theta = 35$, other conditions remaining the same, showed a similar pattern. However, it is yet unclear whether this is a general result or a coincidence restricted to this parameter range. The final paper and presentation will include extended results and more in depth analysis.

References

[1] Rossiter J. E. Wind-tunnel experiments on the flow over rectangular cavities at subsonic and transonic speeds. London, 1964
[2] de Vicente J., Basley J., Meseguer-Garrido F., Soria J., Theofilis V. Three-dimensional instabilities over a rectangular open cavity: from linear stability analysis to experimentation. *J Fluid Mech*. **748**:189–220, 2014
[3] Citro V., Giannetti F., Brandt L., Luchini P. Linear three-dimensional global and asymptotic stability analysis of incompressible open cavity flow. *J Fluid Mech*. **768**:113–40, 2015
[4] Yamouni S, Sipp D, Jacquin L. Interaction between feedback aeroacoustic and acoustic resonance mechanisms in a cavity flow: a global stability analysis. *J Fluid Mech*. **717**:134–65, 2013
[5] Mathias M. S. Medeiros M. The Influence of the Boundary Layer Thickness on the Stability of the Rossiter Modes of a Compressible Rectangular Cavity. *2018 Fluid Dynamics Conference Internet. Reston, Virginia: American Institute of Aeronautics and Astronautics*, 2018.
[6] Mathias M. S. Medeiros M. Direct Numerical Simulation of a Compressible Flow and Matrix-Free Analysis of its Instabilities over an Open Cavity. *J Aerosp Technol Manag*. **10**:1–13, 2018.

SOUND GENERATION IN A HOLE-TONE CONFIGURATION

Javier Sierra Ausin*[1,2], David Fabre[1], Vincenzo Citro[2], and Flavio Giannetti[2]
[1]Institutde Méanique de sfluides de Toulouse (IMFT),Toulouse 31400,France
[2]Dipartimento di Ingegneria (DIIN),Universitá degli Studi diS alerno,Fisciano 84084,Italy

Summary The purpose of this work is to investigate the flow dynamics in a "hole-tone" configuration, namely the flow through two successive apertures (Fig. 1), a configuration which is known to lead to powerful tonal noise at moderately low Reynolds numbers. Thresholds of instability are determined using fully compressible linear global stability analysis. The resulting nonlinear saturated state is then characterized through a weakly nonlinear asymptotic method starting from compressible equations. Results of these global approaches are then compared to direct numerical simulations using an augmented incompressible model, which consists of considering the flow as locally incompressible (under the hypothesis of acoustic compactness), and introducing compressibility into the boundary conditions to model the impedance of a resonant cavity and of a monopolar radiation in the downstream domain. The augmented model confirms the existence of a bistable range of Re leading to two possible fundamental frequency, in accordance with observations from a previous an experimental campaign.

INTRODUCTION

The problem of a flow passing through two circular holes in a plate (known as the hole-tone configuration) is encountered in many practical applications, including human whistling, wind instruments, whistling of a tea kettle [1] or birdcalls (devices used by hunters to imitate bird singing) [2, 3].

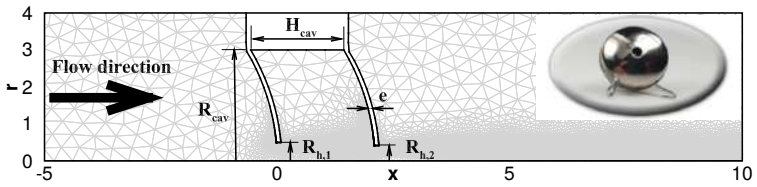

Figure 1: Sketch of the hole-tone configuration, frame of reference and definition of geometrical parameters. An example of computational mesh is also reported in light gray. An actual birdcall is depicted in the upper right corner. e denotes the thickness of the cavity wall, radius of holes $R_{h,i}, i = 1, 2$, radius and length of the cavity are denoted by R_{cav} and H_{cav} respectively. Values of geometrical parameters can be found in Longordardi et al. [3].

The physical mechanism responsible for whistling made the object of debates among acousticians the second half of the 19th century. [4, 5, 6]. Early attempts approached the problem mainly from a purely acoustic point of view, the influence of the mean flow was neglected. Another possibility are the so called lumped models, where the hydrodynamical component of the system is modeled by a system of a limited number of degrees of freedom. Recently, the problem of sound generation has been tackled with linearized Navier Stokes equations. The instability mechanism at the threshold has been analyzed on the one-hole [7, 8] and the two-hole configuration [2] using incompressible Navier Stokes equations where the compacity of acoustic sources is assumed and with compressible [3] LNSE. These efforts allowed to identify the difficulties associated to boundary conditions which has been addressed in [9, 10]. An experimental campaign on the hole-tone configuration carried out by [11] has shown the appearance of complex dynamics such as quasi-periodic or chaotic behaviours for low to moderate Reynolds numbers. Theoretical and numerical determinations should provide some answers to the reason behind dynamics and the underlying physical mechanism.

PRELIMINARY RESULTS

Most of sound generating devices are in essence self-sustained oscillators composed of two parts: An *acoustic system* which acts as a resonator and a *hydrodynamic system* which can be a shear flow. The purpose of this work consists in the analysis of dynamics of the double hole tone configuration with an special emphasis on the hydrodynamic part. Four approaches are carried out. The first is a stability analysis based on *linearised compressible Navier Stokes equations* (LNSE) [3] which allow the determination of the Threshold Reynolds numbers. The second is *weakly nonlinear asymptotic* method based on multiple-scale approach[12, 13] allowing to characterize the saturated state for values of Re slightly above the threshold. The third is a direct numerical simulation (DNS) of the full compressible equations. This strategy leads to strong constraints on the time step and domain dimensions in the range $M \ll 0.05$, making a parametric study costly. To overcome this limitation, a fourth approach is proposed, namely a DNS based on an *augmented incompressible*

*Corresponding author. E-mail: javier.sierra@imft.fr

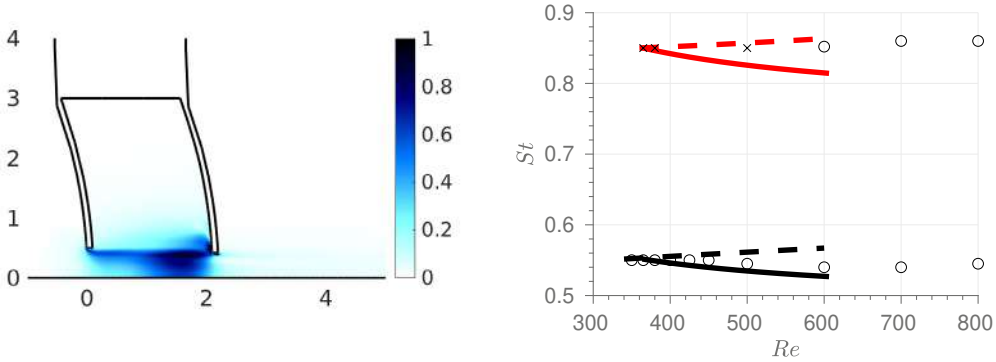

(a) (b)

Figure 2: (a) Structural sensitivity of the flow field [14]. (b) Prediction of the whistling fundamental harmonic frequency at $M = 0.02$. Dashed lines corresponds to the frequency determined via compressible linearised Navier Stokes equations, solid lines to compressible weakly nonlinear stability, crosses (×) to unstable frequencies and circles (○) to stable frequencies determined by augmented model

model [2, 3] assuming the flow as locally incompressible and incorporating the effect of compressibility as impedance-like boundary conditions at the inlet, outlet, and bottom of the cavity. Underlying assumptions of the methodology are compactness and monopolar radiation, and these assumptions have been verified in experiments [11]. The inlet and the cavity are modelled as a Helmhotz resonator whereas at the outlet a radiation boundary condition is imposed.

$$\int_{\Gamma_i} \Big[\frac{\partial p'}{\partial t} + \frac{S_i}{V_i M^2}\mathbf{u}' \cdot \mathbf{n}\Big] dS = 0, \quad (i = \text{inlet or cavity}); \qquad \int_{\Gamma_{out}} \Big[\frac{\partial^2 \mathbf{u}' \cdot \mathbf{n}}{\partial t^2} + \frac{8}{M S_{out}} p'\Big] dS = 0 \tag{1}$$

This fourth approach has previously been validated in the linear regime [3]. In the present work, validation will be done by comparison with fully compressible results (linear, weakly nonlinear and fully nonlinear). Once validated, the augmented incompressible model will be used for parametric exploration of the parametric space. Particular attention will be paid to ranges of parameters where experiments show rich nonlinear dynamics, including bistable behavior (with hysteretic transition between two modes with different frequencies), quasi-periodic, and chaotic regimes. Preliminary results have already confirmed the existence of a range of Reynolds number Re of bistability, characterized by the existence of two stable limit cycles with different frequencies. The properties of these states are in good accordance with linear and weakly nonlinear approaches close to the thresholds, but deviations are observed for larger values of Re.

Furthermore, compressible linear and weakly non linear stability allow to characterize the instability mechanism using structural sensitivity tools. The results indicate a purely hydrodynamic feedback mechanism originating from a "wavemaker" region localized along the shear layer in the region between the two holes, see Fig. 2.

References

[1] RH Henrywood and A Agarwal. *Physics of fluids*, 25(10):107101, 2013.
[2] D Fabre, P Bonnefis, F Charru, S Russo, V Citro, F Giannetti, and P Luchini. In *International Symposium on Musical Acoustics (ISMA), Le Mans, France, July*, pages 7–12, 2014.
[3] Raffaele Longobardi, David Fabre, Paul Bonnefis, Vincenzo Citro, Flavio Giannetti, and Paolo Luchini. In *IUTAM Symposium on Critical flow dynamics involving moving/deformable structures with design applications*, 02 2018.
[4] John William Strutt and Baron Rayleigh. *The theory of sound*. Dover, 1945.
[5] H Helmholtz. The theory of sound, 1878.
[6] H Bouasse. *Instruments à vent*. Impr Delagrave, 1929.
[7] David Fabre, Raffaele Longobardi, Paul Bonnefis, and Paolo Luchini. The acoustic impedance of a laminar viscous jet through a thin circular aperture. *Journal of Fluid Mechanics*, 864:5–44, 2019.
[8] D Fabre, R Longobardi, V Citro, and P Luchini. Acoustic impedance and hydrodynamic instability of the flow through a circular aperture in a thick plate. *Journal of Fluid Mechanics*, 885, 2020.
[9] Javier Sierra, David Fabre, and Vincenzo Citro. Efficient stability analysis of fluid flows using complex mapping techniques. *Computer Physics Communications*, page 107100, 2019.
[10] J Sierra, D Fabre, and V Citro. In *International Symposium on Fluid-Structure-Sound Interactions and Control (FSSIC), Crete, Greece, August*, 2019.
[11] D Fabre, P Bonnefis, S Marragou, Raffaelle Longobardi, V Citro, F Giannetti, P Luchini, David LoJacono, and Benjamin Fry. The whistling jet instability: experimental investigation and global stability modelling of a birdcall. In *ERCOFTAC Sig33 conference, La certosa di Pontignano, Siena Italy, June 2017*, 2014.
[12] Denis Sipp and Anton Lebedev. Global stability of base and mean flows: a general approach and its applications to cylinder and open cavity flows. *Journal of Fluid Mechanics*, 593:333–358, 2007.
[13] D. Fabre, V. Citro, D. Ferreira Sabino, P. Bonnefis, J. Sierra, F. Giannetti, and M. Pigou. *Appl. Mech. Rev.*, 70(6):060802, 2019.
[14] Flavio Giannetti and Paolo Luchini. Structural sensitivity of the first instability of the cylinder wake. *Journal of Fluid Mechanics*, 581:167–197, 2007.

ONSET OF SUSTAINED TURBULENCE IN CHANNEL FLOW AND PLANE COUETTE FLOW

Masaki Shimizu*[1] and Paul Manneville[2]
[1]Graduate School of Engineering Science, Osaka University, Toyonaka, Japan
[2]Hydrodynamics Laboratory, CNRS-UMR 7646, Ecole Polytechnique, Palaiseau, France

Summary We investigate the onset of turbulence in channel flow (CF) and in plane Couette flow (PCF). The spatiotemporally fluctuating turbulent patterns in both systems experience a continuous transition. The critical values for sustained turbulence are $\mathrm{Re_g} \simeq 712$ in CF and $\mathrm{Re_g} \simeq 337$ in PCF. In the vicinity of $\mathrm{Re_g}$, the two systems obey directed-percolation (DP) universality however with different spatial dimensionality, 1D for CF and 2D for PCF. This comes from the symmetry difference in the minimal turbulent elements of the two systems. In CF they correspond to downstream active heads, which move obliquely at a constant speed along a chosen direction, yielding an asymmetrical, effectively 1D, turbulent pattern. On the other hand, the minimal elements in PCF, the spots, have the potential to extend in either span-wise direction and form a symmetrical, effectively 2D, pattern.

INTRODUCTION

In several kinds of wall-bounded flows, the transition to turbulence has recently been shown to be continuous and obey directed-percolation (DP) universality in the sense of critical phenomena [1–5]. In channel flow (CF) and Waleffe flow (WF), which are flows between two-parallel planes, the transition to turbulence was reported to belong to the spatially two-dimensional DP (2D-DP) universality class [1, 3]. In the case of CF, several studies have however experimentally and/or numerically proven the existence of sustained turbulence significantly below the DP critical point [6–9]. We scrutinized this inconsistency in [5], gave evidence of a symmetry-breaking bifurcation of the turbulence pattern, and showed that the transition does not follow 2D-DP below the bifurcation point. On the other hand, a discontinuous transition around $\mathrm{Re_g} \sim 325$ was observed in plane Couette flow (PCF) [11, 12]. On the basis of their study of WF, Chantry *et al.* [3] attributed this discontinuous character to size effects and advocated a 2D-DP continuous transition at $\mathrm{Re_g}$ in PCF, but in a very narrow range of Reynolds number and in a (very) long time limit, $t \sim O(10^5)$. In the following we summarize our numerical findings on the characteristics of the transition to turbulence around $\mathrm{Re_g}$ in CF and PCF.

CHANNEL FLOW

In transitional CF various turbulent patterns are observed depending on the Reynolds number. Figure 1 displays two kinds of pattern below and above $\mathrm{Re_2} \simeq 1010$. For $\mathrm{Re} < \mathrm{Re_2}$ all localized turbulent bands (LTBs) point to the same direction. On the other hand, for $\mathrm{Re} > \mathrm{Re_2}$ LTBs of both directions exist and the turbulent pattern is statistically symmetrical. This change is associated with a pitchfork bifurcation controlled by the 'transversal splitting' rate [5]. Above $\mathrm{Re_2}$ turbulence expansion becomes intrinsically two-dimensional and obeys 2D-DP (Fig.2 left). On the other hand, turbulence spread below $\mathrm{Re_2}$ follows 1D-DP (Fig.2 right), because the LTB density only fluctuates in the direction perpendicular to their main orientation, under the control of the 'longitudinal splitting' rate.

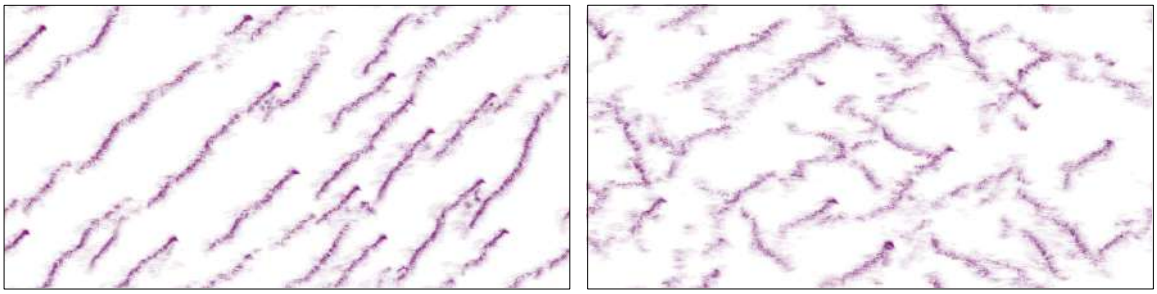

Figure 1: Symmetry-broken pattern at Re=850 (left) and symmetry-restored pattern at Re=1050 (right). The flow direction is from left to right. The domain size is (1000,2,500).

PLANE COUETTE FLOW

In PCF's transitional range, two kind of turbulent patterns are found: the tight-banded pattern [12, 13], Fig. 3 (right), and the spatiotemporally fluctuating pattern, Fig. 3 (left). The band pattern is only obtained upon quasi-static decrease of Re. Both types of pattern seem to coexist around $\mathrm{Re_g}$ at least over our observation time $O(10^5)$. Whereas the band pattern is seen to decay abruptly, the fluctuating pattern goes through a continuous, seemingly 2D-DP, transition at $\mathrm{Re_g} \simeq 337$ though the statistics over sampling durations $O(10^5)$ is not yet good enough (Figure 4).

*Corresponding author. E-mail: shimizu@me.es.osaka-u.ac.jp

Unlike in CF but like in WF, the fluctuating pattern in PCF remains statistically symmetrical in the vicinity of $\mathrm{Re_g}$ (Fig. 3, left). This is because turbulent spots keep a tail-head symmetry that leaves them the potential to stretch into either oblique direction equally [12].

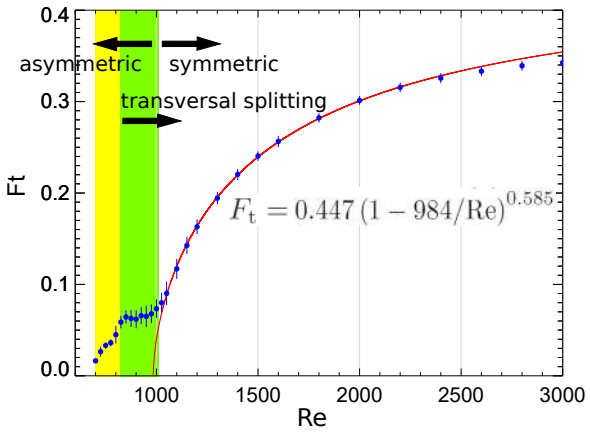

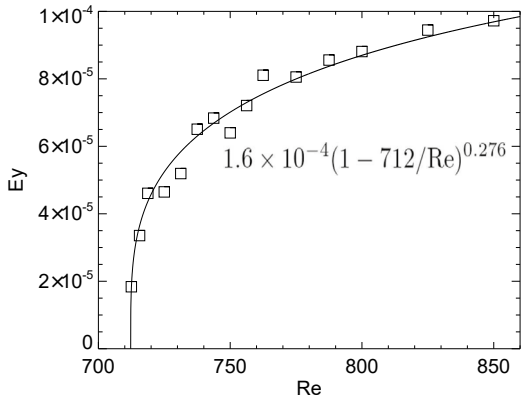

Figure 2: (left) Turbulent fraction as a function of Reynolds number. (right) Turbulent energy as a function of Reynolds number.

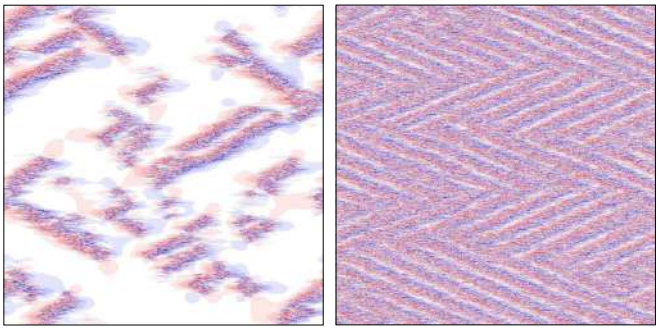

Figure 3: Flow patterns in plane Couette flow at Re=338 (left) and Re=400 (right). The flow direction is from left to right. The domain size is (1000,2,1000).

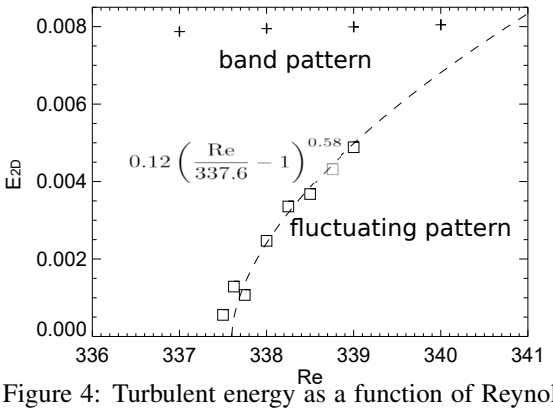

Figure 4: Turbulent energy as a function of Reynolds number.

CONCLUSIONS

Our numerical simulations showed that the onset of fluctuating turbulent patterns is continuous in CF and PCF although in PCF the band pattern stably persists for long durations around $\mathrm{Re_g}$. The transition in CF starts with an asymmetrical one-sided flow pattern while following 1D-DP. By contrast, in PCF the fluctuating turbulent pattern is always symmetrical and the transition follows 2D-DP. This difference comes from the characteristics of minimal elements that maintain turbulence. The minimal element in CF corresponds to the downstream active head (DAH) [10], which is necessary to maintain an LTB and shows relative periodic motion while traveling to one side of the span-wise direction. The collective motion of DAHs without frequent transversal splittings results in the one-sided flow pattern illustrated in Fig. 1 (left) [5]. On the other hand, the turbulent spot in PCF shows chaotic motion, keeps the symmetry with respect to stream-wise and span-wise directions, and leads the symmetrical pattern (Figure 3 left). This symmetry difference is at the origin of the observed universality-dimension discrepancy between these two flows.

References

[1] Sano M., Tamai K. A universal transition to turbulence in channel flow. *Nature Physics* **12**: 249–253, 2016.
[2] Lemoult G. *et al.* Directed percolation phase transition to sustained turbulence in Couette flow. *Nature Physics* **12**: 254–258, 2016.
[3] Chantry M. *et al.* Universal continuous transition to turbulence in a planar shear flow. *J. Fluid Mech.* **824**: R1, 2017.
[4] Hiruta Y., Toh S. Subcritical laminar-turbulence transition with wide domains in simple two-dimensional Navier–Stokes flow without walls. *arXiv preprint* 1805.04257, 2018.
[5] Shimizu M., Manneville P. Bifurcations to turbulence in transitional channel flow. *Phys. Rev. Fluids* **4**: 113903, 2019.
[6] Xiong X. *et al.* Turbulent bands in plane-Poiseuille flow at moderate Reynolds numbers. *Physics of Fluids* **27**: 041702, 2015.
[7] Tsukahara T., Ishida T. Lower bound of subcritical transition in plane Poiseuille flow. *Nagare* **34**; 383–386, 2015.
[8] Hof B. *Workshop on Extreme Events and Criticality in Fluid Mechanics: Computations and Analysis* Toronto, Jan. 25–29, 2016.
[9] Kanazawa T. *et al.* Two-dimensionally localized turbulence in plane channel flow. *9th JSME-KSME Thermal and Fluids Eng. Conf.*, 2017.
[10] Xiao X., Song B. The growth mechanism of turbulent bands in channel flow at low Reynolds numbers. *J. Fluid Mech.* **883**: R1, 2020.
[11] Bottin S. *et al.* Discontinuous Transition to spatio-temporal intermittency in the plane Couette flow. *Europhys. Lett.* **43**: 171–176, 1998.
[12] Duguet Y. *et al.* Formation of turbulent patterns near the onset of transition in plane Couette flow. *J. Fluid Mech.* **650**: 119–129, 2010.
[13] Manneville P. On the growth of laminar-turbulent patterns in plane Couette flow. *Fluid Dyn. Res.* **44**: 031412, 2012.

TOWARDS GLOBAL PERTURBATION ANALYSIS OF LIQUID/GAS FLOWS

Simon Schmidt*[1], Lutz Lesshafft[2], Outi Tammisola[3], and Kilian Oberleithner[1]
[1] Laboratory for Flow Instability and Dynamics, Technische Universität Berlin, 10623 Berlin, Germany
[2] LadHyX, CNRS/Ecole Polytechnique/Institut Polytechnique de Paris, 91128 Palaiseau, France
[3] FLOW, Engineering Mechanics, KTH Royal Institute of Technology, SE-100 44 Stockholm, Sweden

Summary We develop a framework to compute linear global modes for interfacial liquid/gas flows by linearising a state-of-the-art nonlinear flow solver. Eigenpairs of the the underlying linearised Navier-Stokes operator are extracted by time-stepping of the linearised solver. The methodology is applied to compute global modes of a planar two-phase wake. The linear model is able to accurately predict the onset of global instability and the frequencies of the leading eigenvalues compare excellently to the observed frequencies of the nonlinear flow. The flexibility of the framework further allows straightforward extensions to more complex flow scenarios.

INTRODUCTION

Shear flows of two immiscible fluids can exhibit distinctively different and potentially more complex stability characteristics compared with their single-phase equivalents. This can be due to the presence of not only a momentum gradient of the adjacent fluids but also a density and viscosity gradient. Furthermore, the presence of a surface tension force can influence the stability of the flow.

While surface tension usually acts stabilizing in plane flow configurations, a study by [2] found that for certain configurations, surface tension destabilises a plane wake or jet flow which is stable in its absence. These somewhat surprising results are partially confirmed in a subsequent study by [1] who found an unstable global mode for some of the configurations of the former study. However, for other configurations they found no global instability, thereby raising doubts concerning the validity of the surface tension-induced destabilisation found by [2]. Assessment of the stability of such flows is usually done through the framework of linear stability analysis, which seeks solutions of the Navier-Stokes operator, linearised around a steady base flow. In a local analysis, the underlying base flow is assumed to be parallel and therefore only dependent on one spatial coordinate, whereas for a global analysis it might be inhomogeneous in all spatial coordinates.

Although global analysis has become a standard tool for analysing single-phase flows, its application to multi-phase flow has not found widespread attention, yet. The work of [2] is one of the very few reported applications of global stability for liquid/gas flows. In their approach, the linearised operator is constructed explicitly. Here, we explore a different approach, by developing a framework which allows for computation of global modes by means of time-stepping of a linearised DNS solver, capable of computing two-phase flows. For our study, we choose the open-source code BASILISK [3], which offers an adaptive quad/octree spatial discretisation and a geometrical Volume-Of-Fluid (VOF) interface representation, combined with a well-balanced surface tension scheme. We perform nonlinear and linear computations to shed more light on the surface tension induced instability investigated by [2].

LINEARISATION PROCEDURE FOR INTERFACIAL FLOWS

We decompose the flow into a basic state and an infinitesimal perturbation $\epsilon \ll 1$, which gives $\mathbf{u} = \mathbf{U} + \epsilon\mathbf{u}'$ and $p = P + \epsilon p'$ for the velocity and pressure respectively. A continuous level-set function ϕ can be derived from the discontinuous volume fraction c and is perturbed as $\phi = \Phi + \epsilon\phi'$. Therewith associated are a perturbed curvature $\kappa = K + \epsilon\kappa'$ and a normal vector $\mathbf{n} = \mathbf{N} + \epsilon\mathbf{n}'$. Inserting this decomposition into the nonlinear Navier-Stokes equations, and the transport equation of the level-set function, while retaining only leading-order terms in ϵ, we arrive at

$$\begin{aligned}[\tilde{\rho} + H_\epsilon(\Phi)(1-\tilde{\rho})](\partial_t\mathbf{u}' + \mathbf{u}'\cdot\nabla\mathbf{U} + \mathbf{U}\cdot\nabla\mathbf{u}') + 2[\delta_\epsilon(\Phi)\phi'(1-\tilde{\rho})](\mathbf{U}\cdot\nabla\mathbf{U}) \\ = -\nabla p' + \frac{1}{Re}\nabla\cdot\left[(\tilde{\mu} + H_\epsilon(\Phi)(1-\tilde{\mu}))\left(\nabla\mathbf{u}' + \nabla^T\mathbf{u}'\right)\right] + \frac{1}{Re}\nabla\cdot\left[(\delta_\epsilon(\Phi)\phi'(1-\tilde{\mu})\left(\nabla\mathbf{U} + \nabla^T\mathbf{U}\right)\right] \\ + \frac{1}{We}\left[\kappa'\mathbf{N}\delta_\epsilon(\Phi) + K\mathbf{n}'\delta_\epsilon(\Phi) + K\mathbf{N}\phi'\partial_\Phi\delta_\epsilon(\Phi)\right], \quad (1a)\end{aligned}$$

$$\partial_t\phi' + \nabla\cdot(\Phi\mathbf{u}') + \nabla\cdot(\phi'\mathbf{U}) = 0, \quad (1b)$$

where $H_\epsilon(\Phi)$ is the Heaviside function and $\delta_\epsilon(\Phi)$ the Dirac Delta function, derived from the zero contour of Φ.

*Corresponding author. E-mail: schmidt.simon01@gmail.com

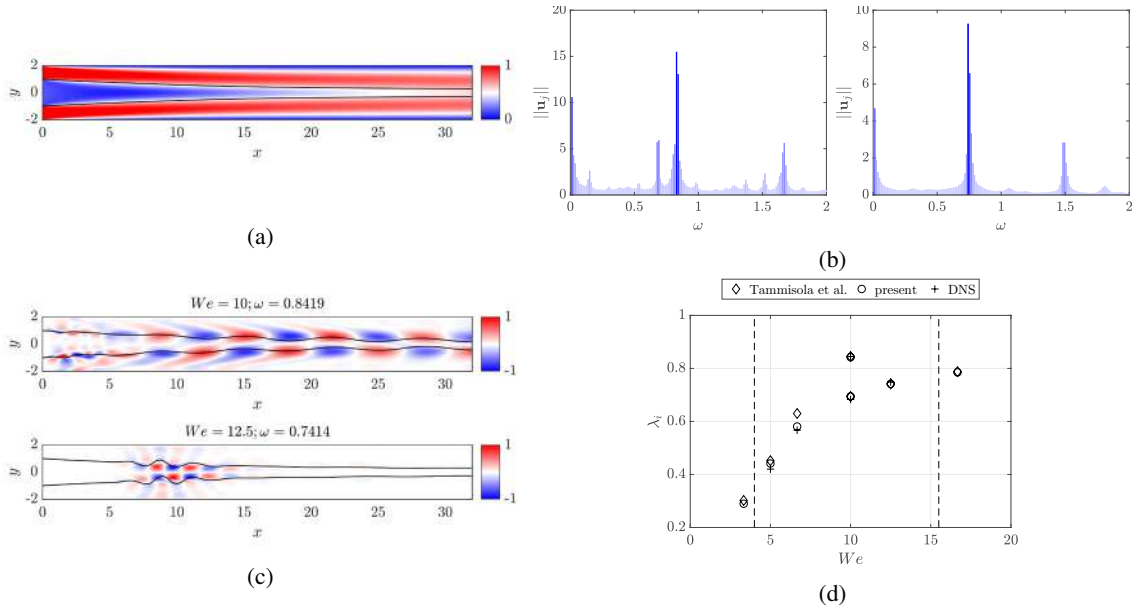

Figure 1: (a) Baseflow velocity field U and interface for $We = \infty$. (b) Frequency spectrum for $We = 104$ (left) and $We = 12.5$ (right) (c) Mode shapes of the most unstable global mode, top: $We = 10$; bottom: $We = 12.5$. (d) Comparison of the frequencies ω of the DNS , λ_i of the linear stability analysis and results of [2]. Configurations inside the dashed lines correspond to a supercritical nonlinear flow.

GLOBAL MODES OF A PLANAR TWO-PHASE WAKE

Nonlinear simulation

In the study of [2] no validation of the studied configurations is performed. Therefore, it remains to be shown whether the computed linear modes really are present in the nonlinear flow, and if so, whether their shapes and frequencies are accurately predicted by linear theory. We therefore present nonlinear results for selected wake-type configurations of their study. All flows are confined in a channel with $h = h_2/h_1 = 1$ where $h_1 = h_2 = 1$ are the heights of the respective fluid streams in the half-channel at the inlet, and subscripts 1,2 refer to the inner and outer fluid stream, respectively. The plug flow velocity ratio of both streams at the inlet is $\Lambda^{-1} = (U_1 + U_2)/(U_1 - U_2) = -1.4$. The density and viscosity ratios are $\rho_2/\rho_1 = 1$ and $\mu_2/\mu_1 = 1$. We fix $Re = \frac{\rho_2 U_2 h_2}{\mu_2} = 316$ and compute results for Weber numbers $We = \frac{\rho_2 U_2^2 h_2}{\sigma}$, ranging from $We = 16.\bar{6}$ to $We = 3.\bar{3}$. Indeed, the nonlinear simulations show an unsteady flow in this regime as is seen in figures 1b, 1c. In particular, the flow at $We = 12.5$ oscillates at a single frequency while for $We = 10$ two frequencies are present which are destabilised solely through surface tension.

Linear Stability Analysis

For the linear stability analysis, a steady base flow is computed for $We = \infty$, as shown in figure 1a. The computation of linear global modes is done by constructing a low-dimensional subspace representation of the linearised Navier-Stokes operator using an Arnoldi procedure. The Krylov vectors spanning the subspace are obtained by time-stepping of the linearised solver. Following the nonlinear analysis, we compute linear global modes for the same range of Weber numbers. The predicted frequencies in all cases are close to those computed for the nonlinear flow and compare well to the results of [2] (figure 1d). The growth rates are consistent with the onset of growth in the nonlinear computations.

CONCLUSIONS

We investigated the global linear stability of a plane two-phase wake and compared the results to nonlinear simulations. The linear analysis is able to accurately capture the bifurcation point of the flow and the global mode frequencies are in excellent agreement with the predicted frequencies of the nonlinear flow. To the authors knowledge, the present study is among the first applications of global linear stability analysis using the full set of linearised Navier-Stokes equations to interfacial flows. The methodology of time-stepping of a linearised DNS-solver further offers the flexibility for application to more complex and potentially three-dimensional flows without much difficulty.

References

[1] Biancofiore, L., Gallaire, F., Laure, P. & Hachem, E. 2014 Direct numerical simulations of two-phase immiscible wakes. *Fluid Dyn. Res.* **46** (4), 041409.

[2] Tammisola O., Lundell F., Söderberg L. D. Surface tension-induced global instability of planar jets and wakes. *J. Fluid Mech.* **713**: 632–658, 2012.

[3] BASILISK, web site **http://www.basilisk.fr**.

ABSOLUTE AND GLOBAL INSTABILITY INDUCED BY THREE-DIMENSIONALITY IN LAMINAR SEPARATION BUBBLES

Daniel Rodríguez*[1], Elmer M. Gennaro[2], and Leandro F. Souza[3]
[1]ETSIAE-UPM (School of Aeronautics)-Universidad Politénica de Madrid,Spain.
[2]São Paulo State University (UNESP),Campus São João da Boa Vista SP,Brazil.
[3]Institute of Mathematical and Computer Sciences,University of São Paulo,São Carlos-SP, Brazil.

Summary Laminar separation bubbles (LSBs) are dominated by inflectional instability of disturbance waves. Under certain conditions, this instability can become of absolute nature, leading to self-excited flow oscillations and vortex shedding. Analyses of 1D velocity profiles show that a peak reversed flow $> 15\%$ is required for the onset of absolute instability. This threshold is larger than the reversed flow reported for most LSBs, and that the $\sim 7-8\%$ required for self-sustained 3D instability. The absolute/convective instability of separated flows is revisited here. Spanwise distortion of separated shear layers is shown to have a strong destabilizing effect, leading to absolute instability for LSBs with mean reversed flow much lower than 10%. This absolute instability gives rise to a 3D global oscillator, that triggers laminar-turbulent transition without requiring external disturbances.

INTRODUCTION

Laminar flow separation is an usual phenomenon on aerodynamic surfaces that takes place when strong enough adverse-pressure-gradients and moderate Reynolds numbers are present. Flow instability and laminar-turbulent transition dominate the evolution and dynamics of the separated flow and the formation of a laminar separation bubble (LSB). Failure of the detached flow to reattach within a short distance, forming what is known as a long LSB, implies important detrimental modifications of the aerodynamic performance. This process, named bursting, and the search for a criterion for its prediction have been an active topic of research since Gaster [1]. The analysis of the flow instabilities occurring in separated flow has successfully guided many research efforts. LSBs are dominated by convective amplification of instability waves by the inflectional mean velocity profiles [2, 3]. Intriguingly, a similar scenario is recovered in direct numerical simulations in which the convective instability is neglected by prescribing undisturbed inlet conditions (e.g. [4, 5]). Pauley *et al.* [4] postulated that the onset of spontaneous vortex shedding, related to the shift from convective to absolute nature of the inflectional instability, could be used as an indication of bursting. Using the peak reversed flow $u_{rev} = -u_{min}/U_\infty$ to quantify the intensity of the recirculation region, different works (e.g. [6]) attempted to determine a threshold for the onset of absolute instability in velocity profiles representative of separated boundary layers; a general agreement exists that $u_{rev} \geq 15\%$ is required. However, most of the works in the literature report peak reversed flows substantially lower than 10%. The prominent amplifier behavior manifested by LSBs does not fully explain the very rich physics observed in experiments and numerical simulations, suggesting that other instability mechanisms must be at play. Indeed, instability analyses considering global eigenmodes have identified at least two self-excited mechanisms in nominally 2D LSBs: a 3D instability of centrifugal type and an oscillator-type instability arising from regions of local absolute instability. Rodríguez *et al.* [8] showed that the three-dimensional instability becomes active for $u_{rev} \sim 7-8\%$ and thus should play a role in the dynamics of relatively weak separation bubbles: the flowfields would develop a spanwise modulation and become fully three-dimensional, even in the absence of external excitations [7].

This contribution revisits the absolute/convective inflectional instability of separated shear layers. First, a new criterion for the existence of absolute instability in this kind of flows is proposed, that depends on the location of the inflection point relative to the separation streamline. Second, fully three-dimensional, spanwise-modulated LSBs arising from the self-excited centrifugal instability are analyzed using (i) an extension of the classical WKBJ analysis to cross-stream planes (as opposed to 1D velocity profiles) and (ii) direct numerical simulations.

METHODOLOGY

The stability of three-dimensional (spanwise-periodic) LSB flows of the form $\bar{\mathbf{q}}(x, y, z)$ is studied, where x, y and z are the streamwise, wall-normal and spanwise directions. Assuming that the base flow properties evolve along the streamwise direction much slower than on the cross-stream plane, separation of scales allows a local analysis of 2D X-planes, where $X = \gamma x$ is the slow variable and $\gamma \ll 1$. At each X-plane, disturbances behave locally as $\hat{\mathbf{q}}(y, z; X)\exp[\mathrm{i}(\alpha(X)x - \omega t)]$. A partial-derivative-based eigenmode problem is obtained by substitution of the former modal disturbance form in the linearized Navier-Stokes equations. Successive solutions of the eigenvalue problem determine the dispersion relation $D(\alpha, \omega, X) = 0$, with α and ω being complex quantities, that describes the local behavior of disturbance waves.

The absolute/convective analysis proceeds then in the classical manner [9]. The character of the disturbances at each X is determined by the complex frequency ω_0 at the zero-group-velocity condition $0 = c_g = \partial\omega/\partial\alpha$. If the growth rate (imaginary part, $\omega_{0,i}$) is positive, then a disturbance introduce at X will grow in time at the location of introduction, and the base flow is said to be absolutely convective at X. If $\omega_{0,i} < 0$, the flow is either stable or convectively unstable at X. The existence of absolute instability over a sufficiently large spatial region can result in self-excited, synchronized

*Corresponding author. E-mail: daniel.rodriguez@upm.es

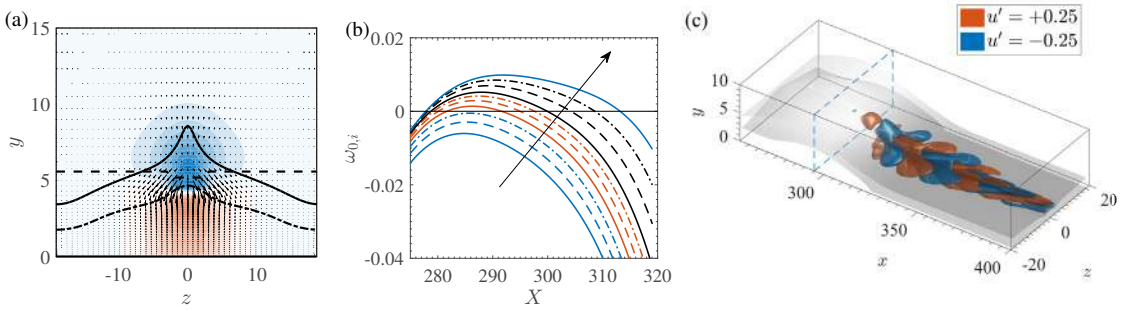

Figure 1: (a) Streamwise velocity contours of the absolute inflectional instability, at $X = 284$. Solid, dashed and dashed-dotted lines correspond to the separation streamsurface, the inflection points and the boundary of the reversed flow. (b) Absolute growth rates $\omega_{0,i}$ for different LSB flows with increasing u_{rev}. (c) Streamwise isosurfaces of the secondary instability global oscillator.

oscillations over all X planes, i.e. a global oscillator. Such a global oscillator is analyzed by further proceeding with the WKBJ expansion and applying the saddle-point condition $\partial\omega/\partial X = 0$.

Direct numerical simulations based on the non-linear Navier-Stokes equations in disturbance form are also solved in this work to (i) compute the three-dimensional LSB flows subject of analysis, (ii) validate the results of the WKBJ analysis, and (iii) investigate the non-linear regimes and laminar-turbulent transition subsequent to the appearance of absolute instabilities of the 3D flows.

SUMMARY OF RESULTS AND CONCLUSIONS

A geometrical criterion for absolute inflectional instability: As opposed to previous research in which a quantitative threshold for the onset of absolute instability was sought, a geometrical criterion based on the local relative location of the inflection point with respect to the separation streamline is proposed. For analytic 1D velocity profiles, it is found that the inflection point must be within the recirculation region for absolute instability. While this is formally a necessary condition, it is found to approximate reasonably well the critical curve for $\omega_{0,i}$ for a broad range of parameters [10].

Absolute instability resulting from spanwise distortion of LSBs: DNS with selective frequency damping was used to compute the steady, 3D LSB flows resulting from the non-linear saturation of the primary centrifugal instability. The spanwise modulation of the reversed flow region increases locally the peak reversed flow at some locations, attaining values above $u_{rev} = 15\%$. The separation streamsurface is distorted, being displaced from the wall at the same locations, while the inflection point moves towards the wall, satisfying the geometrical criterion stated above (figure 1(a)). These spanwise modifications enable the appearance of absolutely unstable inflectional waves, at conditions under which either the initial 2D LSB or the spanwise average of the 3D distorted LSB are only convectively unstable (figure 1(b)). This finding is also of application to LSBs that become 3D due to mechanisms different from the centrifugal instability, e.g. by streaks or Klebanoff modes introduced by free-stream turbulence [5].

A 3D global oscillator and transition to turbulence: Following from the absolute inflectional instability, a self-excited global oscillator appears whose properties are well predicted by the WKBJ analysis (figure 1(c)) [11]. DNS is used to study the subsequent non-linear evolution, showing the formation of vortex loops akin to those observed by Watmuff [2], and transition to turbulent regime. In this scenario, laminar-turbulent transition in separation bubbles is shown to be possible in the total absence of external disturbances.

The authors acknowledge funding from the brazilian public agencies CNPq (grants 305512/2016-1, 423846/2016-7), FAPESP (grant 2017/01586-0) and FAPERJ (grant E-26/010.000356/2017).

References

[1] Gaster M. The structure and behaviour of separation bubbles. **Tech. Report 3595**, *NPL Reports and Memoranda*, 1967.
[2] Watmuff J. H. Evolution of a wave packet into vortex loops in a laminar separation bubble. *J. Fluid Mech.* **397**, 119-169, 1999.
[3] Diwan S. S. and Ramesh O. N. On the origin of the inflectional instability of a laminar separation bubble. *J. Fluid Mech.* **629**, 263–298, 2009.
[4] Pauley L. P., Moin, P., and Reynolds, W. C. The structure of two-dimensional separation. *J. Fluid Mech.* **220**, 397–411, 1990.
[5] Hosseinverdi S. and Fasel H. F. Numerical investigation of laminar-turbulent transition in laminar separation bubbles: the effect of free-stream turbulence. *J. Fluid Mech.* **858**, 714–759, 2019.
[6] Hammond D. A. and Redekopp L. G. Local and global instability properties of separation bubbles. *Eur. J. Mech. B/Fluids* **17**, 145–164, 1998.
[7] Rodríguez D. and Theofilis V. Structural changes of laminar separation bubbles induced by global linear instability. *J. Fluid Mech.* **655**, 280–305, 2010.
[8] Rodríguez D., Gennaro E. M. and Juniper M. P. The two classes of primary modal instability in laminar separation bubbles. *J. Fluid Mech.* **734**, R4, 2013
[9] Monkewitz P. A., Huerre P. and Chomaz, J. M. Global linear stability analysis of weakly non-parallel shear flows. *J. Fluid Mech.* **251**, 1–20, 1993.
[10] Avanci M. P., Rodríguez D. and Alves L. S. B. A geometrical criterion for absolute instability in laminar separation bubbles. *Phys. Fluids* **31**, 014103, 2019.
[11] Rodríguez D., Gennaro E. M. and Souza L. F. Self-excited primary and secondary instability in laminar separation bubbles. *J. Fluid Mech.* accepted for publication, 2020.

EFFECTS OF IMPINGING SOUND WAVES ON LINEAR AND NONLINEAR INSTABILITY OF SUPERSONIC BOUNDARY LAYERS

Fufeng Qin*[1] and Xuesong Wu[1]
[1]Department of Mathematics, Imperial College London, London, UK

Summary This paper investigates linear and nonlinear evolution of radiating modes in supersonic boundary layers under the influence of impinging sound waves. It is found that the ensuing boundary-layer response is extraordinarily large for a subset of the parameters, the sound frequency ω_s and the incident angle θ_s. Moreover, for a particular pair of (ω_s, θ_s), resonant over-reflection, corresponding to the reflection coefficient being infinite, occurs with the reflected wave taking on the character of the neutral radiating mode. The linear and nonlinear evolution of the radiating mode is significantly affected by the incident sound wave.

INTRODUCTION

Laminar-turbulent transition of super- and hyper-sonic boundary layers is crucial for the design of vehicles as the aerodynamic drag and thermal loading differ drastically depending on whether the flow state is laminar or turbulent. Linear stability theory [1] shows that a supersonic boundary layer may support two types of inviscid modes. One is the subsonic mode travelling relative to the mean flow at a phase velocity smaller than the sound speed. This mode is associated with the generalized inflection point of the mean flow, and its energy is trapped in the boundary layer. The other is the supersonic mode, which propagates faster than the sound relative to the mean flow. The corresponding eigenfunction is oscillatory while attenuating, or remaining bounded in the far field when the mode is neutral. This implies that a supersonic mode emits sound to the far field [2,3], and so it is also termed a radiating mode.

Wind tunnel experiments suggest that acoustic waves play a significant role in the onset of transition. These acoustic disturbances are emitted from the turbulent boundary layers on the nozzle and tunnel walls, and/or radiated due to the wall inhomogeneities (e.g. roughness). Transition positions in conventional and quiet tunnel are notably different [4]. There are at least two mechanisms by which an incident acoustic wave influences transition. One is receptivity and the other is the direct effects on the amplification of instability modes. In the present work, we focus on the latter.

THEORETICAL ANALYSIS

We consider a supersonic boundary layer that forms over a semi-infinite plate due to a uniform stream with velocity U_∞. The flow is described by the Cartesian coordinate system (x, y), where x and y are along and normal to the wall respectively, both non-dimensionalized by a characteristic boundary-layer thickness δ^*. We assume that the Mach number $M = O(1)$, and the Reynolds number $R = \rho_\infty U_\infty \delta^*/\mu_\infty \gg 1$. A sound wave impinges on the boundary layer at an angle of incidence, and is reflected by the latter so that the pressure in the far field takes the form

$$p_s \sim \epsilon_s p_I [\mathrm{e}^{\mathrm{i}\gamma_s y} + \mathscr{R}\mathrm{e}^{-\mathrm{i}\gamma_s y}]\mathrm{e}^{\mathrm{i}\alpha_s(x-c_s t)} + \text{c.c.}, \tag{1}$$

where ω_s is the frequency, α_s and γ_s are the streamwise and normal wavenumbers respectively of the incident wave. They satisfy the acoustic dispersion relation $c_s \equiv \omega_s/\alpha_s = 1 - \sqrt{1 + (\gamma_s/\alpha_s)^2}/M$. The intensity of the incident sound wave is denoted by p_I, while $\mathscr{R}$ is the reflection coefficient. We are interested in the slow acoustic wave with wavelength comparable with δ^* so that $\alpha_s = O(1)$.

Reflection and Resonant Over-reflection The boundary-layer response to an incident slow acoustic wave is described by a double-layered structure consisting of a main layer and a critical layer; the latter is a thin region surrounding the critical level y_c at which the base flow velocity $U(y)$ equals the phase speed, that is, $U(y_c) = c$. In the main layer, the pressure of the sound wave satisfies the compressible Rayleigh equation. The boundary-layer response may be measured by $p_s(y_c)$, the pressure at the critical level y_c. Both of $\mathscr{R}$ and $p_s(y_c)$ are determined by integrating the Rayleigh equation supplemented by a jump condition from the analysis of the critical layer. In general, $\mathscr{R}$ is finite. However, for a certain angle of incidence and frequency, $\mathscr{R}$ becomes infinite, which is referred to as resonant over-reflection.

Direct Effects on the Linear and Nonlinear Instability For the incident acoustic wave with α_s and ω_s satisfying the dispersion relation of a neutral radiating mode (with possible detuning), resonance takes place between them. The excitation and evolution of the radiating mode can be described by using the nonlinear critical-layer theory in the non-equilibrium regime [5]. Crucially, due to the resonance the sound wave with an $O(\epsilon_s)$ magnitude excites a radiating mode with a much larger $O(\epsilon_s R^{1/3})$ amplitude. The pressure and streamwise velocity in the main layer can be written as

$$(u, p) = \epsilon_s R^{1/3} A(\tilde{x})(\hat{u}_0, \hat{p}_0)\mathrm{e}^{\mathrm{i}\alpha(x-ct)} + \epsilon_s p_I [\mathrm{e}^{\mathrm{i}\gamma_s y} + \mathscr{R}\mathrm{e}^{-\mathrm{i}\gamma_s y}]\mathrm{e}^{\mathrm{i}\alpha_s(x-c_s t)} + \text{c.c.}, \tag{2}$$

where $\tilde{x} = R^{-1/3}x$ is the slow variable describing the evolution of the mode. The acoustic wavenumber α_s is allowed to differ from that of the neutral radiating mode by $O(R^{-1/3})$, that is, $\alpha_s = \alpha + R^{-1/3}\alpha_d$ with $\alpha_d = O(1)$ representing the

*Corresponding author. E-mail: f.qin17@imperial.ac.uk

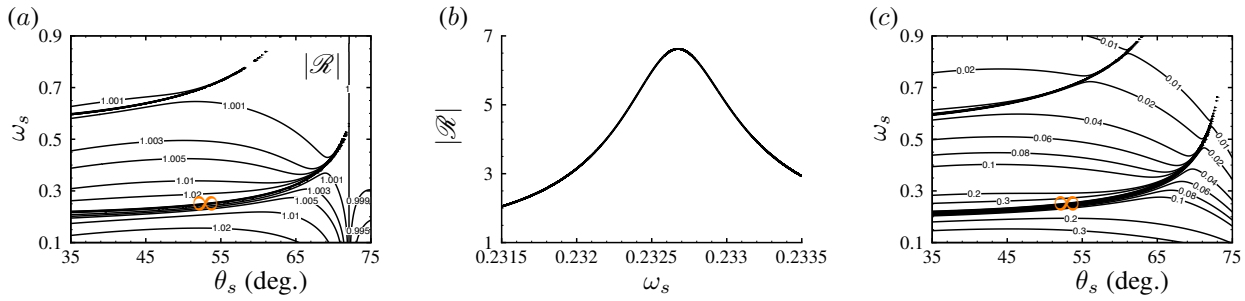

Figure 1: Reflection and absorption of incident sound waves: (a) contours of $|\mathscr{R}|$ in the $\theta_s - \omega_s$ plane with the incident angle θ_s defined by $\cos\theta_s = \alpha_s/\sqrt{\alpha_s^2+\gamma_s^2}$ and the resonant point is indicated with the symbol '∞'; (b) variation of $|\mathscr{R}|$ with ω_s at $\theta_s = 40°$; (c) the pressure $|p_s(y_c)|$ at the critical level.

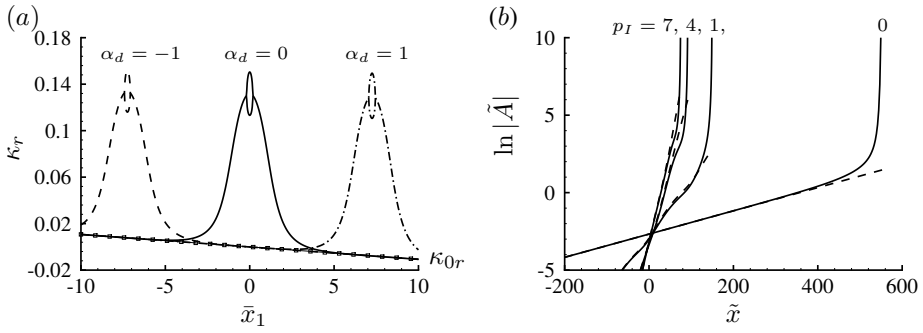

Figure 2: Effects of the incident sound on instability: (a) the modified growth rate in the linear stage when $p_I = 7$, with symbols representing the local growth rate κ_{0r} in the absence of incident sound; (b) nonlinear evolution of the mode in the presence of incident sound waves with different amplitude p_I. The dashed lines represent the corresponding linear solutions.

detuning. The excitation and evolution become nonlinear. After analysing the nonlinear interactions in the critical layer [5], we derive the evolution equation governing the amplitude function $A(\tilde{x})$,

$$A'(\tilde{x}) = \kappa_0 \tilde{A} + \mathscr{N} + \tilde{F} e^{i\alpha_d \tilde{x}}, \tag{3}$$

where κ_0, $\mathscr{N}$ and $\tilde{F}$ represent the unperturbed growth rate, nonlinear term and effective forcing respectively. The amplitude equation admits an equilibrium solution $A_e e^{i\alpha_d \tilde{x}}$, which represents the nonlinear response. The general solution for A can be written as $A_e e^{i\alpha_d \tilde{x}} + \tilde{A}$, with A_e entering the equation for $\tilde{A}$. When $\tilde{A} \ll 1$, $\tilde{A} \sim e^{\kappa \tilde{x}}$. The response A_e modifies κ_r, the growth rate in the linear stage. The nonlinear evolution equation is solved numerically.

RESULTS AND CONCLUSIONS

Results are given for a $M = 6$ boundary layer as a representative. Figure 1(a) depicts contours of $|\mathscr{R}|$ in the $\theta_s - \omega_s$ plane. The reflection coefficient is almost unity for most parameters, but it increases rapidly when the parameters approach the two strips, where very steep gradients are present. Figure 1(b) shows that the reflection coefficient soars to a large but finite value in a small range of the frequency for a fixed incident angle, suggesting the sensitivity of the response. Figure 1(c) shows that the strong critical-layer pressure appears as well in the two strips, indicating that the boundary layer acts as a sound board to magnify the incident acoustic waves. Figure 2(a) shows that the modified growth rate κ_r can be larger than the unperturbed growth rate by one order of magnitude. Figure 2(b) shows that increasing the intensity of sound waves promotes nonlinear amplification and advances the eventual blow-up. Further results will be presented at the Congress.

References

[1] Mack, L. M. 1984 Boundary-layer linear stability theory. AGARD Rep. 709, Chap. 3, pp. 1-81.
[2] Wu, X. 2005 Mach wave radiation of nonlinearly evolving supersonic instability modes in shear layers. *J. Fluid Mech.* **523**, 121-159.
[3] Chuvakhov, P. V. & Fedorov, A. V. 2016 Spontaneous radiation of sound by instability of a highly cooled hypersonic boundary layer. *J. Fluid Mech.* **805**, 188-206.
[4] Schneider, S. P. 2001 Effect of high-speed tunnel noise on laminar-turbulent transition. *J. Spacecr. Rockets* **38** (3), 323-333.
[5] Wu, X. 2019 Nonlinear theories for shear flow instabilities: physical insights and practical implications. *Annu. Rev. Fluid Mech.* **51**, 451-485.

OPTIMAL OBLIQUE TRANSITION IN COUETTE FLOW

Jan O. Pralits*[1], Alessandro Bottaro[1], and Stefania Cherubini[2]
[1]Department of Civil, Chemical and Environmental Engineering, University of Genoa, Genoa, Italy
[2]Department of Mechanics, Mathematics and Management, Polytechnic University of Bari, Italy

Summary A weakly nonlinear approach is described to identify the couple of oblique waves capable to optimally excite transition to turbulence in plane Couette flow. Optimal oblique wave pairs of finite amplitude are found in a wavenumber range substantially different from their linear counterpart, and lead to rapid breakdown past a threshold value of the disturbance amplitude. Direct numerical simulations of the Navier-Stokes equations corroborate the weakly nonlinear results.

BACKGROUND

The breakdown of laminar shear flows is a central problem in fluid mechanics since the early experiments by Osborne Reynolds [1] in pipe flow. Despite the simplicity of unidirectional shear flows (plane Poiseuille and Hagen-Poiseuille, Couette), the physical processes by which environmental effects trigger transition to turbulence are still largely unexplained; this is partly due to the fact that such flows undergo transition at Reynolds numbers for which the linear hydrodynamic stability equations predict a stable behavior, and to the non-normal nature of the equations themselves. The transition phenomenon in such flows must thus be based on nonlinear mechanisms, possibly exploiting transient disturbance energy amplification. A recent approach to identify initial disturbances of finite amplitude capable to optimally initiate the transition process relies on nonlinear optimization theory [3, 2]. Such a theory is very powerful, the main drawback being that it is virtually impossible to explore the full parameter space, because of the computational cost of carrying out many direct simulations in the adjoint looping procedure until convergence of the chosen cost functional, for each set of parameters.

The need for an alternative optimization strategy is here coupled to the investigation of a physical mechanism believed to be central to turbulence breakdown in parallel shear flows: the growth and interaction of oblique waves. In a recent paper, Pralits et al. [4] have described a weakly nonlinear approach capable to identify disturbances growing optimally on top of a mean flow distorted by the Reynolds stresses produced by the disturbances themselves. The results of that study depart significantly from previous, linear, optimal perturbation analyses and point to very receptive regions of wavespace which can support a self-sustaining cycle, as demonstrated by companion numerical simulations. That analysis was based on the self-interaction of a single oblique wave. The goal which we set in the present paper is to extend that work to identify the couple of obliquely travelling waves capable to optimally trigger transition via mutual interactions.

The role and importance of oblique waves in the breakdown of shear flow is by-now well established. The original work on the issue dates to the early nineties, when Schmid & Henningson [5] described a transition scenario in plane Poiseuille flow which occurred on a much faster time scale than that based on the three-dimensional destabilization of initially two-dimensional streamwise travelling waves. Interestingly, this oblique transition scenario was sped up by an increase in initial amplitude and wave angle; waves with a spanwise wavenumber β larger than the streamwise one (α) experienced more rapid amplification and faster spreading of the spectral energy into modes with high streamwise wavenumbers. Here, the oblique transition scenario is optimized by focussing on the oblique waves and on the ensuing streamwise streak/vortex mode; the initial (algebraic) growth of the oblique waves in subcritical conditions is enhanced by the presence of a strong mean flow distortion, in a process which feeds onto itself.

WEAKLY NONLINEAR MODEL

The decomposition of the whole field starts by considering a pair of oblique waves of wavevector $(\alpha, \pm\beta)$ and amplitude ϵ. First-generation interactions yield two ϵ^2 terms: one represents the mean flow correction, denoted with subscript 00, and the second, which behaves like $e^{2i\beta z}$, represents a streamwise-independent streak/vortex. Other first-generation terms of wavevectors $(2\alpha, 0)$ and $(2\alpha, \pm 2\beta)$ are not included on account of the numerical results by Schmid & Henningson [5] which show that such terms are of smaller amplitude than the others. The decomposition reads:

$$\begin{bmatrix} U(y) \\ 0 \\ 0 \\ P(x) \end{bmatrix} + \epsilon \begin{bmatrix} u_{1\pm1}(y,t) \\ v_{1\pm1}(y,t) \\ w_{1\pm1}(y,t) \\ p_{1\pm1}(y,t) \end{bmatrix} e^{i(\alpha x \pm \beta z)} + \epsilon^2 \begin{bmatrix} u_{00}(y,t) \\ v_{00}(y,t) \\ w_{00}(y,t) \\ p_{00}(y,t) \end{bmatrix} + \epsilon^2 \begin{bmatrix} u_{02}(y,t) \\ v_{02}(y,t) \\ w_{02}(y,t) \\ p_{02}(y,t) \end{bmatrix} e^{2i\beta z} + c.c., \tag{1}$$

where *c.c.* indicates the complex conjugate of a complex vector. Replacing into the Navier-Stokes equations, collecting like-order terms we obtain a hierarchy of equations. In particular at leading order we have the equations for the base flow

*Corresponding author. E-mail: jan.pralits@unige.it

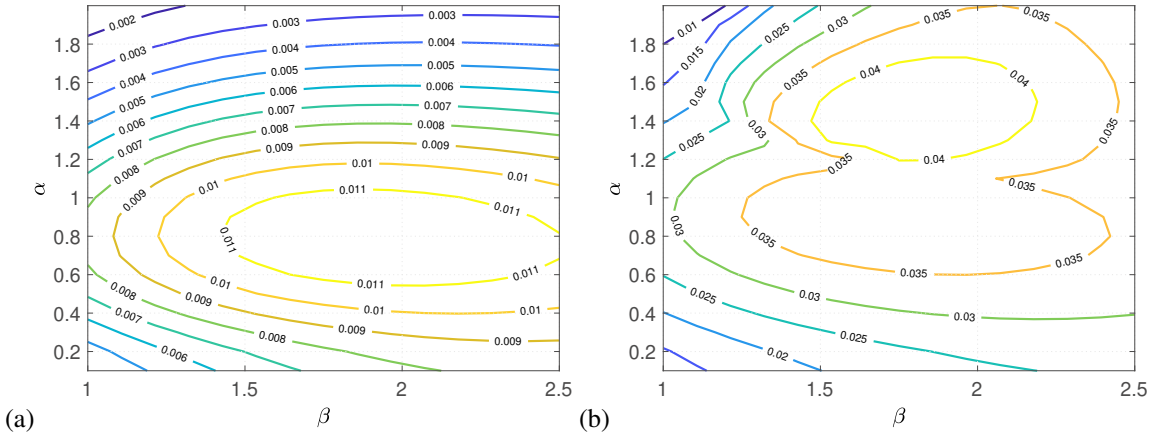

Figure 1: Contours for $e(T)$ at $Re = 400$ and $T = 10$, (a) $\epsilon = 0.01$, (b) $\epsilon = 0.02$.

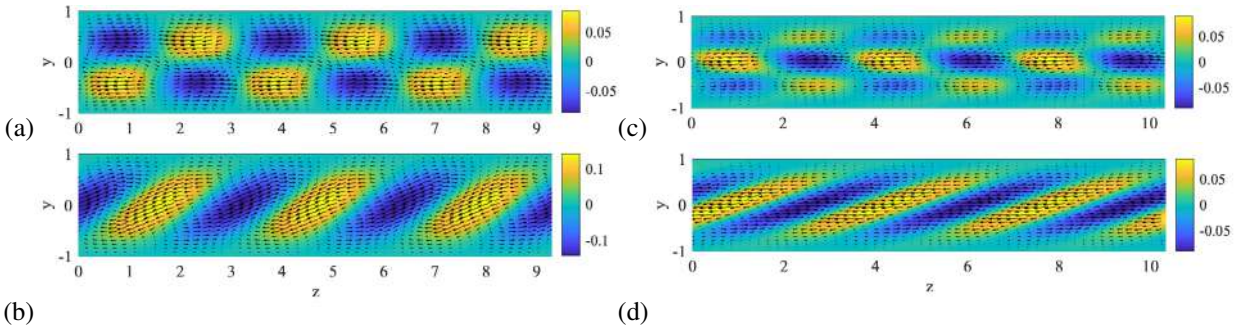

Figure 2: The shaded contours represent the positive and negative streamwise velocity components, whereas the vectors represent wall-normal and spanwise components of the oblique waves. (a) and (b) show solutions at $t = 0$ and $t = T$, respectively, for $\epsilon = 0.01$ and (α, β) from the energy peak in Figure 1(a). (c) and (d) show solutions at $t = 0$ and $t = T$, respectively, for $\epsilon = 0.02$ and (α, β) from the energy peak in Figure 1(b).

correction, forced by the Reynolds stress; at order ϵ we find homogeneous equations for modes $(\alpha, \pm\beta)$, and at order ϵ^2 equations for mode $(0, 2\beta)$ appear. Homogeneous boundary conditions are imposed for all solutions. The system of equations is solved in a direct-adjoint procedure with the objective to optimize the total energy of the unsteady perturbation $e(t) = e_{1,1}(t) + e_{1,-1}(t) + e_{0,2}(t)$ evaluated at a given target time $t = T$. The target time is chosen small on account of the rapidity of the phenomenon being investigated, and not to cover time periods over which further interactions (not accounted for by the weakly nonlinear model) might occur. Such interactions, giving rise to higher modes, are observed in companion direct numerical simulations.

RESULTS

Sample results are shown here for the case in which the Reynolds number (Re) is 400 and $T = 10$. As the amplitude ϵ is increased the maximum response energy $e(T)$ is found for oblique waves which are substantially different from the optimals of the linear case. This can be observed in Figure 1, where we report the response energy $e(T)$ in the (α, β) plane for two values of ϵ. As ϵ increases above a certain threshold, a second energy peak appears at a value of the streamwise wavenumber which is about twice that of the linear case. Optimal oblique waves and their response at the target time are presented in Figure 2, with ϵ, α and β taken from the energy peaks in Figure 1.

These oblique optimal perturbations lead to rapid breakdown past a well defined threshold value of the disturbance amplitude. Direct numerical simulations of the Navier-Stokes equations substantiate the weakly nonlinear results, providing thresholds for transition close to the predictions of the weakly nonlinear model.

References

[1] Reynolds, O. An experimental investigation of the circumstances which determine whether the motion of water shall be direct or sinuous and of the law of resistance in parallel channels. Proc. R. Soc. Lond. Ser. A, **35**, pp. 84-99, 1883

[2] Kerswell R. R., Pringle C. C. T., Willis A. P. An optimisation approach for analysing nonlinear stability with transition to turbulence in fluids as an exemplar *Rep. Prog. Phys.*, **77**:085901, 2014.

[3] Luchini P.,Bottaro A. Adjoint equations in stability analysis. *Annual Review of Fluid Mechanics*, **46**:493–517., 2014.

[4] Pralits J. O., Bottaro A., Cherubini, S. Weakly nonlinear optimal perturbations. *J. Fluid Mech.* **785**:135–151, 2015

[5] Schmid P. J., Henningson D. S. A new mechanism for rapid transition involving a pair of oblique waves. *Physics of Fluids A* **4**:1986–1989, 1992

STATIONARY AND TRAVELLING CROSSFLOW MODES IN LOW TURBULENCE ENVIRONMENTS

Marco Placidi*[1], Chetan Jagadeesh[2], and Chris J. Atkin[3]
[1]Department of Mechanical Engineering Sciences, University of Surrey, Guildford, UK
[2]Department of Mechanical Engineering and Aeronautics, City, University of London, London, UK
[3]School of Engineering, University of East Anglia, Norwich, UK

INTRODUCTION

Controlling the transition from laminar to turbulent flow represents one of the possible strategies to achieve the IATA 2050 emission targets due to climate change. At least in principle laminar flow can deliver a reduction in the skin friction drag, which minimises fuel burn per mile and pollutant emission. However, many processes affect the laminar/turbulent transition; these are not yet fully understood. Here, we investigate the role that the environmental disturbances (i.e the level of FreeStream Turbulence intensity (FST or Tu) have on the crossflow instability, which is typical of three-dimensional boundary layers.

Summarising the state of the art, Crouch et al. (2015) reported that consensus is that for low-turbulence environments ($Tu << 0.2\%U_\infty$) the transition process is dominated by roughness-induced stationary crossflow, while for high turbulence levels ($Tu > 0.2\%U_\infty$) the same process is dominated by the travelling disturbances. This behaviour is corroborated by a number of studies in the literature (Deyhle and Bippes, 1996; Bippes and Lerche, 1997; White et al., 2001; Dagenhart and Saric, 1999; Hunt, 2011; Eppink, 2014; Schrader et al., 2010; Downs and White, 2013). Is it also well-known that the flight environment is characterised by extremely low levels of turbulence intensity (Saric et al., 2011), however, due facility limitations most of the previous experimental work was not be conducted in such environments. Herewith, we aim to further explore the sensitivity of stationary and travelling modes to FST by exploiting the extremely low FST in our facility ($Tu = 0.01\%U_\infty$) and by enhancing it via the means of two turbulence screens, which produced $Tu = 0.33\%U_\infty$ and $Tu = 0.41\%U_\infty$, respectively.

EXPERIMENTAL FACILITY AND SETUP

Experiments were conducted in the closed-circuit 'Gaster low-turbulence wind tunnel' at City, University of London. The turbulence intensity, measured in the empty tunnel, was less than 0.006% of the free-stream velocity, U_∞, within the frequency range $4Hz - 4kHz$ at $U_\infty = 16\ ms^{-1}$. The tunnel test section measures $3\ ft \times 3\ ft \times 6\ ft$ and is equipped with a 3-axis traverse system.

To create favourable conditions for the development of crossflow instability, a combination of a $45°$ swept flat plate and equally swept displacement bodies were used. The plate measured $1535\ mm$ in chord. Further details on this experimental setup are reported in Placidi et al. (2017) and van Bokhorst (2018). To investigate the effect of FST two different turbulence grids were employed to increase the level of environmental disturbances.

Time-resolved velocity measurements are obtained via a *Dantec* Constant Temperature Anemometry, with a miniature boundary layer hot wire sensor. Mean velocity and root-mean-squared (rms) of the bandpass filtered velocity are denoted by capital letters and a prime, respectively. The freestream velocity was set to $16\ m/s$, with uncertainty determined following Hutchins et al. (2009), below 2%.

PRELIMINARY RESULTS AND DISCUSSION

Preliminarily, the quantity $rms[(U - \overline{U})/Ue]$ is evaluated to represent the stationary mode amplitudes as in Hunt (2011). These are shown in figure $1(a)$ to (d) for different chordwise locations from $x/c = 27\%$ to $x/c = 31\%$. At all chordwise locations, the amplitude of the primary stationary modes is affected by the level of FST. At $x/c = 27\%$ in figure $1(a)$, the amplitude of the stationary disturbance is halved by the presence of the grids, and its growth is much hindered compared to the clean low-turbulent case (see figures $1(a)$ to (d)). Bippes and Lerche (1997) and Downs and White (2013) pointed out that while the initial amplitude of the travelling mode is set by the FST, the initial amplitude of the stationary modes is due to the roughness. In the current case, however, the first measurement location was $x/c = 27\%$ and, therefore, it is not to be considered a true initial amplitude given the location of the neutral stability point. It is however clear from figure $1(d)$, that while in the low-FST case the stationary mode amplitude magnitude has reached $rms[(U - \overline{U})/Ue] \approx 0.25$, this has barely increased in the presence of the screens (i.e. in the enhanced Tu cases). This behaviour preliminary confirms that the environmental disturbance level does have an impact on the amplitude and growth of the standing waves, which are hindered for high Tu levels. We will discuss during the presentation how, by increasing the FST, the travelling crossflow modes begin dominating the transition process.

*Corresponding author. E-mail: m.placidi@surrey.ac.uk.

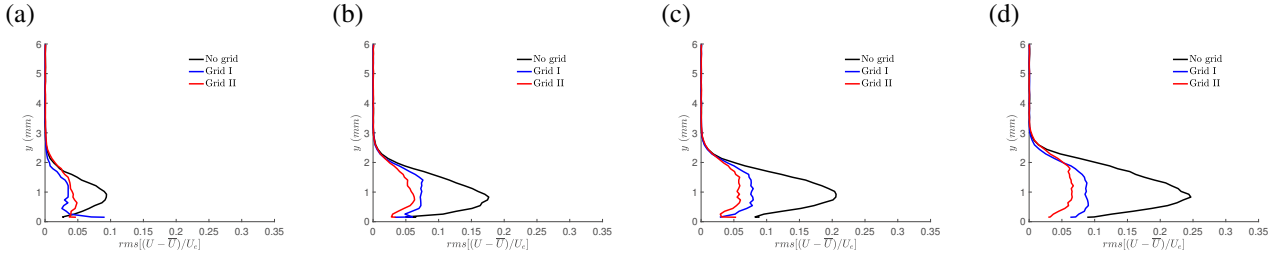

Figure 1: Amplitude of the primary stationary CF mode at (a) $x/c = 27\%$, (b) $x/c = 29\%$, (c) $x/c = 30\%$, and (d) $x/c = 31\%$ for the different Tu levels.

CONCLUSIONS

This study confirms that, at low FST (i.e. $Tu \leq 0.01\%$), the transition process is dominated by the stationary modes; whilst travelling modes are still present, their influence on the transition process is marginal. However, when the level of FST is enhanced ($Tu \geq 0.33\%$), the travelling modes acquire more importance and tend to dominate the laminar/turbulent transition process. This work adds to the sparse literature on low levels of freestream turbulence (i.e. $Tu < 0.01\%$).

References

Bippes, H. and Lerche, T. (1997). Transition prediction in three-dimensional boundary-layer flows unstable to crossflow instability. In *AIAA - 28th Fluid Dynamics Conference,Snowmass Village, CO, U.S.A.*, pages AIAA 97–1906, Reston, Virigina. American Institute of Aeronautics and Astronautics.

Crouch, J. D., Ng, L. L., Kachanov, Y. S., Borodulin, V. I., and Ivanov, A. V. (2015). Influence of surface roughness and free-stream turbulence on crossflow-instability transition. *Procedia IUTAM*, 14:295–302.

Dagenhart, J. R. and Saric, W. S. (1999). Crossflow Stability and Transition Experiments in Swept-Wing Flow. *NASA/TP-1999-209344*.

Deyhle, H. and Bippes, H. (1996). Disturbance growth in an unstable three-dimensional boundary layer and its dependence on environmental conditions. *Journal of Fluid Mechanics*, 316:73–113.

Downs, R. S. and White, E. B. (2013). Free-stream turbulence and the development of cross-flow disturbances. *Journal of Fluid Mechanics*, 735:347–380.

Eppink, J. (2014). *The interaction of crossflow instabilities and a backward facing step in swept boundary layer transition*. PhD thesis, Mechanical Engineering, Tufts University.

Hunt, L. E. (2011). *Boundary-Layer Receptivity to Three-Dimensional Roughness Arrays on a Swept-Wing*. PhD thesis, Texas A&M University. Aerospace Engineering Department, Texas A&M University.

Hutchins, N., Nickels, T. B., Marusic, I., and Chong, M. S. (2009). Hot-wire spatial resolution issues in wall-bounded turbulence. *Journal of Fluid Mechanics*, 635:103–136.

Placidi, M., van Bokhorst, E., and Atkin, C. (2017). Advanced Laminar Flow Enabling Technologies (ALFET) Technical Report. Technical report, City, University of London.

Saric, W. S., Carpenter, A. L., and Reed, H. L. (2011). Passive control of transition in three-dimensional boundary layers, with emphasis on discrete roughness elements. *Philosophical Transactions of the Royal Society A*, 369(1940):1352–1364.

Schrader, L. U., Tempelmann, D., Brandt, L., Hanifi, A., and Henningson, D. S. (2010). Numerical study of boundary-layer receptivity on a swept wing. Technical report, Swedish Defence Research Agency, Stockholm, Sweden.

van Bokhorst, E. (2018). *Forcing of the primary and secondary crossflow instability*. PhD thesis, City, University of London, Aerodynamics and Flow Control.

White, E. B., Saric, W. S., Gladden, R. D., and Gabet, P. M. (2001). Stages of Swept-Wing Transition. In *AIAA 2001 39th Aerospace Sciences Meeting & Exhibit, 8-11 January 2001, Reno, Nevada*, pages AIAA 2001–0271.

STABILITY ANALYSIS OF PERFECTLY EXPANDED AND UNDER-EXPANDED SUPERSONIC JETS

Michael Karp and M. J. Philipp Hack*
Center for Turbulence Research, Stanford University, Stanford, USA

Summary The stability properties of supersonic perfectly and under-expanded jets are investigated by means of global linear stability theory. Weakly nonparallel jets are known to be convectively unstable in the absence of the nozzle. Our focus is on assessment of the effects of the nozzle and shock cells on the instability mechanism. It is found that the explicit representation of the nozzle within the computational domain gives rise to absolute instability owing to a coupling between the downstream-propagating Kelvin-Helmholtz mode and the upstream-traveling acoustic wave, which occurs in the vicinity of the nozzle lip. The presence of shock cells in under-expanded jets has a stabilizing effect on the absolute instability, although the instability mechanism is qualitatively similar to the perfectly expanded case.

INTRODUCTION

Understanding the mechanism of unsteadiness in supersonic jets may aid in developing quieter and more capable jet engines. In this work, the stability properties of perfectly expanded and under-expanded jets are investigated by means of global linear stability theory. In particular, we are interested in analyzing the effect of the nozzle on the instability mechanism and the role of the shock cells.

In global stability analyses, unstable eigensolutions represent absolute instabilities, which may be triggered spontaneously in the flow, while convective instabilities, which require persistent excitation, are associated with stable eigensolutions [1]. Nichols & Lele [2] investigated a perfectly expanded non-parallel jet using global stability analysis, albeit excluding the nozzle from the computational domain. In line with local stability theory, all eigensolutions were found to be stable with the least stable eigenfunction describing an upstream-traveling acoustic mode.

METHODOLOGY

We perform global stability analyses of axisymmetric supersonic jets, with the aim of assessing the role of the nozzle and the shocks on the instability mechanism. To isolate the effect of the nozzle lip and the shock cells, we consider three distinct setups. The first case represents a plain weakly non-parallel jet, serving as a reference case for comparisons with the literature (e.g., Ref. [2]). The second case corresponds to a fully expanded jet and includes the nozzle in the computational domain. The third considered case describes an under-expanded jet and allows assessment of the role of shock cells.

Our aim is to obtain and compare the most unstable eigensolutions for each of the setups. We compute the base flows as axisymmetric, steady, and laminar solutions of the nonlinear compressible Navier-Stokes equations for an ideal gas. Since the laminar base state may be globally unstable, a steady solution to the governing equations is recovered by the application of selective frequency damping [3]. The stability analysis employs the linearized compressible Navier-Stokes equations, with application of numerical sponge layers to ensure the dampening of the perturbations towards the boundaries of the computational domain. A detailed description of the direct numerical solver is given in Ref. [4].

RESULTS

The nozzle exit mach number is set to $M_e = 1$ and the acoustic Reynolds number, based on the nozzle exit radius, is $Re = 10,000$. The laminar base flows are presented in Figure 1, in terms of contours of the Mach number. Only the region in the vicinity of the nozzle exit is shown. The base flow for the case without the nozzle (Figure 1(a)) matches that of the fully expanded jet (Figure 1(b)) in the region downstream of the nozzle. The base flows for the cases with nozzle are calculated by setting the ratio of the nozzle exit pressure and the ambient pressure to 1 for the fully expanded jet (Figure 1(b)) and 2.4 for the under-expanded jet (Figure 1(c)).

The most unstable eigenmodes for each of the base flows are described below. Here, we focus on axisymmetric perturbations since local stability theory predicts that the mechanism extracting energy from the shear layer is most effective for such disturbances. The most unstable eigensolutions are $\omega = 0.395 - 0.004i$, $\omega = 0.399 + 0.136i$, and $\omega = 0.687 + 0.090i$ for the baseflows in Figure 1(a), Figure 1(b), and Figure 1(c), respectively. The reference case without the nozzle is globally stable, indicative of a convective instability, whereas the fully expanded and under-expanded cases are unstable, implying absolute instability. Thus, for the plain jet without explicit representation of the nozzle, we recover the classical result of convective instability in cold jets previously reported by [2]. The representation of the nozzle within the computational domain introduces an absolute instability, even in the absence of shock cells. The under-expansion reduces the growth rate of the instability, although the configuration remains absolutely unstable.

*Corresponding author. E-mail: mjph@stanford.edu

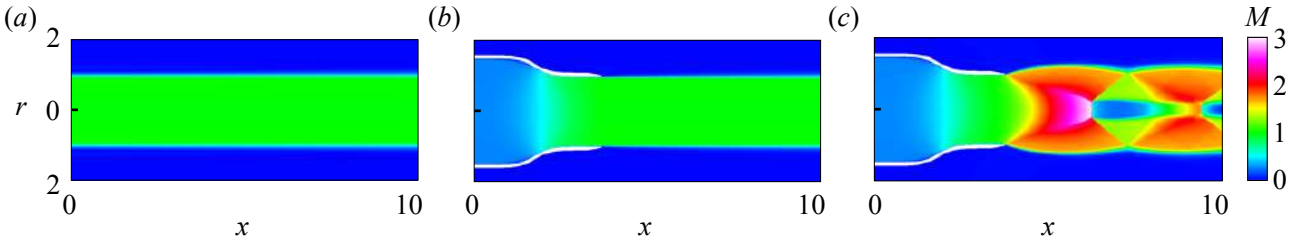

Figure 1: Base flow Mach number contours. Only the region in the vicinity of the nozzle is shown. (a) Without nozzle. (b) Fully expanded nozzle. (c) Under-expanded nozzle.

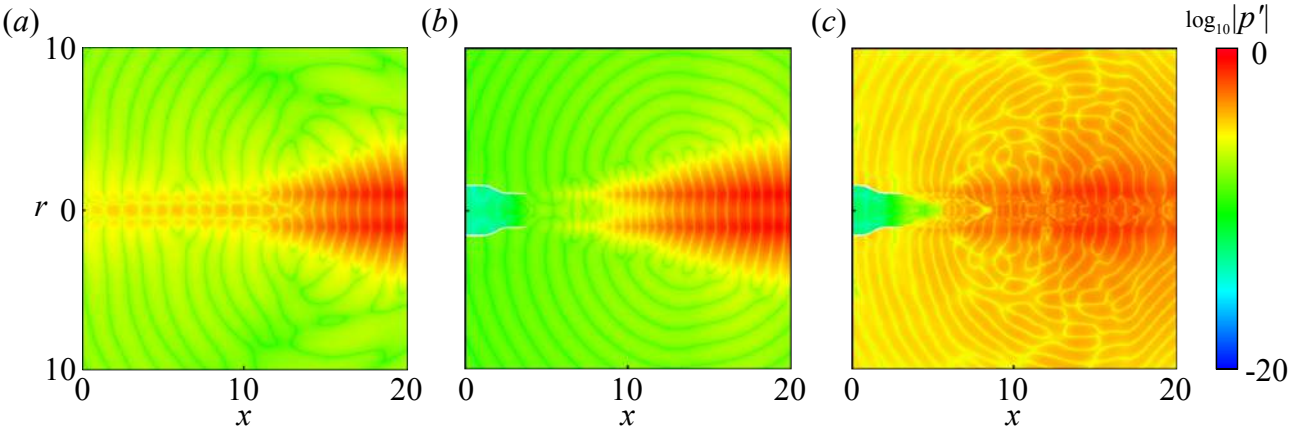

Figure 2: Pressure eigenfunction. The contours correspond to the decimal logarithm of the magnitude of the real part. Only the region in the vicinity of the nozzle is shown. (a) Without nozzle. (b) Fully expanded nozzle. (c) Under-expanded nozzle.

The corresponding eigenfunctions are presented in Figure 2. The pressure is chosen as a representative quantity, and the decimal logarithm of the magnitude of the real part is shown for the three considered cases. For the plain jet (Figure 2(a)), high magnitudes are obtained within the shear layer, where downstream spatial amplification occurs. Outside of the core of the jet, an upstream-traveling acoustic wave is observed, qualitatively similar to the least stable mode reported by Nichols & Lele [2]. Similar features can be seen for the fully expanded nozzle jet (Figure 2(b)). That case exhibits a coupling between the upstream-traveling acoustic wave and the shear layer mode in the vicinity of the nozzle lip, which leads to absolute instability. For the under-expanded nozzle jet (Figure 2(c)) qualitatively similar features are observed; however, the magnitudes in the region outside of the jet core are significantly elevated compared to the other cases, suggesting that the part of the eigenfunction associated with the shear layer is appreciably weaker than that in the other cases.

CONCLUSIONS

Global linear stability analysis of supersonic jets is conducted to determine the role of the nozzle lip and the shock cells in the instability mechanism. Three setups are considered to isolate the effect of the nozzle lip and shock cells. It is found that while the plain non-parallel jet is only convectively unstable, the representation of the nozzle within the computational domain introduces absolute instability. Inspection of the most unstable eigenfunction points to a coupling between the shear layer mode and the upstream-traveling acoustic wave in the vicinity of the nozzle. The effect of the under-expansion is a reduction in the instability growth rate. Nevertheless, the mechanisms of instability are qualitatively similar for both fully expanded and under-expanded jets.

References

[1] Huerre, P. & Monkewitz, P. A. 1990 Local and global instabilities in spatially developing flows. *Annu. Rev. Fluid Mech.* **22**, 473–537.
[2] Nichols, J. W. & Lele, S. K. 2011 Global modes and transient response of a cold supersonic jet. *J. Fluid Mech.* **669**, 225–241.
[3] Åkervik, E., Brandt, L., Henningson, D. S., Hœpffner, J., Marxen, O. & Schlatter, P. 2006 Steady solutions of the Navier-Stokes equations by selective frequency damping. *Phys. fluids* **18**, 068102.
[4] Flint, T. & Hack, M. J. P. 2018 A computational framework for stability analysis of high-speed flows in complex geometries. *Annual Research Briefs*, Center for Turbulence Research, Stanford University, pp. 221–235.

TOWARD PHYSICS-BASED TRANSITION MODELING FOR SUBSONIC TO HYPERSONIC BOUNDARY LAYERS

Pedro Paredes*[1], Balaji Venkatachari[1], Meelan M. Choudhari[2], Fei Li[2], Nathaniel Hildebrand[2], Chau-Lyan Chang[2], Muhammad I. Zafar[3], and Heng Xiao[3]
[1]National Institute of Aerospace, Hampton, VA 23666, USA
[2]Computational AeroSciences Branch, NASA Langley Research Center, Hampton, VA 23681, USA [3]Aerospace and Ocean Engineering, Virginia Tech, Blacksburg, VA 24061, USA

Summary An accurate physics-based boundary layer transition (BLT) prediction method integrated with computational fluid dynamics (CFD) solvers is pursued for a range of aerospace applications. An important aspect of this work involves an approach that employs linear stability computations for a canonical set of configurations to train physics based, data driven models. The performance of a data driven model is evaluated for the planar Mack modes over a blunt, circular cone at zero degrees angle of attack and flow conditions selected to match the HIFiRE-1 flight test with Mach numbers in the range of 3.8 to 5.5. An additional study pertains to the modeling of TS and CF instabilities over the swept wing boundary layer of the CRM-NLF aircraft configuration at the conditions of a recent wind tunnel experiment at the NASA LaRC. The results of this study will be included in the final presentation.

EXTENDED SUMMARY

According to the CFD Vision 2030 [1], the most critical area in CFD simulation capability that will remain a pacing item for the foreseeable future is the ability to adequately predict viscous flows with transition-to-turbulence and flow separation. A majority of CFD computations are carried out under the assumption that the flow is turbulent everywhere, allowing the use of the computationally efficient Reynolds-averaged Navier-Stokes (RANS) based turbulence models throughout the flowfield. However, for several applications ranging from wings with natural laminar flow (NLF) technology, high-lift configurations, rotorcraft flows, unmanned aerial vehicles, and even more importantly in supersonic and hypersonic vehicles, the strong assumption involving a fully turbulent flow can lead to significant errors in the prediction of relevant performance metrics. Furthermore, most of the RANS models are incapable of modeling the process of transition from laminar to turbulent flow because of the complexity involved in the physics of the transition onset process.

Semiempirical correlations based on the linear stability theory (LST) and parabolized stability equations (PSE), such as the e^N method [2, 3], remains one of the most widely used approaches for the transition prediction in aircraft design computations. The LST and PSE track the evolution of small amplitude disturbances. The e^N method does require the specification of a critical N-factor that must be obtained from correlations against experimentally measured transition locations. Both LST and PSE can account for the amplification of the dominant primary instabilities encountered on aircraft wings, i.e., the Tollmien-Schlichting (TS) and crossflow (CF) waves, or in 2D high-speed configurations, i.e., the planar Mack mode waves. However, the application of these approaches toward a coupled computation of laminar and turbulent parts of a flowfield entails an increased computational cost and complexity, suffers from a lack of robustness, and often requires adequate understanding of transition physics and hydrodynamic stability theory that typical users of CFD solvers may not know.

The present research seeks to blend the so-called physics-based approach for transition modeling with the RANS-based approaches, with the eventual goal of developing a reliable and cost efficient, yet robust and user-friendly approach for CFD integrated modeling of BLT. To that end, two separate flow configurations are considered in the present work:

- Axisymmetric boundary layer over a 7° half-angle, circular cone with a nose radius of $r_n = 2.5$ mm at zero degrees angle of attack in a hypersonic free stream that corresponds to the ascent phase of the HIFiRE-1 flight test [4] with freestream Mach numbers in the range of $3.8 - 5.5$ and freestream unit Reynolds numbers in the range of $3.3 \times 10^6 - 21.4 \times 10^6$ m^{-1}. Earlier research [5] had shown that the onset of transition during the HIFiRE-1 flight experiment correlated with an amplification factor of $N \approx 13.5$ for the planar Mack modes.

- Swept wing boundary layer over the common research model with natural laminar flow (CRM-NLF) aircraft at flow conditions selected to match those from a recent wind tunnel experiment in the National Transonic Facility (NTF) at the NASA Langley Research Center [6]. In this configuration, TS instability, and potentially, the CF instability as well, may be expected to play an important role in transition, provided that the attachment line remains laminar.

An important aspect of the physics-based approach for transition modeling involves N-factor correlations based on a data driven surrogate model for linear amplification characteristics of the relevant classes of instability waves. A commonly used approach of this type is based on curve fits or multi-dimensional interpolation of an a priori database of stability characteristics for locally similar profiles. However, the application of this approach to hypersonic boundary layers over blunt spherical nose-tip cones leads to large, unacceptable errors in the predictions of amplification factors, mainly due to its failure in accounting for the effects of the entropy layer on the boundary-layer profiles along the length of

*Corresponding author. E-mail: pedro.paredes@nasa.gov.

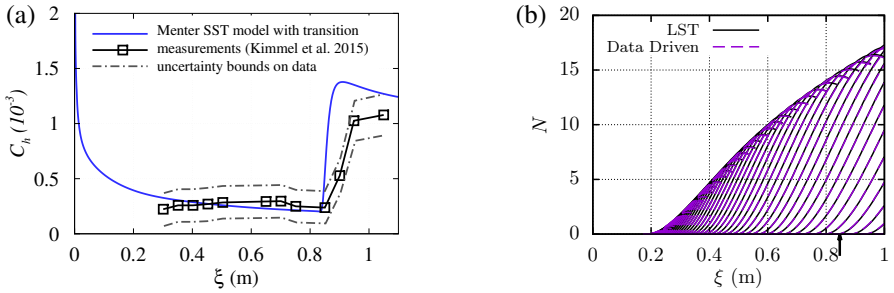

Figure 1: (a) Streamwise evolution of the heat-transfer coefficient and (b) N-factor curves for planar Mack-mode disturbances for HIFiRE-1 at $t = 21.5$ s. The vertical arrow indicate the transition location.

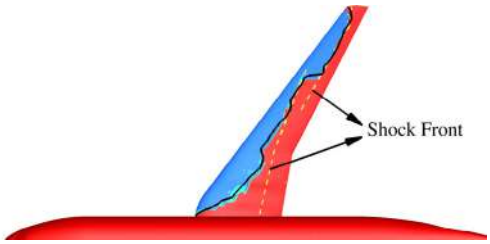

Figure 2: Surface contours of the turbulent index in the CRM-NLF configuration. Blue and red colors denote laminar and turbulent regions, respectively.

the model. We propose and demonstrate an alternate approach that provides substantially improved transition predictions for hypersonic flow configurations with entropy-layer effects. The performance of this model for the HIFiRE-1 vehicle at the flight ascent time of 21.5 s is illustrated in Figure 1. Specifically, Fig. 1(a) shows the evolution of the heat-transfer coefficient with a prescribed transition location, whereas Fig. 1(b) shows the comparison of the N-factor curves based on the data driven model with the results based on the LST, for selected disturbance frequencies in increments of 10 kHz. The excellent performance of the proposed model has also been confirmed over a broad set of flow conditions as well as for cone configurations with nose radius and half-angle values that do not fall within the database used to develop the model. Finally, the same model is shown to outperform the LST calculations for underresolved basic states [7]. Requiring little expertise on the user's part, such data driven models can make physics-based transition prediction accessible to nonexpert users. Furthermore, on a practical front, the highly efficient transition predictions based on this model can be used for accurate estimates of the temporal variations in the heat load on the vehicle as the latter flies through several candidate trajectories, making it a useful, physics-based tool during trajectory analysis.

An additional component of the ongoing research involves the modeling of transition in swept wing boundary layer flows that are relevant to subsonic, commercial transport aircraft. Transition under these conditions may be attributed to TS and CF instabilities, provided that the attachment line flow remains laminar. Highly useful transition measurements for a canonical flow configuration of this type were obtained during NASA's recent experiments on the CRM-NLF that was tested in the NTF. In such flow configurations, the transition onset location can have a significant impact even on the surface pressure distribution, and hence, an integrated modeling of the laminar and turbulent parts of the flow field becomes essential. Figure 2 indicates the mean flow characteristics on CRM-NLF model, computed with NASA's OVERFLOW 2.2o by using Menter's SST-2003 two-equation turbulence model along with an imposed transition front based on the experimental measurements. The transition front is visualized via surface contours of the turbulence index at the flow conditions of $M_\infty = 0.856$, $Re_{MAC} = 15 \times 10^6$ and $AoA = 1.5°$. The meeting presentation will include the results of transition analysis for the computed boundary layer flow over the CRM-NLF configuration.

This research was sponsored by the NASA Transformational Tools and Technologies (TTT) Project of the Transformative Aeronautics Concepts Program (TACP) under the Aeronautics Research Mission Directorate (ARMD).

References

[1] J. Slotnick, A. Khodadoust, J. Alonso, D. Darmofal, W. Gropp, E. Lurie, and D. Mavriplis. CFD vision 2030 study: A path to revolutionary computational aerosciences. Technical Report CR-2014-218178, NASA, 2014.
[2] A.M.O. Smith and N. Gamberoni. Transition, pressure gradient and stability theory. Technical Report ES-26388, Douglas Aircraft Division, 1956.
[3] J.L. van Ingen. A suggested semi-empirical method for the calculation of the boundary layer transition region. *Technische Hogeschool Delft, Vliegtuigbouwkunde, Rapport VTH-74*, 1956.
[4] R. Kimmel, D. Adamczak, A. Paull, R. Paull, J. Shannon, R. Pietsch, M. Frost, and H. Alesi. HIFiRE-1 ascent-phase boundary-layer transition. *Journal of Spacecraft Rockets*, 52(1):217–230, 2015.
[5] F. Li, M. Choudhari, C.L. Chang, R. Kimmel, D. Adamczak, and M. Smith. Transition analysis for the ascent phase of HIFiRE-1 flight experiment. *Journal of Spacecraft Rockets*, 52(5):1283–1293, 2015.
[6] M.B. Rivers, M.N. Lynde, R.L. Campbell, S.A. Viken, D.T. Chan, A.N. Watkins, and S.L. Goodliff. Experimental investigation of the NASA common research model with a natural laminar flow wing in the NASA Langley National Transonic Facility. AIAA Paper 2019–2189, 2019.
[7] P. Paredes, B. Venkatachari, M.M. Choudhari, F. Li, C.-L. Chang, M.I. Zafar, and H. Xiao. Toward transition modeling in a hypersonic boundary layer at flight conditions. AIAA Paper 2020-0000, 2020.

INSTABILITY AND TRANSITION OF A BOUNDARY LAYER FLOW ALONG AN ARROW: RELAMINARIZATION IN FREE-FLIGH TESTS

Julio Ortiz*[1], Toshinari Hasegawa [1], Atsushi Serino [1], Takeshi Miyazaki [1]and Hiroki Sugiura [2]
[1]Department of Mechanical Engineering and Intelligent Systems, University of Electro-Communications, Tokyo, Japan
[2]JAXA, Tokyo, Japan

Summary The laminar-turbulent and turbulent-laminar transitions of an archery arrow's boundary layer flow are explored experimentally. Two types of experimental procedures were carried out to measure the arrow's drag coefficient (C_D): wind tunnel tests in the JAXA's 60 cm × 60 cm Magnetic Suspension & Balance System (MSBS) and free-flight tests. During the free-flight tests, an acceleration sensor was fixed inside the arrow's shaft to measure the instantaneous aerodynamic loads exerted on the projectiles. From the acceleration sensor data, the laminar-turbulent transition and the relaminarization of the boundary layer flow were found in the range $1.6\times10^4 < Re < 1.8\times10^4$.

INTRODUCTION

The trajectory of an arrow is highly sensitive to the aerodynamic properties, such as the drag, lift and pitching moment coefficients. More than half of the contribution to the drag comes from the frictional drag exerted on an arrow shaft. The frictional drag increases if the boundary layer flow along the arrow shaft becomes turbulent.

Recently, two support-interference-free measurements were performed, i.e. wind tunnel tests with JAXA's 60 cm × 60 cm Magnetic Suspension & Balance System (MSBS) and free-flight tests [1,2]. The state of the boundary layer was inferred from the value of the angle of attack. A transition region was found in the Reynolds number range $1.2 \times 10^4 < Re < 1.9 \times 10^4$, in which both the laminar and turbulent values of the drag coefficient (C_D) were observed. It was concluded that even a very small angle of attack developed during the arrow's flight could trigger the laminar to turbulent transition. In this paper, the results of free-flight tests using an acceleration sensor are given compared with those from the MSBS wind tunnel tests.

EXPERIMENTAL APPARATUS

Arrow's description

Modern commercial arrows are slender and light bodies composed by three main elements: a shaft, point and vanes. The shaft utilized in the present study is the aluminium alloy-based A/C/E (Easton: Figs. 1a and 1b). Its external radius is 2.62×10^{-3} m. A bulge-type point is attached at the front part of the shaft. At the rear part of the arrows, 3 straight vanes are fletched to give stabilization during the free-flight. The model of the vanes is the Easton Diamond Vanes size 175. The length of the arrow is 0.638 m and its total mass is 14.2×10^{-3} kg.

(a) (b)

Figure 1. (a) Arrow suspended magnetically in the MSBS and (b) acceleration sensor being inserted in the arrow's shaft.

MSBS tests

The MSBS is a wind tunnel in which arrows can be suspended magnetically against gravity [1], as shown in Fig. 1a. A valuable advantage of the MSBS is that it allows to fix the arrows without any mechanical support that would disturb the measurements. The arrow's drag coefficient was obtained from the MSBS tests. The experiments were carried out in a Reynolds number range $0.28\times10^4 < Re < 1.41\times10^4$. The Reynolds number is defined as $Re=2Ur/\nu_{air}$, where U is the wind velocity, r the arrow's radius and ν_{air} is the air's kinematic viscosity at room temperature.

Free-flight experiments

The second type of experiment consists of shooting arrows using a compressed air launching system to measure the aerodynamic loads exerted during free-flight. An acceleration sensor was introduced in the arrow's shaft allowing us to measure the exerted force and angular velocity in the three spatial components.

The indoor free-flight tests were carried out with two different distances of 17.7 m and 55 m between the shooting and the target positions. For both cases, any type of air conditioning system was turned off to avoid the influence of wind

*Corresponding author. E-mail: ortiz.julio@uec.ac.jp.

gusts. The arrow's trajectories were recorded using high-speed video cameras located at the launching and target positions. From the recorded videos were obtained the initial and final arrow's velocity and angle of attack. The free-flight experiments were carried out in a Re number range 1.2×10^4 <Re< 2.1×10^4.

The acceleration sensor was designed by Logical Product (LP-UUEC002) and has a total length of 0.069 m, including the holders located at the two ends of the sensor (Fig.1b). The holders are designed to avoid excessive vibration. The total mass of the sensor (including the holders and battery) is 1.37×10^{-3} kg. The measurement frequency is 200 Hz and it can record deceleration up to16g (g denotes the gravitational acceleration) and a maximum rotation rate of 2250 dps.

RESULTS

Figure 2a shows the instantaneous deceleration values measured with the acceleration sensor, for shots with initial velocities of 47.3 ms^{-1} and 56.9 ms^{-1} with closed squares (■) and the summation symbols (+), respectively. The shots were carried out in the 55 m archery range. The flying times for the faster and slower shots were 0.95 s and 1.05 s, respectively. Interestingly, a relaminarization of the arrow's boundary layer was found to take place during free-flight for a shot with an initial velocity of 52.8 ms^{-1} (●). The transition from turbulent to laminar boundary layer was evidenced by the reduction in the deceleration during the time range 0.45 s < t < 0.85 s. For t > 0.9. A laminar-turbulent transition took place again due to uncontrolled instabilities in the boundary layer induced by unexpected air flow near the target.

Figure 2b shows C_D as a function of Re obtained from the two tests. In open circles (○) are shown the results corresponding to a shaft with no vanes. Such results agree with the theoretical predictions for a laminar boundary layer around a semi-infinite non-rotating cylinder. The small difference between the theoretical predictions and the MSBS measurements arises from the pressure drag. Open squares (□) show the larger C_D values obtained for an arrow aligned with the wind flow (θ =0). The C_D values correspond to a laminar boundary layer. It is possible to appreciate that the 3 straight vanes yield the drag increase of almost 100%. Open diamonds (◇) show the results when an angle of attack of θ =0.75° was fixed during the MSBS tests. An abrupt increase in the value of C_D suggests a laminar-turbulent boundary layer transition at Re = 1.2×10^4.

Closed symbols show the instantaneous C_D computed as $C_D = F_D/\left(\frac{1}{2}\pi\rho_{air}r^2{v_s}^2\right)$, where F_D is the exerted drag force, ρ_{air} is the air's density and v_s is the instantaneous arrow's velocity. Since the initial velocities are determined from the high-speed video camera recordings, it is possible to compute v_s by integrating the deceleration information. The laminar values of around 1.5 were obtained for Re ≈ 1.3×10^4, which is consistent with the MSBS results. Turbulent values around 2.6 are found for the shots of 47.3 ms^{-1} (■) and 56.9 ms^{-1} (+). In contrast, C_D reduced from a turbulent value 2.65 to a laminar value 1.3, when the relaminarization takes place (●).

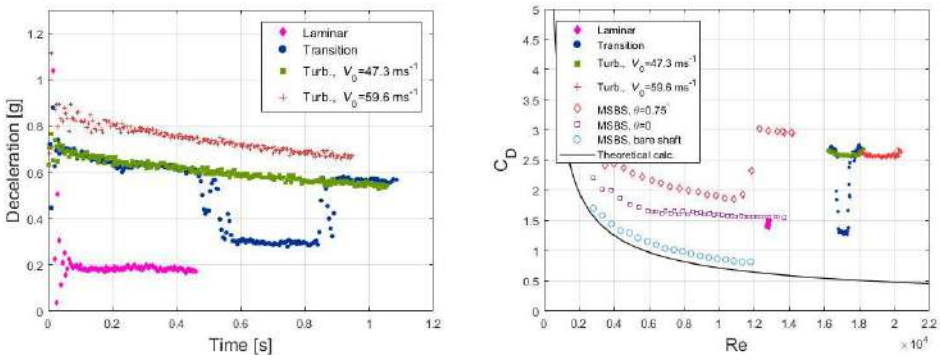

(a) (b)

Figure 2. (a) Time evolution of the arrow's deceleration and (b) C_D as a function of Re.

CONCLUSIONS

In the present study, the static and instantaneous values of the drag coefficient of archery arrows were measured experimentally. Laminar and turbulent boundary layers were found for shots with different launching conditions. The process of laminar-turbulent and turbulent-laminar transitions was found to take place experimentally from the data provided by an acceleration sensor mounted inside an arrow in free-flight. Further theoretical approaches are required to elucidate the detailed mechanism of the boundary layer transition process.

References

[1] Miyazaki, T.; Mukaiyama, K.; Komori, Y.; Okawa, K.; Taguchi, S.; Sugiura, H. Aerodynamic properties of an archery arrow. *Sports Eng.*, **16**: 43-54, 2013.

[2] Miyazaki, T.; Matsumoto, T.; Ando, R.; Ortiz, J.; Sugiura, H. Indeterminacy of drag exerted on an arrow in free flight: arrow attitude and laminar-turbulent transition. *Europhysics*. **38**: 6, 2017.

EFFECT OF GAP WIDTH ON VISCOUS FINGERING INSTABILITY IN HELE-SHAW CELL

Sada Nand* Vandita Sharma,and Manoranjan Mishra†
Department of Mathematics, Indian Institute of Technology Ropar, Punjab, India

Summary The flow through a Hele-Shaw cell with a very fine gap between the glass plates is equivalent to the two dimensional porous media flows. In this work, we focus on experimentally and numerically understanding the effect of the gap in the Hele-Shaw cell on viscous fingering instability observed in various applications like enhanced oil recovery, chromatography separation etc. For the experimental investigation, a radial Hele-Shaw cell with T-section for liquid infusion is used. For a small gap width, rigorous fingering patterns with tip splitting are observed, which disappear on increasing the gap between the glass plates. In order to understand three dimensional effects, numerical simulations are performed using Stokes equation in contrast to commonly used Darcy's law. The numerical results are in qualitative agreement with the experiments.

INTRODUCTION

Displacement of miscible fluids in porous media finds huge applications in many industrial, environmental and engineering areas such as enhanced oil recovery, contaminant transport in geological aquifers etc. Mobility gradient between the displaced fluids in porous media flows results in a hydrodynamic instability called viscous fingering (VF). A less viscous fluid displacing a more viscous one deforms the interface into finger like patterns termed as VF [1]. The understanding of these chaotic patterns is of critical importance in the generation of interfacial instabilities. In the laboratory, VF is visualised and analysed using a Hele-Shaw cell [2], which comprises of two transparent glass plates separated by a gap. For gap width much smaller than the other dimensions of the cell, the flow through Hele-Shaw cell is equivalent to the two dimensional porous media flows [1]. We aim to explore how small the gap width must be in order to neglect the three dimensional effects. In this work, we vary the gap width in the Hele-Shaw cell and analyse its effect on VF patterns. Further, non-linear simulations are performed using COMSOL Multiphysics® [3] to support the experimental findings. As we are interested in the variation in gap to understand the flow dynamics, the gap-averaged Darcy's law may not be able to capture the physical mechanism [4]. As such, we use the Stokes equation for the conservation of momentum. Two different COMSOL Multiphysics® modules are coupled in order to model the hydrodynamic instability.

EXPERIMENTAL SET UP & MODELLING

We use a radial Hele-Shaw cell with glass plates of dimensions 300mm $\times$ 300mm $\times$ 10 mm to experimentally understand various facets of miscible VF on varying the gap width b, between the glass plates. Experiments are performed with the point source. The two fluids are prepared using different concentration by volume of Glycerol in water. The less viscous fluid has less concentration of glycerol in water and also contains dye for visual contrast. It is verified that the dye does not affect the viscosity of the fluid. The experiments are performed by initially filling the cell with high viscous fluid, followed by continuous injection of the less viscous fluid at a constant flow rate Q using a COLE-PARMER-D201253 pump. For an effective infusion of fluids we fabricated a T-section [5], which is attached to the Hele-Shaw cell. There is no need to change the pipes for injection of different fluids when using a T-section. Dynamics are captured with the help of the Sony FDR-AX40 camera fixed above the cell. Viscosity contrast is defined by log-mobility ratio R, defined as the natural logarithm of the ratio of the viscosity of the displaced fluid to that of the displacing fluid (here less viscous).
For the numerical study, we perform a three-dimensional study using COMSOL Multiphysics®. To model the porous media flows, Darcy's law is used in literature [1, 6]. But the Darcy's law encorporates gap-averaged quantities. Consequently, to study the effects of gap width on viscous fingering dynamics, we use Stokes equation coupled with the convection-diffusion equation for solute concentration for the mathematical modelling. The governing equations by considering Newtonian, incomressible and homogenous fluids are:

$$\nabla \cdot (\vec{u}) = 0, \tag{1}$$

$$0 = \nabla.[-p\mathbf{I} + \mu(c)(\nabla\vec{u} + (\nabla\vec{u})^{\mathbf{T}})], \tag{2}$$

$$\epsilon_p \frac{\partial c}{\partial t} + \vec{u} \cdot \nabla c = \epsilon_p D \nabla^2 c \tag{3}$$

where $\vec{u} = (u, v, w)$ is the velocity vector, p is the hydrodynamic pressure, D is the diffusion coefficient and μ is the dynamic viscosity of fluid and ϵ_p is the porosity of the medium. Arrhenius type relation is assumed between viscosity and concentration, defined as $\mu(c) = \mu_1 e^{R\,(c-c_1)/(c_2-c_1)}$, where $R = \ln\left(\frac{\mu_2}{\mu_1}\right)$ is the log-mobility ratio. $\mu_i, c_i, i = 1, 2$ respectively denote the viscosity and concentration of two fluids ($i = 1$ for displacing fluid). If $R > 0$ then $\mu_2 > \mu_1$:

*Corresponding author. E-mail: sadanand@iitrpr.ac.in
†Corresponding author. E-mail: manoranjan@iitrpr.ac.in

which is favourable for VF. The continuity equation (equation(1)) and Stokes equation (equation(2)) are solved using Creeping flow (spf) module which is coupled with the Transport of Diluted Species (tds) module for the convection-diffusion equation (equation(3) for solute concentration. For the numerical study a cylindrical geometry of 300 mm diameter and gap width, b, in mm scale is used. The meshing of the domain is done using user-controlled mesh. We use a free triangular mesh, with swept distribution for capturing the three dimensional effects.

RESULTS AND DISCUSSION

For the experiments, we fix the flow rate Q and log mobility ratio R and vary the gap width. We first specify a gap width $b = 0.5$ mm, for which rigorous fingering patterns are observed when less viscous (blue) fluid displaces the more viscous (transparent) fluid as evident in figure 1(a). The tip splitting mechanism in which the tip of a single finger splits into multiple fingers is clearly visible for $b = 0.5$ mm. On increasing the gap width further, a suppression in instability is observed. For instance when we double the gap width, $b = 1$ mm, a few bumps at the interface are observed up to $t = 7$ sec. which develop into toe shaped fingers at later time (see figure 1(b). Further we numerically explore the gap width effect by considering a three dimensional study. We show a quarter of the fluid injection plane in figure 1(c,d) which are in good qualitative agreement with the experimental findings. With an increase in gap width, the instability is abated for a larger gap width. Thus, the gap width has a significant effect on the VF dynamics and must be clearly chosen in the Hele-Shaw cell experiments to understand the porous media flows and avoid three dimensional effects.

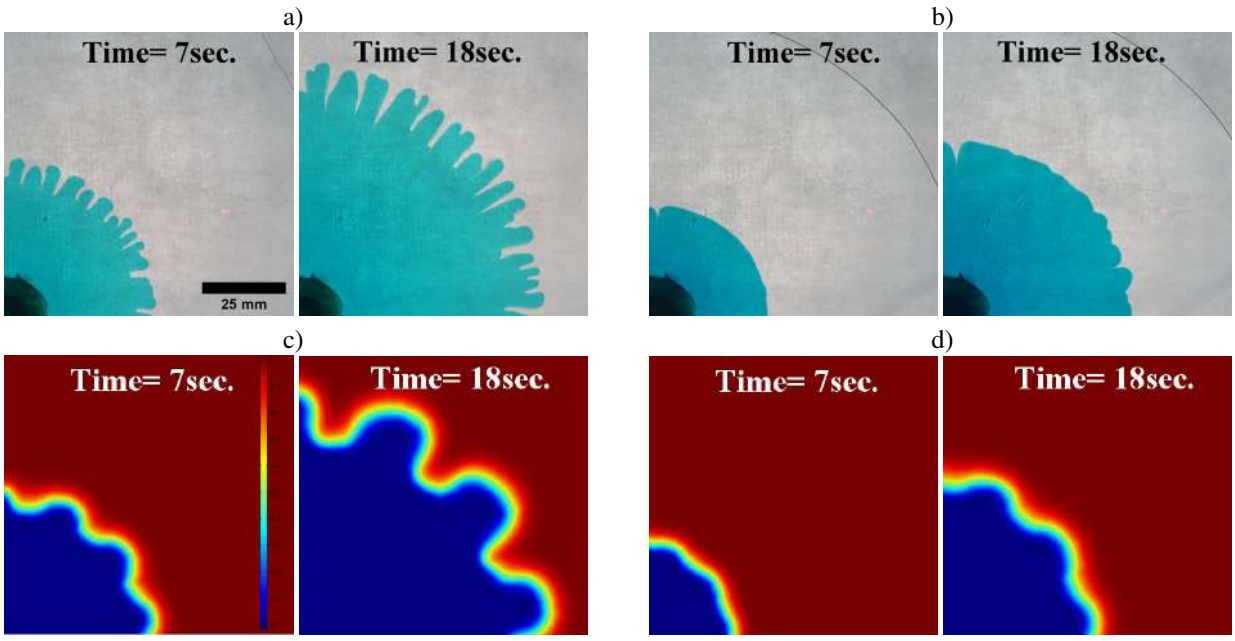

Figure 1: Comparison of the VF patterns observed in experiments (a), b)) with the results of numerical simulations (c), d)). Rigorous fingers are observed for a gap width of 0.5 mm (a,c) in comparison to a gap width of 1 mm (b,d).

CONCLUSIONS

The effect of gap width between the glass plates in the Hele-Shaw cell on the VF dynamics is explored using a deligently designed experimental set up. A range of VF dynamics from rigorous to toe shaped fingers are observed on varying the gap width. An increase in gap width results in an abated instability. The experimental results are in good qualitative agreement with the numerical simulations performed using Stoke's equation.

Acknowledgement MM acknowledges the financial support from SERB, Government of India through project grant number MTR/2017/000283.

References

[1] Homsy G.M. Viscous fingering in porous media. *Annu. Rev. Fluid Mech.*, **19(1)**: 271-311, 1987.
[2] Chen J.D. Radial viscous fingering patterns in hele-shaw cells. *Exp. Fluids*, **5**: 363-371, 1987.
[3] COMSOL Multiphysics® v. 5. 4. **www.comsol.com**. COMSOL AB, Stockholm, Sweden.
[4] Oliveira R. M., Meiburg E. Miscible displacements in Hele-Shaw cells: three-dimensional Navier-Stokes simulations. *J. Fluid Mech.*, **687**: 431-460, 2011.
[5] Sharma V. et al. Control of radial miscible viscous fingering. *J. Fluid. Mech.*, **884** : A16-1, 2020.
[6] Nase, J., Derks D., Lindner, Dynamic evolution of fingering patterns in a lifted Hele-Shaw cell. *Phys. Fluids*, **23**: 123101, 2011.

BOUNDARY LAYER TRANSITION ON BLUFF BODIES DUE TO TRIP AND ITS IMPLICATION IN CRICKET

Gaurav Chopra[1], Aditya Desai[1], and Sanjay Mittal[*1]
[1]Department of Aerospace Engineering, Indian Institute of Technology Kanpur, India

Summary The transition of boundary layer on cylinder and sphere, by a trip, is investigated via computations and experiments. The effect of location and height of the trip on transition is studied. It is found that the formation of the laminar separation bubble (LSB) is bypassed for trips larger than a critical height. The flow on both the trip- and non-trip-side of the body is affected. The swing and reverse-swing of a cricket ball are explained.

INTRODUCTION

"Drag-crisis" in bluff body flows refers to the transition of boundary layer from a laminar to turbulent state and is associated with a steep drop in drag with increase in Reynolds number (Re) beyond a certain critical value. On smooth bodies, the transition is accompanied with the formation of LSB ([1, 2, 3]). An early transition can be engineered via a boundary layer trip or surface roughness. This is utilized in sports projectiles. For example, [4] investigated the role of seam/surface roughness in swing and reverse-swing of a cricket ball. The objective of the present work is to study the effect of the location (θ_T) and height (d_T with respect to diameter) of a trip on the transition of boundary layer on bluff bodies. The study utilizes large eddy simulations (LES) via a stabilized finite element method with a sigma model ([2]) and a very fine grid to resolve the flow, an as well as experiments in the low-speed and low turbulence National Wind Tunnel Facility (NWTF) at Indian Institute of Technology Kanpur. Force, surface pressure measurements, oil flow visualization & PIV are carried out in the experimental study ([3, 4, 5]). The trip on the cylinder is a wire along its span located on one side at an angle θ_T from the stagnation point. On the other hand, it resembles the seam of a cricket ball for the study on a sphere.

RESULTS

It is found that the location and height of the trip affect the transition of flow very significantly. Only a few results are described here: computational for the cylinder, and from experiments for the sphere. Detailed results will be presented at the conference. The variation of time-averaged coefficient of drag ($\overline{C}_D$) with Re for a smooth and cylinder with trip at $\theta_T = 55^o$ and $d_T = 0.25\%$ and 1.0% is shown in figure 1 (a). The drag crisis begins at $Re = 1.0 \times 10^5$ for the smooth cylinder. The transition on the upper and lower surfaces are very similar. In contrast, the drag crisis for the cylinder with $d_T = 1\%$ trip is a two-staged phenomenon. The first stage corresponds to transition on the trip side (TrS) at a relatively lower Re, compared to a smooth cylinder, while the flow on the non-trip/smooth side (SmS) stays laminar. Natural transition of the flow on the non-trip side constitutes the second stage. The Re for this transition is close to that for a smooth cylinder.

Figure 1 (b) shows the variation of time- and span-averaged coefficient of peak suction pressure ($-\overline{C}_{Ppeak}$) with Re. It is observed that the 1% trip affects the suction on not just the trip-side (TrS) but the smooth-side (SmS) as well. Transition on TrS, causes $-\overline{C}_{Ppeak}$ to be larger on TrS and smaller on SmS compared to that during natural transition on a smooth cylinder. On the other hand, transition on SmS causes $-\overline{C}_{Ppeak}$ to be much larger on SmS and lower on TrS compared to that on the smooth cylinder. These two phenomenon, respectively, explain "swing" and "reverse swing" of a cricket ball ([4]). Figure 1 (c) shows the time- and span-averaged streamlines for cylinder with 0.25% and 1% trips at $Re = 3.0 \times 10^5$. An LSB forms between the points of laminar separation (LS) and turbulent reattachment (TR). These along with the point of turbulent separation (TS) are marked in the figure. LSB forms in all cases when there is no trip. However, it does not form on the trip-side for the 1% trip. The large trip leads to a by-pass transition. For the case of 0.25% trip, the LSB on the TrS forms at a lower Re compared to the smooth cylinder.

Figures 2 (a) and (b) show the variation of time-averaged coefficient of drag ($\overline{C}_D$) and side force ($\overline{C}_Z$) with Re, respectively, for smooth sphere and cricket ball at an seam angle (θ_{Tr}) of 20^o. Qualitatively, the phenomenology of drag-crisis is similar to that of the flow past a cylinder. With increase in speed, the cricket ball goes through three regimes (2 (b)). In the regime of no-swing (NS), which occurs for Re less than that for transition, the trip has no effect on the boundary layer and it undergoes Laminar Separation (LS). Therefore, the side-force on the ball is close to zero. In the regime of conventional-swing, the boundary layer on trip-side of the ball undergoes transition while that no the smooth side remains laminar. An LSB forms on the trip-side. This is followed by the regime of reverse-swing (RS), wherein the boundary layer undergoes a natural transition on the smooth-side leading to the formation of an LSB, while the LSB on the seam-side disappears.

*Corresponding author. E-mail: smittal@iitk.ac.in.

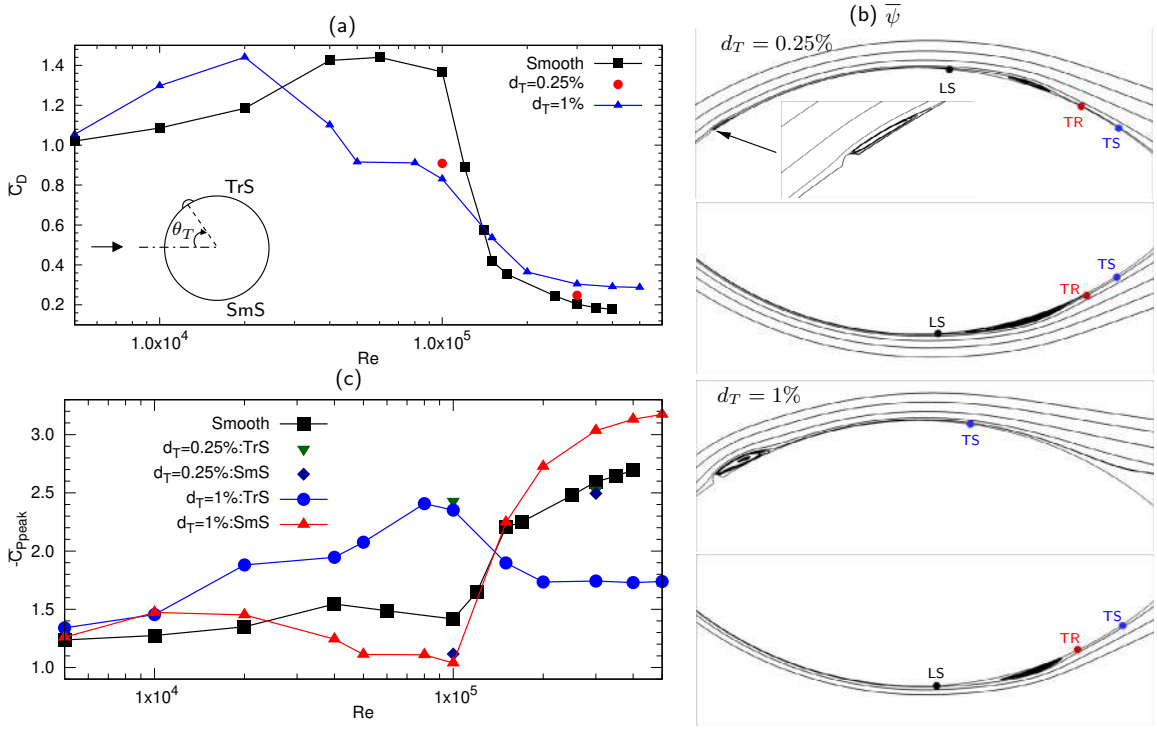

Figure 1: Flow past a cylinder with trip at $\theta_T = 55^o$ and $d_T = 0.25\%$ & 1% (computational study): (a) variation of time-averaged coefficient of drag ($\overline{C}_D$), and (b) time and span-averaged coefficient of peak suction pressure ($-\overline{C}_{Ppeak}$) with Re. Also shown is the data for smooth cylinder. (c) Close up view of time- and span-averaged streamlines of the TrS and SmS for $Re = 3.0 \times 10^5$.

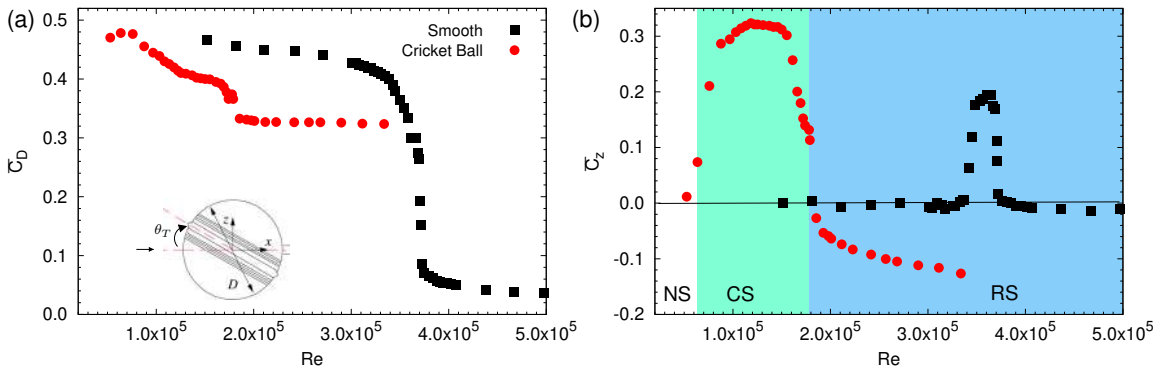

Figure 2: Flow past a smooth sphere and cricket ball (experimental study): (a) variation of time averaged coefficient of drag ($\overline{C}_D$), and (b) coefficient of side force ($\overline{C}_Z$) with Re.

CONCLUSIONS

The effect of a trip on the transition of boundary layer on bluff bodies has been investigated via experiments and computations. The trip prepones the transition. However, the location and height of the trip have a profound effect on the nature of transition. As in natural transition, LSB forms on the trip side if the height of the trip is relatively low. On the other hand, a by-pass transition occurs for a larger trip height. The trip appears to affect the flow not only on the side it is present, but also on the non-trip side of the bluff body. The seam and surface roughness are responsible for the side force on the cricket ball leading to swing and reverse-swing.

References

[1] Singh S. P., Mittal S. Flow past a cylinder: shear layer instability and drag crisis. *Int. J. Numerical Methods Fluids* **47**: 75-98, 2005.
[2] Chopra G., Mittal S. The intermittent nature of the laminar separation bubble on a cylinder in uniform flow. *Computers & Fluids* **142**: 118-127, 2017.
[3] Deshpande R., Kanti V., Desai A., Mittal S. Intermittency of laminar separation bubble on a sphere during drag crisis. *J. Fluid Mech.* **812**: 815-840, 2017.
[4] Deshpande R., Shakya R., Mittal S. The role of the seam in the swing of a cricket ball. *J. Fluid Mech.* **851**: 50-82, 2018.
[5] Desai A., Mittal S., Mittal S. Experimental investigation of vortex shedding past circular cylinder in the high subcritical regime. *Physics of Fluids*: 2019.

EXPERIMENTAL STUDY OF AN EFFECTIVE MECHANISM OF DISTRIBUTED EXCITATION OF UNSTEADY GÖRTLER VORTICES BY LOW-FREQUENCY FREESREAM TURBULENCE

Dmitry Mischenko*[1], Vladimir Borodulin[1], Andrey Ivanov[1], and Yury Kachanov[1]
[1]Khristianovich Institute of Theoretical and Applied Mechanics, SB RAS, Novosibirsk, Russia

Summary The paper is devoted to experimental investigation of a distributed vortex receptivity mechanism that is able to efficiently excite unsteady (in general) Görtler vortices in boundary layers on curved walls. The quantitative study is carried out in a broad range of problem parameters in a Blasius type boundary layer developing on a concave surface. The receptivity coefficients are estimated. The problem of linear unsteady Görtler instability of this particular boundary layer is studied in complementary experiment. All main stability characteristics are obtained and compared with calculations based on linear stability theories.

INTRODUCTION

The Görtler instability is widespread in various shear flows with curved streamlines at sub-, super-, and hypersonic speeds. The instability is caused by centrifugal force, which action is essentially nonuniform in the cross-flow direction due to presence of a strong cross-flow mean-velocity gradient. The paper presents results of a systematic quantitative experimental study of, apparently, one of the most important mechanisms of excitation of unsteady (in general) Görtler vortices [1] in cases of boundary layers developing at conditions of enhanced level of freestream vortex disturbances. This mechanism is associated with distributed scattering of longitudinal low-frequency and stationary freestream vortices on the natural streamwise nonuniformity of the growing boundary layer and is able to excite unsteady Görtler modes and to affect significantly their downstream evolution. Distributed excitation of Görtler modes by freestream vortices was studied quantitatively for the first time in [2]. Similar mechanisms at excitation Cross-Flow and Tollmien-Schlichting instability modes in boundary layers were successfully investigated experimentally in [3-5]. The present work is devoted to a systematic study of distributed excitation of Görtler modes and complements preliminary results obtained in [2].

EXPERIMENTAL SETUP

Two paired series of measurements were performed in the low-turbulence wind tunnel T-324 of ITAM SB RAS (Novosibirsk, Russia) at one and the same base-flow conditions: (1) a main experiment on distributed vortex receptivity and (2) an additional experiment devoted to obtaining experimental linear stability characteristics (increments and phase velocities) of unsteady Görtler modes. The data of the experiment (2) were necessary for obtaining quantitative characteristics of the receptivity mechanism studied in experiment (1) – the coefficients of the distributed vortex receptivity. Detailed hot-wire measurements were carried out in a boundary layer of the Blasius type developing on a concave surface of the high-precision experimental model (with radius of curvature R of 8.37 m) at freestream velocity U_e = 9.18 m/s. The two experiments were carried out using completely controlled unsteady disturbances (of both the boundary layer and of the incident flow), which were generated by special disturbance sources. The results were obtained for Görtler vortices of three frequencies f = 8, 13, and 17 Hz (the corresponding frequency parameter F = 9.29; 15.09 and 19.73) with spanwise wavelengths λ_z = 7 to 24 mm (the corresponding dimensionless spanwise scale Λ = 119 to 758) in a range of Görtler numbers G^* = 8.6 to 21.0. Estimates of the distributed receptivity coefficients at excitation *steady* Görtler modes were also obtained (see below).

MAIN RESULTS

It has been found that the results of experiment (2) are in a good agreement, in general, with the results of calculations based on the locally-parallel and nonlocal non-parallel theories of unsteady Görtler linear instability by A.V. Boiko [1]. (Figure 1*a* shows calculations based on locally-parallel theory only.) The growth of spanwise scale and frequency of unsteady Görtler modes is found to lead to worsening of correlation of experimental and calculated data (which is consistent with [1]). New experimental data complement previous studies [1] (carried out only for three spanwise scales of disturbances) and are suitable for verification of various theories of unsteady Görtler linear instability of boundary layers on concave walls.

It has been found in experiments (1) that the distributed vortex receptivity mechanism is capable of efficient excitation both steady and unsteady Görtler vortices and modifies significantly laws of downstream evolution of unsteady (at least) Görtler modes (Figure 1). As a result, the distributed receptivity can lead to either amplification or suppression of unsteady Görtler modes and, in particular, is able to provide the growth of almost neutrally stable Görtler vortices.

*Corresponding author. E-mail: D.A.Mischenko@itam.nsc.ru.

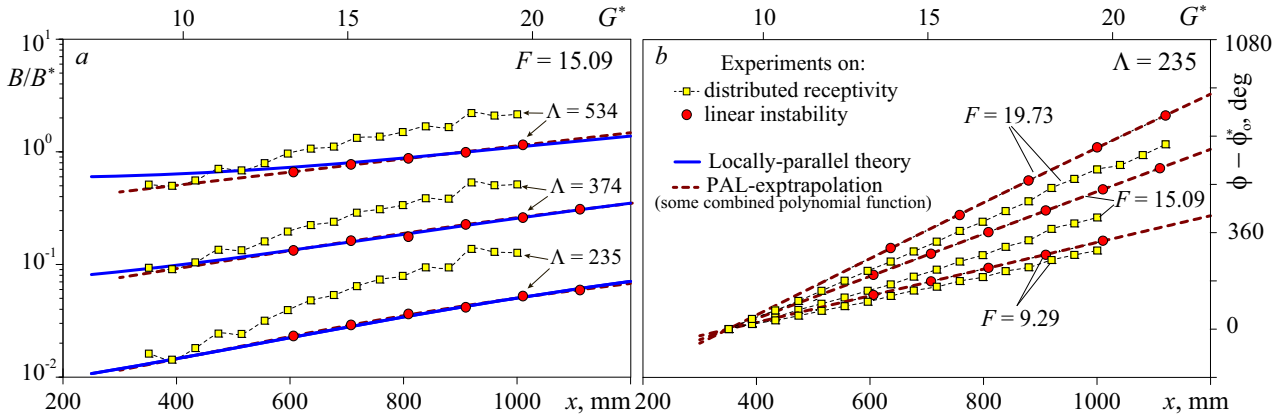

Figure 1. Example of comparison of streamwise distributions of spectral amplitudes (*a*) and phases (*b*) of unsteady Görtler modes developing under action of distributed vortex receptivity mechanism (squares) and of the linear stability mechanism only (circles).

Estimates of quantitative values of the coefficients of distributed vortex receptivity were obtained in present work by solving the corresponding complex, mathematically incorrect problem (similar to [5]). It was found that the amplitudes and phases of these coefficients are independent on streamwise coordinate. In the studied range of parameters, the amplitudes of the coefficients increase (in a linear way) with disturbance frequency, as well as with their spanwise scale (especially in the high-frequency region, see Figure 2). It was found that, due to a number of reasons, it is impossible to obtain directly, in a similar way, the corresponding estimates of the experimental distributed receptivity coefficients at excitation of *steady* Görtler vortices. Nevertheless, they were obtained by means of linear approximation the frequency dependence of the coefficients amplitudes at excitation of *unsteady* Görtler vortices with subsequent extrapolation to the zero frequency. It turned out that the distributed vortex receptivity responsible for excitation of stationary Görtler modes is much weaker compared to the case of nonstationary modes.

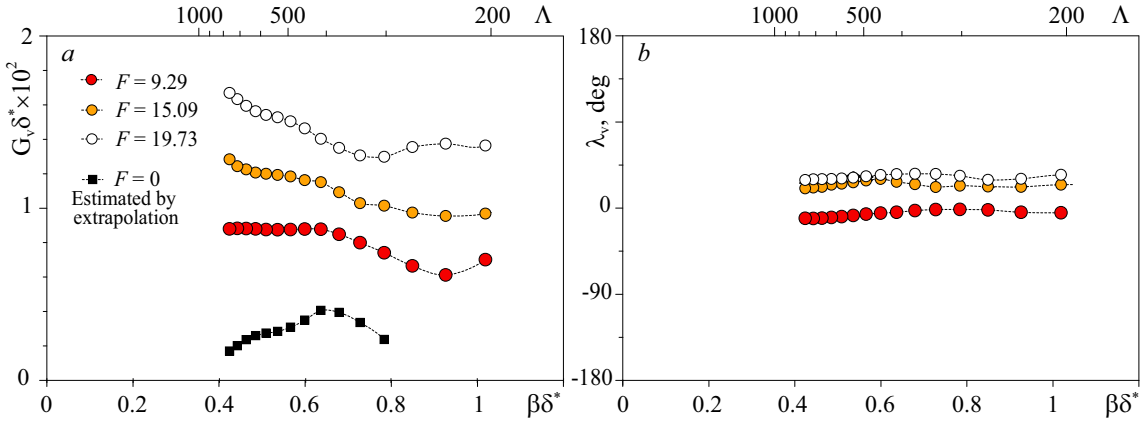

Figure 2. Amplitudes (*a*) and phases (*b*) of distributed vortex receptivity coefficients versus spanwise wavenumber of Görtler modes β. Here $\delta^* = 1.6$ mm is a boundary layer displacement thickness corresponding approximately to the center of region of obtaining of the coefficients.

The results obtained in the present experiments can be used for verification of various theories of distributed excitation of unsteady and steady Görtler modes by freestream vortices and can be applied to estimations of locations of the laminar-turbulent transition in boundary layers on concave walls. The enhancement of power of the studied receptivity mechanism with frequency, along with simultaneous weakening of the linear Görtler instability mechanism [1], is able to lead to a significant expansion of the frequency range, in which freestream vortices can affect the laminar-turbulent transition in various practical applications.

This work is supported by the Russian Foundation for Basic Research (grant No. 12-01-31211).

References

[1] Boiko A.V., Ivanov A.V., Kachanov Y.S., Mischenko D.A., Eur. J. Mech. B Fluids **29**: 61-83, 2010
[2] Ivanov A.V., Kachanov Y.S.,Mischenko D.A., Thermophys. Aeromech. **21**, 663–678, 2014.
[3] Borodulin V.I., Ivanov A.V., Kachanov Y.S., V. M. Fomin (Ed.), XV Internat. Conf. Methods of Aerophysical Research, RAS. Sib. Branch Inst. Theoret. Appl. Mech., Novosibirsk, 2010.
[4] Borodulin V.I., Ivanov A.V., Kachanov Y.S., XV Internat. Conf. Methods of Aerophysical Research, RAS. Sib. Branch Inst. Theoret. Appl. Mech., Novosibirsk, 2010.
[5] Borodulin V.I., Ivanov A.V., Kachanov Y.S., Mischenko D.A., Fedenkova A.A., AIP Conf. Proc. 1770, 030041, 2016.

RESOLVENT ANALYSIS OF BOUNDARY-LAYER FLOWS INTERACTING WITH FINITE-EXTENT VISCO-ELASTIC INSERT

Jean-Lou Pfister[1], Nicolo Fabbiane[1], and Olivier Marquet[*1]
[1]ONERA, DAAA, University Paris Saclay, France

Summary Based on linear fluid-solid stability analysis, we investigate the attenuation of Tollmien-Schlichting waves in a boundary-layer flow developing on a wall with a finite-extent visco-elastic insert. A resolvent analysis of the fluid perturbation in the rigid-wall configuration is first performed to determine the optimal amplification and forcing. The harmonic fluid-solid response to the optimal fluid forcing is then computed for the compliant-wall configuration, based on the linearization of the Arbitrary-Lagrangian-Eulerian formulation [3]. The attenuation of Tollmien-Shlichting waves obtained at low frequencies relies on a wave-cancellation mechanism. The amplification of Travelling-Wave Flutter at high frequencies relies on the existence of nearly unstable solid modes excited by the fluid forcing.

The use of compliant walls to delay the laminar/turbulent transition in boundary layers ([1],[2]) was inspired by the skin properties of animals, like dolphins. It is now well established that three types of instabilities occur in laminar boundary-layer flows developing over *infinite-length* compliant walls: Tollmien-Schlingthing (TS) waves, Travelling Waves Flutter (TWF) and Static Divergence instability. The effect of compliant walls has been mainly investigated using local stability analysis, reyling on the assumption of an infinite extent of the elastic wall in the streamwise direction. Based on resolvent analysis and harmonic fluid-solid linear response, we here investigate the effect on the flow perturbation of a finite-extent visco-elastic insert in the wall.

RIGID-WALL CONFIGURATION AND RESOLVENT ANALYSIS

The nominal flow configuration is a two-dimensional boundary-layer flow developing over a rigid wall. The local Reynolds number $Re(x) = U^*_\infty \delta^*(x)/\nu$, based on the freestream velocity U^*_∞ and the local displacement thickness $\delta^*(x)$ at the streamwise position x from the leading edge of the wall, varies in the range $3000 \leq Re(x) \leq 3179$ between the inlet and the outlet of the computational domain. For such Reynolds numbers, the Blasius boundary layer is convectively unstable to Tollmien Schlichting waves at any streamwise position. In the following, all variables are made non-dimensional using U^*_∞ and the displacement thickness at the inlet $\delta^*(x_i)$, as the velocity and length scales, respectively. The flow, modelled with the incompressible Navier-Stokes equations, is decomposed into a steady component $[\mathbf{U}, P]$ and an infinitesimally small perturbation $[\mathbf{u}, p] = [\hat{\mathbf{u}}, \hat{p}]\, e^{i\,\omega t}$, where $[\hat{\mathbf{u}}, \hat{p}]$ is the harmonic flow response at frequency ω to the harmonic momentum forcing $\hat{\mathbf{f}}$. The linear input-ouput relation between the momentum forcing and the harmonic flow velocity $\hat{\mathbf{u}}$ is formally written

$$\hat{\mathbf{u}} = \mathbf{R}(\omega)\,\hat{\mathbf{f}} \quad , \quad \mathbf{R}(\omega) = \mathbf{C}\,\left(\mathrm{i}\omega\,\mathbf{M} + \mathbf{L}(\mathbf{U})\right)^{-1}\mathbf{B}, \tag{1}$$

where $\mathbf{R}(\omega)$ is the hydrodynamic resolvent operator, $\mathbf{L}$ is the linearized Navier-Stokes operator around the base flow velocity $\mathbf{U}$, $\mathbf{M}$ is the mass matrix accounting for the time-independence of the divergence-free condition, while $\mathbf{B}$ and $\mathbf{C}$ are prolongation and extension operators, respectively. The no-slip condition imposed at the rigid wall is embedded in the definition of the resolvent operator. The resolvent analysis then consists in determining the largest singular values of this operator. They can be computed as the largest (positive) eigenvalues λ_k^2 of the following eigenvalue problem

$$\mathbf{R}(\omega)^H \mathbf{R}(\omega)\,\hat{\mathbf{f}}_k = \lambda_k^2\,\hat{\mathbf{f}}_k \tag{2}$$

Ordered by decreasing values, these eigenvalues represent the gain between the kinetic energy of the flow perturbation (output) and a norm of the focing (input), i.e. $\lambda_k^2 = \hat{\mathbf{u}}_k^H \hat{\mathbf{u}}_k / \hat{\mathbf{f}}_k^H \hat{\mathbf{f}}_k$. The harmonic flow response associated to the largest energy gain λ_0^2 is plotted as function of the frequency in Figure 1, with the solid curve. The large energy gains obtained in the frequency range $0.05 \leq \omega \leq 0.15$ are associated to the amplification of low-frequency Tollmien-Schlichting waves, displayed in Fig.2(a) using the pressure field. The shorter-wavelength Tollmien-Schlichting waves obtained at higher frequency are not amplified, as those displayed in Fig.2(b) at $\omega = 0.45$.

HARMONIC FLUID-SOLID RESPONSE IN THE VISCO-ELASTIC-WALL CONFIGURATION

To attenuate the Tollmien-Schlichthing waves that are amplified at low-frequencies, we insert in the rigid wall a solid patch of non-dimensional length 100 and thickness 5 at the distance 25 of the inlet domain. This solid patch is made of an incompressible visco-elastic material, modelled by a generalization of the one-dimensional Kelvin-Voigt constitutive relation. The elastic component of this stress tensor is proportional to the non-dimensional Young modulus E_s, while the viscous component is proportional to the non-dimension damping D_s. These non-dimensional parameters are fixed

*Corresponding author. E-mail: olivier.marquet@onera.fr

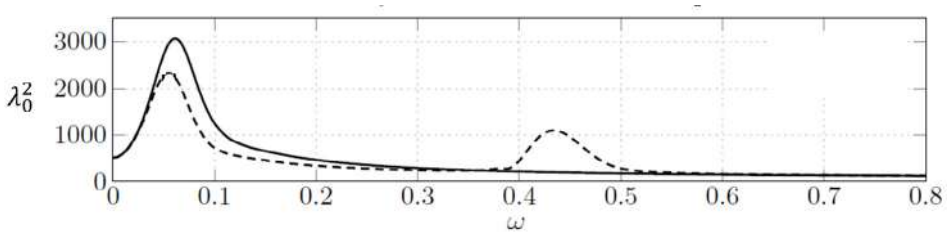

Figure 1: Energy gain as a function of the frequency ω. The solid line depicts the optimal energy amplification of the rigid-wall boundary-layer flow. The dashed line is the linear response to the optimal fluid amplification. The low-frequency and high-frequency peaks corresponds to the amplification of Tollmien-Schlichting (TS) and Travelling-Wave-Flutter (TWF) instabilities.

to $E_s = 1$ and $D_s = 0.2$ in the following (see [4]). The attenuation of the Tollmien Schlichting waves induced by the visco-elastic coating is assesed by computing the linear harmonic response of the fluid-solid perturbation to the optimal flow forcing $\hat{\mathbf{f}}_0$ previously determined. Formally, this is written

$$\left(\mathrm{i}\omega \begin{bmatrix} \mathbf{M}^f & 0 \\ 0 & \mathbf{M}^s \end{bmatrix} + \begin{bmatrix} \mathbf{A}^f(\mathbf{Q}) & \mathbf{C}^{fs} \\ \mathbf{C}^{sf} & \mathbf{A}^s(E_s, D_s) \end{bmatrix} \right) \begin{bmatrix} \hat{\mathbf{q}}^f \\ \hat{\mathbf{q}}^s \end{bmatrix} = \begin{bmatrix} \mathbf{P}\,\hat{\mathbf{f}}_0 \\ 0 \end{bmatrix} \tag{3}$$

In the first line that represents the linear harmonic equation governing the fluid perturbation $\hat{\mathbf{q}}^f$, $\mathbf{A}_f$ is the linearized Navier-Stokes operator written in the Arbitrary-Lagrangian-Eulerian formulation (see [3] for more details) and $\mathbf{C}_{fs}$ represents all the coupling terms with the solid perturbation $\hat{\mathbf{q}}_s$. In the second line that represents the linear harmonic equation governing the solid perturbation, the operator $\mathbf{A}_s$ represents the stress-strain elation of the visco-elastic patch and $\mathbf{C}_{sf}$ accounts for all the couplings with the flud perturbation, as for instance the hydrodynamic loading at the fluid-solid interface. Solving the above linear problem for several frequencies, one can define the energy gain between the input and the output of the fluid-solid configuration, i.e. $\lambda_0^2 = \hat{\mathbf{u}}^{f\,H}\hat{\mathbf{u}}^f / \hat{\mathbf{f}}_0^H \hat{\mathbf{f}}_0$, where $\hat{\mathbf{u}}^f$ is the velocity component of the fluid perturbation $\hat{\mathbf{q}}^f$. This quantity is plotted in Fig. 1 with the dashed curve. It clearly shows the attenuation of low-frequency Tollmien-Schlchting waves and the amplification of higher-frequency waves, kwown as the Travelling-Wave-Flutter waves. They are respectively depicted Fig. 2(c) and (d), with contours of the vertical displacement in the visco-elastic patch. For the low-frequency Tollmien-Schlichting Waves, the vertical displacement of the visco-elastic patch is in-phase with the flow pressure perturbation, and out-of-phase for the Travelling Wave Flutter.

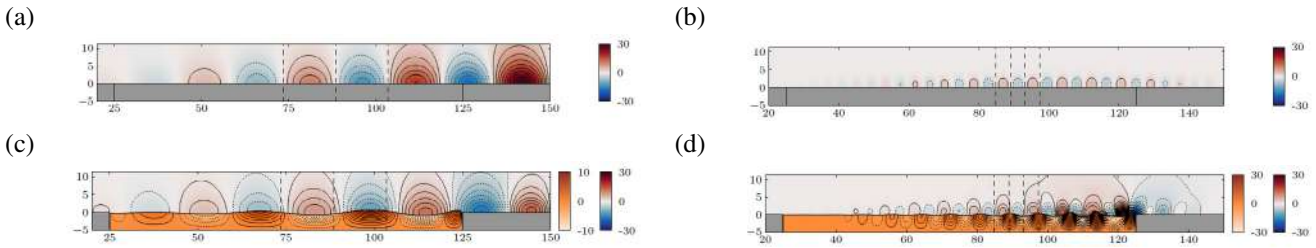

Figure 2: . Attenuation of low-frequency TS instability by the visco-elastic patch. (a) Optimal response of the flow for the rigid-wall configuration. (b) Response of the compliant-wall configuration to the optimal flow forcing. Isolines of the pressure and vertical discplacement are shown in the fluid and solid, respectivley.

A decomposition of the linear fluid-solid harmonic response, not detailed here, allows better understanding the attenuation of low-frequency waves and the amplification at high-frequency waves. In particular, we will show that the attenuation of TS waves relies on a wave-cancellation mechanism, while the amplification of TWF is related to the excitation by the flow of nearly unstable solid eigenmodes. We will further discuss the fluid-solid response to the sub-optimal fluid forcing, thus highlightenig the interest of performing a resolvent analysis of the fluid-solid operator. Results of this fluid-solid resolvent analysis will be compared to the harmonic fluid-solid response to optimal fluid forcing, described above.

References

[1] Benjamin, T. Brooke. Effects of a flexible boundary on hydrodynamic stability. *Journal of Fluid Mechanics*, **9**: 513-532, 1960.

[2] Landahl, Marten T. On the stability of a laminar incompressible boundary layer over a flexible surface. *Journal of Fluid Mechanics* **13**: 609-632, 1962.

[3] Pfister, J. L., Marquet, O., & Carini, M. Linear stability analysis of strongly coupled fluid-structure problems with the Arbitrary-Lagrangian-Eulerian method. *Computer Methods in Applied Mechanics and Engineering*, **355**: 663-689, 2019.

[4] Tsigklifis, K., & Lucey, A. D. The interaction of Blasius boundary-layer flow with a compliant panel: global, local and transient analyses. *Journal of Fluid Mechanics*, **827**: 155-193, 2017.

TRANSITION TO TURBULENCE IN PLANE COUETTE-POISEUILLE FLOW WITH EXTERNAL NOISE

Tao Liu[1], Lukasz Klotz[2], Benoît Semin[1], Ramiro Godoy-Diana[1], José Eduardo Wesfreid[*1], and Tom Mullin[3]
[1]Physique et Mécanique des Milieux Hétérogènes (PMMH),UMR 7636 CNRS,ESPCI,Sorbonne University,University of Paris, 7 Quai Saint Bernard, Paris, France
[2]Institute of Science and Technology, Am Campus 1, 3400 Klosterneuburg, Austria
[3]Mathematical Institute, University of Oxford, Oxford OX2 6GG, UK

Summary We report the results of an experimental investigation of the effects of noise on the critical Reynolds number required for sustained turbulence in plane Couette-Poiseuille flow. We establish the critical point by decreasing the Reynolds number from a fully turbulent state. At $Re_c = 650$, the characteristic decay time approaches infinity and this is found to be independent of the level of noise. On other hand, the time and space averaged amplitude of the statistical permanent state after the decay is sensitive to the external noise level.

INTRODUCTION

The transition to turbulence in confined shear flow is sub-critical and characterized by the coexistence of laminar and turbulent regions at moderate Reynolds number. In order to study this scenario, we have built a plane Couette-Poiseuille flow (CPF) experimental set-up [1]. The CPF shares similarities with plane Couette flow (PCF), plane Poiseuile flow, flow in shallow lake induced by wind and boundary layer (BL) etc. However, the presence of noise in the set-up has an influence on the transition [3]. The noise effects are studied by varying the noise level in the system. The critical Reynolds number Re_c of CPF is defined using the life time of transient turbulent decay; the time and space averaged amplitude is characterized as a function of Re for different noise levels.

EXPERIMENTAL SET-UP

The sketch of the set-up is illustrated in Fig. 1 (a). It consists of two parallel glass plates with a distance $2h = 11mm$ between a glass plate and a moving belt, a length of $L_x/h = 390$ and a height of $L_z/h = 90$. The belt with a velocity U_{belt} induces a shear flow that results in a pressure gradient driving the counter flow (see Fig. 1 (b)). The flow profile is Couette-Poiseuille in laminar regime. The Reynolds number is defined as $Re = U_{belt}h/\nu$, where ν is kinematic viscosity of water. The coordinates x^*, z^* and the time t^* are made dimensionless by h and U_{belt} respectively.

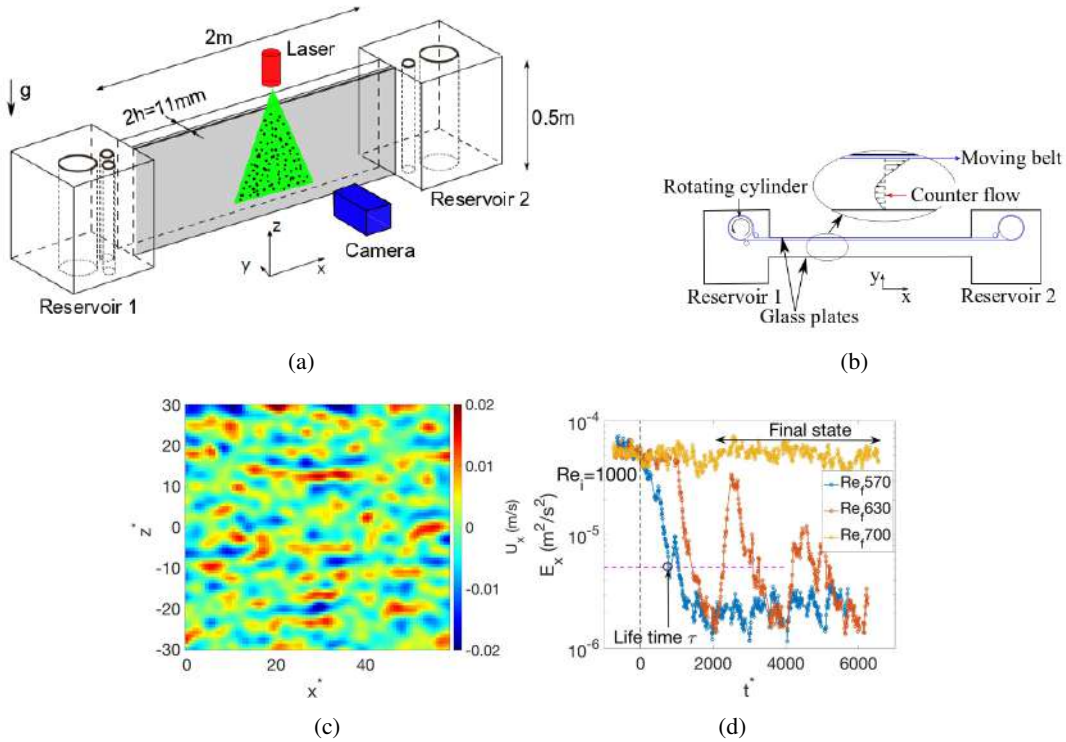

Figure 1: (a) Experimental set-up. (b) Bottom view. (c) 2D velocity field of streamwise small scale flow U_x from PIV measurments at initial Reynolds number $Re_i = 1000$ after spatial filtering with a cutoff wavelength $\lambda^* \leq 14.8h$ which removes large scale flows. (d) Temporal energy evolution of streamwise small scale flow E_x using quench experiments for final Reynolds number $Re_f = 570, 630, 700$, dashed magenta line indicates 10 percent of the energy level at $Re_i = 1000$, definition of life time τ and final state.

*Corresponding author. E-mail: jose-eduardo.wesfreid@espci.fr

The noise is created in the reservoir where the belt turns around and enters the channel from the reservoir 1. We have investigated two levels of noise: 1) with grids at the entrance of channel (low noise) and 2) without grid (high noise). Particle image velocimetry (PIV) is used to measure the velocity field in xz plane at the y^* position where the velocity is zero in CPF profile; the velocity field is filtered spatially to remove large scale flows induced by the position variation of the belt (Fig 1 (c)). The experimental protocol is the following: the flow is initialized at $Re_i = 1000$ (fully turbulent) and then suddenly decreased to lower Re_f, which is referred to as quench experiments.

RESULTS

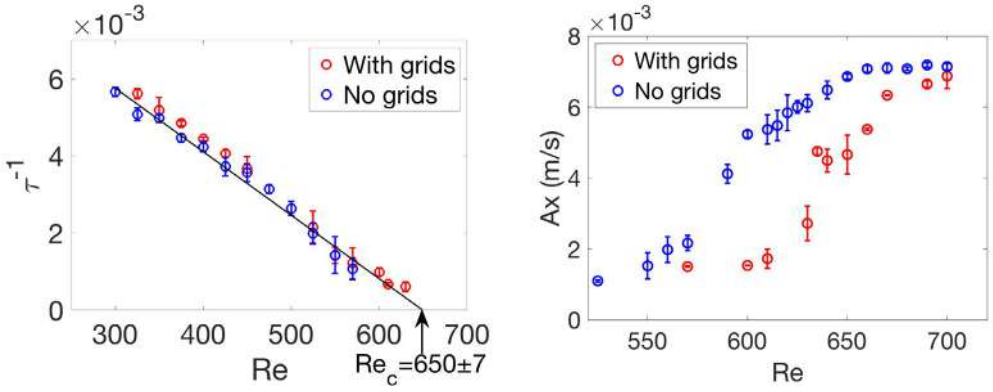

(a) (b)

Figure 2: (a) The inverse of life time τ^{-1} as a function of Re for the measurements with grids in red and without grids in blue, solid line fit $\tau^{-1} \propto (Re_c - Re)$ fit with ($Re_c = 650$), error bar is standard deviation of several realizations. (b) Time and space averaged amplitude of final state $A_x = \sqrt{E_x}$ as a function of Re for measurements without and with grids, error bar is standard deviation of several realizations.

The typical energy evolution $E_x(t^*)$ for different final Reynolds number Re_f is presented in Fig. 1 (d). The life time τ is defined as the first time when $E_x(t^*)$ decreases to a threshold of 10 percent of initial energy level. The final state is the period after the initial transient decay (Fig. 1 (d)). Fig. 2 (a) shows the inverse of life time τ^{-1} is proportional to Re which has been observed in other confined shear flows [4][5]. The intersection point bewteen the fit $\tau^{-1} \propto (Re_c - Re)$ and the Re axis give the critical point at $Re_c = 650$. The Re_c is independent of the external noise. In contrast, the time and space averaged amplitude A_x as a function of Re shows that the apparent threshold is shifted and the final state is modified by different noise levels. We are currently exploring the possibility of modelling the phenomena using a 1D spatio-temporal dynamical systems model with noise [3].

CONCLUSIONS

A critical value of Re for plane Couette-Poiseuille flow is found to be $Re_c = 650$ using quench experiments irrespective of the external noise in the system. By way of contrast, the amplitude has different apparent thresholds and final states for various external noise level. The amplitude diagram is not suitable to define the threshold in a system with pronounced noise. While a definite threshold cannot yet be ascribed to transition in the presence of noise, we are working on a low-dimensional model with multiplicative noise to progress our understanding.

References

[1] Klotz L., Lemoult G., Frontczak I., Tuckerman L.S., Wesfreid J.E. Couette-Poiseuille flow experiment with zero mean advection velocity: Subcritical transition to turbulence. *Phys. Rev. Fluids* **2**: 19, 2017.

[2] Klotz L., Wesfreid J.E. Experiments on transient growth of turbulent spots. *J. Fluid Mech.* **829**, R4. 2017.

[3] Jordi G.O., José M.S. Noise in Spatially Extended Systems. *Springer* 1999.

[4] Bottin S., Chaté H. Statistical analysis of the transition to turbulence in plane Couette flow. *The European Physical Journal B* **6**, 143-155, 1998.

[5] Peixinho J., Mullin T. Decay of Turbulence in Pipe Flow. *Phys. Rev. Lett.* **96**, 094501, 2006.

THE EFFECT OF STREAKS ON THE INSTABILITY OF JETS

Chuhan Wang[1], Lutz Lesshafft*[1], Petrônio A.S. Nogueira[2], André V.G. Cavalieri[2], and Peter Jordan[3]
[1]Laboratoire d'Hydrodynamique, CNRS / Ecole Polytechnique / Institut Polytechnique de Paris, Palaiseau, France
[2]Instituto Tecnológico de Aeronáutica, São José dos Campos, Brazil
[3]Institut Pprime, CNRS / Université de Poitiers / ENSMA, Poitiers, France

Summary The presence of streaks in the shear layer of jets, issuing from a round nozzle, breaks the axisymmetry of their steady-state solution. If the streaks are considered to be part of the base flow, for the purpose of linear instability analysis, the instability eigenmodes are thus affected by their presence. The resulting change of growth rates and spatial shapes of eigenmodes, related to the shear instability in jets, is investigated here for the setting of parallel base flows. The shape of *optimally* growing streak structures inside an initially axisymmetric jet are identified first, and their nonlinear growth to finite amplitude is simulated in time. Linear perturbation eigenmodes of the streaky base flow are then computed in the two-dimensional cross-plane. Consistent with similar studies in plane shear layers, it is found that sinuous streaks have a stabilising effect on the shear instability, whereas varicose streak structures lead to stronger instability growth.

STREAKS IN JETS

Rolls and streaks, and their role for instability dynamics and laminar-turbulent transition, have been extensively studied in the context of wall-bounded shear flows. *Rolls*, as vortices in the cross-plane of the flow, transport high-speed fluid towards the wall and low-speed fluid away from the wall, thereby creating *streaks* in the main flow velocity. These streaks are themselves subject to instabilities, and are even assumed to be responsible for the self-sustained process of wall-bounded turbulence. However, the very presence of rolls and streaks in *free* shear flows such as jets has hardly been recognised until very recently. Nogueira *et al.* [1] documented the appearance of streaky structures in the turbulent velocity field of a high-speed jet, by processing of experimental data, and showed how these could be modelled through transient-growth and resolvent analysis.

Jiménez-González & Brancher [2] computed "optimal" roll shapes for streak creation in jets, in the sense of maximum streak energy growth, but these authors did not investigate the modal instability of the resulting streaky jet flow. Marant & Cossu [3] carried out linear instability calculations for a parallel plane shear layer with streaks; a similar study of jet dynamics has been completed recently [4]. Another recent study, by Pickering *et al.* [5], investigates the formation of streaks in developing jets in response to forcing input, concluding that streaks may be suspected to dominate perturbations in jets at low frequencies.

SCOPE AND METHODOLOGY

The objective of our work is to characterise how, and under what conditions, rolls and streaks may enhance or decrease the shear instability of jets from an axisymmetric nozzle. Our approach follows in several aspects the shear-layer study [3]. In order to reduce the complexity of computations and the number of influence parameters, parallel base flows (invariant in the main flow direction) are considered. Temporal instability eigenmodes in a strictly axisymmetric base flow are characterised by an integer azimuthal wave number m, but this decoupled dynamics of different m is bound to disappear with the introduction of azimuthal base flow modulations, via the appearance of streaks.

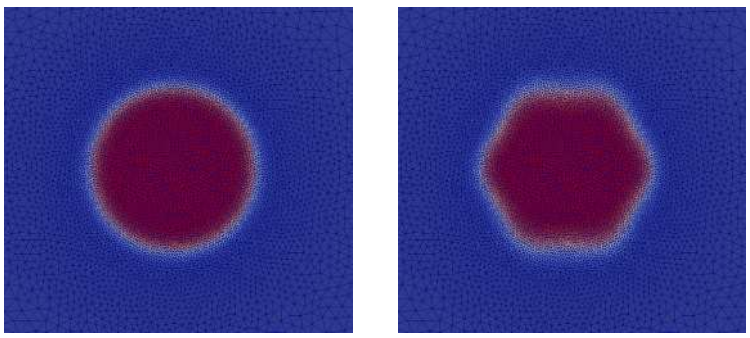

(a) without streaks (b) with six streaks

Figure 1: Base flow velocity in the cross-plane of parallel jets with and without streaks. The shear layer momentum thickness is 5% of the jet radius.

*Corresponding author. E-mail: lesshafft@ladhyx.polytechnique.fr

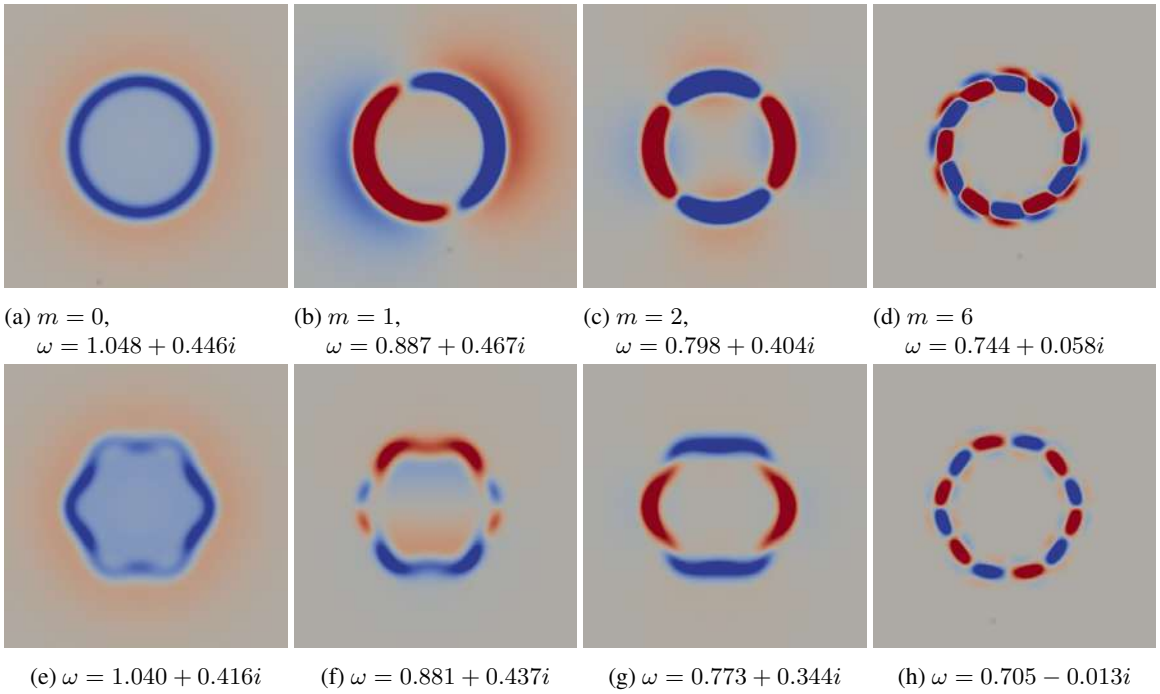

(a) $m = 0$, $\omega = 1.048 + 0.446i$ (b) $m = 1$, $\omega = 0.887 + 0.467i$ (c) $m = 2$, $\omega = 0.798 + 0.404i$ (d) $m = 6$ $\omega = 0.744 + 0.058i$

(e) $\omega = 1.040 + 0.416i$ (f) $\omega = 0.881 + 0.437i$ (g) $\omega = 0.773 + 0.344i$ (h) $\omega = 0.705 - 0.013i$

Figure 2: Some eigenmodes (streamwise velocity) of the axisymmetric base flow (top row) and the streaky base flow (bottom row) from figure 1. The imaginary part of ω is the temporal growth rate.

We first identify the roll/streak structures that experience the strongest transient energy growth due to the lift-up effect. Recovering the results of Jiménez-González & Brancher [2], we find that *sinuous* perturbations, which represent wavy deformations of the jet shear layer, grow the fastest. *Varicose* perturbations, which lead to azimuthal variations of the shear layer thickness, also grow, but at a lower rate. Consistent with earlier results for plane shear layers, the linear sensitivity of shear instability growth rates in jets is zero at first order.

We then consider the effect of finite-amplitude rolls and streaks in the base flow. The nonlinear character of this problem leads to several influence parameters, including the roll and streak amplitudes. Roll shapes are imposed, characterised by the number of vortices along the azimuth, by their radial distribution and individual circulation, and the creation of streaks is obtained by nonlinear time-stepping in the jet cross-plane. Frozen instances of this time-dependent streaky parallel jet are taken as base flows for linear instability analysis. An example of such a streaky base flow (with *sinuous* streaks) is shown in figure 1b.

CURRENT RESULTS

When finite-amplitude rolls are introduced into an axisymmetric jet flow, the ensuing streaks appear in the form of symmetric distortions of the shear layer. For the example shown in figure 1, optimal rolls were computed according to the criterion of maximum streak growth [2], and the number of rolls was fixed as six. The Reynolds number was set to 1000.

Temporal eigenmodes of the non-streaky axisymmetric base flow and its streaky counterpart are represented side by side in figure 2, with their eigenvalues given in the caption. Note that the presence of streaks breaks the azimuthal symmetry of mode shapes, except for $m = 6$, which corresponds to the number of streaks. In this example, as for all sinuous streak perturbations, the streaks have a stabilising effect on all eigenmodes. The opposite is true for *varicose* rolls and streaks: when such structures are present in the base flow, the unstable modal growth rates are increased, and an enlarged interval of axial wavenumbers is unstable.

Absolute instability in streaky base flows has also been investigated: it has been found that streaks of any spatial shape lead to a *stabilisation* of the absolute growth rate, over all tested parameter ranges. Streaks therefore do not seem to promote the occurrence of self-excited oscillations in jets.

References

[1] Nogueira P. A. S., Cavalieri A. V. G., Jordan P., Jaunet V. Large-scale streaky structures in turbulent jets. *J. Fluid Mech.* **873**: 211-237, 2019.
[2] Jiménez-González J.I., Brancher P. Transient energy growth of optimal streaks in parallel round jets. *Phys. Fluids* **29**(11): 114101, 2017.
[3] Marant M., Cossu C. Influence of optimally amplified streamwise streaks on the KelvinHelmholtz instability. *J. Fluid Mech.* **838**: 478-500, 2018.
[4] Wang C., Lesshafft L., Cavalieri A. V. G., Jordan P. The effect of streaks on the instability of jets. *J. Fluid Mech.*, to appear.
[5] Pickering E., Rigas G., Nogueira P. A. S., Cavalieri A. V. G., Schmidt O. T., Colonius T. Lift-up, Kelvin-Helmholtz and Orr mechanisms in turbulent jets. *arXiv preprint*: 1909.09737, 2019.

TAILS OF TURBULENT SPOTS IN SHEAR FLOWS

Pavan KASHYAP*[1], Yohann DUGUET [1], and Matthew CHANTRY[2]
[1]LIMSI-CNRS, Université Paris Saclay, Orsay, France
[2]Department of Physics, Oxford, UK

Summary The far field of localized turbulent patches (spots) and the associated large-scale flow are investigated in various wall-bounded shear flows. A computational study is performed in large periodic domains using the efficient parallel spectral code *Channelflow 2.0*. The large-scale flow generated by the localized spots is observed to be structured according to the symmetries of the laminar base flow. Simulations show that the velocity fluctuations decay algebraically away from the spot, with a decay exponent depending on the structure of the large-scale flow but independent of the Reynolds number.

INTRODUCTION

Localized turbulent spots are routinely interpreted as seeds of turbulence in wall bounded shear flows, in a manner analogous to the nucleation of the liquid phase during condensation. They have been studied in numerical simulations [1][2] and experiments for different wall bounded shear flows such as plane Couette flow (pCf) [3][4], plane Poiseuille flow (pPf) [5] and Couette-Poiseuille flow (CPf)[6]. Growth mechanisms have been documented in these studies [7]. Simulations in moderate-sized numerical domains have previously suggested that the tails of localized structures [8, 9] display exponential decay for the velocity field. However proper numerical investigation of the far field of these spots requires even larger domains, necessitating parallel computing. Besides, the impact of the Reynolds number on the behavior for each of these flow cases still remains an open question.

In order to effectively analyse the far field of the spots, numerical simulations have been performed in large domains using the open source parallelized spectral code Channelflow 2.0 (*https://www.channelflow.ch/*). The dimensions of the domain used for the simulations are Lx, Ly, Lz=1280,2,1280 for a spectral resolution of up to Nx, Ny, Nz=5120,65,10240, where x, y and z stand for the streamwise, wall-normal and spanwise coordinates, respectively. A parametric study in the Reynolds number was also performed for pCf, pPf, CPf and for the recently considered Model Waleffe flow (mWf) [10].

RESULTS AND DISCUSSION

The large-scale flow generated by these localized turbulent spots features a quadrupolar structure for pCf and mWf while it exhibits a dipolar structure for the case of pPf and CPf. The tails were found to decay algebraically away from the spot. This algebraic decay is observed over one and a half decade, thereby conclusively characterizing the nature of the tails. The decay exponents have been measured as ≈ -3 for the quadrupolar structure and ≈ -2 for the dipolar structure with negligible error bars. A visualization of the quadrupolar structure for pCf is shown in Figure 1 together with the algebraic decay. The exponents are summarized in Table 1.

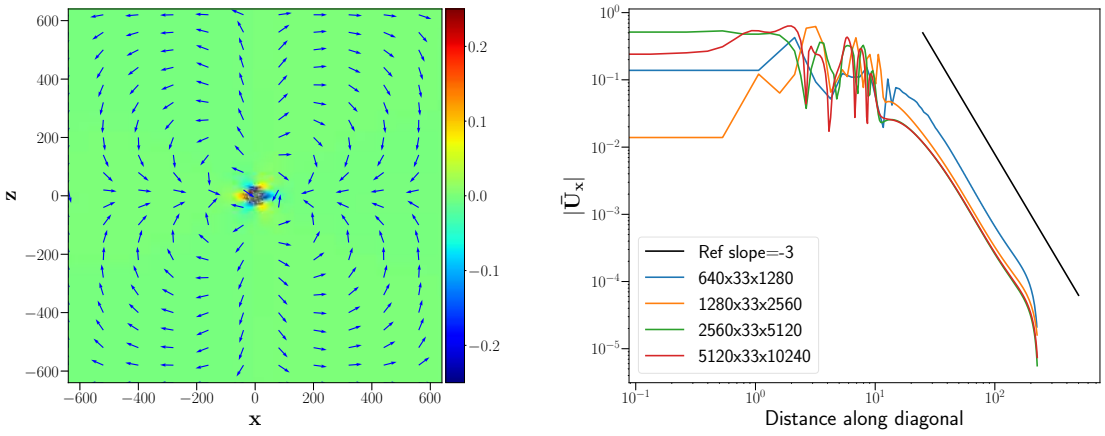

(a) (b)

Figure 1: Turbulent spot in plane Couette flow, Re=400 (a) directional vector field for the large-scale flow represented by unit vectors, (b) spatial decay of streamwise velocity along the diagonal $X = Z$ of the domain.

*Corresponding author. E-mail: kashyap@limsi.fr

The quadrupolar flow appears in the cases featuring approximate central symmetry in the plane parallel to the plates, such as pCf and mWf. The dipolar structure, on the other hand, dominates when the bulk pressure gradient driving the flow breaks this central symmetry and the large-scale flow changes its structure accordingly. A parametric study in terms of the Reynolds number (Re) has been carried out for all the shear flow cases (3 different values of Re for each flow case). The exponent is found to be independent of the Reynolds number.

Sl No.	Type of Flow	Structure of Large-scale flow	Decay Exponent
1.	pCf	Quadrupolar	≈ -3
2.	mWf	Quarupolar	≈ -3
3.	pPf	Dipolar	≈ -2
4.	CPf	Dipolar	≈ -2

Table 1: Algebraic decay exponents for in-plane velocities in the far field.

CONCLUSION

The large-scale flow generated by localized turbulent spots in wall bounded shear flows is found to correspond to a quadrupolar structure in pCf and mWf, but to a dipolar structure in pPf and CPf, respectively. Simulations in large domains conclusively show algebraic decay for the velocity tails of these spots in all four wall-bounded shear cases examined herein. The computed exponents are found to be independent of the Reynolds number of the flow.

References

[1] Kashyap, Pavan V. and Duguet, Yohann and Chantry, Matthew, *Phys. Rev. Fluids* **5** : 103902, 2020
[2] Lundbladh A. , Johanssonn A. V., *J. Fluid Mech.* **229** : 499, 1991
[3] Dauchot O. , Daviaud F. , *Phys. Fluids*, **7** : 335, 1995
[4] Couliou M. , Monchaux R. , *Phys. Fluids*, **27** : 034101, 2015
[5] Carlson D. R. , Widnall S. E. , Peeters M. F. , *J. Fluid Mech.* **121** : 487, 1982
[6] Klotz L. , Lemoult G. , Frontczak I. , Tuckerman L. S. , Wesfreid J. E. , *Phys. Rev. Fluids* **2** : 043904, 2017
[7] Duguet Y. , Schlatter P. , *Phys. Rev. Lett.* **110** : 0304502, 2013
[8] Schumacher J. , Eckhardt B. , *Phys. Rev. E* **63** : 046307, 2001
[9] Gibson J. F. , Brand E. , *J. Fluid Mech.* **745**: 25, 2014
[10] Chantry M. , Tuckerman L. S. , Barkley D. , *J. Fluid Mech.* **791** : R8, 2016

DYNAMICS OF AN AXISYMMETRICALLY EXCITED JET IN CROSSFLOW

Elijah Harris[1], David D. W. Ren[1], Stephen Schein[1], Robert M'Closkey[1], Luca Cortelezzi[2], and Ann Karagozian[1*]
[1]Department Mechanical and Aerospace Engineering, UCLA, Los Angeles, CA 90095-1597, USA
[2]Department of Aerospace Science and Technology, Politecnio di Milano, Milano, Italy

Summary The present experimental study involves a gaseous jet issuing into a uniform crossflow, where the resulting upstream shear layer (USL) is naturally absolutely unstable. The jet is axisymmetrically excited with sinusoidal, square wave, and multi-pulse square wave temporal waveforms to explore implications of such forcing on structural, mixing, and dynamical characteristics. Analysis of the USL shows evidence of synchronization of the flow to the forcing as the forcing amplitude increases, the critical conditions for which differ amongst the waveforms. These analyses are made via snapshot POD of the velocity field extracted from stereo PIV and time delay embedding of velocity fluctuations along the USL. PLIF imaging is utilized for quantification of excitation effects on molecular mixing, where the synchronized jet is shown to significantly enhance mixing compared with the unforced jet.

BACKGROUND AND CONTEXT OF PRESENT STUDIES

The transverse jet or jet in crossflow (JICF) has been extensively studied in the past due to its numerous engineering applications, especially those pertaining to propulsion systems[1,2]. One main interest of prior studies has been to quantify the rate of mixing between the jet and crossflow for a range of flow conditions[3,4]. In the absence of external excitation, the natural instabilities along the upstream shear layer of the jet transition from a relatively weak convective instability at higher jet-to-crossflow momentum flux ratios (J) to that of a strong pure-tone absolute instability at lower J values[5,6,7]. The critical transition in the USL is seen to occur, for a fixed Reynolds number, as J is reduced below approximately 10 and/or if the jet-to-crossflow density ratio (S) is reduced below around 0.4. The nature of these shear layer instabilities plays a significant role in the overall development of jet vortical systems, structural characteristics, and hence mixing dynamics, particularly influencing the structure of the counter rotating vortex pair (CVP) associated with the jet cross-section[8,9,10]. When the jet is convectively unstable, the weak instabilities result in weaker vorticity rollup along the shear layer, in some cases resulting in cross-sectional asymmetry of the jet and generally poorer mixing, while an absolutely unstable USL, with stronger pure-tone instabilities, typically produces strong vortex rollup along the shear layer, a more symmetric cross-sectional CVP, and improved overall mixing[4].

In controlling the JICF, earlier experimental studies on axisymmetric excitation of the jet indicate that one can significantly augment the spread and penetration, depending on the flow regime[11,12,13]. For a convectively unstable jet at higher J values, the flow readily responds to sine wave or square wave excitation, but for the naturally absolutely unstable jet at lower J values, temporal square wave excitation within a range of prescribed temporal pulsewidths typically has a more significant effect on jet penetration and spread than that of a sine wave[13]. Yet improved jet penetration and spread via square wave excitation is not always associated with improved molecular mixing, as documented via acetone planar laser induced fluorescence (PLIF) imaging[14]. More recently it has also been documented that when axisymmetric sinusoidal excitation is applied, the jet USL can synchronize to the forcing frequency via complex dynamical processes[15], with attendance implications for mixing[16]. For a particular forcing frequency, as the transverse jet's USL becomes absolutely unstable (J is lowered), the forcing amplitude required to synchronize or "lock-in" to the forcing becomes much larger, and in some cases produces states of quasiperiodicity between the forcing and natural instability frequencies.

Building on the above-noted JICF axisymmetric excitation studies, it is of interest to explore the influence of alternative temporal waveforms, including those generating multiple vortex rings which can collide or otherwise interact, to determine the effects on jet dynamics as well as molecular mixing within the flowfield. The dynamics are analyzed through PLIF imaging so that the relationship to changes in structural characteristics and mixing may be made. Proper orthogonal decomposition (POD) of data extracted from particle image velocimetry (PIV) as well as hotwire-based time series analysis also enable investigation of synchronization dynamics under various forcing conditions.

EXPERIMENTAL APPROACH AND SAMPLE RESULTS

The present experiments are conducted in a low speed air wind tunnel, where the transversely injected, nozzle-generated jet has constituent species consisting of He, N_2, acetone, and DEHS-oil, the latter two of which are tracers for PLIF and PIV imaging, respectively. For the laser diagnostics, a dual cavity Q-switched Nd:YAG laser (Quantel Evergreen 30266) is triggered at rates relative to the excitation frequencies such that phase advancing data are acquired. For the results shown here, the jet Reynolds number is fixed at Re_j=1800, with S = 1 and J=6, corresponding to a naturally absolutely unstable USL. Axisymmetric excitation is applied via a loud speaker mounted in a plenum upstream of the jet nozzle exit. Adaptive feedforward control for the jet excitation system[14] is implemented to enable formation of relatively accurate temporal waveforms, including sine wave, square wave, double or triple pulse square wave (2 or 3 pulses per period with adjustable pulsewidths and amplitudes), and sawtooth waveforms.

Figures 1 (a-f) depict representative phase portraits generated from time delay embedding of the vertical velocity fluctuations measured via hotwire anemometry at 1.5 diameters along the jet USL. Figures 1(a-c) correspond to the sinusoidally excited JICF forced at f_f=110 Hz, while Figures 1(d-f) correspond to an excitation waveform which has two square wave pulses in a single forcing period, where f_f=55 Hz. For each series, the forcing amplitude, quantified by the

* Corresponding author. Email: **ark@seas.ucla.edu**

RMS of the mean subtracted jet velocity ($u_{j,rms}$), increases from $u_{j,rms}$=0.07 m/s to $u_{j,rms}$=1.70 m/s. The sine wave forcing results in a quasiperiodic USL (Fig. 1(a), with a corresponding power spectral density or PSD plot in Fig. 1(g)), and does not lock-in until $u_{j,rms}$=0.55 m/s. In contrast, for double-pulse square wave excitation, even at the lowest forcing amplitude, the jet is already locked-in to the double pulse forcing (Fig. 1(d), with a corresponding PSD plot shown in Fig. 1(h)). As the forcing amplitude increases, the phase portraits for both excitation waveforms become much cleaner, yet more with complex closed loop trajectories and shapes. Interestingly, the double pulse forcing begins to resemble that of a period doubling loop formation (e.g., seen in Figs. 1(e) and 1(f)), though here this could simply result from the two distinct pulses being formed in a single period.

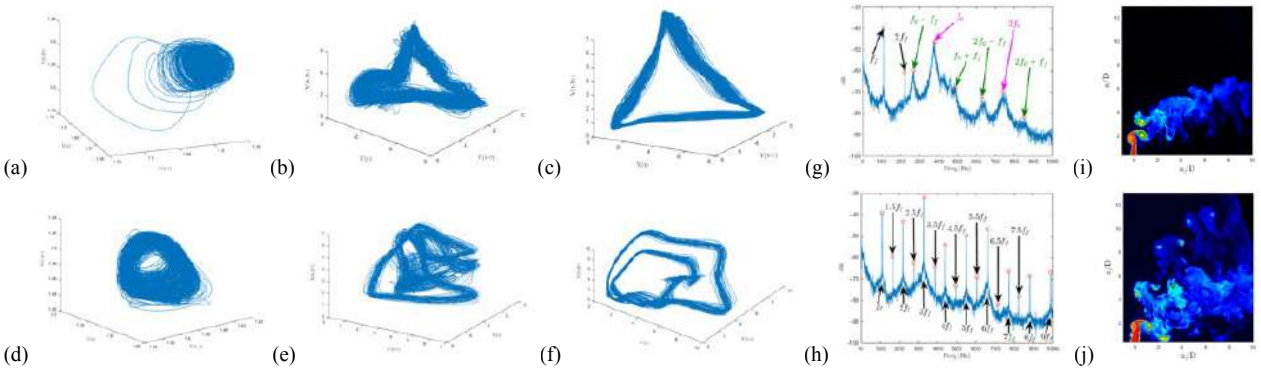

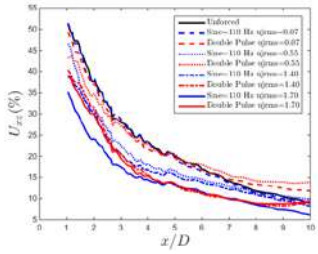

(k)

Figure 1. Resulting effects of axisymmetric jet excitation in a naturally absolutely unstable transverse jet (J=6 at Re_j=1800) with sinusoidal (a-c and g, i) and double pulse (d-f and h, j) temporal perturbations. Phase portraits of vertical velocity fluctuations at 1.5 diameters along the jet USL are shown for $u_{j,rms}$=0.07 m/s (a & d), 0.55 m/s (b & e), and 1.70 m/s (c & f), with a mean jet exit velocity of $U_j \sim 3.4$ m/s. Power spectral density (PSD) plots for forcing at $u_{j,rms}$=0.07 m/s are shown in (d) & (i). Instantaneous centerplane PLIF images for $u_{j,rms}$=1.70 m/s are shown in (i) and (j). Centerplane-based Unmixedness as a function of downstream location x/D for these waveforms with variable excitation amplitudes is shown in (k).

Structural changes in the jet also differ based on different excitation conditions. Instantaneous centerplane PLIF images such as those in Figures 1(i-j) show that sinusoidal excitation produces minimal alteration from the unforced case, even at a larger amplitude, while double pulse forcing substantially bifurcates the jet at the same amplitude. Such images enable quantification of molecular mixing via the Unmixedness parameter[4], where lower Unmixedness corresponds to improved mixing. Downstream Unmixedness evolution shown in Figure 1(k) demonstrates that either of the excitation waveforms can enhance mixing as compared to that for the unforced jet. But at a fixed excitation amplitude, in several cases sinusoidal excitation produces better overall mixing than the double pulse square wave forcing, potentially due to the nature of synchronization of the jet and the sometimes deleterious effects of jet bifurcation on mixing. These and related findings for other waveforms and excitation conditions suggest there may be combinations of excitation parameters, in many cases related to the degree of vortex ring interactions and shear layer synchronization, which may be used to optimize transverse jet dynamics and mixing.

References

[1] Margason R.J.: Fifty Years of Jet in Cross flow Research. AGARD-CP-534 1:1-141, 1993.
[2] Karagozian A.R.: Transverse Jets and Their Control. **Prog. Energy Comb. Science** 36(5):531-553, 2010.
[3] Smith S.H., Mungal M.G.: Mixing, Structure and Scaling of the Jet in Crossflow. **JFM**, 357:83-122, 1998.
[4] Gevorkyan, L., Shoji, T., Getsinger, D.R., Smith, O.I., and Karagozian, A.R.: Transverse Jet Mixing Characteristics, **JFM**, 790:237-274, 2016.
[5] Megerian S., Davitian J., Alves L.S. de B., Karagozian A.R.: Transverse Jet Shear Layer Instabilities. Part I: Experimental Studies. **JFM**, 593:93–129, 2007.
[6] Davitian J., Getsinger D., Hendrickson C., Karagozian, A.R.: Transition to Global Instability in Transverse Jet Shear Layers. **JFM**, 661:294-315, 2010.
[7] Getsinger D.R., Hendrickson C., Karagozian A.R.: Shear Layer Instabilities in Low-density Transverse Jets. **Expts in Fluids** 53:783–801, 2012.
[8] Getsinger, D. R., Gevorkyan, L., Smith, O. I., and Karagozian, A. R.: Structural and Stability Characteristics of Jets in Crossflow. **JFM,** 760, 342-367, 2014.
[9] Kelso R.M., Lim T.T., Perry A.E.: An Experimental Study of Round Jets in Cross-flow. **JFM**, 306:111-144, 1996.
[10] Cortelezzi L. and Karagozian A.R.: On the Formation of the Counter-Rotating Vortex Pair in Transverse Jets. **JFM**, 446:347-373, 2001.
[11] M'Closkey R.T., King J., Cortelezzi L., Karagozian A.R.: The Actively Controlled Jet in Crossflow. **JFM**, 452:325-335, 2002.
[12] Shapiro S., King J., M'Closkey R.T., Karagozian A.R.: Optimization of Controlled Jets in Crossflow. **AIAAJ**, 44:1292-1298, 2006.
[13] Davitian J., Hendrickson C., Getsinger D., M'Closkey R.T., Karagozian A.R.: Strategic Control of Transverse Jet Shear Layer Instabilities. **AIAAJ**, 48(9):2145-2156, 2010.
[14] Shoji T., Besnard A., Harris E., M'Closkey R.T., Karagozian A. R.: Effects of Axisymmetric Square-Wave Excitation on Transverse Jet Structure and Mixing. **AIAAJ**, 57, 2019.
[15] Shoji T., Harris E., Besnard A., Schein S., Karagozian A.R.: Transverse Jet Lock-in and Quasiperiodicity. **Phys. Rev. Fluids,** 5, 013901, 2020.
[16] Shoji, T., Harris, E. W., Besnard, A., and Karagozian, A. R.: Effects of Sinusoidal Excitation on Transverse Jet Dynamics, Structure and Mixing. Submitted for publication.

ON THE BOUNDARY-LAYER FLOW OVER A ROTATING CONE: ENERGY EIGENMODE COMPARISONS

Zahir Hussain*[1], Stephen Garrett[2], and Sophie Calabretto[3]
[1]School of Engineering, University of Leicester, Leicester, UK

Summary We investigate boundary-layer flow over a rotating cone by perturbing the mean flow leading to disturbance equations that are solved via a more accurate spectral method involving Chebyshev polynomials. The formulation enables an energy analysis of production and dissipation terms for any eigenmode, which lends further physical insight into the energy signatures within the flow. For both techniques, the results obtained show that reducing the cone half-angle destabilises the flow by decreasing the critical Reynolds number, which lends further support to the authors' earlier hypothesis that an alternative mode is the most dangerous for slender rotating cones. Importantly, favourable comparisons are yielded with existing experiments and theoretical investigations in the literature. Meanwhile, further details will be provided of comparisons with DNS simulations in the pipeline.

INTRODUCTION

There has been considerable research on the flow over rotating geometries, particularly the Von Kármán flow over a rotating disk, which has long been used as a model for flow over a swept-wing, since the early work of [6]. Recently, the stability of rotating boundary layer flows has experienced increased attention in the literature and has been investigated within a wide range of flow setups and variations. In particular, the flow over a rotating cone represents a complex generalisation of rotating disk flow, and involves the introduction of a cone half-angle, which is equal to 90° for a rotating disk. Recently, research on this geometry has accelerated, with theoretical global linear instability [13], numerical simulations [12] and experimental investigation of broad cones [10], which follows on from earlier experimental work on the rotating-disk boundary layer [9]. In this paper, we will build upon the investigation of boundary-layer transition over rotating cones. Specifically, we consider a family of rotating cones in still fluid, with major emphasis on the parameter values represented by the crossflow instability, for which the cone half-angle ψ is large, typically greater than 40° and less than 90°. Conversely, cones with half-angles in the parameter regime less than 40° are referred to as slender cones, where the boundary-layer flow is instead susceptible to a centrifugal instability [8]. In particular, following recent findings, we focus on the changing nature of the dominant instability mechanism, which has been observed to transition from crossflow to a centrifugal instability mechanism as the half-angle is reduced from 90°. The methods used in this study develop a linear stability analysis of the full disturbance equations via a spectral numerical code, which is subsequently used to analyse the energy production and dissipation terms for the crossflow instability modes. The approach follows that of [2] for a compliant rotating disk, and has been verified successfully for related investigations on the rotating disk by [1].

ENERGY ANALYSIS

Continued and long-standing research on the rotating disk, in particular by the late Prof. Carpenter and co-workers has led to the possibility of analysing energy production and dissipation terms for any eigenmode. The energy analysis of [2] for a rotating disk enables the calculation of various energy sources using the Chebyshev–tau technique. It should be noted that the various energy production and dissipation terms identified represent the various energy signatures, namely: (i) the Reynolds stress energy production terms, P_i; (ii) the viscous dissipation energy removal term, D; (iii) the pressure work term, PW_i; (iv) contributions from work done on the wall by viscous stresses, S_i; (v) terms arising from streamline-curvature effects and the three-dimensionality of the mean flow, G_i. The total energy, TE, is then given by the sum of these individual contributions, which are either positive (production) or negative (dissipation). The method facilitates an accurate quantitative analysis of the energy as it passes through the flow, and has been applied successfully to the flow over rough rotating disks by [3, 5], as well as for the BEK family of flows by [1].

In figure 1, we present an analysis of the various significant energy source terms for a range of ψ as it is decreased from 90° to 20°. Positive values indicate energy production, whereas negative values denote energy dissipation, with the sum of each source term giving the total mechanical energy (TE), which is normalised to ensure consistent comparisons of energy production and dissipation. From the results, we observe that there are two major contributors to the energy signature of the flow over a rotating cone in still fluid, most notably the Reynolds stress energy production term P_2 and the viscous dissipation energy removal terms D. The overall total mechanical energy TE is positive. Meanwhile, there is a small contribution to energy reduction attributed to terms arising from streamline-curvature and the three-dimensionality of the meanflow, such as G_1, but in general other contributions are negligible compared with P_2 and D.

*Corresponding author. E-mail: zahir.hussain@leicester.ac.uk

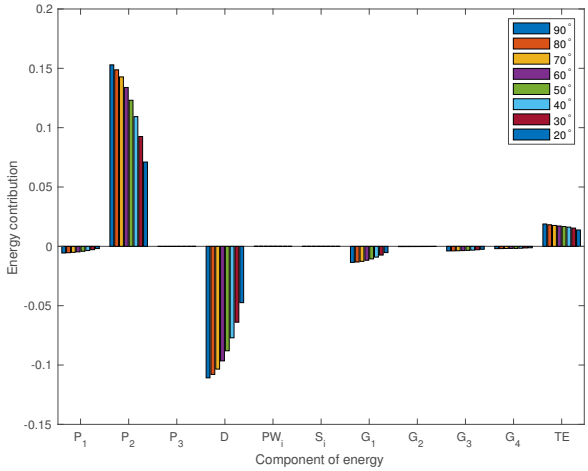

Figure 1: Energy distribution of the Type I mode with maximum total energy at 25 units of Reynolds number from the mode's onset for a range of values of ψ. Energy bars move from left to right for each source of energy as ψ is reduced from $90°$ to $20°$. Contributions from P_3, PW_i, S_i and G_2 are non-zero but negligible.

CONCLUSIONS

We discuss the variation of energy sources as ψ is decreased from $90°$ to $20°$. While the Reynolds stress production term P_2 and viscous dissipation terms D dominate the overall energy distribution, the difference between energy generated and dissipated remains positive $TE > 0$ corresponding to unstable disturbances. Furthermore, TE decreases only marginally with reduced ψ. However, we see very rapidly decaying values of P_2 and D with reduced ψ. Essentially, the dominant energy signatures are leaving the crossflow 'type I' disturbance mode as ψ is decreased, with minimal overall difference. As less energy is produced by P_2, in similar fashion less energy is dissipated by D. We may ask the question, where has this energy moved to? Physically, energy is transferred between the base flow and type I disturbance mode, and it appears that, as ψ is reduced, less energy is produced and dissipated. Therefore, it may be that these energy signatures move into an alternative mode, such as that identified by [7, 8] for slender rotating cones. Hence, we propose the hypothesis that these energy signatures move from interacting between the base flow and type I mode to instead interacting between the base flow and an alternative mode governed by the centrifugal instability mechanism, as described mathematically in [7] and [8]. It can be argued that this finding yields possibly stronger evidence of the emergence of the alternative mode as ψ is decreased than the previous argument based on the reduction in growth rates observed in [4]. Such findings are in agreement with developing DNS simulations in progress, which show the gradual reduction of modal energies as ψ is reduced from $90°$. Furthermore, we observe contrasting behaviour as ψ is decreased below the critical value of $40°$ as the modal energies gradually increase. This interesting finding may indicate the strengthening of the hypothesised alternative centrifugal mode below $40°$ and as such requires further careful investigation.

References

[1] ALVEROGLU, B., SEGALINI, A. & GARRETT, S.J. 2017 An energy analysis of convective instabilities of the Bödewadt and Ekman boundary layers over rough surfaces, *Eur. J. Mech. B*, **61**, 310–315.
[2] COOPER, A.J. & CARPENTER, P.W. 1997 The stability of rotating-disc boundary-layer flow over a compliant wall. Part 1. Type I and II instabilities, *J. Fluid Mech.* **350**, 231–259.
[3] COOPER, A.J., HARRIS, J.H., GARRETT, S.J., THOMAS, P.J. & ÖZKAN, M. 2015 The effect of anisotropic and isotropic roughness on the convective stability of the rotating disk boundary layer, *Phys. Fluids* **27**, 014107.
[4] GARRETT, S. J., HUSSAIN, Z. & STEPHEN, S. O. 2009 The crossflow instability of the boundary layer on a rotating cone, *J. Fluid Mech.* **622**, 209–232.
[5] GARRETT, S.J., COOPER, A.J., HARRIS, J.H., ÖZKAN, M., SEGALINI, A. & THOMAS, P.J. 2016 On the stability of von Kármán rotating-disk boundary layers with radial anisotropic surface roughness, *Phys. Fluids* **28**, 014104.
[6] GREGORY, N., STUART, J. T. & WALKER, W. S. 1955 On the stability of three-dimensional boundary layers with application to the flow due to a rotating disk, *Phil. Trans. R. Soc. Lond.* A **248**, 155–199.
[7] HUSSAIN, Z., STEPHEN, S. O. & GARRETT, S. J. 2012 The centrifugal instability of a slender rotating cone, *Journal of Algorithms & Computational Technology*, Vol. 6, No. 1.
[8] HUSSAIN, Z., GARRETT, S. J. & STEPHEN, S. O. 2014 The centrifugal instability of the boundary-layer flow over slender rotating cones, *J. Fluid Mech.* **755**, 274–293.
[9] IMAYAMA, S., ALFREDSSON, P. H., & LINGWOOD, R. J. 2012 A new way to describe the transition characteristics of a rotating-disk boundary-layer flow, *Phys. Fluids*, **24**, 031701.
[10] KATO, K., KAWATA, T., ALFREDSSON, P. H., & LINGWOOD, R. J. 2019 Investigation of the structures in the unstable rotating-cone boundary layer, *Phys. Rev. Fluids*, **4**, 053903.
[11] KOBAYASHI, R. & IZUMI, H. 1983 Boundary-layer transition on a rotating cone in still fluid, *J. Fluid Mech.* **127**, 353–364.
[12] SEGALINI, A. & CAMARRI, S. 2019 Flow induced by a rotating cone: Base flow and convective stability analysis, *Phys. Rev. Fluids*, **4**, 084801.
[13] THOMAS, C. & DAVIES, C. 2019 Global linear instability of rotating-cone boundary layers in a quiescent medium, *Phys. Rev. Fluids*, **4**, 043902.

THE EFFECT OF LARGE PARTICLES ON THE LAMINAR-TURBULENT TRANSITION

Willian Hogendoorn*[1], Bidhan Chandra[1], and Christian Poelma[1]
[1]Multiphase Systems (3ME, P&E), Delft University of Technology, Delft, The Netherlands

Summary In this study the effect of finite size particles on laminar-turbulent transition in pipe flow has been investigated. In particular the influence of particle concentration and diameter on the behaviour of turbulent puffs is studied, which has not been investigated in depth before. Particle Image Velocimetry is applied in addition to pressure drop measurements in order to quantify the flow field around the particles. By using Particle Tracking Velocimetry the velocity of the finite size particles is measured. At the same time, the local particle concentration is measured as well. These unique and synchronous measurements gives us a complete picture of the effect of particles on the change in transition behaviour.

INTRODUCTION

Transition to turbulence in pipe flow has been extensively studied since Reynolds discovery in 1883. Also polymer addition to (pipe) flows and the drag reduction it realises has been studied in depth as well. Less attention, however, has been given to the laminar-turbulent transition of particle-laden flows. Particle-laden flows are very relevant, as these flows are ubiquitous in nature and industry. Recently [1, 2] it has been shown that particles completely alter laminar-turbulent transition behaviour. For higher particle concentrations, a gradual transition is observed, without turbulent puffs in the intermittent region. This is different compared to the classical, single-phase transition. The results we present, involve a more detailed analysis of particle induced transition behaviour. For this study relatively big particles are used to increase the particle-to-pipe diameter ratio, in order to investigate the effect of particle diameter on this change in transition behaviour. In addition, by using relatively big particles, Particle Image Velocimetry (PIV) is feasible to obtain flow field characteristics.

EXPERIMENTAL SETUP

Experiments are performed in a slightly adapted version of the setup which is described in [1]. In short, a 1-cm diameter pipe (D) with a total length of 310D is used. Salt (Na_2SO_4) is added to the water to match the densities of the fluid and the polystyrene particles. The flow is pressure driven by means of an overflow tank. An orifice plate, comparable with Wygnanski et al. [3] is used as a trigger mechanism. After this trigger there is 125D development length, followed by the measurement section. A schematic of this measurement section is shown in Fig. 1. At first a pressure drop measurement over 125D is applied (Δp_1). This Δp_1 is used for average pressure drop measurements. Another pressure drop measurement (Δp_2) is performed directly after Δp_1. As this pressure drop sensor is used to measure local pressure fluctuations, the differential distance is 5D. For low particle concentrations, Particle Image Velocimetry is applied to measure the velocity field around the particles and the corresponding disturbance which is introduced by the particles. In addition to the laser light sheet, LED back-illumination is used. By doing so, the velocity of the finite size particles can be determined by using Particle Tracking Velocimetry (PTV). Moreover, by identifying all the finite size particles in the camera image, the local particle concentration (ϕ) is measured synchronously.

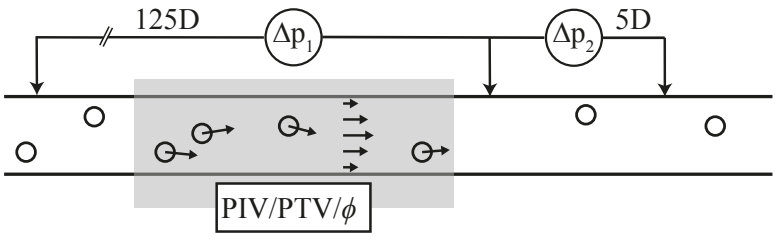

Figure 1: Schematic of the measurement section of the experimental setup. Two different differential pressure sensors are used, which measure the pressure drop over 125D and 5D, respectively. A few diameters before Δp_2, Particle Image Velocimetry, Particle Tracking Velocimetry and a concentration measurement is applied.

RESULTS

A typical result for the streamwise centerline velocity, the corresponding local particle concentration and the pressure drop (Δp_2) as function of τ, for a transition flow is shown in Fig. 2. Here, τ is defined as $t\frac{\overline{u}}{l}$, where t is the time, $\overline{u}$ is the mean flow velocity and l is a typical length scale, for which we used 20D. Note that the pressure drop data is

*Corresponding author. E-mail: W.J.Hogendoorn@tudelft.nl.

recorded after (spacewise) the PIV and concentration data. However, by correcting the pressure drop data with the mean advection velocity of the flow and the spatial lag, all three measurements can be regarded as being measured at the same location. Because the spatial lag is only a few diameters, it is assumed by using Taylors frozen turbulence hypothesis that the structure of the flow remains similar. The maximum particle concentration (center panel) in this time series occurs for $\tau \approx 5$. At the same time, a drop and rise of the centerline velocity (upper panel) can be observed. This drop and rise of the centerline velocity resembles a characteristic sawtooth shape which is typical for a puff (see e.g. [1, 4]). In the timeseries for the pressure drop (bottom panel) also a characteristic fluctuation, which is corresponding with a passing puff, can be seen.

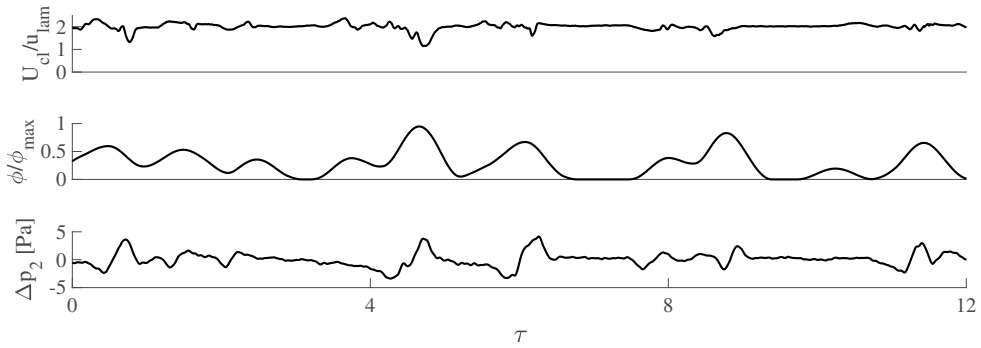

Figure 2: Steamwise centerline velocity, particle concentration and pressure drop signal as function of dimensionless time, τ.

In addition to the synchronous timeseries from Fig. 2, PIV data is recorded. An instantaneous flow field, corresponding with $\tau \approx 5$ in Fig. 2 is shown in Fig. 3. The color of the vectors represents the radial velocity component. This flow field is superimposed on the particle image in which the finite size particles appear in black. From the particle image, the particle position, velocity and concentration can be determined. The results of this data processing will be presented at the Congress.

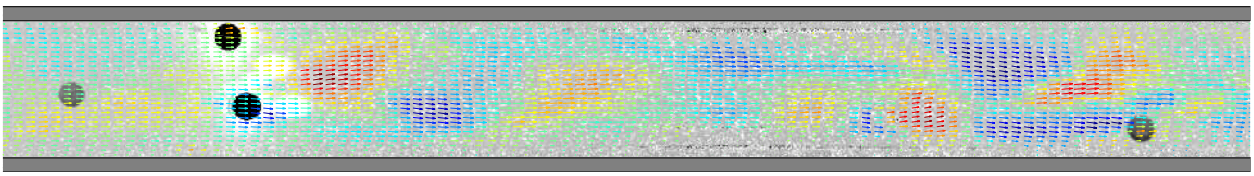

Figure 3: Instantaneous flow field of a typical puff in a dilute suspension, corresponding with $\tau \approx 5$ in Fig 2. This flow field is superimposed on the particle image, in which the finite size particles appear in black. The color of the vectors represents the radial velocity component.

CONCLUSIONS

Experiments are performed in particle-laden, transitional pipe flow. The effect of relatively big particles on the change in laminar-turbulent transition behaviour is investigated by using different, combined measurement techniques. Synchronous velocity, concentration and pressure drop measurements are performed. Particle Image Velocimetry is applied to measure the overall flow field and Particle Tracking Velocimetry is used in addition, to obtain the velocity of the particles. Combining all the data gives us a wealth of information about the effect of particles on the change in transition behaviour.

References

[1] Hogendoorn W., Poelma C. Particle-Laden Pipe Flows at High Volume Fractions Show Transition Without Puffs. *Phys. Rev. Lett.* **121(19)**: 194501, 2018.

[2] Agrawal, Nishchal, George H. Choueiri, and Björn Hof. Transition to turbulence in particle laden flows. *Phys. Rev. Lett.* **122(11)**: 114502, 2019.

[3] Wygnanski, Israel J., and F. H. Champagne. "On transition in a pipe. Part 1. The origin of puffs and slugs and the flow in a turbulent slug." *J. Fluid Mech.* **59.2 (1973)**: 281-335.

[4] D. J. Kuik, C. Poelma, and J. Westerweel, *J. Fluid Mech.* **645**: 529-539, 2010.

FRACTAL NEUTRAL STABILITY CURVES IN TAYLOR'S THREE-LAYERED FLOW

Jonathan J Healey*[1]
[1]Department of Mathematics, Keele University, Keele, Staffs. ST5 5BG, UK

Summary In 1931 Taylor published a pioneering study of the linear stability of stratified shear layers, i.e. horizontal flows where gravity is in the vertical direction, and fluid density varies vertically. The resulting buoyancy term is important in many geophysical applications. In one example, Taylor considered a uniform shear with three layers, each of constant density, with densities increasing downwards, and showed that this flow is unstable. We revisit this flow, but with smoothed density profiles, thus including effects of density diffusion neglected by Taylor. This minor change is shown to create infinitely many new instability modes, and their neutral curves have a self-similar fractal structure, even though they are determined by the linear Taylor-Goldstein equation. We indicate how the presence of such a structure may influence laminar-turbulent transition scenarios.

INTRODUCTION AND PROBLEM FORMULATION

Fractal behaviours are usually associated with nonlinear dynamical systems, so it is of interest to observe that they can also be produced by linear stability equations arising in hydrodynamic stability theory. The Taylor-Goldstein equation, see [1], describes the stability properties of linearized inviscid waves in horizontal parallel shear layers of Boussinesq fluid where density varies in the vertical direction, which is a common scenario in geophysical flows. It can be written

$$(U-c)\left[v''-k^2v\right]-U''v-\frac{g\bar{\rho}'\sec^2\phi}{\bar{\rho}(U-c)}v=0, \tag{1}$$

where $U=U(y)$ is the basic velocity in the x direction, $\bar{\rho}=\bar{\rho}(y)$ is the basic density profile, g is acceleration due to gravity, k is the magnitude of the wavevector, ϕ is the waveangle ($\phi=0$ for two-dimensional waves), c is the complex phase velocity, $v=v(y)$ is the vertical component of the disturbance velocity, and primes denote differentiation with respect to the vertical coordinate y. In homogeneous flow, where $\bar{\rho}'=0$ everywhere, (1) reduces to the Rayleigh equation. However, the presence of $\sec^2\phi$ in the buoyancy term shows that buoyancy effects are important for highly oblique waves with $\phi\to\pi/2$, even when $\bar{\rho}'$ is small.

Although (1) has been studied in detail for many years, and for many geophysical flows, the author recently observed a new phenomenon for this equation (and perhaps for linear ordinary differential equations in general), in which the neutral stability curves were found to have an underlying fractal structure, see [2]. Plane Couette flow was considered, and $\bar{\rho}'/\bar{\rho}$ was taken to be a quadratic function of y. In the present paper we investigate whether such unusual behaviour occurs in other flows, especially in flows of practical importance. We also suggest mechanisms whereby the fractal structure of the linear stability problem might produce novel laminar-turbulent transition scenarios.

We consider a flow first introduced by Taylor in his 1931 paper, [1], in which the flow is an infinite uniform shear, with two interfaces where there are step changes in density, as shown in figure 1(a). Taylor used this example to illustrate how even stable stratification ($\bar{\rho}'\leq 0$ everywhere) can destabilize an otherwise stable flow. In fact, this flow turns out to be a useful model for flows encountered in the ocean, where a well-mixed layer of intermediate density lies between a less dense upper layer and a more dense lower layer, see [3], and references therein. The instability resulting from a shear flow with this density structure is sometimes called the Taylor-Caulfield instability.

Suppose that a dynamical process at an earlier time has resulted in the layered structure described by Taylor, but the fluid is now at rest. Allowing diffusion of density across the originally sharp interfaces results in a density profile like that in figure 1(b). When the total density change is small, the buoyancy coefficient, $-\bar{\rho}'/\bar{\rho}$, has a profile like that in figure 1(c), which can be conveniently modelled by

$$Ri(y)=-\frac{g\bar{\rho}'}{\bar{\rho}U'^2}=\left(Ri_0+Jy^2\right)\mathrm{e}^{-y^2+y_0y}, \tag{2}$$

where Ri is the local Richardson number (a dimensionless quantity formed from a ratio of buoyancy frequency and shear) and U' is the constant shear. Subsituting (2) into (1) and imposing homogeneous boundary conditions, $v\to 0$ as $y\to\pm\infty$, gives an eigenvalue problem for c, with instability if $\mathrm{Im}(c)>0$ for $k>0$. When $y_0=0$, Ri is symmetric about $y=0$, and when $y_0\neq 0$ the density jumps across each interface are different, as in the cases shown in figure 1. We consider $J>0$ and $Ri_0\geq 0$, giving stable stratification.

*Corresponding author. E-mail: j.j.healey@keele.ac.uk.

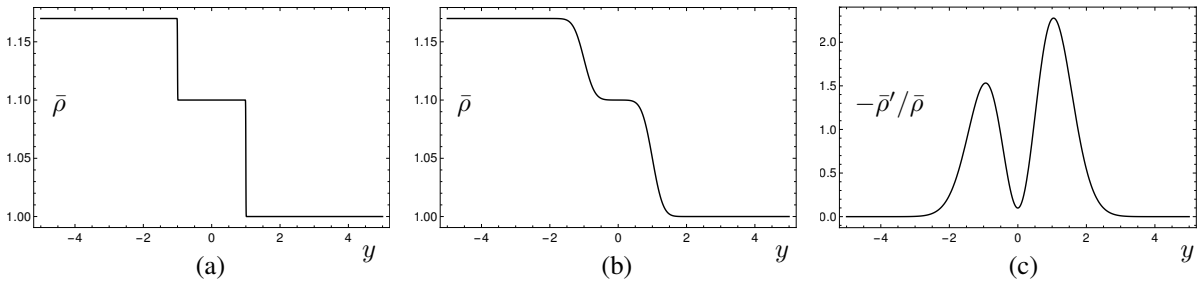

Figure 1: (a) Step density profile for Taylor's flow; (b) density for Taylor's flow with diffusion; (c) qualitative variation of buoyancy term for profile (b).

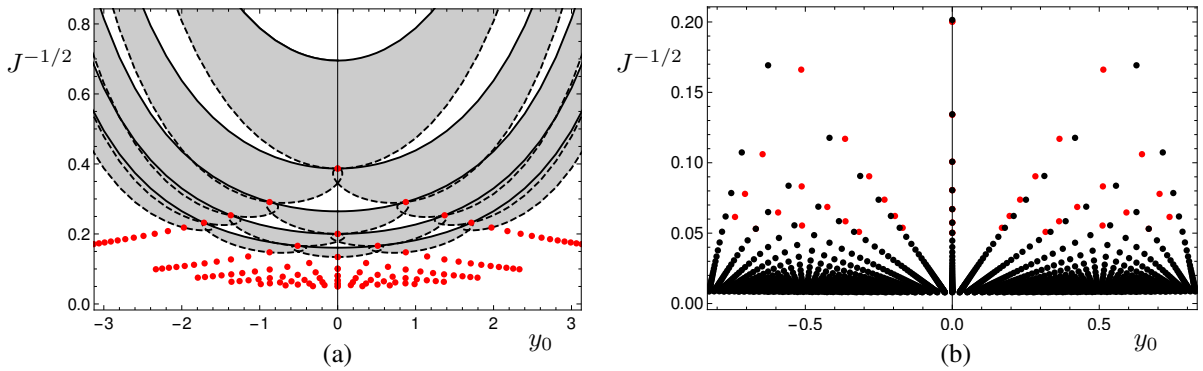

Figure 2: (a) Neutral curves for $k = 1$, $\phi = 0$, $Ri_0 = 0$. Solid lines have $c = 0$; dashed lines have $c \neq 0$; red dots are points where three different neutral curves cross each other. (b) Red dots as in (a); black dots are asymptotic predictions for the red dots where neutral curves cross each other based on WKB theory when $J \gg 1$ and $|y_0| \ll 1$.

RESULTS AND CONCLUSIONS

Note that the step density changes in figure 1(a) allow dispersion relations to be derived analytically, giving a quartic in c, see [1]. But the smooth density profile in figure 1(b) supports arbitrarily many unstable modes when $J \sec^2 \phi$ is large. This case has been solved numerically, and neutral curves are shown in figure 2(a). The following pattern can be observed: Working down from the top of the diagram, there is one large unstable region below the top solid neutral curve, there are two unstable regions below the second solid neutral curve, there are three unstable regions below the third solid neutral curve, etc. There is one red dot along the second solid neutral curve, there are two red dots along the third solid neutral curve, there are three red dots along the fourth solid neutral curve, etc. This pattern has been verified numerically down to the fifth solid neutral curve. A numerical search procedure has been developed for locating the points where three neutral curves cross, marked by red dots, and many more of these points have been obtained than the neutral curves themselves.

A WKB theory has been developed for obtaining asymptotic solutions to (1) with (2) for $J \gg 1$ and $|y_0| \ll 1$, and this theory produces explicit expressions for J and y_0 at the red dots. These predictions are shown in figure 2(b) as black dots. These black dots follow the same fractal pattern found in [2], and predict the positions of red dots more and more accurately as J increases and $|y_0|$ decreases, i.e. towards the origin of figure 2(b).

In the presentation we also show neutral curves in the wavenumber plane for fixed sets of profile parameters with streamwise wavenumbers and spanwise wavenumbers on the axes. There are multiple bands of unstable wavenumbers, with the number of unstable regions increasing from one for $Ri_0 \to 1/4$, to arbitrarily many as $Ri_0 \to 0$. By adjusting profile parameters we can tune resonant wave interactions involving any desired number of resonant waves. This gives the possibility of novel weakly nonlinear amplitude equations that may produce chaotic spatio-temporal dynamics.

In this paper we have shown that the fractal behaviour found for a special flow in [2], also appears in a diffused version of Taylor's three-layered flow, and so can be expected in a variety of flows of practical importance. The associated multiple unstable bands in wavenumber planes can generate many types of weakly nonlinear behaviour which may be important in the laminar-turbulent transition of these flows.

References

[1] Taylor G. I. Effect of variation in density on the stability of superposed streams of fluid. *Proc. R. Soc. Lond.* A **132**: 499-523, 1931.
[2] Healey J. J. Fractal sets of neutral curves for stably stratified plane Couette flow. *J. Fluid Mech.* **872**: 697-728, 2019.
[3] Eaves T. S. & Caulfield C. P. Multiple instability of layered stratified plane Couette flow. *J. Fluid Mech.* **813**: 250-278, 2017.

DECAY AND SPLITTING PATHWAYS IN TRANSITIONAL CHANNEL FLOW

Sébastien Gomé*[1], Laurette Tuckerman[1], and Dwight Barkley[2]
[1] Laboratoire de Physique et Mécanique des Milieux Hétérogènes (PMMH), CNRS, ESPCI Paris, PSL Research University, Sorbonne Université, Université Paris Diderot, Paris 75005, France
[2] Mathematics Institute, University of Warwick, Coventry CV4 7AL, United Kingdom

Summary Transition to turbulence in shear flows is characterized by intermittent laminar-turbulent patterns, which statistically proliferate or decay depending on the Reynolds number. We study the time evolution of turbulent bands in a tilted plane channel flow geometry via direct numerical simulations using pseudospectral code ChannelFlow. Turbulence decay or spreading processes are exponentially distributed, which is the signature of a memoryless process. Statistically estimated time scales for decay or splitting of a band are plotted as a function of the Reynolds number and lead to the estimation of a critical Reynolds number $Re_{\mathrm{cross}} \simeq 950$, with an associated time scale of 10^6 advection times. With such a large time scale, the use of statistical mechanics methods such as the rare event approach is necessary to evaluate the mean decay or splitting time. Spectral analysis of a band during a decay or a splitting event is helpful to determine the stochastic pathway followed by a turbulent band, and to disentangle deterministic and stochastic behaviors during laminarization.

STATISTICAL TEMPORAL EVOLUTION OF A TURBULENT BAND

Transition to turbulence in wall-bounded flows follows a globally subcritical route far below the Reynolds number at which laminar flow linearly destabilizes. For plane channel, plane Couette or pipe flows, turbulence is sustained after finite amplitude perturbations, and takes the form of intermittent turbulent-laminar patterns. In a pipe, these turbulent puffs are shown to be metastable. They can decay or split obeying stochastic mechanisms [1]. In planar shear flows such as plane Poiseuille or Couette flows, the intermittent turbulence takes the form of oblique bands in the streamwise-spanwise plane. Direct numerical simulations of plane Couette flow in a slender but long tilted domain show that transition also follows the 1D Directed Percolation class, and that turbulent bands are memoryless as their lifetimes or splitting times are exponentially distributed [2]. The characteristic time scales for decays (τ^d) or splittings (τ^s) depends on the Reynolds number Re. A critical Reynolds number can be defined at the crossing of the two curves $\tau^d(Re)$ and $\tau^s(Re)$. In pipe and plane Couette flows, these critical Reynolds number are respectively approximately 2000 and 325.

Direct numerical simulations of plane channel flow are carried out in an oblique geometry, via the pseudo-spectral code ChannelFlow. A statistical study of band decay or splitting is performed in a long ($L_z = 100h$) narrow ($L_x = 6.6h$) domain, tilted with an angle $\theta = 24°$ with the streamwise direction (h denotes the half-gap between the two rigid plates) [3]. Snapshots from an a band at $Re = 1050$ are used as initial conditions for simulations at higher or lower Re. Decay or splitting are observed to occur at times that are exponentially distributed:

$$P(\text{decay or splitting at T} \geq \text{t})) = \exp(-(\text{t} - \text{t}_0)/\tau^{\text{d/s}})$$

The slope of the distribution $\tau^{d/s}(Re)$ for decay or splitting cases is estimated via a maximum likelihood estimator, and its dependence on Re is shown on Figure 1. Time scales seem to follow super-exponential trends, and their crossing point is estimated to be $Re_{\mathrm{cross}} \simeq 950$.

The trend $\tau^{d/s}(Re)$ is similar to the one obtained in pipe flow [1], and differs from that of plane Couette flow [2]. This could be due to their inherent different local shear rates, especially near the walls, which could induce more sustained turbulent rolls in channel flow.

Since time scales are very large, computing the statistical evolution of the band is presumably expensive between $Re = 900$ and 1100. Therefore, a rare event approach is desirable to bridge the gap between these Reynolds numbers. This requires adequate score functions to measure the distance between a state A (*e.g* a turbulent band) and another state B (*e.g* the laminar state), in order to select preferentially trajectories between A and B.

TRANSITION PATH DURING SPLITTING AND DECAY EVENTS

A turbulent-laminar pattern in plane channel flow acts as a metastable state, which can either transit to the laminar state (decay), or to another pattern with a different wavelength (splitting). The evolution of the flow field during these transitions is monitored via spectral quantities, which are obtained through Fourier transforms. Large-scale structures are characterized by spectral coefficients $\hat{u}_{0,1}$ and $\hat{u}_{0,2}$ which respectively represent a one and a two-band structure.

Laminarization of a turbulent band is shown to proceed by a sharp disappearance of small-scale structures (streaks and rolls) and by a slow decay of the one-band pattern $\hat{u}_{0,1}$, which becomes prominent after a specific time.

Figure 2a presents the decay process for different initial conditions, with a shifted time t^* so that each final t^* is the same in all the cases. For all the simulations, $\hat{u}_{0,1}$ collapse to the same exponential slope at the end of the decay

*Corresponding author. E-mail: sebastien.gome@espci.fr

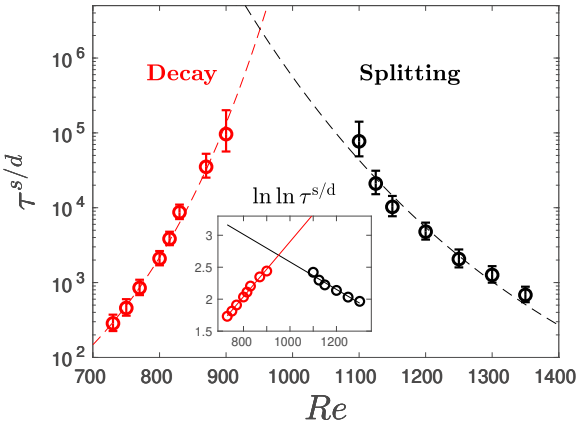

Figure 1: Evolution of mean lifetimes (red) and splitting times (black) with Reynolds number Re. The error bars correspond to 95% confidence intervals for the estimated parameter τ. Insight: $\ln\ln\tau^{s/d}$ versus Re and associated linear interpolations.

process. This is also the case for $\hat{u}_{0,2}$, but with an expected higher slope. Each spectral quantity undergoes a loss of effective randomness after a certain time, that differs for each wave number. From this time on, flow structures follow a deterministic route to the laminar state, governed by linear dissipation.

In the case of a band splitting, the system transits from a one-band ($\hat{u}_{0,1} > \hat{u}_{0,2}$) to a two-band pattern ($\hat{u}_{0,2} > \hat{u}_{0,1}$). All simulations seem to statistically follow the same path, as illustrated in Figure 2b: from the one-band attractor (1), $\hat{u}_{0,2}$ decreases and then grows to finally outpace $\hat{u}_{0,1}$. Meanwhile, the third harmonic $\hat{u}_{0,3}$ reaches a maximum nearly at the half of the trajectories, as a result of $\hat{u}_{0,1}$ and $\hat{u}_{0,2}$ interactions. These trends are currently under investigation by applying a rare events approach to turbulent band splitting.

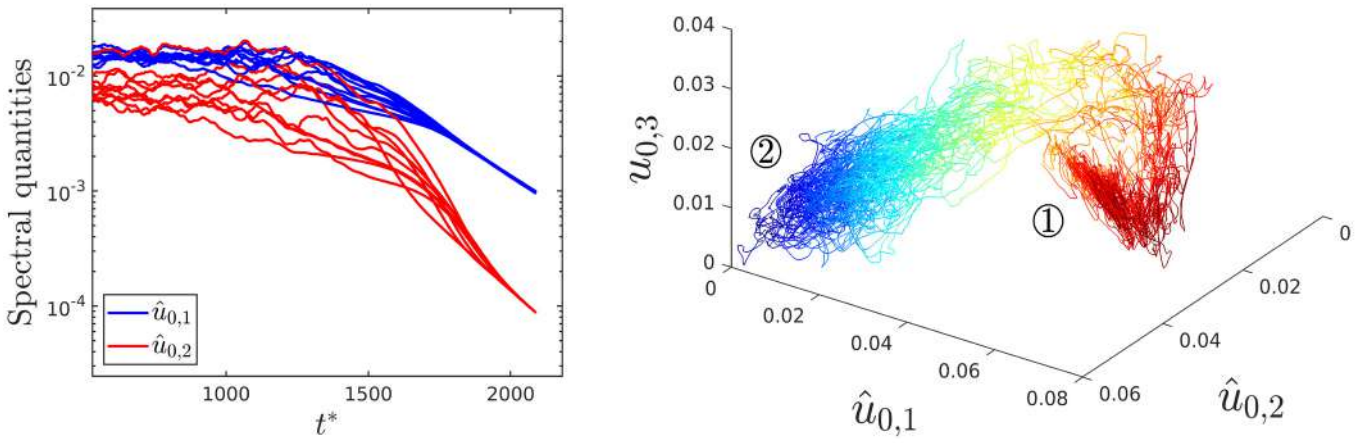

(a) (b)

Figure 2: Evolution of spectral quantities during (a) 10 decays at $Re = 830$ and (b) 10 splittings at $Re = 1200$.

References

[1] Avila, K., Moxey, D., de Lozar, A., Avila, M., Barkley, D., Hof, B. The onset of turbulence in pipe flow, *Science*, **333** (6039): 192-196, 2011.

[2] Shi, L., Avila, M., Hof, B. Scale invariance at the onset of turbulence in Couette flow, *Phys. Rev. Letters*, **110** (20): 204502, 2013.

[3] Tuckerman, L. S., Kreilos, T., Schrobsdorff, H., Schneider, T. M., Gibson, J. F. Turbulent-laminar patterns in plane Poiseuille flow. *Physics of Fluids*, **26** (11): 114103, 2014

[4] Bouchet, F., Rolland, J., Simonnet, E. Rare event algorithm links transitions in turbulent flows with activated nucleations, *Phys. Rev. Letters*, **122** (7): 074502, 2019.

A COMPREHENSIVE STUDY ON THE INSTABILITIES ARISING IN THE WAKE OF A ROTATING CYLINDER

Javier Sierra Ausin*[1,2], David Fabre[1], Vincenzo Citro[2], and Flavio Giannetti[2]
[1]Institut de Mécanique des fluides de Toulouse (IMFT),Toulouse 31400,France
[2]Dipartimento di Ingegneria Industriale (DIIN),Università degli Studi di Salerno,Fisciano (SA),84084,Italy

Summary A complete description of the bifurcation scenario of a uniform flow past a rotating circular cylinder is aimed. Linear stability theory is used to depict neutral curves and analyze the arising unstable global modes. Special emphasis is paid to the identification of bifurcations with codimension higher than one. Three codimension-two bifurcation points are detected, namely a Takens-Bogdanov, a cusp and generalized Hopf, which are closely related to qualitative changes in orbit dynamics. The occurrence of the cusp and Takens-Bogdanov bifurcations for very close parameters (corresponding to an imperfect co-dimension-3 bifurcation) is shown to be responsible for the emergence of multiple steady states. Direct numerical simulations confirmed the presence of homoclinic and heteroclinic orbits which are classical in the presence of Takens-Bogdanov bifurcations. Finally, a weakly nonlinear analysis is accomplished in the neighborhood of the Generalized Hopf bifurcation to determine the fold of two limit cycles of opposing stability in the vicinity the subcritical Hopf bifurcation curve.

INTRODUCTION

The flow past a circular cylinder is one of the classical flow configurations which has long received attention from the fluid dynamics community. This kind of flow has direct implications for flow control by using wall motion and has recently received particular attention [1, 2, 3, 4] .

Linear stability approaches, see i.e. [5, 6], have precised the picture, showing the existence of two separated regions of instability in the (Re, α) plane, where α is the nondimensional rotation rated and Re the Reynolds number. At large rotation rates $\alpha \geq 4.5$, there is a region in the plane of parameters (Re, α) where multiple steady states coexist [5, 7, 8]. It has been conjectured by [7] the fact that multiple steady states collapse into a *cusp* bifurcation point. In the vicinity of *cusp* bifurcation, three coexisting steady states exist. The counting of steady states supports the hypothesis of a *cusp* bifurcation. However, near a *cusp* bifurcation one should not find an unsteady transition as it is the case of Mode II. The presence of a connection between a Hopf bifurcation and a saddle-node is an indicator of other type of codimension-two bifurcation, a 0^2 or *Takens-Bogdanov* bifurcation. Nevertheless, the generic type of this bifurcation does not explain the existence of three steady states. Actually, in the neighbourhood of the onset at which multiple steady states arise, dynamics are driven by the third-order normal form of the unfolding of the TB bifurcation.

Furthermore, it has been identified a third codimension-two point, namely a Generalized Hopf (GH) bifurcation.

PRELIMINARY RESULTS

Cusp-Takens Bogdanov normal form The Cusp-Takens Bogdanov normal form reads:

$$\frac{dy_1}{dt} = y_2, \qquad \frac{dy_2}{dt} = \beta_1 + \beta_2 y_1 + \beta_3 y_2 + \epsilon y_1^3 + c_1 y_1 y_2 - y_1^2 y_2 \tag{1}$$

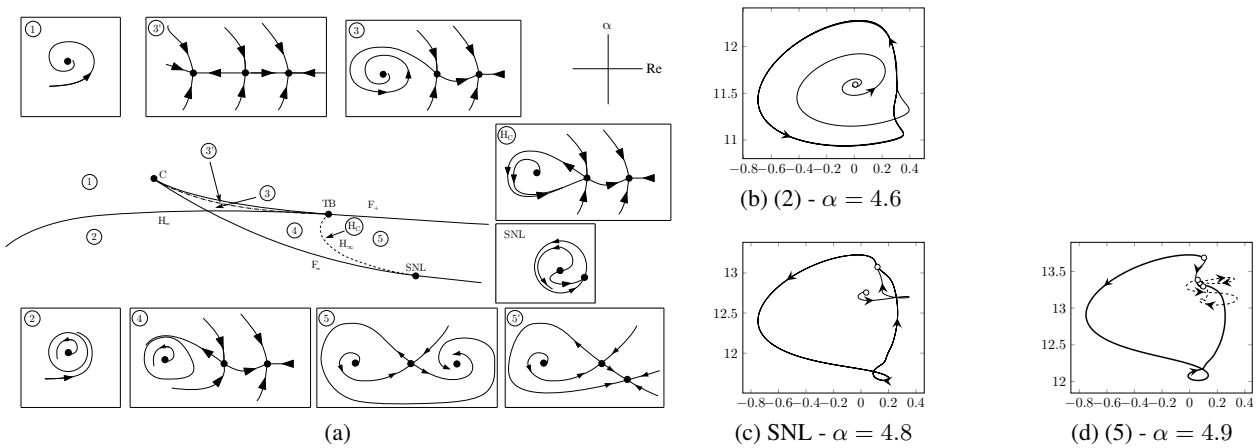

Figure 1: (a) Bifurcation diagram predicted using the normal form 1 in the stable focus case (adapted from [9]), and qualitative phase portrait in regions (1), (2), (3), (3'), (4) , (5), (5') and along curve H_∞. (b-d) Phase portrait (F_x, F_y) of the dynamics of the rotating cylinder at $Re = 170$, where empty dots denote steady state solutions.

*Corresponding author. E-mail: javier.sierra@imft.fr

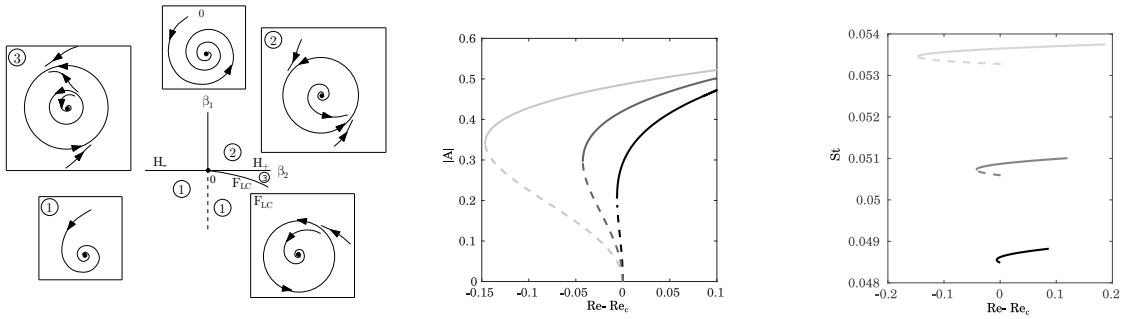

(a) (b) (c)

Figure 2: (a) Qualitative bifurcation scenario in the vicinity of the GH bifurcation. (b) Comparison of the amplitude of stable (solid line) and unstable (dashed line) limit cycles for three Re_c, where Re_c denotes the Reynolds number at the subcritical Hopf bifurcation. Light grey curve corresponds to $Re_c = 250$, dark grey to $Re_c = 200$ and black to $Re_c = 170$. (c) Strouhal number for each limit cycle is shown.

where β_1, β_2 and β_3 are unfolding parameters (mapped from the physical parameters (Re, α)), c_1 and ϵ (which can be rescaled to ± 1) are fixed coefficients which depend on the nonlinear terms of the underlying system. Note that this normal form Eq. 1 generalizes both the normal form of the standard TB bifurcation (which is recovered for $\beta_1(Re, \alpha) = 0$) and the one of the fold bifurcation (which is recovered for $\beta_3(Re, \alpha) = 0$). The occurrence of both these codimension-2 conditions for very close values of the parameters is characteristic of an imperfect codimension-3 bifurcation and justifies the relevance of the associated normal form.

The dynamics of the normal form has been explored by [9, 10] who classified the possible phase portraits and the associated bifurcation diagrams as a function of the unfolding parameters $(\beta_1, \beta_2, \beta_3)$ along a spherical surface. They showed that all possible bifurcation diagrams fall into three possible categories, called *focus, saddle and node* according to the values of the coefficients c_1 and ϵ. The situation $0 < c_1 < 2\sqrt{2}$ and $\epsilon = -1$ corresponds to the *stable focus case* and is found to lead to a bifurcation diagram Fig. 1. In order to confirm the global stability results, we performed also a parametric study by using time-stepping simulations for several rotation rates at a fixed Re, see Fig. 1 (b-d).

Generalised Hopf bifurcation The governing equation is a Stuart Landau equation, depending on a small parameter $\epsilon^2 = Re_c^{-1} - Re^{-1}$:

$$\frac{dA}{dt} = (i\omega_0 + \epsilon^2\lambda_0 + \epsilon^4\lambda_1)A + (\nu_{1,0} + \epsilon^2\nu_{1,1})|A|^2A + \nu_{2,0}|A|^4A \tag{2}$$

From Eq. 2, a GH bifurcation occurs on the Hopf bifurcation curve and whenever $Re(\nu_{1,0}) = 0$. When $Re(\nu_{1,0}) < 0$ (resp. $Re(\nu_{1,0}) > 0$) the Hopf bifurcation is subcritical (resp. supercritical). The amplitude of the limit cycle $|A|_\pm = \sqrt{-\frac{Re(\nu_1)}{2Re(\nu_2)} \pm \sqrt{\frac{Re(\nu_1)^2}{4Re(\nu_2)^2} - \frac{Re(\lambda)}{Re(\nu_2)}}}$ and its frequency $\omega\pm = \omega_0 + Im(\nu_1)|A|_\pm + Im(\nu_2)|A|_\pm^2$ where $\nu_1 = \nu_{1,0} + \epsilon^2\nu_{1,1}$, $\lambda = \epsilon^2\lambda_0 + \epsilon^4\lambda_1$ are directly computed from Eq. 2 via Weakly NonLinear analysis, see Fig. 2 (b-c). When the Hopf bifurcation is subcritical ($Re(\nu_{1,0}) < 0$) there is a range in ϵ^2 where both solutions are positive real solutions, $|A|_\pm \in \mathbb{R}_+$. The inner unstable (resp. outer stable) limit cycle increases (resp. decreases) its amplitude as the distance from the Hopf bifurcation increases until both periodic orbits collide and disappear, that occurs when $\frac{Re(\nu_1)^2}{4Re(\nu_2)^2} = \frac{Re(\lambda)}{Re(\nu_2)}$.

References

[1] Sangmo Kang, Haecheon Choi, and Sangsan Lee. Laminar flow past a rotating circular cylinder. *Physics of Fluids*, 11(11):3312–3321, 1999.
[2] D Stojković, M Breuer, and F Durst. Effect of high rotation rates on the laminar flow around a circular cylinder. *Physics of fluids*, 14(9):3160–3178, 2002.
[3] D Stojković, P Schön, M Breuer, and F Durst. On the new vortex shedding mode past a rotating circular cylinder. *Physics of Fluids*, 15(5):1257–1260, 2003.
[4] S Mittal. Three-dimensional instabilities in flow past a rotating cylinder. *Journal of applied mechanics*, 71(1):89–95, 2004.
[5] Jan O Pralits, Luca Brandt, and Flavio Giannetti. Instability and sensitivity of the flow around a rotating circular cylinder. *Journal of Fluid Mechanics*, 650:513–536, 2010.
[6] Jan O Pralits, Flavio Giannetti, and Luca Brandt. Three-dimensional instability of the flow around a rotating circular cylinder. *Journal of Fluid Mechanics*, 730:5–18, 2013.
[7] Anirudh Rao, JS Leontini, MC Thompson, and Kerry Hourigan. Three-dimensionality in the wake of a rapidly rotating cylinder in uniform flow. *Journal of Fluid Mechanics*, 717:1–29, 2013.
[8] MC Thompson, A Rao, JS Leontini, and K Hourigan. The existence of multiple solutions for rotating cylinder flows. 2014.
[9] Freddy Dumortier, Robert Roussarie, Jorge Sotomayor, and Henryk Zoladek. *Bifurcations of planar vector fields: Nilpotent Singularities and Abelian Integrals*. Springer, 2006.
[10] Yu A Kuznetsov. Practical computation of normal forms on center manifolds at degenerate bogdanov–takens bifurcations. *International Journal of Bifurcation and Chaos*, 15(11):3535–3546, 2005.

FROM HYDRODYNAMIC INSTABILITY TO THE ONSET OF LAGRANGIAN CHAOS

S. W. Gepner*[1] and J. M. Floryan[2]
[1]Warsaw University of Technology, Institute of Aeronautics and Applied Mechanics, Warsaw, Poland
[2]Department of Mechanical and Materials Engineering, The University of Western Ontario, London, Canada

Summary It is demonstrated that channel modifications in the form of longitudinal grooves lead to a decrease of hydraulic drag and to the onset of a travelling wave instability at very low Reynolds numbers ($Re < 10^2$). The growth of these waves leads to the formation of saturation states which are both time- and space-periodic and have the form of downstream-travelling vortex pairs combined with periodic, in-plane motions. Secondary flows remain laminar and relatively uncomplicated but result in complex advection patterns leading to chaotic particle trajectories, thus creating the potential for low Reynolds number mixing enhancement. The qualitative and quantitative analyses of particles trajectories demonstrate the onset of Lagrangian chaos and enhanced mixing.

INTODUCTION

The mixing of fluids is a two-stage phenomenon composed of molecular transport processes (such as diffusion and reaction) overlaid on top of mechanical stirring [2]. Molecular transport depends on material properties and is in general slow. The stirring part is due to the kinematics of the flow and its role is to create stretching and folding of material interfaces leading to the increase in concentration gradients and in contact area. This enables the otherwise slow diffusion to act more rapidly and across shorter distances [4]. Consequently, efficient stirring is associated with flow kinematics that results in complicated flow patterns. While flow turbulization is an effective way to achieve such flows [5], its use is infeasible in a number of problems [5], either due to size constraints or the fragile nature of the fluid, e.g., when biological macromolecules are present in the flow. Such flows are typically laminar and their effective stirring remains a challenge.

For laminar flows, effective stirring can be achieved by means of *chaotic advection* [1, 2, 3], a phenomenon in which fully laminar, relatively simple velocity fields (in the Eulerian representation) result in a chaotic response in the Lagrangian view [1, 2]. The high complexity of motion results from the fact that the dynamical system that describes the motion of individual fluid particles might be non-integrable, leading to chaotic trajectories and, consequently, to improved stirring.

The principles of chaotic advection have been applied to various designs and studies (see [3] for an extensive review). Both passive and active methods have been proposed to generate a chaotic response. The former approach relies on the use of obstacles such as bars or blades, wall patterns or various geometry modifications that force turning and redirection of the flow. The latter require external actuation, e.g., some form of stirrers and/or external body forces.

In this work, we propose a new method to induce chaotic advection by means of naturally occurring hydrodynamic instabilities. This method has not been previously proposed to the best of our knowledge [3]. The onset and amplification of the unstable modes eventually leads to a time-dependent saturation state which is still laminar. These instabilities are promoted through the introduction of wall corrugations of different spatial distributions and amplitudes. Geometrical modifications of the conduit geometry place this approach in the passive flow control category. It should be stressed that the mechanism leading to the onset of chaos is due to the flow three-dimensionalization and its non-stationarity rather than due to the flow modifications created directly by the surface grooves.

PROBLEM STATEMENT

Corrugation patterns which are especially suitable for low-Reynolds ($Re < 10^2$) number destabilization leading to three-dimensional, time-periodic nonlinear states that do not cause a large drag penalty are regular grooves oriented in such a manner that lines of constant elevation run parallel to the direction of the flow [6, 7]. The geometry considered here is periodic in the span-wise direction, formed by a sequence of diverging-converging sections as illustrated in Figure 1a. The pattern of surface topography is characterized by the amplitude S and the wave number α, and the mean channel

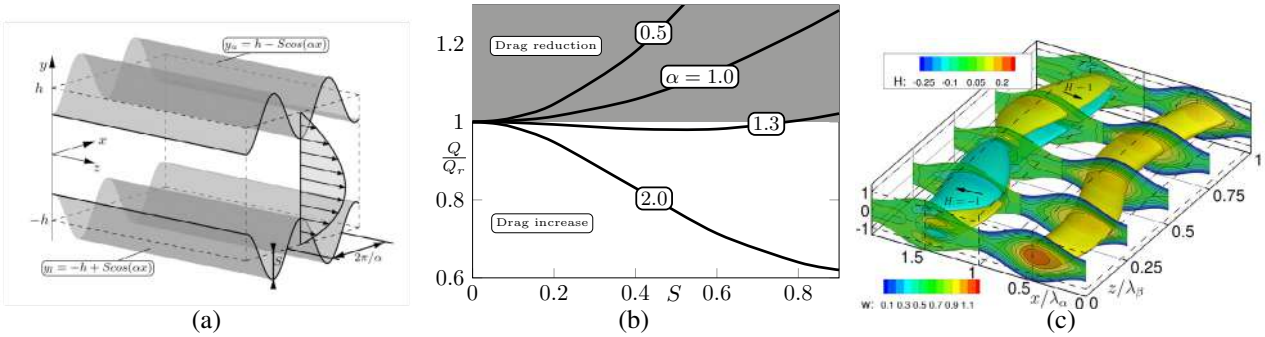

(a) (b) (c)

Figure 1: (a) Channel geometry; (b) Variation of the flow rate related to plane Poiseuille reference with corrugation amplitude; (c) Topology of the nonlinear state for $(\alpha, S) = (1, 0.4h)$ at Reynolds number $Re = 110$ showing downstream travelling, vortex pairs coloured by helicity (left) and iso-surface of the streamwise velocity (right).

*Corresponding author. E-mail: stanislaw.gepner@pw.edu.pl.

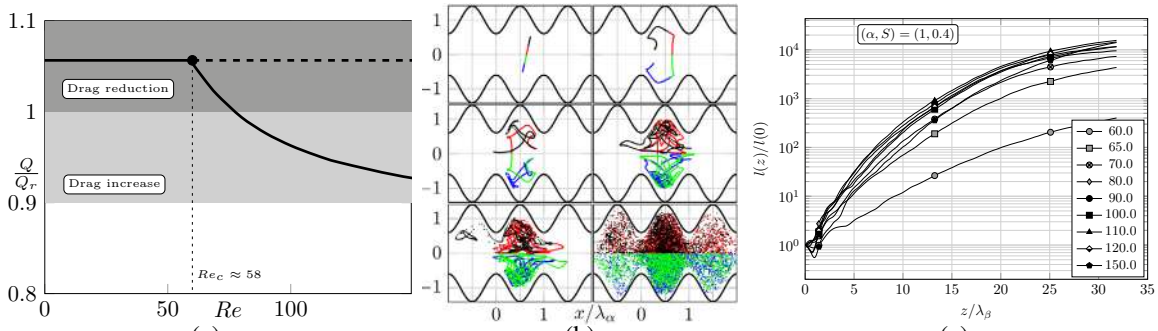

(a) (b) (c)

Figure 2: (a) Flow rate related to plane Poiseuille reference as a function of the Reynolds number for $(\alpha, S) = (1, 0.4h)$, bifurcation point marked at $Re \approx 58$.; (b) Downstream intersections of particle trajectories for $(\alpha, S) = (1, 0.4h)$ at $Re = 110$ initially positioned as a segment and coloured by initial position of the particle. Left to right and top to bottom intersections taken at $z = 0, 3, 5, 8, 10, 30$ wavelengths of the unstable mode; (c) Stretching of the initial segment captured at downstream intersections for selected Reynods numbers.

opening is $2h$. The flow is driven by a specified pressure gradient and, depending on geometrical parameters, can lead to a decrease in hydraulic drag relative to the reference plane Poiseuille flow. Figure 1b illustrates variations of the flow rate Q as a function of the corrugation amplitude for selected corrugation wave numbers.

The growth of an unstable mode activates nonlinear effects which eventually limit the disturbance growth and lead to the formation of a saturation state. The nonlinear saturated state is characterized by a system of three-dimensional vortices with a downstream propagating wave superimposed on them. The resulting three-dimensional flow pattern travels in the downstream direction, resulting in a periodic redirection of the velocity vector. An example of the topology of such a state determined for $(\alpha, S) = (1, 0.4h)$ at a Reynolds number $Re = 110$ is illustrated in Figure 1c. The two vortex pairs travelling downstream are identified by different colours associated with the helicity of the velocity field. These colours identify different directions of vortex rotation. The iso-surfaces of the streamwise velocity component illustrate periodic flow redirection. The formation of the saturated state is accompanied by a slight slowdown of the flow and an overall increase in the hydraulic drag. This process is illustrated in Figure 2a displaying variations of the flow rate as a function of the Reynolds number for a representative geometry $(\alpha, S) = (1, 0.4h)$.

Although the saturated state is rather simple, its three-dimensional and time dependent character more than satisfies the necessary conditions for the onset of chaotic advection [2]. The onset of Lagrangian chaos is verified by tracking trajectories of individual particles advected downstream by the velocity field of the saturated state. Integration of particle paths is performed using the classical RungeKutta (RK4) method, with the numerical error controlled by asserting appropriately small integration time steps. Qualitative insight into the character of the flow is given in Figure 2b, which shows intersections of particle trajectories by planes perpendicular to the streamwise direction taken at selected downstream positions and marked using colours which depend on the initial particle position (at $z = 0$). In this example, the channel geometry is given by $(\alpha, S) = (1, 0.4h)$ and $Re = 110$, with particles initially distributed uniformly within a single periodic section of the channel (top left in Figure 2b). One may observe that the initially straight segment of tracer particles is both stretched and bent, and the particles are eventually uniformly distributed throughout the channel section where they were initially placed, with some of the particles being advected to neighbouring channel sections. Such behaviour indicates that stirring associated with the saturated state results in complex patterns of particle movements and that it is indeed a case of chaotic advection. An attempt to quantify the stirring effectiveness of the saturated state is illustrated in Figure 2c, which shows elongation of the initially straight segment of tracer particles with the downstream distance, with $l(z)$ representing length of the deformed segment reproduced from trajectory intersections at position z and $l(0)$, the initial length.

CONCLUSIONS

The onset of chaotic dynamics is illustrated for the case of a low Reynolds number flow. This onset relies on the formation of a natural flow instability whose growth leads to the formation of a saturated state which is periodic both in time and space. The resulting chaotic advection [1] provides the means for achieving an effective stirring and results in enhancement of transport processes.

References

[1] H. Aref. Stirring by chaotic advection. *Journal of Fluid Mechanics*, 143:121, 1984.
[2] H. Aref. Chaotic advection of fluid particles. *Philosophical Transactions of The Royal Society A: Mathematical, Physical and Engineering Sciences*, 333:273–288, 11 1990.
[3] H. Aref, J. R. Blake, M. Budišić, S. S. S. Cardoso, J. H. E. Cartwright, H. J. H. Clercx, K. El Omari, U. Feudel, R. Golestanian, E. Gouillart, G. F. van Heijst, T. S. Krasnopolskaya, Y. Le Guer, R. S. MacKay, V. V. Meleshko, G. Metcalfe, I. Mezić, A. P. S. de Moura, O. Piro, M. F. M. Speetjens, R. Sturman, J.-L. Thiffeault, and I. Tuval. Frontiers of chaotic advection. *Rev. Mod. Phys.*, 89:025007, Jun 2017.
[4] J. M. Ottino. *The kinematics of mixing: stretching, chaos, and transport*, volume 3. Cambridge university press, 1989.
[5] J. M. Ottino. Mixing, chaotic advection, and turbulence. *Annual Review of Fluid Mechanics*, 22(1):207–254, 1990.
[6] N. Yadav, S. W. Gepner, and J. Szumbarski. Instability in a channel with grooves parallel to the flow. *Physics of Fluids*, 29(8):084104, 2017.
[7] N. Yadav, S. W. Gepner, and J. Szumbarski. Flow dynamics in longitudinally grooved duct. *Physics of Fluids*, 30(10):104105, 2018.

EXPERIMENTAL CONFIRMATION OF LINEAR STABILITY ANALYSIS FOR A SUBMERGED JET

Julia Zayko[1], Alexander Reshmin[1], Vladimir Trifonov[1], Linar Gareev[*1], and Vasily Vedeneev[1]
[1]Institute of Mechanics, Lomonosov Moscow State University, Moscow, Russia

Summary In this study, theoretical and experimental analysis of perturbation growth in submerged air jet is conducted. For the first time for this type of flows the comparison with linear stability theory is done. Both growth rates and wave lengths are measured experimentally. Both branches of growing perturbations are in excellent agreement with theory.

INTRODUCTION

In the linear stability theory of shear flows, only a few classical results have been tested experimentally, e.g. Blasius boundary layer [1, 3], Poiseuille flow in a round pipe [2], the plane Poiseuille flow [4, 5]. Stability of free shear flows, e.g. jets and wakes, and perturbation growth in such flows are much less studied experimentally, because of low critical Reynolds numbers and free jets breakdown near the orifice. Recently, a new method for the formation of laminar jets of $D = 0.12$ m in diameter, which stays laminar at the distance $5.5D$ from the orifice for the Reynolds number $\sim 10\,000$ was proposed [6]. In this study, by comparing experimental results with theoretical stability analysis, we conclude that the perturbation growth follows the prediction of the linear stability theory.

THEORETICAL STABILITY ANALYSIS OF A JET

To theoretically analyse the evolution of artificial axisymmetric perturbations, we performed the spatial stability analysis of the jet.

For each frequency $\omega \in \mathbb{R}$ and azimuthal wave number $n = 0$ the boundary-value problem for the Rayleigh equation defines an eigenvalue problem to find axial wave number $\alpha(\omega, n) \in \mathbb{C}$. Then the perturbation wave length is found as $\lambda = 2\pi/Re(\alpha)$, and $\delta = -Im(\alpha)$ is the perturbation growth rate.

For the considered velocity profiles [6] near the orifice (fig. 1a) two branches of growing perturbations exist (fig. 1b). The first branch is generated by two inflection points farthest from the jet axis, the second one by the infection point closest to the jet axis. The frequency range of growing perturbations is similar for both branches and corresponds to $0 < \Omega < 14$ Hz. The frequencies $\Omega = 4 - 6$ Hz corresponding to the maximum growth are also similar for both branches. However, wavelengths are different (fig. 2a)

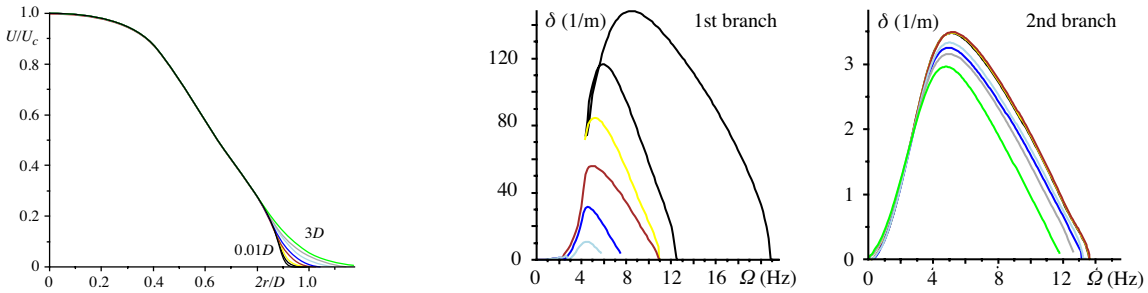

(a) (b)

Figure 1: (a) Mean velocity profile for $U_c = 1.5$ m/s ($Re = 5680$) at the distances $x/D = 0.01$, 0.04, 0.1, 0.25, 0.5, 1, 2, 3 from the orifice. (b) Theoretical spatial growth rate δ versus excitation frequency Ω at different distances from the diffuser (color coding corresponds to fig. 1a).

EXPERIMENTAL STUDY OF PERTURBATION GROWTH

Experimental apparatus

In figure 1a jet velocity profiles at different distances x/D from the diffuser are shown; x is the coordinate along the jet axis, U is the velocity component along the jet axis, U_c is the velocity at the jet axis. The jet visualization system consists of laser and video camera. Light-reflecting glycerin particles of ~ 10 μm in diameter are generated at the aerosol generator and introduced to the flow. A segment of the jet is illuminated by the laser light sheet. The image is taken by the camera, whose optical axis is normal to the plane of the laser light sheet (figure 2b). Perturbations are introduced into the jet by a wire ring installing close to the orifice. The ring oscillates with specified amplitude and frequency, which is governed by a controller. Two rings, whose radii are equal to inner and outer inflection point locations, were used.

*Corresponding author. E-mail: gareev.lr@yandex.ru.

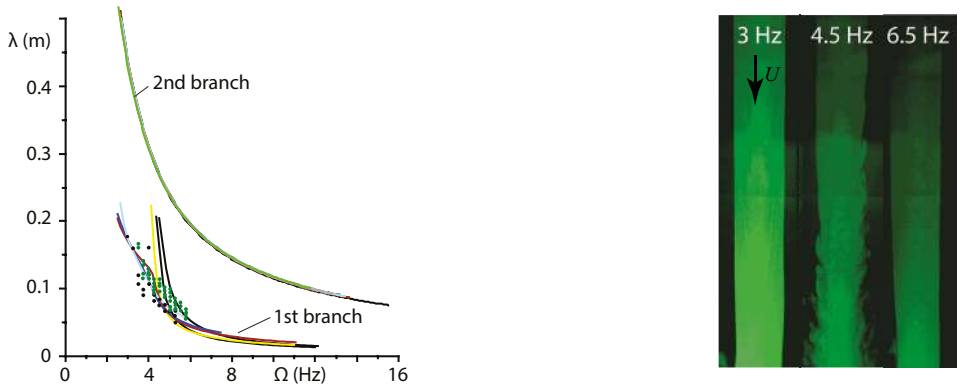

(a) (b)

Figure 2: (a) Theoretical (color curves) and experimental (points) wavelengths λ versus excitation frequency Ω. (b) Visualization of the jet for different values of the ring oscillation frequency.

Results

We study the perturbation growth in the laminar jet at the Reynolds number $Re = 5680$ (the velocity at the jet axis $U_c = 1.5$ m/s), for which the length of the laminar jet portion in the unperturbed condition is ~ 0.6 m. We aim to show that introduced perturbations with the frequencies from the range $4 - 6$ Hz (corresponding to the theoretical maximum growth rates) grow spatially and yield the maximum shortening of the laminar jet length, whereas, for the frequencies beyond this range the influence of the introduced perturbations on the laminar jet is not as essential.

Visualized flow patterns for various perturbation frequencies are shown in figure 2b. In the absence of oscillations the ring presence in the jet does not affect the laminar region length. The visualization shows that the shortest laminar portion of the jet occurs for the frequencies from the range $4 - 6$ Hz.

Theoretically and experimentally obtained wavelengths are compared in figure 2a for ring radius corresponding to the outer inflection point. Experimental points are close to theoretical curves, thus we may conclude that experimental values are in agreement with modal theory predictions. Experimentally measured growth rates are also in a good agreement with theory.

The analysis of the second mode, excited by a smaller ring is conducted by PIV. Measured wavelenghts are also close to the theoretical prediction.

CONCLUSIONS

An axisymmetric laminar jet stability is theoretically analyzed for the jet profile [6]. For the regime $Re = 5680$, two branches of growing perturbations exist, for both of them growth rates and wavelengths have been studied.

The influence of the perturbations produced by the oscillating ring on the laminar jet is experimentally investigated. It is shown that experimental wavelengths and growth rates of perturbations are in good agreement with linear stability theory predictions.

ACKNOWLEDGEMENTS

The work is supported by Russian Science Foundation (project No. 20-19-00404).

References

[1] A.V. Boiko, K.J.A. Westin, B.G.B. Klingmann, V.V. Kozlov and P.H. Alfredsson. Experiments in a boundary layer subjected to free stream turbulence. Part 2. The role of TS-waves in the transition process. *J. Fluid Mech.* **281**: 219-245, 1994.

[2] B. Eckhardt. Introduction. Turbulence transition in pipe flow: 125th anniversary of the publication of Reynolds paper. *Phil. Trans. R. Soc. A.* **367**: 449-455, 2009.

[3] H. K. Skramstad, G. B. Schubauer. Laminar-Boundary-Layer Oscillations and Transition on a Flat Plate. Technical report, 1948

[4] V.V. Kozlov and M.P. Ramazanov. An experimental investigation of the stability of Poiseuille flow. *Izv. Akad Nauk SSSR, Tech. Sci.* **8**: 45-48, 1981.

[5] M. Nishioka, S. Iida and Y. Ichikawa. An experimental investigation of the stability of plane Poiseuille flow. *J. Fluid Mech.* **72**: 731-751, 1975

[6] J. Zayko, S. Teplovodskii, A. Chicherina, V. Vedeneev and A. Reshmin. Formation of free round jets with long laminar regions at large Reynolds numbers. *Physics of Fluids* **30**: 043603, 2018

MODELING OF INSTABILITY WAVE PACKETS AND MACH WAVE RADIATION IN A SUPERSONIC JET

Yihong Fang*[1,2], Shu Meng[1]& Cheng Cheng[1]
[1]Department of Mechanics, School of Mechanical Engineering, Tianjin University, Tianjin, China
[2]State key Laboratory of Hydraulic Engineering Simulation and Safety, Tianjin University, Tianjin, China

Summary The modelling and simulation of wave packet and its Mach wave radiation are presented in this paper. It involves a wave packet of instability modes calculated by disturbance equation. And Mach wave radiation field is computed based on a matched-asymptotic-expansion. Reasonable predictions of the acoustic field can be made by present hybrid approach.

INTRODUCTION

The study of jet noise has a long history and received renewed interest in recent years, in particular for the aviation industry. Since the 1970s, the discover of coherent structures opens a way for analysis of the sound-producing mechanisms. Several previous theoretical researches have described that large-scale coherent structures constitute a dominant source of jet noise. Tam & Burton [1] [2] extended linear stability theory into the far field on relates sound to the growth and decay of instability waves in supersonic jet. More Recent work has focused attention on the nonlinear development of instability waves and more complex models, these coherent wave-packets structures were first employed by Avital et al. [3] and reviewed by Jordan & Colonius [4]. Additionally, Wu [5] regarded the nonlinear effects of supersonic instability waves on Mach wave radiation by using a matched asymptotic expansion combined with the multiple scale method, and accounted for the nonlinear spatial evolution of instability waves through nonlinear terms arising from the critical layer. Cheung & Lele [6] analysed a forced two-dimensional shear layer by linear and nonlinear PSE models. The influence of nonlinear mechanisms in sound generation has also been examined by Suponitsky et al. [7].

For predicting the acoustic far field, there are three techniques: directly, an equivalent source base on acoustic analogy, or Kirchhoff surface. But the latter two methods require some prior knowledge about far field sound source. The primary objective of current study is to develop a hybrid approach for analysis and prediction of acoustic radiation process in supersonic jet. In this effort, the nonlinear disturbance equation is employed to simulate the evolution of instability wave packets. Afterwards, we extent the theoretical method that has been previously explored by Wu [5] to compute the associated Mach wave radiation. Results from our current calculations are compared against experiment data and similar DNS calculations for accuracy.

COMPUTATIONAL TECHNIQUE

In this section we provide a brief description of the approach. Conceptually, the domain is divided into two regions: a near-field and a far-field. In near-field, the hydrodynamic motions are dominant, while acoustic propagation has a predominant effect in far-field. An axisymmetric jet is computed from experimental fitting function in [1], for Reynolds number $Re = 70000$, Mach number $Ma = 2.1$, Prandtl number $Pr = 1$. In addition, the steady base flow is artificially excited by particular instability waves, which obtained by linear stability problem defined by Orr-Sommerfeld equation.

$$\phi(x,r,t) = \hat{\phi}(r)e^{i(\alpha x-\omega t)} + c.c \tag{1}$$

The behaviour of the instability waves can be determined through the direct computation of nonlinear, compressible, axisymmetric disturbance equations (2) for the density ρ, velocities u_i, temperature T, and pressure p. The code was developed by our group. Details regarding the simulations are omitted for space reason.

$$\frac{\partial U'}{\partial t}+\frac{\partial E'}{\partial x}+\frac{\partial rG'}{r\partial r}=\frac{\partial E_v'}{\partial x}+\frac{\partial rG_v'}{r\partial r}+k \tag{2}$$

The near-acoustic field is an overlap region, here, the local solution of wave equation matched to the inner hydrodynamic pressure fluctuations, and to the outer, behaviour of propagating acoustic. By theoretical analysing, the radiation process is clear. While a Mach wave front propagates along the characteristics line ζ=constant, its acoustic energy propagates along the other line ξ=constant. For wave packets consist of a train of instability waves, we introduce an extrapolation of integral suggested by Wu [5]. The acoustic pressure in far-field can be determined by the following formula:

$$\hat{p}_0\left(\bar{\xi},\tilde{\omega},\tilde{r}\right)=\frac{e^{-\pi i/4}}{\tilde{r}}\left(\frac{\alpha q^3}{2\pi M_a^2c^2}\right)^{1/2}\ell_\infty\hat{Q}\left(\bar{\xi},\tilde{\omega},\tilde{r}\right)\exp\left\{-\frac{iM_a^2\tilde{\omega}^2\tilde{r}}{2\alpha q^3}\right\}\int_{-\infty}^{\infty}A(\zeta)\exp\left\{\frac{\alpha q^3}{2M_a^2c^2\tilde{r}}\left(\bar{\xi}-\zeta\right)^2\right\}d\zeta \tag{3}$$

*Corresponding author. E-mail: yhfang@tju.edu.cn.

RESULTS AND DISCUSSION

The numerical result of pressure contour at a certain frequency was displayed in figure 1. It can be seen obviously that Mach wave radiation (acoustic energy) is highly directivity along a fixed line. One can trace the line back to a location where the "sound emission", which coincides approximately to the saturation of peak frequency. Figure 2 to figure 4 show the results of wave packets with *St=0.3~0.5*, for natural jet and excited jet (excited at *St=0.4*). Comparing with relevant experimental data [8], results are in a good degree of quantitative agreement.

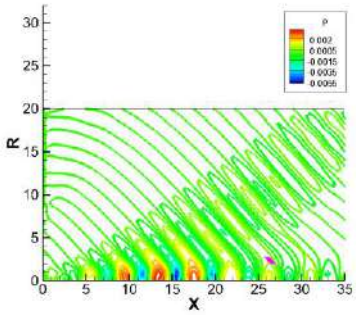

Figure 1. Pressure contour of Mach waves in near-field.

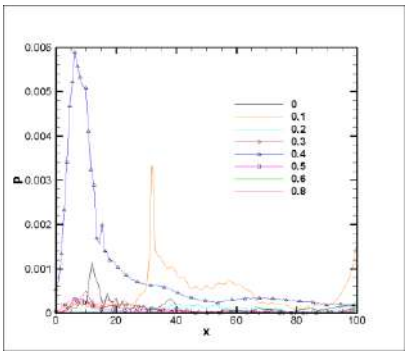

Figure 2. Pressure fluctuations for excited jet.

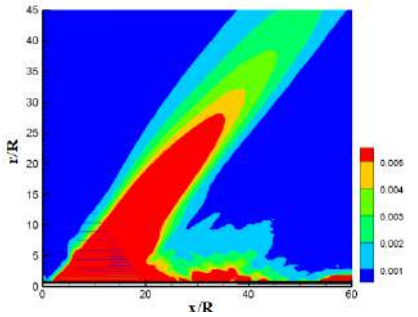

Figure 3. The time-averaged acoustic intensity for excited jet.

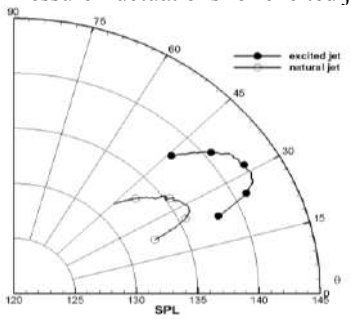

Figure 4. Overall sound-pressure level directivity.

Figure 2 demonstrated that instability with frequencies around *St=0.4* grow initially, then nonlinear effects become apparent. Afterwards the overall fluctuation amplitude attains a saturated situation and spectral content shifts to lower frequencies. This can also be seen in figure 3. Even though spectral are broaden, the downstream lobe pattern is quite directivity. Directivity patterns of noise in downstream region for both excited and natural jet are shown in figure 4. There is a considerable increase in the SPL with excitation for a given frequency, but a very little change in the directivity of radiation between natural and excited jets. This implies that two cases may have same mechanism responsible for noise generation path.

It can be note that present approach can successfully predict the features of Mach wave radiation associated with instability wave packets, quantitatively as well as qualitatively.

A more complete analysis of wave packets and their Mach wave radiations will be presented at the Congress.

ACKNOWLEDGEMENTS

This work is being supported by National Natural Science Foundation of China (Grant 91852110) and State key Laboratory of Hydraulic Engineering Simulation and Safety (HESS-1812).

References

[1] Tam, C. K. W.; Burton, D. E.: Sound generated by instability waves of supersonic flows. Part 1: Two-dimensional mixing layers. J. Fluids Mech. 138:249-271, 1984. Part 2: Axisymmetric jets. J. Fluids Mech. 138: 273-295, 1984.

[2] Tam, C. K. W. Supersonic jet noise. Annu. Rev. Fluid Mech. 27, 17–43,1995.

[3] Avital, E. J., Sandham, N. D. & Luo, K. H. Mach wave radiations by mixing layers. Part I: Analysis of the sound field. Theor. Comput. Fluid Dyn. 12 (2), 73–90,1998

[4] Jordan, P., Colonius, T.: Wave packets and turbulent jet noise. Annu. Rev. Fluid Mech. 45, 173-195, 2013.

[5] Wu, X.: Mach wave radiation of nonlinear evolving supersonic instability modes in shear layers. J. Fluids Mech. 523: 289-313, 2005.

[6] Cheung LC, Lele SK. Linear and nonlinear processes in two-dimensional mixing layer dynamics and sound radiation. J. Fluid Mech. 625:321–51, 2009.

[7] Suponitsky V, Sandham N, Morfey C. Linear and nonlinear mechanisms of sound radiation by instability waves in subsonic jets. J. Fluid Mech. 658:509–38, 2010.

[8] Troutt T R, McLaughlin D K., Experiments on the flow and acoustic properties of a moderate-Reynolds-number supersonic jet. J. Fluid Mech. 116:123-156, 1982.

OBLIQUE SOLITARY WAVES IN CHANNEL FLOW

Yohann Duguet*[1], Chaitanya Paranjape[2], and Björn Hof[2]
[1]LIMSI, University Paris-Saclay, Orsay, France
[2]IST Austria, Klosterneuburg, Austria

Summary In subcritical fluid flows such as channels and pipes, the way turbulence manifests itself at the lowest possible flow rates has been a long-standing question. It appears possible to sustain turbulent flow in experiments and numerics at much lower values of the Reynolds number Re than previously thought. The flow takes the form of isolated stripes of turbulence oblique with respect to the flow. The angle of these stripes saturates at 45° as Re is decreased towards the critical point of the system. This talk addresses the self-sustaining mechanisms for such complex flows by identifying relative equilibrium and periodic orbit solutions of the full Navier-Stokes equations with analogous properties.

INTRODUCTION

The nature of the simplest non-trivial flow occuring in a channel as the Reynolds number is decreased has remained mysterious for decades. Recently it was established numerically that it consists of isolated stripes of turbulence oblique with respect to the flow, with an angle close to 45° [1, 2]. Equally recently this numerical prediction has been validated in the experimental set-up developed at IST Austria using localised disturbance applied over a finite time (see fig 1).

Figure 1: Experimental realisation of growing turbulent stripe at Re=750 (flow from left to right).

Since the laminar Poiseuille flow is linearly stable, it is desirable to understand which mechanisms cooperate to sustain such non-trivial flow structures. Tollmien-Schlichting waves predicted by linear stability theory at higher flow rates have a radically different spatial structure and are no relevant candidates to explain the growth and nonlinear saturation of oblique turbulent stripes.

NOVEL INVARIANT SOLUTIONS

The appropriate bifurcation scenario rationalising the appearance and sustenance of such oblique turbulent structures has not been clarified yet. We expect it to start from a branch of nonlinear solutions with the following properties : a) spatial localization, b) an oblique orientation with respect to the mean flow, with angles comparable to experimental observations, c) composed of quasi-streamwise vortices and streaks not aligned with the interface. In the present study, we demonstrate numerically the existence of unstable travelling waves satisfying all the above properties at once. These travelling waves form a large family of nonlinear states parametrized by two wavelengths and by their angle with respect to the streamwise direction.

We use a deterministic approach in terms of unstable solutions of the Navier-Stokes equations in a slanted periodic domain, where the angle becomes one of the control parameters [3]. Edge states in the form of localised travelling waves, and their subsequent bifurcations, act as a scaffold for the turbulent dynamics down to very low values of Re consistent with the experimental thresholds. Numerical simulations are based on the freely available code *channelflow.org*. Invariant solutions are identified numerically using edge tracking coupled with a Newton-Krylov method and arc-length continuation. A complete parametric study is performed including their stability, the investigation of their large-scale flow, and the robustness to changes of numerical domain. The solutions display robust spatial localisation as the width of the numerical domain is increased, which demonstrates their relevance to the solitary states identified in experiments. All solutions emerge in saddle-node bifurcations at values of Re lower than the previously found solutions. Relative periodic orbit solutions bifurcating from each branch of travellling waves have also been computed. For each of the solutions found, a large-scale is present parallel to the interface [4]. It coexists with a stripe core dominated by a regular array of quasi-streamwise vortices streaks. Outside the stripe core the streamwise orientation streaks is deviated by the large-scale flow.

*Corresponding author. E-mail: duguet@limsi.fr

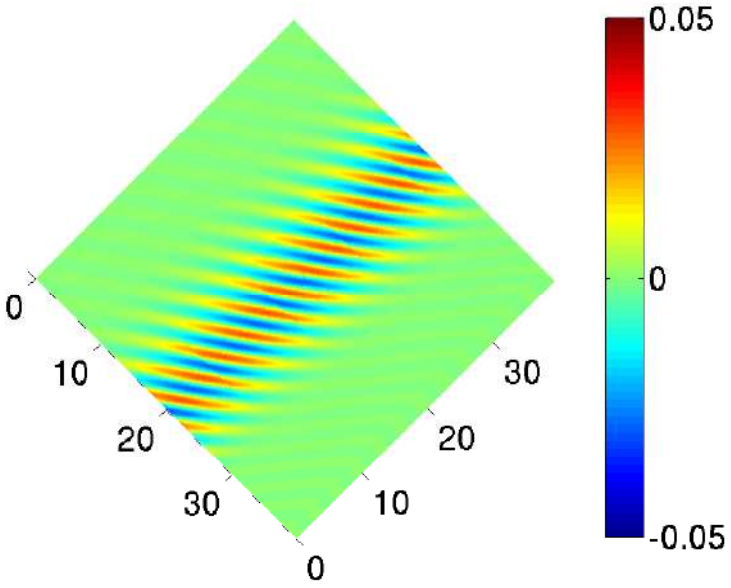

Figure 2: Nonlinear travelling wave solution found with an orientation of 45° for Re=720 (flow from left to right).

CONCLUSIONS

We have presented new families of nonlinear travelling wave solutions of channel flow featuring spatial localization, oblique orientation with respect to the mean flow direction, and streamwise vortices and streaks [5]. All the solutions reported here are linearly unstable although the number of unstable directions is generally very low, ranging from one for edge states up to six for upper branch solutions near their onset. The multitude of possible angles displayed by turbulent stripes falls within the range of angle values where the travelling waves and their bifurcated states exist. A natural question that arises is whether the range of angles of the TWs bears a direct relation to the selection process of stripe angles in turbulent flows.

References

[1] Xiong, X. et al., Turbulent bands in plane Poiseuille flow at moderate Reynolds numbers. . *Phys. Fluids* 27, **4**: 041702, 2015.
[2] P. Kashyap, Y. Duguet, O. Dauchot, Flow statistics in the transitional regime of plane channel flow, *Entropy* 22, **9**, 1001, 2020.
[3] Tuckerman, L. S. et al.. Turbulent-laminar patterns in plane Poiseuille flow. *Phys. Fluids* 26, **11**: 114103, 2014.
[4] Duguet, Y. and Schlatter, P.. Oblique laminar-turbulent interfaces in plane shear flows. *Phys. Rev. Lett.* **110**: 034502, 2013.
[5] Paranjape, C., Duguet, Y. and Hof, B.. Oblique stripe solutions of channel flow. *J. Fluid Mech.* **897**: 2020.

LOCAL RECEPTIVITY THEORY FOR GENERATION OF INVISCID MODES IN SUPERSONIC/HYPERSONIC BOUNDARY LAYERS

Ming Dong*[1], Yinhui Liu[1], and Xuesong Wu[2]
[1]Department of Mechanics, Tianjin University, Tianjin, China
[2]Department of Mathematics, Imperial College London, UK

Summary This paper studies the receptivity of inviscid first and second modes in a super/hypersonic boundary layer due to the interaction between a freestream acoustic wave and a small isolated surface roughness element. A large-Reynolds-number asymptotic theory is developed, which reveals the key process of the local receptivity. Through parametric study, the dependence of the receptivity efficiency on the relevant parameters is provided. The numerical results are compared with the finite-Reynolds-number calculation and direct numerical simulation, and favourable agreement is achieved for sufficiently large Reynolds numbers. An improved asymptotic theory is further developed to render high-accuracy predictions at moderate Reynolds numbers.

PHYSICAL MODEL AND ASYMPTOTIC SCALING

As is sketched in Fig. 1-(a), we consider a thin flat plate inserting into a supersonic uniform perfect-gas flow, and an isolated roughness element, with a height much lower than the boundary-layer thickness, is located at a distance L downstream of the leading edge. We introduce a sound wave in the freestream, which propagates at an incident angle θ, and simultaneously, a reflection occurs due to the presence of the plate. We define the characteristic length as the boundary-layer thickness at the roughness $\delta = \sqrt{\nu_\infty L/U_\infty}$, where the subscript ∞ denotes the quantities of the oncoming flow, and U and ν represent the velocity and the kinetic viscosity, respectively. The oncoming Mach number M and the Reynolds number R are defined as $M = u_\infty/a_\infty$, and $R = U_\infty\delta/\nu_\infty$, respectively, with a being the sound speed. We are interested in the supersonic regime with $M > 1$, and assume $R \gg 1$.

The roughness height h^* is taken to be of $O(R^{-1/3}\delta)$ or smaller, then the mean-flow distortion is governed by a double-deck structure, consisting of the main layer with $O(\delta)$ width and a much thinner wall layer in an $O(R^{-1/3}\delta)$ vicinity of the wall; see regions I and II of Fig. 1-(b), respectively. A direct consequence is that the mean-flow distortion in the main layer is of $O(hR^{-1/3})$, where $h \equiv h^*/\delta$. Both the freestream acoustic waves and the inviscid Mack modes have phase speeds and frequencies of $O(U_\infty)$ and $O(U_\infty/\delta)$, respectively, and their wavelengths are comparable with the local boundary-layer thickness δ. Therefore, in order to satisfy the 'resonance condition', we take the roughness width to be of $O(\delta)$. Additionally, a thinner Stokes layer driven by the inviscid acoustic wave appears in the $O(R^{-1/2}\delta)$ vicinity of the wall, shown as region III in Fig. 1-(b), which also acts as an active layer in the receptivity process.

Through scaling analysis, the first two orders of receptivity are revealed. (i) The leading-order receptivity is caused by the deformation of the sound-generated Stokes layer by the curved wall. For an acoustic wave with an infinitesimal amplitude $\mathcal{E}_a \ll 1$, the Stokes-layer streamwise velocity near the roughness is amplified to $O(\mathcal{E}_a hR^{1/2})$, in order to satisfy the no-slip condition. The continuity equation indicates that the associated transverse velocity is $O(\mathcal{E}_a h)$, and generates an unsteady outflux of the same size to the main layer. Such a forcing on the main-layer Rayleigh equation leads to the excitation of an inviscid Mack mode with amplitude of $O(\mathcal{E}_a h)$. This process is in principle the same as an canonical receptivity problem induced by an unsteady blowing and suction. (ii) The second-order receptivity is due to the interaction between the acoustic signature and the roughness-induced mean-flow distortion. The roughness induces an $O(R^{-1/3}h)$ steady perturbation in the main layer, where this perturbation interacts with the $O(\mathcal{E}_a)$ acoustic signature, producing a volumetric unsteady forcing of $O(\mathcal{E}_a R^{-1/3}h)$, and simultaneously, an unsteady outflux of the same size is driven from the viscous wall layer.

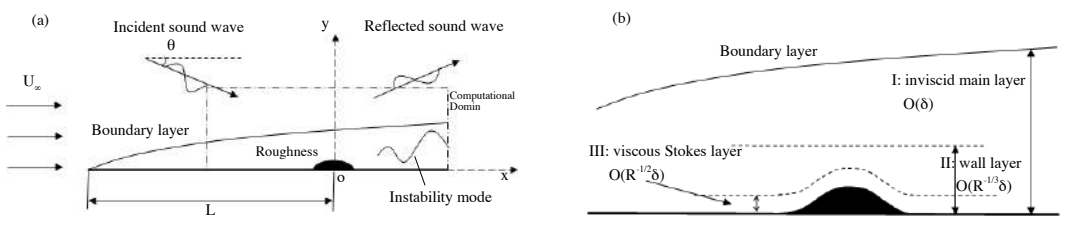

Figure 1: (a): Sketch of the physical model; (b): the asymptotic structure of the receptivity problem.

*Corresponding author. E-mail: dongming@tju.edu.cn.

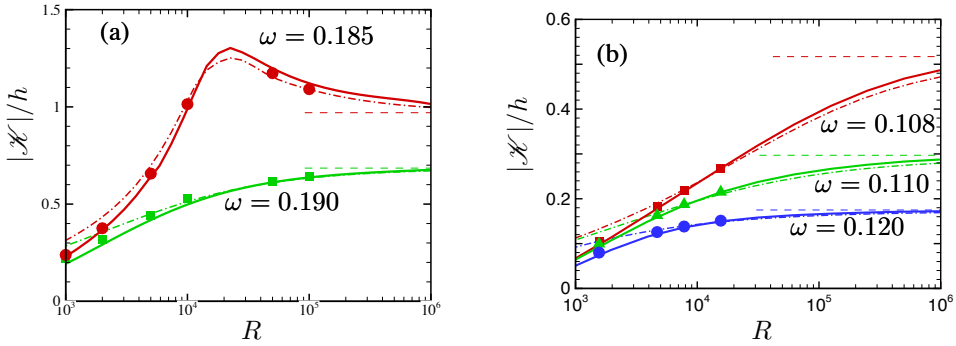

Figure 2: Comparison of the receptivity coefficient to planar fast acoustic waves with wave angle $\theta = 45°$ for $M = 4.5$ (a) and 5.92 (b). Solid lines: finite-R calculations; dashed lines: asymptotic predictions; dot-dashed lines: improved asymptotic predictions; symbols: DNS results.

A LARGE-REYNOLDS-NUMBER THEORY AND ITS IMPROVED VERSION

In the main layer, the flow field ϕ (where ϕ represents any flow quantity) is decomposed as a base flow ϕ_B, a mean-flow distortion $h\bar{\phi}$, an acoustic signature $\mathcal{E}_a\hat{\phi}_a$ and the excited perturbation $h\mathcal{E}_a(\tilde{\phi}_0 + R^{-1/3}\tilde{\phi}_1 + \cdots)$,

$$\phi = \phi_B + h\bar{\phi} + \mathcal{E}_a\hat{\phi}_a + h\mathcal{E}_a(\tilde{\phi}_0 + R^{-1/3}\tilde{\phi}_1 + \cdots). \tag{1}$$

The Fourier transformed perturbations $\hat{\phi}_{0,1}$ are governed by $\mathbf{L}\hat{\phi}_0 = 0$, and $\mathbf{L}\hat{\phi}_1 = \mathbf{F}$, where $\mathbf{L}$ is the Rayleigh operator and $\mathbf{F}$ is the volumetric forcing in the second-order receptivity. Both equations satisfy an attenuation condition at the far field and an unsteady outflux condition at the wall. The Rayleigh operator poles when the frequency and wavenumbers satisfy the dispersion relation of the eigenmodes, and the receptivity coefficient $\mathscr{K}$ is obtained by evaluating the residual contributions from the poles. Such a treatment is the same as that in the finite-R theory[1].

Since the Rayleigh equation is less accurate in a moderate Reynolds number due to the viscous effect, we also develop an improved large-R asymptotic theory, which takes into account the $O(R^{-1/2})$ correction induced by the Stokes layer to the inviscid perturbation in the main layer. In the improved theory, an $O(R^{-1/2})$ term obtained by analysing the transverse velocity of the flat Stokes layer is added in the wall boundary condition of the Rayleigh equation, which predicts a more accurate dispersion relation of the eigenmodes as compared to the Orr-Sommerfeld equation.

NUMERICAL RESULTS

For case studies, we select two typical oncoming Mach numbers, i.e. $M = 4.5$ and 5.92. A systematical parametric study is carried out for the excitation of both the first and second modes by both the freestream fast and slow acoustic waves, and the dependence of the receptivity efficiency on the relevant parameters is provided. Fig. 2 compares the receptivity efficiency to a typical incident acoustic wave obtained by the asymptotic theory (dashed lines), finite-R calculation[1] (solid lines) and direct numerical simulation[2] (symbols). The finite-R calculations agree with the DNS results almost precisely at moderate Reynolds numbers, while in the large-R limit, they approach the large-R asymptotic predictions. Such a phenomenon indicates the consistency of the three approaches. One may criticize the accuracy of the asymptotic theory although it can reveal the intrinsic receptivity mechanism. However, if we improve the asymptotic theory by taking into account the $O(R^{-1/2})$ viscous correction (dot-dashed lines), then the predictions can agree with the finite-R calculations even when R is a few thousands.

CONCLUSIONS

This paper develops a large-R asymptotic theory to predict the receptivity efficiency of supersonic/hypersonic inviscid modes due to roughness-sound interaction. The key receptivity process is clearly demonstrated. Additionally, an improved asymptotic theory that accommodates the $O(R^{-1/2})$ correction from the viscous Stokes layer is developed, which can yield a more accurate prediction on receptivity in comparison with the finite-R theory even when R is a few thousands.

References

[1] Choudhari M., Streett, C. L. A finite Reynolds-number approach for the prediction of boundary-layer recepvitity in localized regions. *Phys. Fluids A* **4**: 2495, 1992.

[2] Liu, Y., Dong, M., Wu, X. Generation of first Mack modes in supersonic boundary layers by slow acoustic waves interacting with streamwise isolated wall roughness. *J. Fluid Mech.*, accepted.

INSTABILITIES AND INTERMITTENCY IN A CUBIC SHEAR-DRIVEN CAVITY

Pierre-Emmanuel des Boscs*[1] and Hendrik C. Kuhlmann [1]
[1]Institute of Fluid Dynamics and Heat Transfer, TU Wien, Vienna, Austria

Summary The incompressible fluid flow confined in a cubic box, driven at the top surface by a constant shear stress is investigated using a spectral-element method. The steady basic flow loses its reflection symmetry through a pitchfork bifurcation at $\mathrm{Re}_P = 53478$, where two steady flows emerge which are antisymmetric to each other. Both asymmetric flows become linearly unstable to oscillatory perturbations at $\mathrm{Re}_H = 55720$, giving rise to limit cycles. At $\mathrm{Re} = 57300$, the limit cycles are destabilized by nonlinear bursts, allowing the system to visit both limit cycles. As in the lid-driven cavity, the transition to turbulence follows a Pomeau–Manneville scenario.

INTRODUCTION

Flows in cavities are of particular interest in fluid mechanics. For instance, the *lid-driven cavity* (LDC) serves as a canonical benchmark for CFD codes, exhibits complex flow patterns, and shows a non-trivial dynamical evolution to turbulence. The transition to chaos in the cubic LDC arises through a slightly subcritical Hopf bifurcation [1] followed by nonlinear bursts [2]. The limit cycles play an important role in the nonlinear dynamics [3] which was further explored considering flow symmetries and finding a Neimark–Sacker bifurcation [4].

The *shear-driven cavity* (SDC) in which a constant stress is prescribed on one boundary, instead of a constant velocity in the LDC, has received much less attention. The SDC serves as an approximation to the flow over an open [5] or liquid-filled cavity [6]. It is also equivalent to a thermocapillary flow in an open differentially-heated cube in the limit of a small Prandtl number, which has some application in open-boat crystal growth. Here we investigate the structure and the dynamics of the flow in the SDC as the shear stress is increased. Of interest are differences and similarities of the scenario with the one in the lid-driven cavity (LDC).

PROBLEM FORMULATION AND NUMERICAL METHODS

We consider the Navier-Stokes equations for an incompressible fluid of density ρ and kinematic viscosity ν confined in a cubic cavity of edge length L. The flow is driven by a constant shear stress τ imposed on one side of the cube and parallel to the edge. The only dimensionless parameter is the Reynolds number $\mathrm{Re} = \tau L^2/\rho\nu^2$ in which the velocity scale $\tau L/\rho\nu$ is derived from τ and the viscous time scale L^2/ν.

The flow is computed using the spectral-element code `Nek5000`. It is based on a $\mathbb{P}_N/\mathbb{P}_{N-2}$ formulation with the polynomial order $N = 6$. The tensor-product mesh is compressed towards all boundaries to be able to resolve the boundary layers on the solid walls and the free surface where the stresses are high. To obtain the basic flow the `BoostConv` algorithm proposed by [7] is used. The implementation of latter algorithm does not require major adaptations of the transient solver as it modifies the flow variables only at some specific time steps. `BoostConv` is typically faster than a selective-frequency-damping approach. To solve the eigenvalue problem which arises in the linear stability analysis the Arnoldi method is employed, using a time-marching technique.

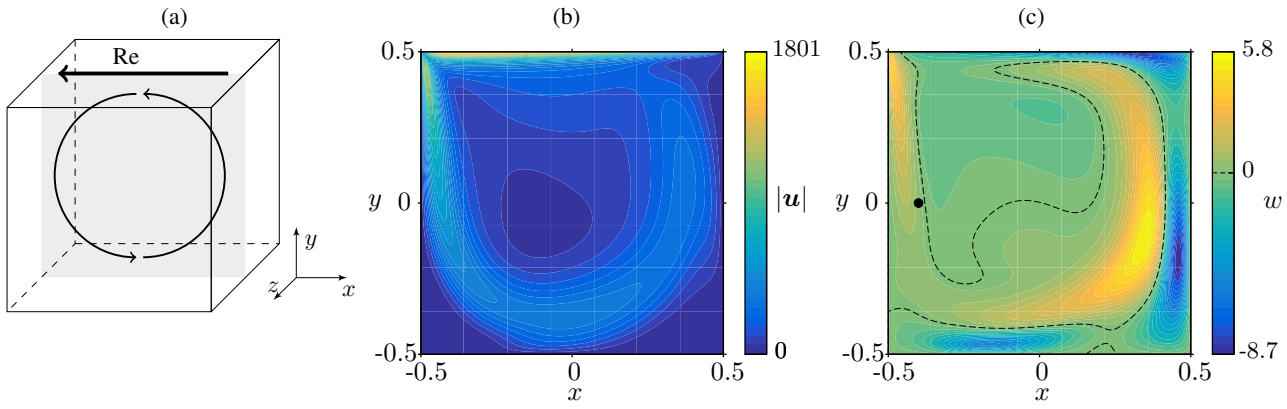

Figure 1: (a) Sketch of the setup. The direction of the shear stress is indicated by the top arrow. The symmetry plane is shown in gray. (b) Velocity magnitude of the basic flow in the symmetry plane $z = 0$ for $\mathrm{Re} = 54000$. (c) Spanwise velocity component w in the symmetry plane $z = 0$ for $\mathrm{Re} = 54000$. The black circle (•) indicates the monitoring point $\boldsymbol{x}_p$ used in fig. 2(a).

*Corresponding author. E-mail: pierre-emmanuel.boscs@tuwien.ac.at

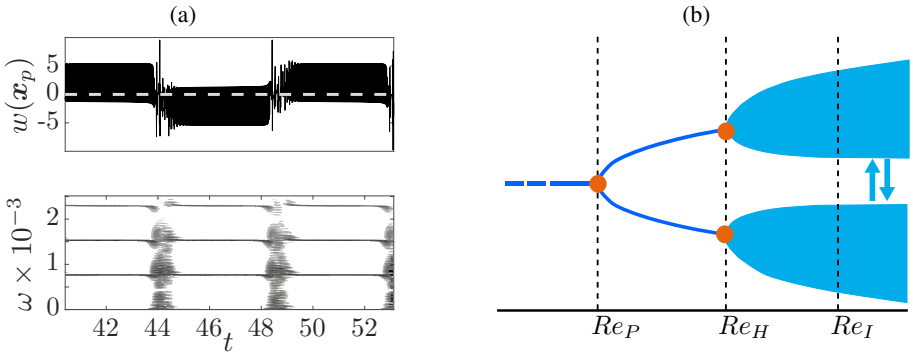

Figure 2: (a) Spanwise velocity $w(\boldsymbol{x}_p)$ (top) at the monitoring point from fig. 1(b) for Re $= 57300$ and sliding FFT (bottom) for a time interval $T = 0.6$. (b) Sketch of the transition to a chaotic regime.

RESULTS AND DISCUSSION

Bifurcation scenario

As the Reynolds number is increased a pitchfork bifurcation arises at $\mathrm{Re}_P = 53478$ and the flow loses its reflection symmetry with respect to $z = 0$. Figure 1(c) shows the distribution of the spanwise velocity component of one of the steady asymmetric solution branches in the plane $z = 0$ at a supercritical Reynolds number. As a measure for the symmetry breaking we consider the asymmetry parameter $S = \int_V |\boldsymbol{u} - \mathcal{S}(\boldsymbol{u})|^2 \mathrm{d}V$, where $\mathcal{S} : (u, v, w)(x, y, z) = (u, v, -w)(x, y, -z)$ is the symmetry map. We find $S^2 \sim \mathrm{Re} - \mathrm{Re}_P$ (not shown), which is indicative of a supercritical pitchfork bifurcation. A linear stability analysis of the basic flow confirms the above results of the above numerical simulations. The critical mode is very similar to the deviation of the slightly supercritical finite-amplitude flow from the symmetric flow. The critical mode consists of a single steady Taylor–Görtler vortex, centered on the symmetry plane, whose velocity magnitude takes a maximum close to the downstream bottom corner of the cavity. The two critical modes are distinguished by the sense of rotation of the Taylor–Görtler vortex.

Further increasing the Reynolds number the translation invariance in time is broken. For $\mathrm{Re}_H \geq 55720$ small deviations from any of the steady asymmetric flow states start growing until the amplitude of oscillation saturates, defining two limit cycles. These limit cycles are related to each other *via* the operation $\mathcal{S}$. The peak-to-peak amplitude $P[S(t)]$ of the time-dependent asymmetry parameter $S(t)$ is found to grow with the square root from the second critical point, i.e. $P[S(t)]^2 \sim \mathrm{Re} - \mathrm{Re}_H$, indicating a Hopf bifurcation. The eigenmode consists of series of Taylor-Görtler vortices which are advected downstream while slowly drifting in the spanwise direction. The latter effect is caused by the steady symmetry-broken flow. The two limit cycles towards which the system can evolve are stable at least up to $\mathrm{Re}_I = 56200$. For $\mathrm{Re} > \mathrm{Re}_I$ intermittency can set in.

For $\mathrm{Re} > \mathrm{Re}_I$ bursting events can be observed even though the system sits on a limit cycle for a long time (several viscous time units). This is demonstrated in fig. 2(a). The bursts arising at $t \approx 44$ and $t \approx 48$ enable the system to visit wide regions of the phase space and thus allow the system to switch between the two limit cycles. The bursts are characterized by a lower frequency than the fundamental frequency of the limit cycles (fig. 2), suggesting the existence of one or a couple of additional low-frequency limit cycles.

Conclusions

Similar to the cubic LDC the transition in the SDC follows a Pomeau–Manneville scenario where intermittent bursts progressively destabilize the system. However, the behavior of the system is significantly different: In the LDC the flow undergoes subcritical Hopf and Neimark–Sacker Bifurcations involving the limit cycles of different nature (one is antisymmetric, the other is not). In the SDC the flow is progressively destabilized by a sequence of supercritical pitchfork and Hopf bifurcations which are both antisymmetric to each other.

References

[1] Feldman Yu., Gelfgat A. Yu. Oscillatory Instability of a Three-dimensional Lid-driven Flow in a Cube. *Phys. Fluids*. **22(9)**:093602, 2010.
[2] Kuhlmann H.C., Albensoeder S. Stability of the Steady Three-dimensional Lid-driven Flow in a Cube and the Supercritical Flow Dynamics. *Phys. Fluids*. **26(2)**:024104, 2014.
[3] Loiseau J-Ch., Robinet J-Ch., Leriche E. Intermittency and Transition to Chaos in the Cubical Lid-driven Cavity Flow. *Fluid Dyn. Res.* **48(6)**:061421, 2016.
[4] Lopez J. M., Welfert B.D., Wu. K., Yalim. J. Transition to Complex Dynamics in the Cubic Lid-driven Cavity. *Phys. Rev. Fluids* **2(7)**074401, 2017.
[5] Yoshida T., Watanabe T. Numerical Simulation of Flow over an Open Cavity with Self-Sustained Oscillation Mode Switching . *Open Jour. Fluid. Dyn.***6**: 361–370,2016.
[6] Kalaev V. V. Liquid flow in a cubic cavity generated by gas motion along the free surface. *Intl Jour. Heat Mass Transfer*. **55**:5214–5221, 2012.
[7] Citro, V., Luchini P., Giannetti F., Auteri F. Efficient Stabilitization and Acceleration of Numerical Simulation of Fluid Flows by Residual Recombination. *J. Comp. Phys.* **344**:234–246, 2017

EXPERIMENTAL CONTROL OF TOLLMIEN-SCHLICHTINGWAVES USING PRESSURE SENSORS AND PLASMA ACTUATION

Pedro P.C.B. Brito*[1], Pierluigi Morra[2], André V.G. Cavalieri[1], Thiago B. Araújo[1], Ardeshir Hanifi[2], and Dan Henningson[2]
[1]Aerodynamics Department, Instituto Tecnológico de Aeronáutica (ITA), São José dos Campos, Brazil
[2]Linné FLOW Centre, KTH Royal Institute of Technology, 10044 Stockholm, Sweden

Summary An IFFC (*Inverse Feedforward Control*) technique was applied to the boundary layer around a NACA 0008 airfoil at zero angle of attack aiming to delay the transition to turbulence by cancelling Tollmien-Schlichting (TS) waves. Experiments were carried out in an open-circuit wind tunnel. Microphones were used as sensors instead of hot-wires, which is an affordable option, especially for 3D disturbances requiring a higher number of sensors, and the actuation was performed with modulated plasma. Different penalizations were applied to the control law to minimize spurious actuation signals caused by zeros of the transfer functions. The results show that closed-loop control leads to attenuation of TS-wave spectra of about one order of magnitude, showing the good performance of IFFC with the present choice of sensors and actuators.

INTRODUCTION

This work focus on the delay of transition to turbulence in boundary layers due to its significant impact in the aerodynamics area. The transition delay means a reduction of the friction coefficient, which is responsible for more than half of the total drag on aircraft in cruise flight (Schrauf, 2005), therefore, the advances in transition delay represent a potential way for improving the fuel consumption on aircraft.

The control technique for transition delay tested here is a first try of the Inverse Feedforward Control (IFFC) proposed by Sasaki et al. (2018), which is used to cancel the Tollmien-Schlichting (TS) waves by taking advantage of its linearity and acting via destructive interference.

The control strategy of the IFFC is based on the obtention of the transfer functions between the inputs d (disturbance) and u (actuation) and two sensors y and z, which leads to the obtention of the control kernels (K), which depends on the open-loop transfer function G_{yz} and the actuation transfer function G_{uz}. The former can be obtained with stochastic excitation of disturbances d, while the latter is taken with white-noise actuation. Such transfer functions do not require calibration of sensors or determination of detailed actuator properties, as their intrinsic properties may be absorbed in the determined amplitudes and phases. The control is performed with a superposition of open-loop operation with the actuation (u) to cancel the output (z). The downstream output can be written in the frequency domain as

$$Z(\omega) = [G_{yz} + K(\omega)G_{uz}(\omega)]Y(\omega) \tag{1}$$

and the actuation signal in the frequency domain is taken as $U(\omega) = K(\omega)Y(\omega)$.

The control law is thus amenable to experimental applications. This is attempted here, with a plasma actuator and a pair of flush-mointed microphones. The latter replace hot wires often used in transition studies, and offer an affordable option for sensing TS waves. However, microphones are also sensitive to other disturbances, such as acoustic waves, and an objective of this study is to determine their applicability to transition control.

EXPERIMENTAL SETUP

Experiments were carried at Instituto Tecnológico de Aeronáutica (ITA) at the Kwei Lien Feng laboratory in an open-circuit wind tunnel. The test section has 4.0m x 1.28m x 1.0m and the level of turbulence is less than 0.1%. The experiments were performed on a NACA 0008 airfoil for a Reynolds number of $5.7{\cdot}10^5$. The wing was made of composite materials and had a plexiglass plate mounted at the center to allow easy assembling of different sensors and actuators. A slit situated at $x/c = 0.1$ was connected, with 37 tubes of equal length, to a 200W loudspeaker outside the wind tunnel, which was used to trigger the TS waves. Figure 1 shows the model placed in the test section.

The primary sensors used in the experiment at the wall of the wing were microphones, instead of hot wires. The microphones had a diameter of 1/4", and the purpose of using them was to prove their capability of behaving well in boundary layer transition control experiments. The advantages of using them rely on the fact that they are less intrusive than typical hot-wires due to the fact of being placed inside and tangent to the wall. Perhaps more importantly, electret microphones have a very low cost, which makes them suitable for flight test campaigns and situations were a large number of sensors need to be placed.

A Minipuls 2.1 system, manufactured by GBS Elektronik®, was used as the high voltage source to generate plasma for actuation. The system generates AC voltage up to 20kV (Vpp) with an operational frequency range of 5-20 kHz. The

*Corresponding author. E-mail: pedropcb@ita.br.

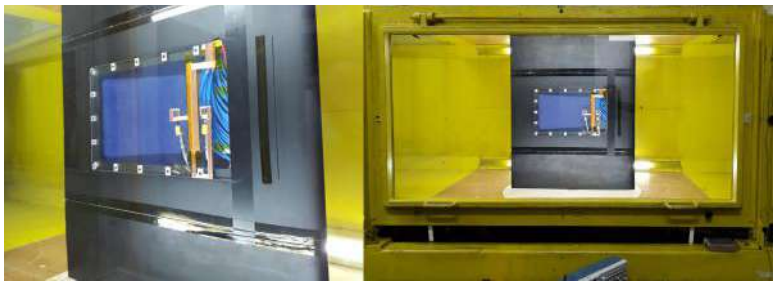

Figure 1: Zoom view of the wing (left) and side view of the test section with the loudspeaker on its top (right).

system provided a potential difference around 10kV at the dielectric (plexiglass plate) throughout two thin strips of copper that worked as electrodes along the span of the wing, so that plasma could be generated.

Acquisition and control were carried out usind a dSpace system, where the control law was implemented in real time. The actuation signal was used as an amplitude modulation for plasma excitation, which is felt in the flow as a fluctuating body force.

RESULTS

The results for the attenuation of the TS waves using closed-loop control are summarized in Figure 2, where the PSD of the signals of the z sensor show attenuation of one order of magnitude when a penalization R = 200 is applied.

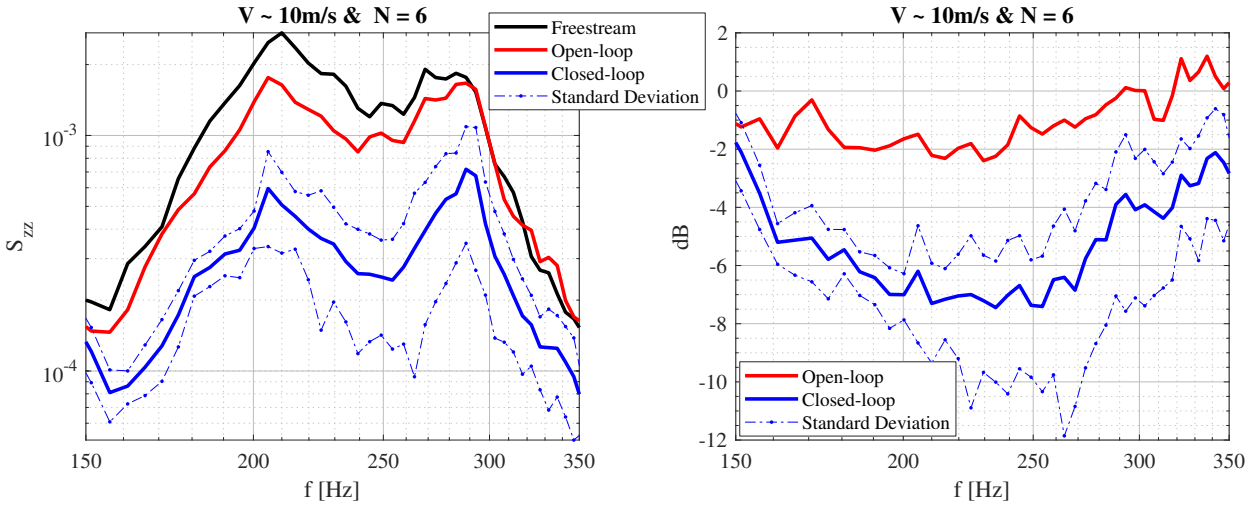

Figure 2: PSD signal for z sensor (left) and attenuation in dB (right)

In Figure 2, six experimental runs were carried out, and the full lines represent the mean value for the whole frequency range. A considerable standard deviation is noticed around the closed-loop data due to the free-stream velocity fluctuations ($\pm 0.5 m/s$) at the open-circuit wind tunnel. Therefore, most of the time, the control law was applied for velocities different from the design value. When the wind tunnel velocity is close to the target velocity of the control law design, attenuations of 10dB are obtained.

CONCLUSIONS

The present results show how closed-loop control can help to delay the transition to turbulence on boundary layers. Inverse feedforward control (IFFC) was shown to be robust, with significant attenuation of TS waves even with fluctuations of free-stream velocity. Finally, the present work shows how microphones can be used as sensors for closed-loop control of transitional boundary layers. Their relative low cost opens new possibilities for the application of multiple sensors in experimental implementations of control, which is relevant for complex 3D disturbances.

References

[1] Schrauf. G,. Status and Perspectives of Laminar Flow. *The Aeronautical Journal*, 2005.
[2] Sasaki et. al. On the Wave Cancelling Nature of Boundary Layer Flow Control. *J. Theor. Comput. Fluid Dyn.*, 2018.

RECENT DEVELOPMENTS ON THE ONE-WAY NAVIER-STOKES EQUATIONS

Omar Kamal[1], Georgios Rigas[2], Matthew Lakebrink[3], and Tim Colonius[*1]
[1]Division of Engineering and Applied Science,Caltech,Pasadena,CAUSA [2]Department of Aeronautics, Imperial College London,UK
[3]The Boeing Company, Hazelwood, MO USA

Summary The One-Way Navier-Stokes equations (OWNS), based on a approximate parabolization of the linearized, compressible Navier-Stokes equations in frequency space, are a fast alternative to global methods for stable, weakly non-parallel base flows. The method alleviates ambiguities and inaccuracies associated with streamwise marching in the parabolized stability equations (PSE). In this work, we generalize the method originally developed for weakly compressible free shear flows to flows at all speeds, from incompressible to hypersonic, and for three-dimensional wall-bounded flows in arbitrary, body-fitted generalized coordinates. We demonstrate DNS-like accuracy for the evolution of inlet disturbances in the hypersonic boundary layer on a 7-degree half-angle sharp cone, and we use OWNS to investigate worst-case disturbance growth in hypersonic boundary layers on flat plates.

INTRODUCTION

Current methods to track the spatial evolution of linear disturbances in boundary layers and other weakly non-parallel shear flows are direct numerical simulations (DNS), linear stability theory (LST), and parabolized stability equations (PSE). DNS, although most accurate, is computationally intensive, especially with complex geometries. LST is more computationally efficient but typically employs the parallel-flow assumption which introduces error as seen in [2], which studies the stability characteristics of a Mach 4.5 flat-plate boundary layer. PSE may seem as the optimal method between DNS and LST but there are intrinsic disadvantages. Instead of formally deriving a one-way operator, PSE achieves a stable spatial march by numerically damping all upstream propagating waves, as well as a subset of the downstream propagating ones, by using an implicit axial discretization along with a restriction on the minimum step size, or by explicitly adding damping terms to the equations [7]. In either form, the associated damping prevents the upstream waves from destabilizing the spatial march, but also has the unintended consequence of damping and distorting, to differing degrees, all of the downstream waves. This has, in turn, profound negative consequence for non-modal instabilities that are associated with an interacting group of modes [7].

Thus, we introduce a novel technique, the One-Way Navier-Stokes (OWNS) equations, which represents a path forward to overcoming the deficiencies of PSE. Originally developed for hyperbolic equations (e.g. Euler), OWNS employs a rigorous parabolization technique to generate well-posed, one-way approximations [6]. Efficient (fast) approximations of the resulting operator can then be made using recursive filters that were originally developed for non-reflecting boundary conditions. Aside from the parabolization itself, and unlike PSE, the numerics are convergent and not restricted to a dominant wavelength. The only restriction is the parabolization itself–meaning that OWNS can be applied in flows such as boundary and free shear layers that are dominated by downstream propagation, i.e. flows lacking feedback. Originally developed for free shear flows, the method was extended to wall bounded flows and validated by comparison with PSE and DNS for a variety of flow speeds [3]. We now include temperature-dependent fluid properties and a general non-orthogonal curvilinear coordinate system and apply this methodology to transitional hypersonic boundary layers. In the present work, we compare results from DNS of a sharp cone to validate the newly developed fully-compressible OWNS.

After linearizing the compressible Navier-Stokes equations about some time-independent base flow and discretizing in the curvilinear cross-stream directions (η, ζ), we can transform the equations into the characteristic space and obtain a one-way equation in the frequency domain via the Laplace transform yielding

$$\frac{\mathrm{d}\widehat{\phi'}}{\mathrm{d}\xi} = M\widehat{\phi'} + \widehat{g}, \tag{1}$$

Where ξ is streamwise direction. Note that we employed the thin shear-layer approximation by ignoring streamwise viscous diffusion. Since Eq. 1 is a linear ODE with $\widehat{g}$ being evaluated explicitly, we can instead assume a homogeneous ODE, i.e. $\widehat{g} = 0$, without a loss of generality. Using an eigenvalue decomposition of $M = VDU$, the exact parabolization in terms of characteristics with differential-algebraic equation (DAE) of index 1 is

$$\frac{\mathrm{d}\phi_+}{\mathrm{d}\xi} = M_{++}\phi_+ + M_{+-}\phi_-, \qquad U_{-+}\phi_+ + U_{--}\phi_- = 0. \tag{2}$$

Performing the spatial march with the exact parabolization would be computationally intractable and thus we use an approximate one-way marching using a high-order recursive filter. Derivation of the recursive parameters and the approximate one-way equation can be found in [6, 5] with the final DAE system being

$$\frac{\mathrm{d}\phi_+}{\mathrm{d}\xi} = M_{++}\phi_+ + M_{+-}\phi_-, \quad (M - ib_+^j I)\phi^j = (M - ib_-^j I)\phi^{j+1}, \quad \phi_-^{N_b} = 0. \tag{3}$$

*Corresponding author. E-mail: colonius@caltech.edu.

RESULTS

We validate the newly developed hypersonic OWNS framework in curvilinear coordinates by analyzing the boundary layer flow over an axisymmetric 7-degree half-angle sharp cone from [4]. The results for the wall-pressure perturbations are compared to their DNS solutions in Figure 1.

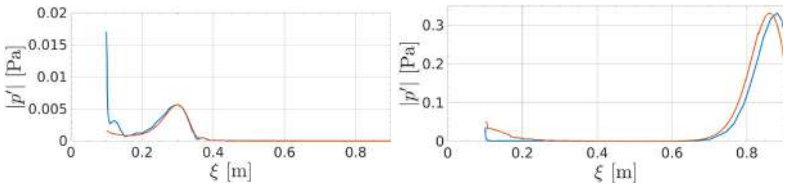

(a) $\mathrm{Re}_\infty = 1.46 \times 10^6\ \mathrm{m}^{-1}$ (b) $\mathrm{Re}_\infty = 4.06 \times 10^6\ \mathrm{m}^{-1}$

Figure 1: Comparing wall-pressure perturbations between OWNS (red) and DNS (blue) from [4] with mode S initialized at the inlet at $f = 400$ kHz. Flow over an axisymmetric 7-degree half-angle sharp cone with wall temperature of 300 K and Mach 7.3, $p_\infty = 789$ Pa, $T_\infty = 267$ K (left), and Mach 7.4, $p_\infty = 2129$ Pa, $T_\infty = 268$ K. (right)

Apart from the initial transient associated with the choice of inlet perturbation, we see excellent agreement between OWNS and DNS. To visualize the disturbance field, we plot the temperature perturbations for $\mathrm{Re}_\infty = 4.06 \times 10^6\ m^{-1}$ and $f = 475$ kHz in Figure 2.

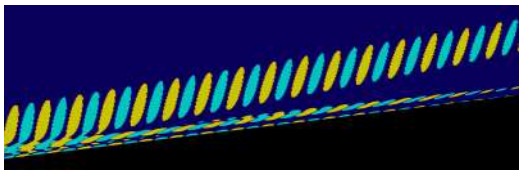

Figure 2: Temperature perturbations from OWNS at $\mathrm{Re}_\infty = 4.06 \times 10^6\ \mathrm{m}^{-1}$ and $f = 475$ kHz. Same flow conditions as Figure 1 (right).

We see the trapped acoustic waves between the wall and relative sonic line along with the subsonic "rope-like" structures in the region where the disturbances travel subsonically with respect to the freestream. However, due to substantial wall-cooling ($T_w/T_e = 0.8635$), there is an additional mode – the supersonic mode. This mode occurs when the phase speed of the disturbances in the freestream is slow enough such that they travel supersonically *upstream* relative to the freestream and creates an acoustic radiation from the boundary layer. This is qualitatively corroborated from [1].

CONCLUSION AND FUTURE WORK

We applied linear OWNS in studying transitional hypersonic boundary layers with full compressibility in general curvilinear coordinates. We demonstrated excellent agreement to DNS of 7-degree half-angle sharp cone from [4]. In the presentation, we will demonstrate how OWNS can be used an an efficient tool to investigate worst-case disturbance growth in hypersonic boundary layers on flat plates.

References

[1] Carleton P. Knisely and Xiaolin Zhong. "Sound radiation by supersonic unstable modes in hypersonic blunt cone boundary layers. II. Direct numerical simulation". In: *Physics of Fluids* 31.2 (2019), p. 024104.

[2] Yanbao Ma and Xiaolin Zhong. "Receptivity of a supersonic boundary layer over a flat plate. Part 1. Wave structures and interactions". In: *J. Fluid Mech* 488 (2003), pp. 31–78.

[3] Georgios Rigas, Tim Colonius, and Michael Beyar. "Stability of wall-bounded flows using one-way spatial integration of Navier-Stokes equations". In: *55th AIAA Aerospace Sciences Meeting* (2017).

[4] Victor C.B. Sousa et al. "Numerical Investigation of Second-Mode Attenuation over Carbon/Carbon Porous Surfaces". In: *Journal of Spacecraft and Rockets* 56 (2018), pp. 319–332.

[5] Aaron Towne and Tim Colonius. "Improved Parabolization of the Euler Equations". In: *19th AIAA/CEAS Aeroacoustics Conference* (2013).

[6] Aaron Towne and Tim Colonius. "One-way spatial integration of hyperbolic equations". In: *J. Comput. Phys.* 300 (2015), pp. 844–861.

[7] Aaron Towne, Georgios Rigas, and Tim Colonius. "A critical assessment of the parabolized stability equations". In: *Theo. Comput. Fluid Dyn* 33 (2019), pp. 359–382.

PARAMETRIC ANALYSIS OF 3D RECEPTIVITY IN LAMINAR SEPARATION BUBBLES VIA A NOVEL MULTI-FREQUENCY ITERATIVE METHOD

Eduardo Martini*[1,2], Daniel Rodríguez[3], André V. G. Cavalieri[1], and Peter Jordan[2]
[1]Instituto Tecnológico de Aeronáutica, São José dos Campos/SP-Brazil
[2]Département Fluides, Thermique et Combustion, Institut Pprime, CNRS, Université de Poitiers, ENSMA, 86000 Poitiers, France
[3]ETSIAE-UP M(School of Aeronautics)-Universidad Politécnica de Madrid, Spain.

Summary When formed, laminar separation bubbles (LSBs) typically lead to boundary layer transition to turbulence. Two-dimensional receptivity analyses show large gains, indicating that transition may occur via non-normal amplification of external perturbations. However, stability analysis reveals that the flow first becomes unstable via three-dimensional perturbations, and since in experiments such flows typically exhibit three-dimensional structures, a two-dimensional pathway to transition may not describe the appropriate dynamics. The sensitivity analysis of three-dimensional perturbations is addressed using a novel strategy, which provides optimal gains and modes for all frequencies using a single iterative scheme, resulting cost reduction of an order of magnitude lower in comparison with previous methods. These low computational costs allow for a parametric investigation of gains with frequency and LSB strength.

INTRODUCTION

The input-output analysis of flows provides useful insights into the system's dynamics. Optimal force and response modes, and the associated gains, can be used to explain by-pass transition: in flows which exhibit very large receptivity, small-but-finite perturbations are amplified up to the point where non-linear interactions become relevant and initiate the transition of the flow to a turbulent state.

Such mechanism have been explored to explain transition in laminar-separation bubbles (LSBs), which are formed by strong adverse-pressure gradients in laminar boundary layers. The bubbles are highly unstable, and when formed, frequently lead to transition. Different pathways to transition are possible: the flow can become globally unstable, leading to modal perturbation growth, or large receptivity can trigger non-linear dynamics, as mentioned before. Two-dimensional receptivity in LSBs exhibits large gains for the optimal forcing [1]. Rodríguez *et al* [2] showed that laminar separation bubbles are intrinsically unstable to three-dimensional perturbations, even in the absence of continuous external excitation, which is probably connected to the three-dimensionality typically seen for these flows in experiments. Due to computational cost, and the need to perform large parametric analyses to quantify the impact of the LSB mean properties on the development of perturbations, three-dimensional receptivity of LSBs has not yet been explored.

High computational cost makes direct singular-value decomposition (SVD) of system matrices, which can be used to compute optimal force and response modes, applicable only to small systems. To approach more complex systems, model reduction [3] and matrix-free methods have been proposed [4]. The choice of reduction basis is crucial for reduction strategies. For instance, eigenmodes, though they form a complete basis, may be a poor choice, as a large number of modes is frequently necessary to describe the dynamics of non-orthogonal systems. Such poor convergence was observed by Alizard *et al* [1]. Matrix-free methods compute modes and gains directly for the full system for a given frequency, not requiring model reduction. But high computational cost nonetheless hinders large parametric studies.

METHODS

Here we propose a variation of the method proposed by Monokrousos *et al*, using a matrix-free iterative method based on the system's transient response to compute optimal force and response modes for all frequencies simultaneously. The method is based on an iterative integration of the following set of equations

$$\frac{d}{dt}u_n(t) = Au_n(t) + f_{n-1}(-t) \tag{1}$$

$$\frac{d}{dt}f_n(t) = A^\dagger f_n(t) + u_n(-t) \tag{2}$$

with A and $A^\dagger$ representing the linearized Navier-Stokes operator and its adjoint, respectively. In the frequency domain the n-th iteration can be written as $\hat{f}_n(\omega) = (R^\dagger(\omega)R(\omega))^n \hat{f}_0(\omega)$, with $R = (-A - \mathrm{i}\omega)^{-1}$. Thus $\hat{f}_n(\omega)$ and $\hat{u}_n(\omega)$ converge to optimal force and response modes. The first iteration is set as spatial white noise, and as an impulse in time. Temporal filters are used to perform a frequency-dependent normalization, and a variation of the Arnoldi method is proposed as a way to accelerate convergence and compute sub-optimal modes and gains. Computational requirements are an order of magnitude lower than those associated with the method used by Monokrousos *et al* when results for many frequencies are desired.

*Corresponding author. E-mail: emartini@ita.br

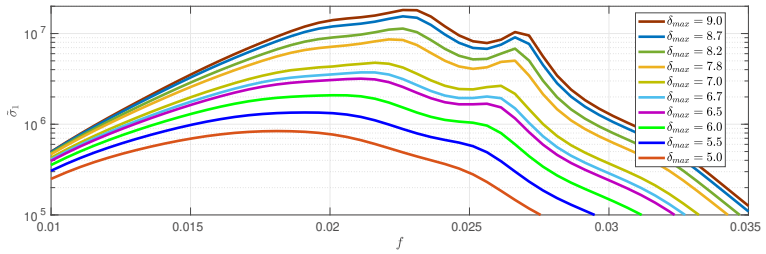

Figure 1: Gains for several LSBs, showing large increase with δ_{max} .

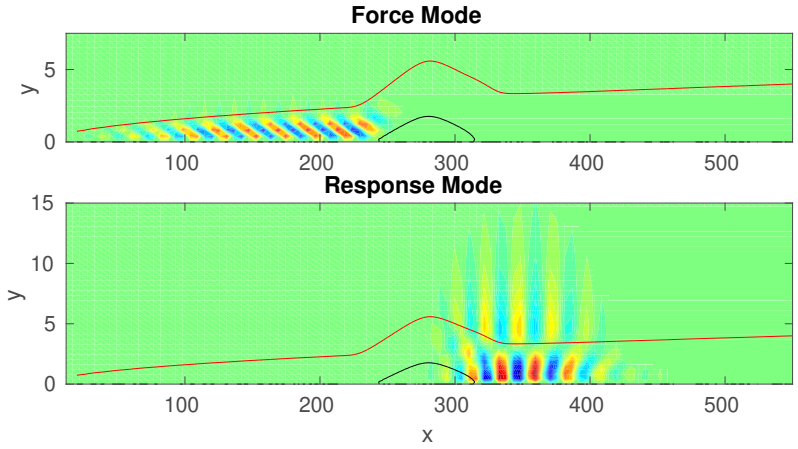

Figure 2: Force and response modes for $f = 0.018$, for a flow with $\delta_{max} = 5.0$ (colour map). Black and red lines indicate iso-contours of the baseflow streamwise velocity for $U = 0.0$ and 0.9.

RESULTS

Optimal force and response modes for laminar-separation bubbles are computed, with a large parametric study involving the bubble strength, frequency and three-dimensionality effects. An inverse formulation of the boundary-layer equations is used for the computation of steady two-dimensional bubbles, as in Rodríguez *et al* [2]. A distribution of the displacement thickness is imposed, reproducing the features of an adverse-pressure gradient separation bubble. The maximum separation thickness in boundary-layer units, δ_{max}, is used to parametrize the flow. Preliminary results for two-dimensional perturbations for different values of δ_{max} are presented in figure 1, with the optimal force and response modes for $\delta_{max} = 5.0$ presented in figure 2. Modes show excitation of TS waves in the downstream part of the bubble.

Using the proposed method, a three-dimensional sensitivity analysis for these flows is possible with moderate computational cost. The transition of the dominant mode from a planar TS wave, for boundary layers with zero pressure gradients, to three-dimensional structures related to TS-KH instability, seen in larger separation bubbles, can then be mapped. Such calculations are ongoing, and results will be presented at the conference.

The input-output framework has also been used in the study of turbulent flows. Working with the Navier-Stokes equations linearized around the mean flow, where the remaining non-linear terms are treated as an unknown external force, Mckeon & Sharma showed that large gain separation between the optimal and suboptimal modes can lead to a flow response which is insensitive to details of these external forces [5]. The approach has been used to construct low-rank flow modes and predicting large scale coherent structures in many flows. The method here presented has thus potential to assist in the study of both transitional and turbulent flows.

References

[1] Frédéric Alizard, Stefania Cherubini, and Jean-Christophe Robinet. Sensitivity and optimal forcing response in separated boundary layer flows. *Physics of Fluids*, **21(6)**:064108, June 2009.

[2] Daniel Rodríguez, Elmer M. Gennaro, and Matthew P. Juniper. The two classes of primary modal instability in laminar separation bubbles. *Journal of Fluid Mechanics*, **734**:R4, November 2013.

[3] Espen Åkervik, Jérôme Hœpffner, UWE Ehrenstein, and Dan S Henningson. Optimal growth, model reduction and control in a separated boundary-layer flow using global eigenmodes. *Journal of Fluid Mechanics*, **579**:305–314, 2007.

[4] Antonios Monokrousos, Espen Åkervik, Luca Brandt, and Dan S. Henningson. Global three-dimensional optimal disturbances in the Blasius boundary-layer flow using time-steppers. *Journal of Fluid Mechanics*, **650**:181, May 2010.

[5] B. J. McKeon and A. S. Sharma. A critical-layer framework for turbulent pipe flow. *Journal of Fluid Mechanics*, **658**:336–382, September 2010.

GLOBAL STABILITY OF AXISYMETRIC LIQUID-LIQUID FLOW FOCUSING

M. Rubio[1],N. Rebollo-Muñoz[1],M.G. Cabezas[*1],M.A. Herrada[2],and J.M. Montanero[1]
[1]Departamento de IngenieríaMecánica,Energética y de los Materiales and Instituto de Computación Científica Avanzada (ICCAEx),Universidad de Extremadura,Avda.de Elvass/n,E-06071 Badajoz,Spain
[2]Escuela Técnica Superior de Ingenieros,Universidad de Sevilla,Avda.de los Descubrimientoss/n, E-41092-Sevilla, Spain

Summary We study both numerically and experimentally the stability of the steady jetting regime of liquid-liquid flow focusing. The base flow is calculated by solving the full Navier-Stokes equations and boundary conditions for arbitrary values of the viscosities and flow rates. The linear stability analysis of the base flow is conducted by calculating its global eigenmodes. The minimum flow rate is determined as that for which the growth factor of the dominant mode becomes positive. We find good agreement between this theoretical prediction and preliminary experimental values. Numerical results will be used to analyze the mechanisms responsible for the instability.

INTRODUCTION

The axisymmetric liquid-liquid flow focusing configuration has been frequently studied because of its very diverse applications, such as fabrication of particles encapsulating different actives [1], or emulsions with high monodispersity [2]. In the most common operation mode, the outer flow stretches an inner liquid droplet or meniscus, which is attached to the feeding capillary, and forces the ejection of a microjet (steady jetting tip streaming, SJTS). This jet eventually breaks up into droplets due to the capillary instability. The SJTS mode keeps running if the expelled volume is properly replaced by injecting liquid into the tapering droplet/meniscus. The diameter of the emitted jet can be reduced by decreasing the injected flow rate. If the rest of parameter conditions are fixed, there is a minimum value of the flow rate below which SJTS becomes unstable.

The stability analysis of the steady tip streaming produced by axisymmetric liquid-liquid flow focusing has received very little attention. Gañán-Calvo and Riesco-Chueca [3] studied the jetting-to-dripping transition when the liquid stream is focused by another liquid current in the presence of a circular orifice, and compared the critical inner-to-outer flow rate ratios in the experiments with those leading to the convective-to-absolute instability transition in the jet. More recently, Mu *et al.* [4] studied the stability of the same configuration both experimentally and theoretically. They successfully explained their experimental observations and direct numerical simulations by distinguishing the instability originated in the emitted jet from that localized in the tapering meniscus.

The calculation of the linear global modes [5] is an adequate tool to predict the instability of SJTS. The idea is to assume that an infinite jet tapers from the liquid meniscus, and to interrogate this basic flow about its response to small-amplitude perturbations [6]. SJTS becomes unstable if the largest growth rate of the eigenfrenquency spectrum is positive. In this case, the system evolution is asymptotically (i.e., for sufficiently large times) dominated by the corresponding mode whose growth leads to either the interruption of the ejection or self-sustained oscillations. The complexity of the global stability analysis probably explains why it has been applied to very few SJTS configurations, including axisymmetric liquid-liquid flow focusing.

Cruz-Mazo *et al.* [7] and Ponce-Torres *et al.* [8] have recently obtained the stability limits of SJTS in gaseous flow focusing and the cone-jet mode of electrospray, respectively. The theoretical predictions agreed remarkably well with the experimental data for all the cases of electrospray analyzed [8]. However, SJTS became unstable for flow rates larger than those predicted by the asymptotic linear stability in gaseous flow focusing with small applied pressure drops [7]. This instability is caused by the short-term superposition of the eigenmodes. A natural question is which of these two possible scenarios the liquid-liquid flow focusing configuration corresponds to.

RESULTS

The pressure and velocity fields are calculated from the axisymmetric and incompressible Navier-Stokes equations, which are integrated taking into account the kinematic compatibility and equilibrium of tangential and normal stresses at the interface. We impose fully developed velocity profiles at the inlet section. The non-slip boundary condition is prescribed at the solid walls. The free surface shape is obtained as part of the solution by considering the anchorage condition of the triple contact line at the edge of the feeding capillary. We impose the standard regularity conditions at the symmetry axis, and the outflow conditions $u_z^{(k)} = w_z^{(k)} = F_z = 0$ at the right-hand end of the computational domain. We verified that the results are not significantly affected by this last condition by comparing the stability limits for different lengths of the discharge cell. The fluid domain is mapped onto a fixed numerical domain through a coordinate transformation. We conducted simulations for different mesh sizes to ensure that the results did not depend on that choice.

*Corresponding author. E-mail: mguadama@unex.es.

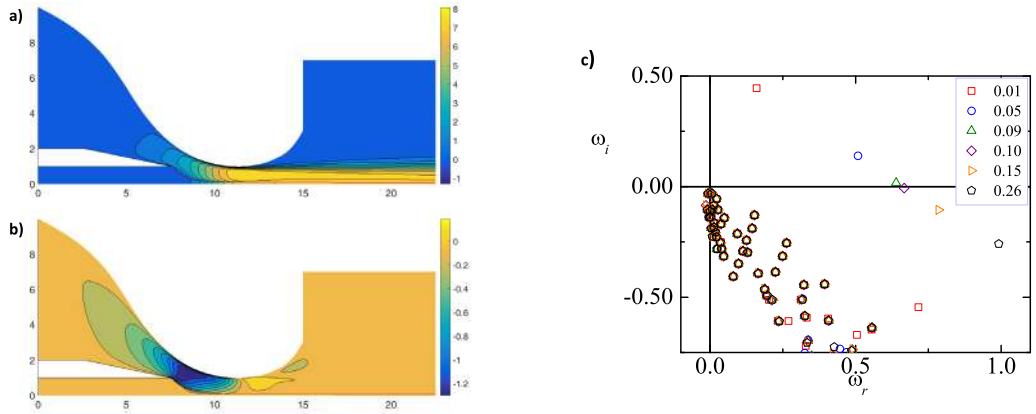

Figure 1: a) Axial and (b) radial adimensional velocity field of the base flow for Q_A=0.15 and Q_B= 20.7. c) Eigenfrequencies for Q_B= 20.7 and different internal flow rates Q_A (symbols).

Q_B	Numerical		Experiments	
	Q_A	R_j	Q_A	R_j
15.78	0.098	0.075	0.1	0.073
20.66	0.097	0.066	0.1	0.064
24.58	0.103	0.063	0.1	0.056
28.21	0.109	0.060	0.1	0.064

Table 1: Minimum inner flow rate and jet radius for different outer flow rates obtained numerically and in experiments. The liquids are 100 cSt silicone oil (inner) and water (outer).

First, the base solution of the problem is calculated, and then, the linear global modes are calculated by assuming the temporal dependence $U(r,z;t) = U_0(r,z) + \varepsilon\delta U(r,z)\, e^{-i\omega t}$ $(\varepsilon \ll 1)$, where $U(r,z;t)$ represents any hydrodynamic quantity, $U_0(r,z)$ and $\delta U(r,z)$ stand for the base (steady) solution and the spatial dependence of the eigenmode, respectively, while $\omega = \omega_r + i\omega_i$ is the eigenfrequency. Both the eigenmodes δU and the corresponding eigenfrequencies ω are obtained as a function of the governing parameters. The dominant eigenmode is that with the largest growth factor ω_i. If that growth factor is positive, the base flow is asymptotically unstable [5].

The experimental setup was similar to that described in [3] but for the flow focusing device. In our experiments, a capillary tube, with inner radius $R_c = 100$ μm, is located coaxially inside a glass converging-diverging nozzle at a distance $H = 380$ μm to its neck of diameter $D = 199$ μm. We focused a 100cSt silicone oil jet using a water stream.

For the sake of illustration, Fig. 1 shows numerical results for the configuration and system of the experiments. The variables are made dimensionless with the capillary radius R_c, the liquid density ρ_i, and the capillary time $t_c = \rho_i R_c^3/\sigma$, where σ is the interfacial tension. The discharge cell radius R and Length L are 7 and 7.5 times the capillary radius respectively. The dimensionless inner and outer flow rates are Q_A and Q_B, respectively. Fig. 1.a) and b) show the axial and radial dimensionless velocity of the base flow and the dimensionless interface shape F_z (red line) for Q_A= 0.15 and Q_B= 20.7, corresponding to SJTS. It can be observed how the outer stream speed in the nozzle orifice considerably exceeds that of the inner current. This makes the jet accelerate in that region, which produces the flow focusing effect. Fig. 1.c) shows the eigenfrequencies for different values of the inner flow rate Q_A and Q_B= 20.7. The sign change in the growth factor of the eigenfrequency responsible for the instability is used to determine the minimum stable flow rate Q_A= 0.97. Table 1 compares minimum flow rates and the corresponding jet radii R_j obtained numerically with those measured in experiments.

Acknowledgements: The authors thank Ministerio de Economía y Competitividad and Gobierno de Extremadura (Spain) for their support through Grants No. DPI2016-78887 and GR18175.

References

[1] Nabavi S. A., Vladisavljevic G. T. and Manovic V. *Chem. Eng. J.* **322**: 140-148, 2017.
[2] Gu H., Duits M. H. G. and Mugele F. *Int. J. Mol. Sci.* **12**: 2572-2597, 2011.
[3] Gañán-Calvo A. M. and Riesco-Chueca P. *J. Fluid Mech.* **553**: 75-84, 2006.
[4] Mu K., Ding H. and Si T. *Microfluid Nanofluidics* **22**: 138, 2018.
[5] Theofilis V. *Annu. Rev. Fluid Mech.* **43**: 319-352, 2011.
[6] Cabezas M. G., Herrada M. A. and Montanero J. M. *Phys. Rev. E* **100**: 053104, 2019.
[7] Cruz-Mazo F., Herrada M. A., Gañán-Calvo A. M. and Montanero J. M. *J. Fluid Mech.* **832**: 329-344, 2017.
[8] Ponce-Torres A., Rebollo-Muñoz N., Herrada M. A., Gañán-Calvo A. M. and Montanero J. M. *J. Fluid Mech.* **857**: 142-172, 2018.

TRANSITION TO TURBULENCE OF ELECTRICALLY CONDUCTING LIQUID FLOW DRIVEN BY A ROTATING MAGNETIC DIPOLE IN A RING CHANNEL

Didzis Berenis* and Ilmars Grants
Institute of Physics, University of Latvia, Salaspils, Latvia

Summary Electrically conducting liquid flow driven by a rotating magnetic dipole in a cylindrical ring channel is studied numerically with a focus on the hydrodynamical instability and transition to turbulence. In a narrow ring the flow itself and its instability resembles the related rotating magnetic field driven flow in a cylinder. That changes in a wide ring when an intense radial jet develops on the mid-plane. This jet looses stability either to wave-like three-dimensional deformation or to axially symmetric vertical displacement depending on ring's geometry. In the latter case two stable steady solutions emerge. As the flow intensity increases the jet switches chaotically between two mirror-symmetric patterns.

INTRODUCTION

Suppose that we wish to create possibly strong flow with a rotating permanent magnet in a confined volume. Evidently the best would be to insert the magnet in the middle of the volume since the magnetic field would then close almost entirely through the liquid. We arrive naturally to the ring channel configuration with conducting liquid surrounding a magnet. It has similarities with the traditional RMF configuration where magnetic inductor surrounds the liquid [1]. In both cases the magnetic field lines propagate in the azimuthal direction creating a time-averaged azimuthal body force [2]. The motion of liquid is expectedly similar, however, we find that it is not always the case.

FORMULATION AND METHODS

Incompressible Navier-Stokes equation with axially symmetric azimuthal body force is used to study electrically conducting liquid flow in a ring channel. Half-height of the ring H and momentum diffusion time H^2/ν are used as distance and time-scales, respectively, where ν is the kinematic viscosity. For definiteness, ring inner radius is set equal to H. Thus, only ring outer radius R and magnetic Taylor number Ta are free parameters which serve as the geometrical and dimensionless force parameter respectively.

Flow is driven by a rotating magnetic dipole on the ring axis creating a time-averaged azimuthal body force with an analytical expression [2]. Linear instability problem is addressed numerically with spectral methods by time integration of the axially symmetric base flow and infinitesimal azimuthally periodic perturbation. Weakly turbulent regimes are calculated with direct numerical simulation using spectral methods. Large eddy simulation using finite volume fluid dynamics software is performed for flow calculations in developed turbulence regimes.

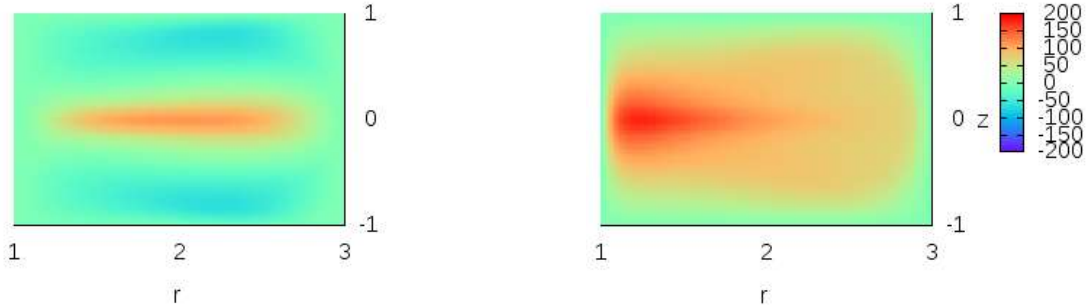

Figure 1: Velocity distribution in the ring cross section before the instability occurs ($R = 3$, $Ta = 1.7 \cdot 10^5$): (a) radial; (b) azimuthal

RESULTS

In the traditional RMF configuration magnetic inductor surrounds the liquid [1], time-averaged azimuthal body force drives the primary swirl and the presence of vertical solid walls creates secondary flow via so-called Ekman pumping [3]. It may be expected in the ring channel too that interplay of the secondary recirculation with the primary swirl eliminates vertical variation of the rotation outside thin Bödewadt boundary layers. However, it is so only for small outer ring radius $R < 2$. In which case the instability also is similar to the RMF counterpart.

*Corresponding author. E-mail: didzis.berenis@lu.lv

For $R > 2$ a radial jet develops on the mid-plane (Fig. 1) with high radial velocity. Magnetic force is overwhelmed by convective and viscous forces in the jet. Strong vertical variation of azimuthal flow persists in the core of the flow. For $R < 3$ jet instability manifests itself as a wave in the azimuthal direction. The critical magnetic Taylor number $Ta_{\rm cr}$ drops sharply at $R \approx 3.2$ with the flow's maximum dimensionless velocity ($Re_{\rm cr}$) falling below 70 (Fig. 2). Two new axially symmetric steady solutions emerge in the result of a monotonic ($\omega_{\rm cr} = 0$) instability. These solutions have vertically displaced radial jet and they are mirror images of each other with respect to the mid-plane.

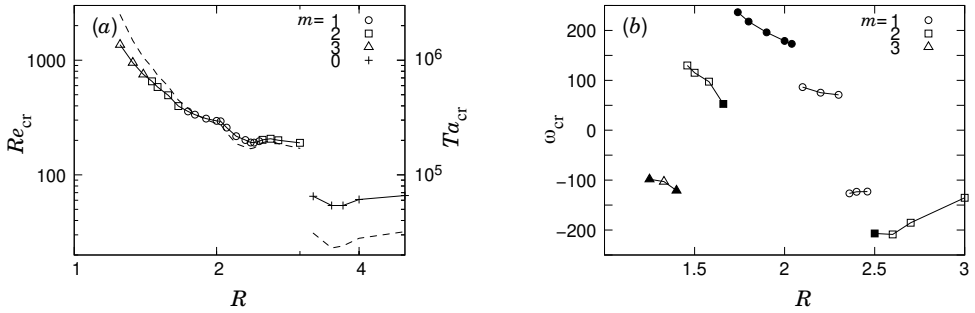

Figure 2: Instability conditions (a) shown in terms of critical Reynolds number (solid line) and magnetic Taylor number (dashed line). Frequency of the least unstable mode at the instability onset (b). Negative frequency values imply co-rotation with the magnetic field. Filled and open dots in (b) mark vertically symmetric and un-symmetric instability, respectively.

Direct numerical simulation shows that the radial jet also dominates weakly turbulent flow causing chaotic switching between two patterns as flow intensity increases (Fig. 3). Large eddy simulation is used to investigate the flow at yet higher velocities. Continuation simulations are in progress with an aim to explore conditions leading to switching events as well as probability density function of the time interval in between.

Estimates show that the flow regime as in Fig. 3 with $Ta = 10^6$ may be reached in an experiment with a transparent electrolyte with characteristic values of material properties: electrical conductivity – $50 S/m$, density – $1.2 \cdot 10^3 kg/m^3$, kinematic viscosity – $1.2 \cdot 10^{-6} m^2/s$. Taking characteristic size $H = 0.05m$ and magnetic field magnitude at the inner radius – $0.2T$ the necessary radial frequency of the magnet is $\approx 300 rad/s$ which can be easily achieved.

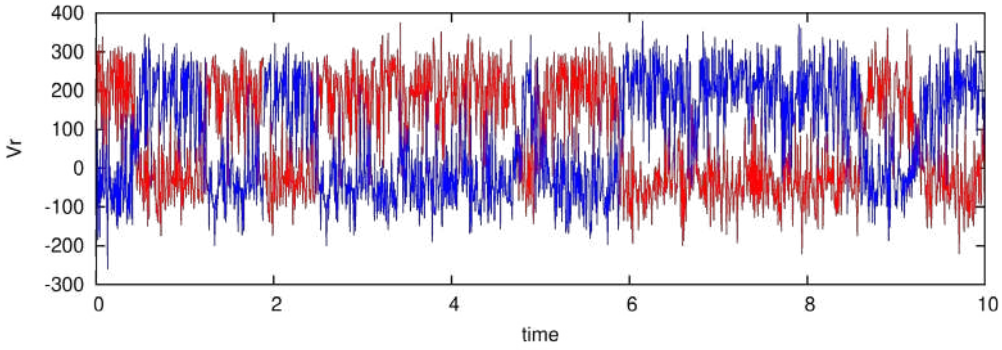

Figure 3: Time series of the radial velocity in two points at $z = \pm 1/3$; $Ta = 10^6$, $R = 4$.

CONCLUSIONS

The rotating magnetic dipole creates azimuthal body force in a conducting liquid ring surrounding it. This force drives primary swirl and secondary recirculation. In a wide enough ring $R > 2$ the flow develops mid-plane radial jet being a detached boundary layer by nature of the force balance. By exchange of stabilities two new mutually symmetric stable steady states arise for $R > 3.2$. These solutions are reflected in the turbulent flow as two symmetric patterns between which the flow wanders randomly. Stirring efficiency of the considered configuration allows to observe the phenomenon experimentally in a transparent electrolyte.

References

[1] P. A. Davidson, Swirling flow in an axisymmetrc cavity of arbitrary profile, driven by a rotating magnetic field, *J. Fluid Mech.* **245**, 669, 1992.
[2] D. Berenis and I. Grants, Analytical induced force solution in conducting cylindrical bodies and rings due to a rotating finite permanent magnet, *J. Magnetism and Magn. Mat.* **497**, 165856, 2020.
[3] P. A. Davidson, D. J. Short and D. Kinnear, The role of Ekman pumping in confined, electromagnetically-driven flows, *Eur. J. Mech., B/Fluids* **14**, 795, 1995.

FLOW REGIMES IN ROTATIONAL MOTIONS OF IMMISCIBLE PURE VISCOUS AND VISCOELASTIC FLUIDS

Diana Broboana and Corneliu Balan*
REOROM Laboratory, Department of Hydraulics, University Politehnica of Bucharest, Bucharest, Romania

Summary The goal of the present paper is to investigate the transitory flow regime between two immiscible liquids in rotational flows: water-oils and water-viscoelastic fluid, respectively. The qualitative differences between the two cases are analyzed. For the tested range of spin velocity, three distinctive flow regimes are observed in the case of Newtonian liquids: (i) linear, (ii) transitory and (iii) chaotic. Direct visualization of the interface's evolution is correlated with the torque measurements and the numerical simulations. The onset of the transitory regime is characterized by a sharp decreasing of the torque and the appearance of the Kelvin-Helmholtz instability at the interface between water and the tested liquids. The final aims of the study are: (i) to determine the elasticity influence on the flow dynamics, (ii) to correlate the interface pattern with the fluids rheology.

INTRODUCTION AND GOAL OF THE STUDY

The rotational flow of immiscible liquids in confined symmetric vessel might be considered a benchmark problem for the modelling of fluid interfaces. In the previous published works, the focus was mainly the analysis of the wavy interface between pure viscous fluids, when the bottom wall of the vessel is rotated, [1], [2]. The present paper is a starting study of the transitory rotational flow regime between immiscible viscoelastic fluids, associated to the Kelvin-Helmholtz (KH) instability of the interface. The correlation of the measured torque on the upper disk with the patterns of the wavy interface and the fluid elasticity is the main goal of the work.

EXPERIMENTAL, FLOW VISUALIZATION AND NUMERICAL SIMULATIONS

The immiscible fluid samples of different densities and viscosities, with measured interfacial tensions in the range of 0.025 – 0.045 N/m, are initially at rest in a confined cylindrical transparent vessel with diameter d = 66 mm. The height of water in the vessel is 20 mm, twice the height of the less dense liquid sample. The moving upper disk is connected to the MC 301 Anton Paar rheometer; the input are continuous or discrete ramps of pre-selected rotational speeds (n) and the output is the measured torque (T). The dynamics of the interface is simultaneously visualized with two digital cameras: (i) Nikon J5 (60 fps at 10 Mpixel resolution) and (ii) Photron UX100 (4000 fps at 1.3 Mpixel resolution), respectively. In Fig. 1 and Fig. 3.a are shown the dependences $T(n)$ for the tested samples and the corresponding evolutions of the interface are presented in Fig. 2 and Fig. 3.b, respectively.

In the case of water – Newtonian oil contact, there are observed 3 well defined regimes (Fig. 1). During the linear regime (split in 2 regions) T is increasing with n (almost linear), the oil keeps the contact with the upper rotated disk and the interface has a symmetric shape (I.1-I.3 in Fig. 2). The onset of the transitory regime starts at the sharp decreasing of the measured torque, when water is removing the oil from the rotational disk and the interface becomes wavy, similar in shape with the periodic KH pattern (II.1-II.3 in Fig. 2); this regime is characterized by almost constant T. In the third regime, defined as chaotic (III.1-III.3 in Fig. 2), the shape of KH waves are deformed and progressively, as the spin rotation is increasing, the emulsion is formed in the vessel. In this regime high fluctuations of the torque are recorded.

The numerics performed with the Fluent code (using the VoF method for the interface modelling) give a fair representation of the flow dynamics (both qualitatively and quantitatively) in the linear and transitory regimes, Fig. 1.b.

The first 2 regimes are also observed during the evolution of the water – viscoelastic fluid interface, Fig. 3. Due to the presence of elasticity, the magnitude of the experimental time (t_e) at fixed input velocity step plays an important role in the dynamics of the interface. The perturbation is amplified by elasticity even at constant low spin velocity, so the shape of the interface at n = const. may be changed from patterns I.1 to II.1 (Fig. 3.b) at any of the input steps from Fig. 3.a., if t_e is long enough. The fluctuations of T are high during t_e = 100 s (Fig. 3.a) at all velocities, with the exception of the regime II (100 rot/min $> n >$ 75 rot/min), where the wavy interface is lack of periodic symmetry.

This behavior is qualitatively similar with the Newtonian fluid, since in both cases the onset of a stable KH patterns (i.e. wavy interfaces, II.2 in Fig. 2 and II.1 in Fig. 3.b) is associated with a sharp decreasing of the torque. However, the high fluctuations of T are observed for the Newtonian fluid only in the regime III. But this is not the only difference between the analysed cases. As spin velocity is increasing, the wavy viscoelastic interface becomes more close to the bottom of the vessel, but at the same time only the viscoelastic fluid remains in contact with the moving disk, contrary to the Newtonian case. As consequence, the water is almost completely covered inside the vessel with a viscoelastic membrane, with the exception of the bottom wall.

CONCLUSIONS

The performed experimental investigations proved the direct relation between: (i) the sharp decreasing of the torque and the onset of the KH instability at the interface, (ii) the fluid elasticity and the torque/interface fluctuations at constant spin

* Corresponding author. E-mail: corneliu.balan@upb.ro

velocity. In the case of viscoelastic interface, the time variation of the measured torque, corroborated with the analysis of the parametric plot $T(dT/dt)$, suggests the existence of at least three attractors (no shown in this abstract).

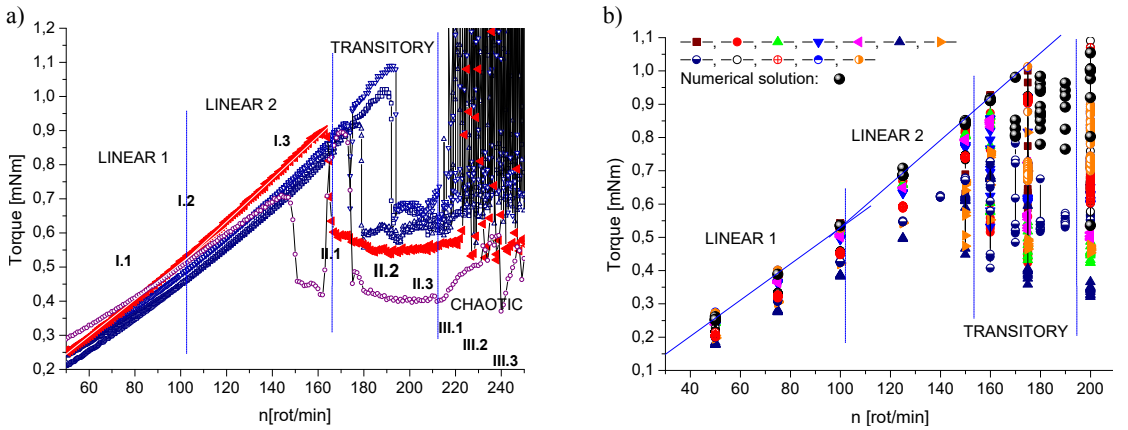

Figure 1. Measured torque at different inputs of the rotational velocity: different ramps (a) and steps (b). Numerical solutions are obtained during 5s/step; samples: water ($\rho = 995 kg/m^3$, $\eta = 13$mPas) – silicon oil ($\rho = 850 kg/m^3$, $\eta = 0.16$Pas).

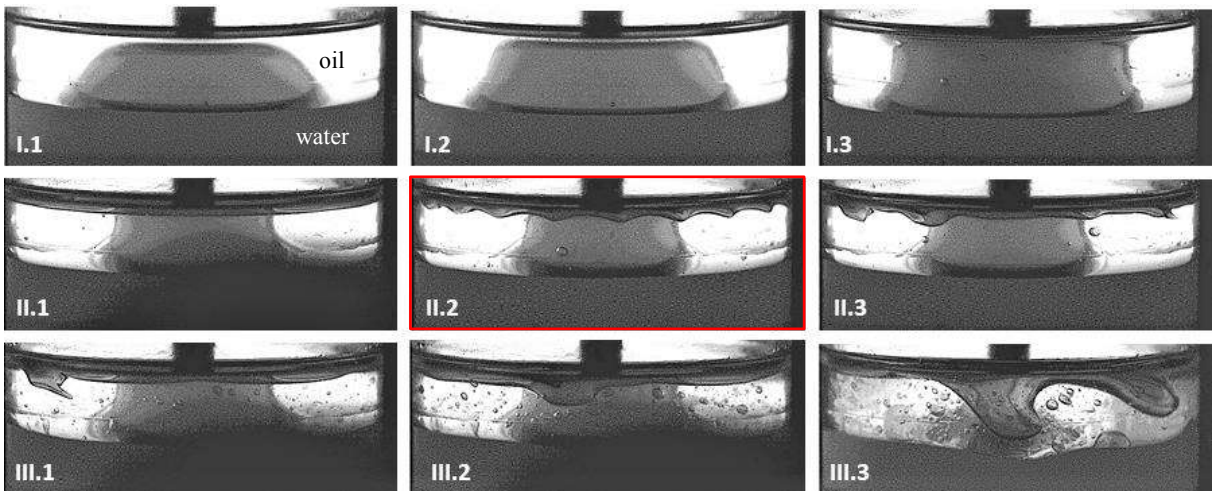

Figure 2. Interface configurations corresponding to the zone I, II and III from Fig. 1 (pictures at 4000 fps).

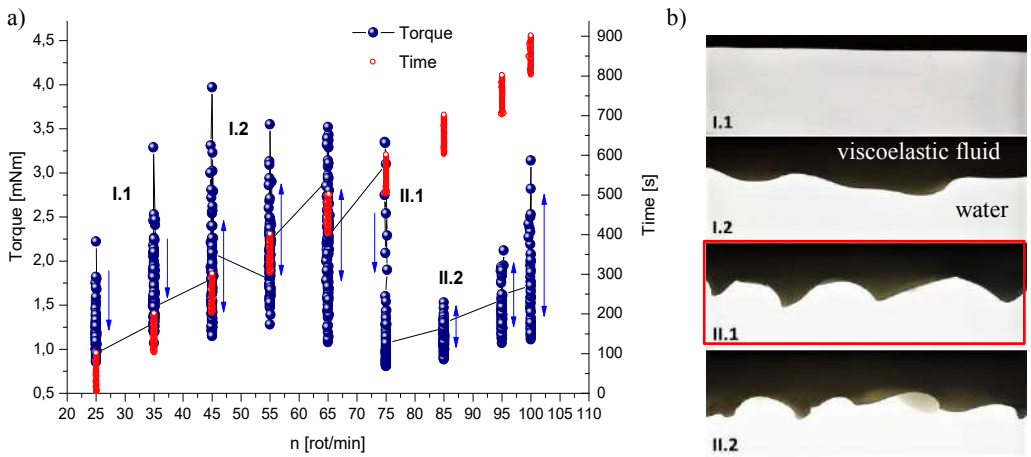

Figure 3. Measured torque at different input steps of the rotational velocity (a) and the corresponding interfaces (b); the samples: water ($\rho = 995 kg/m^3$, $\eta = 13$mPas) – viscoelastic shear thinning fluid ($\rho = 865 kg/m^3$; $\eta_0 = 40$Pas, $\eta_\infty \cong 1$Pas, first normal stress difference coefficient $\psi_{10} = 3000 Pas^2$, crossing point $G' = G''$ at frequency $\omega = 25 s^{-1}$).

References

[1] Fujimoto S. et al. Visualization of transient interfacial waves induced by spin-up of two immiscible fluid layers, *J. Vis.***13**: 17-23, 2010.
[2] Brady P.T., Herrmann M. Two-fluid confined in a cylinder driven by a rotating endwall, *Phys. Rev.* **E 85**: 016308, 2012.

THE EFFECT OF WALL COMPLIANCE UPON THE STABILITY OF ANNULAR POISEUILLE-COUETTE FLOW

Avni Chotai*[1] and Andrew Walton[1]
[1]Department of Mathematics, Imperial College London, South Kensington Campus, London, SW7 2AZ, UK

Summary Driven by a constant axial pressure gradient, the viscous flow through the concentric annular region between a stationary outer cylinder and a sliding inner cylinder is known as annular Poiseuille-Couette flow (APCF). The linear stability of this flow to infinitesimal, axisymmetric disturbances is studied asymptotically at large Reynolds numbers and computationally at finite Reynolds numbers when the inner cylinder possesses a degree of flexibility. A brief description of the asymptotic structure of lower-branch neutral modes will be followed by illustrations of the resulting asymptotic solutions, and it will be seen that the compliant nature of the inner cylinder results in the existence of unstable elastic modes that are not present in the rigid counterpart of the problem.

INTRODUCTION

APCF can be characterised by the constant sliding velocity V of the inner cylinder and the ratio of radii of the inner to outer cylinder δ, where $0 < \delta < 1$. The linear stability of APCF (with a rigid inner cylinder) to axisymmetric disturbances has been studied extensively by Walton [1], who confirmed that multiple neutral curves co-exist for certain choices of the parameters V and δ. This flow is of particular relevance in medicine; thread-injection is a minimally invasive technique for the transportation of medical implants into the body. In view of this application, the inner cylinder is modelled as compliant in this study and the effect of this on the linear stability of APCF is investigated.

Consider steady, incompressible APCF between two infinitely long cylinders. With horizontally orientated cylinders that are concentric, the geometry of this problem naturally lends itself to the use of a cylindrical coordinate system whose axial axis aligns with that of the cylinders; (x, r, θ) represent the non-dimensional axial, radial and azimuthal directions respectively. Assumed to be unaffected by the inner cylinder's compliance, the basic flow has only an axial component given by

$$U_0(r) = 1 - r^2 + \left(V - 1 + \delta^2\right)\ln(r)/\ln(\delta), \quad \delta \leq r \leq 1. \tag{1}$$

The flow is perturbed by axisymmetric disturbances of the travelling-wave form $\epsilon\hat{q}(r)\exp(\mathrm{i}\alpha(x-ct)) + c.c.$ where $\epsilon \ll 1$ and $\hat{q}(r)$ is the disturbance amplitude. The wavenumber α and wavespeed c are assumed to be real and complex respectively. Typical no-slip boundary conditions apply on the wall of the rigid outer cylinder. The inner cylinder, which flexes only radially so as to preserve the axisymmetry of the problem, is described by a spring-backed plate model [2]. Thus the following kinematic and dynamic conditions are to be satisfied on the inner cylinder:

$$\mathrm{i}\alpha(V-c)\hat{u}(\delta) + \hat{v}(\delta){U_0}'(\delta) = 0, \qquad \hat{p}(\delta) = \frac{2}{R}\hat{v}'(\delta) + \left(-\alpha^2 c^2 m + \frac{K}{R^2}\right)\frac{\hat{u}(\delta)}{{U_0}'(\delta)}. \tag{2}$$

Here, m and K represent the mass per unit area and spring stiffness per unit area of the inner cylinder respectively. We have neglected damping, tension and flexural rigidity. $\hat{u}(r), \hat{v}(r)$ and $\hat{p}(r)$ correspond to the axial, radial and pressure perturbations respectively. The Reynolds number R has been defined to be proportional to the axial pressure gradient in light of our 'thread-injection' application. This system results in a generalised eigenvalue problem for α that can be solved numerically via a Chebyshev collocation method. The system can also be analysed asymptotically at large R.

ASYMPTOTIC ANALYSIS AND COMPARISON WITH FINITE REYNOLDS NUMBER RESULTS

As a first step, the inner cylinder is assumed to be stationary to enable us to focus on the effects of compliance. At asymptotically large Reynolds numbers, we anticipate that the bulk of the flow is dominated by inertial forces. Near the cylinder walls, however, viscous forces become significant and there is a balance between the inertial, pressure and viscous terms in the governing linear disturbance equations. The lower-branch mode behaviour is captured by a three-zone structure (see figure 1) consisting of an inviscid core surrounded by viscous wall layers of thickness $O(R^{-2/7})$. Critical layers, where the basic velocity is equal to the wavespeed of the mode, are embedded in the viscous layers. The wavenumber and wavespeed of the lower-branch neutral mode are found to be such that $\alpha \sim R^{-1/7}\alpha_0$ and $c \sim R^{-2/7}c_0$. Seeking a balance of pressure and compliant terms in the dynamic condition, we fix $K \sim R^{12/7}K_0$ and $m \sim R^{4/7}m_0$. With these scalings, the inner cylinder's flexibility has a leading order effect on the lower-branch mode. Near $r = \delta$, we have $U_0 \sim R^{-2/7}\lambda_-^{(0)}y$ for a scaled radial coordinate y and $\lambda_-^{(0)} = 2 + (1-\delta^2)/\ln\delta$. In the lower viscous layer, let the variables u_-, v_- and p_- represent the appropriately scaled leading order terms of the axial velocity, radial velocity and pressure disturbances respectively. Substitution of these variable expansions into the governing linear disturbance equations gives, to leading order,

$$\mathrm{i}\alpha_0 u_- + \frac{\mathrm{d}v_-}{\mathrm{d}y} = 0, \quad \frac{\mathrm{d}^2u_-}{\mathrm{d}y^2} - \mathrm{i}\alpha_0\left(\lambda_-^{(0)}y - c_0\right)u_- - \lambda_-^{(0)}v_- = \mathrm{i}\alpha_0 p_-, \quad \frac{\mathrm{d}p_-}{\mathrm{d}y} = 0, \tag{3}$$

*Corresponding author. E-mail: avni.chotai13@imperial.ac.uk

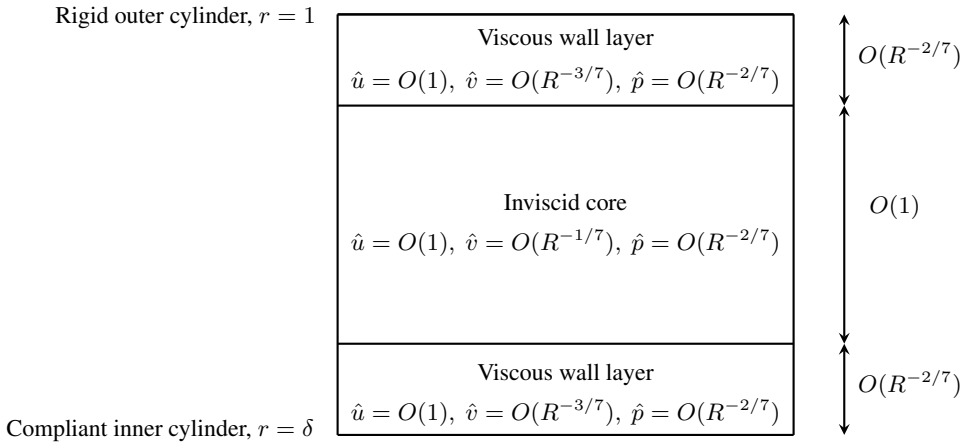

Figure 1: Schematic of the asymptotic structure of the lower-branch mode, where $\alpha = O(R^{-1/7}),\ c = O(R^{-2/7})$.

subject to matching the disturbance behaviour in the core as $y \to \infty$ and

$$\lambda_-^{(0)} v_- - \mathrm{i}\alpha_0 c_0 u_- = 0, \quad \lambda_-^{(0)} p_- = \left(K_0 - {\alpha_0}^2 {c_0}^2 m_0\right) u_- \quad \text{on} \quad y = 0. \tag{4}$$

We note the compliance affects the lower-branch mode through the boundary conditions only. The analysis of the lower-branch structure results in a complex-valued eigenrelation that describes how α_0 and c_0 depend on the problem parameters. This can be solved numerically using a Newton-Raphson method for fixed δ, K_0 and m_0. Figure 2 shows solutions α_0 of the lower-branch eigenrelation for various values of the expression $\tilde{K} = K_0 - {\alpha_0}^2 {c_0}^2 m_0$ and fixed $\delta = 0.5$.

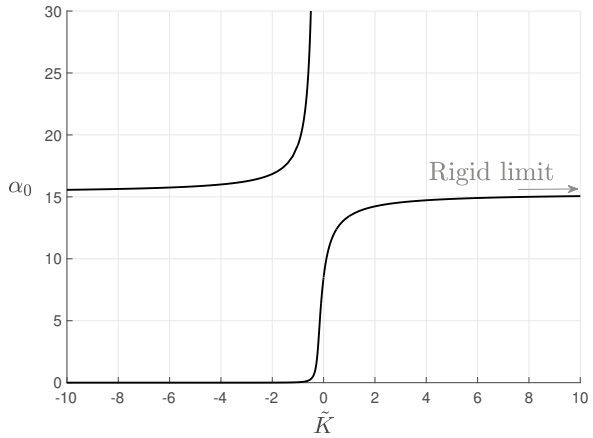

Figure 2: Solutions α_0 of the lower-branch eigenrelation for various $\tilde{K} = K_0 - {\alpha_0}^2 {c_0}^2 m_0$ and fixed $\delta = 0.5, V = 0$.

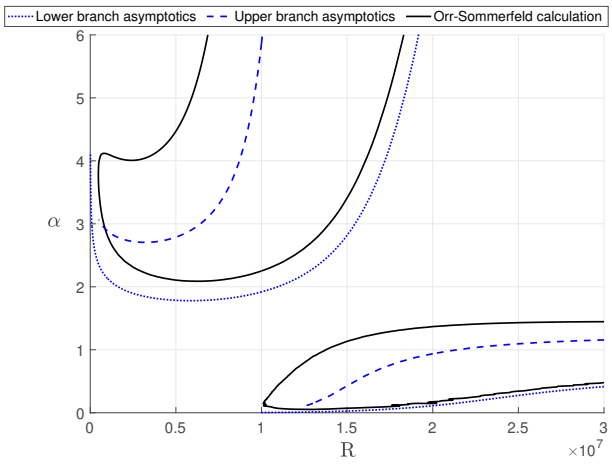

Figure 3: $\delta = 0.5, V = 0, \tilde{K} = -10^{12}$. Comparison of neutral stability curves obtained by asymptotic analysis with those obtained by solving an appropriate Orr-Sommerfeld type equation.

CONCLUSIONS

Illustrating the scaled wavenumbers of the lower-branch neutral modes, figure 2 unveils the existence of two neutral 'elastic' modes that arise from the flexibility of the inner cylinder, specifically when $\tilde{K}$ is negative. There exists only one neutral mode for positive $\tilde{K}$, and the wavenumber in the rigid limit is approached from below as $\tilde{K}$ is increased. Figure 3 shows the neutral stability curves obtained from solving an appropriate Orr-Sommerfeld type equation using a Chebyshev collocation method. These are compared to the neutral curves found from the asymptotic analysis of the lower and upper-branch structures. Agreement between the two methods increases at larger R. The upper-branch asymptotic structure, for which $\alpha = O(R^{-1/11})$ and $c = O(R^{-2/11})$, is obtained by an approach similar to that used for the lower-branch mode.

References

[1] Walton A. G. Stability of circular Poiseuille–Couette flow to axisymmetric disturbances. *J. Fluid Mech.* **500**: 169-210, 2004.
[2] Carpenter, P. W. and Garrad, A. D. The hydrodynamic stability of flow over Kramer-type compliant surfaces. Part 1. Tollmien-Schlichting instabilities. *J. Fluid Mech.* **155**: 465–510, 1985.

ON THE INSTABILITY OF THE FLOW AROUND RECTANGULAR CYLINDERS

Alessandro Chiarini*[1], Maurizio Quadrio[1], and Franco Auteri[1]
[1]Department of Aerospace Sciences and Technologies, Politecnico di Milano, via La Masa 34, 20156 Milano,Italy

Summary In this work we perform a Floquet stability analysis of the two-dimensional symmetric periodic flow past rectangular cylinders with aspect ratio (AR) between 1 and 5. We show that the occurrence and/or the nature of the secondary instability strongly depends on the aspect ratio of the cylinder. In particular, three ranges of AR can be identified: (i) for $AR \in [1, 2]$, the well known "mode A" three-dimensional synchronous instability is found at a spanwise length scale $\beta \approx 1.6D$ (for $AR = 1$ a further instability of quasi-periodic nature, usually called "mode B", is found for larger Reynolds number at $\beta = 2.6D$); (ii) for $AR \in [3, 4.75]$, the base flow is found to be stable to three-dimensional perturbations, but a secondary two-dimensional instability of the flow occurs; (iii) for $AR \geq 5$, a three-dimensional instability of (almost) subharmonic nature is found at $\beta \approx 2.1D$.

The investigation of the stability of the steady flow around bluff bodies is of great interest to a number of different applications, especially in the field of vortex-induced oscillations [1]. While the circular cylinder is a natural prototype of bluff body, extensively investigated [2], rectangular cylinders are also very interesting both from the viewpoint of applications and that of basic research, since they display flow features that are different with respect to the circular cylinder case: they have sharp edges where flow separation occurs and, depending on the aspect ratio of the rectangle AR, flow reattachment can be present on its lateral sides. In this work we are particularly interested in the effect of the aspect ratio of the cylinder on the secondary instability of the cylinder wake, usually leading to a three-dimensional flow.

The three-dimensional instability of blunt bluff-body wakes has been first investigated by Robichaux et al. [3]. For a square cylinder ($AR = 1$), they reported a three-dimensional instability classified as a subharmonic instability. Blackburn and Lopez [4] then showed this kind of instability to be precluded by the spatio-temporal symmetry of the base flow, and provided new evidence of the quasi-periodic nature of this instability. The subharmonic character of the instability is however recovered when the symmetry of the base flow is broken by slightly rotating the cylinder [5]. The impact of the aspect-ratio on the 3D secondary instability has been investigated in [6] for $0 < AR < 1$, but a comprehensive overview of the effects of the aspect ratio for $AR > 1$ is still lacking. This work addresses the stability of the flow past rectangular cylinders with aspect ratios $AR \in [1, 5]$, investigating both the first instability that leads to a periodic flow as well as the secondary one, by a Floquet stability analysis.

We found several interesting phenomena for both the first and secondary instabilities. In particular, we found that the quantitative and, more importantly, the qualitative nature of the secondary instability of such flows strongly depends on the aspect ratio of the cylinder. In this respect, three subranges of AR can be identified: (i) $AR \in [1, 2]$, (ii) $AR \in [3, 4.75]$, (iii) $AR \geq 4.85$.

For $AR \in [1, 2]$, the first three-dimensional instability is found to occur at $Re = U_\infty D/\nu \approx 200$ (U_∞ is the free-stream velocity, D is the cross-stream size of the cylinder and ν the kinematic viscosity). This a synchronous instability with spanwise length scale $\beta \approx 1.5D$, as shown in the left panel of figure 1 where the Floquet multipliers (μ) for $AR = 1$, $Re = 200$ and $\beta \approx 1.5D$ are plotted: the unstable Floquet multiplier with $|\mu| > 1$ is real and positive. The unstable mode in this case is usually referred to as "mode A" [5]. For the flow past the cylinder with $AR = 1$, a second three-dimensional

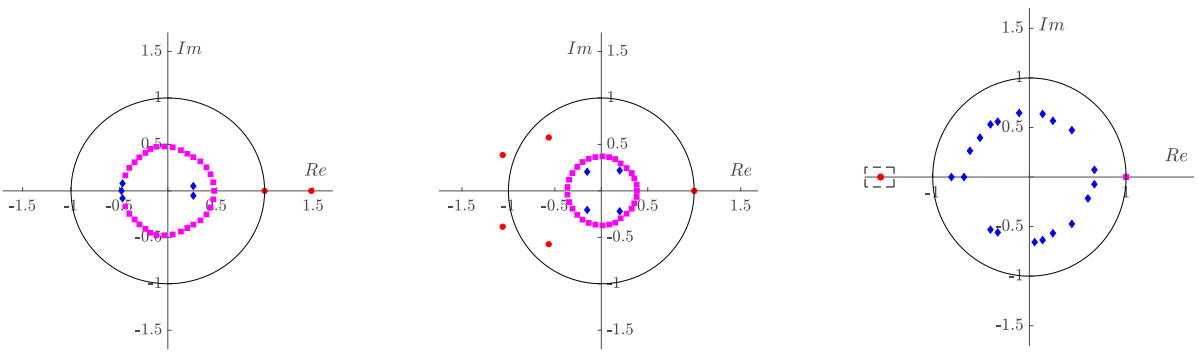

Figure 1: Left: Floquet multipliers for $AR = 1$, $Re = 200$ and $\beta = 1.5D$. Centre: Floquet multipliers for $AR = 1$, $Re = 225$ and $\beta = 2.6D$. Right: Floquet multipliers for $AR = 5$, $Re = 550$ and $\beta = 2.1D$

*Corresponding author. E-mail: alessandro.chiarini@polimi.it

instability is found at larger Reynolds number ($Re \approx 225$). This instability has a spanwise length scale $\beta \approx 2.6D$ and is of quasi-periodic nature, as shown in the central panel of figure 1: the unstable Floquet multipliers form a complex conjugate pair with negative real part. Interestingly enough, this instability is not found for $AR = 2$.

For $AR \in [3, 4.75]$, no 3D instability is found by Floquet linear stability analysis for $Re < 400$, and DNS shows that no three-dimensionality arises up to $Re = 450$. However, a second two-dimensional instability seems to occur in this range of aspect ratio and Reynolds number, which makes the flow loose the spatio-temporal symmetry of the wake. This is shown in figure 2, where a snapshot of the $2D$ flow for $AR = 4$ at $Re = 450$ is plotted.

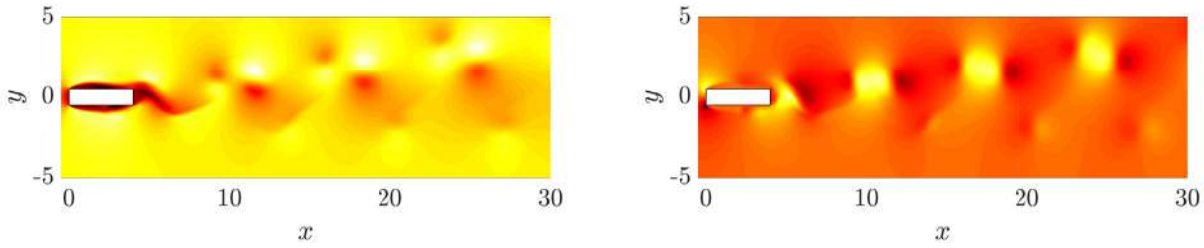

Figure 2: Baseflow for $AR = 4$ at $Re = 450$, without any stabilisation. Left: streamwise of the velocity. Right: cross-stream component of the velocity

For $4.85 \leq AR \leq 5$, a three-dimensional instability is found for $Re \approx 500$. In contrast with what found for $AR \in [1, 2]$, the instability is almost subharmonic and has a spanwise length scale $\beta \approx 2.1D$. This is shown in the right panel of figure 1 where the Floquet multipliers for $AR = 5$, $\beta = 2.1D$ and $Re = 550$ are plotted: the unstable multipliers form a complex conjugate pair with negative real part and imaginary part almost null (in the figure they seem to collapse to the real axis as $\text{Im}(\mu) \approx 10^{-3}$).

Aiming at investigating the nature of such instabilities, we exploit several tools: e.g a detailed investigation of the $2D$ base flows, $3D$ DNSs, linear stability analysis of snapshots of the base flows. An interesting result that further highlights the different nature of the three-dimensional instabilities found for $AR \in [1, 2]$ and $AR \geq 4.85$ is provided by the structural sensitivity [7] that allows one to locate the flow region where the instability is triggered. The structural

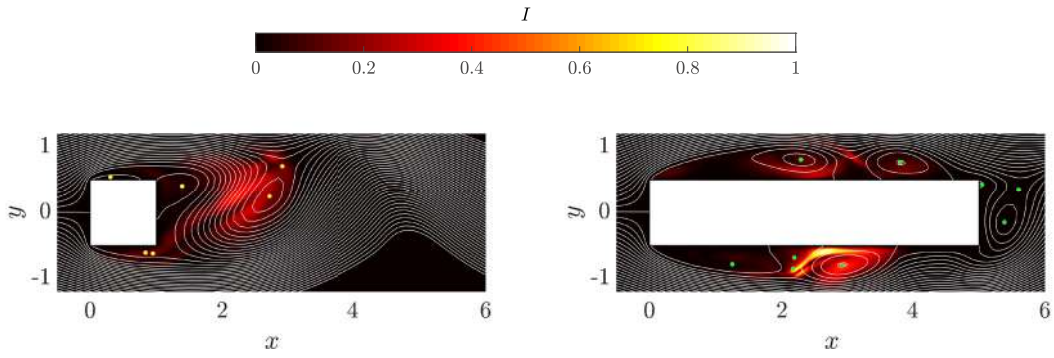

Figure 3: Snapshots of the structural sensitivity at one phase along the period of the base flow for $AR = 1$, $Re = 200$, $\beta/D = 1.5$ (left) and $AR = 5$, $Re = 550$, $\beta/D = 2.1$ (right). Streamlines and stagnation points are show superimposed on the sensitivity map.

sensitivity, figure 3, highlights the completely different nature of the instability mechanisms. For $AR \in [1, 2]$, the instability is triggered downstream the trailing edge: this is similar to what found for the flow past a circular cylinder [7]. For $AR \geq 4.85$, instead, the three-dimensional instability is triggered in a region close to the streamwise edges of the cylinder, where the recirculation occurs.

References

[1] Williamson C.H.K., Govardhan R., A brief review of recent results in vortex-induced vibrations. *J. Wind Eng. Ind. Aerodyn.* **96**: 713-735, 2008
[2] Zdravkovich M.M. *Flow Around Circular Cylinders*. Oxford University Press, 1997.
[3] Robichaux J., Balachandar S., Vanka S. P. Three-dimensional Floquet instability of the wake of a square cylinder. *Phys. Fluids* **11**: 560, 1999.
[4] Blackburn H. M., Lopez J. M. On three-dimensional quasiperiodic Floquet instabilities of two-dimensional bluff body wakes. *Phys. Fluids* **15**(8): L57-L60, 2003.
[5] Blackburn H.M., Sheard G.J. On quasiperiodic and subharmonic Floquet wake instabilities. *Phys. Fluids* **22**: 031701, 2010.
[6] Choi C.-B., Yang K.-S. Three-dimensional instability in flow past a rectangular cylinder ranging from a normal flat plate to a square cylinder. *Phys. Fluids* **26**: 061702, 2014.
[7] Giannetti F., Camarri S., Luchini P. Structural sensitivity of the secondary instability of the cylinder wake. *J. Fluid Mech.* **651**: 319-337, 2010.

EXPERIMENTS ON INSTABILITY AND BREAKDOWN OF VISCOUS SUBLAYER IN WALL TURBULENCE OVER RIBLETS

Masahito Asai[*1], Ayumu Inasawa[1], and Shohei Takagi[1]
[1]Department of Aeronautics and Astronautics, Tokyo Metropolitan University, Hino, Tokyo, Japan

Summary Instability and breakdown of the flow very close to streamwise riblets were examined experimentally using a hot-wire rake of 48 sensors with high spanwise resolution to clarify the mechanism of viscous breakdown leading to degradation of the drag reducing effect of riblets in wall turbulence. The result showed that high-frequency (small-scale) fluctuations developed on the ribbed surface distinctly around $s^+ = 16$, the optimal riblet spacing leading to the maximum drag reduction, which strongly suggested that instability of wall shear layer over riblets was intensified for $s^+ \geq 16$, leading to the breakdown of riblet flow.

INTRODUCTION

Surface manipulation with riblets (or longitudinal grooves) is one of the most successful passive means to reduce friction drag in wall turbulence. Several cross-sectional geometries of riblets including triangular, sawtooth, scalloped, blade and trapezoidal, have been proposed and tested, and the optimal riblet spacing (distance between neighboring ridges) was found to lie over 10–20 in wall units, depending on the riblet geometry, as summarized by Bechert [1]. In the viscous regime of $s^+ \leq 10$–15, turbulent vortices have no significant impact on the flow insude grooves, and thus the viscous sublayer over the riblets is laminar-like and the drag reduction due to a viscous effect is linearly proportional to s^+. Beyond this value of s^+, the viscous regime breaks down and drag reducing effect of riblets is saturated at $s^+ = 15$–20. In this concern, Garcia-Mayoral and Jimenez [2, 3] pointed out on the basis of direct numerical simulations and stability analysis of a model flow (having a inflectional profile) over riblets that the flow close to riblets became unstable when the riblet spacing exceeded a threshold value. Their stability result is consistent with studies on the stability of laminar flow over riblets/grooves [4, 5, 6]. However, no experiment detected such an instability event over riblets in wall turbulence thus far. In the present paper, we try to visualize the disturbance field in the viscous sublayer very close to riblets with $s^+ = 13$–24 using a hot-wire rake with high spatial resolution to identify the instability phenomenon in the riblet flow.

EXPERIMENTAL SETUP

The whole experiment was conducted in a rectangular channel of 10 m long with the cross section of 900×100 mm^2. The flow was tripped at the channel entrance by isolated roughness elements and fully developed to turbulent flow for the center velocity $U_c \geq 2.5$ m/s. Riblets had triangular ridges with ridge angle of 45° and trapezoidal valleys, and the height (h) and spacing (s) of the riblets were respectively 1 and 2 mm and therefore the height-to-spacing ratio (h/s) was 0.5, as illustrated in Fig. 1. In order to capture instantaneous velocity field very close to the ribbbed surface, a hot-wire rake consisting of 48 sensors aligned at an equal interval of 1 mm in the spanwise direction was used. Each sensor was a 1-mm-long tungsten wire with diameter of 5 μm. Hot-wire anemometers were operated in a constant current mode for the 48-sensor rake. The hot-wire rake was inserted into the flow from the downstream end of the channel.

RESULTS

We first confirmed that the maximum drag reduction was obtaind for $s^+ \approx 16$ for the present riblets. Figure 2 compares instantaneous streamwise velocity fields in the viscous sublayer (y^+=6), measured by a hot-wire rake, over the smooth surface and ribblets with $s^+ = 19$ (just above the optimal size). We see only a streaky structure consisting of low- and high-speed streaks on the smooth surface. On the other hand, high-frequency (small-scale) fluctuations appeared other than the streaky structure on the ribbed surface, which no doubt resulted from due to instabiliy nature of the riblet flow. We carefully examined the riblet flow for various values of s^+ and confirmed that development of such high-frequency fluctuations could be observed frequently only for $s^+ \geq 16$. Figures 3 (a)–(c) display y-distributions of rms values of low-frequency ($f^+ \leq 0.02$) and high-frequency ($f^+ \geq 0.04$) components of streamwise velocity fluctuations, $u_L^{'+}$ and $u_H^{'+}$ on the riblets with s^+= 13, 16 and 19, respectively, by comparing to the smooth-surface data. The maximum values of the low-frequency component ($u_L^{'+}$) were not different over the smooth and ribbed surfaces for $s^+ \leq 16$, while the high-frequency component ($u_H^{'+}$) for $y^+ < 20$ increased considerably over the riblets compared to the smooth surface data. Interestingly, the increase in $u_H^{'+}$ was the largest for the optimal-sized riblets with $s^+ = 16$, which was considered to be due to the instability of riblet flow.

*Corresponding author. E-mail: masai@tmu.ac.jp

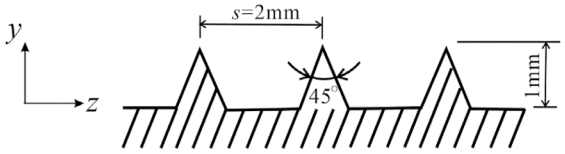

Figure 1: Cross-section geometry of riblets.

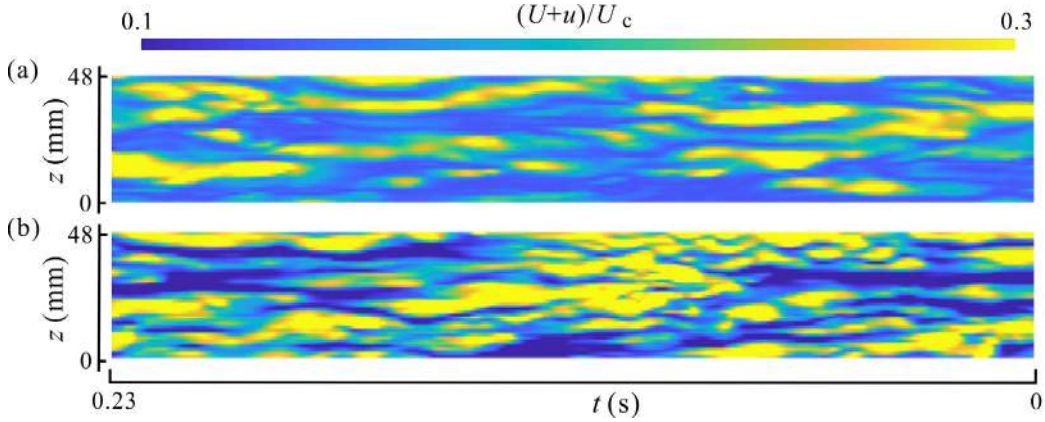

Figure 2: Instantaneous streamwise velocity in the (x, z) plane at $y^+ = 6$, measured by hot-wire rake ($Re_\tau = 470$). (a) Smooth surface, (b) riblets ($s^+ = 19$). Time t runs from right to left so as to simulate the flow from left to right.

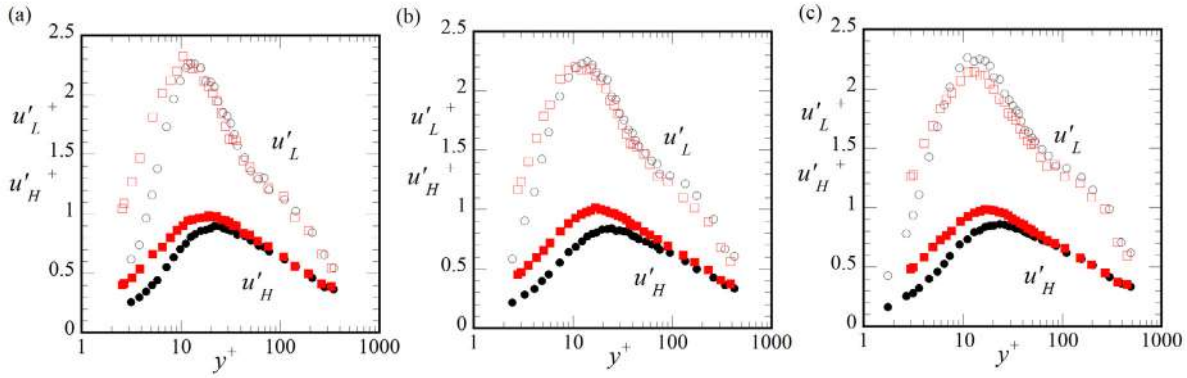

Figure 3: Comparisons of y^+-distributions of $u_L^{'+}$ ($f^+ \leq 0.02$) and $u_H^{'+}$ ($f^+ \geq 0.04$) between smooth and ribbed surfaces. (a) $s^+ = 13$ ($R_\tau = 330$), (b) $s^+ = 16$ ($R_\tau = 400$), (c) $s^+ = 19$ ($R_\tau = 470$) . Black and red symbols denote data for smooth-surface and riblets, respectively.

CONCLUSIONS

We successfully visualized occurrence of high-frequecy (small-scale) fluctuations in the viscous sublayer over the optimal-sized riblets for drag reduction, using a hot-wire rake with high spatial resolution. Increase of such small-scale turbulence strongly suggested that instability of shear layer adjacent to the ribbed surface was responssible for the viscous breakdown of the riblet flow.

This work was in part supported by JSPS Grant-in-Aid for Scientific Research 19H02350.

References

[1] Bechert D. W., Bruse M., Hage W., Van Der Hoeven J. G. T. and Hoppe G. Experiments on drag-reducing surfaces and their optimization with an adjustable geometry. J. Fluid Mech. 338: 59-87, 1997.
[2] Garcia-Mayoral R. and Jimenez J. Hydrodynamic stability and breakdown of the viscous regime over riblets. J. Fluid Mech. 678: 317-347, 2011.
[3] Garcia-Mayoral R. and Jimenez J. Scaling of turbulent structures in riblet channels up to $Re_\tau \approx 550$. Phys. Fluids 24: 105101, 2012.
[4] Luchini P. and Trombetta G. Effects of riblets upon flow stability. Appl. Sci. Res. 54 (4): 313-321,1995.
[5] Moradi H. V. and Floryan J. M. Stability of flow in a channel with longitudinal grooves. J. Fluid Mech. 242: 411-474, 2014.
[6] Ho H. Q. and Asai M. Experimental study on the stability of laminar flow in a channel with streamwise and oblique riblets. Phys. Fluids 30: 024106, 2018.

IDENTIFYING AND INTERPRETING MULTIPLE EQUILIBRIA OF AN OCEANIC INERTIAL JET

Kunihiro Aoki*[1], Yasumasa Miyazawa[1], Tsutomu Hihara[1], and Toru Miyama[1]
[1]Japan Agency for Marine-Earth Science and Technology, Yokohama, Japan

Summary This study addresses an objective identification of multimodal states in the Kuroshio, which is an oceanic inertial jet being a part of North Pacific western boundary current. The solutions of an ensemble simulations with 80 members conducted in a realistic situation are classified by the Gaussian mixture distribution model, an unsupervised machine learning technique. This model is successful in identifying two distinctive meander current paths, which have been bifurcated from a nearly straight path in the initial state. The spatiotemporal evolutions of a baroclinic energy conversion rate suggests that this bifurcation is induced by baroclinic instability. In addition, two clusters corresponding to each of the bistate in a phase space are located almost along the left singular vector for a tangential linear operator defined at a time just before the bifurcation. Those features suggests that the transition of the Kuroshio state is governed by the dynamical system permitting the pitchfork branch through a symmetry breaking by baroclinic instability.

INTRODUCTION

Multi-equilibria of the current paths in Kuroshio has been recognized in observation since 1960s and is generally thought to have a straight path, middle path, and a large meander path [1] (see also Fig. 1). Previous theoretical studies have explained the transition among the Kuroshio paths as a bimodal regime shift between the straight and large meander paths [e.g., 2, 3, 4, 5]. The transition to the large meander is, recently, thought to be achieved by baroclinic instability triggered by a small disturbance generated to the upstream [e.g., 5]. The remaining middle path has been interpreted as a transient phenomenon from the straight path [e.g., 6]. Given that a single system generally can have multiequilibria in the same scale under the control of nonlinearity, a theory comprehensively describing the trimode in the Kuroshio is expected to be developed. There are no sufficient circumstantial evidences that can lead to elaborating the theory, because the sufficient experiments producing the trimode in the Kuroshio under an uniform condition have not be done so far. The recent advance in computational technology, however, enables us to conduct an ensemble experiment with a larger ensemble size. In this study, therefore, we aim at identifying and interpreting the multiequilibria of the Kuroshio state produced in an ensemble simulation.

METHOD

A regional numerical simulation is developed on the basis of a parallelized version of the Princeton Ocean Model [7]. The model covers the region of 28°–36°N and 128°–142°E with the resolution of 1/36° horizontally and 21 sigma levels vertically. The model topography is derived from 1/120° gridded product. Targeting the large meander event in 2017, ensemble runs with 80 members start from 1 January 2017. For the first one month, the forecasts of the ensemble simulation are converges near optimal values by assimilating the observational data using the technique of the Local Ensemble Transformation Kalman Filter [8]. Free runs are conducted from 1 February 2017 to 14 June 2017. All the ensemble members experience the unique atmospheric forcing and boundary conditions in the entire ensemble simulation.

The ensemble solutions in the free run are classified by the Gaussian mixture distribution model (MDM) [e.g., 9]. The Gaussian MDM method is applicable to find clusters with their means, variances, and occurrence probabilities in a data sample. We apply this method for sea surface height (SSH) at the end-date, which gives the streamfunctions for the geostrophic velocity in the upper ocean. In short, our clustering analysis is a pattern recognition in the geostrophic streamfunction. The optimal number of clusters is determined by the test using information criteria (AIC and BIC). The classification of the SSH fields needs treating a large dimension with the size of the total number of horizontal grids of the numerical model. We classify the SSH fields on a phase space composed of some dominant modes derived from principle component analysis (PCA) performed in the ensemble space for the SSH data. The PCA mode provides a characteristic field in the deviations from the ensemble mean.

RESULTS

All the members have the straight path in the initial state in the free run, reflecting assimilation to the observational data. Some members, however, begin to have the large meander path in a couple of months, while most of the remaining members show the middle path. The Gaussian MDM with 2-class decomposition well-identifies the large meander and non-large meander states occurring with a similar probability (Fig. 1). Those two states is found to be discernible on the first PCA mode axis. Note that the 2-class decomposition is validated by the information criteria. A large part of the non-large meander cluster is composed of the members having the middle path, but some members still have straight

*Corresponding author. E-mail: kaoki@jamstec.go.jp

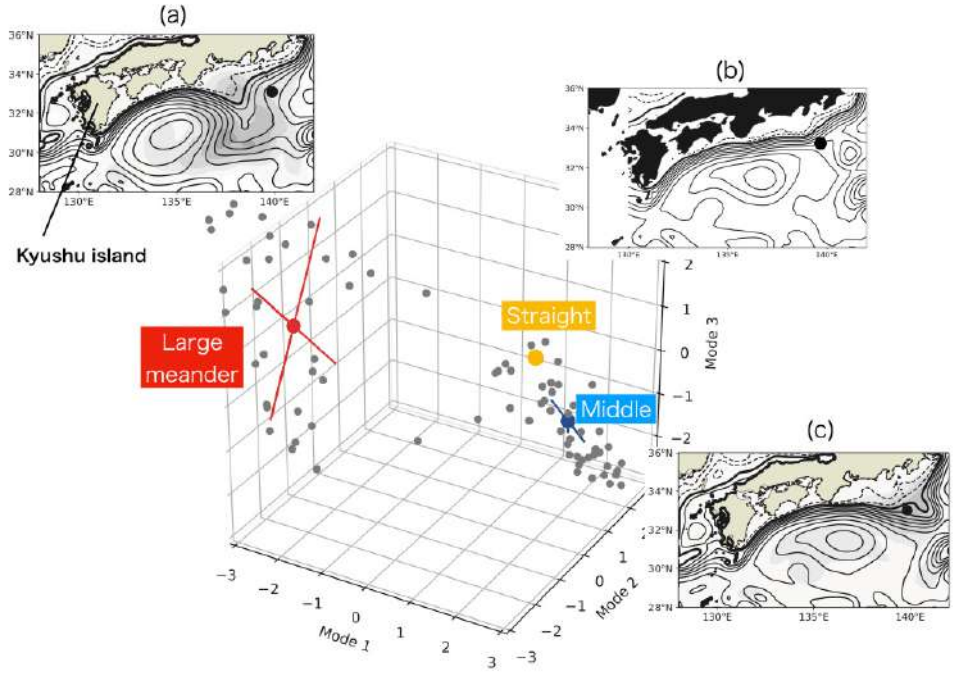

Figure 1: Scatter plot of ensemble solutions for SSH and the means of clusters estimated by Gaussian MDM in the phase space of three PCA modes at the end-date. Lines denote standard deviations. The panels show the SSH field corresponding to the means of the clusters: a) large meander path, b) straight path, and c) middle path.

path. Those two fractions in the non-large meander state is distinguishable on the third PCA mode axis although it is not statistically significant.

Both transitions to the large meander and middle paths is triggered by a small perturbation occurring to the southwest of Kyushu island. A slight difference is that the trigger perturbation for the middle paths appears at somewhat downstream side, compared to the case of the large meander path. The both cases, however, are found to be developed by a systematic baroclinic energy conversion that transfers the potential energy from the background to the anomalous fields. In contrast, some members stably keep the straight path to the end-date in spite of an occurrence of small disturbance. This suggests that the transitions to the large meander and middle paths are allowable for the jet being baroclinically unstable.

DISCUSSIONS

The bifurcation to the bistate suggests that the multiequilibria in the Kuroshio is governed by a system having super-critical instability. Although similar idea has been proposed in previous theoretical studies, they predict the bimodality between the straight and large meander paths [e.g., 4]. Our first PCA mode is obtained statistically, but can be mathematically proven to be equivalent to the left singular vector having the largest groth rate for the tangential linear operator at a time just before the bifurcation. This suggests that the large meander path and middle path can be interpreted as two possibilities that the order parameter characterized by the largest growing mode can take in a fully nonlinear circumstance.

References

[1] M. Kawabe. Variations of Current Path, Velocity, and Volume Transport of the Kuroshio in Relation with the Large Meander. *J. Phys. Oceanogr.* **25**: 3103 -3117, 1995.
[2] W. B. White and J. P. McCreary. On the formation of the Kuroshio meander and its relationship to the large-scale ocean circulation. *Deep Sea Research.* **23**: 33 - 47, 1976.
[3] A. Masuda. An interpretation of the bimodal character of the stable Kuroshio path. *Deep Sea Research.* **29**: 471 - 484, 1982.
[4] T. Yamagata and S. Umatani. The capture of current meander by coastal geometry with possible application to the Kuroshio current. *Tellus.* **39**: 161 -169, 1987.
[5] T. Endoh and T. Hibiya. Numerical simulation of the transient response of the Kuroshio leading to the large meander formation south of Japan. *J. Geophys. Res.* **106**: 26833 -26850, 2001.
[6] T. Waseda, H. Mitsudera, B. Taguchi, and Y. Yoshikawa. On the eddy-Kuroshio interaction: Meander formation process. *J. Geophys. Res.* **108**: C7, 2003.
[7] sbPOM: A parallel implementation of Princenton Ocean Model, web site **http://www.ccpo.odu.edu/POMWEB**
[8] B. R. Hunt, E. J. Kostelich, and I Szunyogh. Efficient data assimilation for spatiotemporal chaos: A local ensemble transform Kalman filter. *Physica D.* **230**: 112 -126, 2007.
[9] C. M. Bishop. Pattern recognition and machine learning. *springer-verlag new york.*, 2006.

SUBCRITICAL TRANSITION IN WALL-BOUNDED SHEAR FLOWS

Jacob Cohen*[1], Jimmy Philip[2], Franco Auteri[3] and Michael Karp[4]
[1]Faculty of Aerospace Engineering, Technion- Israel Institute of Technology, Haifa, Israel
[2]Department of Mechanical Engineering, The University of Melbourne, Parkville, Australia
[3]Department of Aerospace Science and Technology, Politecnico di Milano, Milano, Italy
[4]Center for Turbulence Research, Stanford University, Stanford, USA

Summary The sub-critical transition in wall bounded simple-geometry shear flows: Couette, Hagen-Poiseuille, and Plane-Poiseuille, is investigated theoretically. The transition process is initiated by a linear transient growth. This stage is well approximated by four decaying normal modes. Because of the minimal number of modes participating in the transition process, it is possible to follow most of the key stages analytically. The theoretical predictions are compared with direct numerical simulations, and very good agreement with respect to the growth of the disturbance energy and associated vortical structures is observed, up to the final stage just before the breakdown to turbulence. This procedure reveals the role of the different boundary conditions associated with these flows in the transition process.

The current study focuses on a sub-critical transition scenario of wall-bounded shear flows, which are stable with respect to infinitesimally small disturbances. We consider Couette flow (CF), Hagen-Poiseuille flow (HPF) and Plane-Poiseuille flow (PPF). The first two of which are predicted by Linear Stability Theory (LST) to be stable at all Reynolds number whereas the last one is predicted to be stable up to Re=5772. In practice, however, these flows transition to turbulence at finite Reynolds numbers, lower than those predicted by LST. Following the analytical procedure outlined for transition in Couette flow[1,2], here we investigate the transition to turbulence of CF, HPF and PPF, where the process is initiated by a Linear Transient Growth (LTG). We compare the evolution of the transition in these three shear flows associated with simple geometries but different boundary conditions.

The first stage of the transition is that of a LTG. It has been shown that the optimal linear disturbance, leading to the maximum transient growth of energy, is associated with a counter rotating vortex pair (CVP) which is independent (or almost independent) of the streamwise coordinate. Taking advantage of this characteristic, we can approximate the LTG process by following the sum of only four normal (decaying) modes. The modes and their three summation coefficients are obtained analytically. Figure 1 shows the LTG for Couette flow (a) and Hagen-Poiseuille flow (b) for Re=3000. Based on previous studies, the respective spanwise wavenumber (β) and azimuthal wavenumber (n) for CF and HPF are chosen to be 1.66 and 1. In both cases the analytical curves associated with the four modes approximate well the optimal LTG obtained numerically by a singular value decomposition. Furthermore, it is clear from the figure that the LTG is much more effective for CF than for HPF with the maximum energy gain ratio larger by a factor of more than 16. Also, the time at which the maximum is achieved is shorter for the HPF (~0.05) compared to that of CF (~0.14). This can be accounted for by defining the Reynolds number based on the shear and viscous diffusion time scales[3], $Re = (U/h)(2h)^2/\nu = 4Re_{CF}$, where U is one of the wall velocities and h the half channel height. Now, since the energy gain ratio and the time to reach maximum energy are respectively proportional to $1/Re^2$ and $1/Re$, the source for the TG difference between the CF and HPF is clear. More importantly, because of the minimal number of modes participating in the transition process, it is possible to follow most of the key subsequent stages analytically. Following the LTG of the four modes, the evolving modified base flow is subjected to an infinitesimally small disturbance. However, it turns out that the combination of the LTG and the four modes may not be enough to generate strong inflection points, necessary for the initiation of a significant secondary inviscid instability. Thus, the nonlinear mutual interactions between the four modes cannot be neglected. Using a series expansion, these nonlinear contributions are accounted for by utilizing Duhamel's principle. The inviscid (Rayleigh's type) instability is known to be sensitive to the base-flow velocity profiles, and indeed the effect of the four modes' mutual interactions on the velocity profiles is significant. This has been established by comparing the linear and nonlinear velocity profiles along the radial coordinate with the ones obtained by DNS results (see figure 2).

In the secondary stability analysis, we take advantage of the fact that the streamwise component of the base flow is O(Re) greater than the velocity components in the cross-section. Furthermore, we use the fact that there is a separation of time scales between the slowly evolving modified base flow, t=O(Re), and the rapidly evolving secondary disturbance, t=O(1). Accordingly, we employ the method of multiple scales to derive the temporal evolution of the disturbance, where at each "frozen time" step, the stability problem is solved by Floquet theory as the modified base flow is periodic along the spanwise/azimuthal directions. Figure 3 demonstrates the effect of Reynolds number on the above described transition scenario in Couette flow. Our analytical model (solid blue) describing the disturbance energy gain is compared with the corresponding DNS results (solid red). As Re is increased from 1000 to 2000 and to 3000, a lower initial disturbance amplitude is required for transition. Moreover, the difference between the two curves, observed for Re=1000, is reduced for Re=2000 and almost disappears for Re=3000. This difference is associated with a high-order nonlinear transient growth effect that has not been accounted for. Nevertheless, this small difference has a negligible effect on the transition. The vortical structures evolving during the transition process are identified using Q

*Corresponding author. E-mail: aerycyc@gmail.com

(the second invariant of the velocity gradient tensor)-criterion and are successfully compared with the DNS results. In the presentation, a detailed comparison will be made between the transition scenarios associated with CF, HPF and PPF.

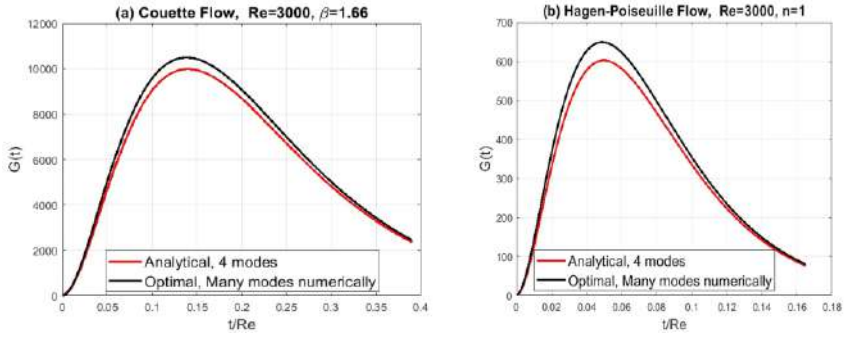

Figure 1. Linear Transient Growth: comparison between optimal solutions obtained numerically using many modes (black curves) and analytical solutions obtained by four modes (red curves). (a) Couette flow; (b) Hagen-Poiseuille flow.

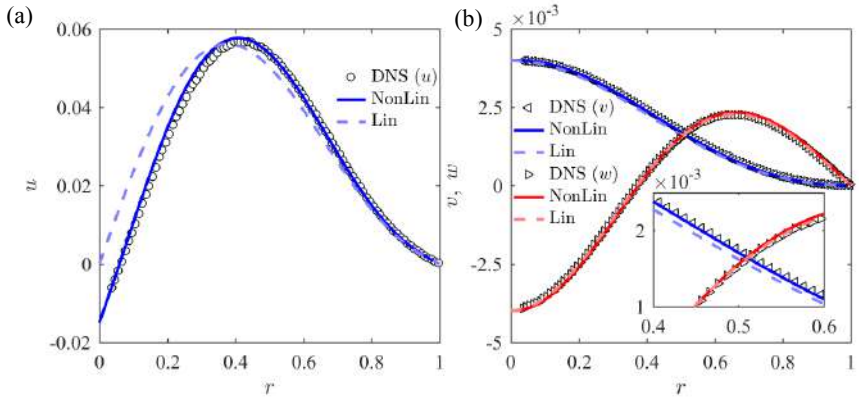

Figure 2. Comparison between DNS and analytical expressions with and without nonlinear interactions for Hagen-Poiseuille flow, Re=3000, n=1. (a) disturbance axial velocity (u); (b) disturbance radial (v) and azimuthal (w) velocities.

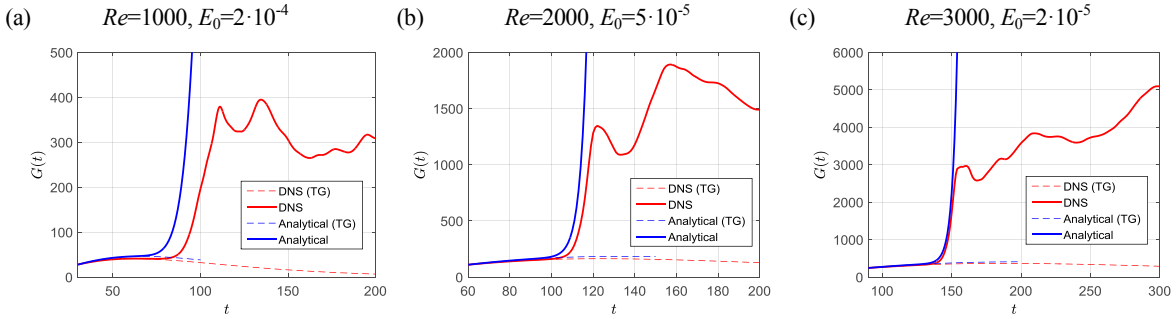

Figure 3. Effect of Reynolds number on the transition scenario in Couette flow. α=1, β=1. Comparison between the energy gain obtained from DNS (red) and an analytical model based on a multiple time scale analysis (blue).

CONCLUSIONS

In all three shear flows (CF, HPF and PPF) the linear transient growth can be approximated by few normal decaying modes. It is demonstrated that the kinetic energy growth of the initial disturbance is not the key parameter in this transition mechanism. Rather, it is the ability of the transient growth process to generate an inflection point in the wall-normal or spanwise/azimuthal directions and consequently to make the flow susceptible to a three-dimensional disturbance leading to transition to turbulence.

References

1. Karp, M., and Cohen, J. Tracking stages of transition in Couette Flow analytically. *J. Fluid Mech.* **748**, 896-931, 2014.
2. Karp, M., and Cohen, J. On the secondary instabilities of transient growth in Couette Flow. *J. Fluid Mech.* **813**, 528-557, 2017.
3. Manneville, P. IUTAM Symposium on Laminar-Turbulent Transition and Finite Amplitude Solutions, T. Mullin & R. Kerswell eds. Fluid Mechanics and its Applications, **77**, Springer, 1-33, 2005.

ASYMPTOTICS OF THE LOCALIZED PERTURBATION OF A VISCOUS FLUID FLOW DOWN AN INCLINED PLANE

Andrey Kulikovskii[1] and Julia Zayko*[1]
[1]Department of Mechanics, Steklov Mathematical Institute of Russian Academy of Sciences, Moscow, Russia

Summary The study is devoted to the asymptotic behavior of the linear localized perturbation of the laminar slope flow of a viscous fluid. The flow is described by equations in hydraulic approximation, which can be used to model certain natural flows, for example, dense snow avalanches. The localized perturbation is expressed by a double Fourier integral over the streamwise and transverse wave vector components. The asymptotics at large time for this integral is obtained analytically by the steepest descent method. The asymptotic shape of the region of the growing perturbation is found, as well as the wave crests and the lines of constant growth rate of the perturbation.

INTRODUCTION

The stability of thin liquid films has been widely studied since the middle of the 20th century. Most of the results on linear and nonlinear analyses of thin falling films are described in [1–4]. In [5] Benjamin studied the asymptotic behavior of the three-dimensional localized perturbation of a viscous fluid film down an inclined plane. It was shown that the perturbation is concentrated within the elliptical region in the coordinate system moving with dimensionless velocity $U = 3$. The asymptotic behavior of the localized perturbation of the film, described by the integral boundary-layer model [6], was studied numerically using the saddle point approach in [7]; the film was assumed to flow along the vertical wall so that the pressure gradient across the flow was not taken into account.

Equations in hydraulic approximation are widely used to model natural slope flows (see, for instance, [8]). The pressure gradient across the flow plays a significant role in this approach. In this study, we analytically conduct a linear analysis of the asymptotic behavior of a localized perturbation of the slope flow. The flow is described by two-dimensional equations in hydraulic approximation. The steepest descent method and the saddle point approach are used to obtain the asymptotic evolution of the perturbation as $t \to \infty$.

STATEMENT OF THE PROBLEM

Governing equations and dispersion relation

The uniform laminar flow of a viscous fluid down a slope of constant inclination angle is considered. It can be described by equations in hydraulic approximation if the longitudinal wavelength is much larger than the flow depth. For instance, it can be suitable for modeling of dense snow avalanches [9]. The governing equations in dimensionless form are given in [10]; the geometry of the flow is shown in Figure 1(a).

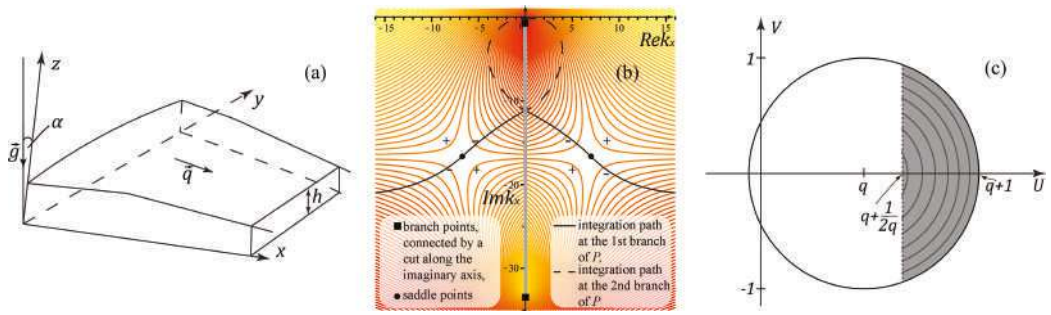

Figure 1: (a) Coordinate system. (b) Topology of the level lines of the function $\mathrm{Im}P = \mathrm{const}$ at the complex plane k_x. The squares define branch points; the gray bold line is the branch cut, lying along the imaginary axis; the circles define saddle points; and the continuous and dashed lines are the deformed integration paths at the 1st and 2nd branches of P, respectively. (c) The gray portion is the region of growing perturbation. The dashed line defines the line where $\mathrm{Im}P = 0$, and the gray circle segments are the wave crests.

We conduct a classical linear stability analysis of the unperturbed flow; the instability condition is $\mathrm{Fr} > 1/2$, where $\mathrm{Fr} = q_0/\sqrt{gh_0\cos\alpha}$ is the Froude number. Here $q = \sqrt{u^2+v^2}$ is the modulus of the velocity vector $\vec{q} = \{u, v\}$, h is the flow depth, α is the constant inclination angle of the slope, g is the gravity acceleration, and subindex 0 denotes the values of the unperturbed flow; h_0 and q_0 are taken as dimensionally independent parameters. The solutions of the dispersion equation are

$$\omega_1 = k_x - iF_0, \quad \omega_{2,3} = k_x - \frac{iF_0}{2} + \sqrt{\frac{k_x^2+k_y^2}{\mathrm{Fr}^2} + 2iF_0k_x - \frac{F_0^2}{4}}. \tag{1}$$

*Corresponding author. E-mail: zayko@imec.msu.ru.

Dimensionless function F_0 represents the friction at the bottom and for the laminar flow of a viscous fluid is $F_0 = 3/Re$, where $Re = q_0 h_0/\nu$ is the Reynolds number and ν is the kinematic viscosity coefficient. All values in (1) and below are dimensionless. In (1) the square root is the double value complex function with two branches; k_x and k_y are the components of the wave vector $\vec{k}$.

Expression for localized perturbation and methods of the study

Denote the localized perturbations of the basic flow depth and velocity components as $w(x, y, t)$. It is expressed by the double Fourier integral

$$w(x, y, t) = \sum_{n=1}^{3} \int_{-\infty}^{\infty} G_n(k_x, k_y) e^{i(k_x x + k_y y - \omega_n t)} dk_x dk_y. \tag{2}$$

For the perturbation of h, u, and v the function w differs by $G_n(k_x, k_y)$. To find the shape of the region of growing perturbation, we must obtain the growth rate of the disturbance for each pair of rays $x = Ut$, $y = Vt$ for all real U, V. Introducing the moving coordinate system $x' = x - Ut$, $y' = y - Vt$, we rewrite the exponent power in (2) as $k_x x' + k_y y' - Pt$, where $P = \omega - k_x U - k_y V$. The imaginary part of the function $P(U, V)$ defines the growth rate of the disturbance for given U, V. The asymptotics of the integral (2) can be obtained by the Laplace method. The function $\mathrm{Im}P$ reaches its maximum in the saddle points, which are obtained from the equations $\partial P/\partial k_x = 0$ and $\partial P/\partial k_y = 0$. For a growing frequency of the dispersion relation (1), the saddle points do not lie at the real axes k_x and k_y so that the steepest descent method is used to transform the integration paths of the integral (2). We apply this procedure subsequently to the integral over k_y and, after it, to the integral over k_x. For the problem considered, we analytically find the saddle points and the topology of the level lines $\mathrm{Im}P = \mathrm{const}$ in the complex planes k_y and k_x. By employing this method, we find the perturbation growth rate for different U and V, the shape of the growing perturbation region, and the wave crests.

RESULTS OF THE STUDY

Note that equations in hydraulic approximation are hyperbolic, so the localized perturbation lies in the circle $(U - q_0)^2 + V^2 \le \mathrm{Fr}^{-2}$. An example of the topology of $\mathrm{Im}P = \mathrm{const}$ level lines in the complex plane k_x and the deformed integration path are shown in Figure 1(b); for this case, $U - q_0 > 0$. It is interesting to note that for the case $U = q_0$ there is an analogy between the function $P(k_x|_{k_y^{saddle}})$ and the complex potential of a flat plate flow, and the critical points of this flow are saddle points for $P(k_x)$.

Introducing the notations $\hat{U} = U\mathrm{Fr}$, $\hat{V} = V\mathrm{Fr}$, $\hat{q} = q_0\mathrm{Fr}$, $\hat{P} = P\mathrm{Fr}$, and $f = F_0\mathrm{Fr}$ and omitting the sign $\hat{}$, we prove that the region of growing perturbation is the portion of the circle given by the following two equations: $(U-q)^2+V^2 \le 1$, $U > q + 1/(2q)$ (the gray region in Figure 1(c)). The growth rate $\mathrm{Im}P$ is independent of V,

$$\mathrm{Im}P = -\frac{f}{2} - fq(q - U), \tag{3}$$

and reaches the maximum in the point $U = q + 1$. The crests of the growing waves are circle segments with the center $U = q$, $V = 0$ (see Figure 1(c)).

CONCLUSIONS

The behavior of the localized perturbation as $t \to \infty$ of a viscous flow down an inclined plane is considered. The asymptotic shape of the growing perturbation region is obtained analytically (the gray region in Figure 1(c)). The result can be useful for natural slope flows and the modeling of thin films.

Acknowledgments. This work is supported by the Russian Science Foundation under grant 19-71-30012.

References

[1] Alekseenko S.V., Nakoryakov V.E., Pokusaev B.G. Wave Flow in Liquid Films. Begell House, NY 1994.
[2] Chang H.-C., Demekhin E.A. Complex Wave Dynamics on Thin Films. D. Möbius and R. Miller. Elsevier, Amsterdam 2002.
[3] Craster R.V., Matar O.K. Dynamics and Stability of Thin Liquid Films. *Rev. Mod. Phys.* **81**: 1131-1198, 2009.
[4] Kalliadasis S., Ruyer-Quil C., Scheid B., Velarde M.G. Falling Liquid Films. Springer, London 2012.
[5] Benjamin T.B. The Development of Three-Dimensional Disturbances in an Unstable Film of Liquid Flowing Down an Inclined Plane. *J. Fluid Mech.* **10**: 401-419, 1961.
[6] Shkadov V.Ya. Wave Flow Regimes of a Thin Layer of Viscous Fluid Subject to Gravity. *Izv. Akad. Nauk SSSR, Mech. Idk. Gaza* **1**: 43-51, 1967. (English translation in *Fluid Dynamics* **2**: 29-34, Faraday Press, NY 1970.)
[7] Demekhin E.A., Kalaidin E.N., Kalliadasis S., Vlaskin S.Yu. Three-Dimensional Localized Coherent Structures of Surface Turbulence: II. Λ Solitons. *Phys. Fluids* **19**: 114104, 2007.
[8] Zanutting B., Lamberti A. Instability and Surge Development in Debris Flows. *Rev. Geophys.* **45**: RG3006, 2007.
[9] Dent J.D., Lang T.E. Modeling of Snow Flow. *J. Glaciol.* **26**(94): 131-140, 1980.
[10] Zayko J., Eglit M. Stability of Downslope Flows to Two-Dimensional Perturbations. *Phys. Fluids* **31**: 086601, 2019.

INSTABILITY PHENOMENA IN SHORT ASYMMETRIC TAYLOR-COUETTE CAVITY

Ewa Tuliszka-Sznitko
Institute of Thermal Engineering, Poznan University of Technology, Poznan, Poland

Summary The paper reports on the numerical investigations of Taylor-Couette flow with rotting inner cylinder and bottom disc, and with stationary outer cylinder and top disc over the range of radius ratio η=0.25-0.6, (Re=100-200). In the investigations the fully 3D DNS code based on the spectral Chebyshev–Fourier approximation is used. Many interesting phenomena are uncovered including the modulated rotating wave, the period doubling cascade and the homoclinic/heteroclinic collision. The period doubling bifurcation is dominated in the flow cases of radius ratio close to η=0.375.

INTRODUCTION

The main purpose of the present numerical research (DNS) is to determine the influence of radius ratio $\eta=R_1/R_2=0.25$-0.6 on the bifurcation phenomena observed by Mullin and Blohm [1] and Lopez et al. [2] in the short Taylor-Couette configurations of η=0.5. The present investigations are thought as complimentary to these results. The DNS computations are performed using code based on the spectral Chebyshev – Fourier approximation (the precision of this method has allowed to gain insight into very complicated flow cases, [3]). To verify the present DNS results the computations obtained for η=0.5 and selected aspect ratios $\Gamma=H/(R_2-R_1)$ have been compared with experimental results of Mullin and Blohm [1]. The comparison has confirmed that for η=0.5 the flow dynamics is governed by a pair of codimension-2 bifurcation points: the double Hopf bifurcation point and the cusp point. The Hopf and Neimark-Sacker bifurcation lines have been reconstructed and the obtained RW_1 and RW_2 flow structures agree with those presented by Lopez et al. [2]. The DNS research has been preceded by the calculations of the saddle-node bifurcation lines along which the transition from the 3-cell structure to the 1-cell structure (and vice versa) takes place (the ENTFIVE code, [4]). These results have shown that the cusp points occur in the wide range of radius ratio η=0.1-0.75 and that the line connecting the cup points creates a parabola in the (Re, Γ) plane with extreme point near η=0.375, [5]. The attention is focused on the modulated rotating wave (MRW) which appears near the cusp point. Following Lopez et al. [2] the investigations of MRW have been based on the one-dimensional parameter path. Lopez et al. [2] have presented (Re=120) the MRW period as a function of Γ. They have found that at lower Γ the increase of T_{MRW} is slow, then it becomes exponential and for the critical value of Γ the MRW period goes to infinity $T_{MRW}\rightarrow\infty$. With increase of Γ (starting from stable state) they have observed consecutively: the stable RW_1 wave, the modulated rotating wave, then, the MRW wave undergoes several saddle-node bifurcations and finally a homoclinic/heteroclinic collision occurs (the MRW wave disappears). Lopez et al. [2] have determined the critical value of Γ at which the MRW wave appears and the value of Γ at which the homoclinic/hereroclinic collision takes place for different Re (see the N_M and C lines in Fig. 25, [2]).

THE RESULTS

The most information on the flow dynamics comes from the velocity components time series (obtained using DNS) - based on the time series the profiles of squared amplitudes $(A)^2$ of the radial velocity component u as a function of Re have been determined for the subsequent values of Γ and η ($(A)^2$ changes linearly with Re in accordance with Hopf bifurcation theory). Then, the unstable areas have been determined for η=0.25-0.6, [5]. Figure1 show time dependent behavior at η=0.475, Γ=3.0404, Re=119.7 (the considered point is very close to the homoclinic collision). Figure1a shows changes of the kinetic energy $k=(u^2+v^2+w^2)/2$ (black line) and the modal energy $\mathbf{u}_0\cdot\mathbf{u}_0^*/2$, $\mathbf{u}_1\cdot\mathbf{u}_1^*/2$ in one period T_{MRW} ($\mathbf{u}_0^*$ and $\mathbf{u}_1^*$ indicate complex conjugate, grey and red lines, respectively). During most of T_{MRW} k and $\mathbf{u}_0\cdot\mathbf{u}_0^*/2$, $\mathbf{u}_1\cdot\mathbf{u}_1^*/2$ have almost constant values. Figure1b shows the variations of u in time obtained in 100 azimuthal sections – it is visible that the flow is 2D during most of T_{MRW} (except for the narrow range of time where $\mathbf{u}_1\cdot\mathbf{u}_1^*/2$ reaches large values). In the investigations of MRW the changes of T_{MRW} with increase of Γ (Re fixed) have been studied. For η=0.475-0.6 the same phenomena have been observed as in Lopez et al. [2], as is evidenced by the similarities of the time series, the phase portraits and the one-parameter path. In the range of η=0.475-0.6 there is no the period doubling bifurcation phenomena and the phase portraits show spiraling orbits. For the flow cases of η=0.375-0.42 the strong period doubling phenomena occur. For η=0.42 a large diversity of phenomena is observed depending on Reynolds number: For small values of Re the one-parameter path shows the occurrence of the period doubling cascade bifurcation, but, for higher Reynolds numbers Re ≥126 the one-parameter paths resemble the solutions observed for η=0.475-0.6. The cascade time series are very complex but in most cases they are regular, see [5]. In such flow cases the strong three-dimensionality is observed – the 3D flow structures coincide with the time ranges in which the modal energy $\mathbf{u}_1\cdot\mathbf{u}_1^*/2$ reaches large values. For the flow cases of η=0.375 the period doubling bifurcation is dominant in the whole MRW area. For η=0.3 the changes of T_{MRW} are milder and all observed unsteady processes are much weaker in comparison to those observed for higher η.

For the flow cases of η=0.375, 0.475, 0.6 the lines of the RMW appearance and the homoclinic collision (above which the flow becomes steady) have been determined for different Re and compared to the corresponding N_M and C lines in Lopez et al. [2]. The comparison shows that scenario proposed by Lopez et al. [2] for η=0.5 is valid for wide range of

radius ratio η (regardless of the differences in the bifurcation phenomena mentioned above, [5]). The investigations have also shown that regardless of the complexity of some time series the elementary flow parameter profiles in the circumferential direction are always smooth, see Figure 1c.

For comparison, the DNS studies have also been performed for the short Taylor-Couette configurations with two rotating end-walls (Re=90-150, Γ=3.7-4.2, η=0.5, 0.45). In these flow cases the rotating discs cause the strong outward motion along the end-walls (two strong Ekman vortices occur) and thus produce a strong symmetric forcing on the flow. The unsteady area results from the interaction of the Hopf bifurcation and the steady-state fold bifurcation. Many interesting phenomena have been uncovered. The results are compared with experimental data published by Mullin [6]. All bifurcation lines presented in [6] (Fig. 2) have been reconstructed.

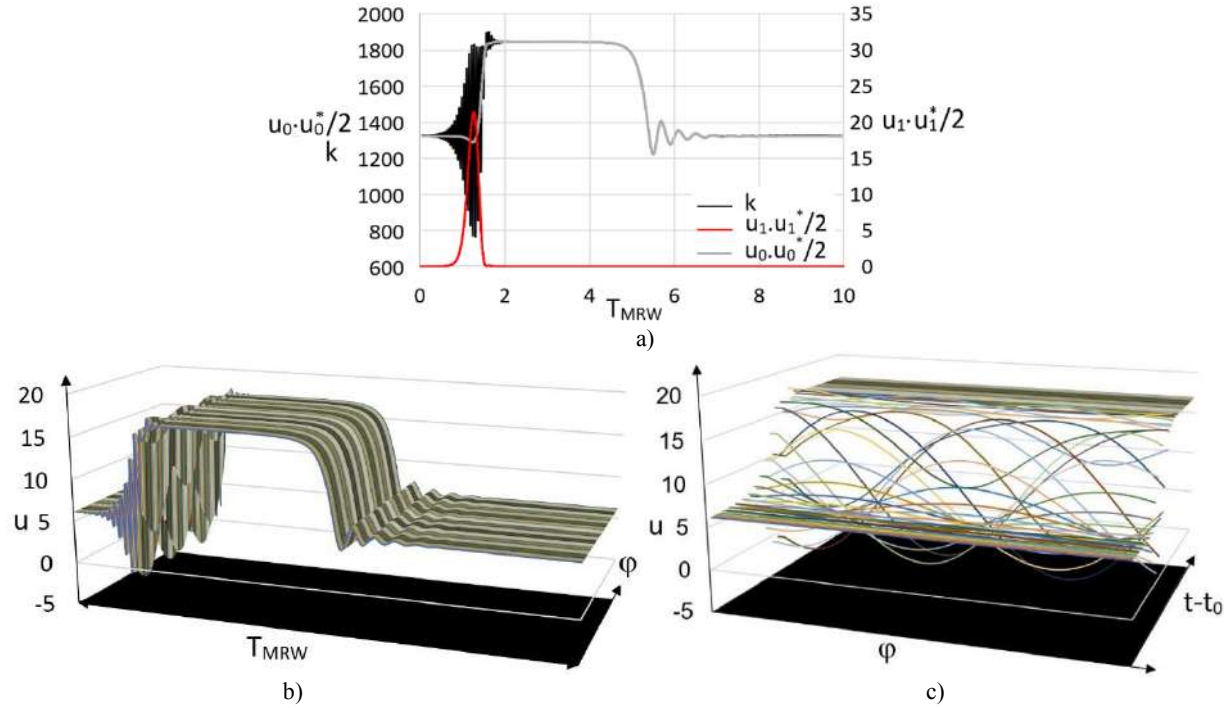

Figure 1. a) The time series (one period) of the kinematic energy k (black line) and the modal energy $\mathbf{u}_0\cdot\mathbf{u}_0^*/2$ (grey line), $\mathbf{u}_1\cdot\mathbf{u}_1^*/2$ (red line), c) the time series of the radial velocity component u obtained for 100 azimuthal sections, c) the azimuthal profiles of the radial velocity u = f(φ) obtained in this part of T_{MRW} where $\mathbf{u}_1\cdot\mathbf{u}_1^*/2$ reaches large values. η=0.475, Re=119.7, Γ=3.0404, [5].

CONCLUSIONS

The presented DNS results clearly show the directions of changes occurring in the short asymmetric Taylor-Couette flow dynamics with changes of radius ratio η. The research has shown that the scenario of bifurcation processes presented by Lopez et al. [2] for radius ratio η=0.5 is valid for a very wide range of η. The most interesting phenomena have been found for η=0.375-0.42 where the period doubling bifurcation is observed.

Acknowledgement

The author is grateful to Prof. Tom Mullin from Oxford University for inspirations, research help and discussion. The DNS computations have been performed in Poznan Supercomputing and Networking Center, which is gratefully acknowledged.

References

[1] Mullin T., Blohm, C. Bifurcation phenomena in a Taylor-Couette flow with asymmetric boundary conditions, *Phys. Fluids*, **13**, 136-140, 2001.
[2] Lopez J.M., Marques F., Shen J. Complex dynamics in a short annular container with rotating bottom and inner cylinder, *J. Fluid Mech.*, **501**, 327-354, 2004.
[3] Serre E., Pulicani J.P. A three-dimensional pseudo-spectral method for rotating flows in a cylinder, *J. Computers and Fluids*, **30**, 49, 2001.
[4] Tuliszka-Sznitko E., Mullin T. Numerical investigation of bifurcation phenomena in Taylor-Couette flow with the asymmetric end-wall boundary conditions, Book of abstract, ETC, Stockholm, 2017.
[5] Tuliszka-Sznitko E. Flow dynamics in the short asymmetric Taylor-Couette cavities at low Reynolds numbers, *Int. J. Heat and Fluid Flow*, **46**, 2020.
[6] Mullin T. An experimental and numerical study of a codimension-2 bifurcation in a rotating annulus, *EUROPHYSICS LETTERS*, **8** (3), 1989.

COMPLEXITY OF PHASE DISTRIBUTION IN TWO-PHASE FLOW USING COMPOSITE MULTISCALE ENTROPY

Gabriela Rafałko*[1], Romuald Mosdorf[1], Grzegorz Litak [2], Grzegorz Górski[1]
[1]Faculty of Mechanical Engineering, Bialystok University of Technology, Bialystok, Poland
[2]Department of Automation, Lublin University of Technology, Lublin, Poland

Summary The paper presents two-phase flow analysis using Composite Multiscale Entropy (CMSE). The two-phase flow of water-glycerol and air phases in a 3 mm, circular minichannel was taken into consideration. The video frames were extracted for particular flows and further computed in order to perform a phase distribution complexity examination in such flow. Finally, CMSE curves and complexity indexes were obtained for the analysed series. It can be concluded that CMSE and CI enable flow pattern analysis and further identification.

INTRODUCTION

During two-phase flow in minichannel changes of gas and liquid phase distribution are observed. The form of gas phase organisation in a minichannel determines certain flow pattern. The analysis of two-phase flow is crucial in understanding different mechanisms of this phenomenon [1, 3]. The flow patterns observed in a minichannel are complex and instable. Numerous studies have shown different approaches to the identification of two-phase flow patterns such as: image analysis methods [2, 7], nonlinear methods [6, 8], or for instance, certain two-phase flow parameters determination [5]. There are numerous two-phase flow analysis methods, however there still is a need of deep investigation of the phenomena observed in a two-phase flow due to the instabilities and changes in phase distribution. Thus, in the paper the concept of composite multiscale entropy (CMSE) is applied in order to analyse the complexity of phase distribution in two-phase flow.

EXPERIMENTAL SETUP AND DATA CHARACTERISTICS

In the experiment two-phase flow patterns in a circular minichannel (3 mm x 3 mm x 60 mm) have been taken under consideration. The flow consisted of two phases, liquid phase: water – glycerol solution (solution's concentration: 45 %) and air phase. The experimental schema is shown in Fig. 1. A pump (4 – Fig. 1) generated compressed air which passed through an air tank (5 – Fig. 1) and a valve (6 – Fig. 1). Next it was directed into the constant pressure air tank (5 – Fig. 1), a flow meter (8 – Fig. 1) and a special micro-bubble generator (1 – Fig. 1). A water tank (7 – Fig. 1) was also a part of the setup. The two-phase flow patterns were recorded using the Phantom v. 1610 high speed camera (2 – Fig. 1). The light (3 – Fig. 1) was directed onto the minichannel.

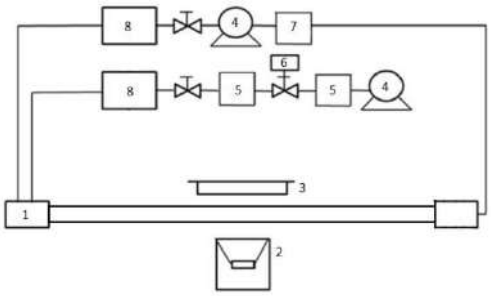

Figure 1. The experimental schema: 1 – a special micro-bubble generator [8], 2 - Phantom v. 1610 high speed camera, 3 –lightning system, 4 – pumps, 5 – a constant pressure air tank, 6 – a valve, 7 – a water tank, 8 – flow meters.

The videos of the flow were recorded using the Phantom v. 1610 high speed camera with a frequency of 5000 fps. The films were divided into the frames which presented grayscale flow pattern images (64 pixels x 1280 pixels) (Fig. 2). The gathered two-phase flow video frames (10 for each observed flow) have been converted into pixel matrices. First, a central part of the frame was extracted (24 pixels x 800 pixels).
Next, each data set presenting observed flow was calculated using CMSE formula for m=2, k=1:49, r=0.2 [9]. Additionally, the complexity index value (CI) [9], which is defined as integral of the CMSE curve was assessed. Figure 3 shows CMSE curves and CI indexes for flows presented in Fig. 2 a-c and Fig. 2 g.

*Corresponding author. E-mail: rafalkogabriela@gmail.com.

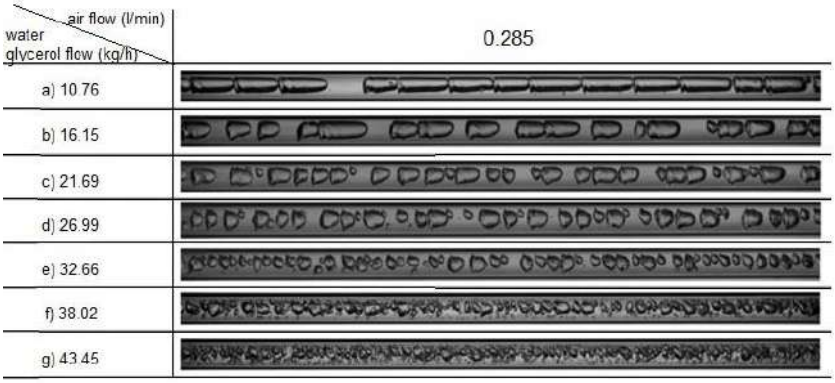

Figure 2. The analysed two-phase flow patterns (water-glycerol and air flow) characterised by constant air flow rate (0.285 l/min) and different water – glycerol flow rates; observed flow patterns: a) long slugs, b) slugs, c) slugs and cap bubbles, d) short slugs and cap bubbles, e) cap bubbles and bubbles, f) bubbles, g) minibubbles.

RESULTS

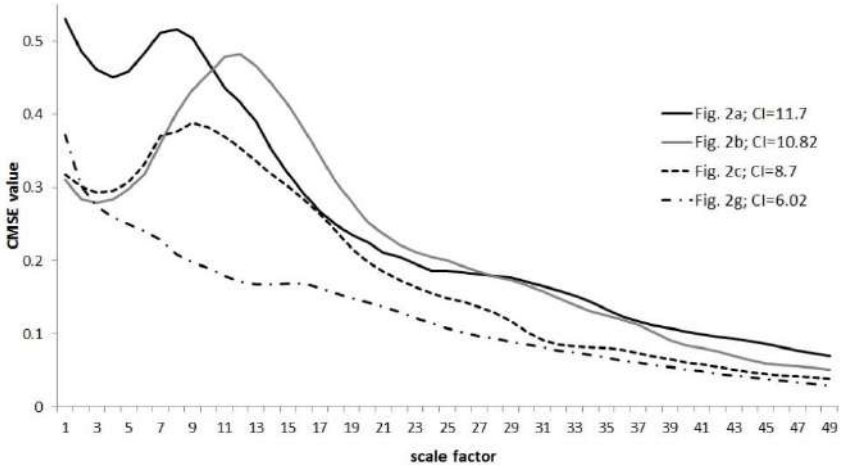

Figure 3. The CMSE curves and CI of four different observed flows.

CONCLUSIONS

Results show that CMSE curves and CI value can unable distinguishing two-phase flow patterns. In the Fig. 3 CMSE for slug flow is similar to a CMSE curve of correlated noise while CMSE for minibubbles presents a curve similar to an uncorrelated noise. The level of CMSE determines the flow pattern order, the lower the CMSE level, the more chaotic/stochastic the observed flow is. As the scale factor increases the level of CMSE decreases – less and less details are observed in the flow.

Acknowledgment

This work was supported by International scholarship exchange of PhD candidates and academic staff.

References

[1] Cheng, L., Ribatski, G., Thome, J. R.. Two-Phase Flow Patterns and Flow-Pattern Maps: Fundamentals and Applications. *Applied Mechanics Reviews*. **61**(5): 050802, 2008.
[2] do Amaral. C.E.F., Alves, R. F., da Silva M. J., Arruda, L.V.R., Dorini L., Morales R.E.M., Pipa D.R. Image processing techniques for high-speed videometry in horizontal two-phase slug flows. *Flow Measurement and Instrumentation*. **33**:257–264, 2013.
[3] Grzybowski, H., Mosdorf, R., Dynamics of pressure drop oscillations during flow boiling inside minichannel. *International Communications in Heat and Mass Transfer:* **95**:25–32,2018.
[4] Hansen C. et al. Sample Entropy, Univariate, and Multivariate Multi-Scale Entropy in Comparison with Classical Postural Sway Parameters in Young Healthy Adults. *Front in Hum Neuroscience*. **11**:206, 2017.
[5] Kim T.H., Kommer E., Dessiatoun S., Kim J. Measurement of two-phase flow and heat transfer parameters using infrared thermometry. *International Journal of Multiphase Flow*. **40**:56-67, 2012.
[6] Litak G., Górski G., Mosdorf, R., Rysak, A., Study of dynamics of two-phase flow through a minichannel by means of recurrences. *Mechanical Systems and Signal Processing*: **89**: 48–57, 2017.
[7] Masiukiewicz, M., Anweiler, S. Two-phase flow phenomena assessment in minichannels for compact heat exchangers using image analysis methods. *Energy Conversion and Management*: **104:** 44–54, 2015.
[8] Mosdorf, R., Górski, G. Identification of two-phase flow patterns in minichannel based on RQA and PCA analysis. *International Journal of Heat and Mass Transfer*. **96**: 64–74, 2016.
[9] Wu S. et al. Time Series Analysis Using Composite Multiscale Entropy. *Entropy*. **15**: 1069-1084, 2013.

NAVIER-STOKES SOLUTIONS WITH SYMMETRY RESTRICTIONS AND THEIR RELATION WITH TRANSITIONAL AND TURBULENT PIPE FLOWS

V.G. Priymak*
A.M.Obukhov Institute of Atmospheric Physics, Russian Academy of Sciences, Moscow, Russia

Summary The problem of Poiseuille flow stability in an infinite circular pipe is a model one for subcritical transition studies since Osborne Reynolds results. The prevailing mathematical model describing all the related physics consists of incompressible unsteady Navier-Stokes equations in cylindrical coordinates (r, φ, x), streamwise periodic velocity, no-slip conditions at the walls, constant mass flux (or constant pressure gradient) driving and naturally 2π-periodic velocity along the azimuthal direction. Navier-Stokes solutions are also assumed to satisfy suitable regularity conditions at $r = 0$. Calculations using this model are very expensive, also the computed dynamics is chaotic and too complex to decode the transition scenario. Therefore, it may be relevant to simplify the mathematical model. In the present study we consider certain simplifications, including popular cases restricting the dynamics to reflectional (about the meridional plane $\varphi = 0$) and rotational (e.g., π-rotational) symmetries. We show that in these two cases certain flow characteristics cannot be properly computed, whereas others are only weakly sensitive to symmetry constraints. Accurate calculations are carried out at two Reynolds numbers Re= 2000 and 4000 corresponding to spatially intermittent flow and essentially uniform turbulence.

PROBLEM FORMULATION

The flow of an incompressible viscous fluid in a pipe $\Omega = \{\mathbf{r} = (r, \varphi, x) : 0 \leqslant r < R, 0 \leqslant \varphi < 2\pi, |x| < \infty\}$ is described here by the Navier-Stokes equations

$$\partial_t \mathbf{v} = -\nabla(p/\rho + \mathbf{v}^2/2) + \nu\nabla^2\mathbf{v} + \mathbf{v}\times\boldsymbol{\omega}, \quad \nabla\cdot\mathbf{v} = 0 \quad \text{in } \Omega, \tag{1}$$

where $\mathbf{v} = (v, w, u)$ is the velocity, $\boldsymbol{\omega} = \nabla\times\mathbf{v}$, and p, ν, ρ are respectively, pressure, kinematic viscosity and constant density. Equations (1) are supplemented with certain initial conditions for velocity. The boundary conditions are periodicity in the axial direction $\mathbf{v}(r, \varphi, x, t) = \mathbf{v}(r, \varphi, x + X, t)$ and no-slip on the wall $\mathbf{v}|_{r=R} = 0$, satisfying the volume flux conservation constraint $U(t) = (1/\pi R^2)\int_0^R r\,dr\int_0^{2\pi} d\varphi u(r, \varphi, x, t) = const$.

Spatial discretization of (1) involves Galerkin trigonometric approximation in x, φ and pseudospectral technique with Chebyshev collocation nodes $r_j = R\cos(\pi j/2Q)$, $j = 0, 1, \ldots, Q$ in radial direction. We represent solution by the truncated Fourier series

$$\mathbf{v} = \sum_{n=-N}^{N}\sum_{m=-M}^{M} \mathbf{v}_{nm}(r, t)\, exp(i\alpha_m x + in\varphi), \alpha_m = 2\pi m/X. \tag{2}$$

For Eqs. (1) written in terms of $\mathbf{v}_{nm}$ there is no physical boundary at $r = 0$, therefore suitable regularity conditions are imposed at the polar axis. These conditions exploit (but do not meet exactly) special behaviour of analytic functions in the vicinity of $r = 0$, established by Theorem 1 of [1]. We require the weaker condition that the Navier-Stokes equations be nonsingular at the origin [1]. Direct numerical simulation using the above mathematical model adequately describes (see [2]) both intermittent and turbulent flow regimes at $1950 \leqslant \mathrm{Re} \leqslant 4000$ without *a priori* requirements of certain rotational or reflectional symmetries.

These long-term and high resolution calculations are very expensive, also the computed dynamics is chaotic and often too complex to decode the transition scenario. Therefore, it may be relevant to simplify the mathematical model. In the present study we consider certain simplifications, including popular cases restricting the dynamics to the reflectional symmetry

$$[v, w, u](r, \varphi, x, t) = [v, -w, u](r, -\varphi, x, t), \tag{3}$$

and π-rotational symmetry

$$[v, w, u](r, \varphi, x, t) = [v, w, u](r, \varphi + \pi, x, t). \tag{4}$$

NUMERICAL EXAMPLES

To understand if the long-life (with an extensive statistically stationary stage) Navier-Stokes solutions with symmetry restrictions do exist and what is their relationship with transitional and turbulent flows in Ω, we carried out special calculations at two Reynolds numbers Re= 2000 and 4000 with $X = 120\pi R$ and $(Q+1)\times(2N+1)\times(2M+1) = 33\times81\times2401$ spectral modes in r, φ, x. Previous work briefly concerns only the cases of reflectional symmetry and turbulent flow regime [1]. We show that the use of symmetry relations (3),(4) turns out to be rather insidious: certain flow characteristics cannot be properly computed, whereas others are only weakly sensitive to symmetry constraints (see Fig. 1, Re= 4000). The same is true in the core region of turbulent puffs at Re= 2000.

*E-mail: vgpriymak@mail.ru.

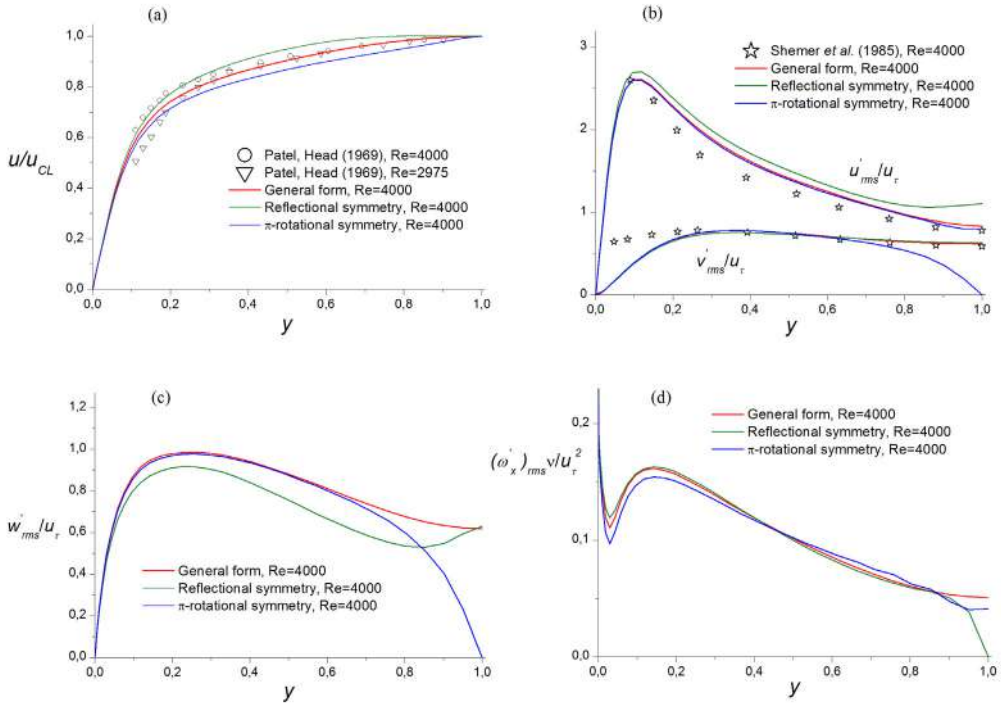

Figure 1: Comparison of flow characteristics corresponding to solutions of the Navier-Stokes equations without symmetry constraints (i.e. of general form), with reflectional symmetry and with π-rotational symmetry. (a) Mean velocity profiles normalized by the centreline velocity. (b) Root-mean-square streamwise and radial velocity fluctuations as functions of distance $y = 1 - r/R$ from the pipe wall. (c) R.m.s. azimuthal velocity fluctuations profiles. (d) R.m.s. streamwise vorticity fluctuations distributions.

CONCLUSIONS

The appeal of using symmetries (3),(4) is due to the fact that the complexity of calculations may be considerably reduced: one half of Fourier modes in (2) is equal to zero both for (3) and (4) conditions.

At the same time we show here that numerical Navier-Stokes solutions with symmetry restrictions cannot accurately describe basic turbulence statistics for actual pipe flow. This fact is sometimes overlooked when constructing simplified mathematical models (see, e.g., [3, 4, 5]): time-periodicity (in a comoving frame) of limiting solutions on the separatrix between laminar and turbulent attraction regions is the result of *a priori* requirements of a π-rotational and reflectional symmetries. Perhaps this is an oversimplification of the mathematical model.

Let us note in conclusion the following technical point. If the initial velocity field satisfies the symmetry conditions, then these conditions are reproduced at arbitrary times even when using universal computer code. Rounding errors cease to play a destabilizing role in this case: the result of multiplying the non-zero value of a variable by a machine zero (when calculating quadratic nonlinear terms) is interpreted by the computer as a machine zero. As a result, we may not even suspect that we are calculating symmetric solutions of the Navier-Stokes equations.

References

[1] Priymak V.G., Miyazaki T. Accurate Navier-Stokes investigation of transitional and turbulent flows in a circular pipe. *J. Comput. Phys.* **142**: 370-411, 1998.

[2] Priymak V.G. Direct numerical simulation of quasi-equilibrium turbulent puffs in pipe flow. *Phys. Fluids* **30**: 064102, 2018.

[3] Avila M., Mellibovsky F., Roland N., Hof B. Streamwise-localized solutions at the onset of turbulence in pipe flow. *Phys. Rev. Lett.* **110**: 224502, 2013.

[4] Chantry M., Willis A. P., Kerswell R. R. Genesis of streamwise-localized solutions from globally periodic traveling waves in pipe flow. *Phys. Rev. Lett.* **112**: 164501, 2014.

[5] Nikitin N. V., Pimanov V. O. Numerical study of localized turbulent structures in a pipe. *Fluid Dynamics* **50**: 655-664, 2015.

[6] Patel V. C., Head M. R. Some observations on skin friction and velocity profiles in fully developed pipe and channel flows. *J. Fluid Mech.* **38**: 181-201, 1969.

[7] Shemer L., Wygnanski I., Kit E. Pulsating flow in a pipe. *J. Fluid Mech.* **153**: 313-337, 1985.

RESPONSE OF A LAMINAR SEPARATION BUBBLE TO CONTROLLED DISTURBANCES WITH MODULATED AMPLITUDE

Pedro B P Panisset[1], Igor B de Paula[1], and Omar H O Pinedo [1]
[1]Department of Mechanical Engineering, Pontifícia Católica do Rio de Janeiro, RJ, Brazil

Summary Laminar separation bubbles are highly influenced by disturbances upstream the separation location. Here, time-resolved velocity fields are measured with PIV in order to resolve variations of bubble topology when subjected to changes in the level of background disturbances. Experiments are carried out in a low turbulence and close return water tunnel. Disturbances are introduced with a vibration ribbon and phase locked acquisitions with respect to excitations enable to use ensemble averaging techniques. Spectra of fluctuations near the inflection point showed amplification of fluctuations in a narrow bandwidth with dominant non dimensional frequencies within a range of 0.08<St<0,1. Proper orthogonal decomposition analysis showed that the most energetic modes reach around 15% of total disturbance energy at the final stages of the separated flow. Spatial distribution of the most energetic modes suggests that the transition was governed by Kelvin Helmholtz instability mechanisms.

INTRODUCTION

Following the technological advances in aerial vehicles and low pressure turbines, improvements of the aerodynamic performance has become essential. Due to the low chord-based Reynold number (from 104 to 106), the flow over an airfoil may separate from the surface and laminar to turbulent transition occur. The laminar separation bubble appears in this context as a result of the transition process result on the separated shear layer. LSB is responsible for changes in the dynamic behavior of the airfoil.

Some works showed that the presence of LSB creates a plato on the coefficient pressure profile [1,2], increasing drag and reducing lift. Reynold number, freestream disturbances (such as acoustic disturbances), freestream turbulence, pressure gradient, surface roughness, geometric discontinuities are the main parameters that promote significant topological changes in the bubble [3]. Depending on the Reynold number and the angle of attack, imposed external disturbances modify the bubble structure [4]. It's a result of the amplification of small-convective perturbations that trigger the laminar-to-turbulent transition process [5]. Optimal effect of the disturbances is linked to the amplitude and frequency which it is generated. However, the selection of the best frequency range is even difficult. Conform the perturbations are introduced, the deformation of the mean flow alter the spectral profile. In this way, more experimental result are needed to confirm this nature of the flow.

The experiment in this work was carried out on a flat plate subjected to an adverse pressure gradient, in a low turbulence and close return water channel. Controlled disturbances were introduced by means of a vibrating ribbon displaced just upstream of the separation point. The vibrating ribbon was induced by a surface-mounted magnetic actuator. Planar, time-resolved PIV technique was used for measurements of quasi-steady state of the bubble. The objective of this study is to examine the free stream turbulence effect on the mean topological feature of the bubble. First, geometrical parameter are compared with the literature. Then, spectral analysis and proper orthogonal decomposition (POD) are performed to give more information about LSB stability characteristics.

EXPERIMENTAL METHODOLOGY

The experiment of this paper was conducted on a low turbulence level and close return water tunnel. With the aid of a frequency inverter ranging 0.1-20Hz, a motor fan generates the flow in the range of 0.05-0.15m/s. The measured turbulence level in the test section is about 0,15%. To this end a hot film and a TSI IFA3000 system were employed. It is important to mention that a great part of turbulent fluctuations lay is within the electronic noise level of the anemometer circuit. A flat plate having 3000mm long was inserted in the test section at 600mm downstream from the test section inlet. The plate is made of transparent polycarbonate. The plate is equipped with a flap for adjustment of the stagnation point on the leading edge. Above the flat plate a false wall was built in order to create a variable pressure gradient on the plate. In the present configuration, the false wall created a convergent, divergent channel over the plate. The angle of divergent wall could be adjusted in order to provide a prescribed constant adverse pressure gradient. The throat height at the vertex of convergent-divergent channel was fixed in 200mm. On the divergent part suction slots were machined on the false wall in order to avoid separation. Centrifugal pumps Sarlo2000 were used for boundary layer suction. The water was pumped to the tunnel corner downstream from the test section.

Controlled disturbances were created using a vibrating ribbon made of steel. The oscillation of the ribbon was provided by an electrical magnet with a controlled current. The magnet was placed in a sealed case that was flush mounted with the flat plate surface.

Time resolved velocity fields were measured using a planar PIV system. High sampling frequency was achieved using a double cavity laser LITRON LDY-300, which provides 30mJ/pulse at 2kHz, and a MotionPro X3Plus, which has a resolution of 1280x1240 and can run at frequencies up to 2000frames per second. Illumination and imaging systems were synchronized by a TSI 610036 synchronizer. For present measurements the sampling frequency was set to

250Hz. A set of spherical and cylindrical lens was used to create the illumination plan for PIV measurements. Polyamide particle tracers with diameters of about 20um and density of 1.03kg/m3 were used for flow seeding. Routines developed in LabView and Matlab platforms allow to control the image acquisition and the PIV processing.

PRELIMINAR RESULTS

According to [6], some topological parameters of LSB are relevant to describe the bubble nature. In this work the Falkner Scan parameter was constant and equals -0.22. The Reynolds number based on the momentum thickness at separation is 332 which do also display a good agreement with the literature. In this study, (γs) was obtained following the methodology proposed by [6]. The empirical correlation proposed in that work predicts an angle of 0.034 rad for a ratio LI /Ld = 0.068. In current experiments an angle γs = 0.038 rad was found which is in agreement with the model proposed for bubbles measured in wind tunnels. Figure 1 show the inflectional velocity profile along the bubble and power spectrum density of the disturbances. As expected, inflection of the profile is more pronounced from near the separation point until the reattachment point. Downstream of the reattachment the velocity profile asymptotically tends to a fully turbulent one.

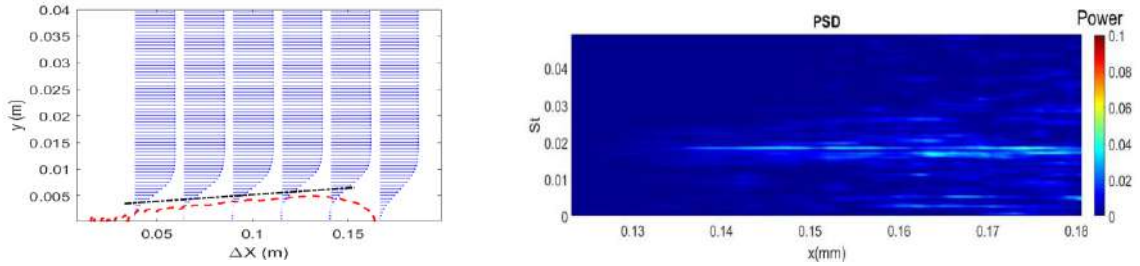

Figure 1. Right: Bubble contour (dashed red), mean velocity vectors (blue vector) and inflection of mean velocity profile (dashed-dot black line). Left: Contour of power density spectrum of the streamwise velocity.

The dominant frequencies on the velocity fluctuations along the separation region can be observed in Figure 1. In this case, no controlled excitations were introduced in the boundary layer. The figure shows a clear energy peak in narrow frequency bandwidth. Near the reattachment point the most prominent perturbations are within the range of nondimensional frequencies of 0.016<St<0.019, where St is the Strouhal number given by St=fδ*/U∞. These spatial structure of flow fluctuations in this frequency range are also characterized. In the full paper, similar results will be presented for the case with controlled excitations.

In order to analyze spatial structure of the fluctuations 2000 instantaneous velocity fields were analyzed using Proper Orthogonal Decomposition (POD) technique. The analysis is done only in the region of reattachment bubble. The first two modes shown in the Fig. 4 represent the same type of structure and show rapid growth of perturbations. These structures resemble those of Kelvin-Helmholtz instability [7]. In the full paper the role of controlled excitation and the transient growth of the bubble will be assessed and the results will be presented accordingly.

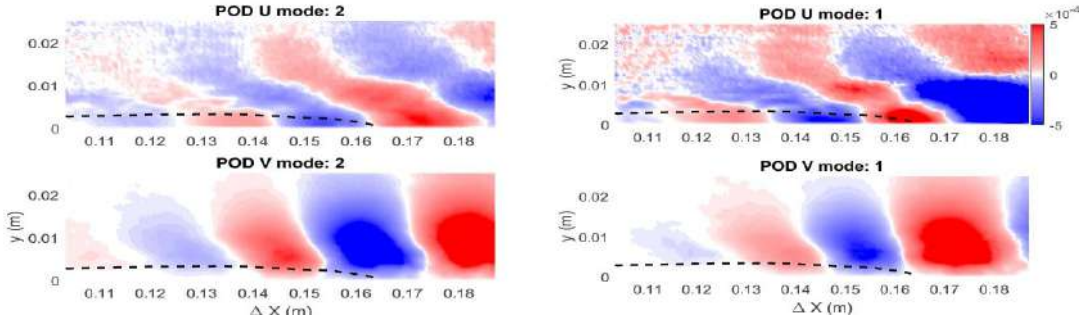

Figure 2. Most energetic POD modes of streamwise and wall normal fluctuations.

References

[1] Tani, I. 1694. “Low speed flows involving separation bubbles”, Prog. Aeronaut. Sci. 5, pp. 70-103.
[2] Gaster, M. 1969. “The structure and behavior of laminar separation bubbles”, Rep. Mem. No. 3595. Aeronautical Research Council.
[3] Akpolat, T., et. al. 2012. “Low Reynolds number flows and transition”, Low Reynolds Number Aerodynamics and Transition, Mustafa Serdar Genc, IntechOpen, DOI: 10.5772/31131.
[4] Yarusevych, S., Kotsonis, M. 2017. “Steady and transient response of a laminar separation bubble to controlled disturbances” J. Fluid Mech. , vol. 813, pp. 955-990.
[5] Diwan, S. S. and Ramesh, O. N. 2009. “ On the origin of the inflectional instability of a laminar separation bubble”. J. Fluid Mech. 629, 263–298.
[6] Serna, J., Lázaro, B. J. 2015. “On the laminar region and initial stages of transition in transitional separation bubble“, Eur. J. Mech B/Fluids, v. 49, pp. 171-183.
[7] Lengani, D., Simoni, D., Ubaldi, M., & Zunino, P. (2014). “POD analysis of the unsteady behavior of a laminar separation bubble”. Experimental Thermal and Fluid Science, v. 58, pp 70-79.

INFLUENCE OF NOISE ON THE WAVE NUMBER CHOICE AFTER FIRST INSTABILITY IN THE SPHERICAL COUETTE FLOW

Olga Krivonosova*[1], Maria Gritsevich [2,3,4], Dmitry Zhilenko [1]and Peter Read [5]
[1]Institute of Mechanics, Lomonosov Moscow State University, Moscow, Russia [2]Finnish Geospatial Research Institute (FGI), Masala,Finland
[3]Department of Physics, Helsinki University, Helsinki,Finland
[4]Institute of Physics and Technology, Ural Federal University, Ekaterinburg, Russia [5]Department of Physics, Atmospheric, Oceanic and Planetary Physics, University of Oxford, Oxford, United Kingdom

Summary In this study we carried out investigations on wave number selection for rotating spherical flow, when its state changes from subcritical to supercritical one in the presence of noise and forcing. Noise is injected to the flow by irregular in time perturbations in the imposed rotational rate and forcing – by rotation with acceleration. The obtained results provide insights into nonlinear interactions and energy exchange between competing modes in model flows and can be extended to flows in astrophysical objects, such as pulsars, and also to the selection of circulation regimes in the atmosphere.

PROBLEM UNDER STUDY

Numerous examples have been reported among experiments and calculations in fluid flows in which multiple stable solutions with different wave numbers can be observed at the same Reynolds numbers [1-3]. In this study experiments [4] and preliminary DNS were carried out to study how the selection of one from two possible wave numbers in the onset of azimuthal waves following the first instability depends on noise amplitude in the presence of the inner sphere acceleration. The acceleration is determined by the initial and final Reynolds numbers and the time of transition between them. The flow of viscous incompressible fluid in the gap between concentric spherical boundaries, induced by their rotation about common axis, is under study. The outer sphere was held stationary, while the inner sphere rotational speed was increased linearly from a subcritical flow (further denoted as 0) to a supercritical one, with azimuthal wave numbers m=3 or m=4 (further denoted as 3 or 4). Noise perturbations were added to the flow by introducing small (not more than 1.5%) irregular in time disturbances into the rotational speed signal. The noise which was used in experiments looks like white noise in accordance with its kind of spectrum. The flow velocity measurements were conducted by using laser Doppler anemometer to investigate the behaviour of competing modes in their stages of damping and growth.

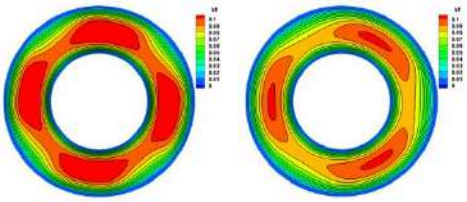

Figure 1. Contour lines of radial velocity component in equatorial plane for azimuthal waves with m = 4 (left) and m = 3 (right)

RESULTS

With an increasing of noise amplitude, a change in the dominant m value was found to occur at the same initial and final Reynolds numbers and acceleration values. It was revealed that several scenarios for wave number transition as a function of noise amplitude can be observed with increasing acceleration rate. At relatively “small” and “large” noise amplitudes, the favoured wave numbers may remain constant - m=3 in the first case and m=4 in the second case independently of the acceleration rate. The values of “small” and “large” noise amplitudes were found to be dependent on initial Re number, corresponding to the beginning of acceleration phase. At intermediate noise level, one change in wave number (from transition $0 \rightarrow 4$ to transition $0 \rightarrow 3$) or two (starting from transition $0 \rightarrow 4$ to transition $0 \rightarrow 3$ and then from $0 \rightarrow 3$ to $0 \rightarrow 4$) were observed with accelerating rate increasing. Effects on wave number transitions with increasing acceleration for constant noise intensity, and with noise intensity increasing at constant acceleration, as obtained in our work, were also observed in experiments [5] on surface water waves, generated under the action of sinusoidal forcing. The imposed noise increases the total time-scale of competing linear mode interactions, ranging from the beginning of ultimate growth of the preferred mode to the time when the damping mode reaches its maximum amplitude. The latter was confirmed by preliminary DNS, as well as change in wave number (from transition $0 \rightarrow 4$ to transition $0 \rightarrow 3$) with accelerating rate increasing.

* Corresponding author. E-mail: olga@imec.msu.ru

CONCLUSIONS

It was shown that the action of imposed noise leads to energy transfer from the initially preferred to the corresponding damped mode, increasing both its maximum amplitudes and increments of growth. The noise destroys the results of an acceleration in the boundary conditions and the persistence of the preferred number m=4 is observed.

This work was partially supported by the Russian foundation for basic research, Projects Nos. 18-08-00074 and 19-05-00028.

References

[1] Coles D. Transition in circular Couette flow. *J. Fluid Mech.***21,** 385-425, 1965.

[2] Frueh W. and Read P. Experiments on a barotropic rotating shear layer. Part1. Instability and steady vortices. *J. Fluid Mech.***383,** 143-173, 1999.

[3] Erenburg V., Gelfgat A., Kit E., Bar-Yoseph P. and Solan A. Multiple states, stability and bifurcations of natural convection in a rectangular cavity with partially heated vertical walls. *J. Fluid Mech.***492,** 63-89, 2003.

[4] Zhilenko D., Krivonosova O., Gritsevich M, and Read P. Wave number selection in the presence of noise: Experimental results. *Chaos* **28**, 053110, 2018.

[5] Berthet R., Petrossian A.,Residori S., Roman B and Fauve S. Effect of multiplicative noise on parametric instabilities. *Physica D,* **174**, 84-99, 2003.

BOUNDARY LAYER TRANSITION DETECTION USING ADVANCED INFRARED THERMOGRAPHY

A.V. Ivanov*[1], A.V. Boiko[1], D.A. Mischenko[1]
[1]Khristianovich Institute of Theoretical and Applied Mechanics, SB RAS, Novosibirsk, Russia

Summary The problem of accurate experimental detection of boundary layer transition position in wind-tunnel tests is discussed. A new robust and highly resolving technique using IR-thermography is suggested. The developed techniques are successfully applied for boundary layer transition detection in a broad range of base flow parameters and wing model configuration. Thus, a significant and valuable experimental database for verification of boundary layer transition position prediction tools is obtained.

INTRODUCTION

The highest potential for increasing of aircraft efficiency usually attribute to reduction of turbulent friction drag that is the greatest part (about 50%) of total drag of modern commercial aircraft. The most natural way of turbulent drag reduction is flow laminarization, i.e. enlargement of laminar flow run and consequently reduction of turbulent flow regions. The main targets of laminarization are aircraft wings, vertical and horizontal tails. Transition of boundary layer flow from laminar to turbulent state in flight conditions on these wings usually happens due to amplification of boundary layers waves and vortexes triggered by different wing surface imperfectness (like surface roughness, waviness etc) or maybe by different external flow factors like enhanced turbulence level of the free stream or high acoustic level. In order to reach the required laminarization the engineers need new reliable and well verified approaches for calculations of boundary layer flows and prediction of the laminar-turbulent transition position.

In frame of the current experimental study it is supposed to create experimental database for verification of the developed computational transition prediction code. Creation of such verification database suggests exact detection of the beginning and the ending of the laminar-turbulent transition process at significant variation of the base flow parameters (velocity and turbulence level of incident flow) and in a wide range of wing model configuration (attack angle, nondimensional amplitudes of wing surface roughness). In all studied cases the potential flow and boundary layer flow have to be documented accurately together with model geometry and accurate documentation of environmental perturbations (free stream turbulence level, surface roughness etc). Since the present study suggests multiple variations of the model and flow parameters, for detection of transition position we have chosen IR-thermography since this method is non-contact, fast and provides panoramic view of the transition picture.

EXPERIMENTAL SET-UP

The experiments were performed in subsonic low-turbulence wind tunnel T-324 of ITAM SB RAS (Novosibirsk, Russia). The model of 45 degree swept wing (SW45) installed in the test section of T-324 is shown in Fig.1. The model has comprehensive structure including rigid frame (comprising ribs and stringers), outer wing skins made of transparent acrylic sheets (fixed to the frame) and attachable CNC milled leading edge. SW45 model has modified profile NACA 67 1-215 (the same as in studies [1], [2]) and the chord length C=0.8 m in direction normal to the leading edge (LE). The pressure distributions over the model was measured with help of 34 static pressure taps available on the model surface. The integral boundary layer characteristics, potential flow streamlines, streamwise distributions of velocity over the model and freestream turbulence levels were documented with help of hot-wire technique for various angles of attack. The model surface roughness was documented with help of laser displacement sensor. The incident flow turbulence level was varied from low level Tu~0.09% up to enhanced level Tu~0.8%. The incident flow velocity Q_∞ was varied in a wide range from 10 to 50 m/s in order to observe and document transition position shift due to Reynolds number variation.

AN APPROACH FOR INFRARED THERMOGRAPHY FOR LAMINAR-TURBULENT TRANSITION DETECTION

To increase the thermal contrast between laminar and turbulent regions the swept-wing model SW45 was externally preheated before each wind tunnel run with help of array of halogen lamps up to +6°C above ambient air temperature. Then the wind-tunnel starts together with the start of model surface temperature records performed by IR-camera FLIR SC 7300 (with the frame rate about 100 fps). The processing of the recorded IR-movies have shown that in case of low free stream turbulence level, when transition to turbulence caused by amplification of stationary cross-flow vortices only, the IR-images (movie frames) have their maximum temperature contrast in 10-20 seconds after the wind tunnel reach the desired incident flow speed. In this case the averaged transition position can be assessed from a single IR-frame, even if the frame is somehow spoiled by different artefacts caused by initial non-uniformity of the model preheating and significant non-uniformity of the model parts thermal capacity. It was demonstrated here and earlier in [1] that using of time derivative of surface temperature dT_s/dt instead of surface temperature T_s itself provides significant improvement of the transition imaging and helps to get rid of the mentioned artefacts. One should note that when the IR-frames reach their

*Corresponding author. E-mail: andi@itam.nsc.ru .

maximum contrast (10-20 sec after the wind tunnel speed settling) the values of derivatives dT_s/dt usually differ in laminar and turbulent areas not very significantly.

Much harder cases for transition detection by IR-technique are found in the studied regimes with cross-flow dominated transition in cases of enhanced levels of free stream turbulence. In these cases, the transition process becomes unsteady due to significant presence of unsteady, traveling cross flow modes excited due to receptivity to the free-stream turbulence. As a result, the temperature contrast of IR-frames in laminar and turbulent areas become much less pronounced, the number and levels of artefacts growth significantly (see Fig.2 left). The calculation of time derivative dT_s/dt from the recorded IR-movies somehow helps to improve the transition imaging, however the signal to noise ratio still remains low and insufficient for successful transition position detection.

The solution of the experimental problem was found due to detailed temporal analysis of the model surface temperature records. It was found that just after the wind tunnel speed settling, there is a very short time period (1-4 sec only) when the model surface in turbulent areas cools significantly faster than in laminar ones. In fact, during this short period forms the main surface temperature difference between areas with laminar and turbulent flows. The derivatives dT_s/dt calculated in this specified period differ in laminar and turbulent areas with factor of 4(!) that allow detection not averaged transition position only, but also clear detection the beginning and the ending of the laminar-turbulent transition process (see Fig. 2 right)

RESULTS

The present experimental study resulted to development of highly resolving technique for detection of laminar-turbulent transition stages with help of IR-thermography. Application of this technique allowed evaluation of the laminar-turbulent transition position in numerous regimes with various model attack angles and flow speeds including cases of Tollmien-Schlichting waves dominated transition, cross-flow dominated transition (and combination of both), as well at the low and enhanced turbulence levels of the free-stream. The quantitative results of the study will be given in the presentation.

This study is financially supported by Russian Science Foundation, grant No. 18-19-00460

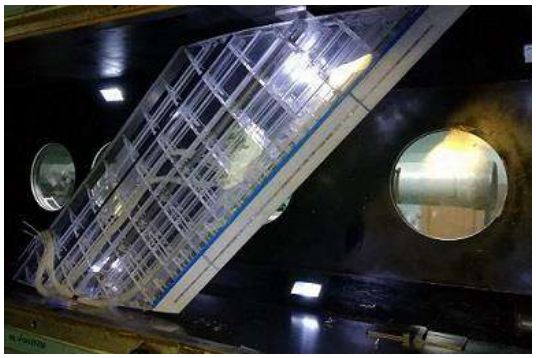

Figure 1. Swept-wing model SW45 installed in the test section of laminar wind tunnel T-324.

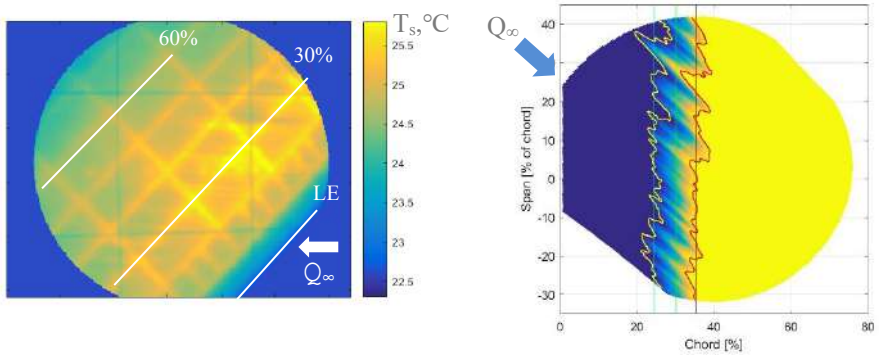

Figure 2. One of the most contrast IR-frame showing wing model surface temperature T_s (left) and the final results of the advanced IR-movie processing - normalized logarithmic derivative of the surface temperature (right). Deep blue color – area of laminar flow state, yellow – turbulent state, intermediate colors – laminar-turbulent transition. The lines at 24.6% and 35,4% of the chord length are automatically evaluated beginning and the ending of the transition process. Tu=0.83%, Q_∞=30m/s.

References

[1] V. I. Borodulin, A. V. Ivanov, Y. S. Kachanov, A. Hanifi. Laminar-turbulent transition delay on a swept wing, AIP Conference Proceedings 1770, 030065 (2016)

[2] V. I. Borodulin, A. V. Ivanov, Y. S. Kachanov, D. A. Mischenko, R. Örlü, A. Hanifi, S. Hein. Experimental and theoretical study of swept-wing boundary-layer instabilities. Unsteady crossflow instability, Phys. Fluids 31, 064101 (2019)

ON THE SIMULATION OF TS WAVES OVER VERY SMALL ISOLATED ROUGHNESS AND ITS RESULTS

Fernando H. T. Himeno*[1], Marlon S. Mathias [1], and Marcello A. F. de Medeiros[1]
[1]Department of Aeronautical Engineering, University of São Paulo, São Carlos, São Paulo, Brazil

Summary Experiments demonstrate that interactions of TS waves of amplitudes about 1% of free-stream velocity with minuscule roughness can trigger transition. Simulating this phenomenon can be difficult as many numerical procedures cannot mesh such small roughness. In acoustic receptivity studies a Taylor-expansion-based non-homogeneous boundary condition on a smooth wall has been successfully used for this purpose. Here we show that such an approach overestimates the roughness effect on the TS wave in a 2D incompressible flow. The study also investigates the effect of roughness on a TS wavepacket in 2D incompressible flows using meshed roughness and will be extended to 3D compressible ones.

INTRODUCTION

The transition to turbulence can be sensitive to very small surface irregularities. [1] investigated experimentally the interaction of a monochromatic TS wave with an isolated cylindrical roughness. They found that for a TS wave of amplitude in the order of 0.5 to 1%, even the smallest roughness still affects the transition. The present study aimed at numerically investigating this phenomenon and extend the analysis to more generic types of TS waves, such as wave packets. Modelling very small excrescences with body fitted grids require high mesh refinement which increases computational cost. Moreover, for many numerical methods including such small roughness can be impossible [4]. Hence, several studies represent small irregularities by a non-homogeneous boundary condition on the wall based on a Taylor expansion of the flow without any roughness. This has been done not only for steady flows [4], but also for unsteady flows in the context of receptivity to acoustic waves [3], both showing that up to roughness heights of $0.1 \times \delta^*$ the results are indistinguishable from body fitted solutions. Here, however, we consider the interaction of a roughness with a TS wave generated upstream of the roughness. We could not find numerical studies of this kind in the literature. To test the approach, simulations were carried out for a small roughness with a body fitted roughness and also with a non-homogeneous boundary condition based on a Taylor expansion for comparison.

METHODS

We used an in-house DNS code in a structured mesh. The time-marching is performed by 4th order Runge-Kutta scheme and the spatial differentiation by a 4th order spectral-like method. A 10th order spatial anti-aliasing filter was applied and buffer-zones were included at the open boundaries to prevent spurious oscillations. The code is parallelized and solves the compressible Navier-Stokes equations as we intend to extend into the compressible regime. Details of the code implementation and validation are found in [2].

PRELIMINARY RESULTS AND CONCLUSIONS

As a preliminary study, we considered a two-dimensional simulation of a flat plate with a rectangular roughness element and verified its influence on the evolution of a TS wave. Parameters were non-dimensionalized by the displacement thickness at the roughness center, δ^*_R, and by the free-stream speed. Based on the experiments from [1], the Reynolds number was $Re_R = 950$. The physical domain was $0 \leq X \leq 800$ and $0 \leq Y \leq 20$ in non-dimensional variables. The disturbance was located at $X_D = 200.51$ and was composed by 10 time-harmonic modes of the fundamental frequency $F = 90 \times 10^{-6}$. The excitation strip had a length $\Delta X_D = 20$. The roughness was centered at $X_R = 320.82$ with length $\Delta X_R = 13.37$ and height $h_R = 0.1 \times \delta^*_R$. The Mach number $M = 0.3$, which can still reasonably represent an incompressible flow, with much reduced simulation time in our code. The velocity derivatives for the Taylor expansion roughness representation were obtained from a numerical simulation of the packet evolution on a corresponding smooth plate. This provided the velocity fields in space and time from which the time varying derivatives were calculated to enforce the non-homogeneous boundary condition not only on the mean flow, but also on the TS waves. Nonlinear effects directly associated with the roughness height cannot be accounted for by this model, but they were not expected to be relevant at such small heights. Figure 1(a) shows the evolution of δ^*. It is seen that the roughness affects the boundary layer thickness and the non-homogeneous boundary condition captured the effect accurately. The approach reproduced the flow precisely, except very close to the roughness, Fig. 1(b). The roughness has only a local effect and the boundary layer returns to the smooth case shortly downstream.

Figure 2(a) shows a comparison of the packet evolution for the roughness models used and for the smooth surface reference case while 2(b) gives the corresponding frequency spectra. The roughness has a small destabilizing effect on the packet evolution which is similar at all unstable frequencies. The Taylor-expansion model substantially overestimated

*Corresponding author. E-mail: fernando.himeno@usp.br.

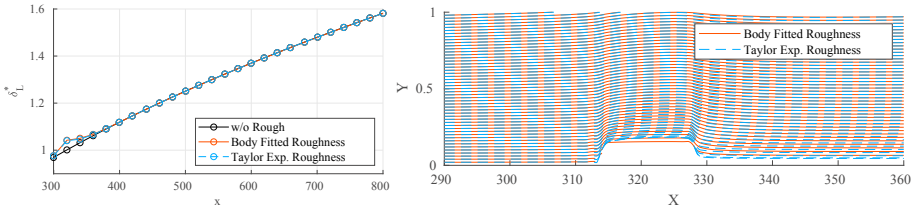

(a) (b)

Figure 1: Mean flow results. a) Displacement thickness evolution. b) Streamlines for the different roughness modelling approaches.

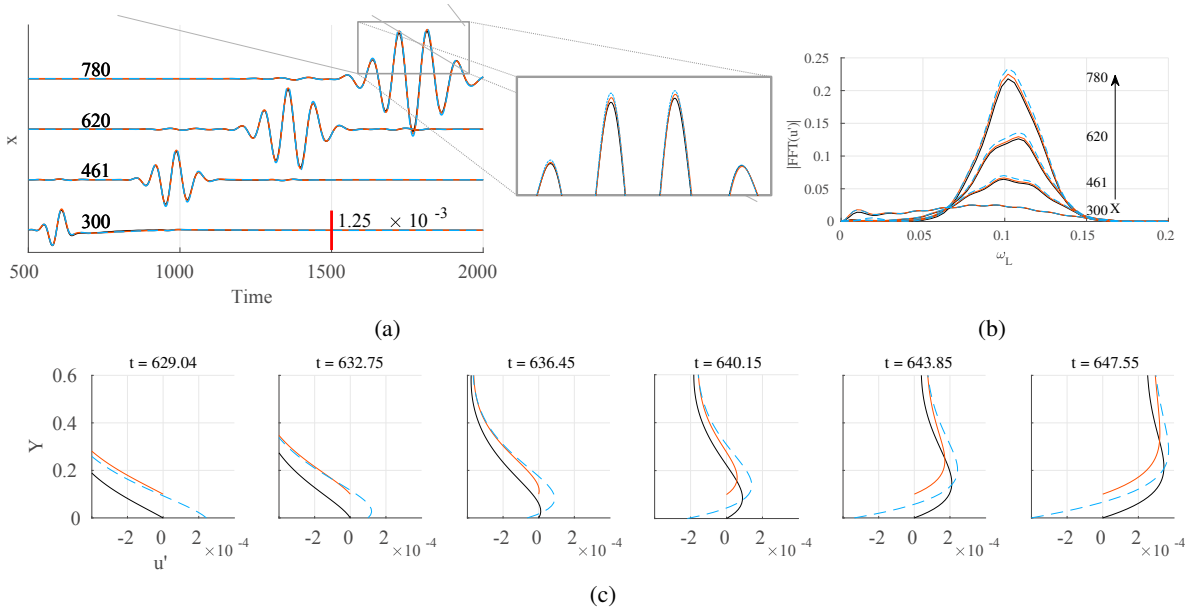

(a) (b)

(c)

Figure 2: Results of TS wave evolution. a) u' acquired at $y = 0.6 \times \delta^*$ and b) its corresponding spectra. c) u' profile showing the phase delay of the Taylor expansion model.

the roughness effect. Figure 2(c) shows profiles of the streamwise velocity fluctuation close to the wall at selected times. It appears that the Taylor model suffers from a phase delay yielding higher oscillations close to the wall. This was not observed on receptivity studies where the flow disturbance did not have a such a complex structure as the TS wave close to the wall. We are currently performing similar tests for smaller roughness where the agreement should improve. We are also trying to reproduce the experiments of [1] with body fitted and Taylor expansion models. The results are not shown due to space limitations, but will be presented at the conference.

ACKNOWLEDGMENTS

The authors would like to thank the Sao Paulo Research Foundation (FAPESP/Brazil), for grants 2018/02542-9 and 2018/04584-0; National Council for Scientific and Technological Development (CNPq/Brazil) for grants 134722/2016-7 and 304859/2016-8; the US Air Force Office of Scientific Research (AFOSR) for grant FA9550-18-1-0112, managed by Dr. Geoff Andersen from SOARD.

References

[1] IB de Paula, W Würz, MT Mendonça, and MAF Medeiros. Interaction of instability waves and a three-dimensional roughness element in a boundary layer. *Journal of Fluid Mechanics*, 824:624, 2017.

[2] Marlon Sproesser Mathias and Marcello Medeiros. Direct Numerical Simulation of a Compressible Flow and Matrix-Free Analysis of its Instabilities over an Open Cavity. *Journal of Aerospace Technology and Management*, 10:1–13, jul 2018.

[3] Henrique Raposo, Shahid Mughal, and Richard Ashworth. Acoustic receptivity and transition modeling of tollmien-schlichting disturbances induced by distributed surface roughness. *Physics of Fluids*, 30(4):044105, 2018.

[4] David Tempelmann, Lars-Uve Schrader, Ardeshir Hanifi, Luca Brandt, and Dan S Henningson. Swept wing boundary-layer receptivity to localized surface roughness. *Journal of Fluid Mechanics*, 711:516–544, 2012.

TRANSITION IN A LAMINAR BOUNDARY LAYER CONTAINING A SUSPENDED SQUARE ROD

Wei He *[1] and Larry K. B. Li[2]
[1]School of Enginnering, University of Liverpool, Liverpool, UK
[2]Department of Mechanical and Aerospace Engineering, Hong Kong University of Science and Technology, Hong Kong, Hong Kong SAR

Summary Boundary layer transition is an important phenomena in engineering. For example, in aeronautical and automotive engineering, the predicted drag is known to depend strongly on the location of transition. Transition in a flat-plate boundary layer has been extensively studied. In its early stages, transition is governed by Tollmien-Schlichting waves induced by background disturbances and wall roughness. Another possible route to transition is via the formation of a separation bubble in the boundary layer, which can alter the adverse pressure gradient. Previous numerical studies have involved generating a separation bubble by imposing a multi-segment velocity function along the far boundary [1], or by placing an inverted airfoil at the inflow boundary to accelerate the flow downstream [3]. These methods, however, only affect the boundary layer indirectly. The effect of surface roughness on boundary layer transition can be modelled by introducing small surface elements, such as bumps and cavities. The mechanisms behind this, however, are still not fully understood. In this numerical-theoretical study, we investigate transition in a non-inclined flat-plate laminar boundary layer containing a suspended square rod. The inflow is defined as $Re_{\delta^*} = 421.5$, with Re_x at around 2.4 million, as estimated at the outlet of the computational domain. The square rod has sides of length $2\delta^*$ and is placed $213\delta^* \leq x \leq 220\delta^*$ downstream from the leading edge of the plate, with a clearance height of $y = 0.71\delta^*$ (0.1 in dimensionless units) from the plate surface. The square rod is fully immersed in the boundary layer, causing the inner layer flow to be more disturbed than the outer layer flow. When the rod is at $x = 213\delta^*$, the wake immediately downstream of the rod oscillates periodically as a result of the Kelvin-Helmholtz instability. The shed vortices propagate to around $70\delta^*$ before landing on the plate and forming a vortex street along it (see figure $1a$). When the rod is moved to $x = 220\delta^*$, the downstream wake becomes more stable (see figure $1b$). The steady state and mean flows of this boundary layer system will be examined in detail using a linear stability analysis.

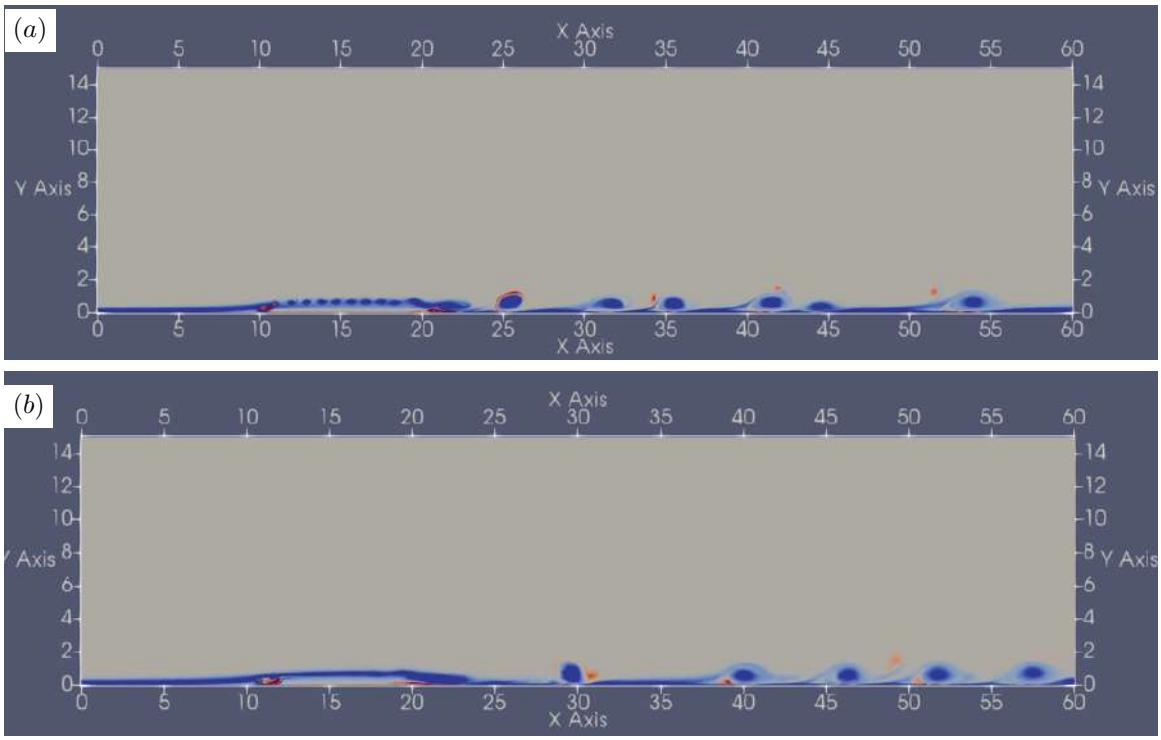

Figure 1: Instanteneous snapshots of the vorticity field behind a square rod immersed in a boundary layer

References

[1] Theofilis V., Hein S. and Dallmann U., On the origins of unsteadiness and three-dimensionality in a laminar separation bubble, *Phil. Trans. R. Soc. Lond. A*, **358**: 3229-3246, 2000.
[2] Schlichting H., Boundary Layer Theory, 7th, McGraw-Hill, 1979.
[3] Hosseinverdi S. and Fasel H. Laminar-turbulent Transition in a Laminar Separation Bubble in the Presence of Free-stream Turbulence, *Procedia IUTAM*, **14**: 570-579, 2015

*Corresponding author. E-mail: whe@liverpool.ac.uk.

AN IDENTYFICATIONOF TWO-PHASE FLOW PATTERNS IN TWO PARALLEL MINICHANNELS

Hubert Grzybowski[1*], Iwona Zaborowska[1], Romuald Mosdorf [1]
[1]Faculty of Mechanical Engineering, Bialystok University of Technology, Białystok Poland

Summary In the paper, the two-phase flow patterns in two parallel circular minichannels with a diameter of 1 mm was identified. The analysis was performed on the pressure drop fluctuations. The data were collected using MPX50DP pressure sensors. In the present experiment the oscillations caused by one type of two-phase flow instability are superimposed to another type, leading to chaotic pressure oscillations. The Principal Component Analysis and Recurrence Quantification Analysis methods were used to the identification two-phase flow patterns in two parallel minichannels in flow boiling. Flow patterns maps were obtained for each of the channels that identified 5 dominant flow patterns.

INTRODUCTION

During non-stationary flow boiling in minichannels there are pressure drop oscillations which are associated with the formation of various chaotically changing flow patterns [1,2]. The continuous transitions between various types of flow patterns make it difficult to set the precise boundaries on flow pattern maps. Additionally flow boiling in parallel channels is associated with flow maldistribution, due to dynamic interaction between channels. Local pressure changes generated by explosive growth of bubbles influences flow in other channel. Many authors use nonlinear analyses to identify flow patterns and assess their complexity [3–5]. From these research methods, most authors use the Recurrence Quantification Analysis (*RQA*). The idea of using the Principal Component Analysis (*PCA*) for *RQA* has been presented in the papers [6-8]. In these papers authors used these methods to create flow pattern maps.

In the paper, *PCA* and *RQA* methods were used to the identification two-phase flow patterns in two parallel minichannels in flow boiling. In the present experiment the short-period density wave oscillations superimposed on long-period pressure drop oscillations were analysed. Flow patterns maps were obtained for each of the channels that identified 5 dominant flow patterns.

EXPERIMENTAL AND DATA CHARACTERISTICS

The scheme of the experimental setup is shown in Figure 1. The distance between minichannels was equal to 5 mm and the inner diameter was equal to 1 mm. During the experiment distilled water was supplied to the heated minichannels from individual surge tanks (Figure 1 - 6, 7). The water flow rate was regulated by a ball valve (Figure 1 - 5). The pressure inside the supply tank (Figure 1 - 3) was kept constant by using the proportional pressure regulator. The heated section consisted of two 150 mm long circular brass pipe with an inner diameter of 1 mm. The two-phase flow patterns at the outlet of the heated section were observed in the glass tube (with an inner diameter of 1 mm) and recorded by a high-speed camera (Figure 1 - 8). The outlet of the glass tube was connected to the overflow tank (Figure 1 - 9). Signals were acquired by the data acquisition system at a rate of 1 kHz. The data recorded for constant heat input equal to 55.8 W and the average mass flux equal to 38.8 kg/m^{2}s was analysed. The observed flow patterns are mainly bubbly, slug, elongated slug or wavy annular flow which also differed in flow velocities. When local pressure exceeds the upstream pressure also flow reversal was observed.

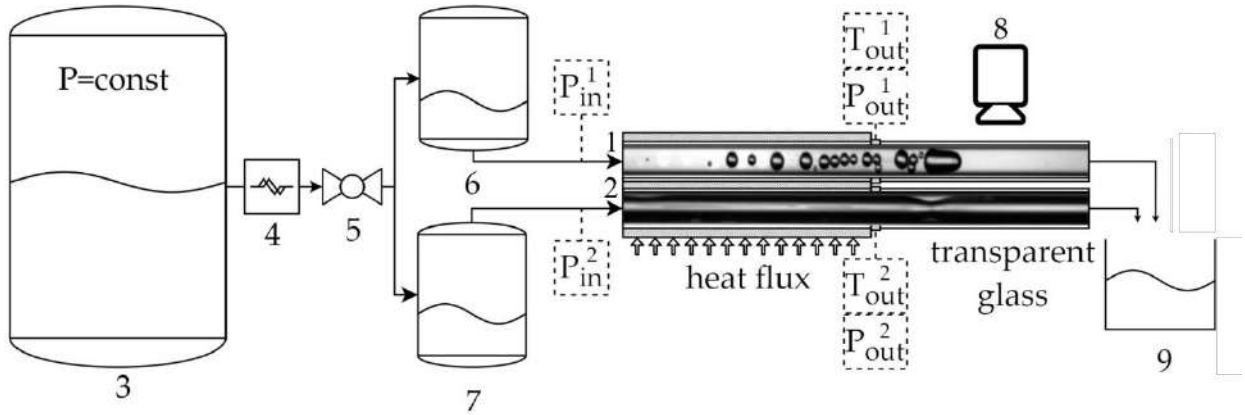

Figure 1. The experimental setup. 1, 2 – minichannels, 3 – supply tank; 4 – flow meter; 5 – ball valve; 6, 7 – surge tank; 8 – high speed camera; 9 – overflow tank.

*Corresponding author. E-mail: h.grzybowski@pb.edu.pl

RESULTS

Single cycle of pressure drop oscillations recorded in each channel was analysed using nonlinear data analysis methods. The results the showed that the system is prone to various flow instabilities that usually superimposed on each other. The analysis of the dynamics of chaotic pressure oscillations and recorded videos show that a certain dominant flow patterns can be identified. The *RQA* and *PCA* [6] were used to analyse the pressure drop fluctuations in each minichannel. The *RQA* coefficients were used to obtain the set of independent variables characterising the dynamics of two-phase flow patterns [9]. The analysis allowed to obtain the flow-pattern maps. In Figure 2 the flow pattern maps for both channels are shown. The proposed results allowed to the identification of dominant patterns in the flow in each parallel horizontal channel: I – liquid/wavy annular flow, II – liquid flow, III – bubbly flow, IV – slug/wavy annular flow, V – wavy annular flow. The obtained maps can be used for an analysis of synchronization of appearance of flow patterns in the parallel minichannels.

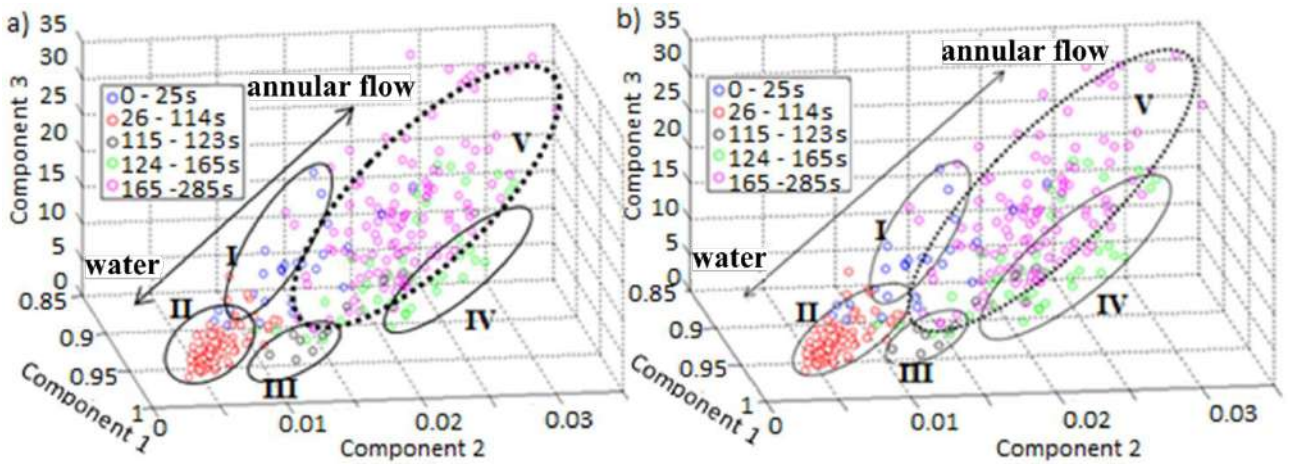

Figure 2. The flow pattern maps for both channels. (a) 1st channel, (b) 2nd channel: I – liquid/wavy annular flow, II – liquid flow, III – bubbly flow, IV – slug/wavy annular flow, V – wavy annular flow.

CONCLUSIONS

To accurately determine the transition of changes in flow patterns within each minichannel, the *RQA* and *PCA* analysis was used. During experiment the flow boiling was affected by several instabilities at once. It was observed that the points representing similar dynamics of the system forms a specific group on the flow pattern maps. Those specifics groups indicate dominant flow pattern which was visible in the minichannels.

Acknowledgment

This work was supported by the National Science Centre, Poland UMO-2015/17/N/ST8/03079 and International scholarship exchange of PhD candidates and academic staff.

References

[1] M. Masiukiewicz, S. Anweiler, Two-phase flow phenomena assessment in minichannels for compact heat exchangers using image analysis methods, Energy Conversion and Management. **104** 44–54, 2015.

[2] P. Valeh-e-Sheyda, M. Rahimi, E. Karimi, M. Asadi, Application of two-phase flow for cooling of hybrid microchannel PV cells: A comparative study, Energy Conversion and Management. **69** 122–130, 2013.

[3] G. Górski, G. Litak, R. Mosdorf, A. Rysak, Dynamics of a two-phase flow through a minichannel: Transition from churn to slug flow, Eur. Phys. J. Plus. **131**, 111, 2016.

[4] S.F. Wang, R. Mosdorf, M. Shoji, Nonlinear analysis on fluctuation feature of two-phase flow through a T-junction, International Journal of Heat and Mass Transfer. **46**, 1519–1528, 2003

[5] G. Górski, R. Mosdorf, Detection of two-phase flow patterns in a vertical minichannel using the laser–phototransistor sensor, in: EUROTHERM Seminar101: Transport Phenomena in Multiphase Systems, Kraków, p. 4, 2014.

[6] H. Grzybowski, R. Mosdorf, Dynamics of pressure drop oscillations during flow boiling inside minichannel, International Communications in Heat and Mass Transfer. **95** 25–32, 2018.

[7] R. Mosdorf, G. Górski, Identification of two-phase flow patterns in minichannel based on RQA and PCA analysis, International Journal of Heat and Mass Transfer. **96**, 64–74, 2016.

[8] J. P. Zbilut, A. Giuliani, Ch. L. Webber Jr., Recurrence quantification analysis and principal components in the detection of short complex signals, Phys. Lett. A **237**: 131–135, 1998.

[9] N. Marwan, M. C. Romano, M. Thiel, J. Kurths: Recurrence Plots for the Analysis of Complex Systems, Physics Reports, **438**(5-6), 237-329, 2007.

ON THE DEVELOPMENT OF METHODS OF LAMINAR-TURBULENT TRANSITION PREDICTION IN AERODYNAMIC FLOWS

Andrey Boiko*[1], Kirill Demyanko[1], Andrey Ivanov[1], Stanislav Kirilovskiy[1], Dmitry Mishenko[1], Yury Nechepurenko[1], and Tatiana Poplavskaya[1]
[1]Khristianovich Institute of Theoretical and Applied Mechanics of SB RAS, Novosibirsk, Russia

Summary Actual fundamental and computational problems of finding the position of laminar-turbulent transition in aerodynamic flows are discussed. Modern popular methods of engineering prediction of transition to turbulence for flows around 2D and 3D aerodynamic configurations for sub- and transonic speeds are reviewed. An original approach based on e^N-method is described and the results of experimental and numerical work aimed at clarifying its calibration for complex flows are highlighted.

INTROFUCTION

Interest in forecasting the position of laminar-turbulent transition on the surface of transport aircraft in cruise regime of flight is actual since the 50s of XX century. Over the past decade, the studies to improve the forecast accuracy has intensified significantly as the traditional means to reduce the drag aiming to save fuel consumption and/or increase the range of flight by profiling and eliminating the flow separation approach their limit. Hence, laminarization of the flow at some elements of aircraft is considered as one of the promising ways in designing modern aircraft was in order to reduce the drag caused by turbulent boundary layer. To this end, engineers and designers need to have appropriate approaches to predict the position of laminar-turbulent transition in aerodynamic applications with a required accuracy.

Currently, engineering gas-dynamic packages as ANSYS Fluent and OpenFOAM are widely used to solve various problems of gas dynamics and heat transfer. These packages do not have built-in tools to analyze the position of laminar-turbulent transition based on the theory of hydrodynamic stability. However, that the position of laminar-turbulent transition mainly depends on the dominant types of the boundary-layer instability as the Tollmien-Schlichting waves and cross-flow vortices. The development of Tollmien-Schlichting waves is typical for the boundary layers occurring at the most elements of the aircraft as fuselage, wings, etc. The appearance of strong cross-flow on a swept wing can lead to the predominance of cross-flow vortices in the laminar-turbulent transition. The wide interest to the engineering e^N-method of laminar-turbulent transition prediction in aerodynamic applications is stipulated by the physically sound linear theory of hydrodynamic stability, which is the foundation for the method, and which correct for both two-dimensional and three-dimensional incompressible and compressible flows, if the level of free-stream turbulence is low enough (low-noise and low-turbulence wind tunnels or cruise flight conditions).

In this presentation, using computations of subsonic and transonic laminar-turbulent flows the operation of software package for the laminar-turbulent transition prediction using the e^N-method in conjunction with the engineering gas-dynamic packages is demonstrated. The complete linearized heat and mass transfer equations for compressible flows, original matrix algorithms for stability analysis, and original pre-processing technologies of data on the flow under study are used. Comparisons are made of the computed transition positions for different flows obtained using the package, the Transition SST empirical model and experimental data. The purpose of these comparisons is both to verify the computed data experimentally and to estimate the limits of the applicability of the Transition SST model and the e^N-method for some aerodynamic applications.

RESULTS

The results are illustrated in Fig. 1 by the computed and experimentally estimated skin-friction coefficients for one of the cases under consideration. For the experimental data [4] the start and the onset of the transition were determined by the behaviour of the intermittency; the skin-friction coefficients were obtained by processing the digitized velocity profiles. The computed data were obtained for the flow past a flat plate under the same external conditions in ANSYS Fluent for the laminar flow, using the empirical Transition SST model, and using the e^N-method in conjunction with the k-ω SST turbulence model. As seen, the data obtained using the e^N-method are consistent with the experimental ones, particularly the difference between them in the streamwise coordinate does not exceed 10%. The difference in the onset of transition between the data obtained using the Transition SST model (associated with the local maximum in the skin friction) and the experimental value (associated with the disturbance maximum) is about 22%. Moreover, the Transition SST model shows significantly narrower transition area than it is obtained in the experiment and in the e^N-method computations.

*Corresponding author. E-mail: boiko@itam.nsc.ru.

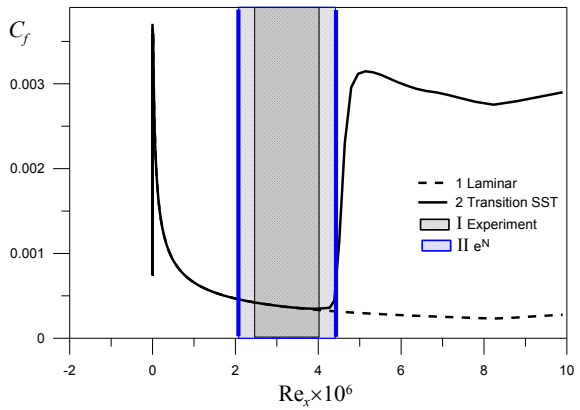

Figure 1. Skin friction coefficients as functions of Reynolds number Re_x at free stream turbulence level Tu=0.03%: computed data for the laminar flow (1); Transition SST model prediction (2); the transition region according to the experiment [4] (I), and the transition region estimated using the transition prediction package under consideration (current study)

One of the main problems in calibrating and verifying the e^N-method is a lack of broad experimental data for different flows and flow conditions. To obtain such data, along with detailed documentation of the parameters of the flow (speed, free-stream turbulence level, etc.) and the parameters of the object (geometry, degree of roughness, angle of attack, etc.), it is necessary statistically accurately to document the position of laminar-turbulent transition on the object surface under study. In experiments with a swept wing model conducted in the low-turbulent wind tunnel T-324 of the Khristianovich Institute of Theoretical and Applied Mechanics of SB RAS, Novosibirsk, Russia, sequences of thermograms of the surface in time were recorded and an advanced algorithm to determine the transition lines was developed [5]. It was observed that using the algorithm the position of transition can be reliably detected in the entire documented area that allows a direct parametric comparison of the experimental data with computations using the e^N-method in conjunction with gas-dynamic packages. The results of this comparison are quite successful. The details will be shown in the presentation during the Congress.

CONCLUSIONS

Thus, the numerical simulation of several two-dimensional and three-dimensional transitional flows at different aerodynamic objects at subsonic and transonic speeds was carried out using the developed software package. The accuracy of the package in determining the transition position was estimated by comparing with experimental data and results of other techniques. To this end an experimental method of conducting parametric measurements in various flow regimes at three-dimensional aerodynamic objects (in general case) with predominance of either Tollmien-Schlichting waves or cross-flow vortices was developed and used successfully in order to statistically accurately document the position of laminar-turbulent transition in a swept-wing boundary layer.

The study was supported by the Russian Science Foundation (grant No. 18-19-00460).

References

[1] Boiko A.V., Nechepurenko Y.M., Zhuchkov R.N., Kozelkov A.S. Laminar-turbulent transition prediction module for LOGOS package. *Thermophys. Aeromech*. **21**(2): 191–210, 2014.

[2] Boiko A.V., Nechepurenko Y.M., Abalakin I.V., Bobkov V.G. Numerical prediction of laminar–turbulent transition on an airfoil. *Russ. J. Numer. Anal. Math. Modelling*. **29**(4): 205-218, 2014.

[3] Boiko A.V., Demyanko K.V., Nechepurenko Y.M. On computing the location of laminar–turbulent transition in compressible boundary layers. *Russ. J. Numer. Anal. Math. Modelling*. **32**(1): 1–12, 2017.

[4] Schubauer G.B., Klebanoff P.S. Contributions on the mechanics of boundary-layer transition: NACA TN-3489, 1955.

[5] Boiko A.V., Dovgal I.I., Dronov A.D., Ivanov A.V., Mischenko D.A. On the problem of quantification of the transition to turbulence in three-dimensional flows. *AIP Conf. Proc*. **2125**: 030040, 2019.

LINEAR STABILITY OF SHEAR-IMPOSED FLOW DOWN A SLIPPERY INCLINED PLANE

Farooq Ahmad Bhat*[1] and Arghya Samanta [1]
[1]Department of Applied Mechanics, Indian Institute of Technology Delhi, New Delhi 110016, India

Summary Linear stability of a shear imposed fluid falling down a slippery inclined plane is scrutinized based on the Orr-Sommerfeld equation. An analytical solution is determined by using the long-wave analysis and the technique of Padé approximation and compared with the numerical solution obtained from the Chebyshev spectral collocation method. It is found that the solution of Padé approximation is more accurate than the solution of asymptotic long-wave expansion. Further, the destabilizing effect of wall slip on the primary instability can be reduced by introducing a constant surface shear stress in the counter-flow direction.

INTRODUCTION

The thin film flows are often encountered in natural and technical set-ups, and thus, warrant a special scholarly interest. In particular, the attention in the study of falling film instability has been increased in the last few decades owing to its numerous applications in coating technology, heat exchangers and chemical reactors [1], etc. In this context, a simple shear-imposed free surface flow can be modelled when a falling film flow is bounded by an air-flow, because the free surface is no longer a shear free [2]. Further, in specific practical situations, like flow over super-hydrophobic substrates and porous substrates, the velocity at the solid-fluid interface does not satisfy no-slip boundary condition, and therefore, a semi-empirical Navier-slip boundary condition is necessary at the fluid-solid interface to accurately capture the dynamics of fluid-solid interactions [3]. Here our aim is to decipher the combined effect of slip and imposed shear on the primary instability.

GOVERNING EQUATION AND MATHEMATICAL FORMULATION

Consider a fluid with dynamic viscosity μ, density ρ, and surface tension σ, flowing down a slippery inclined plane with inclination angle θ. Suppose, the free surface is subjected to a constant tangential shear τ_t. Origin of the Cartesian coordinate system is placed on the plane, while x and y axes are levelled along streamwise and cross-stream directions respectively (see fig. 1(a)). Here g is the acceleration due to gravity, $U(y) = \left[\frac{2y-y^2+2\beta}{1+2\beta} + (y+\beta)\tau\right]$ is the base flow velocity, d is the height of the base film, and $h(x,t)$ is the height of the disturbed free surface. Here β is the dimensionless slip length [4] and τ is the dimensionless imposed shear stress [2]. The Orr-Sommerfeld boundary value problem in terms

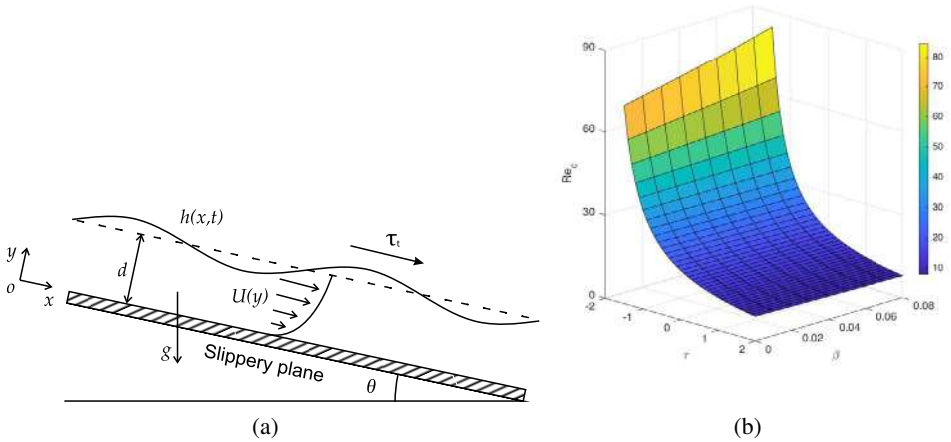

(a) (b)

Figure 1: (a) Schematic diagram of a shear-imposed film flow over a slippery plane. (b) Variation of critical Reynolds number Re_c with slip length and imposed shear stress when $\theta = 4°$.

of the amplitude of stream function ϕ corresponding to the infinitesimal disturbance can be expressed as

$$(\mathcal{D}^2 - k^2)^2\phi(y) - ikRe[(U-c)(\mathcal{D}^2-k^2) - \mathcal{D}^2U]\phi(y) = 0, \quad (1)$$

$$\phi(0) = 0, \ \ \mathcal{D}\phi(0) - \beta\mathcal{D}^2\phi(0) = 0, \quad (2)$$

$$(\mathcal{D}^2 + k^2)\phi(1) + \eta\mathcal{D}^2U(1) = 0, \quad (3)$$

$$(\mathcal{D}^3 - 3k^2\mathcal{D})\phi(1) - ikRe[\{U(1)-c\}\mathcal{D}\phi(1) - \tau\phi(1)] - k[2i\cot\theta/(1+2\beta) + ik^2/Ca + 2k\tau]\eta = 0, \quad (4)$$

$$\phi(1) + [U(1)-c]\eta = 0, \quad (5)$$

*Corresponding author. E-mail: farooq@am.iitd.ac.in

where k is the wavenumber, c is the wave speed and η is the amplitude of deformed free surface. $Re = \rho U_s d/\mu$ is the Reynolds number and $Ca = \mu U_s/\sigma$ is the Capillary number. The above Orr-Sommerfeld boundary value problem (1)-(5) is solved analytically in the long-wave regime ($k \to 0$) and the critical Reynolds number Re_c is computed

$$Re_c = \frac{(1 + 5\beta + 6\beta^2)5\cot\theta}{(2 + 10\beta + 15\beta^2)[2 + \tau + 2\beta(1 + \tau)]}.$$

Note that the critical Reynolds number Re_c decreases in the presence of wall slip but increases if the imposed shear stress acts in the counter-flow direction (see fig. 1(b)). Following Lange *et al.* [5], the technique of Padé approximation is further employed to improve the result of long-wave approximation. Accordingly, the complex wave speed c can be expressed as a ratio of polynomials in terms of wavenumber k

$$c = \frac{P(k, Re, Ca, \tau, \beta)}{Q(k, Re, Ca, \tau, \beta)} = \frac{\sum_{i=0}^{m} p_i(Re, Ca, \tau, \beta)k^i}{1 + \sum_{j=0}^{n} q_j(Re, Ca, \tau, \beta)k^j}, \tag{6}$$

where $p_i(Re, Ca, \tau, \beta), q_i(Re, Ca, \tau, \beta)$ are the coefficients of polynomials to be determined analytically. Figure 2 demonstrates the temporal growth rate kc_i and phase speed c_r of the infinitesimal disturbance when k varies.

RESULTS

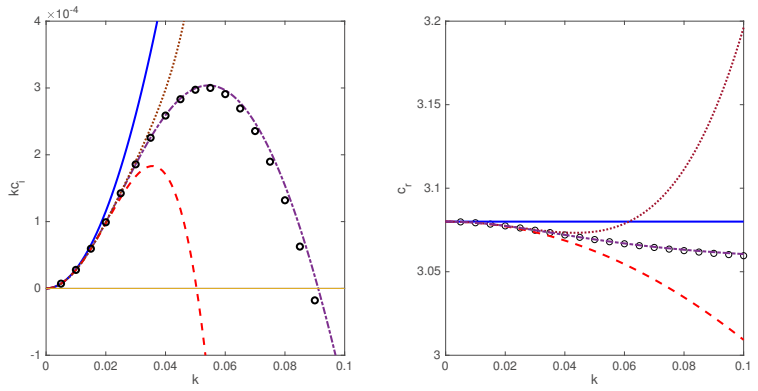

(a) (b)

Figure 2: Variation of (a) temporal growth rate kc_i and (b) phase speed c_r with wavenumber k when $\theta = 4°$, $Re = 11$, $Ca = 2$, $\beta = 0.08$ and $\tau = 1$. Solid, dashed and dotted lines represent 1st, 3rd and 5th order long-wave results respectively. Dash-dotted lines represent the result of Padé approximation, and circular points stand for the numerical result.

In fact, we have compared the analytical results of Padé approximation and different orders long-wave approximation with the numerical results obtained from the Chebyshev spectral collocation method [4]. Obviously, the results acquired from the Padé approximation is more accurate than the different orders long-wave results because it arrests the numerical results very well for a larger range of k, while the long-wave results are valid only in the vicinity of $k \approx 0$. In other words, the Padé approximation enhances the domain of convergence of the long-wave asymptotic expansion.

CONCLUSIONS

A study of linear stability for a shear-imposed flow is accomplished when the bottom wall is slippery. Different orders long-wave solutions and the solution from Padé approximation are computed analytically and verified with the numerical solution procured from the Chebyshev spectral collocation method. It is found that Padé approximation solution is more accurate and matches very closely with the numerical solution over a wider range of wavenumber. In addition, it is noticed that the destabilizing effect of slip length on the most unstable mode will be attenuated as soon as the constant shear stress is applied in the counter-flow direction.

References

[1] S.Kalliadasis, C. Ruyer-Quil, B. Scheid, and M.G. Velarde, Falling liquid films (Vol. 176). Springer Science & Business Media, 2011.
[2] M. K. Smith, The mechanism for the long-wave instability in thin liquid films, J. Fluid Mech. **217**, 469, 1990.
[3] A. Samanta, C. Ruyer-Quil, and B. Goyeau. A falling film down a slippery inclined plane, J. Fluid Mech., **684**, 353383, 2011.
[4] F. A. Bhat, and A. Samanta, Linear stability of a contaminated fluid flow down a slippery inclined plane. Phys. Rev. E, 98(3), 033108, 2018.
[5] U. Lange, K. Nandakumar, and H. Raszillier. Symbolic computation as a tool for high-order long-wave stability analysis of thin film flows with coupled transport processes. J. Comp. Phys. **150**, 116, 1999.

STEADY-STATES FOR STATIONARY AND CONVECTIVELY UNSTABLE FLOWS

Ricardo Dias dos Santos, Mateus Sanglard Schuabb Nunes, Rodrigo Tavares Veloso, and Leonardo Santos de Brito Alves*
Department of Mechanical Engineering (TEM),Universida de Federal Fluminense (UFF),Niterói-RJ,Brazil

Summary Many three-dimensional boundary layers are convectively unstable to stationary modes. Crossflow vortices in swept wings and cones and Görtler vortices in concave surfaces are examples of such modes. This is a challenge to current time integration schemes because these modes will contaminate the steady-state if introduced in a simulation. Due to the physical nature of these modes, any stationary excitation is capable of doing so. As simulated geometries become more complex, it is increasingly more difficult to generate a mesh with a spatial error distribution that is smooth enough to not act as a stationary excitation source. Hence, steady-state contamination often ensues. Recent methodologies have been able to damp oscillatory modes under convectively and absolutely unstable conditions but still need to be evaluated for stationary modes as well. This is the goal of the present study.

INTRODUCTION

Accurate base flows are required for linear stability analysis. For many studies, they should be a disturbance free steady-state of the governing equations. A few methods exist today for the construction of such steady-states. The most traditional one is the class of Newton iteration methods, usually adapted to use continuation techniques as well [1]. However, they are very sensitive to initial conditions, require heavy computational resources for large systems and have severe convergence difficulties for globally unstable problems. Selective frequency damping (SFD) was developed to overcome these difficulties [14]. However, this method has been applied to flows that only have a single dominant self-excited frequency that needs to be filtered and cannot damp stationary modes. Minimal Gain Marching (MGM) Schemes [2] were developed by altering the coefficients of a marching scheme so it becomes linearly numerically stable under linearly physically unstable conditions. Achieving this at the smallest possible time steps prevents nonlinear effects from jeopardizing convergence towards steady-state. Recently, inspired by the use of Krylov-subspaces, a new method has been introduced [3]. Known as BoostConv, it is based on the minimization of the residual norm at each iteration step. The stabilization of dynamical systems is achieved with a small increase in computation time. Furthermore, it can be easily implemented into pre-existing codes with a call to a single black-box subroutine.

A recent comparative study of these different methods applied to the nonlinear and viscous Burger's equation has shown that none of them are able to remove stationary and convectively unstable modes from the steady-state [4]. Such modes are typical of three-dimensional boundary layers with a strong inflectional velocity profile that appear in flows around swept-wings, elliptic cones and circular cones at an angle of attack. They are known as stationary crossflow vortices. Stationary Görtler vortices are another example. They appear on concave surfaces due to an instability of the viscous boundary-layer modified by centrifugal effects induced by the curvature [5]. Crossflow vortices were visualized in experiments [6, 7] and also with direct numerical simulations during the transition process of a swept flat plate boundary layer [8, 9] and of a subsonic realistic swept-wing [10, 11]. Steady-state simulations of a hypersonic flow around the elliptic cone using an implicit Euler scheme could not be grid converged independent of the scheme employed [12] due to these stationary and convectively unstable vortical structures. This was true even when employing a highly dissipative first-order scheme for the spatial discretization. This was likely due to the fact that any changes in grid size and numerical scheme would change the excitation location and amplitude of the stationary crossflow vortices. Later studies were forced to fine tune the grid to excite these stationary crossflow structures at fixed locations independently of the grid employed [13]. These examples illustrate the importance of assessing how these different steady-state generation methods deal with stationary and convectively unstable modes, which is the main motivation of the present study.

PRELIMINARY RESULTS

In order to illustrate these issues, a test case was simulated to evaluate the ability of the discussed methods to reach a steady-state when it is convectively unstable to stationary disturbances. The performances of the implicit Euler (IE), Newton method, MGM, SFD and BoostConv are compared. A modified, one-dimensional transient, dimensionless and viscous Burger's type equation is considered now for this purpose. It is given by

$$\frac{\partial u}{\partial t} = f(u) = \frac{1}{Re}\frac{\partial^2 u}{\partial x^2} - u\frac{\partial u}{\partial x} + R(u - u_s) \tag{1}$$

where R is the source term control parameter, Re is the Reynolds number, x is the dimensionless spatial coordinate, t is dimensionless time, u is the flow velocity field and f is the steady-state residue. The linear and modal stability analysis shows that it becomes convectively unstable at $R = 0$ and transitions to absolutely unstable at $R = Re/4$. Here, $Re = 32$ is used. Both onsets of instability are due to stationary and spatially uniform disturbances.

*Corresponding author. E-mail: lsbalves@id.uff.br.

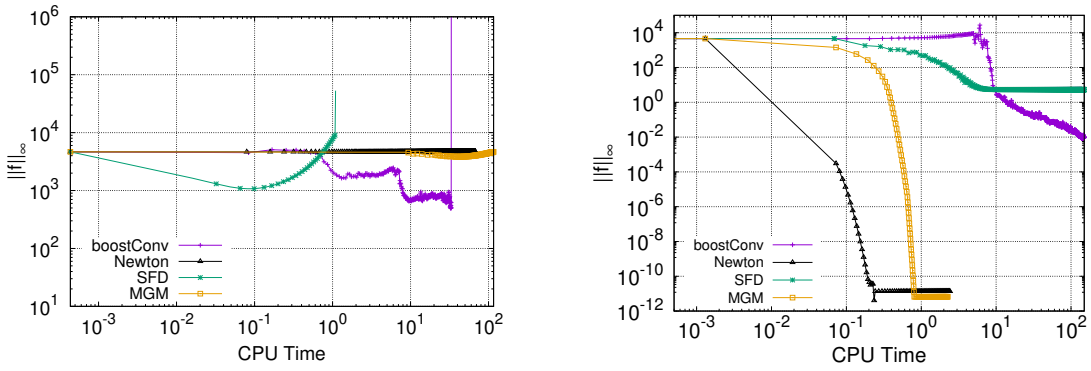

Figure 1: CPU time versus maximum residue norm for each steady-state generation scheme (left) without and (right) with an adaptation designed to allow damping of stationary and convectively unstable modes.

Simulations employed periodic boundary condition and $u(x) = 1$ as initial condition. A sufficiently large domain, $L = 16$ with $N_x = 4001$ grid points, is chosen in order to guarantee enough spacial growth of the disturbance. The time-step was set to $\Delta t = 5 \times 10^{-5}$. The parameter $R = 7.2$ was chosen to ensure that the dominant mode is stationary and convectively unstable. The flow is disturbed by a Gaussian source therm, with a small amplitude, added to the governing equation. Discrete approximations used were a fifth-order WENO scheme [15] for the advective term and fourth-order central scheme for the diffusive term. The explicit Euler scheme was used to march the solution to $t = 4$, where nonlinear saturation occurs and a shock wave is formed. From this point forward, steady-state generation was turned on.

Figure 1 (left) shows that none of the aforementioned schemes is capable of reaching steady-state, since $||f||_\infty$ cannot be reduced to acceptable tolerances. This can only be achieved if the governing equation is modified by a special source term that turns the dominant disturbance into an oscillatory one instead. Figure 1 (right) shows that all schemes achieve a disturbance free steady-state in this case. The implicit Euler scheme with a very large time step (i.e. Newton's method) performs best, followed by MGM. Although they are implicit marching schemes, having a high cost per iteration, they converge with just a few iterations. SFD generates a solution with higher errors and BoostConv converges quite slowly.

CONCLUSIONS AND ADDITIONAL WORK

All existing schemes fail to recover a disturbance free steady-state for a convectively unstable flow dominated by a stationary mode, unless properly modified to turn this mode oscillatory. Two additional test cases involving such modes will be included for the presentation. They use our more advanced in-house codes to evaluate the three-dimensional unsteady boundary-layers susceptible to both Görtler and crossflow instabilities.

References

[1] Tuckerman, L. S., and Barkley, D., *Numerical Methods for Bifurcation Problems and Large-Scale Dynamical Systems*, The IMA Volumes in Mathematics and its Applications, 2000, Vol. 119, Chap. Bifurcation Analysis for Time Steppers, pp. 453–466.

[2] Teixeira, R. S., and Alves, L. S. B., Minimal Gain Marching Schemes: Searching for Unstable Steady-States with Unsteady Solvers, *Theoretical and Computational Fluid Dynamics*, Vol. 31, No. 5-6, 2017, pp. 607–621.

[3] Citro, V., Giannetti, P. L. F., and Auteri, F., Efficient stabilization and acceleration of numerical simulation of fluid flows by residual recombination, *Journal of Computational Physics*, Vol. 344, 2017, pp. 234–246.

[4] Veloso, R. T., Santos, R. D., and Alves, L. S., Comparative Analysis Between Steady-State Generation Methods, *25th International Congress of Mechanical Engineering*, ABCM, 2019.

[5] Saric, W., Görtler Vortices, *Annual Review of Fluid Mechanics*, Vol. 26, 1994, pp. 379–409.

[6] Reed, H. L., and Saric, W., Stability of three-dimensional boundary layers, *Annual Review of Fluid Mechanics*, Vol. 21, 1989, pp. 235–284.

[7] W. Saric and L. Yeates. Experiments on the stability of crossflow vortices in swept-wing flows. In *AIAA Paper*,85-0493

[8] Wassermann, P., and Kloker, M. (2002). Mechanisms and passive control of crossflow-vortex-induced transition in a three-dimensional boundary layer. In *Journal of Fluid Mechanics*. Vol. 456, pp. 49-84.

[9] Wassermann, P., and Kloker, M. (2003). Transition mechanisms induced by travelling crossflow vortices in a three-dimensional boundary layer. In *Journal of Fluid Mechanics*. Vol. 483, pp. 67-89

[10] Duan, L., Choudhari, M. M. and Li, F. (2013). Direct numerical simulation of transition in a swept-wing boundary layer. In *43rd Fluid Dynamics Conference*

[11] Duan, L., Choudhari, M. M. and Li, F. (2014). DNS of laminar-turbulent transition in swept-wing boundary layers. In *CTR Proc. of the Summer Program*

[12] Dinzl, D. J., and Candler, G. V., Analysis of Crossflow Instability on HIFiRE-5 using Direct Numerical Simulation, *53rd AIAA Aerospace Sciences Meeting*, 2015, pp. 1–10.

[13] Dinzl, D. J., and Candler, G. V., Direct Simulation of Hypersonic Crossflow Instability on an Elliptic Cone, *AIAA Journal*, Vol. 55, No. 6, 2017, pp. 1769–1782.

[14] Åkervik, E., Brandt, L., Henningson, D. S., Hoepffner, J., Marxen, O., and Schlatter, P., Steady Solutions of the Navier-Stokes Equations by Selective Frequency Damping, *Physics of Fluids*, Vol. 18, No. 6, 2006, p. 068102.

[15] Jiang, G.S. and Shu, C.W., 1996. Efficient implementation of weighted eno schemes. *Journal of Computational Physics*, Vol. 126, pp. 202–228.

ON THE SENSITIVITY OF LEADING EDGE PRESSURE GRADIENT TO FREE-STREAM TURBULENCE INDUCED BOUNDARY-LAYERTRANSITION

André Weingärtner*, Santhosh B. Mamidala, and Jens H.M. Fransson
Department of Engineering mechanics, KTH-Royal Institute of Technology, Stockholm, Sweden

Summary The region of highest boundary layer receptivity to free-stream turbulence is believed to be the nose region of the leading edge, where the boundary layer is thinnest. Thus, the velocity field and the boundary layer shape in this region are expected to be of relevance for the process, even if transition appears further downstream. However, the effect of varying the flow around a given leading edge on transition remains largely unexplored. A unique experimental setup incorporating a multitude of streamwise microphones on a flat plate is employed to elucidate this influence, allowing a large variation of parameters. Results show a twofold effect, depending on free-stream turbulence parameters.

INTRODUCTION

In most experimental studies on the transition to turbulence in zero-pressure gradient boundary layers (BLs), a flat plate in combination with a rounded leading edge (LE) and a trailing flap are utilized. The LE is known to be an important receptivity region for free-stream turbulence (FST) induced BL transition, where streamwise streaky structures (Klebanoff modes) originate (e.g. [1]). Hence, the flow around the LE is expected to be of significance for the transition process, even if the actual transition location is further downstream.

The effect of bluntness of an elliptical LE on transition has been examined by Kendall [1], showing that a decrease in aspect ratio of the ellipse does not affect the Klebanoff mode instabilities, but increases the amplitude of Tollmien-Schlichting waves. Nagarajan et al. [2] performed numerical simulations, revealing different mechanisms taking place, depending on FST conditions. It was concluded that, in general, a blunter LE leads to an earlier onset of transition for given FST conditions.

Elliptical LEs will inevitably generate a suction peak, leading to a region of adverse pressure gradient. This has been shown to destabilize the BL and cause increased disturbance growth rates [3]. In order to eliminate this suction peak, the usage of asymmetrical LEs for BL transition experiments has been proposed (e.g. [4],[5]). The aim with these LEs is to eliminate the suction peak and to minimize the region of non-zero pressure gradient along the LE, in order to quickly reach a Blasius-like BL velocity profile.

Besides the shape of the LE, the second parameter to alter the LE pressure gradient on a BL plate is the angle of the trailing flap. Variation of the flap angle will cause a change in overall circulation of the boundary-layer plate and thus shift the position of the stagnation line. In order to optimize the C_p distribution on the LE and to avoid periodic fluctuations, it is usually desired to position the stagnation line slightly on the measurement side of the LE [5].

It was already reported by Westin et al. [4], although merely as a side note, that the angle of the trailing flap can have a significant effect on the transition location. However, the quantitative effect of flap angle variation – and therefore the shape and severeness of the LE pressure gradient region – on zero-pressure gradient BL transition due to FST remains unclear and is the topic of this paper.

EXPERIMENTAL SETUP

Experiments were conducted in the MTL wind tunnel at the Department of Engineering Mechanics at KTH. The cross-sectional area of the test section is 0.8×1.2 m and its length 7 m. For the present experiments, the reference free-stream speed was held constant at 8 m/s throughout all cases, measured in the zero-pressure gradient region sufficiently far downstream of the LE. Several different turbulence-generating grids were interchanged and installed upstream the LE in order to produce various conditions of FST intensity (Tu) and integral length scale (Λ_x).

The employed flat plate has a total length of 4.5 m (of which 0.26 m is the LE) and fills out the whole width of the tunnel (1.2 m). The mounted LE is from Fransson [5]. The trailing flap has a length of 1.6 m and it was mounted in the diffuser section of the wind tunnel. The unique feature of the BL plate that enabled this type of examination is the method of transition location determination. Embedded inside the plate are a total of 100 electret microphones, ranging in streamwise direction all the way from the LE to the end of the plate. All microphones can be sampled simultaneously, so that the intermittency distribution along the whole plate can be acquired in a single run.

Additionally, a total of 56 pressure taps (of which 16 are located on the LE) are used to determine the static pressure distribution along the plate. Furthermore, hot-wire anemometry was employed in order to measure streamwise velocity profiles of the BL on the LE.

*Corresponding author. E-mail: andrewei@kth.se.

RESULTS

As expected, the C_p distribution along the LE shows a strong dependence on the flap angle ϕ (Fig. 1). The determined optimal flap angle of $\phi = 14.3°$ (black line in Fig. 1) features at first a sharp decrease in C_p and then a gradual approach to $C_p = 0$ without undershoot (i.e. no adverse pressure gradient). A significantly higher flap angle of $\phi = 17°$ causes the stagnation line to move further downstream on the measuring side of the plate, resulting in a strong negative C_p at the nose of the LE and a much slower recovery of the pressure. On the other hand, a low flap angle results in the stagnation line moving further upstream or even to the lower side of the plate. This leads to an even sharper pressure drop, which is proceeded by an undershoot and thus an adverse pressure gradient. The C_p range in this set of experiments is limited by flow separation and turbulent reattachment above $\phi = 17°$ and below $\phi = 12°$.

To quantify the transition location in a non-dimensional manner, the transitional Reynolds number Re_{tr} is introduced. It is defined as $Re_{tr} = U_\infty x_{tr}/\nu$, where U_∞ is the free-stream speed, ν the kinematic viscosity of air and x_{tr} the transition location, i.e. the point where the intermittency of the time signals measured by the microphones was 50%.

The effect of ϕ on Re_{tr} show two separate trends (Fig. 2). For a constant turbulence intensity and integral length scales in the range of 13.6 to 27.5 mm, Re_{tr} appears rather robust against small changes in flap angle around the optimum. Only a significant increase in ϕ causes the transition to appear notably earlier, likely due to destabilizing effects on the boundary layer. The case of $\Lambda_x = 8.4$ mm, however, shows a remarkably different trend. In the range of 12.4 to 14.5°, transition appears noticeably later compared to the higher Λ_x cases. Furthermore, the transitional Reynolds number appears to be sensitive to even slight changes in flap angle around the maximum at about 13.8°. Looking in more detail at the $\Lambda_x = 13.6$ mm case reveals some similarities to the 8.4 mm integral length scale, such as a decrease in Re_{tr} towards very low flap angles or a slight global maximum around $\phi = 14.8°$.

Attempting to reproduce the results of low Λ_x revealed high sensitivity of the measurements to small changes in Λ_x, but where relative changes still can be large. Even dismounting the turbulence-generating grid and positioning it again at seemingly the same upstream distance from the LE resulted in changes in Λ_x of ± 1 mm, that lead to variations in Re_{tr} of around $\pm 1 \times 10^5$. However, the general shape incorporating a global maximum somewhere close to the optimum ϕ remained.

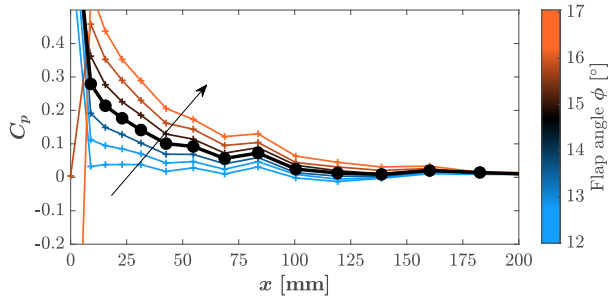

Figure 1: Pressure distribution along the LE for different flap angles ϕ (the arrow indicates increasing ϕ)

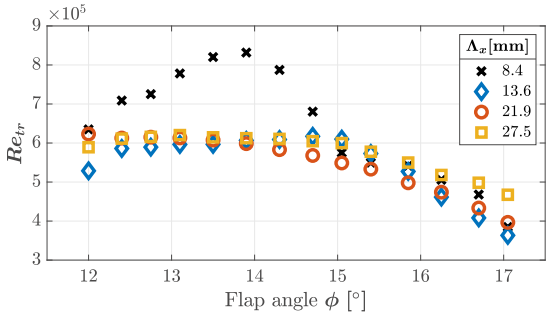

Figure 2: Transitional Reynolds number vs. flap angle for different Λ_x, $Tu = 2\%$ for all cases

CONCLUSIONS AND OUTLOOK

An experimental investigation of the sensitivity of FST-induced BL transition to the LE pressure gradient, altered by changing the trailing edge flap angle, has been performed. At a constant Tu of 2%, the transition location is insensitive for small variations in flap angle for a large range of Λ_x. However, below a certain threshold of integral length scale, Re_{tr} increases significantly and becomes sensitive to small variations in ϕ. Hot-wire measurements of the BL on the LE, which is expected to be a region important for receptivity, will be presented together with a larger database, including variation of Tu.

References

[1] Kendall, JM (1991). Studies on laminar boundary-layer receptivity to freestream turbulence near a leading edge. Boundary Layer Stability and Transition to Turbulence, 23-30

[2] Nagarajan, S., Lele, S., & Ferziger, J. (2007). Leading-edge effects in bypass transition. *J. Fluid Mech.* 572, 471-504. doi:10.1017/S0022112006001893.

[3] Zaki, T., & Durbin, P. (2006). Continuous mode transition and the effects of pressure gradient. *J. Fluid Mech.* 563, 357-388. doi:10.1017/S0022112006001340

[4] Westin, K., Boiko, A., Klingmann, B., Kozlov, V., & Alfredsson, P. (1994). Experiments in a boundary layer subjected to free stream turbulence. Part 1. Boundary layer structure and receptivity. *J. Fluid Mech.* 281, 193-218. doi:10.1017/S0022112094003083

[5] Fransson, J.H.M. Leading edge design process using a commercial flow solver. *Exp Fluids* 37, 929–932 (2004). https://doi.org/10.1007/s00348-004-0858-3

TRANSITION AND SPATIO-TEMPORAL INTERMITTENCY IN PULSATILE PIPE FLOW

Daniel Morón*[1], Daniel Feldmann[1], and Marc Avila[1]
[1]University of Bremen, Center of Applied Space Technology and Microgravity (ZARM), Am Fallturm 2, 28359 Bremen, Germany

Summary Despite its importance in cardiovascular diseases and engineering applications turbulence in pulsatile pipe flow remains little comprehended. The question remains on how they transition to turbulence and how turbulence behaves once triggered. In this project we explore both. First, using non-modal methods, we look for perturbations that are optimum for triggering turbulence in pulsatile pipe flows. Second we test these perturbations and the turbulence they trigger by performing Direct Numerical Simulations. We consider flows driven by a single harmonic and flows driven by a physiological wave form. We show how the shape of the pulsation dramatically increases the chances for turbulence transition and turbulence survival. Our results suggest that turbulence transition in cardiovascular flows is more likely and widespread than previously thought.

INTRODUCTION

Cardiovascular diseases represent one of the major causes of death worldwide [1]. Their increasing danger has sparked the interest on understanding their causes. One seems to be the presence of turbulence in cardiovascular vessels [2]. This turbulence may exert random shear stresses on the walls that, in the worst scenarios, can lead to the formation of aneurysms in the aorta or other serious injuries.

Ignoring hemodynamic and flexible wall effects, cardiovascular flow may be regarded to as the pulsatile flow of a Newtonian fluid in rigid pipes. This type of flow is not steadily driven rather driven by the heart pulsation, which is composed of a mean and an oscillatory driving force. In this case the bulk velocity is periodically varied as:

$$u_b\left(t\right) = u_s \cdot \left[1 + A\sin\left(2\pi \cdot t/T\right)\right] \tag{1}$$

Transition to turbulence in pulsatile pipe flows depends on three parameters, [3]:

- The (mean) Reynolds number $Re = u_s D/\nu$ which compares inertia and viscous forces on the flow, being u_s the one period averaged bulk velocity, D the pipe diameter and ν the fluid kinematic viscosity.
- The Womersley number $Wo = 0.5 \cdot D \cdot \sqrt{2\pi/\left(\nu \cdot T\right)}$ which represents the relation between pulsation period T and viscous time.
- The amplitude of the pulsation A.

While transition in steady driven pipe flow $A = 0$ is relatively well understood, transition to turbulence for pulsatile pipe flow is not. Linear stability analysis claim the flow is stable for $Re < 10^4$, but experiments and simulations suggest otherwise. In this project we aim to study transition in pulsatile pipe flows and also how turbulence behaves once triggered at physiologically relevant flow regimes.

METHODS

We consider an incompressible viscous Newtonian fluid confined in a straight smooth rigid pipe of circular cross-section and diameter D. The fluid is driven by a time dependent pressure gradient which ensures that the bulk velocity coincides with the desired pulsation at each time step. Two different pulsations have been considered, a simple sinusoidal function as in equation 1 and a physiological like pulsation.

There is an analytical solution to this kind of flows for the idealised case of laminar, axisymmetric, fully developed flow through a smooth pipe and single harmonic driving, the so called Sexl–Womersley flow. The only non zero velocity component is the axial one, which only depends on radial position and time. The SW velocity profile can be added to itself and/or the (parabolic) Hagen–Poiseuille profile to obtain an analytical (laminar) solution for any combination of Wo, A and pulsation waveform

In order to find optimum perturbations that disturb that flow the most, we perform a transient growth analysis as the one used by Xu *et al.* [3]. The method seeks the perturbation that grows the most in terms of energy on top of a laminar flow from the linear point of view. Thus the laminar flow ignores the evolution of perturbations on top of it. For each Re, Wo and A the method points to the most dangerous perturbation out all initial shapes, and initial times.

We then test those optimum perturbations by performing Direct Numerical Simulations where the Navier Stoke's equations are solved.

*Corresponding author. E-mail: daniel.moron@zarm.uni-bremen.de

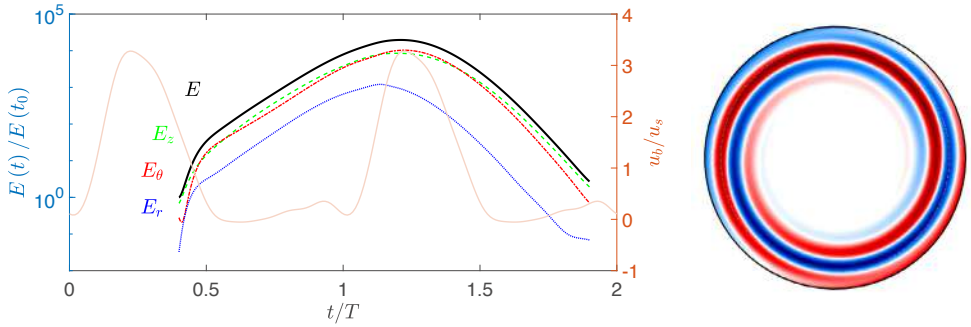

Figure 1: To the left energy of the perturbation that resulted in the biggest transient growth for $Re = 1277$ and $Wo = 12$. See in **black** the total energy, in blue, red, and green, the corresponding radial, azimuth and axial components of that energy. In the background, in orange, the bulk velocity u_b. To the right the axial vorticity of the perturbation at a given pipe (r, θ) cross section. In red, positive values, in blue negative values.

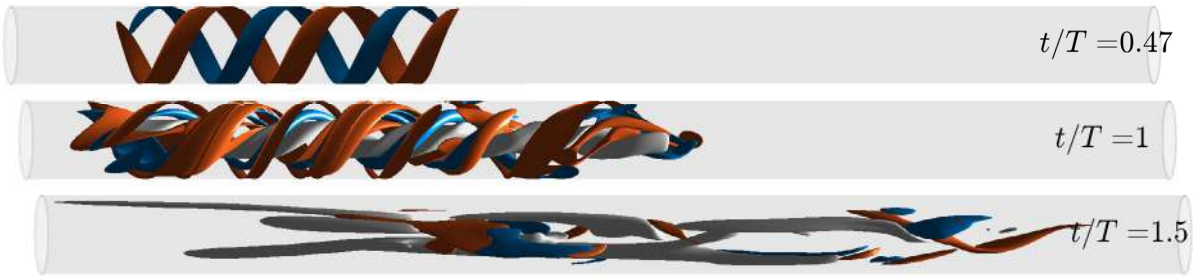

Figure 2: Three different snapshots of the flow in a section of $15 \times D$ axial length for a DNS with a $40 \times D$ long pipe for $Re = 1277$ and $Wo = 12$. The observer is moving with the pulsation speed. The initial perturbation is introduced localized in a $z = 5 \times D$ axially long section. In red $\omega_z \approx 3u_s/D$, in blue $\omega_z \approx -3u_s/D$ in grey low speed velocity streaks with $-0.3 \cdot u_s$.

PERTURBATION ON CARDIOVASCULAR FLOW

In this short abstract we summarise some results for a pulsatile pipe flow driven by a physiologic-like pulsation. See the shape of the pulsation in the background of figure 1. The amplitude is fixed by the pulsation shape itself. In order to model a physiological-like pulsation a particular signal presented in [4] has been selected. In that study they measured the mean velocity of the blood flow at different sections of the aorta of different patients. In our study the signal for the descending aorta section of a young volunteer has been selected. Inspired by the blood flow in the human descending aorta we here focus on $Re = 1277$ and $Wo = 12$.

For this particular case the perturbation that grows the most according to the non-modal analysis, is a helical like perturbation, close to the wall. See the evolution of its energy and its initial shape in figure 1 Then we initialize direct numerical simulations at $t_0/T = 0.4$ with the corresponding laminar SW profile and on top of it the optimum perturbation scaled to $4 \times 10^{-2} \cdot u_s$ in a given axial section.

The perturbation grows in magnitude while it is convected by the flow, see figures 2. At some point it looses its initial helix shape, and results in a set of low velocity streaks. Overall the perturbation is able to survive more than one period as it evolves.

OUTLOOK

We are further analysing results for flows driven by a physiological like pulsation and comparing them with results for a single harmonic pulsation. At the conference we will present how both compare and how on the two cases, perturbations are able to survive longer than a period. We will also show how small geometric imperfections that do not trigger turbulence in steady pipe flow, are able to perturb pulsatile pipe flow enough to intermittently trigger turbulence.

References

[1] World Health Organization WHO, 2017. `https://www.who.int/news-room/fact-sheets/detail/cardiovascular-diseases-(cvds)`, *Online; accessed 2-July-2020*

[2] Freis, Edward D and Heath, William C, Hydrodynamics of aortic blood flow, *Circulation research*, volume 14, number 2, 105-116, 1964.

[3] Xu D., Song B. and Avila M., Non-modal transient growth of disturbances in pulsatile and oscillatory pipe flow, *Submitted*, 2020 `http://arxiv.org/abs/2008.04616`

[4] Bürk J., Evaluation of 3D blood flow patterns and wall shear stress in the normal and dilated thoracic aorta using flow-sensitive 4D CMR, *Journal of cardiovascular magnetic resonance*, volume 14, number 1, 1–11, 2012.

TRANSITIONAL BOUNDARY LAYERS DRIVEN BY FREE-STREAM TURBULENCE

Santhosh B. Mamidala*, André Weingärtner,and Jens H.M. Fransson
Department of Engineering mechanics, KTH-Royal Institute of Technology, Stockholm, Sweden

Summary Challenges in understanding the intricacies of transitional boundary layers (BLs) emanating under free-stream turbulence (FST) over a flat-plate have intiated a renewed interest over the recent years. The present study includes a unique dataset with a big parameter space, providing with incisive experimental renderings on the importance of FST integral length scale (Λ_x) in FST induced transition and not only the turbulence intensity (Tu). We believe that the streamwise unsteady streaks play a vital role in the onset of transiton and their spanwise wavelength strongly depend on the intial FST conditions at the leading-edge (LE). A substantial correlation is observed between the aspect ratio of the streaky structures and a FST Reynolds number. Furthermore, we derive empirical prediction models to forecast the spanwise wavelength and the aspect ratio of the streaks merely based on the FST conditions.

INTRODUCTION

One of the most intrinsic problems in BL reasearch is a flow over a simple geometry like flat-plate with zero-pressure gradient condition. The FST penetrating the BL developing over the flat-plate is a strong disturbance to the laminar BL which will lead to a rapid transtion to turbulence. Since the thirties of the last century, a significant number of studies have been performed on FST induced transition. Despite this, modeling this transition scenario has always been an intricate task. Heretofore, mostly Tu alone was considered in predicting the transitional Reynolds number Re_{tr} ($Tu = u_{\mathrm{rms}}/U_\infty$ & $Re_{\mathrm{tr}} = x_{\mathrm{tr}}U_\infty/\nu$, where u_{rms}, U_∞, x_{tr}, ν are the root-mean square velocity, free-stream velocity, the transition location and the kinematic viscosity, respectively). Not until the studies of [1, 4, 5], where the effect of Λ_x was first examined, it is now believed that Tu is not sufficient enough to model Re_{tr}, the length scale Λ_x should also be treated in future prediction models [2]. It is apparent from recent experiments [2] & direct numerical simulations (DNS) [6], that introducing a Reynolds number based on Λ_x namely $Re_\Lambda = \Lambda_x U_\infty/\nu$ accomodates more flexibility in choosing the parameter space for the investigation. However, for a more explicit interpretation of how FST conditions influence this transition scenario, we need to define a FST Reynolds number as $Re_{\mathrm{fst}} = \Lambda_x u_{\mathrm{rms}}/\nu$ as examined in [2].

Experimental results from [2, 3] ascertain the presence of the elongated streamwise unsteady streaks, which we here believe is of prime importance for the onset of transition. With this stated, it is reasonable that the spanwise scale of streaks λ_z induced by FST is influential for the breakdown to turbulence. Although, the well cited works of [3, 4, 6] indicate that the spanwise scale λ_z fully adapts to the BL thickness which routes to the BL structures with an aspect ratio of one, contrarily it is obscure to interpret that λ_z assymptotes to a same spanwise scale based on BL displacement thickness δ_1 i.e., $\lambda_z/2 \approx 3\delta_1$. Evidently, [2] specificates that the spanwise length scale of the streaks λ_z holds a strong correlation with the LE conditions in the free-stream namely Λ_x & Tu indicating the assymptotic value of λ_z is not crucial for the transition process since for most of the FST conditions, transition takes place far upstream of this value. This symbolizes the vitality of establishing accurate prediction models for spanwise scale λ_z and to explore how the aspect ratio of the streamwise structures behave with FST conditions.

EXPERIMENTAL SETUP

A thorough experimental campaign was performed in the Minimum Turbulence Level (MTL) wind tunnel at KTH-Royal Institute of Technology. The setup consists of a 4.5 m long flat-plate where the base flow was adjusted to zero-pressure gradient conditions by means of the ceiling of the test-section. Several turbulence generating grids were inter-changed and mounted upstream of the leading edge to generate different FST characteristics. The experiments incorporate both single-point and two-point correlation measurements using single sensor hot-wire probes and electret sub-miniature microphones. The initial FST conditions at the leading edge were adjusted using a single hot-wire probe mounted in the free-stream. A new approach using electret microphones mounted inside a cavity under a pinhole orifice was investigated and established to detect transtion location. A total of 100 microphones mounted in the streamwise direction provided a full streamwise intermittency distribution within a simultaeneous sampling time of 60 seconds. The parameter space includes a systematic variation of Λ_x from 4 mm - 36 mm at different levels of Tu (1%-7% in steps of 0.5%). Also, the free-stream speed U_∞ was varied from 6 m/s to 15 m/s unlike other existing FST induced transition experimental studies [1, 2] or DNS [4, 5, 6]. This combination of Re_Λ, Tu and U_∞ provided a total of 83 unique FST conditions at the LE.

RESULTS

The transition onset and the transition location were determined as the position where the intermittency factor (γ) of the microphone signals is 0.05 and 0.5, respectively, where $\gamma = 0$ and 1 indicate a fully laminar and a fully turbulent flow. Two-point correlation measurements along spanwise direction allowed for the estimation of spanwise wavelength

*Corresponding author. E-mail: mamidala@kth.se.

λ_z, where two single-wire probes were placed at the same wall-normal location, one probe being fixed and the other being traversable (minimum resolution between the probes is less than 1 mm). The minimum of the correlation function (of negative sign) corresponds to the averaged half spanwise wavelength of the unsteady streaks [2, 3].

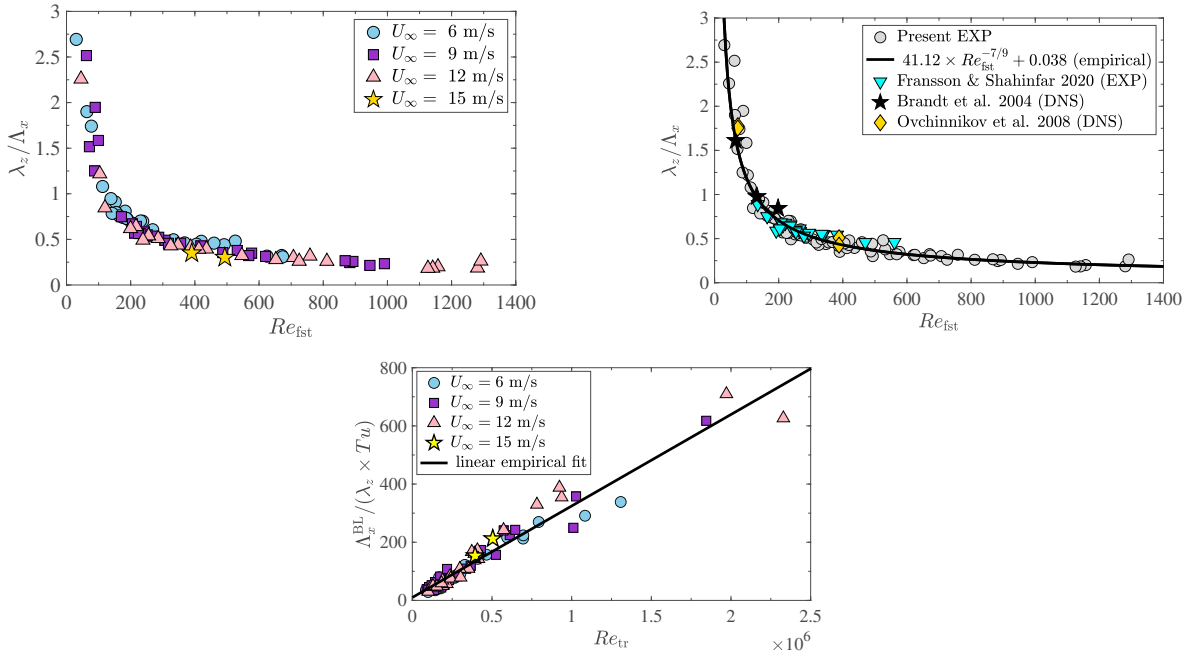

Figure 1: (*a*) Scaled λ_z at the transition onset as a function of FST Reynolds number. (*b*) Present experiments (EXP) compared with previous experiments and DNS. Solid line indicates a curve fit to the data according to eq. (1). (*c*) Aspect ratio of streaks $\lambda_x^{\mathrm{BL}}/\lambda_z$ normalised with Tu versus Re_{tr}. Solid line corresponds to a linear fit to the data as per eq. (2).

In figure 1(*a*), the spanwise wavelength λ_z at $x_{\gamma=0.05}$ is scaled with Λ_x, and is plotted against the FST Reynolds number Re_{fst}. The data obtained at all free-stream speeds agree well with the previous experimental works of [2] and DNS data [4, 6], and collapse onto a single emprical power law (figure 1*b*) defined as:

$$\lambda_z/\Lambda_x = 41.12\, Re_{\mathrm{fst}}^{-7/9} + 0.038\,. \tag{1}$$

The above equation is substantially simpler than eq. (3.7) of [2]. The length scale Λ_x^{BL} measures how large the structures are inside the BL i.e., the maximum streamwise length of the streaks. We can define the aspect ratio of the streaks as $\Lambda_x^{\mathrm{BL}}/\lambda_z$, which corresponds to ratio of maximum length scales inside BL. Figure 1 (*c*), clearly depicts that this ratio when normalised with Tu at the LE, the data closely falls onto a straight line and we see an increased scatter with Re_{tr} according to:

$$\Lambda_x^{\mathrm{BL}}/(\lambda_z \times Tu) = 3.146 \times 10^{-4} Re_{\mathrm{tr}} + 9.981\,. \tag{2}$$

CONCLUSIONS

Current experimental results provide further evidence that the spanwise wavelength of the streaks λ_z as well as the aspect ratio $\Lambda_x^{\mathrm{BL}}/\lambda_z$ strongly correlate with the FST conditions (Λ_x & Tu) at the LE. The empirical model as in eq. (1) aid to predict λ_z solely based on Reynolds number Re_{fst}. The new results promote the emphasis of Λ_x for the transition prediction, indicate that a rooted effort is required in developing future prediction models for Re_{tr}. We believe that, this dataset provides a great potential to prospect further into BL receptivity coefficients which can simply be extracted purely from the parameter space of Re_Λ & Re_{fst}.

References

[1] Jonáš P., Mazur O. & Uruba V. On the receptivity of the by-pass transition to the length scale of the outer stream turbulence. *Eur. J. Mech.* **B19**: 707-722, 2000.
[2] Fransson J. H. M., Shahinfar S. On the effect of free-stream turbulence on boundary-layer transition. *J. Fluid Mech.* **899**: A23, 2020.
[3] Matsubara M., Alfredson P. H. Disturbance growth in boundary layers subjected to free-stream turbulence. *J. Fluid Mech.* **430**: 149-168, 2001.
[4] Brandt L., Schlatter P. & Henningson D. S. Transition in boundary layers subject to free-stream turbulence. *J. Fluid Mech.* **517**: 167-198, 2004.
[5] Ovchinnikov V., Piomelli U.& Choudhari M. M. Inflow conditions for numerical simulations of bypass transition. *AIAA Pap.* 2004-0591, 2004.
[6] Ovchinnikov V., Choudhari M. M. & Piomelli U. Numerical simulations of boundary-layer bypass transition due to high-amplitude free-stream turbulence. *J. Fluid Mech.* **613**: 135-169, 2008.

THE INTERACTION BETWEEN THE FREE-STREAM TURBULENCE AND A 3D ROUGHNESS ELEMENT IN BOUNDARY LAYERS

Masumeh Gholamisheeri*Kristina Đurović,Santhosh Babu Mamidala,Jens Fransson,Ardeshir Hanifi,and Dan Henningson
Engineering Mechanics, FLOW, KTH Royal Institute of Technology, Stockholm, Sweden

Summary The dynamics of transition-to-turbulence induced by an isolated cylindrical roughness element immersed in the boundary layer subjected to the free-stream turbulence (FST) is investigated through direct numerical simulation (DNS) and hot-wire measurements. The roughness element is located on a flat plate with an asymmetrical leading edge. The flow Reynolds number and aspect ratio of the roughness are chosen such that in the absence of FST it induces a steady wake with high- and low-speed streaks. An impulse response analysis is performed to find the frequencies of the unstable disturbances behind the roughness element. The imposed free-stream turbulence has an intensity of about 2% at the plate leading edge. To find the dynamics behind the roughness element in the presence of FST, the stability and proper orthogonal decomposition (POD) analyses are considered. Numerical results are compared with the hot-wire anemometry (HWA) measurements which are performed at the Minimum Turbulence Level (MTL) wind tunnel at KTH.

INTRODUCTION

Predicting or controlling the laminar-turbulent transition is of great importance. The flow characteristics, surface roughness, and environmental noises can affect the onset of transition. The experimental work by Klebanoff & Tidstrom [1] showed that the natural transition can be promoted with the spanwise-invariant roughness elements. The modified stability properties of the boundary layer flow was known as the cause of the early transition. With the fully three-dimensional roughness elements, however, the transition can be delayed due to the streamwise velocity streaks. Fransson et al. [3] employed an array of the cylindrical roughness elements to delay the transition, however, beyond a threshold the streaks induced by the roughness elements could become unstable. Therefore, their height, shape, aspect ratio, and, the spacing between them have to be chosen carefully. In order to broaden the knowledge of effects of FST on the transition onset, various levels of free-stream turbulence have been experimentally and numerically investigated. A boundary layer subject to FST develops unsteady streaky structures with high and low streamwise velocities [4]. Breakdown to turbulence is caused by a secondary instability that develops on the streaks leading to the formation of turbulent spots. As explained by Schlatter et al. [2], the secondary instabilities appear as growing wave packets situated on the low speed streaks, their magnitude increases as they are dispersing in the streamwise direction. It was noted that although low speed streaks extend high in the boundary layer, where they are susceptible to the disturbances in the FST, other possible breakdown triggering mechanisms such as pressure fluctuations should be considered [2].

The aim of the present study is to assess the interaction between the two above-mentioned mechanisms, *i.e.* FST and isolated roughness element, and also how they influence the transition onset. To this end, high-fidelity direct numerical simulations (DNS) are performed for an isolated cylindrical roughness element, on a flat plate with asymmetric leading edge. At the first stage, the impulse response analysis is performed using the solution in the absence of FST and the frequencies behind the roughness element are identified. The POD analysis is planned for the simulation with the FST in order to find the structures behind the roughness element. Numerical results are compared with the hot-wire anemometry (HWA) measurements which will be performed in the KTH MTL wind tunnel.

NUMERICAL AND EXPERIMENTAL SETUPS AND APPROACHES

The dynamics of a three-dimensional incompressible flow is described by the Navier-Stokes equations which reads as:

$$\mathbf{u}_t + (\mathbf{u}\cdot\nabla)\mathbf{u} = -\nabla p + \frac{1}{Re}\nabla^2\mathbf{u}\,, \tag{1}$$

$$\nabla\cdot\mathbf{u} = 0\,, \tag{2}$$

where, $\mathbf{u}$, p and Re are the velocity vector, pressure and the free-stream Reynolds number, respectively. The roughness element has the diameter $d = 6\,mm$ and height $h = 1.3\,mm$. The computational domain size is equal to $L_x = 200d$, $L_y = 33d$ and $L_z = 13d$ in the streamwise, wall-normal and spanwise directions, respectively.

The plate leading edge is located at approximately $L_{le} = 34d$ downstream of the domain inlet and the roughness element is placed at $75d$ downstream of the plate leading edge and is centered in the spanwise direction. In order to set the simulation conditions, a few experimental measurements were conducted based on which a roughness Reynolds number $Re_{hh} = U_h h/\nu = 250$ is chosen for current studies. Further, based on the size and location of the roughness element, the freestream velocity is set to $6.38\,m/s$. The initial experiments also suggest that with the chosen velocity and roughness aspect ratio, the flow over the roughness element remains in the laminar region.

*Corresponding author. E-mail: masumeh@kth.se.

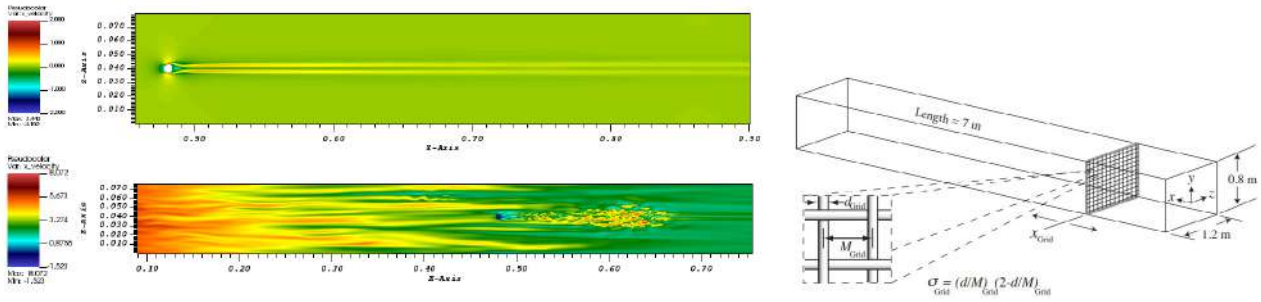

(a) (b)

Figure 1: High- and low-speed streaks behind the roughness element (a-top), FST-induced streaks before and after the roughness element (a-bottom), and the wind tunnel setup with the grid installed (b).

The DNS are performed using the open-source CFD solver Nek5000 [5]. Spatial discretisation is performed by a spectral element method with the polynomials of order 9 in each spatial direction at each element. The number of spectral elements in the mesh is of the order of 325000 which leads to 325 million degrees of freedom. For time integration, a backward differentiation scheme of order 3 combined with an extrapolation of the same order (together called BDF3/EXT3) is employed.

The experimental measurements will be carried out at the MTL wind tunnel facility at KTH. The test section of the wind tunnel is $1.2\,m$ wide, $0.8\,m$ high, and $7\,m$ long. A trailing flap at the end of the plate allows for positioning the stagnation line at the leading edge, on the upper side of the plate, in order to avoid unsteadiness. To measure the velocity, HWA is used. The traverse system in the wind tunnel allows the probe to be moved along the test section, normal to the plate and in the spanwise direction. The freestream turbulence is generated by turbulence generating grids. The turbulence intensity is proportional to the pressure drop over the grid and the FST length scales are defined by the mesh width, M, and bar diameter d_{bar} of the grid. The desired FST intensity at the leading edge of the plate is achieved by adjusting the distance between the grid and the leading edge. A schematic of an empty test section with a FST grid is shown in Figure 1 (b).

PRELIMINARY RESULTS

Our numerical simulations and the initial experimental results show that with the chosen freestream velocity and roughness aspect ratio, in the absence of FST, the flow remains laminar, although, high- and low-speed streaks are generated behind the roughness element, as is shown in Figure 1 (a-top). The base-flow simulation agrees well with the experiments. Introducing an initial perturbation (wave packet-like disturbance) upstream the roughness element and solving the linearised Navier-Stokes equations reveal that the flow is convectively unstable and in the limit of long times, the disturbances are advected away from the location of origin.

The FST generated streaks are shown in Figure 1, (a-bottom). Fransson and Shahinfar [6] showed that the aspect ratio of the streaky structures correlates with the FST Reynolds number, Re_{FST}, where,

$$Re_{FST} = \frac{u_{rms}\Lambda_x}{\nu} = Tu \cdot Re_\Lambda\,, \quad \text{and} \quad Re_\Lambda = \frac{U_\infty \Lambda_x}{\nu}\,. \tag{3}$$

Here, u_{rms} is the root-mean-square value of the velocity, Tu denotes the FST intensity, Λ_x is the integral length scale, U_∞ represents the free-stream velocity and ν is the kinematic viscosity of the flow. The correlation between the size of the cylindrical roughness element and aspect ratio of the streaky structures will be investigated in the present study.

To further investigate the instabilities behind the roughness element in the presence of FST, stability and POD analysis are to be performed.

References

[1] Klebanoff P. S. and Tidstrom K. D., Mechanism By Which A Two-Dimensional Roughness Element Induces Boundary-Layer Transition: Roughness Induced Transition. *Phys. Fluids*, 1972.

[2] Schlatter P, Brandt L., Lange D. HC., and Henningson D., On Streak Breakdown in Bypass Transition. *Phys. Fluids* **20**, 2008.

[3] Fransson J., Brandt L., Talamelli A. and Cossu C., Experimental Study of the Stabilization of Tollmien-Schlichting Waves by Finite Amplitude Streaks. *book title*, IUTAM Symposium on Laminar-Turbulent Transition, 2006.

[4] Matsubara M. and Alfredsson P. H., Disturbance Growth in Boundary Layers Subjected to Free Stream Turbulence. *J. Fluid Mech.* **430** 2001.

[5] Fischer P. and Mullen J., Filtered-Based stabilization of Spectral Element Methods. *J. Comptes Rendus de l'Academie des Science - Series I - Mathematics*, **32**: 2001.

[6] Fransson J. and Shahinfar S., On the effect of Free-Stream Turbulence on Boundary-Layer Transition. *J. Fluid Mech.* **899**, A23, 2020.

EXCITATION OF WATER WAVES BY IMPULSIVELY APPLIED WIND: ORR-SOMMERFELD COMPUTATIONS VS. EXPERIMENTS

Meital Geva and Lev Shemer[1]
School of Mechanical Engineering, Tel-Aviv University, Tel-Aviv, Israel

Summary The stability of flow resulting from impulsively applied turbulent wind over initially quiescent water surface is analysed by coupled viscous Orr-Sommerfeld equations. This linear stability analysis is applied to describe the initial development of wind-waves. The computational results are compared with comprehensive experimental data accumulated in a wind-wave facility at wind velocities ranging from 5.5 m/s to 8.5 m/s. The wind velocity profiles and friction velocities at air-water interface in the simulations are taken from separate measurements performed under steady wind forcing. Instantaneous wave energies were obtained by a reliable ensemble-averaging of multiple independent realizations. The direct comparison of computations with experiments reveals differences indicating that this stability analysis needs to be amended to describe accurately the initial growth of wind-waves.

EXPERIMENTAL AND NUMERICAL RESULTS

Coupled Orr-Sommerfeld equations (OSE) with appropriate boundary conditions at the air-water interface are applied to analyse the interaction of impulsively applied turbulent flow with initially calm water surface in a test section of wind-wave facility. Turbulent log-linear wind profile measured in the facility [1] and an exponential velocity profile in the water were used following the approach applied in [2, 3]. Different numerical schemes were used to solve OSE and assess the initial growth of gravity-capillary wind waves [4, 5].

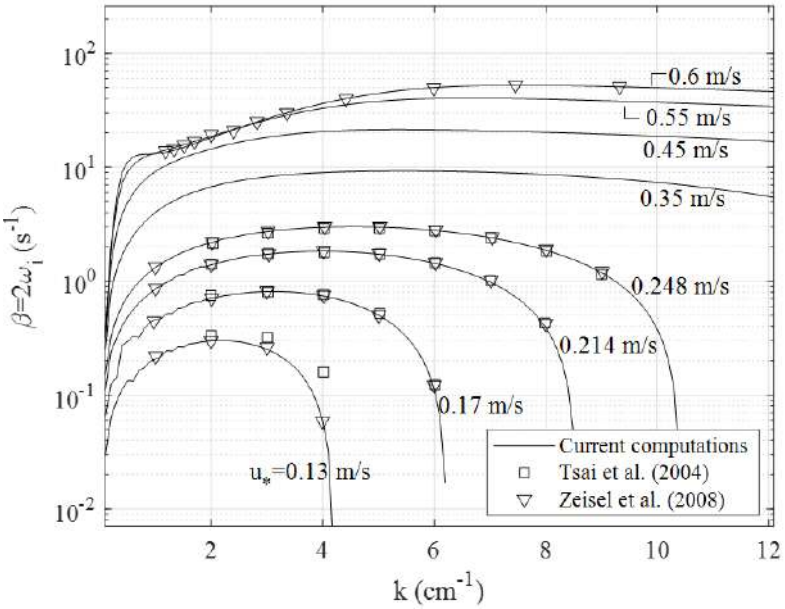

Figure 1. Energy growth rate vs. wavenumber k: validation by comparison with available results.

The Chebyshev polynomials method used in [5] was somewhat modified in this study. The energy growth rates are defined as $\beta_i=2Im(\omega_i)$, where ω_i represents the solution eigenvalues. Fig. 1 demonstrates that the present results are in agreement with earlier studies. It should be stressed that the only existing combined experimental and numerical study on temporal growth of wind-waves by Kawai [3] is limited to very low wind velocities. In the present investigation, the theoretical predictions are compared with the detailed data on the initial growth of wind waves under impulsive wind forcing reported in [6].

The measured wave energy growth at the initial stages of evolution are presented in Fig. 2 for three wind velocities and at three distances from the inlet, x. The representative wave energy at each instant relative to the initiation of the wind, t, was calculated by ensemble-averaging of the instantaneous squared surface elevations $<\eta^2>$ measured in multiple independent experimental realizations. The results clearly demonstrate that during the initial stage following the impulsive application of wind forcing that lasts for few hundred milliseconds, the measured wave energy growth is indeed exponential at all fetches and wind velocities.

[1]Corresponding author. E-mail: shemerl@tauex.tau.ac.il.

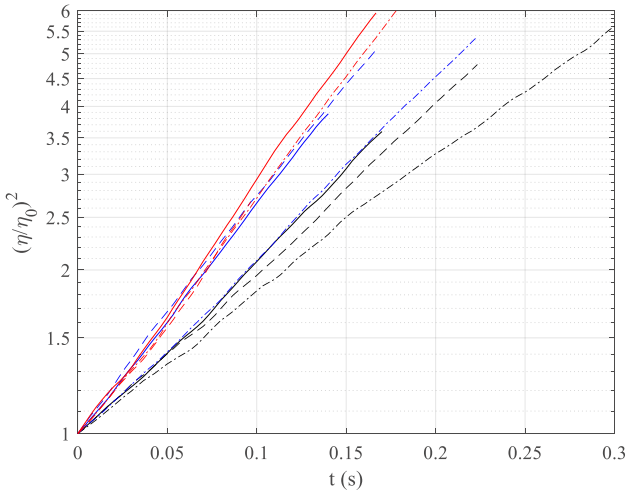

Figure 2. The measured temporal growth of wave energy relative to the initial state. Black: friction velocity u_*=0.35 corresponding to wind velocity U=6.5 m/s, blue u_*=0.45 m/s, U=7.5 m/s, red u_*=0.55 m/s, U=8.5 m/s; solid lines (-): x=120 cm, dashed line (--): x=220 cm, dashed-dot line (-.): x=340 cm [6].

The corresponding growth rates are presented in Table 1. In simulations as well as in experiments, the growth rates β increase with wind velocity. The numerical results are fetch-independent, whereas certain scatter is observed in the measured values of β. It should be stressed that the most unstable mode is usually considered in the OSE analysis, while the experimental results represent the variation in time of $<\eta^2>$. The values representing the growth of the energy of all unstable harmonics are therefore also presented in Table 1. Note that for all wind velocities, growth rates based on the total wave energy and on the most unstable harmonic differ insignificantly.

Table 1. Growth rates β (s^{-1})

		u_*=0.35 m/s	u_*=0.45 m/s	u_*=0.55 m/s
Experiment	x=120 cm	7.63	9.84	10.94
	x=220 cm	7.04	9.77	10.18
	x=340 cm	5.77	7.69	10.19
OSE	most unstable	9.25	21.07	40.34
	sum of harmonics	8.07	19.01	38.09
	sum of harmonics with $-4k^2\nu$	7.14	18.11	36.85

Reasonable agreement between the results of the linear stability based on OSE and experiments for lower wind velocity is demonstrated in Table 1. However, for stronger wind forcing, the theoretically predicted wave energy growth rates are notably higher than those obtained in the experiments. An attempt to account for viscous dissipation by adding the viscous dissipation term $-4k^2\nu$ as done in [5] does not improve the agreement significantly. Alternative dissipation mechanisms are discussed in the full version of the paper.

CONCLUSIONS

The experimental results indicate that the initial ripple grows exponentially in time under application of impulsive forcing. This suggests that linear stability analysis is applicable for the description of the early stage of the temporal wind-wave evolution. The numerical simulations based on OSE take advantage of the availability of carefully accumulated experimental data that describe the actual conditions encountered in the experiments. For relatively weak wind forcing, the agreement of the numerical predictions with measurements is indeed reasonable. However, for stronger wind the present results indicate that accounting for additional dissipation mechanism is essential to obtain not only qualitative but also quantitative agreement with the measurements.

References

[1] Zavadsky A. and Shemer L. *J. Geophys. Res. Oceans.* **117** (C11), 2012.
[2] Valenzuela G. R. *J. Fluid. Mech.* **76**: 229-250, 1976.
[3] Kawai S. *J. Fluid. Mech.* **93**: 661-703, 1979.
[4] Tsai W. T. and Lin M. Y. *J. Mar. Sci. Technol.* **12**: 200-208, 2004.
[5] Zeisel A., Stiassnie M. and Agnon Y. *J. Fluid. Mech.* **597**: 343-369, 2008
[6] Zavadsky A. and Shemer L. *J. Fluid. Mech.* **828**: 459-495, 2017

TRANSITION IN BOUNDARY LAYERS INFLUENCED BY FREESTREAM TURBULENCE

Kristina Đurović, Philipp Schlatter, Ardeshir Hanifi and Dan S. Henningson
Department of Engineering Mechanics, FLOW, KTH Royal Institute of Technology, Stockholm, Sweden

Summary We aim at examining and understanding the physics behind the influence of free-stream turbulence (FST) on the boundary-layer transition. A recent experiment by Fransson & Shahinfar (2020) shows significant effects of FST scales. They found that, for the low values of turbulence intensity, an increase in the integral length scale advances the transition, which agrees with literature. However, for high turbulence intensities, the trend is reported to be the opposite. Here we want to understand these results by performing a series of high-fidelity direct numerical simulations. The obtained detailed data will help to understand why the FST integral length scale affects the transition location differently depending on the intensity. This knowledge is crucial for the development of the transition models, which are commonly used in the field of turbomachinery and aeronautics.

INTRODUCTION AND RESULTS

Laminar-turbulent transition induced by the free-stream turbulence is of great relevance due to its occurrence in many practical situations like turbo-machinery flows, flow mixers and also understanding results of the experiments in the conventional wind tunnels. In the two-dimensional boundary-layer flows subjected to FST intensities of 1% or higher, transition usually occurs rapidly bypassing the classical scenario triggered by the Tollmien–Schlichting waves. This type of transition is characterised by the occurrence of the streamwise elongated streaky structures inside the boundary layer. As these streaks travel downstream, they break down into the turbulent spots due to their secondary instability. These spots grow and merge until the flow is fully turbulent.

This type of flow has been extensively studied in the past [2], but always using certain simplifications compared to the real setup (e.g. removing the leading edge, simplified FST generation etc.). With the availability of large-scale computers and corresponding simulation codes, we can now perform computations of the complete physical case, extracting flow details at unprecedented detail, and putting the focus on details potentially neglected previously. Here, we study the effects of the FST characteristic length scales and intensity on the transition in an incompressible flat-plate boundary layer using direct numerical simulation (DNS). The numerical setup corresponds to the experimental investigations by Fransson & Shahinfar (2020) [1].

To accurately simulate a wide range of temporal and spatial scales in the flow, a high-order numerical method is necessary. The code chosen for the proposed project is Nek5000, developed by Fischer et al. [3], and based on the spectral element method (SEM) [4]. The spatial discretization is done using the Galerkin approximation, following the P_N-P_{N-2} formulation. The solution is interpolated within a spectral element employing Lagrange interpolants of orthogonal Legendre polynomials on the Gauss-Lobatto-Legendre (GLL) quadrature points. The non-linear terms are treated explicitly by third-order extrapolation (EXT3), whereas the viscous terms are treated implicitly by a third-order backward differentiation scheme (BDF3). Dealiasing of the non-linear terms is performed using overintegration.

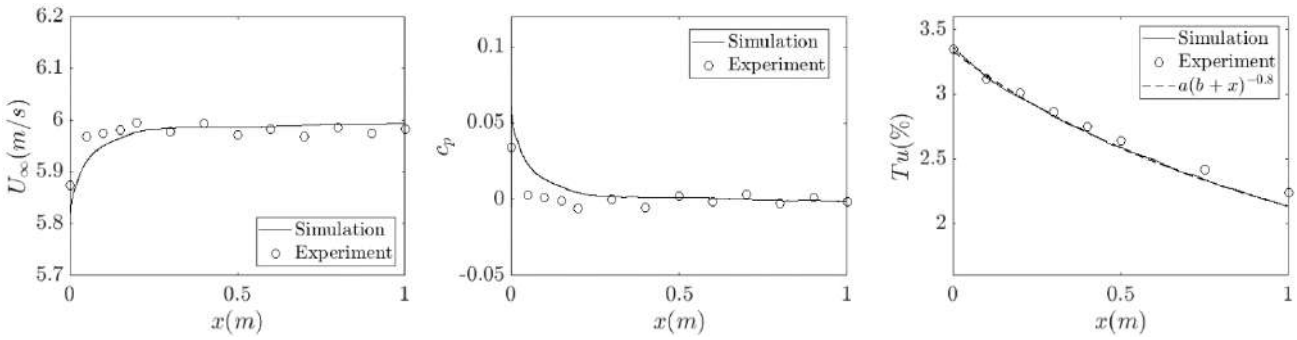

Figure 1. Comparison of the simulation data with the measured data from the experiment: Streamwise distribution of streamwise velocity component (left) and pressure coefficient (middle); decay of the turbulence intensity in the free-stream together with a fit to a power law with exponent -0.8.

FST generation is done in such a way to mimic the isotropic, homogeneous free-stream turbulence generated behind the grid in the wind tunnel. FST is prescribed in the volume section close to the inlet boundaries as a superposition of Fourier modes. The numerical methodology that is used allows us to define the energy spectrum (von Kármán energy spectrum) of the turbulent inflow and thereby to control the integral length scale and turbulence intensity of the FST.

To validate the flow simulation, we first examine behaviour of generated FST. Isotropic grid turbulence is known to follow a decay as a power law. The decay rate is, dependent on the source, between 0.5 and 1 [5]. A least-square fit on the decay of the turbulence intensity was performed (Figure 1, right) yielding a decay rate of 0.8. Thus, the decay of the simulated FST is similar to that of the grid-generated. On figure 1 (left), we show a comparison of velocity distribution in the streamwise direction with data from the experiments. As it can be seen there, we have achieved a good agreement with the experiments, which confirms that we have modelled our simulation with correct boundary conditions. We can also confirm this by looking and pressure coefficient distribution in Figure 1 (middle). A uniform pressure distribution near the leading edge cannot usually be obtained using elliptic or wedge-shaped leading edges, although careful attention to this problem can minimize undesirable effects. From the figure, we see that the pressure decreases smoothly within the first 50 mm, as the flow accelerates from the stagnation point, without producing a suction peak. Based on these data, we can conclude that our model of the experiments, including the plate leading edge and the generation of free-stream turbulence, are in a good agreement with the experiments, thus allowing us to perform the DNS with high fidelity.

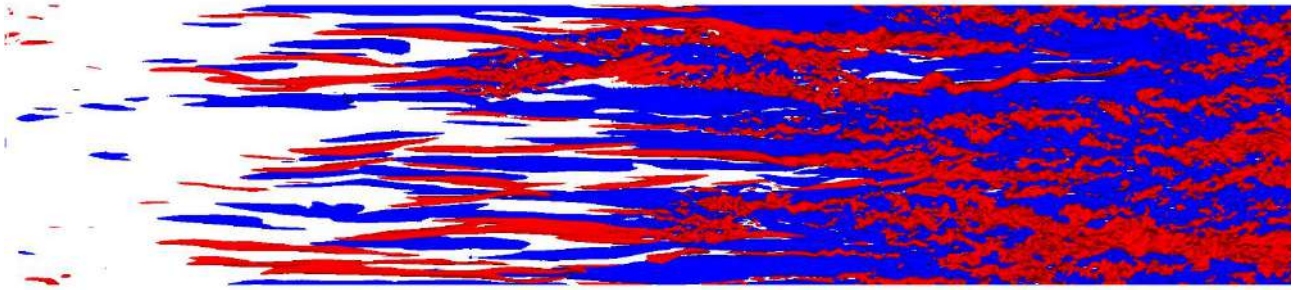

Figure 2. Isocontours of positive (red) and negative (blue) streamwise disturbance velocities.

A snapshot of the flow is shown in Figure 2. The isocontoures of the instantaneous streamwise velocities perturbations are plotted in a plane parallel to the wall close to the surface. From this picture the overall transition mechanism can be deduced. Starting from the inlet position, the perturbations in the boundary layer appear mainly in the streamwise velocity component, in the form of elongated structures. Patches of irregular motion, turbulent spots, are observed further downstream. As these spots travel downstream, they become broader and more extended. Note also that laminar streaks can be observed even downstream of the spots. At the end of the domain, the turbulent region is created by the enlargement and merging of the various spots and therefore the streamwise position at which the flow is turbulent varies with time. Transition location is determined based on an intermittency function similar to that used by Fransson & Shahinfar (2020). Further, we will analyse the streak breakdown by investigating the snapshots of the instantaneous 3D flow configurations and tracing the location of the spot formation. The turbulence spots are identified using the wall-normal derivatives of the spanwise velocity following the process suggested by Kreilos et al [6]. This data can then serve as a basis for a new data-driven version of the nucleation model[6]. By devising such a model, the full dynamics of the transitional boundary layer can be simulated for varying conditions appearing in reality at a greatly reduced computational cost.

Outlook

The final conference contribution will contain a detailed description of the influence of FST scales on laminar to turbulent transition location for four different sets of integral length scales and turbulence intensities. The results will be validated and compared against experiments [1]. These results will be used to improve cellular automaton representation model for a laminar-turbulent transition[6]. Especially the nucleation model, for which the local conditions (turbulence intensity, length scales, etc.) are taken into account, can be improved by employing the new data sets.

References

[1] Fransson, J.H.M., Shahinfar, S. On the effect of free-stream turbulence on boundary-layer transition. *J. Fluid. Mech*. **899**: A23, 2020.
[2] Brandt, L., Schlatter, P. and Henningson, D. S. Transition in boundary layers subject to free-stream turbulence. *J. Fluid. Mech*. **517**: 167–198, 2004.
[3] Fischer, P. F., Lottes, J. W. and Kerkemeier, S. G. "Nek5000", web site, **http://nek5000.mcs.anl.gov**
[4] Patera, A.T. A spectral element method for fluid dynamics: laminar flow in a channel expansion. *J. Comput. Phys* **54**:468–488,1984.
[5] Westin, J. Laminar-Turbulent Boundary Layer Transition Influenced by Free Stream Turbulence. *PhD Thesis*, Royal Institute of Technology (KTH), Stockholm, Sweden, 1997.
[6] Kreilos, T., Khapko, T., Schlatter, P., Duguet, Y., Henningson, D.S. and Eckhardt, B., Bypass transition and spot nucleation in boundary layers, *Phys. Rev. Fluids* **1** (4) 043602, 2016

EXPERIMENTAL EVALUATION OF THE OPTIMIZED AERO-STRUCTURE-CONTROL MORPHING WING TECHNOLOGY FEASIBILITY FOR A FULL-SCALE PORTION OF A REGIONAL AIRCRAFT WING

Ruxandra Mihaela Botez[1], Michel Joël Tchatchueng Kammegne[1], Lucian Teodor Grigorie[1,2], Mahmoud Mamou[3], Yousef Mébarki[3]
[1]*École de Technologie Supérieure, Montréal, Québec H3C 1K3, Canada*
[2]*Military Technical Academy "Ferdinand I", Bucharest 050141, Romania*
[3]*National Research Council, Ottawa, Ontario K1A 0R6, Canada*

Summary The paper presents some of the results obtained during the wind tunnel testing of a morphing wing experimental model representing a full-scale portion of a regional aircraft wing equipped with an aileron. The work is a part from a major morphing wing project realized in an international collaboration Canada-Italy, involving industry (Bombardier Aerospace and Thales from Canada, and Alenia from Italy), research entities (National Research Council Canada and CIRA Italy), but also university partners (Ecole de Technologie Supérieure in Montréal, which was the project coordinator, École Polytechnique de Montréal, and University of Naples Frederico II). The research team developed a system for active control of the morphing wing in order to extend the laminar flow over the upper surface of the wing, and also built an evaluation system which has been used to detect the airflow characteristics using pressure sensors installed on the upper surface of the morphing wing. On the other way, to capture the transition region over the entire wing model surface, infra-red (IR) thermography method was applied.

MORPHING WING PROJECT DESCRIPTION

Called "Multi-Disciplinary Optimization" 505 (MDO 505) the project aimed at the development of morphing architectures and related technologies for wing efficiency improvement to reduce the operating costs for the new generation of aircrafts through a fuel economy in flight, and also to improve aircraft performances, expand its flight envelope, replace conventional control surfaces, reduce drag to improve range and reduce vibrations and flutter.

The developed model of the morphing wing is a portion of an existing regional aircraft wing, its interior consisting of spars, stringers, and ribs, and having a structural rigidity similar to the rigidity of a real aircraft wing. The deformable part is provided by a flexible skin piece mounted on the upper surface of the wing, made of composite materials, and directly actuated in four points by using electrical miniaturized actuators in house manufactured. In order to evaluate the aerodynamic improvement of the morphing configuration, a detection system that gives information about the characteristics of the flow has been built by installing 32 Kulite pressure sensors on the flexible skin. Also, to capture the transition region over the entire wing model surface, infra-red (IR) thermography method was applied ([1], [2]).

As a preliminary step in the project, starting from the reference airfoil of the wing (un-morphed airfoil), a numerical optimization was performed by the aerodynamic team in order to establish some optimized airfoils (morphed airfoils) for various flow cases ([3], [4]). A number of 97 flow cases were considered in the optimization step, and were obtained as combinations of incidence angles (α) (nineteen values, between -3 and +3 degrees), Mach numbers (three values: 0.15, 0.2 and 0.25) and aileron deflection angles (δ) (thirteen values, between –6 and +6 degrees).

The developed experimental model, with a chord and a span both of 1.5 meters in length, was equipped with an adaptive upper surface placed between 20% and 65% of the wing chord. The designed actuation mechanism includes four similar actuators disposed on two lines along two wing ribs, which are at 37% and 75% of the wing's span. Also, along the two actuation lines, the actuators were fixed at 32% and 48% of the local chord (Fig. 1).

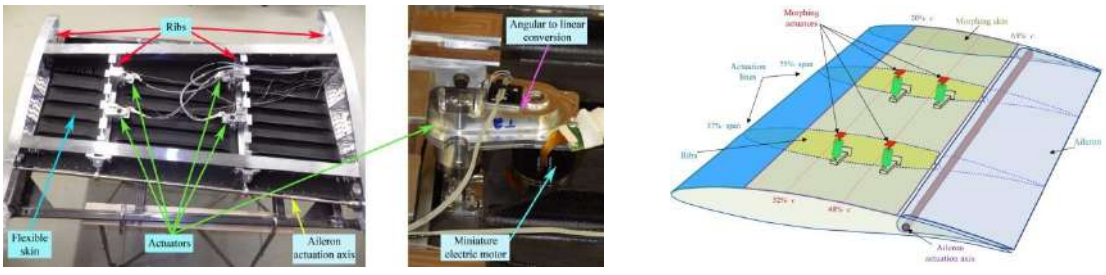

Figure 1. Morphing skin and actuators' positioning on the experimental model.

INSTRUMENTATION AND TESTING OF THE EXPERIMENTAL MODEL

The experimental tests were performed both in the lab conditions, on bench, with no aerodynamic load on the wing, but also, in the NRC wind tunnel facility in Ottawa, for each of the optimized flow cases. The wind tunnel testing aimed at the validation of all stuff integration in the developed model, with aerodynamic loads similar to the real flight conditions, but also at the evaluation of the aerodynamic gain brought by the morphing technology for our project. In these aims, all ninety-seven flow cases have been run in the wind tunnel for both un-morphed and morphed airfoils. For each analysed flow case, the optimization stage provided four linear displacements corresponding to the differences

between the optimized shape and the original shape (un-morphed) of the wing in the actuation points. The development of the control system for the morphing wing supposed the design of a controller able to control each of the four actuators in order to reproduce the required displacements, and in this way a morphed wing shape as close as possible to the optimized one, for each flow case. Several variants of control systems were designed, implemented and experimentally tested for the morphing wing model. The system interfacing the remote computer and the morphing wing experimental model was designed by using a National Instruments Real Time (RT) Target (Fig. 2) ([5]).

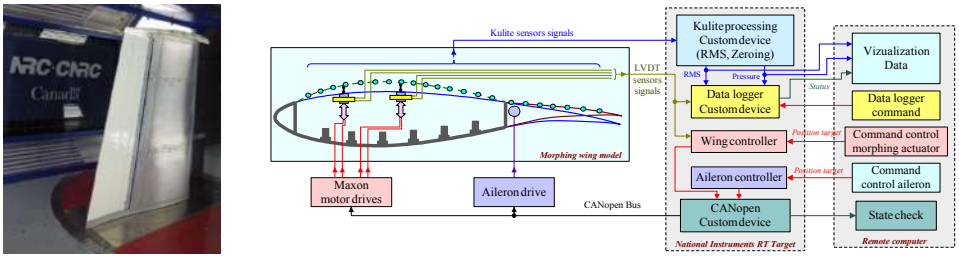

Figure 2. Wind tunnel testing of the experimental model and the interface of the model with the remote computer.

To detect the airflow characteristics and to evaluate the position of the laminar to turbulent transition over the upper surface of the wing the date from the 32 Kulite pressure sensors were used. The Standard deviation and Power spectrum visualization of the pressure data were the main approaches used both in real time, but also in a post-processing phase, to perform this evaluation. The pressure data were recorded at 20 kHz rate, for both un-morphed and morphed airfoils, and were analyzed using the Fast Fourier Transforms (FFT) decomposition to detect the magnitude of the noise in the surface air flow. Both mechanisms allow the estimation of the laminar to turbulent transition point position in the Kulite span-wise station. To capture the transition region over the entire wing model surface the IR thermography method was applied. In the flow case characterized by Mach=0.15, $\alpha=1^\circ$ and $\delta=0^\circ$ the IR thermography technique provided the results presented in Fig. 3. For un-morphed configuration the averaged position of the laminar to turbulent transition over the entire wing surface was estimated to be at 48% of the wing chord, while for the morphed configuration it was estimated to be at 51% of the wing chord. Therefore, for this case, the morphing configuration produced a displacement of the averaged position of the laminar to turbulent transition over the entire wing surface with 3% of the wing chord.

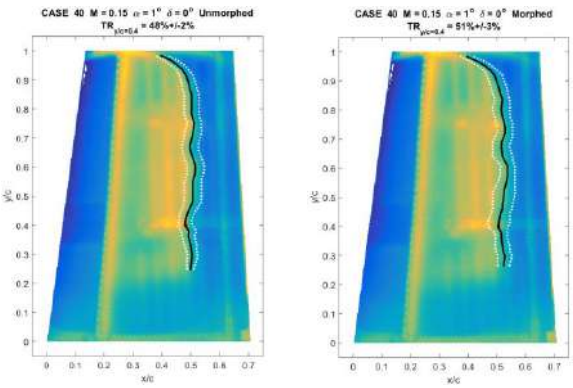

Figure 3. IR thermography results for Mach=0.15, $\alpha=1^\circ$ and $\delta=0^\circ$ flow case.

CONCLUSIONS

Both, the IR analysis and the processing of Kulite data validated the numerical predicted transition location. Therefore, the experiments confirmed the feasibility of the morphing wing technology and created the premises for a future application of this technology on real aircraft, having in mind that our project was based on a real wing segment.

References

[1] Tchatchueng Kammegne, M.J., et al., Experimental wind tunnel testing of a new multidisciplinary morphing wing model. *18th International Conference on mathematical methods, computational techniques and intelligent systems (MAMECTIS '16)*, Venice, Italy, January 29-31, 2016.

[2] Tchatchueng Kammegne, M.J., Grigorie, T.L., Botez, R.M., Design, numerical simulation and experimental testing of a controlled electrical actuation system in a real aircraft morphing wing model. *Aeronaut J.* **119**(1219): 1047-1072, 2015.

[3] Koreanschi, A., et al., Optimization and Design of an Aircraft's Morphing Wing-Tip Demonstrator for Drag Reduction at Low Speeds, Part I - Aerodynamic Optimization using Genetic, Bee Colony and Gradient Descent Algorithms, *Chinese J Aeronaut* **30**(1): 149-163, 2017.

[4] Koreanschi, A., et al., Optimization and Design of an Aircraft's Morphing Wing-Tip Demonstrator for Drag Reduction at Low Speeds, Part II - Experimental Validation using Infra-Red Transition Measurement from Wind Tunnel Tests, *Chinese J Aeronaut* **30**(1): 164-174, 2017.

[5] Tchatchueng Kammegne, M. J., et al., Proportional Fuzzy Feed-Forward Architecture Control Validation by Wind Tunnel Tests of a Morphing Wing, *Chinese J Aeronaut* **30**(2): 561-576, 2017.

SELF-SIMILAR COALESCENCE OF LIQUID LENSES

Jacco H. Snoeijer [1], Michiel A. Hack[1], Walter Tewes [1], Qingguang Xie[2], Charu Datt[1], Kirsten Harth[1,3], and Jens Harting[2,4]
[1]Physics of Fluids Group, Faculty of Science and Technology, University of Twente, P.O. Box 217, 7500 AE Enschede, The Netherlands
[2]Department of Applied Physics, Eindhoven University of Technology, P.O. Box 513, 5600 MB Eindhoven, The Netherlands
[3]Institute of Physics, Otto von Guericke University, 39106 Magdeburg, Germany
[4]Helmholtz Institute Erlangen-Nürnberg for Renewable Energy (IEK-11),Forschungszentrum Jülich,FürtherStr. 248, 90429 Nuremberg,Germany

Summary A basic feature of liquid drops is that they can merge upon contact to form a larger drop. In spite of its importance to various applications, drop coalescence on pre-wetted substrates has received much less attention then coalescence on dry substrates or of freely suspended drops. Here, we experimentally and theoretically reveal the dynamics of drop coalescence on a thick layer of liquid [1]. It is shown that these so-called "liquid lenses" merge by the self-similar growth of a bridge connecting the two lenses. Using a slender analysis, we derive similarity solutions corresponding to the viscous and inertial limits. Excellent agreement is found with the experiments without any adjustable parameters, capturing both the spatial and temporal structure of the flow during coalescence. Finally, we consider the crossover between the two regimes and show that all data collapse on a single curve capturing the full range of the coalescence dynamics.

References

[1] Michiel A. Hack, W. Tewes, Q. Xie, C. Datt, K. Harth, J. Harting, J.H. Snoeijer, Self-similar liquid lens coalescence, arXiv:1912.06420.

AN ACOUSTO-GRAVITATIONAL BALANCE IN CLIMBING FILMS OF WATER AND OIL

Amihai Horesh, Daniel Khaikin, Mackenzie Karnilaw, Anna Zigelman, and Ofer Manor
Department of Chemical Engineering, Technion – Israel Institute of Technology, Haifa, Israel

Summary We study the contributions of acoustical stresses to wetting. We employ MHz-frequency surface acoustic waves (SAWs), which we generate in an acoustic actuator in the form of a SAW device. When a vertical device is in contact with a liquid reservoir, the SAW supports the climb of silicon oil and water up the device. The fully wetting oil climbs as a nearly flat film. The film supports resonance-enhanced radiation pressure, which satisfies gravitational stresses. Hence, the climbing velocity of oil is mainly determined by an interplay between acoustical and viscous stresses and appears to be independent of gravity. Unlike oil, the partially wetting water meniscus is curved and does not support enhanced radiation pressure. As a result, the water meniscus climbs up the device to a finite height, which is determined from an interplay between acoustical, capillary, and gravitational stresses.

Introduction

In recent years, there is a growing interest in the excitation of films at thicknesses that range from nanometres to micrometres by MHz-frequency vibrations [1]. Recent studies employed surface acoustic wave (SAW) devices, which generate Rayleigh type SAWs, to manipulate liquid films. The excitation of silicon oil by MHz SAWs gives rise to the dynamic wetting of the substrate of the device. Oil films spread along and opposite the path of the SAW [2,3]. Further studies showed that partially wetting water films may undergo similar dynamics should the acoustic stresses in the films exceed the strong capillary stresses at the free surface of water [4,5]. Moreover, SAWs are found to actuate thin films of liquid in different applications. Examples include the SAW induced draining of liquid films and thus the enhancement of the attachment of bubbles to substrates [6], the actuation of dynamic wetting in nanochannels, [7] and the actuation of a nanofiltration process [8]. The contribution of gravity to SAW induced dynamic wetting was ignored to date. Here, we present a study on the balance between acoustical and gravitational stresses in climbing films, which are under the influence of SAWs [9].

Experiment

We present the climb of water menisci and silicon oil films up a vertical SAW device. The experimental system is comprised of a 20 MHz-frequency SAW device, which is mounted on a vertical stage. The edge of the device is submerged in a reservoir of liquid. See Figure 1 for further details. Upon the application of power, a SAW propagates down the device to eventually enter the liquid reservoir. Using a video camera, we monitor the response of the liquid.

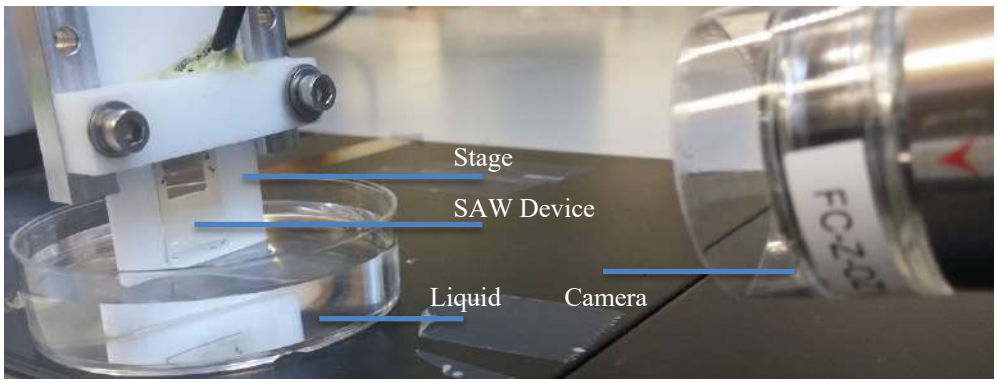

Figure 1. The experimental systems: A SAW device mounted on a vertical stage and touching a reservoir of liquid below.

Findings and Conclusions

Upon the excitation of a propagating 20 MHz-frequency SAW, we observe the climb of liquid atop the solid substrate of the device. Partially wetting water and surfactant solutions satisfy a finite three phase contact angle between the liquid, vapor, and the solid substrate of the device, which gives rise to curved liquid menisci. In the presence of a SAW, the menisci rise up the device to obtain steady state heights above the level of liquid in the reservoir. A theoretical analysis predicts that the steady state heights are determined by a balance between acoustical, capillary, and gravitational stresses. In contrast, silicon oil is a fully wetting liquid. It supports a vanishing contact angle with the SAW device, which gives rise to flat films. In the presence of a SAW, silicon oil films are found to continuously climb up the device (In the absence of the SAW, the oil supports an approximately 1 mm high meniscus with the substrate of the device). Moreover, the climbing velocities of the oil films appear to be steady. They are comparable to the dynamic wetting velocities of oil on a horizontal SAW device. On vertical and horizontal devices, the measured velocities of the oil films are in agreement with a balance between acoustical and viscous stresses. A clue to deciphering the lack of gravitational contributions to the climbing velocity of oil films is that the nearly flat films may support high levels of acoustic radiation pressure. The pressure varies with the film thickness due to acoustic resonance effects. We show that the resonance-enhanced radiation pressure may satisfy the gravitational stresses in the climbing films at any film height. As a result, in the presence of the SAW, the oil films will continuously climb up the device.

References

[1] Morozov M. and Manor O. Vibration-driven mass transfer and dynamic wetting. Curr. Opin. Colloid Interface Sci., **36**: 37, 2018
[2] Rezk A., Manor O., et al. Unique fingering instabilities and soliton-like wave propagation in thin acoustowetting films. Nat. Commun., **3**: 1167, 2012
[3] Rezk A., Manor O., et al. Double flow reversal in thin liquid films driven by megahertz-order surface vibration. Proc. Roy. Soc. A, **470**: 20130765, 2014
[4] Altshuler G. and Manor O. Spreading dynamics of a partially wetting water film atop a MHz substrate vibration. Phys. Fluids, **27**: 102103, 2015
[5] Altshuler G. and Manor O. Free films of a partially wetting liquid under the influence of a propagating MHz surface acoustic wave. Phys. Fluids, **28**: 072102, 2016
[6] Horesh A. Morozov M. et al. Enhanced drainage and thinning of liquid films between bubbles and solids that support surface waves Phys. Rev. E **95**: 052803, 2017
[7] Connacher W., Zhang N., et al. Micro/nano acoustofluidics: materials, phenomena, design, devices, and applications. Lab Chip **18**: 1952, 2019
[8] Ang K. M., Yeo L.Y. et al. Acoustially-mediated microfluidic nanofiltration through graphene films. Nanoscale **9**: 6497, 2017
[9] Horesh A., Khaikin D., Karnilaw M., Zigelman A., Manor O. Acoustogravitational balance in climbing films. Phys. Rev. Fluids **4**: 022001, 2019

COMPETITIVE EVAPORATION OF MULTIPLE THIN DROPLETS

Stephen K. Wilson*[1], Alexander W. Wray[1], Brian R. Duffy[1], Feargus G. H. Schofield[1], and David Pritchard[1]
[1]Department of Mathematics and Statistics, University of Strathclyde, Livingstone Tower, 26 Richmond Street, Glasgow G1 1XH, United Kingdom

Summary A combination of analytical and numerical methods is used to analyse two different but related scenarios in which evaporating sessile droplets influence each other via the concentration of vapour in the atmosphere, namely the evaporation of multiple thin droplets in three dimensions and the evaporation of one or two thin droplets in two dimensions.

INTRODUCTION

The evaporation of one or more sessile droplets is a very exciting and dynamic area of interdisciplinary study in fluid mechanics, with worldwide activity across many different subject disciplines, including physics, chemistry, mathematics, biology and engineering (see, for example, [1]). In particular, in recent years considerable attention has been paid to aspects of evaporation such as the coffee-ring effect [2] and droplet lifetimes [3]. However, while the vast majority of the previous work has concerned a single droplet, in practice most droplets do not occur in isolation, and so interactions between droplets are of great practical and scientific interest. In particular, the critical difference between the evaporation of single and of multiple droplets is the occurrence of the so-called "shielding effect", namely that the presence of other evaporating droplets increases the local vapour concentration in the atmosphere, and so each droplet evaporates more slowly than it would in isolation. In order to better understand this phenomena, in the present contribution we investigate two different but related scenarios, namely the evaporation of multiple thin droplets in three dimensions and the evaporation of one or two thin droplets in two dimensions.

EVAPORATION OF MULTIPLE THIN DROPLETS IN THREE DIMENSIONS

An asymptotic model is derived for the competitive diffusion-limited evaporation of multiple thin sessile droplets in three dimensions under the assumption that the droplets are well separated. Exact solutions of the model are obtained for a pair of and for a polygonal array of identical droplets, and the model is found to perform well even outside its formal range of validity, up to and including the limit of touching droplets. Figure 1 shows the excellent agreement between the exact and asymptotic solutions for the fluxes from a pair of identical droplets. The shielding effect of droplets on each other is demonstrated, and the model is used to investigate the effect of this shielding on droplet evolutions and lifetimes, as well as on the coffee-ring effect. The theoretical predictions of the model are found to be in good agreement with recent experimental results for seven relatively closely-spaced droplets, suggesting that the model could be a useful tool for studying a wide range of other droplet configurations [4].

EVAPORATION OF ONE OR TWO THIN DROPLETS IN TWO DIMENSIONS

We also consider the diffusion-limited evaporation of thin two-dimensional sessile droplets either singly or in a pair. A conformal-mapping technique is used to calculate the vapour concentrations in the surrounding atmosphere, and thus to obtain closed-form solutions for the evolution and the lifetimes of the droplets in various modes of evaporation. Figure 2 shows contours of the vapour concentration for both the one-droplet problem and the two-droplet problem. These solutions demonstrate that, in contrast to in three dimensions, in large domains the lifetimes of the droplets depend logarithmically on the size of the domain, and more weakly on the mode of evaporation and the separation between the droplets. In particular, they allow us to quantify the shielding effect that the droplets have on each other, and how it extends the lifetimes of the droplets [5].

CONCLUSIONS

In the present contribution, we used a combination of analytical and numerical methods to analyse two scenarios in which evaporating sessile droplets influence each other via the concentration of vapour in the atmosphere. There are, of course, many other configurations and other physical mechanisms (such as, for example, via the distribution of temperature in the substrate and/or the atmosphere) via which they can influence each other that are also worthy of investigation.

*Corresponding author. E-mail: s.k.wilson@strath.ac.uk

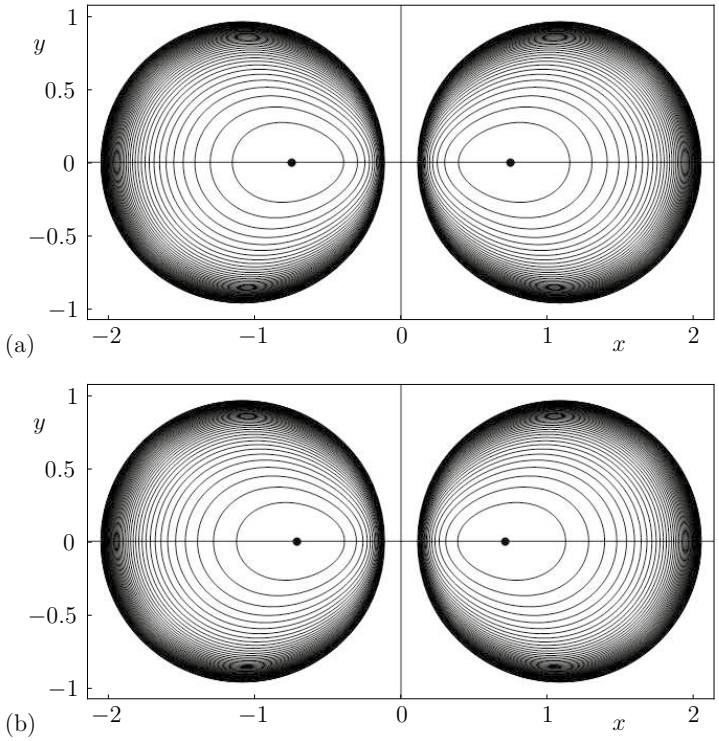

Figure 1: Comparison of (a) the contours of the exact solutions for the fluxes with (b) the corresponding contours of the asymptotic solutions for a pair of identical droplets in three dimensions.

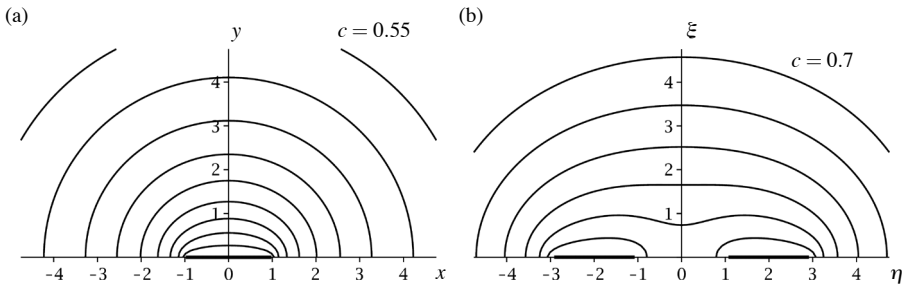

Figure 2: Contours of the vapour concentration for (a) the one-droplet problem and (b) the two-droplet problem in two dimensions.

Acknowledgements

The authors are very grateful to Ms Hannah-May d'Ambrosio (University of Strathclyde) and Prof. Khellil Sefiane (University of Edinburgh) for insightful discussions about various aspects of droplet evaporation.

References

[1] Brutin D., Starov V. Recent advances in droplet wetting and evaporation. *Chemical Society Reviews* **47**:558–585 (2018)
[2] Deegan R.D., Bakajin O., Dupont T.F., Huber G., Nagel S.R., Witten T.A. Capillary flow as the cause of ring stains from dried liquid drops. *Nature* **389**(6653):827–829 (1997)
[3] Stauber J.M., Wilson S.K., Duffy B.R., Sefiane K. On the lifetimes of evaporating droplets. *J. Fluid Mech.* **744**:R2 (2014)
[4] Wray A.W., Duffy B.R., Wilson S.K. Competitive evaporation of multiple sessile droplets. *J. Fluid Mech.* **884**:A45 (2020)
[5] Schofield F.G.H., Wray A.W., Pritchard D., Wilson S.K. The shielding effect extends the lifetimes of two-dimensional sessile droplets. To appear in *J. Eng. Math.* (2020)

THIN LIQUID FILM FORMATION ON HEMISPHERICAL AND CONICAL SUBSTRATES

Markus Scholle*[1], Philip H. Gaskell[2], Florian Marner[1], and Amy Morris[2]
[1]Institute for Flow in Additively Manufactured Porous Media, Heilbronn University, Heilbronn, Germany
[2]Department of Engineering, Durham University, Durham, UK

Summary The deposition and coating of thin films onto curved rigid substrate, involving displacement of air by a liquid, has numerous applications within the technology sectors but faces two major challenges: (i) control of the local film thickness; (ii) ensuring that the coating remains stable. The work reported here investigates the full coverage of two- and three-dimensional curved geometries, of cylindrical, hemispherical and conical shape, by a continuously fed, gravity-driven, thin liquid layer. The modelling approach adopted utilises a first integral formulation of the Navier-Stokes equations leading to a variational formulation in the case of steady flow and an advantageous re-formulation of the dynamic boundary condition at the free surface. Asymptotic analysis, underpinned by the long-wave approximation, enables analytic solutions for the local film thickness and the internal flow to be obtained.

The new results are placed in context by comparing them with recently acquired experiments and flow visualisations specific to film flow on conical surfaces, prior to the onset of and post instability. A perspective is provided in relation to how the findings form the basis for a corresponding stability analyses.

FORMULATION

Problem definition

We consider gravity-driven steady incompressible Newtonian liquid film flow over different two- and three-dimensional shapes, namely a horizontally aligned cylinder, a hemisphere and a cone, see Fig. 1, fed continuously, $\dot{V}$, from above, investigating both the internal flow structure and the free surface shape.

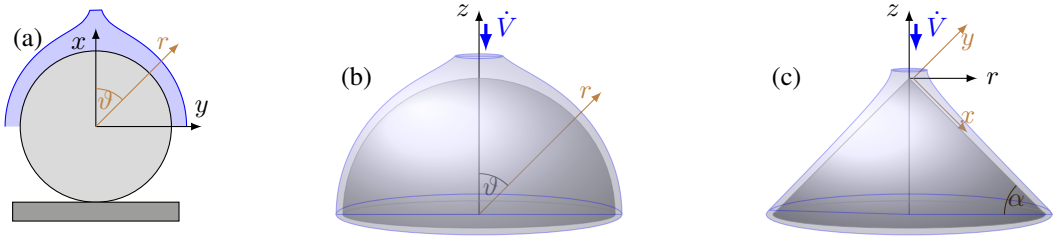

Figure 1: Continuously fed film flow over (a) a horizontally aligned cylinder, (b) a hemisphere and (c) a cone.

First Integral variational approach for steady 3D flow

In [1] a first integral of the Navier-Stokes (NS) equation is derived in an analogous fashion to Maxwell's use of potential fields in developing his classical electro-magnetic theory and governing equations. As is well-known for steady incompressible flow, the streamfunction vector Ψ_k constituting the velocity via $u_i = \varepsilon_{ijk}\partial_j\Psi_k$ with Levi-Civita symbol ε_{ijk} can be introduced to fulfil the continuity equation $\partial_i u_i = 0$ automatically. In a similar manner a traceless symmetric tensor potential $\bar{a}_{ij}$ and a scalar potential Φ are introduced as auxiliary unknowns allowing derivation of the Navier-Stokes equations from the variational principle:

$$\delta \iiint_V \ell\left(\bar{a}_{ij}, \partial_n\Psi_m, \partial_k\bar{a}_{ij}, \partial_i\Phi\right) \mathrm{d}V = 0\,, \qquad \ell = \varrho\bar{a}_{ij}u_iu_j + 2\left[\eta u_j - \partial_j\Phi\right]\partial_i\bar{a}_{ij} + \frac{1}{2}\varepsilon_{ilk}\varepsilon_{jpq}\partial_l\bar{a}_{ij}\partial_p\bar{a}_{kq}\,. \tag{1}$$

By computing the divergence of the tensor equation resulting via variation with respect to $\bar{a}_{ij}$, the Navier-Stokes equations are recovered [1]. Likewise the dynamic boundary condition related to stress equilibrium at a free surface can also be recasted in a first integral form for the tensor potential:

$$\varepsilon_{ikl}\left[\partial_k a_{lm}\mathrm{d}x_m + \left(\sigma_s n_k - \int U\mathrm{d}x_k\right)\mathrm{d}x_l\right] = 0\,, \tag{2}$$

with surface tension σ_s and potential energy density U for an external conservative force. The mathematical formulation is completed by the kinematic boundary condition at a free surface and the no-slip/no-penetration condition at solid walls.

*Corresponding author. E-mail: markus.scholle@hs-heilbronn.de.

Implementation for axisymmetric flows

Using spherical coordinates $q_1 = r, q_2 = \vartheta, q_3 = \varphi$ for hemispheres and cylindrical coordinates $q_1 = z, q_2 = r, q_3 = \vartheta$ for cones, the independence of the azimuthal angle φ in both cases allows for a reduction of complexity by assuming:

$$\Psi_k = \psi \partial_k q_3 \,, \qquad \bar{a}_{ij} = a_{\mu\nu} \partial_i q_\mu \partial_j q_\nu \,, \qquad \mu, \nu = 1, 2 \,, \tag{3}$$

with a scalar streamfunction ψ and only two[1] additional potentials a_{11}, a_{12}, depending only on the two coordinates q_1, q_2, like also the scalar potential Φ. Making use of the above assumptions, the Lagrangian (1) simplifies to:

$$\ell = \varrho a_{\mu\nu} u_\mu u_\nu + \left[\eta u_\nu - G_{\nu\kappa} \partial_\kappa \Phi\right] \left[2 \left\{G_{\mu\lambda} \partial_\lambda + \Delta q_\mu\right\} a_{\mu\nu} + \partial_\nu G_{\mu\lambda} a_{\mu\lambda}\right] \tag{4}$$

with metric tensor $G_{\mu\nu} = \partial_i q_\mu \partial_i q_\nu$ and the velocity in the μ-direction, expressed via the stream function, $u_\mu = u_i(\partial_\nu \psi)$. The dynamic boundary condition (2) becomes a condition for the scalar potential (with tangential and normal vector t_ν, n_ν):

$$\partial_\nu \Phi + \frac{\sigma}{2} n_\nu - \frac{1}{2} \int U t_\nu \mathrm{d}s = 0 \,. \tag{5}$$

SOLUTION METHOD, RESULTS AND DISCUSSION

The two relevant field equations for ψ and Φ, derived as Euler-Lagrange equations of (4) w.r.t. a_{11}, a_{12}, become integrable by (i) neglecting inertia and (ii) applying an asymptotic analysis, underpinned by the long-wave approximation, as demonstrated in [2] for 2D film flows. Following the same steps as in [2], a single equation for the local film thickness $h = h(\vartheta)$ finally results. Neglecting capillary effects and using r_0 for length scale, this procedure leads to the equation:

$$\left(1 + \frac{3h}{4}\right) h^3 \sin^2\vartheta = \frac{3Q}{2} \left[1 + \frac{h^2}{1+h} \frac{\sin^2\vartheta - 2}{2\sin^2\vartheta}\right] \tag{6}$$

for the flow over a hemisphere with non-dimensional flow rate $Q = 2\eta \dot{V} / \varrho g r_0^4$; the corresponding equation for the thickness $h = h(x)$ for flow over a cone reads:

$$\left(1 - \frac{h'''}{\mathrm{Ca}}\right) \left(\frac{5}{4} \tan\alpha\, h + x\right) h^3 + \left(\frac{h}{\frac{5}{4}\tan\alpha\, h + x}\right)^2 = 1 \tag{7}$$

with the capillary number given as: $\mathrm{Ca} = \sqrt{6\eta\varrho g \dot{V} \tan\alpha}/\sigma$, using $L = \sqrt[4]{12\eta\dot{V}/\varrho g \sin(2\alpha)}$ for length scale and $U = \sqrt{3\varrho g \dot{V} \tan\alpha / 2\eta}$ for velocity scale. Resulting thickness profiles are presented in Fig. 2.

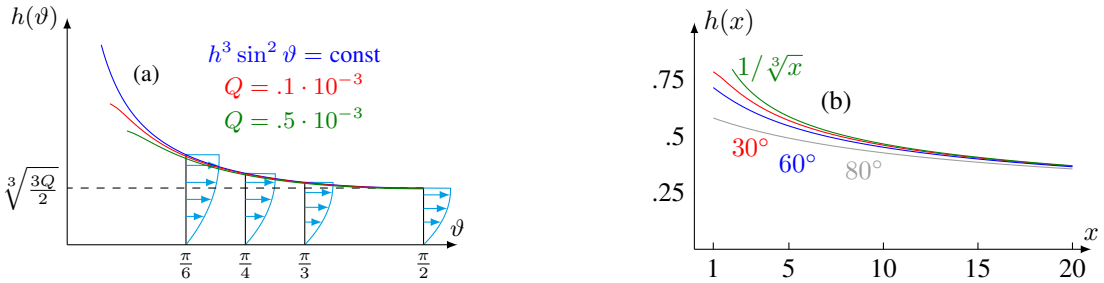

Figure 2: Film thickness predictions for film flow over: (a) a hemisphere and (b) a cone.

Corresponding analytic solutions for unsteady flows with a constant volume instead of a constant flux can also be obtained within the framework of the lubrication approximation by replacing the kinematic boundary condition for steady flow by its unsteady analogue. The above new results are placed in context by comparing them with recently acquired new experiments and flow visualisations specific to film flow on conical surfaces, prior to the onset of and post instability. In conclusion, a perspective is provided in relation to how the findings form the basis for corresponding stability analyses to study the onset of unsteady phenomena such as solitary waves and, in the case of incomplete wetting, rivulet formation.

References

[1] M. Scholle, P. H. Gaskell, and F. Marner. Exact integration of the unsteady incompressible Navier-Stokes equations, gauge criteria, and applications. *Journal of Mathematical Physics*, 59(4):043101, Apr 2018.

[2] Markus Scholle, Philip H. Gaskell, and Florian Marner. A potential field description for gravity-driven film flow over piece-wise planar topography. *Fluids*, 4(2), 2019.

[1] The other two potentials a_{21}, a_{22} result from symmetry and vanishing trace of the tensor potential.

ROLLING OF NON-WETTING DROPLETS DOWN A GENTLY INCLINED SURFACE

Ory Schnitzer*[1], Anthony M. Davis[2], and Ehud Yariv[3]
[1]Department of Mathematics, Imperial College, London, UK

Summary In their pioneering 1991 paper [1], Mahadevan & Pomeau argued that small non-wetting drops roll, rather than slide, down gently inclined surfaces. Using contact-mechanics arguments, they showed that the rolling speed possesses an anomalous scaling with an inverse dependence upon drop size, in contrast with conventional modes of drop mobility. The Mahadevan-Pomeau scaling was corroborated by the experiments of Quere and coworkers. Here, we go beyond scaling arguments, providing an asymptotic approximation for the speed of rolling droplets. The theory agrees well with experiments and provides a detailed description of the flow field within the drop and close to the moving contact line in particular.

BACKGROUND

Consider a sessile drop on a solid surface, whose size is small relative to the capillary length and whose contact angle is 180 degrees. Under these conditions, the drop adopts a near-spherical shape with a small flat spot in contact with the surface. Mahadevan & Pomeau [1] showed that such small non-wetting droplets roll, rather than slide, down a gently inclined surface. Thus, by balancing the rate of change in potential energy of the drop with an order-of-magnitude estimate for the viscous dissipation in the vicinity of the flat spot, they derived the scaling

$$\mathcal{U} \sim \mathcal{C} \times \frac{\gamma}{\mu} \frac{\alpha}{B^{1/2}}, \tag{1}$$

in which $\mathcal{U}$ is the drop speed, α is the inclination angle, γ is the interfacial tension, μ is the liquid viscosity and $\mathcal{C}$ is an unkown numerical constant; the Bond number is defined as $B = (\kappa a)^2$, wherein a is the drop "radius" defined based on volume and $1/\kappa = \sqrt{\gamma/\rho g}$ is the capillary length, ρ being the liquid density and g the gravitational acceleration. The scaling law of Mahadevan & Pomeau predicts, counterintuitively, that the drop speed is inversely proportional to its size. It was corroborated by the experiments of Quere and coworkers, where the non-wetting conditions assumed in [1] were realised approximately using either superhydrophobic surfaces [2] or liquid marbles [3].

The stress-dissipation singularity usually expected at a moving contact line does not occur for a perfectly non-wetting droplet. Thus, with this assumption, the problem of a rolling drop becomes purely hydrodynamic. To date, the rolling-drop hydrodynamic problem has only been analyzed in two dimensions. In particular, assuming a two-dimensional droplet and the limits $\alpha, B \ll 1$ underlying their three-dimensional scaling analysis, Mahadevan & Pomeau [1] proposed a *local* solution to the flow field close to the contact line. Hodges *et al.* [4], who analyzed a family of related problems, suggested a two-dimensional counterpart of the scaling law (1) and argued that a quantitative analysis of the rolling-drop problem would necessarily be numerical. The two-dimensional problem was later solved numerically in the PhD thesis of Wang [5], who also disputed the validity of the local solution found in [1].

TWO-DIMENSIONAL ROLLING DROPLETS [6]

Recently, Yariv and Schnitzer [6] carried out a detailed asymptotic analysis of the two-dimensional problem. Following [1], their analysis is based on the smallness of the inclination angle α and the Bond number B. First, the problem is linearized for small α, which allows formulating the hydrodynamic problem with respect to the stationary drop shape. Then, both the stationary drop shape and the linearized hydrodynamic problem are analyzed for $B \ll 1$ using the method of matched asymptotic expansions. In particular, the linearized flow field is found by matching a rigid-body rotation in the "outer" drop-scale region, where the drop shape is nearly circular, with the flow field in an "inner" region close to the flat spot of the drop. Besides matching with the outer flow, the flat-spot flow satisfies no-slip and impermeability on the solid flat spot, and kinematic and zero-shear-stress conditions on the fluid interface, which appears flat to leading order (although the local curvature of the interface enters the leading-order problem through the kinematic condition). The flat-spot flow problem was solved analytically using integral transforms. A key feature of the analysis is that the linearized flow problem and the leading-order drop velocity are uniquely determined based on integral force and energy-dissipation relations, which circumvent the need to consider higher orders in the asymptotic scheme. The analysis yields a leading-order approximation for the drop speed:

$$\mathcal{U} \sim \frac{\gamma}{\mu} \frac{\alpha}{2B \ln \frac{1}{B}}. \tag{2}$$

*Corresponding author. E-mail: o.schnitzer@imperial.ac.uk

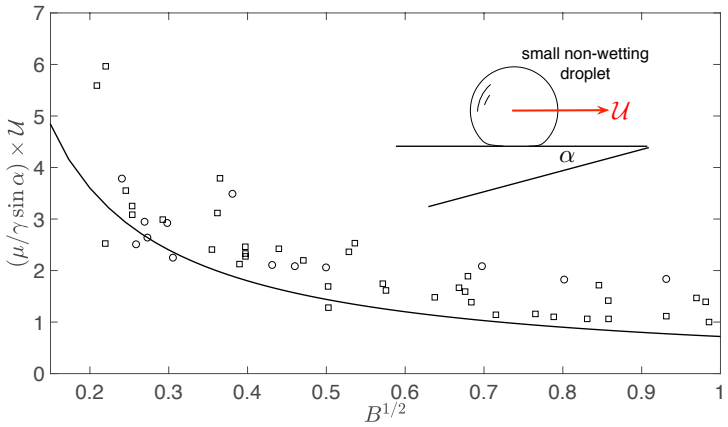

Figure 1: Speed of droplet rolling down an inclined substrate (see text for definitions). Circles: Experiments with glycerol drops on superhydrophobic surfaces [2]. Squares: Experiments with liquid marbles [3]. Line: Eq. (1) with $\mathcal{C}$ given by Eq. (3).

The scaling $1/B \ln B$ differs from that suggested in [4] by the logarithmic factor. The analysis in [6] shows that that logarithmic factor arises because the contribution of the drop-scale region to the total dissipation, which is associated with the deviation of the flow from a rigid-body rotation, is actually not negligible in two dimensions; rather, both the drop-scale and flat-spot regions contribute at the same order, with the leading-order contribution arising from their overlap. It is also shown in [6] that an expansion of the flat-spot flow field close to the contact line agrees with the local solution proposed by Mahadevan & Pomeau [1].

THREE-DIMENSIONAL ROLLING DROPLETS

Here we report on new results of a comparable asymptotic analysis of the hydrodynamic problem governing a three-dimensional rolling droplet. Our approach is similar to than in [6], though the three-dimensional problem is conceptually simpler than the two-dimensional one, as dissipation is dominated by the flat-spot region. Accordingly, calculating a leading-order approximation to the drop speed boils down to formulating and solving the appropriate flat-spot flow problem (and evaluating the associated dissipation). Moreover, the error in this procedure is algebraic in both α and B, in contrast to the logarithmic accuracy of (2). Using a suitable ansatz (see concluding remarks), we obtained a solution to the three-dimensional flat-spot flow field in terms of integral functions of the coordinates. Fortunately, it turns out that the associated dissipation quadrature can still be evaluated in closed form. This gives the prefactor in (1),

$$\mathcal{C} = \frac{3\pi}{16}\sqrt{\frac{3}{2}} \approx 0.72, \tag{3}$$

which gives good agreement with the experiments of Quere and coworkers (see Fig. 1). Furthermore, the behaviour of the flat-spot flow field near the circular contact line can also be obtained in closed form by asymptotic expansion of the integral representations. This shows that near the contact line the flow is mainly in the plane locally normal to the contact line; the flow in that plane is similar to the local flow found in the two-dimensional case up to the multiplicative factor $2\cos\theta$, θ being the azimuthal angle. This analogy breaks down only for $\theta \approx \pm\pi/2$, where the contact line propagates parallel to itself and the local flow is genuinely three-dimensional.

CONCLUDING REMARKS

In both the two- and three-dimensional problems, the flow field in the flat-spot region has the peculiar feature that, in the lab frame, the velocity field happens to satisfy the no-slip and no-shear-stress conditions simultaneously over both the solid flat spot and the mobile fluid interface. This observation allows, in hindsight, enormous simplification in the solution of both flow problems. It also suggests a unique 'peeling' mechanism by which the contact line propagates in the non-wetting case. Remarkably, it also suggests that the asymptotic theory remains unchanged if the no-slip condition on the solid flat spot is replaced by a Navier-slip condition.

References

[1] L. Mahadevan, Y. Pomeau, *Phys. Fluids*, **11** 2449, 1999
[2] D. Richard, D. Quere, *Europhys. Lett.*, **48** 286, 1999
[3] P. Aussillous, D. Quere, *Nautre*, **411** 924, 2001
[4] S. R. Hodges, O. E. Jensen, J. M. Rallison *J. Fluid Mech.*, **512** 95, 2004
[5] X. Wang, PhD thesis supervised by M. Siegel, NJIT 2008
[6] E. Yariv, O. Schnitzer, *Phys. Rev. Fluids*, **4** 093602, 2019

AN EXPANSIVE SINGULARITY IN A JUST DETACHED DEVELOPED LIQUID LAYER AND THE TEAPOT EFFECT

Bernhard Scheichl *[1,2], Robert I. Bowles[3], and Georgios Pasias[3]
[1]Institute of Fluid Mechanics and Heat Transfer,Technische Universität Wien,Vienna,Austria
[2]AC2T research GmbH (Austrian Excellence Center for Tribology), Wiener Neustadt, Austria
[3]Department of Mathematics, University College London, London, United Kingdom

Summary We present a rigorous explanation of the celebrated teapot effect via asymptotic analysis of a developed liquid layer passing the trailing edge of a flat plate. Its slenderness, i.e. the reciprocal Reynolds number, represents the primary perturbation parameter. The passage of the flow over the edge is governed by the characteristic "jet-type" viscous–inviscid interaction mechanism, implying a myriad of different phenomena, such as the onset of standing capillary waves, under variation of the appropriately defined Froude and Weber numbers of $O(1)$. Interestingly, for a certain range of these parameters, the fully detached interacting flow hits an expansive singularity whose regularisation on an Euler stage enforces the layer to reattach at the downstream continuation of the plate, guiding the oncoming layer, so as to stay stationary—like poured tea sticking to the underside of a spout.

MOTIVATION AND ESSENCE

Consider the steady, planar flow of a slender Newtonian (liquid) film of uniform properties passing the sharp trailing edge of a horizontal, perfectly smooth and impervious rigid plate in a quiescent (gaseous) environment of constant pressure as gravity acts towards the flow against the vertical direction. We scrutinise the flow in the vicinity of the plate edge, i.e. by taking the vertical height $\tilde{H}$ of the incident unperturbed film at the edge as the reference length scale. This flow configuration, of fundamental concern as ubiquitous in real-world situations, is essentially governed by a complex interplay of inertia with viscosity, gravity, and surface tension and hence controlled by the inverse local Reynolds, Froude and Weber numbers ϵ, g and τ respectively, with ϵ taken as asymptotically small. How a developed, very supercritical free-surface film anticipates the plate edge in terms of viscous–inviscid short-scale interaction was addressed first in [1]. Specifically, there $G := g\epsilon^{-4/7} = O(1)$ and $T := \tau/J_0 = O(1)$, J_0 is the dimensionless undisturbed momentum flux, parametrise the least-degenerate flow description. In the following, we refer to the sketch in figure 1 (a) throughout.

As a start, it is expedient to outline most concisely the basic "jet" interaction law underlying this asymptotic theory and its current extension. To this end, let some viscous flow, initially firmly attached to the plate, undergo an interaction process in order to negotiate locally an upstream influence. Hence, we let all lengths and flow components and the local pressure variation Δp be non-dimensional with its vertical depth, here identified with $\tilde{H}$, the according reference flow speed, and the (locally) uniform fluid density. With interaction at play over some horizontal (streamwise) distance δ_x ($\gg 1$), significant viscous action and plate irregularities remain confined to a sublayer of some vertical depth δ_y ($\ll 1$). Therein, the streamwise flow speed of $O(\delta_y)$ exhibits some perturbation Δu about its base state so that the streamwise component of the Navier–Stokes equations implies the order-of-magnitude balances $\Delta u\,\delta_y/\delta_x \sim \Delta p/\delta_x \sim \epsilon\Delta u/\delta_y^2$. The sought interaction law relating the pressure disturbance Δp, predominantly varying in streamwise direction, to Δu provides a third one finally recovers the well-known dependencies of δ_x and δ_y on ϵ. If we consider a genuine boundary layer, the potential flow induced on its top exerts Δp (triple-deck structure). Otherwise, the pressure vanishes there as for a wall jet or developed free-surface layer (present double-layer structure) so that Δp is typically governed by streamline curvature, i.e. the inviscid lateral momentum transfer, when we first ignore the effect of body/surface forces (hydrostatic pressure and capillarity). Since continuity induces a lateral flow speed in the core layer of $O(\Delta u\,\delta_y/\delta_x)$, the respective momentum balance entails the missing estimate $\Delta u/\delta_x^2 \sim \Delta p$, thus $\delta_y = \delta_x^{-2} = \epsilon^{2/7}$ and the parametrisation of the arising interaction law by G and T, measuring the impact of those forces. In leading order, we describe the flow in the sublayer in terms of horizontal and vertical coordinates X and Z directed respectively from the trailing edge and the lower free streamline, its X-component $U(X,Z)$, the pressure disturbance $P(X)$, and the Z-displacements $H_\pm(X)$ of the lower, detaching $(-)$ and the upper $(+)$ free streamline; all quantities are scaled to $O(1)$ by δ_y, δ_y, δ_y/δ_x^2 and δ_y respectively. In turn, $U \sim Z + A(X)$ as $Z \to \infty$, and for the detached portion of the flow ($X > 0$) and $T \gg \epsilon^{12/7}$

$$\{P, H_-, H_+\} = \left\{ \frac{T}{2T-1}\left[G + \mathrm{sgn}(T-1)A''\right],\ \frac{T-1}{2T-1}\left[A - A(0) - A'(0)X + \mathrm{sgn}(T-1)\frac{GX^2}{2}\right],\ H_- - A \right\}. \quad (1)$$

Here in the first interaction or P/A-law closing the interactive feedback loop capillarity counteracts streamline curvature to cancel it if $T = 1$. We currently investigate this degenerate and the case $T = 1/2$ (capillary waves at vanishing speed).

Compressive interactive branching from the unperturbed wall-bounded flow has proven central in the rational description of the susceptibility of the latter to local corrugations of and separation from the wall: originally established for jet flows [2], it was later applied to gravity-driven free-surface layers [3, 4]; see also the references therein. In contrast, the much less appreciated expansive branching has the numerical marching solution of the interaction problem inevitably

*Corresponding author. E-mail: b.scheichl@tuwien.ac.at.

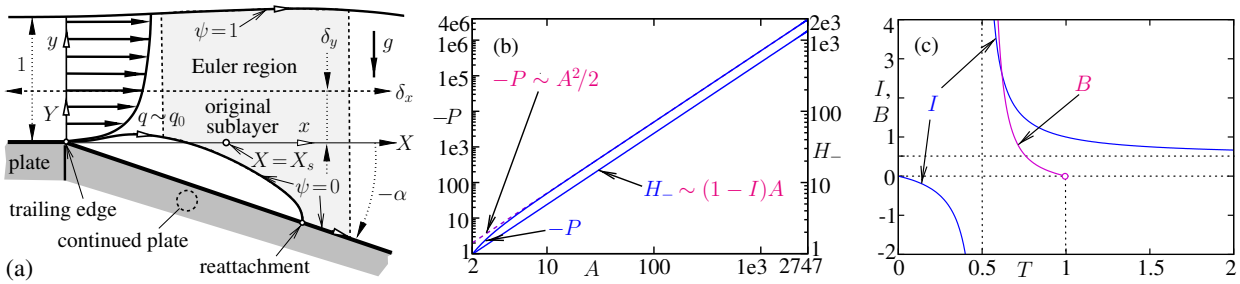

Figure 1: (a) Configuration (not to scale); (b) blow-up past detachment, log-log plot of interpolated numerical data (*solid*, terminate at $A \simeq 2747$, $G = 1$, $T = 0.51$, $I = 25.5$) and asymptote (*dashed*); (c) strengths of interaction I and blow-up B in detached flow.

terminate in a finite-X singularity of generic type [2]. Its physical interpretation was not clarified earlier as in [1] in the context of the attached film anticipating the plate edge. However, we demonstrate that a close counterpart of this blow-up is also met in the detached layer at some $X = X_s(G,T)$ by virtue of the P/A-law for $1/2 < T < T^*(G) < 1$ with X_s increasing towards infinity as T approaches some threshold T^*. Most importantly, this blow-up is regularised over a streamwise extent of relative $O(1)$ by a full Euler stage. Given the smallness of g, this is solely driven by capillarity active on both free surfaces. Moreover, in any physically admissible stationary solution of the elliptic Euler problem initiated by the blow-up, the oncoming flow must turn through some overall angle α ($-\pi \le \alpha \le \pi$) before it recovers as the unperturbed parallel one. However, its vertical linear momentum associated with a non-trivial solution ($\alpha \neq 0$) must be compensated by a pressure net force. In the current setting, this requires the flow to impinge onto a rigid wall. If this represents a continuation of the plate and forms a convex corner (downturn, $\alpha < 0$), we arrive at an unprecedented and exciting rational explanation of the so-called teapot effect, corroborating the original heuristic one [5]: for a sufficiently weak momentum flux J_0, the blow-up prevents the "tea" jet achieving the gravity-driven parabolic downfall, see (1), as it clings to the "spout" due to a local interplay of inertia with capillarity. For a larger one ($T < 1/2$), the interaction mechanism predicts a free jet exhibiting a capillary wave crest; for a smaller one ($T > 1$) and strikingly different capillarity-dominated flow picture, the onset of the waves already above the plate approaches the plate edge as $T \to 1+$.

The existing rigorous *model* of the teapot effect resorts to a capillarity-free ideal-fluid flow [6]. It describes this phenomenon qualitatively correctly, without the need of pre-separation. However, the assumption of a developed incident layer surmounts a deficient and intrinsic parametric non-uniqueness that originates in the artificial neglect of viscosity.

BLOW-UP AND REGULARISING EULER STAGE

Our numerical solutions of the interaction problem confirm excellently the predominantly inviscid nature of the expansive singularity; see figure 1 (b): $-P \sim A^2/2$, $H_- \sim (1-I)A$ as $A \to \infty$ and $I := T/(2T-1)$ measures the strength of the P/A-law, cf. (1). Denote x and y coordinates, non-dimensional with $\tilde{H}$ and aligned with X and Y respectively and originating in $(X,Y) = (X_s, 0)$, and q the streamwise flow component in the core layer, assuming its unperturbed state q_0 above the plate edge, we find $q \sim q_0(y) + Bq_0'(y)/x^2$ where $B := (12/J_0)T^2(1-T)/(2T-1)^2$; see figure 1 (c).

A novel and numerically appealing representation of the free-surface Euler problem regularising the blow-up reads

$$\frac{\partial}{\partial\phi}\Big(\frac{\chi}{q^2}\frac{\partial q}{\partial\phi}\Big) + \frac{\partial}{\partial\psi}\Big(\frac{q}{\chi^2}\frac{\partial\chi}{\partial\psi}\Big) = 0, \quad \chi(\phi,\psi) := q\exp\int_1^\psi \frac{\omega(t)\,\mathrm{d}t}{q^2(\phi,t)}, \quad \begin{cases} \psi = 0\colon\ \theta(-\phi)q^3/(2\tau) + q\partial_\psi q = -\omega(0), \\ \psi = 1\colon\ q^2 = q_0^2 + 2\tau\partial_\psi q. \end{cases} \tag{2}$$

Herein, q is considered as a function of a pseudo-potential ϕ and the streamfunction ψ ($0 \le \psi \le 1$), $\psi = 0$ denotes the lower and $\psi = 1$ the upper free streamline, $\omega(\psi)$ the vorticity impressed by q_0, and θ the Heaviside step function. We discuss the numerical solutions to (2) supplemented with a matching condition reflecting the bifurcation from $q = q_0$ due to the blow-up as $\phi \to -\infty$. It is seen that we force the streamline $\psi = 0$ to reattach in the origin of the (ϕ,ψ)-plane at a flat plate, thus modelling the "spout of the teapot" in a first and most simple manner. Hence, a wedge-flow singularity emerges in the origin, parametrised by the plate angle equal to α. Prescribing α then selects a unique solution for q.

We finally envisage the interesting long-wave limit $\gamma := T - 1 \to 0$, stretching the Euler regime in streamwise direction to $O(\gamma^{-1/2})$. When γ is reduced to $O(\delta_x^{-2})$, i.e. $O(\epsilon^{2/7})$, it collapses with the encompassing interactive stage such that the teapot effect sets in already at the original trailing edge without pre-separation in the accordingly extended theory.

References

[1] Scheichl B., Bowles R. I., Pasias G. Developed liquid film passing a trailing edge under the action of gravity and capillarity. *J. Fluid Mech.* **850**: 924–953, 2018.
[2] Smith F. T. Upstream interactions in channel flows. *J. Fluid Mech.* **79** (4): 631–655, 1977.
[3] Gajjar J. S. B. Fully developed free surface flows—Liquid layer flow over a convex corner. *Comput. Fluids* **15** (4): 337–360, 1987.
[4] Bowles R. I., Smith F. T. The standing hydraulic jump: theory, computations and comparisons with experiments. *J. Fluid Mech.* **242**: 145–168, 1992.
[5] Reiner M. The teapot effect ... a problem. *Phys. Today* **9** (9): 16–20, 1956.
[6] Vanden-Broeck,J. M., Keller J. B. Pouring flows with separation. *Phys. Fluids A* **1** (1): 156–158, 1989.

STABILITY OF A PARTICLE-LADEN FILM FALLING DOWN AN INCLINE

Darish Jeswin Dhas S*[1] and Anubhab Roy [1]
[1]Department Applied Mechanics, Indian Institute of Technology Madras, Chennai, India

Summary The stability of particle-laden thin film falling down an incline is investigated using a nonlinear wave theory and a linear stability analysis. In absence of particles, the stability of a gravity-driven thin film has been extensively studied. Yih (1963) [5] in his pioneering study carried out a linear stability analysis and identified a long wavelength instability in a falling film. Subsequently Benney (1966) [1] performed an expansion in wave amplitude and derived a nonlinear wave equation describing the evolution of the film height that reproduced the linear stability findings as a limiting case. The presence of particles alters the rheology of the fluid with the non-uniformity of particle concentration altering the local shear viscosity leading to a coupling with the momentum balance. Using a Benney-like amplitude expansion, a set of coupled nonlinear equations are derived describing the evolution of film height and particle concentration. The modified Benney equation is solved numerically and the threshold of instability is calculated. However, the Benney equation is known to have a finite time blowup beyond the stability threshold. This is countered using a weighted residual approach in conjunction with the lubrication approximation. On linearizing the governing equations, a generalized Orr-Sommerfeld system of equations is derived. The predictions of linear stability analysis are then compared with the results from the nonlinear long wave theories.

INTRODUCTION

Thin liquid films are observed in a wide range of scenarios, of both natural and engineering importance. Tear film formation, glaciers flowing down mountains and coating flows are some of the classical examples of thin liquid films [2]. A lot of work has been done in the case of gravity driven falling films. However, introcuction of particles brings in new physics which is not much understood. In this work, we study the dynamics of a Brownian particle-laden gravity driven falling film. The particles evolve by being both advected by the background flow while also diffusing due to Brownian motion. Both the linear and the non-linear regimes are studied by developing models using the lubrication approximation.

LONG-WAVE THEORY

Consider a particle-laden two-dimensional viscous incompressible thin film falling down an inclined plane under the action of gravity. The particles are colloidal and neutrally buoyant and are assumed to be rigid. The substrate is inclined at an angle α and the height of the film is taken as $h(x,t)$. With the suspensions, the effective viscosity becomes a function of the particle volume fraction (ϕ). Using a Benney-like amplitude expansion about the film aspect ration (ϵ), a set of coupled nonlinear equations are derived describing the evolution of film height and particle concentration.

$$\frac{\partial h}{\partial t}+\frac{\partial}{\partial x}\left(\kappa h^3\right)+\epsilon Re\frac{\partial}{\partial x}\left\{\kappa\left(-\kappa_t\frac{2}{5}h^5+\kappa\kappa_x\frac{8}{35}h^7+\kappa^2\frac{6}{5}h^6\frac{\partial h}{\partial x}-\frac{\cot\alpha}{Re}h^3\frac{\partial h}{\partial x}+\epsilon^2We\frac{h^3}{3}\frac{\partial^3 h}{\partial x^3}\right)\right\}=0 \quad (1)$$

$$\frac{\partial(h\phi)}{\partial t}+\frac{\partial}{\partial x}\left(\phi\kappa h^3\right)+\epsilon Re\frac{\partial}{\partial x}\left\{\phi\kappa\left(-\kappa_t\frac{2}{5}h^5+\kappa\kappa_x\frac{8}{35}h^7+\kappa^2\frac{6}{5}h^6\frac{\partial h}{\partial x}-\frac{\cot\alpha}{Re}h^3\frac{\partial h}{\partial x}+\epsilon^2We\frac{h^3}{3}\frac{\partial^3 h}{\partial x^3}\right)\right\} \quad (2)$$
$$=\frac{1}{Pe_l}\frac{\partial}{\partial x}\left(\chi(\phi)h\frac{\partial\phi}{\partial x}\right)$$

where κ denotes the non-dimensional part of the viscosity such that $\mu=\mu_s\kappa(\phi)^{-1}$, χ denotes the non-dimensional part of the particle diffusivity, Reynolds number defined as $Re=\rho h_0u_0/\mu_s$, Peclet number as $Pe_l=u_0l/D_0$ and the Weber number as $We=\gamma/\rho u_0^2h_0$. This modified Benney equation is solved numerically and the stability threshold is calculated. However, the Benney equation has a major drawback of having a finite time blowup while beyond the stability threshold [3]. Also, the equation remains valid only for a small range of Re. To counter such problems, a depth averaged weighted residual based technique [4] is used to obtain boundary layer equations. Using the Galerkin weighted residual method in this case, the model equations can be written as

$$\frac{\partial h}{\partial t}+\frac{\partial q}{\partial x}=0 \quad (3)$$

$$\epsilon Re\frac{\partial q}{\partial t}=\frac{5}{2}h-\frac{5}{2}\kappa(\phi)\frac{q}{h^2}+\epsilon Re\left(\frac{9}{7}\frac{q^2}{h^2}\frac{\partial h}{\partial x}-\frac{17}{7}\frac{q}{h}\frac{\partial q}{\partial x}-\frac{5}{2}\frac{\cot\alpha}{Re}h\frac{\partial h}{\partial x}+\frac{5}{6}\epsilon^2Weh\frac{\partial^3 h}{\partial x^3}\right) \quad (4)$$

$$\frac{\partial(h\phi)}{\partial t}+\frac{\partial\left(q\phi\right)}{\partial x}=\frac{1}{Pe_l}\frac{\partial}{\partial x}\left(\chi h\frac{\partial\phi}{\partial x}\right) \quad (5)$$

Here, q denotes the flow rate. The above system is solved numerically as done with the modified Benney equations.

*Corresponding author. E-mail: sdarishjeswindhas@gmail.com

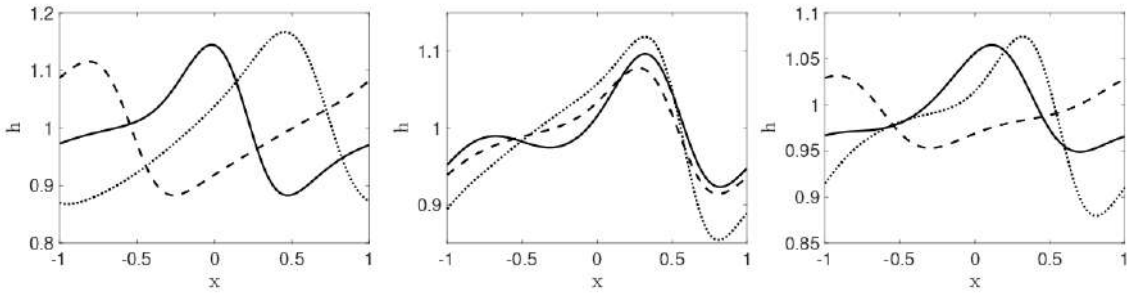

Figure 1: Free-surface wave-forms with $k = k_c/2$ for the corresponding initial particle concentrations (—)$\phi = 0.01$; (- - -) $\phi = 0.05$; $(\cdots)$ $\phi = 0.1$ for different time instances.

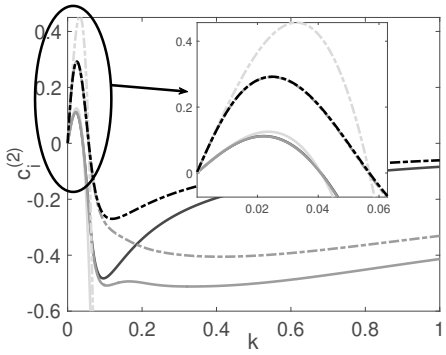

Figure 2: Comparison between linear Benney (light grey lines), boundary layer equation (grey lines) and Numerical Orr-Sommerfeld (black lines) for the case of $Re = 20$, $\phi = 0.01$ (-.-.-), $\phi = 0.1$ (—), $\phi = 0.2$ (- - -) and $\phi = 0.3$ $(\cdots)$

LINEAR STABILITY ANALYSIS

For the linear stability analysis, the base state is taken to be that of a Nusselt flow with $h = 1$ and constant particle concentration $\phi = \phi_b$. A normal mode analysis is done by perturbing the variables, say X in the form $X = X_b + X_1 e^{ik(x-ct)}$ with X_b referring to the base flow and X_1 to the infinitesimal amplitude of the wave. This form of linearisation in the momentum equations leads to the Orr–Sommerfeld equation and the same on the concentration equation leads to a similar linear equation, both together forming an eigenvalue problem.

$$\psi''''\kappa_b - 2k^2\psi''\kappa_b + k^4\psi\kappa_b + \kappa_{b1}(\phi U')'' = ikRe\left[(U-c)(\psi'' - k^2\psi) - U''\psi\right] \tag{6}$$

$$\chi_b\phi'' - k^2\chi_b\phi - ikPe_l\,(U-c)\,\phi = 0 \tag{7}$$

Here ψ denotes the stream function and the primes denotes the differentiation with respect to y and $\kappa_{b1}(\phi_b)$ is a consequence of expansion of the viscosity term. The eigenvalue problem can be solved numerically using the Chebyshev spectral collocation method. In the limit of small wavenumbers, the solutions of the full Orr-Sommerfeld system should be equal to the linear solutions of the long-wave theory based models as is shown in figure 2.

CONCLUSIONS

The effect of particles on the stability of a falling liquid film driven by gravity down an inclined plane is studied. Using the lubrication approximation, modified Benney equations and a depth averaged boundary layer equations were obtained and their consistency with the full governing Navier Stokes equations with the particle concentration evolution was check in the linear long-wave limit and shown to be consistent. The finite amplitude disturbances are explored by solving the nonlinear coupled PDEs (equations 1 & 2 and 3, 4 & 5) numerically in a periodic domain.

References

[1] D. Benney. Long waves on liquid films. *Journal of mathematics and physics*, 45(1-4):150–155, 1966.
[2] R. V. Craster and O. K. Matar. Dynamics and stability of thin liquid films. *Rev. Mod. Phys.*, 81:1131–1198, Aug 2009.
[3] A. Pumir, P. Manneville, and Y. Pomeau. On solitary waves running down an inclined plane. *Journal of Fluid Mechanics*, 135:27–50, 1983.
[4] A. Samanta, C. Ruyer-Quil, and B. Goyeau. A falling film down a slippery inclined plane. *Journal of Fluid Mechanics*, 684:353–383, 2011.
[5] C.-S. Yih. Stability of liquid flow down an inclined plane. *The physics of Fluids*, 6(3):321–334, 1963.

AUGMENTED SKEW-SYMMETRIC SYSTEM FOR THIN FILM FLOWS

Didier Bresch*[1], Nicolas Cellier[2], Fred Couderc[3], Marguerite Gisclon[1], Pascal Noble[3], Gael Richard[4], Christian Ruyer-Quil[2], and Jean-Paul Vila[3]
[1]LAMA Laboratoire de Mathématiques, Université Savoie Mont Blanc, Chambéry, France
[2]LOCIE Laboratoire d'Optimisation de la Conception et Ingénierie de l'Environnement, Université Savoie Mont Blanc, Chambéry, France
[3]IMT Instut de Mathématiques de Toulouse, Toulouse, France [4]Univ. Grenoble Alpes, INRAE, ETNA, Grenoble, France

Summary In this paper, we introduce a new extended version of the shallow water equations with surface tension which is skew-symmetric with respect to the L^2 scalar product and allows for large gradients of fluid height.

INTRODUCTION

Thin film flows are encountered in a large number of industrial applications due to their low resistance to heat or mass transfers. The hydrodynamic regime that is promoted in such applications is a wavy laminar regime for which a significant enhancement of transfers has been observed. Yet, the mechanisms responsible for this enhancement are far from being well understood due to the high numerical cost required to investigate such flows. Indeed, the long-wave nature of the hydrodynamic instability, the weakly turbulent organization of the flow by solitary waves in interaction, the 3D nature of the flow, and the extension of the entrance thermal region (high Peclet numbers) require simulations on extended domains and over extended periods of time, that are still out of reach. A promising approach is offered by the derivation of consistent Saint-Venant-like equations to describe the film flows [1]. Such approaches are based on the long-wave nature of the instability generating surface waves. Elimination of the "rapid variable", here the cross-stream coordinate, leads from the 3D incompressible Navier-Stokes equations with a free-surface to 2D equations where the film thickness h plays a role similar to density and surface tension appears along with third-order terms. These third-order terms are problematic numerically and therefore generally linearized to be dealt with more easily. As a consequence, numerical investigations of these Saint-Venant-like models are limited to regular meshes, which severely impairs their use with complex geometries, for instance when a wall topography is considered. A cure to this problem has been proposed by Vila and coworkers [2, 3] by introducing an additional variable with the dimension of a velocity whose kinetic energy is equal to the surface energy of the film. By writing a transport equation for this additional variable, these authors have been able to recast shallow-water equations with linearized surface tension terms into an "augmented" system of equations with a skew-symmetric structure with respect to the L^2 scalar product which makes the proof of energy estimates. Additionally, the design of compatible numerical scheme is made easier as surface tension terms are then recast as generalized diffusion terms.

However, this strategy is limited to linearized surface tension terms and is therefore not suitable in cases of partial wetting with large contact angles, as can be encountered for instance in the design of plate exchangers for which dewetting phenomena are detrimental to their efficiency. In this paper, we thus propose to extend the formulation proposed in [3] to account for the full surface tension terms.

FORMULATION

We thus consider shallow-water type equations with a full surface tension term:

$$\left\{\begin{array}{ll} \partial_t h + \operatorname{div}(h\mathbf{u}) = 0 & (i) \\ \partial_t(h\mathbf{u}) + \operatorname{div}(h\mathbf{u}\otimes\mathbf{u}) + \nabla P = -\operatorname{div}(\nabla h \otimes \nabla_{\mathbf{p}} E) + \nabla(h\operatorname{div}(\nabla_{\mathbf{p}} E)) & (ii) \end{array}\right. \tag{1}$$

with h the fluid height, $\mathbf{u}$ the fluid velocity vector field. The internal energy E is defined by

$$E(h,\boldsymbol{p}) = \frac{1}{2} g_z h^2 + \frac{\sigma}{\rho}(\sqrt{1+q^2} - 1) \tag{2}$$

where g_z is the gravitational acceleration normal to the plate, σ is the surface tension, ρ the density, $\boldsymbol{p} = \nabla h$ and $q = \|\boldsymbol{p}\| = \sqrt{\boldsymbol{p}^t\boldsymbol{p}}$. Finally, the pressure P is given by

$$P(h,\boldsymbol{p}) = h\partial_h E(h,\boldsymbol{p}) - E(h,\boldsymbol{p}) = \frac{1}{2} q_z h^2 - \frac{\sigma}{\rho}(\sqrt{1+q^2} - 1) \tag{3}$$

*Corresponding author. E-mail:didier.bresch@univ-smb.fr

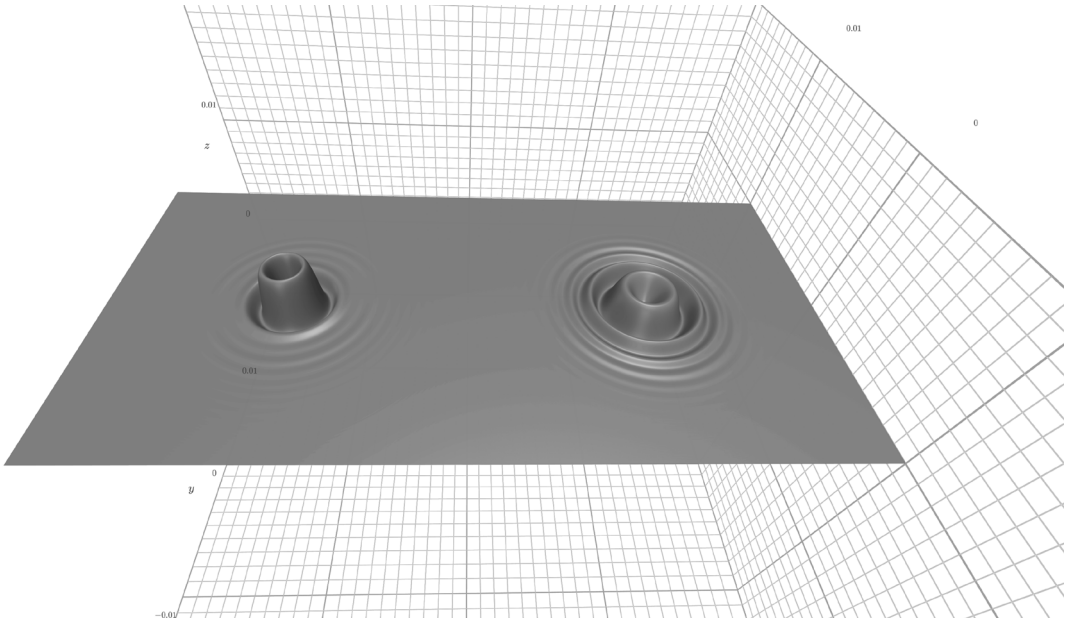

Figure 1: Numerical simulations of capillary-gravity waves considering a two-dimensional Gaussian-shaped deformation of a layer of water; (left) with the full non-linear capillary contribution, (right) with the linearized capillary contribution.

We introduce an additional unknown, denoted $\boldsymbol{v}$, which is co-linear to ∇h and satisfies

$$\frac{1}{2}h\left\|\boldsymbol{v}\right\|^2 = \frac{\sigma}{\rho}(\sqrt{1+\left\|\nabla h\right\|^2}-1) \tag{4}$$

To do so, we define $\mathbf{v}$ as $\boldsymbol{v} = \alpha(q^2)\boldsymbol{p}\sqrt{\frac{\sigma}{\rho}\frac{1}{h}}$ where $\alpha(q^2) = \dfrac{\sqrt{2(\sqrt{1+q^2}-1)}}{q}$.

Note that, in this context, $\boldsymbol{v}$ has the dimension of velocity and transform the capillary energy into some kinetic energy. We show that the augmented system

$$\partial_t U + \operatorname{div}\left(F\left(U\right)\right) = \mathcal{M}. \tag{5}$$

where

$$U = \begin{pmatrix} h \\ h\boldsymbol{u} \\ h\boldsymbol{v} \end{pmatrix}, \qquad F\left(U\right) = \begin{pmatrix} h\boldsymbol{u} \\ h\boldsymbol{u}\otimes\boldsymbol{u} + g_z\frac{h^2}{2}I_d \\ h\boldsymbol{v}\otimes\boldsymbol{u} \end{pmatrix} \qquad \mathcal{M} = \begin{pmatrix} 0 \\ \operatorname{div}\left(h\nabla(f(h,\boldsymbol{v})\boldsymbol{v})^t\right) - \nabla(g(h,\boldsymbol{v})^t\boldsymbol{v}) \\ -f(h,\boldsymbol{v})\operatorname{div}\left(h\nabla\boldsymbol{u}^t\right) \quad -g(h,\boldsymbol{v})\operatorname{div}\boldsymbol{u} \end{pmatrix}. \tag{6}$$

where $f(h,\boldsymbol{v})$ is a symmetric tensor and $g\left(h,\boldsymbol{v}\right)$ a vector field given by

$$f(h,\boldsymbol{v}) = \left(\frac{\sqrt{h}}{\sqrt{1+\frac{\rho h}{4\sigma}\left\|\boldsymbol{v}\right\|^2}}\right)\left(\mathbf{I} - \left(1+\frac{\rho h}{2\sigma}\left\|\boldsymbol{v}\right\|^2\right)^{-1}\frac{\rho h}{4\sigma}\boldsymbol{v}\otimes\boldsymbol{v}\right), \quad g(h,\boldsymbol{v}) = \frac{h\boldsymbol{v}}{2}\left(1+\frac{\rho h}{2\sigma}\left\|\boldsymbol{v}\right\|^2\right)^{-1}$$

verifies: If $(h,\boldsymbol{u})$ is regular enough and the initial velocity $\boldsymbol{v}_0$ satisfies $\boldsymbol{v}_0 = \alpha(\left\|\nabla h_0\right\|^2)\sqrt{\frac{\sigma}{\rho}\frac{1}{h_0}}\nabla h_0$, then $\boldsymbol{v}$ satisfies also (4) and $(h,\boldsymbol{u})$ solves (1)–(3). The proof of this convergence derives from the existence of an energy balance that shows that the total energy of the system is conserved (see [4] for details). Numerical investigations using appropriate schemes have shown that (5) does capture correctly capillary waves (see fig. 1). We now intend to introduce a disjoining pressure to account for dewetting phenomena as proposed by [5].

References

[1] Kalliadasis S., Ruyer-Quil C., Scheid B., Velarde M.G. Falling liquid films Applied Mathematical Sciences 176, Springer London 2012.
[2] Noble P., Vila J.P. Stability theory for difference approximations of Euler-Korteweg Equations and application to thin film flows. *SIAM J. Numerical Analysis* **52**(6): 2770-2791, 2016.
[3] Bresch D., Couderc F., Noble P., Vila J.P. A generalization of the quantum Bohm identity: Hyperbolic CFL condition for Euler-Korteweg equations. *C.R. Acad. Sciences Paris* **354**(1): 39-43, 2016.
[4] Bresch D., Cellier N., Couderc F., Gisclon, M., Noble P., Richard G.L., Ruyer-Quil C., Vila J.P. Augmented Skew-Symetric System for Shallow-Water System with Surface Tension Allowing Large Gradient of Density. arXiv:1911.12217 [math.AP]
[5] Lallement J., Trontin P., Laurent C., Villedieu P. A shallow water type model to describe the dynamic of thin partially wetting films for the simulation of anti-icing systems AIAA AVIATION Forum, June 25-29, 2018, Atlanta, Georgia.

PHASE SEPARATION OF A CONFINED IONIC-LIQUID – WATER MIXTURE IN A TEMPERATURE GRADIENT

Marc Pascual[1], Arthur Poquet [1], Alexandre Vilquin [1], and Marie-Caroline Jullien *[1,2]
[1]Gulliver CNRS UMR 7083, PSL Research University, ESPCI Paris, 10 rue Vauquelin, 75005 Paris, France [2]Université Rennes1,CNRS,IPR,UMR6251,F-35000 Rennes,France

Summary The phase separation of a confined binary mixture induced by a temperature gradient shows surprizing patterns depending on the composition of the mixture. For all three characteristic patterns identified we notice an accumulation of the most wetting phase in the warmer region. This behavior is explained by the presence of a micrometer-thick wetting layer submitted to thermal interfacial gradient.

PHASE SEPARATION IN THERMOCAPILLARY FORCE FIELD

Introduction

Thermoresponsive ionic liquid (IL) - water (W) mixtures (figure 1(a)) have been proposed for various applications such as selective synthesis and extraction of chemical products [1] or desalination [2]. These applications rely on the reversible separation-recombination of the mixture with temperature loops, but do not propose explicitly any means to isolate selectively one phase or the other (aside from gravity effects [3]). Since it has been shown that wetting effects with the walls and initial volume fraction of each components play a significative role in the phase separation kinetics [4], microfluidic-scale systems are relevant as capillary effects are highlighted. In this presentation we investigate the interplay between phase separation and wetting when a temperature gradient is applied to the system.

Experiment on dynamics of separation

We use a thin cylindrical microfluidic cavity (figure 1(b)) of 1 cm diameter and with a height varying from 20 to 500 μm, placed above a micropatterned heating resistor (Joule effect). When the resistor is switched on, the temperature profile increases radially in the cavity and triggers phase separation which propagates from the center towards the edges. The interfaces formed during this separation are submitted to thermal interfacial tension gradients which induce transport along the gradient [5]. Depending on the IL mass fraction of the solution we identify three phase separation regimes (figure 2(a)-(c)). For both three, the wetting phase is accumulated above the heating resistor while the non-wetting phase is driven towards the colder region. Hence, tuning the wall-fluid affinity allows selecting the component to be concentrated. This behaviour is recovered with lutidine-water mixture and is expected to be universal to all binary system.

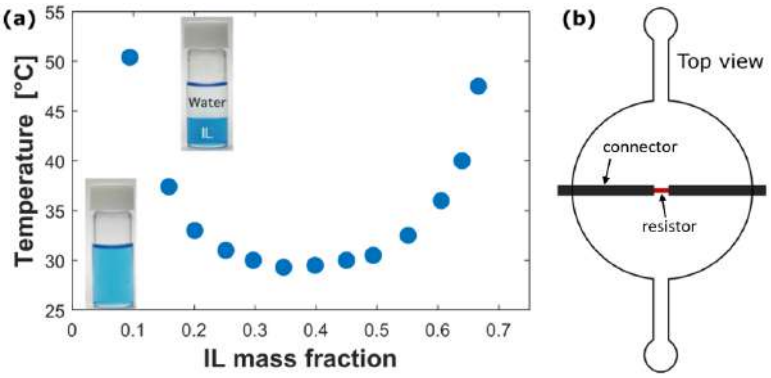

Figure 1: (a) Phase diagram of the LCST (Lower Critical Solution Temperature) IL-water system. The solution is colored with a blue dye. Critical point is at 35 wt% in IL, and 29.2°C. (b) Top view of the microfluidic chip. Diameter is 1 cm. Gold tracks are connecting the chromium microresistor at the center.

The first regime (15 to 35 wt% in IL) depicted in figure 2(a) has been quantitatively studied in more detail. We show that the outer frontier is due to the isotherm propagation, the second frontier is linked to a thermocapillary migration of small droplets and finally the inner frontier corresponds to the accumulation of the phase enriched in IL. Moreover, the complete spreading of the IL-rich wetting phase gives birth to a micrometer-thick film, whom thermal actuation induces a 3D flow which is not obvious in light of figure 2(a). The velocity of droplets dragged by this film are compared to the temperature gradient and film thickness profile. A quantitative description on the model of this 3D flow structure will be discussed during the presentation.
In the second regime (40 to 55 wt% in IL), depicted in figure 2(b), an instability develops at the external frontier. Despite the vertical confinement which drives the viscous dissipation, the instability develops radially. An analogy with the Bénard-Marangoni instability is proposed leading to recirculating cells at the outer frontier.

*Corresponding author. E-mail: marie-caroline.jullien@univ-rennes1.fr.

In the third regime (more than 60 wt% in IL), represented on figure 2(c), water droplets are thermocapillary driven towards the outside, eventually undergo coalescence events but does not lead to an efficient phase separation.
As a whole, we will present experiments, supported by a theoretical model for regime 1, in which phase separation is thermally assisted in a microfluidic cavity and show the richness of physical phenomena involved in the system.

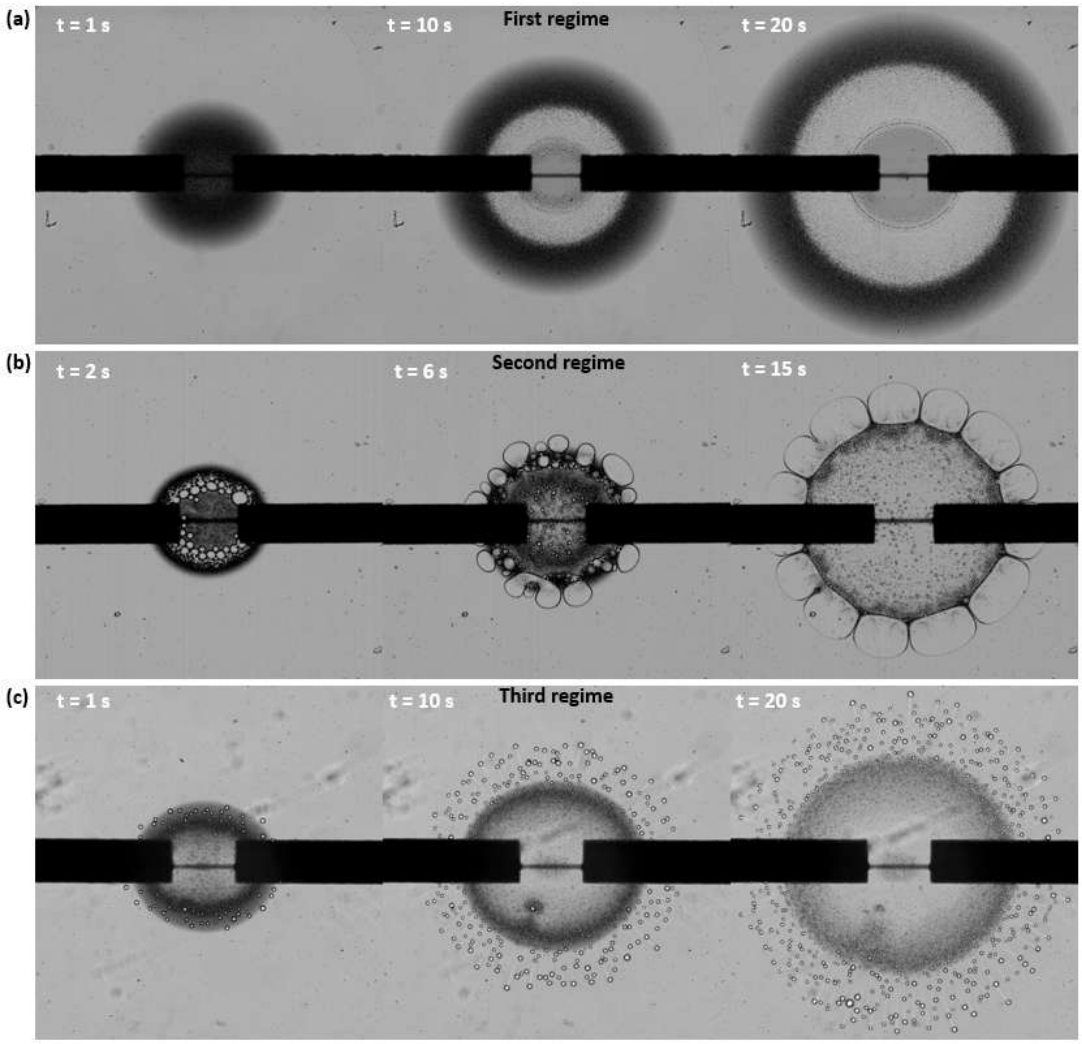

Figure 2: Temporal evolution of the phase separation patterns observed with transmitted light microscopy after resistor switch-on (80 mW). Solutions compositions are respectively: (a) 25 wt% in IL, (b) 45 wt% in IL, (c) 60 wt% in IL. The resistor length is 500 μm for scale.

CONCLUSIONS

Wetting effects coupled to a temperature gradient produce non-trivial patterns during phase separation. Their dynamic is controlled by the interfacial transport which result of thermal Marangoni actuation. It leads systematically to the focusing of the wetting phase at the center of the cavity. This behavior should be universal to all binary systems. This technique can prove relevant for the applications using thermoresponsive binary mixtures.

References

[1] D. Depuydt, L. Liu, C. Glorieux, W. Dehaen, and K. Binnemans. Homogeneous liquid–liquid ex-traction of metal ions with non-fluorinated bis (2-ethylhexyl) phosphate ionic liquids having a lowercritical solution temperature in combination withwater. *Chem. Comm.*. **51** : 14183–14186, 2015.
[2] C.-H. Hsu, C. Ma, N. Bui, Z. Song, A. D. Wilson,R. Kostecki, K. M. Diederichsen, B. D. McCloskey,and J. J. Urban. Enhanced forward osmosis desali-nation with a hybrid ionic liquid/hydrogel thermore-sponsive draw agent system. *ACS Omega*. **4**: 4296–4303, 2019.
[3] T. Araki and H. Tanaka. Hydrodynamic delocal-ization of phase separation in a locally cooled fluidmixture. *EPL*. **65**: 214-218, 2004.
[4] H. Tanaka. Interplay between wetting and phase separation in binary fluid mixtures: roles of hydrodynamics. *J. Phys.: Condens. Matter*. **13**: 4637-4674, 2001.
[5] D. Beysens, Y. Garrabos, V. Nikolayev, C. Lecoutre-Chabot, J.-P. Delville, and J. Hegseth. Liquid-vapor phase separation in a thermocapillary forcefield. *EPL*. **59**: 245-251, 2002.

THE STOKES AND EULER REGIMES OF THIN FILM RUPTURE

Daniel Moreno-Boza*[1], Alejandro Martínez-Calvo [1], and Alejandro Sevilla[1]
[1]Grupo de Mecánica de Fluidos, Universidad Carlos III de Madrid, Spain

Summary Theory and numerical simulations are used to unravel the nonlinear dynamics of non-wetting ultrathin liquid films deposited on solid substrates in the spinodal dewetting regime. The distinguished limits of Stokesian and ideal flow are investigated in detail.

INTRODUCTION

Thin liquid films are ubiquitous in nature and everyday life, and they play important roles in many engineering, medical, and physiological contexts [1]. Here, we shed light on the unstable dynamics of non-wetting ultrathin films of Newtonian liquid of density ρ and viscosity μ deposited on solid surfaces (see Fig. 1a). The liquid film, of initial thickness h_o and constant surface tension coefficient σ at the interface with the surrounding air, is known to become linearly unstable due to the long-range van der Waals (vdW) forces when $h_o \lesssim 100$ nm [2]. The dynamics leading to film rupture has typically been described with lubrication theory, which assumes that the longitudinal length scale is much larger than the film thickness, leading to models with simpler mathematical structure than the Navier-Stokes equations.

Two distinguished limits are addressed in detail, namely that of negligible inertia where the flow is described by the Stokes equations, and the opposite limit of inertial rupture, which admits a potential flow description outside thin viscous boundary layers. The corresponding Stokes and Euler self-similar regimes arising close to rupture are unraveled here for the first time, showing marked differences with respect to previous results obtained with lubrication theory. Regarding the dewetting of very viscous films, the well-known scaling $h_{\text{min}} \propto \tau^{1/5}$, where h_{min} is the minimum film thickness and $\tau = t_{\text{R}} - t$ is the time until rupture [3], cannot be used to describe the local flow close to rupture due to the breakdown of the slenderness assumption close to the singularity. Instead, a non-slender regime with $h_{\text{min}} \propto \tau^{1/3}$ is found upon examination of the complete Stokes equations of motion [4]. The effect of liquid inertia must be retained for metallic film dewetting [5, 6], for which we develop a new self-consistent theory that correctly describes the inertial dynamics close to rupture with the power law $h_{\text{min}} \propto \tau^{2/5}$ stemming from a balance between liquid inertia and vdW forces, the capillary force being asymptotically subdominant. The latter result is in marked contrast with the prevailing descriptions of the inertial limit, which predict $h_{\text{min}} \propto \tau^{2/7}$ from a balance of liquid inertia with capillary and vdW forces [3, 5].

In the general case, the film dynamics is described using the continuity and momentum conservation equations,

$$\nabla \cdot \boldsymbol{v} = 0, \quad \rho\left(\partial_t \boldsymbol{v} + \boldsymbol{v} \cdot \nabla \boldsymbol{v}\right) = -\nabla\left(p + \phi\right) + \mu \nabla^2 \boldsymbol{v}, \tag{1}$$

where $\boldsymbol{v} = (u, v)$ is the liquid velocity field, assumed to be two-dimensional, p is the liquid pressure, $\phi = A/(6\pi h^3)$ is the disjoining pressure, which models the overall effects of the long-range vdW forces, where A is the Hamaker constant. The supplementing boundary conditions include the stress balance and the kinematic condition at the free surface and no-slip at the wall. The appropriate near-rupture scalings for the Stokes and Euler limits are briefly discussed next.

FILM RUPTURE AT SMALL REYNOLDS NUMBERS: SELF-SIMILAR STOKES FLOW

In the limit of negligible inertia, Eqs. (1) and the corresponding boundary conditions were conveniently nondimensionalised by taking $a = [A/(6\pi\sigma)]^{1/2}$, σ/μ, $\mu a/\sigma$, and $A/(6\pi a^3)$ as the relevant scales for length, velocity, time, and pressure, respectively. This choice of scales renders the dimensionless initial film thickness, h_o/a, as the only governing parameter. To unravel the Stokesian dynamics, Eqs. (1) were integrated in time in the inertialess limit, $\rho = 0$, until times very close to rupture, revealing a near-singularity evolution consistent with the power-law $h_{\text{min}} \propto \tau^{1/3}$ as $\tau \to 0$, markedly different from the classical result $h_{\text{min}} \propto \tau^{1/5}$ [3]. Moreover, this difference appears already during the early stages after the onset of the vdW instability, and increases over time. In particular, the 1/5 power law predicted by lubrication theory is only accomplished transiently during a very short intermediate time interval prior to the crossover to the 1/3 power law described in [4] for the first time, to which the reader is referred for more details. To describe the newly discovered self-similar regime, the similarity ansatz $x = \tau^{1/3}\xi$, $y = \tau^{1/3}\eta$, $h = \tau^{1/3} f(\xi)$, $u = \tau^{-2/3} U(\xi, \eta)$, $v = \tau^{-2/3} V(\xi, \eta)$, $p = \tau^{-1} P(\xi, \eta)$, suggested upon consistently balancing the viscous and vdW forces, was introduced into Eqs.(1), allowing us to elucidate the structure of the leading-order flow for $\tau \to 0$. The parameter-free self-similar Stokes equations read

$$U_\xi + V_\eta = 0, \quad U_{\xi\xi} + U_{\eta\eta} = P_\xi - 3 f^{-4} f_\xi, \quad V_{\xi\xi} + V_{\eta\eta} = P_\eta, \quad \text{in} \quad 0 < \xi < \infty, 0 < \eta < f(\xi), \tag{2}$$

in which capillary forces are subdominant. The corresponding self-similar form of the boundary conditions are not included here for brevity [4]. The integration of the latter elliptic system provided the shape $f = f(\xi)$ of the film, with an associated wedge-shaped far-field behavior $f \sim \xi \tan\theta_o$ with an opening angle $\theta_o = 37°$ off the solid. Figure 1(b) shows the self-similar flow along with a transient computation close to rupture, showing excellent agreement.

*Corresponding author. E-mail: damoreno@pa.uc3m.es

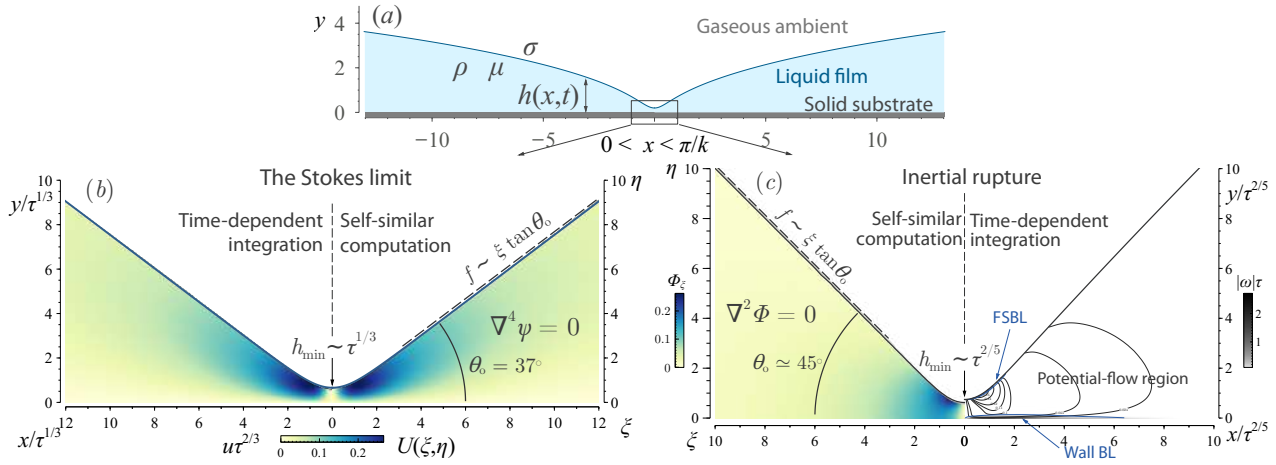

Figure 1: (a) Schematics of a planar thin film approaching the rupture singularity. (b) Stokes self-similar regime: isocontours of U obtained by solving the self-similar system (2), and by using the rescaled velocity $u\,\tau^{2/3}$ for $\log_{10}\tau = -4.62$, and $h_o/a = 4.34$, extracted from the simulation of (1). (c) Euler self-similar regime: filled isocontours of the self-similar potential velocity Φ_ξ and isocontours of the rescaled velocity $u\,\tau^{3/5} \in (0.024, \ldots, 0.16)$ and vorticity $|\omega|\tau$ obtained from the integration of (1) for $h_o/a = 4.34$ and $Oh = 0.188$, for $\log_{10}\tau = -4.62$.

FILM RUPTURE AT HIGH REYNOLDS NUMBERS: SELF-SIMILAR POTENTIAL FLOW

On introducing a, $[A/(6\pi\rho a^3)]^{1/2}$, $(6\pi\rho a^5/A)^{1/2}$, and $A/(6\pi a^3)$ as the relevant scales of length, velocity, time and pressure in Eqs.(1), the relative importance of viscous forces compared with liquid inertia is measured by the Ohnesorge number $Oh = \mu/\sqrt{\rho a\sigma}$ which, together with the dimensionless initial thickness h_o/a, completes the nondimensional description. Numerical integrations of the full Navier-Stokes equations up to very small minimum film thicknesses revealed a well-defined three-region structure (see Fig. 1c). Indeed, the flow displayed a core potential region of vanishing vorticity, surrounded by a pair of viscous boundary layers, one at the solid wall, and another one at the free surface. The minimum film thickness displayed the power law behaviour $h_{\min} \propto \tau^{2/5}$, as deduced from a local dominant balance between inertia and vdW forces described here for the first time. Along the lines of the Stokes analysis, the self-similar ansatz $x = \tau^{2/5}\xi$, $y = \tau^{2/5}\eta$, $h = \tau^{2/5}f(\xi)$, $u = \tau^{-3/5}U(\xi,\eta)$, $v = \tau^{-3/5}V(\xi,\eta)$, $p = \tau^{-6/5}P(\xi,\eta)$ is introduced in Eqs.(1). The leading-order is irrotational, indicating the validity of a potential description in the limit $\tau \to 0$ in terms of self-similar variables. In particular, introducing Φ such that $\Phi_\xi = U$ and $\Phi_\eta = V$, reduces the outer inviscid problem to $\Phi_{\xi\xi} + \Phi_{\eta\eta} = 0$, in $0 < \xi < \infty$, $0 < \eta < f(\xi)$, to be integrated with the boundary conditions

$$\frac{1}{f^3} + \frac{1}{5}\Phi + \frac{2}{5}\left(\xi\Phi_\xi + \eta\Phi_\eta\right) + \frac{1}{2}\left(\Phi_\xi^2 + \Phi_\eta^2\right) = 0, \quad \frac{2}{5}f + \Phi_\eta - f_\xi\left(\frac{2}{5}\xi + \Phi_\xi\right) = 0, \tag{3}$$

accounting for the normal-stress balance and the kinematic condition, respectively, along the unknown free surface $\eta = f$, together with the no-penetration condition $\boldsymbol{n}\cdot\nabla\Phi = 0$ everywhere else. The latter self-similar problem has a similar structure as that derived in [7] to describe the ejection of singular liquid jets from Faraday waves. The integration of this system provided the shape $f = f(\xi)$ of the free surface, with an associated wedge-shaped far-field behavior $f \sim \xi\tan\theta_o$, and an opening angle $\theta_o \simeq 45°$ off the solid. Fig. 1(c) shows the self-similar film shape along with a transient computation close to rupture, showing good agreement. The thicknesses of the wall and free-surface boundary layers were seen to decrease as $\delta_\mu \sim Oh^{1/2}\tau^{1/2}$ and $\delta_\sigma \sim \tau^{6/5}$ as $\tau \to 0$, as deduced by balancing the advective liquid inertia with the viscous forces and with the capillary forces, respectively.

References

[1] Craster, R.V. and Mater, O.K. Dynamics and stability of thin liquid films. *Rev. Mod. Phys.* **81**, 1131, 2009.
[2] Blossey, R. Thin liquif films: dewetting and polymer flow. Springer Science & Business Media 2012.
[3] Zhang, W. W. and Lister J. R. Similarity solutions for van der waals rupture of a thin film on a solid substrate. *Phys.Fluids*, **11**(9):2454–2462, 1999.
[4] Moreno-Boza, D., Martínez-Calvo, A. and A. Sevilla. Stokes theory of thin-film rupture. *Phys. Rev. Fluids*, **5**, 2020.
[5] Garg, V., Kamat, P. M., Anthony, C. R., Thete, S. S., and Basaran, O. A. Self-similar rupture of thin films of power-law fluids on a substrate. *J. Fluid Mech.*, **826**:455–483, 2017.
[6] González, A. G., Diez, J. A. and Sellier, M. Inertial and dimensional effects on the instability of a thin film. *J. Fluid Mech.*, **787**:449–473, 2016.
[7] Zeff, B. W., Kleber, B., Fineberg, J. and Lathrop, D. P. Singularity dynamics in curvature collapse and jet eruption on a fluid surface. *Nature*, **403**(6768):401, 2000.

HOW MANY WAYS A CELL CAN MOVE: THE MODES OF SELF-PROPULSION OF AN ACTIVE DROP

Aurore Loisy*[1,2], Jens Eggers[1], and Tanniemola B. Liverpool *[1]
[1]School of Mathematics, University of Bristol, Bristol, UK
[2]IRPHE (Aix-Marseille Université,CNRS,Ecole Centrale Marseille),Marseille,France

Summary Numerous physical models have been proposed to explain how cell motility emerges from internal activity, mostly focused on boundary-driven crawling motion. Here we take a more fundamental view and offer a classification of self-propulsion mechanisms based on general physical principles. We consider a thin drop of active liquid moving on a planar substrate and obtain, using both numerical simulation and asymptotic analysis, travelling-wave solutions to the lubrication equations. This allows us to fully characterize the three possible modes of autonomous motion of this active drop, thereby showing that crawling is not the only way to move. In particular, we find a new mode of self-propulsion which is driven in the bulk rather than at the boundaries, and which signature is the zero traction exerted everywhere on the substrate except near the contact line.

MOTIVATION

Eukaryotic cells have the ability to move autonomously in a variety of environments, and they do so by adapting their mode of migration to the geometrical and physical properties of their surroundings. A minimal system to study motility is provided by a deformable drop of material with anisotropic components that consume energy (active matter [1]) on a flat rigid surface [2, 3, 4]. Several studies have shown self-propulsion of active drops on a surface with a number of related models, e.g. [5, 6, 3, 4]. However the complexity of the underlying dynamics means that identifying similarities and differences between them is difficult. Besides, these studies are mostly focused on crawling, a mode of motion driven by active processes at the boundaries. In view of the complexity and diversity of cell motility, one may want to ask first: what are the physical requirements for autonomous motion, and what are the possible ways to move?

METHODS

Our model (Fig. 1a) is a 2D drop of active nematic liquid on a rigid substrate and confined by surface tension. The fluid motion inside the drop is governed by the incompressible Stokes flow equations. The stress tensor $\boldsymbol{\sigma} = -p\boldsymbol{I} + \eta[\boldsymbol{\nabla u} + (\boldsymbol{\nabla u})^T] + \boldsymbol{\sigma}^a$ (with η the viscosity) includes an active contribution $\boldsymbol{\sigma}^a = -\alpha \boldsymbol{nn}$ where α is the activity coefficient and where $\boldsymbol{n}$ is the director field (a headless unit vector which describes the coarse-grained orientation of the active units). The mechanical interaction with the substrate is modeled by a partial slip boundary condition (with ℓ_u the slip length) and a free surface boundary condition is applied at the interface (with γ the surface tension coefficient and κ the curvature).

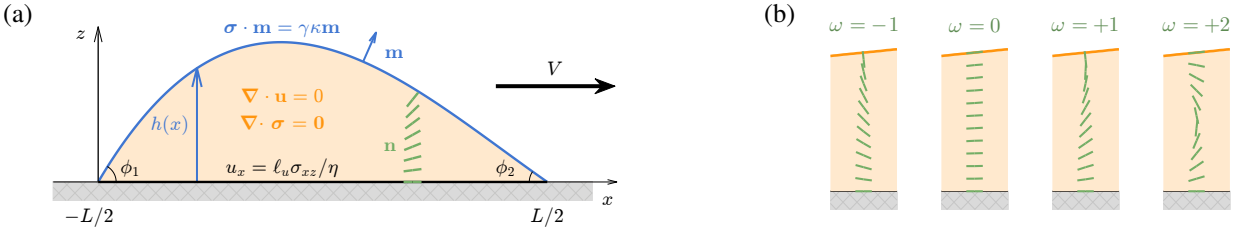

Figure 1: (a) our model is a 2D drop of active fluid moving on a rigid surface, (b) the winding number ω describes the topology of $\boldsymbol{n}$.

We further assume a drop geometry with a small height-to-width ratio and work in the framework of lubrication theory. Restricting to travelling-wave solutions, we can show that the problem reduces to a nonlinear third-order ordinary differential equation for the drop shape $h(x)$:

$$\frac{\gamma}{\eta}\left(\frac{h}{3}+\ell_u\right)hh''' + \frac{\alpha}{2\pi\omega\eta}h = V \qquad \text{if } \omega \neq 0, \tag{1a}$$

$$\frac{\gamma}{\eta}\left(\frac{h}{3}+\ell_u\right)hh''' - \frac{\alpha}{\eta}\left(\frac{h}{3}+\ell_u\right)h' + w_o\frac{\ell_w}{h}\left[1-\exp\left(-h/\ell_w\right)\right] = V \qquad \text{if } \omega = 0, \tag{1b}$$

which involves the drop velocity V as an unknown constant. Here ω is a winding number which counts the number of quarter turns of the director across the drop height (Fig. 1b). The additional term $\propto w_0$ in Eq. (1b) arises from the

*Corresponding author. E-mail: aurore.loisy@bristol.ac.uk
†Corresponding author. E-mail: t.liverpool@bristol.ac.uk

self-advection of active units at a characteristic speed w_0 in a layer close to the substrate of characteristic small thickness ℓ_w (see e.g. [3] for details), and models the effect of cytoskeletal filaments undergoing polymerization and treadmilling. This ODE is supplemented by four boundary conditions: $h(\pm L/2) = 0$, $h'(-L/2) = \phi_1$, $h'(+L/2) = -\phi_2$ where $\phi_{1,2}$ are the contact angles on each side of the drop, and the drop width L is determined from a volume constraint.

RESULTS

Three possible driving sources are embedded in Eq. (1): active stresses ($\propto \alpha$), active self-advection ($\propto w_0$), and a capillary force due to different contact angles [$F_{\text{capillary}} = \gamma(\cos\phi_2 - \cos\phi_1)$] as would result from e.g. an external or self-generated gradient of surface energy. Those give rise to three distinct modes of motion which are illustrated in Fig. 2.

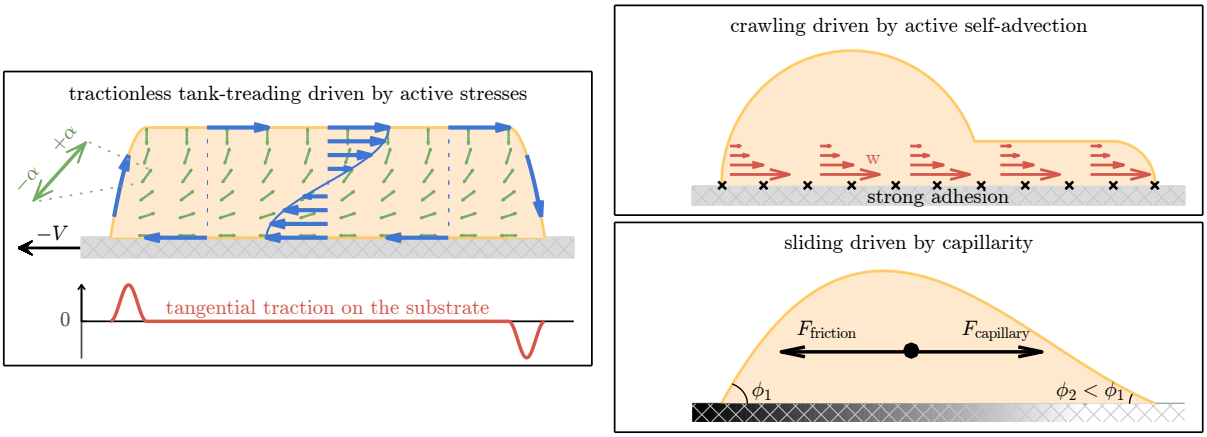

Figure 2: The modes of self-propulsion of a drop of active liquid on a substrate.

We determined travelling-wave solutions to the lubrication equations as a function of a dimensionless activity parameter for each mode of motion. Numerical simulations are used to characterize the drop motion over a wide range of activity magnitudes, and explicit analytical solutions in excellent agreement with the simulations are derived in the weak-activity regime. The main features of each mode of self-propulsion can be summarized as follows.

In self-propulsion driven by active stresses, motion arises from the internal net flow (blue arrows, here drawn in the drop frame of reference) generated by active stresses. The motion direction and speed are controlled by the winding number ω. This mechanism does not require a shape asymmetry and is efficient even in the presence of slip. Remarkably, motion can be achieved without exerting any traction anywhere on the substrate except near the contact line, giving rise to "tractionless tank treading" (see our recent communication [7]). This new mode of motion, driven in the bulk rather than at the boundaries, is particularly suited for moving rapidly through tiny pores, and therefore provides a robust physical mechanism for efficient cell migration in tissues.

In contrast, motion driven by the self-advection of polarized active units at the substrate, known as crawling, is characterized by a strong shape anisotropy and is most efficient in the absence of slip. Therefore this mode of self-propulsion is particularly suited for moving on 2D surfaces which provides strong anchoring points. A prominent example of crawling is mesenchymal migration, a mode of cell motility characterized by strong cell-substrate adhesions, with self-advection provided by actin polymerization in a leading edge protrusion.

In sliding driven by capillarity, the drop is pulled by a capillary force due to gradients. This third mode motion is, unlike the other two, not driven by active processes. Yet it can be coupled to internal activity to create droplets faster than their passive counterparts, thereby giving a new twist to this well-known mechanism.

ACKNOWLEDGEMENTS

Part of this work was funded by Leverhulme Trust Research Project Grant No. RPG-2016-147. T.B.L. acknowledges the support of BrisSynBio, a BBSRC/EPSRC Advanced Synthetic Biology Research Centre (Grant No. BB/L01386X/1).

References

[1] M. C. Marchetti, et al. Hydrodynamics of soft active matter. *Rev. Mod. Phys.*, 85(3):1143–1189, 2013.
[2] T. Sanchez, et al. Spontaneous motion in hierarchically assembled active matter. *Nature*, 491(7424):431–434, 2012.
[3] E. Tjhung, et al. A minimal physical model captures the shapes of crawling cells. *Nat. Commun.*, 6:5420, 2015.
[4] D. Khoromskaia and G. P. Alexander. Motility of active fluid drops on surfaces. *Phys. Rev. E*, 92(6):062311, 2015.
[5] K. Kruse, et al. Contractility and retrograde flow in lamellipodium motion. *Phys. Biol.*, 3(2):130–137, 2006.
[6] D. Shao, H. Levine, and W.-J. Rappel. Coupling actin flow, adhesion, and morphology in a computational cell motility model. *Proc. Natl. Acad. Sci. USA*, 109(18):6851–6, 2012.
[7] A. Loisy, J. Eggers, and T. B. Liverpool. Tractionless Self-Propulsion of Active Drops. *Phys. Rev. Lett.*, 123(24):248006, 2019.

MARANGONI SPREADING OF NON-NEWTONIAN FLUID ON BATH LEADING TO FINGER INSTABILITY

Xue Ma[1], Menglin Zhong[1], Zhanwei Liu, and Zhenzhen Li[*1]
[1]School of Aerospace Engineering, Beijing Institute of Technology, Beijing, China

Summary Marangoni spreading is involved in fields such as coating and drug delivery. We report finger instability occurs during Marangoni spreading of shear thinning and viscoelastic polymer solution on a deep bath. Temporal dependence of spreading diameter shows elastic dominated and viscous dominated regime. Finger formation is accompanied by thickness perturbation of liquid surface of the order of 5 μm, measured by Transmission Lattice method. We delineate a range of Capillary number and viscoelastic relaxation time, which leads to large and flat fingers. The finger number is a function of polymer concentration, and of molecular weight. This study suggests that thin film instability may occur on bath surface with presence of Non-Newtonian fluids. It indicates conditions for homogenous coating, and shows transient behavior during delivery of Non-Newtonian drugs.

EXPERIMENTAL DESCRIPTION AND OBSERVATION

A drop of PEO solution at 5MDa molecular weight with Non-ionic surfactant is deposited on a bath of polymer solution without surfactant, the bath solution is 8 mm deep, in a square container made of Plexiglas with length and width 20 mm. The drop falls from 4 mm above the bath surface, injected by a syringe pump. Reflection and transmission optical methods are used for observation on the free liquid surface, which is illuminated by a Xenon light. Capillary waves propagates outwards firstly, followed by the Marangoni ridge presented by the dark large band, drop contact line falls behind the Marangoni ridge, with fingering instability developed (Figure 1). The fingers are slightly higher than the bath in its vicinity. For comparison, Marangoni spreading of Newtonian fluid does not show finger instability.

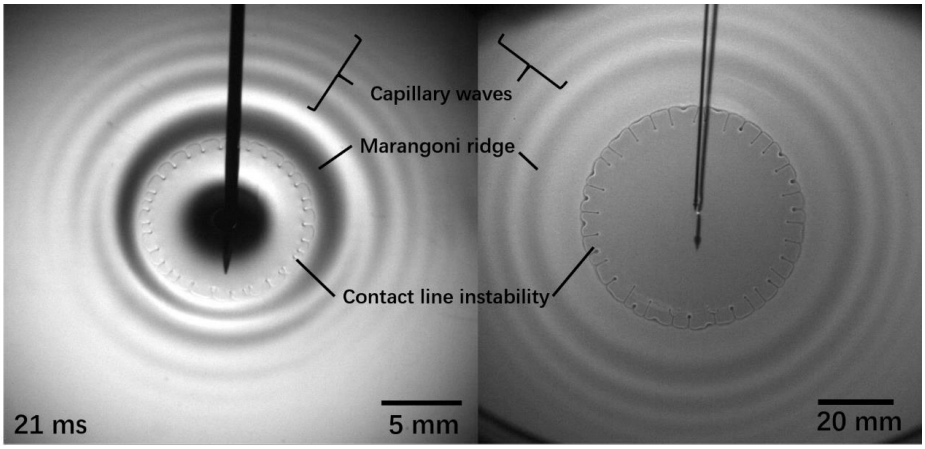

Figure 1: Fingering instability observed with light transmission (left) and reflection (right).

The height perturbation at the position of fingers is determined by Transmission Lattice method [1]. A transparent sheet with black grids is placed under the transparent container, and the LED light for illuminating is under the sheet. Grids frequency on the sheet is 10 lines per mm. Observing the grids above the deformed liquid surface, The grid pattern is distorted by the modulation of the liquid surface topography. Horizontal displacement of the grids pattern caused by liquid surface perturbation is analyzed by sampling Moiré method combined with the phase-shift technique. The propagation of Marangoni ridge [2] is captured during time, with height perturbation at the position of finger tips, which is measured at the order of 5 μm (Figure 2). This indicates that the finger instability is associated with elevation of free liquid surface, which may be caused by viscoelastic property of Non-Newtonian fluid under strong shear [3].

The spreading diameter increases with time. Considering the shear thinning effect of the polymer solution, the shear rate $\dot{\gamma}$ of the free surface flow can be calculated from the equation: $\dot{\gamma}(t)^2 \cdot \left(\eta_\infty + \frac{\eta_0 - \eta_\infty}{1+(k\dot{\gamma}(t))^p}\right) = \frac{\rho \cdot v(t)^2}{t}$, so that to deduce the temporal variation of viscosity. A balance between Marangoni stress and viscous stress gives prediction of spreading diameter $D(t) \sim t^{3/4}$. Figure 3a shows collapsed curves of $D(t) \cdot \eta^{1/4}$, proving the viscosity dominated regime after the time of 10 ms. The spreading is dominated by elasticity before 10 ms. The temporal evolution of finger number is a function of polymer concentration at a fixed molecular weight, and also a function of molecular weight. Figure 3b shows finger number, which is higher for low concentration at a fixed time. This may be due to high spreading velocity for low concentration solution, which has lower viscosity. The average finger width do not change remarkably with solution concentration.

*Corresponding author. E-mail: **zhenzhenli@bit.edu.cn**

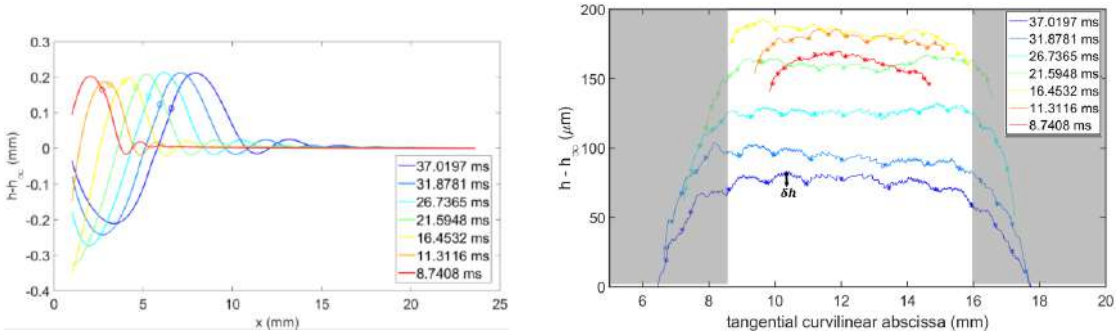

Figure 2: Bath surface deformation induced by Marangoni spreading, measured by Transmission-Lattice method. Left, cross-sectional profile of bath surface at different time steps. Circles on each curve represent x position of finger tips. **Right,** Bath thickness variation $h - h_\infty$ along finger tips on the contact line, for different time steps. Finger height δh above the surrounding bath is the order of 5 μm for the first 37 ms of spreading.

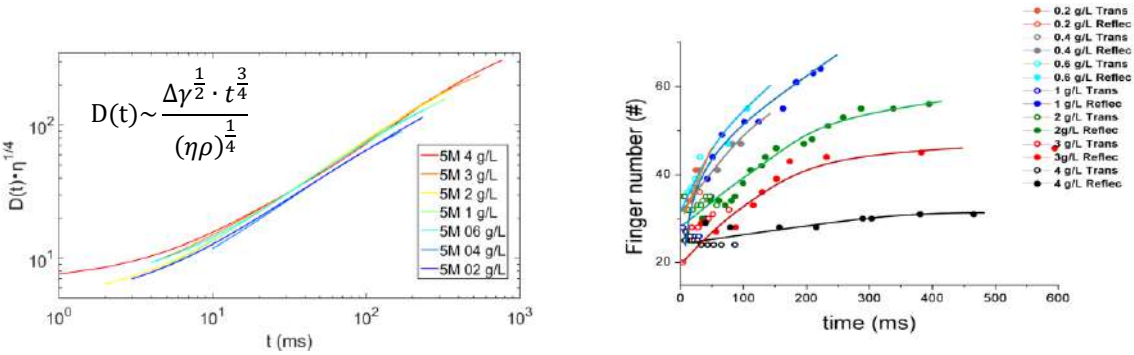

Figure 3: Temporal evolution of spreading diameter (left) and finger number (right).

DISCUSSION

Finger instability is observed under strong shear, caused by Marangoni flow of Non-Newtonian fluid on a free liquid surface of a bath. The elevation of free surface height at the position of finger tips may be caused by normal stress difference at high shear rate. This is consistent with the fact that the height elevation is more pronounced for high concentration of polymer, and for large molecular weight. We think that the elevation of surface height is associated with finger number development, noting that previous studies on thin film instability showed that thicker films produce larger fingers, so that smaller finger number [4]. We also note that the structure of the fingers is reminiscent of crease formation of elastic materials such as hydrogels. An elastic material under compression, which causes accumulation of elastic energy, creases are formed to relieve the elastic energy [5]. In our work, the in-plane strong shear may cause tangential compression in the spreading drop, the first 10 ms second is dominated by elastic response, and energy may be relieved by crease-like finger development.

CONCLUSIONS

Marangoni spreading of viscoelastic and shear thinning polymer solution on a free surface of a bath is studied experimentally. The spreading procedure is elastic dominated at the beginning and viscous dominated later on. The development of fingers is related with the polymer property, which exhibits non-linear effect under strong shear. The origin of the finger development may be thin film finger instability, and/or crease formation to relieve elastic energy. More study on the mechanism of finger formation is needed in the future. This work may provide support on coating technology and lung drug delivery, where Marangoni flow of Non-Newtonian fluid on free surface is important.

References

[1] Shi W., Huang X., Liu Z., Transmission-lattice based geometric phase analysis for evaluation the dynamic deformation of a liquid surface. *Optics Express.* **22,** 9:10559-10569, 2014.

[2] Matar OK, Troian S.M. Linear stability analysis of an insoluble surfactant monolayer spreading on a thin liquid film. Physics of Fluids, **9**, 12: 3645-3657.

[3] Oswald P. Rheophysics The deformation and flow of matter. *Cambridge University Press*, 2009.

[4] Keiser L. Bense H., Colinet P., Bico J., Reyssat E. Marangoni bursting: Evaporation-induced emulsification of binary mixture on a liquid layer. *Physical Review Letters*, **118**: 074504, 2017.

[5] Hong W., Zhao X., Suo Z. Formation of creases on the surfaces of elastomers and gels. *Applied Physics Letters*, **95**, 111901, 2009.

INSTABILITY OF A THIN FILM FLOWING UNDER AN INCLINED PLANE

Pier Giuseppe Ledda*[1], Gaétan Lerisson[1], Gioele Balestra[1], and François Gallaire[1]
[1]Laboratory of Fluid Mechanics and Instabilities, Ecole Polytechnique Fédérale de Lausanne, Lausanne, Switzerland

Summary We study the pattern formation of a thin film of viscous fluid flowing under an inclined plane, in the context of the Rayleigh-Taylor instability. We compare the experimental measurements with numerical simulations and theoretical findings. A steady pattern characterized by structures aligned with the flow arises, so-called rivulets, which saturate after some distance from the inlet. The profile is described using a one-dimensional model that well agrees with a two-dimensional pendant drop shape. The impulse response shows a selection of rivulets even in absence of boundary effects, rationalized using a weakly non-linear approach. The stability of the saturated rivulet profile to streamwise perturbations reveals the presence of an unstable mode characterized by lenses which travel on rivulets.

INTRODUCTION

When a heavier fluid is placed above a lighter fluid, a horizontal flat interface is linearly unstable even in absence of inertial effects and the Rayleigh-Taylor instability occurs[1, 2]. The presence of surface tension stabilizes small wavelengths, while large wavelengths remain unstable. When an upper wall confines the overhanging fluid, the problem can be tackled using the lubrication approximation [3], i.e. the wavelength of the perturbations is much larger than the thickness of the liquid. As a result of the instability, regular patterns of growing lenses are observed [4]. When the substrate is inclined, a complete description of the steps that lead from a flat substrate to dripping drops remains to be analyzed.

Experimental apparatus

A very viscous Newtonian fluid is injected under an inclined glass plate (see fig.1a), with a constant flow rate. The angle with respect to the vertical θ can be varied thanks to an orientable structure. Variations of the flow rate are obtained by the height difference between a closed reservoir connected to the injector slit and an open reservoir continuously overflowing. We can impose a steady spanwise modulated boundary conditions at the inlet using sinusoidal-shaped and comb-like blades. The film thickness is measured using a confocal chromatic sensor located on the upper part of the plate.

STEADY PATTERNS

The rivulet profile

When steady boundary conditions are considered, structures aligned with the streamwise direction (rivulets) dominate the flow. Moreover, for a certain range of flow rate and inclination angle, experiments show that rivulets saturate in the streamwise direction after some distance from the inlet (see fig1b). The experimental measurements of the film thickness are compared with non-linear numerical simulations of the two-dimensional lubrication equation accounting for the experimental boundary conditions, with an overall good agreement. At each cross section, the thickness profile is periodic in the spanwise direction. We develop a one-dimensional model, with periodic boundary conditions, in which

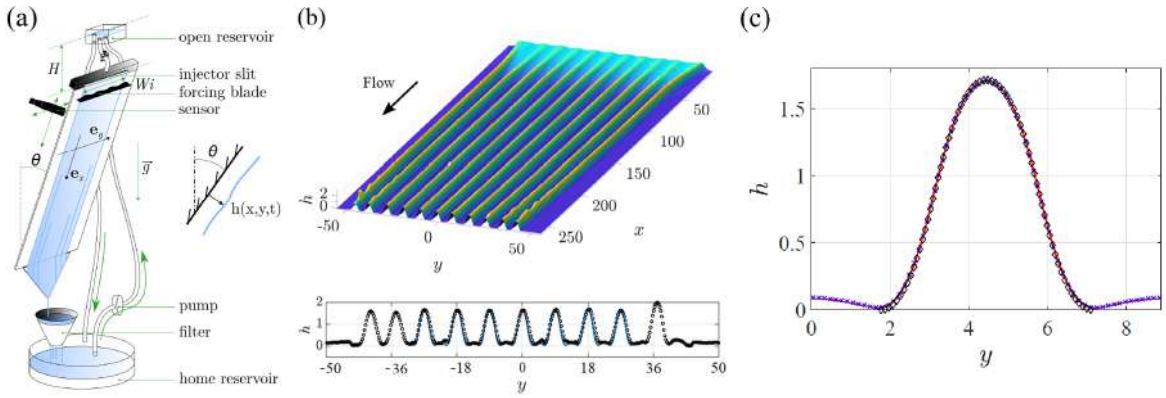

Figure 1: (a) Sketch of the configuration and the experimental apparatus. (b) On the top: typical experimentally measured thickness. On the bottom: comparison between the numerical simulations (blue line) and the experimental measurements (dots) for the saturated rivulets. (c) Comparison of the rivulet profile obtained from the one-dimensional model (red line), the pendant drop shape (black diamonds) and the two-dimensional Stokes simulations with free interface (blue crosses).

*Corresponding author. E-mail: pier.ledda@epfl.ch.

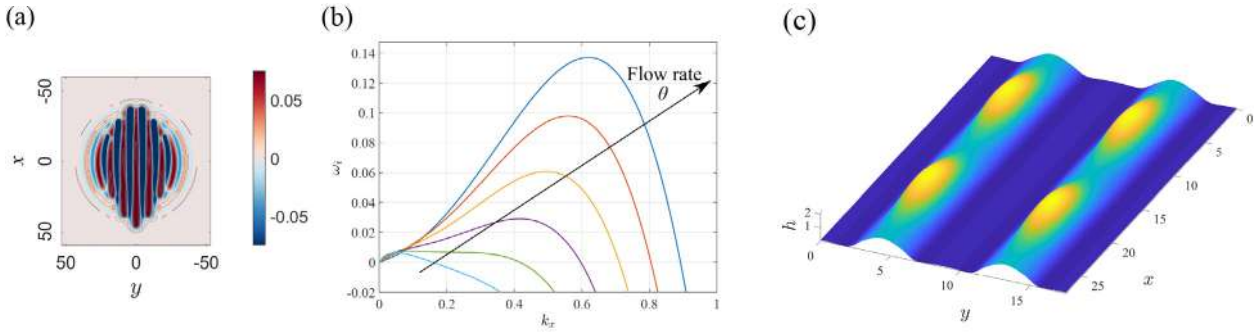

Figure 2: (a) Thickness perturbation iso-contours of the impulse response at long times from the weakly non linear model. (b) Dispersion relations from the rivulet stability analysis. (c) Linear combination of the rivulet profile and its unstable mode from the stability analysis.

the correct flow rate in the direction normal to the rivulet profile is ensured using a Lagrange multiplier. Results show the presence of a region of high thickness (central lobe) which slowly saturates to a constant shape, while the side lobes slowly drain with a power law $h \propto t^{-1/2}$. We thus study the shape of the central lobe imposing the pure static equilibrium between surface tension and hydrostatic pressure, i.e. we consider a two-dimensional static pendant drop. Total wetting conditions are considered, i.e. zero contact angle at the wall where the curvature is set to ensure the correct flow rate in the direction normal to the cross section. The results well agree with the one-dimensional lubrication model and a Stokes simulation with free surface (see fig.1c).

PATTERN SELECTION

Flat film impulse response

Afterwards, we focus on the temporal evolution which leads to a rivulet pattern. We consider the response of the flat film to a perturbation localized in space and time, in absence of boundary effects. While the linearized dynamics of the perturbation η exhibits an isotropic growth of the perturbation, a weakly non-linear model analogous to the Nepomnyashchy equation [3] features the selection of streamwise structures (see fig.2a). The two stages of the temporal evolution, i.e. the linearized isotropic linear growth and the weakly non-linear dynamics, are observed also in the fully non-linear simulations. The flow experiences a natural selection of streamwise structures resulting from the weakly non-linear dynamics, also in absence of boundary effects.

Saturated rivulets stability analysis

We study the survival of the saturated rivulet structures in the context of linear stability analysis. Starting from the rivulet profile $H(y)$ obtained from the one-dimensional model, we consider its stability to perturbations when the profile is perturbed in the streamwise direction with a perturbation of the form $\eta(x, y, t) = \hat{\eta}(y) \exp(k_x x - \omega t)$. In fig.2b we report the growth rate ω_i as a function of the streamwise wavenumber k_x. When lower values of the flow rate and θ are considered, short wavelengths are progressively stabilized until only very large wavelengths are weakly unstable. The unstable mode is characterized by lenses that form on the rivulets and travel on them (fig.2c), in agreement with the experimental observations.

CONCLUSIONS

We built a novel experiment for the flow of a thin film under an inclined plane, analyzing the arising patterns. We compared the experimental measurements with theoretical and numerical results. In the route to dripping, the flat film first destabilizes into a pattern characterized by saturated rivulets. This selection is intrinsic and related to a weakly non-linear mechanism. Subsequently, a secondary instability occurs on rivulets. As the flow rate and θ are decreased the rivulets are progressively stabilized and only very large wavelengths remain weakly unstable. As a result of the instability, rivulets that carry lenses are observed. In a last step, these lenses may eventually drip from the inclined ceiling.

References

[1] Lord Rayleigh. Investigation of the character of the equilibrium of an incompressible heavy fluid of variable density. *Proceedings of the London Mathematical Society* **s1-14 (1)**: 170–177, 1882.

[2] Taylor, G.I. The instability of liquid surfaces when accelerated in a direction perpendicular to their planes. I. *Proceedings of the Royal Society of London, Series A. Mathematical and Physical Sciences* **201 (1065)**: 192–196, 1950.

[3] Kalliadasis, S., Ruyer-Quil, C., Scheid, B., Velarde, M.G. Falling liquid films, vol. 176. Springer Science & Business Media, 2011.

[4] Lister, J.R., Rallison, J.M., Rees, S.J. The nonlinear dynamics of pendent drops on a thin film coating the underside of a ceiling. *Journal of Fluid Mechanics* **708 647**: 239–264, 2010.

SPREADING OF FLUIDS WITH BLADE COATING, MODEL AND EXPERIMENT

Marion Krapez*[1], Anaïs Gauthier[1], Jean-Baptiste Boitte [2], Christophe Kusina [2], Danielle Le Verge [2], Angelina Roudot [2], Odile Aubrun [2], Hamid Kellay [3], Jean-François Joanny [4]andAnnie Colin [1]

[1]*Laboratoire Matériaux Innovants pour l'Energie, Chemistry, Biology and Innovation (CBI) UMR8231, ESPCI Paris, CNRS, PSL Research University, 10 rue Vauquelin, Paris, France*

[2]*L'Oréal Recherche et Innovation, Chevilly-Larue, France*

[3]*LOMA, Laboratoire Ondes et Matière d'Aquitaine (UMR 5798), Université de Bordeaux _ CNRS, 33405 Talence, France*

[4]*Collège de France, 11 place Marcelin Berthelot, 75005 Paris, France*

Summary A new model is presented for soft blade coating of Newtonian fluids in the case of a finite reservoir of liquid. In comparison with previous studies, we show here that a new variable, the wetting length (which quantifies the amount of liquid remaining under the blade), is essential to explain the dynamics of the spreading of Newtonian fluids. Its impact on the thickness of the fluid layer is demonstrated through experiments, simulations and a scaling law model.

INTRODUCTION

The spreading of fluids is a crucial industrial process, for example in the cosmetic field, food industry and construction industry. While most of the spread liquids are non-Newtonian, the parameters that govern the deposit in usual configurations are not well understood, even in the case of simple Newtonian fluids. A better understanding of the spreading dynamics is needed to tackle common issues such as formation of inhomogeneous film or defects.

This subject is of great interest for the cosmetic field which uses complex fluids (i.e. polymers, emulsions, suspensions) for moisturizers or gels. It is a challenge to mimic by a mechanical system the gesture followed by the consumers. A promising technique is blade coating with a soft and deformable blade that compares better to real applications (Figure 1). A pioneering study was first conducted by Seiwert *et al.* [1], who studied the spreading of Newtonian fluids experimentally and theoretically, with an infinite reservoir of liquid. In their model they use an analogy with the dip-coating process by introducing a key parameter, the dynamic length, which corresponds to the length of the blade deformed by the fluid. More recent studies, carried out in our group on complex fluids [2], reveal that another parameter should be considered, which is the *wetting length* l_w, defined as the length of contact between the soft blade and the fluid measured along the spreading movement x, as shown in Figure 1. Our work shows that the wetting length is essential to explain the dynamics of the spreading of Newtonian fluids, and its impact on the thickness of the fluid layer is demonstrated.

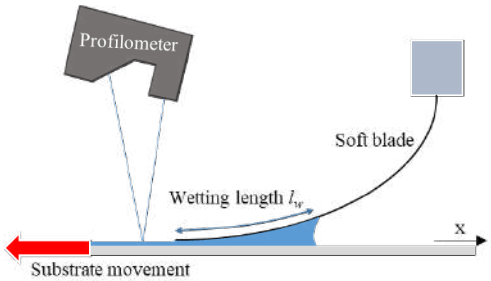

Figure 1. Schematic representation of the soft blade coating experiment.

MATERIALS AND METHODS

The liquids considered here are silicone oils, with viscosity η ranging between 500 and 1000 cSt. They are spread on a PMMA plate using a soft blade made from flexible mylar, with a thickness u =125 µm or 250 µm, cut to a length L of typically 6 cm, with a constant width b = 4cm. The blade is held at a specific height so that its end is just tangent to the surface [1]. A known mass of liquid is deposited under the blade and then spread with a one-way movement, by moving the substrate at a constant speed V (2.5 to 10 mm/s). The changes in the wetting length during spreading are followed from the side and from the top using two optical cameras (at typically 10 frames per second). Finally, the thickness of the liquid layer is measured, using an optical profilometer, at a distance of 2 mm from the end of the blade. Such experimental conditions aimed at correlating the thickness of the film e to the wetting length of the blade l_w. Accordingly, e and l_w are simultaneously recorded during the spreading as a function of the time and treated quasistatically.

*Corresponding author. E-mail: marion.krapez@espci.fr.

RESULTS

Figure 2a shows a typical profile of a liquid film *e(t)* (here silicone oil with viscosity 480 mPa.s), measured parallel to the spreading direction. Two plots are presented: the raw data directly extracted from the profilometer, which exhibits noise due to additionnal reflections, and a filtered curve that was used in the measurements. The film profile exhibits a transitory state in the first 7.5 s, where the thickness increases from 0 to 230 µm, followed by a slow and continuous reduction (from 230 to 15 µm in the last 12.5 s of the spreading experiment). On Figure 2b the corresponding wetting length l_w is presented. It decreases from 22.5 mm to nearly 0 mm while the fluid reservoir is emptied.

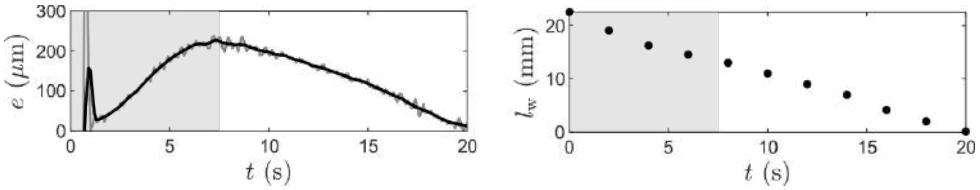

Figure 2. (*a*) Profile of fluid thickness *e* as a function of time *t* for a Newtonian fluid (silicone oil 480 mPa.s, V = 5 mm/s, L = 5.6 cm, u = 125 µm) raw (grey line) and filtered data (black line). (*b*) Evolution of l_w with time for the same experiment

These experiments thus show a clear dependency between the film thickness and the wetting length after a transitory region (in gray) corresponding to the setting in motion of the liquid. This is showed in Figure 3 for two different viscosities. The relation between *e* and l_w is quadratic. To understand how the reservoir size influences the spreading dynamics a full numerical integration of the blade and liquid dynamics was performed by finite difference. The results, obtained with no adjustable parameters, are in good agreement with the experiment (dashed lines).

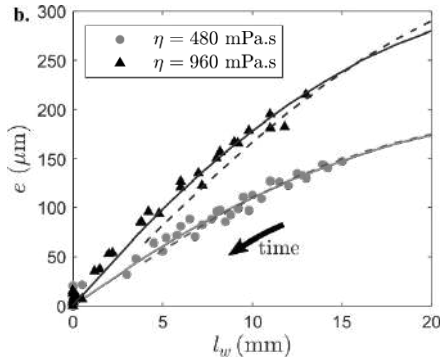

Figure 3. Evolution of the fluid thickness with the wetting length for two different oils with viscosity 480 mPa.s and 960 mPa.s, experiment (markers), simulation (dashed line) and model (line). V = 5 mm/s, u = 125 µm and L = 5.7cm.

The lines represents our model with prefactors 0.15 (for η = 480 mPas) and 0.17 (for η = 960 mPas) corresponding to the best fits (equation 1). To obtain this law, we consider at equilibrium the balance between the torque induced by the lubricating pressure within the film, and the resisting torque coming from blade elasticity (Euler-Bernoulli beam theory) which gives:

$$e \sim l_w \sqrt{\frac{\eta V L^2 b}{EI}} \left(1 - \frac{l_w}{L}\right) \quad (1)$$

where V is the spreading velocity, L the blade length, b the blade width, E the young modulus including the Poisson coefficient correction, and I a geometric factor. By varying also L, V and I we showed a good agreement between the thickness given by the model and the experiments over a wide range of data.

CONCLUSIONS

The present work shows that spreading with a blade cannot be directly compared with the "meniscus" spreading performed in Landau-Levich situations [1]. In particular, the analogy cannot be made when there is a finite reservoir of fluid, for which the distinction between static and dynamic regions is no longer relevant. A new parameter, the wetting length l_w, fully describes the system. Our effort is now focused on expanding the model to shear thinning and yield stress fluids such as carbopol based systems.

References

[1] Seiwert, J., Quéré, D., Clanet, C., Flexible scraping of viscous fluids. J. Fluid Mech. **715**: 424–435, 2013.
[2] Kusina C., Colin A. *(unpublished)*

SOAP FILM DEFORMATIONS: TOWARD A LOCAL RHEOLOGICAL MODEL FOR FOAMS

Adrien Bussonnière[1] and Isabelle Cantat*[1]
[1]Univ Rennes, CNRS, IPR (Institut de Physique de Rennes) - UMR 6251, F- 35000 Rennes.

Summary The highly confined flow of the liquid phase, trapped between the gas bubbles, is at the origin of the large effective viscosity of the liquid foams. Despite the industrial relevance of this complex fluid, the foam viscosity remains difficult to predict, because of the lack of flow characterization at the bubble scale. Using an original deformable frame, we provide an exhaustive characterization of the dynamical behavior of connected soap films, by measuring the film thickness map, the velocity map and the film tensions during and after the imposed deformation. Two important results are obtained: (i) we show that, for our foaming solution based on SDS and dodecanol, the film tension depends on its extension only and, surprisingly, not on its extension rate. (ii) we provide the first experimental evidence of the interface transfer between a compressed film (resp. a stretched film) and its first neighbor, across their common meniscus, and show that the energy dissipated during the whole deformation is dominated by the viscous dissipation induced by this transfer. We finally discuss the way we could built, on the basis of these two results, a model of foam visco-elasticity consistent with surfactant transport and hydrodynamics laws.

EXPERIMENTAL SET-UP

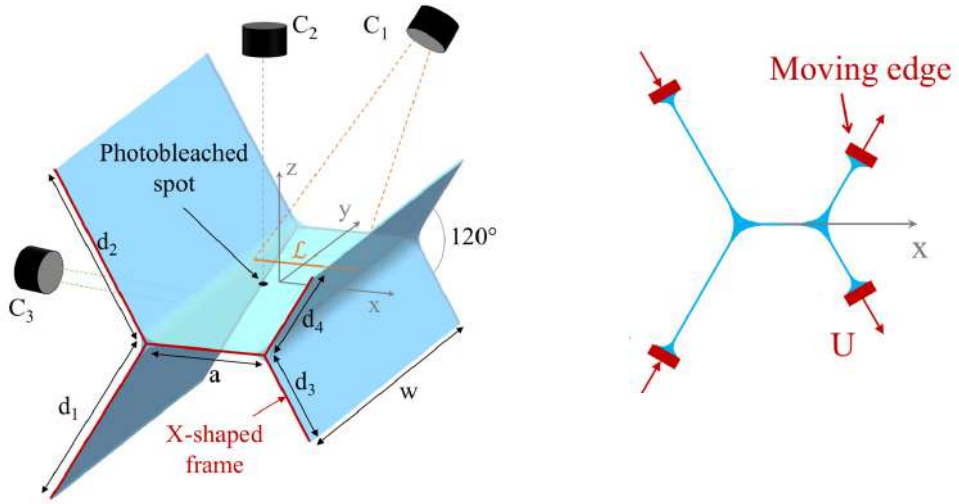

Figure 1: Sketch of the deformable frame on which five soap films, connected along two free menisci, are suspended, and of the position of the different cameras. As shown in the (x, z) plane view on the right, the left films are compressed and the right films are stretched due to the motion of the four moving edges (represented by the red arrows). This leads to a translation of the central film to towards the right meniscus.

The set-up is a deformable frame shown in Fig. 1, on which five flat, rectangular, soap films are produced. The film widths (in y direction) are all $w = 41.5$mm, whereas the length is $a = 6$mm for the central film and a variable length d_i, controlled by four independant piezo-motors, for the lateral films [1]. The foaming solution is made of SDS (2.5 cmc), dodecanol (0.05 g/L), glycerol (15 % in volume) and fluorescein (0.8 g/L). The studied deformation is a compression, during a time τ and at velocity U, for the two films on the left, synchronized with the symmetrical extension on the right. The film thicknesses are measured by an interferometric technique, using a spectral camera recording the reflected light spectrum along the line $\mathcal{L}$ in the (x, z) plane; the velocity field in the same plane is obtained from the motion of a photobleached spot [2] ; and the tension difference between adjacent films is deduced from the meniscus motion [3, 4, 5].

RESULTS

A first observation is that the film extension on the right side is followed by the extraction from the right meniscus of some new film, hereafter called the Frankel's film. This Frankel's film is much thicker than the film initially present (hereafter the initial film) and a sharp frontier between both parts of the film is stable during several seconds, so that the extension of both parts can be easily measured. In the compressed side, we observe a film volume decrease, which indicates that some film has been absorbed by the left meniscus. This absorption / extraction is coupled to an surfactant exchange between the lateral film and the meniscus, and ultimately, between the lateral films and the central film. This transfer induces, in the central film, the extraction of a Frankel's film on the left side and the absorption of the initial film by the meniscus on the right side. The whole central film translate at the velocity U_c. This clearly appears on the film thickness profiles in Fig. 2.

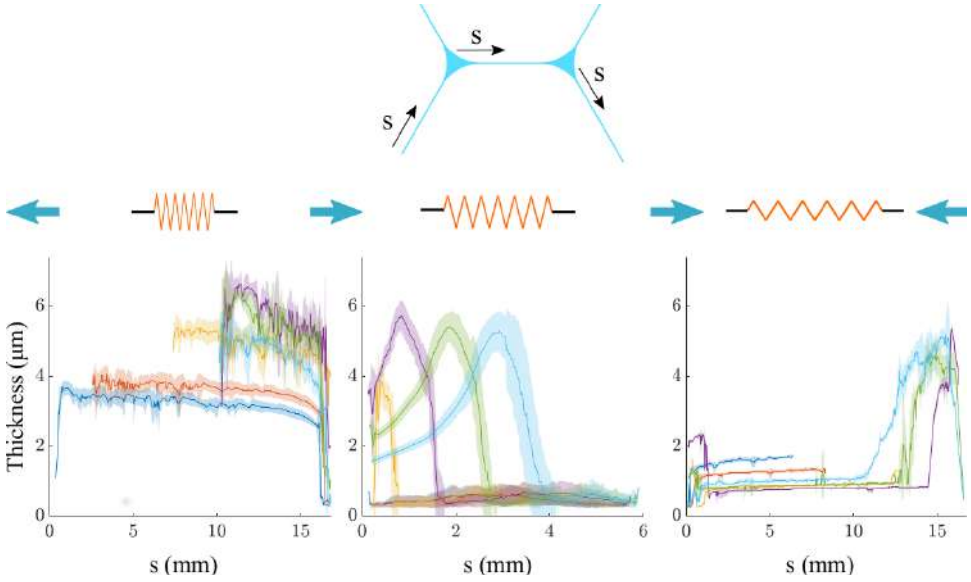

Figure 2: From left to right, film thickness profiles in the bottom left film, central film and bottom right film, at times 0 (blue), 0.04 (red), 0.275 (yellow), 0.475 (purple), 0.776 (green) and 1.25 s (cyan), as a function of the curvilinear abscissa defined above. The films have the mechanical role of elastic springs (represented in red), which tension can relax by transferring some interface to the next film, across their common meniscus (symbolized by the blue arrows). The transfer velocity U_c is ruled by the tension differences by the two films involved, and the meniscus therefore plays the mechanical role of a viscous dashpot.

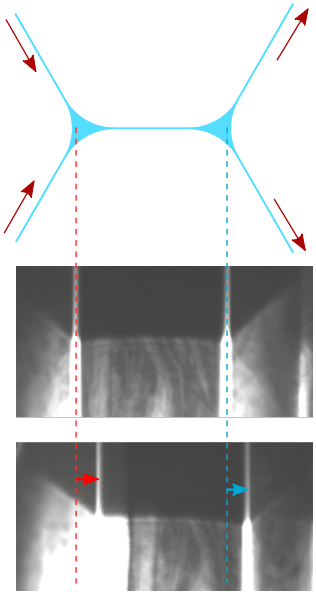

Figure 3: Top view of the experiment showing the small displacement of the free menisci, due to a variation of film tension.

The film tension are uniform on each films [3] and their values σ^-, σ_c and σ^+, respectively in the left, central and right films, can be deduced from the menisci motion shown in Fig. 3. Similarly, the extension ε and extension rate $\dot{\varepsilon}$ are uniform in each film. Importantly, note that, because of the exchanges with the menisci, these quantities are not related to the actual film sizes imposed by the motor motion. They can instead be deduced from the thickness map: if a piece of film is stretched, its thickness decreases, due to the liquid phase incompressibility. A key result we obtained is a master curve representing the film tension σ as a function of its extension ε, with a nice superposition of the all data, whatever the extension rate, in the range $\dot{\varepsilon} \in [1 - 10]\ \mathrm{s}^{-1}$. This shows that, in our parameter range, the intrinsic viscosity of the films is negligible in the apparent viscosity of the whole structure [6]. In contrast, the surface tension difference between the central and lateral films depends on the transfer velocity U_c from one film to its neighbor, which thus appears as a viscous process.

CONCLUSION

Our experiments allowed us to conclude that the thin film are elastic elements in the structure, and that the viscosity arises from the interface transfer from one film to its first neighbour, across the menisci. We propose a model for this viscous contribution, showing that the dissipation is dominated by the shear of a small part of the thin films, located close to the meniscus, as first qualitatively proposed in [7].

This project has received funding from the European Research Council (ERC) under the European Union's Horizon 2020 research and innovation program (grant agreement No 725094).

References

[1] A. Bussonnière, E. Shabalina, X. Ah-Thon, M. Le Fur, and I. Cantat, Phys. Rev. Lett. **124**, 018001 (2020).
[2] J. Seiwert, R. Kervil, S. Nou, and I. Cantat, Phys. Rev. Lett. **118**, 048001 (2017).
[3] M. Durand and H. A. Stone, Phys. Rev. Lett. **97**, 226101 (2006).
[4] S. Besson, G. Debrégeas, S. Cohen-Addad, and R. Höhler, Phys. Rev. Lett. **101**, 214504 (2008).
[5] A. L. Biance, S. Cohen-Addad, and R. Höhler, Soft Matter **5**, 4672 (2009).
[6] A. Bussonnière and I. Cantat, Preprint (2020).
[7] P. Petit, *Déformation d'interfaces complexes: des architectures savonneuses aux mousses de particules*, PhD thesis, 2014.

*Corresponding author. E-mail: isabelle.cantat@univ-rennes1.fr

ENHANCED DIP-COATING ON A SOFT SUBSTRATE

Vincent Bertin*[1,2], Jacco H. Snoeijer[3], Elie Raphaël[2], and Thomas Salez[1,4]
[1]Univ. Bordeaux, CNRS, LOMA, UMR 5798, 33405 Talence, France,
[2]UMR CNRS Gulliver 7083, ESPCI Paris, PSL Research University, 75005 Paris, France,
[3]Physics of Fluids Group, Faculty of Science and Technology, and Mesa+ Institute, University of Twente, 7500AE Enschede, The Netherlands,
[4]Global Station for Soft Matter, Global Institution for Collaborative Research and Education, Hokkaido University, Sapporo, Hokkaido 060-0808, Japan.

Summary A solid, withdrawn from a liquid bath, entrains a thin liquid film. This simple process, first discussed by Landau, Levich and Derjaguin (LLD), is observed in everyday's life and is widely used in industry. However, the liquid flux entrained can be altered by various properties of the withdrawn solid. Here, we develop a model that accounts for the additional presence of a soft solid layer atop the rigid plate. For simplicity, a Winkler's foundation is assumed as an elastic response. A new power-law regime is found for the thickness of liquid entrained $h_\infty \sim \sqrt{\ell_{ec}\ell_{cap}}\,\mathrm{Ca}^{1/2}$ (where Ca denotes the capillary number, ℓ_{cap} the capillary length and ℓ_{ec} an elastocapillary length) at small Ca. At large Ca, the classical LLD scaling law $h_\infty \sim \ell_{cap}\,\mathrm{Ca}^{2/3}$ is recovered. The crossover between the two regimes occurs when the substrate's deformation is comparable to the thickness of the entrained film.

INTRODUCTION

The motion of a liquid meniscus on a wet solid occurs in a wide variety of situations, such as the motion of a confined bubble flowing within a microfluidic channel, or the spreading of a droplet on a substrate [1]. The dip-coating experiment is the canonical example of such phenomena and has important applications in industry [2]. In nature, some animals like humming birds, bees or ants dip their tongue inside liquids to drink, which is argued to be more efficient for viscous liquids (such as nectars [3]) than other drinking processes.

In the last decade, a lot of attention has been devoted to the mechanics of very soft gels (shear modulus $\sim$ kPa), which unveil *e.g.* rich wetting properties as capillary forces can deform such materials over observable microscopic length scales [4, 5]. Nevertheless, the influence of the softness of the wall on a dynamic meniscus is still unknown [2]. Here, we address this question and study theoretically the effect of the softness in the thickness of liquid entrained through a dip-coating process.

MODELING

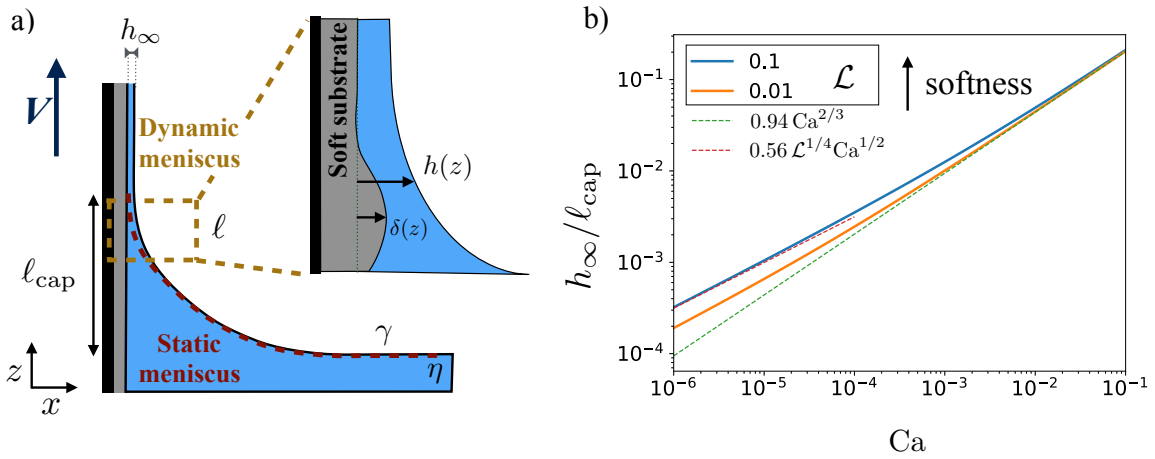

Figure 1: a) Schematic of the dip-coating situation. The inset exhibits a zoom in the dynamic meniscus zone where the flow is localized. The interface curvature imposes a negative Laplace pressure that deforms the soft substrate. b) Normalized entrained liquid thickness versus the capillary number for different values of the dimensionless softness parameter $\mathcal{L} = \rho g s_0/E$. The green dashed line represents the LLD scaling law $h_\infty = 0.94\,\ell_{cap}\,\mathrm{Ca}^{2/3}$, valid at large Ca. The red dashed line is an apparent scaling law $h_\infty \approx 0.56\,\sqrt{\ell_{cap}\ell_{ec}}\,\mathrm{Ca}^{1/2}$.

We consider a two-dimensional plate (see Fig. 1a), withdrawn with a velocity V from a liquid bath of viscosity η, density ρ and surface tension (with air) γ. We assume that the Weber ($\mathrm{We} = \rho V^2 \ell_{cap}/\gamma$, with $\ell_{cap} = \sqrt{\gamma/\rho g}$ the

*Corresponding author. E-mail: vincent.bertin@u-bordeaux.fr

capillary length) and capillary (Ca $= \eta V/\gamma$) numbers are small with respect to 1, so that we can neglect inertia and perform a LLD-like asymptotic matching [6]. Therefore, we describe the flow in the dynamic meniscus zone (see Fig. 1a) using the lubrication approximation. Gravitational drainage is neglected in this regime, and the governing equation for the interfacial profile $h(z)$ is given by the following thin-film equation:

$$\frac{\gamma\Big(h(z)-\delta(z)\Big)^3}{3\eta}h'''(z)+V\Big(h(z)-\delta(z)\Big)=Vh_\infty\,, \tag{1}$$

where the prime denotes the spatial derivative with respect to z, h_∞ is the thickness of the entrained liquid film, and $\delta(z)$ is the displacement field that denotes the normal deformation of the soft substrate induced by the Laplace pressure in the film.

As a minimal description, we use a Winkler's foundation which means that the substrate behaves as a mattress of independent springs – a situation relavant to thin compressible elastic materials. Thus, the displacement field is proportional to the local Laplace pressure, which amounts to $\delta(z) = \frac{s_0\gamma}{E}h''(z)$, where s_0 is a typical length (*e.g.* the length at rest of a spring) and E is an elastic modulus. The natural length scale $\sqrt{s_0\gamma/E} = \ell_{\text{ec}}$ appearing here is called the elastocapillary length. Therefore, a dimensionless softness parameter emerges from this model, as the ratio between elastocapillary and capillary lengths squared: $\mathcal{L} = (\ell_{\text{ec}}/\ell_{\text{cap}})^2 = \rho g s_0/E$.

Injecting the previous elastic law in Eq. 1, we find an ordinary differential equation that is solved here using a 4^{th}-order Runge-Kutta numerical scheme. The entrained liquid thickness h_∞ is found using a shooting algorithm that ensures the curvature matching condition $\lim_{z\to-\infty} h''(z) = \sqrt{2}/\ell_{\text{cap}}$ [6]. We plot in Fig. 1 the resulting entrained liquid thickness versus the capillary number, for two different softness parameters. Two scaling distinct regimes are observed: at large Ca, we recover the LLD scaling law $h_\infty = 0.94\,\ell_{\text{cap}}\,\text{Ca}^{2/3}$, and at small Ca, more fluid is entrained and we find a novel empirical scaling regime $h_\infty = 0.56\sqrt{\ell_{\text{cap}}\ell_{\text{ec}}}\,\text{Ca}^{1/2}$. From the observation of the typical liquid-thickness and displacement fields (not shown here), we observe that the crossover between the two scaling regimes happens when the typical deformation of the substrate is larger than the thickness of the entrained liquid film. Therefore, at small velocity, the wall softness enhances the dip-coating efficiency with respect to the classical LLD scenario.

In future work, the details and potential self-similar properties of this so-called soft-LLD regime will be investigated, as well as other elastic models for the substrate's response.

References

[1] Cantat I. Liquid meniscus friction on a wet plate: Bubbles, lamellae, and foams. *Physics of Fluids* **25**: 031303, 2013.
[2] Rio E., Boulogne F. Withdrawing a solid from a bath: How much liquid is coated?. *Advances in colloid and interface science*, **247**, 100-114. 2017
[3] Kim W., Gilet T., Bush J.W. Optimal concentrations in nectar feeding. *Proceedings of the National Academy of Sciences* **108**(40): 16618-16621, 2011.
[4] Andreotti B., Snoeijer J. H. Statics and dynamics of soft wetting. *Annual Review of Fluid Mechanics.* **52**, 2020.
[5] Style R. W., Jagota A., Hui C.Y., Dufresne E.R. Elastocapillarity: Surface tension and the mechanics of soft solids. *Annual Review of Condensed Matter Physics.* **8**, 99-118, 2017.
[6] Levich B., Landau L. Dragging of a liquid by a moving plate. *Acta Physicochim. URSS* **17**, 1942.

THE DEPENDENCE OF THE SURFACE TENSION AND CONTACT ANGLE ON THE TEMPERATURE, AS DESCRIBED BY THE DIFFUSE-INTERFACE MODEL

Eugene Benilov*[1]
[1]Department of Mathematics and Statistics, University of Limerick, Limerick, Ireland

Summary Two sets of results are reported in this paper. *First*, asymptotic estimates are used to check two conjectures included in the diffuse-interface model for contact lines: that the boundary condition for a fluid bounded by a solid wall should prescribe the fluid's density (which is indeed true) and that liquid–vapor interfaces are nearly isothermal (which is not true for, say, water, but can be true for a more viscous fluid). The non-isothermaility occurs at a microscopic scale, but can still affect the dynamics of contact lines. *Second*, the diffuse-interface model is coupled to a realistic equation of state for water and used to calculate the surface tension and contact angle of a static liquid–vapor interface, as functions of the temperature. The former result agrees quantitatively with the experimental data, but no data are available to verify the latter, so only theoretical predictions are reported. It is shown that, with increasing temperature, the contact angle becomes either 180° (perfect hydrophobicity) or 0° (perfect hydrophilicity); the former occurs when the boundary-presribed density ρ_0 matches that of saturated vapor and the latter, when ρ_0 matches the liquid density. Such behavior presumably occurs in all fluids, not just water, and for any sufficiently strong variation of parameters, not just that of the temperature. This conclusion is supported by existing observations of drops under variable electric field.

DESCRIPTION OF THE PROBLEM

The diffuse-interface model (e.g., [1]) is based on an assumption that the van der Waals force in fluids can be described by a pair-wise potential exerted by the molecules on each other. If the potential's spatial scale is much shorter than that of the flow, the force term in the governing equations can be simplified, yielding the so-called Korteweg stress. The resulting model provides a tool for studying flows involving contact lines, i.e., curves where the gas, liquid, and solid are in simultaneous contact. To this end, one also needs a boundary condition for fluid–solid interfaces, of which several versions exist in the literature. Firstly, Ref. [2] suggested a condition prescribing the density gradient in the direction normal to the solid boundary; secondly, Ref. [1] put forward a condition prescribing a linear combination of the density gradient and the density itself. It was also conjectured in Ref. [1] that, if the solid–fluid interaction is short-ranged by comparison with the fluid–fluid one, the general boundary condition can be simplified, so that just the density is prescribed. This simplest boundary condition is usually employed in applications.

Curiously, the diffuse-interface model (DIM) has never been coupled with a realistic equation of state (EoS): the one typically used is inconsistent with the ideal-gas limit and does not involve temperature (the latter amounts to spatial isothermality). This EoS, however, allows one to find analytically the profile of the liquid–vapor interface, which comes handy when calculating the flow's macroscopic characteristics (the surface tension and contact angle). Still, the use of a non-realistic EoS renders the DIM somewhat phenomenological rather than physics-based.

A model close to, but still not fully, realistic was examined in Ref. [3], where the DIM was coupled with the van der Waals EoS. Interestingly, simulations carried out in this work showed that interfacial flows can be significantly non-isothermal.

THE RESULTS

The shortcomings of, and discrepancies associated with, the non-realistic equations of state incorporated in the existing versions of the DIM are resolved in the present work. The following results have been obtained:

1. It has been shown that the boundary condition prescribing the density value ρ_0 that the fluid should assume at a solid wall can be derived without assuming that the solid–fluid interaction is short-ranged by comparison with the fluid–fluid one (as conjectured in Ref. [1]). In other words, this boundary condition is based on the same physics as the DIM itself.

2. A parameter region has been identified, where interfacial flows without external heating are almost isothermal. It does *not* include water, where the heat production due to viscosity and compressibility of vapor near the interface is too strong.

   Non-isothermality is not observed in fluids whose van der Waals parameters are not too different from those of water, but the viscosity is considerably higher. The latter slows the flow down and, thus, reduces the heat production.

3. The DIM was coupled to a realistic EoS of water and used to compute the surface tension σ of a liquid/vapor interface as a function of the temperature T – see Fig. 1. The theoretical results agree well with the empiric dependence $\sigma(T)$ [4].

*Corresponding author. E-mail: Eugene.Benilov@ul.ie.

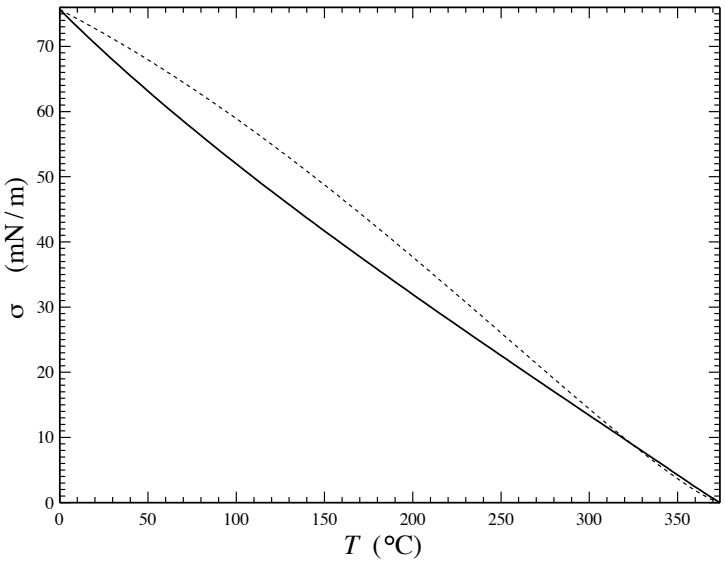

Figure 1: The surface tension σ of the interface between liquid water and its vapor vs. the temperature T. The temperature varies from water's triple-point value to its critical value. The solid curve shows the results computed through the DIM, the dotted curve shows the corresponding empiric results [4].

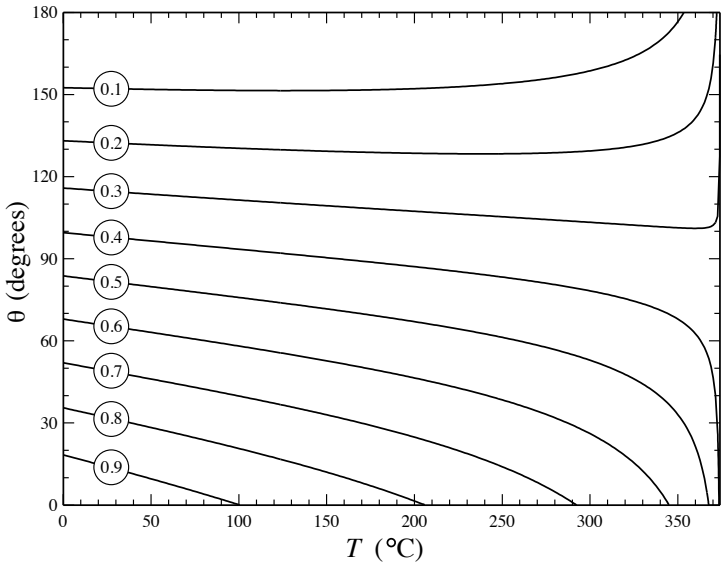

Figure 2: The static contact angle θ vs. the temperature T, for water. The curves are labelled with the corresponding values of ρ_0/ρ_{tp} where ρ_{tp} is the triple-point density of liquid water. The separatrix (dashed line) corresponds to ρ_0 coinciding with the critical density of water.

4. We have also computed the static contact angle θ of a liquid–vapor interface as a function of T for water – see Fig. 2. The results obtained predict that, with increasing T, any substrate would become either perfectly hydrophobic ($\theta = 180°$) or perfectly hydrophilic ($\theta = 0°$): the former occurs at a temperature for which the saturated-vapor density equals ρ_0, and the latter occurs when the liquid density does. It can be argued that states with $\theta = 180°$ or $\theta = 0°$ can be created through *any* parameter variation, not only that of the temperature. To do so, this variation should change either ρ_0 or the densities of the phases – until the former coincides with one of the latter. This argument could explain the observed behavior of droplets under variable electric field [5].

References

[1] Pismen L. M., Pomeau Y. Disjoining Potential and Spreading of Thin Liquid Layers in the Diffuse-Interface Model Coupled to Hydrodynamics. *Phys. Rev. E* **62**: 2480-2492, 2000.
[2] Seppecher P. Moving contact lines in the Cahn-Hilliard theory. *Int. J. Eng. Sci.* **34**: 977-992, 1996.
[3] Onuki A. Dynamic van der Waals theory. *Phys. Rev. E* **75**: 036304.1-15, 2007.
[4] Wagner W., Kretzschmar H.-J. International steam tables. Springer, Berlin 2008.
[5] Brabcova Z., McHale G., Wells G. G., Brown C. V., Newton M. I. Electric field induced reversible spreading of droplets into films on lubricant impregnated surfaces. *Appl. Phys. Lett.* **110**: 121603.1-4, 2017.

RIVULET STRUCTURE IN A HEATED LIQUID FILM DUE TO THERMOCAPILLARITY

Sergey Aktershev[1], Sergey Alekseenko[1]
[1]Kutateladze Institute of Thermophysics, Novosibirsk, Russia

Summary The formation of a 3D rivulet structure in a heated falling liquid film is investigated theoretically. Within the framework of the spatial approach, a linear analysis of the stability of the heated film flow relative to spanwise perturbations is performed for the first time, and the dispersion dependences are obtained. A numerical method is used to study the nonlinear development of instability. It is shown that a small spanwise perturbation evolves into the time-independent developed 3D rivulet structure.

THEORETICAL MODEL AND RESULTS OF CALCULATIONS

Non-isothermal liquid films are the basis of many technological processes. Theoretical researches of the waves in a heated film are based, usually, on the long-wave approximation, but two different approaches are used. In the first one, based on the lubricant approximation, one equation is derived for film thickness evolution, such as the Benney equation [1], but taking into account the tangential stress on the film surface due to the thermocapillarity. Models using this approach are applicable only for small Reynolds numbers. According to another approach, the Reynolds number is not assumed to be small, and the evolution of the heated liquid film is described by a system of equations for the film thickness, flow rate and temperature. Theoretical models [2-4], based on second approach, have a significantly wider range of applicability on Reynolds number since they are directly deduced from the Navier-Stokes equations with the help of some suppositions concerning the velocity and temperature profiles. Using the second approach, we investigate the occurrence of 3D rivulets in a locally heated liquid film. The results of calculations for small and moderate Reynolds numbers are compared with experimental data. We consider 3D liquid film flow on a locally heated vertical wall. The liquid film is in contact with a fixed gas, and the heat exchange on the interface is described by means of a given heat transfer coefficient α. All properties of a liquid are considered to be constant, with the exception of surface tension, which is linearly dependent on temperature: $\sigma = \sigma_0 - \gamma(T - T_0)$. It is assumed that the perturbations in the film are long-wave (i.e. film thickness h is much smaller than the characteristic size of the rivulet structure L). The system of equations derived in [5] for the film thickness $h(x,z,t)$, flow rates $q(x,z,t)$ and $m(x,z,t)$ takes the following form in dimensionless variables:

$$\frac{\partial q}{\partial t} + \frac{\partial J_1}{\partial x} + \frac{\partial J_{1,2}}{\partial z} = \frac{3}{\mathrm{Re}}\left(h - \frac{\mathrm{Ma}}{2}\frac{\partial T_s}{\partial x} - \frac{q}{h^2}\right) + \mathrm{We}h\frac{\partial \Delta h}{\partial x},$$

$$\frac{\partial m}{\partial t} + \frac{\partial J_2}{\partial z} + \frac{\partial J_{1,2}}{\partial x} = -\frac{3}{\mathrm{Re}}\left(\frac{\mathrm{Ma}}{2}\frac{\partial T_s}{\partial z} + \frac{m}{h^2}\right) + \mathrm{We}h\frac{\partial \Delta h}{\partial z},$$

$$\frac{\partial h}{\partial t} + \frac{\partial q}{\partial x} + \frac{\partial m}{\partial z} = 0.$$

Here $J_1 = \frac{6q^2}{5h} - \mathrm{Ma}\frac{qh}{20}\frac{\partial T_s}{\partial x} + \frac{h^3}{120}\left(\mathrm{Ma}\frac{\partial T_s}{\partial x}\right)^2$, $J_2 = \frac{6m^2}{5h} - \mathrm{Ma}\frac{mh}{20}\frac{\partial T_s}{\partial z} + \frac{h^3}{120}\left(\mathrm{Ma}\frac{\partial T_s}{\partial z}\right)^2$,

$J_{1,2} = \frac{6mq}{5h} - \frac{\mathrm{Ma}}{40}h\left(q\frac{\partial T_s}{\partial z} + m\frac{\partial T_s}{\partial x}\right) + \frac{h^3\mathrm{Ma}^2}{120}\frac{\partial T_s}{\partial x}\frac{\partial T_s}{\partial z}$, $\Delta h = \frac{\partial^2 h}{\partial x^2} + \frac{\partial^2 h}{\partial z^2}$, $T_s(x,z) = \frac{T_W}{1+\mathrm{Bi}h}$, $\mathrm{We} = \left(3Fi/\mathrm{Re}^5\right)^{1/3}$ is Weber number, $Fi = \sigma^3/\rho^3 g\nu^4$ is Kapitsa number, $\mathrm{Ma} = \gamma T_m/\mu\iota_m$ is Marangoni number, $\mathrm{Bi} = \alpha h_m/\lambda$ is Biot number, $\mathrm{Re} = gh_m^3/3\nu^2$ is Reynolds number.

Linear analysis of stability relative to the spanwise perturbation. We study the stability of the unperturbed flow using the spatial approach. Let $h = 1 + \tilde{h}$, $q = 1 + \tilde{q}$, $m = m_0 + \tilde{m}$, $T_s = T_{s,0} + \tilde{T}_s$, where $\tilde{h}, \tilde{q}, \tilde{m}, \tilde{T}_s$ are small perturbations of the thickness, flow rate, and temperature of the film surface. Temperature perturbation can be expressed through perturbation of film thickness in the form $\tilde{T}_s = -E\tilde{h}$, where $E = \mathrm{Bi}/(1+\mathrm{Bi})^2$. Perturbations of the film flow are written in the form $\tilde{h}(x,z) = H_a\cos(kz)\exp(\alpha x)$, $\tilde{q}(x,z) = Q_a\cos(kz)\exp(\alpha x)$, $\tilde{m}(x,z) = M_a\sin(kz)\exp(\alpha x)$. Here $k = 2\pi h_m/L_z$ is the real wave number, L_z is the dimensional spatial period, α is the spatial growth rate of the perturbation. Having substituted these expressions in the linearized equations, we have gained analytical expression for spatial growth rate depending on a wave number k. Dependences of a spatial period of rivulet structure L_z for maximum growth perturbations depending on Re are shown in fig. 1 in comparison with experimental data for various fluids. One can see from the figure that in a wide range of Re, the experimental values of L_z are in good agreement with the parameters of the maximum growth perturbations calculated by an analysis of stability.

*Corresponding author. E-mail: asvasus@yandex.ru

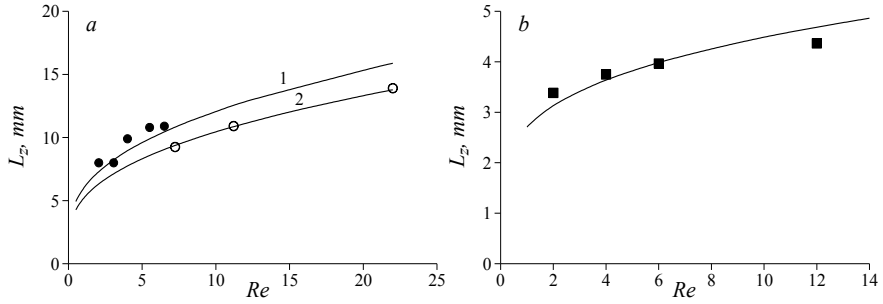

Figure 1. Distance between rivulets L_z, depending on Re for water (*a*) and for liquid MD-3F (*b*). Experimental data of [6]: solid circles for $Ma^* = 150$ and open circles for $Ma^* = 200$. The solid lines mean prediction of the most amplified perturbations (*a*). Squares are experimental data of [7]. The solid line is prediction for $Ma^* = 150$ (*b*).

Nonlinear development of perturbation in a 3D statement. The formation of 3D rivulets in a heated film was modeled by a spanwise perturbation applied to an unperturbed flow. At the inlet (i.e. at $x = 0$) a small z-periodic perturbation of thickness with predetermined wavelength L_z was set: $h = 1 + H_a \cos(kz)$, where H_a is the specified small amplitude of the initial perturbation. The calculations were performed for a film section with a width of one period, i.e. the computational domain represented a rectangle $0 \le x \le X_{end}$, $0 \le z \le L_z$. On the side boundaries of the computing domain (with $z = 0$ and $z = L_z$) the periodicity conditions were set. The calculations have shown that the initial disturbance evolves downstream into the rivulet structure. The calculated developed rivulet structure is shown in fig. 2.

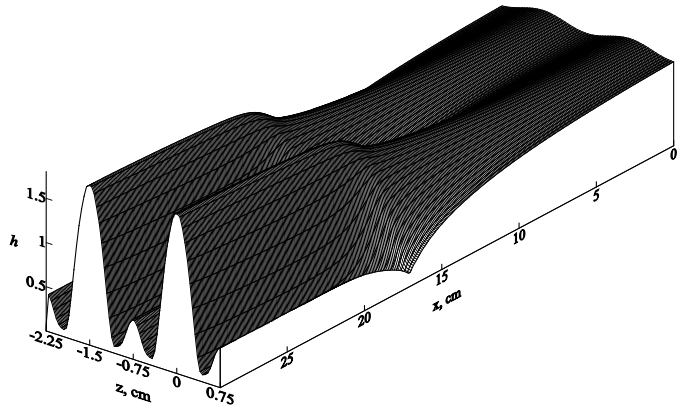

Figure 2. Developed 3D rivulet structure with wavelength $L_z = 1.5$ cm at Re = 5, $Ma^* = 100$, $Bi^* = 0.2$

CONCLUSIONS

The formation of 3D thermocapillary rivulet structure in a heated liquid film was investigated numerically. Using a spatial approach, a linear analysis of the stability was performed with respect to spanwise perturbations, and a spatial growth rate was calculated. Analysis of the experimental data for various liquids and different Reynolds numbers showed that the distance between rivulets agree well with the wavelength of the most amplified perturbation, calculated in accordance to the theory of stability. The stationary rivulet structures were simulated by spanwise perturbations imposed on a pre-calculated stationary 2D flow. Calculation results show that developed rivulet structure has a quasistationary character and very slightly changes downstream. The influence of dimensionless parameters on the developing rivulet structure has been revealed.

References

[1] Benney D.J. *J. Math. Phys.* **45** 150−155, 1966.
[2] Trevelyan M.J., Scheid B., Ruyer-Quil C. and Kalliadasis S. *J. Fluid Mech*. **592** 295–334, 2007.
[3] Scheid B., Kalliadasis S., Ruyer-Quil C. and Colinet P. *Phys. Rev.* E **78** 066311, 2008.
[4] Oron A. *Phys. Fluids* **12** 1633–1645, 2000.
[5] Aktershev S.P, Alekseenko S.V. *Int. J. Multiphase Flow* **114** 115−127, 2019.
[6] Chinnov E.A. and Shatskiy E.N. *Technical Physics Letters* **36** 53–56, 2010.
[7] Kabov O.A. and Chinnov E.A. *Russ. J. Engin. Thermophys.* **7** 1–34, 1997.

LINEAR STABILITY AND LATE TIME EVOLUTION OF AN EVAPORATING LIQUID FILM COMPRISING VOLATILE BINARY MIXTURES

R. K. Nazareth[1], G. Karapetsas[2], K. Sefiane[1], O. K. Matar[3] and P. Valluri[1]
[1]Institute for Multiscale Thermofluids, School of Engineering, The University of Edinburgh, Edinburgh, UK
[2]Department of Chemical Engineering, Aristotle University of Thessaloniki, Thessaloniki, Greece
[3]Department of Chemical Engineering, Imperial College London, London, UK

Here, we consider the evaporation of a thin liquid film which consists of a binary mixture of volatile liquids. Both the components in the mixture can be volatile. The mixture is in contact with a solid substrate below which is heated and is exposed to a gas phase. Using lubrication approximation and accounting for thermo/soluto-capillarity, we derive evolution equations for the interfacial height and concentration. We then perform a linear stability analysis, with a frozen base-state approximation. Our linear theory demonstrates the existence of principally two modes and the growth rates predicted are used to validate our numerical simulations. Our numerical simulations also allow us to examine the dynamics in the nonlinear regime and analyse how these instabilities evolve with time.

INTRODUCTION

Thin liquid films subject to temperature and concentration gradients are ubiquitous in nature and in technological applications such as coating, wetting, and cooling. The efficiency of these applications largely depends on the dynamics and stability of such liquid films. This is particularly true for coolants which are typically liquids comprising mixtures. While work has been done on stability of evaporating liquid films, focus has mainly been on those laden with surfactants (Hatziavramidis,1992; Danov et. al. 1998; Lin et al. 2000). Machrafi et al. (2010) performed linear stability analysis on a horizontal binary film using water/ethanol mixtures but with the evaporation of water being neglected. In this work, we consider competitive evaporation of components owing to the difference in volatilities. This is important as in most applications, like coating or cooling, the liquid comprises of several organic volatile components. Understanding their stability is key to help improve the efficiency of the application being considered.

PROBLEM FORMULATION

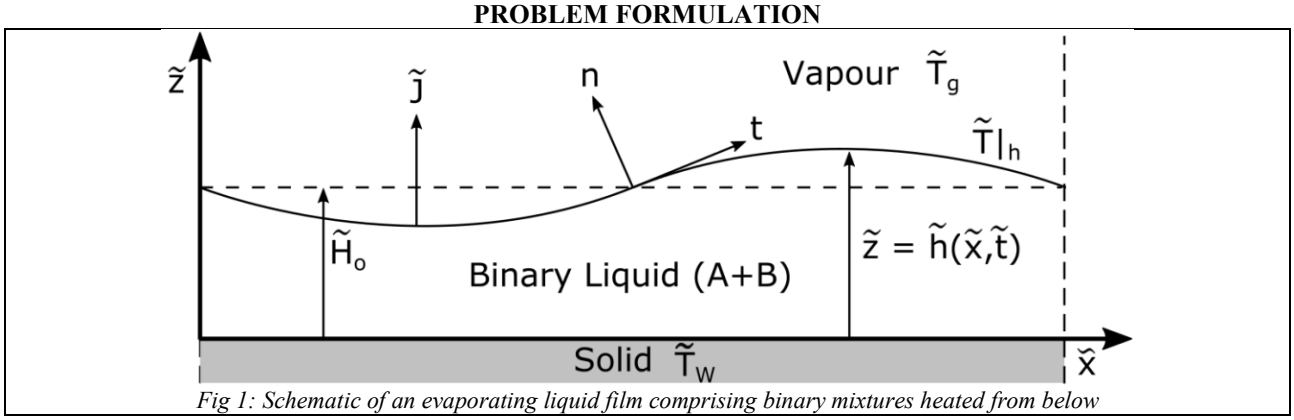

Fig 1: Schematic of an evaporating liquid film comprising binary mixtures heated from below

As shown in Fig 1, a thin liquid film comprising a mixture of volatile liquids A and B is heated from below. The volatilities of the components are dependent on their respective vapour pressures, with the component with highest vapour pressure exhibiting the highest volatility. The mixture is assumed to be ideal while the liquid layer is considered to be Newtonian, with density $\tilde{\rho}$, specific heat capacity $\tilde{c_p}$, thermal conductivity $\tilde{\lambda}$ and viscosity $\tilde{\mu}$, which depend on the local concentration of the two volatile components with the tildes standing for dimensional quantities. The surface tension $\tilde{\sigma}$, also depends on the local concentration as well as the local temperature $\tilde{T}$ given by Eq. (13). The liquid layer is on the top of a horizontal, uniformly heated solid substrate and is in contact with the gas phase with average bulk temperature $\tilde{T_g}$; the gas consists of the vapour of the binary mixture. Initially, the liquid layer has thickness $\tilde{H_o}$ and width $\tilde{L_o}$. Here, we consider a very thin liquid film, giving $\tilde{L_o} \gg \tilde{H_o}$ so that the ratio, $\epsilon = \frac{\tilde{H_o}}{\tilde{L_o}} \ll 1$. This assumption permits the use of lubrication theory. We use $\tilde{H_o}$, $\tilde{U_o} = \frac{\tilde{\nu_A}}{\tilde{H_o}}$ and $\Delta\tilde{T} = \tilde{T_w} - \tilde{T_g}$ as length, velocity and temperature scales. Next, with an assumption of density matched components, the following dimensionless governing equations are obtained.

$$u_x + w_z = 0 \tag{1}$$
$$u_t + uu_x + wu_z = -p_x + (\mu u_x)_x + (\mu u_z)_z \tag{2}$$
$$w_t + uw_x + ww_z = -p_z + (\mu w_x)_x + (\mu w_z)_z \tag{3}$$
$$Pr[(c_pT)_t + u(c_pT)_x + w(c_pT)_z] = (\lambda T_x)_x + (\lambda T_z)_z \tag{4}$$
$$c_t + uc_x + wc_z = Pe^{-1}(c_{xx} + c_{zz}) \tag{5}$$

Considering evaporation of both the components, the following boundary conditions are obtained:
At $z = h(x,t)$;

$$EJ = (-h_x(u-u_s)+w-w_s)(h_x^2+1)^{-\frac{1}{2}} \tag{6}$$

$$-\frac{E^2}{D}J^2 + p - \mathbf{n}\cdot\underline{\underline{\tau}}\cdot\mathbf{n} = p_v + \frac{\mathcal{A}}{h^3} - \left(\frac{\delta}{Ca} + \frac{M_c c}{Pr} - \frac{M_T}{Pr}(\gamma_r + (1-\gamma_r)c)T\right)\frac{h_{xx}}{(h_x^2+1)^{\frac{3}{2}}} \tag{7}$$

$$\mathbf{n}\cdot\underline{\underline{\tau}}\cdot\mathbf{t} = Ca^{-1}(h_x^2+1)^{\frac{1}{2}}(\sigma_x + h_x\sigma_z) \tag{8}$$

$$J_A + \Lambda J_B + \frac{E^2}{2\mathcal{L}D^2}J^3 + \lambda(-h_x T_x + T_z)(h_x+1)^{-\frac{1}{2}} = 0 \tag{9}$$

$$\frac{1}{Pe}\left[\frac{-h_x c_x + c_z}{(h_x^2+1)^{\frac{1}{2}}}\right]_{z=h} = E(cJ - J_A) \tag{10}$$

$$EJ = (w - h_t - uh_x)(h_x^2+1)^{-\frac{1}{2}} \tag{11}$$

$$KJ_A = cT;\quad KJ_B = (1-c)\alpha\beta^{\frac{3}{2}}\Lambda T \tag{12}$$

$$\sigma = c + (1-c)\delta - \Gamma(c + (1-c)\gamma_r)T|_h \tag{13}$$

$$\text{At } z = 0;\ u = w = 0 \text{ and } T = 1 \tag{14}$$

SOLUTION METHODOLOGY

Using long-wave approximations, Eqs (1)-(14) are reduced to evolution equations in interfacial height $H(t)$ and interfacial concentrations $C(t)$. This is then subject to a frozen base state approximation to perform a quasi-steady linear stability analysis. We then undertake transient simulations to understand the non-linear behaviour.

RESULTS

Considering standard ethanol-water solutions and a very thin liquid film (1 micron), we study evolution of the interface height and concentration. With an assumption of slow phase-change, we can consider that the rate of growth of the ensuing soluto-capillary instabilities is faster than the rate of evaporation. Our stability analysis shows that the evaporating film can demonstrate two unique modes of instability: monotonic mode when the most volatile component also has the highest surface tension or an oscillatory mode when the most volatile component has the lowest surface tension. Figure 2 demonstrates the parameter regime (ratio of solutal to thermal Marangoni numbers against relative volatility) where such modes can occur. Further investigation using transient simulations show the late-time behaviour of the film – revealing the nature of pattern formation as these components evaporate.

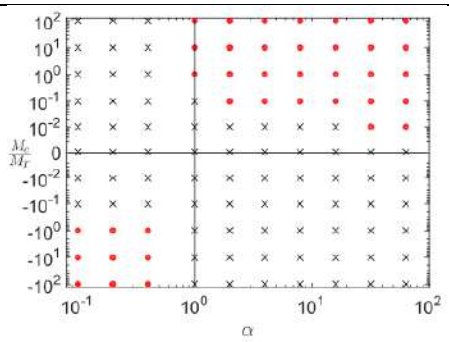

Figure 2: Map showing regions of monotonic instability mode (crosses) and oscillatory instability mode (squares) at $E = 10^{-4}$

CONCLUSIONS

The stability of the evaporation of an horizontal thin liquid layer which consist of a binary mixture of volatile liquids heated from below has been investigated by means of linear stability analysis and transient simulations. Two distinct modes of instabilities, identified from quasi-steady linear stability analysis, are further investigated via transient simulations to understand late-time and non-linear behaviour.

References

[1] D. Hatziavramidis, International Journal of Multiphase Flow 18, 517 (1992).
[2] K. D. Danov, N. Alleborn, H. Raszillier, and F. Durst, Physics of Fluids 10, 131 (1998).
[3] C.-K. Lin, C.-C. Hwang, and W.-Y. Uen, Journal of Colloid and Interface Science 231, 379 (2000).
[4] H. Machrafi, A. Rednikov, P. Colinet, and P. Dauby, Journal of Colloid and Interface Science 349, 331 (2010).

BEDROCK RECONSTRUCTION FROM FREE SURFACE DATA FOR UNIDIRECTIONAL GLACIER FLOW WITH BASAL SLIP

Elizabeth K. McGeorge[1], Mathieu Sellier[*2], Miguel Moyers-Gonzalez[1], and Phillip L. Wilson[1]
[1]School of Mathematics and Statistics, University of Canterbury, Christchurch, New Zealand
[2]Department of Mechanical Engineering, University of Canterbury, Christchurch, New Zealand

Summary In order estimate the volume of ice in a glacier, it is necessary to have a reliable map of its ice thickness distribution. A range of numerical techniques have been developed recently to infer the bedrock location from free surface observations and therefore deduce the glacier thickness. These techniques usually have to make assumptions about the nature of the slip at the base of the glacier. In this contribution, we show that, within the limits of the Shallow Ice Approximation, it is theoretically possible to simultaneously infer the glacier thickness and the basal slip coefficient from the knowledge of the glacier surface altitude and its free surface velocity. Results suggest that the problem of identifying the slip coefficient and the glacier thickness is not an equifinal inverse problem.

INTRODUCTION

The evolution of glaciers and ice bodies have long been known to be a good indicator of climate change. Consequently, much work has been dedicated to predicting their dynamics through mathematical modelling and numerical simulations. Such models require boundary conditions such as bedrock location (DEM) or ice flux at the domain boundaries which are usually unknown a priori. In parallel, the increasing availability of airborne data (satellite, aircraft, or UAVs) providing information about the ice surface altitude or free surface velocity have opened up the prospect of indirectly inferring difficult to measure fields such as the ice thickness from observed free surface observations. A range of numerical methods have been developed in the recent past to solve such inverse problems, see [1,2] and references therein for example, enabling for example the unveiling of the portrait of the contours of the land beneath Antarctica's ice sheet [3]. Such methods often make assumptions about the nature of basal conditions. We show in this contribution, that, within the limits of the Shallow Ice Approximation, it is theoretically possible to simultaneously infer the glacier thickness and the basal slip coefficient from the knowledge of the glacier surface altitude and its free surface velocity.

MATHEMATICAL MODEL

We assume here that the glacier dynamics is well described by the Shallow Ice Approximation [4] and that the flow is unidirectional with x the horizontal direction. Conservation of mass and momentum applied to the glacier requires that

$$\frac{\partial H}{\partial t} = a + \frac{2}{5}(\rho g)^3 \frac{\partial}{\partial x}\left(D \frac{\partial S}{\partial x}\right) \tag{1}$$

where H is the ice thickness, a represents the surface mass balance which is assumed to be known, S is the free surface altitude, ρ the ice density, and g the acceleration of gravity. The diffusion coefficient D is given by

$$S = \left|\frac{\partial S}{\partial x}\right|^2 H^4 \left[AH + \frac{5}{2}\beta A_s\right] \tag{2}$$

In this expression A is Glen law parameter (4.16×10^{-17} $Pa^{-3}yr^{-1}$), A_s the sliding coefficient (5×10^{-14} $m^8N^{-3}yr^{-1}$), and $\beta(x)$ acts as a dimmer switch for the amount of basal slip at the glacier base. Along the length of the glacier $\beta(x) \in [0,1]$. Physically, $\beta(x) = 0$ represents a sticky base and $\beta(x) = 1$ a friction-less base. It is not required for $\beta(x)$ to be constant along the glacier length. This dimmer switch is referred to as the basal slip distribution. Within the assumption of the Shallow Ice Approximation, we find that

$$u_s = -(\rho g)^3 \left(\frac{\partial S}{\partial x}\right)^3 H^3 \left[\frac{1}{2}AH + \beta A_s\right] \tag{3}$$

The free surface altitude S and ice thickness H are related through $S = z_b + H$ where z_b is the bedrock altitude. The governing equations are solved using a simple 1st order explicit, second order accurate in space finite difference scheme.

INVERSE METHODOLOGY

Given two observable variables, u_s and S, it is possible to recover two exact algebraic expressions which allow the direct reconstruction of the unknown variables, $H(x)$ and $\beta(x)$. The first one is obtained by integrating in space eq. (1) assuming a steady-state. This results in

$$0 = \int_0^x a dx - \frac{1}{10}(\rho g)^3 MAH^5 - u_s H + C_0 \tag{4}$$

*Corresponding author. E-mail: mathieu.sellier@canterbury.ac.nz.

where $M = \left(\frac{\partial s}{\partial x}\right)^3$ is known for a given ice surface altitude and C_0 a constant of integration. Eq. (4) combined with a rearranged eq. (3) provide the required two equations which allow the reconstruction of $H(x)$ and $\beta(x)$. A simple Newton's method was implemented to solve the non-linear system of equations.
In order to test the methodology a twin experiment was performed whereby an artificial data set was created by running the model to a steady state for a given distribution of β and z_b. The resulting distribution of ice surface altitude and free surface velocity was then use as the observable data for the inverse problem. An example of the results obtained is illustrated in Figure 1.

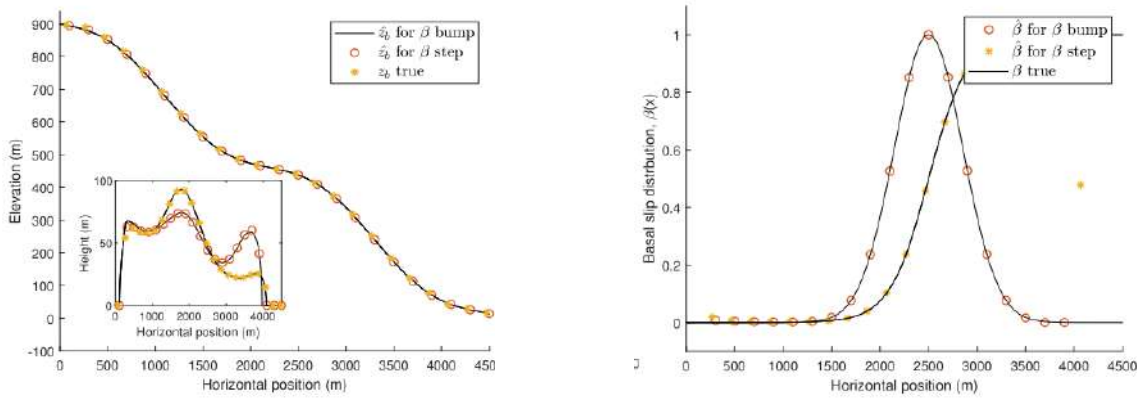

Figure 1: Reconstructed bedrock location (left-hand figure) and reconstructed basal slip distribution. The black lines indicate the true distributions and the symbols the reconstructed ones. Two types of basal slip distribution were tested: a "bump" and a step.

Results confirm the validity of the reconstruction algorithm as the reconstructed fields are indistinguishable from the real ones. Tests with noisy input data confirm that the reconstruction algorithm is also robust to the addition of noise.

CONCLUSIONS

This contribution shows that it is possible to simultaneously reconstruct the bedrock location and basal slip coefficient from observed free surface altitude and velocity. This result suggests that the identification problem is well-posed, i.e. a unique combination of basal slip coefficient and bedrock profiles leads to a unique free surface signature. While the current contribution is limited to uni-directional flow, we believe that it can be extended to three-dimensional flow following a method analogous to [5].

References

[1] Martin, N. and Monnier, J. Inverse rheometry and basal properties inference for pseudoplastic geophysical flows. *European Journal of Mechanics-B/Fluids* **50**: 110-126, 2015.
[2] Gessese, A., C. Heining, M. Sellier, R. Mc Nish, and W. Rack. Direct reconstruction of glacier bedrock from known free surface data using the one-dimensional shallow ice approximation. *Geomorphology* **228**: 356-371, 2015.
[3] Morlighem, M., Rignot, E., Binder, T., Blankenship, D., Drews, R., Eagles, G., Eisen, O., Ferraccioli, F., Forsberg, R., Fretwell, P. and Goel, V. Deep glacial troughs and stabilizing ridges unveiled beneath the margins of the Antarctic ice sheet. *Nature Geoscience*, pp.1-6, 2019
[4] Fowler, A. C. Sliding with cavity formation. *Journal of Glaciology* **33, no. 115**: 255-267, 1987.
[5] Heining, C., and M. Sellier. Direct reconstruction of three-dimensional glacier bedrock and surface elevation from free surface velocity. *AIMS Geosci* **2**: 45-63, 2016.

A SIMULATION OF THIN LIQUID FILM FORMING WITH SURFACTANTS BY FULLY EXPLICIT GAS-LIQUID TWO-PHSE FLOW SOLVER WITH INTERFACE-ADAPTED AMR METHOD

Shintaro Matsushita[1] and Takayuki Aoki [2]
[1]Department of Mechanical Engineering, Tokyo Institute of Technology, Meguro, Japan
[2]Global Scientific Information and Computing Center, Tokyo Institute of Technology, Meguro, Japan

Summary A weakly compressible scheme for solving low-Mach number gas-liquid two-phase flows with interface-adapted AMR (Adaptive Mesh Refinement) method is proposed to achieve high-resolution simulation by avoiding solving pressure Poisson equation. A fully explicit time integration is developed by solving independent hyperbolic pressure evolution equation. We have developed a GPU code of the tree-based AMR method, which can greatly reduce the computational cost to assign high-resolution mesh to the region of moving interfaces. The accuracy of our solver is examined by solving a lot of benchmark problems. To reproduce the stable liquid film on liquid surface in gravity, the Marangoni-effect is introduced by considering the transportation equations of bulk/surface surfactant concentrations with adsorption/desorption effects.

INTRODUCTION

In the numerical studies on gas-liquid two-phase flows, high-resolution meshes are required to describe the gas-liquid interfaces in diffuse interface models. In most cases, mesh convergence has not been achieved yet, however, the simulated results of two-phase flows strongly depend on mesh resolution especially for violent flows. Our target is incompressible flows, which have been widely solved by semi-implicit time integrators to keep a large time step without restricted by the speed of sound. The Poisson equation has to be solved by sparse matrix solver to maintain the divergence-free condition. The iteration convergence becomes poor as the matrix size increases, especially for gas-liquid two-phase flows even if we use preconditioned BiGCSTAB method[1]. Therefore, solving the Poisson equation for a large-scale two-phase flow simulation is a challenging problem. We have developed a fully explicit scheme for solving low Mach number two-phase flows with diffuse-interface model to avoid solving Poisson equation based on characteristic theory[2]. To increase the accuracy of the interface behaviour by applying density-weighted advection evaluation[3], we have changed the numerical methods to solve Compressible Navier-Stokes equations to the independent hyperbolic pressure evolution equation derived from isothermal equation of state. The time step is restricted by the sound speed and we reduce it within the range where the weak compressibility is negligibly small and is acceptable for describing incompressible flows.

The tree-based AMR method can greatly reduce the number of computational costs by assigning high-resolution mesh to the region around the moving interface. To realize the two-phase flow simulations using higher-resolution mesh, the GPU-code have been developed in CUDA language and successfully combined with the weakly compressible scheme. The surfactants transportation equations with adsorption/desorption effects are introduced to consider Marangoni-effect. Our solver has succeeded to simulate the process of forming thin liquid film onto the liquid surface using real physical parameters while having robustness that allows for arbitrary deformation of interfaces.

NUMERICAL METHODS

Compressible Navier-Stokes equations under the isothermal equation of state and low-Mach number conditions are solved on staggered grid system. The density-weighted advection evaluation[3] is applied to advection scheme and 3rd order TVD-Runge-Kutta scheme is used for time integration. We solve conservative Allen-Cahn equation by using finite volume method to maintain mass conservation since the density and viscosity are computed by phase-field variables.

The tree-based AMR method is employed for easy handling of frequent refinement and coarsening since adaptations of mesh is applied to the moving interfaces. The extra reserved memory pool data structure are used to reduce the frequency of allocation/deallocation of the global memory on GPU[4].

RESULTS AND DISCUSSIONS

The accuracy of our solver has been examined by carrying out a lot of benchmark problems of two-phase flows. The applicability of violent two-phase flows is examined by simulating the liquid jet break up problem shown Fig.1. It takes about 11 hours by our solver on single Tesla V100 GPU, while it takes about 350 hours (estimated) using 5760 cores of CPU by incompressible solver on uniform mesh in reference[5]. Fig.2 shows the simulation results of soap bubble forming process using 20% glycerine solution and air properties and the equivalent diameter of soap bubble surrounded by very thin liquid film expands to 7.8 times larger at $t = 5.0\,\mathrm{s}$ compared to initial. The stable thin liquid film onto the liquid

surface, which we can often see in daily life, is reproduced in 2D computational domain by introducing the transportation equations of surfactants and the Marangoni-effect using Triton-X100 solution and air properties (Fig.3).

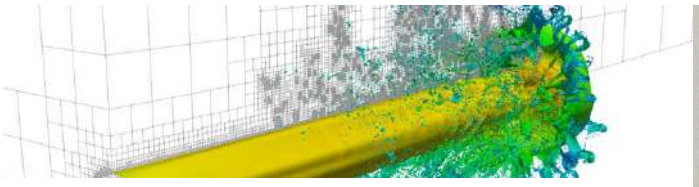

$t^* = 13.6$

Figure 1. The gas-liquid interface of liquid jet breakup problem with 7-level AMR method. The finest width of mesh equals to $\Delta x = D/256$ and the dimensionless time $t^* = Ut/D$, where $U = 100\ \mathrm{m/s}$ is the inlet velocity.

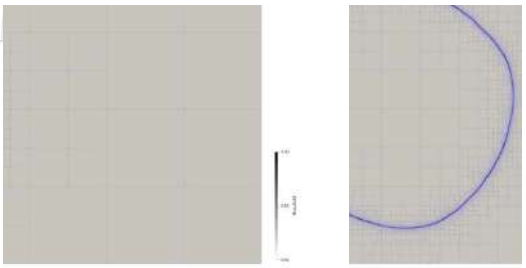

$t = 0.0\ \mathrm{s}$ $t = 5.0\ \mathrm{s}$

Figure 2. The phase-field profile with blue leaf lines for the simulation of forming soap bubble problem. Each leaf has 4^2 meshes and the finest mesh equals to $\Delta x = D/819$, where D is the initial diameter of bubble.

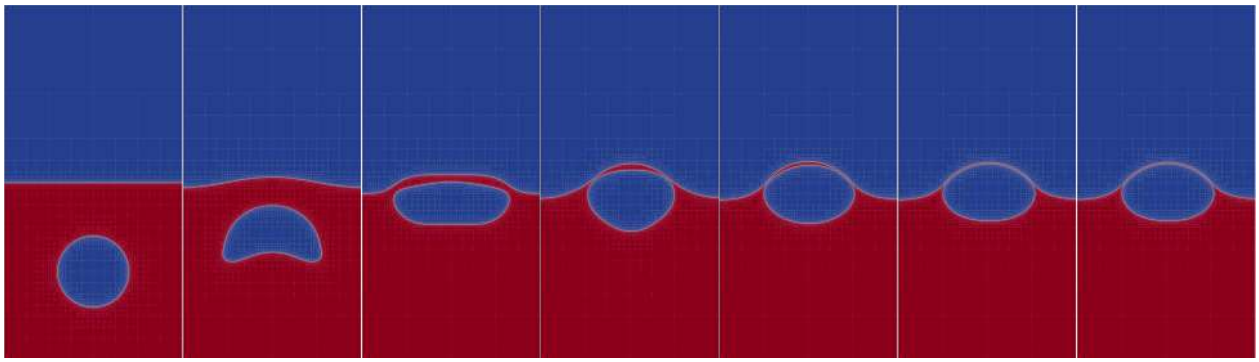

$t = 0.0\ \mathrm{s}$ $t = 0.03\ \mathrm{s}$ $t = 0.06\ \mathrm{s}$ $t = 0.12\ \mathrm{s}$ $t = 0.20\ \mathrm{s}$ $t = 1.0\ \mathrm{s}$ $t = 2.0\ \mathrm{s}$

Figure 3. The phase-field profile with while leaf lines for the simulation of stable thin liquid film onto the liquid surface with surfactant effect. Each leaf has 42 meshes and the finest mesh equals to $\Delta x = D/341$, where D is the initial diameter of bubble.

CONCLUSIONS

We have successfully developed a weakly compressible fully explicit solver for low Mach number gas-liquid two-phase flows combined with tree-based AMR method. Our solver has enough to solve incompressible two-phase flows since the results of benchmarks are in good agreements even if AMR method is applied. Thanks to the efficient GPU-implementation of AMR method and fully explicit scheme, the simulation of liquid jet breakup problem is performed in much shorter time than that of reference's incompressible solver on uniform mesh. In the 2D simulation of forming thin liquid film of soap bubble under the non-gravity, 7.8 times expanding is reproduced by our techniques. The stable liquid film forming onto the liquid surface under the gravity is also achieved by introducing surfactants and Marangoni-effect. By this study, the efficient high-resolution two-phase flow simulation can be achieved and the numerical simulation of forming of thin liquid film can be possible to consider the surfactant effect while keeping numerical stability for violent flows and robustness that allows for arbitrary deformation of interfaces.

Acknowledgements

This research was partly supported by KAKENHI, Grant-in-Aid for Scientific Research (S) 26220002 and 19H05613 from Japan Society for the Promotion Science (JSPS), and "Joint Usage/Research Center for Interdisciplinary Large-scale Information Infrastructures (JHPCN)" jh180035, jh190054 and "High Performance Computing Infrastructure (HPCI)" hp190130 in Japan. The authors thank the Global Scientific Information and Computing Center, Tokyo Institute of Technology for use of the computer resources of the TSUBAME 3.0 supercomputer and Kyushu University for use of the computer resources of the ITO supercomputer.

References

[1] Onodera N., Aoki T. Large-scale simulation of gas-liquid-solid multiphase flow on GPU cluster, *Japanese J. of Multiphase flow* **27 (5)**: 607-613. 2014.
[2] Matsushita S., Aoki T. A weakly compressible scheme with a diffuse-interface method for low Mach number two-phase flows, *J. Comput. Phys*. **376**: 838- 862. 2019
[3] Tan N. Numerical simulation of two-phase ow driven by a rotating object with an interface capturing method, *Ph.D. thesis*, TITECH, 2012.
[4] Matsushita S., Aoki T. A gas-liquid two-phase flow simulation with interface-adapted AMR method, *Japanese J. of Multiphase flow* **33 (1)** : 96-102. 2019.

THIN FILM FLOWS WITH WAVY WALL SHAPE: AN ASYMPTOTIC ANALYSIS

Corinne Rouby*[1], Kim Pham[1], Rogers Cordova[1], and Agnès Maurel[2]
[1]IMSIA, ENSTA Paris, Institut Polytechnique de Paris, 828, boulevard des Maréchaux-91120-Palaiseau
[2]Institut Langevin, CNRS, ESPCI Paris Tech, 1 rue Jussieu, 75005 Paris, France

Summary We extend the lubrication approximation to a fluid flowing in channels with arbitrary shape functions and moderate aspect ratio. The higher-order model is obtained following an asymptotic analysis resulting in closed forms of velocity and pressure involving the derivatives of the shape functions of the walls up to the second-order. Comparisons with full-scale simulations are given and show good agreement as well as improvements from the classical standard lubrication approximation. Extension of this model to more complex channels involving strong curvature such with high angle elbows will be proposed.

The *Classical Lubrication Approximation* (CLA) accounts for the behavior of viscous flows in thin channels under assumptions of small Reynolds numbers and slowly varying walls. Under these hypotheses, the flow is characterized by (i) a constant pressure across the transverse, say vertical, section and with variations along the channel axis governed by the Reynolds equation [1], (ii) a vanishing vertical velocity and a horizontal one of the Poiseuille's type. The CLA, as it avoids to resolve a full-scale fluid calculation, is used in many fields such as film lubricant, hydraulic fracture mechanics or flows in biological systems such as blood cell transport in narrow capillaries. However, its validity as that of the associated Reynolds equation have to be questioned when the curvature of the channel is not negligible anymore. This is the case for wavy walls or high angle elbows in even more compelling situations. A systematic way to derive such approximation is to use asymptotic techniques which are well-adapted due to the small thickness of the channel compared its length. Starting in the 80s, such *Extended Lubrication Approximation* (ELA) has been applied to channels with a single wavy wall [2] and with two symmetric wavy walls [3]. Recently, Tavakol and co-workers have revisited the problem of a single wavy wall using a slightly different approach in which the asymptotic analysis is applied to the Stokes equations [4]. Experimental and numerical results support their analytical result and exemplify the interest of the improved model to capture accurately the velocity profiles and the pressure drop. Our study follows from this work and extends the lubrication approximation to two non-symmetric wavy walls [5].

EXTENDED LUBRIFICATION APPROXIMATION

We consider an incompressible, steady, two-dimensional pressure-driven flow in a channel of length L. The geometry is defined through the introduction of the upper shape function $y = h_+(x)$ and the lower shape function $y = h_-(x)$ for $x \in (0, L)$ with $h_+ > h_-$ (see Fig. 1). These functions are assumed to be at least C^2 continuous. We introduce the mean line level $y_m(x) = \frac{h_+(x)+h_-(x)}{2}$, the local half-thickness $h(x) = \frac{h_+(x)-h_-(x)}{2}$ of the channel as well as the rescaled vertical coordinate defined by $\mathrm{y} = \frac{y-y_m(x)}{h(x)}$. x .

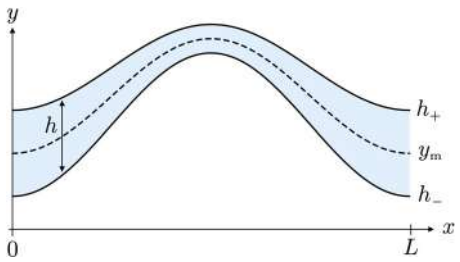

Figure 1: Schematic view of a channel of length L with arbitrary upper and lower shape profiles $h_+(x)$ and $h_-(x)$. The functions $h(x)$ and $y_m(x)$ denote the half-distance between the walls and the average level respectively.

The Reynolds number is assumed to be small so that the flow is governed by the Stokes equations $\nabla \cdot \mathbf{u} = 0$ and $\mu \nabla^2 \mathbf{u} = \nabla p$, where $\mathbf{u} = u\mathbf{e}_x + v\mathbf{e}_y$ and p are the velocity and the pressure fields respectively, and μ is the viscosity of the fluid. Additionally to a no-slip condition on the walls $\mathbf{u}(x, h_+(x)) = \mathbf{u}(x, h_-(x)) = \mathbf{0}$, the boundary conditions are defined as prescribed a Poiseuille inlet velocity profile $\mathbf{u}(0, y) = \frac{3\Phi}{4h(0)} \left(1 - \mathrm{y}^2\right) \mathbf{e}_x$ (Φ being the fluid flux) and a vanishing outlet pressure $p(L, y) = 0$. The lubrification model is obtained by conducting an asymptotic analysis based on

*Corresponding author. E-mail: corinne.rouby@ensta-paris.fr

the introduction of the small parameter $\varepsilon = \frac{h(0)}{L} \ll 1$, which accounts for the slenderness ratio of the channel. The main result of our study is the following approximation of the exact solution up to the second order in the small parameter ε :

$$u(x,y) \simeq \frac{3\Phi}{4h}\left(1-\mathrm{y}^2\right)\left(1+\frac{4h'^2-hh''}{10}\left(1-5\mathrm{y}^2\right)+\frac{2hy_{\mathrm{m}}''-12h'y_{\mathrm{m}}'}{3}\,\mathrm{y}\right), \tag{1}$$

$$v(x,y) \simeq \frac{3\Phi}{4h}\left(1-\mathrm{y}^2\right)\left(h'\mathrm{y}+y_{\mathrm{m}}'\right), \tag{2}$$

$$p(x,y) \simeq \mu\Phi\int_x^L \frac{3}{2h^3}\left(1+\frac{2}{5}\left(h'^2+hh''+5y_{\mathrm{m}}'^2\right)\right)\mathrm{d}x' + \frac{3\mu\Phi}{4h^2}\left(h'(1-3\mathrm{y}^2)-2y_{\mathrm{m}}'\mathrm{y}\right), \tag{3}$$

see [5]. The classical lubrication approximation is obtained from Eqs. (1)-(3) by simply putting the derivative of y_{m} and h to zero. Hence, in the standard case, the velocities and the pressure depend only on the (half) relative distance h between the walls. Note that the prescribed parabolic inlet velocity profile is matched only on *average* by the second-order approximation.

VALIDATION OF THE MODEL TOWARDS DIRECT NUMERICAL SIMULATIONS

To inspect the accuracy of the ELA model specified by Eqs. (1)-(3), we consider a channel profile where both y_{m} and h vary, see Figure 1. The direct problem is solved with COMSOL MultiPhysics. We report in Figure 2 the fields of the velocity components (u, v) and of the pressure p computed numerically from the direct problem and the corresponding fields predicted by the CLA and ELA (note for the CLA, the vertical velocity is negligible).

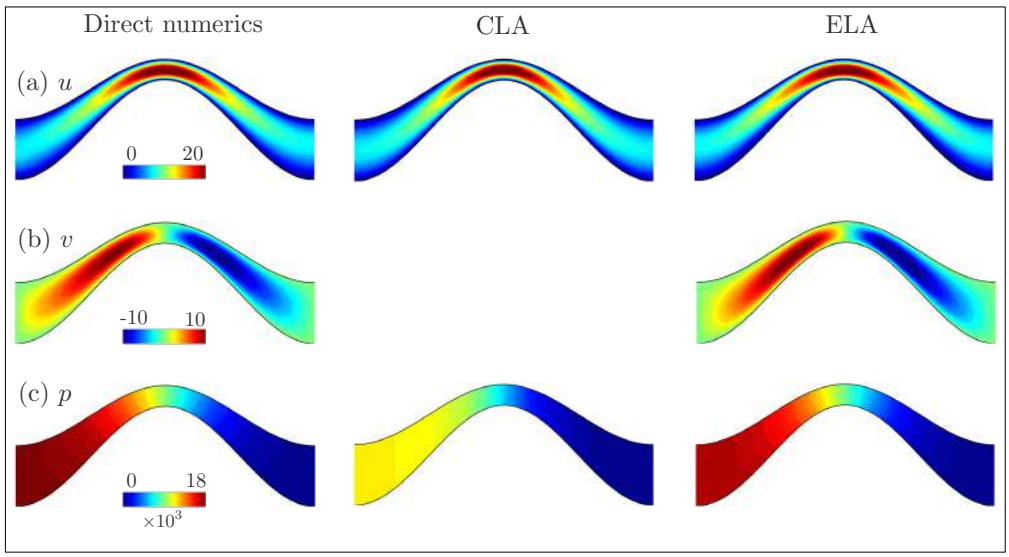

Figure 2: Results for the profile (P1). Fields of the velocity components (u, v) and of the pressure p in full scale simulations, CLA and ELA (note in the CLA theory, the vertical velocity is negligible and thus is not plotted).

It is noticeable that CLA and ELA have the same good accuracy to capture the right variations on the horizontal velocity u since the correction of ELA appears at the second order. On the other hand, the effect on the vertical velocity v is much more significative and again this is expected since the correction appears at the first order. As for the pressure, which is of particular interest since the pressure drop due to expansions/constrictions are important in many practical situations, the gain in the ELA is significant with an error between the prediction and the direct numerics of about 5% for ELA and of about 40% for CLA. Expectedly, ELA offers the most significant improvement with respect to CLA when the channels contain constrictions with large variations of the centerline. This results in high vertical velocities and pressure drops widely underestimated by CLA and accurately reproduced by ELA. The current work aims to be generalized by investigating more complex situations including walls with high angle elbows as well as flows with moderate (yet non-negligible) Reynolds number.

References

[1] Reynolds O. *Philos. Trans. R. Soc.* 177 (1886) 157–234.
[2] Hasegawa E., Izuchi H. *Bulletin of JSME.* 26 (1983) 514–520.
[3] Van Dyke M. *Advances in applied mechanics* 25 (1987) 1.
[4] Tavakol B., Froehlicher G., Holmes D. P., Stone H. A., *Proc. R. Soc. A* 473 (2017) 20170234.
[5] Cordova R., Pham K., Rouby C. *CR Mécanique* 347(5), 389-396.

INFLUENCE OF CORRUGATION ON SURFACE WETTABILITY

Dariusz Asendrych[1]
Institute of Thermal Machinery, Częstochowa University of Technology, Częstochowa, Poland

Summary The paper presents the results of numerical simulation of the liquid flow at the inclined surfaces. The aim of the research was to analyse the influence of surface texture and Reynolds number on the wetting efficiency. The simulations allowed to recover the morphological flow structure being dependent on the inertial and the surface tension forces. Surface corrugation turned out to modify the flow pattern and in turn to influence wetting efficiency. As the result the increased interfacial area enhances the mass, heat and momentum transfer processes in 2-phase flow systems commonly encountered in various industrial applications.

INTRODUCTION

Two-phase gas-liquid flows are commonly encountered in industry. The processes they are involved in are mostly operated in packed bed columns providing large contact area between phases and thus ensuring enhanced mass, momentum and heat transfers. Various designs of structured packings have been offered in recent years (see e.g. [1,3]) allowing to improve hydrodynamic characteristics to better control pressure drop or liquid holdup. However, deeper understanding of gas-liquid-solid interactions is still required to further optimise packing designs. This goal can be achieved with the help of Computational Fluid Dynamics (CFD) allowing to perform parametric studies and to test various parameters. Due to geometrical complexity of packings available commercially most of works deal with simplified cases considering flat [5] or corrugated surfaces [2,3]. Such an approach allows to separate various influences and to formulate optimisation guidelines. One of the key feature of the packing is to ensure high surface wettability and to increase the residence time of liquid within it. This can be improved by surface texture. As shown in [2] the portion of wetted surface can be enlarged by several per cent when compared to the flat one. In contradiction Isoz [3] showed the reduction of wetting efficiency at textured surfaces. Such a lack of consistency seems to convince that further research efforts are needed.

NUMERICAL MODEL

The paper presents the numerical analysis of a flow structure and a surface wettability on flat and corrugated surfaces. The flow was modelled using a classical system of equations including mass and momentum conservation laws. A 3D Eulerian unsteady model combined with Volume of Fluid (VOF) method was developed allowing for reconstruction of a gas-liquid interface [4]. Surface tension was included in the momentum equation as a source term. Water and air at ambient conditions were used as working fluids.

The simulations were conducted for flat and corrugated surfaces inclined to the horizontal direction by the angle of 60°. Plate size (length - 60mm, width - 50mm) were chosen for consistency with literature (e.g. [1,5]). Computational domain took a form of a cuboid with height equal to 10mm. Surface texture had a shape of triangular waviness with a scale 2.8mm and a height varied in the range 0.3-0.9mm. The inflow was simulated with the velocity inlet boundary condition. Liquid entered a domain as a liquid film with prescribed thickness and parabolic velocity profile. At plate the non-slip boundary condition was applied with contact angle 70° characterising a water-steel system. Side boundaries were treated as walls with the slip boundary condition. Pressure outlet was applied at the bottom boundary. Numerical grid, consisting of 1.13 million cells, was selected as a result of relevant tests with various meshes. Time step of 25μs was used for all the cases under consideration.

RESULTS AND DISCUSSION

A series of CFD simulations was conducted for inclined flat and corrugated surfaces for varying Reynolds number and corrugation heights. At first the simulations were performed for flat surface allowing for model verification with literature CFD and experimental data [1,5]. Flow evolution upon Reynolds number (from droplet-like flow through the system of rivulets, up to film flow [4]) was found to be fully consistent with reference results and thus proving model relevance. The simulations for corrugated surfaces showed a qualitative and quantitative modifications of the flow structure. A sample results obtained for Reynolds number 50 are shown in Fig. 1. As can be seen for the flat surface (Fig. 1, left) liquid entering a plate forms a number of small rivulets which are broken into droplets. Surface texture increases resistance to the flow and the rivulets keep higher integrity what prevents them from break up process (see Fig. 1, right). As a result portion of wetted surface slightly increases improving surface wettability. Moreover, detailed analysis of the velocity field showed that for textured plate liquid phase "needs" more time to reach the bottom edge, thus increasing residence time in control volume.

[1] Corresponding author. E-mail: darek@imc.pcz.czest.pl.

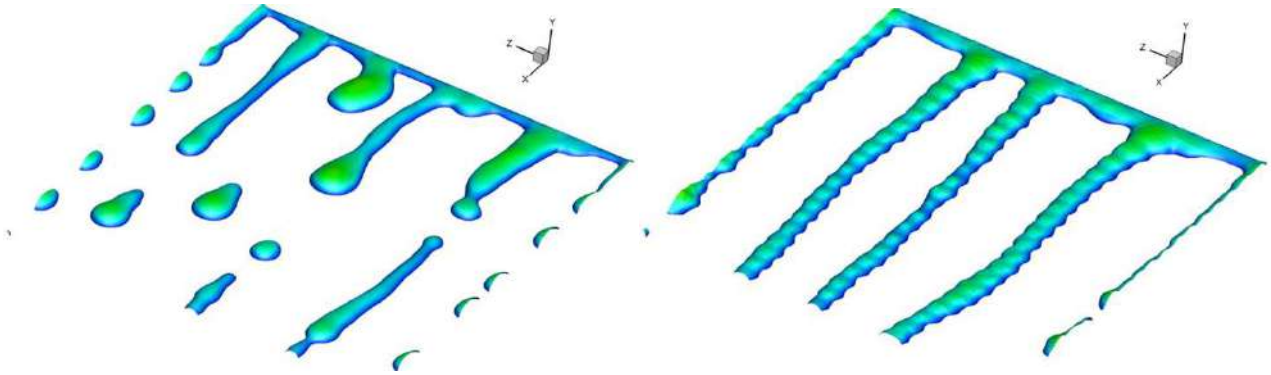

Figure 1. The flow structure on flat (left) and corrugated (right) surface for Re = 50. Surface corrugation - 0.3mm.

Parametric simulations allowed to test the influence the corrugation height can have on a flow structure and surface wettability. As can be seen from data collected in Fig. 2 wetting efficiency increases with Reynolds number reaching 100% at appr. Re=200 for flat surface. Modified flow structure for textured surfaces leads to increase of wetted area, which is hardly visible for corrugation height h=0.3mm while noticeable for h=0.6mm. It shows that corrugation promotes wetting efficiency by additional drag acting against gravity and leading to local liquid accumulations.

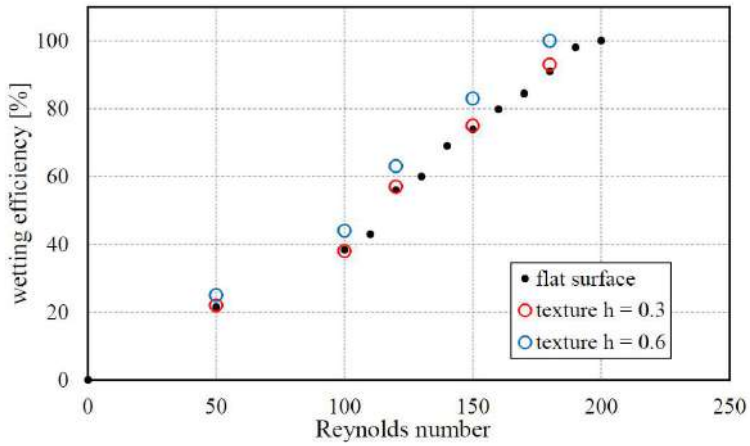

Figure 2. Influence of Reynolds number on wetting efficiency for varying surface texture height.

CONCLUSIONS

The CFD simulations presented in the paper seem to convince that surface corrugation can improve hydrodynamic characteristics of packed beds. However, corrugation shape (wavelength, height, symmetrical/asymmetrical) can still be optimized to further increase wetting ability as well as liquid holdup and its residence time. These parameters are of special importance in separation, distillation or absorption processes taking place in packed bed columns.

Acknowledgements

The present research work was funded by the National Science Centre under the grant UMO-2014/15/B/ST8/04762. The PL-Grid Infrastructure is gratefully acknowledged for providing its computational resources.

References

[1] Haroun Y., Raynal L., Alix P. Prediction of effective area and liquid hold-up in structured packings by CFD. *Chemical Engineering Research and Design* **92:** 2247-2254, 2014.

[2] Iso Y., Huanga J., Katoa M., Matsunoa S., Takano K. Numerical & experimental study on liquid film flows on packing elements in absorbers for PC CO2 capture. *Energy Procedia* **37:** 860-868, 2013.

[3] Isoz M. CFD Analysis of Gas Flow Through Corrugated Sheet Structured Packing. *Proc. 11th OpenFOAM Workshop (Guimarães)*, ed J.M. Nobrega and H. Jasak, Springer Nature, 2018.

[4] Asendrych D. Impact of the Initial Conditions on the Wetting Efficiency on the Flat Inclined Surface. *Technische Mechanik* **39**: 1, 137-147, 2019

[5] Xu Y., Zhao M., Paschke S., Wozny G. Detailed Investigations of Countercurrent Multiphase Flow by 3D CFD. *Ind. Eng. Chem. Res.* **53:** 7797-7809, 2014.

ABSORPTION, FILM FORMING AND RUNOFF DUE TO WIND-DRIVEN RAIN

Aytaç Kubilay*[1], Dominique Derome[2], and Jan Carmeliet [3]
[1]Laboratory of Multiscale Studies in Building Physics, Empa, Switzerland
[2]Department of Civil and Building Engineering, Université de Sherbrooke, Canada
[3]Chair of Building Physics, Department of Mechanical and Process Engineering, ETH Zurich,Switzerland

Summary There is a need for experimental data, specially for model development and validation, of wind-driven rain (WDR) absorption in porous building materials and rainwater runoff. The present study reports field measurements of WDR that are conducted with high spatial and temporal resolution in a test setup consisting of two parallel building models. Porous building materials with varying pore size distributions, water absorption characteristics and thickness are installed and monitored during rain events with different characteristics.

INTRODUCTION

Wind-driven rain (WDR), referring to the droplets carried by the wind and impinged on the building facades, influences the hygrothermal performance and the durability of building facades significantly. Therefore, WDR intensity is used as a main boundary condition in studies for moisture transport in building envelopes. With more extreme rain events expected due to climate change, building damage risks could increase in the coming decades, reinforcing the need for accurate information on the spatial and temporal distribution of WDR.

Distribution of WDR reaching urban surfaces can be quantified by numerically solving for the wind flow around buildings and the trajectories of rain droplets [1]. Once rain droplets impinge on the surface, WDR leads to complex phenomena that involve spreading, splashing, rolling or bouncing, coalescence of droplets, hemiwicking on the surface, absorption in a porous medium, evaporation, film forming and runoff under gravity. While absorption and moisture distribution of WDR have been investigated in the past, few studies have considered film forming and runoff, especially on building materials [2]. Limited quantitative rain runoff data from experiments or numerical modeling are currently available [3]. Development and validation of such numerical models require complete measurement datasets to provide representative validation data for numerical simulations.

This study aims to quantify the moisture content absorbed by the porous building materials and the occurrence of runoff by field measurements. Measurements are performed at a test site at Empa, Dübendorf, Switzerland and compared with one-dimensional numerical results.

METHODOLOGY

Field measurements

The field measurements are performed between April-November 2019 on a setup consisting of two parallel building models as shown in Fig. 1. The building models are formed using cubic structures, each with dimensions of H×H×H = 2×2×2 m^3. The authors presented two earlier measurement campaigns to estimate the spatial and temporal distribution of WDR intensity, one of which featured the same geometry [4]. Here, in addition to the WDR gauges, porous building materials with varying pore size distributions, water absorption characteristics and thickness are installed.

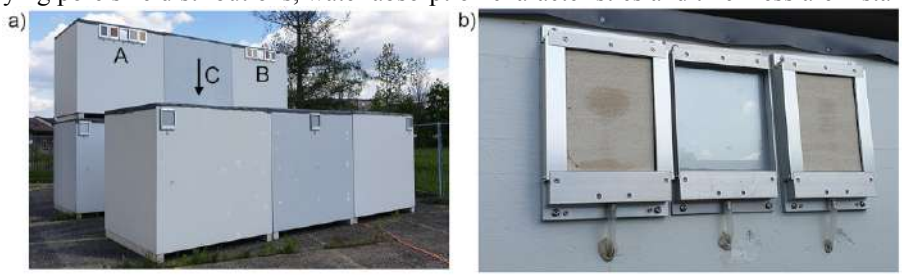

Figure 1. a) Measurement geometry and sensor positions. b) Two Savonnières limestones and the WDR gauge at location C.

The porous materials are placed at locations A, B and C as indicated in Fig. 1a, all on the downstream building. Locations A and B have symmetrical positioning of 4 different porous materials (Pietra Serena sandstone, Meule sandstone, Savonnières limestone and clay brick, from left to right at location A). The materials at location A are 8 mm thick, while the ones at location B are 20 mm. At location C, which is at a lower height behind the upstream building, two Savonnières limestones are installed as shown in Fig. 1b. One of them is 8 mm thick, while the other one is 20 mm. Each of the 10 collectors are equipped with a load cell to measure the absorbed rainwater. A tipping bucket mechanism is used to measure the rainwater that runs off from the surface. The collectors are connected via tubing to the tipping bucket mechanism placed inside the cubes. At each location, an additional WDR gauge is installed at the center to measure the local WDR intensity as reference. Additional WDR gauges are installed on the upstream building.

In order to measure the approach-flow wind direction and wind speed, a meteorological mast is positioned west (upstream) of the measurement site. The meteorological mast is equipped with a 3D ultrasonic anemometer and two cup anemometers to measure the approach wind flow profile. The horizontal rainfall intensity is measured 0.4 m above the

[1]*Corresponding author. E-mail: aytac.kubilay@empa.ch

ground by a rain gauge positioned near the weather mast. Additionally, measurements of relative humidity, air temperature and solar radiation are performed. Different types of rain events have been fully documented.

Numerical modelling

In the current study, the porous materials (20×15 cm^2) are modeled using one-dimensional domains. The coupled heat and moisture transport equations commonly used in building physics applications are given below [5]:

$$\left(c_0\rho_0+c_l w\right)\frac{\partial T}{\partial t}=-\nabla\left(q_c+q_a\right) \quad (1)$$

$$\frac{\partial w}{\partial p_c}\frac{\partial p_c}{\partial t}=-\nabla\left(g_l+g_v\right) \quad (2)$$

where c_0 denotes the specific heat of dry material, ρ_0 the density of dry material, c_l the specific heat of liquid water, w the moisture content, T absolute temperature and p_c capillary pressure. The derivative $\partial w/\partial p_c$ represents the moisture capacity of the porous material. q_c and q_a denote the conductive and advective heat fluxes, while g_l and g_v the liquid and vapor moisture fluxes. The moisture content in the material upper bound is the capillary moisture content. The rain droplets are absorbed via capillary action until saturation occurs. In cases where the surface reaches capillary saturation and the rain flux is larger than the possible absorption by the material, the excess water flows over the surface as runoff.

RESULTS

Fig. 2 shows a rain event with several rain spells that was measured between June 9-16, 2019. The measured absorption and runoff for the two Savonnieres samples, as well as the total WDR amount measured by the WDR gauge, are presented for location C. The measurements show that the 8-mm sample reaches saturation during all three rain spells, while the 20-mm sample is not fully saturated during the initial two rain spells. As a result, a smaller amount of runoff is measured on the thicker sample.

For the numerical simulations, the total WDR amount is used as a flux boundary condition. The comparison of simulations with experiments show that the numerical model underestimates the runoff amount for both samples. For the 8-mm sample in Fig. 2a, numerical model accurately predicts the absorbed rainwater, as well as the rate of evaporation. On the other hand, for the 20-mm sample in Fig. 2b, the absorbed amount of water during the initial two rain spells is overestimated. Furthermore, even though the numerical model reaches near saturation during the first rain spell, the runoff amount is much lower than the measured value. This indicates that the commonly-used flux boundary condition for wetting of building facades due to WDR is unable to capture the fate of discrete raindrops. Further, the droplet physics after impingement on the material can be quite different for dry and wet surfaces. The numerical simulations should take into account droplet spreading and surface film formation in order to accurately estimate the moisture transport during a rain event.

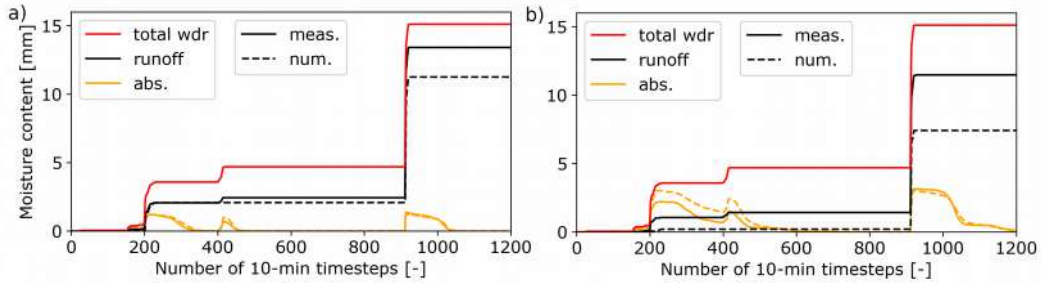

Figure 2. Comparison of the experimental absorption and runoff amounts with the numerical results on the a) 8-mm and b) 20-mm Savonnières stone samples.

CONCLUSIONS

A new measurement campaign for WDR is presented on two parallel buildings, featuring rainwater absorption and runoff measurements. Work is currently on-going both experimentally and numerically. The complete experimental dataset can provide valuable insight in raindrop absorption and runoff mechanisms for porous building materials and can act as a basis for numerical model development.

Acknowledgment

This research project is supported by the Swiss National Science Foundation (SNF) project no. 169323.

References

[1] Kubilay A., Derome D., Blocken B., Carmeliet J. CFD simulation and validation of wind-driven rain on a building facade with an Eulerian multiphase model. *Build. Environ.* ***61***: 69-81, 2013.

[2] Martin M., Defraeye T., Derome D., Carmeliet J. A film flow model for analysing gravity-driven, thin wavy fluid films. *Int. J. Multiphas. Flow.* ***73***: 207-216, 2015.

[3] Derome D., Kubilay A., Defraeye T., Blocken B., Carmeliet J. Ten questions concerning modeling of wind-driven rain in the built environment. *Build. Environ.* ***114***: 495-506, 2017.

[4] Kubilay A., Derome D., Blocken B., Carmeliet J. Wind-driven rain on two parallel wide buildings: field measurements and CFD simulations. *J. Wind Eng. Ind. Aerod.* ***146***: 11-28, 2015.

[5] Janssen H., Blocken, B., Carmeliet, J. Conservative modelling of the moisture and heat transfer in building components under atmospheric excitation. *Int. J. Heat Mass Transf.* ***50***: 1128-1140, 2007.

NUMERICAL SIMULATION OF THE FILM OBLIQUE STRETCHING PROCESS

Mengnan Zhang*[1,2], Jun Zeng [1,2], Erjie Yang [1,2], Fucheng Tian [1,2], andLiangbin Li [1,2,3]
[1]National Synchrotron Radiation Lab, University of Science and Technology of China, Hefei 230029, China
[2]Anhui Provincial Engineering Laboratory of Advanced Functional Polymer Film, University of Science and Technology of China, Hefei 230029,China
[3]CAS Key Laboratory of Soft Matter Chemistry, University of Science and Technology of China, Hefei 230029, China

Summary Finite element methods (FEM) used in the optical film processing field can accelerate the development of film research. The FEM is carried out to simulate the processing of oblique stretching for the first time, the membrane hypothesis is developed and a complete numerical case is given. The stabilization techniques *discrete elastic viscous stress splitting* (DEVSS) is introduced into the simulation and the energy equation, as well as temperature effect, are also considered. The (Phan-Thien and Tanner) PTT viscoelastic constitutive model has been adopted for the simulation, which is regarded as one of the most realistic fluid models. Material parameters of polycarbonate (PC) and proper boundary conditions are given to the simulation. Finally, the contours of the temperature and thickness are present, based on which the effect of the heat transfer coefficient is discussed briefly.

The oblique stretching

The optical film is an essential film in many industrial fields, where oblique stretching is a vital method for the fabrication of optical films such as polarization film. Nonetheless, there is a lack of research and no complete analysis of this method currently, so we aim to analyze the oblique stretching processing in this work. As can be seen in Fig.1, the process of oblique stretching is present. Two rows of closely arranged clamp groups, with variable spacing, grip left and right side edges of the film respectively. Moving those clamps gives the tensile force to the film as well as drives the film forward. That the distance between the clamps is from small to large, leads to the stretching of the film. In addition, the gradual increase of the clamps spacing means the continuous increase of the clamp's velocity, and that is the key to setting the boundary conditions. Additionally, when a delay is imposed on one side (the point at which the stretching starts is *FS* on the right but *LS* on the left in Fig.1), the oblique stretching condition comes into being as a result. Under the membrane hypothesis proposed by Agssant et al [1], the 3D computing domain can be reduced to an in-plane field, all conservation equations are averaged throughout the thickness direction.

The stabilization techniques DEVSS algorithm, presented by Guenette and Fortin [2], which has been proved to improve numerical stability, is applied in this work. The PTT viscoelastic constitutive model [3,4] has been adopted for the simulation, which is regarded as one of the most realistic fluid models. And, the energy equation is also considered, the effects of temperature on rheological properties are taken into consideration. For sake of more realistic input parameters, the polycarbonate (PC) material is taken as the reference. Rheological measurement is performed on PC and the parameters are present as the result. Finally, under the proper boundary conditions of kinematic, thickness, and temperature are set into the model.

To solve those governing equations numerically, spatial discretization is essential. In this work, the computational domain is discretized by quadrilateral elements and the unknown variables are approximated by means of interpolation. The Galerkin weighted residual method is employed and the Newton-Raphson iteration is used for solving sharp nonlinear character governing equation.

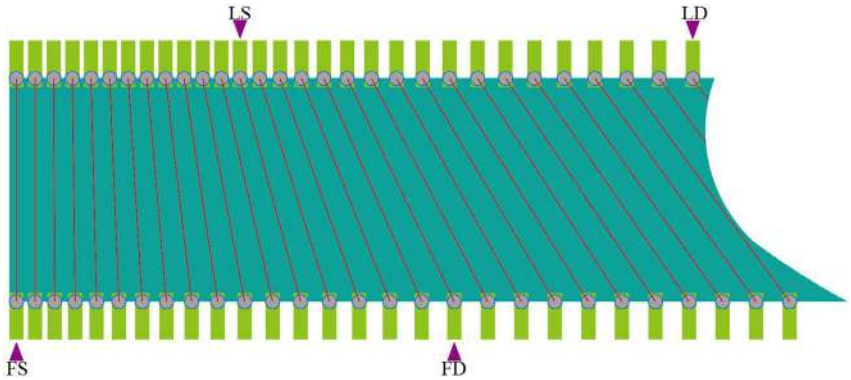

Figure 1. Diagrammatic of oblique stretching

*Corresponding author. E-mail: mnzh@mail.ustc.edu.cn

Result

Taking the parameters and proper boundary conditions above-mentioned, the final result obtained after iterations. Fig.2(a) illustrates the distribution of the temperature and thickness. The temperature drops from the initial 190 ℃ to the ambient temperature 185 ℃ gradually. The thickness uniformity is particularly important for the optical film, from the contour, the thickness distribution appears the “bowing” phenomenon as the result of processing methods (stretching site is located on both sides). Further analysis shows that there is always a couping effect of the physical field (kinematic field, temperature field) in the oblique stretching process.

The variance of the temperature along the width-direction is plotted, as can be seen in Fig.2(b) with the change of heat transfer coefficient (HTC). Every point of the curve in Fig.2(b) represents the variance of the temperature distribution along the width direction. There always be a period in the curve showing an upward trend, on account that the initial temperature is not the same as the ambient temperature. After reaching the peak value, the variance will decline, the location of the peak value and the degree of the decline depend on the HTC as the result. The larger HTC is, the location of the peak value happens early and the reduction gets greater, which means that the variance of temperature becomes small at the end of oblique stretching. But there is no obvious distinction among the variety of HTC. The thickness variance keeps the same trend, it goes up and steadily and then goes up again. The unevenness of the thickness is always rising because the stretching is kept going during the whole process.

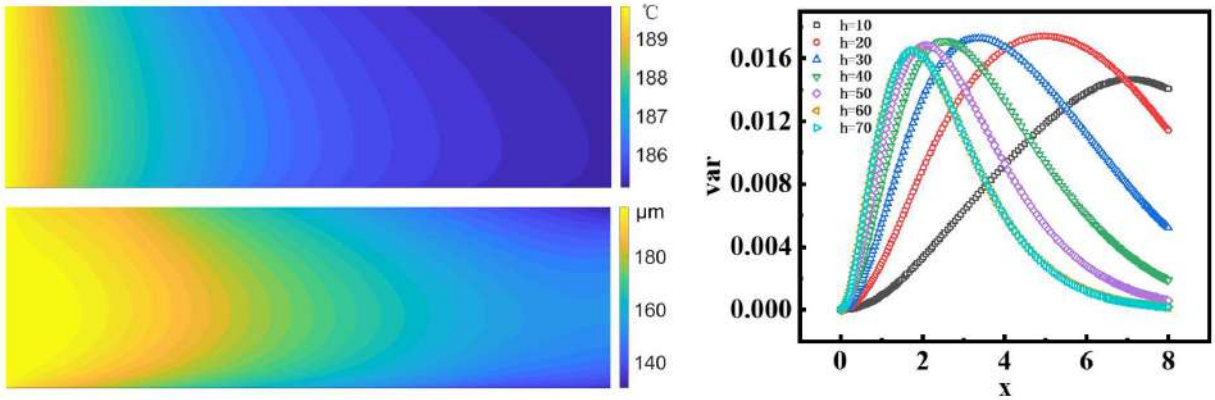

(a) (b)

Figure 2. (a) Contours of temperature and thickness (b) The variance of thickness as heat transfer coefficient changes

The theoretical analysis and numerical implementation are present in this work and the result based on that is discussed briefly at the end. The stretching in the direction of width meanwhile will be considered and more accurate and efficient algorithms will be developed in future work.

References

[1] S. d'Halewyu, J. F. Agassant and Y. Demay, Numerical simulation of the cast film process, Polymer Engineering & Science. 30 (6) (1990) 335-340.
[2] R. Guénette and M. Fortin, A new mixed finite element method for computing viscoelastic flows, Journal of Non-Newtonian Fluid Mechanics. 60 (1) (1995) 27-52.
[3] N. Phan‐Thien, A Nonlinear Network Viscoelastic Model, Journal of Rheology. 22 (3) (1978) 259-283, 10.1122/1.549481.
[4] N. P. Thien and R. I. Tanner, A new constitutive equation derived from network theory, Journal of Non-Newtonian Fluid Mechanics. 2 (4) (1977) 353-365.

HYDRODYNAMICS OF AQUEOUS THIN FILMS OF SURFACTANTS WHILE DRYING

Clément Robert*[1,2,3], L. Maillaud [4], J. Teisseire [4], Frédéric Mondiot [1], Cécile Monteux[2] and Arnaud Antkowiak[3]
[1]Laboratoire Surface du Verre et Interfaces, UMR 125, CNRS/Saint-Gobain, Aubervilliers, France ;
[2]Laboratoire Sciences et Ingénierie de la Matière Molle, UMR 7615, CNRS/ESPCI, Paris, France ;
[3]Institut Jean Le Rond d'Alembert, UMR 7190, CNRS/Sorbonne Université, Paris, France ;
[4]Groupe Revêtements Fonctionnels par voie Liquide, SGR Paris, Aubervilliers, France

Summary We experimentally and theoretically investigate the drying process on flat thin films spread from aqueous solutions of surfactants. The stability of these films is observed to be strongly dependant of the evaporation rate, the film thickness and the surfactant adsorption kinetics. A consistent mechanism based on an evaporation-induced Marangoni instability is suggested and the results are rationalised with a theoretical model and numerical simulations using the Navier-Stokes solver Basilisk.

INTRODUCTION

Wet film deposition is a key process in metallurgy, plastic or glazing industry as it is a quick and efficient way to functionalise large surfaces. Regarding environmental and economical stakes, achieving thin and homogeneous waterborne coatings on glazing is a major challenge. Although attractive, the development of such coatings is still limited by the apparition of defects in the liquid film during the drying step. Yet, in extended flat films Marangoni flows, induced by surface tension gradients, can result in defects in the thin film [1] or film dewetting [2]. In this talk, we tackle how the coupling of solvent evaporation and surfactant adsorption at the surface can induce Marangoni flows and hydrodynamic instabilities in drying flat films. The influence of the coating conditions (evaporation rate, initial thickness, viscosity) and the surfactant adsorption dynamics over the film stability are questioned.

MATERIALS AND METHODS

An automatic blade coater is used to deposit a liquid film of an aqueous solution of surfactant on a horizontal glass plate ($30\ cm3x330\ cm$) laid on a backlight. The initial coating thickness is controlled by adjusting the blade height within the range $[20\ \mu m,\ 150\ \mu m]$. The setup is placed within a hermetic box for controlling relative humidity between 20 % and 90 %.
The drying behaviour of the film is monitored with a camera positioned above the film. To measure and map the film thickness over time, we use the light adsorption method [3]. Nigrosin dye is added to the solution at a concentration of $1\ g.L^{-1}$. This inert dye matches with the Beer-Lambert law of adsorption for a wide range of adsorption. Thus, thickness is calculated from the light adsorption through the film height. As a regular pattern seems to develop on the film, the thickness map is numerically studied to extract the emergent wavelength and the amplitude of the thickness variations.
Most experiments are conducted with sodium dodecyl sulfate (SDS) at a concentration of 82 mM. Critical micelle concentration (CMC) and surfactant adsorption dynamics are studied with a tensiometer, using the pendant droplet method.

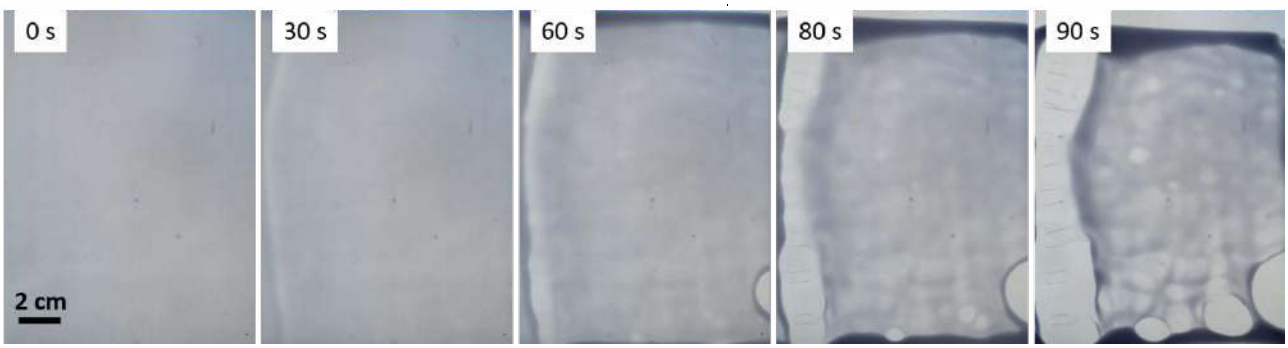

Figure 1. Snapshots of a liquid film of an aqueous solution of SDS (82 mM) that is drying under a relative humidity of 30%. A die is added for observation. An instability develops in the film with an emergent wavelength of the order of the centimetre.

RESULTS & DISCUSSIONS

*Clément Robert. E-mail: clement.robert@m4x.org

As shown in Figure 1, under strong evaporation rate (30% relative humidity), a thin film of an aqueous solution of SDS is unstable. We can observe two phenomena: the development of instability patterns at the surface of the film, leading to hole nucleation, and the receding of the frontline. In the following, we consider the central part of the film (away from the receding frontline).
By a numerical analysis, these patterns may be associated to a characteristic wavelength and an amplitude over time. The characteristic wavelength of the thickness fluctuation in the film remains quite constant over time (Fig 2a.) while the amplitude increases exponentially (Fig 2b.). The exponential growth at constant wavelength is characteristic of the linear regime of an instability. This is studied for different experimental conditions (evaporation rate, initial thickness, viscosity or surfactant concentration) and for surfactants with different adsorption dynamics.
This instability is triggered by solvent evaporation and surface tension gradients. Indeed, liquid films in a humid atmosphere (90% relative humidity), i.e. with a very low evaporation rate, are completely stable and neither instability nor front receding are observed. Likewise, aqueous film without surfactants are quite stable on glass.

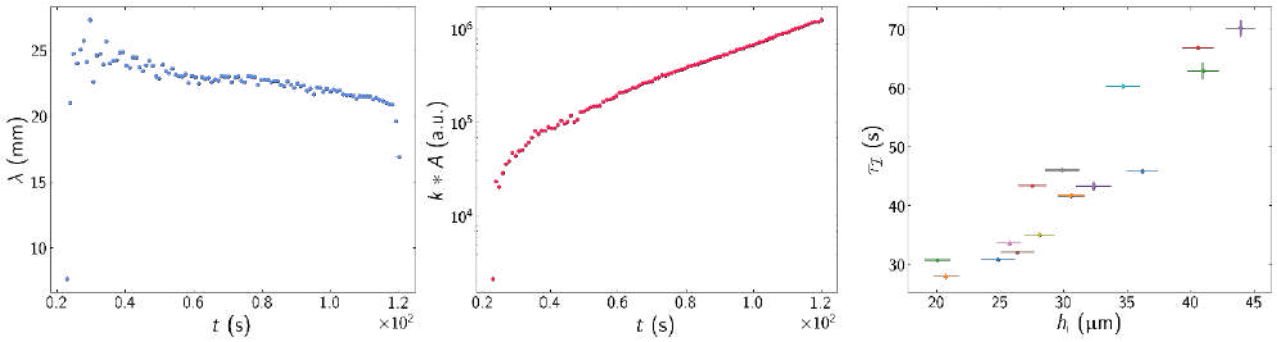

(a) (b) (c)

Figure 2. (a) Wavelength and (b) amplitude along time of the perturbations a drying liquid film of an aqueous solution of SDS. (c) Characteristic time of the instability depending on the initial thickness of the wet film of SDS.

To explore the influence of the thickness on the instability, we spread liquid films at different initial thickness. For each experiment, a characteristic time τ_i can be determined from the amplitude exponential growth. In figure 2c., the characteristic time of the instability is plotted against the initial thickness of the wet film in the corresponding experiment. A growing trend is observed: the thinner the initial film, the quicker the instability develops.
The role of the surface adsorption dynamics of the surfactant in the stability was also studied by deposit solutions containing different surfactants. Solutions of anionic surfactants with a very low adsorption barrier (i.e. with a quasi-immediate adsorption), such as SDS, are unstable. However, surfactants with slow adsorption dynamics, due to energy barriers (cinematically-limited adsorption), appears to be stable when deposit under evaporation. The adsorption dynamics seems then to be crucial in this instability.

CONCLUSIONS

An experimental study of drying aqueous thin films of surfactants brings out an instability responsible of the film destabilisation by amplification of natural perturbations. Our experiments highlights that the coupling of evaporation and surface tension gradients is the driving force of this instability. Besides, a larger thickness of the film or a slow adsorption dynamics are stabilizing parameters in those film.
These observations lead us to propose a mechanism relaying on an evaporation-induced Marangoni instability. Solvent evaporation in a thin film leads to an increasing solute concentration. When the film is perturbed, surfactant concentration increases stronger in the thinner areas of the film than in the thicker areas. If surfactants adsorb quick enough, these bulk concentration gradients result in surface concentrations gradients and thus in surface tension gradients. These induces Marangoni flows and trigger the liquid from thinner areas to thicker areas, hence amplifying the perturbations until hole nucleation.
For a broader comprehension, this phenomenon is rationalised through a theoretical model and with numerical simulations using the Navier-Stokes solver Basilisk [4-5] and a multilayer description [6].

References

[1] H. S. Kheshgi and L. Scriven, Ch. Eng. Sci., 46, 519-526 (1991)
[2] S. Karpitschka, F. Liebig and H. Riegler, Langmuir, 33, 4682-4687 (2017)
[3] Y. Wang, L. Bourouiba, J. Fluid Mech, 814, 510-534 (2017)
[4] http://basilisk.fr/
[5] S. Popinet, J. Comput. Phys, 228, 5839-5866 (2009)
[6] S. Popinet, J. Comput. Phys, 418, 109609 (2020)

VERY-LARGE-SCALE MOTIONS AND DUST CONCENTRATION STRUCTURES IN ATMOSPHERIC BOUNDAR YLAYER

Xiaojing Zheng*[1,2] and Wei Zhu[2]
[1]Research Center for Applied Mechanics, Xidian University, Xi'An, 710071, China
[2]College of Civil Engineering and Mechanics, Lanzhou University, Lanzhou, 730000, China

Summary In this paper, concentrations of PM10 particles with size less than 10 μm and three-component wind velocities are measured synchrounously at various heights by the Qingtu Lake Observation Array (QLOA). Two-point correlation analysis reveal the existence of very-large-scale motions (VLSMs) in the flow fields of the sand-laden flows, and for the first time point out that the PM10 concentration fields also have similar organized structures as the turbulent structures in the flow fields. Through comparing the VLSMs in the flow fields of clean-air and sand-laden flows as well as the structures of PM10 concentration fields from the perspective of streamwise length scales, inclination angles, turbulent kinetic energy and their distributions, the relations and differences of the three types of structures are discussed.

INTRODUCTION

Previous studies on the high-Reynolds-number turbulent flows in the ASL have revealed the existence of the very large scale motions (VLSMs) whose streamwise scales are larger than 3 times the thickness of the boundary layer (δ) [1,2]. Till now, it has been widely accepted that VLSMs contribute more than 50% of the turbulent kinetic energy and Reynolds stress, and have a significant modulation effect on small-scale structures [3,4], which consequently play dominating roles in dust transport [5,6]. In addition, it is found that the structure is at an oblique angle to the free stream [7], and the inclination angles of VLSMs decrease linearly with the increase of the friction wind velocity [8]. However, there have been rare reports up to date concerning the morphological characteristics and energy contribution of VLSMs in sand-laden flows in the ASL, and it has been not clear whether there exist organized structures of particle concentration in sand-laden flows or not. Answer to this question may provide an insight to the mechanism of dust transport with respect to the effect of VLSMs in the ASL.

EXPERIMENTAL SETUP AND DATA PROCESSING

The field measurements were conducted at the Qingtu Lake Observation Array (QLOA) site. The experimental facility and QLOA site were introduced in details in Ref [2]. For wind-velocity measurements, 11 sonic anemometers were installed on the main tower (from 0.9 m to 30 m), with a sampling frequency of 50 Hz. For PM10 concentration measurements, 11 aerosol monitors were installed on the main tower at the same heights as the sonic anemometers and recorded with a frequency of 1 Hz. The sonic anemometers and aerosol monitors were linked by acquisition instruments, which were synchronized in time by the Global Positioning System (GPS). The selection and pretreatment on the raw velocity data are consistent with that in Ref [2], including stratification stability judgement, wind direction adjustment, de-trending manipulation and steady wind selection.

RESULTS AND DISCUSSIONS

Figure 1 illustrates the two-point correlation contours of streamwise fluctuations and PM10 concentrations in the sand-laden flow fields. The black solid line in Figure 1a is the isoline with a correlation coefficient of 0.05. From the positive correlation regions in Figures 1a and 1b, we can clearly identify coherent structures with streamwise scale larger than 3δ in both sand-laden flow fields and PM10 concentration fields, and the two types of structures both present obvious inclination angles to the streamwise direction.

Further, we conducted statistical analysis on the morphological characteristics of VLSMs in sand-laden flow fields and dust concentration structures, including their streamwise scales and inclination angles. Figure 2a shows the variations of the average streamwise scales of the VLSMs respectively in clean-air and sand-laden flow fields and those of dust concentration structures with height. Here the Taylor's frozen hypothesis is used and assuming that the dust particles have the same velocities as the convectional velocities of the local surrounding flow fields. It can be seen that both the streamwise scales of the VLSMs in clean-air and particle-laden flow fields increase with height, while the scales of the PM10 concentration structures are larger than 3δ in our measured region, which are larger than the scales of VLSMs below 14m and basically do not vary with the height; For the region above 14m, the streamwise scales of the three types of structures are statistically equal and all increase with height. Such difference and similarity may come from a combinational effect of surface shear and particles' intertia. The former reduces the energy of low-frequency

*Corresponding author. E-mail: xjzheng@lzu.edu.cn

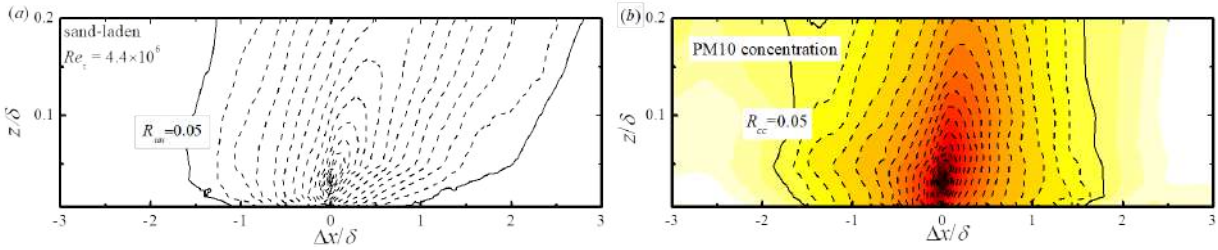

Figure 1: Two-point correlation contours of (a) the steamwise velocity and (b) PM10 concentration fluctuations at z_{ref}=5m and Re_τ=4.4 × 10^6.

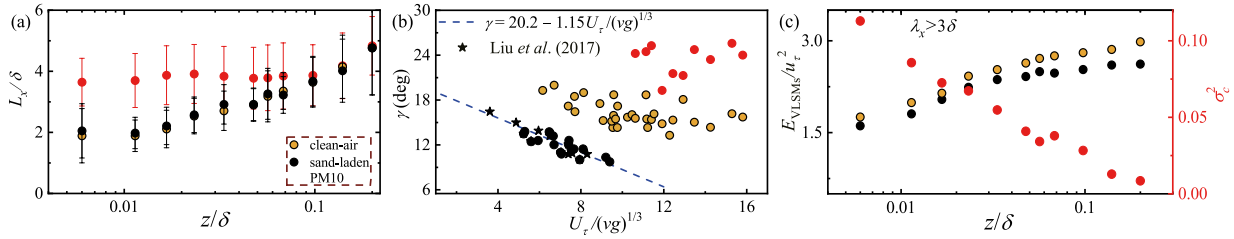

Figure 2: Variations of (a) the streamwise scales (a) the inclination angles and (c) the fluctuation energy of VLSMs and PM10 concentration structures with z/δ and u_τ.

fluctuations (large-scale structures in flow fields) while the latter attenuates the response of PM10 structures to the high-frequency fluctuations of flow fields near surface. In addition, Figure 2b shows that the inclination angles of VLSMs in the sand-laden flows increase with the sand flux and are larger than those in the clean-air flows, which both decrease with the frictional wind velocity u_τ. This is because the angles of VLSMs and PM10 structures are dominated by different factors, the former by the streamwise wind velocity gradient, while the latter by the coherence of the wall-normal wind fluctuations. Besides, Figure 2c shows the comprisons of the energy of the VLSMs in the clean-air and sand-laden flow fields and that of PM10 concentration structures varying with height. It can be found that in both clean-air and sand-laden flow fields, the energy of VLSMs increase with the height, while the energy of PM10 concentration fluctuations presents a decreasing trend with height. For the increase of the energy of VLSMs, it can be explained by the input of the external energy in ASL, in other words, the 'top-down' mechanism. However, the PM10 particles are released from the land surface and the strength of the concentration fluctuations decrease with the height, which make the energy of PM10 concentration structures decrease with height.

CONCLUSIONS

Based on the field measurements of high-Reynolds-number turbulent flows in ASL with dust entrainment, we found the existence of the super-large-scale (>3δ) structures of PM10 concentration fields. The inclination angles of the PM10 structures are larger than that of the VLSMs in flow fields, and the streamwise scales of PM10 structures do not vary with the height and are larger than that of the VLSMs at the lower height. The fluctuation energy of PM10 structures decrease with height, which is qualitatively different from the varying trend of the engergy of VLSMs in the flow fields.

References

[1] Hutchins, N., Marusic, I. Evidence of very long meandering features in the logarithmic region of turbulent boundary layers. *J. Fluid Mech.*, **579**, 1-28, 2007.
[2] Wang, G., Zheng. X. Very large scale motions in the atmospheric surface layer: a field investigation. *J. Fluid Mech.*, **802**, 464-489, 2016.
[3] Mathis, R., Hutchins, N., Marusic, I. Large-scale amplitude modulation of the small-scale structures in turbulent boundary layers. *J. Fluid Mech.*, **628**, 311-337, 2009.
[4] Liu. H., Wang. G., Zheng, X. Amplitude modulation between multi-scale turbulent motions in high-Reynolds-number atmospheric surface layers. *J. Fluid Mech.*, **861**,585-607, 2019.
[5] Zheng, X., Zhang, J., Wang, G., Liu, H., Zhu, W. Investigation on very large scale motions (VLSMs) and their influence in a dust storm. *Science China Physics, Mechanics and Astronomy*, **56(2)**:306-314, 2013.
[6] Wang, G., Zheng. X, Tao, J. Very large scale motions and PM10 concentration in a high-Re boundary layer. *Physics of Fluids*, **29(6)**:1-28, 2017.
[7] Marusic, I, Heuer, W. D. C. Reynolds Number Invariance of the Structure Inclination Angle in Wall Turbulence. *Physical Review Letters*, **99(11)**:114504, 2007.
[8] Liu, H., Bo, T., and Liang, Y. The variation of large-scale structure inclination angles in high reynolds number atmospheric surface layers. *Physics of Fluids*, **29(3)**:035104, 2017.

ON THE GROWTH OF BARCHAN DUNES

Carlos A. Alvarez[1] and Erick M. Franklin*[1]
[1]School of Mechanical Engineering, UNICAMP - University of Campinas, Campinas, Brazil

Summary Barchans are crescent-shaped dunes, with horns pointing downstream, that are found in different environments. We investigate experimentally the formation of subaqueous barchans. Controlled grains were poured in a channel filled with water, forming a conical pile. Afterward, a turbulent water flow was imposed, entraining the grains and forming a single barchan while a high-speed camera recorded the bedform evolution. We show that most of the grains migrating to horns come from upstream regions on the periphery of the dune. These results diverge from the generally accepted description that the barchan horns are formed from the advance of the lateral flanks of the bedform. Our results reveal a new mechanism for barchan formation, valid, at least, for the subaqueous case. A great part of what is presented here can be found in Phys. Rev. Lett. 121, 164503 and Phys. Rev. E 100, 042904

INTRODUCTION

The growth and migration of sand dunes result from the interaction between a fluid flow and a granular bed, when, under moderate shear stresses, grains are entrained by the fluid as a moving layer. This mode of transport is called bedload. Under one-directional flow conditions, crescent-shaped dunes with horns pointing downstream, known as barchan dunes, usually appear. Barchan dunes can be found in environments as different as rivers, Earth's deserts and on the surface of Mars, for example. However, despite being similar in shape, their scales vary from the centimeter and minute under water [1, 2, 3, 4], to the kilometer and millennium on Mars [5]. Because of their smaller length and time scales, subaqueous barchans are the ideal object to study the growth and migration of barchan dunes.

Although frequently found in nature, some aspects of the morphodynamics of barchans are still not fully understood. One of them concerns the trajectories of individual grains over the bedform, and how they affect its shape, inducing the growth and maintenance of barchans. This study investigates experimentally the formation and evolution of subaqueous barchans.

EXPERIMENTAL SETUP

The experimental device consisted of a water reservoir, two centrifugal pumps, a 5-m-long closed-conduit channel, a settling tank, and a return line. The channel was made of transparent material (acrylic) and had a rectangular cross section 160 mm wide by 50 mm high (2δ = 50 mm). The test section started at 3 m (40 hydraulic diameters) downstream the channel entrance, assuring that the water flow was fully developed in the test section. A high-speed camera of complementary metal-oxide-semiconductor type (CMOS) with a spatial resolution of 1280 px $\times$ 1024 px at frequencies up to 1000 Hz was placed above the channel to record the bed evolution. Figure 1(a) shows a photograph of the test section arrangement.

Prior to each test, controlled grains were poured in the test section (previously filled with water), forming a single conical pile at the bottom wall. We used round glass beads (density of grains ρ_s = 2500 kg/m^3 and bulk density of 1500 kg/m^3) with diameters of 0.15 mm $\leq d \leq$ 0.25 mm and 0.40 mm $\leq d \leq$ 0.60 mm, where 2% of them had a different color (but same density and diameter) and were used as tracers. Afterward, a turbulent water flow was imposed, entraining the grains and forming a single barchan while a high-speed camera recorded the bedform evolution. The cross-sectional mean velocities of water U were 0.243, 0.294 and 0.364 m/s, corresponding to Reynolds numbers based on the channel height $Re = \rho U 2\delta/\mu$ of 1.21×10^4, 1.47×10^4 and 1.82×10^4, respectively, where ρ is the fluid density and μ its dynamic viscosity. With this procedure, each experiment concerned one single barchan that loosed grains by its horns, decreasing slowly in size while migrating. By using an image processing code written in the course of this work, the centroids of the tracers and of the barchans were identified, and the trajectories of tracers were computed using particle tracking velocimetry (PTV). Figure 1(b) shows some pathlines of tracers over a developed barchan made of 0.40 mm $\leq d \leq$ 0.60 mm glass beads superposed with a photograph of the barchan dune.

MAIN RESULTS

Figure 1(c) shows the trajectories of some tracers that migrated to horns during the growth of a barchan dune (some movies are available on Ref. [6]), where pathlines are blue at the pile initial position and red at the barchan final position. We observe that a large part of grains migrating to horns was originally in upstream regions on the periphery of the dune, and that their path is described approximately by an arc of circumference with, therefore, significant transverse displacements. Numerical computations using CFD-DEM (computational fluid dynamics - discrete element method) reproduced well these experimental findings [7]. Our results show that most of grains migrating to horns of subaqueous barchans do not come from the lateral flanks of the initial heap or dune, as usually assumed in the aeolian case, providing then a new picture for the growth of subaqueous barchans.

*Corresponding author. E-mail: franklin@fem.unicamp.br.

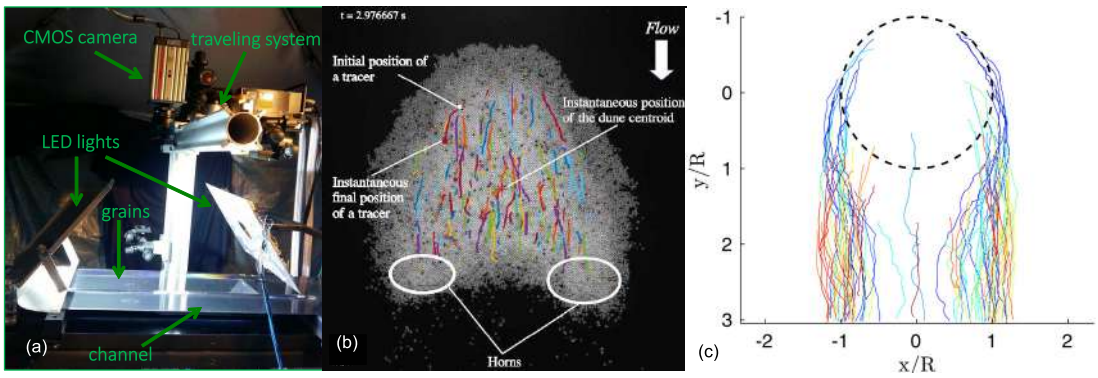

Figure 1: (a) Photograph of the test section; (b) pathlines of tracers over a developed barchan; (c) Trajectories of some tracers that migrated to horns during the growth of a barchan dune, where R is the radius of the initial pile. Adapted from Refs. [1, 2].

CONCLUSIONS

We have shown that most of the grains migrating to horns came from upstream regions on the periphery of the dune, with significant transverse displacements. These results diverge from the generally accepted description that the barchan horns are formed from the advance of the lateral flanks of the bedform. Our results reveal a new mechanism for barchan formation, valid, at least, for the subaqueous case.

ACKNOWLEDGMENTS

Carlos A. Alvarez is grateful to SENESCYT (Grant No. 2013-AR2Q2850) and to CNPq (Grant No. 140773/2016-9). Erick M. Franklin is grateful to FAPESP (Grant No. 2018/14981-7) and to CNPq (Grant No. 400284/2016-2) for the financial support provided.

References

[1] Alvarez, C. A., Franklin, E. M. Role of Transverse Displacements in the Formation of Subaqueous Barchan Dunes. *Phys. Rev. Lett.* **121**: 164503, 2018.
[2] Alvarez, C. A., Franklin, E. M. Horns of Subaqueous Barchan Dunes: A Study at the Grain Scale. *Phys. Rev. E* **100**: 042904, 2019.
[3] Hersen, P., Douady, S. and Andreotti, B. Relevant Length Scale of Barchan Dunes. *Phys. Rev. Lett.* **89**: 264301, 2002.
[4] Franklin, E. M., Charru, F. Subaqueous Barchan Dunes in Turbulent Shear Flow. Part 1: Dune Motion. *J. Fluid Mech.* **675**: 199-222, 2011.
[5] Claudin, P., Andreotti, B. A Scaling Law for Aeolian Dunes on Mars, Venus, Earth, and for Subaqueous Ripples. *Earth Plan. Sci. Lett.* **252**: 30-44, 2006.
[6] `http://www.fem.unicamp.br/%7Efranklin/movies%5Fdunes.html`
[7] Alvarez, C. A., Franklin, E. M. Shape Evolution of Numerically Obtained Subaqueous Barchans. *Phys. Rev. E*, accepted.

IMPULSIVE FORCES FROM SHEARING: NON-EQUILIBRIUM MECHANICS OF DILATANCY IN GRANULAR SNOW AVALANCHES

Othmar Buser and Perry Bartelt*
WSL Institute for Snow and Avalanche Research, SLF, Davos, Switzerland

Summary Snow avalanches represent an important class of granular flows that find a true mechanical equilibrium only under exceptional conditions. For the most part avalanches flow outside the equilibrium state. In the following we find the slope-perpendicular, impulsive forces associated with terrain steepness and roughness that change the flow density of the avalanche. These forces are responsible for the attainment of equilibrium and therefore, in the end, avalanche speed, flow height and runout. Because we consider the acceleration of the center-of-mass of a flowing ensemble of snow particles in the slope-perpendicular direction, the approach can be classified as a computationally reduced, mixed Eulerian-Lagrangian calculation method. Moreover, we adopt a macroscopic approach that can be implemented within the framework of existing shallow-water-type avalanche dynamics models.

INTRODUCTION

The very word *avalanche* invokes a physical system which is mechanically out-of-balance. This impression is nowhere more apparent than when watching snow avalanches descend steep mountain slopes (Fig. 1). The front of the avalanche appears to explode upwards. Plumes of snow particles and ice-dust are pulsed into the air. The particles and dust reach heights of 50m in fractions of a second, indicating large slope-perpendicular accelerations [1]. The heights reached by the powder clouds is all the more perplexing because the upward moving mixture of snow particles and ice-dust must be accelerated *against* gravity and overcome the forces of air-drag.

The mechanical source of the upward movement was identified by Reynolds [2] as early as 1885. Reynolds maintained that a sheared granular ensemble must dilate (expand). In snow avalanches, these dilations are extreme. The high-rate of shearing, caused by the flow of snow particles over rough, steep terrain, leads not only to large slope-perpendicular accelerations, but also to *overshoots*; that is, the amount of energy introduced by shearing in the slope-perpendicular direction is more than needed to maintain the static equilibrium of the ensemble. This idea requires mathematical clarification.

SLOPE-PERPENDICULAR ACCELERATIONS AND GRANULAR DILATANCY

We consider a column of snow particles in the avalanche (Fig. 1). The height of the column h is given by the z-position of the granule located farthest from the running surface (the highest particle in the column). The total mass of the column of particles is M. It is possible to find the z-location of the center-of-mass of the column, which we denote k. The distance k is to be considered a Lagrangian variable that will be transported with the avalanche velocity in the slope parallel direction. Let E represent the potential energy of a granular column which is related to the sum of the force of gravity Mg_z and the inertial force $M\ddot{k}$,

$$E = Fk = M(g_z + \ddot{k})k. \tag{1}$$

The gravity g_z acts in the slope-perpendicular z-direction. The reaction to this force N acts on the ground. The reaction therefore consists of the hydrostatic component Mg_z and the dynamic part $M\ddot{k}$ associated with the acceleration of the center-of-mass $\ddot{k}$. The rate of change of the potential energy is then

$$\dot{E} = \dot{F}k + F\dot{k} = M\dddot{k}k + M\left(g_z + \ddot{k}\right)\dot{k}. \tag{2}$$

Here we adopt the ideas of Reynolds and say that the γ fraction of the shear work $\dot{W}$ is used to change the potential energy of the column, $\dot{E} = \gamma\dot{W}$. Therefore,

$$M\left[\dddot{k}k + \left(g_z + \ddot{k}\right)\dot{k}\right] = \gamma\dot{W}. \tag{3}$$

The third-order equation implies the column ensemble will experience overshoots and, if undamped, will obtain an dynamic, oscillating equilibrium. More importantly, however, is the fact that the state of the column is strongly dependent on the "input" function, $\dot{W}$. Because of the changing terrain and roughness, the work function $\dot{W}$ will continually place the snow avalanche outside equilibrium. A static equilibrium will only be obtained after a certain time when the dynamic oscillations are damped, and the $\dot{W}$ input function disappears, for example on smooth, flat slopes. This energy must be some part of the random kinetic energy (granular temperature) which has movements in the slope-perpendicular z-direction. This approach is explained in detail in [3].

*Corresponding author. E-mail: bartelt@slf.ch.

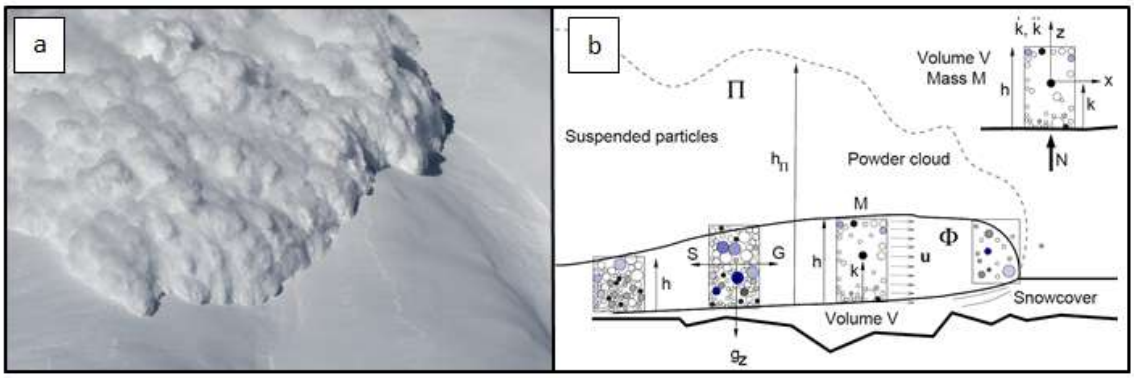

Figure 1: a: The front of a mixed flowing/powder snow avalanche. Behind the cloud Π of ice dust, there is a granular core Φ. The height of the cloud is between 20m and 30m. b: Column model. The avalanche core Φ is divided into columns with mass M and volume V. The height of the column is h, the center-of-mass is located at k. The center-of-mass moves with velocity $\dot{k}$ and $\ddot{k}$.

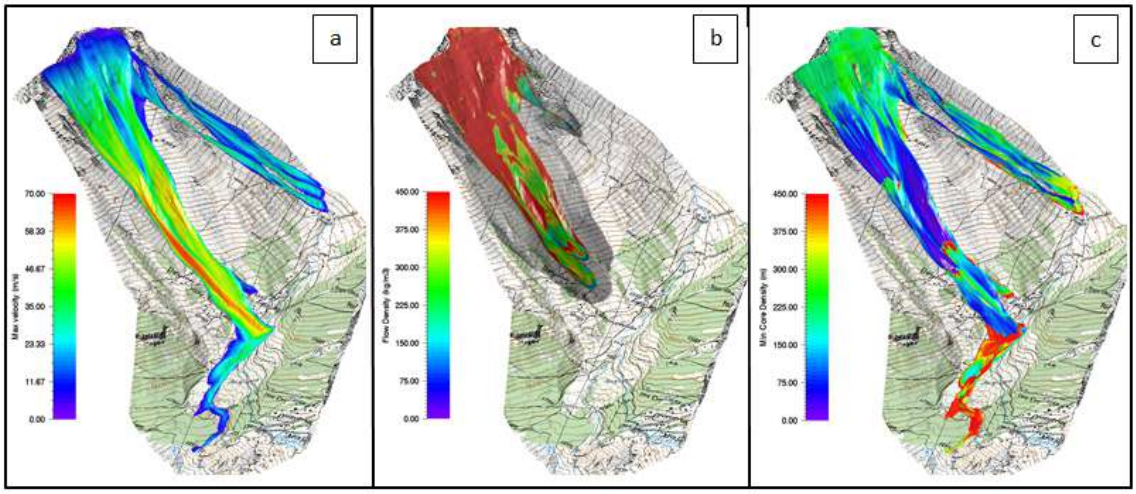

Figure 2: Calculation of the 25.2.1999 Vallée de la Sionne avalanche. a) Calculated flow velocity. d) Flow density of the avalanche core. The front is fluidized, the tail of the avalanche is dense. The location of the cloud is depicted in transparent grey. c) Minimum calculated flow density of the avalanche core.

NUMERICAL RESULTS

We introduced Eq. 3 into a depth-averaged avalanche dynamics program [4]. This was accomplished by breaking the third-order equation down into a system of three-first order equations for k, $\dot{k}$ and $\ddot{k}$. We used the model to simulate a large mixed flowing/powder avalanche measured recorded at the Swiss Vallée de la Sionne test site (Figure 2). The calculated avalanche velocities are in good agreement with measurements. However, the most important improvement of over existing calculations is the prediction of the avalanche flow densities and the formation of the avalanche cloud. The avalanche front is highly fluidized (front density of 100kg/m^3, tail density of 400kg/m^3.) At the end of the event the avalanche transformed into a completely dense flow (lubricated by meltwater). The observed and calculated runout distances are in good agreement.

CONCLUSIONS

Slope-perpendicular accelerations are produced by shear work in the avalanche core. These accelerations dilate the avalanche flow body (fluidization) producing low density flows with extreme runout distances.

References

[1] Dreier, L and others. Comparison of simulated powder snow avalanches with photogrammetric measurements, *Annals of Glaciology*, 57(71), 371-381, 2016.

[2] Reynolds O., On the dilatancy of media composed of rigid particles in contact, with experimental illustrations,*Phil. Mag.*,Ser.5,20,469-481,1885.

[3] Buser O., Bartelt P., An energy-based method to calculate streamwise density variations in snow avalanches, *Journal of Glaciology*, 61(227), 563-575. 2015.

[4] Christen M., Kowalski J., Bartelt P. RAMMS: numerical simulation of dense snow avalanches in three-dimensional terrain, *Cold Regions Science and Technology*, 63(1-2), 1-14.

PHASE TRANSITION OF ENERGY TRANSFER IN NEAR-INERTIAL WAVE–VORTEX INTERACTING TURBULENCE

Jin-Han Xie*[1]
[1]Department of Mechanics and Engineering Science at College of Engineering, State key laboratory for turbulence and complex systems and Beijing Innovation Center for Engineering Science and Advanced Technology, Peking University, Beijing, 100871, PR China

Summary The energy budget of the oceanic mesoscale eddies remains an unsolved problem where the known energy injection is much larger than the discovered energy dissipation. By studying a near-inertial wave–mesoscale eddy coupled model, this work proposes a new mechanism that in the turbulent states wave-vortex interaction induces a downscale energy transfer and finally a small-scale dissipation at the ocean interior. The existence of this new energy path is understood as the emergence of phase transition of changing energy transfer direction in the spectral space. This phase transition is justified and studied in details using forced-dissipative numerical simulations.

INTRODUCTION

The mesoscale eddy, which has horizontal scale from one to hundreds of kilometers, contains a significant part of the ocean energy, however, its energy budget remains not well understood: wind forcing and large-scale circulations injection energy into the mesoscale eddies, and the mesoscale eddies dissipate at the boundaries and be converted to other types of motions, but the known amount of energy injection is much larger than that of the energy dissipation [1, 2]. Several candidates are thought to be responsible for the mesoscale eddy energy closure, such as loss of balance [3] and stimulated wave generation [4].

Another energy reservoir in the ocean is the near-inertial waves (NIWs) which contain around 50% of the wave energy. There are a variety of mechanisms potentially explaining that NIWs can extract energy from balanced flow, and they have been studied in various setups and parameter regimes. Gertz and Straub [5] run numerical simulations in a periodic box with O(1) Rossby number and find that the energy transfer between 2D and 3D motions is crucial. Also with O(1) Rossby number, [6] considers a channel flow with forcing on both low and high frequencies, they find that the Reynolds stresses of NIW act as a kinetic energy sink for mesoscale motions. In [7], numerical simulations in a channel flow with external forcing find the direct extraction dominates while the mechanism of stimulated NIW generation is of subdominant. NIW is also found to absorb mean flow energy in the frontogenesis [8]. In this paper, using the two-dimensional NIW–mesoscale eddy coupled model [4] we study the turbulent wave-vortex interaction and find a new mechanism that the NIW induces downscale energy transfer, and finally the energy dissipates at the interior.

The bidirectional energy transfer has been observed in numerical simulations of the rotating stratified turbulence, which is a key feature of the atmospheric and oceanic flows, e.g. [9]. However, the mechanism for bidirectional energy transfer is less understood. This work on the reduced model of NIW-eddy turbulent interaction uses a simple setup to provide a phase-transition explanation to the wave-induced bidirectional energy transfer.

MODEL

We consider forced dissipative system of the NIW-eddy interaction with single-vertical-mode waves [4]

$$M_t + \mathcal{J}(\psi, M) - \frac{\mathrm{i}N^2}{2m^2 f}\nabla^2 M + \frac{\mathrm{i}}{2}M\nabla^2\psi = F_M + D_M, \tag{1a}$$

$$q_t + \mathcal{J}(\psi, q) = F_q + D_q, \tag{1b}$$

$$\text{with} \quad q = \nabla^2\psi + \frac{\mathrm{i}f}{2}\mathcal{J}(M^*, M) + \frac{f}{4}\nabla^2|M|^2, \tag{1c}$$

where M is the complex wave amplitude such that $u + \mathrm{i}v = -\mathrm{i}fM\mathrm{e}^{-\mathrm{i}ft+\mathrm{i}mz}$ with u and v the two horizontal velocities, $\mathcal{J}$ denotes the Jacobian, N is the Brunt-Väisälä (buoyancy) frequency, m is the vertical wavenumber of the NIW, f is the Coriolis frequency, ψ is the stream function of the quasigeostrophic mean flow corresponding to the eddies. F_M and F_q are random forces acting on the wave and mean fields, respectively, and we define a parameter R such that the energy injection ratio between the wave and mean fields is R^2. D_M and D_q are dissipations of the wave and mean fields, respectively, where both large- and small-scale dissipations are included.

*Corresponding author. E-mail: jinhanxie@pku.edu.cn

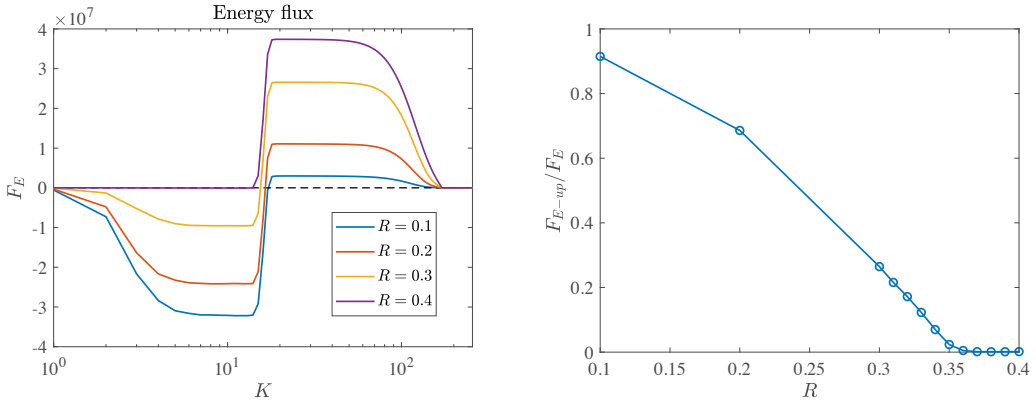

Figure 1: The left panel shows the dependence of total energy flux on parameter R. Negative and positive values of F_E represent upscale and downscale energy transfers, respectively. The black dashed line is 0 for reference. The right panel shows the dependence of the upscale flux ratio on the parameter R.

NUMERICAL RESULTS

We run numerical simulations of the coupled system (1) with different energy injection ratio R^2 and examine the energy transfer scenario of the coupled model. The numerical simulations use a Fourier pseudospectral method with 2/3 dealiasing in space, a resolution 512×512 in a domain of size $2\pi \times 2\pi$ and a fourth-order explicit Runge–Kutta scheme in time, in which the nonlinear terms are treated explicitly, and linear terms implicitly use an integrating factor method. We take the forcing wavenumber to be $k_f = 32$ for both wave and eddy forcings. The large- and small-scale dissipation wavenumbers are designed to be $k_{large} \approx 0.4$ and $k_{small} \approx 100$, respectively.

In figure 1, the left panel shows the dependence of total energy flux in the spectral space on parameter R. As R increases, energy first transfers upscale, then bidirectionally and finally downscale. The right panel of figure 1 shows the dependence of upscale energy flux ratio F_{E-up}/F_E on R, where F_{E-up} and F_E are the magnitudes of the upscale and total energy transfer, respectively. As R increases from zero, the upscale energy flux ratio decreases and reaches zero at a critical value $R \approx 0.36$, implying a second-order phase transition for the direction of energy transfer.

SUMMARY AND DISCUSSION

We run numerical simulations of the NIW-eddy coupled model to study the dependence of energy transfer on the ratio of the energy injection into the wave and vortex components. We find a phase transition of the direction of energy transfer: when the injection of the wave energy is weak, the energy transfers upscale, while when the injection of wave energy is strong, the energy transfers downscale; with intermediate wave energy injection the energy transfers bidirectionally. The transition from the bidirectional energy transfer and the downscale energy transfer shows a second-order phase transition.

The existence of turbulent states with bidirectionally energy transfer is a candidate for explaining the mesoscale energy puzzle: when the effect of (near-inertial) waves is not negligible, energy can transfer to downscales and finally dissipate at the ocean interior. Moreover, we propose that the strength of downscale energy transfer depend on the portion of the wave energy injection. Compared with the previous mechanism of wave absorption of the mean-flow energy (e.g. [3, 4]), this work focuses on the more realistic energy transfer in turbulent states. Three-dimensional numerical simulations are demanded in the future to justify the existence of the new mechanism in the real ocean.

References

[1] Wunsch, C. & Ferrari, R. Vertical mixing, energy, and the general circulation of the oceans. *Annu. Rev. Fluid Mech.* **36**, 281–314, 2004
[2] Ferrari, R. & Wunsch, C. Ocean circulation kinetic energy: reservoirs, sources, and sinks. *Annu. Rev. Fluid Mech.* **31**, 962–971, 2009
[3] Vanneste, J. Balance and spontaneous generation in geophysical flows. *Annu. Rev. Fluid Mech.* **45**, 147–172, 2013
[4] Xie, J.-H. & Vanneste, J. A generalised-Lagrangian-mean model of the interactions between near-inertial waves and mean flow. *J. Fluid Mech.* **744**, 143–169, 2015
[5] Gertz, A. & Straub, D. N. Near-inertial oscillations and the damping of midlatitude gyres: a modeling study. *J. Phys. Oceanogr.* **39**, 2338–2350, 2009
[6] Taylor, S. & Straub, D. Forced near-inertial motion and dissipation of low-frequency kinetic energy in a wind-driven channel flow. *J. Phys. Oceanogr.* **46**, 79–93, 2016
[7] Barkan, R., Winters, K. B. & McWilliams, J. C. Stimulated imbalance and the enhancement of eddy kinetic energy dissipation by internal waves. *J. Phys. Oceanogr.* **47**, 181–198, 2017
[8] Thomas, L. N. On the effects of frontogenetic strain on symmetric instability and inertia–gravity waves. *J. Fluid Mech.* **711**, 620–640, 2012
[9] Marino, R., Pouquet, A. & Rosenberg, D. Resolving the paradox of oceanic large-scale balance and small-scale mixing. *Phys. Rev. Lett.* **114**, 114504, 2015

THE BOUNDARY ZONAL FLOW (BZF) AND ITS IMPORTANCE FOR THE HEAT TRANSPORT IN ROTATING THERMAL CONVECTION

Stephan Weiss*[1,6], Xuan Zhang [1], Marcel Wedi[1], Dennis P.M. van Gils[2], Susanne Horn[3], Lukas Zwirner[1], Guente Ahlers[4], Robert E. Ecke[5], Eberhard Bodenschatz[1], and Olga Shishkina[1]

[1]Max-Planck-InstituteforDynamicsandSelf-Organization,Göttingen,Germany

[2]Twente University, Enschede, The Netherlands

[3]Centre for Fluid and Complex Systems, Coventry University, Coventry, UK

[4]University of California, Santa Barbara, USA

[5]Center for Nonlinear Studies, Los Alamos National Laboratory, Los Alamos, New Mexico, USA

[6]Max Planck - University Twente Center for complex fluid dynamics

Summary For rapidly rotating turbulent Rayleigh–Bénard convection in a slender cylindrical cell, experiments and direct numerical simulations reveal a boundary zonal flow (BZF) that replaces the classical large-scale circulation for the non-rotating case. The BZF is located near the vertical side wall and enables enhanced heat transport there. Although the azimuthal velocity of the BZF is cyclonic (in the rotating frame), the temperature is an anticyclonic traveling wave of mode one whose signature is a bimodal temperature distribution near the radial boundary. The BZF width is found to scale closely as $\delta_{BZF} \propto Ra^{1/4}Ek^{2/3}$ where the Ekman number Ek decreases with increasing rotation rate.

Turbulent convection, where a fluid is driven by a thermal gradient is one of the most important mechanisms for the transport of heat in astro- and geophysical systems, but also plays a crucial role in many industrial applications. In particular in natural systems such as the Earths atmosphere or the convection zone in stars, the flow is not only highly turbulent but also strongly influenced by the rotation of their celestial body due to Coriolis forces. In the laboratory and in numerical simulations, thermal convection is usually studied in the Rayleigh-Bénard setup, where a horizontal fluid layer is confined by a warm plate at the bottom and a cold plate at the top and confined laterally by adiabatic sidewalls [1]. Under Oberbeck-Boussinesq-conditions, i.e., homogeneous fluid properties, this system is governed by only two dimensionless control parameters: the Rayleigh number ($Ra = \alpha g \Delta H^3/(\kappa\nu)$) and the Prandtl number ($Pr = \nu/\kappa$). Here α, ν, and κ denote the thermal expansion coefficient, the kinematic viscosity, and the thermal diffusivity, respectively. Furthermore, g is the gravity and Δ the temperature difference between the bottom and the top. The main integral response parameters that is considered is the Nusselt number $Nu \equiv \langle \mathcal{F}_z \rangle_{t,V}$, where $\langle\cdot\rangle_{t,V}$ denotes the time- and volume-averaging and $\mathcal{F}_z \equiv (u_z(T - T_0) - \kappa\partial_z T)/(\kappa\Delta/H)$ is the normalized vertical heat flux with u_z being the vertical component of the velocity and T_0 the average of the top and bottom temperatures. Under rotation, the rotation rate Ω is incorporated in another dimensionless control parameter, the Rossby number $Ro = \sqrt{\alpha g \Delta H}\ /\ (2\Omega H)$ or, alternatively, the Ekman number $Ek = \nu/(2\Omega H^2)$.

Most studies are conducted in cylindrical systems with aspect ratios between the diameter D and the height H, $\Gamma = D/H$ close to one. When no rotation is present, the flow self-organises in such cylinders into a large-scale convection role (LSC) that spans over the entire cell height [1], and transports warm fluid from the bottom to the top along one side and cold fluid from top to bottom on the opposite side of the cylinder.

In rotating convection, the LSC breaks down and is replaced by vortical structures that are aligned in vertical direction, i.e., along the rotaion axis. The intrinsic linear scale of separation of these vortices is reduced with increasing rotation rate, suggesting that one might reduce the geometric aspect ratio, i.e., $\Gamma < 1$ while maintaining a large ratio of lateral cell size to linear scale; such convection cells are being implemented in numerous new experiments [5].

We present numerical and experimental measurements for rotating RBC in a $\Gamma = 1/2$ cylindrical cell for $Pr = 0.8$, $10^8 \leq Ra \leq 5 \times 10^{14}$, and $1/Ro < 20$. We find that under sufficiently fast rotation, an annular flow, denoted a boundary zonal flow (BZF), occurs that has profound effects on the overall flow structure and on the spatial distribution of the vertical heat flux. In particular, within the BZF the mean azimuthal velocity is positive, i.e., the flow is in cyclonic direction, while the radial core has on average negative azimuthal velocities, i.e., anticyclonic flow. Within the BZF, warm fluid rises along one side, while cold fluid sinks on the opposite sides, creating an azimuthal temperature distribution (see fig. 1a and b), which on the first glance is similar to the LSC. However, in contrast to the LSC, these temperature bands are located only in a region close to the lateral sidewall (at distance $\delta_{BZF} < 0.3R$ away from it). As shown in the space-time plots in fig. 1(a and b), while the velocity is cyclonic, the entire structure drifts in anticyclonic direction. In the experiment one can detect the BZF as two distinct maxima in the temperature probability density function (PDF) when measured sufficiently close to the sidewall at sufficiently large rotation rates ($1/Ro$), as shown in fig. 2a. This bimodality is absent in the PDF of the temperature measured in the radial bulk of the cell (fig. 2b). The heat flux inside the BZF is significantly larger than in the radial bulk, as is shown in fig. 1c.

The size of the BZF (δ_{BZF}) decreases with increasing rotation rates but increases with Ra, following $\delta_{BZF} \propto Ra^{1/4}Ek^{2/3}$. We note, that this scaling is in contrast to the expected scaling of Stewartson layers [2] and thus we believe that the mechanisms responsible for the BZF are not understood [6]. Furthermore, the robustness of the BZF state

*Corresponding author. E-mail: stephan.weiss@ds.mpg.de.

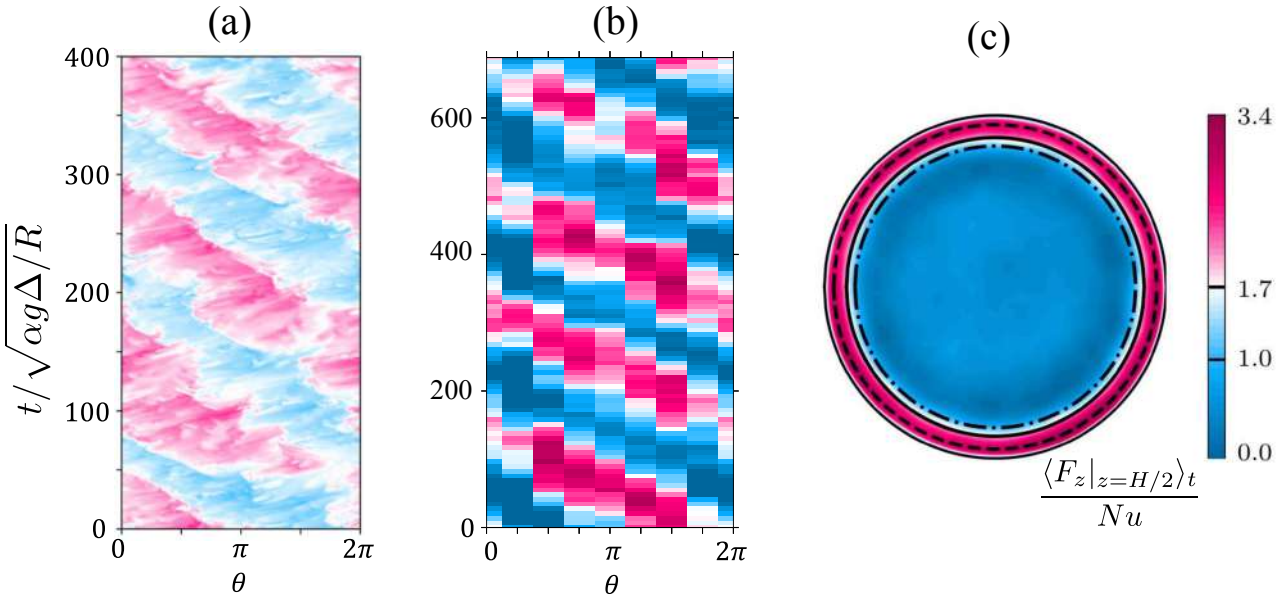

Figure 1: Temperature at the sidewall and vertical distance z=H/2 from the bottom plate as a function of azimuthal position (x-axis) and time (y-axis) in simulation (a, $Ra = 10^9$) and experiment (b, at $Ra = 5 \times 10^{13}$). Warm areas are marked in red. Cold regions are marked in blue. (c): Average heat flux at midheight ($z = H/2$) normalised with the Nusselt number. The heat flux in the BZF is significantly enhanced compared to the heat flux inside the bulk.

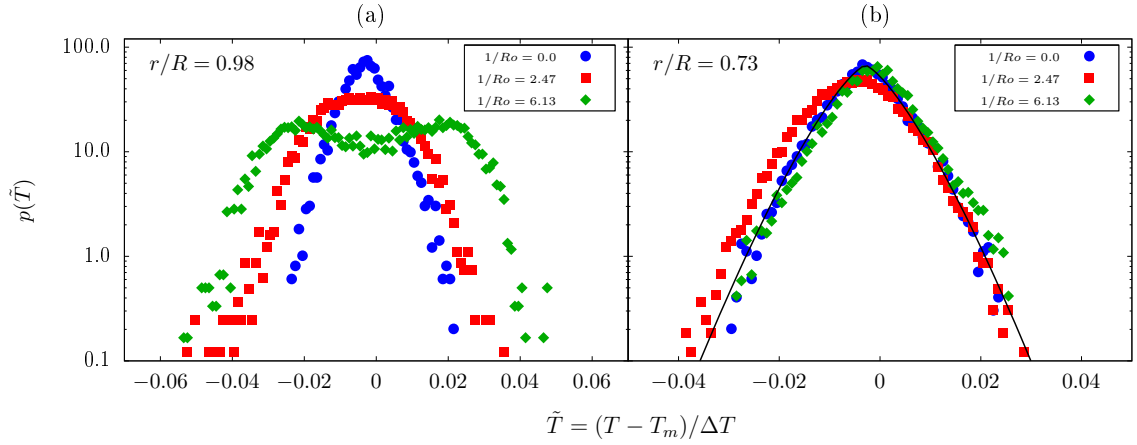

Figure 2: Probability density distribution of the reduced temperature $T - T_m/\Delta T$ at height z/L=0.49 and $Ra = 4.9 \times 10^{13}$ for radial distances from the center line $r/R = 0.98$ (a) and $r/R = 0.73$ (b) and for three different $1/Ro$.

as evidenced by its existence over 7 orders of magnitude in *Ra* in DNS and experiment and over a range $1/2 \leq \Gamma \leq 2$ and $0.1 \leq Pr \leq 4.4$ suggests that this flow structure might play a crucial role for the heat transport in rotating RBC and thus needs to be understood for generalising observations in DNS and experiments.

References

[1] Ahlers G., Grossmann S., and Lohse D. *Rev. Mod. Physics* **81**: 503, (2009).
[2] Kunnen et al., *J. Fluid Mech.* **688**:422, (2011).
[3] Weiss S., and Ahlers G., *J. Fluid Mech.*, **688**:461, (2011).
[4] Horn S., and Shishkina O., *J. Fluid Mech.*, **762**:232, (2015).
[5] Cheng J. et al., *Geophys. Astrophys. Fluid Dyn. Lett.*, **112**:277, (2018).
[6] Zhang X. et al., accepted in *Phys. Rev. Lett.*, 2020.

INITIAL STAGE OF THE LOBE-CLEFT FORMATION AT A GRAVITY CURRENT FRONT

Lin-Sen Zhang and Jian-Jun Tao *
SKLTCS, CAPT, Department of Mechanics Engineering Science, College of Engineering, Peking University, Beijing, 100871, P. R. China

Summary Different from the traditional lock-exchange setup, a rotatable apparatus is designed to study the initial stage of the three dimensional instability that leads to the formation of lobe and cleft structures at the gravity current fronts. It is shown that the measured initial dominating spanwise wavenumbers have a 1/3 scaling law with the Grashof number at moderate Grashof numbers, agreeing with the prediction of a Rayleigh-Taylor Instability (RTI) model. Furthermore, after a Schmidt number modification suggested by the RTI model, the previous results for a small Schmidt number (Härtel *et al*., J. Fluid Mech. 2000) turn to be consistent with the present experimental data with a high Schmidt number, confirming that the initial dominating spanwise wavenumber of lobe and cleft structures depends on the Schmidt number substantially.

INTRODUCTION

Gravity currents are the the flows driven by horizontal density differences, and are common phenomena occurring in nature and industrial applications, e.g. sand storm and avalanche [1]. A key feature of the current front is the lobe and cleft structures, which dominate the local transportation process. Simpson carried out pioneering experiments [2] by using saltwater and freshwater within a lock-exchange tank, and found that the thin light fluid layer beneath the front nose was necessary for the formation of lobes and clefts. Based on the stability analyses of the two-dimensional density and velocity fields obtained numerically in advance [3], the locations and the spanwise wavenumbers of the most unstable modes for different Grashof numbers (Gr) were obtained for unit Schmidt number (Sc), and it was stated that the dependence of the growth rate on Sc was weak unless Sc was very small. Recently, three dimensional numerical simulations and stability analyses revealed that the original formation mechanism of lobes and clefts is the Rayleigh-Taylor instability (RTI), and the initial dominating spanwise wavenumber can be estimated with a RTI model for given Gr and Sc without any details of the density and velocity fields [4],

$$k_{max} = \left(\frac{Gr}{2}\right)^{\frac{1}{3}} \left(\left[2(1+\frac{1}{Sc}) + \sqrt{4(1+\frac{1}{Sc})^2 - 3} \right]^2 - 1 \right)^{-\frac{1}{3}} = \left(\frac{Gr}{2}\right)^{\frac{1}{3}} \mathcal{F}(Sc). \quad (1)$$

However, it has been difficult to examine experimentally the initial linear stage of the mode evolution, because opening the lock gate or suddenly stoping the moving floor plate [2, 5] bring strong disturbances to the front interface and stimulate nonlinear evolutions, which may cause underestimate of the dominating wavenumbers [4]. Therefore, the systematic experiments on the linear stage of the three dimensional instability at the current front have been lacked so far, and this is the main motivation of the present paper.

METHODS AND RESULTS

In order to avoid the strong local disturbances caused by lifting the lock gate, rotatable tanks around their horizontal axles are constructed. The experimental procedure is as follows. The tank is placed vertically at first, then the thin plate separating the bottom denser fluid (solution of $CaCl_2$) and the upper lighter fluid (distilled water) is withdrawn. After the disturbed interface recovers to its equilibrium state, the tank is rotated to its horizontal position and the gravity current will be formed. In the experiments, we used three tanks, which have the same length (500mm) and width (150mm) but different heights h, i.e. 43.4mm, 74.2mm and 117.8mm. The Grashof number is defined as $Gr = 2gAh^3/(\nu^2)$, where g, A, and ν are the gravitational acceleration, the Atwood number, and the kinematic viscosity, respectively. The denser fluid is dyed in order to show the interface clearly, and the influence of the dye addition on the density is considered. The Schmidt number $Sc = \nu/D$ at the laboratory temperature is 833, where D is the concentration diffusivity.

The top views of the front evolution are recorded by a CCD camera mounted above the tank, and the edges of the fronts are extracted and tracked by image processing. As shown in Fig. 1 (a), the current front moves downstream (x direction) with time, and its leading edge changes from a straight line to a curve varied periodically in the spanwise (z) direction, indicating the formation of lobes and clefts. The three-dimensional instability leads to streamwise vortices, which correspond to the dark bands arranged regularly in the spanwise direction. Therefore, the rotatable tank is validated to study the linear stability of the current front at least for moderate Grashof numbers. The time series of the front leading edge are recorded as shown in Fig. 1(b) and the initial dominating spanwise wavenumber k_{max} can be determined.

*Corresponding author. E-mail: jjtao@pku.edu.cn

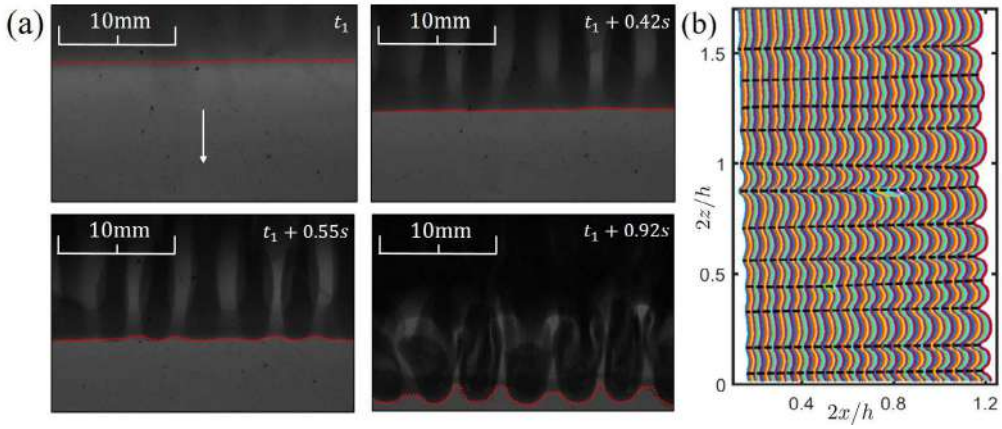

Figure 1: (a) Top view of the current front at different time for $Gr = 5 \times 10^6$. The white arrow indicates the moving direction of the front and the front leading edge is shown by the red line. (b) The front leading edges with a time interval of 0.01s as $Gr = 1 \times 10^6$. The dashed lines represent the tracks of the clefts.

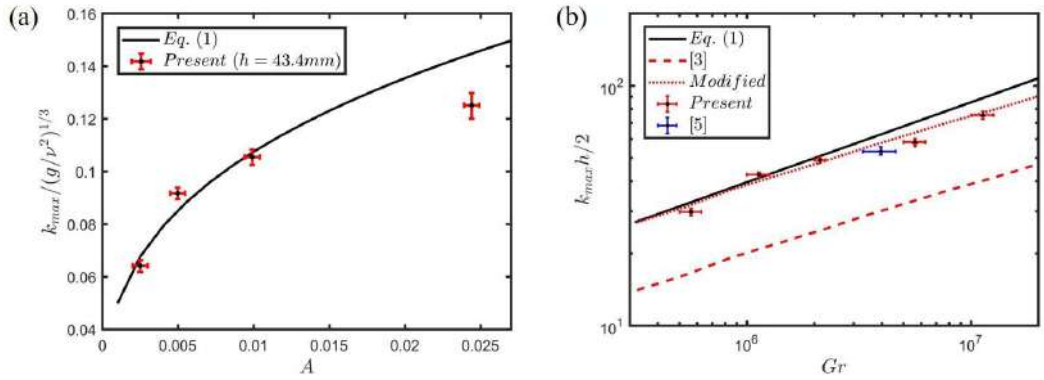

Figure 2: The measured initial dominating spanwise wavenumber as a function of (a) Atwood number and (b) Grashof number in comparison with the theoretical curve of the RTI model. The previous linear result for $Sc = 1$ [3] is shown as the dashed line.

It is shown in Fig. 2(a) that the measured k_{max} varies with A just as predicted by the RTI model (Eq. 1) when A is small, indicating the the original formation mechanism of the lobes and clefts is the Rayleigh-Taylor instability [4]. It is noted that in the present experiments the slight variation of Sc for different solution densities is ignored. According to the RTI model (Eq. 1), k_{max} at the linear stage has a scaling law of 1/3 with Gr, which is confirmed by the present experimental data as shown in Fig.2 (b), especially at moderate Grashof numbers. The previous linear result [3] for $Sc = 1$ is shown as a dashed line in Fig. 2(b), and has large discrepancies with the present measurements and other previous experimental data [5] because of the Schmidt number difference. In fact, based on Eq. (1), we may modify the previous result [3] by simply multiplying $\frac{\mathcal{F}(Sc=833)}{\mathcal{F}(Sc=1)} = 1.92$, and then the dashed line changes to the dotted line as shown in Fig. 2(b), which is consistent with the present experimental data very well, confirming that the Schmidt number has an important effect on the initial spanwise length scale of lobes and clefts.

CONCLUSIONS

In order to experimentally study the linear instability of the gravity-current front, rotatable tanks are designed and used to avoid the strong local disturbances caused by the traditional lock-exchange setup. It is shown that the measured spanwise dominating wavenumber has a 1/3 scaling law with the Grashof number and a dependence on the Schmidt number as predicted by the RTI model, suggesting that the original formation mechanism of lobes and clefts is the Rayleigh-Taylor instability.

References

[1] Simpson J. E. Gravity Currents in the Environment and Laboratory. Cambridge University Press, 1997.
[2] Simpson J. E. Effects of the Lower Boundary on the Head of Gravity Current. *J. Fluid Mech.* **53**: 759-768, 1972.
[3] Härtel C., Carlsson F. & Thunblom M., Analysis and Direct Numerical Simulation of the Flow at a Gravity Current Head. Part 2. the Lobe and Cleft Instability. *J. Fluid Mech.* **418**: 213-229, 2000.
[4] Xie C.Y., Tao J.J., Zhang LS. Origin of Lobe and Cleft at the Gravity Current Front. *Phys. Rev. E*, **100**(3), 031103, 2019.
[5] Neufeld, J. Lobe-cleft Patterns in the Leading Edge of a Gravity Current. Masters thesis, University of Toronto, 2002.

KATABATIC PRANDTL SLOPE FLOWS IN THE VERY-STABLE REGIME

Inanc Senocak*[1] and Cheng-Nian Xiao[1]
[1]Department of Mechanical Engineering and Materials Science, University of Pittsburgh, Pittsburgh, USA

Summary We investigate the nature of patchy turbulence in stably stratified Prandtl slope flows with and without ambient wind forcing using direct numerical simulations. The slope angle, Prandtl number and two newly established dimensionless numbers, namely the stratification perturbation and the wind forcing numbers, form the dimensionless parameter space to realize a turbulent patch that persists over the slope plane. We use conditional statistics to characterize the flow in turbulent and non-turbulent patches in katabatic slope flows to and contrast it against the flow states in the weakly stable regime. Additionally, we demonstrate the ineffectiveness of the gradient Richardson number as a stability parameter and investigate the plausibility of the new dimensionless numbers to serve as an improved criterion of stability.

INTRODUCTION

Turbulence in strongly stratified fluids is one of the least understood subjects in fluid mechanics. Comprehension of the subject matter plays a central role in developing computer models of stable atmospheric boundary layer (SABL), nocturnal winds in mountainous terrain, and winds over large ice sheets in polar regions and glaciers. Stable conditions in atmospheric boundary layer starts to develop around evening hours due to radiative cooling of the surface to clear skies. Conditions within SABL can range from fully developed turbulent to intermittently turbulent and even near calm state, which make it difficult to predict computationally [1].

Ludwig Prandtl was the first to derive an exact solution to idealized slope flows within a stratified medium [2]. The Prandtl solution has been shown to describe qualitatively the vertical profiles of wind speed and temperature of katabatic winds in mountainous terrain or over large ice sheets in polar regions. In the Prandtl model, winds aloft are quiescent. Lykosov and Gutman [3] incorporated the effect of a uniform ambient wind field into Prandtl's original formulation, which we refer to as the *extended* Prandtl model. The vertical profiles of buoyancy and velocity are exponentially damped sinusoidal solutions in the original Prandtl model. The velocity profile in the extended Prandtl model appears as a mere shifting of the velocity profile produced by the original Prandtl model.

In a series of publications [4, 5, 6], we have studied the fluid instabilities in idealized slope flows. We have shown through linear stability analysis and direct numerical simulations that Prandtl slope flows are prone to two types of instabilities: stationary vortical rolls aligned in the along-slope direction and travelling waves propagating in the along-slope direction. The analyses have shown that dynamical stability of slope flows is governed by the slope angle, Prandtl number and the stratification perturbation number, which is a measure of the disturbance to the background stratification due to cooling at the surface. When an ambient wind field aloft exists, wind forcing number emerges as an additional dimensionless number highlighting the uniqueness of the stratification perturbation parameter as a dimensionless number. These new developments have enabled us to argue the ineffectiveness of the current practice of using a single Richardson number to describe the stability of stratified slope flows. In Xiao and Senocak [5], the stratification perturbation number was proposed as a potential quantitative metric to demarcate stably stratified flows into super, very stable and weakly stable regimes.

In the present work, we use the newly established dimensionless parameter space to study a patch of turbulence over an infinitely wide slope with a constant inclination angle and negative heat flux imposed at the surface. The advantage of the present approach is that a unique flow state can be identified such that a patchy turbulence persists at all times over the slope plane. This idealized configuration enable us to study the slope flow in the very-stable regime with the help of conditional statistics and contrast it against fully developed turbulent conditions in the weakly stable regime.

TECHNICAL BACKGROUND

The governing equations for conservation of momentum and energy under the Boussinesq approximation for an incompressible slope flow with a constant ambient wind aloft can be written as follows [3]:

$$\frac{\partial u_i}{\partial t} + \frac{\partial u_i u_j}{\partial x_j} = -\frac{1}{\rho}\frac{\partial p}{\partial x_i} + \frac{\partial}{\partial x_j}\left(\nu \frac{\partial u_i}{\partial x_j}\right) + b g_i, \tag{1}$$

$$\frac{\partial b}{\partial t} + \frac{\partial b u_j}{\partial x_j} = \frac{\partial}{\partial x_j}\left(\beta \frac{\partial b}{\partial x_j}\right) - N^2 g_j (u_j - U_j), \tag{2}$$

where ν is the kinematic viscosity, β is the thermal diffusivity. N is the constant Brunt-Väisälä frequency. Buoyancy b is related to the potential temperature Θ as $b = g(\Theta - \Theta_e)/\Theta_r$, where Θ_r is a reference potential temperature and Θ_e is the environmental potential temperature. Non-dimensional gravity vector is defined as $g_i = [g_1, g_2, g_3] = [\sin\alpha, 0, \cos\alpha]$,

*Corresponding author. E-mail: senocak@pitt.edu

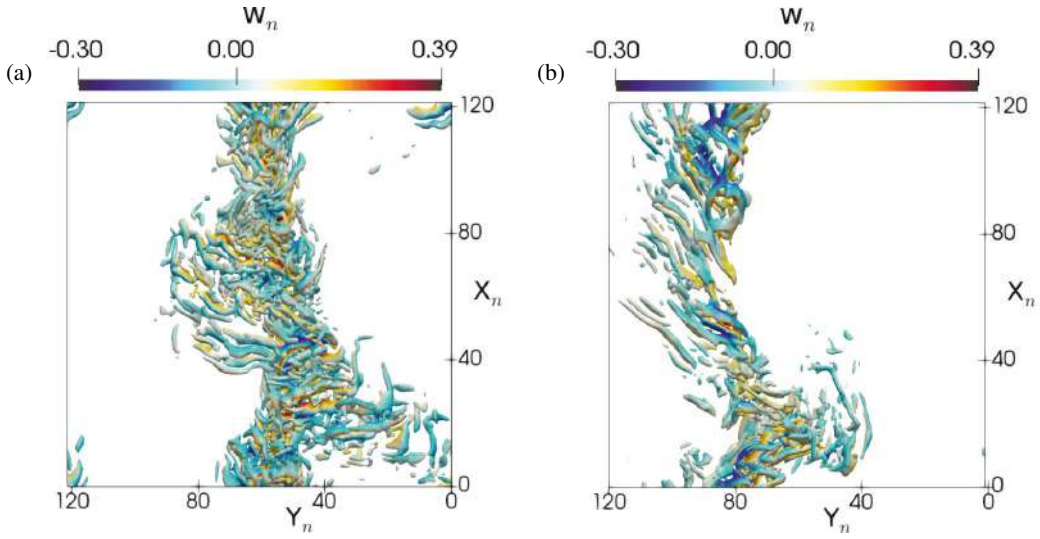

Figure 1: Q-contour visualisations of a patch of turbulent region in slope flows with and without ambient wind forcing. Colour represents for the slope normal velocity. $\alpha = 5^\circ$ (a) $\Pi_s = 25$, $\Pi_w = 0$; (b) $\Pi_s = 19.8$, $\Pi_w = 320$. $Ri_g = 1.14 \times 10^{-3}$ for both cases. Main slope flow direction is from top to bottom.

where α is the slope angle. The ambient wind vector is assumed to be of the form $(U_j) = (U_\infty, 0, 0), U_\infty < 0$. The governing equations are completed by the divergence free velocity field condition for incompressible flows.

The dimensionless numbers involved in the Prandtl slope flow with an ambient wind field can be determined with the help of the Buckingham-π theorem.

$$\alpha, \quad Pr \equiv \frac{\nu}{\beta}, \quad \Pi_s \equiv \frac{|B_s|}{\beta N^2}, \quad \Pi_w \equiv \frac{U_\infty^2}{\nu N}, \tag{3}$$

where B_S is the constant negative heat flux imposed at the surface. Because there is no external length scaled imposed on the Prandtl slope flow familiar dimensionless numbers such as the Reynolds, Richardson, or Froude number do not appear in the above list. Π_s was introduced in [4] as the stratification perturbation number, and Π_w in [6] as the wind forcing number. [6] used the analytical solution of the extended Prandtl model [3] to further show that the gradient number is a function of the four dimensionless numbers given in equation 3 as follows:

$$Ri_g = \frac{N^2}{\left(\frac{\partial u}{\partial z}\right)^2_{\max}} = \frac{\mathrm{Pr}}{\left(\sqrt{2\Pi_w}\mathrm{Pr}^{3/4}\sin^{1/2}\alpha + \Pi_s\right)^2}, \tag{4}$$

The above relationship is significant because it shows that a single gradient Richardson number is insufficient to define the dynamic stability of stratified slope flows.

RESULTS

Figure 1 illustrates the nature of patchy turbulence that can persist in the very-stable slope flow regime. Prandtl number of 0.71 and a slope angle of 5° is used for both cases shown in Figure 1. We use equation 4 to identify flow states with the same Ri_g number but with different Π_w, Π_s. Figure 1a represents a case with no ambient wind aloft, whereas Figure 1b has a wind forcing number of $\Pi_w = 320$ and a smaller $\Pi_s = 19.8$. An instantaneous visualization of the vorticity field via the Q-criterion reveals the differences in the flow states. The flow field corresponding to the larger stratification perturbation $\Pi_s = 25$ is more turbulent like with numerous smaller eddies than its counterpart at the same Ri_g number with a nonzero wind forcing number $\Pi_w = 320$. This illustration serves as a visual evidence of the ineffectiveness of gradient Richardson number to describe the dynamic stability of slope flows. It appears that for a fixed Ri_g, surface buoyancy flux has a stronger destabilization effect than the ambient wind higher aloft. Statistical results from these fields will be compared against the weakly stable regime and presented in the final abstract.

References

[1] L. Mahrt. Stably stratified atmospheric boundary layers. *Annu. Rev. Fluid Mech*, 46:23–45, 2014.
[2] L. Prandtl. *Führer durch die Strömungslehre*. Vieweg und Sohn, 1942.
[3] V. Lykosov, L. Gutman. Turbulent boundary-layer over a sloping underlying surface. *Izv. Acad. Sci. USSR, Atmos. Ocean. Phys.*, 8(8):799, 1972.
[4] C.-N. Xiao, I. Senocak. Stability of the Prandtl model for katabatic slope flows. *J. Fluid Mech.*, 865, 2019.
[5] C.-N. Xiao, I. Senocak. Stability of the anabatic Prandtl slope flow in a stably stratified medium. *J. Fluid Mech.*, 885:A13, 2020.
[6] C.-N. Xiao, I. Senocak. Linear stability of katabatic Prandtl slope flows with ambient wind forcing. *J. Fluid Mech.*, 886:R1, 2020.

BINARY INTERACTIONS BETWEEN BARCHAN DUNES

Willian Righi Assis*[1] and Erick de Moraes Franklin[1]
[1]School of Mechanical Engineering, University of Campinas, Rua Mendeleyev, 200, Campinas, SP, Brazil.

Summary Barchan is a crescentic-shape dune, often organized in dune fields. When in a dune field, dune-dune interactions play a significant role in regulating the dynamics and sizes of barchans. The present work experimentally investigates the different types of interactions between two barchans and which physical aspects govern the behavior of those interactions. The experiments were conducted in a closed-conduit channel of transparent material, where pairs of granular piles were poured in and a high-definition camera used to acquire images of the bedforms. As a result, five different patterns were identified for both aligned and off-centered configurations, and we propose interaction maps that depend basically on the ratio between the number of grains of each dune, Shields number (θ) and alignment of barchans. This paper is based on Ref.[3] and reproduces many of its parts.

INTRODUCTION

Barchans are crescent-shaped dunes that form in areas of unidirectional fluid flow with horns pointing downstream [1]. In nature, they are found in deserts and rivers, for example, and in industry they can be found inside oil pipelines and dredging lines. Although the study of isolated dunes helps to understand their dynamics, barchans generally do not appear isolated, but belong to dune fields, where they can be influenced by their neighbors whose speeds and sizes are different [2].

The contact (or quasi-contact sometimes) of dunes, termed collision [2], that happens in dune fields plays a significant role in regulating the size of barchans, by redistributing sand and also creating small barchans from large ones. In a previous study [3], the short-range interactions occurring between two subaqueous barchans were experimentally investigated and five different patterns were identified and interaction maps that depend basically on the ratio between the number of grains of each dune, Shields number, and alignment of barchans were proposed.

EXPERIMENTAL SETUP

The experimental setup consisted of a water reservoir, two centrifugal pumps, a flow straightener, a 5m long closed-conduit channel with rectangular cross-section (width $\alpha = 160$mm and height $\beta = 50$mm), a settling tank and a return line. The test section is 1m long and starts 40 hydraulic diameters downstream of the channel inlet. A total number of 123 tests were performed, for which we used different populations of grains (not mixed): round glass beads ($\rho_s = 2.500$ kg/m^3) with 0.15mm $\leq$ d $\leq$ 0.25mm and 0.40mm $\leq$ d $\leq$ 0.60mm, angular glass beads with 0.21mm $\leq$ d $\leq$ 0.30mm, and zirconium beads ($\rho_s = 4.100$ kg/m^3) with 0.40 mm $\leq$ d $\leq$ 0.60, where ρ_s and d are, respectively, the density and diameter of grains. Reynolds number based on the channel height, $Re = \rho\overline{U}\beta/\mu$, varied from 1.13×10^4 to 1.82×10^4, where μ is the dynamic viscosity, ρ the density of the fluid and $\overline{U}$ the cross-sectional mean velocity of water. The Shields number $\theta = (\rho u_*^2)/((\rho_s - \rho)gd)$, which is the ratio between drag on grains and their relative weight, varied from 0.019 to 0.106, where u_* is the shear velocity and g is the magnitude of gravity. The total number of grains on each pile was computed as the mass of the initial pile divided by that of one single grain. We identified the different patterns by recording the bedforms with a digital camera and afterwards processing the images.

RESULTS AND DISCUSSION

Five different patterns were observed as resulting from the binary interaction (for both aligned and off-centered configuration): 1) chasing (Figures 1a and 2a), when the upstream dune does not reach the downstream one; 2) merging (Figures 1b and 2b), when the upstream dune collides with downstream one and there is no loss of grains; 3) exchange (Figures 1c and 2c), when, after the collision, a small barchan is ejected and, being the smaller one, outruns the other and migrates downstream; 4) fragmentation-chasing (Figures 1d and 2d), when the downstream dune splits into two or more barchans; and 5) fragmentation-exchange (Figures 1e and 2e), when the fragmentation initiates as in 4), but, the upstream barchan being still faster than the splitting dune, they collide. Once they touch, an off-center exchange occurs, and a small barchan is ejected. Figures 3 (a),(b) and (c),(d) depict points from each test in terms of the Shields number (θ) versus the ratio between the number of grains of each dune $\xi_N = \Delta_N/\Sigma_N$, and boundaries between different patterns for the aligned and off-centered barchans, respectively. The alignment of barchans is represented by the offset parameter σ (dimensionless),

*Corresponding author. E-mail: righiassis@gmail.com

computed as the transverse distance between the centroid of approaching barchans, η, divided by their average width: $\sigma = 2\eta/(W_u + W_d)$, where W_u and W_d are the widths of the upstream and downstream bedforms, respectively. These maps provide a comprehensive and simple classification for the short-range interactions of subaqueous barchans and they may be useful for predicting the collisions of barchans in different environments.

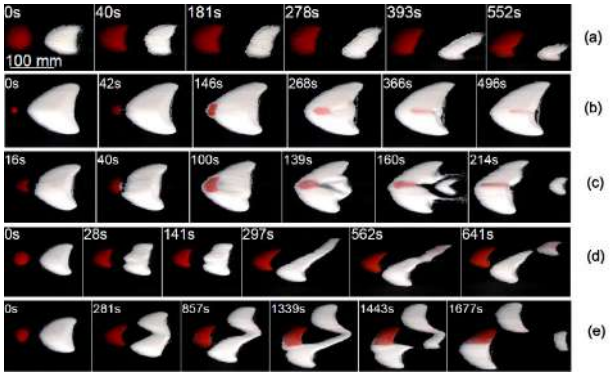

Figure 1: Snapshots of barchan interactions for aligned dunes. In the snapshots, the water flow is from left to right, the upstream pile consisting of red glass beads and the downstream pile of white glass beads. Figure extracted from [3].

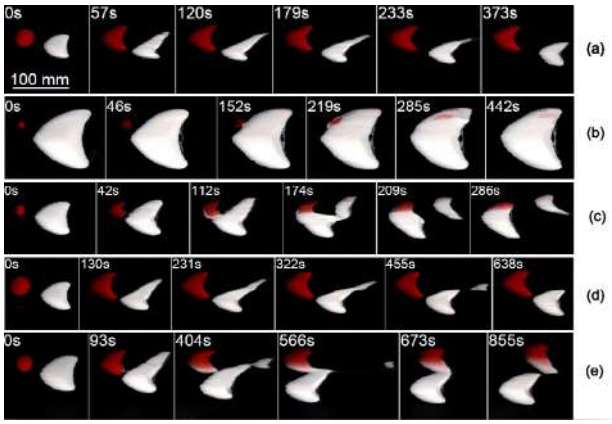

Figure 2: Snapshots of barchan interactions for off-centered dunes. In the snapshots, the water flow is from left to right, the upstream pile consisting of red glass beads and the downstream pile of white glass beads. Figure extracted from [3].

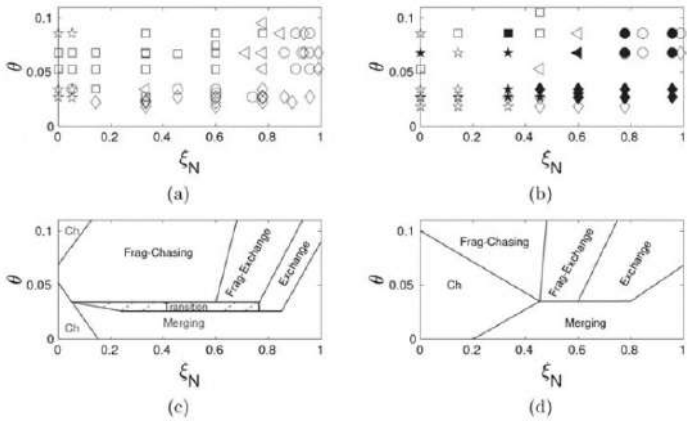

Figure 3: (a and b) Patterns of barchan-barchan interactions as functions of ξ_N and θ for (a) aligned and (b) off-centered barchans. Stars, diamonds, circles, squares, and triangles correspond to chasing, merging, exchange, fragmentation-chasing, and fragmentation-exchange, respectively. In (b), open symbols correspond to $\sigma < 0.5$ and solid symbols to $\sigma \geq 0.5$. (c and d) Boundaries between different patterns for the aligned and off-centered barchans, respectively, where Ch stands for chasing and Frag to fragmentation. Figure modified from [3].

References

[1] Hersen P., Andersen K.H., Elbelrhiti H., Andreotti B., Claudin P., Douady S. Corridors of barchan dunes: Stability and size selection. *Physical Review E.* **69**: 011304, 2004.
[2] Hersen P., Douady S. Collision of barchan dunes as a mechanism of size regulation. *Geophysical Research Letters* **32**: 21, 2005.
[3] Assis W.R., Franklin E.M., A comprehensive picture for binary interactions of subaqueous barchans. *Geophysical Research Letters* **47**, no. 18 (2020): e2020GL089464.

SCENARIOS OF LANDSLIDE TSUNAMI IN THE SOUTH CHINA SEA

Hua Liu*[1], Zhiyuan Ren [2]
[1]Key Laboratory of Hydrodynamics (Ministry of Education), Shanghai Jiao Tong University, Shanghai, China
[2]National Marine Environmental Forecasting Center, Beijing 100081, China

Summary We adopt the Herschel-Bulkley rheological theory to describe the viscoplastic debris landslide flow and the shallow water equations to compute the propagation of tsunamis induced by the time-dependent deformation of the seafloors. The one-way coupled method of the landslide induced tsunami is implemented through satisfying the kinematic bottom boundary condition. With respect of the Baiyun slide, the effects of remolding rate, initial and residual yield strength on landslide and tsunami are studied numerically. To predict the potential landslide tsunami hazard in the South China Sea, the scenarios of the landslides with the different volumes in the Baiyun slide and the Brunei Slide are presented. Comparison with the non-deformation model in the near-field illustrates the crucial role of rheological property in the landslide tsunami modelling. Furthermore, the characteristics of the propagation of landslide tsunami in the South China Sea and coastal hazards are analyzed.

INTRODUCTION

In the past decade, many studies have focused on the potential earthquake tsunami from Manila Trench of the South China Sea[1]. Nevertheless, the landslide tsunami should be included in tsunami hazard analysis based on the historical records and potential submarine landslide in the South China Sea. The mechanism of the tsunami which struck the southwest coast of Taiwan in the eighteenth century was considered as a submarine mass failure[2]. In 1992, earthquake swarms of magnitude 3.4-3.7 occurred near Hainan Island. Two gauges at Yulin port and Sanya port recorded tsunami wave around 0.78 m and 0.5-0.8 m respectively. However, it is still an open question how can such a small earthquake generates a significant tsunami near Sanya.

The past and potential tsunami sources in the South China Sea have been reviewed. The Baiyun slide along the northern margin of the South China Sea and the Brunei slide near the southern margin may generate giant submarine landslide which could be triggered by a seismic activity or hydrate disassociation[3]. It is interesting to understand the potential landslide tsunami to coasts of the South China Sea. Although some preliminary results of the landslide tsunami from the Baiyun slide or the Brunei slide have been studied by using the solid submarine landslide model, it is still necessary to provide a comprehensive analysis of landslide tsunami included deformation and regression process of landslide.

In this study, we mainly focus on numerical study on rheological landslide and potential landslide tsunamis in the South China Sea. The mathematical formulation of the coupling submarine landslide and water wave generation will be discussed.

NUMERICAL MODEL

Based on the Herschel-Bulkley rheological theory, the depth averaged governing equations of the viscoplastic debris flow can be formulated in the horizontal two-dimensional form[4,5],

$$\frac{\partial h}{\partial t}+\nabla\cdot\left(\left(h_p+\alpha_1 h_s\right)\mathbf{u}_\mathbf{p}\right)=0\,, \tag{1}$$

$$\begin{aligned}&\frac{\partial\left(\mathbf{u}_\mathbf{p}\left(h_p+\alpha_1 h_s\right)\right)}{\partial t}+\left(\left(h_p+\alpha_2 h_s\right)\mathbf{u}_\mathbf{p}\cdot\nabla\right)\mathbf{u}_\mathbf{p}+\mathbf{u}_\mathbf{p}\nabla\cdot\left(\left(h_p+\alpha_2 h_s\right)\mathbf{u}_\mathbf{p}\right)\\&+\left(1-\frac{\rho_w}{\rho_d}\right)gh\nabla\left(h+b\right)=-\frac{\tau_y\,\mathrm{sgn}\left(\mathbf{u}_\mathbf{p}\right)}{\rho_d}-\frac{\alpha_3\tau_y}{\rho_d}\mathbf{f}_\mathbf{s}\,,\end{aligned} \tag{2}$$

$$\frac{\partial\mathbf{u}_\mathbf{p}}{\partial t}+\mathbf{u}_\mathbf{p}\cdot\nabla\mathbf{u}_\mathbf{p}+\left(1-\frac{\rho_w}{\rho_d}\right)g\nabla\left(h+b\right)=-\frac{\tau_y\,\mathrm{sgn}\left(\mathbf{u}_\mathbf{p}\right)}{\rho_d h_p}\,, \tag{3}$$

in which, t is the time, ρ_w and ρ_d denote the density of water and debris fluid, b is the still water depth, g is the gravitational acceleration. ∇ is the horizontal gradient operator. τ_y is the yield stress. The parameters α_1, α_2, and α_3 are determined by the Herschel-Bulkley rheological flow model for the case of small slope assumption. $\mathbf{u}_\mathbf{p}$ is the plug layer velocity of the debris flow. Including the remolding progress, the yield strength is written as,

$$\tau_y\left(\gamma\right)=\tau_{y,\infty}+\left(\tau_{y,0}-\tau_{y,\infty}\right)e^{-\Gamma\gamma}\,. \tag{4}$$

in which, the initial yield strength and residual yield strength is noted by $\tau_{y,0}$ and $\tau_{y,\infty}$. γ is the total shear deformation, and Γ is the remolding rate.

The tsunami propagation is simulated by the nonlinear shallow water equations. The numerical model GeoClaw based on the nonlinear shallow water equations is used to simulate the propagation of landslide tsunami. The model has

*Corresponding author. E-mail: hliu@sjtu.edu.cn

been validated in many recent tsunami events.

The slide process of debris flow could last a relatively long duration (10 min to 2 h), while the duration of most earthquake motion only lasts around 5 – 200 s. Compared with tsunami propagation time, the landslide duration can not be ignored. When a submarine landslide occurs, the landslide slide model is firstly used to calculate the evolution of the debris landslide flow. Then the process of the landslide in terms of landslide thickness is coupled with the nonlinear shallow water equation model based on the kinematic boundary condition[3].

The rheological landslide modeling needs to take into account several parameters. The slide thickness depends on the geological measurement. The selection of rheological parameters is based on the numerical experiments and previous studies since it is hard to measure them. The density of 1860 km/m^3 is adopted herein.

RESULTS AND DISCUSSION

The landslide tsunami from the Baiyun slide is studied by the numerical model, concerning the effect of initial and residual yield strength, and remolding rate. The grid solution for landslide tsunami is 15 arc-sec. In tsunami simulation, the grid size is one arc-min in tsunami simulation, and is refined to 15 arc-sec grids near coastal measured locations. Regarding the potential submarine landslide tsunami of the Baiyun slide, the tsunami propagation for the cases of typical volumes of 10 km^3, 50 km^3, 100 km^3, and 200 km^3 is plotted in Fig. 1. The generation and propagation of tsunami are following the slide process. The tsunami wave amplitude and wavelength depend on the volume and maximum thickness of the slide. The slide with a volume of 200 km^3 could generate the most hazardous tsunami.

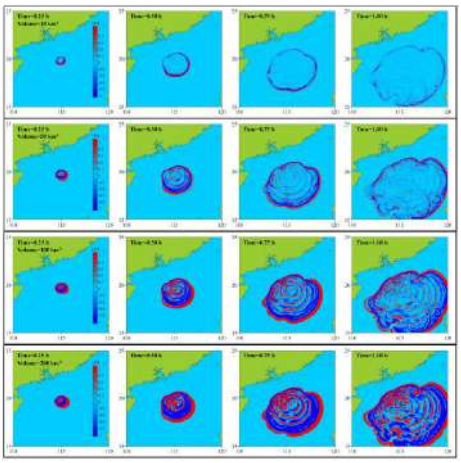

Figure. 1. Evolution of tsunami wave in the near-field for different landslide volumes. The time interval is 0.25 h.

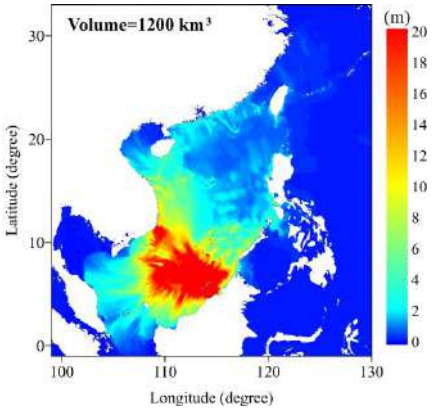

Figure. 2. Distribution of the maximum landslide amplitude induced by Brunei slide of 1200 km^3.

The distribution of the maximum landslide amplitude induced by Brunei slide of 1200 km^3 is shown in Fig. 2. It is noted that the giant landslide could generate a huge tsunami in the South China Sea, especially for the northern part. The tsunami could attack the coast of Brunei, Malaysia, Indonesia, Vietnam, Philippines, and South China. The tsunami in the near-field could exceed 10 m, and still be over 2 m in the far-field. The wave periods for Yongxing island, Zhongsha island, Huangyan Island are 30 min, 20 min, 17 min, respectively.

CONCLUSIONS

A numerical model to deal with tsunami induced by debris flow landslide is developed. The landslide model is described by the Herschel-Bulkley rheological theory including the remolding process, while the tsunami wave propagation is computed by the nonlinear shallow water equations. This paper presents scenarios of the submarine landslide tsunamis in the South China Sea computed by the coupling numerical model of the landslide model and the wave generation model. The details of the validation of the numerical model and the effects of the initial yield strength and the residual yield strength will be discussed in the presentation.

References

[1] Ren Z. Y., Zhao X., Wang N.L., Dias F., and Liu H. Characteristics of Wave Amplitude and Currents in South China Sea Induced by a Virtual Extreme Tsunami. *J. Hydrodyn*. **29**(3): 377-392, 2017.

[2] Li L., Switzer Wang Y., Weiss R., Qiu Q., Chan C.H., and Tapponnier P. What Caused the Mysterious Eighteenth Century Tsunami That Struck the Southwest Taiwan Coast?. *Geophys. Res. Lett*. **42**(20):8498-8506, 2015.

[3] Ren Z., Zhao X., and Liu H. Numerical Study of the Landslide Tsunami in the South China Sea using Herschel-Bulkley Rheological Theory. *Physics of Fluids* **31**:056601, 2019.

[4] Huang X., Garcia M.H. A Herschel–Bulkley Model for Mud Flow Down a Slope. *J. Fluid Mech*. **374**:305-333, 1998.

[5] Løvholt F., Bondevik S., Laberg J.S., Kim J., and Boylan N. Some Giant Submarine Landslides Do Not Produce Large Tsunamis. *Geophys. Res. Lett*. **44**(16):8463-8472, 2017.

MULTI SCALE QUANTITATIVE SIMULATION OF TEMPORAL AND SPATIAL EVOLUTION OF SNOW DISTRIBUTION IN ALPINE REGION

Ning Huang*[1], Guang Li[1], and Jie Zhang[1]
[1]Key Laboratory of Mechanics on Disaster and Environment in Western China, Lanzhou University, Lanzhou, China

Summary The snow distribution in cold mountain area has a profound impact on the earth's climate and ecosystem. Due to the complex underlying surface and the nonuniform wind, the snow distribution in the mountains presents highly inhomogeneity. Based on the simulation of wind field through LES method, we obtain the snow distribution over a complex terrain that considering the effects of snowfall, snowdrift and snowmelt. The Particle Number Concentration Statistical method is introduced into LES to describe the snowfall and obtain the initial snow distribution; the parameterized snowdrift and snowmelt models are applied to characterize the movement and ablation of snow. The simulation results show that the initial snow distribution of complex terrain is obviously inhomogeneous, especially under large wind. The snowdrift and snowmelt processes exacerbate the nonuniform of snow.

INTRODUCTION

Snow is widely distributed in the global with significant interannual and seasonal variations. Snow always shows a nonuniform distribution under the action of the wind, especially in mountainous terrain. So far, these snow products are mainly obtained from remote sensing retrieval, such as multispectral imaging AVHRR and moderate resolution spectral imagingMODIS. The temporal and spatial resolution of remote sensing retrieval is low while the change of snow cover is relatively fast, and the accuracy is usually poor duo to the interference of many nature factors. Additional, as one of the most important fresh water resources, snow distribution have a profound impact on the allocation of freshwater resources. Thus, the real-time snow products (such as snow distribution, snow depth and diameter distribution of snow particles) with high resolution are essential to prevent snow disasters and predict global climate changes in the future.

Recently, numerical simulations were developed (Nemoto & Nishimura, 2004) as computer technology became more and more advanced. However, most of above works are implemented over flat surface. Furthermore, early snow models treat the precipitation simply as an input, which usually comes from one or several meteorological stations. They didn't consider the preferential deposition of precipitation (Lehning et al., 2008; Mott et al., 2014), which refers to the spatially variable deposition of snowfall due to the complex near-surface flow field in mountainous terrain.

In this paper, the Lagrangian dynamic subgrid-scale (SGS) model is introduced into the ARPS in order to match the nonuniform drag force due to the saltating snow particles. Then a Lagrangian particle tracking model was introduced into ARPS and the drifting snow and falling snow deposition over complex terrain with mixed sizes of snow grains were The sublimation of mid-air snow particles is modeled by the sublimation rate formula of ice crystals9, and its feedback effects on the air temperature and moisture is considered through introducing temperature and moisture source terms into the corresponding diffusion equations. simulated. Finally, a drifting snow parameterization scheme considering slope effect is developed so that a snow distribution forecast model in mountain area based on snowfall and snow drifting Simulations is established.

MODEL

The Advanced Regional Prediction System (ARPS5.3.3) is a three-dimensional, non-hydrostatic, compressible Large-eddy simulation (LES) model which is developed by University of Oklahoma. Here is used for a snow drift simulation (Huang and Wang, 2016). The Lagrangian Particle Tracking Method combined with fourth order Ronge-Kutta method is used to track the snow grains (Huang and Wang, 2016). And the effect of sublimation of ice crystal was taken into consideration (Huang and Shi, 2017).

Here we proposed a new formula of snow transport rate over flat surface ($\theta = 0^0$) based on the LES simulations of Huang & Wang 2016), which agrees well with both the wind tunnel experiments and field observations:

$$Q(0) = \frac{\rho u_*^3}{g}\left(1 - \frac{u_{*t0}^2}{u_*^2}\right)\left(3.7 + 4.7\frac{u_{*t0}}{u_*} - 4\frac{u_{*t0}^2}{u_*^2}\right) \quad (1)$$

And then we can get the formula of snow transport rate over slope surface as:

*Corresponding author. E-mail: huangn@lzu.edu.cn.

Thematic Session FM

$$Q(\theta_s) = \frac{\rho u_*^3}{gM}\left(1 - \frac{u_{*t0}^2}{u_*^2}M\right)\left(3.7 + 4.7\frac{u_{*t0}}{u_*}\sqrt{M} - 4\frac{u_{*t0}^2}{u_*^2}M\right) \quad (2)$$

RESULT AND DISCUSSION

For the flat terrain of Fig. 1, the snow depth is fairly uniform, especially in the middle of y=0.8~1km. Although there are some partial recirculation zones and vorticities in the sides, the difference of snow depth is very small. Compared with the ridge terrain, we can draw the conclusion that the blocking effect of large terrain is the main factor which leads to an uneven distribution of snowfall. And the nonuniform wind field due to undulating topography may aggravate the uneven distribution of snowfall.

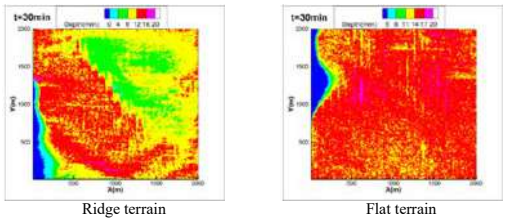

Ridge terrain Flat terrain

Fig. 1 Snow depth distribution of different terrains

Fig.2 shows the time evolution of snowbed for the two cases. Considering the effect of local topography, we found that the erosion events usually happen at the windward side, and deposition at the leeward side, no matter what wind speed is. And it is different from the preferential deposition of snowfall, which has various patterns when wind speed increases (Wang & Huang, 2017). However, the change of snow depth due to drifting snow is sensitive to wind speed, for 2 orders of magnitude is found between 2 cases. It indicates that the distribution of snow deposition caused by drifting snow is dominantly controlled by terrain, but the quantity is governed by wind speed.

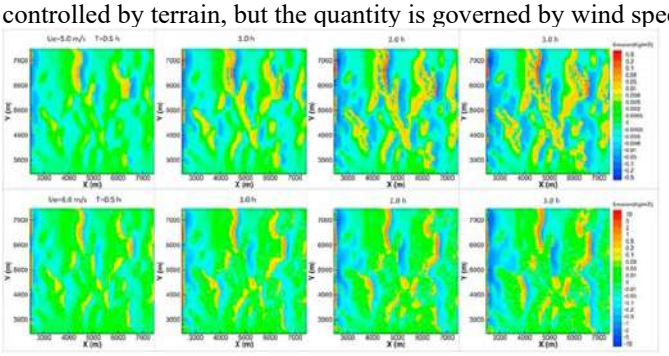

Fig. 2 Erosion and deposition of snow due to drifting snow under different wind speeds.

CONCLUSIONS

In this paper, we proposed a new formula of snow transport rate over flat surface based on the LES simulations of Huang and Wang (2016) and corrected it by take account of slope effect, temperature, and time effect. Then combining it to the snowfall model of Wang and Huang (2017), which introduces a Lagrangian particle tracking model into ARPS to simulate the falling snow deposition over complex terrain, we established a snow distribution model for alpine terrain considering both snowfall and snow drifting processes. The validation wind tunnel experiments and field observations show high accuracy of our model in snow depth evaluation.

References

[1] Nemoto M. and Nishimura K. Numerical simulation of snow saltation and suspension in a turbulent boundary layer. *Journal of Geophysical Research: AtmospheresS*. **109(D18):D18206**, 2004.

[2] Huang N. and Wang Z. The formation of snow streamers in the turbulent atmosphere boundary layer. *Aeolian Research.* **23, 1-10, 2016**

[3] Huang, N., & Shi, G. (2017), The significance of vertical moisture diffusion on drifting snow sublimation near snow surface. *Cryosphere*. **11(6), 3011-3021, 2017.**

OPTIMAL CLOSED-LOOP WIND FARM WAKE STEERING CONTROL UNDER TRANSIENT ATMOSPHERIC CONDITIONS

Michael F. Howland*[1], Aditya S. Ghate[2], Sanjiva K. Lele[2], and John O.Dabiri[3]
[1]Department of Mechanical Engineering, Stanford University, Stanford, CA 94305
[2]Department of Astronautics and Aeronautics, Stanford University, Stanford, CA 94305
[3]GALCIT and Mechanical Engineering, California Institute of Technology, Pasadena, CA 91125

Summary Wake interactions between wind turbines reduce the annual energy production of the collective wind farm as a result of greedy, individual turbine control. The potential for wake steering control, the intentional yaw misalignment of a wind turbine with respect to the incoming wind direction, to increase wind farm power production within large eddy simulations of realistic atmospheric boundary layers (ABL) was investigated. As a result of the atmospheric diurnal cycle, the dynamics of the atmosphere are transient, and therefore, a dynamic, closed-loop wake steering control strategy was selected. While wake steering control is able to increase a six wind turbine wind farm power production approximately 5% in conventionally neutral and transient stable atmospheric conditions, the increase in power production is sensitive to the control architecture, wind farm layout, and surface cooling rate.

MOTIVATION AND LARGE EDDY SIMULATION SETUP

Horizontal axis wind turbines generate turbulent wakes which persist 10-15 wind turbine rotor diameters downstream [1]. With modern utility-scale wind turbine wakes reducing power production for generators kilometers downwind, recent efforts have focused on wind farm control schemes which sacrifice individual wind turbine power production for the benefit of the collective wind farm as a replacement for the contemporary standard greedy turbine operation. While greedy wind turbine operation entails the yaw alignment of the nacelle and the incoming wind direction, wake steering control intentionally misaligns certain turbines with respect to the incoming wind direction in order to laterally deflect the wake region away from downwind generators [2]. The potential for wake steering to increase the power production of a six wind turbine array was recently shown in a full-scale field experiment where increases with respect to baseline greedy operation between 7-13% were found for moderate wind speeds [3]. However, typical studies of wake steering have focused on stationary atmospheric simulations [2] or static wind farm control based on lookup tables [3, 4]. The turbulent ABL, however, is rarely stationary with the quasi-stationary conventionally neutral state infrequently observed in field experiments [5]. As such, the goal of the present study is to assess various wake steering control architectures under transient atmospheric stability conditions associated with the diurnal cycle in large eddy simulations.

Large eddy simulations are performed using the in-house code *PadéOps*[1]. The psuedo-spectral code has been utilized in a number of geophysical applications previously and is described thoroughly in the associated references [6, 7]. Simulations are performed initially in a quasi-stationary conventionally neutral ABL. Six wind turbines are embedded in the ABL with the array designed to approximately represent the layout studied in [3]. The finite wind farm is represented using the concurrent precursor framework where fringe regions [8] are used (Figure 1(a)). Once the wind farm reaches the quasi-stationary state associated with the conventionally neutral ABL, a suite of simulations are performed to analyze the sensitivity of the effect of wake steering on wind farm power production as a function of the control architecture, wind farm layout, and stable ABL surface cooling rate. All power production results are compared to a simulation of the same setup with greedy wind farm control. The closed-loop wake steering controller architecture is shown in Figure 1(b). The optimal controller is the gradient-based wake steering methodology developed by Howland *et al.* [3]. The state estimation utilizes the ensemble kalman filter method developed by [9]. Open-loop control, where the yaw misalignment and power production state are not fed back to the controller, and closed-loop control cases are tested.

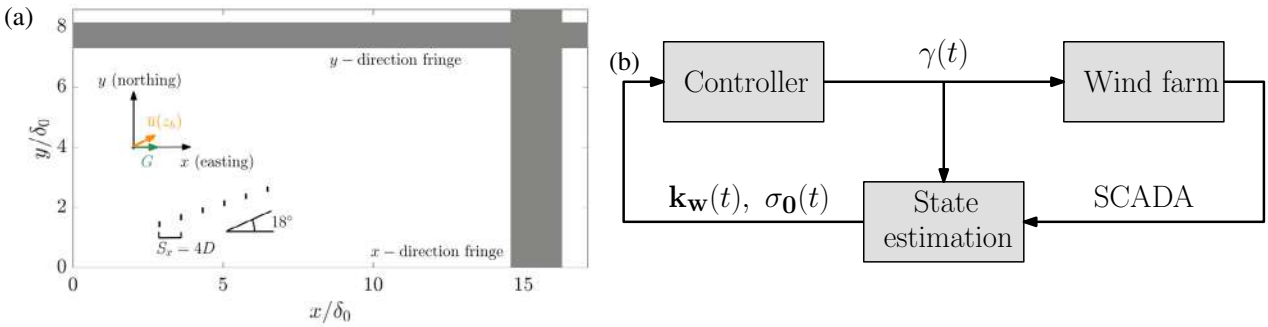

Figure 1: (a) Large eddy simulation computational setup primary simulation. Fringe regions [8] are used in the x and y directions to force the primary simulation to match the concurrent precursor simulation. Six actuator disk model wind turbines are incorporated into the primary domain. The geostrophic wind direction G is shown in green and the mean velocity at wind turbine hub height $\overline{u}(z_h)$ is shown in orange. (b) Closed-loop wake steering controller architecture.

*Corresponding author. E-mail: mhowland@stanford.edu
[1]https://github.com/FPAL-Stanford-University/PadeOps

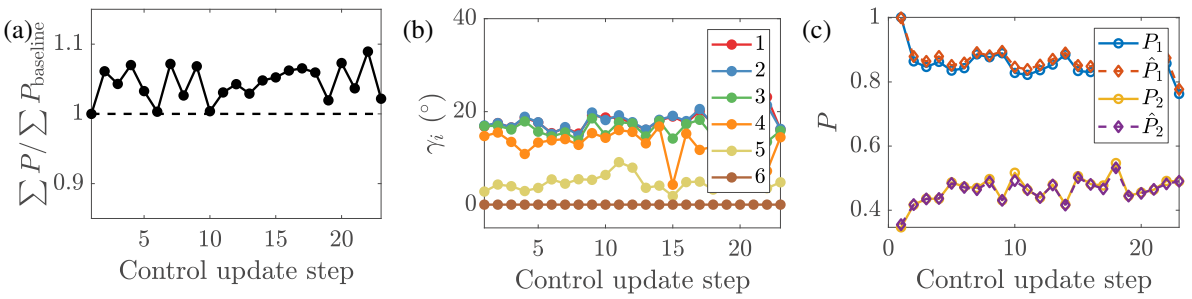

Figure 2: (a) Time averaged wind farm power production as a function of the control update steps for the conventionally neutral ABL case. The wind farm power is normalized by the power of the aligned wind farm case. (b) Yaw misalignment angles and (c) simulation P and state estimated model $\hat{P}$ power production for the first and second upwind turbines in the array as a function of the control update steps. The yaw misalignment is updated with a period of 50 minutes.

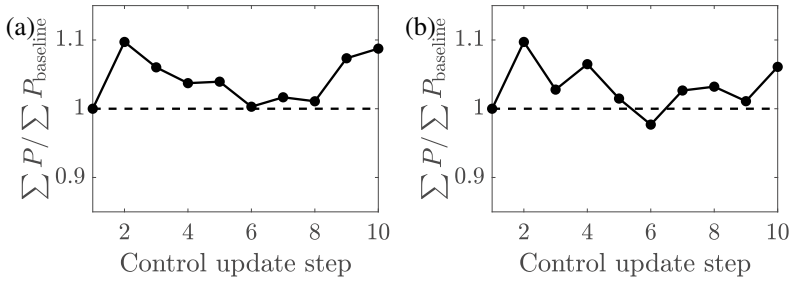

Figure 3: (a) Time averaged wind farm power production as a function of the control update steps for the stable ABL case with (a) closed-loop control and (b) open-loop control. The wind farm power is normalized by the power production of the greedy wind farm case. The yaw misalignment is updated with a period of 30 minutes.

SIMULATION RESULTS

The suite of large eddy simulations reveal sensitivity in the wind farm power production to the choice of control architecture, wind farm layout, and surface cooling rate. In the conventionally neutral ABL, both open-loop and closed-loop control (Figure 2) produce power increases over the greedy operation, with the mean power production increase of approximately 5%. However, when the wind farm alignment is $14°$ instead of the $18°$ shown in Figure 1(a), the wind farm power production increase with wake steering decreases to approximately 1% due to the reduction of partial waking with the mean wind speed at wind turbine hub height of approximately $15°$. In the stable ABL, the wake steering control benefits are larger for the closed-loop (Figure 3(a)) than for open-loop (Figure 3(b)) control, with power production increases over the greedy baseline of 4.7% and 3.5%, respectively. This reveals that closed-loop control is able to dynamically adapt to the changing stability and boundary layer state in transient stable ABL flows. With increased surface cooling, the power production increases over greedy operation are reduced due to a rapid stability transition. Overall, the results suggest that the specific wind farm layout and ABL state will dictate the optimal wake steering strategy and closed-loop, dynamic wake steering increases wind farm power production in transient flows compared to open-loop approaches.

References

[1] Meyers, J., and Meneveau, C. (2012). Optimal turbine spacing in fully developed wind farm boundary layers. Wind Energy, 15(2), 305-317.
[2] Gebraad, P., Thomas, J. J., Ning, A., Fleming, P., and Dykes, K. (2017). Maximization of the annual energy production of wind power plants by optimization of layout and yaw-based wake control. Wind Energy, 20(1), 97-107.
[3] Howland, M. F., Lele, S. K., and Dabiri, J. O.: Wind farm power optimization through wake steering, Proceedings of the National Academy of Sciences, 116, 14 495–14 500, 2019.
[4] Fleming, P., King, J., Dykes, K., Simley, E., Roadman, J., Scholbrock, A., ... and Dam, J. V. (2019). Initial results from a field campaign of wake steering applied at a commercial wind farm–Part 1. Wind Energy Science, 4(2), 273-285.
[5] Hess, G. D. (2004). The neutral, barotropic planetary boundary layer, capped by a low-level inversion. Boundary-layer meteorology, 110(3), 319-355.
[6] Ghate, A. S., and Lele, S. K. (2017). Subfilter-scale enrichment of planetary boundary layer large eddy simulation using discrete Fourier–Gabor modes. Journal of Fluid Mechanics, 819, 494-539.
[7] Howland, M. F., Ghate, A. S., and Lele, S. K. (2020). Influence of the geostrophic wind direction on the atmospheric boundary layer flow. Journal of Fluid Mechanics, 883.
[8] Nordström, J., Nordin, N., and Henningson, D. (1999). The fringe region technique and the Fourier method used in the direct numerical simulation of spatially evolving viscous flows. SIAM Journal on Scientific Computing, 20(4), 1365-1393.
[9] Evensen, G. (2003). The ensemble Kalman filter: Theoretical formulation and practical implementation. Ocean dynamics, 53(4), 343-367.

EXPERIMENTAL STUDY O FZONAL JETS IN PLANETAR YATMOSPHERES: MULTI-STABILITY AND LONG-TERMDYNAMICS

Daphné Lemasquerier *[1], Benjamin Favier[1], and Michael Le Bars[1]
[1]Aix Marseille Univ, CNRS, Centrale Marseille, IRPHE UMR 7342, Marseille, France

Summary The stability and dynamics of gas giants' zonal jets are still poorly understood. Here, we use an experimental approach to address the question of zonal jets formation and long-term evolution. A strong topographic β-effect is obtained inside a rotating water tank thanks to the paraboloidal shape of the upper free surface. A turbulent forcing is performed using small-scale jets at the base of the tank. We identify a subcritical transition and associated hysteresis cycle between two distinct regimes. In the first regime, jets are weak in amplitude, steady and remain spatially locked to the forcing. In the second one, we observe dynamical and dominant jets, independent of the forcing scale. Kinetic energy spectra are in that case consistent with theoretical predictions of so-called zonostrophic turbulence, relevant to planetary applications.

INTRODUCTION

Turbulent flows in planetary atmospheres are constrained by many dynamical effects such as rapid rotation or density stratification which contribute to the rich dynamics observed on many planets. One of the striking features of rapidly-rotating atmospheres is their ability to sustain azimuthal flows whose direction alternates with latitude. The best example is probably Jupiter, for which zonal jets are clearly visible in the weather layer as witnessed by Voyager, Cassini and more recently Juno [1]. The origin, robustness and potential long-term dynamics of these jet-like structures are however still not fully understood. In particular, to which extent they penetrate in the deep interior of Jupiter is still unclear, although recent indirect measurements suggest that they are deeper than initially thought [2].

In this work, improving upon the results of Cabanes *et al.*[3], we explore experimentally the long-term dynamics of zonal jets driven by a topographical effect in a rapidly-rotating water tank. The extreme parameter regime reached by our experiment allows us to vary the intensity of the forcing while remaining in the rotationnally-constrained regime, relevant for these large-scale atmospheric features.

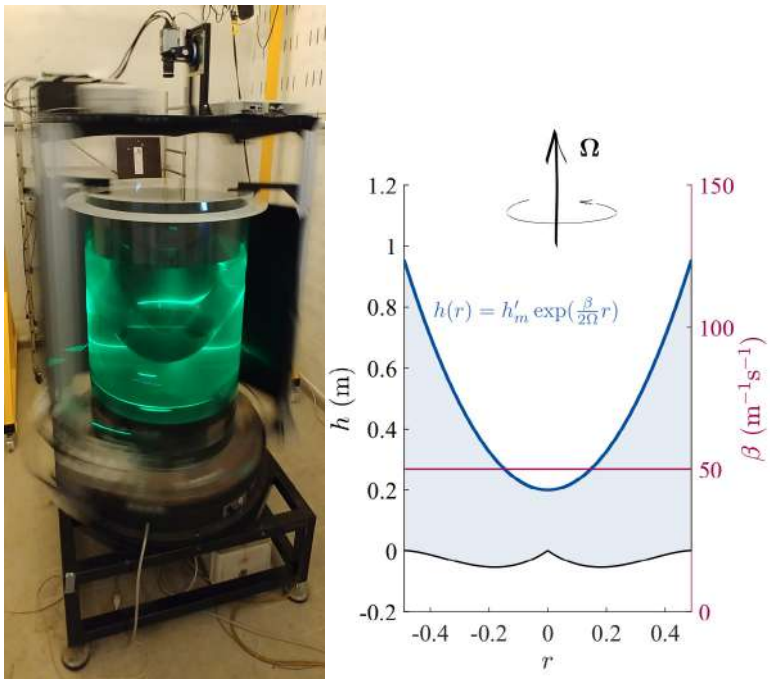

Figure 1: Details of the experimental setup. Left: Picture of the experiment after the spin-up is completed. The tank is 1.6 m high, 1 m in diameter and rotates at 75 rpm. Right: height and β as a function of the cylindrical radius.

EXPERIMENTAL SETUP

A cylindrical transparent container of radius $R = 0.5$ m is filled with 440 litres of water and is rapidly-rotating around its vertical axis. At rest, the water depth is $h = 58$ cm and once the platform is rotating at $\Omega = 75$ rpm, the water height varies parabolically from $h = 20$ cm on the axis of rotation up to $h = 95$ cm at the edge of the domain (see Figure 1). The bottom of the tank is not flat but slightly curved so that the total water column height $h(r)$ varies exponentially with cylindrical radius r. The topographic β-effect, given by $\beta = (2\Omega/h)\mathrm{d}h/\mathrm{d}r$, is thus constant across the experiment, $\beta = 50$ m^{-1}.s^{-1}. An experiment with a flat bottom surface (as in [3]) would lead to a non-uniform β-effect, which is a further complication we want to avoid. Small-scale fluctuations are generated by an array of 64 injection and 64 suction points, with a typical inlet radius of 2 mm, regularly distributed in a non-axisymetric pattern and connected to 6 independent pumps.

Measurements are performed on a fully-immersed horizontal plane using Particle-Image Velocimetry (PIV). The fluid is seeded with 40 μm fluorescent particles which are illuminated with a 2 W 532 nm green laser. Their peak emission is approximately at 607 nm and thus appears orange when excited by the laser. This allows to filter out inevitable reflections from various parts of the experiment and dramatically improves the quality of the PIV measurements.

*Corresponding author. E-mail: lemasquerier@irphe.univ-mrs.fr.

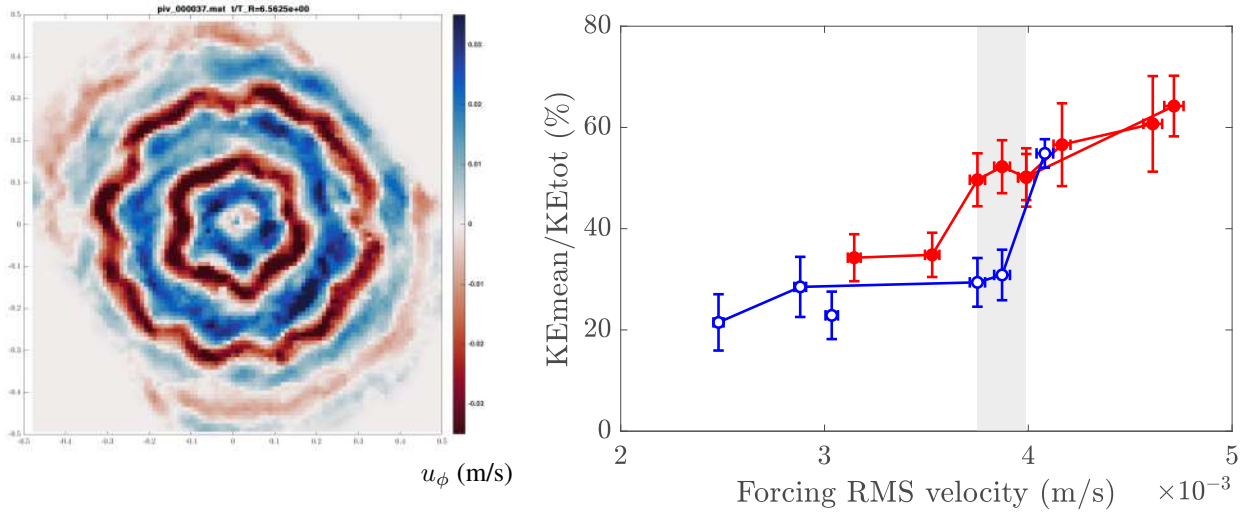

Figure 2: Left: instantaneous azimuthal velocity field as measured by PIV in a horizontal plane across the experiment for the second regime. Red is prograde while blue is retrograde. Right: ratio between the kinetic energy in the azimuthally-averaged flow and in the total flow as a function of the forcing amplitude. Blue corresponds to experiments where the forcing is gradually increased while red corresponds to experiments where the forcing is decreased. Bi-stability is observed inside the grey area.

BI-STABILITY AND LONG TERM DYNAMICS

The rotation rate is fixed to $\Omega = 75$ rpm for all experiments. This corresponds to an Ekman number of $E = \nu/(\Omega R^2) \approx 5 \times 10^{-7}$ where ν is the kinematic viscosity of water. Our control parameter is the intensity of the forcing which we measure as the root-mean-square fluctuating velocity at the beginning of the experiment, when the mean flow has not developed yet. In all cases, the typical velocity is of the order of $u \approx 4 \times 10^{-3}$ m/s, so that the typical Rossby number is approximately $Ro = u/(\Omega R) \approx 10^{-3}$.

For each experiment, once the platform is rotating, we first wait for the fluid to spin-up and reach a solid-body rotation state. The pumps are then activated and we record the spatio-temporal evolution of the velocity field in the PIV plane. This allows to separate the contributions of the azimuthally-averaged zonal flow from those of the small-scale fluctuations. For all cases, we observe the formation of zonal flows which correspond to the azimuthally-averaged part of the flow (see Figure 2). Note that contrary to most previous experiments, we reach the so-called zonostrophic regime characterised by a dominant instantaneous zonal flow (see [3] for more details).

In addition, the detailed PIV measurments allow to distinguish between two dynamical regimes. For low forcing amplitudes, coherent steady zonal flows are obtained, whose typical size matches that of the forcing. As the forcing amplitude increases, the system switches to a much more dynamical regime characterized by stronger and wider zonal flows and merging events. We can even construct the full transition diagram between the two states, and we observe a hysteretic behaviour as shown in Figure 2. Finally, we have performed several realisations of the same experiment and observed that the system is actually multi-stable in the zonostrophic regime: we have found at least three different quasi-steady states with different jet positions and structures, but similar jet sizes and amplitudes.

CONCLUSIONS

Using a large-scale experiment, we have identified a new transition in β-plane turbulence between two different regimes. One is characterised by relatively weak zonal flows locked at the forcing scale while the second regime, more relevant for planetary applications, is characterized by intense large-scale jets. We observed a hysteretic behaviour at the transition between the two regimes, which remains to be explained. The long-term dynamics of the zonal flows in the second regime are now being studied in more details. In particular, these results have been reproduced using a quasi-geostrophic two-dimensional code which confirms the robustness of the transition observed experimentally.

References

[1] Bolton S.J. *et al.*. Jupiter's interior and deep atmosphere: The initial pole-to-pole passes with the Juno spacecraft. *Science* **356**: 821-825, 2017.
[2] Kaspi, Y. *et al.*. Jupiter's atmospheric jet streams extend thousands of kilometres deep. *Nature* **555**: 223-226, 2018.
[3] Cabanes S., Aurnou J., Favier B. & Le Bars M. A laboratory model for deep-seated jets on the gas giants. *Nature Physics* **13**: 387-390, 2017.

ONE-DIMENSIONAL MODELS FOR EXCHANGE FLOWS AND THEIR APPLICATION TO THREE-DIMENSIONAL TURBULENT NUMERICAL SIMULATIONS

Steven J. Kaptein[1], Vincenzo Armenio[2], Herman J.H. Clercx[1], and Matias Duran-Matute*[1]
[1]Fluid Dynamics Laboratory and J.M. Burgers Center for Fluid Dynamics, Department of Applied Physics, Eindhoven University of Technology, Eindhoven, The Netherlands
[2]Dipartimento di Ingegneria e Architettura,Università degli Studi di Trieste,Trieste,Italy

Summary We use two recently developed parametrizations of the horizontal density gradient leading to one-dimensional models to reproduce strongly stratified gravity-driven exchange flows at high and low Schmidt number values. These models were extensively tested against results from laminar two-dimensional simulations and are shown to outperform the models with the classical constant parametrization for the horizontal density gradient. Finally, we use these models as drivers in three-dimensional direct numerical simulations of continuously forced turbulent exchange flows with periodic boundary conditions, and we present the results of the evolution and characteristics of these flows.

INTRODUCTION AND DESCRIPTION OF THE PROBLEM

Modeling and understanding of turbulent strongly stratified flows remains an ongoing problem within environmental fluid mechanics. Exchange flows driven by horizontal density differences occur in many natural environmental situations and are ideal to further our insight into turbulence in strongly stratified flows, but modeling all the relevant scales of such flows poses several challenges. Idealized three-dimensional models with periodic horizontal forcing can be used for such an endeavor. However, the horizontal density differences are often parametrized using an imposed, constant horizontal density gradient that results in the stratification to grow out of bounds: a phenomenon usually called 'runaway-stratification'. In this work, we present a way to overcome this limitation.

The problem set-up (shown in Figure 1) is inspired by different experimental configurations (e.g. [3]) and consists of two reservoirs connected by a channel of height h and length L, with $L \gg h$ (implicitly assuming that end effects at $x = \pm L/2$ can be ignored). Each reservoir contains water with a different initial salt concentration, denoted by the salinity values s_1 and s_2 in the left and right reservoirs, respectively. Initially, the salinity $s(x, z)$ in the channel is uniform in the vertical, and the salinity gradient in the along-channel direction is constant: $\partial s/\partial x = (s_2 - s_1)/L$. In the channel, both the top and bottom boundary are solid boundaries. The aim of our study is to reproduce the flow in the center of the channel (around $x = 0$), first for the laminar case and second for the turbulent case. For the latter, we are resolving all scales using direct numerical simulations (DNS). The flow is governed by three non-dimensional parameters: the gravitational Reynolds number $Re_g = U_g h/\nu$, the Schmidt number $Sc = \nu/\kappa$, and the aspect ration of the channel $\Gamma = h/L$ where $U_g = \sqrt{(\Delta\rho g h)/(\rho_0)}$, with $\Delta\rho$ the density difference between the the water in the two containers, g the acceleration due to gravity, ρ_0 the density at $x = 0$ and $t = 0$, ν the kinematic viscosity, and κ the molecular diffusivity.

ONE-DIMENSIONAL MODELS

To achieve our goal, the key aspect is to decompose the density of the fluid ρ as

$$\rho(x, y, z, t) = \rho_r(x, y, z, t) + xG(z, t), \tag{1}$$

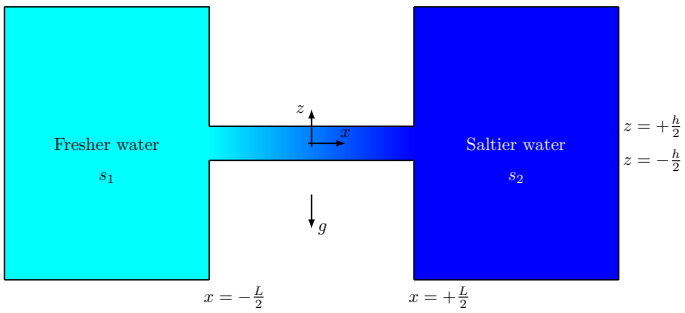

Figure 1: Side-view of the domain, with the initial distribution of salinity. This sketch is not to scale as $L \gg h$, and we assume very large (infinite) salt reservoirs. The salt concentration in the left reservoir is denoted by the salinity s_1 and in the right reservoir it is denoted $s_2 > s_1$. The acceleration due to the gravity g is in the negative z-direction.

*Corresponding author. E-mail:m.duran.matute@tue.nl

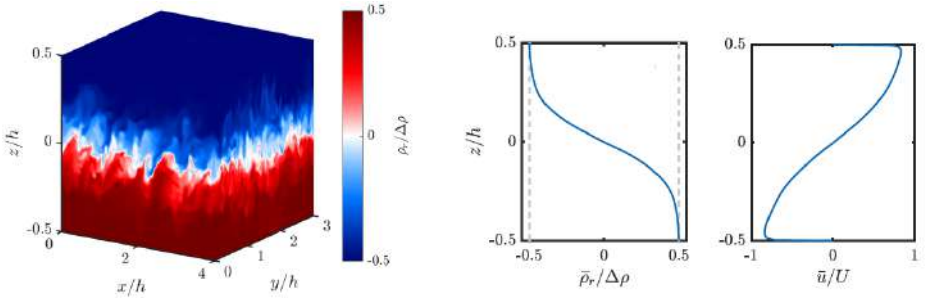

Figure 2: Results of a 3D DNS with horizontally periodic boundary conditions for the turbulent flow around the center ($x = 0$) of the channel with $Re_g = 5 \times 10^6$. Left: snapshot of the three-dimensional distribution of the normalized density. Right: horizontally averaged vertical profiles of the density and of the horizontal velocity.

where ρ_r is the part of the density that has to be solved for and $G(z,t)$ is an imposed horizontal density gradient. For the horizontal density gradient $G(z,t)$, we propose a parameterization of the form

$$G(z,t) = a_0 + a_1 \left|\tilde{\rho}\right| + a_2 \left|\frac{\partial \tilde{\rho}}{\partial z}\right|, \tag{2}$$

where $\tilde{\rho}$ is the horizontal average of ρ_r, and a_0, a_1 and a_2 are constants to be determined. Note that with this parametrization the horizontal density gradient is constant over the vertical in the absence of stratification; it decreases at the boundaries with the onset of stratification; and it increases in the center of the channel once the flow converges to a two-layer system. When $a_1 = 0$ and $a_2 = 0$, the classical constant horizontal density gradient parametrization is recovered, and we refer to this as the 1D0 model. In the case $a_2 = 0$ but $a_1 \neq 0$, the parametrization resembles the one proposed in [1], and we refer to this parametrization as 1D1. Finally, the case where all three parameters are different than zero is referred to as 1D2 [2].

To satisfy the initial condition $a_0 = \Delta\rho/L$, and to satisfy the top and bottom no-slip boundary conditions as $t \to \infty$, $a_1 = -2/L$. Finally, we assume that the shear at $z = 0$ is always such that $a_2 = \Gamma/3$.

Four different flow regimes are found by exploring the parameter space defined by Re_g, Sc, and Γ. The classical 1D0 model, which considers a constant horizontal density gradient, only performs well in the diffusion dominated regime, where the stratification is weak. The new 1D models outperform the classical model in all other regimes, but they perform differently depending on the Schmidt number. For low Sc values the 1D1 model performs best while for high Sc values, the 1D2 model performs best. Most importantly, runaway stratification is prevented with both the 1D1 and the 1D2 models.

IMPLEMENTATION OF 1D MODELS FOR 3D SIMULATIONS OF TURBULENT FLOW

The 1D models are used to force 3D direct numerical simulations with horizontal periodic boundary conditions. These simulations focus on a small enough domain close to the center of the channel to have enough resolution to solve all the relevant scales. The simulations start with the fluid at rest. For small values of Re_g, a steady laminar flow is attained after a short transient time. As the value of Re_g increases, Holmboe waves appear at the interface. Finally, for large enough Re_g values, the flow becomes turbulent and turbulent mixing between the two fluids occurs at the interface. Figure 2 shows results of one 3D DNS for the turbulent flow around the center of the channel. The fact that vertical profiles of neither the density nor the velocity are imposed allows them to vary in time revealing their interplay and the interplay with the turbulence characteristics at the interface.

CONCLUSIONS

In this work, we show how recently developed 1D models of exchange flow can be applied to forced 3D direct numerical simulation set-ups with horizontally periodic domains. This opens a whole new range of possibilities to reproduce, using high-resolution simulations, the dynamics of different environmental situations where other actors such as tides or wind can interact with the exchange flow.

References

[1] Blaise, S., Deleersnijder, E. Improving the parameterisation of horizontal density gradient in one-dimensional water column models for estuarine circulation, *Ocean Sci.* **4**, 239–246.

[2] Kaptein, S. J., van de Wal, K. J., Kamp, L. P., Armenio, V., Clercx, H. J., Duran-Matute, M. Analysis of one-dimensional models for exchange flows under strong stratification. *Ocean Dynam.*, **70**, 41-56, 2020.

[3] Lefauve, A., Partridge, J.L., Zhou, Q., Dalziel, S.B., Caulfield, C.-c.P., Linden, P.F. The structure and origin of confined Holmboe waves, *J. Fluid Mech.* **848**, 508–544, 2018.

CASCADE OF RESONANCES TO ACHIEVE INTERNAL WAVE TURBULENCE

Géraldine Davis[1],Timothée Jamin[1],Julie Deleuze[1],Sylvain Joubaud[1,2],and Thierry Dauxois*[1]
[1]Univ Lyon, ENS de Lyon, Univ Claude Bernard, CNRS, Laboratoire de Physique, Lyon, France [2]Institut Universitaire de France (IUF)

Summary We study experimentally the interaction of weakly nonlinear internal waves in a stratified fluid confined in a trapezoidal tank. The set-up that leads to internal wave attractors has been devised to present ingredients conducive to internal wave turbulence. It eventually achieves a nonlinear cascade in frequencies and wavevectors via triadic resonant interactions, which results at large forcing amplitudes in a k^{-3} spatial energy spectrum.

INTRODUCTION

Fluids stratified in density develop waves beneath the surface, in their bulk. Nowadays these so-called internal gravity waves, whose origin comes from the simple Archimedes' principle, are the center of many theoretical and numerical studies, but also of major scientific cruises across the oceans. In the weakly nonlinear regime, these fluid systems may develop wave turbulence that corresponds to a large number of dispersive and weakly nonlinear interacting waves [1]. Internal waves are distinguishable among waves with a still unclear understanding, in particular due to their very unusual dispersion relation. We present here an experimental set-up that allows us to get efficient nonlinear energy transfers through frequencies and wavelengths and finally internal wave turbulence signatures.

The experimental set-up, sketched in Fig. 1, is a confined trapezoidal domain filled with a linear stratified fluid of density $\rho(z)$, function of the vertical coordinate z. The energy is injected at a very large scale by means of a vertical moving boundary oscillating around its mid horizontal axis, with a half cosine shape $a(t)\cos(\pi z/H)$.

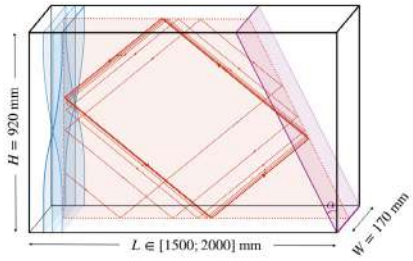

Figure 1: Experimental set-up with the generator (resp. slope inclined with an angle α) on the left (resp. right) of the tank. An example of ray tracing from a single point located on the left hand wall and corresponding to an oscillation at a given frequency $\omega = \pm N \sin\theta$ is shown in the case of a linearly stratified fluid with constant N-value.

INTERNAL WAVE ATTRACTORS

In a confined domain with an inclined slope, internal waves generated at a given frequency will concentrate on a closed loop [2] because of the peculiar reflection mechanism for internal waves. Indeed, even if Fig. 1 presents an example of ray tracing for a single emitting point, any initial point leads to the same loop, provided the frequency is kept constant. Similar to an internal wave billiard, different angles of propagation (*i.e.* different frequencies) lead to different attractors with simple or more complicated shapes.

In laboratory experiments in which viscosity cannot be overlooked, internal wave attractors are preserved but instead of a vanishingly small width, the balance between focalization and dissipation leads to a finite width. The energy, large just after the focusing reflection, is progressively dissipated along the perimeter of the attractor before being focused again by the slope.

It is important to stress that energy focalization and transfer to small scales both have here a pure linear origin since only the linear dispersion relation has been used so far. In the experimental domain presented in Fig. 1, this physical mechanism provides an energy transfer between wavelengths: this is a first important ingredient in the context of wave turbulence as it increases the number of waves with different wavevectors in interaction.

Owing to energy focusing, after each reflection on the slope, the reflected beam has a larger amplitude and is therefore more prone to reach the threshold for triadic resonant instability (TRI) [3]: a beam with primary frequency ω and wavevector $\mathbf{k}$ will generate two subharmonic waves with frequencies $\omega_\pm$ and wavevectors $\mathbf{k}_\pm$, satisfying the temporal and spatial resonance conditions $\omega = \omega_+ + \omega_-$ and $\mathbf{k} = \mathbf{k}_+ + \mathbf{k}_-$. Then, any wave in the domain may again become unstable through TRI and/or interact with any other wave to generate a third one, the latter process being without any amplitude threshold. One thus obtains a necessary ingredient for wave turbulence: a physical mechanism providing multiple nonlinear resonant interactions between waves of various wavelengths and frequencies.

*Corresponding author. E-mail: Thierry.Dauxois@ens-lyon.fr.

FROM THE LINEAR TO THE NONLINEAR REGIME

Let us focus first on the transition to the nonlinear dynamics with a monochromatic forcing. The amplitude of the generator a is gradually and slowly increased. One distinguishes several different regimes: the *linear regime* (a) with a monochromatic response leading to a nice IWA. Then, (b) corresponds to a TRI-perturbed IWA. The third and turbulent-like regime (c) is characterized by a broadband temporal spectrum and a spatial pattern in which one hardly recognizes any IWA. When the amplitude is further increased the temporal spectrum becomes richer. If some peaks are still visible at large forcing (especially at the forcing frequency), a rather continuous temporal spectrum is established (not shown here).

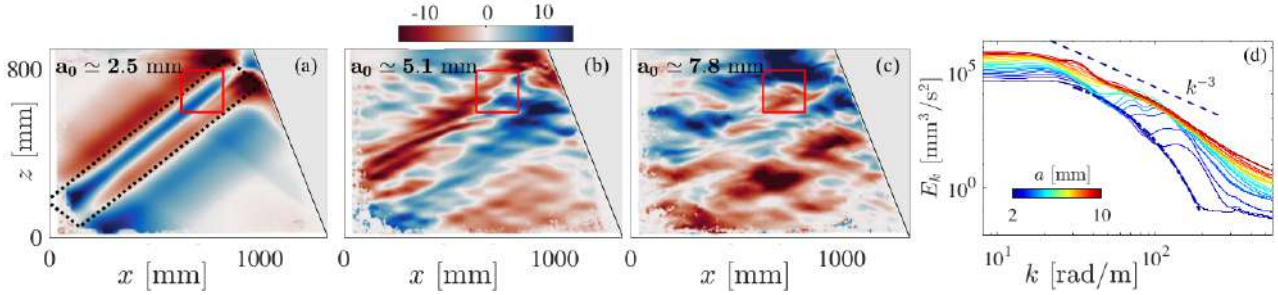

Figure 2: (a-c) Three snapshots of the horizontal velocity fields (in mm/s) measured when $a = 2.5$, 5.1 and 7.8 mm. (d) Energy density $E_k = k\langle\hat{u}(k,\theta,t)^2 + \hat{w}^2(k,\theta,t)^2\rangle_{\theta,t}$ as a function of the wavenumber k for the experiment shown in panels (a) to (c). The different curves correspond to increasing values of the amplitude a from 2 to 10 mm.

SPATIAL SPECTRA

Figure 2(d) presents the evolution of the spatial energy spectrum $E_k(k)$ as a function of the wavenumber $k = |\mathbf{k}|$ as the forcing amplitude is gradually increased. The analysis has been performed only on the low frequency band (*i.e.* $\omega < N$). The velocity field is then essentially composed of propagative waves [4].

In the linear regime, IWA have been shown to have an exponential spatial power spectrum $I_0 \exp(-\beta k)$, when dissipation due to the lateral walls dominates that of the bulk [5]. This behaviour is indeed observed at small amplitude ($a = 2$ mm), as shown by the dashed blue line.

When a is slightly increased, the attractor is destabilized by TRI and a small bump is visible around $k = 150$ rad/m (corresponding to a 4 cm wavelength). It corresponds to subharmonic waves which have a wavelength smaller than the typical width of the attractor [3]. Further increasing a, the bump not only moves towards smaller values of k but also widens.

At large forcing, these different ingredients lead to a richer spectrum that is compatible with a power law decay $E_k \sim k^{-3}$. Notice that the same power law is obtained for the vertical wavenumber k_z (not shown here). To reinforce our point, we checked the exponent for various IWA, using different forcings (monochromatic or modulated in frequency) and different geometrical parameters.

CONCLUSIONS

The trapezoidal and stably stratified domain has been shown to be an excellent experimental set-up to study weakly nonlinear interacting internal waves. Different forcings, monochromatic or stochastic, lead to a well defined power law behavior of the energy spatial spectrum. These are the first experimental signatures of internal wave turbulence.

This work was supported by the grant ANR-17-CE30-0003 (DisET), by the Labex iMUST (ANR-10-LABX-0064) of Université de Lyon and by a grant from the Simons Foundation.

References

[1] Nazarenko S. Wave Turbulence, Lecture Notes in Physics **825**, Springer, 2011.
[2] Maas L.R.M., Lam F.P.A.. Geometric focusing of internal waves. *J. Fluid Mech.* **300**: 1–41, 1995.
[3] Dauxois T., Joubaud S., Odier P., Venaille A. Instabilities of internal gravity wave beams. *Ann. Rev. of Fluid Mech.* **50**: 131–156, 2018.
[4] Brouzet C., Ermanyuk E., Joubaud S., Sibgatullin I., Dauxois T. Energy cascade in internal wave attractors. *Europhysics Letters* **113**: 44001, 2016.
[5] Beckebanze F., Brouzet C., Sibgatullin I.N., Maas L.R.M. Damping of quasi-two-dimensional internal wave attractors by rigid-wall friction. *J. Fluid Mech.* **841**: 614–635, 2018.

MEASUREMENT AND MODELING OF INDEX OF REFRACTION STRUCTURE PARAMETER IN NEAR-MARITIME ENVIRONMENT

Chris Jellen[1], John Burkhardt[1], Charles Nelson[2], Miles Oakley [2], and Cody Brownell[*1]
[1]Mechanical Engineering Department, U.S. Naval Academy, Annapolis, Maryland, USA
[2]Electrical Engineering Department, U.S. Naval Academy, Annapolis, Maryland, USA

Summary To better understand optical propagation through the atmospheric surface layer, measurements of optical and environmental variables have been obtained continuously for more than a year at a site near the Chesapeake Bay in Maryland, USA. With this data, machine learning tools are applied to facilitate the creation of reduced-order models for the index of refraction structure coefficient, C_n^2, used in most optical turbulence estimates.

INTRODUCTION

As an electromagnetic beam propagates through a complex medium such as the atmosphere, fluctuations in the refractive index result in scintillation – increased variance in irradiance at the receiver or target, and excessive beam spreading [1, 2]. These effects are referred to as optical turbulence. Optical turbulence in the atmosphere is caused by the turbulent mixing of natural temperature variations. As a beam passes through regions of varying temperature (and therefore varying refractive index), its wave front becomes perturbed, causing additional beam spread, increased variance, and a reduction in irradiance on target (see Fig. 1).

Optical turbulence is most commonly quantified by C_n^2, the coefficient in the second order structure function for refractive index. The structure function defined in terms of temperature is $D(r) = [T(x) - T(x+r)]^2$, and for isotropic turbulence this is expected to take the form of $\mathrm{D(r)} = {C_T}^2 * \mathrm{r}^{\left(\frac{2}{3}\right)}$ where r is the spatial separation between temperature observations, ${C_T}^2$ is the structure coefficient for temperature, and square brackets denote averaging. Because of the proportionality between temperature and index of refraction, C_n^2 may be calculated directly from temperature measurements via ${C_T}^2$.

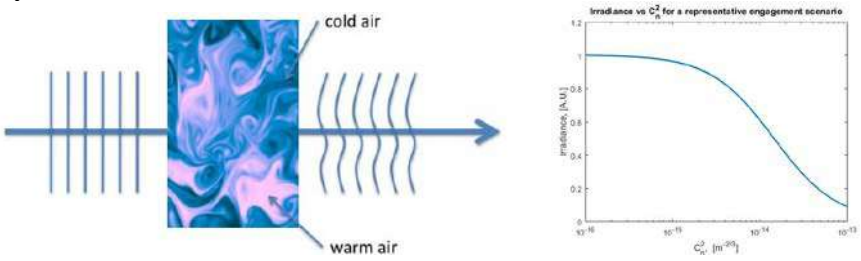

Figure 1. Schematic of light propagation through a complex medium (left) and influence of C_n^2 on irradiance at receiver (right).

Current models for laser beam propagation require path-integrated values of C_n^2, and rely on reduced order estimates of C_n^2 derived from limited physical observations – typically wind speed, time of day, and air-surface temperature difference. These models are effective in high-altitude environments where optical turbulence is low, but predictions become inaccurate close to the ground [3]. In low-altitude maritime environments, a large number of environmental factors affect optical turbulence. Current models assume that factors such as atmospheric temperature and humidity are constant over a beam's path. Due to the assumptions and simplifications inherent in existing physical models, predictions for C_n^2 break down close to sea level. This can significantly reduce the operational effectiveness of naval laser systems. A Naval Postgraduate School study suggested that other environmental factors such as the properties of the ocean below the propagation path made current models inaccurate for maritime environments [1]. An improved model for predicting the refractive index structure parameter using environmental data will enhance the accuracy of current models for laser propagation in maritime environments.

In this work, an extensive measurement campaign has been conducted to obtain C_n^2 values along with corresponding meteorological data in a maritime environment. Using this data, machine learning tools are then applied to understand the most relevent physical parameters and for the fabrication of new models for the prediciton of C_n^2.

MEASUREMENTS

A scintillometer is used to collect field measurements along a fixed propagation path of approx. 1-km over the Chesapeake Bay at the mouth of the Severn River in Annapolis, MD. The scintillometer consists of a transmitter and receiver, can be used to measure C_n^2 between observation stations (see Fig. 2). At each end of the propagation path, a weather station and oceanographic snode were used to measure a variety of environmental parameters, including air and

* Corresponding Author. E-mail: brownell@usna.edu.

water temperature, wind speed and direction, pressure, humidity, rainfall, and wave height. In addition to these weather stations and current profilers, other local atmospheric, oceanographic, and environmental parameters were collected. Atmospheric readings from a NOAA weather station in Annapolis Harbor were compiled to validate those measurements taken by the weather stations at each end of the path. Additional oceanographic parameters were taken from a NDBC data buoy located in Chesapeake Bay, less than two miles from the propagation path. In order to capture diurnal effects, sunrise and sunset times each day were used to determine the time after sunrise (temporal hour weight) for each reading. Sample C_n^2 data is shown in Fig. 3, indicating a wide range of atmospheric conditions over the observation period.

Figure 2. Measurement locations over Severn River.

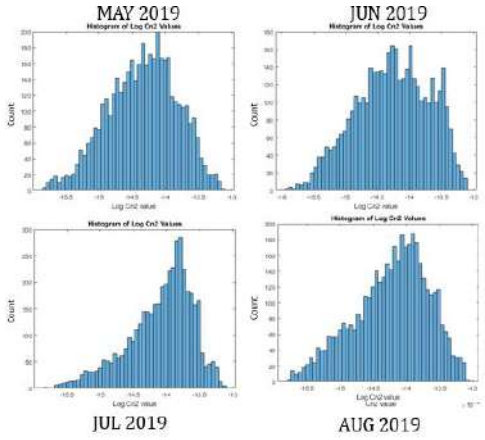

Figure 3. Histograms of (log) C_n^2 data collected over four months.

RESULTS

After training and testing individual regression trees, a random forest model was trained and tested using data from May 2019 to October 2019. This involved generating 500 distinct regression trees, each which used different environmental parameters at different times to make splits. The predicted value of C_n^2 from each final regression tree was averaged to generate an overall prediction for the value of C_n^2 given the environmental measurements in the training set. These predictions were compared to the field measurements of C_n^2 using five-fold cross validation. A plot of predicted C_n^2 vs. measured C_n^2 for the test indices, along with a red line to indicate perfect prediction accuracy, is given in Figure 4. The random forest model performed markedly better than any individual regression tree or multivariate linear model. When predicting the Log of C_n^2, the random forest model had a mean square error of 0.058, a percent error in Log prediction of 1.1%, and a model R^2 of 0.795, indicating that the predictions fell on or near the line of measured C_n^2 values. While the model performed well overall, the performance differed based on how close each test point was to training data in time. This was further investigated by re-training the model on one the subset of May 2019 data, with one day removed, and then testing the model on the removed day observations and observations taken three weeks later, in June of 2019.

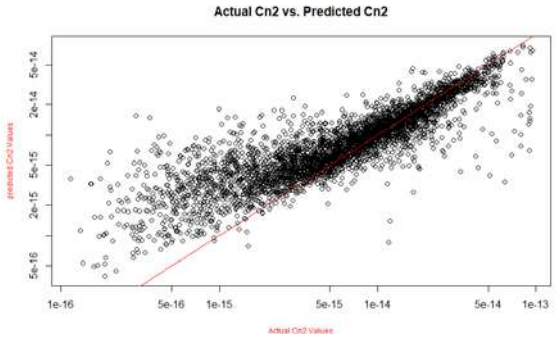

Figure 4. Random forest model, 500 trees, all predictors.

CONCLUSIONS

Linear models showed limited predictive capacity, even when compared to current bulk-atmospheric models. A non-linear regression tree model showed markedly improved predictive performance when compared to three multivariate linear models. This result encouraged investigation into other non-linear and ensemble non-linear machine learning models. The random forest model developed from the training data had the lowest absolute and percent error of any class of model. While the predictive power of the random forest model was better than a single regression tree or linear model, as quantified by the mean square error, the random forest model struggled to generate accurate prediction for data far removed from the training set.

References

[1] Frederickson, P. A., Davidson, K. L., Zeisse, C. R., & Bendall, C. S. (2000). Estimating the refractive index structure parameter over the ocean using bulk methods. *Journal of Applied Meteorology*, 39(10), 1770-1783.

[2] Tunick, A. D. (1998). The refractive index structure parameter/atmospheric optical turbulence model: CN2 (No. ARL-TR-1615). ARMY RESEARCH LABORATORY ADELPHI MD.

[3] Tunick, A., Tikhonov, N., Vorontsov, M., & Carhart, G. (2005). Characterization of optical turbulence (Cn2) data measured at the ARL A_LOT facility (No. ARL-MR-625). US Army Research Laboratory Adelphi United States.

WIND-TUNNEL STUDIES ON MECHANISMS OF GRAINS EMISSION IN TURBULENT BOUNDARY LAYER

Jie Zhang[1,2], Guang Li [1,2], Bo Yang [1,2]and Ning Huang [*1,2],
[1]Key Laboratory of Mechanics on Disaster and Environment in Western China, Ministry of Education of China, Lanzhou University, Lanzhou, China
2College of Civil Engineering and Mechanics, Lanzhou University, Lanzhou, China
*Corresponding author: Ning Huang (huangn@lzu.edu.cn)

Summary Grains emission is an important process of Aeolian transport which is common phenomena on many planets in the solar system and has great impact on landform formations as well as climate and ecosystems. To well understand the mechanisms of grains emission, wind-tunnel, a sophisticated device which is good at reproducing the wind condition of turbulent boundary layer and simulating the Aeolian transport, is generally employed. Here we firstly introduce the wind-tunnel laboratory in Lanzhou University and subsequently illustrate two elaborate wind-tunnel studies on grains emission to reveal the mechanisms of aerodynamic entrainment in turbulent boundary layer and the effect of surface renew in emission process.

WIND-TUNNEL LABORATORY IN LANZHOU UNIVERSITY (LZU)

The multifunctional environmental wind tunnel of Lanzhou University is designed to study scientific issues related to the wind-blown sand process in nature. Therefore, it is required to have the following basic functions: simulate the wind profile similar to the atmospheric boundary layer, and have an enough space for the development of turbulence boundary layer and wind-blown sand stream.

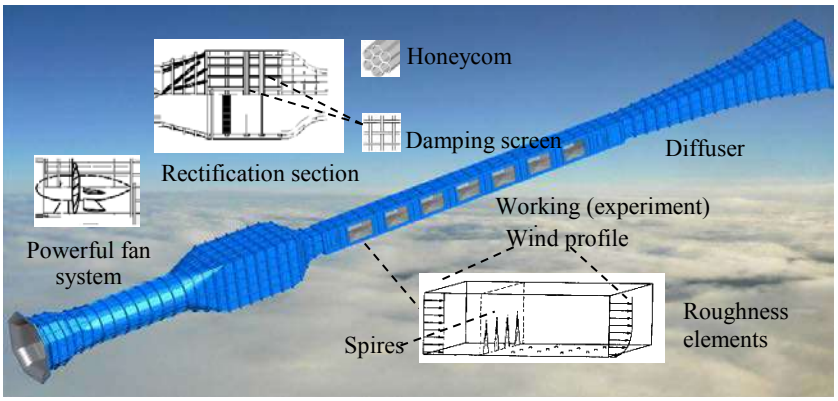

Figure 1: Sketch map of the wind tunnel of LZU.

As shown in Fig. 1, it is a blow-down wind tunnel, which is in total 55 m long, including a powerful fan system, a rectification section, a working section and a diffuser. High-speed and turbulent wind can be generated by a fan of 75 Kw in the first part. Then, the turbulent air flows into the rectification section. Here, the flow speed is slowed down because of a bigger cross-section. Turbulent eddies in the original flow generated by the fan are destructed by a combination of honeycomb and damping screens (rectangular grids) deployed in this part. After passing the rectification section, the air flow becomes uniform. The rectified air flow is accelerated in the working section which has a smaller but uniform cross-section of 1.3 m (width) × 0.45 m (height). The length of the working section is about 22 m, which is enough for the development of turbulence and wind-blown sand stream. Some spires or roughness elements (or both) are set up in the front of this section to generate a turbulent boundary layer. Finally, the air flows out from the diffuser with an increasing cross-section. The wind tunnel is controlled by a computer and the wind speed can be adjusted between 3 and 40 m/s which is normal wind speed range in natural.

WIND-TINNEL EXPERIMENT ON AERODYNAMIC ENTRINMENT

A series of wind tunnel experiments were executed to deepen our understanding of aerodynamic entrainment in turbulence. The experimental data show that the prevalent model cannot even qualitatively predict the aerodynamic entrainment rate. The conventional linear relationship between entrainment rate and mean surface shear stress is only confirmed for continuous flux for sufficiently large surface shear stresses. Additionally, intermittent entrainment, which is sensitively affected by wind turbulence, exists and follows an exponential law (Fig. 2a). We revealed the physical behavior of surface particles exposed in turbulent boundary layer, the regimes of aerodynamic entrainment and three different thresholds. We showed that fluctuations in surface shear caused by turbulence and the variation of the entrainment threshold caused by the spatially varying surface condition can both be represented by distribution functions that should be introduced into the theoretical modeling to fully describe aerodynamic grain entrainment.

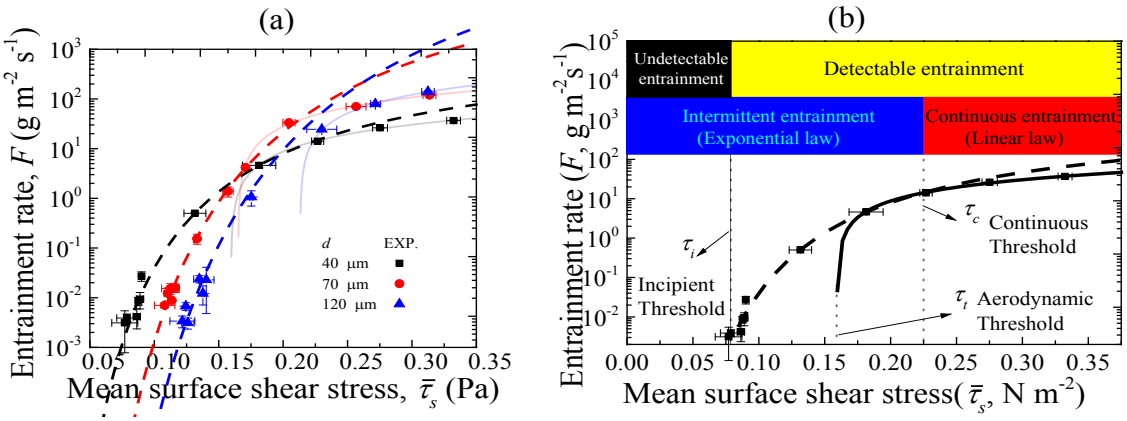

Figure 2: (a) Measured entrainment rate F vs. mean surface shear stress $\bar{\tau}_s$; (b) Regimes of aerodynamic entrainment. Three different thresholds are defined. The incipient threshold is defined as the minimal mean surface shear stress below which grain entrainment could not be detected. The continuous threshold corresponds to the minimal mean surface shear stress above which grain entrainment continuously occurs to activate the linear law. The aerodynamic threshold is the minimal average shear stress required to give rise to the motion of surface particles. The value aerodynamic threshold could be obtained by fitting the data of continuous entrainment to the linear law.

INVERSTIGATION OF DUST EMISSION OVER VARIOUS SOIL SURFACES

Wind-tunnel experiments are carried out on dust emissions from different soil surfaces to better understand dust emission mechanisms. The effects of surface renewal on aerodynamic entrainment and the saltation bombardment are analyzed in detail, and the measurements are used to test published dust models. It is found that flow conditions, surface particle motions (saltation and creep), soil dust content and ground obstacles all significantly affect dust emission, causing dust emission to change in orders of magnitude. Aerodynamic entrainment is highly effective, if dust supply is unlimited, as in the first 2-3 minutes of our wind-tunnel runs (Fig. 3a). While aerodynamic entrainment is suppressed by dust supply limit, surface renewal through the motion of surface particles is found to be an effective pathway to remove the supply limit ((Fig. 3b)). Surface renewal is also found to be important to the efficiency of saltation bombardment. We have thus demonstrated that surface renewal is a significant mechanism affecting dust emission and we recommend that this mechanism be included in future dust model.

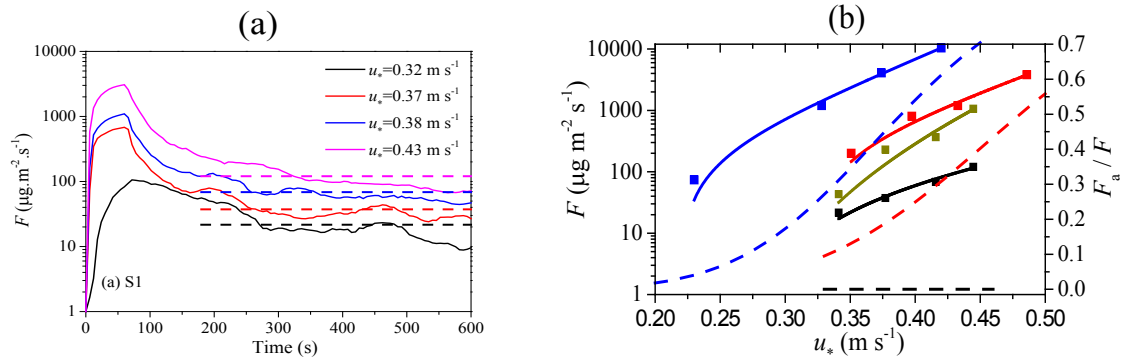

Figure 3: (a) Dust emission flux series over natural soil surfaces; (b) Measured (dots) and predicted (solid lines) dust emission flux vs. friction velocity over different surface. The ratios of aerodynamic emission flux to total flux are shown as the dashed lines and corresponding to the right vertical axis. The contribution of aerodynamic emission increases, because of surface renew.

CONCLUSIONS

The multi-function environmental wind-tunnel with a long working section built in Lanzhou University is a sophisticated device which has been validated to effectively study the mechanisms of Aeolian Process by many successful experiments.

ACKNOWLEDGEMENTS

This work is supported by the National Natural Science Foundation of China (11602100, 11772143, 11702163).

References

[1] Huang, N., & Zhang, J ., Wind-tunnel experiment on dust atmosphere-surface exchange: emission and dry deposition. Procedia IUTAM, 2015, 17, 129-135.

[2] Zhang, J., Teng, Z., Huang, N., Guo, L. , & Shao, Y. P., Surface renewal as a significant mechanism for dust emission. Atmospheric Chemistry and Physics, 2016, 16(24):15517-15528.

[3] G. Li, J. Zhang, H. J. Herrmann, Y. Shao, N. Huang, Study of Aerodynamic Grain Entrainment in Aeolian Transport. (Under review)

STATISTICAL ANALYSIS OF TURBULENT FLOW OVER WAVY SURFACE

Enwei Zhang, Xiaoliang Wang, Wangxia Wu, and Qingquan Liu *
School of Aerospace Engineering, Beijing Institute of Technology, Beijing, China

Summary The turbulent flow over the wavy surface is numerically studied based on LES approach with the dynamic one-equation subgrid-scale stress model. A series of flow variables are extracted and analysed in detail, including the time-averaged flow velocity, turbulent kinetic energy, Reynolds shear stress and the wall pressure. Besides, the properties of flow fields and the statistical characteristics of turbulence are investigated and compared, in the consideration of different ratios between amplitude and wavelength of the wavy surfaces. The results show that, due to the pressure-induced form drag, the streamwise time-averaged velocity decreases with the ratio between amplitude and wavelength of wavy surface in both the viscous and logarithmic regions. The maximum values of turbulent kinetic energy and Reynolds shear stress appear at the region close to the trough of wavy surface.

INTRODUCTION

The turbulent flow over wavy surface exists in a large number of engineering and environmental problems. Both large-scale flow such as atmospheric flow over complex terrain and small-scale flow such as experimental channel flow are examples of this kind of flows. So, understanding the turbulent characteristics of the flow over complex wall geometry is of significance for studying the mechanism of flow, which is valuable for utilization of environmental resources, providing references for the engineering applications.

The last several decades has seen a lot of achievements in this problem, including turbulent boundary layer flow [1,2], heat and mass transfer [3,4], and so on. Experiments by Hamed A.M. et al.[1] provided velocity profile, turbulent kinetic energy and Reynolds shear stress over two dimensional and three dimensional large-scale wavy walls. Takenobu [4] used large eddy simulation to study the flow and gas dispersion over wavy walls with three ratios of wave amplitude to wavelength. However, the mechanism of turbulent flow over wavy walls and the relationship between velocity profile and wall pressure distribution are still not well understood. Therefore, turbulent flow over wavy walls with different ratios of wave amplitude to wavelength are systematically studied by large eddy simulation model (LES).

NUMERICAL METHOD

The problem considered here is a three dimensional fully developed turbulent flow over wavy surface. We define the x, y, z as streamwise, spanwise and vertical direction respectively. The filtered incompressible Navier-Stokes equations and the continuity equation for describing resolvable turbulent flow field are as follow:

$$\frac{\partial u_i}{\partial x_i} = 0, \tag{1}$$

$$\frac{\partial u_i}{\partial t} + u_j \frac{\partial u_i}{\partial x_j} = -\frac{1}{\rho_0}\frac{\partial p}{\partial x_i} + \nu \nabla^2 u_i - \frac{\partial \tau_{ij}}{\partial x_j} \tag{2}$$

where, u_i are the filtered velocity components, τ_{ij} are the subgrid-scale stress modelled by dynamic one-equation model. Periodic boundary conditions are applied in streamwise and spanwise directions, top and bottom boundaries are applied as no-slip walls. In the vertical direction, the first layer of the grids is clustered near the wall with Δz^+= 0.5. The Reynolds number is defined as $Re = U_b h/\nu$(= 4000), where the h is half-height of the channel, U_b is bulk velocity, ν is kinematic viscosity. OpenFOAM is utilized for numerical simulation with the SIMPLE algorithm for pressure-velocity coupling. The time averaging starts after reaching a fully developed turbulence (corresponding to 15 flow cycles) and continues for another additional 30 flow cycles. The LES model is validated by several simulations in agreement with experiment results for turbulent flow over wavy structures. Then the LES model is used to study turbulent characteristics of flow over wavy surface of different ratios of wave amplitude to wavelength.

RESULTS AND DISCUSSIONS

Figure.1 shows turbulent characteristic information of flow over wavy surface of ratio 0.05. The separation zones behind the wave crest expand with increase of the wavy surface ratio (a/λ_x). The region of separation zones locate at $x/\lambda_x \in$[0.3, 0.55] for a/λ_x= 0.025, $x/\lambda_x \in$[0.2, 0.7] for a/λ_x= 0.05, $x/\lambda_x \in$[0.15, 0.75] for a/λ_x= 0.075, $x/\lambda_x \in$[0.1, 0.8] for a/λ_x= 0.1. The direction of vertical time-averaged velocity profile for cases $a/\lambda_x > 0.05$ is in contrast from cases $a/\lambda_x < 0.05$ at the position of x/λ_x= 0.7. In the near wall region, the distribution of streamwise time-averaged velocity along the wavy wall appears to be out-of-phase with wall geometry as shown in Figure 1(a). In Figure 1(b), the high upward velocity occurs at the stoss side of the wall near wave crest while the high downward velocity region locates

*Corresponding author. E-mail: liuqq@bit.edu.cn

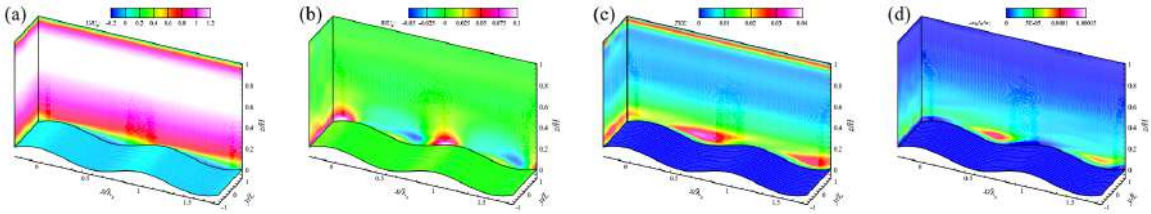

Figure 1: (a) Streamwise time-averaged velocity (b) vertical time-averaged velocity (c) turbulent kinetic energy and (d) Reynolds shear stress contour with a/λ_x= 0.05.

at the lee side expanding to the next stoss side of the wall. As shown in Figure 2, the streamlines exhibit a quasi-elliptical pattern in the separation zone, which locate under the elevation of wave crest. Above the wave crest, the streamlines are horizontal. But at the reattachment region, streamlines are a little bit concave which are consistent with other study [4].

Turbulent kinetic energy and Reynolds shear stress increases with ratio of a/λ_x. For the small ratio case, the region of high turbulent kinetic energy is also small. But for the other cases, the regions of high turbulent kinetic energy locate approximately between $x/\lambda_x \in$[0.3, 0.7] and $z/H \in$[0, 0.1] for a/λ_x= 0.05, $x/\lambda_x \in$[0.2, 0.9] and $z/H \in$[0, 0.15] for a/λ_x= 0.075, $x/\lambda_x \in$[0.1, 1.1] and $z/H \in$[0, 0.2] for a/λ_x= 0.1. And the regions of high Reynolds shear stress occur between $x/\lambda_x \in$[0.3, 0.7] and $z/H \in$[0, 0.1] for a/λ_x= 0.075, $x/\lambda_x \in$[0.2, 0.8] and $z/H \in$[0, 0.15] for a/λ_x= 0.1. In addition , the maximum turbulent kinetic energy and Reynolds shear stress occur at $x/\lambda_x \approx 0.5$ as shown in Figure 1(c) and Figure 1(d), which are approximately distributed symmetrically in one wavelength range.

The dimensionless streamwise time-averaged velocity decreases in both viscous region and logarithmic region with increase of ratio of a/λ_x as a result of the impediment of the wavy wall. The flow over wavy surface is different from the flat wall turbulent flow in viscous region, and the dimensionless velocity U^+ of the former is smaller than the latter [5].

The pressure distribution for different ratios of a/λ_x is diversified. As shown in Figure 3, there is negative pressure zone starting from wave crest and expanding to the stoss side, and a small positive pressure zone occurs at the stoss side of the wall near wave crest. In Figure 4, the form-drag induced by pressure distribution increases with increase of ratio of a/λ_x, while the viscous drag decreases.

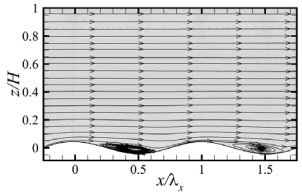

Figure 2: Time-averaged field streamline.

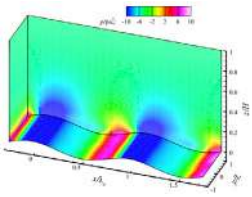

Figure 3: Pressure distribution contour with a/λ_x= 0.05.

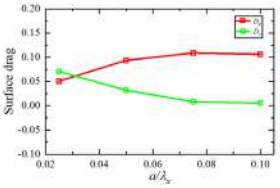

Figure 4: Form drag and viscous drag with different ratio of a/λ_x.

CONCLUSIONS

A large eddy simulation (LES) model for turbulent flow over wavy surface is constructed and validated. Then, it is used to study the turbulent characteristics of flow over various wavy surfaces. Main conclusions can be drawn as follows:

Separation zones behind the wave crest expand with increase of ratio of wave amplitude to wavelength.

The region of high turbulent kinetic energy and Reynolds shear stress expand with increase of ratio of wave amplitude to wavelength. $x/\lambda_x \approx 0.5$ is the position where the maximum turbulent kinetic energy and Reynolds shear stress occur.

The dimensionless time-averaged velocity decreases with increase of ratio of wave amplitude to wavelength. In viscous region and logarithmic region, the dimensionless velocity U^+ are lower compared with flat wall turbulence.

The form-drag occurs owing to the pressure distribution near wall and increases with the wavy surface ratio, while the viscous drag decreases.

References

[1] Hamed A.M., Kamdar A., Castillo L., Chamorro L.P. Turbulent boundary layer over 2D and 3D large-scale wavy walls. *Phys. Fluids.* **27(10)**: 106601, 2015.

[2] Martins S.V., Ormiston S.J., Tachie M.F. Experimental and numerical investigation of developing turbulent flow over a wavy wall in a horizontal channel. *Eur. J. Mech. B-Fluids.* **68**: 128-143, 2018.

[3] Michioka T. Large-eddy simulation for turbulent flow and gas dispersion over wavy walls. *Int. J. Heat Mass Transf.* **125**: 569-579, 2018.

[4] Yang D., Shen L. Direct numerical simulation of scalar transport in turbulent flows over progressive surface waves. *J. Fluid. Mech.* **819**: 58-103, 2017.

[5] Kim J., Moin P., Moser R. Turbulence statistics in fully developed channel flow at low Reynolds number. *J. Fluid. Mech.* **177**: 133, 1987.

PHASE-DEPENDENT SEDIMENT CONCENTRATION CARRIED BY NONLINEAR WAVES

Yiqin Xie[1,2], Yanrong Kuai[2], Jifu Zhou *[1,2], and Xu Wang[2]
[1]School of Engineering Sciences, University of Chinese Academy of Sciences, Beijing, China
2Key laboratory for Mechanics in Fluid Solid Coupling Systems, Institute of Mechanics, Chinese Academy of Sciences, Beijing, China.

Summary A sediment transport model coupled with numerical wave flume is built to simulate the hydrodynamic characteristics of nonlinear waves by using the Reynolds-averaged Navier-Stokes equations and the *k-ε* turbulence model. The model is validated by experimental data. It is shown that the model can well reproduce the spatial and temporal distribution of sediment concentration carried by nonlinear waves. Then, the variation of sediment concentration is studied. The results show that sediment carrying capacity increases almost linearly with wave height, whereas it increases more slowly with wave period. The averaged sediment concentration in different phase stages behaves similarly, and the averaged sediment concentration of the wave crest stages is higher than that of the wave tough stages.

INTRODUCTION

Sediment movement is one of the fundamental problems in coastal engineering research, which has a significant impact on ecological environment and human activities. In the process of wave propagation in the coastal region, the wave surface steepens with increasing wave height, and may eventually break. Then the nonlinearity becomes very strong, which plays an important role in the distribution of sediment concentration and further influences sediment carrying capacity carried by waves. Therefore, it is of significant implication to analyse the distribution law of sediment concentration carried by nonlinear waves.

A great progress has been made in the investigation of sediment carrying capacity with many empirical formulas obtained. For example, Dou Guoren [1] derived a formula of sediment carrying capacity under waves and currents by means of energy superposition. Liu Jiaju [2] analysed the data of sediment concentration profile near coastal areas and acquired a formula via dimensional analysis. Li Ruijie [3] obtained a formula based on sediment concentration profile obtained from the solution of two-dimensional sediment transport model. However, these formulas are limited to either linear waves or currents. Few attention is paid to the effect of nonlinearity of waves.

In the present paper, a sediment transport model coupled with numerical wave flume is built to simulate the hydrodynamic characteristics of nonlinear waves by using the Reynolds-averaged Navier-Stokes equations and the k-ε turbulence model. Then, sediment transport process induced by nonlinear waves is investigated. The variation of sediment concentration with wave parameters is analysed. The averaged concentration in different phase stages is discussed.

SEDIMENT TRANSPORT MODEL

The numerical wave flume for unsteady incompressible fluid is governed by the two-phase RANS equations:

$$\frac{\partial u_i}{\partial x_i} = 0 , \tag{1}$$

$$\frac{\partial \rho u_i}{\partial t} + \frac{\partial \rho u_i u_j}{\partial x_j} - \frac{\partial}{\partial x_j}\left(\mu_{eff}\frac{\partial u_i}{\partial x_j}\right) - \frac{\partial u_i}{\partial x_j}\frac{\partial \mu_{eff}}{\partial x_j} = -\frac{\partial p_d}{\partial x_i} - \left(g_j \cdot x_j\right)\frac{\partial \rho}{\partial x_i} , \tag{2}$$

where u_i is velocity in the ith direction, ρ is the fluid density, g_j is the jth component of the gravitational acceleration, p_d is the fluid dynamic pressure, and $\mu_{eff} = \mu + \rho\nu_t$ is the dynamic viscous coefficient, composed by the molecular dynamic viscosity and the turbulent viscosity, ν_t is obtained by solving the *k-* ε turbulence model. The VOF method is used to track the free surface location.

The suspended sediment concentration is acquired from the advection-diffusion-settling equation:

$$\frac{\partial c}{\partial t} + \frac{\partial\left(u_i - w_s\delta_{i3}\right)c}{\partial x_i} = \frac{\partial}{\partial x_i}\left(\varepsilon_s\frac{\partial c}{\partial x_i}\right) , \tag{3}$$

where w_s is the sediment settling velocity and can be determined by Van Rijn's method [4], ε_s is the sediment diffusivity.

The boundary conditions are specified as follows for wave motion and sediment transport, respectively. Nonlinear waves are generated using the stream function theory at the inlet of the wave flume. A sponge layer is employed to eliminate wave reflection at the outlet of the flume. No-slip condition is adopted for the velocity field at the bottom. No-flux of sediment is applied at the free surface. At the flume bottom, an empirical pickup function is adopted, which specifies the sediment flux as a function of bed shear stress.

RESULTS AND DISCUSSION

* Jifu Zhou. Email：zhoujf@imech.ac.cn

The numerical model is verified by experimental data from Amoudry, et.al[5], as shown in Table 1. In Figure 1, it is shown that the simulation results agree well with experimental data.

Table 1. The parameters of the cases to verify numerical model

Case	h/m	H/m	T/s	d/mm	λ_r /m	η_r /m	w_s /(m/s)
A	4.5	0.85	5	0.329	0.37	0.04	0.017
B	4.5	1.11	5	0.329	0.43	0.05	0.017

To analyse the influence of wave height and period on the sediment carrying capacity, several cases are specified based on case A and case B respectively with the wave height changing from 0.5 m to 2 m and the wave period from 4 s to 8 s. By double integrating sediment concentration over one wave period and the whole water depth, one can easily obtain the sediment carrying capacity of a wave. Figure 1 and Figure 3 show the variation of sediment carrying capacity with wave height and wave period, respectively. It is found that sediment carrying capacity increases with wave height and wave period as well.

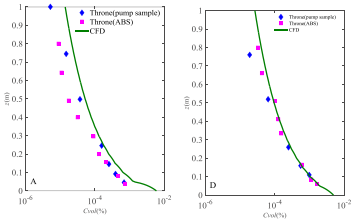

Figure 2. The vertical distribution of period-averaged concentration.

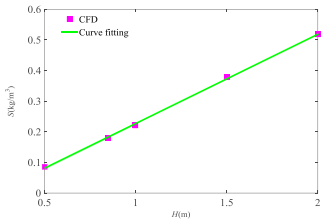

Figure 3. Sediment carrying capacity varying with wave height.

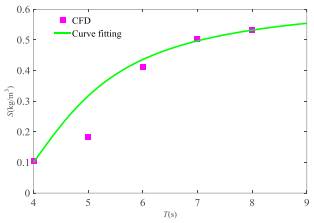

Figure 4. Sediment carrying capacity varying with wave period.

Further analysis goes for the variation of averaged sediment concentration with wave height and period in different phase stages. One wave period is divided into four stages as shown in Figure 4. Figure 5 and Figure 6 present the numerical results. It is obvious that the averaged concentration in different stages varies similarly to the sediment carrying capacity. Nonetheless, the averaged sediment concentration in wave crest stages (stage 1 and stage 4) is higher than that in tough stages (stage 2 and stage 3). This result is probably of implication for parameterizing sediment carrying capacity of nonlinear waves.

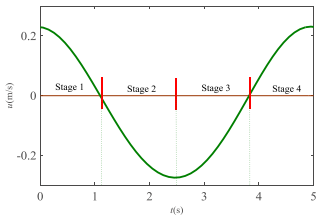

Figure 6. Schematic diagram of stage division in one wave period.

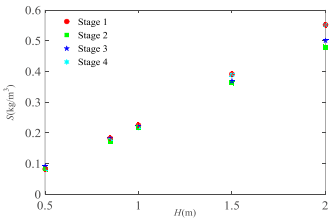

Figure 7. Averaged concentration varying with wave height.

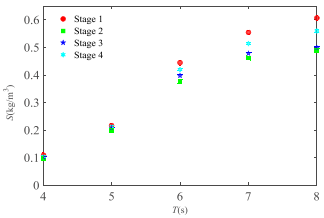

Figure 8. Averaged concentration varying with wave period.

CONCLUSIONS

A sediment transport model coupled with numerical wave flume is built and validated by experimental data. Based on this model, sediment carrying capacity of nonlinear waves is analysed. The numerical results demonstrate that the sediment carrying capacity of nonlinear waves increases almost linearly with wave height, whereas it increases more slowly with wave period. The averaged concentration in different phase stages behaves similarly. The averaged concentration in wave crest stages is higher than that in wave tough stages. This is probably of implication for parameterizing sediment carrying capacity of nonlinear waves.

ACKNOWLEDGEMENTS

We very much appreciate the financial support of the National Key R&D Program of China (2017YFC1404202) and the National Natural Science Foundation of China (11602274).

References

[1] Dou Guoren, Dong Fengwu, The sediment carrying capacity of currents and waves, [J]. Chinese Science Bulletin. Vo1.40, No 5. 1995. (in Chinese).
[2] Liu Jiaju. Determination of sediment concentration in muddy shoals under the action of wind waves and tidal current, [J]. Scientific research on water conservancy and transportation, 69-73, 1988. (in Chinese).
[3] Li Ruijie, Dong Dexin, Zheng Jun, Zhang Weiyi. Discussion on the inshore sediment carrying capacity, [J]. Journal of Sediment research. No 5. 2011. (in Chinese).
[4] Van Rijn, L. C., Unified view of sediment transport by currents and waves. II: Suspended transport, [J]. Hydraul. Eng.. 133(6), 668–688, 2007.
[5] Amoudry, L. O., P. S. Bell, P. D. Thorne, and A. J. Souza. Towards representing wave-induced sediment suspension over sand ripples in RANS models, [J]. Geophys. Res. Oceans, 118, 2378–2392, 2013.

EFFECT OF UPDRAFT ON NON-SUPERCELL TORNADO GENESIS

Koji Sassa[1], and Haruna Nagano [1]
[1]Faculty of Science and Technology, Kochi University, Kochi, Japan

Summary The present experimental study aims to clarify the effect of updraft on tornado genesis. We tested three updraft fans with different diameter at three bottom heights and at three driving voltages settled on a cold outflow intruding into environmental flow. The results showed that tornado-like vortices changed their rotation direction and size depending on the characteristics of updraft. The vortices were sometimes unstable and a pair of counter rotating vortex also was appeared. These facts shows that the characteristics of updraft affect tornado genesis. The updraft slightly smaller than the width of cold outflow is found to be suitable for tornado genesis.

INTRODUCTION

Tornadoes frequently occur in Japan and cause damages. Most of them are non-supercell ones which are classified as Type III by Agee and Jones (2009). Although such type tornadoes are relatively weak, they brake houses and plants. Different form supercell tornadoes, the parent clouds of non-supercell tornadoes do not have meso cyclones. Moreover such tornadoes sometimes occur at the same time of the development of parent clouds. Therefore, it is difficult to catch the tornado genesis by weather radars. We need to understand the flow condition of tornado genesis in order to predict the occurrence of tornadoes.

We have made the laboratory experiments to reproduce the environment of tornado genesis (Sassa and Watanabe 2016, Sassa and Komatsubara 2017). We showed the flow condition suitable for tornado genesis, in which the velocity of cold outflow is slightly higher than that of the environmental flow. In this case, the local front between the cold outflow and the environmental flow is fixed and the tornado-like vortex is formed at the end of the local front. The updraft velocity was also confirmed to affect the tornado genesis. However, we have still not examined how the other characteristics of the updraft, e.g., its diameter and height, affect the tornado genesis.

The present experimental study aims to investigate the effect of the updraft characteristics to the tornado genesis.

EXPERIMENT

The experimental set up is composed of our original outflow simulator reproducing cold outflow from cumulonimbus, the environmental flow simulator and a fan generating updraft as shown in Fig. 1. Our experimental system is quite different from traditional tornado simulators (e.g., Church et al. 1977). We do not need any chamber to keep tornado-like vortex. The outflow simulator is a kind of blow down type wind tunnel having cooling system. The height and width of its outlet are h = 40 mm and b = 100 mm, respectively. The cooling system is composed of thin aluminum heat sink, Peltier elements and water tank. We can easily control the velocity and temperature of cold outflow. The environmental flow simulator is also a kind of blow down type wind tunnel. Its outlet is 120 mm in height and 500 mm in width. The outlet of the outflow simulator faced the outlet of the environmental flow simulator. The gap between both simulators is 1050 mm. Then, it is simulated that the cold outflow intrudes in environmental flow. The origin of the coordinate system is set at the centre bottom of the outlet of outflow simulator and the coordinates are x: downstream, z: upward and y: perpendicular to x and z. Three updraft fans were examined. Their diameters, d, of fan A, B, C are 50, 90 and 150 mm, respectively. They were set at x = 150 mm and y = 80 mm. Their bottom height was set at z = 50, 100, 150 mm. Applied voltage driving fan was set to 12, 14, 16 V. Totally, we made 27 cases of experiment at various updraft conditions. In the present study, we set the outflow velocity, Uo = 0.3 m/s and the environmental flow velocity, Ug = 0.2 m/s. One Peltier element was driven at 5 V in the present experiment. Horizontal plane at z/h=0.125 was illuminated by laser sheet light and filmed by hi-speed cameras at 1000 fps in frame rate. The mist from ultrasonic humidifier was used as tracer for visualization. Horizontal velocity components, u, v, were measured by using dynamic PIV method. We also filmed the flow fields by ordinal video camera at 30 fps in order to examine flow situation.

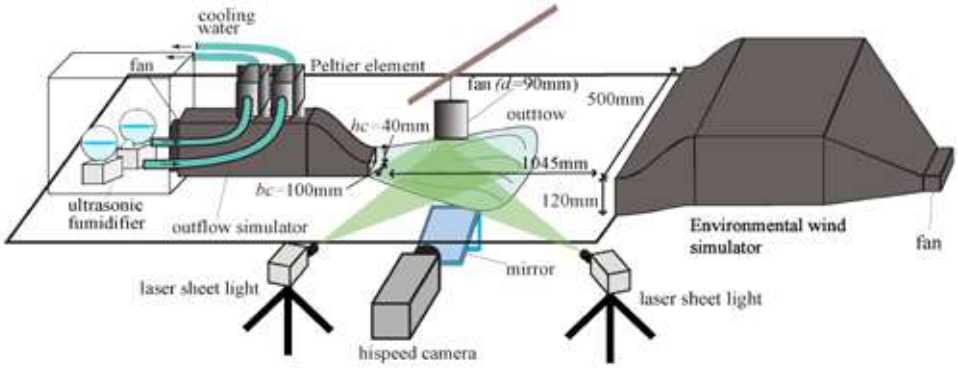

Figure 1. Experimental setup. Base plate is made of

RESULT AND DISCUSSION

The smallest updraft by fan A cannot stretch the cyclonic vorticity of horizontal shear at the local front in most of cases. The small tornado-like vortex is generated only in the lowest height, z = 50 mm as shown in Fig.2a. In this case, the updraft is quite localized, then cold outflow flows downstream and the local front is not formed. The tornado-like vortex was formed in the mixing layer between the cold outflow and the environmental flow.

In the case of fan B, the diameter of updraft region is slightly smaller than the width of the cold outflow. Such situation is similar to that relation between the actual updraft of cumulonimbus and the cold outflow. As shown in Fig.2b, the local front is clearly formed and the tornado-like vortex appears at the left hand side edge of the local front. The tornado-like vortex is the most stable in all cases and its intensity is also highest. Such situation was observed in relatively larger heights. The updraft of fan B is too strong to generate the tornado-like vortex at z = 50 mm. In this case, the rotation direction of the tornado-like vortex frequently changed cyclonic to anticyclonic and vice-versa as the direction of horizontal shear changes.

Fan C simulates the situation that the updraft region is larger than the width of cold outflow like the mesocyclone in a supercell. Most of cold outflow is sucked up due to strong updraft and the local front becomes not to be clear as shown in Fig. 2c. In this case, the rest of the cold outflow forms counter rotating vortex pair. It is similar to the pair of cyclonic and anticyclonic tornadoes observed in a supercell (Bluestein et al. 2007). But the tornado-like vortex becomes to be relatively stable at z =150 mm. These facts show that the effective region of updraft is changed by the height of fan and the characteristics of tornado-like vortex is also altered depending on the width of updraft.

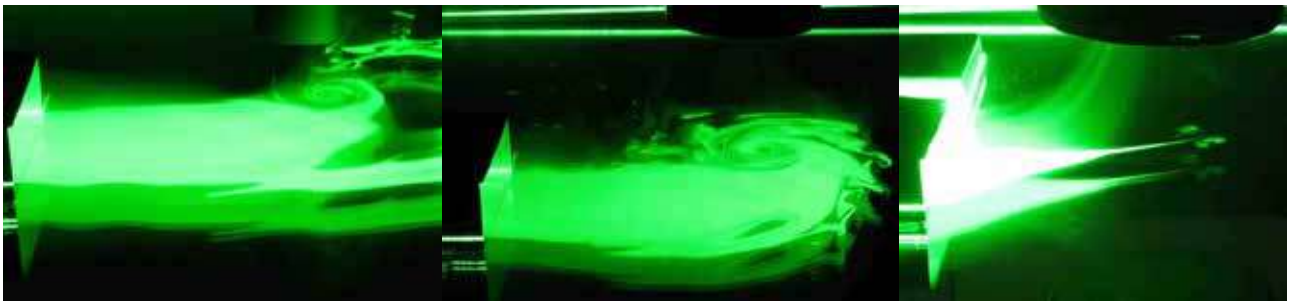

(a) fanA:d=50 mm at z=50 mm (b) fan B:d=90 mm at z=100 mm (c) fan C:d=150 mm at z=100 mm

Figure 2. Typical example of tornado-like vortex

CONCLUSIONS

The width and height of updraft were found to affect the structure of tornado-like vortex. Despite the location of the updraft fan was fixed at the left hand side edge of the cold outflow, cyclonic and anti-cyclonic vortices appeared depending on the updraft situation. Even the counter rotating vortex pair was observed. These facts shows that the present experiment can simulate not only non-supercell tornado but also supercell tornado. The most suitable condition for tornado genesis was found that the updraft region is slightly smaller than the cold outflow as observed in actual cumulonimbi.

ACKNOWLEDGMENT

The present study was supported by JSPS KAKENHI No. 18H01682.

References

[1] Agee E., Jones E., Proposed Conceptual Taxonomy for Proper Identification and Classification of Tornado Events. *Wea. Forcusting.* **24**: 609-617, 2009.

[2] Sassa K., Watanabe H., Laboratory Experiment on the environment for non-supercell tornadogenesis,. Proc. of the 11th ERCOFTAC symposium on ETMM, Palermo, Italy, 6pages, 2016.

[3] Sassa K., Komatsubara M., Laboratory Experiment of Non-Supercell Tornado Genesis on Local Front. Proc. of the 9th APCWE, Auckland, New Zealand, 4pages, 2017.pdraft

[4] Church C. R., Snow J. T., Agee E. M., Tornado vortex simulation at Purdue University, Bull. Amer. Meteor. Soc., 58-9, 900-908, 1977.

[5] Bluestein H.B., French M.M. Tanamachi R.L., Close-Range Observations of Tornadoes in Supercells Made with a Dual-Polarization, X-Band, Mobile Doppler Radar, Mon. Wea. Rev., 135, 1522-1543, 2007.

FLOW THROUGH A POROUS MEDIUM AND GROUND HEAT EXCHANGERS

Iosifina Iosif Stylianou[1], Paul Christodoulides[2a)], Lazaros Aresti[2], Savvas Tassou[1]& Georgios A. Florides[2]
[1]Institute of Energy Futures, Brunel University London, Uxbridge, Middlesex UB8 3PH, UK
[2]Faculty of Engineering and Technology, Cyprus University of Technology, Limassol, Cyprus

Summary The thermal response of vertical Ground Heat Exchangers (GHEs) is examined when the ground sublayer involves underground water flow. A numerical model constructed to allow for the presence of porous media regions and a consequent validated computational finite elements model in FlexPDE software lead to an analysis of several factors effecting the efficiency of the GHE, such as summer and winter mode of operation, underground temperature variation in small depths, borehole radius, borehole grout properties, U-tube diameter, U-tube leg and borehole centers distance, groundwater flow velocity.

INTRODUCTION

Geothermal energy, the thermal energy generated and stored in the Earth, is a fast-growing Renewable Energy Source. It has been used since Paleolithic times for bathing, through the use of water from hot springs, as well as since ancient Roman times for space heating. It is nowadays used for electricity generation as well, in addition to district heating, space heating, spas, industrial processes, desalination and agricultural applications. Depending on the depth geothermal energy systems (GES) can be classified as deep or shallow. One of the most common approaches for lower and mid-depth applications for shallow GES is the borehole vertical Ground Heat Exchanger (GHE), where using a Ground Source Heat Pump (GSHP) fluid circulates through pipes (U-tubes) and an indirect thermal contact is achieved between the fluid and the subsurface. GHE technology is of higher efficiency for air-conditioning compared to conventional systems as the underground environment provides lower temperature for cooling and higher temperature for heating, with the underground temperature being approximately equal to the mean annual atmospheric temperature of the year [1–2].

A GHE system is controlled by the effective area, the thermal conductivity of the subsurface, the velocity of the circulating fluid, the equipment involved, (type and size of pipes, the grouting material, etc.), the presence of underground water in the form of an aquifer, and so on. A parametric analysis of the aforementioned factors using simulations and validation tools can lead to the optimization of the GHE system. For more on the design aspects of GHEs the reader is referred to [3]. An aquifer is the saturated permeable geologic unit that can transmit significant quantities of water under ordinary hydraulic gradients [4]. In order to describe the flow through a porous medium, Darcy's law needs to be applied. The theory, allowing the estimation of the velocity or flow rate within an aquifer was firstly established by Darcy [5] based on experimental results. Model results with various seepage velocities (i.e. Darcy's velocity over porosity) indicate that groundwater flow influences the average GHE temperature, and in the water-baring layer the average temperature is lower than in the dry regions [6]. It is also noteworthy that the temperature of the affected ground layer reaches a steady-state much sooner than in other regions.

The effect of an aquifer on a GHE is examined in this paper through numerical modeling in the FlexPDE software based on the convection-diffusion equation and Darcy's law. FlexPDE is a general-purpose software that builds a mesh, constructs a system finite-elements model (FEM), solves it, and presents an easy to use graphical output for steady-state, time-dependent and free boundary problems.

MATHEMATICAL MODEL OF GHEs IN POROUS MEDIA

The basic three-dimensional equation governing the convective and conductive heat transfer is given as

$$\rho c_p \frac{\partial T}{\partial t} + \rho_f c_{pf} u_{in} \cdot \nabla T + \rho_w c_{pw} u_p \cdot \nabla T + \nabla \cdot (-\lambda \nabla T) = Q, \quad (1)$$

where ρ denotes the density [kg m^{-3}], u the velocity [m s^{-1}], T the temperature [K], c_p the specific heat capacity [J kg^{-1} K^{-1}], λ the thermal conductivity (W m^{-1} K^{-1}), Q the power density of the heat source [W m^{-3}]. Subscript f denotes fluid, w denotes water, in denotes inside tube and p denotes porous media. At the boundary between the fluid and the tubes (Darcy's regime) the convective heat flux is $h\Delta T$, where h is the convective heat transfer coefficient of the process [W m^{-2} K^{-1}] and ΔT is the temperature difference at the boundary. The convection heat transfer coefficient h can be estimated to be $h = \lambda \mathrm{Nu}/\mathrm{D_H}$, where $\mathrm{D_H}$ is the hydraulic diameter (in this case the tube-inside diameter) and Nu is the Nusselt number. The Nusselt number in this case can be expressed through the Dittus–Boelter correlation as $\mathrm{Nu} = 0.023\mathrm{Re}^{0.8}\mathrm{Pr}^{n}$, where $\mathrm{Pr} = \mu c_p/\lambda$ is the Prandtl number, $\mathrm{Re} = \rho c_p d_{in}/\mu$ is the Reynolds number, μ is the dynamic viscosity [kg m^{-1} s^{-1}, and porosity $n = 0.4$ for heating and 0.33 for cooling. For more on the fluid properties necessary for the application of the equations above and the various boundary layers of the GHE the reader is referred to [7–8].

COMPUTATIONAL MODEL AND RESULTS

The desired model based on the numerical model above was created in the FlexPDE environment with the following meshed ground layers (zones) from top to bottom: 80 m of dry well area; 25 m of high water-velocity area (0.00005 m s^{-1}); 55 m of low water-velocity area (0.0000000116 m s^{-1}); 5 m of base area shown in purple. The configuration above is a model for an existing borehole GHE in Lakatameia area, Cyprus, and has been validated through Thermal Response Testing (TRT) [7]. The underground temperature in the Lakatameia BH, for depths over 7 m is 22°C, with 1°C increase per 100 m. The best-fit equations for the temperature gradient were imposed on the numerical model to match the ground

*Corresponding author, E-mail: paul.christodoulides@cut.ac.cy

temperatures used in simulations to the actual temperatures of the ground during the experiments (Figure 1 for deep zone). The results for the computational model show a good agreement with TRT measured values (Figure 2).

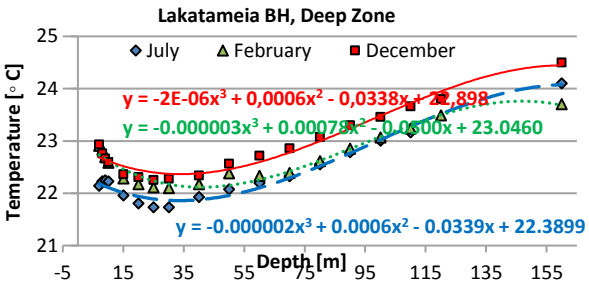

Figure 1. Recorded underground temperature at the Lakatameia borehole (BH) deep zone (7–160m), shown is the best-fit equation.

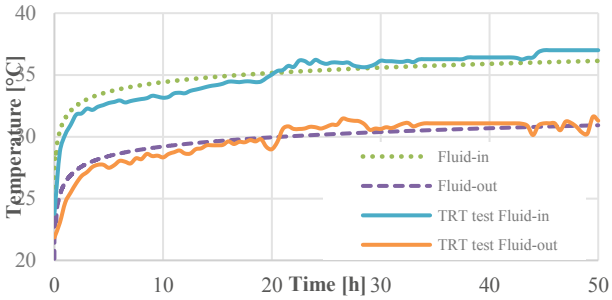

Figure 2. TRT recorded temperatures (December) at the Lakatameia BH (TRT Fluid-in/out) in comparison with the FlexPDE script calculated values (Fluid-in/out).

The thermal response of the GHE can then be examined with confidence for both cooling and heating regimes (see [7] for details). For cooling, one can conclude that the greater the difference between the input water temperature and the ground temperature, the greater the rejected heat to the ground, while the higher the exiting water temperature, the greater the rejected heat to the ground. Similarly, for heating, the greater the difference between the input water temperature and the ground temperature, the greater the absorbed heat from the ground, while the lower the exiting water temperature, the greater the absorbed heat from the ground.

The effect of the groundwater velocity is examined through a parametric analysis for various BH radiuses. Results show that a smaller BH radius keeps a lower temperature of the fluid of the GHE (cooling mode) due to the thermal properties of the grout used in the specific geological formation. It turns out that the relation of the absorbed power per m (= $mc_w\Delta T$) of BH length to the BH radius (Figure 3), reveals that although the total power absorbed by the ground is kept the same (5710 W) in all cases, the dry layer and the low underground water-velocity layer respond rather uniformly in absorbing power, as opposed to the high underground water-velocity layer that decreases exponentially with radius.

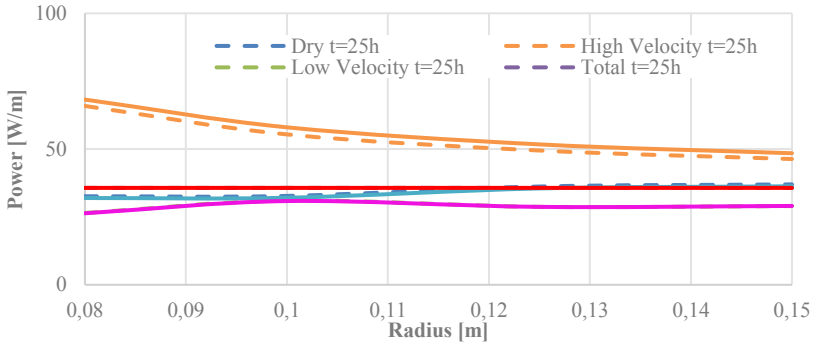

Figure 3. Absorbed power per m against the BH radius for the three layers of the BH for 25h of GHE operation.

CONCLUSION AND DISCUSSION

A more complete parametric analysis, for the cooling mode of the GHE, can involve the analysis of (i) the grout thermal conductivity, (ii) the U-tube size, (iii) the distance between BH and tube leg centers, (iv) underground water velocities [7]. The study presented in here is an important step toward investigating the importance of the presence of an aquifer in the construction of a BH GHE and can be further extended for factors such as the summer and winter mode of operation, the underground temperature variation due to seasonal changes, the BH thermal resistance and multiple BHs [6].

References

[1] Busby J. UK shallow ground temperatures for ground coupled heat exchangers. Geological Society of London, 2015.
[2] Heath R.C. Basic ground-water hydrology. US Geological Survey, 1983.
[3] Aresti L, Christodoulides P, Florides G. A review of the design aspects of ground heat exchangers. *Renewable and Sustainable Energy Reviews* **92**:757-773, 2018.
[4] Freeze R.A., Cherry J.A. Groundwater. Prentice-Hall, 1979.
[5] Darcy H. Les Fontaines Publiques de la Ville de Dijon. Paris: Dalmont, 1856.
[6] Aresti L., Christodoulides P., Florides G.A. Computational modelling of a ground heat exchanger with groundwater flow. *Bulgarian Chemical Communications* **48**:55-63, 2016.
[7] Stylianou I.I., Tassou S., Christodoulides P., Aresti L., Florides G. Modeling of vertical ground heat exchangers in the presence of groundwater flow and underground temperature gradient. *Energy and Buildings* **192**:15-30, 2019.
[8] Iosif-Stylianou I., Christodoulides P., Aresti L., Tassou S.A., Florides G.A. Borehole Ground Heat Exchangers and The Flow of Underground Water. *International Journal of Industrial Electronics and Electrical Engineering* **6**(9):69-72, 2018.

DUNE-DUNE INTERACTIONS IN A QUASI-TWO-DIMENSIONAL CORRIDOR

Karol A. Bacik[1], Colmcille P. Caulfield[2,1], and Nathalie M. Vriend [2]
[1]Department of Applied Mathematics and Theoretical Physics, University of Cambridge, Cambridge, UK
[2]BP Institute, University of Cambridge, Cambridge, UK

Summary: Sand dunes rarely occur in isolation, but usually form vast collectives known as dune fields or dune corridors. The large scale organisation of the dune fields cannot be explained by the properties of individual dunes, but it is controlled by the mesoscale dune-dune interactions. The physics of these interactions is poorly understood, not least due to the shortage of prolonged geophysical observations. To circumvent the limitations of field observations, we investigate the dynamics of a quasi-two-dimensional dune corridor. We discuss wake-induced interactions and show how they control the structural stability of a dune corridor.

INTRODUCTION

Sand dunes spanning several orders of magnitude can be found in deserts, on river beds, as well as on other planets [1]. Dunes often form larger collectives known as dune fields. Notwithstanding significant progress in our understanding of single dune dynamics, the morphologies of dune fields are still poorly understood. Most importantly, it is not clear if the configurations we observe in the field are steady or transient [2]. At the same time making accurate predictions on dune field evolution is of chief societal importance. Migrating dunes not only enhance desertification, but they also regularly bury roads, rail tracks or even buildings.

Here, in order to uncover fundamental physical principles governing dune field dynamics, we investigate a train of quasi-two-dimensional moving over an unerodible substrate.

EXPERIMENTAL SET-UP

The experimental set-up consists of a 2 m diameter annular flume fixed to a turntable and a paddle assembly (see Fig. 1). Counter-rotation of the two components induces a turbulent water flow in the 9 cm wide channel. Sufficiently vigorous flows can mobilise glass beads (d = 1mm), which rest at the bottom arranged in discrete dunes. By using circular geometry, we avoid practical problems of fluid and sediment resupply at the boundaries. Moreover, rotating systems facilitate data collection with a stationary cameras, which can be used to record the topography evolution and image the flow field through particle tracking.

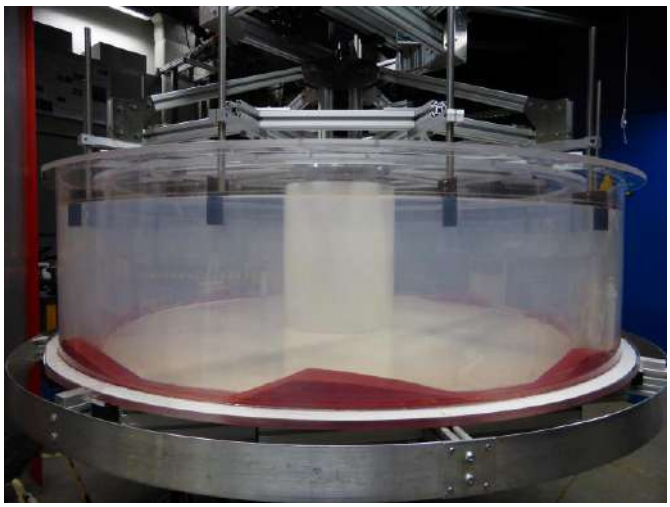

Figure 1. **Experiment.** A spider assembly of 12 paddles counter-rotating with the tank mounted on a turntable. The topography corresponds to a quasi-2D dune corridor with 8 dunes.

WAKE-INDUCED INTERACTIONS

Previous experiments revealed that two dunes, one directly upstream of the other, can interact at large distances even if they are not in direct contact [3]. The feedback is induced by the wake forming behind the upstream dune. Turbulent fluctuations in the wake enhance sediment flux over the downstream dune and thus increase its migration rate. This change in the migration rate can be described as an effective dune-dune repulsion, which prevents dune collisions.

In this study, instead of probing pairwise interactions, we consider sand dunes arranged in a quasi-two-dimensional periodic train. Specifically, we test how the morphology and migration rate of the corridor depends on the distance between neighbouring dunes. For sparse arrangements, the dunes are dynamically independent but as the gap between the dunes narrows, wake-induced effects ensue. We investigate the physical underpinnings of the inter-dune coupling and explore its consequences for the structural stability of the dune corridor.

CONCLUSIONS

Laboratory aqueous experiments show that wake-induced effects can affect the properties of sand dunes embedded in a dense dune field. Velocity field fluctuations in the wake enhance sediment transport and thus affect the shape and the migration rate of individual dunes.

References

[1] Charru F., Andreotti B. & Claudin P. Sand ripples and dunes. Annu. Rev. Fluid Mech. 45, 469 (2013)

[2] Hersen P., Andersen K.H., Elbelrhiti H., Andreotti B., Claudin P. & Douady S. Corridors of barchan dunes: Stability and size selection. Phys. Rev. E 69, 011304 (2004)

[3] Bacik K.A., Lovett S., Caulfield C.P. & Vriend N.M. Wake induced long range repulsion of aqueous dunes. *Phys. Rev. Lett.* (in press) (2020)

SIMULATION OF EFFECTS OF ELECTRIC FIELD ON THE SNOW PARTICLE TRAJECTORY

Hongxiang Yu[1,2], Guang Li[1,2], and Ning Huang[*1]
[1]School of Civil engineering, Lanzhou University, Gansu, China
[2]School of Architechture, Civi l and Environmental Engineering, Ecole Polytechnique Federal de Lausanne, Lausanne, Switzerland

Summary Snow particles will be charged due to the collisions with each other or with the ground in snow drifting, and form a strong electric field compared to the atmospheric electric field. This field will also have an impact on the trajectory of snow particles. In this work, we set up the charge separation model for calculating the charge caused by the asymmetric collision. We simulate the single particle's trajectory in the flow field, and analysis the factors that affect the saltation trajectory.

INTRODUCTION

Snow drifting is a common phenomenon in high and cold regions, and has an important impact on the local environment and socioeconomic consequences (Bartelt and Lehning, 2002). It affects the mass balance of snow cover, thereby impacting on the radiation balance and hydrological processes (Luce et al., 1999). It changes snow distribution, forming snow patterns like snow ridges, ripples and dunes, as well as cornices (Vogel et al., 2012). The uneven accumulation due to snow drifting also lead to disasters such as avalanches, building collapse, road and rail traffic safety problems, and agricultural production damages (McClung et al., 2006).

Since the snow particles are charged, the additional associated electric field also has impact on their motion trajectories. Schmidt (1999) estimated the electric field force of snow particle with 0.14 mm size at a height of 0.5 cm above the bed and found that it could counterbalance gravity, which exceeds the gravity, and the direction is opposite. However, Schmidt only calculated the first hop of the snow particle in the electric field. Omiya (2012) calculated the influence of electric field force on the jump length and jump height of moving particles under the assumption that all particles are negatively charged, and, but all the particles are negative charged. the resulting electrostatic force creates an acceleration of 0.0004g (g: gravitational acceleration), this small value could be caused by calculate charges using bulk-method during the experiment. And But in most of snow drifting snow models, the electric effects are ignored. Thus, it is necessary to accurately study the trajectories of snow particles of different polarities in drifting snow electric field. In this contribution, we develop a model that describes the influence of charge separation on particle trajectories in drifting snow.

METHOD AND MODEL

In this manuscript, we calculate the single particle's trajectory moving in a neutral atmospheric boundary layer. As is shown in Fig. 1, snow particles jump with an initial velocity, after falling back to the ground and bouncing back to the air, after multiple collisions with ground, the saltation trajectory becomes stable.

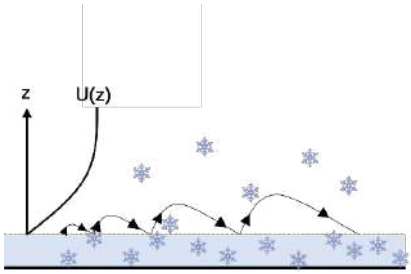

Fig.1 Schematic diagram of calculation.

Charge separation model of collision snow particles

Assuming a mixed-size granular system composed on N particles, and the particle size distribution is Φ(R). During the transportation, the repeat collisions between two particles and the multi-collisions among different types of particles can happen. According to the assumption proposed by Latham and Mason (1961) that it is either H^+ or OH^- that can transfer during the contact, and the mobility of H^+ is higher than OH^-. Here we also assume that the particles are covered totally by H^+ and OH^- ions, as is shown in Fig. 1, and assume that the transferred charge carrier as H+.

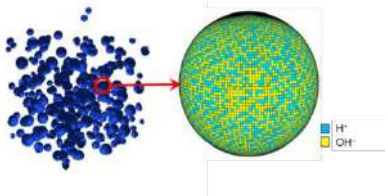

Fig 2. The schematic of H^+ and OH^- distribution on the snow particle surface

Assume the $c_{H+,i}$(n) and $c_{H+,j}$(m_j) are the ion concentration of particle i after nth collision and particle j after m^{th} collision. The net transferred charge from particle j to particle i can be calculated as:

$$\langle Q_i(n)\rangle = \rho_0 A_0 C_{i,j}\{\alpha(m_j)S_j c_{H+,j}(m_j-1)[1-c_{H+,i}(n-1)]3 - \alpha(n)S_i c_{H+,i}(n-1)[1-c_{H+,j}(m_j-1)]\} \quad (1)$$

In which, S_i and S_j are the maximum deformation area of the two particles, respectively, α is the H^+ transfer probability. The detailed derivation is available from (Yu et al., 2017). After Li times of collision, the mean charge on the particle *i* is:

$$\langle Q_i(L_i)\rangle = \rho_0 A_0 \sum_{n=1}^{L_i}\sum_{j=1,j\neq i}^{N} C_{i,j}\{\alpha(m_j)S_j c_{H+,j}(m_j-1)[1-c_{H+,i}(n-1)]3 - \alpha(n)S_i c_{H+,i}(n-1)[1-c_{H+,j}(m_j-1)]\} \quad (2)$$

In which, the initial hydrogen ion concentration $c_{H+,i/j}(0)$ is related to air humidity.

CONCLUSION AND DISCUSSION

The complete saltation trajectory of these three different polarities of particles are shown in Fig 3, when the saltation movement are trend to be stable, the saltation height of positive particle is 54.6% larger than the neutral particle, and that of the negative particle is 54.6% smaller than the neutral particle. The height of suspension particle is the lowest, the suspension height is 88.2% smaller than the neutral particle.

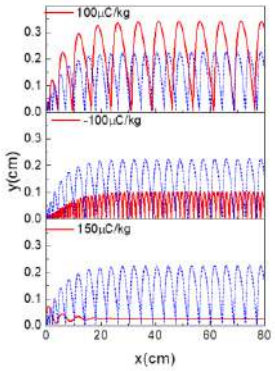

Fig 3. Four kinds of charge to mass ratio of particles' trajectory (the blue dash represents the neutral particle's trajectory).

During the wind blow snow, the charge separation happens during the asymmetric collision between particles and the ground. The polarity of snow particles is positive or negative, which is dependent on the size distribution. The charged snow particles moving in the electric field can change its trajectory with the effect of the electrostatic force.

References

[1] Latham, J., & Mason, B. J. (1962). Electrical charging of hail pellets in a polarizing electric held. Proceedings of the Royal Society of London. Series A. Mathematical and Physical Sciences, 266(1326), 387-401.

[2] Latham, J., & Montagne, J. (1970). The possible importance of electrical forces in the development of snow cornices. Journal of Glaciology, 9(57), 375-384.

[3] Luce, C. H., Tarboton, D. G., & Cooley, K. R. (1999). Sub - grid parameterization of snow distribution for an energy and mass balance snow cover model. Hydrological Processes, 13(12 - 13), 1921-1933.

[4] McClung, D., & Schaerer, P. A. (2006). The avalanche handbook. The Mountaineers Books.

[5] Naaim, M., Naaim-Bouvet, F., & Martinez, H. (1998). Numerical simulation of drifting snow: erosion and deposition models. Annals of glaciology, 26, 191-196.

TSUNAMI WAVE RUNUP ON A NON-UNIFORMLY SLOPING BEACH

Arghya Bandyopadhyay*[1] and Dipannita Maji[1]
[1]Department of Mathematics, Khalisani College, Chandannagar, India

Summary Ocean bottom bathymetry plays an important role in tsunami propagation [1, 2]. In an earlier work [3], the first author analytically studied tsunami waves in a continuously sloping non-uniform bottom profile of the form $y = -qx^r$, $q > 0$, $0 < r < 2$. The complete analysis of the wave integral involving double Hankel integrals leads us to a four-wave structure, one component of which gives rise to forerunner and another component provides a new expression for wave runup. This study also unfolds other characteristics of wave underlining the effect of bottom bathymetry in a tsunami wave motion generated by a periodic bottom disturbance.

PROBLEM AND ITS SOLUTION

For a two-dimensional linear shallow water waves due to a sudden bottom upheaval past a sloping beach $y = h_0(x)$ (Figure 1), the surface displacement $\eta(x,t)$ satisfies the differential equation

$$\eta_{tt} - gh_0(x)\eta_{xx} - gh_0'(x)\eta_x = \eta_{0tt} \tag{1}$$

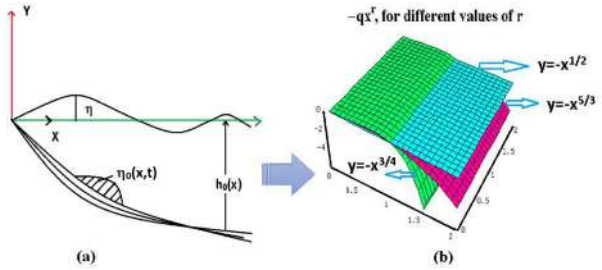

Figure 1: Illustration of bed profile $y = -qx^r$ with choice of axes (a) Cross-sectional view (b) Three dimensional view

The solution of which subject to appropriate initial condition can be obtained with the use of Hankel transform as

$$\eta(x,t) = (\gamma\sqrt{gq})^{-1} \int_0^\infty x^{(1-r)/2} J_\nu(\xi\gamma^{-1}x^\gamma)d\xi \int_0^\infty \alpha^{(1-r)/2} J_\nu(\xi\gamma^{-1}\alpha^\gamma)d\alpha \int_0^t \ddot{\xi}_1(\alpha,s)\sin\sigma(t-s)ds \tag{2}$$

where $\sigma = \xi\,(gq)^{\frac{1}{2}}$, $\gamma = 1 - \frac{r}{2}$, $\nu = \frac{r-1}{2-r}$ and $h_0(x) = qx^r$. An analysis of the expression in (2) over $0 < t < \tau$ for a periodic ground motion shows that η may be regarded as the superposition of four distinct waves $\eta \equiv \eta_1 = \eta_{11} + \eta_{121}^{\pm} + \eta_{122} + \eta_{123}^{\pm}$, where $\pm$ signs indicate that the corresponding expressions are different for $\nu \geq 0$ and $\nu < 0$ respectively while η_{11} and η_{122} remain unchanged. The forms of the above four waves when analysed provide us a full view of the wave structure. The detailed mathematical calculation involved in the whole process is daunting and beyond the scope of this submission, instead we only mention the form of the wave components η_{11} and η_{123} which are the reasons of the forerunner and wave runup respectively. A brief discussion on the significance of these four wave structure and its interaction with the ocean bed is provided subsequently.

The component η_{11} of η identified as forerunner [3] of the wave system

$$\eta_{11} = \frac{\sqrt{\pi}\xi_0^{2\nu+2}}{\Gamma(\nu+1)(2\gamma)^{(2\nu+1)}} \sum_{m=0}^\infty (m+1)^{-1}(\omega t/2)^{m+3/2}\left[J_{m+1/2}(\omega t) + iJ_{m+3/2}(\omega t)\right] \sum_{n=0}^\infty \frac{(-1)^n}{n!}\left(\frac{\xi_0\gamma^{-1}x^\gamma}{2}\right)^{2n} \times$$
$$\times \frac{1}{\Gamma(n+m+\nu+2)} \int_0^\infty {}_2F_1\left(-n,-n-\nu;\nu+1;\left(\frac{\alpha}{x}\right)^2\gamma\right)\zeta_1(\alpha)d\alpha$$

The component $\eta_{123}^{\pm}$ of η

$$\eta_{123}^{\pm} = \gamma\Gamma_k z_0^{2\nu+2} x^{-\nu\gamma}\left[1 + i\omega\int_0^t dt\right]\left[\sum_{n=0}^\infty \frac{(-1)^n}{\Gamma(2n-2\nu+1)}\left\{\sum_{l=0}^{N_k}(-1)^l\binom{N_k}{l}(\omega t)^{N_k-l}\int_0^1 x_1^{-L_k} z_0^l \frac{\partial^l P_1}{\partial z_0^l} e^{j(\omega t x_1 + l\pi/2)}dx_1 + \right.\right.$$
$$\left.\left. + (-1)^{n+k}\cos\omega t \int_0^1 x_1^{-2n-1} z_0^{N_k}\left(\frac{\partial}{\partial z_0}\right)^{N_k} P_1 dx_1\right\}\right]$$

Here k=1, 2 refers to $\nu > 0$, $\nu < 0$, $N_k = 2n, 2n+1$, $L_k = l+1, l$, $P_1 = z_0^{-2\gamma} J_\nu(z_0 x^\gamma x_1)\bar{f}_\nu(z_0 x_1)$, $\Gamma_k = \Gamma(1-2\nu)Re\left[e^{j(\omega t x_1 + l\pi/2)}\right], \Gamma(-2\nu)Im\left[e^{j(\omega t x_1 + l\pi/2)}\right]$.

*Corresponding author. E-mail: b.arghya@gmail.com

The analysis of η-integral for t >τ : paired four wave composition of η

For the part of the motion when $t > \tau$, it can be shown that $\eta \equiv \eta_2 = \eta_1(x,t) + \eta_1(x,t-\tau)$. This means to each of the four wave-system consisting of η_1, there correspond two similar wave forms; of these two, one follows the other with a time-lag of τ.

DISCUSSION OF THE RESULTS

To illustrate the above results, we consider one particular periodic bottom disturbance with amplitude $\zeta_1(x) = \sqrt{x}e^{-\sqrt{x}}$. The nature of η_{11} and η_{12} are depicted near the shore for a time period of $t < \tau$, that is at the sub-quake range, it is clear that η_{11} dominates the spectrum for small time. This η_{11} is the forerunner which comes ahead of the forced wave (Figure 2).

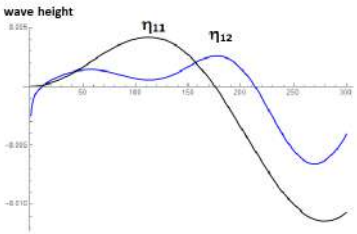

Figure 2: Illustration of the forerunner η_{11} at the shore which clearly shows the dominance of η_{11} over η_{12} for $t < \tau$(= 150 s)

Again, this dominance of η_{11} in the spectrum is even more prominent if the small-time behaviour of the comparable component η_{122} is in same phase with η_{11} or not. This perhaps explain the existence of forerunners or otherwise in many of the tsunami events. The wave component η_{123} is the reason of wave evolution at the shore and it dominates the spectrum after certain time, to be precise after $t > \tau$. To our understanding, the expression of η_{123} may be taken as the analytical measure for runup in case of generation of tsunami waves in a physical setting like the one considered here (Figure 3).

Another thought-provoking fact is realized with the ocean bed profile where we find different wave forms reaching the shore - elevation or depression according as the ocean bed profile is convex downward (i.e. with r = 1.1 or $\nu > 0$) or convex upward (i.e. with r = 0.8 or $\nu < 0$), all other parameters remaining same (Figure 4).

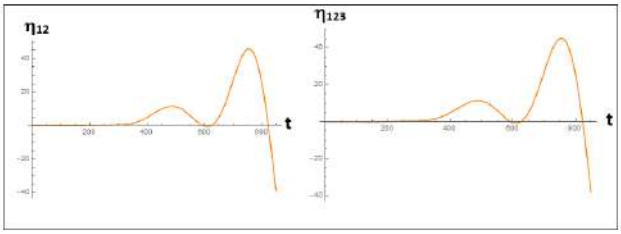

Figure 3: Equivalence of η_{123} and η_{12} for large time depicting dominance of η_{123} at shore.

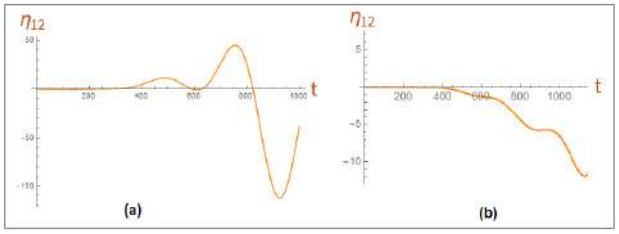

Figure 4: (a) wave elevation when the ocean bed is convex downward (b) wave depression when the ocean bed is convex upward

CONCLUSIONS

The analytical solution found here highlights the following - (i) waves behave in a quartet (ii) from this quartet forerunners can be isolated and (iii) the expression of runup can be determined. Further, (iv) ocean bathymetry effects in wave evolution and acts as one determining factor whether an elevation or a depression wave would reach the shore. In 2011 Tohuku tsunami, forerunners were observed in Japan sea [5], this observational finding matches with our mathematical finding.

References

[1] Jinadasa S., Interaction of tsunami wave propagation with coastal bathymetryand geo-morphology; a case study in Sri Lanka. NARA. 2008.
[2] Kanoglu U., Synolakis C.E., Long wave runup on piecewise linear topographies. J.Fluid Mech, **374**: 1-28, 1998.
[3] Bandyopadhyay A., Identification of forerunners and transmission of energy to tsunami waves generated by instantaneous ground motion on a non-uniformly sloping beach, International Journal of Geosciences., **4**: 454-460, 2013.
[4] Gradshteyn I. S. and Ryzhik I. M., Table of Integrals, Series, and Products, 4th ed., Academic Press, New York, 1965.
[5] Murotani S. et. al, Tsunami Forerunner of the 2011 Tohuku Earthquake Observed in the Sea of Japan., Pure Appl. Geo.,**172**: 683-697, 2014.

PARTICLE MOTION NEARBY ROUGH SURFACES

Christina Kurzthaler[1], Lailai Zhu[1,2], Amir Pahlavan[1], and Howard A. Stone*[1]
[1]Department of Mechanical and Aerospace Engineering, Princeton University, NJ 08544, USA
[2]Linné Flow Centre and Swedishe-Science Research Centre (SeRC),KTH Mechanics,SE-10044,Sweden

Summary Interactions between particles and boundaries are ubiquitous in nature and play a pivotal role in microfluidic applications. For low-Reynolds-number motions we study the hydrodynamic couplings between particles and solid, rough boundaries, which are characterized by periodic and random surface textures. Using the Lorentz reciprocal theorem, we derive analytical expressions for the grand mobility matrix of a spherical particle and find that roughness-induced velocities vary non-monotonically with the characteristic wavelength of the surface. In contrast to motion near a plane wall, we predict particle translation perpendicular to the applied force. Also, we find that particles drift along tilted, grooved surfaces, which makes possible particle separation with respect to size.

INTRODUCTION

Transport processes at low Reynolds number are significantly altered by confining geometries omnipresent in biological environments and microfluidic devices. These topics include transport of red blood cells in microchannels [1], active motion of microorganisms in their natural habitats [2], and diffusion of macromolecules in crowded cells [3]. A well-known consequence of the reversibility of Stokes flows is that a rigid spherical particle that sediments nearby a vertical planar wall does not experience a hydrodynamic force perpendicular to the wall and thus maintains a constant distance from the wall [4, 5]. This behavior has been shown to change dramatically once time-reversal symmetry is broken. In particular, elastohydrodynamic couplings between a spherical particle and a deformable boundary induces a lift force and, thus, motion away from the surface [6, 7]. Furthermore, hydrodynamic couplings between swimming microorganisms and boundaries lead to surface accumulation or repulsion depending on the flow fields produced by the propulsive mechanisms [8].

In contrast to plane, smooth surfaces, biological surfaces display a large variety of surface features, including rough and structured topologies. These corrugated surface textures alter the surrounding flow fields and thereby hydrodynamically impact nearby particle motion, which represents the main topic of this study.

THEORETICAL FRAMEWORK

We consider the translational and rotational motion of a spherical particle with radius a in an incompressible flow of a viscous fluid of viscosity μ nearby a rough surface, S_w (see Fig. 1). In the presence of an external force $\mathbf{F}$ and torque $\mathbf{L}$, the particle translates at a velocity $\mathbf{U}$ and rotates with angular velocity $\mathbf{\Omega}$. For low-Reynolds-number flow, the quasi-steady fluid velocity $\mathbf{u}(\mathbf{r})$ and pressure fields $p(\mathbf{r})$ are described by the continuity and Stokes equations,

$$\nabla \cdot \mathbf{u} = 0 \quad \text{and} \quad \mu \nabla^2 \mathbf{u} = \nabla p, \tag{1}$$

with associated stress field, $\boldsymbol{\sigma} = -p\mathbb{I} + \mu\left(\nabla\mathbf{u} + \nabla\mathbf{u}^T\right)$ and no-slip boundary conditions on the particle surface, S_p, and rough wall, S_w. The translational and rotational velocities of the sphere, $\mathbf{U} = \mathbf{U}(\mathbf{r}_S, h)$ and $\mathbf{\Omega} = \mathbf{\Omega}(\mathbf{r}_S, h)$, depend on its instantaneous position, $\mathbf{r}_S(t) = (x_S(t), y_S(t))$, and distance from the surface, $h(t)$.

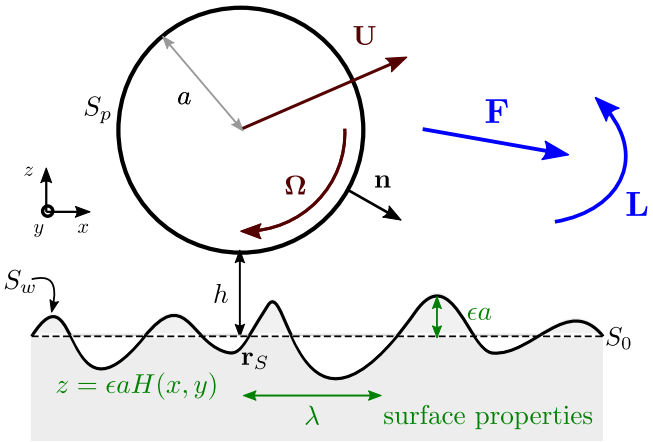

Figure 1: Model set-up for the motion of a sphere near a random rough surface.

We describe the small height fluctuations of the surface by $z = \epsilon a H(x, y)$, where $H(x, y)$ denotes the shape function and ϵa the surface amplitude with small dimensionless parameter $\epsilon \ll 1$, which permits expansion of the velocity field, $\mathbf{u} = \mathbf{u}^0 + \epsilon\mathbf{u}^1 + \mathcal{O}(\epsilon^2)$, and similar expansions for other fields. Due to the linearity of the Stokes equations and the rigid boundaries of the suspended particle and the rough wall, the velocity field generated by the particle motion must be coupled linearly to the applied forces and torques. Consequently, the translational and rotational velocities, $\mathbf{U}$ and $\mathbf{\Omega}$, are related to the forces and torques of the problem, $\mathbf{F}$ and $\mathbf{L}$, via the grand mobility tensor $\mathbf{M}$.

By employing the method of domain perturbations and utilizing the Lorentz reciprocal theorem for viscous flows, we arrive at the general form for the *grand mobility matrix* of the sphere next to a rough wall

$$\mathbf{M} = \mathbf{M}^0 - \epsilon a \int_{S_0} H(x, y)\mathbf{K}\, \mathrm{d}S + \mathcal{O}(\epsilon^2), \tag{2}$$

*Corresponding author. E-mail: hastone@princeton.edu.

which represents the principal finding of this work. Here, $\mathbf{M}^0$ denotes the mobility tensor corresponding to the well-established problem of a sphere translating and rotating near a plane, smooth wall [4, 5, 9, 10]. The coupling tensor $\mathbf{K}$ can be assumed known as it depends on the zeroth-order problem only. As a main consequence, the velocities of the externally driven sphere, up to the second order in the surface roughness, can be obtained for arbitrary surface shapes $H(x, y)$.

RESULTS

Roughness-induced velocities

We apply the theoretical predictions to elucidate the roughness-induced velocities of a sphere near a random rough wall characterized by a wavelength λ and random surface amplitudes (see Ref. [11] for more details). The particle velocities are determined by the local geometry of the underlying, random surface, and, therefore, we are interested in average quantities such as the variance of particle velocities near rough surfaces. The variance is determined by the distance of the particle from the wall h/a and the characteristic wavelength of the surface λ/a. We find that velocity fluctuations decay rapidly with respect to the particle-surface distance. Thus, for increasing distances transport is governed by the average wall contribution rather than details of the surface structure.

Furthermore, the variances of the velocities perpendicular and transverse to the applied force display a maximum at a characteristic wavelength λ that depends on the particle distance from the wall. These findings can be rationalized, since for a particle close to the surface, $h/a \ll 1$, the fluid flow in the lubrication layer between the rough surface and the particle dominates the hydrodynamic couplings. However, the velocities of particles that are located further away $h/a \gtrsim 1$ are affected by hydrodynamic interactions with larger parts of the underlying surface texture. For large and small wavelengths roughness-induced velocities become small and the particle essentially experiences the presence of a smooth wall.

Particle trajectories near a grooved surface

We study the trajectories of spheres with different radii a near a grooved surface with characteristic wavelength λ, see Fig. 2. In particular, the particles follow the shape of the underlying surface and display a drift along the grooves. The drift velocity varies with particle sizes and makes possible separation of particles. Moreover, drift is determined by the strength of the hydrodynamic interaction with the surface, which varies non-monotonically with λ/a and separates, e.g., $a/\lambda = 1/4$ from other (even larger) spheres. Thus, by varying the wavelength of the grooves a particular particle size can be selected from others.

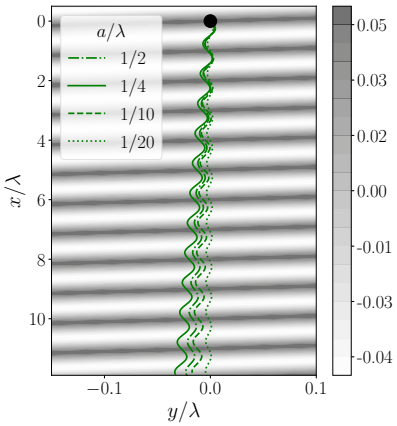

Figure 2: Trajectories, $x_S(t), y_S(t)$, for particles of different radii a near a grooved surface with tilt angle of $\pi/4$ between the force $\mathbf{F} = F\mathbf{e}_x$ and the oriented grooves and distance $\lambda/h(0) = 20$. The colorbar indicates hills (dark) and valleys (white) of the surface and the black dot the initial particle position.

CONCLUSION

We have presented an analytical expression for the mobility of a sphere near a textured surface. In particular, we find that roughness-induced velocities decay rapidly with the particle-surface distance and exhibit a non-monotonic behavior with respect to the characteristic wavelength of the corrugated surface. Our findings indicate that details of the surface roughness impact fluid flow and transport phenomena locally and are therefore expected to be important for surface-accumulation of particulate matter, e.g. biofilm formation. We anticipate that our predictions may allow novel particle separation methods and may allow non-invasively inferring surface properties by monitoring transport of particles near rough surfaces. Our theoretical predictions can be further extended to elucidate the impact of surface roughness on the motion of self-propelled agents.

References

[1] Secomb T. W., Skalak R., Özkaya N., Gross J. F. Flow of axisymmetric red blood cells in narrow capillaries. *J. Fluid Mech.* **163**: 405–423, 1986.
[2] Bechinger C., Di Leonardo R., Löwen H., Reichhardt C., Volpe G., Volpe G. Active particles in complex and crowded environments. *Rev. Mod. Phys.* **88**: 045006, 2016.
[3] Höfling F., Franosch T. Anomalous transport in the crowded world of biological cells. *Rep. Prog. Phys.* **76**: 046602, 2013.
[4] O'Neill M. E., Stewartson K. On the slow motion of a sphere parallel to a nearby plane wall. *J. Fluid Mech.* **27**: 705–724, 1967.
[5] Goldman A. J., Cox R. G., Brenner H. Slow viscous motion of a sphere parallel to a plane wall—I Motion through a quiescent fluid. *Chem. Eng. Sci.* **22**: 637–651, 1967.
[6] Sekimoto K., Leibler L. A mechanism for shear thickening of polymer-bearing surfaces: elasto-hydrodynamic coupling. *EPL* **23**: 113, 1993.
[7] Rallabandi B., Oppenheimer N., Zion M. Y. B., Stone H. A. Membrane-induced hydroelastic migration of a particle surfing its own wave. *Nat. Phys.* **14**: 1211, 2018.
[8] Berke A. P., Turner L., Berg H. C., Lauga E. Hydrodynamic attraction of swimming microorganisms by surfaces. *Phys. Rev. Lett.* **101**: 38102, 2008.
[9] Dean W. R., O'Neill M. E. A slow motion of viscous liquid caused by the rotation of a solid sphere. *Mathematika* **10**: 13–24, 1963.
[10] Blake J. R., Chwang A. T. Fundamental singularities of viscous flow. *J. Eng. Math.* **8**: 23–29, 1974.
[11] Savva N., Kalliadasis S., Pavliotis G. A. Two-dimensional droplet spreading over random topographical substrates. *Phys. Rev. Lett.* **104**: 084501, 2010.

RHEOLOGY OF A CONCENTRATED MONOLAYER OF SPHERICAL SQUIRMERS

Takuji Ishikawa[1], Douglas Brumley[2], and Tim Pedley*[3]
[1]Department of Finemechanics, Tohoku University, Sendai, Japan
[2]School of Mathematics and Statistics, University of Melbourne, Australia
[3]Department of Applied Mathematics and Theoretical Physics, University of Cambridge, U.K.

Summary A concentrated, vertical monolayer of identical spherical squirmers, which may be bottom-heavy, and which are subjected to a horizontal shear flow, is modelled computationally by two different methods: Stokesian Dynamics, and a lubrication-theory-based method. The effective shear viscosity is found in general to be increased by the squirming motions.

BACKGROUND

Suspensions of swimming micro-organisms exhibit fascinating collective behaviour, ranging from steady, regular patterns, as in bioconvection [1], to random coherent structures, sometimes referred to as bacterial turbulence [2], with many variants in between. There have been many models of such behaviour, most of which have been developed to see if the observations can be explained by physical processes alone, without requiring an understanding of biological or chemical signalling or intracellular processes. Continuum models have been very successful for dilute suspensions, in which the cells interact with their environment but not with each other: bioconvection results from either a gravitational instability when the upswimming of dense cells leads to a gravitationally unstable density profile, or a gyrotactic instability in which the cells' non-uniform density or geometric asymmetry causes them to be reoriented in a shear flow [2]. Even when gravity is unimportant the stresses applied by the cells' swimming motions (a swimmer acts as a force dipole or stresslet) lead to instability and random bulk motions [3,4].

In this paper we wish to consider concentrated suspensions, in which the flow is dominated by cell-cell interactions. Continuum models fail because there is no agreed way of incorporating cell-cell interactions into the model equations – in particular the particle stress tensor $\mathbf{\Sigma}^{(\mathbf{p})}$ – even when the interactions are restricted to near-field hydrodynamics together with a repulsive force to prevent overlap of model cells. We seek to understand the rheological properties of an idealised suspension from direct numerical simulations. The cells are modelled as identical steady spherical squirmers [5,6,7]: spheres of radius a which swim by means of a prescribed tangential velocity on the surface, $u_\theta = \frac{3}{2}V_s \sin\theta(1+2\beta\cos\theta)$, where θ is the polar angle from the cell's swimming direction, V_s is the cell swimming speed and β represents the stresslet strength; inertia is negligible. The suspension is taken to be a monolayer, embedded in an infinite fluid, in which the sphere centres and their trajectories are confined to a single plane, which is vertical in cases for which gravity, $\mathbf{g}$, is important. The spheres may be bottom-heavy, so that when the swimming direction of a sphere, $\mathbf{p}$, is not vertical the sphere experiences a gravitational torque $\mathbf{L}$, where $\mathbf{L} = -\rho v h \mathbf{p} \times \mathbf{g}$ and v, h are the cell volume and the displacement of the centre of mass from the geometric centre; ρ is the average cell density, assumed the same as that of the fluid. The monolayer is taken to be driven by a simple shear flow in the same, $x-y$, plane: $\mathbf{U} = (\gamma y, 0, 0)$, with shear-rate γ; we will also take $\mathbf{g} = -g(\sin\alpha, \cos\alpha, 0)$, so the flow is horizontal if $\alpha = 0$.

METHODS

We have previously studied the rheology of semi-dilute (three-dimensional) suspensions of squirmers – volume fraction $c \leq 0.1$ - in which every cell interacted only with its nearest neighbour [8]. General pairwise interactions could be computed exactly using the boundary element method, supplemented by lubrication theory when cells were very close together. Cells were prevented from overlapping computationally by the inclusion of a repulsive interparticle force $\mathbf{F} = \mu a^2 \gamma F_0 \tau e^{-\tau\epsilon}/(1+e^{-\tau\epsilon})\hat{\mathbf{r}}$ where $\hat{\mathbf{r}}$ is the unit vector along the line of centres and ϵ is the minimum permitted dimensionless spacing [9]. In [8] τ was taken equal to 10^3 and F_0 was varied. It was found that the swimming activity made very little difference to the effective shear viscosity when the spheres were non-bottom-heavy, but the suspension showed significant non-Newtonian behaviour, such as anisotropic effective shear viscosity and normal stress differences, when the cells were bottom-heavy.

Here we use two different methods of simulation for very concentrated monolayer suspensions, with areal fraction c up to 0.7. One is a full numerical simulation using Stokesian Dynamics [9,10], while in the other we assume that cells in which every cell interacts with other cells in the domain and mirror domains by assuming additivity of forces. The interaction is described using lubrication theory alone. This model was recently used to investigate the stability of a regular array of bottom-heavy squirmers, swimming upwards in the absence of an imposed shear flow [11]. The point of this is to see if lubrication alone is good enough to account for all the interesting rheological behaviour of a concentrated suspension, or if some effect of more distant particles is necessary, in the case of squirmers. As well as illuminating the physics, this might make related computations significantly cheaper than the full Stokesian Dynamics. For inert and force-free spheres, Leshansky & Brady [12] reported in a footnote that suppressing all far field interactions made less than 5% difference to the quantities they were computing.

*Corresponding author. E-mail: tjp3@cam.ac.uk

RESULTS AND DISCUSSION

In addition to β, α, τ, F_0 and the areal fraction c, the governing dimensionless parameters are: the dimensionless swimming speed, $Sq = \frac{V_s}{a\gamma}$, and $G_{bh} = \frac{\rho v g}{(3\mu a V_s)}$, the 'bottom-heaviness parameter'. The initial objective is to compute the effective shear viscosity, η_{eff}, which in Stokesian Dynamics is obtained from the off-diagonal terms of the particle stress tensor $\mathbf{\Sigma}^{(p)}$, defined as the average over all spheres of the stresslet for a single particle [13]:

$$\mathbf{S} = \int_{A_p} [\frac{1}{2}\{(\sigma \cdot \mathbf{n})\mathbf{x} + \mathbf{x}(\sigma \cdot \mathbf{n})\} - \frac{1}{3}\mathbf{x} \cdot \sigma \cdot \mathbf{n}\mathbf{I} - \eta(\mathbf{un} + \mathbf{nu})]dA, \tag{1}$$

where σ is the stress tensor and $\mathbf{u}$ is the velocity. and A_p is the surface of the particle with outward normal $\mathbf{n}$.Then

$$\eta_{eff} - 1 = 2.5c\frac{< S_{xy} + S_{yx} >}{20\pi/3}. \tag{2}$$

The result of the Stokesian Dynamics simulations for horizontal shear flow ($\alpha = 0$) is that, for non-bottom-heavy spheres ($G_{bh} = 0$) η_{eff} increases with c more rapidly than for non-swimming spheres. Examination of the cell trajectories suggests that this is associated with the interior of the suspension forming horizontal layers when the spheres do not swim, but becoming veryirregular when theydo (presumably increasing the local rate of energy dissipation). The increase in η_{eff} is greater for larger swimming speeds ($Sq = 10$ rather than $Sq = 1$), but is not much affected by the squirming mode β ($-3 \leq \beta \leq 3$) or the magnitude of the inter-particle repulsion, F_0. Bottom-heaviness, in a horizontal flow, reduced η_{eff} in general, but not by much.

In the lubrication theory model η_{eff} is calculated in a different way: a regular array of squirmers is placed between two rigid planes parallel to the x-axis, at $y = \pm H$, and these are translated parallel to each other with speeds $\pm V$; only the cells closest to the planes are set into motion by them, through the stress in the lubricating layer, and these then cause their other neighbours to move too. Once the shear stress on the planes, S_W, has become steady, on average, η_{eff} is calculated as $\eta_{eff} =< S_W > H/V$. Preliminary results indicate that η_{eff} is not greatly affected by the squirming alone, in the absence of bottom-heaviness. However, it is significantly reduced for bottom-heavy squirmers in horizontal shear flows. Preliminary results for the normal stress difference will also be presented.

There have been few experimental studies on the effective viscosity of suspensions of microscopic swimmers. Notable among those few are the measurements of Rafai *et al.* [14] on suspensions of motile algae (*Chlamydomonas reinhardtii*), which are close to spherical, are bottom-heavy, and *pull* themselves through the fluid (equivalent in the squirmer model to $\beta > 0$). The effective viscosity in a horizontal shear flow was found to increase with volume fraction much more dramatically than for a suspension of dead cells, in agreement with the above Stokesian Dynamics prediction. On the other hand, Sokolov Aronson [15] measured the effective viscosity of a suspension of bacteria (pushers: $\beta < 0$), and found a significant decrease in shear viscosity with swimming speed. However, this could be attributed to the rod-like geometry of the bacteria. Apparent agreement with our lubrication theory predictions is coincidental.

References

[1] Pedley,T.J. and Kessler,J.O. *Ann.Rev.Fluid Mech.* **24**:313-358, 1992
[2] Dombrowski,C., Cisneeros,L., Chatkaew,S., Goldstein,R.E. and Kessler.J.O. *Phys.Rev.Lett.* **93**:098103, 2004
[3] Simha,R.A. and Ramaswamy,S. *phys.Rev.Lett.*89:058101, 2002
[4] Saintillan,D. and Shelley,M.J. *Phys.Fluids* **20**:123304, 2008
[5] Lighthill,M.J. *Comm.Pure Appl. Math.* **5**:109-118, 1952
[6] Blake,J.R. *J.Fluid Mech.* **46**:199-208, 1971
[7] Ishikawa,T., Simmonds,M.P. and Pedley,T.J. *J.Fluid Mech.* **568**:119-160, 2006
[8] Ishikawa,T. and Pedley,T.J. *J.Fluid Mech.* **588**:399-435, 2007
[9] Brady,J.F. and Bossis,G. *J.Fluid Mech.* **155**:105-129, 1985
[10] Ishikawa,T., Locsei,J.T. and Pedley,T.J. *J.Fluid Mech.* **615**:401-431, 2008
[11] Brumley,D.R. and Pedley,T.J. *Phys.Rev. Fluids* **4**:053102, 2019
[12] Leshansky,A.M. and Brady,J.F. *J.Fluid Mech.* **527**:141-169, 2005
[13] Batchelor,G.K. and Green,J.T. *J.Fluid Mech.* **56**:401-427, 1972
[14] Rafai,S., Jibuti,L. and Peyla,P. *Phys.Rev.Lett.* **104**:098102, 2010
[15] Sokolov,A. and Aronson,I.S. *Phys.Rev.Lett.* **103**:148101, 2009

UNIFYING DISPARATE EXPERIMENTAL VIEWS ON SHEAR-THICKENING SUSPENSIONS

Philippe Bourrianne *[1], Thibaut Divoux[2] and Gareth H. McKinley,
[1]Hatsopoulos Microfluids Lab, Department of Mechanical Engineering, MIT, Cambridge, MA 02139, USA
[2]Department of 1Department of Civil and Environmental Engineering, MIT, Cambridge, MA 02139, USA

Summary: Shear thickening denotes the rapid and reversible increase in the viscosity of a suspension of rigid particles under shear. This ubiquitous phenomenon has been documented in a broad variety of multiphase particulate systems, but the relative contributions of hydrodynamic interactions and frictional contact between particles to the magnitude of shear thickening is still highly debated. We explore here a discriminating experimental study using a model shear-thickening suspension that allows us to tune independently both the surface chemistry and the surface roughness of the particles. We show here that both properties matter when it comes to continuous shear thickening (CST) and that the presence of hydrogen bonds between the particles (which enhance solid friction) is essential to achieve discontinuous shear thickening (DST). Moreover, a simple argument allows us to predict the onset of CST, which for these highly-textured particles occurs at a critical volume fraction much lower than that previously reported in the literature.

INTRODUCTION

Suspensions composed of rigid particles dispersed in a liquid matrix are ubiquitous in daily life, from cosmetics and consumer products (e.g., toothpaste) to foodstuffs (e.g., coffee) and engineering materials such as fresh cement paste. Their flow properties display a broad variety of rheological behavior depending on the volume fraction φ and the nature of the physico-chemical interactions between particles [1, 2]. In the semi-dilute regime, suspensions show a shear-thinning response, *i.e.* their shear viscosity η decreases for increasing applied shear rate $\dot{\gamma}$. Such behavior, which results from long-range hydrodynamic interactions and possible shear-induced structure formation, is amplified in the presence of attractive interactions between particles. Conversely, so-called "dense suspensions" (i.e., suspensions with high volume fractions of dispersed solids) exhibit shear-thinning under weak shearing conditions, followed by a 'shear-thickening transition' for sufficiently large shear, characterized by a rapid and reversible increase of viscosity with applied shear rate, or shear stress [3]. The magnitude of the shear thickening is enhanced by increasing the volume fraction. At intermediate volume fractions, continuous shear thickening (CST) ranges from a mild increase in viscosity that was initially explained by lubricated hard-sphere interactions [4] to a more pronounced effect when particle interactions involve frictional contacts [5]. Finally, for very large volume fractions, closer to the jamming volume fraction φ_J, the viscosity may jump by orders of magnitude at constant shear rate [6]. The nature of local inter-particle interactions, mediated by the suspending solvent, affects this picture. Indeed, the shear-thickening transition is enhanced when particles show moderate attraction [7], and suppressed in presence of strong short-range interparticle attractions due to the presence of a yield stress

The relative contributions of the solid friction and the chemical interactions at the molecular scale to the magnitude and dynamic of the DST remain to be quantified, but are embodied qualitatively in the magnitude of the friction coefficient between particles. Here we report an experimental study on suspensions of colloidal fumed silica particles suspended in a viscous oligomeric polar solvent. We show that these suspensions, which do not exhibit any ageing, drying, migration or settling (in sharp contrast to cornstarch or other non-Brownian suspensions) can display both CST and DST transitions at much lower volume fractions than values traditionally reported in the literature, and by varying surface chemistry and particle roughness we can systematically investigate the conditions required to achieve shear-thickening.

Experimental Fluid Formulation

To study the shear thickening transition, we utilize two distinct fumed silica systems that enable us to vary both the roughness and the hydrophilicity of the particles, while holding the average particle size constant at $D \simeq 300$ nm. These textured fumed silica particles are composed of a large number ($N_u \approx 150$) of small nodules of size R_u that are fused together permanently during the initial flame synthesis. The sintered aggregates confer nanometric textures and high specific areas to the particles [see Fig. 1(a)]. The particles are hydrophilic due to both the presence of surface hydroxyl groups and to their intrinsic submicronic roughness – as seen in the picture in Fig. 1(b) – which, in line with Wenzel theory, amplifies the wettability characteristics. When dispersed in a polar solvent such as polypropylene glycol, the fumed silica particles display a stabilizing solvation layer that prevents irreversible aggregation. The resulting suspensions are transparent and show excellent stability over time with no thixotropy or ageing. We have prepared suspensions at various volume fractions φ by varying the mass ratio of particles dispersed. In order to directly probe the effect of the particle surface chemistry, we also prepare corrresponding suspensions of hydrophobic fumed silica particles. These particles are coated with a nanometric layer of silanes; they display identical geometrical features (R_u, N_u and D) as the hydrophilic particles [see Fig. 1(d)] but have different surface chemistry.

*Corresponding author. E-mail: gareth@mit.edu.

RESULTS

The steady rheological responses of both of the different classes of suspensions are measured by a slowly increasing and then decreasing ramp of shear stress imposed in a cone and plate geometry connected to a stress-controlled rheometer and the results are shown in Figure 1 below.

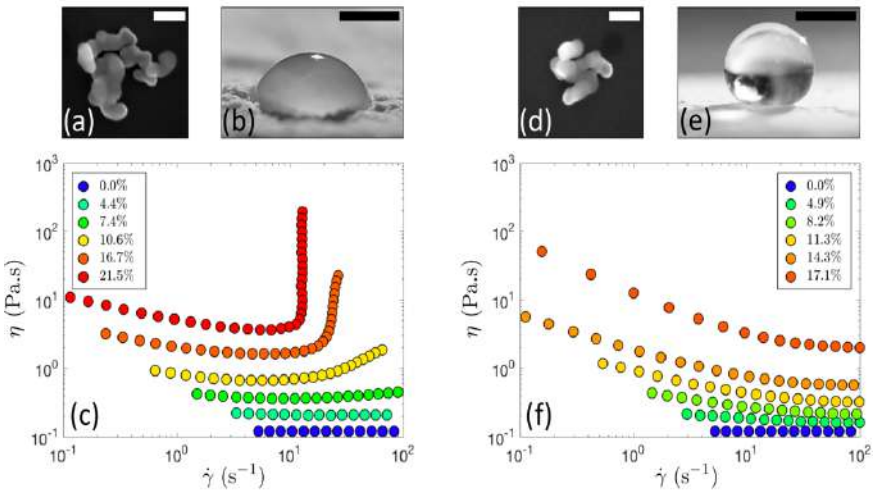

Fig 1(a) SEM image of a hydrophilic fumed silica particle (100nm scale bar). (b) Hydrophilic fumed silica particles coated on a glass slide are wetted by a drop of water. (scale bar 1 mm). (c) Flow curves measured for suspensions of hydrophilic fumed silica particles. (d) SEM picture of a hydrophobic fumed silica particle (100 nm scale bar). (e) A water drop is repelled by a coating made by depositing a layer of hydrophobic fumed silica particles on a glass slide. (1mm scale bar). (f) Viscosity of a suspension of hydrophobic fumed silica as a function of shear rate at various volume fractions φ. The suspensions of hydrophobic particles display a shear-thinning response for all the volume fractions tested.

The rheometric responses of hydrophilic fumed-silica suspensions are reported in Fig. 1(c) for volume fractions ranging between $\varphi = 0\%$ and 21.5%. Increasing the mass fraction of dispersed particles leads to a departure from the Newtonian response of the pure solvent. At low volume fractions, the suspension shows a weakly shear-thinning behavior characterized by a slow decrease of the viscosity for increasing shear rates. At intermediate volume fractions ($\varphi \simeq 7.4\%$), the shear-thinning behavior persists at low shear rates ($\dot{\gamma} \lesssim 20s^{-1}$), whereas the viscosity begins to slowly increase at high shear rates, which is characteristic of continuous shear thickening (CST). This trend is amplified for increasing volume fractions of fumed silica, up to $\varphi = 16.7\%$ for which the viscosity jumps by an order of magnitude over a narrow range of shear rates. Finally, for even larger volume fractions ($\varphi = 21.5\%$), an abrupt shear-thickening transition occurs at an almost constant critical shear rate of about 15 s^{-1}, which corresponds to DST. Strikingly, these volume fractions are significantly lower than that reported in the literature, where shear thickening is usually observed for $\varphi \approx 50\%$ in the vicinity of the jamming point in dense suspensions with more regular shapes. In order to directly probe the effect of the particle surface chemistry, we repeat the same rheological measurements on suspensions of hydrophobic fumed silica particles coated with a nanometric layer of silane. As observed in Fig. 1(f), these hydrophobic suspensions exhibit a strikingly different response from that observed with hydrophilic particles at the same volume fraction. They display a purely shear-thinning response over the entire range of volume fractions explored and the shear-thinning becomes more pronounced for increasing volume fractions, in part due to the gradual appearance of a yield stress at large volume fractions.

CONCLUSIONS & ONGOING WORK

We have formulated a series of suspensions that are transparent, stable with time and can show pronounced shear-thickening (or shear-thinning) at moderate volume fractions of suspended particles The pronounced differences in rheological behavior between two suspensions of particles with similar surface roughness and volume fractions but two different surface chemistries show that the microscopic mechanism for shear thickening is based on a synergy between solid friction and reversible hydrogen bonding; with the latter being crucial for discontinuous shear thickening at moderate volume fractions. To clarify the important contribution of particle surface roughness to the above picture, we have also performed another series of rheological experiments on rougher particles. These particles are composed of a larger number of nodules of smaller size corresponding to a markedly higher specific surface area. However, these "rough" particles possess the same global size as the "smoother" particle suspensions studied here. By combining results for all four systems as well as introducing a quantitative metric for the extent of shear-thickening, we are developing a comprehensive rheological state map for designing bespoke shear-thickening fluid systems with customizable extents of shear-thickening at user-prescribed critical shear stresses.

References

[1] J. Stickel and R. Powell, *Annu. Rev. Fluid Mech.* **37**, 129 (2005).
[2] J. Mewis and N. J. Wagner, Colloidal Suspension Rheology (Cambridge University Press, Cambridge, England, 2011).
[3] N. J. Wagner and J. F. Brady, *Phys. Today* **62**, 27 (2009).
[4] G. Bossis and J. F. Brady, *J. Chem. Phys*. **91**, 1866
[5] S. Jamali and J. F. Brady, *Phys. Rev. Lett*. **123**, 138002 (2019).
[6] R. Seto, R. Mari, J. F. Morris, and M. M. Denn, Phys. Rev. Lett. **111**, 218301 (2013).
[7] N. M. James, E. Han, R. Arturo, L. de la Cruz, J. Jureller, and H. M. Jaeger, *Nat. Mater*. **17**, 965 (2018).
[8] S. R. Raghavan, H. J. Walls, and S. A. Khan, *Langmuir* **16**, 7920 (2000).

RHEOTACTIC VELOCITIES AND ORIENTATION DISTRIBUTIONS OF SWIMMING E. COLI BACTERIA IN SHEAR FLOWS

Andreas Zöttl*[1,2], Guangyin Jing[1,3], Éric Clément[1], and Anke Lindner[1]
[1] Physique et Mécanique des Milieux Hétèrogènes, ESPCI Paris, Paris, France
[2] Institute for Theoretical Physics, TU Wien, Vienna, Austria
[3] School of Physics, Northwest University, Xi'An, China

Summary Understanding the interaction of swimming bacteria with flows is crucial for societal and environmental challenges such as infections, soil contamination and cell sorting. Here we present a combined experimental, numerical and theoretical study on bacterial bulk rheotaxis *i.e.* the non-trivial orientation of bacteria in shear flows at low Reynolds number. Using tracking of a large number of bacteria we obtain high-accuracy spatially dependent velocity and orientation distributions for a wide range of flow rates, in excellent agreement with our kinematic model which includes both hydrodynamic and stochastic effects. Theoretical analysis reveals the relevant scaling laws using a dimensionless chirality parameter and which explains the full reorientation dynamics including a very slow saturation at large shear rates due to the existence of a marginally stable fixed point in orientation phase space.

INTRODUCTION

It has been found more than half a century ago that some microorganisms swimming close to surfaces orient with respect to flow gradients and break the left-right symmetry (rheotaxis). Interestingly, bacterial rheotaxis in bulk has been discovered by Marcos *et al* [1] recently who have shown that surface interactions are not required for bacteria to drift towards the positive vorticity direction ("to the right") but the helical flagella shape leads to chirality-induced lift forces. In combination with the viscous drag on the bacteria head this leads to a rheotactic torque reorienting bacteria in flows which eventually cross streamlines by swimming along their direction of orientation. Brownian noise or bacteria tumbling randomizes the shear induced orientation dynamics but does not destroys the effect.

Despite the fact that quantitative observations of mean rheotactic velocities of bacteria have been reported and reproduced by numerical simulations [1] the details of the underlying physical mechanisms were not fully revealed. Here we combine an experimental, numerical and theoretical analysis to systematically investigate bulk rheotaxis of *E. coli* bacteria. Microfluidic experiments are performed in wide channels and a large number of bacteria tracks are recorded as projections into planes parallel to the bottom wall at different distances from the latter. Careful tracking of active bacteria as well as passive tracers allows then to obtain precise rheotactic velocities and orientation distributions at different positions in Poiseuille flow at various flow rates. Our findings constitute a full characterization of bacteria rheotaxis under shear flow, spanning the complete space of the Poiseuille channel flow and a comprehensive understanding of the physical mechanisms and relevant parameters behind it [2].

RESULTS

A dilute suspension of *E. coli* bacteria was injected at a given flow rate Q into a microchannel (Fig. 1(a)) which imposes a planar Poiseuille flow sufficiently away from the side walls. Using a high magnification objective lens bacteria tracks were recorded as projections into the x-y plane at different distances z from the bottom wall (Fig. 1(b)).

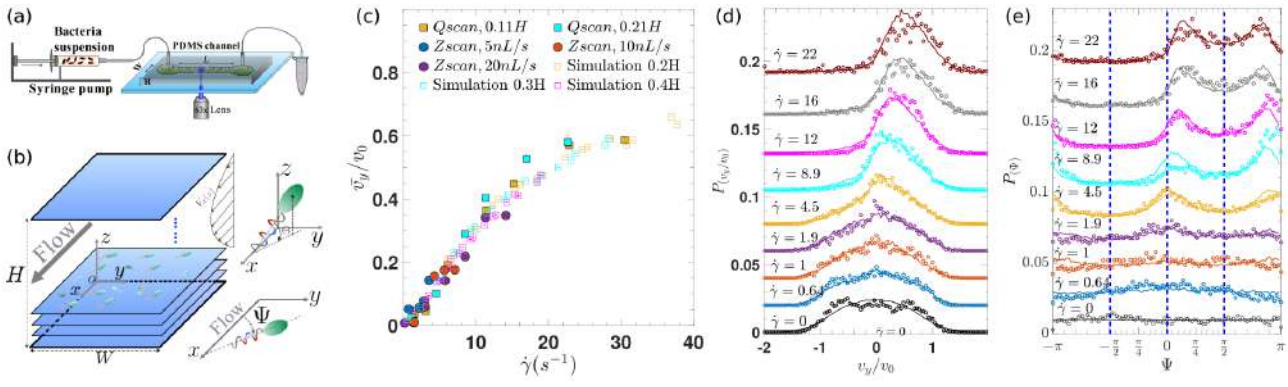

Figure 1: (a) Experimental microfluidic setup; (b) Coordinate system, definition of bacteria orientation (ψ, θ), and sketch of the different z-layers used to track bacteria in Poiseuille flow; (c) Mean scaled rheotactic velocity depending on the local shear rate at different flow rates Q and positions z; (d,e) Bacterial probability distribution of the rheotactic velocity (d) and orientation ψ (e). Open circles are experimental data, and solid lines obtained from Brownian dynamics simulations.

*Corresponding author. E-mail: andreas.zoettl@tuwien.ac.at

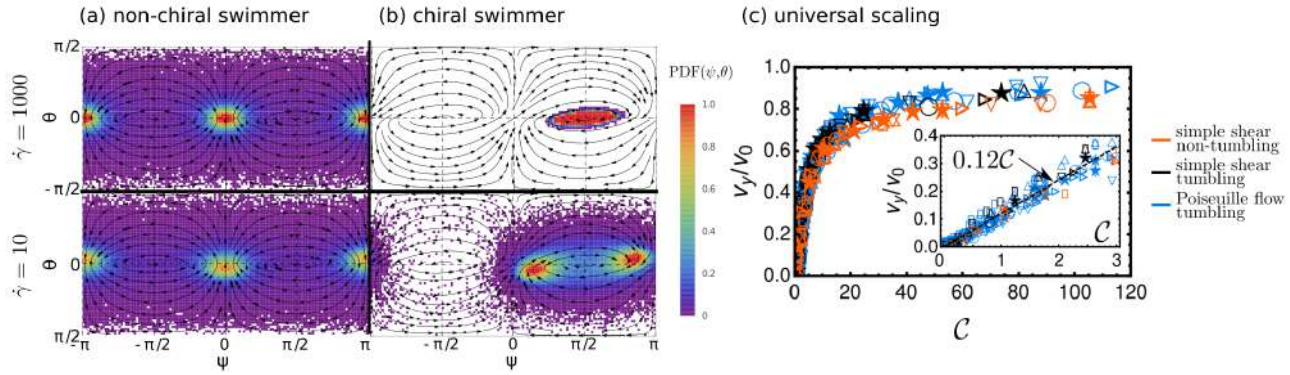

Figure 2: (a,b) Phase space curves and orientatioin probability function for a non-chiral (a) and a chiral (b; $\nu = 0.06$) microswimmer at different shear rates $\dot{\gamma}$; (c) master curve of rheotactic velocities for a wide range of different systems parameters (represented by different symbols) reveals universal scaling using the dimensionless chirality number $\mathcal{C}$.

Different local shear rates $\dot{\gamma}$ can be obtained in two ways, either by varying the imposed flow rate Q or by varying the position z inside the channel. Fig. 1(c) shows mean drift velocities $\bar{v}_y$ as a function of local shear rates from different data sets, scaled by the average intrinsic bacteria velocity $v_0 = 25\mu m s^{-1}$, and which almost collapse to a single curve. The large amount of recorded data allowed us for the first time to determine the velocity distributions $p(v_y)$ and in-plane orientation distributions $p(\psi)$ of bacteria away from surfaces with high accuracy (Fig. 1(d,e)).

In order to understand the detailed physical mechanisms behind bacterial rheotaxis we develop a theoretical framework which captures the dynamics of individual bacteria. We account for the elongated and chiral shape of the flagellated bacteria, their self-propulsion, tumbling, translational and rotational noise, and their advection and rotation in Poiseuille flow. In the absence of noise the coupled equations for the in-plane (ψ) and out-of-plane (θ) orientations read [2, 3]

$$\dot{\psi} = \frac{\dot{\gamma}}{2}(1+G)\sin\psi\tan\theta + \dot{\gamma}\nu\cos\psi\frac{\cos 2\theta}{\cos\theta}, \qquad \dot{\theta} = \frac{\dot{\gamma}}{2}(1-G\cos 2\theta)\cos\psi + \dot{\gamma}\nu\sin\psi\sin\theta. \tag{1}$$

where $0 < G < 1$ depends on the swimmer aspect ratio, and ν is the dimensional chiral strength which only depend on bacterial shape. Fig. 2(a,b) show the orientation phase space curves (black arrowed lines) for a non-chiral ($\nu = 0$) and a chiral ($\nu = 0.06$) microswimmer and the probability distributions at high ($\dot{\gamma} = 1000$) and low ($\dot{\gamma} = 10$) shear rates when Brownian and tumbling noise is included. Non-chiral swimmers exhibit bimodal, left-right symmetric distributions with peaks aligned and anti-aligned with the flow, similar as for passive microscopic elongated particles [4]. In contrast, the solution of Eq. (1) for chiral swimmers reveals an attractive phase space region for orientations to the right ($\psi > 0$) which includes a linearly marginally stable fixed point, which effectively traps low-noise trajectories at relatively high amplitudes and is resonspible for the slow saturation of the rheotactic velocity at high shear rates. At lower shear rates bimodal peaks occur, in agreement with experiments (Fig. 1(e)), as a consequence of the competition between swimmer alignment with flow due to their elongation, and attraction towards the right [2].

A theoretical analysis and linearization both near the flow-aligned peaks and the marginally stable fixed point allows us to extract the relevant scaling laws which determine the strength of the rheotactic velocity depending on the swimmer aspect ratio, the chiral strength, the local shear rate, and Brownian and tumbling noise [2]. Our analysis now suggests to introduce a dimensionless *chirality number*

$$\mathcal{C} = \frac{\dot{\gamma}\nu}{D_r^{\text{eff}}} \tag{2}$$

as the main relevant physical quantity which regulates rheotaxis. Here we use D_r^{eff} as the effective rotational diffusion constant steming from rotational Brownian motion and tumbling. In Fig. 2(c) we show the rheotactic velocity for a wide range of different parameters as a function of the chirality number $\mathcal{C}$ which indeed collapse.

CONCLUSIONS

Here we have demonstrated experimentally, numerically and theoretically the detailed orientation and velocity distribution of swimming *E. coli* bacteria in shear flows at low Reynolds number. Our results contain the first comprehensive analysis of bacterial rheotaxis in bulk, of possible relevance for various biomedical and technological applications.

References

[1] Marcos, H. C. Fu, T. R. Powers, and R. Stocker, Proc. Nat. Acad. Sci. **109**, 4780 (2012).
[2] G. Jing, A. Zöttl, É. Clément, and A. Lindner, Sci. Adv. **6**, eabb2012 (2020).
[3] A. J. T. M. Mathijssen, N. Figueroa-Morales, G. Junot, É. Clément, A. Lindner, and A. Zöttl, Nat. Commun. **10**, 3434 (2019).
[4] A. Zöttl, K. E. Klop, A. K. Balin, Y. Gao, J. M. Yeomans, and D. G. A. L. Aarts, Soft Matter **15**, 5810 (2019).

BENDING OF FLEXIBLE FIBERS IN SHEAR FLOW IS OFTEN DRIVEN BY THEIR ENDS

Pawel J. Zuk*[1,2], Agnieszka M. Slowicka[1], Maria L. Ekiel-Jezewska[1], and Howard A. Stone[2]
[1]Institute of Fundamental Technological Research, Polish Academy of Sciences, Warsaw, Poland
[2]Department of Mechanical and Aerospace Engineering, Princeton University, Princeton, USA

Summary We present a numerical study of the dynamics of an elastic fiber in shear flow. The simulations are done in the bead-spring framework including hydrodynamic interactions in two theoretical schemes: the Generalized Rotne-Prager-Yamakawa model and a multipole expansion corrected for lubrication. We focus on the evolution of an initially straight fiber oriented in the flow direction. In the simulations fibers have aspect ratio from 20 to 200 and various bending stiffnesses: fiber shape vary from highly bent to straight. We discover variations of the fiber shapes and dynamics that follow powers, e.g. the fiber curvature changes as fiber stiffness to the power -1/4, and show that time scales of fiber rotation (length dependent) and fiber bending (stiffness dependent, length independent) determine the fiber motion. The numerical results are further supported with an analytical elastica model.

INTRODUCTION

The behavior of fibers immersed in the shear flow is a phenomena studied experimentally [1, 2], theoretically and numerically [3, 4, 5] in the context of fundamental understanding and technological applications of fibrous materials [6]. Here we focus on the dynamics of a single, flexible fiber that is initially stretched in the direction of the shear flow. We perform numerical simulations for different lengths and stiffnesses using a bead-spring model of a fiber. The results demonstrate that for a finite aspect ratio the fiber end effects are important to understand the shape of the fiber and its evolution, at least in part because they introduce a separate time scale.

METHODS

In simulations we use the bead-spring model common to studies of the dynamics of suspensions in the regime of small Reynolds numbers [7]. The fiber consists of N beads (with diameter d, position $\mathbf{R}_i$) that are interacting with stretching and bending potentials, and the fiber is placed in a fluid of viscosity η undergoing a shear flow with shear rate $\dot{\gamma}$. Between every two consecutive beads in the chain we impose the FENE stretching potential with equilibrium distance d between the bead centers and maximum stretch $0.1d$, which has a stretching resistance large enough to mimic an inextensible structure. Indeed, the observed changes in the fiber length does not exceed 0.1% of the total fiber length. The bending potential E_{bi} acts between every three consecutive beads $(i-1, i, i+1)$ restricting the shape of the fiber. We used harmonic $E_{bi} = \frac{A'}{2}(\theta_i - \pi)^2$ and cosine $E_{bi} = A'(1+\cos(\theta_i))$ bending potentials, where $\theta_i = \text{arc cos}\left(\frac{(\mathbf{R}_{i-1}-\mathbf{R}_i)\cdot(\mathbf{R}_{i+1}-\mathbf{R}_i)}{|\mathbf{R}_{i-1}-\mathbf{R}_i||\mathbf{R}_{i+1}-\mathbf{R}_i|}\right)$. The dimensionless bending stiffness $A = A'/(\pi\eta\dot{\gamma}d^3)$ and the number of beads N are treated as parameters. We used two different hydrodynamic interactions (HI) models: the Generalized Rotne-Prager-Yamakawa (GRPY) [8] and the Hydromultipole algorithm [4] based on the multipole expansion corrected for lubrication. In case of the GRPY approximation, to prevent sphere overlap, spheres that are more distant than nearest neighbors interact with the repulsive part of the Lennard-Jones potential. We focus here on GRPY with harmonic bending potential.

RESULTS

The quantity that we investigate in detail is the maximum curvature κ over the fiber length at every instant of time. For each consecutive three beads $(i-1, i, i+1)$ the local curvature κ_i is the inverse of a radius of a circle circumscribed on points $\mathbf{R}_{i-1}, \mathbf{R}_i, \mathbf{R}_{i+1}$. For each time we take the maximum of κ_i over all nearest neighbor triplets in the fiber and denote this quantity κ. An example of κ as a function of time is shown in Figure 1A. We will focus on two characteristic features of $\kappa(t)$: a time τ_b that is needed for a fiber to bend (interval from the beginning of the simulation to the rapid increase in κ) and maximum of κ observed over time that we will denote κ_b. In Figure 1B the corresponding shapes of the fiber are shown during the time instances marked in Figure 1A.

The maximum bending curvature κ_b as a function of dimensionless bending stiffness A is presented in Figure 1C. Generically a fiber of a given length will have three distinct behaviors as a function of A. First, in the regime of the smallest A, κ_b is limited primarily by the excluded volume of the beads. Second, in the regime of the intermediate A, κ_b is best described by the local bending. In this regime the shape follows the scaling law $\kappa_b \propto A^{-1/4}$ that can be understood from the interplay between the shear flow and elasticity, as we demonstrate with the elastica model. Third, in the regime of large A the fiber bends globally leaving the scaling law typical for the second regime. The transition between the second and third regimes depend on N and for larger N occurs at larger A.

*Corresponding author. E-mail: pzuk@ippt.pan.pl.

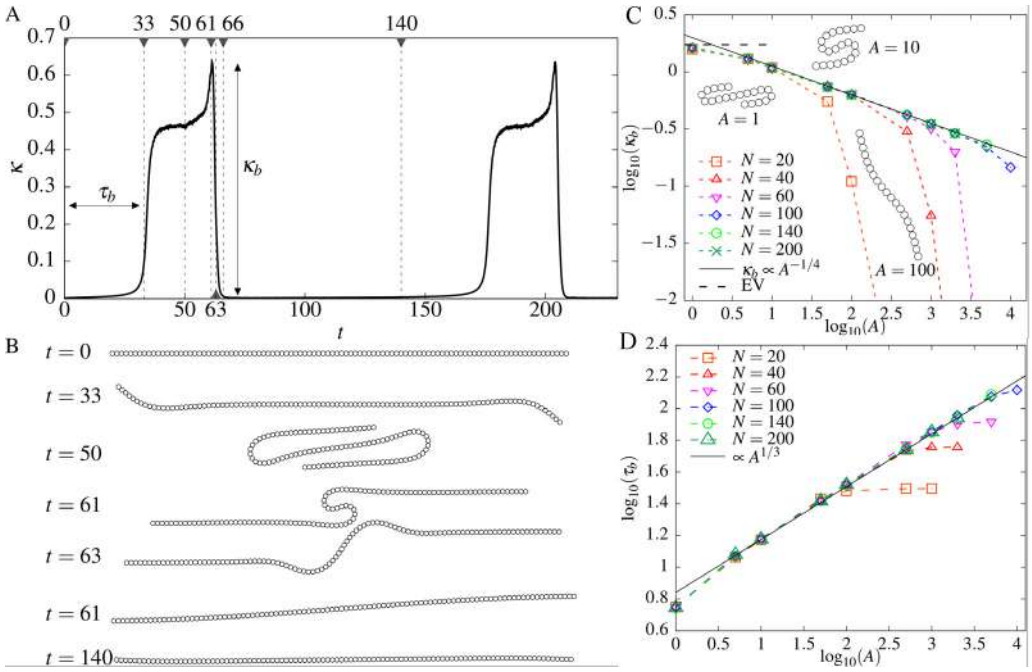

Figure 1: Flexible fiber in the shear flow calculated with the GRPY model. (A) The maximum curvature chosen over the fiber length as a function of time for the fiber of length $N = 100$ and $A = 100$. (B) Fiber shape corresponding to the time instants marked in the panel A and the same simulation. (C) The maximum curvature κ_b that a fiber reaches during simulation as a function of A for different N. The EV denotes the curvature limit from the excluded volume of the spheres. In the insets the characteristic bent shapes of the fiber with $N = 20$ are shown. (D) The bending time τ_b as a function of A and N.

Another aspect of the transition between the second and third regimes of fiber bending arises from the detailed inspection of the bending times τ_b. In Figure 1D we show τ_b as a function of A for different N. Again, for a given fiber length we can distinguish three regimes: regime of small A, regime of intermediate A ($\tau_b \propto A^{1/3}$) and regime of large A (τ_b saturates). To justify the slope in Figure 1D we use the elastica model with an additional assumption: at the fiber end a constant hydrodynamic force is present. It is perpendicular to the fiber direction and oriented as the rotational component of the shear flow. This assumption is justified by the results obtained from the bead-spring approach.

The τ_b does not depend on the fiber length in the low and intermediate regimes of A (owing to the local nature of bending), however the transition between the local and global bending does depend on N. This can be understood from a competition of the two time scales present in the system. The time scale τ_r that a straight and stiff fiber needs to perform a quarter of periodic rotation in the shear flow and the time scale τ_b that the fiber end needs to bend from the stretched, flow aligned configuration. The behavior $\tau_r \propto N$ and its values are visible as saturation times in Figure 1D. Furthermore, using the τ_b the phase space of the shapes of elastic fiber evolving in the plane of shear flow can be explained.

ACKNOWLEDGEMENTS

We acknowledge a partial support of project ITHACA (nr PPI/APM/2018/1/00045/U/001) founded by Polish National Agency for Academic Exchange.

References

[1] Forgacs O. L., Mason S. G. Particle motions in sheared suspensions: IX. Spin and deformation of threadlike particles. *J. Coll. Sci.* **14(5)**:457-472, 1959.
[2] Perazzo A, Nunes J. K., Guido S., Stone H. A. Flow-induced gelation of microfiber suspensions. *P. Natl. Acad. Sci. USA* **114(41)**:E8557–E8564, 2017.
[3] Tornberg A.-K., Shelley M. J. Simulating the dynamics and interactions of flexible fibers in Stokes flows. *J. Comput. Phys.*, **196(1)**:8–40, 2004.
[4] Słowicka A. M., Wajnryb E., and Ekiel-Jeżewska M. L. Dynamics of flexible fibers in shear flow. *J. Chem. Phys.* **143(12)**:124904, 2015.
[5] Słowicka A. M., Stone H. A., Ekiel-Jeżewska M. L. Flexible fibers in shear flow approach attracting periodic solutions. *Phys. Rev. E* accepted, 2020; https://arxiv.org/abs/1905.12985.
[6] Du Roure O., Lindner A., Nazockdast E. N., Shelley M. J. Dynamics of flexible fibers in viscous flows and fluids. *Annu. Rev. Fluid Mech.* **51**:539–572, 2019.
[7] Gruziel M., Thyagarajan K., Dietler G., Stasiak A., Ekiel-Jeżewska M. L., Szymczak P. Periodic motion of sedimenting flexible knots. *Phys. Rev. Lett.* **121**:127801, 2018.
[8] Wajnryb E., Mizerski K. A., Zuk P. J., Szymczak P. Generalization of the RotnePragerYamakawa mobility and shear disturbance tensors. *J. Fluid Mech.* **731**, 2013.

INSTABILITIES AND DYNAMICS OF PHORETIC SUSPENSIONS

Tullio Traverso*[1], Sébastien Michelin [1]
1LadHyX, Ecole Polytechnique, Palaiseau, France

Janus phoretic colloids self-propel as a result of self-generated chemical gradients, and influence each other hydrodynamically and chemically. The shape and surface chemical properties of the particles, which are design parameters, determine the relative importance of such interactions which, in turn, characterize the large-scale collective dynamics of the suspension in a fundamental way. We use a kinetic model to investigate the competition and interaction of self-propulsion with hydrodynamic and chemical couplings. Using linear stability analysis we discuss the role of such design parameters in determining the onset of instabilities. Nonlinear numerical simulations are then used to investigate the subsequent nonlinear collective dynamics in dilute suspensions of chemically-active Janus swimmers.

INTRODUCTION

A fascinating analog to biological signalling is provided by the collective behaviour of synthetic autophoretic Janus particles (JPs). Unlike living cells, their motion is governed by deterministic laws which relate the hydrodynamic forcing to the chemical environment of the particle. We exploit this relationship to derive a self-consistent kinetic model which we use to assess the relative importance of hydrodynamic and chemical interactions in the dilute regime for different particles configurations.

FROM SINGLE-PARTICLE DYNAMICS TO THE KINETIC MODEL OF A SUSPENSION

Self-diffusiophoretic particles, such as JPs, drive an apparent slip velocity on their surface, $\mathbf{u}_s$, in the presence of a local chemical gradient along their surface, ∇C, which can be self-generated (e.g. by asymmetric activity) or due to the presence of other swimmers. The chemical properties and the shape of the particle determine its self-propulsion velocity u_0, the coefficient for the drift and rotation into an external chemical gradient, ξ_t and ξ_r (orange arrows in Fig.1), and the far-field chemical and hydrodynamic signature (background colour field and thin blue arrows in Fig.1 respectively), the latter being characterised by an active stress tensor $\boldsymbol{\sigma}_a$ [1].

We represent the configuration of a suspension of auto-phoretic swimmers by means of a distribution function $\Psi(\mathbf{x},\mathbf{p},t)$ of the particle position $\mathbf{x}$ and director $\mathbf{p}$ [2]. The evolution of the suspension is described by a Smoluchowski equation

$$\frac{\partial \Psi}{\partial t} = -\nabla \cdot (\Psi \dot{\mathbf{x}}) - \nabla_p \cdot (\Psi \dot{\mathbf{p}}) \quad (1)$$

where ∇_p is the gradient operator on the unit sphere and the fluxes are determined by the particles response to the hydrodynamic and chemical fields, $\mathbf{u}(\mathbf{x},t)$ and $C(\mathbf{x},t)$, through the particles velocities $\dot{\mathbf{x}}$ and $\dot{\mathbf{p}}$. They read

$$\dot{\mathbf{x}} = u_0\mathbf{p} + \mathbf{u} + \xi_t \nabla C - D\nabla(\ln\Psi) \quad (2)$$

$$\dot{\mathbf{p}} = \boldsymbol{\Omega} \times \mathbf{p} + \xi_r(\nabla C \times \mathbf{p}) \times \mathbf{p} - d_r \nabla_p(\ln\Psi) \quad (3)$$

where $\boldsymbol{\Omega}$ is half the vorticity vector while D and d_r are the particles translational and rotational diffusion. The chemical concentration evolves according the an advection-diffusion equation with a source term proportional to the particle density $\Phi(\mathbf{x},t) = \int \Psi(\mathbf{x},\mathbf{p},t)\,\mathrm{d}\mathbf{p}$ and a decay term, $-\beta C$. Finally, the hydrodynamic field follows the incompressible Stokes flow equations forced by the active stress, which, at the suspension level, is approximated by $\boldsymbol{\Sigma}(\mathbf{x},t) = \int \boldsymbol{\sigma}_a \Psi \,\mathrm{d}\mathbf{p}$. The connection between the properties of the particle and the model for the suspension is encapsulated in u_0, ξ_t and ξ_r (through which $\boldsymbol{\sigma}_a$ can be determined) all of which are functions of the first two moments of the activity and mobility distribution on the surface of the particles.

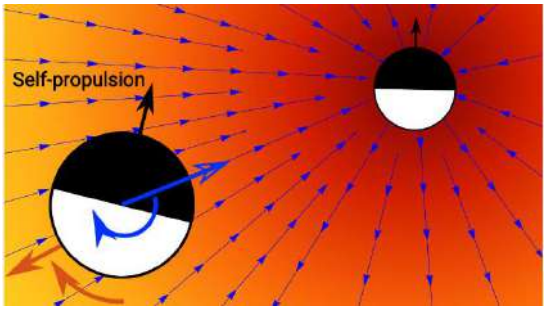

Figure 1: schematic of the motion induced on a hemispherical JP by another swimmer (only the self-generated flow field is depicted, thin blue arrows). Thick blue arrows: hydrodynamically induced motion.

*traverso@ladhyx.polytechnique.fr

LINEAR STABILITY AND THE ROLE OF SELF-PROPULSION

We analyse the linear stability of the uniform and isotropic state and study two destabilising mechanisms associated with attractive chemical interactions (i.e. when either ξ_t or ξ_r are positive) which we refer to as chemotactic limit, due to $\xi_r > 0$ while $\xi_t < 0$, and phoretic limit, due to $\xi_t > 0$ while $\xi_r \approx 0$. The main difference between these mechanisms is that the former induces particles to polarize first and then to swim towards regions of higher particles concentration (Fig.2a), while the latter induces particle aggregation without polarization and occurs also for $u_0 = 0$. Interestingly, we find that self-propulsion stabilise long-wavelength modes in the phoretic limit [5], which could explain why experimentally observed clusters never coalesce [3]. High values of u_0 will eventually stabilize the suspension in both the chemotactic and phoretic limit. Within a realistic range of D, the linear stability is solely determined by an interplay between phoretic interactions and self-propulsion, which also determines the most unstable wavelength.

HYDRODYNAMICALLY INDUCED DISORDER

The long term dynamics are investigated by numerically integrating equation (1) coupled with the Stokes flow equations and the advection-diffusion equation for C, in a square periodic 2D domain. Due to the fact that a nonzero active stresslet, $\boldsymbol{\sigma}_a$, is associated with $\xi_r \neq 0$ we focus on the chemotactic limit, where the interplay between chemical and hydrodynamic interaction characterize long term dynamics, as opposed to the phoretic limit, where $\boldsymbol{\sigma}_a, \xi_r \approx 0$.

In the chemotactic limit polar order must emerge for aggregates to form (Fig.2a), which allows the hydrodynamic perturbations of many particles to positively superimpose, driving a large scale flow that prevents ordered structures to appear (Fig.2b). If the hydrodynamic interactions are not taken into account, the patterns in Fig.2a appear circular and static with the mean director field always pointing radially toward the centre of the aggregates. We consider this behaviour as the precursor to cluster formation, as observed in particle-based simulations even at low area fraction [4].

We define $\mu_{2,2}(t)$ as an intrinsic measure of how scattered the energy density is on the Fourier plane, i.e., of the variety of length scales in the particle distribution. As we can see from Fig.2c, the presence of an induced flow field continuously depletes energy from the chemically unstable modes, which is injected at other wavenumbers, including at higher spatial frequency, which are chemically-stable modes and where particle diffusion dominates [5].

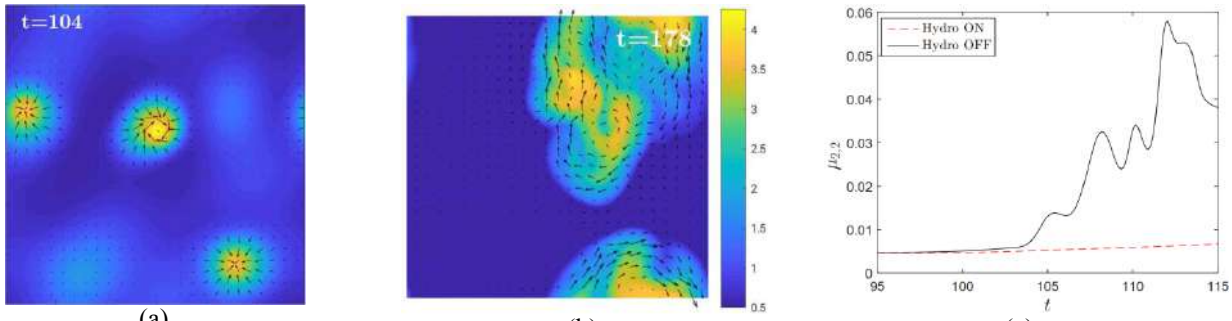

Figure 2. (a-b) Colour: Particle density Φ; arrows: (a) Mean particles orientation; (b) flow velocity u. (c) Amplitude of $\mu_{2,2}(t)$. Black and red line correspond to simulations with and without hydrodynamic interactions, respectively.

CONCLUSIONS

Based on the stability analysis, we clarify the role of self-propulsion at the onset of collective motion: while it is a necessary ingredient for the chemotactic mechanism, it has a purely stabilising effect to those modes promoted by attractive phoretic drift. Our numerical simulations suggest that strong self-generated hydrodynamic field within suspensions of auto-chemotactic JPs ($\xi_r > 0$) smoothen the energy spectrum and ordered long-wavelength structures cannot form [5].

References

[1] Lauga E., Michelin S. Stresslet induced by active swimmers, *Phys. Rev. Lett.* **117**, 148001, 2016.
[2] Saintillan D. and Shelley M. J. Instabilities, pattern formation and mixing in active suspensions, *Phys. Fluids* **20**, 123304, 2008
[3] Theurkauff I. & Co. Dynamic clustering in active colloidal suspensions with chemical signalling, *Phys. Rev. Lett.* **108**, 268303, 2012
[4] Liebchen B., Marenduzzo D. and Michael E. Cates Phoretic interactions generically induce dynamic clusters and wave patterns in active colloids, *Phys. Rev. Lett.* **118**, 268001, 2017
[5] Traverso T., Michelin S., Hydrochemical interactions in dilute phoretic suspensions: From individual particle properties to collective organization, *Phys. Rev. Fluids* **5**, 104203, 2020

HYDRODYNAMIC INTERACTIONS OF MOTILE CELLS WITH A SOLID SURFACE

Abel-John Buchner[1], Junaid Mehmood[1], Koen Muller[1], and Daniel Tam*[1]
[1]Laboratory for Aero and Hydrodynamics, TU Delft, Delft, Netherlands

Summary Motile micro organisms swim through complex environments and often interact with solid surfaces. Their swimming is influenced by the proximity to solid substrates, through hydrodynamic and steric interactions. The influence of hydrodynamic forces on cell-wall interactions remains unclear and previous studies have often been limited to 2-dimensional flow cells, confining the trajectories of the swimming cells. Here, we investigate the interaction of free-swimming cells with surfaces in an unconstrained 3-dimensional flow chamber. Our tracking experiments focus on C. reinhardtii. Motile cells are recorded simultaneously by four separate cameras and triangulated in 3-dimensions. Kinematic statistics are calculated from approximately 30,000 swimming tracks. Our results provide evidence for long-range hydrodynamic interaction, which induces orbiting behaviour in the near-surface region.

MOTIVATION

On the micron scale, motile cells swim through environments with complex topographies and their motion is affected by interactions with solid surfaces. Elucidating these interactions is key to the understanding of biophysical processes such as fertilization, surface colonisation and biofilm growth. The mechanical interactions between motile cells and solid walls have been the focus of previous experimental [1, 2, 3] and theoretical studies[4]. In particular, investigations of the ciliated cells of Chlamydomonas Reinhardtii in microfluidic Hele-Shaw cells has highlighted the importance of contact interactions between the cilia and the solid wall [2, 3]. In these studies, the depth of the Hele-Shaw cell is of a few body lengths. This geometry constrains the natural motion of the cells to mostly two-dimensional trajectories, which can be tracked with an optical microscope. Here, we use a multi-view microscope, which supports the three-dimensional tracking of unconstrained swimming micro-organisms. Our experimental setup has a sufficiently large depth of field to record freely swimming cells over long time periods. The accurate calibration of the experimental setup [5] supports tracking within one body length accuracy in all directions, which enables us to resolve the near boundary cell dynamics and to distinguish between the cells that come in direct contact with the wall and the cells that do not.

Near the wall, we find two distinct cell-wall interactions, contact and non-contact interactions, leading to different scattering dynamics. From the long time recording, we also characterize an orbiting behaviour within 10-20 body lengths of the wall, whereby cells repeatedly return to the surface.

METHODOLOGY

We track *Chlamydomonas reinhardtii*, a green alga and common model organism for motility studies of size approximately 10μm and swimming at $\sim 100\mu\text{m.s}^{-1}$. We introduce a dilute suspension of cells at a density of 2×10^4 cells.mL^{-1} in a large flow chamber, whose smallest dimension is approximately 2mm in the direction of the optical axis. This cell suspension is illuminated by an LED light source at a wavelength beyond the phototactic range of the cells, and recorded simultaneously by four sCMOS cameras at 50 fps, see figure 1a. Each camera records the motion of the swimming cells off centre through a single large objective lens, such that the viewing axes of the four camera converge on the measurement domain from varying angles, see figure 1b. The depth of field is large and the entire 2mm depth of the flow cell is in focus. We developed an accurate calibration method within the framework of projective geometry using tools from computer vision [5]. This calibration supports the accurate triangulation of the three dimensional position of the cells and allows us to track all the cells in the suspension over the entire depth of field, see figure 1c. Our tracking algorithm is robust, and we track cells over long periods of time. Here, we report data extracted from $\sim$ 30000 individual tracks.

RESULTS

We first consider cell trajectories within a near wall region of 10 body lengths. We find two distinct dynamics at the wall, which can be identified as contact and non-contact interactions and lead to different scattering dynamics. First, cells approaching the wall with a higher angle come in direct contact with the solid surface and leave it at a fixed angle. Such contact interactions are characterized by a decrease in swimming velocity at the point of nearest approach and are associating with a scattering angle in the wall plane. Second, cells approaching the wall with a shallower angle often do not approach the wall within contact region and are scattered at a shallow angle. For non-contact interactions, the velocity remains constant through the wall interaction and the swimming direction in the wall plane remains unchanged. Our results are consistent with cell scattering at lower angle due to hydrodynamic interactions.

We then consider the trajectories of cells tracked over longer time intervals, and identify an orbiting behaviour, whereby cells repeatedly approach the wall, see figure 1d. Such cells are captured within 10-30 body lengths of the wall for long periods of time. We find this orbiting behaviour to be mostly due to an increase in the swimming angle towards the wall for cells within this region. This observation is qualitatively consistent with the hydrodynamic capturing of puller type cells through hydrodynamic interactions.

*Corresponding author. E-mail: d.s.w.tam@tudelft.nl

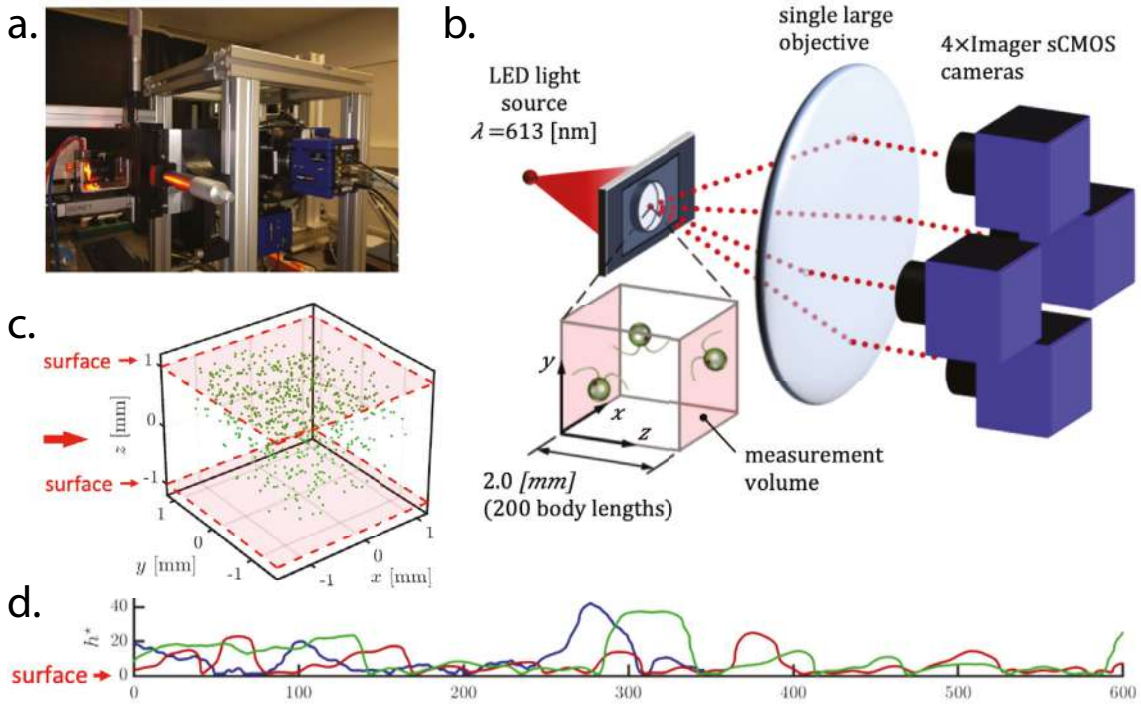

Figure 1: a. Multiview microscope. Each of the four sCMOS cameras image the flow chamber through the same objective but at an offset of the optical axis, allowing viewing of the sample from four different camera views. b. Schematic representation of the experimental setup. c. Triangulation of the postions of the cells in the flow chamber. d. z-position away from the solid wall of several cells as a function of time.

References

[1] Berke, Allison P., Linda Turner, Howard C. Berg, and Eric Lauga. "Hydrodynamic attraction of swimming microorganisms by surfaces". *PRL* **101**: 3, 038102. 2008.

[2] Kantsler, Vasily, Jorn Dunkel, Marco Polin, and Raymond E. Goldstein. "Ciliary contact interactions dominate surface scattering of swimming eukaryotes." *PNAS* **110**: 4, 1187-1192. 2013.

[3] Contino, Matteo, Enkeleida Lushi, Idan Tuval, Vasily Kantsler, and Marco Polin. "Microalgae scatter off solid surfaces by hydrodynamic and contact forces." *PRL* **115**: 25, 258102. 2015

[4] Spagnolie, Saverio E., and Eric Lauga. "Hydrodynamics of self-propulsion near a boundary: predictions and accuracy of far-field approximations." *JFM* **700**:105-147. 2012

[5] Muller, K., C. K. Hemelrijk, J. Westerweel, and D. S. W. Tam. "Calibration of multiple cameras for large-scale experiments using a freely moving calibration target." *Experiments in Fluids* **61**1. 2020.

AZIMUTHAL MOTION OF LARGE NEUTRALLY BUOYANT PARTICLES IN POISEUILLE FLOW

Sudarshan Sridharan*[1] and Christian Poelma [1]
[1]Department of Mechanical, Maritime & Materials Engineering, Delft University of Technology, Delft, The Netherlands

Summary Poiseuille flow in a pipe with neutrally buoyant particles is investigated using Shadowgraphy-PTV. The considered pipe to particle diameter ratios (D/d) are 20 and 5.5. The bulk Reynolds number is varied between Re_b = 200 and Re_b = 800. As expected, the particles are observed to migrate radially to a location corresponding to the Segré-Silberberg annulus. In addition, we observe unexpected behaviour, as the D/d = 5.5 particles in the annulus move in a helical motion with a constant azimuthal velocity. This behaviour persists throughout the pipe. The effect of particle size and the Reynolds number on this azimuthal velocity is investigated.

INTRODUCTION

Wall-bounded particle-laden flows at low Reynolds number are known for particles inertially migrating to the Segré-Silberberg annulus [2]. This is predominantly due to the effect of shear around the particle resulting in a lift force acting radially towards the annulus [2]. Modelling these flows is challenging when the inertial contribution becomes significant, even at very low particle concentration [4]. Experiments at bulk Reynolds numbers $Re_b > 100$ show the dependence of the location of the stable annulus on the Reynolds number and pipe to particle diameter ratios (D/d) [1]. Furthermore, particles take longer to accumulate in the annulus than that predicted in the Stokes limit. An unstable annulus along with the stable annulus is also reported at Re_b = 600-800 [3]. These experimental results are generally based on stochastic analysis of particle radial positions at different streamwise locations from the entrance of the pipe and thus do not provide insight on the Lagrangian track of a particle.

In order to study the nature of particle trajectories, the particles are tracked along the pipe using a Shadowgraphy-PTV setup. The flow is imaged along two perpendicular directions resulting in three-dimensional reconstruction of particle tracks. Based on our observations, particles with D/d = 5.5 exhibit peculiar behaviour spiralling along the azimuthal direction after they have migrated to a radial position at 0.3D from the centre of the pipe.

EXPERIMENTAL SETUP

A flow loop is constructed at the Laboratory for Aero & Hydrodynamics in TU Delft for this study, with a 3.8 m long pipe with 10 mm diameter (D). The flow is driven by a constant head maintained in the overflow tank employed. The suspension enters the pipe through an inlet chamber containing a flow conditioner, followed by a smooth contraction. The suspension is collected in a reservoir from the pipe and pumped back to the overflow tank using a peristaltic pump, forming a closed loop. The considered bulk Reynolds numbers (Re_b) are 300, 400, 500, 600, and 700, based on flow rate measurements. A neutrally buoyant solution is prepared using the calculated amount of water and glycerol to match the density of the Polystyrene particles ($\rho_p = 1035\ kg/m^3$). The suspension has a kinematic viscosity of 1.53 x $10^{-6}\ m^2/s$ at 18.5 ^{o}C. The particle concentration is kept below 0.1% in order to avoid particle-particle interaction.

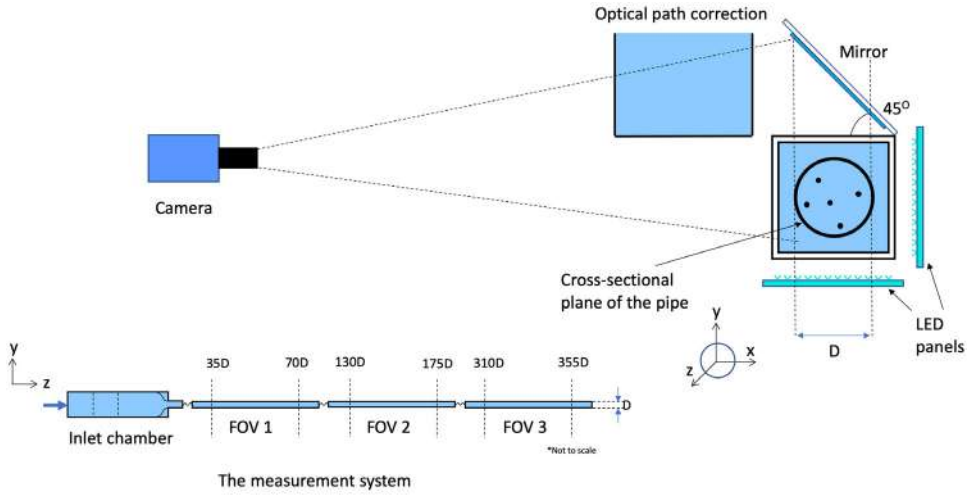

Figure 1: A schematic diagram of optical system used to reconstruct the three dimensional position of a particle in the pipe in the cross-sectional ($x - y$) plane. The particles are tracked in three field of views: FOV 1, FOV 2, and FOV 3 corresponding to 35-70D, 130-175D, and 310-355D from the pipe entrance respectively.

*Corresponding author. E-mail: S.Sridharan@tudelft.nl.

The imaging system employed is designed to image the suspension in two perpendicular planes using a single camera. An Imager sCMOS camera with 50 mm lens is placed perpendicular to the $(y-z)$ plane. A mirror is placed at 45^o with the horizontal (x-axis) over a rectangular PMMA section enclosing the pipe. This system provides two images simultaneously along perpendicular directions in the $(y-z)$ and $(x-z)$ planes with the $z-axis$ as the epipolar line, allowing three dimensional reconstruction of any particle in the field of view. The difference in optical path between the two views is compensated by employing a water filled container (Figure 1). The particles are tracked along 45D of pipe length at three different field of views, 35D-70D, 130D-175D, and 310-355D from the entrance with a spatial resolution of 0.22 mm and a temporal resolution of 0.02 s.

RESULTS

The particle positions reconstructed are used to generate radial probability distribution functions (PDFs) and the trajectories are used to determine the particle velocity. The particles with D/d = 20 and D/d = 5.5 accumulate in a stable annulus at 0.4D and 0.3D from the centre of the pipe respectively. However, the trajectory of particles with D/d = 20 and D/d = 5.5 show a sharp contrast. Particles with D/d = 20 are observed to travel mostly parallel to the pipe centreline in the measured field of view, migrating slowly in the radial direction. However, particles with D/d = 5.5 are observed to also undergo displacement along azimuthal direction (Figure 2). These motions are consistently observed in all the three field of views, from 35D-350D.

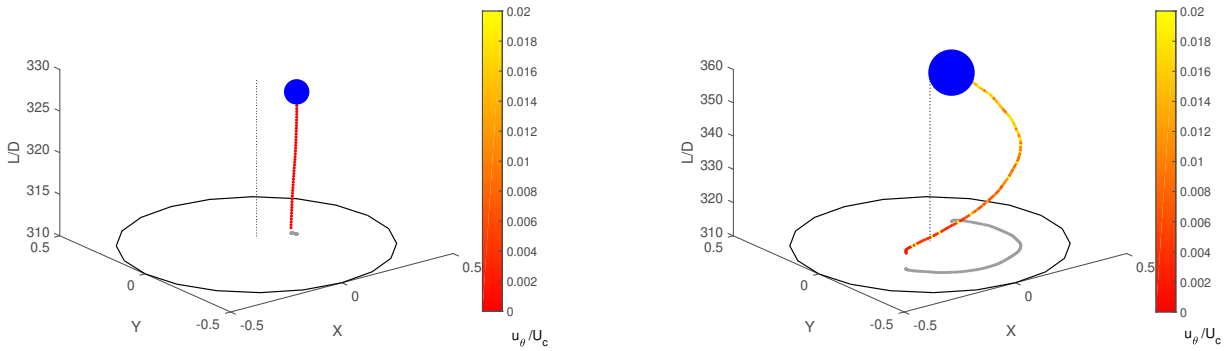

(a) D/d = 20. (b) D/d = 5.5.

Figure 2: Particle trajectories reconstructed in three-dimensional space at Re_b = 600. The flow direction is from bottom to top. The colormap denotes the azimuthal velocity (u_θ) of the particle normalized with the centreline velocity (U_c). The circle indicates the flow domain and the gray line represents the projection of tracks in the $(x-y)$ plane.

The particles moving along azimuthal direction rotate over 300 degrees in the measured field of view and have a constant azimuthal velocity after they migrate to the stable annulus. No preferred direction of the azimuthal displacement is observed as the particles move either in clockwise or anti-clockwise direction around the z-axis. As Re_b increases, more particles are observed to spiral in the azimuthal direction. Moreover, the azimuthal velocity of particles in the annulus increases with Re_b proportionally, with $u_\theta/U_c \approx 0.02$. This behaviour is briefly mentioned recently [3] in suspension with particles of D/d = 8. We will investigate this behaviour further with different pipe to particle sizes and supplement the PTV results with fluid velocity field measurements.

CONCLUSION

Large neutrally buoyant particles (D/d = 5.5) in Poiseuille flow migrate radially to a stable annulus as expected. However, they also move along azimuthal direction in contrast to particles of D/d = 20. The azimuthal velocity of the particle accumulated in the annulus is proportional to the bulk Reynolds number. The nature of such motions will be further investigated in suspensions with different pipe to particle diameter ratios.

References

[1] Matas, Jean-Philippe and Morris, Jeffrey F and Guazzelli, Élisabeth. Inertial migration of rigid spherical particles in Poiseuille flow. *J. Fluid Mech.* **515**: 171-195, 2004.

[2] Asmolov, Evgeny S. The inertial lift on a spherical particle in a plane Poiseuille flow at large channel Reynolds number. *J. Fluid Mech.* **381**: 63-87, 1999.

[3] Nakayama, Saki and Yamashita, Hiroshi and Yabu, Takuya and Itano, Tomoaki and Sugihara-Seki, Masako. Three regimes of inertial focusing for spherical particles suspended in circular tube flows. *J. Fluid Mech.* **871**: 952-969, 2019.

[4] Hood, Kaitlyn and Lee, Sungyon and Roper, Marcus. Inertial migration of a rigid sphere in three-dimensional Poiseuille flow. *J. Fluid Mech.* **765**: 452-479, 2015.

UNIFIED CALCULATION OF THE FAR-FIELD FLOW AROUND AN INERTIAL SWIMMER

Tommaso Redaelli*[1], Fabien Candelier[2], Bernhard Mehlig[3], and Christophe Eloy[1]
[1]Aix Marseille Univ, CNRS, Centrale Marseille, IRPHE, Marseille, France
[2]Aix Marseille Univ, CNRS, IUSTI, Marseille, France
[3]Department of Physics, Gothenburg University, Sweden

Summary Hydrodynamic signalling is widely used at the planktonic scale. To understand how millimetric organisms use hydrodynamic signals to perceive their environment, we need to model how both inertial and unsteady effects influence the flow field produced by an active organism swimming in a viscous flow. Here, to address this question, we propose a model based on the method of Matched Asymptotic Expansions. This model allows us to calculate, as an expansion, the flow field produced by an active spherical particle, for an arbitrary time-dependent motion. The present technique unifies previously known results and extend them to the case of an active particle.

CONTEXT

Copepods are widespread millimetric crustaceans living in almost all waters on Earth. Although copepods are blind, they are able to detect preys, predators and mates by using hydrodynamic signalling. However, we do not know how they process and extract relevant information from the turbulent flow background. To address this question, we need a mathematical model of the hydrodynamic signals produced by their targets (Fig. 1b).

Copepods targets have a typical size of the order of $a = 1\,\mathrm{mm}$ and move with typical velocity of the order of $U = 1\,\mathrm{mm\,s^{-1}}$. Their Reynolds number, $\mathrm{Re} = aU/\nu$, is thus of order 1. Moreover, their motion is affected by unsteady effects of typical timescale τ, and the associated Strouhal number, $\mathrm{St} = a/(U\tau)$, is in many cases of order 1. In this context, both inertia and unsteadiness affect the disturbance flow produced by a millimetric swimmer.

STATEMENT OF THE PROBLEM

Let us assume that the swimming organism is moving with velocity $\mathbf{u}$. In the framework moving at velocity $\mathbf{u}$, the disturbance flow field, $\boldsymbol{v}$, is a solution of the following Navier–Stokes equation

$$\mathrm{Re}\,\mathrm{St}\frac{\partial \boldsymbol{v}}{\partial t} - \mathrm{Re}\,(\boldsymbol{u}\cdot\nabla\boldsymbol{v} - \boldsymbol{v}\cdot\nabla\boldsymbol{v}) = -\nabla p + \nabla^2\boldsymbol{v}, \quad \nabla\cdot\boldsymbol{v} = 0, \tag{1}$$

where typical length, velocity and density are taken to be a, U and ρ to make the problem dimensionless. This equation is complemented with the boundary conditions $\boldsymbol{v} = \boldsymbol{u} + \boldsymbol{u}_s$ on the particle surface (where $\boldsymbol{u}_s$ is the active velocity on the particle surface) and $\boldsymbol{v} \to 0$ at infinity.

In the asymptotic limit $\mathrm{Re} \ll 1$ and $\mathrm{St} \lesssim 1$, equation (1) is the Stokes equation. In that case, inertia and unsteadiness can be neglected and classical methods can be used to obtain the force acting on the swimming organism and the flow produced (Fig. 1a) [1, 2]. In contrast, when fluid inertia is taken into account (when $\mathrm{Re} = O(1)$ and $\mathrm{St} \ll 1$) or when unsteadiness is taken into account (when $\mathrm{Re}\,\mathrm{St} = O(1)$ with $\mathrm{Re} \ll 1$), the problem complexity increases drastically.[3, 4]

In the past, some important works have addressed how to solve the Navier–Stokes equation (1) in some particular limits (Table 1). However, when both inertial effects and unsteady effects are taken into account, we do not known how these effects combine for an active particle. This is the main question we want to address in this communication.

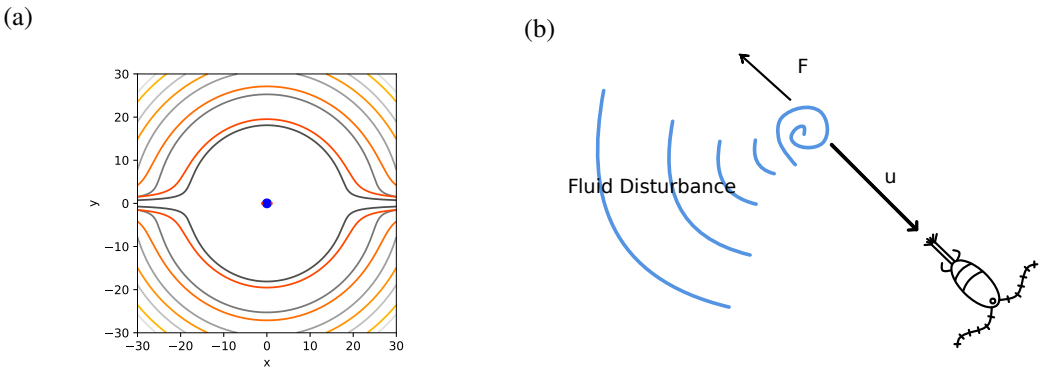

Figure 1: (a) Streamlines of the Stokes solution (grey) and Oseen approximation (red) for a sphere (blue) moving at constant velocity ($a = 1$ and $\mathrm{Re} = 8$). (b) Sketch of a millimetric organism swimming unsteadily. The force $\mathbf{F}(t)$ is force exerted on the fluid by the swimmer and $\mathbf{u}(t)$ is its instantaneous velocity.

*Corresponding author. E-mail: tommaso.redaelli@irphe.univ-mrs.fr

	passive particle	active particle
Stokes equation ($\mathrm{Re} \ll 1$, $\mathrm{St} \lesssim 1$)	Stokes [5] $\circ$ $\star$	Lauga & Powers [2] $\circ$ $\star$
unsteadiness ($\mathrm{Re}\,\mathrm{St} = O(1)$, $\mathrm{Re} \ll 1$)	Basset–Boussinesq–Oseen [6] $\circ$	Wang & Ardekani [7] $\circ$
inertia ($\mathrm{Re} = O(1)$, $\mathrm{St} \ll 1$)	Oseen [8] $\circ$ $\star$	Khair & Chrisholm [9] $\circ$ $\star$
unsteadiness and inertia ($\mathrm{Re} = O(1)$, $\mathrm{St} = O(1)$)	Lovalenti & Brady [10] $\circ$	present work $\circ$ $\star$

Table 1: Partial review of the analytical studies on a spherical particle moving in a fluid at rest. The first column gives the approximation of the Navier–Stokes equation used. The second and the third columns correspond to references addressing passive or active particles. We use symbols to refer to analytical expressions of the flow field ($\star$) or the force acting on the particle ($\circ$).

MATCHED ASYMPTOTIC EXPANSION METHOD

We apply a method that relies on Matched Asymptotic Expansion of the flow field $\boldsymbol{v}$. In the outer region, $\boldsymbol{v}$ is expanded as a series of the small parameter $\epsilon = \sqrt{\mathrm{Re}\,\mathrm{St}}$. We then match the outer solution to an inner solution near the active particle. This method allows us to calculate both the force acting on the particle and the flow field $\boldsymbol{v}$ including corrections due to inertia and unsteadiness.

The proposed solution can be seen as a generalisation to active particle of the force derived by Lovalenti and Brady for passive particles [10]. We can also recover the results of Wang and Ardekani [7] on the force acting on an active unsteady particle. The novelty of the present method, is that it allows us to calculate the flow field produced by an active particle, a result that is not accessible with methods based on the reciprocal theorem.

This method will be used to compute the flow field generated by a millimetric organism that produces a time-periodic active force. It will then be compared to the experimental data of Kiorboe and Jiang [11] on swimming copepods.

References

[1] Blake J. R. A spherical envelope approach to ciliary propulsion. *J. Fluid Mech.* (**46**):pp.199-208, (1971).
[2] Lauga E.,Powers M.T., The hydrodynamics of swimmming microorganisms. *Re3p. Prog. Phys.* **72**, (2009).
[3] Wang S., Ardekani A. M., Inertial squirmer. *Physics of fluids*, (2012).
[4] Maxey M.R., Riley J.J., Equation of motion for a small rigid sphere in a nonuniform flow. *American Institute of Physics*, (1982).
[5] Stokes G. G., On the effect of internal friction of fluids on the motion of pendulums. *Transactions of the Cambridge Philosophical Society*, (1851).
[6] Boussinesq J., Théorie de l'écoulement tourbillonnant et tumultueux des liquides dans les lits rectilignes a grande section. *Gauthier-Villars*, (1897).
[7] Wang S., Ardekani A. M., Unsteady swimming of small organisms *J. Fluid Mech.* (2012).
[8] Oseen C.W., Ueber die Sotkes'sche Formel, und uver eine verwandte Aufgabe in der Hydrodynamik. *Ark. Math. Astronom. Fys.* (**6**) No 19 pp. 154-155, (1910).
[9] Khair A.S., Chrisholm N.G., Expansion at small Reynolds numbers for the locomotion of a spherical squirmer. *Phys. of Fluids*, (2014).
[10] Lovalenti P.M., Brady J.F.,The hydrodynamic force on a rigid particle undergoing arbitrary time-dependent motion at small Reynolds number. *J. Fluid Mech.* (**256**):pp.561-605, (1993).
[11] Kiorboe T., Jiang H., Colin S.P., Danger of zooplankton feeding: the fluid signal generated by ambush-feeding copepods. *Proc. R. Soc. B.*, (2010).

RECIPROCAL FRAMEWORK FOR THE SELF-PROPULSION OF CHEMICALLY ACTIVE COLLOIDS

Bhargav Rallabandi*[1], Fan Yang[2], and Howard A. Stone[2]
[1]Department of Mechanical Engineering, University of California, Riverside, USA
[2]Department of Mechanical and Aerospace Engineering, Princeton University, Princeton, USA

Summary Active colloids generate chemical gradients through surface chemical activity, using which they then can self-propel via phoretic mechanisms. Here, we discuss a framework to model the self-propulsion of N non-Brownian active colloids that interact chemically and hydrodynamically. This is achieved by combining multipole expansions for the chemical transport with the Lorentz reciprocal theorem for low-Reynolds-number hydrodynamics. The framework yields explicit analytic predictions for the particle velocities that are shown to be in good agreement with exact results where available. We then apply the model to a binary mixture of particles with different mobilities and find behaviors that include pair-chasing, attraction and aggregate formation. The framework is computationally advantageous in that it circumvents the matrix inversion common in problems involving colloidal suspensions.

BACKGROUND

The self-propelled motion of particles suspended in viscous fluid has widespread applications in biological systems and for microscale assembly. In synthetic microscale systems, chemical gradients are often used to drive the motion of suspended particles with engineered surface properties. A particle whose surface interacts with the solute through a short-range potential will translate when exposed to a gradient of a chemical potential. This type of motion, known as diffusiophoresis, can be generated by several physical mechanisms, including van der Waals forces, steric interactions or an electrostatic potential between a charged particle and ions in solution [1]. Chemically active colloids are typically designed with materials that catalyze chemical reactions, generating chemical species whose gradients drive particle motion through phoretic mechanisms.

PROBLEM SETUP AND APPROACH

Here, we consider the low-Reynolds-number motion of N rigid, self-propelling colloids suspended in a Newtonian fluid. Each particle i translates with velocity $\mathbf{V}_i$ and rotates with angular velocity $\mathbf{\Omega}_i$ as a result of surface chemical flux $\varphi_i(\mathbf{x})$ at the particle surfaces S_i (due to surface chemical reactions). We are interested in determining the motion of the particles given their positions and the surface chemical fluxes. We assume that the flow is sufficiently slow that the transport of chemical $c(\mathbf{x})$ is diffusion dominated. Thus, each particle experiences a gradient of chemical concentration $\nabla c(\mathbf{x})$ that is a function of the positions of all of the particles and chemical in the system. The local chemical concentration gradient causes the development of a thin slip layer around each particle, that ultimately leads to its motion. We use the common modeling framework in which we model the slip layer using an effective slip velocity condition

$$\mathbf{v} = \mathbf{v}_s(\mathbf{x}) = M(\mathbf{x}, c(\mathbf{x}))\nabla \mathbf{c}(\mathbf{x}) \quad \text{for} \quad \mathbf{x} \in S_i. \tag{1}$$

Here, M is a phoretic mobility that can depend explicitly on the position along the particle surface as well as on the local concentration field.

Past studies have solved the coupled chemical-hydrodynamic problem by directly solving the Stokes equations subject to the slip conditions and a balance of forces and torques, for example using multipole expansions [3]. Here, we develop an alternative framework that utilizes the Lorentz reciprocal theorem to circumvent the solution to the detailed fluid velocity and pressure fields and instead directly yield the kinematics of the problem. The result is that the the translation and rotation ($\mathbf{V}$ and $\mathbf{\Omega}$) of the particles can be expressed directly as integrals of the slip velocity over the particle surfaces in N- particle systems. In contrast with other approaches in the literature for N-body hydrodynamics [2], the framework developed here does not involve the inversion of a grand mobility matrix and thus is computationally advantageous.

We apply the framework to the common case of spherical particles in unbounded flow. We further focus on particles with uniform surface chemical fluxes, so any motion of the particles is a direct consequence of either chemical or hydrodynamic interactions between the particles. We apply our framework to two particles in an electrolyte solution (where $M(c) \propto c^{-1}$ for which the particles co-move or counter-move depending on the relative sign of their mobility. We find our theory to be in excellent agreement with exact solutions [4] up to the time when the particles make contact. We then apply the framework to multiple particles, exploring the behavior of the system for a binary mixture of two populations of particles – one with positive mobility (chemical seeking) and the other with negative mobility. In these multi-particle binary systems, we observe the formation of particle pairs and propelling clusters that transiently change geometry as the system evolves in time (Fig. 1). At long times, we generally find that the positive-mobility particles form a single large aggregate, expelling the negative-mobility ones. However, we also encounter situations in which the large aggregate may trap negative-mobility particles as "inclusions". We find the presence of these inclusions to greatly enhances the propulsion speed of these aggregates, which may prove useful as a strategy for microscale assembly.

*Corresponding author. E-mail: bhargav@engr.ucr.edu

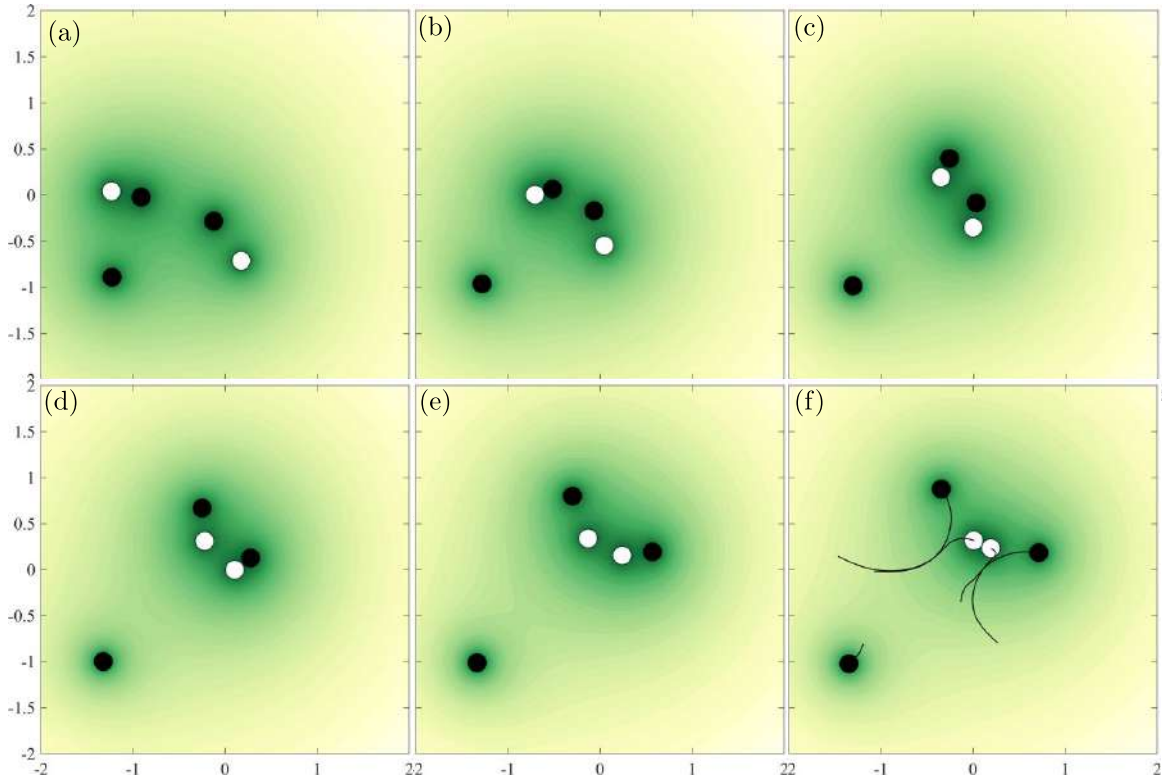

Figure 1: Sample trajectories of 5 particles with uniform surface chemical flux; light particles are attracted to the chemical while dark particles are repelled from it. The shading indicates the concentration field (dark indicates higher concentration) which is generated by the particles and diffuses away. Particle behaviors include transient pairing (b), chasing (c–d) and aggregation (f).

CONCLUSIONS

Our main result is the development of a versatile formalism that accurately and efficiently models the motion of hydrodynamically interacting active particles. We use the Lorentz reciprocal theorem in our work, which circumvents the construction of the detailed velocity fields in the fluid volume, in contrast with earlier approaches. We build on results in the literature to evaluate the motion of widely separated spheres, retaining contributions up to the level of force and torque quadrupoles. We then apply the theory to problems with multiple spheres with uniform surface fluxes, recovering results of earlier work in the literature and demonstrating new effects due to chemical inhomogeneities in the system.

References

[1] J. L. Anderson. Colloid transport by interfacial forces. *Ann. Rev. Fluid Mech.*, 21:61–99, 1989.

[2] J. W. Swan, J. F. Brady, R. S. Moore, and C. 174. Modeling hydrodynamic self-propulsion with Stokesian Dynamics. Or teaching Stokesian Dynamics to swim. *Phys. Fluids*, 23(7):071901, 2011.

[3] A. Varma, T. D. Montenegro-Johnson, and S. Michelin. Clustering-induced self-propulsion of isotropic autophoretic particles. *Soft Matter*, 14:7155–7173, 2018.

[4] F. Yang, B. Rallabandi, and H. A. Stone. Autophoresis of two adsorbing/desorbing particles in an electrolyte solution. *J. Fluid Mech.*, 865:440–459, 2019.

MODELING CONCENTRATION POLARIZATION AND FOULING LAYERS IN CROSSFLOW ULTRAFILTRATION

Gun Woo Park* and Gehard Nägele
Institute of Complex Systems (ICS-3), Forschungszentrum Juelich

Summary We present a boundary layer approximation (BLA) method for calculating the concentration-polarization (CP) layer and dispersion flow in crossflow ultrafiltration with a cylindrical membrane [1]. Results are discussed for various feed dispersions of colloidal particles, namely hard spheres, charge-stabilized particles [2], solvent-permeable non-ionic microgels [3, 4], and deswelling ionic microgels [5]. State-of-the-art methods are used for the gradient diffusion coefficient and viscosity entering the calculation of filtration profiles [3, 5]. We show that the BLA profiles are in quantitative agreement with predictions by a finite-element method [1]. The BLA results are compared with predictions by a similarity solution [4]. The BLA method is extended to conditions where a filter cake is formed at the membrane, with permeate flux results presented for a hard-sphere system [6].

INTRODUCTION

Crossflow ultrafiltration (UF) is a pressure-driven separation and enrichment process for colloidal dispersions where the feed dispersion is continuously pumped through a membrane pipe (Fig. 1, left). The applied transmembrane pressure (TMP) causes the solvent to flow out of the membrane, while the colloidal particles are retained inside the tube. Consequently, a particle-enriched diffuse layer is formed near the membrane, which reduces the filtration efficiency. This concentration-polarization (CP) layer is due to the balance of flow advection of particles towards, and gradient diffusion away from the membrane. The CP layer reduces the permeate flux, which can be attributed to the particles-created osmotic pressure counteracting the TMP. With increasing TMP, the particles near the membrane become immobilized, forming a crystalline so-called cake layer (Fig. 1, right). The cake layer is commonly believed to be at the origin of the limiting flux behavior, i.e., the experimentally observed horizontal flattening of the mean permeate flux at large TMP.

We have developed an efficient boundary layer approximation (BLA) method for accurately calculating the flow and concentration profiles in the UF of colloidal dispersions, on accounting for the concentration dependence of transport properties and osmotic pressure inside the inhomogeneous CP layer [1]. The BLA method is easily applied to feed dispersions including hard spheres (HS), solvent-permeable non-ionic microgels (MG), and ionic microgels (ion-MG) which deswell with increasing concentration [5]. To illustrate the importance of the concentration dependence of gradient diffusion and dispersion viscosity, we also report concentration profiles for constant transport (CT) coefficients. Fig. 2 shows BLA results for the particle volume fraction profile $\phi_w(z)$ at the membrane wall for different dispersions, in comparison with finite-element method (FEM) results (symbols), demonstrating the excellent agreement between both methods. We further compare with CP layer predictions for hard spheres by an earlier boundary layer similarity solution (sBLA) [4], which differs significantly from the FEM/BLA results. Gradient diffusion away from the membrane is the largest (smallest) for hard spheres (ionic microgels). Hence, hard spheres have the most strongly developed CP layer and osmotic pressure for equal operation conditions, and hence the lowest permeation efficiency. For hard spheres, there is only a moderate increase of gradient diffusion with increasing concentration, differently from charge-stabilized particles. Regarding the filtration efficiency, this is over-compensated by an accordingly increasing viscosity, resulting in a $\phi_w(z)$ curve only mildly larger than that for constant transport (CT) coefficients of values taken at the feed concentration.

We have extended the BLA to conditions where a crystalline filter cake is formed (Fig. 1, right). The cake layer contributes to the hydraulic resistance entering the employed Darcy-Starling law relating permeate flux to TMP and osmotic pressure. For hard spheres, Fig. 3 illustrates the effect of the cake layer on the pipe-length averaged permeate flux $\langle v_w \rangle$, as a function of the length-averaged TMP. According to the figure, the cake is responsible indeed for an (apparent) limiting flux behavior at large TMP where a large fraction of the membrane is covered by the cake (inset).

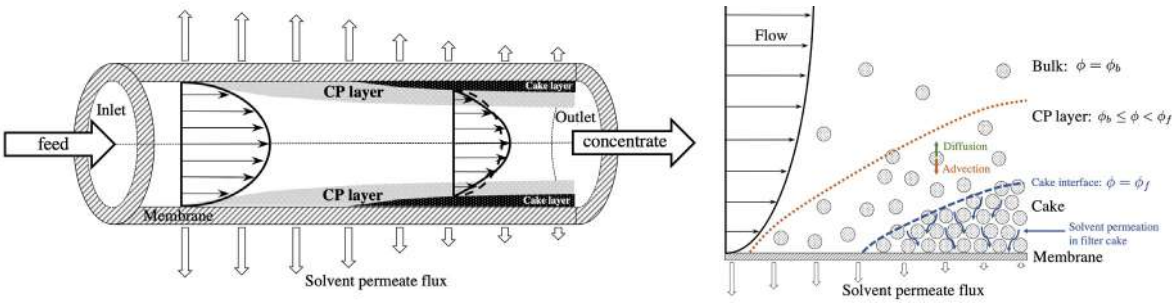

Figure 1: Left: Sketch of inside-out crossflow in a cylindrical membrane pipe. Right: CP and cake layers of particles near a perfectly retentive membrane, with an axially declining solvent permeate flux. In our model, a cake is formed for particle volume fractions ϕ exceeding the freezing transition value ϕ_f, which for hard spheres is equal to 0.494.

*Corresponding author. E-mail: g.park@fz-juelich.de

THEORY AND MODEL

We consider crossflow of a monodisperse feed dispersion inside a cylindrical membrane (see Fig. 1), for a small feed volume fraction and constant pressure values $p_{in} > p_{out} > p_{perm}$ at the inlet, outlet and inside the permeate, respectively. The particles are small enough that diffusion is dominated by Brownian motion, and sedimentation is negligible (ultrafiltration regime). The suspension-averaged incompressible flow and the particles flux are described macroscopically by coupled effective Stokes and diffusion-advection equations, respectively, incorporating a concentration-dependent gradient diffusion coefficient and effective viscosity, which we calculate with the salient hydrodynamic interactions included. The permeate flux through the fully particle-rejective membrane is described by the Darcy-Starling law, using an accurate input for the osmotic pressure derived microscopically from the particle interactions [1], and using the width-dependent hydraulic resistance due to the cake layer determined by the Carman-Kozeny relation for hard spheres [6]. The FEM results were generated using the COMSOL Multiphysics software for meshing and numerical solution [1].

CONCLUSIONS

The CP layer predictions by the simplifying BLA method based on a leading-order matched asymptotic expansion were shown to be in quantitative agreement with elaborate FEM results, for all considered feed dispersions and operating conditions. This justifies the approximations in the BLA method. The differences in the wall concentration curves of the similarity solution (sBLA) can be attributed to the less accurate pressure profiles obtained by the latter method.

The CP layer influence on ultrafiltration is small for ionic microgels since the gradient diffusion coefficient is distinctly larger than the one for neutral particles (e.g., HS and MG), with the accordingly small viscosity contribution by the charged particles. We have shown that the additional hydraulic resistance due to the cake layer leads to an apparent limiting flux behavior. The qualification apparent is used since the permeate flux is still weakly increasing with increasing at large TMP values where most ($> 80\%$) of the membrane wall is covered by the filter cake. If only the permeate flux reduction due to the osmotic pressure is considered, the permeate flux profile in Fig. 3 with an inflection point is obtained, showing linear growth at large TMP of slope inversely proportional to the hydraulic resistance of the bare membrane.

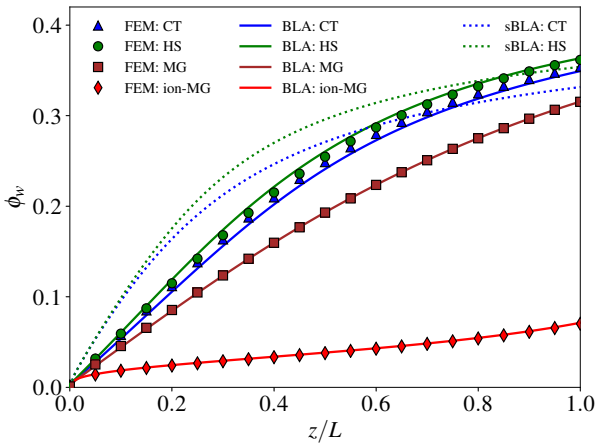

Figure 2: CP layer particle volume fraction $\phi_w(z)$ at membrane wall, as function of distance z to the inlet of the tube of length L. Results are shown by the finite-element method (FEM: symbols), boundary layer method (BLA; solid curves), and similarity solution (sBLA: dashed curves), respectively. The considered aqueous dispersions are hard spheres with concentration-dependent (HS: green color) and constant transport properties (CT; blue color), solvent-permeable non-ionic microgels (MG: brown color), and ionic microgels (ion-MG: red color). See [1].

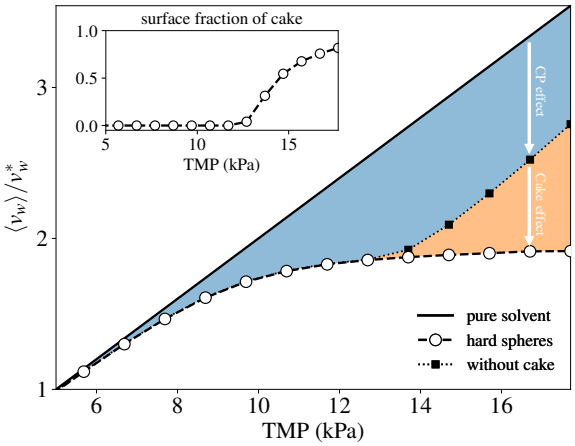

Figure 3: CP and cake layer effects on the tube-length averaged permeate flux $\langle v_w \rangle$ as a function of length-averaged TMP, quantified using the BLA method. The permeate flux is normalized by its value v_w^* at 5 kPa (open circles). The pure solvent line is the permeate flux for vanishing CP and fouling layers. The colored areas hallmark the flux reduction due to the CP (blue) and cake (sepia) layers. Filled squares: permeate flux including CP layer effect (see text). Dashed and dotted lines are guides to the eyes.

References

[1] G. W. Park and G. Nägele, Modeling concentration-polarization effect in crossflow ultrafiltration (to be submitted).
[2] R. Roa *et al.*, Ultrafiltration of charge-stabilized dispersions at low salinity, *Soft Matter* **11**: 4638-4653, 2016.
[3] J. Riest, T. Eckert, W. Richtering, and G. Nägele, Dynamics of suspensions of hydrodynamically structured particles: analytic theory and applications to experiments, *Soft Matter* **11**: 2821-2843, 2015.
[4] R. Roa, E. K. Zholkovskiy, and G. Nägele, Ultrafiltration modeling of non-ionic microgels, *Soft Matter* **11**: 4106-4122, 2015.
[5] M. E. Brito, A. R. Denton, and G. Nägele, Modeling deswelling, thermodynamics, structure, and dynamics in ionic microgel suspensions, *J. Chem. Phys* **151**, 2019.
[6] G. W. Park and G. Nägele, Cake layer effect in crossflow ultrafiltration with cylindrical membrane (manuscript in preparation).

PARTICLE CAPTURE IN A MICROCHANNEL: TAKING INERTIAL EFFECTS INTOACCOUNT

Donatien Mottin[1,2], Florence Razan[2], Frédéric Kanoufi[3], and Marie-Caroline Jullien*[1]
[1]Univ Rennes, CNRS, IPR (Institut de Physique de Rennes) – UMR 6251, F-35000 Rennes, France
[2]ENS Rennes, SATIE, UMR-CNRS 8029, Campus de Ker Lann, 35170 Bruz, France
[3]UniversitédeParis, ITODYS, CNRS, UMR7086, Paris, France

Summary **In the growing field of bioassays, there is a crucial need to determine *a priori* the experimental conditions that would lead to an efficient particle capture. In this presentation, we investigate the capture of density matched particles on a surface in a straight microchannel and underline the importance of inertial effects at low Reynolds numbers. A theoretical model for particle capture is proposed, supported by experimental and numerical results. More precisely, we will present a statistical model that allows predicting the distribution of the particle concentration in a cross-section, leading to a predictive model for the particle capture for any Reynolds number below 15.**

INTRODUCTION

The question we address is how many particles are captured on a specific surface in a microchannel when a particle-ladden liquid is continuously injected. This question is of fundamental interest in many domains. Typically, a lot of biological processes involve nano or micro-particles that might link to a reactive surface under flow [1]; predicting the capture rate is crucial in such a context. Oppositely, the adsorption of particles on the wall in a porous media may lead to clogging, profoundly changing the flow conditions [2]. The capture of molecules by a reactive surface has already been extensively studied, especially in the electrochemistry community [3], the question being whether this approach applies for particles. In this experimental, numerical and theoretical work, we propose to fill the gap by establishing a new capture law suitable for particles. We show that the fluid inertia has to be taken into account, even at very low Reynolds number, as it is responsible for a force that repels particles away from the walls.

EXPERIMENTS

Experiments are performed in a microfluidic channel of height H and width W_c, represented on Figure 1. Water is injected in the channel at a flow rate Q, laden with polystyrene particles of radius a that are density matched with the water solution, of diffusion coefficient D, and at a concentration c_0. The particles are coated with a carboxylate layer COOH, exhibiting negative surface charge COO^- in water. A gold surface of length L and width W_s, coated with a positively charged polymer, is located on one wall of the channel. The two charged surfaces (the particle surface and the gold surface) create a short range electrostatic force that makes the particle adhere definitively to the capture surface.

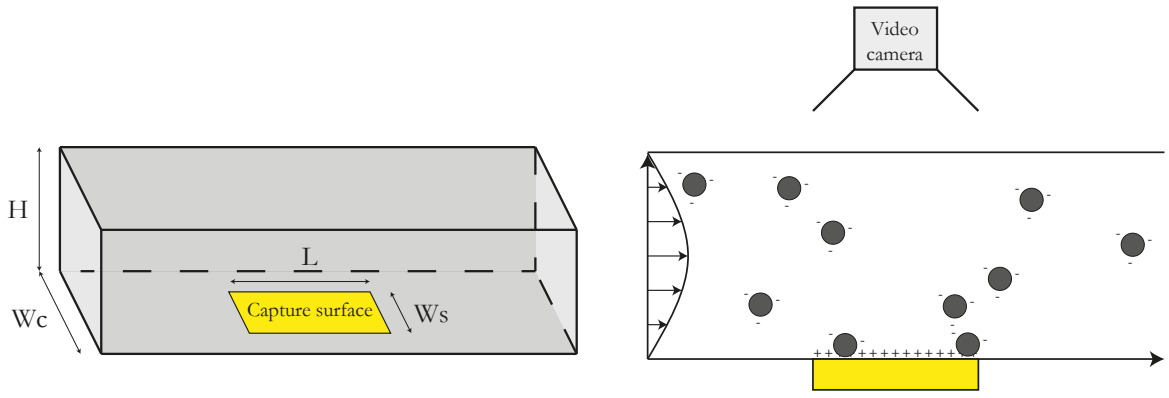

Figure 1: Sketch of the experimental setup. The particle-ladden water is injected at a flow rate Q and the negatively charged particles, of radius a and diffusion coefficient D, are injected at a concentration c_0. In the channel, of width W_c and height H, stands a positively charged capture surface, of width W_s and length L, located on one of the wall of the channel. Observation is done via a video camera through a reflective microscope.

Observation is carried out using a reflection microscope. The gold capture surface reflects light while polystyrene particles do not, making image processing easy. The number of adsorbed particles versus time is obtained and a linear fit allows the extraction of the capture rate J, *i.e.* the number of particles which adsorb on the capture surface per second.

Results of such experiments for molecule capture, subject only to diffusion and convection, have been extensively presented in the literature and have been rationalized by Squires *et al.* [3]. Several regimes exist, discriminated by the

*Corresponding author. E-mail: marie-caroline.jullien@univ-rennes1.fr

channel Péclet number $Pe = \frac{QH}{DLW_c}$ and the Péclet number related to the capture surface length $Pe_S = \frac{QL^2}{DW_cH^2}$. Applying this theory directly to particles, due to a low diffusion coefficient, implies $Pe \gg 1$ and $Pe_S \gg 1$. This corresponds to a regime called Partial Capture limited by Convection (PCC), represented on Figure 2a for molecule capture. In that case, the capture rate has been computed by [5] and is equal to $J_0 = 1.468\, c_0 DW_s Pe_S^{1/3}$.

The results of our experiments are presented on figure 2b. The black line corresponds to the theoretical prediction for molecule capture in the PCC regime, while our experiments for particles are represented by purple dots. These results clearly show that while some of the points are well predicted by the theoretical model for molecule, most of them are well below the curve showing that the actual capture rate is way smaller. An accurate model calls for deriving the particle concentration profile in a cross-section along the channel.

DISCUSSION

In the presentation, we propose a statistical model that takes into account additional forces, first observed by Segré and Silberberg [4] that act on particles flowing in a Poiseuille flow. These forces are linked to fluid inertia. One force tends to push the particle away from the walls and the other away from the center of the channel, as computed in [6]. The balance of the two forces focuses the particles at intermediate position. These effects lead to a depletion of the particles in the vicinity of the wall. Conversely, the particles are also submitted to diffusion that tends to restore a homogeneous concentration profile. By solving this complete problem we will show that we can reproduce the experimental data without any adjustable parameter. In fact, the PCC theory has to be amended by introducing a correction factor ξ, such that $J = \xi J_0$. The ξ factor takes into account the depletion of particle near the capture surface due to a balance between diffusion and lift forces. Figure 2c displays the concentration profiles for the two highlighted experimental data obtained by Lagrangian numerical simulations, and clearly shows that the concentration profile is deformed due to the flow and affects the capture rate.

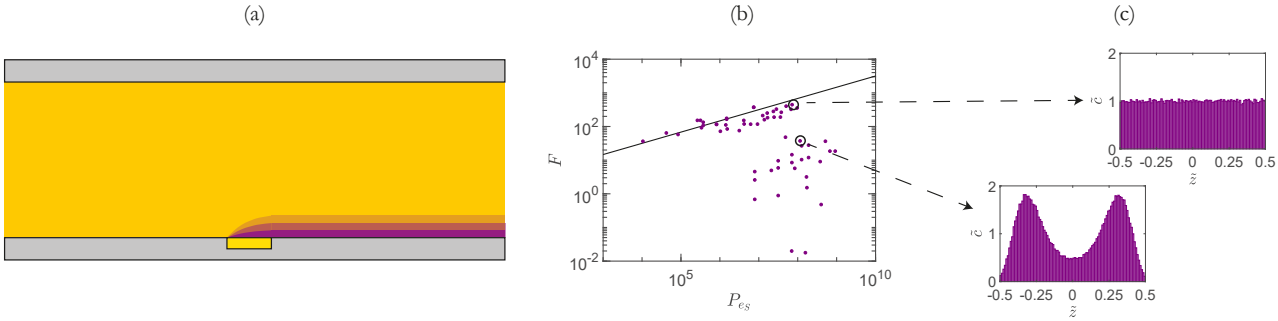

Figure 2: **(a)** Lagrangian simulation of molecule capture in the PCC regime, side view. Flow goes from left to right. In the liquid, yellow corresponds to high molecule concentration and purple to low molecule concentration. The gold rectangle represents the capture surface. **(b)** Dimensionless capture rate $F = J/(DW_s c_0 Pe_S^{1/3})$ versus the surface Péclet number $Pe_S = QL^2/(DH^2W_c)$. (Purple dots) Experiments. (Black line) Theoretical model for molecule capture in the PCC regime. **(c)** Particle normalized concentration $\tilde{c} = c/c_0$ profiles along the height of the channel $\tilde{z} = z/H$, obtained via Lagrangian simulations for the two highlighted experimental parameters.

As a whole, we propose a new law for particle capture at low Reynolds numbers. This work predicts both the particle concentration profile in the channel, but also the capture rate on a specific surface for spherical, rigid, and density matched particles. This work paves the way for ongoing research on more complex particles. This work should also have direct applications, for example in biological processes involving nano or microparticles capture. We will also present a free-of-access user friendly software. Based on the work, it allows an automatic computation of the particle concentration profile and capture rate in a channel. We expect this software to be an important tool for experiment design.

References

[1] Ren, X., Meng, X., Chen, D., Tang, F. & Jiao, J. Using silver nanoparticle to enhance current response of biosensor. *Biosensors and Bioelectronics* **21**, 433–437 (2005).

[2] Dressaire, E. & Sauret, A. Clogging of microfluidic systems. *Soft Matter* **13**, 37–48 (2017).

[3] Squires, T. M., Messinger, R. J. & Manalis, S. R. Making it stick: convection, reaction and diffusion in surface-based biosensors. *Nature biotechnology* **26**, 417 (2008).

[4] Segré, G. & Silberberg, A. Behaviour of macroscopic rigid spheres in poiseuille flow part 1. determination of local concentration by statistical analysis of particle passages through crossed light beams. *Journal of fluid mechanics* **14**, 115–135 (1962).

[5] Amatore, C., Da Mota, N., Sella, C. & Thouin, L. Theory and experiments of transport at channel microband electrodes under laminar flows. 1. steady-state regimes at a single electrode. *Analytical chemistry* **79**, 8502–8510 (2007).

[6] Schonberg, J. A. & Hinch, E. Inertial migration of a sphere in poiseuille flow. *Journal of Fluid Mechanics* **203**, 517–524 (1989).

INTERACTIONS AND COLLISIONS OF CHEMICALLY-ACTIVE DROPLETS

Kevin Lippera[1],Matvey Morozov[1],Michael Benzaquen[1],and Sébastien Michelin*[1]
[1]LadHyX, Ecole Polytechnique, Institut Polytechnique de Paris, 91128 Palaiseau, France

Summary Chemically-active droplets swim by exploiting the non-linear transport of chemical solutes they consume or release by the Marangoni flows induced by such solutes. Experimentally, their hydrodynamic and chemical interactions result in complex avoidance dynamics and trajectories, and are a canonical example of active matter. The present work proposes for the first time a complete quantitative modeling and analysis of the head-on collision of two droplets, providing a significant insight in the non-linear rebound dynamics as well as the resulting collective behaviour emerging from variability in the droplets' size.

CHEMICALLY-ACTIVE SWIMMING DROPLETS

Active particles and droplets have recently attracted much attention from the physics and fluid mechanics communities, as canonical examples of synthetic swimmers that can self-propel at the micron scale without relying on any external actuation such as a macroscopic magnetic field or mechanical forcing. Instead, the isotropic emission of large swollen reverse micelles from their surface during their slow solubilization provides them with a chemical activity, which can be turned into self-propulsion when coupled to the transport of such large molecular compounds by the Marangoni flows they create.

For an isolated droplet, when advection is large enough compared to molecular diffusion (i.e. above a critical Péclet number Pe_c), the isotropic steady state becomes unstable and a new self-propelling branch arises through a transcritical bifurcation. The broken directional symmetry results in a net polarity Π of the surface concentration distribution, which is directly proportional to the swimming velocity V in the case of an isolated droplet in a fluid at rest [1, 3].

The Marangoni flows generated by a swimming droplet induce the hydrodynamic drift of other droplets, as for any other suspended body at microscopic scale. Furthermore, the chemical activity of the droplet also modifies the solute content, generating additional chemical gradients on its neighbours. These chemical interactions are repulsive: indeed, these droplets display negative auto-chemotaxis (they swim away from their own chemical wake). As a result, swimming droplets interact both hydrodynamically and chemically, and these two routes are intrinsically coupled through the non-linearity of the system. As a result, an accurate and complete modeling of active droplets' collective dynamics has so far remained elusive and relies mostly on far-field approximations.

COLLISION AND REBOUND OF A SINGLE DROPLET AND A RIGID WALL

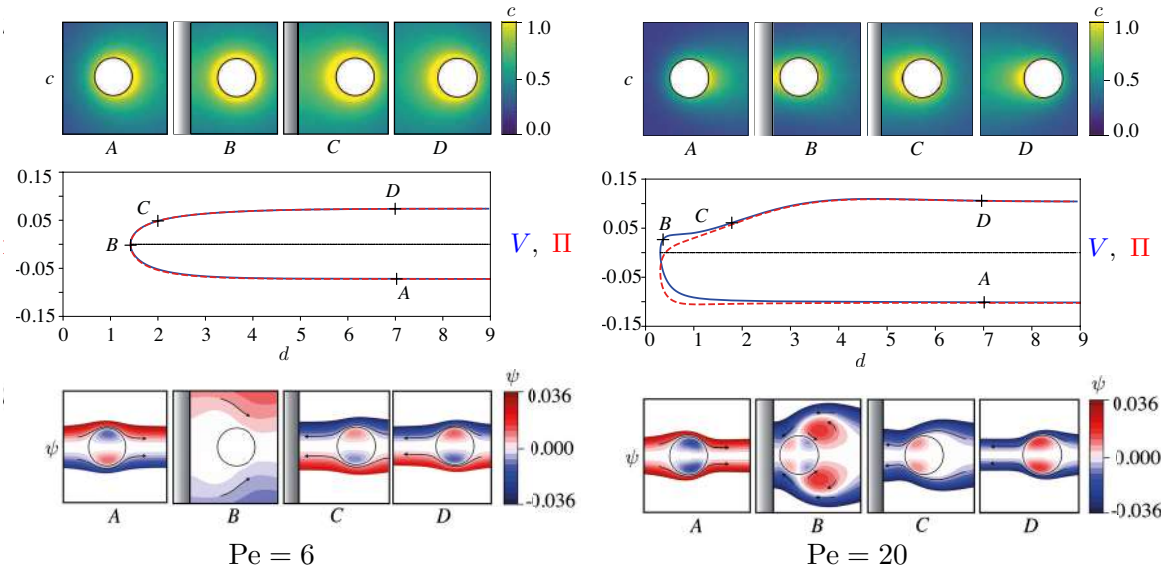

Figure 1: Collision dynamics of a chemically-active droplet and a rigid wall for intermediate (left, $\mathrm{Pe} = 6$) and large advection-to-diffusion ratio (right, $\mathrm{Pe} = 20$). In each case, the evolution of the droplet velocity and chemical polarity is presented, as well as snapshots of the concentration distribution and streamfunction at four successive stages of the collision (A–D).

*Corresponding author. E-mail: sebastien.michelin@ladhyx.polytechnique.fr.

In this work, we exploit the axisymmetry of a head-on collision of a single droplet onto a rigid wall to analyse the fully-coupled hydro-chemical dynamics for arbitrary wall-to-drop distance. A novel modeling and simulation framework based on a time-dependent body-fitted bi-spherical grid is used to compute the hydrodynamic and chemical fields exactly regardless of the droplet-wall distance [4]. The same approach further allows us to demonstrated that all the conclusions below are directly applicable to the head-on collision of two identical droplets.

The wall-drop collision is characterized on Figure 1 for intermediate and large Péclet number. In both cases, the approaching droplet is slowed down by the solute accumulating between its active surface and the confining wall. Eventually, this repulsion reverses the chemical polarity of the droplet, which rebounds and starts swimming away. The relative importance of advection and diffusion in the solute transport (Pe) plays however a critical role in the detailed collision dynamics. For moderate Pe, the collision is almost symmetric and droplet polarity and velocity match exactly, suggesting that the hydrodynamic influence of the wall is negligible: the entire collision is dominated by chemical interactions.

In contrast, for larger Pe, the front-back asymmetry of the droplet's chemical footprint is more pronounced [3] and, as a result, the rebound distance of the droplet (i.e. its minimum distance to the wall) decreases with Pe. Additionally, the rebound is highly non-symmetric: the reacceleration of the droplet is significantly slowed down by its internal quadrupolar Marangoni flow, which maintains an accumulated solute content away from the wall and holds the droplet back. Eventually, chemical repulsion by the wall overcomes this effect and the droplet completes its rebound. Yet, this nonlinear effect significantly delays the droplet's departure, e.g. in comparison with an elastic shock.

ASYMMETRIC COLLISIONS OF TWO DROPLETS AND LONG-TERM DYNAMICS

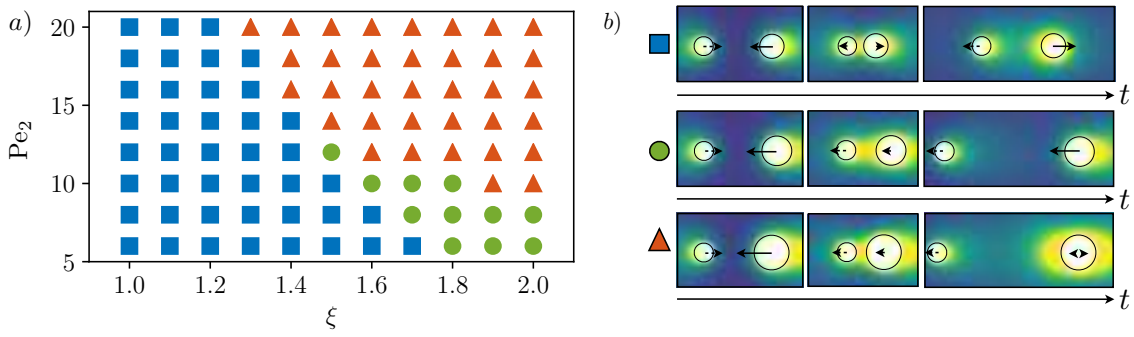

Figure 2: (a) Phase diagram of the collision of two droplets of different radii in terms of the Péclet number and size ratio ξ. (b) Illustration of the three dynamical regimes identified in (a).

We finally extend this study to the asymmetric head-on collision of two droplets with different radii, which are thus characterized by different chemical footprints [5]. Using the same modeling approach, three different dynamical regimes are identified depending on Pe and the size ratio ξ (Figure 2). When both droplets have a similar radius (ξ not too large), both rebound under the effect of the chemical repulsion induced by the other. Their collision is asymmetric, with the smaller droplet rebounding first.

However, for larger size contrast, the larger droplet is still swimming fast enough toward the smaller one, when the latter starts swimming away, leading to the emergence of two new and complex dynamical regimes. In the first one, observed for small enough Pe, the chasing of the smaller droplet by its larger neighbour eventually leads to the formation of a bound state where both droplets swim at the same velocity and in the same direction. In contrast, when Pe is large enough, the collision may provoke a mode switch for the larger droplet which stops swimming and starts pumping fluid symmetrically along its axis. This non-swimming state is however likely unstable and further interactions with other droplets will likely set it again into motion. Its pre-collision directionality will however be lost. This effect is expected to play a critical role in the long-term collective dynamics of such active droplets.

References

[1] Z. Izri, M. N. van der Linden, S. Michelin & O. Dauchot, *Phys. Rev. Lett.*, **113**: 248302, 2014
[2] C. C. Maass, C. Krüger, S. Herminghaus and C. Bahr, *Ann. Rev. Condens. Matter Phys.*, **7**:171–193, 2016
[3] M. Morozov & S. Michelin, *J. Fluid Mech.*, **860**: 711–738, 2019
[4] K. Lippera, M. Morozov, M. Benzaquen & S. Michelin, *J. Fluid Mech.*, **886**: A17, 2020
[5] K. Lippera, M. Benzaquen & S. Michelin, *Phys. Rev. Fluids*, **5**: 032201, 2020

PRE-SHEAR HOLDS THE KEY IN UNDERSTANDING DISCONTINUOUS SHEAR THICKENING

Tabish Khan[1] and Prabhu Nott *[1]
[1]Department of Chemical Engineering, Indian Institute of Science, Bangalore, India

Summary The phenomenon of discontinuous shear thickening (DST) in dense non Brownian suspensions has gained considerable attention in the last few years. The dominant opinion expressed in previous studies is that it is a stress controlled transition from lubricated to frictional state, modulated by short range repulsion between the particles. Typically, most of the experiments are done in such a way that the suspension is first pre-sheared, typically for an hour longer, before rheological measurements are made. However, little is known about what happens during the pre-shear, and why it need to be done for such long times. We provide clear evidence that pre-shear holds the key to understanding the change in response from continuous shear thickening (CST) to DST, and finally 'shear jamming', where the suspension shows Newtonian behaviour at lower shear stresses but shears at constant high shear stress, like dry granular materials. We provide arguments as to why large strains are required, and comment on the implication of our findings on slurry transportation in industries.

INTRODUCTION

Shear thickening is a non-Newtonian behaviour, generally exhibited by suspensions, in which the shear stress increases faster than linearly with shear rate. The rise in viscosity with shear rate could be continuous (CST) or discontinuous (DST), depending on the volume fraction (ϕ) of particles. The phenomenon of shear thickening has fascinated scientists and children alike, stemming from videos where a person is seen running on cornstarch suspension[1]. This behavior has been captured in various types of systems and is now believed to be the generic feature of dense suspensions.

Shear thickening is now believed to be a shear stress dependent transition from lubricated to frictional state, controlled by short range repulsions between the particles. A recent phenomenological theory was proposed by Wyart and Cates [2], where stress dependent jamming volume fraction relates DST with S shaped transition. Although, experiments on non Brownian suspensions [3,4] fits well for lower ϕ rheology, highly concentrated suspensions of spherical particles seems to diverge from the theory [2]. A common protocol in most experiments [4,5] is that the suspension is pre-sheared for an hour or so before rheological measurements are performed. Cwalina and Wagner [5] pre-sheared their suspenions for an hour and Pan et al [4] also points out the need of long shearing for DST. Here, we show that pre-shear holds the key in understanding DST and captured the evolution the microstructure by shear stress/rate sweep experiments. We report the transition of the microstructure from CST to DST to shear jamming, where a suspension behaves like a Newtonian fluid at low stress but creeps at higher stress, like granular matter. By performing series of experiments on non-Brownian suspensions like shear stress/rate sweep, constant shear rate and shear rate reversal, we report that the non Brownian concentrated suspensions of spherical particles show much slower dynamics than two body lubrication theory prediction, which we attribute to collective behaviour shown by N particle system.

Materials and methods

The experiments were conducted on polystyrene particles of 80 μm diameter in a Newtonian solvent of water and glycerol mixture. The composition was chosen such that the fluid is neutrally buoyant with the particles and tested using centrifugation at 2000 rpm for 5 minutes. This was done to prevent sedimentation or creaming during the experiments. Experiments were performed on parallel plate and concentric cylinder with temperature control and solvent trap to prevent evaporation.

Experimental conditions are maintained such that Re = $\frac{\rho\dot{\gamma}a^2}{\mu}$ is small enough ($< 10^{-3}$) to neglect inertia and Pe = $\frac{6\pi\mu a^3\dot{\gamma}}{k_BT}$ is large enough ($> 10^7$) to neglect thermal motion.

RESULTS AND DISCUSSION

Fig 1 shows the response during shear stress sweeps between $\tau = 0.01$ Pa to $\tau = 300Pa$ for ϕ =0.58. Various colours represent consecutive forward stress sweeps and the direction of the arrow represents the increasing number of sweeps. Dense suspensions always undergoes CST in the first few sweeps, followed by S shaped curve, associated with DST. Finally, the suspension behaves like Newtonian fluid at low stress but creeps at higher stress, like granular matter. At this stage, any attempts to increase $\tau > 300Pa$ accelerates the system to high shear rates. Constant shear rate experiments were also performed which exemplified the effect of pre-shear. It was found that dense suspensions underwent jamming at constant shear rate as well, but large strains O(100) were required. Shear reversal experiments on pre-sheared sample support our findings of slow microstructural buildup, dominated by frictional contacts. The viscosity rise was found to be independent of shear rate, although large strains O(10) were required, signifying the slow collective behaviour shown by spherical particles in dense suspensions.

*Corresponding author. E-mail: [prnott@iisc.ac.in]

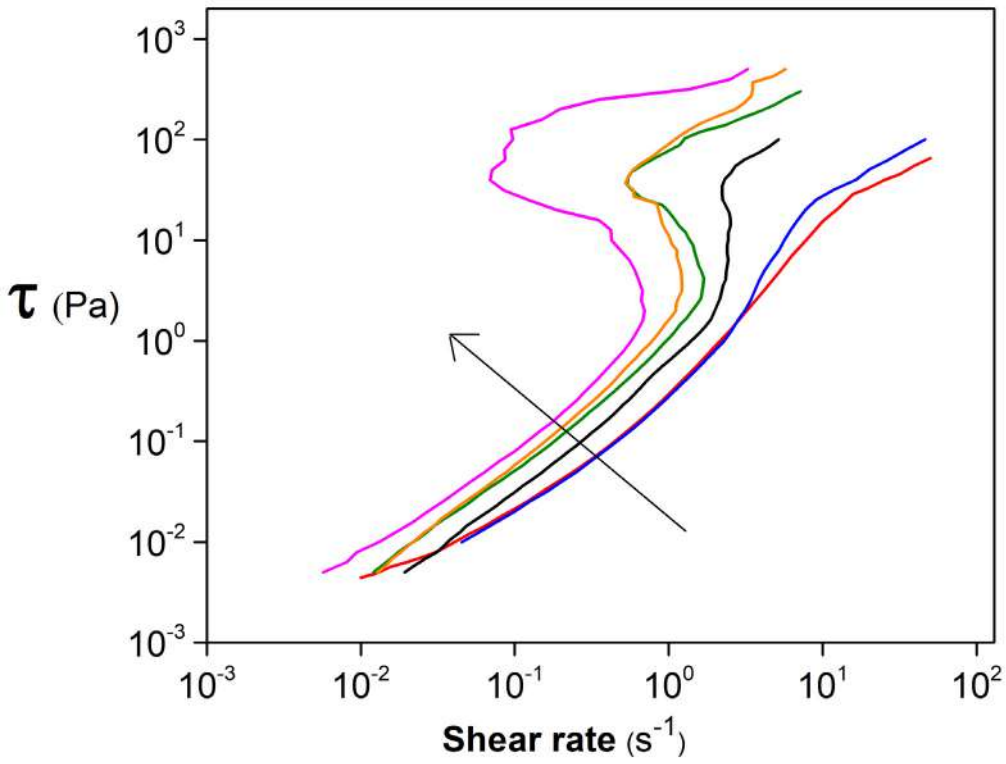

Figure 1: Shear rate sweep

CONCLUSIONS

Pre shear holds the key in obtaining DST and here we have shown the evolution of the microstructure that results in the transition from CST to DST to rate independent plastic shear during shear stress/rate controlled experiments. To exemplify the effect of pre shear, experiments were performed at constant shear rate such that low shear rate require less strain to undergo jamming. Friction forces dominate shear thickened rheology and the microstructure requires larger strain units to jam from lubricated state during shear reversal experiments. These observations imply a slow collective microstructural rearrangement of concentrated non Brownian suspensions.

References

[1] Eric Brown and Heinrich M Jaeger 2014 Rep. Prog. Phys. 77 046602.
[2] Wyart M, Cates ME. 2014. Discontinuous shear thickening without inertia in dense non-Brownian suspensions. Phys. Rev. Lett. 112:098302.
[3] . Guy BM, Hermes M, Poon WC. 2015 Towards a unified description of the rheology of hardparticle suspensions. Phys. Rev. Lett. 115, 088304. (doi:10.1103/PhysRevLett.115.088304).
[4] Z. Pan, H. de Cagny, B. Weber, and D. Bonn, Phys. Rev. E 92, 032202 (2015).
[5] Cwalina CD, Wagner NJ. 2014. Material properties of the shear-thickened state in concentrated near hardsphere colloidal dispersions. J. Rheol. 58:949–67

TRANSITIONS IN A TAYLOR-COUETTE FLOW OF DILUTE NON-COLLOIDAL SUSPENSIONS

Changwoo Kang[1,2] and Parisa Mirbod [*1]
[1]Department of Mechanical and Industrial Engineering, University of Illinois at Chicago, Chicago, USA
[2]Department of Mechanical Engineering, Jeonbuk National University, Jeonju-si, Republic of Korea

Summary

Flow transitions of neutrally buoyant and non-colloidal particles confined in a Taylor-Couette system have been numerically investigated by numerical simulations using suspension-balance model and rheological constitutive laws. It has been shown that particles destabilize the flow of dilute suspensions (ϕ_b=0.1). Furthermore, the circular Couette flow transitions to wavy vortex flow via non-axisymmetric spiral vortex flow and wavy spiral vortex flow have been observed.

INTRODUCTION

Particle-laden or suspension flows in a Taylor-Couette system, in which flows are contained between two coaxial cylinders, encounters in numerous applications; food processing, bio and chemical reactors, micro-mixers, micro-reactors, and engineering processes. In particular, shear-induced particle migration occurring by the rotating cylinder has been a crucial issue since it can affect the flow field leading to a change of velocity profile of suspensions [1]. Moreover, the Taylor-Couette flow is known to reveal various stable regimes as the rotation rate of the inner and outer cylinders varies. However, very few works have analysed the effect of finite size particles on flow transitions. Ali et al. [2] performed the linear stability analysis for a suspension in circular Couette flow and showed that the particles destabilize the flow of dilute suspensions ($\phi_b \leq 0.005$). They showed that the critical Taylor number decreases as the particle concentrations increases, and increasing the ratio of particle density to fluid density decreases the stability of the flow [2]. Majji et al. [3] performed experiments on the inertial flow transitions of a particle-fluid suspension in the Taylor-Couette flow with rotating inner and stationary outer cylinders. They found that the primary effects of the particles are a reduction of the maximum Reynolds number (Re) for the circular Couette flow. They also reported the onset of non-axisymmetric flow states not seen for a pure fluid where only inner cylinder rotates. In addition, when Re was decreased, for dilute suspension flows ($0.05 \leq \phi_b \leq 0.15$) the sequence of flow transitions followed by wavy Taylor vortex flow (WTV) → Taylor vortex flow (TVF) → spiral vortex flow (SVF) → ribbons (RIB) → circular Couette flow (CCF). However, for higher volume fractions (ϕ_b=0.2 and ϕ_b=0.3), a non-axisymmetric flow structure the so-called wavy spiral vortex flow (WSV) was observed. For ϕ_b=0.2, the flow transitions followed the sequence of WSV → WTV → WSV → TVF → SVF → RIB → CCF with decreasing Re. On the other hand, the sequence simplified for ϕ_b=0.3. It involved only non-axisymmetric flow structures: WSV → SVF → CCF.

We numerically examine flow transitions for a Taylor-Couette flow of dilute suspensions in the present study. The flow of neutrally buoyant and non-colloidal spherical particles between infinite two coaxial cylinders, in which the inner cylinder rotates at a constant angular velocity and the outer one is stationary, is considered (Fig. 1). We revisit the work reported by Majji et al. [3] where the radius ratio of cylinders is $\eta(=r_i/r_o)$=0.877, the particle size $\epsilon(=d/a)$ which is the ratio of annular gap (d) to the radius of particles (a) is 60, and the bulk particle volume fraction (ϕ_b) is fixed with ϕ_b=0.1. The Reynolds number is defined as $Re=\rho r_i \Omega_i d/\mu_o \mu_s(\phi_b)$ where $\mu_s=(1-\phi/\phi_m)^{-1.82}$ with ϕ_m=0.68 and μ_o is the solvent viscosity [3].

MATHEMATICAL FORMULATION

In this study, the suspension balance model (SBM) [4] is introduced for suspensions modelling. The SBM considers the suspension as a continuum consisting of solid and fluid phases. We assume that the particles suspended in an incompressible fluid are non-colloidal and non-Brownian. Using the SBM, the flow of non-colloidal hard-sphere suspensions is governed by incompressible continuity and momentum conservation equations written as

$$\nabla \cdot \langle \mathbf{u} \rangle = 0 \tag{1}$$

$$\frac{D\langle \rho \mathbf{u} \rangle}{Dt} = \langle \mathbf{b} \rangle + \nabla \cdot \langle \mathbf{\Sigma} \rangle \tag{2}$$

$\langle \mathbf{\Sigma} \rangle$ is the average suspension stress. For non-Brownian suspensions, the constitutive law for the suspension stress can be given by $\langle \mathbf{\Sigma} \rangle = -\langle p \rangle_f \mathbf{I} + 2\mu \langle \mathbf{S} \rangle + \langle \mathbf{\Sigma} \rangle_p$. $\langle \mathbf{\Sigma} \rangle_p$ is the particle stress and defined as $\langle \mathbf{\Sigma} \rangle_p = -\mu_o \mu_n(\phi) \dot{\gamma} \mathbf{Q} + 2\mu \mu_p(\phi) \langle \mathbf{S} \rangle$ [5]. Here, μ_n is the normal stress viscosity expressed as $\mu_n(\phi)=K_n(\phi/\phi_m)^2/(1-\phi/\phi_m)^2$ with K_n=0.75 [5] and $\dot{\gamma}=\sqrt{2\mathbf{E}\mathbf{E}}$ is the local shear rate. The tensor parameter ($\mathbf{Q}$) considers the anisotropy of the normal stress [4].

The particle-phase mass balance is given by

*Corresponding author. E-mail: pmirbod@uic.edu

$$\frac{\partial \phi}{\partial t} + \mathbf{u} \cdot \nabla \phi = -\nabla \cdot \mathbf{j} \quad \text{where} \quad \mathbf{j} = \frac{2a^2}{9\mu_o} f(\phi) \nabla \cdot \Sigma^p. \tag{4}$$

The sedimentation hindrance function, $f(\phi)=(1-\phi/\phi_m)(1-\phi)^3$, indicates the mean mobility of the particle phase [4].

The governing equations (Eqs. (1), (2) and (4)) were discretized in the cylindrical coordinate system using a finite volume method. A second-order central difference scheme was used for spatial discretization of derivatives except for the convective term ($\mathbf{u} \cdot \nabla \phi$) of Eq. (4), which utilized the QUICK scheme for the discretization. A hybrid scheme is applied for time advancement with a third-order Runge-Kutta scheme and Crank-Nicolson method. A fractional-step method is employed for time integration and the Poisson equation that resulted from the second stage of the fractional-step method is solved by a fast Fourier transform (FFT).

Computations are carried out on a cylindrical grid system with $96(r)\times512(\varphi)\times64(z)$ grid points and $L_z = 4d$. The grid cells are uniform in the azimuthal (φ) and axial (z) directions, while more grid points are allocated near walls in the radial direction (r). The no-slip condition is imposed on both cylindrical surfaces, and the migration flux of particles is set to be zero at the walls. The flow and particle concentration are assumed to be periodic in the axial direction (z).

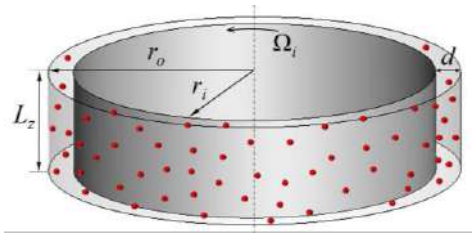

Figure 1. Schematic diagram of suspensions in a Taylor-Couette flow.

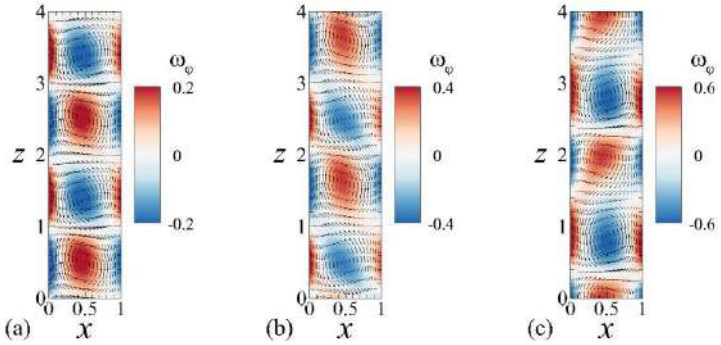

Figure 2. Contours of azimuthal vorticity component (ω_φ) with velocity vectors in a r-z plane for $\epsilon=30$; (a) Re=125, (b) Re=140, (c) Re=165 and $x=(r-r_i)/d$. Velocity vectors were plotted for every four and two points in the radial (r) and axial (z) directions, respectively.

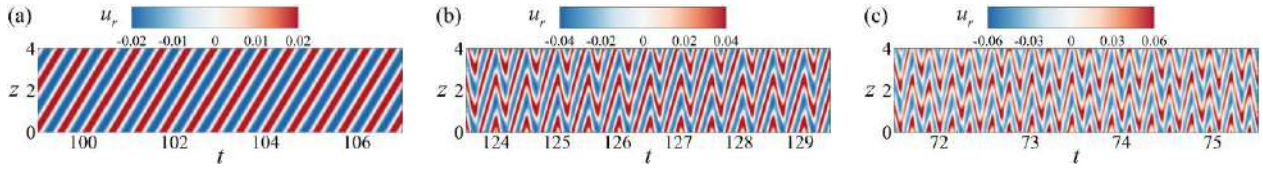

Figure 3. Space-time diagram of radial velocity (u_r) at the midgap (x = 0.5) and a given φ for $\epsilon=30$; (a) Re=125, (b) Re=140, (c) Re=165.

RESULTS

Figure 2 shows instantaneous flow field in a r-z plane for several Re, and space-time diagram of radial velocity (u_r) corresponding to the Re are plotted in Fig. 3. As the Reynolds number increase, the flow becomes unstable and non-axisymmetric counter-rotating vortices are developed in the annulus (Figs. 2(a), 3(a)). These vortices have a spiral mode (SVF) showing the inclination of vortices and the traveling to the axial direction. With increase in the Reynolds number to Re=140, an oscillation occurs in the axial traveling wave (Fig. 3(b)). These oscillations arise from the appearance of wavy pattern propagating to the azimuthal direction in spiral vortices. We refer these non-axisymmetric flow structure as wavy spiral vortex flow (WSVF). A transition to wavy vortex flow (WVF) occurs at higher Re=165 where the space-time diagram clearly shows an oscillation of vortices in time (Fig. 3(c)). The oscillation propagates in both axial and azimuthal directions resulting from the rotating wave of wavy vortices.

Acknowledgement

This work has been supported in part by the National Science Foundation award #1854376 and partially by the Army Research Office award #W911NF-18-1-0356.

References

[1] Lyon M.K., Leal L.G. An Experimental Study of the Motion of Concentrated Suspensions in Two-Dimensional Channel Flow. Part 1. Monodisperse System. *J. Fluid. Mech.* **363**: 25-56, 1998.
[2] Ali M.E., Mitra D., Schwille J.A., Lueptow R.M. Hydrodynamic Stability of a Suspension in Cylindrical Couette Fow. *Phys. Fluids* **14**: 1236-1243, 2002.
[3] Majji M.V., Banerjee S., Morris J.F. Inertial Flow Transitions of a Suspension in Taylor-Couette Geometry. *J. Fluid. Mech.* **835**: 936-969, 2018.
[4] Miller R.M., Morris J.F. Normal Stress-Driven Migration and Axial Development in Pressure-Driven Flow of Concentrated Suspensions. *J. Non-Newtonian Fluid Mech.* **135**: 149-165, 3006.
[5] Morris J.F., Boulay F. Curvilinear Flows of Noncolloidal Suspensions: The Role of Normal Stresses. *J. Rheol.* **43**: 1213-1237, 1999.

BIFURCATION AND STABILITY OF A SUSPENSION OF GYROTACTIC SWIMMER IN A VERTICAL PIPE

Lloyd Fung*[1], Rachel N. Bearon[2], and Yongyun Hwang[1]
[1]Department of Aeronautics, Imperial College London, London, UK
[2]Department of Mathematical Sciences, University of Liverpool, Liverpool, UK

Summary It is well known that a downflowing suspension of bottom-heavy swimming microalgae (e.g. *Chlamydomonas*) forms a beam-like structure, known as a gyrotactic plume, which is prone to a blip instability. In this study, we employ population-level continuum models, such as the Fokker-Planck (FP) and Generalised Taylor-Dispersion (GTD) models, and perform bifurcation and stability analyses for a downflowing suspension through a vertical pipe. It was found that the steady basic-state plume solution robustly exhibits a sophisticated two-parameter bifurcation composed of transcritical and cusp bifurcations. The stability analysis is also performed around the computed solution. It revealed that the GTD model provides more realistic predictions than the FP model when compared with experimental observations. However, the GTD model is only applicable to unidirectional shear flow. To this end, we will present a new model that only perform just as well as the GTD model in vertical shear flows, but also remains applicable in other scenarios.

INTRODUCTION

Bottom-heavy swimming microalgae, such as *Chlamydomonas*, *Dunaliella* and *Volvox*, are commonly found in nature and industrial bioreactors. These microorganisms are 'gyrotactic': their swimming orientation is determined by the balance between the gravitational torque posed by the bottom heaviness and the viscous torque of the background shear. Through a series of pioneering experiments where bottom-heavy microalgae are suspended in a downflowing vertical pipe, Kessler [1] showed that the swimmers move towards the pipe centre and a beam-like structure (known as a plume), demonstrating their gyrotactic nature. Furthermore, under certain condition, the gyrotactic plume was found to spontaneously break down into multiple blips along the streamwise direction [2, 3] due to instability.

The precise continuum description for the behaviours of suspensions of swimming microorganisms has been understood as a long-standing challenge. As such, even the pioneering experiment by Kessler [1] has not been fully analysed with any existing continuum model. Only recently, a similar set up was analysed in a vertical channel flow [4]. The objective of this study is to revisit the original experiment of Kessler in a vertical pipe and perform a comprehensive theoretical analysis using continuum models. A particular emphasis of this study is given to the assessment of the performance of the continuum models. For this purpose, we consider three types of continuum models: the Fokker-Planck (FP) model [5, 6], the Generalised Taylor Dispersion (GTD) theory [7, 8] and a new model recently developed by the authors. The most important difference between the three models is the form of the diffusivity tensor for the cell transport equation: the FP model is a simplified approximation of the covariance-matrix form of the diffusivity expression with a constant correlation time scale [5, 6], whereas the GTD model is obtained by considering the dispersional relationship between the swimmer's translational and orientational motility [7, 8]. Recently, there has been a growing body of evidence that the GTD model shows superior performance over the FP model, especially when the background shear rate is high [9, 10]. In this study, we shall demonstrate that the use of the GTD model is essential to provide a theoretically consistent description for the plume structure and the blip instability observed experimentally.

Meanwhile, we shall also demonstrate the performance of the new model we have developed. Coincidentally, the GTD model and the new model share the same results in this example with vertical shear flows. However, we shall demonstrate that the new model is more applicable and accurate in other flow cases.

RESULTS AND DISCUSSION

As in the experiment of Kessler [1], we consider a downflowing suspension of bottom-heavy swimmers in a vertical pipe. All the results shown here are based on the parameters obtained for *Chlamydomonas nivalis*. They are made dimensionless with the swimming velocity of each swimmer, the averaged cell number density and the pipe radius.

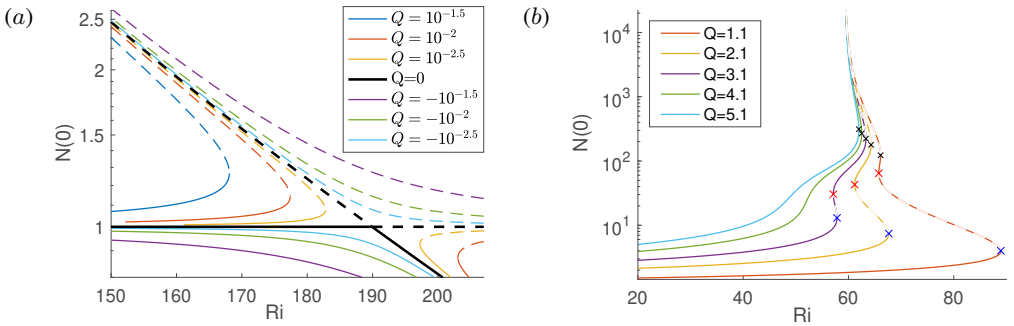

Figure 1: Bifurcation of steady basic-state plume solution for the GTD model at (a) low and (b) high flow rates. Here, the blue, red and black crosses (x) indicate the first, second and third saddle-node points, respectively. In both figures, ———, stable; - - - -, unstable. Also, in (b), $N(0) \to \infty$ when $Ri = Ri_s (\simeq 59)$

*Corresponding author. E-mail: lloyd.fung@imperial.ac.uk

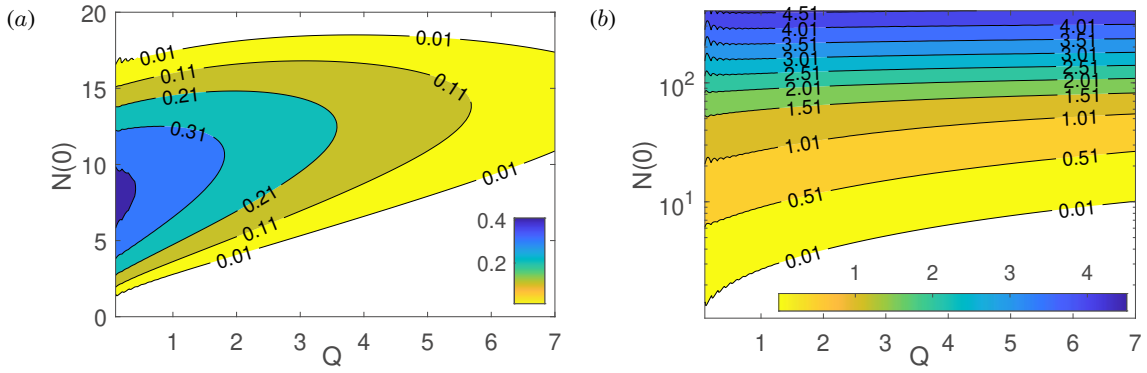

Figure 2: The maximum growth rate of the axisymmetric mode in the $N(0) - Q$ plane from (a) the FP model and (b) the GTD model.

Bifurcation of basic state (steady plume solution)

The steady parallel basic state is computed for the three models. We note that when the flow rate is low, the three models share almost identical result due to their same asymptotic behaviour in the limit of zero background shear. Figure 1 shows its bifurcation diagram represented by the cell number density at the pipe axis ($N(0)$) for several flow rates (Q) with respect to the Richardson number (Ri) which would represent the averaged total cell number density. When the suspension is stationary ($Q = 0$ in figure 1(a)), there exist two solutions, one of which is the stationary uniform suspension ($N(0) = 1$), while the other non-trivial solution ($N(0) \neq 1$) is characterised with a non-uniform cell number density and a non-zero flow velocity. These two solutions meet at $Ri = Ri_c(\approx 190)$ and interchange their stability, forming a transcritical bifurcation. As Q is increased, the transcritical bifurcation point turns into a saddle-node point (i.e. imperfect bifurcation) through an imperfect bifurcation (figure 1(a)). Another cusps bifurcation in the $Q - Ri$ parameter space is shown for at moderately large flow rates ($Q = 1.1$) in figure 1(b) with the GTD model. The bifurcation is an artefact of the GTD model and can be removed when the Smoluchowski equation is resolved directly instead. However, as the solution is continued, it becomes singular (i.e. $N(0) \to \infty$ at $Ri_s \approx 59$). The singularity is a robust behaviour originating from the diminishing diffusivity at increasingly strong shear, as we shall demonstrate analytically. As Q is increased further, the saddle-node points merge for both models, implying a cusp bifurcation occurring in the $Q - Ri$ parameter space.

Stability analysis

Linear stability analysis is performed with the steady plume solutions computed, and the maximum growth rate for the axisymmetric case (relevant to the blip instability) is presented in the $N(0)$-Q space in figure 2. The FP model gives a stabilising result at high $N(0)$. This is not consistent with experimental observation, and is found to be an artefact of the inaccurate diffusivity of the FP model at high shear rate. Meanwhile, the GTD model gives a growth rate that is strongly correlated with $N(0)$. This indicates the instability is likely localised at the high shear region near the centreline of the pipe. Finally, for the stability for non-axisymmetric modes, the FP model exhibits an instability, the growth rate of which is comparable with that for the axisymmetric case. This is in contrast to the GTD model, which exhibits a highly suppressed non-axisymmetric instability, as well as to the experimental observation where such instability has never been reported previously.

CONCLUDING REMARK AND THE NEW MODEL

In this study, we have performed a bifurcation and stability analysis for the experiment of Kessler [1] using both the FP and GTD models. The results evidently indicate the better predictive nature of the GTD model, consistent with the previous observations [9, 10]. However, the GTD model is only applicable in unidirectional shear flows and the linearised stability around a unidirectional flow profile. To extend the use of continuum modelling, we have developed a new model. It shares the same result as the GTD model in this example, meaning it is at least as accurate as the GTD model. However, in a more general flow case where the GTD model is not applicable, the new model remains accurate.

References

[1] Kessler J. O. Hydrodynamic focusing of motile algal cells. *Letters to Nature* **313**: 218-220, 1985.
[2] Kessler J. O. Individual and collective fluid dynamics of swimming cells. *J. Fluid Mech.* **173**: 191-205, 1986.
[3] Denissenko P., Lukaschuk S. Velocity profiles and discontinuities propagation in a pipe flow of suspension of motile microorganisms. *Phys. Lett. A* **362(4)**: 298-304, 2007.
[4] Hwang Y., Pedley T. J. Stability of downflowing gyrotactic microorganism suspensions in a two-dimensional vertical channel. *J. Fluid Mech.* **749**: 750-777, 2014.
[5] Pedley T. J., Kessler J. O. A new continuum model for suspensions of gyrotactic micro-organisms. *J. Fluid Mech.* **212**: 155-182, 1990.
[6] Pedley T. J. Instability of uniform micro-organism suspensions revisited. *J. Fluid Mech.* **647**: 335-359, 2010.
[7] Hill N. A., Bees M. A. Taylor dispersion of gyrotactic swimming micro-organisms in a linear flow. *Phys. Fluids* **14(8)**: 2598-2605, 2002.
[8] Manela A., Frankel I. Generalized Taylor dispersion in suspensions of gyrotactic swimming micro-organisms. *J. Fluid Mech.* **490**: 99-127, 2003.
[9] Croze O. A., Sardina G., Ahmed M., Bees M. A., Brandt L. Dispersion of swimming algae in laminar and turbulent channel flows: consequences for photobioreactors. *J. R. Soc. Interface* **10(81)**: 20121041, 2013.
[10] Croze O. A., Bearon R. N., Bees M. A. Gyrotactic swimmer dispersion in pipe flow: Testing the theory. *J. Fluid Mech.* **816**: 481-506, 2017.

STOKESIAN DYNAMICS SIMULATIONS OF A SHEAR-INDUCED AGGREGATION PROCESS: AGGREGATION KINETICS AND CLUSTER MORPHOLOGY

Graziano Frungieri*[1] and Marco Vanni[1]
[1]Department of Applied Science and Technology, Politecnico di Torino, Torino, Italy

Summary We investigate the shear-induced aggregation phenomenon occurring in a dilute suspension of colloidal particles. A Discrete Element Method (DEM) built in the framework of Stokesian Dynamics (SD) is employed. The method takes into account both hydrodynamic and colloidal forces between particles and it is able to simulate in detail each aggregation event occurring in the suspension. Simulations were run coupling the DEM with a Monte Carlo algorithm in order to study the aggregation kinetics and the morphology of a large population of colloidal aggregates.

INTRODUCTION

In a sheared suspension the aggregation of colloidal particles occurs as a result of the binary encounters induced by the gradient of the flow field [1]. However, the occurrence of aggregation is not easily predictable, in that complex interaction between the approaching aggregates establishes; far field and near field (i.e. lubrication) hydrodynamic interactions may in fact deviate the relative aggregate trajectories to the point of preventing the formation of a contact; on the contrary, colloidal interactions (for instance due to Van der Waals attraction forces) act favouring the aggregation.

A detailed view of the aggregation process can be obtained by running Stokesian Dynamics (SD) simulations. This technique, by using a first order multipole expansion of the flow field around each primary particle, allows one to properly model the whole spectrum of the hydrodynamic interaction between particles; for this reason SD has been extensively used to predict aggregation dynamics [2], aggregate restructuring [3] and aggregate breakup [4].

In this work we make use of Stokesian Dynamics, coupled with proper models for the adhesive interactions, to study the aggregation process occurring in a dilute suspension of colloidal particles. To overcome the typically large computational cost of multi-particle Stokesian Dynamics simulations, a Monte Carlo (MC) approach has been developed. The role of the MC algorithm is to sample a statistically expected sequence of encounter events. Each of these events is then individually simulated by Stokesian Dynamics to ascertain the occurrence of aggregation and to obtain the morphology of the new generated aggregate. The advantage of such a combination is that Stokesian Dynamics is used to track the motion of just two aggregates at a time, allowing one to obtain detailed information about the aggregation dynamics at a reasonable computational cost.

NUMERICAL METHOD

We coupled Stokesian Dynamics simulations with an event-driven, rejection-free Monte Carlo algorithm [2]; the MC algorithm is used to reproduce a particular realization of the process through the sampling of a statistically expected sequence of encounter events. To setup the MC algorithm we use the shear-induced Smoluchowski encounter rate $f_{ij} = \frac{4}{3}\dot{\gamma}\left(R_i + R_j\right)^3 / V$, where $\dot{\gamma}$ represents the shear rate intensity, R_i and R_j are the external radii of the considered aggregates and V is the total volume of the suspension. The outcome of the encounter event is ascertained deterministically by using detailed Stokesian Dynamics simulation, counting for both colloidal and hydrodynamic interactions. The calculation scheme is depicted in Figure 1: At the beginning of the simulation, the solid fraction of the suspension, an

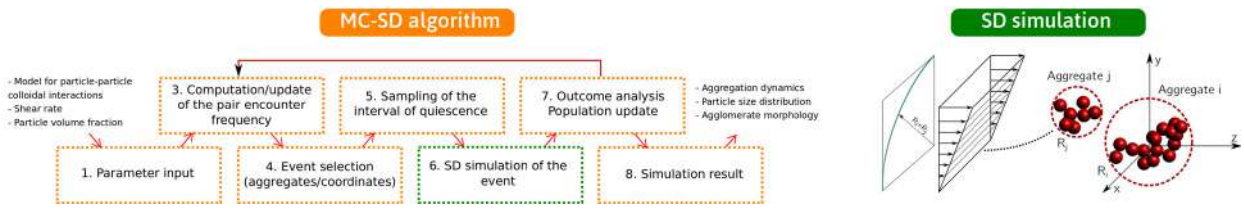

Figure 1: left) Monte Carlo - Stokesian Dynamics algorithm used for the simulation of a shear-induced aggregation process. right) Qualitative representation of a Stokesian Dynamics simulation.

initial distribution for the size and the morphologies of the aggregates and the shear rate conditions are chosen. The simulation is initialized by computing the encounter frequencies relative to all the pairs of suspended particles and, based on these, the details of the encounter are determined, in terms of involved aggregates and initial positions in the flow. At this stage, the Stokesian Dynamics simulation of the event is performed and, based on the outcome, the population is updated and the procedure repeated until the desired number of events is simulated. Between events, an interval of quiescence is imposed. Such an interval represents the time elapsing between two subsequent encounters, during which the population is assumed to remain unaffected.

*Corresponding author. E-mail: graziano.frungieri@polito.it

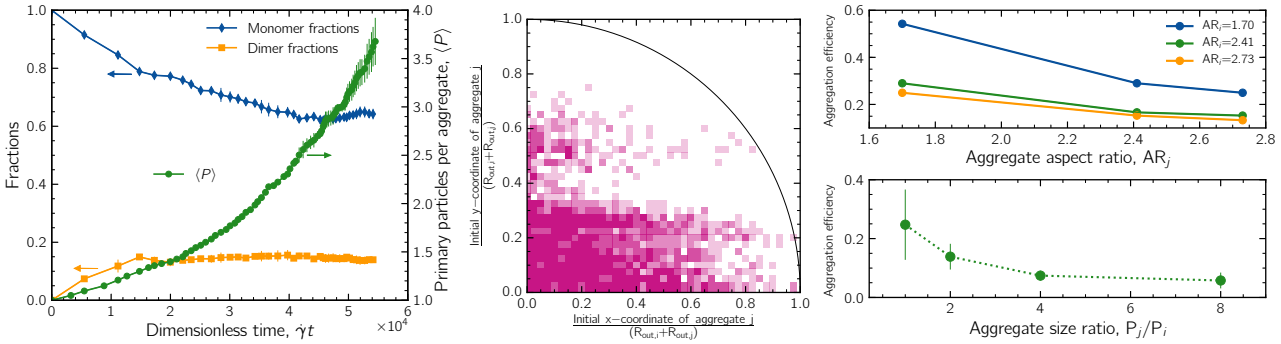

Figure 2: left) Monomer and dimer fractions as a function of time. The green curve reports the temporal trend of the population average size in terms of number of primary particles. middle) Encounter cross section for a pair of aggregates composed by 12 primary particles in uniform shear flow of intensity $\dot{\gamma} = 10\,\mathrm{s}^{-1}$. The shade intensity scales according to the fraction of events turned into an aggregation event. The circumference represents the radius of the theoretical aggregation section. top right) Aggregation efficiency between two aggregates i and j as a function of their aspect ratio. Both aggregate are made by 12 monomers. bottom right) Aggregation efficiency as a function of the aggregate size ratio.

RESULTS AND DISCUSSION

Simulations were run starting from a monodisperse population of 200 simulated primary particles with radius equal to $0.5\,\mu\mathrm{m}$, dispersed in a suspension with a solid fraction equal to 10^{-4} and subject to a uniform shear rate of intensity $\dot{\gamma} = 10\,\mathrm{s}^{-1}$.

The most direct consequence of aggregation is the reduction of the number concentration of the suspended particles and the generation of new, larger aggregates. The left plot in Figure 2 shows the concentration of monomers and dimers as a function of time. As apparent, the monomer concentration drops rapidly in the first stage of the process and a significant fraction of dimers is promptly produced. However, both the classes are still present in a significant amount for long times. This can be explained by the fact that the shear-aggregation dynamics is governed by the larger aggregates, which, once generated, because of their larger cross section, are the most likely to intercept and aggregate other suspended clusters. This is made apparent also by the self-accelerating behaviour of the population average size (green curve). Thus, from the plot one can conclude that, at the end of the simulation, monomers, dimers and other small clusters coexist along with few large aggregates. It is worth to point out however that over a certain size breakup phenomena set in, dampening the aggregate growth.

To obtain further insights into the aggregation dynamics additional Stokesian Dynamics simulations were run according to a grid-based scheme: the encounter cross section (of radius $R_i + R_j$) is divided by using an equally spaced grid. Each node of the grid is used as a release point of an aggregate j, which moves, with the imposed flow field, towards an aggregate i. After scanning the whole grid space, an aggregation cross section can be constructed (middle plot in Figure 2) and the aggregation efficiency evaluated as the ratio between the flow rate of aggregates through the effective aggregation cross section and the flow rate through the aggregation section one would obtain by neglecting hydrodynamic and colloidal interactions. The results of this analysis for the encounter between two aggregates composed by 12 primary particles and with different aspect ratios are reported in the top right plot of Figure 2. It can be noticed that as the aspect ratio of the aggregates increases the aggregation efficiency reduces. This can be explained in the light of a lower time-averaged cross section of elongated aggregates, which reduces the chances of contact. In the bottom right plot of Figure 2 the case of the encounter between two differently sized aggregates is addressed; in this case the size disproportion appeared to be most detrimental factor on the aggregation efficiency. This can be explained by considering that as the size of the aggregates increases a larger disturb is induced in the surrounding flow field; this disturb makes the approaching cluster to substantially deviate from the the rectilinear streamline, finally preventing aggregation.

In conclusion, Stokesian Dynamics have been shown to represent a valuable tool to study the aggregation phenomena occurring in a colloidal suspension. The technique can be used to get precise information about the aggregation mechanism, the morphology of the aggregates and the kinetics of the process. However, the relatively large computational cost suggests to employ such information to fine tune computationally cheaper population balance models.

References

[1] Kusters, K. A., Wijers, J. G., Thoenes, D. Aggregation kinetics of small particles in agitated vessels. *Chem. Eng. Sci.* **52**: 107-121, 1997.

[2] Frungieri G., Vanni M. Shear-induced aggregation of colloidal particles: A comparison between two different approaches to the modelling of colloidal interactions. *Can J. Chem. Eng.* **95**: 1768-1780, 2017.

[3] Seto R., Botet R., Auernhammer G., Briesen H. Restructuring of colloidal aggregates in shear flow. *Eur. Phys. J. E* **35**: 128-140, 2012.

[4] De Bona J., Lanotte A. S., Vanni M., Internal stresses and breakup of rigid isostatic aggregates in homogeneous and isotropic turbulence. *J. Fluid Mech.* **755**: 365-396, 2014.

AN ELASTIC SWIMMER NEAR A BOUNDARY

S. Arman Abtahi[1], Babak Nasouri[2], Saverio E. Spagnolie[3], and Gwynn J. Elfring *[1]
[1]University of British Columbia, Vancouver, British Columbia V6T 1Z4,Canada
[2]Max Planck Institute for Dynamics and Self-Organization,37077 Göttingen,Germany
[3]University of Wisconsin Madison, 480 Lincoln Drive, Madison, WI 53706,USA

Summary In this work we study the trajectories of swimming microorganisms near boundaries. In particular, we explore the effect of shape change due to bending on the trajectories of swimmers near walls. For this analysis we use a simple toy model of a swimmer formed by two spheres linked by a torsional spring. The spheres capture hydrodynamic interactions of a head and tail while the torsional spring allows the swimmer to bend. We see that in the presence of a wall, swimmers can bend leading to substantially altered dynamics and trajectories. We illustrate a number of trajectories varying the initial orientation, geometry and flexibility of the swimmer.

INTRODUCTION

Swimming microorganisms are routinely found near surfaces. Confining surfaces can dramatically alter the trajectories of microswimmers such as bacteria or spermatozoa [1,2] and the interaction between swimmers and a nearby surface may lead to the formation of a biofilm through the attachment of colonist of bacteria to the surface [3]. Far-field hydrodynamics are frequently utilized to explain interactions between a swimmer with nearby boundaries [4,5]. Using this method a number of studies have quantified the dynamics of the swimmers close to walls and have showed that swimmers tend to accumulate walls [6, 7]. Most studies keep the geometry of swimmers fixed despite the fact that many swimmers tend to be quite flexible [8] and flexibility can alter trajectories [9]. In this work we investigate the trajectories of flexible swimmers near boundaries.

MINIMAL MODEL

In order to capture the effects of shape change due to bending, on the trajectories of swimmers, we use a minimal hydrodynamic model. As shown in Figure 1, we use two spheres, one to capture the hydrodynamic drag of a head and another to capture the drag and thrust generated by a tail. Spheres have radii r_B and r_A, for head and tail respectively, and we define the ratio $\lambda = r_A/r_B$. Sphere A propels the swimmer by an imposed fixed thrust $\mathbf{F}_T = F_T\hat{\mathbf{e}}_1$ and is called a pusher for $F_T > 0$ or a puller for $F_T < 0$. The centres of these two spheres are connected by hydrodynamically insignificant thin rods (each length $L/2$) and a linear torsional spring (stiffness k) in the middle. Sphere A is at distance h_A from the wall and we refer to the angle between the unit vector from sphere A to sphere B, $\hat{\mathbf{r}}$, and a unit vector parallel to the wall $\hat{\mathbf{e}}_\parallel$ as the swimming angle θ. The angle between $\hat{\mathbf{r}}$ and the thrust direction $\hat{\mathbf{e}}_1$ is called bending angle δ, which takes positive or negative values corresponding to bending towards the wall or away from the wall, respectively. For simplicity, the sizes of the spheres are assumed to be considerably smaller than the scale of the body ($\beta = r_B/L << 1$). The flow field induced by the motion of each sphere is approximated by a point force Stokeslet, and a source doublet. In order to capture the effect of nearby surface using far-field approximations, the swimmer is assumed to be far away from the wall, $\alpha = L/H_A << 1$, where H_A is the initial distance to the wall. We use image solutions to satisfy the no-slip boundary condition on the wall. Each sphere interacts with the nearby sphere and the nearby wall as if in a background flow field $\mathbf{u}_\infty(\mathbf{x})$ according to Faxén's laws. To leading order the swimmer bends in response to a torque dipole on the swimmer induced by the background flow field.

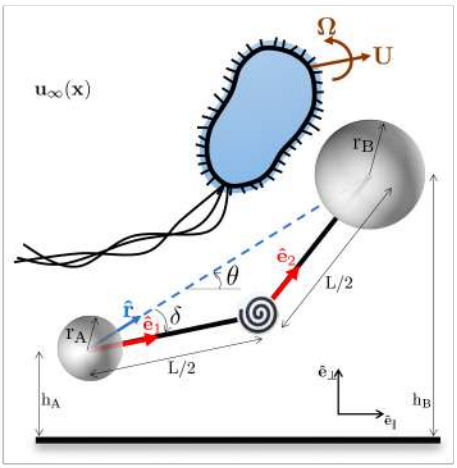

Figure 1: Schematic of the elastic swimmer.

*Corresponding author. E-mail: gelfring@mech.ubc.ca.

RESULTS

We define the initial orientation of the swimmer as θ_i where the thrust is pushing (pulling) the swimmer towards (away from) the wall for $\theta_i < 0$ and away from (towards) the wall for $\theta_i > 0$. Figure 2(a,b) show the contour plots of normal velocity, rotation direction, and bending angle, as a function of the initial orientation θ_i, and the aspect ratio λ for pullers and pushers. The simple picture is that due to hydrodynamic interaction with the wall, a flexible swimmer will bend, a curved swimmer will then experience an angular velocity to direct the swimmer either toward the wall or away from it, for example, when a pusher bends toward the wall $\delta < 0$, the angular velocity re-orients it downward $\Omega < 0$. The grey area in figure 2(a,b) shows the terminus attraction zone after some time, starting at θ_i (the darker grey area is for a rigid swimmer). A straight rigid swimmer ($\delta = 0$ and $k \to \infty$) can maintain a parallel trajectory over long times. On the other hand, elastic swimmers that are initially swimming parallel to the wall, display repulsion or attraction for pushers and pullers respectively. In general swimmers' trajectories tend to have a sensitive dependence on the initial configuration. Figure 2c) shows that a pusher which is initially pointing slightly towards the wall, swims for a long time near the wall with an initial attraction but eventually escapes. In contrast, pullers tend to move towards the wall.

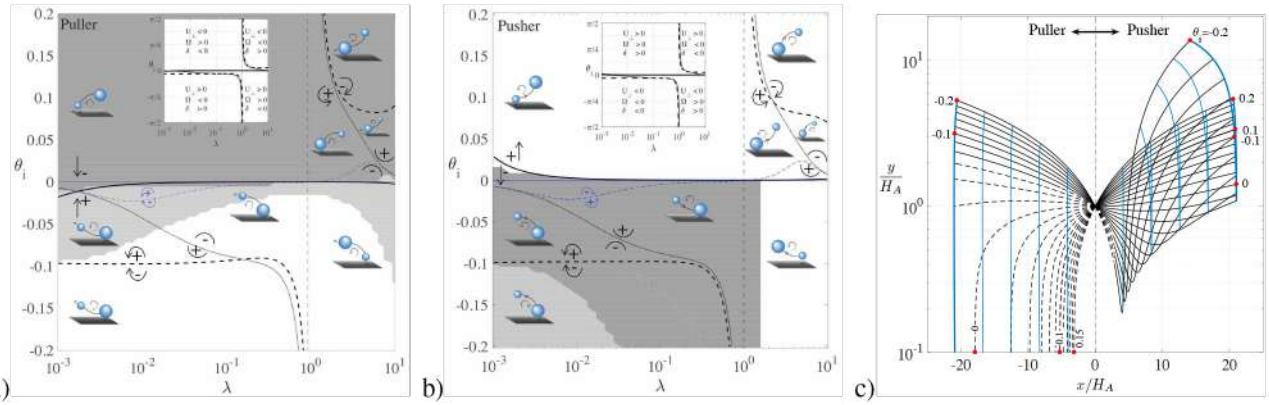

Figure 2: (a,b) Contour plots of normal velocity $\mathbf{U}_\perp = 0$ (solid lines), angular velocity $\mathbf{\Omega} \cdot (\hat{\mathbf{e}}_\parallel \times \hat{\mathbf{e}}_\perp) = 0$ (dashed lines), and bending angle $\delta = 0$ (dotted lines) as a function of aspect ratio λ and initial orientation θ_i. Blue lines are for a rigid swimmer. Grey (white) area is the terminus attraction (escape) zone. (c) Trajectories for initial orientations θ_i. Blue lines correspond to the position of the swimmer after times $t/H_A/U = 1, 2, 3, 4, 5$. Dashed lines in c) correspond to bending towards the wall. Results are obtained for $|F_T|/\mu H_A U = 1, \theta_i = 0, \lambda = 0.1, k/\mu H_A^2 U = 10^{-4}, \alpha = \beta = 0.1$ unless mentioned otherwise.

CONCLUSIONS

Near-wall dynamics of swimmers is a very rich and complex phenomenon. In this paper, we explored the dynamics of an elastic swimmer near a no-slip wall and demonstrated that wall-trapping dynamics of microorganisms can be significantly altered by shape change due to flexibility.

References

[1] Lauga E., DiLuzio W. R., Whitesides G. M., Stone H. A. *Biophys. J.* **90**: 400-412, 2006.
[2] Ezhilan B., Saintillan D. *J. Fluid Mech.* **777**: 482-522, 2015.
[3] O'Toole G., Kaplan H. B., Kolter R. *Annu. Rev. Microbiol.* **54**: 49-79, 2000.
[4] Spagnolie S. E., Lauga E. *J. Fluid Mech.* **700**: 105-147, 2012.
[5] Blake J. R. *Math. Proc. Camb. Philos. Soc.* **70**: 303-310, 1971.
[6] Berke A. P., Turner L., Berg H. C., Lauga E. *Phys. Rev. Lett.* **101**: 038102, 2008.
[7] Lushi E., Kantsler V., Goldstein R.E. *Phys. Rev. E* **96**: 023102, 2017.
[8] Son K., Guasto J.S., Stocker R. *Phys. Rev. E* **96**: 023102, 2017.
[9] Montenegro-Johnson T.D., Gadêlha H., Smith D.J. *Phys. Rev. E* **96**: 023102, 2017.

ELASTIC RINGS SEDIMENTING IN A VISCOUS FLUID

Magdalena Gruziel-Słomka[1], Paweł Kondratiuk[2], Piotr Szymczak[2], and Maria L. Ekiel-Jeżewska*[1]
[1]Institute of Fundamental Technological Research, Polish Academy of Sciences, Pawińskiego 5B, 02-106, Warsaw, Poland
[2]Institute of Theoretical Physics, Faculty of Physics, University of Warsaw, 02-093, Pasteura 5, Warsaw, Poland

Summary Dynamics of elastic rings settling under gravity at low-Reynolds-number are analyzed numerically. The bead model is used with Rotne-Prager-Yamakawa approximation of the hydrodynamic mobility matrix for the beads. Several attracting dynamical modes are found for a wide range of values of the elasto-gravitational number, and for many different initial configurations. The modes are stationary configurations, stationary shapes with the beads moving periodically along the ring, rotating rigid configurations or periodically changing shapes. Very stiff rings are circular and orient vertically. Less stiff ones tend to form almost circular and almost flat structures that are inclined with respect to gravity. Even more flexible rings deform significantly and reach one of several characteristic periodic orbits. Mean sedimentation velocities of different modes in general are different.

INTRODUCTION

Recently, there has been a lot of interest in topology and dynamics of deformable, closed, thin and long elastic chains (here called rings) moving in a viscous fluid. The motivation for developing theoretical models comes from biological systems such as DNA, proteins or ring polymers that spontaneously form similar structures [1, 2, 3]. Moreover, elastic rings can serve as simple models of vesicles, red blood cells [4], or swimming microorganisms, e.g., bacteria or algae [5]. Theoretical models of sedimenting elastic rings help to investigate the influence of gravity on the dynamics of microorganisms, to design new diagnostic tools in medicine and to apply ultracentrifugation to sort proteins or DNA.

SYSTEM AND ITS THEORETICAL MODEL

Here we focus on sedimentation of an elastic unknotted ring. We assume that the Reynolds number is much smaller than unity and that the Brownian motion is negligible. We report our recent results [6] on characteristic attracting dynamical modes and their shapes. Additionally, we evaluate and discuss the corresponding sedimentation speeds. An elastic ring is modeled as a chain of N overlapping identical spherical beads of diameter d. Centers of the consecutive beads are connected by springs of equilibrium length $l_0 = 0.6d$ and a large spring constant $50F_0/d$, where F_0 is a gravitational force, corrected for buoyancy, acting on each of the beads. The harmonic bending potential energy equals to $-\sum_{i=2}^{N-1} A^*\phi_i^2/(2l_0)$, where ϕ_i is the angle between the springs attached to the bead i, and A^* is the bending stiffness. A wide range of values of the stiffness ratio $\tilde{A} = 6 \times 10^4 \times A^*/(F_0 N^3 l_0^2)$ is studied, where $A^*/(F_0 N^3 l_0^2)$ is the inverse elasto-gravitational number. To prevent a chain self-crossing, Lennard-Jones potential energies $\epsilon[(\sigma/r_{ij})^{12} - (\sigma/r_{ij})^6]$ are summed up over non-consecutive beads i, j with center-to-center distances $r_{ij} < 2^{1/6}\sigma$, where $\sigma = d/2$ and $\epsilon = dF_0/4$.

The dynamics is based on the Stokes equations. The motion of center $\boldsymbol{r}_i$ of bead i satisfies $\dot{\boldsymbol{r}}_i = \sum_{i=1}^{N} \boldsymbol{\mu}_{ij} \cdot \boldsymbol{F}_j$, with the force $\boldsymbol{F}_j$ determined from the sum of the spring, bending and Lennard-Jones potential energies presented above, plus the gravitational force (corrected for buoyancy), $\boldsymbol{F}_g = (0, 0, F_0)$. We adopt the Rotne-Prager-Yamakawa approximation for the mobility matrix $\boldsymbol{\mu}_{ij}$ [7] and solve the dynamics numerically.

RESULTS

Initially horizontal circle remains circular and horizontal while sedimenting. Therefore, we start our analysis from evaluating evolution of elastic rings that initially form flat circular rings in elastic equilibria, slightly inclined with respect to the horizontal plane. We observe that an elastic ring tends to one of several attracting orbits, depending on the stiffness ratio $\tilde{A}$. Rings with a large stiffness ratio $\tilde{A}$ after a long time become *vertical* and remain circular. When $\tilde{A}$ decreases, the final stationary shapes become more and more *tilted* from vertical, and deviations from circular and planar shape increase. Then, for even more flexible rings, other attracting modes are observed. In the *swinging* and *flapping* modes, the ring shape changes periodically with time, as illustrated in Fig. 1. One of shapes from each sequence in Fig. 1 is also

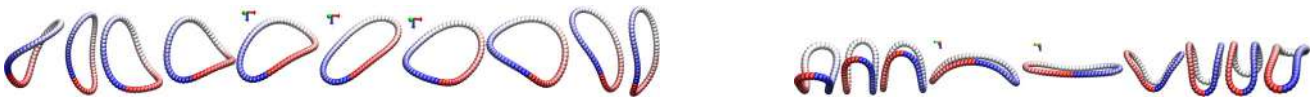

Figure 1: Snapshots from the swinging (left) and flapping (right) modes [6]. Gravity points down.

*Corresponding author. E-mail: mekiel@ippt.pan.pl

shown in Fig. 2a where names of all the modes are associated with certain characteristic shapes. In the *frozen rotating* and *figure eight* modes, the rigid shapes, shown in Fig. 2a, rotate around vertical axis. In the *tank-treading* mode, the beads move periodically along the configuration shown in Fig. 2a. In the *toroidal* modes with *two* or *three coils* ($\mathcal{T}_{2,1}$ or $\mathcal{T}_{3,1}$), the beads swirl in the poloidal direction and rotate in the toroidal direction, i.e., around vertical axis. In Fig. 2a, we also demonstrate that for the chosen class of the initial configurations, the smaller $\tilde{A}$, the more compact is the ring, with the smaller radius $\bar{R}_g$ of gyration (evaluated with respect to the center-of mass), averaged over many periods. Here $R_0 = Nl_0/(2\pi)$ is the radius of the initially circular and inclined ring.

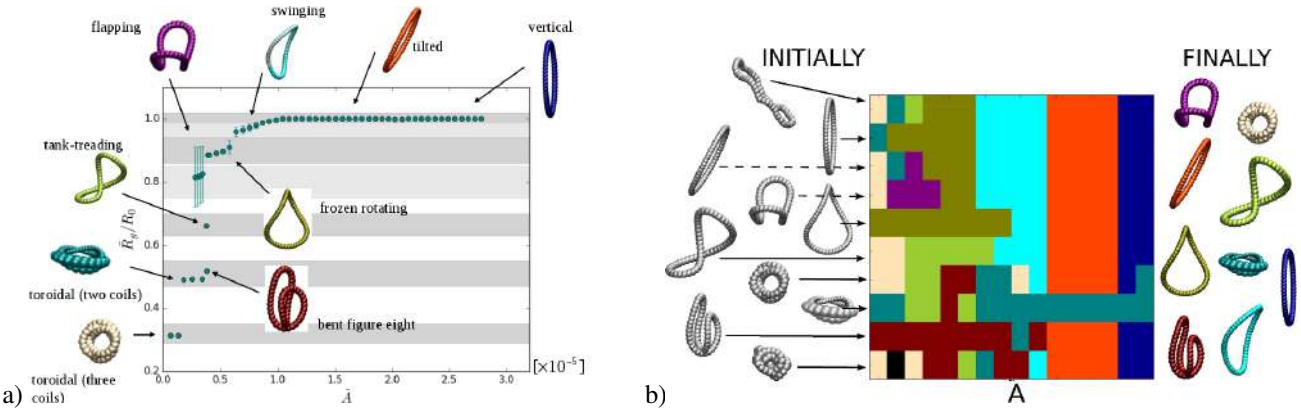

Figure 2: Shapes of sedimenting elastic rings, characteristic for different attracting dynamical modes with $N = 60$ and different values of the stiffness ratio $\tilde{A}$ [6]. Gravity points down except the toroidal, three coils mode for which it points towards the reader. The initial configurations are: a) flat circular ring in elastic equilibrium, inclined by $\beta_0 = 16^\circ$ to the horizontal plane; b) characteristic shapes from the attracting dynamical modes, shown in panel a). In panel b), $\tilde{A} \in [0.23, 2.37]$, with a nonlinear scale shown in Fig. 20 of Ref. [6].

In Fig. 2b, we present simulations performed for another family of initial conditions. Each row in Fig. 2b corresponds to an initial configuration (indicated by arrow), that appeared in a different long-time dynamical mode shown in Fig. 2a. The colors correspond to the final stages of the evolution, shown at the right. The initial configuration in the last row and black color of the final stage correspond to an irregular coil.

The results shown in Fig. 2 illustrate very rich dynamics of sedimenting elastic loops. We have found many different attracting dynamical modes for the stiffness ratio $0.1 \leq \tilde{A} \leq 2.5$. Moreover, for a given value of $\tilde{A}$, different modes can emerge from different initial configurations. To complete the analysis performed in Ref. [6], we have also evaluated and analyzed sedimentation speeds of elastic loops in different modes, and for different values of $\tilde{A}$. Shapes, gyration radii and sedimentation velocities of elastic rings from the same mode only weakly depend on the stiffness ratio $\tilde{A}$, but in general they are significantly different for different dynamical modes observed for the same value of $\tilde{A}$. For example, as shown in Fig. 2b, a very compact shape of the toroidal mode with two coils has been observed in a wide range of the stiffness ratio, coexisting with almost circular vertical and tilted modes for $\tilde{A} \geq 1.22$. A more compact toroidal mode with three coils has been also detected for larger values of $\tilde{A}$. As the result, for a larger value of $\tilde{A}$, gyration radii and sedimentation velocities of different modes can differ even as much as by a factor of 3 and 2, respectively.

We analyzed dynamics of elastic loops made of different numbers of beads N. For $N > 15$, elastic rings behave similarly in similar ranges of the stiffness ratio $\tilde{A}$, i.e., in similar ranges of the elasto-gravitational number. This finding indicates that the attracting dynamical modes described here are generic for dynamics of very elastic sedimenting rings.

ACKNOWLEDGMENTS

M. G.-S. and P. S. were supported in part by Narodowe Centrum Nauki under grant 2015/19/D/ST8/03199. The VMD package [8] was used to visualize shapes.

References

[1] Stasiak A., Katritch V., Bednar J., Michoud D. and Dubochet J. Electrophoretic mobility of DNA knots. *Nature* **384**, 122, 1996.
[2] Ercolini E., Valle F., Adamcik J., Witz G., Metzler R., Rios P. D. L., Roca J. and Dietler G. Fractal Dimension and Localization of DNA Knots. *Phys. Rev. Lett.* **98**: 058102, 2007.
[3] Poier P., Likos C. N., Moreno A. J. and Blaak R. An Anisotropic Effective Model for the Simulation of Semiflexible Ring Polymers. *Macromolecules* **48**: 4983-4997, 2015.
[4] Jay A. W. L. and Canham P. B. Sedimentation of single human red blood cells. Differences between normal and glutaraldehyde fixed cells. *J. Cell. Physiol.* **80**, 367372, 1972.
[5] Rizvi M. S., Farutin A. and Misbah C. Three-bead steering microswimmers. *Phys. Rev. E* **97**: 023102, 2018.
[6] Gruziel-Słomka M., Kondratiuk P., Szymczak P. and Ekiel-Jeżewska M. L. Stokesian dynamics of sedimenting elastic rings. *Soft Matter* **15**: 7262-7274, 2019.
[7] Rotne J. and Prager S. Variational treatment of hydrodynamic interaction in polymers. *J. Chem. Phys.* **50**, 48314837, 1969.
[8] Humphrey W., Dalke A. and Schulten K. VMD: visual molecular dynamics. *J. Mol. Graphics* **14**: 33-38, 1996.

SURPRISING HYDRODYNAMICS OF BACTERIA NEAR SURFACES

Debasish Das*and Eric Lauga
Department of Applied Mathematics and Theoretical Physics, Centre for Mathematical Sciences, University of Cambridge, Wilberforce Road, Cambridge CB3 0WA, UK.

Summary Recent experiments [1] have shown that a sulfide-oxidizing bacterium named *T.majus* can transition from swimming in circles to a surface-bound state where it stops swimming while remaining free to move laterally along the surface. In this bound state, the cell rotates perpendicular to the surface with its flagella pointing away from it. Using simulations and theory, we demonstrate the existence of a fluid-structure interaction instability that causes cells with relatively short flagella to become surface bound [2]. In both the bound and dynamic states, we find that bacterium gets attracted to the wall consistent with far-field force dipole assumption [3]. However, on simply changing the shape of the cell body from a sphere *T.majus* to a prolate spheroid, relevant for cells such as *E.coli*, we find that the cell swims in circular trajectories but at a certain height above the surface.

INTRODUCTION

Bacteria are one of the most important life-forms on Earth. Being one of the first organisms to have appeared on the planet, they have evolved to thrive in a variety of environments. Peritrichous (multi-flagellated) bacteria, such as *T. majus* or *E. coli*, self-propel in fluids by using specialized rotary motors to rotate multiple helical filaments, enabling swimming of the whole cell. In the present work, we focus on the surface interactions mechanisms of bacteria such as *T. majus* that have a large spherical cell body compared to their flagellar length, in contrast with *E. coli* that have a relatively smaller but elongated prolate-spheroidal cell body.

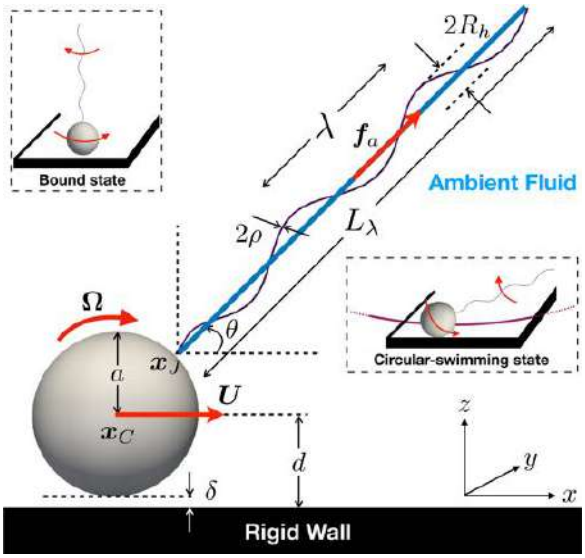

Figure 1: Schematic diagram of a flagellated bacterium swimming near a plane surface. The cell body is modeled as a rigid sphere (case of *T. majus* bacteria) or a prolate spheroid (*E. coli*) and the flagellar filament as a rigid right-handed (*T. majus*) or a right-handed (*E. coli*) helix rotating along its axis for the numerical simulations. The cell body undergoes rigid body translation and rotation at velocities $\boldsymbol{U}$ and $\boldsymbol{\Omega}$, respectively. The flagellum tilt angle is denoted by θ. The two possible final steady states of a bacterium near a surface are shown as insets: surface-bound (top left) and circular swimming (bottom right).

In recent experiments, the swimming behavior of *T. majus* cells was studied near surfaces [1]. Quite surprisingly, it was found that instead of swimming along the surface in circles (as well established for many species), many freely swimming cells became dynamically surface-bound. In this bound state, cells remained free to move laterally along the surface and their bodies continuously rotated around their center in the direction perpendicular to the surface while their flagellar filaments pointed away from the surface, rotating in the opposite direction. The bound state is in stark contrast to the classical situation of bacteria swimming in circular paths near surfaces [4]. The question therefore arises regarding the mechanism at the origin of this transition to a bound state.

Mathematically, we define the cell to be in the surface-bound state when the flagellum axis is perpendicular to the surface, i.e. $\theta = \pi/2$ (Fig. 1), and consequently, the radius of circular trajectory is $R = 0$. In the bound state, a small perturbation in the tilt angle of the flagellum is expected to destabilize the cell and cause it to swim parallel to the surface in circles. What exactly makes this state stable? Using a combination of theory and simulations, we show that the transition from swimming to a bound state can be rationalized as an instability due to fluid-structure interaction. We then focus on the question: how does changing the shape of the cell body from a sphere to a prolate spheroid change these swimming dynamics near surfaces?

BIOMECHANICAL MODELING

The fluid dynamics of bacteria are described by the incompressible Stokes equations solved using a combination of slender body theory [5, 6] and boundary element method [7]. *T. majus* cells rotate in a counterclockwise direction when viewed from the posterior side, which motivates us to model the fraction of flagella on the cell-surface that cause propulsion bundled together as a single right-handed clockwise rotating helix in the numerics, or as a rigid active pushing rod for the theory (details of the theory can be found in Ref. [2]). This assumption holds particularly well for *E. coli* as their flagella are known to be in a bundled configuration when swimming. The cell body of *T. majus* is assumed to be a sphere of radius a, also chosen as the relevant length scale for the problem. For *E. coli* cells, we have an additional dimension for body width, $b = \alpha a$, where α is the cell body aspect ratio. The cell body is centered at $\boldsymbol{x}_C$ while the

*Corresponding author. E-mail: dd496@cam.ac.uk.

flagellum is attached to the cell body surface at the junction point, $\boldsymbol{x}_J$ (Fig. 1). The minimum distance between the cell-body surface and the plane rigid wall is δ and the distance between the center of the cell-body and the wall is $d = a + \delta$. The tilt angle of the flagellum measured with respect to the horizontal direction is denoted by θ, so that $\theta = \pi/2$ and $\theta \neq \pi/2$ correspond to surface-bound and circular-swimming state, respectively.

RESULTS AND CONCLUSIONS

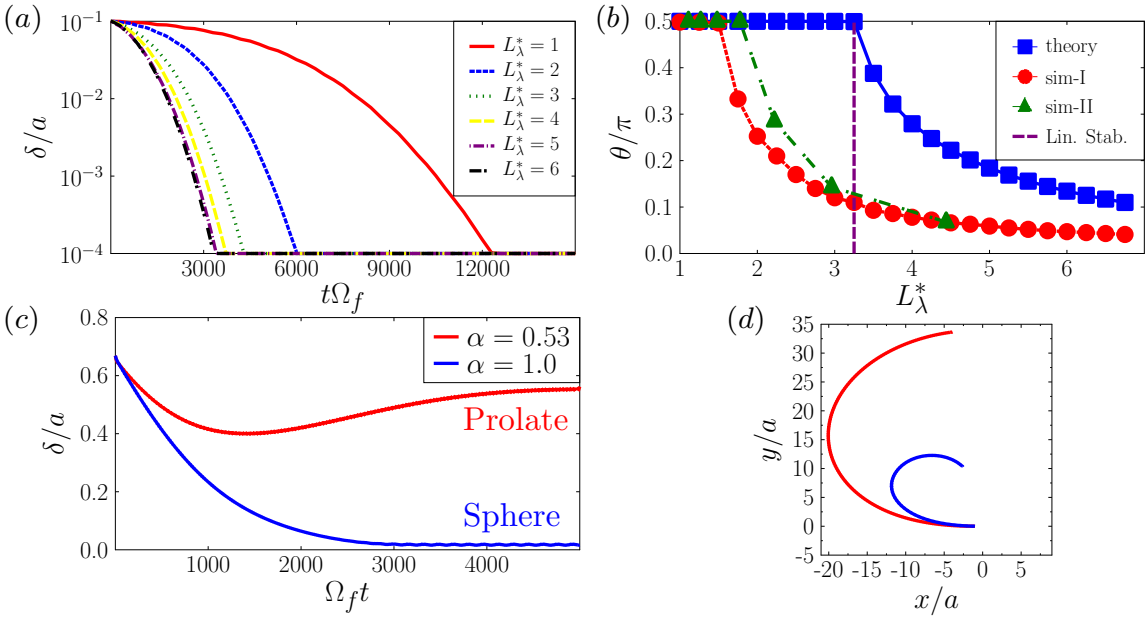

Figure 2: (a) Temporal evolution plot of δ/a for various flagellar lengths L_λ^*; (b) Pitchfork bifurcation of the tilt angle, θ/π, plotted against the flagellum axial length, L_λ^*; (c) temporal evolution of δ/a for a swimming bacterium with spherical and prolate-spheroidal cell body; (d) trajectories in the $x - y$ plane corresponding to (c).

In the numerical simulations, the cell body is placed at a distance $\delta^* = 0.1$ from the wall with its flagellar filament initially parallel to the wall ($\theta = 0$). The geometrical parameters of the flagellar filament are assumed to be similar to that of *E. coli*. In the first set of simulations (sim-I), the axial length of the filament is varied from $L_\lambda = 1.0\,\mu\text{m}$ to $6.75\,\mu\text{m}$ while the cell body radius is fixed at $a = 1\,\mu\text{m}$. In the second set of simulations (sim-II), we fix the number of turns at $N = 2$ and axial length at $L_\lambda = 4.44\,\mu\text{m}$ while the cell body radius is varied from $a = 1\,\mu\text{m}$ to $4\,\mu\text{m}$. We plot in Fig. 1a the dynamics of $\delta(t)$ for six values of the flagellum length, L_λ^*, for sim-I. In each case, the cell gets attracted to the wall regardless of the flagellar filament length. As the cell gets closer to the wall, the coupling between translation and rotation becomes stronger which causes the filament to tilt away from the wall, see Fig. 1b. This tendency to tilt away from the wall due to cell body-wall interaction is resisted by the viscous torque experienced by the translating flagella as well as an attractive torque that tends to align the helix parallel to the wall arising from helix-wall hydrodynamic interactions. As a result, the tilt angle reaches a dynamical steady state whose value depends on L_λ^*. Hence, a large ratio of cell body size to flagellar length can cause a transition from circular swimming along the surface to a bound state.

The results in Fig. 2a & b are obtained using a semi-analytical approach [2], while those in Fig. 2c & d are obtained using a full boundary element method. Here, we show next that on simply changing the shape of the cell body from a sphere (relevant for *T. majus*) to a prolate spheroid (relevant for *E. coli*), the cells swimming parallel to the surface in circular trajectories do so at a finite height above the surface of magnitude similar to the width of the body (Fig. 2(c)). The trajectories viewed from above the surface are shown in Fig. 2(d). This is a rather surprising result as bacteria are force-free organisms and, as force-dipoles swimming in a fluid medium, they should always be attracted towards no-slip surfaces [8]. Similar observations were made in a previous work [9] but only for $\alpha < 0.7$. The development of a simple mathematical model to explain these curious findings is under progress.

References

[1] A. P. Petroff, X.-L. Wu, and A. Libchaber, Phys. Rev. Lett. **114**, 158102 (2015).
[2] D. Das and E. Lauga, Phys. Rev. E **110**, 043117 (2019).
[3] S. E. Spagnolie, E. Lauga, J. Fluid Mech. **700**, 105–147 (2012).
[4] E. Lauga, W. R. DiLuzio, G. M. Whitesides, and H. A. Stone, Biophys. J. **90**, 400 (2006).
[5] J. Dauparas, D. Das, and E. Lauga, Biomicrofluidics **12**, 014108 (2018).
[6] E. E. Riley, D. Das, and E. Lauga, Sci. Rep. **8**, 10728 (2018).
[7] D. Das and E. Lauga, Soft Matter **14**, 5955 (2018).
[8] A. P. Berke, L. Turner, H. C. Berg and E. Lauga, Phys. Rev. Lett. **101**, 038102 (2008).
[9] D. Giacche, T. Ishikawa and T. Yamaguchi, Phys. Rev. E **82**, 82, 056309 (2010).

THE SEDIMENTATION OF CLOUDS OF SPHERICAL PARTICLES IN VORTICAL FLOWS

Laurence Bergougnoux*[1], Benjamin Marchetti[1], and Elisabeth Guazzelli[2]
[1]Aix Marseille Univ, CNRS, IUSTI, Marseille, France 2MSC, CNRS, University of Paris, Paris, France

Summary We present a jointed experimental and numerical study examining the influence of vortical structures on the settling of clouds of solid spherical particles under the action of gravity at low Stokes numbers. The two-dimensional model experiments use electroconvection to generate a two-dimensional array of controlled vortices which mimics a simplified vortical flow. The motion of the clouds are tracked when settling through this vortical flow. The interplay between the multibody particle interactions and the interaction between the particles and the spatial structures of the flow is examined by comparing the experimental cloud dynamics to the predictions of point-particle numerical simulations.

INTRODUCTION

In many natural phenomena or industrial applications, heavy particles are transported in complex flows. The flow structures may happen to promote the stirring and dispersion of the particles. But the opposite can also take place and the flow configuration may contribute to the focussing and accumulation of particles within specific regions of the flow. A typical example in the natural environment is the observed patchiness of plankton concentration caused by wind-induced Langmuir cells occurring at the surface of lakes and oceans. The objective of this work is to examine the settling of a collection, i.e. a cloud, of solid spherical particles through the local spatial structures of the flow, i.e. large vortices. The key question is whether this cloud maintains a cohesive entity or disintegrates and spreads when settling through this complex flow structure. The present work considers a simple vortical flow, specifically a cellular flow consisting of counter-rotating vortices, which is a model flow capturing key features of vortical effects on the particles. It addresses the interaction of these controlled vortices with the individual particles of the settling cloud as well as the particle interactions between themselves. The focus here is on flow regimes ranging for negligible to small but finite inertia but at low Stokes numbers.

EXPERIMENTS

Following [1], we use electroconvection to generate a two-dimensional array of controlled vortices and track settling clouds using a set of synchronized cameras located below and in front of the cell as depicted in figure 1 (a). The transparent cell is filled with an aqueous mixture of citric acid (UCON® oil can be added to increase the viscosity). The magnetic field is generated by a checkerboard of magnets placed behind the back wall of the cell. The electric current is created by two electrodes placed on the opposite small sides of the cell. The coupling between the magnetic field and the uniform electric current gives rise to an electromagnetic force in the fluid. The flow generated by this force is a periodic flow of counter-rotating vortices that is characterized by particle image velocimetry (PIV). Clouds are prepared by mixing a weighted amount of spherical particles with the same fluid as that filling the cell. Different fluids and particles (polystyrene or polymethyl methacrylate spheres having different radii, $a = 70, 115$, and $175\,\mu$m) are used to explore regimes going from that of Stokes to that of small inertia. The clouds are injected at the top of the cell and their time-evolution can be tracked when settling through the vortices.

NUMERICAL MODELING

We adopt the simplest model containing the minimum physics to describe the problem. At low Reynolds number, the particles of the clouds are represented by identical point forces. The velocity of a given sphere is then its own terminal velocity (such as when the single particle falls in a quiescent fluid) incremented by the local fluid velocity [2] and the sum of the velocity disturbances (only represented by its far-field portion, i.e. the Stokeslet) coming from the other particles [3, 4]. When inertia becomes finite, the crudest approximation is to replace the far-field Stokes interactions between the particles by the steady far-field Oseen interactions (i.e. the Oseenlet), i.e. assuming steady Oseen wake interactions between the particles [5, 6].

RESULTS AND COMPARISON

When settling in a quiescent fluid in the Stokes regime (i.e. regime of negligible inertia), a cloud of spheres remains first roughly spherical with a leakage of particles in a vertical tail and then evolves into a torus. After falling at least 500 times its radius, it can become unstable and break up into secondary droplets which deform into tori themselves and break

*laurence.bergougnoux@univ-amu.fr

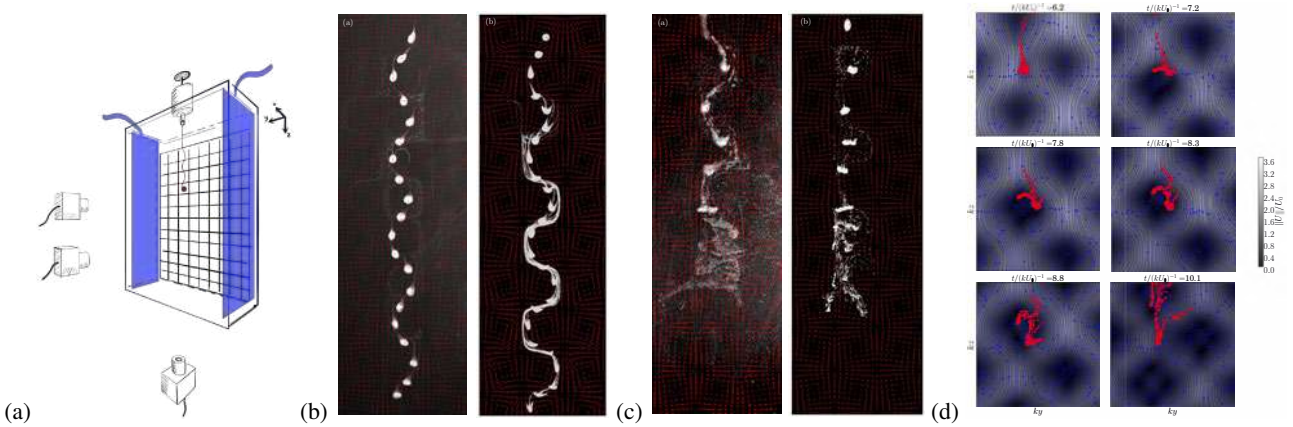

Figure 1: (a) Sketch of the experimental apparatus. (b) Comparison of the experimental (left) and numerical (right) chronophotographies of a cloud in the Stokes regime. (c) Comparison of the experimental (left) and numerical (right) chronophotographies of a cloud in a finite-inertia regime. The time between successive photos is kept constant (2 s in the experiments and a corresponding interval in the simulations) in order to indicate the difference in velocities along the trajectory. (d) Cloud break-up in the inertial regime: flow field computed at successive times in the vertical plane in the cloud reference frame for a typical Oseenlet simulation. High (low) velocity is indicated in white (dark). The quasi periodic structure of counter-rotating vortices has a velocity U_0 and a spatial wavenumber k.

in a repeating cascade. The key feature of this Stokes cloud is the chaotic motion of the particles which leads to escapes from the cloud toroidal circulation and to particle leakage [3, 4]. When inertia is small but finite, the cloud deforms into a flat torus that eventually destabilizes and breaks up into a number of secondary droplets but particle leakage is much weaker. The inertial cloud evolution is strongly determined by the importance of Oseen-wake-mediated interactions [5, 6].

When the cloud settles in the vortical flow in the Stokes regime, it follows the downstream flow of the successive vortices and displays zigzagging motions due to the modulations caused by the periodic cellular flow as illustrated in figure 1 (b). It does not maintain a spherical shape as it is slightly stretched in the elongational region of the flow, in particular close to the stagnation points surrounding the purely rotational regions at the centers of the vortices. A significant leakage of particles at the cloud rear is observed. The small particles released into the vortical flow can become trapped inside the vortices. Break-up does not occur as the travel distance of the cloud is not long enough. Similar qualitative evolution is found by the point-particle simulation using the Stokeslet approximation. When inertia is increased and becomes finite, the flow structure induces a stronger cloud deformation as evidenced in figure 1 (c). The cloud eventually widens in the elongational portions of the flow and breaks into multiple pieces. Point-particle simulations using an Oseenlet (instead of Stokeslet) approximation can capture this phenomenon.

A more quantitative comparison between experiments and simulations can be obtained by examining the time evolution of the vertical and horizontal coordinates of the cloud centre of mass as well as quantities such as the cloud projected surface in the horizontal plane normalized by its initial value. Point-particle simulations, which contain the minimal physics to describe the coupling between particle-particle and particle-flow interactions, capture well the cloud dynamics. A significant leakage of particles is observed at the rear of the clouds. It is greatly amplified by the vortical flows by comparison with clouds settling in quiescent fluids. It is also intensified when inertia is increased and becomes finite.

An important output of the present work is that the vortical structures induce a faster break-up of the clouds into multiple shatters in the finite inertia case. This phenomenon is evidenced by visualizing the flow field surrounding the cloud in the cloud reference frame for a typical Oseenlet simulation, see figure 1 (d). The cloud successively expands and contracts when falling in the consecutive upward and downward, respectively, elongational portions of the flow. When inertia is finite, the oscillation between the expansion and contraction phases is no longer reversible and the cloud expansion becomes stronger. When the cloud reaches an upward elongational region of the flow wherein there is a slow-down of the velocity, break-up then happens as the widened cloud winds around the vortical structure. The remaining pieces of the cloud spread in the flow structures and can undergo the same break-up process.

References

[1] Bergougnoux L., Bouchet G., Lopez D. & Guazzelli É. The motion of solid spherical particles falling in a cellular flow field at low Stokes number. *Phys. Fluids* **26**: 093302-15, 2014.

[2] Stommel H. Trajectories of small bodies sinking slowly through convection cells. *J. Mar. Res.* **8**: 24-29, 1949.

[3] Nitsche J. & Batchelor G. Break-up of a falling drop containing dispersed particles. *J. Fluid Mech.* **340**: 161-175, 1997.

[4] Metzger B., Nicolas M. & Guazzelli É. Falling clouds of particles in viscous fluids. *J. Fluid Mech.* **580**: 283-301, 2007.

[5] Subramanian G. & Koch D. L. Evolution of clusters of sedimenting low-Reynolds-number particles with Oseen interactions. *J. Fluid Mech.* **603**: 63-100, 2008.

[6] Pignatel F., Nicolas M. & Guazzelli É. A falling cloud of particles at a small but finite Reynolds number. *J. Fluid Mech.* **671**: 34-51, 2011.

THE EFFECT OF SURFACE ATTACHMENT OR GRAVITATIONAL TETHERING ON PLANKTONIC FEEDING FLOWS

Anders Andersen[1*] and Thomas Kiørboe[1]
[1]National Institute of Aquatic Resources and Centre for Ocean Life, Technical University of Denmark, DK-2800 Kgs. Lyngby, Denmark

Summary We use a simple low Reynolds number flow model to examine and explain the effect of attachment or gravitational tethering on the flow in interception feeding plankton. We show that under general assumptions it is favourable to be freely swimming instead of tethered to a surface or gravitationally attached since the resulting feeding flow past the cell is more intense, leading to a larger clearance rate.

INTRODUCTION

Marine zooplankton feed in a nutritionally dilute environment. To enhance prey clearance rates many species swim through the water or create a feeding current. Many species are non-motile when feeding, either due to gravitational tethering (many copepods) or by direct attachment to a surface (many unicellular organisms). Several authors have independently suggested that attachment or gravitational tethering leads to a more efficient feeding flow [1-5], whereas two recent computational fluid dynamics (CFD) studies of attached and freely swimming choanoflagellates have suggested the opposite, that freely swimming flagellates have higher clearance rate than those attached to a surface [6, 7]. What causes this difference is not evident. Here, we use an analytical flow model to explore and quantify the effect of attachment on the prey encounter rate of the feeding flow in an interception feeding model flagellate, and we show that free swimming is superior to attachment in terms of clearance rate.

POINT FORCE MODEL

To model and compare feeding flows of tethered and freely swimming planktonic organisms we apply a flow model based on the Oseen solution for the low Reynolds number flow due to a point force next to a solid sphere [8-10]. As model organism, we consider a uniflagellate pulled by a single flagellum (figure 1a). The thrust force $\boldsymbol{T}$ represents the force on the flagellum from the water whereas the force $\boldsymbol{F}$ represents the force from the flagellum on the water. The force $\boldsymbol{F}$ gives rise to a flow past the no-slip sphere that represents the spherical cell body, and the resulting stress on the surface of the cell leads to the force $\boldsymbol{K}$ that is opposite to the thrust force and smaller in magnitude. If the cell is tethered, the stalk provides an external force that holds the cell in place and the flow past the cell is simply the flow due to the force $\boldsymbol{F}$. In the case of a freely swimming cell, the flagellum pulls the cell through the surrounding water with a constant velocity $\boldsymbol{U}$ that is determined such that the resulting Stokes drag $\boldsymbol{D}$ makes the net force on the model flagellate vanish.

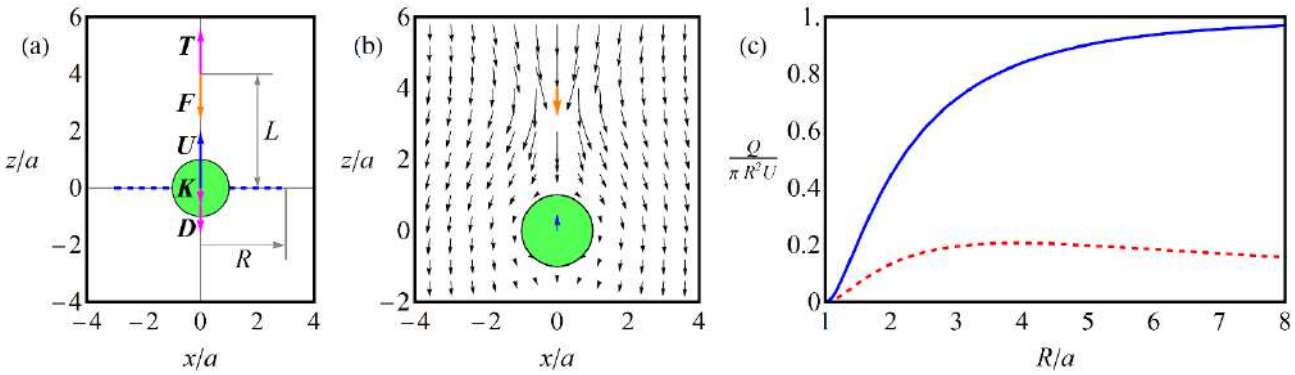

Figure 1. Point force model, flow field, and prey clearance rate. (a) Point force model and prey encounter zone of freely swimming flagellate. The thrust force $\boldsymbol{T}$ represents the flagellum that pulls the spherical cell (green) with velocity $\boldsymbol{U}$. The radius of the cell is denoted a, and the thrust force acts at a distance $L = 4\,a$ from the centre of the cell. The annular prey encounter zone in the equator plane (blue, dashed) represents tentacles extending form the cell and has outer radius R. (b) Velocity field relative to the cell when the model flagellate is freely swimming. (c) Clearance rate as function of the outer radius of the prey encounter zone when the model flagellate is tethered (red, dashed) and freely swimming (blue, solid), respectively.

*Corresponding author. E-mail: aanders@aqua.dtu.dk

FEEDING FLOW AND CLEARANCE RATE

The flow relative to the cell body of the freely swimming flagellate is directed backwards, and it is most intense past the front half of the surface of the cell (figure 1b). Depending on the detailed morphology of the flagellate, prey particles may be intercepted by the flagellate either directly on the cell body or on tentacles extending from it. Here we consider an annular encounter zone of outer radius R in the equator plane around the cell (figure 1a), and we assume that the clearance rate is equal to the flow rate Q relative to the cell and through the annular encounter zone. The flow rate Q depends on the outer radius R of the encounter zone, but it is always larger by at least a factor of three when the flagellate is freely swimming in comparison with the tethered situation (figure 1c).

DISCUSSION

In contrast to the commonly accepted view [1-5], our model demonstrates that tethering decreases rather than increases the clearance rate of interception feeding zooplankton, consistent with the recent CFD simulations of tethered and freely swimming choanoflagellates [6, 7]. The clearance rate of a zooplankton organism of course depends on the detailed architecture of the flow generation apparatus and the structures on which prey particles are intercepted. Our simple model relies on the assumption that the flagellum generates the same force whether or not the flagellate is tethered or freely swimming, and we further assume that the prey encounter zone is at rest relative to the cell. Our presumption is that our qualitative conclusion is correct as long as these two key assumptions are satisfied, and that it is therefore valid for a large class of ecologically significant zooplankton.

FUNDING

This work is supported by The Independent Research Fund Denmark (grant no. 7014-00033B) and by the Villum Foundation through the Centre for Ocean Life.

References

[1] J. R. Strickler, Calanoid Copepods, Feeding Currents, and the Role of Gravity, Science **218**, 158-160 (1982).
[2] R. B. Emlet and R. R. Strathman, Gravity, Drag, and Feeding Currents of Small Zooplankton, Science **228**, 1016-1017 (1985).
[3] T. Fenchel, Protozoan Filter Feeding, Progress in Protistology **1**, 65-113 (1986).
[4] P. Tiselius and P. Jonsson, Foraging behaviour of six calanoid copepods: observations and hydrodynamic analysis, Mar. Ecol. Prog. Ser. **66**, 23-33 (1990).
[5] K. K. Christensen-Dalsgaard and T. Fenchel, Increased filtration efficiency of attached compared to free-swimming flagellates, Aquat. Microb. Ecol. **33**, 77-86 (2003).
[6] J. B. Kirkegaard and R. E. Goldstein, Filter-feeding, near-field flows, and the morphologies of colonial choanoflagellates, Phys. Rev. E **94**, 052401 (2016).
[7] H. Nguyen, M. A. R. Koehl, C. Oakes, G. Bustamante, and L. Fauci, Effects of cell morphology and attachment to a surface on the hydrodynamic performance of unicellular choanoflagellates, J. R. Soc. Interface **16**, 20180736 (2019).
[8] C. W. Oseen, Neuere Methoden und Ergebnisse in der Hydrodynamik (Akademische Verlagsgesellschaft Leipzig, 1927).
[9] H. Jiang, T. R. Osborn, and C. Meneveau, The flow field around a freely swimming copepod in steady motion. Part I: Theoretical analysis, J. Plankton Res. **24**, 167-189 (2002).
[10] J. Dölger, T. Bohr, and A. Andersen, An analytical model of flagellate hydrodynamics, Phys. Scr. **92**, 044003 (2017).

THE EFFECT OF LOCAL FLUID RHEOLOGY ON PHORETIC MODES

Patrick S. Eastham[1] and Kourosh Shoele*[2]
[1]Department of Mathematics, Florida State University, Tallahassee, FL, USA
[2]Department of Mechanical Engineering, Florida State University, Tallahassee, FL, USA

Summary Many micro-swimmers, either biological or artificial, affect the local environments through which they move. For bacteria, this is done through feeding on surrounding nutrients; for micro-robots, this is done through surface heat dissipation or chemical reaction as a byproduct of swimming actuation. These mechanisms have the theoretical potential to alter the local material properties of the surrounding fluid. This raises the question of whether it is possible for a swimmer to modify local fluid rheology in order to enhance its locomotion. Our work intends to answer this question by providing asymptotic and numerical categorization of the effect of different modes of swimming. Additionally, experimental exploration of the role of a fluid's local rheology on swimming performance is an active area of research, and our analysis should aid in the interpretation of experimental results.

INTRODUCTION

In published work over the past several years, we have investigated the role of nutrient-dependent viscosity on the swimming and feeding performance of microswimmers [2]. To introduce variable viscosity, we assume that the fluid is governed by a variable-viscosity Stokes equation and the nutrient is transported by an advection-diffusion equation. The coupling of these PDEs is through the nutrient-dependent viscosity:

$$\mu\big(c(\mathbf{x})\big) = \mu_0\left[1 + k\,c(\mathbf{x})^{\xi}\right] \tag{1}$$

where μ_0 is the far-field viscosity, k measures the sign and strength of the coupling, and ξ governs the nonlinearity of the relationship. The form of the nutrient-dependent viscosity is chosen in the form of a "power-law" so that it may capture both the strength and sign of the coupling as well as the potentially non-linear relationship between concentration and viscosity. All of these components are well-motivated, as demonstrated in Fig. 1(c), by comparisons to real-world materials.

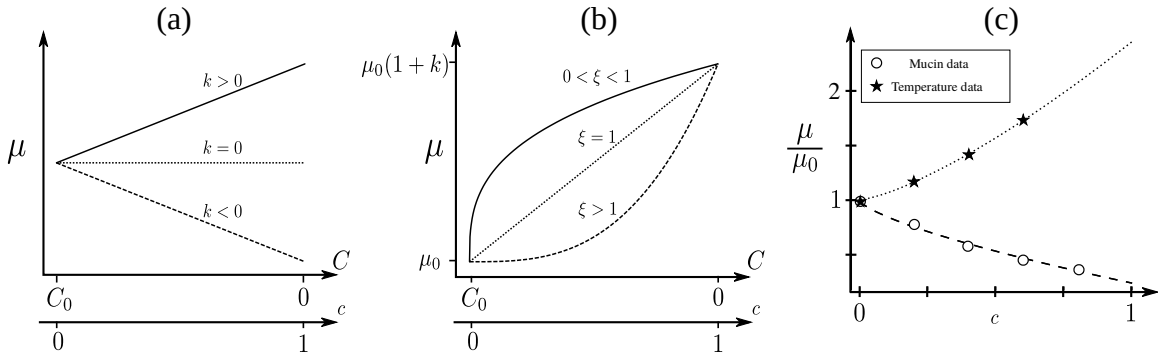

Figure 1: The nutrient-viscosity relationship for (a) various k, fixed $\xi = 1$, and (b) various ξ, fixed $k > 0$, and (c) fit to two real materials, using Eq. 1. Fitting the data for viscosity vs. concentration of Mucin, a protein, gives $k = -0.76$ and $\xi = 0.70$ [3]; fitting the data for viscosity vs. water temperature gives $k = 1.45$ and $\xi = 1.35$ [1]. The power-law coefficient ξ determines the nonlinearity of relationship, while the magnitude and sign of k determines the strength of the relationship and whether the viscosity increases or decreases near the surface of the squirmer ($C = 0$, $c = 1$), respectively. Note that C is the dimensional nutrient variable and c is its dimensionless counterpart

This coupling also eliminates the ability to find an analytic solution. Through both asymptotic and numerical methods, it is possible show that the swimming speed, feeding rates and power expenditure are all affected by nutrient-dependent viscosity. Additionally, the mode of swimming is also found to affect the locomotion performance. In particular, the major force difference between the variable- and constant-viscosity cases was through modification of the fluid pressure gradient, as opposed to the rate-of-strain tensor (see Fig. 2). This modification to the pressure gradient either helps or hurts swimming performance based on whether the modified pressure force was working "for" or "against" the swimming body. This major modification to a "volume force" like pressure, with little modification to "surface force" of the velocity gradient was surprising and is the focus on the work presented here.

Statement of Problem

We present our findings about the competing effects of surface forces (slip velocities, rate-of-strain forces) and volume effects (pressure gradients, variable viscosity) on the locomotion performance of a Janus particle. In particular, it will be discussed whether an organism or artificial micro-robot could actively control the presence of volume effects in order to aid their locomotion.

*Corresponding author. E-mail: kshoele@fsu.edu.

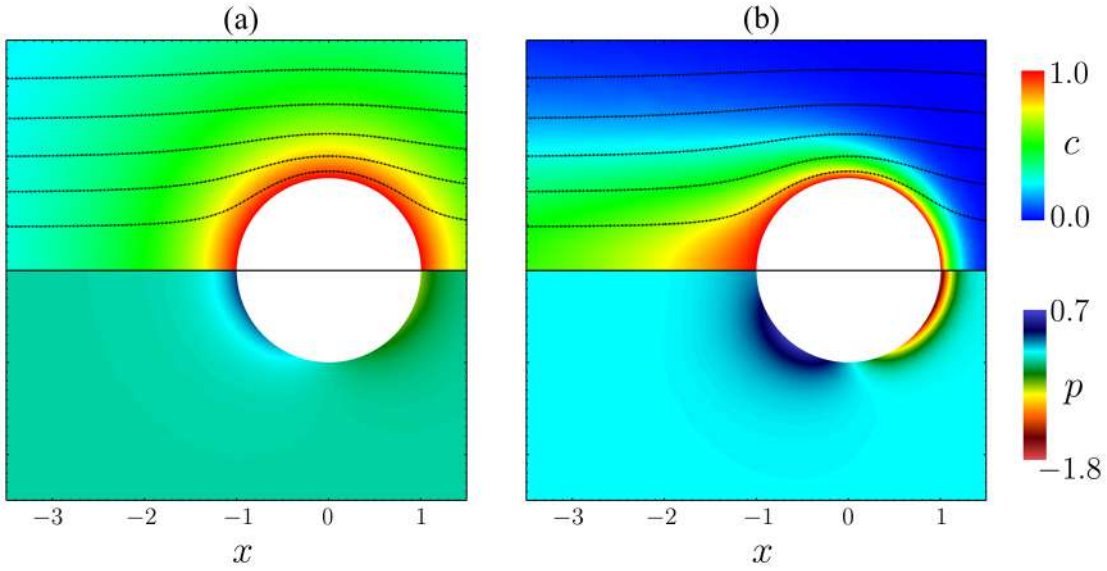

Figure 2: Effect of Pe on a treadmill squirmer with $\xi = 1.0$ and $k = 0.5$; nutrient field with streamlines on top and pressure field on bottom. (a) Pe $= 0.01$, both nutrient and pressure are symmetric due to the diffusion-dominated regime. (b) Pe $= 10$, advection-dominated regime causes an asymmetry in pressure and nutrient fields which results in larger modifications to swimming speed and nutrient flux. This pressure change for large Pe is *not* present in the constant-viscosity case.

CONCLUSIONS

In this abstract, we briefly present the connection between local versus non-local effects on the locomotion efficiency of Janus particles. While the local effect are found to modify the local gradient of the scalar and as a results induces a surface tangential forces which changes the phoretic locomotion efficiency of the particle, the non-local effect primarily modifies the pressure field around the object and induce more asymmetric pressure forces on the body. The combined use of both mode of locomotion can be leveraged to enhance the transport of Janus particles using phoretic locomotion mode.

References

[1] E. Lemmon, M. McLinden, and D. Friend. Thermophysical properties of fluid systems. In *NIST Chemistry WebBook, NIST Standard Reference Database*, number 69. Nat. Inst. Stand. Tech. Gaithersburg, 1998.

[2] K. Shoele and P. S. Eastham. Effects of nonuniform viscosity on ciliary locomotion. *Physical Review Fluids*, 3(4):043101, 2018.

[3] H. Winet. Ciliary propulsion of objects in tubes: wall drag on swimming tetrahymena (ciliata) in the presence of mucin and other long-chain polymers. *Journal of Experimental Biology*, 64(2):283–302, 1976.

RHEOLOGY OF NON-BROWNIAN DENSE SUSPENSIONS: AN OPTIMISED IMPLEMENTATION OF THE FICTITIOUS DOMAIN METHOD IN OPENFOAM®

Michel Orsi*[1], Laurent Lobry[1], Stany Gallier[2], and François Peters[1]
[1]Institut de Physique de Nice, CNRS UCA, Parc Valrose, 06108 Nice CEDEX 2, France
[2]ArianeGroup, Le Bouchet Research Center, 91710 Vert le Petit, France

Summary Non-Brownian concentrated suspensions of particles embedded in low-Reynolds-number flows are ubiquitous in industry (e.g. food, transport and civil engineering) as well as in biological or natural flows (blood, mud or lava flows). Fresh concrete or uncured rocket fuel are two examples of concentrated suspensions for which the highest particle volume fraction is desired, while specific rheological and flowing properties are required. These dense suspensions exhibit a complex rheological behaviour that is far from being totally understood. Numerical simulations can help shed light on the intricate physics of suspensions at the particle scale. The aim of the present work is to provide a highly optimised parallel implementation of a fictitious domain method (FDM) in OpenFOAM®, in order to give the opportunity to simulate large systems with a high amount of particles.

INTRODUCTION

The complexity characterising the rheology of dense suspensions mainly stems from the wide variety of fluid-particle or particle-particle interactions (Brownian, hydrodynamic, frictional or collisional) as well as from the physical properties of particles (roughness, shape, size distribution, etc.) [4]. Even idealised cases involve strong non-Newtonian effects such as shear-thinning, shear-thickening, particle migration and anisotropic normal stresses and microstructures [2, 5, 6].

Due to the importance of flow-particle interactions, particle-scale numerical methods are of primary interest. For low-Reynolds-number suspensions, different techniques have been previously developed; some of them are highly specialised and may not tackle any kind of flow or fluid [4, 7]. Therefore, direct numerical simulations (DNS) have emerged as an attractive alternative, allowing to solve particulate flows with arbitrary particle shape, Reynolds number or rheological constitutive equation [4]. The very first class of DNS methods dedicated to particulate flows followed a boundary-fitted approach wherein only the domain occupied by the fluid is meshed. For sheared concentrated suspensions, in which particle separation can be vanishingly small, remeshing becomes extremely involved and makes this approach impractical for more than a few particles. In contrast, non-boundary-fitted methods are much more suited for the simulation of suspensions with a high number of particles: the whole domain is mapped onto an Eulerian fixed grid and particles are embedded in this regular non-moving mesh. These techniques include different methods, such as the immersed boundary method, the lattice Boltzmann method or the fictitious domain method, being the latter considered in the present work.

In the fictitious domain method, particles are modelled via a body-force introduced in the momentum equation to enforce a rigid body motion. For the sake of computational efficiency, the body-force quantities are defined in the present approach at the Eulerian grid points and an advection step is inserted into the method, so that the body-force remains attached to the particles as they move along.

A peculiar feature of concentrated suspensions is that the average separation distance between particles becomes extremely small. The so-called lubrication forces arise between particles in near-contact because of the draining of interstitial fluid in the gap, and it is singular in the limit of touching particles. Consequently, the rheology of suspensions is modified by lubrication forces and important effects occur [3, 4]. Keeping the grid spacing high enough for large scale simulations while accounting for the low-scale lubrication effects requires the modelling of the latter [3]. A last essential ingredient for accurate simulations of non-Brownian suspensions is the modelling of contact interactions between particles, as contacts inevitably occur despite lubrication because of particle roughness [3].

FICTITIOUS DOMAIN METHOD

Let $\mathcal{D}$ be the computational domain including the fluid domain $\mathcal{D}_f$ and the solid particle domain $\mathcal{D}_p$, so that $\mathcal{D} = \mathcal{D}_f \oplus \mathcal{D}_p$; each of the N particles is assumed to be rigid and homogeneous with density ρ_p; the boundary between fluid and particle domains is noted $\partial\mathcal{P}$. The idea of the fictitious domain method is to extend the Navier-Stokes equations in the whole domain $\mathcal{D}$, including particles. They are thus supposed to be filled with the fluid, which is supposed here to be Newtonian and incompressible with density ρ_f and viscosity μ. Continuity and momentum equations for an incompressible flow in the whole domain $\mathcal{D}$ read:

$$\begin{gathered} \nabla \cdot \mathbf{u} = 0 \\ \rho_f \left(\frac{\partial \mathbf{u}}{\partial t} + \mathbf{u} \cdot \nabla \mathbf{u} \right) = \nabla \cdot \boldsymbol{\Sigma} + \rho_f \boldsymbol{\lambda} \end{gathered} \tag{1}$$

where $\mathbf{u}$ is the velocity field and $\boldsymbol{\Sigma} = -p\mathbf{I} + 2\mu\mathbf{E}$ is the fluid stress tensor for a Newtonian fluid, being p the fluid pressure and $\mathbf{E} = \frac{1}{2}\left(\nabla\mathbf{u} + \nabla\mathbf{u}^T\right)$ the rate-of-strain tensor; the term $\rho_f\boldsymbol{\lambda}$ is a body-force that enforces the rigid body motion inside

*Corresponding author. E-mail: michel.orsi@univ-cotedazur.fr.

the particles which is non-zero in the particle domain $\mathcal{D}_p$ and zero in the fluid domain $\mathcal{D}_f$. So, the velocity field inside particles is given by a rigid body motion $\mathbf{u} = \mathbf{U} + \mathbf{\Omega} \times \mathbf{r}$, where $\mathbf{U}$ and $\mathbf{\Omega}$ are the particle translational and rotational velocities, respectively, and $\mathbf{r}$ denotes the position vector with respect to the particles centre of gravity $\mathbf{r} = \mathbf{x} - \mathbf{x}_G$.

Particles motion is given by Newton's equations and reads:

$$\begin{aligned} M\frac{d\mathbf{U}}{dt} - \left(1 - \frac{\rho_f}{\rho_p}\right) M\mathbf{g} &= \mathbf{F}^{hyd} + \mathbf{F}^{sub}(\mathbf{U}, \mathbf{\Omega}) + \mathbf{F}^{int} \\ \mathbf{J} \cdot \frac{d\mathbf{\Omega}}{dt} + \mathbf{\Omega} \times (\mathbf{J} \cdot \mathbf{\Omega}) &= \mathbf{T}^{hyd} + \mathbf{T}^{sub}(\mathbf{U}, \mathbf{\Omega}) + \mathbf{T}^{int} \end{aligned} \tag{2}$$

where M and $\mathbf{J}$ stand for the particles mass and inertia tensor and $\mathbf{g}$ is the gravity acceleration. $\mathbf{F}^{int}$ and $\mathbf{T}^{int}$ are the force and the torque due to contact interactions between particles: they take into account elastic interactions as well as friction and are implemented as shown by Gallier et al. (2014) [3]. $\mathbf{F}^{hyd}$ and $\mathbf{T}^{hyd}$ are the hydrodynamic force and torque exerted by the fluid on the particles, respectively, and read:

$$\begin{aligned} \mathbf{F}^{hyd} &= \int_{\partial\mathcal{P}} \mathbf{\Sigma} \cdot \mathbf{n}\, dS \\ \mathbf{T}^{hyd} &= \int_{\partial\mathcal{P}} \mathbf{r} \times (\mathbf{\Sigma} \cdot \mathbf{n})\, dS \end{aligned} \tag{3}$$

where $\mathbf{n}$ is the outward-pointing unit normal vector on the boundary $\partial\mathcal{P}$. $\mathbf{F}^{sub}$ and $\mathbf{T}^{sub}$ are the sub-grid hydrodynamic force and torque correction, respectively: they are computed from the linear and angular velocities of the particles using theoretical expressions and account for the unresolved (sub-grid) part of the flow. Denoting the $6N$ vectors $\boldsymbol{\mathcal{F}}^{sub} = (\mathbf{F}^{sub}, \mathbf{T}^{sub})$ and $\boldsymbol{\mathcal{U}} = (\mathbf{U}, \mathbf{\Omega})$, the generalized sub-grid force reads [1, 3]:

$$\boldsymbol{\mathcal{F}}^{sub} = -\boldsymbol{\mathcal{R}}^{sub}_{FU} \cdot \boldsymbol{\mathcal{U}} \tag{4}$$

where the resistance matrix $\boldsymbol{\mathcal{R}}^{sub}_{FU}$ depends on the particles position. Integrating the momentum equation on a particle $\mathcal{P}$ and using the rigidity constraint and the definitions of the hydrodynamic force and torque yields:

$$\begin{aligned} \mathbf{F}^{hyd} &= -\rho_f \int_{\mathcal{P}} \boldsymbol{\lambda} d\mathbf{x} + \frac{\rho_f}{\rho_p} M\frac{d\mathbf{U}}{dt} \\ \mathbf{T}^{hyd} &= -\rho_f \int_{\mathcal{P}} \mathbf{r} \times \boldsymbol{\lambda} d\mathbf{x} + \frac{\rho_f}{\rho_p} \left[\mathbf{J} \cdot \frac{d\mathbf{\Omega}}{dt} + \mathbf{\Omega} \times (\mathbf{J} \cdot \mathbf{\Omega})\right] \end{aligned} \tag{5}$$

Finally, using these expressions in Eqs. 2 provides:

$$\begin{aligned} \rho_f \int_{\mathcal{P}} \boldsymbol{\lambda} d\mathbf{x} &= \frac{(\rho_f - \rho_p)}{\rho_p} M \left[\frac{d\mathbf{U}}{dt} - \mathbf{g}\right] + \mathbf{F}^{int} + \mathbf{F}^{sub}(\mathbf{U}, \mathbf{\Omega}) \\ \rho_f \int_{\mathcal{P}} \mathbf{r} \times \boldsymbol{\lambda} d\mathbf{x} &= \frac{(\rho_f - \rho_p)}{\rho_p} \left[\mathbf{J} \cdot \frac{d\mathbf{\Omega}}{dt} + \mathbf{\Omega} \times (\mathbf{J} \cdot \mathbf{\Omega})\right] + \mathbf{T}^{int} + \mathbf{T}^{sub}(\mathbf{U}, \mathbf{\Omega}) \end{aligned} \tag{6}$$

The system of equations is split into two sub-problems. The fluid sub-problem – Eqs. 1 – is a standard Navier-Stokes problem in $\mathcal{D}$ whereas the particle sub-problem corresponding to Eqs. 4 and 6 together with the rigid body motion mainly consists in enforcing the rigid body motion inside the particles and in coupling the interaction and the sub-grid forces to the flow. These coupled sub-problems are solved using the algorithm described by Gallier et al. (2014) [3].

RESULTS

In the present study, the fluid sub-problem is solved using the open-source finite volume library OpenFOAM® on an isotropic Cartesian mesh with a constant grid spacing. The idea is to take benefit from the parallelisation facility available in OpenFOAM® to make the simulation of large systems with a high amount of particles possible. The algorithm described by Gallier et al. (2014) [3] is adapted to work under the OpenFOAM® environment, paying particular attention to the optimisation of the code. Different classical particle configurations are studied in order to validate the method.

References

[1] Ball R.C., Melrose J.R. A simulation technique for many spheres in quasi-static motion under frame-invariant pair drag and Brownian forces. *Physica A: Statistical Mechanics and its Applications* **247**: 444-472, 1997.
[2] Denn M.M., Morris J.F. Rheology of non-Brownian suspensions. *Annu. Rev. Chem. Biomol. Eng.* **5**: 203-28, 2014.
[3] Gallier S., Lemaire E., Lobry L., Peters F. A fictitious domain approach for the simulation of dense suspensions. *J. Comput. Phys.* **256**: 367-387, 2014.
[4] Gallier S., Lemaire E., Peters F., Lobry L. Rheology of sheared suspensions of rough frictional particles. *J. Fluid Mech.* **757**: 514-549, 2014.
[5] Guazzelli E., Pouliquen O. Rheology of dense granular suspensions. *J. Fluid Mech.* **852**: P1, 2018.
[6] Lobry L., Lemaire E., Blanc F., Gallier S., Peters F. Shear thinning in non-Brownian suspensions explained by variable friction between particles. *J. Fluid Mech.* **860**: 682-710, 2019.
[7] Maxey M. Simulation Methods for Particulate Flows and Concentrated Suspensions. *Annu. Rev. Fluid Mech.* **49**: 171-193, 2017.

ON THE BOUNDARY CONDITIONS IN CELL MODELS OF FILTRATION IN MEMBRANES

Daria Khanukaeva*, Leonid Ostrer, Anatoly Filippov
Department of Higher Mathematics, Gubkin Russian State University of oil and gas, Moscow, Russia

Summary The cell model used for the simulation of filtration flows in membranes requires the statement of boundary conditions on solid, porous and hypothetical liquid surfaces. In the present work the mechanical aspects of boundary conditions are discussed. The effect of slip and no-slip is analysed for a micropolar flow across a solid cylinder. Two types of conditions are compared for the porous-liquid cylindrical surface. Various types of conditions at the outer cell surface are compared for a spherical cell. Their impact on the membrane hydrodynamic permeability is demonstrated, the condition of their equivalence is formulated.

INTRODUCTION

Membrane technologies are among the most intensively developing branches of science. They deal with micro level interaction of fluids with porous media. So, understanding the specifics of these processes is of crucial importance for the development, production and exploitation of membranes.

A cell model technique introduced by Happel and Brenner [1] has become an instrument for a simulation of hydrodynamic processes in membranes. It considers a membrane as a set of identical cells. Each cell includes solid or porous or composite core and liquid shell. A filtration problem is replaced by a flow problem for a separate cell. The influence of cells on each other is taken into account by setting corresponding boundary conditions at the outer surface of the cell. The solution of the problem is used further for the evaluation of the membrane hydrodynamic permeability - a macro-characteristics which can be measured in an experiment. Recently the cell model was extended to the filtration of micropolar liquids, that is liquids with microstructure [2]. The obtained solution includes classical results as a limiting case.

All cell models consider boundary value problems (BVPs) with boundary conditions some of which are set phenomenologically. This internal property of the model influences the solution and, in turn, the interpretation of the experiment. Therefore an adequate choice of the boundary conditions in a cell model is responsible for a correct simulation of the membrane operation. The present work is devoted to the mechanical consideration, comparison and discussion of various conditions at the boundaries of the cell.

CONDITIONS ON A SOLID SURFACE

Original Happel and Brenner's cell model included a solid core and liquid envelope. The filtration flows are slow enough for the Stokes approximation to be valid. So, in the absence of the external body forces this flow is governed by the continuity and the Stokes equations:

$$\begin{aligned} &\nabla \cdot \mathbf{v} = 0, \\ &\mu \Delta \mathbf{v} = \nabla P, \end{aligned} \tag{1}$$

where $\mathbf{v}$ is the velocity vector, P is the pressure, μ is the liquid viscosity coefficient. The most widely used condition on the solid surface is the no-slip condition, while various types of slips are more and more actively used in modern models. If one considers a cylindrical cell in a uniform flow perpendicular to its axis both mentioned boundary conditions give unique solutions of the corresponding BVPs. Meanwhile, in the case of a single cylindrical obstacle in an infinite uniform flow one obtains the Stokes paradox for the no-slip boundary condition and some solution depending on the unknown slip parameter if the slip condition is used. This inconsistency is traditionally attributed to the extra simplification of the model by the Stokes approximation. On the other hand, the reason may be in the extra simplification of the liquid representation. A simple swarm of material points used for the description of a fluid in classical hydrodynamics may not represent all the aspects of a flow interaction with a solid surface.

We consider a uniform micropolar liquid flow in the same statement with the following governing equations:

$$\begin{aligned} &\nabla \cdot \mathbf{v} = 0, \\ &-(\mu + \kappa)\nabla \times \nabla \times \mathbf{v} + 2\kappa \nabla \times \boldsymbol{\omega} = \nabla P, \\ &-(\delta + \varsigma)\nabla \times \nabla \times \boldsymbol{\omega} + 2\kappa \nabla \times \mathbf{v} - 4\kappa \boldsymbol{\omega} = 0, \end{aligned} \tag{2}$$

where the viscosity coefficients $\kappa, \delta, \varsigma$ and microrotation velocity vector $\boldsymbol{\omega}$ are introduced. The hyper stick conditions ($\mathbf{v} = \mathbf{0}, \boldsymbol{\omega} = \mathbf{0}$) on the cylinder surface also lead to the Stokes paradox. No-slip only for the linear velocity results in a growth of microrotation velocity on the boundary. Besides, the slip condition for the tangential velocity component along with the impermeability condition is satisfied automatically. There is no need to introduce an artificial slip parameter, because tangential stress is proportional to the tangential component of the velocity. So, we have demonstrated that for a micropolar liquid the slip condition is equivalent to the no-slip for the linear velocity, because the energy of the translational motion transfers into microrotation on the solid-liquid boundary.

*Corresponding author. E-mail: khanuk@yandex.ru.

CONDITIONS AT THE POROUS-LIQUID INTERFACE

A composite cell with a solid-porous core represents a partially degraded membrane. The coupled flow problem should be considered for the regions occupied by liquid and by porous medium. System (1) in the case of Newtonian liquid flow or system (2) in the case of micropolar liquid flow should be supplemented with an appropriate system for a flow in porous medium. It includes the continuity equation and the Brinkman equation for the Newtonian liquids and the continuity equation, the Brinkman-type equation and the moment of momentum equation for the micropolar liquids [3]. The coupled liquid-porous flow problem in the framework of a cell model for a micropolar liquid and composite solid-porous-liquid cell was set and solved in [2]. In the case of fully degraded membrane the core may become fully porous, so the flow takes place in the whole volume of the membrane and porous-liquid interface plays a principal role in the formation of a flow pattern.

In the present work the problem of a uniform infinite micropolar flow across a single porous cylinder is considered. The most natural conditions on its surface are the continuity of all the velocity components and the continuity of the normal stress. The last condition can be the continuity of the couple stress or the continuity of the tangential stress. They are not equivalent and represent different mechanical properties of the considered interface. The former leads to the tangential stress on the cylinder surface and minimal disturbance of the flow when it passes the obstacle. So, the uniform flow in this case slightly deforms depending on the permeability coefficient of the porous medium. The latter, on the opposite, simulates a gel-like inclusion with zero drag. The streamlines circulate inside the cylinder like in the Hadamard-Rybchinscky problem of flow over a droplet of one liquid in another liquid.

CONDITIONS AT THE HYPOTHETICAL OUTER SURFACE OF THE CELL

Four boundary conditions at the outer surface of the cell are known in the classical cell models. They are Happel's no-stress condition, Kuwabara's vorticity-free condition, Kvashnin's condition of the velocity profile symmetry and Cunningham's condition of the flow uniformity. Analytical solution is known for each of them as well as the expression for the hydrodynamic permeability of the membrane. The question is which of them should be taken for the characterisation of the membrane and for the comparison with the flow experiment results.

In the present work all the mentioned conditions are considered in the problem of flow in a spherical cell both for Newtonian and micropolar liquid flow. All of the obtained solutions possess the following peculiarity: the tangential velocity profiles intersect in one point, that is there exists a surface inside a cell where the value of the tangential velocity is independent of the boundary condition at the outer cell surface. The existence and uniqueness of this surface was proved for a solid-liquid cell in Newtonian liquid flow [4], but it is also observed in a composite solid-porous-liquid cell and for the micropolar liquid flow.

Basing on the found peculiarity, we have formulated a hypothesis that all four mentioned conditions give equivalent estimate for the hydrodynamic permeability. In [2] it was demonstrated that the membrane porosity gives the strongest effect on the hydrodynamic permeability. So, we investigate the dependence of the hydrodynamic permeability on the membrane porosity using known solutions with the aforementioned conditions. For low porosity values (less than 20%) three of the considered conditions were found to give equal estimates of the hydrodynamic permeability in the linear approximation, while Cunningham's condition is not equivalent to them. Besides, it was proved that all conditions give substantially different estimates of the hydrodynamic permeability for high values of the membrane porosity. So, the inner structure of highly porous membranes should be analysed for an adequate choice of the mechanical model for flow modelling in them.

CONCLUSIONS

The effect of boundary conditions in classical macro scale problems is restricted by the area adjacent to the boundary. In the micro scale problems the whole flow domain is the vicinity of boundaries. Thus, the conditions set at the boundaries influence the flow dramatically. We have considered peculiarities of solid-liquid, porous-liquid interaction and specifics of the outer surface boundary conditions in cell models for the filtration processes. The micro mechanism of no-slip on a solid surface is modelled for a micropolar liquid flow. The membrane degradation process and its influence on the flow pattern was formulated using boundary condition at porous-liquid interface. The influence of the boundary conditions at the outer surface of the cell on the hydrodynamic permeability was investigated. Equivalence of three conditions was proved for low porous membranes. Substantial effect of any boundary condition was demonstrated for highly porous membranes.

The work is supported by the RFBR (grant no. 19-08-00058).

References

[1] Happel J., Brenner H. Low Reynolds number hydrodynamics. Martinus Nijoff Publishers, The Hague 1983.

[2] Khanukaeva D.Yu., Filippov A.N., Yadav P.K., Tiwari A. Creeping flow of micropolar fluid through a swarm of cylindrical cells with porous layer (membrane*). J. Molec. Liq*. **294**: 111558, 2019.

[3] Hamdan M.H. & Kamel M.T. Polar fluid flow through variable-porosity, isotropic porous media, *Special Topics & Reviews in Porous Media — An Int. J.* **2** (2): 145–155, 2011.

[4] Khanukaeva D.Yu., Ostrer L.A. On the boundary conditions in the Stokesian flows, *Theoretical and Computational Fluid Dynamics* DOI 10.1007/s00162-020-00552-w.

STRUCTURE AND DYNAMICS OF HYDRODYNAMICALLY INTERACTING BROWNIAN PARTICLES IN A SPHERICAL CAVITY

Xikai Jiang*[1]
[1]Institute of Mechanics, Chinese Academy of Sciences, Beijing, China

Summary The structure and dynamics of confined suspensions of particles with arbitrary shapes are of interest in many disciplines. A numerical study on the diffusion of spherical and cylindrical particles in a spherical cavity is presented here. A general geometry Ewald-like method is used to capture hydrodynamic interactions between particles with arbitrary shapes, satisfy the fluctuation-dissipation theorem, and include appropriate no-slip boundary condition at the confining wall. We explore how hydrodynamic interaction, particle volume fraction and shape, and fraction of cylinders affect the equilibrium structure and diffusion of particles. We found that particles form layered aggregates near the wall that can influence particle dynamics. Hydrodynamic interactions strongly affect the particle diffusion. Our results offer fundamental insights into the dynamics and structure of proteins in cells.

INTRODUCTION

Diffusion under confinement is central to multiple physical, chemical, and biological systems, including colloidal and protein suspensions, devices for particle separation, and transport through membranes. A model system to study the diffusion and structure of highly concentrated particles under confinement could offer insights into the dynamics of crowded macromolecules, such as proteins, inside cells where they typically occupy 20 to 40% of the cytoplasm volume. Previous studies have shown that crowding between macromolecules hinders the diffusion of intra-cellular particles [1]. A previous review discussed several factors that could lead to the hindrance, including the viscosity of cytoplasm, steric effects, hydrodynamic interactions (HI), and other shortrange interactions between particles [1]. Recently, a theoretical study was used to model the behavior of a concentrated colloidal dispersion confined in a spherical cavity [2]. The authors studied the structure and diffusion of hydrodynamically interacting spherical particles confined in a spherical cavity following a Stokesian dynamics (SD) approach [3]. They concluded that confinement, particle concentration, and HI jointly contribute to the short- and long-time equilibrium transport properties of the confined suspensions. Their results included the prediction of the critical particle volume fraction where crowding effects begin to emerge. At high volume fractions, the diffusion coefficient of the particles was found to be affected by particle structure within the cavity. That study was limited to spherical particles. In this work, a numerical approach is used to study structure and dynamics of spherical and cylindrical particles in a spherical cavity.

METHOD

Let's consider N_P finite-size particles in a viscous fluid of viscosity μ, confined in a spherical cavity of radius R. The surface of each suspended particle is discretized into a set of N_S nodes that constitute a mesh. On the surface nodes, we define structural spring potentials that maintain particle shape, volume and surface. Assuming external forces/torques are zero, the force balance in the N_P particles under a zero Reynolds number condition is then translated into the $N_{IB} = N_P \times N_S$ surface nodes as follows,

$$\boldsymbol{f}_\nu^H + \boldsymbol{f}_\nu^B + \boldsymbol{f}_\nu^C + \boldsymbol{f}_\nu^{EV} = \boldsymbol{0}, \tag{1}$$

for every node $\nu = 1, \ldots, N_{IB}$; where $\boldsymbol{f}_\nu^H$ is the $3N$ hydrodynamic force, $\boldsymbol{f}_\nu^B$ is the $3N$ Brownian force, $\boldsymbol{f}_\nu^C$ is the $3N$ constitutive force and $\boldsymbol{f}_\nu^{EV}$ is the $3N$ vector with all the excluded volume interactions: particle-particle and particle-wall. Assuming that the probability density for nodal positions is continuous for the Fokker-Planck equation, an equivalent stochastic differential equation for the motion of nodes is written as follows [4],

$$d\boldsymbol{R} = \left[\boldsymbol{M}\cdot\boldsymbol{F} + \frac{\partial}{\partial \boldsymbol{R}}\cdot\boldsymbol{D}\right]dt + \sqrt{2}\boldsymbol{B}\cdot d\boldsymbol{W}, \tag{2}$$

where $\boldsymbol{R} = (\mathbf{x}_1, \mathbf{x}_2, \ldots, \mathbf{x}_N)$ denotes a $3N$ vector containing the spatial coordinates of the nodes, $\boldsymbol{D} = k_B T \boldsymbol{M}$ is the $3N\times3N$ diffusion tensor, k_B is Boltzmann constant, T is the absolute temperature, and $\boldsymbol{M}$ is the $3N\times3N$ mobility tensor. In addition, $\boldsymbol{U} = \boldsymbol{M}\cdot\boldsymbol{F}$ contains the $3N$ fluctuating velocities from the hydrodynamic interactions and $\boldsymbol{F}$ is the $3N$ vector that contains the non-HI and non-Brownian forces on the nodes. The divergence of the diffusion tensor $\frac{\partial}{\partial \boldsymbol{R}}\cdot\boldsymbol{D}$ is the drift resulting from the configuration-dependent mobility of the confined particles and $d\boldsymbol{W}$ is a random vector, the components of which are obtained from a real-valued Gaussian distribution with zero mean and variance dt; $d\boldsymbol{W}$ is coupled to the diffusion tensor through the fluctuation-dissipation theorem: $\boldsymbol{D} = \boldsymbol{B}\cdot\boldsymbol{B}^{\boldsymbol{T}}$. The force distributions at moving solids are discretized as distributions of regularized point-forces. The smoothing function for the delta function scales as the distance between surface nodes that are used to represent moving particles. At each node a purely repulsive Lennard-Jones potential is used for particle-particle and particle-wall excluded volume interactions. Method details are described in Ref. [4].

RESULTS AND DISCUSSIONS

At low concentrations, the particle number density distribution is uniform in the interior of the cavity. As the concentration increases, a layered structure appears for both spherical and cylindrical particles (see left panels in Fig. 1). From right panels in Fig. 1, it was also found that long-range HI leads to a position-dependent diffusion of the particles inside the cavity; the particles diffuse faster near the center of the cavity and slower near the walls. The HI also decrease the global mobility of the suspended particles, when compared with their diffusion in the bulk. The increase in particle concentration also results in a decrease of the particles' diffusion coefficients; this effect is observed for free-draining and HI particles. However, the concentration decrease of the diffusion rate is stronger when HI are considered. Lubrication forces, or short-range HI, influence the dynamics of highly concentrated suspensions; they generate a direction dependent diffusion, where particles diffuse at a lower rate when moving towards the walls than when moving parallel to the walls. The no-slip conditions at the walls, i.e. zero particle mobility, work synergistically with lubrication forces, resulting in an stronger wall dependence of the diffusion coefficients in the radial direction. Importantly, lubrication gives rise to a sub-diffusive regime (crowded mobility) at high particle concentrations. The sub-diffusive regime, characterized by the diffusion-to-crowded transition time and the mobility power law exponent, becomes more prominent as the concentration increases.

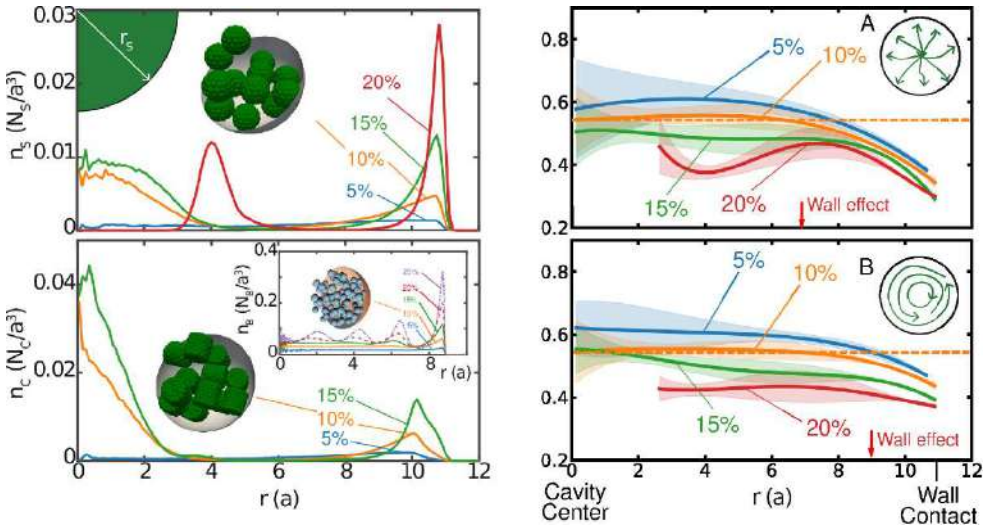

Figure 1. (left) Number density of particles in a spherical cavity of radius R = 15 as a function of particle concentration. (left-top) Spheres with radius r_S = 3; (left-bottom) cylinders with radius r_C = 2.62 and height $h_C = 2r_C$. Snapshots for volume fraction ϕ_{HI} = 10% are shown for both systems, while number density of HI "beads" is included in the inset. (right) Short-time diffusion coefficients for spherical particles (r_S = 3) that are confined in a spherical cavity with R = 15. (right-top) Radial diffusivity and (right-bottom) tangential diffusivity. The coefficients are normalized by the diffusivity of a spherical particle in bulk at infinite dilution, $k_BT/(6\pi\mu r_S)$. The orange dashed line represents averaged "inner" diffusivities for ϕ_{HI} = 10%. The filled shadow area around each curve represents their statistical errors.

CONCLUSIONS

The structure and dynamics of hydrodynamically interacting Brownian particles in a spherical cavity were studied using numerical simulations. Results for spherical and cylindrical particles were obtained and compared. It was found that particle volume fraction, particle shape, and hydrodynamic interactions between particles have important effects on particle density distributions and short- and long-time diffusions.

References

[1] Skolnick J. On the importance of hydrodynamic interactions in the subcellular dynamics of macromolecules. *J. Chem. Phys.* **145**, 100901, 2016.
[2] Aponte-Rivera C., Zia R. N. Simulation of hydrodynamically interacting particles confined by a spherical cavity. *Phys. Rev. Fluids* **1**, 023301, 2016.
[3] Aponte-Rivera C., Su Y., Zia R. N. Equilibrium structure and diffusion in concentrated hydrodynamically interacting suspensions confined by a spherical cavity. *J. Fluid Mech.* **836**, 413450, 2018.
[4] Zhao, X., Li, J., Jiang, X., Karpeev, D., Heinonen, O., Smith, B., Hernandez-Ortiz J. P., de Pablo, J. J. Parallel O(N) Stokes'solver towards scalable Brownian dynamics of hydrodynamically interacting objects in general geometries. *J. Chem. Phys.*, **146**, 244114, 2017

EFFECTIVE VISCOSITY OF A DILUTE SUSPENSION OF SPHERES BETWEEN PARALLEL SLIP WALLS

Néjiba Ghalya[1], Antoine Sellier*[2], Maria L. Ekiel-Jeżewska[3], and François Feuillebois[4]
[1]Laboratoire de Modélisation Mathématique et Numérique pour les Sciences de l'Ingénieur-LAMSIN, Université de Tunis El Manar, Ecole Nationale d'Ingénieurs de Tunis, BP37, 1002 Tunis Le Belvédère, Tunisia
[2]LadHyX, Ecol ePolytechnique, 91128 Palaise au cedex. France
[3]Institute of Fundamental Technological Research, Polish Academy of Sciences, Pawińskiego 5b, 02-106 Warsaw, Poland
[4]LIMSI-CNRS, UPR 3251, BP 133, 91403 Orsay cedex, France

Summary The energy cost for transporting suspensions in micro-channels may be reduced by using slipping walls. A theoretical model is presented here for the effective viscosity, μ_{eff}, of a dilute suspension of freely suspended identical solid no-slip spherical particles carried by a Poiseuille flow between parallel slip walls. Compared with no-slip walls (Feuillebois et al., *J. Fluid Mech.*, 800:111, 2016), this viscosity strongly depends on the ratio of the wall slip length to particle radius, λ/a, for given ratio of the gap between walls to particle diameter $H/(2a)$: in the very confined case $H/(2a) = 2$ and for a very large slip $\lambda/a = 1$, the suspension intrinsic viscosity $[\mu] = (\mu_{\text{eff}} - \mu_0)/(\mu_0\phi)$, where μ_0 is the fluid viscosity and ϕ is the low suspension volume fraction, is divided by 3 compared with the no-slip case and divided by 5 compared with Einstein's result (5/2) for an unbounded suspension.

The effective viscosity of a confined flowing suspension is the relevant quantity to consider for particle transport (see e.g. [1] [2]). This viscosity depends on the suspension volume fraction and on the ambient flow field. Assuming a dilute suspension (i.e. at small volume fraction $\phi \ll 1$) of either spherical or elongated particles and a high-frequency ambient flow field, in the sense that all particles occupy all possible positions and orientations with equal probability, made it possible to calculate the suspension effective viscosity in Couette [3] and Poiseuille [4] flows between two parallel planar no-slip walls.

The same approach is used here for slip walls and no-slip spherical particles. On each wall the impermeability condition reads $\mathbf{u} \cdot \mathbf{n} = 0$ where $\mathbf{u}$ is the fluid velocity and $\mathbf{n}$ is the unit vector normal to the wall and pointing into the liquid. The usual Naviers's [5] slip boundary condition is applied on each wall:

$$\mathbf{u} = \lambda \frac{\partial \mathbf{u}}{\partial n}\,, \tag{1}$$

where $\lambda \geq 0$ is the wall slip length, assumed to be uniform and identical for both walls and n is the normal coordinate along $\mathbf{n}$. The Poiseuille flow velocity profile $u_0(z)$ with these slip conditions (1) on walls W_1, W_2 is sketched in Fig. 1.

The average pressure drop for driving particles in this flow field is derived by using Lorentz reciprocal theorem. The suspension effective viscosity is obtained from the relationship between this pressure drop and the volume flow rate. The result for the suspension intrinsic viscosity $[\mu]$ (defined in the summary) is:

$$[\mu] = \frac{9}{4\pi\left(1 + 6\dfrac{\widetilde{\lambda}}{\widetilde{H}}\right)\left(\widetilde{H} - 2\right)} \int_1^{\widetilde{H}-1} \left[\left(1 - 2\frac{\widetilde{z}_c}{\widetilde{H}}\right)\widetilde{S}_{xz} - \frac{1}{\widetilde{H}}\widetilde{Q}_{xzz}\right] d\widetilde{z}_c\,, \tag{2}$$

where $\tilde{H}, \tilde{\lambda}, \tilde{z}_c$ are made dimensionless with a sphere radius a. We denote $\widetilde{H}$ the normalized gap between walls and $\widetilde{z}_c$ the normalized position of the centre of a test particle (see Fig. 1). Eq. (2) involves (as is classical for the viscosity of suspensions) the stresslet component S_{xz} on a particle, that is a symmetric first moment of stresses on its surface. It also involves the quadrupole component Q_{xzz}, second moment of stresses. The normalized components of the stresslet $\widetilde{S}_{xz}$ and quadrupole $\widetilde{Q}_{xzz}$ appearing in (2) are defined as $\widetilde{S}_{xz} = S_{xz}/(\mu_0 a^3 k_1)\,, \widetilde{Q}_{xzz} = Q_{xzz}/(\mu_0 a^4 k_1)$, where k_1 is the linear shear rate at wall W_1.

Taking into account the full interactions of a sphere with both slip walls is not presently accessible. Two single-wall models are used here: the "nearest wall" (nw) and "wall superposition" (ws) approximations. The stresslet and quadrupole on a sphere near a single slip wall are calculated from analytical solutions of the Stokes equations in bispherical coordinates [6, 7]. Both nw and ws models are validated by comparing to earlier accurate results [3, 4] in the case of no-slip walls.

The suspension intrinsic viscosity $[\mu]$ is evaluated in the range $2 \leq H/(2a) \leq 100$ and $\widetilde{\lambda} \leq 1$. It depends strongly on $\widetilde{\lambda}$ for small $H/(2a)$, as detailed in the summary and shown in Fig. 2. The main contribution to the dependence on $\widetilde{\lambda}$ comes from the factor $1/(1 + 6\widetilde{\lambda}/\widetilde{H})$ in (2), which is independent of particle-wall interaction. This strong variation of $[\mu]$ on $\widetilde{\lambda}$ may have practical applications for particle transport in microfluidics. A handy fitting formula for $[\mu]$ is provided. Finally, outlooks for experiments are proposed: for instance, a non-optical microcapillary rheometer [8] may allow to measure first the slip length in pure fluid and then the suspension effective viscosity for comparison with the present theory. Details of this paper are available in [10].

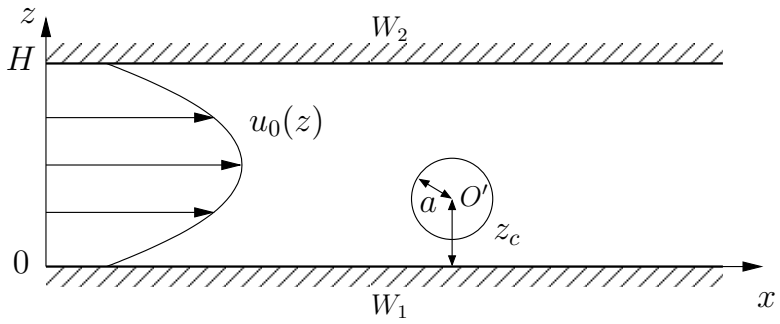

Figure 1: Sketch of a single sphere with centre O' and radius a freely suspended in a Poiseuille flow between two parallel solid slip walls W_1 and W_2.

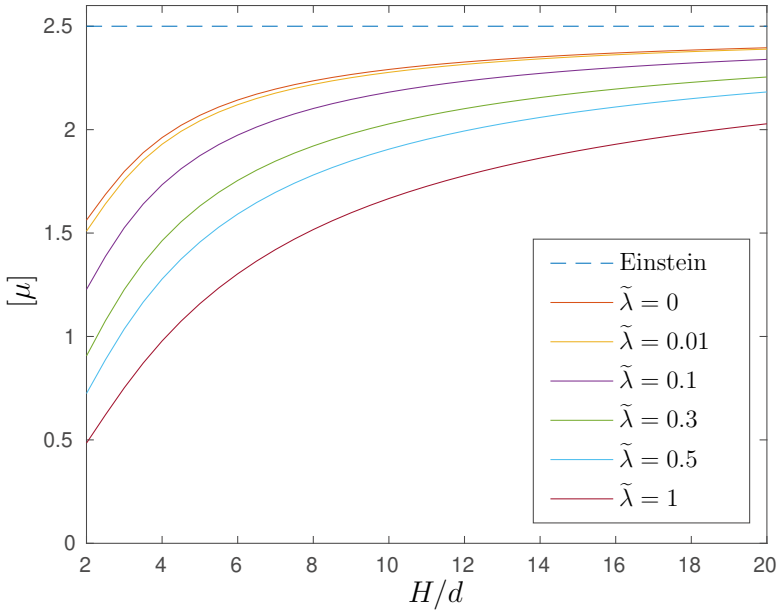

Figure 2: Variations of the suspension intrinsic viscosity $[\mu]$ calculated with the "wall superposition" model versus H/d (with $d = 2a$) for various values of $\widetilde{\lambda}$. From top to bottom: Einstein's [9] result 5/2 for an unbounded suspension and present results for a bounded suspension with $\widetilde{\lambda} = 0, 0.01, 0.1, 0.3, 0.5, 1$.

Acknowledgements

A.S., M.E.J. and F.F. benefited from the ITHACA project PPI/APM/2018/1/00045 financed by the Polish National Agency for Academic Exchange. M.E.J. was supported in part by the National Science Centre under grant UMO-2018/31/B/ST8/03640.

References

[1] S. Navardi and S. Bhattacharya. Effect of confining conduit on effective viscosity of dilute colloidal suspension. *J. Chem. Phys.*, 132(11):114114, 2010.
[2] P. Peyla and C. Verdier. New confinement effects on the viscosity of suspensions. *Europhys. Lett.*, 94:44001, 2011.
[3] F. Feuillebois, M. L. Ekiel-Jeżewska, E. Wajnryb, A. Sellier, and J. Bławzdziewicz. High-frequency viscosity of a dilute suspension of elongated particles in a linear shear flow between two walls. *J. Fluid Mech.*, 764:133–147, 2015.
[4] F. Feuillebois, M. L. Ekiel-Jeżewska, E. Wajnryb, A. Sellier, and J. Bławzdziewicz. High-frequency effective viscosity of a dilute suspension of particles in Poiseuille flow between parallel walls. *J. Fluid Mech.*, 800:111–139, 2016.
[5] C. L. M. H. Navier. Mémoire sur les lois du mouvement des fluides. *Mémoires de l'Acad. des Sciences de l'Institut de France*, 6:389–416, 1823. http://gallica.bnf.fr/ark:/12148/bpt6k3221x/f577.pagination, page 415.
[6] H. Loussaief, L. Pasol, and F. Feuillebois. Motion of a spherical particle in a viscous fluid along a slip wall. *Quart. J. Mech. Applied Math.*, 68(2):115–144, 2015.
[7] N. Ghalia, F. Feuillebois, and A. Sellier. A sphere in a second degree polynomial creeping flow parallel to a plane, impermeable and slipping wall. *Quart. J. Mech. Applied Math.*, 69(4):353–390, 2016.
[8] G. Vleminckx and C. Clasen. The dark side of microrheology: Non-optical techniques. *Current Opinion in Colloid & Interface Science*, 19(6):503 – 513, 2014.
[9] A. Einstein. Eine neue Bestimmung der Moleküldimensionen. *Ann. Phys.*, 19:289–306, 1906.
[10] N. Ghalya, A. Sellier, M. L. Ekiel-Jeżewska, and F. Feuillebois. Effective viscosity of a dilute homogeneous suspension of spheres in Poiseuille flow between parallel slip walls. *J. Fluid Mech.*, 899(A13):1–36, 2020.

*Corresponding author. E-mail: sellier@ladhyx.polytechnique.fr

INCLUSION OF HYDRODYNAMIC WALL EFFECTS IN CONTINUUM MODELS OF MICROORGANISM SUSPENSIONS

Michael Gravatt[1], Alys Clark[2], Vinod Suresh[1,2], and Richard Clarke*[1]
[1]Department of Engineering Science, University of Auckland, Auckland, New Zealand
[2]Auckland Bioengineering Institute, University of Auckland, Auckland, New Zealand

Summary The absence of hydrodynamic interactions between swimming microorganisms and solid boundaries is a known issue with existing continuum models for cell suspensions. Using flow singularity representations, together with their image systems, we simulate the extent to which hydrodynamic wall effects influence average cell orientations. We then proceed to show that existing continuum models can give accurate predictions for cell concentrations in confined suspensions when they use these cell orientation fields.

INTRODUCTION

In recent years there has been a great deal of interest and activity in developing continuum-level models capable of describing suspensions of swimming microorganisms. Such models are useful since these kinds of active suspensions pervade almost every facet of daily life, and have implications in areas ranging from healthcare to bioprocessing. While the existing models have enjoyed success in describing a number of phenomena, one recognised shortcoming is the neglect of hydrodynamic interactions between cells and solid surfaces in confined settings, which are known to affect the swimming motion of individual cells. We address this issue here by providing a means by which wall hydrodynamics can be incorporated into existing continuum models.

FORMULATION

Microorganism Flowfield

We adopt the following flow singularity approximation for the flow field $\boldsymbol{V}$ generated by a squirming microorganism of radius $a \ll 1$, located at $\boldsymbol{x}'$ and swimming with constant speed V_c in a direction $\boldsymbol{p}$ in the vicinity of a nearby horizontal solid surface [1]

$$V_i(\boldsymbol{x}) = a^3 B_1 p_j D_{ij} + a^2 B_2 S_{jk} U_{ijk} + V_i^I + O(a^4) \tag{1}$$

where

$$S_{ij} = \frac{4\pi}{3}\left(p_i p_j - \frac{\delta_{ij}}{3}\right), \quad U_{ijk} = \frac{3\hat{x}_i\hat{x}_j\hat{x}_k}{\hat{r}^5}, \quad D_{ij} = -\frac{\delta_{ij}}{3\hat{r}^3} + \frac{\hat{x}_i\hat{x}_j}{\hat{r}^5} \tag{2}$$

($\hat{\boldsymbol{x}} = \boldsymbol{x} - \boldsymbol{x}'$, $r = |\hat{\boldsymbol{x}}|$, δ_{ij} is the Kronecker delta) are, respectively, the squirmer stresslet, the symmetric component of the force-dipole and the potential dipole flow field. The coefficients B_1 and B_2 characterise the cell's swimming action. The image systems for these singularities that make up V_i^I ensure that no-slip and no-penetration conditions are satisfied on the nearby wall, and are given by [2], [3]. By comparison with full numerical simulation of finite-sized cells near a solid boundary, we can show that the above singularity representation provides a reasonable approximation.

Cell Conservation Model

We now consider a semi-dilute suspension of squirming micro-organisms contained between no-slip walls at $z = \pm H_z$. We assume that the suspension is homogeneous in the horizontal directions (x, y), and that vertical variations in cell concentrations, $n(z)$, satisfy the classical steady cell conservation model [4]

$$\frac{dJ}{dz} = 0, \quad J = D\frac{dn}{dz} - \left(V_c \langle p_3(z)\rangle + W\right) n \tag{3}$$

subject to $J(\pm H_z) = 0$, where $\langle p_3(z)\rangle$ is the steady average vertical component of orientation. Cell-wall and cell-cell hydrodynamic interactions lead to an additional advective flow $\boldsymbol{W}$. However, the hydrodynamic effect of the wall is much greater on $\langle p_3(z)\rangle$, and consequently it is on this that we focus in what follows. In the standard cell conservation model $\langle p_3(z)\rangle$ is governed by a Fokker-Planck equation, while observing appropriate kinematics. In the absence of any biases (as is the case here) this approach predicts $\langle p_3(z)\rangle = 0$. We instead use Discrete Particle Simulations (DPS) to determine $\langle p_3(z)\rangle$ in the presence of cell-wall hydrodynamic interactions.

*Corresponding author. E-mail: rj.clarke@auckland.ac.nz

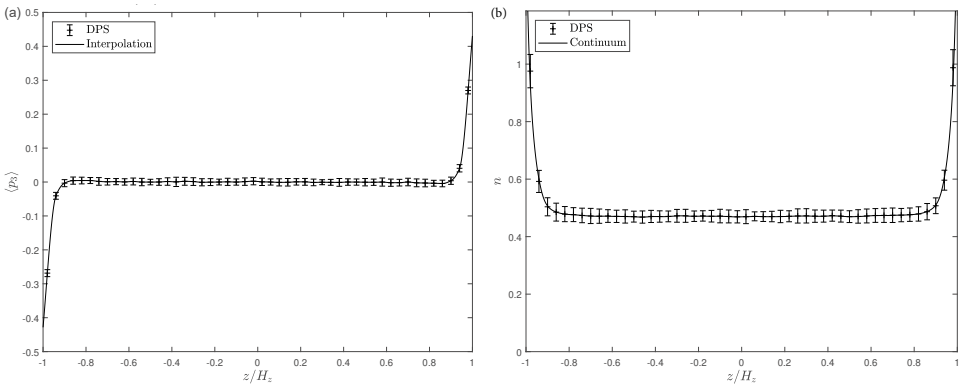

Figure 1: (a) Average vertical component of orientation as a function of vertical position, as computed using Discrete Particle Simulations (walls lie at $z/H_z = \pm 1$) (b) Cell concentration as function of vertical position, as computed explicitly using both Discrete Particle Simulation (markers) and the cell conservation model (3) with cell orientation field informed by DPS (solid line). In both cases the cell is swimming at one body length per second, $D_r = 0.13$, $D = 1.3$ and $B_2/B_1 = -1$. Bars indicate 95% confidence intervals.

Discrete Particle Simulations

The Discrete Particle Simulations explictly track the dynamics of N squirmers, their motions being governed by:

$$\frac{d\boldsymbol{x}_j'}{dt} = V_c \boldsymbol{p}_j + \boldsymbol{\eta}_j + \sum_{k=1}^{N} \boldsymbol{V}_k^I + \sum_{k=1,k\neq j}^{N} \boldsymbol{V}_k, \quad \frac{d\boldsymbol{p}_j}{dt} = \boldsymbol{\xi}_j + \frac{1}{2}\sum_{k=1}^{N} \boldsymbol{\Omega}_k^I \times \boldsymbol{p}_k + \frac{1}{2}\sum_{k=1,k\neq j}^{N} \boldsymbol{\Omega}_k \times \boldsymbol{p}_k \tag{4}$$

($j = 1, \ldots, N$) where $\boldsymbol{V}_k$ and $\boldsymbol{\Omega}_k$ are, respectively, the flow velocity and vorticity fields generated by the kth squirmer, i.e. in addition to their self-motility, cells are advected by the flows due to the other cells, and flow field images in the walls. Diffusion is captured via stochastic terms $\boldsymbol{\xi}_j$ and $\boldsymbol{\eta}_j$, sampled from the conditional probability distributions

$$P_1(\theta, t|\theta_0, t_0) = \frac{A}{\sqrt{D_r(t-t_0)}} \exp\left(-\frac{(\theta-\theta_0)^2}{4D_r(t-t_0)}\right) \sin(\theta - \theta_0), \tag{5}$$

$$P_2(z, t|z', t_0) = \frac{1}{\sqrt{4\pi(D(t-t_0))}} \left[\exp\left(-\frac{(z-z')^2}{4D(t-t_0)}\right) + \exp\left(-\frac{(z+z'+2H_z)^2}{4D(t-t_0)}\right) + \exp\left(-\frac{(z+z'-2H_z)^2}{4D(t-t_0)}\right)\right], \tag{6}$$

respectively. P_2 accounts for non-hydrodynamic cell-wall interactions through a biased random walk in z (randon walks in x and y are unbiased), and D_r is the rotational diffusivity. Long-time averages over multiple realisations are then taken to determine $\langle p_3(z) \rangle$ and $n(z)$.

RESULTS

Figure 1(a) shows the average vertical component of the cell orientation field as a function of depth within the suspension as computed using DPS. Whereas classical continuum models, which do not account for wall hydrodynamics, would predict no orientational bias ($\langle p_3(z) \rangle = 0$), we can see that these hydrodynamics interactions lead to an average turning of the cells towards the walls. The consequences of this effect on the cell concentration can be seen in Figure 1(b), where an elevation in cell levels close to the walls is observed. By contrast, the continuum model (3) with $\langle p_3(z) \rangle = 0$ would predict a constant cell concentration profile through the suspension. However, we see that when the $\langle p_3(z) \rangle$ computed using DPS is used, the non-constant cell concentration predicted by DPS can be recovered.

CONCLUSIONS

These results illustrate the extent to which hydrodynamic interactions with solid surfaces can affect the bulk concentration of cells, and also suggest that these effects can be captured in the standard continuum models when the wall-influenced cell orientations are used. Here we have computed these steady orientations by numerically time evolving (4), however, it may be possible to derive these more directly by setting to zero the left-hand side of (4b) and solving.

References

[1] Gravatt, M., Suresh, V., Clark, A. and Clarke, R.J. Important of irrotational flow components of swimming flows on the stability of a suspension of weakly-squirming microorganisms *IMA J. of Applied Math.* **83**: 720-742, 2018.
[2] Blake, J. R. and Chwang, A. T. Fundamental singularities of viscous flow *J. Eng. Math.* **8**: 2329. 1974
[3] Gimbutas, Z., Greengard, L. and Veerapaneni, S. Simple and efficient representations for the fundamental solutions of stokes flow in a half-space *J. of Fluid Mech.* **776**: 2015
[4] Pedley, T.J., Kessler, J.O. A new continuum model for suspensions of gyrotactic micro-organisms *J. Fluid Mech.* **212**: 155-182 1990.

TRANSITION FROM CLOGGING TO CONTINUOUS FLOW IN CONSTRICTED PARTICLE SUSPENSIONS

Mathieu Souzy*[1], Iker Zuriguel[2], Alvaro Marin[1]
[1]Physics of Fluids, University of Twente, The Netherlands
[2]Departamento de Física, Facultad de Ciencias, Universidad de Navarra, Spain

Summary When suspended particles are pushed by liquid flow through a constricted channel they might either pass the bottleneck without trouble or encounter a permanent clog that will stop them *forever*. However, they may also flow intermittently with great sensitivity to the neck-to-particle size ratio D/d. In this work, we experimentally explore the limits of the intermittent regime for a dense suspension through a single bottleneck as a function of this parameter. Using high-resolution and high-speed optical video microscopy in a microfluidic constriction, we reveal that there is a sharp transition from a clogged state to a continuous flow, where clog does not develop at all.

MANUSCRIPT PREPARATION

When people, animals, or particles are forced through a constriction, the flow may become intermittent due to the development of clogs that obstruct the constriction. Despite the diverse nature and scale of these systems – including hungry sheep herds [1], pedestrian crowds trying to escape a room in a life-and-death situation[2], discharge of dry granular silos [3], suspended hydrated particles transported through pipelines, electrons passing through nanoconstrictions on a liquid helium surface, sand hourglasses[4], or mice escaping a water pool – a distinctive phenomenology is always observed: particles or bodies flow in erratic bursts separated by short period of arrest (see Fig 1). The analogy is not only qualitative, and in all cases the number of escapees per burst follows an exponential distribution, and the probability distribution of time lapses separating the passage of consecutive bodies seems to exhibit a power-law tail with characteristic exponents that depend on diverse system parameters [1].

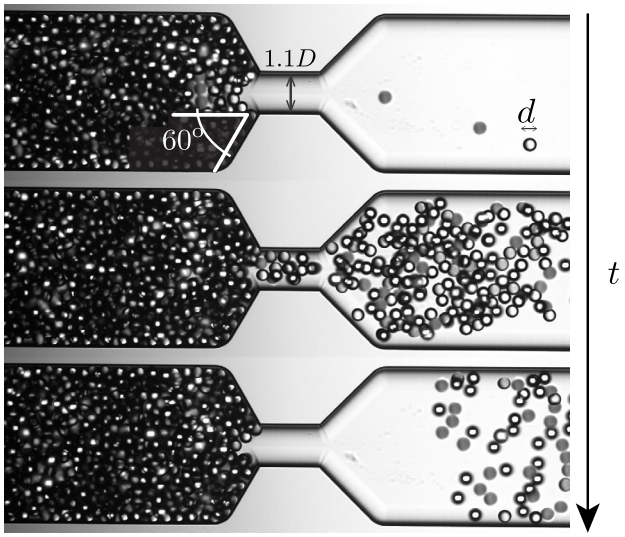

Figure 1: Successive snapshots of a burst in a suspension of particles with a diameter d that intermittently flow through a constriction – having a neck width $1.1D$ and height D – by a volume-driven flow ($D/d = 3.03$). From top to bottom: clog previous to the burst, burst, and clog after the burst.

In our work [5], we experimentally investigate the flow of a suspension getting through a constriction. We explore the critical sensitivity of the intermittent particle flow on the neck-to-particle size ratio D/d by using high-resolution and high-speed optical video microscopy in a microfluidic device. The fluidic system consists of a transparent straight channel of borosilicate glass with a rectangular cross-section which reduces to an almost square cross-section of $100 \times 110\,\mu\text{m}^2$ to form the neck.

As can be seen on Figure 2, the spatio-temporal diagrams at the constriction neck reveal a qualitative difference in the flow behavior: from a blocked situation (top diagram) to uninterrupted particle flows (bottom diagram). For $D/d \leq 2.43$ only few particles (which appear in dark) escape before a clog is formed. As D/d is increased, the intermittent particle flow regime emerges and the flowing intervals become longer and more abundant. This regime persists until the flow becomes continuous, so the bursts intermittency becomes unmeasurable. In our system, the intermittent flow is thus observed for $2.43 < D/d < 5.26$.

*Corresponding author. E-mail: m.p.j.souzy@utwente.nl

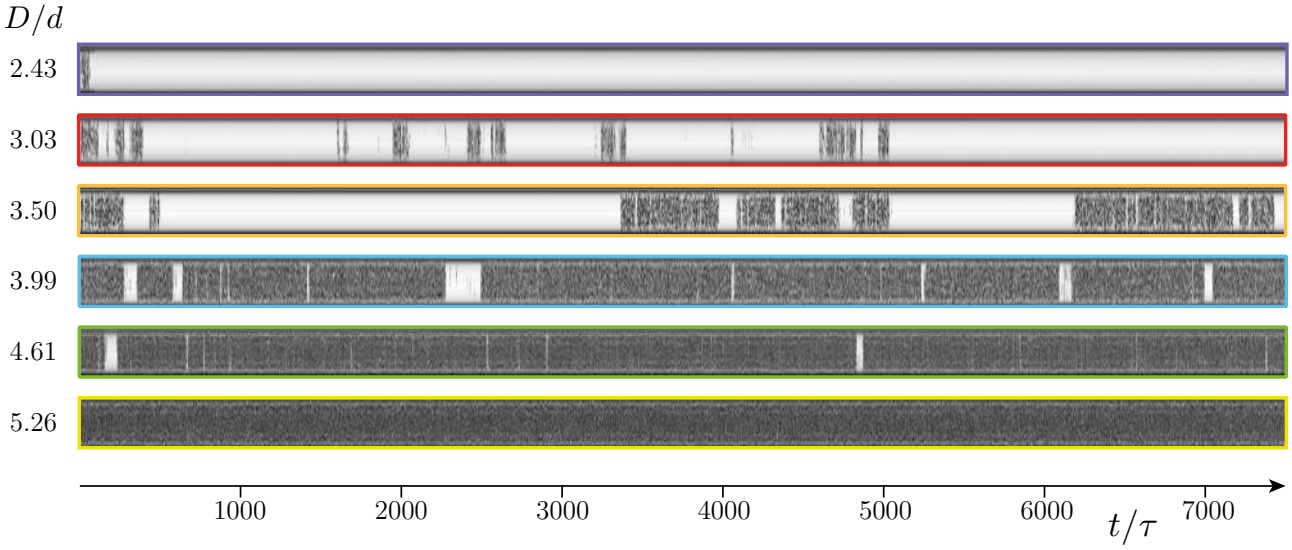

Figure 2: Spatio-temporal diagrams at the constriction neck for various D/d. For $D/d \leq 2.43$ only few particles (which appear in dark) escape before a permanent clog is formed. When increasing D/d, intermittent particle flow is observed, eventually reaching particle continuous flow for $D/d \geq 5.26$. Time is normalized by the Stokes time τ a particle takes to travel its own diameter.

Furthermore, we make use of high time- and space-resolution experiments to obtain the distributions of arrest times (T) between successive bursts, which display power-law tails ($\propto T^{-\alpha}$) with characteristic exponents. These exponents compare well with the ones found for as disparate situations as the evacuation of pedestrians from a room, the entry of a flock of sheep into a shed or the discharge of particles from a silo. Nevertheless, the intrinsic properties of our system (i.e. channel geometry, driving and interaction forces, particle size distribution) seem to introduce a sharp transition from a clogged state ($\alpha \leq 2$) to a continuous flow, where clogs do not develop at all. This contrasts with the results obtained in other systems where intermittent flow, with power-law exponents above two, were obtained.

In addition, we also plan to address the question of the physics behind clogging arches break out by investigating the pressure signal during both clog-construction and clog destruction process. This should help to clarify furthermore the crucial role of the driving force (the suspending fluid dragging the dispersed particles). Indeed, although the phenomenological behavior of a suspended flow is similar to that of dry cases (like the discharge of a silo), the interactions between the particles are strongly affected by the presence of the fluid. By monitoring the pressure signal, we ambition to investigate if there is a signature of the clogging process which could be used to predict clogging, which would make a remarkable diagnostic tool to avoid clogging (by interrupting the flow for instance) for a broad range of applications.

CONCLUSIONS

To conclude, our study [5] show that volume-driven flow of dense non-adhesive particle suspension going through a constriction exhibits intermittent flow behavior with a striking similarity as in dry granular matter [3, 4], human crowds [2], or animal herds [1]. At low Reynolds number and in the absence of particle aggregation or particle/wall adhesion, the geometry of the system (neck-to-particle size ratio and constriction angle) prescribes the flow regime entirely. At low D/d the flow is quickly interrupted by the formation of stable particle arches spanning the constriction, while at large D/d the flow is continuous and no stable arches develop (at least in the experimental timescale). A transitioning intermittent regime is reported for $2.43 < D/d < 5.26$, for which we have investigated the distribution of the time lapse T/τ between the passage of consecutive particles. The distribution displays a characteristic power-law tail $\propto (T/\tau)^{-\alpha}$ with values of α below two in all cases. This is an unexpected result which implies that for our system, even when flow is intermittent, a permanent clog may occur. Therefore, our system exhibit a remarkable sharp transition from a clogged state (when there is a non-zero probability that a permanent clog eventually occurs) to a continuous flow for $D/d \approx 5$.

References

[1] I. Zuriguel, D. R. Parisi, R. C. Hidalgo *et al.* Clogging transition of many-particle systems flowing through bottlenecks. *Sci. Rep.* **4** 7324 (2014).
[2] D. Helbing, L. Buzna, A. Johansson, and T. Werner, Self-organized pedestrian crowd dynamics: Experiments, simulations, and design solutions. *Transp. Sci.*, **39(1)** 1-24 (2005).
[3] K. To, P. Y. Lai, and H. K. Pak, Jamming of granular flow in a two-dimensional hopper. *Phys. Rev. Lett.*, **86(1)** 71 (2001).
[4] X. L. Wu, K. J. Måløy, A. Hansen *et al.* Why hour glasses tick. *Phys. Rev. Lett.*, **71**(9) 1363 (1993).
[5] M. Souzy, I. Zuriguel, A. Marin, Transition from clogging to continuous flow in constricted particle suspensions. *Phys. Rev. E*, **101**(6) 060901 (2020).

DYNAMICS OF SEMIFLEXIBLE POLYMERS IN OSCILLATORY SHEAR FLOWS

Francesco Bonacci[1], Anke Lindner*[1], Du Roure Olivia[1], David Saintillan[3], and Brato Chakrabarti[2]
[2]Department of Another Author, University of Another Author, City, Country
[1]PMMH, CNRS, ESPCI Paris, Université PSL, Sorbonne Université, Université de Paris, F-75005, Paris, France
[2]Center for Computational Biology, Flatiron Institute, New York, New York 10010, USA
[3]Department of Mechanical and Aerospace Engineering, University of California San Diego, La Jolla, California 92093, USA

Summary Elucidating the physics behind the morphological and orientation dynamics of single, elastic polymers in viscous flows is key to the understanding of the complex rheological phenomena found in polymer solutions (shear thinning, normal stress differences, etc) and of a wealth of biophysical processes (cilia and flagellar propulsion, intracellular streaming). In the last decades, the study of elastic filaments in shear flows at low Reynolds number has been mainly limited to simple shear [1, 2] and straining flows [3]. Depending on the mechanical properties of the polymer, various dynamics have been reported. Together with tumbling motion, flexible and semi-flexible polymers usually show morphological transitions, which stems from a balance between flow induced stresses, bending elasticity and thermal fluctuations. Examples include the coil–stretch [4] and stretch–coil [3] transitions in pure straining flows, and elastic shear-induced transitions [1, 2] and irregular tumbling motion in simple shear flows. In this work, we combine fluorescence microscopy experiments and computational modeling to study the dynamics and conformation transitions of elastic Brownian actin filaments in oscillatory flows in a microfluidic channel. The use of a pulsatile flow adds a new time scale associated with the oscillation, and is motivated by the relevance of non-steady flows in biological processes [5] (cardiovascular flows, nutrient and waste transport in animals, growth and motion of cells) and on-chip applications [6] (particle sorting, focusing and mixing, microrheology and clog mitigation).

MATERIALS AND METHODS

We follow standard protocols for the polymerization of fluorescent actin filaments. They are observed in an inverted microscope equipped with an high NA water-immersion objective, at a distance of $\approx$150 µm from the bottom wall of a vertical Hele-Shaw cell, whose width W =150 µm, is much larger than the typical dimension of the deformed filaments (5 to 20 µm). In these conditions, the filaments experience a 2-D flow gradient in the observation plane, with a shear rate that can be approximated as uniform along the centerline. A sinusoidal shear rate $\dot{\gamma}(t) = \dot{\gamma}_M sin\left(\frac{2\pi}{T}t\right)$, with amplitude $\dot{\gamma}_M$ of 0.5-5 s^{-1}, is imposed by applying an oscillatory external pressure using a couple of commercially available pressure controllers. We vary the oscillations period T from 1 to 10 s. The filaments centerline $r(s,t)$, parametrized by arclength s, is extracted from time-lapse images through a custom-made image segmentation algorithm. We compute the gyration tensor as:

$$G_{i,j}(t) = \frac{1}{L}\int_0^L \left[r_i(s,t) - \bar{r}_i(t)\right]\left[r_j(s,t) - \bar{r}_j(t)\right] ds \tag{1}$$

where $\bar{r}(t)$ is the instantaneous center-of-mass position and L the filament contour length. The eigenvectors of the gyration tensor are used to find the mean filament orientation angle χ with the flow direction, while its eigenvalues (λ_1,λ_2) are used to compute a sphericity parameter $\omega = 1 - 4\lambda_1\lambda_2/(\lambda_1 + \lambda_2)^2$, which varies from $\omega = 1$ for a straight shape to $\omega = 0$ for a nearly isotropic configuration.

RESULTS

A constant shear rate can be represented as a linear superposition of a rotational flow and an elongational flow, with equal magnitude. While the pure rotational part is responsible for the tumbling motion of the filament, the elongational part can be further split into a compression region and an extensional region. In a sinusoidal flow, however, every half period the flow reverses its direction, leading the compression and extensional quadrant to be inverted. In Fig.1a are reported two typical image sequences of a 12 µm actin filament during a single oscillation. Here, the imposed maximum viscous stresses ($\dot{\gamma}_M = 3.7\,s^{-1}$) are large enough to overcome bending resistance [2], and hence we observe strong deformations. In both cases, the initial orientation ($\chi_0 = \chi(t=0)$) lies in the compression quadrant ($\pi/2 \leq \chi_0 \leq \pi$). Despite a small difference in χ_0, one can observe a different evolution of the orientation angle. The filament in the upper panel is trapped in the compression and extensional quadrants for $0 < t < T/2$ and $T/2 < t < T$, respectively. As a consequence, a continuous buckling of the polymer is found in the first half cycle, while a continuous stretching occurs in the remaining part of the period. We call this deformation dynamics as a CB-CS pair (Continuous Buckling-Continuous Stretching). A different situation is found in the second example (lower panel). Here, the rotation induced by the shear is large, and the filament crosses the boundary between the compression and extensional quadrant. As a result, at the

*Corresponding author. E-mail: ictam2020@aimgroup.eu.

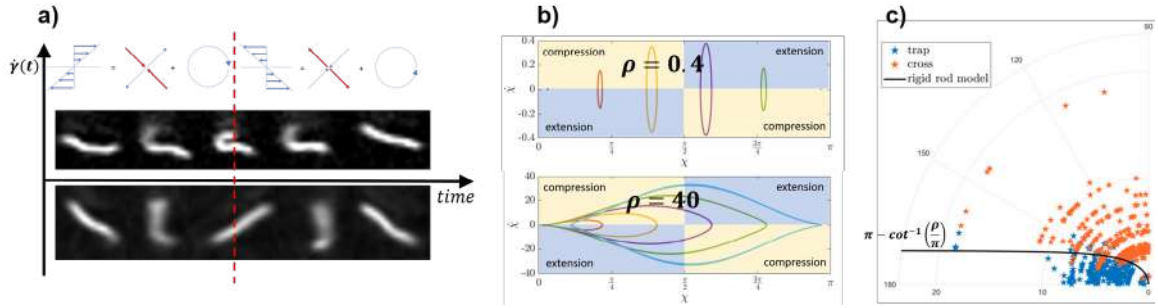

Figure 1: (a) Typical image sequences of a deformed actin filament during a sinusoidal shear rate. (b) Orbits in the (χ,$\dot{\chi}$) phase space of a rigid rod in an oscillatory shear flow, for two different dimensionless periods ρ (see text). (c) Polar plot showing the probability for a filament of being trapped in the compression quadrant, as a function of initial orientation and dimensionless period.

beginning of each half period, it is always initially oriented along the compression axis, and thus can be deformed and stretched twice during one period. We call this event as a Buckling-then-Stretching pair (BTS-BTS). In order to describe the orientation and deformation dynamics of the filaments, we first consider the simplest possible model for a fiber in a simple shear flow: the rigid rod model, which can be derived by the solution of Jeffery's equation in the limit of infinite aspect ratio. The evolution of the rod orientation in 2-D is governed by:

$$\dot{\chi}(t) = \dot{\gamma}(t) sin^2(\chi(t)) \tag{2}$$

The solution to the above ODE:

$$\chi(t) = cot^{-1}\left[cot(\chi_0) + \frac{\rho}{2\pi}\left(1 - cos(\frac{2\pi}{T}t)\right)\right], \tag{3}$$

with $\rho = \dot{\gamma}_M T$, is independent of the filament length L. In the (χ,$\dot{\chi}$) phase space, Eqs. 3 and 2 correspond to closed orbits, whose shape depends on the initial orientation χ_0 and dimensionless period ρ. As illustrated in the upper panel of Fig. 1b, for small ρ, the oscillations are confined to a small range of orientation around the initial configuration. As ρ increases (bottom panel), the phase-portraits extend and eventually span the whole orientation quadrant. Based on such orbits, we compute the probability to change shear quadrant during a semi-period, given any initial filament orientation $\chi_0 \in [\pi/2, \pi]$. For a given ρ, we found two distinct angular intervals, separated by:

$$\chi_0^\star(\rho) = \pi - cot^{-1}\left(\frac{\rho}{\pi}\right) \tag{4}$$

When $\chi_0 \geq \chi_0^\star$, the filament is trapped in the compression quadrant, while if $\chi_0 < \chi_0^\star$, it can sample the whole phase space. Eq. 4 determines a boundary between two regions in a polar plot (ρ,χ_0), which can be tested against our experimental data, obtained for different combination of $\dot{\gamma}_M$ and T, and for various L. As shown in Fig. 1c, the agreement is excellent, suggesting that the orientation dynamics of semi-flexible filaments is not strongly affected by the deformation, as also reported in a recent work [1].

Based on the above observations, we expect the deformation dynamics to dependent on the couple (ρ,χ_0). In particular, we expect the trapping region to be associated with CB-CS events, while the crossing region to BTS-BTS pairs. We have tested these predictions. The scenario is qualitatively in accordance with our expectations, although the transition is blurred from the presence of rotational diffusion. Moreover, a second transition to simple tumbling motion is found for initial angles close to $\pi/2$. In these region, filaments rotate so fast that they rapidly reach the extensional quadrant before any deformation is possible. We also perform numerical simulations matching the experimental conditions, using inextensible Euler–Bernoulli beam theory and nonlocal slender-body hydrodynamics in the presence of thermal fluctuations [2]. We observe a good agreement between experimental results and simulations.

References

[1] M. Harasim, B. Wunderlich, O. Peleg, M. Kröger, and A. R. Bausch, "Direct observation of the dynamics of semiflexible polymers in shear flow," *Phys. Rev. Lett.*, vol. 110, p. 108302, Mar 2013.

[2] Liu2018, "Morphological transitions of elastic filaments in shear flow," *Proceedings of the National Academy of Sciences*, vol. 115, no. 38, pp. 9438–9443, 2018.

[3] V. Kantsler and R. E. Goldstein, "Fluctuations, dynamics, and the stretch-coil transition of single actin filaments in extensional flows," *Phys. Rev. Lett.*, vol. 108, p. 038103, Jan 2012.

[4] C. M. Schroeder, H. P. Babcock, E. S. G. Shaqfeh, and S. Chu, "Observation of polymer conformation hysteresis in extensional flow," *Science*, vol. 301, no. 5639, pp. 1515–1519, 2003.

[5] J. M. Tarbell, Z.-D. Shi, J. Dunn, and H. Jo, "Fluid mechanics, arterial disease, and gene expression," *Annual review of fluid mechanics*, vol. 46, pp. 591–614, Jan 2014. 25360054[pmid].

[6] B. Dincau, E. Dressaire, and A. Sauret, "Pulsatile flow in microfluidic systems," *Small*, vol. 16, no. 9, p. 1904032, 2020.

HYDRODYNAMICS OF OPTO-ELECTROTHERMAL TWEEZERS

Rajorshi Paul[1], Aloke Kumar[2], and Tian Tang[*3]
[1]Department of Mechanical Engineering, Stanford University, Stanford, USA
[2]Department of Mechanical Engineering, Indian Institute of Science, Bangalore, India
[3]Department of Mechanical Engineering, University of Alberta, Edmonton, Canada

Summary Simultaneous use of a high frequency alternating electric field and a laser induced heat source generates vortex flows inside microfluidic channels which can be used for manipulating particles at the micro- and nano- length scales, including live cells and biomolecules. Here, we present a theoretical model to describe the hydrodynamics of this phenomenon. Semi-analytical solutions for the temperature, pressure and velocity fields have allowed us to systematically analyse the effect of relevant material properties and experimental parameters. Further we have studied the flow patterns under the influence of two heating sources to address their potential interference. Results from this work provide useful insights into the design of efficient rapid electrokinetic patterning techniques using opto-electrothermally induced vortex flows.

INTRODUCTION

Opto-electrothermal tweezers (OETTs) represent an interesting hydrodynamic phenomenon, wherein opto-electrothermally activated and maintained microscale vortices can be used effectively as tweezers for manipulating matter at the micro- and nano- length scales. The typical experimental set-up for generating such flows consists of two Indium tin oxide (ITO) coated glass slides separated by spacers forming a microfluidic channel. The ITO acts as the electrodes to which an external high frequency AC field is applied. The microfluidic channel is filled with an electrolyte solution, typically aqueous KCl. On simultaneous application of a highly focused laser beam (wavelength: 1064nm) on the surface of the electrode, vortices are generated inside the microfluidic channel, with a stagnation zone on the optical axis at the surface of the irradiated electrode (Figure 1a). Particles of micron and sub-micron length scales suspended in the electrolyte are transported via viscous drag and subsequently trapped in the stagnation zone. By modulating the optical landscape, the aggregation of trapped particles can be manipulated non-invasively. This phenomenon, originally devised for manipulating colloidal assemblies, is also known as Rapid Electrokinetic Patterning (REP) [1].

The physical mechanism behind the phenomenon is as follows. The incident laser creates localized heating of the electrode, generating thermal gradients of the order of 10^5 K/m in the electrolyte. This creates local perturbations in the electrical permittivity and conductivity of the fluid, which is manifested in the form of a volumetric force. As a result, toroidal micro-vortices form which are capable of trapping particles. The strength of the micro-vortices, measured in terms of the fluid velocity is a function of the material properties of the electrode and electrolyte such as electrical and thermal conductivities, as well as experimental parameters, such as the frequency of the AC field, and the heating profile of the laser source. Despite experimental efforts and some direct simulations of particular systems, there has not been a systematic investigation on the nature of the governing equations and dependence of the temperature and velocity fields on physical parameters. We fill this gap by developing a rigorous theoretical model, semi-analytical solution and detailed parametric analysis.

MATHEMATICAL MODEL

The OETT problem can be decomposed into two sub boundary value problems (BVPs), which are thermal and hydrodynamic respectively. The thermal problem describes the temperature field in the fluid which is essential for computing the volumetric opto-electrothermal force. Heat transfer in the fluid is conduction dominated as the thermal Peclet number is small, $\sim O(10^{-3})$. The hydrodynamic problem describes the fluid flow in the system due to the volumetric force, which is coupled to the thermal problem by the Stokes equation, as the Reynolds number for the flow is small, $\sim O(10^{-3})$. Non-dimensionalization of the BVPs identifies six governing dimensionless parameters: ϕ (ratio of thermal conductivity of the fluid to that of the electrode), ν (dimensionless absorption coefficient of the electrode towards laser radiation), δ (dimensionless electrode thickness), λ (dimensionless width of the laser beam), κ (a dimensionless Coulombic forcing which depends on the electrical conductivity and permittivity of the fluid, and the AC frequency) and the Biot number Bi accounting for thermal convection between environment and the device. ϕ and ν can be modulated by the selection of materials, δ and λ are mainly controlled by experimental set-up, and κ is influenced by both materials and operating conditions. Noting axisymmetry about the optical axis, the thermal BVP can be solved using the Hankel transformation resulting in a semi-analytical solution in closed-form. The hydrodynamic BVP has been solved using the finite volume method in the cylindrical coordinate system.

RESULTS

Flow pattern predicted from the proposed model agrees well with experimental results; a qualitative comparison can be seen from Figures 1b and 1c. Using the same non-dimensionalization introduced in the modelling we can collapse the

*Corresponding author. E-mail: ttang1@ualberta.ca

experimental data (temperature and velocity obtained with different AC fields and laser powers) onto a single curve which agrees well with the solution from the model (comparison not shown). The model also allows us to systematically study the effects of the six dimensionless parameters identified earlier. The parametric analysis is useful in understanding how the hydrodynamics of opto-electrothermal micro-vortices can be modulated by designing material and experimental parameters. For example, a linear relationship is found between κ and the magnitude of dimensionless velocity (see Figure 1d for the point located on the optical axis midway between the two electrodes). Because κ depends on the frequency of the AC field, this allows for precise control of the velocity using the AC frequency, compared to the commonly used control using voltage.

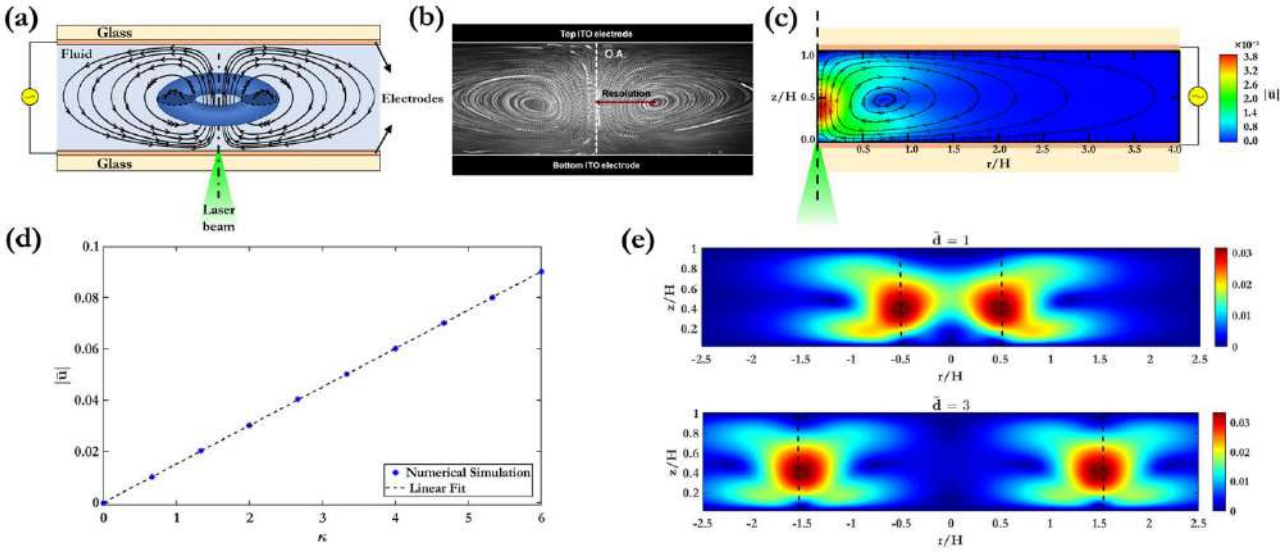

Figure 1. (a) Schematic of the experimental set-up for creating an OETT. (b) A visual representation of the OETT vortex obtained by Kwon et al experimentally [2]. (c) Solution of the governing BVPs showing the velocity field and streamlines which resemble the experimental observation in (b). (d) The influence of non-dimensional parameter κ on the magnitude of the dimensionless fluid velocity, for the point located on the optical axis midway between the two electrodes. (e) The interference between two adjacent opto-electrothermal vortices when the dimensionless separation between the optical sources are 1 and 3 respectively.

The system of governing equations is linear and homogeneous, therefore, by superposition of the solutions, we have studied the effect of multiple optical sources on the hydrodynamics. Figure 1e shows strong interference between two optical sources when their separation is the same as the height of the microfluidic channel, and no interference when their separation is three times the height. This implies that each optical source is associated with a quantifiable resolution beyond which the addition of another optical source will have little influence and the two vortices will essentially be independent of each other. This resolution can be interpreted as the radius of the stagnation zone of the micro-vortex, and therefore, can be correlated to the size of the particle cluster trapped in an OETT device. It is hence possible to control the size of the particle aggregation by modulating the flow patterns resulting from interacting vortices.

CONCLUSIONS

The present study proposes a mathematical model for the hydrodynamics of opto-electrothermal tweezers used to manipulate micro- to nano- particles. Predictions from the model are in good agreement with experimental results. The systematic analysis of material and experimental parameters would offer precise control of the process which would be pertinent in sensitive operations, e.g., those involving live cells. Non-dimensionalization and grouping of the physical parameters into dimensionless forms allow for wide applicability of our results.

ACKNOWLEDGMENT

Authors would like to thank Dr. Eric Murphy and Dr. Avanish Mishra for their valuable insights in model development and experimental results.

References

[1] Williams S. J., Kumar A., Wereley S. T. Electrokinetic patterning of colloidal particles with optical landscapes *Lab Chip* **8**: 1879-1882, 2008.
[2] Kwon J. S., Wereley S. T. Light-actuated electrothermal microfluidic motion: experimental investigation and physical interpretation *Microfluid Nanofluid* **19**: 609-619, 2015.

DYNAMICS OF PARTICLES SUSPENDED IN VISCOELASTIC LIQUIDS IN CONFINED FLOWS IN MICROFLUIDIC APPLICATIONS

Gaetano D'Avino and Pier Luca Maffettone
Dipartimento di Ingegneria Chimica, dei Materiali e della Produzione Industriale, Università di Napoli Federico II, P.le Tecchio 80, 80125 Naples, Italy

Summary Solid particles suspended in viscoelastic fluids are encountered in a variety of industrial applications. Viscoelasticity of the suspending medium has a strong influence on the particle motion leading to phenomena not observed in Newtonian fluids [1]. In the last years, our group developed efficient numerical methods based on the Arbitrary Lagrangian-Eulerian technique to accurately compute the flow and stress fields around rigid or deformable particles of arbitrary shape immersed in a viscoelastic fluid subjected to a general flow field [2-4].
We here present an overview of the recent results on the dynamics of particle dynamics in microfluidics channels with specific emphasis on their self-assembly in ordered trains.

INTRODUCTION

The focusing of particles at the centerline of a microfluidic channel induced by fluid viscoelasticity has been of great interest over the last years [5]. Particle alignment in a viscoelastic medium can be achieved in a simple straight microchannel avoiding extra components and/or complex designs of the device. In brief, a particle suspended in a viscoelastic medium experiences a motion with a component transversal to the main flow direction. Since the 'transversal velocity' is 2–3 orders of magnitude lower than the main flow velocity, very long channels (compared to the cross- section characteristic dimension) are required to achieve highly efficient alignment. Microfluidics is, then, a very well-suited framework to exploit the migration phenomenon. To date, 3D particle focusing induced by fluid viscoelasticity is a well established, finely controllable technique to manipulate trajectories of particles with spherical shape. Two aspects are of interest in this presentation: what happens when the spherical particles are close enough to hydrodynamically interact, and what happens when the particles are non-spherical.

Spherical Particle Self-Assembly in Ordered Trains

Very recent experiments and simulations have shown that when inertia is negligible viscoelasticity is able to rearrange the microstructure and promote ordering [6]. The formation of a train of particles at approximately equal distances has been observed in a shear-thinning viscoelastic fluid, while no ordering has been reported for constant viscosity fluids. The relevant parameters are: the confinement ratio R/H (see Fig.1), Weissenberg number $Wi=\lambda/t_f$ (the characteristic time λ of the fluid and the characteristic time t_f of the flow), solid volume fraction ϕ.

The sketch of the experimental situation is reported in Fig. 1. Three phenomena are observed: Caging of the particle at the channel axis for the crossflow migration; Ordering of the particles to form a train with a specific interparticle distance; possible pairing of particles to form doublets.

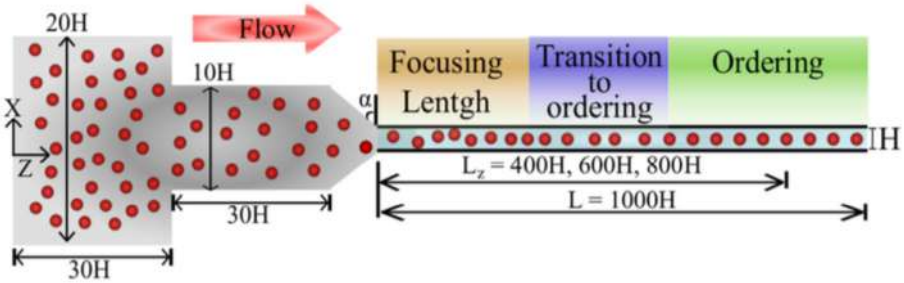

Figure 1. Microfluidic device with relevant dimensions. Particles of radius R converge gently to the glass channel, align after a certain length, and then self-order.

The main experimental outcomes are: i) fluid viscoelasticity drives self-assembly of particle trains in a straight microfluidic channel; ii) Throughput up-to 2400 particle/second; iii) Shear-thinning required to achieve the ordering; iv) Dominant distance between ordered particles does not depend on *Wi*-values; v) larger *Wi*-values enhance the fraction of ordered particles at a given dimensionless distance from inlet; vi) at larger loadings formation of particles doublets.

MODELING

Figure 2 shows the basics of the modelling efforts. We assume that caging is already occurred in the inlet section of the cylindrical tube of Fig. 1. The tube is extremely long (L/D>>1) and the number of particles flowing at the channel axis is very large. Relative velocity between consecutive particles is three orders of magnitude lower than the main flow velocity.

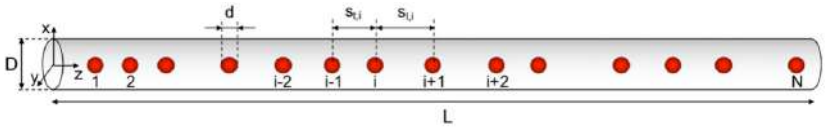

Figure 2. The simplified modelling situation with a train of particles at the channel axis.

We assume that each particle hydrodynamically interacts only with the leading and trailing one. Complete direct numerical finite element simulations of the problem with just three particles on a line are numerically solved to yield particle translational velocity for different interparticle distances.
The results show that the spatial evolution of the microstructure strongly depends on the particle volume fraction and initial distance distribution. In general, at very low volume fractions, weak hydrodynamic interactions prevent significant changes of the initial microstructure. At intermediate values of the particle concentration, ordering is possible. At high volume fractions, strings of nearly-touching particles form. A partially ordered structure in inflow strongly increases the ordering efficiency. On the contrary, the *Wi*-value has a small effect on the ordering phenomenon as in the experiments. A simple stability analysis justifies this scenario.

SPHEROIDAL PARTICLES

Similar analysis has been carried out with couples of spheroidal particles, which are assumed to lay on the channel axis with the largest dimension aligned with it as confirmed by recent numerical simulations [7]. Preliminary results show that, at a moderate confinement ratio, spheroids with small aspect ratio behave very similar to spherical particles. The most relevant quantitative difference concerns the attraction region at small distances: for spheroids, the critical Weissenberg number is slightly lower and, more importantly, the attraction region is narrower than the spherical particle case. A behavior similar to spherical particles is also observed when the confinement ratio is reduced. In this case, the attraction region at large distances is never observed whereas attraction at small distances is always present except for high values of the Weissenberg number. As the aspect ratio of the spheroid is increased, a relevant qualitative difference from the spherical case is observed: the attraction region at small distances is not present, i.e., the relative particle velocity is always positive at small interparticle distances. Hence, regardless of the Weissenberg number, two close spheroids always repel and reach an equilibrium distance or a sufficiently large distance such that hydrodynamic interactions become negligible. Hence, in this case, the formation of doublets is reduced.

A possible explanation for the attraction/repulsion dynamics at small distances can be based on the local stress field in the fluid domain around the particles. In the fluid between two spherical particles at a relatively large distance, the stress field is found to be qualitatively similar to the one expected for an isolated particle. The stress distribution is, of course, quantitatively different from the isolated case because the particles are still relatively close one to each other. On the contrary, as the interparticle distance is reduced, the stress is more uniform in the gap. In this case, indeed, the fluid between the two particles travels at approximately the same velocity of the particles leading to a small velocity gradient that, in turn, produces low viscoelastic stresses. In the former case, the normal stress gradient at the internal particle surfaces counteracts the stress around the external part of the particles, giving rise to a net force that pushes the particles away. On the other hand, the weak stress gradient between the particles in the second case of is not able to contrast the external stresses resulting in particles attraction. The local stress field for spheroidal particles confirms this argument. The shear rate between two close spheroids (that repel) is found to be not uniform. This is likely due to the particle shape and, more specifically, to the large curvature near the tips of the spheroids. Such effect is similar to what observed for the lateral migration of a spheroid where, around the tip, the normal stresses are larger as compared to spherical particles, leading to wall repulsion even when the spheroid is very close to the wall [7].

Ordering of spheroidal particles is under investigation.

References

[1] D'Avino G., Maffettone P.L., *J. non-Newtonian Fluid Mech.*, **215**, 80-104, 2015.
[2] Hu H.H., Patankar N.A., and Zhu M.Y., *J. Comp. Phys.*, **169**, 427–462, 2001.
[3] D'Avino G., Maffettone P.L., Greco F., and Hulsen M.A., *J. non-Newtonian Fluid Mech.*, **165**, 466-474, 2010.
[4] D'Avino G., Romeo G., Villone M.M., Greco F., Netti P.A. and Maffettone P.L., *Lab Chip*, **12**, 1638-1645, 2012.
[5] D'Avino G., Greco F. and Maffettone P.L., *Ann. Rev. Fluid Mech.*, **49**, 341-360, 2017.
[6] Del Giudice F., D'Avino G., Greco F.., Maffettone P.L., Shen A.Q., *Phys Rev Appl* **10**:064058, 2018
[7] D'Avino G., Hulsen M.A., Greco F., Maffettone P.L., *J. non-Newtonian Fluid Mech.*, **263**, 33-41, 2019

REORIENTATION OF PASSIVE AND ACTIVE CHIRAL PARTICLES IN MICROFLOWS

Francesca Tesser[1], Olivia du Roure[1], Justine Laurent[1], Andreas Zöttl[2], Anke Lindner*[1]
[1]PMMH, ESPCI, Paris, France
[2]Institute for Theoretical Physics, TU Wien, Vienna, Austria

Summary We investigate the dynamics of passive and active chiral microparticles in viscous shear flows. In such flows, helical particles are known to drift in the vorticity direction, with the sign of the rheotactic drift being function of the handedness. When a sphere is added to the helical particle, the sphere acts like and anchoring point and the rheotactic drift becomes a rheotactic torque now orienting particles into the vorticity direction. Here we use microprinted helices with a spherical "head" with perfect control of the helix shape as well as the handedness. Using this model system, we investigate the effect and the strength of the rheotactic torque. Due to the comparable shapes of E-coli bacteria, formed by a helical flagella bundle and a body, our study can also shed light on bacterial dynamics close to surfaces, being inherently more complex compared to the passive microparticles.

INTRODUCTION

Helical particles in viscous shear flows migrate across streamlines as a result of their shape and the shear flow [1]. Such chirality-induced effects are also at the origin of rheotactic effects in E.coli bacteria, due to the helical structure of their flagellar bundle. In this case, the rheotactic drift in combination with viscous friction on the bacterial head produces what is known as rheotactic torque, acting as a bias on the orientation of the cell [2]. For elongated particles, this torque applies at the same time as the usual Jeffery tumbling and its effect is to modify dramatically the periodic closed orbits of the Jeffery dynamics into spiral orbits. By using a high-resolution micro-printing technique, we fabricate micro-particles with a controlled and tuneable chiral shape, like the one of a simplified but passive bacterium. We use them to perform experiments where the re-orientation dynamics can be observed under shear flow as the particle is transported in a micro-fluidic channel close to a surface. In other words, we print both left-and-right handed helices attached to a spherical body and follow them individually as they move away from their initial Jeffery orbit, eventually flip and are stabilized perpendicularly to the flow direction with the helix on the right or left according to their handedness. We show how this stabilization mechanism depends on the shear rate and the helix geometry and compare the experimental results with a theoretical model including the rheotactic torque and Jeffery dynamics. Finally, we discuss similarities of the observed dynamics of micro-printed helices with a head to the swimming of E-coli bacteria close to surfaces [3].

EXPERERIMENTAL SET-UP AND METHODS

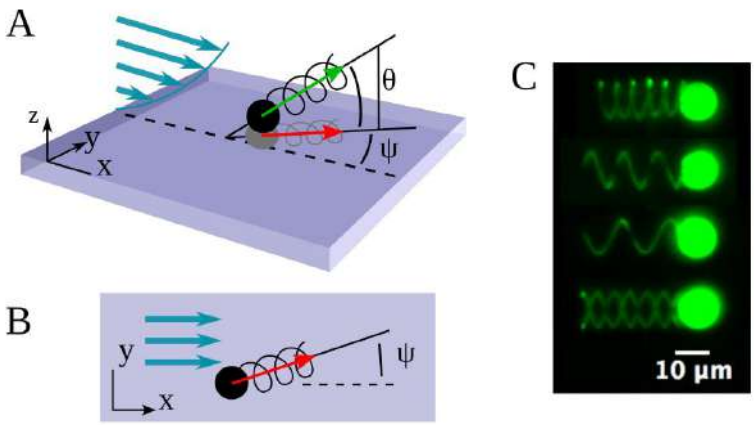

Figure 1. (A) Sketch of the experimental set up. The particle is transported by the flow in the vicinity of the bottom substrate, its orientation is characterised by the in plane angle Ψ and dipping angle Θ describing, respectively, the orientation with the flow direction and the orientation with the horizontal wall. (B) The particle projection as it is seen by the camera. The red arrow represents the particle projected length. (C) Fluorescent particles with different geometries (same radius 5 µm). From top to bottom: pitch values 5,10,15µm and a particle having two helices with opposite handedness with pitch 10 µm. From [4].

Fig. 1 shows the experimental set-up. Particles are flown close to the bottom of a microfluidic chamber far away from bounding side walls and thus experience a viscous shear flow in the z-direction. We follow the particles while they are transported downstream and record their tumbling and reorientation dynamics. Flow is imposed via a syringe pump.

The micro-particles are fabricated using a Nanoscribe 3D printer at the highest resolution possible. Helices are formed by less than 1 µm thick filaments and are of typical radius of 5 µm for a length of 1 µm. The pitch can be varied from 5 to 15 µm. A spherical particle is attached to the helices and has in all cases a radius of 5 µm. The densities of the particles

and the surrounding fluid are closely matched such as to only induce very weak sedimentation bringing the particles towards the channel bottom and maintaining them there.

RESULTS

We first investigate the reorientation dynamics of the helical particles as a function of their shape properties. The tumbling and reorientation dynamics are shown on fig. 2 for one Jeffery orbit on the top row and for the slow reorientation dynamics in subsequent oscillation periods on the bottom row. One observes a clear reorientation towards an orientation perpendicular to the flow direction, in this case with the helix pointing downwards. When the handedness is inversed (not shown) the orientation is also inversed, now with the helix pointing upwards.

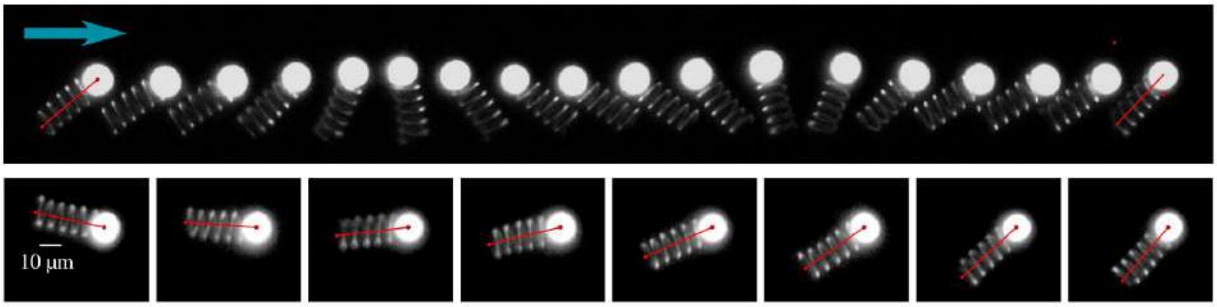

Figure 2. Top: subsequent snapshots of a particle over one period tumbling. The flow direction is from left to right. Bottom: snapshots of the particle orientation at its maximum oscillation amplitude, one image is shown every 5 oscillating periods. This series shows the slow reorientation of the particle to a direction more and more perpendicular to the flow, with the helix pointing down (left handed helix here). From [4].

We investigate the typical timescales for these orientation dynamics as a function of helix shape and show that they are function of the strength of the rheotactic torque. By performing a large number of experiments, we establish that for each handedness there is a stable orientation and that particles are able to switch orientation when initially positioned along an unstable orientation. Finally, we discuss an extra stabilizing effect given by the particle density inhomogeneity that, together with the presence of the wall, prevents the flip from happening from a limited range of initial conditions.

Finally, we compare our findings to recently discovered oscillatory surface rheotaxis of E-coli bacteria and show that those partially have the same origin as the particle reorientation of the passive objects discussed above.

CONCLUSION

Here we have investigated the dynamics of micro-printed left-and-right handed helices attached to a spherical body transported in a shear flow close to a surface. We followed these particles individually as they move away from their initial Jeffery orbit, eventually flip and stabilized perpendicularly to the flow direction with the helix on the right or left according to their handedness.

We showed how this stabilization mechanism depends on the shear rate and the helix geometry and compared the experimental results with a theoretical model including the rheotactic torque and Jeffery dynamics. Very good agreement has been obtained. Finally, we have shown the similarities between the observed dynamics of micro-printed helices with a head and the swimming of E-coli bacteria close to surfaces under flow.

References

[1] Marcos *et. al.,* Phys. Rev. Lett. (2009)
[2] Marcos *et al*., PNAS 2012
[3] Mathijssen *et al.,* Nature Comm. (2019)
[4] Tesser *et al.* in preparation (2020)

PARTICLE DYNAMICS DURING DIRECTED ASSEMBLY INTO BANDS

Andrew Yee[1] and Minami Yoda[*1]
[1]Woodruff School of Mechanical Engineering, Georgia Institute of Technology, Atlanta, GA USA

Summary Evanescent-wave visualizations have shown that suspended colloidal particles assemble into near-wall structures—"bands"—in combined Poiseuille and electroosmotic counterflow through microchannels. A small fraction of tracer particles are used to estimate particle concentrations and velocities during the various stages of band assembly. The number of particles attracted to the wall in the initial accumulation stage appears to grow exponentially, while the particle velocities are significantly less than the superposition of the flow and electrophoretic velocities throughout assembly.

INTRODUCTION

The manipulation and assembly of suspended particles flowing through a microchannel is of current interest in microfluidics and nanotechnology [1; 2]. This work studies a novel type of directed assembly driven by shear flow and dc electric fields (of magnitude $|E|$) where particles of radius $a = O(10^{-7}$ m) in dilute (bulk volume fraction $\varphi_\infty < 5\times10^{-3}$) suspensions are attracted to, then assemble into periodic elongated structures, which we call bands, near the channel wall (Fig. 1). This assembly occurs in Poiseuille and electroosmotic (EO) "counterflow" when these flows are in opposite directions and when $|E|$ exceeds a minimum value, $|E_{min}|$, which depends upon the near-wall shear rate $\dot{\gamma}$ and φ_∞ [3]. A number of banding characteristics, such as the time for bands to form after applying the electric field, appear to depend upon the electric field offset $|E|-|E_{min}|$, or how $|E|$ compares with the minimum value for band assembly [3]. Unlike previous reports of colloidal assembly [5], band assembly occurs in a flowing solution and very far from the electrodes.

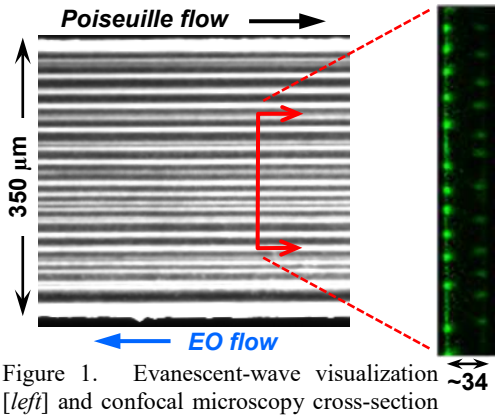

Figure 1. Evanescent-wave visualization [*left*] and confocal microscopy cross-section [*right*] of bands in a channel with a cross section of 34 µm × 350 µm [4].

Based on observations, band assembly is comprised of three stages: 1) (particle) accumulation; 2) band formation; and 3) steady-state (bands). Initial analyses based on spatially averaged grayscales of images of these structures obtained with evanescent-wave visualization suggest that the particle concentration grows exponentially during the initial accumulation stage [6]. Since the particle concentration is too high to allow detection of individual particles, these studies used "two-color" particle visualizations, where ~1% of the particles were tracers labeled with a different fluorophore to investigate particle dynamics over time for a range of flow conditions and determine if the number of near-wall particles also has an exponential growth during the accumulation stage.

EXPERIMENTS

These studies considered Poiseuille and EO flow of a dilute suspension through the central straight section of a S-shaped fused-silica microchannel of length 2.8 cm and cross section 34 µm × 320 µm at $\dot{\gamma} < 1800$ s^{-1} and $|E| < 500$ V/cm; in all cases, the flow Reynolds number was $O(10^{-1})$ (Fig. 2). A mixture of $a = 240\pm5$ nm polystyrene (PS) particles labelled with a red fluorophore with ζ-potential $\zeta_p = -55\pm7$ mV at $\varphi_\infty = 1.7\times10^{-3}$, plus tracer particles labelled with a green fluorophore with $\zeta_p = -60\pm7$ mV at $\varphi_\infty = 1.7\times10^{-5}$, were suspended in 1 mmol/L sodium tetraborate solution. The flow was illuminated by evanescent waves through the bottom channel wall and green particles with centers within 0.5 µm of the wall were imaged at three different distances from the channel inlet, namely $x = 0.61$ cm, 1.4 cm and 2.2 cm. Individual green particles can be discerned in the typical image over a field of view 203 µm square during the steady-state stage (Fig. 3), along with faint images of the bands which are mainly comprised of red particles.

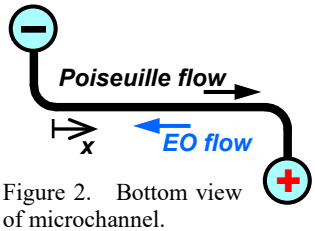

Figure 2. Bottom view of microchannel.

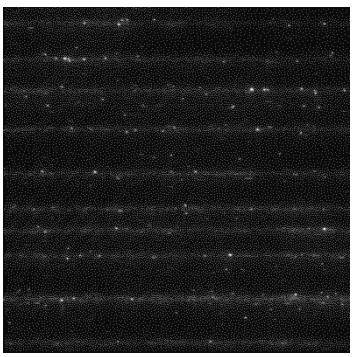

Figure 3. Contrast enhanced image of bright green tracers and faint red particles at $\dot{\gamma} = 1760$ s^{-1}, $|E|-|E_{min}| = 40$ V/cm.

All of the experiments started with "pure" Poiseuille flow, and then a dc electric field was applied at time $t = 0$. Images were acquired with an electron multiplying CCD camera at 10 Hz to estimate the number of tracer particles, and with a CMOS camera at 500 Hz to estimate the velocity of these tracer particles as a function of $t > 0$.

*Corresponding author. E-mail: minami@gatech.edu.

SUMMARY OF RESULTS

In all cases, particles are attracted to, and accumulate near the, microchannel wall before the particles assemble into bands. Tracer particle centers were detected in images where the background was minimized by subtracting off an average image. The average number of tracer particles N_p over the 203 μm square field of view was then determined as a function of time t (after the electric field is applied) over four independent realizations, and appears to grow exponentially during the accumulation stage for different $|E|-|E_{min}|$ at $\dot{\gamma} = 1760\ s^{-1}$ (Fig. 4), suggesting that the total number of particles also increases exponentially (assuming that the tracers are a consistent fraction throughout the flow). The band formation stage appears to start when $N_p \approx 50–80$, decreasing as $|E|-|E_{min}|$ increases.

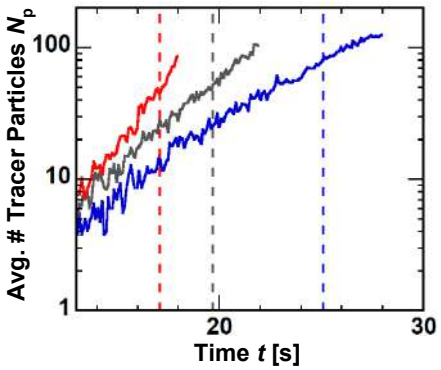

Figure 6. Semilog plot of the average number of particles *vs.* time t at $|E|-|E_{min}|$ = 16 [*blue*], 40 [*gray*], and 63 V/cm [*red*]; the dashed lines denote the end of the accumulation stage for each case.

The average tracer particle velocities U_p, determined using multilayer nano-particle tracking velocimetry at different particle-wall separations h (where a particle at $h = 0$ touches the wall) [7], are consistently lower than those predicted by the exact solution, *i.e.*, the superposition of the flow and particle electrophoretic velocities, during the accumulation stage, although U_p appears to increase slightly over time (Fig. 5). Interestingly, the slopes of the velocity profiles 3 s before the end of the accumulation stage and in steady state are within 10% of $\dot{\gamma}$.

During the steady-state stage, the particle velocities were analysed for particles within, and between, the band structures. The velocities of the tracer particles between the bands are essentially identical to those observed near the end of the accumulation stage, but those for the tracer particles within the bands are much lower, and essentially independent of h (Fig. 6). This suggests that the motion of the particles within the bands is severely hindered by interparticle interactions. Although the estimates of h for the particle velocities within the bands may be flawed because the high density of particles there will convert most of the evanescent-wave illumination to propagating waves, which do not have an exponential decay in their intensity, this result also indicates that the particles within the bands are moving *en masse*, irrespective of their distance from the wall.

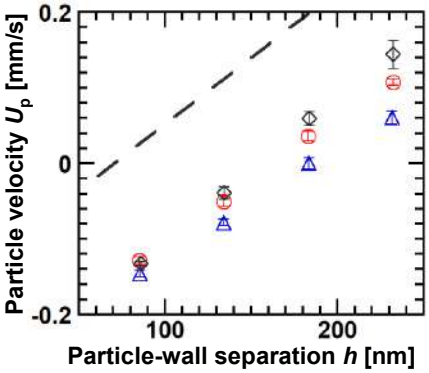

Figure 5. Particle velocity profiles 7 s (△) and 3 s (○) before the end of accumulation, during steady-state (◇), and compared with the expected particle velocity [*dashed line*] at $\dot{\gamma} = 1760\ s^{-1}$, $|E|-|E_{min}| = 16$ V/cm. The error bars denote standard deviations.

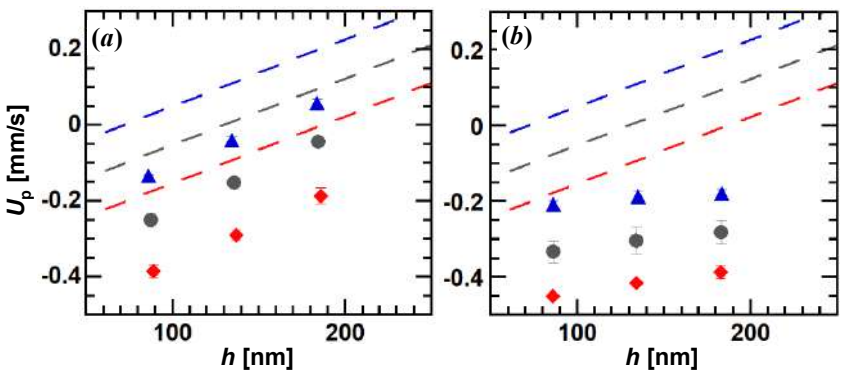

Figure 6 Particle velocity profiles between the bands (***a***) and within the bands (***b***) during the steady-state stage at $\dot{\gamma} = 1760\ s^{-1}$ and $|E|-|E_{min}| = 16$ (▲), 40 (●), and 63 (◆) V/cm and compared with the expected particle velocity [*dashed lines*]. Both graphs have the same vertical axis label; the error bars denote standard deviations.

References

[1] Sajeesh P., Sen A.K. Particle Separation and Sorting in Microfluidic Devices: A Review. *Microfluid. Nanofluid.* **17**:1-52, 2014.
[2] Hou X., *et al.* Interplay Between Materials and Microfluidics. *Nat. Rev. Mater.* **2**:17016, 2017.
[3] Yee A., Yoda M. Experimental Observations of Bands of Suspended Particles Subject to Shear Flow and Steady Electric Field. *Microfluid. Nanofluid.* **22**:113, 2018.
[4] Lochab, V., *et al.*. Dynamics of Colloidal Particles under Combined Pressure and Electric Potential Gradients. *Microfluid. Nanofluid.* **23**:134, 2019.
[5] Velev O.D., Bhatt K.H. On-chip Micromanipulation and Assembly of Colloidal Particles by Electric Fields. *Soft Matter* **2**:738-750, 2006.
[6] Yee A., *et al*. Determining Time Scales for Directed Assembly of Particles into Bands by Shear Flow and Electric Fields. Submitted to *Exp. Fluids*, 2019.
[7] Yoda, M., Kazoe, Y. Dynamics of Suspended Colloidal Particles Near a Wall: Implications for Interfacial Particle Velocimetry. *Phys. Fluids* **23**:111301, 2011.

BREAKUP OF SHEAR ACTIVATED NANO-THERAPEUTICS IN A MICROFLUIDIC DEVICE BY A CFD-STOKESIAN DYNAMICS APPROACH

Lorenzo Vasquez Giuliano[1], Graziano Frungieri *[1], Antonio Buffo[1], and Marco Vanni[1]
[1]Dipartimento di Scienza Applicata e Tecnologia, Politecnico di Torino, Torino, Italy

Summary The treatment of arterial obstructions can be strongly improved by the development of drug carriers with a highly localized action. Our research focuses on the investigation of Shear Activated Nano-Therapeutics, a novel class of drug carriers consisting in aggregates of nanoparticles, which are locally activated by the breakup induced by the viscous stress acting on them as they travel in obstructed blood vessels. We adopted a coupled Computational Fluid Dynamics - Stokesian Dynamics technique able to compute the history of the viscous shear forces experienced by the aggregates and to study the dynamics of breakup. We investigate the behaviour of different potential morphologies of the aggregates, in order to identify the most suitable for such a delivery strategy and to identify the critical structural properties to be taken into account when designing such carriers.

INTRODUCTION

Arterial obstructions represent one of the main causes of disease and death worldwide [1]. When treating this disease, the dose of active agent that can be administered to the patient has to be carefully chosen in order to limit the potential adverse effects due to the free circulation of the drug in the blood stream. For this reason, targeted drug delivery techniques have received considerable attention over the last years. One of the most promising delivery strategy is based on the observation that in obstructed blood vessel abnormally large shear stress are present. This feature of the hemodynamic condition has therefore pushed research towards the development of Shear Activated Nano-Therapeutic (SANT) particles [2]. SANTs are micro-metric agglomerates of polymeric primary nanoparticles on which a clot-lysing drug is deposited. As the nanoparticles are held together mainly through relatively weak Van-der-Waals forces, SANTs can be engineered in such a way that they break up into smaller fragments when they enter a high shear zone; these fragments, because of their smaller size, experience lower hydrodynamic drag forces, thus they are more likely to adhere to the obstruction and to perform their clot-lysing action.

In this work we use a coupled Computational Fluid Dynamics - Stokesian Dynamics approach able to investigate the breakup dynamics of aggregates of primary particles [3, 4]. We tested our method on a microfluidic device designed in such a way as to mimic a pathological vessel obstruction. CFD simulations are performed to compute the flow field in the device and to extract a set of particle trajectories including the history of experienced shear stresses. Stokesian Dynamics simulations are instead carried out to compute the distribution of mechanical stress inside the aggregate structure, from which the occurrence of breakup can be predicted. We investigate different potential SANTs morphologies by comparing them in terms of conditions for the onset of breakup and size distribution of the generated fragments.

METHODS

Computational Fluid Dynamics

We used ANSYS Fluent 19.2 to simulate the flow field of a Newtonian fluid with viscosity $\mu = 1 \times 10^{-3}\,\mathrm{Pa \cdot s}$ flowing in a rectangular microchannel. The presence of the clot is modelled by introducing a 90% lumen obstruction. The domain is divided in 10^5 hexahedrical cells (left panel in Figure 1). The flow rate is adjusted in order to obtain the typical values of shear stress in a blood vessel (10 Pa in the unrestricted vessel and 100 Pa in the obstructed vessel).

The computed flow field is used to extract the trajectories of a set of 1000 aggregates. Being their Stokes and Reynolds numbers much lower than the unity, the aggregates can be treated as tracer particles, i.e. massless particles with negligible inertia; their equation of motion therefore reads as:

$$\dot{\mathbf{x}}_\mathbf{p}(t) = \mathbf{u}(\mathbf{x}_\mathbf{p}(t)) \tag{1}$$

where $\dot{\mathbf{x}}_\mathbf{p}(t)$ is the velocity of the particle and $\mathbf{u}(\mathbf{x}_\mathbf{p}(t))$ is the velocity of the flow at the particle position.

Stokesian Dynamics

In Stokesian Dynamics (SD) simulation, the morphology of the aggregates is taken into full account. This technique, by using a first order approximation of the flow field, allows one to evaluate the hydrodynamic forces acting on each primary particle composing the aggregate and, based on these, to evaluate the normal stress acting at each inter-particle contact [4]. In order to identify the most suitable morphology for our delivery strategy, three classes of clusters characterized by different shape and porosity are studied; we analyze the behaviour of aggregates obtained by a diffusion limited aggregation (DLCA), Random Close Packing aggregates (RCP) and hollow RCP aggregates. In order to get statistically robust results, for every class we studied 100 aggregate realizations. Therefore, a statistical analysis has been conducted in order to count for the variety of aggregate morphologies and aggregate trajectories.

*Graziano Frungieri. E-mail: graziano.frungieri@polito.it.

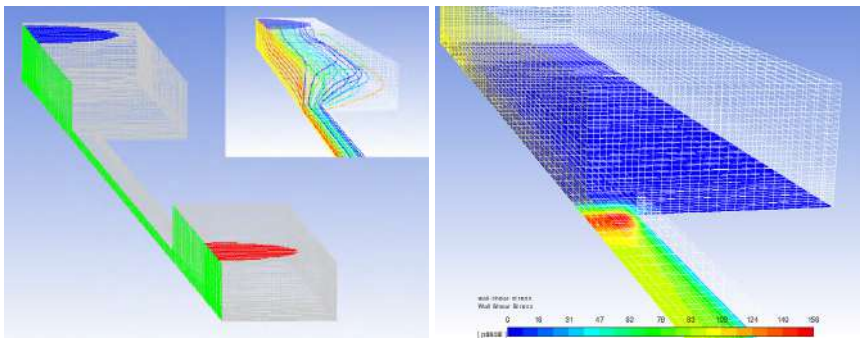

Figure 1: Left) Microchannel with inlet (blue surface), outlet (red surface), symmetry plane (green surface) and walls (grey surfaces). The inset shows the trajectories of a subset of tracer particles. Right) Wall shear stress on the bottom wall of the microchannel.

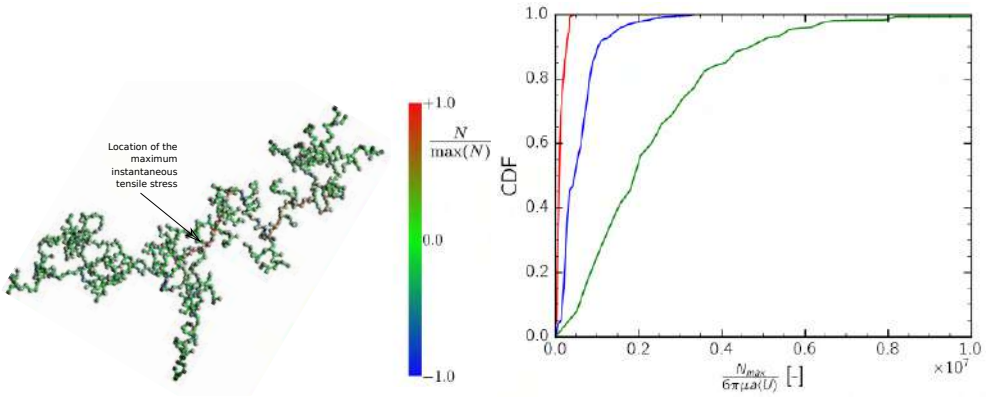

Figure 2: Left) Distribution of normal force in a DLCA cluster. A ball and stick representation has been used to highlight the inter-particle bonds. Right) Cumulative Distribution Function of the maximum tensile force experienced by RCP clusters (red), DLCA (blue) and hollow RCP (green). On the x-axis, a is the radius of the NPs, $\langle U \rangle$ is the average velocity in the constricted section.

RESULTS

The flow field in the microdevice and the trajectories of a set of tracer particles were obtained by running CFD simulations. Figure 1 right) reports the contour plot of the shear stress evaluated at the bottom wall of the microchannel. It can be noticed that the shear stress is relatively mild ($\approx$ 10 Pa) in the unrestricted section, it reaches a peak value ($\approx$ 150 Pa) at the entrance of the constricted section and then goes down to a value of 100 Pa in the narrowed region.

By Stokesian Dynamics we computed the distribution of the normal forces at the inter-particle contacts of the aggregates, as they move along the microchannel. A sample instantaneous distribution for a DLCA cluster is shown on the left side of Figure 2. For this class of aggregates, the highest tensile forces are observed in the internal region, thus suggesting that the expected dominant mechanism of breakup should be the fragmentation in two almost equally sized fragments. On the contrary, in the case of RCP and hollow RCP clusters, the highest tensile forces are observed in the external region, so that a progressive erosion of the cluster should instead be expected [4]. In the right plot of Figure 2 the mechanical responses of three different populations of aggregates are compared through the Cumulative Distribution Functions of the maximum experienced tensile stress. Hollow RCP aggregates emerged as the most fragile structure (i.e. the highest internal tensile force were observed for this class), RCP aggregates as the most resistant, whereas DLCA aggregates had an intermediate behaviour.

Results are encouraging and show the feasibility of such a deliver strategy. The CFD-Stokesian Dynamics approach appears as a promising tool to identify the fundamental properties of the aggregates to take in account when designing shear-activated drug carriers.

References

[1] C.J.L. Murray, A.D. Lopez. Mortality by cause for eight regions of the world: Global burden of disease study. *The Lancet*, **349**:1269-1276, 1997

[2] N. Korin, M. Kanapathipillai, B.D. Matthews, M. Crescente, A. Brill, T. Mammoto, K. Ghosh, S. Jurek, S.A. Bencherif, D. Bhatta, A.U. Coskun, C.L. Feldman, D.D. Wagner, D.E. Ingber, Shear-activated nanotherapeutics for drug targeting to obstructed blood vessels. *Science* **337**: 738-742, 2012.

[3] J. De Bona, A. S. Lanotte, M. Vanni, Internal stresses and breakup of rigid isostatic aggregates in homogeneous and isotropic turbulence. *J. Fluid Mech.* **755**: 365-396, 2014.

[4] M. Vanni. Accurate modelling of flow induced stresses in rigid colloidal aggregates.*Computer Physics Communications*, **192**: 70-90, 2015

ON THE INFLUENCE OF THE SECONDARY FLOW ON THE EFFICIENCY OF A MEMBRANELESS MICROFLUIDIC FUEL CELL

Wiebke Rösing*, Jörg König, and Christian Cierpka
Department of Mechanical Engineering, Technische Universität Ilmenau, Ilmenau, Deutschland

Summary The efficiency of membraneless microfluidic fuel cells is limited by the formation of concentration boundary layers at the electrodes, resulting in low power density and low fuel utilization. This work demonstrates a novel method to enhance the diffusion-limited mass transport by decreasing the size of the concentration boundary layer using a transversal secondary flow. The so-called Dean vortices are induced by a curved microchannel and enhance the mass transport of fresh reactant towards the electrodes. In this study, numerical simulation, electrochemical characterization methods and astigmatic particle tracking velocimetry (APTV) are used to characterize the correlation between the fuel cell efficiency and the transversal secondary flow.

Introduction

Novel microfluidic fuel cells have arouse enormous interest due to their possible application in portable electronic devices, such as mobile phones or clinical diagnostic devices [1,2]. They are a possible alternative to conventional batteries, because of their high energy density, low weight and the ability to be used without charging for a long period of time [1,3]. In microfluidic fuel cells, fuel and oxidant flow in parallel at low Reynolds number without convective mixing. The membraneless architecture eliminates problems such as ohmic losses of the membrane, the complex water management of the membrane and the challenge to miniaturize the membrane. Since the first published work in 2002 [3], numerous studies were published in the field of microfluidic fuel cell technology. However, it is still difficult to commercialize microfluidic fuel cells, because at practical flow rates and useful cell voltages poor fuel utilizations below 10% and low power densities persist problematic [4]. This is mostly caused by the formation of concentration boundary layers at the electrodes as shown in Figure 1. A possibility to reduce the size of the concentration boundary layers is to increase the flow rate. However, this results in a further decrease in fuel utilization due to a shorter residence time of the fuel and oxidant at the respective electrode. A simple alternative method for the suppression of the concentration boundary layer expansion is a passive flow control by using a curved microchannel, which induces a transversal secondary flow as sketched in Figure 2b) [5]. The generated counter rotating vortices, known as Dean vortices, enhance the transport of fresh reactant from the center of the channel to the concentration boundary layers. The strength of the Dean vortices can be characterized by the Dean number *De* [6]

$$De = Re3\sqrt{\frac{D_h}{2R}}3.$$

The Dean number depends on the radius of curvature R (see insert in Figure 4), the Reynolds number Re and the channel geometry expressed in terms of the hydraulic diameter D_h. In microfluidic fuel cells a controlled supply of reactant towards the electrodes is required, which can be easily achieved by adjusting the strength of the transversal flow by the variation of the Reynolds number for a channel with given radius of curvature.

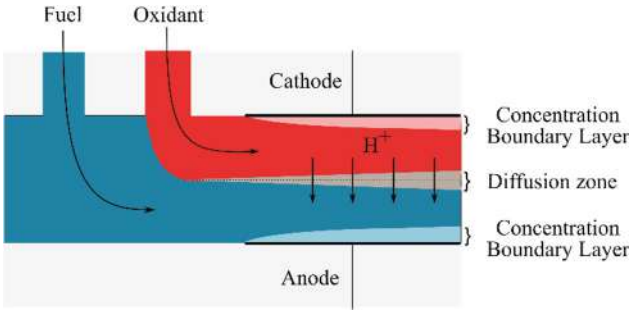

Figure 1. Schematic of the membraneless microfluidic fuel cell.

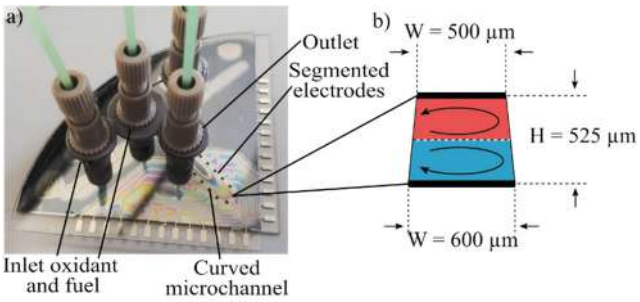

Figure 2. a) Photograph of the microfluidic device with segmented platinum electrodes on the top and the bottom of a curved microchannel. b) Cross-sectional view of the microchannel with sketched Dean-vortices.

In order to characterize the correlation between the performance of a microfluidic fuel cell and the transversal secondary flow, a partly curved microchannel with integrated segmented electrodes on the top and bottom of the microchannel was fabricated (Figure 2). This microfluidic fuel cell was characterized by using electrochemical measurement methods, astigmatic particle tracking velocimetry (APTV) [7] and numerical simulations.

Results

Numerical simulations were used to compare the performance of a straight and a curved microfluidic fuel cell. Hence, a numerical model including fluid dynamics, mass transport, charge conservation and chemical reaction kinetics with appropriate boundary conditions was applied. The numerical simulation demonstrate that by using a curved microfluidic fuel cell instead of a straight microfluidic fuel cell an increase of current density of about 8% at low flow rates (30 ml h^{-1}; De = 6.69) and an increase of 30% at higher flow rates (100 ml h^{-1}; De = 22.32) can be achieved, due to the induced counter rotating vortices [5]. To validate the results of the numerical simulation, astigmatic particle tracking velocimetry measurements were carried out to measure volumetrically all velocity components in the straight and curved channel part in between the segmented electrodes of the microfluidic device. The APTV measurement verifies the formation of two counter rotating vortices in the curved channel part, which are in good agreement with the numerical results. Furthermore, the microfluidic device with segmented electrodes enables a comparison of the electric current density obtained without the influence of Dean vortices in the straight channel part and with the enhanced mass transport induced by the Dean vortices in the curved channel part. Within this device electrochemical measurements were performed at first using a simple redox pair ferrocyanide/ferricyanide. The electrochemical measurements show that the formation of the concentration boundary layer diminishes the electrochemical reaction and thus decrease the current density along the straight part of the microchannel by about 20%. However, the Dean vortices appearing in the curved channel part enhance the mass transport and, therefore increase the current density (Figure 4). The higher the flow rate and thus the Dean number, the higher the current density of the electrodes (6,7,8) at the curved channel part compared to the current density of the electrodes (1,2,3) at the straight channel part.

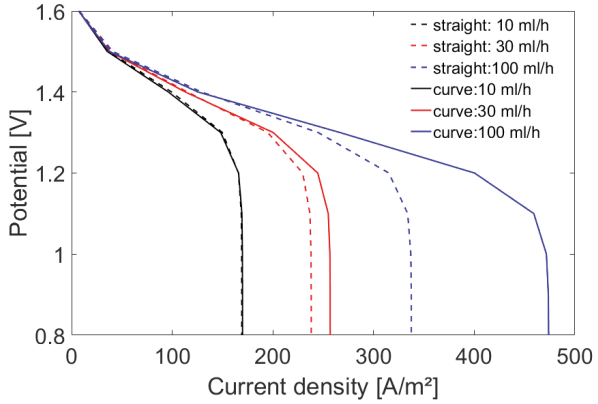

Figure 3. Simulated polarization curves for straight and curved microfluidic fuel cell at the three volumetric flow rates.

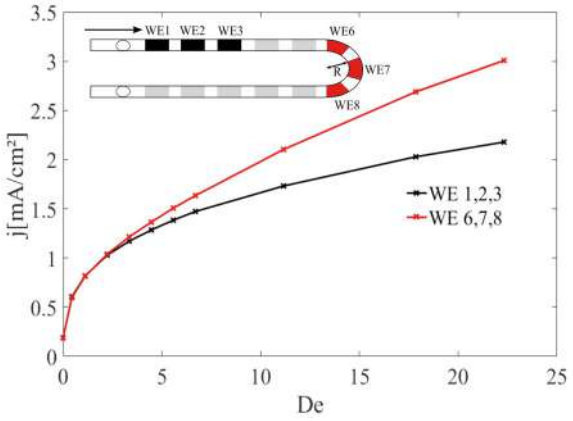

Figure 4. Experimental results for the current density measured simultaneously at working electrode 1 (WE1), WE2 and WE3 and at WE6, WE7 and WE8. Data were obtained by applying a potential of 400 mV in 5 mM potassium ferrocyanide and 5 mM potassium ferricyanide using 1 M KCl as supporting electrolyte with various flow rates resulting in Dean numbers ranging from 0 to 22.

Conclusion and Outlook

This study shows the performance improvement of a microfluidic fuel cell by decreasing the size of the concentration boundary layer at the electrodes using a curved microchannel, which induces counter-rotating vortices. Further experimental results, including polarisation curves and additional APTV measurements will be discussed at the conference to get a better understanding of the correlation between fuel cell efficiency and the flow physics.

References

[1] E. Choban. Microfluidic fuel cell based on laminar flow. *J Power Sources* **128**: 54–60, 2004.
[2] J. Massing, N. van der Schoot, C. J. Kähler, C. Cierpka. A fast start up system for microfluidic direct methanol fuel cells. *Int J Hydrogen Energ*. **44**: 26517–26529, 2019.
[3] R. Ferrigno, A.D. Stroock, T.D. Clark, M. Mayer, G.M. Whitesides. Membraneless Vanadium Redox Fuel Cell Using Laminar Flow. *J Am Chem Soc.* **124**: 12930–12931, 2002.
[4] E. Kjeang, N. Djilali, D. Sinton. Microfluidic fuel cells. *J Power Sources* **186**: 353–369, 2009.
[5] W. Rösing, T. Schildhauer, J. König, C. Cierpka. Passive control of the concentration boundary layer in microfluidic fuel cells using Dean vortices. *Microfluid Nanofluid.* **23**: 110, 2019.
[6] W. R. Dean. Fluid Motion in a Curved Channel. *P Roy Soc London* **121**: 402–420, 1928.
[7] C. Cierpka, R. Segura, R. Hain, C.J. Kähler. A simple single camera 3C3D velocity measurement technique without errors due to depth of correlation and spatial averaging for microfluidics. *Meas Sci Technol.* **21**: 45401, 2010.

DROPLETS IN SHEAR FLOWS

Marco Edoardo Rosti*[1] and Shu Takagi[2]
[1]Okinawa Institute of Science and Technology Graduate University, Onna, Kunigami, Okinawa, Japan
[2]The University of Tokyo, Department of Mechanical Engineering, The University of Tokyo, Tokyo, Japan

Summary We study the rheology of a two-fluid emulsion in semi-concentrated conditions; the solute is Newtonian while the solvent an inelastic power law fluid. The problem at hand is tackled by means of direct numerical simulations using the volume of fluid method. The analysis is performed for different volume fraction and viscosity ratio under the assumption of negligible inertia and zero buoyancy force. Several carrier fluids are considered encompassing both the shear-thinning and thickening behaviours. We show that the effective viscosity of the system increases for shear-thickening fluids and decreases for the shear-thickening ones for all the viscosity ratios considered. The changes in the emulsion viscosity are due to modifications of the coalescence in the system obtained by changing the carrier fluid property.

INTRODUCTION

Emulsions are mixtures of two or more liquids that are partially or totally immiscible. They are present in many biological and industrial applications such as waste treatment, oil recovery and pharmaceutical manufacturing and are also relevant in the field of colloidal science where the accuracy and the control of the production process of functional materials rely on the knowledge of the complex microstructure of the suspension [1]. In this work we focus on the rheology of biphasic emulsions by means of direct numerical simulations.

The study of rheology is motivated by the many fluids in nature and industrial applications which exhibit a non-Newtonian behavior, i.e., a nonlinear relation between the shear stress and the shear rate; the relation between these macroscopic behaviors and the microstructure is often studied assuming suspensions of objects in a Newtonian solvent with dynamic viscosity μ. Einstein [2] was the first to provide a closure for the effective viscosity μ_e of a dilute rigid particle suspensions with vanishing inertia, and showed theoretically that μ_e is a linear function of the particle volume fraction Φ. Non-rigid and deformable objects, such as deformable particles, capsules and droplets behave differently because of their deformation and in the latter case also coalescence and breakup. Taylor [3] took into account the deformation and extended Einsten's relation by introducing the viscosity ratio between the two phases λ (defined as the disperse phase over the matrix phase viscosity), and more recently Pal [4] derived expressions to evaluate the effective viscosity of infinitely dilute and concentrated emulsions using the effective medium approach. These relations assume limiting cases to model surface tensions effects (either going to zero or infinite) and thus direct numerical simulations are a valuable tool to overcome these limitations. De Vita et al. studied the effect of coalescence [5] and showed that the effective viscosity is a concave function of Φ, i.e., μ_e has a maximum for an intermediate value of Φ and then decreases with the volume fraction. The volume fraction for which the maximum is reached decreases with the viscosity ratio λ and μ_e is again a convex function of Φ in the case of droplets when the coalescence of the solute phase is suppressed; in this case, their behaviour resembles what found for deformable particles, thus confirming that coalescence is a key mechanism that can dramatically change the rheology of emulsions.

In this works we account for the coalescence and study how it affects the rheology of emulsions adding an additional complexity to the system by considering non-Newtonian solvents. To be best of our knowledge, no systematic study of the rheology of concentrated emulsions are available in the literature and the present work is aimed to fill in this gap.

NON-NEWTONIAN FLUID MODELS

Several models have been developed to capture the different behaviours of various non-Newtonian fluids and in the current study, we focus on the simple inelastic power law models, where the local viscosity of the fluid is a function of the sole local value of shear rate. A relation that can be used to summarize the behaviors previously described for complex fluids is

$$\mu_{pl} = K\dot{\gamma}^{n-1}, \tag{1}$$

where n is the flow index and K the fluid consistency index. A Newtonian behavior is recovered when $n = 1$ and $K = \mu$, while values of the flow index above and below unity, $n > 1$ and $n < 1$, denote shear-thickening and shear-thinning fluids, respectively. In general, the local viscosity of the non-Newtonian fluid increases with $\dot{\gamma}$ for shear-thickening fluids, while it reduces for shear-thinning ones, which means that the fluidity of shear-thickening fluids reduces increasing the shear rate, while the opposite is true for shear-thinning fluids. The viscosity of a power law shear-thinning fluid becomes infinite for null shear-rate; to overcome this numerical issue, the Carreau fluid model is used instead in which the local viscosity is computed as

$$\mu_{ca} = \mu_\infty + (\mu_0 - \mu_\infty)\left[1 + (k\dot{\gamma})^2\right]^{(n-1)/2}. \tag{2}$$

*Corresponding author. E-mail: marco.rosti@oist.jp.

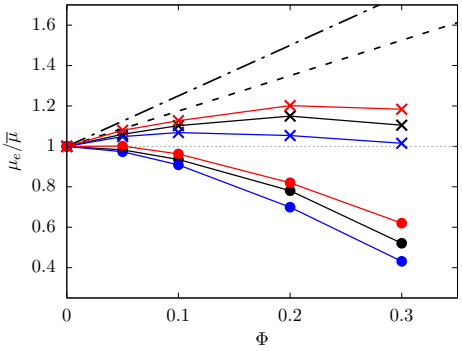

Figure 1: Normalised effective viscosity μ_e as a function of the droplets volume fraction Φ for different fluids and viscosity ratios. The blue, black and red colors indicate $n = 0.5$, 1 and 1.5, while the cross $\times$ and circle $\bullet$ symbols are used to distinguish λ equal to 1 and 0.01.

In this equation, μ_∞ and μ_0 indicate the lower and upper limits of fluid viscosity at infinite and zero shear rates. The flow index n characterizes the behaviour of the fluid: for $n < 1$ the fluid is shear thinning and the material time constant k represents the degree of shear-thinning.

RESULTS

We study the rheology of a droplet suspension immersed in power law fluids and compare the results with those obtained in a Newtonian fluid. The suspended fluid is Newtonian with uniform constant viscosity μ_1, while three different kinds of carrier fluids are studied: Newtonian fluids with viscosity $\mu_2 = \overline{\mu}$, shear-thickening fluids with viscosity $\mu_2 = \mu_{pl}$ defined by equation (1) and shear-thinning fluids with viscosity $\mu_2 = \mu_{ca}$ defined by equation (2). We consider the effective viscosity μ_e which is the viscosity of a Newtonian fluid that gives the same shear stress at the same shear rate, and is thus defined as $\mu_e = \langle \sigma_{12}^w \rangle_{xz,t} / \dot{\gamma}$. σ_{12}^w is the shear component of the stress tensor evaluated at the walls. In general, we expect the rheology of a two fluid system to be a function of the Reynolds number Re, the capillary number Ca, the viscosity ratio λ, the solute volume fraction Φ, the confinement ratio $2\mathcal{R}/2h$ and the non-Newtonian property of the carrier fluid here summarised by the power flow index n. In the present work, we limit our analysis to inertialess flows, i.e., $Re \lll 1$, the capillary number Ca is not varied and fixed to be in a range where breakup is avoided, and the domain size is chosen such that confinement effects are negligible. Thus, we can simply the analysis to $\mu_e \approx \mathcal{F}(\Phi, \lambda, n)$.

Figure 1 shows the effective viscosity μ_e as a function of the droplet volume fraction Φ for two different viscosity ratio λ and for three different power flow index n. In the Newtonian carrier fluid (black color), the behaviour is the same observed by [5]: when the viscosity of the two fluids is the same, i.e., $\lambda = 1$, the effective viscosity μ_e first grows with the volume fraction similarly to a rigid particle suspension, then reaches a maximum value for an intermediate Φ and then starts decreasing again. When the viscosity of the dispersed phase is reduced, i.e., λ decreases, the volume fraction for which the maximum effective viscosity is reached reduces, and for a sufficiently low λ the maximum is reached at $\Phi \approx 0$ and the effective viscosity curve decreases with Φ. Note that, the effective viscosity μ_e can be even smaller than the carrier fluid one $\overline{\mu}$ in the case of $\lambda < 1$. The non-monotonic behaviour of μ_e with Φ is a direct consequence of the limiting behavior for $\Phi \to 0$ and $\Phi \to 1$ where μ_e is equal to μ_2 and μ_1 by definition [6]. When the carrier fluid is non-Newtonian the situation is further modified. In general, for all the power law index n and viscosity ratio λ considered in the present study, we observe that the non-monotonic behaviour is preserved and that the effective viscosity μ_e is larger for shear-thickening fluids with $n > 1$ and smaller for shear-thinning fluids with $n < 1$ than their Newtonian counterparts with $n = 1$. The difference in μ_e between the Newtonian and non-Newtonian fluids grows with the volume fraction Φ and larger difference are evident between the Newtonian and shear-thinning fluids than what observed with the shear-thickening fluid for both the viscosity ratio λ considered.

References

[1] Y. Xia, B. Gates, Y. Yin, and Y. Lu. Monodispersed colloidal spheres: old materials with new applications. *Advanced Materials*, 12(10):693–713, 2000.
[2] A. Einstein. Berichtigung zu meiner arbeit - eine neue bestimmung der molekuldimensionen. *Annalen der Physik*, 339(3):591–592, 1911.
[3] G. I. Taylor. The viscosity of a fluid containing small drops of another fluid. *Proceedings of the Royal Society of London. Series A*, 138(834):41–48, 1932.
[4] R. Pal. Novel shear modulus equations for concentrated emulsions of two immiscible elastic liquids with interfacial tension. *Journal of Non-Newtonian Fluid Mechanics*, 105(1):21–33, 2002.
[5] F. De Vita, M. E. Rosti, S. Caserta, and L. Brandt. On the effect of coalescence on the rheology of emulsions. *Journal of Fluid Mechanics*, 880:969–991, 2019.
[6] M. E. Rosti, F. De Vita, and L. Brandt. Numerical simulations of emulsions in shear flows. *Acta Mechanica*, 230(2):667–682, 2019.

DRYING OF ELEMENTARY NETWORKS WITHIN AN ARTIFICIAL LEAF

Philippe Marmottant[1], Benjamin Dollet [1]
[1]Laboratoire Interdisciplinaire de Physique, CNRS and University Grenoble Alpes, France

Summary The hydraulic networks of leaves are of prime importance to supply water for photosynthesis. This function is at risk when a cavitation bubble develops in the case of excessive evaporative stress, leading to an embolism, which dries the network. We have designed elementary networks in artificial microfluidic leaves to understand the speed at which the drying occurs. We found that in the case of an intersection leading to several branches, the interface between air and water divides into two several parts. The drying rate is reduced just after the splitting since axial fluxes of water vapour interact. We have developed a model to qualitatively predict this behaviour.

INTRODUCTION

Leaves are the pumping elements in plants since they drive sap water in the hydraulic circuit. Evaporation results in a strong negative pressure that tends to pull the water upwards, until it reaches the leaves and participates into photosynthesis. Unfortunately the pressure becomes so negative, of the order of tens of bars, that cavitation bubbles can occur, forming a so-called embolism, and grow. Here we are interested in the growth of the embolism in the hydraulic circuit of the leaf under evaporation. When the embolism is growing several menisci move into the conduits of the leaf. Here we are interested in unravelling the basic physical laws that drive the menisci in complex architectures.

ELEMENTARY NETWORKS

For this purpose we have developed microfluidic experiments using artificial leaves in transparent PDMS elastomer bounded on glass (method by [1]), under a continuous flux of dry air. Such networks are visible on figure 1. The networks are filled from the large disc, cut with a scalpel to create an opening. To reproduce the normal function of a leaf, water would be supplied to this entrance and would then flow, diffuse through the very thin layer of PDMS and evaporate, which mimics water transport between the sap network and the atmosphere through the body of real leaves.

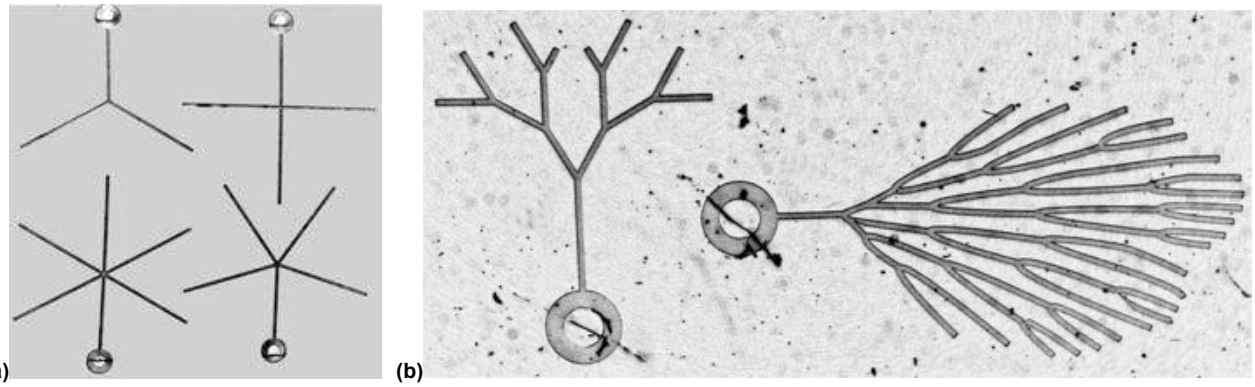

Figure 1. Microfluidic artificial leaves of thin PDMS with elementary networks with: (a) simple intersections. (b) trees of intersections inspired from Adiantum ferns leafs. In all networks, the drying starts from the disk, open to air.

We simulate an embolism by stopping the injection of water through the open disc and let an air bubble enter and invade the drying network. In biological leaves it was indeed found that embolism always starts at the base of the leaf (the petiole [2]).

DRYING IN A SINGLE CHANNEL

In simple single straight channels (not shown here) we found that the remaining length L of water in a dead end decreases during drying decreases with a velocity given by $\frac{dL}{dt} = -\frac{L+L_g}{\tau}$, where τ is a characteristic time linked to the diffusivity of water though the cover layer of PDMS, and to its thickness, and where L_g is a characteristic length due to the axial flux of evaporation through the air in the channel before diffusion in PDMS elastomer [3].

DIVISION INTO MULTIPLE MENISCI AT INTERSECTIONS

Here we first consider branched channels, as on figure 1a. When bubble grows, arriving from the left from a branch to a junction into two secondary branches, the meniscus divides into two menisci (figure 2ab and 2ef). In junction with more branches, the meniscus equally divides in several menisci (figure. 2cd).

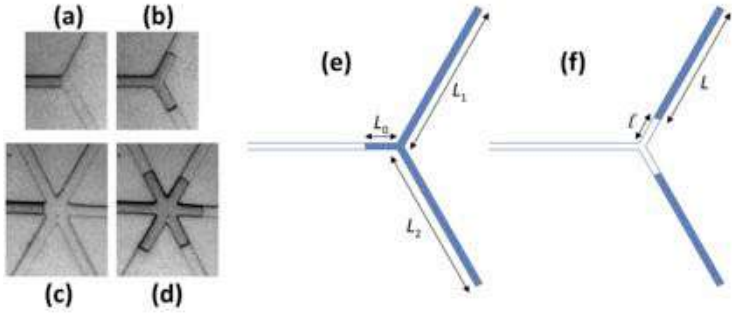

Figure 2. Division of a bubble when arriving at a intersection leading to N other branches.

The menisci velocity reduces abruptly after the junction, as seen on figure 3a. It is explained by the fact that all the evaporative flux was driving the initial single meniscus before the division. After division the velocity in each branches obeys a law that is very close to that of a single branch, see figure 3b, except at the beginning when menisci are close to each other and interact. Indeed the presence of neighbour menisci decreases the evaporative flux in the axis of the channel. We predict that the drying velocity writes $\frac{\mathrm{d}L}{\mathrm{d}t} = -\frac{L+fL_g}{\tau}$, where f is geometrical prefactor ($f < 1$) that writes $f = \frac{\cosh[\ell/L_g]+N\sinh[\ell/L_g]}{\sinh[\ell/L_g]+N\cosh[\ell/L_g]}$ using ℓ the distance to junction. This prediction qualitatively describes the observation that the velocity is smaller just after the division, when the secondary branches are full with a water length of about 4 mm.

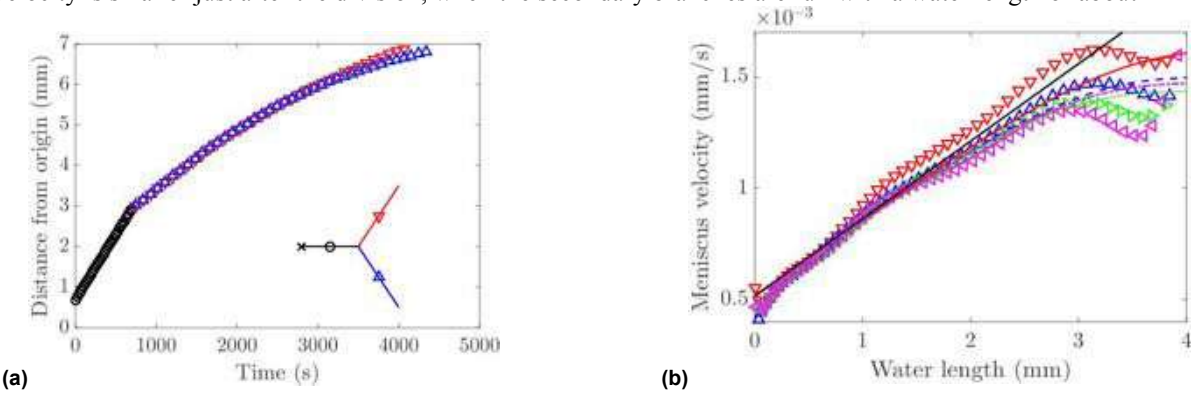

Figure 3. (a) Position of the meniscus as a function of time. (b) Velocity as a function of the remaining water length (initially 4mm), after the junction into two (◦), three (∗), four (+) and five (×) branches. Prediction for a meniscus in a single channel (black line), and taking into account the interaction between branches (colored lines).

This model helps deriving precisely the motion of water in even more complex networks such as the ones of figure 1b.

DIVISION IN THE CASE OF CONNECTED ENDS

In real leaves channels presents loops. If the secondary channels after the junction are topologically connected (imagine the ends of channels in figure 2ef being connected by water), we found surprisingly there is an inequality of velocities in secondary branches, with sometimes pinning of one meniscus due to a slight imperfection. But the total flux of water evaporating is conserved and the sum of velocities $\frac{\mathrm{d}L_1}{\mathrm{d}t} + \frac{\mathrm{d}L_2}{\mathrm{d}t}$ after the junction is evolving smoothly.

CONCLUSION AND PERSPECTIVES

We found that the axial evaporative flux is dependant on the proximity of other interfaces. Having understood the basic laws driving the motion of menisci in simple configurations we aim to tackle more complex geometries, in particular channels presenting constrictions, as is the case in real leaves. Preliminary experiments showed stop and go behaviour at constriction, with fast jumps when the pinned interface is released, consistently with biological observations.

References

[1] Noblin X., Mahadevan L., Coomaraswamy I.A., Weitz D.A., Holbrook N.M., Zwieniecki M.A. Optimal vein density in artificial and real leaves. *Proc. Natl Acad. Sci. USA* **105**: 9140 – 9144, 2008.

[2] Brodribb T. Bienaimé D., Marmottant P. Revealing catastrophic failure of leaf networks under stress *Proc. Natl Acad. Sci. USA* **113**: 4865, 2016.

[3] Dollet B., Louf J.-F., Alonzo M., Jensen K. H. and Marmottant P. Drying of channels by evaporation through a permeable medium mimicking embolism in plant leaves *J. Roy. Soc. Interface* **16**, 20180690, 2019.

FLOW-INDUCED VIBRATIONS DUE TO THE FLOW OF A VISCOELASTIC FLUID BETWEEN TWO CANTILEVERED MICROCYLINDERS

Cameron C. Hopkins*[1], Simon J. Haward[1], and Amy Q. Shen[1]
[1]Micro/Bio/Nanofluidics Unit, Okinawa Institute of Science and Technology Graduate University, Onna-son, Okinawa, Japan

Summary In this work, the flow of a viscoelastic wormlike micellar solution between two cantilevered microcylinders and their resulting flow-induced vibrations is studied. At moderate Weissenberg number, the microcylinders are laterally deflected due to elastic forces and undergo highly periodic and synchronized oscillations in time that are governed by the relaxation time of the fluid. At high Weissenberg number, one of the posts is dramatically deflected towards the other post, ultimately resulting in them sticking together and vibrating erratically due to elastic turbulence. The study on the motion of the posts is analyzed together with the flow behaviour of the fluid measured using micro-Particle Image Velocimetry and Flow-Induced Birefringence experiments.

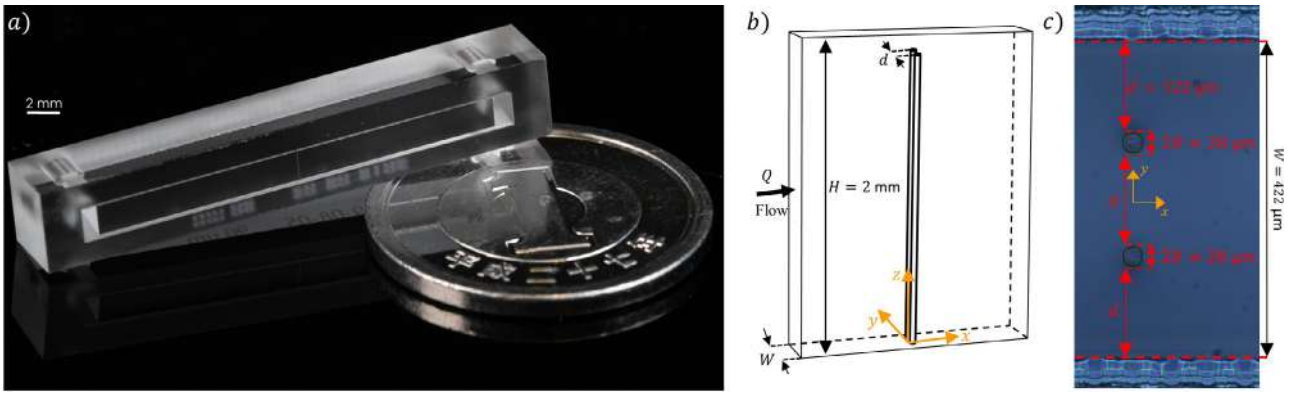

Figure 1: a) Photograph of a glass microfluidic channel with a single microcylinder in the center of the channel. 1-yen coin included for scale. b) Schematic diagram of the microfluidic channel used in this work with two cantilevered microcylinders situated at the same streamwise (x) position in the channel with equal spacing in the y direction between the cylinders and walls of the channel. c) Micrograph of the glass microchannel focused on the tips of the microcylinders.

INTRODUCTION

Microfluidics has recently emerged as a promising new technique for use in fluid dynamics and rheology [1]. One system of particular interest to this work is flow around a cylinder. The flow of a Newtonian fluid around a cylinder is characterized by the ratio of inertial to viscous forces in the fluid using the Reynolds number $\mathrm{Re} = \rho U R/\eta$, where ρ and η are the fluid density and viscosity, respectively, U is a characteristic flow velocity, and R is the radius of the cylinder. Many fluids however, including biological fluids (e.g., mucus, synovial fluid, semen), are not Newtonian, but are viscoelastic, meaning they possess a combination of solid-like (elastic) and liquid-like (viscous) properties. Elasticity in viscoelastic fluids arises from the deformation and relaxation of macromolecules in the fluid, and the elastic response of the fluid depends on the timescale for the relaxation of these molecules. The flow of a viscoelastic fluid around a cylinder can be characterized by the ratio of elastic to viscous forces in the fluid using the Weissenberg number $\mathrm{Wi} = \lambda U/R$ where λ is the relaxation time of the fluid. Due to the small lengthscale achieved in a microchannel ($R = O(10\mu\mathrm{m})$), it is therefore possible to study flows that are simultaneously inertia-less ($\mathrm{Re} \ll 1$) with high elasticity ($\mathrm{Wi} \gg 1$).

Using state-of-the-art selective laser-induced etching of glass [1], we fabricated microchannels containing slender cantilevered microcylinders. Fig. 1a shows a photograph of an example glass microchannel with height $H = 2$ mm and width $W = 400$ μm that contains a single microcylinder. For the work presented here, the microchannel used contains two cantilevered microcylinders with heights ≈ 1.95 mm positioned at the same streamwise (x) position in the channel, with equal spacing between the cylinders and walls, as in the schematic diagram shown in Fig.1b. A micrograph focused on the tips of the cylinders is shown in Fig 1c along with the dimensions of the channel.

In a previous study, we investigated the flow of a viscoelastic wormlike micellar solution around a rigid microcylinder that is fixed at both the top and bottom of the microchannel [2] as in Fig. 1a. Above a critical Wi, the flow destabilizes and the fluid preferentially flows around one side of the cylinder. At higher Wi, the flow becomes time dependent and pulses with a period equal to λ. If the microcylinder is cantilevered, the same flow instability exerts a force on the cylinder, deflecting it off the flow axis and causes complex two-dimensional oscillations [3].

In this work, we present a study on the flow of a viscoelastic wormlike micellar solution between two cantilevered microcylinders located at the same streamwise position in the channel with equal gaps between the cylinders and walls. The flow of the fluid will be investigated using micro-Particle Image Velocimetry and Flow-Induced Birefringence imaging techniques. The behaviour of the cantilevered microcylinders will be studied using high-speed video microscopy.

*Corresponding author. E-mail: cameron-hopkins1@oist.jp.

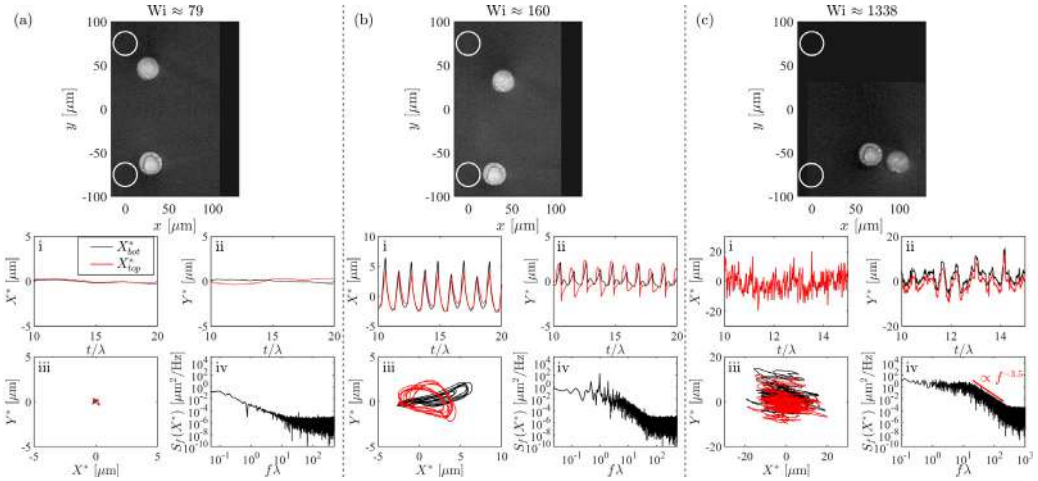

Figure 2: High-speed video microscopy and cylinder tracking. The three columns show data at three Weissenberg numbers (a) Wi $\approx$ 79, (b) Wi $\approx$ 160, and (c) Wi $\approx$ 1338. In each column, a video snapshot at each Wi is shown in the top panel. Flow is from left to right. The white circles show the initial rest positions of the cylinders. In the lower four panels, i) and ii) show X^* and Y^* for both posts, where the black curve is the bottom post and the red curve is the top post. iii) shows the $X^* - Y^*$ orbits of the posts, and iv) shows $S_f(X^*)$ for the bottom cylinder.

RESULTS

Figure 2 shows high-speed video microscopy of the motion of the microcylinders at three Weissenberg numbers illustrating distinct behaviour. At the lowest Wi (Fig 2a), the posts deflect downstream by approximately the same distance and are also deflected in the y direction, compressing the posts together. Their x and y positions with their means subtracted, denoted X^* and Y^*, are plotted vs. normalized time t/λ in Figs. 2 a-i and a-ii; they are steady in time. The posts' $X^* - Y^*$ orbits, shown in Fig. 2 a-ii are effectively points at the origin. The power spectrum of the top cylinder's x-position, $S_f(X^*)$, is plotted vs normalized frequency $f\lambda$ in Fig. 2 a-iv. In this case, $S_f(X^*)$ shows no notable features.

At slightly higher Wi, shown in Fig. 2 b, compared to the previous case, both posts are deflected more significantly in the $-y$ direction, with the top post deflecting the most. As shown by their x and y positions in Fig. 2 b-i and b-ii, the posts undergo highly periodic and synchronized oscillation in time. Their x positions follow sawtooth-like oscillations, while their y positions trace out a much more irregular, but still periodic, shape. Their orbits, plotted in Fig. 2 b-iii, trace our complex two-dimensional oval-like shapes. The power spectrum plotted in Fig. 2 b-iv reveals a strong primary peak at normalized frequency $f\lambda \approx 1$ along with higher integer harmonics in agreement with previous work [3]. In addition, half-integer harmonics are also present that were not observed in previous work, which may be evidence of a period doubling cascade towards elastic turbulence, or a modification of the flow instability due to the arrangement of the posts.

At the highest Wi shown here, in Fig. 2 c, both posts deflect more significantly downstream, with the top post deflecting over 100 μm in both the x and $-y$ directions. Note that the post that is furthest in the x direction in the top panel of Fig. 2c is the top post. The posts' x and y trajectories, plotted in Fig. 2 c-i and c-ii, are highly erratic in time, showing no clear periodicity. The posts' trajectories are virtually identical because they are effectively stuck together, showing only a slight separation in the y direction due to their relative displacement. Their orbits shown in Fig. 2 c-iii are also identical with a slight y offset, and trace out a random back-and-forth path. The power spectrum shown in Fig. 2 c-iv reveals strong broad-spectrum amplitude at low-frequency with a power-law decrease in amplitude with increasing frequency that follows a -3.5 slope which is evidence of elastic turbulence, similar to that observed in previous work [3].

OUTLOOK

The results presented above reveal that the flow of a viscoelastic wormlike micellar system between two cantilevered microcylinders results in complex spatiotemporal oscillations of the posts. The analysis of the Wi-dependent behaviour of the posts was presented in terms of their $x - y$ oscillations. Further insight can be obtained by casting the geometry of the problem in terms of the separation vector $\vec{r}$, and the angle θ, between the posts. In addition, using micro-Particle Image Velocimetry and Flow-Induced Birefringence data, the motion of the posts can be correlated with the flow behaviour of the fluid.

References

[1] Burshtein, N., Chan, S. T., Toda-Peters, K., Shen, A. Q., Haward, S. J. 3D-printed glass microfluidics for fluid dynamics and rheology, *Curr. Opin. Colloid Interface Sci* **43**:1-14, 2019.

[2] Haward, S. J., Kitajima, N., Toda-Peters, K., Takahashi, T., Shen, A. Q. Flow of wormlike micellar solutions around microfluidic cylinders with high aspect ratio and low blockage ratio, *Soft Matter* **15**: 1927, 2019.

[3] Hopkins, C. C., Haward, S. J., Shen, A. Q. Purely elastic fluid-structure interactions in microfluidics: implications for mucociliary flows, *Small* 1903872, 2019.

CONFIGURABLE DEFORMATIONS OF A THIN LIQUID FILM GENERATED BY THE THERMOCAPILLARY EFFECT

Ran Eshel[1,¥], Valeri Frumkin[1,¥], Matan Nice[1], Omer Luria[1], Khaled Gommed[1], Maxim Shusteff[1,2], and Moran Bercovici[1]
[1]Faculty of Mechanical Engineering, Technion – Israel Institute of Technology, Haifa, Israel
[2]Lawrence Livermore National Laboratory, 7000 East Ave, Livermore, CA 94550, USA

Summary: We present a novel method for deforming thin liquid-films into desired topographies, driven by a photo actuated thermocapillary effect. Our system consists of a thin liquid film, resting on a flat substrate patterned with an array of metal pads, and a DMD-based illumination system that projects light onto the metal array. Upon projecting a desired pattern, light absorbed by the array is converted to a heat pattern on the bottom surface. This heat pattern induces surface tension gradients at the liquid-air interface, which deform the free surface. By using this effect, we can achieve complex structures with deformations as large as 10 µm over cm-scale actuation regions. The deformed liquid can be dynamically modulated from one configuration to another or be polymerized to yield extremely smooth solid structures. We believe that this method opens the door to generating complex structures that can be leveraged to rapidly create phase masks and other freeform optical components.

INTRODUCTION

The Marangoni effect describes the motion of a liquid due to tangential stresses induced by surface tension gradients on one or more of its liquid-fluid interfaces. A subset of Marangoni flows, where the surface tension gradients are induced by non-uniform temperature is known as the thermocapillary effect. If a non-uniform temperature profile is imposed (for example) on a gas-liquid system, liquid will spontaneously flow along the free-surface from warmer regions with lower surface tension to colder regions with higher surface tension [1]. Since at the microscale, effects of capillary forces become dominant over convective and gravitational forces, thermocapillary flow has the potential to serve as an effective method for the control and manipulation of liquids at such scales. The study of induced deformations on horizontal liquid films dates back to Davis et al. who first derived an evolution equation of the interface of a uniformly heated but perturbed liquid film, and later provided both an analytical model and experimental results for the steady-state deformation of a thin liquid film subjected to a spatially periodic temperature distribution [2,3]. A number of studies have considered the use of the thermocapillary effect for patterning of polymers, and those are discussed extensively in a recent review by Singer [4]. In particular, McLeod and Troian demonstrated deformations of nanoscale films using temperature-controlled structural elements brought in close proximity to the film. Nejati et al. [5] demonstrated shaping of thin polymer films into periodic arrays of lenses by suspending a thick layer of another liquid on top of a thin polymer film and leveraging the Benard-Marangoni instability of the top interface to drive short-wavelength deformation in the polymer, followed by successful UV-polymerization of the structure. In this work, we demonstrate for the first time a thermocapillary-based system, which allows for reconfigurable patterning of a thin liquid (polymer) film in real time, using arbitrary light-projected actuation. We provide details of its concept and design, characterize its performance, and demonstrate its use for creation of useful phase masks and other structural elements.

EXPERIMENTAL SYSTEM

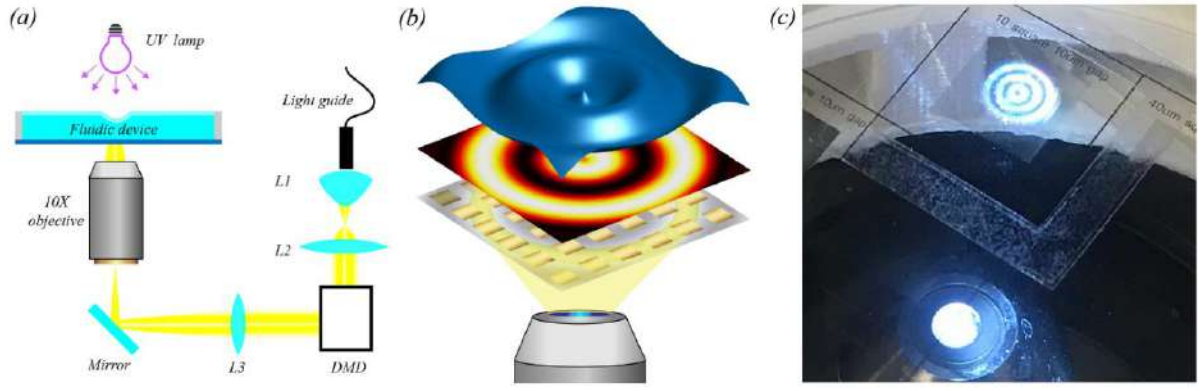

Figure 1. (a) Schematic illustration of the experimental setup. The fluidic device consists for 2x2 cm frame made of 60um thick tape, attached to a glass wafer patterned with absorbing metal squares and with a UV light curable polymer. A desired heating pattern is irradiated onto the surface using a DMD-based projection system. The light originates from a LED source coupled to a liquid guide, and we collimate it onto the DMD using a 25 mm aspheric condenser f=16 mm (L1) and a 50.8mm bi convex lens f=60mm (L2). The DMD is imaged onto the patterned surface of the chamber using a microscope objective and Kohler lens f=300 mm (L3) that focuses the light onto its back focal plane. (b) Schematic illustration of fluidic shaping via light illumination. The pattern is projected on the metal squares, which absorb the light and generate the thermal pattern to induce the thermocapillary effect, which deforms the interface between the liquid polymer and the air. We polymerize the UV curable polymer using a UV lamp located above the device. (c) An image of the device on top of the projection system.

Figure 1 presents a schematic illustration and image of the experimental setup we used to generate the thermocapillary deformations. The device consists of a 2 cm x 2 cm x 60 µm (WxLxH) fluidic chamber whose floor is made of a glass wafer patterned with an array of metal squares that absorb the light projected from below. We fabricated the squares using a standard photolithography process where we deposited a 100 nm of chrome followed by another 100 nm of gold, yielding good absorption of light in the visible spectrum. The size and spacing of the squares provide a tradeoff between spatial resolution and efficiency of heating. A desired temperature pattern is achieved by using a high intensity (4W output) LED source collimated onto a digital mirror device (DMD). We fill the chamber with a UV curable liquid polymer, and after obtaining the desired shape, we cure the polymer to obtain the final shape. To measure the topography of the resulting polymerized surface we use a digital holographic microscope (DHM) [6].

RESULTS

Figure 2 presents the experimental results of projection of three concentric rings onto wafer patterned with 20 um x 20 um metallic squares, spaced at a distance of 80 um (edge to edge), using a projection intensity of approximately 0.67 W/cm^2. The projected rings heated the surfaces on the bottom of the chamber, which then induced a gradient in the surface tension above the rings. The topography of the resulting surface, captured by the DHM, shows a set of concentric rings, whose 'valleys' correspond, as expected, to heated region where surface tension is reduced, with a deformation magnitude of several micrometers

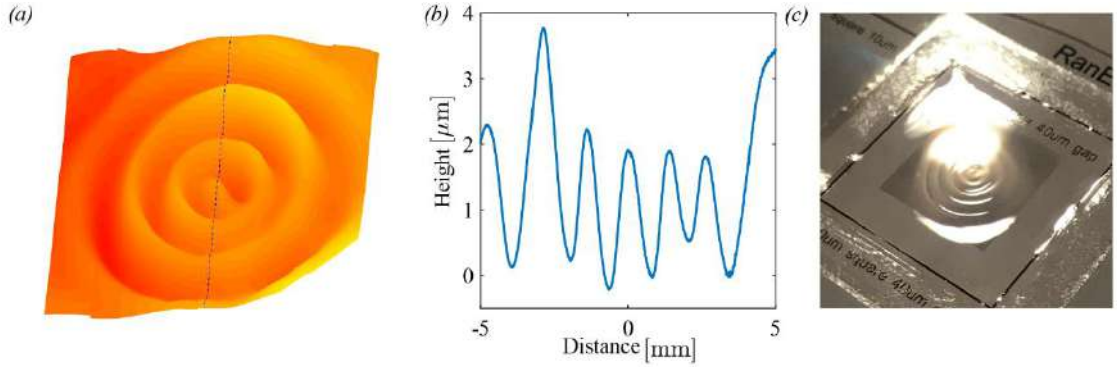

Figure 2. Experimental results showing the polymerized pattern resulting from the projection of three concentric rings. (a) A 3D view of the surface over a field of view of 10by 10 mm, as captured by a DHM. (b) The deformation pattern across the centerline of the pattern, as indicted by a dash line in 'a' (c) An image of the polymerized surface, taken using a consumer-grade camera.

References

[1] S. H. Davis, *Thermocapillary Instabilities.*, in *Annual Review of Fluid Mechanics* (Annual Reviews Inc, 1987), pp. 403–435.
[2] J. Burelbach, S. Bankoff, and S. H. Davis, *Steady Thermocapillary Flows of Thin Liquid Layers. II. Experiment*, Physics of Fluids A: Fluid Dynamics **2**, 322 (1990).
[3] M. Tan, S. Bankoff, and S. H. Davis, *Steady Thermocapillary Flows of Thin Liquid Layers. I. Theory*, Physics of Fluids A: Fluid Dynamics **2**, 313 (1990).
[4] J. P. Singer, *Thermocapillary Approaches to the Deliberate Patterning of Polymers*, Journal of Polymer Science Part B: Polymer Physics **55**, 1649 (2017).
[5] I. Nejati, M. Dietzel, and S. Hardt, *Exploiting Cellular Convection in a Thick Liquid Layer to Pattern a Thin Polymer Film*, Applied Physics Letters **108**, 051604 (2016).
[6] E. Cuche, P. Marquet, and C. Depeursinge, *Simultaneous Amplitude-Contrast and Quantitative Phase-Contrast Microscopy by Numerical Reconstruction of Fresnel off-Axis Holograms*, Applied Optics **38**, 6994 (1999).

DYNAMICS OF MICRO-PARTICLES IN VORTEXFLOWS

Noa Burshtein*[1,2], Simon J. Haward[2], Amy Q. Shen[2], and Anke Lindner[1]
[1]Physique et Mécanique des Milieux Hétérogènes, ESPCI Paris, France
[2]Okinawa Institute of science and technology, Onna-son, Okinawa, Japan

Summary The presence of microparticles (MPs) in fluids may affects the flow properties and dictate MP distribution and transport, which are important in industrial, biological and environmental flows. To understand the underlying mechanisms affecting MP distribution in flows, we disentangle their response to specific element of flows. Here, a microfluidic cross-slot geometry, configured for observations over the cross-section of streamwise planes, is used to generate a stationary streamwise vortex at moderate Reynolds numbers to study MP distribution and dynamics in Newtonian and complex fluids. Findings from this study provide fundamental contributions about MP–flow interactions, improving techniques for particle sorting and transport with applications in medicine and environmental measurements and may provide insights to turbulence attenuation mechanisms.

INTRODUCTION

Microparticles (MPs) are prevalent in different flows such as biological (as cells and microorganisms in blood flow and lymph system [1]), industrial (as plastic MPs scrubbers for cleaning products [2] and textile fibers [3]) and environmental processes (such as dust, sand and degraded plastic debris [4]). Natural and synthetic MPs are a risk for human health due to the constant exchange of water and air flows between the environment and the human body (via ingestion and inhalation) [5]. Due to their high prevalence in diverse flow regimes, it is important to understand the fundamental interaction between MPs and their suspending fluids, particularly non-Newtonian fluids which are common in biological and industrial flows. Vortices are a main building block of turbulent flows, but they also represent an intermediate flow regime that is common in flows involving corners and obstacles (i.e., flows in the heart and vein intersections). Due to the unstable and dynamic nature of vortices, it is challenging to create and study them under controlled and precise conditions. Hence, most current studies focus is on laminar [6] or fully turbulent [7-8] flows. In this ongoing study we aim to explore the interaction between MPs and intermediate vortex flows of both Newtonian and complex fluids. For this purpose, a microfluidic cross-slot geometry, configured for observations over the cross-section of the outflow, is used to generate a well-controlled, stationary vortex. This vortex will serve as a model to study the dynamics of MPs in both Newtonian and complex fluids. Findings from this study provide fundamental contributions to the knowledge about MP–flow interactions, improving techniques for particle sorting and transport with applications in medicine and environmental measurements and potentially provide new insights to turbulence attenuation mechanisms by MPs.

FORMATION AND PROPERTIES OF A STEADY ISOLATED STREAMWISE VORTEX

Intersecting flows, such as the flow in the cross-slot geometry, tend to become unstable and break symmetry at low Reynolds numbers ($\mathrm{Re} = \rho U w/\eta$ where ρ is the density and η is the viscosity of the fluid) resulting in the formation of vortices. In a cross-slot geometry with a low aspect ratio ($\alpha = d/w$ where d and w are the depth and width of the geometry), a single streamwise vortex forms around a stagnation point at the center of the geometry for Re above a moderate critical value (Re_c, Fig. 1 a) [9-10]. By employing the selective laser induced etching micro-fabrication technique in fused silica (Lightfab$^{\mathrm{TM}}$) it is possible to fabricate a fully transparent, highly resistant cross-slot channel, that can be vertically mounted on an inverted microscope (Fig. 1 b). The microscope is equipped with a long working distance objective, enabling a direct observation of the formation of a streamwise vortex (Fig. 1 a-b). The device is washable, reusable, withstands high pressure and is completely transparent, allowing the observation from different planes.

One of the ways to control the vortex properties is by adding elastic forces to the fluid with flexible polymers (4 MDa polyethyleneoxide, PEO). While Newtonian fluids have no elastic properties, even slight addition of polymers, in parts per million (ppm by weight) concentration, increases the relaxation time of the fluid and hence its elasticity increases ($El = (1-\beta)(\lambda\eta/\rho w^2)$), where β is the solvent-to-total viscosity ratio and λ is the relaxation time of the polymer). Slight changes in fluid elasticity may have strong effects on the flow field which lead to a reduction in Re_c and in vortex intensity [11]. Additionally, when $El > 0.011$, the vortex flow becomes unsteady and when El approaches 1, the vortex formation is suppressed.

PARTICLE ARRANGEMENT IN VORTEX FLOW OF NEWTONIAN AND COMPLEX FLUIDS

In order to study the response of MPs to vortex flows, we control the significant factors that influence these interactions. By controlling fluid properties (i.e., density, viscosity and elasticity) and particle properties (i.e., size, shape, density and flexibility) we are able to determine the nature of the interaction between the MPs and the underlying flow. The relative importance of the influencing parameters is commonly described by the non-dimensional Stokes number ($St = t_0 U/w$

*Corresponding author. E-mail: noa.burshtein@espci.fr

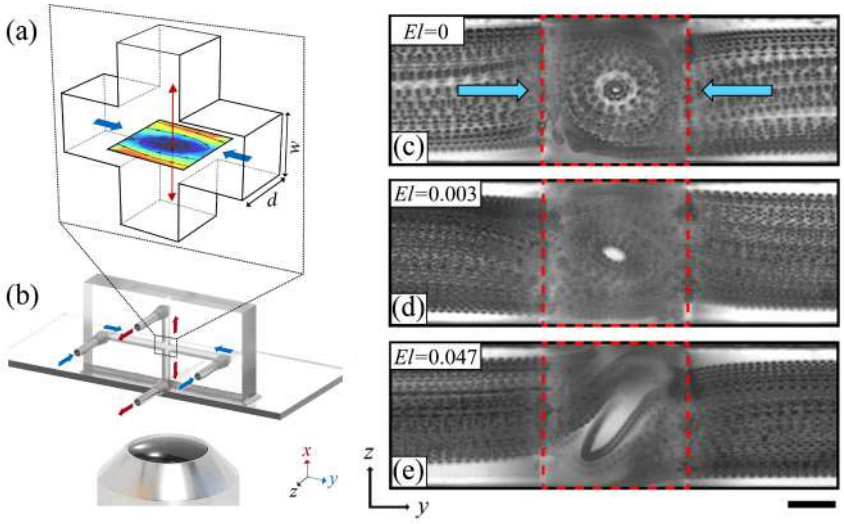

Figure 1: (a) Streamwise vortex formation at the $x = 0$ plane of the cross-slot geometry; (b) A schematic diagram of a microfluidic cross-slot device, used for streamwise vortex visualization, vertically mounted on an inverted microscope. The device is fabricated using laser induced etching technique in fused silica (Lightfab™). Stacks of 500 images of the $x = 0$ plane of the cross-slot channel. Red dashed line marks the borders of the outflow channel. Fluids are 25 wt% glycerol in water with (c) 0 ppm PEO ($El = 0$, $St = 0.03$); (d) 100 ppm PEO ($El = 0.003$, $St = 0.02$) and; (e) 400 ppm PEO ($El = 0.047$, $St = 0.01$). Inflow and outflow are indicated by blue and red arrows, respectively. Scale bar 300 μm.

where t_0 is the time scale of the particle, U is the average flow velocity and w is the characteristic length scale of the flow). The time scale of the particle is estimated by $t_0 = R^2/3\nu$, where R is the diameter of the MP and ν is the dynamic viscosity. Note that St does not account for the changes in the elasticity of the fluid.

MPs response to a single vortex flow is first studied by changing the levels of El of the fluid. We conduct a series of experiments using a microfluidic cross-slot channel with dimensions of $w = d = 1100$ μm ($\alpha = 1$). The flow is driven by 4 individually controlled neMESYS syringe pumps (Cetoni GmbH, Germany) fitted with Hamilton Gastight syringes, ensuring equal volumetric flow rates in the inlets and outlets. Neutrally buoyant spherical polystyrene MPs ($d_p = 80$ μm) are added to 25 wt% glycerol in water at a low concentration (0.2 wt%) in order to avoid interaction between particles. Re is set above Re_c, leading to formation of a stable and steady vortex at Re = 55. Images are captured with a high speed "Photron" camera at a rate of 1000 fps. A single figure is assembled from a stack of all captured images, providing an indication of the path of the MPs in the flow (Fig. 1 c-e). The flow field is shown for three different cases in Fig. 1 c-e with $El = 0$ ($St = 0.03$), $El = 0.03$ ($St = 0.02$) and $El = 0.047$ ($St = 0.01$), respectively. These initial observations demonstrate the effect of weak elasticity on the flow field and the MPs response, leading to non-homogeneous distributions of MPs in a vortex flow field. Although we might expect that particles with $St < 1$ will follow the streamlines of the flow, this is clearly not the case when elastic forces are at play. These experiments provide a simplification for turbulent flows and they represent the possible distribution of particles in intersections of biological flows.

CONCLUSIONS

In this study, a single steady streamwise vortex is formed around a stagnation point in the cross-slot geometry upon exceeding a critical Re for Newtonian and weakly elastic fluids. Adding elasticity to the fluid results in a decrease of the critical Re and in vortex intensity. Although the fluid elasticity is weak (i.e. $El \ll 1$), the non-Newtonian effects lead to distinctly non-homogeneous particle distributions in the vortical flow fields resulting in absence of particles within the vortex core.

References

[1] Shet A. & S., Vasc. Health Risk Manag.; 4(4):769–774 (2008).
[2] Zitko V. and Hanlon M., Mar. Pollut. Bull., 22:41–42 (1991).
[3] Henry B., Sci. Total Environ., 652: 483-494 (2019).
[4] Antão Barboza L.G., Marine Poll. Bull., 133: 336-348 (2018).
[5] Wright S.L. & Kelly F. J. Environ. Sci. Technol. 51, 12:6634-6647 (2017).
[6] Di Carlo, D., PNAS, 104.48: 18892-18897 (2007).
[7] Balachandar s. & Eaton K., Ann. Rev. Fluid Mech. 42: 111-133 (2010).
[8] Toschi F. & Bodenschatz E., Ann. Rev. Fluid Mech., 41:375-404 (2009).
[9] Haward S., Phys. Rev. E, 93, 031101 (2016).
[10] Burshtein N., Phys. Fluids, 31, 034104 (2019).
[11] Burshtein N., Phys. Rev. X, 7, 041039 (2017).

REVERSIBLE ACCUMULATION OF COLLOIDAL PARTICLES IN MICROGROOVES BY DIFFUSIOPHORESIS

Naval Singh[1],Goran Vladisavljević[1],Francois Nadal[2],Cecile Cottin-Bizonne[3],Christophe Pirat[3],and Guido Bolognesi[*1]
[1]Department of Chemical Engineering, Loughborough University, Loughborough, United Kingdom
[2]Wolfson School of Mechanical, Electrical and Manufacturing Engineering, Loughborough University, Loughborough, United Kingdom
[3]Institut Lumière Matière,Université de Lyon,Université Claude BernardLyon1,CNRS,Villeurbanne, France

Summary This work presents a new strategy, based on solute-driven transport mechanism, for the accumulation of colloidal nanoparticles in microgrooves under steady-state and continuous flow settings. Experimental and numerical analysis show how colloids can be steadily accumulated within the grooves of a microfluidic device due to combined hydrodynamics and diffusiophoresis effects.

INTRODUCTION

In recent years, the transduction of chemical energy in the form of solute concentration gradient into particle motion (i.e. diffusiophoresis) and liquid motion (i.e. diffusioosmosis) has been exploited by researchers for the manipulation of nano-/micro-particles in microfluidic devices [1, 2, 3]. Transient salt concentration gradients within dead-end microchannels have been successfully used to achieve enhanced particle transport, into these dead-end structures, driven either by diffusioosmosis [2] or diffusiophoresis [3]. Alternatively, the combination of pressure-driven multicomponent flows and diffusiophoresis directed against these flows was exploited to enable particle accumulation near a junction [4] and within open-ended nanochannels [6].

Here, a novel mechanism for particle accumulation in dead-end micro-structures in continuous flow settings is proposed [5]. Multicomponent flows past transverse microgrooves were used to generate a steady-state salt concentration gradient, which caused the particles to be directed by diffusiophoresis towards the grooves and get trapped therein by recirculation flows induced by the microstructured surface.

METHODS AND MATERIALS

A Ψ-junction microchannel, made of an adhesive polymer (NOA-81), was fabricated and glued to a silicon substrate with parallel microgrooves. Syringe pumps were used to inject an aqueous solution of fluorescent polystyrene nanoparticles (PS-NP), 200 nm in diameter, into the inner channel of the junction, and either deionised (DI) water or an aqueous solution of 10 mM LiCl salt into the outer channels. The outer flow was switched between the DI water and electrolyte solution by means of a flow valve (Figure 1a). A confocal microscope was used to measure the 3D particle concentration field within the main channel and the grooves (Figure 1b). Numerical simulations were performed in Comsol Multiphysics to solve the following PDEs for adimensional pressure p, velocity $\mathbf{u}$ and salt concentration c fields

$$\mathrm{Re}\,\mathbf{u}\cdot\nabla\mathbf{u} = -\nabla p + \nabla^2\mathbf{u} \quad ; \quad \nabla\cdot\mathbf{u} = 0 \quad ; \quad \mathrm{Pe_s}\,\mathbf{u}\cdot\nabla c = \nabla^2 c \tag{1}$$

The adimensional quantities were calculated according to the following scaling relationships: $u \propto U_0$, $x \propto W$, $p \propto \frac{\mu U}{W}$, $c \propto c_{max}$, with U_0 the average fluid velocity, W the channel and groove width, μ the fluid viscosity, c_{max} the salt

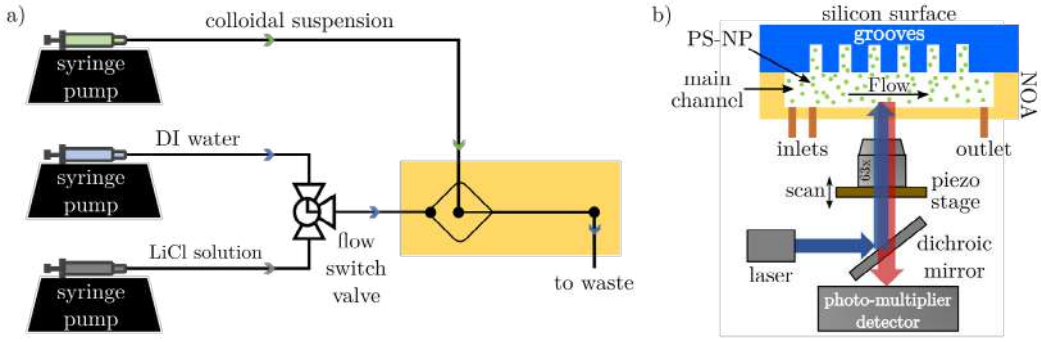

Figure 1: Experimental set-up. a) Syringe pumps and a flow valve were used to create parallel multicomponent flows in a Ψ-junction device. b) Schematic of the confocal microscope rig for particle concentration measurements within the microdevice.

*Corresponding author. E-mail: g.bolognesi@lboro.ac.uk.

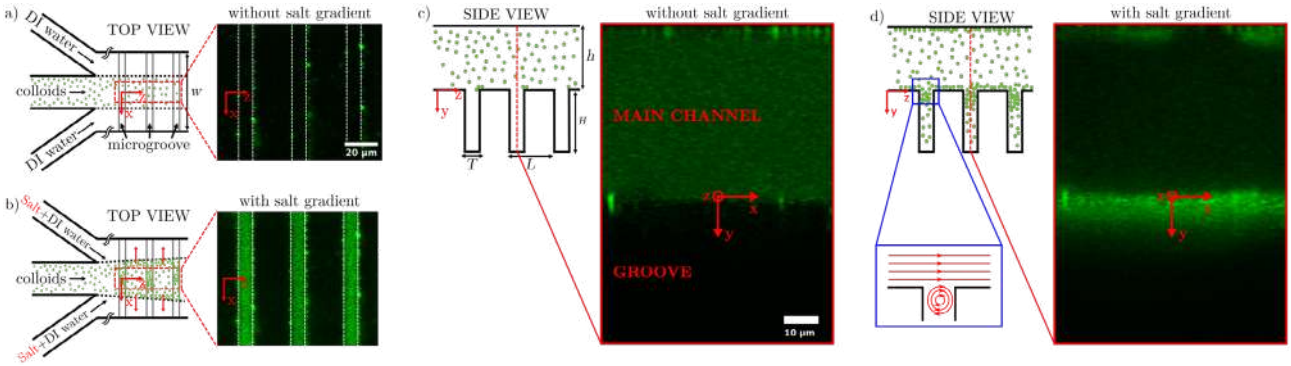

Figure 2: Top/side view channel schematics and confocal micrographs showing fluorescence particle distribution in the absence (a,c) and presence (b,d) of a salt gradient. In the blue close-up, a schematic showing the flow streamlines at the entrance of the groove.

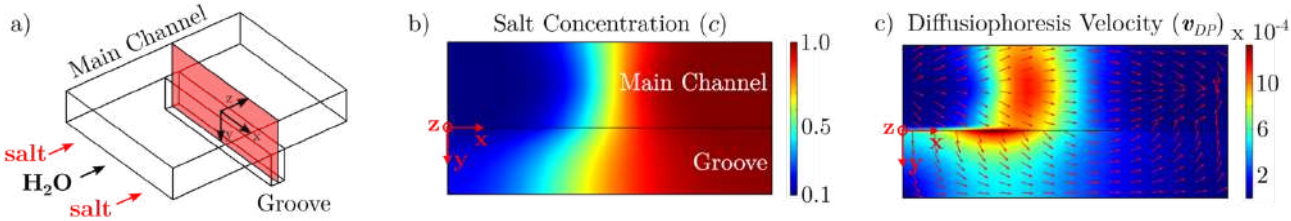

Figure 3: Computational domain (a) and adimensional salt concentration (b), and particle's diffusiophoresis velocity (c) fields at the red-shaded cross-section area in panel (a). Color maps represent the field intensity and the unit arrows the field direction. In panel (b) and (c), only half channel is shown, with $x = 0$ being the axis of symmetry.

concentration of the LiCl solution injected into the device. Reynolds and salt Peclet number are defined as $\mathrm{Re} = \frac{\rho U_0 W}{\mu}$ and $\mathrm{Pe}_s = \frac{W U_0}{D_c}$, respectively, with ρ the fluid density and D_c the salt diffusivity. No salt flux boundary condition and diffusioosmosis slip velocity $\mathbf{v_{DO}} = -\xi_{DO}\frac{\nabla c}{c}$ were imposed at all solid walls, with ξ_{DO} the diffusioosmosis coefficient normalised by $U_0 W$. The nanoparticle's diffusiphoresis (adimensional) velocity field was calculated as $\mathbf{v}_{DP} = \xi_{DP}\frac{\nabla c}{c}$ with ξ_{DP} the particle's diffusiophoresis coefficient normalised by $U_0 W$.

RESULTS AND DISCUSSION

In the absence of salt gradient, particles were simply advected by the flow and the high particle Peclet number hampered their passive diffusion into the grooves (Figure 2a,c). Conversely, when a salt gradient was established by injecting the LiCl solution into the outer channels, particles were accumulated at the entrance of the microgrooves (Figure 2b,d). This phenomenon was stationary and ceased only when the salt gradient was removed. The numerical simulations show that particles were driven by diffusiophoresis from the centre of the main channel downwards towards the grooves and then outwards towards the groove sides (Figure 3c). At the same time, recirculation flows occurring right at the entrance of the grooves, as shown in the blue close-up in Figure 2, trapped the particles within the closed flow streamlines, thereby causing their accumulation at the center of the recirculation region. By alternating electrolyte flows with different and same salinity levels, it is possible to cyclically accumulate and release the particles within the grooves.

To conclude, a new approach for the manipulation of charged nanoparticles in microgrooves based on the combined effects of diffusiophoresis and hydrodynamics (i.e. flow recirculations) was presented. This method offers great potential for microfluidic bio-analytical testing applications, including bio-particle pre-concentration and sorting, signal amplification and highly sensitive biomarker detection. This work was supported by EPSRC grant (EP/S013865/1).

References

[1] Abécassis B., Cottin-Bizonne C., Ybert C., Ajdari A., Bocquet L., Boosting migration of large particles by solute contrasts. *Nat. Mater.* **7**: 785–9, 2008.

[2] Kar A., Chiang T., Rivera I. O., Sen A., Velegol D., Enhanced transport into and out of deadend pores. *ACS Nano.* **9**: 746–753, 2015.

[3] Shin S., Um E, Sabass B, Ault J.T., Rahimi M., Warren P.B., Stone H.A., Size-dependent control of colloid transport via solute gradients in dead-end channels. *Proc. Natl. Acad. Sci.* **113**: 257–261, 2016.

[4] Shin S., Ault J.T., Warren P.B., Stone, H.A., Accumulation of colloidal particles in flow junctions induced by fluid flow and diffusiophoresis. *Phys. Rev. X* **7**: 41038, 2017.

[5] Singh N., Vladisavljević G., Nadal F., Cottin-Bizonne C., Pirat C., Bolognesi G., Reversible trapping of colloids in microgrooved channels via steady-state solute gradients. *arXiv*: 2007.11114, 2020.

[6] Rasmussen, M.K., Pedersen, J.N. and Marie, R., Size and surface charge characterization of nanoparticles with a salt gradient. *Nature communications* **11**:, 2337, 2020.

INSECT MICROFLUIDICS: HEARING AND BREATHING WHILE TINY

Anne E. Staples*[1] and Maxwell R. Mikel-Stites[1]
[1]Engineering Mechanics Program, Department of Biomedical Engineering and Mechanics, Virginia Tech,Blacksburg, VA, USA

Summary Insects have evolved to handle fluids using strategies that vary significantly from those used by larger animals since, by virtue of their size, they interact with fluids in the microscale regime, where surface forces dominate. Here we discuss two examples from insect microfluidics: flow actuation in insect respiration, and the amplification of acoustic sound localization cues in a parasitoid fly. We review behavioral data and present the mathematical, computational, and microfluidic device models we have developed to represent idealized versions of these systems that retain the salient features. In both examples, the insects appear to make use of finely tuned structural and material properties in the organs that come into contact with the fluids in question. In the case of the fly, we show that a tympanal asymmetry of just 5% may lead to order-of-magnitude gains in its hearing abilities.

INTRODUCTION

Bioinspired engineering has been a flourishing field of research for decades. From a mechanics perspective, much bioinspired research occurs in the realm of bioinspired materials and locomotion. Bioinspired fluid dynamics has primarily dealt with external flows at the macroscale, where inertial and viscous forces are both important. There are fewer examples of bioinspired internal and microscale flows, in which viscous and surface tension forces dominate. As integrated circuit cooling and lab-on-a-chip technologies develop, it may be fruitful to look to nature for inspiration for handling fluids efficiently at the microscale. Insects provide a particularly relevant group of model organisms. Here, we present two examples from insect microfluidics that we have studied in our laboratory, insect respiratory pumps and the hearing apparatus of the parasitoid fly, *Ormia ochracea*.

Fluid pumping in insect respiratory systems

Insects have the highest metabolic range in the animal kingdom, owing to their unique respiratory systems that do not use blood as an intermediate oxygen carrier. Instead of using lungs, insects take air in through pairs of openings around their body called spiracles. The air passes through the spiracles into a complex network of tracheal tubes that ramify and eventually reach the tissues (See Figure 1). Although the size of the largest tracheal tubes depends on the size of the insect, the size of the smallest tracheal tubes, located next to the tissues, is fixed at around $0.5 - 1$ μm.

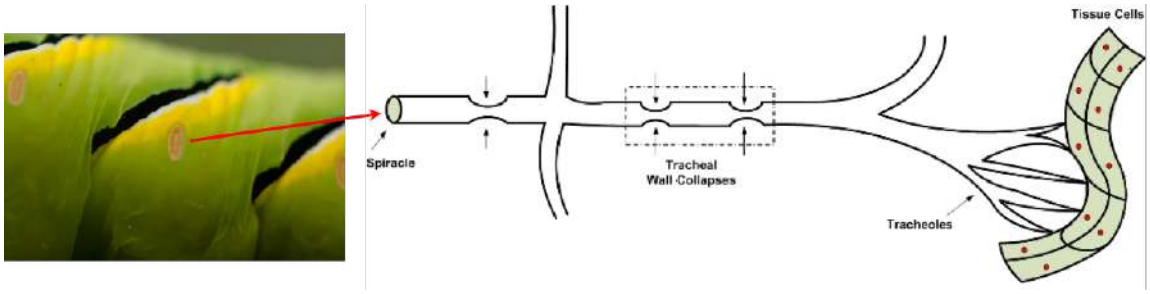

Figure 1: (Left) Close-up of spiracles on a *Manduca sexta* caterpillar. [Steve Begin, Spiracles, Creative Commons (2009); used in accordance with the Creative Commons Attribution (CC BY-NC-SA 2.0) license [1].] (Right) A schematic of the insect pathway for oxygen from spiracle to tissues. Modified with permission from [2].

It has been determined that in many insect species, portions of the tracheal tubes collapse rhythmically during active ventilation [3]. This is indicated by the boxed section labeled "Tracheal Wall Collapses" In Figure 1 (Right). We have developed mathematical, computational, and microfluidic device models that capture the salient features of tracheal-collapse driven respiratory flows (see, e.g., [2, 4]).

Sound localization in a parasitoid fly

Ormia ochracea is a parasitoid fly that relies on phonotaxis to locate its hosts in the horizontal plane. Gravid females locate their cricket hosts with astonishing precision, equal to that of horizontal sound localization in humans, though their small size should preclude this due to fundamental constrains from the physics of sound propagation [6]. Miles *et al.* demonstrated that the fly's two tympanal membranes (highlighted in Figure 2, Left) are mechanically coupled via a cuticular bridge, which increases the interaural time delay (ITD) between the tympana, allowing her to resolve nanosecond time differences, and greatly increasing the precision with which she can locate her larval hosts [5]. Below, we present new experimental and mathematical modeling results that demonstrate that small asymmetries in the tympanal system may lead to large gains in *O. ochracea*'s sound localization abilities.

*Corresponding author. E-mail: staplesa@vt.edu.

METHODS

The classical model for hearing in *O. ochracea* can be written as:

$$\begin{bmatrix} k_1+k_3 & k_3 \\ k_3 & k_2+k_3 \end{bmatrix} \mathbf{x} + \begin{bmatrix} c_1+c_3 & c_3 \\ c_3 & c_2+c_3 \end{bmatrix} \dot{\mathbf{x}} + \begin{bmatrix} m & 0 \\ 0 & m \end{bmatrix} \ddot{\mathbf{x}} = \mathbf{f}, \tag{1}$$

where $\mathbf{x} = (x_1(t), x_2(t))$ is the unknown tympanal amplitude vector, the force applied from the incident sound pressure wave is $\mathbf{f} = (f_1(t), f_2(t))$, and $\dot{(\,)}$ represents differentiation with respect to time, t. The parameters k_i and c_i are spring stiffnesses and dash-pot constants, respectively, and the parameter m is the effective mass of all the moving parts of the auditory system and is assumed to be concentrated at the ends of the intertympanal cuticular bridges. The subscripts 1 and 2 refer to the ipsi- and contralateral tympanal membranes, respectively. [5].

We introduced a size asymmetry between the left and right tympanal membranes into the mathematical model of hearing in *O. ochracea*. Additionally, we made 38 tympanal measurements of 19 *O. ochracea* specimens obtained from the Virginia Tech Insect Collection and the collection of the Smithsonian Museum of Natural History. The specimens were decapitated in order to expose the tympana, photographed with a high resolution camera (Canon 6D dSLR camera with a 65mm MP-E macro lens) and the tympanal areas were measured using ImageJ analysis software [7].

RESULTS

Measurements of the 38 *O. ochracea* tympana demonstrated a mean left-right asymmetry in tympanal area of approximately 5.6% (Figure 2, Center). With the modified mathematical model, we demonstrated that an asymmetry of just 5% in tympanal area can increase the ITD by a factor of 15 compared to the symmetric case (see Figure 2, Right). An additional result from the model, not shown here, is that a 5% asymmetry can also introduce interaural amplitude differences (IAD) four times greater than for the symmetric case, depending on the incident angle of the sound, θ.

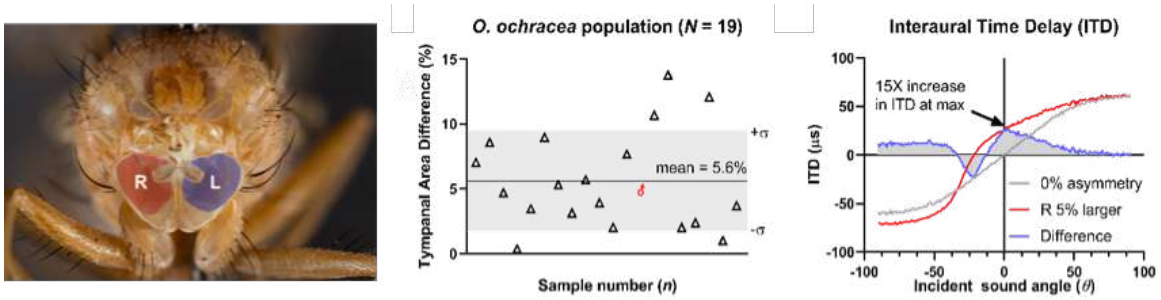

Figure 2: (Left) A headless *O. ochracea* fly with left (L) and right (R) tympanal membranes highlighted. (Center) Percent difference between left and right tympanal membrane areas for 19 *O. ochracea* samples. (Right) Interaural time delay (ITD) between the two tympana as a function of incident sound angle. An asymmetry of just 5% in tympanal area can increase the ITD by a factor of 15.

CONCLUSIONS

The mechanical coupling of the tympana in *O. ochracea* provides a significant advantage to the animal, allowing it to overcome fundamental physical constraints in locating its prey with precision. Here we demonstrate that 1) *O. ochracea*'s tympanal membranes have an average asymmetry of approximately 5.6% in area, and 2) that this asymmetry may allow for an order-of-magnitude additional increase in *O. ochracea*'s ITD and a similarly significant increase (factor of 4) in O. ochracea's interaural amplitude differences (IAD), the two quantities used by the fly to determine its prey's azimuthal location.

References

[1] Begin S. https://www.flickr.com/photos/33763901@N08/3860022559, 2009.
[2] Aboelkassem Y., Staples A. E., Socha J. J. Microscale flow pumping inspired by rhythmic tracheal compressions in insects. *Proc. ASME Press. Vess. Pip. Conf.* **PVP2011-57061**: 471-479, 2011.
[3] Westneat M. W., Betz O., Blob R. W., Fezzaa K., Cooper, W. J., Lee W.-K. Tracheal respiration in insects visualized with synchrotron x-ray imaging. *Science* **299**(5606): 558-560, 2003.
[4] Aboelkassem Y., Staples A. E. A three-dimensional model for flow pumping in a microchannel inspired by insect respiration. *Acta Mech.* **225**(2): 493-507, 2014.
[5] Miles R. N., Robert D., Hoy R. R. Mechanically coupled ears for directional hearing in the parasitoid fly *Ormia ochracea*. *J. Acoust. Soc. Am.* **98**: 3059-3070, 1995.
[6] Mason A. C., Oshinsky M. L., Hoy R. R. Hyperacute directional hearing in a microscale auditory system. *Nature* **410**: 686-690, 2001.
[7] Mikel-Stites M., Marek P. E., Staples A. E. Can you hear better if you're lopsided? Tympanal asymmetry may enhance hearing in a parasitoid fly. *Bull. Am. Phys. Soc* **64**(13): M03.00015, 2019.

DYNAMICAL WETTING IN HYDROPHOBIC NANOPORES DOWN TO ANGSTROM SCALE

Loïc Michel[1],Valentin Gérard[1],Romain Bey[1],Benoit Coasne[1],Elisabeth Charlaix[1],and Cyril Picard*[1]
[1]Laboratoire Interdisciplinaire de Physique, Université Grenoble Alpes, Grenoble, France

Summary Water in hydrophobic confinement is a topic of general importance for industrial applications. Ordered hydrophobic nanoporous materials have been used to study water confined between hydrophobic surfaces in well defined geometries. These materials behave as anti-sponges. The liquid, that can be forced to enter the nanopores at high pressure, is spontaneously expelled out of the pores when the pressure is released. To study the filling and emptying of hydrophobic nanopores, a high pressure apparatus has been built that covers three decades of intrusion/extrusion time at pressures up to 100 MPa. Considering several materials with pore sizes comprised between 0.3 nm to a few nm we study quantitatively the dynamics of filling and drying of the pores and illustrates specificity when going beyond the limits of continuous medium world.

Hydrophobic nanoporous material behave as anti-sponges when immersed within aqueous solutions. The liquid, that can be forced to enter the nanopores at high pressure, is spontaneously expelled out of the pores when the pressure is released. Based on forced intrusion and spontaneous extrusion, the process converts mechanical energy into interfacial energy (see figure 1(a)). Such systems have been envisioned for energy damping or recovery at the macroscale for applications in automotive transport or aerospace [1]. They are appealing for quick operations with a power density larger than the one of supercapacitors. According to the nature of the solid matrix and the fluid, the cycle may have a negligible hysteresis with an extrusion pressure close from the intrusion pressure, of interest for energy storage, or may present a significant hysteresis with an extrusion pressure much smaller than the intrusion pressure of interest for energy damping (see figure 1(b)). In the end, these systems make a bridge between nano or even angstrofluidic phenomena and macroscopic world. The physical grounds of the various observed behaviors are of interest as they are related to general questions concerning transport and wetting phenomena in hydrophobic confinement. Water in hydrophobic confinement is a topic of major importance for industrial applications, such as boiling, heat or mass transfers at interfaces, but also for the general understanding of hydrophobic interactions mediated by water in biological matter and biomolecular responses under osmotic stress.

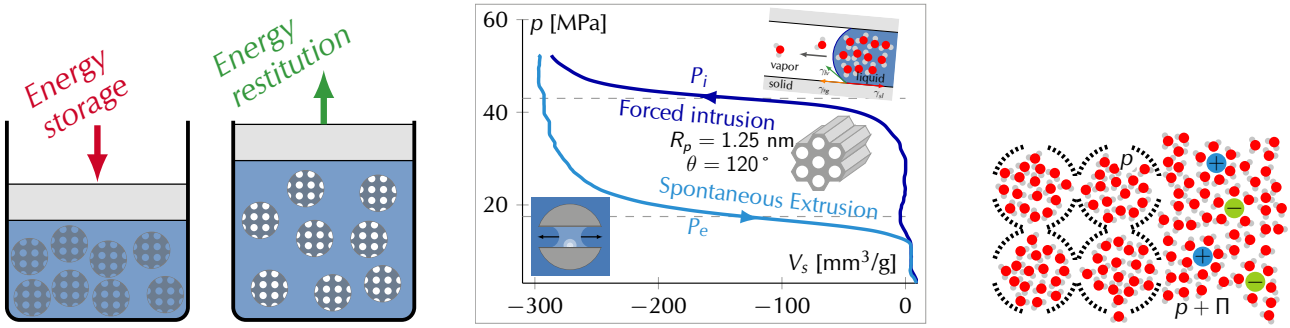

Figure 1: (a) Schematic of the intrusion extrusion process within pulverulent nanoporous material for energy applications. (b) Pressure dependence according to volume during an intrusion/extrusion cycle within hydrophobic nanopore with a radius of 1.2 nm. (c) Schematic of exclusion effect with subnanometric pores.

In this presentation we will focus on ordered nanoporous materials coupled with water or aqueous solutions. Such systems with crystalline structures are well suited to get quantitative insight on the transport of water confined between hydrophobic surfaces. Selecting the nanopore size, the impact of the confinement can be studied down to the limit of validity of the continuum approach and beyond. Among the large family of nanoporous structure, we consider Micelle Templated Silica (MCM-41) developed in the early 90's through condensation of alcoxysilicates and Periodic mesoporous organosilicas (PMOs) a new class of organic-inorganic nanocomposites. These two materials form honeycomb structures of ordered cylindrical parallel nanochannels with pore diameter which can be tuned between 1 to 10 nm. The length of the pore is of the order of 1 micron (see inset of figure 1(b)). These materials, which are natively hydrophilic, are functionnalized with silanol chains to become ultra hydrophobic. The typical intrusion pressure for pure water is of the order of 50 MPa. Additionally we worked with subnanometric pores using a metal organic frameworks (ZIF 8) which presents 1.2 nm spherical cavities interconnected through 0.3 nm gates. This material stable with water is known for its natural hydrophobicity and does not require any functionnalisation. For this material the intrusion pressure is of the order of 25 MPa.

*Corresponding author. E-mail: cyril.picard@univ-grenoble-alpes.fr

To finely characterize the filling and emptying of hydrophobic nanopores, a specific apparatus has been built working up to pressures larger than 100 MPa in dynamical regime. This apparatus gives access to the time dependence of the bulk pressure of the liquid surrounding the pores and the volume of the system during an intrusion/extrusion cycle. Three decades of time scale down to intrusion/extrusion duration of the order of a few ms are covered. Moreover temperature can be varied between -5° to 70° C. The measured bulk pressure is directly linked to average forces required to promote the liquid flow within the nanopores. The volume variation is related to the amount of liquid stored into the pores. This experimental tool allows to study the dynamics of aqueous complex liquids under strong hydrophobic confinement.

For naporous materials of pore diameter larger than typically ten water molecules, macroscopic concepts still hold. For instance in the cylindrical pores of hydrophobic mesoporous silicas, such as silalized MCM41 interfacial phenomena control both the forced wetting and spontaneous drying of the pores (figure 1(b)). The intrusion pressure p_i obeys mainly the Laplace-Washburn law of classical capillarity and scales as the inverse of the pore radius $1/R_p$ [2]. Intrusion characterized on a large range of intrusion time, in MCM41 and recently PMOs, gives access to the excess pressure to be overcome beyond the Laplace static pressure to force the liquid into the pores. This additional contribution gives the ability to study quantitatively dynamical wetting in model hydrophobic confinement and can be related to theoretical description of contact line dynamics The spontaneous extrusion at pressure p_e, on the other hand was shown to be triggered by the heterogeneous nucleation of nanobubbles in the pore, with a strong contribution of line tension[3]. Incidentally, the study of this process provide a novel technique to measure line tension up to values much lower than the measurement limit, of the order of 100 pN, of current dedicated experimental tools. The negative line tension obtained in MCM-41 is consistent with recent numerical simulation carried out in our group [4].

With sub nanometric pores, such as ZIF-8, a breakdown occurs. Macroscopic concepts, especially the notion of bidimensional interface becomes blur as the range of interactions produced by the wall becomes comparable with the pore diameter. From mechanical measurements done in dynamical regime at various temperature, the pure water case shows intriguing behavior such as a strong impact of isotopic composition. Moreover we demonstrate from macroscopic measurements on electrolyte solutions that molecular sieving of hydrated ions leads to giant osmotic pressures that have to be overcome to be able to fill the pores [5] (see figure 1(c)). This fundamental understanding provide a way to control intrusion and extrusion pressures. Concerning the intrusion process in dynamical regime, a major change with respect to nanometric cylindrical pores is observed, with an excess pressure which presents an unexpected dependence with the intrusion duration and a major dependance on temperature.

References

[1] Y. Grosu et al. “Synergetic effect of temperature and pressure on energetic and structural characteristics of ZIF-8 + water molecular spring”. In: *Nanoscale* 7.19 (2015), pp. 8803–8810.

[2] B. Lefevre et al. “Intrusion and extrusion of water in hydrophobic mesopores”. In: *J. Chem. Phys.* 120.10 (2004), pp. 4927–4938.

[3] L. Guillemot et al. “Activated drying in hydrophobic nanopores and the line tension of water”. In: *Proc. Natl. Acad. Sci.* 109.48 (2012), p. 19557.

[4] R. Bey, B. Coasne, and C. Picard. “Probing the concept of line tension down to the nanoscale”. In: *arXiv* 2001.02896 (2020).

[5] M. Michelin-Jamois et al. “Giant osmotic pressure in the forced wetting of hydrophobic nanopores”. In: *Phys. Rev. Lett.* 115 (2015), p. 036101.

PARTICLE MIGRATION IN A MICROFLUIDIC DEVICE ROAD TO CHARACTERIZE VISCOELASTIC LIQUIDS

X. Salas-Barzola[1], A. Naillon[1,2], W. Chevremont[1], C. De Loubens[1] and H. Bodiguel[*1]
[1]Laboratoire Rhéologie et Procédés (UMR 5520), Université Grenoble Alpes, Grenoble, France
[2]Laboratoire sols, solides, structures, risques (UMR 5521), Université Grenoble Alpes, Grenoble, France

Summary Microparticles suspended in liquids are often used to characterize fluids, having a lot of applications in several fields of science *i.e physical, chemical, biological processes*. Polymer solutions are non newtonian viscoelastic solutions. Contrary to Newtonian fluids for which the particles follow the streamlines while flowing in a confined channel, in those liquids they migrate transversely, due to the gradient of normal force at the scale of the particle. The scope of this project is to characterize the viscoelastic properties of very dilute polymer solutions by approaching the behavior of the normal force N_1 through microparticle migration experiments. These experiments are sensitive to very small normal forces (Weissenberg numbers on the order 10^{-3} to 1), a range which is not accessible in traditional rheometry. We have developed for that purpose a dedicated 3D particle tracking velocimetry technique, which allows to determine efficiently the probability density function of the particle position (PDF) and thus lead to a quantitative characterization of the viscoelastic migration phenomenon.

THERORETICAL DEFINITIONS

In 1974, Ho and Leal [1] derived for a second order fluid a theoretical prediction of the transverse viscoelastic force acting on a particle in a confined pressure driven flow. This expression can be rewritten in the following form

$$F_{e,th} = -K\eta\bar{v}_x a Wi \beta^2 z^* \qquad \textbf{Eq. 1}$$

where $\beta = 2a/H$ is the confinement ratio (particle diameter over channel height), a is the particle diameter, v_x is the mean velocity, η is the solution viscosity, $z^* = z/H$ is the reduced height of the particle and Wi is the Weissenberg number, defined as the ratio of the first normal stress difference over the shear stress. Balancing Eq. 1 with the viscous drag force $F_v = 6\pi\eta a V_z$ and assuming that particles flow at liquid velocity in x direction, using Poiseuille law and describing $N_1 = 2\eta\tau\dot{\gamma}^2$, the trajectories of the particle is found to be:

$$\frac{dz}{dx} = \frac{V_z}{V_x} = 2K\beta^2 Wi \frac{z^*}{(1-4z^{*2})} \qquad \textbf{Eq. 2}$$

With this expression we are able to predict the migration phenomena knowing the viscoelastic properties of the polymer solutions. In this work, we first test the above prediction accurately, before enlarging the scope of the problem towards shear-thinning solutions.

EXPERIMENTAL SET-UP

The experimental set-up implemented in this work consists in a thin rectangular capillary channel (Figure 1) mounted in an inversed microscope [2]. Mixing the different viscoelastic solutions with polystyrene fluorescence particles (with different sizes) and letting them flowing imposing a pressure drop with a pump we will be able to track the particles (using a PTV technique) as a function of the travelled distance along the channel.

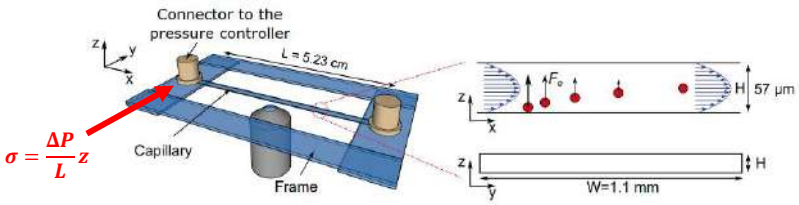

Figure 1. Microfluidic device implemented in particle migration experiments.

In practice, we compute the Probability Density Function of the position of the particles (PDF) at several location, and vary the pressure drop, the particle size and the polymer solutions.

RESULTS

Testing Bogger fluids (Polyacrylamide (PAM) : 150 kDa, 8 to 10% and Polyvinylpyrrolidone (PVP) : 360 kDa, 5 to 10%), we find that the theoretical definitions for the trajectories of the particles well described the migration phenomena, up to a prefactor which is 20% slower than predicted. This discrepancy is probably due to the fact that the theory is valid only for very small confinement. As shown in Figure 2, we are able to account for the evolution of the PDF of the z-

*Corresponding author. E-mail: hugues.bodiguel@univ-grenoble-alpes.fr

position of the particles along the without any fitting parameter. As expected, we find that the greater the pressure drop and the bigger the particles, the quicker the focalisation of the particles in the midplane of the channel.

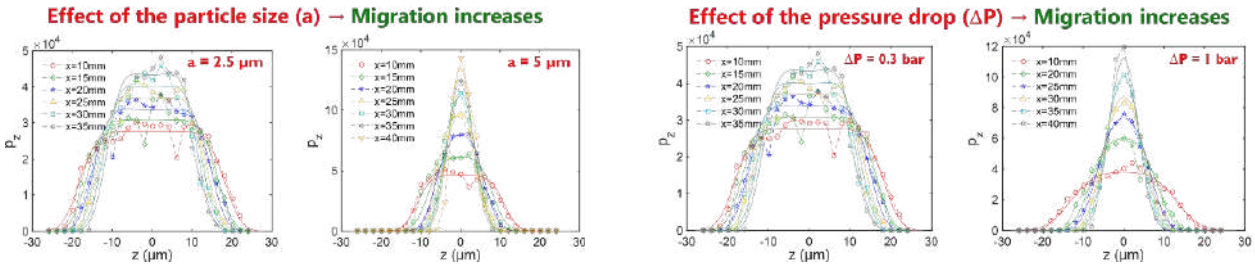

Figure 2. Effect of the particle size (a) and the pressure drop in the dynamics of the migration for Bogger fluids.

To analyse the imprint of the pressure drop in the dynamics of the particle migration, we compute the relative standard deviation of the particle z-position (which is a direct measure of the focalisation efficiency) in function of the pressure gradient. Here, we realise that the tendency is to increase the focalization when the pressure drop is higher for all the tested solutions (Figure 3).

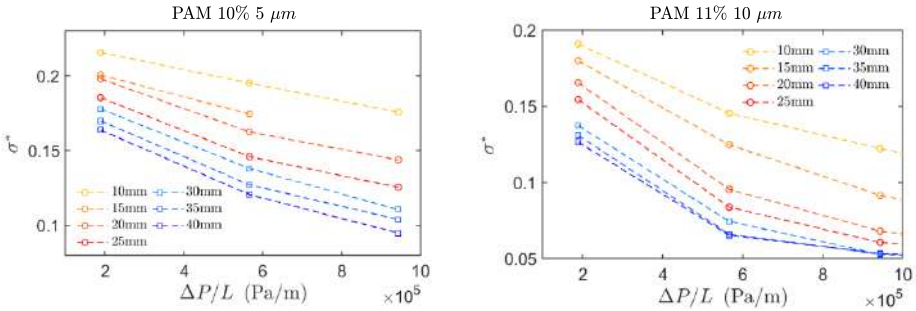

Figure 3. Relative standard deviation of the particle z-position, function of the pressure drop for tested Bogger liquids.

The dynamics of particle migration in shear thinning fluids are quite different from Bogger fluids. Testing FLOPAAM 3630s 6 g/l Na Cl: 18 MDa, 500 1000 and 2000 ppm, we find that the relative standard deviation of the particle is non-monotonic and eventually increases when increasing the pressure drop, as shown in Figure 4. We also found some rolling and sticking particles close to the walls.

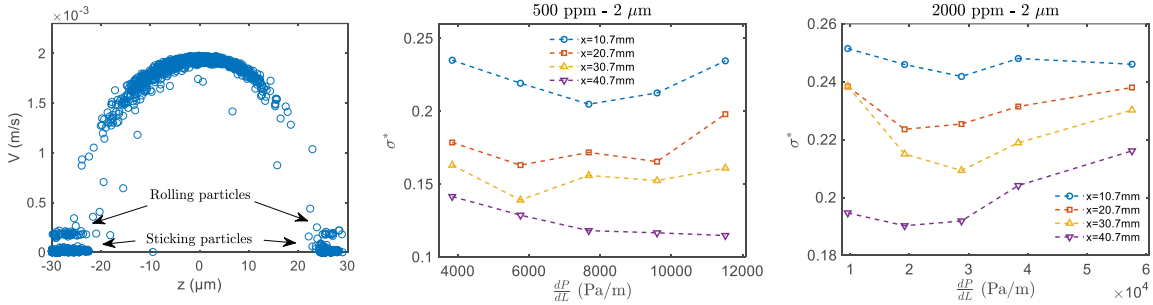

Figure 4. Left: Rolling and sticking particles. Right: Effect of the pressure drop on the migration for shear thinning solutions.

CONCLUSIONS AND OUTLOOKS

All the results presented in this work let us to conclude that the PTV3D method is well suited to study particle migration. We have performed a quantitative experimental validation of the theory for Bogger fluids, where the prediction of the evolution of the PDF along the channel could be used for a range of small $Wi \approx [10^{-3}3–3]10^{-1}]$.
For shear thinning solutions, the fact that the focalization exhibits a minimum when varying the pressure drop is puzzling. We will perform advanced rheometric characterization and direct numerical simulations to better understand these observations.

References

[1] Ho, B., & Leal, L. (1974). Inertial migration of rigid spheres in two-dimensional unidirectional flows. *Journal of Fluid Mechanics, 65*(2), 365-400. doi:10.1017/S0022112074001431.

[2] Naillon A., de Loubens C., Chevremont W., Rouze S., Leonetti M., Bod-iguel H. (2019). Dynamics of Particle Migration in Confined Viscoelastic Poiseuille Flows. *Phys. Rev. Fluids 4, 053301.*

DEVELOPMENT OF UNSTEADY HYDRODYNAMIC STRESS FIELD MEASUREMENT METHOD USING PHOTOELASTIC TECHNIQUE

Masakazu Muto*[1] and Yoshiyuki Tagawa [1]
[1]Department of Mechanical Systems Engineering, Tokyo University of Agriculture and Technology, Tokyo, Japan

Summary The experimental system for measuring the unsteady stress field in the liquid bulk is required to clarify the mechanism of the aneurysm which induces the human brain damage. In this study, the focus is on photoelasticity, which enables the measurement of the retardation that is proportional to the stress. This manuscript explains the process of the established visualization of the stress field in the fluids. The unsteady retardation field in the liquid polymer is measured by using a Venturi-shaped channel while the normalized values of retardation and stress calculated using numerical simulation under the same condition as the experiment are compared. In addition, the retardation field of the polymer liquid column extended by a CaBER-Dos system is also measured. From these examples of the experiment, the proposed method indicates to be a versatile hydrodynamic stress measurement system for various purposes.

INTRODUCTION

The measurement of hydrodynamic stress field is crucial in numerous situations. In medical field, clarifying the mechanism of aneurysm is critical for early diagnosis of brain damage. Recent work [1] suggested that the wall shear stress at the inner wall of aneurysm may be the principal cause of brain injury. Therefore, the development of experimental visualization of real-time stress field is necessary. This study proposes liquid polymers with photoelastic effects for the visualization of the hydrodynamic stress field. Photoelasticity is an optical method based on the retardation obtained by changes in the polarization state of the polymer solution, which results in proportional stress field values [2]. This method is a non-contact optical measurement with the potential to overcome current problems. However, the proposed method can only measure the retardation proportional to the principal stress difference (i.e., the total of vectors of normal stress and shear stress). Here, the visualization of the retardation field using two different target objects is reported.

METHOD

Figure 1(a) shows a schematic of the experimental setup. The proposed method requires a simple system: a target object located between a high-speed polarization camera (CRYSTA PI-1P, Photron Ltd.) and an incident LED light source (520 nm). The high-speed polarization camera contains an array of micro linear polarizers with four incident angles (0°, 45°, 90°, 135°). Each polarizer is attached to each pixel of the image sensor. Therefore, the polarization camera is capable of capturing the photoelasticity phenomena at frame rates up to 1.55 Mf.p.s. The visualization of photoelasticity requires a liquid polymer with a relatively long molecular chain. When external stress is imposed on the liquid polymer, an increase of the retardation is observed. This is generally known as the effect of the orientation state of the molecular chain [3]. In this experiment, xanthan gum and CNC (cellulose nanocrystal) are used as photoelastic materials. In addition, two different target objects are measured. The first target object is the unsteady flow field of the polymer liquid at the flow rate of 30 ml/min in a Venturi-shaped milli-channel as shown in Figure 1(b). On the other hand, the second target object is the polymer liquid column during the extension due to pure extension stress (normal stress) exerted by a CaBER-Dos (the dripping-onto-substrate capillary breakup extensional rheometry) system [4] as shown in Figure 1(c).

RESULTS & DISCUSSION

The result of the retardation distribution using the xanthan gum solution in the milli-channel is shown in Figure 2 (a). It is confirmed that by the proposed method, retardation can be observed in the fluid flow, as the effect of increased stress in the liquid. Moreover, this method can reveal the area of hydrodynamic stress concentration in the liquid. In addition, the retardation near the inner wall is the highest because of the large wall shear stress. Here, in order to investigate whether both have the same spatial intensity distribution, the normalized retardation measured with the proposed method and the normalized stress calculated with numerical simulation using COMSOL Multiphysics® are compared. From the comparison, at the same measurement area of the center cross-section of the channel, it is confirmed that normalized values and slopes are in close agreement. Therefore, the spatial intensity distribution of the phase difference corresponds to the hydrodynamic stress field.

Figure 2 (b) shows the visualization result of the polymer liquid column during extension with the retardation map in the y- and x-direction. It is confirmed that there is inconsistency in the intensity of retardation between the center and the other parts of the liquid column. The red-shaded regime in the retardation map in the y-direction shows a fixed value of retardation. However, there is a big error in the other regime, because the high curvature of the liquid column prevents the camera from capturing the transmitted light from the light source. On the other hand, the red-shaded regime in the retardation map in the x-direction shows a curve. This is due to the change of the optical length of transmitted light along the circular cross-section. From these results, for the target object with curvature, it is necessary to extract the appropriate area including the correct value of retardation.

*Corresponding author. E-mail: mmuto@go.tuat.ac.jp

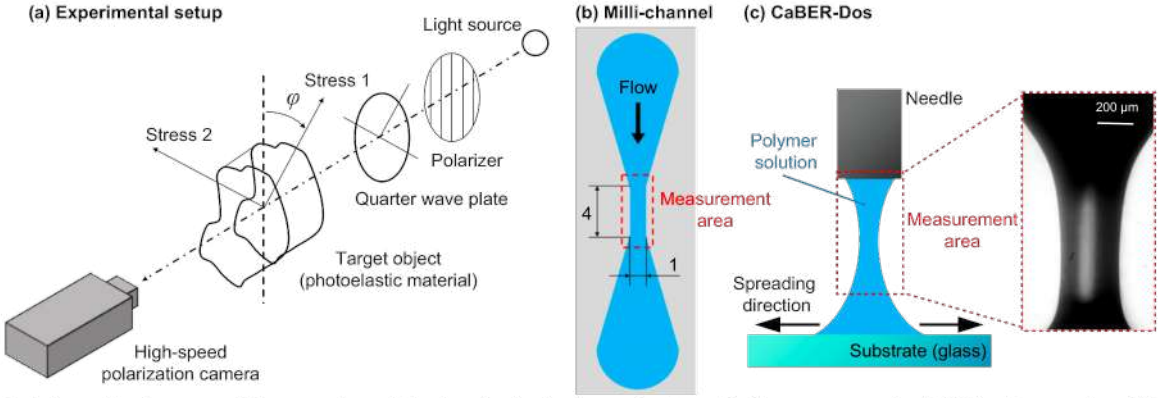

Figure 1. Schematic diagram of the experimental setup for hydrodynamic stress field measurements. (a) The frame rate of the high-speed polarization camera is 5,000 f.p.s. The backlight consists of a green LED light with a wavelength of 520 nm and circular polarization sheet. (b) The liquid polymer flows into the milli-channel is designed with a Venturi-structure with a narrow segment of a rectangular cross-section (1×1 mm^2). The flow is controlled by a syringe pump with a maximum flow rate of 30 ml/min. (c) A CaBER-Dos system generally used for the measurement of elongational viscosity that has a correlation for the neck diameter of liquid column spreading on substrate. Here, pure normal stress field at the state of extension before pinch-off is visualized.

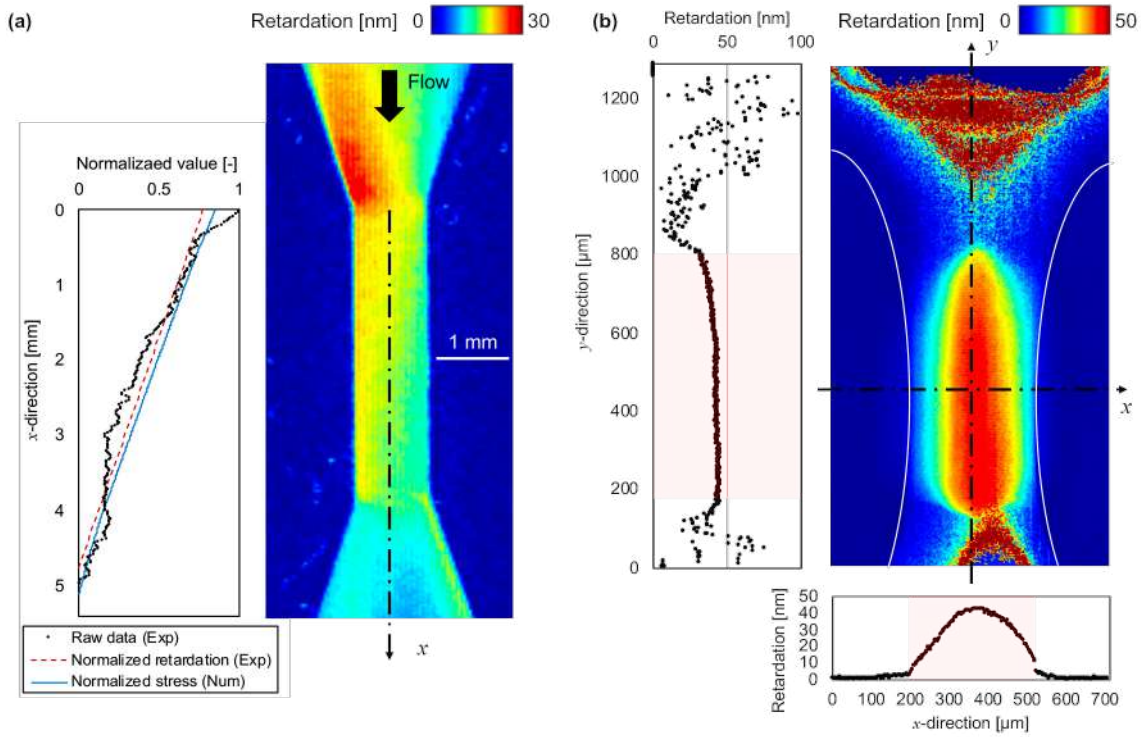

Figure 2. Visualization results of retardation distribution in (a) steady flow field of xanthan gum solution (0.5 wt% in ultrapure water) and (b) extensional stress of the polymer liquid column (mixture of xanthan gum of 0.1 wt% and CNC of 1 wt% in ultrapure water).

CONCLUSIONS

Experimental visualization of retardation proportional to hydrodynamic stress is implemented by the proposed photoelastic technique with a high-speed polarization camera and polymer solution. For the stress visualization using the milli-channel, the calibration between the experimentally measured retardation and the numerically simulated stress is required. However, with the new measurement technique using the CaBER-Dos system, even without numerical simulation, calibration is possible because both retardation and pure normal stress can be measured experimentally.

References

[1] Shojima M., Oshima M., Takagi K., Torii R., Hayakawa M., Katada K., Morita A., and Kirino T. Magnitude and role of wall shear stress on cerebral aneurysm: computational fluid dynamic study of 20 middle cerebral artery aneurysms. *Stroke*. **35**: 2500-2505, 2004.

[2] Onuma T., Otani Y. A development of two-dimentional birefringence distribution measurement system with a sampling rate of 1.3 MHz. *Optics Communications*. **315**: 69-73, 2014.

[3] Saito H., Inoue T. Chain orientation and intrinsic anisotropy in birefringence-free polymer blends. *Journal of Polymer Science Part B: Polymer Physics*, **25**: 1629-1636, 1987.

[4] Dinic J., Jimenez L.N., and Sharma V. Pinch-off dynamics and dripping-onto-substrate (DoS) rheometry of complex fluids. *Lab on a Chip*. **17**: 460-473, 2017.

SURFACTANT INDUCED BACKFLOW ON UNDERWATER LIQUID-GAS INTERFACE

Huiling Duan[1,*], Pengyu Lv[1], Hongyuan Li[1],
[1]State Key Laboratory for Turbulence and Complex Systems, Department of Mechanics and Engineering Science, College of Engineering, Peking University, Beijing, P. R. China

Summary Particle image velocimetry (PIV) is regarded as a typical nonintrusive method for fluid measurements. However, the current work demonstrates that trace amounts of surfactant added to the tracing particle solution induce an unexpected backflow at the liquid-gas interface, which results in an "observer effect" that significantly influences the accuracy of PIV measurements. Here, we reveal the formation mechanism of the backflow, characterize the backflow behavior, and evaluate the quantitative impact of the backflow on the PIV measurements. Our work draws attention to the potential deviations between the measurements and the reality in fluid measurements, especially for studies on liquid-gas interfaces such as slip boundaries, drag reduction, and superhydrophobicity.

INTRODUCTION

"Observer effect" refers to the influence of an observer on reality by the act of watching in the process of experiments, which results in a deviation between the measured value and the true value. The observer effect has been widely demonstrated in both the natural and social sciences, such as quantum mechanics, psychology, sensor performance, and material characterization. Specifically, in fluid measurements, intrusive methods (e.g., Pitot static, hot wire) that involve placing a probe as the observer in the flow field invariably affect the measured value, reflecting the observer effect. Thus, nonintrusive methods (e.g., laser Doppler velocimetry, PIV) are employed to visualize and quantify the flow field, which are presumed to introduce negligible effects on the characteristics of the flow.

Particle image velocimetry (PIV) is a typical nonintrusive method. Through the addition of flow-tracing particles in PIV measurements, the fluid motion becomes observable and measurable. Properties of particles, such as the size, density, following behavior, light scattering, and dispersity in the fluid, are essential to the PIV measurements. For most commercial flow-tracing particles, surfactants must be added to the particle solution to inhibit the agglomeration of particles and ensure stable and well-dispersed particles. However, even trace amounts of surfactant have been demonstrated to have a significant influence on the local flow near the boundary. At the liquid-gas interfaces in the flow, surfactants accumulate at downstream stagnation points, which induces Marangoni stresses opposite to the mainstream direction and thus limits the drag reduction. The slippage is also sensitive to the presence of surfactants, which causes the measured local slip length to be two orders of magnitude smaller than the theoretical prediction. As the flow field is changed by adding surfactants, the accuracy of PIV measurements is significantly affected, which should no longer be ignored, especially for studies on liquid-gas interface phenomena such as the slip boundary, drag reduction, and superhydrophobicity [1-3]. Although previous attempts have been made to investigate the influence of surfactants on the flow, the underlying mechanisms for this strong observer effect are still not clear, and a well-designed experiment is required to systematically visualize, quantify, and evaluate this effect, which is the scope of the current work.

"OBSERVER EFFECT" IN FLUID MEASUREMENTS: BACKFLOW AT LIQUID-GAS INTERFACES

In this work, backflow at the liquid-gas interface is directly observed during PIV measurements, which changes the original flow field and thus reveals a strong observer effect. The surfactant in the particle solution along with the geometric features of the microchannel is demonstrated to be crucial to the formation of this backflow. The backflow behavior is also characterized, in which a kinematic similarity is characterized to predict the backflow behavior under different flow rates. Importantly, the observer effect of the backflow on the PIV measurements is evaluated through quantification of the local slip length. The negative local slip length indicates the loss of accuracy of the PIV measurements. The current work can serve as a model system for investigating the backflow and aims to attract attention to the observer effect in fluid measurements.

References

[1] Xue Y. H., Chu S. G., Lv P. Y., Duan H. L., Importance of hierarchical structures in wetting stability on submersed superhydrophobic surfaces. *Langmuir* **28**: 9440-9450, 2012.
[2] Lv P. Y., Xue Y. H., Shi Y. P., Lin H., Duan H. L. Metastable states and wetting transition of submerged superhydrophobic structures. *Phys. Rev. Lett.* **112**: 196101, 2014.
[3] Xiang Y. L., Huang S. L., Lv P. Y., Xue Y. H., Su Q., Duan H. L. Ultimate stable underwater superhydrophobic state. *Phys. Rev. Lett.* **119(13)**: 134501, 2017.

*Corresponding author. E-mail: hlduan@pku.edu.cn

MASS PRODUCTION OF MULTI-SCALE FEATURES FOR MICROFLUIDIC AND NANOFLUIDIC APPLICATIONS

Michael D. Gilchrist*and Nan Zhang
School of Mechanical & Materials Engineering, University College Dublin,Ireland MiNAN Technologies, Dublin,Ireland

Summary Injection moulding of polymers with sub-micron and nanometre scale features is an ideal process for the mass production of microfluidic and nanofluidic devices for life science applications. However manufacturing tool inserts with inverted sub-micron and nanometre scale features is a challenge for industry. Recent research has led to the development of a method of using Bulk Metallic Glasses (BMGs) as tool materials that allow for nano-features to be incorporated into a replicating mould tool. BMGs have similarly high strength and wear resistance to Nickel, but they have no minimum microstructural size limits because of their amorphous nature. These tools can be used for manufacturing for over 20,000 moulding cycles while retaining the definition of sub-micron sized features. The smallest features that we have machined in BMGs are 85nm.

MOTIVATION

Compared to conventional tool steels, Ni is softer and develops pitting defects during moulding cycles, which may transfer toxic elements to moulded plastic devices. Furthermore, electroforming of Ni is not an environmentally friendly manufacturing process. Bulk Metallic Glasses (BMGs) are a class of amorphous metals without an intrinsic grain structure. FIB milling (focussed ion-beam) can be used to machine metallic glasses as mould tools to prototype multi-scale features that range in size from microns to nanometers.

A traditional disadvantage of manufacturing with BMG tools is the higher cost of raw materials and the need for a master, when compared to Ni electroforming. This prohibits the large uptake of BMG tools. In methods that we have developed recently, an environmentally friendly BMG tool can be used in batch manufacturing production of micron-scale features while also reducing tool cost dramatically, matching commercial Ni tool prices. We have demonstrated the use of these newly developed methods to manufacture microfluidic features with complex shapes that are tens of microns in size. This provides new opportunities to produce polymeric microfluidic and nanofluidic devices suitable for life science applications targeted at bacteria and viruses with dimensions that correspond to these sizes, as indicated in Figure 1.

FOCUSSED ION-BEAM MILLING

Figure 2 (left and middle) shows FIB milled patterns on BMG tools. The minimum feature that was successfully replicated was c. 85 nm on the UCD logo pattern (spacing between individual harp strings). The maximum aspect ratio of the corresponding ridges is c. 2. The mean height of ridge 3 was selected to indicate the quality of replication [1].

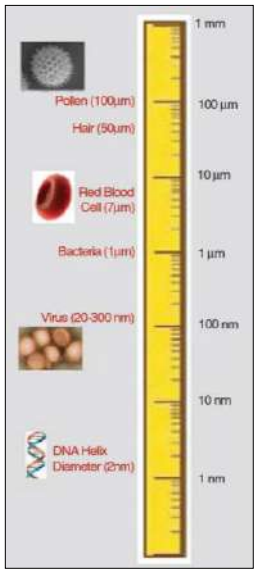

Figure 1: Biological length scales

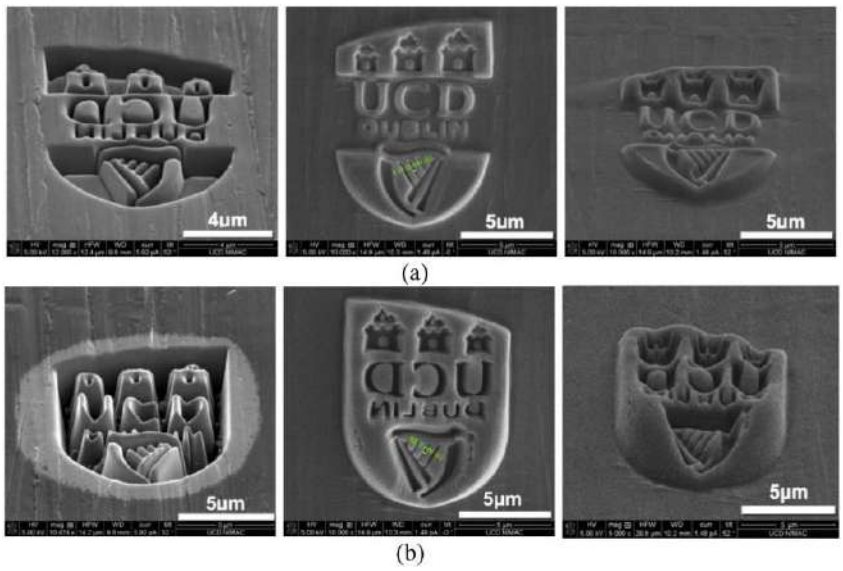

Figure 2 Surface patterns of BMG and replica: positive (a) and negative (b).

THERMOPLASTIC FORMING

Except for FIB milling, BMGs can be hot-embossed like plastics in their super cooled liquid region. Figure 3 (left) shows thermoplastically formed BMG ridge patterns that are 100 um high and that are spaced 300 um to 1 um apart. Ridges are well replicated when the spacing is larger than 10 um. Figure 3 (right) is an array of 10x10x10 um pillars embossed using BMG with a Si master.

Conventional thermoplastic forming process of BMGs uses a Si master and etches Si away after hot embossing; the master is not reusable. Si is brittle and easy to break when subjected to non-uniform pressure. Etching Si using KOH solutions causes tool surface oxidation and reduces tool life. Relatively expensive raw materials, a disposable Si master and the risk of breakage make it expensive to manufacture reliable BMG tools. Recently, however, we have developed a process to manufacture BMG tools via a reusable master and high pressures at moderate cost and without any risk of etching-induced oxidation, as shown in Figure 4. This technology is potentially useful for producing nanometer-scale fluidic tool inserts.

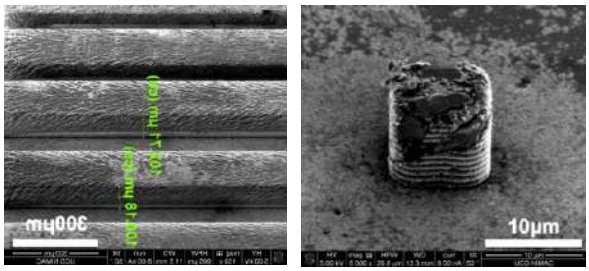

Figure 3. BMG tools embossed using Si master: ridges (left) and pillar (right).

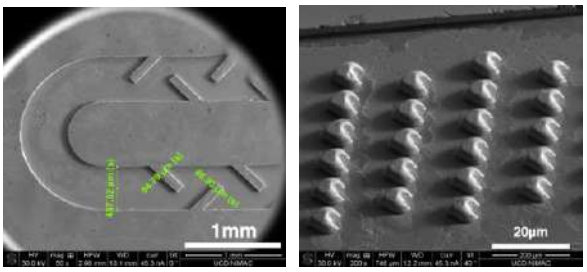

Figure 4. BMG tools produced using developed technology.

Figure 5 compares the hardness of various tool materials. Unhardened Stavax stainless steel tool had a hardness of 223HV and was hardened to 649HV. Nickel tool mechanical properties relies on electroforming conditions with hardness from 166~257HV. BMG has a hardness of 509HV and shows better mechanical properties than Ni. When used in injection moulding, a BMG tool with features smaller than 10 um can sustain ~20000 cycles [2]. By comparison, Ni inserts start to exhibit surface pitting defects and fracture after 130 moulding cycles, depending on process conditions [1].

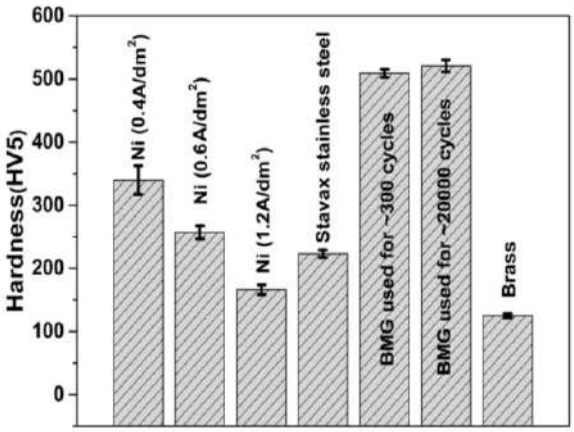

Figure 5. Hardness of various microfluidic tool insert materials.

CONCLUSIONS

Multi-scale mould tools that can be used for the mass manufacturing of polymer microfluidic and nanofluidic devices require precise definition of features that range in dimensions from c. 100 nm to centimeters. We have shown how the use of amorphous metals, specifically BMGs, are appropriate tool materials that allow for nanometer scale features to be incorporated into a mould tool, and that such a tool can be used to replicate more than 10,000 moulding cycles with high accuracy and repeatability, both quickly and cost-effectively.

References

[1] Zhang N., Srivastava A., Kirwan B., Byrne R., Fang F.Z., Browne D.J., Gilchrist M.D., Manufacturing microstructured tool inserts for the production of polymeric microfluidic devices using microinjection molding, *Journal of Micromechanics and Microengineering*, 25 (2015) 095005.

[2] Zhang N., Chu J.S., Byrne C.J., Browne D.J., Gilchrist M.D., Replication of micro/nano scale features by micro injection molding with Bulk Metallic Glass (BMG) mold insert, *Journal of Micromechanics and Microengineering*, 22 (2012) 065019.

ANOMALOUS DIFFUSION OF NANOPARTICLES IN LIPID MONOLAYERS

Xu Zheng*[1], Yang Liu[1], Dongshi Guan[1], Xikai Jiang[1] and Guoqing Hu [2]
[1]State Key Laboratory of Nonlinear Mechanics (LNM), Institute of Mechanics, Chinese Academy of Science, Beijing, China
[2]School of Aeronautics and Astronautics, Zhejiang University, Hangzhou, China

Summary The diffusion of membrane inclusions is crucial for various cell functions; however, its physical mechanism remains ambiguous due to the complex membrane structures. Herein, we investigate the diffusive motions of two different nano inclusions in dipalmitoylphosphatidylcholine (DPPC) monolayers. The first inclusion is the self-assembled microdomains of DPPC molecules, by which we can measured two-dimensional diffusion of an inclusion with molecular thickness. The second case is polystyrene nanoparticles embedded in DPPC monolayers, by which we can simulate nanoparticles dynamics in various biological membranes. Our results show that the diffusion of nanoparticles in lipid monolayer not only presents behaviour distinct from previous hydrodynamic prediction, but also manifests intriguing statistical features.

INSTRUCTION

Lipid membranes, such as cell membranes or lung surfactant membranes, are ubiquitous in biological systems. Despite their different functions, lipid membranes have a common structure - a thin film consisting of lipid and protein molecules. An early fluid-mosaic model treated the live cell membrane architecture as a two-dimensional (2D) fluid matrix in which the lipids and proteins are randomly dispersed. These membrane inclusions are inherently dynamic; thus, deciphering their diffusion is essential for understanding many cellular processes, such as signal propagation, membrane trafficking, and protein sorting [1]. From a physical perspective, the viscosity of the membrane and the mobility of membrane inclusions can both be determined from the lateral diffusions of the inclusions in the plane of the membrane.

The hydrodynamic description of the flow resistance of diffusive inclusions in a two-dimensional (2D) membrane has been a critical challenge [2-3]. The diffusion coefficient of membrane inclusions was initially given by Saffman-Delbrück (SD) [2]. By assuming that a uniform membrane at air-water interface has a 2D viscosity, the diffusion coefficient of a membrane inclusion in the SD model has been proposed. However, the SD model is a linear approximation. Later, Hughes, Pailthorpe, and White (HPW) extended the SD model [3] and applied it to describe the diffusion of larger inclusions, such as condensed microdomains in synthetic lipid membranes. However, it was recently found that the dispersed condensed domains formed by phase separation appeared not only on the micrometer scale but also on the nanometer scale that are in the continuous fluid phase [4-5]. Unless the membrane can be treated as homogeneous, the diffusions in membranes with heterogeneity will become more complicated than the descriptions of the SD and HPW models. Hence, it is vital to study the diffusion of membrane inclusions by considering the dynamic impact from the surrounding heterogeneous structures.

In this study, we first measured the diffusion of microdomains in the monolayers of DPPC, which is the predominant constituent of a lung surfactant film. As a well-controlled 2D model membrane system, the DPPC monolayer can help disentangle the out-of-membrane effects that are difficult to avoid in live biological membranes. After that, we dispersed polystyrene nanoparticles in the DPPC membrane on the air-liquid interface.

RESULTS

1. The 2D diffusion of DPPC domains

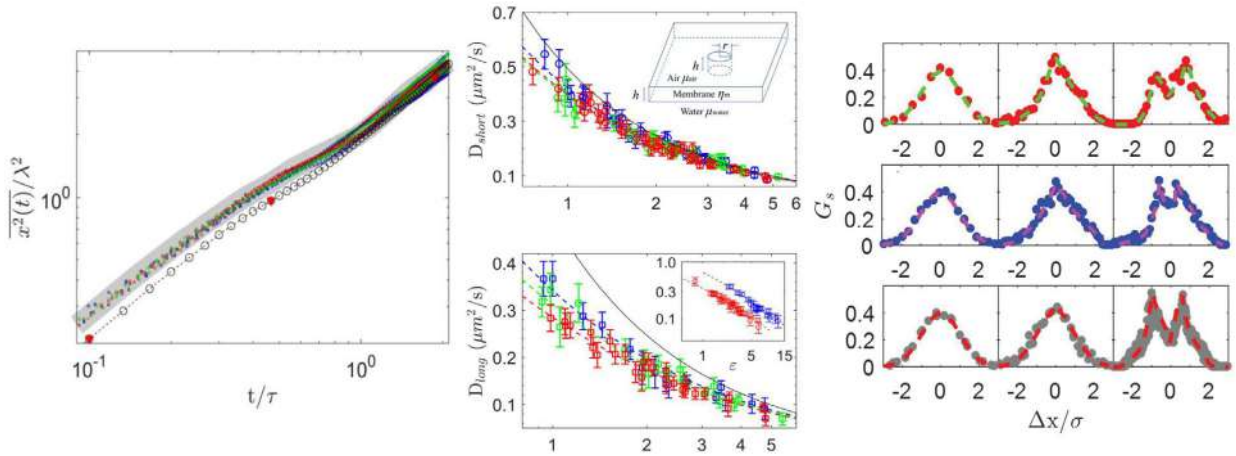

Figure 1. The characteristics of 2D membrane diffusion. (a) two-staged MSD; (b) the long-time and short-time diffusivity; and (c) the double peaked displacement probability distribution (DPD).

*Corresponding author. E-mail: zhengxu@lnm.imech.ac.cn

We find that the self-asembled domains nearby significantly impact the hydrodynamic mobility and the statistical feature of the diffusion, which are different from the existing theories considering the membrane as homogeneous. The diffusion can be divided into multiple stages (Fig.1a): short-time linear motion, then confined diffusion, and finally "anomalous yet Brownian" behavior that shows a linear MSD but an unusual double-peaked DPD. Thus, two membrane viscosities (Fig.1b, viscosity can be calculated from diffusivity) are needed to describe the hydrodynamic mobility of the microdomains: the short-time one describes the local continuous phase, which is found to be independent of the surface density of DPPC; while the long-time one describes the global phase taking into account the nanodomains, which is approximately three times larger than the local viscosity and increases with the DPPC density. Despite of the multistage MSD, the short-time or long-time diffusion coefficient can be described by HPW's hydrodynamic theory respectively (Fig.1b). Our results also unveil unusual displacement probability distributions (DPDs) of the diffusion in DPPC monolayer with heterogeneous nanodomains, which contain valuable information of the diffusion dynamics and domain-domain interactions. The temporal evolution of the DPD demonstrates that the interaction between a microdomain and the surrounding nanodomains varies at different time scales. In the early stage, the confinement from nearby nanodomains dominates, which can be described and quantified by the energy barrier theory. In the late stage, the dynamic nature of the nanodomains induces a disturbance of the positions of the nanodomains relative to the microdomain, and the nonuniformity of nanodomains causes a net dipolar repulsive force on the microdomain and generates the double-peaked DPD. We unveil the double-peaked DPD as a distinct feature of the "anomalous yet Brownian" behavior in monolayer, which differs from previously reported non-Gaussian DPDs in other complex systems that exhibit a central sharp peak or heavy tails.

Diffusion of nano polystyrene particles in the DPPC monolayer

We still use the same DPPC monolayer, and disperse polystyrene nanoparticles (radius R is from 50 nm to 500 nm) in the membrane. By particles tracking, we measure the MSD, diffusivity, and DPD of the nanoparticles based on the same experimental method as before. As the diffusivity D can be expressed as $D = k_BT/f\mu R$, we can estimate the drag coefficient f from diffusivity, and compare it with previous theory [6]. We found that the drag coefficient f is consistent with the theoretical prediction when R = 500 nm. However, the drag coefficients f of R =50 nm and R =100 nm are found to be 5-10 times larger than the theoretical prediction. We attribute the deviation to the microscopic moving contact line of the interface on the particle and the dynamically variation of the interface.

CONCLUSIONS

The diffusion of nanoparticles in biological membranes remains unclear, especially due to the complex structure of the membrane. Our results show that the diffusion of nanoparticles in lipid monolayer not only presents behaviour distinct from previous hydrodynamic prediction, but also manifests intriguing statistical features.

References

[1] Shi, Z., Graber, Z. T., Baumgart, T., Stone, H. A. & Cohen, A. E. Cell membranes resist flow. *Cell* **175**: 1769-1779, 2018.
[2] Saffman, P. G. & Delbrück, M. Brownian motion in biological membranes. *Proc. Natl. Acad. Sci. USA* **72**: 3111–3113, 1975.
[3] Hughes, B. D., Pailthorpe, B. A. & White, L. R. The translational and rotational drag on a cylinder moving in a membrane. *J. Fluid. Mech.* **110**: 349–372, 1981
[4] Zuo, Y. Y., Chen, R., Wang, X., Yang, J., Policova, Z. & Neumann, A. W. Phase transitions in Dipalmitoylphosphatidylcholine monolayers. *Langmuir* **32**: 8501–8506, 2016.
[5] Cruz, A., Vázquez, L., Vélez, M. & Pérez-Gil, J. Influence of a fluorescent probe on the nanostructure of phospholipid membranes: Dipalmitoylphosphatidylcholine interfacial monolayers. *Langmuir* **21**: 5349–5355, 2005.
[6] Dorr, A. et al., Drag and diffusion coefficients of a spherical particle attached to a fluid-fluid interface. *J. Fluid. Mech.* **790**: 607-618, 2016

A SCALING LAW FOR THE NECK-SHAPE IN MICROFLUIDIC FLOW-FOCUSING DEVICE

Tetuko Kurniawan[1,2], Piotr M. Korczyk[1*]
[1]Institute of Fundamental Technological Research, Polish Academy of Sciences, Warsaw, Poland.
[2]President University, Bekasi, Indonesia.

Summary Droplets in microfluidic devices are generated by crossing flows of two immiscible fluid in a confined space. The core point of models describing droplet detachment process from a stream of the droplet phase is the formation of the so-called neck – the constriction of the droplet phase, which finally breaks, releasing a new droplet. In low Capillary number (Ca) range, the neck shrinks through a series of quasi-static shapes that were determined by the instantaneous volume behind the neck and the geometrical confinement of the junction. Surprisingly, the squeezing model predicts that the droplet size is independent of the shear. Here, we reveal that in flow-focusing device, the geometrical confinement is unable to ensure the evolution of quasi-static shapes, such that the neck becomes dramatically prone to the magnitude of shear. We provided a scaling analysis to explain this dependency.

DEPENDENCY OF AREA UNDER THE NECK TO CAPILLARY NUMBER

The squeezing model, firstly introduced in the seminal paper of Garstecki et. al.[1], is the formation of droplet at low Ca (= $\mu_C Q_C / \gamma HW$, where μ_C and Q_C are the viscosity and flow rate of continuous phase respectively, γ is interfacial tension, H and W is the height and width of channel respectively). It is understood that droplet size produced in this squeezing regime, either in T-junction or in flow-focusing device (FFD) is insensitive to Ca, as long as flow rate ratio $q = Q_C / Q_D$ (where Q_D is the droplet phase flow rate) is kept constant, as stated by its scaling law: $\ell_D = \ell_0 + v_{N0} q$ (where ℓ_D is the dimensionless droplet length, with ℓ_0 and v_{N0} as constant parameters represent droplet's initial volume filling the outlet channel and total volume displaced by the neck, respectively). The insensitivity to flow rate parameters makes the squeezing regimes convenient for microfluidic application. However, earlier reports[2], [3]have shown that at some point the droplet size increases greatly as Ca is decreased further. This leads to the new leaking model[4]:

$$\ell_D = \ell_0 + q\, v_{N0} + \frac{\phi}{\mathrm{Ca}} . \qquad (1)$$

The strong dependency to Ca (see last term of Eqn. 1) is due to the leaking process, where the continuous-phase flows around the droplet through the corners of the channel (the so called gutter).

Our experimental analysis of the formation of droplet in FFD revealed that besides the effect of leaking there is another source of Ca dependence – the variation of the size of the neck. In case of T-junction the neck evolution is well localized and the break-up always occurs in the edge of T-junction. So in the case of T-junction the parameter v_{N0} associated with the volume of the continuous phase accumulated behind the neck is assumed to be constant. In contrary, in case of FFD, we observed that the neck is much longer than the width of the channel and it's final length (prior to break-up) becomes very large at very low Ca (see Fig. 1(a)). This behavior is allowed in FFD because the edges in the cross-junction does not play any role in the development of neck, supported by the observation that the position of break-up does not seems to be correlated to the edge position. As a consequence, in FFD the coefficient v_{N0} in Eqn. 1 is not constant and increases sharply as Ca decreases. This is confirmed by measurement of ℓ_D as a function q at fixed value of Q_C (i.e. constant Ca) as shown in Fig. 1(b). Assuming that v_{N0} is solely function of Ca, we can approximate it as the slope of the linear relation ℓ_D versus q . Fig. 1(c) shows the v_{N0} extracted using this assumption and taken from the experimental data of five distinct rectangular cross-section devices (shown as different aspect ratio(W/H)) and one

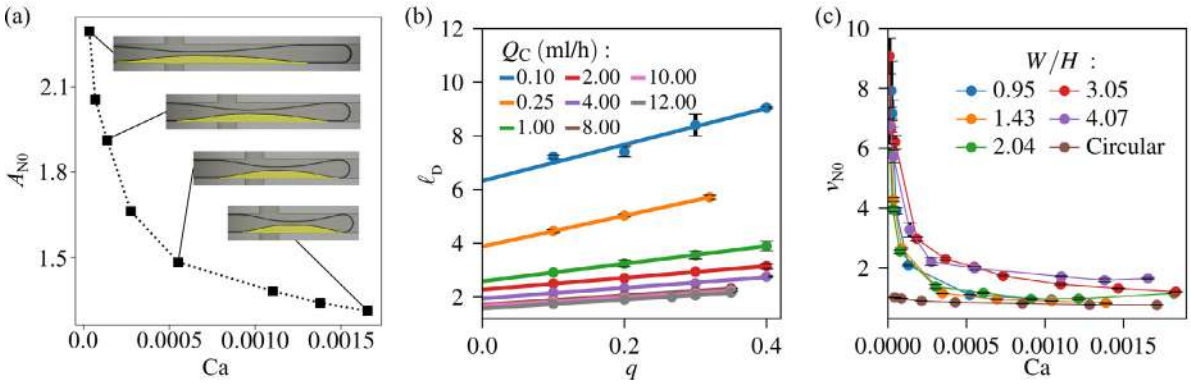

Fig. 1. (a) Visualization and measurement of neck area, A_{N0} , that drastically increases at vanishing Ca. (b) the slope of ℓ_D versus q at fixed Q_c can be use to approximate v_{N0} . The slope is higher for lower Q_c (i.e. lower Ca). Data is taken from device with W/H = 4.07. (c) Comparison of v_{N0} at low Ca from various rectangular cross-sectional devices and single circular device with radius of cross-section 0.2 mm.

* Corresponding author: piotr.korczyk@ippt.pan.pl

circular cross-section channel. v_{N0} increases drastically at decreasing Ca in rectangular cross-section devices but not in a circular cross-section device. This confirms the importance this effect in the leaking regimes of commonly used rectangular cross-section microfluidic devices. Note that although dependency of v_{N0} to flow rate parameters were indicated in previous T-junction[5] and FFD[6]literature, the changes of v_{N0} is not very significant at higher Ca flows (squeezing or dripping regime), such that it's effect is usually neglected. The non-negligible dependency of v_{N0} to Ca in the leaking regime has lead us to revise the previous assumption and modify the scaling law.

SCALING ANALYSIS OF v_{N0}

To explain the observations of v_{N0} variation we explored the simplified model of the evolution of the cosine-like profile of the neck (see Fig. 2). The analysis of the distribution of the capillary stress on such a profiles reveals that such a shape tends to increase its width for the relaxation of the stored potential energy. We Assume that the magnitude of capillary action depends on the maximal amplitude of the curvature - λ/ω^2 (where λ and ω are the height and the width of the profile respectively). The motion of the side edge points of the profile is supposed to be slowed by the viscous friction proportional to the speed of the edge propagation. Finally, balancing both interactions acting on the profile we obtained the following relation $\mathrm{d}\omega/\mathrm{d}t = c\,\lambda/\omega^2$, where $c = \xi\gamma/\mu_C$ and ξ is a constant coefficient of the length dimension corresponding to the height of the channel. Further analysis revealed Ca-dependency of neck shape as:

$$v_{N0} \propto \mathrm{Ca}^{-1/2} . \tag{2}$$

The scaling law was able to describe the exponential increase of v_{N0} at low Ca regime, as shown in Fig. 3 (a). Introduction of this relation into Eqn. 1 gives the extended leaking model, which is in very good agreement with the experiment results, as shown in Fig. 3 (b).

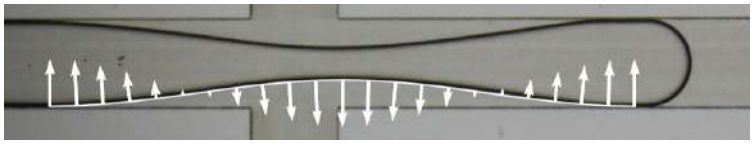

Fig. 2. The cosine-like neck profile shown as the white curve. The arrows are the $\kappa\hat{\mathbf{n}}$ vectors, where κ is the instantaneous curvature at any point along the curve and $\hat{\mathbf{n}}$ is the unit normal vector.

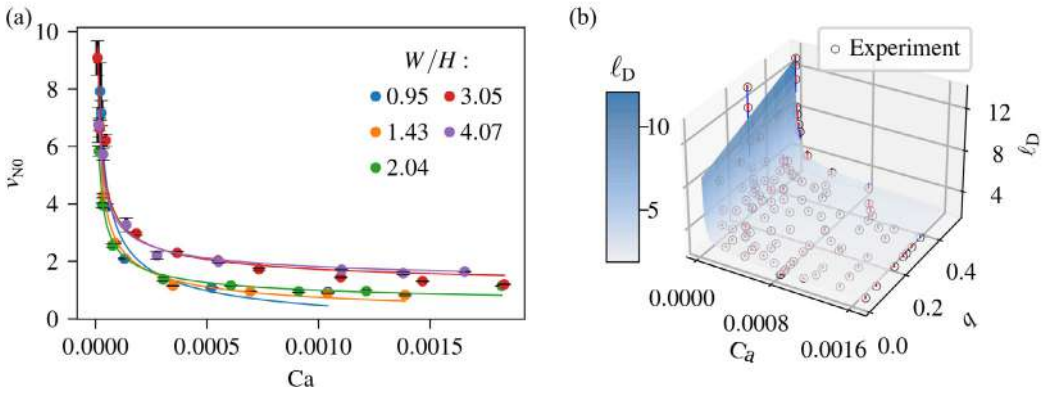

Fig. 3. (a) solid lines is the fitting results of v_{N0} based on Eqn. 2. (b) Theoretical prediction of ℓ_D by modified model of Eqn.1 is shown as the surface plot. Data shown is from device with $W/H = 4.07$.

Acknowledgment

Project operated within the Grant First Team Program No. First TEAM/2017-3/22 by Foundation of Polish Science (FNP).

References

[1] P. Garstecki, M. J. Fuerstman, H. A. Stone, and G. M. Whitesides, "Formation of droplets and bubbles in a microfluidic T-junction—scaling and mechanism of break-up," *Lab. Chip*, vol. 6, no. 3, pp. 437–446, Feb. 2006, doi: 10.1039/B510841A.

[2] T. Cubaud and T. G. Mason, "Capillary threads and viscous droplets in square microchannels," *Phys. Fluids*, vol. 20, no. 5, p. 053302, May 2008, doi: 10.1063/1.2911716.

[3] T. Fu, Y. Wu, Y. Ma, and H. Z. Li, "Droplet formation and breakup dynamics in microfluidic flow-focusing devices: From dripping to jetting," *Chem. Eng. Sci.*, vol. 84, pp. 207–217, Dec. 2012, doi: 10.1016/j.ces.2012.08.039.

[4] P. M. Korczyk, V. van Steijn, S. Blonski, D. Zaremba, D. A. Beattie, and P. Garstecki, "Accounting for corner flow unifies the understanding of droplet formation in microfluidic channels," *Nat. Commun.*, vol. 10, no. 1, Art. no. 1, Jun. 2019, doi: 10.1038/s41467-019-10505-5.

[5] V. van Steijn, C. R. Kleijn, and M. T. Kreutzer, "Predictive model for the size of bubbles and droplets created in microfluidic T-junctions," *Lab. Chip*, vol. 10, no. 19, pp. 2513–2518, 2010, doi: 10.1039/C002625E.

[6] S. van Loo, S. Stoukatch, M. Kraft, and T. Gilet, "Droplet formation by squeezing in a microfluidic cross-junction," *Microfluid. Nanofluidics*, vol. 20, no. 10, p. 146, Oct. 2016, doi: 10.1007/s10404-016-1807-1.

COLLABORATIVE DRAG REDUCTION OF MIXED SURFACTANTS AND POLYMERS

Jinjia Wei*[1,2], Dongjie Liu[2] and Fei Chen[1]
[1] School of Chemical Engineering and Technology, Xi'an Jiaotong University, Xi'an 710049, China.
[2] State Key Laboratory of Multiphase Flow in Power Engineering, Xi'an Jiaotong University, Xi'an 710049, China.

Summary Drag reduction performance and mechanism of mixed cationic surfactant and nonionic polymer were studied by using experiments and coarse-grained molecular dynamics simulation. The results showed that the mixed solutions have an intensified drag reduction performance, especially in low and high Reynolds number ranges. The addition of polymers can facilitate the coalescence of small micelles to form larger size micelles, and it can also help to share the shear action and balance the energy distribution of the micelle, to postpone the appearance of the energy extreme point and delay the rupture of the micelle structures, thus leading to the strengthened drag reduction performance.

INTRODUCTION

It is well known that the addition of small amounts of additives can cause a significant drag reduction effectiveness in turbulent flow[1].The phenomenon can reduce energy consumption and has immense applied value in industry. Polymers and surfactants are two most efficient types of additives in drag reduction. However, they have their own advantages and disadvantages. Polymers cause a drag reduction effectiveness by adding few parts per million by weight, but subject to mechanical degradation. The greatest strength of surfactants is its revisable mechanical degradation characteristics, however, surfactants need concentration above the critical micelle concentration (CMC) to form micelle structures, and showed deteriorated drag reduction performance under high Reynolds numbers due to the destruction of micelle structures. Because of the complementarity between polymers and surfactants, we want to combine them to form a mixed solution for a better drag reduction effect. It is generally believed that the formation of complexes or aggregates of polymer and surfactant is the main reason for drag reduction. For revealing the mechanism of surfactant-polymer drag reduction, some investigations have been performed on the microstructures and dynamic properties of surfactant-polymer aggregates by modern experimental techniques, such as light scattering, NMR spectroscopy surface tensiometry, viscometry and so on. However, most of the relative research is at the macro-level. To explore the phenomenon in surfactant-polymer systems at a molecular-level. The molecular dynamics (MD) simulation is an effective research method and a powerful tool to investigate such phenomena from molecular scale [2,3]. The aim of this work is to investigate the intensification of drag reduction effect caused by the mixtures of cationic surfactant and nonionic polymer solution, and to reveal the corresponding mechanism by simulating the microstructures of the mixed solution.

MEASUREMENT AND SIMULATION

Test facility

The experimental apparatus was a closed loop system consisted of a storage tank, a heater, a centrifugal pump, a setting chamber, a smooth two-dimensional (2D) channel, a diffuser and other measurement instruments. The fluid was pumped into the smooth channel and the flow rates were measured by electromagnetic flowmeters. The 2D channel was 10mm in height(H),125mm in width(W) and 3m in length. The pressure drop of the test section was measured by a differential pressure transmitter.

Surfactant and Polymer

A cationic surfactant - cetyltrimethyl ammonium chloride (CTAC) was used,and Sodium salicylate (NaSal) was used as the counter-ion salt with the same weight concentration as that of surfactant. Both solutes were added to the tap water and the mixed solution was left to stand at least 24 hours before mixing with the polymer solution. A kind of nonionic polymer - nonionic polyacrylamide (PAM) with the molecular weight of $Mv=6*10^6$g/mol was used. PAM was swelled in water for 12 hours first and then stirred in the 50℃water bath at a constant speed for 4 hours until it was dissolved. Then these two solutions (polymer and surfactant) were mixed by a stirrer and left to stand for 24h.

Molecular model

A Coarse-grained (CG) model was employed to simulate the microstructures and rheology of surfactant/polymer solution. Each site represents a group of atoms and the rank of CG sites is based on the MARTINI force field. Four main types of interaction sites are considered in this force field: polar (P), nonpolar (N), apolar (C) and charged (Q).The simulations are performed with LAMMPS simulation package. The simulations started from a random distribution of surfactants, salts, polymers and water molecules in a 23.1nm*23.1nm*23.1nm simulation box. The original distribution was obtained from PACKMOL. The system was minimized and then NPT simulation was performed. At last, the NVT simulation was performed to obtain the final structures. The temperature was 300 K and the pressure was maintained at 1 bar. Particle-Particle Particle-Mesh (PPPM) solver was used to compute long-ranged electrostatic interactions.

*Corresponding author. E-mail: jjwei@mail.xjtu.edu.cn.

RESULTS AND DISCUSSION

Drag reduction of mixed surfactant and polymer solutions

Four concentration combinations of mixed solution were tested at 6 different temperatures range from 25℃ to 50℃ at different Reynolds numbers. The mass concentration of polymer solution is 60ppm and that of CTAC solution is 100ppm. The results indicate that the curve of mixed solution is similar to that of pure CTAC solution, but different to that of pure PAM solution. Before the critical Reynolds number, surfactant micelles play a leading role in drag reduction while after the critical Renolds number, the micelles play a supporting role, on the contrary, polymer molecules dominate the rest experiment. The drag reduction behavior can be divided into three parts: enhanced drag reduction zone, stable drag reduction zone and destroyed drag reduction zone.

Coarse-grained molecular dynamics of mixed surfactant-polymer solutions

Figure 1 shows the sequential snapshots of microstructures. Initially, CTAC and polymer randomly distribute in the box (Figure 1(a)). At the first stage, CTAC molecules aggregate each other and PAM chains curl up, shown as Figure 1(b). This behavior is similar to the CTAC/PAM system. In the second step (Figure 1(c)), CTAC molecules form bigger spherical micelles and conglutinate with PAM chains. The presence of NaSal makes the both hydrophilic head groups arrange more closely as the charges are neutralized. In the third stage, PAM polymer chains drive CTAC micelles get closer to each other and worm like micelles form. Finally, the PAM polymer chains entangle with CTAC surfactant micelles and form surfactant-polymer complex interconnected network structures, reducing contact area with water (Figure 1(d)). Figure 2 shows Cyro-TEM image of the mixed solution, we can clearly see that the polymer can condense the surfactant micelle structures locally, which validates the molecular dynamics simulation.

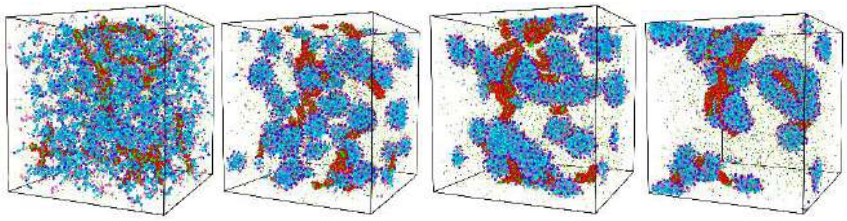

(a) 0 ns (b) 40 ns (c) 190 ns (d) 460 ns

Figure 1 Snapshots of the mixed solution.

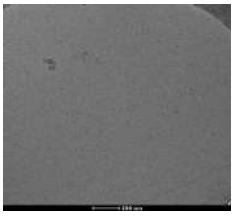

Figure 2. Cyro-TEM image of the mixed solution

Mechanism of the formation of surfactant-polymer network structures and drag reduction

It is found in the mixed solution that the CTAC micelles and PAM chains can form interesting complexes with interconnected network structures. The mechanism of the formation of the aggregates can be attributed to the the attraction between acylamino group and the head of CTAC, and the attraction between Sal^- and acylamino group. The addition of PAM can help facilitate larger size micelles, help to share the shear action and balance the energy distribution of the micelle, to postpone the appearance of the energy extreme point and delay the rupture of the micelle structures, thus leading to the strengthened drag reduction performance.

CONCLUSIONS

We investigated the intensification of drag reduction performance caused by mixtures of cationic surfactant and nonionic polymer solutions by experiments, and revealed the corresponding mechanism by simulating the microstructures of the mixed solution. The mixed solution systems can increase drag reduction efficiency by providing a wider range of Reynolds numbers, especially in enhanced zone and destroyed zone. It was found in the mixed solution that the CTAC micelles and PAM chains can form interesting complicated network structures, in which the polymer helps to form larger micelles and strengthen the network and protect surfactant micelles from being destroyed by shear stresses, improving the drag reduction performance.

References

[1] Toms B. A.Some observations on the flow of linear polymer solutions through straight tubes at large Reynolds numbers. *Proc. 1st Intl Congr. Rheol.*, 2:135-141, 1949.

[2] Cao Q., Zuo C., Li L., He H. Self-assembled nanostructures of bottle-brush polyelectrolytes with oppositely charged surfactants: a computational simulation study. *Soft Matter*, 7 : 6522-6528, 2011.

[3] Yan H.,Guo X. L.,Yuan S. L.,Liu C. B. Molecular Dynamics Study of the Effect of Calcium Ions on the Monolayer of SDC and SDS Surfactants at the Vapor/Liquid Interface, *Langmuir*, 27 :5762-5771, 2011.

CONTROLLING PURELY-ELASTIC INSTABILITIES

Robert J. Poole*[1], and Mahdi Davoodi[1,2]
[1]School of Engineering, University of Liverpool, Liverpool, L69 3GH, UK
[2]Schlumberger Cambridge Research, High Cross, Madingley Road, Cambridge, CB3 0EL, UK

Summary Complex fluid flows are ubiquitous in both the natural and man-made worlds. For such complex fluids the underlying microstructure can give rise to flow instabilities which are often totally absent in "simple" Newtonian fluids such as water or air. For example, beyond a critical flow speed in viscoelastic fluids, driven by elastic normal-stresses, the flow may break symmetry, become time dependent or even chaotic (so-called "elastic turbulence") in the total absence of inertia i.e. creeping-flow. Often such instabilities are unwelcome, for example in rheometric devices when the aim is to measure material properties or in simple pumping operations when they can give rise to unacceptably large pressure drops and prevent pumping. In the current paper we discuss a number of ways such onset conditions can be altered in order to control their onset.

INTRODUCTION

Complex fluids such as emulsions, colloidal gels, polymer or surfactant solutions are all characterized by the existence of an internal "microstructure". Often the timescales associated with this microstructure (a relaxation time say) are sufficiently large – on the order of milliseconds to seconds – that they may couple with every day processing or flow time scales (say the reciprocal of a typical shear rate in the process) and lead to instabilities. These instabilities, so-called "purely-elastic" flow instabilities, may arise even under relatively weak shear flows that correspond to vanishingly small Reynolds numbers where equivalent simple (Newtonian) fluids remain laminar and stable. Such purely-elastic flow instabilities, which are transitions in flow stability driven by elastic normal stresses in the absence of significant inertial effects, have been observed, primarily for dilute polymer solutions, in a range of flows both viscometric and complex. In this regime the Reynolds number is small and the Deborah, or Weissenberg (Wi) numbers, which characterize the degree of elasticity in the flow, large. It is now well known that such instabilities can arise as a consequence of the combination of elastic stresses and streamline curvature captured in what is known as the "Pakdel-McKinley" criterion [1]. The aim of the current paper is to understand, via studying two different prototypical geometries, if it is possible to "control" – either delaying or enhancing – the onset conditions of such instabilities. Such control is, practically, of importance in various technological applications. For example, a number of microfluidic rheometers have been proposed to measure material properties of complex fluids, see e.g. viscometers [2] and rheometers to measure time-dependent or extensional properties by [3]. In such microfluidic rheometer geometries, purely-elastic instabilities are often unwanted as they will modify the assumed (viscometric) flow and corrupt any attempt to extract meaningful material properties through them via pressure-drop measurements for example. Alternatively, it may be possible to use the fundamental understanding of the instability to relate the onset conditions to a given material property such as Zilz et al [4] where the flowrate at onset of the time-dependent instability in a microfluidic serpentine channel was used to measure relaxation times down to 1 ms for dilute polymer solutions. Creating instabilities in microfluidic geometries – to enhance heat or mass transfer for example – is also a strong motivation for better fundamental understanding in this area [5]. Firstly, we investigate Taylor-Couette flow, but with a finite aspect ratio, such that the flow is shear-dominated (but not, strictly, viscometric outside of the one-dimensional "infinite" aspect ratio case) and a modified "cross-slot" geometry with a cylinder at the geometric centre of the domain, which can be characterised as being a flow of mixed kinematics. In both cases we show how an understanding of the scaling mechanisms, coupled with the ability to vary the geometry of each problem, allows passive control of the onset conditions.

CONSTITUTIVE EQUATIONS AND NUMERICAL METHODS.

The governing equations for this problem are conservation of mass, assuming incompressibility, and momentum:

$$\nabla \cdot \tilde{\boldsymbol{u}} = 0,$$
$$\tilde{\rho}\left(\frac{\partial \tilde{\boldsymbol{u}}}{\partial \tilde{t}} + \tilde{\boldsymbol{u}} \cdot \nabla \tilde{\boldsymbol{u}}\right) = -\nabla \tilde{p} + \nabla \cdot \tilde{\boldsymbol{\tau}} + \tilde{\eta}_s \nabla^2 \tilde{\boldsymbol{u}},$$

where ρ is the density of the fluid, $\boldsymbol{u}$ is the velocity vector, η_s is the solvent viscosity and $\boldsymbol{\tau}$ is the extra-stress tensor containing the polymeric contribution to the stress which is determined using the simplified Phan-Thien and Tanner model (sPTT):

$$f_1 \tilde{\boldsymbol{\tau}} + \tilde{\lambda} \overset{\nabla}{\tilde{\boldsymbol{\tau}}} = \tilde{\eta}_p (\nabla \tilde{\boldsymbol{u}} + \nabla \tilde{\boldsymbol{u}}^{\mathrm{T}}),$$

where λ is the relaxation time of the fluid and η_p is the polymeric contribution to the viscosity. $\overset{\nabla}{\tilde{\boldsymbol{\tau}}}$ is the usual upper-convective derivative of the extra-stress tensor (see e.g. [6]). Here we use the linear form of the f_1 function:

*Corresponding author. E-mail robpoole@liv.ac.uk.

$$f_1 = 1 + \alpha \frac{\tilde{\lambda}}{\tilde{\eta}_p} Tr(\tilde{\tau}),$$

where α is the extensibility parameter. This constitutive equation was originally derived from network theory by Phan-Thien & Tanner [7]. Here we use the rheoFoam solver in the OpenFOAM platform which was previously introduced by Pimenta & Alves [8] to solve the above equations using a finite-volume methodology.

RESULTS AND DISCUSSION

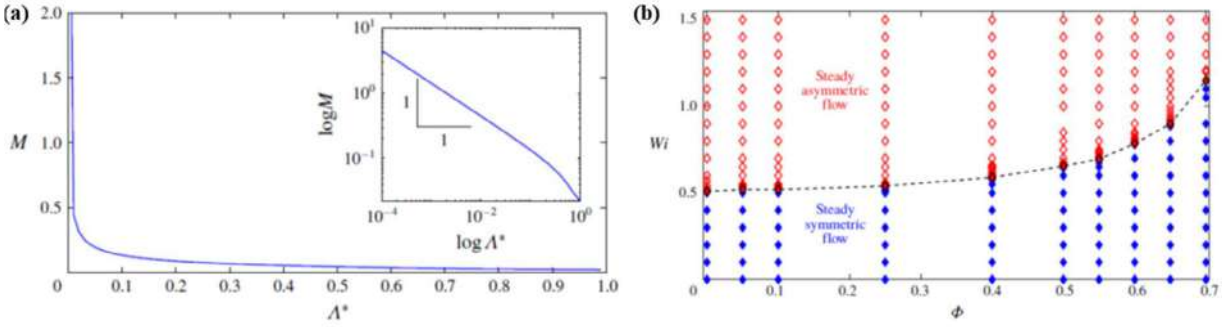

Figure 1. (a) Effect of normalised aspect ratio Λ* on the Pakdel-McKinley [1] "M" parameter for the Taylor-Couette geometry. Oldroyd-B fluid (α=0) , solvent-to-total viscosity ratio β=0.5 and radius ratio= Wi = 0.1. (b) Modified cross-slot flow; boundary between the symmetric and asymmetric flow states for different Wi and blockage ratio for α = 0.02 and β=1/9.

Taylor Couette flow

The effect of finite depth aspect ratio (Λ) on Taylor-Couette flow [9] shows that the shear rate along the centreline can be significantly influenced by the effect of the confining walls. In Fig. 1(a) the effect of the modified aspect ratio (Λ/(Λ+1)) on the Pakdel-McKinley "M" parameter [1] is depicted along the centreline (based on a zeroth-order analytical solution) for a nominal situation of radius ratio and Wi both equal to 0.1. For this particular case, the M parameter for modified aspect ratios of 0.2, 0.5 and 0.8 are calculated as 0.02745, 0.0448 and 0.08941, respectively. Here, setting a constant M_{cr} = 5.92 (i.e. the value calculated from a linear stability analysis in the 1D limit) provides an estimate of the critical values of Wi for instability onset, which are 26.56, 21.57, 13.21 and 6.62 for modified aspect ratios of 1 (1D case), 0.8, 0.5 and 0.2, respectively. The strongly destabilising effect of confining side walls is apparent.

Cross-slot flow

The effect of adding a cylinder of diameter D to the geometric centre of cross-slot width W [10] shows that the critical Wi for the onset of a steady symmetry-breaking instability is modified by this cylinder as characterised by a "blockage" ratio (D/W) as shown in Fig. 1(b). At higher blockage, i.e. a larger cylinder, steady-symmetric conditions can be maintained until much higher Wi which, all else being equal, corresponds to a direct increase in the critical flowrate through the geometry before symmetric conditions are lost.

CONCLUSIONS

For Taylor-Couette flow, our analysis would indicate that purely elastic instabilities are more likely to occur at lower Weissenberg numbers for lower-aspect-ratio geometries. Thus, if one wanted to promote such instabilities, for example to enhance mixing, this could be achieved via small-aspect-ratio geometries. This result may also have important applications for small-angle neutron scattering or flow birefringence studies, which tend to use smaller-aspect-ratio devices. For cross-slot flow, a cylinder added to the geometric centre can enable an increase in the critical flowrate of about two before symmetry is lost. The negligible effect of a vanishingly small cylinder in this geometry highlights the importance of shear-dominated flow away from the central stagnation point as being the driving mechanism for instability in this geometry, suggesting this flow too falls under a "Pakdel-McKinley" curved streamlines paradigm.

References

[1] Pakdel, P., McKinley,G.H., *Phys. Rev. Letts*., 1996, 77, 2459–2462.
[2] Guillot, P., et al, *Langmuir*, 2006, 22, 6438–6445.
[3] Ober, T.J., et al, *Rheologica Acta*, 2013, 52, 529–546.
[4] Zilz, J. et al, *Lab on a Chip*, 2014, 14 (2), 351-358.
[5] Stroock, A.D., et al, *Science*, 2002, 295, 647-551.
[6] Bird, R.B., et al., *Dynamics of Polymeric Liquids,* 1987, New York, Wiley
[7] Phan-Thien, N., Tanner, R.I., *J. Non-Newt Fluid Mech,* 1977, 2(4), 353-365.
[8] Pimenta, F., Alves, M.A., *J. Non-Newt Fluid Mech*, 2017, 239, 85-104.
[9] Davoodi, M., et al.., *J. Fluid Mech.*, 2018, 857, 823-850.
[10] Davoodi, M., .et al.., *J. Fluid Mech.*, 2019, 881, 1123-1157.

OPENFOAM FRAMEWORK FOR PARTIALLY MISCIBLE LIQUIDS

A .Ghaemi[1],M. Hübner[2],M.Mincheva[2],and N. Germann*[1]
[1]Fluid Dynamics of Complex Biosystems, School of Life Sciences Weihenstephan, Technical University of Munich, Germany
[2]Biothermodynamics, School of Life Sciences Weihenstephan, Technical University of Munich, Germany

Summary We present a robust and versatile OpenFOAM framework for partially miscible binary systems. Our solver was successfully validated using prior numerical benchmark studies and in-house microfluidics experiments. We found that this toolbox can reliably predict the interfacial dynamics and mixing characteristics of binary viscous systems. Future work will focus on ternary systems as well as viscoelasticity.

INTRODUCTION

Many flows encountered in industrial applications are composed of multiple components. Important factors affecting the mass- and momentum transport of mixtures include the physicochemical and microstructural characteristics of the individual components as well as their degree of miscibility. An important application where partial miscibility plays a crucial role is liquid-liquid extraction (LLE). This is a purification technique used to separate compounds based on their relative solubilities in two immiscible (or partially miscible) solvents. As an industrial process, LLE is frequently employed in the downstream recovery of proteins and other biomolecules because of its low cost and ease of scale-up. The industrial design of such types of processes requires a proper understanding of the flow kinematics and mass transfer characteristics of the individual components in the mixtures, which can be gained by physical modeling and numerical simulations.

Phase-field methods are well suited to describe the interfacial kinematics of multicomponent systems. Contrary to interface-tracking techniques, e.g., volume-of-fluid (VOF), level-set, and front-tracking, the diffusion of the components is adequately addressed by assuming a diffusive interface layer of finite thickness. This helps with avoiding the non-physical assumption of abrupt changes of the properties at the interface and allows for mass transfer across it. Whereas it has become standard practice to simulate systems with immiscible or fully miscible viscoelastic components, partial miscibility has not been a major focus so far.

In this talk, we present our latest developments in this area. Based on the generalized bracket approach of nonequilibrium thermodynamics, we formulated a phase-field modeling framework for viscoelastic materials. The chemical potential is expressed through a nontrivial velocity difference between the components. In this manner, the transport of the phase fractions can be accurately solved without excessive numerical diffusion by employing a multidimensional universal limiter with explicit solution method. In addition to stress-induced migration, the inertial terms are kept in the final formulation as they can be of relevance in specific applications. The nonideal part of the mixing energy, described by, e.g., a non-random-two-liquid (NRTL)-type equation, controls the phase behavior. Comparison with other numerical studies and in-house microfluidics experiments confirmed the accuracy and reliability of our numerical implementation. Future simulation work will focus on applications involving viscoelasticity, multiple components, and living microorganisms.

METHODS

Based on previous non-equilibrium thermodynamic modeling work [3, 4, 5], we proposed a new phase-field framework to explain the phase dynamics of viscoelastic mixtures with partial miscibility while accounting for the influences of inertia and gravity. In this framework, the chemical potential is expressed through nontrivial velocity differences between the components. By doing so, we can implicitly account for diffusion and obtain more accurate numerical solutions. In the limit of two viscous immiscible components, our framework yields a model similar to NSCH (Navier-Stokes-Cahn-Hillard). We implemented the model equations into the OpenFOAM finite-volume solver. A multidimensional universal limiter with explicit solution method is used to evolve the phase fractions in time accurately.

BENCHMARKING WITH NUMERICAL STUDIES

As a first assessment of our framework, we focused on viscous binary systems with immiscible, partially miscible, and fully miscible components. For the immiscible scenario, we considered the well-known rising bubble problem and compared our predictions with published VOF data [1, 2]. The benchmark setup is displayed along with the comparison in Fig. 1. A two-dimensional rectangular domain whose width to length ratio is $x/y = W/L = 0.5$ is filled with phase-1. The other phase, phase-2, is taken to be a circular bubble of radius ratio $r_{b0}/W = 0.25$. This bubble is placed inside the matrix fluid at the initial position $(x/W, y/W) = (0.5, 0.5)$. The comparison was performed at a dimensionless

*Corresponding author. E-mail: natalie.germann@tum.de

time $\tilde{t} = tU_g/W = 3$, where $U_g = \sqrt{2gr_{b_0}}$ is the characteristic velocity with g being the gravitational acceleration. We find that the rise and deformation of the bubble are accurately captured in both immiscible cases. The formation of the filaments and the satellite bubbles in the system with more significant density and viscosity contrast indicate good agreement.

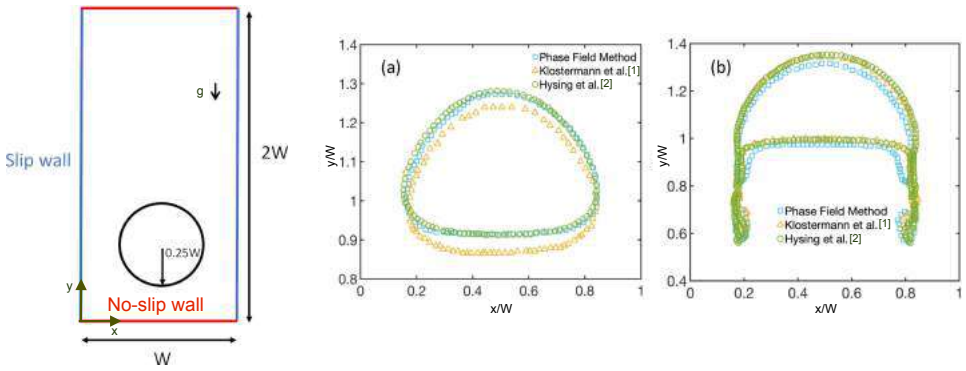

Figure 1: Rising bubble benchmark setup (left) and validation results (right). Comparison of our phase-field predictions with VOF benchmark data at the time instant $\tilde{t} = 3$. a) Bubble rise and deformation. b) Bubble breakup in a system with more significant density and viscosity contrast.

COMPARISON WITH IN-HOUSE MICROFLUIDIC EXPERIMENTS

For the more complicated case of partially and fully miscible viscous components, we compared the numerical results of our solver with in-house microfluidics data. The laboratory data were obtained at room temperature near the inlets and outlet of a Y-shaped microchannel using an optical microscope. For the miscible system, the numerical results are in full agreement with experimental observation. The interface of the two components dissolves along the channel until it disappears, showing complete mixing. The selected partially miscible system is immiscible at room temperature and miscible at an elevated temperature of 330 K. The solver nicely reproduces the experimental data at room temperature. Artificially increasing the temperature in the numerical simulation makes this system miscible, as expected from the binary phase diagram.

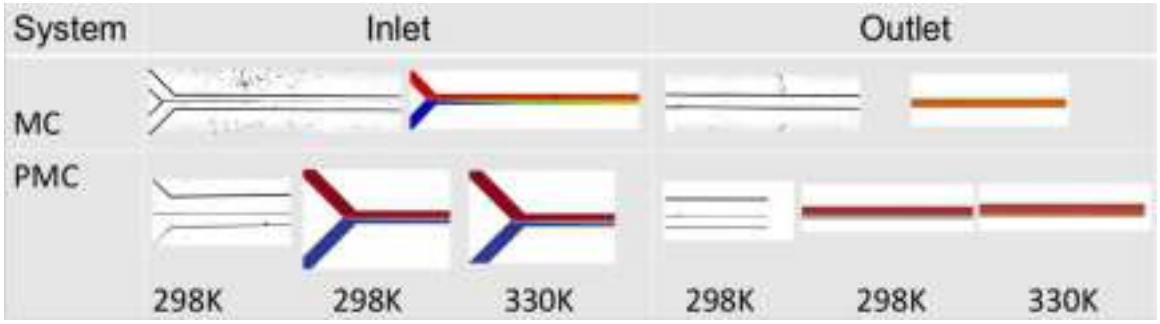

Figure 2: Validation of our solver with optical data recorded near the inlets and outlet of the Y-shaped microchannel. Miscible case (MC): Water/MeOH. Partially miscible case (PMC): MeOh/n-Hexane. All laboratory experiments were conducted at room temperature. An additional simulation was performed at an increased temperature of 330 K to capture the single-phase behavior of MeOh/n-Hexane.

ACKNOWLEDGMENT

The authors acknowledge the Bavarian Research Foundation for their financial support (AZ-1285-17).

References

[1] J. Klostermann, K. Schaake, and R. Schwarze. Numerical simulation of a single rising bubble by VOF with surface compression. *Int. J. Numer. Methods Fluids,* **71**(8):960-982, 2012.
[2] S. Hysing, S. Turek, D. Kuzmin, N. Parolini, E. Burman, S. Ganesan, and L. Tobiska. Quantitative benchmark computations of two-dimensional bubble dynamics. *Int. J. Numer. Methods Fluids,* **60**(11):1259-1288, 2008.
[3] A. Ghaemi and N. Germann. Nonequilibrium thermodynamic modeling of ternary fluid flows. *Int. J. Multiphase Flow,* **111**:310-314, 2019.
[4] S. Hooshyar and N. Germann. A thermodynamic study of shear banding in polymer solutions. *Phys. Fluids,* **28**(6):063104, 2016.
[5] N. Germann, L. P. Cook, and A. N. Beris. A differential velocities-based study of diffusion effects in shear-banding micellar solutions. *J. of Non-Newton. Fluid Mech.,* **232**:43-54, 2016.

TWO-DIMENSIONAL NUMERICAL SIMULATIONS OF VISCOELASTIC JETS

K. Zinelis*, T. Abadie, R. Constante-Amores, and O. K. Matar
Department of Chemical Engineering, Imperial College London, London, UK

Summary The numerical simulation of spray formation in a non-Newtonian fluid offers substantial challenges and is central to numerous industrial applications such as spray-drying. The aim of the present work is to set out the basis for the numerical examination of viscoelastic spray systems. To achieve this, we begin with two-dimensional axisymmetric numerical simulations of a impulsive jet into a stagnant gaseous phase using the volume-of-fluid technique to capture the interface and the log-conformation transformation for the solution of the viscoelastic constitutive equation. This permits the exploration of parameter space, capturing the effect of the elastic, viscous, and inertial forces on the ejected droplet size. In particular, the dependence of the rate of thinning on the injected flow rate, the relaxation time, as well as the finite extensibility of the polymeric chains is investigated.

BACKGROUND

Sprays are the result of atomisation processes, following a number of different types of instabilities, which occur when a jet of liquid discharges into a gaseous phase. The ultimate objective of the present research is the development of numerical simulations about the atomisation process of viscoelastic (i.e. dissolved polymers) fluids. The first step towards this direction is the thorough investigation and capture of phenomena of smaller length-scales that take place during a spray formation. An indicative example of these physical phenomena is the ligament breakup into smaller droplets, which leads to the typical "beads-on-a-string" morphology in the case of viscoelastic jets [1]. The viscoelastic filament thinning and breakup is one of the major problems which exhibit strong complexities due to the emerging non-linearities derived from elastic stresses and gradients of stresses and velocity. Specifically, capillarity is the driving force for the process of breakup. The filament breakup of a Newtonian liquid is a really fast process due to a delicate interplay among viscous, elastic and inertia stresses enhancing the resistance to the action of capillarity. However, in the case of viscoelastic materials, the temporal evolution of a thread is governed by the balance between elastic and capillary forces. Consequently, it is crucial to develop an adequate understanding of the emerging visco-elasto-capillary thinning process [2].

Both experimental and numerical work has been carried out so far on the breakup of a viscoelastic filament. In particular, the thinning dynamics of a viscoelastic thread has been extensively examined through the capillary breakup extensional rheometry (CaBER) and the Rayleigh-Ohnesorge jetting extensional rheometer (ROJER), which are the two predominant experimental methods for jetting processes of viscoelastic fluids [3]. Moreover, several Computational Fluid Dynamics (CFD) simulations have confirmed the CaBER measurements, as well as the effect of elasticity and inertia [4,5], but there is still a lack of advanced and robust numerical tools for studying the jetting process of viscoelastic filaments in both low (ROJER experiment) [6] and high (turbulent jets) Reynolds (Re) numbers.

FORMULATION AND PROBLEM STATEMENT

Using a Volume-of-Fluid (VOF) approach, we solve the two-dimensional (2D) axisymmetric, two-phase, incompressible Navier-Stokes equations with surface tension [7]. The polymeric contribution in the total stress balance is modelled with a constitutive equation, $\boldsymbol{\sigma_p} = (\mu_p/\lambda)\,(\mathbf{f_R}(\mathbf{A})\mathbf{A} - \mathbf{I})$, where $\boldsymbol{\sigma_p}$ is the polymeric stress, μ_p is the polymeric viscosity, λ is the relaxation time of the polymer, $\mathbf{A}$ is the conformation tensor of the viscoelastic fluid and $\mathbf{f_R}(\mathbf{A})$ is the relaxation function equal to $\mathbf{A} - \mathbf{I}$ for the often used Oldroyd-B model and to $\frac{\mathbf{A}}{1-\mathrm{tr}(\mathbf{A})/L^2} - \mathbf{I}$ for the non-linear FENE-P model with L being the finite extensibility of the polymeric chains. For overcoming the numerical challenges emerging in the case of high relaxation times, known as the "High-Weissenberg number problem" (HWNP), the log-conformation formulation is implemented, where the aforementioned equations account for the logarithm of the conformation tensor $\mathbf{A}$ instead, $\boldsymbol{\Psi} = \log \mathbf{A}$ [8].

The complexity of the viscoelastic fluids arises from the different macroscopic and microscopic time-scales that characterise the flow. Specifically, the jetting process of a viscoelastic fluid can be thoroughly described by the following non-dimensional groups, which can be obtained from the governing equations normalised by using the initial filament radius R_0 as length scale, the capillary time scale, $t_c = \sqrt{\rho R_0^3/\gamma}$, with γ being the surface tension, $u_s = R_0/t_c$ as characteristic velocity scale, and finally $\sigma_s = \rho u_s^2$ as characteristic stress scale:

$$De = \frac{\lambda}{t_c} = \frac{\lambda}{\sqrt{\rho R_0^3/\gamma}}, \quad Oh = \frac{t_v}{t_c} = \frac{\mu_0}{\sqrt{\rho\gamma R_0}}, \quad \beta = \frac{\mu_s}{\mu_0}, \quad \frac{\rho_a}{\rho_s}, \frac{\mu_a}{\mu_s}, \quad We = \frac{2\rho u_{jet}^2 R_0}{\gamma}, \tag{1}$$

where De is the Deborah number determining the elasticity effects, Oh is the Ohnesorge number which characterises the relevant importance of the viscous and the inertial forces, t_v is the viscous-capillary time scale, β is the solvent viscosity ratio accounting for the contribution of the polymeric viscosity in the total zero shear viscosity μ_0 of the fluid, μ_a/μ_s and ρ_a/ρ_s are the air-liquid viscosity and density ratios, We is the Weber number which determines the transition between dripping and jetting regime, and u_{jet} is the average jet velocity.

*Corresponding author. E-mail: k.zinelis17@imperial.ac.uk.

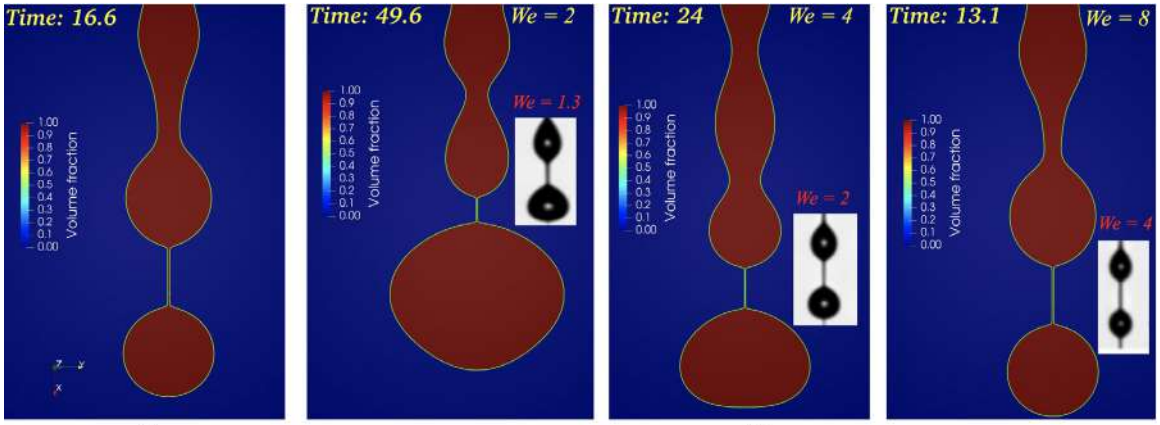

Figure 1: *(a)* The "beads-on-string" morphology of a viscoelastic jet of $De = 1$, $Oh = 0.2$, $\beta = 0.85$, $\rho_a/\rho_s = 0.01$, $\mu_a/\mu_s = 0.01$ and $We = 8$, where *Time* = t/t_c. *(b)* Qualitative comparison of CFD simulations and experimental data for different We numbers [3].

RESULTS

In this study, we perform 2D axisymmetric numerical simulations using the open source code *basilisk* [9], which permits the application of an Adaptive Mesh Refinement (AMR) for a highly-resolved development of the very thin viscoelastic thread. We manage to capture the typical "beads-on-a-string" structure, as Figure 1(a) indicates, that a viscoelastic jet exhibits during a ROJER experiment defined by the parameters shown in Table 1. The size of the simulation domain is $0 \leqslant z/R_0 \leqslant 20$, the jet is injected with a velocity perturbation $u(z,0)/u_s = u_{jet}/u_s + \sin(0.5\pi(t/t_c))$ and the maximum level of AMR is 12. Subsequently, we investigate the effect of the flow rate by applying three different We numbers ($We = 2, 4, 8$) and comparing qualitatively the results of the CFD simulation with available experimental data [3], as Figure 1*(b)* presents. We observe that for lower We number, which is indicative of the "dripping to jetting transition" regime ($We \approx 1$), there is a strong coalescence of the formed droplets just before the breakup time, leading to a large droplet size and a breakup closer to the inlet. For a large We number, the coalescence is less pronounced and thus the jet breaks into droplets over a longer distance from the nozzle and in shorter times. Finally, during this research, the effect of De and L on the thinning dynamics of a viscoelastic jet are also examined. More specifically, in the first case as De increases, thin viscoelastic threads of longer length, as well as larger lifespan are expected, whilst when FENE-P model is applied, for larger L (i.e. $L >$100) a FENE-P filament approaches the Oldroyd-B dynamics, which provides the best agreement with the theoretical predictions so far.

Table 1: Dimensionless parameters of the jetting process of a viscoelastic fluid.

De	Oh	β	ρ_a/ρ_s	μ_a/μ_s	We
1	0.2	0.85	0.01	0.01	8

CONCLUSIONS

2D axisymmetric CFD simulations are performed for studying the thinning dynamics of a ROJER experiment. The numerical simulations can effectively capture the "beads-on-string" structure of the viscoelastic fluids, but also how the thinning dynamics change due to the Weber and Deborah numbers, as well as the finite extensibility of the polymer. A remaining challenge is the development of fully three-dimensional Direct Numerical Simulations where all the scales in space and time are resolved, especially for viscoelastic flows of high Re numbers.

References

[1] C. Clasen, J. Eggers, M. A. Fontelos, J. Li, and G. H. McKinley. The beads-on-string structure of viscoelastic threads. *J. Fluid Mech.* **556**: 283-308, 2006.
[2] A. M. Ardekani, V. Sharma, and G. H. Dynamics of bead formation, filament thinning and breakup in weakly viscoelastic jets. *J. Rheol.* **62(5)**: 1135-1153, 2018.
[3] W. Mathues, S. Formenti, C. McIlroy, O. G. Harlen, and C. Clasen. CaBER vs ROJER—Different time scales for the thinning of a weakly elastic jet *J. Fluid Mech.* **655**: 46-56, 2010.
[4] P. P. Bhat, S. Appathurai, M. T. Harris, M. Pasquali, G. H. McKinley, and O. A. Basaran. Formation of beads-on-a-string structures during break-up of viscoelastic filaments. *Nat. Phys.* **6(8)**: 625-631, 2010.
[5] E. Turkoz, J. M. Lopez-Herrera, J. Eggers, C. B. Arnold, and L. Deike. Axisymmetric simulation of viscoelastic fiilament thinning with the Oldroyd-B model. *J. Fluid Mech.* **851**: 1-13, 2018.
[6] B. Keshavarz, V. Sharma, E. C. Houze, M. R. Koerner, J. R. Moore, P. M. Cotts, P. Threlfall-Holmes, and G. H. McKinley. Studying the effects of elongational properties on atomization of weakly viscoelastic solutions using Rayleigh Ohnesorge Jetting Extensional Rheometry (ROJER). *J. Nonnewton. Fluid Mech.* **222**: 171-189, 2015.
[7] S. Popinet. Numerical models of surface tension. *Annu. Rev. Fluid Mech.* **50(1)**: 49-75, 2018.
[8] R. Fattal and R. Kupferman. Time-dependent simulation of viscoelastic flows at high Weissenberg number using the log-conformation representation.*J. Nonnewton. Fluid Mech.* **126(1)**: 23-37, 2005.
[9] S. Popinet. A quadtree-adaptive multigrid solver for the Serre–Green–Naghdi equations. *J. Comp. Phys.* **302**: 336-358, 2015.

CONSTRAINING THE ORIGIN OF FORE-AFT ASYMMETRICAL SHAPE OF BUBBLES RISING IN YIELD STRESS FLUIDS

Marjan Zare*[1], Ali Pourzahedi[2], and Ian Frigaard[1,2]
[1]Department of Mathematics, University of British Columbia, Vancouver, BC, Canada
[2]Department of Mechanical Engineering, University of British Columbia, Vancouver, BC, Canada

Summary A series of novel experiments are conducted exploring a potential cause of fore-aft asymmetry of a rising bubble in a simple yield stress fluid. It has been believed that the yield stress could prevent bubbles injected from a nozzle to freely adjust their shape and smooth the developed cusp on their lower side. This possibility is investigated by introducing a bubble, with controlled shape, and speed, into a yield stress fluid, Carbopol, without direct injection from a nozzle. Our results rule out this possibility and show that a slight change in the rheology can have significant effect on the shape of rising bubbles, though still fore-aft asymmetric.

INTRODUCTION

A significant number of fluids used in our daily life like toothpaste, hair gel and peanut butter, as well as working fluids in geophysical and industrial settings, such as magma and cement slurry, are categorized as viscoplastic fluids. The key feature of viscoplastic fluids is their characteristic yield stress. More precisely if such fluids are subjected to a stress more than their yield stress they deform and flow, otherwise they exhibit a solid-like behavior. The transition from a solid-like regime to a fluid-like regime is often approximated using rheological models such as Bingham, and Herschel-Bulkley constitutive laws. In these models, the build-up and breakdown of structure are assumed to be reversible and instantaneous, i.e., the material regains its value of the yield stress upon the flow reversal. This ideal yield-stress behavior implies that elastic and thixotropic effects are negligible. Upon adopting this assumption, the rise of a bubble and creeping motion of a sphere settling in a yield stress fluid have been studied numerically, e.g. [1, 2]. Their results confirmed that the developed flow in the yielded envelope zone enclosing moving objects or bubbles is symmetric, when the particles/bubbles are symmetric.

However, the experimental observations published in [3, 4, 5, 6] started researchers thinking that real yield stress fluids might not be as simple as predicted from the aformentioned constitutive laws. The results published in [3, 4] dramatically illustrated the fore-aft asymmetry of flow around a spherical particle settling in a yield stress fluid. And the cusp shape at the bubble's lower side, observed in [6], markedly contradict the fore-aft symmetry expected theoretically in Stokes flows. These results were more surprising since the yield stress fluid used in those experiments, Carbopol, was often assumed to be a simple yield-stress fluid, with negligible thixotropic behaviour.

The inverted teardrop shape could be attributed to a number of reasons. One of which is the elasticity of the Carbopol before yielding and a little sign of thixotropy/hysteresis in its flow curves around the yielding point. There have been many studies aiming to address this shortcoming by including time-dependent parameters into the constitutive law equations. Assuming the bubble is injected from a nozzle, one other possibility is that the shape is formed at the origin and the yield stress of material prevents evolution of bubble's shape and causes the shape to remain 'frozen' [2]. The goals in this paper are to explore the potential contribution of the entry point on the bubble shape in a yield stress fluid and constrain the origin of fore-aft asymmetry. We have investigated this potential cause in a series of experiments. In the following sections, we will describe the experimental setup and the rheological characterization of fluids which have been used. We end the paper with a brief summary of results and conclusion.

EXPERIMENTAL SETUP AND MATERIAL

A simple experimental setup is used to introduce a bubble into a yield stress fluid without injecting direclty from a nozzle. We designed a three-layer fluid system as shown in Fig. 1. A bubble is injected to the lower layer and then in accordance with the properties of fluids in the lower and middle layers develops its shape, speed and volume as it rises. The lower layer is to control the size of bubble injected. The shape and speed are adjusted in the middle layer. Using this setup a bubble with a specified shape, size and speed enters the upper layer which is our test section. A syringe pump is used to inject air into the lower layer and fluids are placed inside a long plexiglas box of width $\hat{W} = 9.525$ cm $(3.75'')$ and length $\hat{L} = 63.5$ cm $(25'')$, with sealed base. The injection point for the invading fluid is via a hole of radius $\hat{R}_h \approx 0.32$ mm $(r_h \approx 0.01)$ positioned centrally in the base of the column.

We used carbopol, densified with Glycerin and sugar, in the lower layer to control the volume of the bubble. The bubble then deforms to an ellipsoidal shape in the middle layer consisting of pure glycerin. We are interested to see

*Corresponding author. E-mail: marjan.zare@math.ubc.ca

how the bubble's shape varies as it enters a yield stress fluid. Hence, the top layer which is our test section is filled with Carbopol. The experiments have been repeated for three concentrations of carbopol and various other parameters. The Herschel-Bulkley (see eq. 1) fits of the yield stress $\hat{\tau}_y$, consistency $\hat{\kappa}$ and power-law index n of the Carbopol in the test section are summarized in table . The Herschel-Bulkley model describes the constitutive equation of a yield stress material after yielding with the following equation:

$$\hat{\boldsymbol{\tau}} = (\hat{\kappa} + \frac{\hat{\tau}_y}{\hat{\dot{\gamma}}})\hat{\dot{\boldsymbol{\gamma}}}^{n-1}, \quad \Leftrightarrow \hat{\tau} > \hat{\tau}_y \tag{1}$$

where $\hat{\boldsymbol{\tau}}$ and $\hat{\dot{\boldsymbol{\gamma}}}$ are the deviatoric stress tensor and the rate of deformation tensor, respectively.

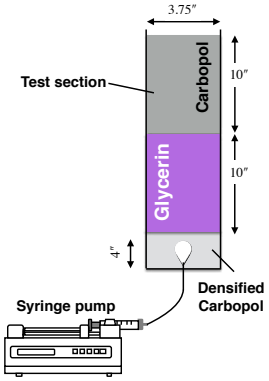

Figure 1: Schematic of the experimental setup.

Concentration $(wt/wt\ \%)$	$\hat{\tau}_y$ (Pa)	$\hat{\kappa}$ $(Pa\ s^n)$	n
0.1	3.88	3.37	0.4
0.15	13.86	8.07	0.39
0.2	24.55	13.73	0.41

Table 1: Herschel-Bulkley fits of the Carbopol solutions.

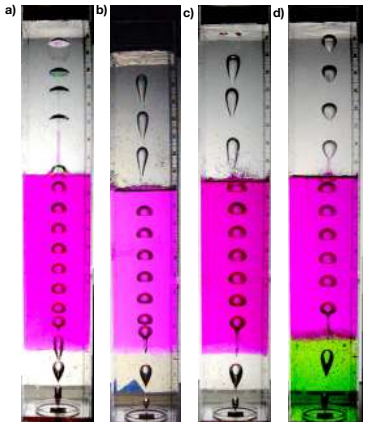

Figure 2: Spatiotemporal images of bubble's motion through our 3-layer fluid system comprising a densified Carbopol (DC) (lower layer), pure Glycerin (middle layer) and Carbopol (C) (upper layer): a) DC=0.15, C=0.06, b) DC=0.15 , C=0.2; c) DC=0.18, C=0.15; and d) DC=0.18, C=0.1 $wt/wt\ \%$.

RESULTS

Some experimental results showing how the shape of a bubble changes as it rises in Glycerin and moves up into a Carbopol solution are presented in Fig. 2. Given the properties of Glycerin,$\hat{\mu} = 0.4Pa.s$ and $\hat{\rho} = 1.18g.m^{-3}$, the bubble develops an ellipsoidal shape at each pair of (Bo, Re) and reaches a steady state before crossing the Glycerin-Carbopol interface. Interestingly, once the bubble enters the Carbopol it adjusts its shape and develops a cusp at the lower side in concentrations above 0.1 $wt/wt\ \%$. Results clearly confirm the fore-aft asymmetry of a bubble in Carbopol is not a nozzle effect. The shape of bubble also varies in Carbopol solutions with different concentrations as well; the bubble becomes elongated as it rises in higher concentrations of Carbopol.

CONCLUSIONS

A novel set of experiments was performed to investigate the 'nozzle effect' on the formation of a cusp at the tail of bubbles rising in Carbopol solution, which is often used as a simple yield stress fluid. Our results restrain potential causes of fore-aft asymmetrical bubble shape and confirm that it is not related to the injection method and the shape of entry point. It might originate from the temporal structure and elasticity of fluid which leads to development of time-dependant behaviours.

References

[1] A. N. Beris, J. A. Tsamopoulos, R. C. Armstrong, and R. A. Brown. Creeping motion of a sphere through a bingham plastic. *J. Fluid Mech.*, 158:219–244, 1985.

[2] J. Tsamopoulos, Y. Dimakopoulos, N. Chatzidai, G. Karapetsas, and M. Pavlidis. Steady bubble rise and deformation in newtonian and viscoplastic fluids and conditions for bubble entrapment. *J. Fluid Mech.*, 601:123–164, 2008.

[3] A.M.V. Putz, T.I. Burghelea, I.A. Frigaard, and D.M. Martinez. Settling of an isolated spherical particle in a yield stress shear thinning fluid. *Phys. Fluids*, 20(3):033102, 2008.

[4] D. Tokpavi, P. Jay, A. Magnin, and L. Jossic. Experimental study of the very slow flow of a yield stress fluid around a circular cylinder. *J. Non-Newtonian Fluid Mech.*, 164(1-3):35–44, 2009.

[5] D. Sikorski, H. Tabuteau, and J.R. de Bruyn. Motion and shape of bubbles rising through a yield-stress fluid. *J. Non-Newtonian Fluid Mech.*, 159(1-3):10–16, 2009.

[6] N. Mougin, A. Magnin, and J.M. Piau. The significant influence of internal stresses on the dynamics of bubbles in a yield stress fluid. *J. Non-Newtonian Fluid Mech.*, 171:42–55, 2012.

COEXISTING INERTIA-DRIVEN AND ELASTO-INERTIAL TURBULENCE DURING MULTISTAGE TRANSITIONS IN POLYMER DRAG REDUCTION

Lu Zhu[1] and Li Xi*[1]
[1]Department of Chemical Engineering, McMaster University, Hamilton, Ontario, L8S 4L7, Canada

Summary Elasto-inertial turbulence (EIT) has been believed to be the state responsible for maximum drag reduction (MDR). We show that EIT can coexist with inertia-driven turbulence starting from much lower Weissenberg number Wi and only takes over when the latter is suppressed. Different from the common belief, MDR is not converged EIT but involves more complex dynamical cycles that are non-asymptotic in nature. Relationship between EIT and other transition stages in turbulent drag reduction is our ongoing focus.

INTRODUCTION

A small amount of polymer additives are known to cause significant turbulent drag reduction (DR). At constant Re and with increasing fluid elasticity, measured by the Weissenberg number Wi, turbulence undergoes several transitions between different dynamical stages [1]. At lowest Wi, no DR is observed. After the onset of DR, the flow enters a low-extent DR (LDR) regime where DR is confined to the buffer layer. At higher Wi, transition to high-extent DR (HDR) occurs where DR is felt across the flow domain. Finally, it converges to an asymptotic upper limit called the maximum DR (MDR). MDR indicates the existence of a new self-sustaining turbulent state with lower drag than Newtonian turbulence, whose mean flow, surprisingly, becomes invariant with polymer elasticity (and all polymer solution properties). Understanding these transitions, in particular, the mysterious MDR asymptote, has motivated researchers for decades.

Recent discovery of the so-called elasto-inertial turbulence (EIT) [2] provided promising leads for the new self-sustaining process (SSP) of MDR. This is a unique state of turbulence where both elasticity and inertia support turbulence. It is self-sustaining even in 2D [3]. Later experiments [4] found that at relatively low Re close to the laminar-turbulent transition for Newtonian flow, classical inertia-driven turbulence (IDT) will first be suppressed by polymer elasticity, causing the laminarization of the flow. Turbulence would resurge in a new form at higher Wi, which was presumed to be EIT. Mean flow was found to reach an asymptotic level in this resurgent regime, which has supported a now prevailing view that MDR reflects the complete suppression of IDT and convergence to EIT.

Recently, we have shown [5] that EIT itself does not give asymptotic DR. Rather, it shows continued drag enhancement with increasing Wi. Asymptotic DR requires 3D flow where IDT grows intermittently from EIT. In this study, we further explore the coexistence between IDT and EIT as well as the role of EIT in various stages of DR.

METHODOLOGY

The Navier-Stokes equation is coupled with the FENE-P constitutive equation

$$\frac{D\boldsymbol{v}}{Dt} = -\boldsymbol{\nabla} p + \frac{\beta}{\mathrm{Re}}\nabla^2\boldsymbol{v} + \frac{2\,(1-\beta)}{\mathrm{ReWi}}\left(\boldsymbol{\nabla}\cdot\boldsymbol{\tau}_p\right), \quad \boldsymbol{\nabla}\cdot\boldsymbol{v} = 0, \tag{1}$$

$$\frac{\mathrm{Wi}}{2}\left(\frac{D\boldsymbol{\alpha}}{Dt} - \boldsymbol{\alpha}\cdot\boldsymbol{\nabla}\boldsymbol{v} - (\boldsymbol{\alpha}\cdot\boldsymbol{\nabla}\boldsymbol{v})^{\mathrm{T}}\right) = -\frac{b}{b+5}\boldsymbol{\tau}_p, \quad \boldsymbol{\tau}_p = \frac{b+5}{b}\left(\frac{\boldsymbol{\alpha}}{1-\frac{\mathrm{tr}(\boldsymbol{\alpha})}{b}} - \left(\frac{b}{b+2}\right)\boldsymbol{\delta}\right) \tag{2}$$

and solved for plane Poiseuille flow (domain size in inner units: $L_x^+ \times L_y^+ \times L_z^+ = 720 \times 2\mathrm{Re}_\tau \times 230$) under fixed pressure drop, where $\boldsymbol{\tau}_\mathrm{p}$ and $\boldsymbol{\alpha}$ are polymer stress and conformation tensors. $\mathrm{Wi} \equiv 2\lambda U/l$ is the product between polymer relaxation time and mean wall shear rate. The friction Reynolds number $\mathrm{Re}_\tau = 84.85$, viscosity ratio $\beta \equiv \eta_\mathrm{s}/\eta = 0.97$ (ratio between solvent "s" and solution zero-shear viscosities), and $b = 5000$ (b is the upper limit of $\mathrm{tr}(\alpha)$, which measures the extent of polymer extension) are constant for all simulations. A finite-difference/pseudo-spectral hybrid scheme is used where the $\boldsymbol{v}\cdot\boldsymbol{\nabla}\boldsymbol{\alpha}$ term is discretized with a conservative total variation diminishing (TVD) method and all other terms use a pseudo-spectral approach. The scheme avoids the need for artificial diffusion. Details on the numerical method and other numerical details are found in [6].

RESULTS AND DISCUSSION

Since IDT only exists in 3D, 2D DNS can completely preclude IDT and obtain EIT in its cleanest form. One such solution at $\mathrm{Wi} = 64$ is shown in fig. 1(a), which, compared with IDT (see 3D DNS of $\mathrm{Wi} = 30$) has much reduced Reynolds shear stress (RSS) and a mean velocity (measured by A_{25}^*) higher than MDR. As reported in [5], EIT solution is not invariant with polymer properties and with increasing Wi, the drag will increase – i.e., the solution will move left in the plot. At high Wi, its mean velocity will be significantly lower than MDR. This indicates that MDR cannot be a single converged EIT state.

*Corresponding author. E-mail: xili@mcmaster.ca

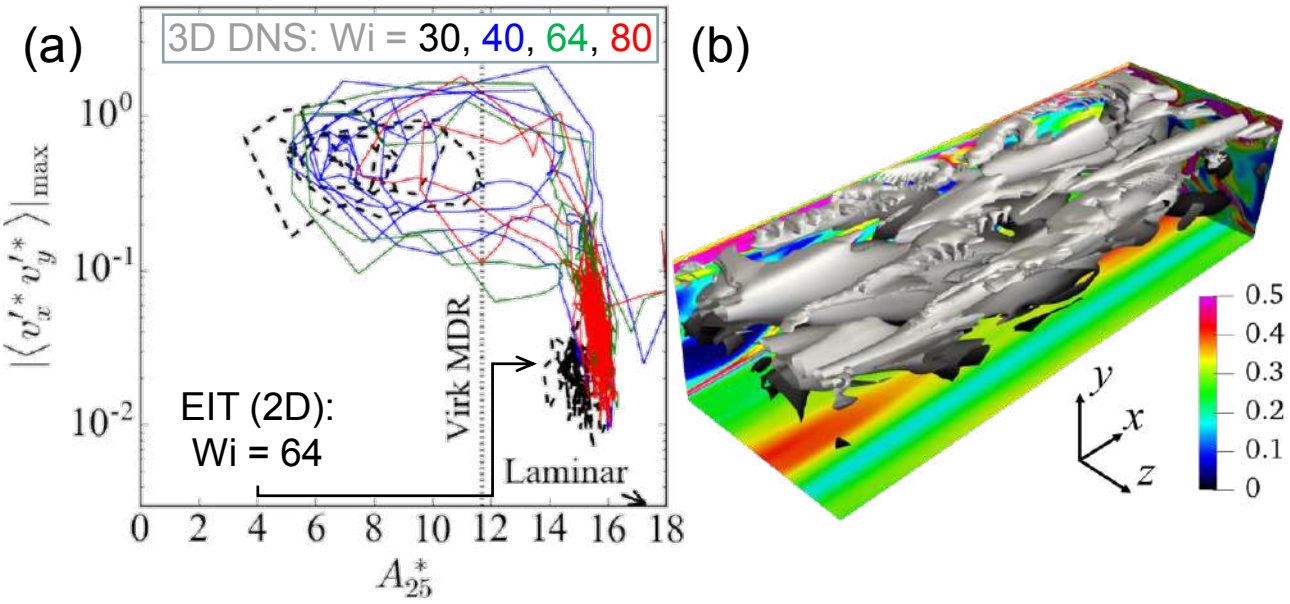

Figure 1: (a) state-space projection of 2D EIT and 3D DNS trajectories: $A^* \equiv y^*(\partial U_{\mathrm{m}}^*(y^*,t)/\partial y^*)$ is the slope in a logarithmic relation of $U_{\mathrm{m}}^* = A^* \ln y^+ + \text{const.}$ (A_{25}^* is its value at $y^* = 25$) and $|\langle v_x'^* v_y'^* \rangle|_{\max}$ is the instantaneous Reynolds shear stress profile peak [7]; (b) vortex configuration at $Q = 0.004$ [8] (top half channel only; darker color for larger wall distance) and color contours of $\mathrm{tr}(\alpha)/b$ for a typical instant of active turbulence ($\mathrm{Wi} = 40$).

Solutions from 3D DNS represent realistic turbulent dynamics and are shown for several Wi. At $\mathrm{Wi} = 30$, the trajectory samples frequently a well-defined region of strong turbulence (high RSS), which represents the kernel of IDT or active turbulence [9]. Occasional excursions away from the kernel can be found, sometimes reaching the MDR level. This is the earlier-studied hibernation phenomenon [9] and is termed type A cycles in [5]. At $\mathrm{Wi} = 40$, some excursions extend far over the MDR level and clearly approach the EIT region (type B cycles [5]), indicating that polymer elasticity is strong enough to disrupt the SSP for IDT and EIT must act as a barrier that blocks the flow from laminarization. With further increasing Wi, the IDT kernel moves toward lower drag (higher A_{25}^*) and the trajectory spends less time therein. At $\mathrm{Wi} = 80$, the highest reported here, the trajectory spends most time in a region near the EIT without fully converging to it. Rather, it frequently jumps back and forth between EIT and a state of higher drag (higher RSS and lower A_{25}^*). This state, according to [5], is also IDT and such cycles were classified as type C.

What we have observed so far is the coexistence of multiple solution objects in the state space, including the kernel of IDT (active turbulence [9]), EIT, and a yet unknown IDT state that forms type C cycles with EIT. Results from higher Wi would show that visits of active turbulence (i.e., types A and B cycles) eventually diminish but type C cycles persist. This transition occurs within the asymptotic DR regime: i.e., flow states with the same average drag display different dynamical characteristics, which indicates that despite the converging mean velocity, MDR is fundamentally underlay by non-asymptotic dynamics [5].

A representative moment when the trajectory returns to active turbulence is shown in fig. 1(b). The flow field shows streamwise vortices which are typical of IDT at this Re. Interestingly, structures near the wall show small protrusions extending sideways. Spanwise vortices in the form of rolls and threads are typical of EIT [2, 5] and our finding indicates that EIT can coexist with IDT not only at different moments of the trajectory, but at different regions of the same moment.

It appears that EIT occurs upon a critical Wi. An EIT layer occurs at Wi much lower than those shown here. When IDT dominates, EIT is confined in a thin-layer near the wall where shear is high and IDT is insignificant. At higher Wi, where active turbulence is suppressed, EIT can spread to the whole channel to keep turbulence sustained. Active turbulence becomes intermittent (for Wi shown here) and eventually disappears (for higher Wi shown in [5]), but another form of IDT still exists. We have so far revealed the role of EIT in the transition to MDR, but its existence at lower Wi makes it possible to affect earlier transitions, which is a focus of our ongoing research.

References

[1] Xi, L. *Phys. Fluids* **2019**, *31*, 121302.
[2] Samanta, D.; Dubief, Y.; Holzner, M.; Schäfer, C.; Morozov, A. N.; Wagner, C.; Hof, B. *Proc. Natl. Acad. Sci. U. S. A.* **2013**, *110*, 10557–100562.
[3] Sid, S.; Terrapon, V. E.; Dubief, Y. *Phys. Rev. Fluids* **2018**, *3*, 011301.
[4] Choueiri, G. H.; Lopez, J. M.; Hof, B. *Phys. Rev. Lett.* **2018**, *120*, 124501.
[5] Zhu, L.; Xi, L. **2020**; arXiv:2001.01638.
[6] Zhu, L.; Ph.D. thesis; McMaster University; 2019.
[7] Zhu, L.; Bai, X.; Krushelnycky, E.; Xi, L. *J. Non-Newton. Fluid Mech.* **2019**, *266*, 127–142.
[8] Zhu, L.; Xi, L. *J. Fluid Mech.* **2019**, *866*, 169–215.
[9] Xi, L.; Graham, M. D. *Phys. Rev. Lett.* **2010**, *104*, 218301.

WATER ENTRY OF VISCOPLASTIC DROPLETS

Anselmo Pereira[1], Mazi Jalaal[2], Romain Castellani[1], Elie Hachem[1], and Rudy Valette[1]
[1]MINES ParisTech, PSL Research University, CEMEF, CNRS UMR 7635, Sophia-Antipolis, France
[2]University of Cambridge, Dept. of Applied Mathematics and Theoretical Physics, Cambridge, UK

Summary We study through experiments and direct numerical simulations the water entry of viscoplastic (yield-stress fluid) droplets. Following the impact on water free surfaces, these Non-Newtonian fluids undergo at least three stages: a spreading one (1), related to the formation of a water crater, driven by viscous dissipation in the droplet and during which the droplet reaches its maximum deformation; a droplet-water interaction stage (2) along which the viscoplastic material tends to recover, at least partially, a spherical shape due to the crater reclosing, before sedimentation (3), being finally dominated by the yield-stress, which prevents further deformations. Different final shapes are observed as a function of the inertial, capillary, viscous and plastic effects. Their link with the fluid rheology is discussed in the light of scaling laws, kinematic and energy exchange analyses.

CONTEXT

The impact of non-Newtonian fluids (microgels, suspensions, emulsions etc.) on free liquid surfaces represents a fundamental and scarcely explored topic in interfacial hydrodynamics and soft matter rheology directly related to extremely important environmental and industrial situations, such as pesticides deposition, ceramic beads production, as well as encapsulation processes [1]. Typically impact flows involve, as illustrated in figures 1-left and 1-right, a falling non-Newtonian drop passing through a liquid-air interface and forming an air cavity, which later retracts, while the non-Newtonian material penetrates the liquid. During the penetration, the drop undergoes deformations as a consequence of the impact on the liquid surface and its interactions with the aforementioned air cavity, inducing different final shapes. These final morphologies vary from pears, Mexican hats (figure 1-left), bowls, up to capsules (figure 1-right) depending on the impact velocity, U_0, and the rheological properties of the drop.

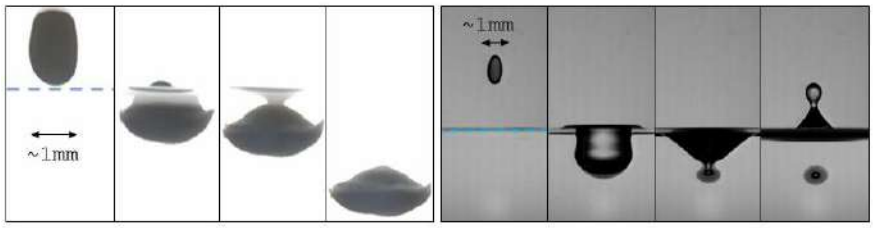

Figure 1. Deformation of viscoplastic drops at different times (typical timescale is 10 *ms*) during and after penetrating a water bath (bath surfaces are shown in blue dashed lines), forming a Mexican hat (left) at low impact velocitiy $U_0 = 0.5m.s^{-1}$ of an alumina suspension and a capsule (right) at a larger impact velocity $U_0 = 2.0m.s^{-1}$ of a Carbopol gel.

A recent attempt to highlight the impact of non-Newtonian drops on liquids was reported by Jalaal et al. [2], who performed experiments on the water-entry of Carbopol solutions (polymer microgels), obtaining a variety of final shapes, similar to the ones displayed in figure 1. Despite the importance of their study, the physical mechanism correlating the viscoplasticity with the drop final morphologies has not been addressed.

MODELLING

In the current work, the relevance of the viscoplastic nature of this phenomenon is demonstrated using both numerical simulations from a homemade finite element code [3, 4] and scaling arguments related to the three aforementioned key-stages (figure 2-left): (1) the drop impact; (2) the formation and retraction of the air cavity; and (3) the descent of the drop. Numerical simulations were performed for different drop diameters D_0, impact velocities U_0, Herschel-Bulckley rheological parameters (consistency k, power law exponent m and yield stress τ_0) and air/bath surface tension σ in order to obtain a large screening of Reynolds numbers $Re = \rho U_0^2/\bar{\tau}$, where ρ and $\bar{\tau}$ are the drop density and characteristics Herschel-Bulckley stress ($\bar{\tau} = k[U_0/D_0]^m + \tau_0$), capillary numbers $Ca = \bar{\tau}D_0/\sigma$, Froude numbers $Fr = U_0^2/gD_0$ (g being the gravity acceleration) and Bingham numbers $Bi = \tau_0/k[U_0/D_0]^m$.

An example of the simulation of an initially spherical viscoplastic drop after its impact at large velocity on a water bath is shown on figure 2-left at different instants within each key-stage, showing that its dimensionless diameter increases in the first stage, deceases in the second one up to 1, meaning that a capsule was formed, and finally kept constant in the last

stage, which preserves the capsule shape. When using low to high impact velocities in numerical simulations, we were able to retrieve all the final shapes observed experimentally (bowls, Mexican hats etc..), as shown on figure 2-right.

Finally, using dimensional arguments similar to previous studies on drop impacts [5, 6], we show and validate through numerical simulations that the drop shape is controlled by the Reynolds number in stage 1, its diameter decreasing in stage 2 is obtained if $Re > Fr^{1/5}/Ca$ and its final shape is preserved if the Reynolds number in the last stage is bounded by the Bingham number. These criteria lead to a single master curve giving the final aspect ratio D_f/D_0 as a function of all Re, Ca, Fr and Bi non-dimensional numbers.

.

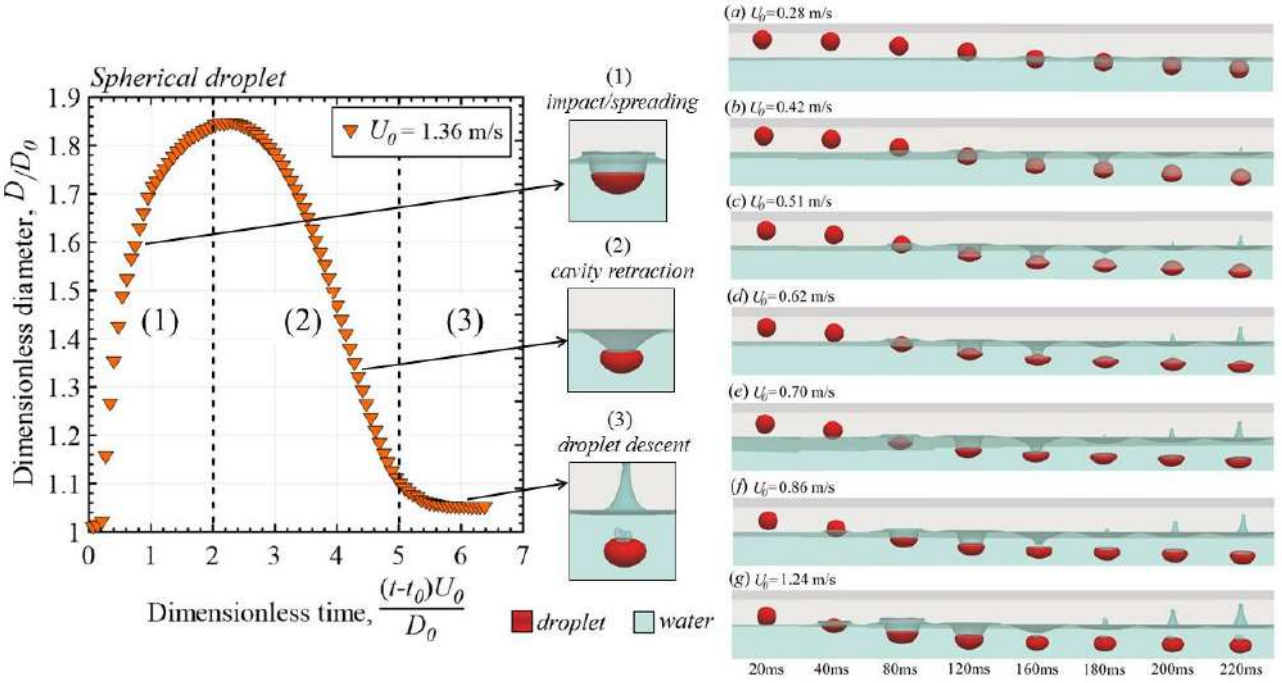

Figure 2. Left: simulation of an initially spherical viscoplastic drop after its impact on the water surface at large velocity and corresponding dimensionless diameter vs. dimensionless time curve. Right: simulations of viscoplastic drops after their impact on the water surface at different velocities, leading to different final shapes (spherical, bowl, Mexican hat, capsule, from low to high velocity).

References

[1] Godefroid J., Complex fluids dripped into a liquid bath: impact, relaxation and gelation dynamics, PhD Thesis, ESPCI-Paris, 2019
[2] Jalaal M., Kemper D., Lohse D., Viscoplastic water entry. *J. Fluid. Mech.* **864**: 596-613, 2019.
[3] Valette R., Hachem E., Khalloufi M., Pereira A., Mackley M.R., Butler S.A., The effect of viscosity, yield stress, and surface tension on the deformation and breakup profiles of fluid filaments stretched at very high velocities, Journal of Non-Newtonian Fluid Mechanics, **263**, 130-139, 2019.
[4] Khalloufi M., Valette R., Hachem E., Adaptive Eulerian framework for boiling and evaporation**.** J. Computational Physics, **401**, 109030, 2020.
[5] Luu L.-H., Forterre Y., Drop impact of yield-stress fluids. *J. Fluid. Mech.* **632**: 301-327, 2009.
[6] Oguz H.N., Prosperetti A., Bubble entrainment by the impact of drops on liquid surfaces. *J. Fluid. Mech.* **219**: 143-179, 1990.

MULTILAYER FLOWS OF VISCOPLASTIC FLUIDS IN AXIALLY ROTATING PIPES

Shan Lyu and Seyed-Mohammad Taghavi*
Department of Chemical Engineering, Université Laval, Quebec, QC, Canada

Summary This experimental work studies the removal of a viscoplastic fluid by a Newtonian fluid in an axially rotating pipe, with applications in the cementing process of oil and gas wells. The experiments are performed in a long inclined pipe. The fluids involved are of different rheological properties, they are miscible and they have different densities. The key parameters are the physical properties of the fluids, such as the density difference, the rheological properties, the imposed flow velocity, and the pipe rotation. The results reveal that the pipe rotation changes the flow patterns significantly, namely from inefficient to efficient removal flow regimes, as the rotating speed increases. The critical transition is well described by dimensionless groups, i.e. the modified Froude number (Fr) and the Rossby number (Rb).

INTRODUCTION

Multilayer displacement flows of viscoplastic fluids have a variety of industrial applications, an example of which is the cementing process in the construction/completion of oil and gas wells. One of the main objectives of this process is the zonal isolation, to hydraulically seal the well. A key step in this process is to completely displace/remove viscoplastic drilling mud by another fluid (e.g. cement slurry, spacer, etc) within the casing (i.e. a pipe) and the annulus parts of the well. To improve the displacement process, casing rotation can be used. However, a significant lack of solid laboratory studies limit our understanding of this process with casing rotation and constrain the wide application of casing rotation in the oil and gas industry. Thus, extending the previous works on viscoplastic displacements in static flow geometries [1, 2], we experimentally analyze the effects of a pipe rotation on the flow features, using the dimensionless groups that describe the flow.

EXPERIMENT

The displacement flow experiments were performed in an acrylic inclined pipe, mounted on a robust frame. The dimensions and some of the flow parameters can be found in Figure 1. An automated gate valve was used to initially separate the displacing and displaced fluids. A system of a stepper motor and various connectors, controlled by LabView, produced stable pipe rotations. A high-resolution digital camera (Basler acA2040) was used to acquire image sequences of the displacement flow process at the frequency of 5 Hz. The post-processing image analysis was done via in-house Matlab codes.

The preparations of the test solutions strictly followed the technical instructions. The displaced fluid was a Carpobol gel, i.e. viscoplastic fluid (i.e.a shear-thinning and yield stress fluid). The displacing fluids were simply salt-water. Fluid characterization was made using a rheometer DHR-3 (TA Instruments). For all cases studied, the temperature was held constant at room temperature.

RESULTS AND DISCUSSIONS

The experiments are performed at various flow parameters, such as the density difference ($At = \frac{\hat{\rho}_H - \hat{\rho}_L}{\hat{\rho}_H + \hat{\rho}_L}$ with $\hat{\rho}_H$ and $\hat{\rho}_H$ being the heavy and light fluid's densities, respectively, 0.0035 - 0.016), pipe inclination angle (β, 83° and 60°), yield stress ($\hat{\tau}_y$, 1.14, 3.80, and 9.20 Pa), imposed flow velocity ($\hat{V}_0$, 10 - 60 mm/s), and rotating speed ($\hat{\omega}$, 0 - 6.28 rad/s).

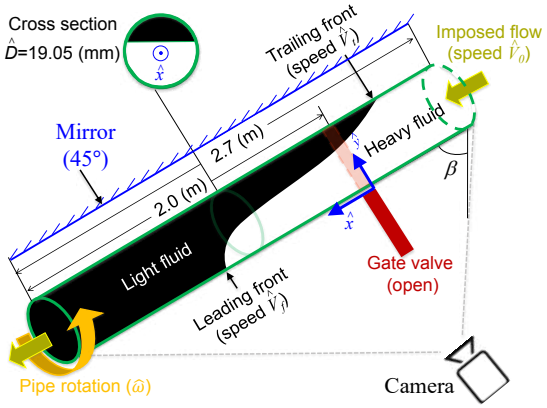

Figure 1: Schematic view of the experimental set-up. The interface is illustrative only.

*Corresponding author. E-mail: Seyed-Mohammad.Taghavi@gch.ulaval.ca

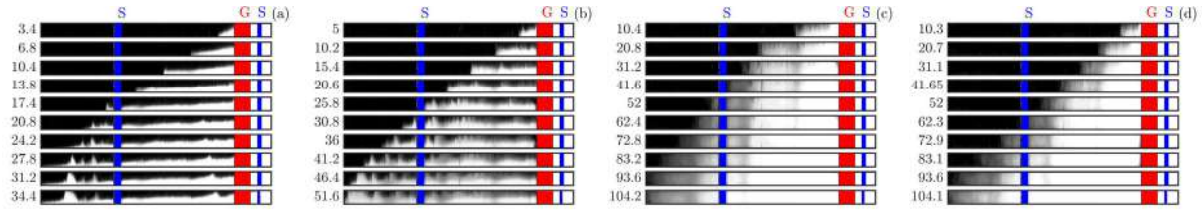

Figure 2: Sequence of experimental snapshots at $\beta = 83°$, $\hat{V}_0 = 20$ mm/s, and $At = 10^{-2}$, with pipe rotating speeds: $\hat{\omega} =$ (a) 0, (b) 2.09, (c) 3.14, and (d) 4.19 rad/s. The yield stress of the displaced fluid is 3.80 Pa. Experimental times in seconds, $\hat{t}$, are indicated beside each snapshot. Field of view in each snapshot is 19.05×2000 mm^2. Displacement is from right to left in each snapshot. Gate valve and pipe supports are marked by G and S, respectively.

The effects of the pipe rotation on the flow patterns of viscoplastic fluid displacement flows are shown in Figure 2. When the pipe is kept static ($\hat{\omega} = 0$), a clear slumping interface exists between the displacing and displaced fluids. A fast leading front leads to the breakage of the viscoplastic layer and flows underneath it. The unyielded viscoplastic gel with an irregular thickness remains immobile on the upper part of the pipe wall. The formation of the ripped displacement is shown in Figure 2a. As the Carbopol gel cannot be removed by the displacing fluid, an "inefficient removal regime" is observed in this figure. By introducing a weak pipe rotation (e.g. $\hat{\omega} = 2.09$ rad/s, see Figure 2b), the weak rotational inertia notches the immobile viscoplastic gel in unsteady bursts. Once the initial burst of the gel layer has occurred, the segments of the Carbopol gel are non-uniform. Figure 2c-d shows continuous unsteady bursts of the Carbopol gel at moderate-high rotating speeds. Some of the large pieces of the Carbopol gel are isolated and they remain as stationary residual deposits; however, the large isolated segments can also be pushed downstream by the slower trailing front. It appears that the pipe rotation can promote an *efficient* displacement regime. In this regime, called "efficient removal regime", the yield stress effect is negligible and the buoyant effects seem to be less relevant. All the Carbopol gel is removed by the displacing fluid.

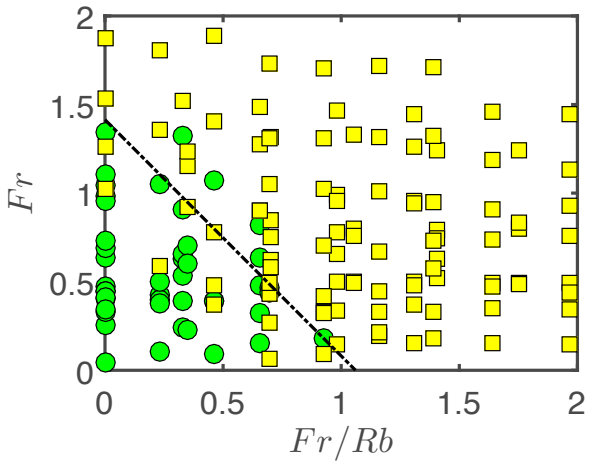

Figure 3: Displacement flow regime classification of viscoplastic fluid. The inefficient (●) and efficient flow regime (■) are roughly separated by the dashed line (empirical) passing through $Fr = \sqrt{2}$ and $Fr/Rb = \frac{3\sqrt{2}}{4}$.

Appropriate dimensionless groups are used to classify our results into efficient and inefficient removal flow regimes (see Figure 3), i.e. Fr and Fr/Rb, where the modified Froude and Rossby numbers are defined as $Rb = \hat{V}_0/\hat{\omega}\hat{R}$ and $Fr = \hat{V}_0/\sqrt{(At)\,\hat{g}\hat{R}\sin\beta}$, respectively, where $\hat{R}$ is the pipe radius and $\hat{g}$ is the gravitational acceleration. Note that Fr shows a balance of the imposed inertia and buoyancy while Fr/Rb represents the balance between rotational inertia and buoyancy. This regime classification can bring novel insights to improve the displacement efficiency using the pipe rotation in the cementing process.

References

[1] S.M. Taghavi and K. Alba and M. Moyers-Gonzalez and I.A. Frigaard. Incomplete fluid–fluid displacement of yield stress fluids in near-horizontal pipes: experiments and theory. *J. Non-Newton. Fluid*, 167:59–74, 2012.

[2] I.A. Frigaard and K.G. Paso and P.R. de Souza Mendes. Binghams model in the oil and gas industry. *Rheol. Acta*, 56(3):259–282, 2017.

VISCO-PLASTICALLY LUBRICATED TRIPLE-LAYER CORE-ANNULAR FLOWS

Parisa Sarmadi[1], Sarah Hormozi[2], and Ian A. Frigaard *[3]
[1]Department of Mechanical Engineering, University of British Columbia, Vancouver, Canada
[2]Department of Mechanical Engineering, Ohio University, Athens, USA
[3]Department of Mechanical Engineering and Mathematics, University of British Columbia, Vancouver,Canada

Summary We present a novel triple-layer core-annular flow method in which we purposefully position an unyielded skin of a visco-plastic fluid between the core and the lubricating fluid to eliminate the possibility of interfacial instabilities, see [1, 2, 3, 4]. Specifically, the skin layer is shaped which allows for lubrication force to develop as the core rises under the action of buoyancy forces. The objective is to reduce the frictional pressure gradient while avoiding interfacial instabilities [5, 6]. Here we address the issue of how in practice to develop a triple-layer flow with a sculpted/shaped visco-plastic skin, all within a concentric manifold by control of the flow rates of the individual fluids. An axisymmetric triple-layer simulation establishes that these flows may be stably established in a controlled way with a desired interface shape. Then, we extend the feasibility of the method to large pipes and higher flow rates by considering the effects of inertia and turbulence in the lubricating layer [7].

MODELING FLOW DEVELOPMENT

Our aim in this paper is to establish the feasibility of developing steady periodic triple-layer flows with a shaped interface of the type illustrated in Fig. 1 as studied in [5]. The development flow is assumed to occur in an inflow manifold, with a concentric arrangement, through which the three fluids may be pumped at controlled flow rates. We consider a horizontal pipe which is periodic in streamwise $\hat{z}$-direction, with period $\hat{l}$. Figure 1 indicates schematically the positions of the 3 fluids, within a cross-section of the pipe at fixed $\hat{z}$. Fluid 1 denotes the core fluid (viscous Newtonian heavy oil), with viscosity $\hat{\mu}^{[1]}$ and density $\hat{\rho}^{[1]}$. The skin layer is fluid 2, modeled simply as a Bingham fluid, with $\hat{\mu}^{[2]}$, $\hat{\tau}_y^{[2]}$, and $\hat{\rho}^{[2]}$ denoting its viscosity, yield stress, and density, respectively. Fluid 3 is the lubrication layer (a low viscosity Newtonian fluid) with viscosity $\hat{\mu}^{[3]}$, and density $\hat{\rho}^{[3]}$.

The outer radius of the skin may vary with $\hat{z}$: $\hat{r}_2 = \hat{r}_{2,0} + \Delta\hat{r}_2\Phi(\hat{z})$, i.e. $\Phi(\hat{z})$ captures the sculpted streamwise skin profile. The inner radius ($\hat{r} = \hat{r}_1$) is assumed to be uniform. The skin fluid is assumed to have a sufficiently high yield stress that it remains rigid (unyielded), except during a flow development region in which the interface shape is sculpted, as studied by [6]. Thus, fluids 1 and 3 remain separated. In general, we might assume that the required yield stress is moderately large (estimated later) and that surface tension effects are negligible in comparison to the other stresses; note that the radii of curvatures are relatively large.

The governing equations for the flow are the Navier-Stokes equations, in each fluid domain. The core fluid is assumed lighter than the lubricant. As shown by [8], both eccentricity and axial variation in lubrication layer are necessary to generate a transverse lift force via viscous lubrication. The lubrication pressure generated is larger where the gap is smaller and hence eccentricity towards the top of the pipe results in a net downward force to balance the buoyancy.

EXTENSIONAL MODEL

Here we exploit the aspect ratio of the flow to derive a simplified model to estimate the minimal yield stress required to maintain the skin rigid. We derive the model under the assumption of small aspect ratio. We suppose that the desired

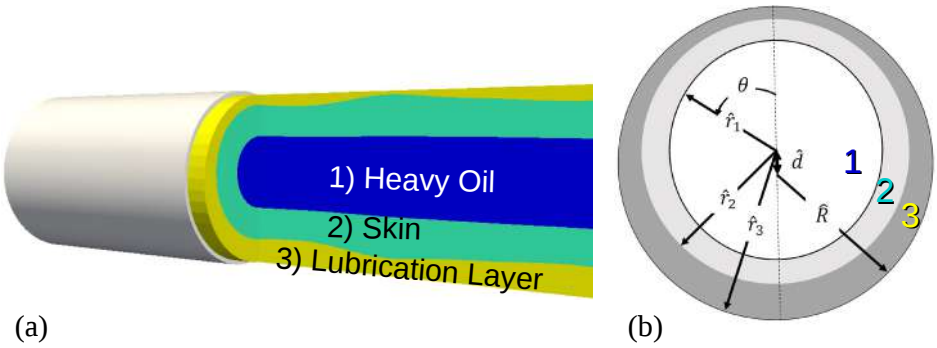

Figure 1: a) Shaped skin profile in 3D; b) cross section of the pipe with triple-layer configuration, illustrating the coordinates.

*Corresponding author. E-mail: frigaard@math.ubc.ca.

sculpted interface is to be periodic in $\hat{z}$, with period $\hat{L}$. Variations in the downstream flow of the skin and lubricant occur due to variations in interface shape, hence layer thickness, which have amplitude $\hat{R}(1-r_{2,0})$. Therefore, an appropriate aspect ratio ϵ to consider is $\epsilon = \frac{\hat{R}(1-r_{2,0})}{\hat{L}}$. We scale $\hat{z}$ with $\hat{L}$: $\tilde{z} = \hat{z}/\hat{L}$. In the lubricant and skin layers we scale radial distances onto x:

$$\hat{r} = \hat{r}_{2,0} + (\hat{R} - \hat{r}_{2,0})x \quad \Rightarrow \quad x = \frac{r - r_{2,0}}{1 - r_{2,0}}.$$

In terms of the x-coordinate the skin occupies $x_1 \leq x \leq x_2$. The lubricant occupies $x_2 \leq x \leq 1$. The core fluid layer is not assumed thin: hence $r = \hat{r}/\hat{R}$ for fluid 1.

We split the pressure into two parts: $\hat{P} = -\hat{G}\hat{z} + \hat{P}_l$, where the constant axial pressure gradient $\hat{G}$ drives the flow and $\hat{P}_l$ is the lubrication pressure. For the latter we use a classical lubrication scaling of the equations. Core and lubrication layers are mainly shear flow and velocity scaling implies $\hat{\tau}_{xx} \sim \hat{\tau}_{zz} \sim \epsilon\hat{\tau}_{xz} \sim \epsilon^2\hat{P}_l^*$. Within the skin layer, as we are interested in large yield stresses where the skin is unyielded or just yielded, we expect an extensional flow. The pressure in the Newtonian layers is balance by the total normal stress, i.e. part of the pressure generated in the lubrication layer may be absorbed by $\hat{\tau}_{rr}^{[2]}$, i.e. $\hat{\tau}_{rr}^{[2]} \sim \hat{\tau}_{zz}^{[2]} \sim \hat{P}_l^*$.

Leading order momentum equations and leading order constitutive equation of the skin result in a system of equations for skin velocity and normal stresses within the skin.

INERTIAL EFFECTS

The effect of inertia can be neglected for long-thin geometries when the product of aspect ratio and Reynolds number is small. However, inertial effects can become important both for large Reynolds numbers and in trying to balance larger core fluid density differences with larger amplitude sculpting. Both effects occur in larger pipelines and with higher flow rates: common industrial objectives. Thus, extension of the triple-layer concept to wider parameter regime means that we need to understand the main effects of inertia and turbulence in lubricating layer in particular on the generated lubrication force. For this purpose, we investigate a single periodic wavelength of fully developed flow, in which the buoyancy of the core fluid is balanced by the generation of hydrodynamic lubrication pressures. Different scaling for different flow regimes of the lubricating layer is used and leading order N-S equations are derived. We have used an analytical method to estimate inertial effects by assuming self-similarity of the velocity profile in thin layer flow. The study shows that inertia can have a significant effect on the pressure field and consequently lubrication force. In addition, careful choice of the waveshape can result in counterbalancing lubrication force.

CONCLUSIONS

We introduced a novel methodology for efficient transport of heavy oil via a triple-layer core-annular flow. We positioned a shaped unyielded skin of a visco-plastic fluid between the transported oil and the lubricating fluid layer. We addressed the important issue of how in practice to develop a triple-layer flow with shaped viscoplastic skin. Computational studies of [6] showed that these flows may be stably established and the shaped interface induces extensional stresses in the skin layer. We studied this directly by developing a long-wavelength analysis of the extensional flow. This allowed us to predict the minimal yield stress required to maintain the skin rigid.

We extended the feasibility of the method by considering the effects of inertia and turbulence in the lubrication layer. We showed that the method can generate enough lubrication force to balance the buoyancy force for wide range of density differences and pipe sizes if the proper shape is imposed on the unyielded skin.

References

[1] Frigaard I. A. Super-stable parallel flows of multiple visco-plastic fluids. *J. Non-Newton. Fluid Mech.* **100**(1): 49-75, 2001.
[2] Moyers-Gonzalez M., Frigaard I. A., Nouar C. Nonlinear stability of a visco-plastically lubricated viscous shear flow. *J. Fluid Mech.* **506**: 117-146, 2004.
[3] Hormozi S., Wielage-Burchard K., Frigaard, I. A. Entry, start up and stability effects in visco-plastically lubricated pipe flows. *J. Fluid Mech.* **673**: 432-467, 2011.
[4] Hormozi S., Wielage-Burchard K., Frigaard, I. A. Multi-layer channel flows with yield stress fluids. *J. Non-Newton. Fluid Mech.* **166**(5): 262-278, 2011.
[5] Sarmadi P., Hormozi S., Frigaard I. A. Triple-layer configuration for stable high-speed lubricated pipeline transport. *Phys. Rev. Fluids* **2**: 044302, 2017.
[6] Sarmadi P., Hormozi S., Frigaard I. A. Flow development and interface sculpting in stable lubricated pipeline transport. *J. Non-Newton. Fluid Mech.* **261**: 60-80, 2018.
[7] Sarmadi P., Frigaard I. A. Inertial effects in triple-layer core-annular pipeline flow. *Phys. Fluids* **321**(10): 103102, 2019.
[8] Ooms G., Pourquie M. J. B. M., Beerens J. C. On the levitation force in horizontal core-annular flow with a large viscosity ratio and small density ratio. *Phys. Fluids* **25**(3): 032102, 2013.

TURBULENT DRAG REDUCTION WITH SURFACTANT SOLUTIONS AT A HIGH CONCENTRATION

Rodrigo S. Mitishita*[1], Jordan MacKenzie[2], Gwynn J. Elfring[1], and Ian A. Frigaard[1,3]
[1]Department of Mechanical Engineering, University of British Columbia, Vancouver, Canada
[2]Department of Chemical and Biological Engineering, University of British Columbia, Vancouver, Canada
[3]Department of Mathematics, University of British Columbia, Vancouver, Canada

Summary We present a comparative experimental investigation of turbulent drag reduction with surfactant based micellar solutions at high concentrations. Experiments are performed with a rotational rheometer and a flow loop in the fully turbulent regime. We analyse the rheology of the micellar fluid in order to characterize its viscoelastic behaviour and compare with that of xanthan gum and Carbopol solutions. The surfactant shows a gel-like response to oscillatory shear that is consistent with entangled gel systems, which is further corroborated by a scaling of G' with concentration, as well as Cryo-TEM visualizations. We analyse these results with LDV measurements of turbulent, drag reducing flows to characterize and better understand the mechanisms of drag reduction with high concentration viscoelastic systems.

INTRODUCTION

As it is well known from the experimental results by Toms, the addition of a few ppm of polymers or surfactants to water can reduce drag in turbulent flows by as much as 70% [1]. Such small additions grant viscoelasticity to the fluid but do not alter the shear viscosity significantly, in most cases. This discovery has brought significant energy savings in practical applications such as fire fighting, HVAC systems and hydraulic fracturing [2,3]. Industrial applications in the oil and gas industry such as gravel packing seek to benefit from both turbulent drag reduction (TDR) as well as high shear viscosities, useful for gravel suspension [4]. While the mechanisms of TDR with dilute polymer or surfactant solutions have been extensively investigated over the years with experimental and computational methods [5], fewer studies have been performed with high viscosity micellar viscoelastic fluids. Considering this gap in literature, we present an experimental investigation of turbulent flows with high viscosity polymer and surfactant fluids. In this study, we compare a Carbopol solution (an ideal yield stress fluid with negligible elasticity after the yielding point [6]),with a mostly shear-thinning fluids (xanthan gum) and a viscoelastic, shear thinning surfactant solution. We present rheological results for the fluids, turbulent friction factor, pressure drop and velocity measurements from Laser Doppler Velocimetry (LDV), and other turbulence characteristics.

EXPERIMENTAL SETUP

Turbulent flow experiments are conducted in a horizontal, pump driven flow loop with two transparent 7.5 *m* test sections, with both cylindrical and rectangular cross sections, as presented in Figure 1. The rectangular test section ("Channel") is made of three 2.5 *m* long, clear acrylic channels with dimensions of (W x H) 50.8 *mm* by 25.4 *mm*, and hydraulic diameter $D_h = 2WH/(W+H)$ of 33.8 *mm*. The circular test section ("Pipe") is composed of five 1.5 *m* borosilicate glass pipes with outer diameter (OD) of 60 *mm* and inner diameter (ID) of 42 *mm*. The fluid in the 200 *L* storage tank is driven by a Netzsch NEMO progressing cavity pump, capable of a maximum flow rate of 1000 *L/min*. An Omega FMG 606 magnetic flow meter is used to measure the average flow rate. The pressure drop along 2.5 *m* of the rectangular test section and 3.1 *m* of the circular test section is measured by an Omega DPG 409 differential pressure transducer (*DP1* and *DP2*). The temperature of the fluid in the tank is measured by an Omega TC-NPT pipe thermocouple. Two-component velocity measurements are performed with an LDV system (*FlowExplorer, Dantec Dynamics*) in the *measurement box* (a rectangular tank surrounding the pipe filled with glycerol to minimize the effects of beam refraction), and also the channel test section.

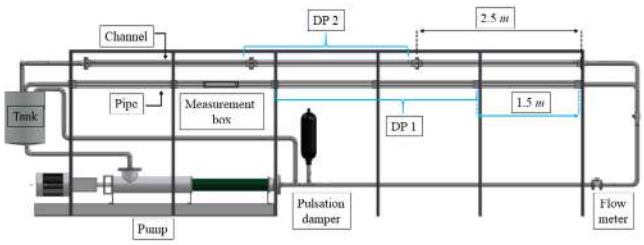

Figure 1: Flow loop schematic.

*Corresponding author. E-mail: rodrigo.seiji06@gmail.com

RESULTS AND FUTURE WORK

Rheological measurements are performed with a Malvern Kinexus Ultra+ rheometer, with a C34 roughened Couette geometry. The surfactant employed in this study is EDAB (erucic dimethyl amidopropyl betaine + isopropanol) mixed with tap water. The rheology of the surfactant system is initially probed by frequency sweeps in the linear regime at different concentrations from 1%w to 10%w concentrations, after a pre-shear of 100 s^{-1} for 6 *mins* and a resting time of 30 *mins* for a reproducible initial condition. We note here that the range of concentrations for industrial applications is usually from 3% to around 6% [4]. The data from Figure 2 (a) indicates that the surfactant system behaves as a viscoelastic solid at room temperature, with storage modulus G′ at least an order of magnitude greater than the loss modulus G″. This also implies very long relaxation times at room temperature and also the presence of a yield stress, which is confirmed by steady flow curves. In the inset of Figure 2 (b), we see that G′ scales with concentration with a power law index of approximately 2.2, which is also seen in other entangled gel-like materials, such as actin. More evidence of an entangled system is seen through Cryo-TEM analysis in Figure 2 (b), which shows a structure of very long micelles greater than 1μm in length. The structure seems to be exclusively formed by entanglements without crosslinks or branching. This evidence of highly elastic material could help to explain drag reduction such as measured by Goyal et al [4] with high concentration surfactant solutions.

Rheology data, as well as comparisons with better known polymers such as a Carbopol fluid, which is an inelastic gel-like material in the linear viscoelastic regime, is used to interpret flow loop experiments with surfactants at concentrations between 1 and 4.5 %w, performed with the setup described in the previous section. Experiments are executed at a Reynolds number of over 10000 to ensure a fully turbulent flow. We present friction factor measurements over a range of turbulent Reynolds numbers in both pipe and channel test sections, for both Carbopol and the surfactant fluid. The percentage of drag reduction is calculated as $\%DR = (\Delta P_{water} - \Delta P_{measurement})/\Delta P_{water}$. In order to quantitatively investigate TDR with polymers and surfactant fluids, we present Reynolds stress measurements as well as spectra of velocity fluctuations near the wall, to show how the additives affect the energy cascade and thus energy dissipation during a statistically steady turbulent flow.

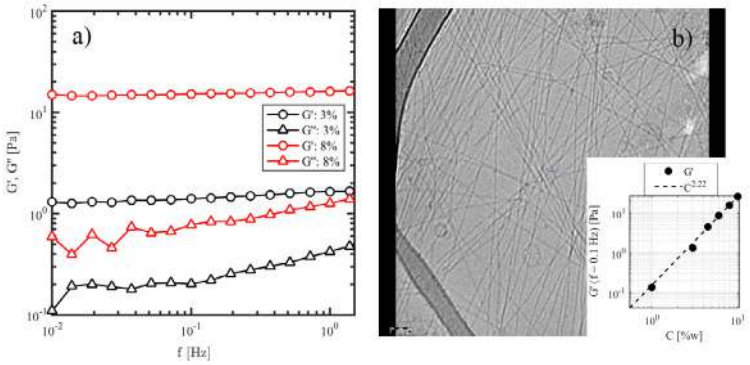

Figure 2: (a) Storage (G′) and loss modulus (G″) vs frequency, showing only results for 3%w and 8%w concentrations. (b) Cryo-TEM of 4.5% EDAB along with scaling of G' with concentration, at a frequency of 0.5 Hz.

Acknowledgments

We would like to acknowledge funding from Schlumberger and the Natural Sciences and Engineering Research Council under the CRD program, project 505549. Experimental infrastructure was funded by the Canada Foundation for Innovation and the BC Knowledge Fund, grant number CFI JELF 36069. This funding is gratefully acknowledged. R.S. Mitishita also acknowledges funding from the University of British Columbia via the 4 Year Fellowship programme.

References

[1] Toms, B. A., On the early experiments on drag reduction by polymers. *Physics of Fluids 20 (10)*, 1977.
[2] Pereira, A. S. & Soares, E. J., Polymer degradation of dilute solutions in turbulent drag reducing flows in a cylindrical double gap rheometer device. *Journal of Non-Newtonian Fluid Mechanics 179-180*, 9-22, 2012.
[3] Zakin, J. L., Myska, J. & Chara, Z., New Limiting Drag Reduction and Velocity Profile Asymptotes for Nonpolymeric Additives Systems. *AIChE Journal, 42 (12)*, 3544-3546, 1996.
[4] Goyal, G., Elfring, G. J. & Frigaard, I. A., Rheology and flow studies of drag-reducing gravel packing fluids. *Rheologica Acta 56 (11)*, 905-91, 2017
[5] White, C. M. & Mungal, M. G., Mechanics and prediction of turbulent drag reduction with polymer additives. *Annual Review of Fluid Mechanics 40 (1)*, 235-256, 2008.
[6] Balmforth, N. J., Frigaard, I. A. & Ovarlez, G., Yielding to stress: recent developments in viscoplastic fluid mechanics. *Annual Review of Fluid Mechanics 46*, 121-146, 2014.

A LAGRANGIAN VORTEX MODEL FOR VISCOELASTIC FLUID FLOWS

Fumihiko Mikami*[1]
[1]Department of Mechanical Engineering, Chiba University, Chiba, Japan

Summary A Lagrangian vortex model is proposed that describes the vorticity transport in a two-dimensional flow of a Maxwell fluid in which elastic shear waves propagate. A point vortex created at the surface of the body translates with the uniform flow velocity, and its vorticity occupied area expands at the shear wave speed according to the two-dimensional Green's function of the telegraph equation. The viscoelastic Mach number determines the size of the expanding area. In contrast, the Deborah number determines the radial distribution of the vorticity that can be classified into diffusion type and traveling-wave type. The model offers an intuitive understanding of the viscoelastic fluid flows around a body.

INTRODUCTION

Vorticity plays an important role in fluid dynamics. In the case of a two-dimensional incompressible flow, the vorticity form of the Navier-Stokes equations describes the convection and diffusion of the vorticity, which provides useful insights into the understanding of the flow of a Newtonian fluid. In contrast, a clear explanation of the vorticity transport mechanisms in the flow of a viscoelastic fluid has not been found, in particular, the one corresponding to the viscous diffusion. In a viscoelastic fluid, elastic shear waves or vorticity waves propagate in certain conditions. Joseph[1] studied the problem of the flow of a viscoelastic fluid past a body, which is the viscoelastic analog to the aerodynamic flow problem associated with sound waves. With linearization around uniform flow, he obtained an equation that describes the propagation of vorticity. Such an equation was shown by Joseph et al. [2] to change type in steady flow depending on the viscoelastic Mach number M defined as the ratio of the uniform flow speed U to the shear wave speed c in the fluid. Besides, the problem depends on another parameter, such as the Deborah number De, the ratio of the fluid relaxation time τ to characteristic flow time. It is thus desirable to understand the vorticity transport in the flow of viscoelastic fluids in terms of these parameters. In this study, a Lagrangian vortex model is proposed based on the linearized equations of a Maxwell fluid, with which we discuss the vorticity transport mechanisms in the flow around a body.

VORTICITY TRANSPORT IN A MAXWELL FLUID

A vortex model

Based on the governing equations linearized around a uniform flow, and with the notation $D_0/Dt = \partial/\partial t + U \cdot \partial/\partial x$, Joseph[1] has derived the following vorticity equation for a Maxwell fluid,

$$\frac{D_0^2 \boldsymbol{\omega}}{Dt^2} + \frac{1}{De}\frac{D_0 \boldsymbol{\omega}}{Dt} = \frac{1}{Re\, De}\nabla^2 \boldsymbol{\omega}, \tag{1}$$

where $\boldsymbol{\omega}$ is the vorticity. This equation describes the propagation of vorticity waves in a medium moving with uniform speed U. From equation (1), the shear wave speed relative to the surrounding fluid is given by $c = 1/\sqrt{ReDe} = 1/M$. By using the coordinate system moving with the fluid and by including a source term $\gamma(\boldsymbol{x}, t)$ introduced in this study to denote creation of vorticity at the body surface, equation (1) is now replaced by the following telegraph equation,

$$\left(\nabla^2 - M^2\frac{\partial^2}{\partial t^2} - \frac{M^2}{De}\frac{\partial}{\partial t}\right)\boldsymbol{\omega}(\boldsymbol{x}, t) = -\gamma(\boldsymbol{x}, t). \tag{2}$$

In the case of two-dimensional flow, a point vortex created at the point $\boldsymbol{x} = \boldsymbol{x}'$ on the body surface at $t = t'$ translates with the uniform flow velocity U, and its vorticity occupied area expands at the wave speed c according to the two-dimensional Green's function of equation (2), which is described, with $t - t'$ replaced by t, as[3]

$$G_2(r, t) = \frac{1}{2\pi\sqrt{t^2 - M^2 r^2}}\exp\left(-\frac{t}{2De}\right)\cosh\left(\frac{\sqrt{t^2 - M^2 r^2}}{2De}\right)H(t - Mr), \tag{3}$$

where $r = |\boldsymbol{x} - \boldsymbol{x}'|$. This Green's function for a Maxwell fluid is essentially different from that of seismic S waves[4, 5]. Figure 1 shows a schematic of this process. The viscoelastic Mach number $M = U/c$ determines the radius of the area occupied by the vorticity as it is observed at a fixed point of the domain downstream of the body. The vorticity occupied areas are assumed to retain the same shape for all times.

On the other hand, the Deborah number De determines the radial profile of vorticity. Figure 2 shows the plots of equation (3) for two different Deborah numbers, presenting the difference in the feature of the point vortex. At $De = 0.1$ (Figure 2(a)), the vorticity spreads, keeping the feature of the vortex core, like viscous diffusion in a Newtonian fluid, with the exception that the vorticity occupied area is restricted within a non-dimensional radius $r = t/M$, whereas at $De = 0.4$ (Figure 2(b)), traveling waves with tails are readily observable, where the wave carries the vorticity with its maximum at the wavefront. The radial profile of vorticity is attenuated with time due to a loss term in the equation (2) and tends to the profile of the Newtonian case.

*Corresponding author. E-mail: fmikami@faculty.chiba-u.jp

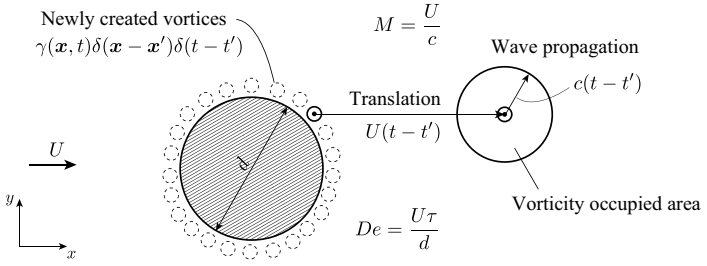

Figure 1: A Lagrangian vortex model for vorticity transport in the flow of a Maxwell fluid.

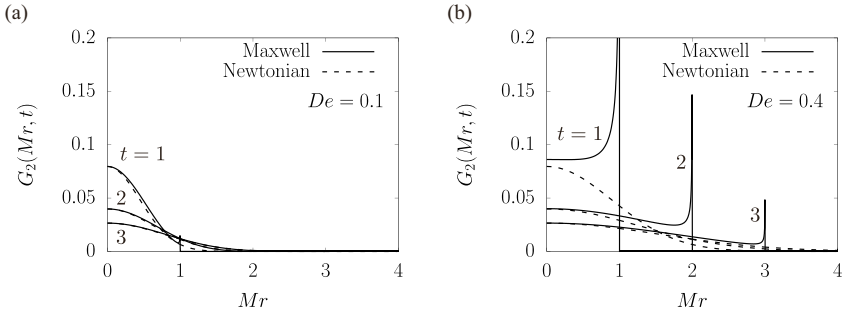

Figure 2: Equation (3) at various non-dimensional times $t = 1, 2$ and 3, showing the expansion of the vorticity occupied area. The dashed lines denote the Newtonian cases at the equivalent Reynolds number $Re = M^2/De$. (a) $De = 0.1$. (b) $De = 0.4$.

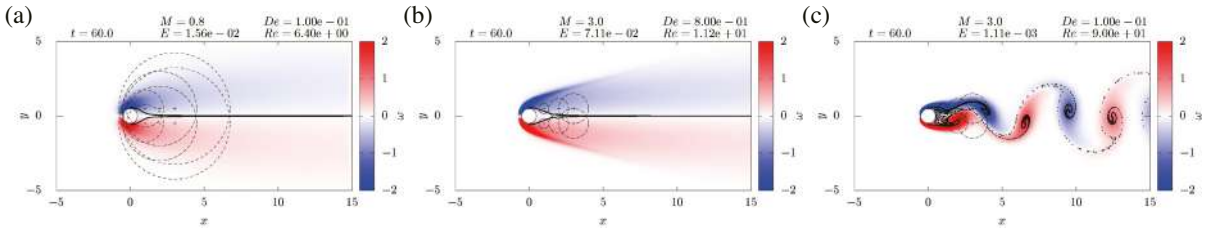

Figure 3: Snapshots of vorticity contours and streaklines. The dashed lines denote examples of the wavefronts of the previously created vortices, only showing those originated from the top and bottom of the circular cylinder and at positions corresponding to the times shown in Figure 2. (a) The flow exhibits a low Reynolds number character at $M = 0.8, De = 0.1$. (b) A clear Mach cone is observed at $M = 3.0, De = 0.8$. (c) The flow exhibits a vortex street wake at $M = 3.0, De = 0.1$.

Comparison with numerical results

The impulsively started flow of a UCM (upper convected Maxwell) fluid around a circular cylinder is numerically simulated using a finite-difference method, with a Cartesian mesh and the staggered variable arrangement. The solid obstacle is taken into account by the penalization method. The governing equations are the stream function-vorticity formulation of the momentum equation and the constitutive relations for the UCM fluid.

The flow exhibits a steady and low Reynolds number character at $M = 0.8$ and $De = 0.1$ (Figure 3(a)), where the vorticity in the wake is located near the center, as shown in Figure 2(a), of a larger expanding area, whereas at $M = 3.0$ and $De = 0.8$ (Figure 3(b)), a formation of a Mach cone, i.e., a V-shaped wake is observed, where the peak vorticity is located at the wavefront as shown in Figure 2(b). The flow exhibits a vortex street wake at $M = 3.0$ and $De = 0.1$ (Figure 3(c)), where the vorticity is located near the center of an expanding area of relatively small radius displaying low dissipation (that is, high Reynolds number).

CONCLUSIONS

A vortex model which describes the vorticity transport in a two-dimensional flow of a Maxwell fluid is proposed. The viscoelastic Mach number determines the size of the expanding area occupied by the vorticity, whereas the Deborah number determines the radial distribution of the vorticity, which can be classified into diffusion type and traveling-wave type. The model successfully describes the main characteristics of the numerical results based on the specified parameters, which offers an intuitive understanding of the viscoelastic fluid flows around a body.

References

[1] Joseph, D. D. Fluid dynamics of viscoelastic liquids. Springer, Berlin Heidelberg 1990.
[2] Joseph, D. D., Renardy, M. and Saut, J. C. Hyperbolicity and change of type in the flow of viscoelastic fluids. Archive for Rational Mechanics and Analysis, **87**(3): 213-251, 1985.
[3] Morse, P. M. and Feshbach, H. Methods of theoretical physics. McGraw-Hill 1953.
[4] Aki, K. and Richards, P. Quantitative seismology: Theory and methods. W. H. Freeman & Co, Vol.1, Chap.4: 74-75, 1980.
[5] Bercoff, J., Tanter, M. and Fink, M. Sonic boom in soft materials: The elastic Cerenkov effect. Applied Physics Letters, **84**(12): 2202-2204, 2004.

YIELD STRESS EFFECTS ON FLOW ONSET AND ARREST

Kunal D. Jadhav[1], Pietro Rossi[1], and Ida Karimfazli*[1]
[1]Department of Mechanical, Industrial & Aerospace Engineering, Concordia University, Montreal, QC, Canada

Summary We conduct experimental studies of internal buoyancy-driven flow of yield stress fluids to characterize the effect of the yield stress on flow features. We compare our findings with theoretical predictions to assess the accuracy of hydrodynamic models. We verify the existence of a critical yield stress (sufficient to prevent steady flow) but identify other phenomenological differences in the predicted and observed flow development patterns.

BACKGROUND

Yield stress fluids (*YSF*), first introduced by Bingham [1], are characterized by their solid-body-like behaviour below a certain shear stress known as the yield stress. Above the yield stress, the material *yields* and starts to flow.

For any flow setup there is, inevitably, a critical yield stress below which the fluid does not flow. Energy stability analysis and numerical studies [2, 3] have shown that the motionless background state is always linearly stable and that, if disturbed, stable disturbances decay and the motionless state is recovered within a finite time. Although these initial studies focused on unidirectional shear flows, more recent studies demonstrated the same results in different multidimensional buoyancy-driven flows (see e.g. [4, 5, 6]). Numerical results also revealed episodic flow development in yield stress fluids (including delayed flow onset and temporary flow arrest) [7, 8].

Figure 1: Illustration of the flow domain.

Contrary to the plethora of theoretical studies on buoyancy-driven flows of YSF, experimental studies are quite scarce and the distinct features of YSF predicted theoretically have not been validated with experimental studies. We consider natural convection in a square cavity with differentially heated sidewalls and use time resolved Particle Image Velocimetry (*PIV*) to investigate the existence of a critical yield stress and flow development and arrest in YSF (see Fig.1).

EXPERIMENT SETUP

A square box of size $15cm$ was made of acrylic. The sidewalls (on the hot and cold side) are made of Aluminum to facilitate heat transfer. Hot and cold side temperatures were maintained using feedback-controlled Peltier modules. See Fig.2 for an illustration of the setup. Temperature variation on each wall was monitored and found to be always less than 1^oC. Carbopol solutions of concentration 0.3 to $0.4g/L$ with yield stress values ranging from 0.05 to $0.2Pa$ were used as the working fluid. Experiment was started with the system at room temperature and the fluid at rest. Peltier modules were turned on and data collection started at $t = 0s$. Once the flow reached steady state, the Peltier modules were turned off while data collection continued until flow stoppage.

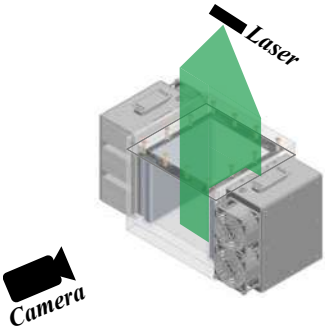

Figure 2: Schematic of the experimental setup.

CRITICAL YIELD STRESS

For each carbopol solution, the temperature difference across the cell was changed between 3^oC and 30^oC. The L^2 norm of the velocity field, $||u||$, was used as a measure of the kinetic energy of the flow to determine the existence of steady advective currents. Figure 3 illustrates the outcome of the experiments. When the ratio of the yield stress to the buoyancy stresses is above a certain *critical* value, the steady state is motionless; however, when the ratio is below the critical value, steady flow is observed (see Fig.3).

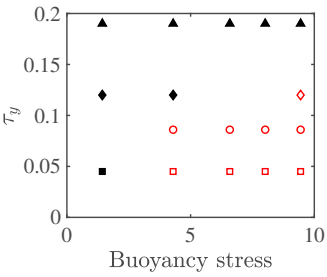

Figure 3: Effect of the yield stress on development of advective currents. Filled (empty) markers indicate motionless (flowing) regimes.

FLOW ONSET AND ARREST

An illustrative case of flow development is presented in Fig.4: (a,b,c,d) show snapshots of the velocity field at different stages of flow development and (e,f) flow decay (after the Peltier modules are turned off). Figure 4 (g) and (h) show the evolution of the temperatures of the hot and cold walls and the velocity norm during the experiment. In an apparent contrast with the theoretical predictions, flow appears to start immediately, initially developing slowly before accelerating and approaching the steady state.

*Corresponding author. E-mail: ida.karimfazli@concordia.ca.

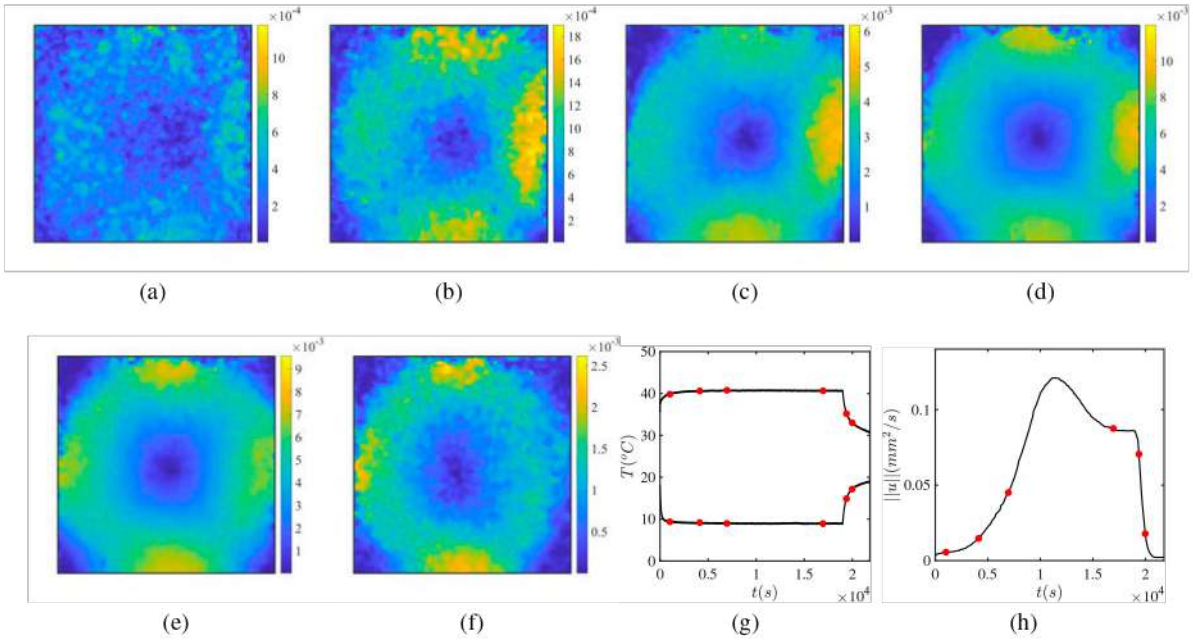

Figure 4: (a-f) show snapshots of the velocity field (in mm/s). (g) and (h) show the time evolution of hot and cold wall temperatures and the velocity norm, respectively. The red circles indicate the times of the snapshots (carbopol concentration $0.38g/L$).

We present different quantitative measures of advective currents to show that, although some experiments comply with the theoretical predictions (see e.g. Fig.5), depending on the magnitude of the yield stress there can also be marked differences between experiment and theory.

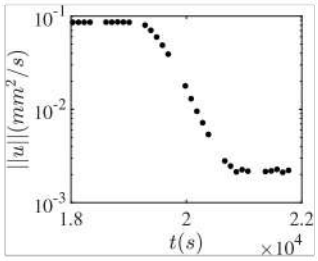

Figure 5: Decay of the velocity norm after the heating and cooling units are turned off. Carbopol concentration $0.38g/L$; for temperature boundary conditions see Fig. 4g.

CONCLUSIONS

We conduct experiments to investigate buoyancy-driven flow in a square cavity. We use time-resolved PIV to characterize flow onset, development and arrest. Experimental observations confirm the existence of a threshold yield stress above which there is no steady flow. Contrary to the theoretical predictions, however, below the critical limit flow onset appears to be immediate; this does not seem to depend on the value of the yield stress. Flow arrest is theoretically expected to take place within a finite time. Our experimental observations contradict this prediction. Increasing the yield stress, however, decay trends appear to approach the theoretical predictions.

References

[1] Bingham, E.C. *Fluidity and plasticity*. Vol. 2. McGraw-Hill, 1922.
[2] Glowinski, R., Lions, J.-L. & Tremolieres, R. Numerical analysis of variational inequalities. North-Holland (trans. from French), 1981.
[3] Huilgol, R. R., Mena B., & Piau. J. M. Finite stopping time problems and rheometry of Bingham fluids. *J non-Newt Fluid* **102(1)**: 97-107, 2002.
[4] Zhang, J., Vola, D. & Frigaard, I.A.. Yield stress effects on Rayleigh–Bénard convection. *J Fluid Mech* **566**: 389-419, 2006.
[5] Balmforth, N.J. & Rust, A.C.. Weakly nonlinear viscoplastic convection. *J non-Newt Fluid*, **158(1-3)**: 36-45, 2009.
[6] Karimfazli, I., Frigaard, I.A. & Wachs, A. A novel heat transfer switch using the yield stress. *J Fluid Mech*, **783**: 526-566, 2015.
[7] Davaille, A., Gueslin, B., Massmeyer, A. and Di Giuseppe, E. Thermal instabilities in a yield stress fluid: existence and morphology. *J non-Newt Fluid*, **193**, 144-153, 2013.
[8] Karimfazli, I., & Frigaard, I. A. Flow, onset and stability: Qualitative analysis of yield stress fluid flow in enclosures. *J non-Newt Fluid* **238**: 224-232, 2016.

CHOCOLATE FOUNTAIN: MULTI-PHYSICS, MULTI-PHASE, AND MULTI-SCALE MODELING

Lyes Kahouadji*[1], Seungwon Shin[2], Jalel Chergui[3], Damir Juric[3], and Omar K. Matar[1]
[1]Department of Chemical Engineering, Imperial College London, South Kensington Campus, London SW7 2AZ, UK
[2]Department of Mechanical and System Design Engineering, Hongik University, Seoul 121-791, Republic of Korea.

Summary We present a three-dimensional direct numerical simulation of a heated chocolate fountain using physical properties of melted chocolate (60°C) flowing in an ambient atmosphere (20°C). We solve both the Navier-Stokes and the energy equation using a front-tracking-based multiphase method that accounts for both the Newtonian (ambient air) and Non-Newtonian (melted chocolate) fluids, and a direct forcing method technique for fluid-structure interaction. The numerical framework employed circumvents numerous meshing issues normally associated with constructing complex geometries within typical computational fluid dynamics packages. The device considered in the present work, a static chocolate fountain structure with a rotating vertical Archimedes Screw that are both constructed via a module that defines solid objects by means of two distance functions, which are positive for the fluid and negative for the solid. The construction combines primitive objects, such as a cylinder, a plane, and an ellipsoid, for instance, using simple geometrical operations. Finally, we present a new approach to explore the resulting computational fluid dynamics data through a virtual reality environment in which it will be possible to 'dive' inside the chocolate fountain and explore the underlying physics through a multi-sensory process.

INTRODUCTION

A chocolate fountain encompasses many topics in fluid mechanics such fluid-structure interactions, heat-transfer, and multiphase flow. A typical chocolate fountain is composed of (*i*) a large plate at the bottom filled with molten chocolate, (*ii*) a central vertical tube in which a vertical Archimedes Screw is rotating in order to pump up the heated molten chocolate from the bottom plate, and (*iii*) some domes fixed to the vertical tube over which the molten chocolate flows. When the chocolate fountain is activated, people enjoy dipping pieces of fruit (strawberries, bananas,...) and also some sweets such as marshmallows through the falling chocolate curtain between two domes. Townsend and Wilson [1] have considered both Newtonian and Non-Newtonian types of molten chocolate and studied the flow occurring in a chocolate fountain by isolating three mechanisms in it: (*i*) the pumped pipe flow as a traditional Poiseuille flow, (*ii*) a chocolate film flowing on a typical dome, and finally (*iii*) the curtain flow between two domes. Our approach is to combine all these isolated mechanisms through a single numerical setup that also takes into account heat-transfer effects and a complex type of pumping mechanism via the rotation of an Archimedes screw.

CONFIGURATION, PROBLEM FORMULATION, AND DISCUSSION

The specific Chocolate Fountain configuration used in this study is a 4-tier device illustrated in Figure 1-(a), represented in a cubical Cartesian domain (x, y, z) of size $0.5m \times 0.5m \times 0.5m$. Our approach for the construction of a similar structure circumvents the need for time-consuming construction, meshing, and remeshing of this geometry. Instead, we proceed in a modular manner that enables us to build the geometry from primitive geometrical objects using a static distance function that takes into account the interaction of these objects with the flow for both single and two-phase flows. The final structure in the computational domain, viz. Fig. 1-(a) and (d) to (j), consists of the iso-value $\psi(x, y, z) = 0$; the static distance function, $\psi(x, y, z)$, is positive for the fluid part and negative for the solid part. In a similar way, the Archimedes screw is also constructed with a distance function (see figure 1-(c)) and its rotational motion via a direct forcing method technique [3]. The temporal evolution of the chocolate fountain exhibits many physical mechanisms such as Poiseuille flow (see Fig 1-(d)), laminar falling film during the dome envelopment (g), radial retraction of the chocolate curtain (g and h), curtain coiling when reaching a larger dome (h and i) followed by an interfacial instability in the azimuthal direction (i), and finally curtain breakup (j).

The Archimedes screw shown in figure 1-(c) is also built using distance functions. The rotation of its helicoid geometry provides an axial motion that pumps the molten chocolate from bottom to top. The activation of the Archimedes screw rotation requires the implementation of the so-called Direct Forcing Method, which is a technique that incorporates a fluid-solid interaction force defined numerically using the latest step of the temporal integration [3] for two types of molten chocolate rheology (a highly viscous Newtonian and a shear-thinning non-Newtonian model [1]).

When the chocolate fountain is activated, the molten chocolate falls from one dome to a larger dome and the liquid curtain becomes thinner and colder (see figure 1-(b)). Moreover, the simulation correctly predicts the inward falling of the chocolate curtain due to the presence of a pressure difference between its external and internal sides, the gravity, and the surface tension force.

*Corresponding author. E-mail: l.kahouadji@imperial.ac.uk

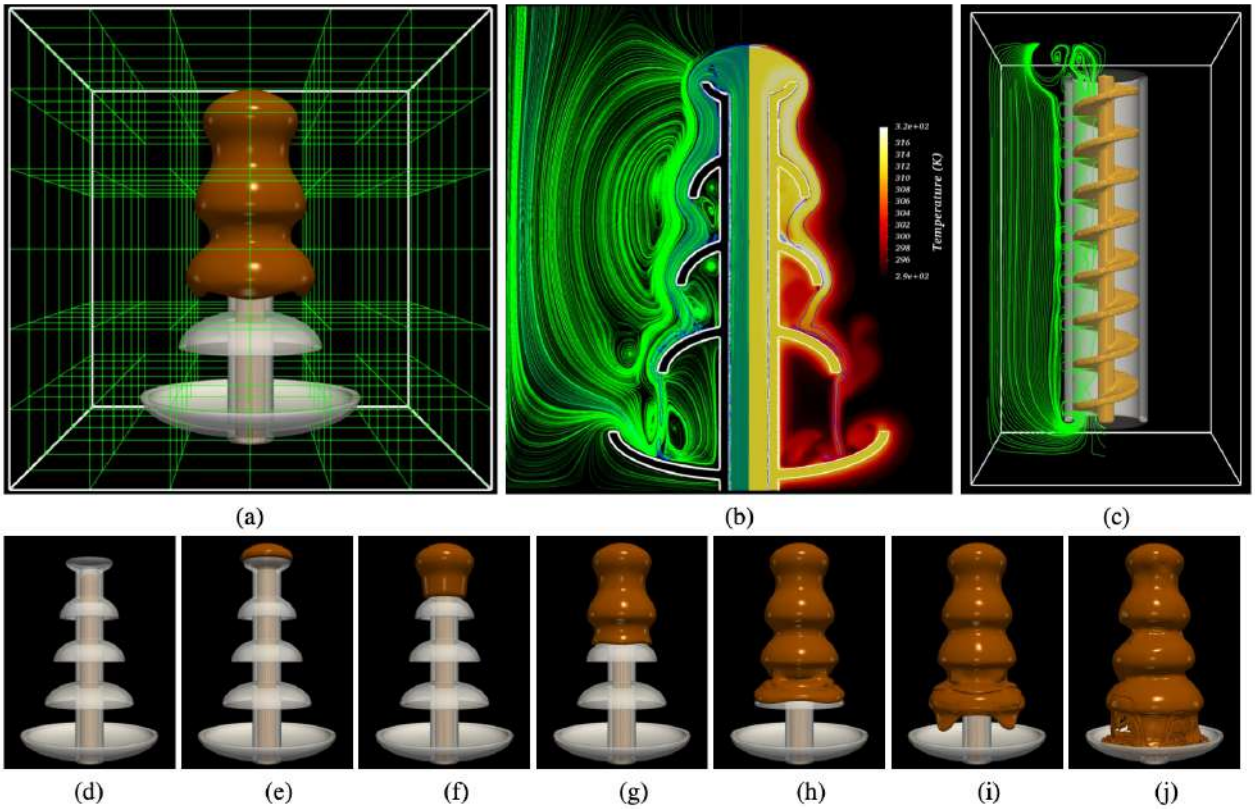

Figure 1: Typical chocolate fountain (a): Computational domain of 0.5^3 m^3 divided onto $216 = 6 \times 6 \times 6$ subdomains. Each subdomain has a resolution of 64^3 grid cells which gives a global resolution of 384^3. (b): A typical vortical structure and temperature field in the solid, liquid and in the gas. (c): A vertical Archimedes screw confined inside a cylindrical tube. (d-j): Temporal evolution of chocolate fountain flow until reaching the bottom plate.

CONCLUSIONS

This work studies the dynamics of a chocolate fountain in a single computation that combines fluid structure interaction, heat-transfer, and in the context of a front-tracking based multiphase method for both Newtonian and non-Newtonian fluids.

ACKNOWLEDGEMENTS

This work is supported by the Engineering & Physical Sciences Research Council, United Kingdom, through the MEMPHIS program grant and by computing time at HPC facilities provided by the Research Computing Service (RCS) of Imperial College London. Simulations have been performed using code BLUE and the visualisations have been generated using Paraview.

References

[1] Townsend A. K., Wilson H. J. The fluid dynamics of the chocolate fountain. *Eur. J. Phys.* **35**: 015803, 2016.

[2] Kahouadji L., Nowak E., Kovalchuk N., Chergui J., Juric D., Shin S., Simmons M. J. H., Craster R. V., Matar O. K. Simulation of immiscible liquid-liquid flows in complex microchannel geometries using a front-tracking scheme. *Microfluidics and Nanofluidics* **22** 126, 2018.

[3] Russell A. W., Kahouadji L., Mirpuri K., Quarmby A., Piccione, P. M., Matar O. K., Luckham P. F., Markides C. N.. Mixing viscoplastic fluids in stirred vessels over multiple scales: A combined experimental and CFD approach. *Chemical Engineering Science* **208**: 115129, 2019.

[4] De Graef V., Depypere F., Minnaert M., Dewettinck, K. Chocolate yield stress as measured by oscillatory rheology. *Food Int. Res.* **44**: 2660-2665, 2011.

[5] Kahouadji, L. Fabulous, flowing, and folding fountain of chocolate. *UK Fluids Network video award, 2019. (https://www.fluids.ac.uk)*

ENERGY TRANSFER IN VISCOELASTIC DILUTE POLYMER SOLUTIONS MODELED BY A HYBRID CONTRAVARIANT-COVARIANT DUMBBELLS

Kiyosi Horiuti*[1], Carlos B. da Silva[1], and Fernando T. Pinho[2]
[1]LAETA/IDMEC/Instituto Superior Técnico, Universidade de Lisboa, Portugal 2CEFT, FEUP, Universidade do Porto, Portugal

Summary We conduct an analysis of the energy transfer and polymer configuration in homogeneous isotropic turbulent flow (HIT) of dilute polymer solutions. The polymer chains are modeled by new nonlinear elastic dumbbells in which the constraint of affinity of motion of the bead-spring configuration with the macroscopic deformation of the solvent fluid is removed. Slippage of the strand and variation in the slip parameter α are allowed. When the complete affine dumbbell ($\alpha = 0$) is rotated to the maximum non-affine ($\alpha = 1$) direction, the value of α is adjusted to represent the renewed orientation. Assessment is numerically conducted by dispersing the dumbbells in HIT, where their motion is pursued by Brownian dynamics. The macroscopic motion of solvent fluid is determined by DNS and with the proposed model with variable slip, enhancement of drag reduction is achieved in comparison to the complete affine case. This is associated with the conversion of the connector vector of dumbbell between contravariant ($\alpha = 0$) and covariant ($\alpha = 1$) states, which takes place alternately and quasi-periodically in time with an interval comparable to the relaxation time. The largest elastic energy production is achieved in the elongated covariant dumbbells ($\alpha \approx 1$) with the elastic energy accumulating in the region adjacent to the vortex sheets. Large elastic energy is attained in the dumbbells aligned in the direction normal to the vortex sheets. When $\alpha \approx 0$, the elastic energy accumulates along the vortex sheets, and large elastic energy is attained in the dumbbells oriented in the direction transverse to the vorticity.

Drag reduction (DR) by addition of small amounts of long-chain polymers into Newtonian solvent is an important theoretical and practical problem. Molecules of polymer in dilute solution are commonly modeled as dumbbells, i.e. sets of two beads connected by a nonlinear spring. It is generally assumed that the fluid surrounding this bead-spring configuration moves affinely with an equivalent continuum. The polymer chains, however, may slip through the solvent which is normally observed with rigid particles [1]. Actually, when complete affinity is assumed, the elasto-inertial turbulence (EIT) regime arises as shown in [2] using the FENE-P constitutive equation for the polymer stress. Molecular motions may not precisely correspond to the macroscopic deformation when straining is large [3], and slip may be accounted for through slip parameter α $(0 \leq \alpha \leq 1)$. This rigidity effect was considered in [4] assuming that α may not be fixed but variable subjected to elongation and reorientation of the dumbbells. This paper aims to develop a new dumbbell model in which the variation of α is incorporated and to elucidate its impact on the energy transfer and DR.

We utilize the multi-scale BDS-DNS in which a mesoscopic description of an ensemble of dumbbells is connected to a macroscopic DNS of the solvent [5]. Non-affinity is introduced by allowing the slippage of strand motion in the dumbbell model. When $\alpha = 0$, the governing equation for the end-to-end vector of the dumbbell $\boldsymbol{R}$ becomes $dR^i/dt = R^j \partial_j u^i$, and $\boldsymbol{R}$ is contravariant. $\boldsymbol{R}$ tends to become parallel to the vorticity vector $\boldsymbol{\omega}$ and distributes along the vortex sheet. When non-affinity is maximum $(\alpha = 1)$, it becomes $dR_i/dt = -R_j \partial_i u^j$, and $\boldsymbol{R}$ is covariant. $\boldsymbol{R}$ aligns orthogonally to the vortex sheet [6].

Using the steady solution for the governing equation of the conformation tensor $c_{ij}(\equiv R_i R_j)$, the production term for c_{ii}, $P_c(= (1-2\alpha)c_{ij}S_{ji})$, is approximated as $P_c \approx 4\tau_s(1-2\alpha)^3 S_{ik}S_{kj}S_{ji}$ [6], where S_{ij} is the strain rate tensor and τ_s is the relaxation time. The generation term of the solvent dissipation rate (ε) is given as $P_\varepsilon \approx -\nu S_{ik}S_{kj}S_{ji}$, where ν is the viscosity. Since $\mathcal{S}_\mathrm{S}(\equiv -S_{ik}S_{kj}S_{ji})$ is predominantly positive [7], when $\alpha = 0$, $P_c \propto$ -$\mathcal{S}_\mathrm{S} < 0$ and $P_\varepsilon \propto \mathcal{S}_\mathrm{S} > 0$. Thus, the contravariant dumbbells transfer the elastic energy back into the solvent where it is then dissipated and EIT arises. This energy transfer can be reversed only when $\mathcal{S}_\mathrm{S} < 0$. We use the eigenvalues of S_{ij}, $\sigma_+, \sigma_-, \sigma_s$. σ_s corresponds to the eigenvector $\boldsymbol{e}_s$ maximally aligned with $\boldsymbol{\omega}$, the largest remaining ones as σ_+ and $\boldsymbol{e}_+$, and the smallest ones as σ_- and $\boldsymbol{e}_-$. $\boldsymbol{e}_s \parallel \boldsymbol{\omega}$, and $\boldsymbol{e}_s$ and $\boldsymbol{e}_+$ span the vortex sheet, while $\boldsymbol{e}_-$ is perpendicular to the vortex sheet [6]. When $\alpha = 0$, $\boldsymbol{R} \parallel \boldsymbol{e}_s$ or $\boldsymbol{R} \parallel \boldsymbol{e}_+$ and $\mathcal{S}_\mathrm{S} < 0$ is achieved when $\sigma_+ > 0, \sigma_- < 0, \sigma_s < 0$. By altering the orientation of $\boldsymbol{R}$ from $\boldsymbol{e}_s$ to $\boldsymbol{e}_+$, large P_c is restored [7]. When $\alpha = 1$, $\boldsymbol{R} \parallel \boldsymbol{e}_-$, $P_c \propto \mathcal{S}_\mathrm{S} > 0$ and $P_\varepsilon \propto \mathcal{S}_\mathrm{S} > 0$. The energy transfer can proceed to both elastic energy and dissipation.

Evolution of $\boldsymbol{R}$ is governed by the $\Omega_{ij}R_j$ term which gives rotation of $\boldsymbol{R}$ but preserves the length of $\boldsymbol{R}$, and the $S_{ij}R_j$ term which yields stretching of $\boldsymbol{R}$, where Ω_{ij} is the vorticity tensor. Noting that the $\Omega_{ij}R_j$ term is independent on α, we incorporate the effect of reorientation of $\boldsymbol{R}$ due to $\Omega_{ij}R_j$ term into the renormalized value of α. The increment of α in time can be determined as $\delta\alpha = -C_\alpha(\Delta t/\tau_s)(R_pR_jS_{ip}\Omega_{ij})/2(R_pR_jS_{ip}S_{ij})$ (Variable-α model) where Δt is the time increment.

The polymer stress tensor τ_{ij} due to the force acting on the fluid from the dumbbells and solvent is directly obtained by averaging over the dumbbells in the configurational space as $\tau_{ij} = C_\tau \sum_{n=1}^{N_t}(1-2\alpha)\left\{f(|\boldsymbol{R}|^*)(R_i^{(n)}R_j^{(n)})/r_{eq}^2 - \delta_{ij}\right\}\delta(\boldsymbol{x} - \boldsymbol{r}_g^{(n)})$, where N_t is the number of dumbbells, r_{eq} is the equilibrium length of the dumbbell and $\boldsymbol{r}_g$ is the vector connecting the center of $\boldsymbol{R}$. The FENE damping function $f(x) = 1/(1-x^2)$ is applied. The linear interpolation scheme is applied for averaging [5]. Transfer of the solvent energy to the polymers is evaluated by the production term $P_e(\equiv \tau_{ij}S_{ij})$.

*Corresponding author. Email: kiyosi.horiuti@tecnico.ulisboa.pt

We carried out three cases in HIT with 128^3 grid points, $\tau_s = 2.4$s, Weissenberg number $W_i = 10$ and $N_t = 10^9$: α was fixed to 0 in case Fix-B, fixed to 1 (case Fix-A) and allowed to vary between 0 and 1 (Variable-α). Figure 1 (a) compares the p.d.f. of the length of the dumbbells $|\boldsymbol{R}|$ in the three cases. Not only is Variable-α not intermediate to the two fixed cases, but the largest elongation is attained in Variable-α. In this study, steady state is maintained by imposition of external random force f_i. Figure 1 (b) shows the p.d.f. of the work provided by the external force f_i, $u_i f_i$. The tails of p.d.f. obtained in all cases are decimated compared with the Newtonian case, i.e., steady state is sustained by supplying smaller work due to f_i in viscoelastic cases and DR is achieved. Solvent dissipation (ε) was smaller in Fix-A (0.226) than in Fix-B (0.263) and P_e was larger in Fix-A (0.149) than in Fix-B (0.115). In Variable-α, P_e was close to Fix-A (0.146), while ε was between Fix-A and Fix-B (0.243). DR exceeding Fix-B is obtained in Variable-α.

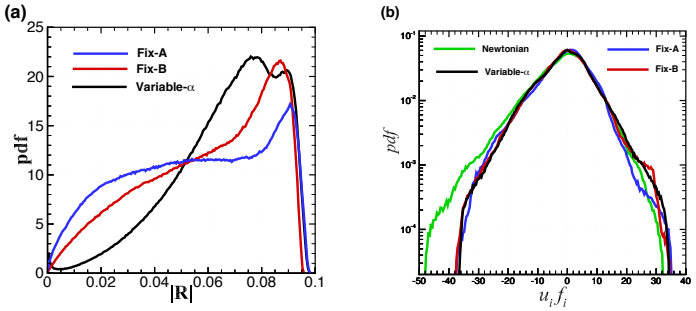

Figure 1: (a) Distributions of p.d.f. of the dumbbell length $|\boldsymbol{R}|$ obtained in Fix-A (blue line), Fix-B (red), Variable-α (black).; (b) Distribution of p.d.f. of the $u_i f_i$ term obtained in Newtonian (green line), Fix-A (blue), Fix-B (red), Variable-α (black).

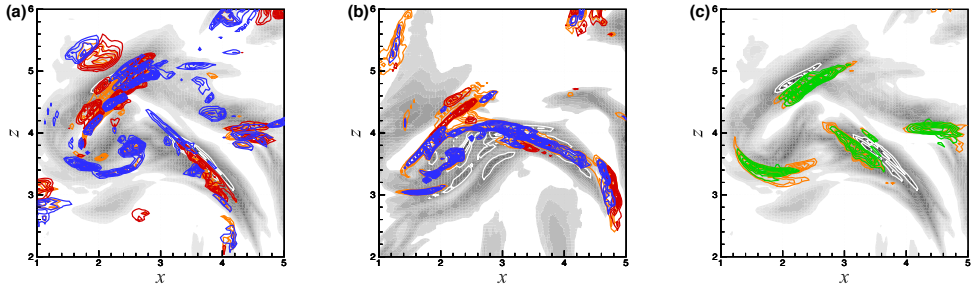

Figure 2: Contours of vortex sheets (gray flood and white lines), the polymer energy τ_{kk} (orange lines) and the polymer energy production term P_e (blue, red, green lines) in the $x-z$ plane at $y = 2.21$ at (a) $t = 586.5$, (b) $t = 587.0$, (c) $t = 586.5$.

Figure 2 show the distributions of vortex sheets (gray flood), the polymer energy τ_{kk} (orange lines) and P_e in which conditional sampling of $|\boldsymbol{R}|^2 \geq 0.75 L^2_{\max}$ is applied on the dumbbells to derive τ_{ij}, where $L_{\max}$ is the maximum dumbbell length. In Fig. 2 (a) and (b), P_e is sampled on $0 \leq \alpha \leq 0.2$, and Fig. 2 (c) on $0.8 \leq \alpha \leq 1$. Blue, red and green lines show P_e further sampled on the dumbbells with $\boldsymbol{R} \parallel \boldsymbol{e}_+$, $\boldsymbol{R} \parallel \boldsymbol{e}_s$, $\boldsymbol{R} \parallel \boldsymbol{e}_-$, respectively. In the contravariant dumbbells, initially in (a), the dumbbells with $\boldsymbol{R} \parallel \boldsymbol{e}_s$ are responsible for large P_e, but later in (b), P_e by $\boldsymbol{R} \parallel \boldsymbol{e}_s$ annihilates and P_e by $\boldsymbol{R} \parallel \boldsymbol{e}_+$ becomes predominant. Large P_e is restored by turning $\boldsymbol{R}$ from $\boldsymbol{e}_s$ to $\boldsymbol{e}_+$, and τ_{kk} distributes upon the vortex sheets. In the covariant dumbbells in Fig. 2 (c), τ_{kk} concentrates in the region outside and adjacent to the vortex sheets and P_e by $\boldsymbol{R} \parallel \boldsymbol{e}_-$ is predominant. The dumbbells are orthogonal to the vortex sheets and the sheet is under tension, leading to large DR [6].

CONCLUSIONS

We proposed new dumbbell model with variable α. Its impact on the motion of polymers and energy transfer is studied using BDS-DNS in HIT. Correlation between the alignment of the dumbbells and polymer energy production is presented. Contravariant polymers release the polymer energy back into the solvent when highly stretched and dissipation increases. This transfer is alleviated by altering the orientation of the dumbbell to the transverse direction. Covariant polymers distribute orthogonally to the vortex sheets and the largest elastic energy is retained when highly elongated, which leads to larger DR.

References

[1] A.N. Beris and B.J. Edwards: Thermodynamics of Flowing Systems: Oxford Univ. Press, New York 1994.
[2] P. C. Valente, C. B. da Silva and F. T. Pinho: J. Fluid Mech 760, 39-62, 2014.
[3] P.G. de Gennes: Physica, 140A,:9-25, 1986.
[4] E.J. Hinch: Phys. Fluids 20, 10: S22-S30 1977.
[5] T. Watanabe, and T. Gotoh: J. Fluid Mech. 717, 535-575, 2013.
[6] K. Horiuti, K. Matsumoto and K. Fujiwara: Phys. Fluids 25: 015106, 2013.
[7] K. Horiuti and S. Suzuki: Proc. ICTAM 2016: 2016.

SLIPPERY WEISSENBERG EFFECT?

Udita U. Ghosh,[1] Navin K. Chandra,[1] and Aloke Kumar*[1]
[1]Department of Mechanical Engineering, Indian Institute of Science, Bangalore, India.

Summary We investigate the effect of a slippery interfacial layer on the climbing of a viscoelastic fluid onto a partially immersed rotating rod (Weissenberg effect). The bare rods are replaced by silicone and castor oil dipped rods and the maximum free surface deformation ($\bar{h}$) of the polymeric suspensions is used as a characterization parameter. It is found that the polymeric suspensions not only continue their ascent onto the rod but can also exhibit rod-dipping state for polymeric concentration $c = 0.5$ (w/w%) for a range of rod rotation velocity of $\omega = 400$ to $\omega = 1000$ RPM. Thus, fluid behavior has been demarcated into three regimes (rod-climbing, rod-dipping, absence of Weissenberg effect) as a function of type of oil, polymeric concentration and rod-rotation velocity.

INTRODUCTION

Weissenberg effect [1] is the 'climbing' by a fluid onto a partially immersed rotating shaft. Weissenberg [1] postulated that such deformation in the meniscus profile is driven by the non-zero value of the normal stress differences under shear flow [2-4]. There are multiple parameters that influence the magnitude of climb and can be enumerated as the properties of the fluid properties like surface tension, viscosity, experimental variables (angular velocity) and geometrical parameters (rod radius, extent of rod immersion in fluid) [5]. However, the effect of altering the interfacial condition (rod-fluid interface) on the climbing is still unexplored. In this article, we alter the interfacial condition by introducing an oil layer at the rod-fluid interface and outline its effect on the maximum free surface deformation, h of the fluid as a response to the applied angular velocity ω.

Aqueous polymeric suspensions of polyethylene oxide (PEO, viscosity average molecular weight ~ 5×10^6, *Sigma Aldrich*) are employed as a model fluid in the present study and subjected to rotating rods dipped in castor/silicone oils. The polymer concentration is varied as $c_{0.5}, c_1$ where represent the 0.5 and 1 are the polymer weight percentage (w/w) resp. in the suspension. Effect of such 'slippery-rods' on the occurrence of the Weissenberg effect are outlined as a function of two parameters, (i) polymer weight concentration in the fluid, c and (ii) varying angular rotation speed, ω. It is surprisingly found that the polymeric fluid not only exhibits the rod-climbing in presence of oily rods but can also show rod-dipping for $c_{0.5} + castor\ oil$!

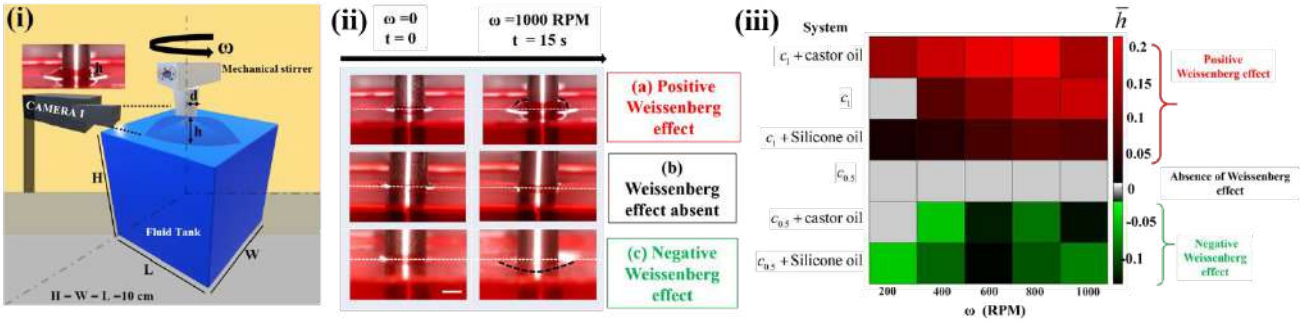

Figure 1. (i) Schematic of the experimental setup, h is the height of rod climbed/dipped by the fluid on a rod of diameter, d (= 1 cm) (ii) Image sequence demarcating the three states of (a) classical rod-climbing/ positive Weissenberg effect shown by aqueous suspension of 1% (w/w) of polyethylene oxide (c_1) (b) absence of Weissenberg effect shown by aqueous suspension of 0.5% (w/w) of polyethylene oxide ($c_{0.5}$) (c) dipping of the meniscus or the negative Weissenberg effect shown by ($c_{0.5}$ + castor oil). All the three regimes are shown for $\omega = 1000$ RPM. Scale bar: rod diameter, d = 1 cm (iii) Heat map display demarcating the observed regimes based on the absence/occurrence of Weissenberg effect (positive and negative) in presence of oil coated (slippery) rod surface as a function of rod rotation rate, ω and polymer concentration ($c_{0.5}, c_1$). The maximum deformation, $\bar{h} = h/d$ of the fluid meniscus (climbing or dipping) is used as the characterizing parameter in the heat map display.

The experimental setup comprises of a cuboid acrylic tank of dimensions (H =W= L = 10 cm) as shown in Figure 1(i), placed symmetrically with respect to an overhead stirrer. A digital camera (Camera I) was aligned with the stirrer axis to track the interfacial profile at 50 fps (front view). Polymeric fluid in the tank (fluid level ~ 4 cm) in the tank, rod immersion depth ~ 3.5 cm was kept constant) was dyed with Phenol red (*Sigma Aldrich*) and the maximum free surface deformation, h of the fluid is quantified via image analysis (*ImageJ v:1.52a*). It is non-dimensionalized ($\bar{h} = h/d$) by the rod diameter, d to classify the three regimes (positive, absence, negative Weissenberg effects) of polymeric response observed in the experiments. Figure 1(ii) shows these regimes for an applied angular velocity $\omega = 1000$ RPM.

*
Corresponding author. E-mail: alokekumar@iisc.ac.in

RESULTS AND DISCUSSIONS

A heat map (Figure 1(iii)) is constructed to classify the systems into these three states based on the maximum free surface deformation, $\bar{h}$ over the range of the applied angular velocity ω provided by the overhead stirrer, ramped externally from 200 to 1000 RPM in increments of 200 RPM. The first regime of classical rod-climbing can be observed for c_1 for $\omega \geq 400$ till $\omega = 1000$ RPM. It is expected intuitively that an oil layer will promote slip allowing the polymer molecules to slip over the rod which in turn acts as a hindrance to the upward climb of the fluid. However, we found that the polymeric fluid continued to exhibit rod-climbing even for an oily-rod for c_1. Also, a decrease in the rod-climbing angular velocity from $\omega = 400$ RPM for a bare rod to $\omega = 200$ RPM is observed for an oily rod. The influenced the magnitude of climb, $\bar{h}$ is found to be dependent on the type of the oil layer. Specifically, castor oil enhanced the magnitude of climb, for e.g., at $\omega = 800$ RPM, it increased from ~ 0.1 to ~ 0.2. Silicone oil had an opposite influence on the rod-climbing magnitude, it decreased the climbing height e.g., at $\omega = 800$ RPM from ~ 0.1 to ~ 0.05. The second regime is the control state which is the absence of either rod-climbing /rod-dipping observed uniformly for $c_{0.5}$ for the entire range of ω and for c_1 at $\omega = 200$ RPM. This control state remains unaltered on introduction of oily-rod for $c_{0.5}$ only at the lowest operational velocity, $\omega = 200$ RPM for castor oil. At the rest of the operational velocities, an oily-rod with either of the oils (Silicone and castor) changes the control state to third regime of rod-dipping in $c_{0.5}$ systems! The trend in the magnitude of dip for a specific angular rotation speed can be stated as, $\left|\bar{h}_{(c_{0.5}+silicone\ oil)}\right| > \left|\bar{h}_{(c_{0.5}+castor\ oil)}\right|$ except for the highest operational speed, $\omega = 1000$ RPM. To summarize the effect of oily-rod for the range of operating velocities, $\omega = 200$ to $\omega = 800$ RPM, castor oil assists in maintaining the existing state of rod-climbing in c_1 system and also increases the magnitude of climb whereas in $c_{0.5}$ system, it changes the fluid response from absence of Weissenberg to rod-dipping or Negative Weissenberg state. Therefore, alteration in the interfacial condition affects the free-surface response in terms of its directionality i.e. rod-climbing, rod-dipping, control as well as the magnitude of the response, $\bar{h}$.

CONCLUSIONS

Weissenberg effect in the presence of an oil-dipped rod is investigated and the interfacial dynamics is represented by a heat map. This heat map demarcates three states of positive (rod-climbing), negative (rod-dipping) and absence of Weissenberg effect on the basis of polymer concentration and applied shear rates (rod rotational velocity). Thus, the alteration of the interfacial condition by introduction of an oily rod affects the rod climbing phenomenon in terms of the magnitude of the response.

References

[1] K. D. Weissenberg, *Nature*, 1947, 159, 310–311.
[2] G. S. Beavers, J. Y. Yoo and D. D. Joseph, *Rheol. Acta*, 1980, **19**, 19–31.
[3] J. D. Daniel, *Applied Mathematical Sciences*, 1973, vol. 84.
[4] D. D. G. S. B. & R. L. F. C. Joseph, *Arch. Ration. Mech. Anal.*, 1980, **49**, 381–399.
[5] D. D. Joseph and G. S. Beavers, *Rheol. Acta*, 1977, **16**, 169–189.

LOCAL NORMAL STRESSES MEASUREMENT IN NON-NEWTONIAN FLUIDS

Anaïs Gauthier*[1], Michaël Pruvost[1], Olivier Gamache[1] and Annie Colin [1]
[1]MIE,Chemistry,Biology and Innovation Laboratory (CBI) UMR8231,ESPCI Paris,CNRS,PSLR esearch University, 10 rue Vauquelin, Paris,France

Summary We present a new experimental approach to obtain a local measurement of normal stresses in non-Newtonian fluids. We use a 4x4 cm^2 array of 25 highly sensitive sensors (with a precision of 5 Pa) that we built and integrated to the bottom plate of a rheometer. We use this system to characterize the flow of a shear-thickening liquid: a non-Brownian suspension of cornstarch particles. We demonstrate that the flow becomes heterogeneous in the discontinuous shear thickening region. Intriguingly, the sensors evidence the presence of a single, stable object rotating with the surrounding fluid. We characterise in detail this heterogeneity: we show how its shape and its relative velocity varies with the solid fraction of the suspension, the gap height and the nature of the particles. We finally discuss its origin.

INTRODUCTION

The flow of complex fluids is often associated with highly non-linear phenomena, such as the development of normal stresses, with dramatic effects. Polymer suspensions, for example climb along spinning rods (the well-known Weissenberg effect), which is a consequence of the elasticity of the polymer chains. Another example is the growth of normal stresses in shear-thickening suspensions, which is an important industrial issue: strong and local normal stresses can break mixers or blenders. The characterisation of these complex flows is greatly improved by local measurements, which can be used to measure the pressure profile in the geometry [1], or to detect heterogeneities [2]. Here, we develop a new capacitive sensor, inspired from "soft electronics" and adapt it to a rheology geometry to measure the local normal stresses. The sensors are sensitive to the pressure $P = -\sigma_{zz}$, with σ_{zz} the zz component of the stress deviator tensor. Pressures as small as 5 Pa can be detected, so that a precise 2D mapping of the normal stress can be established. We use this system to characterize the flow of a shear-thickening liquid: a cornstarch suspension, at high solid fraction ϕ.

MATERIALS AND METHODS

The core of the sensor is a piezo-capacitive soft solid foam, filled with carbon black particles [3]. The dielectric material is placed between two electrodes: a soft one, at the top and a solid electrode network, at the bottom. When a pressure P is applied on the sensor, the foam slightly bends and compresses, which increases its capacitance C. We measure C by applying a low-voltage AC current (1V, 1000 Hz) between the top electrode and one of the bottom electrodes. As presented in Figure 1a, 25 of these sensors are built into a 4x4 cm^2 matrix (figure 1b), which replaces the bottom plate of a torsional rheometer. The blue disk on Figure 1b indicates the size and position of the upper plate (with diameter 4 cm). In a typical experiment, the suspension is sheared between two parallel plates separated by a distance h = 1 mm. Using the sensor array, we record the normal stress measured by each of the 12 sensors covered by the fluid. The suspension considered here consists of a large volume fraction of solid particles of cornstarch (here, 40% in weight) in an isodensity salt of CsCl in water. This suspension exhibits a discontinuous shear thickening, for applied shear stress $\sigma > 20$ Pa. In each experiment, we apply a series of step-like shear stresses σ of increasing values and record the pressure measured by each sensor. In the following, we focus on two points placed diagonally in the geometry, as indicated in Figure 1b, in red and blue.

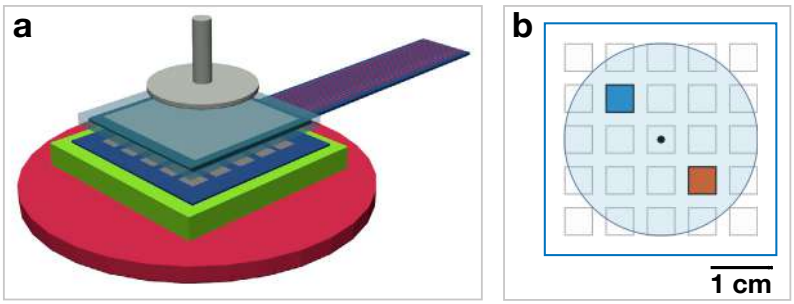

Figure 1. **a.** Schematic of a capacitive pressure sensor. It consists of two layer: the top one is a soft solid polymeric foam filled with conductive carbon black particles, and covered with a soft electrode. At the bottom, an electrode network of 25 measurement points, with size 4x4 mm^2. The sensor is placed on the bottom plate of the rheometer (in red), in a parallel plate configuration. **b.** Array of 25 sensors: the circle in blue shows the position and size of the upper disk, with a diameter of 4 cm. The two measurement points (used in Figure 2) are shown in red and blue.

*Corresponding author. E-mail: anais.gauthier@espci.fr

RESULTS

Figure 2a shows the viscosity η of a 40% (in weight) cornstarch suspension for increasing shear stresses $\dot{\gamma}$: this system is shear-thinning at low shear rates ($\dot{\gamma} < 5$ s^{-1}) and strongly shear thickening above at critical shear rate $\dot{\gamma}_c = 40$ s^{-1}, with a viscosity η increasing by more than one order of magnitude. As reported earlier [4], the shear thickening is associated with a strong increase of the mean normal stress, associated with very large fluctuations. For the first time, our sensor arrays give access to the local normal stresses associated with these fluctuations. We use here two sensors, placed at opposite directions below the rotating plate (see Figure 1b, in red and blue), and record the pressure at a high frequency of 100 Hz. We present in Figure 2b and c the sensors measurement during steps of constant shear stress σ, either before the discontinuous shear thickening region (Figure 2b, for $\sigma = 1$ and 16 Pa) or in the discontinuous shear thickening region (Figure 2c, $\sigma = 125$ Pa).

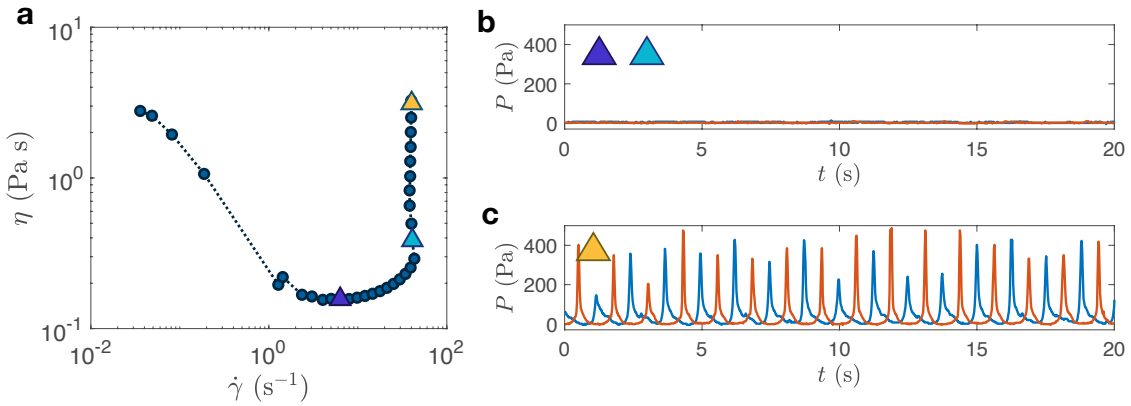

Figure 2. **a.** Viscosity η of a 40% cornstarch suspension as a function of the shear rate $\dot{\gamma}$. The triangles indicate the points in the plot where the pressure is recorded by the sensors. **b-c**. Pressure measurement of the sensors as a function of time, for varying imposed constant stresses σ. Two 4x4 mm^2 sensors (red and blue lines) are placed in opposite directions on a diagonal (as shown in Figure 1b). **b**: σ = 16 Pa and **c**: σ = 125 Pa.

Below the discontinuous shear-thickening region, the pressure is constant, close to zero and identical for both sensors (figure 2b). However, as soon as the discontinuous shear thickening region is reached, normal stress oscillations become visible, as presented in Figure 2c. Very interestingly, the pressure fluctuations are extremely regular: the red and blue signals exhibit perfectly out of phase peaks, of similar amplitude. This indicates the presence of one large structure, rotating here at a velocity $\Omega_a \approx 5$ rad/s, which is 60% faster than the angular velocity of the geometry. Our experiments show that this signal is extremely stable, and that its relative velocity (with respect to the geometry) does not depend on the imposed stress. However, the peak pressure P_{max} does increase with σ, from $P_{max} \approx 10$ Pa for $\sigma = 50$ Pa to $P_{max} \approx 400$ Pa for $\sigma = 125$ Pa (Figure 2c). This unique structure is observed in every experiment we performed. It also appears when varying the solid fraction ϕ of the suspension (from 37% to 42%) as long as the system undergoes discontinuous shear thickening. Its size (measured by the width of the signal) and velocity, however, do vary with ϕ, which might indicate a different nature or origin.

CONCLUSION

The sensor array that we present here is a new tool that brings a new insight into heterogeneous flows. It gives access to the local value of σ_{zz}, an important parameter that is much less studied than the shear components of the stress tensor. We use here the sensors to characterize the flow of a cornstarch suspension, a popular shear thickening system. We evidence for the first time a unique normal stress front propagating within the flow, in the discontinuous shear thickening regime. Its exact nature and origin (is it an aggregate with a larger density, a stress front propagating within the flow?), and their stability are still to be understood. It would also be interesting to see if such objects are specific of cornstarch suspensions or if they can also be detected in other non-brownian, shear-thickening systems.

References

[1] T. Dbouk, L. Lobry and E. Lemaire Normal stresses in concentrated non-Brownian suspensions. J. Fluid. Mech., 715, 239-272, 2013.

[2] V. Rathee, D. Blair & J. Urbach. Localized stress fluctuations drive shear thickening in dense suspensions. *Proc. Nat. Acad. Sci. USA*, **114**(33), 8740-8745, 2017.

[3] M. Pruvost, W. Smit, C. Monteux, P. Poulin & A. Colin. Polymeric foams for flexible and highly sensitive low-pressure capacitive sensors. *npj Flexible Electronics*, **3**(1), 7, 2019.

[4] B. Saint-Michel, T. Gibaud, S. Manneville, Uncovering instabilities in the spatiotemporal dynamics of a shear-thickening cornstarch suspension. *Phys. Rev. X*, **8**, 03100, 2018.

FLOW AND STABILITY OF A VISCOELASTIC LIQUID CURTAIN

Antoine Gaillard*[1,2], Matthieu Roché [1], Sandra Lerouge[1], Cyprien Gay[1], and Laurent Limat[1]
[1]Universitéde Paris,Laboratoire MSC-CNRSUMR 7057,Paris,France
[2]MCND and Department of Physics & Astronomy, University of Manchester, UK

Summary Liquid curtains are sheets of liquid falling freely from an extrusion die. We investigate the flow of curtains made of polymer solutions and we show that gravity is initially balanced by the elastic stress arising from the stretching of polymer chains, after which the classical free-fall behaviour is recovered. We show how this is analogue to Newtonian curtains in which gravity is initially balanced by viscous dissipation. We also describe a varicose modulation of the sheet observed for the most shear-thinning solutions, which is linked to a unsteady three-dimensional flow instability at the planar contraction in the extrusion die.

INTRODUCTION

Liquid curtains are used in industry for precision coating of surfaces. This curtain coating technique consists in forming a liquid sheet by extruding a liquid from a slot, and let it impact on a substrate moving underneath. This free-surface extensional flow has been investigated in the case of Newtonian liquids [1]. The evolution of the liquid velocity U with the distance z from the slot outlet is given by the force balance equation

$$U\frac{\mathrm{d}U}{\mathrm{d}z} = g + \frac{4\eta U}{\rho}\frac{\mathrm{d}}{\mathrm{d}z}\left(\frac{1}{U}\frac{\mathrm{d}U}{\mathrm{d}z}\right) \tag{1}$$

where g is the gravitational acceleration and ρ and η are the liquid density and dynamic viscosity respectively. Viscosity affects the flow over a characteristic distance $z_v = ((4\eta/\rho)^2/g)^{1/3}$ from the slot outlet. Within this distance, the liquid acceleration is less than g. More precisely, for extrusion velocities $U_0 \ll \sqrt{gz_v}$, the flow close to the slot ($z \ll z_v$) is a balance between gravitational acceleration and viscous dissipation where $U \propto \rho g z^2/8\eta$ and the flow far from the slot ($z \gg z_v$) is a free-fall where inertia dominates over viscosity, i.e. $U \propto \sqrt{2gz}$.

In most Newtonian industrial curtains, $z_v \ll L_c$ due to low liquid viscosity where L_c is the distance over which the liquid falls before impacting the substrate. The flow can then be approximated by a free fall $U^2 = U_0^2 + 2gz$. Since most industrial coating liquids are non-Newtonian, a natural question is whether or not z_v is still the relevant length scale of the transition to free-fall. The case of viscoelastic liquids is of particular importance. Recent experimental works have been dedicated to the study of curtains made of polymer solutions, but they mainly consider the effect of viscoelasticity on the stability of the sheet without fully exploring its effect on the liquid velocity field [2].

In this work, investigate the effect of viscoelasticity on the flow and stability of curtains made of polymer solutions.

EXPERIMENT

We use aqueous solutions of polyethylene oxide (PEO) of varying polymer concentration. We also use solutions of partially hydrolysed polyacrylamide (HPAM) in salted water of varying salt concentration to tune the flexibility of the polymer chains. The liquid is extruded at constant flow rate Q from a die sketched in figure 1 (a) where the flow undergoes a planar contraction of ratio 14 before entering a slot of thickness $2a = 1$ mm. The liquid then forms a rectangular curtain falling vertically in ambient air over a distance $L_c > 15$ cm before impacting a motionless horizontal solid substrate. The liquid velocity in the curtain is measured by particle image velocimetry.

Liquid shear viscosity is measured by a shear rheometer equipped with a cone-plate geometry and the experimental data is fitted by a Carreau law of the form $\eta = \eta_0(1 + (\dot\gamma/\dot\gamma_c)^{a_1})^{(n-1)/a_1}$ where η_0 is the zero-shear viscosity and n represents the degree of shear-thinning. Our solutions range between Boger-like liquids with $n = 1$ (dilute PEO solutions) to strongly shear-thinning solutions with $n = 0.2$ (HPAM solution in unsalted water). Extensional rheology measurements are performed using a Capillary Breakup Extensional Rheometer (CaBER) which is a filament thinning technique allowing the measurement of the polymer relaxation time τ_{fil} relevant in strong extensional flows [3].

RESULTS

Curtain flow

Like in Newtonian curtains, we observe that the liquid acceleration is initially less that g close to the slot, and finally reaches the classical free-fall regime of constant acceleration g beyond some characteristic distance from the slot outlet, provided that the sheet is long enough and doesn't impact the substrate before reaching this regime. This characteristic length z_e is however much larger than the Newtonian viscous length $z_v = ((4\eta_0/\rho)^2/g)^{1/3}$ based on the zero-shear viscosity η_0 of the liquid. Among all rheological parameters, we show that the flow is mostly influenced by the value of the extensional relaxation time τ_{fil} of the polymers.

*Corresponding author. E-mail: antoine0gaillard@gmail.com

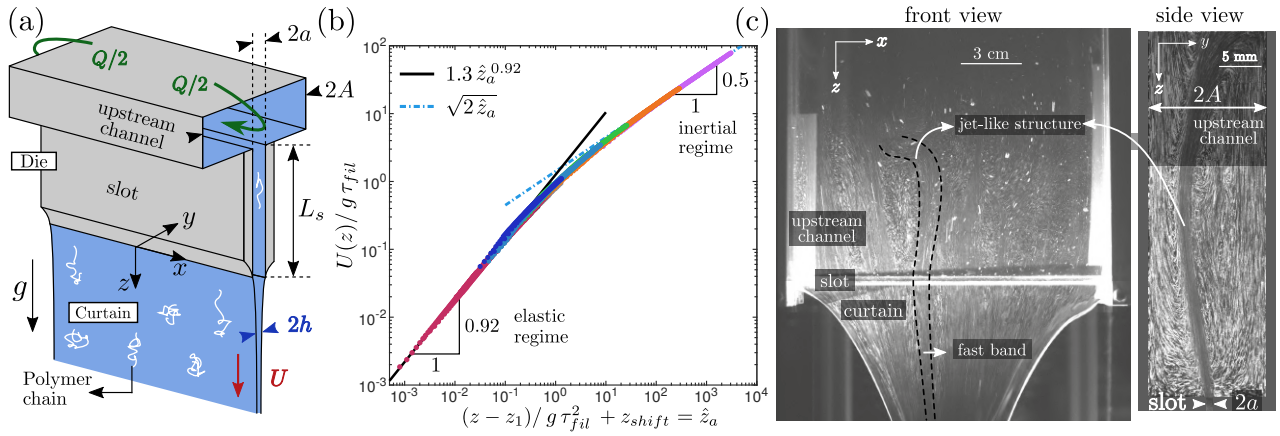

Figure 1: (a) Schematic of the slot die. (b) Master curve for the flow of viscoelastic curtains, showing an initial elastic regime followed by an inertial free-fall regime. Velocity profiles $U(z)$ (where z is the distance from the slot outlet) are scaled by length and velocity scales $g\tau_{fil}^2$ and $g\tau_{fil}$, where τ_{fil} is the polymer extensional relaxation time, and translated along the x-axis by a quantity z_{shift} linked to the dimensionless extrusion velocity. (c) Front and side views of the unsteady and three-dimensional instability observed in the die for a solution of HPAM in unsalted water. "Jet-like" portions of fluid move faster than their surrounding, leading to a modulation of the curtain thickness and velocity field downstream. Note that the transparent die used in (c) is not the one sketched in (a) and that for lighting purposes, the curtain in (c) is exceptionally not guided by the edge wires normally used to get a rectangular sheet.

As displayed in figure 1 (b), all experimental velocity profiles $U(z)$ collapse on a single master curve when using $z_e = g\tau_{fil}^2$ and $\sqrt{gz_e}$ as characteristic length and velocity scales of the problem. This scaling can be explained by simple physical arguments. A polymer molecule following a free-fall trajectory $U \propto \sqrt{2gz}$ is in a spatially decreasing strain-rate field $\dot{\epsilon} = \mathrm{d}U/\mathrm{d}z \propto \sqrt{g/2z}$. Polymer chains are expected to exhibit large stresses for $\dot{\epsilon}\tau_{fil} > 1/2$ which corresponds to the coil-stretch transition value [4]. This translates into $z < z_e = g\tau_{fil}^2$ (without prefactor). Hence, for extrusion velocities $U_0 \ll \sqrt{gz_e}$, the flow is characterised by an initial elastic regime where gravity is balanced by the elastic stresses arising from the stretching and unravelling of polymer molecules. As shown in figure 1 (b), the flow in this regime is close to a linear velocity field where $U \propto z/\tau_{fil}$ with a prefactor close to 1, which gives $\dot{\epsilon}\tau_{fil} = O(1)$. These results are fairly well predicted by a simple model using the Oldroyd-B constitutive equation for polymer molecules. See [5, 6] for details.

Curtain stability

We show that polymer addition enhances the stability of the curtain by reducing the minimum flow rate required to maintain a continuous sheet. However, our results suggest no significant influence of viscoelasticity on the dynamics of sheet retraction after being punctured. Indeed, a continuous sheet forms when the extrusion velocity exceeds the classical Taylor-Culick velocity $\sqrt{\gamma/\rho h}$ where γ is the surface tension and h is half the sheet thickness [7].

We also report a flow instability characterised by an unsteady and horizontally modulated curtain, both in thickness and velocity [6]. This varicose instability is only observed for the most shear thinning solutions with typically $n < 0.7$. Visualisation of the flow inside the die reveals that this phenomenon is linked to a flow instability at the contraction plane upstream of the slot where the flow is unsteady and three-dimensional. Figure 1 (c) shows the typically observed "jet-like" structures formed in the die where the liquid is faster than its surrounding. This leads to an non-uniform feeding of the slot and therefore to a horizontal modulation of the curtain downstream.

CONCLUSIONS

The flow of viscoelastic liquid curtains is characterised by an initial balance between gravity and the elastic stresses arising from the stretching of polymer molecules, followed by the classical free-fall behaviour with constant acceleration g. The characteristic transition length between these two regimes is $g\tau_{fil}^2$ where τ_{fil} is the polymer extensional relaxation time measured by a filament thinning technique. Polymer addition has a stabilising effect on the sheet, unless the solution is too shear-thinning as it may trigger a flow instability in the extrusion die, leading to non-uniform curtains.

References

[1] Brown D. R. A study of the behaviour of a thin sheet of moving liquid. *J. Fluid Mech.* **10**: 297–305, 1961.
[2] Mohammad Karim A., Suszynski W. J., Griffith W. B., Pujari S., Francis L. F., Carvalho M. S. Effect of viscoelasticity on stability of liquid curtain. *J. Non-Newtonian Fluid Mech.* **257**: 83–94, 2018.
[3] Anna S. L., McKinley G. H. Elasto-capillary thinning and breakup of model elastic liquids. *J. Rheol.* **45**: 115–138, 2001.
[4] De Gennes P-G. Coil-stretch transition of dilute flexible polymers under ultrahigh velocity gradients. *J. Chem. Phys.* **60**: 5030–5042, 1974.
[5] Gaillard A., Roché M., Lerouge S., Gay C., Lebon L., Limat L. Viscoelastic liquid curtains: experimental results on the flow of a falling sheet of polymer solution. *J. Fluid Mech.* **873**: 358–409, 2019.
[6] Gaillard A. Flow and stability of a viscoelastic liquid curtain. *PhD Thesis*, Univ. Sorbonne Paris Cité, Paris, 2018.
[7] Culick F. E. C. Comments on a ruptured soap film. *J. Appl. Phys.* **31**: 1128–1129, 1960.

EFFECT OF BLOOD THIXOTROPY AND VISCOELASTICITY ON THE HEMODYNAMICS IN LARGE VESSELS: ADVANCED HEMORHEOLOGICAL MODELLING AND SIMULATION

Konstantinos Giannokostas[1], Pantelis Moschopoulos[1], Yannis Dimakopoulos[*1], Andreas Anayiotos[2] and John Tsamopoulos[1]
[1]Department of Chemical Engineering, University of Patras, Patras, Greece
[2]Department of Mechanical Engineering and Materials Science and Engineering, Cyprus University of Technology, Limassol, Cyprus

Summary Blood exhibits pronounced non-Newtonian behaviour that comes from the proteinic and lipidic structure of the red blood cell (RBC) membrane along with its interaction with the ionic environment of the blood plasma and the shear-rate dependent bridging of neighboring cells. Thus, RBCs can deform and consequently store elastic energy, and also, they can form aggregates that break in quite high shear-rates. The current work deals with the advanced constitutive modelling of human blood samples using the mesoscopic theory proposed by Varchanis et al. (2019) for thixo-elasto-visco-plastic complex materials. The proposed model provides accurate calculations of the yield stress, the shear module, the relaxation time, the dependence of the rouleaux aggregation and the disaggregation rates on the hemodynamic environment as well as realistic predictions of the blood response under different non-linear rheometric protocols (e.g., LAOS, Triangular Ramp experiments). Finally, we apply the model in multidimensional flows where the effect of viscoelasticity and thixotropy is critical due to the development of normal stresses that affect the configuration of the tissue layers or the local viscosity (e.g., flow in a saccular aneurysm).

INTRODUCTION

Human blood is a suspension in plasma of formed elements, mainly erythrocytes, that exhibits plasticity, elasticity, shear-thinning, and thixotropic behaviors[1,2]. Thus, it can be classified as a thixo-elasto-visco-plastic (TEVP) material. Complications in its flow are more pronounced when the size of the vessel, wherein blood flows, is comparable to the radius of a Red Blood Cell (e.g., microvessels and aneurysms). Also, the non-Newtonian effects arise in rheometric flows even under steady or transient conditions, and they are responsible for the development of structural and kinematic instabilities that cannot be represented by previous hemorheological models[3,4,5]. Specifically, for low shear-rates, blood kinematic can never reach a steady-state, and experimental measurements depend strongly on the initial configuration of the blood sample[6,7]. Moreover, under steady flow conditions, there is a non-linear relationship between stresses and velocity-gradient, dependence of the viscosity on the shear rate, existence of a finite yield stress value, and development of slip phenomena due to the formation of plasma layer[8]. Also, under transient flow conditions (e.g., startup shear flow), there is a lag shear-stress and velocity gradient, formation of stress-overshoot in sudden start-up, and hysteretic responses. In the present work, we test previous hemorheological models[3,4,5], which can selectively represent some of the mechanisms mentioned above, and employ our recently proposed macroscopic model for TEVP materials[9], which fits non-linear hemorheological data perfectly. After the successful rheological characterization of various samples of human blood from different donors, we perform flow simulations in large vessels where the effect of thixotropy and viscoelasticity play significant roles (e.g., hemodynamics in and around terminal aneurysm).

MODEL and RESULTS

The TEVP model[9] is an extension of the Elasto-Viscoplastic Model by Saramito[10], accounting for the transient response of the microstructure (e.g., individual RBCs and rouleaux) according to the principles introduced by Dimitriou and Mckinley[11], We et al.[12] and Armstrong et al.[13]. In particular, our model couples the tensorial constitutive model by Saramito for EVP materials with thixotropy, extending the ideas of Isotropic Hardening (IH), and with Kinematic Hardening (KH). We also adopt a scalar variable that describes the level of structure at any instance and a modified Armstrong-Frederick KH equation, thus providing rules governing the dynamics of the apparent yield stress. The material viscosity, yield stress, and back stress modulus feature a nonlinear dependence on the structural parameter, enabling the model to make accurate predictions with a single structural parameter.
We apply the constitutive model in the rheometric data of all donors presented in Ref. [1]. In all cases, the model provided very realistic predictions of basic hemorheological parameters. Indicatively, the basic properties for Donor 1 are: shear model G = 0.597 Pa, viscosity η_p=0.084 Pa s, and yield stress τ_y=0.004 Pa. The predictions of the TEVP model against the experimental data under steady and transient conditions are shown in Figures 1 (a) & (b), respectively. Apart from the excellent capability of the model on reproducing the data, it can also provide an accurate prediction of the transient response of blood under homogenous rheometric conditions. Figure 1(c) depicts the variation of the shear stress in a sequence of shear-rate pulses. The initial response before the overshoot corresponds to the reorganization of the rouleaux, while the overshoot represents the maximum stress value before the breaking up of the rouleaux, while the plateau represents an equilibrium state where RBCs are isolated particles. The cessation of the flow at t=2.5 s causes the gradual formation of new three-dimensional structures. The latter is a long-lasting process causing the reduction of the maximum stress when a second shear pulse is applied at t =5.0 s.

*Corresponding author. E-mail: dimako@chemeng.upatras.gr.

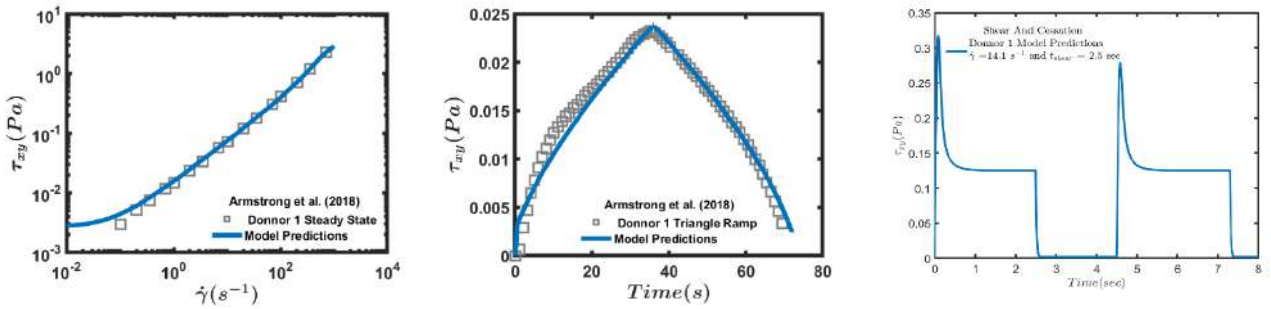

(a) (b) (c)

Figure 1. The TEVP model ([9]) can accurately capture the rheometric data for all Donors in Ref. [1]. (a) & (b) depict the predictions of the model (solid lines) and experimental measurements (hollow symbols) of Donor 1 at steady-state conditions and in time-dependent triangular ramp, respectively. (c) depicts the thixotropic response of blood sample of Donor 1 in a sequence of shear-rate pulses ($\dot{\gamma} = 14.1\ s^{-1}\big(H(t) - H(t-2.5s)\big) + 14.1s^{-1}(H(t-4.5s) - H(t-7.5s))$.

Also, we apply the model in flow domains (e.g., saccular aneurysm) where the structural dynamics and the distribution of the rouleaux vary significantly (e.g., inside and outside the aneurysm). In particular, Figure 2 shows snapshots of the velocity and the Wall-Shear-Stress fields in the cardiac circle under physiological flow conditions. The results are mesh-size independent and they are based on the hemorheological properties of Donor 1 in Ref. [1].

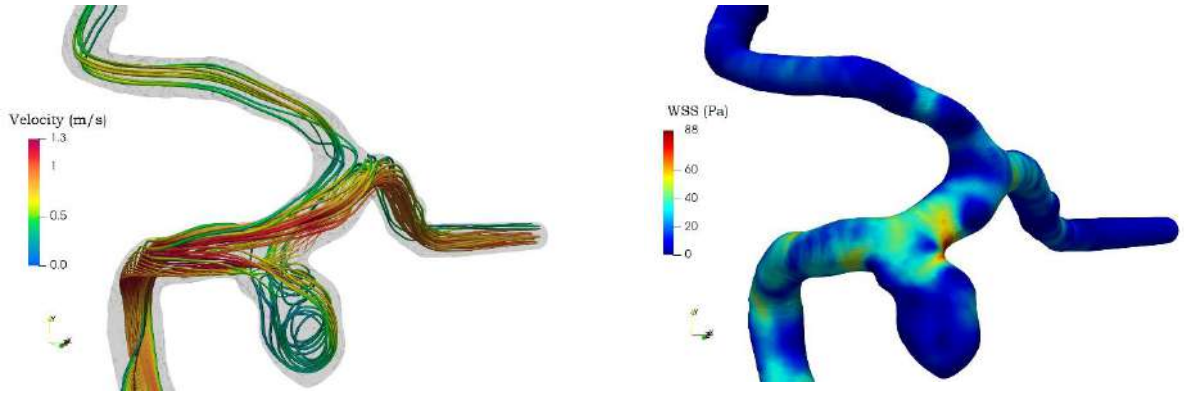

(a) (b)

Figure 2. Snapshots of (a) the velocity field and (b) the distribution Wall-Shear-Stress for Donor1 of Ref. [1].

ACKNOWLEDGMENT

Professors Y. Dimakopoulos, A. Anayiotos, and J. Tsamopoulos are participants of the CARE project funded by National and European resources of H.F.R.I., under the framework "1st Call for H.F.R.I. Research Projects to Support Faculty Members & Researchers".

References

[1] J. S. Horner, M. J. Armstrong, N. J. Wagner, and A. N. Beris, J. Rheol. 62, 577-591 (2018).
[2] J.M. Sherwood, E. Kaliviotis, J. Dusting, S. Balabani, Biomechanics and modeling in mechanobiology, 13 (2), 259-273 (2014).
[3] M. Armstrong, J. Horner, M. Clark, M. Deegan, T. Hill, C. Keith, L. Mooradian, Rheol. Acta 57(11), 705-728 (2018).
[4] R.G. Owens, J. Non-Newt. Fluid Mech. 140, 57-70 (2006).
[5] A. Sequeira, and J. Janela, An overview of some mathematical models of blood rheology, in A Portrait of State-of-the-Art Research at the Technical University of Lisbon, edited by M. S. Pereira (Springer, Dordrecht, 2007).
[6] J.F. Stoltz, M. Lucius, Biorheology 18, 453-473 (1981).
[7] D. Quemada, R. Droz, Biorheology 20, 635-651 (1983).
[8] S. Varchanis, Y. Dimakopoulos, C. Wagner, J. Tsamopoulos, Soft Matter 14 (21), 4238-4251 (2018).
[9] S. Varchanis, G. Makrigiorgos, P. Moschopoulos, Y. Dimakopoulos, J. Tsamopoulos, J. Rheol., 63(4), 609-639 (2019).
[10] P. Saramito, J. Non-Newtonian Fluid Mech. 145(1), 1–14 (2007).
[11] C.J. Dimitriou, G.H. McKinley, J. Non-Newtonian Fluid Mech. 265, 116-132 (2019).
[12] Y. Wei, M.J. Solomon, R.G. Larson, J. Rheol. 60(6), 1301–1315 (2016).
[13] M.J. Armstrong, A.N. Beris, S.A. Rogers, N.J. Wagner, J. Rheol. 60 (3), 433-450 (2016).

EXPERIMENTAL STUDY OF ROLL WAVES IN MUD

Simon Dagois-Bohy*[1],Djibrilla Noma[1],Séverine Millet[1],Valéry Botton[1],Daniel Henry[1],and Hamda Ben Hadid[1]
[1]Laboratoire de Mécanique des Fluides et d'Acoustique,CNRS,UMR 5509,Université Claude Bernard Lyonl,Ecole Centrale de Lyon,INSA Lyon, 43 boulevard du 11 novembre1 918,F-69100,VILLEURBANNE, France

Summary We study experimentally the stability of a film of a viscoplastic fluid down an incline. We set up a model experiment to measure the primary instability of these roll waves : in an inclined channel ($5° - 15°$ slope angle), we established a permanent flow of viscoplastic fluid. By perturbing the inlet flow rate, we generated surface waves at a controlled frequency, and we observed their evolution downstream with direct thickness measurement. Growth rates and wave numbers were calculated, and neutral frequencies were determined, from which a critical Reynolds number was extracted. We found this experimental Reynolds number to be in good agreement with existing theoretical work, provided that the Bingham number is carefully calculated.

Introduction

Viscoplastic fluids are characterized by a yield stress, under which no flow can occur. They usually also exhibit shear-thinning properties. In many engineering applications (coating processes in paint, paper, food, plastic, etc. industries) or geophysical phenomena (glaciers, mud and debris flows), the liquids involved present this viscoplastic behavior. In particular, during mud or debris flows, the surface can destabilize and develop into roll waves, that should be taken into account in any risk assessment study. In this study, we focus on the primary stability of viscoplastic fluids that follow the Herschel-Bulkley law $\sigma = \sigma_y + k\dot{\gamma}^n$, with σ the total shear stress, $\dot{\gamma}$ the shear rate, σ_y the yield stress, k the constistency, and n the rheological index. Such surface waves, also called Kapitsa waves, are well known when the fluid is Newtonian. It is known since the pioneering work of Benjamin (1957) and Yih (1963) that the critical Reynolds number, under which the waves are always stable, is given by $Re_c = \frac{5}{6}\cot\phi$, with ϕ the slope angle. This result has been later confirmed experimentally by Liu and Gollub (1990). To our knowledge, no experimental work on the stability of Herschel-Bulkley fluids has been performed yet, there is only the theoretical study of Balmforth and Liu in 2004. They proposed a linear stability analysis, at the order 0 in the thickness parameter, and they found a critical Reynolds number that depends solely on B, the Bingham number, and n, the fluid power index.

Experiment setup

The experiments were carried out in an inclined channel of length 2 m and width 0.5 m, in which a flowing film of carbopol 980 was perturbed at the inlet, and waves recorded further downstream, as presented figure 1-a). In each experiment, we imposed the frequency f, the flow rate q and the angle ϕ. The perturbation was recorded by measuring the local thickness with a laser position sensor at various positions along the flow direction. A careful Fourier analysis allowed us to extract both the wave number k and attenuation factor α. The rheological properties of the fluid were measured with a cone-plate rheometer several times during the experiments, and found constant over the relevant time scales (1 day).

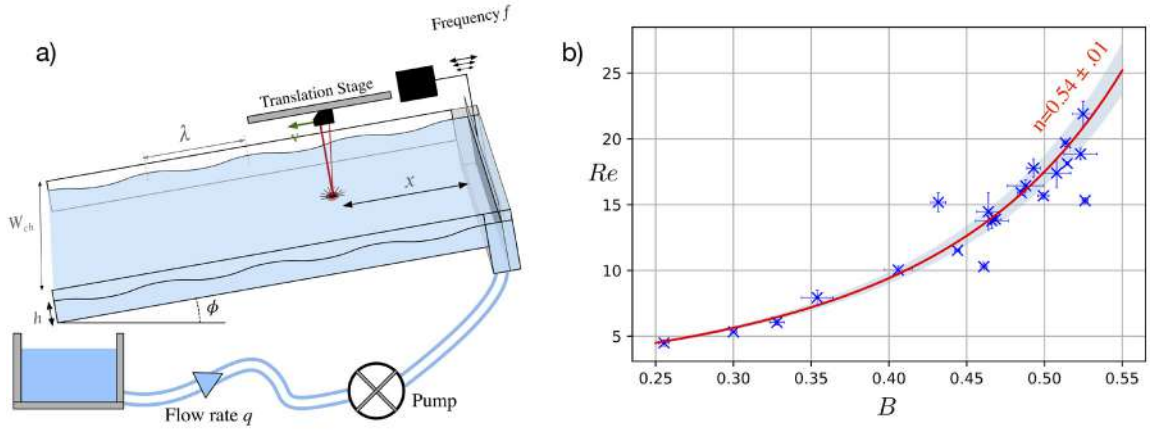

Figure 1: a) scheme of the experimental setup. b) Critical Reynolds number vs Bingham number. Blue crosses : experimental points. Red line : theory by Balmforth and Liu for $n = 0.54$.

*Corresponding author. E-mail: simon.dagois-bohy@univ-lyon1.fr.

Results

By varying the frequency at constant flow rate and angle, we determined the neutral frequency for a given flow rate (i.e. the frequency for which waves are neither amplified nor damped). By repeating these measurements for different flow rates, we were able to determine a critical Reynolds number Re_c and Bingham number B_c, for which this neutral frequency drops to zero. When $Re < Re_c$ or when $B > B_c$, the film is always stable. Finally, we repeated this analysis at different angles and for different concentration of carbopol, in order to measure different couples of (Re_c, B_c). In figure 1-b), we present our measurements together with the prediction of Balmforth and Liu for $n = 0.54$, showing a very good agreement between the two.

References

[1] Benjamin, T. B., Wave formation in laminar flow down an inclined plane. *J. Fluid Mech.* **2** (06), 554–573, 1957.
[2] Liu, J., Paul, J. D. & Gollub, J. P. Measurements of the primary instabilities of film flows. *J. Fluid Mech.* **250**, 69–101.1993
[3] Balmforth N.J, Liu J.J, Roll waves in mud, *J. Fluid Mech.*, **519** : 33–54, 2004

ANISOTROPIC EFFECTIVE VISCOSITY OF SHORT-FIBER SUSPENSIONS

Róbert Bertóti*[1], Daniel Wicht[1], Matti Schneider[1], and Thomas Böhlke[1]
[1]Chair for Continuum Mechanics, Institute of Engineering Mechanics, Karlsruhe Institute of Technology (KIT), Karlsruhe, Germany

Summary For mold filling simulations of short-fiber suspensions, it is efficient to model the fiber-matrix mixture as a homogenized fluid with effective tensorial viscosity which can be anisotropic. Mean-field homogenization theories, based on different assumptions, can be used to predict the anisotropy of the effective viscosity depending on the microstructure parameters: matrix shear viscosity, fiber length to diameter aspect ratio, fiber volume content and fiber orientation distribution. But as far as the authors know, there are no real experiments – because of complexity – which could be used to evaluate the predicted anisotropy of these theories. For this reason numerical experiments, i.e. full-field simulations are performed. The numerical results are used to evaluate and improve the analytical predictions of a mean-field homogenization theory.

ANISOTROPIC EFFECTIVE VISCOSITY

For mold filling simulations of incompressible fiber suspensions the effective, deviatoric Cauchy-stress $\bar{\boldsymbol{\sigma}}'$ is assumed to be the linear mapping of the effective viscosity tensor $\bar{\mathbb{V}}$ and the deviatoric strain rate tensor $\bar{\boldsymbol{D}}'$, noted in tensor and in index notation as

$$\bar{\boldsymbol{\sigma}}' = \bar{\mathbb{V}}[\bar{\boldsymbol{D}}'], \qquad \bar{\sigma}'_{ij} = \bar{V}_{ijkl}\bar{D}'_{kl}, \tag{1}$$

respectively. The effective viscosity tensor $\bar{\mathbb{V}}$ can be parameterized with the help of four variables [1], namely the effective scalar viscosity $\bar{\eta}$, the shear number $\bar{N}_\mathrm{s}$, the particle number $\bar{N}_\mathrm{p}$ and the fourth-order fiber orientation tensor $\bar{\mathbb{N}}$ as

$$\bar{\mathbb{V}}(\bar{\eta}, \bar{N}_\mathrm{s}, \bar{N}_\mathrm{p}, \bar{\mathbb{N}}) = \mathbb{P}_2 \left(2\bar{\eta}\left(\mathbb{P}_2 + \bar{N}_\mathrm{s}\left(\bar{\boldsymbol{N}}\square\mathbf{1} + \mathbf{1}\square\bar{\boldsymbol{N}}\right) + \bar{N}_\mathrm{p}\bar{\mathbb{N}}\right)\right)\mathbb{P}_2, \tag{2}$$

where $\mathbb{P}_2$ is the deviatoric identity tensor of fourth order, $\bar{\boldsymbol{N}} = \bar{\mathbb{N}}[\mathbf{1}]$ is the second-order fiber orientation tensor, $\mathbf{1}$ is the second-order identity tensor and the boxproduct $\square$ is defined by $(\boldsymbol{A}\square\boldsymbol{B})[\boldsymbol{C}] \mathrel{\widehat{=}} A_{ij}C_{jk}B_{kl}$. The viscosity parameters $\bar{\eta}$, $\bar{N}_\mathrm{s}$ and $\bar{N}_\mathrm{p}$ depend on the microstucture of the suspension, i.e. on the matrix viscosity η_m, on the fiber volume fraction $\bar{c}_\mathrm{f}$ and on the fiber aspect ratio l/d, where l denotes the fiber length and d the fiber diameter.

MEAN-FIELD HOMOGENIZATION

Let $\bar{\mathbb{V}}^\mathrm{mf}$ note the viscosity tensor determined by mean-field homogenization [2]. The directional dependency of the effective elongational viscosity $\bar{\eta}_\mathrm{el}$ and of the effective shear viscosity $\bar{\eta}_\mathrm{sh}$ qualifies and quantifies the anisotropy of $\bar{\mathbb{V}}^\mathrm{mf}$. The dimensionless $\bar{\eta}_\mathrm{el}/\eta_\mathrm{m}$ and $\bar{\eta}_\mathrm{sh}/\eta_\mathrm{m}$ are depicted in Fig. 1, considering horizontally aligned short-fibers in the suspension.

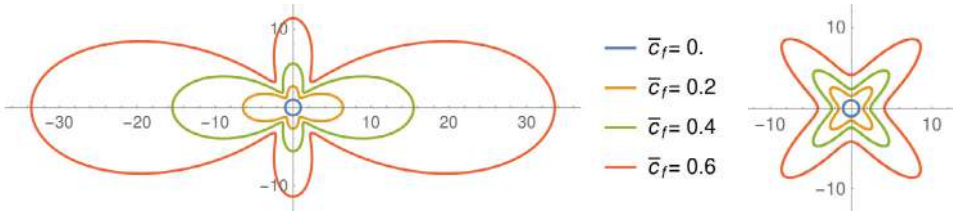

Figure 1: The directional dependency of the effective elongational viscosity $\bar{\eta}_\mathrm{el}$ (left) and of the effective shear viscosity $\bar{\eta}_\mathrm{sh}$ (right) relative to η_m, considering horizontally aligned short-fibers in the suspension, for $l/d = 10$ and different $\bar{c}_\mathrm{f}$ fiber volume fractions. The polar angel corresponds to the direction and the radius to the value.

FULL-FIELD HOMOGENIZATION

To involve more information about the microstrocture in $\bar{\mathbb{V}}$, it is also determined through numerical full-field homogenization based on [3]. With the full-field approach the spatial distribution of the fibers and the effect of the investigated volume element size can also be considered. For the full-field homogenization 128 representative microstructures are generated based on [4], see for examples Fig. 2, depicting the three extreme, i.e. unidirectional (ud), planar isotropic (piso), isotropic (iso), and a frequently formed (7715) fiber orientation state [5]. The corresponding fiber orientation tensors are

$$\boldsymbol{N}_\mathrm{ud} \mathrel{\widehat{=}} \mathrm{diag}(1,0,0),\ \boldsymbol{N}_\mathrm{piso} \mathrel{\widehat{=}} \mathrm{diag}(0.5,0.5,0),\ \boldsymbol{N}_\mathrm{iso} \mathrel{\widehat{=}} \mathrm{diag}(0.33,0.33,0.33),\ \boldsymbol{N}_{7715} \mathrel{\widehat{=}} \mathrm{diag}(0.77,0.15,0), \tag{3}$$

respectively. The numerically determined viscosity tensor $\bar{\mathbb{V}}^\mathrm{num}$ is considered as reference solution. Assuming that the viscosity tensor has the form (2), a fitted viscosity tensor $\bar{\mathbb{V}}^\mathrm{fit}(\bar{\eta}, \bar{N}_\mathrm{s}, \bar{N}_\mathrm{p}, \bar{\mathbb{N}})$ and the errors e^fit and e^mf are determined through

$$e^\mathrm{fit} := ||\bar{\mathbb{V}}^\mathrm{fit} - \bar{\mathbb{V}}^\mathrm{num}||/||\bar{\mathbb{V}}^\mathrm{num}|| \to \min_{\bar{\eta}, \bar{N}_\mathrm{s}, \bar{N}_\mathrm{p}}, \quad e^\mathrm{mf} := ||\bar{\mathbb{V}}^\mathrm{mf} - \bar{\mathbb{V}}^\mathrm{num}||/||\bar{\mathbb{V}}^\mathrm{num}||, \tag{4}$$

*Corresponding author. E-mail: robert.bertoti@kit.edu.

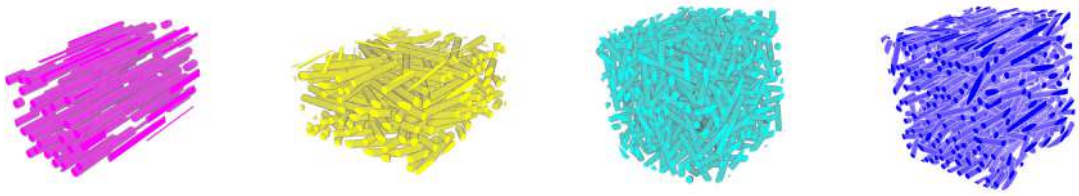

Figure 2: Examples for synthetic microstructures, from left to right: unidirectional (ud), planar isotropic (piso), isotropic (iso) and a frequently formed (7715) fiber orientation state, belonging to the fiber orientation tensors of (3).

respectively, where $\bar{\mathbb{V}}^{\mathrm{mf}}$ is the viscosity tensor determined by mean-field homogenization [2]. The viscosity parameters $\bar{\eta}$, $\bar{N}_{\mathrm{s}}$ and $\bar{N}_{\mathrm{p}}$ of the fitted viscosity tensor $\bar{\mathbb{V}}^{\mathrm{fit}}$ are determined through minimizing the error e^{fit} (4) by a sequential least square algorithm.

COMPARISON OF THE MODELS

The fast predictions of the mean-field approach and the expensive results of the full-field simulations will be compared in the presentation. The similarities and the differences will be shown on hand of the viscosity parameters and the errors e^{mf} vs. e^{fit}. The results considering all four orientation states of Fig. 2 will be discussed in the talk.

CONCLUSIONS

The expensive, numerically determined $\bar{\mathbb{V}}^{\mathrm{num}}$ is almost exactly reproduced by fitting the parameters of (2) to the numerical solution. Through the fitting a relative error $e^{\mathrm{fit}} < 3.5\%$ is reached which is notably smaller than the relative error of the mean-field model $e^{\mathrm{mf}} < 18\%$, considering all investigated orientation cases. Further investigations are needed for higher aspect ratios and to judge, whether the performance of the fitted model is similarly good in the case of non-Newtonian matrix material as in the investigated Newtonian case.

References

[1] Tucker C. Flow regimes for fiber suspensions in narrow gaps. *Journal of Non-Newtonian fluid mechanics* **39**(3):239-268, 1991.

[2] Bertóti R., Böhlke T. Flow-induced anisotropic viscosity in short FRPs. *Mechanics of Advanced Materials and Modern Processes* **3**(1):1-12, 2017.

[3] Schneider M. On the effective viscosity of a periodic suspension–analysis of primal and dual formulations for Newtonian and non-Newtonian solvents. *Mathematical Methods in the Applied Sciences* **39**(12):3309-3327, 2016.

[4] Schneider M. The sequential addition and migration method to generate representative volume elements for the homogenization of short fiber reinforced plastics. *Computational Mechanics* **59**(2):247-263, 2017.

[5] Köbler J., Schneider M., Ospald F., Andrä H., Müller R. Fiber orientation interpolation for the multiscale analysis of short fiber reinforced composite parts. *Computational Mechanics* **61**(6):729-750, 2018.

THE EFFECT OF VISCOELASTICITY IN LUBRICATED CONTACTS

Humayun Ahmed*[1] and Luca Biancofiore[1]
[1]Department of Mechanical Engineering, Bilkent University, Ankara, Turkey

Summary Lubrication is essential to improve the performance of sliding surfaces. Lubricants are carefully designed to account for thermodynamic and *flow* conditions. Particularly, they can exhibit strong viscoelastic effects, if polymers are added. In this study a novel 1D viscoelastic Reynolds equation is derived based on the Oldroyd-B constitutive relation. The model is compared with direct numerical simulations of thin films for a parabolic slider. The results are in good qualitative and quantitative agreement indicating that the simplified model is valid within the context of lubrication theory. The load carrying capacity of the film increases as the lubricant elasticity becomes significant, but stagnates as the polymer relaxation time becomes large compared to the characteristic flow time.

INTRODUCTION

Viscoelasticity within the context of lubrication has received some attention within the past few decades. It has been demonstrated both experimentally [1] and theoretically [2] that the load carrying capacity of the film can be enhanced in the presence of viscoelastic effects. For these reasons, there is a need to improve the models describing viscoelastic lubricants.

Continuum models of viscoelastic fluids consist of a coupling between the Navier-Stokes equations and a constitutive relation describing the growth of the polymeric stress. Hence, the direct numerical simulation (DNS) involves a highly non-linear system of equations and requires special numerical techniques, such as e.g. the Log Conformation Representation (LCR) to obtain accurate solutions if viscoelastic effects are reasonably strong [3].

A linearized model can be achieved by an asymptotic expansion of the Navier-Stokes equations and the constitutive relation, see for example Ref. [2]. However, the only known non-linear model available is the generalized Reynolds equation (an integral-differential equation) [5] which considers only a portion of the material derivative [4]. In this work, a new 1D (spatial) model is proposed which can accurately describe the temporal evolution and spatial distribution of the polymeric stress across the contact and the allowable load for fluids obeying the Oldroyd-B constitutive relation.

MODEL AND NUMERICAL METHOD

The full set of coupled equations for an incompressible, isoviscous fluid consist of the continuity equation (1a), the momentum equation (1b) and the Oldroyd-B constitutive relation (1c)

$$\nabla \cdot \mathbf{u} = 0, \tag{1a}$$

$$Re\frac{D\mathbf{u}}{Dt} = -\nabla p + \beta\nabla^2\mathbf{u} + \nabla\cdot\boldsymbol{\tau}, \tag{1b}$$

$$\boldsymbol{\tau} + De\left(\frac{D\boldsymbol{\tau}}{Dt} - (\nabla\mathbf{u}\boldsymbol{\tau} + \boldsymbol{\tau}\nabla\mathbf{u}^T)\right) = (1-\beta)(\nabla\mathbf{u} + \nabla\mathbf{u}^T), \tag{1c}$$

where $\mathbf{u}$ is the velocity vector, p is the pressure, $\boldsymbol{\tau}$ is the polymeric stress tensor, $\beta = \frac{\mu_s}{\mu_0}$ is the solvent concentration, $Re = \frac{\rho U h_0}{\mu_0}$ is the Reynolds number, μ_s is the solvent viscosity, μ_0 is the total viscosity, h_0 is the maximum height of the film, ρ is the density and U is the surface speed. The Deborah number $De = \lambda\frac{U}{h_0}$, i.e. the ratio of the polymer relaxation time (λ) and characteristic flow time ($\frac{h_0}{U}$), is used to measure the strength of the viscoelastic effects.

Firstly, we assume that (i) the film thickness h is much smaller than the contact length ℓ and (ii) $Re << 1$, hence inertial effects are ignored. Our proposed model stems from the thin film approximation (lubrication theory) of Eqs. 1a-1c, in which we retain the polymer normal stress unlike the GR model (see Ref. [5]). The reduced x-momentum equation is integrated and an explicit equation for pressure is obtained via the reduced continuity equation

$$\frac{d}{dx}\left(\frac{h^3}{12}\frac{dp}{dx}\right) = \frac{\beta}{2}\frac{dh}{dx} + \frac{d}{dx}\left(\int_0^h \frac{y}{h}\int_0^h\int_0^y \frac{d\tau_{xx}}{dx}dy''dy'dy - \int_0^h\int_0^y\int_0^y \frac{d\tau_{xx}}{dx}dy''dy'dy\right)$$
$$+ \frac{d}{dx}\left(\int_0^h \frac{y}{h}\int_0^h \tau_{xy}dy'dy - \int_0^h\int_0^y \tau_{xy}dy'dy\right). \tag{2}$$

where p is the film pressure, τ_{xx} is the normal stress, τ_{xy} is the shear stress and h is the channel height. The integral form of Eq. 2 is further simplified via two key numerical simplifications: (i) we approximate the stress components via polynomials in y ($\tau_{xx} = \sum_{i=1}^{n} F(x,t)y^{i-1}$, $\tau_{xy} = \sum_{i=1}^{n+1} G(x,t)y^{i-1}$ and $\tau_{yy} = \sum_{i=1}^{n+1} K(x,t)y^{i-1}$) and (ii) decouple the stress from the pressure by assuming that the velocity field does not depend on De. Therefore, we obtain the stresses by solving the thin film constitutive equation and obtain the pressure from Eq. 2.

To test the quality of our new model, we have conducted direct numerical simulations of the Eqs. (1a-1c) via *rheoTool* an OpenFOAM based C++ library which takes advantage of LCR [6].

*Corresponding author. E-mail: humayun.ahmed@bilkent.edu.tr

RESULTS

We simulate the lubricant behaviour in a typical parobolic slider, illustrated in fig. 1a. Particularly, we compare for different models the film pressure and the maximum allowable load (L) in Figs. 1b and 1c respectively. The film pressure increases due to an increase (i) in the bulk pressure distribution and (ii) a shift in the positive pressure region. This difference is significant since the pressure within the contact can reach several MPa in magnitude. Finally, a noticeable distortion is symmetry manifests due to the viscoelastic polymers is observed.

Furthermore, all models predict an increase of the load adding viscoelasticity (see Fig. 1c), at least at moderate De. However the degree of increase varies significantly depending on the models. In addition, it should be noted that DNS do not converge at high De due to (i) the high non-linearity of Eqs. 1a-1c and (ii) the strong aspect ratio of the geometry ($\frac{h_0}{\ell} \sim 10^{-3}$). Moreover for the same reasons DNS present some uncertainty as $De \geq 30$ depicted by the gray region in Fig. 1c.

At small De the linearized model predicts the variation accurately but departs from the DNS as De increases, whereas, the generalized Reynolds equation (GR) strongly underestimates the load. Our proposed model (VR) provides excellent quantitative and qualitative agreement with DNS for low to moderate values of De. At large values, it remains within the estimated tolerance region (gray band). From VR, we find a strong non-linear trend in the load which exhibits a maximum value around $De \approx 55$ and eventual saturation at high De. The proposed viscoelastic model imposes no restriction on (i) the value of Deborah number, (ii) the complexity of the surface profile and (iii) mesh size, hence it is computationally appealing.

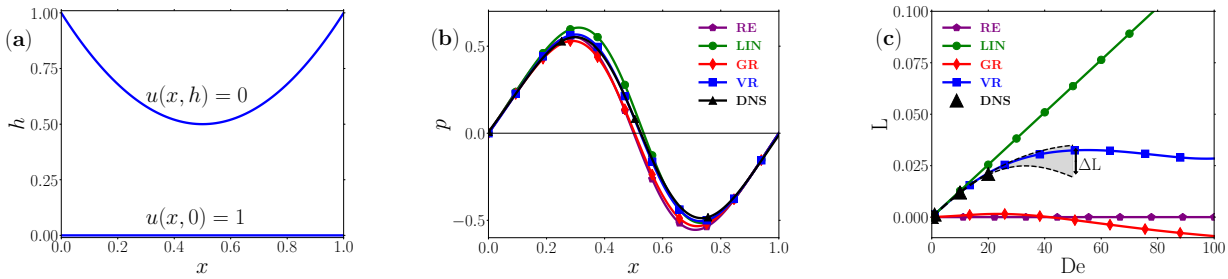

Figure 1: (a) A typical parabolic profile mimicking a lubricated contact in a roller bearing. (b) The film pressure along the channel for $De = 40$ and (c) the load versus De for different models: the Newtonian Reynolds equation (RE), the linearized model (LIN, Ref. [2]), generalized Reynolds equation (GR, Ref. [5]), viscoelastic Reynolds equation (VR) and DNS for $\beta = 0.8$.

CONCLUSIONS

Viscoelasticity can increase the load carrying capacity of the lubricant film. While for small De the linearized model accurately captures the viscoelastic behavior, it fails at moderate to strong De. The new viscoelastic model can capture high-order effects without the complexity, and so with significantly less computational cost, of the existing non-linear models. Furthermore, VR can couple other complex phenomena that can be found in lubricated contacts such as piezo-viscosity (viscosity variation due to pressure), compressibility (density variation) and shear thinning (viscosity variation due to shear stress).

References

[1] Tichy, J. A., and Winer W. O., Journal of Lubrication Technology, 100.1, (1978), 56-64.
[2] Tichy, J. A. Journal of Tribology, 118.2, (1996), 344-348.
[3] Hulsen, M, A., Fattal R., and Kupferman R., Journal of Non-Newtonian Fluid Mechanics, 127.1, (2005), 27-39.
[4] Johnson, K. L., and Tevaarwerk J. L., Proceedings of the Royal Society of London A, 356.1685, (1977), 215-236.
[5] Wolff, R., and Kubo A., Journal of Tribology, 118.1 (1996), 74-82.
[6] Pimenta, F., and Alves M. A., Journal of Non-Newtonian Fluid Mechanics, 239, (2017), 85-104.

INFLUENCE OF POLYMER ADDITIVES ON INVARIANTS OF THE VELOCITY GRADIENT NEAR A TURBULENT/NON-TURBULENT INTERFACE STUDIED BY DIRECT NUMERICAL SIMULATIONS

Hugo Abreu*[1], Fernando T. Pinho[2], and Carlos B. da Silva[1]
1LAETA,IDMEC,Instituto Superior Técnico,Universidade de Lisboa,Lisboa,Portugal2CEFT,FEUP, Universidade do Porto, Porto, Portugal

Summary The motivation for this work is study the influence of the polymer additives on the microscales of a turbulent flow, namely on the turbulent entrainment process. In order to achieve this, the attention is given to the T/NT interface separating the turbulent and the irrotational flow regions. The objective is perform a DNS simulation of a shear free turbulence (SFT) and observe the physical mechanisms and dynamics present at this interface, the ones responsible for turbulent entrainment. The study of the invariants across this interface allows a detailed characterization of the dynamics, geometry and topology of the flow during the entrainment. Viscoelastic solutions simulated by means of the FENE-P model, show to produce interfaces with smoother features and larger scales, more importantly turbulent fronts in dilute polymer solution propagate less than their Newtonian equivalents.

DNS: SHEAR FREE TURBULENCE WITH AND WITHOUT POLYMER ADDITIVES

In order to gain physical insight into the phenomenon the use of Direct Numerical Simulations (DNS) has gained prominence with the evolution of computational resources, since DNS of viscoelastic fluid flows is significantly more expensive than its Newtonian counterpart for a number of reasons. Most of these simulations have been carried out for fluids described by the Finitely Extensible Non-linear Elastic[1] constitutive equation with the dumbbell spring force described through the simplified Peterlin's closure[2], henceforth denoted as the FENE-P model.

More recent investigations on the effect of viscoelasticity upon inertial turbulence has benefited from a more fundamental approach in which the effects of walls and inhomogeneities have been removed in order to focus on the inherent turbulent processes, as in the DNS investigations of forced homogeneous isotropic turbulence of Liberzon et al. [3], De Angelis et al. [4], Ouellette et al. [5] and Valente et al. [6]. In particular, the most recent investigations of FHIT with polymer solutions have shown the reduction of the classical energy cascade with a concomitant increase of the energy directly dissipated by the polymer[6],[7].

Our current understanding of these polymer-induced modifications has not been accompanied by equally relevant issues that have been poorly investigated. Specifically, if the turbulence exists in a sea of irrotational fluid how does the propagation of the turbulence of polymer-laden fluid takes place and how are the mechanisms of entrainment modified by the presence of the polymer? These are important issues to understand, amongst others, the growth rate of a turbulent jet of a polymer solution, its rates of mixing, heat or momentum transfer. Through DNS of viscoelastic fluids described by the FENE-P model, in this work, we precisely investigate the effects of flow viscoelasticity upon the characteristics of the turbulent/ non-turbulent interface, its propagation and the inherent mechanisms associated with turbulence entrainment.

Figure 1 shows that as compared with Newtonian fluid case, much less but wider tube-like vortex structures in the SFT for the polymer solution cases. This appearance of vortex tube structure also reflects a decrease in enstrophy, since the enstrophy indicates the strength of the tube-like vortex structures and mainly is generated by the stretching of the tube-like vortex structures.

(a) (b) (c)

Figure 1: (Isometric view) Constant Q isosurface ($Q = 100s^{-2}$) for a Newtonian fluid (a), viscoelastic fluid with $\tau_p = 0.025$s (b), and viscoelastic fluid with $\tau_p = 0.200$s (c).

Through the analysis of the physical meanings represented by Q and R, clear physical images for the topological dynamics characteristics can be obtained, such as the joint PDFs plots of Q and R in Figure 2. However, it can be seen that the tails of the teardrop shapes have been changed for the polymer solution cases compared its Newtonian fluid counterpart: the large-R and Q regions have shrunk greatly, which indicates the inhibition of small-scale vortices.

*Corresponding author. E-mail: hugo.abreu@tecnico.ulisboa.pt.

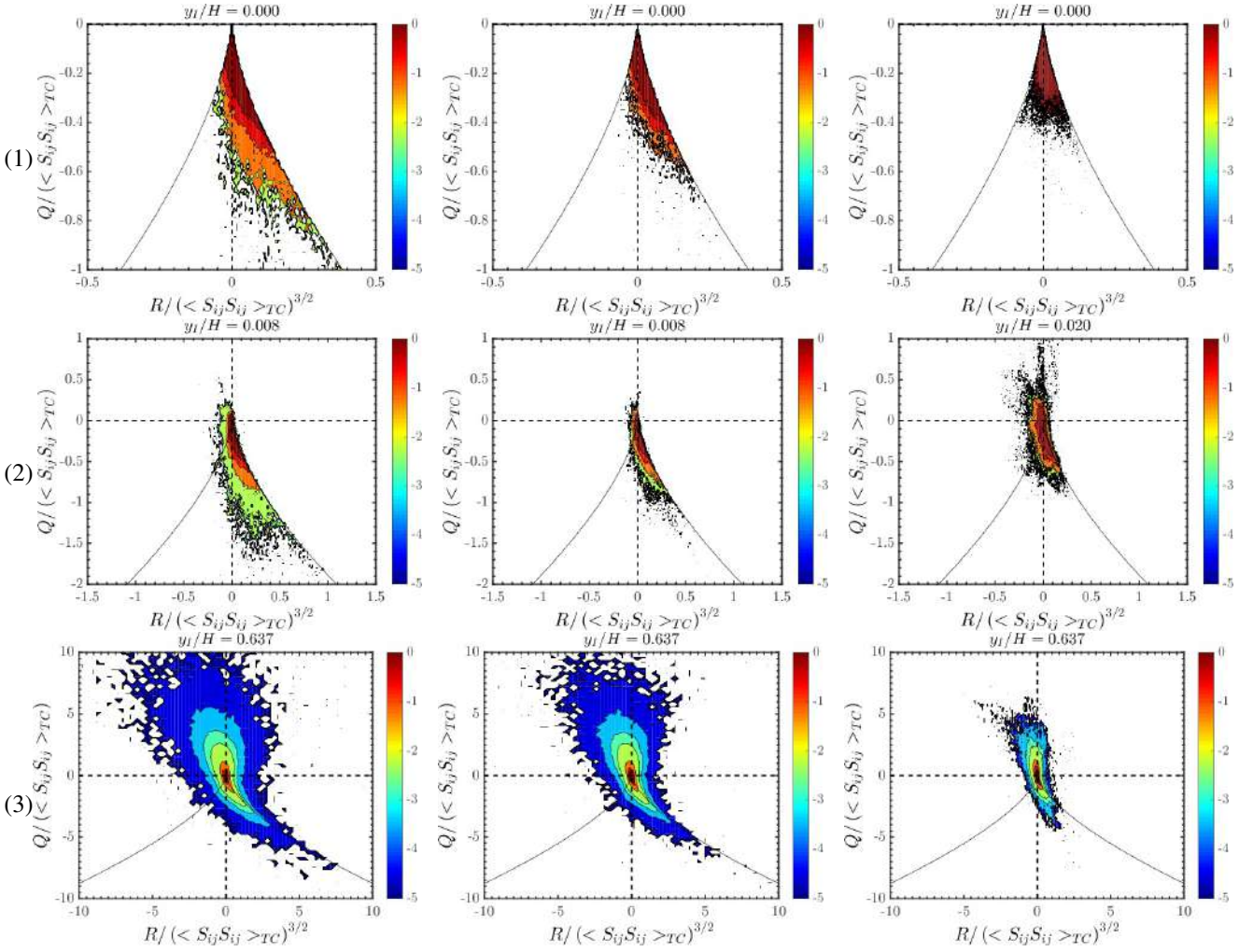

Figure 2: Joint PDFs of R and Q at turbulent non-turbulent (T/NT) interface (1), point of maximum diffusion of the enstrophy (2) and turbulent core (3), for a Newtonian fluid (a), viscoelastic fluid with $\tau_p = 0.025$s, and a viscoelastic fluid with $\tau_p = 0.200$s (c).

CONCLUSIONS

The topological dynamics analysis for the velocity gradient tensor of the shear free turbulence with/without polymer additives has been performed in this paper to the explore the effect of viscoelasticity on the turbulence structures near of the turbulent/non-turbulent interface.

References

[1] Bird R. B., Curtiss C. F., Armstrong R. C., Hassager O. Dynamics of polymeric liquids. Volume 2: Kinetic theory. John Wiley & Sons, 1987.
[2] Bird R. B., Dotson P. J., Johnson N. L. Polymer solution rheology based on a finitely extensible bead-spring chain model. *J. Non-Newtonian Fluid Mech.* **7**: 213-235, 1980.
[3] Liberzon A., Holzner M., Luthi B., Guala M., Kinzelbach W. On turbulent entrainment and dissipation in dilute polymer solutions. *Phys. Fluids* **21**: 035107, 2009.
[4] de Angelis E.,Casciola C. M., Benzi R., Piva R. Homogeneous isotropic turbulence in dilute polymers. *J. Fluid Mech.* **53**: 1-10, 2005.
[5] Ouellette N. T., Xu H., Bodenschatz E. Bulk turbulence in dilute polymer solutions. *J. Fluid Mech.* **629**: 375-385, 2009.
[6] Valente P. C., da Silva C. B., Pinho F. T. The effect of viscoelasticity on the turbulent kinetic cascade. *J. Fluid Mech.* **760**: 39-62, 2014.
[7] Valente P. C., da Silva C. B., Pinho F. T. Energy spectra in elasto-inertial turbulence. *Phys. Fluids* **28**: 075108, 2016.

AN IDEA FOR NON-INVASIVE IN-LINE RHEOMETRY BASED ON SPATIO-TEMPORAL VELOCITY INFORMATION

Yuji Tasaka*[1], Taiki Yoshida[1], Kohei Ohie[1], and Yuichi Murai[1]
1Laboratory for Flow Control, Faculty of Engineering, Hokkaido University, Sapporo, Japan

Summary A novel algorithm for realizing non-invasive in-line rheometry was proposed based on spatio-temporal velocity information that will be measured by ultrasonic velocity profiling. The main concept is substituting velocity data into the equation of motion and a constitutive equation describing rheology, on frequency domain, and thus the rheological properties are determined by minimizing the residual in the equations. The algorithm was evaluated using theoretically derived velocity data of pulsatile pipe flows.

INTRODUCTION

Rheological evaluation of complex materials in manufacturing processes is one of the important issues of rheology, and development of rheometry that is able to do the evaluation in-line and real time has great importance to improve productivity, quality and safety in the processes. Recent developments of ultrasonic velocity profiling provided invention of UVP-PD method that evaluates non-Newtonian viscosity utilizing time-averaged velocity profile information measured by ultrasonic velocity profiling (UVP) and pressure difference (PD) along a pipe [1]; rheological properties are determined as best fit parameters on a constitutive equation of rheology by comparing between the measured velocity profiles and those derived from the equation of motion, the constitutive equation and PD information. The method is, however, still in development for practical use in industry; PD measurement requires insert of pressure transducers in a pipe getting avoided in factories for safe issue; using time-averaged velocity profile cannot access viscoelastic characteristics of materials. Here we propose a novel algorithm of ultrasonic in-line rheometry to avoid PD measurement and to allow characterization of viscoelastic materials using unsteadiness of fluid motion. Main concept of the algorithm is from our recent development of ultrasonic spinning rheometry [2, 3] that evaluates rheology of test fluids by analyzing spatio-temporal velocity information measured by UVP in an oscillating cylindrical vessel on the equation of motion for unsteady flows.

ALGORITHM OF IN-LINE RHEOMETRY

Unsteady laminar pipe flows of general fluids with density ρ under assumption of one-directional flow can be described by following equation of motion,

$$\rho\frac{\partial u}{\partial t} = \alpha(t) + \frac{\partial \tau}{\partial r} + \frac{\tau}{r}, \tag{1}$$

where $\alpha(t) = -\partial p/\partial x$ demotes unsteady pressure gradient in the flow direction. Relation between Shear stress τ and shear rate $\dot{\gamma}$ is expressed by rheological model as constitutive equation,

$$\tau = h(\dot{\gamma}; \Pi_1, \Pi_2, \Pi_3, \cdots), \ \dot{\gamma} = \frac{\partial u}{\partial r} \tag{2}$$

with some constants, $\Pi_1, \Pi_2, \Pi_3, \cdots$, as rheological properties. Assuming that the velocity profile $u(r,t)$ is given by measurements, the equation system on Eq. (1) and (2) has unknowns, $\alpha(t)$ and rheological properties; Given information of the velocity profiles cannot close the system. Here we take Fourier transform on Eq. (1), and assuming that the unsteady flow has dominant frequency component $\omega = \omega_0$. The equation of motion is reduced into ordinal differential equation,

$$i\rho\omega_0\hat{u}(r;\omega_0) = \hat{\alpha}(\omega_0) + \left(\frac{d}{dr} + \frac{1}{r}\right)\hat{\tau}(r;\omega_0), \tag{3}$$

where $\hat{}$ denotes Fourier-transformed function, and $\hat{\alpha}(\omega_0)$ is complex constant. Velocity profiles are given as N-points discrete data in the radial direction, $u(r_n,t),\ n = 1, 2, \cdots, N$, and thus the equation can be closed. To determine the multiple unknowns, cost function,

$$F[\hat{\alpha}(\omega_0), \Pi_1, \Pi_2, \Pi_3, \cdots] = \sum_{n=0}^{N}\left| i\rho\omega_0\hat{u}(r_n;\omega_0) - \hat{\alpha}(\omega_0) - \left(\left.\frac{d}{dr}\right|_{r_n} + \frac{1}{r_n}\right)\hat{\tau}(r_n;\omega_0)\right|^2 \tag{4}$$

is used, and thus the unknowns are determined by minimizing the function, i.e.,

$$\min F[\hat{\alpha}(\omega_0), \Pi_1, \Pi_2, \Pi_3, \cdots] \Longrightarrow \Re[\hat{\alpha}(\omega_0)], \Im[\hat{\alpha}(\omega_0)], \Pi_1, \Pi_2, \Pi_3, \cdots .$$

*Corresponding author. E-mail: tasaka@eng.hokudai.ac.jp

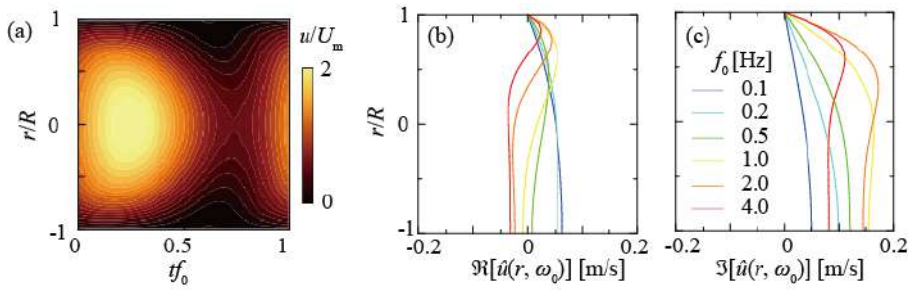

Figure 1: Samples of velocity information calculated from analytic solution of pulsatile flow ($\nu = 100$ mm^2/s, $U_\mathrm{m} = 0.2$ m/s, $U_\mathrm{o} = 0.1$ m/s); (a) spatio-temporal velocity map for one period ($f_0 = 0.5$ Hz), radial profiles of (b) real and (c) imaginary part of Fourier component corresponding to $f = f_0$ for different f_0

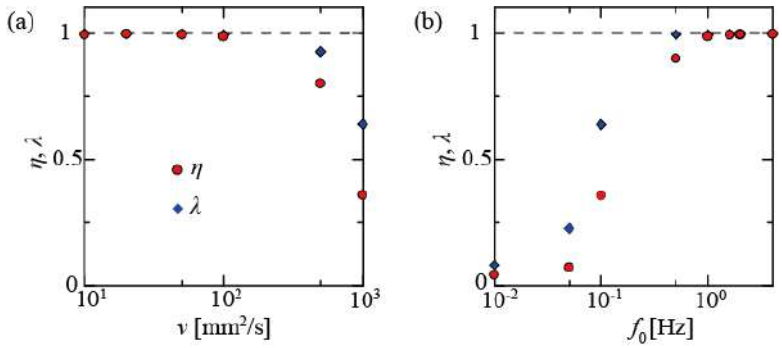

Figure 2: Influence of (a) viscosity and (b) oscillation frequency on estimated values of viscosity and pressure amplitude for $f_0 = 1$ Hz and $\nu = 100$ mm^2/s in each investigation

DEMONSTRATION OF VISCOMETRY ON IDEAL NUMERICAL VELOCITY DATA

We demonstrate the algorithm adopting Newton's law of viscosity, $\tau = \rho\nu\partial u/\partial r$ with kinematic viscosity ν, in this system, as viscometry to simplify the problem. Numerical data sets of velocity are calculated from analytically derived unsteady velocity profile of pulsatile flow, combination of steady Poiseuille flow $u_\mathrm{m}(r)$ and periodically oscillating flow $u_\mathrm{o}(r,t)$ as $u(r,t) = u_m(r) + u_\mathrm{o}(r,t)$. In the data set, maximum velocities of u_m and u_o are set constant, $U_\mathrm{m} = 0.2$ m/s and $U_\mathrm{o} = 0.1$ m/s, respectively, while ν and oscillation frequency of the pulsatile flows $f_0 = \omega_0/(2\pi)$ are modified to evaluate capability of the algorithm. Two normalized values, $\eta = \nu_\mathrm{est}/\nu_\mathrm{set}$ and $\lambda = |\hat{\alpha}_\mathrm{est}|/|\hat{\alpha}_\mathrm{set}|$, are investigated as indicators of successful evaluation of rheology, where subscripts "set" and "est" are given and evaluated values.

A sample of spatio-temporal velocity data and Fourier components of velocity information, real $\Re$ and imaginary $\Im$ part, calculated for $\nu = 100$ mm^2/s and different frequencies are shown in Fig. 1, where R (= 25.4 mm) denotes radius of the pipe. It is easily deduced that velocity data obtained at out of viscous layer, $r > \delta_\mathrm{v} \approx \sqrt{\nu/\omega_0}$, has less information about viscosity, while the pressure estimation is not affected. Here we evaluate applicability of algorithm; how large viscosity or how low frequency conditions can be dealt with. Results of evaluation for influences of the viscosity and the frequency are summarized in Fig. 2, where f_0 and ν are kept constant at 1 Hz and 100 mm^2/s in each evaluation. The both fractions η and λ detach from unity around ν =100 mm^2/s and 1 Hz for high viscosities and low frequencies, where the points are close to conditions $\delta_\mathrm{v} \approx R$ in the set conditions. These results suggest that cases of viscosities dominating behaviors of the frequency modes reduce the quality of estimation.

CONCLUSIONS

We proposed a novel algorithm to realize non-invasive in-line rheometry utilizing spatio-temporal velocity data, and applicability of the algorithm was evaluated in viscosity estimation using velocity data calculated from theoretically derived formula of pulsatile flows. The algorithm has certain measurable range of viscosity determined by thickness of viscous layer. More detailed discussions will be given in the corresponding talk.

References

[1] Ouriev B., Windhab E. J. Rheological study of concentrated suspensions in pressure-driven shear flow using novel in-line ultrasound Doppler method. *Exp. Fluids* **32**: 204–211, 2002.

[2] Tasaka Y., Yoshida T., Rapberger R., Murai Y. Linear viscoelastic analysis using frequency-domain algorithm on oscillating circular shear flows for bubble suspensions. *Rheol. Acta* **57**: 229–240, 2018.

[3] Yoshida T., Tasaka Y., Murai Y. Efficacy assessments in ultrasonic spinning rheometry: Linear viscoelastic analysis on non-Newtonian fluids. *J. Rheol.* **63**: 503-516, 2019.

A NOVEL MULTIPLE RHEOLOGY MAPPING BY ULTRASONIC SPINNING RHEOMETRY

Kohei Ohie*[1], Taiki Yoshida[2], Hyun Jin Park[2], Yuji Tasaka[2] and Yuichi Murai[2]
[1]Laboratory for Flow Control, Graduate School of Engineering, Hokkaido University, Sapporo, Japan
[2]Laboratory for Flow Control, Faculty of Engineering, Hokkaido University, Sapporo, Japan

Summary We propose a novel rheological property map representing both shear rate and frequency dependence of viscoelasticity evaluated by ultrasonic spinning rheometry, which can extract rheological properties from velocity distribution in an oscillating cylindrical vessel through the equation of motion. Rheological properties of carboxymethyl cellulose aqueous solution were evaluated as a typical demonstration of rheological evaluations using the map. Usefulness of the map on evaluations is discussed through considering complex rheological properties of the solution.

INTRODUCTION

Rheological properties measurement has great importance on design optimization of industrial plants, quality control of food processing and performance evaluation of working fluids. Fluidity materials targeted by rheology have complexities which have risks to collapse ideal conditions regarded in conventional torque rheometer, such as wall slip, shear banding and jamming. Ultrasonic spinning rheometry (USR), which is based on velocity information obtained by ultrasonic velocity profiler (UVP), has conquered these fatal problems. Success stories of USR have been reported for measurement of fluids with yield stress and temporal change of rheological properties [1, 2]. These complex fluids have microscopic inner structures, and they induce shear rate and frequency dependence of rheological properties. For better understanding rheology of complex fluids, we propose a novel rheological property map by USR. The map reveals both shear rate and frequency dependence of rheological properties.

EXPERIMENTAL APPARATUS AND ANALYTICAL METHOD

An acrylic cylindrical vessel (diameter: 154 mm, height: 300 mm, thickness: 3 mm) filled with a test fluid up to 240 mm from the bottom is installed centre of a water bath for propagation of ultrasonic wave and for temperature control [Fig. 1]. The vessel is driven by a stepping motor with oscillation frequency f_0 and angle Θ. Spatiotemporal velocity distribution u_ξ along propagation line of the wave is obtained by UVP, where the ultrasonic transducer is installed at off-axis Δy. Linear viscoelastic analysis, an analytical method to quantify viscoelasticity from velocity distribution [3] is adopted, and here, essence of the method is summarized below. Assuming that the flow in the vessel is axisymmetric and radial velocity component is negligible, u_ξ is converted to the azimuthal velocity u_θ along the radial direction by geometric relation $u_\theta = u_\xi\, r/\Delta y$, where the velocity should satisfy Cauchy's equation of motion, $\rho \partial u_\theta/\partial t = (\partial/\partial r + 2/r)\,\tau$; τ indicates the shear stress. Maxwell model, $\tau + (\mu/E)\,\partial\tau/\partial t = \mu\,(\partial/\partial r - 1/r)\,u_\theta$ is utilized just for separation of viscous and elastic contributions to the shear stress, where μ and E denote viscous coefficient and elastic modulus, respectively. Fourier transform is utilized for suppression of measurement noise of UVP. Combining these equations, cost function $F(\mu, E; r) = [i\omega\rho\hat{u}_\theta - (\partial/\partial r + 2/r)\hat{\tau}]^2_{\omega = 2\pi f0}$ is defined where $\hat{u}_\theta$ and $\hat{\tau}$ indicate Fourier-transformed velocity and shear stress, $\mathscr{F}[u_\theta(r, t)]$ and $\mathscr{F}[\tau(r, t)]$, respectively. In optimization problems based on the cost function, μ and E making the cost function minimum are the most proper rheological properties. Solving the optimization problems at every radial position, spatial distributions of μ and E are acquired. Spatiotemporal distribution of shear rate is derived as $\dot{\gamma} = (\partial/\partial r - 1/r)\,u_\theta$, and effective shear rate $\dot{\gamma}_{\mathrm{eff}}(r)$ is obtained by taking effective value of $\dot{\gamma}$ as a representative shear rate at each radial position.

EXAMPLE OF RESULTS

As a demonstration of rheological evaluation using the property map, a viscoelastic fluid, carboxymethyl cellulose (CMC) 1.0 wt.% aqueous solution (Daicel Chemical Co., Ltd., Japan) was chosen as a test fluid. Temperature of the fluid was kept at 25.0 °C by a thermostatic chamber during experiments. Fine particles of highly porous polymer (CHP 20P, Mitsubishi Chemical Co., Ltd., Japan, diameter: 75−150 μm) were added a little to the test fluid as tracer particles for ultrasonic reflection. Ultrasonic transducer (emission frequency is 4 MHz) was set at Δy = 15 mm and 150 mm height from bottom of the vessel. The set height is an adequate height for assumptions in linear viscoelastic analysis. The effective shear rate $\dot{\gamma}_{\mathrm{eff}}(r)$ takes the maximum $O(10\ \mathrm{s}^{-1})$ on the side wall and decreases to $O(1\ \mathrm{s}^{-1})$ toward inner region. USR therefore can obtain $\dot{\gamma}_{\mathrm{eff}} - \mu$ and $\dot{\gamma}_{\mathrm{eff}} - E$ curves which express shear rate dependence only by a set of oscillation parameters (f_0, Θ). Frequency dependence of the rheological properties can be examined by increasing oscillation frequency little by little. Five oscillation conditions were selected as (f_0, Θ) = (0.25 Hz, 480°), (0.50 Hz, 240°), (0.75 Hz, 160°), (1.00 Hz, 120°), (1.25 Hz, 96°). Integrating the results of linear viscoelastic analysis, the rheological property map was obtained [Fig. 2. (a)]. Continuous lines in the map indicates contour of E.

Based on the map, mainly five typical characteristics of the CMC solution can be confirmed. (1) The isolines rising to the right means that the CMC solution expresses more elastic behaviour in higher frequency oscillations. (2) Horizontal

*Corresponding author. E-mail: ohie@ring-me.eng.hokudai.ac.jp.

colour strips of viscosity coefficient are confirmed, which indicates that the CMC solution has no frequency dependence of viscosity in oscillation frequency from 0.25 Hz to 1.25 Hz. (3) Monotonous decrease of viscous coefficient toward high shear rate direction reflects shear thinning characteristic. (4) The CMC solution can be treated as pure viscous fluid on the area surrounded by dotted line [Fig. 2. (b)]. (5) Viscous coefficient on top side of pure viscous area is constant, which means that the CMC solution behaves like a Newtonian fluid in the area.

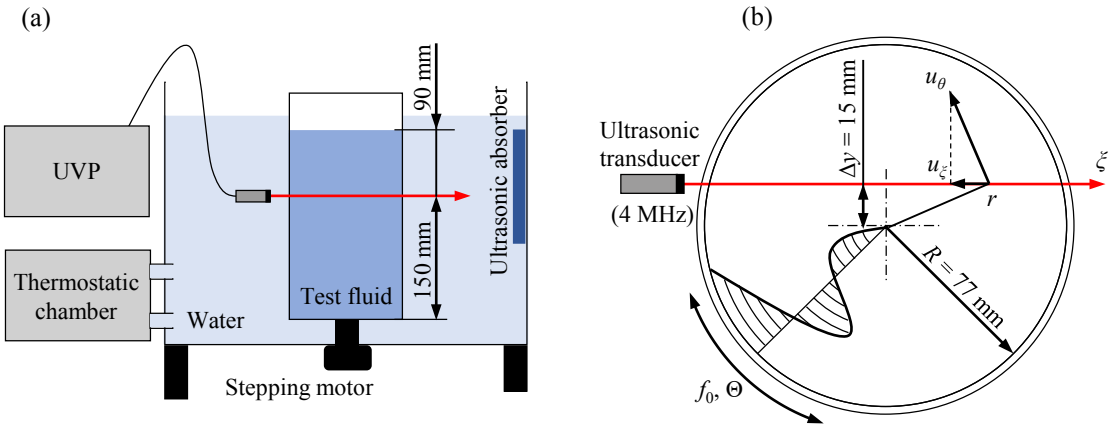

Figure 1. A schematic diagram of experimental setup: (a) side view, and (b) top view.

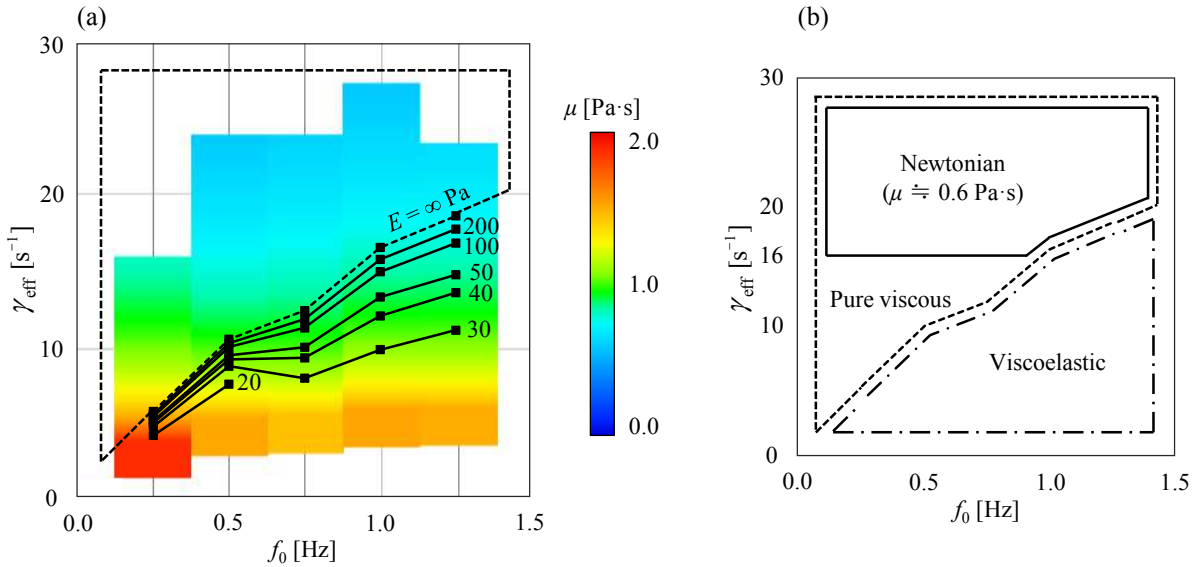

Figure 2. Rheological property map of CMC 1.0 wt.% aqueous solution at 25.0 °C: (a) distribution of viscosity coefficient and elastic modulus, and (b) classification of flow characteristics.

CONCLUSIONS

The CMC solution has usually been treated as a simple shear thinning fluid. However, it widely expresses from viscoelastic to pure viscous, Newtonian behaviours, depending on shear rate and oscillation frequency [Fig. 2]. USR can acquire these rheological properties by measurements with a few oscillation parameters, whereas conventional torque rheometer needs to set not only oscillation frequency conditions but also shear rate conditions. Furthermore, the map obtained by USR is applicable to evaluate more complex fluids such as fluids containing solid or gas phases and fluids with yield stress. Evaluations using the map have high potential for better understanding rheology of complex fluids.

References

[1] Yoshida T., et al., Rheological evaluation of complex fluids using ultrasonic spinning rheometry in an open container, J. Rheol., 61(3), 537-549, 2017.
[2] Yoshida T., et al., Ultrasonic spinning rheometry test on the rheology of gelled food for making better tasting desserts, Phys. Fluids, 31(11), 113101, 2019.
[3] Tasaka Y., et al., Linear viscoelastic analysis using frequency-domain algorithm on oscillating circular shear flows for bubble suspensions, Rheologica Acta, 57(3), 229-240, 2018.

SOLUTION OF TRANSIENT VISCOELASTIC FLOW PROBLEMS APPROXIMATED BY A VMS STABILIZED FINITE ELEMENT FORMULATION USING TIME-DEPENDENT SUBRID-SCALES

Laura Moreno[1], Ramon Codina[1,2], and Joan Baiges *[1]
[1]UniversitatPolitècnicadeCatalunya,JordiGirona1-3,EdificiC1,08034,Barcelona,Spain
[2]Centre Internacional de Mètodes Numèrics en Enginyeria,Gran Capità S/N,08034,Barcelona,Spain

Summary Recent studies indicate that classical residual-base stabilized methods for unsteady incompressible flows may experience difficulties when the time step is small in relation with the spatial grid size. The aim of this work is the design of finite element stabilized techniques based on the Variational Multiscale (VMS) method that allow to compute time-dependent viscoelastic flow problems with high elasticity and considering an anisotropic space-time discretization. Although the main advantage is achieve stable solutions for anisotropic space-time discretizations, other benefits related with elastic problems are proved in this study. In particular, the proposed methods are designed for the standard and logarithmic formulations in order to deal with high Weissenberg number problems, ensuring stability in all cases. A comparison between formulations and stabilization techniques will be performed to demonstrate the efficiency of time-dependent sub-grid scales and the term-by-term methodologies.

INTRODUCTION

Bochev et al. [1] argue that spatial stabilization in conjunction with finite differencing in time implies destabilizing terms and that $\delta t > Ch^2$ (where δt is the time step size, C a positive constant and h the spatial grid size) is a sufficient condition to avoid instabilities. Nevertheless, for anisotropic space-time discretizations, this inequality is not necessarily satisfied, and in fact complications in residual-based stabilized methods are reported. These problems can happen, for instance, when small time steps result from the necessity of accuracy to solve transient problems due to the presence of non-linear terms in the differential equations, a very common issue in viscoelastic flow formulations. In particular, the approximations used in Variational Multiscale (VMS) methods [2] usually neglect the time derivative of the sub-grid scales, resulting in the inequality $\delta t > Ch^2$ being required to obtain stable solutions. Consequently, anisotropic space-time discretizations cannot guarantee stability, as it is argued by Codina et al. [3]. By following these ideas, the present work pursues to expand transient subgrid-scale methods to the viscoelastic flow problem, such as it is presented in [4] for the Navier-Stokes incompressible problem using a split term-by-term method. The computation of viscoelastic flows leads to its own difficulties, especially when elasticity becomes dominant, i.e., when the dimensionless number known as the *Weissenberg number* is high: the so called High Weissenberg Number Problem (HWNP). A new formulation was proposed by Fattal and Kupferman in order to deal with these shortcomings: the so called Logarithmic Conformation Representation. In this sense, in [5] the authors apply this reformulation using a stabilized formulation based on the VMS method.

VISCOELASTIC FLOW PROBLEM

The governing equations for the viscoelastic flow problem in incompressible and isothermic conditions, are the conservation of momentum and mass and a constitutive equation which can be expressed as

$$\rho\frac{\partial \boldsymbol{u}}{\partial t} + \rho\boldsymbol{u}\cdot\nabla\boldsymbol{u} - \nabla\cdot\boldsymbol{T} + \nabla p = \boldsymbol{f} \text{ in } \Omega, t \in]0, t_{\mathrm{f}}[, \tag{1}$$

$$\nabla\cdot\boldsymbol{u} = 0 \text{ in } \Omega, t \in]0, t_{\mathrm{f}}[, \tag{2}$$

$$\frac{1}{2\eta_p}\boldsymbol{\sigma} - \nabla^s\boldsymbol{u} + \frac{\lambda}{2\eta_p}\left(\frac{\partial\boldsymbol{\sigma}}{\partial t} + \boldsymbol{u}\cdot\nabla\boldsymbol{\sigma} - \boldsymbol{\sigma}\cdot\nabla\boldsymbol{u} - (\nabla\boldsymbol{u}^T)\cdot\boldsymbol{\sigma}\right) = \boldsymbol{0}, \text{ in } \Omega, t \in]0, t_{\mathrm{f}}[, \tag{3}$$

where Ω is the domain considered of $\mathbb{R}^d$ (d=2 or 3), whose boundary is $\partial\Omega$, during the time interval $[0, t_{\mathrm{f}}]$, where ρ denotes the constant density, p is the pressure field, $\boldsymbol{u}$ is the velocity field, $\boldsymbol{f}$ is the force field and $\boldsymbol{T}$ is the deviatoric stress tensor. In general, $\boldsymbol{T}$ is defined in terms of a viscous and a viscoelastic contribution as $\boldsymbol{T} = 2\eta_e\nabla^s\boldsymbol{u} + \boldsymbol{\sigma}$. Effective (or solvent) viscosity is denoted by η_e and the polymeric viscosity by η_p. The third equation of the system is the constitutive equation for the viscoelastic stress tensor. We have considered the Oldroyd-B model where λ is the relaxation time. The logarithmic reformulation of the equations is derived basically from a change of variables, where the stress tensor is replaced by $\boldsymbol{\sigma} = \frac{\eta_p}{\lambda_0}(\exp(\boldsymbol{\psi}) - \mathbf{I})$ in (1), (2) and (3). Particularly, λ_0 is linearly dependent with λ and is defined as $\lambda_0 = \max\{k\lambda, \lambda_{0,\min}\}$, being $k \leq 1$ a constant and $\lambda_{0,\min}$ a given threshold. Note that the complete development employed is extensively explained in [5].

*Corresponding author. E-mail: joan.baiges@upc.edu

P1 elements	**Time step** (δt)			
Method	0.050	0.0250	3.125×10^{-3}	1.562×10^{-3}
Static-OSS	Solved	Failed	-	-
Dyn-OSS	Solved	Solved	Solved	Solved
Static-SOSS	Solved	Solved	Solved	Failed
Dyn-SOSS	Solved	Solved	Solved	Solved

Table 1: Solved and failed cases We $= 0.125$, $\alpha_{1,\min} \approx 1.156 \times 10^{-3}$.

	Weissenberg (We)			
Formulation	0.125	0.165	0.25	0.5
Std-Static	Solved	Failed	-	-
Std-Dyn	Solved	Solved	Solved	Failed
Log-Static	Solved	Solved	Failed	-
Log-Dyn	Solved	Solved	Solved	Solved

Table 2: Solved and failed cases for S-OSS formulations,dynamic and quasi-static, $\delta t = 0.1$.

STABILIZED FINITE ELEMENT FORMULATION

The stabilization method departs from the framework described in [2], which consists in splitting the unknowns $\boldsymbol{U}$ in the sum of two components, $\boldsymbol{U}_h$ (component which can be captured by the finite element space) and $\tilde{\boldsymbol{U}}$ (the remainder, called sub-grid scale). Let us suppose that $\mathcal{L}(\hat{\boldsymbol{u}};\cdot)$ is a linear operator for a given $\hat{\boldsymbol{u}}$. Introducing the sub-grid scale decomposition and integrating by parts, the method leads to find $\boldsymbol{U}_h :]0, t_{\mathrm{f}}[\longrightarrow \boldsymbol{\mathcal{X}}_h$ such that

$$\mathcal{G}(\boldsymbol{U}_h, \boldsymbol{V}_h) + B(\boldsymbol{u}_h; \boldsymbol{U}_h, \boldsymbol{V}_h) + \sum_K \langle \tilde{\boldsymbol{U}}, \mathcal{L}^*(\boldsymbol{u}_h; \boldsymbol{V}_h) \rangle_K = L(\boldsymbol{V}_h), \tag{4}$$

for all $\boldsymbol{V}_h \in \boldsymbol{\mathcal{X}}_h$, where B is the bilinear form of the problem and $\mathcal{G}$ the temporal terms, $\mathcal{L}^*(\boldsymbol{u}_h; \boldsymbol{V}_h)$ is the formal adjoint of the operator $\mathcal{L}(\hat{\boldsymbol{u}};\cdot)$ typically without considering boundary conditions, $\tilde{\boldsymbol{U}}$ is the sub-grid scale, which needs to be approximated and has components $\tilde{\boldsymbol{U}}$=$[\tilde{\boldsymbol{u}}, \tilde{p}, \tilde{\boldsymbol{\sigma}}]$. Particularly, $\mathcal{L}(\hat{\boldsymbol{u}};\cdot)$ is the operator associated to the viscoelastic flow problem and $L(\boldsymbol{V}_h)$ comes from the RHS terms in (1) - (3). Once operators $\mathcal{G}$ and $\mathcal{L}$ are defined for both formulations, the sub-grid scales are now the solution of this equation, written in terms of the finite element component:

$$\mathcal{D}_t(\tilde{\boldsymbol{U}}) + \boldsymbol{\alpha}^{-1}\tilde{\boldsymbol{U}} = \tilde{P}[\boldsymbol{F} - \mathcal{G}(\boldsymbol{U}_h) - \mathcal{L}(\boldsymbol{u}_h; \boldsymbol{U}_h)], \tag{5}$$

where we denote $\tilde{P}$ as the L^2 projection onto the space of sub-grid scales, $\mathcal{D}_t(\tilde{\boldsymbol{U}})$ is defined as the temporal derivative of the sub-grid scale and $\boldsymbol{\alpha}$ is taken as a diagonal matrix of stabilization parameters. Apart from the purely residual-based stabilization (denoted by OSS), we propose a term-by term stabilization motivated by the fact that not all the terms of some products provide stability, denoted by S-OSS. The idea of this method is to replace the solution of (5) in (4) but keep only the terms of the form one operator term applied to the unknown by the same operator term applied to the test function, thus neglecting the products of different operators.

NUMERICAL RESULTS AND CONCLUSIONS

The flow over a cylinder problem is used to achieve several objectives: firstly, to compare the various stabilization methods proposed (dynamic and quasi-static formulations) in terms of stability when the time step is small, and when the Weissenberg number increases. In first case, Table 1 shows us that the dynamic method is the most efficient. In the second study, Table 2 we can conclude that dynamic formulations are more effective avoiding elastic instabilities, allowing the computation of fluid flows with a higher Weissenberg number.

The results obtained are particularly remarkable due to the high Weissenberg number reached with the dynamic formulation, which remains stable even if the standard formulation is considered, apart from evident benefits in anisotropic space-time discretizations when the time step is small. The combination of dynamic sub-grid scales and the logarithmic formulation is capable of solving problems with higher elasticity.

References

[1] P. B. Bochev, M. D. Gunzburger, and J. N. Shadid. On inf–sup stabilized finite element methods for transient problems. *Computer Methods in Applied Mechanics and Engineering*, 193(15-16):1471–1489, 2004.

[2] T.J.R. Hughes, G. R. Feijóo, L. Mazzei, and J. Quincy. The variational multiscale method. A paradigm for computational mechanics. *Computer methods in applied mechanics and engineering*, 166(1-2):3–24, 1998.

[3] R. Codina, J. Principe, O. Guasch, and S. Badia. Time dependent subscales in the stabilized finite element approximation of incompressible flow problems. *Computer Methods in Applied Mechanics and Engineering*, 196(21-24):2413–2430, 2007.

[4] E. Castillo and R. Codina. Dynamic term-by-term stabilized finite element formulation using orthogonal subgrid-scales for the incompressible navier–stokes problem. *Computer Methods in Applied Mechanics and Engineering*, 349:701–721, 2019.

[5] L. Moreno, R. Codina, J. Baiges, and E. Castillo. Logarithmic conformation reformulation in viscoelastic flow problems approximated by a vms-type stabilized finite element formulation. *Computer Methods in Applied Mechanics and Engineering*, 354:706–731, 2019.

A PHENOMENOLOGICAL EQUATION FOR THE FRICTION FACTOR OF TURBULENT FLOW OF VISCOELASTIC FLUIDS: FROM THE NEWTONIAN TO THE MAXIMUM DRAG REDUCTION LIMIT

H.R. Anbarlooei[1], C.M.M.Santos[2], F. Ramos[1], and D.O.A. Cruz*[2]
[1]Department of Applied Mathematics, Institute of Mathematics, Federal University of Rio de Janeiro, Brazil
[2]Mechanical Engineering Program, Federal University of Rio de Janeiro (COPPE/UFRJ), Brazil

Summary A novel friction equation is developed for the fluids which follow Oldroyd-B model, using the phenomenological model of Gioia and Chakraborty [1] which connects the Kolmogorov's micro-scales to the wall shear stress. To accomplish this, the kolmogorov's micro-scales for the Newtonian case are extend to the non-Newtonian visco-elastic Oldroyd-B model. The resulted friction equation is then compared with experimental data, where very good agreement has been observed. Finally, the developed friction equation reduces to Blasius equation (Newtonian) and maximum drag reduction asymptote in the limits.

INTRODUCTION

It is well known that the friction coefficient of a turbulent flow, can be reduced by the addition a small amount of some substances to the liquid. Despite the extensive research done since that phenomenon was discovered in the late 40's , no definite explanation for the friction factor drop or even a theoretical approach was developed, that can provide a useful friction equation for this type of flow. In their work of Gioia and Chakraborty (GC) [1], proposed a phenomenological approach that can be used to formulate a variety of frictions equations for different types of non Newtonian fluids turbulent flows [2]. In this work, a friction factor equation is proposed for the turbulent flow of viscoelastic fluids using the Oldroyd B model. The resulting expression is valid from the Newtonian to the maximum drag reduction regime.

PHENOMENOLOGICAL MODEL

In the present work, the phenomenological model developed by Gioia and Chakraborty [1] is extended for the viscoelastic Oldroyd-B model. This model is a combination of the upper convected maxwell (UCM) model with the solvent contribution. The UCM model is described as:

$$\lambda\dot{\tau_p} + \tau_p = \eta_p\dot{\varepsilon}, \tag{1}$$

where λ, η_s, τ and $\dot{\varepsilon}$ are the relaxation time, polymer viscosity, shear stress and strain rate respectively. Assuming a scale analysis of the equation (1) such as $\lambda\tau_p\omega + \tau_p \approx \eta_p\varepsilon\omega$, with frequency scale as $\omega \approx 1/t$, the shear stress can be expressed as:

$$\tau_p \approx \frac{\omega\eta_p}{1+\omega\lambda} \tag{2}$$

Equation (2) represents the polymer stress equation. The solvent stress contributions (τ_s) is given by $\tau_s \approx \omega\eta_s$ (η_s is the solvent viscosity). Therefore, the total shear stress would be:

$$\tau_T \approx \tau_p + \tau_s \approx \frac{\omega\eta_p}{1+\omega\lambda} + \omega\eta_s \tag{3}$$

Following the lines of [2] to obtain Kolmogorov's microscales for the Oldroyd-B model, two conditions must be met: 1- balance between the inertial and the viscous effect ($Re \sim 1$), and 2- dissipation of the input energy at viscous scale ($\varepsilon \sim \tau_T\omega$). Using these two, one could find the following equations for the ω and velocity at Kolmogorov's microscale.

$$\beta\left(\frac{1+\omega\lambda}{1+\beta\omega\lambda}\right)\frac{u^2}{\nu_s\omega} \approx 1 \tag{4}$$

$$\frac{U^3}{L} = \varepsilon = \left(\frac{\omega\eta_p}{1+\omega\lambda} + \omega\eta_s\right)\omega \tag{5}$$

Here, ν_s, u, U and L are the solvent kinematic viscosity, Kolmogorov's velocity scale, integral velocity and integral length scale, respectively. Also the parameter β is defined as $\beta = \eta_s/(\eta_s+\eta_p)$.

Finally, defining the solvent Reynolds number as $Re = \frac{UL}{\nu_s}$, and Deborah number as $De = \frac{\lambda U}{L}$, equations (4) and (5) can be solved for ω_k and u_k as follows:

$$\omega_k^2\left(\frac{1+\beta\omega_k\,De}{1+\omega_k De}\right) = \beta Re \tag{6}$$

$$\frac{u_k}{U} = \sqrt{\frac{\omega_k}{Re\,\beta}\left(\frac{1+\beta\omega_k\,De}{1+\omega_k De}\right)} \tag{7}$$

*Corresponding author. E-mail: doac@mecanica.coppe.ufrj.br.

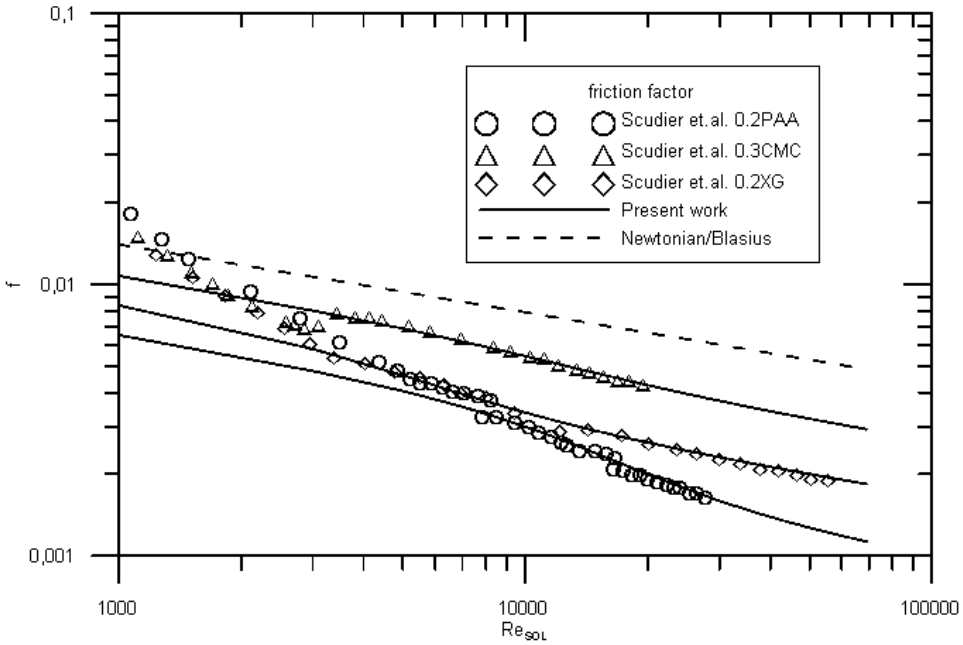

Figure 1: The predictions of the friction factor equation for the visco-elastic fluids compared with experimental data.

According to the phenomenological model of [1], the wall shear stress in pipe can be expressed as $\tau \sim \rho u_k U$. Therefore, the friction factor will be

$$f = \frac{2\tau}{\rho U^2} = \alpha \frac{u_k}{U} = \alpha \sqrt{\frac{\omega_k}{Re\,\beta}\left(\frac{1+\beta\omega_k\,De}{1+\omega_k De}\right)} \tag{8}$$

Figures (1) shows the predictions of the this friction factor, compared with the experimental data of [3]. Here the horizontal axis is the Reynolds based on the wall viscosity. As evident, this simple friction predicts the behaviour of such a complicated fluid successfully. It must noticed that the cases shown here did not reach to the maximum drag reduction limit.

As evident in Equation (8), for the case $De = 0$ this equation reduces to the well-known Blasius equation for the Newtonian fluids ($f \propto Re^{-1/4}$). On the other hand, for $\beta \ll 1$, $De > 1$ and $\omega > 1$, the equation (8) reduces to:

$$f_{MDR} \propto \sqrt{\frac{1}{Re}} \tag{9}$$

This result is similar to the empirical equation proposed in [4] for the maximum drag reduction, and also by Virk's asymptote.

References

[1] Gioia G., Chakraborty P. Turbulent friction in rough pipes and the energy spectrum of the phenomenological theory. *Phys. Rev. Lett.* **96**, 2006.
[2] Anbarlooei H.R., Cruz D.O.A, Ramos F., Santos C., FreireA. S. On the connection between kolmogorov microscales and friction in pipe flows of viscoplastic fuids. *Physica D: Nonlinear Phenomen.* **69**, 2018.
[3] M.P. Escudier M.P., Presti F., Smith S. Drag reduction in the turbulent pipe flow of polymers, *J. Non-Newtonian Fluid Mech.* **81**, 1999.
[4] Aguilar G., Gasljevic K., Matthys E.F. Drag reduction in the turbulent pipe flow of polymers, *Int. J. Heat Mass Transf.* **44**, 2001.

BLOOD RHEOLOGICAL MODELING: UNCERTAINTY QUANTIFICATION OF THE REGRESSION CALIBRATED PARAMETERS

Christos Psevdos[1], George Makrigiorgos [2], Yannis Dimakopoulos [1*], John Tsamopoulos[1]
[1]Department of Chemical Engineering, University of Patras, Patras, Greece
[2]Chemical and Biomolecular Engineering Department, University of California, Berkeley, USA

The following work presents a start-to-finish procedure for performing uncertainty quantification tasks on a tensorial differential hemorheological model that accounts for blood thixotropy, elasticity and viscoplasticity, utilizing open-source tools that researchers and professionals can expect to use with relative ease. This study is based on a specific model but can also provide a detailed roadmap for conducting uncertainty quantification related tasks on similar models encountered in several areas of science and engineering.

INTRODUCTION

Being a complex suspension of various types of cells and proteins, blood demonstrates a profoundly non-Newtonian rheological behaviour [1]. Due to its importance in human physiology, this behaviour has been under heavy scrutiny over the last decades, resulting in the development of multiple rheological models that describe it from different aspects and to various degrees of accuracy. Despite the undeniably great effort put into developing such models, there seems to be a relatively small number of works focused on validating their ability to discriminate between healthy and pathological cases via means of sensitivity analysis (SA). This is especially true for the more complex models that encompass a large number of adjustable parameters in order to accurately depict the changes in blood shear and normal stresses as well as in viscosity under a plethora of varying conditions. Unlike simple constitutive models, whose few parameters are usually acquired directly from experimental data, the tuning of most multi-parametric differential models relies on some form of regression. While this procedure aids greatly in selecting a suitable set of parameters for the given experimental conditions, it provides no readily available information about their statistical properties (distribution shape, confidence intervals, etc.). This lack of information discourages the usage of powerful and widely available SA tools, which, no matter how sophisticated, are heavily reliant on such knowledge [2]. In this work, we present a methodology of conducting uncertainty quantification (UQ) tasks on flows utilizing a thixo-elastoviscoplastic hemorheological model [3,4] that has been calibrated through Least-Squares Regression (LSR) on steady-state and transient experimental data of blood under different shear regimes.

ESTIMATING PARAMETER DISTRIBUTIONS FROM REGRESSION DATA

The data utilized for the LSR of the model parameters originate from three types of experiments, namely: simple shear steady-state, rectangular shear step, and triangular shear step. Accordingly, the shear stress calculated by the model under these experimental conditions is fitted on the aforementioned data. It should be noted that the model also outputs the normal stress along with a blood structure parameter, both of which indirectly affect the shear stress profiles.

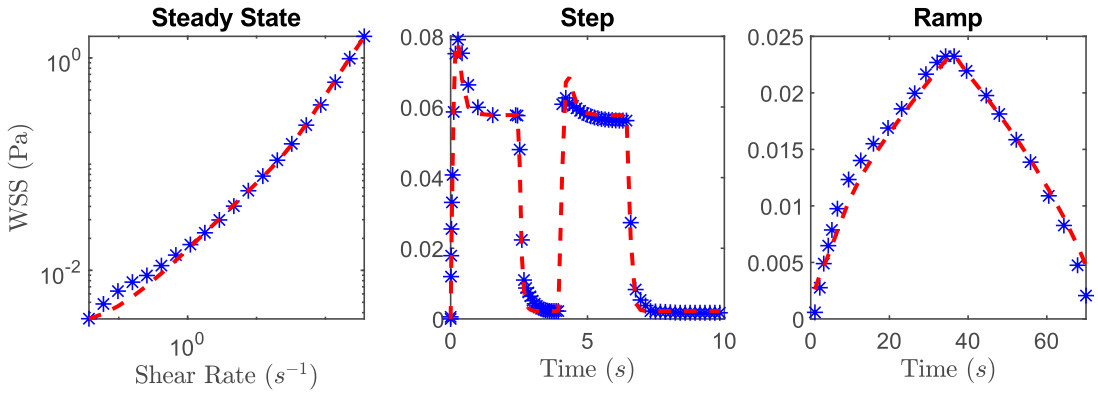

Figure 1: Model predictions (red) vs. experimental data (blue) after calibration with LSR

When performing LSR, it is possible to calculate the estimated parameters' variances, under the assumption that the model error is independent and normally distributed [5]. As expected, the usage of such assumptions leads to a crude approximation of the parameters' probability distributions (PDs). Nevertheless, this is the only source of information on the uncertain parameters' PDs, it is therefore imperative to improve these estimates if they are to be used for SA purposes.

Bayesian Inference (BI)

BI enables the update of *prior* knowledge of uncertain parameters as more data becomes available (*evidence*). In our case, the prior PDs are considered to be gaussian, characterized by the variance that has been computed from the LSR results.

*Corresponding author: **dimako@chemeng.upatras.gr**

The same experimental data used for the LSR serve as the evidence. Using the same data to obtain a first estimate of the PDs and then improve them may seem paradoxical, but the logic is very similar to solving a system of nonlinear equations using an iterative method that requires an initial guess of the solution: The experimental data are first used to perform the LSR and derive the prior PDs. Then, utilizing both the data and the priors, the posteriors are calculated through BI. All computations regarding the BI are carried out using the UQLab Matlab toolbox [6], which offers a user-friendly interface to perform such tasks without requiring from the user to be familiar with the complex mathematical concepts involved.

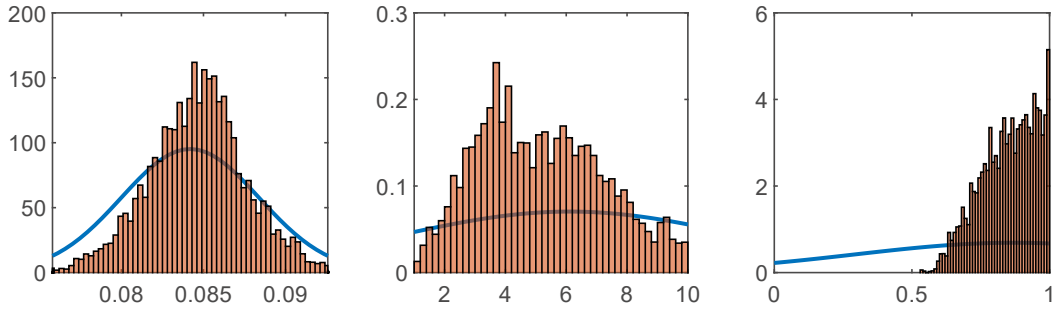

Figure 2: Prior (solid line) and posterior (histogram) PDFs for 3 of the model parameters

GLOBAL SENSITIVITY ANALYSIS (GSA)

Having extracted the PDs of the uncertain parameters, we opt to perform GSA via variance-based methods, to quantify their impact on model predictions. The first step in this endeavour is deciding which model outputs are to be studied (termed Quantities of Interest – QoIs) and the conditions under which the study will take place. Obviously, conditions similar to those encountered in the experimental data used for LSR have to be avoided since it is expected that highly identifiable parameters (parameters that showed minimal variance during LSR) will also be deemed as the most important by GSA. Instead, it is of more substance to perform the GSA under steady-state and transient extensional flow regimes, allowing for the evaluation of model fidelity in drastically different conditions to the ones it has been calibrated on. As for the QoIs, we consider all 3 model outputs.

The next step lies in choosing the most suitable method. The PDs calculated through BI indicate a strong correlation between some of the model parameters. We choose to proceed with Analysis of Covariance (ANCOVA), whose results offer a relatively approachable and clear interpretation [7]. The main disadvantage of ANCOVA is that its current realizations only take into account first-order effects, leaving out the interaction effects that occur due to the model's structure. Luckily, the magnitude of parameter correlation effects on the variance of the output is shown to be minimal, meaning that we can safely utilize methods designed for GSA of models with uncorrelated parameters. We calculate the 1st order and Total order Sobol' indices for each parameter in the set of conditions discussed previously, presenting a clear view of their effects on the variation of the QoIs.

Surrogate Models - Metamodeling

Variance-based methods require a relatively large number of model evaluations in order to produce accurate results. This feature can be problematic when the simulation is computationally expensive, resulting in prohibitively long runtimes to perform a single analysis. A possible solution is to use data from a small number of model evaluations in order to develop a much simpler model that sufficiently mimics the original model's behaviour. This obstacle can be overcome by deriving a data-driven mapping between the predicted QoIs and the uncertain parameters, based on polynomial chaos expansions of the original model and using it to perform the analysis. We utilized this approach to great effect, reducing the total runtime of all the analyses performed from a few days to overnight, achieving an almost 10-fold time saving (including the time needed to train the PCE surrogates).

References

[1] Chien S., Usiami S., Dellenback R.J., Gregersen M.I. Shear-dependent interaction of plasma proteins with erythrocytes in blood rheology. *American Journal of Physiology*. **219**: 143-153, 1970

[2] Salteli A., Ratto M., Andres T., Campologno F., Cariboni J. Global Sensitivity Analysis. The Primer. Wiley & Sons, West Sussex 2008.

[3] Varchanis S., Makrigiorgos G., Moschopoulos P., Dimakopoulos Y., Tsamopoulos J. Modeling the rheology of thixotropic elasto-visco-plastic materials. *Journal of Rheology*. **63**: 609-639, 2019

[4] Giannokostas K., Moschopoulos P., Varchanis S., Dimakopoulos Y., Tsamopoulos J. Advanced Constitutive Modeling of the Thixotropic Elasto-Visco-Plastic Behavior of Blood: Description of the Model and Rheological Predictions. *Materials*. **13**: 4184, 2020.

[5] Bensic M. Properties of the Generalized Nonlinear Least Squares Method Applied for Fitting Distribution to Data. *Probability & Statistics*. **35**: 75-94, 2015

[6] Marelli S., Sudret B. UQLab: A Framework for Uncertainty Quantification in MATLAB. *ICVRAM 2014*, University of Liverpool, United Kingdom

[7] Sudret B., Caniou Y. Analysis of covariance (ANCOVA) using polynomial chaos expansions. *ICOSSAR'2013*, New York, USA

FROM MICROSTRUCTURE TO RHEOLOGY OF SOFT DENSE SUSPENSIONS

Nicolas Cuny*[1], Romain Mari[1], and Eric Bertin[1]
[1]Université Grenoble Alpes,CNRS,LIPhy,38000 Grenoble,France

Summary Our work aims to develop a constitutive model allowing for the description of the rheology of soft dense suspensions below and above jamming. While most attempts to get such a constitutive model are purely phenomenological ones, based on symmetries like frame indifference, we developed such a constitutive model from the particle-level dynamics, using statistical physics tools to get a non-linear tensorial equation linking the stress tensor to the strain-rate and vorticity tensors. The coefficients appearing in this equation are expressed in terms of particle-level parameters. We are thus able to describe the behaviour of dense suspensions under simple shear deformation and to get predictions on various rheological protocols.

CONTEXT

Soft dense suspensions, as microgels for example, cover a large spectrum of materials made of soft particles immersed in a liquid phase. Although the nature of those solid particles can be very different, dense suspensions share some common rheological properties under simple shear. We distinguish two density regimes for the rheology of those materials. For low enough density, particles at rest have enough space to organize themselves without developping contact one with another. Applying shear to the material, the latter flows with a viscosity decreasing with the shear-rate, a phenomenon known as shear-thinning[1]. When increasing the density, particles have to overcome elastic energy barriers to move and the material thus exhibits a yield-stress: for shear-stress above this threshold materials behave as solid materials whereas overcoming this yield-stress makes the materials flow according to the Herschel-Bulkley law linking stress and shear-rate[2]. The transition density between these two regimes is known as the jamming density.

Establishing an evolution equation for the stress tensor as a response to a given time-dependent deformation is of great importance in order to describe the flow of such systems. Most attempts to obtain a constitutive model are phenomenological. They are typically based on symmetries, such as frame indifference[3, 4, 5], and while usually motivated by a microscopic physical picture, they do not directly relate the parameters they rely on to microscopic (i.e., particle-level) quantities. The goal of our work is to derive a constitutive model directly from the microscopic dynamics.

METHOD

In this work we are interested in getting such a constitutive model starting from the particle dynamics in order to connect the microscopic particle properties to the rheology. We assume two-dimensional, athermal and overdamped particles interacting one with another by radial contact repulsion forces only. We consider the influence of fluid through a Stokes drag and the external deformation of the material is assuming to generate a velocity field $\mathbf{U}^\infty$ in the fluid. The gradient of this velocity field is assumed to be homogeneous, for simplicity.

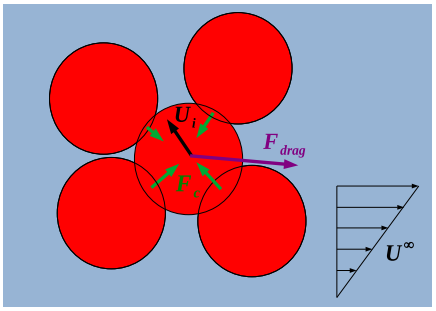

Figure 1: Illustration of the microscopic model used to describe our material.

Inspired by some similar work on hard sphere suspensions[6], we write the equation of conservation of the N-body probability density function associated to this microscopic description. We derive from the latter an equation on the pair correlation function g, thus reducing the number of variables of the equation, g being only function of $\mathbf{r}$ the center-to-center vector between two particles. However, this equation is not closed because of the presence of the three-body correlation function $g^{(3)}$. We solve this problem using a simple and standard closure relation between $g^{(3)}$ and g, known as the Kirkwood closure[7]. In order to translate this equation describing the microscopic structure into an equation on the macroscopic rheology, we use the virial relation linking the stress-tensor to the pair-correlation function.

Then, using a parameterization of the pair correlation function in terms of the deviatoric part $\mathbf{\Sigma}'$ of the stress tensor $\mathbf{\Sigma}$, we eventually obtain a tensorial equation on $\mathbf{\Sigma}$ that we can decompose into two equation. The first equation is a Ginzburg-Landau-type tensorial equation on $\mathbf{\Sigma}'$ with advection terms satisfying frame indifference. This first equation is

*Corresponding author. E-mail: nicolas.cuny@univ-grenoble-alpes.fr.

coupled to a non-linear evolution equation for the pressure, thereby providing a full characterization of the stress tensor. The pressure equation has a fixed point which depends on density and shear rate. All the coefficients appearing in these two coupled equations are expressed in terms of microscopic parameters, through a systematic approximation scheme motivated by observations made in LAMMPS simulations. Note that the cases below and above the jamming density have to be considered separately. One of the originalities of our approach is that it naturally provides a non-linear term in the tensorial equation on $\mathbf{\Sigma}'$ that induce a yield-stress behaviour above jamming.

The resulting macroscopic equations describing the rheology are quite promising. We display in Fig. 2 some preliminary results. By numerically integrating the macroscopic equations above the jamming density, we get a time evolution of the shear-stress qualitatively similar to what one can observe in simple shear experiments, with the presence of an overshoot before the shear-stress tends to some stationnary value. Turning to the steady-state rheology, we obtain a flow-curve with the presence of a yield-stress and a linear dependence of shear-stress with shear-rate for low shear-rate, resulting in a Bingham-fluid behavior.

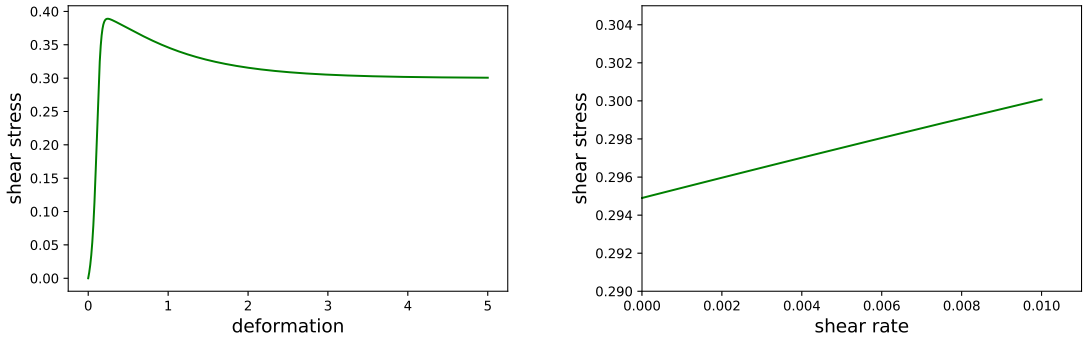

Figure 2: *(left)* Evolution of the shear-stress with time for a shear-rate of 10^{-2} and area fraction of 1.3 obtained by numerical resolution of our model, *(right)* Flow-curve obtained by numerical resolution of our model for area fraction of 1.3. Shear-rate is adimensionned by $f_{\text{el.}}/3\pi\eta a^2$ and stress by $f_{\text{el.}}/a^2$, where $f_{\text{el.}}$ is the caracteristic elastic contact force, a the radius of particles and η the viscosity of the Newtonian fluid.

References

[1] Barnes H. A., Thixotropy- a Review. *J. Non-Newtonian Fluid Mech.* **70**: 1-33, 1997.

[2] Bonn D., Denn M. M., Berthier L., Manneville S. Yield Stress Materials in Soft Condensed Matter. *Rev. Mod. Phys.* **89**: 035005, 2017.

[3] Hand G. L., A Theory of Anisotropic Fluids. *J. Fluid Mech.* **13**: 33-46, 1962.

[4] Saramito P., A New Elastoviscoplastic Model Based on the Herschel–Bulkley Viscoplastic Model *J. Non-Newtonian Fluid Mech.* **158**: 154-161, 2009.

[5] Bénito S., Bruneau C.-H., Colin T., Gay C., Molino F. An Elasto-visco-plastic Model for Immortal Foams or Emulsions *Eur. Phys. J. E* **25**: 225-251, 2008.

[6] Nazockdast E., Morris J. M. Pair-particle Dynamics and Microstructure in Sheared Colloidal Suspensions: Simulation and Smoluchowski Theory. *Phys. Fluids* **25**: 070601, 2013.

[7] Kirkwood J. G., Statistical Mechanics of Fluid Mixtures. *J. Chem. Phys* **3**: 300-313, 1935.

IMMERSED METHOD AND ANISOTROPIC MESH ADAPTATION FOR MULTIPHASE FLOW DYNAMICS

Thierry Coupez[1],
[1]CEMEF, Mines-ParisTech, Sophia Antipolis, France

Summary CFD is still strongly depending on the construction of meshes. Moreover, the flow equations are containing different scales filtered by the local mesh size, adding difficulties to tailor accurately the mesh a priori. For complex flow situation as liquid gas or fluid structure interaction involving discontinuity in the primal variables the sensitivity to the mesh can become a bottleneck. Mesh adaptation is a way of to simplify both the initial mesh construction, as the a posteriori dependency of solution to the mesh. In order to simplify CFD simulation, in particular for multiphase flows, we present here a general approach that combines immersed method and anisotropic mesh adaptation with an error estimate original technique in view to embed completely the mesh construction into the solution calculated with a stabilised optimally Finite element solver. . .

INTRODUCTION AND CONTEXT

A wider use of numerical simulation is still depending on meshing and adaptive meshing capabilities when complex geometry, multi-domain, moving interface and multiphase flow are involved. This task becomes more and more difficult when it is combined with a posteriori adaptive meshing or/and dealing with moving interfaces and boundary layers and also when running on massively parallel computers. In order to overcome the lack of flexibility of the common body fitted method, the alternative proposed here, is based on an implicit representation of the interfaces by a local distance function using a hyperbolic tangent filter. Therefore, the geometries can be interpolated and contribute to the numerical error which is detected by an a posteriori error estimator technique. This approach favours the full usage of anisotropic adaptive meshing techniques providing an optimal capture of the interfaces within the volume mesh, whatever is the complexity of the involved geometries. From the flow solver side, unstructured meshes with highly distorted elements (however solution aligned) need to rely on a robust solution framework. The interface condition transfer is enforced by following the immersed boundary/volume (IVM) methodologies for fluid/fluid and or fluid/structure interaction. The proposed multiphase flow solver, including a related local level set technique is based on a stabilized finite element method (VMS with residual based stabilisation) that can afford with anisotropic meshing with high aspect ratio elements. For transient flow a complete stabilization approach including the interface stabilization term and the dynamic of the subscales will be proposed with a quasi-optimal calculation of the stabilization parameter. The error estimation and the metric calculation will be presented and various application examples will be proposed.

METRIC STABILITY APPROXIMATION ERROR AND IMMERSED METHOD

The presentation will follow the following issues:
First we go back to the definition of a metric field, denoted by M, following the technique introduced in [5] to calculate a unit continuous metric field associated with a certain class of meshes. Moreover, we will show that the metric provides a very simple recovery operator and it enables on one hand, to retrieve the classical interpolation error and to elaborate an approximation erro on the other hand. We focus on the numerical calculation of the incompressible Navier-Stokes equation by using a mixed velocity pressure formulation with equal order finite element, mainly P1/P1 at this stage because of the current unstructured anisotropic meshing technology, well established for straight simplex elements and being under development for curved tetrahedra. The stabilisation theory gives rise to a unique framework to fulfil the infsup condition and to control the convective term. In brief, we introduce the Petrov-Galerkin formulation in which the stabilisation parameter providing the stability condition will depend on h, a mesh size field. In fact, and it is part of the novelty of this presentation, by using a duality argument (looking at the adjoint problem) h can be defined as the square root of the trace of the metric, $\text{trace}(M)^{-1/2}$, which is clearly dominated by the smallest height of elements and consequently opening clearly the door to anisotropic meshing. Indeed, the added artificial diffusion is controlled by the smallest width of the element and consequently at the least possible level.

This leads to a convergence between the residual based stabilisation method and the approximation error estimate.
The basic idea of immersed method is to represent the interfaces between domains or phases by an implicit function, here the zero value of a level set function. The parameter jumps are averaged by a smooth Heaviside function depending on thickness parameter [2]. The classical way to choose the thickness is to account for a certain number of elements. We change this point of view by fixing a priori the thickness and expecting that the mesh adaptation will give the right number of element we need to achieve the best possible accuracy. Here again it requires a well suited metric construction that must combine the solver error and the interpolation of the geometry? exactly evaluated by the a posteriori error estimate of the interpolated or calculated distance fields.

APPLICATIONS

In order to show the calculation possibility of this approach, several examples will be presented in order to explain the methodology and results obtained for challenging applications. We will focus on a target industrial process in which the spatial scales and time scales can be considered as extreme for the actual state of the art. The process is the coating of an iron strip by a liquid (molten zinc) with impacted by a very high speed air jet. It combines high Reynolds effect with high capillary effect with air liquid interaction and liquid solid interaction with jump in rheology parameters at more than one to thousands. Moreover, the target layer of the liquid film is about ten micron meters related to the meter which is the scale of the entire process and effectively, the meshes can vary from one to the micron meter in certain direction.

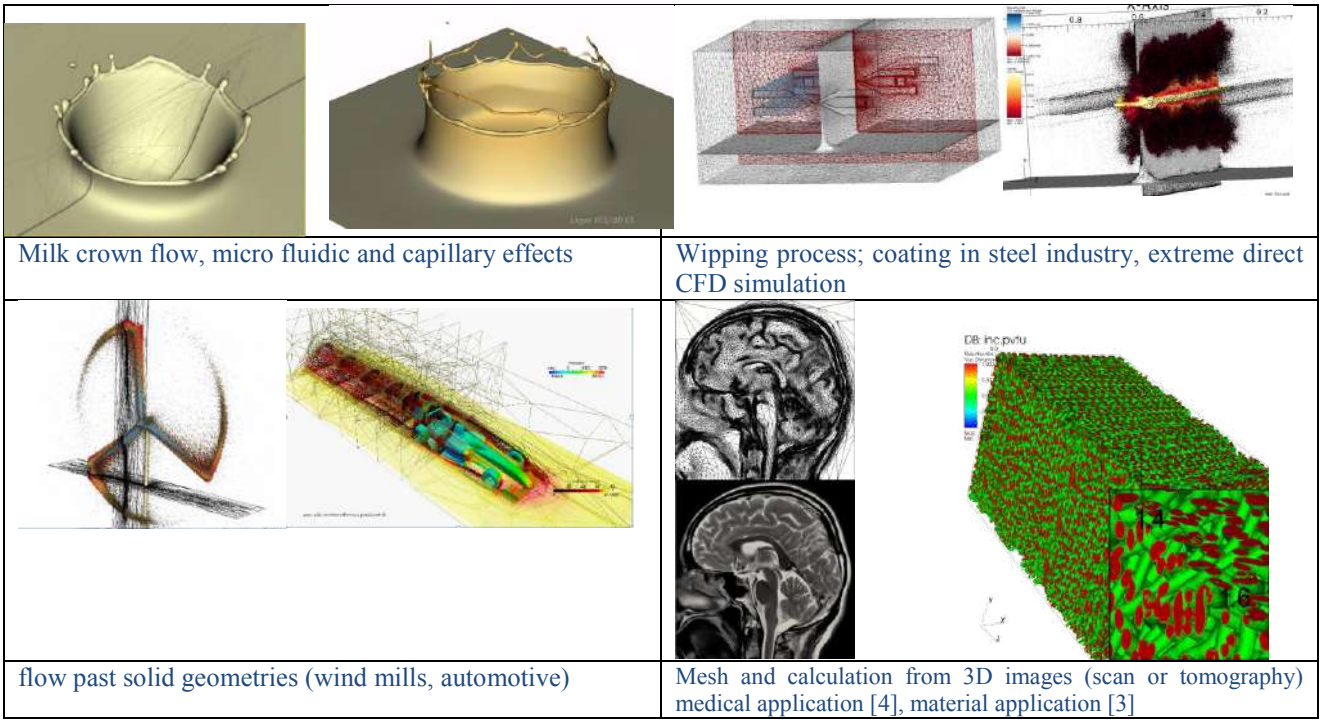

Milk crown flow, micro fluidic and capillary effects

Wipping process; coating in steel industry, extreme direct CFD simulation

flow past solid geometries (wind mills, automotive)

Mesh and calculation from 3D images (scan or tomography) medical application [4], material application [3]

Figure 1. Various applications using a monolithic approach for fluid-fluid or fluid-solid with a single adapted mesh and the implicit representation of interfaces. Dynamic anisotropic parallel mesh adaptation.

CONCLUSIONS

Immersed method can be combined with anisotropic mesh adaptation providing a unique mesh on which a monolithic formulation can be written for various multiphase applications. In that case, the geometries involved can be integrated in the error estimate for Navier stokes by using an extension of our earlier work on the metric construction.
The inherent thickness of the interfaces of immersed methods can be well controlled a priori and the mesh adaption process delivers the optimal mesh size in the vicinity of the interfaces. Clearly, this artificial thickness gives rise to certain regularity to the solution that aims to ensure a mesh convergence. 3D complex applications show the potential of this framework.

References

[1] Coupez T, Hachem E., "Solution of high Reynolds Incompressible Flow with Stabilized Finite Element and Adaptive Anisotropic Meshing", *Comp. Meth. in App. Mech. and Engng* Vol. 267, pp. 65-85, 2013

[2] Coupez T., Silva L., Hachem E., Implicit boundary and adaptive anisotropic meshing, *SEMA SIMAI Springer Series*, Vol. 5, pp. 1-18, 2014.

[3] Silva L, Coupez T, Digonnet H, Massively parallel mesh adaptation and linear system solution for multiphase flows, *International Journal of Computational Fluid Dynamics* 30 (6), 431-436,

[4] Zhao JX, Coupez T, Decencière E, Jeulin D, Cárdenas-Peña D, Silva L (2016) Direct multiphase mesh generation from 3D images using anisotropic mesh adaptation and a redistancing equation *Computer Methods in Applied Mechanics and Engineering* 309, 288-306, 2016

[5] Coupez T., Metric construction by length distribution tensor and edge based error for anisotropic adaptive meshing, *J. of Comp. Physics* 230: 2391-2405, 2011

REDUCED ORDER METHODS FOR FLUID-STRUCTURE INTERACTION PROBLEMS

Gianluigi Rozza*[1], Monica Nonino[1], and Francesco Ballarin[1]
[1]SISSA, International School for Advanced Studies, Mathematics Area, mathLab, Trieste, Italy

Summary This work focuses on overcoming the problem of slowly decaying Kolmogorov n-widths in the framework of reduced basis method (RBM). This slow decay represents an additional difficulty since it decreases the efficiency of reduction methods: this happens, for example, in transport dominated problems. In this work we implemented a preprocessing procedure, to be carried out during the offline phase of the reduced basis method; this procedure has been introduced in [1], and it has mainly been studied in the 1D framework. We tested its performance in the 2D setting, on three different test cases [2], the representative one being a transport dominated FSI problem. The multiphysics problem has been solved with a monolithic procedure; future work will concern partitioned procedures for RBM in FSI [3].

INTRODUCTION AND MOTIVATION

Let $\mathcal{M}$ be the solution manifold of the problem of interest, embedded in some normed linear space $(X, ||\cdot||_X)$. A fundamental assumption of the reduced basis method is that $\mathcal{M}$ can be well approximated by a sequence of finite dimensional linear spaces. This assumption translates in the mathematical hypothesis that the Kolmogorov n-width D_n of $\mathcal{M}$ decays fast, as a function of n, being D_n defined as:

$$D_n(\mathcal{M}, ||\cdot||_X) = \inf_{E_n} \sup_{p\in\mathcal{M}} \inf_{q\in E_n} ||p-q||_X,$$

where E_n is any linear subspace of X of $\dim(E_n) = n$. Unfortunately hyperbolic or convection dominated problems represent quite a challenge for the reduced basis method, since a linear setting is not suited to represent complex phenomena such as shocks or wave propagation. Our investigation focuses on transport dominated problems, and it aims at overcoming the problem of the slow decay of D_n by implementing an additional feature in the offline phase of the reduced basis method, called 'preprocessing procedure', which has been first introduced in [1].

FLUID–STRUCTURE INTERACTION PROBLEM FORMULATION

Given the time interval $[0, T]$, we have a thin (1D) structure Σ_t, situated at the top and at the bottom of a 2D rectangle filled with a newtonian fluid Ω_t^f. We adopt an Arbitrary Lagrangian Eulerian (ALE) formulation for the coupled problem, which now reads as follows: find $\mathbf{u}_f(\cdot;t)\colon \Omega_t^f \to \mathbb{R}^2$, $p_f(\cdot;t)\colon \Omega_t^f \to \mathbb{R}$ and $d_s(\cdot;t)\colon \Sigma \to \mathbb{R}$ such that:

$$\begin{cases} J\rho_f(\partial_t \mathbf{u}_f + F^{-1}(\mathbf{u}_f - \partial_t d_f \mathbf{e}_y)\cdot\nabla)\mathbf{u}_f) - \mathrm{div}(J\sigma^f F^{-T}) = \mathbf{b}_f & \text{in } \Omega^f \times [0,T], \\ \mathrm{div}(JF^{-1}\mathbf{u}_f) = 0 & \text{in } \Omega^f \times [0,T], \\ \rho_s h_s \partial_{tt} d_s - c_0 \partial_{xx} d_s + c_1 d_s = -\sigma^f \mathbf{n}\cdot\mathbf{n} & \text{in } \Sigma, \end{cases}$$

subject to the coupling conditions:

$$\begin{cases} d_f = d_s & \text{in } \Sigma_t, \quad \text{continuity of the displacement} \\ \mathbf{u}_f = \partial_t d_s \mathbf{e}_y & \text{in } \Sigma_t, \quad \text{continuity of the velocity.} \end{cases}$$

Here σ_f is the fluid Cauchy stress tensor and d_f is a suitably defined extension of the structure displacement on the whole domain. F is the gradient of the map T that maps the reference fluid domain Ω^f to the current domain Ω_t^f, and J is the determinant of F. Figure 1 shows three snapshots for the fluid pressure, for which we clearly see that there is a dominating transport phenomenon.

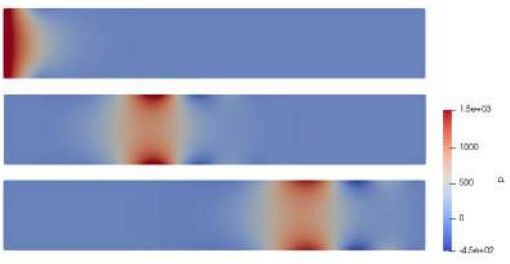

Figure 1: Fluid pressure p_f behaviour at different timesteps. The peak of the pressure wave (red) propagates in the domain: we have a transport dominated behaviour.

*Corresponding author. E-mail: gianluigi.rozza@sissa.it

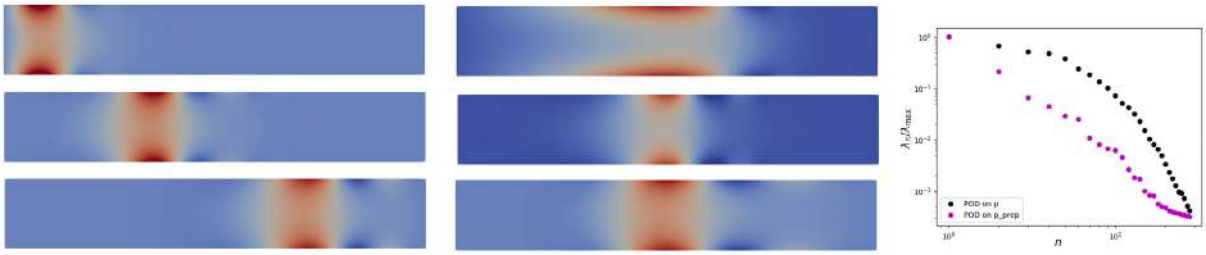

Figure 2: Example of snapshots of p_f before (left column) and after (central column) the preprocessing. The peaks of the waves are all aligned at the same point. Right column: comparison of the rate of decay of eigenvalues given by POD on $\mathcal{M}_{p_f}$, and on $\mathcal{M}_{p_f,\mathcal{F}}$.

PREPROCESSING PROCEDURE

For the sake of the simplicity of the exposition we briefly outline the preprocessing procedure applied on the solution manifold $\mathcal{M}_{p_f}$ for the fluid pressure p_f. The idea is to build a family of *smooth* and *invertible* maps $\mathcal{F} = \{F : \Omega^f \to \Omega^f\}$ s.t. $\forall t \in [0;T]$, $\exists F_t \in \mathcal{F}$ s. t.

$$\mathcal{M}_{p_f,\mathcal{F}} = \{p_f(F_t^{-1}(\cdot), t); t \in [0;T]\}$$

has a smaller Kolmogorov n-width.
We outline in the following the entire algorithm:

Reduction method with the preprocessing procedure
Offline phase

- FEM: compute M snapshots $p_f(t_1), \dots, p_f(t_M)$, where $\{t_1, \dots, t_M\}$ is a discretization of the time interval $[0, T]$;
- $\forall n = 1, \dots, M$, compute a preprocessing map $F_n^{-1}\colon \Omega^f \to \Omega^f$ that alignes the peaks of the wave at the same point;
- run a POD on the set of preprocessed snapshots and obtain N basis functions $\{\Phi_1^{p_f}, \dots, \Phi_N^{p_f}\}$, N small.

Online phase

- at timestep $n+1$ look for coordinates $\{\alpha_k^{n+1}\}_{k=1}^N$ and a suitable map $F_{n+1} \in \mathcal{F}$ such that $p_f(\cdot, t^{n+1})$ is well approximated by:

$$p_N^{n+1} = \sum_{k=1}^{N} \alpha_k^{n+1} \Phi_k^{p_f} \circ F_{n+1}.$$

RESULTS

In the test case considered results show that we are able to gain an important improvement in the efficiency of the RBM by adding the preprocessing of the snapshots in the offline phase. This is shown in Figure 2, where we have plotted the decay of the eigenvalues returned by the POD, normalized by the greatest eigenvalue, against the number N of modes, with (magenta) and without (black) the preprocessing procedure. As we can see the results are promising: with just $N = 5$ modes we obtain an improvement of more than one order of magnitude, and with just $N = 15$ modes we reach a magnitude of 10^{-3} thanks to the preprocessing procedure. Other remarkable results have been obtained for other two test cases, as detailed in [2]. The undergoing extension of this work is in collaboration with Efthymios Karatzas (NTUA Athens, Greece), and Yvon Maday (Sorbonne Université, Paris, France).

References

[1] Cagniart N., Maday Y., Stamm B. Model order reduction for problems with large convection effects. *Comp. Meth. in Appl. Sci.* Springer Int. Pub. **47**: 131–150, 2019.
[2] Nonino M., Ballarin F., Rozza G., Maday Y. Overcoming slowly decaying Kolmogorov n-width by transport maps: application to model order reduction of fluid dynamics and fluidstructure interaction problems. *Preprint arXiv*, 1911.06598, 2019.
[3] Ballarin F., Rozza G., Maday Y. Reduced–order semi–implicit schemes for fluid–structure interaction problems. *MS&A.* Springer Int. Pub. **17**: 149–167, 2017.

A COMPUTATIONAL FLUID DYNAMICS STUDY OF BLOOD FLOWS IN THE HUMAN LEFT HEART

Luca Dede'*[1], Alberto Zingaro[1], Marco Fedele[1], and Alfio Quarteroni[1,2]
[1]MOX–Modeling and Scientific Computing, Department of Mathematics, Politecnico di Milano, Milano, Italy
[2]Institute of Mathematics,E´cole Polytechnique Fédérale de Lausanne,Switzerland (Emeritus Professor)

Summary We propose a computational fluid dynamics study of blood flows in the human left heart. Our model considers the incompressible Navier-Stokes equations in the ALE framework where domain displacement is prescribed, or possibly obtained from cardiac electromechanics simulations. We use the Variational Multiscale method within the Large Eddy Simulation paradigm to model turbulence, the finite element method for space discretization, and BDF formulas for time discretization. Our numerical study highlights that, in healthy hearts and normal conditions, the cardiac blood flows are transitional and characterized by complex and peculiar features.

INTRODUCTION

Recent years have seen an increasingly use of *in-silico* studies to assess and characterize blood flows in the cardiovascular system. While hemodynamics of arteries, its interaction with the arterial walls (both in physiological and several pathological conditions) have been extensively addressed, numerical studies of blood flows in the human heart as an organ are less common. Indeed, the focus is often on a single chamber – typically the left ventricle or atrium [4, 11] – or, even more commonly, numerical studies target valvular dynamics and their pathological conditions [2, 7]. As a matter of fact, computational fluid dynamics of the heart is a very challenging task [1, 8], mainly due to: i) the very large and complex deformations of the cardiac chambers during the heartbeat; ii) the topological changes occurring in the domain wherein the equations are defined when valves open and close; iii) the very large pressure gradients across chambers and changes occurring over time, mainly related to cardiac electromechanics and valve dynamics [10]; iv) the blood flow dynamics exhibiting multiscale behavior both in space and time, thus namely calling for a intensive use of computational resources. Moreover, as blood flows in the heart can reach in physiological conditions Reynolds numbers around 5000 or above, cardiac hemodynamics is characterized by a distinguishing behavior; this can be further exacerbated in pathological conditions or simply under exercise. As a matter of fact, blood flows in the left heart appear to be neither laminar nor fully turbulent, but rather transitional. The latter is a peculiar condition that has received so far a limited attention in computational fluid dynamics studies of internal flows.

We propose in this work a detailed computational fluid dynamics study of the whole left heart including the left atrium and ventricle, the mitral and aortic valves, the pulmonary veins, and the aortic root. In particular, we characterize the blood flows developing in a healthy heart that operates in normal conditions; our study takes into consideration the whole heartbeat and, for a more complete assessment, several heart cycles. In addition, we study blood flows through meaningful fluid dynamics indicators in cardiac configurations and working conditions that are departing from the reference one.

MATHEMATICAL MODELS

As our focus is on blood flow dynamics in the heart chambers, we model it by means of the incompressible Navier-Stokes equations in the Arbitrary Lagrangian Eulerian (ALE) framework, wherein the displacement of the chambers' walls in prescribed. In this respect, we consider two approaches. In the first one, the endocardium wall displacement is assigned compatibly with the behavior of the chambers' volume vs. time that is depicted in a typical Wiggers diagram. In the second one, the wall displacement is instead obtained as output of electromechanical simulations [9] for which the Navier-Stokes equations are surrogated by 0D models of the chamber and the whole circulation.

Accounting for the valves and their dynamics is an essential part of blood flow modeling in the heart. In particular, for the left heart, the aortic and mitral valves take a leading role in shaping cardiac hemodynamics. In this work, we account for valve leaflets and their dynamics by means of surrogate models. In addition, we use the resistive method [5] to mimic the effect of the valves on the blood flows; this boils down adding to the Navier-Stokes equations a (zero order) term that weakly enforces blood velocity adherence to that of the valve leaflets.

NUMERICAL METHODS

In principle, turbulence should be taken into account in cardiac hemodynamics. This can be done according to Direct Numerical Simulations, for which the whole range of spatio-temporal scales of the velocity and pressure fields are numerically solved by using space and time discretizations that fully match Kolmogorov lengths. Instead, Large Eddy Simulations (LES) directly solve only the largest scales of the velocity and pressure fields, whereas the smaller scales are modeled. In this work, we define a sub-grid model for LES by means of the Variational Multiscale (VMS) method [6], a stabilization technique for the Navier-Stokes equations that: i) yields inf-sup stable approximations when considering the same finite element spaces for velocity and pressure fields; ii) controls numerical oscillations in flow regimes at locally large Reynolds numbers; and iii) provides LES modeling of turbulence.

*Corresponding author. E-mail: luca.dede@polimi.it

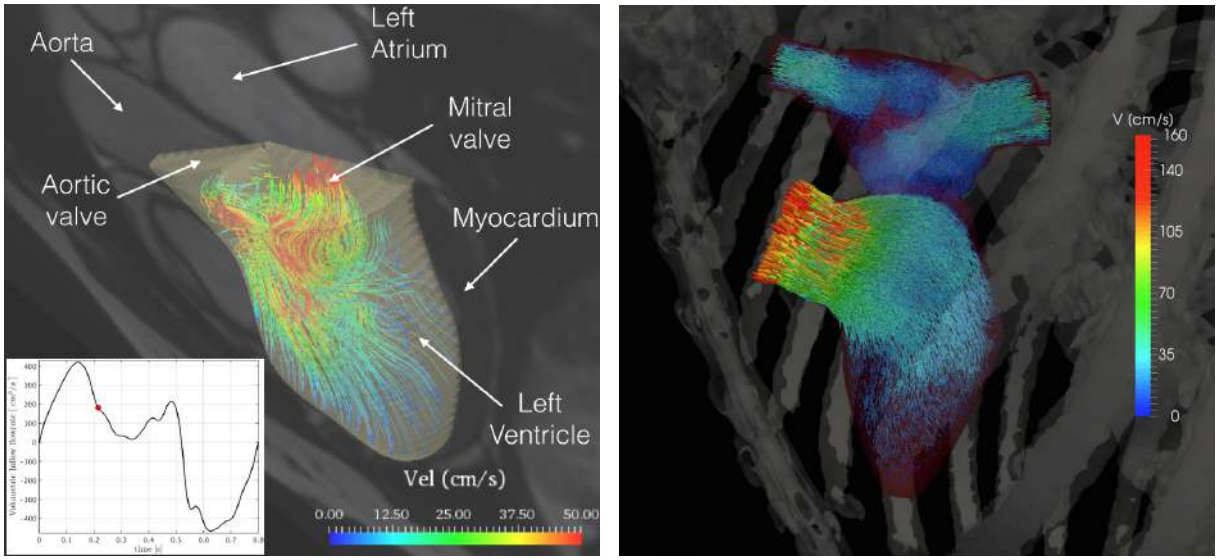

Figure 1: Blood flows in a patient-specific left ventricle during diastole (left) and in an idealized left heart during systole (right); colors highlight the magnitude of the velocity field.

Our numerical approximation scheme is therefore based on the VMS-LES method for which we consider space discretization by the finite element method and semi-implicit or implicit schemes involving BDF formulas for the time discretization [6]. We consider for our VMS-LES formulation both quasi-static and dynamic modeling of the sub-grid (fine) scales of the velocity and pressure fields.

NUMERICAL RESULTS AND DISCUSSION

We use our VMS-LES computational models to assess and characterize the blood flow dynamics in a realistic left heart in normal conditions (Figure 1). Our study involves both instantaneous and phase averaged quantities, other than several clinically meaningful fluid dynamics indicators as kinetic energy, fluctuating kinetic energy, enstrophy, and Wall Shear Stress [3]. In particular, we confirm that the blood flow regime in a healthy heart is transitional or nearly turbulent. Indeed, fully developed turbulence does not sustain for a significant amount of time during the heartbeat; moreover, we highlight that blood flows are characterized by instabilities and complex interactions of vortexes involving different spatio-temporal scales. In this respect, we finally critically compare and assess the numerical performances of VMS-LES formulations with quasi-static and dynamic approximations of sub-grid scales.

ACKNOWLEDGMENTS

This project has received funding from the European Research Council (ERC) under the European Unions Horizon 2020 research and innovation programme: grant agreement No 740132, iHEART – "An integrated Heart Model tor the Simulation of the Cardiac Function", 2017–2022.

References

[1] Chafna C., Mendez S., Nicoud F. Image based Large-Eddy Simulation in a realistic left heart. *Comput. Fluids* **94**: 173-187, 2014.
[2] De Tullio M. D., Cristallo A., Balaras E., Verzicco R. Direct numerical simulation of the pulsatile flow through an aortic bileaflet mechanical heart valve. *J. Fluid Mech.* **622**: 259-290, 2009.
[3] Dedè L., Menghini F., Quarteroni A. Computational fluid dynamics of blood flow in an idealized left human heart. *Internat. J. Numer. Methods Biomed. Engng.* 2019; doi: 10.1002/cnm.3287
[4] Domenichini F., Pedrizzetti G., Baccani B. Three-dimensional filling flow into a model left ventricle. *J. Fluid Mech.* **539**: 179-198, 2005.
[5] Fedele M., Faggiano E., Dedè L., Quarteroni A. A patient-specific aortic valve model based on moving resistive immersed implicit surfaces. *Biomech. Model. Mechanobiol.* **16**(5): 1779-1803, 2017.
[6] Forti D., Dedè L. Semi-implicit BDF time discretization of the Navier-Stokes equations with VMS-LES modeling in a High Performance Computing framework. *Comput. Fluids* **117**: 168-182, 2015.
[7] Griffith B. E. Immersed boundary model of aortic heart valve dynamics with physiological driving and loading conditions. *Internat. J. Numer. Methods Biomed. Enging.* **28**(3): 317-345, 2012.
[8] Mittal R., Seo J. H., Vedula V., Choi Y. J., Liu H., Huang H. H., Saurabh J., Younes L., Abraham T., George R. T. Computational modeling of cardiac hemodynamics: current status and future outlook. *J. Comput. Phys.* **305**: 1065-1082, 2016.
[9] Quarteroni A., Dede' L., Manzoni A., Vergara C. *Mathematical Modelling of the Human Cardiovascular System. Data, Numerical Approximation, Clinical Applications*. Cambridge University Press, 2019.
[10] Sugiura S., Washio T., Hatano A., Okada J., Watanabe H., Hisada T. Multi-scale simulations of cardiac electrophysiology and mechanics using the University of Tokyo heart simulator. *Progre. Biophys. Molec. Biol.* **110**: 380-389, 2012.
[11] Tagliabue A., Dedè L., Quarteroni A. Complex blood flow patterns in an idealized left ventricle: a numerical study. *Chaos* **27**: 093939, 2017.

HIGH FIDELITY COMPUTATIONAL FRAMEWORK FOR CONTROL CO-DESIGN OF UTILITY SCALE WIND FARMS: REDUCING THE LEVELIZED COST OF ENERGY VIA ADVANCED TURBINE CONTROLS

Xiaolei Yang[1], Christian Santoni[2], and Fotis Sotiropoulos*[2]
[1]Institute of Mechanics, Chinese Academy of Sciences, Beijing, China
[2]Department of Civil Engineering, College of Applied Sciences, Stony Brook University, Stony Brook, United States

Summary A large-eddy simulation approach incorporating advanced turbine controls is developed for control co-design of large wind farms. The methodology is employed to evaluate the effect of individual blade pitch control (IBPC) on the fatigue loads of wind turbine blades for 1) a finite-size wind turbine array, 2) an infinitely-large wind turbine array and 3) a utility-scale wind farm. It is shown for the first time that IBPC can significantly reduce the fluctuations of blade bending moments for all three cases.

INTRODUCTION

With the increase in penetration of wind energy in the world's energy portfolio, the levelized cost of energy (LCOE) has to be further reduced for wind energy to remain competitive [1]. Advanced turbine controllers have the potential to greatly reduce the LCOE by lowering the capital and operational expense of wind farms. However, such advanced controllers have to be designed taking into account the nonlinear aerodynamics, hydrodynamics (for offshore wind) and structural dynamics of wind turbines that cannot be taken into account by existing engineering design tools (e.g. FAST, Bladed, HAWC2, etc.). The goal of our work is to use high-fidelity numerical simulations to develop and evaluate the performance of advanced turbine controllers for the nonlinear dynamics of wind turbines following the concept of the control co-design (CCD) approach [2], which integrates turbine control in the design process of wind turbines and wind farms.

In general, at wind speeds below rated, the turbine controller varies the generator torque to keep the angular velocity at optimum to maximize the power extraction (region 2). For higher wind speeds, region 3, the blades are pitched to mitigate mechanical and electrical loads. As it rotates, the turbine blade loads fluctuate due to the heterogeneity of the wind speed at the rotor caused by the vertical shear and large-scale turbulence structures. The collective blade pitch control (CBPC) commonly used in Region 3 cannot reduce such load fluctuations as it pitches all the blades together to the same angle. On the other hand, the individual blade pitch control (IBPC) has the potential to reduce the blade load fluctuations. However, the effectiveness of the IBPC on reducing blade load fluctuations cannot be tested easily in the field. As a first step towards developing advanced turbine controllers using the CCD approach, we evaluate the performance of IBPC on reducing blade load fluctuations using high-fidelity simulations.

METHODOLOGY

Large-eddy simulations of a finite-size turbine array, an infinitely large turbine array and a utility-scale wind farm have been performed using the Virtual Flow Simulator (VFS) code [3, 4]. Fully developed turbulent flow is applied at the inlet of the finite-size turbine array with periodic boundary conditions along the crosswind direction. For the infinitely large wind turbine array, periodic boundary condition was given along the streamwise and crosswind direction. The utility-scale wind farm consists of 100 turbines located in a complex terrain at Pleasant Valley, Minnesota, United States. The wind turbines are modeled using the actuator line/surface for the rotor and nacelle. For all cases the turbines operate in Region 3, where the blade pitch control is activated. Both CBPC and IBPC are tested for each case. A description on the IBPC of the EOLOS turbine can be found in [7]. VFS has been successfully validated and applied to utility-scale wind farm including the Horns-Rev offshore wind farm [5] and a wind farm in complex terrain [6] located in Vantage, Washington, United States.

RESULTS

Figure 1 show the contours of the instantaneous downwind velocity and the temporal variation of the blade bending moment for the finite-size turbine array case. As seen, the fluctuations of the bending moments are reduced significantly by using IBPC. Similar levels of reductions on the fluctuations of the blade bending moments are observed for the infinitely-large turbine array case as shown in figure 2. Figure 3 show the results from the utility-scale wind farm case. The wind blows from left to right in figure 3. The bending moments from two turbines, turbine T98 located in the upwind and the turbine T11 located deep in the farm, respectively, are examined. Reduction on the fluctuations of blade bending moments are observed for both turbines, although the temporal variations of the bending moment of T11 are more complex because of the terrains and the upwind turbine wakes.

*Corresponding author. E-mail: fotis.sotiropoulos@stonybrook.edu.

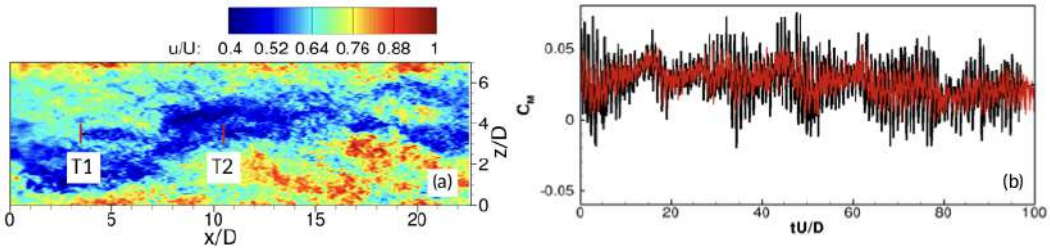

Figure 1: Finite-size turbine array case for (a) contour of instantaneous downwind velocity at turbine hub height and (b) temporal variations of blade bending moments. In (b), the black and red lines are for CBPC and IBPC, respectively.

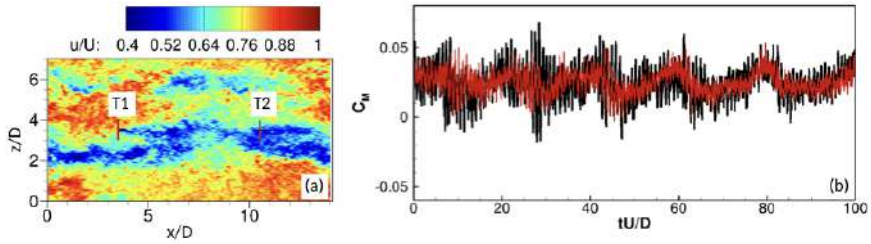

Figure 2: Infinitely-large turbine array case for (a) contour of instantaneous downwind velocity at turbine hub height and (b) temporal variations of blade bending moments. In (b), the black and red lines are for CBPC and IBPC, respectively.

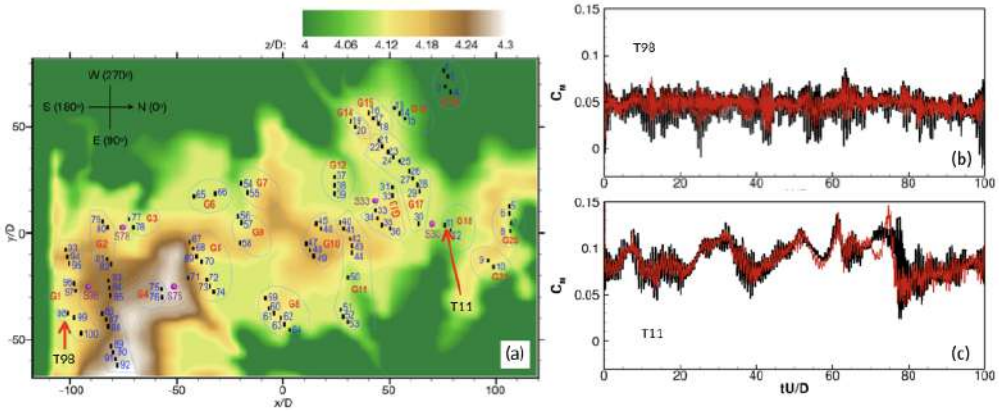

Figure 3: Utility-scale wind farm case for (a) contour of terrain elevations, and (b) and (c) temporal variations of blade bending moments for turbines T98 and T11, respectively. In (b) and (c), the black and red lines are for CBPC and IBPC, respectively.

CONCLUSIONS

We have performed large-eddy simulations with actuator line/surface to model the wind turbine rotor to investigate the effect of IBPC on the blade bending moment fluctuations. A finite-size turbine array case, an infinitely large turbine array case and a utility-scale wind farm case are considered. Comparison of the IBPC against CBPC have shown that the fluctuations of the bending moment are reduced. This study suggests the possibility of using IBPC to reduce the maintenance cost of wind farms, shows the importance of considering IBPC in the design process of wind farms and paves the way for significant reduction in the levelized cost of energy by incorporating advanced control strategies in large wind farms.

References

[1] Veers, Paul, Katherine Dykes, Eric Lantz, Stephan Barth, Carlo L. Bottasso, Ola Carlson, Andrew Clifton et al. Grand challenges in the science of wind energy. *Science* **366** (6464): eaau2027, 2019.

[2] Garcia-Sanz, Mario. Robust control engineering: practical QFT solutions. CRC Press, 2017.

[3] Yang, Xiaolei, Fotis Sotiropoulos, Robert J. Conzemius, John N. Wachtler, and Mike B. Strong. Large-eddy simulation of turbulent flow past wind turbines/farms: the Virtual Wind Simulator (VWiS). *Wind Energy* **18** (12): 2025-2045, 2015.

[4] Yang, Xiaolei, and Fotis Sotiropoulos. A new class of actuator surface models for wind turbines. *Wind Energy* **21** (5): 285-302, 2018.

[5] Foti, Daniel, Xiaolei Yang, Lian Shen, and Fotis Sotiropoulos. Effect of wind turbine nacelle on turbine wake dynamics in large wind farms. *Journal of Fluid Mechanics* **869**: 1-26, 2019.

[6] Yang, Xiaolei, Maggie Pakula, and Fotis Sotiropoulos. Large-eddy simulation of a utility-scale wind farm in complex terrain. *Applied energy* **229**: 767-777, 2018.

[7] Ossmann, Daniel, Julian Theis, and Peter Seiler. Load reduction on a clipper liberty wind turbine with linear parameter-varying individual blade pitch control. *Wind Energy* **20** (10): 1771-1786, 2017.

EFFECT OF ASPECT RATIO ON THE INTERACTION BETWEEN WING-TIP VORTEX AND VORTEX SHEDDING AT LOW REYNOLDS NUMBER

Jawahar Sivabharathy Samuthira Pandi[1], Yuvraj[1], and Sanjay Mittal*[1]
[1]Department of Aerospace Engineering, Indian Institute of Technology Kanpur, INDIA

Summary The effect of aspect ratio ($0.5 \leq AR \leq 10$) on the flow past a rectangular wing with NACA 0012 section is studied numerically. The angle of attack of the wing to the freestream is 14 deg and the Reynolds number based on its chord is 1000. The flow is steady for very low AR. Cellular shedding is observed on the wing for higher AR; one cell for $AR \leq 6$ and two cells for larger AR. The dislocations at the boundary of the cells as well as the end-cell structures are studied. Very interesting variations in flow structure with change in AR are observed. Contrary to the flow at large Re, $\overline{C_D}$ increases with an increase in AR, and it is lower than that for an airfoil.

INTRODUCTION

The wing is the main lifting body in an aircraft. The parameters that govern the flow of wing are: Reynolds number (Re), angle of attack (α), section of the wing (airfoil profile), wing planform and aspect ratio (AR). An interesting feature of the flow is the wing-tip vortex which is generated due to the pressure difference between the lower and upper surface of the wing. The wing-tip vortex leads to downwash and reduction in the effective angle of attack. There have been several experimental and computational studies on flow past wing, but mostly at larger Re. Taira and Colonius [1] studied the flow past flat plate low aspect ratio wing at $0^o \leq \alpha \leq 60^o$ for $Re = 300$ and 500. It was found that the wing-tip vortex plays a significant role in the stability and shedding frequency of the primary vortices. Jantzen *et al.* [2] carried out numerical and experimental investigation on pitching rectangular flat plates for $AR = 2$ and 4 at $Re = 300$. It was found that the fully developed wing-tip vortex significantly affects the vortex structures in the flow. The vortices remain relatively close to the surface at the mid-span for $AR = 2$ due to the stronger influence of the wing-tip vortex while for $AR = 4$ the vortices remain separated. Six wing planforms were investigated by Chen and Qin [3] at various α and $Re = 10^5$. The tapered wing with high sweep angle experiences a drastic stall. On the other hand the low sweep angle wing exhibits a gradual stall. Among all the planforms considered in their study the Zimmerman planform achieves high lift to drag ratio. The present study is conducted on rectangular wing in the pre-stall regime and for $\alpha = 14^o$. The governing flow equations are solved using a stabilized finite element method [4].

EFFECT OF ASPECT RATIO

At $Re = 1000$, strong vortex shedding is observed for an end-to-end/infinite wing. However, a wing-tip vortex is expected to weaken the shedding. Figure 1 shows the $Q(= 0.1)$ iso-surface for the fully developed unsteady flow for various aspect ratio. The presence of wing-tip vortex is evident from the picture. The wing-tip vortex completely suppresses the vortex shedding and steady flow is observed for $AR = 0.5$. Cellular vortex shedding is observed at larger AR. The frequency of vortex shedding recorded by probes placed at certain spanwise locations is used to identify the cell structures in the flow. One cell structure is observed for $AR \leq 6$ whereas two cell structures are observed for larger AR. The primary vortices observed in $AR = 10$ are almost parallel to the wing-axis at the mid-span of the wing (Figure 1(c)).

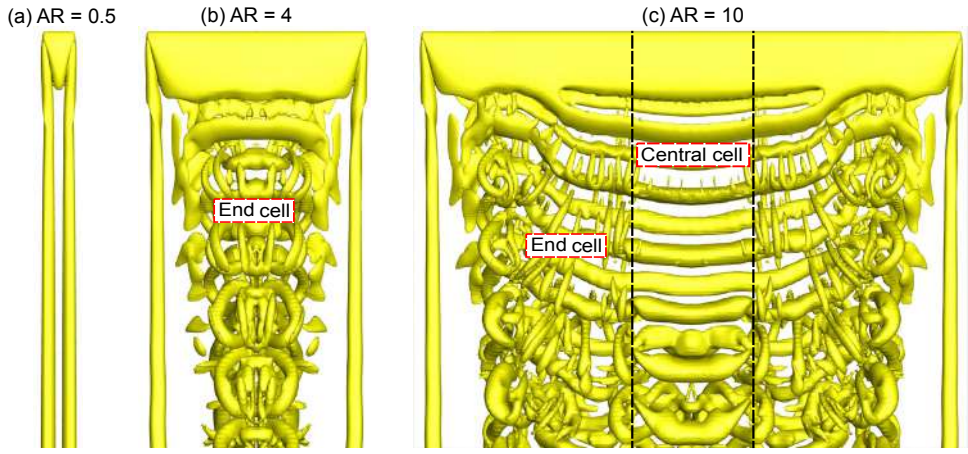

Figure 1: Flow past wing at $Re = 1000$ and $\alpha = 14^o$: $Q(= 0.1)$ iso-surface for various AR. Also marked in the picture are the cellular structures. The dashed black line in (c) is used to show the central cell region.

*Corresponding author. E-mail: smittal@iitk.ac.in

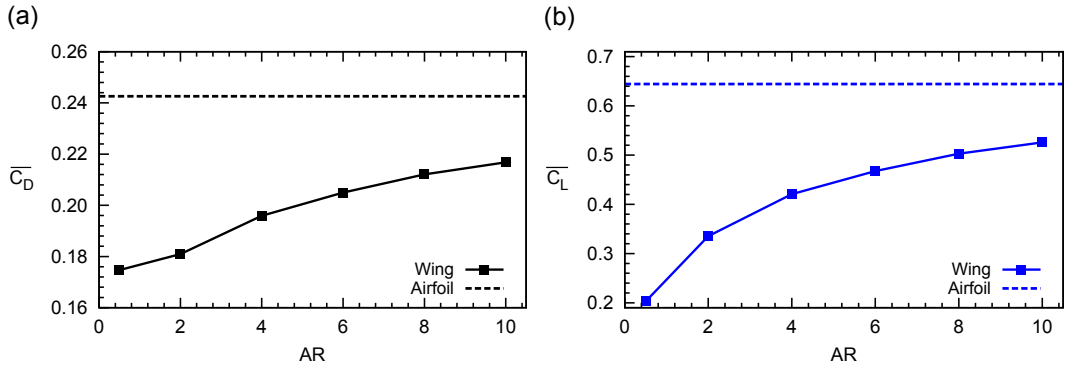

Figure 2: $Re = 1000$ and $\alpha = 14^o$: variation of (a) $\overline{C_D}$ and (b) $\overline{C_L}$ with AR. Also plotted is the data of NACA 0012 airfoil.

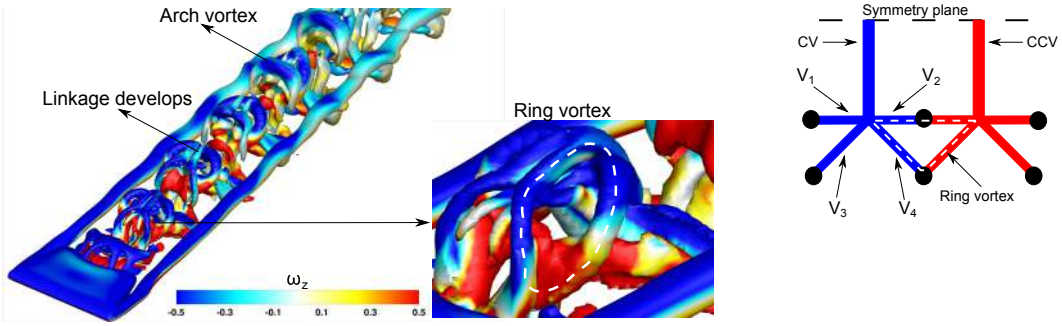

Figure 3: $Re = 1000$, $\alpha = 14^o$ and $AR = 2$: Q(= 0.1) iso-surface of the flow colored with spanwise vorticity. A schematic representation of the connectivity observed between the spanwise vortices is also shown. CV and CCV represents clockwise and counter-clockwise vortices.

The variation of aerodynamic force coefficient with AR is presented in figure 2. Also plotted is the data for airfoil. Both $\overline{C_D}$ and $\overline{C_L}$ increase with an increase in AR. According to the finite wing theory, at large Re, the wing-tip vortices create downwash which are responsible for induced-drag and lowering the lift. The effect of wing-tip vortex decrease with increase in AR of the wing. Therefore, for large Re wing, the induced-drag as well as the total drag experienced by a wing reduces with increase in AR. In contrast the present study shows that drag of wing is lower than the airfoil and with an increase in AR the value approaches airfoil. It is found that the unsteadiness in the flow increases with AR.

Q iso-surface colored with spanwise vorticity (ω_z) and schematic representation of the connectivity between the spanwise vortices is presented in figure 3 for $AR = 2$. The primary vortices (CV and CCV), near the wing-tip, split into four branches V_1, V_2, V_3 and V_4 and form a ring vortex. The ring vortex present on either side of the symmetry plane forms an additional linkage as the vortex is shed. This results in the formation of arch vortex in the far wake. Unlike $AR = 2$, the ring vortex in $AR = 4$ (please refer figure 1(b)) collapses and forms loop like structure in the far wake. The undulations in wing-tip vortex is dominant in $AR = 2$ (Figure 1 and 3). For $AR \geq 6$, the vortices split into V_1 and V_2 and forms linked vortex structure. Details of the Reynolds stress distribution across the span, along with the variation of strength of wing-tip vortex for various AR and dislocations observed at large AR will be presented in the conference. In addition the data obtained for steady flow simulation will be compared with the unsteady results.

CONCLUSIONS

The flow past rectangular wing for various aspect ratio placed at $Re = 1000$ and at $\alpha = 14^o$ has been numerically investigated via a stabilized finite element method. The wing-tip vortex weakens the vortex shedding, specially near the wingtip. The $AR = 0.5$ flow remains steady. Cellular vortex shedding is observed for wing with larger AR. Two cell vortex shedding occurs for $AR > 6$. The drag coefficient of wing is found to be lower than the airfoil. Ring vortex structures are seen for $AR \leq 4$. The linkages between the counter-rotating vortices at the end cell show complex structures for $AR \geq 6$.

References

[1] Taira K., Colonius. T. Three-dimensional flows around low-aspect-ratio flat-plate wings at low Reynolds numbers. *J. Fluid Mech*, vol. 623, pp. 187207, 2009.
[2] Jantzen R.T., Taira K., Granlund K.O., Michael V. Ol. Vortex dynamics around pitching plates. Phys. Fluids 26, 053606, 2014.
[3] Chen Z.J., Qin N. Planform effects for low Reynolds number thin wings with positive and reflex cambers. Journal of aircraft, Vol. 50, No. 3, MayJune 2013.
[4] Tezduyar T.E., Mittal S., Ray S.E., Shih R. Incompressible flow computations with stabilized bilinear and linear equal-order-interpolation velocity-pressure elements. Computer Methods in Applied Mechanics and Engineering, volume 95, pages 221242, 1992.

DEFINING A NEW VARIABALE-ORDER TEMPERED FRACTIONAL DERIVATIVE FOR MODELING TURBULENT FLOWS

Pavan P. Mehta[1] andGeorge Em Karniadiakis *[1]
[1]Division of Applied Mathematics, Brown University, Providence, United States of America

Summary A fractional derivative is used to model non-local effects in turbulence. However, as the second moment does not exist, tempering the Levy distribution leads to finite moments, and thus, a new tempered fractional derivative free from all assumptions is formulated for non-local modelling of turbulent flows. The total shear stress is modelled here as opposed to commonly modelled unclosed terms in turbulence modelling; also, working in wall units does not introduce any coefficient for representing the shear stresses. We demonstrate this new concept for turbulent Couette flow, where the error found in total shear stress is very low compared to results of direct numerical simulations.

INTRODUCTION

In an experiment for a rotational flow, for long enough time, the tracer particles exhibited Levy distribution [1]. In the context of non-Fickian law, it is a super-diffusion phenomenon where the spatial scales spreading are larger than the temporal scales, a rather non-local phenomenon. Furthermore, Kolmogorov's 5/3 spectra described the inertial ranges [2]. The Hurst scaling, $H = 1/3$ with fractional Brownian motion, a stochastic process models the Kolmogorov's 5/3 spectra [3], while, a tempered fractional derivative, with a fixed order and a tempering length models the entire spectra [4]. Despite this evidence of non-locality in turbulence, modelling has mostly received local treatment. Thus, in this study a non–local closure model is established with the use of fractional derivatives.

Fractional derivatives were first introduced by Leibniz soon after their integer counter parts [5]. Chen speculated that the Reynolds Stresses behaved as fractional laplacian of fixed order 2/3 [6]. Our group extended it to a variable-order fractional derivative to address the multiple scales [7][8], whilst discovering a *universal scaling law*. A variable-order as a function of the distance from the wall, provides further robustness to model it, as the energy containing wave-numbers will vary. Furthermore, our group also modelled the total shear stress as opposed to Reynolds stresses using one sided Caputo fractional derivative for turbulent Couette flow [7]; the advantage of working in wall units was emphasised as modelling required no additional scaling coefficient. In the present study, a new approach for the fractional Reynolds-averaged Navier-Stokes equations (F-RANS) is established for turbulent flows.

TEMPERED FRACTIONAL TWO SIDED DERIVATIVE

For an infinitely long turbulent Couette flow, the Reynolds-averaged Navier-Stokes (RANS) equations reduce to (1) in wall units [7]. Upon integration and using the fact that $\overline{uv}^+ \approx 0$ near the wall, while $U^+ \approx y^+$, the constant of integration is then elevated as $\left.\frac{\partial U^+}{\partial y^+}\right|_{y^+=03} = \tau^+ = 1$, thus we have (2).

$$\frac{\partial}{\partial y^+}\left(\frac{\partial U^+}{\partial y^+} - \overline{uv}^+\right) = 0^33 \tag{1}$$

$$\frac{\partial U^+}{\partial y^+} - \overline{uv}^+ = \tau^+ = 1^33 \tag{2}$$

The newly formulated definition for tempered F-RANS is given by (3), where λ_l and λ_r are associated with the tempering length of the left- and right-sided fractional derivative, respectively (4,5). The total shear stress is modelled directly with the use of these derivatives (3). As $\lambda \to 0$, the tempered definition becomes a standard fractional Caputo derivative. Tempering the Levy distribution ensures that the second moment exists, thus a finite variance, as observed in real world phenomenon. In contrast to a sharp cut-off, the exponential term appearing in (4,5) is smoother cut-off.

$$\left({}_0^C D_{y^+}^{\alpha(y^+),\lambda_l} - 3\,{}_{y^+}^C D_{2Re_\tau}^{\alpha(y^+),\lambda_r}3\right)U^+ = \tau^+ = 1; 3\alpha(y^+) \in (0,1], 3\lambda_l, \lambda_r \in [0,\infty)3 \tag{3}$$

$${}_0^C D_{y^+}^{\alpha(y^+),\lambda_l} U^+ = 3\frac{1}{\Gamma(1-\alpha(y^+))}3\int_0^{y^+} 3(y^+ - \xi)^{-\alpha(y^+)}3U^+(\xi)'3e^{-\lambda_l(y^+-3\xi)/Re_\tau}3d\xi 3 \tag{4}$$

$${}_{y^+}^C D_{2Re_\tau}^{\alpha(y^+),\lambda_r} = 3-\frac{1}{\Gamma(1-\alpha(y^+))}3\int_{y^+}^{2Re_\tau} 3(\xi - y^+)^{-\alpha(y^+)}3U^+(\xi)'3e^{-\lambda_r(\xi 3-3y^+)/Re_\tau}3d\xi \tag{5}$$

The variable order ($\alpha(y^+)$) appearing in (3) is found by employing the fractional – physics informed neural networks [9] for a fixed tempering length on both sides ($\lambda_l = \lambda_r = \lambda$) as shown in [7] with the aid of velocity data from direct

*Corresponding author. E-mail: george_karniadakis@brown.edu.

numerical simulations (DNS) of turbulent Couette flow [10]. The horizon of non-local interactions is computed by decomposing the integral appearing in (4, 5) into a sum of integrals over infinitesimally small domains. The fraction of the original domain associated with first n-integrals computed to 0.99999 times the original value of the fractional derivative is where the non-local interactions take place. Since the fractional order is a variable, the horizon then can be determined for all points in space.

RESULTS

Beyond the viscous sub-layer, the flow is non-local as indicated by the low fractional order values (figure 1(a)). While in the viscous sub-layer the fractional order (α) converges to unity, irrespective of the tempering length (figure 1(a)), as the flow is dominated by the *local interactions* governed solely by the viscous forces. Thus, the horizon near wall for both left- and right-length-scale are negligible (figure 1(b)). However, for $\lambda = 0$ (standard definition) the horizon shows other than zero; this is due to the fact that the second moment for a Levy distribution does not exists, or in other words, there could be infinite jump lengths, hence it takes the information of the entire available domain. However, for real applications there are only finite jump lengths and tempering the Levy distribution thus addresses real world phenomenon. The linear regions observed for $\lambda = 13$(figure 1(b)) indicates that the tempering length is too large to have an effect and it returns to a standard Levy distribution. The error in total shear stress is appreciably low (figure 1(c)) for any given tempering length. The error is primarily due to the use of first-order schemes for evaluating the integral (4, 5).

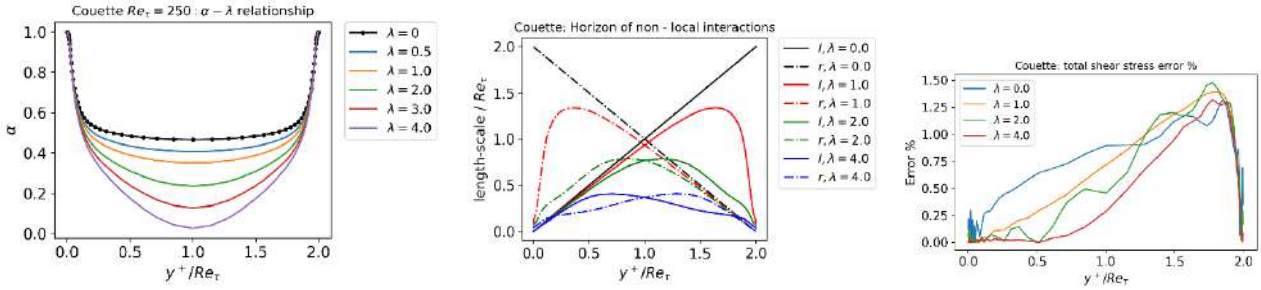

(a) (b) (c)

Figure 1: Results for Couette flow, $Re_\tau = 250$ (a) The effect of tempering length (λ) over fractional order (α). (b) Horizon of non-local interaction for various tempering lengths (λ), here, the length-scale, l and r are associated with the left- and right-sided fractional derivative, respectively. (c) The percentage error in total shear stress when compared to DNS [10] for various λ.

One of the major advantages of the tempered F-RANS is that it can be readily applied to unbounded flows, where the tempering length is tuned for the free stream beyond which non-local interactions do not occur. This has useful consequences, as a large number of engineering flows also uses free stream boundary conditions, such as a flow over an aerofoil. In a nutshell, this new model represents a generalized approach applicable to any type of flow.

CONCLUSIONS

Turbulence is governed by both local and non-local phenomenon, thus it has been cumbersome on a mathematical standpoint to address it with proper mathematical objects. The introduction of a variable–order fractional derivative is thus highly suitable to address such complex phenomenon, while tempering ensures its variance is finite, mimicking the real world. As a first step its merit is shown for turbulent Couette flow, however, this model does not inherently use any assumptions, thus this new definition is a general one and can be applied to any flow, which includes unbounded flows too.

References

[1] T. H. Solomon, E. R. Weeks, and H. L. Swinney, "Observation of anomalous diffusion and Lévy flights in a two-dimensional rotating flow," *Phys. Rev. Lett.*, vol. 71, no. 24, pp. 3975–3978, 1993.
[2] S. B. Pope, *Turbulent Flows*. Cambridge University Press, 2000.
[3] B. B. Mandelbrot and J. W. Van Ness, "Fractional Brownian Motions, Fractional Noises and Applications," *SIAM Rev.*, vol. 10, no. 4, pp. 422–437, Oct. 1968.
[4] M. M. Meerschaert, F. Sabzikar, M. S. Phanikumar, and A. Zeleke, "Tempered fractional time series model for turbulence in geophysical flows," *J. Stat. Mech. Theory Exp.*, vol. 2014, no. 9, Sep. 2014.
[5] I. Podlubny, "Fractional Derivatives and Integrals," in *Fractional Differential Equations: An Introduction to Fractional Derivatives, Fractional Differential Equations, to Methods of Their Solution and Some of Their Applications*, 1st Editio., Academic Press, 1998, pp. 41–62.
[6] W. Chen, "A speculative study of 2/3-order fractional Laplacian modeling of turbulence: Some thoughts and conjectures," *Chaos*, vol. 16, no. 2, 2006.
[7] P. P. Mehta, G. Pang, F. Song and G. E. Karniadiakis, "Discovering a universal variable-order fractional model for turbulent Couette flow using a physics-informed neural network," *Fract. Calc. Appl. Anal.*, vol. 22, no. 6, pp. 1675–1688, 2019.
[8] F. Song and G. E. Karniadakis, "A Universal Fractional Model of Wall-Turbulence," Aug. 2018.
[9] G. Pang, L. Lu, and G. E. Karniadakis, "FPinns: Fractional physics-informed neural networks," *SIAM J. Sci. Comput.*, vol. 41, no. 4, pp. A2603–A2626, 2019.
[10] V. Avsarkisov, S. Hoyas Calvo, M. Oberlack, and J. P. García Galache, "Turbulent plane Couette flow at moderately high Reynolds number," *J. Fluid Mech.*, vol. 751, pp. 1–10, 2014.

USING COMPUTATIONAL PHYSISCS TO PERFORM QUALITY CONTROL OF 4D FLOW MRI SYSTEMS

Franck Nicoud*[1], Thomas Puiseux [2], Anou Sewonu[2], Ramiro Moreno[2] andSimon Mendez[1]
[1]IMAG, Univ Montpellier, CNRS, Montpellier, France
2ALARA Expertise, Strasbourg, France

Summary A numerical pipeline is developed to compute the outcome of Phase Contrast Magnetic Resonance Imaging, a modality able to characterize the hemodynamics of large vessels under *in vivo* conditions. The methodology requires solving the Navier-Stokes (for the flow dynamics) and Bloch (for the spins magnetisation) equations simultaneously and makes use of a semi-analytic solution for the Bloch equations as well as an original particle re-injection strategy. After being validated, the methodology is applied to the pulsatile flow within an *in vitro* experiment designed to represent the typical flow features in the largest vessels of the cardiovascular system. The simulated Magnetic Resonance Images compare favourably with the experimental and computational unsteady 3D flow and allows explaining some of the systematic errors related to Phase Contrast Magnetic Resonance Imaging.

MOTIVATION

Hemodynamics in large vessels is closely related to several diseases of the cardiovascular systems such as aneurysm generation and rupture, stenosis or thromboembolism. Time-resolved 3D phase-contrast Magnetic Resonance Imaging (or 4D Flow MRI) is a promising tool for non-invasive blood flow quantification under *in vivo* conditions [1]. As for its morphological counterpart, the basic principles of 4D flow MRI arise from the magnetic properties of the protons. This imaging technique takes advantage of the nuclear spin of the hydrogen atoms, widely present in tissues like vessels or blood, and consists in analyzing the response of the spins after they are excited by the Radio-Frequency signal (RF) and immersed in a properly designed time-dependent and inhomogeneous magnetic field (the so-called MRI sequence). If morphological MRI is now part of the clinical routine, the 4D flow modality still belongs to clinical research and requires more assessment/characterization before it can be widely used by non-experts. Several artifacts have been identified which are related to either MRI principles (e.g.: partial volume effect, acceleration induced error, intra-voxel phase dispersion, spatial misregistration) or technology (e.g.: Gibbs artifacts, magnetic field distortion, coil sensitivity profile). A way to better understand and quantify these measurement errors consists in numerically simulating the MRI experiment in order to reconstruct synthetic images in which technological errors are either absent or controlled. On top of identifying the effects of the different types of errors on the velocity measurements, the ability to build *in silico* 4D flow images could serve as a support to optimize MRI sequences at low price. The main objective of this work is thus to develop an efficient numerical pipeline able to represent the outcome of actual 4D flow MRI systems.

METHODS

The macroscopic behaviour of a collection of spins is governed by the Bloch equations [2] which read

$$\frac{d\mathbf{M}}{dt} = \gamma \mathbf{M} \times \mathbf{B} + \frac{M_0 - M_z}{T_1}\mathbf{e_z} - \frac{M_x}{T_2}\mathbf{e_x} - \frac{M_y}{T_2}\mathbf{e_y} \qquad (1)$$

where $\mathbf{B}(t) = B_0\mathbf{e_z} + \mathbf{B_1}(t)$ is the magnetic field generated by the MRI system to excite the spins, γ is the gyromagnetic ratio which equals 267.513×10^6 rad $s^{-1}T^{-1}$ form the hydrogen atoms, T_1 and T_2 are the longitudinal and transverse relaxation times of the tissues and $\mathbf{M}(t) = M_x\mathbf{e_x} + M_y\mathbf{e_y} + M_z\mathbf{e_z}$ is the magnetization vector expressed in the cartesian basis $(\mathbf{e_x}, \mathbf{e_y}, \mathbf{e_z})$. When submitted to the stationary magnetic field $B_0\mathbf{e_z}$, the spins rotate around the z-axis at the Larmor angular frequency γB_0 and generate the magnetization vector $M_0\mathbf{e_z}$. A common approach is to solve the Bloch equations within the Eulerian framework in order to avoid solving for a very large number of particles and reduce the computational time [3], [4]. Since the equations for fluid mechanics are most often solved within the Eulerian framework as well, this choice also simplifies accounting for the spins convection by the blood motion when phase contrast MRI is dealt with. In turn, the Lagrangian formalism offers the possibility to use analytical solutions for the Bloch equations once the MRI sequence has been properly idealized [5], but requires to track a large number of particles to avoid spurious images due to spins density inhomogeneity. In any case, the usual strategy is to decouple the magnetization and fluid problems, solving and storing the information from the Navier-Stokes equations in a first step and solving Eq. (1) in a second round [6]. This approach is well suited for stationary cases but requires a huge amount of data storage when dealing with pulsatile flows. Indeed, the 4D flow MRI acquisition requires simulating several (a few tens or hundreds) cardiac cycles; it turns out that, to the best of our knowledge, no *in silico* 4D MRI of complex flow configuration has been presented so far.

* Corresponding author. E-mail: franck.nicoud@umontpellier.fr

An Eulerian (fluid) - Lagrangian (spins) simulation strategy is proposed to generate *in silico* the kind of images that a 4D Flow MRI system would produce. The data storage issue is avoided by solving the Bloch equations on Lagrangian particles with "on the fly" coupling to the flow solver. In this view, each Lagrangian particle represents a sample of spins (isochromat) transported by the turbulent velocity field, as computed by Large Eddy Simulation with proper sub-grid scale model [7]. For each isochromat, a semi-analytic formulation of Eq. (1) is then used to speed up the computation of the magnetization vector. Eventually, an original volume particle reinjection strategy is implemented that mimics the periodic removal of the transverse magnetization (the RF-spoiling in actual 4D Flow MRI) and allows keeping the particle distribution homogeneous in space, independently of the number of particles considered. This allows generating non-spurious images while tracking less than 50 particles per voxel while 1000 was recently recommended [6] in the classical framework without reinjection. The pipeline was implemented in the in-house YALES2BIO solver (imag.umontpellier.fr/~yales2bio/) dedicated to the computation of blood flows [7-8] and verified by considering several elementary configurations (e.g.: [10]).

RESULTS AND CONCLUDING REMARKS

The *in vitro* flow phantom designed and studied by computational fluid dynamics (CFD) as well as experimentally by 4D flow MRI in [11] was then simulated by the numerical pipeline proposed. As illustrated in Fig. 1 (left), the configuration includes an aneurysm, a curved channel as well as a bifurcation; it produces, under pulsatile conditions, a complex flow with several features typical of the cardiovascular hemodynamics (recirculation, periodic turbulence generation, shear layer, boundary layer separation, jetting flow). Fig. 1 (middle) shows that the outcome of the proposed pipeline (the reconstructed hemodynamics from *in silico* 4D flow MRI) is in very good agreement with the phase-averaged CFD velocity field. Note that the latter is very well correlated (approx. 97 %, [11]) with the flow measurement obtained with an actual imaging system (1.5 T Siemens) operated at University Hospital of Toulouse-Rangueil. Fig. 1 (right) shows that the largest discrepancies are located near the exit of the collateral vessel. A deeper analysis suggests that this large error site is a consequence of neglecting acceleration in 4D Flow MRI sequences (not shown). Overall the discrepancies are larger for the experimental 4D Flow MRI, reflecting that the experimental noise due to magnetic field inhomogeneities and off-resonance effects are not present in the MRI simulations. This illustrates how the pipeline can be used to better understand and control the different sources of errors when measuring the hemodynamics of large vessels.

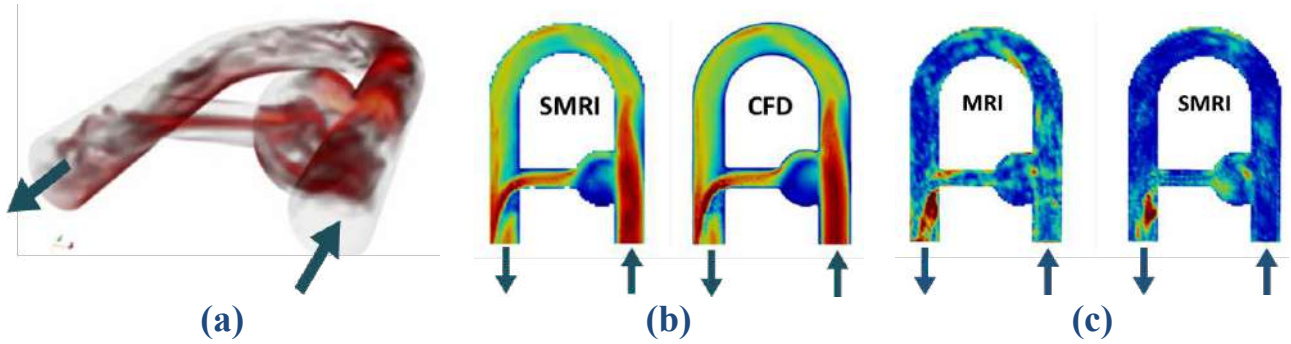

Figure 1. Outcomes of the CFD and MRI simulations at peak systole. The arrows indicate flow direction at inlet/outlet. **(a)** : 3D view (positive vorticity) of the flow within the phantom designed in [11]. **(b)** : Magnitude of the velocity from *in silico* 4D Flow MRI (SMRI) and predicted by CFD at peak systole. Scale is from 0 (blue) to 0.12 m/s (red). **(c)** : L2-norm of the discrepancies between the CFD velocity field and the experimental (MRI) or *in silico* (SMRI) 4D Flow MRI. Scale is from 0 (blue) to 0.12 m/s (red).

References

[1] M. Markl *et al.*, "Advanced flow MRI: emerging techniques and applications," *Clin. Radiol.*, 2016.
[2] F. Bloch, "Nuclear induction," *Phys. Rev.*, **70**, pp. 460–474, 1946.
[3] A. Hazra, G. Lube, and H.-G. Raumer, "Numerical simulation of Bloch equations for dynamic magnetic resonance imaging," *Appl. Numer. Math.*, **123**, pp. 241–255, 2018.
[4] S. Lorthois, J. Stroud-Rossman, S. Berger, L. Der Jou, and D. Saloner, "Numerical simulation of magnetic resonance angiographies of an anatomically realistic stenotic carotid bifurcation," *Ann. Biomed. Eng.*, **33**, no. 3, pp. 270–283, 2005.
[5] C. Xanthis, I. Venetis, A. Chalkias, and A. Aletras, "MRIsimul: A GPU-based parallel approach to MRI simulations," *IEEE Trans. Med. Imaging*, **33**, pp. 607–617, 2014.
[6] A. Fortin, S. Salmon, J. Baruthio, M. Delbany, and E. Durand, "Flow MRI simulation in complex 3D geometries: Application to the cerebral venous network," *Magn. Reson. Med.*, **80**, no. 4, pp. 1655–1665, 2018.
[7] F. Nicoud, H. Baya Toda, O. Cabrit, S. Bose, and J. Lee, "Using singular values to build a subgrid-scale model for large eddy simulations," *Phys. Fluids*, **23**, no. 8, p. 085106, 2011.
[8] C. Chnafa, S. Mendez, R. Moreno, and F. Nicoud, *Using image-based CFD to investigate the intracardiac turbulence*, **14**. 2015.
[9] F. Nicoud, C. Chnafa, J. Siguenza, V. Zmijanovic, and S. Mendez, *Large-Eddy simulation of turbulence in cardiovascular flows*, **84**. 2018.
[10] C. Yuan, G. Gullberg, and D. Parker, "The solution of Bloch equations for flowing spins during a selective pulse using a finite difference method," *Med. Phys.*, **14**, pp. 914–921, 1987.
[11] T. Puiseux *et al.*, "Reconciling PC-MRI and CFD: an in-vitro study," *NMR Biomed.*, **32**, no. 5, p. e4063, 2019.

RECENT PROGRESS IN COMPUTATIONAL PREDICTION OF HEMOCOMPATIBILITY

Marek Behr*[1], Anna Maria Ranno[1], and Stefan Haßler[1]
[1]Chair of Computational Analysis of Technical Systems (CATS) Center for Simulation and Data Science (JARA-CSD) RWTH Aachen University, 52056 Aachen, Germany

Summary Simulation-based biomedical engineering relies on a variety of physical and physiological models to represent the reality. In addition to macro-scale biomechanics, models extend now increasingly to cellular and molecular scales. For prediction of blood damage, the averaged red blood cell behavior is modeled in the form of coupled partial differential equations, exhibiting certain similarities to macroscopic models of constitutive behavior of microstructured fluids. The numerical approaches also follow the paths established in the viscoelastic flow community, from stabilized finite element formulations to logarithmic transformation of primary variables.

INTRODUCTION

Modeling and computational analysis play an increasingly-important role in bioengineering, particularly in the design of implantable ventricular assist devices (VAD) and other blood-handling devices. Numerical simulation of blood flow and associated physiological phenomena has the potential to shorten the design cycle and give the designers important insights into causes of blood damage and suboptimal performance [1,2].

METHODOLOGY

A set of modeling techniques is presented which are based on stabilized space-time finite element formulation of the Navier-Stokes equations. An Arbitrary Eulerian Lagrangian (ALE) moving mesh approach combined with a limited remeshing technique – shear-slip mesh update method – are used to represent the movement of the rotating parts of the pump. Alternate methods that represent the rotating components in an averaged sense using a rotating frame of reference have been compared to the high-fidelity ALE approach, and showed adequate representation of the flow field at a greatly reduced computational cost [3].

Tensor morphology model

In order to obtain quantitative hemolysis prediction, cumulative tensor-based measures of strain experienced by individual blood cells must be developed; red blood cells under shear can be modeled as deforming droplets, and their deformation tracked along pathlines of the computed flow field. Originally, these models were based on integrating the evolution of the droplet shapes over a representative sample of pathlines. Although this approach has some advantages, such as the possibility to account for the tank-treading motion of the membrane, it was relatively inefficient, and it was difficult to provide adequate coverage of the entire flow volume. An efficient continuum-based approach was developed as an alternative, where a tensor field is undergoing an evolution in every part of the fluid domain. As such, this continuum representation of the RBC shape shows similarities to some common viscoelastic constitutive models (Fig. 1).

Log-morph transformation

A reformulation in terms of logarithm of the morphology tensor, analogous to the log-conf formulations which are finding use in flow rheology [4], is shown to improve the numerical behavior of the hemolysis quantification tools. This reformulation is able to represent the very sharp boundary and internal layers which tend to develop in the tensor field. Moreover, it guarantees by construction the positive definiteness of the conformation tensor, precluding the numerical difficulties normally associated with the local loss of such definiteness. A downside is that the morphology equation in the log-morph form becomes relatively complex.

Stabilized finite element formulation

A critical aspect is the proper stabilized formulation of this transport equation. Here, a Variational Multiscale (VMS) approach was found to be beneficial, allowing for the first time robust simulation of the blood cell deformation across the broad range of flow fields, including those found in actual devices which are of engineering and clinical interest.

Concentration equation transformation

Another area where reformulation of the governing equations may be useful is the hemoglobin concentration equation. Regardless of modeling approach to quantify release (source) of hemoglobin, local concentration and accumulation is governed by a strongly non-linear advection-diffusion-reaction equation. The standard form of such an equation does not guard against non-physical values of concentration, such as negative or extremely high concentrations which may result from numerical artifacts. A restating of the equation in terms of tailored functions of concentration [5] improves the numerical behavior, and often makes the model more suitable for model order reduction.

*Corresponding author. E-mail: behr@cats.rwth-aachen.de.

RESULTS AND CONCLUSIONS

The methods are applied to several rotary blood pump configurations. One of them is a simplified centrifugal pump, which was recently the subject of an FDA round-robin study. A second device undergoing computational analysis with these tools is a prototype centrifugal blood pump now in development and in clinical trials [6]. For both the FDA and the prototype pump, a variety of experimental data is becoming available, ranging from PIV-generated averaged flow fields, to the measures of hemolysis.

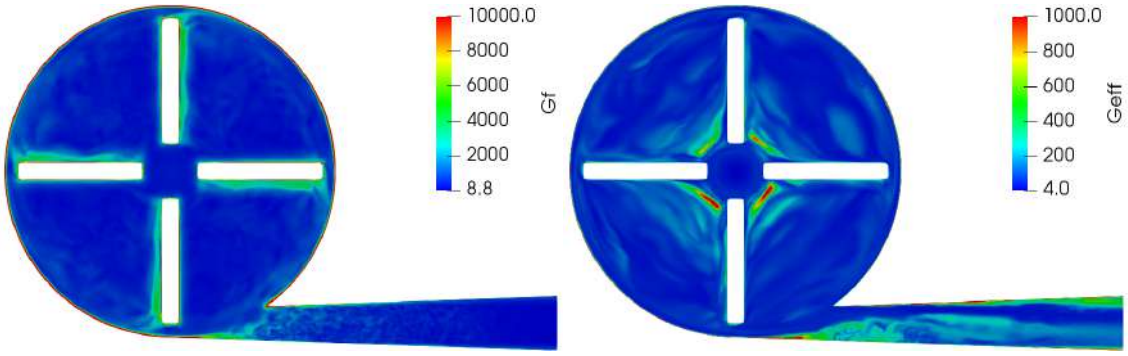

Figure 1. Actual shear rate in a cross-section of a simplified centrifugal blood pump (left) shows potential hemolysis areas but does not take into account the delay between flow shear stress and red blood cell deformation. The cell deformation is correlated to the effective shear rate in a morphology model (right). This more accurately identifies the areas where excessive shear and higher residence time combine to deform red blood cells, thus promoting pore formation and hemoglobin release.

References

[1] Vitale F., Nam J., Turchetti L., Behr M., Raphael R., Annesini M.C., Pasquali M. A Multiscale Biophysical Model of Flow-Induced Red Blood Cell Damage, *AIChE Journal,* **60**:1509-1516, 2014.

[2] Gesenhues L., Pauli L., Behr M. Strain-Based Blood Damage Estimation for Computational Design of Ventricular Assist Devices, *International Journal of Artificial Organs*, **39**:166-170, 2016.

[3] Pauli L., Both J., Behr M. Stabilized Finite Element Method for Flows with Multiple Reference Frames, *International Journal for Numerical Methods in Fluids*, **78**: 657–669, 2015.

[4] Knechtges P., Behr M., Elgeti S. Fully-Implicit Log-Conformation Formulation of Constitutive Laws, *Journal of Non-Newtonian Fluid Mechanics*, **214**: 78–87, 2014.

[5] Hassler S., Ranno A.M., Behr M., Finite-Element Formulation for Advection–Reaction Equations with Change of Variable and Discontinuity Capturing, *Computer Methods in Applied Mechanics and Engineering*, **369**:113171, 2020.

[6] Hassler S., Pauli L., Behr M. The Variational Multiscale Formulation for the Fully-Implicit Log-Morphology Equation as a Tensor-Based Blood Damage Model, I*nternational Journal for Numerical Methods in Biomedical Engineering*, **35**:e3262, 2019.

HYBRID LEVEL-SET/EMBEDDED BOUNDARY NUMERICAL METHOD FOR THE SIMULATION OF SOLIDIFICATION/MELT PROBLEMS

Alexandre Limare*[1], Stéphane Popinet[2], and Christophe Josserand[1]
[1]Laboratoire d'Hydrodynamique de l'Ecole polytechnique, Institut Polytechnique de Paris, Palaiseau, France
[2]Institut Jean lerond d'Alembert, CNRS & Sorbonne Université, Paris, France

Summary In this paper, we present a novel way to represent the interface for two-phase flows with phase change. We combine a level-set method with an embedded boundary method and take advantage of both. This is part of an effort to obtain a numerical strategy relying on Cartesian grids allowing the simulation of complex boundaries with possible change of topology while retaining a high-order representation of the gradients on the interface and the capability of properly applying boundary conditions on the interface. This new numerical method is then applied to some validation test cases.

INTRODUCTION

Flows with moving interfaces between two phases are quite commonly encountered in engineering and fundamental fluid physics studies and are of interest to a wide community of researchers. Having a computational tool able to deal with such flows accurately and efficiently has been the goal that gave birth to several families of numerical methods which started with Harlow and Welch's marker and cell (MAC) method [1], Volume of Fluid [2] (VOF), phase field [3] and level-set methods [4]. Most of the time, in a two-phase flow simulation, one method is best suited, depending on the main properties of the flow: possible phase change, shear of the interface, complex topological changes of the interface (splitting/merging). This is because they treat the interface differently by construction. Thus, the development of numerical methods combining the best properties of the aforementioned techniques is still an open field of research. Levelset methods are for example known to provide simple access to geometric quantities while not exactly conserving mass, in contrast to VOF methods. This lead Sussman and Puckett [5] to combine a VOF method with a level-set in order to remove this limitation. Our work is the direct continuity of such endeavours. We developed a numerical approach combining a level-set function used as an embedded boundary method [6] for phase change simulations. We present a few preliminary results on validation test cases.

NUMERICAL METHOD

Let ϕ be a level-set function, whose zero level-set is a hypersurface which represents the interface Γ. Subscripts $_L$ and $_S$ will denote the liquid and the solid respectively. The equation describing the motion of the interface is the following:

$$\partial_t \phi + \mathbf{u_{pc}}|_\Gamma \cdot \nabla \phi = 0 \tag{1}$$

$\mathbf{u_{pc}}|_\Gamma$ is the phase-change velocity which is given by a Dirichlet boundary conditions on the interface, the so-called Stefan condition:

$$L_H \ \mathbf{u}_{pc}|_\Gamma = k_L \ \nabla T_L|_\Gamma - k_S \ \nabla T_S|_\Gamma \tag{2}$$

where L_H is the latent heat, k_i are the thermal diffusivities. The normal derivative of the temperature, are obtained by imposing the interface temperature following the relation:

$$T_\Gamma = T_m - \epsilon_\kappa \kappa - \epsilon_u u_{pc}, \tag{3}$$

where κ is the curvature of the interface, ϵ_κ is the surface tension coefficient and ϵ_u is the molecular kinetic coefficient. This condition consists of imposing the temperature of the interface to be the melting one, corrected by the Gibbs-Thomson (curvature term) and kinetic (velocity term) corrections [7].

A level-set approach requires solving the heat equation in a complex domain with Dirichlet boundary conditions on the interface Eq. (3), then computing the jump in the normal derivative of the temperature, and then extending this to the region around the front. The extension of the velocity off the interface is necessary to obtain a continuous field that can be used in Eq. (1). In our approach the level-set function is used as an embedded boundary method [6]. Thus, this can be seen as two-fluid approach where, from the perspectibe of each phase, the embedded boundary is the interface between the two fluids. Therefore each phase has its own set of variables. The embedded boundary method gives us the tools needed to compute high-order approximations of the gradients on the interface (Fig. 1(a)) and, Eq. (2) and Eq. (3) :

$$\nabla \phi|_\Gamma = \frac{1}{d_2 - d_1} \left(\frac{d_2}{d_1}(\phi_f - \phi_1) - \frac{d_1}{d_2}(\phi_f - \phi_2) \right) \tag{4}$$

In our method u_{pc} is a cell-centered velocity defined in both phases. The initial values on the interface centroids in red on Fig. 1(b) are given by relation (3) and the method of Chen *et al.* [8] is then used to extend the velocity off the interface. We use an iterative method to correct the cell-centered values u_{pc} (in black) so that their bilinear interpolation matches the correct interfacial boundary condition $u_{pc}|_\Gamma$.

*Corresponding author. E-mail: alexandre.limare@polytechnique.edu

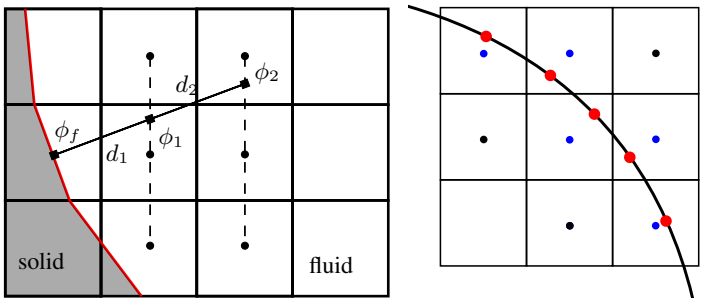

(a) Gradients calculation (b) u_{pc}

Figure 1: Embedded boundary approach

TEST CASES

We validated our method with some test cases, such as 1D solidification, the stable solidification of a Gaussian bump and the melting of a starry-shaped ice particle. We show the evolution of the interface at different times on Fig. 2(a) and 2(b) . We are planning to do a proper stability analysis corresponding to the Mullins–Sekerka instability and we also would like to study dendrite growth and run a few cases combining solidification and convection.

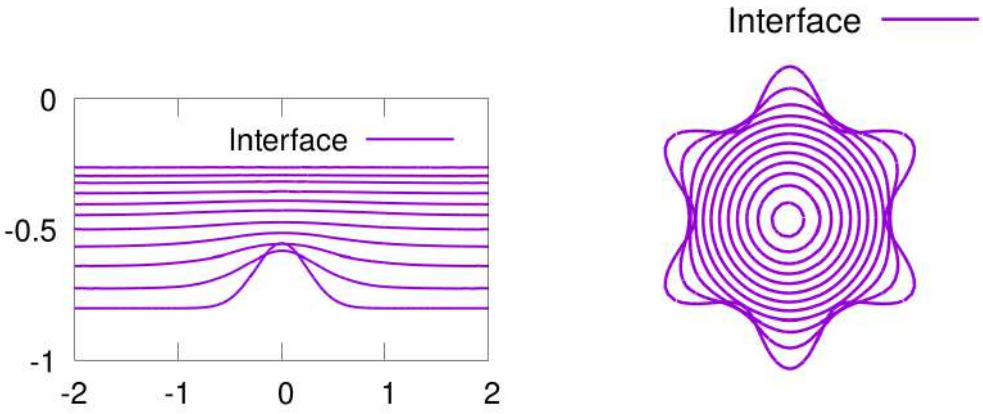

(a) Solidification of an initial Gaussian bump (b) Melting of a starry-shaped ice particle

Figure 2: Test cases

References

[1] F. Harlow and J. E. Welch, "Numerical calculation of time-dependent viscous incompressible flow of fluid with free surface," *The physics of fluids*, vol. 8, no. 12, pp. 2182–2189, 1965.

[2] C. W. Hirt, A. A. Amsden, and J. L. Cook, "An arbitrary Lagrangian-Eulerian computing method for all flow speeds," *Journal of Computational Physics*, vol. 14, no. 3, pp. 227–253, 1974.

[3] J. Langer, "Models of pattern formation in first-order phase transitions," in *Directions in Condensed Matter Physics: Memorial Volume in Honor of Shang-Keng Ma*, pp. 165–186, World Scientific, 1986.

[4] S. Osher and J. A. Sethian, "Fronts propagating with curvature-dependent speed: algorithms based on Hamilton-Jacobi formulations," *Journal of computational physics*, vol. 79, no. 1, pp. 12–49, 1988.

[5] M. Sussman and E. G. Puckett, "A coupled level set and volume-of-fluid method for computing 3d and axisymmetric incompressible two-phase flows," *Journal of Computational Physics*, vol. 162, pp. 301–337, aug 2000.

[6] H. Johansen and P. Colella, "A Cartesian grid embedded boundary method for Poisson's equation on irregular domains," *Journal of Computational Physics*, vol. 147, no. 1, pp. 60–85, 1998.

[7] M. Worster, *Perspectives in Fluid Dynamics a Collective Introduction to Current Research*, ch. Solidification of Fluids. Cambridge Univ. Press, 2000.

[8] S. Chen, B. Merriman, S. Osher, and P. Smereka, "A simple level set method for solving Stefan problems," *Journal of Computational Physics*, vol. 135, no. 1, pp. 8–29, 1997.

ONLINE REDUCED-ORDER MODEL AND ITS APPLICATION ON ADJOINT-BASED MESH ADAPTATION FOR LARGE EDDY SIMULATION

Xiaodong Li*, Steven John Hulshoff, and Stefan Hickel
Department of Aerodynamics, Wind Energy, Flight Performance and Propulsion, Delft University of Technology, Delft, the Netherlands

Summary We present a mesh adaptation strategy based on adjoint method to improve the performance of Large Eddy Simulation (LES) so as to address the difficulties of mesh generation in high-fidelity simulations. The adjoint method is employed to facilitate Adaptive Mesh Refinement (AMR) by controlling local contributions to an physical quantity of interest (such as lift, drag). Since solving the adjoint problem for unsteady simulations requires the access to flow states, an online reduced-order model, which is implemented by an enhanced incremental singular value decomposition, is considered to tackle this issue instead of storing them. The ROM-enabled AMR approach is verified in a Burgers problem with a multiple-frequency forcing term compared to those from full-order flow solutions. Numerical results validate the efficiency and effectiveness of the ROM-enabled AMR approach for LES.

INTRODUCTION

Large Eddy Simulation (LES) has the potential to deliver reliable flow predictions for cases involving mixing layers, large pressure gradients or high unsteadiness. The main challenge of LES for practical applications is how to make its computing cost tractable while keeping a good accuracy of the Quantity of Interest (QoI), e.g. lift or drag. Constructing such meshes, however, usually involves experience and trial even for engineering experts. Adaptive Mesh Refinement (AMR) [1] provides the ability to automatically change the computational mesh, resulting in a considerable reduction of computing cost. Thus, it has been widely used to improve the computing efficiency. On the other hand, adjoint methods can be used to facilitate the AMR by connecting local mesh contributions with the error of approximating a QoI so that the adapted mesh can provide the highest accuracy per degree of freedom. Through doing this, a posterior estimation can be developed for AMR, which has been investigated largely in steady laminar and turbulent flow problems [2].

In unsteady simulations, the primal flow problem is advanced forward in time, while the adjoint problem needs to be solved backward in time. Due to the non-linearity of Navier-Stokes equations, flow states from LES are required for completely solving the adjoint problem. Unfortunately, the resources required to record these solutions would be very huge, even prohibitive, for practical problems. Hence, a Reduced-Order Model (ROM) is considered to address this difficulty, which will be elaborated in following sections.

AN AMR STRATEGY BASED ON ADJOINT METHOD AND ROM FOR LES

In present work, the Proper Orthogonal Decomposition (POD) is utilized to build ROM because POD is capable of extracting optimal low-dimensional bases, viz. POD modes, to represent the high-dimensional flow field while retaining important dynamic features of the full-order system [3]. The procedure of building a ROM is stated as follows, (i) POD analysis to obtain POD modes, (ii) computing the coefficients of ROM, and (iii) reconstructing the flow solution in a low-order space. In order to make it feasible for practical problems, the POD implemented by incremental Singular Value Decomposition (SVD) [4] is introduced to achieve an online ROM as shown in Algorithm 1. One improvement of this algorithm is that an enhanced step is added by truncating the number of selected POD modes on-the-fly as well (stated in Line 5).

Algorithm 1 Incremental weighted SVD

Input: $V \in \mathbb{R}^{n\times k}, \Sigma \in \mathbb{R}^{k\times k}, W \in \mathbb{R}^{m\times k}, c \in \mathbb{R}^{n}, \mathrm{tol}, \mathrm{tol}_{\mathrm{sv}}, \mathrm{nModes}$

1: **Get the dimension:** $k = \mathrm{nColumns}(V)$.
2: **Project of a new column into an existing space:** $d = V^{\intercal}c, \quad p = \|c - Vd\|_2$.
3: **Neglect the small projection** ($< \mathrm{tol}$)**.**
4: **Apply standard SVD analysis on an updated matrix** Q**:** $V_Q, \Sigma_Q, W_Q = \mathrm{SVD}(Q)$.
5: **Truncation 1: truncate on the selected number of POD Modes** (nModes)**:**
$k = \mathrm{nModes}, \quad \Sigma = \Sigma_{(1:\mathrm{nModes},1:\mathrm{nModes})}, \quad V = V_{(:,1:\mathrm{nModes})}, \quad W = W_{(:,1:\mathrm{nModes})}$.
6: **Truncation 2: neglect small singular values** ($< \mathrm{tol}_{\mathrm{sv}}$)**.**
7: **Re-orthogonalize the modes if necessary.**

The QoI used here is chosen as an volume-integrated function of flow variables. Variational Multiscale Method (VMM) is applied as a LES model and the error estimation is accomplished by representing the actual solution by resolved and

*Corresponding author. E-mail: X.Li-12@tudelft.nl.

unresolved scales. The error estimation is constrained on each element to form elemental error indicator by which the cell will be marked in whether to be refined or not. We use a mesh adaptation strategy to refine 10% cells with largest errors and an auxiliary algorithm to keep the smoothness of the adapted mesh. Finally, a novel AMR strategy is formulated based on adjoint method and ROM for LES.

NUMERICAL RESULTS

This novel technique is validated on an 1D unsteady Burger problem with a multiple-frequency forcing term, which is designed to produce flow solutions with large fluctuations. Figure 1 shows the approximation of a QoI by uniform, full-order solution-based and one-mode ROM-enabled AMRs. These results demonstrate that the AMR-based computation is more efficient than the uniform refinement and the ROM-enabled AMR has a reasonable agreement with full-order solution-based AMR although only one POD mode is used to construct the ROM. Furthermore, online POD analysis does not alter the convergence of the computation, which has the same accuracy of calculations from the AMR technique based on a standard ROM. Overall, ROM-driven AMR does not affect the computing accuracy of the QoI and online ROM can keep this property as long as the significant modes are considered. Figure 2 depicts the comparison of first eigenvalue between standard and online ROMs. We can observe that they tally well with each other except for the last two AMR levels. This results from the limited number of selected POD modes, which means that one POD mode is not enough to capture significant flow features on fine meshes. Thus, the discrepancy of computations occurs. This can be improved by increasing the number of selected POD modes, as shown from the results of a four-mode ROM in this figure.

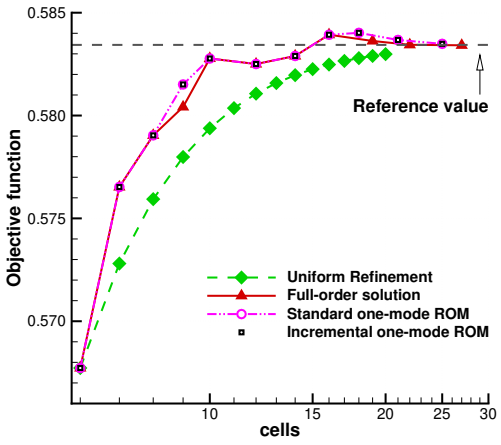

Figure 1: QoI's approximations by different AMRs. Green, red and purple lines and black square denote results from the uniform refinement, full-order solution-based AMR, ROM-based AMR, and online ROM-based AMR, respectively.

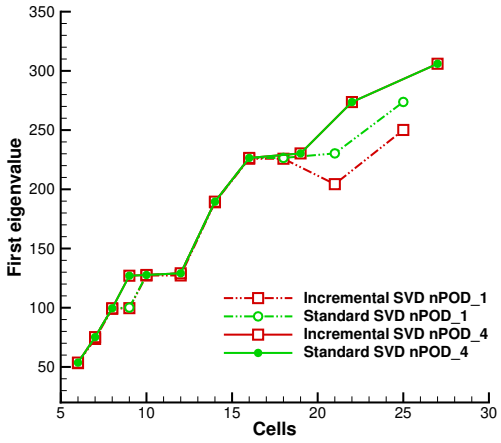

Figure 2: Eigenvalue evolutions of one-mode (dashdotdot lines) and four-mode (solid lines) ROMs during AMR from online (red) and standard (green) SVD

CONCLUSIONS

To summarize, adjoint-based AMR can be used to significantly reduce the computing cost of LES regarding to an interested output function. The ROM-driven AMR preserves the efficiency of solution-driven AMR in the current case and reducing the number of POD modes has a slight impact on QoI's convergence. Thus, ROM can give a correct prediction of primal flow solutions. As long as the POD modes are able to capture major flow structures, the ROM-driven AMR is effective and will acquire a good accuracy of the QoI. The online algorithm further improves the feasibility of ROM-enabled AMR for more challenging problems without losing the accuracy of the computation.

References

[1] J. Slotnick et al. *CFD vision 2030 study: a path to revolutionary computational aerosciences*. Report NASA/CR–2014-218178. Washington, DC 20546-0001: National Aeronautics and Space Administration, 2014, p. 58.

[2] K. J. Fidkowski and D. L. Darmofal. "Review of Output-Based Error Estimation and Mesh Adaptation in Computational Fluid Dynamics". In: *AIAA Journal* 49.4 (2011), pp. 673–694.

[3] K. Taira et al. "Modal Analysis of Fluid Flows: An Overview". In: *AIAA Journal* 55.12 (2017), pp. 4013–4041.

[4] H. Fareed et al. "Incremental proper orthogonal decomposition for PDE simulation data". In: *Computers & Mathematics with Applications* 75.6 (2018), pp. 1942–1960.

COUPLING ADJOINT SENSITIVITY ANALYSIS WITH THE POLYNOMIAL CHAOS EXPANSION FOR EFFICIENT UNCERTAINTY QUANTIFICATION

Kyriakos D. Kantarakias[1] andGeorge Papadakis *[1]
[1]Department of Aeronautics, Imperial College London, London, United Kingdom

Summary We present a method for Uncertainty Quantification (UQ) that uses the Polynomial Chaos Expansion (PCE) coupled with the adjoint method. In contrast to the standard PCE, where the computational cost scales in a power law with the number of stochastic parameters, N, in the coupled method the cost is independent of N. The method works for small input uncertainties, and takes advantage of widely available software for solving PDEs and the corresponding adjoint problem. The method is applied to a transonic airfoil with uncertain geometry, and results are compared with traditional UQ methods, such as Monte Carlo.

UNCERTAINTY QUANTIFICATION WITH THE POLYNOMIAL CHAOS EXPANSION

In Computational Fluid Dynamics, as well as in general mechanics problem, we consider systems in the form

$$\frac{d\mathbf{u}}{dt} = \mathbf{f}(\mathbf{u}, \mathbf{s}) \tag{1}$$

where $\mathbf{u}$ are the field variables and $\mathbf{s}$ denotes a set of design parameters. In many practical cases, such as turbulent flows, it is of interest to compute quantities that are integrals of the field $\mathbf{u}$, in the form

$$J = \int_{\Omega} h(\mathbf{u}, \mathbf{s}) d\Omega \tag{2}$$

In the case of fluid mechanics, (1) represents the Navier–Stokes equations and J is for example the drag or lift coefficients of an airfoil. If the vector $\mathbf{s}$ is of stochastic nature, uncertainty will propagate through the flow field $\mathbf{u}$ and introduce uncertainties into the Quantity of Interest (QoI) of eq. 2. These uncertainties are of interest since they characterise the performance of the system. In real world applications, spectral approaches such as the PCE, are the state of the art for conducting UQ, due to their low cost for a small number of uncertain variables. In such methods, the QoI is written in spectral form

$$J(\xi) = \sum_{i=0}^{\infty} J^i \Psi_i(\xi) \tag{3}$$

where ξ is a vector modelling the stochastic behavior of $\mathbf{s}$ and Ψ_j refers to polynomials that are orthogonal to the PDF of $\mathbf{s}$. Here J^i is computed by the the Galerkin integral

$$J^i = \int_{\mathcal{E}} J \Psi_i d\xi \approx \sum_{j=1}^{\alpha} \omega_j J(\xi_j) \Psi_i(\xi_j) \tag{4}$$

where the value of a depends on the integration grid chosen. This method, first presented in [2] is accurate, however its computational cost has a power law scaling with the number of uncertain parameters.

DECOUPLING THE COST OF THE PCE FROM THE NUMBER OF UNCERTAIN VARIABLES

The computational cost of conducting UQ with the PCE can be decoupled from the number of uncertain parameters, by employing the adjoint sensitivity analysis, as in [1]. The sensitivities of 2 with respect to $\mathbf{s}$ can be computed by solving the adjoint equation of 1 to find the Lagrange multipliers of $\mathbf{u}$. The adjoint sensitivity analysis can compute the sensitivity of the QoI (2) with respect to multiple parameters, with a computational cost that is decoupled from the dimension of $\mathbf{s}$. This property can be employed to compute the statistics of the QoI, by approximating the spectral coefficients of the expansion in eq. 4 using the information from the sensitivities, namely

$$J(\xi_j) = J_\mu + (\xi_j - \xi_\mu)^T \nabla J_\mu \tag{5}$$

Where ∇J_μ is computed with adjoint sensitivity analysis at the mean value of the stochastic inputs, ξ_a. With eq. 5, we approximate the values of J at eq. 4, while ω_j and Ψ_j are given by the PCE. This approach implies the locality of the adjoint and is therefore not suitable for UQ of large uncertainties. However, in most aerodynamic applications, such as the quantification of uncertainties in the geometry of airfoils uncertainties are usually small and global UQ is of no practical interest, therefore implying an equivalence between local UQ and sensitivity analysis.

*Corresponding author. E-mail: k.kantarakias@imperial.ac.uk

TRANSONIC INVISCID 2D NACA0012 WITH UNCERTAIN GEOMETRY

This test case for the method deals with the inviscid flow around a NACA0012 airfoil, at $M_\infty = 0.8$ and $a_\infty = 1.25°$, which is a common benchmark problem for methods focusing on aerodynamics. The geometry of the airfoil is written as

$$y_{airfoil} = y_{base} + \sum_{i=1}^{N} a_i f_i(x) \tag{6}$$

where $f_i(x)$ are the Hicks–Henne bump functions, commonly used in shape optimization problems in aerodynamics [3]. For the purposes of demonstration, we consider Gaussian uncertainties in the set of weights $(a_1, a_2, \dots a_N)$, with a standard deviation equal to 1% of their mean value. In figure 1 we see that the Monte–Carlo simulation converges to the mean value and standard deviation predicted by the adjoint enhanced PCE. A comparison of the moments predicted by

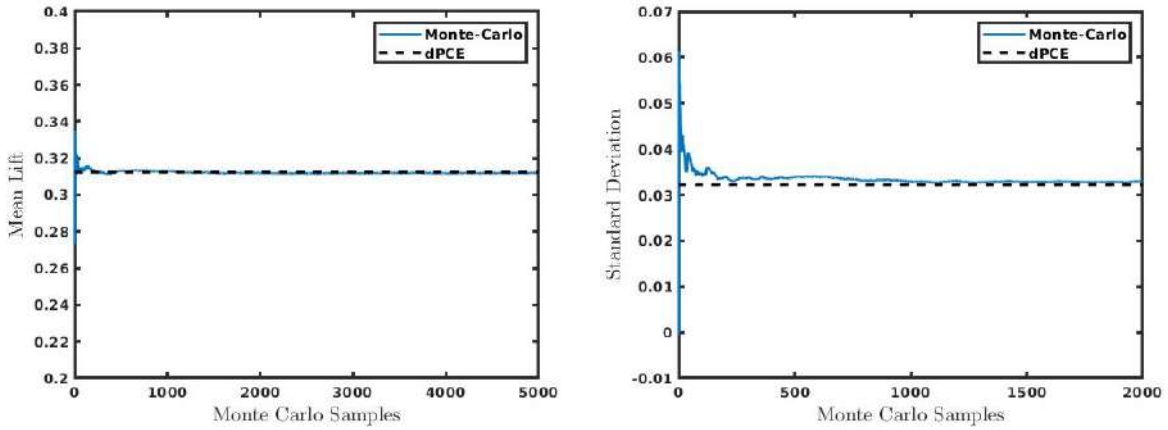

Figure 1: Monte–Carlo convergence and comparison with adjoint–enhanced PCE.

the adjoint enhanced PCE and the Monte–Carlo is seen in table 1. Notice that results are in very good agreement with the compared methods, with the computational cost of the adjoint-PCE approach being orders of magnitude smaller than the PCE and the MC. As an example, in the case of $N = 19$ uncertain variables, for a full tensor product computation of the integral of eq. 4, $a = 524288$ CFD runs would be required for the PCE, while in the adjoint enhanced PCE only one CFD and one adjoint evaluation were conducted.

Parameters N	μ_{C_L}		σ_{C_L}		Error (%) μ_{C_L}	Error (%) σ_{C_L}
	MC	adjoint PC	MC	adjoint PC		
1	0.3339	0.3289	0.0333	0.0326	1.51	2.06
2	0.3451	0.3421	0.0352	0.0358	0.86	1.70
3	0.3128	0.3144	0.0313	0.0317	0.53	1.39
19	0.3156	0.3124	0.0316	0.0322	1.01	1.92

Table 1: UQ in the NACA0012 airfoil. The QoI is the lift coefficient. Uncertainty is introduced through the coefficients of the Hicks–Henne bump conditions. A comparison is made with the Monte–Carlo simulation.

CONCLUSIONS

A new method, capable of conducting accurate UQ for a high number of uncertain variables is introduced. It is found that the statistical moments of a QoI can be computed, provided that the input uncertainties are relatively small. The method, introduces small errors due to the linear approximations introduced by the adjoint, but at a massively reduced computational cost.

References

[1] J. Reuther, A. Jameson, J. Farmer, L. Martinelli and D. Saunders. Aerodynamic shape optimization of complex aircraft configurations via an adjoint formulation. *AIAA Meeting Papers* 1996.

[2] Dongbin Xiu, George Em Karniadakis. The Wiener-Askey Polynomial Chaos For Stochastic Differential Equations. Society for Industrial and Applied Mathematics, 2002.

[3] D. Kumar, J. Miranda, M. Raisee, C. Lacor. Adjoint based multi-objective shape optimization of a transonic airfoil under uncertainties. EngOpt 2016, Brazil, 2016.

DEMONSTRATION OF MACHINE LEARNING-BASED REDUCED ORDER MODELING USING UNSTEADY FLOWS AROUND BLUFF BODIES WITH VARIOUS SHAPES

Kazuto Hasegawa*[1,2], Kai Fukami[1], and Koji Fukagata [1]
[1]Department of Mechanical Engineering, Keio University, Japan
[2]Dipartimento di Scienze e Tecnologie Aerospaziali, Politecnico di Milano, Italy

Summary We use machine learning (ML) methods to build a framework of reduced order modeling for complex flows. Two ML methods are unified for the present modeling: a convolutional neural network-based autoencoder (CNN-AE) and long short term memory (LSTM). The CNN-AE is utilized to map a high-dimensional flow field into low-dimensional latent space. The LSTM is then employed to predict a temporal evolution of low-dimensionalized field via the CNN-AE. By combining these methods, a temporal evolution of high-dimensional dynamics can be represented by following only that of low-dimensionalized vector, because a CNN decoder which is part of the CNN-AE can re-map to original dimension. The present scheme is demonstrated using a flow around bluff bodies with various shapes. The reconstructed fields show statistical agreement with the reference data obtained by a direct numerical simulation.

INTRODUCTION

In recent years, the enthusiastic uses of machine learning have been seen in fluid dynamics due to its great affinity between accumulated fluid big data generated under complex and chaotic nature, and machine learning which is good at dealing with a large amount of data while considering nonlinearlity [1]. In particular, the applications to reduced order modeling (ROM) have been attracting attention. Srinivasan *et al.* [2] demonstrated the ability of a multi-layer perceptron and a long short-term memory (LSTM) by predicting a temporal evolution of nine-shear turbulent flow equation. A spatial low-dimensionalization with a customized convolutional neural network-based autoencoder (CNN-AE) was presented by Murata *et al.* [3]. These works reported that considering nonlinearity into the internal schemes of machine learning enables us to have a possibility to overcome drawbacks of the conventional linear-theory based ROM.

Here, we present a new framework of machine learning based reduced order modeling (ML-ROM) unifying a CNN-AE and an LSTM, then demonstrate its ability using a flow around bluff bodies with various shapes defined randomly.

MACHINE LEARNING METHODS

Let us first introduce a CNN-AE utilized for dimension reduction of the present study. With the use of the autoencoder (AE) [4], the problem setting is usually set to output the same data as the input data $\boldsymbol{q}$ through the model $\mathcal{F}$ such that $\boldsymbol{q} \approx \mathcal{F}(\boldsymbol{q};\boldsymbol{w})$, where $\boldsymbol{w}$ denotes the weights of the AE. Although it looks like a copy machine now, the noteworthy structure of the AE here is to have the intermediate latent space $\boldsymbol{r}$ which has lower dimension than input or output data. In other words, $\boldsymbol{r}$ can be a low-dimensionalized representation of input high-dimensional data $\boldsymbol{q}$ if we can obtain the same data as the output with the input data. The parts of the AE for dimension reduction and extension are called an encoder $\mathcal{F}_e$ and a decoder $\mathcal{F}_d$, respectively. In this study, we use a convolutional neural network (CNN) [5]-based model called multi-scale CNN [6] to construct the AE so that a multi-scale nature of complex flows can be considered [7].

An LSTM [8] is known as a prominent data-driven tool to apply to time-series prediction, e.g., speech recognition [9]. We here utilize the LSTM $\mathcal{F}_L$ to predict the temporal evolution of the latent dynamics. Although the details are skipped here, a flag map of the bluff body (i.e., 1 for the bluff body region, 0 for the fluid region) is also utilized as the input of the LSTM model to give the information of boundary condition.

The present combination of CNN and LSTM for reduced order modeling are shown in figure 1. A high-dimensional flow field $\boldsymbol{q}$ is mapped into a low-dimensional latent vector $\boldsymbol{r}$ using the CNN-AE. Then, the temporal evolution of latent dynamics are predicted by the LSTM with recursive input so that the temporal evolution of high-dimensional flow can be also represented with the use of CNN decoder. Summarizing above, the proposed modeling can be mathematically expressed as

$$\boldsymbol{q} \approx \mathcal{F}(\boldsymbol{q}) = \mathcal{F}_e(\mathcal{F}_d(\boldsymbol{r})), \tag{1}$$

$$\boldsymbol{r}^{(n+1)\Delta t} = \mathcal{F}_L(\boldsymbol{r}^{n\Delta t}). \tag{2}$$

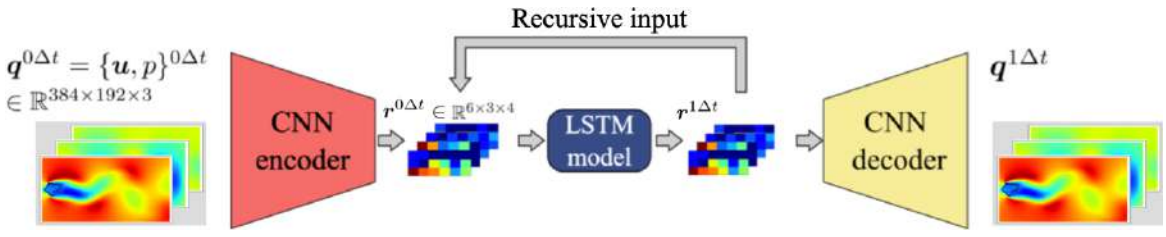

Figure 1: Present reduced order modeling with CNN-AE and LSTM.

*Corresponding author. E-mail: kazuto.hasegawa@kflab.jp

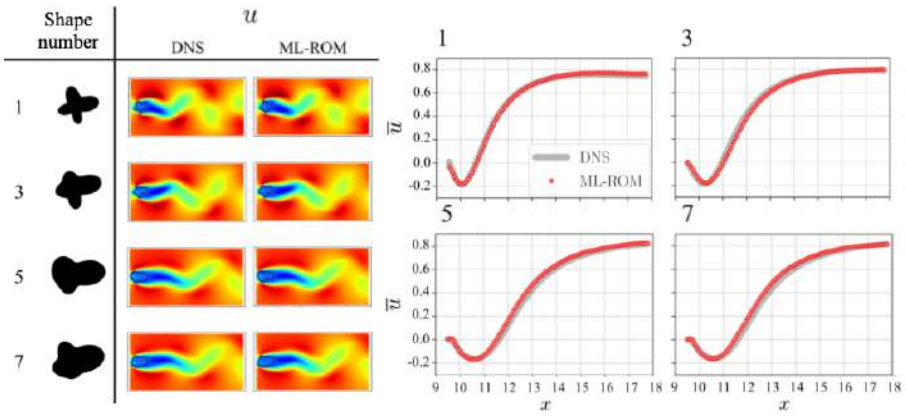

Figure 2: Streamwise velocity contour and the mean centerline velocity in the wake.

RESULTS

Let us consider flows around various bluff bodies, whose shapes are defined randomly. Training data is prepared with a two-dimensional direct numerical simulation by solving incompressible Navier–Stokes equations,

$$\nabla \cdot \boldsymbol{u} = 0, \quad \frac{\partial \boldsymbol{u}}{\partial t} + \nabla \cdot (\boldsymbol{u}\boldsymbol{u}) = -\nabla p + \frac{1}{Re_D}\nabla^2 \boldsymbol{u}, \tag{3}$$

where $\boldsymbol{u}$, p, and t denote the velocity, pressure, and time, respectively. All variables are made dimensionless by the fluid density ρ^* , the uniform velocity U^*_∞, and the frontal length D^* of the body, where the superscript $*$ represents dimensional variables. The Reynolds number is set to $Re_D = U^*_\infty D^*/\nu^* = 100$, where ν^* is the kinematic viscosity. The length of computational domain is set to $(L_x, L_y) = (25.6D, 20.0D)$. The number of grid points is $(N_x, N_y) = (1024, 800)$ and the time step is set to $\Delta t = 2.5 \times 10^{-3}$. A ghost-cell method [10] is used to satisfy the no-slip boundary condition on the bluff body surface. To investigate whether the proposed model can learn the Navier-Stokes equation under various conditions as a proof concept for unseen flow data, we consider various bluff bodies, whose shapes are defined as

$$r = 0.5 + \sum_{n=1}^{4} a_n \sin n\theta + \sum_{n=1}^{4} a_{n+4} \cos n\theta, \quad \sum_{n=1}^{8} a_n = 0.5, \tag{4}$$

where r is the distance between the center and the surface, θ represents the angle from the inflow (i.e., x) direction, and a_n denotes random numbers normalized to satisfy equation (4). Fifty different shapes are generated for training data and the generated fields are rotated around the x-axis symmetry to increase the amount of training data, i.e., 100 kinds of flows.

Let us present in figure 2 an example of flow fields around bluff bodies with untrained shapes. As the data attributes, we use velocities and pressure $\boldsymbol{q} = \{u, v, p\}$. The dimension of the latent space here is set to 72 which corresponds to 0.03% compression against original data dimension. The flow fields reconstructed by the present ML-ROM show excellent agreement with the reference DNS data. In addition, the mean centerline velocity profiles of the present model are also in good agreement with the DNS data. Note that we can see nice agreement for the other test shapes and other attributes, i.e., v and p, although not shown here.

CONCLUSIONS

We presented machine-learning based reduced order modeling by unifying a CNN and an LSTM. The CNN was employed to map a high-dimensional flow field into low-dimensional latent space. The LSTM was then utilized to predict a temporal evolution of latent dynamics. By combining the predicted latent vectors with the CNN decoder, the time-evolved high-dimensional dynamics can be represented. The proposed method was demonstrated unsteady flows around bluff bodies with various random shapes. The reconstructed flow fields were in excellent agreement with the reference data. We refer enthusiastic readers to Hasegawa *et al.* [11] for more details.

References

[1] Brunton S. L., Noack B. R., and Koumoutsakos P. Machine Learning for Fluid Mechanics. *Annu. Rev. Fluid Mech.* **52**: 477–508, 2020.
[2] Srinivasan P. A. *et al.* Predictions of turbulent shear flows using deep neural networks. *Phys. Rev. Fluids* **4**: 054603, 2019.
[3] Murata T. *et al.* Nonlinear mode decomposition with convolutional neural networks for fluid dynamics. *J. Fluid Mech.* **882**: A13, 2020.
[4] Hinton G. E. and Salakhutdinov R. R. Reducing the dimensionality of data with neural networks. *Science* **313**(5786): 504–507, 2006.
[5] LeCun Y. *et al.* Gradient-based learning applied to document recognition. *Proc. IEEE* **86**(11): 2278–2324, 1998.
[6] Du X. *et al.* Single image super-resolution based on multi-scale competitive convolutional neural network. *Sensors* **789**(18): 1–17, 2018.
[7] Fukami. K. *et al.* Super-resolution reconstruction of turbulent flows with machine learning. *J. Fluid Mech.* **870**: 106–120, 2019.
[8] Hochreiter S. and Schmidhuber J. Long short-term memory. *Neural Comput.* **9**: 1735–1780, 1997.
[9] Graves, A. *et al.* Hybrid speech recognition with deep bidirectional LSTM. *IEEE Workshop on Automatic Speech Recognition and Understanding* Olomouc, Czech, Dec. 8–12, 2013.
[10] Kor, H. *et al.* A unified interpolation stencil for ghost-cell immersed boundary method for flow around complex geometries, *J. Fluid Sci. Technol.*, **12**: JFST011, 2017.
[11] Hasegawa, K. *et al.* Machine-learning-based reduced order modeling for unsteady flows around bluff bodies of various shapes, *Theor. Comp. Fluid Dyn.*, in Review 2019.

IMMERSED BOUNDARY PROJECTION METHOD FOR THE IMCOMPRESSIBLE NAVIER-STOKES EQUATION WITH ARBITRARILY SHAPED NAVIER SLIP BOUNDARIES

Takehiro Fujii*[1], Takeshi Omori[2], and Takeo Kajishima[1]
[1]Department of Mechanical Engineering, Osaka University, Suita, Japan
[2]Department of Mechanical and Physical Engineering, Osaka City University, Osaka, Japan

Summary Immersed boundary methods that have been used to simulate flows with arbitrary-shaped boundaries on the Cartesian grid have not been established for the Navier slip boundary condition. We present a new method to impose the Navier boundary condition based on the immersed boundary projection method by introducing the regularization operator which is the sum of the conventional regularization operator and its gradient. Using the present regularization operator to regularize the boundary forces, the velocity gradient in the Navier boundary condition is appropriately evaluated with interpolation. Results from the simulations of the plane Poiseuille flow and Couette flow inside the two concentric cylinders with Navier slip walls show good agreement with the analytical solutions.

INTRODUCTION

In recent progress in the micro- and nanofluidics, the prediction of the flow confined by intricately shaped walls with slip velocity plays a significant role [1,2], and the numerical methods for the flows around the arbitrarily shaped Navier slip walls are needed.

The immersed boudary method is one of the most popular method to simulate the flows around the arbitrarily shaped surfaces where the no-slip conditions are imposed. However, the immersed boundary methods for the Navier boundary conditions have not been established. In this study, we present a new method that imposes the Navier boundary conditions on the immersed surfaces, based on the immersed boundary projection method by Taira and Colonius [3], which is appropriate for simulating the flows with rigid bodies. We present a discrete description of the Navier boundary condition using interpolations and introduce a new regularization operator, which smears the boundary forces on the Cartesian grid, to appropriately evaluate the velocity gradient in the Navier boundary condition using interpolation. To validate the present method, the plane poiseuille flow and the Couette flow inside the two concentric cylinders are calculated.

GOVERNING EQUATIONS

We consider the two dimensional imcompressible flow of Newtonian fluids around the arbitrarily shaped walls. The wall position and velocity are assumed to be known. The non-dimensional governing equations are the Navier-Stokes equation $\partial \boldsymbol{u}/\partial t + \boldsymbol{u}\cdot\nabla\boldsymbol{u} = -\nabla P + (1/\mathrm{Re})\nabla^2\boldsymbol{u} + \boldsymbol{f}_{ext}$, together with the continuity equation $\nabla\cdot\boldsymbol{u} = 0$. Here P is the non-dimensionalized pressure, Re is the Reynolds number and $\boldsymbol{f}_{ext}$ is the acceleration due to external forces. The boundary conditions on the walls are the Navier boundary conditions [4]

$$(1+\mathcal{L}_s\kappa)u_t - u_t^B = \mathcal{L}_s\left(\frac{\partial u_t}{\partial x_n} + \frac{\partial u_n}{\partial x_t}\right), \tag{1}$$

together with the impermeability conditions $u_n = u_n^B$, where the subscripts t and n indicate tangential and normal, respectively, the superscript B represents the quantities defined on the walls, $\mathcal{L}_s$ is the non-dimensional slip length, and κ is the curvature of the walls. For the second term on the right hand side of the Eq. (1), $\partial u_n/\partial x_t = \partial u_n^B/\partial x_t$ holds using the impermeability conditions $u_n = u_n^B$.

NUMERICAL METHODS

In the immersed boundary projection method [3], the immersed boundaries are described as the sequence of Lagrange points, where the boundary condisions are imposed, and the positions and the velocities of these points are assumed to be known. The discretized no-slip boundary condition is described as $\hat{E}\boldsymbol{u} = \boldsymbol{u}^B$, where $\hat{E}$ is the interpolation operator which interpolates the quantities defined on the Cartesian grid onto the Lagrange points. In order to enforce the discretized no-slip conditions on the immersed boundaries, the boundary forces $\boldsymbol{F}^B$ defined on the Lagrange points act on the Cartesian grid via the regularization operator $\hat{H}$. Both $\hat{E}$ and $\hat{H}$ are linear operators and constructed from the regularized discrete delta function.

In case of the Navier boundary condition, the evaluation of the tangent velocity and its normal gradient at the Lagrange points is needed. The velocity profile near the immersed boundaries depends on the distribution of the boundary forces on the Cartesian grid, namely, the regularization operator. The conventional combination of the operators $\hat{E}$ and

*Corresponding author. E-mail: fujii@fluid.mech.eng.osaka-u.ac.jp

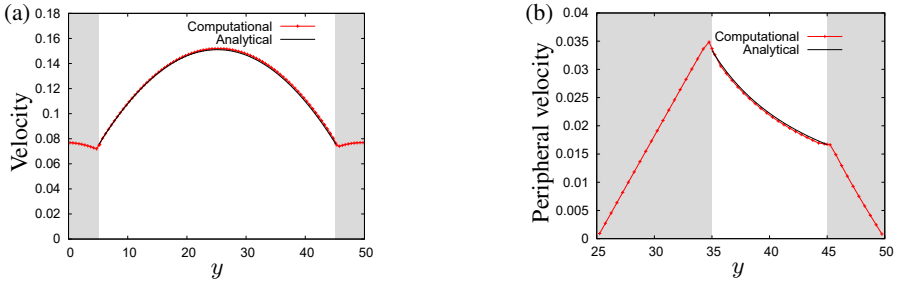

Fig. 1: The velocity profile for the case (a) the plane Poiseuille flow at $t = 10$ and (b) the Couette flow inside the two concentric cylinders at $t = 200$. The shaded regions represent the walls.

$\hat{H}$ underestimates the velocity gradient. We introduce a new regularization operator $\hat{H}^* = \hat{H} + \Delta\hat{G}_n\hat{H}$, where Δ is the grid space, to appropriately evaluate the tangent velocity and its gradient at the Lagrange points using interpolation. $\hat{H}^*$ regularizes the tangential boundary force corresponding to the Navier boundary condition, and the normal boundary force imposing the impermeability condition is regularized with $\hat{H}$. The Navier boundary condition and the impermeability condition are described as $(1 + \mathcal{L}_s\kappa)\hat{E}u_t - \mathcal{L}_s\hat{E}\hat{G}_n u_t = u_t^B + \mathcal{L}_s(\partial u_n^B/\partial x_t)$ and $\hat{E}u_n = u_n^B$, respectively, and these descriptions are reduced to an equation $\hat{B}\boldsymbol{u} = \boldsymbol{u}^B$, where $\hat{B}$ is a linear operator. For the discrete delta function constructing the interporlation and regularization operator, we use the three-grid cell delta function by Roma et al. [5], which is appropriate for the staggered grids.

The discretized governing equations and the boundary conditions are described as follows:

$$\frac{\boldsymbol{u}^{n+1} - \boldsymbol{u}^n}{\Delta t} = \frac{1}{2}\left(3\boldsymbol{A}^n - \boldsymbol{A}^{n-1}\right) - \hat{G}P^{n+1} + \frac{1}{2\mathrm{Re}}\left(\hat{L}\boldsymbol{u}^{n+1} + \hat{L}\boldsymbol{u}^n\right) + \boldsymbol{f}_{ext}^{n+1} + \hat{K}\boldsymbol{F}^{B,n+1}, \tag{2}$$

$$\hat{D}\boldsymbol{u}^{n+1} = 0, \tag{3}$$

$$\hat{B}\boldsymbol{u}^{n+1} = \boldsymbol{u}^{B,n+1}, \tag{4}$$

where $\hat{G}$, $\hat{L}$ and $\hat{D}$ are gradient, Laplacian and divergence operators, respectively, $\hat{K}$ composes of $\hat{H}^*$, $\hat{H}$ and coodinate transformation, and $\boldsymbol{A}^n = -\boldsymbol{u}^n \cdot \hat{G}\boldsymbol{u}^n$. Eqs. (2), (3) and (4) are solved in the same way as the immeresed boundary projection method [3].

RESULTS

For a two-dimensional test problem, we simulate (a) the plane Poiseuille flow driven by the constant external force $\boldsymbol{f}_{ext} = 0.04\boldsymbol{e}_x$ and (b) the Couette flow inside the two concentric cylinders with peripheral velocity $U = 0.1$ of the inner cylinder. The flows are initially stationary. We take a periodic computational domain of size $[0, 50] \times [0, 50]$, spatial resolution $\Delta x = \Delta y = 0.5$, Reynolds number $\mathrm{Re} = 0.01$ and non-dimensional slip length $\mathcal{L}_s = 10$ for the both cases, and time step $\Delta t = 1 \times 10^{-2}$ for the case (a) and (b) $\Delta t = 1 \times 10^{-1}$. The positions of the Lagrange points are $(0.25 + (i-1)\Delta x, 4.65)$ and $(0.25 + (i-1)\Delta x, 44.65)$, $(i = 1, 2, \cdots, 100)$ for the case (a). For the case (b), the 372 Lagrange points are located on the circumferences $(x-25)^2 + (y-25)^2 = 10^2$ and $(x-25)^2 + (y-25)^2 = 20^2$ at the equal intervals.

Fig. 1 shows the velocity profile for the case (a) at $t = 10$ and (b) along $x = 25$, $y \in [25, 50]$ at $t = 200$. The results are in good agreement with the analytical solutions.

CONCLUSIONS

We presented a new numerical method that imposes the Navier boundary condition on the immersed surface, based on the immersed boundary projection method. In order to appropriately evaluate the velocity gradients using interpolation, the regularization operator which is the sum of the conventional regularization operator and its gradient was introduced. To validate this method, the plane Poiseuille flow and the Couette flow inside the two concentric cylinders with Navier slip walls were computed. The resulting velocity profile shows a good agreement with the analytical solution.

References

[1] Omori T., Kajishima T. Apparent and Microscopic Dynamic Contact Angles in Confined Flows. *Phys. Fluids* **29**: 112107, 2017.
[2] Omori T., et al. Full Characterization of the Hydrodynamic Boundary Condition at the Atomic Scale Using an Oscillating Channel: Identification of the Viscoelastic Interfacial Friction and the Hydrodynamic Boundary Position. *Phys. Rev. Fluids* **4**: 114201, 2019.
[3] Taira K., Colonius T. The Immersed Boundary Method: a Projection Approach. *J. Comput. Phys.* **225**: 2118-2137, 2007.
[4] Chen W., Zhang R., Koplik J. Velocity slip on curved surfaces. *Phys. Rev. E* **89**: 023005, 2014.
[5] Roma A. M., Peskin C. S., Berger M. J. An Adaptive Version of the Immersed Boundary Method. *J. Comput. Phys.* **153**: 509-534, 1999.

PROJECTION-BASED REDUCED ORDER MODELS FOR A CUT FINITE ELEMENT METHOD IN PARAMETRIZED DOMAINS

Efthymios N. Karatzas[1,2], Francesco Ballarin*[1], and Gianluigi Rozza[1]
[1]SISSA, International School for Advanced Studies, Mathematics Area, mathLab, Via Bonomea 265, Trieste, 34136, Italy
[2]Current address: Department of Mathematics, National Technical University of Athens, Zografou 15780, Greece

Summary This work presents a reduced order modeling technique built on a high fidelity embedded mesh finite element method, as proposed in [1]. Such methods, and in particular the CutFEM method, are attractive in the generation of projection-based reduced order models thanks to their capabilities to seamlessly handle large deformations of parametrized domains and in general to handle topological changes. The combination of embedded methods and reduced order models allows us to obtain fast evaluation of parametrized problems, avoiding remeshing as well as the reference domain formulation, often used in the reduced order modeling for boundary fitted finite element formulations. The resulting novel methodology is presented on linear elliptic and Stokes problems, together with several test cases to assess its capability. The role of a proper extension and transport of embedded solutions to a common background is analyzed in detail. We will then further discuss ongoing extensions to fluid-structure interaction problems [2], in collaboration with M. Nonino and Y. Maday.

INTRODUCTION AND MOTIVATION

A wide variety of numerical methods for the solution of problems governed by partial differential equations is nowadays available. However, in many cases either the solution of the governing equations or the solution of associated inverse problems becomes impractical or unfeasible using standard discretization techniques, such as the Finite Element Method. For instance, complicated topology of the problem or a complex geometry may pose a challenge in the discretization of complex phenomena, and ultimately affect the quality of the resulting simulation. Moreover, repeated queries to the underlying solver in the context of an iterative solution of inverse problems may result in unbearably large computational times. Such situations occur, for example, when a large number of different configurations are in need of being tested, such as in uncertainty quantification, optimal control and shape optimization. The overall objective of this presentation (and the associated manuscript [1]) is to investigate how the recently introduced unfitted mesh finite element methods can be used in combination with reduced order modeling techniques for parametrized partial differential problems. Indeed, unfitted methods are very useful in cases characterized by complex geometrical configurations; however, as their Finite Element counterparts, they usually require large computational efforts. A combination with reduced order methods, able to widely decrease the overall computational time, would result in a very compelling methodology to be possibly applied in several different fields.

HIGH FIDELITY CUTFEM APPROXIMATION

For simplicity, for most of the presentation we will tackle stationary (but parametrized) problems, of the form find $u(\mu) \in V(\mu)$ such that

$$a_\gamma(u(\mu), v; \mu) = \ell_\gamma(v; \mu) \text{ in } V(\mu), \tag{1}$$

where $a_\gamma(\cdot, \cdot; \mu)$ is the weak form of an operator defined on a domain $\mathcal{D}(\mu) \subset \mathcal{B} \subset \mathbb{R}^d$, for $d = 2, 3$, while $\ell_\gamma(\cdot, \mu)$ is the right hand side of the system of equations related to the forcing term. The forms $a_\gamma(\cdot, \cdot; \mu)$, $\ell_\gamma(\cdot, \mu)$, the domain $\mathcal{D}(\mu)$, as well as the Sobolev space $V(\mu)$, depend on the parameter $\mu \in \mathcal{K}$, being $\mathcal{K} \subset \mathbb{R}^K$ the set of possible outcomes, which we assume to be a compact set in $\mathbb{R}^K$, $K \in \mathbb{N}$. In contrast, the bounding box $\mathcal{B}$ is not parameter dependent. Since CutFEM discretizations usually require suitable penalty and stabilization procedures, for the sake of exposition we will denote by $a_\gamma(\cdot, \cdot; \mu)$ and $\ell_\gamma(\cdot, \mu)$ the forms with penalty and stabilization, where γ represents the penalty and stabilization coefficients. We refer to e.g [1] for the expressions of the forms $a_\gamma(\cdot, \cdot; \mu)$ and $\ell_\gamma(\cdot, \mu)$ for common problems in fluid dynamics.

REDUCED ORDER MODELS FOR EMBEDDED METHODS

Using embedded methods, such as CutFEM, as high fidelity method of projection based reduced order models is certainly attractive, e.g. because (i) it offers a more versatile shape parametrization (for instance, based on level sets), (ii) which is capable of seamlessly handle large deformations, (iii) and which does not require a reference domain formulation typical of standard reduced basis methods (see for instance [3]). The main challenge however comes from the need to efficiently reduce (possibly localized) snapshots moving (due to parametric dependence) throughout the global domain. We will compare the two following options:

*Corresponding author. E-mail: fballarin@sissa.it.

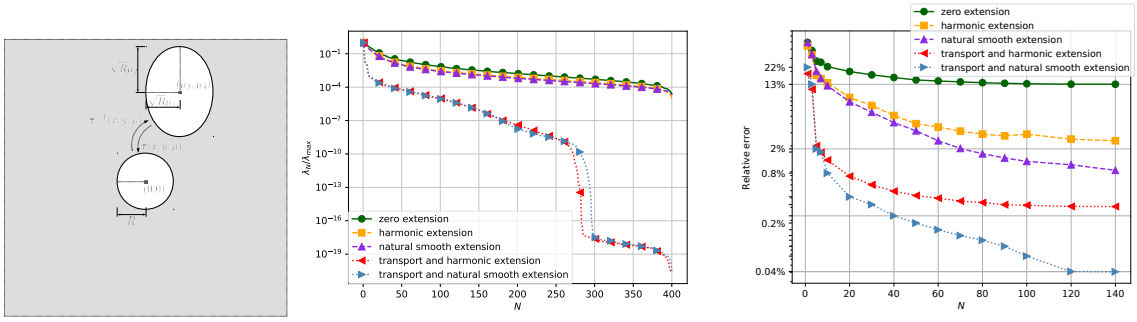

Figure 1: Example of transport map (left), comparison of POD eigenvalue decay (middle) and comparison of error analysis (right) between linear and nonlinear POD-Galerkin methods

Standard (linear) POD-Galerkin methods

Offline phase (POD):

- query CutFEM for $M \gg 0$ representative values $\mu^1, \dots, \mu^M$ of the parameter μ;
- note that $u(\mu^m) \in V_h(\mu^m)$, where the FE space $V_h(\mu^m)$ is defined *just* over (a neighbrood of) $\mathcal{D}(\mu^m)$, $m = 1, \dots, M$,
- introduce the background FE space $\widehat{V}_h$ defined over $\mathcal{B}$, of dimension $\mathcal{N}_h$;
- extend $u(\mu^m) \in V_h(\mu^m)$ to $\widehat{u}(\mu^m) \in \widehat{V}_h$ (three simple options will be presented);
- compute a POD of the (extended) snapshots $\mathcal{S} = [\widehat{u}(\mu^1), \dots, \widehat{u}(\mu^M)] \in \mathbb{R}^{\mathcal{N}_h \times M}$;
- collect the first POD modes $\varphi_1, \dots, \varphi_N$ and define the RB space $\widehat{V}_N = \text{span}\{\varphi_1, \dots, \varphi_N\}$;
- note that $V_h = V_h(\mu)$ depends on μ, $\widehat{V}_N$ *does not*.

Online phase (Galerkin):

- seek a RB solution of the form $u_N(\mu) = \sum_{i=1}^N \alpha_i(\mu)\, \varphi_i$, such that $\sum_{i=1}^N \alpha_i(\mu) a_\gamma(\varphi_i, \varphi_j; \mu) = \ell_\gamma(\varphi_j; \mu), \quad \forall j = 1, \dots, N$.

Nonlinear variant of POD-Galerkin methods

The nonlinear variant is based on the following assumption: for a fixed $\overline{\mu} \in \mathcal{K}$, assume to have $\boldsymbol{\tau}(\mu) : \mathcal{B} \to \mathcal{B}$ be a bijective map chosen such that $\mathcal{D}(\overline{\mu})$ is mapped into $\mathcal{D}(\mu)$, and let $\boldsymbol{\tau}^{-1}(\mu)$ denote its inverse with respect to the spatial coordinates (see e.g. Figure 1 (left)).

Offline phase (POD + transport^{-1}):

- query CutFEM for $M \gg 0$ representative values $\mu^1, \dots, \mu^M$ of the parameter μ;
- extend $u(\mu^m) \in V_h(\mu^m)$ to $\widehat{u}(\mu^m) \in \widehat{V}_h$;
- transport^{-1} $\widehat{u}(\mu^m) \in \widehat{V}_h$ to $\widehat{u}_{\boldsymbol{\tau}}(\mu) = \widehat{u}(\mu) \circ \boldsymbol{\tau}^{-1}(\mu)$;
- compute a POD of the (extended and transported^{-1}) snapshots and collect the first POD modes $\varphi_1, \dots, \varphi_N$

Online phase (Galerkin + transport):

- define the RB space $\widehat{V}_N^{\boldsymbol{\tau}}(\mu) = \text{span}\{\varphi_1 \circ \boldsymbol{\tau}(\mu), \dots, \varphi_N \circ \boldsymbol{\tau}(\mu)\}$, by transporting the computed POD modes;
- note that $\widehat{V}_N^{\boldsymbol{\tau}}(\mu)$ now depends on μ;
- seek a RB solution via Galerkin projection on the space $\widehat{V}_N^{\boldsymbol{\tau}}(\mu)$.

Numerical results

Numerical results on elliptic and fluid dynamics cases show that the nonlinear variant outperform the linear one. The results of the offline stage for a representative test case are shown in Figure 1 (middle) where POD eigenvalues (normalized to the maximum eigenvalue) are plotted against the number of modes. Results show that small reduced basis spaces cannot be obtained relying only on linear methods; indeed, Figure 1 (middle) shows a very slow eigenvalue decay, with negligible differences among the different extension options. A faster decay is obtained instead thanks to the transportation introduced by the nonlinear variant. In particular an improvement of almost three orders of magnitude is obtained for $N = 100$, more than four for $N = 200$; furthermore, the transport POD drops below numerical precision at $N = 300$. Results of the online stage are then shown in Figure 1 (right), where the average of the relative error over the testing set is plotted against the reduced basis size. The reduced solution obtained from the best linear method results in relative errors that are of the order of 10^{-2} for the maximum value of N. In contrast, the combination with inverse transportation of nonlinear methods allows to sensibly improve results, up to errors of 10^{-4} for $N = 140$. Ongoing extensions to fluid-structure interaction problems will be mentioned as well [2].

References

[1] Karatzas E. N., Ballarin F., Rozza G. Projection-based reduced order models for a cut finite element method in parametrized domains. *Computers & Mathematics with Applications* **79(3)**: 833–851, 2020.

[2] Nonino M., Ballarin F., Rozza G., Maday Y. Overcoming slowly decaying Kolmogorov n-width by transport maps: application to model order reduction of fluid dynamics and fluid–structure interaction problems. *Preprint arXiv* 1911.06598, 2019.

[3] Hesthaven J. S., Rozza G., Stamm B. Certified Reduced Basis Methods for Parametrized Partial Differential Equations. *Springer Briefs in Mathematics*, 1st edition, 2015.

A MULTISCALE MODEL FOR PREDICTING THE VASCULAR TRANSPORT AND ADHESION MECHANICS OF NANOMEDICINES

Federica Laurino[1,2], Alessandro Coclite*[3], Paolo Decuzzi[2], and Paolo Zunino[1]
[1]Department of Mathematics (MOX), Politecnico di Milano, Milano, Italy
[2]Laboratory of nanotechnology for precision medicine. Italian Institute of technology. Genova, Italy
[3]Scuola di Ingegneria,Università degli studi della Basilicata,Potenza,Italy

Summary In the Nanomedicine community, there is a pressing need for predictive, quantitative tools to rationally design and optimize carriers for therapeutic and imaging applications. Current nano/micro-fabrication technologies allow us to control a large number of parameters, namely size, shape, surface properties and mechanical stiffness (4S parameters). Indeed, the biophysical behavior of such nanomedicines is greatly affected by these parameters. Reliable, multiscale and multiphysics computational models are crucial to guide the fabrication process towards optimal delivery systems. Here, a computational model for describing blood flow in the microvasculature, particle transport and molecular interaction with the vascular walls is presented. The model predicts particle deposition within a tumor microvasculature as a function of different design parameters.

INTRODUCTION

THE MULTISCALE COMPUTATIONAL MODEL

The aim of the present work is to study the dynamics of injectable particles (nanomedicines) within a microvascular network. Such particles travel along the vascular tree and interact with the endothelial cells. The vascular transport and adhesion of particles depend on various factors, over different scales. These include the geometry of the vascular network, the local Reynolds number, Re (which governs the hydrodynamic forces) and the ligand-receptor interaction (which modulates vascular adhesion). Here, a hierarchical, multiscale computational approach is developed, based on continuum and statistical mechanics, to predict and quantify the vascular concentration of blood-borne particles and their vascular deposition as a function of the above factors. Our long term vision is to develop a computational model consisting of three different modules: the organ level module, the vascular transport module and the particle-wall interaction module. These three modules with their characteristic governing equations and the exchange parameters are schematically shown in **Figure.1**.

In this work, we explicitly address the vascular transport module and the particle-wall interaction module only. A top-down strategy is used starting from the continuum macroscale description of the fluid flow and particle transport at the level of the whole network [1] to the molecular scale with the individual particle-wall interactions [2]. The model is formulated as a particle transport problem regulated by the blood flow. For this reason, the blood flow problem is first studied in terms of hydrodynamic velocities and pressures. Then, the actual particle transport problem in the vascular network is addressed. To combine these models with the organ level module, we are planning to adopt an approach based on numerical homogenization in order to upscale the current simulations to the level of the whole organ. Very encouraging preliminary results based on this strategy are obtained in the work by Vidotto et al. [3]. We believe that models based on averaged tissue-vasculature should be used in combination with the approach presented here, with the ultimate aim to tackle organ level simulations.

In particular, the present model couples two numerical approaches for different length scales. The detailed dynamics of micro-carriers with different stiffness and surface properties is computed by an Immersed-BoundaryLattice Boltzmann approach. On the other hand, larger scales are carried out by means of a finite element (FE) discretization of a real vasculature and the within flow filed (taken from http://physiology.arizona.edu/people/secomb/network). These two computational schemes are off-line coupled and hierarchical multiscale approach is obtained.

Vascular and extra-Vascular Transport

To model a network of arterioles, we start form the vascular data for R3230AC mammary carcinoma developed in a rat dorsal skin flap preparation. Precisely, the dataset named rat93 is chosen, which describes a network of 28 branches, with variable diameters. The network is embedded into a biological tissue modeled as a homogeneous continuum. This material is called the interstitial volume. The fluid dynamic problem is defined in a three-dimensional domain, which is split in two subdomains: the tissue and the vasculature. The tissue is assumed to be an isotropic porous medium and the flow is governed by the Darcys law combined with mass conservation for incompressible fluids. The blood is considered ad a non-Newtonian biphasic suspension consisting of plasma and blood borne cells. Precisely the model provides the flow of plasma and haematocrit on the basis of conservation of mass and momentum principles, combined with constitutive laws for the blood rheology such as Fahraeus-Lindqvist effect, plasma skimming and variable apparent viscosity. To mitigate the computational cost of such model, a dimensionality reduction technique is adopted and the full 3D vessels are replaced by their central axis.

*Corresponding author. E-mail: alessandro.coclite@unibas.it.

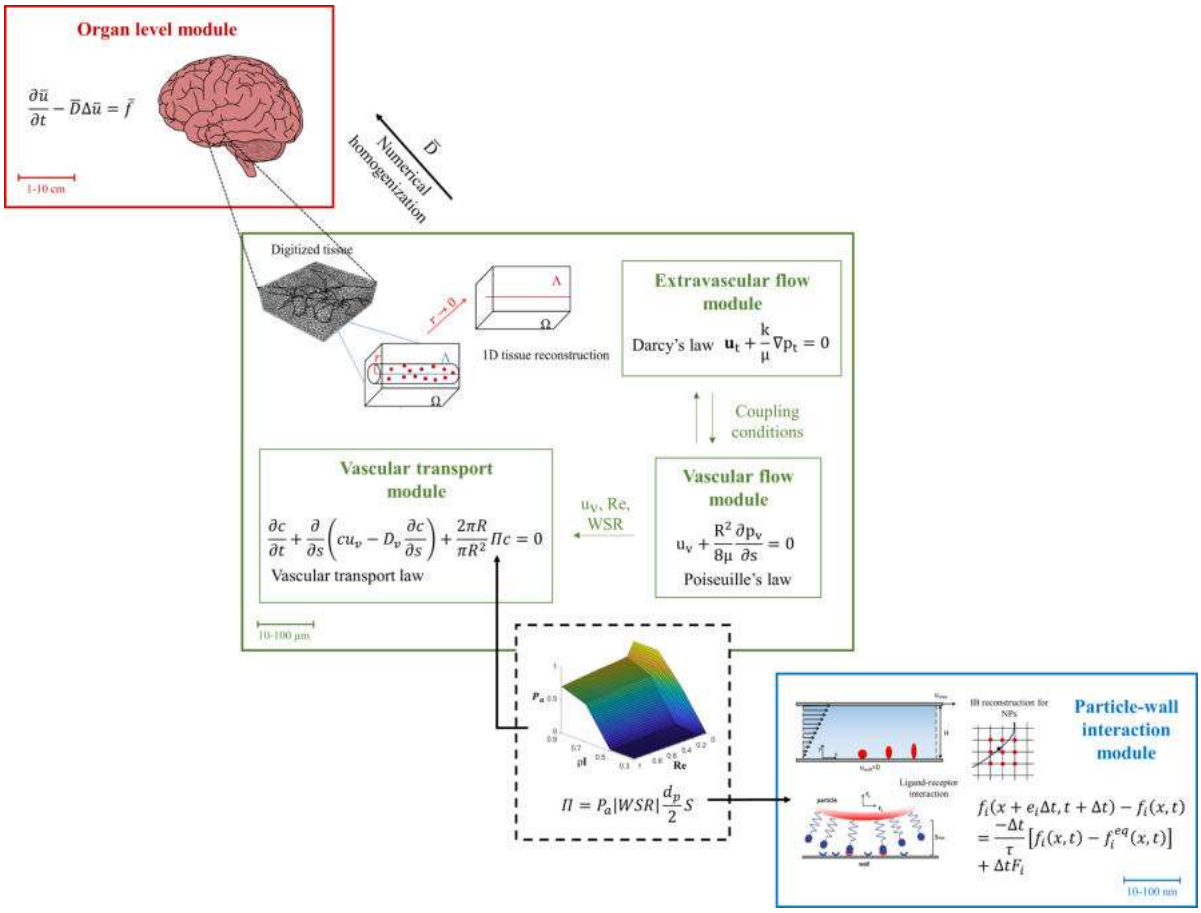

Figure 1: **Schematic representation of the hierarchical computational model.** A vision of the complete multiscale model for vascular and extravascular transport of nanoparticles. In this work we address the green and the blue boxes.

Micro-transport and particle-wall interaction module

A dynamic-Immersed–Boundary (IB)/Lattice Boltzmann (LB) scheme is employed to analyze particle transport and adhesion mechanics with micro-and meso-lenght scales. Such membranes are modeled as a collection of mass-spring elements responding to a bending potential, a worm-like chain potential and the area conservation constraint. Furthermore, on particles' surfaces are uniformly distributed adhesive molecules (ligands) interacting with their counterpart (receptors) disposed on vascular walls. For the lattice Boltzmann modeling, a Gauss-Hermite projection is used to derive the lattice equation; wall boundary conditions are imposed through the Zou-He framework; and a moving least squares algorithm accurately reconstructs the forcing term accounting for the immersed boundary.

CONCLUSIVE REMARKS

The present model has the unique ability to combine a physically sound mechanistic description of micro-particles transport and adhesion dynamics with an affordable computational cost. It represents an ideal framework to optimize the such carriers rational design. Moreover, it has to be stressed that the model is open to interesting generalizations without changing its general structure. It has to be stressed that the present model is based on fundamental physical laws of particle dynamics, which are put into action through advanced computational models. In perspective the aim of the work is twofold; firstly, this technique can be adapted on a number bio-inspired problems, then such approach as it is could significantly foster the development of nanomedicine, for more effective and personalized treatments.

References

[1] Possenti L. et al., A computational model for microcirculation including Fahraeus-Lindqvist effect, plasma skimming and fluid exchange with the tissue interstitium. International Journal for Numerical Methods in Biomedical Engineering, 2019. 35(3).
[2] Coclite A. et al. Predicting different adhesive regimens of circulating particles at blood capillary walls, Microfluidics and Nanofluidics, 2017 21(11)
[3] Vidotto E. et al., Hybrid models for simulating blood flow in microvascular networks. Multiscale Modeling & Simulation. 2019 17(3)

A FINITE VOLUME METHOD FOR NAVIER-STOKES EQUATIONS ON OVERSET GRID

Michele Giuliano Carlino*[1,2], Michel Bergmann[1,2], and Angelo Iollo[1]
[2,1]MEMPHIS team, INRIA Bordeaux Sud-Ouest, Talance, France
[2]Institut de Mathématiques de Bordeaux,Université de Bordeaux,Talance,France

Summary In the present work, we propose a Finite Volume (FV) approach for the solution of Navier-Stokes equations for incompressible flows over a Chimera configuration of meshes. In particular, a Chimera configuration (or overset grid) is a composition of meshes allowing to overcome the problem of the geometrical adaptation of the computational domain with a unique block of mesh. These meshes overlap each other and can move and deform during the simulation. The Navier-Stokes equations are solved through a projection method (*Chorin-Temam*). For this reason, we present two solvers for the steady diffusive problem and the unsteady advection-diffusion problem. For the last problem we present a proper adaptation of the ADER method.

INTRODUCTION

One of the difficulties in the simulation of a fluid flow problem is the representation of the computational domain with a unique block mesh. As a matter of fact, not only the geometry could be particularly complex in itself, but it could change during the simulation and this necessary involves an *in itinere* geometrical adaptation of the mesh, with consequent high computational costs. One of the ways to overcome this problem is to use multiple overlapping mesh blocks that together define a *Chimera* or *overset* grid [1]. Once the different mesh blocks are generated, they are properly composed by the creation of holes and, consequently, an *overlapping zone* between two overlapping blocks is defined. In our simulations, the Chimera grid is composed of a background and a foreground mesh (see Figure 1). In particular, the foreground mesh can move and deform (consequently, the hole in the background mesh can change its configuration).
Let $\Omega \subset \mathbb{R}^2$ be the computational domain and let us consider the Navier-Stokes equation for incompressible flow

$$\partial_t \boldsymbol{u} - \nu \Delta \boldsymbol{u} + (\boldsymbol{u} \cdot \nabla)\boldsymbol{u} + \nabla p = \boldsymbol{f} \quad \text{in } \Omega \times [0, T], \tag{1}$$

with $\nabla \cdot \boldsymbol{u} = 0$ in $\Omega \times [0, T]$ and properly completed with initial and boundary conditions; with $\boldsymbol{u}$ and p the fluid velocity field and pressure, respectively, $\nu = 1/Re$ the inverse of Reynolds number and $\boldsymbol{f}$ the force term. System (1) is solved through a projection method (*Chorin-Temam*) [2, 3], thus we propose in the sequel a finite volume (FV) method for the steady diffusion equation and the unsteady advection-diffusion (AD) equation on a Chimera configuration. For both methods, the error of the mismatch between the exact solution and its FV approximation in L^∞- and L^2-norm shows schemes are second order accurate. The overlapping zone is necessary for the the communication and data transfer from one mesh to another. With respect to the methods available in the literature for overset grids, the ADER approach allows to transmit data from one mesh to another through fluxes and not through strong conditions on the boundary of the overlapping zone, by improving computational costs and timing.

THE POISSON EQUATION AND ADER METHOD FOR ADVECTION-DIFFUSION EQUATION

Let the Poisson equation be $\Delta u = f$ in $\Omega \subset \mathbb{R}^2$, completed with adequate boundary conditions. Let Ω_i be the quadrilateral i-th cell (either in the background or foreground mesh); thus its boundary is denoted by $\partial\Omega_i = \bigcup_{l=1}^4 \Gamma_{il}$. By integrating the Poisson equation over cell Ω_i, it reads

$$\sum_{l=1}^{4} \int_{\Gamma_{il}} \nabla u \cdot \boldsymbol{n}_{il} \, \mathrm{d}\Gamma = \int_{\Omega_i} f \, \mathrm{d}\Omega, \tag{2}$$

where $\boldsymbol{n}_{il}$ is the outer unit normal to Γ_{il}. For the computation of the gradient, we adopt two different strategies: if the cell is not at the boundary of the overlapping interface, the reconstruction is *geometrically* achieved, otherwise, an *analytical* reconstruction is employed. The analytical approach consists of an interpolation of the gradient by using the information of neighboring cells to Ω_i by minimizing a convex functional [4]. On the other hand, the geometrical approach is based on the projection of the gradient along the direction $\boldsymbol{n}_{il}$ by using the approximations of the gradient along the directions linking the cell centers and the extremes of sides Γ_{il}.
Regarding the unsteady advection-diffusion equation, let us consider problem

$$\begin{aligned} \partial_t u + \nabla \cdot \mathcal{F}(u, \nabla u) &= f \quad \text{in } \Omega \times [0, T]; \\ \frac{\mathrm{d}\boldsymbol{x}}{\mathrm{d}t} &= \boldsymbol{V}(\boldsymbol{x}, t; u); \end{aligned} \tag{3}$$

properly completed with initial and boundary conditions. In the above system, $\mathcal{F}(u, \nabla u)$ is the advective-diffusive term and the second line is the *motion equation* for the foreground mesh. In order to solve (3), we adapted the ADER method

*Corresponding author. E-mail: michele-giuliano.carlino@inria.fr.

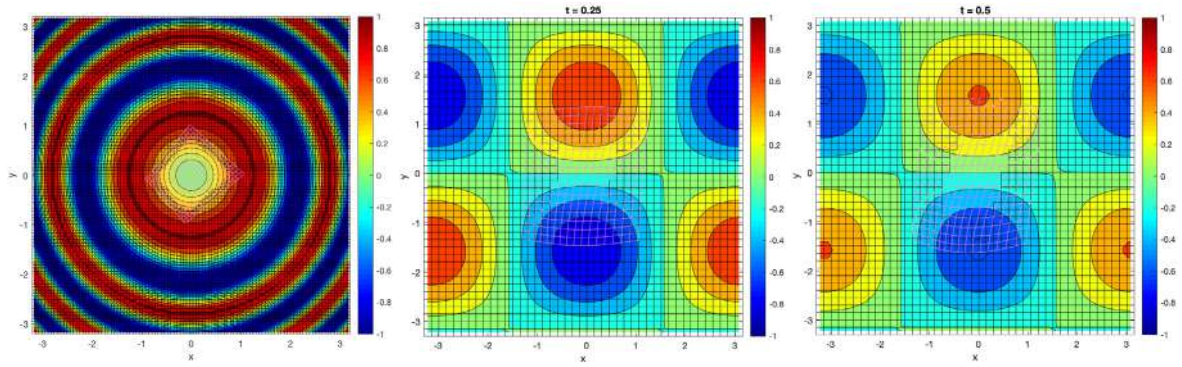

Figure 1: First figure in the left corresponds to the Poisson equation case test. The central and right figures show two time instants of the advection-diffusion case test.

[5, 6] for a Chimera configuration. First, we solve the motion equation in the space-time cell $\mathcal{C}_i^n = \Omega_i(t) \times [t^n, t^{n+1}]$, with Ω_i the usual spatial cell, in a weak sense by a Galerkin projection. This allows to both solve $(3)_2$ and define a map $\mathcal{M}_i$ from the physical space-time cell $\mathcal{C}_i^n$ to the reference space-time cell $\hat{\mathcal{C}} = [0,1]^3$. Through map $\mathcal{M}_i$, we first find a **local predictor solution** of $(3)_1$ in $\mathcal{C}_i^n$ as a Galerkin projection employing the same Lagrangian basis used for solving $(3)_2$ (*isogeometric approach*). Successively, by writing equation $(3)_1$ in a hyperbolic sense, namely $\tilde{\nabla} \cdot \tilde{\boldsymbol{u}} = f$, with $\tilde{\nabla} = [\nabla, \partial_t]^T$ and $\tilde{\boldsymbol{u}} = [\mathcal{F}, u]^T$, we integrate it over $\mathcal{C}_i^n$. Since the boundary $\partial\mathcal{C}_i^n$ of the space-time cell is $\partial\mathcal{C}_i^n = \Omega_i^n \cup \Omega_i^{n+1} \cup \bigcup_{j=1}^4 \Gamma_{ij}^n$, with $\Omega_i^\mu \equiv \Omega_i(t^\mu)$ and Γ_{ij}^n the j-th space-time side of $\mathcal{C}_i^n$, equation $(3)_1$ turns into

$$-|\Omega_i^n| U_i^n + |\Omega_i^{n+1}| U_i^{n+1} + \sum_{j=1}^{4} \int_{\Gamma_{ij}^n} \tilde{\boldsymbol{u}} \cdot \tilde{\boldsymbol{n}}_{ij} \, \mathrm{d}\Gamma = \int_{\mathcal{C}_i^n} f \, \mathrm{d}\mathcal{C}, \tag{4}$$

with $U_i^\mu = |\Omega_i^\mu|^{-1} \int_{\Omega_i^\mu} u(\boldsymbol{x}, t^\mu) \mathrm{d}\boldsymbol{x}$ the spatial average of the solution and $\tilde{\boldsymbol{n}}_{ij}$ the unit outer normal of Γ_{ij}^n. In equation (4), the unknown is U_i^{n+1} and the last term of the left side is the space-time flux to be computed. For this reason, the integral function $\tilde{\boldsymbol{u}} \cdot \tilde{\boldsymbol{n}}_{ij}|_{\Gamma_{ij}^n}$ is approximated through a Local Lax-Friederichs (LLF) formula by using the local predictor solutions over $\mathcal{C}_i^n$ and its neighboring space-time cells. Equation (4) with the approximation of the space-time flux is called **correction stage** of the ADER method. Finally, in order to manage the cells at the boundary of the overlapping zone and the evolution of the cells in the hole of the background mesh, a local polynomial reconstruction over those cells is performed.

Here we present the study of the order of convergence with two test cases for the two problems, respectively. For both test cases, the computational domain is $\Omega = [-\pi, \pi]^2$. For the Poisson equation (see Figure 1 left), the exact solution is $u_{ex} = \sin(x^2 + y^2)$ and Dirichlet boundary conditions are imposed, i.e., $u \equiv u_{ex}$ on $\partial\Omega$. For AD problem, we considered a linear advective-diffusive term, i.e. $\mathcal{F}(u, \nabla u) = \nu \nabla u + \boldsymbol{\beta} u$, where $\nu = 0.1$ is the viscous term and $\boldsymbol{\beta} = [3, 4]^T$ is the advective field. The exact solution reads $u_{ex} = e^{-\nu t} \sin(x) \cos(y)$ and the last time is $T = 1$. We imposed initial and boundary conditions as $u(\boldsymbol{x}, 0) = u_{ex}(\boldsymbol{x}, 0)$ and $u \equiv u_{ex}$ on $\partial\Omega \times [0, T]$, respectively. The foreground mesh fulfills $(3)_2$ with velocity $\boldsymbol{V} = [u, u]^T$ (see Figure 1 center and right). Table 1 resumes the errors and rates of convergence for both problems, confirming the second order accuracy of the methods.

Table 1: Errors (second and third columns) and convergence rates (last two columns) for Poisson (left) and advection-diffusion equations (right). For AD problem, the errors refer to final time $T = 1$.

#CELLS	L^∞-err	L^2-err	$\mathcal{O}(L^\infty)$	$\mathcal{O}(L^2)$
2443	2.4150e-1	4.0000e-2		
9853	1.8500e-2	7.1000e-3	3.68	2.48
39511	6.2000e-3	1.7000e-3	2.34	2.06

#CELLS	L^∞-err	L^2-err	$\mathcal{O}(L^\infty)$	$\mathcal{O}(L^2)$
542	2.2467e-1	8.5193e-3		
1910	4.7015e-3	1.9332e-3	2.77	2.35
7270	1.0103e-3	4.3717e-4	2.30	2.23

References

[1] Meakin, R. L. "Composite overset structured grids." *Handbook of Grid Generation* (1999): 1-20.
[2] Chorin, A. J., The numerical solution of the Navier-Stokes equations for an incompressible fluid. *Bull. Amer. Math. Soc.*, 73(6):928-931, 11 1967.
[3] Temam, R., Une méthode d'approximation de la solution des équations de Navier-Stokes. *Bulletin de la société Mathématiques de France*. 96:115-152, 1968.
[4] Raeli A., Bergmann M., and Iollo A., A finite-difference method for the variable coefficients Poisson equation on hierarchical Cartesian meshes. *Journal of computational Physics*. 355:59-77, 2018.
[5] Dumbser M., Boscheri W., Semplice M., and Russo G., Central weighted ENO scheme for hyperbolic conservation laws on fixed and moving unstructured meshes. *SIAM Journal on Scientific Computing*. 39(6):A2564-A2591, 2017.
[6] Hidalgo A., and Dumbser M., ADER schemes for nonlinear systems of stiff advection-diffusion-reaction equations. *Journal of Computational physics*. 48(1-3):173-189, 2011.

A NEURAL-NETWORK-BASED SYNTHETIC BOUNDARY CONDITION FOR THE SIMULATION OF CHANNEL TURBULENCE

Heesik Yoo[1], Bérengère Podvin*[1], Yann Fraigneau[1], and Alexandre Allauzen[1]
[1]Université Paris-Saclay, CNRS, LIMSI

Summary We describe a method combining Proper Orthogonal Decomposition (POD) and an artificial recurrent neural network to implement an inlet boundary condition for a turbulent channel flow. The boundary condition is reconstructed from POD modes, the amplitudes of which are predicted using a neural network (LSTM). We first assess the quality of the LSTM prediction in POD space. The reconstructed velocity is then used as an inlet boundary condition in a spatially developping channel. Statistics are compared with the reference and are found to be in relatively good agreement.

MOTIVATION

The generation of turbulent inlet boundary conditions is an important question for the simulation of flows around aerodynamic immersed bodies or a spatially developing boundary layer. Fully developed turbulent channel flow can be obtained using periodic boundary conditions, but in general turbulent flows such as boundary layers develop in the spatial direction and more effort is required to construct an inlet velocity condition.

Pamiès *et al.* [1] used a combination of structures to construct the inlet condition - synthetic eddy method. Proper Orthogonal Decomposition (POD) provides a natural reconstruction framework as the velocity field can be approximated as a linear combination of POD spatial modes, the amplitudes of which vary in time. The question of determining inlet boundary conditions thus boils down to predicting the temporal evolution of a relatively limited number of amplitudes. In this framework the issue is to predict the behavior of the amplitudes of the POD spatial modes. Druault *et al.* [2] combined linear stochastic estimation with POD to construct an inlet boundary condition for a spatially developing mixing layer. Perret *et al.* [3] used experimental data to construct a low-order model for the amplitudes of the POD modes and build an inlet condition for large-eddy-simulation (LES) of a mixing layer. In the present work, we predict POD amplitudes using a special type of neural network called a long-term short-term memory network (LSTM) [4]. We first describe the method and show how the network is able to predict the POD amplitudes of the velocity field in a turbulent channel flow. The method is then implemented to reconstruct the velocity field on a plane which is used as an inlet boundary condition for the numerical simulation of a turbulent channel flow. Turbulent statistics in the channel are then compared with those of a reference one.

RECONSTRUCTION METHOD

Description

We consider the numerical simulation of an incompressible turbulent channel flow characterized by a bulk velocity U and a half-height h. The Reynolds number based on channel half-height h and friction velocity u_τ is $Re_\tau = 194$, which corresponds to the reference channel. Application of Proper Orthogonal Decomposition to the velocity field yields

$$\underline{u}(\underline{x}, t) = \sum_n a_n(t)\underline{\phi}_n(\underline{x}) \tag{1}$$

The spatial eigenfunctions $\underline{\phi}_n$ are determined *a priori* from a reference simulation. We consider 300 snapshots separated by a time scale of $\delta t = h/U$, which can be reorganized into a hierarchy of 300 modes.

Constructing an inlet condition at all times consists in predicting the amplitude of these modes. In order to this we use a LSTM. The network is trained on a subset of the snapshots and validated on the remaining subset. The goal of the LSTM is to predict the next values of the amplitudes at $t + \delta t$, given the values at t. It is a recursive procedure, so that the amplitudes can be predicted over a long period of time.

Once the predicted values obtained at regular intervals of δt, the amplitudes can be interpolated in the simulation at any instant within the range spanned by the prediction.

Results

In the results shown below, the LSTM was trained on 180 snapshots. The remaining 120 snapshots constitute the validation basis. The LSTM was iterated over 640-180=480 snapshots - 120 of which can be compared with the reference and 360 of which correspond to entirely new times. We consider only the 100 most energetic POD modes, which capture about 85% of the energy.

We first compare the amplitude of the POD modes predicted with the LSTM to those the reference simulation.

Figure 1 represents respectively the energy content and frequency spectrum of the amplitudes (frequencies are expressed in wall units, denoted with a $+$). Overall the LSTM predicts relatively well the characteristics of the modes.

*Corresponding author. E-mail: podvin@limsi.fr

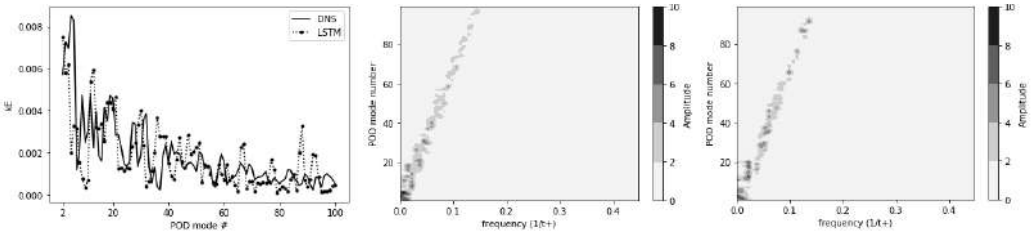

Figure 1: Left: Energy of the POD amplitudes as a function of POD mode number for the reference data and the prediction; Middle: Frequency spectrum of the reference POD amplitudes as a function of POD mode number; Right: Frequency spectrum of the predicted POD amplitudes.

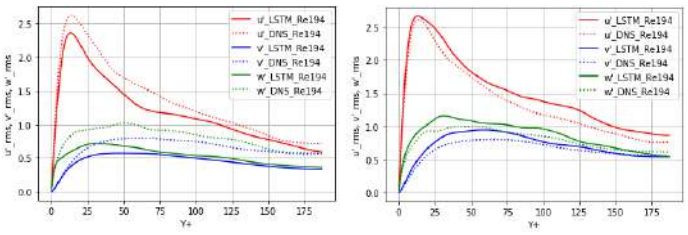

Figure 2: Turbulent intensities averaged over time and the spanwise direction at different streamwise locations as a function of the wall distance y (expressed in wall units +); top: channel inlet; bottom: channel outlet.

INLET BOUNDARY CONDITION

In this section we simulate a spatially developing turbulent channel using as an inlet condition the velocity field reconstructed using the POD eigenfunctions and the amplitudes predicted by the LSTM. A convective boundary condition is used at the outlet of the channel. The dimensions of the channel are $L_x = 2\pi, L - z = 4\pi, L_y = 1$ in respectively the streamwise (x), wall-normal (y) and spanwise (z) direction. The statistics are computed over 24 time units based on channel half-height and bulk velocity in cross-planes at the following streamwise locations: the inlet, the mid-channel $x = \pi$ and the outlet. They are compared with those of a reference simulation at the same Reynolds number with periodic boundary conditions in the streamwise direction.

Figure 2 shows the turbulent intensities (or normal components of the Reynolds stresses). The normal stresses components of the reconstructed velocity condition are slighty under-predicted, which corresponds to the fact that only 85% of the kinetic energy is captured in the reconstruction. However at the outlet of the channel, the stresses are in much better agreement with the reference.

CONCLUSIONS

A new method combining Proper Orthogonal Decomposition and neural approaches was developed in order to build an inlet condition for an turbulent channel flow. The boundary condition was reconstructed using POD modes determined *a priori*. The amplitudes of the POD modes were predicted using a LSTM network. The characteristics of the amplitudes were satisfactorily captured by the LSTM. The statistics of the channel with the synthetic inlet boundary condition were found to match relatively well those of a turbulent channel flow with standard periodic boundary conditions.

References

[1] M. Pamies, P.E.Weiss, E. Garnier, S. Deck, and P. Sagaut. Generation of synthetic turbulent inflow data for large-eddy simulation of spatially evolving wall-bounded flows. *Phys. Fluids*, 21:045103, 2009.

[2] P. Druault, S. Lardeau, J-P Bonnet, F. Coiffet, J. Delville, E Lamballais, J-F Largeau, and L Perret. Generation of three-dimensional turbulent inlet conditions for large-eddy simulation. *AIAA Journal*, 20:075107, 2008.

[3] L. Perret, J. Delville, R. Manceau, and J.P. Bonnet. Turbulent inlet boundary conditions for large-eddy simulation based on low-order empirical model. *Phys. Fluids*, 20:075107, 2008.

[4] M.A. Bucci, O. Semeraro, A. Allauzen, L. Cordier, G. Wisniewski, L. Mathelin. Control-oriented model learning with a recurrent neural network. APS Meeting, 2018.

AN OPTIMAL, FAST, PARALLEL SOLVER FOR THE INCOMPRESSIBLE NAVIER–STOKES EQUATIONS ON COLOCATED GRIDS

Franco Auteri*[1], Alessandro Chiarini[1], and Maurizio Quadrio[1]
[1]Department of Aerospace Sciences and Technologies, Politecnico di Milano, via La Masa 34, 20156 Milano, Italy

Summary A novel colocated finite difference solver for the incompressible Navier-Stokes equations is presented, based on the direction-splitting fractional step method proposed in [Guermond & Minev 2010]. High computational efficiency is obtained using the direction-splitting method; high scalability is obtained thanks to the Schur complement method used for parallelisation. The checkerboard pressure modes have been stabilised using the approach introduced by [Rhie & Chow 1983], which consists in adding a fourth order term to the right-hand side of the pressure equation and using a short stencil for second derivatives in the left-hand side. The obtained solver is found to be second order accurate in time and space. As expected, the new solver is faster than the staggered version and its parallel performance scales extremely well with the number of processors.

The large increase in CPU and memory performance of recent computers leads to new opportunities for Direct Numerical Simulations (DNS) of turbulent flows. An example is the DNS of complex biomedical flows such as the flow in the nasal cavities [2] or the blood stream [3]. These new possible applications of the DNS require large grids – up to 10^9 points – and high geometrical flexibility. Therefore, together with improving computer performance, suitable new DNS programs need to be developed capable of taking advantage of the hardware performance and allowing an increased geometrical flexibility. In this respect, the time and space discretisation methods can be key to fully exploit the available performance to solve problems still elusive. In particular, when fluid structure interaction problems within complex geometries are concerned, such as in biomedical applications, not only high geometrical flexibility is needed, but also the capability to cope with a shape that changes with the flow. Finite elements, despite providing high geometrical flexibility and good accuracy, lack the necessary efficiency when the mesh must be modified in each time step. Finite differences, able to deal with such complex geometries by the immersed boundary method, seem to provide the best trade-off between accuracy and efficiency in these applications.

A very efficient finite difference solver for the incompressible Navier–Stokes equations on staggered grids has been recently introduced by Guermond and Minev [1], the solver has an optimal computational complexity and is highly scalable. The efficiency of this solver hinges on a novel fractional-step method used to decouple the viscous step from the incompressibility constraint that allows the use of the ADI algorithm [4] for both the viscous and the pressure step. Using a Crank–Nicolson time discretisation, the viscous step reads:

$$\frac{\boldsymbol{\xi}^{n+1}-\boldsymbol{u}^n}{\Delta t}-\frac{1}{\mathrm{Re}}\nabla^2\tilde{\boldsymbol{u}}^n=f^{n+1/2}-\nabla p^{*,n+1/2}-\mathbf{nl}(\boldsymbol{u}^{n+1/2}) \tag{1}$$

$$\frac{\boldsymbol{\eta}^{n+1}-\boldsymbol{\xi}^{n+1}}{\Delta t}-\frac{1}{2\mathrm{Re}}\frac{\partial^2}{\partial x^2}\left(\boldsymbol{\eta}^{n+1}-\boldsymbol{u}^n\right)=0 \tag{2}$$

$$\frac{\boldsymbol{\zeta}^{n+1}-\boldsymbol{\eta}^{n+1}}{\Delta t}-\frac{1}{2\mathrm{Re}}\frac{\partial^2}{\partial y^2}\left(\boldsymbol{\zeta}^{n+1}-\boldsymbol{u}^n\right)=0 \tag{3}$$

$$\frac{\boldsymbol{u}^{n+1}-\boldsymbol{\zeta}^{n+1}}{\Delta t}-\frac{1}{2\mathrm{Re}}\frac{\partial^2}{\partial z^2}\left(\boldsymbol{u}^{n+1}-\boldsymbol{u}^n\right)=0 \tag{4}$$

where $\boldsymbol{u}^n$ is the velocity at time t_n, $p^{*,n+1/2}=p^{n-1/2}+\phi^{n+1/2}=2p^{n-1/2}-p^{n-3/2}$ is the pressure prediction at time $t_{n+1/2}$, Re is the Reynolds number and **nl** the nonlinear term. Instead, the pressure step reads:

$$\psi-\frac{\partial^2\psi}{\partial x^2}=-\frac{1}{\Delta t}\nabla\cdot\boldsymbol{u}^{n+1}, \qquad \frac{\partial\psi}{\partial x}|_{x=0,1}=0, \tag{5}$$

$$\varphi-\frac{\partial^2\varphi}{\partial y^2}=\psi, \qquad \frac{\partial\varphi}{\partial y}|_{y=0,1}=0, \tag{6}$$

$$\phi^{n+1/2}-\frac{\partial^2\phi^{n+1/2}}{\partial z^2}=\varphi, \qquad \frac{\partial\phi^{n+1/2}}{\partial z}|_{y=0,1}=0. \tag{7}$$

This method retains the efficiency of $1D$ solvers with banded matrices, hence an optimal computational complexity, in a direct solver. The high scalability is guaranteed by the use of the Schur-complement method [1].

While the capabilities of this solver have been extended to complex geometries by a Moving Least Square immersed boundary procedure [6], the use of a staggered grid to enforce the LBB condition prevents the potential of the solver to be fully exploited when moving geometries and fluid-structure interaction problems are concerned. Indeed, when applying the immersed boundary procedure, the calculation of all the coefficients necessary for the involved interpolations must be computed on the four staggered grids, leading to a significant performance degradation.

*Corresponding author. E-mail: franco.auteri@polimi.it.

These problems motivated us to develop a colocated version of the aforementioned fractional-step solver. The instability related to pressure spurious modes has been cured by the method proposed by Faure et al. [8] which heavily relies on the well known method first proposed by Rhie and Chow [7]. It consists in adding a stabilisation term in the form of a fourth derivative term multiplied by an under-relaxation coefficient in the right-hand side of the equivalent of the Poisson equation for pressure. The stabilisation term reads:

$$\alpha c(\nabla_L^2 p - \nabla_s^2 p) \tag{8}$$

where $\nabla_s^2 p$ is the pressure Laplacian computed on the small stencil – in 2D $(p_W - 2p_C + p_E)/\Delta x^2 + (p_S - 2p_C + p_N)/\Delta y^2$, see fig 1 – and $\nabla_L^2 p$ is the pressure Laplacian computed on the large stencil – $(p_{WW} - 2p_C + p_{EE})/4\Delta x^2 + (p_{SS} - 2p_C + p_{NN})/4\Delta y^2$– and $\alpha \in [0, 1]$ and c a constant.

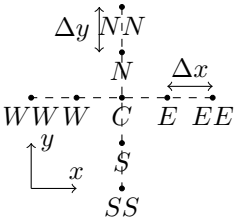

Figure 1: Colocated grid in the 2D case.

The stabilisation term partially substitutes the large-stencil Laplacian of the pressure implicitly present in the right-hand side of the pressure equation with its small-stencil counterpart, thus coupling all grid points.

As expected, the colocated program is slightly less accurate than the staggered one, but second order convergence is obtained in both time and space for velocity and pressure (see figure 2). Moreover, the colocated program displays faster

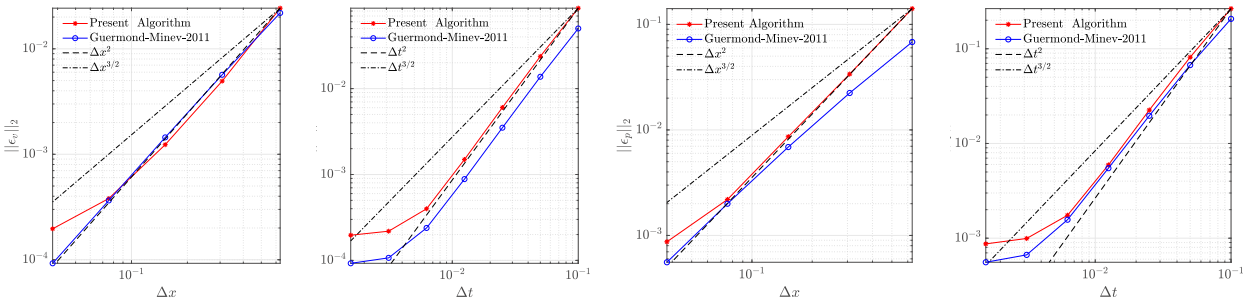

Figure 2: Convergence curves. Top-left panel: spatial convergence of the velocity; top-right panel: time convergence of the velocity; bottom-left panel: time convergence of the velocity; bottom-right: time convergence of the pressure

convergence in space with respect to the original staggered one (see bottom-left in figure 2).

In addition, the colocated version of the program is about 30% faster than the staggered one, and still presents high scalability by virtue of the Schur complement method used for parallelisation.

References

[1] Guermond J.L., Minev P.D. A new class of fractional step techniques for the incompressible Navier–Stokes equations using direction splitting. *Compt. Rendus Math,* **348**: 581-585, 2010.

[2] Covello V., Pipolo C., Saibene A., Felisati G., Quadrio M. Numerical simulation of thermal water delivery in the human nasal cavity. *Comput. Biol. Med.* **100**: 62-73, 2018.

[3] Crosetto P., Deparis S., Fourestey G., Quarteroni A. Parallel algorithms for fluid-structure interaction problems in haemodynamics. *SIAM J. Sci. Comput.* **33**: 1598-1622, 2011.

[4] Douglas J. Alternating direction methods for three space variables. *Numer. Math.* **4**, 41-63, 1962.

[5] Guermond J.L., Minev P.D. A new class of massively parallel direction splitting for the incompressible Navier–Stokes equations. *Comput. Methods Appl. Mech. Engrg.* **2000**: 2083-2093, 2011.

[6] Auteri F., De Tullio M.D., Guermond J.-L., Montagnani D., Konghar P.D. A Massively Parallel, Direction-Splitting Solver for DNS in Complex Geometries. Salvetti M.V., Armenio V., Fröhlich J., Geurts B.J., Kuerten H. eds., *Direct and Large-Eddy Simulation XI*, Springer, 23-29, 2019.

[7] Rhie C.M.,Chow W.L. Numerical Study of the Turbulent Flow past an Airfoil with Trailing Edge Separation. *AIAA J.* **21**: 1525-1532, 1983.

[8] Faure S., Laminie J., Temam R. Colocated finite volume schemes for fluid flows. *Comm. Comput. Phys.* **4**: 1-25, 2008.

A HIGH ORDER COMPACT MESHLESS METHOD FOR MOVING BOUNDARY FLOWS

Y. YAO[1]*, D. Shyam Sundar[2], K.S. Yeo[2]
[1]Midea Corporate Research Center, Midea Group, Foshan, China
[2]Department of Mechanical Engineering, National University of Singapore, Singapore

Summary This article presents the application of a high order meshless method with compact support in moving boundary flow problems. The high order meshless method is applied to a mix of Cartesian and meshless nodes to construct an efficient hybrid high-order scheme. The present scheme was then applied to solve complex moving boundary problems including the ground effect of flapping airfoils and the flow phenomena in clap-and-fling motion.

INTRODUCTION

The meshless or meshfree methods have generated considerable interest among researchers for the treatment of problems with complex geometry [1-3]. Meshless methods are a class of methods that do not rely on a mesh for solution process. These methods require relatively lower cost of geometric and data administration, especially with problems involving complex deforming geometries. However, meshless methods are sensitive to the distribution of support nodes selected for data reconstruction. The problem of instability increases rapidly with increase in the order of meshless methods. In practice, additional supporting nodes are added until the set of nodes result in a valid interpolation.

The requirement for large supporting node set and the sensitivity of interpolation techniques to the distribution of support nodes have restricted the general application of meshless methods. Shyam Sunder et al. [4] presented a high order meshless method with compact support. The utilization of the increased degrees of freedom and corresponding high-order information at nodes results in a significant reduction in the number of support nodes needed for solution reconstruction. High-order accuracy of up to the 6th order was demonstrated in their work.

This research work is an extension and development based on what Shyam Sundar et al. [4] has done. We extended the compact meshless method to Cartesian grid system and constructed a hybrid high-order scheme with a mix of Cartesian and meshless nodes. The high order scheme was then applied in complex moving boundary problems. The results showed that the high order scheme can produce accurate results in small gap and proximity with lesser number of nodes.

NUMERICAL METHODS

Theoretical Formulation of High Order Meshless Method with Compact Support

Consider a meshless grid, where there exists at each node a solution data set, which describes the solution in the vicinity of the node. For a reference node i, N_s supporting nodes will be used to interpolate data set Q^i at node i. Thus, the solution data may be represented in terms of a finite linear expansion in a set of basis functions $Q^i = [\alpha^i]^T[\phi^Q]$. With proper selection of $[\phi^Q]$, we could get the derivatives of Q^i of any order in terms of and their derivatives. Conversely, the same equation can be used to find the coefficient $[\alpha^i]$ if we know the derivatives of solution data.

Let $\mathrm{I}^i = [\beta^i]^T[\phi^I]$ denotes a p_I order interpolant of Q^i. With sufficient number of support nodes, the interpolant coefficients $[\beta^i]$ can be obtained by solving the system of equations

$$\left[\frac{\partial^p \phi^I}{\partial \xi_i^m \partial \eta_i^{p-m}}\right]^T_{(\xi_i,\eta_i)=(\xi_{ij},\eta_{ij})} \left[\beta^i\right] = \left[\frac{\partial^p Q^j}{\partial \xi_i^m \partial \eta_i^{p-m}}\right]^T_{(\xi_i,\eta_i)=(\xi_{ij},\eta_{ij})}, (p \le p_Q) \quad (1)$$

where (ξ_{ij},η_{ij}) denotes the local coordinate of the *j*-th support node for the node *i*. In the present work, we adopt the singular-value decomposition (SVD) method to solve weighted Eq. (1) for $[\beta^i]$. The estimated $[\beta^i]$ then gives the interpolant I^i and its relation with the solution data. With M_Q number of derivatives available at a node, and N_s supporting nodes, $M_Q \times N_s$ number of equations can be constructed for Eq. (1). Thus, the supporting region of reference node could shrink to contain a moderate number of nodes, which allows stable reconstruction at high order of interpolation. The computation procedure for $[\beta^i]$ has been discussed in details by Shyam Sundar et al. in [1].

Governing Equations and Discretization

In this study, we investigate the moving boundary problems in incompressible viscous fluid flow. The present methodology is adopted to discretize the Arbitrary Lagrangian-Eulerian (ALE) form of the incompressible Navier-Stokes equations. Fractional step method is used to integrate the governing equations in time.

The discretized equations are solved on a hybrid Cartesian-cum-messfree grid system. The formulation described in the last section is used to obtain the derivatives on both kinds of nodes. The interpolation on the Cartesian nodes is

*Corresponding author. E-mail: yaoyang@u.nus.edu.

equivalent to that derived in the compact finite difference methods. At time step *n*, the Cartesian nodes overlapped by meshfree nodal cloud or moving body will not participate in the computation. For the overlapped Cartesian nodes that may emerge in the computation in the next time step, the field values on the nodes will be updated with the high meshfree scheme, thus to maintain the order of accuracy of the solution. More details of the 'nodal refreshing' process can be found in [2].

NUMERICAL EXPERIMENTS

Flapping Airfoil

We first studied the aerodynamics of a single 2D flapping elliptic airfoil. The numerical results were compared the experimental results of flapping wings in a free-steam velocity reported by Zhang et al. [4]. The single wing undergoes simple harmonic motion with exactly the same kinematics described in [5]. The time dependent thrust and lift coefficients are compared in Figure 1. The results clearly show that the good agreement between the numerical and experimental results was achieved.

Flapping in Ground Effect

We further studied the performance of the present computational method in ground effect simulation. Numerical results with the 2D flapping wing results of Gao & Lu [6] and experimental results of Lu et al. [7] were compared with the current CFD results. As shown in Figure 2, the variations of resultant lift and drag coefficients in all the three studies follow similar trend and can be categorized into the three regimes: force enhancement, force reduction and force recovery. However, the magnitudes of the resultant force coefficients are different from each other. The lift and drag coefficients obtained in the present study were substantially higher than those in the other flights.

Aerodynamic Effects in Clap-and-Fling

Aerodynamic effects of 2D clap-and-fling flapping motion were investigated at Re=150. The numerical method was carefully modified to allow the stable and accurate computations of rigid wings to be in extreme close proximity and even with physical clap occurring at the wing tips. The lift peak captured and aerodynamic force computed have shown good agreement with existing published results in [10].

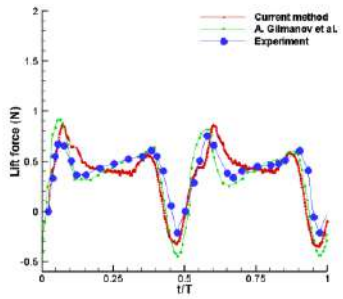

Figure 1 Thrust and lift on a single flapping wing.

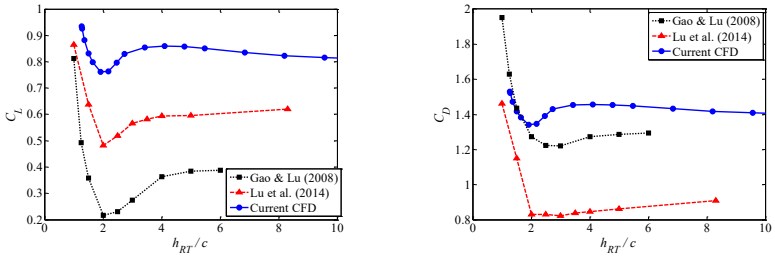

Figure 2. Force coefficients of a flapping wing in ground effect. (a) Lift coefficient, (b) Thrust coefficient.

CONCLUDING REMARKS

In this work, we extended the high order compact meshless method to hybrid meshfree-Cartesian grid with a unified interpolation scheme. The hybrid high order scheme was then applied in complex moving boundary problems involving small gaps. The numerical results proved that the present method could capture fine flow structures with high accuracy in moving boundary flows.

References

[1] Ding H., Shu C., Yeo K.S., Xu D. Development of least-square-based two- dimensional finite-difference schemes and their application to simulate natural convection in a cavity. *Comp. Fluids*. **33**: 137-154, 2004.
[2] Chew C.S., Yeo K.S., Shu C. A Generalized Finite-Difference (GFD) ALE Scheme for Incompressible Flows around Moving Solid Bodies on Hybrid Meshfree-Cartesian Grids. *J Comput. Phys.* **218**: 510-548, 2006.
[3] Yao Y, Yeo K.S. Manoeuvring Flight of a Model Insect – Saccadic Yaw and Sideslip. *Comp. Fluids*. **33**: 137-154, 2019.
[4] Shyam Sundar D., Yeo K.S. A High Order Meshless Method with Compact Support. *J Comput. Phys.* **272**: 70-87, 2014.
[5] Nguyen T.T., Shyam Sundar D., Yeo K.S., Lim T.T. Modelling and Analysis of Insect-Like Flexible Wings at Low Reynolds Number. *J. Fluids Struct.***62**: 294-317, 2016.
[6] Zhang X.H. Aerodynamics of Two-Dimensional Flapping Wings. *PhD Thesis*, National University of Singapore, 2014.
[7] Gilmanov A. Sotiropoulos F., Balaras E. A General Reconstruction Algorithm for Simulating Flows with Complex Immersed Boundaries on Cartesian Grids. *J. Comput. Phys.* **191**: 660-669, 2003.
[8] Gao T., Lu X.-Y. Insect Normal Hovering Flight in Ground Effect. *Phys. Fluids*. **20**: 87101, 2008.
[9] Lu H., Lua K.B., Lim T.T., Yeo K.S. Ground Effect on the Aerodynamics of a Two-Dimensional Oscillation Airfoil. *Exp. Fluids*. **55**: 1787, 2014.
[10] Kolomenskiy, D., Moffatt, H. K., Farge, M., Schneider, K. The Lighthill-Weis-Fogh clap-fling-sweep mechanism revisited. *J Fluid Mech*. **676**: 572–606, 2011.

NUMERICAL MODEL OF THE COLLECTIVE FLIGHT OF METEOROID FRAGMENTS IN THE ATMOSPHERE

Vladislav Lukashenko, Fedor Maksimov
Institute for Computer Aided Design of RAS, Moscow, Russia

Summary We present a numerical model to simulate a collective flight of meteoroid fragments in the atmosphere. The calculation method is based on the system of grids and allows to consider the bodies of different shapes and sizes placed in different positions relative to each other. Collisions of the bodies are simulated with the help of 'billiard balls' model with impact recovery coefficient. Using this method, we studied the dynamics of the system consisting of ten bodies. Initially bodies were placed on the line perpendicular to the flight direction with a short distance between them. It was observed that two head formations appeared from initial configuration and in these formations multiple collisions of the bodies occurred. Eventually the formations merged together into a conical shape that continued to spread apart.

INTRODUCTION

The development of observational technologies shows that the fall of meteor bodies is not as rare occurrence as it was assumed before. It is important to construct accurate models to simulate the events of meteoroids entering Earth's atmosphere and their flight. Initially meteoroid may enter the atmosphere as a single body however it often cracks under the load due to inner defects and heterogeneity of the structure [1]. As a result, fragmentation occurs and a group of closely spaced fragments is formed in the stead of the singular body. These fragments continue their flight together however the difference in forces, acting on each body, should result in the restructuring of these fragments: some fragments may get separated from the group, while others may continue their flight together.

The studies concerning the dynamics of multiple bodies are often carried out by determining aerodynamic properties of the bodies at different relative positions [2]. This approach works relatively well for small number of bodies but becomes inconvenient for big systems due to a large number of potential positions of the bodies and time-consuming calculations. Alternative approach is to solve adjoint aerodynamic and ballistic problems [3]. At first the aerodynamic problem is solved for the current configuration of the bodies, and then coordinates and velocities of the bodies are changed according to the acting forces and moments. In this work we present a newly developed method [4] that allows to simulate dynamics of the collective flight of multiple bodies and can be used to determine the possible change in the trajectory of the fragments. Using this method we studied the problem of the expansion of a system of ten meteoroid fragments that initially formed a line perpendicular to the flight direction and results show that the bodies will restructure and eventually form a conical shape.

METHODOLOGY

A uniform grid with rectangular cells is used to describe the external non-viscous flow field. A set of other smaller grids is used to simulate the flow near the surfaces of the bodies. These grids are connected with each corresponding body and take into account their shape and size (Figure 1). Thin-layer approximation to the Navier-Stokes equations is used to describe the flow field on these grids (i.e. viscous flow is considered). An information exchange is established between the external grid and the grids built in the proximity of the bodies.

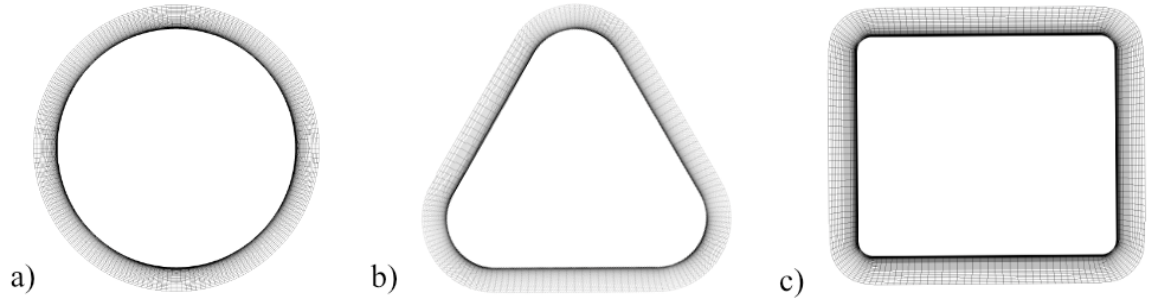

Figure 1. Grids that are built around cylindrical bodies with different shape of the cross section: (a) – circle, (b) – triangle, (c) – rectangle with elongation $\lambda = 1.2$.

Flow field is calculated using a two-step predictor-corrector method. The aerodynamic forces and moments acting on each body are determined from the pressure distribution, and then the state of the whole system is recalculated after a small time interval. Each body is moved together with its own grid to the distance that it should have passed. The flow field is recalculated over the given time interval with bodies having new positions. A new pressure distribution is calculated on the surfaces of the bodies. The whole process is repeated multiple times until calculations are completed.

If one body appears in the area behind another then it will have reduced resistance from the flow and, as a result, it will catch up with the body flying ahead. A collision is bound to occur in this situation as was shown by Barri [3]. The model of 'billiard balls' is used to simulate such collisions. Fragments are considered to be rigid bodies; the impact recovery coefficient is used to calculate the energy exchange and loss.

CALCULATIONS AND RESULTS

Using the method [4] we studied the dynamics of the system consisting of ten bodies that were initially placed near each other on the line perpendicular to the flight direction (Figure 2a). Due to time consuming calculations, two-dimensional plane problem was considered with bodies having a cylindrical shape with circular cross section. It was assumed that each body is an iron fragment with a mass of 1 kg and the flight was happening with a speed of 2 km/s at an altitude of 10 km. The distance between bodies was a variable parameter.

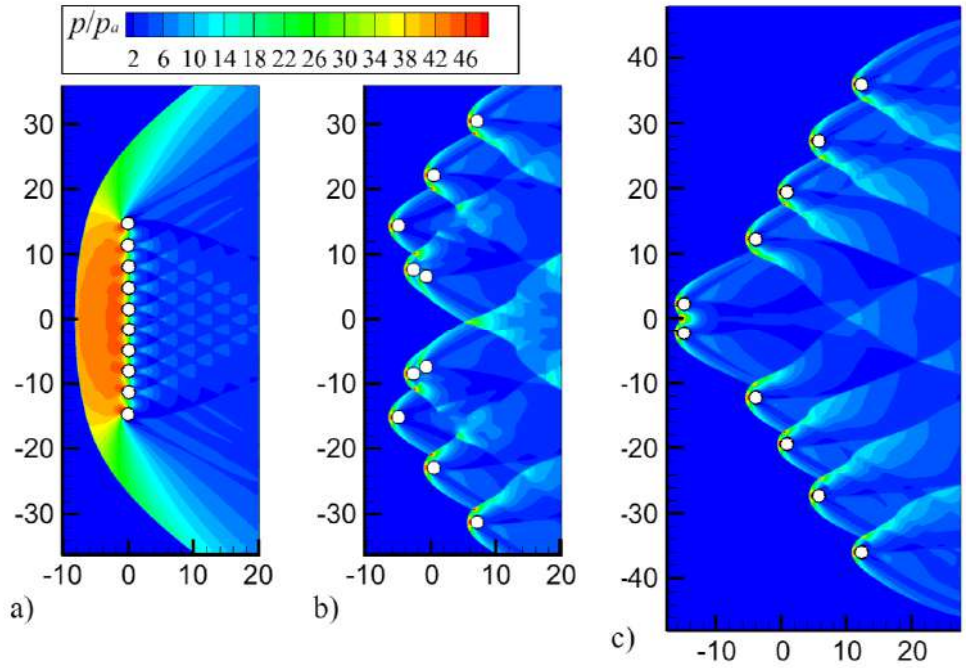

Figure 2. Pressure patterns for the expansion of a system of ten bodies: (a) – initial configuration with a collective head shock wave; (b) – appearance of two head formations in which collisions of the bodies occur; (c) – final configuration of the system that resembles a conical shape and continues to spread apart.

The results of the calculations show that outer bodies of the initial configuration (Figure 2a) fly apart from the group due to the asymmetry of the pressure on their surface, while the bodies in the center get pushed back due to the highest amount of pressure on their front. As the result the central bodies get dragged into the trail of the bodies located further from the middle of configuration and two head formations emerge (Figure 2b). Multiple collisions of the bodies occur in these head formations, however eventually the formations merge together forming a conical shape (Figure 2c). This conical shape remains relatively stable with bodies slowly spreading apart.

CONCLUSIONS

A new comprehensive method has been developed to study dynamics of complex systems of meteoroid fragments. The method allows to consider fragments of different shapes and sizes placed in different positions. The dynamics of the system consisting of ten bodies was studied. Initially bodies were placed near each other on the line perpendicular to flight direction. As a result of restructuring, two head formations appeared in which collisions of the fragments occurred. Eventually these formations merged together forming a conical shape that continued to spread apart.

References

[1] Stulov V.P., Mirskii V.N., Vislyi A.I. Fireball Aerodynamics. Nauka, MSK 1995.

[2] Marwege A., Willems S., Gulhan A. et al. Superposition Method for Force Estimation on Bodies in Supersonic and Hypersonic Flows *J. Spacecraft. Rockets.* **55**: 1166-1180, 2018. https://doi.org/10.2514/1.A34128

[3] Barri N.G. Dynamics of two spherical objects in supersonic flow *Dokl. Phys.* **55**: 516-518, 2010. https://doi.org/10.1134/S1028335810100101

[4] Lukashenko V.T., Maksimov F.A. Numerically simulated model of meteor body fragments distribution after destruction *Eng. J. Sci. Innov.* **69**: 1-14, 2017. https://doi.org/10.18698/2308-6033-2017-9-1669

COUPLED COOLING CHARACTERISTICS ANALYSIS FOR LAMINATED COOLING CONFIGURATION

Honglin Li[1], Lei Li1[1], Wenjing Gao[1], Zhonghao Tang[1], Fujuan Tong[1]
[1]School of Mechanics, Civil Engineering and Architecture, Northwestern Polytechnical University, Xi'an, China

Summary. The coupled cooling, internal cooling and film cooling of laminated cooling configuration are simulated under different blowing ratios using a new method that internal coolant air flows out computational domain at the film hole to decoupled internal cooling and remain the same flow pattern. Results indicate that while the coupled cooling contains the cooling characteristics of internal cooling and film cooling, its performance cannot directly derive from the superposition of internal cooling and film cooling, they will counteract part of cooling performance. Cooling effectiveness analysis under different blowing ratios shows that the internal cooling and film cooling effectiveness are about 98% and 25% that of coupled cooling separately.

Introduction and background

As the increasing requirement of gas turbine engines and aeroengines performance, the turbine inlet temperature gets dramatically raised and thus requires more advanced cooling method for turbine blade. The newly laminated cooling configuration can achieve larger temperature decrease than traditional cooling method since it integrates the advantages of film cooling, impingement cooling and pin fin cooling. Coolant air impinges into the laminated configuration and then flows through pin fins. Finally, it exhausts from film holes and forms the protective film. The external film cooling will influence the heat that transferred into blade from gas and the internal impingement cooling and pin fin cooling will also influence the formation of protective film. Therefore, the cooling process of laminated cooling configuration is a typical coupled cooling including internal cooling and external cooling.

It would be beneficial for the design of laminated cooling configuration to clarify the characteristics of internal and external cooling separately and their coupling property. Limited publications addressed this issue previously. Zhou, et al. [1] obtained the internal cooling effectiveness through directly minus the film cooling effectiveness from coupled cooling effectiveness. They found that the optimum coupled cooling effectiveness does not represent the optimum film cooling effectiveness or internal cooling effectiveness due to their interaction. Rao, et al. [2] conducted the coupled cooling numerical simulation and internal cooling calculations using constant temperature boundary conditions. Result shows that internal heat transfer is insensitive to the external flow. Though their studies have revealed the coupling property of laminated cooling to some extent, furtherly intensive investigation are still needed.

This study presents a new numerical method to calculate internal cooling considering the external flow and retaining the same flow pattern as coupled cooling. Combined with external cooling and coupled cooling calculation, three series of numerical simulations are conducted under different blowing ratios. The temperature distribution of outside surface and the cooling effectiveness under different blowing ratios are analyzed to clarify the coupling property, internal cooling characteristics and external cooling characteristics.

Numerical method

In this paper, a laminated cooling configuration is established which contained 7 cooling units as shown in Fig.1. Based on it, a fluid numerical model is also established which extended the gas flow channel to form gas inlet and outlet boundary, thus to eliminate the influence of boundary condition. In order to study cooling characteristics of internal cooling, external cooling and coupled cooling, three series of numerical method are employed. Simulating the flow and heat transfer between fluid and solid domains to obtain coupled cooling, simulating the flow and heat transfer only in fluid domain to obtain external cooling, simulating the flow and heat transfer both in fluid domain and solid domain with a coolant air outlet near the outside surface as shown in Fig.1 to obtain internal cooling.

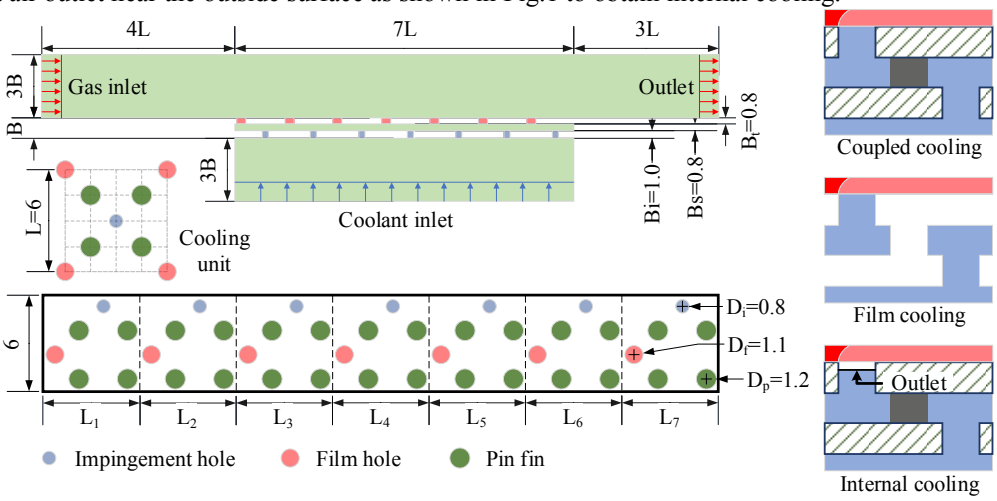

Fig.1 The dimension and three numerical calculation methods of laminated cooling configuration

Hot gas flows into fluid domain at 500 m/s and total temperature of 1800K. Coolant air flows into fluid domain at total temperature 800K and its total pressure varies among 111325Pa~171325Pa to obtain different blowing ratios. The outlet pressure is set to be 101325Pa. Hexahedron grid is used for fluid domain and tetrahedron grid is used for solid domain. SST turbulence model is employed and results shows Y+ value is less than 1 which satisfies requirement. Present numerical method has been verified by grid independence analysis and comparison with experiment.

Results & Discussion

Temperature distribution and effectiveness are analyzed under different blowing ratios which can be calculated by:

$$BR = \rho_c v_c / \rho_g v_g \quad (1) \qquad effectiveness = (T_g - T_w)/(T_g - T_c) \quad (2)$$

Fig.2 presents the temperature distribution of outside surface for three kinds of cooling calculations. When the laminated cooling configuration only has external cooling (film cooling), the film only covers a relatively small region behind film holes. Therefore, only a narrow low temperature region would be formed. At L1~L3 coolant units, when coolant air exhausts from film holes, it will attach outside surface firmly and cause an obviously low temperature region. However, at L4~L7 coolant units, the coolant air jet will penetrate the bulk flow and hence decrease the cooling performance. The low temperature region will disappear. When there is only internal cooling, the temperature distribution of outside surface appears clearly characteristics that it gets lowest at corresponding impingement region and then decreases along radial direction. The overall temperature is significantly lower than that of external cooling and it decreases from left to right due to the effect of hot gas flow. It can be clearly seen that the outside surface temperature distribution of coupled cooling distinctly shows the characteristics of internal cooling and external cooling. The overall temperature level is similar with that of internal cooling.

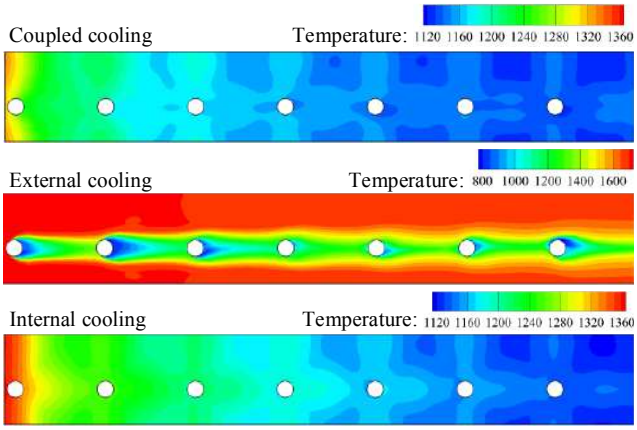

Fig.2 The outside surface temperature distribution (BR=0.62)

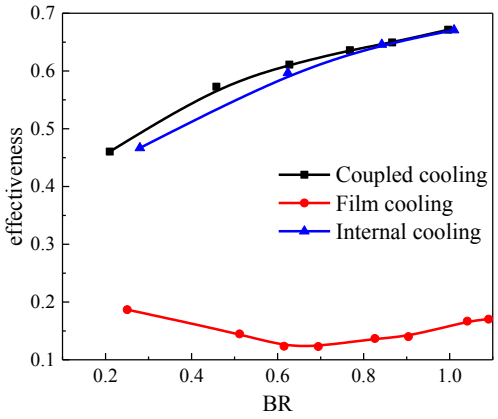

Fig.3 Cooling effectiveness under different blowing ratio

Fig.3 presents the outside surface area-averaged cooling effectiveness of L5~L6 cooling units. Corresponding to the temperature distribution as shown in Fig.2, the internal cooling has similar cooling effectiveness with coupled cooling while there is slightly difference when blowing ratio is lower than 0.6. The film cooling effectiveness is significantly lower than Internal and coupled cooling. When blowing ratio is lower than 0.6, the jet will gradually detach outside surface so that the cooling effectiveness decreases with the blowing ratio rises. When blowing ratio is higher than 0.6, the cooling effectiveness will increase because rising coolant air mass flow rate will furtherly enhance heat transfer. In general, the internal cooling effectiveness is about 98% of that of coupled cooling, meanwhile, the film cooling is about 25% of that of coupled cooling under all calculated blowing ratio. It indicates that coupled cooling performance cannot directly derived from the superposition of internal cooling and film cooling and they will counteract part of cooling performance.

Conclusions

The coupled cooling, internal cooling and film cooling of laminated cooling configuration are simulated under different blowing ratios using a new method that internal coolant air flows out computational domain at the film holes to decoupled internal cooling with the same flow pattern. The results show that coupled cooling contains the cooling characteristics both of internal cooling and film cooling and the internal cooling has similar temperature distribution with coupled cooling. Cooling effectiveness analysis under different blowing ratios shows that the internal cooling and film cooling effectiveness are about 98% and 25% that of coupled cooling separately. Coupled cooling performance cannot directly derive from the superposition of internal cooling and film cooling, they will counteract part of cooling performance.

References

[1] Zhou W, Deng Q, Feng Z. Conjugate heat transfer analysis for laminated cooling effectiveness: part A—Effects of surface curvature[C]//ASME Turbo Expo 2016: Turbomachinery Technical Conference and Exposition. American Society of Mechanical Engineers Digital Collection, 2016.

[2] Rao Y, Liu Y, Wan C. Multiple-jet impingement heat transfer in double-wall cooling structures with pin fins and effusion holes[J]. International Journal of Thermal Sciences, 2018, 133: 106-119.

SUPER-RESOLUTION RECONSTRUCTION OF UNPAIRED TURBULENCE USING GENERATIVE ADVERSARIAL NETWORKS

Junhyuk Kim[1], Hyojin Kim[1], and Changhoon Lee*[1,2]
[1]Department of Mechanical Engineering, Yonsei University, Seoul, Republic of Korea
[2]Department of Computational Science and Engineering, Yonsei University, Seoul, Republic of Korea

Summary We investigated super-resolution reconstruction of turbulent flows using an unsupervised learning method, generative adversarial networks (GANs). Unlike previous studies that have applied supervised learning to predict direct numerical simulation (DNS) data from filtered DNS data, the present study has novelty in the use of unpaired turbulence data. We found that an unsupervised learning adopting GAN model has statistically similar reconstruction capability of turbulent flows to that of supervised learning one. Therefore, super-resolution reconstruction of turbulence could be extended to much wider applications such as translation from large-eddy simulation (LES) to DNS, connection between experiment and simulation, and de-noise.

INTRODUCTION

The equations governing turbulence have long been established as the Navier-Stokes equations, but their solutions are difficult to predict due to their nonlinearity and multi-scale nature. Recently, deep learning has been rapidly developed to find a function that represents the nonlinear correlation of turbulence. In particular, convolutional neural networks (CNNs) effectively represent spatial correlation with fewer trainable parameters than fully connected neural networks (FCNNs). As a result, in addition to turbulence closure modelling, they were applied to various fields such as unsteady flow prediction, super-resolution reconstruction of turbulent flows[1], analysis of spatial relation between turbulence variables[2], and inflow turbulence generation[3].

Especially, super-resolution flow reconstruction is very important in a direct application in simulations and experiments as well as in a fundamental study related to the large-scale motions and their effect on the small-scale modulation. If a high-resolution reconstruction from low-resolution turbulence is possible, it means that there is a connection between the relatively large-scale structures and the small-scale structure. It could be a basis for the sub-grid scale modelling of large-eddy simulation (LES). In addition, from an experimental viewpoint, it will help to overcome the environment where only some data can be measured due to the limitation of measuring equipment.

The CNN model used by Fukami et al.[1] showed the reconstruction ability of isotropic turbulence from filtered one. However, with an increase in resolution ratio, poor representation of small-scale structures was observed because there are too many possible high-resolution solutions from low-resolution data. To overcome this, generative adversarial networks (GANs) proposed by Goodfellow et al.[4] could be used to give a possible high-resolution solution with realistic small-scale structures. Using the GAN training framework, Xie et al.[5] proposed a super-resolution reconstruction model for smoke flows. Deng et al.[6] also applied GAN to high resolution reconstruction of turbulent flow around cylinders and showed statistically accurate results similar to DNS.

However, most studies are restricted to supervised learning frame that low-resolution data is obtained from DNS, and the input (filtered DNS) and the output (DNS) are paired. It is unlikely that the trained model developed under these frames could well reconstruct high-resolution flow field from the LES data or experimental data which were not used for training. That is, there is a strong need for an unsupervised learning methodology that can learn unpaired turbulence data, such as LES data and DNS data, and sparse-measured data and dense-measured data, and could be used in realistic environments.

In this study, we apply GAN, one of the unsupervised learning methods, to reconstruction of super-resolution using unpaired turbulence data. Kim and Lee[3] found that GAN can learn the similarity in turbulence data obtained with different simulation parameters. From this experience, we expect that performance of unsupervised learning might be similar to that of supervised learning by learning the similarity of turbulence structure in unpaired data.

METHODOLOGY

In unsupervised learning, the most different thing from supervised learning is that input (X) and output (Y) data are not paired. Therefore, there is no clear loss such as mean-squared-error (MSE) between predicted field and targeted one. The basic GAN objective function without MSE could be expressed as follows.

$$\min_G \max_D \mathbb{E}_Y\left[\log\left(D(Y)\right)\right] + \mathbb{E}_X\left[\log\left(1 - D(G(X))\right)\right]$$

In our problem, X and Y are low-resolution turbulent flow fields and high-resolution ones which are not paired. After training, $G(X)$ could give a high-resolution flow field. However, $G(X)$ is less dependent on X and has low prediction accuracy compared to supervised learning method because desirable correlation between X and $G(X)$ is not considered in the above objective function. To reflect correlation between low-resolution flow fields and high-resolution ones, an inverse mapping $F : Y \rightarrow X$ is added and a cycle consistency loss is enforced [7].

*Corresponding author. E-mail: clee@yonsei.ac.kr.

RESULTS AND CONCLUSIONS

The framework was applied to two test cases. In the first one, DNS and filtered DNS data of homogeneous isotropic turbulence were used as Y and X, respectively. For the purpose of comparison, supervised learning using direct MSE between reconstructed field and DNS one with GAN was carried out. As a result, unsupervised GAN model could give statistically high reconstruction ability compared with DNS flow fields. It also achieved low MSE between reconstructed field and DNS one, similar to the supervised learning GAN model. In other words, we found that unsupervised GAN model could reflect physical correlation between low-resolution and high-resolution turbulent flows with a level similar to supervised learning.

In second test case, DNS and LES data of fully developed turbulent channel flow were used. Supervised learning framework could not be used for this unpaired problem. Our unsupervised learning model also showed high statistical accuracy with DNS. We could observe high similarity between the LES field and the DNS-like one reconstructed from LES one. Our results indicate that it is possible to match unpaired turbulence data, which was thought to be impossible so far. In addition to changing LES field to DNS one, unsupervised GAN could be applied to connect experiment and simulation, to reconstruct dense-measured data from sparse-measured one, and to reduce noise in the measured data.

References

[1] Fukami K., Fukagata K., Taira K. Super-Resolution Reconstruction of Turbulent Flows with Machine Learning. *J. Fluid Mech.* **870**: 106-120, 2019.
[2] Kim J., Lee C. Prediction of Turbulent Heat Transfer Using Convolutional Neural Networks. *J. Fluid Mech.* **882**: A18, 2020.
[3] Kim J., Lee C. Deep Unsupervised Learning of Turbulence for Inflow Generation at Various Reynolds Numbers. *J. Comput. Phys*. : in press.
[4] Goodfellow I., Pouget-Abadie J., Mirza M., Xu B., Warde-Farley D., Ozair S., Courville A., Bengio Y. Generative Adversarial Nets. In: *NIPS*, 2014, pp.2672-2680.
[5] Xie Y., Franz E., Chu M., Thuerey N. TempoGAN: A Temporally Coherent, Volumetric GAN for Super-Resolution Fluid Flow. *ACM Trans. Graph* **37**(4): 95, 2018.
[6] Deng Z., He C., Liu Y., Kim K. C. Super-Resolution Reconstruction of Turbulent Velocity Fields Using a Generative Adversarial Networks-based Artificial Intelligence Framework. *Phys. Fluids* **31**(12): 125111, 2019.
[7] Zhu J.-Y., Park T., Isola P., Efros A. A. Unpaired Image-To-Image Translation Using Cycle-Consistent Adversarial Networks. In: *ICCV*, 2017, pp.2223-2232.

CFD MODELING OF TWO-PHASE FLOWS IN CONCRETE CRACKS

Germain Davy*[1,2,3], Etienne Reyssat[3], Stéphane Vincent[2], and Stéphane Mimouni[1]
[1]R&D Division, Electricité de France (EDF), Chatou, France
[2]Laboratoire de Modélisation et Simulation Multi-Echelle (MSME), CNRS, Université Paris-Est Créteil, Université Paris-Est Marne-la-Vallée, Marne-la-Vallée, France
[3]Laboratoire de Physique et Mécanique des Milieux Hétérogènes (PMMH), CNRS, ESPCI Paris, PSL Research University, Sorbonne Université, Université Paris Diderot, Paris, France

Summary In the event of a pressurized water reactor loss-of-coolant accident, hot water vapor would infiltrate and condensate into cracks present in the concrete containment structure. The liquid water could form capillary bridges, which would probably modify the leakage rate. This paper presents the latest developments to the NETPUNE_CFD code in the context of the modeling of two-phase flows in concrete cracks under LOCA conditions. Water vapor condensation is affected by the presence of non-condensable gases. Liquid bridges dynamics depends on wettability. Two physical models are proposed. The first one is a condensation model allowing to take into account non-condensable gases. The second one is a wettability model allowing for the imposition of a given contact angle. The results of these numerical models are compared with analytical and experimental studies.

CONTEXT

In the event of a pressurized water reactor loss-of-coolant accident (LOCA), a large amount of water vapor, as well as fission products, would be released in the containment building. The large pressure involved would open up preexisting cracks in the concrete walls, through which potentially dangerous fission products could escape.

The flow of water vapor inside the relatively colder cracks would induce condensation. The liquid water would form drops, films and eventually capillary bridges (see Figure 1), which would counteract the primary flow and thus probably modify the leakage rate of the containment building [1].

This paper aims to present the latest advances in the modeling of gas-liquid flows in concrete cracks with the NEPTUNE_CFD code in the context of a LOCA.

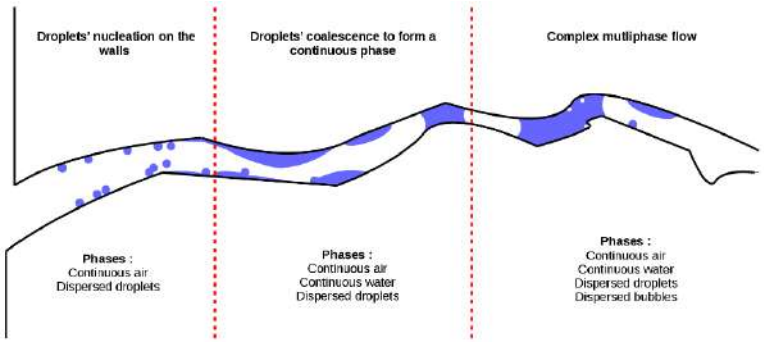

Figure 1. Crack in which water vapor has condensed.

NEPTUNE_CFD

NEPTUNE_CFD is Electricité de France's (EDF) in-house multiphase computational fluid dynamics code. It is based on the two-fluid model of [4] extended to n-fields and allows for three-dimensional calculations of compressible and turbulent flows.

In NEPTUNE_CFD, in the context presented above, the liquid phase can be modeled as a dispersed or as a continuous field. In the latter case, which corresponds to the modeling approach adopted in this paper, the gas-liquid interface is explicitly captured and surface tension can be taken into account [2].

CONDENSATION

Two condensation models are available in NEPTUNE_CFD. The first one is specific to wall condensation. Dispersed liquid droplets nucleate at the wall and grow due to heat and mass transfer in the core flow [5]. The second one is specific to explicitly captured interfaces [2].

Unlike the model by [5], the model by [2] was originally not developed to deal with non-condensable gases. An adaptation of this model for cases involving such gases is proposed. The adapted model has been successfully validated on several test cases, including one corresponding to the well-known Stefan problem.

*Corresponding author. E-mail: germain.davy@edf.fr.

DYNAMICS

The presence of a capillary bridge in a model crack can lead to a no-flow state, depending on the orientation of the walls and on the contact angle (CA) made by the liquid on the solid [6].

Based on the work of [3], a model allowing for the imposition of a given CA of the liquid on the solid has been implemented in NEPTUNE_CFD (see Figure 2). While most of the existing models consist in correcting the interface normal at each time step to match the imposed CA, the model proposed here simply consists in adding a penalization term in one of the equations solved and thus does not require any correction step. This model has been successfully validated both in statics, by comparison with Jurin's law, and in dynamics, by comparison with Wang's experimental data [7].

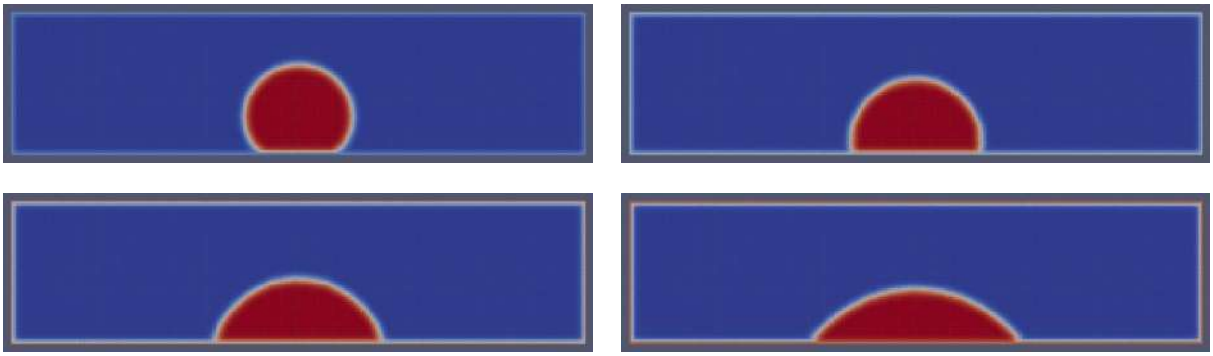

Figure 2. Water droplet at equilibrium. From top to bottom and left to right: $CA = 138°, 111°, 72°, 37°$.

CONCLUSIONS

Two new physical models have been implemented in the NEPTUNE_CFD code in the context of the modeling of two-phase flows in concrete cracks under LOCA conditions. The first one is a condensation model allowing to take into account non-condensable gases. The second one is a wettability model allowing for the imposition of a given contact angle. Both models have been successfully validated by comparison with analytical and experimental results.

Future work will focus on the development of a model for thermal expansion of concrete, phenomenon resulting from condensation and causing the cracks opening to decrease. The three models (condensation, wettability and thermal expansion) will then be coupled. 3D representative calculations at the scale of the cracks will finally be performed and the impact of the flow structures such as the capillary bridges on the leakage rate will be assessed.

Acknowledgments

This work has been achieved in the framework of the CIWAP3 project, financially supported by EDF. The NEPTUNE_CFD code is being developed in the framework of the NEPTUNE project, financially supported by EDF, Commissariat à l'Energie Atomique et aux Energies Alternatives (CEA), Institut de Radioprotection et de Sûreté Nucléaire (IRSN) and Framatome.

References

[1] Davy G., Baconnier P., Mimouni S. Overview of Mitigation Models Dedicated to Severe Accidents and Consequences on Flow Rate Through Concrete Containment Structures. In *18th international Topical Meeting on Nuclear Reactor Thermal Hydraulics*, Portland, Oregon, 2019.

[2] Fleau S. Multifield Approach and Interface Locating Method for Two-Phase Flows in Nuclear Power Plant. *PhD Thesis*, UPEM, Marne-la-Vallée, 2017.

[3] Guillaument R., Vincent S., Caltagirone J.-P. An Original Algorithm for VOF Based Method to Handle Wetting Effect in Multiphase Flow Simulation. *Mech. Res. Commun.* **63**:26-32, 2015.

[4] Ishii M. Thermo-Fluid Dynamic Theory of Two-Phase Flow. Eyrolles, Paris 1975.

[5] Mimouni S., Foissac A., Lavieville J. CFD Modeling of Wall Steam Condensation by a Two-Phase Flow Approach. *Nucl. Eng. Des.* **241:**4445-4455, 2011.

[6] Rastiello G., Leclaire S., Belarbi R., Bennacer R. Unstable Two-Phase Flow Rate in Micro-Channels and Cracks Under Imposed Pressure Difference. *Int. J. Multiph. Flow* **77**:131-141, 2015.

[7] Wang M.-J., Lin F.-H., Ong J. Y., Lin S.-Y. Dynamic Behaviors of Droplet Impact and Spreading – Water on Glass and Paraffin. *Colloids Surfaces A: Physicochem. Eng. Aspects* **339**:224-231, 2009.

A POSTERIORI STABILIZATION OF CONVECTION-DOMINATED FLOWS. SOME APPLICATIONS TO REDUCED ORDER MODELING

Mejdi Azaïez[1],Tomás Chacón Rebollo*[2],and Samuele Rubino[2]
[1]I2M, Institut Polytechnique de Bordeaux
[2]Departamento EDAN & IMUS, Universidad de Sevilla

Summary We present a simple general procedure to stabilize the spurious oscillations due to convection-dominance in the numerical solution of fluid flow problems. We apply it to Finite Element and Proper Orthogonal Decomposition discretizations, for both convection-diffusion problems and Navier-Stokes equations.

INTRODUCTION

The numerical solution of fluid flow problems generates well-known spurious numerical instabilities when the convection term dominates the diffusion one at the discrete level, provoking the failure of the discrete maximum principle. We address in this talk the treatment of this difficulty with conformal discretizations. Typically, to avoid these instabilities, the numerical discretizations need to be modified by means of complex stabilization (projection stabilization, method of characteristics or variational multi-scales among others) techniques, that ultimately need to be non-linear if all spurious oscillations are to be eliminated. These techniques have experienced a vast development in the last decades (Cf. for instance [1, 2, 4]).

In the last years the solution of parametric PDEs by reduced order models (ROM) has experienced a fast development due to its ability to dramatically reduce the computing times to solve the PDE. These ROM are Galerkin methods constructed on structurally-fitted discrete spaces of very low dimension, able to accurately represent the dominant features of the parametric range of the flows to be solved. The construction of the ROM basis requires the solution of the parametric PDE with an accurate numerical method (the full order method, FOM) for a well chosen set of parameters. The solution of flows with convection-dominance by ROM similarly faces the presence of spurious oscillations, that needs to be stabilized as well. Many efforts are being addressed in this sense to let really useful the reduced order solution of fluid flows. The strategy again is to modify the discrete equations by introducing stabilization terms (Cf. [3, 5]).

In this talk we follow a different approach. Our intention is to act on the numerical solution polluted by spurious oscillations, applying a post-processing procedure aimed at damping them. This is not based upon a pure filtering technique that does not take into account the PDE, but rather it is consequence of a self-stabilizing effect that is present in the Galerkin discretization of fluid flow equations on any discrete space. Indeed, the large scales of the discrete solution satisfy a modified variational formulation with additional diffusive terms. The strength of these diffusive terms depends on the actual decomposition of the discrete solution as sum of a large and a small scale component. This lets a large range of possibilities to the user to optimize the post-processed solution.

This post-processing procedure may be applied to any Galerkin method. We here present applications to Finite Element and Proper Orthogonal Decomposition (POD) discretizations. In this last case we will also show the interplay between the a-priori stabilization of the FOM and the a-posteriori stabilization by our method.

We at first describe the post-processing procedure in an abstract framework, then apply it to the finite element solution of Navier-Stokes equations and finally to POD solution of convection-diffusion equations.

A POSTERIORI STABILIZATION

Let us describe the process of a-posteriori stabilization in an abstract framework. Let us consider an elliptic variational problem: Find $x \in X$ such that $b(x,w) = l(w) = \langle f, w\rangle, \quad \forall w \in X$, where X is a Hilbert space. The form b is defined on $X \times X$ and $l \in X'$, being X' the topological dual of X. Consider a family of sub-spaces of finite dimension of X, $\{X_i\}_{i\in\mathcal{I}}$, for some set of indices $\mathcal{I}$. Let us assume that we solve the problem by the Galerkin method on X_i: Find $x_i \in X_i$ such that $b(x_i,w_i) = l(w_i), \quad \forall w_i \in X_i$. Assume that the space X_i is decomposed into $X_i = Y_i \oplus Z_i$, where Y_i and Z_i are subspaces of X_i. Let $x_i = y_i + z_i$ be the unique decomposition that x_i admits with $y_i \in Y_i$ and $z_i \in Z_i$. The Galerkin discretization may be recast as a variational problem for the only unknown y_i, as follows. Denote by $\mathcal{A}$ the operator from X on X' defined by the form b; that is for $v \in X$, $\mathcal{A}v$ is the element of X' defined by: $\langle \mathcal{A}v, w\rangle = b(v,w), \quad \forall w \in X$. Denote by $\mathcal{R}_i : X' \mapsto Z_i$ the "static condensation"operator on Z_i generated by the form b, defined for $\varphi \in X'$ by: $b(\mathcal{R}_i(\varphi), w_i) = \langle \varphi, w_i\rangle, \quad \forall w_i \in Z_i$. Let us introduce the "condensed" variational formulation to the Galerkin discretization: Find $y_i \in X_i$ such that $b_c(y_i,v_i) = l_c(v_i), \quad \forall v_i \in Y_i$, with $b_c(y,v) = b(y,v) - b(\mathcal{R}_i(\mathcal{A}^*v), \mathcal{R}_i(\mathcal{A}y)), \quad l_c(v) = l(v) - b(\mathcal{R}_i(\mathcal{A}^*v), \mathcal{R}_i(f)), \quad \forall y, v \in X$; where $\mathcal{A}^*$ is the adjoint of $\mathcal{A}$.

Let us consider a family of finite-dimensional spaces $\{(Y_i, Z_i)\}_{i\in\mathcal{I}}$, where $\mathcal{I}$ is a set if indices, satisfies the saturation property $\|y_i\|_X + \|z_i\|_X \leq \alpha \|x_i + y_i\|_X, \quad \forall y_i \in Y_i, z_i \in Z_i, \quad \forall i \in \mathcal{I}$, for some $\alpha > 0$. Assume in addition that

*Corresponding author. E-mail: chacon@us.es.

$Y_i \cap Z_i = \emptyset$. Let $x_i = y_i + z_i$ be the unique decomposition of some $x_i \in X_i$, with $y_i \in Y_i$ and $z_i \in Z_i$. Then, x_i is the solution of the Galerkin method if and only if y_i is the solution of the condensed variational formulation, and $z_i = \mathcal{R}_i(l - \mathcal{A}(y_i))$. Moreover, there exists a constant $C > 0$ such that $\|y_i\|_X + \|z_i\|_X \leq C\,\|l\|_{X'}, \quad \|c_i\|_X \leq C\,\|l\|_{X'}$, where $c_i = \mathcal{R}_i(\mathcal{A}(y_i))$. Note that c_i is a representation on Z_i (by means of the static condensation operator) of the small-scale components of the operator $\mathcal{A}$ acting on y_i. Due to the last estimate, c_i is uniformly bounded in X norm. We interpret this bound as an a-posteriori stabilization effect.

In practice, if X_i is a FE space, Y_i could be a subspace of X_i constructed on a sub-grid with coarser elements, or with polynomials of lower degree. This construction may be local in space, acting only on the elements located in a sub-set of the computational domain. Also, if X_i is a POD space, or a more general ROM space, then Y_i could be a subspace formed by a truncated set of basis functions of low frequency. In both cases, Z_i will be a space containing the small scales (or high frequency) components of the space X_i. Anyhow only the restriction operator from X_i onto Y_i is needed to construct the post-processing, space Z_i is not needed. For evolution problems, the post-processing procedure may be applied at a given time step, without need of post-processing the preceding ones.

APPLICATIONS

Figure 1 depicts the effect of the post-processing procedure to the piecewise finite element solution of the steady Navier-Stokes equations in a channel with an obstacle, at $Re = 1000$. The computational domain is$[0, 10] \times [0, 1]$. Fig. 1 shows the stabilized y_i of x_i (the computed velocity) after locally applying the procedure on the domain $[0, 1.2] \times [0, 1]$. The degrees of freedom of y_i are the "even" nodes of the grid. The values of y_i at those nodes are the same as the values of x_i. We observe that all oscillations have disappeared, and that the quality of the numerical solution is improved.

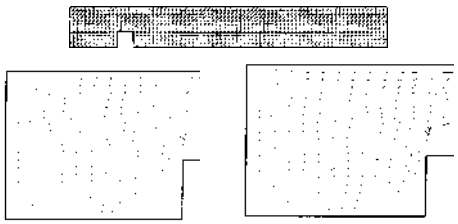

Figure 1: Post-processing of convective instabilities for Navier-Stokes FE produced by a frontal obstacle in a channel

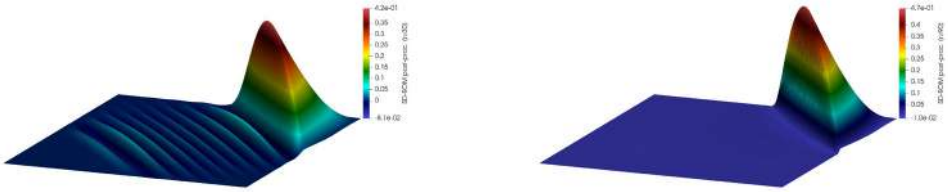

Figure 2: Numerical solution for SD-POD with stabilizing post-processing at $T = 1$ for $r = 30, 90$ (from left to right).

Figure 2 displays the effect of post-processing the POD solution to the evolution convection-diffusion equation with a traveling inner front, with Péclet number 10^8, applied at $T = 1$. The POD basis are constructed from the solutions provided by the FOM: a finite element discretization that, despite including a local projection stabilization of the advection operator, still present large spurious oscillations. We observe that when space Y_i is formed by the $r = 30$ more energetic basis functions out of 100 large oscillations still remain, while when it is formed by the $r = 90$ most energetic basis functions, these are largely reduced. These basis respectively contain 99.71% and 99.96% of the kinetic energy of the POD. The L^2 error is reduced from 0.12 for the Galerkin solution to 0.06 with the post-processed POD solution.

Acknowledgments: Work partially supported by Spanish Government - Feder EU grant RTI2018-093521-B-C31, IdEx Bordeaux project ref. ANR-10-IDEX-03-02, IdEx Bordeaux International Post-Doc Programme and the national Spanish programme Juan de la Cierva-incorporación 2017. Thanks are addressed to Antonio Domínguez for his help with Figure 1.

References

[1] Ahmed N., Chacón Rebollo T., John V., Rubino S. Analysis of a full space-time discretization of the Navier–Stokes equations by a local projection stabilization method. *IMA J. Numer. Anal.* **37**: 1437–1467, 2017.

[2] Arndt D., Dallmann H., Lube G. Local projection FEM stabilization for the time-dependent incompressible Navier–Stokes problem. *Numer. Meth. Part. D. E* **31**: 1224-1250, 2015.

[3] Baiges J., Codina R., Idelsohn S.. Explicit reduced-order models for the stabilized finite element approximation of the incompressible Navier-Stokes equations. *Internat. J. Numer. Methods Fluids* **72**: 1219–1243, 2013.

[4] Benítez M., Bermúdez A. A second order characteristics finite element scheme for natural convection problems. *J. Comput. Appl. Math.* **11**: 3270–3284, 2011.

[5] Giere S., Iliescu T., John V., Wells D. SUPG reduced order models for convection-dominated convection-diffusion-reaction equations. *Comput. Methods Appl. Mech. Engrg.* **289**: 454–474, 2015.

THEORETICAL AND NUMERICAL ANALYSIS OF A MEMBRANELESS REDOX FLOW BATTERY

Désirée Ruiz-Martín[1], Daniel Moreno Boza[1], Marcos Vera[1], Rebeca Marcilla[2], and Mario Sánchez-Sanz*[1]
[1]Departamento de Ingeniería Térmica y de Fluidos, Universidad Carlos III de Madrid, 28911, Leganés, Madrid, Spain
[2]IMDEA Energy Institute, Avda. Ramón de la Sagra, 3, 28935, Móstoles, Madrid, Spain

Summary In this work we present the first mathematical model for the description of a membrane-free redox flow battery formed by two co-flowing immiscible electrolytes. The interface separating the liquid-liquid system is well defined once the physical fluid properties (viscosity and density ratios), Reynolds and mass flow rate are specified. Here we focus on testing the feasibility of a flow battery working in laminar regime. In particular we present the variation of the cell voltage with the state of charge (SoC) for different current intensities I_{app}, to show that the operational range of SoC becomes narrower as I_{app} increases. The performance of the cell is thoroughly assessed varying the flow rate of the electrolytes to show a steady working power of around 1 mW/cm^2 at Reynolds numbers $Re = 20$, comparable to the experimental values reported by [1].

INTRODUCTION

The increasing concern about climate-related issues has stimulated the demand of energy-storage systems to increase the penetration of green energy into sectors that could no benefit yet from the utilization of renewable energy. In this regard, electrochemical storage (batteries) are widely used in stationary applications. In particular, Redox Flow Batteries (RFBs) present several advantages, among which is worth mentioning the total decoupling of power and energy densities and the rapid mechanical charging easily achieved by substituting spent electrolytes with fresh ones. However, most RFBs use an expensive ion-selective membrane to separate the electrolytes and prevent the crossover of active species while providing the exchange of the active charge carriers. The high cost of these membranes has motivated the development of membrane-free designs with two immiscible electrolytes that form a separating interface which allows the exchange of active species [1, 2].

DESCRIPTION OF THE PROBLEM

In this work we present a two-dimensional model of a membrane-less battery formed by two immiscible liquids. The flow geometry under consideration is depicted in Fig. 1. We consider a channel of width h and length $L \gg h$ fed with two liquid streams at flow rates per unit spanwise length Q_1 and Q_2. The traditional vanadium compounds have been replaced with organic molecules in accordance with the previous work of Navalpotro et. al [1]. Thus, the catholyte consists of an acidic solution of hydroquinone (H_2Q), with viscosity μ_2 and density ρ_2, while for the anolythe we considered the redox-active organic molecule parabenzoquinone (pBQ) dissolved in hydrophobic ionic liquid with viscosity μ_1 and density ρ_1. The viscosity ratio between both fluids is large, $\mu_1/\mu_2 = 80$, while the density ratio ρ_1/ρ_1 is assumed to be unity. The interface Γ separating both fluids has been tracked using the Arbitrary Lagrangian-Eulerian (ALE) method [3]. For the sake of simplicity, the dilute solution theory is assumed to decouple the velocity and the species concentration field. Therefore, we first computed the velocity field and, in a second step, we determined the distribution of mobile ionic species as well as the current and electric potential field of the electrolyte. Both geometrical and flow parameters are carefully chosen to avoid the emergence of shear and viscosity driven instabilities that could perturb the shape of the interface $Re = \rho_1 Q_1 h_0/\mu_1 \leq 20$. For this purpose, before obtaining the electrochemical parameters of the RFB, we performed a complete study of the stability of the two-layer, viscosity-stratified Poiseuille flow following the approach used by [4, 5].

CONCLUSIONS

Unlike previous membrane-less designs, limited to work in laminar conditions to avoid the crossover of active species, the operation of the proposed design is not restricted to low Reynolds numbers. Besides, the device can be applied to both aqueous and non-aqueous electrolytes. The model developed provides, under a particular set of fluid and electrochemical parameters, the current-voltage polarization curves as well as the species concentration and ionic potential fields both during charge and discharge. We have verified that the limiting current density increases with Reynolds number both under charge and discharge conditions. Accordingly, higher power densities are achieved as the flow rate increases. The effect of the flow only becomes evident at larger flow rates, when the limiting current density is shifted towards larger values as the gradient concentrations near the electrode surface are reduced. Our results are qualitatively consistent with previous studies, showing during discharge operation a dependency of the limiting current density with the flow rate similar to the $Re^{1/3}$ predicted by Braff et al [2] (see Fig. 2). Besides, the maximum power density obtained at $Re = 20$ is around 1 mW/cm^2, comparable to the experimental values reported by [1]. The effect of the State of Charge (SoC)

*Corresponding author. E-mail: mssanz@ing.uc3m.es

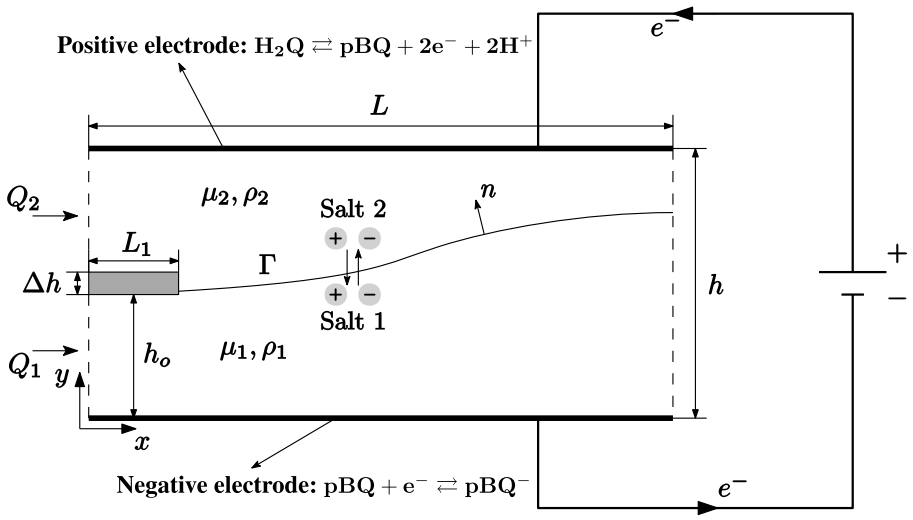

Figure 1: Schematics of the problem, including the geometrical, fluid-dynamical and electrochemical relevant parameters.

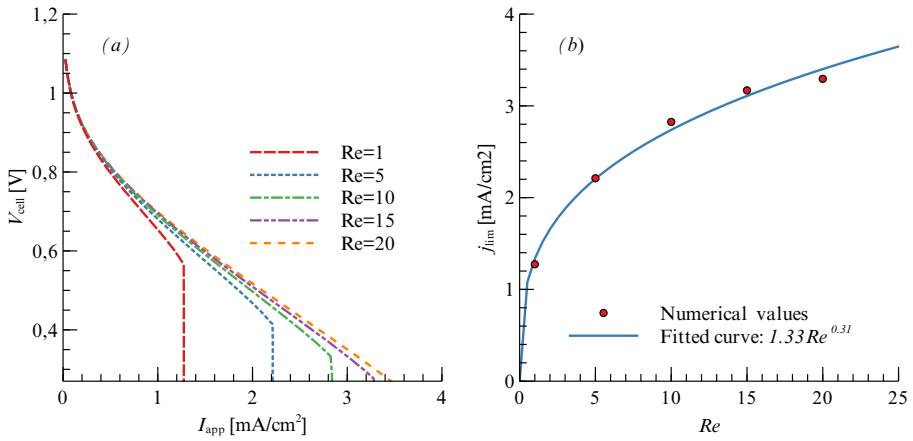

Figure 2: (a) Discharge polarization curves for different Reynolds numbers: 1 (red dashed dotted line), 5 (blue dashed line), 10 (green dotted line), 15 (purple dotted line), 20 (yellow dotted line) . (b) Value of the limiting current density as a function of Reynolds number. Both figures are calculated at 50% SoC.

has also been analysed. Low SoC values lead to fuel depletion at the anode whereas at SoC close to unity the absolute values of the overpotentials at the anode and cathode increase as a result of the high gradient concentrations. Thus, the performance of the device relies closely on the suitable reactant supply to the electrodes.

References

[1] Navalpotro P., Palma J., Anderson M., Marcilla R. A Membrane-Free Redox Flow Battery with Two Immiscible Redox Electrolytes. *Angewandte Chemie* **129**: 12634-12639, 2017.

[2] Braff W.A., Bazant M.Z., Buie C.R. Membrane-less hydrogen bromine flow battery. *Nature communications* **4**: 2346, 2013.

[3] Donea J., Huerta A., Ponthot J.P., Rodríguez-Ferran A. Arbitrary Lagrangian–Eulerian Methods. In Encyclopedia of Computational Mechanics Second Edition. John Wiley & Sons, Ltd, Hoboken, NJ 2017.

[4] Blyth M.G., Pozrikidis C. Effect of inertia on the Marangoni instability of two-layer channel flow, Part II: normal-mode analysis. *Journal of Engineering Mathematics* **50**: 329-341, 2004.

[5] Valluri P., Onaraigh L.,Ding H., Spelt P.D.M. Linear and nonlinear spatio-temporal instability in laminar two-layer flows. *Journal of Fluid Mechanics* **656**: 458-480, 2010.

EFFECT OF AN IMPULSIVELY-ACCELERATED FLOW ON THE PIPE BEND FORCES

Feroz Ahmed *[1], Emad Moeendarbary[1], and Alireza Azarbadegan[2]
[1]Department of Mechanical Engineering, University College London, London, WC1E 7JE, UK
[2]BP Exploration Operating Company Limited, Chertsey Road, Middlesex, TW16 7NL, UK

Summary We studied the influence of strongly impulsively-accelerated flow on the forces in 90-degree pipe bend. This force is characterised by a step change due to high Strouhal number flow. The problem is analytically and numerically analysed at $Re = 2000$, $St = 1$ and $R_c/D = 1.5$. Various contributions to the total bend forces are found: momentum flux (ρU_b^2), time-acceleration ($\rho \mathrm{d}U_b/\mathrm{d}t$), pressure at the bend inlet (p_{bi}) and outlet (p_{bo}).

INTRODUCTION

Unsteady flows (positive branch of sine function $|\sin \Omega_p t|$) along circular pipes are one of the most studied problems in fluid mechanics encompassing a type of geometry (the circular tube) and a type of flow driven by a heart [1] or a pump [2] common in nature and industry. Unlike smoothly varying acceleration in sinusoidal flows ($\sin \Omega_p t$), these flows exhibit an impulsively-accelerated components, and are characterised by large jumps in the acceleration. Impulsively-accelerated flows are especially common in high-pressure high Strouhal number flow systems in the energy sector where high static pressures can only be achieved with reciprocating pumps. The purpose of this paper is to understand the effect of an impulsively-accelerated flow on the forcing characteristics in the pipe bend. These forces are problematic with respect to the stress, vibration and hence fatigue.

MATHEMATICAL FORMULATION

We analyse a duplex configuration of reciprocating pump that consists of a periodic volume flux (see figure 1 (a)) and focus on a 90-degree bend (see figure 1 (b)), a geometry common in the energy sector.

Fluid Mechanical Model

The three-dimensional fluid flow $\boldsymbol{u}$ is driven by the gradient of a pressure field p and resisted by viscous stresses $\boldsymbol{\tau}$. The dynamics of an incompressible Newtonian fluid are described by the Navier-Stokes and the continuity equations,

$$\rho\left(\frac{\partial \boldsymbol{u}}{\partial t} + (\boldsymbol{u}\cdot\boldsymbol{\nabla})\boldsymbol{u}\right) = -\boldsymbol{\nabla}p + \boldsymbol{\nabla}\cdot\boldsymbol{\tau}, \qquad \boldsymbol{\nabla}\cdot\boldsymbol{u} = 0, \tag{1}$$

where ρ is the fluid density. The velocity field is set on the pipe inlet through a volume flux (Q), and by imposing a kinematic constraint on the velocity at the pipe wall surface. The periodic volume flux is set as

$$Q(t) = AU_b|\sin \Omega_p t|, \tag{2}$$

where U_b is the maximum velocity, Ω_p is angular frequency, and A is the pipe cross-sectional area (see figure 1 a). On the pipe outlet surface, the pressure is set as $p = 0$. The key parameters are

$$Re = \frac{U_b D}{\nu}, \quad St = \frac{\Omega_p D}{2\pi U_b}, \quad \frac{R_c}{D}. \tag{3}$$

where Re is Reynolds number, St is Strouhal number, R_c/D is the curvature ratio, ν is kinematic viscosity, R_c is radius of curvature, and D is pipe diameter. Numerically, equation (1) were solved within ANSYS FLUENT 19.0.

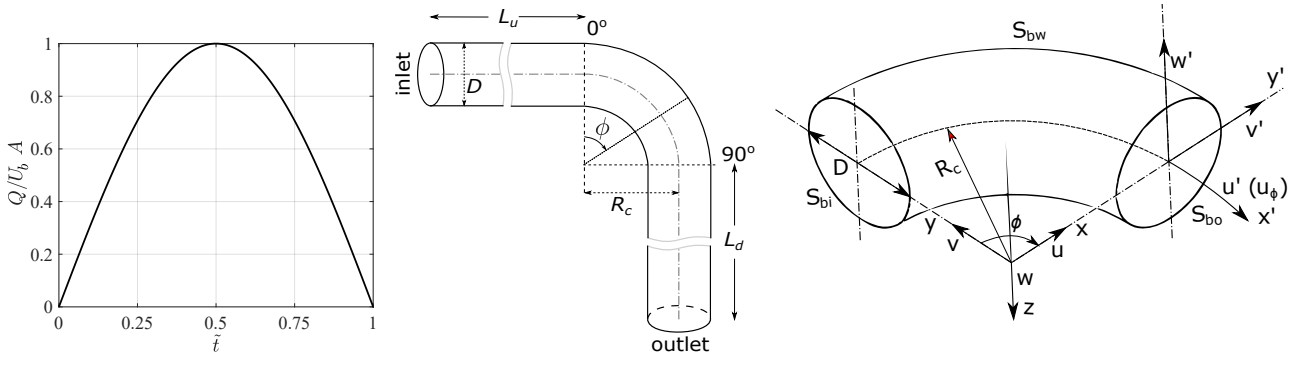

(a) (b) (c)

Figure 1. (*a*) The variation of an inlet volume flux (Q/U_bA) with dimensionless time ($\widetilde{t} = \Omega_p t/\pi$) is shown for one cycle. (*b*) A schematic of the computational domain is shown along with the geometrical length scales. (*c*) The coordinates along with the bend surfaces are shown. The surfaces includes the curved wall (S_{bw}), inlet (S_{bi}) and outlet (S_{bi}) surfaces.

*Corresponding author. E-mail: ucemfah@ucl.ac.uk

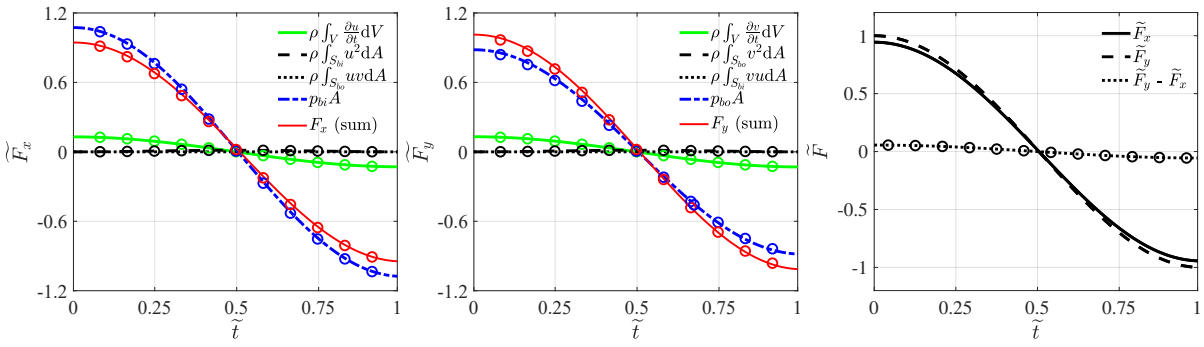

(a) (b) (c)

Figure 2. The pipe bend force in the (a) x- and (b) y- direction are decomposed into integral components and evaluated numerically (solid lines, (4)) and estimated analytically (circular makers, (6)). In (c), the difference in $\widetilde{F}_x$ and $\widetilde{F}_y$ are plotted. The dimensionless force is $\widetilde{F}_x(\text{ or } \widetilde{F}_y) = F_x(\text{ or } F_y)/\rho A\Omega_p U_b(L_d + R_c)$.

Analytical Model

Using the momentum integral approach, the force can be expressed in terms of an integral over the pipe bend inlet and outlet surfaces (S_{bi} and S_{bo}) (see figure 1 (c)), and the pipe bend fluid volume (V)

$$\begin{aligned}\boldsymbol{F}_p\big(=(F_x,F_y)\big) = -\Big(p_{bi}A + \rho\int_{S_{bi}} u_\phi^2\mathrm{d}A + \rho\int_{S_{bo}} u_\phi v'\mathrm{d}A\Big)\hat{\boldsymbol{n}}_i \\ -\Big(p_{bo}A + \rho\int_{S_{bo}} {u_\phi}^2\mathrm{d}A + \rho\int_{S_{bi}} u_\phi v'\mathrm{d}A\Big)\hat{\boldsymbol{n}}_o - \rho\int_V \frac{\partial \boldsymbol{u}}{\partial t}\mathrm{d}V - \int_{S_{bi}+S_{bo}} \boldsymbol{\tau}\cdot\hat{\boldsymbol{n}}\mathrm{d}S,\end{aligned} \tag{4}$$

where p_{bi} and p_{bo} are bend inlet and outlet pressure and $\hat{\boldsymbol{n}}_i\big(=(-1,0)\big)$, $\hat{\boldsymbol{n}}_o\big(=(\cos\phi,-\sin\phi)\big)$ are unit vectors normal to the pipe bend inlet and outlet. [3] applied a momentum approach to evaluate the unsteady forces on a pipe bend due to slugs passing, where the V changed with time due to the slug movement, but the Q was constant. In our example, the V is constant, but Q changed with time. At high Reynolds numbers, the main contributions to the bend force is due to the deflection of the pipe flow arising from the change in $\hat{\boldsymbol{n}}$ and the integral along the bend (from $\int \hat{\boldsymbol{s}}\mathrm{d}V$), with weaker contributions from the secondary flow and viscous effects. At high St, the pressure gradient is dominated by the fluid acceleration $p = -\rho(\mathrm{d}U_b/\mathrm{d}t)\hat{\boldsymbol{s}}$. The pipe bend force is, to leading order,

$$\boldsymbol{F}_p \simeq -(p_{bi}+\rho U_b^2)A\hat{\boldsymbol{n}}_i - (p_{bo}+\rho U_b^2)A\hat{\boldsymbol{n}}_o - \rho\frac{\mathrm{d}U_b}{\mathrm{d}t}\int_V \hat{\boldsymbol{s}}\mathrm{d}V, \tag{5}$$

where $\hat{\boldsymbol{s}}\big(=(\cos\phi,-\sin\phi)\big)$ is the tangential unit vector. The force components for a 90-degree bend ($\phi_m = \pi/2$) are

$$\begin{aligned}F_x &= \Big(p_{bi} - p_{bo}\cos\phi_m + \rho U_b^2(1-\cos\phi_m) - \rho\frac{\mathrm{d}U_b}{\mathrm{d}t}R_c\sin\phi_m\Big)A, \\ F_y &= \Big((p_{bo}+\rho U_b^2)\sin\phi_m - (\cos\phi_m - 1)\rho\frac{\mathrm{d}U_b}{\mathrm{d}t}R_c\Big)A.\end{aligned} \tag{6}$$

RESULTS AND DISCUSSIONS

Figure 2 (a, b) shows a decomposition of the bend force components ($\widetilde{F}_x$ and $\widetilde{F}_y$) into the various terms shown in (4) and compared with with the analytical predictions based on one-dimensional model (6). This shows the relative calculation of pressure at the inlet/outlet of the bend (p_{bi} and p_{bo}), flow acceleration ($\rho\int_V \frac{\partial \boldsymbol{u}}{\partial t}\mathrm{d}V$), momentum flux changes ($\rho\int_{S_{bi}} u^2\mathrm{d}A$ and $\rho\int_{S_{bo}} v^2\mathrm{d}A$) to the total bend force. These bend loading components are dominated by the unsteady impulsive pressure field. The agreement between predictions and computations give a strong justification that the key physics are encapsulated in the simple one-dimensional model (6). The analysis indicates that the force components depend on the length of the pipe exit L_d since this largely determine the pressure in the vicinity of the bend. The model also predicts an asymmetry between $\widetilde{F}_x$ and $\widetilde{F}_y$ (see figure 2 c), and it depends on the bend length.

CONCLUSIONS

The effect of a high St impulsively-accelerated flow on pipe bend forces has been studied using numerical and detailed one-dimensional prediction model. Various force contributions and asymmetry in the force components were found.

References

[1] Najjari, M.R. Plesniak, M.W. Evolution of vortical structures in a curved artery model with non-newtonian blood-analog fluid under pulsatile inflow conditions. Experiments in Fluids 57 (6), 100. 2016.
[2] Singh, P.J Madavan, N.K. Complete analysis and simulation of reciprocating pumps including system piping. In Proceedings of the 4th International Pump Users Symposium. Turbomachinery Laboratories, Department of Mechanical Engineering, Texas AM. 1987.
[3] Xiao, Fei, Jing, Jiaqiang, Han, Li, Yang, Lu Wang, Shuai. Modelling and analysis of impact forces acting on elbow in gas–liquid slug flow. Asia-Pacific Journal of Chemical Engineering 14 (2). 2019.

TURBULENT CHANNEL FLOW AT Re_T=10K

Sergio Hoyas*[1], Martin Oberlack[2], Stefanie Kraheberger[2], and Francisco Alcántara-Ávila[1]
[1]Instituto de Matemática Pura y Aplicada, UP València, Camino de Vera, 46024 València, Spain
[2]Chair of Fluid Dynamics, TU Darmstadt, Otto-Berndt-Str. 2, 64287 Darmstadt, Germany

Summary A direct numerical simulation of a Poiseuille turbulent channel flow was performed at a friction Reynolds number of 10000, in a small box of dimensions $(2\pi h, 2h, \pi h)$. This value is large enough to allow the study of high Reynolds numbers effects. The streamwise mean velocity presents a long logarithmic region, extending from $y^+ \approx 150$ to $y/h \approx 0.2$. The von Kármán constant has a value of $\kappa = 0.389$, which seems to be very close to the final value for this constant. The first maximum of the intensity u' keeps growing and the second maximum is still not present. Mean velocities and intensities can be downloaded from the web page of the FDY

Wall turbulence is probably one of the open problems in physics with most applications in daily life. Even if the equations ruling out these flows have been known for 150 years, we still lack of complete theory. As wall-bounded turbulence is responsible of the 5% of the CO2 dumped by mankind into the atmosphere every year, this is a problem of the uttermost importance. Research of turbulent flows has been dominated by experimental techniques until the eighties of the last century, where supercomputers started to be powerful enough to solve turbulent flows. However, due to the highly non-linear behavior of wall-turbulent flows, Direct Numerical Simulation (DNS) of these flows are restricted to simplified geometries. The most successful of these idealized flows are Poiseuille turbulent channels, where the fluid is confined between two parallel plates and the flow is driven by pressure. Since the seminal paper of Kim, Moin, and Moser, [1], the friction Reynolds number Re_τ has grown steadily. Here, a simulation reaching the $Re_\tau = 10000$ frontier is presented, which would allow the study of high Reynolds numbers effects. This Re_τ is still less than the largest realization of the flow obtained by experimental means, [2], reaching $Re_\tau = 20000$. However, the main advantage is that the DNS allows one to compute any imaginable quantity in the whole domain.

As it is said before, the main control parameter is the friction Reynolds number, defined as $Re_\tau = u_\tau h/\nu$, where h is the semi-height of the channel and ν is the kinematic viscosity. Superscript (+) indicates that the quantities have been normalized by u_τ and ν. h is equivalent to the radius in pipes and δ_{99} in boundary layers. This computation has been performed in a computational box of sizes $L_x = 2\pi$ and $L_z = \pi$. This box is large enough to accurately describe the statistics of the flow [3]. The streamwise, wall-normal, and spanwise coordinates are x, y, and z. The corresponding velocity components are U, V, and W or, using index notation, U_i with $i = 1, 2, 3$. Statistically averaged quantities in x, z, and time t are denoted by an overbar $\overline{\cdot}$, whereas fluctuating quantities are written in lowercase letters, i.e. $U = \overline{U} + u$. Primes are reserved for intensities, e.g. $u' = \overline{(uu)}^{1/2}$.

The flow can be described by means of the momentum and mass balance equations. They have been solved using the LISO code [4]. Briefly, the code uses the same strategy as [1], but using seven-point compact finite differences in y direction with fourth-order consistency and extended spectral-like resolution [6]. The temporal discretization is a third-order semi-implicit Runge-Kutta scheme [7]. The wall-normal grid spacing is adjusted to keep the resolution at $\Delta y = 1.5\eta$, i.e., approximately constant in terms of the local isotropic Kolmogorov scale $\eta = (\nu^3/\epsilon)^{1/4}$, where ϵ is the dissipation rate. In wall units, Δy^+ varies from 0.3 at the wall, up to $\Delta y^+ \simeq 12$ at the centerline. The resolution in x and z is similar to the largest simulations of turbulence.

To accelerate the compilation of statistics, three initial files were prepared and thus three simulations were run at the same time. The initial file of every run was taken from a smaller Reynolds number simulation. In every case, the code was run until some transition phase has passed and the flow had adjusted to the new set of parameters. Once the flow was in a statistically steady state, which can be very time consuming, statistics were compiled. Comparisons are shown with data coming from [4] ($Re_\tau = 2000$, blue),[3] ($Re_\tau = 4200$, red), and [8]($Re_\tau = 5000$, green).

In order to further validate the simulation, figure 1(a) shows the error in the momentum equation,

$$\overline{uv}^+ = \frac{d\overline{U}^+}{dy^+} + y^+ - 1. \tag{1}$$

As the difference between both sides of this equation is still not below $5 \cdot 10^{-3}$, similar to the other large simulations, the simulation is still running. However, we do not expect any major change in the statistics of the simulation.

The mean velocity profile is shown in figure 1(b) in terms of the indicator function, $\Xi = y^+ \partial_y U^+$. This function should show a plateau if the classical scaling for the logarithmic layer, $U^+ = \kappa^{-1} \log(y^+) + B$, holds. Here, κ is the von Kármán constant. For every case, the minimum is reached around $y^+ \approx 70$ calling into question the possibility, or even the relevance, of estimating the extent of the logarithmic layer in this way. The flatter region of the profile starts at $y^+ \approx 150$. The logarithmic layer extends to around $y^+ \approx 2000$ or $y/h = 0.20$. To obtain the values of κ and B, we have restricted ourselves to the region where the indicator function is even flatter, $y^+ = 350$ to $y/h = 0.15$, obtaining $\kappa = 0.389$ and $B = 4.47$. This value for κ is only 0.005 units larger than the one given by [8].

The intensity of the streamwise velocity is shown in figure 2(a). The well known, [4], scaling failure in the buffer layer is still present. The first maximum is still growing, and its value $u'^+ = 3.06$ is in agreement with the experimental

*Corresponding author. E-mail:serhocal@mot.upv.es

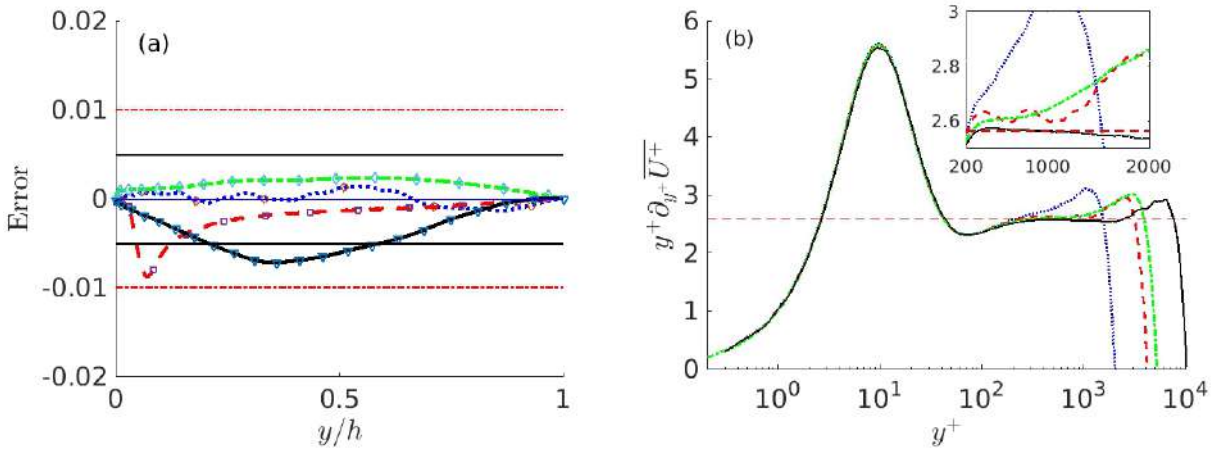

Figure 1: (a) Error in the computation of momentum equation 1 (b). Indicator function, showing an extended log layer, ranging from $y^+ \approx 150$ to $y/h \approx 0.2$

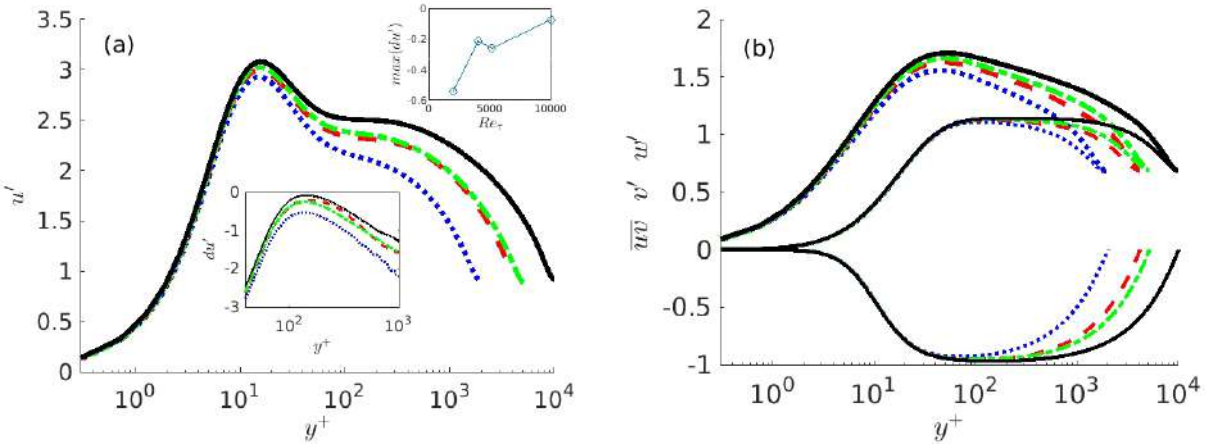

Figure 2: (a) $u'^+ = \sqrt{\overline{uu}}$ for the four cases. The lowest box shows the value of the derivative of u'^+ and the top one the evolution of the maximum with Re_τ. (b) From bottom to top, $\overline{uv}^+$, v'^+ and w'^+.

results of [2]. About the uncertain second maximum of the velocity, located around $y^+ = 120$, the situation is shown in the lowest box of this figure. The derivative of u' is still not zero, and is not clear if the second maximum will ever exist. Again, this is also in agreement with the results of [2].

The collapse of v' and $\overline{uv}$ in the viscous region, figure 2(b), is almost perfect. Also, v' presents a flat behavior in the logarithmic layer. It is remarkable that the maximum of w', first spotted in [4], is still growing. This is possibly the reason of the scaling failure of w'.

As conclusion, a DNS of a Poiseuille turbulent channel has been made at a $Re_\tau = 10^4$. Using symmetry theory, the log layer has been delimited from $y^+ = 150$ to $y/h = 200$. Using this interval a value for $\kappa = 0.389$, has been obtained. Doing the same procedure in previous simulations, κ has basically the same value. About the streamwise intensity, u', its first maximum is still growing and the second one is not yet present. A study of the first derivative of u' shows that is possible that this maximum would never exist. Funally, DNS results suggest that there actually exists a logarithmic scaling of $\overline{U}$ while at the same time this is not true for higher moments. This is the subject of another talk in this session. Mean velocities and intensities can be downloaded from the web page of the FDY. More data will be made available as the postprocessing advances.

References

[1] J. Kim, P. Moin, and R. Moser. *Journal of Fluid Mechanics*, 177:133–166, 1987.
[2] M. Samie, I. Marusic, N. Hutchins, M.K. Fu, Y. Fan, M. Hultmark, and A.J. Smits. *Journal of Fluid Mechanics*, 851:391–415, 2018.
[3] A. Lozano-Durán and J. Jiménez. *Physics of Fluids*, 26(1):011702, 2014.
[4] S. Hoyas and J. Jiménez. *Physics of Fluids*, 18(1):011702, 2006.
[5] Sergio Gandía-Barberá, Sergio Hoyas, Martin Oberlack, and Stefanie Kraheberger. *Physics of Fluids*, 30(4):041702, 2018.
[6] S. K. Lele. *Journal of Computational Physics*, 103(1):16–42, 1992.
[7] Philippe R Spalart, Robert D Moser, and Michael M Rogers. *Journal of Computational Physics*, 96(2):297–324, 1991.
[8] M. Lee and R. Moser. $Re_\tau \approx 5200$. *Journal of Fluid Mechanics*, 774:395–415, 2015.

DROP BREAKUP IN HOMOGENEOUS ISOTROPIC TURBULENCE

Alberto Vela-Martín[1] and Marc Avila*[2]
[1]School o fAeronautics, Universidad Politénica de Madrid, Madrid, Spain
[2]Center of Applied Space Technology and Microgravity (ZARM), University of Bremen, Bremen, Germany

Summary The formation and breakup of drops in turbulent flows is of key importance in chemical, mechanical and aerospace engineering, but their physical mechanisms and time scales remain poorly understood. We investigate drop breakup in homogeneous isotropic turbulence with direct numerical simulations, thereby resolving all temporal and spatial scales. A new GPU code solving the Cahn–Hilliard–Navier–Stokes equations enables the simulation of thousands of independent cases and a detailed analysis of the breakup process. We find that drop breakup is a memoryless process, whose rate depends on the Weber number. Our results allow estimating the evolution of drop-size distributions in the dilute regime and can be used to parametrize population-balance equations.

INTRODUCTION

The emulsification of a disperse phase in a continuous phase under turbulent flow conditions is central in the food and pharmaceutical industries. In stirred tanks, a statistically steady state characterized by the probability density function (pdf) of drop sizes, is approached after initial transients. This pdf is determined by the competition of drop breakup and coalescence processes [6], which are notoriously difficult to parametrize. In this paper, we focus on the breakup of a single drop in homogeneous isotropic turbulence.

The theoretical background of drop breakup in turbulent flows was developed by Kolmogorov[3] and Hinze[2]. Their main assumption was that a drop breaks when the kinetic energy of velocity fluctuations on the drop scale $\overline{u^2(d)}$ (where d is the drop diameter) exceeds the interfacial energy. This happens when the Weber number $We = \rho \overline{u^2(d)} d/\sigma > 1$, where ρ is the fluid density of the continuous phase and σ is the surface tension. In isotropic turbulence the so-defined Weber number can be rewritten as

$$We = 2\rho\epsilon^{2/3} d^{5/3},$$

where ϵ is the average energy dissipation – which is equal to the power input in stirred tanks. The breakup criterion $We \approx 1$ is extremely useful in engineering because it allows to estimate the maximum drop size in an emulsion. However, it does not provide any information on the dynamics of the system and size distributions. In this work, the spatiotemporal dynamics of drop breakup are investigated with direct numerical simulation and statistics are extracted.

METHOD AND SETUP

The Navier–Stokes equations are solved with the pseudo-spectral method of Cardesa *et al.* [1], which was extended to simultaneously solve the Cahn–Hilliard equations governing the conservation of a phase-field variable. Our highly efficient GPU code enables a statistical study of the inherently stochastic breakup process. For simplicity, density- and viscosity-matched fluids are considered, which allows a qualitative comparison with experiments using water as continuous phase and certain oils as disperse phase [4].

The breakup process was investigated by varying the Reynolds number Re_λ and Weber We independently. The initial conditions were taken as snapshots from single-phase turbulence in which a spherical drop was introduced. Numerical resolutions of 128^3 and 256^3 were used and several thousands of independent runs were performed. Results were found to be independent of the interface thickness and numerical convergence was also verified.

RESULTS

The temporal evolution of an initially spherical drop until its breakup is shown in Figure 1. The drop evolves from a sphere to a cigar shape, as described by Hinze [2] in his theoretical considerations. Subsequently the drop progressively stretches until in the final stages it consists of a filament connecting two bulgy bulbous ends – precursors to two large drops emerging after the breakup process. In addition, several small satellite drops form out of the filament. Noteworthy the process is remarkably similar to that of a spherical drop placed in a steady extensional (Stokes) flow [7] and our conditional analysis of velocity gradients close to the interface highlights indeed the importance of the rate-of-strain in the breakup process.

Because of the turbulent nature of the flow, the number and size of daugther drops obey a stochastic process. We found that the breakup times scale with the characteristic drop time

$$t_d = (d^2/\varepsilon)^{1/3}.$$

Surprisingly, at lower Weber numbers the distribution of breakup times is exponential, implying that drop breakup is a memoryless process. The breakup rate diminishes as We is decreased, but remains finite. By contrast, at high Weber numbers the process is fast and sudden (as documented in recent simulations [5]) and the memoryless property is lost. The number of drops increases as We increases.

*Corresponding author. E-mail: marc.avila@zarm.uni-bremen.de.

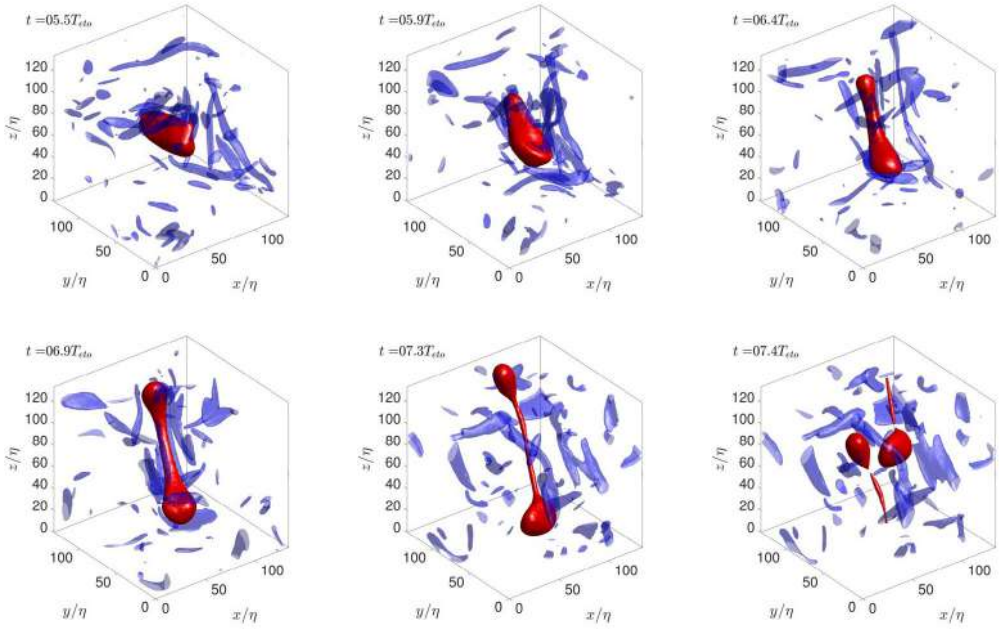

Figure 1: Snapshots of a direct numerical simulation of drop breakup in homogeneous isotropic turbulence with Reynolds number $Re_\lambda = 58$ and Weber number $We = 1.2$. In blue, isosurfaces of intense enstrophy are shown. The box size is 134η, where η is the Kolmogorov scale and time is eddy turnover units, $T_{eto} = L/u'$, where L is the integral scale and u' is the standard deviation of the velocity fluctuations. At $t = 0$ a spherical drop is placed in the turbulent flow and left to evolve until its breakup.

DISCUSSION

The results presented in this work have implications for the physical modeling of binary mixtures. For example, population-balance models require parametrizations of the probability of drop breakup and of the number of children droplets and their surfaces, which were obtained here through direct numerical simulation. Finally, the memoryless property discovered at low Weber numbers implies that in the dilute regime drop size distributions continue to evolve as time passes without reaching steady state.

References

[1] J.I. Cardesa, A. Vela-Martín, and J. Jiménez. The turbulent cascade in five dimensions. *Science*, **357**(6353):782–784, 2017.

[2] J.O. Hinze. Fundamentals of the hydrodynamic mechanism of splitting in dispersion processes. *AIChE Journal*, **1**(3):289–295, 1955.

[3] A.N. Kolmogorov. On the disintegration of drops in turbulent flow. In *Doklady Akad. Nauk. USSR*, **66**, page 825, 1949.

[4] Sebastian Maaß and Matthias Kraume. Determination of breakage rates using single drop experiments. *Chemical Engineering Science*, **70**:146 – 164, 2012.

[5] Changxiao S., Kun L., Yue Y., and J. Fan. Direct numerical simulation of droplet breakup in homogeneous isotropic turbulence: The effect of the weber number. *International Journal of Multiphase Flow*, **107**:263–274, 2018.

[6] R. Shinnar. On the behaviour of liquid dispersions in mixing vessels. *Journal of Fluid Mechanics*, **10**:259–275, 1961.

[7] H. A. Stone and L. G. Leal. Relaxation and breakup of an initially extended drop in an otherwise quiescent fluid. *Journal of Fluid Mechanics*, **198**:399–427, 1989.

MEMORY EFFECT AND QUASI-CYCLIC FRONT PROPAGATION SPEED OF TURBULENT SPOTS DURING PIPE FLOW TRANSITION

Xiaohua Wu*[1], Parviz Moin [2] and Ronald J. Adrian [3]
[1]Department of Mechanical and Aerospace Engineering, Royal Military College of Canada, Kingston, Canada
[2]Center for Turbulence Research, Stanford University, Stanford, USA
[3]Arizona State University, Tempe, USA

Summary We present direct simulation results on a blob of inlet turbulence developing spatially through a 1000 radii-long fully-developed laminar pipe flow at $Re = 2150, 2300$ and 2500, respectively. We observed turbulent spot packet entering processes of splitting, reconnection and re-splitting, indicating a surprising memory and hysteresis effect. Splitting is found to be driven by a sustained zonal axial velocity differential between a spot's downstream front and its center, which causes an elongated zone being frequently shed from the spot leading edge. Viscous dissipation often prevents the detached elongated zone (child embryo) from developing into a child spot (hence full splitting), resulting in a quasi-cyclic peak-valley variation of the spot packet's front instantaneous propagation speed with the axial distance. This suggests that splitting and dissipation are coupled processes rather than two totally independently factors; and mean front propagation speed masks important instantaneous pipe flow transition physics. The constitutive elemental vortex structure of turbulent spots in low Reynolds number pipe flow is primarily reverse hairpin vortex.

BACKGROUND, OBJECTIVE AND METHOD

Compared to pipe transition, boundary layer bypass transition in the narrow sense, a superposition on a Blasius boundary layer by freestream homogeneous isotropic turbulence at an initial turbulence intensity of 1%–4%, has received much more attention from the aeronautical fluid dynamics community. Since pipe transition and boundary layer bypass transition in the narrow sense are both wall-bounded shear flows initiated by finite-amplitude disturbances, it is instructive, and perhaps even imperative, to establish connection between these two branches of study. Much of the pipe transition research to date can be categorized as the Schubauer-Klebanoff type in that the focus was often placed on mean statistics concerning the propagation, development, evolution and fate of deliberately imposed turbulent spots in laminar pipe flow, as was done in [1] for the boundary layer bypass transition in the narrow sense. A more complete investigation of pipe transition should also incorporate the Klebanoff-Tidstrom-Sargent approach to consider both the amplification of inflow three-dimensional disturbance prior to laminar pipe flow breakdown, and the inception of turbulent spots during breakdown, as was done in [2] for the boundary layer by examining the causality of key instantaneous structures in transition.

Lindgren [3] discovered that, at low Reynolds numbers such as $Re = 2800$, based on the bulk velocity V and pipe radius R, some turbulent spots developed a tendency to split into two units with the child spot always appearing downstream of the parent. Avila et al [4] considered turbulent spot splitting in pipe flow as an example of spatial proliferation of chaotic domains. The central underpinning of their idea is that, for $Re < 2400$, turbulent spot splitting is the only mechanism for turbulence to spread; splitting is memoryless, independent of, and competing with, dissipation. A balance between spot decay and splitting yields a critical Reynolds number $Re = 2040$ for pipe flow transition. Barkley et al [5] developed a one-dimensional model to describe the mean front propagation speeds of pipe turbulent spot as a function of the Reynolds number. The essence of the advection-reaction-diffusion model of is one-dimensional transition modeling of certain mean global quantities in pipe flow.

Our objectives here are to examine the hypothesis introduced in the spatial proliferation idea [4] that pipe spot splitting is a memoryless process independent of dissipation, and the underlying assumption made in the advection-reaction-diffusion model [5] that the mean front propagation speeds of turbulent spot encapsulate the pipe transition physics. Such a critical re-examination, in the laboratory reference frame, is also necessary considering the fact the nearly all the previous computer simulations of pipe transition, including [4] and [5], used the numerically expedient axially-periodic boundary condition. The degree of inaccuracy associated with long duration, axially periodic, turbulent spot simulations using short pipe domain $(< 200R)$ can be discerned from [6]. The temporal simulations in [6] correspond to a non-standard situation of imposed turbulent spots developing into an already perturbed (by itself earlier in time) chaotic pipe flow environment. When spot life-time statistics are extracted from such short-length pipe simulations running for very long time, they may be contaminated, see [6]. Our direct simulation design corresponds to the standard and idealized situation of turbulent spot developing spatially into a pristine fully-developed laminar pipe flow environment that has not been perturbed prior to the arrival of the spot. The governing equations are the continuity and the Navier-Stokes equations for incompressible flow in cylindrical coordinates, and they are solved using the fractional step method. The pipe length is $1000R$. Three cases were simulated at $Re = 2150$, 2300 and 2500, respectively. The computational mesh size is $32768 \times 200 \times 256$, $\Delta t = 0.01R/V$. The inlet base flow has the fully-developed parabolic laminar velocity profile, except for $0 \le t \le 20R/V$, within a 60^o numerical wedge, the exact laminar parabolic velocity profile is replaced by a time-dependent, fully-developed turbulent pipe DNS velocity field at $Re = 5300$ to trigger disturbance to generate a spot. For $t > 20R/V$, the laminar velocity profile is restored inside the wedge.

RESULTS

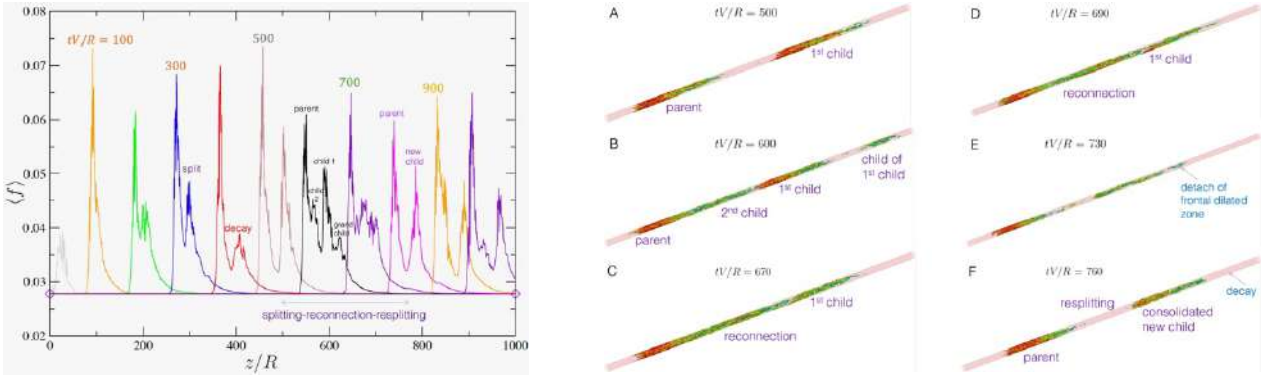

Figure 1. Splitting-reconnection-resplitting at $Re = 2300$ revealed by circumferentially-averaged friction factor $\langle f \rangle$ (Left) and by iso-surfaces of swirling strength $\lambda_{ci} = 0.3V/R$ (Right). Diamond symbols are fully-developed laminar pipe solution. This composite process suggests that after a full splitting event, child spot can still have contact and interaction with its parent; it may also merge and consolidate with other children. Thus, pipe spot splitting may not be memoryless. This is at odds with the prevailing spatial proliferation idea [4] which considers that, for $Re < 2400$, spot splitting is memoryless in the sense that, once split, a child spot has no contact (memory) with its parent and behaves entirely as a standalone new parent. The splitting-reconnection-resplitting process also suggests that, for the purpose of collecting lifetime statistics, it is important to carefully track child spots through three-dimensional vortex structures (as opposed to one-dimensional signals) because their identities can change due to reconnection and re-splitting.

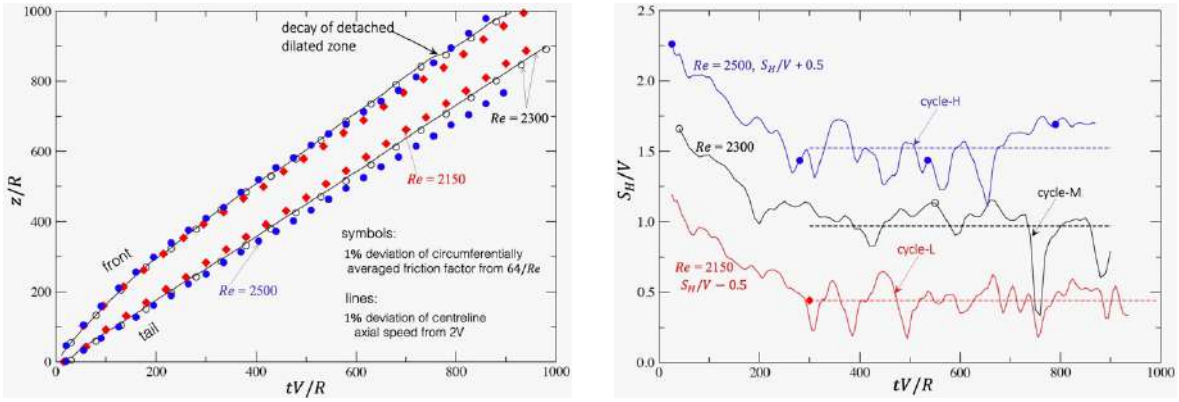

Figure 2. Propagation of turbulent spot packet: Left: Front and tail positions. Right: Instantaneous speed S_H/V of the front. Note the S_H/V profiles exhibit a quasi-cyclic peak/valley characteristic – this is not random stochastic fluctuation. In particular, the deep valley labeled as 'cycle-M' at $Re = 2300$ corresponds to the kink highlighted on the Left pane. The valley at $Re = 2500$, marked as 'cycle-H', is due to the decay of a detached frontal dilated zone. Similarly, the valley labeled as 'cycle-L' at $Re = 2150$ is a result of the decay of a detached frontal dilated zone. Averaged front propagation speed values are represented using the dashed lines. Clearly, the averaged propagation speed misses the important transition physics information conveyed by the quasi-cyclic peak/valley characteristic in the instantaneous front speed data: the frequent development, detachment, decay or growth of a frontal elongated zone. Furthermore, in the event of growth rather than decay, the frontal elongated zone is in essence the embryo of a child spot which will lead to a full splitting. This scenario is somewhat inconsistent with the notion of splitting and dissipation being two completely independent factors in pipe transition [4] because the present results suggest that dissipation may also be an integral part of the splitting process itself.

CONCLUSIONS

Pipe spot splitting at low Reynolds number can have memory and hysteresis effect, splitting and dissipation are coupled rather than totally independent. Variation of a spot-packet's instantaneous front speed with axial distance reflects the physical development processes of splitting, reconnection, re-splitting and decay. Mean propagation speed of spot-packet fronts masks important pipe transition physics. Conditional sampling results demonstrate that the fluid dynamics mechanism of splitting is a sustained zonal axial velocity differential between a pipe spot's leading front and the core.

References

[1] Schubauer G.B., Klebanoff P.S. *NACA Technical Note* 1289, 1956.
[2] Klebanoff P.S., Tidstrom K.D., Sargent L.M. *J. Fluid. Mech.* **12**: 1-34, 1962.
[3] Lindgren E.R. *ARKIV FYSIK* **15**:97-119, 1959
[4] Avila K., Moxey D., de Lozar A., Avila M., Barkley D., Hof B. *Science,* **333**:192-196, 2011.
[5] Barkley D., Song B., Mukund V., Lemoult G., Avila M., Hof B. *Nature,* **526**:550–553, 2015.
[6] Priymak V.G., Miyazaki T. *Phys Fluids* **16**:4221, 2004.

DISENTANGLING LAGRANGIAN TURBULENCE

Lukas Bentkamp[1], Cristian C. Lalescu[1], and Michael Wilczek*[1]
[1]Max Planck Institute for Dynamics and Self-Organization, Am Faßberg 17, 37077 Göttingen, Germany

Summary Lagrangian particles frequently encounter extreme acceleration events in fully developed turbulence. Intense small-scale structures such as vorticity filaments can give rise to acceleration events exceeding the typical root-mean-squared fluctuations by orders of magnitude (see Fig. 1). Here, we introduce the notion of persistent Lagrangian acceleration, quantified by the squared Lagrangian acceleration coarse-grained over a viscous time scale. Conditioning Lagrangian particle data from direct numerical simulations on this coarse-grained acceleration, we find remarkably simple, close-to-Gaussian statistics for a range of Reynolds numbers. Based on this observation, we develop a theory of Lagrangian single-particle statistics covering the acceleration, velocity increments as well as single-particle dispersion.

Introduction A recurrent idea for modeling turbulence is to seek decompositions into simpler sub-ensembles. This idea underlies various modeling approaches such as superstatistics and multifractals. In these approaches, the full ensemble statistics is obtained by superposing simpler statistics characterized by a parameter, which varies statistically across the ensemble. To obtain a physically meaningful description for turbulence, the challenge is to identify the quantity that separates the full statistical ensemble into simpler sub-ensembles.

For the description of the spatial (i.e. Eulerian) statistics of turbulence, the refined similarity hypothesis [1, 2] states that the scale-dependent Eulerian statistics can be reduced to a universal form, solely depending on the dissipation rate volume-averaged (i.e. coarse-grained) on the given scale. Indeed, conditional probability density functions (PDFs) of velocity increments were observed to take a self-similar, or even an approximately Gaussian form when conditioning on the coarse-grained energy dissipation [3, 4] or energy transfer rate [5, 6].

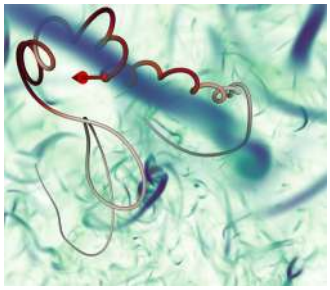

Figure 1: Tracer particle (trajectory color-coded by acceleration magnitude) encountering an intense vortex (blue volume rendering). Figure adapted from [14].

In the analogous Lagrangian refined similarity hypothesis [7–10], it is assumed that Lagrangian statistics can be formulated in a universal form in terms of a locally averaged (in time or space) dissipation rate along tracer particle trajectories. However, conditional statistics appear to remain intermittent and generally depart from Gaussianity [3, 11]. This raises the question whether a physically meaningful quantity exists that separates the intermittent statistics of Lagrangian turbulence into simpler, Gaussian statistics. In this contribution, we provide an answer to this question. We introduce the squared acceleration, coarse-grained over a typical viscous time scale, as a measure of persistence of the Lagrangian acceleration, and show that it decomposes the strongly non-Gaussian and scale-dependent statistics of Lagrangian turbulence into much simpler, close-to-Gaussian sub-ensembles. Based on this observation, we develop a comprehensive theoretical framework of Lagrangian single-particle statistics.

Results The central quantity, which allows us to disentangle the complex Lagrangian statistics, is $\alpha(t)$ – the squared acceleration coarse-grained along Lagrangian tracer trajectories over a few Kolmogorov time scales. On a general level, $\alpha(t)$ can be perceived as a Lagrangian analogue of the coarse-grained dissipation rate in the Eulerian refined similarity hypothesis [1, 2], which essentially measures the degree of small-scale turbulence encountered by a particle.

We find that conditioning Lagrangian statistics on α leads to approximately Gaussian statistics, which implies a significant reduction of complexity. As an example, Fig. 2 shows the PDFs of an acceleration component a both unconditional (red line) and conditional on α (colored lines) from our direct numerical simulations of homogeneous isotropic turbulence at a Reynolds number of $R_\lambda \approx 350$. Whereas the unconditional PDF is extremely heavy-tailed, the conditional acceleration PDFs display a close-to-Gaussian form for all values of α.

Based on this observation, we develop a comprehensive framework of Lagrangian single-particle statistics. The complete statistical information of a Lagrangian trajectory is contained in its characteristic functional $\phi[\vartheta]$, which has been introduced in Hopf's functional approach to turbulence [12]. Exploiting our observation that conditioning on α leads to approximately Gaussian statistics, we propose that the characteristic functional of the full ensemble takes the form [13, 14]

$$\phi[\vartheta] = \int_0^\infty \mathrm{d}\alpha\, f(\alpha)\, \phi_\alpha^{\mathrm{G}}[\vartheta]. \tag{1}$$

Here, $f(\alpha)$ is the PDF of α, and $\phi_\alpha^{\mathrm{G}}[\vartheta] = \exp\left[-\frac{1}{2}\int_{-\infty}^{\infty}\mathrm{d}t\int_{-\infty}^{\infty}\mathrm{d}t'\,\vartheta(t)C_\alpha(t-t')\vartheta(t')\right]$ is a Gaussian characteristic functional, which is fully determined by the conditional autocorrelation function $C_\alpha(\tau)$. The test function $\vartheta(t)$ can be chosen, for example, to project the complete statistics to single- or two-time statistics etc. Overall, this means that the

*Corresponding author. E-mail: michael.wilczek@ds.mpg.de.

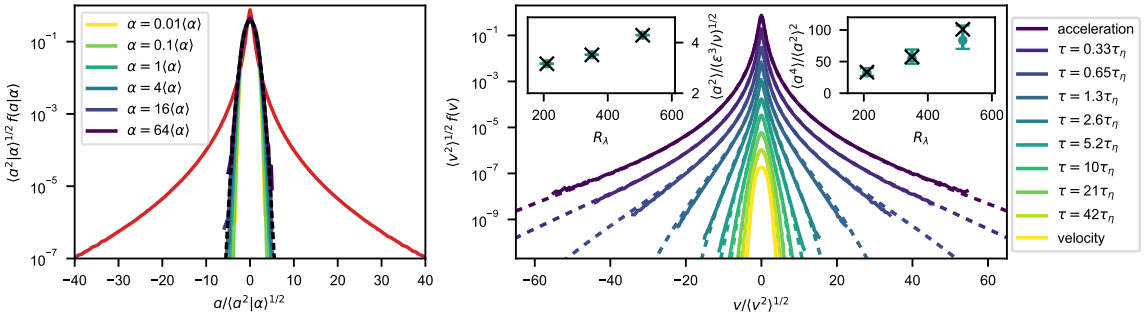

Figure 2: **Left:** The PDFs $f(a|\alpha)$ of an acceleration component conditional on α (colored lines) are all close to Gaussian. The unconditional PDF (red line) and a Gaussian distribution (black, dashed line) are plotted for comparison. **Right:** Comparison of PDFs derived from the model (dashed) with DNS data (solid) ($R_\lambda \approx 350$). From top to bottom: acceleration PDF, velocity increment PDFs, velocity PDF (vertically shifted for clarity). Insets: Acceleration variance (in Kolmogorov units) and flatness from model (dots) compared to DNS (crosses) as a function of Reynolds number. The error bars are obtained by varying the coarse-graining time scale between 1.5 and 4.5 Kolmogorov time scales. Figure adapted from [14].

full Lagrangian ensemble can be considered as a probabilistic mix of Gaussian sub-ensembles with varying correlations. Since the characteristic functional offers a comprehensive statistical description, the complete single-particle statistics of Lagrangian turbulence can be determined from our framework once the PDF of the coarse-grained squared acceleration $f(\alpha)$ and the conditional correlation functions $C_\alpha(\tau)$ are given. For the present results, we take these quantities directly from our DNS data without resorting to further modeling assumptions.

The main challenge in capturing Lagrangian single-particle statistics is intermittency, which can be studied in terms of the statistics of the velocity increment $v = u(t+\tau/2) - u(t-\tau/2)$ taken over a time lag τ. Intermittency manifests itself in a pronounced scale dependence of the PDF $f(v;\tau)$ of the Lagrangian velocity increments. It exhibits heavy tails for small time lags but relaxes to an almost Gaussian distribution for large time lags. These PDFs can be directly computed from our framework [14]. As a quantitative benchmark, we compare the PDFs obtained from (1) to the ones obtained from DNS. Fig. 2 shows the velocity increment PDFs along with the PDFs of velocity and acceleration at $R_\lambda \approx 350$. Very good agreement is found at all scales, which supports our hypothesis that Lagrangian intermittency can be perceived as a consequence of the statistical mixture of different regions of the flow, each characterized by a particular coarse-grained squared acceleration.

Conclusions We showed that Lagrangian single-particle statistics can be decomposed into approximately Gaussian sub-ensembles when trajectories are discriminated with respect to the coarse-grained squared acceleration α. Physically, high values of α correspond to events in which particles encounter intense small-scale structures such as vorticity filaments. Hence the decomposition intuitively separates regions of highly turbulent activity from more quiescent regions.

Based on this, we developed a theoretical model of Lagrangian single-particle statistics, which requires the PDF of α and the conditional Lagrangian velocity autocorrelation functions as input. Formulated in terms of the characteristic functional, our framework offers a comprehensive statistical description of Lagrangian single-particle statistics, which constitutes a conceptual generalization of previous approaches. By projecting it to finite-dimensional statistics such as velocity increment distributions, we find very good agreement with simulation results across a range of Reynolds numbers.

References

[1] A. N. Kolmogorov. *J. Fluid Mech.*, 13(1):82–85, 1962.
[2] A. M. Oboukhov. *J. Fluid Mech.*, 13(1):77–81, 1962.
[3] H. Homann, D. Schulz, and R. Grauer. *Phys. Fluids*, 23(5):055102, 2011.
[4] J. M. Lawson, E. Bodenschatz, A. N. Knutsen, J. R. Dawson, and N. A. Worth. *Phys. Rev. Fluids*, 4:022601, 2019.
[5] Y. Gagne, M. Marchand, and B. Castaing. *J. Phys. II France*, 4(1):1–8, 1994.
[6] A. Naert, B. Castaing, B. Chabaud, B. Hébral, and J. Peinke. *Physica D*, 113(1):73 – 78, 1998.
[7] R. Benzi, L. Biferale, E. Calzavarini, D. Lohse, and F. Toschi. *Phys. Rev. E*, 80:066318, 2009.
[8] H. Yu and C. Meneveau. *Phys. Rev. Lett.*, 104:084502, 2010.
[9] B. L. Sawford and P. K. Yeung. *Procedia IUTAM*, 9(Supplement C):129 – 137, 2013. IUTAM Symposium on Understanding Common Aspects of Extreme Events in Fluids.
[10] B. L. Sawford and P. K. Yeung. *Phys. Fluids*, 27(6):065109, 2015.
[11] P. K. Yeung, S. B. Pope, A. G. Lamorgese, and D. A. Donzis. *Phys. Fluids*, 18(6):065103, 2006.
[12] E. Hopf. *J. Ration. Mech. Anal.*, 1:87–123, 1952.
[13] M. Wilczek. *New J. Phys.*, 18(12):125009, 2016.
[14] L. Bentkamp, C.C. Lalescu, and M. Wilczek. *Nature Commun.*, 10:3550, 2019.

DYNAMICS OF CORNER VORTICES AND FLOW REVERSALS IN TURBULENT RAYLEIGH-BÉNARD CONVECTION

Venugopal T. Vishnu*[1], Arnab K. De[1], and Pankaj K. Mishra[2]
[1]Department of Mechanical Engineering, Indian Institute of Technology Guwahati, Guwahati, India
[2]Department of Physics, Indian Institute of Technology Guwahati, Guwahati, India

Summary We present the dynamics of corner vortices during flow reversals of large-scale circulation (LSC) in turbulent Rayleigh-Bénard convection (RBC) of air inside a cubic cell in the range $2 \times 10^6 \leq Ra \leq 10^9$ using direct numerical simulations. The plane containing LSC is generally aligned along one of the diagonals of the box accompanied by a four-roll structure in the other. In addition to the primary roll, two secondary corner-rolls are also observed in the LSC plane, which grow in size and destabilize the LSC resulting in partial and complete reversals. We observe that these corner vortices are not restricted to the LSC plane, as observed in two dimensional simulations, but they extend much beyond.

INTRODUCTION

Reorientation of large-scale flow, such as wind reversals in atmospheric flows and the change in polarity of magnetic field in Earth and Sun have been an interesting field of research in turbulence since last couple of decades. Understanding the genesis of large-scale circulation and the mechanism that leads to change in its direction still remains a challenge. Although flow reversals have been extensively studied over the years in 2D/quasi-2D systems [1] and cylindrical [2] domains, origin and dynamics of such large-scale structures in a Cartesian box are not well understood, especially for highly turbulent flow. In the present study, we examine the dynamics of LSC with prime focus on its orientation and subsequent reversals in high Rayleigh number range $2 \times 10^6 \leq Ra \leq 10^9$.

NUMERICAL DETAILS

The mathematical model of RBC using Boussinesq approximation consists of the momentum, mass, and energy conservation equations written as

$$\frac{\partial \boldsymbol{u}}{\partial t} + \boldsymbol{u}\cdot\nabla\boldsymbol{u} = -\nabla p + \sqrt{\frac{Pr}{Ra}}\nabla^2\boldsymbol{u} + \theta\hat{\boldsymbol{k}} \quad (1)$$

$$\nabla\cdot\boldsymbol{u} = 0 \quad (2)$$

$$\frac{\partial \theta}{\partial t} + \boldsymbol{u}\cdot\nabla\theta = \frac{1}{\sqrt{PrRa}}\nabla^2\theta \quad (3)$$

where $\boldsymbol{u}$ represents the velocity vector, p pressure, and θ non-dimensional temperature, while Ra and Pr are the Rayleigh number and Prandtl number, respectively. The above coupled Eqs. 1-3 are solved using a predictor-corrector based finite volume formulation with collocated arrangement of variables. No-slip velocity condition is applied on all the boundaries, while for temperature isothermal and adiabatic conditions are applied on the horizontal and vertical walls, respectively. The non-linear convective term is approximated using the 2nd-order Adams-Bashforth scheme, while the buoyancy, pressure and diffusive terms are approximated by the 2nd-order Crank-Nicolson scheme. All the resulting sparse linear systems are solved using BiCGSTAB technique preconditioned by a highly scalable diagonalised version of Stone's Strongly Implicit Procedure. For details of the numerical procedures, readers are referred to Vishnu *et al.* [3].

RESULTS

One of the striking features of turbulent RBC is the presence of LSC, which is a large-scale discernible convection pattern comprising thermal plumes sustained by its own dynamics, depending not only on the state of the turbulence but also on the geometric constraints. In cubic cells LSC is generally aligned along a diagonal plane [4]. It is observed that, with time, the plane containing LSC switches between the diagonals resulting in flow reversals. Here we classify these reversals as partial, where the LSC reorients from one diagonal to another and complete in which the LSC stays in a single diagonal plane but changes its direction of circulation.

Figure 1(a) shows the iso-surfaces of instantaneous temperature for $Ra = 10^9$, where hot plumes erupt from the boundary layer and cold plumes sink along the opposite corners giving rise to a large-scale coherent structure aligned along the diagonal labeled as d_1. The planar view of this diagonal plane is shown in Fig. 1(b) which shows the apparent large-scale circulatory motion of the flow. For better visualization of the large-scale flow structure, time-averaged velocity vectors superimposed on the temperature contours at the diagonal planes are shown in Fig. 2 for $Ra = 10^7$. In the diagonal plane containing LSC, a counter-clockwise rotating primary roll (LSC) along with two corner rolls are observed [see Fig. 2(a)]. Note that the direction of circulation of the corner rolls (clockwise) is opposite to that of the LSC. In the opposite diagonal, a four-roll structure is identified, as shown in Fig. 2(b). It has been well established that these corner vortices play a crucial role in the stability and dynamics of LSC in 2D Rayleigh-Bénard flows. However,

*Corresponding author. E-mail: vishnu.t@iitg.ac.in

in 3D RBC, such dynamics are less explored. To quantify these vortices, the second invariant of the velocity gradient tensor, Q, is shown in Fig. 2(c). Here $Q > 0$ represents regions of strong local rotation, i.e., high vortical motions. It is apparent from Fig. 2(c) that the corner vortices are not restricted to the LSC plane (as are limited in 2D RBC), but they extend along the adjacent faces sharing the diagonal plane to yield a "boomerang" shape.

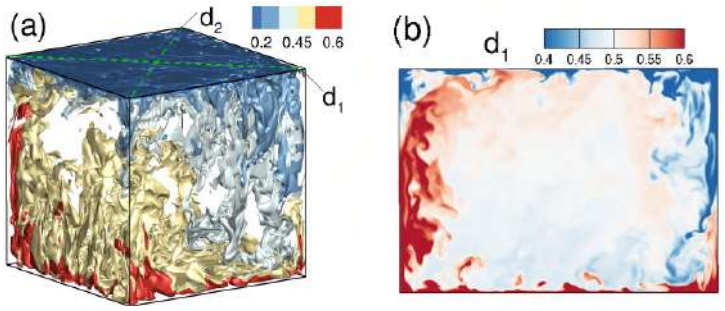

Figure 1: (a) Instantaneous temperature iso-surfaces indicating LSC oriented along the diagonal plane d_1 for $Ra = 10^9$. (b) The contours of temperature in the diagonal plane containing LSC.

Mechanism of flow reversals

Previous 2D/quasi-2D studies [1] on the dynamics of LSC have emphasized the role of corner rolls in flow reversals, though, in such a set-up, LSC is forced to coexist with the rolls at all times in a plane. Alleviating such limitations, we discuss dynamics and reversal of the mean wind in a 3D Cartesian box. At the outset, LSC is oriented along d_1 as a counter-clockwise primary roll accompanied by two clockwise secondary rolls near the corners, while in d_2 a four-roll structure is noticed [see Figs. 2(a) and 2(b)]. During a reversal, the corner rolls in d_1 grow in size and they induce the primary roll to break into two, which results in a four-roll structure. On the other hand, only a set of rolls with same sense of rotation appear to grow and merge in d_2 only to form an LSC retaining the sense of rotation. This effectively shrinks and constricts the remaining two rolls towards the corners. Thus, the LSC and four-roll structure switch between the diagonal planes during a partial reversal. In addition, we observe complete reversals in which the corner rolls in the LSC plane grow in size to yield a four-roll structure which further merge to produce an LSC with opposite sense of rotation. However, on the other diagonal plane, the same four-roll structure is maintained during the entire reversal process. The sequence of flow structures and vortex reconnection in the LSC-plane during a complete reversal is very much similar to that observed in 2D/quasi-2D [1] cases. On the contrary, partial reversals are only realized in 3D geometry.

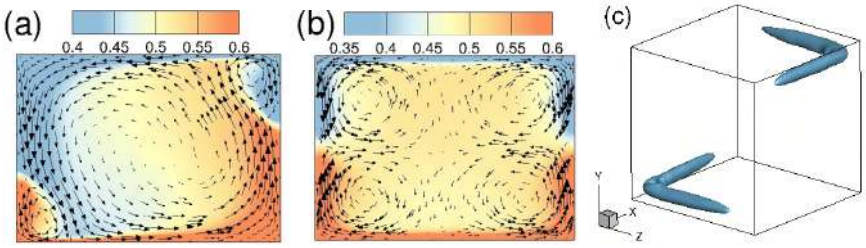

Figure 2: Time-averaged velocity vectors superimposed on the temperature contours at the diagonal planes containing (a) LSC and (b) four-roll structure for $Ra = 10^7$. (c) Time averaged Q structures showing three dimensional structure of the corner vortices.

CONCLUSIONS

Using a series of DNS calculations, dynamics of LSC in turbulent RBC inside a cubic box has been investigated for $2 \times 10^6 \leq Ra \leq 10^9$. LSC is primarily aligned along one of the diagonal planes accompanied by a four-roll structure in the other diagonal. The present study reveals that the corner vortices are not just restricted to the plane containing LSC, but extend much beyond, thus forming a "boomerang" topology. Further, we have analyzed the flow structures in different planes for partial and complete reversals. During a partial reversal, the LSC weakens at the expense of growth of the corner-rolls to form a four-roll structure, while in the opposite plane, two rolls merge together to form LSC.

References

[1] Sugiyama K., Ni R., Stevens R. J. A. M., Chan T. S., Zhou S.-Q., Xi H.-D., Sun C., Grossmann S., Xia K.-Q., Lohse D. Flow reversals in thermally driven turbulence. *Phys. Rev. Lett.*, **105**: 034503, 2010.
[2] Brown E., Ahlers G. Rotations and cessations of the large-scale circulation in turbulent Rayleigh-Bnard convection. *J. Fluid Mech.*, **568**: 351- 386, 2006.
[3] Vishnu V. T., De A. K., Mishra P. K. Dynamics and statistics of reorientations of large-scale circulation in turbulent rotating Rayleigh-Bnard convection. *Phys. Fluids*, **31**: 055112, 2019.
[4] Foroozani N., Niemela J. J., Armenio V., Sreenivasan K. R. Reorientations of the large-scale flow in turbulent convection in a cube. *Phys. Rev. E*, **95**: 033107, 2017.

O108342 - FM15 - Turbulence - Oral

TURBULENT POLY-DISPERSED BUBBLY CHANNEL FLOWS: EFFECTS OF SOLUBLE SURFACTANT AND VISCOELASTICITY

Outi Tammisola*[1], Zaheer Ahmed[2], Daulet Izbassarov[4], M Nufail Farooqi[3], and Metin Muradoglu[2]
[1]Linné Flow Centre and SeRC,KTH Mechanics,Stockholm,Sweden
[2]Department of Mechanical Engineering, Koc¸ University, Istanbul, Turkey.
[3]Department of Computer Engineering, Chalmers University of Technology, Sweden.
[4]Aalto University, Department of Mechanical Engineering, FI-00076 Aalto, Finland

Summary Interface-resolved direct numerical simulations are performed to examine the combined effects of soluble surfactant and viscoelasticity on the structure of poly-dispersed bubbly turbulent channel flows at $Re_\tau = 250$. A soluble surfactant and FENE-P viscoelastic models are coupled to the incompressible flow equations. In the clean case, small bubbles move toward the wall due to the inertial lift force, resulting in the formation of wall-layers and a significant reduction in the flow rate while larger bubbles tend to move toward channel center. An addition of strong enough surfactant alters the direction of lateral migration, i.e., the contaminated bubbles move toward the core region and spread out across the channel. For the viscoelastic case, shear-thinning effects and elastic forces promote formation of bubbly wall-layers leading to a strong decrease in the flow rate. Formation of a wall-layer is determined by the interplay of the inertial lift, elastic and Marangoni forces when they coexist.

NUMERICAL METHOD

The incompressible flow equations are solved in both phases using a second-order finite-difference/front-tracking (FD/FT) method [4]. Following [4] and [1], a single set of governing equations can be written for the entire computational domain provided the jumps in the material properties are taken into account and the effects of the interfacial surface tension are treated appropriately. The momentum equation, accounting for interphase coupling, is given by

$$\begin{aligned}\frac{\partial \rho \mathbf{u}}{\partial t} + \nabla \cdot (\rho \mathbf{u}\mathbf{u}) &= -\nabla p + (\rho - \rho_{av})\mathbf{g} + \nabla \cdot \boldsymbol{\tau} + \nabla \cdot \mu_s(\nabla \mathbf{u} + \nabla \mathbf{u}^T) \\ &+ \int_A \left[\sigma(\Gamma)\kappa \mathbf{n} + \nabla_s \sigma(\Gamma)\right]\delta(\mathbf{x} - \mathbf{x_f})dA, \end{aligned} \quad (1)$$

where $\mathbf{u}$, $\boldsymbol{\tau}$, p, $\mathbf{g}$ ρ, μ_s and σ are the velocity vector, the polymer stress tensor, the pressure, the gravitational acceleration, the density, the solvent viscosity, and the surface tension coefficient, respectively, and A is the surface area. In the last term of Eq. (1), κ is twice the mean curvature, $\mathbf{n}$ is a unit vector normal to the interface and ∇_s is the gradient operator along the interface. The present soluble surfactant methodology is developed by Muradoglu and Tryggvason [4]. The FENE-P model is adopted as the constitutive equation for the polymeric stress $\boldsymbol{\tau}$. The FENE-P model and its numerical solution are described in [1, 2].

COMPUTATIONAL SETUP

We consider vertical turbulent channel flow as shown in Fig. 2. The flow is periodic in the spanwise (x) and streamwise (y) directions, with no-slip/no-penetration boundary conditions at the walls in the z direction. In all the cases, bubbles were placed randomly in a vertical channel with a fully developed turbulent flow. The flow is driven upward by an imposed constant pressure gradient dp/dy with the gravitational acceleration $\mathbf{g}$ acting in the opposite direction. The size of computational domain is $4 \times 8 \times 2$ and it is resolved by a $640 \times 1280 \times 384$ grid in x, y and z directions, respectively. The grid points are uniformly spaced in the spanwise and streamwise direction but stretched in the wall-normal direction. In terms of wall units, defined by $l_0^+ = h/Re_\tau$ (i.e., $l_0^+ = 1/250 = 0.004$ in the present setup), the size of the channel is $1000 \times 2000 \times 500$. For the poly-dispersed flow case, the physical parameters are selected such that the total void fraction is 3%. Further, the void fraction is divided into four equal portions of 0.75% for four different sizes of bubbles, yielding the Eötvös numbers (Eo) ranging from 0.5 to 2.5. The details of this configuration and governing parameters are given in Table 1.

RESULTS

First, simulations are perfomed to achieve fully developed single phase turbulent flow for $Re_\tau = 250$. Statistically steady state results are compared with the DNS data of Lu and Tryggvason [3]. Figure 1 shows that the results are in excellent agreement. Extensive simulations are then performed to investigate the the effects of surfactant and viscoelasticity on the dynamics of turbulent bubbly channel flow. For this purpose, in addition to the clean case ($C_\infty = 0$), computations are carried out for two bulk surfactant concentrations, i.e., $(C_\infty = 0.25 \text{ ppm}, 0.5 \text{ ppm})$ of TritonX-100 to examine the

*Corresponding author. E-mail:outi@mech.kth.se

Thematic Session FM

Table 1: (left) The governing parameters (right) Configuration of poly-dispersed flow. Eo, R_b , V_b and N_b denote the Eötvös number, the initial bubble radius, the bubble volume and number of bubbles.

Parameter	Definition	value
Density ratio	ρ_i/ρ_o	0.1
Viscosity ratio	μ_i/μ_o	0.1
Morton Number	$M = g{\mu_o}^4/\rho_o\sigma^3$	5.75×10^{-10}
Langmuir Number	$La = k_aC_\infty/k_d$	0/0.6/1.2
Elasticity Number	$\beta_s = RT\Gamma_\infty/\sigma$	0.5
Weissenberg Number	$Wi = \lambda W_b/h$	0/10/20
Solvent viscosity ratio	$\beta = \mu_s/\mu_o$	0.9
Extensibility parameter	L	60

Eo	R_b	V_b	N_b	$N_b \times V_b$
0.5	0.08	0.0021	224	0.48
1.0	0.11	0.0055	86	0.48
1.5	0.14	0.0114	42	0.48
2.5	0.18	0.0244	20	0.48

effects of surfactant on the poly-dispersed bubbly flows without viscoelasticity. Then the simulations are performed for the viscoelastic case at Weissenberg numbers of Wi = 0, 10 and 20 in the absence of surfactant to examine the sole effects of viscoelasticity. Finally the combined effects of surfactant and visoelasticity are investigated. Figure 2 shows the results of the clean case ($C_\infty = 0, W_i = 0$). Although the flow has not yet reached to a statistically stationary state (Fig. 2), the clean spherical bubbles move towards the wall due the strong inertial lift force and the formation of a horizontal bubble clusters has already emerged. The formation of these clusters results in the reduction of the flow rate in the channel. The most deformable bubbles are distributed around the core as expected.

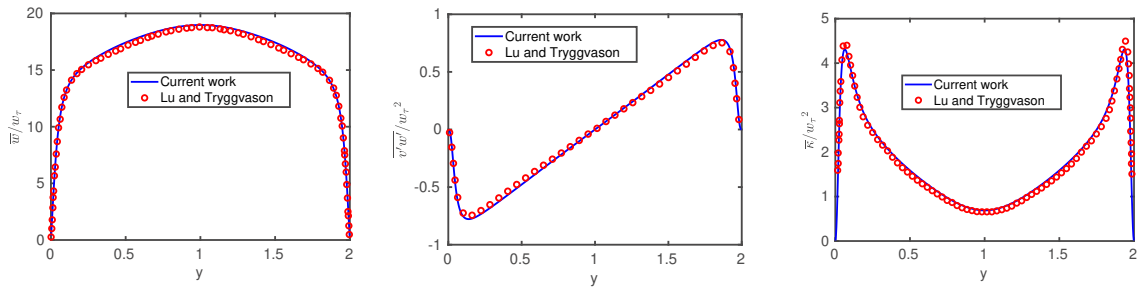

Figure 1: The turbulent single-phase flow. The average bulk velocity profile (left), the Reynolds stresses (middle) and the turbulent kinetic energy (right). The solid lines represent the current results and the symbols are the DNS data of Lu and Tryggvason [3].

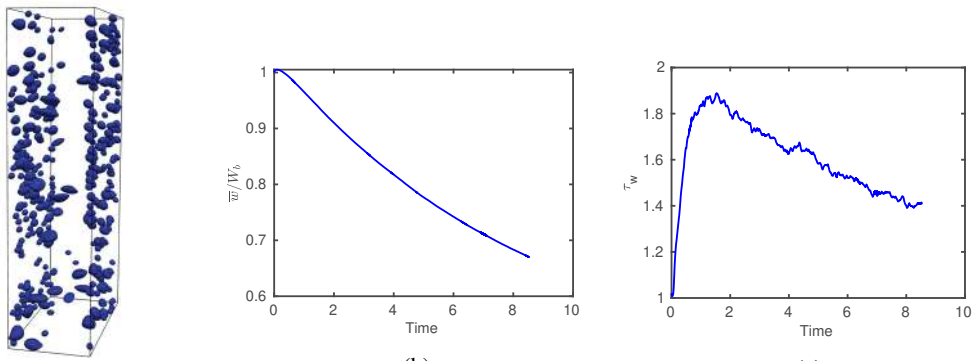

(a) (b) (c)

Figure 2: (a) The bubble distribution at $t = 8$. (b) The average bulk velocity normalized by the average bulk velocity of the single-phase flow and (c) the average wall shear stress.

References

[1] Daulet Izbassarov and Metin Muradoglu. A front-tracking method for computational modeling of viscoelastic two-phase flow systems. *Journal of Non-Newtonian Fluid Mechanics*, 223:122–140, 2015.

[2] Daulet Izbassarov, Marco E Rosti, M Niazi Ardekani, Mohammad Sarabian, Sarah Hormozi, Luca Brandt, and Outi Tammisola. Computational modeling of multiphase viscoelastic and elastoviscoplastic flows. *International Journal for Numerical Methods in Fluids*, 88(12):521–543, 2018.

[3] Jiacai Lu and Gretar Tryggvason. Dynamics of nearly spherical bubbles in a turbulent channel upflow. *Journal of Fluid Mechanics*, 732:166–189, 2013.

[4] Metin Muradoglu and Gretar Tryggvason. Simulations of soluble surfactants in 3d multiphase flow. *Journal of Computational Physics*, 274:737–757, 2014.

WAKES AND TURBULENCE PROPERTIES IN WIND FARMS

Jens N. Sørensen*[1] and Søren J. Andersen [1]
[1]Department of Wind Energy, Technical University of Denmark, Lyngby, Denmark

Summary Large Eddy Simulations (LES) are performed to analyse the influence of turbulence on wakes and power production of wind turbines located in a wind farm. Three farm simulations with different degrees of imposed atmospheric turbulence is presented and compared to results using an analytical wake model. The analytical wake model, which was originally developed for infinite wind farms, is validated against the LES computations in order to check its generality for coping with power production in finite-sized wind farms subject to different levels of inflow turbulence.

INTRODUCTION

Modern wind turbines are often clustered in wind farms in order to reduce the overall installation and maintenance expenses. An unwanted but inevitable side-effect, however, is that the downstream turbines, depending on the wind direction, often operate in the wake of upstream located turbines. A wind turbine operating in the wake of one or more wind turbines yields less power and is subject to greater loadings from the induced turbulence, leading to increased fatigue. The increased turbulence originates from the vorticity created by the rotor loading on the passing rotor blades. Understanding this highly dynamic wake interaction is very important for wind farm optimization. Although large eddy simulations reveal many details regarding wakes and turbulence in a wind farm, for layout optimization of wind farms one has to resort to semi-analytical techniques based on simplified modelling of the wake dynamics, such as those proposed by Jensen [1] and Frandsen et al. [2]. Generally, these models are based on simple assumptions regarding steady state considerations, and are developed with the aim of predicting mean quantities, e.g. the mean velocity deficit in the wake. Therefore, the models exclude the details of the dynamic wake interaction and turbulence properties needed to assess the turbine performance and loadings. Frandsen [3] proposed both a model for the array-effect of the wind farm on the atmospheric boundary layer, and a model for fatigue loading on rotors using the effective turbulence intensity as the only governing parameter, arguing that the various changes in turbulence properties usually correlates with the standard deviation of wind speed fluctuations. The present work concerns an extension of the models by Frandsen, taking the effective turbulence intensity as a design variable, which will be tested against controlled LES results.

NUMERICAL TECHNIQUE

The LES computations presented in this paper are carried out using the 3D flow solver *EllipSys3D* (Michelsen [4]), Sørensen [5]). This code solves the discretized incompressible Navier-Stokes equations in general curvilinear coordinates using a block structured finite volume approach. *EllipSys3D* is formulated in pressure-velocity variables in a non-staggered grid arrangement. In the present work, the pressure correction equation is solved using the PISO algorithm and pressure decoupling is avoided using the Rhie/Chow interpolation technique. The convective terms are discretized using a hybrid scheme combining the third order accurate QUICK scheme and the fourth order CDS scheme. The time discretization is specified such that the tip of a rotor blade during a time step moved less than a half grid spacing. The flow field around the wind turbine rotor is simulated using the actuator line technique developed by Sørensen and Shen [6]. In this model the three-dimensional Navier-Stokes equations are solved with body forces distributed along rotating lines representing the blades of the wind turbine. The flow field is thus determined by solving the three-dimensional Navier-Stokes equations using Large Eddy Simulation (LES), whereas the loading on each blade is computed by calculating the local angle of attack to determine the local forces from tabulated airfoil data.

RESULTS

Three simulations are presented, which all are computed on the same grid. The grid is 200R × 20R × 20R in the streamwise, lateral, and vertical direction, respectively. The grid is constructed of 640 blocks of 803 cells corresponding to a total of approximately 328·106 cells. The grid is uniform in all directions with a resolution corresponding to 17 cells per rotor blade. The lateral boundary conditions are cyclic to simulate wind farms of infinite extent in the lateral direction. The vertical boundary conditions are symmetry planes. Inlet/outlet conditions are applied in the streamwise boundaries. Three LES have been performed with a row of 16 turbines of constant turbine spacing of 12R. The same inflow of 8m/s at hub height has been applied, but the turbulent fluctuations are imposed using body forces, which have been scaled to yield different turbulent intensities of approximately 0%, 3%, and 15%. For more details on the simulation setup, please see Andersen et al. [7]. As an illustration of the flow and turbulence characteristics about the turbines, Fig. 1 depicts instantaneous iso-vorticity contours around the 16 wind turbines that are located around a common line.

*Corresponding author. E-mail: jnso@dtu.dk.

Fig. 1 Vorticity contours showing the wake structure along the wind turbines.

Figure 2 shows box plots of the power production of 51 different 10-min periods of the 16 turbines normalized by the rated power of 2750 MW. The influence of atmospheric turbulence is mainly seen in two aspects. First, the power production of the second turbine is greatly affected by the inflow turbulence, which helps the wake breakdown and recover, see Sørensen et al. [8]. Secondly, the converged level deep inside the farm increases with increasing turbulence as the entrainment is enhanced.

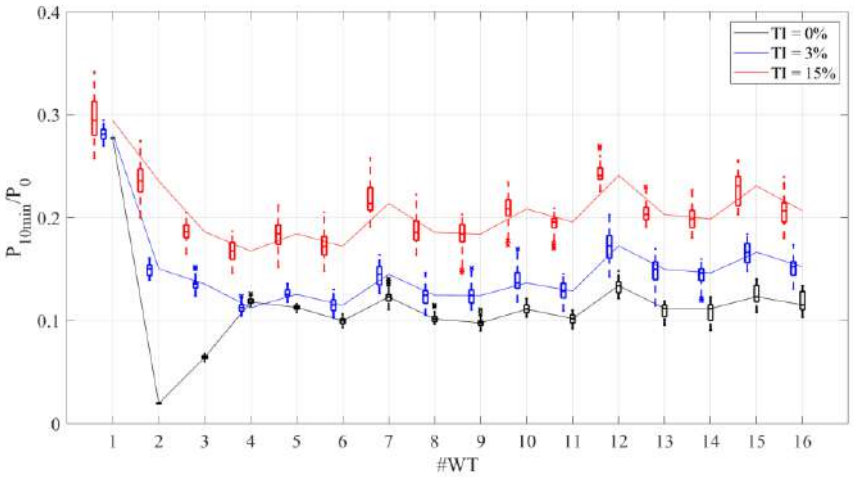

Fig. 2 Averaged power production of the wind turbines for different turbulence intensities.

CONCLUSIONS

Large eddy simulations have been performed to analyse the influence of inflow turbulence on the power production in a wind farm. The turbulence is seen to have a big impact on the power production, in particular on the power produced by the second wind turbine in the array. In the final presentation these results will be compared to an analytical wake model.

References

[1] Jensen, N. O., A Note on Wind Generator Interaction, Risø-M-2411, 1983.
[2] Frandsen, S. and Barthelmie, R. and Pryor, S. and Rathmann, O., and Larsen, S. and Højstrup, J. and Thøgersen, M., Analytical modelling of wind speed deficit in large offshore wind farms, Wind Energy, vol. 9, 2006.
[3] Frandsen, S.T., Turbulence and Turbulence-Generated Structural Loading in Wind Turbine Clusters, Risø-R-1188(EN), Risø National Laboratory, Roskilde, Denmark, 2007.
[4] Sørensen, N. N., General Purpose Flow Solver Applied to Flow over Hills, PhD, Risø-R-827(EN), Risø National Laboratory, Roskilde, Denmark, 1995.
[5] Michelsen JA. Basis3D – a Platform for Development of Multiblock PDE Solvers. Technical Report, Danmarks Tekniske Universitet, 1992.
[6] Sørensen, J. N. and Shen, W. Z., Numerical modelling of Wind Turbine Wakes, *J. Fluids Engineering*, vol. 124, 2002.
[7] Andersen, S. J., Sørensen, J. N., & Mikkelsen, R. F. Turbulence and entrainment length scales in large wind farms. *Philosophical Transactions of the Royal Society A: Mathematical, Physical and Engineering Sciences*, 375 (2091), 2017.
[8] Sørensen, J. N., Mikkelsen, R. F., Henningson, D. S., Ivanell, S., Sarmast, S., & Andersen, S. J. Simulation of wind turbine wakes using the actuator line technique. *Philosophical Transactions of the Royal Society A: Mathematical, Physical and Engineering Sciences*, 373 (2035), 2015.

MALL SCALE UNIVERSALITY IMPRINTED IN THE ENTRAINMENT CHARACTERISTICS OF FREE SHEAR FLOWS

Marco Zecchetto[1] and Carlos B. da Silva*[1]
[1]LAETA,IDMEC,Instituto Superior Ténico,Universidade de Lisboa,Lisboa,Portugal

Summary It is well known that different turbulent flows such as jets, wakes, mixing layers, boundary layers, exhibit different entrainment characteristics as attested by their different spreading rates and entrainment velocities. Several direct numerical simulations (DNS) of free turbulent flows, attaining Reynolds numbers of the order of $Re_\lambda \approx 400$, show that when properly normalised, the small scale turbulence quantities governing the entrainment are universal. Specifically, normalised by the local Kolmogorov scales, the profiles of the small scale turbulence statistics within the so called turbulent/non-turbulent interface (TNTI) layer - which separates the flow into a turbulent and a non-turbulent (or irrotational) region - display exactly the same shape and magnitude in jets, wakes and shear free turbulence.

INTRODUCTION

Turbulent entrainment takes place in free shear flows (jets, wakes, mixing layers) and also in boundary layers, and results in some of the most visible features observed in these flows, namely the growth of the shear layer (or turbulent region). It is well known that the entrainment characteristics in these flows are very different *e.g.* planar jets entrain more fluid than circular jets. This can be attested by the very different spreading rates and entrainment velocities that are observed in different turbulent flows [1]. The turbulent entrainment (TE) mechanism occurs across the so called *turbulent/non-turbulent interface* (TNTI), which is a very thin and highly contorted layer, that separates regions of turbulent and non-turbulent (or irrotational) flow [2]. TE can be described by the mechanism by which packets of non-turbulent flow acquire vorticity across the very thin TNTI layer [3]. The turbulence characteristics vary significantly moving from the irrotational region towards the turbulent bulk *e.g.* the enstrophy and viscous dissipation display extremely high spatial gradients inside the TNTI layer, and become statistically uniform once the turbulent bulk of the flow is reached. However, it has been recently established that the TNTI layer possesses a two layers structures: a viscous superlayer (VSL) where viscous effects dominate, and a turbulent sublayer (TSL) where inertial effects dominate and that the thickness of these two sublayers (as well as the total TNTI layer) scales with the Kolmogorov micro-scale, for sufficiently high Reynolds numbers [4]. This result, together with the close relation between the local shape of the TNTI layer and the intense vortices in its vicinity [5] suggests that the Kolmogorov scales can be the key to describe the characteristics of the TNTI layer arising from very different flows, such as wakes and jets.

The entrainment characteristics of turbulent planar jets (PJET), planar wakes (PWAKE) and shear free turbulence (SFT) are assessed by comparing several turbulence statistics across the TNTI layers in these flows, obtained from direct numerical simulations (DNS) which attain Reynolds numbers, based in the Taylor micro-scale, of up to $Re_\lambda \approx 400$.

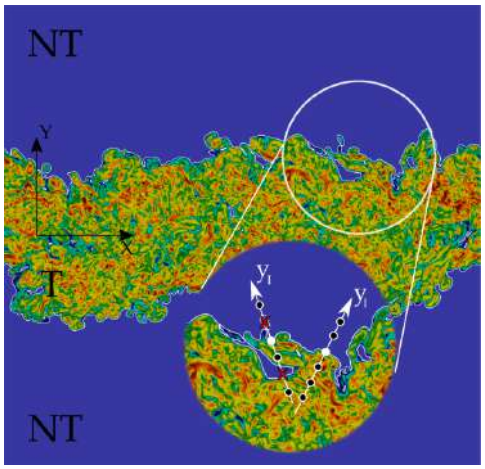

(a)

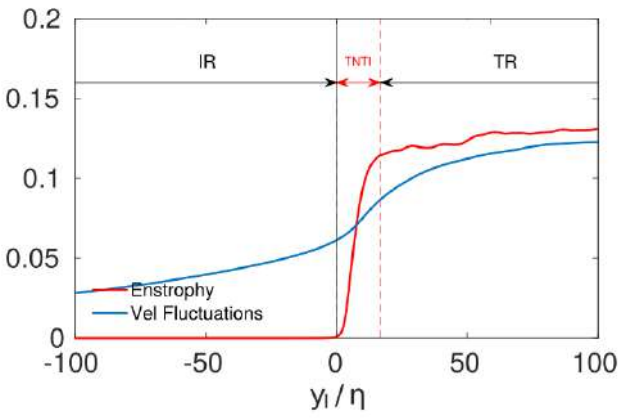

(b)

Figure 1: (a) Planar cut of a 3D vorticity magnitude field of a planar jet representing the TNTI layer separating the turbulent (T) from the non-turbulent (NT) regions. The coordinate system of the plane jet (x, y) and the one used in the conditional statistics in relation to the distance from the TNTI (y_I) are also shown. The conditional points used for the statistics are marked by a black circle whereas the discarded ones are marked by a red cross;(b) Conditional mean profiles of enstrophy and magnitude of the velocity fluctuations (root-mean-square streamwise velocity).

*Corresponding author. E-mail: carlos.silva@ist.utl.pt.

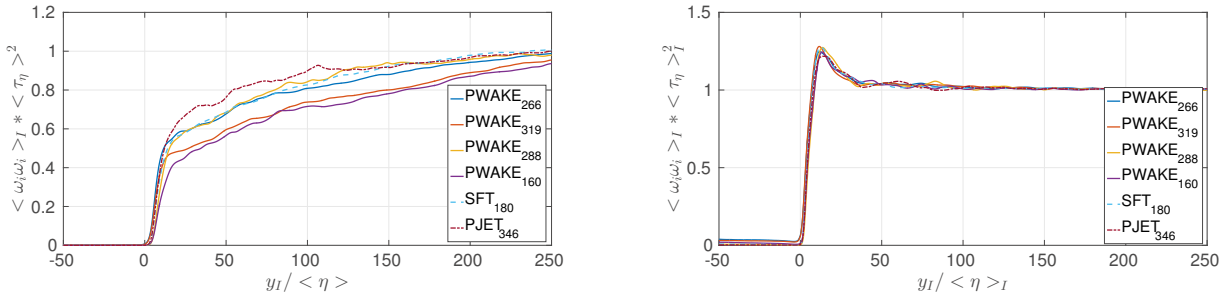

(a) (b)

Figure 2: Conditional mean profiles of enstrophy (normalised by the Kolmogorov velocity u_η, and lenght scale η), in relation to the distance from the irrotational boundary (IB) at the edge of the TNTI layer, y_I, for planar jet (JET), planar wake (WAKE), and shear free turbulence (SFT), normalised by the Kolmogorov micro-scale η: (a) Using a constant Kolmogorov micro-scale η_T taken from the turbulent core region; (b) using a (conditional) mean local Kolmogorov micro-scale $\langle\eta\rangle_I$.

RESULTS AND DISCUSSION

To analyse the TNTI layer it is crucial to use a metric which provides an unambiguous separation between turbulent and irrotational flow data (samples). This is achieved by using conditional statistics in relation to the distance from a given reference point within the TNTI layer. These conditional statistics are obtained rearranging the calculated 3D field as function of the distance from the irrotational boundary (IB), which is the outer surface delimiting the TNTI layer (figure 1 (a)). The conditional mean profiles are then computed in a local coordinate system positioned at the IB (at the edge of the the TNTI layer), and the averaging is computed as function of the distance from the IB. Figure 1 (b) shows the conditional mean profiles of enstrophy and velocity fluctuations normalised by the center line velocity ($\sqrt{\langle u'^2\rangle + \langle v'^2\rangle + \langle w'^2\rangle}/U_c$). The distance to the IB, y_I is normalised by the Kolmogorov length scale η calculated in the turbulent core region of the flow. The IB is fixed at $y_I = 0$, while the irrotational and turbulent regions correspond to $y_I < 0$ and $y_I > 0$ respectively. The enstrophy is zero in the NT region and roughly constant in the T core region, the two regions being linked by characteristic sharp vorticity jump with a thickness close to $\sim 15\eta$. In contrast, the velocities exhibit a very smooth variation across the TNTI layer [6].

Figure 2(a) shows typical conditional mean profiles of vorticity magnitude ($\omega_i\omega_i$) normalised with the mean Kolmogorov time scale obtained from the turbulent core region $\langle\tau_\eta\rangle^2$. In the non-turbulent region, $\omega_i\omega_i$ is zero but advancing towards the turbulent core it grows sharply when crossing the initial part of the TNTI ($\sim 10\eta$). A smoother rise follows until a constant plateau is reached in the turbulent bulk of the shear layer. A relatively good collapse is achieved by normalising these conditional means as $\langle\omega_i\omega_i\rangle_I \cdot \langle\tau_\eta\rangle^2 \approx 1$ due to kinematic constraints. However the profiles obtained from different flows (jets, wakes, shear free turbulence) with different initial conditions, diverges in the proximity of the TNTI layer (i.e. for values of $y_I/\eta \lesssim 150$) due to the different local dynamics of the different flows analysed here. Figure 2(b) plots the conditional profiles of $\langle\omega_i\omega_i\rangle_I$ using local conditional mean Kolmogorov scales $\langle\tau_\eta\rangle_I^2$. It is clear that an excellent collapse is achieved in these figures, which underscores the universality of the small scale motions of different flows within the TNTI layer. Here again $\langle\omega_i\omega_i\rangle_I \cdot \langle\tau_\eta\rangle_I^2 \approx 1$ deep into the turbulent core while it is virtually zero in the non-turbulent region. The steep profiles increment that occur after the IB continue much further until a pronounced peak of $\langle\omega_i\omega_i\rangle_I \cdot \langle\tau_\eta\rangle_I^2 \approx 1.2$ is reached. Afterwards they start decreasing slowly to 1. The peaks location occur in a very narrow range of $y_I/\langle\eta\rangle_I \approx 15$.

More evidences of the universality of small scale motions during the entrainment will be discussed during the presentation.

References

[1] A. A. Townsend. The Structure of Turbulent Shear Flow. Cambridge University Press, 1976.

[2] J. Westerweel and C. Fukushima and J. M. Pedersen and J. C. R. Hunt. Momentum and scalar transport at the turbulent/non-turbulent interface of a jet. In *J. Fluid Mech.*, pp. 199-230, 2009.

[3] C. B. da Silva and J.C.R. Hunt and I. Eames and J. Westerweel. Interfacial layers between regions of different turbulent intensity. In *Annual Review of Fluid Mechanics*, pp. 567-590, 2014.

[4] T. S. Silva, M. Zecchetto and C. B. da Silva. The scaling of the turbulent/non-turbulent interface at high Reynolds numbers. In *J. Fluid Mech.*, pp. 567-590, 2018.

[5] T. Watanabe and R. Jaulino and R. R. Taveira and C. B. da Silva and K. Nagata and Y. Sakai Role of an isolated eddy near the turbulent/non-turbulent interface layer. In *Phys. Rev. Fluids*, 094607, 2017.

[6] M. Holzner and A. Liberzon and N. Nikitin and W. Kinzelbach and A. Tsinober Small-scale aspects of flows in proximity of the turbulent/nonturbulent interface. In *Phys. Fluids*, 071702, 2007.

ON THE TORIC SYMMETRY OF TURBULENT CHANNEL FLOWS

Chiara Pilloton*[1,3], Francesco Fedele[2], Claudio Lugni[3], and Giorgio Graziani[1]
[1]Department of Mechanical and Aerospace Engineering, Sapienza Università di Roma, Roma, Italy
[2]School of Civil and Environmental Engineering, Georgia Institute of Technology, Atlanta, USA
[3]CNR-INM, Institute of Marine Engineering, Via di Vallerano 139, 00128 Roma, Italy

Summary In the last century, the study of turbulence has been approached following the great Kolmogorov's physical insights on the inertial energy cascade and, more recently by investigating the geometry of the state space of the Navier-Stokes equations treated as a dynamical system. Such novel geometric approach arises from the evidence that what is observed in physical space sometimes is not always suggestive of the hidden laws of physics of the turbulent motion. Thus, looking at the turbulent dynamics in state space may lead to new understanding of the associated physical processes. In particular, vortices in a channel flow change shape as they are transported by the mean flow at the Taylor speed, or dynamical velocity. Reducing the translational or Toric symmetry in state space reveals that the shape-changing dynamics of vortices influences their own motion and it induces an additional self-propulsion velocity, the so-called geometric velocity. Thus, in strong turbulence the Taylor's hypothesis of frozen vortices is not satisfied because the geometric velocity can be significant.

RESULTS

Symmetry reduction approaches [1, 2, 3] provide a new way to understand the vortical motion of turbulence. This depends on the inertia of the flow and on its own shape-changing form over time. Because of the inertia of the flow, vortices are transported at roughly the Taylor speed, the so-called dynamical velocity V_{dyn} [2]. If turbulent fluctuations are significant, vortices change shape over time as they are transported by the mean flow. Their shape-changing dynamics induces an additional self-propulsion velocity, the so-called geometric velocity V_{geom} [2]. Thus, in strong turbulence the Taylors hypothesis of frozen vortices is not satisfied since the geometric velocity is not negligible over the Kolmogorov's inertial range.

The Navier-Stokes (NS) equations for channel flows have translational symmetry, that is if the fluid velocity $u(x,t)$ and associated pressure $p(x,t)$ fields are solutions, so are the space-shifted $u(x+L,t)$ and $p(x+L,t)$, where L is the shift. From a dynamical system perspective, if symmetry is present, the velocity V of the vortical motion can be uncoupled in the sum of dynamical and geometric components [2]

$$V = V_{dyn} + V_{geom}. \tag{1}$$

Such uncoupling is clearly observed in state space, and symmetry can be reduced or quotiented out to reveal the pure motion solely due to turbulence. The desymmetrized state space reveals how i) vortices change shape over time and how ii) their shape-changing influences their own motion. The Fourier representation of the velocity field is

$$u(x,t) = \sum_{-N}^{N} z_n(t) e^{ik_0 n x} \tag{2}$$

and the NS state space is $\mathbb{C}^N = \mathbb{R}^{2N}$, where N is the number of Fourier modes. We collect the Fourier modes z_n in a vector z and the NS equations can be rewritten as

$$\dot{z} = F(z), \tag{3}$$

where $F(z)$ is a nonlinear operator of z. Translational symmetry in physical space becomes a Toric symmetry (T-symmetry) in Fourier space, i.e. if the set (z_n) of Fourier modes is a solution of Eq. (4), so is $(z_n \exp(ik_0 L))$, for any shift L. The state space $\mathbb{C}^N$ has the geometric structure of a fiber bundle (see [2] and references therein). The bundle is made of a base or shape manifold $B = \mathbb{C}^N|\mathbb{R}$ of dimensions $\mathbb{R}^{2N-1}$ and 1D fibers along the direction of T-symmetry that attach to any point of B as shown in Figure 1a.

The T-symmetry can be reduced by devising a reduction map π that maps trajectories or orbits $z(t)$ of $\mathbb{C}^N$ onto desymmetrized orbits $Z_D(t)$ of the base manifold B, as illustrated in Figure 1a. The map π is invariant under the T-symmetry and it can be interpreted as a coordinate change transformation that allows for a map representation of the abstract base manifold. There are infinite ways to represent such manifold, i.e Mercatore projection, stereographic projections, etc. The desymmetrized orbit $Z_D(t)$ depends only on the shape-changing dynamics of vortices as in the motion of a jellyfish. Geometric and dynamical velocities allow studying the motion of the vortical motion in the desymmetrized frame. Figure 1b shows the mean velocity profile V of a turbulent channel flow at $Re = 3300$ $(Re_\tau = 180)$. The regime of turbulence is strong and the Taylor hypothesis is not satisfied. The dynamical velocity V_{dyn} is estimated as if vortices are transported by and frozen in the flow. V_{dyn} underestimates the observed mean velocity and the geometric component V_{geom} is not negligible, indicating that the shape-changing of vortices affects their own speed.

*Corresponding author. E-mail: chiara.pilloton@uniroma1.it

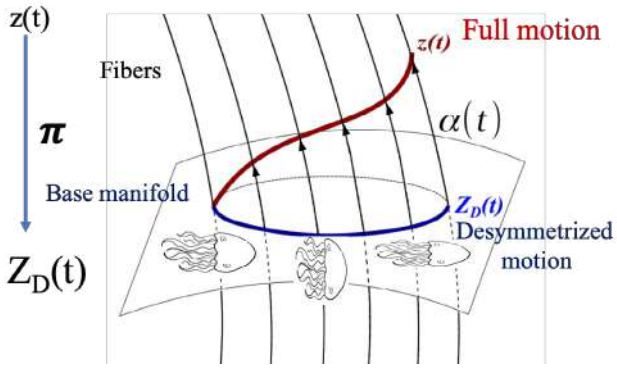

(a) Desymmetrization concepts

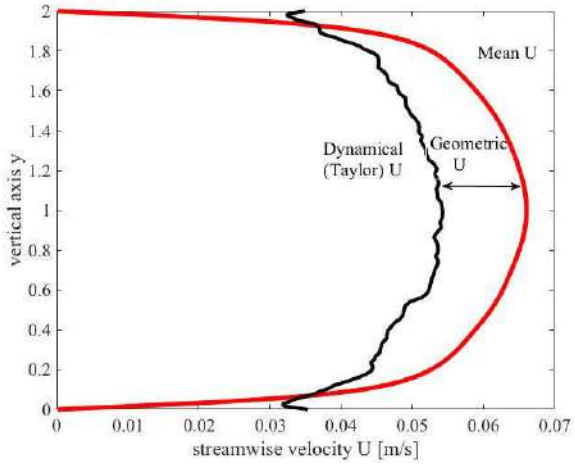

(b) Dynamic and geometric velocity components

The group orbit of a trajectory $z(t)$ is a sheet of the fiber bundle and it is defined as

$$\begin{cases} G(z) = \{G_\alpha(z(t)) \quad \forall\, t\} \\ G_\alpha(z(t)) = \left\{z_n(t)e^{in\alpha}, \quad \alpha \in [0\ 2\pi]\right\} \end{cases} \tag{4}$$

Typical group orbits of $\mathbb{C}^N$, visualized in a 3D subspace, are depicted in Figures 2a and 2b. The simulated full trajectory or orbit $z(t)$ (black line), the orbit in the comoving frame (yellow line) and the desymmetrized orbit $Z_D(t)$ (blu line) are also shown. The comoving frame trajectory is that seen from a frame that moves with the dynamical velocity V_{dyn}. The desymmetrized trajectory is seen from a frame that moves at the total speed $V = V_{dyn} + V_{geom}$, sum of the dynamical and geometrical velocities.

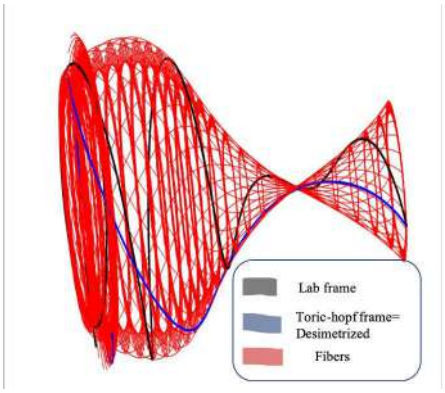

(a) U streamwise velocity component

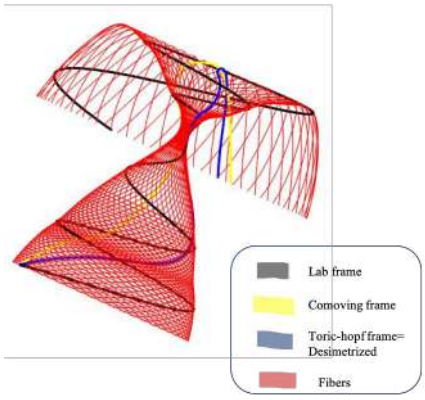

(b) Spanwise vorticity component

Figure 2: Group orbit of DNS turbulent channel flow

CONCLUSIONS

Symmetry reduction approaches are new ways to study the anatomy of the vortical motion in channel flows. Because of the inertia of the flow, vortices are transported at the Taylor speed, the so-called dynamical velocity [2]. When the vortex shape changes over time, it induces an additional self-propulsion velocity, the so-called geometric velocity [2]. Thus, in strong turbulence the Taylor's hypothesis of frozen vortices is not satisfied since the geometric velocity is not negligible.

References

[1] Cvitanović, P., Artuso, R., Mainieri, R., Tanner, G., Vattay, G., Whelan, N., and Wirzba, A. (2005). Chaos: classical and quantum. *ChaosBook. org (Niels Bohr Institute, Copenhagen 2005)*, 69.

[2] Fedele, F., Abessi, O., and Roberts, P. J. (2015). Symmetry reduction of turbulent pipe flows. *Journal of Fluid Mechanics*, 779:390–410.

[3] Willis, A. P., Cvitanović, P., and Avila, M. (2013). Revealing the state space of turbulent pipe flow by symmetry reduction. *Journal of Fluid Mechanics*, 721:514–540.

NETWORK-BASED INVESTIGATION OF TURBULENT MIXING IN AN INHOMOGENEOUS FLOW

Davide Perrone*[1], Hans Kuerten[2], Luca Ridolfi[3], and Stefania Scarsoglio[1]
[1]Department of Mechanical and Aerospace Engineering, Politecnico di Torino, Turin, Italy
[2]Department of Mechanical Engineering, Eindhoven University of Technology, Eindhoven, The Netherlands
[3]Department of Environmental, Land and Infrastructure Engineering, Politecnico di Torino, Turin, Italy

Summary To date, many aspects of turbulent mixing require a better and more detailed understanding. Added clarity may be provided by the use of novel approaches such as those based on complex networks, one of which will be presented in this work. The network here proposed aims specifically to describe turbulent mixing in the inhomogeneous direction of a numerically resolved channel flow at $Re_\tau = 950$; this is done using as a starting point Lagrangian data, in the form of the trajectories of a set of tracers released in the channel. Such an approach makes it possible to thoroughly analyse the transient phase before the Taylor regime, the spatial heterogeneities of tracers and the formation of spatial and temporal zoning.

INTRODUCTION

Turbulent mixing is a primary constituent of a huge variety of different phenomena, such as the diffusion of pollutants in the atmosphere or the blending of chemical reactants. Further investigation is needed to better understand its properties, especially its ability to enhance transport [1]. The Lagrangian perspective appears appropriate for this kind of study, since it makes it possible to directly follow the motion of tracers which experience mixing [4]. Complex networks have been already successfully applied to a range of different fields, including biology and social network [2][3]. Their exploitation in the study of turbulence is rather recent but promising, since they allow one to properly represent the temporal and spatial complexity of turbulent flows and are an innovative tool to enrich classical statistical analysis [5][6][7].

DATASET AND NETWORK DEFINITION

The Lagrangian dataset employed in this work consists of the trajectories of $N_p = 10^4$ non inertial tracers released in a turbulent channel flow. The channel flow is simulated by means of direct numerical simulation at a frictional Reynolds number $Re_\tau = \delta u_\tau/\nu = 950$, where δ, u_τ, and ν are the channel half height, the friction velocity and the kinematic viscosity, respectively [8]. The trajectories are integrated for the entire simulation time, which is $T^+ = 15\,200$. At their release, tracers are disposed in $N_l = 100$ equispaced levels along the inhomogeneous direction, which is y; their position is shown in Figure 1(a). The network is specifically designed to describe the mixing of tracers starting from different levels. Indeed, each level constitutes a node in the network, while a connection between nodes is established according to the motion of tracers along y^+. In details, a link between levels i and j exists at any given time if a tracer, released at $t^+ = 0$ inside level i, reaches level j. This leads to the definition of a network composed by $N_l = 100$ nodes, which is *directed* since it retains information about the directional motion of tracers. Moreover, a weight is associated to each link, namely the number of tracers moving between different levels (normalized by the number of tracers present in each level at their release, that is 100). Figure 1(b) contains a simplified representation of the trajectories of particles in and out of levels located at different y coordinates. The mixing process can be fully described by the transport network $\mathbf{W}(t^+)$; the weight matrix of this simplified representation is shown in 1(c), along with the ingoing strength $s_i^{\mathrm{IN}} = \sum_{j=1}^{N_l} W_{ji}$ of the four nodes, which is the sum of weights of incident links and is proportional to the number of tracers moving inside a node at a given time.

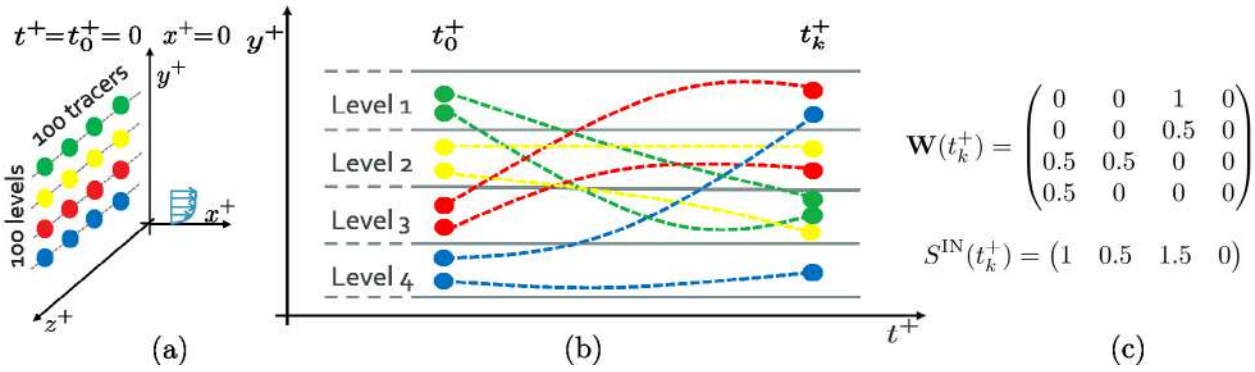

Figure 1: (a) Schematics of the release pattern of tracers, organized in N_l equispaced levels on the $x^+ = 0$ plane; (b) schematics of the motion of tracers between different levels, leading to the definition of the network weight matrix $\mathbf{W}$; (c) network weight matrix $\mathbf{W}$ and ingoing strength s^{IN} for the simplified representation of 1(b). All values in $\mathbf{W}$ are normalized by 2 (*i.e.* the number of particles originally present in each level); the values on the main diagonal are always zero since nodes cannot have self loops.

*Corresponding author. E-mail: davide.perrone@polito.it

RESULTS

The geometrization of the particle dynamics provided by the network definition allows us to highlight several features of the mixing phenomenon. The time dependent weight matrices $\mathbf{W}(t^+)$ immediately characterize the extent of mixing between initially distant levels. While for short times (Figure 2(a), $t^+ = 240$) the motion of tracers is confined to levels close to the release location and thus only the elements of $\mathbf{W}$ close to the diagonal are non-zero, for longer times (Figure 2(b), $t^+ = 14\,250$) particles are diffused everywhere across the channel and any information about their starting coordinates is lost. Applying metrics designed for directed networks to the weight matrix $\mathbf{W}$ enables us to thoroughly describe the motion of particles. For instance, the ingoing strength of each node $s^{\mathrm{IN}}(t^+)$ is directly related to the concentration of tracers at any time. As it is shown in Figure 2(c), two main phases in the evolution of the flow are evident: for short times ($t^+ < T_d^+$, $T_d^+ \approx 4000$) the concentration of tracers is highly inhomogeneous, while for larger times ($t^+ > T_d^+$) the vertical mixing of particles is completed and the Taylor dispersion regime is reached. The network formalism is able to capture both the complexity of the irregular, transient phase, and the onset of the asymptotic behaviour. The tools introduced by graph theory may also be exploited to highlight non trivial features which are difficult to notice using statistical methods. The analysis of the physical length of links measures the spatial extent reached by diffusion and also signals the presence of tracers trapped near the channel walls and far away from their starting level. The increase in link length is related to the displacement of tracers towards the channel walls during the initial transient, as can be seen in Figure 2(c). Additionally, common and fast tools developed to find communities in graphs may be used to partition the network into regions of the channel that exchange a reduced amount of tracers between them. Community detection performed in the channel flow is useful to determine the spatial extent of turbulent mixing at different times and highlights the existence of two separate regions near the channel walls.

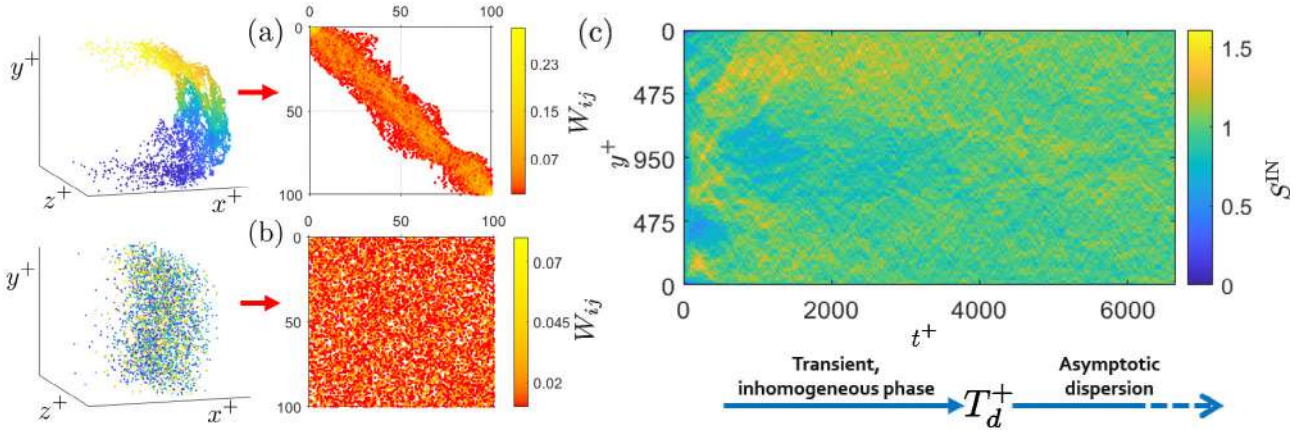

Figure 2: (a) Distribution of particles and network weight matrix at $t^+ = 240$; (b) Distribution of particles and network weight matrix at $t^+ = 14\,250$; (c) the evolution of the ingoing strength s^{IN} of nodes emphasizes both the details of particle motion across the channel and the presence of different regimes in the dispersion process; the onset of the Taylor asymptotic regime ($T_d^+ \approx 4000$) marks the shift between a highly irregular concentration of tracers and a more homogeneous one.

CONCLUSIONS

These findings show both the effectiveness of methods based on network theory and the suitability of the Lagrangian framework for the analysis of turbulent mixing. The complexity of the starting transient and the shift to the asymptotic dispersion regime are well outlined by the network representation of vertical motion inside the channel. Exploitation of the capabilities of the tools presented here offers an in-depth look on the collective and individual behaviour of diffusing tracers in wall bounded turbulence, highlighting their concentration, their trapping in persistent flow structures and their presence in isolated communities [9].

References

[1] Dimotakis P. E. Turbulent mixing. *Annu. Rev. Fluid Mech.*, **37**:329–356, 2005.
[2] Boccaletti, S. et al. Complex networks: Structure and dynamics. *Phys. Rep.* **424.4-5**: 175-308, 2006.
[3] Costa, L. et al. Analyzing and modeling real-world phenomena with complex networks: a survey of applications. *Adv. Phys* **60.3**: 329-412, 2011.
[4] Stelzenmuller N. et al. Lagrangian acceleration statistics in a turbulent channel flow. *Phys. Rev. Fluids* **2.5**:054602, 2017.
[5] Iacobello G. et al. Visibility graph analysis of wall turbulence time-series. *Phys. Lett. A* **382.1**: 1-11, 2018.
[6] Iacobello G. et al. Lagrangian network analysis of turbulent mixing. *J. Fluid Mech* **865**: 546–562, 2019.
[7] Iacobello G. et al. Spatial characterization of turbulent channel flow via complex networks. *Phys. Rev. E* **98.1**:013107,2018.
[8] Kuerten J.G.M., Brouwers J.J.H. Lagrangian statistics of turbulent channel flow at $Re_\tau = 950$ calculated with direct numerical simulation and Langevin models. *Phys. Fluids*, **25**(10):105108, 2013.
[9] Perrone D. et al. Wall-induced anisotropy effects on turbulent mixing in channel flow: A network-based analysis. *Phys. Rev. E* **102.4**:043109,2020.

DYNAMICS OF SHEAR-LAYER COHERENT STRUCTURES IN A FORCED WALL-BOUNDED FLOW

Petrônio A.S. Nogueira[1] and André V.G. Cavalieri*[1]
[1]Divisaõ de Engenharia Aeronáutica, Instituto Tecnológico de Aeronáutica, São José dos Campos, SP, Brazil

Summary A model problem for analysing the interaction between coherent structures in shear flows with the presence of a convective instability is proposed. Starting from Couette flow, a permanent forcing in the shape of a hyperbolic tangent is introduced, leading to a wall-bounded flow with an inflection point, triggering a Kelvin-Helmholtz (KH) hydrodynamic instability. Due to the presence of shear, streaks and rolls are also present in the flow, and these structures interact with KH-vortices via oblique waves. Results from direct numerical simulation exhibit a limit cycle involving streaks, vortices, rolls and oblique waves. The flow dynamics reproduce some of the features of jets and mixing layers, such as jitter and translational instability, showing that the present simplified flow model can potentially clarify some of the phenomenon involved in turbulence dynamics.

INTRODUCING THE FLOW MODEL

The present work focuses on analysing the interaction between streamwise elongated, spanwise organised structures (rolls and streaks) and Kelvin-Helmholtz-like vortices, both coherent structures present in turbulent jets [2, 4]. For that, we introduce a novel flow model in which both structures are present, but with a simpler wall-bounded configuration that prevents streamwise inhomogeneity. We consider a laminar Couette flow between two walls at $y = \pm h$, moving with velocity $\pm U_e$. In this flow we introduce a steady forcing, independent of span and streamwise coordinates, in the shape of a hyperbolic tangent in the wall-normal direction y, which is given by the expression $f_P = P_A \tanh(P_B y)$. By introducing this forcing in the laminar streamwise momentum equation, subject to no-slip boundary conditions, the laminar solution can be directly obtained as a function of the parameters P_A and P_B, and the Reynolds number Re. The body force leads to positive (respectively negative) streamwise forcing for $y > 0$ (respectively $y < 0$), which increases velocity gradients in the central region of the flow and creates an inflection point at the centre of the channel. For the present case, we chose P_A such that $\partial U/\partial y = 0$ on the walls, and $P_B = 5$ for a sharp gradient of the body force around $y = 0$, which may nonetheless be numerically resolved with a low number of grid points, and $Re = 200$. The base flow and its wall-normal derivatives for the present choice of parameters can be seen in figure 1(a).

Despite the simplicity of the model, this is a new baseflow and should be appropriately characterised, especially concerning its stability and the amplification of flow disturbances. This was be assessed by means of linear stability analysis and resolvent analysis, pointing to unstable Kelvin-Helmholtz vortices for streamwise/spanwise wavenumbers $(k_x, k_z) = (0.5, 0)$, which leads to structures with zero phase velocity, and highly amplified streaks for $(k_x, k_z) = (0, 1)$.

DIRECT NUMERICAL SIMULATION

From the results of locally parallel analyses, a computational box for a direct numerical simulation (DNS) was designed. Since we are interested in evaluating the interaction between vortices, streaks and other structures, the computations should allow for the growth of the unstable mode at this Reynolds number. Therefore, a box size of $(L_x, L_y, L_z) = (4\pi, 2, 2\pi)$ was chosen, enabling the growth of modes associated to $k_x = 0.5$, which is the sole unstable mode for this case. The box size also enables structures related to $(k_x, k_z) = (0, 1)$, related to the energetic streaks found using resolvent analysis. The present simulation was performed with $(N_x, N_y, N_z) = (32, 65, 32)$ collocation points before dealiasing.

The simulation was started with spatial white-noise, and velocity fields were stored for post-processing. The importance of streaks and vortices in this flow is reinforced by simply looking at the streamwise/wall-normal velocity field at a given simulation time. Isocontours of 60% of maximum streamwise velocity at a sample time ($t = 1930$) are shown in figure 1(a), and streaky structures similar to the ones found in the analysis of [3] can be clearly spotted; the high energy of such structures facilitate their identification in the raw velocity field. At this time, Kelvin-Helmholtz vortices are less energetic, and can only be seen by taking the spanwise mean of the velocity field. Contours of this structure are depicted in the slices shown in figure 1(b).

Looking at the energy of each combination of wavenumbers in the simulation, a limit cycle could be identified, and the energy of the most relevant modes for a single cycle can be seen in figure 2. Clearly, the streaky mode $(k_x, k_z) = (0, 1)$ has most of the energy of this flow for almost all times, with some regions of sharp decay, pointing to an intermittent cancellation of this mode, with alternating positive and negative streaks in a given position of the channel. The vortex, i.e. $(k_x, k_z) = (0.5, 0)$, on the other hand, has intervals of exponential growth and decay, and is never totally damped in the flow. Other modes are also important in the flow dynamics: the oblique wave mode $(0.5, 1)$, for instance, has a higher energy growth at some times compared to the vortex mode, even though it is also subject to a cancellation at other parts of the cycle. Isolating the (v, w) components of mode $(0, 1)$, the energy related to rolls (streamwise vortices) can be extracted; considering that these structures are closely linked to streaks via the lift-up effect, it is expected that these also

*Corresponding author. E-mail: petronio.augusto@gmail.com.

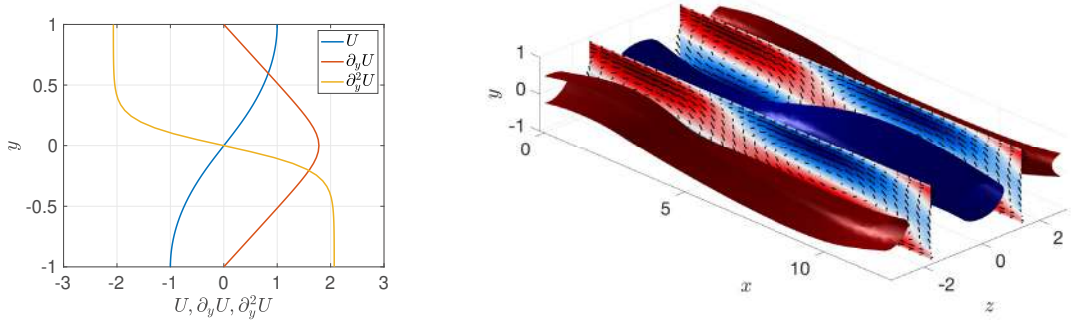

(a) Base flow (b) Streaks and vortices in the flow

Figure 1: (b) Base-flow and its wall-normal derivatives for the present flow case. (a) Isocontours of 60% of positive (red) and negative (blue) maximum streamwise velocity at $t = 1930$. Slices show the field resulting from the spanwise average of the velocity at $t = 1930$, where Kelvin-Helmholtz vortices can be clearly spotted. Colours indicate streamwise velocity fluctuations and arrows depict streamwise and wall-normal. velocity fluctuations.

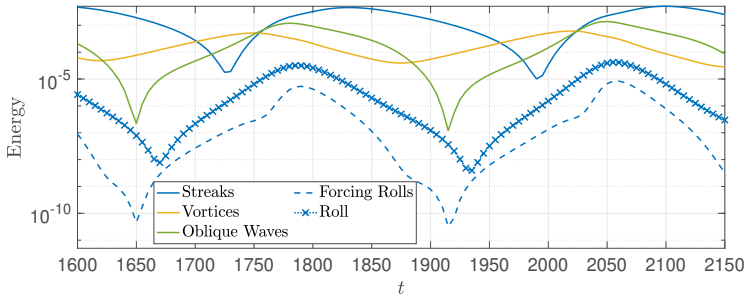

Figure 2: Energy of the different modes involved in the dynamics as a function of time. Dashed line represents the energy related to the forcing of mode $(k_x, k_z) = (0, 1)$ and the symbols depicts the energy related to the (v, w) velocity field of mode $(k_x, k_z) = (0, 1)$.

play a role in this case. Figure 2 also depicts the energy related to the $(0, 1)$ component of the non-linear terms, which also affects directly the time-evolution energy of the rolls. Our current analysis of the limit cycle shows a self-sustaining process, where non-linear interactions of vortices and oblique waves excite rolls of opposite sign of existing ones; rolls cancel existing streaks and create new streaks of opposite sign; and stability of the streaky mean flow leads to new oblique waves of opposite phase, restarting the cycle with a π phase jump.

CONCLUSIONS AND PERSPECTIVES

The present work introduces a flow model that includes the most important coherent structures in jets and mixing layers. To study such flow, a computational box for direct numerical simulation was designed based on the optimal wavenumbers from stability and resolvent analyses. Results from the simulation display a limit cycle involving streaks, vortices, oblique waves and rolls, and a clear dynamics between these modes is observed. We plan to further study this limit cycle by using linear analyses and by computing directly the relevant non-linear terms, so that all the steps of the cycle are clarified. The present results already show several similarities with the behaviour of jets and mixing layers, reproducing a simplified jitter phenomenon [1] and keeping some of the characteristics of a translational instability mechanism [5]. Considering the simplicity of the model and its characteristics (which could be compared to a "minimal jet unity"), such study has considerable potential for the study of coherent structures in free-shear turbulence.

References

[1] A. V. G. Cavalieri, P. Jordan, A. Agarwal, and Y. Gervais. Jittering wave-packet models for subsonic jet noise. *Journal of Sound and Vibration*, 330(18-19):4474–4492, 2011.

[2] A. V. G. Cavalieri, D. Rodríguez, P. Jordan, T. Colonius, and Y. Gervais. Wavepackets in the velocity field of turbulent jets. *Journal of Fluid Mechanics*, 730:559–592, 9 2013.

[3] J. M. Hamilton, J. Kim, and F. Waleffe. Regeneration mechanisms of near-wall turbulence structures. *Journal of Fluid Mechanics*, 287:317–348, 1995.

[4] P. A. S. Nogueira, A. V. G. Cavalieri, P. Jordan, and V. Jaunet. Large-scale streaky structures in turbulent jets. *Journal of Fluid Mechanics*, 873:211–237, 2019.

[5] R. T. Pierrehumbert and S. E. Widnall. The two- and three-dimensional instabilities of a spatially periodic shear layer. *Journal of Fluid Mechanics*, 114:59–82, 1982.

HIERARCHY OF COHERENT STRUCTURES AND ENERGY CASCADE IN WALL-BOUNDED TURBULENCE

Yutaro Motoori*and Susumu Goto
Graduate School of Engineering Science, Osaka University, 1-3 Machikaneyama, Toyonaka, Osaka, 560-8531, Japan

Summary By applying a Gaussian filter to the velocity fields in turbulent channel flow at the friction Reynolds number $Re_\tau \approx 4200$, we decompose the turbulence into different scales. Then, we identify the hierarchy of vortices and low-speed structures depending on the scale and height from the wall. For examining its generation mechanism, we also quantify the inter-scale energy transfer. The largest-scale structures at each height (wall-attached structures) are composed of quasi-streamwise vortices and low-speed streaks. Since these are similar to the well-known coherent structures in the buffer layer, they are likely to be maintained by the hierarchical self-sustaining process, in which the source of the energy is the mean flow. On the other hand, structures smaller than the height are generated by the energy cascade; the energy of these small-scale structures is transferred predominantly from twice-larger-scale structures and reduced by half-scale structures.

BACKGROUND AND SCOPE

The sustaining mechanism of wall-bounded turbulence at low Reynolds numbers is well known (for example, Ref. [1]). However, as the Reynolds number increases, the sustaining mechanism becomes complicated due to the appearance of the hierarchy of multiscale vortices. This is the reason why we must identify the hierarchy of coherent vortices to understand the sustaining mechanism of high-Reynolds-number turbulence. However, the extraction of multiscale vortices is difficult because the magnitude of the velocity gradient is predominantly determined by the smallest scale. In our previous studies [2, 3], by coarse-graining turbulent fields, we overcame this difficulty and identified the hierarchy in a turbulent boundary layer at $Re_\tau \approx 1000$. In the present study, for turbulent channel flow [4] at a higher Reynolds number ($Re_\tau \approx 4200$), we identify the hierarchical structures to understand their sustaining mechanism. For this purpose, we extract the hierarchy of vortices, and also quantify the real-space energy transfer.

HIERARCHY OF VORTICES AND LOW-SPEED STREAKS

To extract the hierarchy in turbulence, we use a band-pass filter, which was also used in our previous study [3]. First, we apply the Gaussian filter

$$u_i^{(\sigma)\mathrm{low}} = C(y) \int_{V(\boldsymbol{x}|\sigma)} u_i'(\boldsymbol{x}') \exp\left(-\frac{2}{\sigma^2}(\boldsymbol{x}-\boldsymbol{x}')^2\right) \mathrm{d}\boldsymbol{x}' \quad (1)$$

to the fluctuating velocity fields u_i', where C is the coefficient to ensure that the integration of the filter gives unity and σ denotes the filter scale. For the wall-normal direction y, we use the method proposed by Lozáno-Durán *et al.* [5]. Next, we take the difference between the low-pass filtered fields $u_i^{(\sigma)\mathrm{low}}$ at two different scales, i.e.

$$u_i^{(\sigma)} = u_i^{(\sigma)\mathrm{low}} - u_i^{(2\sigma)\mathrm{low}}. \quad (2)$$

This filter corresponds to a band-pass filter of the Fourier modes because $u_i^{(\sigma)}$ has the contributions only from around the scale σ. All the scale-decomposed quantities $\cdot^{(\sigma)}$ (e.g., the second invariant $Q^{(\sigma)}$ of the velocity gradient tensor) are evaluated from $u_i^{(\sigma)}$. Figure 1 shows positive isosurfaces of $Q^{(\sigma)}$ at three different scales $\sigma^+ = 960$ (red), 240 (yellow) and 60 (blue). Here, $\cdot^+$ denotes the wall unit. We see that the identified structures are approximately in the filter scale. We emphasize that these hierarchies cannot be identified without a scale-decomposition (see figures 3 and 4 in Ref. [2]).

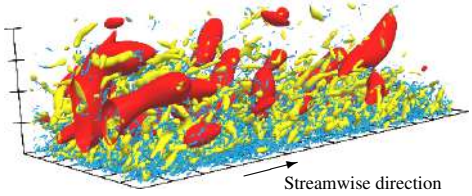

Figure 1: Hierarchy of vortices identified by positive isosurfaces of $Q^{(\sigma)}$ at three scales $\sigma^+ = 960$ (red), 240 (yellow) and 60 (blue). The grid width indicates 1000 wall units.

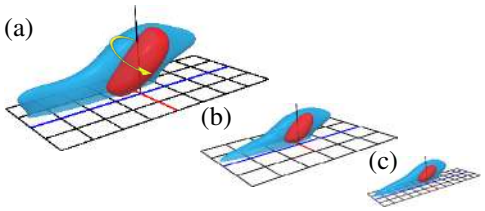

Figure 2: The hierarchy of quasi-streamwise vortices and low-speed streaks identified by isosurfaces of conditional averages of $Q^{(\sigma)}$ (red) and $u^{(\sigma)}$ (blue) at (a) $y_c^+ = \sigma^+ = 960$, (b) 240 and (c) 60. The grid width indicates the filter scale σ.

The analysis of the scale-decomposed fields enables us to reveal the nature of the hierarchy. To show that the largest-scale structures at each height ($\sigma = y$) are similar to coherent structures in the buffer layer, we take conditional averages. When $Q^{(\sigma)}$ at a height y_c is larger than the standard deviation and the streamwise vorticity $\omega_x^{(\sigma)}$ is positive, we take averages of $Q^{(\sigma)}$ and $u^{(\sigma)}$ around the point satisfying these conditions. This conditional averaging leads to the average distributions of $Q^{(\sigma)}$ and $u^{(\sigma)}$ around the largest-scale vortices. Figure 2 shows the isosurfaces of the conditional averages of $Q^{(\sigma)}$ (red) and $u^{(\sigma)}$ (blue) for (a) $\sigma^+ = y_c^+ = 960$, (b) 240 and (c) 60. We see that visualized structures are a quasi-streamwise vortex (red) and low-speed streak (blue), which implies that they are likely to be maintained by the self-sustaining process (SSP). Since such processes occur simultaneously at different heights, we call them the hierarchical SSP.

*Corresponding author. E-mail: y_motoori@fm.me.es.osaka-u.ac.jp

SUSTAINING MECHANISM OF THE HIERARCHY

To investigate the sustaining mechanism of the hierarchy, we quantify two types of the scale-dependent energy transfers. First, we define the energy transfer at the scale $\sigma_{\rm to}$ from the mean flow as

$$Pr(\mathrm{M} \to \sigma_{\rm to}; y) = -\overline{u_i^{(\sigma_{\rm to})} u_j^{(\sigma_{\rm to})}} \frac{\partial \overline{u_i}}{\partial x_j} = -\overline{u^{(\sigma_{\rm to})} v^{(\sigma_{\rm to})}} \frac{\partial \overline{u}}{\partial y}, \tag{3}$$

where $\bar{\cdot}$ denotes the average in the spanwise and streamwise directions and time. We then define the inter-scale energy transfer from $\sigma_{\rm fr}$ to $\sigma_{\rm to}$ as

$$Tr(\sigma_{\rm fr} \to \sigma_{\rm to}; y) = -\overline{u_i^{(\sigma_{\rm fr})} u_j^{(\sigma_{\rm fr})} \frac{\partial u_i^{(\sigma_{\rm to})}}{\partial x_j}} - \left(\overline{-u_i^{(\sigma_{\rm to})} u_j^{(\sigma_{\rm to})} \frac{\partial u_i^{(\sigma_{\rm fr})}}{\partial x_j}} \right). \tag{4}$$

Since these are scale-dependent quantities, they are not in the equation of the (mean) turbulent kinematic energy. However, as Kawata and Alfredsson [6] showed, these terms are in the equation of the scale-dependent energy, which is derived by decomposing the velocity into two scales with an orthogonal filter. Although our decomposition is not orthogonal, similarly to Ref. [6], we interpret $Pr(\mathrm{M} \to \sigma_{\rm to})$ as the energy transfer to the scale $\sigma_{\rm to}$ from the mean flow and $Tr(\sigma_{\rm fr} \to \sigma_{\rm to})$ as the inter-scale energy transfer from $\sigma_{\rm fr}$ to $\sigma_{\rm to}$.

We show, in figure 3, Tr (open circles) and Pr (closed circles) for $\sigma_{\rm to}^+ = 960$ (red), 240 (yellow) and 60 (blue) in the log layer ($y^+ = 960$). Looking at Tr, we see that the contributions from the larger scale ($\sigma_{\rm fr} > \sigma_{\rm to}$) are positive, whereas those from the smaller scale ($\sigma_{\rm fr} < \sigma_{\rm to}$) are negative. This implies that the energy is forwardly transferred on average. Among the contributions, those from the twice larger scale $Tr(2\sigma_{\rm to} \to \sigma_{\rm to})$ and half one $Tr(\sigma_{\rm to}/2 \to \sigma_{\rm to})$ are most important. Note that Pr (closed circles) is larger for larger scales. To investigate the generation mechanism of the energy for a given scale $\sigma_{\rm to}$ and a given height y, we show in figure 4 the ratio Γ of $Tr(2\sigma_{\rm to} \to \sigma_{\rm to})$ to $Pr(\mathrm{M} \to \sigma_{\rm to})$. If $\Gamma > 1$, the energy for the scale $\sigma_{\rm to}$ at height y is generated by the energy cascade; otherwise, the energy is directly produced by the mean flow. The blue dashed line indicates $y = 3\sigma$. We can see that this line is in good agreement with $\Gamma = 1$, which corresponds to the qualitative change of the generation mechanism. Therefore, we conclude that, in the log and buffer layers, the largest-scale ($\sigma \gtrsim y/3$) energy is directly produced by the mean flow, which is related to the SSP, whereas small scales ($\sigma \lesssim y/3$) are generated by the energy cascade.

We have shown that the spatial structures and sustaining mechanism of the hierarchical structures in turbulent channel flow [7]. The keys to these analyses are the scale-decomposition defined by (2) and the quantification of the real-space energy transfer defined by (3) and (4). The main result is the qualitative change (from the hierarchical SSP to the energy cascading process) of the sustaining mechanism at the scale $\sigma \approx y/3$ of vortices of the scale σ at height y (figure 4).

References

[1] Jeong J., Hussain F., Schoppa W. and Kim J. *J. Fluid Mech.* **332**: 185–214, 1997.
[2] Motoori Y. and Goto S. *J. Fluid Mech.* **865**: 1085–1109, 2019.
[3] Motoori Y. and Goto S. *J. Fluid Sci. Technol.* **14**: JFST0016, 2019.
[4] Lozano-Durán A. and Jiménez J. *Phys. Fluids* **26**: 011702, 2014.
[5] Lozano-Durán A., Holzner M, and Jiménez J. *J. Fluid Mech.* **803**: 356–394, 2016.
[6] Kawata T. and Alfredsson P. H. *Phys. Rev. Lett.* **120**: 244501 2018.
[7] Motoori Y. and Goto S. *J. Phys.: Conf. Ser.* to be published in March 2020.

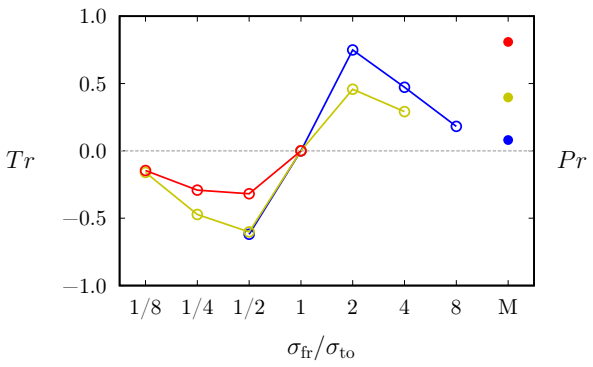

Figure 3: Tr (open circles) and Pr (closed circles) for scales $\sigma_{\rm to}^+ = 960$ (red), 240 (yellow) and 60 (blue) at $y^+ = 960$. Larger-scale energy tends to be produced by the mean flow, whereas smaller-scale energy is transferred from the twice-larger scale.

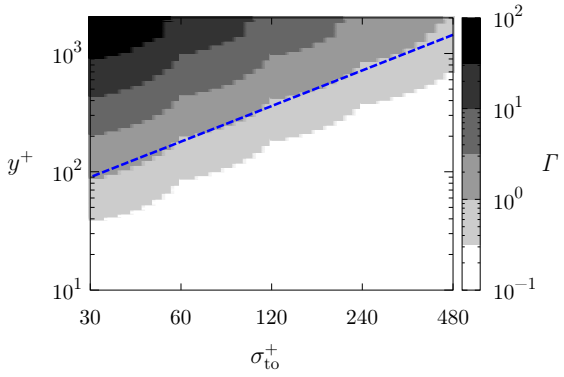

Figure 4: The ratio Γ of $Tr(2\sigma_{\rm to} \to \sigma_{\rm to})$ to $Pr(\mathrm{M} \to \sigma_{\rm to})$. $\Gamma = 1$ indicates the qualitative change of the generation mechanism, which corresponds to $y = 3\sigma$ (blue dashed line). The large-scale ($\sigma \gtrsim y/3$) energy is produced by the mean flow, whereas small-scale ($\sigma \lesssim y/3$) energy is generated by the energy cascade.

SYMMETRY INDUCED TURBULENT MOMENT SCALING LAWS OF ARBITRARY ORDER AND ITS VALIDATION USING CHANNEL FLOW DNS DATA AT $Re_\tau = 10^4$

Martin Oberlack*[1], Sergio Hoyas[2], Stefanie Kraheberger[1], and Francisco Alcántara-Ávila[2]
[1]Chair of Fluid Dynamics, TU Darmstadt, Otto-Berndt-Str.2, 64287 Darmstadt, Germany
[2]Instituto de Matemática Pura y Aplicada, UP València, Camino de Vera, 46024 València, Spain

Summary Using the symmetry-based turbulence theory we derive turbulent scaling laws for arbitrarily high moments of the streamwise velocity U_1. In the region of the log-law, the theory predicts an algebraic law with the exponent $\omega(n-1)$ for moments $n > 1$. The exponent ω of the 2^{nd} moment determines the exponent of all higher moments. Moments here always refer to the instantaneous quantities and not to the fluctuations. For the core region of a Poiseuille flow we find a deficit law for arbitrary moments n of algebraic type with a scaling exponent $n(\sigma_2-\sigma_1)+2\sigma_1-\sigma_2$. Hence, the moments of order one and two with its scaling exponents σ_1 and σ_2 determine all higher exponents. To validate the new theoretical results we have conducted a Poiseuille flow DNS at $Re_\tau = 10^4$. All of the latter theoretical findings could be verified with high accuracy using DNS data.

THE MULTI-POINT CORRELATIONS EQUATIONS AND ITS SYMMETRIES

The basic equations of the following analyses are the infinite set of multi-point correlations equations

$$\frac{\partial H_{i_{\{n+1\}}}}{\partial t}+\sum_{l=0}^{n}\left[\frac{\partial H_{i_{\{n+2\}[i_{(n+1)}\mapsto k_{(l)}]}}[\boldsymbol{x}_{(n+1)}\mapsto\boldsymbol{x}_{(l)}]}{\partial x_{k_{(l)}}}+\frac{\partial I_{i_{\{n\}[l]}}}{\partial x_{i_{(l)}}}-\nu\frac{\partial^2 H_{i_{\{n+1\}}}}{\partial x_{k_{(l)}}\partial x_{k_{(l)}}}\right]=0 \quad \text{for} \quad n=1,\ldots,\infty \ , \tag{1}$$

which directly result from the Navier-Stokes equations (see e.g. [1]), to be extend by continuity, and where $H_{i_{\{n+1\}}} = H_{i_{(0)}i_{(1)}\ldots i_{(n)}} = \overline{U_{i_{(0)}}(\boldsymbol{x}_{(0)},t)\cdot\ldots\cdot U_{i_{(n)}}(\boldsymbol{x}_{(n)},t)}$. $I_{i_{\{n\}[l]}}$ obeys a similar defintion as $H_{i_{\{n+1\}}}$, but at the l-th position the velocity is replaced by the pressure P. Most important it is to note that other than in classical statistical approaches both velocity and pressure refer to the instantaneous and not to the fluctuating quantities. We may note that $H_i = \bar{U}_i$.

For the results to be derived below we need to define symmetries, which indicate a transformation of the independent $\boldsymbol{x}$ and dependent variables $\boldsymbol{y}$ to new variables $\boldsymbol{x}^* = \boldsymbol{\phi}(\boldsymbol{x},\boldsymbol{y})$ and $\boldsymbol{y}^* = \boldsymbol{\psi}(\boldsymbol{x},\boldsymbol{y})$, which map a differential equation (DE) $\boldsymbol{F}(\boldsymbol{x},\boldsymbol{y},\boldsymbol{y}^{(1)},\boldsymbol{y}^{(2)},\ldots,\boldsymbol{y}^{(p)}) = 0$ onto itself, i.e. concretely after the transformation the DE has an identical form, so $\boldsymbol{F}(\boldsymbol{x}^*,\boldsymbol{y}^*,\boldsymbol{y}^{*(1)},\boldsymbol{y}^{*(2)},\ldots,\boldsymbol{y}^{*(p)}) = 0$. The Lie algorithm allows to rigorously calculate the symmetry transformations $\boldsymbol{\phi}$ and $\boldsymbol{\psi}$ from a given DE, which denote a continuous transformation that depends on one or several continuous parameter out of $\mathbb{R}$ and possesses certain group properties. Since the equations (1) is derived from the Navier-Stokes they admit the classical Galilei transformation group, and in the limiting case of large Reynolds numbers, the two scaling symmetries

$$t^* = \mathrm{e}^{a_2}t, \quad \boldsymbol{x}^*_{(l)} = \mathrm{e}^{a_1}\boldsymbol{x}_{(l)}, \quad \mathbf{H}^*_{\{n\}} = \mathrm{e}^{n(a_1-a_2)}\mathbf{H}_{\{n\}}, \quad \mathbf{I}^*_{\{n\}[l]} = \mathrm{e}^{(n+2)(a_1-a_2)}\mathbf{I}_{\{n\}[l]}, \tag{2}$$

which are scaling of space (a_1) and time (a_2). Additionally, the equations (1) admit two statistical symmetries, i.e.

$$t^* = t, \quad \boldsymbol{x}^*_{(l)} = \boldsymbol{x}_{(l)}, \quad \mathbf{H}^*_{\{n\}} = \mathrm{e}^{a_s}\mathbf{H}_{\{n\}}, \quad \mathbf{I}^*_{\{n\}[l]} = \mathrm{e}^{a_s}\mathbf{I}_{\{n\}[l]}, \tag{3}$$

and

$$t^* = t, \quad \boldsymbol{x}^*_{(l)} = \boldsymbol{x}_{(l)}, \quad \mathbf{H}^*_{\{n\}} = \mathbf{H}_{\{n\}} + \mathbf{A}_{\{n\}}, \quad \mathbf{I}^*_{\{n\}[l]} = \mathbf{I}_{\{n\}[l]} + \mathbf{B}_{\{n\}[l]}, \tag{4}$$

where a_s, $\mathbf{A}_{\{n\}}$ and $\mathbf{B}_{\{n\}[l]}$ are group parameter. These statistical symmetries are not admitted by the Navier-Stokes equations and in [2] it has been shown that (3) and (4) respectively define a measure of intermittency and non-gaussianity.

SYMMETRY INDUCED TURBULENT SCALING LAWS

From the above symmetries and using the notion of infinitesimal transformation, we may construct invariant solutions using the invariant surface condition (for details see e.g. [1]), which specifically for plane shear flows reads

$$\frac{\mathrm{d}x_2}{a_1x_2+a_3}=\frac{\mathrm{d}H_1}{[a_1-a_2+a_s]H_1+A_1}=\cdots=\frac{\mathrm{d}H_{1_{\{n+1\}}}}{[n(a_1-a_2)+a_s]H_{1_{\{n+1\}}}+A_{1_{\{n+1\}}}}, \tag{5}$$

where we presently focus on moments of the U_1 velocity, $H_{1_{\{n+1\}}} = H_{\underbrace{11\ldots1}_{n}}$ and, further, we remind that $H_1 = \bar{U}_1$.

Since the equation (1) is a multi-point equation, the moments $n \geq 2$ depends on further points, so that in the general case in (5) further invariant parts of coordinates occur. In the present case we consider only one-point moments, so that the integration constants are true constants. For the integration of (5) we consider two cases.

For the log-law, the friction velocity $u_\tau = \sqrt{\tau_w/\rho}$ is the determining parameter. If we combine the scaling symmetries (2) and (3), which for the mean velocity reads $\bar{U}_1^* = \mathrm{e}^{a_1-a_2+a_s}\bar{U}_1$, u_τ turns out to be symmetry-breaking and hence

*Corresponding author. E-mail: oberlack@fdy.tu-darmstadt.de.

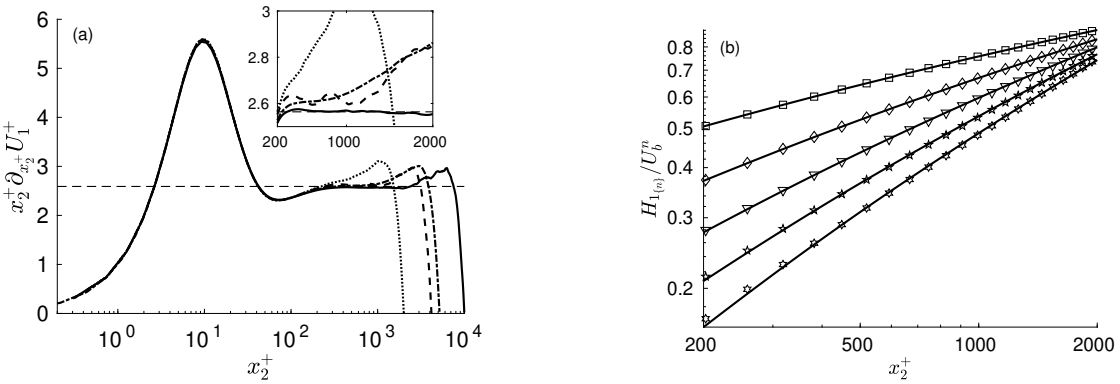

Figure 1: *Left*: Log-indicator function $x_2^+\partial_{x_2^+}\overline{U}_1$ at different Re, with zoom on the log-region. ------ : $Re_\tau = 2000$, – – – : $Re_\tau = 4000$, – - – - : $Re_\tau = 5200$, ——— : $Re_\tau = 10^4$. Horizontal line $\kappa \approx 0.384$. *Right*: Higher moments $H_{1_{\{n\}}}$. From top to bottom: $H_{1_{\{n\}}}$ of order $n = 2, ...6$. ——— : DNS data at $Re_\tau = 10^4$, symbols: Eq. (6) with coefficients fitted to DNS data.

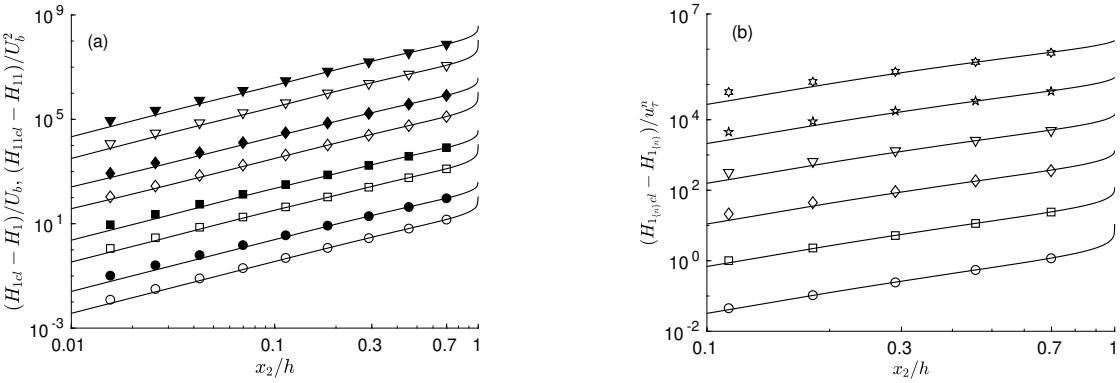

Figure 2: Results refer to the channel core, as x_2 is anchored to the channel center. Solid lines link to DNS data. Symbols are according to Eq. (7). *Left*: 1^{st} and 2^{nd} moments H_1 (open symbols) and H_{11} (closed). From bottom to top: $Re_\tau = 2000, 4000, 5200, 10^4$. Profiles are shifted to increase visibility. *Right*: $H_{1_{\{n\}}}$ of order $n = 1, ...6$, DNS data are at $Re_\tau = 10^4$.

$a_1 - a_2 + a_s = 0$. Using this in (5) and integrate the ODE, we obtain the classical log-law for the mean velocity and an algebraic scaling law for the higher moments

$$\bar{U}_1^+ = \frac{1}{\kappa}\ln\left(x_2^+ + A\right) + B, \quad \text{for } n = 1 \quad \text{and} \quad H_{1_{\{n\}}} = C_{1_{\{n\}}}\left(x_2^+ + A\right)^{\omega(n-1)}, \quad \text{for } n \geq 2 \tag{6}$$

where κ, A, ω, are function of the group parameter defined in (2)-(4) and $C_{1_{\{n\}}}$ are constants of integration. For the deficit-law in the channel center, which was first suggested to be algebraic in [3], we may not invoke a symmetry breaking scale ab initio, and integration of (5) leads to

$$\frac{H_{1_{\{n\}}cl} - H_{1_{\{n\}}}}{u_\tau^n} = D_{1_{\{n\}}}\left(\frac{x_2}{h}\right)^{n(\sigma_2-\sigma_1)+2\sigma_1-\sigma_2} \quad \text{for } n \geq 1. \tag{7}$$

σ_1 and σ_2, which are the scaling exponents of the 1^{st} and 2^{nd} moments, determine all higher moments, and have their origin in the group parameter given in (2)-(4). $H_{1_{\{n\}}cl}$ is the n^{th} moment at the channel center and $D_{1_{\{n\}}}$ are constants of integration.

TURBULENT SCALING LAW VALIDATION USING DNS DATA

Validation of these new scaling laws (6) and (7) have been done using the data of [4], [5], [6] and a new simulation at $Re_\tau = 10^4$ using the code LISO [4]. All computations were conducted on SuperMUC-NG at LRZ in Munich/Garching.

A clear confirmation of (6), especially for the new algebraic law for $n > 2$, is done using the new DNS data at $Re_\tau = 10^4$. Results are shown in figure 1b, leading to the following values $\kappa = 0.386$, $A = 4.487$ and $\omega = 0.12$. Further, the evaluation of the scaling law (7) in the channel centre, even at lower Reynolds numbers, can be taken from the figures 2a and 2b, where the DNS data yield the following values $\sigma_1 = 1.76$ and $\sigma_2 = 1.74$.

References

[1] Oberlack, M., Wacławczyk, M., Rosteck, A., Avsarkisov, V., *Bulletin of the JSME: Mechanical Engineering Reviews*, **2**(2), pp. 1-72, 2015.
[2] Wacławczyk, M., Staffolani, N., M., Oberlack, M., Rosteck, A., Wilczek, M., Friedrich, R., *Phys. Rev. E*, **90**, pp. 013022, 2014.
[3] Oberlack M., *J. Fluid Mech.*, **427**, pp. 299-328, 2001.
[4] Hoyas, S., Jiménez, J. *Physics of Fluids*, **20**(10):101511, 2008.
[5] Lozano-Durán, A. and Jiménez, J. *Physics of Fluids*, 26(1):011702, 2014.
[6] Lee, M., Moser, B.D., *J. Fluid Mech.*, **774**, pp. 395-415, 2015.

REGENERATION OF THE SMALL SCALES IN TURBULENCE WITH 4DVAR: COMPARISON BETWEEN DNS AND LES

Yi Li*[1], Jianlei Zhang[2], and Gang Dong[2]
[1]School of Mathematics and Statistics, University of Sheffield, UK
[2]National Key Laboratory of Transient Physics, Nanjing University of Science and Technology, P. R. China

Summary Variational data assimilation has been applied to CFD research in a number of applications, including inflow condition generation, fields reconstruction, sensor placement, dispersion source identification etc. Here the method is applied to recover small scale fluctuations in 3D turbulent velocity fields from a given time sequence of the velocity data obtained at the large scales. The 4DVAR formalism is used, where the initial velocity field serves as the control, to be chosen to minimize the difference between the measure data and the simulated velocity. Both DNS and LES as the model for the data are considered. The adjoint method is used to find the optimal solutions. The results show that satisfactory recovery can be achieved with DNS as the model. As expected, the recovery with LES as the model is lower, although the accuracy might still be sufficient for some applications.

THE GOVERNING EQUATIONS

Data assimilation (DA) refers to the process where experimental data are merged with simulation data to improve the prediction of a numerical model. In the four-dimensional variational (4DVAR) method, the available data are usually 3D field data given as a time sequence over a time period. The assimilation is accompolished by solving an optimization problem, where a problem-specific control variable is optimized to reduce the error between simulation and measurements. The method has been used, e.g., for field reconstruction [2, 1], to obtain optimal reduced order models [3], to find optimal sensor placement [4] and to reconstruct scalar sources [5]. In this paper, it is assumed some measurements of a time sequence of 3D turbulent velocity fields $\mathbf{v}(\mathbf{x},t)$ are known over a time period $t\in[0,T]$. The measurements are denoted by $\mathcal{F}\mathbf{v}(\mathbf{x},t)$, and is assumed to contain only the large scale velocity field. The question is if it is possible to reconstruct the small scales in $\mathbf{v}(\mathbf{x},t)$ solely based on the large scale data $\mathcal{F}\mathbf{v}$ and the knowledge that $\mathbf{v}(\mathbf{x},t)$ is a solution of either the Navier-Stokes equations (NSEs) or the filtered NSEs. Let $\widetilde{\mathbf{u}}(\mathbf{x},t)$ be the solution of the filtered NSEs with initial condition $\widetilde{\mathbf{u}}(\mathbf{x},0)=\boldsymbol{\phi}(\mathbf{x})$. The problem is thus reduced to finding $\boldsymbol{\phi}(\mathbf{x})$ such that $\mathcal{F}\mathbf{u}(\mathbf{x},t)$ agrees with $\mathcal{F}\mathbf{v}(\mathbf{x},t)$. Since $\widetilde{\mathbf{u}}$ is a solution of the filtered NSEs and $\mathcal{F}\widetilde{\mathbf{u}}$ matches $\mathcal{F}\mathbf{v}$, the small scales of $\widetilde{\mathbf{u}}$ are thus the reconstruction of $\mathbf{v}$. Because 3D turbulent flows are highly chaotic, this problem has not been fully resolved.

Mathematically, we define a cost functional to quantify the difference between $\mathcal{F}\widetilde{\mathbf{u}}(\mathbf{x},t)$ and the measurement data:

$$J\equiv\frac{1}{2}\int_0^T\int_B||\mathcal{F}\widetilde{\mathbf{u}}(\mathbf{x},t)-\mathcal{F}\mathbf{v}(\mathbf{x},t)||^2d^3\mathbf{x}dt, \tag{1}$$

where T is the optimization horizon and B is the solution domain. The initial field $\boldsymbol{\phi}(\mathbf{x})$ is found from a constrained optimization problem in which J is minimized subject to the constraint that $\widetilde{\mathbf{u}}(\mathbf{x},t)$ is the solution of the filtered NSEs given $\boldsymbol{\phi}(\mathbf{x})$ as the initial condition.

Using the adjoint method, the optimal solution can be found as the solution of the KKT conditions. The KKT conditions includes the filtered NSEs:

$$\partial_t\widetilde{\mathbf{u}}+\widetilde{\mathbf{u}}\cdot\nabla\widetilde{\mathbf{u}}+\nabla\widetilde{p}+\nabla\cdot\boldsymbol{\tau}-\nu\nabla^2\widetilde{\mathbf{u}}-\widetilde{\mathbf{f}}=0,\quad\nabla\cdot\widetilde{\mathbf{u}}=0,\quad\widetilde{\mathbf{u}}(\mathbf{x},t=0)=\boldsymbol{\varphi}(\mathbf{x}). \tag{2}$$

where $\boldsymbol{\tau}=\widetilde{\mathbf{u}\mathbf{u}}-\widetilde{\mathbf{u}}\widetilde{\mathbf{u}}$ is the SGS stress tensor. The KKT conditions also include the adjoint equations:

$$\partial_t\boldsymbol{\xi}+\mathbf{u}\cdot\nabla\boldsymbol{\xi}-\nabla\mathbf{u}\cdot\boldsymbol{\xi}+\nabla\mu+\nabla\cdot\boldsymbol{\tau}^{\xi}+\nu\nabla^2\boldsymbol{\xi}=-\mathcal{F}^{+}\mathcal{F}[\widetilde{\mathbf{u}}(\mathbf{x},t)-\mathbf{v}(\mathbf{x},t)],\quad\nabla\cdot\boldsymbol{\xi}=0,\quad\boldsymbol{\xi}(\mathbf{x},t=T)=0, \tag{3}$$

where $\boldsymbol{\xi}$ and μ are the adjoint velocity and pressure, respectively. Using the standard Smagorinsky model, we obtain:

$$\boldsymbol{\tau}=2(C_s\Delta)^2|\widetilde{\mathbf{s}}|\widetilde{\mathbf{s}}\quad\text{and}\quad\boldsymbol{\tau}^{\xi}=2(C_s\Delta)^2\left\{|\widetilde{\mathbf{s}}|^{-1}[(\widetilde{\mathbf{s}}:\widetilde{\mathbf{s}})\boldsymbol{\Sigma}+(\widetilde{\mathbf{s}}:\boldsymbol{\Sigma})\widetilde{\mathbf{s}}]\right\},$$

where $\Sigma=(\nabla\boldsymbol{\xi}+\nabla\boldsymbol{\xi}^T)/2$. It can be shown that the gradient of J is given by

$$\frac{dJ}{d\boldsymbol{\varphi}}=\boldsymbol{\xi}(\mathbf{x},0). \tag{4}$$

If $\mathbf{v}$ is assumed to be the solution of the NSEs instead, the KKT condtions would be the same except that $\boldsymbol{\tau}$ and $\boldsymbol{\tau}^{\xi}$ will be absent. The above sysmtem of equations are solved iteratively using a forward-backward loop. For this investigation, a 3D Kolmogorov flow is considered, so that all equations are solved in the Fourier space with a pseudo-spectral scheme. A second order time stepping is used. The Reynolds number of flow is $Re_\lambda\approx 75$. $\mathcal{F}\mathbf{v}(\mathbf{x},t)$ is assumed to include the Fourier modes of a sequence of DNS data with wavenumbers not bigger than $k_m=4$.

*Corresponding author. E-mail: yili@shef.ac.uk.

RESULTS

The reconstruction quality can be measured by the energy spectrum E_D of the velocity difference $\widetilde{\mathbf{u}} - \mathbf{v}$, as well as the spectral correlation between the Fourier modes of $\widetilde{\mathbf{u}}$ and $\mathbf{v}$, which is defined by

$$\hat{\rho}_{\mathbf{uv}}(k) \equiv \frac{\oint \langle \hat{\mathbf{u}}^*(\mathbf{k},t) \cdot \hat{\mathbf{v}}(\mathbf{k},t) \rangle dS_k}{2\sqrt{E_{\mathbf{u}}(k) E_{\mathbf{v}}(k)}}, \tag{5}$$

where $E_{\mathbf{u}}(k)$ and $E_{\mathbf{v}}(k)$ denote the energy spectrum of the reconstruction $\widetilde{\mathbf{u}}$ and the target velocity $\mathbf{v}$, respectively. The left panel in Fig. 1 plots the integral $\int_0^{k_\Delta} E_D(k)dt$ normalized by a similar integral of $E_{\mathbf{v}}(k)$. The ratio meaures the total difference up to wavenumber k_Δ. The result shows that the reconstruction with DNS as the model is uniformly better, as expected. Nevertheless, the reconstruction with LES can reduce the error down to about 2%. The error is smaller for smaller k_Δ, which implies larger scales are reconstructed better, which again is expected.

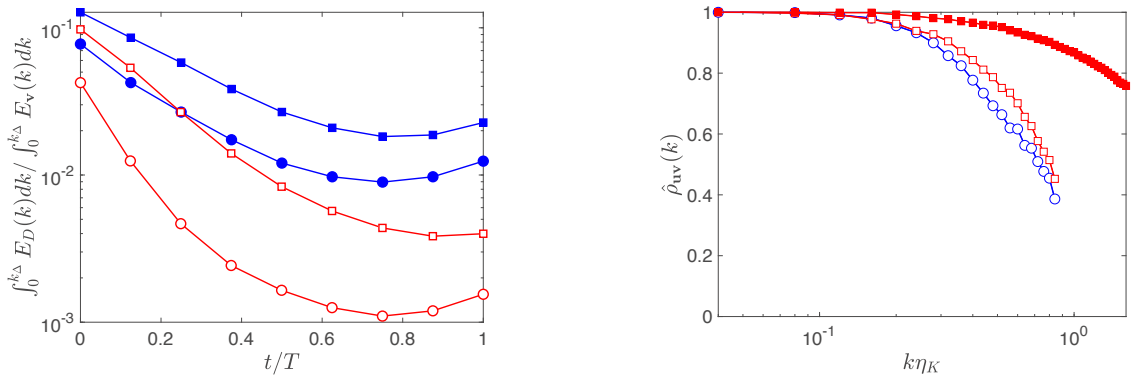

Figure 1: Left: The integrated $E_D(k)$ normalized the integrated $E_{\mathbf{v}}(k)$. Solid symbols: LES; open symbols: DNS. Squares: $k_\Delta \eta_K = 0.5$; circles: $k_\Delta \eta_K = 0.25$. T equals the large eddy turn-over time scale. Right: $\hat{\rho}_{\mathbf{uv}}$ for LES (open symbols) and DNS (solid symbols). Squares: $t/T = 1$; circles: $t/T = 0.5$.

The right panel of Fig. 1 shows the spectral correlation as different times for the LES model, which is compared with the result for DNS at $t = T$. Good correlation is observed for DNS down to the Kolomogorov scale. For LES, the correlation coefficient at the filter scale is approximately 0.4, which shows there is not much correlation with the target data. Good correlation at twice the fitler scale is observed, with the coefficient at about 0.8.

DISCUSSION AND CONCLUSIONS

The ability of the 4DVAR method to reconstruct the small scales of a 3D turbulent field from large scale measurement is investigated. For the given parameters, accurate reconstruction can be obtained if DNS is used as the model and the optimization horizon is approximately one large eddy turn-over time scale. However, to ascertain whether full reconstruction is possible, a longer optimization horizon is needed. The reconstruction with LES has larger errors, which is not unexpected. However, as LES is less expensive, in principle it is possible to extend the optimization horizon to compensate, to some extent, for the error induced by the SGS model. This scenario and the generalization to problems with higher Reynolds number are on-going research.

References

[1] Foures D. P. G., Dovetta, N., Sipp, D. & Schmid, P. J. A data-assimilation method for reynolds-averaged navier-stokes-driven mean flow reconstruction. *J. Fluid Mech.* **759**: 404-431, 2014

[2] Bewley T. R., Protas B. Skin friction and pressure: the "footprints" of turbulencei. *Phys. D* **196**:28-44, 2004

[3] Protas B., Noack, B. R., Osth J. Optimal nonlinear eddy viscosity in Galerkin models of turbulent flows. *J. Fluid Mech.* **766**: 337-367, 2015

[4] Mons V., Chassaing J.-C., Sagaut P. Optimal sensor placement for variational data assimilation of unsteady flows past a rotationally oscillating cylinder. *J. Fluid Mech.* **823**: 230-277, 2017

[5] Wang Q., Hasegawa Y., Zaki T. A. Spatial reconstruction of steady scalar sources from remote measurements in turbulent flow. *J. Fluid Mech.* **870**: 316-352, 2019

SPECTRAL ANALYSIS OF REYNOLDS SHEAR STRESS IN WALL-BOUNDED TURBULENT FLOWS

Myoungkyu Lee*[1] and Robert D. Moser[2,3]
[1]Combustion Research Facility, Sandia National Laboratories, Livermore, California, USA
[2]Oden Institute for Computational Engineering and Sciences, The University of Texas at Austin, Austin, Texas, USA
[3]Walker Department of Mechanical Engineering, The University of Texas at Austin, Austin, Texas, USA

Summary We perform spectral analysis of terms in the transport equation of the Reynolds shear stress (RSS), $\langle u'v' \rangle$, in wall-bounded channel flows to study the dynamics of RSS in the overlap region. It had previously been observed [1], that the RSS spectrum is highly concentrated in streamwise elongated modes with spanwise length scales that grow linearly with wall distance in the overlap region. The RSS transport spectra are studied to identify the reason for this, and investigate other characteristics of the RSS dynamics. Also, to facilitate interpretation, we will revisit the definition of terms in conventional Reynolds stress transport equations.

The wall-bounded flows at high Reynolds number (Re) are important in science and engineering applications, such as atmospheric flows and high-speed transportation system. Yet, our understanding of wall-bounded turbulence is still limited despite recent advances in experimental and computational techniques. As with all turbulent flows are, turbulent fluctuations at different length scales occur in wall-bounded turbulence and their dynamics vary with the distance from the wall. The dynamics of the near-wall turbulence is relatively well explained by the autonomous self-sustaining cycle model [2]. On the other hand, the interaction between the near-wall and outer flows are not well-understood. In this study, we investigate the "life-cycle" of the Reynolds shear stress (RSS) in the overlap region between near-wall and outer layer turbulence. In particular, we perform spectral analysis of the terms in the transport equation of RSS, $\langle u'v' \rangle$.

For this study, we used a set of direct numerical simulations (DNSs) of turbulent channel flows up to friction Reynolds number, Re_τ, 5200 [3]. Here, x, y, and z denote the streamwise, wall-normal and spanwise directions and u, v and w denotes velocity components in each direction, respectively. Using the analysis outlined in [1], we examine the two-dimensional spectra at various distances from the wall of terms in the transport equation for the RSS computed from this DNS. The two-dimensional spectral densities are visualized in polar-log coordinates, as defined in [1].

To start, consider the spectral density of $\langle u'v' \rangle$ itself, as shown in Figure 1a for selected locations in the overlap region. The RSS is highly concentrated in the streamwise elongated modes, that is the spectral density is concentrated along the $k_z^\#$ axis. Further the z wavenumber at which it is concentrated increases linearly with distance from the wall, as expected. Because of the role of the RSS in the production of turbulent kinetic energy, this structure has a profound effect on the spectral dynamics of the turbulence [1].

In Figure 1b-d we examine the spectra of terms in the RSS transport equation to determine what gives rise to this structure. First, as in the $\langle u'v' \rangle$ spectrum, a large portion of production occurs in streamwise elongated motions (near the $k_z^\#$ axis), and the spanwise grows linearly with y (Figure 1b). There is however also production in modes with other orientations consistent with the spectra of the wall-normal fluctuations. The spectrum of the scale transfer term $E^{T^\parallel}_{u'v'}$ indicates the redistribution of RSS from streamwise elongated modes toward more spanwise elongated modes (Figure 1c), which is acting to make the RSS spectrum more isotropic in scale, contrary to structure of the RSS spectrum. Note that the scale-transfer acts from large to small scales or to change orientation. It does not exhibit transfer from small to large scales as suggested in one-dimensional spectral densities [4]. The wall-normal transport of RSS by both turbulent and viscous processes (not shown) is relatively weak, and so does not significantly impact the structure of RSS. Similarly, the dissipation of $\langle u'v' \rangle$ (not shown) is small and in fact acts to strengthen spanwise elongated modes. The only process that provides a significant sink of RSS in the spanwise elongated modes that could produce the observed structure of $\langle u'v' \rangle$ is the pressure-strain (Figure 1d). Of course, the pressure terms arise due to the continuity constraint, and so the rapid and slow pressure strain contributions can be understood as the response to the continuity constraint of the turbulent processes that result in production and scale transfer, respectively.

In summary, the spectral analysis of the RSS transport equation shows detailed pathways for the RSS in length-scales and wall-normal locations. The rich information obtained from spectral transport analysis allows a number of open questions regarding the structure and dynamics of the Reynolds stress to be addressed, where the results outlined above are an example. In this presentation we will discuss the spectral RSS transport analysis in detail and revisit the definition of terms in the Reynolds stress transport equation.

References

[1] Lee M., Moser R. D. Spectral analysis of the budget equation in turbulent channel flows at high Reynolds number. *J. Fluid Mech.* **860**: 886-938, 2019.

*Corresponding author. E-mail: mnlee@sandia.gov.

[2] Jiménez J., Pinelli A. The autonomous cycle of near-wall turbulence. *J. Fluid Mech.* **389**: 335-359, 1999.
[3] Lee M., Moser R. D. Direct numerical simulation of turbulent channel flow up to $Re_\tau \approx 5200$. *J. Fluid Mech.* **774**: 195-415, 2015.
[4] Örlü R. et al. Interscale Transport of the Reynolds Shear Stress in Wall-bounded Flows, *72nd Annual Meeting of the APS Division of Fluid Dynamics*, Seattle, 2019

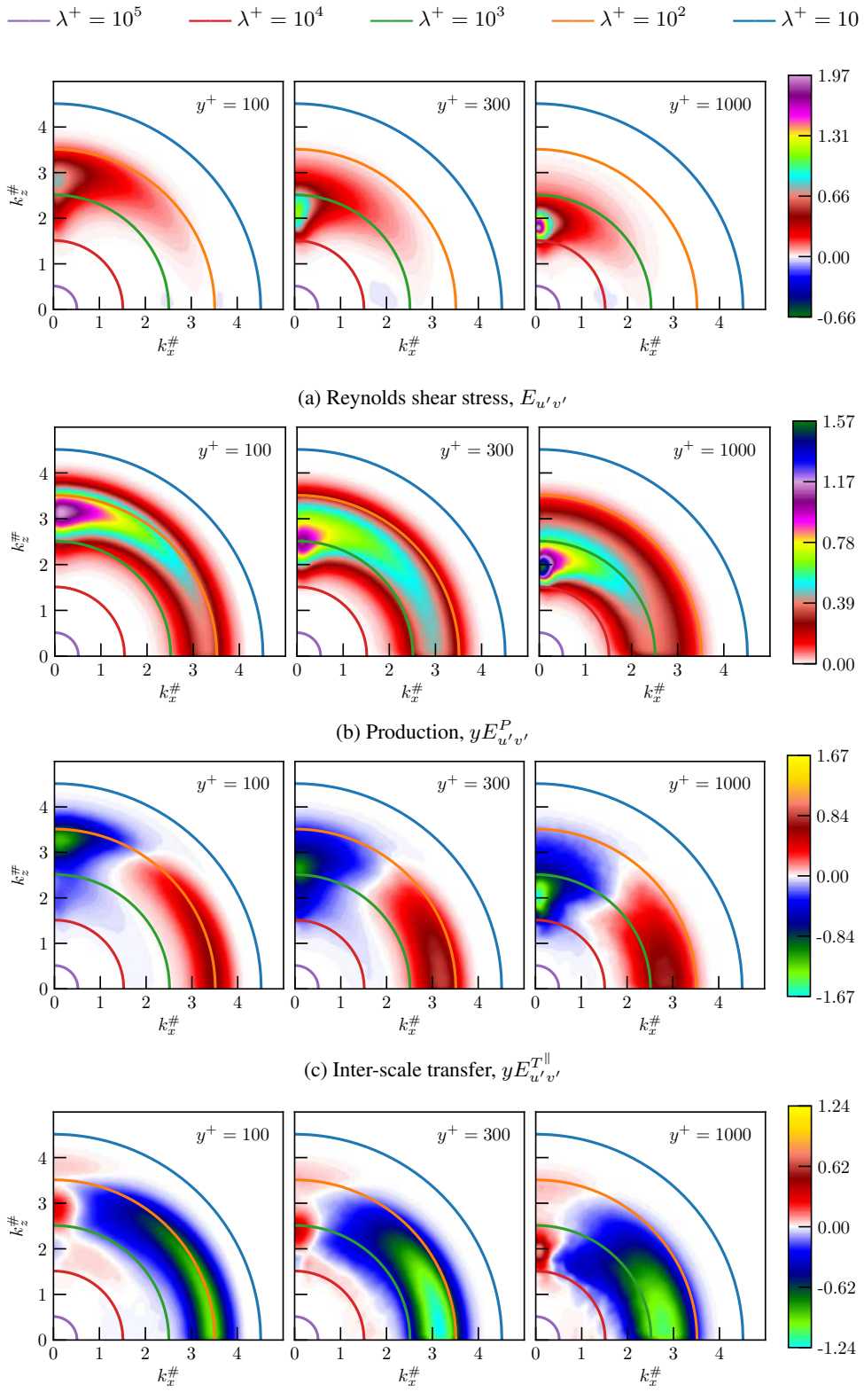

(a) Reynolds shear stress, $E_{u'v'}$

(b) Production, $yE^P_{u'v'}$

(c) Inter-scale transfer, $yE^{T^\parallel}_{u'v'}$

(d) Pressure-strain, $yE^{\Pi^s}_{u'v'}$

Figure 1: Spectral densities of Reynolds shear stress and terms in Reynolds shear stress transport equation. $k_x^\# = (k_x/|k|)\log_{10}(|k|/k_{\mathrm{ref}})$, $k_z^\# = (k_z/|k|)\log_{10}(|k|/k_{\mathrm{ref}})$, $|k| = (k_x^2 + k_z^2)^{1/2}$ and $k_{\mathrm{ref}}\delta = Re_\tau/50000$ where δ is channel-half-width.

SOLUTION PROPERTIES OF THE TURBULENT CHANNEL FLOW MEAN EQUATION

Joe Klewicki[1]
[1]Department of Mechanical Engineering, University of Melbourne, Melbourne, Australia

Summary Multiscale analysis reveals that, under a key assumption, the mean momentum equation for turbulent channel flow admits similarity solutions for the mean velocity and Reynolds shear stress. The solutions are found via analytical integration. High resolution numerical simulations up to friction Reynolds numbers of 8,000 are used to assess the analyses and solutions. At $\delta^+ = 8{,}000$ the key assumption is satisfied to within less than 0.1%. Mathematically well-defined criteria for the start and end points of the log layer are found via use of the leading balances and Reynolds stress similarity solution. The present results indicate that the mean flow structure arises from a self-similar hierarchy of scales, and that this hierarchy is reflected in the shape of the Reynolds stress profile. Ramifications of this structure on the asymptotic value of the von Karman constant are briefly discussed.

BACKGROUND AND MOTIVATION

The broad and lasting technological relevance of turbulent wall-flows motivates developing reliable ways to predict their statistical property variations with Reynolds number [1]. Owing to the dynamical complexity of wall-flows, their Re dependencies occur in ways that are often difficult to anticipate from empirical evidence alone. This study investigates the analytical prediction of turbulent channel flow statistics and their associated scaling behaviours.

Predicting time averaged behaviours typically begins the mean momentum equation, and subsequently seeks to determine the structure of the mean flow – a primary need for engineering applications. This leads to the classical closure problem that inherently accompanies methods founded on the Reynolds Averaged Navier-Stokes (RANS) equations. Indeterminacy, which is addressed herein, results from averaging the nonlinear advective acceleration terms. The inherent non-uniqueness of RANS solutions presents an apparently insurmountable challenge.

Fully developed turbulent channel flow is one of the canonical wall-flows. The simplified form of the mean momentum equation for this flow retains indeterminacy through a single Reynolds stress gradient term. The literature on mean flow prediction approaches for this flow is extensive, with the predominant methods including those that *i*) assume some sort of phenomenological or mathematical closure hypothesis, *ii*) implement (at least partially) the methods of matched asymptotic expansions, or *iii*) exploit the symmetry properties of the equations themselves.

Because scaling is such a prevalent issue in fluid dynamics, symmetry methods hold special importance, e.g., [2]. Approaches that leverage the symmetry properties of the RANS equations retain a clear mathematical basis for describing the solutions to these equations [3]. Central aims of symmetry methods involve identifying and exploiting the invariant forms of the governing equation(s), which also inherently informs Re scaling. To date, however, general methods that address the full RANS equations continue to face a variant of the classical closure problem.

The present study builds upon a multiscale analysis aimed at determining the scaling properties of indeterminate equations. This analysis reveals that the mean equation simplified for the channel asymptotically admits an invariant form over a large wall-normal portion of the flow [4]. Because the analysis yields a self-similar relationship between the derivatives of the mean velocity, U, and the Reynolds shear stress ($T = -\langle uv \rangle$), the indeterminacy of the equation is addressed. As a result, a single invariant form simultaneously yields similarity solutions for both U and T via direct integration. These solutions hold over well-defined subdomains, and for asymptotically large Re simplify to those found via asymptotic matching. Owing to the spatial hierarchy of length scales shown to underlie these solutions, significantly more can be said, and herein some of these findings are described.

ANALYSIS OUTLINE AND THE KEY ASSUMPTION

The mean momentum equation for turbulent channel flow involves three terms that sum to zero; a mean viscous force (VF), a Reynolds shear stress gradient or turbulent inertia (TI), and a mean pressure gradient (PG). The multiscale analysis employed herein begins with an empirical step that reveals how the leading balances of the mean equation are structured across the channel. With this information one can analytically determine how to rescale the equation such that it formally reflects the leading balances. Employing a change of variables and invocating a well-supported assumption yields an invariant form of the mean momentum equation that is operative from a position that is $O(\nu/u_\tau)$ from the wall to a position that is $O(\delta)$. Here, ν is the kinematic viscosity, u_τ is the friction velocity, and δ is the half-channel height.

The invariant equation holds on a continuous hierarchy of scaling layers whose structure depends on the decay rate of the TI term with wall distance. At any position on the hierarchy, TI takes on some value. This TI value uniquely prescribes the wall-normal location, y, and the finite layer width, W(y), anchored at the given y location. The layer widths increase in size with distance from the wall. The local length scale used in the variable normalizations that yield the invariant form on any and all hierarchy layers is this layer width. Thus, the analysis shows that the mean equation admits an invariant form on the layer hierarchy domain when u_τ and W(y) are used as the normalizing parameters.

The analysis uses one key assumption. It is analytically known that on the layer hierarchy the normalized second derivative (curvature) of the T profile remains O(1) for all Re. In addition, from the formulation leading to the invariant form one can surmise that on an interior inertial portion of the hierarchy this derivative should attain constancy at large

Re. The key assumption is that this constancy is realized. Given this, the equation can be integrated to yield solutions for U and T. Results that speak to the asymptotic geometric structure of the flow also emerge.

RESULTS

Results herein pertain to an assessment of the analysis, and the predictive capability of the theory. In the space remaining we describe a few of these using the high-resolution DNS of Yamamoto and Tsuji [5].

The constancy of the normalized Reynolds stress curvature is analytically equivalent to the W(y) profile attaining constant slope on the interior inertial domain (inertial sublayer) noted above. Direct evaluation of dW/dy at $\delta^+ = \delta u_\tau/\nu = 8{,}000$ reveals an interior region where the profile is linear to within less that 1 part in 1000. Use of the leading balance structure and the solution for T(y) allows one to independently identify the beginning and ending locations of the inertial sublayer. Consistently, this region identically coincides with where $dW/dy = 1/\phi_c$ attains constancy. The theory specifies that dW/dy is also directly related to the von Karman constant, $\kappa = 1/\phi_c^2$. On the domain where dW/dy is constant, $U^+(y^+)$ is logarithmic to within a fraction of a percent with a slope that is accurately determined using dW/dy.

Comparisons between the similarity solutions for U and T are made across the range of friction Reynolds numbers, $1{,}000 < \delta^+ < 8{,}000$. These solutions are shown to closely adhere to the finite δ^+ solutions, and with increasing δ^+ increasingly approximate the accepted asymptotic forms. The finite δ^+ form for U^+ is used to clarify why use of the indicator function, $\Xi = ydU^+/dy$, for discerning logarithmic dependence can be misleading.

The scaling on any layer of the hierarchy layer holds over the finite extent of that local W(y). This analytical result lead to a discrete representation of the layer hierarchy. This allows one to algebraically develop new results pertaining to the geometric structure of the flow. One such result is exemplified in Fig. 1, which shows that on the constant dW/dy portion of the hierarchy the geometric mean of the y^+ locations of any fixed T^+ value is equal to y_m^+, the position of maximum T^+. Among other findings, this result affords an alternative means of estimating the von Karman constant.

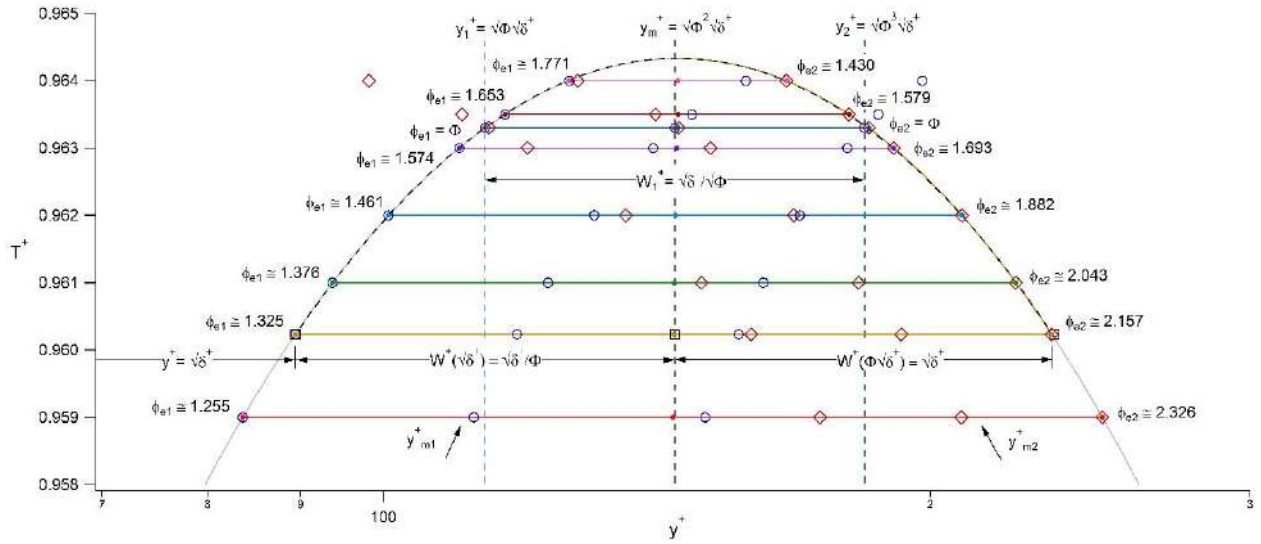

Figure 1. Inner-normalized Reynolds shear stress profile in the vicinity of the peak at $\delta^+ = 7996$. Small dot symbols along the vertical line at y_m^+ are the geometric mean of the points on the solution curve at the same T^+ value.

CONCLUSIONS

An invariant form of the mean momentum equation in channel flow is developed and validated. This invariant form leads to similarity solutions for U and T over an interior portion of the flow, while the mathematical properties underlying its construction provides a basis for understanding the scaling structure of the flow.

References

[1] Klewicki, J.C. Reynolds number dependence, scaling and dynamics of turbulent boundary layers. *J. Fluids Eng.* **132**: 094001, 2010.
[2] Cantwell, BJ. Introduction to Symmetry Analysis. Cambridge University Press, Cambridge UK, 2002.
[3] Oberlack, M., Waclawczyk, M., Rosteck, A. and Avsarkisov, V. Symmetries and their importance for statistical turbulence theory. *Mech Eng. Rev.* **2**: 1500157, 2015.
[4] Fife, P., Klewicki, J. and Wei, T. Time averaging in turbulence settings may reveal an infinite hierarchy of length scales. *J. Discrete and Cont. Dyn. Sys. A* **24**: 781-807, 2009.
[5] Yamamoto, Y. and Tsuji, Y. Numerical evidence of logarithmic regions in channel flow at $Re_\tau = 8000$. *Phys. Rev. Fluids* **3**: 012602, 2018.

TWO-TIME VELOCITY CORRELATION FUNCTION FOR TWO LAGRANGIAN PARTICLES IN TWO-DIMENSIONAL INVERSE ENERGY-CASCADE TURBULENCE

Tatsuro Kishi*[1], Takeshi Matsumoto[1], and Sadayoshi Toh[1]
[1]Division of Physics and Astronomy, Graduate School of Science, Kyoto University, Kyoto, Japan

Summary We investigate both numerically and analytically a two-time correlation function of two Lagrangian particles in two-dimensional inverse energy-cascade turbulence. From our direct numerical simulation data, we propose a self-similar form of the correlation function and the scaling exponents, one of which is not obtainable from dimensional analysis. We then show the non-Kolmogorov scaling law is consistent to the Richardson law of dispersion, t^3.

INTRODUCTION

Correlation function is a fundamental tool of physics. Here our focus is on two-time correlation function of two Lagrangian particles in turbulence,

$$C_{ij}(t_1, t_2) = \langle \delta v_i(t_1) \delta v_j(t_2) \rangle, \tag{1}$$

which is intrinsic to turbulent dispersion and mixing. Here the Lagrangian velocity increment $\delta v_i(t)$ is defined by $\delta v_i(t) \equiv v_i(\boldsymbol{x} + \boldsymbol{r}_0, s|t) - v_i(\boldsymbol{x}, s|t)$, where $v_i(\boldsymbol{x}, s|t)$ is the i-th component of the velocity of a Lagrangian particle at time t, which passed a point $\boldsymbol{x}$ at time s. Notice that it is different from the Lagrangian velocity autocorrelation for a single particle which has been studied and well-understood recently, see, e.g. [1]. In contrast, the property of the particle-pair correlation, Eq.(1), remains open. A notable exception is one measurement in direct numerical simulation (DNS) of three-dimensional homogeneous and isotropic turbulence [2], to the best of our knowledge. Obviously, obtaining converged data of the correlation (1) is more difficult than the single-particle correlation or Eulerian correlation. However with two-dimensional (2D) turbulence, this difficulty can be alleviated.

SELF-SIMILARITY IN TIME OF CORRELATION FUNCTION

We investigate scaling properties of the correlation function, Eq.(1) in detail in the 2D inverse-cascade turbulence. Based on the numerical result, we propose a self-similar form of $C_{ij}(t_1, t_2)$ and determine two scaling exponents. In particular, both of the exponents are different from those obtainable with the Kolmogorov's phenomenology.

We investigate the correlation function, $C_{ij}(t_1, t_2)$, in two-dimensional inverse energy-cascade turbulence both numerically and analytically. Although $C_{ij}(t_1, t_2)$ has four components for two-dimensional turbulence, we here deal only with a longitudinal component, $C(t_1, t_2) \equiv r_i(t) C_{ij}(t_1, t_2) r_j(t) / r^2(t)$, as a first step. Here $r_i(t)$ is a i-th component of relative separation of two Lagrangian particles and $r(t) \equiv |\boldsymbol{r}(t)|$. Also we define the longitudinal relative velocity as $v_l(t) \equiv \delta v_i(t) r_i(t) / r(t)$. This component is directly related to the squared relative separation of Lagrangian particle pairs, namely,

$$\langle r^2(t) \rangle \sim \int_0^t \int_0^t C(t_1, t_2)\, dt_1 dt_2. \tag{2}$$

The celebrated Richardson law [3] is $\langle r^2(t) \rangle \propto \varepsilon t^3$, where ε is the energy flux in the inertial range for the 2D inverse-cascade turbulence.

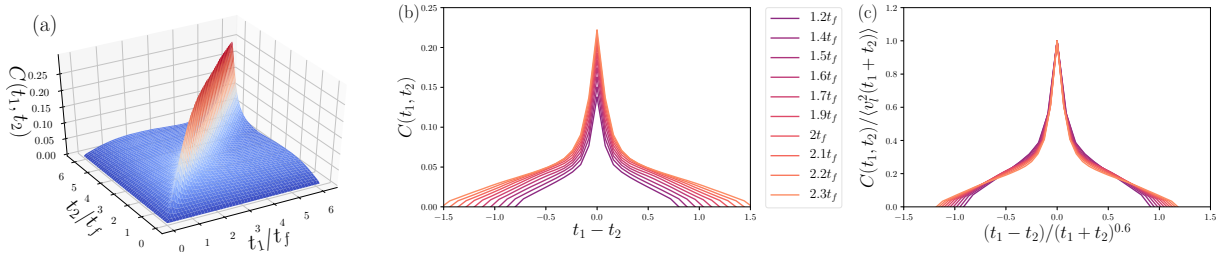

Figure 1: (a) Bird's view of the correlation function, $C(t_1, t_2)$. (b) $C(t_1, t_2)$ vs. $t_1 - t_2$ at different time $(t_1 + t_2)/2$ as shown in the legend. Here t_f is a forcing time scale. (c) Rescaled two-time correlation function by the second-order moment, $\langle v_l^2(t_1 + t_2) \rangle$. The time, $t_1 - t_2$, is also rescaled by $(t_1 + t_2)^{0.6}$.

First, we perform DNS of two-dimensional inverse energy-cascade turbulence with Lagrangian particle tracking involving a velocity interpolation. Our numerical setup of the 2D turbulence is the same as [5]. Figure 1(a) shows DNS

*Corresponding author. E-mail: tatsuro@kyoryu.scphys.kyoto-u.ac.jp

results of the correlation function. Horizontal axis represents the time lag between a two particle, $t_1 - t_2$. As shown in figure 1(b), the correlation function is likely to have a self-similar form,

$$C(t_1, t_2) = r_0^{\frac{2}{3}(\alpha-1)} \varepsilon^{\frac{\alpha+2}{3}} (t_1 + t_2)^{\alpha} F\left(\frac{t_1 - t_2}{r_0^{1-\beta} \varepsilon^{\frac{\beta-1}{2}} (t_1 + t_2)^{\beta}} \right). \tag{3}$$

Here, r_0 is an initial separation of particle pairs. The two scaling exponents of this self-similar form cannot be determined uniquely by dimensional analysis unlike the Kolmogorov's phenomenology. This indeterminancy of the scaling is induced by the fact that $C(t_1, t_2)$ depends on not only $t_1 + t_2$ but also $t_1 - t_2$. The self-similar form, Eq.(3), can be supported by the incomplete similarity analysis. According to figure 1(b), we can determine the scaling exponents as follows:

$$\alpha \simeq 1.3, \quad \beta \simeq 0.6. \tag{4}$$

Note that the exponent α is determined by looking at $\langle v_l^2(t) \rangle$ shown in figure 2(b).

We performed the same DNS but with three different Reynolds numbers. This suggests that the above results are insensitive to the Reynolds number.

RICHARDSON LAW OF SEPARATION & NON-KOLMOGOROV SCALING OF VELOCITY

Now we show numerically that the above results of the correlation function are consistent with the Richardson law, $\langle r^2(t) \rangle \propto t^3$. In figure 2(a), we show $\langle r^2(t) \rangle$ calculated with our DNS data, which indeed show the t^3 law. Combining Eq.(2) with Eq.(3), the observed t^3 law imposes a constraint on the exponents α and β as $\alpha + \beta + 1 = 3$. Our measured exponents (4) are consistent with this constraint.

Contrastively, if we adopt the Kolmogorov's dimensional analysis, the second-order moment of the relative velocity becomes $\langle v_l^2(t) \rangle \propto \varepsilon t$. This is different from our result $\langle v_l^2(t) \rangle \propto t^{1.3}$ (figure 2(b)). This difference is caused by the temporal correlation in $t_1 - t_2$ as shown in figure 1.

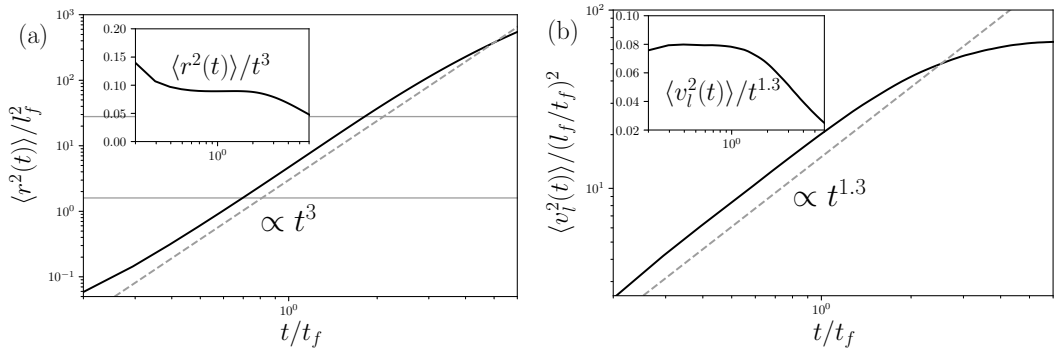

Figure 2: (a) Second-order moments of the relative separations, $\langle r^2(t) \rangle$. The dashed line represents the Richardson t^3 law. The range between the two horizontal gray solid lines is the inertial range estimated with the mean exit time [4]. Inset: the compensated plot by t^3. (b) Second-order moments of the longitudinal relative velocity, $\langle v_l^2(t) \rangle$. The dashed line represents the non-K41 $t^{1.3}$ scaling law. Inset: the compensated plot by $t^{1.3}$.

These DNS results imply that another theoretical consideration beyond the Kolmogorov's phenomenology is needed to understand the scaling behavior of the correlation function. As one way to shed some light, we adopt the Lagrangian renormalized approximation (LRA) [6] to study the above scaling exponents, Eq.(4), which will be reported in the conference. This is different from [2], where they substitute a Lagrangian velocity autocorrelation (single particle) for the correlation function, $C(t_1, t_2)$.

CONCLUSIONS

In this study, we have revealed the self-similar properties of the Lagrangian two-particle, two-time correlation function, $C(t_1, t_2)$, for the first time. We estimated the scaling exponents from DNSs. They are consistent with incomplete similarity analysis and the Richardson law. Moreover the scaling relation leads to the non-Kolmogorov scaling law of the relative velocity.

References

[1] Yeung P.K. Lagrangian investigations of turbulence. *Ann. Rev. Fluid* **34**:115, 2002.
[2] Ishihara T., Kaneda Y. Relative diffusion of a pair of fluid particles in the inertial subrange of turbulence. *Phys. Fluids* **14**: L69, 2002.
[3] Richardson L.F. Atmospheric Diffusion Shown on a Distance-Neighbour Graph. *Proc. R. Soc. London, Ser A* **110**: 709, 1926.
[4] Boffetta G., Sokolov I M. Statistics of two-particle dispersion in two-dimensional turbulence. *Phys. Fluids* **14**: 3224–3232, 2002.
[5] Xiao Z., Wan M., Chen S., Eyink G.L. Physical mechanism of the inverse energy cascade of two-dimensional turbulence: a numerical investigation. *J. Fluid Mech.* **619**: 1, 2009.
[6] Kaneda Y. Renormalized expansions in the theory of turbulence with the use of the Lagrangian position function. *J. Fluid Mech.* **107**: 131, 1982.

TURBULENCE STATISTICS - ADVECTIVE AND VISCOUS TERMS

Yukio Kaneda*[1], Takashi Ishihara [2], Koji Morishita [3], Mistuo Yokokawa [4], and Atsuya Uno [5]
[1]Graduate School of Mathematics, Nagoya University, Nagoya, Japan,
[2]Graduate School of Environmental and Life Sci., Okayama University, Okayama, Japan
[3]SOUM Corporation, Tokyo, Japan
[4]Graduate School of System Informatics, Kobe University, Kobe, Japan
[5]RIKEN Center for Computational Science, Kobe, Japan

Summary Turbulence statistics concerning the vorticity and the advective and viscous terms of the Navier-Stokes equations are studied by analysing the data of high-resolution direct numerical simulation of forced turbulence in a periodic box. The analysis shows that the conditional average of the magnitude of the advective term and that of the viscous term for a given magnitude ω of the vorticity increase with ω at large ω, but the conditional average of the ratio, say R_{loc}, of the former to the latter is almost independent of ω. The analysis also shows that the Reynolds number given by $Re \equiv UL/\nu$ is much larger than the average of the ratio R_{loc}, where U and L are respectively the characteristic velocity and length of the energy containing eddies, and ν is the kinematic viscosity.

INTRODUCTION

High Reynolds number turbulence exhibits strong intermittency at small scales. The magnitude ω of the vorticity $\boldsymbol{\omega}$ is high in some regions and low in others. It would not be surprising if the statistics of the flow field are different in the high- and low-vorticity regions. Among the statistics are those of the advective term $(\boldsymbol{u}\cdot\boldsymbol{\nabla})\boldsymbol{u}$ and the viscous term $\nu\boldsymbol{\nabla^2 u}$, which are the key ingredients of the Navier-Stokes (NS) equations. Here $\boldsymbol{u}=\boldsymbol{u}(\boldsymbol{x},t)$ is the fluid velocity at position $\boldsymbol{x}$ and time t. In order to get some idea on the relation between ω and the statistics, we consider here the joint probability distribution functions (pdf's) $P(\omega^2,|(\boldsymbol{u}\cdot\boldsymbol{\nabla})\boldsymbol{u}|)$, $P(\omega^2,\nu|\boldsymbol{\nabla^2 u}|)$, and $P(\omega^2,R_{loc})$, on the basis of the data of high-resolution direct numerical simulation (DNS), where R_{loc} is the local Reynolds number defined at each position as the ratio of $|(\boldsymbol{u}\cdot\boldsymbol{\nabla})\boldsymbol{u}|$ to $\nu|\boldsymbol{\nabla^2 u}|$.

STATISICS OF ADVECTIVE AND VISCOUS TERMS

The following shows some results of the DNS of forced incompressible turbulent flow obeying the NS equations and the incompressibility condition in a periodic box. The Taylor micro-scale Reynolds number R_λ is 730, and $k_{\max}\eta \approx 2$ in the DNS, where η is the Kolmogorov micro-scale given by $\eta=(\nu^3/\epsilon)^{1/4}$, ϵ is the average of the energy dissipation rate per unit mass, and $k_{\max}$ is the maximum wavenumber retained in the DNS. Readers may refer to Ishihara et al. (2007) for some details of the method of DNS.

Figures 1(a), (b) and (c) show the pre-multiplied joint pdf's $xyP(x,y)$ for $x=\omega^2/|\omega^2|$ and $y=|(\boldsymbol{u}\cdot\boldsymbol{\nabla})\boldsymbol{u}|$, $\nu|\boldsymbol{\nabla^2 u}|$, and R_{loc}, respectively. The solid lines show the conditional averages of y, for a given ω^2. These figures can be compared with Figs. 1 (d), (e) and (f), which plot the same statistics as Figs. 1 (a), (b) and (c), respectively, but for an artificial random field generated by randomizing the phases of the Fourier velocity components $\hat{\boldsymbol{u}}(\boldsymbol{k})$ of the DNS field.

As regards the advective term, the normalized averages $\langle|(\boldsymbol{u}\cdot\boldsymbol{\nabla})\boldsymbol{u}|\rangle/[(u'v_\eta)/\eta)]$ are 0.707 in the DNS and 0.812 in the random field, where u' is the characteristic velocity of the energy containing range given by $3(u')^2=\langle\boldsymbol{u}\cdot\boldsymbol{u}\rangle$, v_η is the Kolmogorov micro-scale given by $v_\eta=(\epsilon\nu)^{1/4}$, and $\langle\boldsymbol{u}\rangle=0$. Thus the average is smaller in the DNS field. The smallness in the NS field is consistent with the phenomenon known as the depression of nonlinearity. A comparison of Fig. 1(a) with Fig. 1(b) shows that the depression of the conditional average $\langle|(\boldsymbol{u}\cdot\boldsymbol{\nabla})\boldsymbol{u}||\omega^2\rangle$ for a given ω^2 occurs only for small $c\equiv\omega^2/\langle\omega^2\rangle$, e.g. $c<1$, but not for large c.

As regards the viscous term, the normalized averages $\langle\nu|\boldsymbol{\nabla^2 u}|\rangle/[\nu v_\eta/\eta^2]$ are 0.283 and 0.405 in the DNS and random fields, respectively. Thus the average is again smaller in the DNS field. A comparison of Fig. 1(b) with Fig. 1(e) shows that the conditional average $\langle\nu|\boldsymbol{\nabla^2 u}||\omega^2\rangle$ is smaller in the DNS than in the random field for small c, e.g., $c<1$, but not for large c. For large c, the conditional average sharply increases with ω^2 in DNS; in the random field, in contrast, the average is almost independent of ω^2.

As regards the local Reynolds numbers, the averages $\langle R_{loc}\rangle$ are 53.6 and 34.9 in the DNS and random fields, respectively. Thus the average $\langle R_{loc}\rangle$ is larger in the NS field. It is remarkable that the conditional average $\langle R_{loc}|\omega^2\rangle$ is almost independent of ω^2 in the DNS field, in contrast to the random field. This implies that there is a certain mechanism in the NS dynamics which suppresses the increase of $\langle R_{loc}|\omega^2\rangle$ with ω^2 at large c as observed in Fig. 1(f).

It is often mentioned in the literature that the Reynolds number $Re\equiv UL/\nu$ is a representative ratio of the advective term to the viscous term, where U and L are respectively the characteristic length and velocity of the flow filed. Given this, one might expect that $\langle R_{loc}\rangle \sim Re$. But this is not so. In fact, the DNS data used in Fig. 1 give $Re\approx 14800$. (Here we used $U=u'$ and $L=$ the integral length scale.) The value 14800 is much larger than $\langle R_{loc}\rangle = 53.6$. This implies that

$$Re\equiv UL/\nu \neq |advective\ term|/|viscous\ term|. \quad (1)$$

The (incorrect) expectation $\langle R_{loc}\rangle \sim Re$ could be derived by assuming $|(\boldsymbol{u}\cdot\boldsymbol{\nabla})\boldsymbol{u}|\sim U^2/L$ and $\nu|\boldsymbol{\nabla^2 u}|\sim\nu U/L^2$ as often assumed in the literature. However, the large difference between $\langle R_{loc}\rangle$ and Re implies it to be wrong or misleading for turbulence. A better estimate of $\langle R_{loc}\rangle$ can be obtained by assuming $|(\boldsymbol{u}\cdot\boldsymbol{\nabla})\boldsymbol{u}|\sim u' v_\eta/\eta$ and $\nu|\boldsymbol{\nabla^2 u}|\sim\nu v_\eta/\eta^2$. We thereby obtain $\langle R_{loc}\rangle\sim u'\eta/\nu \propto (Re)^{1/4}$, which is consistent with an estimate by Orszag (1977). This gives $\langle R_{loc}\rangle\sim$ 13.7 for the DNS data used in Fig.1.

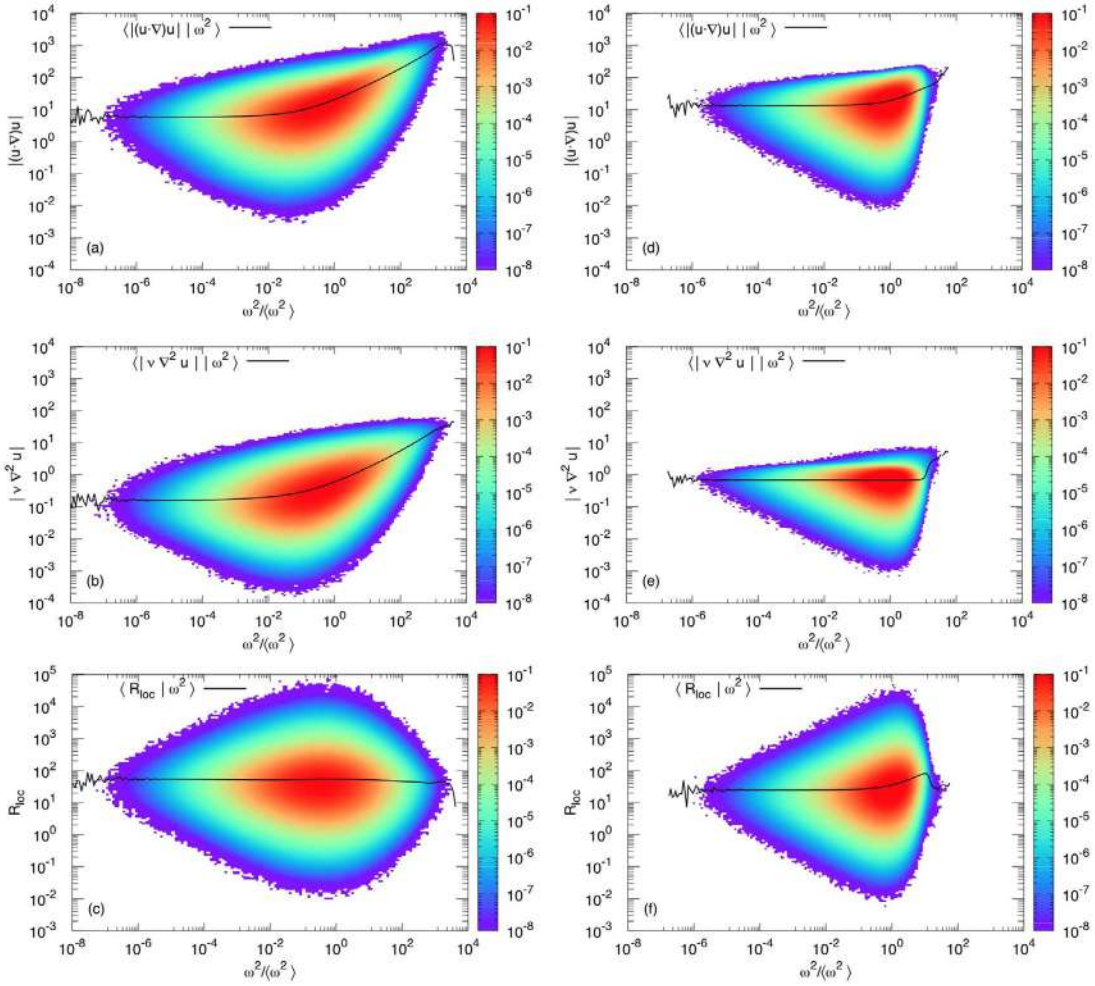

Figure 1. Pre-multiplied joint pdf's of (a)$(\omega^2, |(\boldsymbol{u}\cdot\boldsymbol{\nabla})\boldsymbol{u}|)$, (b)$(\omega^2, \nu|\boldsymbol{\nabla^2 u}|)$, and (c) (ω^2, R_{loc}) at $R_\lambda = 730$. (d), (e), (f): The same as (a), (b), (c), respectively, but for the random field.

CONCLUSIONS

The DNS data suggest the following:
(i) Both of the conditional averages $\langle|(\boldsymbol{u}\cdot\boldsymbol{\nabla})\boldsymbol{u}||\omega^2\rangle$ and $\langle\nu|\boldsymbol{\nabla^2 u}||\omega^2\rangle$ increase with ω^2 at large $\omega^2/\langle\omega^2\rangle$.
(ii) The conditional average $\langle R_{loc}|\omega^2\rangle$ is almost independent of ω^2 in the DNS field, in contrast to the random field.
(iii) The estimates $|(\boldsymbol{u}\cdot\boldsymbol{\nabla})\boldsymbol{u}|\sim U^2/L$, $\nu|\boldsymbol{\nabla^2 u}|\sim\nu U/L^2$, as well as the idea that the Reynolds number $Re \equiv UL/\nu$ is a measure of the ratio of the advective term to the viscous term, are incorrect or misleading for turbulence. (see Eq. (1))
Some results of the analysis of DNS data at lower R_λ were reported at a meeting [3].

This study was partly supported by JSPS KAKENHI Grant Numbers JP19H00641. The computational resources of the K computer provided by the RIKEN Advanced Institute for Computational Science through the HPCI System Research project (Projects ID: hp180109 and ID: hp190076) were partly used in this study. This study was also partly supported by "Joint Usage/Research Center for Interdisciplinary Large-scale Information Infrastructures" (Project ID: jh190068).

References

[1] Ishihara T., Kaneda Y., Yokokawa M., Itakura K., Uno A. Small-scale statistics in high-resolution direct numerical simulation of turbulence: Reynolds number dependence of one-point velocity gradient statistics, *J. Fluid Mech.* **592**:335-366, 2007.
[2] Orszag, S. A. Lectures on the statistical theory of turbulence. *Fluid Dynamics*, Balian, R. and Peube, J. -L. (eds.) 235-374, Gordon and Breach Science Publishers, 1977.
[3] web site: http://online.kitp.ucsb.edu/online/turbulence11/kaneda/

SCALE-SIMILAR ANALYSIS ON MAXIMALLY HELICAL HOMOGENEOUS TURBULENCE

Kazuhiro Inagaki[1]
[1]Institute of Industrial Science, The University of Tokyo, Tokyo, Japan

Summary In the conventional three-dimensional homogeneous turbulence, the direction of energy cascade is forward or large to small scales. Recent studies showed that inverse energy cascade or small to large scale energy transfer occurs even in three-dimensional homogeneous turbulence when the turbulence is highly helical. Through the analysis employing the detailed balance, we can show a possibility that the Navier–Stokes equations have a scale-similar structure accompanied by an inverse cascade of energy under the maximally helical condition. However, the closure approximation does not allow the maximally helical condition. Thus, we conclude that the maximally helical condition cannot be realized through the purely nonlinear dynamics of the Navier–Stokes equations.

SCALE-SIMILAR SPECTRA IN HELICAL TURBULENCE

As the two-dimensional Navier–Stokes equations have two inviscid invariants, energy and enstrophy (squared vorticity), the three-dimensional Navier–Stokes equations also have two inviscid invariants; namely, energy and helicity. Helicity is defined by the inner product of velocity and vorticity. In analog with the enstrophy cascade range in two-dimensional turbulence, Brissaud *et al.* [1] suggested the existence of the following energy spectrum in helicity cascade range:

$$E(k) \propto (\varepsilon^H)^{2/3} k^{-7/3}, \tag{1}$$

where $E(k)$ denotes the energy spectrum which satisfies $\langle \boldsymbol{u}^2 \rangle/2 = \int_0^\infty \mathrm{d}k\, E(k)$, $\langle \cdot \rangle$ denotes the statistical average, and ε^H denotes the dissipation rate of helicity. However, what we often observe in three-dimensional homogeneous turbulence is the conventional Kolmogorov spectrum of $E(k) \propto \varepsilon^{2/3} k^{-5/3}$ where ε denotes the energy dissipation rate (see, e.g., ref. [2]). Moreover, the direction of the energy cascade is forward.

Recently, Biferale *et al.* [3, 4] showed that an inverse energy cascade with Kolmogorov spectrum $E(k) \propto k^{-5/3}$ occurs when we restrict the nonlinear interaction to that inducing the single sign of helical mode. In such a case, the helicity spectrum must satisfy

$$E^H(k) = 2kE(k), \tag{2}$$

where $\langle \boldsymbol{u} \cdot \boldsymbol{\nabla} \times \boldsymbol{u} \rangle = \int_0^\infty \mathrm{d}k\, E^H(k)$. Equation (2) gives the maximally helical condition [1, 5]. They also observed the energy spectrum of the helicity cascade range given by Eq. (1) [4]. Although it is interesting that the inverse cascade occurs even in three-dimensional homogeneous turbulence, there remains a question: does the Navier–Stokes equations without any modulation on the nonlinear interaction also provides an inverse cascade solution? Sahoo *et al.* [6] suggested that inverse cascade occurs only when the nonlinear term is modulated to an almost fully homo-chiral condition. In this study, we investigate the scale-similar laws and the direction of cascade through the statistical property of the Navier–Stokes equations without any modulation.

STATISTICAL PROPERTY OF NAVIER–STOKES EQUATIONS IN MAXIMALLY HELICAL CONDITION

The Navier–Stokes equations with the continuity equation lead to the following energy and helicity spectra equations:

$$\left(\frac{\partial}{\partial t} + 2\nu k^2\right) E(k) = \frac{1}{2}\int_0^\infty \mathrm{d}p \int_0^\infty \mathrm{d}q\, S(k,p,q), \quad \left(\frac{\partial}{\partial t} + 2\nu k^2\right) E^H(k) = \frac{1}{2}\int_0^\infty \mathrm{d}p \int_0^\infty \mathrm{d}q\, S^H(k,p,q), \tag{3}$$

$$S(k,p,q) = -16\pi^2 kpq \Delta_{kpq} M_{ij\ell}(\boldsymbol{k}) \Im[\langle \tilde{u}_i(\boldsymbol{k},t)\tilde{u}_j(-\boldsymbol{p},t)\tilde{u}_\ell(-\boldsymbol{q},t)\rangle], \tag{4}$$

$$S^H(k,p,q) = -16\pi^2 kpq \Delta_{kpq} \left(\epsilon_{ijm}k_\ell + \epsilon_{i\ell m}k_j\right) k_m \Re[\langle \tilde{u}_i(\boldsymbol{k},t)\tilde{u}_j(-\boldsymbol{p},t)\tilde{u}_\ell(-\boldsymbol{q},t)\rangle], \tag{5}$$

where $\tilde{u}_i(\boldsymbol{k},t)$ denotes the Fourier coefficient of the velocity field, $M_{ij\ell}(\boldsymbol{k}) = [k_j P_{i\ell}(\boldsymbol{k}) + k_\ell P_{ij}(\boldsymbol{k})]/2$, $P_{ij}(\boldsymbol{k}) = \delta_{ij} - k_i k_j/k^2$, and Δ_{kpq} takes unity only when k, p, and q can form the sides of a triangle. Note that $S(k,p,q)$ and $S^H(k,p,q)$ satisfy the detailed balance equations,

$$S(k,p,q) + S(p,q,k) + S(q,k,p) = 0, \quad S^H(k,p,q) + S^H(p,q,k) + S^H(q,k,p) = 0, \tag{6}$$

which guarantee the conservation of energy and helicity for the inviscid condition. Now, we assume that the helicity spectrum is given by Eq. (2). In such a case, $S(k,p,q)$ and $S^H(k,p,q)$ satisfy

$$S^H(k,p,q) = 2kS(k,p,q). \tag{7}$$

Thus, the detailed balance for helicity spectrum equation yields

$$kS(k,p,q) + pS(p,q,k) + qS(q,k,p) = 0. \tag{8}$$

This is the analog of two-dimensional turbulence, which yields $k^2S(k,p,q) + p^2S(p,q,k) + q^2S(q,k,p) = 0$. Through the two detailed balance equations (6) and (7) and the scale-similarity assumption,

$$\frac{E(ak)}{E(k)} = a^{-n}, \quad \frac{S(ak,ap,aq)}{S(k,p,q)} = a^{-(1+3n)/2}, \tag{9}$$

we can analyze the scale-similar structures of the Navier–Stokes equations [7, 8]. Consequently, we can show a possibility of an inverse cascade of energy under the maximally helical condition.

STATISTICAL PROPERTY OF CLOSURE EQUATIONS IN MAXIMALLY HELICAL CONDITION

To discuss the scale-similarity of the Navier–Stokes equations, closure theories may be helpful. Now, we consider the helical decomposition of the velocity field [8]:

$$\tilde{\boldsymbol{u}}(\boldsymbol{k},t) = \tilde{u}^+\boldsymbol{h}^+_{\boldsymbol{k}} + \tilde{u}^-\boldsymbol{h}^-_{\boldsymbol{k}}, \quad \boldsymbol{h}^\pm_{\boldsymbol{k}} = \boldsymbol{e}^{(2)} \mp \mathrm{i}\boldsymbol{e}^{(1)}, \quad \boldsymbol{e}^{(1)} = \frac{\boldsymbol{k}\times\boldsymbol{n}}{|\boldsymbol{k}\times\boldsymbol{n}|}, \quad \boldsymbol{e}^{(2)} = \frac{\boldsymbol{k}\times\boldsymbol{e}^{(1)}}{|\boldsymbol{k}\times\boldsymbol{e}^{(1)}|}, \tag{10}$$

where $\boldsymbol{n}$ denotes an arbitrary vector. Under the maximally helical condition where $\tilde{u}^-(\boldsymbol{k},t) = 0$, the equation for $Q^-(k,t)(= \langle|\tilde{u}^-(\boldsymbol{k},t)|^2\rangle)$ yields

$$\frac{\partial}{\partial t}Q^-(k,t) = -\frac{1}{4}\int \mathrm{d}^3p \int \mathrm{d}^3q\, \delta(\boldsymbol{k}-\boldsymbol{p}-\boldsymbol{q})(p-q)\boldsymbol{h}^+_{\boldsymbol{k}}\cdot\boldsymbol{h}^+_{\boldsymbol{p}}\times\boldsymbol{h}^+_{\boldsymbol{q}}\left\langle\tilde{u}^{-*}(\boldsymbol{k},t)\tilde{u}^+(\boldsymbol{p},t)\tilde{u}^+(\boldsymbol{q},t)\right\rangle = 0. \tag{11}$$

However, the closure approximation, e.g., the eddy-damped quasi-normal Markovian (EDQNM)[8, 9] yields

$$\frac{\partial}{\partial t}Q^-(k,t) = \int \mathrm{d}^3p \int \mathrm{d}^3q\, \delta(\boldsymbol{k}-\boldsymbol{p}-\boldsymbol{q})\theta_{kpq}(t)\frac{(k-p-q)^2}{16R^2}(p-q)^2Q^+(p,t)Q^+(q,t) \neq 0, \tag{12}$$

even in the maximally helical condition where $Q^-(k,t) = 0$. Here, $R^2 = (kpq)^2/[2(p^2q^2+q^2k^2+k^2p^2) - k^4 - p^4 - q^4]$ and $\theta_{kpq}(t)$ is the function characterizing a probabilistic relaxation time. The same situation occurs in the direct-interaction approximation based closures [10]. Hence, the maximally helical condition cannot hold in the closure equations. This is because the closure approximations take into account the dynamics of the Navier–Stokes equations that tends to recover the mirror symmetry [2, 11]. Some special helical forcing may alter this situation [12].

CONCLUSIONS

The analysis through the detailed balance equations shows that the Navier–Stokes equations possibly have the scale-similar structures accompanied with an inverse cascade of energy under the maximally helical condition. However, the closure analysis suggests that the maximally helical condition cannot be a root of the statistically averaged Navier–Stokes equations. This is because the dynamics of the Navier–Stokes equations tends to recover the mirror symmetry [2, 11]. Hence, we conclude that the maximally helical condition cannot be realized through the purely nonlinear dynamics of the Navier–Stokes equations. Employing some special helical forcing is a candidate that realized the maximally helical spectra [12].

References

[1] Brissaud A., Frisch U., Leorat J., Lesieur M., Mazure A. Helicity cascades in fully developed isotropic turbulence. *Phys. Fluids* **16**: 1366-1367, 1973.
[2] Chen Q., Chen S., Eyink G. L., Holm D. D. Intermittency in the joint cascade of energy and helicity. *Phys. Rev. Lett.* **90**: 214503, 2003.
[3] Biferale L., Musacchio S., Toschi, F. Inverse energy cascade in three-dimensional isotropic turbulence. *Phys. Rev. Lett.* **108**: 164501, 2012.
[4] Biferale L., Musacchio S., Toschi, F. Split energy–helicity cascades in three-dimensional homogeneous and isotropic turbulence. *J. Fluid Mech.* **730**: 309-327, 2013.
[5] Moffatt K. H. Field Generation in Electrically Conducting Fluids. Cambridge University Press, Cambridge 1978.
[6] Sahoo G., Bonaccorso F., Biferale L. Role of helicity for large- and small-scale turbulent fluctuations. *Phys. Rev. E* **92**: 051002 2015.
[7] Kraichnan R. H. Inertial ranges in two-dimensional turbulence. *Phys. Fluids* **10**: 1417-1423, 1967.
[8] Waleffe, F. The nature of triad interactions in homogeneous turbulence. *Phys. Fluids A* **3**: 350-363, 1992.
[9] Orszag, S. A. Analytical theories of turbulence. *J. Fluid Mech.* 41: 363-386, 1970.
[10] Kraichnan, R. H. The structure of isotropic turbulence at very high Reynolds numbers. *J. Fluid Mech.* 5: 497-543, 1959.
[11] Kraichnan, R. H. Helical turbulence and absolute equilibrium. *J. Fluid Mech.* 59: 745-752, 1973.
[12] Plunian, F., Teimurazov, A., Stepanov, R. & Verma, M. K. Inverse cascade of energy in helical turbulence. *J. Fluid Mech.* 895: A13, 2020.

ANGULAR MOMENTUM TRANSPORT IN TURBULENT TAYLOR–COUETTE FLOW MODIFIED BY SURFACTANT ADDITIVES

Yasufumi Horimoto*, Taisei Hayama, Hiroki Matsukawa, Yosuke Imai, and Yasuo Kawaguchi
Department of Mechanical Engineering, Tokyo University of Science, Noda, Chiba, Japan

Summary To understand the most enhanced angular momentum transport in turbulent Taylor–Couette flow, we conduct laboratory experiments of turbulence suppression by surfactant additives. Turbulent eddies are drastically suppressed by the viscoelasticity of the surfactant solution. Systematic experiments of flow visualization, torque measurements, and particle image velocimetry for this suppressed turbulence provide important information to consider the transport mechanism of turbulence of water.

INTRODUCTION

Experimental approaches are necessary to understand the physics in fully developed turbulence as well as numerical simulations. Taylor–Couette flow, the flow between two concentric cylinders which independently rotate about their axes, is one of the most popular closed flow systems and has been used for fundamental researches of turbulence [1]. In turbulent Taylor–Couette flow where the rotation of the inner cylinder is dominant, it is well-known that there exist large-scale vortical structures, so-called turbulent Taylor vortices which play a quite important role in transport phenomena in this flow system. On the other hand, the rotation of the outer cylinder suppresses these vortices and makes laminar flow more stable. However, interestingly, angular momentum transport is enhanced for the case that the outer cylinder rotates slowly in the opposite direction to that of the inner cylinder, rather than the case of pure inner cylinder rotation [2]. In the present study, we investigate this enhanced turbulence by using a very large experimental apparatus.

Here, we introduce control parameters of Taylor–Couette flow. Note that once we fix geometric parameters such as the radius ratio $\eta = r_o/r_i$ and aspect ratio $\Gamma = L/(r_o - r_i)$ [r_i (r_o) is the radius of the inner (outer) cylinder; L is the length of the inner cylinder], only two independent parameters exist reflecting the fact that we control only the angular velocities of the two cylinders. Although the Reynolds numbers defined by the angular velocities and radii of the cylinders are easy to understand, we use the Taylor number Ta and the ratio a of the angular velocities defined as

$$Ta = \frac{1}{4}\left(\frac{1+\eta}{2\sqrt{\eta}}\right)^4 \frac{(r_o^2 - r_i^2)^2(\omega_i - \omega_o)^2}{\nu^2} \quad \text{and} \quad a = -\frac{\omega_o}{\omega_i}. \tag{1}$$

ω_i (ω_o) is the angular velocity of the inner (outer) cylinder and ν is the kinematic viscosity of a working fluid, respectively. Ta characterizes the magnitude of the centrifugal force relative to the viscous force. A positive value of a means a counter-rotation of the cylinders. As an indication of the magnitude of angular momentum transport, we define a Nusselt number Nu_ω as the ratio of torque T on the surface of the inner cylinder to its value for the laminar case,

$$Nu_\omega = \frac{T}{4\pi L\rho\nu r_o^2 r_i^2(\omega_i - \omega_o)/(r_o^2 - r_i^2)}. \tag{2}$$

ρ is the density of a working fluid.

For a sufficiently high Taylor number, turbulence is sustained in not only a bulk region but also boundary layers on both the cylinders. This turbulence is called *ultimate turbulence* and a scaling law,

$$Nu_\omega \sim Ta^{0.39}, \tag{3}$$

holds [2]. A similarity between this turbulence and the most enhanced heat transfer in Rayleigh–Bénard convection is predicted [3]. Thus, there are many investigations to understand the transport mechanism. We also focus on this problem.

In this study, we employ a strategy based on the view of the rheological properties of fluid. More concretely, we examine turbulence suppression caused by additives. This is an easy method for turbulence control because even a dilute solution of additives has viscoelasticity and turbulent eddies are strongly suppressed [4, 5]. Furthermore, we can drive important information about a physical mechanism of turbulence by systematically investigating this phenomenon [6].

METHODS AND PRELIMINARY RESULTS

We conduct flow visualization, torque measurements, and particle image velocimetry (PIV) by using a large experimental apparatus whose inner and outer cylinders rotate independently. The radii of the inner and outer cylinders are respectively 150 mm and 205 mm, radius ratio η being 0.732. The length of the inner cylinder is 990 mm while that of the outer cylinder is 1014 mm. That is, the aspect ratio Γ of the gap between the cylinders is 18. The end surfaces of the outer cylinder rotate together with it.

As working fluids, we use water and an aqueous solution of cationic surfactant, cetyltrimethyl ammonium chloride (CTAC; the molecular weight 160.10). We add sodium salicylate (NaSal; the molecular weight 320.00) to the solution to

*horimoto@rs.tus.ac.jp

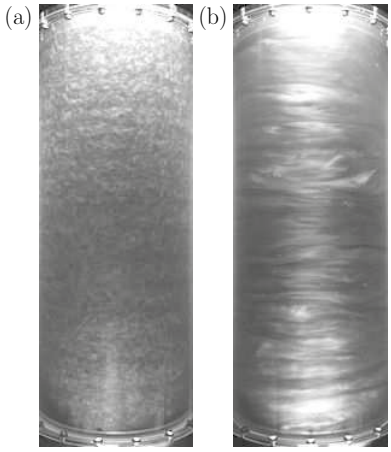

Figure 1: Visualized turbulences of (a) water and (b) the CTAC solution (100 ppm) for $Ta = 2.4 \times 10^8$ and $a = 0.33$. We can observe turbulence suppression by the addition of surfactant in spite of the existence of Taylor vortices which are implied by horizontal stripe patterns.

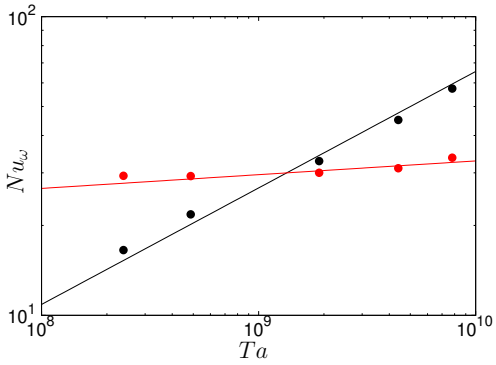

Figure 2: Taylor-number dependence of normalized torque Nu_ω at $a = 0.33$. Black: water; Red: the CTAC solution (100 ppm). Black and red lines are proportional to $Ta^{0.39}$ and $Ta^{0.046}$, respectively. Viscoelasticity of the solution drastically reduces the dependence of angular momentum transport on the effect of the centrifugal force.

supply counterions which stabilize micellar structures of surfactant. Both concentrations of the CTAC and NaSal are 100 ppm by mass (the molar ratio of NaSal to CTAC is 2). Because the solution is quite dilute, we estimate the Taylor number and the Nusselt number for the solution by using the physical property values of water at the same temperature.

The outer cylinder consists of acrylic resin so that we can observe flow visualized by using minute mica flakes and three light sources surrounding the apparatus. Figure 1 shows turbulences of water and the CTAC solution for $Ta = 2.4 \times 10^8$ and $a = 0.33$. For water [Fig. 1(a)], developed turbulence is sustained and angular momentum transport between the two cylinders is the most enhanced by Taylor vortices at this value of a [2]. On the other hand, we can observe the remarkable suppression of turbulent eddies in the CTAC solution [Fig. 1(b)]. Very interestingly, nevertheless, we also see horizontal stripe patterns which imply that Taylor vortices still exist even in such suppressed turbulence.

Figure 2 shows the results of torque measurements. For the CTAC solution, the Taylor-number dependence of the Nusselt number is much weaker than that for water which well coincident with the previous study [see Eq. (3) and Ref. [2]]. This implies that the effect of the centrifugal force is drastically reduced by the viscoelastic property of the solution such as first normal stress difference. To consider these results in more detail, we are conducting parametric experiments which show that the above results also occur for other values of a (results will be shown at the conference).

CONCLUDING REMARKS

To investigate the physical mechanism of angular momentum transport in ultimate turbulence in Taylor–Couette flow, we conduct flow visualization, torque measurements, and PIV for turbulences of water and a dilute surfactant (CTAC) solution by using a large apparatus. Eddies in turbulence of water are strongly suppressed even by a very small amount of surfactant additives. We can consider the dynamics of fully developed turbulence by examining the suppressed turbulence because it is a response of turbulence to the addition of surfactant.

Turbulent eddies are almost vanished by the viscoelasticity of the CTAC solution although Taylor vortices still exist (Fig. 1). Torque measurements reveal that the Taylor-number dependence of the non-dimensional torque, the Nusselt number Nu_ω, is also reduced by the addition of surfactant (Fig. 2). These results imply that angular momentum transport which sustains fully developed turbulence is drastically suppressed due to decreasing the relative magnitude of the centrifugal force by surfactant additives in spite of the existence of Taylor vortices. We are now conducting PIV as well as the methods described above in a more higher Ta-regime. At the conference, we will present a more detail discussion by showing distributions of turbulence statistics obtained by PIV.

ACKNOWLEDGMENT

This work was partially supported by JSPS Grant-in-Aid for Early-Career Scientists, Grant Number 19K14893.

References

[1] Grossmann S., Lohse D., Sun C. High-Reynolds number Taylor–Couette turbulence. *Annu. Rev. Fluid Mech.* **48**: 53-80, 2016.
[2] Van Gils D. P. M., Huisman S. G., Grossman S., Sun C., Lohse D. Optimal Taylor–Couette turbulence. *J. Fluid Mech.* **706**: 118-149, 2012.
[3] Eckhardt B., Grossmann S., Lohse D. Torque scaling in turbulent Taylor–Couette flow between independently rotating cylinders. *J. Fluid Mech.* **581**: 221-250, 2007.
[4] Zakin J. L., Lu B., Bewersdorff H.-W. Surfactant drag reduction. *Rev. Chem. Eng.* **14**: 235-256, 1998.
[5] White C. M., Mungal M. G. Mechanics and prediction of turbulent drag reduction with polymer additives. *Annu. Rev. Fluid Mech.* **40**: 53-80, 2008.
[6] Horimoto Y., Goto S. Sustaining mechanism of small-scale turbulent eddies in a precessing sphere. *Phys. Rev. Fluid* **2**: 114603, 2017.

REYNOLDS STRESS ANISOTROPY IN CANONICAL SHOCK / TURBULENCE INTERACTIONS

Nathan E. Grube[1] and M. Pino Martín *[1]
[1]Department of Aerospace Engineering, University of Maryland, College Park, MD, USA

Summary The disagreement between predictions of linear interaction analysis (LIA) and observations in direct numerical simulation (DNS) and experiments regarding the anisotropy of turbulence emitted by shock/turbulence interactions is a longstanding question. The disagreement arises from nonlinear terms which are neglected by LIA. These terms usually promote isotropy, but here the nonlinearities actually generate the observed anisotropy. We propose that this behavior is due to the wavelengths of vortical waves emitted from the interaction at different inclination angles. The wavelength disparity implies a timescale disparity which in turn causes the waves carrying the transverse Reynolds stress to return to isotropy faster than the waves that carry the streamwise Reynolds stress. A simple model based on this physical understanding agrees with the DNS and experimental observations.

CANONICAL SHOCK / ISOTROPIC TURBULENCE INTERACTIONS (SITI)

Super- and hypersonic flows of engineering interest are complicated by unsteady two-way interactions between shock waves and turbulent fluctuations; the general shock / turbulence interaction is too complicated to be studied theoretically with much success. Instead, the simpler, statistically axisymmetric interaction between isotropic turbulence and a nominally planar shock wave offers a theoretically tractable problem that retains a large subset of the physics of the more general interaction.

This so-called canonical shock / isotropic turbulence interaction (SITI) is characterized by four flow parameters based on the pre-shock conditions: the convective Mach number in the shock-normal direction (M), the turbulence Mach number ($M_t \equiv q'_{\rm rms}/\overline{c}$) based on the r.m.s. velocity fluctuation magnitude $q'_{\rm rms}$ and the mean speed of sound $\overline{c}$, a Reynolds number such as the Taylor microscale Reynolds number Re_λ, and the ratio χ of dilatational turbulent kinetic energy to total TKE.

The interaction leads to the amplification of turbulence and the emission of sound and entropy spots as well as a modification of the mean jumps across the shock. An example is shown in Figure 1 for the case with $(M, M_t, Re_\lambda, \chi) = (2.98, 0.504, 48, 0.026)$. Instantaneous contours of density gradient magnitude are shown at left and Reynolds stress amplification (and isotropy) profiles at right.

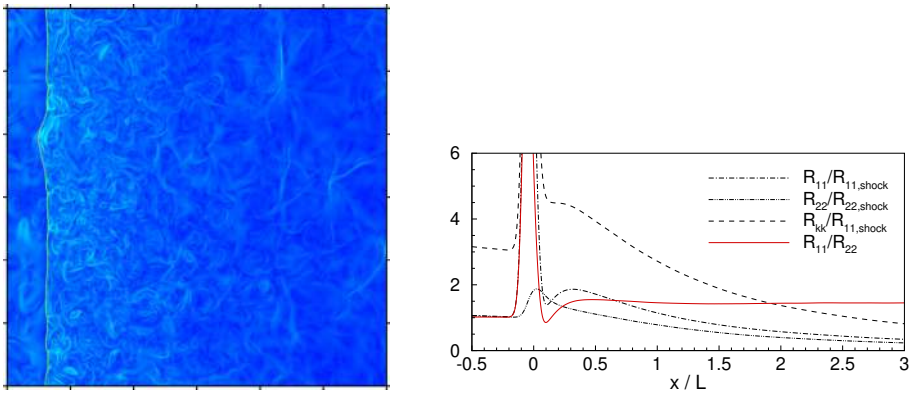

Figure 1: DNS of shock / isotropic turbulence interaction: instantaneous contours of density gradient magnitude (left) and Reynolds stress profiles (right). Distance is normalized by pre-shock turbulence scale L.

Post-Shock Turbulence Anisotropy

In 1998, some forty-five years after the initial publication of his pioneering work on the linear analysis of this problem (so-called linear interaction analysis or LIA), Ribner [5] reflected on the state of agreement between direct numerical simulation (DNS), experiment, and LIA theory. Although experimental results and DNS generally agreed with LIA predictions, Ribner noted that, above Mach 2, a severe qualitative disagreement between the Reynolds stress anisotropy observed by experiment and DNS on the one hand ($R_{11} > R_{22}$) and LIA predictions on the other hand ($R_{22} > R_{11}$) "remain[ed] a puzzle." Here R_{11} and R_{22} denote streamwise and transverse Reynolds stresses, respectively.

DNS profiles of the budget terms for the Reynolds stress equations show that the nonlinear pressure terms (pressure–strain and pressure-diffusion) redistribute TKE from R_{22} to R_{11} until $R_{11} > R_{22}$. These terms are usually observed to drive the turbulence toward isotropy; in fact the slow pressure–strain term is often called the *return-to-isotropy* term. Why, then, do these nonlinear effects drive the Reynolds stress *away* from isotropy in these SITI flows?

An answer to this question would help clarify the acceptable applications for LIA, and the resulting physical insights might aid in the development of turbulence models for STIs. The following section proposes an explanation.

*Corresponding author. E-mail: mpmartin@umd.edu.

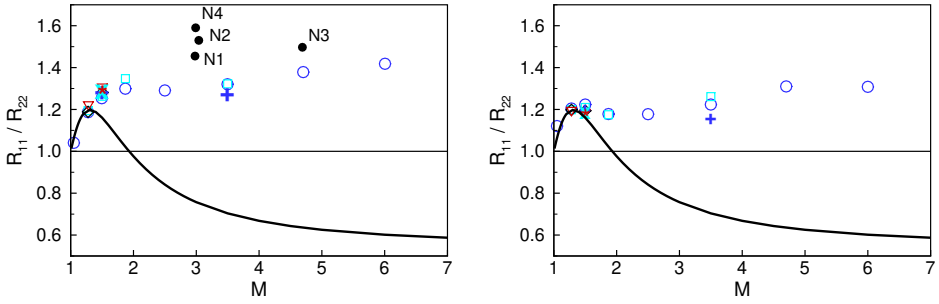

Figure 2: DNS results (left) and model predictions (right) of post-shock Reynolds stress anisotropy R_{11}/R_{22} for the cases of [2] (circles, squares, diamonds, and triangles) and the N-series cases of [1] (+). The LIA prediction is shown as a solid line.

Proposed Explanation

Consider the turbulence field as a superposition of elementary Fourier waves. The angle and wavenumber of an incident vortical wave are linked to those of the resulting emitted wave by a refraction law. The ratio of wavenumber magnitudes for emitted and incident vortical waves (k_2 and k_1, respectively) can be written as

$$\left(\frac{k_2}{k_1}\right)^2 = 1 + \alpha_1^2(\check{m}^2 - 1) = \frac{\check{m}^2}{\check{m}^2 - \alpha_2^2(\check{m}^2 - 1)} \tag{1}$$

where $\alpha_1 \equiv \cos\theta_1$ is the cosine of the incident wave angle, $\alpha_2 \equiv \cos\theta_2$ is the cosine of the emitted wave angle, and $\check{m} \equiv \bar{\rho}_2/\bar{\rho}_1$ is the compression ratio across the shock. The incidence angles θ of the wavevectors are defined relative to the mean flow (x) direction. It follows from (1) that the spatial compression k_2/k_1 of the emitted wavefronts ranges from unity to $\check{m} \equiv \rho_2/\rho_1$ for wavefronts perpendicular ($\alpha_2 = 0$) and parallel to the shock ($\alpha_2 = \pm 1$), respectively. For a specific heat ratio $\gamma = 1.4$ and high Mach number M, the wavefront compression varies from unity to as much as six.

According to LIA, the Reynolds stress in the immediate post-shock region is anisotropic in two senses: First, without regard to lengthscale (and for $M > 2$), there is more energy in R_{22} than in R_{11}. We might call this *global* anisotropy. It also follows from (1) that the energy in R_{22} (i.e., modes with $\alpha_2 \approx \pm 1$) is concentrated at smaller scales than the energy in R_{11} (i.e., modes with $\alpha_2 \approx 0$). In the wavenumber range where R_{22} is concentrated, there is a *local* anisotropy in the sense $R_{22} > R_{11}$, which is in the same direction as the global anisotropy. By contrast, in the largest post-shock scales, those which have not been spatially compressed as much by the shock, the local anisotropy is in the sense $R_{11} > R_{22}$.

In the near post-shock region, the majority of R_{11} lies at lower wavenumbers than the majority of R_{22}. From dimensional analysis, each vortical wave can be associated with a timescale based on its wavelength and perturbation velocity. The result is that the smaller scales isotropize more rapidly, and this process transfers TKE from R_{22} to R_{11}. The largest scales evolve more slowly, and their anisotropy in the sense $R_{11} > R_{22}$ persists longer, resulting in a global anisotropy in the same sense that is observed in DNS.

Based on this understanding, we develop a quantitative model starting with the LIA solution at the shock and using an eddy viscosity representation for the subsequent nonlinear interactions. Figure 2 compares the model predictions against DNS results of Larsson *et al.* [2] and Grube and Martín [1]. The LIA prediction is shown in black. The present model is applicable only to solenoidal incident turbulence; cases N1 through N4, which feature significant incident dilatational TKE, are included to show that the presence of dilatational TKE increases the anisotropy. Note that the simple model offers a vast improvement over LIA; this improvement supports the physical argument based on different timescales for the return to isotropy of the different Reynolds stress components.

ACKNOWLEDGEMENTS

This work was supported in part by the Air Force Office of Scientific Research under award number FA 9550-17-1-0104 monitored by Dr. Ivett Leyva and the Air Force Testing and Evaluation Division under award number FA 9550-10-0535 monitored by Dr. Michael Kendra and Dr. Brett Pokines with the Center for Testing Excellence at the University of Maryland and Mr. Daniel Marren, Mr. John Lafferty and Dr. Eric Marineau of the Arnold Engineering Development Center. Computational resources were provided by the Department of Defense under the High Performance Computing Modernization Program (DoD HPCMP) and by the CRoCCo Laboratory.

References

[1] Grube, N. E. and Martín, M. P., Direct Numerical Simulation of Shock / Highly Compressible Isotropic Turbulence Interactions. *To be published.*
[2] Larsson J., Bermejo-Moreno I., and Lele, S. K., Reynolds- and Mach-number Effects in Canonical Shock–Turbulence Interaction. *Journal of Fluid Mechanics*, **717**:293–321, 2013.
[3] Ribner, H. S., Convection of a Pattern of Vorticity through a Shock Wave. NACA Technical Report 1164, January 1954.
[4] Ribner, H. S., Shock–Turbulence Interaction and the Generation of Noise. NACA Technical Report 1233, January 1954.
[5] Ribner, H. S., Comment on "Experimental Study of a Normal Shock/Homogeneous Turbulence Interaction." *AIAA J.* **36(3)**: 494, 1998.

REALIZABILITY AND METRICS FOR COARSE GRAINED SIMULATION OF THE TURBULENT MIXING TRANSITION

Fernando F. Grinstein* and Filipe S. Pereira
Los Alamos National Laboratory, MS F644, Los Alamos, NM 87545, USA

Abstract In many areas of practical interest we are interested in detailed understanding of the late-time consequences of mixing driven by hydrodynamical instabilities promoted by initial conditions at accelerated material interfaces. Under-resolved simulations of turbulent mixing driven by under-resolved velocity fields are unavoidable, Coarse Grained Simulation is typically the strategy of choice, and there is a practical need to characterize the simulated turbulence and assess macroscopic convergence of quantities of interest. Recently proposed turbulent mixing transition metrics are examined for representative examples of both, fundamental and practical applications.

BACKGROUND

Turbulent mixing can be characterized by the length scales of the fluid physics involved: 1) large-scale entrainment in which advection brings relatively large regions of the pure materials together, 2) an intermediate length scale associated with the convective stirring due to velocity gradient fluctuations, and, 3) much smaller scale interpenetration resulting from molecular diffusion. At high Reynolds number (Re) -- when convective time-scales are much smaller than those of molecular diffusion -- and for Schmidt number, Sc~ 1, primary concern is with the simulation of advection and stirring. The complexity of the high-Re turbulent flow typically requires achieving accurate and dependable large-scale predictions of highly nonlinear processes with under-resolved computer simulation models. All scale-resolving simulation models reduce the range of scales, and presume scale separation between resolved and unresolved scales: Direct Numerical Simulation (as typically practiced) leaves out the longest scales, and CGS [1] (classical and implicit LES) models the effects of the shortest scales.

Transition to turbulence is traditionally viewed in terms of rapid increase in the energy and the enstrophy production by mode coupling of a spectrum of smaller length scale motions. Transition can lead to an inertial range exhibiting Kolmogorov -5/3 power-law in the turbulence kinetic energy spectrum for sufficiently high Re [2,3] above the mixing transition threshold, Re ~ 1-2x10^4 based on the integral scale L (or Re ~ 1-1.4x10^2 based on the Taylor microscale λ) [2]. A higher threshold, Re ~ 1.6x10^5, was proposed to achieve a minimum turbulent state [3] having enough scale separation to ensure robustness of macroscopic flow characteristics. Cascade mechanisms for high Re are believed to be mainly driven by Re-independent equilibrium dissipation, e.g., as indicated by the high-Re constancy of the non-dimensional quantity $D = \varepsilon L / u^3 \sim 1$ [4]. Equilibrium dissipation is regarded as basis for the fundamental turbulence scaling relation $\varepsilon \sim u^3 / L$, where u and L denote characteristic velocity fluctuation magnitude and length scale. However, there is also reported evidence for significant high-Re non-equilibrium dissipation regimes existing in various turbulent flows in which the energy spectrum has Kolmogorov -5/3 wave-number scaling over a wide wave-number range, for which distinctly different scaling relations supporting asymptotically non-constant D apply [5].

TO BE PRESENTED AT XXV ICTAM

On dimensional grounds, if the dissipation rate ε can be estimated the simulated turbulence can be characterized by an effective viscosity defined in terms of strain-rate or enstrophy [6,7], $\nu_{eff} \sim \varepsilon / [2 < s_{ij} s_{ij} >] \sim \varepsilon / \Omega$.

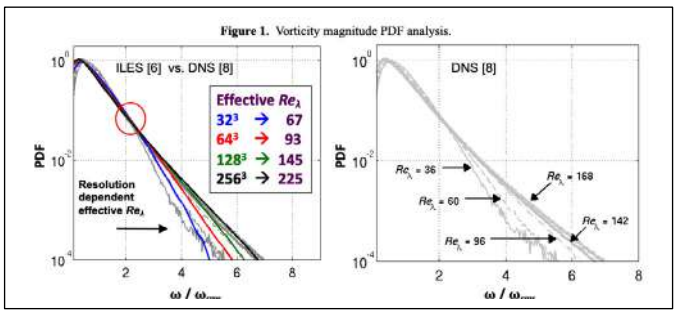

Figure 1. Vorticity magnitude PDF analysis.

The dissipation ε is determined by the prescribed momentum forcing for the homogeneous isotropic turbulence case; it relates to the kinetic energy dissipation for unsteady turbulence, and can be estimated through $\varepsilon \sim u^3 / L$ in the high-Re limit [7]. Effective turbulence Re, is then computed as $\mathrm{Re}_\lambda = u\lambda / \nu_{eff}$, where u is the *rms* value of the velocity and λ is the Taylor microscale of the velocity fluctuations characterizing the CGS cutoff – both evaluated from raw velocity data. Evaluation of ν_{eff} as computed ratio of dissipation and mean squared strain-rate [6,7] is distinct from residual local numerical viscosity (as Newtonian viscosity) associated with algorithm specifics through modified equation analysis. For high-Re inertially dominated flow, ν_{eff} characterizes the simulated turbulence dissipation in the inertial subrange whereas the local (grid level) numerical viscosity characterizes the simulated viscous dissipation subrange.

* Corresponding author. E-mail: fgrinstein@lanl.gov .

In [6], we used established turbulence metrics and DNS data [8] to show that a well-designed ILES can accurately capture the mixing transition and asymptotic high-Re self-similar behaviour (Fig.1), in terms of this effective turbulence Re. Mixing of a passive scalar θ by a fluctuating flow field is a classical problem in turbulence and relevant in many industrial flow applications. Overholt and Pope [9] conducted DNS of Sc~1 mixing of a passive scalar in the presence of a mean scalar gradient, by forced, spatially periodic, isotropic turbulence. In this flow, a statistically steady-state scalar variance is achieved by balancing scalar variance production and dissipation. This problem was first investigated in the LES context by Pullin [10], who predicted that the normalized scalar variance asymptotically approaches a constant value as a function of Re (Fig.2); however, non-constancy of the highest-Re DNS predictions [11] in Fig.2 are clearly apparent, and uncertainties due to sampling time –between 27 and 2.3 eddy-turnover times for Re_λ between 174-586 in [11], remain to be established. The squared-ratio of Taylor microscales – proportional to the velocity-to-scalar dissipation time ratio $\mathcal{R}$, was also reported to be asymptotically constant as function of Re in [10], albeit comparisons with the early DNS [9,12] were inconclusive. Analysis of subsequent results from theory [13], DNS [11], and ILES in [6], shows continued growth of $\mathcal{R}$ consistent with high-Re non-equilibrium dissipation variability [5].

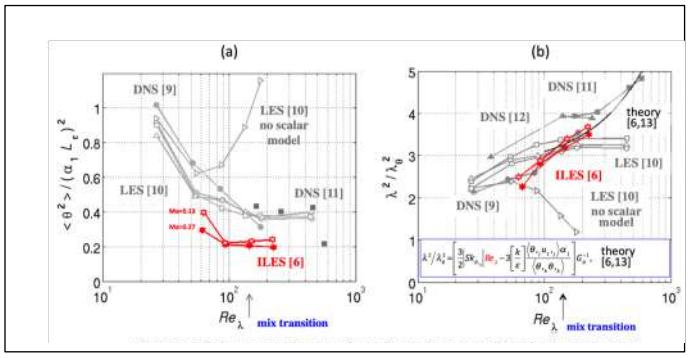

Associated with equilibrium dissipation *built* into the LES modeling, Re-independence of $\mathcal{R}$ for high Re is predicted by Pullin's LES. On the other hand, equilibrium dissipation *not built* into DNS, theory, and ILES, allows variability of $\mathcal{R}$ as function of Re for high-Re. Figures 2 also show that when the explicit scalar SGS model is turned off in LES [10], scalar variance and the ratio predictions rapidly diverge with increasing Re – reflecting inadequacy of the (dispersive) numerics in [10] to ensure by itself correct physical asymptotic behaviour. In contrast, we find that a well-designed ILES allows for asymptotic growth behaviour with Re consistent with the predictions from theory [13], early [9] and more recent DNS [11]. Thus, fundamental constraints appear naturally built into a numerically well-designed ILES, but not necessarily in the mainstream classical LES – *suggesting that further realizability requirements for LES are needed*. More accurate high-Re reference data is also needed to elucidate these issues.

Capturing a target late-time turbulence Re threshold characteristic of the laboratory experiments is crucial in qualifying the impact of the discretization specifics on the simulated flow accuracy for many transitional flows of interest. For example, consider recently revisited ILES of shocked Gas-Curtain experiments with LANL's xRAGE code [14,15]. Simulations agree well with experiments on flow patterns & growth rates before reshock with 2nd order Godunov xRAGE (Fig.3) [14] but are unable to capture the late-time mix-transition after reshock – i.e., late-time Re is too low – as fairly diffusive 2nd order numerics inhibit vortex stretching driving transition. On the other hand, enhanced "smaller-scale" mixing with less-diffusive low-Mach corrected 3rd order xRAGE [15] – allows capturing higher late-time turbulence Re.

Los Alamos National Laboratory is operated by TRIAD National Security, LLC for the US DOE NNSA.

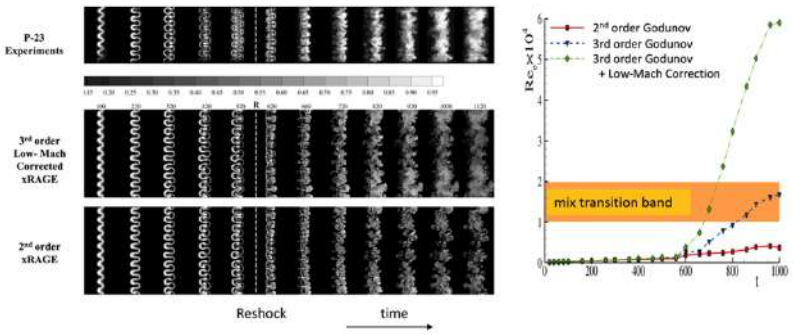

Figure 3: ILES of shocked Gas-Curtain experiments; Re is computed based on a mix width L, and a high-Re effective viscosity as in [15].

References

1. F.F. Grinstein, Coarse Grained Simulation and Turbulent Mixing, Cambridge UP, 2016.
2. Dimotakis, P.E., Journal of Fluid Mechanics, 409, 69-98 (2000).
3. Zhou, Y., Phys. Plasmas, 14, 082701 (2007).
4. Kaneda, Y., Ishihara, T., Yokokawa, M., Itakura, K., & Uno, A., Physics of Fluids, 15, L21 (2003).
5. Vassilicos, J.C., Annual Review of Fluid Mechanics 47, 95-114 (2015).
6. Wachtor, A.J., Grinstein F.F., Devore, C.R., Ristorcelli, J.R., and Margolin, L.G., Physics of Fluids, 25, 025101 (2013).
7. Zhou, Y., Grinstein, F.F., Wachtor, A.J., & Haines, B.M., Physical Review E, 89, 013303 (2014).
8. J. Jimenez, A. A. Wray, P. G. Saffman, and R. S. Rogallo , Journal of Fluid Mechanics 255, 65-90 832 (1993).
9. Overholt, M.R. & Pope, S.B., Phys. Fluids, 8(11), 3128-3148 (1996).
10. Pullin, D.I., Physics of Fluids, 12, 2311 (2000).
11. Gotoh, T. & Watanabe, T., Physica D 241 (2012), 141–148
12. Yeung, P.K., Xu, S. & Sreenivasan, K.R., Physics of Fluids, 14, 4178-4191 (2002).
13. Ristorcelli, J.R., Physics of Fluids, 18, 1-17 (2006).
14. Gowardhan, A.A., and F. F. Grinstein, Journal of Turbulence, 12, No. 43, 1-24 (2011).
15. F.S. Pereira, F.F. Grinstein, and D. Israel, Computers and Fluids, 2019, under review.
16. F.F. Grinstein, et al., Computers and Mathematics with Applications, 78, Issue 2, pp. 437-458 (2019).

TRANSITION OF GRADIENT MOMENTS OF PASSIVE VECTOR IN RANDOMLY STIRRED FLUID

T. Gotoh*[1], J. Yang[1], H. Miura[2], and T. Watanabe[1]
[1]Department of Physical Science and Engineering, Nagoya Inst. Tech., Nagoya, Japan [2]National Institute for Fusion Science, Oroshi, Toki city, Gifu, Japan

Summary Variation of the normalized moments of the gradients of an incompressible passive vector as well as passive scalar and turbulent velocity against the Reynolds number is numerically studied. It is found that the transition of the moments from that of the Gaussian statistics to that of the turbulence occurs at the almost same Reynolds number for three fields and that the power law exponents in the Reynolds number for the passive vector are larger than those of the velocity.

INTRODUCTION

It is recognized that the scaling exponents of passive scalar at high order are smaller than those of the velocity and less universal [1, 2]. In order to explore the physics behind this difference, we have recently studied the statistcial properties of the incompressible passive vector $\boldsymbol{w}$ convected by the isotropic turbulence which obeys an equation very similar to the Navier Stokes equation except the linearity of the convective term [3, 4]. Findings are (1) the spectrum obeys $k^{-5/3}$ in the inertial convective range, (2) the intense pseudo enstrophy $(\nabla \times \boldsymbol{w})^2$ is sheet-like unlike the tube like for the enstrophy as seen in Fig.1, (3) the scaling exponents are in between the velocity and the passive scalar, (4) the pseudo pressure suppresses the intermittency but not as effective as the pressure, and (5) the differences result from whether or not the convective term is nonlinear, (6) the differences bewteen linear and nonlinear become more appreciable at small scales. It has recently been reported that when the Reynolds number R_λ is increased the n-th order moments of the velocity derivatives change from the Gaussian value to increase as a power law $R_\lambda^{\rho(n)}$ and that $\rho(n)$ is related to the scaling exponents in the inertial range [5, 6, 7]. Since the universality of the scaling exponents of the passive scalar is weaker than in the velocity, it is interesting and important to see whether or not such relationship holds for the passive scalar and passive vector.

PASSIVE VECTOR

An incompressible passive vector $\boldsymbol{w}(\boldsymbol{x}, t)$ convected by the homoegenous isotropic turbulence of an incompressible fluid velocity $\boldsymbol{u}(\boldsymbol{x}, t)$ is assumed to obey the following equations:

$$\left(\frac{\partial}{\partial t} + \boldsymbol{u} \cdot \nabla\right) \boldsymbol{w} = -\nabla q + \alpha \nabla^2 \boldsymbol{w} + \boldsymbol{f}^w, \qquad \nabla \cdot \boldsymbol{w} = 0, \tag{1}$$

where α is the diffussive coefficient of the passive vector, and $q(\boldsymbol{x}, t)$ the pseudo-pressure to assure the incompressibility of the passive vector. The external force $\boldsymbol{f}^w$ obeys the Gaussian statistics with zero mean and white in time. Also a passive scalar θ is assumed to be convected by the same turbulent flow. The direct numerical simulation (DNS) of the velocity, passive vector and scalar is performed for very low to moderate Reynolds numbers as $0.126 \leq R_\lambda \leq 120$. In order to assure the enough spatial resolution for high order moments of the gradient fields $k_{\max}\eta$ is kept quite large as $3.73 \leq k_{\max}\eta \leq 67.6$ depending on the Reynolds number. The statistical average is taken as the volume and time average.

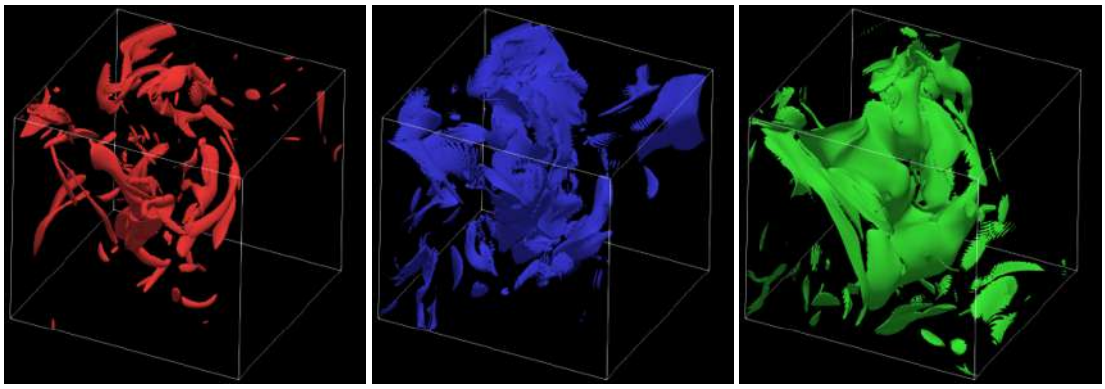

Figure 1: Visualization of $(\nabla \times \boldsymbol{u})^2$ (left), $(\nabla\theta)^2$ (center), and $(\nabla \times \boldsymbol{w})^2$ (right) at $R_\lambda = 120$, respectively.

*Corresponding author. E-mail: gotoh.toshiyuki@nitech.ac.jp.

RESULTS

Figure 1 shows the visularization of $(\nabla \times \boldsymbol{u})^2$, $(\nabla\theta)^2$, and $(\nabla \times \boldsymbol{w})^2$ at $R_\lambda = 120$ in the domain $(L/4)^3$, where L is the box size. It is seen that $(\nabla \times \boldsymbol{u})^2$ is tube like while $(\nabla\theta)^2$ and $(\nabla \times \boldsymbol{w})^2$ are sheet like as reported in [4]. The nth-order normalized moments of the longitudinal and transverse derivatives of the velocity are defined as

$$M_n^{u_L} = \left\langle \left(\frac{\partial u_1}{\partial x_1}\right)^n \right\rangle \Big/ \left\langle \left(\frac{\partial u_1}{\partial x_1}\right)^2 \right\rangle^{n/2}, \qquad M_n^{u_T} = \left\langle \left(\frac{\partial u_1}{\partial x_2}\right)^n \right\rangle \Big/ \left\langle \left(\frac{\partial u_1}{\partial x_2}\right)^2 \right\rangle^{n/2}, \tag{2}$$

respectively. Similarly, the nth-order moments of the corresponding derivatives of the passive vector and passive scalar are defined as

$$M_n^{w_L} = \left\langle \left(\frac{\partial w_1}{\partial x_1}\right)^n \right\rangle \Big/ \left\langle \left(\frac{\partial w_1}{\partial x_1}\right)^2 \right\rangle^{n/2}, \qquad M_n^{w_T} = \left\langle \left(\frac{\partial w_1}{\partial x_2}\right)^n \right\rangle \Big/ \left\langle \left(\frac{\partial w_1}{\partial x_2}\right)^2 \right\rangle^{n/2}, \tag{3}$$

$$M_n^{\theta} = \left\langle \left(\frac{\partial \theta}{\partial x_1}\right)^n \right\rangle \Big/ \left\langle \left(\frac{\partial \theta}{\partial x_1}\right)^2 \right\rangle^{n/2}, \tag{4}$$

For the multivaliate Gaussian statistics, the above moments are $M_{2n}^G \,/\, (M_2^G)^n = (2n-1)!!$. Figure 2 shows the variation of the normalized moments M_n^A, where A denotes $u_L, u_T, w_L, w_T, \theta$, with respect to the Reynolds number. The curves are constant at the Gaussian values M_n^G for $R_\lambda < 2$, begin to rise at around $R_\lambda \approx 5$, and increase as $R_\lambda^{\rho_n^A}$ for $R_\lambda > 30$. Since the transition is not sharp but the trend is clear, it is interesting and worthwhile to estimate the transition point as $R_\lambda \approx 5$ for n up to 10, which is not inconsistent with the previous studies [5, 6]. Corresponding to this transition in the moments, we found that when the Reynolds number increases the probability density functions (PDFs) for the gradient fields change their functional forms and their tails begin to expand. Close examination finds the facts that the curves $M_n^{W_T}$ and M_n^{θ} are close to each other and the same for $M_n^{W_L}$ and $M_n^{u_T}$, while the curve $M_n^{u_L}$ is lowest. The exponents $\rho_n^{u_L}$ are smaller than other ones for up to $n = 8$ but not certain for high order. Careful examination of the exponents and PDFs are now under way and will be reported.

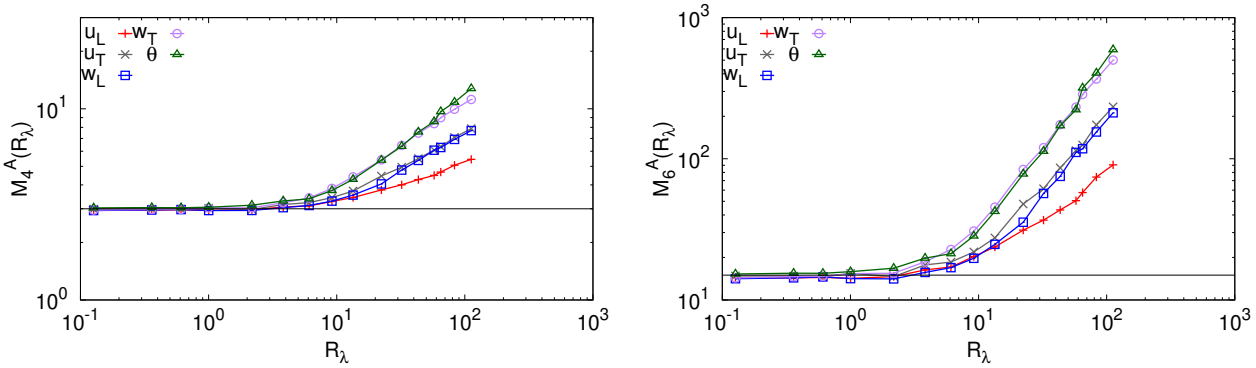

Figure 2: Variation of moments of gradients M_4^A (left) and M_6^A (right) against R_λ for $A = u_L, u_T, w_L, w_T, \theta$. Thin black lines denote the Gaussian values, 3 and 15, respectively.

ACKNOWLEDGMENTS

The National Institute for Fusion Science, Japan (NIFS18KNSS105) and the Networking, Large-scale Data Analyzing and Information Systems (JHPCN) (jh190018) are gratefully acknowledged for providing computational resources. The work of T.G. was supported by MEXT KAKENHI through Grant No.15H02218, and JSPS KAKENHI Grant Nos.17K05734 for H.M and 18K03925 for T.W. are highly appreciated.

References

[1] Watanabe T., Gotoh T., *New J. Phys*. **6**, No.40 2004.
[2] Gotoh T., Watanabe T., *Phys. Rev. Lett*. **115**, 114502, 2015.
[3] Yang J., Gotoh T., Miura H., Watanabe T., *Phys. Rev. Fluids*, **4**, 064601, 2019.
[4] Yang J., Gotoh T., Miura H., Watanabe T., *Phys. Rev. Fluids*, **4**, 114602, 2019.
[5] Yakhot V., Donzis, *Phys. Rev. Lett.* **119**: 044501, 2017.
[6] Schumacher J., Pandey A., Yakhot V., Sreenivasan K., *Phys. Rev. E* **98**: 033120, 2018.
[7] Donzis D., Sreenivasan K., Yakhot V., *APS DFD* B28.00002, 2019.

EMERGENCE OF TRANSPORT DISSIMILARITY BY GROWING TURBULENT SPOT IN PLANE COUETTE FLOW

Koji Fukudome*[1], Takahiro Tsukahara[1], Hiroya Mamori[2], and Makoto Yamamoto[1]
[1]Department of Mechanical Engineering, Tokyo University of Science, Tokyo, Japan
[2]Department of Mechanical and Intelligent Systems Engineering, The University of Electro-Communications, Tokyo, Japan

Summary Direct numerical simulations (DNSs) were performed to study the dissimilarity between the heat and momentum transfer of turbulent spot structures developing in a laminar plane Couette flow. The turbulent spot was generated by pair vortices, and the boundary conditions for velocity and thermal fields were set to be consistent with each other. The Reynolds and Prandtl numbers were 450 and unity, respectively. As a result, we confirmed that the effective heat transfer state is obtained for developing a turbulent spot rather than a fully developed state. It attains the maximum when the turbulent spot grows the half size of the computational domain. Moreover, much effective heat transfer state was obtained for developing in streamwise direction rather than in spanwise direction.

INTRODUCTION

From the engineering view point, there are many concerns for the flow achieving the dissimilarity between heat and momentum transfer because the dissimilarity under higher heat transfer with lower hydraulic friction would improve the efficiency of heat exchangers. Although the transport between heat and momentum has a strong similarity as known as Reynolds or Colburn analogies, the origin of the dissimilarity is coming from the pressure terms of momentum transfer equation, i.e. Navier-Stokes equations [1]. Recently, the authors [2] studied the turbulent stripe in a plane Couette flow, and reported that the more effective heat transfer state is slightly obtained for the turbulent stripe in comparison to the fully-developed turbulence. Here, the turbulent stripe is one of the large-scale intermittent flow structures observed in the transitional region between laminar and turbulence. More recently, the authors [3] reported that the effective heat transfer state is obtained by developing turbulent spot, where the magnitude of dissimilarity is almost proportional to the size of the developing turbulent spot which keeps effective heat transfer state, where the spot grows in both streamwise and spanwise directions. In this study, we perform the DNSs of developing turbulent spot in a plane Couette flow to reveal which is more dominant for the effective heat transfer state of the spot growing in streamwise or spanwise direction.

NUMERICAL PROCEDURE

Objective flow is a plane Couette flow driven by the walls moving in opposing directions at a speed of $\pm U_W$ in the streamwise (x-) direction, where the wall-normal and spanwise directions are y- and z-directions, respectively. The governing equations are incompressible continuity, Navier-Stokes, and energy equations, where the temperature is treated as a passive scalar. For spatial discretization, the spectral method [2] is adopted with Fourier series in the streamwise and spanwise directions, respectively, and the Chebyshev polynomial expansion in the wall-normal direction. The collocation grid used to compute the nonlinear terms in physical space has 1.5 times finer resolution to remove aliasing errors. For time integration, the second-order Adams–Bashforth and Crank–Nicolson schemes are adopted for the nonlinear and viscous terms, respectively, though the explicit Euler scheme is adopted for the first step of the nonlinear terms to compute from the initial flow field. In this study, the Reynolds and Prandtl numbers are 450 and unity, respectively, where the Reynolds number is defined by the wall speed U_W and the channel half width δ. For the thermal boundary condition, the top and bottom walls are set to a constant temperature of $\Theta_H = 1$ and $\Theta_C = -1$, respectively. The computational domains as well as the grid systems are listed in Table 1. Time step size is $\Delta t = 0.01\delta/U_W$. Thereafter, the parameters are normalized by U_W, δ, and the half of the temperature difference, $(\Theta_H - \Theta_C)/2$.

As the initial flow field, we mimic a transient jet from the wall, as a single disturbance, introduced by Lundbradh and Johansson [4]. The flow field is formulated as

$$\Psi = A(1-y^2)^2 z \exp(-x^2-z^2), \quad (1)$$

where Ψ is the stream function. In addition, A is set to be 1.2 where A represents the magnitude of the jet, and the jet position is located at the centre of the computational domain (but note the periodic boundary conditions in x and z). This initial field (as shown in figure. 1(a) discussed later) comprises two vortices near the channel centre, and the initial distribution of temperature T is set to be same with streamwise velocity, so that both the velocity and thermal fields are precisely matched. We would focus on onset of any mismatch, i.e., dissimilarly, between the velocity and thermal fields as the spot disturbance grows with time.

Table 1 Computational domains and the grid system

Cases	Box size	Grid points
2-1	$20\pi\delta \times 2\delta \times 10\pi\delta$	256×65×256
2-2	$20\pi\delta \times 2\delta \times 20\pi\delta$	256×65×512
4-1	$40\pi\delta \times 2\delta \times 10\pi\delta$	512×65×256

*Corresponding author. E-mail: kfukudome@rs.tus.ac.jp.

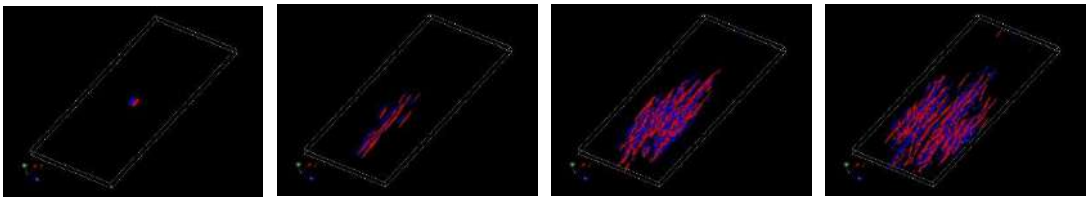

(a) $t = 0$ (b) $t = 100$ (c) $t = 200$ (d) $t = 300$

Figure 1. Temporal evolution of the developing turbulent spots for Case2-1.

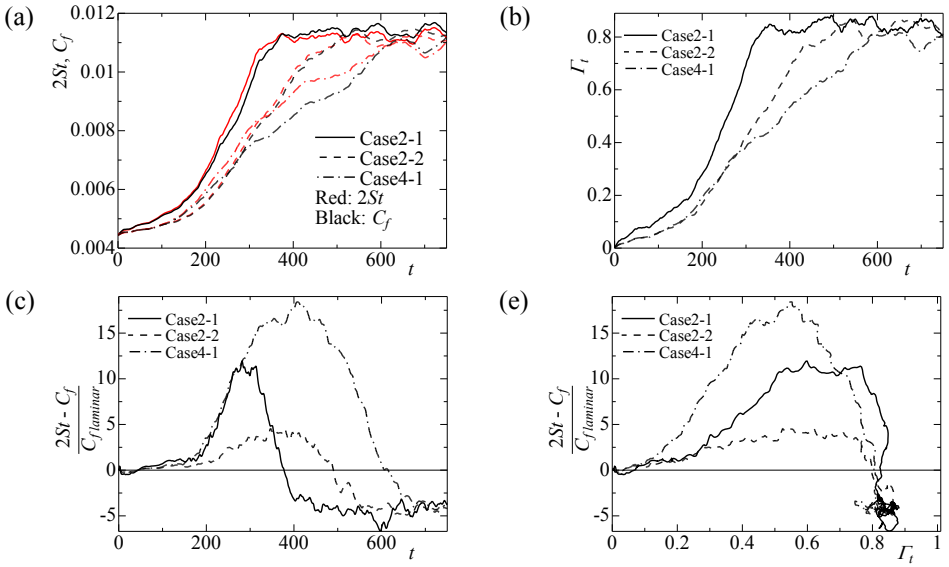

Figure 2. Statistics evolution of the developing turbulent spots.

RESULT AND DISCUSSION

Figure 1 shows the temporal evolution from the pair vortices disturbance as shown in figure 1(a) for Case2-1. Red and blue iso-surfaces represent clockwise and anti-clockwise vortical structures, respectively, identified by second invariant of deformation tensor. The vortices develop and elongated in the streamwise direction at $t = 100$ in figure 1(b). Then, the turbulent spot consists of many small-scale vortices and spatially develops in the streamwise and spanwise directions, as shown in Figure 1(c) at $t = 200$. Thereafter, its dimension becomes comparable with the domain size at t = 300 in figure 1(d). Figure 2 shows the temporal statistics of the developing turbulent spots. The Stanton number St and friction coefficient C_f as shown in figure 2(a) increase with time for all cases and reach to the fully-developed turbulence at $t \approx 400$, 550 and 650 for Case2-1, Case2-2 and Case4-1, respectively. Figure 2(b) represent the temporal evolution of the turbulent fraction Γ_t estimated by the turbulent dissipation [2], and the evolutions show the same trends with the temporal evolutions of St and C_f in each case. Figure 1(c) represents the effectiveness of the heat transfer against the hydraulic friction normalized by the laminar friction coefficient $C_{f\,laminar}$. Here, the equation of $2St = C_f$ is derived by Colburn analogy as the Prandtl number is unity, thus we can judge the effectiveness of the heat transfer by $2St - C_f$. The effectiveness rapidly increases from $t \approx 200$ except Case 2-2 and almost same evolution for Case2-1 and Case4-1 is clearly seen in $t < 250$, thereby much effective heat transfer state was obtained for developing in the streamwise direction rather than in the spanwise direction. Eventually, they become almost constant value of –5 for all cases when Γ_t is saturated in each case. Figure 1(d) shows the effectiveness as a function of Γ_t. The effectiveness increases for $\Gamma_t < 0.5$ in all cases and thereby the effective heat transfer state appears until when the spot grows the half of the computational domain, and it attains the much effective state for growing in the streamwise direction because of the results of Case2-1 and Case4-1.

CONCLUSION

We confirmed the effectiveness of the heat transfer of developing turbulent spot. As a result, it attains the maximum when the turbulent spot grows the half size of the computational domain, and much effective heat transfer state was obtained for developing in the streamwise direction rather than in the spanwise direction.

References

[1] Katoh, K., Sakai, A., Fujii, R., Wakimoto, T., ant Kawahara, G. Trans. Jpn. Soc. Mech. Eng. **79** (806), 2019–2029, 2013. (In Japanese)
[2] Fukudome K., Tsukahara T. and Y. Ogami, Int. J. of Advances in Engineering Sciences and Applied Mathematics **10**(4), 291-298, 2018.
[3] Fukudome K., Tsukahara T., Mamori H. and Yamamoto M., Proc. of 2nd PRTEC **24167**, 5 pages.
[4] Lundbladh A. and Johansson A.V., *JFM* **229**, 499-516, 1991.

TOWARD MACHINE LEARNING BASED CONTROL OF TURBULENCE

Koji Fukagata[1]
[1]Department of Mechanical Engineering, Keio University, Yokohama, Japan

Summary Application of machine learning techniques is one of the hottest topics in the fluid mechanics community. In the present talk, some of our recent efforts to establish the building blocks required to achieve machine learning based control of turbulence are introduced. We adopt the convolutional neural network to extract lower order dynamics of flows, and its performance is demonstrated through some examples such as the spatio-temporal regression of cross-sectional velocity field in a turbulent channel flow and the super-resolution reconstruction of a two-dimensional isotropic turbulence. In addition to the machine learning of turbulent flows, the methodology to extract the lower dimensional dynamics is introduced through simpler flow problems involving laminar vortex shedding.

INTRODUCTION

Modern turbulence research has a history of more than 100 years. Although numerical prediction of turbulence at the laboratory level has made remarkable progress in the recent 50 years, true understanding of turbulence phenomena and their control are still challenging issues due to their inherent strong nonlinearity and multi-scale nature.

Until now, various numerical simulations and experimental measurements have been performed to understand the essence of turbulence. Direct numerical simulations (DNS) can now be performed with billions of degrees of freedom, which produce *big data* of turbulence. In order to understand the dynamics of turbulence from those *big data* and to control it, many attempts have been made primarily based on the linear theory. However, nonlinear mechanisms such as vortex deformation and breakdown, which should be as important as the linear mechanisms such as streak formation in the self-sustaining process, cannot be extracted by the methods based on the linear theory. For instance, in our group, the resolvent analysis [1] has been utilized to analyze and improve the performance of the suboptimal control law developed for turbulent friction drag reduction [2]. In this example, the resolvent based analysis of the control law in the wavenumber-frequency space [3] was successfully utilized to design an improved control law [4], but the amount of improvement was limited likely due to the nonlinearity accounted for just as an external forcing in the resolvent framework. Therefore, development of methods that can directly deal with the nonlinearity of turbulence is awaited. If such methods are successfully developed, those methods can also be applied to construct more efficient control laws.

In the present talk, we introduce some of our recent efforts to establish some building blocks required to achieve machine learning (ML) based control of turbulence. We adopt the convolutional neural network (CNN) to extract lower order dynamics of flows, and its performance is demonstrated through some examples such as spatio-temporal regression of cross-sectional velocity field in a turbulent channel flow [5] and super-resolution reconstruction of a two-dimensional isotropic turbulence [6]. In addition to the machine learning of turbulent flows, the methodology to extract the lower dimensional dynamics [7, 8] is introduced through a simpler flow problem involving laminar vortex shedding. For the recent studies in this field conducted by other research groups, readers are referred to the very recent review paper by Brunton et al. [9].

APPLICATIONS OF CONVOLUTIONAL NEURAL NETWORK TO TURBULENT FLOWS

Spatio-temporal regression of cross-sectional velocity field in a turbulent channel flow [5]

We used an autoencoder-type CNN with a fully connected multilayer perceptron in the middle, as schematically shown in Fig. 1 for spatio temporal regression of the cross-sectional velocity field in a turbulent channel flow at the friction Reynolds number of $Re_\tau = 180$. The ML model was trained using the DNS data so as to work as a surrogate model to the discretized Navier-Stokes equation. From the *a priori* test, the spatio-temporal evolution of cross-sectional structure is found to be reasonably well reproduced only by recycling the output to the input within this ML model. As an *a posteriori test,* we utilized this ML model as the spatio-temporally varying inflow condition for DNS of inflow-outflow turbulent channel flow. It was demonstrated that the present ML model can be used as a turbulent inflow generator with much lower computational cost than the conventional driver DNS.

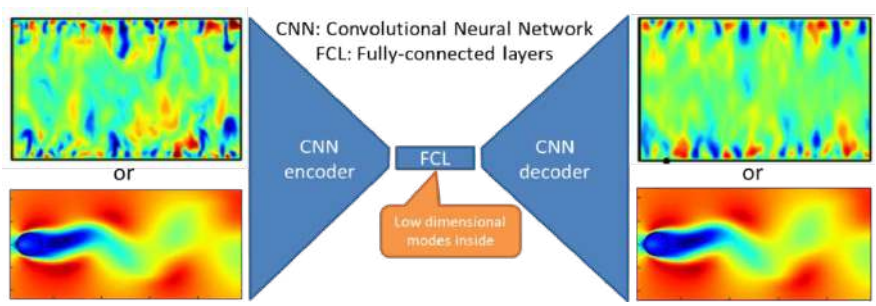

Figure 1. Schematic of the generic structure of the neural network models introduced in the present talk.

Super-resolution reconstruction of two-dimensional isotropic turbulence [6]

In this example, we used a similar CNN-based network for super-resolution reconstruction of flow field from grossly under-resolved flow field data of two-dimensional decaying isotropic turbulence. To account for the multiscale nature of the flow field, a variant of CNN structure called the hybrid downsampled skip-connection/multi-scale (DSC/MS) model was proposed. The present ML-based super-resolution technique was found to be able to reconstruct the flow field with 192×192 resolution with a reasonable accuracy even from an extremely coarse input of 4×4 pixels, in contrast to other reconstruction methods such as the bicubic interpolation and the conventional CNN. The present results imply a great potential of CNN-based networks for revealing subgrid-scale physics.

MACHINE LEARNING BASED REDUCED ORDER MODELING

Nonlinear mode decomposition using CNN autoencoder [7]

Using another variant of CNN autoencoder, called MD-CNN-AE, we proposed a new nonlinear mode decomposition method to visualize the decomposed flow fields. A flow around a circular cylinder at Re = 100 was mapped into two nonlinear modes in the latent space and then these two modes are visualized in the physical space. It was found that each single mode decomposed using the MD-CNN-AE with nonlinear activation contains multiple POD modes in a physically interpretable manner. The same was confirmed for a slightly more complicated problem involving a transient wake. The present results suggest a great potential for the MD-CNN-AE to be used for feature extraction of flow fields in lower dimensions than POD, although its applicability for turbulent flow needs further investigation.

Extracting dynamics of low dimensional nonlinear modes [8]

We also attempted to extract the governing equations for the two extracted nonlinear modes for the above cylinder flow problem using SINDy [10]. It was found that the dynamics of the flow can be successfully extracted as a state equation when the parameter for L_1 regularization is properly chosen. The optimal choice of the parameter, however, is not known *a priori* and needs to be asessed *a prosteriori*, which gives some technical difficulties in using SINDy for extracting nonlinear reduced order dynamics.

OUTLOOK TOWARD MACHINE LEARNING BASED CONTROL OF TURBULENCE

Once a turbulent flow is successfully represented with reasonably few nonlinear modes, it may not be so difficult to extract their dynamics by using either the sparse nonlinear regression techniques such as SINDYc [11] which accounts for control input or an ML based technique such as the long short term memory (LSTM), which has been demonstrated to excellently reproduce the chaotic behaviour of the nine-equation shear flow model [12]. Control using sparsely placed sensors will also be straightforward [13]. However, the major problem is how to drastically reduce the number of nonlinear modes to successfully represent a turbulent flow. Therefore, the key issue toward successful machine learning based control of turbulence should be further improvement in the low dimensionalization part.

References

[1] McKeon, B. J., Sharma, A. S. critical-layer framework for turbulent pipe flow. *J. Fluid Mech.* **658**, 336-382, 2010.
[2] Lee, C., Kim, J., Choi, H. Suboptimal control of turbulent channel flow for drag reduction. *J. Fluid Mech*. **358,** 245–258.
[3] Nakashima, S., Fukagata, K., Luhar, M. Assessment of suboptimal control for turbulent skin friction reduction via resolvent analysis. *J. Fluid Mech.* **828**, 496-526, 2017.
[4] Kawagoe, A., Nakashima, S., Luhar, M., Fukagata, K. Proposal of control laws for turbulent skin-friction reduction based on resolvent analysis. *J. Fluid Mech.* **866**, 810-840, 2019.
[5] Fukami, K., Nabae, Y., Kawai, K., Fukagata, K. Synthetic turbulent inflow generator using machine learning. *Phys. Rev. Fluids* **4**, 064603, 2019.
[6] Fukami, K., Fukagata, K., Taira, K. Super-resolution reconstruction of turbulent flows with machine learning. *J. Fluid Mech.* **870**, 106-120, 2019.
[7] Murata, T., Fukami, K., Fukagata, K. Nonlinear mode decomposition with convolutional neural networks for fluid dynamics. *J. Fluid Mech.* **882**, A13, 2020.
[8] Murata, T., Fukami, K., Fukagata, K. CNN-SINDy based reduced order modeling of unsteady flow fields. The ASME-JSME-KSME Joint Fluids Engineering Conference 2019 (AJKFLUIDS2019), San Francisco, CA, USA, July 28-August 1, 2019, Paper 5056.
[9] Brunton, S. L., Noack, B. R. Koumoutsakos, P. Machine learning for fluid mechanics. *Annu. Rev. Fluid Mech.* **52**, 477-508, 2020.
[10] Brunton, S. L., Proctor, J. L., Kutz, J. N. Discovering governing equations from data by sparse identification of nonlinear dynamical systems. *Proc. Natl. Acad. Sci.* **113**, 3932-3937, 2016.
[11] Brunton, S. L., Proctor, J. L., Kutz, J. N. Sparse Identification of Nonlinear Dynamics with Control (SINDYc). *IFAC-PapersOnLine* **49**, 710-715, 2016.
[12] Srinivasan, P. A., Guastoni, L., Azizpour, H., Schlatter, P., Vinuesa, R. Predictions of turbulent shear flows using deep neural networks. *Phys. Rev. Fluids* **4**, 054603, 2019.
[13] Nair, N. J., Goza, A. Leveraging reduced-order models for state estimation using deep learning. arXiv:1912.10553 [physics.flu-dyn], 2019.

RECOVERY OF TURBULENT PIPE FLOW DOWNSTREAM OF A SQUARE BAR ROUGHNESS

Liuyang Ding*[1] and Alexander Smits[1]
[1]Mechanical and Aerospace Engineering, Princeton University, Princeton, New Jersey 08544, USA

Summary The recovery of turbulent pipe flow at $Re_D = 156,000$ downstream of an axisymmetric square bar roughness is studied. Two bar sizes are tested: $h/D = 0.05$ and 0.1 (bar height h, pipe diameter D). Particle image velocimetry (PIV) is utilized to measure turbulence statistics in an axial-radial plane and over a downstream distance of $100h$. Three stages of recovery are identified: the self-similar development of the shear layer, the diffusion of turbulence towards the center region of the pipe, and the decay of turbulence throughout the pipe cross-section. h is shown to be the length scale governing the flow evolution in the first two stages. R is potentially the length scale for the third stage, which is to be confirmed with data further downstream ($h/D \sim 200$). The recovery is found to be long-lasting and non-monotonic.

INTRODUCTION

Wall-bounded turbulent flows subjected to step or impulse changes in surface conditions are commonly encountered in laboratory experiments and engineering applications. We are interested in small perturbations, i.e. the length scale of the perturbation is small as compared to the integral length scale of the flow. Examples include the flow over the surface of a vehicle where there is a small height mismatch between two panels, a screw, or a change in surface roughness; the flow over the joint of two sections in a pipe or channel. Such flows have been largely overlooked in the past. Scaling laws for the downstream evolution of the flow are lacking. We do not know to what extent these small perturbations challenge the validity of well established experimental methods. Also, it is unclear whether classical modeling approaches for RANS and LES would succeed in predicting the flow.

Past investigations have manifested some intriguing but not fully understood aspects of flows subjected to abrupt changes in surface conditions. First, the recovery to equilibrium is a long-lasting process. For example, a turbulent boundary layer over a fence or step of height h does not return to the ordinary boundary-layer state even at a downstream distance of a few hundreds of h [1]. The length scale on which the flow evolves far downstream is still an open question. Second, the recovery is non-monotonic. Quantities such as the Reynolds shear stress and the friction coefficient typically evolve like a damped harmonic oscillator, with the valley noticeably below the equilibrium-state value [2, 3]. The physical mechanism driving the non-monotonic recovery has not been thoroughly explained.

We study in this work a fully developed turbulent pipe flow over an axisymmetric square bar roughness. The flow recovery to equilibrium is of our primary interest. This flow possesses the advantage of having well defined boundary conditions. Therefore, it provides an ideal test case for computational approaches such as RANS and LES.

EXPERIMENTAL METHOD

The experiment is conducted in a recirculating pipe facility with an inner diameter of D = 19.05 mm in the development and test sections. The development length is approximately $200D$, ensuring the flow being fully developed upstream of the square bar roughness. With water being the working fluid, the bulk Reynolds number is $Re_D = U_b D/\nu = 156,000$, and the friction Reynolds number is $Re_\tau = u_\tau R/\nu = 3,550$. Here, U_b, u_τ, ν and R are, respectively, the bulk velocity, the friction velocity, the kinematic viscosity of water, and the pipe radius. The axisymmetric square bar is held in position by friction, and three bar sizes are tested: h/D = 0.02, 0.05, and 1. The schematic of an axial-radial slice of the test geometry is depicted in figure 1.

Particle image velocimetry (PIV) is utilized to measure the in-plane velocity components in an axial-radial plane. The measurement domain spans over a distance of $100h$ downstream of the square bar roughness. A single PIV camera (LaVision Imager sCMOS) is deployed at multiple downstream stations with a magnification of 0.32 (49 pix/mm). Statistics of the flow are computed with 10,000 realizations.

RESULTS AND BRIEF DISCUSSION

We identify three stages for the evolution of the flow downstream of the square bar roughness. The first stage features the self-similar development of the shear layer arising directly from the separation on the square bar. As seen in figure

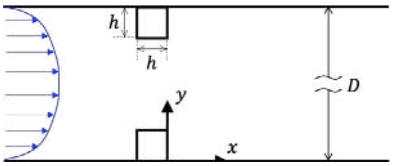

Figure 1: Schematic of an axial-radial slice of the test geometry.

*Corresponding author. E-mail: liuyangd@princeton.edu

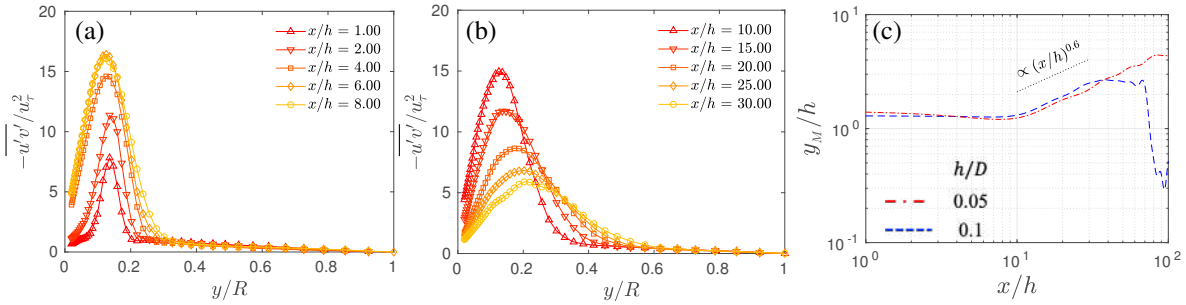

Figure 2: Development of the Reynolds shear stress distribution for $h/D = 0.05$: (a) the self-similar growth of the shear layer until $x/h \approx 10$; (b) the diffusion of turbulence towards the center region of the pipe; (c) the location of peak shear stress, y_M, against the downstream distance, x, suggesting that h is the correct length scale for the early stage of the flow evolution. u_τ is the friction velocity of the upstream fully developed flow.

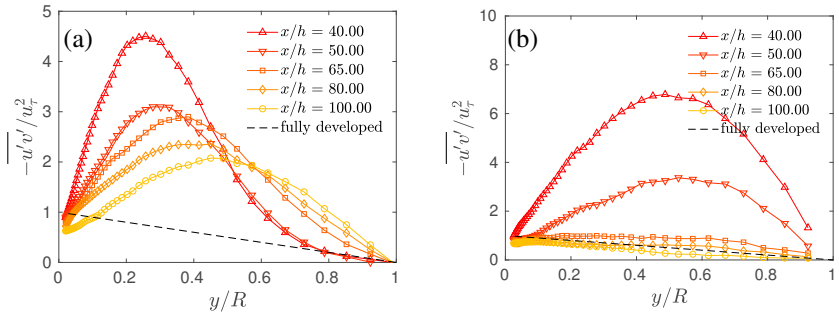

Figure 3: The far-field ($40 < x/h < 100$) evolution of the Reynolds shear stress for h/D = 0.05 (a) and 0.1 (b). u_τ is the friction velocity of the upstream fully developed flow.

2a, the distribution of the Reynolds shear stress ($-\overline{u'v'}$) for $h/D = 0.05$ grows in both its strength and width. The peak location is slightly above $y/D = 0.05$ ($y/R = 0.1$) and moves slowly towards the wall until $x/h \approx 10$. $x/h \approx 10$ marks the beginning of the second stage, during which the shear layer starts to interact with the wall. It is evident in figure 2b that the region of strong turbulence near the wall gradually diffuses into the center region of the pipe. The peak value of $-\overline{u'v'}$ decreases, and the peak location moves away from the wall. Flow evolution in the above two stages originates from the perturbation of scale h on the wall. The presence of the perturbation and the wall directly affects the evolution of the flow, but the confined geometry of the pipe does not. Therefore, it is reasonable to expect h to be the length scale governing the flow evolution in these two stages. This postulation is supported by the result in figure 2c, in which the peak location of $-\overline{u'v'}$, y_M, is plotted against the downstream distance, x. When both quantities are scaled by h, the curves for $h/D = 0.05$ and 0.1 collapse upstream of $x/h \approx 30$. The plot also distinctly shows the two stages divided by $x/h \approx 10$, and the diffusion of turbulence in the second stage follows a power law of $(x/h)^{0.6}$.

The confined geometry of the pipe, i.e. the radius R (or diameter D), kicks in after the second stage. Following the diffusion of turbulence, the third stage is initiated by the merging of turbulence in the center region of the pipe. Thereby, the onset location of the third stage is a function of h/D. It is clear in figure 2c that the second stage for $h/D = 0.05$ continues until at least, and probably beyond, $x/h = 100$, while for $h/D = 0.1$ the third stage starts after $x/h \approx 30$. Consequently, the evolutions of $-\overline{u'v'}$ for the two bar sizes are fundamentally different in the far field ($x/h > 30$). For $h/D = 0.05$, the diffusion of turbulence is still ongoing in $40 < x/h < 100$, as seen in figure 3a. However, $-\overline{u'v'}$ of $h/D = 0.1$ is noticeably dissipated throughout the cross-section of the pipe. At $x/h = 100$, $-\overline{u'v'}$ of $h/D = 0.05$ is significantly above the equilibrium state, whereas $-\overline{u'v'}$ of $h/D = 0.1$ falls below the equilibriums state. These observations are consistent with previous findings that the flow recovery is a long-lasting and non-monotonic process.

Ongoing effort is focused on the length scale of the far-field recovery. R is a potential candidate, which is to be justified with data further downstream ($x/h \sim 200$). Also, the data for the smallest bar size, $h/D \approx 0.02$, is being analyzed to provide more insights into the flow recovery downstream of weak perturbations. We expect to finish data processing in February and have all presentable results ready in May, well before the conference (Aug. 23 – 28, 2020).

References

[1] Bradshaw, P. and Wong, F. Y. F. (1972). The reattachment and relaxation of a turbulent shear layer. Journal of Fluid Mechanics, 52(1), 113-135.

[2] Smits, A. J., Young, S. T. B., and Bradshaw, P. (1979). The effect of short regions of high surface curvature on turbulent boundary layers. Journal of Fluid Mechanics, 94(2), 209-242.

[3] Van Buren, T., Hellström, L. H. O., and Smits, A. J. (2019). Turbulent pipe flow response to rough-to-smooth step change in roughness: flow structure. 11th International Symposium on Turbulence and Shear Flow Phenomena, Southampton, UK.

LARGE EDDY SIMULATION WITH A MACHINE-LEARNING-BASED SUBGRID-SCALE MODEL

Jongwhan Park[1] and Haecheon Choi[1]
[1]Department of Mechanical Engineering, Seoul National University, Seoul, Korea

Summary We apply a neural network (NN) to model the subgrid-scale (SGS) stress and perform large eddy simulation (LES). NNs are trained to predict the SGS stress for two turbulent flows: forced isotropic turbulence and turbulent channel flow. For isotropic turbulence, an NN-SGS model using stencils of velocity components performs better than the Smagorinsky model for the prediction of the energy spectrum. For turbulent channel flow, an NN-SGS model using stencils of velocity components shows the highest correlation coefficient between true and predicted SGS stresses. In actual LES, however, this NN-SGS model provides inaccurate statistics due to overpredicted backscatter. On the other hand, an NN-SGS model using the strain rate tensor shows excellent agreements with the filtered mean velocity and Reynolds shear stress from DNS data, even without any wall damping function or *ad hoc* clipping.

Large eddy simulation (LES) resolves only large-scale turbulent flows, and the effect of subgrid-scale (SGS) flow on the resolved one is modeled. The aim of SGS modeling is to find the relation between the resolved flow and SGS stress. A conventional approach for the SGS modeling is to approximate the SGS stress with the resolved flow in an arithmetic form based on a turbulence theory and hypothesis. For example, the Smagorinsky model assumes that the SGS stress is linearly correlated with the strain rate tensor (Smagorinsky [1]). However, the Smagorinsky model is purely dissipative and cannot predict the energy transfer from unresolved to resolved scale flows (backscatter). In addition, the Smagorinsky model provides low correlations between the SGS stress and the true SGS stress from DNS data. To overcome these limitations, machine-learning-based SGS models without any assumption on the model form have been developed. In the case of two- or three-dimensional isotropic turbulence (Wang *et al.* [2]; Maulik *et al.* [3]; Xie *et al.* [4]), SGS models based on neural networks (NN) showed better performances than the physics-based SGS models. In the case of turbulent channel flow, Gamahara & Hattori [5] conducted LES with an NN using the velocity gradient tensor and wall-normal location and showed high correlations between the SGS stresses from the model and DNS data in *a priori* test. However, this NN-SGS model had no advantages over the Smagorinsky model in the actual LES for predicting the mean velocity and Reynolds stresses.

In the present study, we apply NNs for SGS modeling and conduct LES of two canonical turbulent flows: forced isotropic turbulence at Re_λ=73 and turbulent channel flow at Re_τ=180, respectively. We use NNs to predict pointwise SGS stress (τ_{ij}) with a resolved flow variable: $\tau_{ij}=\overline{u_iu_j}-\bar{u}_i\bar{u}_j=f(\bar{x})$, where $u_i(=u_1, u_2, u_3)$ is the velocity, an overbar denotes a filtering operation, and $\bar{x}$ (resolved flow variable) is a user-defined input variable of NNs. Direct numerical simulations of forced isotropic turbulence at Re_λ=73 and turbulent channel flow at Re_τ=180 are conducted to obtain instantaneous τ_{ij} and $\bar{x}$. We use NNs consisting of two hidden layers and 128 neurons per layer, and optimize them to minimize the mean-squared-error between the SGS stresses from NN-SGS model and DNS data. We test several input flow variables ($\bar{x}$) such as the strain rate tensor, velocity gradient tensor and local stencils of velocity components at 3×3×3 grids. *A priori* and *a posteriori* tests are conducted to investigate the performances of NN-SGS models considered.

For isotropic turbulence, the NN-SGS model with stencils of the velocity components as an input variable outperforms the Smagorinsky model for the predictions of the SGS dissipation, energy spectrum, and vortical structures (figure 1). The NN-SGS model trained is also applied to the LES of different grid resolution and higher Reynolds number (Re_λ=115), resulting in more accurate solution than the dynamic Smagorinsky model (Germano *et al.* [6]; Lilly [7]). The results from other NN-SGS models with the input variables of the strain rate and velocity gradient tensors will be also discussed in the presentation.

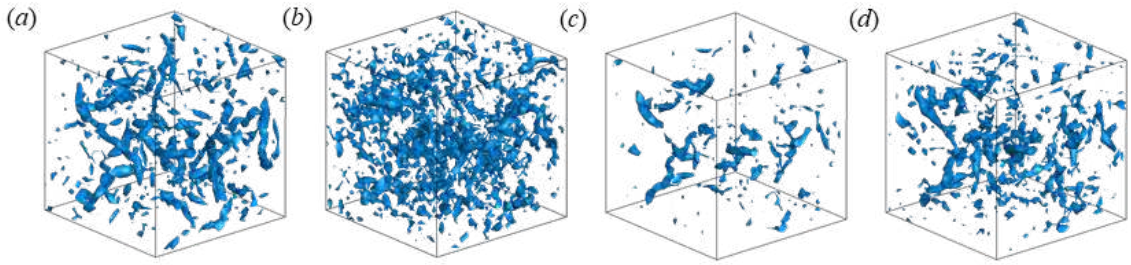

Figure 1. Instantaneous vortical structures of isotropic turbulence: (*a*) filtered DNS; (*b*) coarse DNS; (*c*) LES with dynamic Smagorinsky model; (*d*) LES with an NN-SGS model using stencils of the input velocity components

For turbulent channel flow, an NN-SGS model with stencils of input velocity components provides highly correlated SGS stresses with those from DNS data, and predicts backscatter more accurately than other models considered in *a priori* test. In the actual LES, however, the NN-SGS models that predicted the backscatter very well in *a priori* test severely overpredict the backscatter, resulting in inaccurate statistics. On the other hand, an NN-SGS model with the strain rate tensor as an input variable shows excellent predictions of the filtered mean velocity and Reynolds shear stress, even

without any wall damping function or *ad hoc* clipping (figure 2). The NN-SGS model trained at Re_τ=180 is also applied to the LES at $Re_\tau \approx 720$, and shows a good prediction capability.

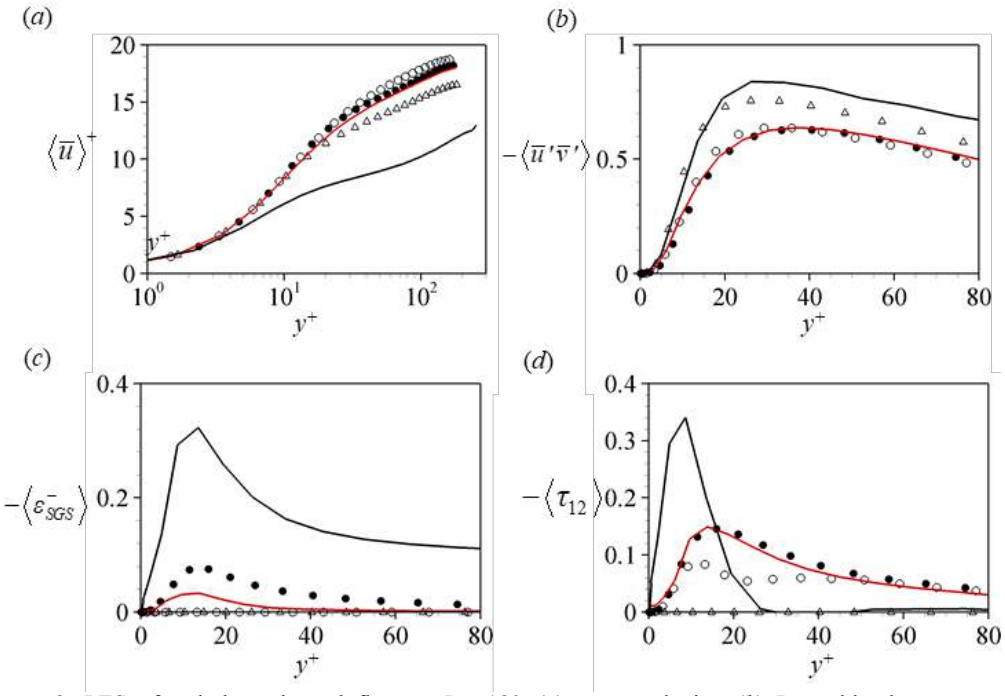

Figure 2. LES of turbulent channel flow at Re_τ=180: (*a*) mean velocity; (*b*) Reynolds shear stress; (*c*) backscatter; (*d*) SGS shear stress. ●, Filtered DNS; Δ, coarse DNS; ○, dynamic Smagorinsky model; —, NN using stencils of the velocity components; —, NN using the strain rate tensor.

Acknowledgements

This work is supported by the National Research Foundation through the Ministry of Science and ICT (no. 2019R1A2C2086237).

References

[1] Smagorinsky J. General circulation experiments with the primitive equations. *Monthly Weather Review* **91**: 99-164, 1963.
[2] Wang Z., Luo K., Li D., Tan J. & Fan J. Investigations of data-driven closure for subgrid-scale stress in large-eddy simulation. *Phys. Fluids* **30**: 125101, 2018.
[3] Maulik R., San O., Rasheed A. & Vedula P. Subgrid modelling for two-dimensional turbulence using neural networks. *J. Fluid Mech.* **858**: 122-144, 2019.
[4] Xie C., Wang J., Li K. & Ma C. Artificial neural network approach to large-eddy simulation of compressible isotropic turbulence. *Phys. Rev. E.* **99**:053113, 2019
[5] Gamahara M. & Hattori Y. Searching for turbulence models by artificial neural network. *Phys. Rev. Fluids* **2**: 054604, 2017.
[6] Germano M., Piomelli U., Moin P. & Cabot W. H. A dynamic subgrid-scale eddy viscosity model. *Phys. Fluids* **3**: 1760-1765, 1991.
[7] Lilly D. K. A proposed modification of the Germano subgrid-scale closure method. *Phys. Fluids* **4**: 633-635, 1992.

EXPLORING ISOTROPIC TURBULENCE RELATIONS WITH CENTERLINE TURBULENCE

Clayton P. Byers*[1], Matt K. Fu[2], Ivan Marusic[3], and Marcus Hultmark[4]
[1]Department of Engineering, Trinity College, Hartford, CT 06106 USA
[2]Department of Civil and Environmental Engineering, Stanford University, Stanford, CA 94305 USA
[3]Department of Mechanical Engineering, University of Melbourne, Victoria 3010, Australia
[4]Department of Mechanical and Aerospace Engineering, Princeton University, Princeton, NJ 08544 USA

Summary Isotropic relations form a cornerstone of turbulence research, but the exact extent of their validity in different flow configurations is always elusive. An investigation of multiple isotropic relations for high Reynolds number turbulence has been performed along the centerline of a turbulent pipe flow. Utilizing a nanoscale crosswire, simultaneous measurements of the streamwise and radial component of velocity were acquired and the consistency of several different isotropic dissipation estimates were evaluated. The estimations indicate that isotropic dissipation relations can work in limited regions, and no universality is found at the moderate Reynolds numbers of the experiments performed. A correction for inhomogeneity is shown to be necessary for increasing separation of the structure functions, but is less prominent with increasing Reynolds number.

INTRODUCTION

The study of high Reynolds number turbulence and turbulence theory often relies upon the assumption of local isotropy of the small scales in the flow. This assumption allows for the estimation of the viscous dissipation, ϵ, from fully resolved measurements of a single fluctuating component of the velocity field. Two commonly obtained examples are the streamwise estimate, ϵ_u, and radial estimate, ϵ_v, both of which are given in equation 1:

$$\epsilon_u = 15\nu \int_0^\infty k_1^2 \phi_{11}(k_1) \mathrm{d}k_1, \quad \epsilon_v = \frac{15}{2}\nu \int_0^\infty k_1^2 \phi_{22}(k_1) \mathrm{d}k_1. \tag{1}$$

Here, k_1 is the streamwise wavenumber, ϕ_{ii} corresponds to the spectrum function in the i direction, u is the $i = 1$ streamwise velocity fluctuation, v is the $i = 2$ radial velocity fluctuation, and ν is the kinematic viscosity of the flow. The refined similarity hypothesis of Kolmogorov [3], seen in equation 2, provides another dissipation estimate:

$$\epsilon_{\langle(\Delta u)^3\rangle} = -\frac{5}{4}\frac{\langle(\Delta u)^3\rangle}{r}, \tag{2}$$

where $\Delta u = u(x + (r/2)) - u(x - (r/2))$ is the streamwise velocity increment at location x with streamwise separation r, and $\langle\cdot\rangle$ indicates ensemble averaging. Though derived in the limit of high Reynolds number turbulence, this relation is often applied to finite Reynolds number flows. More recently, a generalization of equation 2 was proposed by Danaila et al. [1], shown in equation 3, to incorporate the large scale anisotropic contributions from flow inhomogeneities:

$$\underbrace{-\frac{\langle(\Delta u)^3\rangle}{\epsilon r}}_{\text{Term I}} + \underbrace{\frac{6\nu}{\epsilon r}\frac{\mathrm{d}}{\mathrm{d}r}\langle(\Delta u)^2\rangle}_{\text{Term II}} + \underbrace{\frac{6}{\epsilon r^5}\int_0^r s^4 \left(-\frac{\partial\langle v(\Delta u)^2\rangle}{\partial y}\right)\mathrm{d}s}_{\text{Term III}} = \frac{4}{5}. \tag{3}$$

The estimates for dissipation in equations 1 to 3 will be compared and evaluated with Taylor's dissipation estimate of $\epsilon = Au^3/l$, where u and l are relevant velocity and length scales, respectively, and A is a constant, argued to be universal at sufficiently high Reynolds number. These comparisons will provide an indication of the applicability of local isotropy. The five different estimates of ϵ will be calculated by obtaining high resolution measurements of u and v along the centerline in a turbulent pipe flow. A nanoscale crosswire probe (X-NSTAP) with enhanced spatial and temporal resolution is utilized to obtain these measurements [2].

RESULTS

A test of the universality of A is shown in figure 1, following the methodology of Morrison et al. [4]. In this plot, the relevant velocity and length scale is u_τ, the friction velocity, and R, the pipe radius, respectively. Included in figure 1 is the data presented by Morrison et al. in hollow symbols [4].

The spectral dissipation estimates from the nanoscale crosswire measurements and equation 1 (shown in $\triangle$ and $\triangledown$ symbols) demonstrate good agreement with the data of [4], indicating a nearly linear increase in A with Re_λ. Interestingly, the agreement in the evolution of A with Re_λ for the different spectral measurements is significant and consistent with the assumption of local isotropy, indicating that either streamwise or radial velocity fluctuations provide similar estimates, so long as the resolution is sufficient. Similar agreement between the current and previous study is found with equation

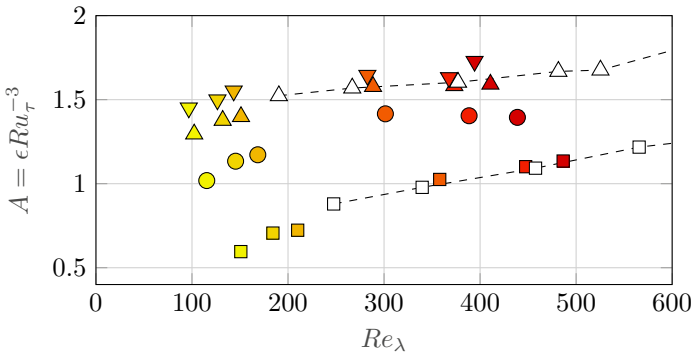

Figure 1: Nondimensional dissipation rate $A = \epsilon R u_\tau^{-3}$. $\triangle$ and $\triangledown$: equation 1. $\square$: equation 2. $\circ$: equation 3 evaluated at the maximum value of the third order structure function. Colors indicate increasing Re_λ from yellow to red. Hollow symbols represent the same parameter from Morrison et al. [4].

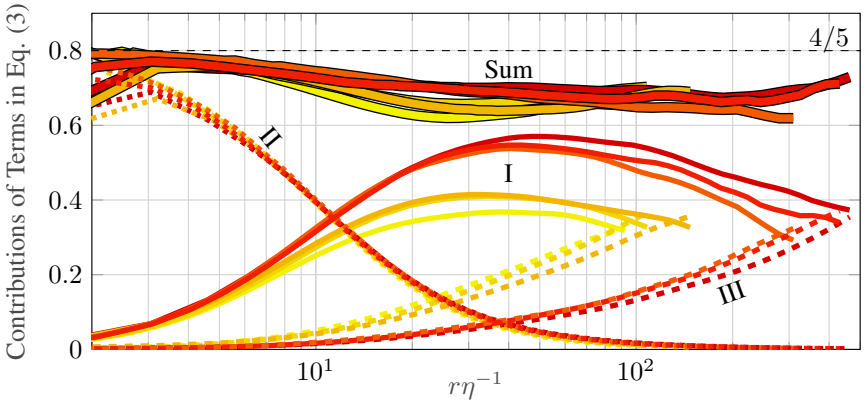

Figure 2: The three terms in equation 3 and their sum as a function of the non-dimensional separation $r\eta^{-1}$, where $\eta = (\nu^3\epsilon^{-1})^{1/4}$ is the Kolmogorov scale. Term I shown in solid lines; Term II shown in dotted lines; Term III shown in dashed lines; the sum of the three terms shown in thick solid lines. Colors of yellow to red indicate increasing Re_λ.

2, shown with $\square$ symbols. A new estimate of A that utilizes equation 3 to extract ϵ at the maximum value of $\langle(\Delta u)^3\rangle$ is shown in $\circ$ symbols and indicates an intermediate estimate between the three other methodologies.

The three terms on the left hand side of equation 3 and their sum are plotted in figure 2. At sufficiently high Reynolds numbers, the sum should equate to $4/5$. Here, we assume that the dissipation in equation 3 is given by the integrated streamwise spectra using equation 1. Consequently, a sum of 4/5 is only observed at the smallest separation where the behavior is entirely dominated by Term II. As the separation increases, the contributions of Term I, representing the inertial contributions, become dominant as predicted by refined similarity hypothesis of Kolmogorov [3]. However, at the abscissa of the maximum value of Term I, the contributions from Terms II and III are non-negligible at these moderate Reynolds numbers.

Despite being able to account for the large scale inhomogeneity along the centerline, the corrected dissipation estimate from equation 3 does not agree with the those obtained from equation 1. The disagreement between the various dissipation estimates even for this nearly isotropic centerline flow motivates the need for further investigation, in particular, measurements of additional velocity components at higher Reynolds number.

References

[1] L. Danaila, F. Anselmet, T. Zhou, and R. A. Antonia. Turbulent energy scale budget equations in a fully developed channel flow. *Journal of Fluid Mechanics*, 430:87–109, 3 2001.

[2] M. K. Fu, Y. Fan, and M. Hultmark. Design and validation of a nanoscale cross-wire probe (X-NSTAP). *Experiments in Fluids*, 60:99, 2019.

[3] A. N. Kolmogorov. A refinement of previous hypotheses concerning the local structure of turbulence in a viscous incompressible fluid at high Reynolds number. *Journal of Fluid Mechanics*, 13(1):82–85, 5 1962.

[4] J. F. Morrison, M. Vallikivi, and A. J. Smits. The inertial subrange in turbulent pipe flow: centreline. *Journal of Fluid Mechanics*, 788:602–613, 2 2016.

*Corresponding author E-mail: clayton.byers@trincoll.edu

THE IMPORTANCE OF POWERFUL DETRAINMENT EVENTS WHEN TURBULENT SHEAR FLOW IS EXPOSED TO AN INTENSELY TURBULENT BACKGROUND

Oliver Buxton*[1], Paweł Baj[2], and Krishna Kankanwadi[1]
[1]Department of Aeronautics, Imperial College London, London, UK
[2]Department of Energy and Process Engineering, NTNU, Trondheim, Norway

Summary Turbulent entrainment is classically studied in flows for which the background is non-turbulent. Whilst the majority of environmental/industrial flows exist within a turbulent background, entrainment for flows exposed to freestream turbulence is not well understood. In particular, when the background turbulence is particularly intense it is not yet clear whether a turbulent/turbulent interface exists demarcating the primary turbulent flow from the background or whether the entrainment rate is enhanced relative to a non-turbulent background. Here we present results proving the existence of such an interface. Further, we show that the presence of freestream turbulence reduces the entrainment rate with the key parameter being the intensity of the freestream turbulence. We show that intense freestream turbulence promotes powerful detrainment events explaining this finding.

INTRODUCTION

Turbulent entrainment is the process by which mass/energy is transferred into a body of turbulent fluid from the background. The rate of entrainment is determined by the dynamics of the flow in the proximity of the outermost boundary of the turbulent portion, which is characterised by a sharp contorted interface of thin, but finite thickness. When the turbulent fluid is surrounded by irrotational fluid, this boundary is known as the turblent/non-turbulent interface (TNTI) which has been extensively studied over the past two decades [e.g. 1]. The seminal work of Corrsin and Kistler [2] postulated that the mechanism by which vorticity is transferred from the turbulent to the irrotational fluid, and hence the entrainment mechanism, is via the direct action of viscosity; a result that has been verified in more recent years [e.g. 3].

In practical applications, however, entrainment rarely takes place from an irrotational background since most industrial/environmental flows exist within a turbulent background. In such cases the boundary between the primary flow, e.g. a turbulent wake, and the background is no longer the TNTI but the turbulent/turbulent interface (TTI). In such circumstances the intuition of Corrsin and Kistler [2] no longer holds since inertial mechanisms may also be responsible for transferring vorticity/mass across the TTI. At present there is no consensus as to whether the presence of freestream turbulence increases [e.g. 4] or decreases [e.g. 5] the rate of entrainment relative to that from an irrotational background. Our uncertainty of the understanding of turbulent/turbulent entrainment (TTE) is particularly acute when the background turbulence intensity is high. In the review paper of da Silva et al. [6] it was even suggested that when the turbulence intensity of the background becomes comparable to that in the primary turbulent flow the TTI breaks down entirely.

EXPERIMENTAL METHODS

Two experimental datasets are presented in this abstract, both of which were acquired using simultaneous particle image velocimetry (PIV) and planar laser induced fluorescence (PLIF) in the Imperial College London hydrodynamics flume [e.g. 7]. In both datasets in excess of 2,500 combined PIV/PLIF snapshots were collected. The two configurations are a two dimensional multi-scale array of rectangular bars (of three different thicknesses) and a circular cylinder exposed to freestream turbuulence produced by an assortment of turbulence-generating grids. The freestream turbulence was categorised into three groups (1, 2 and 3) according to the intensity of the freestream turbulence in the field of view, which was 37-41 cylinder diameters downstream of the cylinder. This abstract specifically considers group 3 in which the freestream turbulence intensity was greater than the turbulence intensity in the wake when no grid was used (9.8%). The first configuration gives us access to TTE between different sized wakes in which there is a strong coherent aspect to the "background" turbulence and the second configuration yields TTE in which the background turbulence is intense but incoherent. A high Schmidt number scalar (Rhodamine 6G, $Sc \approx 2.5 \times 10^3$ in water) is used to mark the primary portion of the flow, which is seeded isokinetically through a small pinhole into the wake of interest (the smallest rectangular bar and the circular cylinder, respectively). More details on the experimental methods can be found in Baj and Buxton [7].

RESULTS AND DISCUSSION

Figure 1(a) shows the mean enstrophy ($\omega^2 = \boldsymbol{\omega} \cdot \boldsymbol{\omega}$, where $\boldsymbol{\omega}$ is the vorticity vector) conditioned on distance normal to the location of the TTI, γ. $\gamma = 0$ corresponds to the outermost boundary between the wake and the background and was determined using a threshold on $|\nabla\phi|$, where ϕ is the signal recorded by the PLIF camera. This threshold detection was validated against the no-grid run and detection of the TNTI using the classical enstrophy threshold technique reported frequently in the literature [e.g. 6]. In a result that is reminiscent of the classical TNTI result it can be seen that there is a jump in the conditional mean enstrophy across the TTI, regardless of the level of the background turbulence - even for the

*Corresponding author. E-mail: o.buxton@imperial.ac.uk.

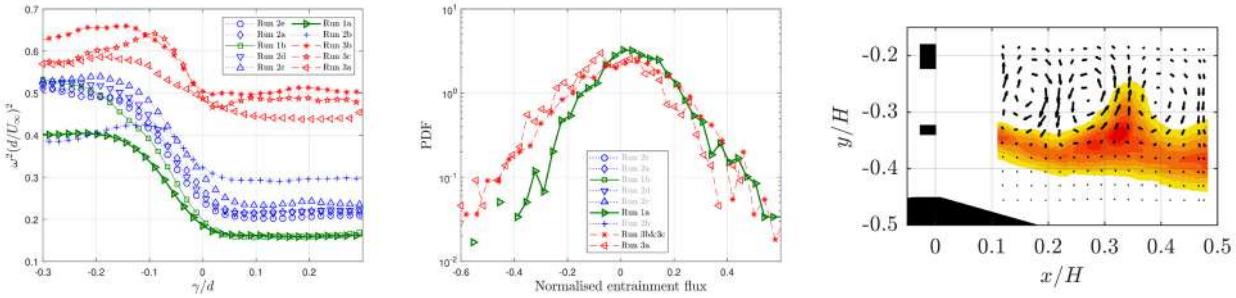

(a) (b) (c)

Figure 1: (a) Conditional enstrophy jump across the TTI for various experimental runs. Note group 3 refers to the runs with intense background turbulence. (b) Probability density functions for the computed normalised entrainment mass flux per snapshot. (c) Phase-averaged velocity and scalar fields for TTE between adjacent wakes in the multi-scale array.

group 3 cases in which the background turbulence intensity is higher than the "natural" turbulence intensity of the wake, i.e. for the wake in which the cylinder was not exposed to any freestream turbulence (no-grid run). This result proves the existence of the TTI even for cases with extreme freestream turbulence intensity, and thereby refutes the postulation in da Silva et al. [6] that the interface may break down entirely in such cases.

The specific "runs" in figure 1(a) correspond to an exploration of the two-dimensional $\{\mathcal{L}, u'\}$ freestream turbulence parameter space, where $\mathcal{L}$ corresponds to the integral length scale and u' corresponds to the rms velocity fluctuation (or turbulence intensity) of the freestream turbulence. Our results (not shown in this abstract for brevity) show that the entrainment mass flux is a decreasing function of u' but it is uncorrelated to $\mathcal{L}$. This is despite the fact that an increase in $\mathcal{L}$ and u' are both correlated to an increased contortion of the TTI and hence an increase in surface area over which entrainment may take place. The explanation for why an increasingly contorted TTI, and hence increased surface area, corresponds to a reduction in entrainment rate is provided in figure 1(b). This shows probability density functions (PDFs) of the normalised entrainment mass flux per snapshot for the reference no-grid run and the group 3 (intense freestream turbulence) runs. It can be seen that whilst the right tails (entrainment events) of the PDFs are similar there is a large discrepancy between the left tails of the group 3 runs and the no-grid run. This shows that intermittent, but powerful detrainment events (fluid is transported across the TTI from the wake to the background) occur significantly more frequently when there is intense freestream turbulence. Multi-scale analysis (again not presented for brevity) shows that the entrainment mass flux is virtually constant as a function of length scale, a result that mirrors classical entrainment from a non-turbulent background. This explains the dependence of the entrainment rate on u' but not $\mathcal{L}$, since the complete spectrum of turbulent length scales are involved in the entrainment processes, not simply the energy-containing scales.

Figure 1(c) shows the phase-averaged combined scalar and velocity fields for the intersection between the wakes produced by the small and medium bars in the multi-scale array. In this configuration the scalar was seeded into the wake of the small bar and the medium wake acts as intense "freestream turbulence" with a periodic/coherent component to it associated with the vortex shedding. The phase averaging is done with respect to the periodic velocity fluctuation of the medium wake, i.e. the "freestream turbulence" as far as the seeded, small wake is concerned. Our results indicate that the coherence of the freestream turbulence drives powerful detrainment events in which fluid is transported from the space occupied by the small wake to that occupied by the medium wake, analogous to the powerful detrainment events evidenced in figure 1(b). Our final paper will present analysis based on a multi-scale triple decomposition, i.e. $\boldsymbol{u} = \overline{\boldsymbol{u}} + \sum_j \tilde{\boldsymbol{u}} + \boldsymbol{u}''$ [see, e.g. 7], which tracks the decomposed scalar and energy exchanges that take place during this detrainment.

References

[1] D.K. Bisset, J.C.R. Hunt, and M.M. Rogers. The turbulent/non-turbulent interface bounding a far wake. *J. Fluid Mech.*, 451:383–410, 2002.

[2] S. Corrsin and A.L. Kistler. Free-stream boundaries of turbulent flows. Technical Report NACA Tech. Rep. TN-1244, 1955.

[3] M. Holzner and B. Lüthi. Laminar Superlayer at the Turbulence Boundary. *Phys. Rev. Lett.*, 106(13):134503, 2011.

[4] C.Y. Ching, H.J.S. Fernando, and A. Robles. Breakdown of line plumes in turbulent environments. *J. Geophys. Res.: Oceans*, 100(C3):4707–4713, 1995.

[5] B. Khorsandi, S. Gaskin, and L. Mydlarski. Effect of background turbulence on an axisymmetric turbulent jet. *J. Fluid Mech.*, 736:250–286, 2013.

[6] C.B. da Silva, J.C.R. Hunt, I. Eames, and J. Westerweel. Interfacial Layers Between Regions of Different Turbulence Intensity. *Annu. Rev. Fluid Mech.*, 46(1):567–590, 2014.

[7] P. Baj and O.R.H. Buxton. Passive scalar dispersion in the near wake of a multi-scale array of rectangular cylinders. *J. Fluid Mech.*, 864:181–220, 2019.

WALL-BOUNDED TURBULENCE OVER HIGHLY POSITIVELY AND NEGATIVELY SKEWED ROUGHNESS

Angela Busse*[1] and Thomas O. Jelly[1,2]
[1]James Watt School of Engineering, University of Glasgow, Scotland
[2]Department of Mechanical Engineering, University of Melbourne, Australia

Summary While most engineering rough surfaces have only moderately skewed height distributions, examples of irregular rough surfaces with very high positive or negative skewness are not unusual. In the current study, the fluid dynamic properties of a set of seven irregular rough surfaces with skewness varying from -2.3 to $+2.3$ are investigated using direct numerical simulations of turbulent channel flow. We observe that the roughness function saturates both for very high positive and very high negative skewness, showing that extrapolation of existing empirical correlations for moderate skewness will overpredict the roughness effect for extremely skewed cases.

INTRODUCTION

The fluid dynamic effects of a rough surface are known to increase with the roughness height but are also influenced by a number of other topographical parameters. Amongst these, the skewness of the height distribution Ssk has been identified as a key topographical parameter [1]. The effect of surface skewness on wall-bounded turbulence has been the subject of both experimental [2] and numerical [3] investigations. However, the skewness values covered in these studies encompass only a relatively narrow range for this parameter not exceeding $Ssk \approx \pm 1$. When surveying the skewness and kurtosis Sku values of typical engineering rough surfaces (see map shown in figure 1(a)), we observe that while many rough surfaces have only moderately skewed height distributions, cases with $Ssk \gg 1$ or $Ssk \ll -1$ commonly occur. For example, surfaces affected by light calcareaous tubeworm-fouling display high skewness and kurtosis [4], as the sparse tubeworm features cause sharp local deviations relative to surrounding smaller-scale roughness features. The aim of the current study is a systematic investigation of rough surfaces with extreme skewness values, and to test existing empirical correlations developed in the context of previous studies for more moderately skewed roughness [1, 2].

NUMERICAL METHOD

The fluid dynamic properties of seven different rough surfaces with Ssk ranging from -2.3 to $+2.3$ have been investigated using direct numerical simulations of turbulent channel flow.

All rough surfaces have been generated using the surface generation algorithm of Patir [5, 6]. The heightmaps are then passed through a low-pass Fourier filter to generate smoothly-varying rough surfaces [7]. Two representative examples of the resulting rough surfaces are illustrated in figure 1(b). All surfaces have been scaled to the same mean-peak to valley height and have closely matched values in effective slope ($ES \approx 0.2$) to allow the current study to focus on the effects of the higher moments of the height distribution. The skewness and kurtosis values of the investigated cases are representative of values typically found for engineering rough surfaces (see figure 1(a)).

For each surface, a direct numerical simulation of turbulent channel flow at $Re_\tau = 395$ with constant mean streamwise pressure gradient has been conducted. Uniform grid spacing ($\Delta x^+ = \Delta y^+ = 4.94$) and periodic boundary conditions were applied in the streamwise and spanwise directions. In the wall-normal direction, uniform grid spacing was used within the roughness layer ($\Delta z^+_{\text{min}} = 0.67$). Above the highest roughness peak, the wall-normal grid spacing was gradually increased reaching $\Delta z^+_{\text{max}} \approx 5$ at the channel centre.

RESULTS

The roughness function, ΔU^+, and mean streamwise velocity profiles (see figure 2) show that the roughness effect increases with Ssk for moderate values of Ssk consistent with trends observed in previous studies. Outer-layer similarity of the mean streamwise velocity profile is recovered in all cases. However, for very highly positively and negatively skewed cases, the roughness effect saturates - no significant further increase in ΔU^+ is observed as Ssk is increased above 1; similarly, ΔU^+ stays constant for high negative values of $Ssk \leq -1.5$. The observed behaviour can be approximately fitted by a $\tanh$-function. Extrapolation of existing empirical correlations for positively and negatively skewed surfaces [2] to $Ssk > 1$ or $Ssk < -1$ would predict an increase in the roughness function for both high positive and high negative skewness. This difference in behaviour between moderately and extremely skewed surfaces could be attributed to the fact that very highly skewed surfaces are typically characterised by a sparse distribution of extreme roughness peaks or very deep roughness pits embedded into a 'background roughness' composed of smaller roughness features. In contrast, moderately skewed surfaces typically display a much more dense distribution of pits ($Ssk < 0$) or peaks ($Ssk > 0$).

*Corresponding author. E-mail: angela.busse@glasgow.ac.uk.

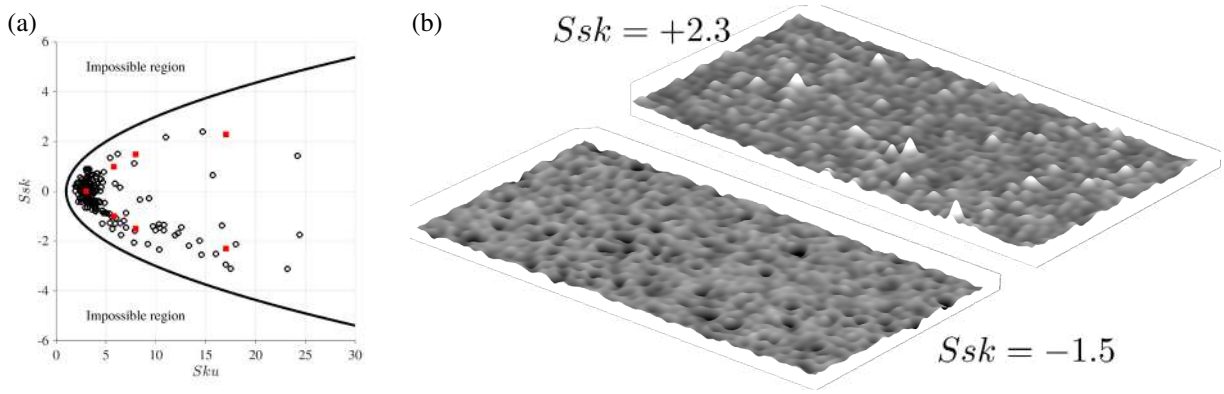

Figure 1: (a) Map of skewness and kurtosis values (black circles) reported for engineering surfaces (for details refer to [8]); the filled red squares indicate the configurations investigated in the current study. (b) Two representative examples of the generated surfaces: case $Ssk = +2.3$ and case $Ssk = -1.5$.

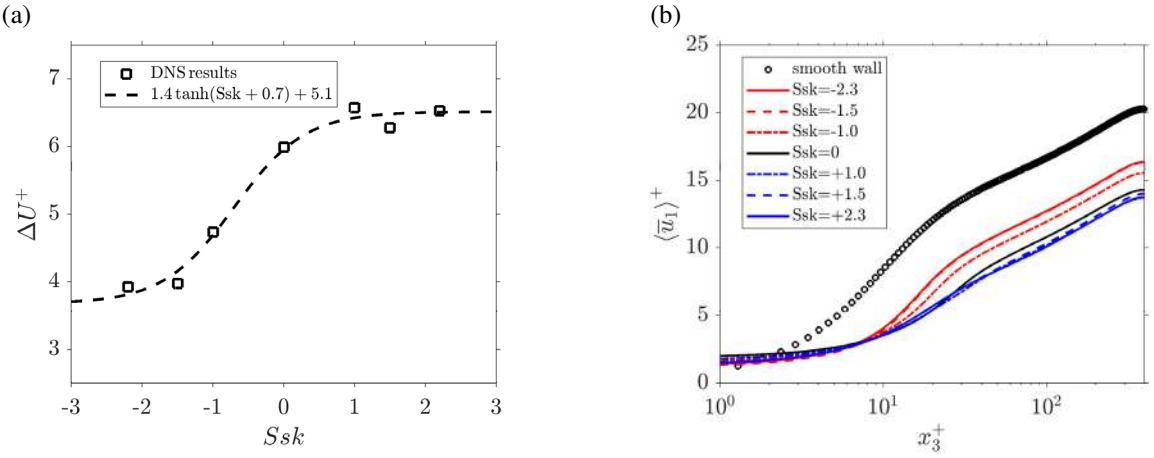

Figure 2: (a) Roughness function ΔU^+ versus skewness Ssk. (b) Mean streamwise velocity profiles.

CONCLUSIONS

Direct numerical simulations of turbulent channel flow over highly positively and negatively skewed surfaces were performed at a friction Reynolds number of 395. The highly skewed surfaces show a saturation in the roughness function for both very high positive and negative values of Ssk (see figure 2). This demonstrates that the fluid dynamic behaviour of highly skewed surfaces cannot be extrapolated from results obtained for more moderately skewed surfaces [1, 2]. A detailed analysis of the turbulent velocity fluctuations, the surface pressure statistics, and their dependence on surface skewness is currently ongoing.

References

[1] Flack K. A., Schultz M. P. Review of hydraulic roughness scales in the fully rough regime. *J. Fluids Eng.* **132**:041203, 2010.
[2] Flack K. A., Schultz M. P., Barros J. Skin friction measurements of systematically-varied roughness: probing the role of roughness amplitude and skewness. *Flow Turbul. Combust.* (2019)
[3] Forooghi P., Stroh A., Schlatter P., Frohnapfel B. Direct numerical simulation of flow over dissimilar, randomly distributed roughness elements: A systematic study of the effect of surface morphology on turbulence. *Phys. Rev. Fluids* **3**:044605 (2018)
[4] Monty J., Dogan E., Hanson R., Scardino A. J., Ganapathisubramani B., Hutchins N. An assessment of the ship drag penalty arising from light calcareous tubeworm fouling. *Biofouling* **32**:451-464, (2016)
[5] Patir N. A numerical procedure for random generation of rough surfaces. *Wear* **47**:263-277, 1978.
[6] Watson W., Spedding T. A. The time series modeling of non-Gaussian engineering processes. *Wear* **83**:215-231, 1983.
[7] Busse A., Lützner M., Sandham N. D. Direct numerical simulation of turbulent flow over a rough surface based on a surface scan. *Comp. Fluids* **116**: 129-147
[8] Jelly T. O. and Busse A. Reynolds number dependence of Reynolds and dispersive stresses in turbulent channel flow past irregular near-Gaussian roughness. *Int. J. Heat Fluid Flow* **80**:108485 (2019)

NON-LOCALITY OF VORTICITY AMPLIFICATION IN TURBULENT FLOWS

Dhawal Buaria*[1,2], Alain Pumir[3,2], and Eberhard Bodenschatz[2,4]
[1]Department of Mechanical and Aerospace Engineering, New York University, New York, USA [2]Max Planck Institute for Dynamics and Self-Organization, Göttingen, Germany
[3]Laboratoire de Physique, Ecole Normale Supérieure de Lyon and CNRS, Lyon, France
[4]Institute for Nonlinear Dynamics, University of Göttingen, Göttingen, Germany

Summary Using highly resolved direct numerical simulations of stationary isotropic turbulence, we investigate the non-local contributions to the process of vortex stretching. In particular, expressing the strain-rate as a Biot-Savart integral over the vorticity field, we decompose it as a sum of a local and a non-local component, and characterize their respective roles in amplifying vorticity. Our results suggest a characteristic length scale of about ten times the Kolmogorov length scale for the non-local effects. We also consider statistics conditioned on vorticity magnitude to understand formation of extreme events.

BACKGROUND AND APPROACH

Small-scale intermittency, which refers to intermittent formation of very localized and intense velocity gradients, is a key characteristic of fluid turbulence [1]. The physical mechanism responsible for the formation of these extreme events is vortex stretching, which results from a non-linear coupling between vorticity and strain-rate. An essential aspect of this coupling is non-locality, whereby vortex stretching in one region of space is affected by the entire flow field, resulting in severe mathematical difficulties. The complexity of the problem is highlighted in Fig. 1, which shows the organization of the intense regions of vorticity and strain rate. Consistent with known results, intense vorticity is found arranged in tube-like structures, surrounded by regions of intense strain, which non-locally amplify the tubes. Thus, a natural question arises, as to what proportion of the stretching acting at a spatial point arises from non-local effects. The objective of the present contribution is to characterize quantitatively this non-locality. To this end, we utilize direct numerical simulations (DNS) of isotropic turbulence with an unprecedented small-scale resolution, going up to 8192^3 grid points and Taylor-scale Reynolds number (R_λ) of 650 [2].

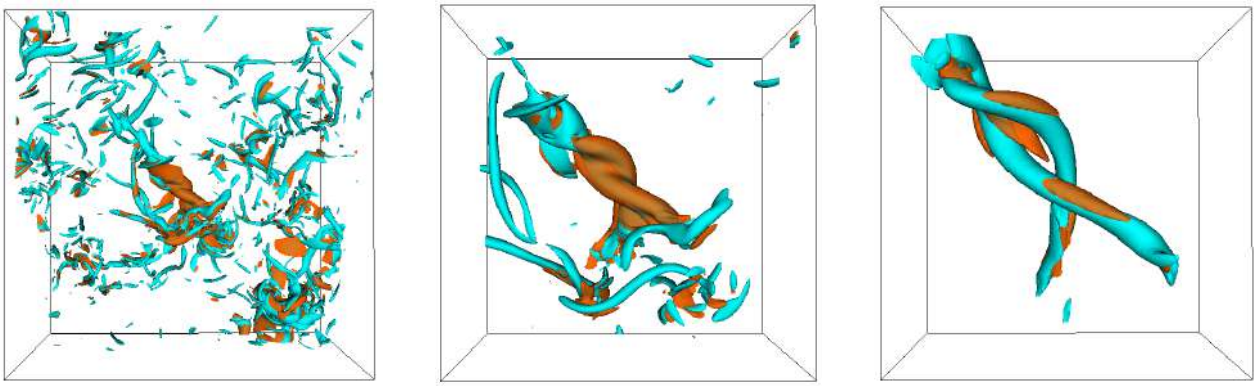

(a) $(250\eta)^3$; $C = 50$ (b) $(100\eta)^3$; $C = 100$ (c) $(50\eta)^3$; $C = 300$

Figure 1: 3D contour surfaces of squared-norm of vorticity (cyan) and strain-rate (red) normalized by their mean-values, from direct numerical simulation at Taylor-scale Reynolds number of $R_\lambda = 650$ on 8192^3 grid (or $(4096\eta)^3$, where η is the Kolmogorov length scale). Panels (a-c) show sub-domains of decreasing size, and increasing contour threshold, C, as indicated in sub-captions. All sub-domains are centered around the same intense vorticity event.

NON-LOCAL STRAIN AND VORTICITY AMPLIFICATION

Quantitatively, the non-locality discussed earlier can be explicitly expressed by writing the velocity $\mathbf{u}(\mathbf{x})$ and hence the strain rate, defined as $\mathbf{S}(\mathbf{x}) = \frac{1}{2}\left[\nabla\mathbf{u} + (\nabla\mathbf{u})^T\right]$, as a global Biot-Savart integral over the vorticity field $\boldsymbol{\omega}(\mathbf{x})$:

$$\mathbf{u}(\mathbf{x}) = \frac{1}{4\pi}\int_{\mathbf{x}'} \boldsymbol{\omega}(\mathbf{x}') \times \frac{\mathbf{x}-\mathbf{x}'}{|\mathbf{x}-\mathbf{x}'|^3} d^3\mathbf{x}' \,. \tag{1}$$

Thereafter, we can decompose the strain-rate at each spatial point as $\mathbf{S}(\mathbf{x}) = \mathbf{S}^L(\mathbf{x}) + \mathbf{S}^{NL}(\mathbf{x})$ [3], where $\mathbf{S}^L(\mathbf{x})$ is the local contribution, obtained by evaluating the Biot-Savart integral in the neighborhood $|\mathbf{x}' - \mathbf{x}| \leq R$, and $\mathbf{S}^{NL}(\mathbf{x})$

*Corresponding author. E-mail: dhawal.buaria@nyu.edu

is the non-local contribution over the background $|\mathbf{x}-\mathbf{x}'| > R$. This allows us to separate the local and the non-local contributions to the strain, hence to the stretching acting on vorticity as a function of the distance R. Note, by definition $\mathbf{S}^L(\mathbf{x}) = \mathbf{0}$ and $\mathbf{S}^{NL}(\mathbf{x}) = \mathbf{S}(\mathbf{x})$ when $R = 0$. Extending the theoretical framework of [3], we show that the non-local strain $\mathbf{S}^{NL}(\mathbf{x})$ can be exactly determined by applying a simple filter to the total strain $\mathbf{S}(\mathbf{x})$, resulting in a very efficient numerical implementation than an explicit computation of the Biot-Savart integral.

Fig. 2a shows the relative amplitude of non-local strain, $\langle|\mathbf{S}^{NL}|^2\rangle/\langle|\mathbf{S}|^2\rangle$, as a function of R at two different R_λ. The relative contribution of $\mathbf{S}^{NL}$ appears to depend only on R/η, (where η is the Kolmogorov length scale, regarded as the size of the smallest eddies), almost independently of R_λ. The local and non-local contribution become comparable for $R \approx 10\eta$. We further diagonalize $\mathbf{S}^{NL}$ into an orthonormal basis, with its eigenvalues given by λ_i, and sorted in decreasing order: $\lambda_1 \geq \lambda_2 \geq \lambda_3$, with $\lambda_1 + \lambda_2 + \lambda_3 = 0$ due to incompressibility; the corresponding eigenvectors are denoted as $\mathbf{e}_i$. Fig. 2a also shows that the ratio between the variances of the eigenvalues of $\mathbf{S}^{NL}$ and those of $\mathbf{S}$ remarkably follows the same decay with R as the strain magnitudes, again without any appreciable dependence on R_λ.

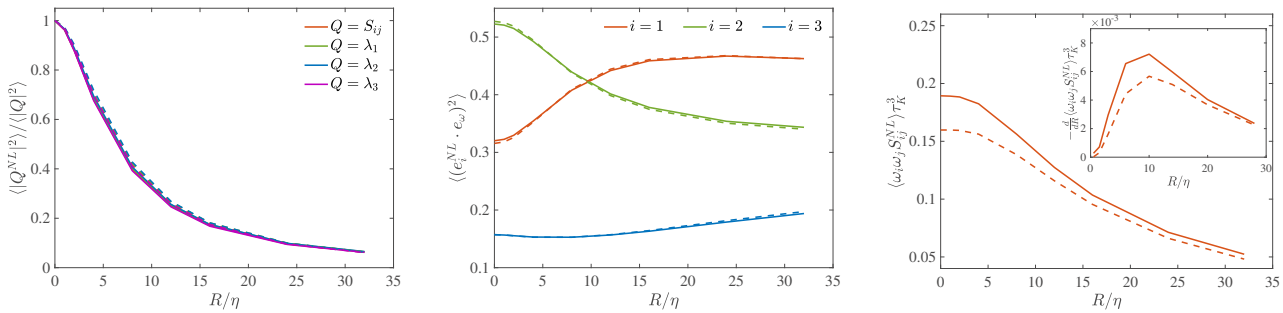

(a) (b) (c)

Figure 2: (a) Relative magnitude of non-local strain and its eigenvalues as a function of R/η (where η is the Kolmogorov length scale), normalized by their respective values corresponding to total strain; (b) Alignment of vorticity with the eigenvectors of the $\mathbf{S}^{NL}(\mathbf{x})$, as a function of R/η; (c) Enstrophy production term normalized by Kolmogorov time scale τ_K as a function of R/η. The rate of production as a function of R (shown in inset), peaks at $\approx 10\eta$. In all plots, solid lines correspond to $R_\lambda = 650$ and dashed lines correspond to $R_\lambda = 140$.

The alignment between $\mathbf{e}_\omega$ $(= \boldsymbol{\omega}/|\boldsymbol{\omega}|)$ and the eigenvectors of $\mathbf{S}^{NL}$, can be characterized by the cosines $\langle(\mathbf{e}_i \cdot \mathbf{e}_\omega)^2\rangle$ (which by definition, add up to unity), and is shown in Fig. 2b as a function of R. Vorticity preferentially aligns with the intermediate strain eigenvector for $R = 0$ ($\mathbf{S}^{NL} = \mathbf{S}$), consistent with know results [4], and with the most extensive eigendirection of $\mathbf{S}^{NL}$ when R exceeds $\approx 10\eta$, consistent with [5]. Finally, the dependence of vortex stretching by $\mathbf{S}^{NL}$, normalized by τ_K^3, and shown as a function of R/η in Fig. 2c, shows an inflexion at $R \approx 10\eta$. Fig. 2 therefore reveals a qualitative change of the properties of $\mathbf{S}^{NL}$ with scale, occurring around $R/\eta \simeq 10$. To summarize, the results presented in Fig. 2 point to a length of about 10η that characterizes the region where non-local effects are important.

CONCLUSIONS

We have documented here the feasibility of decomposing the strain $\mathbf{S}$ as a sum of a local, $\mathbf{S}^L$, plus a non-local contribution, $\mathbf{S}^{NL}$ in a systematic and efficient manner. The preliminary results reveal the existence of a characteristic length scale, $\ell_S \approx 10\eta$, for which the local and non-local contributions are equal. When $R \gtrsim \ell_S$ (respectively $R \lesssim \ell_S$), vorticity aligns with eigenvector corresponding to the most extensive (respectively intermediate) eigenvalue of $\mathbf{S}^{NL}$. Extending the analysis presented here by conditioning on strain or vorticity magnitude will provide new insights on the (local and non-local) mechanism(s) of production of very large gradients in turbulent flows – as we will further discuss in the presentation at the Congress.

We gratefully acknowledge the Gauss Centre for Supercomputing (GCS) for providing the necessary computing time for this work on the GCS Supercomputers JUQUEEN and JUWELS at Jülich Supercomputing Centre (JSC).

References

[1] U. Frisch. Turubulence: the legacy of A. N. Kolmogorov. *Cambridge University Press* 1995.
[2] D. Buaria, A. Pumir, E. Bodenschatz, and P. K. Yeung. Extreme velocity gradients in turbulent flows. *New J. Phys.* **21**:043004, 2019.
[3] P. E. Hamlington, J. Schumacher, and J. A. D. Werner. Local and nonlocal strain rate fields and vorticity alignment in turbulent flows. *Phys. Rev. E*, **77**:026303, 2008.
[4] W. T. Ashurst, A. R. Kerstein, R. M. Kerr, and C. H. Gibson. Alignment of vorticity and scalar gradient with strain rate in simulated Navier-Stokes turbulence. *Phys. Fluids*, **30**:2343–2353, 1987.
[5] P. E. Hamlington, J. Schumacher, and J. A. D. Werner. Direct assessment of vorticity alignment with local and nonlocal strain rates in turbulent flows. *Phys. Fluids*, **20**:111703, 2008.

PASSIVE SCALAR TRANSPORT IN ROTATING COUETTE FLOWS

Geert Brethouwer*[1]
[1]FLOW, Engineering Mechanics, KTH, Stockholm, Sweden

Summary The transport of a passive scalar in rotating plane Couette and Taylor-Couette flow is investigated by DNS. In non-rotating Couette flows the passive scalar transport and (angular) momentum transport are similar, in accordance with the Reynolds analogy. However, if Couette flow is subject to anti-cyclonic system rotation passive scalar transport can be much faster than (angular) momentum transport. The Reynolds analogy can thus be broken if a Coriolis force induced by system rotation is imposed on the flow.

INTRODUCTION

Reynolds [1] postulated almost one and a half century ago that turbulence transports heat and momentum at a similar rate in shear flows. Experiments and numerical simulations have confirmed that this analogy applies to heat and mass transfer in many shear flows. This concept has been very valuable for turbulence modelling and deriving relations between the skin friction and heat or mass transfer in wall-bounded flows. The Reynolds analogy can be physically motivated and is suggested by the similarity between the governing equations for the streamwise velocity and e.g. temperature or concentration. However, the latter similarity is absent if a body force acts on the flow, therefore, the Reynolds analogy applies less obviously to transport processes in flows subject to e.g. buoyancy or Coriolis forces. Indeed, turbulent Prandtl numbers much smaller than unity have been observed in DNS of mixed convection in turbulent channel flow [2] and in turbulent channel flow subject to spanwise system rotation [3, 4]. Also in recent theoretical studies it has been shown that a body force can alter transport processes and make the transport of a passive scalar much faster than the transport of momentum in channel and plane Couette flows [5, 6]. This result is interesting because it implies that it is perhaps possible to make heat and mass transport more efficient and reduce the power consumption by applying a body force in engineering applications with heat and mass transfer. However, the body force was arbitrary in the aforementioned theoretical studies. Consequently, it is not obvious how this body force can be generated and how efficient transport can be realized in practice. The purpose of the present study is to demonstrate that rotation significantly affects the transport of a passive scalar in Couette flows and can make the scalar transport much more efficient in real flows.

DIRECT NUMERICAL SIMULATIONS

To investigate the effect of rotation on transport in Couette flows, I have carried out DNS of incompressible plane Couette flow (PCF) and Taylor-Couette flow (TCF) with a passive scalar. From now on the passive scalar is called temperature for convenience, but note that there are no buoyancy forces. The PCF system rotates about the spanwise direction whereas the TCF system rotates about the axial direction. The governing equations for TCF are solved in cylindrical coordinates using a similar setup as in [7], and the ratio of the radius of the inner and outer cylinder $\eta = r_i/r_o = 0.71$. PCF can be viewed as the limit $\eta \to 1$ of TCF. The velocity at the no-slip and isothermal inner and outer wall is $\pm U_w$, respectively, while the temperature at the inner and outer wall is $\pm T_w$, respectively. The momentum and heat transport are thus driven by a velocity and temperature difference between the plane or cylindrical walls. The Reynolds number is now defined as $Re = \Delta U d/\nu$ and the rotation number as $Ro = 2\Omega d/\Delta U$, where $\Delta U = 2U_w$ is the velocity difference and d the gap width between the walls, ν viscosity and Ω the rotation rate. In PCF the Prandtl number $Pr = 1$ whereas in TCF $Pr = 0.7$. To study the effect of rotation on the transport, I have carried out DNS at a constant Re and varying Ro. I have repeated this procedure at several Re, from low values of Re up to $Re = 40\,000$.

RESULTS

In the statistically stationary state the mean transverse (angular) momentum flux J^m and mean heat flux J^h through a unit area (PCF) or cylindrical shell (TCF) are constant. To quantify the (angular) momentum and heat transport the Nusselt numbers $Nu_m = J^m/J^m_{lam}$ and $Nu_h = J^h/J^m_{lam}$, respectively, are used. Here, J^m_{lam} and J^h_{lam} are the (angular) momentum and heat flux, respectively, when the flow is fully laminar.

PCF and TCF are very suitable systems to study the influence of rotation on momentum and heat transport because the momentum and heat transport are forced in the same way, i.e. by a velocity and temperature difference between the walls. Figure 1(a) and (c) shows Nu_m and Nu_h, respectively, for PCF at $Re = 400$, 1600, 6400, 17 200 and 40 000 as function of Ro while Fig.1.(b) and (d) shows Nu_m and Nu_h, respectively, for TCF at $Re = 400$, 2593, 8750, 19 688 and 40 000 as function of Ro. In both PCF and TCF $Ro > 0$ corresponds to anti-cyclonic rotation whereas $Ro < 0$ corresponds to cyclonic rotation. Fig. 1 shows that both Nu_m and Nu_h increase with Re, as expected, but also change if the rotation rate, i.e. Ro, changes. Starting from $Ro = 0$, i.e. no rotation, the (angular) momentum transfer and, accordingly, Nu_m at first increases with Ro and reaches a maximum at approximately $Ro = 0.2$ in PCF and between $Ro = 0.1$ and 0.3 in TCF.

*E-mail: geert@mech.kth.se

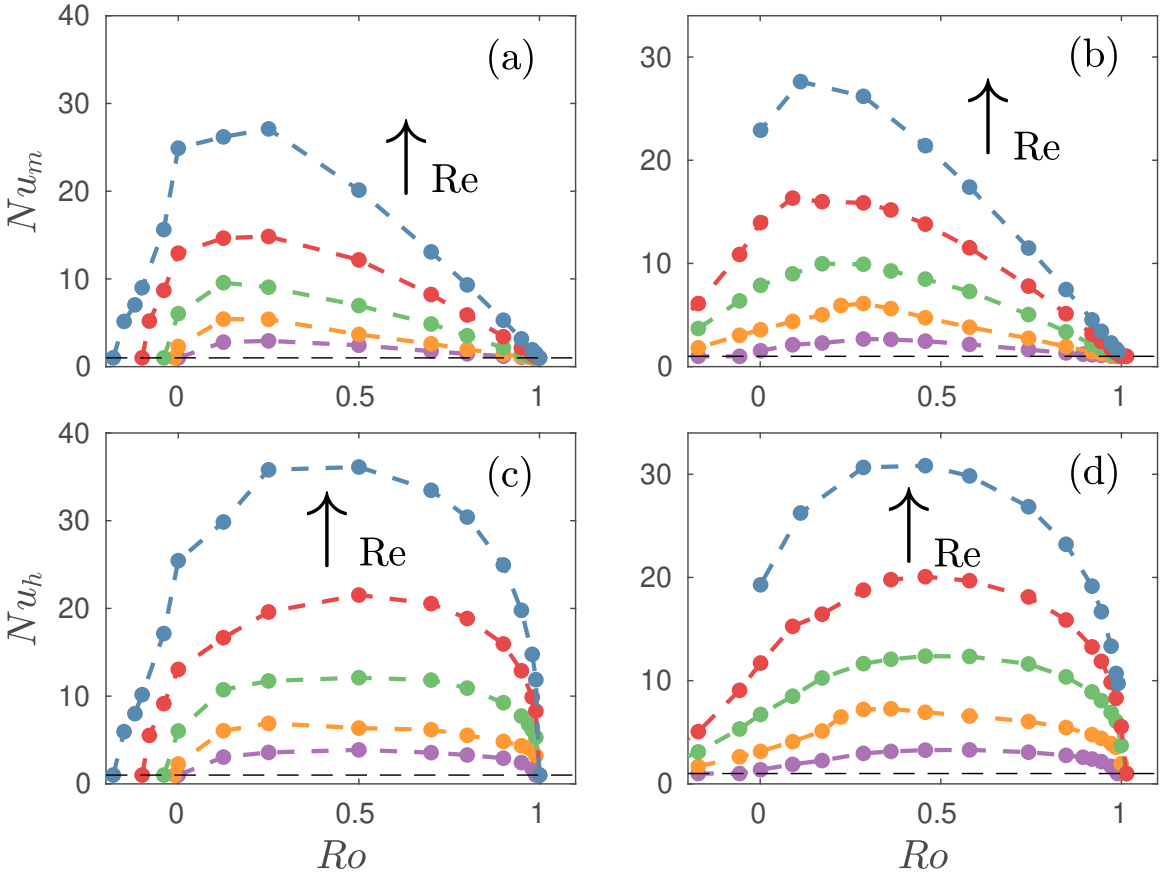

Figure 1: (a) Nu_m and (c) Nu_h for PCF. (b) Nu_m and (d) Nu_h for TCF. Each line/colour represents a different constant Re and dots denote simulation results. Arrows show trends for increasing Re.

Thereafter Nu_m declines and approaches unity when $Ro \to 1$ and the flow becomes laminar. When $Ro \gtrsim 1$ Couette flows are linearly stable and turbulence cannot be sustained. These results for the (angular) momentum transfer are consistent with e.g. the DNS of [7, 8]. At low Re Couette flows are steady and contain large streamwise vortices but at high Re both PCF and TCF are turbulent. The heat transfer expressed in terms of Nu_h is similar to Nu_m at $Ro = 0$ and $Ro < 0$ in PCF and TCF, which implies that the Reynolds analogy is approximately valid for non-rotating and cyclonic rotating Couette systems. However, if $Ro > 0$ and the rotation is anti-cyclonic Nu_m and Nu_h start to differ. The maximum of Nu_h is higher and occurs at a higher $Ro \approx 0.5$ in both PCF and TCF. When Ro further increases the ratio Nu_h/Nu_m increases until Ro approaches unity and both Nu_m and Nu_h become one because the flows becomes laminar. This means that the heat transfer becomes increasingly fast compared to the (angular) momentum transfer until about $Ro = 0.8$ to 0.99, which implies that rapid anti-cyclonic rotation induces a strong violation of the Reynolds analogy in PCF and TCF. At these Ro the mean temperature profiles deviate clearly from the mean streamwise or azimuthal velocity profiles (not shown here). Further analysis reveals that at high Ro the Coriolis force strongly suppresses the streamwise or azimuthal velocity fluctuations and this leads to weak momentum transport. However, Taylor vortices or turbulent eddies are still present and are able to effectively transport the heat across the flow from one wall to the other.

To summarize, anti-cyclonic rotation can lead to a strong violation of the Reynolds analogy between heat and (angular) momentum transfer in Couette flows and can make the heat transport very efficient compared to (angular) momentum transfer. Care should therefore by exercised when modelling heat and mass transfer in flows affected by body forces like the Coriolis force because the Reynolds analogy is not necessarily valid.

References

[1] Reynolds O., *Proc. Lit. Phil. Soc., Manchester* **14**: 7-12, 1874.
[2] Pirozzoli S., Bernardini M., Verzicco R., Orlandi P. *J. Fluid Mech.* **821**: 482-516, 2017.
[3] Brethouwer G., *J. Fluid Mech.* **844**: 297-322, 2018.
[4] Brethouwer G., *Phys. Rev. Fluids* **4**: 104602, 2019.
[5] Alben S., *Phys. Rev. Fluids* **2**: 104501, 2017.
[6] Motoki S., Kawahara G., Shimuzu M. *J. Fluid Mech.* **835**: 1157-1198, 2018.
[7] Brauckmann H. J., Eckhardt B. *J. Fluid Mech.* **718**: 398-427, 2013.
[8] Brauckmann H. J., Salewski M., Eckhardt B. *J. Fluid Mech.* **790**: 419-452, 2016.

FROM ISOTROPIC TURBULENCE TO TRANSITION IN PLANE CHANNEL FLOW

Wouter Bos*[1], Faouzi Laadhari[1], and Wesley Agoua[1]
[1]CNRS, LMFA, Ecole Centrale de Lyon, UCBL, INSA Lyon, Univ Lyon

Summary In plane Poiseuille flow, somewhat beyond a critical value of the Reynolds number, laminar flow co-exists with turbulent stripes. We transpose modeling concepts, which were derived for the case of statistically isotropic turbulence, to this case. Thereby it is shown that the kinetic energy balance around the onset of turbulent flow in plane channel flow can be described by a simple model-equation. We first validate our ideas in the isotropic setting using direct numerical simulation (DNS) and two-point closure technique. Subsequently we assess the ideas applied to channel flow using high resolution DNS.

INTRODUCTION

Transitional shear flows and the modeling of isotropic turbulence are two seemingly different research subjects. Recently, however, it was realized that isotropic turbulence and the laminar-turbulent transition in wall-bounded shear flows share certain features [1]. For instance, it was shown that relaminarization, a feature generally associated with shear flows, such as flow through pipes driven by a pressure gradient, can also be observed in statistically isotropic periodic box turbulence. In the present investigation we first investigate the transitional dynamics of isotropic turbulence. In particular, we will show that in the case of linear forcing a critical Reynolds number exists above which a turbulent flow can be sustained.

ISOTROPIC TURBULENCE

The global kinetic energy of a closed or periodic turbulent flow is fully determined by the production (p) and dissipation (ϵ) mechanisms. Its volume-averaged balance is simply given by the equation

$$\frac{dk}{dt} = p - \epsilon. \tag{1}$$

We consider the Navier-Stokes equations to which we add a linear forcing term [2],

$$\frac{D\boldsymbol{u}}{Dt} = -\boldsymbol{\Pi} + \nu\Delta\boldsymbol{u} + \alpha\boldsymbol{u}. \tag{2}$$

with $\boldsymbol{u}$ the velocity, $\boldsymbol{\Pi}$ the density-normalized pressure gradient and ν the kinematic viscosity. The parameter α determines the strength of the linear forcing. This system allows the exact determination of the energy injection as a function of the kinetic energy. Using an in-depth analysis of triadic closure and comparison with DNS we refine and assess an existing model for the dissipation as a function of the kinetic energy. We show that the analytical solutions to the modeled equation describe accurately the asymptotic behavior of the Reynolds number dependence of the kinetic energy near the onset [3]. Results of this study are shown in figure 1.

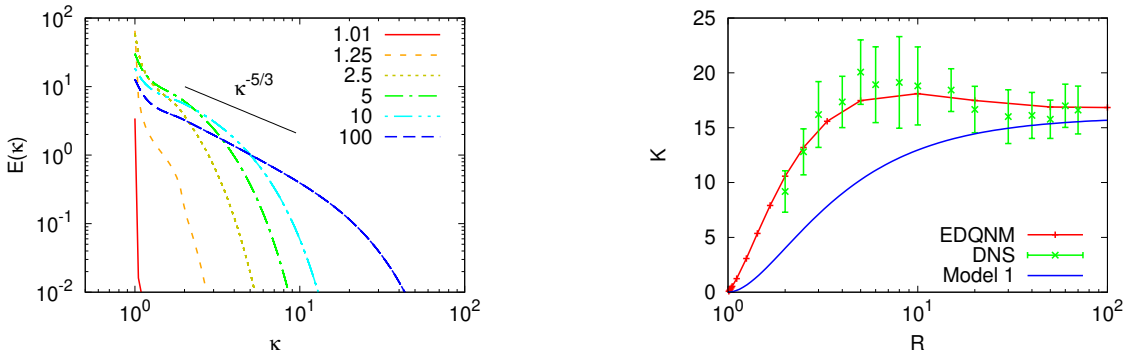

Figure 1: DNS and closure analysis of the linearly forced Navier-Stokes equations allow to assess a simple model for the kinetic energy in steady states above a critical value of the Reynolds number. Left: closure results for energy spectra for forcing-rate-based Reynolds numbers $R = \alpha L^2/\nu = [1.01 : 100]$. Right: kinetic energy as a function of R. A basic model of the dissipation rate leads to an under-prediction of the kinetic energy. We improve the model [3].

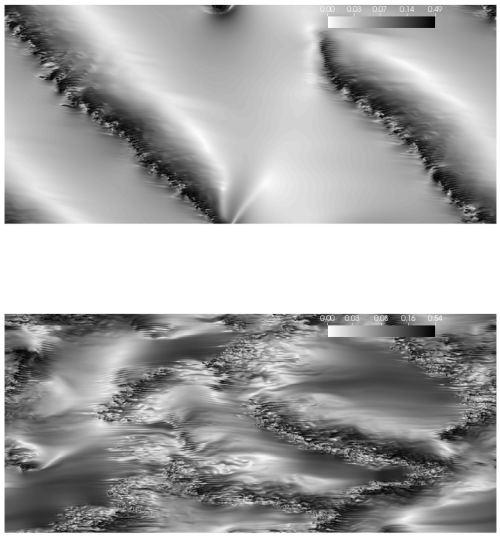

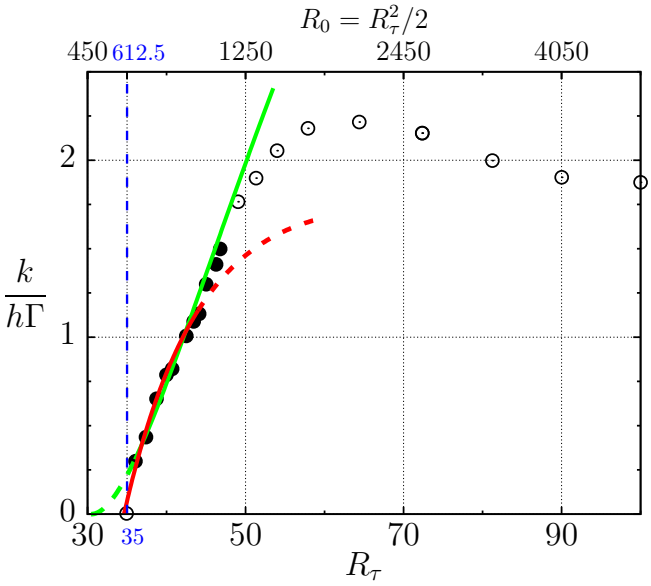

Figure 2: Left: DNS results of velocity-fluctuations in the center-plane of plane Poiseuille flow. The mean flow is directed from left to right. Right: kinetic energy as a function of the Reynolds number $R_\tau = \Gamma^{1/2}h^{3/2}/\nu$. Two distinct models (lines) are compared to the data.

PLANE POISEUILLE FLOW

Subsequently we transpose the ideas to the case of plane Poiseuille flow, i.e. flow between two parallel walls driven by a mean pressure gradient. In this case the evolution of the system is also given by equations (1) and (2), but the forcing of the system is now not determined by the linear forcing term ($\alpha = 0$) but by the imposed pressure gradient which we will call $-\Gamma$. Using the same type of model as for the isotropic case, we can obtain a closed expression for the kinetic energy as a function of the Reynolds number. We checked our ideas by means of a series of 25 pseudo-spectral simulations in a domain of size $L_x \times L_y \times L_z = 350h \times 2h \times 155h$ with periodic boundary conditions in the streamwise (x), and spanwise (y) directions. The domain is discretized using approximately 7×10^8 grid-points. Steady state values were obtained by decreasing stepwisely the Reynolds number starting from a turbulent initial condition.

In Figure 2 (left), we show the RMS velocity fluctuations in the centerplane between the two walls for a Reynolds number close to the critical value below which the flow relaminarizes and a Reynolds number somewhat larger. Coexistence of laminar and turbulent regions is observed in the flow, in particular for the lowest value of the Reynolds number. In Figure 2(b), we show the prediction of our simple models for the kinetic energy as a function of the Reynolds number and good agreement is observed with the numerical results.

CONCLUSIONS

It is shown that the behaviour of the turbulent kinetic energy in both isotropic turbulence and plane Poiseuille flow, near the critical Reynolds number above which turbulence can be sustained, can be described by a simple model equation. What is still to be explored is how the results depend exactly on the size of the domain, and how the shape of the turbulent production term can be derived from the Navier-Stokes equations. Furthermore, in future work we want to assess our ideas in different systems which show subcritical transition, such as plane Couette flow.

References

[1] MF Linkmann and A Morozov. Sudden relaminarization and lifetimes in forced isotropic turbulence. *Physical review letters*, 115(13):134502, 2015.
[2] TS Lundgren. Linearly forced isotropic turbulence. *Annual Research Briefs-2003*, page 461, 2003.
[3] WJT Bos and F Laadhari and W Agoua *Linearly forced isotropic turbulence at low Reynolds numbers. Phys. Rev. E.*, 102, 033105, 2020.

*Corresponding author. E-mail: wouter.bos@ec-lyon.fr.

ASSIMILATION & CLASSIFICATION OF TURBULENCE DATA: PHYSICS-INFORMED AND MACHINE LEARNING TOOLS

L. Biferale[1], F. Bonaccorso[1], M. Buzzicotti[1]and P. Clark di Leoni[2]
[1]Dept. Physics and INFN University of Rome Tor Vergata, Italy
[2]Dept. Mechanical Engineering, Johns Hopkins University, Baltimore, USA

We provide a side-by-side comparison of modern techniques to assimilate, classify and control turbulent data by using equation-based tools, as Nudging, or big-data Machine Learning approaches. We discuss applications to rotating turbulence and fully developed isotropic turbulence. Both Eulerian and Lagrangian cases will be discussed, including optimal navigation problems [1-4].

INTRODUCTION

Measuring, reconstructing, and then predicting the evolution of turbulent flows are highly important tasks for fundamental and applied goals. A key example is given by the problem of state estimation in geophysics, important for numerical weather prediction. The chaotic and complex nature of turbulence makes these tasks very difficult, as any small error in the initial conditions will make predictions impossible on the long run, and as it is impossible to access all active modes in the flow. This is particularly worrying when we consider that in a turbulent flow the number of active degrees of freedom (dof) grows with the Reynolds number as $Re^{9/4}$. Data assimilation (DA) is the family of tools used to reconstruct the states of a dynamical system, out of a series of partial and noisy data, in order to improve future predictions. The key questions that need to be answered are: what is the quality and quantity of information that we need to provide to ensure a perfect (or optimal) data reconstructions? In other words, where, when and what we need to measure to exploit the maximum information from the field data? In this paper we will compare two modern and popular tools to attack this problem. One based on an equation-informed protocol, known as Nudging. The second is a Machine-Learning approach, where (many) partial data are supplied to a machine (a Neural Network) to train the output to reproduce as faithfully as possible the missing data. The final goal is to set-up a series of optimal Eulerian and Lagrangian protocols to reconstruct and control turbulent flows, as well as to learn how to navigate and design optimal measuring campaign in flows of geophysical interest [1-4].

NUDGING

Nudging is a general data-driven algorithm to learn from sparse measurements in a dynamical way and with a broad range of applications. The idea is to use the Navier-Stokes equations with a Newton relaxation feedback term, which imposes a linear reward/penalisation depending if the evolved velocity and/or temperature fields are close/far from the data to be assimilated [1-2]. In our Eulerian and Lagrangian implementation (see Fig. 1 right panel), the Nudging control terms are defined on fixed spatial positions (Eulerian) or along the trajectory, $\mathbf{X}(t)$, of tracer probes passively advected by the flow. In applications triggered from the field, data are affected by errors and one does not know the precise intensity and properties of the forcing mechanisms. As a result, it is key to perform an optimisation of the nudging coefficient (e.g., varying its intensity depending on the space/time probes position and on the quality of the local data). In our presentation, we will show the first application of Nudging to highly turbulent flows, both isotropic and anisotropic (rotating turbulence) providing a systematic assessment of reconstruction performance as a function of the quantity and quality (Eulerian/Largangian/Fourier) of data provided. Transition to full synchronization (perfect reconstruction) will be also studied.

ADVERSARIAL NEURAL NETWORKS

Machine Learning (ML) approaches provide key solutions to many different problems, especially when the goal is to extract significant information out of a large amount of data without control on the equations of motion. In the recent years, ML has been applied to problems related to flow control and modelling, demonstrating a good ability in gathering information about the chaotic and multi-scale evolution of turbulent fields [5]. In this work, we investigate the potential of the generative adversarial neural networks (GANN) to (i) identify the main features of turbulent flows (e.g. intensity of rotation, kinematic viscosity, temperature boundary conditions etc…) and (ii) reconstruct field data satisfying all the features extracted from the supplied partial measurements [6].
The GANN framework, consists in the competition of two different models, the generative model (G) that is trained to reproduce the data distributions of the training dataset and the discriminative model (D) that simultaneously learns to estimate the probability that a given input comes from the training dataset or that it is produced by the generative model. In this way, following an adversarial process the model G aims to maximize the probability of D to be mistaken. The optimal solution in the space of arbitrary G and D is for G to reconstruct exactly the full training data distribution and for D being always 1/2. Following this idea, we compare the GANN performances with the ones of Nudging in the reconstruction of the velocity field. In particular, we focus on the case of turbulent flows on a rotating reference frame,

as for the case of geophysical flows. We perform a quantitative analysis, comparing spectral properties and small-scale statistics involving gradients' distributions.

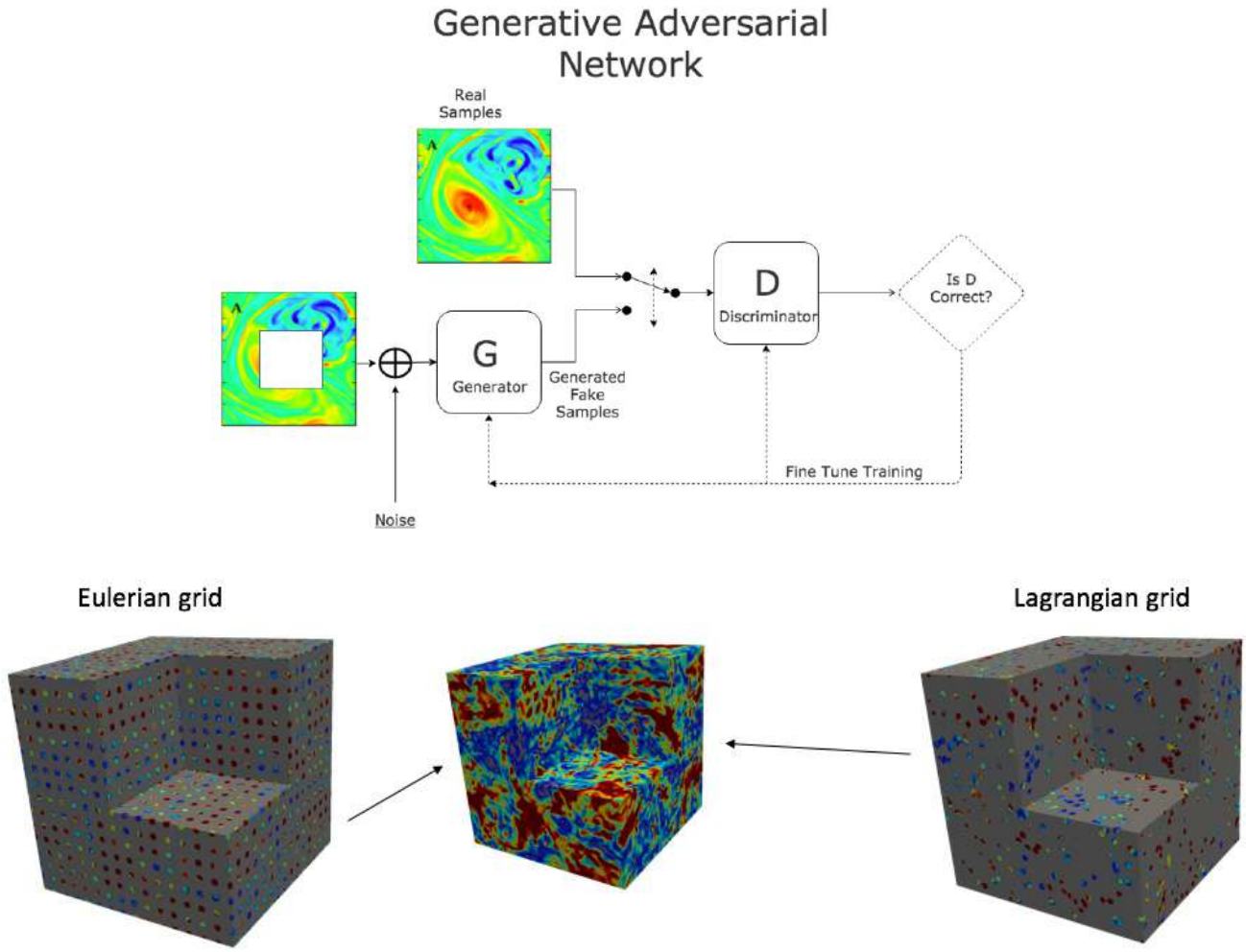

Figure 1. Top: schematic of the GANN approach for data assimilation of 2d turbulent snapshots. The aim is to fill the (squared) gap in the supplied data set. Bottom: data assimilation using Nudging [2], where two different data-sets (from partial Eulerian or Lagrangian measurements) are supplied to the Navier-Stokes equations to reconstruct the flow in the whole volume.

CONCLUSIONS

We present a quantitative comparison among physics-informed data-assimilation tools, based on Nudging techniques [1-2], and ML approaches without imposing any prior knowledge on the equations of motion [6]. We discuss pluses and minuses of both techniques and potential application to flow control using either Eulerian or Lagrangian actuators. The latter problem being also connected to optimal swimming/navigation in complex flows [3-4].

References

[1] Inferring flow parameters and turbulent configuration with physics-informed data-assimilation and spectral nudging. P. Clark Di Leoni, A. Mazzino, L. Biferale. Physical Review Fluids 3, 104604, 2018
[2] Synchronization to big-data: nudging the Navier-Stokes equations for data assimilation of turbulent flows. P. Clark Di Leoni, A. Mazzino, L. Biferale. Physical Review X in press 2020, arXiv:1905.05860
[3] Zermelo's problem: Optimal point-to-point navigation in 2D turbulent flows using Reinforcement Learning. L. Biferale, F. Bonaccorso, M. Buzzicotti, P. Clark Di Leoni, K Gustavsson Chaos 29, 103138, 2019
[4] Smart Inertial Particles. S. Colabrese, K. Gustavsson, A. Celani, L. Biferale. Physical Review Fluids 3 (8), 084301, 2018
[5] S. L. Brunton, B. R. Noack, P. Koumoutsakos Annual Review of Fluid Mechanics 52:1, 2020
[6] M. Buzzicotti, F. Bonaccorso, P. Clark di Leoni and L. Biferale. Machine Learning tools to classify and reconstruct turbulent flows. In preparation (2020)

IS TURBULENCE KNOTTED ?

Carlo F. Barenghi*[1]
[1]School of Mathematics, Statistics and Physics and JQC (Joint Quantum Centre Durham-Newcastle), Newcastle University, Newcastle upon Tyne NE1 7RU, United Kingdom

Summary We address the question as to whether turbulence contains vortex knots in a context which is simpler that ordinary fluids: superfluid helium. Unlike what happens in ordinary Navier-Stokes fluids where vorticity is a continuous field, in superfluid helium quantum mechanics constraints the vorticity to individual vortex lines, aiding the characterization of knots in terms of Alexander polynomials. Numerical simulations confirm that superfluid turbulence is indeed knotted.

INTRODUCTION

The controlled generation of vortex knots in the laboratory [1] motivates this work on knots in turbulent flows. Numerically, turbulent field lines display a high degree of spatial disorder, and appear to be coiled, twisted, even knotted. Our aim is to explore direct ways to quantify this complexity beyond existing measures such as helicity [2], $\mathcal{H} = \int_V \boldsymbol{\omega}(\mathbf{r})\cdot\mathbf{v}(\mathbf{r})d^3\mathbf{r}$, where $\mathbf{v}$, $\boldsymbol{\omega} = \nabla \times \mathbf{v}$, $\mathbf{r}$ and V are respectively the velocity field, the vorticity, the position and the volume of fluid. In the case of thin vortex tubes, $\mathcal{H}$ can be interpreted in terms of writhe, link and twist of the tubes [3], combining geometrical and topological information. Here we seek a measure which is directly related to the knottiness of the vortex lines. In principle, this requires precise identification of instantaneous vortex lines from the numerical solution of the incompressible Navier-Stokes equation; however, starting from the initial position, numerical noise across regions of large and small vorticity may prevent the traced vortex line from joining with itself, forming a closed loop as required by $\nabla \cdot \boldsymbol{\omega} = 0$.

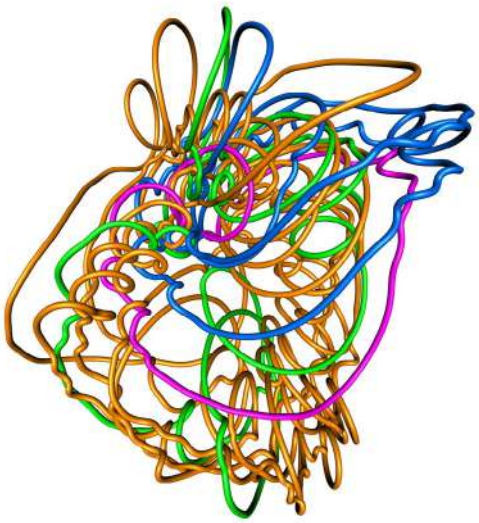

Figure 1: Snapshot of numerically computed turbulent tangle of vortex lines. For clarity, a tubular region of arbitrary radius has been drawn around the axis of each vortex line; the colours distinguish the different vortex loops.

Fortunately there is a fluid, superfluid helium, in which the vorticity is not an unconstrained continuous field, but is concentrated in discrete, physically distinct vortex lines, hence the identification of vortex lines is not a problem (indeed individual vortex lines and their reconnections have been experimentally visualized [4]). Superfluid helium is created in the laboratory by cooling liquid helium to temperatures below the critical temperature for Bose-Einstein condensation, $T_c = 2.17$ K at saturated vapour pressure. For $T < T_c$, a macroscopic fraction of the atoms form a condensate (which, for simplicity, we identify with the superfluid); the remaining thermal atoms form the so-called normal fluid, whose density drops rapidly as T is lowered. The key property [5] of a superfluid vortex line is that its circulation κ takes the fixed value $\kappa = h/m \approx 10^{-7}$ m^2/s where h is Planck's constant and m is the mass of one atom. This property is a consequence of the existence and the uniqueness of a macroscopic wavefunction $\Psi(\mathbf{r})$ governing the system. Physically, a vortex line is a small tubular region of radius $a_0 \approx 10^{-10}$ m around the vortex axis (defined by $\Psi = 0$); the azimuthal velocity around the axis corresponds to the phase of Ψ which changes from 0 to 2π.

Superfluid turbulence, easily generated by mechanical or thermal stirring, consists of a disordered tangle of vortex lines which interact and reconnect when they collide. Because of the discrete nature of vortex lines, this is an ideal context to study the knottiness of turbulence. Additional interest arises from the fact that superfluid turbulence satisfies key properties of ordinary turbulence, for example the same Kolmogorov energy spectrum. Thus what we learn about the knottiness of superfluid turbulence is probably relevant to ordinary turbulence too.

*Corresponding author. E-mail: carlo.barenghi@newcastle.ac.uk

MODEL

In most helium experiments, the average distance between vortex lines, $\ell \approx 10^{-4}$ to 10^{-2} m, is orders of magnitude larger than the vortex core radius a_0, hence vortex lines can be modelled as space curves $\mathbf{s}(\xi, t)$ (where ξ is arclength and t is time) which move according to the classical Euler equation. We are interested in experiments in which the vortex tangle is generated in the centre of the helium sample away from boundaries; in this way all vortex lines form closed loops, which simplifies the analysis. Each vortex line is advected by all other vortex lines (Helmholtz Theorem), and, at $T \neq 0$, interacts with the normal fluid, gaining or losing energy depending on the relative difference between the local normal fluid and superfluid velocities (an effect akin to a positive or negative friction). The governing equation of motion is [6]

$$\frac{d\mathbf{s}}{dt} = \mathbf{v}_s(\mathbf{s}, t) + \alpha \mathbf{s}' \times \mathbf{w}(\mathbf{s}, t) - \alpha' \mathbf{s}' \times [\mathbf{s}' \times \mathbf{w}(\mathbf{s}, t)], \tag{1}$$

where α and α' are small temperature-dependent friction coefficients, $\mathbf{w}(\mathbf{s}, t) = \mathbf{v}_n(\mathbf{s}, t) - \mathbf{v}_s(\mathbf{s}, t)$, $\mathbf{v}_n(\mathbf{s}, t)$ is the normal fluid's velocity, $\mathbf{s}' = d\mathbf{s}/d\xi$ is the unit tangent vector to the vortex line at $\mathbf{s}$, and

$$\mathbf{v}_s(\mathbf{s}, t) = -\frac{\kappa}{4\pi} \int_{\mathcal{L}} \frac{(\mathbf{s} - \mathbf{r}) \times d\mathbf{r}}{|\mathbf{s} - \mathbf{r}|^3}, \tag{2}$$

is the velocity induced by the entire vortex configuration at $\mathbf{s}$. The Biot-Savart integral (2) is desingularised in a standard way based on the core a_0 cutoff. Vortex reconnections are performed algorithmically when vortex lines collide [6, 7].

RESULTS

All numerical simulations start with few seeding random vortex lines driven by a prescribed, time-dependent, solenoidal normal fluid velocity $\mathbf{v}_n(\mathbf{r}, t)$ which is concentrated in a spherical region of radius D. After an initial transient, the vortex tangle settles down to a steady regime in which vortex length Λ and energy E fluctuate around average values which is independent of the initial condition, as driving and dissipation balance out; a snapshot of the vortex tangle in this regime is shown in Fig. (1). Small vortex loops which move away from this spherical region shrink and vanish due to friction in the quiescent normal fluid. We verify that in this regime the energy spectrum obeys the classical Kolmogorov $k^{-5/3}$ scaling (where k is the wavenumber) in the inertial range $2\pi/D < k < 2\pi/\ell$.

To characterize the knottiness of the turbulence, we compute the Alexander polynomial $\Delta(\tau) = c_0 + c_1\tau + \cdots + c_\nu\tau^\nu$ of each vortex loop. A vortex ring has Alexander polynomial of degree $\nu = 0$, a trefoil knot has degree $\nu = 2$, etc; the higher ν, the more complex the knot type [8].

We find [9] that although vortex reconnections keep breaking up long vortex loops, long loops are also continually created; therefore, at each time, the vortex tangle always contains some long, highly knotted vortex loops, with degree of Alexander polynomial ranging from $\nu \approx 10$ to 100 depending on the intensity of the drive. The probability that a vortex loop is knotted increases (and then saturates to unity) with the length of the loop, as found for macromolecules [10]. Finally, we find that the probability of finding a knot with degree ν in the turbulent vortex tangle scales as $P(\nu) \sim \nu^{-3/2}$, independently of the tangle's total vortex length.

CONCLUSIONS

We have demonstrated that superfluid turbulence is knotted, indeed it contains long vortex loops with high degree of Alexander polynomial. This rich topology has a physical meaning, because vortex reconnections (which create the knots in the first place) are associated with energy losses by phonon emission [11]. The natural question is whether these findings also apply to ordinary Navier-Stokes turbulence.

References

[1] Kleckner D. and Irvine W. T. M. *Nature Phys.* **9**: 253, 2013.
[2] Moffatt H. K. *J. Fluid Mech.* **35**: 117, 1969.
[3] Moffatt H. K. and Ricca R. L. *Proc. Roy. Soc. London A* **439**: 411, 1992.
[4] Bewley G. P., Paoletti M. S., Sreenivasan K. R., and Lathrop D.P. *Proc. Nat. Acad. Sci. USA* **105**: 13707, 2008.
[5] Barenghi C.F. and Parker N.G. A Primer on Quantum Fluids. Springer 2016.
[6] Schwarz K. W. *Phys. Rev. B* **38**: 2398, 1989.
[7] Galantucci L., Baggaley A. W., Parker N. G. and Barenghi C. F., *Proc. Nat. sci. USA* **116**: 12204, 2019
[8] Livingstone L. Knot Theory. Cambridge University Press 1993.
[9] Cooper R. G., Mesgarnezhad M., Baggaley A. W. and Barenghi C. F. *Sci. Reports* **9**: 10545, 2019.
[10] Arsuaga J., Vazquez M., Trigueros S., Sumners D.W. and Roca J. *Proc. Nat. Acad. Sci. USA* **99**: 5373, 2002.
[11] Leadbeater M., Winiecki T., Samuels D. C., Barenghi C. F. and Adams C. S. *Phys. Rev. Lett.* **86**: 1410, 2001,

EVOLUTION OF THE DENSITY GRADIENTS IN BUOYANCY-DRIVEN HOMOGENEOUS VARIABLE-DENSITY TURBULENCE

Denis Aslangil*[1,2], Daniel Livescu[1], and Arindam Banerjee[2]
[1]Los Alamos National Laboratory, Los Alamos, NM, USA
[2]Department of Mechanical Engineering and Mechanics, Lehigh University, Bethlehem, PA, USA

Summary Evolution of the density gradients in buoyancy-driven homogeneous variable-density turbulence (HVDT) is studied using high-resolution direct numerical simulations (DNS) data on 2048^3 triply periodic domain size. Turbulent mixing is generated as two incompressible, miscible fluids with different densities, initially at rest and segregated in large random regions, are subjected to acceleration. Mixing is enhanced by the conversion of the potential energy to the turbulent kinetic energy which leads to an increase in density gradients during the flow evolution. We investigate the suitability of the Boussinesq approximation and validity of the incompressible assumption in variable-density (VD) turbulence for both low density ratio (1.1:1) and high density ratio (7:1) cases, as the density gradients increase due to turbulence.

INTRODUCTION

Variable-density (VD) turbulence is of fundamental research interest due to its frequent occurrence in atmospheric and oceanic flows, astrophysics, combustion, and high density energy processes such as inertial confinement fusion [1-4]. DNS studies using a triply periodic configuration of HVDT remove the edge and boundary effects from the flow and allow investigations of the VD turbulent mixing process in the core of the mixing layer [1,2,4-6]. In most engineering models, a Boussinesq kind of assumption is widely used to model density effects; the density variations are neglected except for the buoyancy term in the Navier-Stokes equations (NS). In this study, we examine the suitability of the Boussinesq approximation and the possibility that the density gradients blow up in finite time due to stirring by turbulence.

Governing Equations

The variable-density version of the non-dimensional incompressible Navier-Stokes Equations can be written as [1,4]:

$$\rho^*_{,t} + (\rho^* u^*_j)_{,j} = 0, \tag{1}$$

$$(\rho^* u^*_i)_{,t} + (\rho^* u^*_i u^*_j)_{,j} = -p^*_{,i} + \tau^*_{ij,j} + \frac{1}{Fr^2}\rho^* g_i, \tag{2}$$

where ρ^* is the instantaneous density, u^*_i is the instantaneous velocity in i direction, p^* is the instantaneous pressure term and $\tau^*_{ij,j}$ is the Newtonian stress term where $\tau^*_{ij} = (\rho^*/Re_0)(u^*_{i,j} + u^*_{j,i} - (2/3)u^*_{k,k}\delta_{ij})$, and $g_i = (-1, 0, 0)$ is the gravitational force applied to the flow. In addition, due to the mixing process, the velocity divergence is not zero and is equal to:

$$u^*_{j,j} = -\frac{1}{Re_0 Sc_0} ln\rho^*_{,jj}. \tag{3}$$

The non-dimensional numbers that appear in equations 1, 2 and 3 are the computational Reynolds number, $Re_0 = \rho_0 L_0 U_0/\mu_0$, Schmidt number, $Sc = \mu_0/\rho_0 D_0$, and Froude number, $Fr^2 = U_0^2/gL_0$; where, $\mu_0/(= \mu^*/rho^*)$ is the reference dynamic viscosity, ρ_0 is the mean density, and D_0 is the diffusion coefficient.

Computational Setup

In this study, low density ratio (1.1:1) and high density ratio (7:1) cases are compared to study the influence of the density ratio on the evolution of the density gradients in HVDT. The mean density values are ≈ 1.05 and 4, and Re_0 is equal to 20000 and 3125 respectively for the low and high density ratio cases. Details of the simulations and more information on the initializing procedure can be found in [4-6]. VD NS equations (1) and (2) are solved with periodic boundary conditions and the divergence condition (3) using the CFDNS code [1,2] developed at LANL. The spatial derivatives are evaluated using Fourier transforms and the time advancement is performed with the variable time step third order Adams-Bashforth-Moulton scheme, coupled with a fractional time method.

RESULTS

In HVDT, when the acceleration is applied to the triply periodic domain, pure light and heavy fluids start to move in opposite directions due to differential buoyancy forces. These motions generate turbulence within the flow, which in turn enhances molecular mixing between the fluids. As the pure fluids become molecularly mixed, the buoyancy production weakens and at some instance turbulence dissipation overcomes turbulence production. Hence, buoyancy driven HVDT covers birth, growth, and decay of VD turbulence. This dynamic behavior allows us to connect acceleration driven Rayleigh-Taylor and shock driven Richtmyer-Meshkov instabilities as well as VD mixing layers and jet flows to the different phases of the idealized HVDT flow evolution (more information can be found in [4,6]). Here, we focus on the evolution of the density gradients in HVDT.

*Corresponding author. E-mail: denis.aslangil@gmail.com.

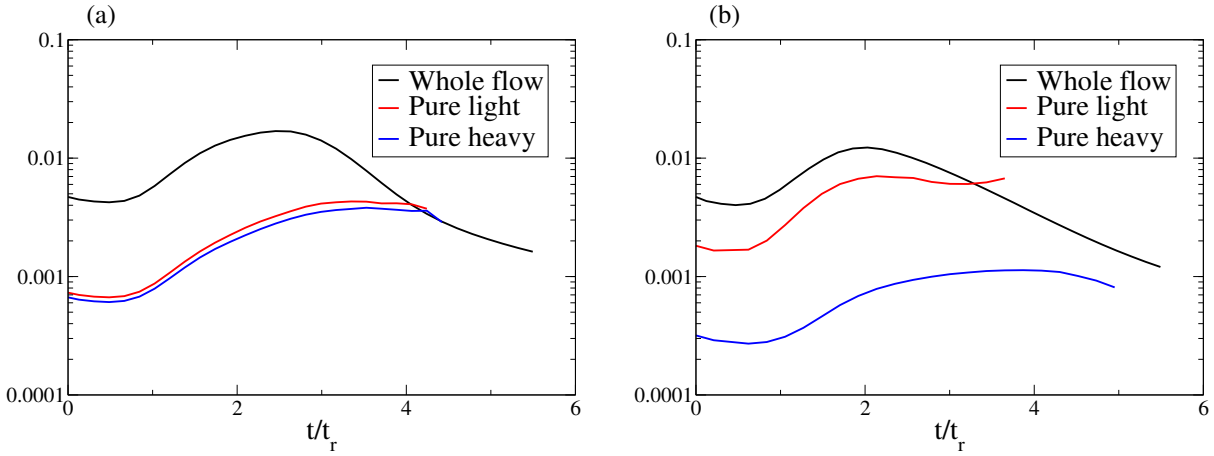

Figure 1: The evolution of the normalized Euclidean norm of the density gradients ($\Omega_{2,\nabla\theta}$) for a) low density ratio (1.1:1) and b) large density ratio (7:1) cases. The black line represents the volume average of the $\Omega_{2,\nabla\theta}$, red and blue lines represent the conditional average of the $\Omega_{2,\nabla\theta}$ for the pure light and pure heavy fluids, respectively.

Non-Boussinesq Effects

In the Boussinesq approximation, density appears in the momentum equation only in the buoyancy term. The usual underlying assumption is that the density fluctuations are much smaller than the mean and can be neglected in the rest of the terms of the momentum equations. However, even when the density fluctuations are small, density field can still have large gradients that could invalidate the Boussinesq approximation [1]. The evolution of the normalized Euclidean norm of the density gradients [$\Omega_{2,\nabla\theta} = (\int_V (\nabla(ln(\rho^*)/\theta_0)^2 dV)^{1/2}$, where θ_0 is the maximum resolved density gradient in DNS] is shown for both low and high density ratios in figure 1. The results indicate that, unlike density fluctuations that continuously decrease during the flow evolution, density gradients are not bounded by the initial conditions. This lack of non-linear depletion of the density gradients suggests that non-Boussinesq approximation may not be valid even for the low density-ratio mixing flows when the turbulence levels become high. Moreover, for the high density ratio case, the evolution of the conditional expectations of the density gradients is significantly different within the pure fluid regions. This indicates that the flow properties can locally be very different than what volume averaged statistics suggest [4] and any conclusion on the validity of Boussinesq approximation relying on the global statistics may be incorrect.

To further examine the evolution of the density gradients, the terms in the transport equations for the L^{2m}-norms of density gradient are bounded from above by simple expressions. The methodology was first used for the low density ratio (1.1:1) case by Rao et al.(2017) [7]. Here, we extend the study to the large density ratio (7:1) case. In addition, we change the normalization for a more meaningful comparison of the norms at late times and replace some of the bounds by tighter expressions. Similar to Rao et al.(2017), the results show that the analysis cannot exclude the possibility of finite time blow-up of the density gradients at sufficiently high Reynolds number, as the fluids are accelerated by differential buoyancy forces. On the other hand, at high Atwood numbers, the larger turbulence intensity in the light fluid regions also leads to much larger density gradients in these regions compared to the rest of the flow. Thus, if a blow-up does occur, it is in the light fluid regions. Of course, such an event would invalidate not only the Boussinesq approximation, but also the incompressibility assumption used to derive the VD euqations.

ACKNOWLEDGEMENTS

A. Banerjee acknowledge financial support from DOE/NNSA SSAA Program (Grant No. DE-NA0003195) and the U.S. National Science Foundation Early CAREER Program (Grant No. 1453056 from CBET-Fluid Dynamics). This work is co-authored by employees of Triad National Security, LLC which operates Los Alamos National Laboratory under Contract No. 89233218CNA000001 with the U.S. Department of Energy/National Nuclear Security Administration. Computational resources were provided by the Institutional Computing Program at Los Alamos National Laboratory and the Argonne Leadership Computing Facility at Argonne National Laboratory through a 2017 ALCC Award.

References

[1] Livescu, D., Ristorcelli, J. R. Buoyancy-driven variable-density turbulence. *J. Fluid Mech.* **591**, 43–71, 2007.
[2] Livescu, D., Ristorcelli, J. R. Variable-density mixing in buoyancy-driven turbulence. *J. Fluid Mech.* **605**, 145–180, 2008.
[3] Livescu D. Turbulence with large thermal and compositional density variations. *Annu. Rev. Fluid Mech.* **52**, 309-341, 2020.
[4] Aslangil D., Livescu D., Banerjee A. Atwood and Reynolds numbers effects on the evolution of buoyancy-driven homogeneous variable-density turbulence. *under review J. Fluid Mech.*, 2020.
[5] Aslangil D., Livescu D., Banerjee A. Variable-density buoyancy-driven turbulence with asymmetric initial density distribution. *under revision Physica D*, 2020.
[6] Aslangil D., Livescu D., Banerjee A. Flow regimes in buoyancy-driven homogeneous variable-density turbulence. In *Progress in Turbulence VIII (ed. Ramis Orlu, Alessandro Talamelli, Joachim Peinke and Martin Oberlack)*, pp. 235–240. C ham: Springer International Publishing, 2019.
[7] Rao, P., Caulfield, C. P., Gibbon, J. D. Nonlinear effects in buoyancy-driven variable-density turbulence. *J. Fluid Mech.* **810**, 362–377 2017.

ALTERNATION OF VERY LARGE SCALE FEATURES IN A TURBULENT CHANNEL FLOW

Yuya Tanada[1], Yuta Akasaka[2], and Masaharu Matsubara *[3]
[1,2,3]Department of Mechanical System Engineering, Shinshu University, 4-17-1, Wakasato, Nagano, Japan

Summary It has been experimentally observed that in turbulent channel flows very large scale features(VLSF), whose scales are ten times larger than the channel width, appear at very low and very high Reynolds numbers, though it is unknown if both Reynolds numbers are classified as the same because there is no scrutiny between them. In the present study, we explore the Reynolds number range existing the VLSFs and their streamwise and spanwise length scales with increasing the Reynolds number up to 10000 (based on the mean velocity and the channel width) in the experiments with the cross spectra of the streamwise velocity fluctuations measured by hot-wire sensors separating in the spanwise direction. Between Reynolds numbers, 3400 and 5000, the VLSF of a wide spanwise scale alters into narrow structure keeping their streamwise length. The narrow VLSF is confirmed up to Reynolds number 10000 and the streamwise and spanwise length scales are in the same order of that Monty et al. (J. Fluid Mech. 289, pp. 147–156, 2007) found in a channel flow.

INTRODUCTION

In the current decade, large-scale turbulent patterns in wall-bounded shear flows have been noticed. Liu et al. [1] performed proper orthogonal decomposition (POD) for two-dimensional particle image velocimetry measurements in a turbulent channel flow at $Re_h = 5378, 29935$ (defined by the bulk velocity and the half channel width), and they demonstrated that modes of the streamwise large-scale in order of the channel width has high contribution to the total kinetic energy. Monty et al. [2] discovered a low-speed region of streamwise length scales larger than ten pipe radii or channel widths in turbulent pipe and channel flows at very high Reynolds number, and they called it 'very large-scale feature' (VLSF). Seki et al [3] observed a low-frequency peak which is very close to the frequency of the turbulent patch appearance in premultiplied frequency spectra of the streamwise velocity fluctuation at $Re = 2660$ (defined by the bulk velocity and the channel width) at which the flow is turbulent with the intermittency factor reaching unity. This peak suggested the existence of the VLSF. Horii et al. [4] conducted similar experiments to theirs using two-channel flow facilities and showed that the spectral peak of the VLSF at low Reynolds number was observed independently of the apparatus and they confirm the peak up to $Re = 4000$. They also performed flow visualization in a water channel facility and observed inclined regions filled with kinked streaks whose streamwise length corresponds to that of the spectral peak.

Though the roles of the VLSFs to a channel flow are not obvious, it is clear that VLSF gives a contribution to the statics such as the spectra of the streamwise velocity. Furthermore, since the VLSFs were observed at only both very-low and very-high Reynolds numbers it is not clear whether these are the same or not. In order to investigate the VLSFs at moderate Reynolds numbers and their streamwise and spanwise length scales, we measure the two-point correlations of the streamwise velocities by hot-wire anemometry with increasing Reynolds number from the upper marginal Reynolds number at which the channel flow sustains a fully turbulent state.

RESULTS AND DISCUSSION

In the present experiment, the channel facility is the same as the larger facility used by Horii et al. [4]. The channel width d is 25 mm. The streamwise and spanwise dimensions of the channel part are about 14 m and 1 m, respectively. The coordinates are defined as x and y in the streamwise and wall-normal directions. Hot-wire anemometry is used for the streamwise velocity measurements. The measurements are conducted at the channel center with a sampling frequency of 20 kHz, and a sampling time of 600 s. The two-point correlations of the streamwise velocity fluctuations are obtained with fixing one hot-wire sensor and moving the other hot-wire in the spanwise direction. All length scales here are normalized by the channel width d.

Figure 1 shows the color maps of the cross-correlation coefficient at $Re = U_b d/\nu = 3400$, 5000 and 10000, where U_b is the bulk velocity and ν is the kinematic viscosity. ΔZ is the non-dimensional distance between the hot-wire sensors and λ_x is the non-dimensional streamwise scale estimated in Taylor's frozen-flow hypothesis with the velocity spectra. Blue shows a negative cross-correlation coefficient and red is positive. It can be estimated that the ΔZ at which the correlation coefficient has a negative minimum is about half the spanwise length scale of the dominant structures. It is inferred that negative minimum regions around $\Delta Z = 0.7$, $\lambda_x = 3$ at all Reynolds numbers are caused by turbulent vortices because their streamwise length scale is in order of the magnitude of d.

At $Re = 3400$, a negative region distributes around $\Delta Z = 3.1$ and $\lambda_x = 20$ indicating the VLSF that has the streamwise and spanwise length scales of about $20d$ and 6, respectively. These sizes correspond to those of the VLSF observed by Seki et al. at $Re = 2660$. Furthermore, the length scales are very close to the scales of the large structure observed by Horii et al. [4]. It is considered that VLSF observed from this experiment is the same as the structure observed by Horii et al. [4] in their flow visualization, suggesting that this VLSF is a cluster of the streaky structures forming an inclined local band.

*Corresponding author. E-mail: mmatsu@shinshu-u.ac.jp

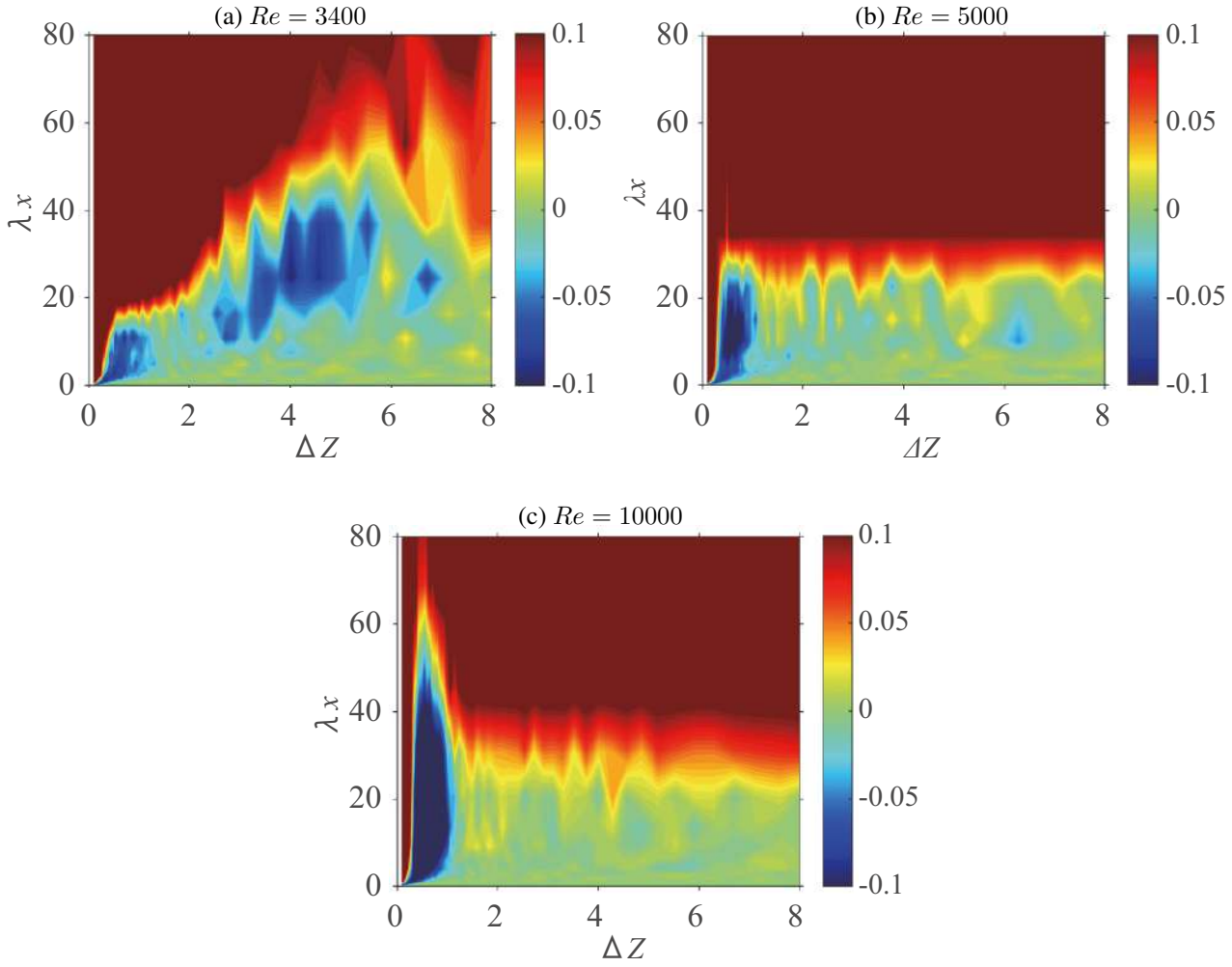

Figure 1: Color maps of the cross correlations of the streamwise velocities.

The negative peak at $Re = 5000$ in the region of $\Delta Z = 0.7$ and $\lambda_x = 10$-20 indicates another VLSF that has the spanwise length scale of $1.4d$ This spanwise length scale corresponds with that of the VLSF obtained by Monty et al. This negative region still exists at $Re = 10000$, though the streamwise length slightly elongates comparing with that at $Re = 5000$. Survey of the color maps with gradually increasing Re shows the drastic change of them around $Re = 4000$, indicating that the VLSF alters to the narrow VLSF. The observation at $Re = 10000$ and the investigation by Monty et al. suggest that the narrow VLSF is ubiquitous in a high Re channel flow.

References

[1] Z. Liu, and R. J.Adrian, T. J. Hanratty, "Large-scale modes of turbulent channel flow: transport and structure", J. Fluid Mech.448, 53-80, (2001).
[2] J. P. Monty, J.A.Stewart, R. C. Williams and M. S. Chomg, "Large-scale features in turbulent pipe and channel flows", J. Fluid Mech.589, 147-156, (2007).
[3] D. Seki, and M.Matsubara, "Experimental investigation of relaminarizing and transitional channel flows", Phys. Fluids, 24, 124102, (2012).
[4] S. Horii et al., "Very large-scale feature of transitional and turbulent channel flows: dependence on facilities", Progress in Turbulence VII.189-195, (2016)

THE ENERGY BUDGET AT THE OUTER PEAK OF $\overline{u^2}$ IN TURBULENT PIPE FLOW

Jonathan Morrison*and José Fernando Vicente
Department of Aeronautics, Imperial College London, London SW7 2AZ, UK.

Summary We use the NSTAP data from the Princeton superpipe [1] to examine the spatial & spectral energy fluxes close to the outer peak in $\overline{u^2}$ in the range of Reynolds numbers, $2.1 \times 10^6 \leq Re_D \leq 6.0 \times 10^6$, for which the ratio of hot-wire length to Kolmogorov length scale is $l/\eta \leq 10$. Previous results [2] suggest that the outer peak emerges at $Re_D \approx 1.1 \times 10^6$, its position exhibiting a locus $y_m^+ = 0.23(Re_\tau)^{0.67}$. We note that this is close to the position of the well-known "mesolayer", which we have also described as the intermediate layer with scaling ($y_m^+ \propto \sqrt{Re_\tau}, u_m$), where u_m is the rms velocity at $y = y_m$ – see [3, 4] and also the presentation in the minisymposium, "Modeling and Controlling Turbulent Shear Flows". It is straightforward to show that the locus of u_m is close to that for the production of $\overline{u^2}$, $P_m(\overline{u^2})$ where the local-equilibrium approximation holds. Therefore, spectral dynamics are most 'Kolmogorov-like' because spatial transport is small there. Here we examine the inertial scaling of the axial velocity spectra and low-order structure functions to help provide a rational basis for the concept of intermediate scaling.

INTRODUCTION

The logarithmic (log) variation of the streamwise mean velocity and variance in the inertial sublayer are two cornerstones in wall turbulence (Eq. 1):

$$U^+ = \frac{1}{\kappa}\ln(y^+) + C, \qquad \frac{\overline{u^2}}{u_\tau^2} = B_1 - A_1 \ln\left(\frac{y}{\delta}\right). \tag{1}$$

Here u_τ is the friction velocity, y is the wall-normal distance and $^+$ indicates scaling on wall variables. δ is the boundary-layer thickness for the turbulent boundary layer or, here, the pipe radius. κ and A_1 in Eq. (1) are the well-known von Kármán and Townsend-Perry [5] 'constants' respectively; C and B_1 are the additive 'constants'.

We have recently demonstrated [3, 4] the importance of a length scale for the intermediate region, $y_m^+ \propto \sqrt{Re_\tau}$ ($Re_\tau \equiv R^+ = u_\tau\delta/\nu$), which is the typical "mesolayer" scaling; the velocity scale is chosen to be the rms turbulence velocity at $y = y_m$. Using the intermediate length scale and velocity scale, we show that the mean-velocity defect and variance profiles achieve a Reynolds-number similarity in the intermediate region for both pipe and boundary-layer flow. This reveals a Reynolds-number invariant log region in wall turbulence, in terms of the intermediate variables. As a consequence, the classical log law is seen to emerge only at sufficiently large Reynolds numbers and the Townsend-Perry 'constant' shows a systematic Reynolds-number dependence and it is plausible that associated eddies scale on the intermediate variables which are local to the inertial sublayer. We have also discussed the consequences of this finding for the Reynolds-number behaviour of κ and A_1.

It is not immediately obvious why y_m should emerge as a natural length scale: in some sense, it is obvious simply through the identification of a maximum on which statistics close to it can be expected to scale. For a more physical reason however, we note that the three-layer asymptotic structure of pipe flow, made explicit by the use of intermediate scaling, suggests Reynolds-number independence for $Re_\tau \gtrsim 10^4$. We further note that previous results [2] suggest that the outer peak emerges with $Re_D \gtrsim 1.1 \times 10^6, Re_\tau \gtrsim 2 \times 10^4$. By extension, a simple dimensional analysis of the near-wall energy budget using wall scaling (u_τ, y) will reduce to the local-equilibrium approximation, for which spatial transport of turbulence kinetic energy is a small fraction of its (local) production and dissipation. We further suppose that, in this region, spectral flux is most 'Kolmogorov-like' because small spatial transport implies a relative absence of energy sources or sinks at each wavenumber. Here we use the turbulent pipe-flow data obtained in Princeton Superpipe using the NSTAP probe [1, 2] for $Re_\tau = 1985 - 98190$. Measurements were performed with NSTAP probes of length, $\ell = 30$ μm and 60 μm, with temporal resolution up to 300 kHz. The ratio of hot-wire length to Kolmogorov length scale is $l/\eta \leq 10$. Figure 1 shows the variance profiles scaled on wall units, the actual peak lying close to the intermediate length scale, $y_m^+ = 3.5\sqrt{Re_\tau}$ with the velocity scale $u_m = \sqrt{\overline{u^2}}(y = y_m)$ – see [3].

SCALING OF THE DISSIPATION RATE NEAR THE OUTER PEAK

We have previously examined [6] the inertial subrange scaling of the axial velocity component for the centreline of turbulent pipe flow for Reynolds numbers in the range $249 \leq Re_\lambda \leq 986$, where λ is the Taylor length scale: we noted that the dimensionless dissipation rate, $A = \epsilon R/u_\tau^3$, increases indefinitely with Reynolds number, in contrast to other similar measures [7]. Here, we extend the analysis to examine the scaling of the inertial subrange in the local-equilibrium region, $y/R = 0.052$. With the assumption of "wall" (u_τ, y) scaling, we expect the log-law and local-equilibrium regions to be approximately coincident. With the assumption of local-equilibrium, and using the momentum equation:

$$-\overline{uv}^+ = 1 - \frac{y}{R} - \frac{1}{\kappa y^+}, \qquad \epsilon^+ = (-\overline{uv}^+)/\kappa y^+. \tag{2}$$

*Corresponding author, j.morrison@imperial.ac.uk. We acknowledge financial support, ESPRC Grant No. EP/I037938/1.

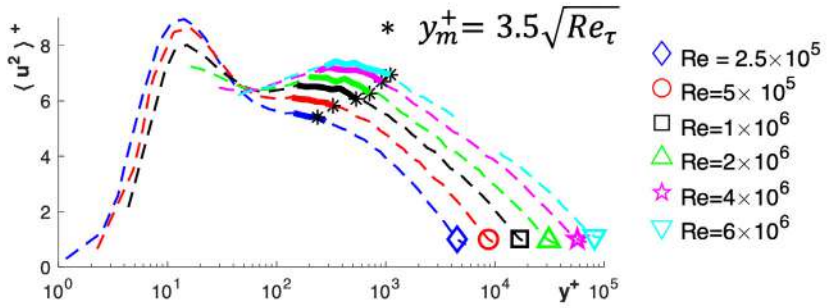

Figure 1: Streamwise variance, $\overline{u^2}^+$, $2.5 \times 10^5 \leq Re_D \leq 6.0 \times 10^6$, locus of actual peak given by $y_p^+ = 0.23 Re_\tau^{0.67}$ [2].

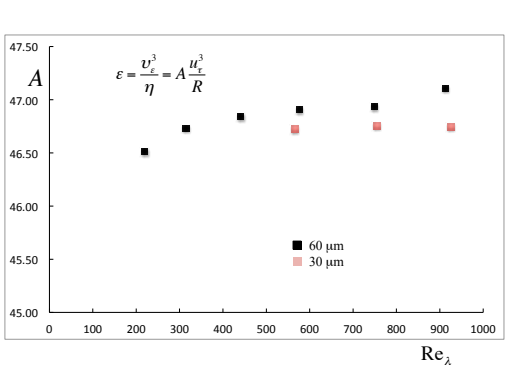

(a) Fixed y, $y^+ = 0.052 Re_\tau$

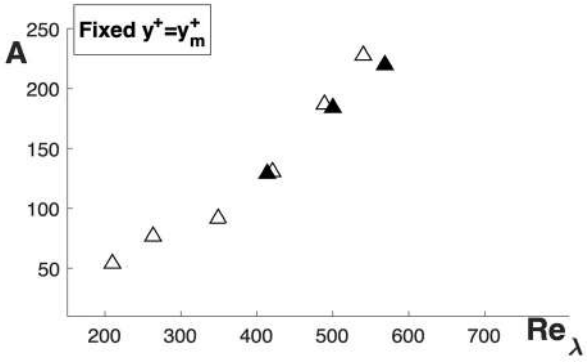

(b) Outer peak, $y_m^+ = 3.5\sqrt{Re_\tau}$. Open symbols, 60$\mu$m; closed 30$\mu$m.

Figure 2: Variation of $A = \epsilon R/u_\tau^3$ with Re_λ.

However, the spectral flux is much more spatially intermittent than either the production or dissipation spectra, and since the energy balance at any point in space is an integration over all wavenumbers, local equilibrium will only ever be an approximation. Figure 2a shows that A in the local-equilibrium region is closer to a constant value than at the centreline over a similar range of Re_λ, [6, 8]. This could be attributed to the fact that the turbulent transport in the local-equilibrium region is a somewhat smaller fraction of production and dissipation than at the centre line. With these assumptions, it is straightforward to show that $A = \epsilon^+ R^+$ and that by inspection of equation (2), A is more nearly constant at $y/R =$constant. Note also that $S = dU/dy$ nondimensionalised as $S^* = \sqrt{\epsilon/S^3}$ becomes $S^{*+} = \kappa y^+$, with the assumption of local equilibrium. With $A =$ constant therefore, the use of u_τ and R to non-dimensionalise ϵ here, suggests that the effect of the outer boundary conditions is represented by these scales, in conformity with the assumptions of local equilibrium.

Figure 2b shows the calculated variation of A following the locus of $y_m^+ = 3.5\sqrt{Re_\tau}$. To leading order, equation (2) may be written as $A = R^+/\kappa y^+$ which, with $y^+ = y_m^+$ gives $A/\sqrt{R^+} =$ constant. Noting that $\sqrt{R^+} \propto Re_\lambda$, figure 2b shows that this is indeed the case. The result is similar for y_p^+ [8]. At the outer peak therefore, we have $A = Re_\lambda \times$ constant. In the full paper, we shall discuss this result, and compare estimates of dissipation rates with locally-isotropic estimates available from integration of the one-dimensional dissipation spectra. We shall also examine the spectral and spatial distribution of energy by reference to scaled and premultiplied inertial subrange spectra as well as the second- and third-order structure functions.

References

[1] Vallikivi, M. Wall-bounded turbulence at high Reynolds numbers. PhD thesis, Princeton University.
[2] Hultmark M., Vallikivi M., Bailey S. C. C., Smits A. J. Turbulent pipe flow at extreme Reynolds numbers. *Phys. Rev. Lett.* **108**: 094501, 2012.
[3] Diwan S. S., Morrison J. F. Reynolds-number dependence of the Townsend-Perry 'constant' in wall turbulence. In *TSFP11 Digital Library Online, Begel House Inc.*, 2019.
[4] Diwan S .S., Morrison J. F. Intermediate Scaling and Logarithmic Invariance in Turbulent Pipe Flow. *arXiv:1909.11951*, 2019.
[5] Marusic I., Monty J. P., Hultmark M., Smits A. J. On the logarithmic region in wall turbulence. *J. Fluid Mech.* **716**: R3, 2013.
[6] Morrison J. F., Vallikivi M. and Smits A. J.: The inertial subrange in turbulent pipe flow: centreline. J. Fluid Mech 788:602-613, 2016.
[7] Sreenivasan, K. R.: On the universality of the Kolmogorov constant. Phys. Fluids 7, 2778-2784, 1995.
[8] Morrison J. F., Vicente J. F. The energy budget at the outer peak of $\overline{u^2}$ in turbulent pipe flow. APS DFD abstract: G11.00006, 2019.

CHARACTERISTICS OF GRID TURBULENCE IN THE FAR DOWNSTREAM REGION

Yulin Zheng*[1], Tomoaki Watanabe[1], and Koji Nagata[1]
[1]Department of Aerospace Engineering, Nagoya University, Nagoya, Aichi, Japan

Summary Characteristics of grid turbulence have been investigated in the far downstream region ($x/M \sim 10^3$: x is the downstream distance from the grid, M is the mesh size of the grid.) through the wind tunnel experiment. It can be concluded that the dissipation coefficient C_ε at large Re_λ (Re_λ is the Taylor microscale Renolds number, based on the r.m.s longitudinal velocity fluctuation $u_{\rm rms}$, the Taylor microscale λ, and the kinematic viscosity ν) tends to be constant and raises rapidly during the final of the transition period of decay. The construction of the vorticity $S + 2G/Re_\lambda$ (S is the skewness of the longitudinal velocity derivative, G is the destruction coefficient) rapidly increases with the streamwise distance in the far downstream region.

INTRODUCTION

Homogeneous isotropic turbulence (HIT) is probably the most fundamental turbulence which has been extensively investigated by theoretical studies, direct numerical simulation (DNS), and wind tunnel experiments[1, 2, 3]. Since grids with various geometries can generate quasi-HIT, they have been applied for the wind tunnel experiments for many decades. Although the development and the initial period of decay of grid turbulence have been analyzed experimentally and theoretically, few experiments have been conducted in the far downstream region to investigate the transition and final period of decay. In this study, the wind tunnel experiment was conducted to investigate the statistics from the initial to the transition period of decay till the far downstream, with the range of Re_λ = 5-114.

EXPERIMENT APPARATUS

The experiment was conducted in an open-type wind tunnel in Nagoya University. The test section has a width of 600 mm, a height of 600 mm and a length of 12 m. Three types of grids with difference mesh size M (Fig. 1) were used. The experiments were conducted 5 times at each point to reduce the statistical errors. The measurements were conducted up to 6 m from the entrance of the test section because of the growth of the boundary layer and secondary flow at the farther streamwise region. Experimental conditions are given in Table 1.

Constant Temperature Anemometer (CTA, DANTEC Streamline) with an I-type hot wire probe (DANTEC 55P11) was used to measure the instantaneous streamwise velocity. The sampling number and frequency are set to 524288 and 20 KHz aiming to acquire reliable derivative quantities. Low pass filter is used to remove the electronic noise.

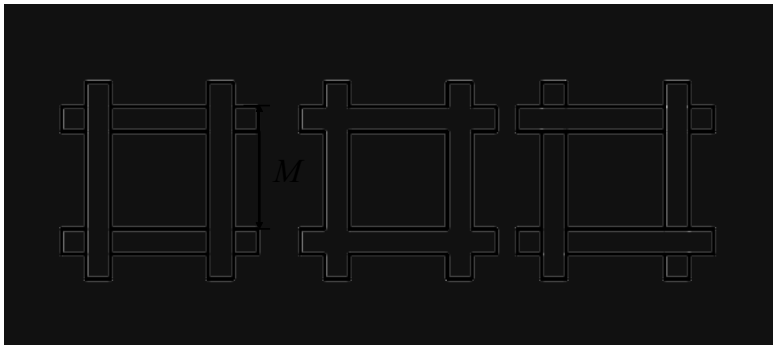

Figure 1: Sketch of (a) square grid of biplane, (b) square grid of single plane, and (c) woven-mesh grid

RESULTS

For HIT, the fundamental equations related to the dissipation rates of energy and enstrophy can be derived from the Karman-Howarth equation as Eq. (1) and Eq. (2)[1]:

$$\varepsilon = -\frac{3}{2}\frac{{\rm d}{u_{\rm rms}}^2}{{\rm d}t} = \frac{C_\varepsilon u_{\rm rms}^3}{L_{uu}} \tag{1}$$

$$\frac{{\rm d}{\omega_{\rm rms}}^2}{{\rm d}t} = -\frac{7}{3\sqrt{5}}{\omega_{\rm rms}}^3 (S + 2G/Re_\lambda) \tag{2}$$

*E-mail: zheng.yulin@k.mbox.nagoya-u.ac.jp

Table 1: Experimental conditions

U_0 (m/s)	Re_M	M (mm)	Solidity σ	Shape
2	680	5 (M5)	0.39	woven-mesh
2	1300	10 (M10)	0.36	square (single-plane)
4	3900	15 (M15)	0.36	square (biplane)
6	5800	15 (M15)	0.36	square (biplane)
10	9600	15 (M15)	0.36	square (biplane)
10	33000	50 (M50)	0.36	square (biplane)

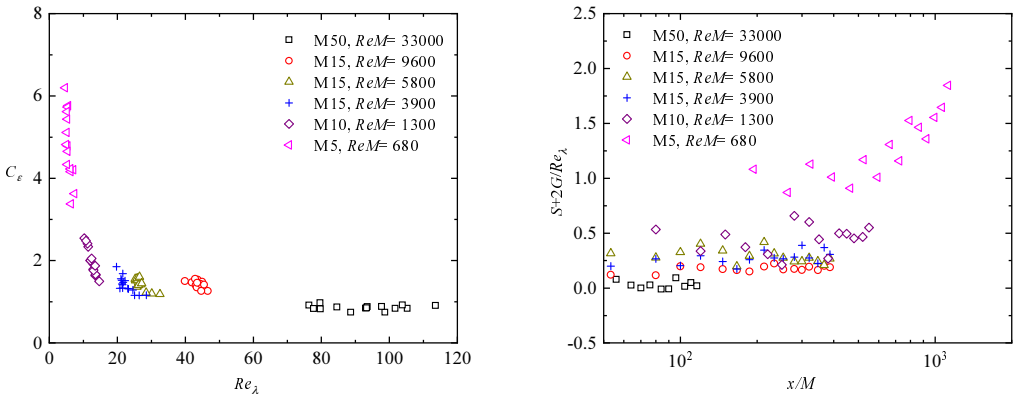

(a) (b)

Figure 2: (a) Relationship between C_ϵ and Re_λ. (b) Variation of $S + 2G/Re_\lambda$ with downstream.

$$S = \overline{\left(\frac{\partial u}{\partial x}\right)^3} \Big/ \left[\overline{\left(\frac{\partial u}{\partial x}\right)^2}\right]^{\frac{3}{2}}, G = {u_{\rm rms}}^2 \overline{\left(\frac{\partial^2 u}{\partial x^2}\right)^2} \Big/ \left[\overline{\left(\frac{\partial u}{\partial x}\right)^2}\right]^2 \tag{3}$$

Here, L_{uu} is the integral length scale, $\omega_{\rm rms}$ is the r.m.s of the vorticity fluctuations. S and G is defined by Eq. (3). From Eq. (1), it is of great significance to investigate the energy decay and the connection between large and small eddies. Thus, it is important to measure the dissipation coefficient C_ε ($C_\varepsilon = \varepsilon L_{uu}/u_{rms}^3$), which is associated with both the characteristics of large eddies and dissipation. The relationship between C_ε and Re_λ is shown in Fig. 2(a). For large Re_λ, $C_\varepsilon \approx 1$ can be seen clearly and this is consistent with the results of past experimental data[5]. Conversely, for small Re_λ, C_ε increases rapidly as Re_λ decreases. The variation of $S + 2G/Re_\lambda$ with the downstream distance from the grid is given in Fig. 2(b). It can be seen that $S + 2G/Re_\lambda$ grows with the downstream distance in the far downstream region only for M5, while the increasing trends of other cases do not appear apparently. This means that the balance between the production and destruction of the enstrophy has been broken down and that the process is under the domination of destruction in the far downstream region for the case M5.

CONCLUSIONS

Velocity measurements in grid turbulence were conducted in the far downstream region of $x/M \sim O(10^3)$ and $Re_\lambda \sim O(1)$. C_ε rapidly increases at the small Re_λ, and the construction of enstrophy ($S + 2G/Re_\lambda$) increases in the far downstream region.

References

[1] Batchelor, G. K. and Townsend, A. A. Decay of vorticity in isotropic turbulence. *Proc. R. Soc. Lond. A* **190**: 534-550, 1947.
[2] Kitamura, T., Nagata, K., Sakai, Y., Sasoh, A., Terashima, O., Saito, H., Harasaki, T. On invariants in grid turbulence at moderate Reynolds numbers. *J. Fluid Mech.* **738**: 378-406, 2014.
[3] Watanabe, T. and Nagata, K. Integral invariants and decay of temporally developing grid turbulence. *Phys. Fluids* **30**: 105-111, 2018.
[4] Djenidi, L. and Antonia, R. A. Transport equation for the mean turbulent energy dissipation rate in low-Re_λ grid turbulence. *J. Fluid Mech.* **747**: 288-315, 2014.
[5] Vassilicos, J. C. Dissipation in Turbulent Flows. *Ann. Rev. Fluid Mech.* **47**: 95-114, 2015.

SKIN-FRICTION DRAG REDUCTION EFFECT OF STREAMWISE LARGE-SCALE VORTEX GENERATED BY WALL HEATING AND COOLING IN TURBULENT PIPE FLOW

Koyo Tanaka[1], Hiroya Mamori [*1], and Takeshi Miyazaki [1]
[1]University of Electro-Communications, 1-5-1, Chofugaoka, Choufu, Tokyo, Japan

Summary Skin-friction drag reduction in wall-turbulence is of importance to reduce energy loss and many flow control techniques to obtain the drag reduction have been studied. It is known that streamwise large-scale vortical structure can decrease the skin-friction drag in the turbulent channel flow. In this study, we performed direct numerical simulations of the turbulent pipe flow controlled by the large-scale vortical structure to investigate its drag reduction effect. To generate the large-scale vortical structure, we impose temperature distribution to generate buoyancy force. A maximum drag reduction rate is 8.7% when two pairs of the large-scale vortices are generated. We found that the turbulent vortical structures are transported and affected by the motion of the large-scale vortical structure.

Background

Reduction of skin-friction drag is of importance in wall-turbulence. Streamwise vortical structures play important role to increase the skin-friction drag and various control techniques to decrease the vortical structures have been studied [1-3]. One of the control techniques, this study focuses on a large-scale control technique for the skin-friction drag reduction in the wall-turbulence.

Schoppa & Hussain[4] made direct numerical simulations (DNS) of turbulent channel flows with streamwise forced vortices. The forced vortices are generated by an imposed velocity distribution mimicking small jet flow from walls or assuming a vortex generator. They reported that the forced vortices decrease the wall-normal vorticity and the regeneration mechanism of the wall-turbulence is weakened. Thus, the skin-friction drag is reduced. Canton et al.[5] imposed an ideal body force distribution into the turbulent channel flow to generate the forced vortices and they confirmed 18% of the skin-friction drag reduction. Our research group, in contrast to the channel flow, has investigated the control effect in turbulent pipe flows, because the pipe flow is an important system in engineering, e.g., pipelines, and the number of forced vortices generated by control is limited due to curvature of pipe.

In this study, we make the DNS of the turbulent pipe flow with the forced vortex to investigate its skin-friction drag reduction effect. To induce the forced vortex, instead of the ideal velocity or body force distribution, we employed the buoyancy force generated by heating and cooling from the wall.

Direct numerical simulation

Figure 1 shows a pipe flow (together with the temperature distribution as discuss later). The length of the pipe was set to $10R$ where the radius R of the pipe is chosen as a reference length. A constant pressure gradient condition is imposed as the driving force of the flow. The friction Reynolds number Re_τ, defined by the friction velocity and R, is set to be 180. In addition, the reference temperature is denoted by T_{ref} in this paper.

A staggered computational grid in a cylindrical coordinate system is employed and the number of computational grid points is 64x128x128. The governing equations are incompressible continuity, Navier-Stokes, and energy equations. As boundary conditions, a non-slip condition is imposed on the wall and a periodic boundary condition is imposed in the streamwise direction. The DNS code is discretized by using a finite difference method[6].

A forced vortex is generated by buoyancy force which appears as a body force term in the Navier-Stokes equation. The buoyancy force using Boussinesq approximation reads,

$$F_b = Ri\Delta T \quad (1)$$

The buoyancy force F_b consists of the Richardson number $Ri = Gr / (\mathrm{Re}_\tau{}^2)$ (where Gr is the Grashof number) and ΔT (difference between the local temperature and the reference temperature). To induce the body force, we impose the wall temperature as the control input and it reads

$$T_{wall}(\theta) = -A\sin(\Omega_{wall}\theta) \quad (2)$$

The wall temperature varies in the azimuthal direction and homogeneous in the streamwise direction. The control parameters are the wave number Ω_{wall} and the amplitude A. In this study, the amplitude A is fixed at $A = 1$, which means the mean temperature averaged on the wall surface equals T_{ref}. To make parametric study, Ω_{wall} is varied from 2 to 4 with the Richardson number of 40, 80, 120, and 160.

Figure 1 also shows an example of the mean temperature distribution at the wavenumber of 3 and the Richardson number of 120, together with the mean velocity vectors. Due to the heating and cooling from the wall, the buoyancy force generates the upward flow (i.e., flow from the wall toward center of the pipe) at $\theta = 0$ and π and the downward flow at $\theta = \pi/2$ and $3/2\pi$. As a result, two pairs of forced streamwise vortices were generated in this case.

*Corresponding author. E-mail: mamori@uec.ac.jp

Simulation results

Figure 2 shows a drag reduction rate as a function of the Richardson number. The drag reduction rate R_D is defined as.

$$R_D = \frac{C_{f0} - C_f}{C_{f0}} \times 100 \quad (3)$$

Here, C_f is a friction coefficient and the subscript of zero indicates the uncontrolled flow. The skin-friction drag reduction is obtained ($R_D > 0$) for $\Omega_{wall} = 2$ and 3 and R_D is maximized ($R_D = 8.7$ [%]) at $\Omega_{wall} = 3$ and $Ri = 120$, whereas the drag increases for $\Omega_{wall} = 4$. We chose the maximum drag reduction case as a reference in the following.

Figure 3 shows turbulent vortical structures visualized by the second invariant value of the velocity deformation tensor at $Q^+ = 0.05$. The plus means wall units. In the uncontrolled case as shown in Fig. 3(a) and (c), the vortical structures are observed near the wall surface. On the other hand, in the reference case as shown in Fig. 3(b) and (d), the vortical structures are gathered around $\theta = 0$ and π. Due to upward flow induced by the buoyancy force the vortical structure is transported to the center of the pipe.

Conclusion and outlook

The skin-friction drag reduction effect by the forced vortex induced by the buoyancy force in the turbulent pipe flow is investigated by means of the direct numerical simulations. The buoyancy force is controlled by the temperature distribution on the pipe wall. The maximum drag reduction rate of 8.7 [%] was obtained at the wavenumber of 3 and the Richardson number of 120, in which two pairs of forced vortices were generated. The force vortices gather the turbulent vortical structures and they are transported toward the center of the pipe. In the presentation, we will discuss the mechanism of the drag reduction in detail.

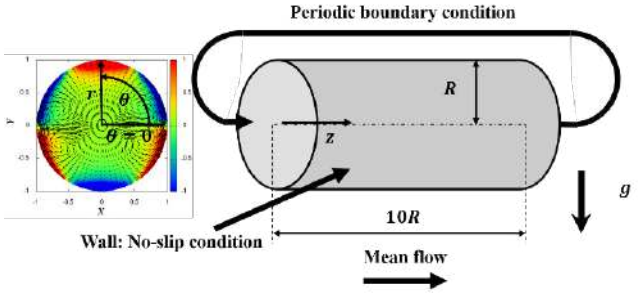

Figure 1. Computational domain.

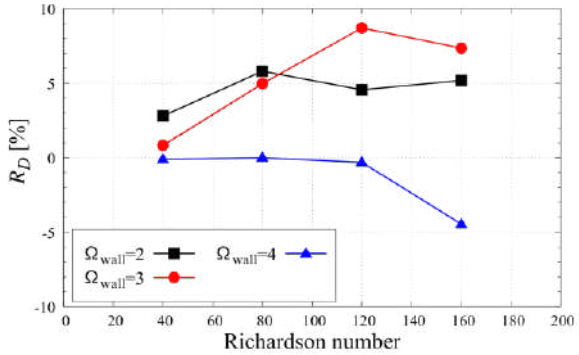

Figure 2. Drag reduction rate as a function of the Richardson number.

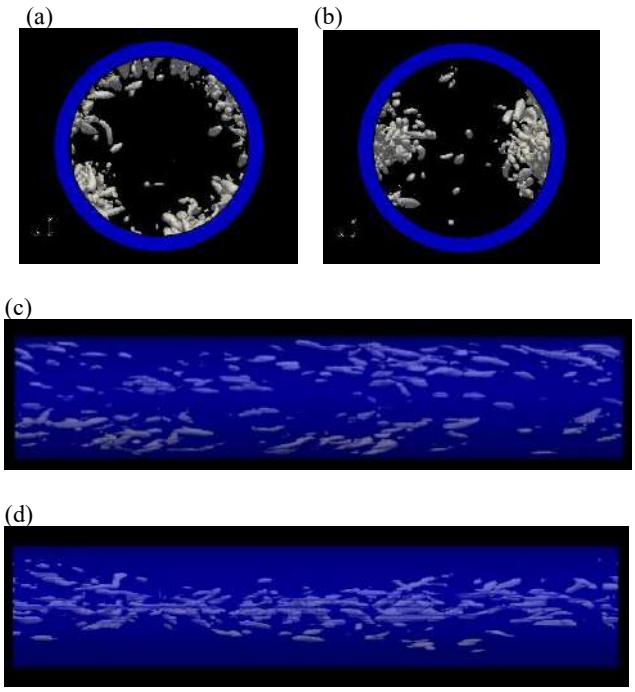

Figure 3. Instantaneous vortical structures: (a) and (c), the uncontrolled flow; (b) and (d), the reference case.

References

[1] Gad-el-Hak, *et al*., "Interactive control of turbulent boundary layers: A futuristic overview", *AIAA. J.,* Vol. 32, pp. 1753-1765, (1994).

[2] Choi, *et al*., "Active turbulence control for drag reduction in wall-bounded flows", *J. Fluid Mech.,* Vol. 262, pp.77-110, (1994).

[3] Schoppa & Hussain, "A large-scale control strategy for drag reduction in turbulent boundary layers", *Phys. Fluids,* Vol.10, pp. 1049-1051, (1998).

[4] Canton, *et al*., "On large-scale friction control in turbulent wall flow in low Reynolds number channels", *Flow Turbul. Comb.,* Vol. 97, pp. 811-827, (2016).

[5] Fukagata, *et al*., "Highly energy-conservative finite difference method for the cylindrical coordinate system", *J. Comput. Phys.,* Vol. 181, pp. 478-498, (2002)

EXPERIMENTAL STUDY ON MIXING AND ENTRAINMENT THROUGH ANISOTROPIC POROUS MEDIA DRIVEN BY A TURBULENT FLOW

Sofia Saoncella*[1], Aidan Rinehart[1], Agastya Parikh[1], Marcus Hultmark[2], and Shervin Bagheri[1]
[1]Department of Engineering Mechanics, KTH, Stockholm, Sweden
[2]Department of Mechanical and Aerospace Engineering, Princeton University, Princeton, USA

Summary This poster presents our current effort to investigate a turbulent flow over an anisotropic micro-structured porous bed. The objective is to characterize modifications in the overlying turbulent flow in terms of turbulent structures and friction drag and to describe quantitatively mixing, entrainment and diffusion of particles inside the porous bed. In particular, we want to understand the link between shear flow instabilities and the interstitial flow for different microscopic features of the porous medium. The work involves the building of water channel facility, the fabrication of a micro-structured surface and the measurement procedure through micro-PIV.

MOTIVATION

Fluid flows over porous media play a central role both in industrial applications as well as in natural settings (geological, environmental, etc). The conditions encountered in different applications are broad enough to cover a large range of Reynolds numbers, both for the overlying turbulent flow and the interstitial flow in the porous media. For example, Stokes flow in porous media may be encountered in ground water flows while turbulent flows are found in application such as heat exchangers or nuclear reactors. Despite their ubiquity, the relationship between the geometry of the porous material, porous size and shape, and the the turbulence over the porous bed is still not known in detail. The present experimental study aims to investigate the interaction between turbulent flows and porous surfaces. In particular, we will characterize surfaces with different geometries and configurations of micro-sized pores. A schematic representation of the configuration is shown in Fig. 1.

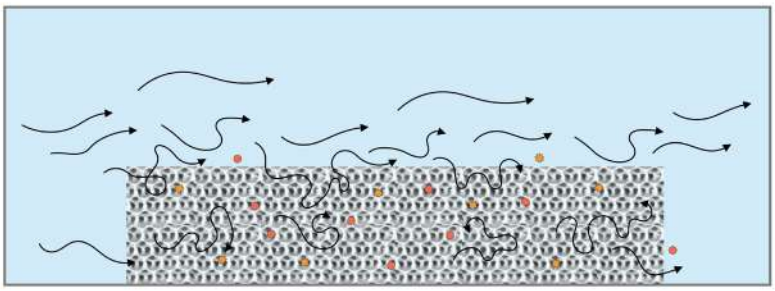

Figure 1: Schematics of the mixing and diffusion of particles induced by a flow over the porous medium. Black arrows indicates possible trajectories of the flow and consequently of the particles.

METHODS

The project involves the fabrication of a complex surface with interconnected and properly sized pores (ranging from 10 to $300\,\mu\mathrm{m}$), followed by the characterisation of its porosity, permeability and geometry and the final test inside a water channel facility. The water channel is being manufactured and designed to sustain flows with Reynolds number up to $Re_\delta \approx 5 \cdot 10^5$. To provide insight into the turbulent transport processes within the porous structure, particle image velocimetry technique at the micro scale (μPIV) will be used. A difficulty common to most optical diagnostic techniques that are applied to fluid-structure studies is the refraction of light passing through the material. This project will use refraction index matching of the liquid (NaI solution) and wall surface (PDMS) to minimize the distortion from the walls. This treatment will allow for measurements to be taken at the interface as well as within the porous structures. The channel has a cross section of $10\,\mathrm{mm} \times 200\,\mathrm{mm}$ and a length of $2160\,\mathrm{mm}$, of which $1440\,\mathrm{mm}$ are counted as the pre-test section development length. The facility has a design bulk flow velocity of $10\,\mathrm{m\,s^{-1}}$ in the test section, which yields a maximum friction Reynolds number $Re_\tau \approx 2.4 \cdot 10^3$. The test section has removable plugs to insert various surfaces as depicted in Fig. 2. The surfaces tested will cover an area of $10\,\mathrm{cm} \times 15\,\mathrm{cm}$ with a maximum of $1\,\mathrm{mm}$ height. Particular attention is dedicated to the choice of the materials which have to meet specific requirements such as; durability, robustness and easy optical access for the water channel. The complex surface must have low refractive index and manufacturing processes that are adaptable allowing for variety of complex surfaces. Several tests have been conduced in order to identify the most suitable and effective technique for surface fabrication. A promising protocol, used in other works (2), consists in the

*Corresponding author. E-mail: sofiasao@kth.se

creation of a sacrificial mold made of pressed white sugar grains which will be then impregnated with the liquid polymer. Once the polymer is cured, the sugar mould is dissolved in water and the structure of a porous scaffold will remain as solid PDMS.

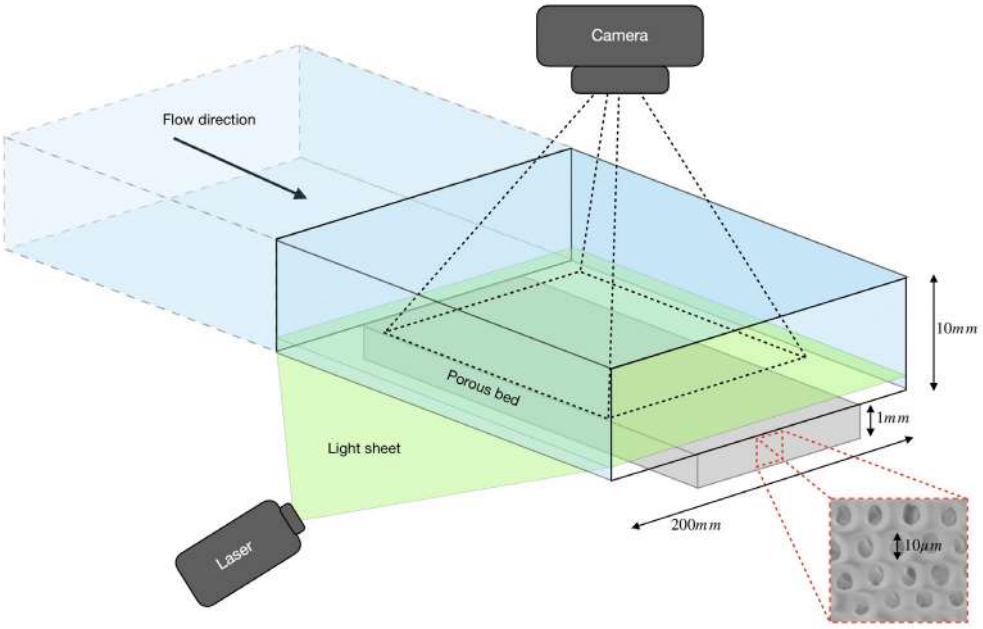

Figure 2: Representation of the water channel test section together with the main elements for the PIV acquisition system. In the sketch the dimensions of the relevant component are also indicated.

OUTLOOK

We will present our initial results of turbulent flow over index-matched porous surfaces. We seek to extend the prior research of turbulent flows over rough and porous surfaces (1) by providing greater detail of the physics near the interface as well as the internal porous flow. The ability to capture continuous flow data from the free fluid into the porous surface will provide greater understanding of the complex physics at the fluid surface interface. This research will increase our understanding of drag modification from porous surfaces. It will also elucidate the role and key parameters that control mixing and entrainment of particles inside the porous medium. These mechanisms are central in applications, such as the mixing and diffusion of marine soil nutrients in the environmental field and delivery of drugs into bone tissue in the biomedical field.

References

[1] Hong, Jiarong and Katz, Joseph and Schultz, Michael P, Near-wall turbulence statistics and flow structures over three-dimensional roughness in a turbulent channel flow. *J. Fluid Mech.* **2011**, 667, 1-37.

[2] Cha, Kyoung Je and Kim, Dong Sung, A portable pressure pump for microfluidic lab-on-a-chip systems using a porous polydimethylsiloxane (PDMS) sponge. *Biomedical microdevices* **2011**, 13, 877-883.

PARTICLE COLLISION STATISTICS IN MULTISCALE TURBULENT FLOW STRUCTURES

Yoshiki Sakurai*[1], Naoki Kobayashi [1], and Takashi Ishihara [2]
[1]Graduate School of Engineering, Nagoya University, Nagoya, Japan
[2]Graduate School of Environmental and Life Science, Okayama University, Okayama, Japan

Summary Collision statistics of inertial particles in multiscale vortical structures in high Reynolds number turbulence are studied using direct numerical simulation data of incompressible turbulence laden with the particles. It was shown recently by Picardo et al. that vortical regions contribute predominantly to slow side-on collisions compared to rapid head-on collisions in straining zones. In this paper, the statistics of the second invariant Q^* of velocity derivatives in coarse grained velocity field $\boldsymbol{u}^*$ at the positions of the inertial particles are studied. The data analysis shows that depending on a given coarse grained level, the PDF of Q^* at the positions of particles with a certain value of the Stokes number (St) is the most negatively skewed and also that the particles with that value of St have a tendency to collide at relatively low speeds when they are in negative Q^* regions.

INTRODUCTION

To elucidate the mechanisms of rain drop growth in cloud and planetesimal growth in protoplanetary disks, particle collision processes in high Reynolds number (Re) turbulence should be properly understood. Especially in the planetesimal formation, it is important to understand how the dust particles collide at low speeds because high-speed collision causes bouncing and fragmentation. Picardo et al. studied the correlation between particle collisions and flow structures in low Re turbulence, and showed that particles in vortical regions can collide at slower speeds than those in straining regions [1]. Recently, the method of data analysis using the eigenframe of the rate-of-strain tensor in turbulence [2] was applied to investigate the relationships between inertial particle clustering and multiscale vortical structures [3,4]. The results suggest that the distribution and the motion of inertial particles around high-vorticity regions defined in coarse-grained turbulent velocity fields have a self-similar property depending on particle inertia and coarse-graining level [4]. These results motivate us to study the relationships between particle collision statistics and coarse-grained turbulence structures. In this paper, we study the statistics of the second invariant Q^* of velocity derivatives in coarse grained velocity field at the positions of the inertial particles using a DNS dataset.

NUMERICAL SIMULATION AND ANALYSIS METHODS

In a study on the turbulent clustering [5], DNSs of incompressible homogeneous isotropic turbulence were performed using an alias-free spectral method and inertial particles were tracked in the time-dependent velocity fields in the DNSs. In this study, we use the datasets of turbulence with the number of grid points $N^3 = 2048^3$ and the Taylor microscale Reynolds number $R_\lambda \sim 730$. The values of the Stokes number (St), which is defined by the ratio of the relaxation time of the particle to the Kolmogorov time scale, are St=0, 0.1, 0.5, 1, 2, 5, 10, and 20, where St=0 corresponds to the fluid particles. For the detail of the computations, see [5] and references therein.

To characterise the multiscale structure of turbulence, we analyse the second invariant Q^* of the velocity derivatives in coarse grained velocity field $\boldsymbol{u}^*$ obtained by spectral low-pass filter. Here Q^* is given by $Q^*=(\Omega)^2-(S)^2$, where $S = (A + A^t)/2$, $\Omega = (A - A^t)/2$, and $A = \boldsymbol{\nabla u}^*$ so that $Q^*>0$ and $Q^*<0$ define the vortical regions and the straining regions, respectively, in the coarse grained field. The cut off wavenumber k_c for the coarse grained velocity $\boldsymbol{u}^*$ are set as $k_c/k_{\max}$ =1, 1/2, 1/4, 1/8, 1/16, and 1/32, where $k_{\max} = \sqrt{2}N/3$ is the maxmum wavenumber in the DNS and the unfiltered field is expressed as $k_c/k_{\max}$=1.

RESULTS

Figure 1 shows the probability density functions (PDFs) of Q^* for the turbulence field and at the particle positions. As shown in Ref [6], the PDFs are asymmetric and have St dependence. The PDF of Q^* at fluid particle positions is positively skewed and agrees well with that obtained for the turbulence field. The shape of the positive part of the PDFs of Q^* at the inertial particle positions strongly depends on the particles' inertia (St value) and the coarse-graining level (k_c). The result indicates small probability for particles with a certain St value (which depends on the value of k_c) to be found in high Q^* region. This may be well explained by considering that the particles with a certain St value are effectively ejected from the high Q^* (vortical) regions.

To quantify the St dependence of the PDFs plotted in Figure 1, we plot the skewness of the second invariant in Figure 2. Note that the positive/negative skewness of Q^* means that vorticity/strain is dominant at the positions of the inertial particles in the filtered field. Figure 2 shows that the value of the skewness is a function of St and k_c and that, for each value of k_c, the function takes the minimum at a certain St value. The fact that the St value that gives the minimum skewness is an increasing function of k_c is consistent with our previous result [4], that is, the particles with larger inertia are effectively and self-similarly ejected from coarser-grained high vorticity regions.

*Corresponding author. E-mail: msakurai@fluid.cse.nagoya-u.ac.jp

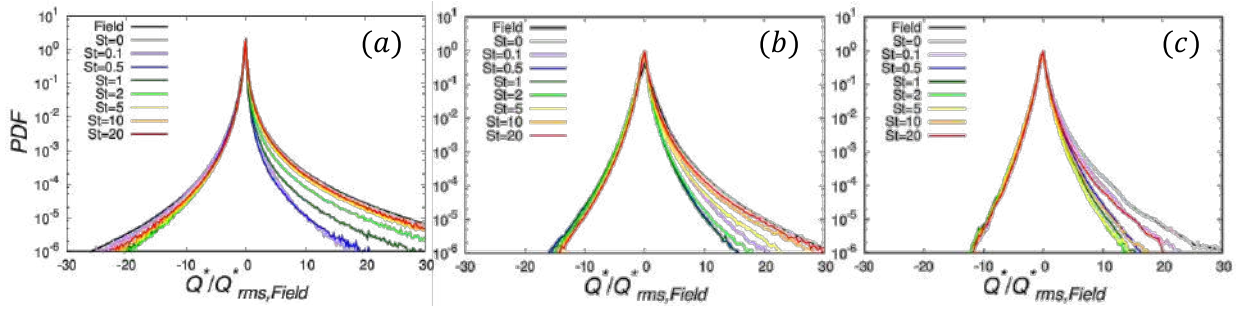

Figure 1. Probability density functions (PDFs) of Q^* for turbulence field and at particle positions. (a)$k_c = k_{\max}$, (b)$k_c = k_{\max}/8$, and (c)$k_c = k_{\max}/32$. The horizontal axis is normalized by the rms value of Q^* for the turbulent velocity field.

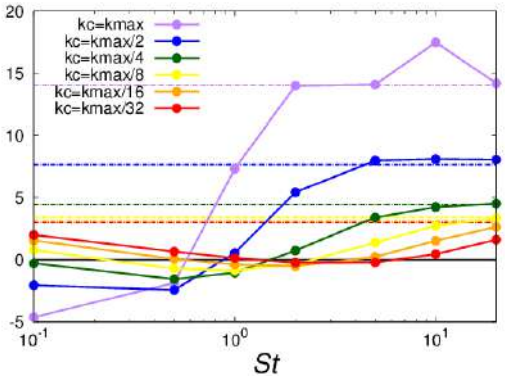

Figure 2. Skewness of the second invariant (Q^*) as a function of St. The dashed lines and solid line parallel to the horizontal axis represent the skewness of the turbulent field and zero skewness.

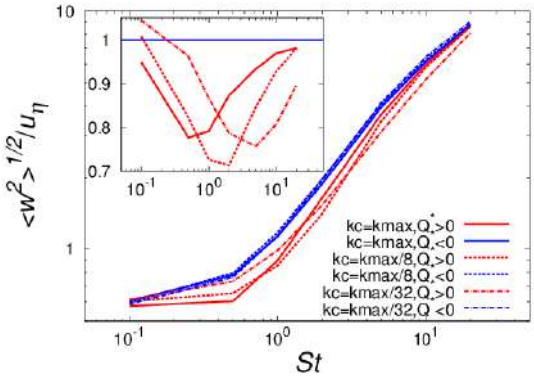

Figure 3. rms relative velocity of particles in vortical regions ($Q^* > 0$) and straining regions ($Q^* < 0$) as a function of St. The data are normalized by the Kolmogorov velocity u_η. Inset represents the ratio of rms relative velocity in vortical regions to that in straining regions.

As one of the particle collision statistics, relative velocities between particles at a distance of Kolmogorov-scale, conditionally averaged over two different zones are plotted separately in Fig. 3: one average was taken over the particles in vorticity dominant (Q*>0) zone and the other was taken over the particles in strain dominant (Q*<0) zone. The result for the case of $k_c = k_{\max}$ is consistent with that reported in [1], that is, the ratio of the average over the strain dominant region to that over the vorticity dominant region is the smallest when the value of St is approximately 0.5. Figure 3 shows that for the cases of $k_c = k_{\max}/8$ and $k_{\max}/32$, the ratios are the smallest at the different values of St: $St = 2$ for $k_c = k_{\max}/8$ and $St = 5$ for $k_c = k_{\max}/32$. Note that this correspondence between the values of St and k_c agrees well with the correspondence between the St value that gives the minimum skewness of Q* and the k_c value that determines the coarse grained level. In the cases of the smallest ratio, the rms relative velocity in vortical zone is 20-30% lower than that in straining zone. The results indicate that depending on the values of St, particle collisions at relatively slow speeds may occur in the vorticity dominant (Q*>0) zone of the corresponding coarse-grained level. In general, the particles' inertia grow due to coalescence. The above results suggest a possibility that coalescing particles may continue to collide at low speeds when they are in the appropriate vorticity dominant (Q*>0) zone at each colliding process.

Acknowledgments

The computational resources of the K computer provided by the RIKEN Advanced Institute for Computational Science through the HPCI System Research project (Projects ID:hp190076, hp190084, and hp190185) were partly used in this study. It also used the FX100 system at the Information Technology Center of Nagoya University and the supercomputer system ITO at R.I.I.T of Kyushu University. This study was also partly supported by "Joint Usage/Research Center for Interdisciplinary Large-scale Information Infrastructures" (Project ID: jh190068). This research was supported in part by MEXT as “Exploratory Challenge on Post-K computer” (Elucidation of the Birth of Exoplanets [Second Earth] and the Environmental Variations of Planets in the Solar System).

References

[1] J. R. Picardo et al.: Flow structures govern particle collisions in turbulence. *Physical Review Fluids*, 4, 032601, 2019.
[2] G. E. Elsinga and I. Marusic: Universal aspects of small-scale motions in turbulence. *J. Fluid Mech*., 662, 514, 2010.
[3] Y. Sakurai and T. Ishihara: Relationships between Small-scale Fluid Motions and Inertial Particle Clustering in Turbulence, *J. Phys. Soc. Japan*, 87, 093401, 2018.
[4] Y. Sakurai, H. Shiraishi, and T. Ishihara: Distribution and motion of inertial particles around high vorticity regions in coarse-grained homogeneous isotropic turbulence, *Japan Society of Civil Engineering*, 75(2):I_509-I_518, 2019 (in Japanese).
[5] T. Ishihara, N. Kobayashi, K. Enohata, M. Umemura, and K. Shiraishi: Dust coagulation regulated by turbulent clustering in protoplanetary disks. *Astrophys. J.*, 854, 81, 2018.
[6] M. Sato, M. Tanahashi, and T. Miyauchi: Particle dispersion and coherent fine scale eddies in turbulence. *J. Fluid Sci. Tech.*, 3(1):149–160, 2008.

TURBULENT FLUID FLOW IN A PRECESSING CYLINDER

Federico Pizzi*[1], André Giesecke[1], and Frank Stefani[1]
[1]Department of Magnetohydrodynamics, Helmholtz-Zentrum Dresden-Rossendorf, Institute of Fluid Dynamics, Bautzner Landstrasse 400, D-01328 Dresden, Germany

Summary In the framework of DRESDYN (DREsden Sodium facility for DYNnamo and thermohydraulic studies) we study the hydrodynamics of a fluid contained in a precessing cylinder. Here we focus on turbulence properties of the flow in dependence of the precession angle as well as Reynolds number and Poincaré number (ratio of the frequency of the precessional system and the cylinder itself). The main result is a characteristic peak in the dissipation around $Po = 0.1$ which goes along with a local maximum of turbulent kinetic energy.

PROBLEM DEFINITION AND METHODS USED

A precessing container performs simultaneous rotations around two different axis (Fig.1). In doing so the fluid in the container experiences a force that drives a non-axisymmetric flow, which becomes turbulent when precession is strong enough.

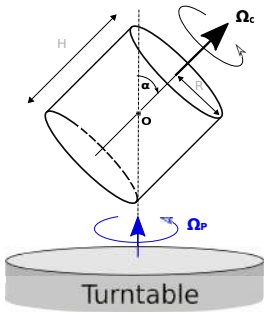

Figure 1: Schematic drawing of the precessing cylinder.

The mathematical problem is described by the Navier-Stokes equations for incompressible flows, which in dimensionless formulation in the precessing frame of reference read:

$$\frac{\partial u_i}{\partial t} + u_j \frac{\partial u_i}{\partial x_j} = -\frac{\partial P}{\partial x_i} - 2Po\,\Omega_j \epsilon_{ijk} u_k + \frac{1}{Re}\frac{\partial^2 u_i}{\partial x_j^2}\,, \qquad \frac{\partial u_i}{\partial x_i} = 0\,, \tag{1}$$

where u_i is the velocity field, P the (reduced) pressure and Ω_j the components of precession angular velocity. The boundary conditions are standard no-slip conditions (Dirichlet) at the wall $u_{r,z} = 0$ and $u_\phi = \Omega_C R$. The dimensionless numbers are respectively the Reynolds number $Re = \Omega_C R^2/\nu$ and the Poincaré number $Po = \Omega_P/\Omega_C$ with Ω_P, Ω_C denoting the precession angular frequency and cylinder angular frequency. We solve equations (1) using the DNS code SEMTEX which is based on a Galerkin Spectral Element Fourier method [2]. In our simulations we fix the aspect ratio, $\Gamma = H/R = 2$ (close to the resonance of the first Kelvin mode), in order to compare the results with a water experiment carried out at HZDR [6] in preparation for a large scale dynamo experiment [1], where liquid sodium will be used as a fluid.

TURBULENCE PROPERTIES

Precession provides a volume forcing that directly drives a flow with azimuthal wave number $m = 1$. Figure $2(a)$ shows the corresponding kinetic energy scaled by the energy of a rigid rotating cylinder $(\Omega_c R)^2$ for $Po = 0.095$. The flow drains energy from the rigid body rotation, and after an initial transient phase a fluctuating but, in the statistical sense, stationary state develops. There is a clear oscillating pattern for the largest precession angle. The contour plots on the right side of Fig. 2 show the correspnding time-average of the axial velocity $\langle u_z \rangle$ Fig. 2 (b) and the fluctuating components $u_z' = u_z - \langle u_z \rangle$ Fig. $2(c)$. The two magnitudes are comparable therefore the fluctuating flow is a non-negligible contribution. Figure $3(a)$ represents the total dissipation of the time-averaged flow $D = \int_V (2\nu S_{ij} S_{ij} - S_{ij} R_{ij})\, dV$, where $S_{ij} = 1/2\,(\partial u_i/\partial x_j + \partial u_j/\partial x_i)$ is the strain rate tensor and $R_{ij} = -\langle u_i' u_j' \rangle$ the Reynolds stress tensor. The discontinuity of the curve around $Po \simeq 0.1$ indicates the transition to a turbulent state, which happens independent of the precession angle. Figure $3(b)$ presents the (integral) turbulent kinetic energy $E_{turb} = \int_v \langle u_i' u_i' \rangle dV/2$ as a function of Po with a peak at $Po \approx 0.1$. The maximum of the corresponding turbulence intensity $I = \sqrt{(2/3)\ E_{turb}/2\pi}$ is around 7%, in accordance with observations performed in a spheroid [7]. For particular combinations of α, Re and Po we find a triadic resonance when free Kelvin modes become resonant simultaneously [3], indicated by the spike localized at small Po in Fig. $3(a)$.

*Corresponding author. E-mail: f.pizzi@hzdr.de

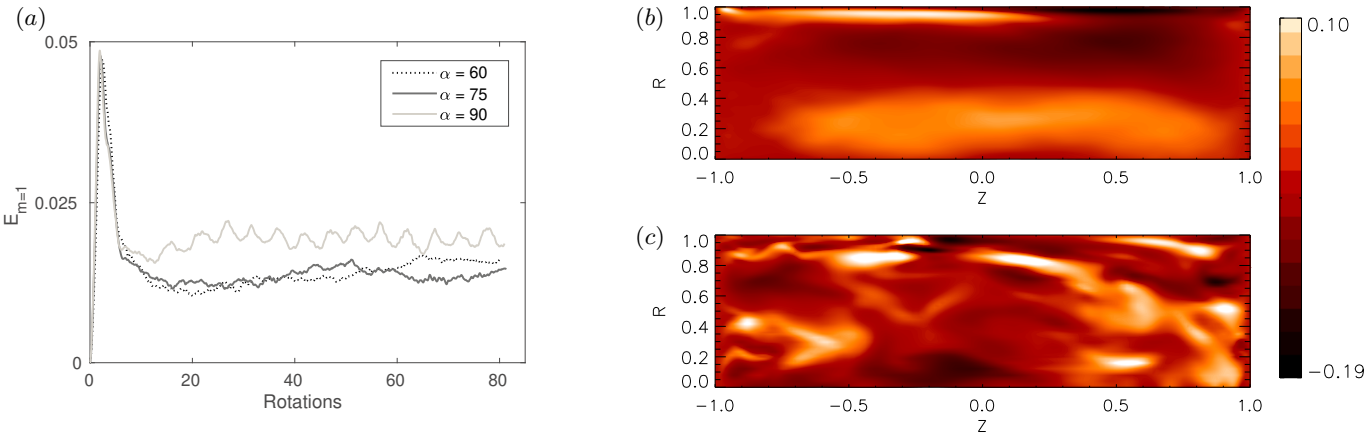

Figure 2: (a) $E_{m=1}$ versus time, for $Re = 6500,\ Po = 0.095$ and three different precession angles. (b) Contour of time average $\langle u_z \rangle$ in a meridional plane. (c) Snapshot of the fluctuating axial velocity $u_z' = u_z - \langle u_z \rangle$ ($Re = 6500,\ Po = 0.095,\ \alpha = 60°$).

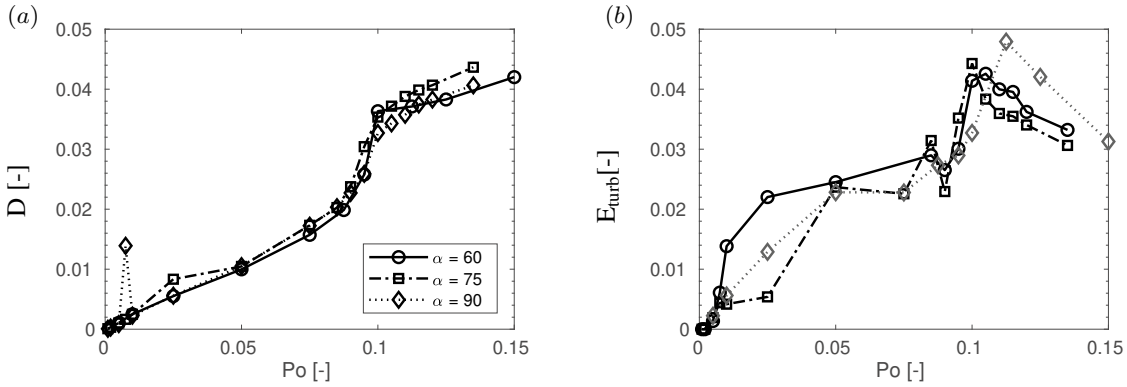

Figure 3: (a) Total Dissipation D and (b) turbulent kinetic energy E_{turb} versus precession ratio for $Re = 6500$.

CONCLUSIONS

Our simulations show that in a precession driven fluid around the transition to turbulence the chaotic fluctuations have a comparable amplitude to the mean flow itself. Moreover, in the turbulent regime the total dissipation increases almost linearly with the forcing. This behavior is found also in our experiments [8]. However Malkus experimentally [5], and Kerswell through a theoretical estimation [4], observed a plateau-shape in the turbulent regime for high precession ratios. Further studies must be done regarding this aspect. The impact of the precession angle α remains small, in contrast to preliminary experimantal studies performed with the water experiment which is probably due to the much smaller Reynolds number used in the numerical simulations compared with experiment.

References

[1] Stefani F., Albrecht T., Gerbeth G., Giesecke A., Gundrum T., Herault J., Nore C., Steglich C. Towards a precession driven dynamo experiment. *Magnetohydrodynamics*, **51**: 275-284, 2015.

[2] Blackburn H. M. and Sherwin S.J. Formulation of a Galerkin spectral element-Fourier method for three-dimensional incompressible flows in cylindrical geometries. *J. Comp. Phys.*, **197**: 759-778, 2004.

[3] Giesecke A., Albrecht T., Gundrum T., Herault J., and Stefani F. Triadic resonances in nonlinear simulations of a fluid flow in a precessing cylinder. *New J. Phys.*, **17**, 113044, 2015.

[4] Kerswell R.R., Upper bounds on the energy dissipation in turbulent precession. *J. Fluid Mech.*, **321**, 335-370, 1996.

[5] Malkus W.V.R. Precession of Earth as cause of geomagnetism. *Science*, **160**, 259-264, 1968.

[6] A. Giesecke, T. Vogt, T. Gundrum, and Stefani F. Nonlinear large scale flow in a precessing cylinder and its ability to drive dynamo action. *Phys. Rev. Lett.*, **120**: 024502, 2018.

[7] Goto S., Matsunaga A., Fujiwara M., Nishioka M., Kida S., Yamato M. Turbulence driven by precession in spherical and slightly elongated spheroidal cavities. *Phys. Fluids.*, **26**, 055107, 2014.

[8] Herault J., Gundrum T., Giesecke A., and Stefani F. Subcritical transition to turbulence of a precessing flow in a cylindrical vessel. *Phys. Fluids.*, **27**, 124102, 2015.

ELECTROMAGNETIC FORCING OF A TIDE-LIKE FLOW IN CYLINDRICAL GEOMETRY

Peter Jüstel*[1],Sebastian Röhrborn[1],Felix Schindler[1],Frank Stefani[1],Tobias Vogt[1],and Rodion Stepanov[2]
[1]Institute of Fluid Dynamics, Helmholtz-Zentrum Dresden-Rossendorf, Dresden, Germany
[2]Institute of Continuous Media Mechanics, 1 Acad. Korolyov str., 614013 Perm Russia

Summary Motivated by a tidal synchronization model of the solar dynamo, we plan to study the influence of a tide-like forcing on the helicity oscillations of the large-scale circulation in a Rayleigh-Bénard experiment. The current paper reflects on preliminary experiments to investigate the flow structure arising from electromagnetic tidal forcing of a liquid metal.

INTRODUCTION

The amazing similarity of the eleven-year solar cycle and the alignment cycle of the tidally dominant planets Venus, Earth, and Jupiter has been known for a long time in the solar science community. Recent papers [1-4] have suggested that a viable synchronization effect could be accomplished by influencing the current-driven, kink-type Tayler instability (TI) with azimuthal wavenumber $m = 1$. The proposed mechanism implies that small tidal forces created by the planets might be sufficient to affect the helicity oscillations of the TI, whereby the chaotic behaviour of the entire solar dynamo could ultimately be synchronized [3]. A liquid metal experiment has been set up at Helmholtz-Zentrum Dresden-Rossendorf to investigate this mechanism. The TI flow structure is actually replaced by a Rayleigh-Bénard (RB) large scale circulation (LSC) with the same $m = 1$ azimuthal dependence. The helicity oscillations are nothing else than the well-known sloshing/torsional oscillations of the LSC. A resonance of those oscillations with external tide-like forces would hint on a rather generic mechanism. As a first step, the Lorentz-force driven m=2 flow was investigated to validate the experimental setup.

THE EXPERIMENTAL SETUP

We have chosen the liquid eutectic GaInSn alloy as the working fluid. The vessel is a cylinder with inner diameter $D = 180\,\mathrm{mm}$ and unit aspect ratio [6]. For the subsequent Rayleigh-Bénard experiments, it can be cooled at the top and heated at the bottom via a thermostat and an electric heater. The cylindrical shell is insulated. Additionally, two electromagnetic coils are situated on opposite sides of the cylinder along a horizontal axis (dashed lines in Fig. 1(a)). They can be used to induce a flow in the liquid metal. For data acquisition, ten Ultrasound-Doppler-Velocimetry probes are arranged around the vessel. They measure velocity values at multiple points on the acoustic path. Those values are projections of the velocity vector onto the path.

FLOW STRUCTURE AND STABILITY

Applying an alternating current between 5 and $49\,\mathrm{A_{RMS}}$ to the coils induces an eddy current in the fluid. The resulting Lorentz-force draws the liquid metal towards the coils and pushes it from the sides towards the centre axis. The fluid motion is generally turbulent while the average flow takes the form of Fig. 1(c). Increasing the coil current at a fixed frequency increases the turbulence and mean velocities. The frequency range of 12.5 to 200 Hz shows different optimum coupling efficiencies for each current setting. Mean flow velocities of up to $3\,\mathrm{cm/s}$ are achieved.
Since for strong forcing the two impinging jets form an unstable system, the stagnation point moves around the centre of the cylinder. This motion is random without any reproducible periodicity. But there seems to be a preference to stagnate away from the centre point. A histogram of the flow in Fig. 1(b) shows a clearly bimodal distribution.

CONCLUSIONS AND PROSPECTS

For weak forcing, the observed fluid motion bears good resemblance to the simplified Stokes flow simulation of Stepanov et al. [5]. We were able to confirm the effectiveness of a symmetric coil polarity to attain the desired flow pattern. Varying the coil current and the frequency leads to the expected behaviour: higher currents increase the Lorentz-forces and induce stronger flows. Higher frequencies tend to get shielded by the skin effect, reducing coupling effectiveness. For the future helicity synchronization experiments, the LSC should not be heavily disturbed by the tide-like forcing. Therefore a setting of around 25 Hz and below $5\,\mathrm{A_{RMS}}$ will be chosen for the Rayleigh-Bénard experiments. For those forcings, we were able to show that there are no internal frequencies present in the system yet. Therefore the chances are high to properly identify a synchronized sloshing motion, without false attribution, if such an effect is detected. Apart from that, the bi-stable impinging jets might form a system susceptible to stochastic resonance. We will further investigate this possibility. Our next step will be to apply a modulated alternating current in order to emulate the tidal forcing. The subsequent experiments with added Rayleigh-Bénard flow will then answer the question of a possible helicity synchronization by tidal forcing.

*Corresponding author. E-mail: p.juestel@hzdr.de.

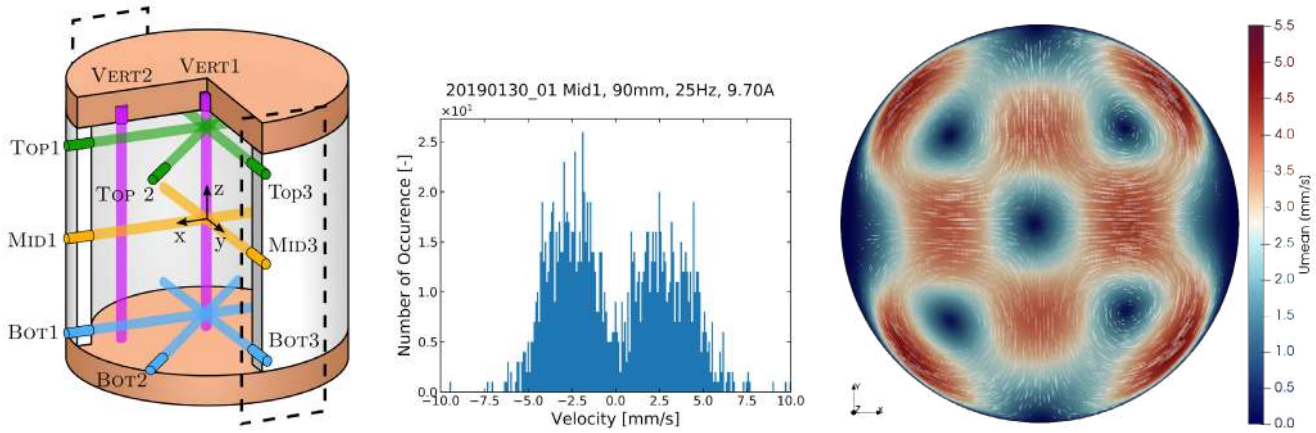

(a) (b) (c)

Figure 1: a) Layout of the experimental vessel. The dashed lines show the position of the electromagnet coils. The small, coloured cylinders represent the ultrasonic transducers. The like-coloured bars indicate their measurement paths. b) Bimodal distribution of velocity in x-direction at the centre of the cylinder within a recording time of 30 minutes. c) Representative mean velocity field in the symmetry plane (from a direct numerical simulation).

References

[1] Weber N. et al. The Tayler instability at low magnetic Prandtl numbers: between chiral symmetry breaking and helicity oscillations. *New Journal of Physics*, **17**: 113013, 2015

[2] Stefani F. et al. Synchronized helicity oscillations: a link between planetary tides and the solar cycle? *Sol. Phys.* **291**: 2197, 2016

[3] Stefani F., Giesecke A. Weier T. On the synchronizability of Tayler-Spruit and Babcock-Leighton type dynamos. *Sol. Phys.* **293**: 12, 2018

[4] Stefani F., Giesecke A., Weier T. A model of a tidally synchronized solar dynamo. *Sol. Phys.* **294**: 60, 2019

[5] Stepanov R., Stefani F. Electromagnetic forcing of a flow with the azimuthal wave number m = 2 in cylindrical geometry. *Magnetohydrodynamics* **55**: No. 1/2, 207-214, 2019

[6] Zürner T. et al. Combined measurement of velocity and temperature in liquid metal convection. *J. Fluid Mech.* **876**: 1108-1128, 2019

TURBULENCE SUPPRESSION IN SPHERICAL COUETTE FLOW

Maria Gritsevich[*1,2,3], Olga Krivonosova[4] and Dmitry Zhilenko[4]
[1]Finnish Geospatial Research Institute (FGI), Masala, Finland [2]Department of Physics, University of Helsinki, Helsinki, Finland
[3]Institute of Physics and Technology, Ural Federal University, Ekaterinburg, Russia
[4]Institute of Mechanics, Lomonosov Moscow State University, Moscow, Russia

Summary We report results from the laboratory experiments investigating the possibilities to control the turbulence in the flow of viscous incompressible fluid in the gap between concentric spherical boundaries, induced by their rotation about the common axis. Turbulent flow states were subjected to periodical modulation of outer sphere rotational rates about unaltered averaged values. With an increase of modulation amplitude, a change of flow state was found to occur in the whole spherical gap: turbulent flow became laminar and exemplified the patterns, preceding the transition to turbulence.

Much attention is currently given to the invention of methods of turbulence suppression in pipes [1] and rotating flows [2]; in nature turbulence destruction can be observed in atmospheric processes, for example, cooling of the surface atmospheric boundary layer at night [3]. The spherical Couette flow (SCF) - the flow of viscous incompressible fluid in the gap between concentric spherical boundaries, induced by their rotation about common axis, is under study in the present work. In the case of turbulence, induced in SCF by periodical modulation of outer sphere rotational rate, it was numerically shown that azimuthal component of kinetic energy remains periodical [4]. In the present study we carried out the experiments to investigate the influence of periodical excitation of outer sphere rotational rate on the possibility of turbulence destruction. The initial turbulent flows in the spherical layer are formed within the gap between the two counter rotating transparent spheres with stationary in time angular velocities Ω_1 and Ω_2, and radii r_1 = 75mm for the inner sphere and r_2 =150mm for the outer sphere. The spherical gap is filled with silicone oil with viscosity $\nu = 5\times10^{-5}$ m^2/s at 22^{0}C temperature. The oil is contaminated with aluminum powder to visualize the flow. The azimuthal flow velocity u_φ measurements were conducted by using laser Doppler anemometer. The more detailed description and picture of the experimental setup are presented in [5]. The chosen turbulent flow states have the following peculiarity: with decelerating inner sphere rotational rate (or Reynolds number $Re_1 = \Omega_1 r_1^2/\nu$ decreasing at constant $Re_2 = \Omega_2 r_2^2/\nu$) the transition to periodical laminar flow state occurs, where pattern is represented by three symmetric about equatorial plane vortices propagating in azimuthal direction. In turbulent flow states, near the threshold of its formation, randomly distributed fragments of mentioned above spatial structures were observed [6]. Chosen turbulent flows (I: Re_1 =434, Re_2 =900, II: Re_1 =382, Re_2 =700, and III: Re_1 =377, Re_2 =700) are subjected to periodical modulation of the outer sphere angular rotational rate Ω_2 (t) about unaltered averaged values Ω_{20}: $\Omega_2(t) = \Omega_{20}(1+A\sin(2\pi ft + \varphi))$, where A is the modulation amplitude, f is modulation frequency. I and II turbulent flow states were received with Re_1 increasing at constant Re_2, III – was obtained from II by decreasing Re_1 at constant Re_2 and occupied the hysteretic area of Re_1 between laminar flow state and turbulent state. Each experiment began from turbulence at A=0, then for a selected value of f amplitude A was increased from 0 to a specified value (but not more than 20% of Ω_{20}). At small A the turbulence remains and its spectra look like “two-dimensional”: with slope -5/3 at lower frequencies and slope -3 at higher frequencies. An increase in A in all the considered cases was found to suppress turbulence, which is replaced by a laminar flow. The structure of the laminar flow is similar to the structure of the above-mentioned periodic flow, which under stationary boundary conditions precedes turbulence. Decrease in A for I and II leads to the restoration of turbulence. In this case, hysteresis is observed with the suppression of turbulence and its restoration. For III the flow remains laminar with A decreasing.

Figure 1 shows fragments of the time dependence Ω_2 (t) and u_φ (t), a) and b) destruction of turbulence and transition to a laminar flow after increasing A, c) turbulence restoration after decreasing A. Fig 1a and 1b present time dependence of amplitudes at the modulation frequency and at natural frequencies of laminar flow states. Amplitudes were calculated from u_φ signal using the same method as in [5] based on the Hilbert transform. The characteristic time of amplitude rising from a local minimum, preceding the stage of final increase, until the moment of turbulence destruction approximately equals to one oscillation period (Fig. 1a, 1b). Destruction of turbulence with A increasing occurs at the moment of time close to the Ω_2 (t) minimum (Fig. 1a, 1b). Turbulence is restored after decreasing A and passing Ω_2 (t) maximum (Fig. 1, c). Hence, the suppression of turbulence occurs in the region of Re that in the case of stationary rotation level of stochasticity is more intense. This result corresponds to the available data for pipe flow, where one of the possible ways to suppress turbulence is to increase its intensity at the entrance to the tube [1]. First of all, due to the limitations in maximal values of A in the experiment (A < 0.2), it was not possible to destroy the turbulence at f > 0.02 Hz. Critical A_1 values, corresponding to the suppression of turbulence, increase with f arising in the range of 0.01-0.018Hz, and the dependence of A_1 from f has a local minimum in the range of f from 0.018 to 0.02Hz. This range is close to one-third of the natural frequency of laminar flow state. Since it contains three vortices, this frequency corresponds to the passage frequency of one vortex. Therefore, we can conclude that turbulence is most sensitive to disturbances with a frequency corresponding to the passage frequency of one vortex of the preceding turbulence periodic flow state.

*Corresponding author. E-mail: maria.gritsevich@nls.fi.

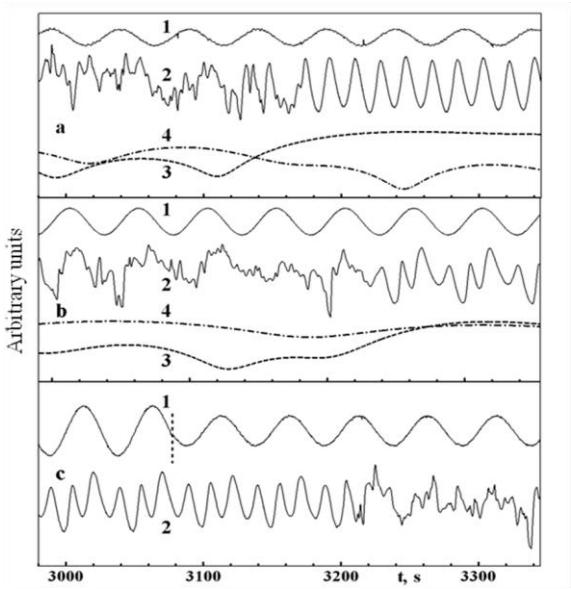

Figure 1. Time dependence of the smoothed signal Ω_2 (t)-1, u_φ (t) -2, amplitudes at the frequency of coherent structures -3, amplitudes at the modulation frequency f=0.02 Hz, a) – III, A=0.02, b)-II, A=0.15, c)- II, transition from A=0.1 to A=0.059 (the moment when A changes is indicated by the vertical dashed line).

CONCLUSIONS

Periodical excitation of outer sphere velocity at a frequency, not exceeding the transit frequency of one vortex in the laminar flow preceding turbulence, can lead to the suppression of turbulence. Turbulence destruction occurs at times near the minimums of the outer sphere rotation rates, while the turbulence recovery at values of amplitude smaller than suppression occurs at times close to the velocity maximum. Suppression of turbulence occurs in the range of Re numbers that in the case of stationary boundary conditions is more displaced from the threshold of turbulence formation compared to the range of Re numbers, corresponding to its restoration.

ACKNOWLEDGMENTS

This work was supported, in part, by the Russian Foundation for Basic Research, Projects Nos. 18-08-00074 and 19-05-00028. MG acknowledges the Academy of Finland project no. 325806.

References

[1] Kuhnen J., Song B., Scarselli D., Budanur N., Riedl M., Willis A., Avila M. and Hof B. Destabilizing turbulence in pipe flow. *Nat. Physics*, **14**, 386-390. 2018.

[2] Leng X., Kolesnikov Y.B., Krasnov D. and Li B. Numercal simulation of turbulent Taylor-Couette flow between conducting cylinders in an axial magnetic field at low magnetic Reynolds number. *Phys. Fluids* **30**, 015107, 2018.

[3] Donda J.M.M., van Hooijdonk I.G.S., Moene A.F., van Heijst G.J.F., Clercx H.J.H. and van de Wiel B.J.H. The maximum sustainable heat flux in stably stratified channel flows. *Q.J.R. Meteorol. Soc.* **142**, 781-792. 2016.

[4] Zhilenko D., Krivonosova O. and Gritsevich M. The different types of turbulence in rotating spherical layers. *J. of Physics: Conf. Series* **955**, 012012, 2017.

[5] Zhilenko D., Krivonosova O., Gritsevich M. and Read P. Wave number selection in the presence of noise: Experimental results. *Chaos* **28**, 053110, 2018.

[6] Zhilenko D. and Krivonosova O. Origination and evolution of turbulent flows in a rotating spherical layer. *Tech. Physics* **55,** 4, 449-456. 2010.

*Corresponding author. E-mail: maria.gritsevich@nls.fi.

SPECTRAL ENERGETICS OF A QUASILINEAR APPROXIMATION IN UNIFORM SHEAR TURBULENCE

Carlos G. Hernández*[1,2] and Yongyun Hwang[2]
[1]Department of Mathematics, Imperial College London, 180 Queen's Gate, London SW7 2AZ, UK
[2]Department of Aeronautics, Imperial College London, South Kensington, London SW7 2AZ, UK

Summary A quasi-linear approximation is employed to study statistically-stationary uniform shear turbulence. The approximation is based on the decomposition of the velocity into a mean component and a two-term fluctuation: a streamwise-averaged part and a second term for the rest of the fluctuation and zero streamwise average. Direct numerical simulations removing the nonlinear product of the latter are performed and compared to resolved DNS. The premultiplied one-dimensional spectra of the velocity fluctuations and pressure-strain spectra are obtained and an energy budget analysis is carried out for production, dissipation and turbulent transport.

INTRODUCTION

The quasi-linear-type modelling incorporates some minimal roles played by the nonlinearity in the resulting self-sustaining velocity fluctuations. Common to all variations of this approach is a decomposition of the given flow into two groups: one in which all nonlinear terms are kept, and the other in which all self-interactions are ignored or suitably modelled (e.g. a stochastic forcing). In parallel wall-bounded shear flows, the former is obtained by averaging the velocity field in the streamwise direction and the latter is considered to be the remaining one. An important feature of this type of model is that it typically activates only a handful number of active streamwise Fourier modes for self-sustaining velocity fluctuations [1], thereby being capable of reducing the computational cost significantly. At high Reynolds numbers, the growing recent evidence has consistently supported that wall-bounded shear flows are composed of a hierarchical organisation of self-similar self-sustaining energy-containing motions. This feature poses an important challenge especially from the perspective of QL modelling, because the role of the nonlinearity is expected to be more important at all the integral length scales in such a high-Reynolds-number regime. The present study aims to explore spectral energy transfer in the aforementioned QL model. For the purpose of bypassing the difficulty arising from the existence of multiple integral length scales in typical high-Reynolds wall-bounded turbulent flows, we consider uniform shear turbulence. The capability of the QL model for the description of the self-sustaining process and its related energy cascade can be fully assessed using a spectral energy-budget analysis without suffering from the issue of having multiple integral length scales like in wall-bounded turbulence.

PROBLEM FORMULATION

We consider a turbulent flow under a uniform mean shear where the density and kinematic viscosity of the fluid are given by ρ and ν, respectively. The time is denoted by t, and the space is by $\mathbf{x} = (x, y, z)$ with x, y and z being the streamwise, transverse and spanwise directions, respectively. We consider the Reynolds decomposition of the velocity $\mathbf{u} = (u, v, w)$ like $\mathbf{u} = \mathbf{U} + \mathbf{u}'$ in which $\mathbf{U}(\equiv \langle \mathbf{u} \rangle_{x,z,t}) = (U(y), 0, 0)$ is the mean velocity. The turbulent velocity fluctuation is further decomposed into a streamwise-averaged and the remaining component $\mathbf{u}' = \mathbf{u}_m + \mathbf{u}_r$ with $\mathbf{u}_r = \langle \mathbf{u}' \rangle_x$. Following [3], we introduce two projection operators, which can decompose the flow variables into the streamwise-averaged part and the remaining one. The projection operators are defined as $\mathcal{P}_m[\mathbf{u}'] \equiv \langle \mathbf{u}' \rangle_x = \mathbf{u}_m$ and $\mathcal{P}_r[\mathbf{u}'] \equiv \mathbf{u}' - \langle \mathbf{u}' \rangle_x = \mathbf{u}_r$. The projection of the equations for turbulent fluctuation onto $\mathcal{P}_m$ and $\mathcal{P}_r$ leads to the equations:

$$\frac{\partial \mathbf{u}_m}{\partial t} + (\mathbf{u}_m \cdot \nabla_{yz})\mathbf{U} = -\nabla_{yz} p_m + \nu \nabla_{yz}^2 \mathbf{u}_m - (\mathbf{u}_m \cdot \nabla_{yz})\mathbf{u}_m - \mathcal{P}_m[(\mathbf{u}_r \cdot \nabla)\mathbf{u}_r] \tag{1a}$$

$$\frac{\partial \mathbf{u}_r}{\partial t} + (\mathbf{U}_m \cdot \nabla)\mathbf{u}_r + (\mathbf{u}_r \cdot \nabla)\mathbf{U}_m = -\nabla p_r + \nu \nabla^2 \mathbf{u}_r - \mathcal{P}_r[(\mathbf{u}_r \cdot \nabla)\mathbf{u}_r], \tag{1b}$$

where $\mathbf{U}_m = \mathbf{U} + \mathbf{u}_m$, and p_m and p_r are defined to enforce $\nabla_{yz} \cdot \mathbf{u}_m = 0$ and $\nabla \cdot \mathbf{u}_r = 0$, respectively, with $p' = p_m + p_r$. For the QL approximation, the self-interaction term in (1b) will be ignored: i.e. RNL model [1,3]. The TKE equation is considered in the streamwise/spanwise Fourier space, so that the inter-scale energy transfer can be studied. For this purpose, one-dimensional Fourier-mode decomposition for the turbulent velocity fluctuations is introduced: $u_j'(t, r) = \int_{-\infty}^{\infty} \widehat{u_j'}(t, k) e^{\mathrm{i}kr} \mathrm{d}k$ for $j = 1, 2, 3$, where $\widehat{\cdot}$ denotes the Fourier-transformed coefficient, $(u_1', u_2', u_3') = (u', v', w')$, $r(= x \text{ or } z)$ is the streamwise or spanwise coordinate, and $k(= k_x \text{ or } k_z)$ the corresponding wavenumber. Taking an average in time, transverse direction and the planar direction along which the Fourier transform is not taken ($r^{\perp}$), the resulting energy balance is given by

$$\left\langle \left\{ -\overline{\widehat{u'}}(k)\widehat{v'}(k)\,\frac{\mathrm{d}U}{\mathrm{d}y} \right\} \right\rangle_{r^{\perp},y,t} + \left\langle -\nu \frac{\partial \widehat{u_i'}(k)}{\partial x_j} \frac{\partial \overline{\widehat{u_i'}}(k)}{\partial x_j} \right\rangle_{r^{\perp},y,t} + \left\langle \left\{ -\overline{\widehat{u_i'}}(k) \left(\frac{\partial}{\partial x_j} \left(\widehat{u_i' u_j'}(k) - \mathcal{P}_r \left[\widehat{u_{r,i}' u_{r,j}'}(k) \right] \right) \right) \right\} \right\rangle_{r^{\perp},y,t} = 0,$$

where the first, second and last terms in the left-hand side are the rate of turbulence production, $\widehat{P}(k)$, viscous dissipation, $\widehat{\varepsilon}(k)$ and (nonlinear) turbulent energy transport, $\widehat{T}(k)$ at a given wavenumber, respectively.

*Corresponding author. E-mail: cg1116@ic.ac.uk.

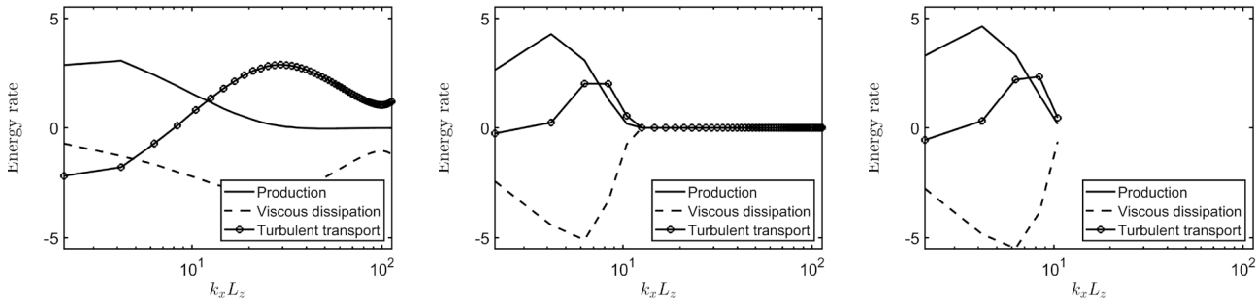

(a) DNS (b) QL-FULL (c) QL-NX16

Figure 1: Streamwise spectral energy budget per unit mean shear for simulation: (a) DNS; (b) QL; and (c) QL-NX16.

Case	$Re_{\tau,Lz}$	Re_λ	$N_{x,F}$	$N_y \times N_z$	dU^*/dy^*	$-\langle u'^* v'^* \rangle_{x,y,z,t}$	u^*_{rms}	v^*_{rms}	w^*_{rms}
DNS	514	63	54	497×108	0.017	0.99	1.72	1.15	1.42
QL-FULL	617	108	54	497×108	0.007	0.99	1.85	1.35	1.30
QL-NX16	628	108	5	497×108	0.006	0.99	1.75	1.35	1.25

Table 1: One-point turbulence statistics.

RESULTS AND DISCUSSION

Uniform shear turbulence is simulated following the approach in [2]. The application of the QL approximation is found to generate more anisotropic velocity fluctuations. In particular, u^*_{rms} and v^*_{rms} are increased in the QL simulations regardless $N_{x,F}$ considered, whereas w^*_{rms} is decreased. The QL simulations are also found not to show any significant changes in the one-point turbulence statistics, if $N_{x,F} \geq 5$ (see table 1). This implies that only a handful number of streamwise Fourier modes are active in the QL simulations. The premultiplied streamwise wavenumber spectra of the energy budget per unit mean shear are shown in figure 1. While the spectra of DNS show the typical features of energy cascade and turbulent dissipation observed in the spanwise spectra, QL simulations do not develop such features. Given the linear nature of (1b), it is not surprising to see the significantly damaged energy cascade in the streamwise wavenumber space. However, it should also be pointed out that there are still a non-negligible number of wavenumbers actively involved in the spectral TKE balance. For example, in the case of QL-FULL, there are still approximately five streamwise Fourier modes highly active, and they form the spectral TKE balance in the streamwise wavenumber space. Furthermore, the nonlinear turbulent transport is not completely inactive in the streamwise wavenumber space either. These observations are found to be associated with the linear instabilities of (1b), consistent with the notion of the self-sustaining process observed in this flow [2]. Finally, the componentwise of TKE transport is studied (not shown). It is found that the QL simulations show a considerable damage in the pressure-strain transport, and this is understood to the lack of slow pressure in (1b).

CONCLUSIONS

The QL model shows a healthy energy cascade in the spanwise wavenumber space. However, it completely inhibits energy cascade in the streamwise wavenumber space due to the proposed linearisation. The latter feature also results in highly elevated spectral energy intensity residing only at the integral streamwise length scale. For the same reason, the velocity field of the QL model has also been found to be anisotropic throughout the entire wavenumber space of the spectra. These features fundamentally differ from the turbulence in DNS, where the spectra in the inertial and dissipation ranges are highly isotropic. It has also been found that the streamwise wavenumber spectra of turbulent transport obtained with the classical Reynolds decomposition statistically well characterizes the instability of the linearised fluctuation equations, as they exhibit a largest intensity at $L_x/L_z = 2 \sim 3$. In the final presentation, we will discuss on how to improve the present QL model based on the understanidng gained from the present analysis.

References

[1] Farrell, B.F. Ioannou, P.J. Jiménez, J. Constantinou, N.C. Lozano-Durán, A. Nikolaidis, M-A A statistical state dynamics-based study of the structure and mechanism of large-scale motions in plane Poiseuille flow. *J. Fluid Mech.* **809**: 290-315, 2016.

[2] Yang, Q. Willis, A. P. Hwang, Y. Energy production and self-sustained turbulence at the Kolmogorov scale in Couette flow. *J. Fluid Mech.* **834**: 531–554, 2018.

[3] Pausch, M. Yang, Q. Hwang, Y. Eckhardt, B. Quasilinear approximation for exact coherent states in parallel shear flows. *Fluid Dyn. Res.* **51**: 011402, 2019.

EXTENDED ORR-SOMMERFELD STABILITY ANALYSIS MODEL

Vilda K. Markeviciute*[1] and Rich R. Kerswell [1]
[1]Department of Applied Mathematics and Theoretical Physics, University of Cambridge, United Kingdom

Summary Using Orr-Sommerfeld stability analysis on turbulent mean flows was first proposed by Malkus (1956). While commonly used to explain the appearance of large scale structures in turbulent flows, this approach can fail when applied to some systems. We extend this naive approach to the next level of sophistication and evaluate its performance by analysing turbulent 2D channel states (metastable asymmetric and symmetric states and an unstable saddle state).

MOTIVATION AND PROBLEM DEFINITION

There is a long history of examining the stability of the turbulent mean profile in shear flows. Originally this was to explore the existence of a possible selection mechanism for the particular form of the mean flow [1] and, latterly, has been used to help rationalise observed large scale structures seen in the turbulence. The stability analysis usually applied consists simply of studying the spectral properties of the Orr-Sommerfeld equation built around the turbulent mean. We extend the notion of 'statistical' stability of turbulent flows by considering the turbulent statistics (mean velocity and correlation matrices) rather than the instantaneous flow fields [2]. Using time-averaging and principal component analysis of the correlation matrices, we derive an embedding back to the primitive variable space producing an extended Orr-Sommerfeld stability model, where the perturbation vector now consists of both the mean and fluctuation fields. We test the model on turbulent 2D channel flow [3] which we found to have two metastable (symmetric and asymmetric) states.

RESULTS AND DISCUSSION

Starting with the statistical flow representation equations, we develop an extended Orr-Sommerfeld stability model in terms of the primitive flow variables (velocity and pressure) decomposed into the streamwise-mean and fluctuation components. We show that the naive Orr-Sommerfeld eigenvalue analysis fails to correctly predict the stability properties of two metastable (symmetric and asymmetric - see Figure 1.) states and one unstable (saddle) state of 2D channel flow. Preliminary application of the extended stability model shows only marginal improvement to the naive approach: the eigenspectrum still does not correctly reflect the stability of the states, but a better understanding of the most unstable eigenvector structure is obtained showing significant energy in the mean velocity component (even if an order of magnitude smaller to the dominant fluctuation component). Two possible shortcomings of the extended Orr-Sommerfeld model are suggested: time-averaging of the velocity correlation matrices neglects the time-evolution of the fluctuation field while singular value decomposition of the time-averaged correlation matrix is an oversimplification of the underlying fluctuation vector. The significance of these shortcomings is examined by performing further numerical experiments. The turbulent base flow and the linear perturbation field are advanced in full and quasi-linear models. This allows us to compute the 'true' value of the growth rate of the most unstable perturbation to the turbulent base flow and thus assess the new extended stability model. Finally, if time permits, we discuss the application of the proposed stability theory on 3D flows.

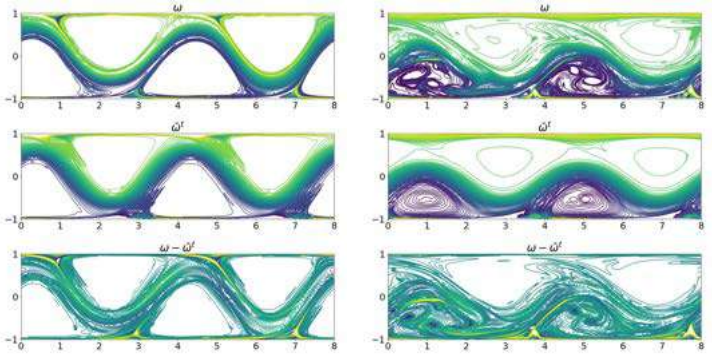

Figure 1: Metastability of states in 2D channel flow. Snapshots of: (top) the vorticity field in the channel $\omega(t)$; (middle) time-averaged vorticity field $\bar{\omega}^t$ in the travelling wave frame; and (bottom) the fluctuation field $\omega(t) - \bar{\omega}^t$ for symmetric (left) and asymmetric (right) states at $Re = 36300$. Dark blue corresponds to minimal vorticity while bright yellow to maximal vorticity levels.

References

[1] Malkus W. V. R. Outline of a theory of turbulent shear flow. *J. Fluid Mech.* **1(5)**: 521–539, 1956.
[2] Farrell B. F, Ioannou P. J. Dynamics of streamwise rolls and streaks in turbulent wall-bounded shear flow. *J. Fluid Mech* **708**: 149-96, 2012.
[3] Falkovich G., Vladimirova N. Turbulence Appearance and Nonappearance in Thin Fluid Layers. *Phys. Rev. Lett.* **121(16)**: 164501, 2018.

*Corresponding author. E-mail: vkm28@cam.ac.uk.

ON A TURBULENT VORTEX RING

Victor Kopiev, Sergey Chernyshev
TsAGI, Moscow Branch, Moscow, Aeroacoustic Department, Russia

Summary It is generally assumed that the short-wave instability of the vortex (the wavelength of the order of the core size) is responsible for the turbulence of the flow near the vortex filaments. This paper draws attention to essentially different instabilities of vortices with a wavelength of the order of the scale of the entire vortex structure (long-wave instabilities), which may be the main reason for the transition to turbulence in vortices and other effects that have verifiable manifestations. The study is based on the theory of long-wave oscillations of a vortex ring, which shows that the eigen-frequency spectrum has a complex structure with accumulation points. Eigen-oscillations are accompanied by the formation of a system of critical layers in which, in the presence of a weak monotonically decreasing vorticity outside the core, perturbations of vorticity intensify through the formation of spiral structures. The obtained results allow to explain the following experimental facts: (i) the existence of a laminar core and turbulent flow regime in the atmosphere of a vortex ring with a sharp boundary between them; (ii) the "impossible" flow regime with the inclination of the plane of the ring; (iii) narrow-band sound radiation by a vortex ring with a main frequency corresponding to the theory prediction and the presence of peaks at multiples of fundamental frequencies; (iv) the structure of the far sound field in three azimuthal quadrupoles n=0, 1, 2. It is shown that the curvature of vortex lines plays a crucial role in the occurrence of long-wave instability.

SETTING THE PROBLEM

The study of vortex ring oscillations is of great interest, as it allows considering the non-stationary processes in the core of localized vortices. The vortex ring can easily be produced for experimental study (Figure 1a,b) and allows the theoretical description of both stationary states and oscillations within the framework of the basic equations of an incompressible ideal fluid. According to the long-wave theory [1] all eigen-oscillations are subdivided into the families of Bessel modes and isolated modes, and the discrete spectrum of eigen-frequencies can degenerate if the isolated mode frequency coincide with the frequency of the Bessel mode (Figure 1c). The influence of a weak monotonically decreasing vorticity outside the main vortex core on the properties of these oscillations was considered [2]. It is shown that the presence of vorticity outside the core leads to multiple instability of oscillations that are neutrally stable in the absence of external vorticity. The mechanism of this instability is similar to the Miles mechanism for surface waves [3]. Miles instability of the vortex ring oscillations occurs due to the complex structure of the eigen-mode shape against vortex column modes. Unstable oscillations are accompanied by the appearance of critical layers outside the vortex core, in which the displacement amplitudes of liquid particles reach a large value. Since many modes are unstable, the entire region of the vortex ring atmosphere is filled with critical layers that provide energy transfer from the average flow to the vortex oscillations (Fig. 1a).

The curvature of the vortex lines causes one more type of the long-wave instability associated with the coupling of the eigen-frequencies of the perturbations with energy of different sign (oscillations with positive and negative energy), as noted in [2]. The characteristics of this new instability were obtained in [4]. This instability is actually a direct verification of long-wave theory on the whole.

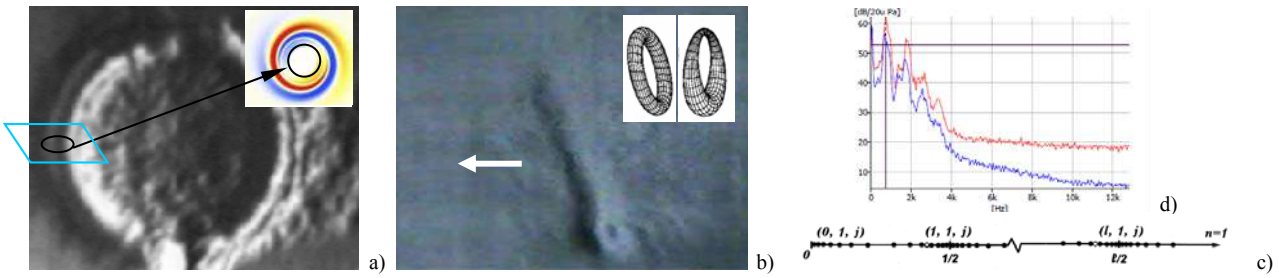

Figure 1. Turbulent vortex ring: a) visualization of laminar vortex core and transport of fluid particles to the vortex tail (front view); in the corner vorticity disturbances in critical layer with the appearance of a spiral structure; b) vortex ring (side view), tilt of the ring, the arrow shows the motion direction; in the corner two phases of slow bulging eigen-mode; c) eigen-osscilations near accumulation points; d) vortex ring noise spectra in large-scale experiment.

Based on the theoretical and experimental results obtained, the paper offers a new scenario of transition to turbulence in a vortex ring. This view is an alternative one to the currently dominant concept of short-wave instability in the cores of large-scale localized vortices [5] or the concept based on an analogy with the elasticity effects of rotating flows [6,7].

METHOD OF PROBLEM SOLUTION

The theory of long-wave oscillations of a thin vortex ring developed in [1] is the basis of the consideration. Due to the extreme complexity of the problem, all theoretical solutions are limited to the case of a thin vortex ring ($\mu \ll 1$).

In the case of short-wave three-dimensional oscillations, when the wavelength has the order of the radius of the core [8,9], the ratio of the wavelength to the vortex ring radius is an additional small parameter, the presence of which allows to obtain a solution, ignoring the mutual influence of perturbations in the distant regions of the vortex ring. In this case, one can limit himself to the main term in the decomposition of the stationary field by the thickness parameter μ, so the question of the existence and structure of the stationary flow does not raise. In contrast to that in the case of long-wave

oscillations the interaction of perturbations is non-local, so the question of the existence and structure in μ of a stationary flow is key question for the asymptotic expansion and oscillation describing.

The stationary flow with vorticity in the toroidal region was considered by Frankel [10]. He proved the existence of stationary solutions for a thin vortex ring with different vorticity distributions, and developed a procedure for obtaining a family of stationary solutions that differ in vorticity profiles in the vortex core. The choice of a stationary flow for which the stability problem would be the simplest is considered and the concept of an isochronous vortex ring was introduced [12], in the core of which the periods of circulation of liquid particles are the same.

The eigen-modes obtained in [1] for an isochronous vortex ring are determined by three integers that characterize the frequency, azimuthal and radial structures of the mode. These modes are the main instrument for turbulent vortex ring structure explanation.

MAIN RESULTS

The main result of this work is a statement and validation of a new scenario for turbulization of a vortex ring. The presented concept is based on a series of results obtained by the authors at different times. It turned out that to describe non-stationary processes in a turbulent vortex ring, it is necessary to consider the long-wave part of the spectrum, where energy can be transferred from the average flow to unstable oscillations with the formation of multiple critical layers. Consideration of the Cauchy problem shows that vorticity perturbations intensify near each critical layer with the appearance of a spiral structures [11] (Fig.1a). At the nonlinear stage, the interaction of perturbations in close critical layers will lead to the transport of vorticity across the streamlines and turbulization of the flow. Thus, for a vortex ring whose spectrum is characterized by the presence of accumulation points, the occurrence of multiple critical layers causes turbulization of the entire flow region outside the vortex core.

Since the critical layers are condensed to the boundary of the vortex core and are absent at the core itself, the boundary between turbulent and laminar domains remains sharp. It can be assumed that this mechanism is also implemented in other vortex flows with intense curved vortex filaments. This would mean that core oscillations of intense vortex filaments serve as a mechanism for turbulization via the formation of small-scale spiral structures around the core with large-scale structure along the filament (pancake like structures). Estimates of the Reynolds number are made for which such a representation can be valid (Re>1000). The proposed concept is validated primarily by experimental observations of the turbulence structure of a vortex ring with a sharp boundary between the laminar core and turbulent atmosphere [6] and an explanation of the existence of modes in which the ring inclinates to the axis of motion in one of the oscillation phase (Fig.1b). These non-trivial experimental facts are explained within the framework of the proposed theory. The theory was also validated by the sound radiation of the vortex ring [2], explaining not only the long-term radiation of the vortex and the high q-factor of the oscillator as a sound energy emitter, but also giving a quantitative comparison with the frequency of the maximum radiation and the presence of several peaks with a multiple frequencies in the radiation spectrum [12].

The new instability of the vortex ring associated with the merging of the eigen-frequencies of the modes with energy of different signs [4] also confirmed the proposed concept [2]. This instability is similar to the Fukumoto's instability obtained earlier for the short-wave disturbances [9]. In spite of the small increment, the instability can be detected in the experiment as having quite special shape. The new instability as well as Miles shear instability of the Bessel oscillations is realized due to the curvature of the vortex line in the vortex ring.

CONCLUSIONS

A new scenario for the transition to turbulence in large-scale 3D vortices with an intense laminar core is proposed. From the point of view of the considered processes, small-scale perturbations, which are certainly present in the considered flows, play the role of a kind of "cover", behind which long-wave processes that have access to the energy of the average flow are hidden. It is remarkable that at the linear stage the solution of the key problems underlying this scenario can be obtained completely analytically based on the equations of an incompressible inviscid fluid.

References

[1] Kopiev V. F., Chernyshev S.A. Vortex-ring eigen-oscillations as a source of sound, J. Fluid Mech.,1997, Vol. 341, 19-47
[2] Kopiev V. F., Chernyshev S.A. Vortex ring oscillations, the development of turbulence in vortex rings and generation of sound // Physics-Uspekhi, 2000, Vol. 43, N7, 663-690.
[3] Miles, J. W. On the generation of surface waves by shear flow. // J. Fluid Mech. 1957, 3, 185–204
[4] Akinshin R.V., Kopiev V.F., Chernyshev S.A. New instability of thin vortex ring in ideal fluid // in Proceedings of 12th All-Russian congress on fundamental problems of theoretical and applied mechanics, Ufa, 2019, Vol.2 "Fluid and gas mechanics", 482-484 (in Russian)/
[5] McKeown R. et al. Turbulence generation through an iterative cascade of the elliptical instability // Sci. Adv. 2020, V.6, N.9, 1-8
[6] Vladimirov, V. A., Lugovtsov, B. A., & Tarasov, V. F. Suppression of turbulence in the cores of concentrated vortices // J. of Applied Mech. and Tech. Phys, 1980, V. 21(n.5), 632-637
[7] Greenspan H.P. The theory of rotating fluids // Cambridge University Press, 1968, 327 p.
[8] Widnall S. E., Tsai S. Y. The Instability of the Thin Vortex Ring of Constant Vorticity // Phil. Trans. R. Soc. London Ser. A, 1977 287 (1344) 273 ()
[9] Fukumoto Y., Hattori Y. Curvature instability of a vortex ring // J. Fluid Mech., 2005. V. 526. P. 77-115.
[10] Fraenkel L. E. On steady vortex rings of small cross-section in an ideal fluid // Proc. Roy. Soc. Lond. A., 1970.Vol. 316. P. 29-62.
[11] Kopiev V. F., Chernyshev S.A., Yudin M. A. Development of Initial Perturbations in the Problem of Motion of a Cylinder in Circulation Flow // Fluid Dynamics, 2019, Vol. 54, №6, pp. 812–820.
[12] Kopiev V. F., Zaytsev M. Yu., Akhmetov D. G., Nikulin V. V. Aerodynamic noise of large-scale vortex ring produced by explosion in cylindrical chamber // AIAA Paper 2019-2739.

EFFECT OF TRAVELING DIRECTION OF WAVE CREATED BY BLOWING AND SUCTION ON RELAMINARIZATION PHENOMENA IN TURBULENT CHANNELFLOW

Minami Kishi[1] and Hiroya Mamori *[1]
[1] Department of Mechanical and Intelligent Systems Engineering, The University of Electro- Communications, Japan

Summary Control techniques for turbulent flows are of importance for improving energy efficiency in manufacturing industry. Recently, a traveling wave control is well-known to induce not only drag reduction effect but also relaminarization phenomenon. In this study, we make direct numerical simulations of turublent channel flows with the traveling wave control to investigate influence of the traveling wave direction on the control effect. In practical situations, the main flow direction may vary due to the unsteadiness of the flow and robustneess is required for the control. The results show that, in some control parameter sets, the relaminarization phenomenon and the skin friction drag reduction effect even in the obliquely traveling waves.

INTRODUCTION

Traveling wave-like blowing and suction control can not only reduce the skin-friction drag reduction but also induce relaminriazation phenomenon on a fully developed turbulent channel flow [1]. The traveling wave control technique is attractive since it is one of predetermined control techniques: apparatus is simple and it doesn't require any sensors [2]. Thus, it is expected to implementation to actual flows. The relaminarization phenomenon by the traveling wave occurs when the wave travels in the downstream direction (i.e., the wave travels in the same direction of the main flow) [3] [4]. However, in practical situations, e.g. ships, the main flow direction may vary due to the unsteadiness of the flow. Therefore, in this study, we make direct numerical simulations to investigate influence of the direction of the traveling wave control on the drag reduction effect and relaminarization phenomenon. The parametric study clarifies the relaminarization range of not only control parameters (amplitude, wavelength, and wavespeed) but also the angle between the traveling wave direction and the main flow.

DIRECT NUMERICAL SIMULATION

In this study, the flow between parallel plates driven by a constant pressure gradient was used. Then, the periodic boundary conditions were applied in the flow direction and the span direction. The calculation area is $L_x \times L_y \times L_z = 2\pi \times 2 \times 2\pi$, and the calculation grid is $N_x \times N_y \times N_z = 256 \times 96 \times 256$. The control formula for the traveling wave-like blowing and suction control is shown as

$$v_w = \mp a \sin\left(\frac{2\pi k}{L_x}(x - ct)\right). \tag{1}$$

The parameters are amplitude a, wave number k, and wavespeed c. On the wall surface, the blowing and suction are given as vertical velocities, and non-slip conditions are given for flow and span velocities. In this study, only varicose mode is investigated. The control effect is evaluated using the skin friction drag coefficient C_f and the total kinetic energy (TKE). Using the continuity equation of an incompressible flow and the Navier-Stokes equation as governing equations, we use friction velocity u_τ^*, channel half width δ^*, and viscous velocity ν^* for non-dimensionalization. The Reynolds number is defined by $Re_\tau = u_\tau^* \delta^* / \nu^*$, and a fully developed turbulent field is used as the initial field at $Re_\tau = 180$.

In this study, the direction of traveling wave control is tilted with respect to the mainstream: the mainstream direction is changed, but the direction of the traveling wave is unchanged. The angle difference between the mainstream and traveling waves is $\theta = 0°, 30°, 45°, 60°$, and $90°$. Figure 1 shows a schematic diagram of the channel flow that changes the mainstream direction.

SAMPLE RESULTS AND OUTLOOK

In previous study, the fully developed turbulent channel flow becomes the laminar flow when the traveling wave travels in the same direction with the mainstream. The relaminarization phenomenon occurred and the so-called

*Corresponding author. Email: mamori@uec.ac.jp

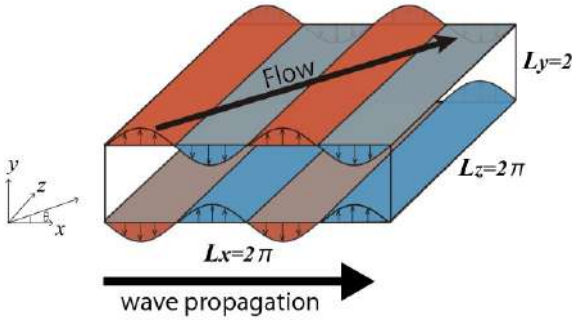

Figure 1: Coordinate system with the traveling wave.

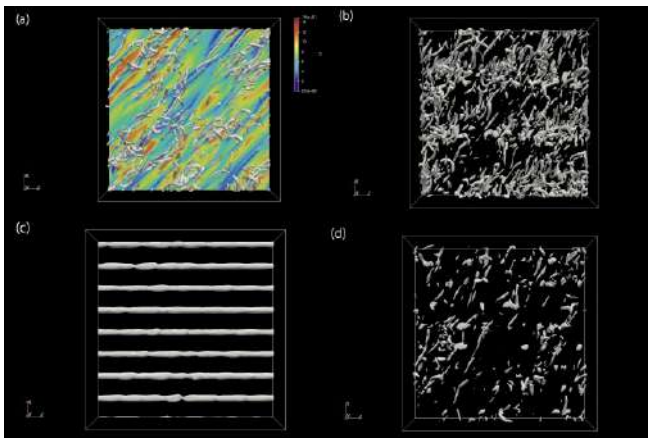

Figure 2: Vortical structure at lower-half of the channel flow: (a) Uncontrolled with $Q = 0.01$; (b) $k = 3$ and $c = 30$ with $Q = 0.03$; (c) $k = 8$ and $c = 30$ with $Q = 0.03$; (d) $k = 8$ and $c = 120$ with $Q = 0.03$. The angle of the main flow direction is $\theta = 45°$.

coherent structures decreased [3, 4]. In contrast, the present study focuses on the control effect of the wave traveling in the diagonal direction to the mainstream.

Figure 2 shows sample results: instantaneous vortical structures visualized using the second invariant of the velocity tensor (so-called the Q value) for uncontrolled and controlled cases. For all the cases, the wave travels in the diagonal direction (i.e., the difference between the direction of the mainstream and the traveling waves is $\theta = 45°$) and the amplitude of the wave is set to be $a = 8$. Figure 2(a) shows the vortical structure together the velocity in the region near the lower wall in the uncontrolled flow. We confirm the turbulent coherent structure (i.e., vortical structures and the streaky structures). Figure 2(b-d) shows controlled cases. All the wave travels in the $x+$ direction and the mainstream direction is 45° on $x - z$ plane. Figure 2(b) shows the reference case of $k = 3$ and $c = 30$. The vortical structures along the mainstream direction remained and the relaminarization phenomenon does not occur. On the other hand, for large wavenumber case as shown in Fig. 2(c) ($k = 8$ and $c = 30$), the vortical structure disappeared where relaminarization phenomenon occurred. As increase of the wavespeed ($k = 8$ and $c = 120$), shown in Fig. 2(d) the vortical structure decreased as compared with the reference case, but they remained and the relaminarization phenomenon did not occur.

In the presentation, we will discuss the flow field in detail, e.g., turbulent statistics and interaction of the control and the coherent structure. Moreover, we will carry out a parametric study to clarify the range of the relaminarization phenomenon and they will be compared with that with the previous study. According them, we will contribute to understand the mechanism of the relaminarization phenomenon by the traveling wave-like control in the fully developed turbulent channel flow.

References

[1] C Lee, T Min, and J Kim. Stability of a channel flow subject to wall blowing and suction in the form of a traveling wave. Physics of Fluids, 20(10):101513, 2008.

[2] T Min, S Kang, J Speyer, and J Kim. Sustained sub-laminar drag in a fully developed channel flow. Journal of Fluid Mechanics, 558:309–318, 2006.

[3] H Mamori, K Iwamoto, and A Murata. Effect of the parameters of traveling waves created by blowing and suction on the relaminarization phenomena in fully developed turbulent channel flow. Physics of Fluids, 26(1):015101, 2014.

[4] R Nakanishi, H Mamori, and K Fukagata. Relaminarization of turbulent channel flow using traveling wave-like wall deformation. International journal of Heat and Fluid Flow, 35:152–159, 2012.

TIME RESOLVED PIV MEASUREMENTS IN FULLY DEVELOPED TURBULENT PIPE FLOW.

Zeinab Hallol*[1], Mohamed Yousry[1], Sebastian Merbold[1], and Christoph Egbers [1]
[1]Department of Aerodynamics and Fluid Mechanics, Brandenburg University for Technology Cottbus- Senftenberg,Germany.

Summary Measurements of time-resolved high-speed particle image velocimetry (HS-PIV) are applied at moderate and high Reynolds numbers in Cottbus Large Pipe facility (CoLaPipe) in Brandenburg University for Technology Cottbus-Senftenberg. The main objective of this experiment is to capture high-spatial instantaneous snapshots of recently explored large coherent structures in log and outer regions of fully developed turbulent pipe flow. PIV measurements in stream-wise wall-normal plane are validated through comparing it with previous single hot-wire anemometry datasets that reveals a good agreement. Among visual inspection, stream-wise coherent structure features are exhibited in the middle of the log region and at the near-wall region.

BACKGROUND

Earlier experimental and numerical studies have explored and documented the existence of coherent structures among the investigation of hairpin-like vortices inclined at an angle to the free stream [7]. Subsequent studies induced that multiple structures of these hairpins are travelled at the same convective velocity forming vortex packets that create large scale structures in internal and external flows [5], [1]. The features of large structures are their alignment in the stream-wise direction to produce regions of low and high stream-wise momentums in the inner and outer layers [3]. Large coherent structures are known to prohibit the log and outer regions of the boundary layer at moderate to high Reynolds number [4] to be responsible for ejection and sweep events generation which are the major contributors to turbulent production and Reynolds shear stress [6].

EXPERIMENTAL SETUP

Although hot wire anemometry proved its effective role in measuring flow in several manners, PIV applications on turbulent flows still stand as one of the most demanding applications due to their wide range of length and time scales [8]. Recent experiment is conducted in CoLaPipe test facility of 190 mm diameter at measuring station L/D = 110 to proceed two dimensional velocity fields of stream-wise /wall-normal plane with accurate temporal and spatial resolutions at Reynolds number range ($10^3 \leq Re_\tau \leq 10^4$). Re_τ is the friction Reynolds number corresponding to the ratio between largest and smallest length scale ($Re_\tau = \mathrm{R}\, u_\tau / \nu$). In this paper, we will present the results of principle statistical moments of $Re_\tau = 1786$. Lavision PIV system is used to capture 1838 snapshots. The system consists of flow visualization by laser illumination of seeding particles, CMOS camera, laser/camera synchronization system, and analysis software (Davis8). The field of view of HS-PIV measurements is 1R in wall-normal and 2R in stream-wise direction. Where R is the pipe radius. Fig.(1) shows the experimental setup.

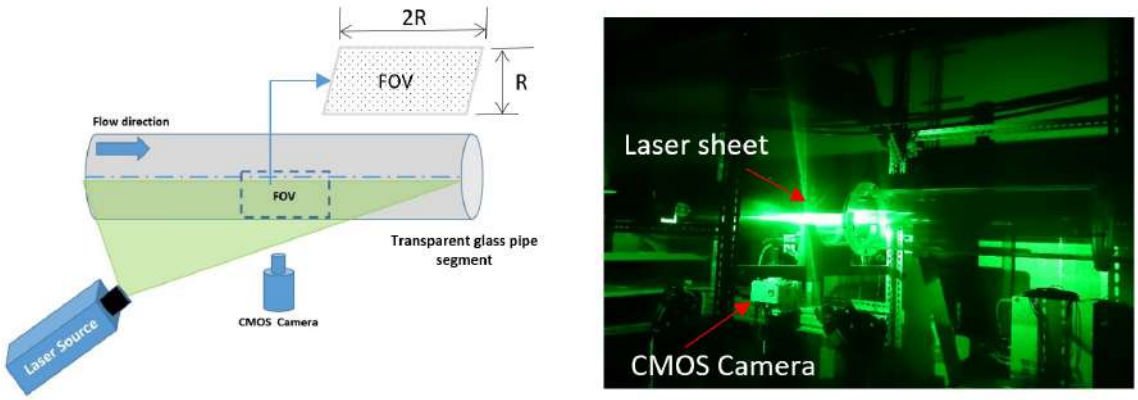

Figure 1: PIV experimental setup in CoLaPipe test facility.

*Corresponding author. E-mail: hallozei@b-tu.de

RESULTS AND CONCLUSION

The flow statistics; mean stream-wise velocity profile (u^+), stream-wise Reynolds stress (u^{2+}) and Reynolds shear stress (uv^+) normalized by friction velocity (u_τ) are presented in figure (2.a). Comparisons for the first and second-order momentum statistics are drawn to single-point prior hot wire anemometry (HWA) measurements of [2] in SuperPipe test facility and recent hot wire datasets in CoLaPipe. The validation reveals good and acceptable agreement between PIV and HWA datasets for the stream-wise fluctuations. The near-wall region $y^+ < 40$ is not clearly captured by PIV system due to the wall turbulence large discrepancies which are the main influence of spatial attenuation and wall reflections. Fluctuation of stream-wise component (u_{rms}) indicates small magnitude in the core region and larger in the near wall region, this is clarified well in fig.(2.b), Also hairpin foot print can be observed near the wall. Temporal and spatial resolutions of the current measurements enable us to visualize large coherent motions known to exist in the near-wall region at moderate to high Reynolds number. Fig.(3.a) extends the instantaneous velocity field contours of stream-wise and wall-normal velocity components. The flow direction is from left to right and the pipe wall is located at the bottom of the image. The visual inspection of the velocity field indicates spatial structures and important stream-wise coherence structure features at the middle of the log region and close to the wall. Velocity fluctuation vector-map image in fig.(3.b) exhibits a high degree of complexity ranging from the smallest resolved scales to structures that are larger than the radius of the pipe. The vortical structures were found to be close to low-speed regions, being responsible to maintain these regions and to induce ejection and sweep events. Protracted flow field is required in future work to obtain sufficient spatial resolution over a longer stream-wise extent. However, large coherent structures (i.e very large scale motions) are recognized to commonly persist with a length greater than 20 R [4].

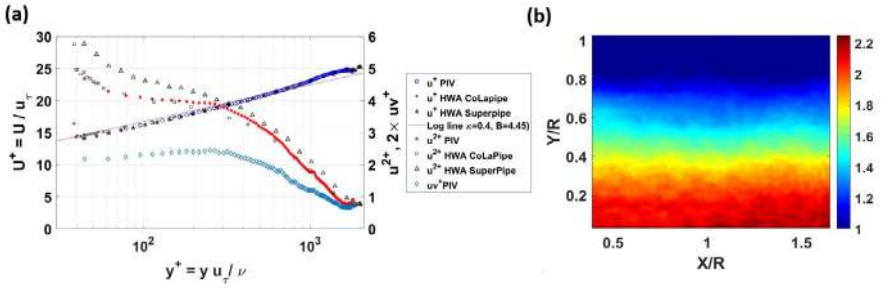

Figure 2: (a) Logarithmic velocity (u^+), stream-wise Reynolds stress (u^{2+}), and shear stress (uv^+) profiles of PIV data compared among CoLaPipe HWA measurement Re_τ= 1786 and SuperPipe HWA measurement Re_τ= 1985 [2]. (b) Contour map for u_{rms} measured by PIV.

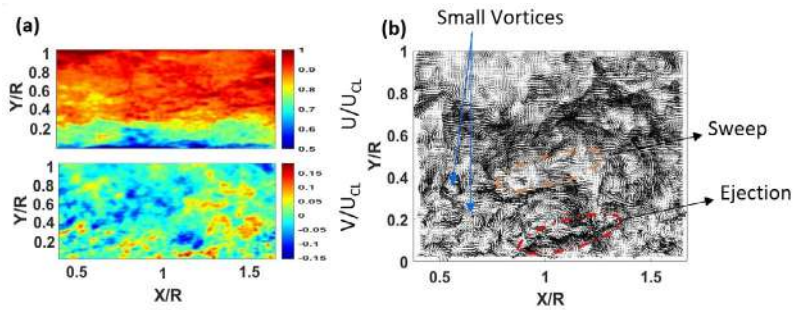

Figure 3: (a) Instantaneous velocity field from the PIV data set for stream-wise (Top) and wall-normal (Bottom) velocity fields normalised by stream-wise velocity at the centreline of the pipe. (b) Vector contour maps at Re_τ= 1786.

References

[1] Balakumar B.J and Adrian R. J.Large- and very-large-scale motions in channel and boundary-layer flows.*Phil. Trans. R. Soc.***365**: 665–681, 2007.
[2] Hultmark M., Vallikivi M., Bailey S.C.C,and Smits A. J.Turbulent Pipe Flow at Extreme Reynolds Numbers. *Phy. Rev. Lett.***108**: 094501, 2012.
[3] Hutchins N., Hambleton WT and Marusic I.Inclined cross-stream stereo particle image velocimetry measurements in turbulent boundary layers. *J. of Fluid Mech.***541**: 21–54, 2005.
[4] Hutchins N. and Marusic I.Large-scale influences in near-wall turbulence.*Phil. Trans. R. Soc.***365**: 645–664, 2007.
[5] Kim C., and Adrian R. J. Very large-scale motion in the outer layer. *Phy. of Fluids***11**: 417, 1999.
[6] Martins F.J.W.A., Foucaut J. M., Stanislas M., and Azevedo L. F. A.Characterization of near-wall structures in the log-region of a turbulent boundary layer by means of conditional statistics of tomographic PIV data.*Exp. thermal and fluid science***105**: 191–205, 2019.
[7] Panton RL. A Reynolds stress function for wall layers. *J. Fluids Eng.***119**:325-330, 1997.
[8] Westerweel J., Elsinga G.E.,and Adrian R.J.Particle Image Velocimetry for Complex and Turbulent Flows.Ann. Rev. Fluid Mech.**45**: 409-436,2013.

BLOWING AND SUCTION CONTROL BASED ON DEEP REINFORCEMENT LEARNING FOR DRAG REDUCTION IN FULLY DEVELOPED TURBULENT CHANNEL flOW

Ryota Aoki[1] and Hiroya Mamori *[1]
[1]Department of Mechanical and Intelligent Systems Engineering, The University of Electro-Communications, Tokyo, Japan

Summary For energy efficiency, flow control techniques to reduce skin-friction drag in the wall-turbulence are investigated by means of direct numerical simulations (DNS). While the coherent structures dominate the near-wall turbulence, it is very difficult to design control based on them due to non-linearity. To make the flow control for the turbulent flow, the present study employs blowing and suction from the wall based on a deep reinforcement learning. The deep reinforcement learning has recently attracted much attention in the community of control. We have given a task to search for the parameters of the blowing and suction from the wall and the control scheme is examined in the turbulent channel flow by means of the DNS. As a result, we were able to learn a parameter that can achieve a 28% drag reduction effect about 600 times out of more than 3000 combinations of parameters.

INTRODUCTION

For energy efficiency, many control techniques to reduce the skin-friction drag in the wall-turbulence have been preformed. A direct numerical simulation (DNS) is powerful tool to investigate the control effect in the turbulent flow, because it can compute without using any turbulence models. For example, Choi *et al.* [1] made the DNS of turbulent flow with so-called an opposition control. The opposition control means the blowing and suction from the wall based on the near-wall velocity to decrease the activity of the vortical structures. Based on the opposition control, many study has been tried to design and construct an optimal (or better at least) control method. In the present study, we employ deep reinforcement learning (DRL) to construct the control scheme for opposition control. Recently, the DRL has been attracting attention in the control community and several studies have demonstrated the effectiveness. In contrast with previous studies, we employ the DRL for the fully developed and three-dimensional turbulent flow for the opposition control. The DRL is applied to search for the detection plane of the opposition control.

NUMERICAL METHOD

Direct Numerical Simulation

Figure 1 shows a schematic diagram of the turbulent channel flow. The governing equations are the continuity equation and the Navier-Stokes equation for incompressible flow. The computational domain size is $(2\pi \times 2 \times \pi)$ in the x, y, and z direction and the number of grid points is $(128 \times 96 \times 128)$. The grid spaces are uniform in the homogeneous directions and non-uniform in the wall-normal direction. The mean pressure gradient is set to be constant and the friction Reynolds number Re_τ based on the half channel width and the friction velocity is set to 180. A no-slip condition is imposed on the wall except the wall-velocity in the controlled case. All the simulation starts from the fully developed turbulent channel flow. In addition, the temperature is treated as a passive scalor with the uniform heat generation condition. The Prandlt number is $Pr = \nu/\alpha = 1.0$ where α is a thermal diffusivity.

Opposition Control and Deep Reinforcement Learning

Opposition control is one of the turbulence control methods performed by Choi *et al.* [1]. A schematic diagram is shown in Fig. 2. This control reduces the skin-friction drag by controlling blowing and suction from the wall to cancel the streamwise vortical structures. Specifically, the wall-normal velocity is detected at 'detecting plane' and the blowing and suction from the wall is used them with opposite sign. In this control, the drag reduction rate depends on the height of the detecting plane: the maximum drag reduction is obtained when the detecting plaine is located at $y^+ \approx 15$ [2]. In the present computational setting, when the detection plane height is set to $y^+ = 15$, the flow becomes steady in about 6 dimensionless time and the drag reduction rate of 25% was obtained.

Figure 3 shows schematic of the DRL. The DRL consists of agents and environment. The agent selects the 'action' and repeatedly tries to maximize the 'reward' based on the 'state' of the environment. In other words, the behavior is determined by the conditions and rewards of the environment. Although various algorithms have been proposed for the DPL, we employ PPO [3] and the DRL framework ChinerRL [4] for its implementation.

In this study, we divide the transitional regime (6 seconds in dimensionless time) from the initial to the steady state under the control into five segments. At the beginning of the segmented time domain, the agent selects the detection plane height and repeats the control for 1.2 seconds in 5 steps. The state-space was set to bulk velocity and bulk temperature, and the action space is set to the detecting plane height of $0 - 20$. The rewards are sum of the increment (or decrement) of the drag reduction rate of each step for one episode.

*Corresponding author. E-mail: mamori@uec.ac.jp

RESULTS

The time history of skin friction drag coefficient C_f during 600 episodes of training is shown in Fig. 4. The red line shows the case of the conventional opposition control (i.e., without using the DRL): the detection plane height is fixed at $y^+ = 15$ and blowing and suction are performed for 6 seconds. On the other hand, the blue line shows the reference DRL case: the detection plane height is changed by the deep reinforcement learning. The number in the figure represents the detection plane height selected by the DRL at each step. In this case, the detection plane height varies 4→ 15 → 15→ 14 → 15. In the conventional case, C_f significantly decreases at $t < 3$ and slightly recovers at $3 < t < 6$. For the DRL case, C_f rapidly drops at the second step when the detection height is $y^+ = 15$. From the third to fifth time steps, the detection heights of 15, 14, and 15 are selected and C_f is maintained around 0.57 where 28% drag reduction is obtained.

Instantaneous vortical structures of the uncontrolled and the DRL case (forth and fifth steps) are visualized in Fig. 5. The vortical structures, which cause the large skin-friciton drag, are observed in the uncontroleed flow. However, number of them decreases in the DRL cases, which corresponds the skin-friction drag reduction.

OUTLOOK

The control learned in this study takes longer than the conventional method to reduce the skin friction drag, so it does not completely outperform the conventional method. Also, the task of selecting the detection plane height is discrete. We are going to develop better control methods by designing the reward system according to the purpose and assigning tasks to learn continuous blowing and suction control.

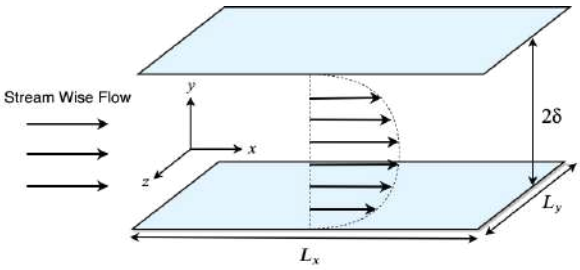

Figure 1: Schematic diagram of turbulent channel flow.

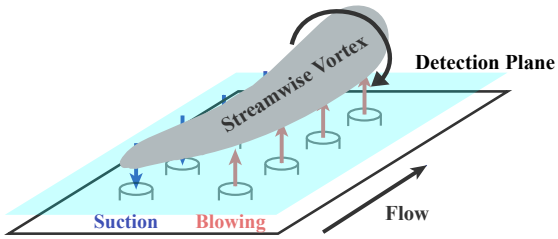

Figure 2: Schematic diagram of opposition control.

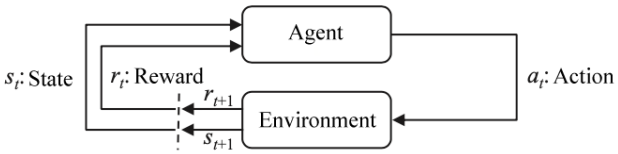

Figure 3: Schematic of Reinforcement learning.

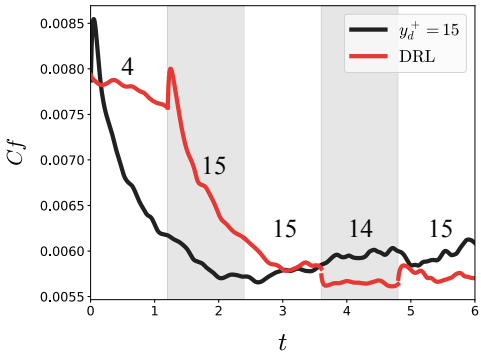

Figure 4: Time history of skin friction drag.

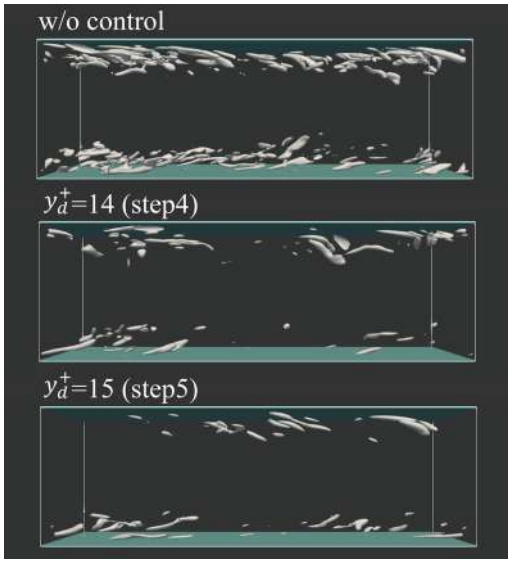

Figure 5: Instantaneous vortical structure defined by the iso-surface of the second invariant of the velocity gradient tensor at $Q^+ = 0.03$

References

[1] Choi, *et al.*, "Active turbulence control for drag reduction in wall-bounded flows", *J.Fluid Mech*, Vol. 262, pp.77-110, (1994).
[2] Hammond, *et al.*, "Observed mechanisms for turbulence attenuation and enhancement in opposition-controlled wall-bounded flows", *Phys. Fluids*, Vol. 10, pp.2421-2423, (1998).
[3] Schulman, *et al.*, "Proximal policy optimization algorithms", *arXiv preprint arXiv:1707.06347*, (2017).
[4] ChainerRL, web site **https://github.com/chainer/chainerrl**.

VORTICES AS PARTICLES IN RAPIDLY ROTATING TURBULENT FLOWS

Ke-Qing Xia*[1,2], Kai Leong Chong[2], Jun-Qiang Shi[3], Guang-Yu Ding[1,2], Shan-Shan Ding[3], Hao-Yuan Lu[3], and Jin-Qiang Zhong[3]
[1]Center for Complex Flows and Soft Matter Research and Department of Mechanics and Aerospace Engineering, Southern University of Science and Technology, Shenzhen, China
[2]Department of Physics, The Chinese University of Hong Kong, Hong Kong, China
[3]School of Physics Science and Engineering, Tongji University, Shanghai, China

Summary Using rotating Rayleigh-Bénard convection as a paradigmatic model system, we demonstrate through both experiment and numerical simulations that the movement of vortices in a rotating turbulent flow resembles that of inertial Brownian particles, the motion of which changes from ballistic to diffusive after certain critical time. Moreover, the transition from ballistic to diffusive behaviors is direct, free from the so-called hydrodynamic memory effect, as predicted by Langevin. The transitional timescale and the effective diffusivity of the vortices can be collapsed excellently onto a master curve for all parameters explored. When the centrifugal buoyancy is present, the cyclonic (anticyclonic) vortices are expected to move radially inward (outward). Surprisingly, as centrifugal buoyancy becomes dominant, anomalous outward motion of cyclones is observed in a centrifugation-dominant flow regime. Moreover, the relative motion of the vortices within a cluster resembles that of scale-free collective motion in systems of active particles. We interpret this phenomenon as a symmetry-breaking of both the population and vorticity magnitude of the vortices brought about by the centrifugal buoyancy.

STOCHASTIC MOTION OF COLUMNAR VORTICES

We present an experimental and numerical study of the motion of columnar vortices in rotating convective thermal turbulence, where the vortices advect horizontally in a stochastic manner. The traditional view of vortex motion is that the effect of inertia should be neglected since the vortex does not have distinct density or mass difference from their environment. Our results demonstrate that the movement of vortices resembles that of inertial Brownian particles, i.e. they initially move ballistically, and then diffusively after certain critical time. Moreover, the transition from ballistic to diffusive behaviors is direct, as predicted by Langevin, without first going through the hydrodynamic memory regime. It is also found that the transitional timescale and the effective diffusivity of the vortices can be collapsed excellently onto a master curve for all our explored parameters.

VORTEX MOTION UNDER CENTRIFUGAL FORCE

When centrifugal buoyancy becomes significant the vortices are found to undergo radial motions, i.e. cyclones move radially inward and anticyclones outward. Unexpectedly, when the centrifugal buoyancy becomes dominant anomalous outward motion of cyclones are observed. This phenomenon is interpreted as a symmetry-breaking of the vorticity field induced by the centrifugal buoyancy. Consequently the cyclones submit to the collective motion dominated by the strong anticyclones. Further studies of this anomalous vortex motion reveal that the vortices self-organize into coherent clusters, in which their velocity fluctuations exhibit scale-free correlations. Scale-free collective motions have been found in many natural systems consisting of large number of objects, such as bird flocks, fish schools, and bacteria swarms.

CONCLUSIONS

We have made systematic studies of the motion of columnar vortices in thermally-driven rotating turbulent flows from ballistic to diffusive regimes. When centrifugal force becomes dominant, anomalous outward motion of cyclones are observed, which can be interpreted as a symmetry-breaking of the vorticity field. Our study brings new perspectives on the phenomenon of collective motion, and may have broad implications in the studies of soft condensed matter, fluid physics and biological systems. This work was supported in part by the Hong Kong Research Grants Council under Grant No. 14302317 and in part by the National Science Foundation of China under Grant Nos. 12072144, 11572230, 11772235, and a NSFC/RGC Joint Research Grant No.11561161004.

References

[1] Chong K. L., Shi J.-Q., Ding G.-Y., Ding S.-S., Lu H.-Y., Zhong J.-Q. and Xia K.-Q., Vortices as Brownian Particles in Turbulent Flows. *Science Advances*, **6**, *eaaz1110 (2020).*
[2] Ding S.-S., Chong K. L., Shi J.-Q., Ding G.-Y., Lu H.-Y., Xia K.-Q., Zhong J.-Q., Inverse centrifugal effect induced by collective motion of vortices in rotating turbulent convection. *Under review.*

*Corresponding author. E-mail: xiakq@sustech.edu.cn.

SIMULATION AND ANALYSIS OF VORTICAL FLOWS

Xiyun Lu*[1]
[1]Department of Modern Mechanics, University of Science and Technology of China, Hefei, Anhui 230026, China

Summary The fluid flows encountered in nature and technology come from the coexistence of three nonlinear fundamental processes, i.e. shearing process, compressing process, and thermal process, and their couplings both in the interior of the fluid flow and on boundaries. These processes are typically measured by vorticity, dilatation and entropy, respectively, and characterized by their respective localized but strong structures and interactions which can dominate the global flow performances. In this talk, I will attempt to introduce a general theoretical framework for multiple-process splitting and coupling and to apply it to examine the key flow structures and interactions based on our numerical simulations. I will demonstrate its applications to some typical flows covering the incompressible, transonic and supersonic flow regimes. The analysis in terms of the fundamental processes provides a physical insight into the understanding of the mechanisms underlying in these vortical flows.

FRAMEWORK FOR FUNDAMENTAL PROCESSES OF VORTICAL FLOWS

Any practical external or internal engineering vertical flow has a set of global performances as its design objectives, e.g. the lift and drag of a wing or the pressure ratio and efficiency of a compressor, as well as the stable operation ability of the flow. Contrary to the early-stage development of fluid dynamics focusing on structure-free potential flows, it has now been well recognized that all global performances are dominated by various local dynamic structures, such as boundary layers, free shear layers, vortices, turbulent coherent structures, shock waves and other nonlinear acoustic waves, as well as entropy waves [1-8]. The richness of local flow structures makes a big variety of complex flows in nature and technology.

Then, a fundamental fact on flow structures is: all of them are measured not by primary variables themselves (e.g., velocity, pressure, and entropy) but their spatial-temporal derivatives, e.g. vorticity, dilatation, pressure gradient, and entropy gradient. These derivatives appear in the local balances of mass, momentum, and energy, and thereby interact each other to produce various dynamic effects, for example the aerodynamic force.

In a multi-dimensional, viscous and compressible flow, the local structures as exemplified above come from three fundamental dynamic processes: the (transverse) shearing process, the (longitudinal) compressing process, and the thermal process. The first two processes are the fundamental bulk dynamic processes in fluid motion which are measured by the vorticity field and dilatation field, and their characteristic behaviors are governed by the Reynolds number and Mach number, respectively. These two fundamental process are inherently coupled both in the interior of the flow field via the nonlinear terms of the governing equations, and on flow boundary owing to the adherence condition. In addition, the thermal process is inevitably involved as long as the flow is compressible. It can be conveniently measured by the entropy field which is inherently coupled with both compressing and shearing processes. Therefore, we introduce a general theoretical framework for multiple-process splitting and coupling and further apply it to examine the key flow structures and interactions based on our numerical simulations below [3-7].

ANALYSIS OF THE FUNDAMENTAL PROCESSES BASED ON NUMERICAL SIMULATION

The forces exerted on a body moving through a fluid depend strongly on the local dynamic processes and structures generated by the body motion, such as flow separation, vortices, etc. A detailed and quantitative understanding of the effects of these processes and structures on the instantaneous overall force characteristics is of fundamental significance, and may improve our capabilities for flow analysis and control. We apply alternative unconventional force expressions to analyze numerical solutions of unsteady and viscous circular-cylinder flows [4,8]. The results confirm the exactness of the expressions and, more importantly, provide a unified understanding of the specific influence on the force of each individual flow structure at its different evolution stages.

The force of flapping plates is studied by vortex dynamic analysis [1,4]. Based on the dynamic analysis of the numerical results of viscous flow past three-dimensional flapping plates, it is found that the force is strongly dominated by the vortical structures close to the body. Further, the dynamics of the flapping plate is investigated in terms of viscous vortex-ring model. It is revealed that the model can reasonably reflect the essential properties of the ring-like vertical structure in the wake, and the energy of the plate transferred to the flow for the formation of each vortical structure possesses a certain relation. The results also provide the understanding of the dynamic mechanisms relevant to flapping locomotion [1,2].

*Corresponding author. E-mail: xlu@ustc.edu.cn

Numerical simulation and analysis of compressible vertical flows past cylinder and foil are also carried out to deal with the fundamental dynamic processes and the relevant flow behaviors [5-7]. Various fundamental mechanisms dictating the intricate flow phenomena, such as turbulent boundary layer characteristics, kinematics of coherent structures, flow separation and separated shear-layer instability, have been studied systematically. The local flow structures are reasonably captured using the instantaneous Generalized Lamb vector divergence and curl, and the underlying dynamical processes are clarified. The results provide physical insight into the understanding of the mechanisms relevant to compressible vortical flows.

References

[1] Peng Z.R., Huang H.B., Lu X.Y. Hydrodynamic Schooling of Multiple Self-Propelled Flapping Plates. *J. Fluid. Mech.* **853**: 587-600, 2018.
[2] Peng Z.R., Huang H.B., Lu X.Y. Collective Locomotion of Two Closely Spaced Self-Propelled Flapping Plates. *J. Fluid. Mech.* **849**: 1068-1095, 2018.
[3] Chu Y.B., Lu X.Y. Topological Evolution in Compressible Turbulent Boundary Layer. *J. Fluid. Mech.* **733**: 414-438, 2013.
[4] Li G.J., Lu X.Y. Force and Power of Flapping Plates in a Fluid. *J. Fluid. Mech.* **712**: 598-613, 2012.
[5] Chen L.W., Wang G.L., Lu X.Y. Numerical Investigation of a Jet from a Blunt Body Opposing a Supersonic Flow. *J. Fluid. Mech.* **684**: 85-110, 2011.
[6] Xu C.Y., Chen L.W., Lu X.Y. Large-Eddy Simulation of the Compressible Flow past a Wavy Cylinder. *J. Fluid. Mech.* **665**: 238-273, 2010.
[7] Chen L.W., Xu C.Y., Lu X.Y. Numerical Investigation of the Compressible Flow past an Aerofoil. *J. Fluid. Mech.* **643**: 97-126, 2010.
[8] Wu J.Z., Lu X.Y., Zhuang L.X. Integral Force Acting on a Body due to Local Flow Structures. *J. Fluid. Mech.* **576**: 265-286, 2007.

VORTICAL STRUCTURES AND HEAT TRANSFER ENHANCEMENT IN ROTATING RAYLEIGH-BÉNARD CONVECTION

Yantao Yang*[1], Roberto Verzicco[2,3,4], Detlef Lohse[2], and Richard J.A.M. Stevens[2]
[1]SKLTCS and Department of Mechanics and Engineering Science, BIC-ESAT, College of Engineering, and Institute of Ocean Research, Peking University, Beijing 100871, China
[2]Physics of Fluids Group, Department of Science and Technology, MESA+ Institute, Max Planck Center Twente for Complex Fluid Dynamics, and J. M. Burgers Center for Fluid Dynamics, University of Twente, 7500 AE Enschede, The Netherlands
[3]Dipartimento di Ingegneria Industriale, University of Rome "Tor Vergata", Via del Politecnico 1, Roma 00133, Italy
[4]Gran Sasso Science Institute - Viale F. Crispi 7, 67100 L'Aquila, Italy

Summary Buoyancy-driven convection plays a crucial role in turbulent mixing. It is well known that, for certain parameter ranges, background rotation may enhance the heat transfer in Rayleigh-Bénard convection turbulence, mainly due to the Ekman pumping near the boundary and the tall vortical structures in the bulk. Here we present our results on the vortical structures in rotating RB flows for a fixed Prandtl number $Pr = 4.38$ and different Rayleigh numbers Ra. We identify the optimal rotation rate which generate the highest heat transfer enhancement. We reveal that the vortical structures may take different forms at the optimal rotation rate. For low Ra, the vortical structures at the optimal rotation rate occupy the whole height of the domain, while for high Ra these structures cannot extend through the bulk. Therefore, different behaviors of the heat transfer enhancement are observed.

INTRODUCTION

Rayleigh-Bénard (RB) convection, which happens when a fluid layer is heated from below and cooled from above, has been extensively studied to improve our understanding of turbulent transport and mixing [1]. Meanwhile, since the seminal work of Rossby [2], it is well-known that background rotation may improve the heat transfer in certain parameter range due the Ekman pumping, namely, rising or falling plumes of hot or cold fluid are stretched into vertically aligned vortices that suck fluid out of the thermal boundary layers adjacent to the bottom and top plates. The Ekman pumping process depends strongly on the control parameters [3].

In this talk we study the rotating RB flow and focus on the heat transfer enhancement and corresponding vortical structures in the field. Consider a fluid layer bounded by two parallel plates, which are perpendicular to the direction of gravity and separated by a height H. The bottom plate has higher temperature than the top one. The whole domain rotates about an axis which is parallel to the direction of gravity. The control parameters include the Prandtl number $Pr = \nu/\kappa$, namely the ratio of viscosity to diffusivity, the Rayleigh number $Ra = \beta g \Delta H^3/\kappa\nu$ which measures the strength of thermal driving, and the Rossby number $Ro = \sqrt{\beta g \Delta/H}/(2\Omega)$ which indicates the relative strength of rotation, respectively. Here β is the thermal expansion coefficient, g the gravitational acceleration, Δ the temperature difference between two plates, and Ω the rotation rate, respectively.

MAIN RESULTS

We numerically solve the incompressible Navier-Stokes equation within the Oberbeck-Boussinesq approximation by using our finite-difference code [4]. The two plates are no-slip and with constant temperature. In the horizontal directions we use periodic conditions. For rotation we only include the Coriolis force in the governing equations. Throughout this study we fix Pr at 4.38 and considered two Rayleigh numbers $Ra = 10^8$ and 2.3×10^9. Then for each Ra we gradually increase the rotation rate, or equivalently $1/Ro$, from zero to sufficiently large values. A general trend as $1/Ro$ increasing is that the heat flux, first increases from the value of non-rotating case and then rapidly decreases, and the heat transfer enhancement is achieved only for intermediate rotation rates. We refer to the rotation rate with the highest heat flux as the optimal rotation rate.

We first show the vortical structures at the optimal rotation rate for each Ra in figure 1. Clearly, the structures have very different morphology for the two cases. For $Ra = 10^8$ the optimal rotation rate is $1/Ro = 5$, and the vortical structures extend the whole bulk and are almost in the vertical direction. For $Ra = 2.3 \times 10^9$ the optimal rotation rate is $1/Ro = 1.6$, and the corresponding vortical structures are much less pronounced and much shorter. Thus, at the optimal rotation rate, the vortical structures are much more coherent at $Ra = 10^8$ than that at $Ra = 2.3 \times 10^9$.

In order to quantify the above observation we characterize the coherence of the flow structures by calculating the following cross-correlation:

$$C(\delta z) = \frac{\langle w(x,y,\lambda_u) w(x,y,\lambda_u + \delta z)\rangle_{x,y}}{\langle (w(x,y,\lambda_u))^2\rangle_{x,y}}, \quad (1)$$

*Corresponding author. E-mail: yantao.yang@pku.edu.cn

where $\langle\cdot\rangle_{x,y}$ indicates the average in horizontal direction. As we are interested in the vertically aligned vortices, we calculate the correlation using the horizontal plane at the viscous boundary layer height ($z = \lambda_u$), where the base of the vortices forms, as reference. Figure 2a,b show the correlation C as a function of the distance from the viscous boundary layer δz for different rotation rates. For all cases the correlation C first increases from 1 for $\delta z = 0$ to some maximum value before it decreases below 1 further away from the boundary layer. The reason for the maximum is that the vertical velocities are higher at some distance above the viscous boundary layer height than at $z = \lambda_u$.

We take the δz value at which the maximum occurs as a measure for the height of the vertically aligned vortices and the magnitude C_m of the peak of $C(\delta z)$ as a measure of the coherence of the vortices. Figure 2c,d show that the variation of C_m with $1/Ro$ is similar for both Ra, which suggests that the flow coherence mainly depends on the rotation rate. However, the height of the plumes or vertically aligned vortices, which is indicated by δz_m, is very different for the low and the high Ra's. For the low Ra the height of the vertically aligned vortices is larger at smaller $1/Ro$ than that for the high Ra. For $Ra = 2.3 \times 10^9$ the height at which the vertical coherence is highest is similar for the non-rotating case and the optimal rotation rate. In contrast, the vertical coherence at the optimal rotation rate is significantly higher than that for the non-rotating case at $Ra = 10^8$.

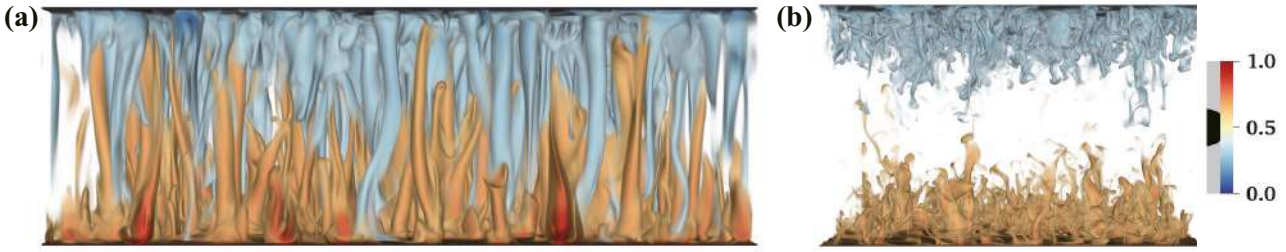

Figure 1: olume renderings of the temperature field at the optimal rotation rate for simulations with $Pr = 4.38$ at (a) $Ra = 10^8$ and (b) $Ra = 2.3 \times 10^9$. The colormap in both panels is identical. The figure shows that the flow structure at the optimal rotation rate is very different in the low and high Ra regime.

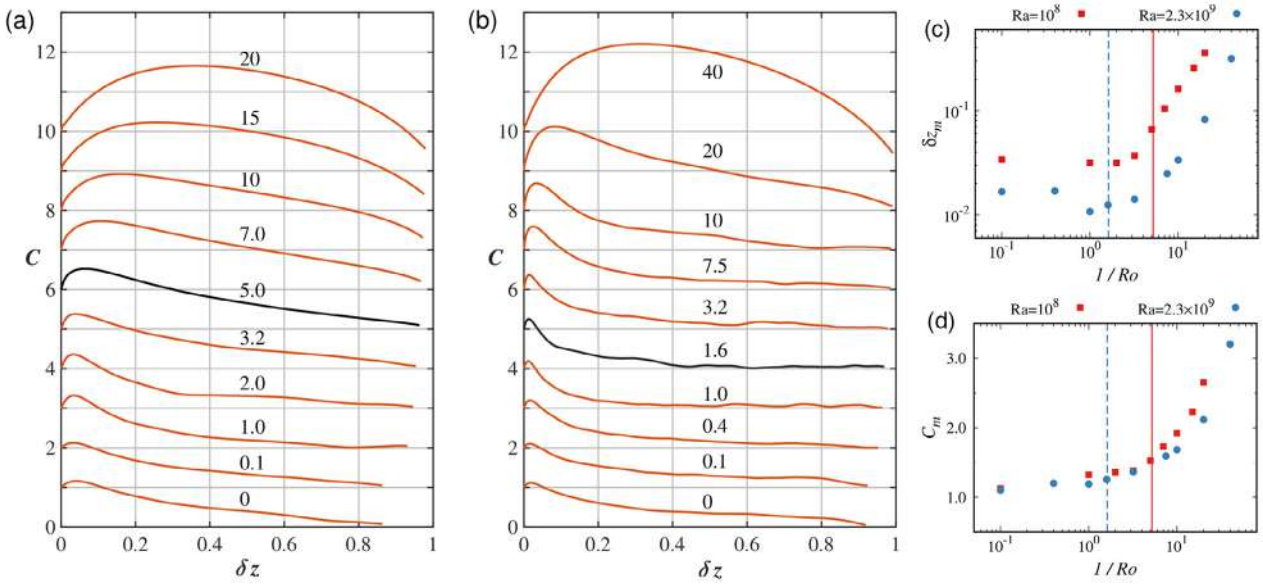

Figure 2: Correlation C as function of δz for different rotation rates in periodic domains in the (a) low ($Ra = 10^8$ and $Pr = 4.38$) and the (b) high Ra regime ($Ra = 2.3 \times 10^9$ and $Pr = 4.38$). The numbers indicate the value of $1/Ro$. The lines for each successive $1/Ro$ are shifted upward by 1 for visibility. The black line indicates the optimal inverse Rossby number. The (c) location δz_m and (d) magnitude C_m for the peak of the correlation function $C(\delta z)$ versus $1/Ro$ for $Pr = 4.38$ and two different Ra in periodic domains. The optimal rotation rate for $Ra = 10^8$ and $Ra = 2.3 \times 10^9$ is indicated by the solid and dashed line, respectively.

References

[1] G. Ahlers, S. Grossmann, and D. Lohse, Heat transfer and large-scale dynamics in turbulent Rayleigh-Bénard convection. *Rev. Mod. Phys.* **81**: 503-537,2009.

[2] H.T. Rossby, A study of Bénard convection with and without rotation, *J. Fluid Mech.* **3**:309, 1969.

[3] J.-Q. Zhong, R. J. A. M. Stevens, H. J. H. Clercx, R. Verzicco, D. Lohse, and G. Ahlers, Prandtl-, Rayleigh-, and Rossby- number dependence of heat transport in turbulent rotating Rayleigh-Bénard convection, *Phys. Rev. Lett.* **102**: 044502, 2009.

[4] R. Ostilla-Monico, Y. Yang, E.P. van der Poel, D. Lohse, and R. Verzicco, A multiple-resolution strategy for Direct Numerical Simulation of scalar turbulence. *J. Comp. Phys.* **301**: 308-321, 2015.

CHARACTERIZING THREE-DIMENSIONAL FEATURES OF VORTEX SURFACES IN FLOWS PAST A PLATE

Wenwen Tong[1] and Yue Yang[*1]
[1]State Key Laboratory for Turbulence and Complex Systems, College of Engineering, Peking University, Beijing 100871, China

Summary We extend the vortex-surface field (VSF), a Lagrangian-based structure identification method, to investigate vortex dynamics in flows past a plate simulated by the immersed boundary method. For the flow past an impulsively started translating plate, we quantitatively distinguish two types of vortical structures and refer them to as the leading edge vortex (LEV) and the tip vortex (TIV). We demonstrate that the lift generated from the LEV is suppressed by the finite growth of TIVs. In the wake region, we quantify the geometry of helical vortex lines in TIVs and the contribution of the helical vorticity component to the streamwise vortical impulse. Furthermore, we characterize the evolution of ring-like vortex lines and two series of inclined and distorted vortex rings in the wake of a flapping plate.

INTRODUCTION

The high lift and efficiency in unsteady flight relies on the generation of coherent vortical structures with strong three-dimensional features, e.g., the leading edge vortex (LEV) and tip vortex (TIV). The flow past a finite plate is a useful model for understanding the relationship between the vortical structures and forces and further improving flow control techniques. The interaction of LEV and TIV plays an important role in unsteady flight of finite wings, and the development of LEV can be suppressed by TIV [1]. In order to characterize the continuous evolution of vortical structures, Yang and Pullin [2] developed the vortex-surface field (VSF), whose isosurface is a vortex surface consisting of vortex lines. In the present study, we extend the VSF method to the flow past a finite plate. Then we characterize three-dimensional features of vortex surfaces in the flow evolution. In particular, we distinguish the LEV and TIV by introducing a mathematical definition of their boundary. Then we quantify the competition between LEV and TIV and the helical development of TIV tubes in the wakes.

NUMERICAL CONSTRUCTION OF VSFS

The immersed boundary method with the discrete stream function [3] is used to solve Navier-Stokes equations to get the velocity-vorticity field. The immersed boundary is represented by Lagrangian markers and the Lagrangian force is exerted on the immersed boundary to satisfy the no-slip condition. The calculation of VSFs is implemented as a post-processing step based on a times series of velocity-vorticity fields. We extend the VSF, which was only applied to flows with simple boundary conditions, to the immersed boundary condition which can have complex geometries. Since the plate is a vortex surface with all the vortex lines attached on its surface, thus we enforce the Dirichlet boundary condition for VSF on the plate by adding a source term to the VSF evolution equation. The two-time method [4] is used for calculating a Lagrangian-like temporal evolution of VSFs.

Using the numerical VSF solution, we characterize the temporal evolution of VSF isosurface for the flow past a translating plate (see Fig. 1). Based on the morphology of vortex surfaces and lines, we divide the VSF evolution into three-stages: (1) streamwise stretching of vortex lines on the plate; (2) rolling up of near-wall vortex surfaces; (3) formation of the hairpin-like vortex and helical vortex tubes.

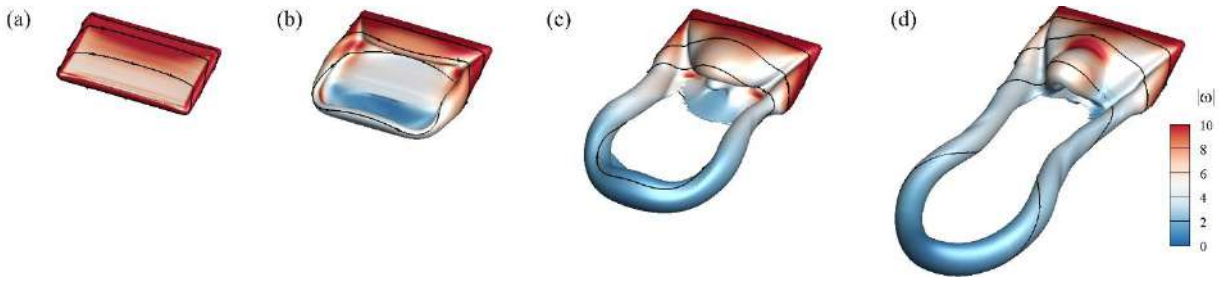

Figure 1. VSF isosurface color-coded by the vorticity magnitude at (a) $t = 0.1$, (b) $t = 1.0$, (c) $t = 3.0$, and (d) $t = 5.0$.

THREE-DIMENSIONAL FEATURES OF VORTEX SURFACES

The flow past a translating plate has two distinct three-dimensional features. Around the tip region, the LEV and TIV compete with each other. We distinguish LEV and TIV by mathematically defining the boundary of LEV based on $\omega_x = 0$ on the VSF isosurface in Fig. 2(a). Then we quantify the streamwise development of LEV and the competition between

*Corresponding author. E-mail: yyg@pku.edu.cn

LEV and TIV in Fig. 2(b), indicating that the LEV is suppressed by the finite growth of TIVs. In the wake region, the helical vortex lines evolve with time and form helical TIV tubes at a late time in Fig. 2(c). We apply a helical vortex model to characterize the development of the helical TIV, and we quantify that the helical vorticity component dominates the streamwise vortical impulse and further influences the drag force.

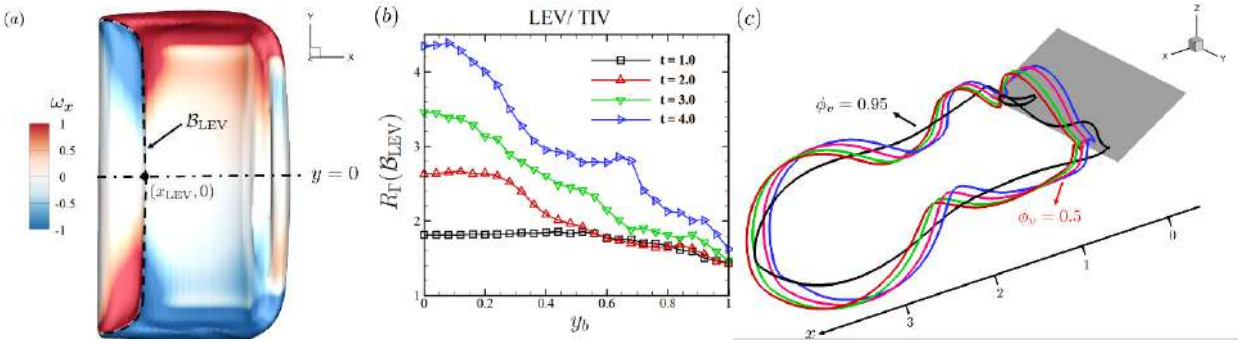

Figure 2. (a) The sketch of boundary of LEV at $t = 0.4$. (b) Relative intensity of LEV and TIV through the boundary of LEV. (c) Visualization of helical vortex lines on VSF isosurfaces at $t = 4.0$.

For the flow past a low-aspect-ratio flapping plate [5], the vortex surfaces with more complex geometry and topology are generated in the wake (see Fig. 3). Two ring-like vortical structures form in each flapping cycle T, and the wake is dominated by two series of distorted vortex rings. The shedding vortex surfaces roll up into vortex rings in further downstream, and generates jets with a pair of oblique rod-like structures. The vortical impulse is generated by inclined vortex rings, and it contributes to the thrust on the flapping plate.

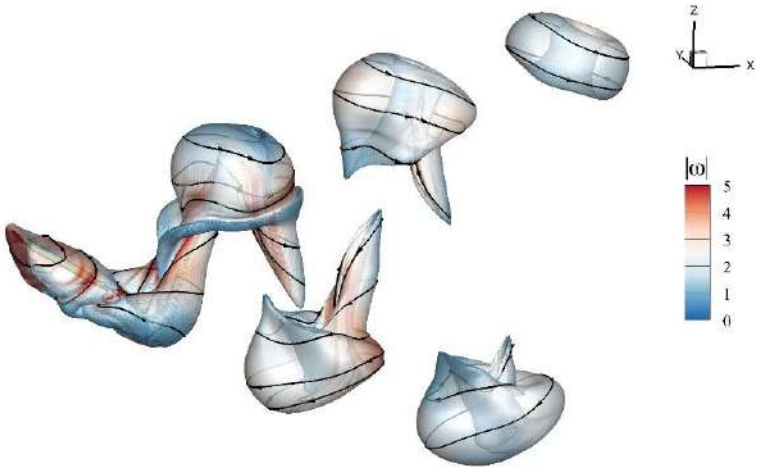

Figure 3. VSF isosurface at $t = 3T$ for the flow past a flapping plate.

CONCLUSIONS

We investigate the evolution of the VSF in the three-dimensional flow past a finite plate. The two-time VSF method is extended to the immersed boundary by adding a source term in the VSF evolution equation, and then the three-dimensional features of vortex surfaces can be characterized by numerical VSF solution. For the impulsively started translating plate, the VSF evolution can be roughly divided into three stages. We quantify the competition between the LEV and TIV, elucidating that the development of the LEV near tips is suppressed by the finite growth of the TIV. In the wake region, we quantify the helical development of TIV and demonstrate that the helical vorticity dominates the drag force. For the flow past a flapping plate, we characterize the evolution of ring-like vortex lines and two series of inclined and distorted vortex rings in the wake region.

References

[1] Taira K., Colonius T. Three-dimensional flows around low-aspect-ratio flat-plate wings at low Reynolds numbers. *J. Fluid Mech.* **623**: 187-207, 2009.
[2] Yang Y., Pullin D. I. On Lagrangian and vortex-surface fields for flows with Taylor-Green and Kida-Pelz initial conditions. *J. Fluid Mech.* **661**: 446-481, 2010.
[3] Wang S., Zhang X. An immersed boundary method based on discrete stream function formulation for two- and three-dimensional incompressible flows. *J. Comput. Phys.* **230**: 3479-3499, 2011.
[4] Yang Y., Pullin D. I. Evolution of vortex-surface fields in viscous Taylor-Green and Kida-Pelz flows. *J. Fluid Mech.* **685**: 146-164, 2011.
[5] Dong H., Mittal R., Najjar F. M. Wake topology and hydrodynamic performance of low-aspect-ratio flapping foils. *J. Fluid Mech.* **566**: 309-343, 2006.

EVOLUTION OF A VORTEX IN A STRATIFIED-ROTATING SHEAR FLOW

Iman Toghraei*[1] and Paul Billant[1]
[1]LadHyX, CNRS, Ecole Polytechnique, F-91128 Palaiseau CEDEX, France

Summary The dynamics of a vertical vortex subjected to an ambient shear flow has been studied numerically in a stratified-rotating fluid. Two distinct behavior have been observed depending on the Rossby number Ro, Froude number F_h and non-dimensional wavenumber K_z^* of the shear flow. When $K_z^* F_h \ll Ro$, the vortex is torn apart by the shear flow while in the opposite case, it resists to the shear flow and remains coherent. This result is explained thanks to the quasi-geostrophic scaling.

INTRODUCTION

Tropical cyclones such as the Hurricane Katrina (Figure 1) are the most deadliest vortices in nature. Their development can be prevented by the presence of a large ambient vertically sheared flow [2, 3]. This sensitivity to a shear flow has been reported to depend on the latitude [4]: cyclones at high latitudes (i.e. with higher Coriolis parameters) being less sensitive. In order to better understand these effects, we have investigated the dynamics of a single vortex in a sinusoidal shear flow as a function of the background rotation and the stratification.

Figure 1: Hurricane Katrina at peak intensity in the Gulf of Mexico [1]

NUMERICAL METHOD

The Navier-Stokes equations under the Boussinesq approximation has been simulated with a pseudo-spectral code (NS3D) in a rectangular box. The vortex is initially columnar with a Lamb-Oseen profile with vorticity $\omega_z = \Gamma/(\pi a_0^2)\exp(-r^2/a_0^2)$, where Γ is the circulation and a_0 the radius of the vortex. The shear flow has the profile $\boldsymbol{U} = U_s \sin(K_z z)\boldsymbol{e_x}$ where U_s is the shear flow amplitude and K_z is the vertical wavenumber (Figure 2). The height of the box l_z is set so as to simulate a single wavelength $K_z = 2\pi/l_z$ [5]. A buoyancy field is also associated to the shear flow due to the thermal wind balance.

The control parameters are the Rossby Ro, Froude F_h and Reynolds Re numbers, the rescaled vertical number K_z^* and shear flow amplitude:

$$Ro = \frac{\Gamma}{4\pi a_0^2 \Omega_b}, \quad F_h = \frac{\Gamma}{2\pi a_0^2 N}, \quad Re = \frac{\Gamma}{2\pi\nu}, \quad K_z^* = K_z a_0, \quad U_s^* = U_s \frac{2\pi a_0^2}{\Gamma}, \tag{1}$$

where Ω_b is the background rotation rate, N the Brunt-Väisälä frequency and ν the viscosity. The Schmidt number $Sc = \nu/\kappa$ is set to unity.

RESULTS

Figure 2 shows the evolution of the potential vorticity $\Pi = (\boldsymbol{w} + 2\Omega_b \boldsymbol{e_z}).\boldsymbol{\nabla} b_t$ in a strongly stratified fluid ($F_h = 0.5$) for weak rotation, $Ro = 5$, (top row) and strong rotation, $Ro = 1.67$, (bottom row). In the first case, the vortex is advected and completely torn apart by the shear flow. However, it's not only displaced in the direction of the shear flow but also in the perpendicular direction due to the self induction of the vortex. In contrast, when the rotation is higher $Ro = 1.67$, the vortex is not largely deformed by the shear flow but resists to it. Its bending deformation executes a rotation in the same direction as in the vortex core as reported previously [2]. Hence, the vortex displacement can be at some instant in the opposite direction of the shear flow.

The behaviour observed in several simulations for different parameters K_z^*, F_h and Ro are summarized in the parameter space $(K_z^* F_h, Ro)$ in figure 3. Typically the vortex resists to the shear flow (white circles) when $Ro \lessapprox K_z^* F_h$ and is torn apart otherwise (red circles). This result can be understand qualitatively by comparing the wavelength of the shear flow l_z to the quasi-geostrophic vertical length scale $a_0 F_h/Ro$. When $l_z \gg a_0 F_h/Ro$, i.e. $K_z^* F_h \ll Ro$, three-dimensional effects are weak and the vortex is not able to resist against the shear flow. On the other hand, when $Ro \ll K_z^* F_h$, three-dimensional effects are strong and keep the vortex coherent despite the effect of the shear flow.

The effects of the other parameters, (Re, U_s^*), the evolution of the minimum Richardson number as well as the evolution of the energy and enstrophy of the vortex have been also investigated.

*Corresponding author. E-mail: iman.toghraei@ladhyx.polytechnique.fr

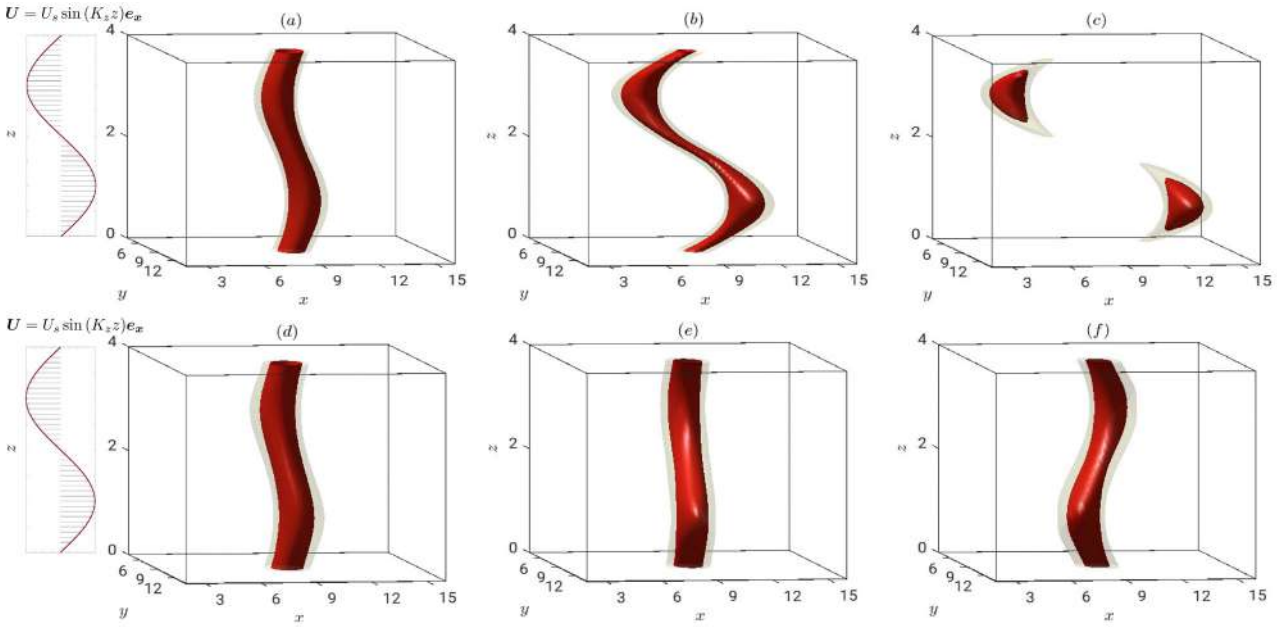

Figure 2: Evolution of the potential vorticity for $Re = 1000$, $K_z^* = \pi/2$, $F_h = 0.5$, $U_s^* = 0.2$ and $Ro = 5$ (top row) and $Ro = 1.67$ (bottom row) at $t = 5$ (a,d), $t = 20$ (b,e) and $t = 35$ (c,f)

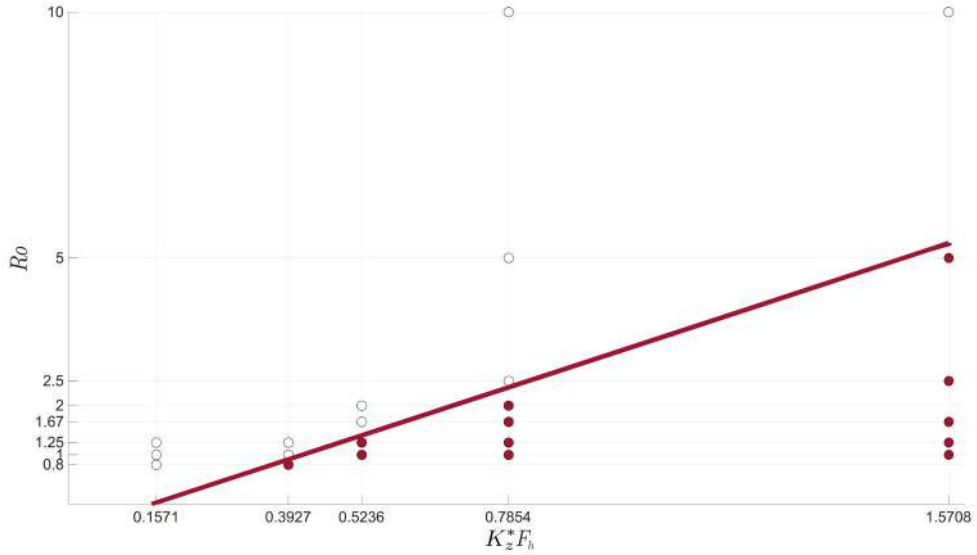

Figure 3: Summary of the simulations for $Re = 1000$ and $U_s^* = 0.2$ as a function of the rescaled wavenumber of the shear flow $K_z^* F_h$ and the Rossby number Ro. White circles indicate the simulations where the vortex is torn apart into two separated parts while the grey circles represent the simulations where the vortex remains coherent.

CONCLUSIONS

The evolution of a vortex in a stratified-rotating sinusoidal shear flow has been studied. Two different regimes have been identified. When three-dimensional effects are weak, the vortex is advected and torn apart by the shear flow. When three-dimensional effects are strong, the vortex resists the shear flow but it's bending deformation executes a rotation in the same direction as the vortex core.

References

[1] Wikipedia contributors. Cyclone, web site **https://www.wikipedia.org/**.

[2] Jones S. C. The evolution of vortices in vertical shear. i: Initially barotropic vortices. *Quarterly Journal of the Royal Meteorological Society*, 121(524):821–851, 1995.

[3] Finocchio, P. M., Majumdar, S. J., Nolan, D. S., Iskandarani, M. Idealized tropical cyclone responses to the height and depth of environmental vertical wind shear. *Monthly Weather Review*, 144(6), 2155-2175, 2016.

[4] DeMaria M. The effect of vertical shear on tropical cyclone intensity change *Journal of the atmospheric sciences*, 53(14):2076–2088, 1996.

[5] Bonnici J. Vertical decorrelation of a vortex by an external shear flow in a strongly stratified fluid *PhD Thesis*, Université Paris-Saclay, April 2018.

ON THE STABILITY OF '2P' POINT VORTEX STREET EQUILIBRIA

Mark A. Stremler*
Department of Biomedical Engineering and Mechanics, Virginia Tech, Blacksburg, VA USA

Summary When a submerged bluff body oscillates transversely with respect to a uniform fluid flow at moderate Reynolds number, the wake structure that develops is most frequently of '2S' type or '2P' type. A useful reduced-order model of the wake consists of relative equilibrium configurations of $N = 2$ or $N = 4$ point vortices, respectively, in a singly-periodic strip. Th. von Kármán and others determined conditions for linear stability of '2S' point vortex streets with $N = 2$. We will discuss a linear stability analysis of '2P' point vortex street relative equilibria with $N = 4$.

BACKGROUND

Over a century ago [5, 6], von Kármán introduced his classic point vortex model of the flow pattern that appears frequently in the wake of a bluff body at moderate Reynolds number. This '2S' wake pattern (following the notation introduced in [11]) is formed when two single, counter-rotating vortices are shed alternately and periodically from a bluff body; an example is shown in Figure 1(a). The point vortex model of a general 2S street consists of two infinite parallel rows of oppositely-signed, periodically-spaced vortices or, equivalently, two oppositely-signed vortices in a singly-periodic domain of width h, as illustrated in Figure 1(b). The vortices move together as a relative equilibrium configuration for all values of the horizontal spacing a and vertical spacing b. The special case of the Bénard-Kármán vortex street corresponds to taking $a = h/2$, in which case the vortex motion is parallel to the rows.

A key aspect of von Kármán's analysis is the determination that the staggered configuration with $a = h/2$ is unstable to infinitesimal perturbations that preserve the energy and impulse of the system (to leading order) unless the vortex positions satisfy *von Kármán's criterion*, given by $\sinh(\pi b/h) = 1$, in which case the configuration is neutrally stable in the linearized analysis. The analysis has been extended to include obliquely translating 2S vortex street relative equilibria with $a \neq h/2$ [2, 7]. A linear stability analysis shows these configurations to be neutrally stable only when the vortex separations satisfy the *Dolaptschiew–Maue criterion*, $\sinh(\pi b/h) = \sin(\pi a/h)$; this criterion reduces to von Kármán's criterion when $a = h/2$.

It can be shown that instabilities with wavelength $2h$ are the most unstable [8]. Physically it can be argued that this is the most unstable mode because it is the mode of shortest extent that produces relative vortex motion. If this mode is not unstable to linear order, other modes of longer wavelength do not produce instability. Maue states [7]: "The proof is rather long and for a general understanding of the situation it is of secondary importance... The corresponding proof for the special case of von Kármán ... is indicated by Lamb."

'2P' POINT VORTEX STREET EQUILIBRIA

When a wake-producing body oscillates transversely with respect to the flow, more than two vortices may be generated per shedding cycle. The most common of these 'exotic' wakes is the '2P' wake [10], in which two pairs of vortices are shed per cycle; an example is shown in Figure 1(c). As a reduced-order model of the 2P-type wake, consider a system of $N = 4$ point vortices with positions $z_\alpha = x_\alpha + \mathrm{i}\, y_\alpha$ and circulations Γ_α in a singly-periodic strip of width L, as illustrated in Figure 1(d). In general, these vortices will move relative to one another, and there are sufficient degrees of freedom for the motion to be chaotic.

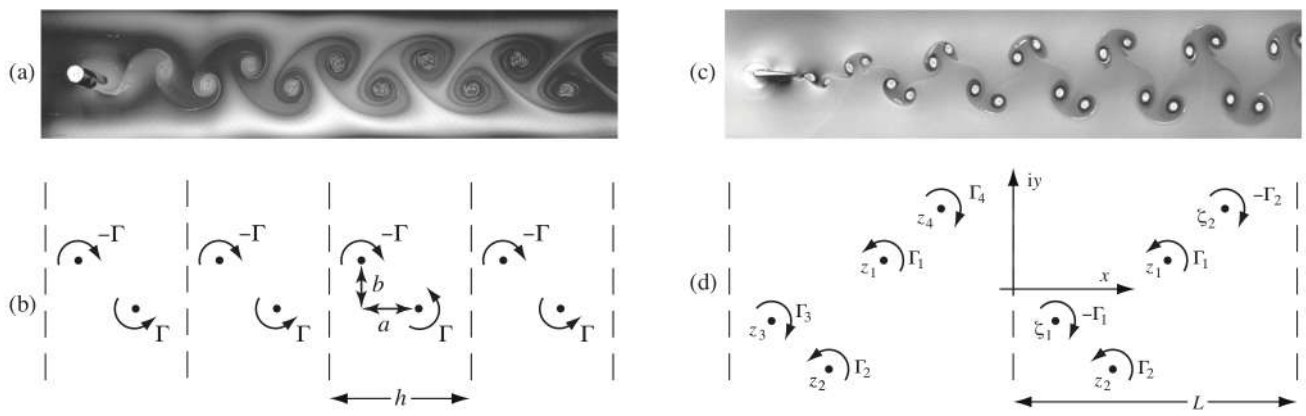

Figure 1: (a) 2S vortex wake behind a circular cylinder in a flowing soap film; photo by W. Yang (private communication). (b) A 2S point vortex street model. (c) 2P vortex wake behind a flapping foil in a flowing soap film, from [9]. (d) A 2P point vortex street model.

*E-mail: stremler@vt.edu.

Based on the shedding symmetries observed experimentally in 2P wakes, we assume that these $N = 4$ vortices are related via $\Gamma_3 = -\Gamma_1$ and $\Gamma_4 = -\Gamma_2$. As a further simplification, consider only those point vortex configurations that are moving in relative equilibrium, so that the inter-vortex spacing remains constant in time, analogous to the behavior of the classic 2S vortex streets. Finding these relative equilibrium configurations amounts to requiring that the translating velocity of each vortex be the same (complex) value V, giving the system of equations

$$V^* = \frac{1}{2Li} \sum_{\beta=1}^{N}{}' \Gamma_\beta \cot\left[\frac{\pi}{L}(z_\alpha - z_\beta)\right]. \tag{1}$$

Without any loss of generality, we assume $\Gamma_1, \Gamma_2 > 0$, and denote the locations of the negatively-signed vortices by $\zeta_1 \equiv z_3$ and $\zeta_2 \equiv z_4$. Under the vortex strength restriction $\Gamma_3 = -\Gamma_1, \Gamma_4 = -\Gamma_2$, the relative equilibrium configurations can be determined as a function of the parameters $\gamma = \Gamma_1/(\Gamma_1 + \Gamma_2)$, which is a dimensionless vortex strength, and

$$Z_0 = \tfrac{1}{2}(\Gamma_1 + \Gamma_2)\left[\gamma(z_1 - \zeta_1) + (1-\gamma)(z_2 - \zeta_2)\right], \tag{2}$$

which is proportional to the linear impulse for the vortex system. A few representative examples of relative equilibria for the special case $\mathrm{Im}(V) = 0$ are shown in Figure 2. Determination and characterization of exotic wake relative equilibria with $N = 4$ will be discussed.

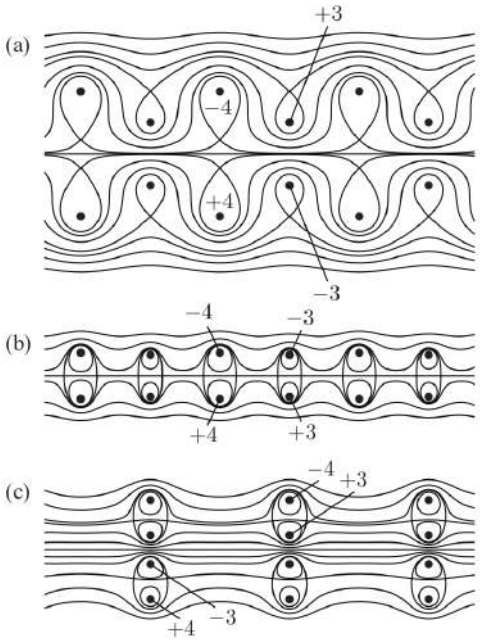

Figure 2: Example point vortex relative equilibria and representative streamlines in a co-moving frame for $N = 4$ and the parameters $\gamma = 3/7$ and $Z_0 = -1/2$. From [1].

STABILITY OF '2P' POINT VORTEX STREET EQUILIBRIA

The relevant stability analysis consists of (periodic, infinitesimal) perturbations in the (constant strength) point vortex locations from relative equilibrium states that preserve the energy and linear impulse of the system (to leading order). Based on the linear stability results for the 2S vortex streets, assume that the most unstable perturbations of the 2P vortex streets are those with the shortest wavelength that lead to relative vortex motion. For the 2P streets, superharmonic perturbations with wavelength L lead to relative motion, and thus it is these perturbations that form the basis of the linear stability analysis to be discussed.

Preserving the energy and linear impulse of the point vortex system under perturbation is a challenge that can be addressed in this case by adopting the 'Domm variables' [3] as used by Eckhardt & Aref [4] to analyze the motion of two vortex pairs in the plane, given here by Z_0 from (2), which is a constant of the motion, and

$$\hat{Z}_0 = \tfrac{1}{2}(z_1 + z_2 + \zeta_1 + \zeta_2), \quad Z_+ = \tfrac{1}{2}(z_1 - z_2 + \zeta_1 - \zeta_2), \quad Z_- = \tfrac{1}{2}(\Gamma_1 + \Gamma_2)\left[\gamma(z_1 - \zeta_1) - (1-\gamma)(z_2 - \zeta_2)\right]. \tag{3}$$

The vortex separations are independent of $\hat{Z}_0$, and as a result the system can be described by a Hamiltonian function $\mathcal{H}(Z_+, Z_-; Z_0)$ with equations of motion given by $\mathrm{d}Z_+^*/\mathrm{d}t = \mathrm{i}\,\partial\mathcal{H}/\partial Z_-$ and $\mathrm{d}Z_-^*/\mathrm{d}t = \mathrm{i}\,\partial\mathcal{H}/\partial Z_+$.

In the Domm system, the desired perturbations are achieved by holding Z_0 fixed while perturbing the Domm variables as $Z_+ + z_+$ and $Z_- + z_-$. Solutions of the resulting equations of motion for the (infinitesimal) perturbations z_+ and z_- show, to leading order, that there exist (neutrally) stable relative equilibrium configurations for the 2P vortex street, similar to the classic results for the von Kármán street. This linear stability analysis will be presented and discussed.

References

[1] Basu, S., Stremler, M. A. Exploring the dynamics of '2P' wakes with reflective symmetry using point vortices. *Journal of Fluid Mechanics* **831**: 72–100, 2017.
[2] Dolaptschiew, B. Störungsbewegungen (Bahnen) der einzelnen Wirbel der Kármánschen Wirbelstraße. *Z. Angew. Math. Mech. (ZAMM)* **18**: 263–271, 1938.
[3] Domm, U. Über die Wirbelstraßen von geringster Instabilität. *Z. Angew. Math. Mech. (ZAMM)* **36**: 367–371, 1956.
[4] Eckhardt, B., Aref, H. Integrable and chaotic motions of four vortices II. Collision dynamics of vortex pairs. *Philosophical Transactions of the Royal Society of London A* **326**(1593): 655–696, 1988.
[5] von Kármán, T. Über den Mechanismus des Widerstandes, den ein bewegter Körper in einer Flüssigkeit erfährt. 1. Teil. *Nachr. Ges. Wiss. Göttingen. Math.-Phys. Kl.* **1911**(5): 509–517, 1911.
[6] von Kármán, T. Über den Mechanismus des Widerstandes, den ein bewegter Körper in einer Flüssigkeit erfährt. 2. Teil. *Nachr. Ges. Wiss. Göttingen. Math.-Phys. Kl.* **1912**: 547–556, 1912.
[7] Maue, A. W. Zur Stabilität der Kármánschen Wirbelstrasse. *Z. Angew. Math. Mech. (ZAMM)* **20**(3): 129–137, 1940.
[8] Saffman, P.G. Vortex Dynamics. Cambridge University Press, 1992.
[9] Schnipper, T., Andersen, A., Bohr, T. Vortex wakes of a flapping foil. *Journal of Fluid Mechanics* **633**: 411–423, 2009.
[10] Williamson, C. H. K., Govardhan, R. Vortex-induced vibrations. *Annual Review of Fluid Mechanics* **36**: 413–455, 2004.
[11] Williamson C. H. K., Roshko A. Vortex formation in the wake of an oscillating cylinder. *J. Fluids Struct.* **2**: 355–381, 1988.

NUMERICAL INVESTIGATION OF THE STABILITY OF A LAMB-OSEEN VORTEX IN TWO-WAY COUPLED PARTICLE-LADEN FLOWS

Shuai Shuai[1] and M. Houssem Kasbaoui[1]
[1]School for Engineering of Matter, Transport and Energy, Arizona State University, Arizona, U.S.A

Summary This paper investigates the stability properties of the particle-laden Lamb-Oseen vortex. We conduct DNS simulation of the two-phase flow in the Eulerian-Lagrangian framework. Unlike the single-phase case where the Lamb-Oseen vortex is hydrodynamically stable to small perturbations, the presence of inertial particles leads to the emergence of an instability characterized by a concentration wave that expands radially from the core of the vortex. We examine how the interaction between inward fluid motion and outward particle ejection by the preferential concentration mechanism modifies the stability of the two-phase vortex.

INTRODUCTION

The swirling motion of a vortex is most often modeled using the Lamb-Oseen profile, a full solution to the Navier-Stokes equations. In a single-phase flow, a constant density Lamb-Oseen vortex is hydrodynamically stable [1]. This remarkable property explains why vortex tubes shed by an aircraft remain stable for long times.

When inertial particles are dispersed, the stability properties of the flow may be altered. Owing to the preferential concentration mechanism, inertial particles tend to accumulate in regions of low vorticity and high strain rate [2]. When dispersed in a vortex, such particles are ejected from the vortical core resulting in an outward momentum transport. The relative motion of particles and fluid leads to a configuration that could be subject to a Rayleigh-Taylor instability.

In this study, several 2D simulations are conducted to investigate the behavior and characteristics of the particle-laden Lamb-Oseen vortex flow. We show from numerical simulations that an instability exists when the full coupling between the two phases is considered. If the particle-feedback is neglected, the Lamb-Oseen vortex remains stable.

PHYSICAL MODEL

Vortex tubes can be represented using the Lamb-Oseen profile given by

$$\boldsymbol{u}_f(r,\theta) = \frac{\Gamma}{2\pi r}\left(1-\exp(-\frac{r^2}{r_c^2})\right)\boldsymbol{e}_\theta \tag{1}$$

where $\boldsymbol{e}_\theta$ represents the azimuthal direction, Γ is the vortex circulation and r_c is the vortex core radius. As demonstrated in [1], a two-dimensional Lamb-Oseen vortex is stable to small perturbations. However, little is known about the stability properties of the flow when inertial particles are present.

We explore the stability of the particle-laden Lamb-Oseen vortex with Eulerian-Lagrangian numerical simulations. In this framework, the governing equations for the fluid and the "i"-th Lagrangian particle are

$$\frac{\partial}{\partial t}\left(\rho_f(1-\phi)\right) + \nabla\cdot\left((1-\phi)\rho_f\boldsymbol{u}_f\right) = 0 \tag{2}$$

$$\frac{\partial}{\partial t}\left((1-\phi)\rho_f\boldsymbol{u}_f\right) + \nabla\cdot\left((1-\phi)\rho_f\boldsymbol{u}_f\boldsymbol{u}_f\right) = \nabla p + \mu_f\nabla^2\boldsymbol{u}_f + \boldsymbol{F}_p \tag{3}$$

$$\frac{d\boldsymbol{x}_p^i}{dt} = \boldsymbol{u}_p^i; \quad \frac{d\boldsymbol{u}_p^i}{dt} = f_D\frac{(\boldsymbol{u}_f-\boldsymbol{u}_p^i)}{\tau_p} \tag{4}$$

where ϕ is the particle volume fraction, $\boldsymbol{F}_p$ is the interphase momentum exchange term due to the force exerted by particles on fluid, f_D is the drag correction term. In the semi-dilute regime considered here, the remaining fluid-particle and particle-particle forces can be neglected.

The dynamics of Lamb-Oseen vortex in the semi-dilute regime are determined by 4 non-dimensional numbers. The Reynolds number based on the vortex circulation is defined as $\mathrm{Re}_\Gamma = \Gamma/2\pi\nu_f$ and determines the strength of the vortex swirl velocity. The Stokes number determines the particle inertia and is given by $\mathrm{St} = \rho_p\Gamma d_p^2/36\pi\mu_f r_c^2$. The coupling between the two phases is determined by the mass loading $M = \langle\phi\rangle\rho_p/\rho_f$, where $\langle\phi\rangle$ is the mean volume fraction. A measure of the discrete Lagrangian effects is given by the ratio of the vortex core radius and particle diameter. Simulations where the particle feedback force on the fluid is considered are identified as two-way coupling simulations, otherwise the simulations are labeled as one-way coupling. A summary of runs and parameters is given in Tab. 1. In all cases considered, $0.2 \leq \mathrm{St} \leq 1$ and $M = 1$ corresponding to significant particle inertia and strong interphase coupling. Effects due to the discrete nature of Lagrangian particles are negligible owing to a large ratio $r_c/d_p \simeq 625$. The Reynolds and Stokes numbers are varied by adjusting the vortex circulation.

Table 1: Non-dimensional parameters considered in this study.

	Case 1	Case 2	Case 3	Case 4
Re_Γ	1×10^3	1×10^3	3×10^3	5×10^3
M	1	1	1	1
St	0.2	0.2	0.6	1
r_c/d_p	625	625	625	625
Coupling type	One–way	Two–way	Two–way	Two–way

NUMERICAL SETUP

The simulations are conducted in a square domain of size $60r_c \times 60r_c$ with a grid of size 1536×1536. The computational domain is split in four quadrants where four anti-symmetrical vortices with randomly distributed Lagrangian particles are initialized. This approach allows the use of straightforward periodic boundary conditions while providing simultaneously 4 realizations of the flow. The governing equations are solved with the Eulerian-Lagrangian strategy in the flow solver NGA [3].

RESULTS AND CONCLUSION

The Eulerian-Lagrangian simulations point towards the existence of an instability that damps the core vorticity when two-way coupling is considered. Snapshots in Fig. 1 show how particles migrate outwards due to the swirling flow. In case 1 (one-way coupling), a sharp volume fraction front forms and the vortex structure is unchanged. In case 2 (two-way coupling), the volume fraction front is disrupted by azimuthal modes due to the formation of particle clusters and void bubbles. The interphase coupling leads to an outward dispersion of vorticity.

(1a) (1b) (1c) (1d)

Figure 1: Particle volume fraction and vorticity magnitude at $t^* \approx 1$: (a,b): one-way coupling; (c,d): two-way coupling.

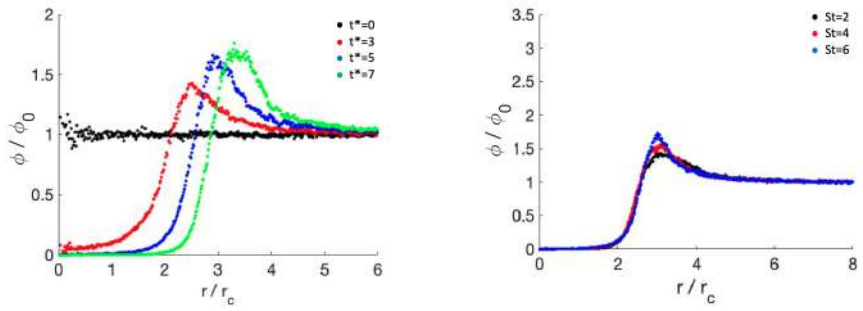

(2a) (2b)

Figure 2: Particle volume fraction profile: (a) case 2 at various non-dimensional times, (b) various St at $t^* = 5$.

Fig. 2a shows the radial evolution of the volume fraction front. Owing to the preferential concentration mechanism, particles are ejected from the vortex core leading to the outward transport of momentum and unstable coupling with the fluid. This process is controlled by a time scale $\tau_f = 2\pi r_c^2/(\Gamma \mathrm{St})$ as evidenced by the collapse of curves from all cases considered in Fig. 2b.

These preliminary simulations shed light on a novel instability that occurs in particle-laden vortex tubes. In future work, we will quantify the azimuthal mode that emerge and analyze the energy transfer between the two-phases.

References

[1] F. W. Warren. A comment on Gans' stability criterion for steady inviscid helical gas flows. *Journal of Fluid Mechanics*, 68(2):413–415, March 1975.

[2] Kyle D. Squires and John K. Eaton. Particle response and turbulence modification in isotropic turbulence. *Physics of Fluids A: Fluid Dynamics*, 2(7):1191–1203, July 1990.

[3] Jesse Capecelatro and Olivier Desjardins. An Euler–Lagrange strategy for simulating particle-laden flows. *Journal of Computational Physics*, 238:1–31, April 2013.

OBSERVATIONS OF VORTEX INSTABILITIES IN THE WAKES OF COAXIAL ROTORS

Mehmet Fatih Konus, and Ömer Savas,*
Department of Mechanical Engineering, University of California, Berkeley, CA 94720-1740 USA

Summary The stability characteristics of helical vortex filaments are studied experimentally in a water tank in the wakes of a coaxial rotor model, of 26-cm diameter at rotor separations of 0.25-1 radius and speeds of 2-8 rps. The vortices from the lower rotor experience extreme distortions. At small separations, lower rotor filaments develop longwave vortex pairing instabilities while upper rotor filaments do not have sufficient space to develop mutual interactions. At a separation of half radius, hairpin vortices form beneath the lower rotor during the development of the longwave instability. Shortwave instabilities form quickly along the helical filaments at 2 & 4 rps cases whereas at 6 & 8 rps filaments develop them long after their formation simultaneously with the longwave instability mode where filaments develop large distortions beneath the lower rotor.

INTRODUCTION

Rotorcraft trail helical vortex filaments, generating an unsteady three-dimensional wake structure [1], which create a nonuniform inflow distribution over the rotor disk and continue to affect this distribution as they move downstream [2]. The characteristics of this inflow is greatly affected by the geometry of the wake and the behavior of the vortices below the rotor. Presence of second rotor introduces more complexities into the flow field. Interactions among the helical filaments of the same rotor and the different rotors as well as interactions of helical filaments from one rotor with the blades of the other rotor largely affect the stability and wake characteristics of coaxial rotor filaments. Even though the stability characteristics of two parallel vortex filaments are well studied [3], those of helices, however, have not been explored to same degree since the pioneering work Widnall [4]. Effect of coaxial rotor parameters, rotor spacing and rotor speed, on the stability and wake characteristics of the helical filaments is investigated through flow visualization and PIV measurements, an extension of the work on a single rotor by Ohanian *et al.* [5].

APPARATUS

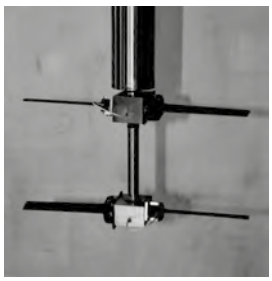

Figure 1: Coaxial rotors at separation $H/R = 1$.

Figure 1 shows the coaxial rotor model consisting of two $2R = 26$-cm diameter counter-rotating two-bladed rotors with a root cut-out of 3.2 cm, which are driven by a microstepper motor though a gearbox. The rotor separation H is set by using shaft extensions, H/R ranging from 0.25 to 1. The untapered blades, twisted 5°, are molded from carbon fiber reinforced plastic with length of $l = 9.5$ cm and chord of $c = 1.9$ cm, hence of solidity of $\sigma = 2cl/\pi R^2$ for a single rotor and $2\sigma = 0.136$ when in the coaxial configuration. The cores of the blade-tip vortices are rendered visible by injecting dye into the flow from the blade tips through tubes embedded in the blades. The collective angle is set to $\theta = 13.5°$. The experiments are done in a 1.2 m wide, 2.4 m long, and 1.2 m deep water tank.

GENERAL VORTEX WAKE CHARACTERISTICS

Figure 2 shows a sample flow at $H/R = 0.41$ and 6 rps. The first frame is an instantaneous picture of the wake where the filaments off the tips can be traced. The helices off the upper rotor maintain their helical form until the interact with lower rotor. The vortices off the lower rotor start out nearly helically, but soon, along with those off the upper rotor, undergo severe distortions. The second frame is the time average of the images over 25 revolutions of the rotors. The radius of the wake of the upper rotor contracts to about $0.75R$ by the time it reaches the lower rotor while the initial contraction of the wake of the lower rotor is to about $0.90R$. Further downstream, the combined wake expands and becomes diffuse due to the interaction of the vortex filaments. The third frame is the phase averaged image at the rotor phase corresponding to the first frame. The phase averaged vortex positions are indistinguishable from the instantaneous ones in the first frame, with almost no dispersion, which indicates a nearly deterministic behavior of the vortex interactions in these flows, the long wave instabilities in particular.

Figure 2: An instantaneous image, time averaged image and phase averaged image (25 samples) at $H/R = 0.41$ and 6 rps.

*Corresponding author. E-mail: savas@berkeley.edu.

VORTEX INSTABILITIES

Longwave instabilities

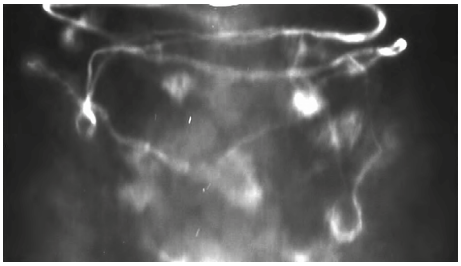

Figure 3: Two hairpins below the lower rotor. $H/R = 0.5$ at 8 rps.

In the longwave instability mode, which is also referred to as leapfrogging process, two adjacent vortices trailed from the blade tips of the lower rotor start to orbit around each other as they travel together in the streamwise direction. This is when these vortices start to develop unusual deformations as the turns of the trailing vortex leapfrog through the turns of the leading vortex. The contribution from the vortices trailed from the upper rotor affect the behavior of the lower vortices significantly, resulting in extreme deformation of the latter. The lower vortices get stretched in the streamwise direction and at certain rotor spacings they deform to into hairpin vortices, losing their orderly helical shapes. The most notable example of this kind of vortex structure formation is observed at rotor spacing of $H/R = 0.5$, an example of which is shown in Figure 3 where two hairpin vortices are visible on either side of the figure. Regardless of the rotor separation, the lower rotor continually operates in the wake of the upper rotor, resulting in mutual interactions between the vortices trailed from both rotor. Also, as the upper rotor filaments pass through the plane of the lower rotor, they interact with the lower rotor blades, which, in turn, cause them to become diffuse and make their subsequent trajectories hard to follow.

Shortwave instabilities

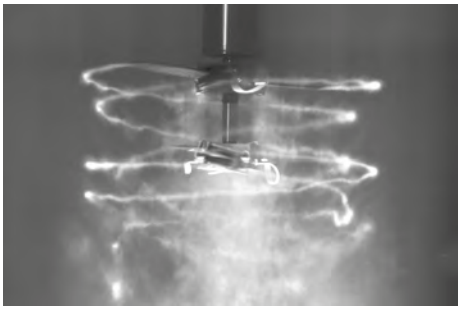

Figure 4: Shortwaves.$H/R = 0.5$ at 4 rps.

At rotor speeds of 2 & 4 rps, shortwave instabilities develop along all filaments. At 6 & 8 rps, however, filaments exhibit shortwave instability characteristics long after their generation and only locally, which become superimposed with the dominant longwave instability mode in the downstream locations of the wake (Figure 4). Figure 5 shows the shortwave instability wavelength λ/R against the vortex age ψ, which are extracted from flow images. The average wavelength in the wake of the upper rotor is $\lambda/R = 0.21 \mp .05$ and $0.25 \mp .08$ in the wake of the lower one. The wavelength data suggest that there is not a particular pattern for shortwave instability wavelengths at a particular rotor, rotor separation or speed, even though the average wavelengths along the upper rotor filaments is slightly lower than those along the lower rotor filaments. Although the wavelength data do not suggest a clear distinction between the upper and the lower rotor filaments, it is clear from the flow visualization images that the amplitude of the short waves along the lower rotor filaments grow in amplitude more rapidly than those along the upper rotor filaments.

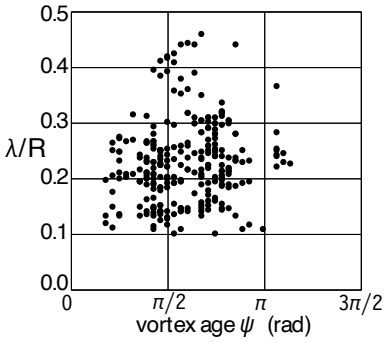

Figure 5: Consolidated shortwave instability wavelengths.

CONCLUSIONS

The tip vortices trailed from the lower rotor experience extreme distortions. At smaller rotor spacings $H/R < 0.5$, lower rotor filaments develop longwave vortex pairing instabilities along with extreme distortions. At $H/R = 1$, the upper rotor filaments develop longwave pairing instabilities similar to a single rotor, whereas those from lower rotor become unstable within first rotor revolution. At $H/R = 0.5$, hairpin vortices form beneath the lower rotor during the longwave instability mode developed by the lower rotor filaments. Similar deformations of the vortex filaments are observed at all rotor spacings. However, the clearest hairpin vortex structures are seen at the rotor spacing of $0.5R$. Regardless of the rotor spacing, shortwave instabilities formed along the helical filaments at 2 & 4 rps cases from their generation whereas at 6 & 8 rps filaments are only observed to develop these types of instabilities long after their formation and not as clearly as those observed in the wake of a single rotor [5], as they become superimposed with longwave instability mode.

References

[1] Conlisk, A. T., Modern helicopter aerodynamics, Annual Review of Fluid Mechanics, **29**:515-567, 1997.
[2] Leishman, J. G., Principles of Helicopter Aerodynamics, Cambridge University Press, New York, NY, 2006, pp. 257-260.
[3] Leweke, T., Le Dizès, S., Williamson, C. H. K. Dynamics and instabilities of vortex pairs. Annual Review of Fluid Mechanics, **48**:507-541, 2016.
[4] Widnall, S. E. The stability of a helical vortex filament. *J. Fluid Mech.* **54**: 641-663, 1972.
[5] Ohanian, C. V., McCauley, G. J., Savaş, Ö. A visual study of vortex instabilities in the wake of a rotor in hover. *J*AHS. **57**, 1-8, 2012.

TRANSIENT BEHAVIOR IN SPIN-UP OF THERMAL CONVECTION

Daisuke Noto*[1], Yuji Tasaka[1], Takatoshi Yanagisawa[2,1], Takehiro Miyagoshi[2], and Yuichi Murai[1]
[1]Laboratory for Flow Control, Hokkaido University, Sapporo, Japan
[2]Japan Agency for Marine-Earth Science and Technology (JAMSTEC), Yokosuka, Japan

Summary Transient behavior in spinning-up of Rayleigh–Bénard convection (RBC) was experimentally investigated by giving an impulsive rotation to non-rotating RBC. For comprehensive understanding of the transient flow structures, the thermochromic liquid crystal particles were seeded into test water, and velocity and temperature fields were quantified. Thermal turbulent structures were blown away due to the impulsive rotation, and subsequently the concentric roll structures emerged from side walls to center of the fluid containers. Depending on the thermal and rotational force intensity, the roll structures were found to take two different states, spiral and ring structures. In both cases, the rolls collapsed into azimuthally aligned vortices along the roll boundaries. The size of the vortices emerged at the time is equivalent to that of the columnar vortices formed in equilibrium rotating RBC.

INTRODUCTION

Rotating thermal convection

Rayleigh–Bénard convection (RBC) in a rotating field has attracted many researchers in various research fields, e.g. fluid physics, geo-/astrophysics, and so on. Rotating RBC can be mainly characterized by two nondimensional parameters; Rayleigh number expresses the thermal force intensity as $Ra = g\beta\Delta T H^3/(\nu\kappa)$, where g, β, ΔT, H, ν, and κ are the gravity acceleration, the thermal expansion coefficient, the vertical temperature difference, the vertical gap between top and bottom plates, the kinematic viscosity, and the thermal diffusivity. Taylor number indicates the Coriolis force intensity as $Ta = (2\omega H^2/\nu)^2$, where ω is the angular velocity of the system. It is well known that the flow structure in rotating RBC is governed by columnar vortices with tall and narrow structures stretched into the rotational axis when both the thermal and rotational forces possess equivalent intensity to each other. Past studies have revealed flow morphologies, heat transfer characteristics and its scaling laws in detail at fully developed, i.e. equilibrium states of rotating RBC.

Transient states during spin-up of thermal convection

On the other hand, some researchers focused on the transient states appeared during spinning-up of thermal convection, not the equilibrium states. Boubnov and Golitsyn [1] reported formation of concentric convection rolls which aligned from center to wall inside a open cylindrical fluid container heated from the bottom. Vorobieff and Ecke [2] investigated quantitatively the flow structures during spinning-up of RBC (confined both top and bottom boundaries), and found that columnar vortices are formed by the Kelvin–Helmholtz (KH) instability. Zhong et al. [3] conducted a similar experiment in an open rectangle cavity only cooled by the air and reported the same transient phenomena; formation of concentric roll structures and columnar vortex formation due to KH instability. What they have in common is the formation of ring shaped convective roll structures regardless of the container geometry and the initiation order of convection or rotation. Although these experimental works explained these phenomena qualitatively and quantitatively in their intrinsic conditions, a comprehensive understanding of all the transient phenomena is still missing and valuable to be investigated.

EXPERIMENTAL INVESTIGATIONS ON SPIN-UP OF THERMAL CONVECTION

We conducted visualization experiments in two different radii cylinders with the same height (aspect ratio $\Gamma = 2.00$ and 4.75) confined with degassed water ($Pr \sim 7$). For visualization, thermochromic liquid crystal (TLC) particles were seeded into the test fluid, and a horizontal cross-section at the mid-height was illuminated by a white light sheet. TLC particles scatters specific coloration corresponding to the temperature, and its motion can be utilized for the velocity measurement. Two Rayleigh number $Ra = 2.0 \times 10^6$ and 1.0×10^7 with 5 different Taylor values $3.0 \times 10^6 \leq Ta \leq 2.0 \times 10^8$ are explored for both cylinders, and 20 parameters are compared in total. By giving an impulsive rotation to a fully developed non-rotating RBC at the specific Ra, transient states were observed until the equilibrium states of rotating RBC were realized.

Formation of concentric convective rolls

Soon after the initiation of the impulsive rotation, the thermal turbulent structures were blown away due to intense rotation, and concentric roll structures are formed as shown in Fig. 1(a) and (b). We found that two types of roll structures can be formed; spiral and ring, and they are easy to be distinguished to each other from the coloration of the visualized images. Types of roll structures of all the explored parameters are summarized in Fig. 1(c) as a regime diagram in Ra-Ta domain. The diagram clearly shows Ta and Γ dependence of the roll type, i.e. faster rotation and smaller cylinder tends to form ring-type rolls. Interestingly, two types of rolls can be roughly divided by the convective Rossby number at $Ro = \sqrt{Ra/(Pr\,Ta)} = 0.1$. Also, considering the fact that larger Γ was hard to form rings, the relatively stronger centrifugal force than the thermal force must have influenced the types of the roll formation.

*Corresponding author. E-mail: noto@ring-me.eng.hokudai.ac.jp.

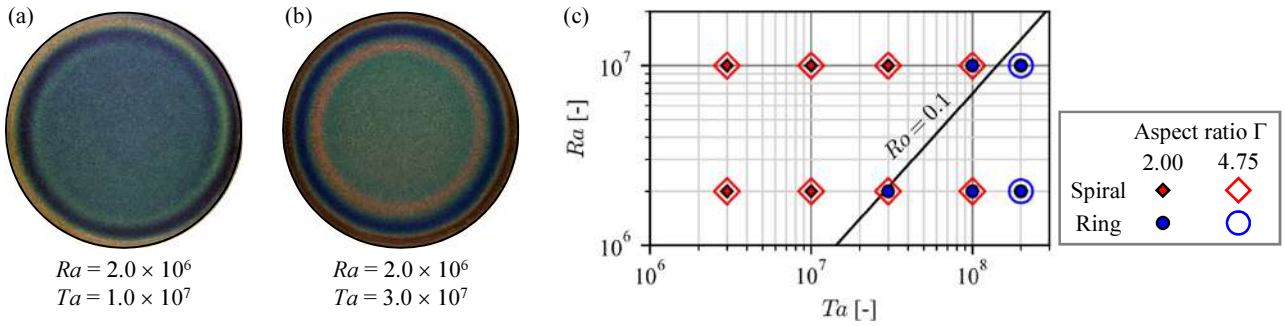

Figure 1: Two types of concentric roll structures visualized by TLC particles in the same cylinder ($\Gamma = 2.00$): (a) spiral ($Ra = 2.0 \times 10^6$, $Ta = 1.0 \times 10^7$) and (b) ring ($Ra = 2.0 \times 10^6$, $Ta = 3.0 \times 10^7$), and (c) a regime diagram for roll formation types of all the explored parameters in Ra-Ta domain.

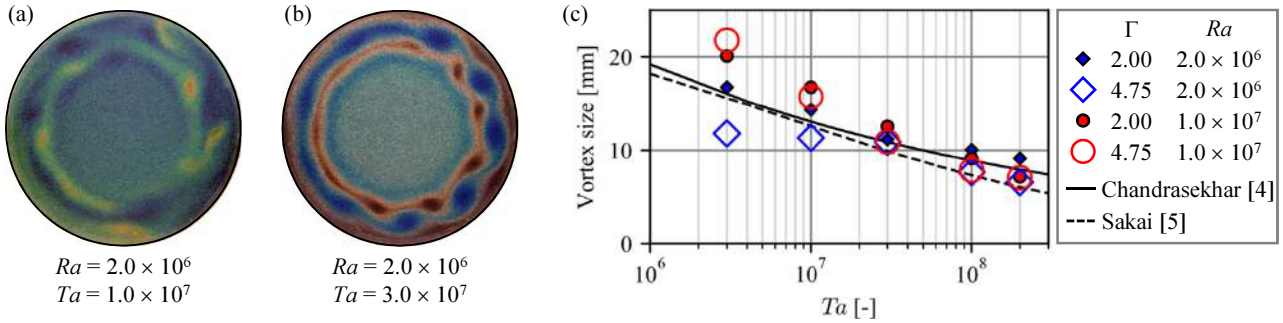

Figure 2: Formation of vortical structures along roll boundaries due to the KH instability ($\Gamma = 2.00$): (a) spiral ($Ra = 2.0 \times 10^6$, $Ta = 1.0 \times 10^7$) and (b) ring ($Ra = 2.0 \times 10^6$, $Ta = 3.0 \times 10^7$), and (c) horizontal size of vortical structures.

Emergence of azimuthally aligned vortices

After the formation of concentric roll structures, vortical structures emerged at roll boundaries as shown in Fig. 2(a) and (b). This is due to strong shear at the roll boundaries and KH instability is induced. The horizontal size of the vortices appeared at this moment is plotted in Fig. 2(c), which can be obtained using the tangential wavenumber and the radial positions of them. What should be pointed out here is that the horizontal vortex size during this transient state matches well with the cell size at the convection onset theoretically estimated by Chandrasekhar [4]. In addition, the columnar vortex size under the equilibrium state of rotating RBC estimated by Sakai [5] also shows good agreement with the present results. The columnar vortices under the equilibrium state are originated in the thermal plumes and their size are automatically determined to transport heat throughout the fluid container. And thus, the vortices formed by the KH instability and the columnar vortices in rotating RBC should have different formation mechanism.

CONCLUSIONS

Transient flow structures during spinning-up of Rayleigh–Bénard convection (RBC) were investigated experimentally. As former works showed previously, there are stepwise transitions from non-rotating RBC to rotating RBC; emergence of concentric roll structures and following formation of vortical structures. Two types of concentric roll structures were found: spiral and ring structures. Relatively weak centrifugal force to the thermal force tends to induce inperfection of ring roll formation. It is required to investigate the mechanism of spiral and ring roll formation more detail. Subsequently to the roll formation, azimuthally aligned vortical structures were formed along the roll boundaries due to the Kelvin–Helmholtz (KH) instability regardless of the type of the roll. The vortical structures possessed equivalent horizontal size to that of the columnar vortices formed under the equilibrium state of rotating RBC, even though the formation mechanism of them cannot be identical. The reason why the KH induced vortices and the columnar vortices possessed the same size is still an open issue and should be clarified.

References

[1] Boubnov B. M., Golitsyn G. S. Experimental study of convective structures in rotating fluids. *J. Fluid Mech.* **167**: 503-531, 1986.
[2] Vorobieff P., Ecke R. E. Transient states during spin-up of a Rayleigh–Bénard cell. *Phys. Fluids* **10**: 2525, 1998.
[3] Zhong J.-Q., Patterson M. D., Wettlaufer J. S. Streaks to Rings to Vortex Grids: Generic Patterns in Transient Convective Spin Up of an Evaporating Fluid. *Phys. Rev. Lett.* **105**: 044504, 2010.
[4] Chandrasekhar S. Hydrodynamic and Hydromagnetic Stability. *Oxford University Press* 1961.
[5] Sakai S. The horizontal scale of rotating convection in the geostrophic regime. *J. Fluid Mech.* **333**: 85-95, 1997.

VORTICAL STRUCTURE IN A HOMOGENEOUS ISOTROPIC TURBULENCE

Katsuyuki Nakayama[1]
[1]Department of Mechanical Engineering, Aichi Institute of Technology, Toyota, Japan

Summary Velocity structure of a vortex in a homogeneous isotropic turbulence is investigated including the vortical flow symmetry characteristic associated with the stability, pressure minimum and vortex stretching. The swirlity specifies the vortex center as its local maximum point, and the swirl plane and direction of the elliptic geometry of the vortical flow are given by the local geometry at the center. The statistical analysis shows that a vortex is not axisymmetric irrespective of the intensity of swirling. In the development of a vortex, its scale, vortical flow symmetry and pressure minimum codevelop. However, the vortex stretching component for the swirling is more intense in a weaker vortex. An intense vortex influences the turbulent flow more greatly, while the support of self-sustaining/reinforcing by the stretching become less.

INTRODUCTION

Vortices play important roles in a turbulent flow, and their dynamics change the turbulent features. The particular characteristics of vortices such as stability [1] or pressure minimum are derived from the velocity structure of the vortices. It has been shown that the statistical velocity structure of vortices in a homogeneous isotropic turbulence is similar to the Burgers vortex [2] that has axisymmetric velocity structure and can hold its structure as a steady state.

On the other hand, the several topological (geometrical) quantities have been defined in terms of the local flow given by the velocity gradient tensor $\nabla \boldsymbol{v}$, which enable to specify the precise flow geometry. The swirlity and sourcity specify the unidirectionality and intensity of the respective azimuthal and radial flows in a plane, i.e., swirl plane, and the vortical flow symmetry quantity identifies the skewness or elliptic shape of the vortical flow [3]. Specifically, it is noted that the vortical flow symmetry is an important quantity for pressure minimum characteristic and vortex stretching [4, 5]. These quantities have shown that, in the local geometry, vortices in the aforesaid turbulence are not axisymmetric [5].

The present study investigates the velocity structure of a vortex with a finite scale in a homogeneous isotropic turbulence with a low Reynolds number. In the statistical analysis, unifying the elliptic direction of vortical flow derives the precise vortical structure and characteristics. The analysis in different intensities of swirlity shows that vortical flow symmetry and scale of the vortex codevelop with the swirlity. On the other hand, effective vortex stretching to strengthen the swirling is more intense in the weak vortex. This is consistent with a vortex model of a vortex life in terms of the local flow where the more intense vortex has less benefit in the vortex stretching for swirling in this turbulence [5].

ANALYSIS AND DISCUSSION

Vortical structure is analyzed in a homogeneous isotropic decaying turbulence at the Taylor Reynolds number $Re_\lambda = 36$, where the pseudo-spectral method with the phase-shifting method is applied with the wavenumber $k < 121$ in the region $(2\pi)^3$ composed of 256^3 nodes [5]. The local maximum point of swirlity φ, as a center of a vortex, is identified using the spacial derivative and the Hessian (Hesse matrix) of φ at the node of the numerical analysis. The swirl plane Π is defined by the real and imaginary vectors of the complex conjugate eigenvectors of $\nabla \boldsymbol{v}$ [2].

Figures 1 and 2 show the velocity distributions $\boldsymbol{v}_{pl}$ of statistical intense and weak vortices in Π, respectively, where the velocity at the center is set to be zero. It is noted in all figures that x_1 and x_2 axes in Π are parallel to the complex conjugate eigenvectors of $\nabla \boldsymbol{v}$ [3-5]. φ at the center in the intense and weak vortices are approximately $\varphi_{ave} + \delta_\varphi$ and $\varphi_{ave} - \delta_\varphi$, respectively, where φ_{ave} and δ_φ denote the average and deviation of φ in vortical region ($0 < \varphi$), respectively. Their velocity distributions show that the scale of vortical flow depends on the intensity of swirling (φ). They also indicate that the vortical flows are not symmetric (axisymmetric) and exhibit skewed (elliptic) geometry. The decomposed azimuthal and radial flows in $\boldsymbol{v}_{pl}$, $\boldsymbol{v}_\theta$ and $\boldsymbol{v}_r$, clearly show that both $\boldsymbol{v}_\theta$ and $\boldsymbol{v}_r$ are not symmetric irrespective of the intensity of vortices. Specifically, although they are inflow (convergent) vortices, $\boldsymbol{v}_r$ has weak outflow in some directions (parallel to the eigenvector of $\boldsymbol{v}_r$ [3, 5]), which indicates that both vortices are difficult to have the efficient vortex stretching that strengthens both swirling and orthogonality of the vortical axis [5]. The vortical flow symmetry quantities c ($0 \le c < 1$) and sourcity σ at the center in the intense and weak vortices are $(c, \sigma) = (0.73, -7.8)$ and $(0.55, -3.1)$, respectively. It is noted that $c = 0$ and 1 indicate the shear and axisymmetric vortical flows, respectively.

Figures 3 and 4 show the contours of φ, pressure minimum ι_2, and vortex stretching component $\boldsymbol{nS\omega}$ in terms of swirling, in Π of the respective intense and weak vortices. ι_2 denotes the (negative) Hessian of the pressure in terms of flow kinematics (vortical flow) in Π [4], and is given by: $\iota_2 = (\varepsilon_R^2 - \varphi^2) + |(c - 1/c)\varepsilon_R|\varphi$ where ε_R denotes the average intensity of $\boldsymbol{v}_r$ that is equal to the real part of the complex conjugate eigenvalues of $\nabla \boldsymbol{v}$ [3] (note $\iota_2 < 0$ for pressure minimum feature). $\boldsymbol{nS\omega}$ denotes the inner product of the unit normal vector n_i of Π and vortex stretching vector $S_{ij}\omega_j$, where S_{ij} and ω_i ($i, j = 1,2,3$) denote the rate-of-strain tensor and vorticity vector, respectively. The weak vortex has approximately a quarter of φ in the intense vortex and slight pressure minimum feature, however, it has more intense vortex stretching effect for swirling, i.e., as twice as that in the intense vortex. This characteristic that more intense vortex has higher flow symmetry but less benefit of the stretching for swirling is similar to that in vortices in terms of the local geometry [5].

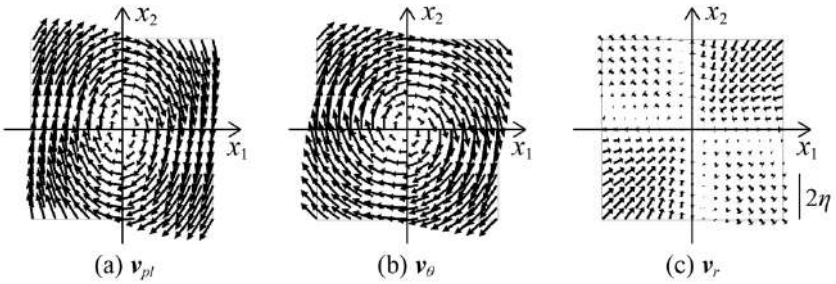

Figure 1. Velocity distribution of an intense vortex in Π. (a) $\boldsymbol{v}_{pl}$, and decomposed (b) $\boldsymbol{v}_{\theta}$ and (c) $\boldsymbol{v}_{r}$.

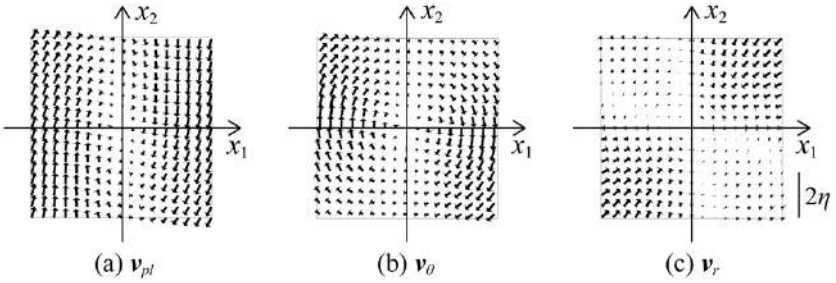

Figure 2. Velocity distribution of a weak vortex in Π. (a) $\boldsymbol{v}_{pl}$, and decomposed (b) $\boldsymbol{v}_{\theta}$ and (c) $\boldsymbol{v}_{r}$.

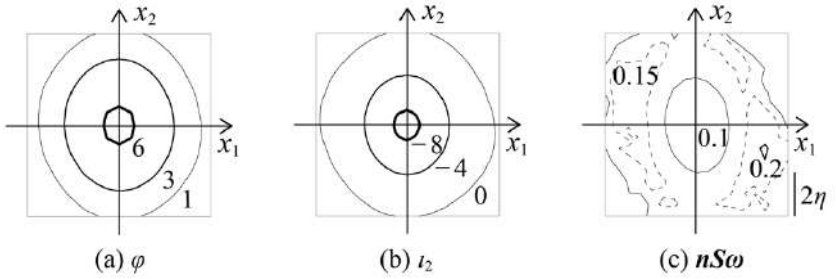

Figure 3. Distributions of (a) φ, (b) ι_2, and (c) $\boldsymbol{nS\omega}$ of an intense vortex in Π.

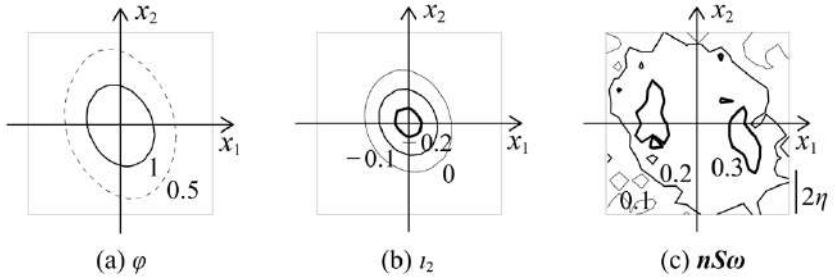

Figure 4. Distributions of (a) φ, (b) ι_2, and (c) $\boldsymbol{nS\omega}$ of a weak vortex in Π.

CONCLUSIONS

Vortices in a homogeneous isotropic turbulence is not axisymmetric and develop with both scale and vortical flow symmetry. An intense vortex has higher vortical flow symmetry and pressure minimum, however, the vortex stretching effect for swirling becomes less. A developed vortex that has a bigger scale and more intense swirlity and pressure minimum may influence greatly the turbulent flow, but decreases the support of self-sustaining/reinforcing function that may be associated with the limit of the growth.

References

[1] Lundgren T. S. Strained spiral vortex model for turbulent fine structure. *Phys. Fluids* **25**: 2193-2203, 1982.

[2] Tanahashi M., Miyauchi T., Ikeda J. Identification of Coherent Fine Scale Structure in Turbulence. *IUTAM Symp. Simulation and Identification of Organized Structures in Flows*: 131-140, 1999.

[3] Nakayama K. Physical properties corresponding to vortical flow geometry. *Fluid Dyn. Res*. **46**: 055502, 2014.

[4] Nakayama K., Sugiyama K., Takagi S. A unified definition of a vortex derived from vortical flow and the resulting pressure minimum. *Fluid Dyn. Res*. **46**: 055511, 2014.

[5] Nakayama K. Topological features and properties associated with development/decay of vortices in isotropic homogeneous turbulence. *Phy. Rev. Fluids* **2**: 014701, 2017.

FORMATION AND SCALING OF PRIMARY AND SECONDARY VORTICES

Guillaume de Guyon, Diego Francescangeli, and Karen Mulleners*
Institute of mechanical engineering,E cole polytechnique fédérale de Lausanne,Switzerland

Summary Vortices do not grow indefinitely. Depending on how they are generated, vortices reach different dimensional sizes and strengths, but their formation process is bounded by the same energetic constraint. The formation time of a primary vortex generated by accelerating objects from rest or impulsively ejecting fluid through holes has been studied extensively. The secondary vortices that form from the vorticity rejected by the primary vortex have received less attention. We present time-resolved experimental data of the formation process of primary and secondary vortices behind translating and rotating objects being uniformly accelerated from rest. We found a scaling law for the vortex circulation that predicts a constant limiting non-dimensional value for all acceleration and velocity values tested. Based on this scaling, the secondary vortices are 4 times weaker than the primary vortex.

INTRODUCTION

When a bluff body is accelerated from rest or a slug of fluid is impulsively ejected through an orifice or a nozzle in a quiescent fluid, a primary vortex is formed in the wake of the body or behind the orifice or nozzle exit. Due to the motion of the body or the slug of fluid with respect to the quiescent flow, vorticity is generated at the solid walls and accumulates in a shear layer that rolls up into a coherent vortex [1]. As the motion continues, this primary vortex grows in size and strength up to a certain limit at which it will no longer take up additional circulation and will pinch-off from the shear layer that feeds it. The dimensionless time at which the vortex pinch-off occurs is referred to as the vortex formation time or number. For various canonical flows with vortex shedding, a formation time of $T^* \approx 4$ can be observed, but the universal nature of vortex formation is not primarily tied to this magical number [2, 3]. It is the result of a more fundamental limiting physical process known as the Kelvin-Benjamin variational principle that states that vortex growth is governed by maximising the impulse-normalised energy. Any additional vorticity that is transported through the shear layer beyond the growth limit is rejected by the primary vortex and accumulates in a series of trailing secondary vortices. These secondary vortices are similar to each other in size and strength and they are generally substantially smaller and weaker than the primary vortex. The most prominent example is probable a completed vortex ring and its trailing jet generated by a piston cylinder [2].

The formation time scales of the primary vortices generated by accelerating a bluff body from rest or impulsively ejecting fluid by a piston cylinder have been studied extensively in the past [4, 5, 6]. The secondary vortices that form from the vorticity rejected by the primary vortex have received considerably less attention. If the vortex formation process is truly universal, it should also apply to the formation of the secondary vortices. To understand and characterise the differences in timing, strength, and size between primary and secondary vortices, we have experimentally studied the formation process of vortices behind a translating cone and around a rotating flat plate in water. In both cases, the objects were uniformly accelerated from rest up to a given constant translational or rotational velocity. The uniform acceleration, final translation or rotational speed, and the object geometries have been varied to investigate their influence on the timescales of the vortex formation process and on the circulation and size of the shed primary and secondary vortices. This information was extracted from time-resolved particle image velocity measurements around the objects.

RESULTS

Two exemplary snapshots of the vorticity field behind the translating cone and the rotating flat plate are presented in figure 1. The cone in figure 1(a) has been moving upwards from its starting position at $y/D = 0$ and has reached a constant velocity of $0.35\,\mathrm{m\,s^{-1}}$ above $y/D = 0.33$. An axisymmetric vortex ring is forming directly behind the cone with an aperture of $60°$ and base diameter $D = 61.5\,\mathrm{mm}$. The Reynolds number for this configuration is 2×10^4 based on the base diameter and the final constant translation velocity. The ridges of the positive and negative finite-time Lyapunov exponent (FTLE) are overlaid on the vorticity field and indicate the transport boundaries of the vortex. Only vorticity on the inside of the positive enveloping FTLE ridge will end up in the vortex, the rest will not be entrained and remains behind. The temporal evolution of the total circulation and the vortex circulation within the FTLE ridge is presented in figure 1(b). The total circulation in the flow field continues to increase while the cone is translating. The vortex circulation, normalised by the translation velocity and the base diameter, converges to a constant value of $\Gamma/(UD) \approx 2.2$ after a formation time $T^* = L/D \approx 3.5$ with L the vertical distance travelled before reaching a constant vortex circulation. The end of the vortex formation time corresponds exactly to the time at which the non-dimensional energy $E^* = E\sqrt{I\Gamma^3}$ drops below the critical value of 0.33 in accordance with the work of Gharib et al. [2]. Here, E, I, Γ are the vortex kinetic energy, impulse, and circulation.

The flat plate in figure 1(c) has been rotated $90°$ in clockwise direction from its initial vertical location at rest. At this time, the primary vortex has shed as well as three secondary vortices. The primary vortex is substantially larger in size and

*Corresponding author. E-mail: karen.mulleners@epfl.ch

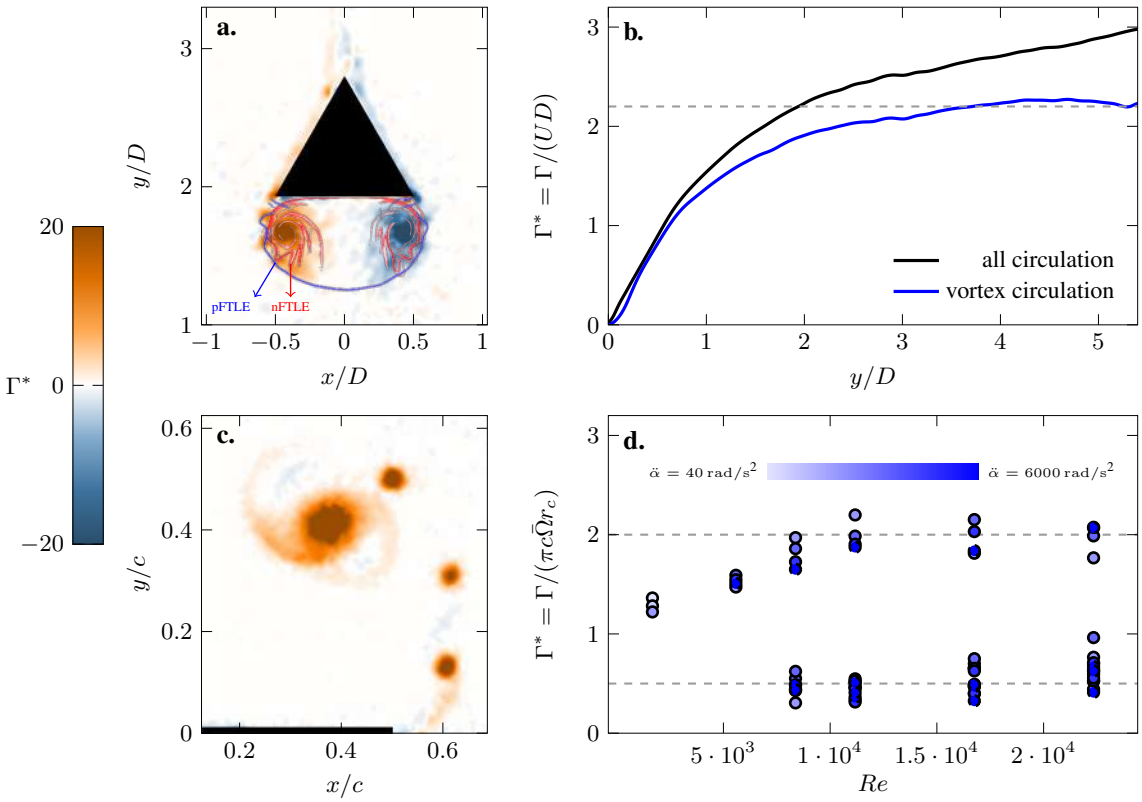

Figure 1: Snapshot of the vorticity fields generated by a translating cone (a.) and a rotating flat plate (b.) in a quiescent fluid. Temporal evolution of the circulation within the primary vortex and in the entire wake behind the translating cone (b.). Scaling of the circulation of the primary and secondary vortices created by the rotating flat plate for various rotation rates and acceleration values (d.).

strength that the secondary structures. A scaling of the vortex strength is proposed as $\Gamma^* = \Gamma/(\pi c\bar{\Omega} r_c)$, with c the width of the plate, $\bar{\Omega}$ the equivalent velocity inspired by Glezer [7], and r_c the size of the vortex core non-dimensionalised by the shear layer thickness. The normalised circulation values after a $90°$ rotation for the primary and secondary vortices for various rotational speeds and accelerations are presented in figure 1(d). The colours of the markers indicate the uniform acceleration value. The rotational speed is expressed through the Reynolds number based on the width and the tip speed of the plate. Two groups can be distinguished. The markers with values of non-dimensionalised circulation above 1 correspond to primary vortices and the other markers below correspond to the secondary vortices. Above $Re \approx 7 \times 10^3$, the primary vortices all have a non-dimensional circulation of $\Gamma^* \approx 2$ and for the secondary vortices $\Gamma^* \approx 0.5$. Below $Re \approx 7 \times 10^3$, the non-dimensional circulation of the primary vortex is lower that 2 and no secondary vortices are observed. For these lower Re conditions, the primary vortex has not reached its limiting size and strength yet after a rotation of $90°$ and will continue to take up vorticity when the motion continues.

OUTLOOK

Based on the analysis of the vortex formation processes behind the translating and rotation objects we derived a new kinematic argument for the closure of the primary vortex that will be presented as an alternative to the energetic argument based on the Kelvin-Benjamin principle. We will also present a model for the vortex growth behind the cone and discuss the vorticity leaking phenomenon that causes the vortex circulation to increase slower that the total circulation. The timing of the vortex shedding around the rotating flat plate has been analysed and core sizes of the primary and secondary vortices will be compared.

References

[1] Morton B. R. The generation and decay of vorticity. *Geophys. Astrophys. Fluid Dyn.* **28**(3-4): 277–308, 1984.
[2] Gharib M., Rambod E., Shariff K. A universal time scale for vortex ring formation. *J. Fluid Mech.* **360**: 121–140, 1998.
[3] Dabiri J. O. Optimal vortex formation as a unifying principle in biological propulsion. *Annu. Rev. Fluid Mech.* **41**(1): 17–33, 2009.
[4] Jeon D., Gharib M. On the relationship between the vortex formation process and cylinder wake vortex patterns. *J. Fluid Mech.* **519**: 161–181, 2004.
[5] Sattari P., Rival D., Martinuzzi R., Tropea C. Growth and separation of a start-up vortex from a two-dimensional shear layer *Phys. Fluids* **24**107102: 1–14, 2012.
[6] Onoue K., Breuer K. Vortex formation and shedding from a cyber-physical pitching plate. *J. Fluid Mech.* **793**: 229–247, 2016.
[7] Glezer, A. The formation of vortex rings. *Phys. Fluids*, **31**(12): 3532–3542, 1988.

THEORETICAL PREDICTIONS FOR THE DRAG FORCE DUE TO EXOTIC WAKES

Emad Masroor*[1] and Mark A. Stremler [2]
[1]Engineering Mechanics Program, Virginia Tech, Blacksburg VA
[2]Department of Biomedical Engineering and Mechanics, Virginia Tech, Blacksburg VA

Summary We present a generalized formulation of von Kármán's analysis of the drag on a bluff body with a vortex-street wake, allowing for the existence of exotic wakes with more than 2 vortices per period. This formulation recovers von Kármán's formula as a special case. We apply the method to exotic wakes by considering systems of N point vortices and their periodic images in relative equilibrium, allowing us to make quantitative comparisons of the drag due to exotic wakes with von Kármán's canonical drag formula.

INTRODUCTION

In 1911, von Kármán considered the drag (or thrust) on a two-dimensional body in uniform flow whose wake takes the form of what is now known as the Bénard - von Kármán vortex street: two rows of counter-rotating vortices [5]. Using the momentum flux through a contour surrounding the cylinder and cutting through the wake, and representing the wake as a series of point vortices in an ideal fluid, he developed the famous formula known by his name that relates the drag on a bluff body to the characteristics of its wake. In dimensionless form, this formula was given by [2] as

$$C_D = \frac{4}{\pi}\frac{L}{d}\frac{U_s^2}{U_\infty^2}\left[\coth^2\frac{\pi h}{L} + \left(\frac{U_\infty}{U_s} - 2\right)\frac{\pi h}{L}\coth\frac{\pi h}{L}\right], \tag{1}$$

where U_s is the self-induced velocity of the double row of vortices, U_∞ is the velocity of the free stream, L is the wavelength of the system, d is the length scale of the bluff body, e.g. the diameter of a cylinder, h is the transverse distance between the two rows, and C_D is the predicted coefficient of drag.

There is a wealth of recent work showing that the Bénard - von Kármán street is not the only arrangement of vortices that persists in the wakes of immersed bodies. The wakes of several moving and/or stationary bluff bodies are known to take on other, repeatable vortex patterns, which were first extensively classified by [8] according to the number and pairings of the vortices in each period of motion. Thus, the '2S' mode was assigned to wakes with two single vortices shed per period, the 'P+S' mode for a pair of vortices together with a single vortex per period, and the '2P' mode for two pairs of vortices per period. These modes are the most extensively documented ones, although more recent work has even found wakes with up to sixteen vortices per period [6]. Theoretical predictions for the forces exerted on a body whose wake takes these complicated forms, analogous to (1) for a Bénard - von Kármán street, are not currently available. Our work aims to fill this gap by generalizing (1) for more complicated vortex-street wakes.

The well-documented experimental observation of discrete, almost-spatially-periodic, temporally persistent vortical structures in bluff-body wakes, such as the 'P+S' and '2P' modes, is mirrored in ideal hydrodynamics by the existence of relative equilibrium solutions to the dynamical system comprised of $N = 3$ and 4 point vortices, respectively, in a singly-periodic vertical strip. The vortex trajectories associated with these equilibrium and near-equilibrium solutions have been shown [7] to approximate the behavior of real vortices in the wakes of bluff bodies reasonably well. Often, the time scale of relative motion of vortices (in a co-moving frame) is of approximately the same order as the convective time scale. Hence, many real vortex-street wakes can be fruitfully analyzed using equilibrium configurations of point vortices in a periodic strip, even when the vortices in the wake are exhibiting relative motion.

EXAMPLE: A PERIODIC VORTEX-STREET WAKE WITH N VORTICES PER PERIOD

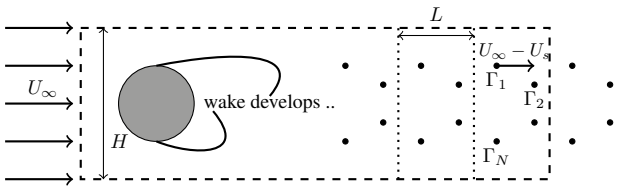

Figure 1: A periodic vortex-street wake with $N = 4$

We consider a wake that, in the well-developed region, can be approximated by a system of N point vortices (together with their periodic images to the left and right), as indicated in figure 1. The strengths $\mathbf{\Gamma} = (\Gamma_1, \Gamma_2, \ldots \Gamma_N)$ and locations in the complex plane $\mathbf{z} = (z_1, z_2, \ldots z_N)$ of the vortices are assumed to be such that the vortices are in *relative equilibrium*; these equilibria can be found using methods given by, e.g., [1]. The vortices tend to move to the left under their mutual induction at a speed U_s, but they are swept to the right with a velocity $U_\infty - U_s$ under the influence of the free stream.

We then write Newton's second law for the control volume defined by the dashed rectangle, supposing that the width H of the rectangle is made large enough that all disturbances die down at the horizontal boundaries; then, [3] gives the average drag force on the body as the sum of two terms,

$$F_D = \rho \oint y\zeta(\vec{v}\cdot\vec{n})\mathrm{d}s - \frac{1}{2}\rho\mathrm{Re}\int_{-H/2}^{+H/2}(u - iv)^2\mathrm{d}y = F_{D_1} + F_{D_2}, \tag{2}$$

*Corresponding author. E-mail: emad@vt.edu

where ζ is the vorticity, ρ is the fluid density, and $u - iv$ is the complex velocity induced by the system of vortices.

The first term, F_{D_1}, represents the flux of '$y \times \zeta$' out of the control volume, averaged over one period. For a system of point vortices, this is identical to the imaginary part of the linear impulse of the N vortices that leave the contour every period, i.e. the flux of $P = \sum_i^N \Gamma_i y_i$ averaged over one period.

The second term, F_{D_2}, requires the evaluation of the velocity induced by the point vortices at the right-side boundary of the control volume. Although the value of the velocity at any point will change with time, by Cauchy's residue theorem the integral in (2) will not change under certain symmetry conditions; thus, it is sufficient to calculate for any one instant the value of the integral in F_{D_2}.

These two terms can then be non-dimensionalized and added to give the expression for the coefficient of drag as

$$C_D = \frac{4}{\pi}\frac{L}{d}\frac{U_s^2}{U_\infty^2} \cdot f_1 \left[f_1 f_2 + \mathcal{P}\left(\frac{U_\infty}{U_s} - 1\right)\right], \tag{3}$$

where $\mathcal{P}$ is a non-dimensionalized form of P, and the non-dimensional quantities f_1 and f_2 are defined by the relations

$$U_s = \Gamma/(2L) \cdot f_1(\mathbf{z}, \mathbf{\Gamma}),$$
$$f_2(\mathbf{z}, \mathbf{\Gamma}) = \pi L/(\Gamma) \int (u - iv)^2 \mathrm{d}y.$$

Scalar Γ is the sum of the strengths of all vortices with positive circulations (or, equivalently, the sum of the strengths of all vortices with negative circulations). Thus f_1 expresses the relationship of $\mathbf{z}$ and $\mathbf{\Gamma}$ with U_s, and f_2 expresses the relationship of $\mathbf{z}$ and $\mathbf{\Gamma}$ with the integral in F_{D_2}.

Equation (3) is a generalized form of von Kármán's drag formula, and it can be applied to any spatially-periodic wake with the vortices in relative equilibrium by determining f_1, f_2, and $\mathcal{P}$ as a function of the vortices' positions and strengths. For the Bénard - von Kármán street, the three terms have straightforward closed forms: $f_1 = -\coth \mathcal{P}$, $f_2 = 1 - \mathcal{P}\tanh \mathcal{P}$ and $\mathcal{P} = -\pi h/L$. By substituting these expressions, we verify that (1) is indeed a special case of (3).

CONCLUSIONS

We use this method to give theoretical predictions for the drag force exerted on a body whose wake takes the often-observed 'P+S' or '2P' forms, using relative equilibrium configurations for $N = 3$ and 4 respectively. A representative example for a system of 4 vortices and their periodic images in relative equilibrium, representing a '2P' wake, is given in figure 2, where we show the predicted coefficient of drag as a function of Strouhal number $St \equiv f \cdot d/U_\infty$, with f the frequency of vortex shedding. The Strouhal number is itself an empirically-known, increasing function of the Reynolds number — as documented by, e.g. [9] — that varies between about 0.18 and 0.25 in the Reynolds number range $100 < Re < 1000$.

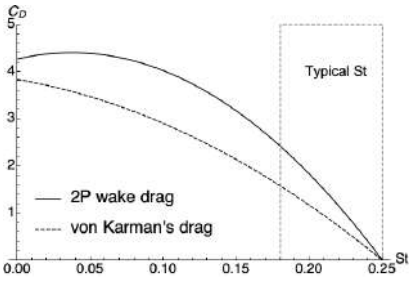

Figure 2: Predicted drag as a function of Strouhal number

It has long been known that abrupt changes in the mode of vortex shedding are related to changes in the forces experienced by the shedding body [4]. This work allows us to classify exotic wakes such as the '2P' and 'P+S' modes according to whether they lead to an increase or decrease in the drag force they cause on the body compared to the standard Bénard - von Kármán -type wake. Our model therefore suggests a theoretical basis for possible drag reduction or thrust-enhancement due to a 'switch' from one vortex-shedding mode to another.

References

[1] Basu, S. and Stremler, M. A. (2017). Exploring the dynamics of '2P' wakes with reflective symmetry using point vortices. *J. Fluid Mech.*, **831** 72–100.

[2] Bearman, P. W. (1967). On vortex street wakes. *J. Fluid Mech.*, **28** 625–641.

[3] Goldstein, Sydney. Modern Developments in Fluid Dynamics 625–641. Clarendon Press, 1938.

[4] Govardhan, R. and Williamson, C. H.K. (2000). Modes of vortex formation and frequency response of a freely vibrating cylinder. *J. Fluid Mech.*, **420** 85-130.

[5] Kármán, Theodore V. (1911). Über den Mechanismus des Widerstandes, den ein bewegter Körper in einer Flüssigkeit erfährt. *Nachrichten von der Gesellschaft der Wissenschaften zu Göttingen*, **12** 509-546.

[6] Schnipper, Teis and Andersen, Anders and Bohr, Tomas (2009). Vortex wakes of a flapping foil. *J. Fluid Mech.*, **633** 411–423.

[7] Stremler et al. (2011). A mathematical model of 2P and 2C vortex wakes. *J. Fluid. Struct.*, **27** 774–783.

[8] Williamson, C. H.K. and Roshko, A. (1988). Vortex formation in the wake of an oscillating cylinder. *J. Fluid. Struct.*, **2** 355–381.

[9] Williamson, C. H.K. and Brown, G. L. (1998). A series in $1/\sqrt{Re}$ to represent the Strouhal-Reynolds number relationship of the cylinder wake. *J. Fluid. Struct.*, **12** 1073–1085.

VISUALIZATION OF MACROSCOPIC VORTEX RINGS IN SUPERFLUID ^{4}HE

Patrik Švančara and Marco La Mantia*
Faculty of Mathematics and Physics, Charles University, Prague, Czech Republic

Summary Macroscopic vortex rings are generated thermally in superfluid ^{4}He, by applying a brief heat pulse. The rings form above a circular tube and propagate upward with velocities of the order of 10 mm s^{-1}, resulting in Reynolds numbers up to 10^5. We visualize their cross-section, of size comparable with the 5-mm tube diameter, by capturing the ring-induced motions of small solid particles. We employ the latter to compute the Lagrangian pseudovorticity, which can be seen as a measure of the ring strength. We thus obtain information on the size, position and velocity of the vortex rings. We show that, in the range of investigated parameters, these rings behave as if they were turbulent vortex rings moving in classical viscous fluids, at least in the direction of ring propagation.

INTRODUCTION

The superfluid phase of liquid ^{4}He, which occurs at temperatures below 2.17 K, at the saturated vapour pressure, is often called He II and is characterized by unique properties, such as an extremely small kinematic viscosity, see, for example, [1] and references therein. Its turbulent flows are defined by the presence of quantized vortices, which are line singularities within the liquid, and quantum turbulence is the name usually given to the phenomenon originating from the mutual interaction between quantized vortex tangles and flows of superfluid ^{4}He.

We report here an experimental investigation on the motion of macroscopic vortex rings in a quiescent He II bath, following [2], where macroscopic means at scales larger than the mean distance between quantized vortices. The rings are thermally generated above a circular nozzle, after a short heat pulse, and have sizes of the order of the nozzle diameter, see figure 1(a). They are visualized by using relatively small solid particles, dispersed in the experimental volume and illuminated by a planar laser sheet. The particle time-dependent positions are collected by a digital camera and processed by using the Particle Tracking Velocimetry (PTV) technique, see, for example, [3] and references therein.

Specifically, we observe the ring cross-section, appearing as a pair of counter-rotating vortices. In order to characterize the ring strength we employ the concept of Lagrangian pseudovorticity pv, which was introduced in [4] to account for the fact that the PTV technique does not give access to the classical Eulerian vorticity. We calculate the parameter on a square mesh and obtain relevant pv-maps, see an example in figure 1(b). As it is clear from the latter, the tool is adequate for the visualization of the generated vortex rings, which can be identified as regions of relatively large $|pv|$ values, and, consequently, it is possible to quantitatively track their motion.

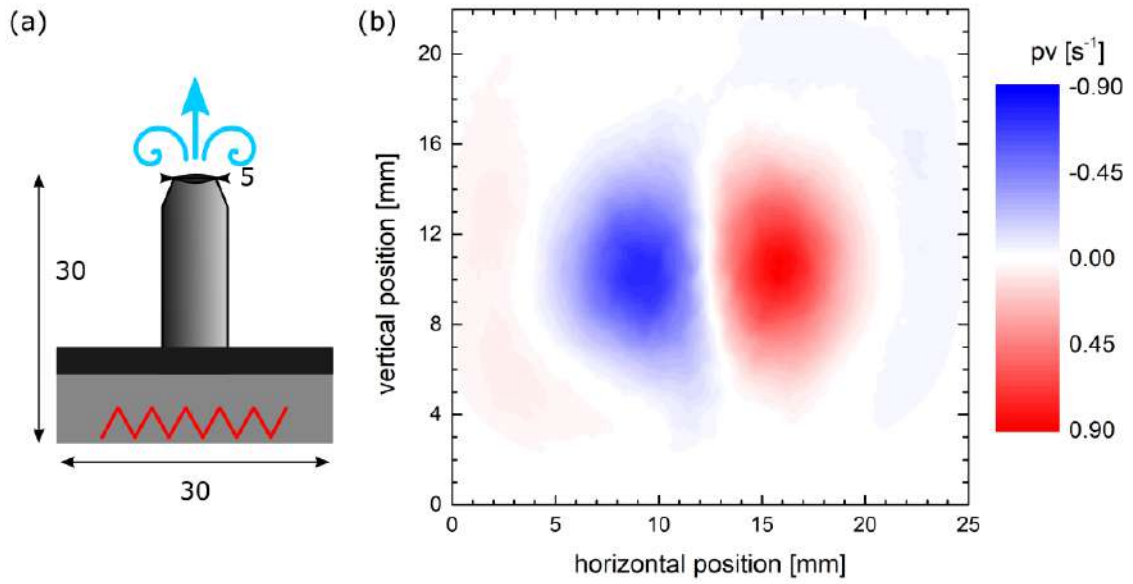

Figure 1: Panel (a) displays a scheme of the nozzle used for thermal generation of macroscopic vortex rings in He II; the red line indicates the planar resistive heater; dimensions are in millimeters. Panel (b) shows an example of pv-map; the cross-section of a macroscopic vortex ring, seen here as a pair of counter-rotating vortices, is well resolved; positive pv values indicate clockwise rotation; in this case the temperature was 1.50 K and a heat pulse of 278 mW cm^{-2} was applied for 500 ms, resulting in a Reynolds number of approximately 1.1×10^5; the displayed pv-map was obtained 1.1 s after the end of the heat pulse; the top of the nozzle matches the bottom of the field of view.

*Corresponding author. E-mail: lamantia@mbox.troja.mff.cuni.cz.

RESULTS

We experimentally investigate the early development of these macroscopic vortex rings, where early means at distances between 1 and 6 times the nozzle diameter. The rings were generated thermally, by applying a short heat pulse, at temperatures ranging from 1.28 to 1.95 K, and with heat fluxes between 35 and 450 mW cm^{-2}, resulting in Reynolds numbers of the order of 10^4, which indicates that they can be regarded as turbulent rings [5].

We observe that, as the distance from the nozzle and the time from the end of the heat pulse increase, the rings show the tendency to become larger and decrease their velocity, which is of the order of 10 mm s^{-1}. The outcome is consistent with the classical behaviour of vortex rings propagating in viscous fluids – see, e.g., [6, 7] – and reinforces therefore the view that, at sufficiently large scales, that is, at scales larger than the mean distance between quantized vortices, turbulent flows of superfluid ^{4}He may display distinctive classical-like features, as discussed, for example, in [8].

In order to further substantiate the claim we apply to our data the similarity theory developed in [9] for turbulent vortex rings, see also [10]. We find that the data obtained in He II closely follow the theory predictions in the direction of ring propagation. However, the agreement between the theory and the data is less satisfactory if one considers the self-similar ring evolution in the radial direction.

The outcome can be related to the fact that, in the range of investigated parameters, the experimentally obtained Lagrangian pseudovorticity does not appear to be suitable to capture the fine details of the ring structure, that is, the corresponding spatial distribution of the ring vorticity, while it seems adequate to resolve more general features, such as the ring position and propagation velocity.

In order to address the issue in a quantitative way we are currently processing existing numerical simulations of classical vortex rings propagating in a viscous fluid. Fluid particles are added to the obtained Eulerian flow fields and the corresponding pseudovorticity values are computed. Preliminary results show that, in order to get a closer agreement between the vorticity and pseudovorticity trends, one should likely employ a larger number of particles compared to that used in the present experiments.

CONCLUSIONS

We experimentally investigated the early development of macroscopic vortex rings, thermally generated in superfluid ^{4}He. The rings were identified and tracked by using the concept of Lagrangian pseudovorticity, recently introduced to quantify the strength of large vortical structures in the absence of Eulerian data [4]. We found that the ring features can be quantitatively assessed by using this method and can therefore be used to perform relevant comparisons.

Our aim was indeed to give a significant contribution to the active line of scientific enquiry focusing on the study of similarities and differences between classical and He II flows. We found that, in the range of investigated parameters, our rings behave as if they were turbulent vortex rings moving in a viscous fluid, at least in the direction of ring propagation. The claim is mainly based on the remarkable agreement between our experimental results and the similarity theory developed in [9] for turbulent vortex rings.

The results therefore reinforce the view that, at scales larger than the mean distance between quantized vortices, turbulent flows of superfluid ^{4}He may display distinctive classical-like features, regardless of the flow generation mechanism, as discussed, for example, in [8]. On the other hand, the reason why He II behaves in such a way is still largely unknown and further studies are needed to address the problem. Another research route, which is potentially not only relevant to quantum turbulence, could focus on clarifying the relation between the Lagrangian pseudovorticity and the Eulerian vorticity, which is yet to be quantitatively established.

We thank A. Andrýsková, P. Hrubcová, O. Outrata, J. Hron, M. Rotter, L. Skrbek and B. Vejr for valuable help. The support of the Czech Science Foundation (GAČR) under grant no. 19-00939S is acknowledged.

References

[1] Mongiovì M. S., Jou D., Sciacca M. Non-equilibrium thermodynamics, heat transport and thermal waves in laminar and turbulent superfluid helium. *Phys. Rep.* **726**: 1-71, 2018.
[2] Stamm G., Bielert F., Fiszdon W., Piechna J. Counterflow-induced macroscopic vortex rings in superfluid helium: visualization and numerical simulation. *Physica B* **193**: 188-194, 1994.
[3] Švančara P., Hrubcová P., Rotter M., La Mantia M. Visualization study of thermal counterflow of superfluid helium in the proximity of the heat source by using solid deuterium hydride particles. *Phys. Rev. Fluids* **3**: 114701, 2018.
[4] Duda D., Švančara P., La Mantia M., Rotter M., Skrbek L. Visualization of viscous and quantum flows of liquid ^{4}He due to an oscillating cylinder of rectangular cross section. *Phys. Rev. B* **92**: 064519, 2015.
[5] Glezer A. On the formation of vortex rings. *Phys. Fluids* **31**: 3532-3542, 1988.
[6] Maxworthy T. Turbulent vortex rings. *J. Fluid Mech.* **64**: 227-239, 1974.
[7] Sullivan I. S., Niemela J. J., Hershberger R. E., Bolster D., Donnelly R. J. Dynamics of thin vortex rings. *J. Fluid Mech.* **609**: 319-347, 2008.
[8] Švančara P., La Mantia M. Flight-crash events in superfluid turbulence. *J. Fluid Mech.* **876**: R2, 2019.
[9] Glezer A., Coles D. An experimental study of a turbulent vortex ring. *J. Fluid Mech.* **211**: 243-283, 1990.
[10] Gan L., Nickels T. B. An experimental study of turbulent vortex rings during their early development. *J. Fluid Mech.* **649**: 467-496, 2010.

DOUBLE-DIFFUSIVE INSTABILITIES IN ROTATING FLOWS: PSEUDO-HERMITICITY AND EXCEPTIONAL POINTS

Oleg N. Kirillov*[1]
[1]Northumbria University, Newcastle upon Tyne, United Kingdom

Summary The Prandtl number, i.e. the ratio of the fluid viscosity to a diffusivity parameter of other physical nature such as thermal diffusivity or ohmic dissipation, plays a decisive part for the onset of instabilities in hydrodynamic and magnetohydrodynamic flows. The studies of many particular cases suggest a significant difference in stability criteria obtained for the Prandtl number equal to 1 from those for the Prandtl number deviating from 1. We demonstrate this for a circular Couette flow with a radial temperature gradient and for a differentially rotating viscous flow of electrically conducting incompressible fluid subject to an external azimuthal magnetic field. Furthermore, in the latter case we find that the local dispersion relation is governed by a pseudo-Hermitian matrix both in the case when the magnetic Prandtl number, Pm, is $\mathrm{Pm}=1$ and in the case when $\mathrm{Pm}=-1$. This implies that the complete neutral stability surface contains three Whitney umbrella singular points and two mutually orthogonal intervals of self-intersection. At these singularities the double-diffusive system reduces to a marginally stable G-Hamiltonian system. The role of double complex eigenvalues (exceptional points) stemming from the singular points in exchange of stability between modes is demonstrated.

INSTABILITIES OF A CIRCULAR COUETTE FLOW WITH RADIAL TEMPERATURE GRADIENT

Circular Couette flow of a viscous Newtonian fluid between two coaxial differentially rotating cylinders is a canonical system for modelling instabilities leading to spatio-temporal patterns and transition to turbulence in many natural and industrial processes. Modern astrophysical applications require understanding of basic instability mechanisms in rotating flows with the Keplerian shear profile in accretion- and protoplanetary disks that are hydrodynamically stable according to the centrifugal Rayleigh criterion. Usually, these instabilities are a consequence of additional factors such as electrical conductivity of the fluid and the magnetic field of the central gravitating object. However, in the so-called dead-zones of protoplanetary disks that are characterized by high electrical resistivity due to very low ionization levels, some magnetohydrodynamic (MHD) instabilities become inefficient (e.g. the standard VelikhovChandrasekhar magnetorotational instability (MRI) in an axial magnetic field). Alternative mechanisms include MRIs caused by azimuthal or helical magnetic fields that work well also in the inductionless limit at a very low conductivity as well as pure hydrodynamic finite-amplitude nonlinear instabilities. Some recent studies indicated a possibility that Keplerian disks with strong mean radial temperature gradients can support the so-called Goldreich-Schubert-Fricke (GSF) instability, which is the instability of short-radial-wavelength inertial modes [1, 2, 3]

In [1] we applied the geometric optics stability analysis to circular Couette flow of a viscous Newtonian fluid with a temperature gradient in the absence of gravity, but retaining the term of the centrifugal buoyancy. We derived a system of characteristic equations that includes the transport equations for the lowest-order amplitude of the envelope of the localized perturbation and find a dispersion relation that takes into account the radial variation of the angular velocity and the temperature as well as the kinematic viscosity and the thermal diffusivity.

Using algebraic stability criteria for localization of the roots of polynomials in the left half of the complex plane, we obtained two stability conditions in compact and explicit form; one of them generalizes the Rayleigh discriminant for stationary axisymmetric instabilities to include viscosity effects, and the other provides a marginal stability curve in the parameter plane for oscillatory instabilities. In the case of a sole outer cylinder rotation, solid body rotation, and rotating flow with Keplerian shear we found a destabilizing effect of the inward temperature gradient that leads to oscillatory instability at small values of the Prandtl number ($\mathrm{Pr}<1$) and to stationary instability at $\mathrm{Pr}>1$ [1].

DOUBLE-DIFFUSIVE AZIMUTHAL MAGNETOROTATIONAL INSTABILITY

In [4, 5] we studied local instabilities of a differentially rotating viscous flow of electrically conducting incompressible fluid subject to an external azimuthal magnetic field. It was found that in the presence of the magnetic field the hydrodynamically stable flow can demonstrate non - axisymmetric azimuthal magnetorotational instability (AMRI) both in the diffusionless case and in the double-diffusive case with viscous and ohmic dissipation. It was shown in [4] that the dispersion relation for the double-diffusive AMRI is $p(\lambda):=\det(\mathbf{H}_0+\mathbf{H}_1-i^{-1}\mathbf{G}_1\lambda\mathbf{I})=0$, where $\mathbf{I}$ is the 4×4 identity matrix, $\mathbf{G}_1$ and $\mathbf{H}_0$ are Hermitian matrices and $\mathbf{H}_1$ is a complex non-Hermitian matrix of dissipative perturbations to a G-Hamiltonian (with a pseudo-Hermitian Hamiltonian) [6, 7] system of ideal MHD. Performing stability analysis based on the dispersion relation, we established that the threshold of the diffusionless AMRI via the Hamilton-Hopf bifurcation is a singular limit of the thresholds of the viscous and resistive AMRI corresponding to the dissipative Hopf bifurcation and manifests itself as the Whitney umbrella singular point. A smooth transition between the two types of instabilities is possible only if the magnetic Prandtl number is equal to unity, $\mathrm{Pm}=1$. At a fixed $\mathrm{Pm}\neq1$ the threshold of the double-diffusive AMRI is displaced by finite distance in the parameter space with respect to the diffusionless case even in the zero dissipation limit, see Fig. 1(left).

*Corresponding author. E-mail: oleg.kirillov@northumbria.ac.uk

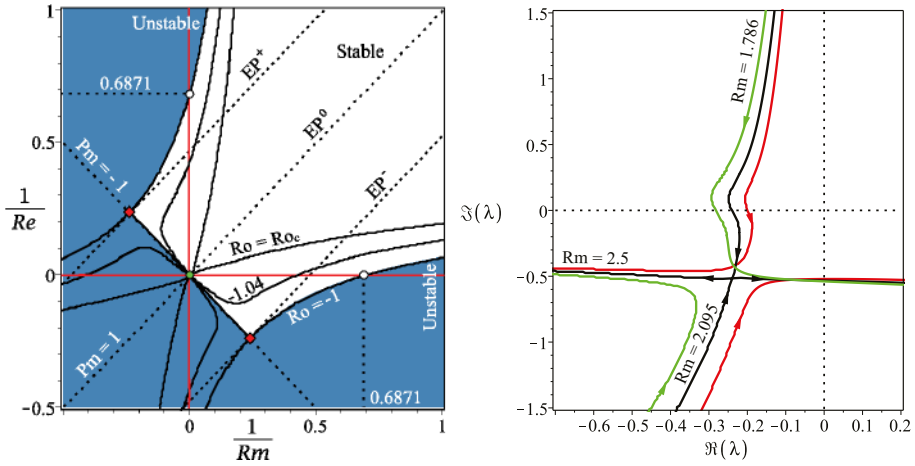

Figure 1: (Left) Contour plots of the neutral stability surface in the plane of inverse Reynolds numbers at (cuspidal curve) $\mathrm{Ro} = \mathrm{Ro}_c \approx -1.07855$, (filled area) $\mathrm{Ro} = -1$, and (intermediate curve) $\mathrm{Ro} = -1.04$. Two singular Whitney umbrella points (filled diamonds) exist at the intersection of the line $\mathrm{Pm} = -1$ and the neutral stability curve at $\mathrm{Ro} = -1$ and another one exists at the origin when $\mathrm{Ro} = \mathrm{Ro}_c$. From these singularities the lines $\mathrm{EP}^{\pm}, \mathrm{EP}^0$ of exceptional points are stemming that govern the transfer of modes shown in the right panel. (Right) For $\mathrm{Rb} = -1$, $\mathrm{S} = 1$, $n = \sqrt{2}$, and $\mathrm{Re} = 1000$ the movement of eigenvalues with decreasing Ro at various Rm chosen such that $\mathrm{Pm} < 1$. At $\mathrm{Rm} < 1000$ and up to $\mathrm{Rm} = \mathrm{Rm}_{\mathrm{EP}-} \approx 2.095$ it is the branch corresponding to perturbed imaginary eigenvalues with positive Krein sign that causes instability. When $\mathrm{Rm} = \mathrm{Rm}_{\mathrm{EP}-}$ two simple eigenvalues approach each other to merge exactly at $\mathrm{Ro} = -1$ into a double eigenvalue whose corresponding matrix is a Jordan block, $\lambda_{\mathrm{EP}-} \approx -i0.5086 - 0.2391$. At $\mathrm{Rm} < \mathrm{Rm}_{\mathrm{EP}-}$ the instability shifts to the branch of perturbed imaginary eigenvalues with negative Krein sign.

Let $\Omega(r)$ be the radial profile of the angular velocity of the fluid, $\mathrm{Ro} = \frac{r\partial_r\Omega}{2\Omega}$ the hydrodynamic Rossby number, $\mathrm{S} = \frac{\omega_{A_\phi}}{\Omega}$ the Alfvén angular velocity in the units of Ω, $\mathrm{Rb} = \frac{r\partial_r\omega_{A_\phi}}{2\omega_{A_\phi}}$ the magnetic Rossby number, Re the hydrodynamic Reynolds number, Rm the magnetic Reynolds number, and $\mathrm{Pm} = \mathrm{Rm}/\mathrm{Re}$ the magnetic Prandtl number.

Consider the following particular case: $\mathrm{Ro} = \mathrm{Rb} = -1$, $\mathrm{S} = 1$, and $\mathrm{Re} = -\mathrm{Rm}$ (that is $\mathrm{Pm} = -1$). Then, the dispersion relation for the double-diffusive AMRI takes the form $p(\lambda) := \det(\mathbf{H} - i^{-1}\mathbf{G}\lambda\mathbf{I}) = 0$, where $\mathbf{H}$ and $\mathbf{G}$ are Hermitian matrices

$$\mathbf{H} = \begin{pmatrix} n & 0 & \frac{i}{\mathrm{Rm}} - n & 0 \\ 0 & \alpha^2 n & -\frac{2\alpha}{n\mathrm{Rm}} & \frac{i\alpha^2}{\mathrm{Rm}} - n\alpha^2 \\ -\frac{i}{\mathrm{Rm}} - n & -\frac{2\alpha}{n\mathrm{Rm}} & n & 0 \\ 0 & -\frac{i\alpha^2}{\mathrm{Rm}} - n\alpha^2 & 0 & \alpha^2 n \end{pmatrix}, \quad \mathbf{G} = \begin{pmatrix} 0 & 0 & 1 & 0 \\ 0 & 0 & \frac{2i\alpha}{n} & \alpha^2 \\ 1 & -\frac{2i\alpha}{n} & 0 & 0 \\ 0 & \alpha^2 & 0 & 0 \end{pmatrix}$$

with $n = \frac{m}{\alpha}$ the modified azimuthal wavenumber and α the coefficient depending on wavenumbers of the perturbation. Hence, in the case of $\mathrm{Pm} = -1 < 0$ the dispersion relation is governed by a G-Hamiltonian system, which implies neutral stability on an interval in the plane of inverse Reynolds numbers, see Fig. 1(left). The loss of the neutral stability is accompanied by the Krein collision of two modes with the opposite Krein/action signs when the parameters correspond to singular Whitney umbrella points. The sets of parameters stemming form the singular points and corresponding to complex double eigenvalues determine transfer of stability between modes, see Fig. 1(right). This picture provides the detailed mechanism of the destabilization of the Chandrasekhar equipartition solution in the case when $\mathrm{Pm} \neq 1$ [4, 8, 9, 10].

References

[1] Kirillov O. N., Mutabazi I. Short wavelength local instabilities of a circular Couette flow with radial temperature gradient. *J. Fluid Mech.* **818**: 319–343, 2017.
[2] Singh S., Mathur M. Effects of Schmidt number on the short-wavelength instabilities in stratified vortices. *J. Fluid. Mech.* **867**: 765–803, 2019.
[3] Vidal J., Cebron D., ud-Doula A., Alecian E. Fossil field decay due to nonlinear tides in massive binaries. *Astron. & Astrophys.* **629**: A142, 2019.
[4] Kirillov O. N. Singular diffusionless limits of double-diffusive instabilities in magnetohydrodynamics. *Proc. R. Soc. A*, **473**(2205): 20170344, 2017.
[5] Zou R., Labarbe J., Kirillov O. N., Fukumoto Y. Analysis of azimuthal magnetorotational instability of rotating magnetohydrodynamic flows and Tayler instability via an extended Hain-Lüst equation. *Phys. Rev. E* **101**: 013201, 2020.
[6] Zhang R., Qin H., Davidson R. C., Liu J., Xiao J. On the structure of the two-stream instabilityComplex G-Hamiltonian structure and Krein collisions between positive- and negative-action modes. *Phys. Plasmas* **23**: 072111, 2016.
[7] Zhang R., Qin H., Xiao J. PT-symmetry entails pseudo-Hermiticity regardless of diagonalizability. *J. Math. Phys.* **61**(1): 012101, 2020.
[8] Rüdiger G., Schultz M., Stefani F., Mond M. Diffusive magnetohydrodynamic instabilities beyond the Chandrasekhar theorem. *Astrophys. J.* **811**(2): 84, 2015.
[9] Gellert M., Rüdiger G., Schultz M., Guseva A., and Hollerbach R. Nonaxisymmetric MHD instabilities of Chandrasekhar states in Taylor-Couette geometry. *Astrophys. J.* **823**(2): 99, 2016.
[10] Deguchi K. Subcritical magnetohydrodynamic instabilities: Chandrasekhar's theorem revisited. *J. Fluid Mech.* **882**: A20, 2020.

NEW PERSPECTIVE ON MASS CONSERVATION LAW AND ROTATIONAL WAVES

Tsutomu Kambe*
Former Professor, University of Tokyo, Tokyo, Japan

Summary This is a new approach hinted by new finding of a general representation of rotational flows of an ideal compressible fluid satisfying Euler's equation of motion. In this representation, four independent fields are introduced. This fact is understood to predict existence of a new field interacting with the flow field. The action describing the interaction is, amazingly, analogous to that of Electromagnetism. The mass conservation law is closely associated with the symmetry of gauge invariance which the new field possesses inherently. Present combined system of fluid flow and gauge field enables excitation of *rotational* waves within shear flow field. An example is given for rotational waves superimposed on a streaky flow.

INTRODUCTION

Concerning the *mass* conservation law, a question may be raised whether it has been given *due* appreciation concerning its dynamical role. A symmetry implies a conservation law, and *vice versa* (*Noether's theorem* [2]). In the background of the mass conservation law, there exists the gauge symmetry [6, 7]. In fact, with respect to traditional formulations on the basis of action principle, a certain kind of weakness is recognized concerning the mass conservation condition. We approach this fundamental question from a quite unexpected direction by learning from the *Electrodynamic* theory (Landau & Lifshitz [3]). A general solution of rotational flow satisfying the Euler's equation of motion was given by Kambe [4] for an ideal compressible fluid. The action formulation that lead to this solution accords with the *gauge theory* of theoretical physics partly. The solution is regarded as an extended version of the Clebsch representation [1]. It is important to recognize that four independent fields are introduced in this new representation. This fact is understood to predict *existence* of a system of new fields governing those as a whole. Total action S of this system [4] was proposed to consist of two actions, S_{fl} for the fluid motion and S_{int} describing interaction. Thus we have $S = S_{fl} + S_{int}$:[1]

$$S_{fl} = \int_M \rho \left(\tfrac{1}{2} v^k v^k - \epsilon(\rho) \right) c_*^{-1} \mathrm{d}\Omega, \qquad S_{int} = -\int_M a_\nu j^\nu \, \mathrm{d}\Omega, \qquad \mathrm{d}\Omega = c_* \mathrm{d}t \, \mathrm{d}^3\boldsymbol{x}, \tag{1}$$

where $\boldsymbol{v} = (v^k)$ is the fluid velocity, $\epsilon(\rho)$ is the specific internal energy, ρ is the fluid density. It is assumed that $\partial\epsilon/\partial s = 0$ (where s denotes the specific entropy), because no entropy change occurs in the assumed uniform ideal (inviscid) fluid, and c_* is a parameter representing a phase velocity. For the expression of S_{int}, see the Appendix.

From an infinitesimal 4-vector $\mathrm{d}x^\nu = (c_*\mathrm{d}t, \mathrm{d}x^1, \mathrm{d}x^2, \mathrm{d}x^3)$ in the 4-dim space-time ($x^0 = c_* t$), one can form a current 4-vector $j^\nu = \rho \, \mathrm{d}x^\nu/\mathrm{d}t = (\rho c_*, \rho v^k)$. The four fields which were introduced in the solution (9) define a co-vector $a_\nu = (a_0, -a_1, -a_2, -a_3)$ in *component-wise*, with its vector counterpart being a^ν defined by $g^{\nu\lambda}a_\lambda = (a_0, a_1, a_2, a_3)$. Using a_ν, one-form $\mathcal{A}$ is defined by

$$\mathcal{A} = a_\nu \mathrm{d}x^\nu = g_{\nu\lambda}a^\lambda \mathrm{d}x^\nu = a_0\mathrm{d}x^0 - a_1\mathrm{d}x^1 - a_2\mathrm{d}x^2 - a_3\mathrm{d}x^3. \tag{2}$$

Then it is seen that the integrand $a_\nu j^\nu$ of S_{int} is a scalar quantity represented by the scalar product $g_{\nu\lambda}j^\nu a^\lambda$.

Consider a transformation $a_\nu \to a_\nu - \partial_\nu \Psi$ (a certain kind of *gauge* transformation; see below). Then the one-form $\mathcal{A}$ is transformed to $\mathcal{A} - \mathrm{d}\Psi$. The interaction action S_{int} is also transformed as

$$S_{int} \to -\int_M a_\nu j^\nu \, \mathrm{d}\Omega + \int_M (\partial_\nu j^\nu) \, \Psi \, \mathrm{d}\Omega - \int_M \partial_\nu (j^\nu \Psi) \, \mathrm{d}\Omega. \tag{3}$$

The last term drops out because it is transformed to surface integrals over ∂M surrounding the volume M of 4D spacetime. Then, the *gauge invariance* of S_{int} requires $\partial_\nu j^\nu = 0$ for arbitrary scalar function $\Psi(x^\nu)$:

$$\partial_\nu j^\nu = \partial_t \rho + \partial_k(\rho v^k) = 0, \tag{4}$$

where $\partial_\nu = (c_*^{-1}\partial_t, \partial_k)$. Thus the equation of mass conservation is required by the gauge invariance. Conversely, the mass conservation equation (4) assures the gauge invariance of S_{int}.

ACTION FORMULATION WITH TAKING ACCOUNT OF A BACKGROUND FIELD A_ν

Learning from the *electromagnetic* theory, it is proposed as hinted above that there exists a gauge field a_ν supporting the mass conservation law in the background. On the analogy with the electromagnetism [3] (EM in short), the present action formulation for fluid flows is represented by a three-component action S:

$$S = S_{fl} + S_{int} + S_F; \qquad S_F = -\frac{1}{4\mu} \int F_{\nu\lambda} F^{\nu\lambda} \, \mathrm{d}\Omega. \tag{5}$$

where μ and c_* are constant parameters. The first two actions are defined by (1): S_{fl} for the fluid motion and S_{int} for interaction. Each of the integrands of S_{fl} and S_{int} satisfies local gauge invariance with respect to both transformations

*Corresponding author. Email: kambe@ruby.dti.ne.jp *Home*: Meguro-ku, Tokyo, Japan 153-0043

[1] Latin indices $i, k, \cdots$ take the values $1, 2, 3$; while Greek indices $\lambda, \nu, \cdots$ take the values $0, 1, 2, 3$. Using the metric tensor $g_{\nu\lambda} = \mathrm{diag}(1, -1, -1, -1)$, a co-vector a_ν corresponding to a vector a^λ is given by $a_\nu = g_{\nu\lambda}a^\lambda = (a^0, -a^1, -a^2, -a^3)$.

of translation and rotation (note that mass element $\mathrm{d}m = \rho\,\mathrm{d}^3\boldsymbol{x}$ is invariant). Hence they are consistent with the gauge theory. The third action S_F should describe the new gauge field a_ν existing in the background of flow field.

Remembering the one-form $\mathcal{A}$ of (2) and taking its external differential d, we obtain the *field strength* two-form $\mathcal{F} = \mathrm{d}\mathcal{A} = \sum F_{\nu\lambda}\,\mathrm{d}x^\nu \wedge \mathrm{d}x^\lambda$, analogous to the EM case [5] where two EM-like fields are introduced by $\boldsymbol{e} = -\partial_t\boldsymbol{a} - \nabla\phi$ and $\boldsymbol{b} = \nabla\times\boldsymbol{a}$. Using the field strength tensor $F_{\nu\lambda}$, one can form a scalar by the scalar product $F_{\nu\lambda}F^{\nu\lambda}$. Thus the third action is defined *gauge-theoretically* by the form of S_F given in (5).

To find the *dynamical* equation of fluid motion by the principle of least action, we vary only the trajectory $\boldsymbol{x}_p(t,\boldsymbol{\alpha})$ of fluid particle $\boldsymbol{\alpha}$ with fixing both of the particle-label $\boldsymbol{\alpha}$ and the field strength $F_{\nu\lambda}$, finding

$$\partial_t\boldsymbol{v} + (\boldsymbol{v}\cdot\nabla)\boldsymbol{v} + \rho^{-1}\nabla p = \boldsymbol{f}, \qquad \boldsymbol{f} \equiv \boldsymbol{e} + \rho^{-1}\boldsymbol{j}\times\boldsymbol{b} \quad (\boldsymbol{j} = \rho\boldsymbol{v}). \tag{6}$$

On the other hand, to obtain the *field* equations, we assume the fluid motions (v^k and j^ν) given (fixed) and vary only the potentials a_ν (serving as the coordinates of the system). Thus we find a set of Maxwell-like equations [5]:

$$\nabla\cdot\boldsymbol{b} = 0, \qquad \partial_t\boldsymbol{b} + \nabla\times\boldsymbol{e} = 0, \qquad \nabla\cdot\boldsymbol{d} = \rho, \qquad -\partial_t\boldsymbol{d} + \nabla\times\boldsymbol{h} = \boldsymbol{j}, \tag{7}$$

where $\boldsymbol{d} = \epsilon\boldsymbol{e},\ \boldsymbol{h} = \mu^{-1}\boldsymbol{b}$ with $\epsilon = 1/(\mu c_*^2)$.

The greatest merit of the present formulation is that the four fields $(\boldsymbol{e},\ \boldsymbol{b}, \boldsymbol{d},\ \boldsymbol{h})$ are invariant with respect to the gauge transformation described at the paragraph above Eq.(3) and, in addition, the last two equations of (7) assure the mass conservation equation (4): $\partial_t\rho + \nabla\cdot\boldsymbol{j} = 0$ (with operating ∂_t and $\nabla\cdot$ respectively and summing up). Thus the mass conservation law is naturally connected with the symmetry of gauge invariance [6, 7]. This is consistent with the Noether's theorem mentioned in the beginning. It should be emphasized that there is no particular mathematical device (except the gauge invariance) assumed to derive the mass conservation.

Let us consider an application of the above formulation, showing an example of *rotational*-waves propagating through a shear flow along a straight channel or a pipe. The wave is characterized as *transversal*, compared with the acoustic wave studied extensively in the fluid mechanics which is *longitudinal*. There exist ample evidences of streamwise rotational-streaks and long meandering wavy-structures in streaky wall-turbulence.

Unperturbed state is a steady streaky flow with streamwise vorticity toward the x-axis. The unperturbed velocity is expressed as $\boldsymbol{U}_s(y,z)$ in the Cartesian frame with $(\nabla\times\boldsymbol{U}_s)_x \neq 0$. Fluid is assumed *incompressible*, for simplicity, with the uniform density ρ_0. The field vectors $\boldsymbol{e}$, $\boldsymbol{b}$ and $\boldsymbol{a}$ are governed by wave equations:

$$\nabla^2\boldsymbol{e} - c^{-2}\partial_t^2\boldsymbol{e} = \mu\,\partial_t\boldsymbol{j}', \qquad \nabla^2\boldsymbol{b} - c^{-2}\partial_t^2\boldsymbol{b} = -\mu\nabla\times\boldsymbol{j}', \qquad \nabla^2\boldsymbol{a} - c^{-2}\partial_t^2\boldsymbol{a} = -\mu\boldsymbol{j}', \tag{8a, b, c}$$

($c = c_*$ for simplicity), where $\boldsymbol{e} = -\partial_t\boldsymbol{a}$ and $\boldsymbol{b} = \nabla\times\boldsymbol{a}$ with $\phi = const$ owing to the incompressibility. These are wave equations with forcing terms derived from the current perturbation $\boldsymbol{j}' = \rho_0\boldsymbol{v}'$ with μ a coupling constant introduced in S_F. The waves propagate to the streamwise direction with frequency ω and wavenumber k: $\boldsymbol{e}, \boldsymbol{v}', \boldsymbol{b} \propto \exp[i(kx-\omega t)]$. Expressing the x-components of $\boldsymbol{e}$ and $\boldsymbol{v}'$ as $e_x = \tilde{e}(y,z)\exp[i(kx-\omega t)]$ and $v_x' = \tilde{u}(y,z)\exp[i(kx-\omega t)]$, we obtain a connecting relation for their amplitudes:

$$\tilde{u}(y,z) = (i/\mu\rho_0\omega)\,(\partial_y^2 + \partial_z^2)\tilde{e}(y,z) \qquad \text{from (8a)},$$

where the amplitudes $\tilde{u}$ and $\tilde{e}$ depend on cross-flow coordinates (y,z). The cross-flow modes of $\tilde{u}$ and $\tilde{e}$ are to be determined from (linear) analyses of the equation (6). There exist plenty of evidences of existence of cross-stream modes (not *irrotational*) in channel flows or pipe flows, both laminar and turbulent, to which this formulation may be applied.

References

[1] Clebsch A. Über die Integration der hydrodynamischen Gleich.*J. Reine und Angew. Math.* **56**: 1-10, 1859.
[2] Noether E. Invariant variations problem, *Nachr d König Gesellsch d Wiss zu Göttingen, Math-Phys. Klasse*, 235-257, 1918; English transl. by Tavel M A: *Transport Theory and Statistical Physics*. **1**: 186-207, 1971.
[3] Landau L.D., Lifshitz E.M. The Classical Theory of Fields (Chap. 3 & 4). Pergamon Press, 1975.
[4] Kambe, T. New representation of rotational flow fields satisfying Euler's equation of an ideal compressible fluid. *Fluid Dyn. Res.* **45**: 015505 (16pp), 2013.
[5] Kambe T. New scenario of turbulence theory and wall-bounded turb.: Theoretical significance, *Geophys. Astrophys. Fl. Dyn.* **111**: 448-507, 2017.
[6] Kambe T. Part I. Landscape of JSFM 50 Years Ago; Part II. New Perspectives on Mass Conservation Law and Waves in Fluid Mechanics. ながれ (*Nagare*) **37**: 436-441, 2018. *web site*: **http://www.nagare.or.jp/download/noauth.html?d=37-5_sinpo2.pdf&dir=13**
[7] Kambe, T. New perspectives on mass conservation law and waves in fluid mechanics. *Fluid Dyn. Res.* **52**: 1-34, 2020.

Appendix: The interaction action S_{int}

The interaction part $S_{int} = -\int a_\nu j^\nu \mathrm{d}^3\boldsymbol{x}\,\mathrm{d}t$ was proposed originally by Kambe (2013) [4] as

$$S_{int} \equiv -\int_M \Big(\mathrm{D}_t\psi + \mathrm{D}_t\langle\boldsymbol{U},\ \boldsymbol{Z}\rangle\Big)\,\rho\,\mathrm{d}^3\boldsymbol{x}\,\mathrm{d}t, \quad = -\int_M \Big(a_\nu j^\nu + \partial_k Q^k\Big)\,\mathrm{d}^3\boldsymbol{x}\,\mathrm{d}t, \quad Q^k \equiv \rho Z^k\,(U_i v^i),$$
$$j^\nu = (\rho c_*, \rho\boldsymbol{v}), \quad a_0 = c_*^{-1}(\partial_t\psi + Z^k\partial_t U_k), \quad (-a_1, -a_2, -a_3) = \nabla\psi + \boldsymbol{Z}\times(\nabla\times\boldsymbol{U}), \tag{9}$$

Each of the three factors (ψ, $\langle\boldsymbol{U},\boldsymbol{Z}\rangle$ and D_t) in the definition of S_{int} satisfies local gauge invariance with respect to translation and rotation since first two are scalars and the operator D_t is gauge-invariant ([4], §5 (ii)). Hence it is consistent with the gauge theory.

VORTEX DYNAMICS ON A UNIT ROTATING SPHERE

Pankaj Jagad[1] and Ravi Samtaney *[1]
[1]Mechanical Engineering, Physical Science and Engineering Division, King Abdullah University of Science and Technology, Thuwal, SaudiArabia

Summary We study the effect of rotation on vortex dynamics on a unit sphere, for an incompressible and inviscid flow, using a Discrete Exterior Calculus (DEC) scheme. For a given initial vorticity distribution, we vary the rate of rotation of the sphere from zero (non-rotating case, corresponding to infinite Rossby number (Ro)) to 20 (corresponding to Ro = 0.025), and investigate the evolution with time. For the non-rotating case, the vortices evolve in to thin filaments due to so-called forward enstrophy cascade, and at late times much of these structures cascade beyond the smallest scale resolved in the simulation, and a quadrupolar vortical structure emerges. For finite Rossby number, rotation suppresses the forward cascade of enstrophy and the flow does not evolve in to a quadrupolar vortical structure at late times. Moreover, rotation aligns the vortices along the azimuthal direction.

INTRODUCTION

Incompressible, inviscid flow investigations on a unit sphere are usually performed to investigate atmospheric flows. These flows are characterized by two-dimensional (2D) turbulence wherein there is direct cascade of enstrophy to smaller scales and inverse cascade of energy to larger scales. In the investigations of such planetary atmospheric flows, it is important to include the effect of rotation of the planet. We investigate the effect of rotation on vortex dynamics on a unit sphere and investigate the direct cascade of enstrophy in 2D turbulence using a DEC method [1]. Exterior calculus deals with the calculus on differential geometries, hence differential forms, and provides an alternative to the vector calculus. DEC is numerical exterior calculus and deals with the discrete differential forms. A discreet differential form is an integral quantity on a mesh object, e.g., integral of a vector along a mesh edge $\int \mathbf{v} \cdot \mathbf{dl}$ represents a discrete 1-form. DEC retains at the discrete level many of the identities of its continues counter part. It is coordinate independent, therefore suitable for solving flows over curved surfaces. More details about DEC can be found in some of the representative references such as [2, 3].

EQUATIONS AND NUMERICAL METHOD

The governing Euler equations in rotating frame of reference and in DEC notations read

$$\left[\left(-\frac{1}{\Delta t}\right) I - \frac{1}{2}\left(W_V\right)^{n+1} *_0^{-1} \left[-d_0^T\right] *_1\right] \left(U^*\right)^{n+1} + *_1^{-1} d_1^T \left(P^d\right)^{n+1} = F, \tag{1}$$

with

$$F = \left(-\frac{1}{\Delta t}\right)\left(U^*\right)^n + \frac{1}{2}\left(W_V\right)^{n+1} *_0^{-1} d_b\left(V\right)^{n+1} + \frac{1}{2}\left(W_V\right)^n *_0^{-1} \left(\left[-d_0^T\right] *_1 \left(U^*\right)^n + d_b\left(V\right)^n\right) + \frac{1}{2}\left[\left(W_V\right)^{n+1} + \left(W_V\right)^n\right] *_0^{-1} f_{dual2}, \tag{2}$$

$$\left[d_1\right]\left(U^*\right)^{n+1} + \left[0\right]\left(P^d\right)^{n+1} = 0, \tag{3}$$

where U^* is the vector containing mass flux primal 1-form for all mesh primal edges, V is the vector containing the discrete primal velocity 1-forms for all mesh primal edges, and P^d is the vector containing discrete dynamic pressure 0-forms for all mesh dual vertices, Δt is the discrete time interval, d_0, $\left[-d_0^T\right]$, d_1^T are the discrete exterior derivative operators, $*_0^{-1}$, $*_1$, $*_1^{-1}$ are discrete Hodge star operators. The dual-2 form f_{dual2} corresponds to the Coriolis parameter $f = 2\Omega\cos\theta$, where Ω is the rate of rotation of the sphere, and θ is the colatitude. The details of the DEC discretization, the definition and expressions of the discrete operators as well as that of the matrix W_V and the operator d_b are available in [1]. The present discretization uses the energy-preserving time integration [4]. We employ a biharmonic viscosity as a means to filter and dissipate very high wavenumber content. The set of non-linear equations represented by equations (1) - (3) are solved using Picard's iterative method for the mass flux 1-form and dynamic pressure degrees of freedom.

RESULTS AND DISCUSSION

The time evolution of the vorticity field from a given initial vorticity distribution was studied for a non-rotating unit sphere as well as a rotating one at the rate of rotation (Ω) of 5, 10, and 20. The initial stream function distribution at the mesh primal nodes is computed as

$$\psi\left(\theta,\phi\right) = \sum_{l=4}^{10}\sum_{m=-l}^{l} \psi_{lm} Y_l^m\left(\theta,\phi\right), \tag{4}$$

where θ is the colatitude, ϕ is the longitude, Y_l^m is the spherical harmonic function of degree l and order m, and ψ_{lm} are the expansion coefficients with $\psi_{l-m} = (-1)^m \psi_{lm}^*$. Here ψ_{lm}^* is the complex conjugate of ψ_{lm}. The ψ_{lm} values as given in [5] were used. The initial mass flux 1-form for a primal edge was then computed as $u^* = d_0\psi$. The scalar (since, here, there is only one component of vorticity normal to the surface) vorticity distribution at the primal nodes was computed

*Corresponding author. E-mail: ravi.samtaney@kaust.edu.sa.

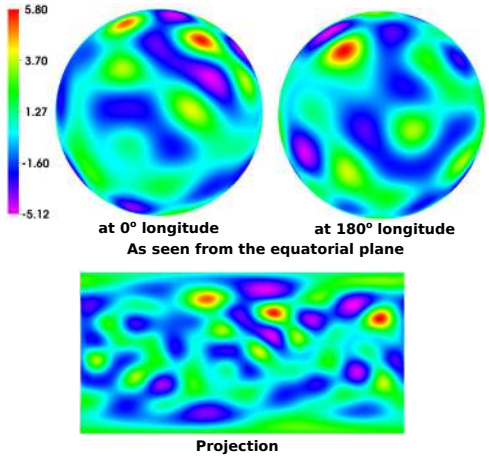

Figure 1: Initial vorticity distribution.

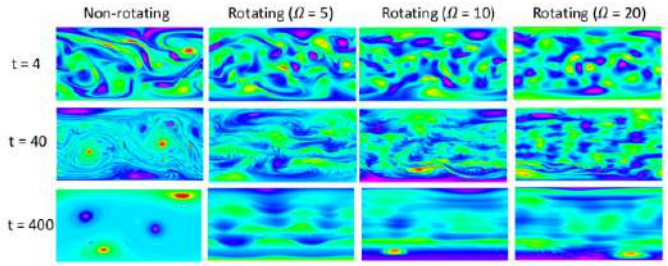

Figure 2: Vorticity distribution at later times.

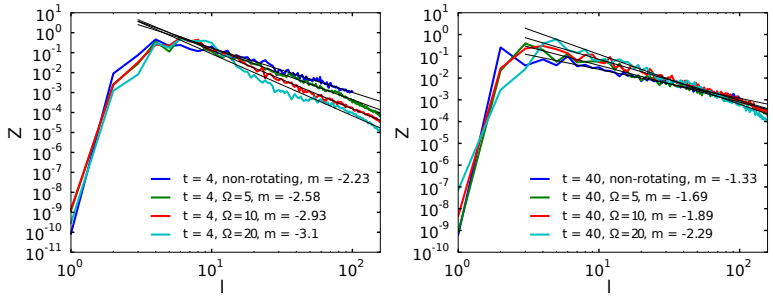

Figure 3: Vorticity power spectra.

from the relation $\omega = *_0^{-1}\left[-d_0^T\right] *_1 u^*$ for post-processing. Figure 1 shows the initial vorticity distribution. Figure 2 shows the vorticity distribution for different rates of rotation at later times. The plots show that for the non-rotating case, the vortices evolve in to thin filaments due to so-called forward enstrophy cascade by time $t = 40$, and at late times ($t = 400$) much of these structures cascades beyond the smallest scale resolved in the simulation and hence dissipate, and a quadrupolar vortical structure evolves. However, not much evolution in to the thin filaments is seen for the rotating cases, and at late times no quadrupolar vortical structure is formed. Thus, rotation suppresses the forward cascade of enstrophy. Moreover, alignment of vortices along the azimuthal direction is seen for the rotating cases. In order to quantify the effect of rotation, vorticity power spectra, vorticity probability density, probability density function (PDF) of aspect ratio (ratio of major to minor axis length of vortical structures), and that of the cosine of the angle between the major axis and the azimuthal direction (which is a measure of orientation of the vortical structures) are determined. Figure 3 shows vorticity power spectra. At $t = 4$, the slope of the spectrum is 2.23 for the non-rotating case for $10 \leq l \leq 100$. The slope increases with increasing Ω, and at $\Omega = 20$ it is 3.1, implying decrease of the enstrophy cascade to smaller scales with increasing Ω. Similarly at $t = 40$, the slope of the spectrum is 1.33 for the non-rotating case, and it increases with increasing Ω, showing suppression of the forward enstrophy cascade with increasing Ω. Moreover, for each Ω, the slope of the spectrum decreases from $t = 4$ to $t = 40$, showing forward cascade of enstrophy with time. The plots of vorticity probability density, and PDF of aspect ratio, not included here due to space limitation, also confirm the suppression of enstrophy cascade with rotation. The plots of PDF of cosine of the angle between the vortex major axis and the azimuthal direction, not included here due to space limitation, confirms that the rotation orients the vortices along the azimuthal direction.

CONCLUSIONS

We investigated the effect of rotation on the enstrophy cascade for a 2D turbulence on a unit sphere using a DEC scheme. Rotation suppresses the cascade and aligns the vortices along the azimuthal direction.

References

[1] Mohamed M. S., Hirani A. N., Samtaney R. Discrete exterior calculus discretization of incompressible navier-stokes equations over surface simplicial meshes. *Journal of Computational Physics* **312**: 175-191, 2016.

[2] Perot J. B., Zusi C. J. Differential forms for scientists and engineers. *Journal of Computational Physics* **257**: 1373-1393, 2014.

[3] Hirani A. N. Discrete Exterior Calculus. *PhD Thesis*, California Institute of Technology, 2003.

[4] Mullen P., Crane K., Pavlov D, Tong Y., Desbrun S. Energy-preserving integrators for fluid animation. *In ACM Transactions on Graphics (TOG)* **28**: 1-38, 2009.

[5] Dritschel D. G., Qi W., Marston J. B. On the late-time behavior of a bounded, inviscid two-dimensional flow. *J. Fluid Mech.* **783**: 1-22, 2015.

CROSSOVER FROM INTERACTION TO DRIVEN REGIMES IN QUANTUM VORTEX RECONNECTIONS

Luca Galantucci*[1], Andrew W. Baggaley[1], Nick G. Parker[1], and Carlo F. Barenghi[1]
[1]School of Mathematics, Statistics and Physics, Newcastle University, Newcastle upon Tyne, United Kingdom

Summary Reconnections of coherent filamentary structures play a key role in the dynamics of fluids, redistributing energy and helicity among the length scales, triggering dissipative effects and inducing fine-scale mixing. Unlike ordinary (classical) fluids where vorticity is a continuous field, in superfluid helium and in atomic Bose-Einstein condensates (BECs) vorticity takes the form of isolated quantised vortex lines, which are conceptually easier to study. New experimental techniques now allow visualisation of individual vortex reconnections in helium and condensates. It has long being suspected that reconnections obey universal laws, particularly a universal scaling with time of the minimum distance between vortices δ. Here we perform a comprehensive analysis of this scaling across a range of scenarios relevant to superfluid helium and trapped condensates, combining our own numerical simulations with the previous results in the literature. We reveal that the scaling exhibit two distinct fundamental regimes: a $\delta \sim t^{1/2}$ scaling arising from the mutual interaction of the reconnecting strands and a $\delta \sim t$ scaling when extrinsic factors drive the individual vortices.

Quantum vortex reconnections play a fundamental role in quantum fluid dynamics. In particular, reconnecting events redistribute energy and helicity amongst scales, trigger a turbulent energy cascade generating the same Kolmogorov spectrum of classical turbulence and, in the low-temperature limit, quantum vortex reconnections represent the ultimate mechanism for the dissipation of incompressible kinetic energy via acoustic emission.

In past studies, many authors have focused on the potential existence of a universal route to reconnections, which may take the form of a vortex ring cascade [4, 5], a particular rule for the reconnecting cusp angles [1, 9] or, more promising, a special scaling with time of the minimum distance $\delta(t)$ between the reconnecting vortex strands [6, 11, 7, 10, 2].

In the present work [3], we focus on the last property showing that $\delta(t)$ can obey *two* distinct scalings. In addition to the already observed $\delta \sim t^{1/2}$ scaling, we predict and observe a new linear $\delta \sim t$ behaviour [Fig. 1]. In our study we show how these two scalings arise from rigorous dimensional arguments and then demonstrate their existence in a vast campaign of numerical simulations performed with both the Gross-Pitaevskii (GP) model and the Vortex Filament (VF) method. Distinctive of our simulations are the larger initial distance compared to past numerical studies and the extension of the investigations to experimentally accessible trapped Bose-Einstein Condensates (BECs) (both box- and harmonically trapped), where vortex reconnections can now be studied with unprecedented resolution [8].

The numerical results obtained show that the $\delta(t)$ scaling is determined by the balance between the vortex mutual interaction (responsible for the $\delta \sim t^{1/2}$ scaling) and extrinsic factors (vortex curvature, density gradients, vortex images) driving the individual vortices towards reconnection (leading to the $\delta \sim t$ behaviour). The relevance of these two scalings arises from their observation in experimentally accessible condensates and in the two limiting, yet fundamental, cases of vortex reconnections in homogeneous systems, namely the reconnection of orthogonal vortices and the vortex ring - vortex line interaction.

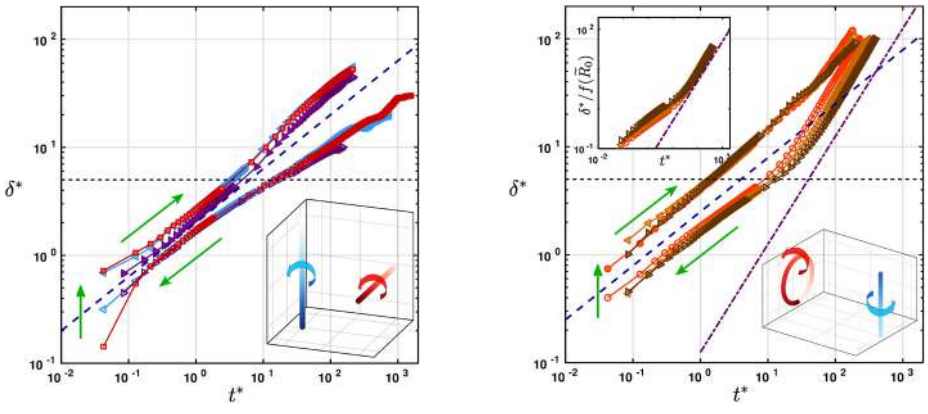

Figure 1: **GP simulations: homogeneous unbounded BECs.** Evolution of the rescaled minimum distance $\delta^* = \delta/\xi$ (with ξ being the healing length) between reconnecting vortices as a function of the rescaled temporal distance to reconnection $t^* = (t - t_r)/\tau$. Empty (filled) symbols correspond to pre (post) reconnection dynamics. **Left**: orthogonal vortices reconnection with rescaled initial distance δ_0^* equal to 10 (▷), 20 (◁) and 30 (□). **Right**: ring-line reconnection for constant initial distance $\delta_0^* = 100$ and vortex ring radii R_0^* equal to 5 (○), 7.5 (◁) and 10 (▷). In both sub figures: the horizontal dashed black line indicates the width of the vortex core ($\approx 5\,\xi$), the blue-dashed line shows the $t^{*1/2}$ scaling. Dot-dashed violet line in the right panel indicates the t^* scaling.

*Corresponding author. E-mail: luca.galantucci@newcastle.ac.uk

References

[1] ATAM De Waele and RGKM Aarts. Route to vortex reconnection. *Phys Rev Lett*, **72**(4):482, 1994.

[2] E Fonda, KR Sreenivasan, and DP Lathrop. Reconnection scaling in quantum fluids. *Proc Nat Acad Sci*, **116**(6):1924–1928, 2019.

[3] L. Galantucci, A. W. Baggaley, N. G. Parker, and C. F. Barenghi. Crossover from interaction to driven regimes in quantum vortex reconnections. *Proc Natl Acad Sci USA*, **116**:12204, 2019.

[4] RM Kerr. Vortex stretching as a mechanism for quantum kinetic energy decay. *Phys Rev Lett*, **106**(22):224501, 2011.

[5] M Kursa, K Bajer, and T Lipniaki. Cascade of vortex loops initiated by a single reconnection of quantum vortices. *Phys Rev B*, **83**:014515, 2011.

[6] S Nazarenko and R West. Analytical solution for nonlinear schrödinger vortex reconnection. *J Low Temp Phys*, **132**:1, 2003.

[7] C Rorai, J Skipper, RM Kerr, and KR Sreenivasan. Approach and separation of quantum vortices with balanced cores. *J Fluid Mech*, **808**:641, 2016.

[8] S Serafini, L Galantucci, E Iseni, T Bienaime, R Bisset, CF Barenghi, F Dalfovo, G Lamporesi, and G Ferrari. Vortex reconnections and rebounds in trapped atomic bose-einstein condensates. *Phys Rev X*, **7**:021031, 2017.

[9] R Tebbs, A J. Youd, and CF Barenghi. The approach to vortex reconnection. *J Low Temp Phys*, **162**(3-4):314, 2011.

[10] A Villois, D Proment, and G Krstulovic. Universal and nonuniversal aspects of vortex reconnections in superfluids. *Phys Rev Fluids*, **2**(4):044701, 2017.

[11] S Zuccher, M Caliari, AW Baggaley, and CF Barenghi. Quantum vortex reconnections. *Phys Fluids*, **24**:125108, 2012.

INSTABILITY OF A VORTEX ROLL-UP AT A FLUID-FLUID INTERPHASE

G. Le Doudic*[1], I. Cantat[2], A. Saint-Jalmes[2], C. Tregouet[2], S. Perrard[3], M. Labousse[4], and M. Roché[1]
[1]Matière et Systèmes Complexes, Université de Paris, CNRS UMR 7057, Paris, France
[2]Institut de Physique de Rennes, University Rennes 1, Rennes, France
[3]LPENS, Université PSL, Paris France
[4]Gulliver, CNRS UMR 7083, ESPCI Paris and PSL University, Paris, France

Summary A local deposition of a droplet of soluble surfactant solution on a water layer creates a surface tension difference along the air/water interphase. The resulting surface tension gradient sets the fluid in motion on each side of the water/air interphase. This effect is called the Marangoni effect. A continuous injection of the surfactant solution at the interphase leads to a quasi-steady Marangoni flow of finite size. The finite size results from the competition between the transport of surfactant molecules by the flow and their diffusion into the bulk water after their desorption from the interphase. The Marangoni stress at the fluid/fluid interphase creates a boundary layer which is advected outwards. When it reaches the edge of the Marangoni region, where the flow decelerates dramatically, the boundary layer winds up generating a stationary vorticity roll-up. In this study, we characterise the flow and the key parameters that play a role within its complex structure and its dynamic. To do so, we use surface flow visualisation and bulk water flow measurements with a 3D Particle Image Velocimetry technique. We propose a model that predicts the growth of the vorticity roll-up. Eventually, we discuss the destabilisation of the vorticity roll-up due to its interaction with a solid wall (bottom of the tank) and the free surface.

EXPERIMENTAL SETUP

We create a quasi-steady solutal Marangoni flow by injecting an aqueous solution of the surfactant Tetradecyltrimethylammonium bromide (TTAB) at a constant molar flow rate $0.2 < Q_\mathrm{a} < 2\ \mu\mathrm{mol}\cdot\mathrm{s}^{-1}$ at the surface of a water layer contained in a tank (Fig. 1.a.) in a fashion similar to refs [1, 2]. Since the surfactant solution is transparent, we visualise the flow by adding tracers, olive oil droplets, to the surfactant solution. These $50\ \mu\mathrm{m}$ droplets diffract light and make the flow visible (Fig. 1.b.). The Marangoni flow has been well characterised in refs. [1,2]. Indeed, the flow is axisymetric and oriented from the point of injection outwards up to a distance R_M with a velocity $U_\mathrm{s} \approx 0.1\ \mathrm{m}\cdot\mathrm{s}^{-1}$. At $r = R_\mathrm{M}$ the surface velocity decreases abruptly by more than one order of magnitude. This flow remains stationnary during several tens of minutes, until the concentration of surfactants in the water layer reaches the critical micellar concentration.

OBSERVATIONS

In this abstract, we present results corresponding to the study of the outer region of the Marangoni flow *i.e.* the region beyond R_M. Figure 1.b. shows several pairs of in-plane vortices emerging and growing from the Marangoni border outwards along the perimeter of the Marangoni border. These vortices are emitted periodically with a period t_w.

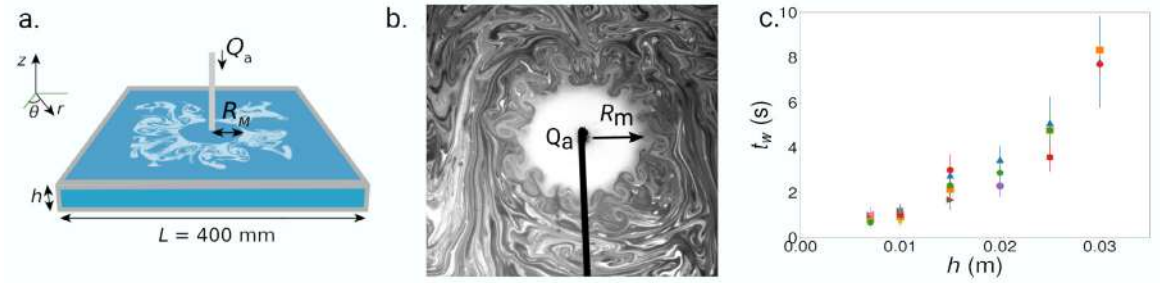

Figure 1: a) Sketch of the experimental setup. The surfactant solution is injected through the needle with a constant molar flow rate Q_a. Once the first drop of surfactant touches the free surface the Marangoni flow starts and reaches its maximum size R_M. We perform the experiments in a $400\ \mathrm{mm} \times 400\ \mathrm{mm} \times 40\ \mathrm{mm}$ tank. b) Top view of a continuous Marangoni flow created at constant flow rate $Q_\mathrm{a} = 1.8\ \mu\mathrm{mol}\cdot\mathrm{s}^{-1}$ and height of water $h = 15\ \mathrm{mm}$. Oil droplets accumulate at $r = R_\mathrm{M}$ allowing us to see the flow outside the Marangoni region. c) Whirl pair emission period t_w as a function of h for a range of flow rates.

Figure 1.c. shows that t_w depends mostly on the thickness of the water layer h. Other parameters such as Q_a have no influence. Tracers allow us to probe the surface part of the flow and Fig. 1.c. highlights the need to investigate flow in the bulk. To do so, we use a laser-scanning particle image velocimetry (LS-PIV) (Fig. 2.a.). that allows to reconstruct 3D maps of the velocity field. A moving mirror deviates the vertical laser sheet used to shine light on particles dispersed in the water layer in a periodic fashion at a 200 Hz rate. We record movies with a high-speed camera at a 5 kHz rate. Thus, we obtain PIV information for 25 planes in the volume of the layer at a rate of 20 fps.

*Corresponding author. E-mail: gabriel.le-doudic@univ-paris-diderot.fr

VORITICITY ROLL-UP

Recirculation in the bulk of a liquid over which another liquid spreads is expected,[3, 4, 5, 6, 7]. Its existence is confirmed by LS-PIV measurements (Fig. 2.b). The boundary layer starts to roll-up near the interphase at time $t = t_0$ and then diffuses into the bulk towards the bottom of the tank. Growth occurs untill roll-up size is comparable to h, at which point the roll-up interacts with the bottom of the tank and destabilises. The duration of this process is similar to t_w (Fig 3.c.).

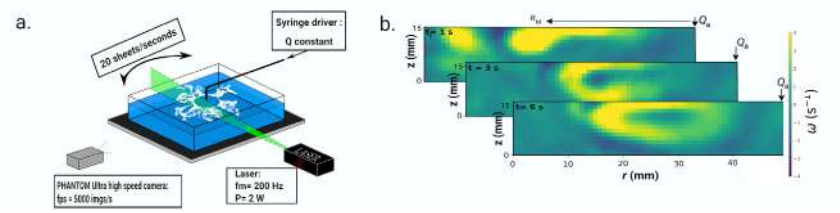

Figure 2: a) Sketch of LS-PIV. b) Vortex strength fields deduced from LS-PIV measurements in a single plane. $Q_\mathrm{a} = 0.5\ \mu\mathrm{mol} \cdot \mathrm{s}^{-1}$ at $h = 15$ mm. The boundary layer rolls up at $t_0 = 1$ s, near the interphase. At $t = 3$ s, the roll-up has diffused in the bulk towards the bottom of the tank. At $t = 6$ s it touches the bottom and start destabilising.

We can predict the growth of the vortex over time. We assume that the vorticity roll-up is fed by the output of the boundary layer located at R_M. Mass and angular momentum coming out of this layer are conserved and transferred to the roll-up. The vortex roll-up is characterized by its radius $r(t)$ and its angular velocity ω. Writing conservation laws for mass, momentum and angular momentum with azimuthal invariance, the time evolution of r obtains:

$$r(t) = \delta\sqrt{1 + \frac{ut}{\delta}}. \tag{1}$$

From Eq. 1, we can also deduce the time t_b that it takes to the vortex to reach the bottom *i.e.* $r(t_\mathrm{b}) = \frac{h}{2}$, it yields:

$$t_\mathrm{b} = \frac{\delta}{u}\left(\frac{h^2}{4\delta^2} - 1\right). \tag{2}$$

Equation 1 agrees well with the experimental results as long as the roll-u is free of interactions with the bottom wall of the tank (Fig. 3.b.). We also show that Eq. 2 predicts the correct scaling for t_w with h (Fig 3.c.). When the vorticity roll-up destabilises and interacts with the free surface it creates a second generation of vortices: the in-plane vortices.

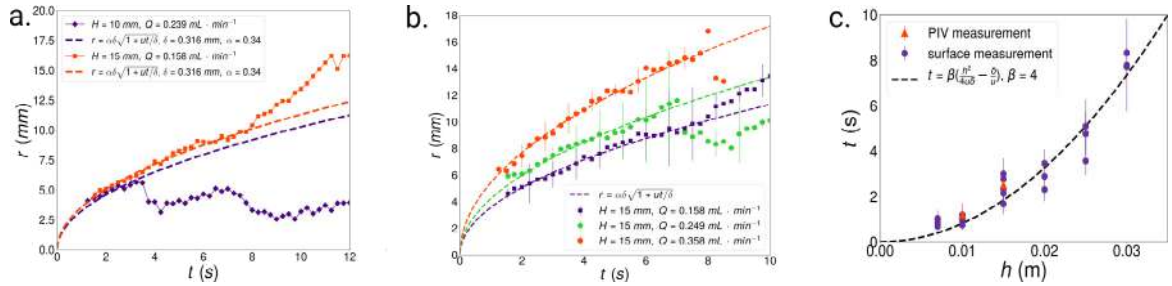

Figure 3: a) Growth of the voriticity roll-up as a function of time. The time of destabilisation increases with h. b) Thickness h is fixed and we increase Q_a. The vortex rolls up faster for higher Q_a but destabilises almost at the same instant t. c) Comparison between experimental emission times and Eq. 2 up to a prefactor.

CONCLUSION AND FUTURE WORK

We have the opportunity to study a soluto-capillary flow that generates beautiful in-plane vortices which are the consequence of the interaction between a vorticity roll-up and a free surface. This is shown by a simultaneous destabilisation of a 3D flow corresponding to a vorticity roll-up below the edge of the Marangoni flow. The future work will consist in studying the stability of the roll up in the frame of the Rayleigh criterion [8]. Therefore, I am looking forward to present and discuss our work at the International Congress of Theoretical and Applied Mechanics of 2020 in Milan.

References

[1] M. Roché, Z. Li, I. M. Griffiths, Ian M., S. Le Roux, I. Cantat, A. Saint-Jalmes, H. A. Stone. Phys Rev Lett,**20**, 208302, (2014).
[2] S. Le Roux, M. Roché, I. Cantat, A. Saint-Jalmes. Physical Review E (2016).
[3] D. G. Suciu, O. Smigelschi, and E. Ruckenstein, AIChE J **13**, 1120 (1967).
[4] A.D. Dussaud and S.M. Troian, Phys. Fluids, **10**, 23 (1998).
[5] A.D. Dussaud, S.M. Troian, and S.R. Harris, Phys. Fluids **10**, 1588 (1998).
[6] H. Kim, J. Lee, T.H. Kim, and H.Y. Kim, Langmuir **31**, 8726 (2015).
[7] J. Kim, K. Muller, O. Shardt, S. Afkhami, and H.A. Stone, Nat. Phys **13**, 1105 (2017).
[8] P.G. Drazin, Introduction to Hydrodynamic Stability, Cambridge Texts In Applied Mathematics.

COMPRESSIBILITY EFFECT ON VORTICITY PRODUCTION AND DARRIEUS-LANDAU INSTABILITY OF A PREMIXED FLAME FRONT

Yasuhide Fukumoto*[1] and Keigo Wada[2]
[1]Institute of Mathematics for Industry, Kyushu University, Fukuoka, Japan
[2]Center of Coevolutionary Research for Sustainable Communities, Kyushu University, Fukuoka, Japan

Summary The Darrieus-Landau instability (DLI) is a linear instability of a premixed flame front, for which the vorticity production plays an important role. We address the effect of compressibility on the DLI, based on a set of equations modeling a one-step overall reaction process of the Arrhenius type, which take account of the heat conduction and the diffusion of a deficient species as well as the viscosity. The method of the matched asymptotic expansions for analyzing the hierarchical thin structure of a flame front, the preheat zone and the reaction zone in it, is extended to second order in the Mach number Ma. The compressibility is shown to act to weaken the DLI. We focus on the Mach-number effect on the baroclinic vorticity production in a flame front of a reacting fluid.

INTRODUCTION

The Darrieus-Landau instability (DLI) is a linear instability of a planar flame front which is identified as a density discontinuous surface. The original analysis of the DLI concluded that a planar flame front is necessarily unstable with larger growth rate for disturbances of shorter wavelengths. This is not consistent with experimental observations, and stabilizing mechanisms have been pursued as exemplified by the Markstein effect of front curvature on the laminar flame speed [1]. The effect of weak compressibility has been considered for long wave disturbances, without entering into the reaction zone [2].

We address the effect of compressibility on the DLI, based on a set of equations modeling a one-step overall reaction process of the Arrhenius type, which takes account of the heat conduction and the diffusion of a deficient species as well as the viscosity. We pursue the large-activation-energy asymptotics under the assumption of large Zeldovich number β. The method of the matched asymptotic expansions [3] in the small parameter β^{-1}, which resolves the fine-scale structure inside a flame front, consisting of the preheat and the reaction zones, is extended to the square in the Mach number $Ma(\ll 1)$.

STABILIZING EFFECT OF COMPRESSIBILITY ON DLI

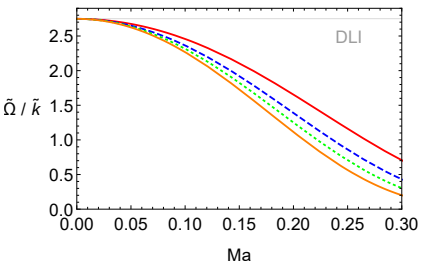

Figure 1: Ω divided by wavenumber k v.s. Mach number Ma. Prandtl number $P_r = 0$ (dot-dashed), 2/4 (dashed), 3/4 (dotted), and 4/4 (bold).

A detailed analysis of the reaction zone, a very thin layer sandwiched by the preheat zones, reveals remarkable effects of compressibility origin, a volumetric heat loss and a dramatic decrease in the laminar flame speed S_L. The spatial variation of pressure plays the role of heat source (sink) and naturally brings in the heat loss, temperature decrease at the edge of the reaction zone on the burned side.

This is seen from the heat-conduction equation, expressed in dimensionless form, as

$$R\left(\frac{\partial T}{\partial t}+(\boldsymbol{V}\cdot\nabla)T\right)=\delta\Delta T + \frac{\gamma-1}{\gamma}\left(\frac{\partial}{\partial t}+\boldsymbol{V}\cdot\nabla\right)P+qQ. \qquad (1)$$

Here R, $\boldsymbol{V}$, T, P and Q are respectively the density of mixture, the velocity field, the temperature, the pressure and the reaction rate of the Arrhenius type, with γ and q being the specific-heat ratio and the heat release, respectively. The dimensionless diffusion coefficient δ provides the scale factor of the preheat zone relative to the hydrodynamic one. The spatial variation of pressure plays the role of heat source (sink) and naturally brings in the heat loss, temperature decrease at the edge of the reaction zone on the burned side. It is noteworthy that the pressure terms couple (1) to the Navier-Stokes equation as opposed to the case of the low-Mach-number limit.

Associated with the heat loss is the decrease of the laminar flame speed S_L, through the burning rate eigenvalue problem [5]. The growth rate of the DLI is proportional to S_L, and therefore the decrease of S_L has a direct influence on stabilizing the DLI as shown in Figure 1. The growth rate Ω divided by the wavenumber k, is plotted as a function of Ma, for several values of the Prandtl number Pr. Figure 1 shows a dramatic decrease of the growth rate with Ma, even to close to zero. This trend is enhanced by viscosity (Pr).

*Corresponding author. Email: yasuhide@imi.kyushu-u.ac.jp

VORTICITY PRODUCTION INSIDE A FLAME FRONT

The vorticity produced in a flame front, by the baroclinic effect, has a stabilizing effect on the DLI [5, 6]. The vorticity jump is affected by the pressure in the low-Mach-number limit [3]. With compressibility, the temperature and the mass flux take part in the vorticity production as illustrated in Figure 2. In the low-Mach-number limit, the normal component of the vorticity vector $\boldsymbol{\Omega}$, produced inside a flame front, is well known to be continuous at the leading order in δ. On the other hand, the tangential component of $\boldsymbol{\Omega}$ is discontinuous across a flame front. It is this component that has a stabilizing effect on the hydrodynamic instability [6]. The compressibility brings a novel effect of the temperature and the mass flux on the tangential jump of $\boldsymbol{\Omega}$ (Figure 2). We reveal that a viscous effect, of compressibility origin, plays a vital role for the suppression of DLI.

The vorticity jump across a flame front is derived from the following equation for the vorticity $\boldsymbol{\Omega}$.

$$\frac{\partial \boldsymbol{\Omega}}{\partial t} - \nabla \times (\boldsymbol{V} \times \boldsymbol{\Omega}) = \frac{1}{\gamma Ma^2} \frac{\nabla R \times \nabla P}{R^2} + \delta Pr \left(\frac{\Delta \boldsymbol{\Omega}}{R} - \frac{\nabla R \times \Delta \boldsymbol{V}}{R^2} - \frac{1}{3} \frac{(\nabla R) \times \nabla (\nabla \cdot \boldsymbol{V})}{R^2} \right). \tag{2}$$

Integrating (2) over the reaction and the preheat zones, we deduce the following jump condition for the tangential component of the vorticity vector.

$$\left[\!\left[\frac{M}{R} \boldsymbol{n} \times (\boldsymbol{\Omega} \times \boldsymbol{n}) \right]\!\right] = - \left[\!\left[\frac{1}{R} \right]\!\right] (\boldsymbol{n} \times \nabla) \left((1 + \gamma Ma^2) P_M + T - \frac{q^2}{2} \left(1 + \frac{4}{3} Pr \right) M \right), \tag{3}$$

where M and q are the mass flux and the non-dimensional heat release, and the double brackets means the difference of values between behind and ahead of a flame front on the hydrodynamic scale, for example, $[\![\phi]\!] = \phi_+ - \phi_-$ for a given function ϕ. The quantities on the right hand side of (3) are evaluated at the upstream unburned edge of a flame front. The pressure is expanded to square of the small Mach number ($Ma^2 \ll 1$) as

$$P = 1 + \gamma Ma^2 P_M; \quad P_M = P_{2M} + Ma^2 P_{4M}, \tag{4}$$

where P_{2M} was considered in the low-Mach-number limit [3] and P_{4M} is new, being tied with the velocity field of $O(Ma^2)$.

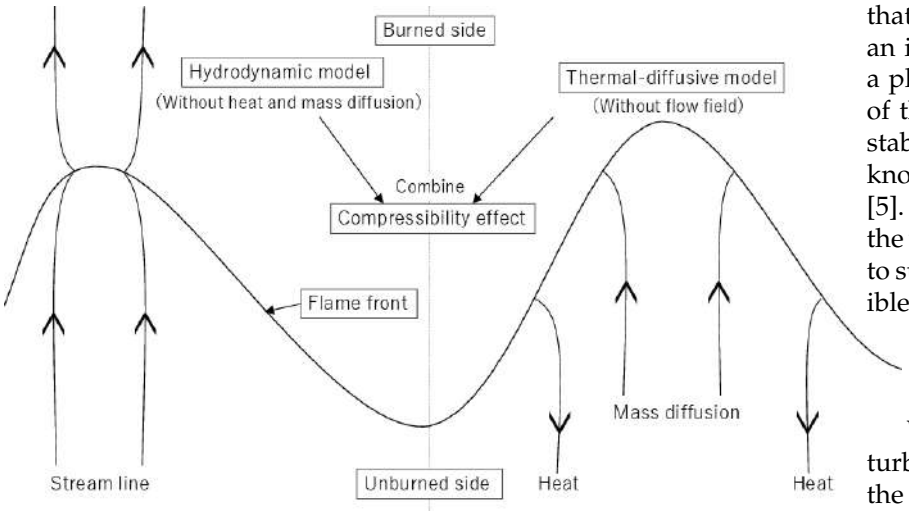

Figure 2: Compressibility combines two independent models.

The jump condition (3) suggests that the Prandtl number Pr plays an important role in the stability of a plane flame because the existence of the vorticity generically brings a stabilizing effect on the DLI as is known in zero-Mach-number limit [5]. We confirm that this is true and the viscous effect acts to weaken and to suppress the DLI in the compressible case as shown in Figure 1.

CONCLUSIONS

We show, by the singular perturbation method, the influences of the temperature and the mass flux on the vorticity production accompanied by the viscous effect. The higher-order term of the pressure in the Mach number is derived, with P_{4M} containing the Prandtl number. These results are obtained by combining the thermal-diffusive model with the hydrodynamic equation. The weakening and even the suppression of the DLI can occur in the coefficient of the linear, in wavenumber, terms in the growth rate.

References

[1] Markstein G. H. Experimental and Theoretical Studies of Flame-Front Stability. *J. Aero. Sci.* **18**: 77-85, 1951.
[2] Wada K., Fukumoto Y. Expansion for Effect of Compressibility on Darrieus-Landau Instability of a Premixed Flame with Translational Symmetry. *preprint*, 2020.
[3] Matalon M., Cui C., Bechtold J. K. Hydrodynamic Theory of Premixed Flames: Effects of Stoichiometry, Variable Transport Coefficients and Arbitrary Reaction Orders. *J. Fluid Mech.* **487**: 179-210, 2003.
[4] Fukumoto Y., Izuyama T. Thermal Attenuation and Dispersion of Sound in a Periodic Emulsion. *Phys. Rev. A* **46**: 4905–4921, 1992.
[5] Joulin G., Vidal P. An Introduction to the Instability of Flames, Shocks and Detonations, in *Hydrodynamics and Nonlinear Instabilities*, Cambridge University Press, 1998.
[6] Sivashinsky G. I., Clavin P. On the Nonlinear Theory of Hydrodynamic Instability in Flames. *J. Physique* **48**: 193-198, 1987.

GENERAL SOLUTIONS FOR CLOSELY SPACED CO-ROTATING HELICAL VORTICES

Andrés Castillo-Castellanos*[1], Eduardo Durán Venegas[1], and Stéphane Le Dizès[1]
[1]Aix Marseille Univ, CNRS, IRPHE, Marseille, France

Summary We extend the work of [2] and present solutions describing the interaction of helical pairs of closely spaced co-rotating vortices using a vortex filament approach. For these structures the helical symmetry is broken, but still display a form of spatial periodicity and are stationary in a rotating and translating frame. A low order approximation is proposed and compared against numerical results. Finally, we discuss how our results may be used to describe the far wake generated by a rotor.

CONTEXT

Rotating blades, such as the ones of a helicopter main rotor or those of a horizontal-axis wind turbine, generate concentrated vortices at their tips, which are transported downstream creating a helical geometry. These helical vortices are associated with several practical issues actively investigated. One concerns the interaction between a tip vortex and a following blade (Blade-Vortex Interaction, BVI), responsible in part for the accelerated wear in wind turbines and undesirable noise in helicopters during forward and descending flight [6]. One successful approach to mitigate BVI is to modify the flow structure by introducing a modified vane tip to split tip vortices in two [1].

Interactions between closely spaced co-rotating helical vortices are controlled by the separation distance d and core size a. If the ratio d/a is smaller than a threshold, vortices merge into a single entity (see, for instance [4]). This process can be accelerated by the development of short-wave instabilities [5]. For this work, we consider a is small enough to neglect the inner core structure and describe vortices as filaments [3, 2]. We also consider d/a is large enough prevent merging, but small enough for the vortices to twist around each other. For these vortices, we show there exist a unique moving frame where structure is steady, i.e. vortex elements are moving along the structure without distorting it. In this work, we present general solutions and characterize the tip vortex dynamics in this special configuration.

PROBLEM DESCRIPTION AND MAIN PARAMETERS

To identify the main parameters of our problem, consider a simple case of vortex interaction: a pair of equal vortices of circulation Γ which rotate around each other with constant angular velocity $\omega = \Gamma/(\pi d^2)$. If we impose an axial flow U_z, the vortices are passively transported streamwise creating a helical pattern. If we also introduce an eccentric rotation with angular velocity Ω, the resulting pattern describes a cycloidal curve defined by the distance between the axes of rotation R, the separation distance d and twist parameter $\beta \equiv 2\pi/\tilde{\theta}$ which compares the rotation of the vortex pair to the rotation around the eccentric axis (figure 1a). The ensemble is transported streamwise creating a helical pair with pitch $h = (\pi d^2 U_z)/\Gamma$ inscribed on top of a helix with pitch $H = U_z/\Omega$ (figure 1b).

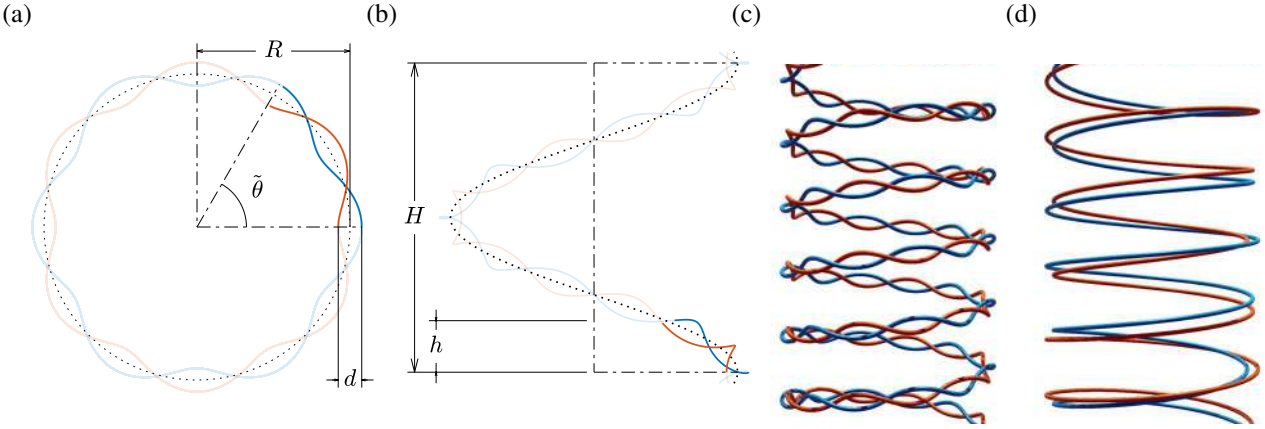

Figure 1: Representation of closely spaced helical pairs. (a) Top and (b) front view illustrate main parameters: radius R, separation distance d, pitch H, and $\beta = 2\pi/\tilde{\theta} = H/h$. Solutions describe a (c) braided pattern for $|\beta| > 1$, and (d) leapfrog pattern for $|\beta| < 1$.

From these parameters we identify the following dimensionless geometric parameters:

$$R^* = \frac{R}{d} \qquad H^* = \frac{H}{d} \qquad \varepsilon = \frac{a}{d} \qquad \beta = \frac{H}{h} \tag{1}$$

We consider $R^* = 9.5$, $\varepsilon = 0.2$, β between -8 and 8, and decrease H^* between 100 and a minimum value ranging between 3 and 6 depending on β. The resulting configuration may describe a braided pattern (figure 1c) or a leapfrog-type pattern where interior and exterior vortices trade places every $1/\beta$ turns (figure 1d).

*Corresponding author. E-mail: castillo@irphe.univ-mrs.fr

DEFORMED SOLUTIONS

While the example above is based on (2-D) point vortices, we show that is indeed possible to obtain similar solutions which incorporate the complete 3-D vortex dynamics using the free-vortex method [3]. Different properties, such as radial deformation, frame velocity or induced flow, are provided from numerical simulations. Numerical results are compared with analytic expressions at zero- and first-order of approximation. In both cases, we assume the locally axial flow is decoupled from the axial vorticity dynamics. Zero-order expressions are deduced from (2-D) point vortex dynamics transported along the axial direction as in the example above. First-order corrections are introduced by considering the vortex pair to be transported along a direction locally tangent to a helix of radius R^* and pitch H^*. For this latter, a good qualitative and quantitative agreement is observed for values of H^* and β where mutual interaction is predominant (see, for instance frame velocities shown in figures 2a and 2b).

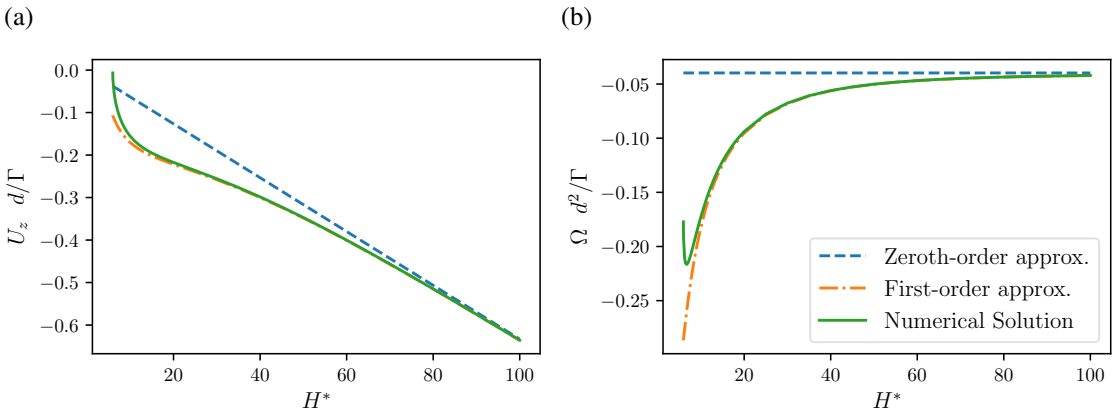

Figure 2: Dimensionless frame velocities for a closely spaced helical pair as function of H^* for $R^* = 9.5$, $\varepsilon = 0.2$, and $\beta = 8$. Numerical solutions are compared to expressions at zero- and first-order of approximation.

Finally, we discuss how these solutions may be used to represent the far wake generated by a rotor with a modified vane tip. If the flow was created by a rotor, the moving frame where each solution is stationary is necessarily attached to a rotor blade. By analyzing the direction of propagation of the vortices relative to that of the external wind, the general solutions are associated to a particular rotor flow regime.

References

[1] Brocklehurst, A. & Pike, A.C. Reduction of BVI noise using a vane tip. *AHS Aeromechanics Specialists Conference* 1994.
[2] Durán Venegas, E. & Le Dizès, S. Generalized helical vortex pairs. *J. Fluid Mech.* **865**: 523–545, 2019.
[3] Leishman, J.G. Principles of Helicopter Aerodynamics. Cambridge University Press, 2016.
[4] Leweke, T., Le Dizes, S. & Williamson, C.H.K. Dynamics and instabilities of vortex pairs. *Annual Review of Fluid Mechanics* **48**: 507–541, 2016.
[5] Meunier, P & Leweke, T. Elliptic instability of a co-rotating vortex pair. *J. Fluid Mech.* **533**: 125–159, 2015.
[6] Yung, H. Y. Rotor blade–vortex interaction noise. *Progress in Aerospace Sciences* **36 (2)**: 97–115, 2000.

TORRICELLI'S DISCHARGE LAW MODIFIED BY THE BATHTUB VORTEX

Aurore Caquas[1,2], Luc Pastur[1], Alain Genty[2]
[1]Institute of Mechanical Sciences and Industrial Applications, ENSTA Paris, Institut Polytechnique de Paris, France
[2]Den-Service de thermo-hydraulique et de mécanique des fluides (STMF), CEA, Université Paris-Saclay, F- 91191 Gif sur Yvette, France

Summary We study the discharge flow in presence of a bathtub vortex and compare it to the Torricelli's law $v = \sqrt{2gH}$, where v is the flow rate velocity, g the gravity constant and H the height of the water column [1]. The experimental set-up is composed of a cylindrical tank, a container and measuring devices, all embarked on a rotating platform. Mass measurements, particule image velocimetry (PIV) and ombroscopy give respectively access to the flow rate velocity, the vortex circulation and the shape deformation due to the vortex. Deviations to the Torricelli's law are observed only when the surface is deformed.

INTRODUCTION

The Torricelli's law [1,2] has been known now for over 300 years and predicts well the emptying speed of a tank whose orifice's size is very small in comparison to its own size [3]. Under this condition, the law only has to be corrected by a multiplicative constant $\alpha < 1$, owing to the *vena contracta* phenomenon and the singular pressure drop associated with it [4].

Vortex formation while emptying can appear in a simple bathtub but can also be present on much larger scales, as for example in the study of vortex flow in hydroelectric dams or in RNR-Na reactors. Yet, it is not clear how the vortex that commonly forms modify the discharge.

EXPERIMENTAL SETUP

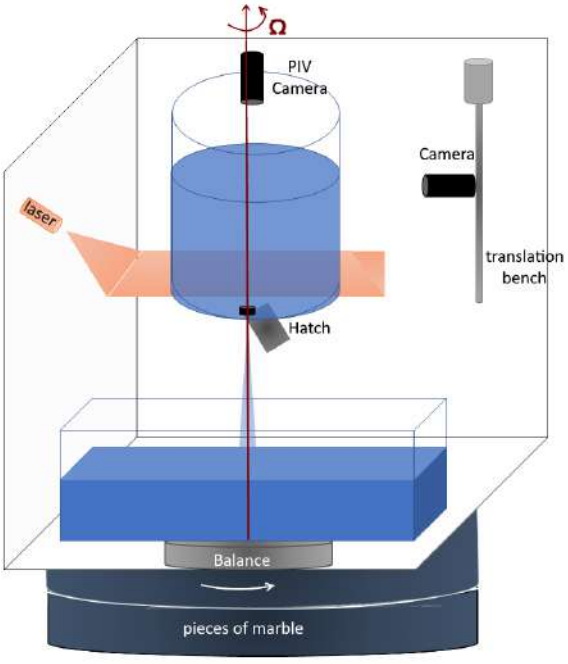

Figure 1. Experimental set-up (see text below).

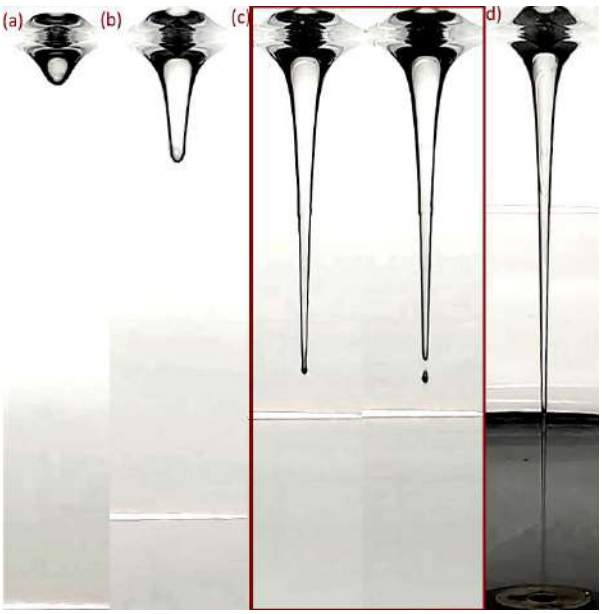

Figure 2. Pictures of the different states of the surface.

The plexiglas tank (fig.1) is a cylinder with radius $R = 300 \pm 1$ mm and height $L = 393$ cm, with a hole centred at the bottom. The diameter of the outlet section can be adjusted by means of cylindrical taps that clip into the hole. These taps have an internal diameter varying from 1 to 43 mm. The start of the draining process is controlled remotely by opening a watertight hatch under the tank. The tank is mounted on a rotating platform and is centered on the axis of rotation. The platform consists of two 20 cm thick cylindrical pieces of marble of diameter 1.5 m, piled up together and separated by a 1 mm thick film of pressurized air, which allows the upper part to rotate above the lower part without solid friction. The rotation speed can be continuously changed from 0 to 1 rad. s^{-1} (10 round. min^{-1}).

The cumulative loss of liquid in the tank is measured by a scale Ohaus Ranger 7000 with a precision of 0.5 g and a sampling frequency of 0.5 Hz. The balance is centered on the axis of the rotating frame, such that no inertial correction be required for the measurement of the weight. The height of water H is determined from the measurement of the mass loss M. The flowrate Q follows from the analytic derivative of $M(t)$ by using a Savitzky-Golay [5] polynomial interpolation of M over 20 points of measurement, yielding an estimated flow rate precision of about 0.03 L. min^{-1}.

The circulation Γ of the vortex is determined by averaging 3 to 10 successive velocity fields every 3 to 10 s, obtained by particle image velocimetry (PIV) with an acquisition frequency of 3 to 60 fps. The free surface shape is obtained by ombroscopy using a camera on a motorized translation bench. The translation bench is controlled in order to follow the interface and avoid parallax errors.

RESULTS

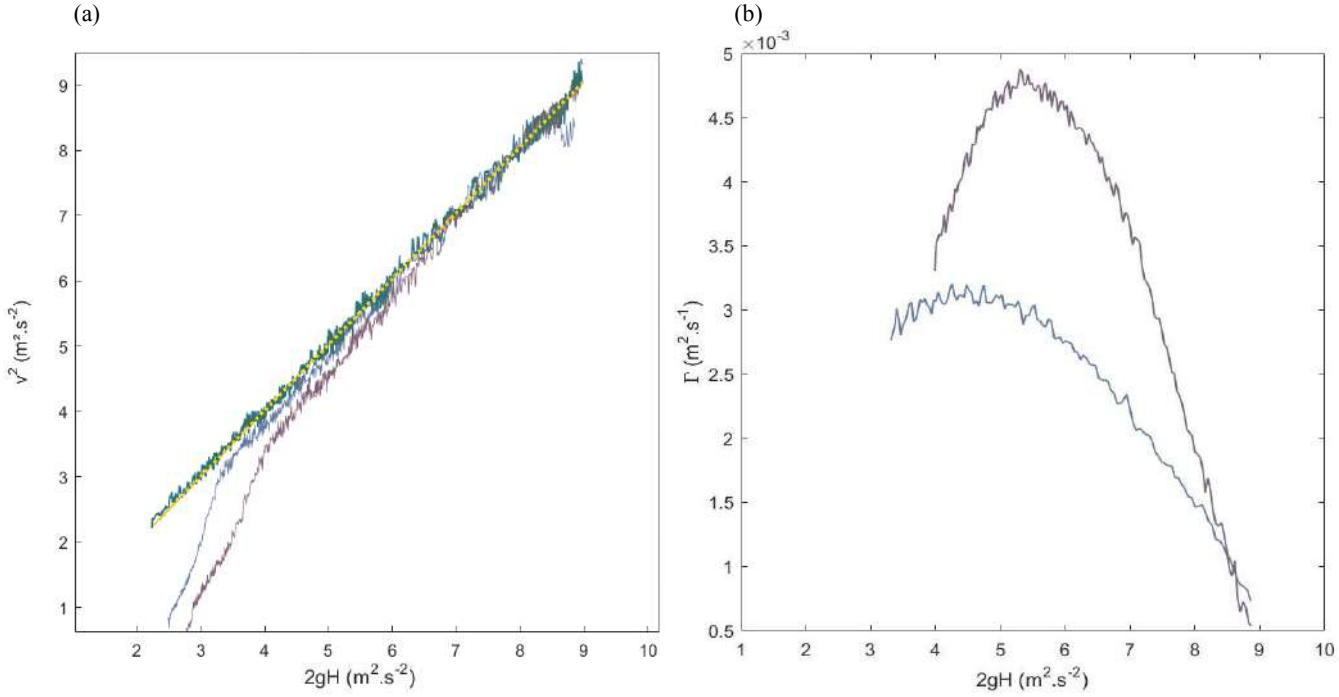

Figure 3 (a) Evolution of the velocity square as a function of $2gH$. The curve in green is the Torricelli's experimental case, the curve dashed in yellow is the theorical law. In grey, the tank rotation velocity is 1.03 round. s^{-1} and in burgundy 1.53 round. s^{-1}.
(b) Evolution of the circulation of the vortex as a function of $2gH$. In grey, the tank rotation velocity is 1.03 round. s^{-1} and in burgundy 1.53 round. s^{-1}.

At the beginning of the emptying, we have not measured any significant differences between the draining with a vortex and the Torricelli's case with water at rest before emptying (fig. 3.a.). In this first regime (3 $2gH > 7$), the free surface is not deformed, despite the presence of a vortex in the flow (fig. 3.b.). When the circulation of the vortex Γ increases and the fluid depth decreases, the free surface takes shape (fig. 2 a. and b.) and a deviation from the Torricelli's law is observed (see fig. 3.a for 4 $< 2gH < 7$). In this regime, the flow rate decreases. Then, bubbles are ripped off the tip of the gaseous core (fig. 2.c). Just after that, the tip quickly moves down to the drain section. As a result, the outlet section is reduced by the gaseous core, as shown in figure. 2.d and the emptying flow rate is further decreased (see fig. 3.a for 2 $2gH < 4$).

PERSPECTIVES

Surprisingly, the flow rate did not appear to be influenced by the presence of the vortex in itself but rather by the shape of the interface created by the vortex. This deformation depends on the vortex strength, the height of the water and the emptying flow rate. We are currently setting up a new experiment to confirm these initial results and refine them in a stationary regime. The new set-up will consist of a closed water circuit to keep the surface height constant.

References

[1] Torricelli E. De motu gravium naturaliter accelerato. Firenze, 1643.
[2] Bernoulli D. Hydrodynamica, sive de viribus et motibusfluidorum commentarii. Strasbourg, 1738.
[3] C. Clanet. Clepsydrae, from Galilei to Torricelli. *Physics of Fluids*, **12(11)**, 2743-2751,2000.
[4] Thomson M., Melville L. Theoretical hydrodynamics. Courier Corporation, 1996.
[5] Savitzky A., Golay M. J. E., *Analytical Chemistry* **8** (1964), 1627.

NONLINEAR EVOLUTION OF VERTICALLY CONFINED INTERNAL GRAVITY WAVES IN NONUNIFORM STRATIFICATION

Bruce R. Sutherland*[1], Ton S. van den Bremer[2], Houssam Yassin[3], and Lois E. Baker[4]
[1]Departments of Physics and of Earth & Atmospheric Sciences, University of Alberta, Edmonton, Canada [2]Department of Engineering Science, University of Oxford, Oxford, England
[3]Department of Physics, University of Alberta, Edmonton, Canada (presently at Princeton University) [4]Department of Civil and Environmental Engineering, Imperial College London, London, England

Summary Because the density of the ocean increases with depth, internal gravity waves can propagate within it, moving under the influence of buoyancy forces. One mechanism for the generation of these waves is through the action of the tides periodically crossing submarine topography. Far from these sources, these "internal tides" are observed to propagate horizontally as vertically confined modes. It remains an open question as to how these internal tides ultimately break down - transferring energy from large scales to sufficiently small scales capable of mixing. Besides interacting with topography, currents and eddies, a well-studied mechanism for the spontaneous breakdown of internal gravity waves is through triadic resonant instabilities (with parametric subharmonic instability being a specific example). Although this readily occurs in uniform stratification, this work will show through theory and numerical simulations that in realistic (non-uniform) ocean stratification the dominant mechanism for energy transfer is through nonlinear self-interaction leading to the generation of mean flows and superharmonics.

THEORY

We restrict ourselves to the examination of two-dimensional, vertically confined Boussinesq internal waves, including the effects of background rotation, but neglecting diffusion and viscosity. The fully nonlinear equations may be combined to give a single equation for the evolution of the streamfunction, $\psi(x,z,t)$ [1]:

$$\underbrace{\left(\partial_{tt}(\partial_{xx}+\partial_{zz})+N^2\partial_{xx}+f^2\partial_{zz}\right)}_{\equiv\, L}\psi = \underbrace{\nabla\cdot\left[\partial_t(\zeta\vec{u})-\partial_x(b\vec{u})+f\partial_z(v\vec{u})\right]}_{\equiv\, \mathcal{N}}. \qquad (1)$$

Here $\vec{u}=(u,w)$ is the velocity velocity vector in the along-stream and vertical directions, ζ is the spanwise vorticity, and b is the buoyancy. The Coriolis parameter, f, is assumed to be constant, while the squared buoyancy frequency, $N^2(z)$, is an arbitrary function of height.

At leading order in amplitude, the right-hand side of (1) can be neglected and the resulting linear equation in $\psi_1 = A\hat{\psi}(z)e^{i\phi}$ (with $\phi\equiv kx-\omega t$) can be solved numerically to give the vertical structure function of the "parent mode" and its corresponding dispersion relation $\omega(k)$. From this result, the polarization relations give the corresponding leading-order expressions for u, v, w, ζ and b.

Our interest here is in the self-interaction of a mode-1 parent wave whereby products of the linear fields on the right-hand side of (1) acts as an order amplitude-squared forcing to the streamfunction, provided N^2 is non-constant. The products of the linear fields provide forcing both to superharmonics, with phase 2ϕ, and to a mean Eulerian flow (with zero phase).

Superharmonics

In the examination of superharmonics, the amplitude, A, of the parent mode can be taken as constant. Through use of Sturm-Liouville theory, the vertical structure of the forcing can be decomposed into vertical modes. Despite the complex vertical structure of the forcing, a straightforward analysis reveals that the most of forcing acts to excite a mode-1 disturbance. Furthermore, the natural frequency of the superharmonic mode is comparable to twice the frequency of the parent mode (which is the forcing frequency, 2ω). Consequently, the superharmonic is found to grow and decay periodically with a frequency determined by the difference of the forcing frequency and the natural frequency of the superharmonic [2]. If this difference is very small, the superharmonics can grow to amplitudes comparable with the parent wave, leading to possible irreversible extraction of energy from the parent mode through dynamics beyond weakly nonlinear theory. Such dynamics should be most significant close to the equator which is where, from the dispersion relation, the frequency has a near-linear dependence upon wavenumber.

Eulerian and Lagrangian Mean Flows

In order to determine the Eulerian flow induced by the parent mode, it is convenient to assume that the amplitude, A, is a slowly varying function of horizontal space and time. Then one can find corrections to the polarization relations that account for spatial variations in the amplitude envelope. This procedure was followed by van den Bremer et al [3] in the case of no background rotation. As with the study of superharmonics, with realistic ocean stratification it is found that the Eulerian mean flow induced by a mode-1 parent wave is predominantly mode-1 and these flows can be substantial

*E-mail: bruce.sutherland@ualberta.ca.

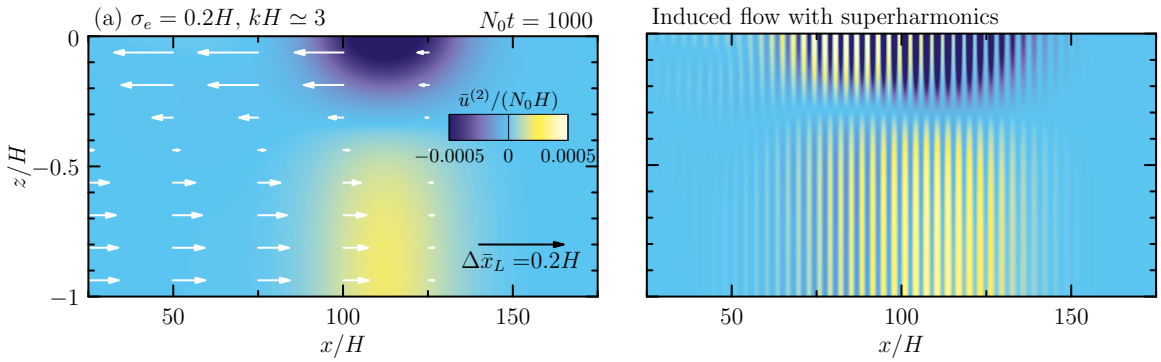

Figure 1: For numerical simulations with stratification decreasing exponentially with depth (with e-folding scale $\sigma_h = 0.2H$), snapshots from simulations: (a) Fourier-filtered horizontal flow at time $N_0 t = 1000$ and filtered parcel displacements, and (b) Horizontal flow with wave-packet removed to reveal the induced Eulerian flow superimposed with superharmonics. The Gaussian wave-packet has amplitude $a_0 = 0.01H$, $\sigma = 20H$ and $kH = 1$.

for a horizontally long parent wave. This has significant implications for the nonlinear evolution of the parent wave, which becomes Doppler shifted by the vertically varying horizontal currents associated with the induced Eulerian flow. Separately, the Stokes drift associated with the parent wave can be computed, but this is negligible compared with the induced Eulerian flow if the waves are long. Hence, for oceanic internal tides, the Lagrangian transport (the sum of the induced Eulerian flow and the Stokes drift [4]) is dominated by the Eulerian induced flow. Besides the interest in the influence upon the modulational stability of modulated internal modes, this study provides a step towards improved predictions for the transport of microplastics in the open ocean.

SIMULATION RESULTS

As an illustration of the theoretical predictions, Figure 1 shows a) the induced flow and b) superharmonics excited by a horizontally Gaussian small-amplitude internal wave packet with half-width 20 times the depth, H, of the domain. The background stratification is exponentially decreasing with depth having maximum buoyancy frequency N_0 at the surface and e-folding depth $\sigma_h = 0.2H$. This simulation was initialized with relatively short horizontal wavelength waves in the wave-packet such that $k = \pi/H$. In simulations with more representative oceanic values of $k \sim 0.2/H$, the induced Eulerian induced flow and superharmonic amplitudes are closer to that of the parent mode, leading to non-trivial nonlinear interactions between the disturbances.

CONCLUSIONS

This analysis presented here provides the starting point for a more thorough examination of the evolution and ultimate breakdown of the internal tides in the ocean. While there has been some observational [5, 6] and numerical [7] evidence for the occurrence of parametric subharmonic instability of low-mode internal tides, this is such a slow-growing process compared with self-interaction in non-uniform stratification [8] that its importance for the transfer to small scales of energy associated with internal tides is questionable. The relatively unexplored phenomenon of self-interacting internal modes in non-uniform stratification provides a fruitful ground in which to explore novel mechanisms for the breakdown of internal tides. Ongoing studies include examining the influence of the finite spanwise extent of the waves, their modulation by solar and lunar tidal forcing and their meridional propagation, accounting for changes in f with latitude.

References

[1] S. Wunsch. Harmonic generation by nonlinear self-interaction of a single internal wave mode. *J. Fluid Mech.*, 828:630–647, 2017.
[2] L. Baker and B. R. Sutherland. The evolution of superharmonics excited by internal tides in non-uniform stratification. *J. Fluid Mech.*, under review.
[3] T. S. van den Bremer, H. Yassin, and B. R. Sutherland. Lagrangian transport by vertically confined internal gravity wavepackets. *J. Fluid Mech.*, 864:348–380, 2019. doi:10.1017/jfm.2019.30.
[4] O. Bühler. *Waves and Mean Flows*. Cambridge University Press, Cambridge, UK, 2nd edition, 2014.
[5] T. Hibiya and M. Nagasawa. Latitudinal dependence of diapycnal diffusivity in the thermocline estimate using a finescale parameterization. *Geophys. Res. Lett.*, 31:L01301, 2004.
[6] M. H. Alford, J. A. MacKinnon, Z. Zhao, R. Pinkel, J. Klymak, and T. Peacock. Internal waves across the Pacific. *Geophys. Res. Lett.*, 34:L24601:1–6, 2007. doi:10.1029/2007GL031566.
[7] J. Hazewinkel and K. B. Winters. PSI of the internal tide on a β plane: Flux divergence and near-inertial wave propagation. *J. Phys. Oceanogr.*, 41:1673–1682, 2011.
[8] B. R. Sutherland and R. Jefferson. Triadic resonant instability of horizontally periodic internal modes. *Phys. Rev. Fluids*, under review.

ENERGY-FLUX VECTORS OF INERTIAL WAVES IN STRONGLY ROTATING TURBULENCE

Naoto Yokoyama *[1] and Masanori Takaoka[2]
[1]Department of Mechanical Science and Bioengineering, Osaka University, Toyonaka, Japan
[2]Department of Mechanical Engineering, Doshisha University, Kyotanabe, Japan

Summary The weak turbulence theory of inertial waves in strongly rotating turbulence tells us that the resonant interactions transfer energy to waves which have small scales perpendicular to the rotational axis without changing its scales parallel to the rotational axis. The energy flux determined at each wave number in the wave-number space is expected to reproduce that predicted by the weak turbulence theory. In this abstract, the energy-flux vector in anisotropic turbulence is proposed based on the net locality and the efficiency of the energy transfer. The energy-flux vector is confirmed to successfully reproduce the energy flux in the inertial-wave turbulence.

INTRODUCTION

In strongly rotating turbulence, anisotropy appears in a small wave-number range, where the inertial waves dominate and the weak turbulence theory can be applied. The weak turbulence theory predicts that the resonant interactions transfer energy to waves which have small scales perpendicular to the rotational axis without changing its scales parallel to the rotational axis. To quantitatively validate the prediction, it is indispensable to investigate the energy flux at each wave number.

In homogeneous isotropic turbulence, the quantitative feature of the flux for sufficiently large Reynolds numbers has been extensively examined. On the other hand, the flux in anisotropic turbulence still provokes a lot of debate, partially because the flux should be treated as a vector. In this abstract, the definition of the local energy-flux vectors in anisotropic turbulence is proposed. The vectors are compared with the prediction of the weak turbulence theory of the inertial waves in strongly rotating turbulence.

METHOD

In Navier-Stokes turbulence, the energy flux plays a key role in energy-cascading process, and is defined for a wave number in isotropic turbulence systems as

$$P(k) = -\int_0^k T(k')dk', \tag{1}$$

where the isotropic energy transfer $T(k)$ is obtained from $T_{\boldsymbol{k}} = \sum_{\boldsymbol{k}_1,\boldsymbol{k}_2} \mathcal{T}(\boldsymbol{u}_{\boldsymbol{k}};\boldsymbol{u}_{\boldsymbol{k}_1},\boldsymbol{u}_{\boldsymbol{k}_2})$ by integration of the triad-interaction function $\mathcal{T}(\boldsymbol{u}_{\boldsymbol{k}};\boldsymbol{u}_{\boldsymbol{k}_1},\boldsymbol{u}_{\boldsymbol{k}_2})$ over the solid angle of $\boldsymbol{k}$, and is assumed to be continuous as a function of $k = |\boldsymbol{k}|$. The triad-interaction function denotes the energy transfer from or to the wave number $\boldsymbol{k}$ via the triad $\boldsymbol{k} + \boldsymbol{k}_1 + \boldsymbol{k}_2 = \boldsymbol{0}$, and

$$\mathcal{T}(\boldsymbol{u}_{\boldsymbol{k}};\boldsymbol{u}_{\boldsymbol{k}_1},\boldsymbol{u}_{\boldsymbol{k}_2}) = -\frac{i}{4}\left\langle (\boldsymbol{k}_1\cdot\boldsymbol{u}_{\boldsymbol{k}_2})(\boldsymbol{u}_{\boldsymbol{k}}\cdot\boldsymbol{u}_{\boldsymbol{k}_1})\right\rangle \delta_{\boldsymbol{k}+\boldsymbol{k}_1+\boldsymbol{k}_2} + \text{c.c.} + (1\leftrightarrow 2), \tag{2}$$

where $(1 \leftrightarrow 2)$ respectively represent the terms with the suffices 1 and 2 interchanged in the preceding ones.

In this abstract, the rotational axis is denoted by z, and the isotropy in the x and y directions perpendicular to the rotational axis is assumed. Then, the energy transfers can be investigated in the $k_\perp$–$k_\parallel$ space, where $k_\perp = \sqrt{k_x^2 + k_y^2}$ and $k_\parallel = |k_z|$. The integrated energy fluxes perpendicular and parallel to the rotational axis

$$P_\perp(k_\perp) = -\int_0^{k_\perp} dk'_\perp \int_0^\infty dk'_\parallel T(k'_\perp,k'_\parallel), \qquad P_\parallel(k_\parallel) = -\int_0^\infty dk'_\perp \int_0^{k_\parallel} dk'_\parallel T(k'_\perp,k'_\parallel) \tag{3}$$

have been conventionally used, respectively. The anisotropic energy transfer $T(k_\perp,k_\parallel)$ is obtained from $T_{\boldsymbol{k}}$ by integration over the azimuthal angle of $\boldsymbol{k}_\perp$ and the sign of k_z. Because $P_\perp(k_\perp)$ and $P_\parallel(k_\parallel)$ are respectively obtained by integration of $k_\perp$ and $k_\parallel$, these integrated fluxes inevitably consist of contributions from all the turbulence regions, i.e., the weak-wave turbulence, the three-dimensional isotropic turbulence, and the dissipation. Thus, detailed local structures of the energy-cascading process in the wave-number space cannot be captured directly by the integrated energy fluxes.

To investigate the detailed local structure of the energy-cascading process, the energy flux is required to be a local geometric vector, because the energy flux can depend on the directions as well as the magnitudes of the wave numbers. Because of the energy cascade, the local energy conservation in the wave-number space

$$T_{\boldsymbol{k}} + \nabla_{\boldsymbol{k}}\cdot\boldsymbol{P}(\boldsymbol{k}) = 0 \tag{4}$$

*Corresponding author. E-mail: yokoyama@me.es.osaka-u.ac.jp

is assumed to hold as is implicitly assumed in the cascade theory of the isotropic turbulence. Here, $\boldsymbol{P}(\boldsymbol{k})$ is the energy-flux vector that quantifies the local energy flux. Unfortunately, $\boldsymbol{P}(\boldsymbol{k})$ cannot be determined uniquely yet because the degree of freedom of $\boldsymbol{P}(\boldsymbol{k})$ is approximately three times larger than the that of $T_{\boldsymbol{k}}$.

In this work, to uniquely determine the energy-flux vector in anisotropic turbulence, we employ the generalized (Moore-Penrose) inverse. The continuity equation of energy (4) is rewritten in a matrix form as $\mathsf{DP} = -\mathsf{T}$, where D is a fat matrix that corresponds to the divergence operator, and P and T respectively represent the generalized vectors consisting of all the wave-number components of $\boldsymbol{P}$ and T. Then, the vector P_* that has the minimal Euclidean norm among solution vectors is selected by using the generalized inverse matrix D^+ as

$$\mathsf{P}_* = -\mathsf{D}^+\mathsf{T} = \mathrm{argmin}\|\mathsf{P}\|_2, \quad \text{where } \mathsf{D}^+ = \mathsf{D}^T(\mathsf{D}\mathsf{D}^T)^{-1}. \tag{5}$$

The selection of the minimal-norm vector corresponds to the assumption that the energy transfer is "efficient". The minimal-norm solution P_* is irrotational. It results from the fact that the Moore-Penrose solution does not have the null-space component P_0 that satisfies $\mathsf{DP}_0 = 0$, and D corresponds to the divergence operator.

NUMERICAL RESULTS

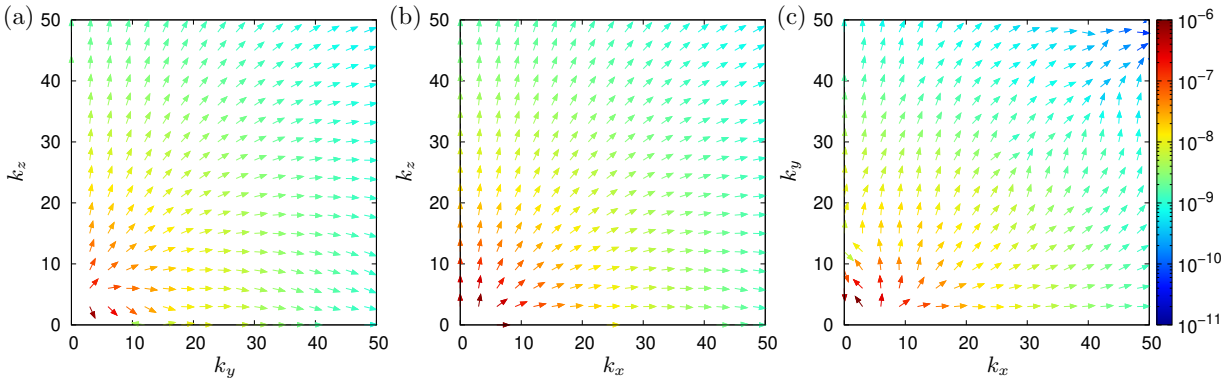

Figure 1: Energy fluxes on the planes of (a) $k_x = 0$, (b) $k_y = 0$ and (c) $k_z = 0$. The lengths of the energy-flux vectors are normalized, and the magnitudes of the vectors are expressed by color. Only the range $0 \le k_x, k_y, k_z \le 50$ is shown.

A direct numerical simulation of rotating turbulence is performed by using the pseudo-spectral method. The perpendicular wave numbers, k_x and k_y, are discretized with the spacing $\Delta k_x = \Delta k_y = 1$, while the parallel wave number k_z is discretized with $\Delta k_z = 1/4$. To obtain the statistically steady state, three-dimensional three-component random forces is added to the wavenumber mode in $k_\mathrm{f} - 1/2 \le |\boldsymbol{k}| < k_\mathrm{f} + 1/2$, where the forced wavenumber k_f is set to 4. The anisotropic energy-flux vectors are obtained from the energy transfer rate in the direct numerical simulation by using the Moore-Penrose inverse.

The energy-flux vectors on the planes of $k_x = 0$, $k_y = 0$ and $k_z = 0$ are drawn in Fig. 1. As the perpendicular wave numbers, k_y and k_x, become large, the energy-flux vectors become more parallel to the k_y and k_x axes in Figs. 1(a) and (b), respectively. It indicates that the energy is transferred to the wavenumbers having the same $k_\parallel$, and is consistent with the energy transfer due to the resonant interactions appearing in the weak turbulence theory of the inertial waves [1, 2, 3]. The alignment of the two-dimensional columnar vortex causes anisotropy on the $k_z = 0$ plane shown in Fig. 1(c), but this anisotropy should disappear if the large ensemble averaging were performed.

CONCLUSION

In this abstract, based on the net locality and the efficiency of the nonlinear energy transfer, the minimal-norm energy-flux vector obtained by using the generalised Moore-Penrose inverse is proposed to uniquely determine the energy-flux vector. It has been confirmed that the minimal-norm vector proposed here well reproduces the direction of the energy flux of the inertial-wave turbulence. In the presentation, the energy-flux vector will be shown to be consistent also with the prediction of the weak turbulence theory in stratified turbulence as well as the isotropy in the isotropic turbulence. In addition, the energy-flux vector is compared with the prediction of the critical balance in the buffer region between the weak turbulence and the strong turbulence.

References

[1] S. Galtier. Weak inertial-wave turbulence theory. *Phys. Rev. E*, **68**:015301, 2003.
[2] F. Bellet, F. S. Godeferd, J. F. Scott, and C. Cambon. Wave turbulence in rapidly rotating flows. *J. Fluid Mech.*, **562**:83–121, 2006.
[3] E. Yarom, and E. Sharon. Experimental observation of steady inertial wave turbulence in deep rotating flows. *Nature Physics*, **10**:510–514, 2014.

AXISYMMETRIC INERTIA LATTRACTOR MODES IN A SPHERICAL SHELL AT LOW EKMAN NUMBERS

Lorenzo Valdettaro*[1] and Michel Rieutord[2,3]
[1]MOX - Department of Mathematics, Politecnico di Milano, Milano, Italy
[2]Université de Toulouse;UPS-OMP;IRAP;Toulouse,France
[3]CNRS; IRAP; 14, avenue Edouard Belin, F-31400 Toulouse, France

Summary We investigate the asymptotic properties when viscosity tends to zero of axisymmetric inertial attractor modes propagating in a spherical shell. These modes are made of thin shear layers adjacent to the periodic orbit traced by attractors of characteristics. We investigate them numerically using a pseudo-spectral linear eigenvalue solver of the linearized fluid dynamics equations. Using quadruple precision arithmetics we are able to extend the analysis done in [2] to those modes that are prone to round-off error. A simple quantization pattern emerges, although the quantum number is limited to a few values.

ATTRACTOR MODES IN A SPHERICAL SHELL

Attractor modes are eigenmodes associated with a specific attractor represented by a periodic orbit of characteristics. In a spherical shell these modes were first studied in [1] and their analytic form has been given by [2]. They are shaped by a fast oscillating wave whose typical wavelength scales like $\mathcal{O}(\mathrm{E}^{1/3})$ ($\mathrm{E} = \frac{\nu}{2\Omega R^2}$ is the Ekman number with ν the kinematic viscosity coefficient of the fluid and Ω the angular velocity, while R is the major radius of the spherical shell) trapped in a nearly gaussian envelope of characteristic width $\mathcal{O}(\mathrm{E}^{1/4})$. The wave packet remains at a distance $\mathcal{O}(E^{1/6})$ from the asymptotic attractor, which is reached at $\mathrm{E} = 0$. Numerical computations in [2] showed that a simple dispersion relation applies to eigenvalues of attractor modes. That dispersion relation was obtained using double precision arithmetics, by which only the first few damped eigenmodes are accessible, since it was shown that high order modes are very sensitive to round-off errors and cannot be properly computed using double precision.

In this presentation we make use of extended precision arithmetics. The range of the accessible eigenvalues increases and we find a simple governing law that extends the one found in [2], namely

$$\lambda_n = i\omega_0 - \sum_{k=0}^{\infty} \hat{\tau}_k \left(n + \frac{1}{2}\right)^k e^{i\phi_k} E^{\frac{1}{3}+\frac{k}{6}} \tag{1}$$

In this expression, ω_0 is the asymptotic frequency of the attractor, while $\hat{\tau}_k$ are positive real numbers that depend on the shape of the attractor. $n = 0, 1, \cdots$ is the quantum number that characterizes the mode.

We have found such families of eigenvalues in association with various attractors. Table 1 gives the parameters for six sets of such modes. In this table, we gathered the families of modes by pairs of families where we associated the attractor at ω_0 with the symmetric one at $\alpha_0 = \sqrt{1-\omega_0^2}$; in the table η is the shell aspect ratio, that is the ratio between radius of internal and external spheres.

We show in figure 1(a) the numerical evidence of formula (1) for the attractor 0.55537 at $\eta = 0.35$. We recall that double precision arithmetics is enough only for the first few damped eigenmodes (corresponding to $n \leq 3$ in formula (1)). Thus we make use of extended precision for all the computations.

We remark that as n increases the numerical resolution needs to be increased in order to resolve the eigenvector. This can be clearly seen on figure 1(a): the red eigenvalues (computed using resolution $L_{\max} = 800$ and $N_r = 300$, where $L_{\max}$ is the maximum of the index of Legendre polynomial expansion used in latitude and N_r is the number of radial Chebyshev nodes) are correct up to quantum number $n = 14$, but for $n \geq 15$ they are no more valid. Increasing the resolution to $L_{\max} = 1000$ and $N_r = 370$ we are able to obtain four more eigenvalues, and increasing further the resolution we can capture up to eigenmode $n = 19$. However, beyond $n = 19$, no matter the increase of resolution, we

η	ω_0	α_0	$\hat{\tau}_0$	ϕ_0	$\hat{\tau}_1$	ϕ_1	$\hat{\tau}_2$	ϕ_2
0.35	0.555369	0.831694	1.02	$+0.996\,\pi/3$	3.20	$+1.013\,\pi/4$	0.67	$+0.554\,\pi/12$
0.35	0.831694	0.555369	1.61	$-1.002\,\pi/3$	2.57	$-1.012\,\pi/4$	0.52	$-0.534\,\pi/12$
0.35	0.622759	0.782413	1.13	$+1.004\,\pi/3$	2.97	$+0.956\,\pi/4$	0.23	$+1.657\,\pi/12$
0.35	0.782413	0.622759	0.97	$-0.998\,\pi/3$	2.60	$-0.986\,\pi/4$	0.36	$-0.642\,\pi/12$
0.50	0.466418	0.884564	0.970	$+\pi/3$	5.59	$+\pi/4$		
0.50	0.884564	0.466418	1.290	$-\pi/3$	4.31	$-\pi/4$		

Table 1: Best fit of asymptotic parameters of some attractor modes following dispersion relation (1).

*Corresponding author. E-mail: lorenzo.valdettaro@polimi.it

E	$n_{\max}$
10^{-7}	11
5×10^{-8}	16
4×10^{-8}	18
3×10^{-8}	18
10^{-8}	16

Table 2: Maximum number of n for eigenvalues satisfying formula (1).

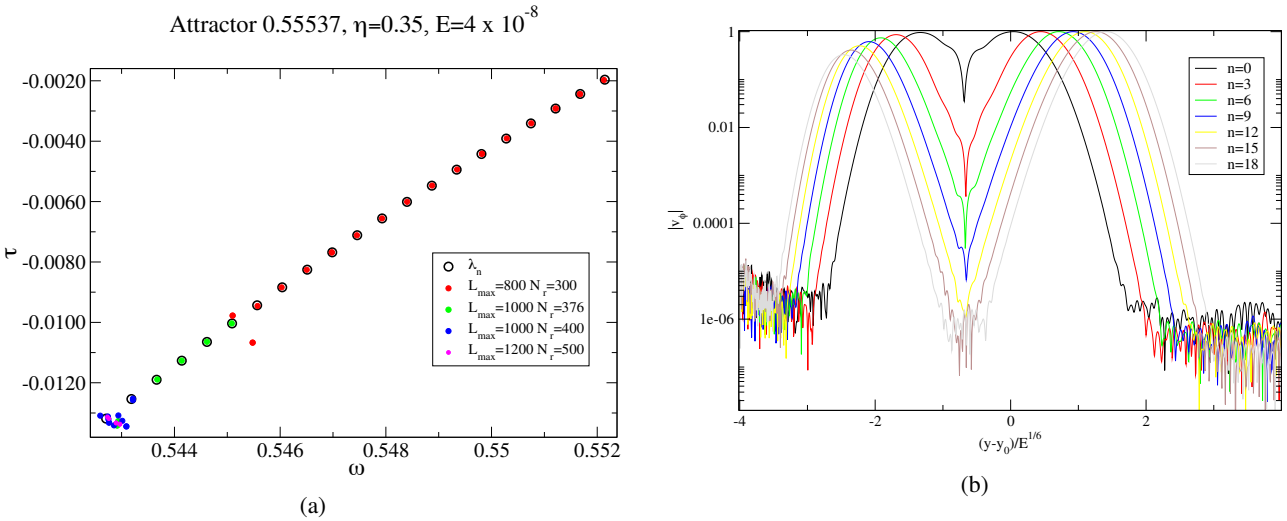

(a) (b)

Figure 1: (a) Eigenvalues at $E = 4 \times 10^{-8}$ for attractor 0.55537 at $\eta = 0.35$. Centers of black circles are given by the formula (1). (b) $|v_\phi|$ for some internal modes at $E = 4 \times 10^{-8}$.

obtain several dispersed eigenvalues that appear to be randomly positioned aroud the corresponding eigenvalue of formula (1). This can be seen in figure 1(a) for the eigenvalue corresponding to $n = 20$. This is reminiscent of the behaviour of eigenvalues that was obtained using double precision arithmetics and might suggest that round-off error affects extended precision computations for such eigenvalues. In table 2 we report such values: the total number of eigenvalues that are not affected by round-off error does not seem to increase when E decreases.

In figure 1(b) we plot the modulus of toroidal component of velocity v_ϕ in the direction normal to shear layer. It thus shows the envelope of the two shear layers adjacent to the attractor. We notice that increasing n the two adjacent rays become more and more separated, until for $n = 18$ (that is $n_{\max}$) they become separated by an interval where $|v_\phi|$ takes values of the order of the background noise. So for sufficiently small values of n the two adjacent rays interact and this might be the key to the dispersion relation. For large values of n instead this interaction is lost and the spectrum of eigenvalues changes shape. The way in which the spectrum is affected will be the subject of further study.

References

[1] M. Rieutord and L. Valdettaro. Inertial waves in a rotating spherical shell. *J. Fluid Mech.*, 341:77–99, 1997.
[2] M. Rieutord and L. Valdettaro. Axisymmetric inertial modes in a spherical shell at low ekman number. *J. Fluid Mech.*, 844:597–634, 2018.

COMBINED NUMERICAL AND EXPERIMENTAL STUDY OF SPATIALLY EVOLVING WIND-WAVE FIELD

Santosh Kumar Singh[1] and Lev Shemer*[1]
[1]School of Mechanical Engineering, Tel-Aviv University, Tel-Aviv, Israel

Summary: The present study focuses on numerical simulations of waves evolving under steady wind forcing that is based on a new model that accounts for effects of nonlinearity, wind input and dissipation. The performance of the model and of the computational procedure is assessed by comparison of the numerical results with associated detailed measurements in a wind-wave tank.

INTRODUCTION

Different aspects of wind waves are of great interest for engineers, mathematicians and physicists due to the complexity of those waves and their importance for applications and basic science. Therefore, a substantial effort was made by the scientific community over the recent decades to accumulate extensive sets of reliable and accurate experimental data that will allow to study various aspects of the wind wave-problem. Despite advances in measurement techniques and instrumentation, the process of excitation of waves on the water surface and of their evolution and growth due to the action of wind is still far from being fully understood. Extensive reviews of the current state of the art on the subject were presented in [1], whereas the effects related to the limited fetch and duration are emphasized in [2].

MATERIALS AND METHODS

Experiments were conducted in the Tel-Aviv University wind-wave facility that has a 5 m long, 0.4 m wide and 0.5 m high test section. The facility is equipped with a closed-loop wind tunnel to generate waves at desired wind velocity; it is described in detail in [3]. Four capacitance type wave gauges made of 0.5 mm thick anodized tantalum wire were used simultaneously. The probes were placed on a bar with a spacing of 10 cm between the adjacent sensors, and supported by an instrument carriage. Each individual record lasted for 3600 s at the sampling rate of 300 Hz. Measurements were performed at eight carriage positions effectively covering the whole length of the test section. At each carriage location, measurements were performed for several mean wind speeds U ranging from 5.5 m/s to 11.5 m/s. The corresponding friction velocities u_* at the air-water interface for different values of U were measured in the present facility and reported in [4].

In order to carry out quantitative comparison of the experimental results with the theoretical predictions, the set of unidirectional discretized spatial Zakharov equations [5] that describes evolution of amplitude of each frequency harmonic in the spectrum with the distance x from inlet was used; the equation was modified to account for wind input and dissipation:

$$c_{g,j}\frac{\partial A_j(x)}{\partial x} = -i \sum_{\omega_j+\omega_l=\omega_m+\omega_n} V_{j,l,m,n} A_l^* A_m A_n e^{-i(k_j+k_l-k_m-k_n)x} + \beta_j A_j(x) - \alpha_j A_j(x) \qquad (1)$$

Here A_j is the complex wave amplitude, β_j and α_j are the wind input and viscous dissipation source terms, $c_{g,j} = d\omega/dk$ is the group velocity of the j^{th} spectral component and ω_j is the frequency related to its wave number k_j by the dispersion relation for gravity-capillary waves, $\omega^2 = gk(1+\gamma k^2/g)tanh(kd)$, where γ is the ratio of surface tension to water density and $d = 0.19$ m is the water depth. The measured at a short fetch $x_0 = 0.67$ m amplitude spectra were used to determine the initial conditions; for the relation between the measured initial amplitudes of the spectral harmonics $\hat{\eta}(\omega_j, x_0)$ and the corresponding initial complex amplitudes $A_j(x_0)$ see [5]. The nonlinear spatial evolution of the prescribed initial amplitude spectra was determined by solving numerically the discretized spatial Eq. (1) using 4th order Runge-Kutta numerical scheme.The wind input parameterization is adapted from [6, 7], however, it is applied here within the selected window:

$$\beta_j = \begin{cases} a_1\left(\frac{u_*}{c_{p,d}}\right)^2 f_d & \text{for } f_d - \Delta f < f_j < f_d + \Delta f \\ 0 & \text{otherwise} \end{cases} \qquad (2)$$

where a_1 is the wind input coefficient, f_d is the dominant frequency and $c_{p,d} = \omega_d/k_d$ is the phase velocity corresponding to the local dominant frequency. The size of the wind input window is defined as $\Delta f = f_d s_w$, where s_w is the coefficient related to spectral width which is calculated from the spectral moments. The wind input coefficient a_1 is chosen empirically to provide sufficient supply of energy by wind as determined in the experiments. In Eq. (1), α_j is the damping term of short waves that for the viscous damping at the water surface is $\alpha_j = -2\nu k^2$ [8], where ν is the molecular kinematic viscosity of water. To account for turbulence under wind waves, effective kinematic viscosity ν_{eff} is introduced instead of ν, with simulations performed for a range of effective viscosities $\nu \le \nu_{eff} \le 10\nu$. The value of the wind input coefficient a_1 is adjusted for ν_{eff} to retain energy growth compatible with the experimental result. The obtained simulation results suggested that the viscosity plays a significant role in frequency downshifting with fetch of young

*Corresponding author. E-mail: shemerl@tauex.tau.ac.il.

wind waves studied here and that the value of the effective kinematic viscosity ν_{eff} increases somewhat with increase in U up to $8\nu_{eff}$. In the present simulations the effective viscosity is taken as 0.08 cm^2/s for all the simulation runs.

RESULTS AND DISCUSSIONS

The wave amplitude and dominant frequency can be related to the fetch x and the friction velocity u_* of the wind using the dimensionless parameters based on the spectral moments m_j of the measured power spectrum $F(f)$ that are defined as $\int_{f_{min}}^{f_{max}} f^j F(f) df$ [9]. The dimensionless parameters are $\hat{m}_0^{1/2} = g m_0^{1/2}/u_*^2$, $\hat{f}_d = u_* f_d/g$ and $\hat{x} = gx/u_*^2$. The $\hat{m}_0^{1/2}$ and $\hat{f}_d$ may be written in terms of $\hat{x}$ as $\hat{m}_0^{1/2} = c_1 \hat{x}^{b_1}$ and $\hat{f}_d = c_2 \hat{x}^{-b_2}$, where c_1 and c_2 are the non-dimensional constants. Figs. 1 and 2 show that the experimental data fit a linear dependence in log-log coordinates and thus exhibit power-law behavior for two wind velocities. The characteristic wave amplitude $\hat{m}_0^{1/2}$ increases with the dimensionless fetch as $\hat{x}^{0.528}$ and $\hat{x}^{0.536}$ in experiments and simulations, respectively, while the corresponding decrease in dominant frequency $\hat{f}_d$ is $\hat{x}^{-0.33}$ and $\hat{x}^{-0.27}$, accordingly. These values of exponents are in a reasonable agreement with those obtained in numerous experiments and numerical simulations that vary in the ranges $0.35 < b_1 < 0.55$ and $0.23 < b_2 < 0.3$ [10]. The present results are in agreement with wind wave channel measurement at a comparable range of fetches $\hat{x}$ [9].

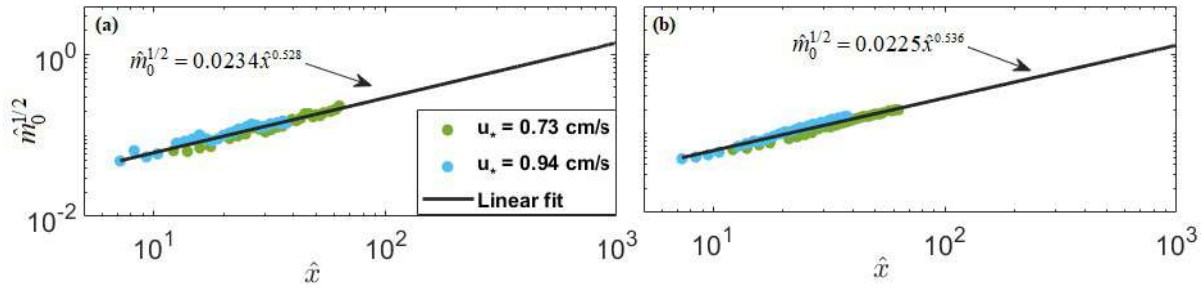

Figure 1. Dimensionless wave amplitude growth with dimensionless fetch: (a) experiment and (b) simulation.

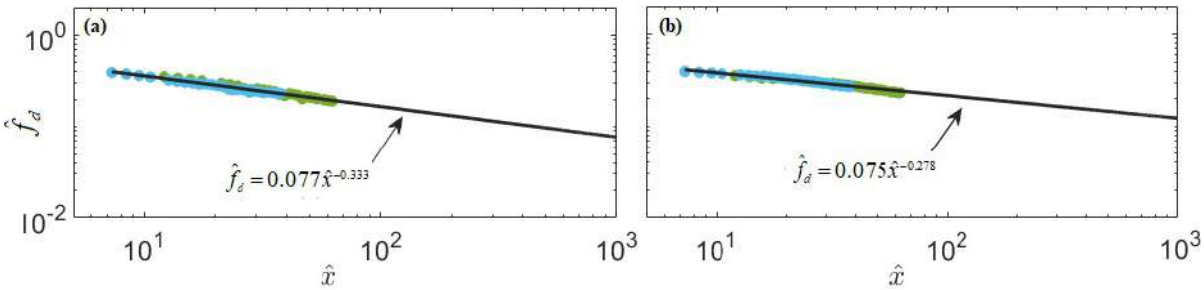

Figure 2. Dimensionless frequency down shifting the dimensionless fetch: (a) experiment and (b) simulation.

CONCLUSIONS

Results of numerical simulations of the spatial evolution of young waves under steady wind forcing are directly verified by comparison with measurements in a wind wave tank. A novel model to account for wind input is suggested. Good agreement between numerical simulations and measurements is obtained for the spatial evolution of global parameters such as dominant frequency downshifting and wave energy growth, as well as for the evolution along the tank of the wave spectra. It is shown that while nonlinearity plays an essential role in the peak frequency downshifting, the effect of dissipation and wind input on the spectral variation of young wind waves cannot be disregarded.

References

[1] Shemer L. On evolution of young wind waves in time and space. *Atmos.* 10, 1-54, 2019.
[2] Young I.R. Wind Generated Ocean Waves. Elsevier, Amsterdam, the Netherlands, 1999.
[3] Liberzon D., Shemer L. Experimental study of the initial stages of wind waves'spatial evolution. *J. Fluid Mech.* 681: 462–498, 2011.
[4] Zavadsky A., Shemer, L. Characterization of turbulent air flow over evolving water-waves in a wind-wave tank. *J. Geophys. Res.* 117, C00J19,2012.
[5] Shemer, L., Goulitski, K., Kit, E. Evolution of wide-spectrum wave groups in a tank: an experimental and numerical study. *Eur. J. Mech. B/Fluids* 26, 193-219, 2007.
[6] Plant W.J. A relationship between wind stress and wave slope. *J. Geophys. Res.* 87(C3), 1961-1967, 1982.
[7] Hwang P.A., Sletten, M.A. 2008 Energy dissipation of wind-generated waves and whitecap coverage. *J. Geophys. Res.* 113, C02012, 2008.
[8] Lamb H. Hydrodynamics, 6th edn. Cambridge UP 1932 (Reprinted by Dover, 1945)
[9] Mitsuyasu H. On the growth of the spectrum of windgenerated waves I. Rep. Res. Inst. Appl. Mech. Kyushu Univ. 16, 459–482, 1968.
[10] Badulin S.I., Babanin A.V., Zakharov V.E., Resio D. Weakly turbulent laws of wind-wave growth. *J. Fluid Mech.*591, 339–378, 2007.

OBSERVATIONS OF TRANS-INFRAGRAVITY (30 MIN) OSCILLATIONS IN THE NORTHERN ADRIATIC

Alex Sheremet*[1], Maurizio Brocchini[2], Rossella Ferretti[3], and Joseph Calantoni[4]
[1]Engineering School For Sustainable Infrastructure and Environment (ESSIE), University of Florida, 365 Weil Hall, Gainesville, FL 32611, USA
[2]Department of Ingegneria Civile,Edile e Architettura,Università Politecnica delle Marche,Ancona,Italy
[3]CETEMPS - Department of physics and Chemistry, Univeristy of L'Aquila, L'Aquila, Italy
[4]Marine Geosciences Division, U.S. Naval Research Laboratory, Stennis Space Center, MS, USA

Summary An array of oceanographic instruments deployed in a cross-shore transect on the Senigallia shelf offshore Misa River Mouth captured persistent (≈ 2 days), low-frequency oscillations of sea level and cross-shore velocity, following the strong Bora event of Jan, 24-25th, 2014. Meteorological data and numerical modeling suggest that the oscillations character is consistent with transversal Adriatic seiching, likely forced by a combination of Bora gustiness and convection instability. This study highlights poorly-understood aspects of air-sea interaction processes associated with Bora events.

INTRODUCTION

Due to its basin shape and topography, the Adriatic may exhibit both longitudinal and transversal seiches. Longitudinal seiches are typically associated with intense winds out of SE, large frontal systems, or with cyclonic activity ([5]). The 22-hour fundamental mode typically dominates the sea-level power spectrum (e.g., [8]), and persists for days, losing energy through basin friction and radiation at the Strait of Otranto (e.g., [2]). Transversal seiches occur on smaller scales, most likely associated transversal forcing such as Bora events. Earlier studies (e.g., [11, 9]) identify periods 8.5, 5, 3.5 and 3 hours in sea level oscillations at Trieste and Venice. They are also less energetic, and due to their local structure, less studied and less understood (details of Bora events themselves have only recently been clarified; [6]).

Here, we investigate observations of 30-min oscillations of sea level and cross-shore velocity observed during a 2-day calm period following the strong Bora event of January 25, 2014.

OBSERVATIONS

The field experiment is described in detail in [1, 7]. The array of sensors (figure 1 a-b) captured on the Jan. 25th., 2014 a strong Bora event, which generated remarkably energetic waves (10-s peak period, 3-m significant height). Following the storm, pressure and velocity records show trans-infragravity (≈ 30 min) oscillations, with periods in the range of 20 to 120 min, with amplitudes in the order of 10-20 cm/s, associated with free-surface oscillations in the order of 2-10 cm (figure 1 c-i). The oscillations were exactly in phase across the entire 1.2-km array. The spectrum of the pressure and cross-shore velocity during this period shows well-defined, distinct peaks at frequencies ≈ 0.005, 0.01, 0.02, 0.03, 0.04, 0.05 min^{-1}, consistent with transversal seiches. The cross-shore velocity has two main peaks at 25 and 33 min, while the pressure spectrum exhibits additional peaks at 50 min and 100 min, a behavior consistent with the vicinity of an antinode. We investigate the generation mechanism using "conceptual", 2D numerical tests based on FUNWAVE-TVD Boussinesq model ([10]), and full 3D simulations covering the entire Adriatic using ROMS.

DISCUSSION

Similar oscillations have been observed in the wake of a cold-front passage at the Port of Rotterdam, the Netherlands, and identified as long-waves likely generated through a Proudman resonance mechanism, associated with strong wind-speed fluctuations and convection cells produced by an unstable atmospheric stratification over the North Sea [4]).

The Adriatic oscillations discussed here have a cross-shore standing-wave structure, discrete spectrum, and periods (harmonics of the fundamental ≈ 100 min) consistent with transversal Adriatic seiches. The generation mechanism is likely a combination of stress fluctuations in the Bora wind, and possibly convection cells associated with unstable atmospheric stratification in the wake of the Bora event. Bora wind develops as parallel narrow jets that exhibit significant instability (10-min oscillations between 15 and 25 m/s; [6]), possibly associated with N-S ocean circulation cells (e.g., [3]). Meteorological data supports this hypothesis. The weather forecast for Jan 25th, 2014 issued by the ESTOFEX (European Storm Forecast Experiment), called for a level 2 alert for the Adriatic sea area. Satellite ASCAT wind (figure 1 k) shows strong wind out of NW active till late evening of 25th Jan, 2014, while radar data shows convective cells developing to a convective line during the late Jan 24th and the early Jan 25th (figure 1 l). Like longitudinal seiches, once generated, transversal seiches would be expected to slowly dissipate due to basin friction, perhaps over several days, consistent with observations.

The study highlights aspects of the relation between Bora events and transversal seiches that are not well documented and poorly understood, but relevant in relation with other air-sea interaction processes that have a significant shoreline impact, such as wave activity, meteotsunamis, and flooding induced by storm surges.

*Corresponding author. E-mail: alex.sheremet@essie.ufl.edu

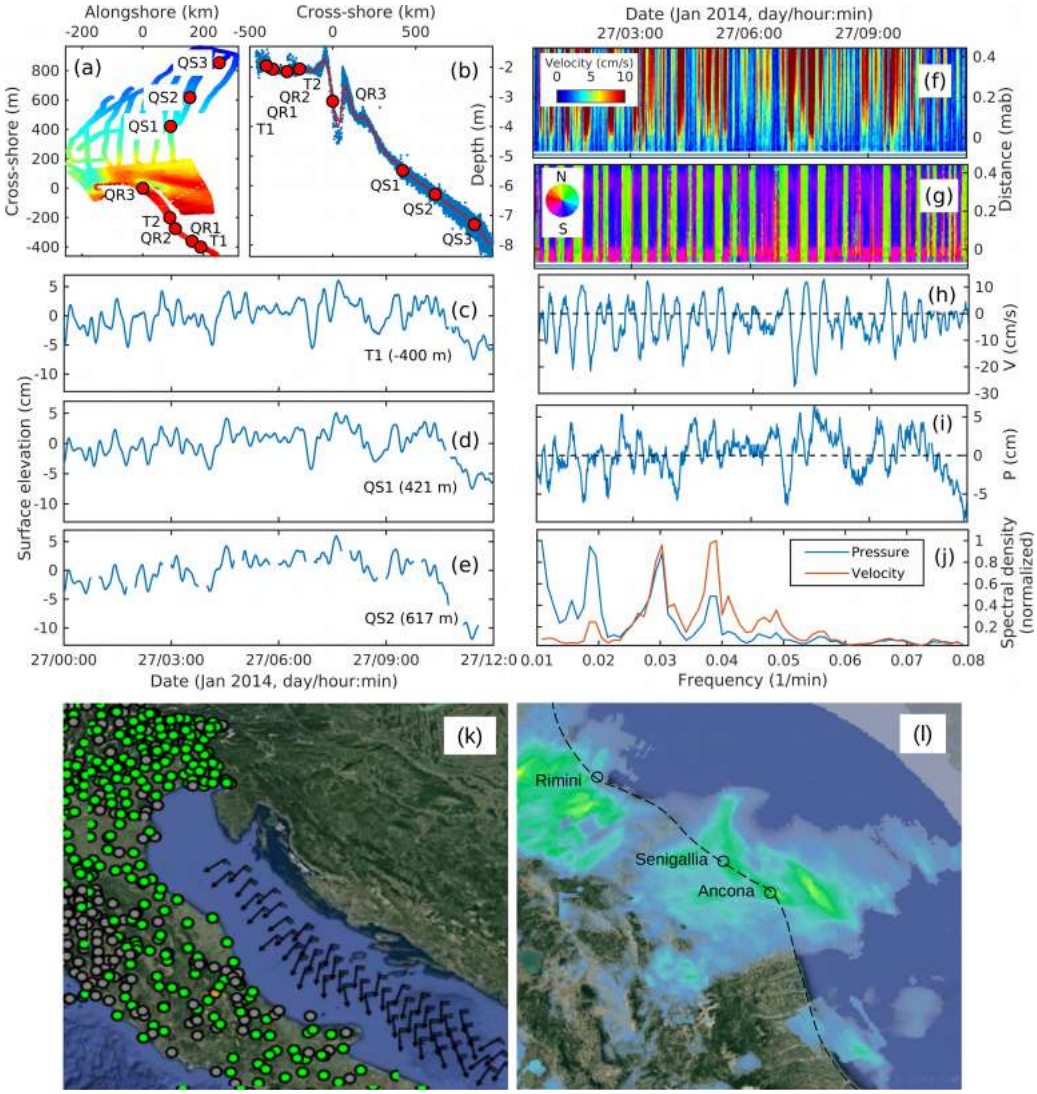

Figure 1: a-b) Bathymetry of the experiment site, plan view and profile; sensors marked by red circles. The offshore bathymetry was surveyed using a 240-kHz ODOM ES3 multibeam with 90 beams with a 1.5 spacing and a $<$ 3 cm RMS accuracy. c-e) Free-surface elevation at sensors T1, QS1, and QS2, respectively. f-g) Vertical structure of speed and direction of the flow at QR1 (Sontek Pulse-coherent ADP). h-i) Corresponding time series of free-surface elevation and top-bin cross-shore velocity. j) Spectral analysis of free-surface elevation and top-bin cross-shore velocity at QR1. k) Satellite ASCAT wind, and warning thresholds form Dewetra-CFA on Jan 25th, 2014 at 20:00 UTC (green means "safe"). l) Radar national mosaic from DEWETRA-CFA showing VMI on Jan 24th, 2014 at 00:00 UTC.

References

[1] Brocchini M., J. Calantoni, M. Postacchini, A. Sheremet, T. Staples, J. Smith, A.H. Reed, E.F. Braithwaite, C. Lorenzoni, A. Russo, S. Corvaro, A. Mancinelli, L. Soldini (2017), Marine Geology 385, 2740, doi: 10.1016 /j.margeo.2016.12.005
[2] Cerovecki, I., M. Orlic, and M.C. Hendershott (1997), Deep-sea Research I, 44/12, 2007-2029.
[3] Cushman-Roisin, B., and K. A. Korotenko (2007), J. Geophys. Res., 112 , C11S91, doi:10.1029/2006JC003516.
[4] de Jong, M.P.C., and J.A. Battjes (2004), J. Geophys. Res., 109, C01011, doi:10.1029/2003JC001931.
[5] Franco, P., L. Jeftic, P. Malanotte Rizzoli, A. Michelato, and M. Orlic (1982) Ocean. Acta 5/3, 379-389.
[6] Grisgono, B. and D. Belusic (2008), Tellus, 61A, 116.
[7] Melito, L., M. Postacchini, A. Sheremet, J. Calantoni, G. Zitti, G. Darvini, and M. Brocchini (2020), Estuarine, Coast. Shelf Sci (in review).
[8] Leder, N., and M. Orlic (2004), Annales Geophysicae 22, 14491464.
[9] Poretti G., (1974), Atti Accad. Naz. Lincei, Quad. N. 206, 153-157.
[10] Shi, F., J.T. Kirby, J.C. Harris, J.D. Geiman, and S.T. Grilli (2012), Ocean Modelling, 43: 3651.
[11] Stravisi F. (1972), Accad. Naz. Lincei, Rend., 8, 52, 2, 187-196.

ANALOG EXPERIMENT AND 1D MODEL OF THE QUASI-BIENNIAL OSCILLATION

Benoît Semin*[1,2], François Pétrélis[2], and Stephan Fauve[2]
[1]PMMH, CNRS ESPCI Sorbonne Université, Université de Paris, 7 quai saint-Bernard, 75005 Paris, France
[2]LPENS, Ecole Normale Supérieure, CNRS, Sorbonne Université, Université de Paris, 24 rue Lhomond, 75005 Paris, France

Summary The quasi-biennial oscillation (QBO) is the nearly periodic reversal of the large scale flow generated by internal waves in the equatorial stratosphere. Using a laboratory analog experiment and a 1D model, we study the instability that generates the QBO. We report the first quantitative measurements of the nonlinearly saturated velocity of the flow. We show both experimentally and using the 1D model that the bifurcation is either supercritical or subcritical depending on the dominant dissipative process.

INTRODUCTION

The quasi-biennial oscillation (QBO) is the periodic reversal of the wind in the lower equatorial stratosphere [1]. The period of the oscillation is 28 months on average, and is not linked to the year duration. This wind is known to be generated by atmospheric waves, in particular internal gravity waves.

We have set up an experiment which reproduces this phenomenon in the laboratory and solved a related 1D model.

EXPERIMENTAL SET-UP

A schematic view of the experimental set-up is shown in figure 1a. It has been described in detail in [4], and is inspired by previous works [2, 3]. The set-up is made of two transparent concentric vertical cylinders. The gap h between these two cylinders is filled with a linearly density-stratified solution of NaCl or $MgCl_2$ in water. The stratification is characterized by the Brunt–Väisälä frequency, $N = \sqrt{(g/\rho_0)\,\mathrm{d}\rho_0/\mathrm{d}z}$, where g is the acceleration of gravity, ρ_0 is the background density and z is the vertical axis.

Internal waves inside the fluid are forced using 16 silicone membranes which are in contact with the top of the fluid and move up and down in a sinusoidal manner. Two neighboring membranes are driven by motors in opposition of phase so that the forcing is a standing wave whose azimutal wavelength $\lambda_x = 200\,\mathrm{mm}$ is twice the curvilinear distance between 2 motors. We note M the amplitude of the motion of the membranes and $T_f = 15 - 17\,\mathrm{s}$ the forcing period.

The fluid velocity is measured using particle image velocimetry (PIV). The local velocity as a function of time is fitted with a sine function. The value of the mean flow, the amplitude and the phase of the wave are obtained from this fit.

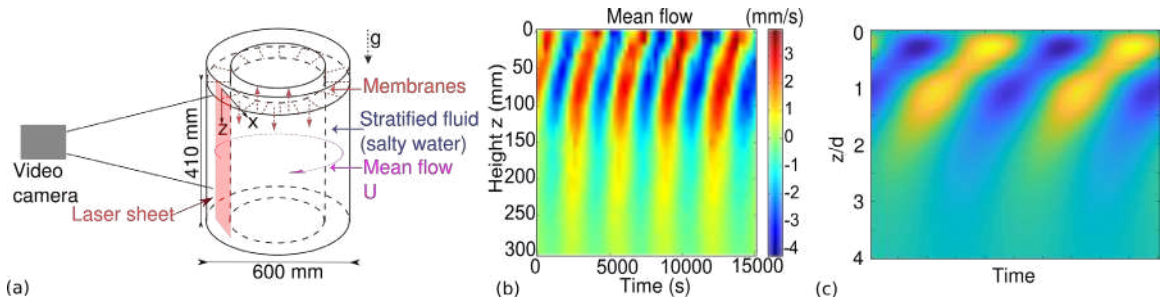

Figure 1: (a): schematic of the experimental set-up. (b): space-time diagram of the mean flow, forcing amplitude: $M = 13.5\,\mathrm{mm}$, forcing period $T_f = 17\,\mathrm{s}$, Brunt–Väisälä frequency, $N = 1.5\,\mathrm{Hz}$, observed mean flow period $T_{\mathrm{QBO}} = 3\,200\,\mathrm{s}$ (c) space-time diagram corresponding to the linearly unstable mode of the model.

MODEL

We have solved analytically the 1D model of Plumb and McEwan close to the QBO threshold. [2]. This model is an effective equation for the mean flow U, which takes into account the forcing by the waves and the dissipation of the mean flow. It is given in dimensionless form by:

$$\frac{\partial U}{\partial T} = -\frac{\partial D}{\partial \xi} + \Lambda_1 \frac{\partial^2 U}{\partial \xi^2} - \Lambda_2 U$$

where:

$$D(\xi) = \exp\left(-\int_0^\xi \frac{1}{(1-U)^4}\mathrm{d}\xi\right) - \exp\left(-\int_0^\xi \frac{1}{(1+U)^4}\mathrm{d}\xi\right)$$

*Corresponding author. E-mail: benoit.semin@espci.fr

traces back to the forcing of the mean flow by the waves. ν is the kinematic viscosity, γ is the wall friction, $F = \overline{u'\,v'}$ is the time average of the product of the vertical velocity associated to the wave (v') by the horizontal one (u'), $c = \omega/k_x$ is the horizontal phase velocity, $d = k_x c^4/(N^3\nu)$ is the vertical dissipation length, $\xi = z/d$ is the dimensionless height,u is the mean flow (which is horizontal), $U = u/c$ is the dimensionless mean flow, $\Lambda_1 = \nu c/(F(0)d)$ is the dimensionless friction corresponding to the bulk dissipation of the mean flow and $\Lambda_2 = \gamma cd/(F(0))$ the dimensionless friction corresponding to the dissipation in the boundary layer on the lateral walls. Time is made dimensionless using $cd/(F(0))$, which gives the order of magnitude of the mean flow period.

RESULTS

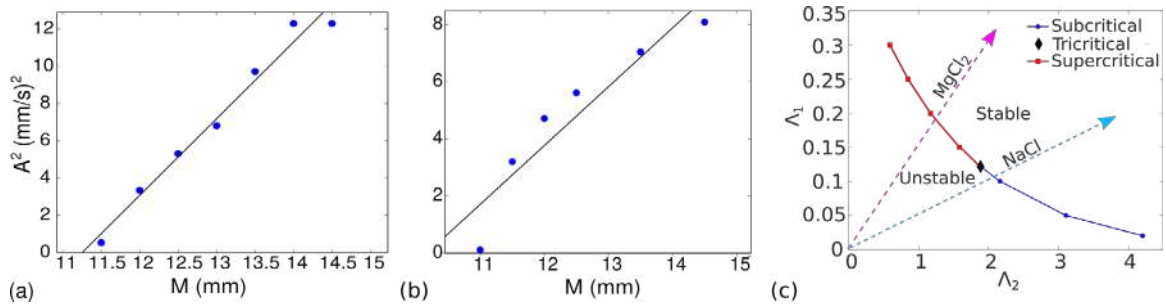

Figure 2: (a): Square of the amplitude of the mean flow as a function of the forcing amplitude M, for $N = 2.15\,\mathrm{Hz}$, i.e. with $MgCl_2$. The blue disc are the experimental measurements, the line is a linear fit (b): similar results for $N = 1.5\,\mathrm{Hz}$, i.e. with NaCl (c): stability diagram. Lines and points are theoretical results, the dashed lines indicate the possible values for the two different salts.

Below a forcing amplitude $M \sim 11\,\mathrm{mm}$, there is no mean flow generated by the waves in the experimental set-up. Above this threshold, there is a symmetry breaking and a mean flow is measured (see figure 1b). At a given height, this mean flow oscillates with a period which is much larger than the period of the waves. The observed pattern is in agreement with both the atmospheric observations [1] and the prediction of the model (figure 1c).

To investigate quantitatively the bifurcation, we decrease stepwise the amplitude of the forcing M. The amplitude of the mean flow A can then be measured for different values of M. The square of A as a function of M is displayed in figure 2a (for $MgCl_2$) and b (for NaCl). The experimental data are fitted with a linear function. The fit is good in figure 2a, indicating that the bifurcation is supercritical. This is not the case in figure 2b, showing that the bifurcation is subcritical in that case.

The effect of the salt is related to a change in the value of N, which modifies d and thus the ratio between Λ_1 and Λ_2. The 1D model predicts that the bifurcation may be supercritical or subcritical, depending on this ratio. The theoretical behavior agree well with the experimental one, without adjustable parameter (figure 2c).

CONCLUSION

We have characterized the bifurcation between a state with a mean flow and a state with no mean flow, in an experimental analog of the quasi-biennial oscillation. The measurements are in agreement with a 1D model. We found that the bifurcation is either supercritical or subcritical, depending on the dominant dissipation mechanism.

A perspective it to link this result with the atmospheric QBO, and to determine the nature of the bifurcation in general circulation models and in the atmosphere.

References

[1] Baldwin M. at al. The quasi-biennial oscillation *Rev. Geophys.* **39** 179-229 (2001)
[2] Plumb R., McEwan A. The instability of a forced standing wave in a viscous stratified fluid: A laboratory analogue of the quasi-biennial oscillation. *J. Atmos. Sci.* **35:** 1827–1839 (1978).
[3] Otobe N., Sakai S., Yoden S., Shiotani, M. Visualization and WKB analysis of the internal gravity wave in the QBO experiment. *Nagare: Japan Soc. Fluid Mech.* **17** (1998)
[4] Semin B., Facchini G., Pétrélis F., Fauve S. Generation of a mean flow by an internal wave. *Phys. Fluids.* **28**, 096601 (2016).
[5] Semin B., Garroum N., Pétrélis F., Fauve S. Nonlinear saturation of the large scale flow in a laboratory model of the quasibiennial oscillation. *Phys. Rev. Lett.* **121:** 134502 (2018)

COASTAL WAVES IN A DEPTH-AVERAGED MODEL WITH AN ANISOTROPIC TURBULENCE AND A WEAKLY COMPRESSIBLE APPROACH

Gaël L. Richard*[1], Maria Kazakova[2], Benoit Fabrèges[3], and Arnaud Duran [3]
[1]Univ. Grenoble Alpes, INRAE, ETNA, 38000 Grenoble, France [2]Normandie Univ, INSA Rouen Normandie, LMI, 76000 Rouen, France
[3]Institut Camille Jordan, CNRS UMR 5208, Université Claude Bernard Lyon 1, 69100 Villeurbanne, France

Summary We introduce two new approaches to model coastal waves and tsunamis. Firstly, averaging over the depth the LES equations enables to include explicitly in the model the anisotropic large-scale turbulence arising in breaking waves while the small-scale turbulence is modelled with a turbulent viscosity hypothesis. Secondly, a depth-averaged weakly compressible approach allows us to derive a fully hyperbolic model with dispersive properties, on a varying bottom. This enables to remove the time-consuming non-local step in the numerical schemes, which is due to the incompressible hypothesis, and to obtain a compressible extension to the Boussinesq-type models. The resulting depth-averaged model is used to perform efficient and accurate numerical simulations of shoaling and breaking waves in various situations. The numerical resolution shows also the decrease of the tsunami propagation speed due to compressibility.

INTRODUCTION

The Boussinesq-type models are one of the approaches for an efficient computation of waves propagation in nearshore areas. They are typically obtained by averaging over the fluid depth the equations of fluid mechanics. This procedure decreases the dimension of the system by one and incorporates the boundary equations at the bottom and at the free surface in the model equations, resulting in a reduced computational cost. The Serre-Green-Naghdi equations are a fully nonlinear variant where the waves amplitude is not supposed to be small with respect to the depth. They are more accurate than the Boussinesq equations in the final stages of coastal waves propagation. However all Boussinesq-type models are weakly dispersive because of the shallow water assumption i.e. the fluid depth is small compared to the wavelength. As a result, the deviation of the predicted linear dispersive properties to the Airy waves theory becomes significant if the depth increases. Another feature of the Boussinesq-type models is the existence of an elliptic or a non-local step in the numerical scheme of the equations. This is related to the presence of mixed space-time third-order derivatives in the equations. This step is highly time-consuming in the numerical resolution since a global system must be solved at each time step over the whole computational domain. Physically, this non-local effect is due to the incompressibility hypothesis which implies that the pressure variations propagate instantaneously at an infinite velocity. One of the goals of this work is to derive a depth-averaged model for coastal waves with a weakly compressible assumption to remove all non-local effects in order to reduce the computational time. Another goal is to obtain a compressible extension to the Boussinesq-type models to capture the reduced propagation speed of tsunamis due to compressibility [1].

To model breaking waves in the surf zone, dissipation effects must be added to the Boussinesq-type models. Some strategies have been proposed to achieve this result, in particular roller models, which involve many empirical parameters, or the switching approach, which is sensitive to mesh size and which can lead to numerical instabilities. Another approach is to model the turbulence with an eddy viscosity hypothesis. This is valid if the turbulence is not too far from isotropy and from an approximate balance between production and dissipation. Further, as for the roller and switching approaches, it is necessary to have a breaking criterion. In the case of the models with a turbulent viscosity, this criterion determines when the viscous terms are activated or deactivated. We propose to include the turbulence of breaking waves by averaging over the depth the Large-Eddy Simulation (LES) equations. The small-scale turbulence is modelled with an eddy-viscosity hypothesis but the anisotropic large-scale turbulence is explicitly resolved.

WEAKLY COMPRESSIBLE APPROACH

As for the Serre-Green-Naghdi model, the derivation uses the shallow water assumption and is fully nonlinear. The model is obtained with the assumption of a weak compressibility, using a low Mach number approximation. The pressure is divided into a hydrostatic part and a non-hydrostatic part. The variations of the depth-averaged density are due to the variations of the hydrostatic pressure caused by depth variations. An equation for the non-hydrostatic pressure is derived from the first law of thermodynamics with the assumption of a homentropic flow. A standard depth-averaging procedure gives the equations of the model for the fluid depth, the average horizontal velocity, the average vertical velocity and an average non-hydrostatic pressure. The model, even with a varying bottom, is hyperbolic. The solutions of the dispersive relation divide into a slow branch governing gravity waves and a rapid branch governing acoustic waves. The equations include the possibility of a mobile bottom, enabling the simulation of tsunamis generated by seabed vertical movements. If the compressibility is negligible, a pseudo-compressible approach using a much slower sound velocity than its physical value can be implemented. The model admits an exact conservation of energy, even on an arbitrary bathymetry. The linear dispersive properties are consistent with the linear theory of compressible fluids at the long-wave limit. The model can be extended to a hyperbolic system with improved dispersive properties.

* Corresponding author. E-mail: gael.richard@univ-grenoble-alpes.fr.

BREAKING WAVES

To average over the depth the LES equations, the filtered horizontal velocity is decomposed as the sum of its depth-averaged value and of the deviation to this average velocity due to large-scale turbulence and shearing effects. These phenomena are taken into account in the depth-averaged equations by a symmetrical and anisotropic tensor, called enstrophy tensor, with the same dimension as the square of a vorticity. The small-scale turbulence, modelled with a turbulent-viscosity hypothesis, gives, after the depth-averaging procedure, viscous terms with the same structure as in a compressible fluid. The closure of the model is obtained by modelling the small-scale eddy viscosity and the turbulent dissipation. The breaking criterion is replaced with the virtual enstrophy concept. This quantity satisfies the same tensor equation as the physical enstrophy, except that its only influence on the system is to define the breaking threshold.

NUMERICAL SIMULATIONS

The numerical scheme is based on a splitting between a slow part treated explicitly and a fast part solved implicitly, but without any global linear system to solve. Numerical simulations are presented for a wide range of situations including coastal waves and tsunamis. The model is able to simulate with a very good accuracy the experiments of Beji & Battjes [2] with irregular waves propagating and breaking over a submerged bar (Figure 1a), or the propagation of a wave over a complex bathymetry, including a conical reef and a beach, with breaking, submersion of the island and run-up (simulation of the experiments of Swigler [3], Figure 1b). The simulations are able to calculate the delay of the arrival time of a tsunami in the far field due to compressibility (Figure 1c).

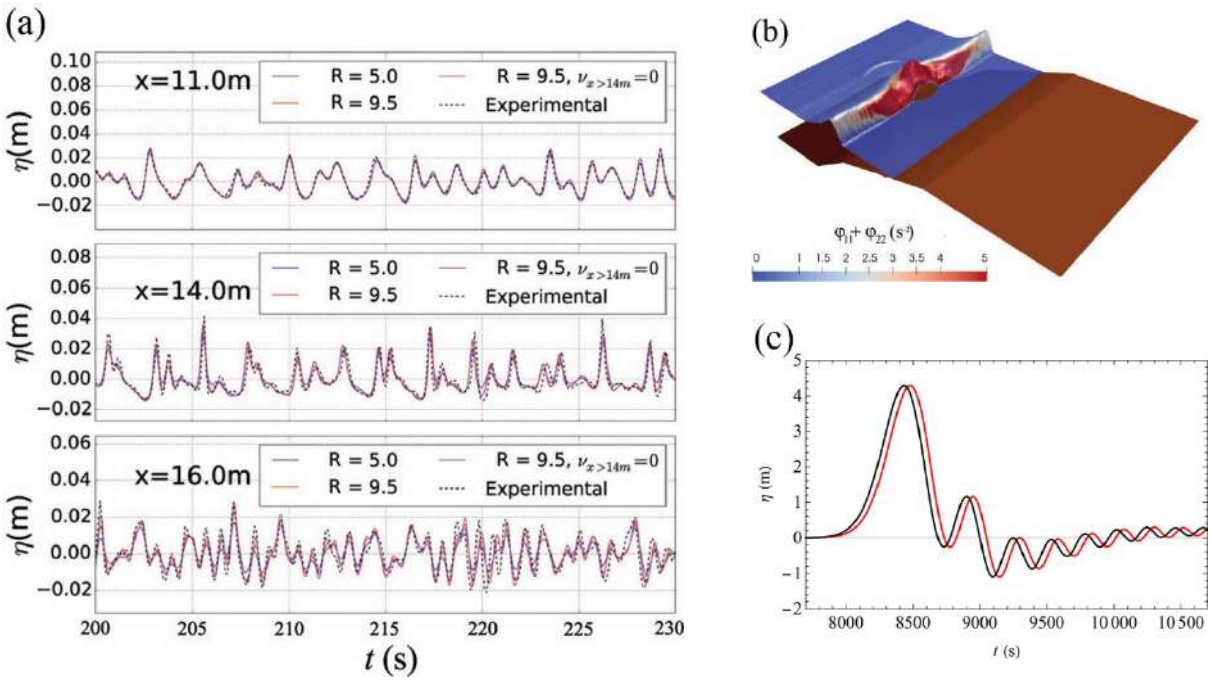

Figure 1 (a): Time evolution of the free surface before (top), above (middle) and after (bottom) a submerged bar in the case of irregular waves with comparison to the experiments of Beji & Battjes [2]. (b): A snapshot of the free surface for the simulation of the propagation of a wave on a complex bathymetry with a beach and a conical island. The red colour indicates the presence of large-scale turbulence (breaking wave). (c) Water elevation of a 1D-tsunami in the ocean after a propagation of 2000 km for the compressible case (red curve) and the incompressible case (black curve).

CONCLUSIONS

The depth-averaged LES approach enables to include explicitly the anisotropic large-scale turbulence in the model. These new approaches give efficient and accurate numerical simulations of shoaling and breaking coastal waves. The weakly compressible approach leads to a fully hyperbolic dispersive model on a varying bottom and can capture compressibility effects in a compressible Boussinesq-type model.

References

[1] Abdolali, A. and Kirby, J. T. Role of compressibility on tsunami propagation. *J. Geophys. Res.-Oceans.* **122**: 9780-9794, 2017.
[2] Beji, S. and Battjes, J. A. Experimental investigations of wave propagation over a bar. *Coast. Eng.* **19**: 151-162, 1993.
[3] Swigler, D. T. Laboratory study investigating the three-dimensional turbulence and kinematic properties associated with a breaking solitary wave. *PhD Thesis*, Texas A&M University, 2009.

THE UNDULAR HYDRAULIC JUMP IN INVISCID AXISYMMETRIC FLOW

Dominik Murschenhofer*[1] and Wilhelm Schneider[1]
[1]Institute of Fluid Mechanics and Heat Transfer, TU Wien, Vienna, Austria

Summary Steady inviscid free-surface flow over a horizontal bottom is considered. The results of an asymptotic analysis for slightly supercritical upstream Froude numbers show that undular hydraulic jumps can exist if the flow is axisymmetric. Provided the origin of the jump is located at a very large radius, the free surface is described by the steady-state version of an extended Korteweg–de Vries (KdV) equation. A numerical solution of the extended KdV equation is shown in comparison with the corresponding one-dimensional flow approximation, indicating that the supercritical branch of the latter is prone to develop into an undular hydraulic jump.

INTRODUCTION AND PROBLEM DESCRIPTION

In hydraulics the transition from slightly supercritical to subcritical free-surface flow is characterized by a wavy surface known as the undular hydraulic jump. In *plane* flow, e.g. in open channels, the undular hydraulic jump is inherently associated with dissipation and cannot exist in inviscid flow [1]. In the present paper it is shown that in the case of *axisymmetric* flow the situation changes, and the governing equations of inviscid flow permit an undular hydraulic jump.

Steady inviscid axisymmetric free-surface flow over a horizontal bottom is considered. The basic equations are the continuity equation for incompressible flow and the Euler equations. Cylindrical coordinates are introduced, with r and z in radial and vertical direction, respectively. The free surface is defined by a streamline, and the ambient pressure is set to zero. The bottom is assumed to be impermeable for the liquid.

ASYMPTOTIC ANALYSIS AND HYDRAULIC APPROXIMATIONS

An asymptotic analysis of the governing equations for slightly supercritical upstream Froude numbers is performed, i.e. $(2/3)(\mathrm{Fr_r}-1)=\varepsilon\ll 1$, with the reference Froude number $\mathrm{Fr_r}:=Q/(r_\mathrm{r}\sqrt{gh_\mathrm{r}^3})$. Here Q, g and h denote, in this order, the constant discharge per unit azimuth angle, the acceleration due to gravity and the height of the free surface above the bottom. The subscript r refers to a reference state. A non-dimensional radius $R=\delta r/h_\mathrm{r}$ is introduced, with $\delta=3\varepsilon^{1/2}$ serving as a contraction parameter. The non-dimensional reference radius R_r is assumed to be very large such that R can be decomposed in $R=R_\mathrm{r}+\eta$ with $\mathrm{d}R=\mathrm{d}\eta$. In the present analysis R_r is chosen as $R_\mathrm{r}=\tilde{R}\varepsilon^{-5/2}$ with $\tilde{R}=\mathrm{const}=\mathrm{O}(1)$. The analysis for reference radii of other orders of magnitude, e.g. $\mathrm{O}(\varepsilon^{-2})$, is beyond the scope of the present paper and will be discussed elsewhere. Expanding all dependent variables in terms of powers of ε, e.g. $H(\eta)=h/h_\mathrm{r}=1+\varepsilon H_1(\eta)+\ldots$ for the non-dimensional height of the free surface, leads to a set of first-order equations that allow to express all unknowns in terms of the free-surface elevation H_1. The latter remains undetermined in the framework of the first-order equations. This requires an investigation of the second-order equations, leading to the solvability condition

$$H_1'''+H_1'(H_1-1)=\varepsilon^{1/2}/3\tilde{R}\,, \tag{1}$$

i.e. an ODE for $H_1(\eta)$. Equation (1) is a steady-state version of an extended Korteweg–de Vries (KdV) equation, with the constant term of order $\varepsilon^{1/2}$ on the right-hand side representing the extension due to axisymmetric flow. According to the present analysis, (1) can be expected to be uniformly valid.

The asymptotic analysis leads to the interesting result $U(\eta,Z)=u/u_\mathrm{r}=1+\varepsilon[c_1(Z)-H_1(\eta)]+\ldots$ for the non-dimensional radial velocity. The function of integration $c_1(Z)$ defines the velocity profile and can be chosen freely, as it does not affect the final result for H_1. If the reference velocity u_r is defined as the volumetric mean velocity, the integral of $c_1(Z)$ over the non-dimensional vertical coordinate $Z=z/h_\mathrm{r}$ has to vanish, i.e. $\int_0^1 c_1(Z)\mathrm{d}Z=0$.

For the purpose of comparison it is of interest to consider a one-dimensional flow approximation, known as the "hydraulic approximation". It is based on the equation of motion in radial direction with hydrostatic pressure distribution. Continuity is expressed as $urh=Q=\mathrm{const}$. Combining the continuity equation and the equation of motion gives

$$\frac{r}{r^*}=\frac{R}{R^*}=\frac{(2+\mathrm{Fr}^2)^{3/2}}{3\sqrt{3}\mathrm{Fr}}\,, \tag{2}$$

i.e. an implicit equation for the local Froude number, which is defined as $\mathrm{Fr}(r):=Q/(r\sqrt{gh^3})$. The asterisk refers to the critical state, where $\mathrm{Fr}=1$. Note that the relation (2) is "universal", as it is free of parameters describing the upstream state.

A near-critical version of the hydraulic approximation is obtained by expanding (2) for $|\mathrm{Fr}-1|\ll 1$. The result is

$$\mathrm{Fr}=1\pm\sqrt{3(R/R^*-1)/2}\,. \tag{3}$$

*Corresponding author. E-mail: dominik.murschenhofer@tuwien.ac.at.

Introducing the reference radius R_r instead of R^* in (3), using the relation $\mathrm{Fr}(\eta) = 1 + 3\varepsilon(1 - H_1)/2$ and expanding for $\varepsilon \ll 1$ gives

$$H_1 = 1 \mp \sqrt{1 + 2\varepsilon^{1/2}\eta/3\tilde{R}}\,. \tag{4}$$

The upper and lower signs in (3) and (4) correspond to the supercritical and subcritical branch, respectively. Both (3) and (4) are near-critical hydraulic approximations. They differ from each other due to the different reference states, i.e. $\mathrm{Fr} = 1$ at $R = R^*$ for (3) and $H_1 = 0$ at $\eta = 0$ for (4). It follows from (4) that the condition $H_1 = \mathrm{O}(1)$ for the validity of the asymptotic expansion is only satisfied if $\varepsilon^{1/2}\eta = \mathrm{O}(1)$. It may be of interest to observe that differentiating (4) with respect to η leads to an equation that is equal to (1) without the term H_1''', i.e. the extended KdV equation without the third-order term is equivalent to the near-critical hydraulic approximation.

RESULTS

In Fig. 1 a solution of the extended KdV equation (1) is shown in black. The red curve represents the solution of the hydraulic approximation, (2). In Fig. 1a) the sub- and supercritical branches of the near-critical hydraulic approximation according to (4) are shown as blue dotted and dashed lines, respectively. The initial conditions for the black curve are chosen such that initial value, initial slope and initial curvature are in accord with the *super*critical branch of (4) in the reference state, i.e. $\eta = 0$. Within a short distance from the reference radius the solution of (1) develops into a wavy solution oscillating around the *sub*critical branch of (4). Such a transition is a characteristic property of undular hydraulic jumps. In Fig. 1b) the radial coordinate is referred to the critical radius. The solution of the near-critical hydraulic approximation according to (3) is shown in green. In order to plot the solution of (1), the critical radius is determined from (2) using the parameter values of the reference state $\mathrm{Fr}_\mathrm{r} = 1.15$ and $R_\mathrm{r} = 2214$, corresponding to $\varepsilon = 0.1$ and $\tilde{R} = 0.7$. If, for instance, the discharge is chosen to be $Q = 10$ l/s, these parameters give the reference values $h_\mathrm{r} = 10.72$ mm, $r_\mathrm{r} = 2.50$ m, $u_\mathrm{r} = 0.37$ m/s, which appear reasonable for applications.

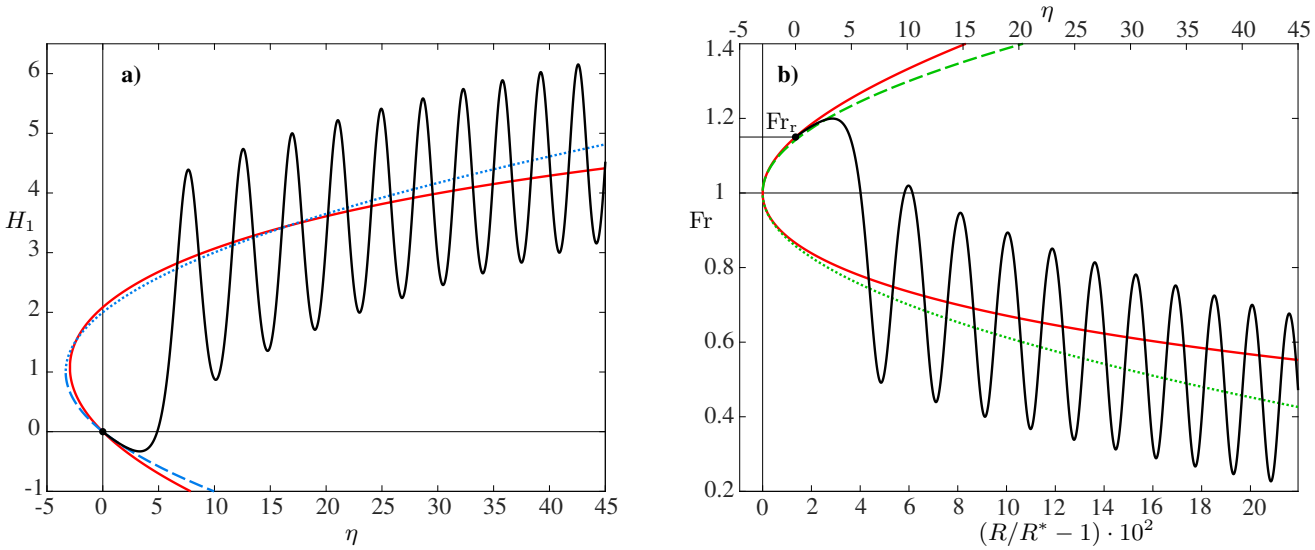

Figure 1: Results for an undular hydraulic jump in inviscid axisymmetric flow over a horizontal bottom; $\varepsilon = 0.1$, $\tilde{R} = 0.7$. a) Non-dimensional surface elevation, H_1. b) Local Froude number, Fr. Black: Numerical solution of (1) for $H_1(0) = 0$, $H_1'(0) = -0.15$, $H_1''(0) = 2.27 \cdot 10^{-2}$. Red: Full hydraulic approximation according to (2). Dotted and dashed: Sub- and supercritical branches, respectively, of the near-critical hydraulic approximation according to (3) in green, according to (4) in blue.

CONCLUSIONS

The present analysis demonstrates that – in contrast to inviscid plane flow – undular hydraulic jumps are possible in inviscid axisymmetric flow. The free-surface elevation is described by an extended steady-state version of the KdV equation. It turns out that the velocity profile can be chosen freely via a function of integration $c_1(Z)$, provided $c_1(Z) = \mathrm{O}(1)$. The velocity profile does not affect the final result for the surface elevation. The numerical solution of (1) shows that the supercritical branch of the hydraulic approximation is prone to develop into an undular hydraulic jump. The validity of the results is limited to non-dimensional distances from the reference radius up to $\eta = \mathrm{O}(\varepsilon^{-1/2})$.

Financial support by Androsch International Management Consulting GmbH (AIC) is gratefully acknowledged.

References

[1] Grillhofer W., Schneider W. The undular hydraulic jump in turbulent open channel flow at large Reynolds numbers. *Phys. Fluids* **15**(3): 730–735, 2003.

ENERGY, BUBBLE AND DROPLET STATISTICS IN BREAKING OCEAN WAVES

Wouter Mostert[1], Stéphane Popinet [2], and Luc Deike [*1,3]
[1]Department of Mechanical and Aerospace Engineering, Princeton University, Princeton NJ, USA
[2]Institut Jean Le Rond d'Alembert, Sorbonne Université, Paris, France
[3]Princeton Environmental Institute, Princeton University, Princeton NJ, USA

Summary We present three-dimensional (3D) direct numerical simulation of breaking ocean waves at various Reynolds (Re) and Bond (Bo) numbers with resolved bubble and droplet size distributions and comprehensive budgets for kinetic, gravitational potential and dissipated energies. The budgets are compared with equivalent 2D simulations to determine the effect of dimensionality in the dissipation rate. At low Bo and Re, 2D and 3D energy budgets for the wave are similar, consistent with the literature. This breaks down at larger Bo with increasingly rapid transition to fully 3D flow. Bubble size distributions are well-resolved, including the Hinze scale r_H at small Bo, and we recover expected distributions of $r^{-10/3}$ for $r>r_H$ while extending somewhat to $r<r_H$. Numerical resolution of droplet size distributions remains challenging and well-resolved droplet ejection only occurs for larger Bo and Re.

BACKGROUND

Breaking ocean waves constitute a diverse and important means of mass, momentum and energy transfer between ocean and atmosphere which is incompletely understood in climate modelling [1]. First, the energy dissipation of breaking waves has been widely studied both experimentally [2] and numerically [3] for the purposes of incorporation into parameterization for regional of global scale wave modelling [4]. In particular, direct numerical simulation has been performed for two-dimensional waves based on the observation that, at small wavelengths, the measured dissipation rates correspond well to three-dimensional experimental counterparts [5]. This is explained by the delayed formation of three-dimensional structures in the breaking wave so that the most intense dissipation occurs during a time when the flow is mostly two-dimensional [5]. This hypothesis has not however been tested directly.

Second, bubble and droplet size distributions are important for understanding the mass transfer between sea and air. While experimental data exists for bubbles [6] and droplets [7], only bubbles have been resolved directly to a limited extent in a recent numerical study [3]. The Hinze scale, which sets the length scale at which bubble surface tension resists the deforming action of turbulent shear, has not been resolved and the bubble statistics below this scale remain elusive. Moreover, droplet size distributions are difficult to determine numerically because they proliferate only for large wavelengths, which are difficult to resolve satisfactorily in direct simulation, and the formation mechanisms occur at smaller length scale, probably of order tens of micrometres.

High-resolution direct numerical simulation (DNS) provides an avenue to investigate each issue. At low wavelengths, the sub-Hinze-scale bubble statistics can be more easily resolved, while at high wavelengths, both the dimensionality of energy dissipation and converged statistics for droplets can be more determined.

RESULTS

Methodology

We use the open-source package Basilisk [8] to perform DNS of the two-phase Navier-Stokes equations with surface tension and viscosity, using adaptive mesh refinement (AMR) to allow for high effective numerical resolutions of the flow field while retaining comparatively low computational costs. This allows us to resolve a wide range of length scales in the breaking wave, including the viscous sublayer and, for appropriate conditions, the Hinze scale in the bubble size distributions. The air-water interface is reconstructed and advected using a volume of fluid scheme with momentum conservation, so that bubbles and droplets are captured directly by the solver. We choose physical and numerical parameters to allow these bubbles and droplets to be fully resolved across a wide range of length scales.

We define the wave Bond number, $Bo = \Delta\rho g/(\gamma k^2)$, and wave Reynolds number, $Re = \sqrt{g\lambda^3}/\nu$, where $\Delta\rho$ is the density difference between the water and gas phases, g is gravitational acceleration, γ is surface tension, λ is the wavelength and k the wavenumber of the breaker, and ν is kinematic viscosity. Larger values of Bo and Re generally correspond with larger breaker wavelengths [9]. In this study we present breakers over a range $Bo = 200, 500, 1000$ and $Re = 40 \times 10^3, 100 \times 10^3$. The breaker is initialized by a high-slope third-order Stokes wave on a domain of a size λ, and the effective numerical cell size in the domain is set by $\Delta x = \lambda/2^L$, where $L = 9,10,11$.

Figure 1 shows a sample rendering of the evolution of the breaking wave, for the case Bo=1000, Re=100000. As the wave steepens nonlinearly, it overturns and breaks, generating a turbulent cloud underneath the surface, ingests air in the form of bubbles into the water, and ejects spray in the air.

Dimensionality of dissipation

The total dissipated energy in the domain of the breaking wave is given by the integral of the squared elements of the deformation tensor, $\dot{E} = 2\nu \int_v \sum_i \sum_j D_{ij}^2 dV$. Linearity of integration allows us to define $\dot{E}_{ij} = \int_V D_{ij}^2 dV$ without implicit summation such that $\dot{E} = 2\nu \sum_i \sum_j \dot{E}_{ij}$. In Cartesian coordinates where indices $i = 1,2,3$ correspond with

streamwise, spanwise and depthwise directions respectively, the dissipation constrained within the plane of the wave is given by the sum $\dot{E}_{in} = \sum_{i=1}^{2}\sum_{j=1}^{2} E_{ij}$, while the out-of-plane (essentially three-dimensional) contribution $\dot{E}_{out}$ is given by the sum of all other components. With these definitions we compare two-dimensional with three-dimensional simulations for the various Bo and Re tested here. By analysing the relative contributions of $\dot{E}_{in}$ and $\dot{E}_{out}$ to the total dissipation for various Re and Bo, we show that contrary to the understanding in the literature, the dissipation becomes properly three-dimensional at an early stage of the breaking process, so that numerical two-dimensional breakers cannot be effectively used to predict the real dissipation beyond the smallest wavelengths, approximately Bo<200. The transition to three-dimensional flow can be directly visualized by highlighting isosurfaces of the λ-2 criterion, featuring longitudinal filaments that form underneath the developing breaker. These filaments suggest the presence of a transverse instability which is probably mediated by surface tension and viscosity, and which constitutes an intermediate state between the initially two-dimensional flow and the terminal three-dimensional, turbulent flow.

Bubble size distributions below the Hinze scale

Figure 2 (left) shows the bubble size distributions for strong breaking waves and two Bond number. Above the Hinze scale, $r > r_H$, we recover $N(r) \sim r^{-10/3}$ in agreement with theory [10] and consistent with a previous study [3], but we emphasize in particular that the distribution also extends below the Hinze scale. Given that there is no known mechanism for bubbles to break up below the Hinze scale, it follows that the bubbles in that range can only be produced by the breakups of super-Hinze bubbles or direct entrainment of tiny bubbles at impact and can only be destroyed by rising to the water surface and bursting. The sub-Hinze distribution follows a slightly shallower power law. The super Hinze scale bubble size distribution appears independent of the Reynolds and Bond number, suggesting that only the size of the injected cavity and the strength of the wave impact control this range of bubble scale creation.

Droplet size distributions

We investigate droplet size distributions (Figure 2, right), averaged over the active breaking period, for various Bond and Reynolds numbers. Since the flow field in the air phase is not turbulent, and hence does not imply relevance to the Hinze scale, we consider the capillary length scale l_c as a relevant length scale. Depending on the Bond number, we can resolve droplets down to $0.14l_c$. We observe a sharp dependence in the total number of droplets being created as a function of Bond number, with very few droplets created at Bo=200. At higher Bond number, we observe a statistically meaningful distribution which follows two power laws, consistent with the observations of [7], although a theoretical argument to explain the approximate $N_d(r) \sim r^{-2.3}, r^{-5}$ dependences or the approximate transition at $r \sim l_c$ has not to our knowledge been developed.

To conclude, we present in this study high fidelity DNS of breaking waves at high Reynolds number, shedding light on the droplet and bubbles creation processes as well as the transition from a two-dimensional wave flow to a three-dimensional turbulent flow.

Figure 1. Snapshots of a breaking wave, Bo=1000, Re=100000.

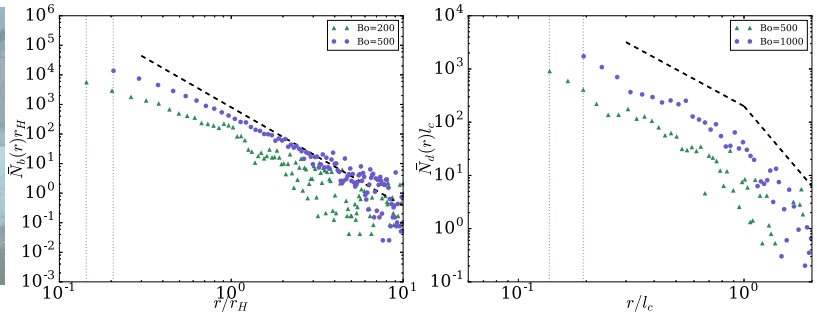

Figure 2. Bubble size distributions for Bo=200, 500; Re=40000,100000 (left) and droplet size distributions for Bo=500, 1000, Re=100000 (right) for various cases.

References

[1] Melville W.K. The role of surface-wave breaking in air-sea interaction. *Ann. Rev. Fluid Mech.* **28** (1): 279-321, 1996.
[2] Romero L., Melville W.K., Kleiss J.M. Spectral energy dissipation due to surface wave breaking. *J. Phys. Ocean.* **42**, 2012.
[3] Deike L., Popinet S., Melville W.K. Air entrainment and bubble statistics in breaking waves. *J. Fluid Mech.* **801**: 91-129, 2016.
[4] Romero L., Distribution of surface wave breaking fronts. *Geophys. Res. Lett.* **46**(17-18): 10463-10474, 2019.
[5] Iafrati A. Numerical study of the effects of the breaking intensity on wave breaking flows. *J. Fluid Mech.*. **622**: 371-411, 2009.
[6] Deane G.B., Stokes M.D. Scale dependence of bubble creation mechanisms in breaking waves. *Nature* **418**: 839-844, 2002.
[7] Erinin M.A., Wang S.D., Lui R., Towle D., Liu X., Duncan J.H. Spray generation by a plunging breaker. *Geophys. Res. Lett.* **46**(14):8244-8251. 2019
[8] Basilisk Flow Solver and PDE library, web site **http://basilisk.fr**.
[9] Deike L., Popinet S., Melville W.K. Capillary effects on wave breaking. *J. Fluid Mech.* **769**: 541-569, 2015.
[10] Garrett C., Li M., Farmer D. The connection between bubble size spectra and energy dissipation rates in the upper ocean. *J. Phys. Ocean.* **30**: 2000.

ON INSTABILITIES OF FINITE-AMPLITUDE INERTIA-GRAVITY WAVES

Michael V. Kurgansky*[1]
[1]A.M. Obukhov Institute of Atmospheric Physics, Russian Academy of Sciences, Moscow, Russia

Summary The instability of monochromatic inertia-gravity waves (IGWs) of finite amplitude, propagating at small angles either to the vertical or horizontal, is studied. The corresponding angle serves as a small parameter in the problem, and instability is investigated using the Galerkin method. For IGWs that propagate at a small angle to the vertical, it is shown that stable density stratification is a stabilizing factor, and fluid rotation is destabilizing. The opposite is true for IGWs that propagate at a small angle to the horizontal. The previous analysis of the short wave instability of the internal gravity waves of finite amplitude that propagate at small angles to the vertical is generalised to the case of the IGW. As an auxiliary problem, the stability of a monochromatic inertial wave of finite amplitude in a fluid of uniform density is investigated in the same mathematical formulation.

INTRODUCTION

In geophysical fluid dynamics, the task of investigating the hydrodynamic instability of inertia-gravity waves (IGWs), which play an important role in the atmosphere and the ocean, is of interest. This is also closely related to the problem of generating and maintaining turbulence in these media. The instability of the IGW, both its wave packets and monochromatic waves of finite amplitude, has been studied repeatedly in the literature [1, 2]. The closest to the proposed study is, apparently, the work of Yau et al. [3], who, using Floquet's theory, investigated the three-dimensional instability of a monochromatic IGW of large amplitude. The proposed study is simpler in that we refuse to fully consider three-dimensionality and assume that fluid dynamic variables are independent on one of the horizontal co-ordinates, although the three velocity components remain nonzero. This 2½-dimensional formulation of the problem allows to fully utilizing the analogy between the effects of stratification and rotation and the resulting perfect mathematical symmetry of the problem. In this work, first, we set the objective of extending the previous analysis of instability of internal gravity waves [4] onto the case of monochromatic IGW of finite amplitude that propagates in the atmosphere at a small angle θ to the vertical when the buoyancy frequency N is much greater than the inertial frequency f. The second task is to use a small parameter in the problem, either θ, if an IGW propagates nearly vertically, or $\varpi = (\pi/2) - \theta$, if the IGW propagates nearly horizontally, for an asymptotic analysis of IGW instability at an arbitrary ratio of f and N. As an auxiliary problem, in the same 2½-dimensional formulation and for small angles θ and ϖ we study the stability of a monochromatic IW of finite amplitude in a fluid of uniform density.

RESULTS

We study the instability of a monochromatic IGW of finite amplitude with the phase velocity vector at an angle θ to the axis of rotation of the fluid, which coincides with the direction of acceleration of gravity, that is, with the vertical. The dependence of the fluid dynamic variables on one of the Cartesian horizontal co-ordinates is neglected and it is assumed that the three velocity components depend on two co-ordinates (x,z). In this 2½-dimensional formulation, the Boussinesq equations for a fluid heterogeneous in density and rotating at a constant angular velocity $f/2$ around the vertical axis z have the exact solution in the form of a monochromatic IGW of finite amplitude, with the frequency σ that satisfies the dispersion relation $\sigma^2 = N^2 \sin^2\theta + f^2 \cos^2\theta$. A linear stability of this exact solution is considered, the perturbation equations are taken in a non-dimensional form and transformed to the co-ordinate system, $X = x\cos\theta - z\sin\theta$, $Z = x\sin\theta + z\cos\theta - t$, co-moving with the IGW in the Z-direction.

A simpler case of an inertial wave (IW) that propagates in a neutrally stratified fluid is analysed. First, the case when an IW propagates vertically is considered. Following the Galerkin method with three basis functions, $\cos Z, \sin Z, 1$, and with the X-dependence as $\exp(\mathrm{i}\alpha X)$, a system of six differential equations with six unknowns is obtained. The wave is unstable only when $\alpha^2 < 2/\sqrt{3}$ and the instability, in the first place, develops with respect to long wave perturbations $\alpha^2 << 1$.

In IW applications to the deep ocean and the outer liquid core of the Earth, the second limiting case of $\theta \to \pi/2 -$ is of interest when the wave vector $\mathbf{k} = (k,q)$ is nearly perpendicular to the direction of fluid rotation and IWs have frequencies $\sigma << f$. Such a problem formulation is also relevant to laboratory experiments [5]. In this case, instability is of a short wave nature. In the middle of the instability interval, the increment of the growth of unstable disturbances is proportional to the square of the amplitude of the IW. A mathematically identical result is obtained, up to replacements $f \leftrightarrow N$, $k \leftrightarrow q$, for the instability of an internal gravity wave, which propagates at a small angle to the vertical [4].

*Corresponding author. E-mail: kurgansk@ifaran.ru.

We now take into account both the fluid rotation around the vertical axis and its stable density stratification and consider the problem of the hydrodynamic instability of IGWs. Specifically, we consider a case when f and N are comparable in magnitude. First, a limiting case when the IGW propagates at $\theta \ll 1$ is considered. Using the Galerkin method we obtain a system of nine equations with nine unknowns, which admits long-wave instability only if $Y < 1$, where $Y = N^2/f^2$. Density stratification is a stabilizing factor, but rotation, on the contrary, is destabilizing. For IGWs that propagate nearly horizontally, long-wave instability is possible only if $Y^{-1} < 1$, i.e., $N^2 > f^2$, and the fluid rotation is in this case a stabilizing factor, whereas the density stratification is destabilizing.

Interesting for applications to atmospheric dynamics is a case of approximate equality of the terms $N^2 \sin^2\theta$ and $f^2 \cos^2\theta$ in the dispersion relation for the IGW, when also $N^2 >> f^2$ and $\theta \ll 1$. Here, we ultimately arrive at the same characteristic equation as that for internal gravity waves. Thus, the conclusion about short-wave instability of internal gravity waves is generalized onto the range of such small θ that the effect of the Earth rotation in the IGW's dispersion relation is comparable in magnitude with the effect of atmospheric stable stratification.

To complement the analytical results a numerical stability analysis was performed at $\theta \ll 1$. We seek the solution with time dependence $\propto \exp(\lambda T)$ and use Maplesoft Maple 10 to calculate the roots of the ninth-order characteristic equation. The numerical results generally confirm the analytical prediction on the long-wave nature of instability that arises at $Y < 1$, if $Y = O(1)$. Very interesting is the appearance of a robust shortwave instability domain at $Y \ll 1$. This shows that the limit transition $Y \to 0$ should be investigated in more detail, since a pure IW that propagates vertically only exhibits long-wave instability. Therefore, we revisit the case of a pure IW, with $Y = 0$, and compare two options numerically: (i) $\theta = 0$ and (ii) $\theta = 10^{-2}, 10^{-1}$. In full compliance with the analytics, the numerical calculations reveal a long-wave nature of the instability of IWs at $\theta = 0$. However, they show at $\theta = 10^{-2}, 10^{-1}$ both long-wave and shortwave instability of IWs. It means that the limit transition $Y \to 0$ is regular, but the limit $\theta \to 0$ for the IW itself is singular, i.e. for small but finite θ-values a short-wave instability domain arises with the lower threshold wavenumber γ-value decreasing along with increase in θ in accordance with the law $\theta^{1/2}\gamma \cong const$

CONCLUSIONS

Attempts have been made to investigate, by applying simple analytical tools, the instability of monochromatic inertia-gravity waves (IGWs) of finite amplitude in two limiting cases when the IGW propagates either at a small angle θ to the vertical or at a small angle $\varpi = (\pi/2) - \theta$ to the horizontal. A particular methodically important case of instability of a pure inertial wave in a homogeneous fluid is also analysed in the same mathematical formulation.

In [4], the shortwave instability of an internal gravity wave was analysed for $\theta_0 \ll \theta \ll 1$, where $\theta_0 = \arctan(f/N)$. It is shown here that the same shortwave instability of IGWs is present for $\theta \sim \theta_0$, that is, when the Coriolis force is taken into account, if only $\theta_0 \ll 1$, as is the case in the atmosphere.

In the case of $f \sim N$ that matches with possible oceanic applications and also corresponds to conditions in intense vertical atmospheric vortices the situation changes radically. The instability of an IGW that propagates at $\theta \ll 1$ acquires a generally long wave nature. The condition $N < f$ must necessarily be met, that is, the stable density stratification is generally a stabilizing factor, and the general rotation of the fluid is destabilizing. The situation is reversed for IGWs that propagate at $\varpi \ll 1$, where inverse inequality $N > f$ must be maintained for long-wave instability.

The analytical results have been complemented with numerical calculations. In general, a fairly good agreement has been obtained with analyses. Interesting, is the appearance of short-wave instability at small θ and $N \ll f$, since a pure IW that propagates strictly vertically only experiences long wave instability. It is argued that the inclusion of an arbitrarily small turbulent viscous dissipation effectively dampens short-wave disturbances at indefinitely small but finite angles θ without noticeably affecting long-wave disturbances, which makes the limit transition $\theta \to 0$ regular.

The work was supported by the Russian Foundation for Basic Research through a grant 18-05-00414-a.

References

[1] Achatz U., Schmitz G. Shear and Static Instability of Inertia–Gravity Wave Packets: Short-term Modal and Nonmodal Growth. *J. Atmos. Sci.* **63**: 397-413, 2006.

[2] Achatz U., Schmitz G. Optimal Growth in Inertia–Gravity Wave Packets: Energetics, Long-term Development, and Three-Dimensional Structure. *J. Atmos. Sci.* **63**: 414-434, 2006.

[3] Yau K.-H., Klaassen G. P., Sommor L. J. Principal Instabilities of Large Amplitude Inertio-Gravity Waves. *Phys. Fluids* **16:** 936-951, 2004.

[4] Kurgansky M. V. On the Instability of Internal Gravity Waves Propagating at Small but Finite Angles to the Vertical *Geophys. Astrophys. Fluid Dyn.* **112**(4): 265-276, 2018.

[5] Seelig T., Harlander U. Can Zonally Symmetric Inertial Waves Drive an Oscillating Zonal Mean Flow? *Geophys. Astrophys. Fluid Dyn.* **109**(6): 541-566, 2015.

DAMPED INTERFACIAL WAVE MECHANICS IN ORBITALLY SHAKEN CYLINDERS

Gerrit Maik Horstmann*[1], Sten Anders[1], Wietze Herreman[2], and Tom Weier[1]
[1]Institute of Fluid Dynamics, Helmholtz-Zentrum Dresden - Rossendorf, Dresden, Germany
[2]LIMSI, CNRS, Université Paris-Sud, Université Paris-Saclay, Orsay, F-91405, France

Summary We present a new theoretical model describing damped gravity-capillary waves in orbitally shaken cylinders. Our model can account for both free-surface and two-layer interfacial waves and is therefore versatilely applicable to two different devices: to study interfacial wave instabilities in liquid metal batteries and to better predict mixing regimes in orbitally shaken bioreactors. We complement a potential model with viscous damping rates to incorporate energy dissipation. This approach allows us to calculate explicit formulas for the responding amplitudes and the phase shifts between wave and shaker, which are in good agreement with our experiments. As an unexpected result, the model predicts the formation of novel spiral wave patterns under the influence of strong damping. By employing a Background-Oriented Schlieren method we can experimentally verify their existence.

Introduction

The theoretical and experimental work presented in this talk originates from the growing interest in liquid metal batteries (LMB)s. LMBs are discussed today as one option for economic grid-scale energy storage, as required for the deployment of fluctuating renewable energies. These batteries incorporate stratified three-layer fluid systems consisting of two liquid metal electrodes separated by a thin molten salt electrolyte. Due to their completely liquid interior, LMBs are highly susceptible to various kinds of fluid dynamical instabilities [4]. Induced fluid flows can endanger the operational safety on the one hand, but they can also have beneficial effects such as increasing the mixing efficiency on the other hand. In particular, Lorentz force-driven interfacial wave instabilities, widely known from aluminum reduction cells (ARCs), have emerged as to be crucial for the operational safety of the batteries. They can arise from the interaction of external or self-induced magnetic fields with internal cell currents. Although such waves are destabilized by rotational Lorentz forces, parts of the evolving wave mechanics can be understood by entirely neglecting electrodynamics and applying classic irrotational wave theories. This was shown in the paper [1], where we have used a potential flow model to describe the wave coupling between the upper and lower interface. One of the most important unresolved questions in connection with these types of interface instabilities concerns the influence of mechanical dissipation. Dissipation effects are neglected in most theoretical models, as it is justified in large-scale aluminum reductions cells. But viscous damping is expected to have a strong influence on the instability onsets in lab-size LMBs. Similar as for the wave coupling mechanics, viscous damping mechanisms can be studied without considering the magnetohydrodynamic origin of the interfacial waves.

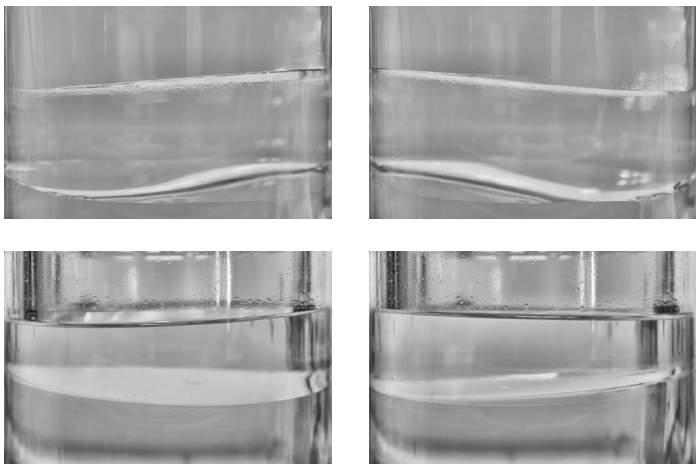

Figure 1: Symmetric (top) and antisymmetric (bottom) coupling modes shown for two different times in one period (left and right). The symmetric mode was realized by using a paraffin oil|silicon oil|water stratification, where the density differences at both interfaces are of similar magnitude. For the antisymmetric coupling we have employed an air|paraffin oil|silicon oil system, where the density differences are of different orders, see [2] for more details.

These two facts have inspired us to create a purely hydrodynamic analogy experiment, presented in [2]. The idea was to fill a cylindrical container with two or three inmiscible liquids and placing it on a shaking table prescribing circular translations. The resulting centripetal forces are known to excite approximately the same rotational gravity wave mode as it is commonly induced by magnetohydrodynamic instabilities closely beyond the linear instability onset. The experiment is therefore capable to imitate the resulting wave mechanics as they can arise due to Lorentz forces in LMBs.

*Corresponding author. E-mail: g.horstmann@hzdr.de

This is emphasized in Figure 1 showing the well-known symmetric (waves are in-phase) and antisymmetric (waves are phase-shifted by 180 °) coupling modes realized within different three-layer stratifications. The waves behave exactly as predicted in [1]: the symmetric mode is dominating when the density jumps at both interfaces are of similar magnitude, while the antisymmetric modes prevails when the density jumps are appreciably different.

Beside the coupling dynamics, we [2] have placed the main focus on measuring damped wave mechanics in two-layer systems. Since damping rates are usually very high for oil-water stratifications, measurements of exponential decay rates are difficult to achieve. Instead, it is advantageous to measure amplitude curves as a function of the shaking frequency. The peak amplitudes around the eigenfrequencies provide insights into the wave mode-dependent dissipation rates. However, we have noted that wave theories [5] for orbitally shaken cylinders entirely lack of any damping mechanism, such that the most interesting amplitudes close to resonance are not captured. Such inviscid approaches are insufficient to describe the measured highly-damped resonance curves presented in [2].

Theoretical model and experiments

Aiming to fill this gap, we have substantially extended the forced wave theory by [5]: the model is re-formulated for two-layer systems, expanded to account also for capillary forces and, most importantly, supplemented with viscous damping rates. Viscous damping rates for interfacial waves in upright circular cylinders have been recently derived by [3] using a perturbation method. The damping rates can account for dissipation arising in the Stokes boundary layers at the side wall, top and bottom walls as well as the interfacial layers above and below the interface. These damping rates provide many new insights into the nature of interfacial wave damping and fully explain the resonant wave amplitudes of the first wave mode measured in [2].

When restricting to the one-layer free-surface limit, our model can be exploited to better predict the wave dynamics in orbitally shaken bioreactors. We present explicit formulas for the phase shift between wave and shaker, which is known to considerably affect the mixing efficiency. Further, we can show that the often assumed linear scaling of the wave amplitudes with the Froude number for small excitation frequencies does not exist. The scaling only *appears* to be linear but results from different shifted resonance curves.

Finally, as an intriguing result, the model predicts the existence of linear spiral wave solutions, which arise due to a damping-induced symmetry breaking mechanism. Representative spiral wave patterns are shown in Figure 2 for the first four orbital wave modes. In contrast to the inviscid classical wave modes, the crests and troughs are connected to an one-armed spiral, which can be explained by the different mode-dependent phase shifts causing a twisting of the nodal cycles. By employing a Background-Oriented Schlieren method, we were recently able to experimentally verify the existence of these spiral wave patterns. We will present first measurements in this talk.

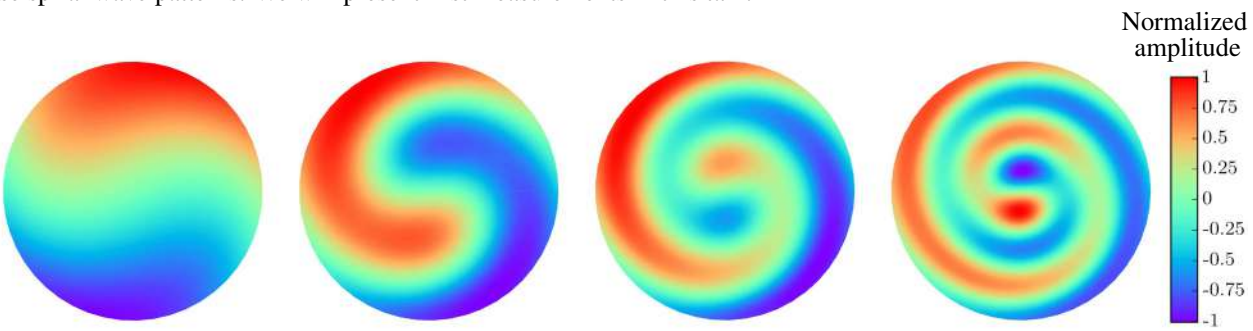

Figure 2: Normalized interface elevations of the first four orbital wave modes (compare with Figure 2 in [2]) under the influence of damping.

Conclusion

By complementing the forced wave theory by [5] with viscous damping rates, we have derived analytical formulas for wave amplitudes, phase shifts and fluid velocities of two- and one-layer gravity-capillary waves in orbitally shaken upright circular cylinders. The theory can explain the damped resonance curves presented by [2] and is helpful to get some new insights into interfacial wave dynamics in liquid metal batteries or to better predict mixing regimes in orbitally shaken bioreactors. As an surprising result, the model predicts the formation of novel spiral wave patterns we experimentally verify using a Background-Oriented Schlieren method.

References

[1] Horstmann, G. M., Weber, N. & Weier, T. *J. Fluid Mech.* **845**: 1-35, 2018.
[2] Horstmann, G. M., Wylega, M. & Weier, T. *Exp. Fluids*. **60**, 56, 2019.
[3] Herreman, W., Nore, C., Guermond, J.-L., Cappanera, L., Weber, N. & Horstmann, G. M. *J. Fluid Mech.* **878**: 598-646, 2019.
[4] Kelley, D. H. & Weier, T. *Appl. Mech. Rev.* **70** (2): 020801, 2018.
[5] Reclari, M., Dreyer, M., Tissot, S., Obreschkow, D., Wurm, F. M. & Farhat, M. *Phys. Fluids* **26**: 052104, 2014.

RAPID TSUNAMI FORECASTS UTILISING THE EXTENDED GREEN'S LAW

Daniel Giles*[1], Audrey Gailler[2], and Frédéric Dias[1]
[1]School of Mathematics and Statistics, University College Dublin, Dublin, Ireland
[2]CEA, DAM, DIF, F-91297 Arpajon, France

Summary Tsunamis are rare but extremely destructive events. Owing to their speed of propagation, accurate and timely warnings are imperative in the mitigation of their damage. Tsunami Warning Centres are tasked with deciding the level of threat posed by an event and the areas at risk. These decisions are often based on regional forecasts of the maximum wave heights. Unfortunately, due to runtime constraints, high resolution localised forecasts are usually unfeasible. Transfer functions which generate localised wave heights from the regional forecasts by incorporating a site's response to an incoming tsunami have been developed. These functions are extensions of the classical Green's Law, which describes the evolution of long waves over varying bathymetry. The extended Green's Laws are shown here to be powerful tools which can provide extremely rapid and accurate localised tsunami forecasts.

INTRODUCTION

Tsunamis can travel at extremely high speeds in deep water, thus arrival times at the coastline are often on the $\mathcal{O}$(mins). Tsunami Warning Centres (TWC) are therefore under severe time constraints when deciding the level of warning and areas at risk from an event. To aid in this decision process, TWCs currently deploy a variety of tools which produce regional levels of warnings. One such tool is launching a faster than real time simulation (Fig 1). In order for these simulations to be completed in the required timeframe a coarse grid resolution must be used.

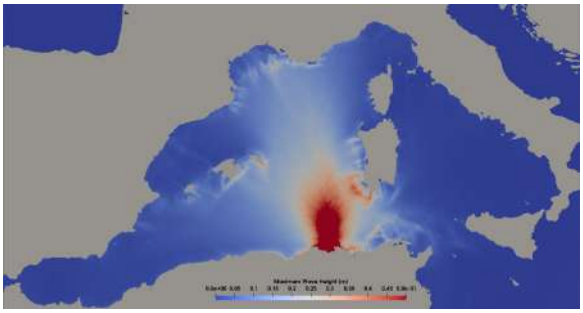

Figure 1: Faster than real time simulation of a tsunami event in the Mediterranean. Figure shows a regional maximum tsunami wave height forecast. Results obtained using Volna-OP2 [1] (4 hours of simulated time in 13s runtime on 2 GPUs)

The local bathymetry can have a large effect on the amplification or diminishment of an incoming wave. Thus, providing localised forecasts at strategic locations would help in the mitigation of damage. However, traditional high resolution simulations which can capture these localised effects are too costly to run from a TWCs perspective. Dealing with the run-up and amplification of long waves on beaches, shelves and shorelines has been extensively dealt with in the literature. However, these works mainly deal with the analytical solution of prescribed wave forms or experimentally derived relationships [2, 3, 4]. Green's Law (Eq. 1) is a classical result in this area of shallow ocean waves propagating over varying bathymetry.

$$\eta_2 = \eta_1 \left(\frac{h_1}{h_2}\right)^{\frac{1}{4}} \tag{1}$$

where η_2 and η_1 are the wave heights at a shallower and deeper point respectively, while h_2 and h_1 are the corresponding water depths at these points. The theory, however, neglects various physical phenomena, such as reflection and refraction which play an extremely important role in the amplification of shallow water waves. Recently, extended versions of Green's Law have been developed [5, 6], which aim to account for the localised effects on the tsunami amplification. These extended versions of Green's Law can capture local variability in tsunami wave height and allow for extremely rapid localised forecasts. Here is an extended version of Green's Law [5],

$$\eta_2 = \alpha\eta_1 \left(\frac{h_1}{h_2}\right)^{\frac{1}{4}} \tag{2}$$

where η_2, η_1, h_2 and h_1 are the same as above (Eq. 1), and α is defined as the local amplification factor. An empirically derived extended version of Green's Law [6] is given by,

$$\eta_2 = \eta_1 \left(1 + \beta\frac{h_E - h_2}{h_2}\right)\left(\frac{h_1}{h_2}\right)^{\frac{1}{4}} \tag{3}$$

*Corresponding author. E-mail: daniel.giles@ucdconnect.ie.

where again η_2, η_1, h_2 and h_1 are the same as above (Eq. 1) with h_E defined as a threshold depth and β is a local amplification factor.

Both versions of the Extended Green's Law incorporate site specific amplification parameters, defined as α and β in (Eq. 2) and (Eq. 3) respectively. The (Eq. 3) extension has been used to forecast maximum tsunami wave heights along the French Polynesia [7] and Mediterranean coastlines [8]. In these works a homogeneous site specific parameter was obtained for a whole site (harbour/bay area) via a 'trial and error' approach. A fully automated method which optimises for a heterogenous amplification parameter (i.e highlights variability within a site) has been developed here. A comparison between the two different formulations of the Extended Green's Law and between the two methods of calculating the site specific parameters has been made. Further, as these site specific parameters play a vital role in the accuracies of the localised forecasts, a robustness study of the values has also been carried out. The results below simply highlight the benefits of utilising the Extended Green's Law approach.

RESULTS

The high resolution sites studied here are located along the French mediterranean coastline. However, due to the lack of tsunami data for the Mediterranean area a collection of scaled historical events and hypothetical scenarios are simulated to capture a site's response to an incoming tsunami. The amplification parameters have been calculated within both formulations of the extended Green's Law (Eq. 2 and Eq. 3) using a fully automative method which optimises for the parameter via a gradient descent approach. A localised forecast is then compared to a computational expensive high resolution simulation (*ground truth*) of the same event. The localised forecasts can be run on a laptop for 5/6 sites within $\approx 30s$ and obtain a relative error of $\approx 10\%$ when compared to the *ground truth* (Fig 2). These results show the utility of this approach for providing extremely rapid localised forecasts.

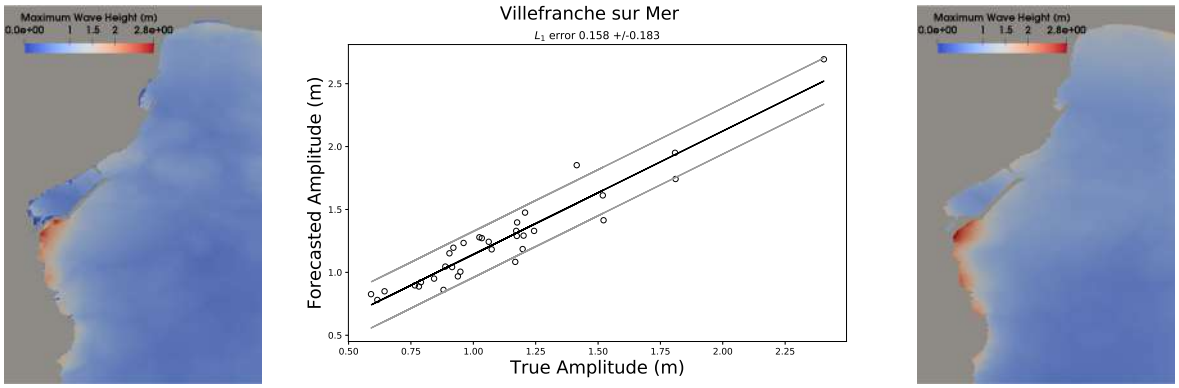

Figure 2: Comparison between the forecasted and true maximum wave heights along the Villefranche sur Mer coastline. Only results obtained with the Eq. 3 formulation of the Extended Green's Law are shown here. Left - Plot of the *ground truth* maximum wave heights. Middle - Comparison of the maximum wave heights at gauge points along the coastline. Right - Plot of the forecasted maximum wave heights. Please note that the forecast method doesn't predict wave heights on land, this explains some of the discrepancies between the left and right plots.

CONCLUSIONS

In the context of a TWC, providing localised maximum wave heights would help mitigate the risks of a tsunami event. One could provide localised forecasts for beaches, harbours or other strategic infrastructure located on the coast. The extended Green's Law approach has been shown to be a powerful tool in this context. The approach is extremely quick and provides an adequate level of accuracy. The various formulations and methods have been compared and a robustness study of the site specific amplification parameters has been carried out.

References

[1] I. Z. Reguly, et al.,The VOLNA-OP2 tsunami code (version 1.5). *Geosci. Model Dev*, (2018), **11(11)**, 4621–4635.
[2] Carrier, G. F. and Greenspan, H. P., Water waves of finite amplitude on a sloping beach. *J. Fluid Mech*, (1958), **4**, 97—109.
[3] Synolakis, C. E., Runup of solitary waves. *J. Fluid Mech*, (1987), **185**, 523–545.
[4] Knowles, J., and Yeh, H., On shoaling of solitary waves. *J. Fluid Mech*, (2018), **848**, 1073–1097.
[5] Lalli F., Postacchini M., Brocchini M., Long waves approaching the coast : Green's law generalization. *J. Ocean Eng. Mar. Energy* , (2019).
[6] Reymond D., Okal E. A., Hébert H., et al, Rapid forecast of tsunami wave heights from a database of pre-computed simulations, and application during the 2011 Tohoku tsunami in French Polynesia. *Geophysical Research Letters* , (2012), **39**, 11: 1–6.
[7] Jamelot A. and Reymond D. New Tsunami Forecast Tools for the French Polynesia Tsunami Warning System Part II: Numerical Modelling and Tsunami Height Estimation. *Pure and Applied Geophysics* , (2015), **172**, 805–819.
[8] Gailler A., Hébert H., Schindelé F., Reymond D. , Coastal Amplification Laws for the French Tsunami Warning Center: Numerical Modeling and Fast Estimate of Tsunami Wave Heights Along the French Riviera. *Pure and Applied Geophysics*, (2017), **175**, 1429.

ASYMPTOTIC STRUCTURE OF ACOUSTIC WAVE SCATTERING BY FINITE-SCALE CYLINDRICAL VORTEX

Dmitry Gadzhiev*[1,2] and Alexander Gaifullin[1,2]
[1]Department of Aeromechanics and Flight Engineering, Moscow Institute of Physics and Technology, Dolgoprudny, Russia
[2]Central Aerohydrodynamic Institute, Zhukovsky, Russia

Summary The asymptotic solution to the two-dimensional problem of a plane sound wave scattering by an axisymmetric vortex with zero circulation at infinity is obtained for the case when the vortex effective radius L is much greater than the wavelength $2\pi/k$. The two well-known solutions for the non-zero circulation case [1] and [2], [3], [4], qualitatively different from each other, are included as separate limiting cases. There is a profound analogy between the patterns observed in the scattering problem and in problems of short-wavelength diffraction. The issue of sound scattering at small angles is resolved: the peak order of the scattered wave intensity is maintained within the elongated "wake" behind the vortex. The longitudinal size of the wake is the Fraunhofer distance kL^2.

OVERVIEW

Scattering of a plane monochromatic acoustic wave by a cylindrical vortex with a given distribution of circulation is a well-known problem in fluid mechanics and aeroacoustics studied since 1950s. In a two-dimensional scattering problem the scattered wave, a time-periodic addition to the superposition of the vortex and the incident wave, is expected to be an outgoing cylindrical wave with the amplitude fading as $1/\sqrt{r}$ at infinity. The common statement assumes that the vortex has non-zero circulation at infinity like the rectilinear point/Rankine/Lamb-Oseen vortex. There are two known solutions qualitatively different from each other. The first is singular on the line behind the vortex center [1]. The second is regular but maintains a non-decreasing amplitude at arbitrarily large distances [2], [3], [4], [5]; this seems to be confirmed by numerical solutions [6]; note that there is a prominent quantum mechanical problem illustrating the Aharonov-Bohm effect where the solution has the similar form [7]. The peculiar behaviour at small angles is related to the fact that sound interaction with the irrotational vortex is nonlocal because the vortex velocity field is decreasing at infinity slowly. As a consequence, the problem is ill-posed: there is no far field where the outgoing wave boundary condition can be imposed. This is naturally connected to infinitely large kinetic energy of the irrotational vortex, which can not exist in an unbounded fluid.

For a regularization, instead of the irrotational vortex with the constant circulation $\Gamma = \Gamma_*$ we take the vortex with the circulation distribution $\Gamma(r) = \Gamma_* (r/\delta)^2$ at $r \leq \delta$ and $\Gamma(r) = \Gamma_* e^{-\varepsilon^2 r^2}$ at $r > \delta$, which can be generated by the infinitely elongated hollow circular cylinder of radius δ rotating in a viscous fluid for a long time $1/(4\nu\varepsilon^2)$, where ν is kinematic viscosity. The similar idea appeared in [8]. We call such flow the *quasi-irrotational vortex*, as it is approximately irrotational when $\delta << r << \varepsilon^{-1}$ and exponentially weak at infinity (figure 1). This allows to model the problem of sound scattering by the irrotational vortex as the limiting case $\delta \to 0$, $\varepsilon \to 0$ of the well-posed boundary-value problem for the quasi-irrotational case.

SOLUTION

The flow obeys the two-dimensional Euler equations, the initial condition being the steady field of the quasi-irrotational vortex and the boundary condition at infinity being the field of the plane acoustic wave. We move to dimensional variables $k\vec{r} \to \vec{r}$, $\omega t \to t$, $\rho \to \rho_\infty \rho$, $\vec{v} \to c_\infty \vec{v}$, $p \to p_\infty p$. where $\vec{r}$ is the position vector, t is time, $\vec{k}$ and ω are the incident wave wavevector and frequency, ρ, $\vec{v}$, p are density, velocity and pressure, ρ_∞, c_∞, p_∞ are density, sound speed and pressure of the unperturbed fluid. We consider the vortex and the incident wave as independent perturbations of the

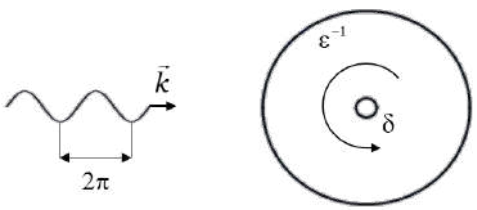

Figure 1: The problem statement in dimensionless variables. The wavelength is much smaller than the vortex outer scale and much larger than the inner one.

*Corresponding author. E-mail: gadzhiev@phystech.edu.

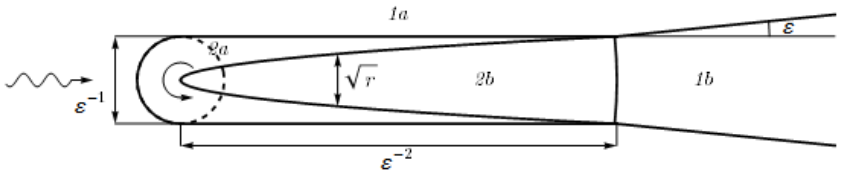

Figure 2: The asymptotic structure of the solution in the case $\varepsilon << 1$. The domain *1* is the far field where $|\rho_{11}| << 1$, with $|\rho_{11}| \sim 1/\sqrt{r}$ in the subdomain *1a* and $|\rho_{11}| \sim \varepsilon^{-1}/\sqrt{r}$ in the subdomain *1b*. The domain *2* is the near field where $|\rho_{11}| = O(1)$, with the sound intensity change much less than $O(1)$ in the subdomain *2a* and $O(1)$ in the subdomain *2b*. Inside the dashed circle, the solution is reduced to one obtained in [2], [3], [4], [5] for the case $\varepsilon = 0$.

homogeneous fluid, with the respective Mach numbers $M_0 = \Gamma_* k/2\pi c_\infty$ and M' assumed to be small. The solution for density perturbations is represented as

$$\rho = \sum_{i=0}^{\infty}\sum_{j=0}^{\infty} M_0^i (M' \mathrm{e}^{-\mathrm{i}t})^j \rho_{ij}(\vec{r};\varepsilon,\delta). \tag{1}$$

The scattered wave is a product of the wave-vortex interaction described in the main approximation by the term of the order $O(M_0 M')$, being much weaker than the vortex and the incident wave superposition. The solution satisfies the equation

$$\Delta\rho_{11} + \rho_{11} = -2i(\vec{k}\cdot\nabla)\left(\frac{(\vec{e}_z,\vec{r},\vec{k})}{r^2} e^{-\varepsilon^2 r^2} e^{i(\vec{k}\cdot\vec{r})}\right) \tag{2}$$

and the outgoing wave boundary condition at infinity, where $\vec{e}_z$ is the unit vector along the vortex axis. The solution for the case $\varepsilon > 0$ is unique and can be represented as convolution of the right-hand side of (2) with the Green's function $-\frac{i}{4}H_0^{(1)}(r)$ or using the Fourier transform method developed in [3], [4].

In the case $\varepsilon << 1$, the asymptotic structure of the scattered wave is profoundly analogous to the structure observed in the problem of the plane wave diffraction by a slit of the width ε^{-1} (figure 2). In the far field *1*, the solution is the outgoing cylindrical wave

$$\rho_{11} = \sqrt{\frac{\pi}{2r}} e^{ir - i\pi/4} \cos\theta \cot\frac{\theta}{2}\left(1 - e^{-\theta^2/4\varepsilon^2}\right), \tag{3}$$

peaking within the region *1b* with the order $\varepsilon^{-1}/\sqrt{r}$. In the near field *2*, the solution is the sophisticated wave with the amplitude $|\rho_{11}|$ maintaining the order $O(1)$. The near field includes the vortex region $r \sim \varepsilon^{-1}$ and the "wake" behind the vortex whose length is $O(\varepsilon^{-2})$. It can be divided into the parabolic zone $\theta \sim 1/\sqrt{r}$, where the maximum change of the sound intensity is reached; and the remaining zone *2a*, where the sound intensity change is small and only the phase shift is significant. At small scattering angles, the far field $r >> \varepsilon^{-2}$ corresponds to the Fraunhofer region while the near field $r \sim \varepsilon^{-2}$ to the Fresnel region. The detection of the characteristic scale extended far beyond the vortex is crucial for numerical/experimental modelling of the considered problem, as it imposes the lower limit on the computational/measurement domain size.

The solution for the formal limit $\varepsilon = 0$ confirms the fairness of the solution [2], [3], [4], [5] with reference to the irrotational vortex case: within the domain $r << \varepsilon^{-1}$ where the quasi-irrotational vortex is close to the irrotational one, the order of the scattering wave amplitude is constant. The singular solution [1] is equivalent to the far-field solution (3) at large angles; however, the far field is absent in the case of the irrotational vortex.

ACKNOWLEDGEMENTS

The reported study was funded by RFBR, project number 19-31-90057.

References

[1] Pitaevskii L. P. Calculation of the phonon part of the mutual friction force in superfluid helium. *Sov. Phys. JETP* **35**: 1271-1275, 1958.
[2] Sakov P. V. Scattering of sound by a vortex filament. *Acoust. Phys.* **39**: 280-282, 1993.
[3] Ford R., Llewellyn Smith S. Scattering of acoustic waves by a vortex. *J. Fluid Mech.* **386**: 305-328, 1999.
[4] Howe M. S. On the scattering of sound by a rectilinear vortex. *J. Sound Vib.* **227**: 1003-1017, 1999.
[5] Belyaev I. V., Kopiev V. F. On the statement of the problem of sound scattering by a cylindrical vortex. *Acoust. Phys.* **54**: 699-711, 2008.
[6] Colonius T., Lele S. K., Moin P. The scattering of sound waves by a vortex: numerical simulations and analytical solutions. *J. Fluid Mech.* **260**: 271-298, 1994.
[7] Aharonov Y., Bohm D. Significance of electromagnetic potentials in the quantum theory. *Phys. Rev.* **115**: 485-491, 1959.
[8] Berthet R., Lund F. The forward scattering of sound by vorticity. *Phys. Fluids* **7**: 2522-2524, 1995.

DAMPING OF SLOSHING WAVES BY CONTACT ANGLE HYSTERESIS

Benjamin Dollet*[1], Elise Lorenceau[1], and François Gallaire[2]
[1]Laboratoire Interdisciplinaire de Physique, CNRS and Université Grenoble Alpes, Grenoble, France
[2]Laboratory of Fluid Mechanics and Instabilities, EPFL, Lausanne,Switzerland

Summary The influence of wetting conditions on the damping of sloshing remains elusive, although it is been long shown to have a significant effect. We conducted controlled experiments on the simplest sloshing configuration, studying the oscillations of a liquid column in U-shaped tubes with different surface treatments. We show that the effect of wetting conditions is dramatic, and we propose a simple predictive model with contact angle hysteresis as the key ingredient explaining the additional friction at the contact line.

INTRODUCTION AND CONTEXT

Sloshing describes the oscillations of liquids in reservoirs [1, 2]. It is often detrimental and can lead e.g. to liquid spilling, or to destabilisation of spacecrafts, especially in its large-amplitude, nonlinear regimes. Therefore, understanding and optimising its damping is of primary importance for many spatial and terrestrial applications.
Existing theories of sloshing include viscous effects in the liquid bulk and along liquid/solid boundaries. However, already early studies have revealed that dissipation predicted as such underestimates experimental measurements of damping [3, 4], which also indicate a dependence on the solid material of the reservoir walls. Although this mismatch between theory and experiments has been qualitatively ascribed to interfacial effects such as contact line pinning, no satisfactory quantitative prediction of such effects is yet available.
We propose to bridge this gap, by leading controlled experiments of freely decaying liquid oscillations in the simple configuration of a U-shaped tube with controlled surface properties, and by proposing a model including contact angle hysteresis as the key ingredient for contact line friction.

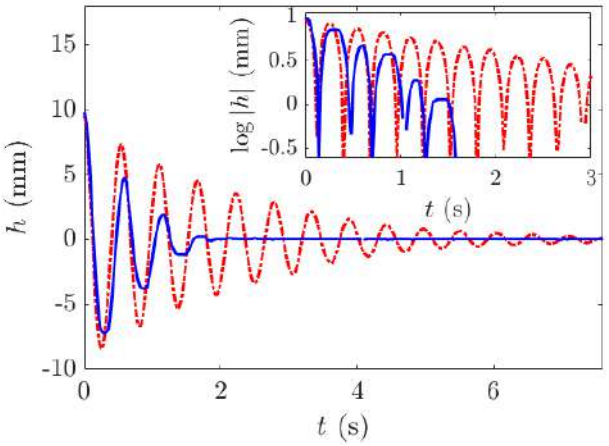

Figure 1: Plot of the height difference of one interface in a U-shaped tube with respect to its equilibrium height, as a function of time, for water in a hydrophobic tube (plain blue curve) and in a hydrophilic tube (dashed red curve). The length of the liquid column in the tube equals l = 10.6 cm. Inset: same data in semi-log. The dotted red line is a guide for the eyes.

EXPERIMENTS

We studied the freely decaying oscillations of liquids in two U-shaped glass tubes, one which was rendered hydrophobic with a silanisation surface treatment, and one hydrophilic with a plasma treatment. We focused on two simple liquids: water and ethanol; we mention results only for water in this abstract. The two surface treatments induced very distinct wetting conditions. In the hydrophobic tube, water displays a large contact angle and a strong hysteresis between an advancing contact angle (θ_a = 93°) and a receding one (θ_r = 68°), the contact line being pinned in between these two angles [5]. In contrast, on the hydrophilic tube, perfect wetting was almost achieved.
The effect of wetting conditions on the damping of oscillations of these two liquids is striking: for water, the oscillations are much more quickly damped for water than for ethanol (Fig. 1). Moreover, the dynamics of damping is quite different: while the oscillations are exponentially damped in the hydrophilic tube, they decay faster in the hydrophobic tube, with a finite-time arrest, in marked contrast with the classical description of oscillations damped by viscous effects.
We studied the influence of the length l of the liquid column and of the initial amplitude h_0 (i.e. the initial height difference between the liquid/gas interfaces within the two arms of the tube) on the oscillations. This revealed another qualitative difference between the two surface treatments. For the hydrophilic tube, at given liquid column length, the

*Corresponding author. E-mail: benjamin.dollet@univ-grenoble-alpes.fr.

oscillations collapsed on a master curve once rescaled by the initial amplitude, as expected for linear damping. This was not the case for the hydrophobic tube, where larger damping was measured as the initial amplitude was decreased.
All these results suggested a nonlinear damping mechanism associated to contact line sliding, which we modelled as follows.

MODELLING AND COMPARISON WITH EXPERIMENTS

Since we observed that the contact line remains horizontal at all times, we proposed a simple dynamical model with a single degree of freedom: the difference h between the current height of one of the two contact lines and its equilibrium height. We included as physical effects: (i) the inertia of the liquid, (ii) gravity as the restoring force, (iii) a viscous term scaling linearly with the velocity $\dot{h}$, and (iv) contact line friction. The latter was modelled by projecting the forces acting at the contact line along the direction of motion, which naturally yields the contact angle hysteresis as a friction coefficient, with the same functional form as solid friction. These ingredients yield the following ODE for the dynamics of motion of the contact line, in dimensionless form:

$$\frac{d^2\bar{h}}{d\bar{t}^2} + \bar{h} = -\alpha\frac{d\bar{h}}{d\bar{t}} - \mu \times \text{sign}\left(\frac{d\bar{h}}{d\bar{t}}\right),$$

with $\bar{h} = h/h_0$ the height rescaled by the initial amplitude, $\bar{t} = \omega_0 t$ the time rescaled by the eigenfrequency $\omega_0 = \sqrt{2g/l}$ (with g = 9.8 m/s² the gravity acceleration), and two dimensionless dissipation parameters: α accounting for viscous dissipation, and $\mu = \gamma(\cos\theta_r - \cos\theta_a)/(\rho g a h_0)$ accounting for contact line friction (with γ the surface tension, ρ the density and a = 8.15 mm the tube radius).
The model was solved analytically by the multiple-scale method. The corresponding solution captured all qualitative trends found in experiments, notably the finite time of arrest of the oscillations, and the influence of the initial amplitude.
To go beyond this qualitative agreement, we fitted all our experiments by fixing the aforementioned prediction of the friction coefficient μ with the measured value of the contact angle hysteresis, and by treating the viscous prefactor α as a fitting parameter. We found a quantitative agreement with our experiments, confirming the relevance of our modelling.
However, the viscous parameter was found to be quite large. Complementary experiments revealed that its value was about 50% larger in the first phase of the experiments, where the contact line slides, than in a second phase where the contact line gets pinned while the interface is still oscillating and relaxes slowly. This suggests that dynamical contact angle effects should be accounted for. However, using the classical Cox-Voinov law quantifying this effect [6] did not fully explain the large difference of viscous damping between the sliding phase and the pinned phase. We discuss possible reasons for this discrepancy, which has been previously remarked in other studies on drop motion.

CONCLUSIONS AND OUTLOOK

We have confirmed that surface properties can drastically increase the damping of liquid oscillations, and shown that the key parameter to quantify this increase is the contact angle hysteresis.
This study was led in the simple configuration of a U-shaped tube, where the liquid oscillation can be described by a single degree of freedom, namely the height difference between the liquid/gas interfaces within the two arms of the tube.
An obvious perspective is the extension to reservoirs, for which we will present preliminary experiments. These show that not only do wetting conditions influence the total damping, but they also modify the very shape of the sloshing modes.
The eventual goal of this study is to provide an operational prediction of the extra dissipation present at the interfaces, which could be used for sloshing applications in aerospace and mechanical engineering; the main theoretical challenge is to extend our simple approach based on a single degree of freedom to the infinity of sloshing modes associated to a given tank shape.

References

[1] R. A. Ibrahim, *Liquid Sloshing Dynamics: Theory and Applications*, Cambridge University Press (2005).
[2] O. M. Faltinsen, A. N. Timokha, *Sloshing*, Cambridge University Press (2009).
[3] G. H. Keulegan, Energy dissipation in standing waves in rectangular basins, *J. Fluid Mech.* 6 (1959) 33-50.
[4] B. Cocciaro, S. Faetti, M. Nobili, Capillarity effects on surface gravity waves in a cylindrical container: wetting boundary conditions, *J. Fluid Mech.* 231 (1959) 325-343.
[5] P. G. de Gennes, F. Brochard-Wyart, D. Quéré, *Gouttes, bulles, perles et ondes*, Belin (2002).
[6] J. H. Snoeijer, B. Andreotti, Moving contact lines: scales, regimes, and dynamical transitions, *Annu. Rev. Fluid Mech.* 45 (2013) 269-292.

DEFORMATIONS OF AN AIR-WATER FREE SURFACE BY HYDRODYNAMIC TURBULENCE.

Timothée Jamin[1,2], Eric Falcon[1], and Michael Berhanu*[1]
[1]MSC, CNRS, Université Paris Diderot, Université de Paris, France
[2]Univ Lyon, ENS de Lyon, Univ Claude Bernard, CNRS, Laboratoire de Physique, F-69342 Lyon, France

Summary The interaction between a turbulent flow and a deformable interface constitutes a difficult fundamental problem, which is seldom addressed. The free surface modifies the structure of the turbulence and the turbulent flow deforms in turn the free surface increasing its roughness. This situation typically occurs at the surface of rivers. Here, we investigate experimentally the deformation of an air-water free surface in response to a subsurface turbulent flow. Using randomly actuated jets, a turbulent flow with a small mean flow is produced in the water phase. The corresponding three-dimensional deformation of the free surface is measured by Fourier Transform Profilometry. The free-surface dynamics is interpreted as the combination of a passive response to the turbulence and of the propagation of excited waves.

Turbulence is ubiquitous in most of environmental flows of water like the sea currents, the rivers or the streams. We note in these examples the presence of a top free surface at the interface between the liquid and the atmosphere. The behavior of this deformable and renewable interface constitutes a very complex problem especially in presence of turbulence in the liquid phase. The free surface modifies the structure of the turbulence below and the turbulent flow deforms in turn the free surface and increases its roughness. Brocchini and Peregrine proposed a qualitative description of the turbulent dynamics of a free surface [1]. Its deformation results from the respective contributions of the pressure field, of the viscous stresses associated to the vorticity and of the propagation of surface waves, which corresponds to the natural response of the interface to perturbations. The roughness created by the turbulence in flow has tremendous consequences for the gas, heat and mass exchanges between the atmosphere and the water body. Facing the complexity of the dynamics of a turbulent free surface, a first step consists in understanding fundamentally the behavior of hydrodynamics turbulence at the vicinity of a free surface. To better distinguish the effect of the hydrodynamics turbulence on a free surface from the advection of perturbations by the mean current, we focus our study to the case of hydrodynamics turbulence dominated by the velocity fluctuations.

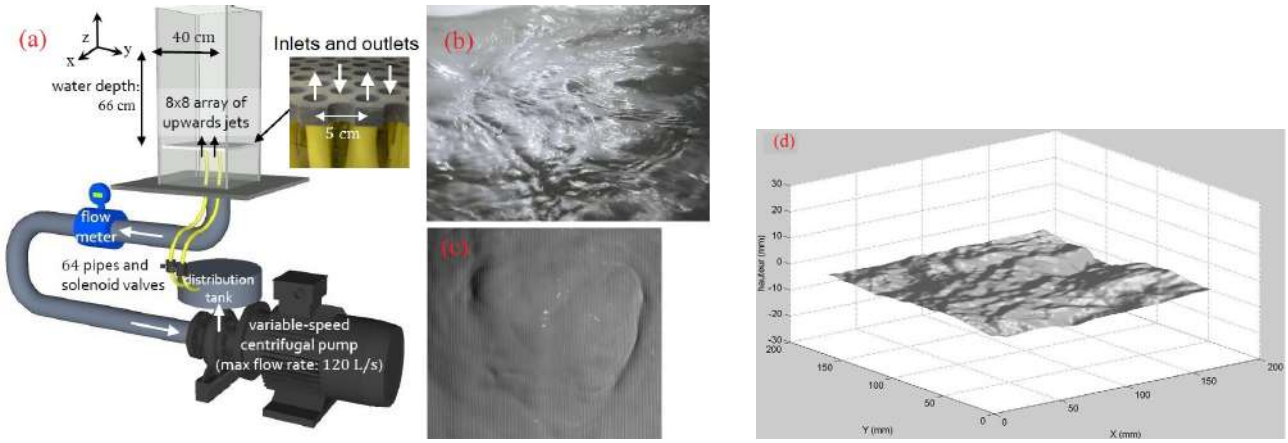

Figure 1: (a) Schematic of the experimental setup. (b) Photography of the free surface agitated by the turbulence. (c) Fringes projection in order to use the Fourier Transform Profilometry method. (d) Example of reconstruction of the deformed surface with this method.

Randomly actuated jets [2] is a convenient method to generate homogeneous and isotropic turbulence more efficiently than with oscillating grids. Our experimental setup [3, 4], consists in a tank of lateral dimensions 40×40 cm filled to a water depth of 66 cm (Fig. 1 (a)). The turbulent flow is produced by an array of 8×8 jets randomly actuated at the bottom and connected to a large pump with a controlled flow-rate. The intensity of the turbulence $\mathcal{U}_{rms}$ varies typically from 1 to 10 cm s^{-1} corresponding to a turbulent Reynolds number between 500 and 5000 and to an integral length L of order 5 cm. Using PIV measurements, we find the phenomenology of isotropic homogeneous turbulence in the bulk [4]. In contrast, the turbulence becomes anisotropic when approaching the free surface on a depth of order the integral length. Here, we investigate the deformations of the free surface $\eta(x, y, t)$ generated by the turbulence below. We observe a complex free surface dynamics (Fig. 1 (b)), with intermittent bumps of few centimeters similar to the "splats" described in the numerical simulations of Guo and Shen [5] accompanied with propagation of free surface waves and ripples. To measure $\eta(x, y, t)$, we use the Fourier Transform Profilometry method [6]. After adding a white pigment in the water, a fringe pattern is projected on the surface and imaged with a fast camera (Phantom V10) located above (Fig. 1 (c)). From the deformation of the fringe pattern, the free-surface dynamics is reconstructed with a good accuracy Fig. 1 (d).

*Corresponding author. E-mail: michael.berhanu@univ-paris-diderot.fr

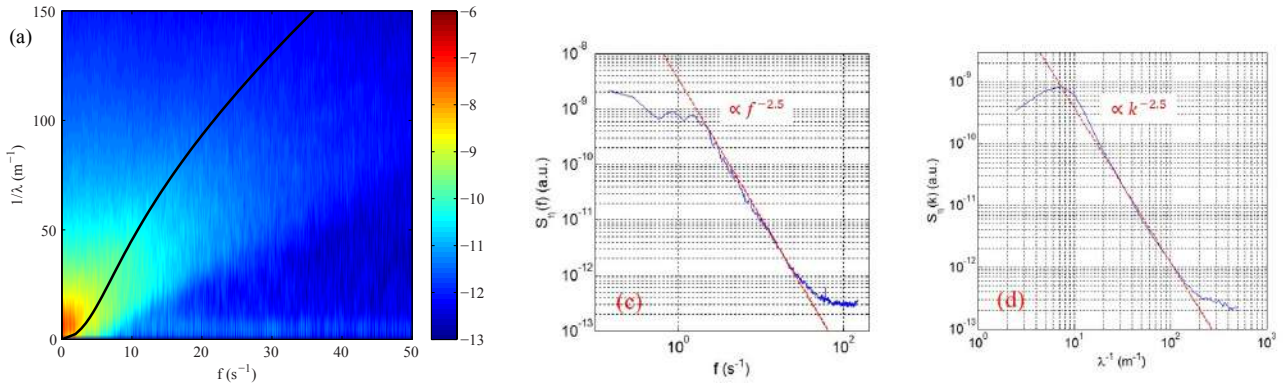

Figure 2: (a) Angular averaged, space-time spectrum of free surface deformation $S_\eta(f, 1/\lambda = k/(2\pi))$ for $\mathcal{U}_{rms} = 6.6$ cm/s. Colorscale log_{10} (arbitrary units). Black line, linear dispersion of surface waves. (b-c) Respectively, time and space spectrum S_η of free-surface fluctuations for $\mathcal{U}_{rms} = 10.5$ cm/s.

The root mean square amplitude of free-surface fluctuations σ_η increases nearly linearly with the turbulence intensity $\mathcal{U}_{rms}$, to reach about 2 mm for $\mathcal{U}_{rms} \approx 10$ cm s^{-1}, corresponding to a steepness $\langle|\nabla\eta|\rangle \approx 0.1$ and Froude number $Fr = \mathcal{U}_{rms}/\sqrt{2\,g\,L} \approx 0.1$. According to the qualitative analysis of free-surface deformations in presence of turbulence by Brocchini and Peregrine [1] and taking the integral length as the typical size of free-surface deformations, these measurements belong to the "wavy" domain, for which the interface is strongly distorted but does not break.

The free-surface dynamics is analyzed in the Fourier space by computing the spatio-temporal power spectrum $S_\eta(k_x, k_y, \omega)$. The angular averaged spectrum displays in Fig. 2 (a) more intensity at large scale and low frequency in a region not precisely defined but compatible with an advection cone of free-surface structures by the randomly fluctuating turbulent velocity field. However, for $S_\eta(k_x, k_y, \omega)$ plotted for a specific axis (not shown), we observe in addition presence of branches which are interpreted as dispersion relations of free-surface waves. Nevertheless, due to the Doppler effect these dispersion relations are broadened by the random advection of the flow and can be shifted if the surface mean flow is non exactly zero in the window of measurement. Due to their random advection, disentangling the waves from the deformation induced by turbulent pressure fluctuations constitutes a difficult task. Moreover, for sufficient turbulent intensity, time and space power spectra $S_\eta(f)$ and $S_\eta(k)$ both exhibit a well defined power law with a same exponent -2.5 in Fig. 2 (b-c), which argues that time dynamics result mainly from the turbulent sweeping of spatial fluctuations. Theoretically, the spectrum of pressure fluctuations for homogeneous isotropic turbulence follows in the inertial range a power law in $k^{-7/3} \approx k^{-2.33}$. The action of the turbulent pressure on the free surface may thus explain its dynamics. Following this idea and inspired by the recent work of Perrard et al.[7], we propose a simple model in Fourier space computing the linear response of the free surface submitted to turbulent fluctuations. The natural response of the free surface corresponds to the propagation of surface waves. However, in presence of sufficient wave dissipation due to viscosity and also here to the loss of correlation by the random advection, the free surface can show a significant response outside the wave linear dispersion relation. In these conditions, the model provides the correct order of magnitude of σ_η and predicts the linear relation with $\mathcal{U}_{rms}$. Using the hypothesis of random sweeping, the qualitative shape of the spectrum $S_\eta(k, f)$ shown in Fig. 2 (a) is recovered. Theoretical spectra $S_\eta(k)$ and $S_\eta(f)$ display also by construction power laws in $k^{-7/3}$ and $f^{-7/3}$.

Our measurements and the subsequent analysis demonstrate for the first time, that the fluctuations of an air-water interface subjected to a subsurface turbulent flow can be interpreted as the linear response of the surface to the turbulent pressure fluctuations. If the wave dissipation is not too important, surface waves are also excited. However, the random advection induces a strong widening of the experimental dispersion relations by Doppler effect. Using our experimental setup in the same range of parameters, we have also investigated the effect of turbulence on mechanically generated surface gravity waves in sinusoidal and random regimes. The dispersion relations are significantly broadened and the waves strongly attenuated due to the random advection by the turbulent flow.

References

[1] Brocchini M. and Peregrine D. H. The dynamics of strong turbulence at free surfaces. Part 1. Description. *J. Fluid Mech.* **449**: 225-254, 2001.
[2] Variano E. and Cowen A. random-jet-stirred turbulence tank *J. Fluid Mech.* **604**: 1-32, 2008.
[3] Jamin T. Interactions between free-surface waves and hydrodynamic flows. *PhD Thesis*, Université. Paris Diderot, Paris, 2016.
[4] Jamin T., Berhanu M. and Falcon E. Experimental study of hydrodynamic turbulence under a free surface *in preparation*, 2020.
[5] Guo C. and Shen L. Interaction of a deformable free surface with statistically steady homogeneous turbulence *J. Fluid Mech.* **658**: 33-62, 2010.
[6] Cobelli P., Maurel A., Pagneux V. and Petitjeans P. Global measurement of water waves by Fourier transform profilometry *Exp. Fluids* **46** 1037-1047, 2009.
[7] Perrard S., Lozano-Durán, Rabaud M., Benzaquen M. and Moisy F. Turbulent windprint on a liquide surface *J. Fluid Mech.* **873**: 1020-1054, 2019.

WIND SUSTAINED VISCOUS SOLITONS

Marine Aulnette*[1], Marc Rabaud[1], and Frédéric Moisy[1]
[1] Université Paris-Saclay, CNRS, FAST, 91405, Orsay, France.

Summary We investigate the generation of wind waves at the surface of a highly viscous liquid. Contrarily to the classical low-viscosity case, we observe the intermittent formation of large localized structures that propagate rapidly downstream, which we call viscous solitons. These strongly nonlinear coherent structures propagate at a velocity given by the balance between the aerodynamic drag in the air and the viscous drag in the liquid. We propose here a model to describe their dynamics based on a subcritical bifurcation governed by the wind shear stress.

INTRODUCTION

When wind blows over water, small disorganized surface deformations, called wrinkles, first appear [1, 2]. These structures, elongated in the direction of the wind, are the random wakes generated by the turbulent pressure fluctuations traveling in the air flow. When the wind velocity is increased above a critical value, theses wrinkles evolve into nearly periodic waves propagating in the direction of the wind, with slowly increasing amplitude and wavelength.

This general picture remains unchanged for viscosity up to approximately 100 times the water viscosity. However, for more viscous liquids, the nature of the waves dramatically changes: the initial wave-packet becomes violently unstable and forms a large asymmetrical fluid bump pushed by the wind [3, 4]. While the energy of the disturbance is homogeneously distributed in the low-viscosity case, it is strongly focused in these large bumps at large viscosity. We call these nonlinear objects, first qualitatively described by Francis in 1954 [5], *viscous solitons*. They are illustrated in figure 1 for a liquid of kinematic viscosity ν_l =1000 mm^2 s^{-1} and wind velocity U_a = 9.6 m s^{-1}. They are typically 2 to 4 mm high, 4 cm in the propagation direction, and 5 to 10 cm in the transverse direction, with a steep rear facing the wind and a weaker slope at the front.

LIFE CYCLE OF VISCOUS SOLITONS

To characterize the viscous solitons, we set up an experiment consisting in a 1.5 m long tank filled with silicon oil of kinematic viscosity $\nu_l = 1000$ mm^2 s^{-1}, fitted to the bottom of a wind tunnel of rectangular cross-section. Wind is blown at velocity between 0 and 15 m/s, and the depth of the liquid tank h is varied from 20 to 150 mm. The surface deformation is measured by laser sheet profilometry, with a vertical resolution of 0.1 mm.

The life cycle of viscous solitons is characterized using spatio-temporal diagrams, as illustrated in figure 2. Above a critical wind velocity, of the order of 9 m/s, a small-amplitude wave packet of a few wavelengths is first formed at small fetch. This wave packet remains spatially confined but it is temporally unstable (figure 2 (a)): the wave amplitude slowly grows until one of its crests reaches a critical height and rapidly evolves into a viscous soliton. Once formed, the soliton accelerates, leaves the wave packet region, and travels along typically 30-50 cm with constant shape and a slightly decreasing velocity (figure 2 (b)). The initial wave packet disappears after the emission of a soliton, but it reforms after a

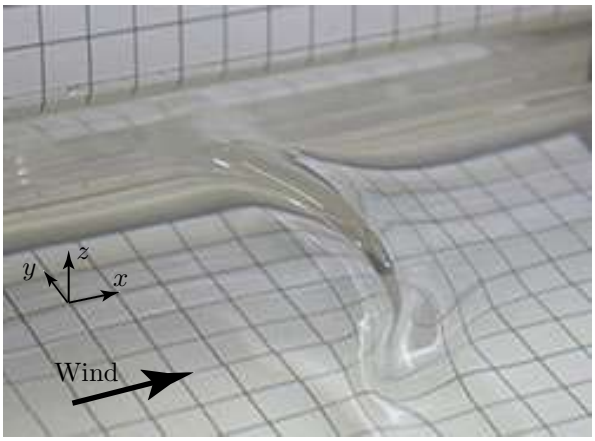

Figure 1: Viscous soliton propagating from left to right, generated by a wind velocity U_a = 9.6 m/s at the surface of silicon oil of kinematic viscosity $\nu_l = 1000$ mm^2 s^{-1}. The size of the grid pattern is 1.3 cm. From Ref. [4].

*Corresponding author. E-mail: marine.aulnette@u-psud.fr

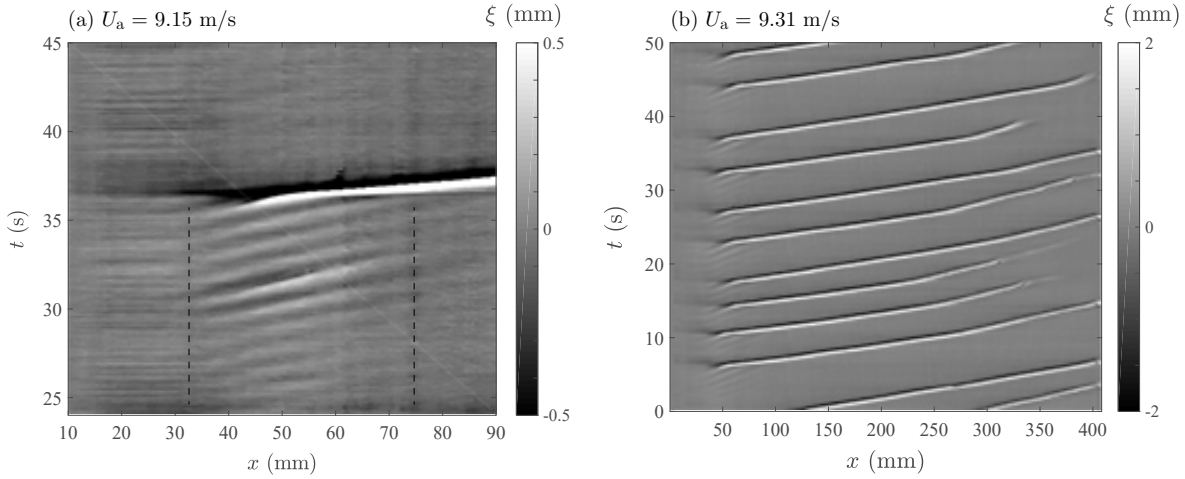

Figure 2: Spatiotemporal diagrams of the surface elevation $\xi(x,t)$ for a liquid depth $h = 35$ mm showing the emission, propagation and decay of viscous solitons. Figure (a) shows a zoom on the generation of a soliton from the instability of the initial wave packet for a wind velocity close to the onset ($U_a = 9.15$ m s^{-1}). Figure (b) shows the propagation and interaction of viscous solitons at larger velocity ($U_a = 9.31$ m s^{-1}): mature downstream solitons are slowed down because of the sheltering by newly created upstream solitons.

while and the process repeats. The waiting time between solitons is of order of 1 min close to the onset, but it decreases down to about 1 s at larger wind velocity.

The finite amplitude (about 2 mm) of the viscous solitons even close to the critical wind velocity suggests that they result from a subcritical instability. This is confirmed by additional experiments, in which solitons are excited for a wind slightly lower than the natural onset by using a small immersed wavemaker producing a finite-amplitude disturbance.

Systematic measurements of the soliton amplitude as a function of the downstream distance and wind velocity show that their dynamics is governed by the local wind shear stress: In the absence of mechanical forcing, viscous solitons spontaneously emerge from the initial wave packet that forms at small fetch, for a local shear stress above a first threshold $\tau_1 \simeq 0.25$ Pa. Solitons then escape from this initial wavepacket and propagate in the subcritical region over an appreciable distance, but because of the thickening of the turbulent boundary layer, the shear stress decreases with downstream distance and solitons disappear when the shear stress reaches a secondary threshold $\tau_2 \simeq 0.21$ Pa. The return to the base state is either natural, if the soliton is isolated and reaches the distance where the shear stress is below τ_2, or forced, when the air drag on the soliton is reduced by the nucleation of a new upstream soliton.

Viscous solitons provide a striking example of out-of-equilibrium coherent structures, resulting from a balance between external forcing and dissipation. These observations raise a number of questions: How their nontrivial asymmetric shape is selected by the liquid viscosity and surface tension? What governs the minimum viscosity to switch from the classical weakly non-linear wind-wave regime to the strongly non-linear soliton regime?

References

[1] A. Paquier, F. Moisy, and M. Rabaud, Surface deformations and wave generation by wind blowing over a viscous liquid, *Phys. Fluids* **27**, 122103 (2015).
[2] S. Perrard, A. Lozano-Duran, M. Rabaud, M. Benzaquen, F. Moisy, Turbulent windprint on a liquid surface, *J. Fluid Mech.* **873**, 1020-1054 (2019).
[3] A. Paquier, F. Moisy and M. Rabaud, Viscosity effects in wind wave generation, *Phys. Rev. Fluids* **1**, 083901 (2016).
[4] M. Aulnette, M. Rabaud, F. Moisy, Wind sustained viscous solitons, *Phys. Rev. Fluids* **4**, 084003 (2019).
[5] J. R. D. Francis, Wave motions and the aerodynamic drag on a free oil surface, *Philos. Mag.* **45**, 695 (1954).

SUPERHARMONIC EXCITATION BY SELF-INTERACTION OF INTERNAL WAVE MODES IN NONUNIFORM STRATIFICATIONS

Dheeraj Varma*[1], Vamsi K. Chalamalla[2], and Manikandan Mathur[1]
[1]Department of Aerospace Engineering, Indian Institute of Technology Madras, Chennai, India
[2]Department of Applied Mechanics, Indian Institute of Technology Delhi, New Delhi, India

Summary Superhamonic internal wave excitation due to self-interaction of internal wave modes in a nonuniform stratification is investigated using a combination of theoretical and numerical analysis. Weakly nonlinear theoretical framework is used to identify triadic resonance resulting from modal interactions of primary internal waves. Two dimensional numerical simulations are done using Stratified Ocean Model with Adaptive Refinement (SOMAR), and the spontaneous excitation of theoretically predicted superharmonic internal wave mode due to resonant/near-resonant interaction of an isolated primary mode is studied.

INTRODUCTION

In the recent past, generation of superharmonic waves due to nonlinear interactions has grabbed much attention. Theoretical studies (Varma *et al.* 2017, Wunsch 2017) and numerical simulations (Sutherland 2016) have investigated the generation of superharmonic waves due to modal interactions in nonuniform stratifications. This could be a potential mechanism by which tidally generated internal waves can transfer energy to smaller spatial and temporal scales. Most of the prior studies (see review papers by Staquet & Sommeria 2002 and Dauxois *et al.* 2018) have focused on the generation of subharmonic internal waves due to Parametric Subharmonic Instability (PSI). The relative importance of excitation of subharmonic and superharmonic waves is not well understood.

THEORETICAL FRAMEWORK

Weakly nonlinear constant-amplitude theory (Varma *et al.* 2017) predicts the superharmonic internal wave mode that would be excited due to resonant interaction of internal wave modes. The method of multiple scales is then used to quantify the spatial/temporal evolution of energy associated with each wave in the triad.

NUMERICAL SIMULATIONS

Numerical simulations are performed using SOMAR, which solves a set of conservation equations for momentum and buoyancy on a composite grid consisting of several levels. For details about the adaptive mesh capabilities of SOMAR, see Santilli & Scotti 2015. SOMAR uses second-order, central finite differences for the spatial discretization of viscous and diffusion terms, computed semi-implicitly for time advancement. Advection terms are computed using the finite volume Piecewise-Parabolic Method (PPM). The computational domain and the boundary conditions are shown in Figure 1(b).

RESULTS AND DISCUSSION

For the nonuniform stratification shown in Figure 1(a), we consider a case where a self-interacting mode-3 at $\omega_0/N_0 = 0.4466$ is in triadic resonance with mode-2 at the superharmonic frequency $2\omega_0$ as predicted by the constant-amplitude weakly nonlinear theory. In numerical simulations, mode-3 at the resonant frequency is continuously forced from the left end of the computational domain, and the wave field is filtered at the forcing frequency ω_0 and the superharmonic frequency $2\omega_0$ (shown in Figure 2(a) & 2(c)) after steady state is attained throughout the domain. The vertical mode shapes of the respective filtered velocity fields is shown in Figure 2(b) & 2(d), and the superharmonic wave has a mode-2 structure in corroboration with the theoretical prediction.

Furthermore, the spatial evolution of the modal amplitudes in the numerical simulations will be compared with the numerical solutions of the amplitude evolution equations obtained using the method of multiple scales. Numerical simulations are also performed at off-resonant frequencies to identify the range of primary wave frequencies (around the resonant frequency) over which spontaneous superharmonic wave excitation occurs.

References

[1] Staquet, C. & Sommeria, J. 2002 Internal gravity waves: from instabilities to turbulence. Annu. Rev. Fluid Mech. 34 (1), 559-593.
[2] Sutherland, B.R. 2016 Excitation of superharmonics by internal modes in non-uniformly stratified fluid. J. Fluid Mech. 793, 335-352.
[3] Varma, D. & Mathur, M. 2017 Internal wave resonant triads in finite-depth non-uniform stratifications. J. Fluid Mech. 824, 286-311.
[4] Wunsch, Scott 2017 Harmonic generation by nonlinear self-interaction of a single internal wave mode. J. Fluid Mech. 828, 630-647.
[5] Dauxois, Thierry, Joubaud, Sylvain, Odier, Philippe & Venaille, Antoine 2018 Instabilities of internal gravity wave beams. Annu. Rev. Fluid Mech. 50, 131-156.

*Corresponding author. E-mail: nldvrm@gmail.com

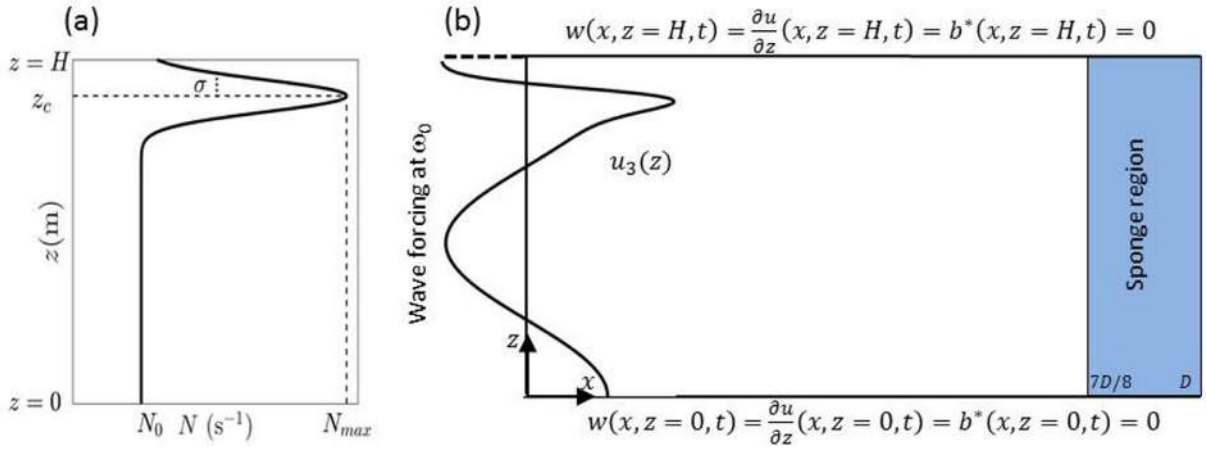

Figure 1: (a) Vertical stratification profile $N(z)$ used in the numerical simulations. The various parameters were set at the following values: $N_0 = 5.477 \times 10^{-3}$ rad/s, the maximum pycnocline stratification $N_{max} = 4N_0$ at $z_c = 3400$ m, and the pycnocline half-width $\sigma = 250$ m. (b) Schematic of the computational set-up for the numerical simulations. A mode-3 internal wave at frequency ω_0 is forced at $x = 0$, and is allowed to evolve over the domain length D.

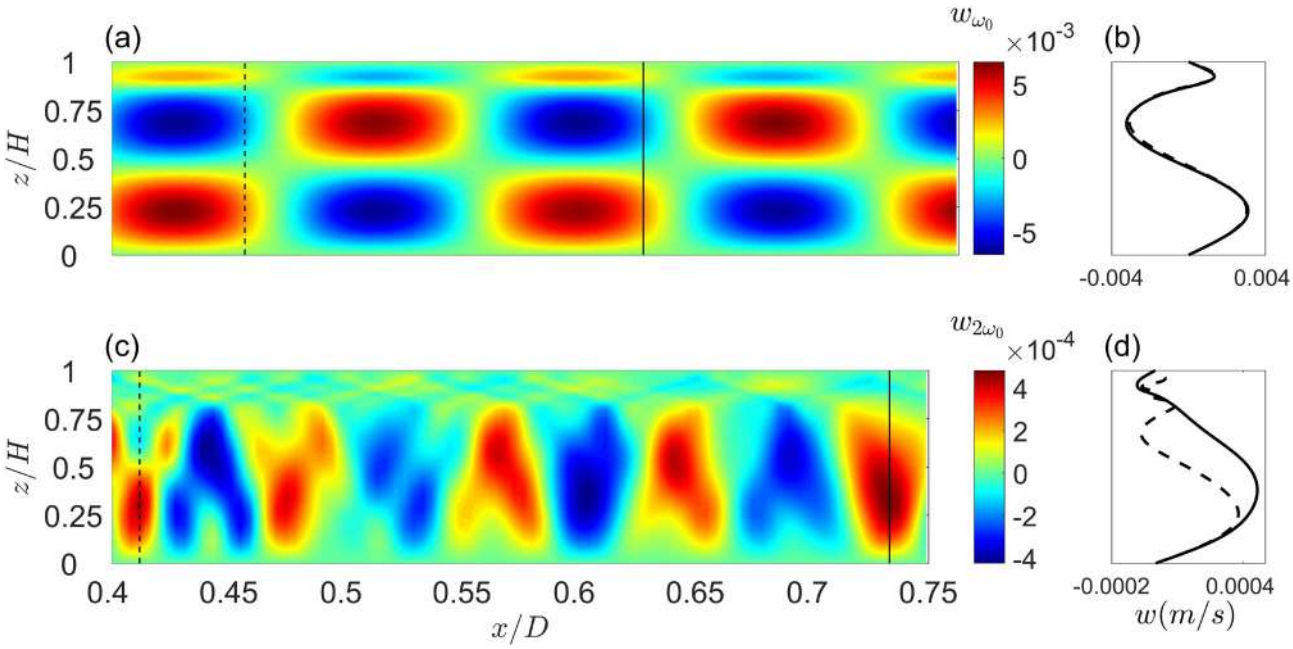

Figure 2: (a) Vertical velocity field w_{ω_0} after filtering the raw time series at the forcing frequency ω_0. (b) Vertical profiles of w_{ω_0} at the two spatial locations corresponding to the vertical dashed and solid lines in (a). (c) Vertical velocity field $w_{2\omega_0}$ after filtering the raw time series at the superharmonic frequency $2\omega_0$. (d) Vertical profiles of $w_{2\omega_0}$ at the two spatial locations corresponding to the vertical dashed and solid lines in (c).

NUMERICAL SIMULATION OF FLOW FIELD CAUSED BY UNDERWATER ULTRASONIC WAVE USING GLOBALLY CONSERVATIVE SCHEME

Masaya Orisaki*[1] and Takeo Kajishima[2]
[1]Department of Mechanical Engineering, Osaka University, Suita, Japan [2]Department of Mechanical Engineering, Osaka University, Suita, Japan

Summary We have developed the globally conservative scheme for analyzing acoustic and flow field in an adiabatic system. By using this scheme, the propagation and reflection of ultrasonic wave are properly simulated and we can maintain the conservation property of the mass of the entire computational domain. It enables the analyses of multiple phenomena involved in industrial applications of underwater ultrasonic wave such as waveform distortion, acoustic shock wave, acoustic streaming and interfacial phenomena. To elucidate the mechanism of the interfacial phenomena, underwater ultrasonic wave propagation considering the reflection at free surface and rigid wall is numerically investigated by using the proposed scheme. The results show that the interfacial deformation caused by underwater ultrasonic waves is mainly dominated by the acoustic streaming.

BACKGROUND

The interaction between ultrasonic wave and gas-liquid interface has attracted attention because of the applicability in industrial as well as medical techniques. Examples include ultrasonic atomization[1] for separation of solute from aqueous solutions. But the mechanism is not completely explained. For better understanding of the interfacial phenomena, the numerical investigation is expected together with experimental observations. To this end, it is necessary to organize the accurate methods to deal with nonlinear propagation and reflection of acoustic wave, interfacial deformation, and acoustic energy transfer at the interface. In other words, it is necessary to construct the computational scheme which maintains the conservation property of the entire system.

COMPUTATIONAL SCHEME

To simulate the phenomena we focus on, it is necessary to set moving boundaries such as sound source and water surface. We use fixed cartesian grid over the entire computational domain to capture the complex deformation of the water surface. Although a treatment of the sound source suitable for fixed cartesian grid has already been proposed[2], the conservation property of the entire computational domain is not enough due to using interpolation. To construct the treatment of the moving boundaries with excellent conservation property, we devised a new method to treat the sound source. To verify the conservation property of this method, we assume a situation in which plane acoustic waves are emitted from a oscillating plate to an adiabatic system consisting of an infinite rigid wall at $x = L_x$ as shown in Figure 1. In Figure 1, a and ω are an amplitude and an angular frequency of the oscillating plate.

We introduce the computational grids with equal interval Δ and time step Δt and denote the conservative quantity at $(x_i, y_j, t_n) = (i\Delta, j\Delta, n\Delta t)$ as $\boldsymbol{Q}^n_{i,j}$, as shown in Figure 2. $\boldsymbol{Q}^n_{l,j}(l = i, i+1, \cdots)$ and $\boldsymbol{Q}^{n+1}_{m,j}(m = i+1, i+2, \cdots)$ are computed by TVD (Total Variation Diminishing) and conservative scheme such as Chakravarthy-Osher scheme[3] .

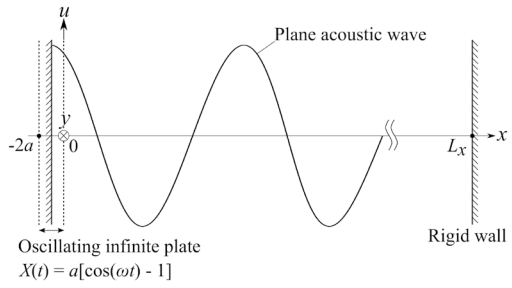

Figure 1: Set up for plane acoustic wave propagation simulation.

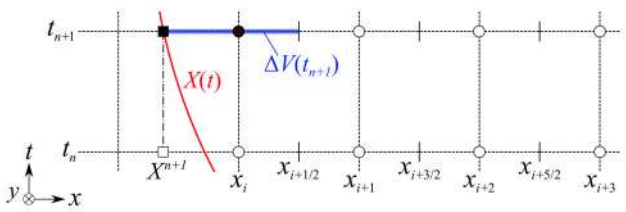

Figure 2: The mesh point near the oscillating infinite plate.

First, $\tilde{\boldsymbol{Q}}^{n+1}_{i,j}$ that is predict value of $\boldsymbol{Q}^{n+1}_{i,j}$ is determined by the moving boundary treatment[2] using interpolation and theory of characteristics. Next, to assume that the conservation error occurs in the computational cell containing the predict value, we can define a correction amount for the predict value of the density given by following equation.

$$\Delta\rho = \frac{M(t_0) - \tilde{M}(t_{n+1})}{\Delta V(t_{n+1})} \tag{1}$$

Where $M(t_0)$ is the initial total mass of the medium, $\tilde{M}(t_{n+1})$ is the total mass containing the predict value of the density, $\Delta V(t_{n+1})$ is the volume of the computational cell containing the predict value. $\tilde{\boldsymbol{Q}}^{n+1}_{i,j}$ is corrected as follows by $\Delta\rho$.

$$\boldsymbol{Q}^{n+1}_{i,j} = (\tilde{\rho}^{n+1}_{i,j} + w_{i,j}\Delta\rho)\left(\frac{\tilde{\boldsymbol{Q}}}{\tilde{\rho}}\right)^{n+1}_{i,j} \qquad \left[w_{i,j} = \frac{|\tilde{\rho}^{n+1}_{i,j} - \rho_0|}{N_y^{-1}\sum_{j=1}^{N_y}|\tilde{\rho}^{n+1}_{i,j} - \rho_0|}\right] \tag{2}$$

*Corresponding author. E-mail: orisaki@fluid.mech.eng.osaka-u.ac.jp

Where ρ_0 is the density in an initial undisturbed medium and $w_{i,j}$ is the weight function which is decided according to the magnitude of the density fluctuation (in the situation shown in Figure 1, $w_{i,j} = 1$).

We executed the numerical computation by using the existing method[2] and present method. The medium was an inviscid compressible fluid that can be described by Modified Tait EOS[4] and $\mathrm{Ma} = 0.01$ (Ma is acoustic Mach number), $L_x = 100\pi$, $\Delta = 2\pi/200$, and $\Delta t = 0.1\Delta$ were used for the computation. In both methods, waveform distortion and acoustic shock wave due to the nonlinear effect were properly simulated (Figure 3). The Figure 4 show the evaluation results of the conservation property of the mass and $\varepsilon_m = M(t_n) - M(t_0)$ in the Figure represent the error of the mass conservation of the entire computational domain. In the existing method, the error oscillates at an interval of the period of the acoustic waves, and the error accumulates over time. In the present method, the error was eliminated and ε_m was maintained at a small value ($\varepsilon_m \sim 10^{-14}$).

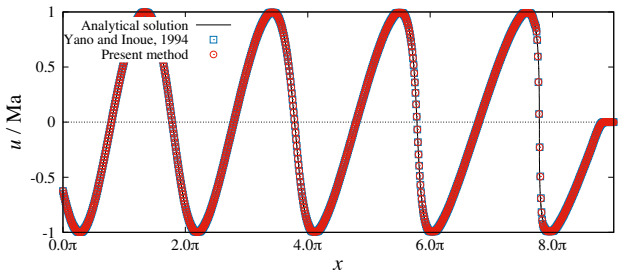

Figure 3: Velocity waveform at shock formation time.

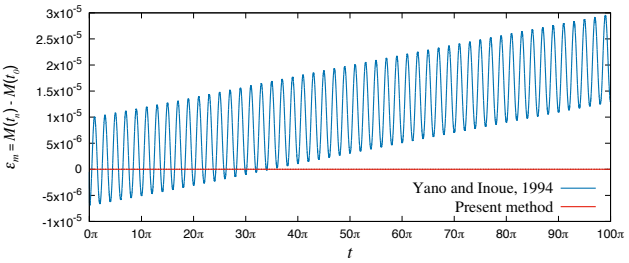

Figure 4: Conservation property of the mass.

RESULT AND CONCLUSION

To analyze the interfacial deformation that can be observed in advance of the ultrasonic atomization, we numerically simulated the situation in which underwater ultrasonic waves are emitted toward the free water surface from an ultrasonic oscillator set at the bottom of a cylindrical container (see Figure 4).The radius and acoustic Mach number of the ultrasonic oscillator are 2π and 0.005, respectively and the initial water level is $y = 8.5\pi$. The proposed method represented by eqs.(2) is applied to the simulation of the ultrasonic oscillator and the free water surface is simulated by height function method[5] using the interfacial velocity that satisfies mass conservation law. While the numerical computation was executed, the conservation property of the mass of the entire computational domain was being small value ($\varepsilon_m / M(t_0) \sim 10^{-8}[\%]$).

We successfully reproduced the water surface uplift above the sound source experimentally observed. It was elucidated that the acoustic streaming mainly dominates the interfacial deformation (see Figure 4). In addition, it was suggested that the remarkable acoustic streaming toward the water surface is caused by the increase in the nonlinear effect due to the reflection of ultrasonic waves.

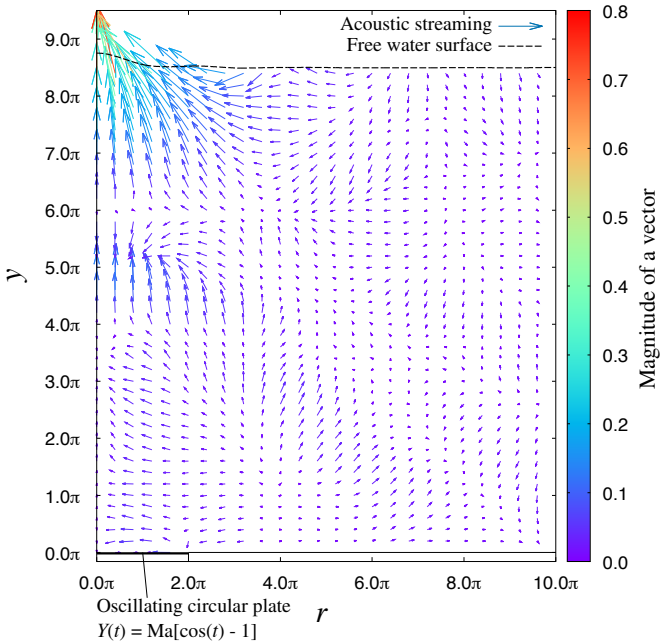

Figure 4: Acoustic streaming in the (r, y) plane at $t = 100\pi$.When the magnitude of the acoustic streaming is equal to Ma, the magnitude of the vector is equal to 1.0.

References

[1] F.Barreras, H.Amaveda, and A.Lozano Transient High-Frequency Ultrasonic Water Atomization. *Exp. Fluids* **33**: 405-413, 2002

[2] T.Yano, Y.Inoue Numerical study of strongly nonlinear acoustic waves, shock waves, and streaming caused by a harmonically pulsating sphere. *Phys. Fluids* **6**: 669-679, 1994

[3] S.R.Chakravarthy, S.Osher A new class of high accuracy TVD schemes for hyperbolic conservation laws. AIAA paper No. 85-0363, 1985

[4] J.Ross Macdonald Some simple isothermal equations of state. *Reviews of Modern Physics* **38**.4: 2831-2844, 1966

[5] C.W.Hirt, B.D.Nichols, and N.C.Romero SOLA-Numerical Solution Algorithm for Transient Fluid Flows. Los Alamos Scientific Laboratory Report LA-5852 (1975)

A SCHEME FOR INTERFACE ANALYSIS OF MAGNETIC FLLUID VALIDATED BY PHYSICAL LAWS

Yo Mizuta*[1]
[1]Department of Applied Physics, Hokkaido University, Sapporo, Japan

Summary For the stability or dynamic analysis in real time and in real space of the interface phenomena of magnetic fluids as the Rosensweig instability, quantities such as magnetic fields, stresses and fluid velocity on the interface are investigated numerically. The magnetic induction $\boldsymbol{b}$ is obtained efficiently by using the indirect boundary element method (IBEM). IBEM is used also for analyzing the fluid described by the velocity potential. The effect of nonlinear magnetization is incorporated in the magnetic stress difference T calculated from $\boldsymbol{b}$. Quantities on the interface in a two-layered system of fluid and vacuum domain under a homogeneous vertical magnetic field are shown. Though the magnetic stress or the gravity acts to grow or decay a raised interface for sure, actual behavior of the interface depends delicately on the change of the sum of interface stresses S.

INTERFACE ANALYSIS OF MAGNETIC FLUID

When we analyze the interface phenomena of incompressible, irrotational and inviscid magnetic fluid with all nonlinear effects but with no limitations on the interface profile, we use the following **equation for interface motion (EIM)** which is derived from Bernoulli's equation and the dynamic boundary condition on the interface [1]:

$$\rho\frac{\partial\varphi}{\partial t}+S=0,\quad S\equiv D+G+C+T+p_0, \tag{1}$$

where ρ, φ, D, G, C, p_0 are the fluid density, velocity potential, dynamic pressure, gravity potential, surface tension and atmospheric pressure, respectively. We omit hereafter D and p_0 in the sum of interface stresses S supposing slowly-moving interface and homogeneous atmospheric pressure.

The magnetic stress difference T representing the action from the magnetic field to the fluid is affected by the **nonlinear magnetization** [1], and determined as

$$T=-2\mu_0\left(Mb_Z\right)^2-\mu_0\frac{M_S}{\gamma}\ln\left(\frac{\sinh\gamma H}{\gamma H}\right),\quad H=\sqrt{h_X^2+h_Y^2+\left(\frac{b_Z}{\mu_1}\right)^2}, \tag{2}$$

where $M\equiv(1/\mu_0-1/\mu_1)/2$ with the permeability μ_J of the fluid (J=1) or the vacuum (J=0), and $\gamma\equiv 3\chi_0/M_S$ with the saturation magnetization M_S and the initial susceptibility χ_0.

The tangential magnetic field $h_{X,Y}$ and the normal magnetic induction b_Z are calculated from the magnetic potential ϕ and the normal magnetic induction b_Z. Through the Indirect Boundary Element Method (IBEM) [1], they are obtained rigorously as well as efficiently compared with the FEM, under arbitrary interface profiles and applied magnetic field distributions.

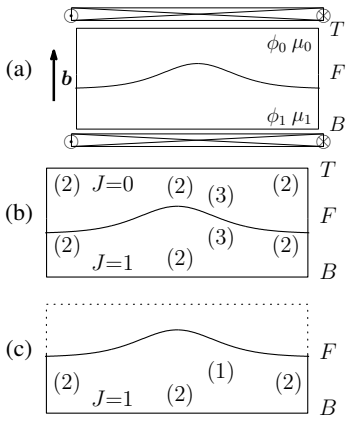

Figure 1: (a) Two-layered system under homogeneous vertical magnetic field. Boundary conditions for (b) magnetic analysis and (c) fluid analysis. (1), (2) or (3) denote boundaries where Dirichlet condition, Neumann condition or interface conditions are imposed, respectively.

TWO-LAYERED SYSTEM UNDER HOMOGENEOUS VERTICAL MAGNETIC FIELD

As shown in Fig. 1(a), a homogeneous vertical magnetic induction with the intensity $b_{\rm app}$ is applied on a two-layered system composed of fluid and vacuum domains with the same depth, and physical quantities are calculated on the axially-deformed solitary-wave-like interface F with the height $\zeta_{\rm pro}$ and the width $w_{\rm pro}$.

After [3], the magnetic fluid of gravity acceleration g=9.81 ms^{-2}, fluid density ρ=1.17 $\times10^3$ kgm^{-3}, capillary coefficient σ=3.09 $\times10^{-2}$ Nm^{-1}, saturation magnetization M_S=2.32 $\times10^4$ $\mathrm{A\,m}^{-1}$ and initial susceptibility χ_0=3.57 is supposed. From these values, critical parameter values where the interface linear wave becomes unstable are obtained as: wavenumber $k_{\rm C}=(\rho g/\sigma)^{1/2}$ =6.09 $\times10^2$ m^{-1}, wavelength $\lambda_{\rm C}=2\pi/k_{\rm C}$=1.03 $\times10^{-2}$ m. The intensity $b_{\rm app}$ changes between 15 mT and 25 mT. The height $\zeta_{\rm pro}$ is changed up to 3 mm, and its width $w_{\rm pro}$ is kept at $\lambda_{\rm C}$.

Boundary conditions to obtain ϕ and b_Z are shown in Fig. 1(b), where the known intensity $b_Z=b_{\rm app}$ is given on T and B, b_Z=0 on the side boundaries, and the interface conditions $\phi_1=\phi_2$ and $b_{Z1}+b_{Z2}=0$ are imposed on F. The magnetic induction vector $\boldsymbol{b}$ for the fluid domain (J=1) (Fig. 2(a),(b)) is obtained as $\boldsymbol{b}=\boldsymbol{b}_t+\boldsymbol{b}_n$ where $\boldsymbol{b}_t=\mu_J\nabla\phi_J\times\boldsymbol{t}_{ZJ}=b_{tx}\boldsymbol{x}+b_{tz}\boldsymbol{z}$ and $\boldsymbol{b}_n=b_{ZJ}\boldsymbol{t}_{ZJ}=b_{nx}\boldsymbol{x}+b_{nz}\boldsymbol{z}$ are the tangential magnetic induction vector, the normal magnetic induction vector and their components, respectively, where $\boldsymbol{t}_{ZJ}$ is the normal unit vector.

Once the magnetic analysis by the IBEM is established, incompressible, irrotational and inviscid fluid is readily analyzed by using the velocity potential φ which satisfies the Laplace equation $\nabla'\cdot(\nabla'\varphi')=0$. The law of conservation of volume is considered now. Figure 1(c) shows boundary conditions for the fluid analysis. On B and side boundaries, the normal fluid velocity v_n=0. On the free surface F, by contrast, the value of φ from the integration in time of the EIM (1) is given as the Dirichlet boundary condition, and the normal fluid velocity v_n is obtained which determines the interface elevation. To obtain v_n just after a short time Δt of the fluid initially at rest, we set here $-S\Delta t/\rho$ for φ. Figure 2(g) shows the fluid velocity $\boldsymbol{v}$ on the free surface, which is composed of the tangential fluid velocity $\boldsymbol{v}_t\equiv\nabla\varphi\times\boldsymbol{t}_Z$ and the normal fluid velocity $\boldsymbol{v}_n\equiv v_n\boldsymbol{t}_Z$.

*Corresponding author. E-mail: yomizuta@eng.hokudai.ac.jp.

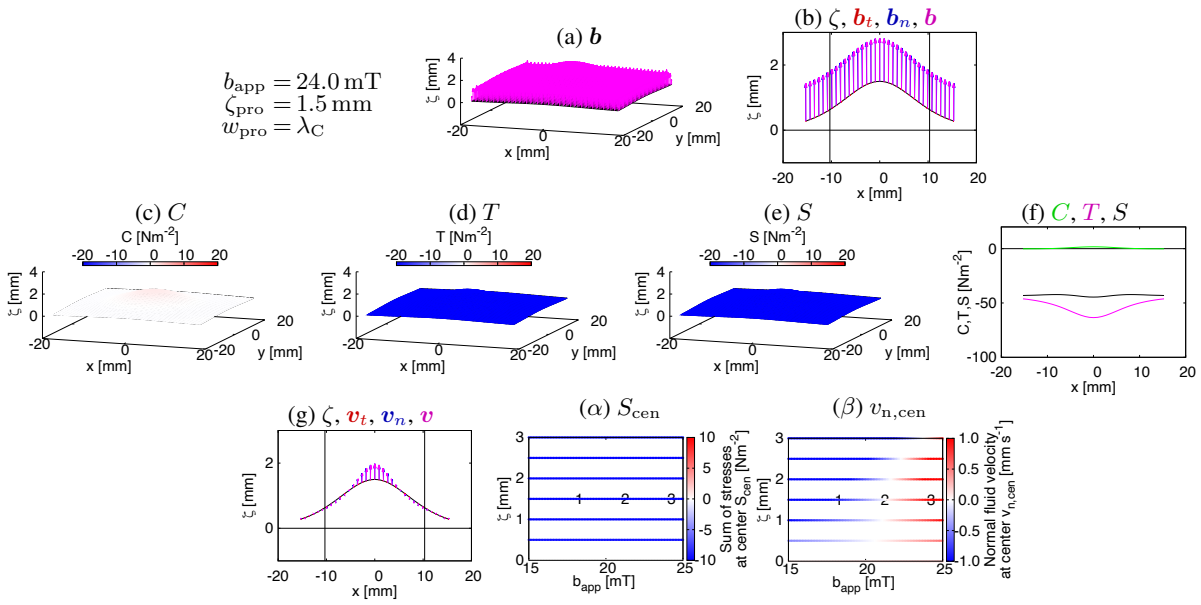

Figure 2: Distribution on the interface ((a),(c),(d),(e)) and within the cross section at y=0 ((b),(f),(g)) of (a),(b) tangential magnetic induction vector $\boldsymbol{b}_t$, normal magnetic induction vector $\boldsymbol{b}_n$, their composite $\boldsymbol{b}$, (c),(f) surface tension C, (d),(f) magnetic stress difference T, (e),(f) sum of interface stresses S including gravity potential G, and (g) tangential fluid velocity $\boldsymbol{v}_t$, normal fluid velocity $\boldsymbol{v}_n$ and their composite $\boldsymbol{v}$. (α) and (β) show dependence of sum of interface stresses S and normal fluid velocity v_n at the center of interface profile on intensity of applied magnetic induction $b_{\rm app}$ and height of interface profile $\zeta_{\rm pro}$.

Calculated quantities on the interface are shown in Fig. 2, and for visibility, their distribution within the cross section at y=0 in (b),(f),(g). The mean curvature H for the surface tension C=$-2\sigma H$ in (c),(f) is calculated through the differentiation in the interfacial direction of the function interpolating the interface profile. The magnetic stress difference T in (d),(f) is from (2), and the sum of interface stresses S in (e),(f) includes the gravity potential G. The correctness of these stresses are verified by the relation between interface stress and interface energy density (RELA) [2].

When the interface is flat, the same $b_{\rm app}$ as applied on T and B is expected to appear on F. Before F is deformed, it was confirmed that obtained ϕ and b_Z on F are continuous across the interface, and they are symmetric after rotated at a right angle due to the geometric configuration.

Figure 2(α),(β) show the value of the sum of interface stresses $S_{\rm cen}$ and the normal fluid velocity $v_{\rm n,cen}$ at the center of the interface profile, by changing $b_{\rm app}$ and $\zeta_{\rm pro}$. The results in (a)–(g) are those at the symbol 3.

DISCUSSION

When $\partial v_z/\partial t \simeq 0$, $\partial\zeta/\partial t \propto \partial\varphi/\partial t = -S/\rho$ holds, since $\varphi = \int_{-\infty}^{\zeta} {\rm d}z v_z$ with the interface elevation ζ and the vertical component of fluid velocity v_z. As Fig. 2(f) shows, under the present condition, T is always negative, positive G cancels it partly, and C is small compared with T and G in S. As the result, S changes gently in the central area, but is still negative. Then, the magnetic stress is expected to grow the interface against the gravity in all the range of $b_{\rm app}$ as shown in Fig. 2(α). In spite of this speculation, the interface decays ($v_n < 0$) in the range between 1 and 2 of Fig. 2(β), and larger $b_{\rm app}$ is needed to be $v_n > 0$ at 3 where v_n is positive in the limited central area as Fig. 2(g) shows.

In the case of 3, the curve of S in Fig. 2(f) is observed to change convex downward in the central area, in contrast to the case of 1 and 2 where convex upward in all area. This behavior of S directs the tangential fluid velocity toward the center, and generates the outward normal fluid velocity together with the conservation of volume. Though the preliminary speculation paid attention mainly on the sign of S, the change of S on the interface should be investigated carefully for discussing the behavior of the interface which is determined from C in addition to T on the basis of the magnetic analysis.

An amplitude equation $\partial A/\partial t = f(\varepsilon, A)$ with $\varepsilon = (B/B_0)^2 - 1$ is reconstructed and used for the nonlinear relaxation dynamics in the neighborhood of the Rosensweig instability [3, 4]. In the phase space spanned by the pattern amplitude A and magnetic induction B, the bifurcation curve is obtained from $f(\varepsilon, A)$=0, which is a stable (unstable) branch when $f(\varepsilon, A) < 0$ in the neighbor above (below) it. Also in Fig. 2(β), this branch is likely to be drawn by connecting the points with $v_{\rm n,cen}$=0 by the correspondence between A, B, $\partial A/\partial t$ and $\zeta_{\rm pro}$, $b_{\rm app}$, $v_{n,cen}$. However, it should be noted that this marginal curves is that for the initial fluid at rest at t=0, and the stable bifurcation curve is to be determined from the stationary v_n=0 at t=∞. After all, dynamic analysis from t=0 to t=∞ is needed considering the changes in $\zeta_{\rm pro}$, $w_{\rm pro}$ and S on the way.

References

[1] Mizuta Y.: Numerical platform for the interface analysis of magnetic fluids by use of the Boundary Element Method. *J. Magn. Magn. Mater.* **514**:167118, 2020.
[2] Mizuta Y.: Dynamic Analysis on Magnetic Fluid Interface Validated by Physical Laws. *J. Magn. Magn. Mater.* **431**:209–213, 2017.
[3] Gollwitzer C., Rehberg I. and Richter R.: From phase space representation to amplitude equations in a pattern-forming experiment. *New Journal of Physics* **12** (9):093037, 2010.
[4] Lloyd D.J.B., Gollwitzer C., Rehberg I. and Richter R.: Homoclinic snaking near the surface instability of a polarisable fluid. *J. Fluid Mech.* **783**:283–305, 2015.

TWO COUPLED NONLINEAR EVOLUTION EQUATIONS OF OBLIQUELY INTERACTING CAPILLARY GRAVITY WAVES OVER INFINITE DEPTH

Shibam Manna*[1], and A.K. Dhar [1]
[1]Department of Mathematics, Indian Institute of Engineering Science and Technology, Shibpur, India

Summary Two coupled nonlinear Schrodinger (CNLS) equations have been employed to discuss the modulational instability (Benjamin-Fier instability) due to unidirectional as well as bidirectional perturbations for two obliquely interacting capillary gravity waves over infinite depth of water under the circumstance of crossing sea states. Graphs and three-dimensional contour plots are demonstrating the fact that the rate of growth of instability G_r for two obliquely interacting wave trains is much elevated compared to the instance of modulation of one wave train. Therefore, freak waves may be created as a consequence of Benjamin-Fier instability. We have also examined a stabilising influence on modulational instability (MI) due to the effect of capillarity.

INTRODUCTION

Freak waves, first introduced by Draper [1], are exceptionally large amplitude waves, localised both in space and time which can be accompanied by deep holes that occur before and after the maximum crest. The devastating power of freak waves are liable for the destruction of numerous ships and lives [2], and resulting depreciation of offshore engineering structures have guided researchers to perform research works for acquiring sufficient information regarding the generation, formulation-mechanism, dynamics of amplification along with other relevant features of such waves. Freak waves may be formed due to both statistical and nonlinear effects, may exist both in shallow and deep water [3]. Employing Zakharov's integral equation, Onorato et al. [4] developed two CNLS equations for two nonlinearly interacting waves in deep water with two separate channels of spread. They presented an investigation of the instability growth rate for one dimensional two wave systems utilising those equations and observed that the growth rates rely on not just the wavelength of the perturbation and steepness of the primary waves yet in addition on the angle between the two wave frameworks. This outcome was then extended by Shukla et al. [3] for investigating the rate of growth of instability for bidirectional perturbations employing two CNLS equations as derived by Onorato et al. [4]. After investigating weakly nonlinear interaction of two wave systems spreading along with two separate directions in deep water, Laine-Pearson [5] inferred that the rate of growth of long-wave instability of two obliquely interacting waves is more significant than those due to resonant interaction of short-crested waves. Senapati et al. [6] determined two CNLS equations in the case of crossing sea states in the presence of uniform wind flow in deep water. All these analyses made by the aforesaid authors are for gravity waves. The present paper is an extension of Shukla et al. [3] to incorporate capillarity using multiple scale method unlike Onorato [4] and Shukla et al. [3]. Thus our paper deals with two CNLS equations for two capillary gravity wave packets in crossing sea states over infinite depth of water.

Evolution equations, Modulational instability:

Here two capillary gravity wave trains having carrier wave numbers $\boldsymbol{k}_1 = (k, l)$ and $\boldsymbol{k}_2 = (k, -l)$ respectively are propagating obliquely and making equal angle θ with the positive direction of x axis. Let $z = \eta(x, y, t)$ represents the equation of the undulating free surface at time t in perturbed state. The perturbed velocity potential $\phi(x, y, z, t)$ satisfies the Laplace equation. At the free surface, the kinematic boundary condition is, $\phi_z - \eta_t = \phi_x\eta_x + \phi_y\eta_y$ on $z = \eta$ (1)

The condition of continuity of pressure at the free surface is, $\phi_t + g\eta = -\frac{1}{2}(\nabla\phi)^2 + s\left[\frac{\eta_{xx}(1+\eta_y^2)+\eta_{yy}(1+\eta_x^2)-2\eta_{xy}\eta_x\eta_y}{(1+\eta_x^2+\eta_y^2)^{3/2}}\right]$, (2)

where $s = \frac{T}{\rho}$ represents the coefficient of surface tension and g is the gravitational acceleration, $\phi \to 0$ as $z \to -\infty$. To solve (1) and (2), we employ $P = P_{00} + \sum_{(m,n)\neq(0,0)}\left[P_{mn}e^{i(m\psi_+ + n\psi_-)} + P_{mn}^* e^{-i(m\psi_+ + n\psi_-)}\right]$, (3)

where $\psi_\pm = kx \pm ly - \omega t$ represent the phase functions of first and second wave trains respectively, P stands for ϕ, η. Here ϕ_{00}, ϕ_{mn} and ϕ_{mn}^* are slowly varying functions of $(x_1, y_1, t_1) = (\delta x, \delta y, \delta t)$ and z; η_{00}, η_{mn} and η_{mn}^* are functions of x_1, y_1, t_1 and $*$ denotes complex conjugate, δ is a small ordering parameter. The linear dispersion relation is $f(\omega, k, l) \equiv \omega^2 - gk_0 - sk_0^3 = 0$, $(k, l) = (k_0\cos\theta, l_0\sin\theta)$. Proceeding similarly as Senapati et al. [6], the evolution equation of the 1st wave train is: $i\frac{\partial\eta_{10}}{\partial t_1} + i\gamma_1\frac{\partial\eta_{10}}{\partial x_1} + i\gamma_2\frac{\partial\eta_{10}}{\partial y_1} + \gamma_3\frac{\partial^2\eta_{10}}{\partial x_1^2} + \gamma_4\frac{\partial^2\eta_{10}}{\partial y_1^2} + \gamma_5\frac{\partial^2\eta_{10}}{\partial x_1 y_1} = \Lambda_1\eta_{10}^2\eta_{10}^* + \Lambda_2\eta_{10}\eta_{01}\eta_{01}^*$ (4)

The coefficients of (4) are available in the Appendix. Similarly, for the 2nd wave train with carrier wave number $(k, -l)$ the evolution equation is: $i\frac{\partial\eta_{01}}{\partial t_1} + i\gamma_1\frac{\partial\eta_{01}}{\partial x_1} - i\gamma_2\frac{\partial\eta_{01}}{\partial y_1} + \gamma_3\frac{\partial^2\eta_{01}}{\partial x_1^2} + \gamma_4\frac{\partial^2\eta_{01}}{\partial y_1^2} - \gamma_5\frac{\partial^2\eta_{01}}{\partial x_1 y_1} = \Lambda_1\eta_{01}^2\eta_{01}^* + \Lambda_2\eta_{01}\eta_{10}\eta_{10}^*$ (5)

In the absence of capillarity (s = 0), the coefficients of equations (4) and (5) are in agreement with the corresponding coefficients of the equations made by Onorato et al. [4], as well as those of Senapati et al. [6] for $(U, r) = (0, 0)$. We choose the uniform wave train solutions of (4), (5) in the form $\eta_{10} = \alpha_0 e^{-it_1\Delta\omega_1} \equiv \eta_{10}^{(0)}$, $\eta_{01} = \beta_0 e^{-it_1\Delta\omega_2} \equiv \eta_{01}^{(0)}$, (6)

where α_0 and β_0 are real constants indicating the wave steepness of two wave trains and the nonlinear frequency shifts $\Delta\omega_1$ and $\Delta\omega_2$ satisfy the following relations: $\Delta\omega_1 = \Lambda_1\alpha_0^2 + \Lambda_2\beta_0^2$, $\Delta\omega_2 = \Lambda_2\alpha_0^2 + \Lambda_1\beta_0^2$ (7)

The nonlinear dispersion relation is $[(\Omega - Q_+)^2 - P_+(P_+ - 2\Lambda_1\alpha_0^2)][(\Omega - Q_-)^2 - P_-(P_- - 2\Lambda_1\beta_0^2)] = 4P_+P_-\Lambda_2^2\alpha_0^2\beta_0^2$, (8)

where $P_\pm = -(\lambda^2\gamma_3 + \mu^2\gamma_4 \pm \lambda\mu\gamma_5)$, $Q_\pm = (\lambda\gamma_1 \pm \mu\gamma_2)$ and equation (8) is in agreement with the equation (2) of Shukla et al. [3]. For $\mu = 0$, from (8) we get $(\Omega - \lambda\gamma_1)^2 = (\lambda^2\gamma_3)^2 + \lambda^2\gamma_3\Lambda_1(\alpha_0^2 + \beta_0^2) \mp \lambda^2\gamma_3\sqrt{(\Lambda_1(\alpha_0^2 - \beta_0^2))^2 + 4\Lambda_2^2\alpha_0^2\beta_0^2}$, (9)

*Corresponding author. E-mail: mannashibam31@gmail.com.

which is again an agreement with the equation (11) of Onorato et al. [4].

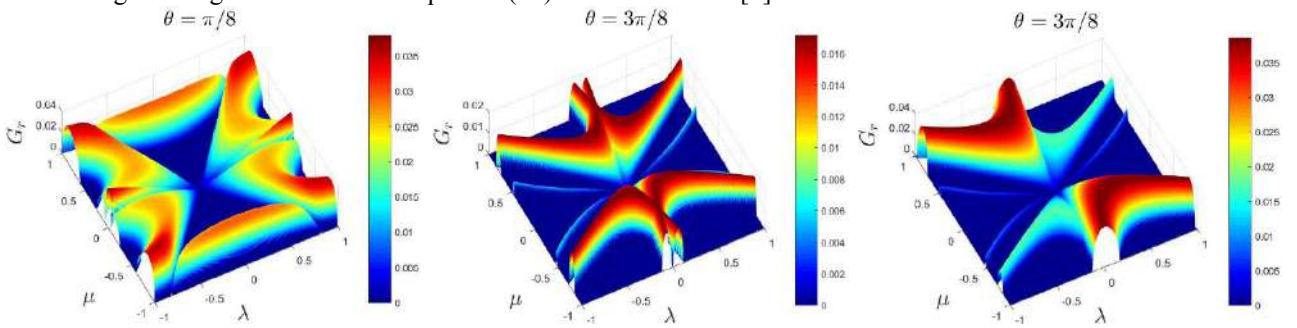

Fig-1: 3D Contour plot of $G_r = Im\Omega$ in (λ, μ) plane for $s = 0.035$, $\alpha_0 = \beta_0 = 0.15$(first two) and $\alpha_0 = 0.1, \beta_0 = 0.15$ (last one).

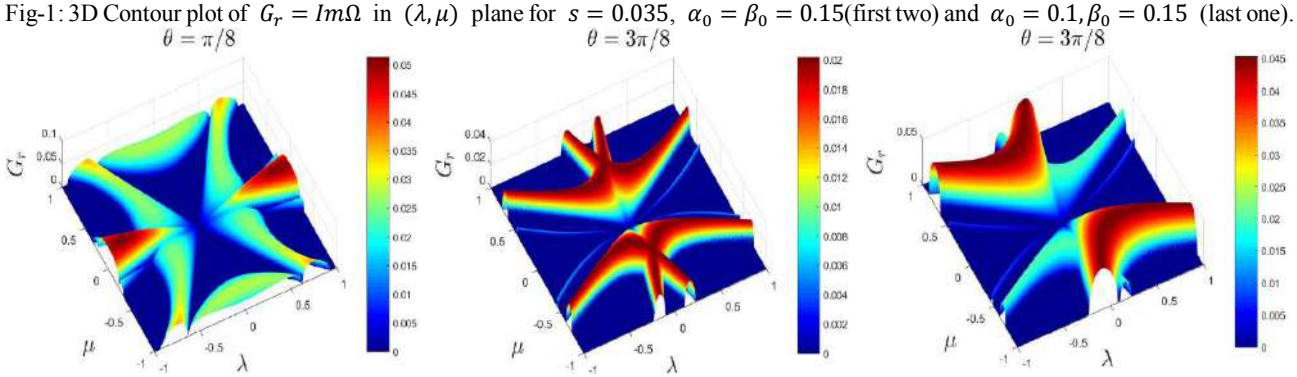

Fig-2: 3D Contour plot of $G_r = Im\Omega$ in (λ, μ) plane for $s = 0$, $\alpha_0 = \beta_0 = 0.15$ (first two) and $\alpha_0 = 0.1, \beta_0 = 0.15$ (last one).

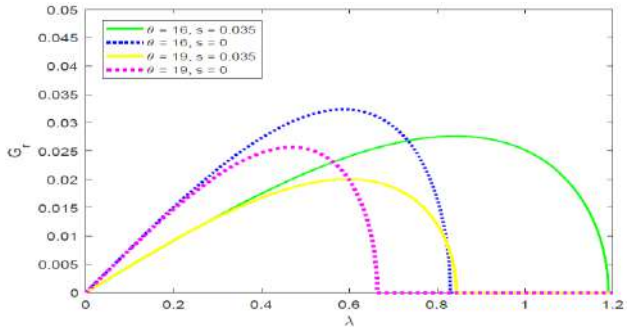

Fig-3: $G_r = Im\Omega$ as a function of λ, $\alpha_0 = 0.1, \beta_0 = 0.15$

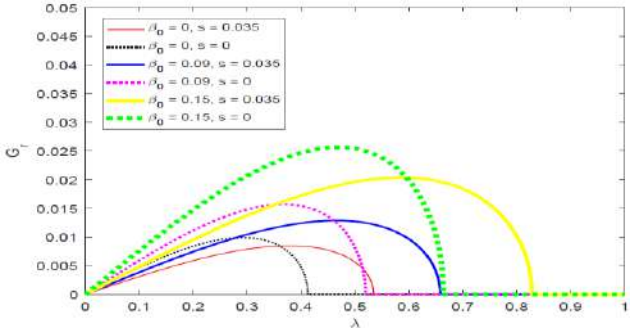

Fig-4: G_r as a function of λ, $\theta = 19°$ (…$s = 0$, __$s = 0.035$)

Fig-1, 2 exhibit that the effect of capillarity results in a decrease in the growth rate producing a stabilising influence. For $\theta = \frac{3\pi}{8}$ comparing Fig-1 with Fig-5 of Senapati et al. [6], we have inferred that due to capillarity G_r decreases. Further, the instability regions for $\alpha_0 = \beta_0$ are symmetric about $\lambda = 0$, $\mu = 0$ whereas for $\alpha_0 \neq \beta_0$ it is not so. Fig-3 exhibits that the capillarity effect produces a decrease in G_r up to a certain value of λ giving a stabilising influence and G_r increases as θ decreases. Finally, Fig-4 demonstrates that G_r increases with the increase of β_0 for a fixed value of θ.

CONCLUSIONS

Comparing Fig-1 with Fig-2, we conclude that the effect of capillarity produces a decrease in the growth rate of instability G_r. Figures 3 and 4 exhibits that G_r decreases due to the effect of capillarity up to a certain value of the wave-number λ and then G_r increases. Further, Fig-4 demonstrating the fact that G_r for two obliquely operating wave packets is much elevated than the instance of modulation of a single ($\beta_0 = 0$) wave packet [7]. Thus freak waves can be produced as a consequence of MI. Furthermore, G_r becomes higher as θ becomes smaller.

Appendix:

$$\gamma_1 = \frac{k(1+3s)}{2\omega}, \gamma_2 = \frac{l(1+3s)}{2\omega}, \gamma_3 = -\frac{k^2}{8\omega^3} + \frac{l^2+3s(l^2+2k^2)}{4\omega}, \gamma_4 = -\frac{l^2}{8\omega^3} + \frac{k^2+3s(l^2+2k^2)}{4\omega}, \gamma_5 = -\frac{kl}{4\omega^3} + \frac{(1+3s)kl}{2\omega}, \Lambda_1 = 2\omega + \frac{\omega(3\omega^2-3-12s)}{(2\omega^2-1-4s)} - \frac{s}{2\omega}\left\{3l^2k^2 - \frac{3}{2}(l^4+k^4)\right\}, \Lambda_2 = \frac{s}{2\omega}\{2l^2k^2 + 3(l^4+k^4)\} + \omega(3k^2-l^2) - \frac{\omega^3 l^2(k^2-l^2-2)}{2(1+4l^2s)} - \frac{\omega k(k^2+l^2-2k)^2}{k+4sk^2-2\omega^2}.$$

References:

[1] Draper L., "'FREAK' OCEAN WAVES", Weather 21(1), pp. 2-4 (1966).
[2] Kharif C., Pelinovsky E., "Physical mechanisms of the rogue wave phenomenon", European Journal of Mechanics B/Fluids 22, 603-634 (2003).
[3] Shukla P. K., Kourakis I., Eliasson B., Marklund M. and Stefano L., "Instability and evolution of nonlinearly interacting water waves", Phys. Rev. Lett. 97, 094501-1-4 (2006).
[4] Onorato M., Osborne A. R. and Serio M., "Modulational instabilities in crossing seas: A possible mechanism for the formation of freak waves", Phys. Rev. Lett. 96, 014503-1-4 (2006).
[5] Laine-Pearson F. E., "Instability growth rates of crossing sea states", Phys. Rev. E 81, 036316-1-7 (2010).
[6] Senapati S., Kundu S., Debsarma S., Das K. P., "Nonlinear evolution equations in crossing seas in the presence of uniform wind flow", European Journal of Mechanics B/Fluids 60, 110-118 (2016).
[7] A. K. Dhar and K. P. Das, "A fourth-order evolution equation for deep water surface gravity waves in the presence of wind blowing over water", Phys. Fluids A 2(5), pp. 778-783 (1990).

RADIATION-INDUCED INSTABILITY OF A MEMBRANE INTERACTING WITH A UNIFORMLY MOVING FREE SURFACE FLOW OF FINITE DEPTH

Joris Labarbe[1] and Oleg N. Kirillov[1]
[1]Northumbria University, NE1 8ST Newcastle upon Tyne, UK

Summary In a recent study [1], we investigate the motion of waves emitted due to flutter of an elastic membrane being at the bottom of a uniform horizontal potential flow of an inviscid and incompressible fluid of finite depth with free surface. The membrane is rigidly fixed at both extremities and placed at the center of a solid floor. The membrane has an infinite span in the direction perpendicular to the direction of the flow and a finite width along the flow axis. In the case where the length of the membrane is supposed infinite, we managed to derive a full dispersion relation that is valid for arbitrary depth of the fluid layer and find conditions for the flutter of the membrane due to emission of surface gravity waves. We describe this radiation-induced instability by means of the wave energy of the flow related to the concept of negative energy waves and study its relation to the anomalous Doppler effect. An extension to the case of a membrane with finite chord is also subject of a discussion in terms of stability, despite the more complex settings and analysis involved.

MEMBRANE FLUTTER DUE TO SURFACE GRAVITY WAVES EMISSION

Flutter of membranes is a classical subject for at least seven decades. Membranes submerged in a compressible gas flow and their flutter at supersonic speeds have been considered already in the works [2, 3]. Recent works on the membrane flutter are motivated by such diverse applications as stability of membrane roofs in civil engineering [4], flutter of traveling paper webs [5] and aerodynamics of sails and membrane wings of natural flyers [6, 7].

Surface gravity waves on a motionless fluid of finite depth is a classical subject as well, going back to the seminal studies of Russell and Kelvin [8]. Numerous generalizations are known taking into account, for instance, a uniform or a shear flow and surface tension [9], flexible bottom or a flexible plate resting on a free surface [10]. The latter setting has a straightforward motivation in dynamics of sea ice and a less obvious application in analogue gravity experiments [8].

Remarkably, another phenomenon that is being analysed from the analogue gravity perspective is super-radiance [8] and its particular form, discovered by Ginzburg and Frank [11], known as the anomalous Doppler effect (ADE) [12, 13]. In electrodynamics, the ADE manifests itself when an electrically neutral overall particle, endowed with an internal structure, becomes excited and emits a photon during its uniform but superluminal motion through a medium, even if it started the motion in its ground state; the energy source is the bulk motion of the particle [12].

Anomalous Doppler effect in hydrodynamics was demonstrated for a mechanical oscillator with one degree of freedom, moving parallel to the boundary between two incompressible fluids of different densities [14]. It was shown that the oscillator becomes excited due to radiation of internal gravity waves if it moves sufficiently fast. In [15] the ADE for such an oscillator was demonstrated due to radiation of surface gravity waves in a layer of an incompressible fluid.

Nemtsov [16] was the first who considered flutter of an elastic membrane being on the bottom of a uniform horizontal flow of an inviscid and incompressible fluid as an anomalous Doppler effect due to emission of long surface gravity waves. In the shallow water approximation, he investigated both the case of a membrane that spreads infinitely far in both horizontal directions and the case when the width of the membrane in the direction of the flow is finite whereas the span in the perpendicular direction is infinite. Nevertheless, the case of the flow of arbitrary depth has not been studied in [16] as well as no numerical computation supporting the asymptotical results has been performed. Another issue that has not been addressed in [16] is the relation of stability domains for the membrane of the finite width to that for the membrane of the infinite width.

Vedeneev studied flutter of an elastic plate of finite and infinite widths on the bottom of a uniform horizontal flow of a compressible gas occupying the upper semi-space. He performed analysis of the relation of stability conditions for the finite plate with that for the infinite plate using the method of global stability analysis by Kulikovskii [17, 18]. However, no connection has been made to the ADE and the concept of negative energy waves.

In the present work [1] we reconsider the setting of Nemtsov in order to address the finite height of the fluid layer as it is presented in FIG. 1. We managed in that setting to derive a full dispersion relation for the case of infinite membrane and find the flutter domains in the parameter space. Using perturbation of multiple roots of the dispersion relation, we analyze the character of the instability to determine the wave motion due to flutter of the membrane. We also investigate dependence of the flutter onset on the width of the membrane and we seek relations with the infinite membrane case by using a numerical model developped in [19] and new expressions for the pressure and the potential of the fluid derived in this work. Finally, we will explain the instabilities via the interaction of positive and negative energy waves by finding explicit formulations of kinetic and potential energy of the flow, and relate these results to the anomalous Doppler effect.

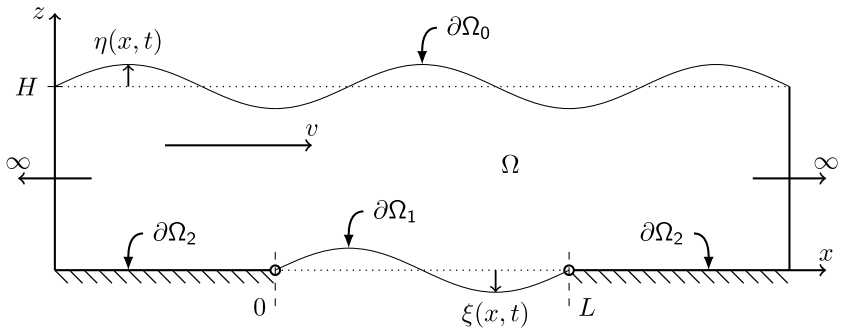

Figure 1: Sketch of the system considered.

References

[1] Labarbe, J. and Kirillov, O. N. 2020. Membrane flutter induced by radiation of surface gravity waves on a uniform flow. *J. Fluid Mech.*, **901**, A4.
[2] Benjamin T. B. (1963) The threefold classification of unstable disturbances in flexible surfaces bounding inviscid flows. *J. Fluid Mech.*, **16**: 436–450.
[3] Bolotin V. V. (1963) *Nonconservative Problems of the Theory of Elastic Stability.* Pergamon Press, Oxford.
[4] Sygulski R. (2007), Stability of membrane in low subsonic flow. *Int. J. Non-Linear Mech.*, **42**(1): 196–202.
[5] Banichuk N., Barsuk A., Jeronen J., Tuovinen T., Neittaanmäki P. (2019) *Stability of Axially Moving Materials*, Springer, Berlin.
[6] Newman B. G., Paidoussis M. P. (1991) The stability of two-dimensional membranes in streaming flow. *J. of Fluids and Struct.* **5**: 443–454.
[7] Tiomkin S., Raveh D. E. (2017) On the stability of two-dimensional membrane wings. *J. Fluids Struct.*, **71**: 143–163.
[8] Carusotto I., Rousseaux G. (2013) The Cerenkov Effect Revisited: From Swimming Ducks to Zero Modes in Gravitational Analogues. In: Faccio D., Belgiorno F., Cacciatori S., Gorini V., Liberati S., Moschella U. (eds) Analogue Gravity Phenomenology. Springer, Cham.
[9] Maissa P., Rousseaux G., Stepanyants Y. (2016) Negative energy waves in a shear flow with a linear profile. *Eur. J. Mech. B/Fluids*, **56**: 192–199.
[10] Das S., Sahoo T., Meylan M. H. (2018) Dynamics of flexural gravity waves: from sea ice to Hawking radiation and analogue gravity. *Proc. R. Soc. A* **474**: 20170223.
[11] Ginzburg V. L., Frank I. M. (1947) On the Doppler effect at the superluminal velocity. *Dokl. Akad. Nauk SSSR* **56**: 583–586.
[12] Bekenstein J. D. , Schiffer M. (1998) The many faces of superradiance. *Phys. Rev. D* **58**: 064014.
[13] Nezlin M. V. (1976) Negative-energy waves and the anomalous Doppler effect. *Sov, Phys. Uspekhi* **19**: 946–954.
[14] Gaponov-Grekhov A. V., Dolina I. S., Ostrovskii L. A. (1983) The anomalous Doppler effect and the radiation instability of oscillator motion in hydrodynamics, *Doklady Akad. Nauk SSSR* **268**(4): 827–831. In Russian.
[15] Abramovich B. S., Mareev E. A., Nemtsov B. E. (1986) Instability in the oscillations of a moving oscillator while it radiates surface and internal waves. *Fluid Dynamics* **21**(1): 147–149.
[16] Nemtsov B. E. (1986) Flutter effect and emission in the region of anomalous and normal Doppler effects. *Radiophys. Quant. Elect.*, **28**(12): 1076–1079.
[17] Doaré O., de Langre E. (2006) The role of boundary conditions in the instability of one-dimensional systems, *Eur. J. Mech. B/Fluids*, **25**: 948–959.
[18] Vedeneev V. V. (2016) On the application of the asymptotic method of global instability in aeroelasticity problems. *Proc. Steklov Inst. Math.* **295**: 274–301.
[19] Vedeneev V. V. (2012) Pannel flutter at low supersonic speeds. *J. of Fluids and Struct.* **29**: 79–96.

BIHARMONIC WAVE ATTRACTORS IN STRATIFIED OR ROTATING FLUIDS

Daniil Riazanov[1], Ilias Sibgatullin *[1,2], and Evgeny Ermanyuk[2]
[1]Ivannikov Institute for System Programming of the RAS, Moscow, Russia
[2]Shirshov Institute of Oceanology of the RAS, Moscow, Russia
[3]Lavrentyev Institute of Hydrodynamics of SB RAS, Novosibirsk, Russia

Summary Simultaneous appearance of different wave attractors in the same tank, which are formed due to external forcings with different frequencies are studied by direct numerical simulation. Structure of the flow for small amplitudes correspond to the linear theory only if the frequencies are not close to each other. For larger amplitudes the dependence of dynamical behaviour, transition to chaotic motion, level of kinetic energy and its pulsations on difference between the frequencies is discussed.

In stratified or rotating fluids accumulation of wave energy along closed paths or surfaces can occur due to peculiarities of dispersion relation of internal or inertial waves, which result in new rules of wave beam billiard in bounded domains. A necessary condition of formation of wave attractors is the presence of a surface inclined with respect to gravity direction or rotations axis. In oceanology and astrophysics it is quite a general situation, when there are several simultaneous tidal forcings from multiples sources, also there may be modifications of stratification or rotation rate affecting wave beams directions. This is why studies of flows with multiple external forcings with different frequencies are of considerable interest both for quite separated frequencies, and close frequencies. In this work we will conventionally call the flows with accumulation of wave energy and subject to two external periodic forcings by biharmonic attractors. In case of finite difference between the frequencies one can expect that there will be independent attractors, corresponding to different frequencies, because inside the domain the beams propagate linearly, and nonlinear effects occur only near the boundaries. In case of close frequencies the regime is less obvious since beating effect can change the regime, and the mean level of kinetic energy and its pulsations are quite different from monochromatic regime. Also viscosity effects, which define the width of the attractors, change the flow of closely interacting attractors. For unstable and turbulent flows the scenarios of transitions and spectra of final regimes are substantially different for monochromatic forcing, biharmonic forcing and slow change of external frequency.

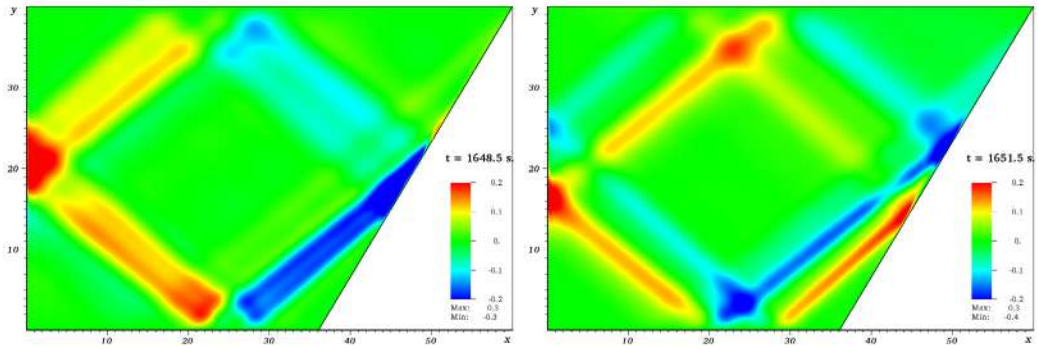

Vertical component of velocity for small-amplitude biharmonic forcing (laminar mode) with frequencies different by 1/20 of the first frequency.

References

[1] I. N. Sibgatullin and E. V. Ermanyuk. Internal and inertial wave attractors: A review. *Journal of Applied Mechanics and Technical Physics*, **60(2)**:284–302, 2019.
[2] C. Brouzet, I. N. Sibgatullin, E. V. Ermanyuk, S. Joubaud, and T. Dauxois. Scale effects in internal wave attractors. *Physical review fluids*, **2(11)**:114803, 2017.
[3] C. Brouzet, E. V. Ermanyuk, S. Joubaud, I. Sibgatullin, and T. Dauxois. Energy cascade in internal-wave attractors. *Europhysics Letters*, **113**:44001, 2016.
[4] T. Dauxois, S. Joubaud, P. Odier, and A. Venaille. Instabilities of Internal Gravity Wave Beams. *Annual Review of Fluid Mechanics*, **50**:131-156, 2018.

*Corresponding author. E-mail: sibgat@ocean.ru.

NUMERICAL INVESTIGATION OF WIND WAVE INTERATION

Jiarong Wu[1] and Luc Deike *[1,2]
[1]Department of Mechanical and Aerospace Engineering, Princeton, USA [2]High Meadows Environmental Institute, Princeton, USA

Summary In this study, we seek better physical understanding of surface wave interacting with a turbulent air flow by direct numerical simulations of the two phase Navier-Stokes equation with adaptive mesh refinement (AMR). A turbulent boundary layer flow interacts with a traveling wave train in a fully coupled manner, and we analyze the dynamics of the turbulent air and water flow, as well as the wave growth. We analyze the energy budget, in particular the wave growth rate, as well as the momentum budget, in particular the pressure and shear stress partition. We explore a wide range of controlling parameters in terms of wave age (ratio of wave speed over friction velocity) and wave slope.

INTRODUCTION

Wind wave interaction happens when wind blows across the water surface. The physics of this common but complex phenomenon is a long standing problem that attracts interests from both theoretical and practical point of view [1][2][3]. The complexity arises from the two-way coupling between turbulent air flow and gravity-capillary surface waves. As wind blows, it excites and amplifies waves and current through viscous shear stress and pressure forcing [4]; at the same time, the presence of a moving wavy boundary alters the turbulent boundary layer above significantly [5][6].

The momentum and energy transfer during this process provides valuable information for wave-resolved air-sea interaction modeling and has been the focus of many studies. However a detailed understanding of the small-scale dynamics including the coupling between the turbulent air and water flow through the waves is still incomplete. Indeed, it is very hard to obtain high resolution three dimensional experimental data near the moving water surface in field campaign and laboratory experiments to access the fluxes directly [6]. Numerical simulation presents an appealing alternative but the large range of scales involved has limited the ability to investigate the fully coupled two-phase flow problem. Direct numerical simulation (DNS) [5] and large eddy simulation (LES) [3] have been performed over the years, however, various degrees of simplifications were often made due to technical constraints and consideration of computational cost, typically resolving the waves with either the air or water turbulent layer, and use prescribed boundary conditions to represent the other side. Numerical simulation also enables investigation of the dynamics across a wider range of parameters, which is important because the dominant forcing mechanism can change under different flow conditions.

The present work leverages progress in adaptive mesh refinement algorithm for two-phase flows with the Basilisk framework to present simulations of the full coupling between idealized wave and the water and air turbulent boundary layer, without any prescribed boundary condition at the interface.

NUMERICAL SETUP

We solve the two phase Navier Stokes equation using volume of fluid (VOF) method to reconstruct the interface and with a momentum conserving AMR solver Basilisk[7] which has been extensively used and validated for complex multiphase flows [9]. Density and viscosity ratio between air and water ρ_a/ρ_w and μ_a/μ_w are kept constant using the realistic values across all simulations, while μ_w is varied to study Reynolds number effect. The problem can be described in terms of non-dimensional parameters: inverse wave age u_*/c, slope ak, friction Reynolds number Re_τ, and Bond number Bo defined as

$$Re_\tau = \frac{\rho_a u_* H}{\mu_a}, \; Bo = \frac{(\rho_w - \rho_a)g}{\sigma k^2} \tag{1}$$

u_*, c, H, a, k, g, σ are the friction velocity, wave phase speed, half channel height, initial amplitude, wave number, gravitational acceleration and surface tension respectively. We are restricted in the highest Re_τ we can reach because of the increasing resolution required to resolve the thinning viscous sub-layer. The numerical procedures are as follows:
Step 1: The air phase is initialized with a smooth wall turbulence profile and some random noise. The flow is driven by a constant bulk pressure gradient. The nominal air friction velocity u_* is related to the pressure gradient by

$$\rho_a u_*^2 = H \frac{\partial p}{\partial x} \tag{2}$$

The wavy boundary is initialized with a monochromatic Stokes wave of wave number k and amplitude a. The "wall" is kept stationary until the turbulence has reached a statistically stationary state.
Step 2: The water phase is initialized with solution based on third order Stokes wave orbital velocity [8] and released. The air and water phase evolve and interact without any prescribed kinematic or dynamic boundary conditions at the interface.

*Corresponding author. E-mail: ldeike@princeton.edu

We verify that the AMR grid is able to capture the turbulent boundary layer mean profile and statistics near the wall relatively well while keeping the total number of grids at a reasonable level. As shown in Figure 1, both the viscous linear profile and logarithmic profile are captured. The use of AMR and reasonably low resolution in the air layer will be used with higher resolution on the wave field to capture its development.

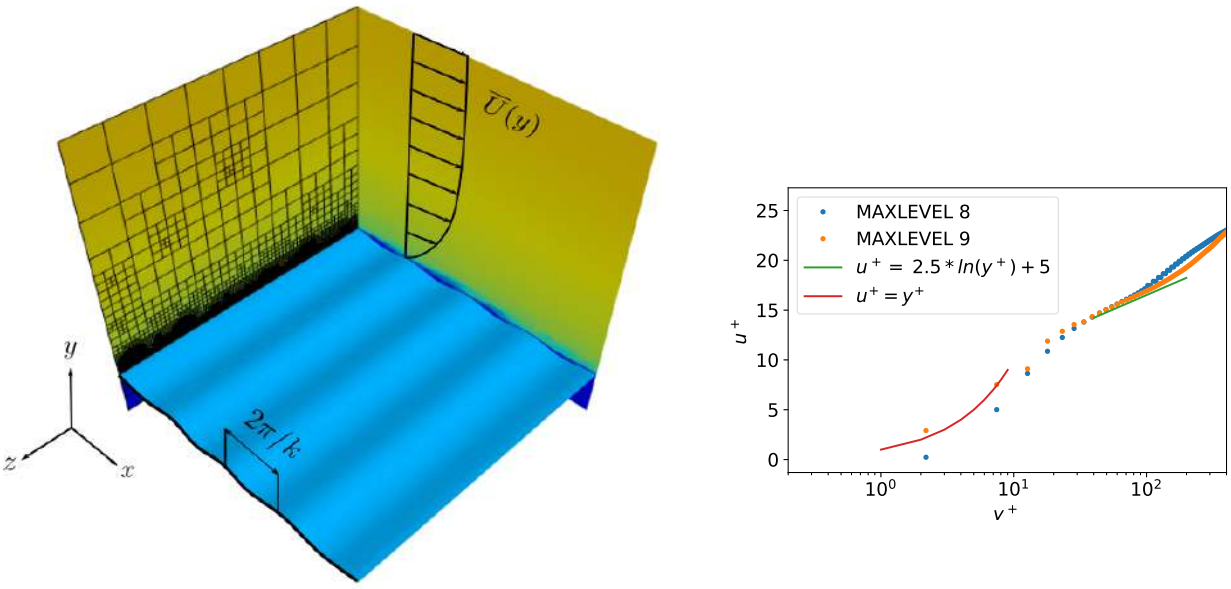

Figure 1: Left: numerical setup; right: reproduction of law of wall without the presence of waves. Refinement level convergence is verified. The friction Reynolds number Re_τ is 160.

RESULTS

The wave energy can be extracted from the mean square surface elevation and the non-dimensional growth rate $\overline{\beta}$ is computed as

$$E(t) = \rho_w g \langle \eta(t)^2 \rangle, \ \overline{\beta} = \frac{1}{\omega E(0)} \frac{dE}{dt} \tag{3}$$

We will discuss the scaling between $\overline{\beta}$ and the aforementioned parameters. From preliminary results at low initial amplitude, we recover the classic $\beta \propto (u_*/c)^2$, while observing threshold for wave growth that depends on the water viscosity. We observe and analyse the formation of a thin drift layer beneath the water surface.

DNS also provides us with detailed flow field data, therefore the momentum and energy partition between shear stress and pressure can be readily computed taking the value at the interface. Preliminary result confirms that most contribution to wave growth comes from pressure forcing. In addition, the time scale of wave growth is much bigger than the turbulence eddy turnover time, indicating that some of the averaging arguments are indeed applicable.

References

[1] Miles, J.W., 1957. On the generation of surface waves by shear flows. J. Fluid Mech. 3, 185.
[2] Phillips, O.M., 1957. On the generation of waves by turbulent wind. J. Fluid Mech. 2, 417.
[3] Sullivan, P.P., McWilliams, J.C., 2010. Dynamics of Winds and Currents Coupled to Surface Waves. Annu. Rev. Fluid Mech. 42, 19–42.
[4] Grare, L., Peirson, W.L., Branger, H., Walker, J.W., Giovanangeli, J.-P., Makin, V., 2013. Growth and dissipation of wind-forced, deep-water waves. J. Fluid Mech. 722, 5–50.
[5] Yang, D., Shen, L., 2010. Direct-simulation-based study of turbulent flow over various waving boundaries. J. Fluid Mech. 650, 131–180.
[6] Yousefi, K., Veron, F., Buckley, M.P., 2020. Momentum flux measurements in the airflow over wind-generated surface waves. J. Fluid Mech. 895, A15.
[7] Popinet, S., 2009. An accurate adaptive solver for surface-tension-driven interfacial flows. Journal of Computational Physics 228, 5838–5866.
[8] Deike, L., Melville, W.K. and Popinet, S., 2016. Air entrainment and bubble statistics in breaking waves.
[9] Mostert, W. and Deike, L., 2020. Inertial energy dissipation in shallow-water breaking waves. J. Fluid Mech. 890, A12.

ON WAVES ARISING FROM DRY GRANULAR COLLAPSE INTO WATER

Wladimir SARLIN*[1], Cyprien MORIZE[1], Alban SAURET[2], and Philippe GONDRET[1]
[1]Université Paris-Saclay,CNRS,Laboratoire FAST,F-91405 Orsay,France
[2]University of California, Santa Barbara, Department of Mechanical Engineering, USA

Summary Tsunami-like waves can arise from significant geological events such as the collapse of a mountain flank or a volcano into a lake or an ocean. We reproduce here this situation at the laboratory scale. The landslide is modeled by the sudden release of a rectangular granular column, which then impacts a still water layer and generates a wave. Through experiments varying both the column dimensions and the initial water height, three regimes of nonlinear waves of different shapes are reported.

INTRODUCTION

Tsunamis generated by landslides, debris avalanches or rockslides are highly destructive phenomena, with several occurrences in the last decades. Caused by major geological events involving large volumes of debris such as mountain or volcano collapses, they may result in the generation of high amplitude water waves. A well-known example is the case of Lituya Bay (Alaska, USA) in 1958 [1], when a rockslide volume of $30.10^6 m^3$ fell into water and produced the largest wave runup recorded in history, destroying neighbouring coastal areas up to an altitude of 524 m.
To describe the wave generation accurately, the granular nature of the falling mass needs to be taken into account [2, 3]. In the present work, we investigate experimentally the collapse of granular columns into water. Various initial conditions for the column dimensions and the initial water depth are considered, which generate waves of different shapes.

EXPERIMENTAL SETUP

Waves induced by granular collapses are experimentally reproduced using a setup described in [4]. A rectangular granular column of initial height H_0 and width L_0 is located above a water layer of height h_0, on the left-hand side of a tank of length 2 m and transverse width 0.15 m [Fig. 1 (a)]. The water is colored with fluorescein in order to enhance the contrast between water, air, and grains. Lifting the vertical sliding gate quickly releases the granular column, which impacts the water free-surface and generates a wave, as presented in Fig. 1 (b)-(d) for different initial conditions. The time evolution of the collapse and the wave is recorded with a camera, and image processing allows to extract the water free-surface and the dry and wet granular profiles. For the granular material, glass beads of diameter 5 mm and density 2500 $kg.m^{-3}$ are used. For different column aspect ratios $a = H_0/L_0$, the water height is varied to investigate the wave generation process in a large range of global Froude number $\mathrm{Fr}_0 = \sqrt{H_0/h_0}$, between 0.5 and 4.4. This dimensionless number compares the typical vertical free fall velocity of the grains $\sqrt{gH_0}$ to the classical velocity of linear waves in shallow water $\sqrt{gh_0}$.

RESULTS

The following parameters are systematically extracted from the movies of the experiments : the maximum wave amplitude A_m, the corresponding wave mid-height width λ_m, and the maximum horizontal velocity v_f of the granular front at the interface $z = h_0$. Doing so, it is possible to estimate a local Froude number $\mathrm{Fr}_f = v_f/\sqrt{gh_0}$, which compares the typical velocity of the collapse to the water wave velocity [4].

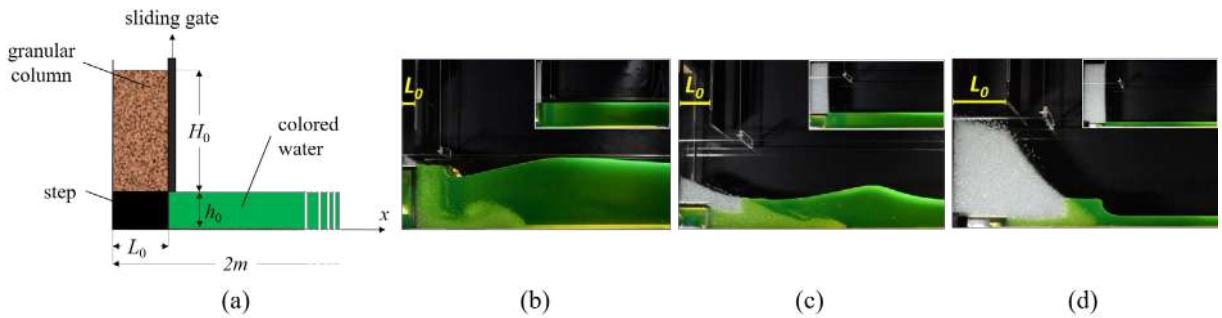

Figure 1: (a) Sketch of the experimental setup, and pictures of the different wave shapes observed for different initial conditions : (b) nonlinear transition wave ($H_0 = 39$ cm, $L_0 = 5$ cm, $h_0 = 25$ cm), (c) solitary wave ($H_0 = 29$ cm, $L_0 = 10$ cm, $h_0 = 9$ cm), and (d) hydraulic jump ($H_0 = 39$ cm, $L_0 = 14.5$ cm, $h_0 = 3$ cm). The inset of each figure shows the initial state of the experiment.

*Corresponding author. E-mail:wladimir.sarlin1@universite-paris-saclay.fr.

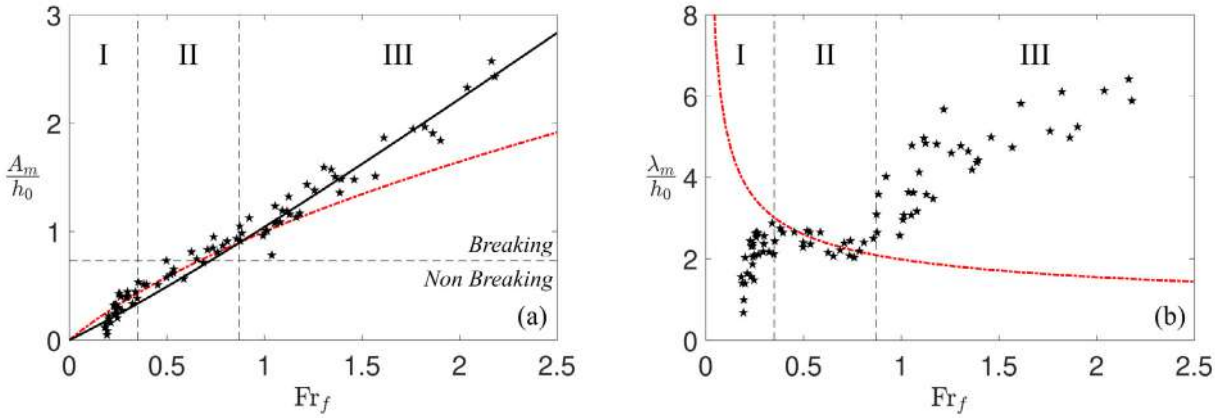

Figure 2: Evolution of (a) the relative amplitude A_m/h_0 and (b) the relative mid-height width λ_m/h_0 of the wave with the local Froude number Fr_f for all experiments (★), with predictions from Korteweg-de Vries solitary wave model (– – –), and from a hydraulic jump model (—); The two vertical dashed lines correspond to the transitions at $\mathrm{Fr}_f = 0.35$ between nonlinear transition waves (I) and solitary waves (II), and $\mathrm{Fr}_f = 0.87$ between solitary waves (II) and hydraulic jumps (III); The horizontal dashed line corresponds to the breaking criterion $A_m/h_0 = 0.73$.

For a given initial granular column, three distinct wave regimes are found when varying the initial water depth h_0, and thus the Froude numbers. For low values of the Froude numbers, a long primary wave followed by a weak dispersive wave train is observed (Fig. 1(b), for $\mathrm{Fr}_0 = 1.25$ and $\mathrm{Fr}_f = 0.19$), which corresponds to the nonlinear transition waves reported by [2] and [5]. At moderate Froude numbers, quasi-symmetrical solitary waves are observed (Fig. 1(c), for $\mathrm{Fr}_0 = 1.80$ and $\mathrm{Fr}_f = 0.52$), that can either break or not depending on the value of A_m/h_0 reached by the wave. Finally, for high Froude numbers, waves are close in shape to hydraulic jumps, breaking near the collapse region, due to the shock produced at the interface between grains and water (Fig. 1(d) for $\mathrm{Fr}_0 = 3.61$ and $\mathrm{Fr}_f = 1.86$).
Based on the local Froude number Fr_f, all data collapse onto a master curve for the relative wave amplitude A_m/h_0 [Fig. 2 (a)]. The first regime [I] observed for $\mathrm{Fr}_f \lesssim 0.35$, is very similar to the solution described by [6]. Waves are found to be highly unsteady, growing in amplitude until reaching a maximum, before flattening with a decreasing amplitude and a growing width. For $0.35 \lesssim \mathrm{Fr}_f \lesssim 0.87$ (regime [II]), waves are in good agreement with the Korteweg-de Vries theory (dash-dotted red curve in Fig. 2(a) and Fig. 2(b)), for both the amplitude and the mid-height width. Finally, for $\mathrm{Fr}_f \gtrsim 0.87$ (regime [III]), the hydraulic jump theory predicts well the maximum wave amplitude (solid black curve in Fig. 2(a)).

CONCLUSIONS

In this study, tsunami waves generated by a granular collapse display different shapes governed by a local Froude number Fr_f based on the horizontal velocity of the granular collapse at the water surface. For $\mathrm{Fr}_f \lesssim 0.35$, nonlinear transition waves are generated, whereas for $0.35 \lesssim \mathrm{Fr}_f \lesssim 0.87$, solitary waves are observed and well described by Korteweg-de Vries theory. Finally, for $\mathrm{Fr}_f \gtrsim 0.87$, hydraulic jumps arise in response to the strong shock at the interface. These experiments allow to characterize the hydrodynamics of landslide generated waves, for a range of initial conditions that cover most of the real cases observed in Nature [7].

References

[1] Fritz H., Hager W., Minor H. : Lituya Bay case: Rockslide impact and wave run-up. *Science of Tsunami Hazards* **19** : 3-19, 2001.
[2] Fritz H., Hager W., Minor H. : Near Field Characteristics of Landslide Generated Impulse Waves. *Journal of Waterway Port Coastal and Ocean Engineering* **130** : 287-302, 2004.
[3] Viroulet S., Sauret A., Kimmoun O. : Tsunami generated by a granular collapse down a rough inclined plane. *Europhysics Letters* **105**, 2014.
[4] Robbe-Saule M., Morize C., Henaff R., Bertho Y., Sauret A., Gondret P. : Experimental investigation of tsunami waves generated by granular collapse into water. *Journal of Fluid Mechanics* **907** : A11, 2021.
[5] Viroulet S., Cébron D., Kimmoun O., Kharif C. : Shallow water waves generated by subaerial solid landslides. *Geophysical Journal International* **193** : 747-762, 2013.
[6] Pelinovsky E., Talipova T., Kharif C. : Nonlinear-dispersive mechanism of the freak wave formation in shallow water. *Physica D: Nonlinear Phenomena* **147** : 83-94, 2000.
[7] Robbe-Saule M., Morize C., Bertho Y., Sauret A., Hildenbrand A., Gondret P. : Tsunamis generated by granular landslides: From laboratory experiments to geophysical events. *Submitted to Geophysical Research Letters*.

TRANSFER BETWEEN WAVES AND EDDIES IN STRATIFIED OR ROTATING TURBULENCE

Henri Lam*[1], Alexandre Delache[1,2], and Fabien S Godeferd[1]
[1]Laboratoire de Mécanique des Fluides et d'Acoustique, Univ Lyon, École centrale de Lyon, INSA Lyon, Université Claude Bernard Lyon I, CNRS, France
[2]Laboratoire de Mécanique des Fluides et d'Acoustique, Univ Lyon, site de Saint-Étienne, Université Jean Monnet de Saint-Étienne, CNRS, France

Summary We propose to separate the waves and eddies in stratified and/or rotating turbulence by using an extended method exposed in Lam et al. (2020) [1]. This separation takes into account the spatial and temporal distortion due to the advecting flow, which modifies the dispersion relation of the waves through the sweeping effect. From this separation, we analyse the transfers and interactions that occur between eddies and waves. Furthermore, this permits the analysis of the detailed energy cascade and fluxes from the input scale to the dissipative ones.

INTRODUCTION

Internal gravity waves (IGW) in the case of stratified turbulence and inertial waves (IW) in the case of rotating turbulence are waves sharing some remarkable properties. They both satisfy a dispersion relation linking their angular frequency ω and the direction of the wavevector $\mathbf{k}$. For IGW $\omega_r = \pm N \cos\theta$ and for IW $\omega_r = \pm 2\Omega \sin\theta$, where N is the Brunt-Väisälä frequency, Ω is the rotation rate and θ is the angle made by the wavevector $\mathbf{k}$ against the horizontal plane. This was experimentally shown in experiments and in simuations of IW propagation [3, 4], likewise for IGW in stratified flows [2]. However, the frequency of the waves can be modified by the sweeping effect (similar to the Doppler shift). This corresponds to the advection of the waves by a large scale, slowly varying in time background flow. In stratified turbulence, this corresponds to the vertically shear horizontal flow (VSHF) composed of large velocity band invariant in the horizontal direction and in rotating turbulence to the geostrophic mode (GM) composed of two opposite vortices invariant in the z direction. In a rotating experiment [4], the geostropic mode is shown to be the main responsible of the modification of the frequency of the waves through the sweeping effect. A new 4D decomposition has been proposed [1] that takes into account the frequency of the waves ω and its wave vector $\mathbf{k}$ to make an estimation of the sweeping effect to separate the waves from the eddies. It requires the estimation of a uniform and constant in time advecting velocity $\mathbf{c}$ responsible of the sweeping effect. Using this estimation the waves are separated from the eddies because the waves are expected to satisfy the inequality $\omega_r - |\mathbf{c}\cdot\mathbf{k}| \leq \omega \leq \omega_r + |\mathbf{c}\cdot\mathbf{k}|$.

SEPARATION TECHNIQUE OF WAVES AND EDDIES

We propose a new separation technique for waves and eddies where the advecting velocity $\mathbf{c}(\mathbf{x},t)$ varies in time and space. This allows us to take into account the non-uniform and the slow variation in time of the expected advecting velocity. This algorithm requires two stages:

1. The advecting flow of the DNS is extracted to convect the response of a linear Navier-Stokes equation forced by a series of Dirac forces in time and space. The dispersion relation of the waves is modified by the advecting flow $\mathbf{c}(\mathbf{x},t)$. A filter $\zeta(\omega,\mathbf{k})$ is created which considers waves to be in areas of the (ω, $\mathbf{k}$) space with a high level of energy. On the contrary eddies are expected to be in areas of the (ω, $\mathbf{k}$) space with a low level of energy.

2. The filter $\zeta(\omega,\mathbf{k})$ is applied to the original DNS to separate the waves from the eddies.

The Navier-Stokes equation with the Boussinesq approximation are solved on a pseudo-spectral code with a three-dimensional 2π periodic domain size. The forcing is done on the kinetic part of the Navier-Stokes equation, it consists of a constant influx of energy P. From this algorithm the velocity vector $\mathbf{u}$ and buoyancy field b are separated in a wave (superscript w), an eddy (superscript e) part and a large scale flow like the VSHF or GM (superscript L). We obtain $\mathbf{u} = \mathbf{u}^w + \mathbf{u}^e + \mathbf{u}^L$ and $b = b^w + b^e + b^L$.

ENERGY BUDGET AND TRANSFER IN STRATIFIED TURBULENCE

We illustrate here the results of our wave-eddy decomposition only for IGW in stratified turbulence, but similar results are obtained for IW in rotating flows. In a statistically stationary flow, with constant injected power P, we have an equation of energy budget for waves and eddies on a large period T_0 . In stratified turbulence whithout considering the VSHF flow, it is:

*Corresponding author. E-mail: henri.lam@ec-lyon.fr

$$0 = \partial_t E^w = T^w_{ee} + T^w_{we} + \epsilon^w + P^w$$
$$0 = \partial_t E^e = T^e_{ww} + T^e_{ew} + \epsilon^e + P^e \quad (1)$$

where the total dissipation is $\epsilon^l = \frac{1}{T_0}\int_{T_0}\sum_k \frac{\nu k^2}{2}(|\mathbf{u}^l|^2 + \frac{|b^l|^2}{N^2})$, the total energy is $E^l = \frac{1}{T_0}\int_{T_0}\sum_k \frac{1}{2}(|\mathbf{u}^l|^2 + \frac{|b^l|^2}{N^2})$ and the total transfer is $T^l_{ij} = \frac{1}{T_0}\int_{T_0}\sum_k(\mathbf{u}^i \times \boldsymbol{\omega}^j)\mathbf{u}^l - \frac{(\mathbf{u}^i\cdot\nabla b^j)b^l}{N^2}$. T^l_{ij} means that i interacts with j to give or take energy to l (the subscripts or superscripts i, j, l stand for w or e). The input of energy P due to the forcing is separated in an eddy P^e and a wave P^w input of energy.

The energy budget can be represented by a Sankey diagram (see Figure 1) where the width of the bar is proportional to the flow rate. The injected power P on the left is dissipated by ϵ^w and ϵ^e on the right and subject to different interactions T^l_{ij} where the color indicates the origin of the flow (red=w, blue =e). The overall energy transfer is from the waves with the transfers T^w_{ee} and T^w_{we}, and to the eddies with the transfers T^e_{ew} and T^e_{ww}. By exploring different values of Froude and buoyancy Reynolds numbers, we show that the maximum of energy transfer from waves to eddies occurs when both are of similar magnitudes (at $\mathrm{Re}_b \sim 1$). Similar analyses will be presented for rotating flows.

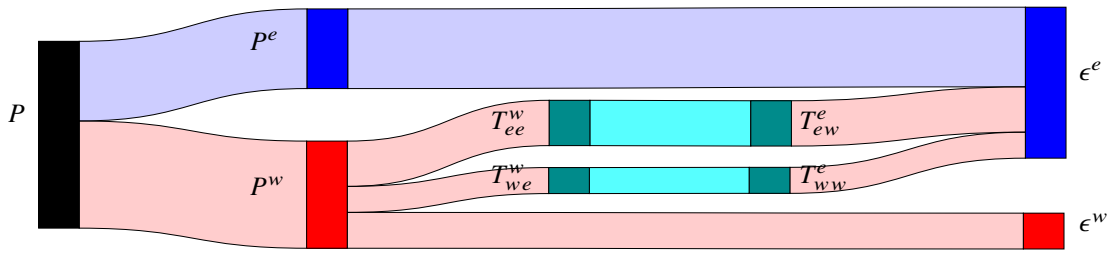

Figure 1: Energy budget for a DNS with buoyancy Reynolds number $\mathrm{Re}_b = 0.9$ and horizontal Froude number $\mathrm{Fr} = 0.015$.

It is hard to draw a clear pattern from the direct study of the fluxes of waves and eddies because they fluctuate a lot. Therefore, we decide to study these statistics through four values (see Figure 2):

- the total positive T^+ (resp. negative T^-) transfer, which correspond to the amount of energy given (resp. taken) from waves or eddies.
- the average scale of positive k^+ (resp. negative k^-) transfer T^+ (resp. T^-), which correspond to the scale at which on average the positive (resp. negative) transfer occurs.

For example, in Figure 2a, the strength of positive and negative transfer T^e_{ee} increases when the Froude number increases. It means that eddies interact more with each other when the flow is more turbulent. In Figure 2b, the transfer T^e_{ee} participates in a forward cascade (as $k^+ > k^-$), and we show that the forward cascade is stronger at high Froude number (when the flow is more turbulent). The same analysis can be done for the wave turbulence transfer T^w_{ww} and for all remaining transfers. Surprisingly, we observe that the wave-eddy interaction results in an inverse cascade for some Froude numbers.

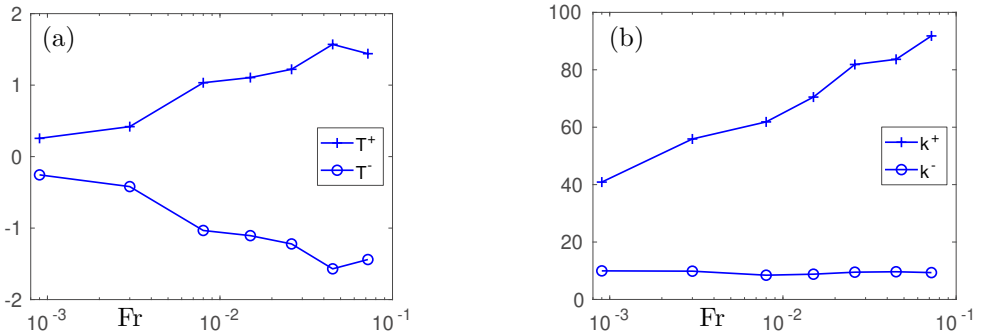

Figure 2: Statistics of the transfer T^e_{ee} for different Froude number. (a) Total positive $T^+$and negative transfer T^-. (b) Average scale of positive k^+ and negative k^- transfer.

References

[1] Lam H., Delache A., Godeferd F. S. Partitioning Waves and Eddies in Stably Stratified Turbulence. Atmosphere 11: 4, 2020
[2] Yarom E., Sharon E. Experimental observation of steady inertial wave turbulence in deep rotating flows Nature, 10: 7, 2014
[3] Le Reun T., Favier B., Barker A. J., Le Bars M. Inertial Wave Turbulence Driven by Elliptical Instability Phys. Rev. Lett., 119: 3, 2017
[4] Campagne A., Gallet B., Moisy F., Cortet P. Disentangling inertial waves from eddy turbulence in a forced rotating-turbulence experiment Phy. Rev. E, 91: 4, 2015

INFLUENCE OF TEMPERATURE ON EHD CONDUCTION PUMPING

Pedro A. Vázquez*[1], M. Talmor[2], and J. Seyed-Yagoobi[2]
[1]Department of Applied Physics III, E.T.S.I, Universidad de Sevilla, Sevilla, Spain
[2]Multi-Scale Heat Transfer Laboratory, Department of Mechanical Engineering, Worcester Polytechnic Institute, Worcester, MA 01609, USA.

Summary The performance of EHD conduction pumps depends on the temperature of the liquid. Seemingly contradictory trends have been reported in experimental works in the literature. We will use an analysis of the working regimes of the EHD pumps used in those papers to explain this behavior.

ABSTRACT

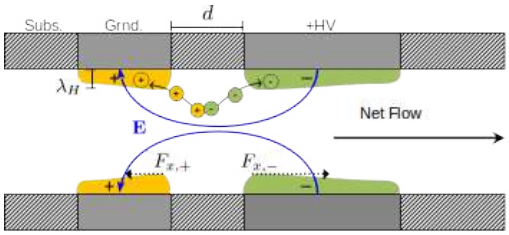

Figure 1: Illustration of the EHD conduction mechanism. The heterocharge layers locations are indicated in green and yellow. The corresponding polarity with respect to the electrodes is shown.

Electrohydrodynamic Conduction Pumping (EHDCP) of weakly conducting liquids is a very interesting practical application of Electrohydrodynamics (EHD) [2]. EHDCP pumps have no moving parts, are easy to miniaturize and to control. In previous works it has been shown that EHDCP works well for a wide range of pump sizes [4, 8, 7], even in absence of gravity [6]. This last feature makes these pumps especially suited for it use in satellites.

EHD flows are generated by electric forces acting on electric charges present in a liquid. In EHDCP systems the ions in the liquid are generated by dissociation of a weak electrolyte[1]. The application of an external electric field generates layers of net electric charge near each electrode, with opposite polarity. These are called heterocharge layers (see Figure 1). Their physical origin is the balance between electric drift and recombination of the ions in the liquid. The electric field acts upon these layers. If the layers have different sizes, the resulting effect is a net electric force that put the liquid into motion.

One of the main applications of EHDCP is the enhancement of heat exchange. Some contradictory results have been reported in the literature. Jeong et al.[3] observed that pressure generation and resultant mass flow rate decreased with increased temperature. However, Nourdanesh et al.[5] studied EHDCP of thin films of R-123 using flush electrodes and

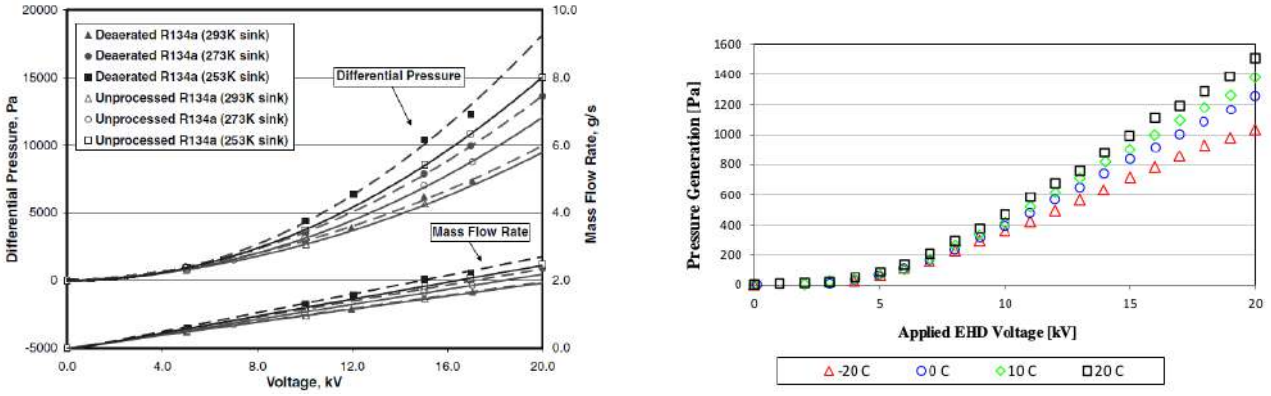

Figure 2: On the left, experimental results from Jeong et al.[3] showing increasing performance with decreasing temperature. On the right experimental results performed by Yang et al.[10] showing increasing performance with increasing temperature.

*E-mail: pvazquez@us.es

found that the generated flow rate increases with the working fluid temperature. Yang et al.[10] obtained similar results than Nourdanesh et al. with different liquids.

We will use the physical model presented in Vazquez et al.[9] to explain these seemingly contradictory results. The physical origin of this discrepancy lies in the different working regimes of these experiments. Two limit regimes can be describe in EHDCP: ohmic and saturation. The working regime can been characterized by two dimensional numbers: the conduction number C_0 and a new number β introduced in that paper. We will show the importance of this number β in the explanation of the different behaviors with temperature.

References

[1] P Atten and J Seyed-Yagoobi. Electrohydrodynamically induced dielectric liquid flow through pure conduction in point/plane geometry. *IEEE Transactions on Dielectrics and Electrical Insulation*, 10(1):27–36, 2003.

[2] A Castellanos, editor. *Electrohydrodynamics*. Springer-Verlag, 1998.

[3] Seong-Il Jeong and Jeffrey Didion. Performance Characteristics of Electrohydrodynamic Conduction Pump in Two-Phase Loops. *Journal of Thermophysics and Heat Transfer*, 22(1):90–97, 2008.

[4] Seong-il Jeong and Jamal Seyed-Yagoobi. Innovative electrode designs for electrohydrodynamic conduction pumping. *IEEE Transactions on Industry Applications*, 40(3):900–904, 2004.

[5] Nader Nourdanesh and Esmaeil Esmaeilzadeh. Experimental study of heat transfer enhancement in electrohydrodynamic conduction pumping of liquid film using flush electrodes. *Applied Thermal Engineering*, 50(1):327–333, 2013.

[6] Viral K Patel and Jamal Seyed-Yagoobi. A Mesoscale Electrohydrodynamic-Driven Two-Phase Flow Heat Transport Device in Circular Geometry and In-Tube Boiling Heat Transfer Coefficient Under Low Mass Flux. *Journal of Heat Transfer*, 137(4):41504, apr 2015.

[7] Matthew R. Pearson and Jamal Seyed-Yagoobi. Experimental study of EHD conduction pumping at the meso- and micro-scale. *Journal of Electrostatics*, 69(6):479–485, 2011.

[8] Muhammad a W Siddiqui and Jamal Seyed-Yagoobi. Experimental study of pumping of liquid film with electric conduction phenomenon. *IEEE Transactions on Industry Applications*, 45(1):3–9, 2009.

[9] Pedro A. Vázquez, Michal Talmor, Jamal Seyed-Yagoobi, Philippe Traoré, and Miad Yazdani. In-depth description of electrohydrodynamic conduction pumping of dielectric liquids: Physical model and regime analysis. *Physics of Fluids*, 31(11):113601, nov 2019.

[10] Lei Yang, Michal Talmor, and Jamal Seyed-Yagoobi. Effect of temperature on electrohydrodynamic conduction pumping performance. In *2014 IEEE 18th International Conference on Dielectric Liquids (ICDL)*, pages 1–4. IEEE, jun 2014.

THE DRESDYN PROJECT: BACKGROUND, STATUS, OUTLOOK

Frank Stefani*[1], Agris Gailitis[2], Gunter Gerbeth[1], André Giesecke[1], Thomas Gundrum[1], Peter Jüstel[1], Vivaswat Kumar[1], George Mamatsashvili[1], Ashish Mishra[1], Jude Ogbonna[1], Federico Pizzi[1], Matthias Ratajczak[1], Sebastian Röhrborn[1], Günther Rüdiger[3], Martin Seilmayer[1], Rodion Stepanov[4], Tobias Vogt[1], Tom Weier[1]

[1]Helmholtz-Zentrum Dresden-Rossendorf, Bautzner Landstr. 400, 01328 Dresden, Germany
[2]Institute of Physics, Latvian University, LV-2169 Salaspils 1, Riga, Latvia
[3]Leibniz-Institut f ür Astrophysik Potsdam, An der Sternwarte 16, D-14482 Potsdam, Germany
[4]Institute of Continuous Media Mechanics,1 Acad. Korolyov str., 614013 Perm, Russia

Summary We report the scientific background, the present construction status, and the prospects of the large-scale liquid sodium platform DRESDYN, which is devoted to experimental research into dynamo action and magnetically triggered flow instabilities.

INTRODUCTION

Magnetic fields are ubiquitous in the cosmos. They are being generated in planetary cores, stars, and entire galaxies by the homogeneous dynamo effect. Once produced, they can trigger instabilities in flows which would otherwise be hydrodynamically stable. The magnetorotational instability (MRI) figures most prominently here, since it can expedite dramatically the accretion process of central objects, such as protostars and black holes, from the accretion disks surrounding them. While widely considered as disjoint effects, self-excitation and magnetically triggered flow instabilities may well "conspire" in massively non-linear processes such as the MRI dynamo or the Tayler-Spruit dynamo.

Against the backdrop of a huge body of theoretical, numerical, observational investigations into cosmic dynamos and magnetically triggered flow instabilities, related experimental results are still scarce [1]. This has mainly to do with the significant technical effort needed to set-up flow experiments with high magnetic Reynolds numbers. The success of the pioneering liquid sodium experiments in Riga [2] and Karlsruhe [3] relied on careful optimizations of underlying paradigmatic models of single-scale and two-scale helical dynamos. The great accomplishments of the Cadarache experiment, in terms of showing field excursions and reversals [4], were achieved only when ferromagnetic propellers were used, which compromised the homogeneous character of this dynamo.

While the unanimous experimental proof of the standard version of MRI, with a purely axial magnetic field being applied, is still elusive, some related instabilities were successfully demonstrated in the liquid metal lab. This applies, in particular, to the helical [5] and the azimuthal [6] version of the MRI, as well as to the current-driven, kink-type Tayler instability (TI) [7]. Since these instabilities are governed by the Reynolds and the Hartmann number, they are much more easily realizable in liquid metal labs than standard MRI, whose onset depends on the magnetic Reynolds and the Lundquist number. As an interesting outcome of the numerical simulations dedicated to instabilities in liquid metals with their typical low magnetic Prandtl numbers, an intrinsic tendency for helicity oscillations was discovered and later exploited in a tidally synchronized Tayler-Spruit-type dynamo model [8], with possible ramifications for the solar dynamo.

THE PRECESSION DYNAMO EXPERIMENT

The most ambitious experiment in the framework of the *DREsden Sodium facility for DYNamo and thermohydraulic studies* (DRESDYN) is a large-scale liquid sodium experiment dedicated to the investigation of dynamo action in a precession-driven flow [9]. With diameter and height of the cylindrical vessel of 2 m each, and a planned rotation rate of 10 Hz, the experiment will attain a magnetic Reynolds number of 700. The turntable can rotate with up to 1 Hz. For maximum rotation and precession rates, the gyroscopic torque will reach values up to 8 MNm, which requires an extremely solid mechanical frame with a ground plate resting on 7 pillars reaching 22 meters into the bedrock. Figure 1 shows some impressions of the recent status of the experiment. First water experiments are planned for the end of 2020.

Besides the significant technical and safety related challenges of this experiment, some basic question about precession driven flows and their dynamo action are non-trivial as well. It has been known for some time that precession driven-flows in cylinders (and, very similarly, also in spheroids) undergo a (hysteretic) transition between a laminar regime and turbulent regime at a precession ratio (or Poincaré number) of around 0.1. Combining numerical simulations with experimental results from a 1:6 downscaled water experiment, this transition was shown to rely on the modified flow rotation profile just becoming Rayleigh-unstable, leading to the formation of a secondary Taylor vortex flow in a narrow window of the precession ratio. It is this Taylor vortex flow, together with the overall rotation and the basic forced m=1 Kelvin mode, which appears to be well suited for dynamo action. Present simulations with a kinematic dynamo code [10] point to a critical magnetic Reynolds number of around 430, which is safely below the technically reachable value of 700. Further detailed experimental and numerical investigations, including the flow structures at further nutation angles between 135° and 45° degrees, will refine the predictions for the large-scale experiment.

---

*Corresponding author. E-mail: F.Stefani@hzdr.de

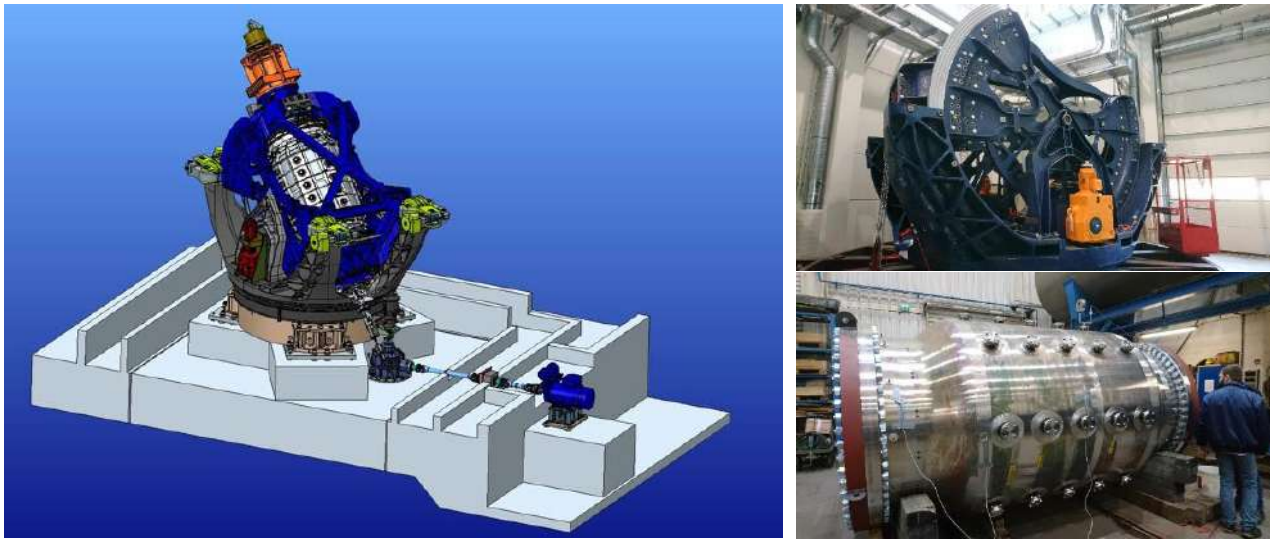

Figure 1. Schematic (left) and some impressions from the construction of the DRESDYN precession dynamo experiment: Test installation of the frame and tilting machine (right top), rotation vessel during pressure test (right bottom).

EXPERIMENTS ON MRI, TI, AND THEIR COMBINATIONS

The second largest experiment in the framework of DRESDYN is a versatile liquid sodium Taylor-Couette experiment for the study of various forms and combinations of MRI and TI. While its design parameters will allow for attaining standard MRI, there is much interesting physics to be studied in the region between the helical MRI and standard MRI, or between azimuthal MRI and TI, for that matter. It remains to be seen whether the recently discovered new form of helical MRI for flows with positive shear [11], which may be highly relevant for the near-equator regions of the solar tachocline, can also be investigated in this experiment.

CONCLUSIONS AND PROSPECTS

DRESDYN builds on the success of recent liquid metal experiments dedicated to dynamo action and magnetically triggered flow instabilities and tries to stretch the relevant parameters to the edge of technical manageability, thereby aiming, in particular, at the experimental demonstration of dynamo action in a truly homogeneous fluid, and at the transition from helical MRI to standard MRI. However, DRESDYN, with its entire sodium and safety infrastructure, is also a flexible platform for further installations, with a large Rayleigh-Bénard experiment under the influence of rotation and/or magnetic fields being one of the most obvious options.

References

[1] Stefani F., Gailitis A., Gerbeth G. Magnetohydrodynamic experiments on cosmic magnetic fields. *ZAMM* **88**: 930-954, 2008.
[2] Gailitis A. et al. Self-excitation in a helical liquid metal flow: the Riga dynamo experiments. *J. Plasma Phys*. **84**: 735840301, 2018.
[3] Müller U. et al. The Karlsruhe two-scale dynamo experiment. *Comptes R. Phys*. **9**: 729-740, 2008.
[4] Monchaux R. et al. The von Kármán sodium experiment: Turbulent dynamical dynamos. *Phys. Fluids* **21**: 035108, 2009.
[5] Stefani F. et al. Helical magnetorotational instability in a Taylor-Couette flow with strongly reduced Ekman pumping. *Phys. Rev. E* **80**: 066303, 2009.
[6] Seilmayer M. et al. Experimental evidence for nonaxisymmetric magnetorotational instability in a rotating liquid metal exposed to an azimuthal magnetic field. *Phys. Rev. Lett.* **113**: 024505, 2014.
[7] Seilmayer M. et al. Experimental evidence for a transient Tayler instability in a cylindrical liquid-metal column. *Phys. Rev. Lett.* **108**: 244501, 2012.
[8] Stefani F., Giesecke A., Weier T. A model of a tidally synchronized solar dynamo. *Solar Phys.* **294**: 60, 2019.
[9] Stefani F. et al. The DRESDYN project: liquid metal experiments on dynamo action and magnetorotational instability. *GAFD* **113**: 51-70, 2019.
[10] Giesecke A. et al. Nonlinear large scale flow in a precessing cylinder and its ability to drive dynamo action. *Phys. Rev. Lett.* **120**: 024502, 2018.
[11] Mamatsashvili G. et al. Two types of axisymmetric helical magnetorotational instability in rotating flows with positive shear. *Phys. Rev. Fluids* **4**: 103905, 2019.

HEAT TRANSFER IN LIQUID METAL DUCT FLOWS UNDER A STRONG UNIFORM MAGNETIC FIELD

Gregory J. Sheard
Department of Mechanical and Aerospace Engineering, Monash University, Melbourne, Australia

Summary Numerical simulation of fluid flow and heat transfer within ducts under a strong, uniform magnetic field is reported, motivated by the need for effective transport of heat from future magnetic confinement fusion reactors. The propensity of the flow to two-dimensionalise in the field direction permits employment of a computationally efficient quasi-two-dimensional model. Heat transfer is enhanced through the inclusion of physical obstacles within the duct designed to invoke convective heat transport. Electrically driven vortices are a promising alternative to physical obstacles, reducing duct pressure drop. Linear optimal growth analysis informs an active mechanism for increased heat transport behind a duct obstacle. Finally, three-dimensional quasi-static low magnetic Reynolds number simulations reveal the shift to quasi-two-dimensional dynamics with increasing Hartmann number.

INTRODUCTION

Hydrogen fusion powers our sun and stars throughout the universe, and has long stood as a tantalising cleaner and safer alternative to nuclear fission for terrestrial power generation. One technology being explored as an avenue towards viable fusion power generation is magnetic confinement, in which very strong magnets confine a hot plasma of the heavier hydrogen isotopes deuterium and tritium sufficiently to facilitate a fusion burn.

The ultimate goal is to harness the emitted heat to produce steam for electricity generation, which could be achieved using heat exchange principles involving coolant flow within ducts surrounding the reactor. Furthermore, the global scarcity of tritium necessitates its production as part of a viable reactor system. This can be achieved via a breeder reaction involving the bombardment of lithium with neutrons released from the fusion reaction (the helium-cooled lithium-lead, HCLL, breeding module to be trialled in the forthcoming ITER reactor is an example, in which a hot liquid lithium-lead alloy flows through ducts facing the plasma). The strong confining magnetic fields dampen and laminarise the flow, inhibiting heat transfer within ducts. This problem motivates the presented research, which seeks to investigate mechanisms for heat transfer enhancement within liquid-metal duct flows under strong magnetic fields.

METHODOLOGY

Given velocity and length scales U and L, this work assumes a small magnetic Reynolds number ($Re_m = UL/\eta$, where magnetic diffusivity $\eta = 1/\mu\sigma$, magnetic permeability is μ and electrical conductivity is σ), such that the magnetic field within the flow is approximately the surrounding uniform field $\boldsymbol{B}$. For a field acting orthogonal to two of the duct walls, Hartmann layers will form having thickness scaling with Ha^{-1}, where Hartmann number $Ha = aB\sqrt{\sigma/\rho\nu}$. Here a is the distance between the Hartmann walls, ρ the fluid density and ν its kinematic viscosity. Where it can be assumed that both the Hartmann number and interaction parameter (representing the ratio of electromagnetic to inertial forces) $N = \sigma B^2 a/\rho U$ are well in excess of unity, [1,2] demonstrate that outside of the Hartmann layers, these flows two-dimensionalise in the magnetic field direction. This permits the three-dimensional duct flow to be solved on a two-dimensional domain, with Hartmann layer friction captured via the addition of a linear braking term in the (two-dimensional) momentum equation. This will be referred to as the SM82 model hereafter. Heat transport is simulated via an advection-diffusion equation. The contributions of viscous dissipation and Joule heating are assumed to be insignificant and are neglected. Where $Ha \gg 1$ or $N \gg 1$ cannot be assumed, full three-dimensional direct numerical simulation using the quasi-static MHD approximation valid for low magnetic Reynolds numbers ($Re_m \ll 1$) is performed. This introduces the electric potential field ϕ.

Flows are predominantly computed using an in-house solver employing a nodal spectral element method on a conforming grid of high-order quadrilateral elements. Three-dimensional quasi-static MHD simulations employ a spectral element discretisation of across the duct cross-section and a periodic Fourier spectral discretisation in the flow direction. Time integration is via a third-order accurate backwards differentiation operator-splitting scheme [3].

RESULTS

To begin, flow in a duct under the SM82 model is computed, with a cold inflow and one hot duct side-wall. Various obstacles and duct widths (transverse to the field direction) are computed, and a range of Reynolds numbers and Hartmann numbers are considered. As reported in [4], a cylindrical obstacle with circular cross-section and axis aligned with the magnetic field is placed in ducts of several blockage ratios (β). Heat transfer was strongly dependent on Re, Ha and β, with the inception of vortex shedding producing a significant uplift in heat transfer (Nusselt number Nu), as demonstrated in Figure 1. This work was developed in [5], identifying an optimal gap between the obstacle and the hot duct wall. Following this, an obstacle of rectangular cross-section is considered [6], in which orientation angle and hot-wall gap ratio are optimised for further enhancement in heat transfer. A comparison between three representative obstacle shapes (circular, square and triangular) is conducted [7], where it is found that the triangular cross-section produces superior heat transfer enhancement.

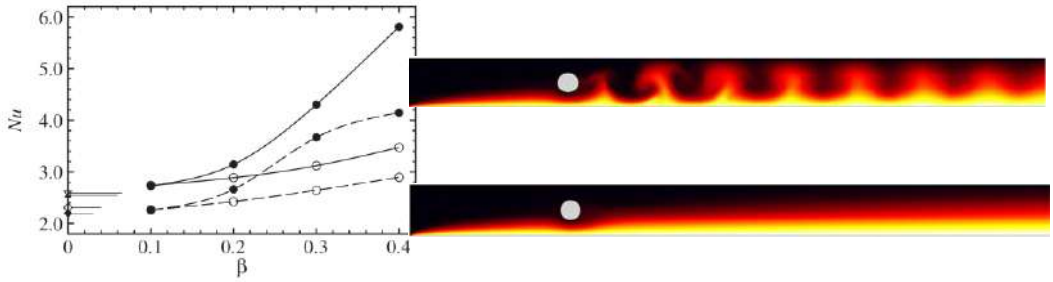

Figure 1. Nusselt number dependence on blockage ratio (β) at $Re = 2000$ (dashed lines) and $Re = 3000$ (solid lines). Inset contour plots of temperature (flow left to right) demonstrate that the uplift in heat transfer is due to mixing induced by vortex shedding convecting hot fluid into the core of the duct at low and high Ha.

An unusual property of these quasi-two-dimensional MHD flows is that electric current injected from an electrode embedded in one of the Hartmann walls spreads radially from the electrode over the Hartmann wall, driving rotation in a two-dimensional column of fluid across the core. An alternating current can then be tuned to produce a vortex street [8,9]. Electrically generated vortex streets are found to be effective for heat transfer enhancement, additionally avoiding the pressure drop penalty created by a physical obstacle. Given the prominent role of vortex shedding in enhancing heat transfer, and the increased suppression of vortex shedding at higher Ha, a linear transient growth analysis is used to better understand the optimal initial disturbances maximising kinetic energy growth over short time intervals [10,11]. A model for wake vortex decay is constructed, revealing conditions where viscous dissipation or Hartmann braking dominate [12].

The role of natural convection on the stability of SM82 duct flows is considered using a one-dimensional linear stability analysis [13]. Finally, an optimal growth analysis of three-dimensional quasi-static MHD duct flow [14] demonstrates the striking fidelity of the SM82 model at high Ha, and reveals the morphology from low-Ha hydrodynamic behaviour to high-Ha quasi-two-dimensional behaviour.

ACKNOWLEDGEMENTS

This presentation draws from the research of former PhD students Wisam K. Hussam, Ahmad H. A. Hamid and Oliver G. W. Cassells and postdoctoral fellow Dr Tony Vo, with contributions from Dr Zhi Ng and Professor Mark C. Thompson. Professor Alban Pothérat has made indelible contributions to this research. G.J.S. is grateful for the support of the Australian Research Council Discovery Project grant scheme (DP120100153, DP150102920, DP180102647), high-performance computing grants availed with support of the Australian Government through the National Computational Merit Allocation Scheme, the Monash eResearch Centre, and international travel support from The Royal Society (grant number IE170034).

References

[1] Sommeria, J., Moreau, R. Why, how, and when, MHD turbulence becomes two-dimensional. *J. Fluid Mech.* **118**: 507–518, 1982.

[2] Pothérat, A., Sommeria, J., Moreau, R. An effective two-dimensional model for MHD flows with transverse magnetic field. *J. Fluid Mech.* **424**: 75–100, 2000.

[3] Karniadakis, G. E., Israeli, M., Orszag, S. A. High-order splitting methods for the incompressible Navier–Stokes equations. *J. Comput. Phys.* **97** (2): 414–443, 1991.

[4] Hussam, W. K., Thompson, M. C., Sheard, G. J. Dynamics and heat transfer in a quasi-two-dimensional MHD flow past a circular cylinder in a duct at high Hartmann number. *Int. J. Heat Mass Transf.* **54** (5): 1091-1100, 2011.

[5] Hussam, W. K., Sheard, G. J. Heat transfer in a high Hartmann number MHD duct flow with a circular cylinder placed near the heated side-wall. *Int. J. Heat Mass Transf.* **67**: 944-954, 2013.

[6] Cassells, O. G. W., Hussam, W. K., Sheard, G. J. Heat transfer enhancement using rectangular vortex promoters in confined quasi-two-dimensional magnetohydrodynamic flows. *Int. J. Heat Mass Transf.* **93**: 186–199, 2016.

[7] Hussam, W. K., Hamid, A. H. A., Ng, Z. Y., Sheard, G. J. Effect of vortex promoter shape on heat transfer in MHD duct flow with axial magnetic field. *Int. J. Thermal Sci.* **134**: 453-464, 2018.

[8] Hamid, A. H. A., Hussam, W. K., Sheard, G. J. Heat transfer augmentation of a quasi-two-dimensional MHD duct flow via electrically driven vortices. *Numer. Heat Transf. A-Appl.* **70** (8): 847-869, 2016.

[9] Hamid, A. H. A., Hussam, W. K., Sheard, G. J. Combining an obstacle and electrically driven vortices to enhance heat transfer in a quasi-two-dimensional MHD duct flow. *J. Fluid Mech.* **792**: 364-396, 2016.

[10] Hussam, W. K., Thompson, M. C., Sheard, G. J. Optimal transient disturbances behind a circular cylinder in a quasi two-dimensional magneto-hydrodynamic duct flow. *Phys. Fluids* **24** (2): 024105, 2012.

[11] Hussam, W. K., Thompson, M. C., Sheard, G. J. Enhancing heat transfer in a high Hartmann number magnetohydrodynamic channel flow via torsional oscillation of a cylindrical obstacle. *Phys. Fluids* **24** (11): 113601, 2012.

[12] Hamid, A. H. A., Hussam, W. K., Pothérat, A., Sheard, G. J. Spatial evolution of a quasi-two-dimensional Kármán vortex street subjected to a strong uniform magnetic field. *Phys. Fluids* **27** (5): 053602, 2015.

[13] Vo, T., Pothérat, A., Sheard, G.J. Linear stability of horizontal, laminar fully developed, quasi-two-dimensional liquid metal duct flow under a transverse magnetic field and heated from below. *Phys. Rev. Fluids* **2** (3): 033902, 2017.

[14] Cassells, O.G.W., Vo, T., Pothérat, A., Sheard, G.J. From three-dimensional to quasi-two-dimensional: Transient growth in magnetohydrodynamic duct flows. *J. Fluid Mech.* **861**: 382-406, 2019.

INTERACTIONS BETWEEN TWO BUBBLES RISING SIDE BY SIDE UNDER THE INFLUENCE OF MAGNETIC FIELD

Jie Zhang*[1] and Mingjiu Ni[2,1]
[1]State Key Laboratory for Strength and Vibration of Mechanical Structures, School of Aerospace, Xi'an Jiaotong University, Xi'an 710049, China
[2]School of Engineering Science, University of Chinese Academy of Sciences, Beijing, China

Summary A series of 3D numerical results are reported about the interactive behaviors between a pair of bubbles rising side by side in the liquid metal, and different magnetic fields are imposed to investigate the magnetohydrodynamics effects on the bubble interactions. It is observed that while a streamwise magnetic field always lead a bounced bubble pair to coalescence, however a horizontal magnetic field has an anisotropic effect on the bubble interaction depending on the direction of the field, particularly, a spanwise magnetic field has an non-monotonous influence on the bubble interaction while a transverse one always spur the two bubble to coalesce. A detailed investigation indicates different bubble interactions come from different vortex evolutions in magnetic fields.

INTRODUCTION AND NUMERICAL METHODS

In the metallurgical industry, external magnetic fields (MFs, hereafter) are one of the rare potential tools to control the motion of bubble plume which are used for metallurgical refining or smelting, objective to homogenize the physical and chemical properties of the liquid metal. Consequently, the combination of external MFs and gas bubble injections enables the liquid metal to produce an optimized environment for the final product quality. Nevertheless, the understanding of such bubbly flows under magnetohydrodynamics (MHD, hereafter) effect is far from satisfactory, and more seriously, how an external MF affect the interactions between the one bubble pair is unclear yet. Previously in ordinary fluids without MFs[1], our numerical results indicate that the increased shear inside the gap between the bubble pair will promote the strength of the double-threaded vortices, which would finally produce a lift force to cause the bubble pair to bounce. This finding, which confirms the importance of the vortex interactions during the bubble collisions, implies that the external MFs will have great influences on the bubble interactions because the vortex structures are known to be sensitive to the MF directions and strengths[2, 3].

Physically, the incompressible bubble flows under the influence of an external MF are governed by the combination of Navier-Stokes equations and the Maxwell equations, and a Lorentz force term is produced due to the coupling of the flow field and the magnetic field, given that $\boldsymbol{F}_l = \boldsymbol{J} \times \boldsymbol{B}$, where $\boldsymbol{J}$ denoting the induced current density and $\boldsymbol{B}$ being the external MF. Note that $\boldsymbol{J}$ is obtained from Ohm's law, given that $\boldsymbol{J} = \sigma_e(-\nabla\varphi + \boldsymbol{u} \times \boldsymbol{B})$ where σ_e being the electric conductivity and φ representinng the induced electric potential, φ is calculated by solving the electric potential Poisson equation due to the divergence-free condition of $\nabla \cdot \boldsymbol{J} = 0$. Typical dimensionless parameters are the Reynolds number (Re), the Weber number (We), the Gallilei number (Ga) and the Bond number (Bo), besides, a variant interaction number of $N_o = \sigma_e B^2 D/\rho u$ is used to characterize the strength of the MF, where D is the bubble diameter and $u = \sqrt{gD}$ is the characteristic velocity.

The numerical solver is as the same as that used in our previous study[1], that a volume-of-fluid approach is used for the interface tracking, and an adaptive mesh refinement (AMR) technique is used to capture the interface more accurately during the bubble motion. Note that besides a spatial resolution of $\Delta_i = D/60$ is set close to the bubble interface, additional local refinement is imposed in vicinity of the thin film between the bubble pair until a minimum mesh size of $\Delta_f = D/400$ is reached, and we will let the two bubbles coalesce numerically if the thickness of the film is thinner than this threshold. Two bubbles with a diameter of $D = 3mm$ are released freely at the bottom of the container which filled with liquid metal GaInSn, then the bubbles will rise under gravity that the shape deformation is permitted. With the help of this numerical tool, we will investigate the interactive behaviors between the bubble pairs when different magnetic fields are imposed externally, and more importantly, the role of the vorticity it plays in the interaction is studies in more details.

RESULTS

Firstly, the influences of the streamwise MF on the interactions between a pair of bubbles are presented, and the MF strength is varied within $N = 0$, $N_y = 0.09$, $N_y = 0.20$ and $N_y = 0.80$, while the corresponding rising trajectories of the bubble pair are presented in Fig. 1. In case of $N = 0$, the two bubbles bounce off at $H = 5.5$, however, if the magnetic field is as strong as $N \geq 0.09$, the two bubbles will coalesce instead of bounce, and clearly, the coalescence height is decreasing with intensified streamwise MFs. It means the streamwise MF weakens the collision between the two bubbles. As already verified previously[1], the bubble interaction is closely related to the vortex developments during bubble the approaching, and strong vortex interactions will produce greater lift force to make the bubble bounce off, otherwise the two bubbles will coalesce. Consequently, the vortex evolutions under the influence of streamwise MF are also studies, as plot in Fig. 2 whereas the dark and light contours denote $\omega_y = \pm 2.0$ repectively. It is clearly observed that streamwise MF tends to reduce the streamwise vortices, and thus the vortex interactions are significantly weakened that the bubble pair is coalesced instead of bouncing.

*Corresponding author. E-mail: j_zhang@xjtu.edu.cn

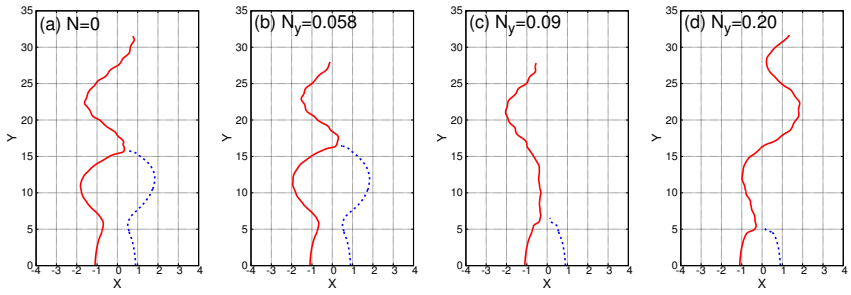

Figure 1: Rising paths of the bubble pairs exposed to different streamwise MFs, within a wide parameter spaces from $N = 0$ to $N_y = 0.80$. With an intensified streamwise MF, it is observed the interactions between the bubble pair to change from bounce to coalescence, indicating that the MF tends to weaken the interactive strengths.

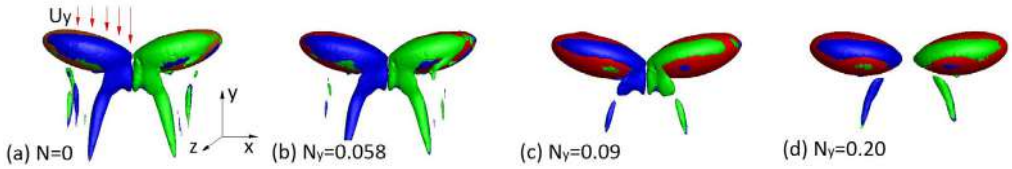

Figure 2: Streamwise vortices behind the bubble pairs at the "kissing" moment while the streamwise MF is varied between $N = 0$ and $N_y = 0.20$, and the iso-contours correspond to $\omega_y = \pm 1$. It is clear that the streamwise MF tends to weaken the double-threaded vortices behind the bubble pair, so that the bubble interaction is also diminished.

On the other hand, the influences of the spanwise (transverse) MF are also studies that the B-lines are parallel (perpendicular) to the line connecting the bubble centroid. The rising trajectories of the bubble pair indicate that the MHD effects are totaly different depending on the field direction, a weak-to-moderate spanwise MF makes the interaction between two bubbles change from bouncing to coalescence, however, a strong spanwise MF cause them to bounce or even repel again. In contrast, the transverse MF always spurs the two bubble to coalesce instead of repelling. After that, detailed investigations are carried out on the vortex evolutions during the bubble motion, and the mechanisms produing such anisotropic effects are detected. It implies developments of the vortices comply to the MHD theory[2, 3], which reveals the vorticity diffusion along the B-lines is enhanced so that a spanwise MF induces much stronger vortex interaction along the B-Lines, consequently, a strong spanwise MF causes the two bubbles to repel rather than coalescence. In contrast, the vortex interaction inside the gap between the two bubbles is nearly uninfluenced, so that the more spheroidal shape under transverse MF makes the bubble pair to coalesce.

References

[1] Jie Zhang, Long Chen, and Ming-Jiu Ni, Vortex interactions between a pair of bubbles rising side by side in ordinary viscous liquids, *Physical Review Fluids* **4**, 043604, 2019.
[2] René J Moreau, *Magnetohydrodynamics*, Vol. 3 (Springer Science andxt Business Media, 2013).
[3] Peter Alan Davidson, *An introduction to magnetohydrodynamics*, Cambridge Press, 2002.

TWIST EFFECTS ON THE EVOLUTION OF KNOTTED FLUX TUBES

Yue Yang*[1] and Shiying Xiong [1]
[1]State Key Laboratory for Turbulence and Complex Systems, College of Engineering, Peking University, Beijing 100871, China

Summary We develop a general method for constructing knotted flux tubes with the finite thickness, arbitrary shape and tunable twist. The helicity of the corresponding knotted field can be explicitly decomposed into the writhe, localized torsion and intrinsic twist. We construct several knotted magnetic flux tubes with various twisting degrees, and reveal twist effects on their evolution in resistive magneto-hydrodynamics flows using direct numerical simulation. The magnetic knot gradually shrinks to a tight stable state for large twist, whereas it splits at early times for small twist. The mechanism of the tube split is then elucidated using the phase portrait of the Lorentz force projected onto divergence-free space.

INTRODUCTION

Understanding the configuration and evolution of magnetic structures in magneto-hydrodynamics (MHD) flows is of fundamental importance for the device design and stability analysis in nuclear fusion and the corona dynamics in astrophysics. The knotted flux tube is a typical magnetic configuration with nontrivial topology and relatively simple geometry, so it is often used for investigating essential dynamics in MHD flows. For characterizing knotted fields, the helicity H is a topological measure of linking and knotting of field lines. In the present study, we extend the methods of Gold and Hoyle [1] and Xiong and Yang [2] to construct knotted flux tubes with the arbitrary shape and tunable twist. The constructed vector fields can be used as the initial magnetic field $\boldsymbol{b}$ in the direct numerical simulation (DNS) of MHD flows. In particular, we reveal the effects of the initial twist T_w of field lines on the evolution of trefoil flux tubes, and elucidate the mechanism of topological changes of magnetic fields in resistive MHD.

CONSTRUCTION OF COILED AND TWISTED FLUX TUBES

From the parametric equation of a given smooth and non-degenerate closed curve, we construct a vector field based on a curved cylindrical coordinate system along the curve. The vector has axial and azimuthal components. The axial component is determined by a given kernel function which decays with the radial distance from the curve. The azimuthal component is derived from our proposed constraints. We prove that this vector field is strictly divergence-free, so it can be used as the initial field of a magnetic tube whose central axis is prescribed by the curve. Within the framework of Chui and Moffatt [3], we derive the expression of H for the constructed vector field. This helicity can be explicitly decomposed into the writhe, localized torsion and intrinsic twist [4]. The sum of latter two components is referred to as the "twist" in this paper. Thus we can isolate the effect of each component in the investigation of helicity.

Corresponding to the theoretical construction, we extend the algorithm in Ref. [2] to construct knotted flux tubes with tunable twist in Cartesian coordinates (see Fig. 1). The relative numerical errors in the helicity calculation of trefoil flux tubes with a range of T_w from 0 to 32.48 are negligible on 512^3 unform grid points in a periodic box.

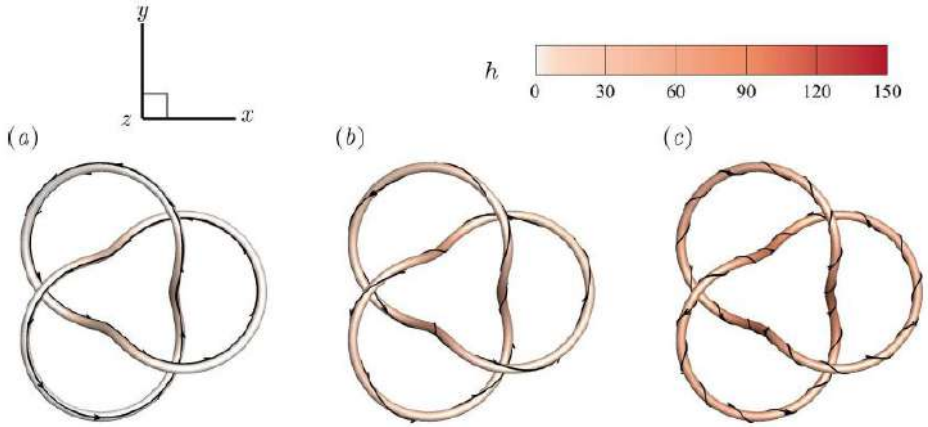

Figure 1. Initial knotted flux tubes with (a) $T_w = 0$, (b) $T_w = 12.48$, and (c) $T_w = 32.48$. The surfaces are color-coded by the helicity density h. Some field lines are integrated on the surfaces.

EVOLUTION OF KNOTTED FLUX TUBES

We use the constructed vector fields as initial magnetic inductions in DNS, and calculate the evolution of trefoil magnetic flux tubes with various T_w in resistive MHD flows. We find that T_w has an impact on the evolution of magnetic

*Corresponding author. E-mail: yyg@pku.edu.cn

knots (see Fig. 2). For large T_w, the magnetic knot gradually shrinks to a tight stable state, similar to the relaxation process in ideal MHD flows. For small T_w, the knotted flux tube splits and reconnects at early times, accompanied by the drastic release of the magnetic energy.

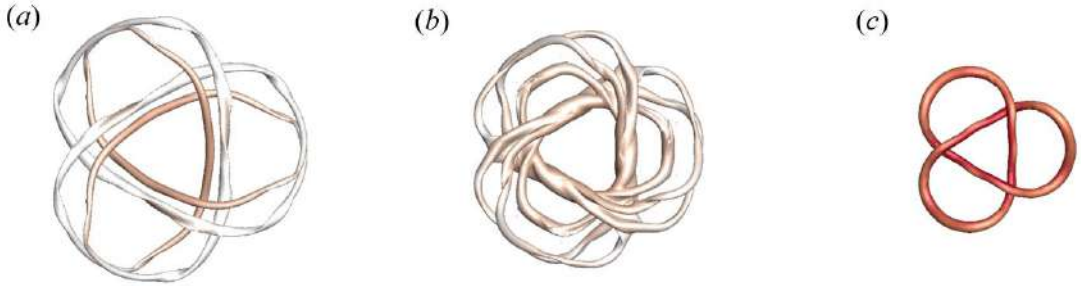

Figure 2. Isosurfaces of $|\boldsymbol{b}|$ in the temporal evolution of trefoil flux tubes with (a) $T_w = 0$, (b) $T_w = 12.48$, and (c) $T_w = 32.48$ at a late time $t = 0.1$. All the isosurfaces are color-coded by the helicity density

The effect of twist on the tube splitting is elucidated by the phase portrait of the Lorentz force $\boldsymbol{f}_p$ projected onto the divergence-free space. The initial counter-rotating $\boldsymbol{f}_p$ drives a bundle of field lines inside the flux tube into two for $T_w = 0$. With increasing T_w, an unstable spiral point of the projected force becomes a limit cycle via the Hopf bifurcation. The field lines inside the limit cycle form invariant tori, whereas the field lines outside the limit cycle become chaotic (see Fig. 3). The split of flux tubes and the chaotic rearrangement of field lines for low T_w lead to the rise of the magnetic dissipation rate.

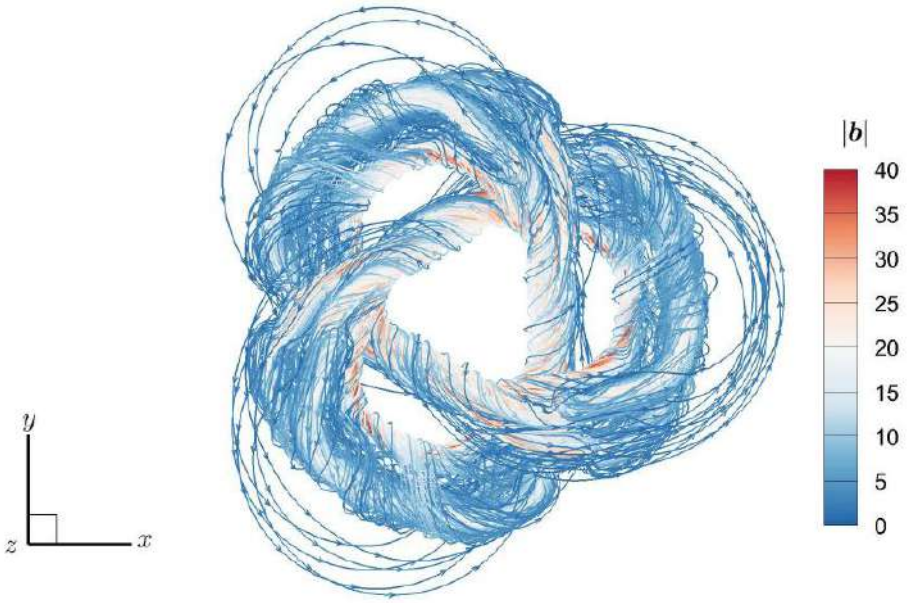

Figure 3. A chaotic field line color-coded by $|\boldsymbol{b}|$ for the magnetic knot with $T_w = 12.48$ at a late time $t = 0.04$ in the evolution.

CONCLUSIONS

We develop a novel method for constructing knotted flux tubes with the finite thickness, arbitrary shape and tunable twist. The central axis of the knotted tube is specified by a smooth and non-degenerated parametric equation, and the helicity of the corresponding knotted field can be explicitly decomposed into the writhe, localized torsion and intrinsic twist. We construct several knotted magnetic flux tubes with various T_w, and investigate the effect of twist on their evolution in resistive MHD flows using DNS. For large T_w, the magnetic knot gradually shrinks to a tight stable state, similar to the relaxation process in ideal MHD flows. For small T_w, the knotted flux tube splits at early times, accompanied by the rise of the magnetic dissipation rate. We find that the Hopf bifurcation of $\boldsymbol{f}_p$ from an unstable spiral point to a limit cycle occurs on the phase plane for finite T_w. In the evolution, field lines inside the limit cycle form invariant tori, whereas they become chaotic outside the limit cycle.

References

[1] Gold T., Hoyle F. On the origin of solar flares. *Mon. Not. R. Astron. Soc.* **120**: 89-105, 1960.
[2] Xiong S., Yang Y. Construction of knotted vortex tubes with the writhe-dependent helicity. *Phys. Fluids* **31**: 047101, 2019.
[3] Chui A. Y. K., Moffatt H. K. The energy and helicity of knotted magnetic flux tubes. *Proc. R. Soc. Lond. A* **451**: 609-629, 1995.
[4] Moffatt H. K., Ricca R. L. Helicity and the Călugăreanu invariant. *Proc. R. Soc. Lond.* A **439**: 411-429, 1992.

INTERPLAY OF SOLUTAL CONVECTION AND ELECTROMAGNETICALLY DRIVEN FLOWS IN LIQUID METAL BATTERY ELECTRODES

Tom Weier*[1], Steffen Landgraf[1], Michael Nimtz[1], Paolo Personnettaz[1], Norbert Weber[1], and Donald Sadoway[2]
[1]Helmholtz-Zentrum Dresden - Rossendorf, Bautzner Landstr. 400, 01328 Dresden, Germany
[2]Department of Materials Science and Engineering, Massachusetts Institute of Technology, Cambridge, MA

Summary Mass transfer in the positive electrode is one of the main factors determining the efficiency of liquid metal batteries. While solutal convection is quite intense during charge, discharge rates are limited by diffusion into a stable density stratification. The resulting concentration polarization can be substantially reduced if electrodynamically driven flows are employed to stir the liquid alloy. This leads to marked improvements in battery performance.

INTRODUCTION

The quest for renewable energy sources entails an increasingly intermittent electricity supply due to the limited potentials of hydropower and biomass that leave basically wind and solar power as options for expanding generation capacity. Since transition grid updates can only partially account for balancing the resulting variations, large-scale stationary storage will gain importance in future energy landscapes dominated by volatile sources.

Given the massive storage capacity needs, its efficiency should be maximized, cost per unit storage should be minimized and storage devices have to be made from abundant and cheap materials. Batteries typically show high energy efficiencies compared to other options and can be flexibly sited, but they have a relatively high price per unit stored energy, are usually of complex construction and often depend on materials of limited availability. Today's battery technologies were, with the notable exception of redox-flow batteries, mainly designed for and driven by mobile applications. Those prioritize properties (energy density, power rating) that are less important for stationary storage. Thus, while particularly Li-ion technologies have shown enormous progress during recent years especially in terms of specific energy and energy specific price, battery technologies developed from the ground up to meet the needs of stationary storage have the potential to much better address the specifics of huge capacity installations.

Liquid metal batteries (LMBs) are a new technology for grid-scale energy storage, see [1] for a comprehensive review. They consist of all liquid cells that operate with liquid metals as electrodes and molten salts as electrolytes. The liquids separate into three stably stratified layers by virtue of density and mutual immiscibility (see the two upper left inserts in Fig. 1a). This conceptually very simple and self-assembling structure has the unique advantage to allow for an easy scale-up at the cell level: single-cell cross sections can potentially reach several square-meters. Such cell sizes enable highly favourable and otherwise unattainable ratios of active to construction material because of the cubic scaling (volume) of the former and the quadratic scaling (surface) of the latter. The total costs should therefore largely be determined by those of the active materials.

While mass transport in most modern battery systems is typically dominated by diffusion and migration in micrometer-scale liquid layers and solids, convection - with exception of the aforementioned redox-flow batteries - rarely plays a role. This is in stark contrast to LMBs were mediated by the fully liquid interior fluid flow can be driven by various mechanisms and has a strong influence on cell performance and operational safety [2]. Electric currents, magnetic fields, and heat and mass transfer are tightly coupled with the cells' electrochemistry. We will concentrate here on the influence of solutal convection in the positive electrode on the cycling behaviour of a cell and on the application of electromagnetically induced convection to improve mixing.

EXPERIMENTAL AND NUMERICAL RESULTS

In the absence of electromagnetic effects and without artificial stirring, natural convection remains as the only source of fluid motion. The bottom of the small cell shown in the top left insert of Fig. 1a is heated keeping the cells' core temperature at 460 °C. To prevent side-reactions the open cell is located in a glove box who's argon atmosphere is at room temperature [3]. The unstable temperature gradient thus created would drive convection. During charge transfer, however, mass transport competes with temperature driven convection. LMBs combine low density, alkaline or earth alkaline metals for the negative electrode (anode; Li in our case) with high density, post-transition metals or metalloids for the positive electrode (cathode; Bi in our case). Cathode metal densities are typically an order of magnitude larger than anode metal ones. In comparison, thermal expansion coefficients are quite small and due to the good thermal conductivity of metals temperature differences tend to be smoothed out quickly. Thus, compositional (i.e. solutal) gradients should dominate over thermal ones and constitute the primary cause or inhibitor of motion in the positive electrode [2].

In the discharged state, the positive electrode consists of a Li-Bi alloy. When charging the cell, low density Li is removed from the top of the positive electrode. This increases locally the density of the alloy and Li-depleted alloy starts to sink down in plumes. Rapidly, solutal convection drives a flow in the whole cathode and intensely mixes the remaining alloy. A snapshot of the concentration distribution and velocity vectors is shown in the lower left insert of Fig. 1a. In

*Corresponding author. E-mail: t.weier@hzdr.de.

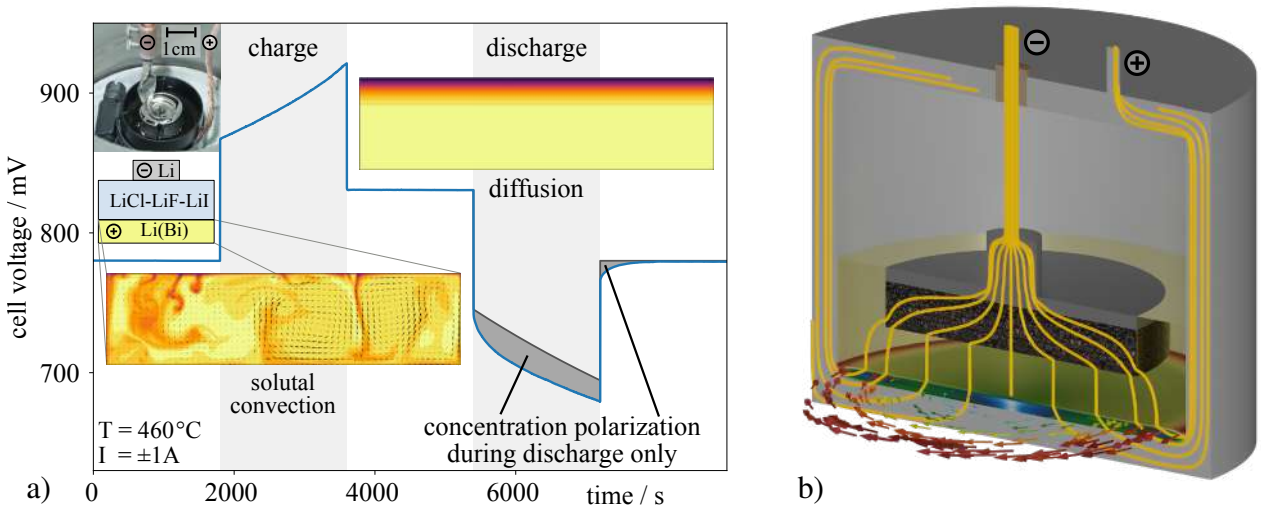

Figure 1: a: Cell voltage during a charge/discharge cycle with intermediate relaxation steps (blue curve) and Li concentration in a section of the positive electrode (insets). b: Exemplary full cell simulation in the presence of a vertical magnetic field with streamlines of the electric current (yellow) in the meridional plane, vectors of the flow velocity in a cross section of the positive electrode and Li concentration in the positive electrode (surface and meridional plane, red: high, blue: low).

thermal convection the analogous effect is sometimes termed 'self-stirring' [4].

LMBs can be understood as concentration cells whose open circuit voltage (OCV) is determined by the activity of the anode metal (Li) in the cathodic alloy (Li(in Bi)) directly at the interface with the electrolyte. During charge, the well mixed cathode guarantees the minimum Li concentration and thereby activity at the interface at every moment. In consequence, only the ohmic resistivity of the electrolyte generates an overvoltage. It results in a shift of the cell potential by a virtually constant value with respect to the OCV. When entering the relaxation step after switching off the charging-current, the cell voltage returns almost instantaneously to the OCV.

During discharge the situation is completely different. Low density Li is deposited on top of the high density cathodic alloy. The stratification is stable and inhibits mixing. The only remain transport mechanism is diffusion. In addition to the ohmic overvoltage, a diffusion overvoltage has now to be overcome that grows with time. After the end of discharge, the cell voltage relaxation happens gradually and with a time response that is again typical for diffusion phenomena.

Obviously, overvoltages diminish cell performance and should be reduced or ideally completely avoided. In addition, disproportionally high alkali or earth alkali metal concentrations in the cathodic alloy can lead to the formation of intermetallics. Depending on the materials combination used, those might be mostly harmless but could in other cases even seriously damage cell integrity. A remedy for these problems can be the application of Lorentz forces that would act as a source of momentum thereby offering a contactless way to stir the alloy. The cell current alone can generate electro-vortex flows. Their shape and magnitude depends on the design of the current collectors and of the feed line contacts. However, overcoming the stable solutal stratification is still a challenge. To improve mixing, addition of a vertical magnetic field component, i.e. by using loops in the feed lines, can be very effective. The resulting swirling flow driven by such a configuration in a numerical model of the 10 cm-diameter Li-Bi cell of Ning et al. [5] is shown in Fig. 1b. As can be inferred from the filled contours showing the Li concentration in the positive electrode, concentration differences do still exist, but regions of high concentration (red) are limited to the cathodes' rim. Mass transport overpotential during discharge can thereby decreased to a few millivolts.

CONCLUSIONS

Liquid metal batteries are a promising concept for large-scale stationary electricity storage. Fluid mechanics can provide valuable insights to optimize cell characteristics. Solutal convection in the positive electrode of an LMB is favorable during charge and enables fast charging. Without additional measures, diffusion overvoltages can arise during high-rate discharge, diminishing cell performance. Electromagnetic stirring is a proper means to improve mixing and to counteract diffusion limitation thereby increasing the cell's energetic efficiency.

References

[1] Kim H., Boysen D. A., Newhouse J. M., Spatocco B. L., Chung B., Burke P. J., Bradwell D. J., Jiang K., Tomaszowska A. A., Wang K., Wei W., Ortiz L. A., Barriga S. A., Poizeau S. M., Sadoway D. R. Liquid Metal Batteries: Past, Present, and Future. *Chem. Rev.* **113**:2075–2099, 2013.

[2] Kelley D. H., Weier T. Fluid Mechanics of Liquid Metal Batteries. *Appl. Mech. Rev.* **70**(2):020801, 2018.

[3] Personnettaz P., Landgraf S., Nimtz M., Weber N., Weier T. Mass Transport Induced Asymmetry in Charge/discharge Behavior of Liquid Metal Batteries. *Electrochem. Comm.* **105**:106496, 2019.

[4] Brown G. C., Mussett A. E. The Inaccessible Earth. Springer Netherlands 1993.

[5] Ning X., Phadke S., Chung B., Yin H., Burke P. J., Sadoway D. R. Self-healing Li-Bi liquid metal battery for grid-scale energy storage. *J. Power Sources* **275**:370–376, 2015.

AXISYMMETRIC VISCOUS MHD FLOW ABOUT A SOLID SPHERE TRANSLATING IN A CYLINDRICAL TUBE

Antoine Sellier*[1] and Selçuk Han Aydin[2]
[1]LadHyX, Ecole Polytechnique, 91128 Palaiseau cedex, France
[2]Department of Mathematics, Karadeniz Technical University, 61080 Trabzon, Turkey

Summary The quasi-steady Stokes MHD flow about a solid insulating sphere translating in a conducting quiescent liquid, bounded by a motionless insulating cylindrical tube and subject to of a uniform ambient magnetic field, is considered. The sphere center is located on the tube axis which is parallel to the magnetic field and the sphere velocity. The axisymmetric fluid velocity and pressure fields are numerically obtained by inverting a boundary-integral equation governing the stress exerted by the flow on the sphere surface, a truncated part of the tube and two far-enough tube cross sections. This key step appeals to two fundamental free-space axisymmetric Stokes MHD flows produced by distributing point forces on a circular ring and obtained elsewhere. For given tube and sphere, the MHD flow is found to deeply depend on the problem Hartmann number Ha based on the sphere radius.

We consider (see figure 1) the quasi-steady Stokes MHD flow about a solid insulating sphere, with radius a and surface S, translating at the velocity $U\mathbf{e}_z$ in a conducting and quiescent Newtonian liquid confined by a cylindrical motionless insulating tube Σ with radius R. The liquid is subject to a uniform steady magnetic field $B\mathbf{e}_z$ which is parallel with the tube axis of revolution to which the sphere center O belongs.

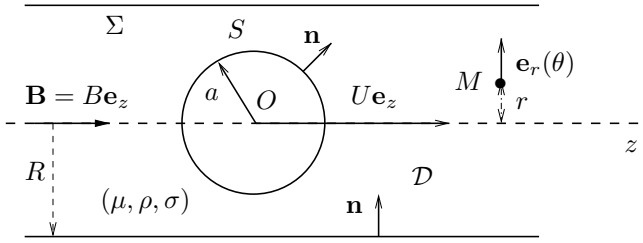

Figure 1: A solid insulating sphere translating, at the velocity $U\mathbf{e}_z$, parallel to a uniform magnetic field $\mathbf{B}$, in a conducting Newtonian liquid confined by a motionless cylindrical insulating tube. The sphere center O is located on the tube axis of revolution.

Assuming a low-Reynolds-number flow and sphere and liquid with equal uniform magnetic permeability ensures that the magnetic field is undisturbed by the sphere and thus equal to $B\mathbf{e}_z$ in the entire liquid domain $\mathcal{D}$. The flow, axisymmetric about the tube axis and without swirl, has velocity $\mathbf{u}(\mathbf{x}) = u_r(r,z)\mathbf{e}_r + u_z(r,z)\mathbf{e}_z$ and pressure $p(\mathbf{x}) = p(r,z)$ with (r,z,θ) the usual cylindrical coordinates and $\mathbf{x} = r\mathbf{e}_r + z\mathbf{e}_z$ (the unit local vector $\mathbf{e}_r(\theta)$ is shown in figure 1). Because both surfaces S and Σ are insulating and the magnetic field is uniform, there is no electric field in the liquid [1, 2, 3, 4]. Accordingly, the quasi-steady viscous flow $(\mathbf{u}, p)$ obeys the following MHD problem

$$\mu\nabla^2\mathbf{u} = \nabla p - \sigma B^2(\mathbf{u}\wedge\mathbf{e}_z)\wedge\mathbf{e}_z \text{ and } \nabla.\mathbf{u} = 0 \text{ in } \mathcal{D}\ , \tag{1}$$

$$\mathbf{u} = U\mathbf{e}_z \text{ on } S,\ \mathbf{u} = \mathbf{0} \text{ on } \Sigma,\ (\mathbf{u},p)\to(\mathbf{0},0) \text{ as } |\mathbf{x}|\to\infty \tag{2}$$

where $\sigma > 0$ and μ denote the uniform liquid conductivity and viscosity, respectively. The flow, with stress tensor $\boldsymbol{\sigma}$, exerts on the sphere surface S, where the unit normal pointing into the liquid is $\mathbf{n}$, the stress $\mathbf{f} = \boldsymbol{\sigma}\cdot\mathbf{n} = f_r(r,z)\mathbf{e}_r + f_z(r,z)\mathbf{e}_z$. Thus, the sphere experiences no torque about its center and a force $\mathbf{F}$, parallel to its translational velocity $U\mathbf{e}_z$, given by

$$\mathbf{F} = \int_S \mathbf{f}dS = [2\pi\int_{\mathcal{C}} f_z(P)r(P)dl(P)]\mathbf{e}_z = -6\pi\mu a\lambda U\mathbf{e}_z,\ \lambda = \lambda(R/a, \mathrm{Ha}). \tag{3}$$

In (3), the contour $\mathcal{C}$ is the half-circle trace of S in the $\theta = 0$ half plane and $\lambda > 0$ designates the so-called drag coefficient. Here, λ solely depends on the tube-sphere size ratio R/a and on the Hartmann number $\mathrm{Ha} = d/a$ which compares the Hartmann layer thickness $d = (\sqrt{\mu/\sigma})/|B|$ (see [5, 6, 7]) with the sphere radius a. Note that $\lambda = 1$ for $a/R = \mathrm{Ha} = 0$.

For a given truncation length $L > a$ the bounded liquid domain $\mathcal{D}_L$ is the set of points of $\mathcal{D}$ for which $|z| < L$. The trace of the boundary $\partial\mathcal{D}_L$ in the half $\theta = 0$ plane is the half-circle $\mathcal{C}$ plus a polyline $\mathcal{C}_L$ of obvious definition. Then, (1)-(2) is replaced with (1) in $\mathcal{D}_L$, $\mathbf{u} = U\mathbf{e}_z$ on S and $\mathbf{u} = \mathbf{0}$ on $\partial\mathcal{D}_L\setminus S$. The worked out procedure appeals, for each point $(\mathbf{x})(r,\theta,z)$ located in $\mathcal{D}_L$, to basic boundary integral representations of u_r, u_z and p. These key representations, derived as done in [4] for the unbounded liquid case, involve the stress $\mathbf{f}$ on $\mathcal{C}\cup\mathcal{C}_L$. More precisely,

$$u_\alpha(\mathbf{x}) = -\frac{1}{8\pi\mu}\sum_{\beta=r,z}\int_{\mathcal{C}\cup\mathcal{C}_L} G_{\alpha\beta}(M,P)f_\beta(P)r(P)dl(P) \text{ for } \alpha = r,z \text{ and } \mathbf{x} \text{ in } \mathcal{D}_L\cup S\cup\partial\mathcal{D}_L, \tag{4}$$

$$p(\mathbf{x}) = -\frac{1}{8\pi}\sum_{\beta=r,z}\int_{\mathcal{C}\cup\mathcal{C}_L} P_\beta(M,P)f_\beta(P)r(P)dl(P) \text{ for } \mathbf{x} \text{ in } \mathcal{D}_L \tag{5}$$

*Corresponding author. E-mail: sellier@ladhyx.polytechnique.fr

with $M(r,z)$ the point of the $\theta = 0$ half plane associated to $\mathbf{x}(r,z,\theta)$ and both Green quantities $G_{\alpha\beta}(M,P)$ and $P_\beta(M,P)$ analytically obtained in [8] in terms of $z - z(P), r, r(P)$ and the Hartmann layer thickness d [5]. Then, enforcing the boundary velocity conditions $\mathbf{u} = U\mathbf{e}_z$ on $\mathcal{C}$ and $\mathbf{u} = \mathbf{0}$ on $\mathcal{C}_L$ yields, using (4), coupled boundary-integral equations for the unknown stress components f_r and f_z on $\mathcal{C} \cup \mathcal{C}_L$. These integral equations are numerically inverted by a collocation method which resorts to quadratic curved boundary elements and N nodal points on $\mathcal{C} \cup \mathcal{C}_L$. Once the stress components f_r and f_z are gained both integral representations (4)-(5) are subsequently employed to efficiently compute the required flow (u_r, u_z, p) in the truncated liquid domain $\mathcal{D}_L$. For given $(R/a, \mathrm{Ha})$, the computed drag coefficient λ sensitivity to both N and the truncation length L is carefully investigated. The values of λ for vanishing Ha have also been convincingly compared with the predictions given in [9] for the pure Stokes flow (absence of magnetic field) case.

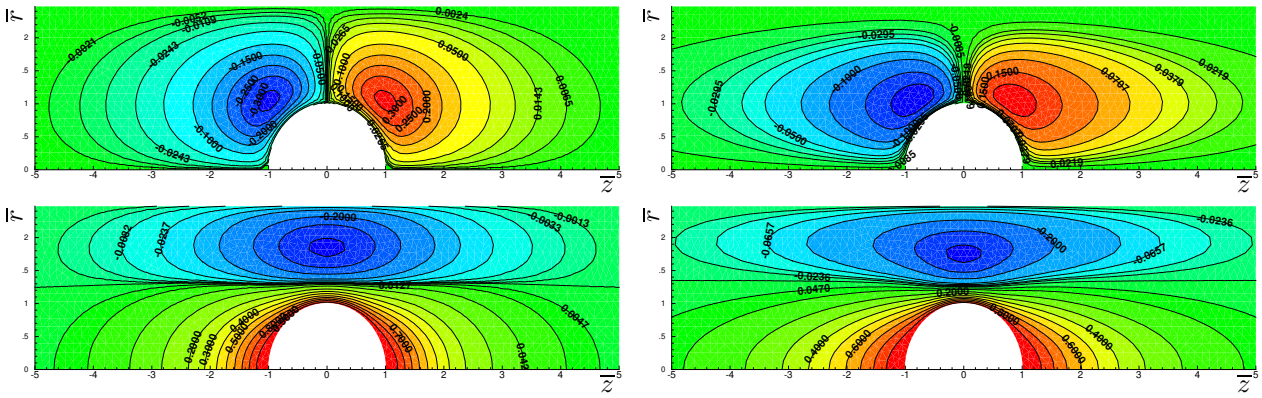

Figure 2: Isolevel curves of the normalized radial velocity u_r/U (top) and axial velocity u_r/U (bottom) for $\mathrm{Ha} = 1$ (left) and $\mathrm{Ha} = 5$ (right). Here $R/a = 2.5$. The selected number of nodal points N and truncation length are $N = 266$ and $L = 7.5a$.

Figure 2 provides for $R/a = 2.5$ and $\mathrm{Ha} = 1, 5$ the isolevel curves of the normalized radial and axial velocities $\overline{u}_r = u_r/U$ and $\overline{u}_z = u_z/U$ in the region $\overline{r} = r/a \leq 2.5$ and $\overline{z} = z/a$ in $[-5, 5]$. The radial component $\overline{u}_r$ vanishes on the sphere and on the tube, quickly decays away from the $(O, \mathbf{e}_z)$ tube axis and remains small especially outside two pockets close the sphere. As Ha increases the previous pockets extends upstream $(\overline{z} > 0)$ and downstream $(\overline{z} < 0)$. The normalized axial velocity $\overline{u}_z$ is positive nearly in a domain $\overline{r} \leq \overline{r}_c$ with $\overline{r}_c$ close to 1.3 and weakly sensitive to Ha. As expected, $\overline{u}_z$ takes the unit value on the sphere and vanishes on the tube. Moroever, its magnitude is less than unity in the entire liquid domain. As Ha increases the regions near the sphere where $\overline{u}_z$ exceeds 0.3 extend away both upstream and downstream the sphere close the $\overline{r} = 0$ axis. As also illustrated in figure 2, each velocity component is strongly sensitive to the value of the Hartmann number.

The drag coefficient values obtained for the flows considered in figure 2 are $\lambda = 3.67$ for $\mathrm{Ha} = 1$ and $\lambda = 5.03$ for $\mathrm{Ha} = 5$. Actually, λ is found to be nearly insensitive to $\mathrm{Ha} \leq 1$ for this size ratio $R/a = 2.5$ ([9] gives $\lambda = 3.60$ for $\mathrm{Ha} = 0$). Finally, our computations (not presented here) also reveal that, not surprisingly, λ increases as R/a decreases (confinement effect) for given Ha. For instance, for the unbounded liquid case addressed in [4] one gets $\lambda = 1$ for $\mathrm{Ha} = 0$, $\lambda = 1.18$ for $\mathrm{Ha} = 1$ and $\lambda = 2.35$ for $\mathrm{Ha} = 5$.

Acknowledgements

A.S. benefited from the ITHACA project PPI/APM/2018/1/00045 financed by the Polish National Agency for Academic Exchange.

References

[1] Chester W. The effect of a magnetic field on Stokes flow in a conducting fluid. *J. Fluid Mech.*, **3**: 304-308, 1957.

[2] Gotoh K. Magnetohydrodynamic flow past a sphere. *Journal of the Physical Society of Japan*, **15 (1)**: 189-196, 1960.

[3] Chester W. The effect of a magnetic field on the flow of a conducting fluid past a body of revolution. *J. Fluid Mech.*, **10**: 459-465, 1961.

[4] Sellier A., Aydin S. H. Creeping axisymmetric MHD flow about a sphere translating parallel with a uniform ambient magnetic field. *MagnetoHydrodynamics,* **53 (1)**: 5-11, 2017.

[5] Hartmann J. Theory of the laminar flow of an electrically conductive liquid in a homogeneous magnetic field. *Det Kgl . Danske Videnskabernes Selskab . Mathematisk-fysiske Meddelelser*, **XV (6)**: 1-28, 1937.

[6] Tsinober A. B. MHD flow around bodies. Fluid Mechanics and its Applications. Kluwer Academic Publisher, 1970.

[7] Moreau R. J. Magnetohydrodynamics. Fluid Mechanics and its applications. Kluwer Academic Publisher, 1990.

[8] Sellier A., Aydin S. H. Fundamental free-space solutions of a steady axisymmetric MHD viscous flow. *European Journal of Computational Mechanics,* **25 (1-2)**: 194-217, 2016.

[9] Haberman W. L., Sayre R. M. Motion of rigid and fluid spheres in stationary and moving liquids inside cylindrical tubes. David W. Taylor Model Basin Report No. 1143, U.S. Navy Dept. 1958.

LARGE-SCALE MAGNETIC FIELD GENERATION BY WAVE INTERACTIONS IN HIGHLY CONDUCTING PLASMA

Krzysztof A. Mizerski*[1]
[1]Department of Magnetism, Institute of Geophysics, Polish Academy of Sciences, Warsaw, Poland

Summary It is well known that a field of random waves in a fluid of non-zero resistivity is capable of exciting a large-scale magnetic field through creation of an electromotive force (EMF) which leads to exponential growth of magnetic energy until the growing Lorentz force reacts back upon the wave field, leading to a saturated state. For highly conducting plasma it is generally found that kinematic fast-dynamos with finite growth rate in the limit of vanishing resistivity, have a pathological structure, non-differentiable wherever they are non-zero; the applicability of fast-dynamo theory to natural physical systems is then questionable. Here we relax the standard simplifying assumptions of stationarity of the background turbulence and introduce new fast-dynamo mechanisms, fully dynamic, that is incorporating the back reaction of the Lorentz force on the flow, for which the growing magnetic field remains smooth during the entire dynamo process. This results from a random superposition of waves, perturbed by the magnetic field. Particularly effective are the interactions of beating waves and nonlinear effects in the mean electromotive force. The MHD equations are renormalized to include the nonlinear effects of turbulent fluctuations on the means and the dynamics of the large-scale field is studied.

INTRODUCTION

The mean field theory (cf. Moffatt 1978) is most commonly used to describe large scale magnetic fields in natural systems. It is based on the following induction equation for magnetic field resulting from the Maxwell laws and the Ohms law and averaged over a statistical ensemble

$$\frac{\partial \langle \mathbf{B} \rangle}{\partial t} = \nabla \times (\langle \mathbf{u} \rangle \times \langle \mathbf{B} \rangle) + \nabla \times \langle \mathbf{u}' \times \mathbf{B}' \rangle + \eta \nabla^2 \mathbf{B}. \tag{1}$$

The ensemble average removes the quickly varying in space and time turbulent fluctuations in magnetic and velocity fields, $\mathbf{B}'$ and $\mathbf{u}'$, leaving the fields $\langle \mathbf{B} \rangle$ and $\langle \mathbf{u} \rangle$ which possess only slowly varying components. The averaged interactions of small scale fluctuations generate a large scale electromotive force (EMF) $\langle \mathbf{u}' \times \mathbf{B}' \rangle$, which is a physical foundation of the mechanism of generation of the large scale magnetic fields. In the isotropic case it takes the form

$$\mathcal{E} = \langle \mathbf{u}' \times \mathbf{B}' \rangle = \alpha \langle \mathbf{B} \rangle, \tag{2}$$

where the coefficient α dependent on the mean field $\langle \mathbf{B} \rangle$ due to the action of the Lorentz force in the flow momentum balance. The presence of the non-negligible Lorentz force is responsible for quenching of the mean EMF and leads to saturation of the large-scale field excited via dynamo action.

INTERACTIONS OF DISTINCT WAVES

The case of linear waves has been extensively studied (cf. Moffatt 1978), with particular attention directed to new mechanisms of the EMF generation based on interactions between distinct waves in Mizerski (2018a,b). The new mechanism results from interactions between fluctuations of the velocity and magnetic fields with the same wavelength but distinct frequencies; in other words, for linear waves, this corresponds to superposition of at least two different eigenmodes, i.e.

$$\mathbf{u}' = A_1 \mathbf{u}'^{(1)} + A_2 \mathbf{u}'^{(2)}, \qquad \mathbf{B}' = A_1 \mathbf{B}'^{(1)} + A_2 \mathbf{B}'^{(2)} \tag{3}$$

$$\begin{aligned} \mathcal{E} &= \frac{1}{2} \Re e \left(\mathbf{u}' \times \mathbf{B}'^{*} \right) \\ &= \frac{1}{2} \sqrt{\mu_0 \rho} \Re e \left[A_1 A_2^{*} \hat{\mathbf{u}}^{(1)} \times \hat{\mathbf{B}}^{(2)*} \mathrm{e}^{\mathrm{i}\Delta\omega t} + A_1^{*} A_2 \hat{\mathbf{u}}^{(2)} \times \hat{\mathbf{B}}^{(1)*} \mathrm{e}^{-\mathrm{i}\Delta\omega t} \right], \end{aligned} \tag{4}$$

where A_1 and A_2 are amplitudes of the eigenmodes and ω_1, ω_2 are the oscillation frequencies of each wave. Such an EMF oscillates on a timescale $1/\Delta\omega$, which can be much larger than that of the mean magnetic field growth and hence can lead to mean field dynamo. In the above $\Delta\omega = \omega_1 - \omega_2$ denotes the difference between the two eigenvalues associated with the two interacting eigenmodes.

Particularly effective are the interactions of beating waves (cf. Mizerski 2018b where waves forced at two disticnt but close frequencies were considered) and nonlinear effects in the mean electromotive force (cf. Mizerski 2018a). Figure 1 depicts an initial period of evolution of magnetic energy amplified by interactions between Lehnert (Magneto-Coriolis) waves; the inset clearly shows initial energy decay in the linear regime, thus demostrating the crucial role of the nonlinear effects from the Lorentz force. The importance of the new mechanism of the EMF generation results from the fact, that contrary to the standard mechanisms invoked in the literature it does not require the magnetic diffusivity to create a phase shift between the kinetic and magnetic components of the fluctuations; the wave interactions are effective at creation of the mean EMF even when the magnetic diffusivity is negligibly small. It follows, that the theory has the potential to be applied to dynamo generation of magnetic fields in the ionised gas of the early universe, for which the resistivity is extremely low (with characteristic diffusion times many orders of magnitude greater than the age of the entire universe); non-resistive dynamo mechanisms are strongly desirable in this context.

*Corresponding author. E-mail: kamiz@igf.edu.pl

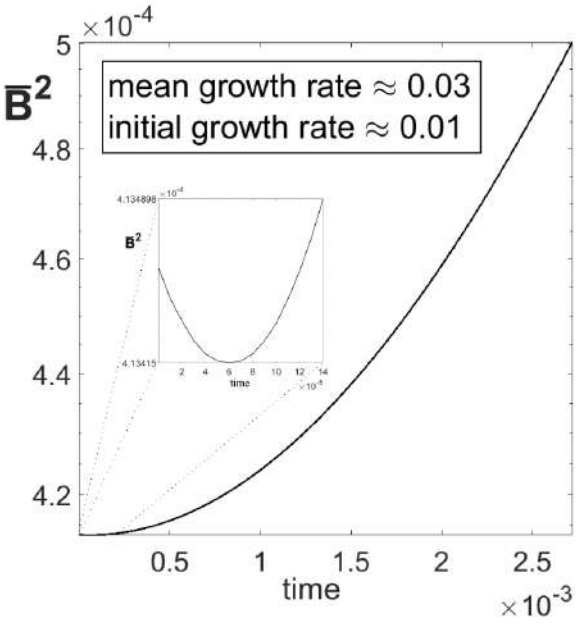

Figure 1: Initial period of growth of the spatially averaged energy of the mean magnetic field generated via interactions between Lehnert waves, in a periodic box; the waves are continuously generated at the top boundary. The inset shows in detail a very short initial stage of magnetic energy drop, before the nonlinear effects due to the Lorentz force (from Mizerski 2018a).

RENORMALIZATION

The theory if further developed by considering the nonlinear effects of waves via the renormalization-group approach, udertaken in a similar manner as in Yakhot and Orszag (1986) and Smith and Woodruff (1998). The assumption of isotropy of turbulence is put forward, but the turbulence remains non-stationary. The full MHD equations are renormalized in order to obtain an effective equation describing the evolution of the mean field, with the explicit form of the mean EMF. A particular dependence of the α coefficient on the large-scale field is obtained, which results from inclusion of the effect of the Lorentz force. In turn the full dynamics of the mean field and its saturation can be studied. The non-stationarity of turbulence turns out to be a crucial factor in the process of large-scale field generation in the limit of low generalized Rossby and Ekman numbers.

Acknowledgements

This work was partially financed as a part of the statutory activity from the subvention of the Ministry of Science and Higher Education in Poland Partial support from the subvention of the Ministry of Science and Higher Education of Poland within statutory activities and of the Polish National Science Centre (Grant No 2017/26/E/ST3/00554) is gratefully acknowledged.

References

[1] Mizerski K. A. Large-scale hydromagnetic dynamo by Lehnert waves in nonresistive plasma, *SIAM J. Appl. Math*, **78**(3), 1402–1421, 2018a.
[2] Mizerski K. A. Large-scale dynamo action driven by forced beating waves in a highly conducting plasma, *J. Plasma Phys.*, **84**, 735840405, 2018b.
[3] Moffatt H. K. Magnetic field generation in electrically conducting fluids. Cambridge University Press, 1978 (available at http://moffatt.tc).
[4] Smith L. M. and Woodruff S. L. Renormalization group analysis of turbulence, *Annu. Rev. Fluid Mech.* **30**, 275–310, 1998.
[5] Yakhot V. and Orszag S. A. Renormalization group analysis of turbulence. I. Basic theory. *J. Sci. Comp.* **1**(1), 3–51, 1986.

INSTABILITIES IN MIXED CONVECTION AT MAGNETIC FIELD

Dmitry Krasnov [1], Yaroslav Listratov[2,3], Ivan Belyaev [2], Yuri Kolesnikov [1]and Oleg Zikanov [4]
[1]Technische Universität Ilmenau, Ilmenau, Germany
[2]Joint Institute for High Temperatures of RAS (JIHT RAS), Moscow, Russia
[3]National Research University (MPEI), Moscow, Russia
[4]University of Michigan-Dearborn, USA

Summary The study addresses, both experimentally and numerically, flow instabilities in a heated vertical duct under a strong transversal magnetic field. Mercury is used as a model liquid metal. The experimental part has studied the temperature signals formed in a strong magnetic field and analyzed their statistical characteristics. The numerical simulations have reproduced the experimental conditions and provided an assessment of the emerging flow structures, determined the characteristic flow regimes. Also, symmetry properties of the system and their influence on the onset of unstable regimes have been studied. Based on the observed results, terminology to describe two different types of temperature fluctuations and associated flow instabilities has been proposed.

INTRODUCTION

This work is performed as a joint experimental-numerical study within a collaboration German-Russian research project, supported by DFG and RFBR. The experimental investigation of the liquid metal downward flow in a vertical duct under the influence of a transverse magnetic field has been performed by the joint group at MPEI and JHIT (Moscow). The geometry corresponds to a flat duct with the aspect ratio 3.5:1 (cross-section of 56×16mm and the length of about 1m), whereas the magnetic field B is applied along the long side of the duct and the heat flux – along the short side. Such configuration is close to the conditions in blanket modules of a tokamak-type thermonuclear reactor. Mercury has been used as a model liquid metal. The experiments have been conducted using an immersion probe with micro-thermocouple, moving inside the duct over a certain cross-section, which can, point by point, restore the profiles of the averaged and fluctuating temperature. It is known that the joint effect of electromagnetic and buoyancy forces may lead to the formation of secondary vortices on top of the main flow [1, 2], which causes fluctuation of temperature with high amplitude and low frequency. Particular attention has been paid to the role of wall heating, i.e. symmetric (two-sided) and non-symmetric (one-side) heating. It has been found that these two configurations of the applied thermal load generate instabilities, which, albeit retaining common features in their nature, are different in their spatio-temporal characteristics. Namely, two temperature signals have been found: quasi-harmonic temperature fluctuations observed at the symmetric heat load, whereas the non-symmetric heat load has led to the appearance of periodic temperature bursts [3]. However, since the velocity fields could not be measured with the necessary accuracy, yet there remained one open question – what are the specific flow structures, which may correspond to the temperature signals, obtained in the measurements [3].

RESULTS AND DISCUSSION

To answer the question above, we have performed a series of numerical simulations with our in-house finite-difference solver [4], aimed to mimic the experimental conditions at the maximum possible capacity. The simulations have been done in the essentially same duct, including the geometry settings and parameter space. Also, to mimic the real experimental conditions, we have implemented a virtual honeycomb installed at the duct inlet, which has also served the purpose of generating turbulent flow before entering the working "experimental" section, where heating and magnetic field are applied. The numerical resolution was 7200×512×128 points in the streamwise x-, spanwise y- and vertical z-directions, correspondingly.

Our numerical simulations have confirmed that the flow of liquid metal in a heated duct can develop at least two different families of instabilities under the transverse magnetic field. Symmetric and non-symmetric heating produces different patterns of fluctuating flow for the downward configuration, as shown in figure 1. We have found that secondary flows naturally develop and keep existing under magnetic field up to the maximum values of $Ha = 200$ accessible in the experiment (here the Hartman number and other parameters are calculated using duct`s half-height). The analysis of the numerical results, both velocity fields, and temperature signals, also fully reveals that symmetric heating of the duct produces quasi-harmonic fluctuations, while non-symmetric leads to quasi-periodic bursts observed at the same combination of parameters (Ra, Ha and Gr numbers) as in the experiment. Moreover, we have conducted a separate investigation on the effect of possible imperfections in the experimental setup, such as deflection from the vertical position and not truly symmetric heating at the two walls. The most interesting outcome here is that even a slight deviation from the ideal heating-symmetry, e.g., by about 5% between the left and right walls, is sufficient to trigger the instability at much lower values of Gr number. The flow patterns and the amplitude of temperature signals at such a slight non-symmetric heat load start to resemble those, identified at the purely one-side heating. At the same time, a 5% deflection from the vertical position did not affect the instability thresholds.

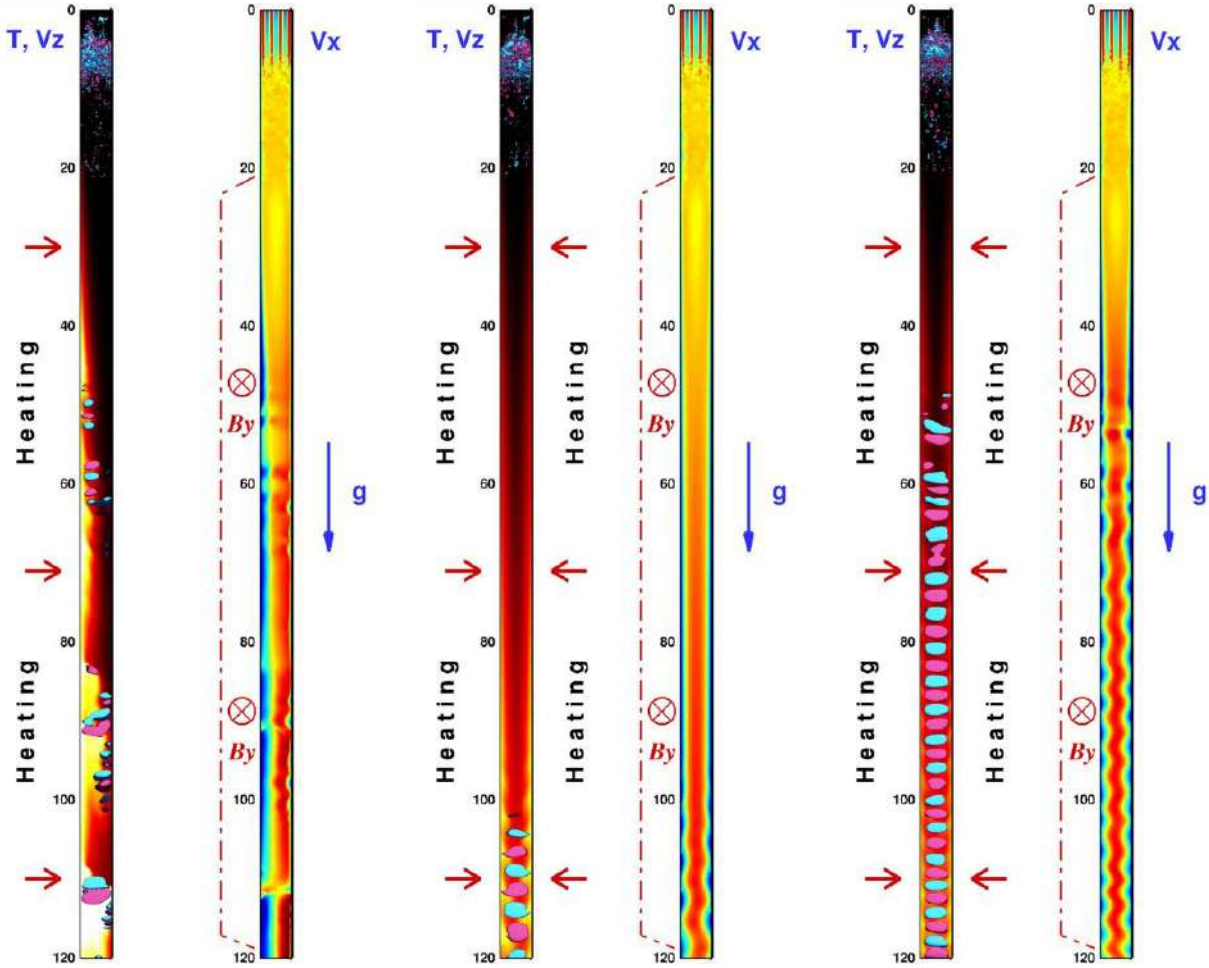

Figure 1. Downward flow in a vertical duct at Re = 5000 and Ha = 200 with (left) one-side heating at Gr = 1.6e6, and (middle and right) two-side heating at Gr = 2.5e6 and 5e6. The plots visualize flow structures in a (x; z)-cross-section of a fully developed state. On each plot, the left panel shows contours of the temperature field T and vertical velocity v_z (cyan and pink), the right panel shows contours of the streamwise velocity v_x.

CONCLUSIONS

The effect of the observed phenomena is actually two-fold. On the one hand, the observed regular 2D structures can produce additional flow mixing and significantly enhance heat transfer, possibly up to the levels observed at a fully developed turbulent state. On the other hand, however, the system appears extremely sensitive to the symmetry properties. Thus, these irregular bursts, observed for the cases of non-symmetric heating (and, to some extent, those with slight non-symmetry), can create unexpectedly high thermal loads or hot spots at the walls, which would pose potential problems for mechanical constructions. Furthermore, it turns out that non-symmetries in positioning are far less critical than those in heating. This may have direct implications for the construction and operation of fusion blankets. In the future work, we plan to address other non-symmetry factors (i.e. experimental or operating imperfections), such as inlet non-uniformity, offsets between both heaters, misalignment of the duct- and *B*-field-axis and finite conductivity of the walls. Finally, we will also provide a more detailed assessment of the observed flow structures and quantify their impact on the integral heat transfer properties.

Acknowledgments
The work is supported by the joint Russian – German project: RFBR NNIO_a 18-508-12005 / DFG KR 4445/2-1

References

[1] S. Smolentsev, N. Vetcha, and M. Abdou. Effect of a magnetic field on stability and transitions in liquid breeder flows in a blanket. Fusion Engineering and Design, vol. 88 (2013), no. 6-8, pp. 607-610.
[2] L. Liu and O. Zikanov. Elevator mode convection in flows with strong magnetic fields. Physics of Fluids, vol. 27 (2015), no. 4, p. 044103.
[3] I.A. Belyaev, N.G. Razuvanov, D.S. Krasnov and V.G. Sviridov, Heating nonuniformity influence on the liquid metal flow characteristics in the presence of a magnetic field during mixed convection in a duct, VANT 5, pp. 86-95, 2018 (in Russian)
[4] O. Zikanov, et al. Patterned turbulence in spatially evolving magnetohydrodynamic duct and pipe flows. Theor. Comp. Fluid Dyn., vol. 28 (2014), pp. 319-334.

VELOCITY-VORTICITY FORMULATION FOR THE MHD TAYLOR-COUETTE FLOW AND THE IMPORTANCE OF THE WIDE-GAP CORRECTION

Y. Velizhanina*, B. Knaepen*

The analysis of the stability of the hydrodynamic Taylor-Couette flow (i.e the flow contained between two concentric rotating cylinders) was first presented in the pioneering work of Taylor[1]. Taylor assumed axisymmetric perturbations but it was later observed experimentally and discussed theoretically that the most unstable modes become non-axisymmetric in case of sufficiently negative $\mu_\Omega = \Omega_{in}/\Omega_{out}$, where Ω_{in} and Ω_{out} denote respectively the rotation rates of the inner and outer cylinders (see e.g. Krueger et al.[2]). The stability of *the hydromagnetic Taylor-Couette flow* was also the subject of numerous studies, mainly in the context of finite magnetic Reynolds numbers and the magnetorotational instability[3]. Here we focus on the limit of small magnetic Reynolds numbers (inductionless limit). The stabilising effect of the uniform axial magnetic field in the axisymmetric case was first described by Chandrasekhar[4] and confirmed experimentally by Donnely & Ozima[5]. The importance of non-axismmetric modes was later concluded from the experiments by Donnelly & Caldwell[6] and investigated further in the framework of the narrow-gap approximation by Chen & Chang[7]. By performing an extensive parametric study these authors were able to separate two important regimes in which non-axisymmetric modes define the stability - first, for moderate values of Ha and negative values of μ_Ω and, second, for large Ha and arbitrary μ_Ω.

Here we present a novel formulation of the hydromagnetic Taylor-Couette flow stability equations based on the variables proposed by Burridge & Drazin[8] in the context of the hydrodynamic pipe flow. This compact system, valid for any gap ratio, is closed in terms of two equations for the wall-normal velocity and the wall-normal vorticity. We compare our numerical results with that of Krueger[2] for the hydrodynamic case and Roberts[9] for the MHD case and find a perfect agreement. The second part of this work concerns the accuracy of the narrow-gap approximation for negative values of μ_Ω where non-axisymmetric modes govern the instability (unfortunately, eventhough Roberts used a wide-gap formulation, the relevant set of parameters for this regime was not considered). For the hydrodynamic Taylor-Couette problem, the narow-gap approximation has proved its validity but it has been shown by Krueger[2] that its accuracy degrades significantly when $\mu_\Omega < 0$ and that the wide-gap correction becomes significant even for $R_{in}/R_{out} = 0.95$. Our results confirm that this observation is also valid in the magneto-hydromagnetic case and we show that the wide-gap correction significantly modifies the results reported by Chen & Chang[7].

*Université Libre de Bruxelles, Blvd du Triomphe CP231, 1050 Ixelles, Belgium

[1] G.I. Taylor, *Phil.Trans. R. Soc. Lond. A* **223**, 289 (1923).
[2] E. R. Krueger et al., *J. Fluid Mech.* **24**, 3 (1966).
[3] R. Rüdiger et al. *Phys. Rep.* **741**, 1 (2018)
[4] S. Chandrasekhar, *Proc. R. Soc. Lond.* **216**, 1126 (1953).
[5] R. J. Donnelly and M. Ozima, *Phys. Rev. Letters* **4**, 10 (1960).
[6] R. J. Donnelly and D. R. Caldwell, *J. Fluid Mech.* **19**, 2 (1964).
[7] C.-K. Chen and M. H. Chang, *J. Fluid Mech.* **366**, 1 (1998).
[8] D. M. Burridge and P. G. Drazin, *Phys. Fluids* **12**, 264 (1969).
[9] P. H. Roberts, *Proc. Camb. Phil.* **60**, 635 (1964).

MAGNETIC FIELD ASSISTED ELECTRODEPOSITION OF METAL ON CONICALLY SHAPED ELECTRODES

Mengyuan Huang*[1], Kerstin Eckert [1,2], Gerd Mutschke [1]
[1]Institute of Fluid Dynamics, Helmholtz-Zentrum Dresden-Rossendorf (HZDR), Dresden, Germany
[2]Institute of Process Engineering, Technische Universität Dresden, Dresden, Germany

Summary The electrodeposition of metal on conically shaped diamagnetic and ferromagnetic electrodes is studied under the influence of a vertical magnetic field. Analytical and numerical results show a beneficial influence of the magnetic field to enhance the cone growth, which can be attributed to the electrolyte flow forced by the Lorentz force and the magnetic gradient force. The influences of cone shape, cone size and distance between neighbouring cones are investigated in detail. The results deliver insights into the feasibility of magnetic field assisted electrodeposition towards nano-structured conical electrodes.

INTRODUCTION

Conical structures at length scales from micrometer to nanometer have numerous applications in areas including super-hydrophobic and electrocatalytic materials [1, 2]. Among the various methods of synthesizing micro- and nano-structured cones, magnetic-field assisted electrochemical deposition could be an important technology [3]. The magnetic forces, i.e. the Lorentz force and the magnetic gradient force, can generate an electrolyte flow that brings fresh electrolyte enriched with electroactive ions towards the cone tip, and thus enhances the local mass transfer [4]. It is therefore possible to support the cone growth during the electrodeposition process by properly adjusting the magnetic field imposed on the electrochemical cell.

For the purpose of separately investigating the influence of the magnetic forces, a homogeneous vertical magnetic field is applied to diamagnetic (Cu) and ferromagnetic (Fe) cathodes of conical shape. The magnetization of the Fe electrodes causes a strong magnetic gradient force near the cones, while for the Cu cones only the Lorentz force is acting. As the cathodes are placed at the bottom of the electrochemical cell, solutal buoyancy needs to be considered as well.

The numerical model consists of a coupled system of equations for mass transport of the ionic species involved, magnetic field, electric potential and electrolyte flow and was implemented in the finite element software COMSOL to study the electrolyte flow and mass transfer during the galvanostatic deposition process [5]. Early simulation results for the Cu case only and compared to experimental findings can be found in [6].

RESULTS AND DISCUSSIONS

Figure 1 shows the electrolyte flow near a Cu and a Fe cone (left) and its influence on the deposit thickness on the conical cathode (right) after 10 s deposition. For the Cu cone, the downward flow due to the Lorentz force is counteracted by the strong upward buoyant flow originating from the bottom of the cone. The magnetic gradient force in case of the Fe cone is creating an additional downward flow that is suppressing the undesirable buoyant flow at the upper part of the cone and therefore supporting the local mass transfer, which explains the enhancement of the deposit thickness on the Fe cone compared to the Cu cone.

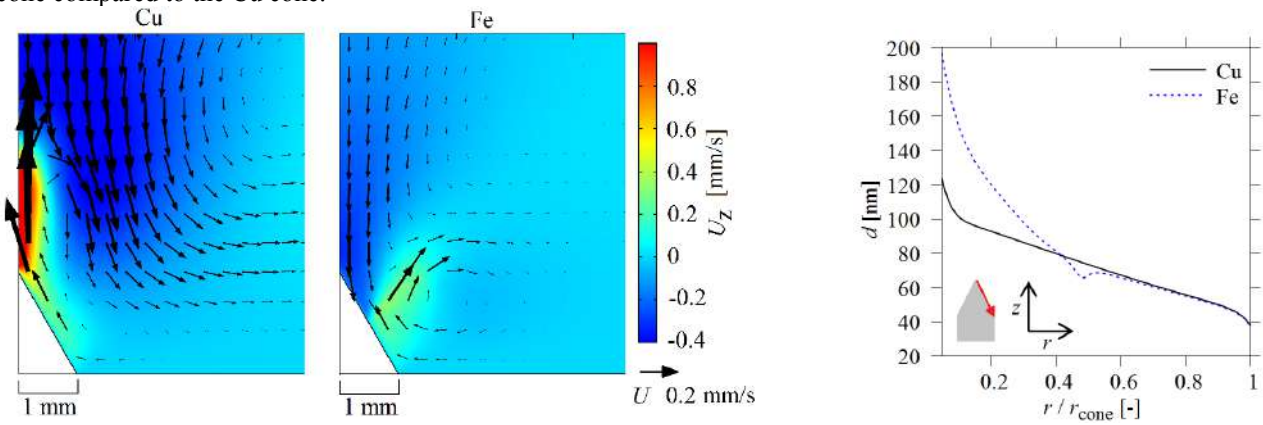

Figure 1. 2D axisymmetric simulation results for single Cu and Fe cones after 10 s deposition. Left: Color surface of the vertical velocity superimposed with the velocity vectors. Right: Deposit thickness on the cone surface. Horizontal axis normalized by the cone radius. The cone grows as the deposit thickness at the cone tip ($r/r_{\mathrm{cone}} = 0$) is higher than at the cone bottom ($r/r_{\mathrm{cone}} = 1$). 0.1 M $CuSO_4$ is used as electrolyte, the average cathode current density is 16 $\mathrm{mA/cm^2}$, the external magnetic field is 200 mT [5].

As the electrodeposition proceeds, the aspect ratio of the cone increases. In this regard, we studied sharp and flat cones to understand the supporting effects of the magnetic field at different stages of the evolution of cone growth. The sharpest

*Corresponding author. E-mail: m.huang@hzdr.de.

cone yields the strongest Lorentz force, which is related to the high current density arising from the geometrical inhomogeneity near the cone tip. For the Fe cones, the intermediate cone tip angle generates the highest magnetic field and the associated magnetic gradient force. These results indicate that in comparison to the Lorentz force, the magnetic gradient force exerts its largest influence at an earlier stage of the cone growth.

Damping effects from neighbouring cones were investigated by varying the distance between cones. While the primary azimuthal flow resulting from the Lorentz force is extending towards the neighbouring cones and is strongly damped when the cones get closer to each other, the meridional flow caused by the magnetic gradient force exists in a smaller region and is less affected by the neighbouring cones.

Scaling studies performed on cones with diameters ranging from 2 mm to 6 µm allow to draw conclusions on the magnetic field effects on the electrodeposition towards micro- and nano-cones. As the cone size shrinks, the geometrical inhomogeneity decreases, and the current density gets more uniformly distributed on the cone, which is making the cone growth more difficult. Furthermore, the flow forced by the magnetic field near smaller cones suffers from higher wall friction. On the other hand, this may partially be compensated by the larger magnetic gradients existing at smaller Fe cones, which is generating a beneficial downward flow also at a 6 µm Fe cone.

CONCLUSIONS AND OUTLOOK

Our work shows the superiority of the magnetic gradient force compared to the Lorentz force in terms of supporting cone growth for single cones of different shape and size, as well as for cone arrays [5]. Although it is more difficult to obtain conical structures when the distance between neighbouring cones decreases and when the cone size shrinks, a beneficial influence of the magnetic field can be stated in general. Future work will focus on optimization of the electrodeposition conditions for different metals and alloys by e.g. applying stronger magnetic fields and pulsed electrodeposition modes.

ACKNOWLEDGEMENTS

Financial support by Deutsche Forschungsgemeinschaft, grant no. 381712986 is gratefully acknowledged.

References

[1] Wang N., Yuan Y., Wu Y., Wang T., Li M. Wetting Transition of the Caterpillar-Like Superhydrophobic Cu/Ni-Co Hierarchical Structure by Heat Treatment. *Langmuir.* **31**: 10807-10812, 2015.

[2] Brinkert K., Richter M. H., Akay Ö., Liedtke J., Giersig M., Fountaine K. T. and Lewerenz H.-J. Efficient Solar Hydrogen Generation in Microsgravity Environment. *Nat. Commun.* **9**: 2527, 2018.

[3] Uhlemann M., Tschulik K., Gebert A., Mutschke G., Fröhlich J., Bund A., Yang X., Eckert K. Structured Electrodeposition in Magnetic Gradient fields. *EPS-Special Topics*. **220**: 287-302, 2013.

[4] Mutschke G., Tschulik K., Weier T., Uhlemann M., Bund A., Fröhlich J. On the Action of Magnetic Gradient Forces in Micro-structured Copper Deposition. *Electrochim. Acta.* **55**: 9060-9066, 2010.

[5] Huang M., Eckert K., Mutschke G. (in press). Magnetic-field-assisted electrodeposition of metal to obtain conically structured ferromagnetic layers. *Electrochimica Acta,* 2020.

[6] Huang M., Marinaro G., Yang X., Fritzsche B., Lei Z., Uhlemman U., Eckert K., Mutschke G. Mass transfer and electrolyte flow during electrodeposition on a conically shaped electrode under the influence of a magnetic field. *J. Electroanal. Chem.* **842**: 203-213, 2019.

PARTICLE DISPERSION IN LIQUID METALS BY MAGNETIC SONICATION

Gunter Gerbeth*[1], Martins Sarma[1], and Ilmars Grants [2]
[1]Helmholtz-Zentrum Dresden – Rossendorf, Institute of Fluid Dynamics, Dresden, Germany
[2]Institute of Physics, University of Latvia, Riga, Latvia

Summary Cavitation in liquid metals is supposed to provide conditions for the desired homogeneous dispersion of small particles, leading for metal matrix composites often to improved mechanical properties. A contactless magnetic field approach to induce cavitation in liquid metals is applied using a combination of AC and DC magnetic fields, which provide a strong oscillating pressure inside the molten sample. New results on the dispersion of a variety of particles in melts such as steel, iron and nickel will be given, including experiments in a high magnetic field laboratory.

INTRODUCTION

Acoustic cavitation by power ultrasound is widely used for the purpose of particle dispersion in room temperature liquids. There are also numerous experimental reports demonstrating that power ultrasound facilitates the dispersion of particles in a molten metal. So far, this technique has been applied for the production of metal matrix nano-composites (MMNC) of light metal alloys [1]. Being extremely violent on the micro-scale, the cavitation degrades also the vibrating surface transmitting the ultrasound into the liquid. A contactless technique for cavitation excitation is, therefore, desirable, in particular for high-melting liquid metals such as steel for which no ultrasonic transducers exist with a reasonable life-time in the melt. A contactless excitation of cavitation is possible by superposition of induction heating with a steady axial magnetic field. This combination creates an alternating radial magnetic body force in a cylinder [2]. The irrotational part of this force produces pressure oscillations. This contactless magnetic excitation of cavitation, which is furtheron called magnetic sonication, was first demonstrated in [3] using a steady magnetic field of up to 0.5 T. Here we report on experiments performed in much stronger steady magnetic fields up to 10 T, while using the same induction heater with an amplitude of up to 0.13 T.

THEORETICAL BACKGROUND

Consider an infinite liquid metal cylinder of radius a in a uniform magnetic field with a steady and an alternating component

$$\mathbf{B} = \left(B_z + b(r)e^{i\omega t}\right)\mathbf{e}_z. \tag{1}$$

The alternating component of the magnetic field induces an azimuthal current, which in combination with the static axial field creates an oscillating radial force. This force is curl-free and, therefore, is balanced by an oscillating pressure field. Suppose the frequency ω is high enough to cause a strong skin-effect ($\sigma\omega\mu_0 a^2 >> 1$, where σ and μ_0 are the electric conductivity and magnetic permeability of the metal, respectively), yet low enough to form a long acoustic wave with a wave length much larger than a. Additionally suppose that the alternating field component is much smaller than the steady one ($b_A << B_z$) where $b_A = |b(a)|$. Under these conditions the alternating magnetic pressure is uniform in the bulk and has the amplitude [3]

$$p = \frac{B_z b_A}{\mu_0}. \tag{2}$$

Acoustic cavitation is recurring non-linear growth and subsequent collapse of small bubbles due to the oscillating pressure in the liquid. In an ideal liquid, where transient voids are only created by thermodynamic fluctuations, the critical tension is comparable to the yield strength of metals. Such tension is out of reach for magnetic sonication. Thus, the observed beneficial effects of power ultrasound on particle dispersion in metal alloys depend on size and density of cavitation nuclei, which is largely unknown and uncontrolled. As bubbles start to cavitate, they emit their own sound containing characteristic sub-harmonics f_0/n, where f_0 is the drive frequency and n = 2,3… [3]. We use this property for the identification of cavitation inception, at least in the low-field case.

The melt flow and its stability during magnetic sonication was numerically analysed in [4]. The magnetic body force of the induction heater drives two symmetrical counter-rotating tori with inward-directed velocity in the midplane. An almost linear scaling with the driving force was observed for the maximum values of the velocity components in a strong steady field, until the flow becomes unstable at some specific control parameter combining both the alternating and steady magnetic field. As expected pronounced side-layers come up for increasing Hartmann number of the steady field. Regarding stability, a transition from the bulk instability mode with comparable low wave number to the side layer mode with larger wave number was observed. Besides steady forces driving a mean flow in the melt, there are force components oscillating with the ac field frequency. For increasing field strengths they may as well contribute to the mean flow by the steady streaming effect. Estimates for it will be presented.

*Corresponding author. E-mail: g.gerbeth@hzdr.de

EXPERIMENTAL SET-UP

A sketch of the experimental set-up in the low magnetic field (LMF) of up to B_z = 0.8 T is shown in Fig. 1. Experiments are made in an evacuated cell (p_0 < 400 Pa) consisting of the quartz tube 5 and water cooled copper caps 3. The cell is placed in a 82 mm wide vertical gap of an electromagnet. Water cooled copper screens 8 are used to protect the ferromagnetic pole shoes 9 from the induced currents. The refractory side support 6 accomodates vertical variations of the magnetic pressure. The electromagnet provides a magnetic flux density of up to 0.8 T in the experimental volume, and the maximum inductor current r.m.s value is I_{AC} = 1300 A that corresponds to b_A = 0.130 T. The AC frequency is f_0 = 14.7 kHz.

In order to reach a significant increase of the oscillating pressure amplitude, additional experiments in a high magnetic field (HMF) were conducted at the High Magnetic Field Laboratory of HZDR. The used magnet is 2290 mm long, has a 150 mm bore diameter and fields up to B_z = 19 T. The coils are immersed in liquid helium and the temperature is around 4 K. A use of the previous set-up was not possible, thus a modified melting cell was constructed. A multi-walled chamber using vacuum for thermal isolation was built. As the maximum field strength is located in the lower part of the bore, the induction coil was fed by 2200 mm long supply bars.

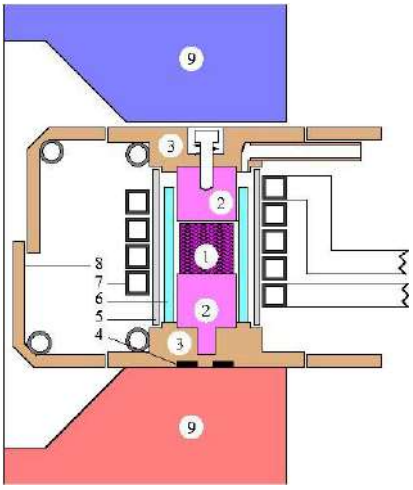

Figure 1: Scheme of the experimental set-up.

RESULTS

The onset of cavitation has been clearly observed in almost all liquid metals under consideration in the LMF experiments. Using piezoelectric sensors at the surface of the bottom cap allowed to display the sound spectrum, which for pressure oscillations above about 30 kPa showed sub-harmonics f_0/n characteristic for cavitation. In case of the HMF experiments this observation was not possible, as the induction coil with the long supply bars was forced to mechanical vibrations in the HMF, which superimposed and dominated the signals from the piezoelectric sensors. Thus, direct cavitation detection as in the LMF case was not possible here.

A multitude of samples have been processed with the high-temperature metals iron, nickel and steel using oxides (TiO_2, Y_2O_3, CeO_2), carbides (TiC, ZrC), nitrides (TiN) and borides (TiB_2, ZrB_2) as particles. For most of those cases the tendency that stronger pressure oscillations result in a better dispersion of the particles has been observed. An example is shown in Fig. 2 for TiB_2 particles (initial size 4 µm) in steel. Without a steady magnetic field large particle clusters are found throughout the matrix (a), whereas the application of an 8 T DC field prevents clustering and both large (empty arrows) and small (solid arrows) precipitates are found (b). More examples and details will be given in the presentation.

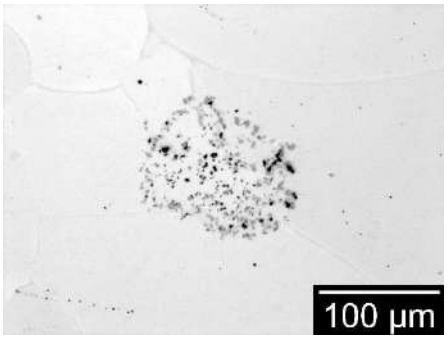

Fig. 2(a): TiB_2 particles in steel without DC field.

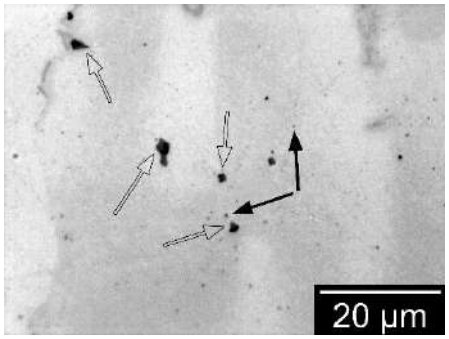

Fig. 2(b): TiB_2 particles in steel in an 8 T DC field.

CONCLUSIONS

Contactless magnetic sonication is capable of avoiding the agglomeration of particles in metal melts, as well as to break-up agglomerated particle clusters. Systematic experiments for a variety of particles in steel, iron and nickel showed this with the clear tendency that stronger pressure oscillations for increasing DC magnetic field improved the particle dispersion.

References

[1] Li X., Yang Y., Weiss D.: Theoretical and exp. study on ultrasonic dispersion of nanoparticles. *Metall. Sci. Technol.* **26**: 12–20, 2008.
[2] Wang Q., et al.: Direct generation of intense compression waves in molten metals. *J. Mater. Sci. Technol.* **19**: 5–9, 2003.
[3] Grants I., Gerbeth G., Bojarevics A.: Contactless magn. excitation of acoust. cavitation in liquid metals. *J. Appl. Phys.* **117**: 204901, 2015.
[4] Grants, I., Gerbeth, G.: Stability of melt flow during magn. sonication in a float. zone configuration. *Phys. Rev. Fluids* **3**: 063902, 2018.

LINEAR STABILITY OF FERROFLUIDS IN DIFFERENT CONFIGURATIONS

Sarah Ferguson Briggs*[1] and Jonathan Mestel[1]
[1]Department of Mathematics, Imperial College, London, United Kingdom

Summary The linear stability of incompressible, isothermal ferrofluids is considered in different configurations. The stability of a column of ferrofluid, surrounded by another with a different magnetic susceptibility, centred on a current-carrying rigid wire that produces an azimuthal magnetic field, is determined. A ferrofluid with a continuous, spatially-dependent susceptibility, subject to a non-uniform field is considered in two configurations; a cylindrical and a planar geometry. Additionally, if the susceptibility varies slowly with space we prove a stability condition for a general configuration.

Ferrofluids are colloidal fluids, consisting of magnetic solids, such as magnetite, dissolved in a surfactant and carrier solution, usually water, kerosene or oils [1]. As a result, the liquid becomes magnetised in the presence of a magnetic field, and to prevent agglomeration, the nanoparticles are either electrically charged, or coated in a surfactant [2]. Technological and industrial applications of ferrofluids include dynamic sealing and heat dissipation, and there have been biomedical advances in their use in hyperthermia treatment and magnetic drug targeting [2]. For these various applications, ferrofluids will be in different domains subject to different magnetic fields. Thus, the theoretical investigation of a variety of configurations can be used in determining the strength and direction of a magnetic field necessary for a stable, real life system.

When a magnetic fluid is subject to a non-uniform magnetic field, the magnetic particles are attracted to a region of highest field intensity as a result of the magnetic dipoles rotating to align with the field, giving the minimal energy configuration [2]. We therefore investigate not only the interfacial stability of two ferrofluids with constant magnetic susceptibility, but also the stability of one ferrofluid with continuous susceptibility that varies spatially, subject to a non-uniform field.

FORMULATION

A ferrofluid (FF) obeys the magneto-static limit of Maxwell's equations, with free current density and Maxwell's displacement current deemed negligible. We assume the magnetisation is colinear with the magnetic field, $\mathbf{H}$. In the momentum equation the force density appears as

$$\mathbf{f} = \int_0^H H \boldsymbol{\nabla}_H \chi dH \tag{1}$$

but, assuming χ does not depend explicitly on H, (1) simplifies to

$$\boldsymbol{f} = \frac{1}{2} H^2 \boldsymbol{\nabla} \chi, \tag{2}$$

where χ is the magnetic susceptibility of the FF and $|\boldsymbol{H}| = H$ [1].

Additionally, when χ varies with space we impose

$$\frac{D\chi}{Dt} = 0,$$

such that χ is advected passively and diffusion processes occur on a large time scale.

CYLINDRICAL DOMAIN

The stability of a column of FF, with susceptibility $\chi = \chi_1$, centred on a rigid wire, surrounded by another FF, with susceptibility $\chi = \chi_2$, is investigated in a fully three-dimensional setting, shown in Figure 1. An electric current runs through the wire, generating an azimuthal magnetic field, $H \sim 1/r$. Since χ is constant, $\boldsymbol{f} = 0$ in the momentum equation, and the forcing acts as a magnetic stress at the interface of the fluids.

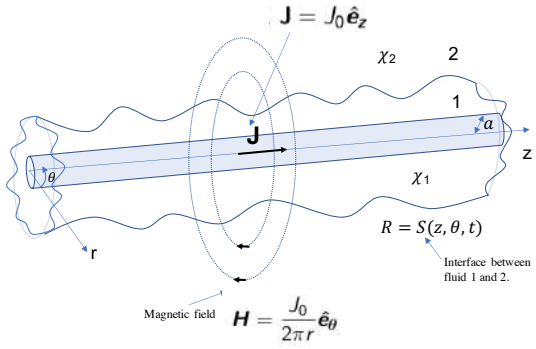

Figure 1: Schematic of the system.

*E-mail: sf218@ic.ac.uk

Results: When $\chi_1 > \chi_2$, it is unstable to axisymmetric perturbations only, and is stabilised by increasing the current in the wire. For $\chi_2 > \chi_1$, the system is unstable to both axisymmetric and non-axisymmetric modes, and increasing the current no longer stabilises the system.

When $\chi_2 > \chi_1$, the region of highest χ is not aligned with the region of highest field intensity, since $dH/dr < 0$, resulting in an unstable system. This motivates the investigation of an infinite column of FF centred around the wire, where $\chi = \chi_0(r)$, shown in Figure 2. For arbitrary Reynolds number, we consider axisymmetric perturbations and prove using variational methods that the system is unstable iff $d\chi_0/dr > 0$ at some point. In the inviscid limit the result holds for non-axisymmetric perturbations also.

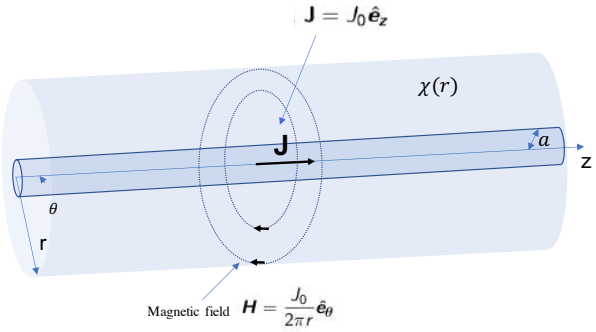

Figure 2: Schematic of the system

Importantly, applying a significantly strong axial field stabilises the system with $\chi = \chi_0(r)$ and when χ is piecewise-constant, irrespective of $\chi_2 > \chi_1$ or $\chi_1 > \chi_2$.

PLANAR DOMAIN

We now consider a FF between two walls, subject to a perpendicular field, $\boldsymbol{H} = H_0(z)\hat{\boldsymbol{e}}_{\boldsymbol{z}}$. For an equilibrium

$$\chi = \chi_0(z) = \frac{A}{H_0(z)} - 1,$$

where A is a constant such that $\chi_0 > 0$. It follows that $dH_0/d\chi_0 < 0$ and we prove the equilibrium is unstable.

Additionally, we prove applying a sufficiently large, rapidly rotating field stabilises the system.

GENERAL χ VARIATION

More generally, given a volume V of FF, where the equilibrium $\chi = \chi_0$, $H = H_0$, is such that χ_0 varies gradually with space and

$$\chi_0 \equiv \chi_0(H_0) \iff \boldsymbol{\nabla} \times \boldsymbol{f} = 0,$$

where $\boldsymbol{f}$ is given by (2). We prove the configuration is unstable iff $dH_0/d\chi_0 < 0$ somewhere in V.

CONCLUSIONS

(1) In the cylindrical, two fluid configuration, a sufficiently large current through the wire stabilises the system when $\chi_1 > \chi_2$, but not when $\chi_2 > \chi_1$. Applying a sufficiently large axial field will stabilise both.

(2) The equilibria considered in the cylindrical and planar geometries, when χ is space dependant, are unstable for $dH_0/d\chi_0 < 0$, and we prove this for a general configuration with $\chi = \chi_0$ varying slowly with space.

(3) For the cylindrical system an axial field will stabilise the system, and for the planar system a rapidly rotating field is needed.

Acknowledgments: Research supported by the Engineering and Physical Sciences Research Council (U.K.)

References

[1] Cowley, M.D.; Rosensweig, R.E.; *The interfacial stability of a ferromagnetic fluid.* Springer,2002.
[2] Scherer,C.; Figueiredo Neto, A.M.; *Ferrofluids: properties and applications.* Braz. J. Phys. vol.35 no.3a São Paulo Sept. 2005
[3] Rosensweig, R.E.; *Ferrohydrodynamics* Cambridge: Cambridge University Press 1985.

STEADY CONVECTION OF DIELECTRIC FLUIDS IN MICROGRAVITY USING NON-UNIFORM AC ELECTRIC FIELDS

Alex Jawichian[1], Laurent Davoust*[1], and Samuel Siedel[1]
[1]Univ. Grenoble Alpes/Grenoble-INP/CNRS,SIMaP,EPMgroup,38402 Saint Martin d'Hères,France

Summary The role of an AC electric field on dielectric liquids confined in a differentially heated cavity is considered. In the purpose of sustaining steady TEHD flows, the electrode arrangement is modified, in contrast to the typical vertical planar case usually investigated in the literature, so as to create non-uniform electric fields. A numerical study is developed in order to investigate such a system in microgravity conditions. Our preliminary results show that a significant and steady perturbation of conductive heat transfers is possible via the use of non-intense and non-uniform electric fields. This suggests a significant improvement in heat transfer efficiency when electric fields are used. The results are compared to scaling laws for the Nusselt number.

INTRODUCTION

A finite volume of dielectric liquid, submitted to a temperature gradient in a closed cavity, experiences a change in its dielectric constant, ϵ_r, such that [1]:

$$\epsilon_r = \epsilon_{ref}(1 - \lambda(T - T_{ref})), \tag{1}$$

where λ is the thermo-dielectric coefficient, T is the temperature, and the ref subscript denotes a reference value. As a consequence, if a thermal gradient is applied upon a dielectric fluid together with an electric field, a joint contribution can be expected which gives rise to a convective motion of thermo-dielectrophoretic (T-DEP) origin [2]. This is all the more true as the dielectric relaxation frequency is always larger than the angular frequency of the applied voltage.

Since the dielectric liquid is considered to be confined, it is more relevant to write the vorticity equation (nondimensional). In microgravity, this writes as,

$$(\vec{u}.\vec{\nabla})\vec{\omega} = \mathrm{Pr}\nabla^2\omega + \mathrm{Pr.L}\,(\vec{E}.\vec{\nabla})\vec{E} \times \vec{\nabla}T, \tag{2}$$

with $\vec{\omega} = \vec{\omega}(0, 0, \omega_z)$ the vorticity, and $\vec{M}_{DEP} = \mathrm{Pr.L}(\vec{E}.\vec{\nabla})\vec{E} \times \vec{\nabla}T$, the DEP torque. The non-dimensional numbers are the Prandtl number, $\mathrm{Pr} = \nu\alpha^{-1}$ and the Roberts number, $\mathrm{L} = \frac{\epsilon_{ref}\epsilon_0\lambda\Delta T\Delta V^2}{\rho\nu\alpha}$. The symbols $\rho, \nu, \alpha, \epsilon_0$, and ΔV are respectively the density, the kinematic viscosity, the thermal diffusivity, the vacuum permittivity, and the voltage applied between the electrodes.

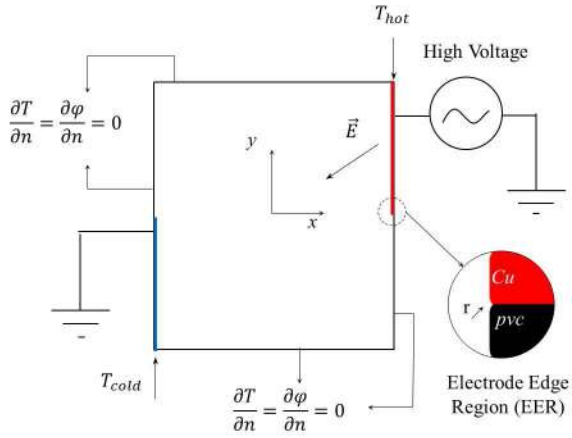

Figure 1: Half electrode pair, electrical, and thermal boundary conditions.

In the case of a differentially heated cavity, where the two isothermal vertical walls are also the electrodes, it can be noticed that in the perfectly conductive regime ($\vec{u} = \vec{0}$), the electric field, its gradient, and the temperature gradient are all aligned: the consequence is that the DEP torque drops to zero. In such a case, the fluid remains stagnant, and a linear temperature profile is established along the cavity [3]. In this communication, the aim is to investigate a new electrode arrangement that can steadily sustain a thermo-electrohydrodynamic (TEHD) flow based on a DEP torque at leading order.

In an attempt to deliver a significant effect of the DEP torque in (2), misaligned planar electrodes are placed along each vertical side wall (fig. 1). Thermally and electrically speaking, the walls in red and blue (pair of half electrodes) in fig. 1 are submitted to Dirichlet conditions, while the complementary part of the walls (in black) are submitted to Neumann conditions. The two half electrodes are not facing each other so that a non-uniform distribution of the electric field is achieved which depends on the electrode to wall lengths ratio, as well as on the curvature radius of the electrode edges (see EER in fig. 1).

*Corresponding author. E-mail: laurent.davoust@grenoble-inp.fr

RESULTS

Numerical simulations confirm that in microgravity conditions and for any value of the Roberts number, $L > 0$, the dielectric liquid is set in motion due to a steady contribution of the DEP torque.

In the presence of an electric field, the DEP force disturbs the stagnant conductive regime and leads to the generation of two counter-rotating vortices (fig. 2). The velocity scale, as well as the vorticity scale, grows with larger and larger electric Grashof numbers. The vortices are not symmetric, which is consistent with the asymmetry of the temperature and the electric potential distributions. Furthermore, the intensification of the angular momentum is present near the electrode edges due to the high intensity of the electric fields in these regions. The angular momentum is later diffused far within the volume under viscosity.

Concerning heat transfer enhancement, the averaged Nusselt number, defined as the ratio of the total heat flux to the conductive heat flux, is displayed in (fig. 2). Its significant increase demonstrates the capability of the DEP-induced convection to improve convective heat transfers. We also notice that for different Pr values, the Nusselt number scales as the Roberts number to the power one fourth $\mathrm{Nu} \sim \mathrm{L}^{0.25}$, while the Nusselt remains independent of the Prandtl number as predicted from the scaling analysis.

One also notices the presence of another regime that is established beyong a critical value of the Roberts number, $\mathrm{L_c} = 10^5$. In this regime, the Nusselt number scales as the Roberts number to the power of 0.15, $\mathrm{Nu} \sim \mathrm{L}^{0.15}$. This means that the heat transfer enhancement due to higher voltages becomes less significant. This can be explained by to the generation of a third vortex within the volume, that counteracts the previously existing counter rotating vortices (viscous damping).

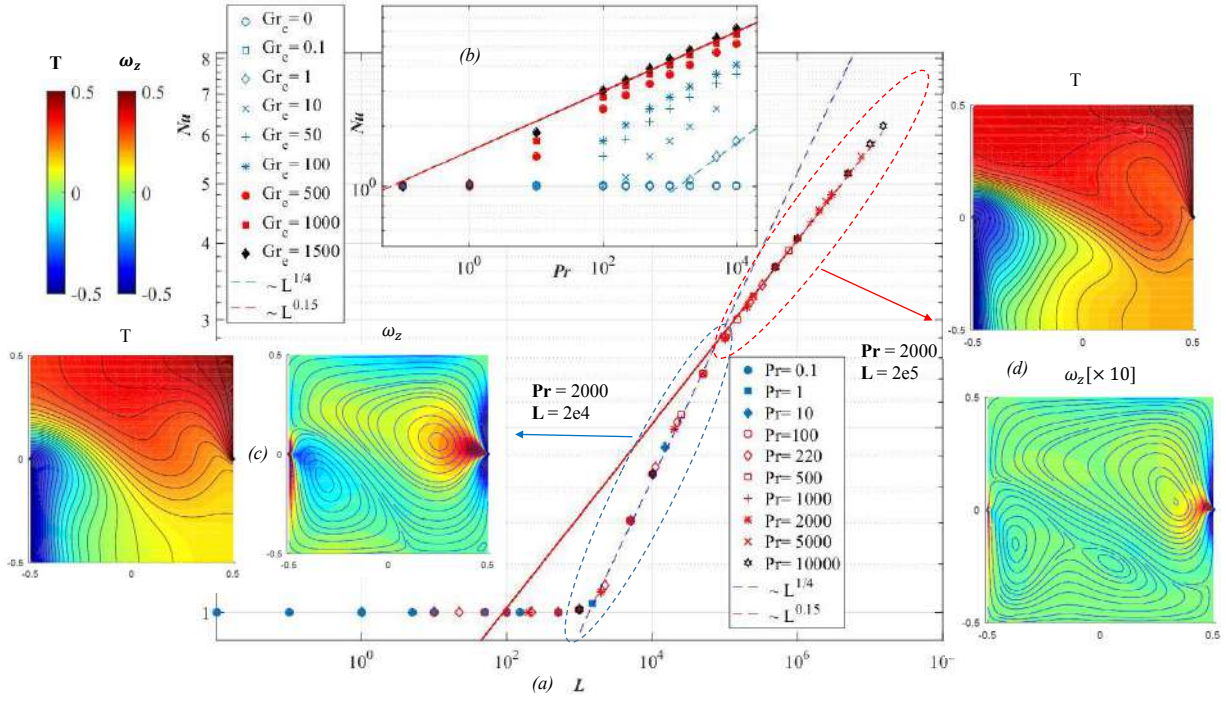

Figure 2: *(a)* Nusselt number as a function of the Roberts number for a range of Prandtl numbers, *(b)* Nusselt number as a function of the Prandtl number for a range of electric Grashof numbers, *(c)* Vorticity and Temperature fields for Pr=2000 and L=2e4, and *(d)* Vorticity and Temperature fields for Pr=2000 and L=2e5.

CONCLUSIONS

In microgravity conditions, it is demonstrated that the imposition of an AC electric field causes steady convective flows of dielectric liquids provided that a temperature gradient is made available, and that the electric field is not uniform. A steady DEP-induced convective flow is provided, which allows heat transfers to be enhanced within on-board systems, in microgravity conditions.

References

[1] Jones T., Electrohydrodynamically Enhanced Heat Transfer in Liquids - A Review. *Advances in Heat Transfer* **14**: 107-148, 1979.
[2] Landau L. D., Lifshitz E. M. Electrodynamics of continuous media. Pergamon Press, Oxford 1993.
[3] Roberts P. H., Electrohydrodynamic Convection. *The Quarterly Journal of Mechanics and Applied Mathematics* **22**: 211-220, 1969.

EHD ACTUATION OF A LIQUID-VAPOR INTERFACE ALONG A CAPILLARY ARRAY IN THE AC REGIME

Nicolas Cardin[1], Laurent Davoust*[1], Samuel Siedel[1], Stéphane Lips[2], and Jocelyn Bonjour[2]
[1]Univ. Grenoble Alpes, CNRS, Grenoble INP, SIMaP, F-38000 Grenoble, France
[2]Univ Lyon, CNRS, INSA-Lyon, Université Claude Bernard Lyon 1, CETHIL UMR5008, F-69621, Villeurbanne, France

Summary The present communication is devoted to the role of an AC electric field on the deformation of a meniscus confined inside a grooved capillary structure. In the presence of an electric field, an electric stress is seen to apply upon liquid-vapor interfaces. The normal component of the electric stress adds to the capillary stress and the gravity force, which leads to a modified pressure jump and therefore to the deformation of the interface. The latter is investigated experimentally thanks to chromatic confocal microscopy. In the presence of an AC electric field, a resonance phenomenon and a double frequency oscillation are observed, depending on the frequency of the electric actuation. A spectral analysis of the interfacial deformation as a function of the frequency is proposed making use of frequency sweep.

INTRODUCTION

This paper addresses the effect of an AC electric field on liquid ridges stretching along an array of U-shaped microgrooves. This study is motivated by the need to enhance the performance and the robustness of stratified two-phase systems such as heat pipes [1] for instance. In such systems, one main limitation is the capillary pumping of the liquid phase along the microgrooves. The capillary structure enables liquid pumping due to a pressure gradient which results from a non-uniform distribution of the interfacial curvature. When the capillary structure cannot provide a capillary pressure difference between the evaporator and the condenser high enough to overcome the pressure drop related to the back flow of the liquid phase, then the capillary limit is reached. This limit is widely encountered in industrial applications. One possible solution to increase the capillary limit is to impose externally an additional stress at the liquid-vapor interface. If an electric field is applied upon a stratified two-phase system, a normal electric stress arises at the interface as an adding contribution to the normal component of the momentum balance. This is expected to extend the capillary limit [2, 3]. A dielectric stress is found to arise at a liquid-vapour interface, which, together with the capillary force, is responsible for changing the pressure jump at the interface [4, 5, 6]. The experiments in the available literature performed with a EHD-enhanced capillary structure indicate an improvement of the thermal performances but neither the effect on the liquid distribution nor the distinctive effects of a DC regime versus a AC regime have been measured [7, 8, 9]. A numerical paper [10] were developed to investigate the effet of a DC electric field on two-phase thermohydraulics. In this paper, the ability of the electric field to change the shape of a meniscus is investigated by means of confocal microscopy. Resonance effects are observed when use is made of an AC field. A length scale selectivity is suspected depending on the frequency of the AC actuation.

GENERAL CONFIGURATION

In this study a sealed cavity is formed from two opposite plates. Because these plates are used as an electrode pair, a planar capacitor is thus obtained and is able to sustain a strong enough electric field. The top plate is flat and connected to a high voltage while the bottom plate is connected to ground. The bottom plate is characterized by a capillary structure made from a series of five squared (400 x 400 μm) grooves filled with HFE 7100, a dielectric fluid. This geometry, presented in Figure 1 is representative of a grooved heat pipe. Here, the length of the groove can be considered as infinite and the configuration is viewed as 2-D. Figure 1 represents the setup with a grooved aluminum plate at the bottom, separated from a glass plate at the top by a gasket seal made with PTFE. The glass plate is coated with an indium tin oxide (ITO) layer on its inner part and used as the high voltage electrode at the top of the cavity. The ITO layer is transparent and therefore allows for optical investigation of the liquid-vapor interface even when the electric field is applied. The ITO layer is connected to the high voltage owing to a very thin layer of copper inserted all around the cavity between the upper plate and the PTFE gasket. A spacing of 1.5 mm is ensured between top and bottom electrodes (Fig.1a). This volume is essentially filled by vapor while the liquid phase is essentially confined within the grooves.

When a voltage is applied between the electrodes in the studied configuration, the vapor and liquid phases behave like two superimposed electric capacitors due to their respective dielectric permittivities. This leads to a jump in the electric field at the fluid interface, as well as to a jump in the electric properties. The electric stress so generated at the interface has two components. Its normal component can actuate the liquid-vapor interface. It should be recalled that the normal electric stress is proportional to the square of the electric field $\tau_n \approx \varepsilon E^2$ (i.e. to the square of the applied voltage).

*Corresponding author. E-mail: laurent.davoust@simap.grenoble-inp.fr.

FREQUENCY SWEEP AND RESONANT FREQUENCIES

To study the effect of the electric stress on the interface, an oscillatory voltage with a time-dependent frequency is imposed between both electrodes (Fig.1b). The time-dependent elevation of the meniscus of the center of the microgroove is measured thanks to confocal microscopy (Fig.1c). A symmetry break-up on the signal delivered by the confocal microscope can be reported in the regime of low frequencies. Depending on the actuation frequency, the peak elevation of the interface can be observed. To analyse the frequency content of the signal, a time-dependent Fourier analysis is applied upon the elevation signal. A fundamental frequency, defined as the most energetic one, is found twice as much as the frequency of the actuation voltage. This is consistent because the oscillatory deformation of the interface is driven by the electric stress which is proportional to the square of the AC voltage. A sub-harmonic frequency, equal to the actuation frequency, is also found which suggests the presence of electric charge density in the liquid volume since the Coulombic force is proportional to the voltage applied. For a frequency large enough, the relaxation of the electrical charges makes possible the arising of multiple harmonic frequencies. This confirms that dielectric effects become prior. These frequencies correspond to the natural resonant modes of the liquid-vapor interface as confirmed from considerations on the dispersion relation. Because the viscous frequency is much smaller than most of the resonant frequencies, a decisive advantage of the AC approach over the DC approach is that it makes possible the local actuation of the liquid-vapor interface independently from the liquid reservoir located at the condenser of a heat pipe.

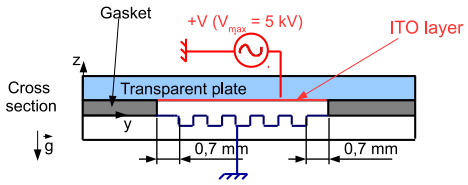

(a) Cross section of the experimental set-up

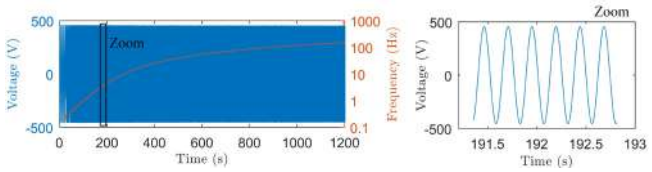

(b) Evolution of the electric voltage

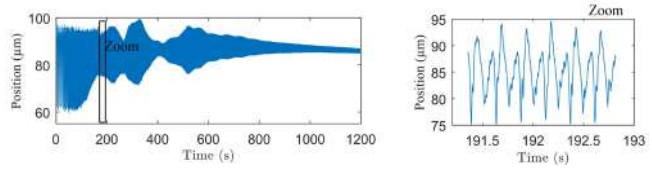

(c) Evolution of the elevation of the center of the meniscus in the groove

Figure 1: a) Cross section of the experimental set up. b) and c) Spectral analysis.

MAIN RESULTS

In this paper, the ability of an AC electric field to change the shape of a meniscus is investigated for the first time by means of confocal microscopy. The experimental bench consists in a slim closed configuration made with one grounded grooved plate at the bottom, facing a flat plate at the top (Figure 1a). The latter is submitted to a high voltage AC regime. The cavity is filled with HFE 7100 as a working fluid. Experimental results highlight the deformation of the liquid-vapor interface in presence of an electric field which is further compared to an in-house numerical method: a good agreement is found. The respective effects of DC vs AC regimes are also investigated: an electro-capillary hysteresis is observed when using a DC electric field whereas resonance effects are observed when use is made of a AC field. A length scale selectivity is suspected depending on the frequency of the AC actuation.

References

[1] Faghri A., Heat pipe science and technology, *Fuel Energy Abstr.*, 285–285, 1995.
[2] Jones T.B., Perry M.P., Electrohydrodynamic heat pipe experiments, *J. Appl. Phys.* **45**: 2129–2132, 1974.
[3] Saad I., Maalej S., Zaghdoudi M.C., Etude de l'effet électrohydrodynamique sur les performances d'un minicaloduc plat comportant une structure capillaire rainurée, *22ème Congrès Fr. Mécanique*, 2015.
[4] Melcher J.R.,Taylor G.I., Electrohydrodynamics: A Review of the Role of Interfacial Shear Stresses, *Annu. Rev. Fluid Mech.* **1**, 1969.
[5] Ramos A., Castellanos A., Equilibrium shapes and bifurcation of captive dielectric drops subjected to electric fields, *J. Electrost.* **33**: 61–86, 1994.
[6] Castellanos A., Electrohydrodynamics, Springer, Vienna, 1998.
[7] Loehrke R., Debs R., Measurements of the performance of an electrohydrodynamic heat pipe, *10th Thermophys. Conf.*, 197–200, 1975.
[8] Cooper P., EHD enhancement of nucleate boiling, *J. Heat Transf.* **112**: 458–464, 1990.
[9] Yu Z., Hallinan K.P., Kashani R.A., Temperature control of electrohydrodynamic micro heat pipes, *Exp. Therm. Fluid Sci.* **27**: 867–875, 2003.
[10] Cardin N. , Davoust L., Lips S., Siedel S., Brik M.E.M., Bonjour J., Effect of a DC electric field on a meniscus in a square groove, *J. Electrost.* **100**: 103350, 2019.

A THEORY OF DISSIPATIVE ALFVÉN WAVES IN A BOUNDED DOMAIN

Guillaume Bermudez*[1] and Alban Pothérat[2]
[1]Département de Physique, Ecole Normale Supérieure, Université PSL, 75005 Paris, France
[2]Center for Fluids and Complex Systems, University of Coventry, Priory Street, Coventry CV1, UK

Summary Magnetohydrodynamics (MHD) wave behaviour can occur under certain conditions due to the coupling between the velocity field of the fluid and the magnetic field; these waves are called Alfvén waves. Alfvén waves exist if their wavelength (proportional to the external magnetic field) is smaller than their dissipation lengthscale (due to viscosity and resistivity). Because the latter is usually very short, Alfvén are commonly assumed to be absent from small-scale laboratory experiments with liquid metals. Previous experimental works showed that this assumption breaks down for sufficiently high magnetic fields, prompting the question of the conditions in which these waves may be observed in laboratory scale experiments with liquid metals, especially when physical boundaries are present. In this paper, we set out to answer this question theoretically.

CONTEXT

Hannes Alfvén showed in 1942 [1], in what one can call a concise article, the existence of magnetohydrodynamic (MHD) waves in perfectly conducing and inviscid fluids due to the two-way coupling of the velocity and magnetic fields. Some later theoretical developments then showed that, under certain conditions, the waves can also be observed in resistive viscous fluids. Although quite challenging due to their high viscosity and resitivity, this fact has been experimentally confirmed throughout the XX$^{\text{th}}$ century [2–5]. These complex wave behaviours would be very promising subjects of research in the lab to model astrophysical phenomenon but are still limited by the highly dissipative tendency of liquid metals. However, most of the theoretical developments on Alfvén waves seem to be limited to open geometries when liquid metal experiments are bounded. Yet, the boundary conditions determine the growth of Alfvén waves, through the phenomenon of reflection *inter alia*.

MODEL AND RESULTS

In the present work, we derive a novel model describing the conditions to observe Alfvén waves in dissipative media. We study a compact geometry, bounded by two horizontal walls called Hartmann walls, and vertical lateral walls of arbitrary shape, allowing variable separation, which describes liquid metal experiments in tanks.

Let us consider a non-relativistic, quasi-neutral, incompressible conducing fluid and introduce its velocity field $\mathbf{v}$ and magnetic field $\mathbf{B}$. The fluid is governed by the full-MHD equations, which are a resourceful rewriting of Navier–Stokes equations and Maxwell equations, which, given our geometry, can be rewritten using alfvénic units as

$$\frac{\partial \mathbf{v}}{\partial t} + (\mathbf{v}\cdot\boldsymbol{\nabla})\mathbf{v} = (\mathbf{B}\cdot\boldsymbol{\nabla})\mathbf{B} + \nu\boldsymbol{\nabla}^2\mathbf{v}, \qquad \boldsymbol{\nabla}\cdot\mathbf{v} = 0,$$
$$\frac{\partial \mathbf{B}}{\partial t} + (\mathbf{v}\cdot\boldsymbol{\nabla})\mathbf{B} = (\mathbf{B}\cdot\boldsymbol{\nabla})\mathbf{v} + \eta\boldsymbol{\nabla}^2\mathbf{B}, \qquad \boldsymbol{\nabla}\cdot\mathbf{B} = 0,$$

ν being the viscosity of the fluid, η the magnetic diffusivity of the fluid, the magnetic field being rescaled as the Alfvén speed.

The fluid, initially at rest, is submitted to an external stationary and homogeneous magnetic field $\mathbf{B}_0 = B_0\hat{\mathbf{e}}_z$ (generated by a magnet for instance) which breaks the symmetry of the system, introducing a preferential direction for Alfvén wave modes alongside its field lines z. As in a bounded geometry the reflection of Alfvén waves — which is nearly total [6] — is a crucial element determining the growth of wave modes, we separate the x, y normal boundaries on the side-walls on the one hand and the z tangential boundaries on the so-called Hartmann walls on the other hand.

To do so, we search for modal Alfvén z-propagating modes and we account for the side-walls boundary conditions expanding over the basis of the eigenmodes $\mathbf{v}_\alpha$ of the normal laplacian $\boldsymbol{\nabla}_\perp^2 = \frac{\partial^2}{\partial x^2} + \frac{\partial^2}{\partial y^2}$ such that $(\boldsymbol{\nabla}_\perp^2 + \alpha^2)\mathbf{v}_\alpha = \mathbf{0}$, satisfying the side-walls boundary conditions. For these modes, the linearly perturbated full-MHD equations yields a complex (k, ω) dispersion relation, $\mathfrak{Re}\, k$ being the z-component of the wavevector, $\mathfrak{Im}\, k$ the corresponding growth rate and ω the frequency, depicted on Fig. 1 overleaf, which has two branches :

- a Hartmann mode k^+, an overdamped mode characterising the MHD boundary layer (red in Fig. 1) ;
- an Alfvén mode k^-, a wave-like mode propagating at the Alfvén speed (blue in Fig. 1).

The control parameters for that dispersion relation are the Prandtl number $\mathcal{P}m = \nu/\eta$ (ratio of kinematic and magnetic diffusivities), the Hartmann number $\mathcal{H}a = \dfrac{B_0\ell}{\sqrt{\eta\nu}}$ (acting as an nondimensional magnetic field) and the eigenvalue α.

Although damped, Alfvén waves can be observed if the damping length is significantly larger than the system size, and the latter is significantly larger than the wavelength which yields the condition that $|\mathfrak{Im}\, k^-| \ll 1/\ell \ll |\mathfrak{Re}\, k^-|$.

*Corresponding author. E-mail: guillaume.bermudez@ens.fr.

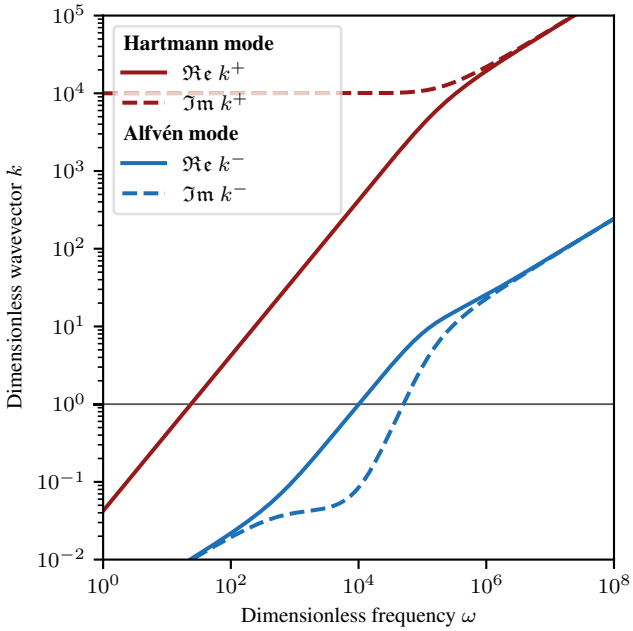

Figure 1: Plot of the dispersion of relation (k, ω) stemming from linearly perturbated full-MHD equations in a bounded geometry. Values of the influence parameters are taken for a typical galinstan experiment from *Alboussière et al.* [4] : $\mathcal{P}m = 10^{-6}$, $\mathcal{H}a = 10^4$, $\alpha = 1$.
The wavevector k has been made dimensionless with the z-characteristic length of the system ℓ and the frequency ω with the effective diffusion time $\ell^2/\sqrt{\eta\nu}$.

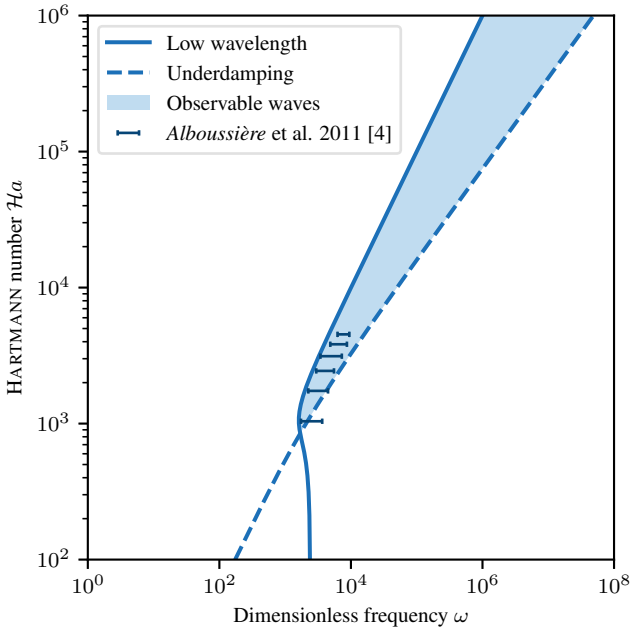

Figure 2: Plot of the region for which the alfvénic mode from the Fig. 1 are observed, compared with experimentally observed Alfvén waves from *Alboussière et al.* [4].
Values of the influence parameters are taken for a typical galinstan experiment [4] : $\mathcal{P}m = 10^{-6}$, $\alpha = 1$.
The frequency ω has been made dimensionless with the effective diffusion time $\ell^2/\sqrt{\eta\nu}$.

Such conditions restrain the observable frequencies to the region plotted in the Fig. 2 above. We have analytically proved that to observe Alfvén waves, the Hartmann number $\mathcal{H}a$ must be higher than a critical value

$$\mathcal{H}a > \mathcal{H}a_c = \alpha\sqrt{\mathcal{P}m^{-1} - 1} \qquad \text{for} \quad \mathcal{P}m \leqslant 1.$$

α can be understood as a geometrical factor. Noteworthily, this critical value is consistent with experimental observations as for a typical galinstan (GaInSn) experiment [4, 5] $\mathcal{H}a_c \simeq 3 \times 10^3$ in which $\alpha \simeq 1$ and $\mathcal{P}m \simeq 10^{-6}$. Indeed, our theoretical prediction matches the range of frequencies and Hartmann numbers where Alfvén waves were experimentally observed by *Alboussiere et al.* and others [4, 5], as it can be seen in the Fig. 2 above.

Finally, to account for the Hartmann walls and the associated no-slip, insulating z-boundary condition there, we decomposed our modes in its $\mathbf{B}_0$-normal and $\mathbf{B}_0$-tangential components to search for natural modes of the cavity. We proved that the tangential mode was forbidden in liquid metals for witch $\mathcal{P}m \ll 1$, which is consistent with the known fact that purely transversal Alfvén waves are actually an exact result of the full-MHD equations.

We showed that the reflection of Alfvén waves is a crucial element conditioning the growth of wave modes. Accounting for side wall boundary conditions, normal to the main magnetic field, allowed us to determine the critical Hartmann number $\mathcal{H}a_c$ to observe Alfvén waves, as well as their frequency range ; while Hartmann wall boundary conditions allowed us to demonstrate that the waves tangential to the main magnetic field are forbidden in such a geometry, both consistently with experimental results.

With this new approach, we expect to be able to identify Alfvén waves in the bulk of a class of wall-bounded MHD flows, from measurements at the walls only.

References

[1] H. Alfvén. Existence of electromagnetic-hydrodynamic waves. *Nature*, 150(3805):405–406, 1942.
[2] J. Hartmann and F. Lazarus. Experimental investigations on the flow of mercury in a homogeneous magnetic field. *Theory of laminar flow of electrically conductive Liquids in a Homogeneous Magnetic Field*, 15(7), 1937.
[3] S. Lundquist. Experimental investigations of magneto-hydrodynamic waves. *Physical Review*, 76(12):1805–1809, 1949.
[4] T. Alboussière, P. Cardin, et al. Experimental evidence of alfvén wave propagation in a gallium alloy. *Physics of Fluids*, 23(9):096601, 2011.
[5] A. Pothérat, L. Davoust, et al. Unpublished experimental measures. SIMaP, LNCMI, EMFL, Grenoble-INP, CNRS, Univ. Grenoble-Alpes.
[6] N. Schaeffer, D. Jault, et al. On the reflection of alfvén waves and its implication for earth's core modelling. *Geophysical Journal International*, 191(2):508–516, 2012.

GENERATION AND REVERSAL OF HELICITY IN CONDUCTING FLUIDS

Wesley Agoua*[1], Wouter Bos[1], Alexandre Delache[1,2], Benjamin Favier[3], and Antoine Briard[4]
[1] CNRS, Univ Lyon, Ecole Centrale de Lyon, Univ Lyon 1 Claude Bernard, INSA Lyon, , Laboratoire de Mécanique des Fluides et Acoustique, UMR5509, 69134 Ecully, France
[2]Univ Lyon, site de Saint-Etienne, Universit Jean Monnet de Saint Etienne, France
[3]Aix Marseille Univ, CNRS, Centrale Marseille, IRPHE UMR 7342, Marseille, France
[4] Centre de Mathmatiques et de Leurs Applications, CNRS, ENS Paris-Saclay, Univ Paris-Saclay, Cachan, France

Summary This paper explains a mechanism for the generation of spatial mean helicity $h = \overline{\mathbf{u}\cdot\boldsymbol{\omega}}$ (with $\mathbf{u}$ the velocity and $\boldsymbol{\omega}$ the vorticity). In a conducting fluid with a vertical unstable stratification and imposed magnetic field, a correlation is established between helicity and spatial mean skew diffusion defined by $\mathbf{q} = \overline{\rho\boldsymbol{\omega}}$ with ρ the density. It is shown using numerical simulations that helicity is generated when the correlation length in the vertical direction becomes significantly larger than the horizontal one. The helicity saturates at a value dependent on the strength of the magnetic field, the mean temperature gradient and the Reynolds number.

STATE OF THE ART

A magnetic field has been protecting against stellar radiations our planet for more than three billions years . According to the laws of electromagnetism, it should have disappeared a few thousand years after the creation of the Earth if only diffusion is taken in account. The exact mechanism which maintains it is an open problem nowadays. However since a conference given by Larmor in 1919 [1] , the theory of the self-sustained dynamo is well accepted. The Earth's outer core is known to be a metallic liquid. Its movement creates an electric field which induces a magnetic field. Most of the proposed dynamical mechanisms which can generate and sustain a large scale field involve helical velocity fields [2]. The origin of this helicity is still a subject of debate [3],[4]. The present investigation focuses on one possible mechanism which can explain spontaneous and statistically homogeneous helicity generation.

UNSTABLE STRATIFICATION AND HELICITY GENERATION

The mechanism proposed in this paper uses the idea that the Earth's inner core is dynamically active, The temperature gradient between the core and the surface creates an unstable stratification. This vertical stratification is characterized by the parameter N defined by $N^2 = -\frac{g}{\overline{\rho}}\frac{\partial \rho}{\partial z}$. The mechanism we propose combines this vertical stratification with a vertical magnetic field leading to the generation of vertical helicity.

From the Navier-Stokes equations and the equation for the density fluctuations, two coupled equations are obtained for average quantities $h_3 = \overline{u_3\omega_3}$ and $q_3 = \overline{\rho\omega_3}$ where u_3, ω_3 and ρ are fluctuations of vertical velocity, vorticity, and density, respectively,

$$\begin{cases} \dfrac{\partial q_3}{\partial t} = N^2 h_3 + \nu\overline{\rho\partial_i^2\omega_3} + \kappa\overline{\omega_3\partial_j^2\rho} + \overline{\rho\omega_i\partial_i u_3} + F^{\omega L} \\ \dfrac{\partial h_3}{\partial t} = \dfrac{g}{\overline{\rho}}q_3 - \dfrac{1}{\rho}\overline{\omega_3\partial_3 p} + \nu\overline{\partial_i u_3\partial_i\omega_3} + F^{uL} \end{cases}$$

with F^{uL} and $F^{\omega L}$ terms associated with the Lorentz force.

In the absence of nonlinearity these equations will lead to an exponential increase of $\overline{u_3\omega_3}$ and $\overline{\rho\omega_3}$ with a growth rate determined by the parameter N.

NUMERICAL SIMULATIONS AND RESULTS

Numerical simulations are performed by using pseudo-spectral methods in a 2π-periodic square box. The fluid is forced with a normalized unstable vertical stratification with a parameter N. The fluid is characterized by its spatial average density $\overline{\rho}$ and viscosity ν. The magnetic field is characterized by the frequency $F = \frac{B^2}{\eta}$ with B the magnetic field strength and η the magnetic diffusivity.

*E-mail: wesley.agoua@ec-lyon.fr.

The first simulations without magnetic field show that the nonlinear damping terms are too strong to allow a generation of helicity in homogeneous stratified turbulence without walls or body forces. It can be shown analytically that these damping terms can be neglected in the case of a fluid which is invariant along the vertical axis, but it seems that the stratification alone is not sufficient to induce this invariance. Subsequently a static vertical magnetic field is therefore applied to the flows using the quasi-static approximation. As can be observed in figure 1 where are represented isosurfaces of helicity, the vertical invariance is enhanced, illustrated by the tube-shaped helicity isosurfaces.

Figure 1: Helicity isosurfaces without and with magnetic field in unstably stratified periodic box turbulence.

The invariance allows an initial exponential evolution of both helicity and skew diffusion with the parameter N as a growth rate, as predicted by the equations. After this linear evolution observed on figure 2, helicity keeps increasing up to a saturation value proportional to the magnetic frequency $\frac{B^2}{\eta}$ and the square root of N.

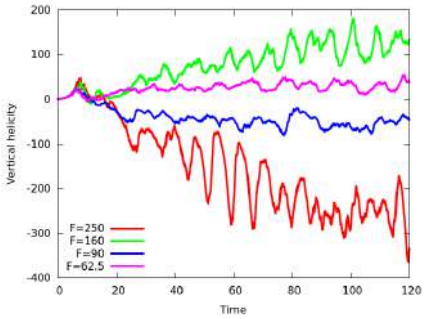

Figure 2: Helicity during the simulation for different values of the magnetic field.

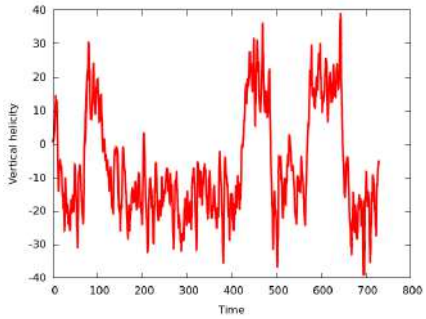

Figure 3: Reversals of the mean helicity are observed for certain parameters.

Another remarkable observation is that reversals of the helicity can be observed along time, (figure 3), more often when the flow is weakly invariant along the vertical axis. Instabilities of the tube-shaped structures for a relative weak magnetic field seem to be at the origin of this phenomenon.

CONCLUSIONS

Numerical simulations confirm the correlation between helicity and skew diffusion in the presence of a unstable stratification and a static magnetic field. The value of the helicity at saturation is determined by parameters characterizing the fluid and the forcing. We think that, possibly, this mechanism can constitute an interesting explanation for the generation of helicity in the outer core of the Earth.

References

[1] Larmor J. How could a rotating body such as the Sun become a magnet? *Report of the British Association for the Advancement of Science, 87th Meeting* , 1919.

[2] Roberts G. O. Spatially Periodic Dynamos. *Philosophical Transactions of the Royal Society of London. Series A, Mathematical and Physical Sciences.* **266(1179)**: 535-558, 1970.

[3] Schaeffer N., Jault D., Nataf H.-C.,Fournier A.Turbulent geodynamo simulations: a leap towards Earths core. *Geophysical Journal International*, **211(1)**: 1-29, 06 2017.

[4] Steenbeck, M. and Krause, F. and Rädler, K.-H., Berechnung der mittleren LORENTZ-Feldstärke für ein elektrisch leitendes Medium in turbulenter, durch CORIOLIS-Kräfte beeinflußter Bewegung., *Zeitschrift Naturforschung Teil A*, **21**:369, 1966.

NUMERICAL MODELLING OF ELECTRO-PULSING

D.E.A. van Odyck*[1]
[1]Tata Steel, R&D, IJmuiden, The Netherlands

Summary Inside a liquid melt one can use electromagnetic forces to manipulate (non-metallic) particles. Recently, experiments have shown promising results in redistributing non-metallic particles inside a liquid melt exposed to an AC current. It is believed that electromagnetophoresis is responsible for accelerating the particles. In this work the model is introduced that describes the liquid metal fluid flow and the particle motion under the influence of an applied current. The model is implemented in OpenFOAM 4.x [9] and some simulation results are presented.

INTRODUCTION

The distribution or removal of (non-metallic) particles in a liquid metal, can be of advantage in the processing of, for example, steel. A major issue in continuous casting is the presence of aluminium oxides. These particles can have a negative effect on process stability and final product quality. The removal or redistribution of these inclusions in such a way that they can not have a negative effect on the process or on the final product is still a topic of active research. A comprehensive overview of these methods is given in [1], [2].

In [3] experiments have been carried out using a rectangular container containing a liquid metal. Two opposing side walls were equipped with electrodes. A homogeneous mixture of liquid melt and small non-metallic particles (average diameter of $8[\mu m]$) was exposed to a pulsed electric current applied to the opposing electrodes. According to their article [3] the main reason for pulsing was to prevent Ohmic heating. The experiment showed a redistribution of particles away from the current density towards the meniscus and the bottom of the container. In their article [3] a free energy argument is used to explain the heterogeneous distribution of particles after electro pulsing. In this study it is proposed to use a more traditional approach, based on electromagnetophoresis [4], and see how well it approaches experimental data.

THEORY

In [4] it is argued that a particle with a different conductivity than the fluid will experience a net force ($\mathbf{F}_{EM}$) if the conducting fluid is exposed to a magnetic field ($\mathbf{B}$) and a current density ($\mathbf{J}$).

$$\mathbf{F}_{EM} = -E_L \mathbf{J} \times \mathbf{B} \ , \quad E_L = \frac{3}{2} V_p \frac{\sigma - \sigma_p}{2\sigma + \sigma_p} \tag{1}$$

where σ, σ_p, V_p are the fluid conductivity, particle conductivity and particle volume, respectively. Even if no external magnetic field is applied the current density alone generates an induced magnetic field that can contribute to the net force experienced by the particle. Particle motion is described by Newton's law:

$$m_p \frac{d\mathbf{u}_p}{dt} = \mathbf{F}_{EM} + \mathbf{F}_d + \mathbf{F}_g + \mathbf{F}_l \tag{2}$$

where $\mathbf{F}_d, \mathbf{F}_g, \mathbf{F}_l$ are the drag, gravity-buoyancy and lift force (detailed expressions for these forces can be found in [8]). According to Ampere's law, the applied current density induces a magnetic field. This magnetic field can be calculated using the so-called $\mathbf{A} - \phi$ formulation [6], where the vector potential ($\mathbf{A}$, $\mathbf{B} = \nabla \times \mathbf{A}$) and the electric potential (ϕ, $\mathbf{E} = -\nabla\phi$) are the unknown variables:

$$\begin{aligned} \tfrac{\partial \mathbf{A}}{\partial t} &= -\nabla\phi + \tfrac{1}{\sigma\mu_0}\Delta\mathbf{A} \\ \Delta\phi &= 0 \end{aligned} \tag{3}$$

where the current density follows from $\mathbf{J} = \frac{1}{\mu_0}\nabla \times \mathbf{B}$ and μ_0 is the vacuum magnetic permeability. The (incompressible) fluid flow is governed by the magnetohydrodynamic (MHD, [6]) equations:

$$\frac{\partial \mathbf{u}}{\partial t} + \mathbf{u} \cdot \nabla \mathbf{u} = -\frac{1}{\rho}\nabla p + \eta \Delta \mathbf{u} + \frac{1}{\rho}\mathbf{J} \times \mathbf{B} \text{ and } \nabla \cdot \mathbf{u} = 0 \tag{4}$$

where ρ, η are the fluid density and kinematic viscosity, respectively. Taking into account the size of the particles, small, the one-way coupled approach is assumed, meaning that the particles do not exert a force on the fluid. Only the fluid affects the particle trajectories.

*Corresponding author. E-mail: Daniel.van-odyck@tatasteeleurope.com

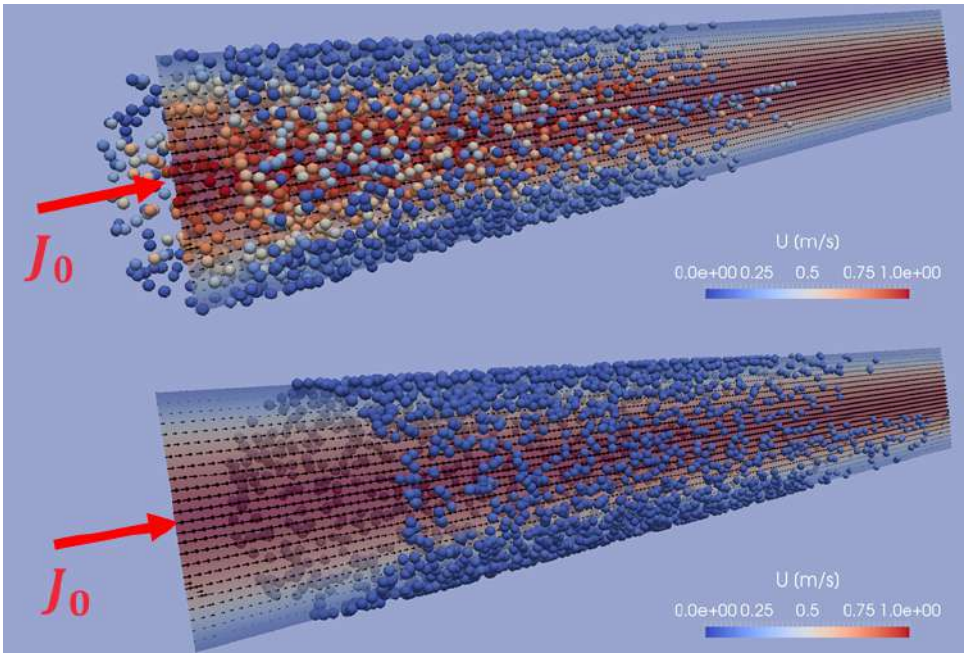

Figure 1: Fluid velocity indicated by arrows and colour scale. Particles indicated by spheres (not real size!) and their velocity is indicated by the colour scale. Top figure: Showing particle distribution during particle injection. Bottom figure: Showing particle distribution after particle injection stopped.

IMPLEMENTATION

The above described model was implemented in OpenFOAM 4.x and concerning the MHD implementation the methodology described in [7] was followed. As a first step, the flow inside an one meter long cylinder subject to a constant current density ($J = 7.13 \cdot 10^6\,[A/m^2]$) applied between the ends of the cylinder was considered. At the inlet of the cylinder a parabolic velocity profile is applied. Particles ($d_p = 70 \cdot 10^{-6}\,[m]$) are injected at random positions at the inlet. After a certain period injection of particles is stopped. Figure (1) shows particle positions at two different times (before and after stopping the injection of particles). It is clear that as time passes more and more particles are migrated towards the cylinder wall because of net Lorentz force ($\mathbf{F}_{EM}$) acting on the particles.

OUTLOOK

A new approach is presented to explain the particle separation between two electrodes as encounter in the work of Zhang [3]. It is based on MHD where the inclusions are modelled as particles subject to forces. During the presentation a more detailed comparison between the proposed model and the experimental results of Zhang [3] will be shown.

CONCLUSIONS

References

[1] Makarov S., Ludwig R., Apelian D. Electromagnetic seperation techniques in metal casting. I conventional methods. *IEEE Trans. Magnetics* **36**: 2015-2021, 2000.
[2] Sun Z. Non-metallic particles manipulation in liquid metals during electromagnetic processing *J. Powder Metall. Min.* **1**: 1-4, 2012.
[3] Zhang X., Qin R. Electric current-driven migration of electrically neutral particles in liquids *App. Phys. Letters* **104**, 2014.
[4] Leenov D., Kolin A. Theory of electromagnetophoresis. I. Magnetohydrodynamic forces experienced by spherical and symmetrically oriented cylindrical particles *J. Chem. Phys.* **22(4)**: 683-688, 1954.
[5] Li M., Guthrie R.I.L. Numerical studies of the motion of particles in current-carrying liquid metals flowing in a circular pipe *Metall. Mat. Trans. B* **31B**: 357-364, 2000.
[6] Moreau R. Magnetohydrodynamics *Kluwer Academic Publishers*, 1990.
[7] Ni M.J., *et al.* A current density conservative scheme for incompressible MHD flows at a low magnetic Reynolds number. Part II: On an arbitrary collocated mesh *J. Comp. Phys.* **227.1**: 205-228, 2007.
[8] Prosperetti A., Tryggvason G. Computational methods for multiphase flow *Cambridge university press*, 2009.
[9] OpenFOAM, web site **https://openfoam.org**.

ELECTROROTATION OF A SPHERICAL CAPSULE IN AN APPLIED UNIFORM CONSTANT ELECTRIC FIELD

Alexander Tyatyushkin*[1]
[1]Institute of Mechanics, Moscow State University, Moscow, Russia

Summary The electrorotation of a capsule in an applied uniform constant electric field is theoretically investigated. The capsule is a rigid spherical shell inside of which a weakly electrically conducting polarizable liquid is contained and suspended in an infinite volume of another weakly electrically conducting polarizable liquid. The influence of the surface conductivity on the internal and external surfaces of the shell is taken into account. With use of the electrohydrodynamic approximation, Stokes approximation, and approximation of quasi-steady flow, the equations are obtained that determine the variation of the electric field and of the flow of the liquids inside and outside the shell. The angular velocity of the steady electrorotation is found.

INTRODUCTION

The study of the electrorotation of various objects attracts attention [1] both due to the fact that this is an interesting phenomenon from the point of view of fundamental science and due to its applications. Melcher and Taylor [2] investigated theoretically the electrorotation of a solid cylinder, Jones [2] investigated the electrorotation of a solid spherical particle. Turcu [4] studied the rotation of a rigid spherical particle in alternating electric fields. Turcu and Lucaciu [5] investigated the rotation a spherical object surrounded by a thin shell both in constant and in alternating electric field. He, Salipante, and Vlahovska [6] studied the electrorotation of a fluid drop.

In order the steady electrorotation occurs in a constant electric field, the solution with constant angular velocity should not only exist, but also be stable. For the electrorotation of a spherical particle, a rather simple situation takes place: if a solution with electrorotation exists, it is stable and the solution without electrortation is unstable; and if a solution with electrorotation does not exist, the solution without electrortation is stable. The situation may be more interesting for more complex objects.

The goal of the present work is to solve the problem about the electrorotation of a spherical capsule and to obtain the conditions of existence and stability for the solutions with electrorotation.

SETTING OF THE PROBLEM

Consider a spherical capsule containing an incompressible viscous weakly electrically conducting polarizable liquid and suspended in another incompressible viscous weakly electrically conducting polarizable liquid in an applied constant uniform electric field with the intensity $\vec{E}_{\mathrm{a}}$. The shell of the capsule is a rigid spherical layer with the external radius R_{e} and the internal radiusR_{i}. The liquids are regarded as sufficiently viscous so that the Stokes approximation is valid and their conductivities are regarded as sufficiently small so that the electrohydrodynamic approximation is valid. Let λ_{e}, λ_{l}, λ_{i} and ε_{e}, ε_{l}, ε_{i} be the conductivities and dielectric permittivities of the liquid outside the capsule, of its shell, and of the liquid inside it, accordingly, η_{e} and η_{i} be the viscosities of the of the liquids outside and inside the capsule, λ_{se} and λ_{si} be the surface conductivities of the external and internal surfaces of the shell of the capsule.

The system of equations for the electric field consists of the Maxwell's equations in the electrohydrodynamic approximations, the law of electric charge conservation, and the material relations. The system of equations for the flow inside and outside the capsule consists of the continuity equation and the Navier–Stokes equation in the Stokes approximation.

The boundary conditions for the electric field on the external and internal surfaces of the shell of the capsule include the continuity condition for the tangential component of the electric field intensity and the conditions for the jumps of the normal components of the electric induction and electric current density vectors. The boundary conditions for the flow on the surfaces of the shell include impenetrability and no-slip conditions and the continuity condition for the tangential component of the stress vector. The stress vector is the total stress tensor, which includes the electric stress tensor, contracted with the external unit normal vector to the surface. At infinity, the electric field intensity tends to the intensity of the applied electric field, $\vec{E}_{\mathrm{a}}$, and the velocity tends to zero. Besides, the electric field intensity and velocity should be bounded for all the values of the radius vector, $\vec{r}$, and time, t.

SOLUTION

The equations for the electric field and for the flow, boundary conditions at infinity, and conditions of boundedness, as well as the continuity condition for the tangential component of the electric field intensity and the impenetrability and

*Corresponding author. E-mail: tan@imec.msu.ru.

no-slip conditions for the velocity on the surfaces of the shell allow one to express the electric field intensity and the velocity of the liquids inside and outside the capsule in the form

$$\vec{E} = -\nabla\varphi, \quad \varphi = \begin{cases} -\vec{E}_{\rm a}\cdot\vec{r} + \vec{D}_{\rm e}\cdot\dfrac{\vec{r}}{r^3} + \vec{D}_{\rm i}\cdot\dfrac{\vec{r}}{r^3}, & r > R_{\rm e}, \\ -\vec{E}_{\rm a}\cdot\vec{r} + \vec{D}_{\rm e}\cdot\dfrac{\vec{r}}{R_{\rm e}^3} + \vec{D}_{\rm i}\cdot\dfrac{\vec{r}}{r^3}, & R_{\rm i} < r \leqslant R_{\rm e}, \\ -\vec{E}_{\rm a}\cdot\vec{r} + \vec{D}_{\rm e}\cdot\dfrac{\vec{r}}{R_{\rm e}^3} + \vec{D}_{\rm i}\cdot\dfrac{\vec{r}}{R_{\rm i}^3}, & r \leqslant R_{\rm i}, \end{cases} \qquad \vec{v} = \begin{cases} \dfrac{R_{\rm e}^3}{r^3}\vec{\Omega}\times\vec{r}, & r > R_{\rm e}, \\ \vec{\Omega}\times\vec{r}, & r \leqslant R_{\rm e}, \end{cases} \tag{1}$$

where the depending on the time parameters $\vec{D}_{\rm e}$ and $\vec{D}_{\rm i}$ and angular velocity of the electrorotation of the capsule $\vec{\Omega}$ are determined by the boundary conditions on the surfaces of the shell. Here, the origin of $\vec{r}$ is at the center of the capsule.

The equations for the variation in time of the parameters $\vec{D}_{\rm e}$ and $\vec{D}_{\rm i}$ follow from the conditions for the jumps of the normal components of the electric induction and electric current density vectors and have the form

$$-\frac{1}{4\pi}\frac{1}{R_{\rm e}^3}(\varepsilon_{\rm l}-\varepsilon_{\rm i})\left(\vec{D}_{\rm e}\times\vec{\Omega}+\frac{{\rm d}\vec{D}_{\rm e}}{{\rm d}t}\right)+\frac{1}{4\pi}\frac{1}{R_{\rm i}^3}(2\varepsilon_{\rm l}+\varepsilon_{\rm i})\left(\vec{D}_{\rm i}\times\vec{\Omega}+\frac{{\rm d}\vec{D}_{\rm i}}{{\rm d}t}\right)=\frac{1}{R_{\rm e}^3}\left(\lambda_{\rm l}-\lambda_{\rm i}-\frac{2\lambda_{\rm si}}{R_{\rm i}}\right)\vec{D}_{\rm e}$$
$$-\frac{1}{R_{\rm i}^3}\left(2\lambda_{\rm l}+\lambda_{\rm i}+\frac{2\lambda_{\rm si}}{R_{\rm i}}\right)\vec{D}_{\rm i}-\left(\lambda_{\rm l}-\lambda_{\rm i}-\frac{2\lambda_{\rm si}}{R_{\rm i}}\right)\vec{E}_{\rm a}-\frac{1}{4\pi}(\varepsilon_{\rm l}-\varepsilon_{\rm i})\,\vec{E}_{\rm a}\times\vec{\Omega}, \tag{2}$$

$$\frac{1}{4\pi}\frac{1}{R_{\rm e}^3}(2\varepsilon_{\rm e}+\varepsilon_{\rm l})\left(\vec{D}_{\rm e}\times\vec{\Omega}+\frac{{\rm d}\vec{D}_{\rm e}}{{\rm d}t}\right)+\frac{1}{4\pi}\frac{1}{R_{\rm e}^3}(2\varepsilon_{\rm e}-2\varepsilon_{\rm l})\left(\vec{D}_{\rm i}\times\vec{\Omega}+\frac{{\rm d}\vec{D}_{\rm i}}{{\rm d}t}\right)=-\frac{1}{R_{\rm e}^3}\left(2\lambda_{\rm e}+\lambda_{\rm l}+\frac{2\lambda_{\rm se}}{R_{\rm e}}\right)\vec{D}_{\rm e}$$
$$-\frac{1}{R_{\rm e}^3}\left(2\lambda_{\rm e}-2\lambda_{\rm l}+\frac{2\lambda_{\rm se}}{R_{\rm e}}\right)\vec{D}_{\rm i}-\left(\lambda_{\rm e}-\lambda_{\rm l}-\frac{2\lambda_{\rm se}}{R_{\rm e}}\right)\vec{E}_{\rm a}-\frac{1}{4\pi}(\varepsilon_{\rm e}-\varepsilon_{\rm l})\,\vec{E}_{\rm a}\times\vec{\Omega}. \tag{3}$$

The continuity condition for the tangential component of the stress vector on the surfaces of the shell yields

$$\vec{\Omega} = \frac{\varepsilon_{\rm e}}{8\pi\eta_{\rm e}R_{\rm e}^3}\vec{E}_{\rm a}\times\left(\vec{D}_{\rm e}+\vec{D}_{\rm i}\right). \tag{4}$$

Substituting the relation (4) into the equations (2) and (3), one obtains the system of ordinary differential equations that completely determines the variation of the parameters $\vec{D}_{\rm e}$ and $\vec{D}_{\rm i}$ if the values of these parameters at some initial instant are given. In particular, stationary solutions of this system of equations can found. With use of the relation (4), then the angular velocity of the steady electrorotation can be found.

The setting of the problem allows existence of both the solutions with electrorotation, for which $\Omega \neq 0$, and those without electrorotation, for which $\Omega = 0$. It follows from the relation (4), that the angular velocity is always normal to the applied electric field intensity vector. Due to the symmetry of the problem, it means that there exist an infinite set of the solutions with electrorotation that are determined by a unique value of the angular speed Ω.

The found formulas expressing the angular speed Ω, as well as the parameters $\vec{D}_{\rm e}$ and $\vec{D}_{\rm i}$ on the parameters of the problem $\vec{E}_{\rm a}$, $R_{\rm e}$, $R_{\rm i}$, $\lambda_{\rm e}$, $\lambda_{\rm l}$, $\lambda_{\rm i}$, $\varepsilon_{\rm e}$, $\varepsilon_{\rm l}$, $\varepsilon_{\rm i}$, $\eta_{\rm e}$, $\eta_{\rm i}$, $\lambda_{\rm se}$, and $\lambda_{\rm si}$ for the stationary solutions are not written down because they are too cumbersome for the present paper.

CONCLUSIONS

The investigation of the equations that determine Ω for the steady electrorotation allowed finding the conditions of existence and Melcher–Taylor's stability [2], based on the force moment balance, of the corresponding solutions. It is established that there always exists the only stationary solution with $\Omega = 0$ and that, depending on the parameters of the liquids and shell, the three cases can take place: 1) solutions with $\Omega \neq 0$ do not exist and the solution with $\Omega = 0$ is alwayes stable, 2) when $E_{\rm a} < E_{\rm c}$, solutions with $\Omega \neq 0$ do not exist and the solution with $\Omega = 0$ is stable, and when $E_{\rm a} > E_{\rm c}$, there exist stable solutions with $\Omega = \Omega_1 \neq 0$ and the solution with $\Omega = 0$ is unstable, 3) when $E_{\rm a} < E_{\rm c1}$, the solutions with $\Omega \neq 0$ do not exist and the solution with $\Omega = 0$ is stable, when $E_{\rm c1} < E_{\rm a} < E_{\rm c2}$, there exist unstable solutions with $\Omega = \Omega_2 \neq 0$ and stable solutions with $\Omega = \Omega_1 \neq 0$ ($\Omega_2 < \Omega_1$) and the solution with $\Omega = 0$ is stable, and when $E_{\rm a} > E_{\rm c2}$, there exist stable solutions with $\Omega = \Omega_1 \neq 0$ and the solution with $\Omega = 0$ is unstable. Here, $E_{\rm c}$, $E_{\rm c1}$, and $E_{\rm c2}$ are some critical values of the electric field intensity.

References

[1] Vlahovska P. M. Electrohydrodynamics of Drops and Vesicles. *Annu. Rev. Fluid Mech.* **51**: 305-330, 2019.
[2] Melcher J. R. and Taylor G. I. Electrohydrodynamics: a Review of the Role of Interfacial Shear Stresses. *Annu. Rev. Fluid Mech.* **1**: 111-146, 1969.
[3] Jones T. B. Quincke Rotation of Spheres. *IEEE T. Ind. Appl.* **IA-20:4**: 845-849, 1984.
[4] Turcu I. Electric Field Induced Rotation of Spheres *J. Phys. A: Math. Gen.* **20**: 3301-3307, 1987.
[5] Turcu I. and Lucaciu C. M. Electrorotation: a Spherical Shell Model *J. Phys. A: Math. Gen.* **22**: 995–1003, 1989.
[6] He H., Salipante P.F., and Vlahovska P.M. Electrorotation of a Viscous Droplet in a Uniform Direct Current Electric Field. *Phys. Fluids* **25**: 032106, 2013.

TRAJECTORIES OF CHARGED PARTICLES IN A TWO-STAGE ELECTROSTATIC PRECIPITATOR

Suantara Darma Gede, Chien-Lin Lai, and Wei-Hsin Tien*
Department of Mechanical Engineering, National Taiwan University of Science and Technology, Taipei, Taiwan

Summary The trajectories of charged particles under the influence of electric field and electrohydrodynamic (EHD) secondary flows were observed separately by Particle Image Velocimetry (PIV) and particle tracking velocimetry (PTV) for a two-stage electrostatic precipitator (ESP). The charging characteristics of the wire-plate charging zones were analysed, and the influence of the EHD secondary flow patterns were compared with the charged particle trajectories.

MOTIVATION

Particulate Matter (PM) has been confirmed to be serious health risks and the removal of PM has been the focus of many recent studies. C. Arden Pope III et al. [1] compiled a study about the effects of human inhaled aerosol, it can be related to effects and pathology of various organs when human inhaled aerosols. Günter Oberdörster et al. [2] showed that human inhaled particles deposited inside the body. Electrostatic Precipitator (ESP) is one of highly efficient and widely used particle collecting technologies for air purifier and industrial filtering system. Experimental studies related to ESP often adopt particle image velocimetry (PIV) to obtain velocity field information of the EHD secondary flow patterns [3-5]. Harmdi et al. [6] investigated various tracer particles used in PIV and showed that some of the tracer particles are not affected much by the electric field, while others may be affected significantly. This finding suggested that it is possible to use different tracers to reveal the EHD flow and the motion of the charged particles, which were the subject to be collected.

METHODS

A transparent acrylic is manufactured as a two-stage ESP model in the current study, as shown in Figure 1(a). The ESP model has dimension of length, width and height of 170 × 80 × 26 mm respectively and 5 mm thickness. In this setup there are 5 pin electrode has a diameter 0.8 mm used to corona discharge. The upper and lower collecting plates of the collection area are 60 × 50 mm, 70 × 50 mm respectively. The model is given two positive and grounded in the charging zone and the collecting zone through two high-voltage DC power supplies. As shown in Figure 1(b), the overall experimental setup includes transparent acrylic model, rectifier, fan, high-voltage power supply, pulsed laser, and high speed camera. Flow field was visualized by the laser light sheet shaped from a double-pulsed Nd-YAG laser, and the images were captured by a high-speed camera and sent to computers for post-processing. During the test, motion of charged particles were test with oil droplets generated by a hazer machine (HZ-350, Antari) and the processed by PTV, and the air flow patterns were measured with Al_2O_3 particles with PIV post-processing routine.

RESULTS AND CONCLUSIONS

This study successfully established a set of quantified flow field visualization settings to observe the particle flow of the two-stage electrostatic precipitator. In the charging zone when the voltage of corona discharge electrode increases, the particles move rapidly toward the excitation electrode due to increase ion wind speed. Electrohydrodynamics (EHD) formed between the corona discharge electrode and the back corona discharge. In the collection area of the electrostatic precipitator model, the movement trajectory will change with the flow velocity and the voltage of the collector plate. As the voltage of the corona discharge electrode increases, the number of charges the particles increases, make particle easier to pass through the collection area. The motion of charged particles has significantly deviation from the EHD influenced air flow.

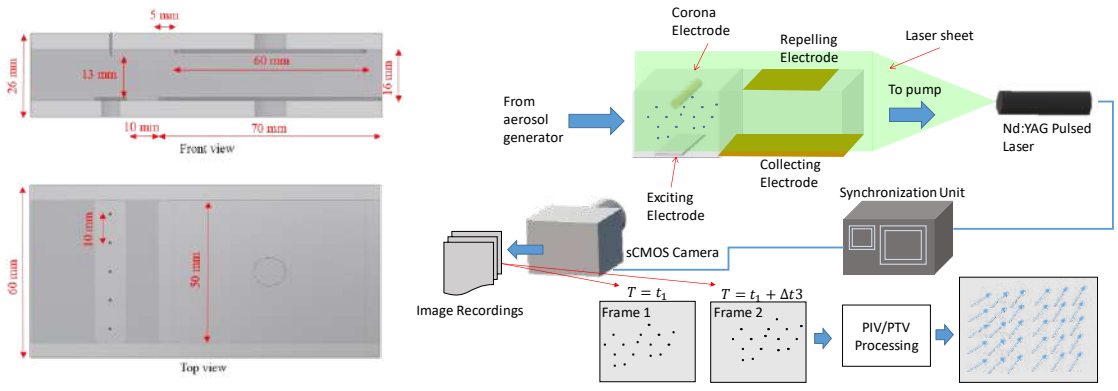

* Corresponding author. E-mail: whtien@mail.ntust.edu.tw

Figure 1. The Experimental Setup of (a) ESP Model (b) PIV/PTV Experiments

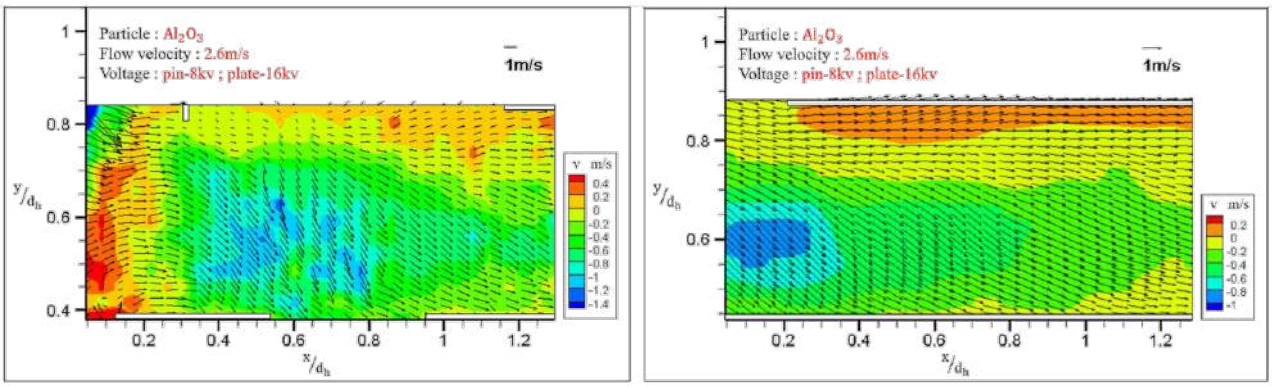

Figure 2. PIV field obtained from the charged aluminium oxide particles

References

[1] Pope C. A., D. W. Dockery, Health Effects of Fine Particulate Air Pollution: Lines that Connect. *J. Air Waste Manage.* **56**(6), 709-742, 2012.

[2] Oberdorster G., Oberdorster E., Oberdorster J. Nanotoxicology: an emerging discipline evolving from studies of ultrafine particles. *Environ. Health Perspect.* **113**(7), 823-839, 2005.

[3] Mizeraczyk J. Measurements of the velocity field of the flue gas flow in an electrostatic precipitator model using PIV method. *J Electrostat*. **51**, 272-277, 2001.

[4] Podliński J., Kocik M., Barbucha.R., Niewulis A., Mizeraczyk J., Mizuno A. 3D PIV measurements of the EHD flow patterns in a narrow electrostatic precipitator with wire-plate or wire-flocking electrodes. *Czechoslovak J. Phys.* **56**, B1009–B1016, 2006.

[5] Podliński J., Dekowski J., Mizeraczyk J., Brocilo D., Urashima K., Chang J. S. EHD flow in a wide electrode spacing spike–plate electrostatic precipitator under positive polarity. *J. Electrostat*, **64**(7-9), 498-505, 2006.

[6] Harmdi M., Havet M., Rouaud O., Tarlet D. Comparison of different tracers for PIV measurements in EHD airflow. *Exp. Fluids*, **55**(4):1702

QUASI-STATIC MAGNETO-HYDRODYNAMIC CONVECTION IN A CYLINDER

Anthony Rouquier*[1], Alban Potherat[1], and Chris C.T. Pringle[1]
[1]Fluid and Complex Systems Research Centre, Coventry University, United Kingdom

Summary We present a numerical study on the topic of magnetoconvection in a cylinder under the quasi-static magneto-hydrodynamic approximation using a spectral-element solver. The aim of this work is to obtain a better understanding of the convection process in planetary cores, in particular the formation of anticyclonic polar inside the tangent cylinder.

INTRODUCTION

The earth background rotation causes the convection of the Earth core to be divided in two zones due to the Taylor-Proudman constraint ; inside and outside of a theoretical cylinder aligned with the Earths rotation axis and touching the solid inner core, the tangent cylinder (TC). The convection process occurring inside this cylinder has garnered significant attention from the scientific community for decades [1]. In particular, the secular variation of the Earths magnetic field points to the existence of anticyclonic polar vortices in the Earths core [2, 3] Indeed, while Busse columns [4], generated outside the TC, are believed to be the main source of the magnetic field, they can not explain the Polar vortex and it's drift, nor the magnetic reversal. Non-magnetic experiments of the TC did not observe a polar vortex [5]. It implies that the addition of the magnetic field to the model is critical to its accuracy.

There are obstacles to accurately simulate the Earth inner core convective process. It is a complex problem with many governing parameters, and physical scales that can not be accurately numerically resolved with the current available processing power. There also are difficulties regarding the modelling the boundary conditions of the magnetic field. We consider the convection inside a cylinder under the quasi-static MHD approximation, thus circumventing the problems arising form the magnetic field boundary conditions. While less accurate than the geodynamo theory, this model should still yields insights regarding the convection in the inner core. The physical model may be expended upon in the future to obtain results closer to the actual physical process.

EQUATIONS FOR THE QUASI-STATIC MHD MODEL

The problem considered is the motion of an electrically conducting fluid in a closed cylinder with electrically insulated boundaries. An external homogeneous magnetic field $\mathbf{B_0}$ is imposed in the vertical direction, across the cylinder length.

In this work is used the quasi-static, low magnetic Reynolds number approximation. While the electric currents induced by the motion of the fluid in the magnetic field are non-negligible, the magnetic field induced by these electric currents can be neglected. Therefore the agglomerated magnetic field is indistinguishable from $\mathbf{B_0}$. It follows that solving the transport equation for the magnetic field is not necessary. We also work under the Boussinesq approximation, where all density differences are neglected with the exception the gravity-affected terms.

The scales used for non-dimensionalisation are the cylinder radius a, peak inlet velocity U_0, pressure ρU_0^2, time a/U_0, the temperature difference between the cylinder inlet and outlet ΔT, the field strength B_0 and electric potential aU_0B_0. The dimensionless system of equations describing our system can be written as:

$$\nabla \cdot \mathbf{u} = 0 \tag{1}$$

$$\frac{\partial \mathbf{u}}{\partial t} = -\nabla p - (\mathbf{u}\cdot\nabla)\mathbf{u} + Pr\nabla^2\mathbf{u} + RaPr\mathbf{e_y} + Ha^2Pr(\mathbf{j}\times\mathbf{e_y}) \tag{2}$$

$$\frac{\partial T}{\partial t} + (\mathbf{u}\cdot\nabla)T = \nabla^2 T\ , \tag{3}$$

$$\mathbf{j} = -\nabla\phi + \mathbf{u}\times\mathbf{e_y}\ , \tag{4}$$

where $\mathbf{u}$ is the fluid velocity, T its temperature, p the pressure, $\mathbf{j}$ the electric density vector and ϕ is the electric potential. , Ha the Hartmann number defined as $Ha = aB_0\sqrt{\sigma/\rho\nu}$. $Ra = g\alpha\Delta T a^3/\kappa\nu$ is the Rayleigh number and $Pr = \frac{\nu}{\kappa}$ the Prandtl number.

In the low magnetic Reynolds approximation, the current density is, for an electrically neutral fluid, solenoidal, such that $\nabla\cdot\mathbf{j} = 0$. Taking the divergence of Eq. 4 yields a Poisson equation:

$$\nabla^2\phi = \nabla\cdot(\mathbf{u}\times\mathbf{e_y})\ , \tag{5}$$

where ϕ is the electric potential. Eq. 5 can be solved to obtain ϕ and $\mathbf{j}$.

*Corresponding author. E-mail: ad4108@coventry.ac.uk.

The boundary conditions are Dirichlet-type conditions at the wall for the velocity :

$$\mathbf{u} = 0 \quad \text{at } r = 1 \,, \tag{6}$$

and Neumann-type boundary conditions for the electric potential, corresponding to electrically insulated horizontal and vertical side walls:

$$\frac{\partial \phi}{\partial r} = 0 \quad \text{at } r = 1 \,. \tag{7}$$

The temperature is fixed to T_1 at the inlet and T_0 at the inlet and lateral walls, with $\Delta T = T_1 - T_0$.

NUMERICAL MODEL

The system of equations (1)-(4) is solved using the spectral-element code Nektar++ [6]. The spectral-element approach is a formulation of the finite element method (FEM). the computational domain is divided into elements where the variables are projected within a polynomial basis within each element. Its specificity of the spectral-element method is that mesh refinement is mainly achieved by increasing the order of the polynomial of much higher order than the standard FEM. Moreover, the interpolation polynomials use GaussLobatto points for collocation points, ensuring spectral convergence as the order of the polynomials is increased. The spectral-element approach can then reach a higher degree of accuracy than other FEM while keeping more flexibility with regards to complex geometries than a spectral method. The time-stepping used is a second-order implicit-explicit (IMEX) method.

CONCLUSIONS

The code is still being developed as of now. In a first time will be conducted a linear analysis of the system is order to find steady states. Then branch tracing will be used from these states to obtain nonlinear solutions of the problem in function of the magnetic field and convection strength and how they compare to experimental data. Other questions of interest are whether the creation anticyclonic polar vortices occurs within the quasi-static MHD approximation and how the magnetic field affects the threshold for convective instability and the flow structures.

References

[1] Chandrasekhar, S. Hydrodynamic and Hydromagnetic Stability, 652 pp., Clarendon. *Oxford, UK*, 1961.

[2] Aujogue, Kélig and Pothérat, Alban and Sreenivasan, Binod and Debray, François. Experimental study of the convection in a rotating tangent cylinder. *J. Fluid Mech.* **843**: 355-381, 2018.

[3] Sreenivasan, Binod and Jones, Chris A *Geophysical and Astrophysical Fluid Dynamics.* **100**: 319-339, 2006. Azimuthal winds, convection and dynamo action in the polar regions of planetary cores.

[4] Busse, Friedrich H. Thermal instabilities in rapidly rotating systems. *Journal of Fluid Mechanics.* **44**: 441-460, 1970.

[5] Aurnou, Jonathan and Andreadis, Steven and Zhu, Lixin and Olson, Peter. Experiments on convection in Earths core tangent cylinder. *Earth and Planetary Science Letters.* **212**: 119-134, 2003.

[6] Cantwell, Chris D and Moxey, David and Comerford, Andrew and Bolis, Alessandro and Rocco, Gabriele and Mengaldo, Gianmarco and De Grazia, Daniele and Yakovlev, Sergey and Lombard, J-E and Ekelschot, Dirk and others. Nektar++: An open-source spectral/hp element framework. *Computer physics communications.* **192**: 205-219, 2015.

THE MECHANISM OF VORTEX INSTABILITY IN ELECTROMAGNETICALLY DRIVEN FLOW IN AN ANNULAR THIN LAYER OF ELECTROLYTE

John McCloughan[1] and Sergey A. Suslov[1]
[1]Department of Mathematics, Faculty of Science, Engineering and Technology, Swinburne University of Technology, Melbourne, Australia

Summary Experimental studies have shown that an azimuthal flow of a conducting fluid in an annular channel driven by a Lorentz force, quite unexpectedly, developed a robust vortex system appearing near the outer cylindrical wall. Our computations have demonstrated that such vortices arise on a background of a steady axisymmetric flow, which consists of two counter-rotating toroidal structures, and that the vortices are formed at the boundary between them. Our subsequent studies use linear stability analysis and disturbance energy balance considerations to pinpoint the physical nature of the instability that leads to the experimentally observed vortices. Specifically, we show that Rayleigh's inviscid centrifugal instability aided by radial shear in the boundary layer near the outer cylindrical wall is the mechanism responsible for vortex formation. While the background flow is driven by the Lorentz force, the electromagnetic effects have virtually no influence on its stability. Therefore, the vortices appear for purely hydrodynamic reasons.

PROBLEM FORMULATION AND GOVERNING EQUATIONS

Consider a layer of incompressible, viscous, weak electrolyte of thickness h, confined to an annular cavity formed by two vertical co-axial cylindrical electrodes of radius R_1 and R_2, $R_1 < R_2$. The bottom of the cavity is solid and non-conducting, while the top is a free surface. This system is placed above a permanent disk magnet that creates a predominantly vertical magnetic field. When an electric potential difference is applied between the electrodes the total current flows predominantly radially through the layer. The interaction between the applied vertical magnetic field $\mathbf{B}$ and the radial electric current $\mathbf{j}$ gives rise to a Lorentz force $\mathbf{F_L} = \mathbf{j} \times \mathbf{B}$ per unit volume which drives the flow circumferentially. Under the small magnetic Reynolds number approximation [1] the steady axisymmetric non-dimensional form of Poissons equation for the electric potential ϕ, and the momentum and continuity equations for an incompressible fluid written in cylindrical coordinates becomes

$$\frac{\partial^2\phi}{\partial z^2} + \epsilon^2\left(\frac{\partial^2\phi}{\partial r^2} + \frac{1}{r}\frac{\partial\phi}{\partial r}\right) = \epsilon^2 Ha^2\left[-B_r\frac{\partial u_\theta}{\partial z} + B_z\left(\frac{\partial u_\theta}{\partial r} + \frac{u_\theta}{r}\right)\right], \tag{1}$$

$$u_r\frac{\partial u_r}{\partial r} - \frac{u_\theta^2}{r} + u_z\frac{\partial u_r}{\partial z} = -\frac{1}{Fr^2}\frac{\partial p}{\partial r} + \frac{1}{\epsilon^2 Re}\left(j_\theta B_z - j_z B_\theta\right) + \frac{1}{Re}\left(\frac{\partial^2 u_r}{\partial r^2} + \frac{1}{r}\frac{\partial u_r}{\partial r} - \frac{u_r}{r^2} + \frac{1}{\epsilon^2}\frac{\partial^2 u_r}{\partial z^2}\right), \tag{2}$$

$$u_r\frac{\partial u_\theta}{\partial r} + \frac{u_r u_\theta}{r} + u_z\frac{\partial u_\theta}{\partial z} = \frac{1}{\epsilon^2 Re}\left(j_z B_r - j_r B_z\right) + \frac{1}{Re}\left(\frac{\partial^2 u_\theta}{\partial r^2} + \frac{1}{r}\frac{\partial u_\theta}{\partial r} - \frac{u_\theta}{r^2} + \frac{1}{\epsilon^2}\frac{\partial^2 u_\theta}{\partial z^2}\right), \tag{3}$$

$$u_r\frac{\partial u_z}{\partial r} + u_z\frac{\partial u_z}{\partial z} = -\frac{1}{Fr^2\epsilon^2}\frac{\partial p}{\partial z} + \frac{1}{\epsilon^2 Re}\left(j_r B_\theta - j_\theta B_r\right) + \frac{1}{Re}\left(\frac{\partial^2 u_z}{\partial r^2} + \frac{1}{r}\frac{\partial u_z}{\partial r} + \frac{1}{\epsilon^2}\frac{\partial^2 u_z}{\partial z^2}\right), \tag{4}$$

$$\frac{\partial u_r}{\partial r} + \frac{u_r}{r} + \frac{\partial u_z}{\partial z} = 0\,. \tag{5}$$

Here the aspect ratio of the electrolyte layer ϵ, the square of Hartmann number Ha^2 characterising electromagnetic effects, the square of Froude number Fr^2 describing the influence of gravity g on a free-surface flow and Reynolds number Re quantifying viscous effects are

$$\epsilon = \frac{h}{R_2 - R_1}, \quad Ha^2 = \frac{\sigma_e B_0^2 h^2}{4\mu}, \quad Fr^2 = \frac{2U_0^2}{gh}, \quad Re = \frac{\rho U_0 (R_2 - R_1)}{2\mu}, \tag{6}$$

where the velocity scale is defined as $U_0 = \left(\sigma_e \Delta\phi_0 B_0 h^2\right)/\left(2\mu(R_2 - R_1)\right)$. Upon the Introduction of a geometric parameter $\alpha = (R_2 + R_1)/(R_2 - R_1)$, the boundary conditions becomes

$$u_r = u_\theta = u_z = 0 \text{ at } z = -1 \text{ and at } r = \alpha \pm 1\,, \tag{7}$$

$$u_z = \frac{\partial u_r}{\partial z} = \frac{\partial u_\theta}{\partial z} = 0 \text{ at } z = 1\,. \tag{8}$$

$$\phi = 0 \text{ at } r = \alpha - 1 \text{ and } \phi = 1 \text{ at } r = \alpha + 1, \tag{9}$$

$$\frac{\partial\phi}{\partial z} = 0 \text{ at } z = -1 \text{ and } \frac{\partial\phi}{\partial z} = -\epsilon^2 Ha^2 u_\theta B_r \text{ at } z = 1\,. \tag{10}$$

BASIC FLOW

The governing equations (1)–(5) and (7)–(10) admit steady axisymmetric solutions referred to as basic flow below. As discussed in [3], when the radial current is applied the resulting Lorentz force drives circumferential flow. The centrifugal force is responsible for the creation of a radial flow component so that the overall flow becomes toroidal. This flow was called a Type 1 solution in [3]. If the Reynolds number is increased to a specific value Re_*, a second axisymmetric solution referred to as a Type 2 solution appears. For example, with fixed $\epsilon = 0.311$, $Ha = 4.59 \times 10^{-5}$ once the Reynolds

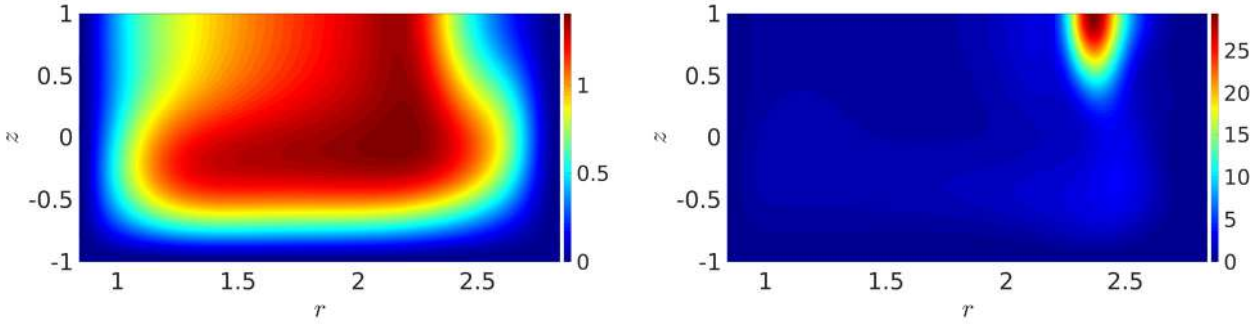

(a) (b)

Figure 1: Meridional distributions of kinetic energy $E_k = u_r^2 + u_\theta^2 + \epsilon^2 u_z^2$ for (a) basic flow and (b) linearised perturbations (arbitrary scale) for the Type 2 basic flow with $m = 2$ for $\epsilon = 0.331$, $Re = 799$, $Ha = 4.59 \times 10^{-5}$.

number reaches $Re_* = 799$ a Type 2 solution appears. The main feature of the Type 2 solution which distinguishes it from the Type 1 counterpart is the existence of a second counter rotating toroidal structure in the meridional plane near the free surface and the outer cylindrical wall. A stagnation point can be identified some distance from the outer cylindrical wall. It has been shown that for some fixed ϵ and Ha the Type 1 and Type 2 solutions can co-exist over a finite interval $Re_* < Re < Re_{**}$.

PERTURBATION ENERGY DISTRIBUTION RESULTS

We investigated the linear stability of the basic flow with respect to infinitesimal periodic perturbations written in the normal mode form

$$[\phi_1(r,z), u_{r,1}(r,z), u_{\theta,1}(r,z), u_{z,1}(r,z), p_1(r,z)]^T \exp(\sigma t + \mathrm{i}m\theta) + \text{c.c.}\,, \quad m = 0, 1, 2, \cdots, \tag{11}$$

where c.c. denotes complex conjugate terms, $\sigma = \sigma^R + \mathrm{i}\sigma^I$ is the complex temporal amplification rate and m is the azimuthal wavenumber. For thin layers of a weakly conducting electrolyte $\epsilon^2 Ha^2 \sim 10^{-7}$, then the perturbation of electric potential equations can be neglected without significant loss of accuracy. We found that only Type 2 basic flow can lead to formation of vortices experimentally observed on the free surface near the outer cylinder [2]. To obtain insight into the mechanisms driving this instability, the linearised perturbation equations corresponding to (2)–(4) were multiplied by the complex conjugate perturbation velocity components $(u_r^\star, u_\theta^\star, u_z^\star)$, respectively, then integrated (by parts where necessary) over the meridional cross section using the corresponding boundary conditions for velocities and the continuity equation to eliminate pressure and obtain an equation representing the conservation of mechanical energy in the system

$$\sigma^R \Sigma_k = \Sigma_{vis} + \Sigma_{Ha} + \Sigma_{cc} + \Sigma_{bf}. \tag{12}$$

where $\Sigma_X = \int_{-1}^{1}\int_{\alpha-1}^{\alpha+1} \Re\left(E_X\right)\, r dr dz$ and $\Re$ denotes real part. Each integral represents different physical characteristics and influences in the system. Only mechanisms corresponding to terms in the right-hand side of (12) that are positive can lead to instability. The term Σ_{vis} is the measure of viscous dissipation. It is negatively defined for all m. The term Σ_k is positively defined and represents the kinetic energy. Figure 1 compares the spatial fields of the basic flow ($E_{k,0}$, panel (a)) and perturbation ($E_{k,1}$, panel (b)) kinetic energies. The basic flow kinetic energy is distributed throughout the meridional cross section while the kinetic energy for the perturbations that lead to the vortices is strongly localised near the free surface and the outer cylindrical wall. We note that vortices are formed in the region where the basic flow is less energetic, and their occurence reduces the kinetic energy deficit there. The term Σ_{Ha} representing the electromagnetic effects is always negative and is several orders of magnitude smaller than any of the other terms. Therefore, it can be concluded that the Lorentz force, which drives the primary flow, makes a negligible contribution to the development of the instabilities. The effects of curvature and radial shear (including Rayleigh centrifugal destabilisation) are represented by Σ_{cc} while the energy exchange between the perturbations and the basic flow via non-radial shear is represented by Σ_{bf}. Both Σ_{cc} and Σ_{bf} are found to be positive and of same order of magnitude, and thus both contribute to the instability. Therefore we conclude that Rayleigh's inviscid centrifugal instability mechanism aided by radial shear in the boundary layer near the outer cylindrical wall is responsible for vortex formation while the electromagnetic effects remain negligible.

References

[1] P. A. Davidson (2017). An introduction to magnetohydrodynamics (2nd ed.). Cambridge University Press.
[2] J. Pérez-Barrera, J. E. Pérez-Espinoza, A. S. Ortiz, E. Ramos and S. Cuevas (2015). Instability of electrolyte flow driven by an azimuthal Lorentz force. *Magnetohydrodynamics*, vol. 51, no. 2, pp. 203–215.
[3] S. A. Suslov, J. Pérez-Barrera, J. and S. Cuevas (2017). Electromagnetically driven flow of electrolyte in a thin annular layer: axisymmetric solutions. *J. Fluid Mech.*, vol. 828, pp. 573–600.

STABILITY ANALYSIS OF THE INTERFACE BETWEEN A NEWTONIAN AND A POWER-LAW FLUID UNDER DC ELECTRIC FIELD

S. Ilke Kaykanat*[1] and A. Kerem Uguz †[1]
[1]Department of Chemical Engineering, Bogazici University, Istanbul, Turkey

Summary The aim of this study is to investigate the practical ways to destabilize the interface between a Newtonian and a power-law fluid flowing in a microchannel under the effect of an electric field applied either normal or parallel to the flat interface. The interface can be practically destabilized by the electric number, the thickness and the viscosity ratios related to the applied voltage, flow rate ratio and the liquid type which can be changed easily in an experiment. Linear stability is conducted to determine the critical point where the interface starts to deflect.

INTRODUCTION

The stability analysis is important for the non-Newtonian fluids due to their applications in petroleum industries, packed bed reactors, etc. Moreover, lithographically-induced self-assembly (LISA) is a technique that uses a mechanical deformation to obtain patterns on the polymer substrate [1]. The linear stability of an interface separating a Newtonian and a power-law fluid has only been partially studied primarily by Khomami [2] in the absence of an electric field. The stability diagrams are obtained for various depth and viscosity ratios. Instead of the Newtonian fluids, additional unstable regions are obtained when the fluids are of power-law type. Sahu *et al.* [3] focused on the linear stability of the pressure-driven flow of two-layer flow where a Newtonian fluid overlays a Herschel-Bulkley fluid. The results show that higher shear-thinning tendency stabilizes the flow. Eldabe [4] studied the interfacial instability between two fluids undergoing a Couette flow and the interface is stressed by an electric field. The inertia affects the stability of the interface which can be considered in terms of the distribution of the vorticity.

PHYSICAL SYSTEM

The physical system consists of two fluids assumed to be immiscible, incompressible and leaky dielectric fluids undergoing a Poiseuille flow. The surface coupled model is employed thus, the electrical terms appear only at the interface conditions. The fluids are assumed to be leaky dielectric [5]. The physical system is depicted in Fig. 1 where a Newtonian fluid flows side by side with a non-Newtonian fluid and they share a common interface. The Newtonian fluid is indicated by $\star$ occupying the region $Z(x,t) < z < h^{\star}$ and the unstarred fluid is the non-Newtonian fluid occupying the region $-h < z < Z(x,t)$. The physical properties of the system are mainly the viscosity, the surface tension, the electrical permittivity and the electrical conductivity which are indicated by μ, γ, $\varepsilon\varepsilon_0$ and α, respectively. Here, ε_0 indicates the vacuum permittivity. To describe the rheological model of the non-Newtonian fluid, power-law model was chosen. An electric field is applied either parallel or normal to deflect the flat interface and at the critical voltage, it starts to deflect.

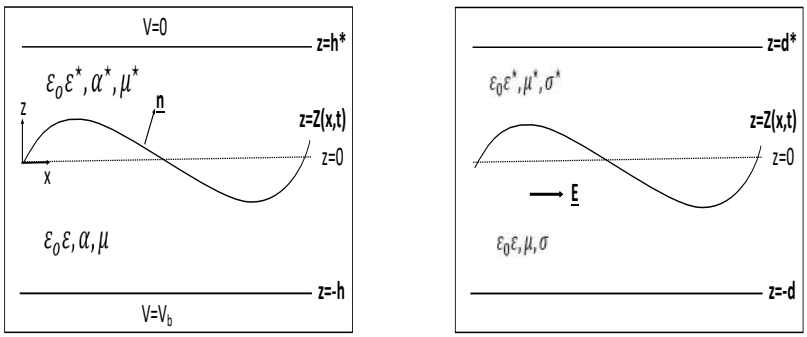

(a) (b)

Figure 1: Physical system depicting a Newtonian and a power-law fluid subjected to (a) a normal electric field (b) a parallel electric field.

*E-mail: seymenilkekaykanat@gmail.com
†E-mail: kerem.uguz@boun.edu.tr

RESULTS

A linear stability analysis is conducted using Chebyshev spectral method in MATLAB. The perturbed governing equations, along with the boundary and the interface conditions are recast into an eigenvalue problem as $Au = \sigma Bu$. Here, σ is the eigenvalue indicating the inverse time constant of the given disturbance. The applied voltage for the parallel electric field is adjusted such that Eb for the normal electric field is equivalent to d^2Eb as described in [6] because of the ratio of the length scales. The results are presented in terms of dispersion curves, i.e. the growth rate, σ versus the wavenumber, k of the disturbance or in terms of neutral curves, e.g., critical wavenumber, k_c versus the electric number d^2Eb. It was shown that the electric number, Eb either stabilizes or destabilizes the system depending on the physical

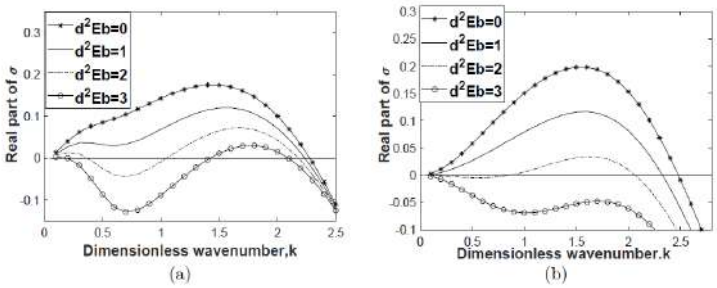

Figure 2: Stabilizing effect of the electric number (a) for the Newtonian/Shear-thinning and (b) for the Newtonian/Shear-thickening fluids

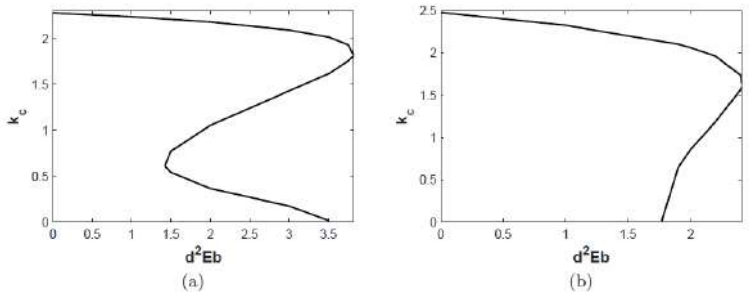

Figure 3: Critical wavenumbers for (a) for the Newtonian/Shear-thinning fluids and (b) for the Newtonian/Shear-thickening fluids

and the electrical properties similar to a system of two Newtonian fluids [6]. When the system is made unstable by the viscosity ratio in the absence of an electric field, e.g. $\lambda = 0.04$, the system can be stabilized by applying an electric field for the Newtonian/Shear-thinning fluids

CONCLUSIONS

In order to investigate the stability characteristics of the interface between a Newtonian and a power-law fluid, an eigenvalue problem is recasted to conduct the linear stability. The applied voltage to the system can stabilize or destabilize the interface depending on the electrical properties of the fluids similar to the Newtonian/Newtonian fluids system. The stable system can be destabilized by adjusting the applied voltage, namely the electric number.

ACKNOWLEDGEMENT

We acknowledge financial support provided by TUBITAK through project No. 116M374.

References

[1] S.Y. Chou, L. Zhuang and L. Guo, Appl. Phys. Lett. **75**, 1004 (1999)
[2] B. Khomami, J. Nonnewton. Fluid Mech. **36**, 289–303 (1990)
[3] K. C. Sahu, P. D. M. Spelt and O. K. Matar, Phys. of Fluids, **19**, 122101 (2007)
[4] N. T. Eldabe, J. Math. Phys. **28**, 2791 (1987)
[5] D. A. Saville, Annu. Rev. Fluid Mech. **29**, 27–64 (1997)
[6] A. K. Uguz, N. Aubry, Phys. Fluids **20**, 092103 (2008)

INVESTIGATION OF DENSITY AND FLOW VELOCITY FIELDOF DBD PLASMA ACTUATOR IN QUIESCENT AIR USING BACKGROUNDORIENTED SCHLIEREN AND PARTICLE-IMAGE-VELOCIMETRYMETHOD

Yutaka Kaneko*[1], Kenta Emori [1], Takaaki Shimazaki [1], Yoshiyuki Tagawa [1], and Hiroyuki Nishida [1]
[1]Department of Mechanical Systems Engineering, Tokyo University of Agriculture and Technology, Tokyo, Japan

Summary DBD plasma actuator is an active flow control device which manipulates the flow utilizing the ionic wind and the Joule heating caused by atmospheric barrier discharge. In this study, we investigate the density and flow velocity field of DBD plasma actuator in the quiescent air using the BOS and PIV method, respectively. As a result, it is confirmed that a wall-surface jet (ionic wind) is induced along the device surface, and low-density field is also formed over the surface. The low-density field is due to the Joule heating at the electrode edge and convection of the heated air by the wall-surface jet. In addition, it is also clarified that both the displacement of the background image and flow velocity has the peak value at some distance from the electrode edge where the discharge occurs.

INTRODUCTION

Dielectric barrier discharge plasma actuator (DBDPA) is an active flow control device using dielectric barrier discharge [1,2]. It consists of two electrodes divided by an insulator; one electrode is insulated coted and the other is exposed to the air. Applying an AC high voltage between the electrodes as shown in Fig. 1, discharge appears, and plasma is generated. DBDPA has two kinds of mechanism manipulating the flow; one is the body force generation due to the momentum transfer between plasma particles and neutral particles (the electrohydrodynamic effect), and the other is the density disturbance caused from the Joule heating. The body force generation has been intensively studied by investigating the flow field (the ionic wind) induced by it. On the other hand, recently, quantitative investigation on the density field also started [3], however, it is not sufficient. It is important to understand the characteristics of not only the body force field but also the density field for further research and development of the DBDPA.

The objective of this study is to investigate the time-averaged density field induced by DBDPA together with the flow field. We adopt the Background Oriented Schlieren (BOS) technique to measure the density field. It is an optical flow visualization technique that enable quantitative and non-contact measurement of the density field [4]. The main advantage is its simple set up as shown in Fig. 2 using only a camera, a background image and a light source. The BOS technique is based on the displacement of the background image caused by the density (refractive index) gradient of the measurement object. The light ray from the background image is deflected by the density gradient, and the background image patterns are displaced. The displacement field can be obtained using an image correlation method and so on. Finally, we can quantitatively obtain the density field by numerical calculation based on the displacement field. Note that in this study, the discussion is made using the displacement field for simply discussing the BOS results. In addition to the BOS measurement, we measure the time-averaged flow field using the PIV method.

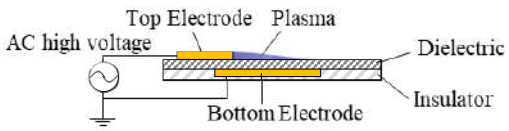

Figure 1. Schematic of the DBDPA.

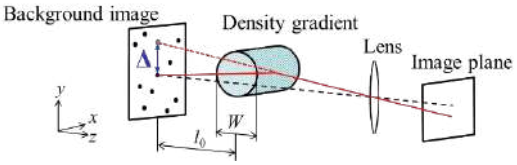

Figure 2. Principle of the BOS technique.

EXPERIMENTAL SETUP

Figure 3 shows the schematic of the DBDPA and the power supply system to drive the plasma actuator. The voltage waveforms from a function generator (Tektronix AFG2021) is amplified by the high voltage amplifier (Trek Model20/20C-HC) and applied to the actuator. The applied high voltage is measured by an oscilloscope (Teledyne Lecroy HDO4034) thorough a high-voltage prove (Tektronix PHV4002-3-Ro). We use the reference plasma actuator provided by the National Institute of Advanced Industrial Science and Technology (AIST). It consists of 0.4 mm thick silicone resin as a dielectric and 18 μm thick copper as two electrodes, and its span length is 100 mm. The applied voltage is 16 kV_{pp}, the frequency is 3 kHz, and the waveform is sinusoidal.

The BOS measurement system is shown in Fig. 4. A background image with random dot patterns, a white LED and a single-lens reflex camera (Nikon D3200) equipped with a single focus lens (Micro-Nikkor 105 mm f/2.8) is used. Imaging resolution and shutter speed is 0.017 mm/pixel and 1/100 s, respectively. Measurements are conducted for 40 times, and the time-averaged displacement field of the background image is calculated using the image correlation method based on the Fast Fourier Transform (FFT), which is often used for the PIV.

In addition, we obtain the time-averaged flow field from 250 instantaneous flow fields using the PIV method.

*Corresponding author. E-mail: s199081s@st.go.tuat.ac.jp

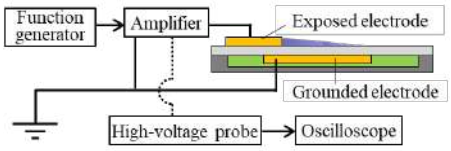

Figure 3. Schematic of the DBDPA and power supply system.

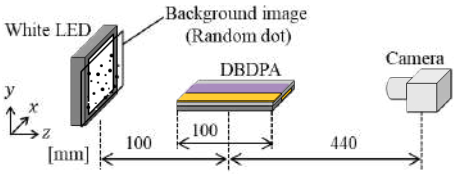

Figure 4. The BOS measurement system.

RESULT

Figure 5 shows (a) the time-averaged displacement field, (b) the time-averaged flow velocity field and (c) x-directional profiles of the displacement (y = 0.5 mm) and flow velocity field (y = 0.2 mm). In Fig.5 (c), the red and blue line indicates the horizontal velocity and displacement, respectively. First, focusing on the displacement field (Fig.5 (a)), it spreads over the dielectric and the exposed electrode surface and is vertically downward. It indicates that the density of the air near the actuator surface is lower than that of the ambient air. In addition, it has the peak value at some distance from the exposed electrode edge (Fig. 5 (c)). Next, focusing on the flow field (Fig. 5 (b)), the suction flow occurs at the exposed electrode edge, and the flow along the actuator surface is generated. The physical reason why such a displacement field was obtained is discussed using Fig. 6. Firstly, the Joule heating and the flow acceleration causes the density disturbance. When the plasma actuator is driven, the discharge occurs at the exposed electrode edge. In the discharge area, both the Joule heating and the acceleration due to the body force occur. The air flowing into the area is heated and the heated air is advected with expanding. As a result, it is considered that lower density area spreads over the dielectric surface, and the lowest density point is at some distance from the electrode edge. It is also considered that the expansion due to the acceleration of the flow is occurring at the same time. Next, focusing on the exposed electrode surface. From comparison with the flow field, there is no flow over the exposed electrode surface, however, the displacement appears. It is considered that the density of the air in this area becomes lower because of the Joule heating of the electrode caused by the current flowing into it.

Second, as observed in Fig. 5 (c), the peak position of the displacement dose not corresponds to that of the horizontal velocity, and we can confirm that the displacement peak position is more downstream of horizontal velocity peak position.

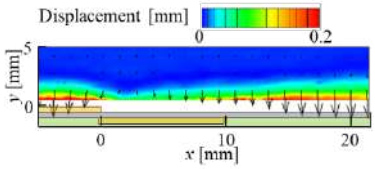

(a) Displacement field.

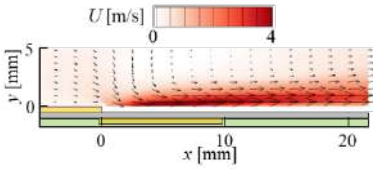

(b) Flow velocity field.

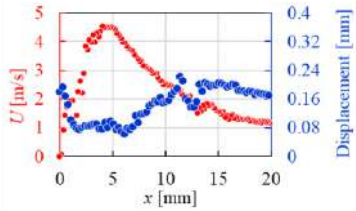

(c) x-directional profiles of the displacement and flow field.

Figure 5. Time-averaged measurement results.

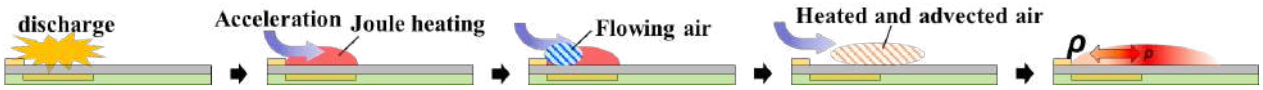

Figure 6. Mechanism of forming the density gradient field.

CONCLUSINOS

In this study, for discussing the density field induced by DBDPA together with the flow field, we adopt the BOS technique in addition to the PIV method and both measurements were conducted to obtain the time-averaged field. As a result, comparing the displacement field of the background image with the flow velocity field, it is confirmed that the BOS result is physically valid, and the peak position of the displacement is downstream of that of the horizontal velocity.

In the future works, for further investigation about the density field of the plasma actuator, we will calculate the density field from the displacement field and conduct the time-resolved measurements of the BOS and PIV. Moreover, we will investigate the effect of the applied voltage waveform on the density and flow field.

References

[1] Benard N., Moreau E. Electrical and mechanical characteristic of surface AC dielectric barrier discharge plasma actuators applied to air flow control. *Exp. Fluids.* **55**: 1846, 2014.

[2] Asa N., Hiroyuki N. The effect of the voltage waveform on performance of dielectric barrier discharge plasma actuator. *J. Appl. Phys.* **126**: 173303, 2019

[3] Atsushi K., Nae O., Momoko I., Taku N., Keisuke A., Akira A. Visualization of density variations produced by alternating-current dielectric-barrier-discharge plasma actuators using the background-oriented shclieren method. *Plasma Sources Sci. Technol.* **28**: 055002, 2019

[4] Keisuke H., Yoshiyuki T., Tianshu L., Masaharu K. Optical-flow-based background oriented schlieren technique for measuring a laser-induced underwater shock wave. *Exp. Fluids.* **57**: 179, 2016

ELECTROMAGNETIC VIBRATIONS INFLUENCE ON DIRECTIONAL SOLIDIFICATION OF METALLIC ALLOYS AND COMPOSITES

Imants Kaldre *[1]
[1]University of Latvia, Institute of Physics, Jelgavas iela 3, Riga LV-1004

Summary Directional solidification is widely used to investigate how various parameters influence solidification structure of the metal materials. It is well known that main parameters influencing the grain structure of metallic alloys are solidification velocity and temperature gradient at the solidification interface. Liquid phase convection is also one of the important parameters which may affect solidification process. Electromagnetically created convection impact on the solidification has been studied and effect has been demonstrated. There are various electromagnetic effects. In this work we focus on the electromagnetically induced vibrations created by simultaneously applied AC and DC magnetic fields to study its impact on metallic alloy microstructure and admixed particle distribution.

INTRODUCTION

Solidification of metallic alloy is an extremely complicated multiphysical process where numerous physical processes take part and influence each other by different ways. Structure of the metal or alloy is also significantly affected by energy and solute transport in the liquid melt at the vicinity of the solidification interface during solidification process. In general, when regular cells are forming at relatively low rates, they grow perpendicular to the liquid-solid interface regardless of crystal orientation. When the growth rate is increased crystallography effects begin to exert an influence and the cell growth direction deviates toward the preferred crystallographic growth direction. Simultaneously the cross section of the cell generally begins to deviate from its previously circular geometry owing to the effects of crystallography. In this case it is called dendritic crystallization, which is the most common type of solidification of metallic alloys in practical metallurgy. Various kinds of dendrite morphologies are known today.

Evenly distributed dielectric particles in metal matrix can significantly improve some of metal properties, like mechanical strength, thermal properties and radiation absorption properties. Particles added to liquid metal tend to form agglomerates due to Van der Waals forces and electromagnetic separation between metal and particles or their ensembles. Dispersion of these agglomerates is a technical challenge which limits the production of these materials in larger quantities. Electromagnetically induced vibrations is one of the means how to disperse particles contactlessly. In previous works it has been shown that combined AC and DC magnetic fields can create sufficiently high pressure amplitude to disperse particles in some metals [1].

Electromagnetic effects on solidification of metal alloys and metal matrix composites has been widely studied. Various electromagnetic effects have different impact on the melt flow, solidification structure and impurity dispersion. Application of magnetic field can be additional mechanism to affect and create convection in the liquid melt and mushy zone of metallic alloy. DC magnetic field creates thermoelectromagnetic convection and melt flow perpendicular to magnetic field leading to anisotropic material structure [2]. Pulsed and DC electromagnetic interaction has been studied showing that electromagnetic vibrations is one of the methods to disperse particles and refine grain structure of the metallic alloys.

EXPERIMENTAL

Small scale experimental setup is designed and built to demonstrate the effect of combined AC and DC magnetic fields on the directionally solidified metallic alloys and metal matrix composites. AC magnetic field is created by high frequency inductor which also melts the sample. The samples are directionally solidified in a Bridgman setup at controlled growth velocities from 10 μm/s to 500 μm/s. Upper part of the sample is melted by the high frequency inductor around the crucible while bottom part is kept solid by water cooled copper ring. Inductor and water-cooled bottom ring are stationary while crucible is lowered by programmable stepper motor. Solidification front is located between heater and cooler at the same location, thus actual solidification velocity is assumed to be equal to the pulling velocity of the crucible. Various electromagnetic interaction parameters and solidification velocities are tested. Experiments are done using low temperature alloys Sn-Pb, Sn-Bi, but in future work with aluminium is foreseen. Numerical model is developed for interpretation of the results and calculation of the actual melt flow in the crucible. It is shown that applied AC and DC electromagnetic fields during directional solidification creates oscillating pressure and drives flow as well. Characteristic velocities of the flow is estimated from the numerical model and analytical estimations. Samples are analysed measuring grain structure and particle dispersion.

CONCLUSIONS

In this work it is demonstrated that applied electromagnetic interaction during directional solidification modifies the grain structure of the metallic alloy and its impact on the particle dispersion in metal matrix composite materials. It is confirmed that AC and DC electromagnetic interaction refines grain structure of the metallic alloys. Electromagnetic contactless technology seems to be promising solution for high temperature metals and aluminium alloys for particle dispersion. Electromagnetic interaction has similar effect that ultrasound. Ultrasound treatment is well known to be used for grain refinement and homogenization.

Acknowledgement

This work is supported by PostDoc Latvia Postdoctoral research grant « Electromagnetic methods for metal matrix nano-composite production » No. 1.1.1.2/VIAA/2/18/264

References

[1] Kaldre, I., Bojarevičs, A., Grants, I., Beinerts, T., Kalvāns, M., Milgrāvis, M., Gerbeth, G. Nanoparticle dispersion in liquid metals by electromagnetically induced acoustic cavitation (2016) Acta Materialia, 118, pp. 253-259

[2] Kaldre, I., Fautrelle, Y., Etay, J., Bojarevics, A., Buligins, L. Influence on the macrosegregation of binary metallic alloys by thermoelectromagnetic convection and electromagnetic stirring combination (2014) Journal of Crystal Growth, 402, pp. 230-233

MODELING THE OSCILLATORY DYNAMICS OF GAS BUBBLES GROWING AT MICROELECTRODES

S. Sahil Hossain*[1], Aleksandr Bashkatov[1], Xuegeng Yang[1], Gerd Mutschke[1], and Kerstin Eckert[1,2]
[1]Institute of Fluid Dynamics, Helmholtz-Zentrum Dresden-Rossendorf, Bautzner Landstrasse 400, Dresden, 01328 Germany
[2]Institute of Process Engineering and Environmental Technology,Technische Universität Dresden,Dresden, 01062 Germany

Summary The working mechanism of the recently observed bubble oscillation on microelectrodes is explained [1]. The force balance includes contributions from a thermocapillary force and a Columb force on the charged bubble. Comparison between model predictions and experimental measurements is presented.

The literature on bubble evolution by water electrolysis dates back decades and over the time, one of the prominent phenomena that remain unresolved is the observation of bubble jump off and return to the electrode surface [3, 4]. Recently we also observed periodic bubble oscillations over Pt microelectrodes [1]. In this contribution, we explain the working mechanism of such phenomena alongwith a comparison of the model estimations with experimental observations.

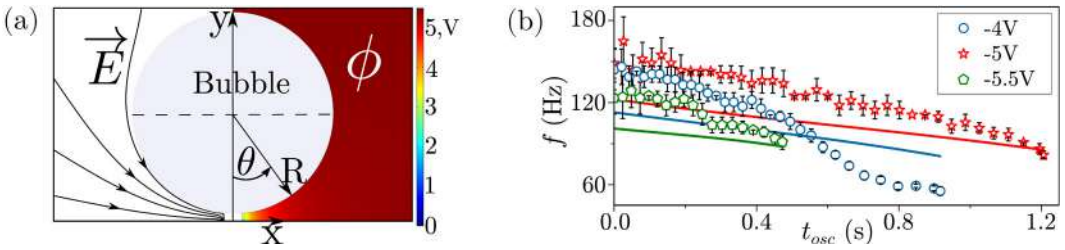

Figure 1: (a) Electric potential distribution and electric field lines in the electrolyte around the bubble, (b) Oscillation frequency estimates (solid line) compared with experimental measurements (open symbols). Reprinted from [1]

Figure 1(a) shows the numerically obtained potential distribution and the electric field lines in the electrolyte around the bubble. Due to the presence of adsorbed ions at the bubble-electrolyte interface, a vertically oriented electric force acts on the bubble. The magnitude of this force depends on the distance between the bubble and the microelectrode at the bottom, and on the surface charge density of the bubble interface. Equilibrium of Marangoni [2], electric and buyoancy forces at the moment of detachment provides an estimation of the interfacial charge density. The distance dependent electric force acts as a restoring force enabling bubble reattachement to the microelectrode. The oscillation frequencies are calculated by approximating the electric force as a linear spring. Figure 1(b) shows a good agreement between the experimentally measured and numerically predicted frequencies for different electrode potentials over the oscillation time.

This project is supported by German Space Agency (DLR) with funds provided by the Federal Ministry of Economics and Technology (BMWi) due to an enactment of the German Bundestag under grant no. DLR 50WM1758 (project MADAGAS).

References

[1] Bashkatov, A., Hossain, S. S., Yang, X., Mutschke, G., and Eckert, K. Oscillating hydrogen bubbles at pt microelectrodes. *Physical Review Letters 123* (2019), 214503.
[2] Massing, J., Mutschke, G., Baczyzmalski, D., Hossain, S. S., Yang, X., Eckert, K., and Cierpka, C. Thermocapillary convection during hydrogen evolution at microelectrodes. *Electrochimica Acta 297* (2019), 929 – 940.
[3] Sides, P. J., and Tobias, C. W. A close view of gas evolution from the back side of a transparent electrode. *Journal of the Electrochemical Society 132*, 3 (1985), 583–587.
[4] Westerheide, D. E., and Westwater, J. Isothermal growth of hydrogen bubbles during electrolysis. *AIChE Journal 7*, 3 (1961), 357–362.

*Corresponding author. E-mail: s.hossain@hzdr.de

CHARACTERISTICS OF DISCHARGE AND JET GENERATION OF PLASMA ACTUATOR UTILIZING DC AND AC DISCHARGES

Asami Hatamoto[1], Kumi Nakai [1], and Hiroyuki Nishida [*1]
[1]Department of Mechanical Systems Engineering, Tokyo University of Agriculture and Technology, Koganei, Japan

Summary Tri-electrode plasma actuator (TED-PA) is an active flow control device utilizing the ionic wind coming from atmospheric discharge. It consists of exposed a DC and AC high voltage electrode, dielectric plate and an covered ground electrode. For high flow controllability, the design optimization is needed to maximize the ionic wind from the DC electrode. In this report, we experimentally investigate the influence of AC discharge state on the DC discharge and DC ionic wind. For this purpose, the discharge photograph and flow velocity field is investigated. As a result, it is found that the DC discharge and ionic wind generation is enhanced by the AC barrier discharge. Increasing the AC frequency is effective for the enhancement.

INTRODUCTION

The Plasma Actuator is one of active flow control devices that induces a jet (ionic wind) using electrohydrodynamic force coming from atmospheric discharge. The Plasma Actuator has many advantages such as thin and light, no mechanical moving parts and excellent rapid controllability so it is expected to be applied to surface flow control of various fluid devices.[1] If the jet can be strengthened, the range of applications can be greatly expanded, and practical application can be accelerated. In order to obtain stronger jet, the Tri-Electrode Plasma Actuator (TED-PA) was proposed. The TED-PA is composed of three electrodes and a dielectric layer as shown in Fig. 1 (a). It induces a jet from both the AC and DC electrodes by applying high voltage to each electrode, and high performance is reported with a thrust of about 10.6 times and a thrust power ratio of about 6.0 times that of the conventional two-electrode plasma actuator.[2] The jet generation of the DC electrode contributes to the high performance of TED-PA, and therefore, for further high performance of TED-PA, it is necessary to optimize the design in order to maximize the DC jet.

The interaction between the AC and DC discharge has significant influence on the performance of TED-PA. Therefore, the objective of this study is to clarify the effect of the AC discharge state on the DC discharge and its jet generation. We investigate two types of plasma actuator; one is the TED-PA (Fig. 1 (a)), the other is the ACDC-PA which has the exposed AC and DC electrode but does not have the covered grounded electrode (Fig. 1 (b)). Depending on the presence or absence of the ground electrode, a dielectric barrier discharge and corona discharge occurs at the AC electrode of TED-PA and of ACDC-PA, respectively. In the experiments, the discharge photographs are taken to investigate the discharge condition, and in addition, flow velocity fields are obtained by the PIV (Particle-Image-Velocimetry) measurement.

(a) TED-PA configuration. (b) ACDC-PA configuration.

Figure 1. Schematic configurations of TED and ACDC plasma actuators.

EXPERIMENTAL SETTINGS

The discharge photographs are taken from the top of the actuator using a single-lens reflex camera (NIKON D3200) with a lens whose focal length is 105 mm. The imaging conditions are as following: the exposure time is 6 s, ISO is 100 and the F-number is 2.8. To quantitatively show the discharge intensity, the value obtained by dividing the brightness of the discharge at the DC electrode in the discharge photograph by the area of the discharge is defined as photo-emission strength around the DC electrode. Furthermore, a time-averaged velocity field is obtained from the 200 flow velocity field images obtained by the PIV method.

For plasma actuator, a copper tape with 0.05 mm thickness for the electrode, a PTFE with 2 mm thickness for the dielectric and a polyimide tape with 0.05 mm thickness and glass epoxy with 1 mm thickness for the Insulator is used, and the gap between the AC electrode and the DC electrode is 20 mm and spanwise length is 80 mm. The overlap between the ground electrode and the AC electrode is 1 mm, and the width of the ground electrode is 10 mm. The DC electrode and AC electrode (top electrode) are cut in a sawtooth shape in order to make the discharge uniform. The AC voltage amplitude is 10 kV_{pp}, the frequency is varied in the range from 0 to 8 kHz and the waveform is sinusoidal, and the DC voltage is 14 kV. Here, 'AC frequency of 0 kHz' indicates that the AC electrode is electrically grounded.

*Corresponding author. E-mail: hnishida@cc.tuat.ac.jp

EXPERIMENTAL RESULTS

Figures 3 (a) and (b) show discharge photographs of TED-PA and ACDC-PA when the AC frequency is 8 kHz. The discharge at the DC electrode is the same for both plasma actuators, which is a corona discharge, but the discharge at the AC electrode is different. In TED-PA, longer propagation of the discharge can be observed at the AC electrode. This indicates that a dielectric barrier discharge occurs between the AC electrode and the ground electrode. In ACDC-PA, many spot discharges are observed. This indicates the occurrence of corona discharge between the AC and DC electrodes.

Figure 4 shows the AC frequency characteristics of the photo-emission strength around the DC electrode. When the AC electrode is electrically grounded (0 kHz in Fig. 4), it can be seen that the photo-emission strength around the DC electrode of TED-PA and ACDC-PA does not change. Therefore, the presence of the lower ground electrode does not affect the DC discharge strength. In the case of TED-PA, the photo-emission strength decreases when the AC frequency is 1 kHz compared to the case that the AC electrode is electrically grounded. This is because the electric field strength around the DC electrode weakened due to the interaction among the DC and AC and ground potential of electrodes. On the other hand, in ACDC-PA, the photo-emission strength increases at 1 kHz. This is because the maximum potential gap between the DC and AC electrode increases, and it strengthen the discharge. Next, in TED-PA, the DC photo-emission strength increases as the AC frequency increases. This is because the barrier discharge at the AC electrode of TED-PA increases with the AC frequency. The electrons generated by the barrier discharge are supplied to the DC electrode, and the discharge at the DC electrode is enhanced. On the other hand, in ACDC-PA, as the AC frequency increases, the DC photo-emission strength decreases and becomes equal to the value for the case that the AC electrode is grounded. This is probably because the ion motion becomes to be not able to follow the high frequency change of electric field and the DC discharge strengthening by the AC high voltage is lost.

Figure 5 shows the AC frequency characteristics of the maximum flow velocity of the jet from the DC electrode obtained from the flow velocity fields. In TED-PA, the DC jet velocity firstly decreases and after that, increases with the AC frequency; this tendency is consistent with that of the photo-emission strength, and at 6 kHz it exceeds the value at the case that the AC electrode is grounded (0 kHz in Fig. 4). In contrast, in ACDC-PA, the value of the DC jet velocity does not change with AC frequency. Therefore, in order to maximize the DC jet, it is effective to generate the barrier discharge using the AC high voltage with high frequency. However, in the TED-PA of Fig. 5, the DC jet velocity decreases as the frequency increases from 6 kHz to 8 kHz. This is thought to be because the jet generated from the AC electrode became stronger as the barrier discharge at the AC electrode became stronger, and collided with the DC jet. This result indicates that there is a possibility that there is an optimum value between the DC voltage and the frequency of AC voltage.

(a) TED-PA. (b) ACDC-PA.

Figure 3. Discharge photographs of TED and ACDC plasma actuators.

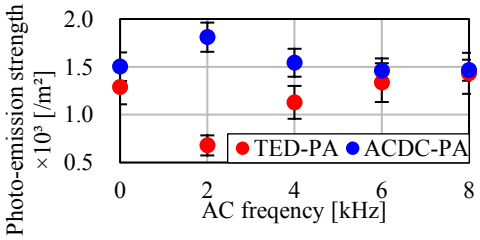

Figure 4. Photo-emission strength around the DC electrode.

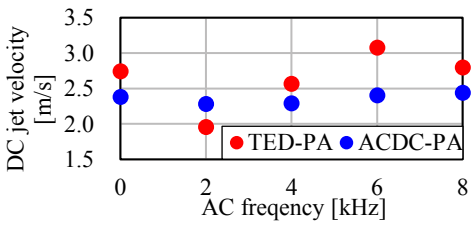

Figure 5. Maximum jet velocity of the DC jet.

CONCLUSIONS

To optimize the driving parameters of TED-PA, we investigated the influence of the AC discharge state on the discharge and jet generation at the DC electrode. From the discharge photographs and flow field measurement, we experimentally showed that it is effective to generate the barrier discharge by AC voltage with high-frequency. Note that, there is a possibility that there is an optimum value between the DC voltage and the frequency of AC voltage.

References

[1] Thomas F., Kozlov A., Corke T. Plasma Actuators for Landing Gear Reducation. AIAA paper 2005-3010, 2005.
[2] Matsuno T., Sugahara M., Kawazoe H., Nishida H., Development of Serrated Multi-Electrode Plasma Actuators for Enhanced Force Production. AIAA paper 2016-1691, 2016.

NUMERICAL STUDY OF NATURAL CONVECTION INDUCED BY PARTICLES UNDERAN IMPOSED AC FIELD AND EXPERIMENTAL MAGNETO-CONVECTION PROCESS WITH LIQUID METAL IN CYLINDRICAL VESSEL

Julien Guillou*[1,2], Philippe Tordjeman[1], Wladimir Bergez[1], Rémi Zamansky[1], Jean-François Haquet[2], Pascal Piluso[2]and Sébastien Renaudière de Vaux[1,2,3]
[1]Institut de Mécanique des Fluides de Toulouse (IMFT)-Université de Toulouse, CNRS-INPT-UPS, Toulouse, France
[2]CEA, DEN/DET/SMTA/LMAG, Cadarache, 13115 Saint-Paul-lez-Durance, France
[3]Saint-Gobain Research Paris, 39 quai Lucien Lefranc, 93303 Aubervilliers, France (present affiliation)

Summary: In this work we study metallic particles diving in a non-electrical conducting fluid under a harmonic magnetic fields with DNS method. Force, torque and Joule heating acting on the particles are calculated with an analytical model. Moreover, an experiment of magneto-convection in Rayleigh-Bénard cell is introduced. Both investigations are dedicated to the understand the hydrodynamic behaviour of a two phases corium with oxide and metal heated by an electromagnetic induction.

INTRODUCTION

In the frame of a hypothetic nuclear accident leading to the partial or the whole destruction of the nuclear fuel, the core could melt and create a high temperature mix named corium. If the mixture were to break through the vessel, it will spread out on a concrete apron and then triggered a reaction mentioned in the literature as Molten Core Concrete Interaction. This interaction result in a gradual concrete ablation intimately linked to the heat flux exchanged.

In order to understand this behavior, experiments using prototypical corium are performed at CEA Cadarache and using induction heating to simulate the residual heating power coming from the fission reaction within the corium in order to match with the reality, the volumetric power heating has concentrated exclusively in the oxide phase and not inside the metallic parts built-in the corium coming from the construction structure melted (cm-sized droplets and/or parietal layers according to the hydrodynamic regime).

The conductivity gap between the two phases raised several questions about the efficiency of the selected heating technology. Spherical droplets and magnetic field interaction may create a force, a torque and heating them up. Consequently, particles trajectory could be bias comparable to the reactor case, as the general hydrodynamic of the bath with the particles feedback on the flow.

NATURAL CONVECTION GENERATED BY INDUCTION HEATING OF PARTICLES

A 3D magneto-hydrodynamic direct numerical simulation investigates when the fluid carrier is neutral and only the metallic particles conduct electricity. An imposed changing magnetic field inside a box which decay exponentially from the bottom to the top of the vessel induced a magnetic levitation force and induction heating when conducting medium spans the changing field. By this means, the unconventional flow patterns shown up and two parameters, the density ratio between the two distinct phases and the concentration of particles may have helped to interpret the global dynamics.

Firstly, scattered particles reached a steady state at predicting position directly link to the balance between the electromagnetic and the gravity force and kickoff expected buoyant flow behavior.

Secondly, huge particles concentration results in heap stuck nearly the lower part of the domain supplying a main thermal plume.

Finally, the intermediate case involves the same conclusions seen previously when the concentration of particles is important. Nevertheless, droplets display high mobility and are ejected intermittently from the hearth following the plumes that they helped create. Picture above describes the last state sum up.

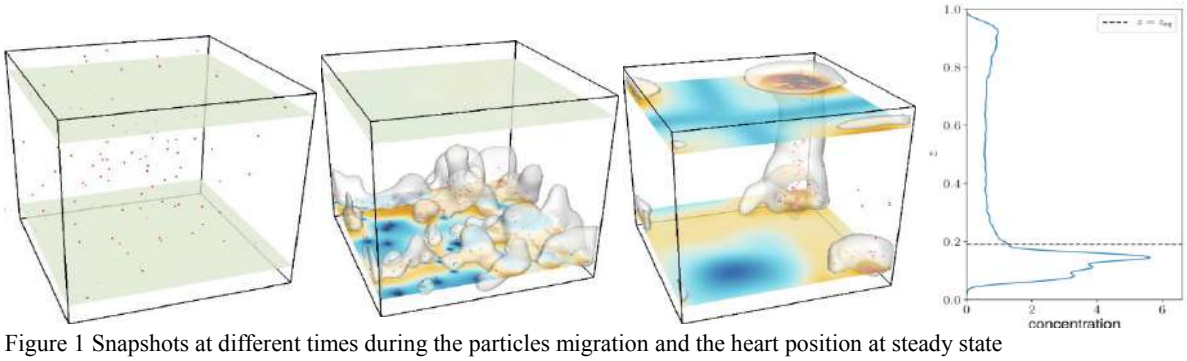

Figure 1 Snapshots at different times during the particles migration and the heart position at steady state

*Corresponding author. E-mail: julien.guillou@imft.fr

MAGNETO-CONVECTION EXPERIMENTATION

An experimental study of a magneto-hydrodynamic flow inside a cylindered vessel filled with a liquid metal under an AC magnetic field and bounded by a vertical temperature gradient is performed. Experimental setup explore a wide range of Rayleigh number based on the induction heating (up to 1.10^4-1.10^8) and Rm (up to 3) and investigate the average Nusselt number of the system.

An electrical and thermal insulated cylinder filled with a liquid metal corresponding to an unity aspect ratio (D/H=1) is manufactured in PEEK (PolyEtherEtherKetone) material in order to avoid electromagnetic power loose outside the fluid and heat loose from the wall. Two distinct flow circulation above a high thermal conducting ceramic (Silicon carbide) imposed a natural vertical thermal gradient ($T_{top}<T_{bottom}$) and sealed our system. Above a critical Rayleigh value, the fluid becomes unstable and it's referred as the Rayleigh-Bénard Instability. The fluid motion is made turbulent regarding the fluid properties, the temperature difference and the geometry length. Many researches have been made about this kind of instability to understand the behavior of the flow and our case is dedicated to study this configuration under the influence of an alternating magnetic field.

The natural convection container seats inside an inductor feed by an AC current supply power in order to induced a non-uniform, time dependent magnetic field within the conducting liquid metal. The frequency of the current flowing in the coil plays a significant role of the distribution in space of the eddy current estimate by the shield parameter (Rw). Playing on the frequency and the intensity of the current inside the coil, eddy current creates Joule heating with different intensity, spread in the whole volume or only distributed on the thin exterior surface of the conducting liquid. The fluid is also submitting to the Lorentz force and its action on the motion on the fluid require an extensive knowledge.

Velocity profile inside the vessel are recorded with UVP technology to catch the flow pattern in an opaque fluid. Several temperature sensors lead to the energy balance of the experiment and finally the average Nusselt number. Picture above describe all the test system.

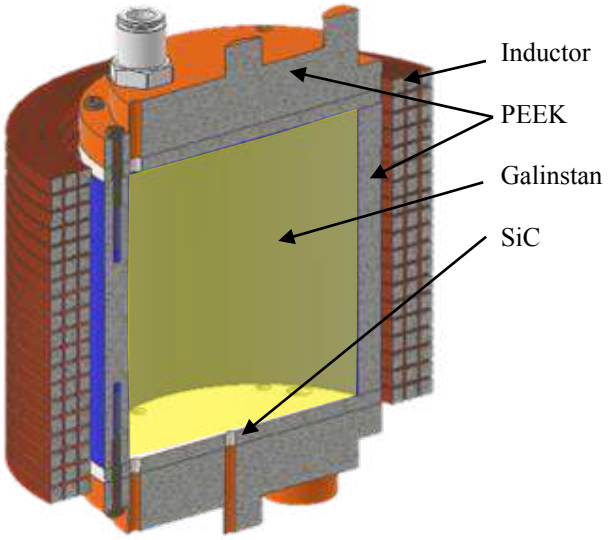

Figure 2 Natural convection cell surrounded by coil

CONCLUSION

In this work magneto-convection DNS of conducting particles in neutral fluid under a harmonic is presented. We find out three different patterns link to the density ratio between the fluid and the particles and the concentration of droplets. Finally, an experimental setup of magneto-convection in Rayleigh-Bénard of two phases with a AC magnetic field is presented.

A NEW EXPERIMENTAL FACILITY FOR IONIC PROPULSION STUDIES

Federico Sottovia[1], Samuele Fiorini*[1], Marco Belan[1], and Filippo Maggi[1]
[1]Dipartimento di Scienze e Tecnologie Aerospaziali, Politecnico di Milano, Milano, Italy

Summary In this work, an experimental setup for ionic propulsion studies is presented. The research aims to better understand the capabilities of a thruster that exploits corona discharge to produce propulsive force. Nowadays, electric propulsion in atmospheric conditions has been tested successfully for heavier-than-air aircrafts; whilst the theoretical principle is well understood at least for a standard corona discharge, the optimization of a thruster requires a wide range of configurations to be experimented and therefore a valid multipurpose experimental setup. For this reason, a test bench that can accommodate different electrodes arrays has been built, with adjustable electrode gaps and spacings. Induced flow can be characterized by means of velocity measurements from which thrust force can be obtained in order to compute the main performance parameters. Results obtained from a first measurement campaign are briefly presented. Using a vacuum vessel, experiments can also be performed with different pressure and gas compositions.

INTRODUCTION

Thrust generation by means of ions acceleration is a propulsion technique often used in space applications but much less studied for atmospheric ones. It allows to develop devices with a thrust per unit power much higher than thermochemical ones. However, this technology in atmospheric applications is used only in few cases, mainly limited by the weight of the high voltage generation system required for ions production and the low values of thrust per unit area achievable [1]. The main application fields are 1) atmospheric system for low orbit satellites, where rarefied gas is captured by a dynamic intake and electrostatically accelerated in order to generate enough thrust to maintain the orbit and 2) proper atmospheric flight system, created exploiting ionic wind produced by corona discharge between two high voltage electrodes.

A test aircraft model has been developed by a research team at MIT [2] showing the capability of sustained flight, having aboard the ionic propulsion system and the power source. The thrusters were designed with airfoil-shaped cathodes in order to optimize the produced force. Another remarkable result has been reached by Khomich and Rebrov [3], who realized a flying thruster with a wireless power source, verifying other possible configurations and applications of this technology.

Despite the knowledge about the underlying physical principle, the problem of increasing thrust efficiently by designing suitable electrodes geometry surely requires further investigations. Moreover, other important studies may arise by considering the use of ionic engines in environments with different gases. Hence, an adaptable setup to fit multiple configurations and environment conditions could help in starting new research lines.

To this purpose, it is presented a test bench that can accommodate arrays of anodes and cathodes with the possibility of varying the gap between opposite electrodes and the distance between similar electrodes. Intermediate electrodes between anodes and cathodes can also be included. The system has been conceived to allow multiple adjustable configurations, in order to explore a wide parameter space seeking for an optimal configuration for thrust generation. Moreover, the test bench can be inserted in a vacuum vessel where pressure and air composition can be controlled, extending the research field to different atmospheres.

A first measurement campaign has been carried out and calculated performances resulted in line with other state of the art devices. Table 1 presents two of the main parameters used during experiments as performance indicators, the thrust to power ratio $T/P = \Theta$ and the thrust to frontal area ratio $T/A = \Psi_A$, for one of the optimal configuration found during the tests and two other systems, the Aeroplane built at MIT [2] and the Ionocraft of Khomich and Rebrov [3].

Device	Θ $[N/kW]$	Ψ_A $[N/m^2]$
PoliMi EHD Thruster	5.62	3.22
Xu et al. EHD Aeroplane [2]	5.16	3.56
Khomich and Rebrov Ionocraft [3]	6.40	1.51

Table 1: Performance comparison between the setup used in the tests and some state of the art devices developed in the last two years. PoliMi data are obtained for a configuration with spacing $s = 30\ mm$ between similar electrodes and gap $g = 20\ mm$ between opposite electrodes.

EXPERIMENTAL SETUP

The experimental setup represented in Figure 1 includes a test bench made entirely of PMMA, which consists in a base of size 300×800 mm with rails screwed to it. The rails provide a sliding coupling with three bridges, each one with a frontal area of 200×355 mm. The vertical columns of each bridge serve as support for the electrodes. In the first

*Corresponding author. E-mail: samuele.fiorini@mail.polimi.it

presented configuration, ground electrodes are made of ABS coated with aluminium and shaped as NACA 0010 airfoils with 100 mm chord and 140 mm span. On both the lateral sides ABS clamps are mounted in order to lock the electrodes at the bridge columns at the desired height. In the same manner, clamps are used to hold tense 30μm diameter wires used as positive electrodes. The test bench is big enough to accommodate five anode-cathode couples or five groups of 3 electrodes, allowing a maximum vertical distance between adjacent electrodes of about 60 mm. Several supply units can be connected to the bench; in the present configuration, the supply voltage ranges up to 20 kV DC.

The test bench is designed to accommodate an almost arbitrary configuration of electrodes, and can be used to study the effect of gap distance on thrust generation or even the interaction between different electrode pairs. Velocity measurements downstream of the ground electrodes can be performed by means of a pitot probe made with a glass tube of diameter 1.2 mm connected to a high accuracy pressure transducer (an example of velocity profile is presented in Figure 2). The pitot can be accurately positioned along the vertical direction by means of a traversing system.

The bench can be entirely placed inside a vacuum vessel; in this case, velocity measurements are performed using a probe traversed inside the vessel thanks to a mechanical feedthrough. Suitable vacuum pumps are connected to the test chamber in order to reach the desired pressure for the experiments, continuously read by vacuum manometers. By means of injectors mounted on the walls, fresh gas can be introduced into the chamber. The desired atmosphere can be created by means of a multistage timer which drives the injectors, balancing their input mass flow with the output due to the main pumps. The same injectors can be used to change the mixture of gases present during the tests. Control over air composition and pressure guarantees a wide range of possible studies, allowing to investigate ionic propulsion in rarefied atmospheres made of different gases.

The system is completed by devices acquiring all the signals of interest, including the outputs of the pressure transducers and the electric quantities as supply voltages and electrodes currents.

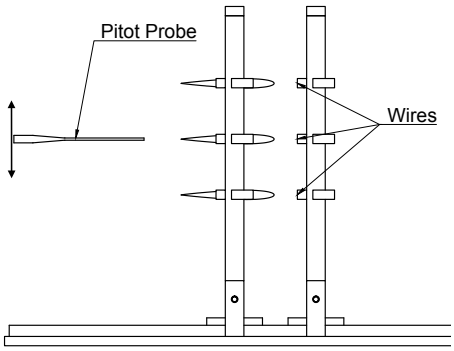

(a) An electrodes array configuration with two bridges and three anode-cathode pairs.

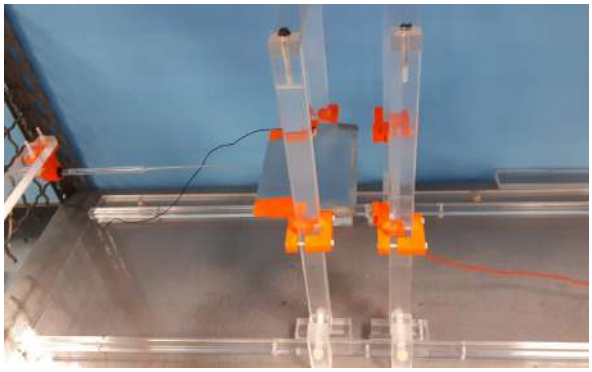

(b) Photo of a single anode-cathode configuration.

Figure 1: Experimental setup

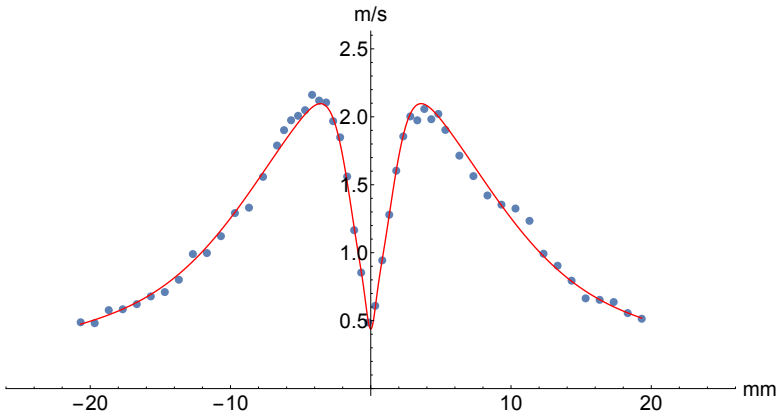

Figure 2: Velocity curve acquired 2 mm downstream of the cathode trailing edge in Figure 1b with 20 kV voltage.

References

[1] Gilmore C.K., Barrett S.R.H., *Proc. R. Soc. A* **471**.20140912, 2015
[2] Xu H., He Y., Strobel K.L., Gilmore C.K., Kelley S.P., Hennick C.C., Sebastian T., Woolston M.R., Perreault D.J., Barrett S.R.H., *Nature* **563**: 532–535, 2018
[3] Khomich V.Y., Rebrov I.E., *J. Electrostat.* **95**: 1–12, 2018

NUMERICAL INVESTIGATION OF THE RICHTMYER-MESHKOV INSTABILITY IN MAGNETO- HYDRO-DYNAMICS

Sheng-Bo Zhang[1], Huan-Hao Zhang *[1], Wei-Tso Wu[2],Zhi-Hua Chen[1]
[1]Key Laboratory of Transient Physics, Nanjing University of Science & Technology, Nanjing, China
[2]School of Mechanical Engineering, Nanjing University of Science & Technology, Nanjing, China

Summary Based on the ideal compressible Magneto-hydro-dynamic (MHD) equations, the Richtmyer-Meshkov instability (RMI) caused by the incident plane shock wave impinging on the heavy gas density interface was numerically studied. The flow characteristics and wave patterns of hydrodynamic (HD, B = 0) and MHD (B = 10, 50, 100) situations are discussed, and verified by the corresponding experiments and numerical results. The suppression mechanism of transverse magnetic field on related interface instability is investigated. In addition, the evolution of the interface under the different transverse magnetic fields is quantitatively analysed.

1 INTRODUCTION

The RMI is produced in a wide range of natural and engineering problems, which include inertial confinement fusion (ICF) [1], supersonic combustion scramjet[2] and underwater explosive explosion[3]. It has the complex physical phenomena involved in the Richtmyer-Meshkov instability (RMI), such as flow stability, vortex, shock-vortex interaction and turbulence transition [3], a lot of attention has been paid on investigating RMI during the last decades. In the meanwhile, in the field of high-energy physics, most of the flowing matter is in a plasma state and is susceptible to the influence of magnetic fields. In recent years, controlling RMI by magnetic field has become a hot and difficult research point.

The effect of a magnetic field on the RMI was firstly analyzed by Samtaney [4] through numerical simulation in 2003 .Recent studies have shown that the growth of RMI can be inhibited from the presence of a magnetic field [3], but their references or data seem to be insufficient to prove this. Therefore, in this paper, we decided to conduct a deeper analysis of the basic mechanism of the transverse magnetic field suppressing RMI.

2 NUMERICAL METHOD AND PHYSICAL MODEL

2.1 Numerical Method

In order to simulate the evolution of the MHD RMI, the Navier-Stokes equations coupled with the Maxwell equations needs to be solved. In this paper, the Richtmyer-Meshkov instability (RMI) caused by the incident plane shock wave impinging on the heavy gas density interface with different transverse magnetic strengths was numerically studied using the ideal compressible Magneto-hydro-dynamic (MHD) equations. Magneto-hydro-dynamic (MHD) equations are solved by the CTU (corner transport upwind) + CT (constrained transport) algorithm which guarantees the divergence-free constraint on the magnetic field, i.e., $\nabla \cdot \mathbf{B} = 0$. Details of the algorithm can be found in Ref. [4].

2.2 Physical Model

As shown in Fig.1, the computational domain is set to [-0.02,0.06]×[0,0.01], and θ is the angle between the density interface and the y axis. Initially, the horizontal distance between the left vertex of the density interface and the left boundary is 0.02, and the plane incident shock wave is located on the left boundary, and then propagates from left to right from the initial position x = -0.02. The density ratio on both sides of the density interface $\eta = \rho_1 / \rho_2 = 3$, the shock Mach number M=2, and the density interface angle θ is 45°.

The upper and lower boundaries of the computational domain are set as reflected wall conditions, the right boundary is the outflow conditions, and a uniformly distributed Cartesian grid is used. After the grid independence test, the total number of grids are 10000×1250. To study the MHD RMI, we suppose the initial transverse magnetic field strength is B=0, 10 and 100. In addition, in order to make the gas affected by the magnetic field, plasma is selected.

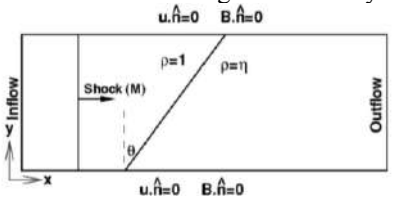

Fig.1 Schematic of computational model.

3 NUMERICAL RESULTS AND DISCUSSIONS

To verify the numerical method of RMI in the above numerical simulation HD, we numerically simulate the instantaneous flow structure of the flow field of the SF6 density interface ($\theta = 60°$), and compared with the corresponding experimental results of Liu [5], as shown in Fig 2. Obviously, the numerical result (down) is a good agreement with the experimental result [5] (up).

The flow characteristics and wave patterns of hydrodynamic (HD, B = 0) and MHD (B = 100) situations are verified by the corresponding numerical results of Samtaney[4], as shown in Fig. 3. The density field for the nonmagnetic RMI is shown in the top half part of the figure, while in the presence of a magnetic field is presented in the lower half. It is obvious that the flow characteristics, wave patterns, contact interface and vortex structures and the other shape density front for both nonmagnetic and magnetic RMI in our numerical results are in good agreement with Ref.

* Corresponding author. Tel.: +8602584303929 E-mail addresses: zhanghuanhao@njust.edu.cn (Zhang, H. H.).

[5].In MHD, the density interface maintains a smooth interface, so the horizontal magnetic field significantly suppresses the RMI at the density interface.

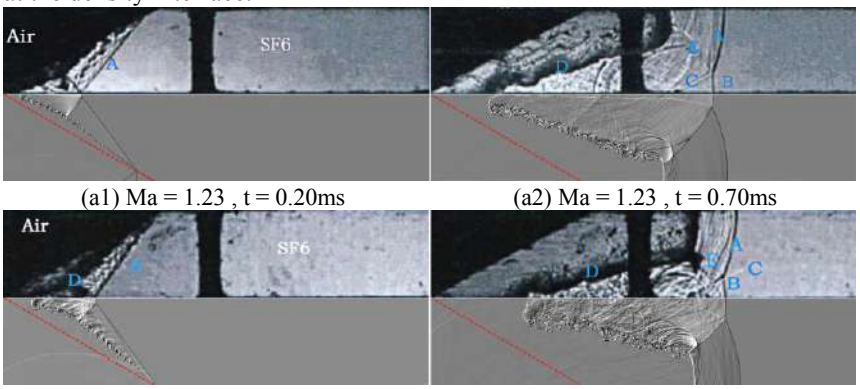

(a1) Ma = 1.23 , t = 0.20ms (a2) Ma = 1.23 , t = 0.70ms

(b1) Ma = 1.41 , t = 0.19ms (b2) Ma = 1.41 , t = 0.59ms

Fig. 2 Comparison of the instantane flow structures of our numerical results with corresponding experimental results of Liu[5].

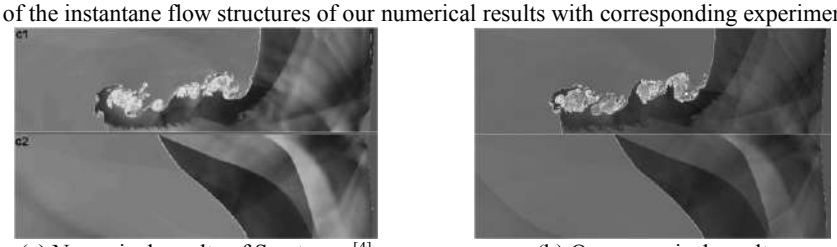

(a) Numerical results of Samtaney [4] (b) Our numerical results

Fig. 3 Comparison of the instantane flow structures of our numerical results with corresponding numerical results of Samtaney [4].

The suppression mechanism of the magnetic field on the interface instability is investigated, and found that the shock wave impinges on the interface, the magnetic field lines exhibit twist on the interface due to the RMI, which leads to the occurrence of the negative longitudinal magnetic field (B_y). The variation in the magnetic intensity on the interface causes the magnetic tension forming on the interface. Since the magnetic tension opposite to the direction of the vorticity generated by velocity shear, seen Fig. 4, the vorticity is attached to the Alfvén shock, and reduces the vortex deposition on the density interface. As show in Fig. 4(c), the strong magnetic field suppresses the later development of RMI more obviously. Therefore, the vorticity is transformed into two vortex sheets travelling away from the density interfaces, and the R-M instability is effectively suppressed.

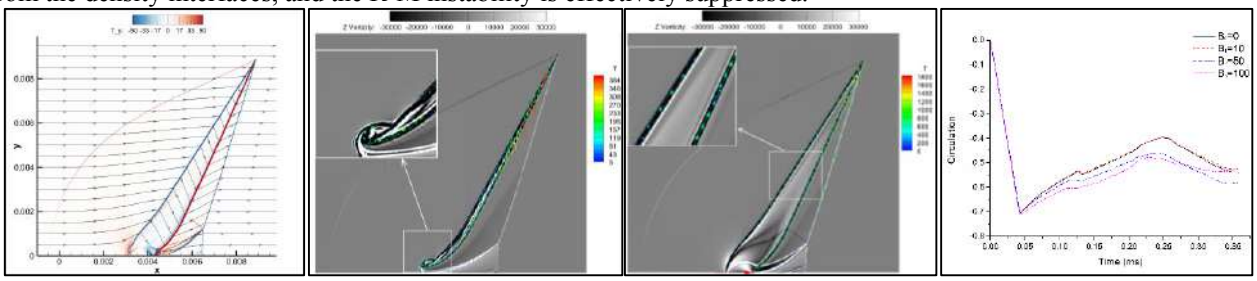

(a)magnetic field lines (b1)B = 10 (b2)B = 50 (c) Circulation

Fig. 4 The influence of different magnetic field strength on interface vorticity.(a)Magnetic field lines exhibit twist(b1)Magnetic tension suppresses the formation of the main vortex; (b2)Magnetic tension is opposite to the direction of the vorticity generated by velocity shear.(c)Change of flow field circulation with time

4 CONCLUSIONS

Based on the ideal compressible MHD equations and CTU+CT algorithm, the Richtmyer-Meshkov instability (RMI) caused by the incident plane shock wave impinging on the heavy gas density interface was numerically studied. Our computational results are in good agreement with the relevant experimental [5] and numerical results [4]. It is found that the suppression mechanism of the magnetic field on the interface instability has two points. Firstly, the direction of the magnetic force is opposite to the direction of the vortex generated by the velocity shear, which suppresses KHI. Secondly, Vortex adheres to the Alfvén shock wave to reduce the deposition of eddy currents on the density interface.

ACKNOWLEDGEMENTS

This work was supported by the National Natural Science Foundation of China (Grant No. 11702005), the Fundamental Research Funds for the Central Universities (Grant No. 30919011260).

References

[1] Cao J., Wu Z., Ren H., Li D. PHY. PLASMAS **16**: 062103, 2009.
[2] Wheatley V., Pullin D. I., Samtaney R. Phys. Rev. Lett. 95: 125002, 2005.
[3] Liu Y., Chen Z. H., Zhang H. H., Lin Z. Y. Phys. Fluids 30: 044102, 2018.
[4] Samtaney R. Phy. Fluids 15(8): 53-56, 2003.
[5] Liu J.H.,Huang W.B.,Tan D.W.,Zou L.Y.,Guo W.C.Journal of Expriments in Fluid Mechanies 24 (06): 27-31 2010.

EXPERIMENTAL INVESTIGATION OF THE TRANSITION TO TURBULENCE IN THE PLANE MAGNETOHYDRODYNAMIC (MHD) COUETTE FLOW

Brahim Moudjed[1] and Alban Pothérat *[1,2]
[1]Fluid and Complex Systems Research Centre, Coventry University, Priory Street, Coventry CV1 5FB, United Kingdom
[2]Laboratoire National des Champs Magn etiques Intenses-Grenoble, CNRS/UGA-UPS-INSA, France

Summary We present an experimental study of the plane MHD Couette flow where pressure and velocity fields are mapped by Particle Image Velocimetry in an electrically conducting electrolyte pervaded by the stray field of a superconducing magnet. We show how the magnetic fields affect the flow patterns compared to the classical Couette flow.

This study aims at characterising experimentally the influence of an externally applied static transversal magnetic field on the transition to turbulence in a plane Couette flow. Without magnetic field, the plane Couette flow is linearly stable for all Reynolds numbers but may be sensitive to finite amplitude perturbations, localised in time and in space: below a lower critical Reynolds number, estimated between 300 and 400 [2, 3, 4] disturbances decay in space and time. Above an upper critical Reynolds number of around 750 the disturbances invade the whole fluid domain and support turbulence. Between these two critical Reynolds numbers, turbulent spots coexist with the laminar flow. The upper and lower critical Reynolds numbers are expected to significantly change under the effect of the magnetic field so that a laminar flow may survive at significantly higher Reynolds numbers than without magnetic field. To investigate this question, a unique experiment was build. A 1600 mm long, 50 mm wide and 40 mm high rectangular glass tank is filled with sulphuric acid at 30 % mass, to ensure the highest conductivity (90 S/m) whilst retaining the necessary transparency for optical velocimetry techniques [1]. A mechanically-driven neoprene belt acts as the moving wall that entrains the fluid so as to generate a half-plane Couette flow between itself and the fixed bottom plate of the tank. The whole setup is placed in the stray-field of a superconducting solenoidal magnet, to apply a transversal continuous magnetic field in the flow of about 1T. A bespoke 2D Particle Image Velocimetry technique is used to map the velocity field and its fluctuations in the vertical and horizontal planes aligned with the streamwise direction.

The problem is controlled by two non-dimensional parameters, the Reynolds number, as in the non-MHD Couette flow, as well as the Stuart number N, that measures the ratio of Lorentz to inertial forces. We present results of the PIV measurement identifying the different regimes we encountered at $0 \leq N < 1$, and Re up to 10^4. We also show how the magnetic field affects the topology of the flow patterns in the intermediate regimes between the lower and upper critical Reynolds numbers.

References

[1] Moudjed B., Pothérat A. and Holdsworth, M. PIV measurements of pressure and velocity fields in the plane MHD-Couette flow, *Exp. Fluids* **61** 255, 2020
[2] Dauchot and Daviaud, *Phys. Fluids* **7**, 2 (1995).
[3] Daviaud et al., *Phys. Rev. Lett* **69**, 17 (1992).
[4] Tillmark and Alfredsson., *J. Fluid Mech* **235**, 89-102 (1992).

*Corresponding author. E-mail: alban.potherat@coventry.ac.uk.

Thematic Session SM

K107833 - SM01 - Biomechanics and Biomaterials - Keynote

CARTILAGE-ON-CHIP:A PHYSIOLOGICALLY INSPIRE DPLATFORM TO REPRODUCE ARTICULAR JOINT COMPRESSION AND SHEAR STRAIN

Carlo Alberto Paggi,[1,2]Bastien Venzac,[2]Jeroen Leijten,[1]Liliana Moreira Teixeira Leijten,[1]Marcel Karperien,[1]and Séverine Le Gac[2]
[1]Department of Developmental BioEngineering, TechMed Center, University of Twente, The Netherlands
[2]Applied Microfluidics for BioEngineering Research, MESA+ Institute for Nanotechnology & TechMed Center, University of Twente, The Netherlands

Summary. Here, we present a cartilage-on-chip platform comprising an innovative multi-modal actuation unit to subject chondrocyte-laden hydrogel to both compression and shear strain. The response of human chondrocytes to both healthy and pathophysiological mechanical stimulation is evaluated.

PURPOSE

Organ-on-chip models allow faithfully mimicking mechanical movements of tissues, as demonstrated for the lung or gut, yet using solely surface strain. However, other tissues such as articular cartilage require 3D multi-axial mechanical mimicry, which current microdevices are incapable of delivering. Moreover, as cartilage is an avascular structure that does not comprise nerves, stimuli received by the chondrocytes are essentially mechanical. Here, we report a versatile platform to exert complex mechanical stimulations on cell-laden hydrogels, in the view of creating a cartilage-on-a-chip model. This platform comprises three independently addressable actuation chambers, separated from a culture chamber by a thin vertical elastomeric membrane (Fig. 1). By applying specific pressure sequences in the three different actuation chambers, uniform compression and/or shear strain can be exerted on a cell-laden hydrogel in a controllable manner.

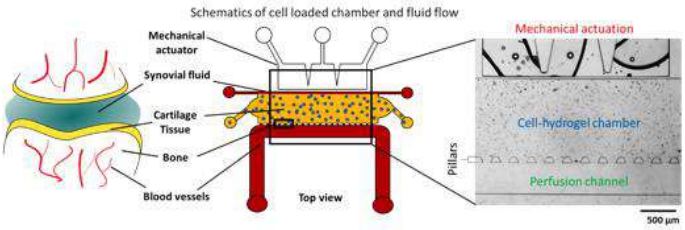

Figure 1: Schematic representation of the knee joint; Schematic and top view of the device comprising a mechanical actuation system, a cell-hydrogel chamber, a set of pillars and a perfusion channel

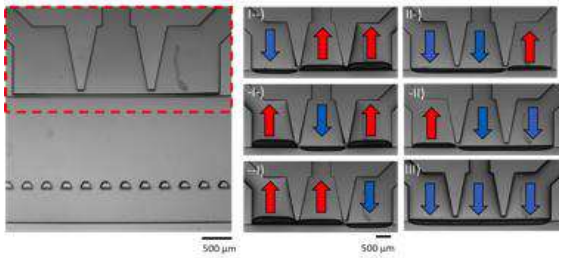

Figure 2: Top view of the system. Left: system at rest. Right: multimodal deformation of the membrane given by positive (blue arrow) and/or negative pressure (red arrow) applied to the individual chambers.

MATERIALS AND METHODS

The cartilage-on-a-chip platform was fabricated from an elastomeric material, polydimethylsiloxane (PDMS), using soft-lithography. The platform comprises three different sections as depicted in Fig. 1: a mechanical actuation unit comprising three individually addressable chambers; a cell-hydrogel section; and a perfusion channel, mimicking the blood circulation to provide nutrients to the cell-laden hydrogel. Compressive strain and shear strain were imposed on the hydrogel by deforming the thin membrane by applying positive and/or negative pressures to the three chambers (Fig. 2). Microbeads (15 µm) added to the hydrogel to evaluate its deformation upon mechanical stimulation and deflection of the elastomeric membrane. Human chondrocytes (hCHs) were cultured in an agarose hydrogel matrix using both proliferation and differentiation medium. The cell projected area was determined for seven different applied pressure amplitudes (100-700 mbar). Cell viability was evaluated using a live/dead assay and specific fluorescent stains, for different applied mechanical stimulation (0, 300, 700 mbar applied at 1 Hz for 1 h per day, starting from day 1). Glycosaminoglycan (GAG) production was assessed using Alcian blue staining, and nuclei were counter-stained with fast-red on histology cryosections after recovery of the 3D cellular constructs from the platform, after 15 days of culture and 14 days of mechanical stimulation at 1 Hz for 1 hour per day at 300 mbar.

RESULTS

Membrane deflection was quantified for various membrane heights and thicknesses, and PDMS formulations, as a function of the applied pressure. Applying higher pressures led to greater membrane deformation. Interestingly, switching pressures, from positive to negative, and vice versa, allowed different and complex membrane deformation patterns (Fig. 2). Hence, full control on the membrane deformation was achieved at the individual chamber level. Agarose deformation was next assessed (Fig. 3): the higher the pressure, the higher the strain. Importantly, both healthy (5-20%) and pathophysiological (>20%) strains could be applied in the vicinity of the membrane on the cell-laden agarose. Moreover,

combined compression and shear strain was obtained by single chamber stimulation. We further determined the projected cell surface area of primary chondrocytes upon increasing applied pressures. This projected surface area was found to decrease, and the closer a cell from the membrane, the larger its surface area decrease. Moreover, the cell surface area decrease correlated to the pressure imposed in the system (Fig. 4). Interestingly, hCHs cultured under hyper-physiological level of compression died after 3 days of stimulation while they maintained their viability under physiological stimulation.

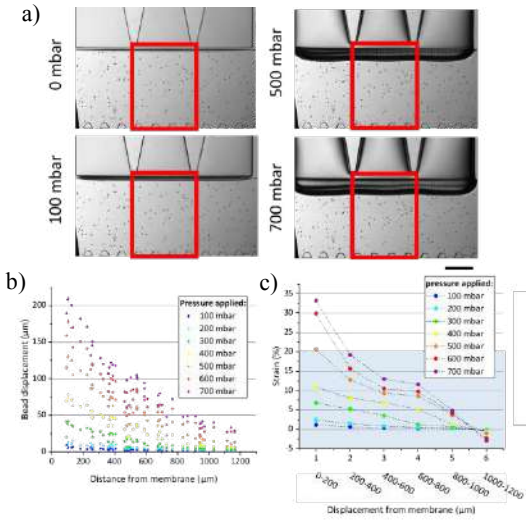

Figure 3: a) Top view of the system with agarose containing 15-µm beads at different pressures; b) Displacement of the microbeads at different pressures and positions in the hydrogel; c) Strain patterns in the hydrogel at different pressures.

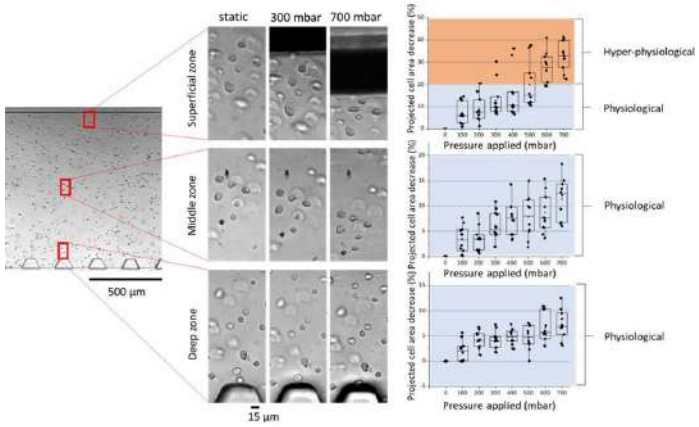

Figure 4: Top view of the middle of the culture chamber; Deformation of cells in different areas in the hydrogel in static conditions or during compression (300 and 700 mbar); Projected cell area deformation of 10 individual cells in the different areas. Light blue indicates physiological deformation; light orange hyper-physiological condition.

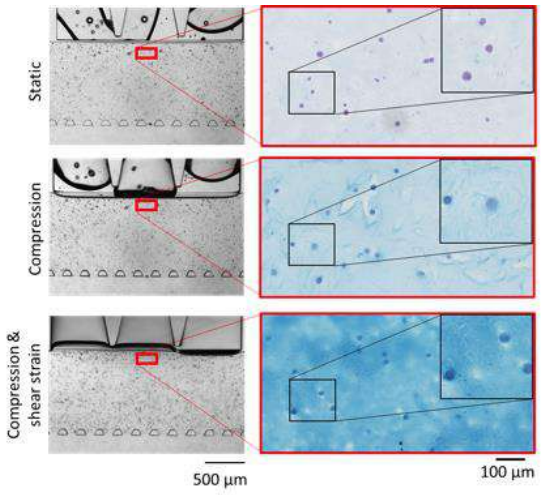

To further evaluate the effect of mechanical stimulation on the cells, hCHs were cultured under static or dynamic conditions, with only compression or a combination of compression and shear strain. Here, the GAG production levels, as analyzed through immunohistochemistry, were enhanced under mechanical stimulation, with formation of a pericellular matrix. Moreover, the combination of compression and shear strain further increased the GAGs production by the hCHs (Fig. 5).

Figure 5: Left, from top to bottom, transmitted image of the system in the three conditions; Right, histological sections after staining for GAGs (Alcian Blue) and cell nuclei (fast red). The ring around the cells corresponds to the pericellular matrix which appear after 15 days of culture (14 days of stimulation at 1 Hz for 1 h at 300 mbar).

To further evaluate the effect of mechanical stimulation on the cells, hCHs were cultured under static or dynamic conditions, with only compression or a combination of compression and shear strain. Here, the GAG production levels, as analyzed through immunohistochemistry, were enhanced under mechanical stimulation, with formation of a pericellular matrix. Moreover, the combination of compression and shear strain further increased the GAGs production by the hCHs (Fig. 5).

CONCLUSIONS

This novel microfluidic platform can be used to explore the impact of various mechanical stimuli on responses of individual cells. In specific, it allows mimicking the healthy and hyper-physiological ranges of stimulation of cartilage and can be used to impose multiple mechanical stimulation patterns on a 3D cellular construct. This platform will be further developed to study disease progression or to screen therapeutic agents. Our final goal is to extend this platform with units mimicking the synovium, ligament, bone and meniscus to engineer a full joint-on-chip.

A MECHANICAL MODEL FOR THE NON-LINEAR HEREDITARINESS OF LIGAMENTS AND TENDONS OF THE HUMAN KNEE

Emanuela Bologna[1], Luca Deseri[2], Kaushik Dayal[3], and Massimiliano Zingales*[1]
[1]Dipartimento di Ingegneria,Università di Palermo,Palermo,Italy.
[2]Dipartimento di Ingegneria Civile,Ambientale e Meccanica,Universitá di Trento,Trento,Italy.
[3]Department of Civil Engineering, Carneige-Mellon University, Pittsburgh, U.S.A.

Summary In this paper the authors introduce a non-linear model for fractional-order hereditariness for ligaments and tendons of the human knee that corresponds to experimental data. Creep and relaxation data on fibrous tissues have been obtained and fitted with logarithmic relations that corresponds to power-laws with non-linear dependence of the coefficients as well as of the order of time-evolution. The use of a proper non-linear transform allows to use Boltzmann superposition in the transformed variables yielding a fractional-order model for the non-linear material hereditariness if the stress/strain dependence of the evolution order is neglected. This approach is extended in the course of the present study resorting to a linear-time dependent mechanical system that corresponds, exactly to the provided time evolution of power-laws and that generalizes the case of stress/strain dependence in the order of the power-laws. Some numerical analysis has been provided to capture the effect of the proposed method with some experimental results in case of non-uniform time evolution of strain and stress.

INTRODUCTION

Material hereditariness is a challenging topic in the field of engineering and physical sciences since the very first observations on the long-term behavior of polymers, rubbers and concrete at the end of the XIX century. Indeed experimental campaigns conducted under long-standing loads (creep tests) and long-standing displacements (relaxation tests) shows that, besides an initial elastic displacement (strain in creep) or load (stress in relaxation) a time evolution of the initially measured strain/stress is clearly observed.

Mathematical modeling of materials time-dependence in terms of creep and relaxation has been intensively investigated since the beginning of the XX century [1, 2]. In such studies the use of Boltzmann superposition assumption yields constitutive equations involving convolution integrals among a kernel function that is material dependent and the material state variables [3]. The observation involving effect superposition corresponds to a linear behavior of the material such that linear hereditariness of engineering materials as wood, glass, bitumen has been extensively studied to account for long-standing loads. In this regard, the use of power-law Kernels to describe experimental material functions led several authors to introduce the fractional-order differ-integral operators to capture the material behavior in linear conditions [4]. Fractional-order constitutive equations have also been extended to three-axial conditions [5] and rheological equivalence has been also introduced [6]

The wide success of fractional-order calculus to deal with linear hereditariness is, however, not justified in the wider field of non-linear material hereditariness. Indeed, it is well-known since the very first long-standing experiments on rubbers and polymers [1, 2] that carbon-based materials undergoes large strains and a significative non-linear behavior is observed from experimental tests [7]. This latter observation has been also more evident in presence of fibrous biological tissues where no linear conditions may be observed even for small level of stress/strain [8].

In some recent papers the authors showed that in case of stress/strain independence of the order of power-laws in creep t^{β_c} and relaxation t^{β_r} by the level of stress or strain applied, a generalization of the well-known theory of quasi-linear hereditariness may be physically extended to fractional-order hereditariness and that a rheological model made by linear springs and linear dashpots fully justifies the assumption of quasi-linear hereditariness with power-law kernel.

In this paper the authors aim to introduce the use of fractional-order calculus to capture the experimental behavior of biological fibrous tissues of the human knee in presence of material non-linear behavior also in the order of the decay of creep $t^{\beta_c(\sigma)}$ and relaxation $t^{\beta_r(\varepsilon)}$ by means of the generalization of the mechanical model proposed. A complete physical and mathematical framework for the relations among creep and relaxation functions in presence of material non-linearities, contrasted with experimental data of a large experimental campaign have been provided by means of fractional-operators formalism.

EXPERIMENTAL CAMPAIGN ON HUMAN PATELLAR AND HAMSTRINGS

The experimental campaign has involved two kind of human tissue, namely patellar (P) and hamstring (H) tendons. The human tissues were obtained by a tissue bank (Lifelegacy Foundation, Arizona, USA) with the requirements that each ensemble of P and H were obtained by the same human knee to avoid donor variability. Biological specimens were stored at 80 $^\circ C$ and thawed in a 37$^\circ C$ water bath for 15 min prior to testing [9], then prepared for the test and finally each specimen was there cut approximately at the same length before clamping for the uniaxial test. commercial

*Corresponding author. E-mail: massimiliano.zingales@unipa.it

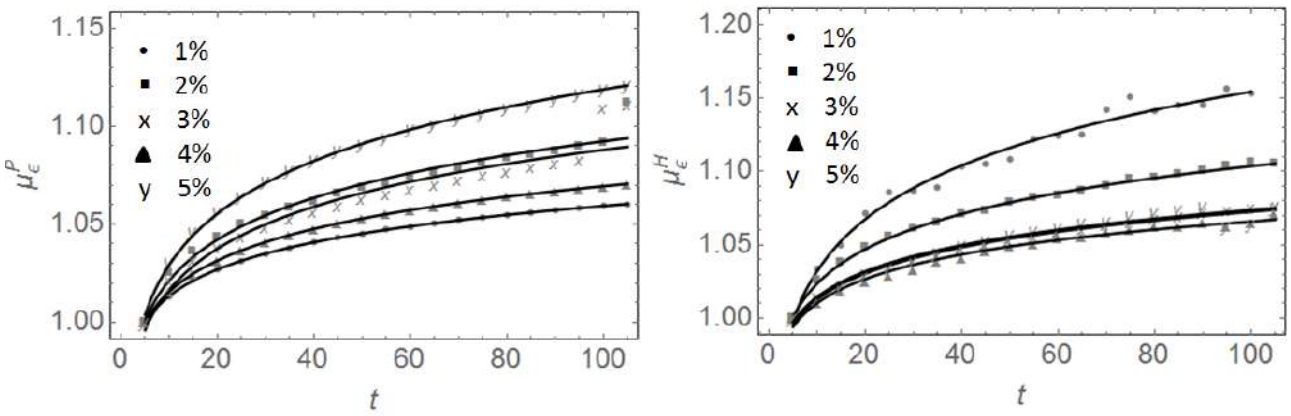

Figure 1: averaged creep functions for patellar and hamstring tendons

electromechanic system (Electroforce, Bose 3330) was used to test both the tendons' groups. We have used a specific protocol for the repeatability of the experimental campaign. Initially, the samples were preconditioned by cycling between 20 and 100 N, for twenty cycles at 0.25 Hz to remove any crimping in the tendon fibrils [**?**]; after preconditioning, we performed relaxation test with prescribed values of the strain level in the range $1-5\%$. We conducted the relaxation tests applying a linear ramp of displacement with speed 250 mm/s and after the hold fixed for 100s at the achievement of preselected value of strain, at the end of relaxation test resting the sample for 15 min in order to achieve the same length of the initial specimen measured at the end of the first phase. In last phase, the creep test obtained applying the same initial stress reached at the end of the relaxation test with a linear load ramp of 315 N/sec and holding the load 100s. During the test, the sample was continuously moistened with saline solution.

Data analysis

The experimental data in terms of the axial engineering strain $\varepsilon(\sigma,t)$ were averaged, for each level of applied stress. The averaged creep functions, namely $\mu_\varepsilon^{(P)}(\bar{\sigma}_i,t)$ and $\mu_\varepsilon^{(H)}(\bar{\sigma}_i,t)$ are reported in fig.(1), respectively. A more detailed representation of the averaged creep functions may be observed in a $log\mu_\varepsilon - logt$ plot reported in figs.(1,2) for the patellar and hamstring tendons, respectively. Data analysis reported in fig.(3,4) for the log-log plots reveals that good candidate to fit averaged values of creep functions $\mu_\varepsilon^{(P)}(\bar{\sigma}_i,t)$ and $\mu_\varepsilon^{(H)}(\bar{\sigma}_i,t)$ is the a linear model with equation:

$$\log \bar{\mu}_\varepsilon^{(j)}(\sigma,t) = \beta_j \log\left(\frac{t}{\tau_c^{(j)}}\right) + \alpha_j \log(\bar{\sigma}_j) \tag{1}$$

where $j = P, H$ denotes the specific tissue considered, $\tau_c^{(j)}$ and $\bar{\sigma}_j$ are respectively a characteristic time and the non-dimensional stress $\bar{\sigma}_j = \sigma_j E$ where E is the tangent elastic modulus obtained at the origin of a monotone test.

CONCLUSIONS

Direct inspection of the creep data shows that the order of evolution of the strain is very influenced by the level of stress applied in the experimental campaign. For this reason single-integral formulations can not be applied to capture the data. In this study the authors will discuss a proper mechanical model that corresponds, exactly, to the time evolution obtained by data analysis and that can be easily generalized to cases of time-variations of the applied stress and strain histories.

References

[1] P.G Nutting.*Adsorption and pycnometry. Journal of the Washington Academy of Sciences*,**1-6**,1936.
[2] A. Gemant. A Method of Analyzing Experimental Results Obtained from Elasto-Viscous Bodies. Physics,311-317, 1936.
[3] F. Mainardi. *Fractional calculus and waves in linear viscoelasticity: an introduction to mathematical models.* World Scientific, 2010.
[4] F. Mainardi, G. Spada. Creep, relaxation and viscosity properties for basic fractional models in rheology. The European Physical Journal Special Topics 193.1: 133-160, 2011.
[5] E. Bologna, F. Graziano, L. Deseri, M. Zingales, Power-Laws hereditariness of biomimetic ceramics for cranioplasty neurosurgery. International Journal of Non-linear Mechanics, **115**, 61–67, 2019.
[6] M. Di Paola, and M. Zingales. Exact mechanical models of fractional hereditary materials. Journal of Rheology 56.5, 983-1004,2012.
[7] D.P.Pioletti, L.R. Rakotomanana. *On the independence of time and strain effects in the stress relaxation of ligaments and tendons.* Journal of biomechanics, 33(12), 1729-1732,2000.
[8] Y. C. Fung*Biomechanics: Mechanical Properties of Living Tissues*. Springer, 1993.
[9] S.D. Abramowitch, S.L. Woo. An improved method to analyze the stress relaxation of ligaments following a finite ramp time based on the quasi-linear viscoelastic theory. Journal of biomechanical engineering, 126.1: 92-97,2004.

WHY THE MUSSEL BYSSAL PLAQUES ARE TINY YET STRONG IN ATTACHMENT

Zhao Qin[1,2]*, Daanish Aleem Qureshi[1,3], Yongtae Kim[4], Yulong Han[5], Ming Guo[5], Seunghwa Ryu[4]
[1] Laboratory for Multiscale Material Modeling, Department of Civil and Environmental Engineering, Syracuse University, 151L Link Hall, Syracuse University, Syracuse, NY 13244, USA
[2] Syracuse Biomaterials Institute (SBI), Syracuse University, NY 13244, USA
[3] WPI Massachusetts Academy of Math and Science, 85 Prescott Street, Worcester, MA 01605, USA
[4] Multiscale Mechanics and Materials Modeling Lab, Department of Mechanical Engineering, KAIST (Korea Advanced Institute of Science and Technology), 291 Daehak-ro, Yuseong-gu, Daejeon, 34141 Korea
[5] Department of Mechanical Engineering, Massachusetts Institute of Technology, 77 Massachusetts Ave., Cambridge, MA 02139, USA

Summary *Mytilus edulis*, commonly referred to as blue mussels, is known for producing byssal threads, which allow them to adhere to rocks and each other in tidal zones. A byssal thread emerges from body tissue and ends with an adhesive plaque that is located at the other end of the thread and attaches to substrates. It is observed that the plaques are usually tiny, and their size does not vary much with different body sizes of mussels, which can cause different impact force in waves. With that said, it is not clear how these byssal plaques are designed for strong attachments. In this study, we combine mechanical testing with 3D printing and numerical modeling to investigate how the size of adhesive plaque affects the adhesion strength. We find that plaques with a diameter 3 to 5 times that of the byssal thread yields optimized strength upon detaching. Interestingly, plaque size larger than this will have a small marginal effect. Our results show that the architecture of byssal plaque is more important than simply increasing plaque size for bonding strength.

Mytilus edulis, commonly known as blue mussels, are known for their capability of hanging to rocky shores by using their bushy "beards", known as byssal threads. Such byssal threads attach to the rock surfaces and the shells of other mussels [1–3]. Each byssal thread has heterogeneous chemical composition and mechanics, making it simultaneously rigid and stretchy, similarly as a bungee cord, which helps to dissipate the repeatedly impact force caused by crashing waves. Both the schooling and the locomotion behaviors of mussels are ensured by the underwater adhesion of the byssal threads to substrates made of different materials, which is guaranteed by the adhesion of the byssal plaque at the far end of the thread, which is a thin film that connects the byssal thread to the rock surface (**Fig. 1A, B**) and it is composed of mussel foot proteins with high concentrations of L-3,4-dihydroxyphenylalanine, which has a strong affiliation with almost any type of material surfaces by forming either non-covalently bonding interactions or covalently bonding interaction to different substrates. Besides molecular mechanics, it is interesting how the entire byssal plaque contributes to the adhesion function. Similar to surface of gecko's toes, mussel byssal plaques are observed to have a clear branching structure, as shown in **Fig. 1C**, as the entire plaque is composed of micrometer fibers distributed in the radial directions that connect from the center of byssal thread to periphery on the substrate. It is intriguing to study how this tiny byssal plaque size (**Fig. 1D**) is beneficial for providing adhesion strength.

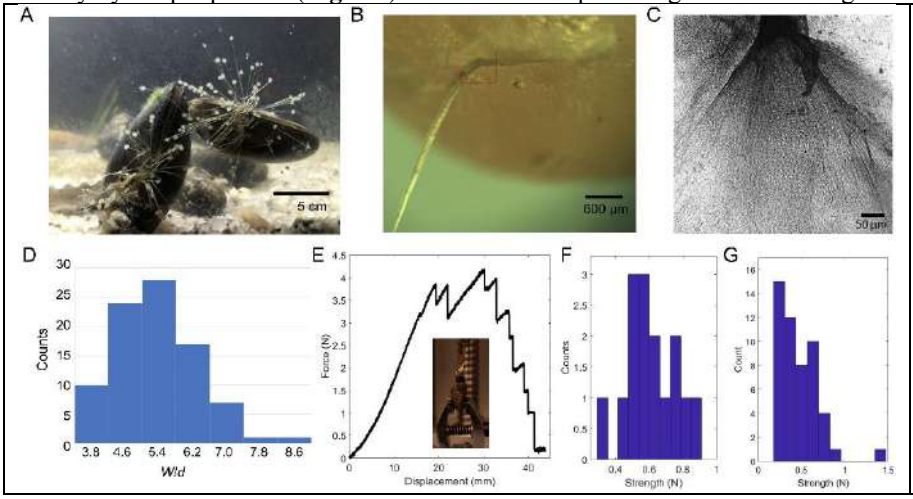

Figure 1. Image of mussels, the multiscale structure of byssal threads and their mechanics in the attachment. A. Snapshot of two mussels. Images of (B) optical microscope (C) laser confocal microscopy. D. measurements of the diameter of byssal plaque. E. A force-displacement curve of detaching a bundle of byssal threads. The histogram of the adhesion strength of detaching a single byssal thread from the rock surface (F) and from the mussel shell surface (G).

Using a mechanical test, we take measurements of the adhesion strength of byssus threads (inset of **Fig. 1E**) by fixing the substrate (rock and mussel shell), clamping their ends at the byssal gland and applying force by slowly moving the grips up with a constant speed. It is noted that the structure failure takes place by the individual detachment of plaques from the rock surface instead of catastrophic rupture, corresponding to each of the saw-tooth and causing significantly more energy dissipation than the area under the J curve. The peak force is 4.2 N as recorded, interestingly, the mean force of each thread (0.47 N) as obtained from detaching of this bundle agree with the strength of each individual byssal thread that is detached from the rock surface (0.61±0.16 N, **Fig. 1F**) and larger than the attachment strength to mussel shells (0.45±0.26 N, **Fig. 1G**). This agreement suggests the unique material composition of the byssal thread can synergistically integrate the strength of each plaque for mussel adhesion. Moreover, considering the area of each byssal plaque is merely 2.8 mm^2, the mean adhesion strength goes up to 215±56 KPa, which is almost one order of magnitude higher than the strength of these bioinspired glues [4–6]. We notice that although the mussel glue is strong, it will never be overused since the plaque size is only 3~6 times that of the byssal thread. (**Fig. 1D**) These

samples are taken from many mussels with their body size varies several tens of times. It seems the byssal thread and plaque of the mussel do not grow together with the mussel body. However, instead of varying the size of each plaque, the growth only affects the number of threads for attachment.

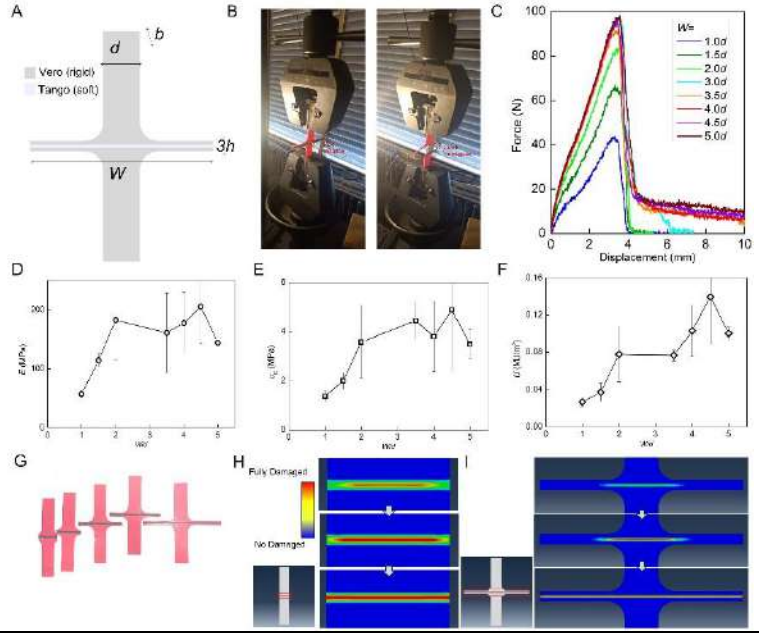

Figure 2. Testing of the size effect in mussel adhesion by using multi-material 3D printing. A. Design sketch of the printing model with parameters as thread diameter (d), plaque width (W), thread thickness (b) and plaque thickness (h). B. The tensile test of the failure process of the 3D printed model. C. Force-displacement curves obtained for mussel models with different W/d values. Featuring mechanical parameters are obtained from the curves including Young's modulus (E) as in D, the ultimate strength (σ_C) as in E and the energy dissipation (U) as in F. G. A summary of all the 3D printed experimental samples with different plaque width. FEM results of the distribution of normal stress within the soft material of the model W/d=1 (H) and W/d=6 (I) by subjecting to different deformations, where the concentrated stress and associated damage at the interface start from the middle and propagate to the two ends

To understand the size effect in mussel plaque, we design and make a series of 3D printed models, by scaling the natural observation up for 100 times, in order to test how the adhesion strength relates to the geometric design of the byssal plaque by using a multi-material 3D printer [7,8]. This model, as schematically shown in **Fig. 2A, G**, takes the 2D profile of a byssal thread near the attachment and is characterized by the diameter (d) and thickness (b) of the rod region that mimics the byssal thread and the width (W) and height (h) of the toe region that mimics the byssal plaque. The rubber-like material layer is defined by $W \times h \times b$ for simplicity and its existence can guarantee the rupture from this region, mimicking the failure of byssal plaque from the interface with substrates. We test the mechanical behavior of these samples with different plaque sizes. Interestingly, as the snapshots shown in **Fig. 2B**, not the entire middle region gets deformed once the structure is subjected to the loading force but the region near the middle of the rod gets more significantly deformed than the two edges. The failure always takes place from the middle of the interface and propagate toward the two ends.

CONCLUSIONS

We record the force-displacement curve as the testing result of models with different W/d ratio, as summarized in **Fig. 2C**. It shows that the larger toe width can increase the structure strength, as the peak of the force, but the effect is limited up to $3.5d$ and the effect becomes very small afterward. However, increasing W can lead to a longer tail region for more energy dissipation, which corresponds to the material failure within the rubber-like material phase by cracking from the center to the two edges. We repeat our test for 4 times for each of the samples and compute the average value and standard deviation of the modulus (E) strength (σ_C) and energy dissipation (U) before the total failure of the structures as shown in Figs. 2D, E, and F, respectively. These test results show a clear trend in common once subjected to tensile loading, as E, σ_C and U almost linearly increase with W/d up to 2 to 3 and thereafter their values trend to converge to a constant value except for U as the energy dissipation can still increase for W/d between 3.5 to 4.5 as the long tail region can grow with W, revealing that W/d from 3 to 5 yields the strong adhesion. Our finite element models (**Fig. 2H, I**) show that before the failure of the interface the stress and deformation largely happen at the middle region below the byssal thread but not the two sides outside this region, as the highest normal stress initiates from the middle point, suggesting the starting of the damage, and propagates toward the two ends. Together, our result shows that the mussel byssal plaque needs to be tiny, as a few times that of the thread for optimized strength.

References

[1] Bell E C and Gosline J M 1996 Mechanical design of mussel byssus: Material yield enhances attachment strength *J. Exp. Biol.* **199** 1005–17
[2] Lee H, Lee B P and Messersmith P B 2007 A reversible wet/dry adhesive inspired by mussels and geckos *Nature* **448** 338–41
[3] Qin Z and Buehler M J 2014 Molecular mechanics of mussel adhesion proteins *J. Mech. Phys. Solids* **62** 19–30
[4] Xu Y, Liang K, Ullah W, Ji Y and Ma J 2018 Chitin nanocrystal enhanced wet adhesion performance of mussel-inspired citrate-based soft-tissue adhesive *Carbohydr. Polym.* **190** 324–30
[5] Fan C, Fu J, Zhu W and Wang D A 2016 A mussel-inspired double-crosslinked tissue adhesive intended for internal medical use *Acta Biomater.* **33** 51–63
[6] Lai E, Keshavarz B and Holten-Andersen N 2019 Deciphering How the Viscoelastic Properties of Mussel-Inspired Metal-Coordinate Transiently Cross-Linked Gels Dictate Their Tack Behavior *Langmuir*
[7] Libonati F, Gu G X, Qin Z, Vergani L and Buehler M J 2016 Bone-Inspired Materials by Design: Toughness Amplification Observed Using 3D Printing and Testing *Adv. Eng. Mater.* **18** 1354–63
[8] Qin Z, Compton B G, Lewis J A and Buehler M J 2015 Structural optimization of 3D-printed synthetic spider webs for high strength *Nat. Commun.* **6**

MEDICAL IMAGE REGISTRATION AND INVERSE MODELING TO UNCOVER FETAL BRAIN FOLDING MECHANISMS

Johannes Weickenmeier*[1], Zhenling Wang[2], Yana Blinkouskaya[1], Blake T. Martin[2], and Krishna Garikipati[2]
[1]Department of Mechanical Engineering, Stevens Institute of Technology, Hoboken, USA
[2]Department of Mechanical Engineering, University of Michigan, Ann Arbor, USA

INTRODUCTION

During fetal development, the human brain undergoes large topological changes and volumetric growth, roughly doubling in size every four weeks [1] and the gyrification index, a ratio related to the real brain surface area over the convex hull, increasing from 1 to 1.6 [2]. Such dramatic changes correspond to the brain changing from a nearly smooth surface to a highly folded structure, as shown in Fig. 1. The corresponding folding of the outer cortex- also known as gyrification- is driven by the migration of neurons from the ventricular zone towards the cortex. The accumulation of neurons in the cortex leads to primary folds that form consistently across all healthy brains during mid-gestation [3]. These neurons originate from the subventricular zone, where they differentiate, proliferate, and ultimately migrate outward to form the cortical layers. The signals driving migration pathways play a critical role in establishing the brain's functional network including the highly complex axon-based connectome [4]. The interconnections between neurons are responsible for the intricate communication between individual brain regions; yet, it remains poorly understood how this network forms, grows, and evolves throughout life.

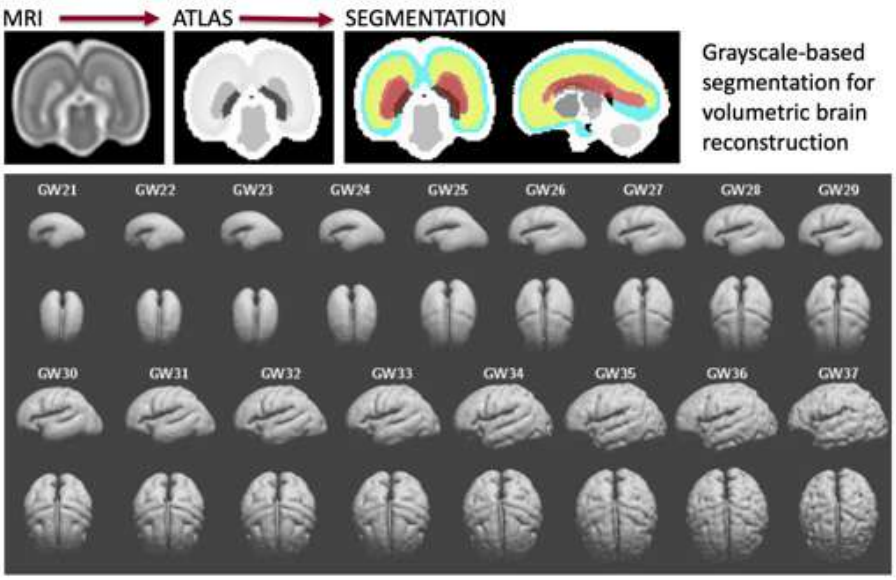

Figure 1: Fetal brain segmentation from medical images between gestational weeks 21 and 37. We differentiate between gray matter, white matter, and the ventricles. Brain volume reconstruction reveals overall growth, ventricular enlargement, and the emergence of primary folds at characteristic gestational timepoints. Based on our segmentations we then created tetrahedra-based finite element meshes for numerical simulations and our inverse problem.

In the present work, we uncover the role of mechanics in understanding the formation of primary folds during gestation. Our approach combines non-rigid image registration and inverse modeling. The former aims at extracting brain shape changes between two consecutive gestational weeks. The latter utilizes a continuum mechanics-based coupled multi-field model of cell migration and morphogenetic growth in order to derive a physics-based mechanism of brain folding.

METHODS AND RESULTS

We extract the spatio-temporal evolution of brain folding in a two-step approach. First, we determine brain shape changes between two consecutive gestational weeks from the longitudinal MRI dataset presented by Gholipour et al [5]. We apply a image registration technique developed by Pawar et al. that minimizes the pixel intensity difference between two medical images by non-rigidly deforming the slave image to coincide with the reference image [6]. The resulting registration mapping contains the deformation field of the brain between the two gestational weeks. As shown in Fig. 2, we are able to obtain physiologically meaningful displacement fields. We can identify the location and timepoint for the onset of primary folds and the overall cortical expansion due to volumetric growth.

*Corresponding author. E-mail: johannes.weickenmeier@stevens.edu.

We use our individual deformation fields as input to our inverse problem. Specifically, our formulation incorporates two fields, i.e. cell density c and deformation $\mathbf{u}$. We follow continuum mechanics theory and assume a hyperlastic behavior according to the Neo-Hookean material model. We prescribe brain growth via a multiplicative split of the deformation gradient, $\mathbf{F} = \text{grad}\,\varphi$, into an elastic and a growth part. We assume purely elastic response, with no viscous effects, while the growth part is coupled to the cell density such that volume increases proportional to cell density. We hypothesize that brain folding is driven by a cell density increase in the cortical layers leading to buckling due to volumetric expansion [7]. Our inverse model uses a gradient descent method to minimize the residual of the energy functional derived for our constitutive model. The registration-based deformation fields are inputs to the inverse model such that we obtain cell density distribution fields $\tilde{c}$ which reveal cell migration patterns during gestation.

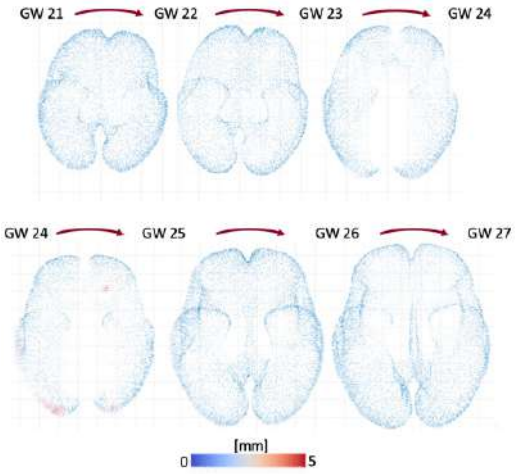

Figure 2: Non-rigid image registration provides brain deformation fields between consecutive gestational weeks. We capture brain deformation as a displacement vector field of our finite element meshes created from brain segmentation and interpolate nodal displacements in the registration maps from our registration tool.

DISCUSSION

Longitudinal MRI data inherently contains information on organ-level morphological changes; yet, reliable physics-driven tools for a quantification of these changes are mostly unavailable. Pawar et al.'s non-rigid framework was modified to deliver weekly brain deformations. Our method identifies the onset of primary folds and quantifies inhomogeneous cortical expansion patterns. The subsequent inverse problem then reveals cell density distributions at discrete gestational weeks that reproduce the displacement fields shown in Fig. 2. Based on our constitutive formulation and the inverse problem, we observe a variation in cell concentration changes between individual gestational weeks of up to $\pm 20\%$. That means, that some regions shrink while others expand producing very inhomogeneous brain volume change patterns which point towards the localization of folds. Fig. 3 shows the result from a forward problem using the initial conditions for for the concentration field based on the output of our inverse problem. It can be observed, that this yields a physiological brain deformation pattern including primary folds. Our method is not without limitations. As such, the solution of the inverse problem is non-unique, and is characterized by a strong dependence on the initial conditions.

CONCLUSIONS

Our work provides a mechanistic rationale for the origin of cortical folding and delivers a novel tool to study the physics behind brain network formation during early development. Our coupling of cell density and brain volume in a continuum framework accurately reproduces spatial folding patterns observed from longitudinal medical image data. Going forward, our approach will be utilized to explain the formation of the brain's complex axon network. Ultimately, we aim at understanding the physical origin of neurological disorders in order to develop novel diagnostic tools and medical interventions.

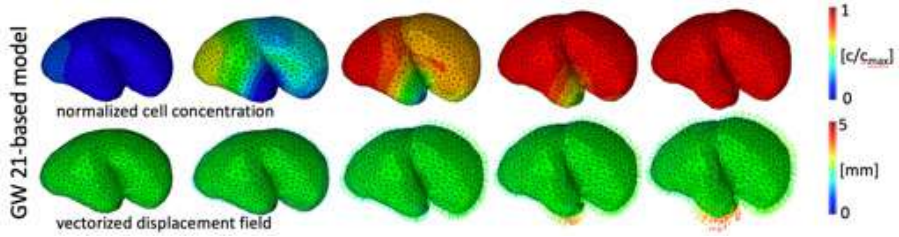

Figure 3: Non-rigid image registration provides brain deformation fields between consecutive gestational weeks. We capture brain deformation as a displacement vector field of our finite element meshes created from brain segmentation and interpolate nodal displacements in the registration maps from our registration tool.

References

[1] J.C. Hsu, Y.C. Wu, P.H. Wang, H.I. Wang, C.M. Juang, Y.J. Chen, C.M. Chang, H.C. Horng, C.Y. Chen, M.J. Yang et al. Quantitative analysis of normal fetal brain volume and flow by three-dimensional power Doppler ultrasound. *Journal of the Chinese Medical Association* (2013) **76**:504–509.

[2] V. Kyriakopoulou, D. Vatansever, S. Elkommos, S. Dawson, A. McGuinness, J. Allsop, Z. Molnr, J. Hajnal, M. Rutherford. Cortical Overgrowth in Fetuses With Isolated Ventriculomegaly. *Cerebral Cortex* (2014) **24**:2141–2150.

[3] S. Budday, P. Steinmann, E. Kuhl. Physical biology of human brain development. *Frontiers in Cellular Neuroscience* (2015) **9**:257.

[4] G.J.A. Ramakers. Neuronal network formation in human cerebral cortex. *Progress in Brain Research* (2005) **147**:1–14.

[5] A. Gholipour, C.K. Rollins, C. Velasco-Annis, A. Ouaalam, A. Akhondi-Asl, O. Afacan, C.M. Ortinau, S. Clancy, C. Limperopoulos, E. Yang, et al. A normative spatiotemporal MRI atlas of the fetal brain for automatic segmentation and analysis of early brain growth *Scientific Reports* (2017) **7**:467.

[6] A. Pawar, Y.J. Zhang, C. Anitescu, Y. Jia, T. Rabczuk. DTHB3D_Reg: dynamic truncated hierarchical B-spline based 3D nonrigid image registration. *Communications in Computational Physics* (2018) **23**:1–12.

[7] S.N. Verner, K. Garikipati. A computational study of the mechanisms growth-driven folding patterns on shells, with application to the developing brain. *Extreme Mechanics Letters* (2018) **18**:58–69.

THE MULTISCALE STIFFNESS OF HUMAN SKIN

Adam Wahlsten*[1], Alberto Stracuzzi[1], Ines Lüchtefeld[2], Alexander E. Ehret[1,3], and Edoardo Mazza[1,3]
[1]ETH Zurich, Institute for Mechanical Systems, Zurich, Switzerland
[2]ETH Zurich, Institute for Biomedical Engineering, Zurich, Switzerland
[3]Empa, Swiss Federal Laboratories for Materials Science and Technology, Dübendorf, Switzerland

Summary The mechanical properties of human skin determine tissue function, they change during wound healing, fibrosis, and aging, and regulate dermal cell behavior. Despite their importance, measuring these properties remains elusive with reported values of the Young's modulus ranging from below one kPa to tens of MPa. This contribution presents a thorough experimental and numerical study of skin stiffness across length scales. The stiffness at the cell-relevant microscale is found to be on the order of 1 kPa, in contrast to macroscopic uniaxial tension measurements on the adjacent tissue showing two orders of magnitude higher modulus. The results are rationalized using discrete and continuum modeling approaches, which highlight the influence of the heterogeneous microstructure of the skin and its nanoscale topography on the measured stiffness.

INTRODUCTION

The skin is the essential barrier that protects our internal organs from excessive damage due to mechanical loading, temperature changes, or irradiation, but also against pathogens and interstitial fluid loss. Its function derives from the layered structural assembly and the microstructural organization within the two main layers: the surface epithelium of differentiated keratinocytes, called the epidermis, and the collagen- and proteoglycan-rich dermis. The dermis is considered to be the load-bearing layer, where the interaction between the collagen fiber network, the proteoglycans, and the interstitial fluid results in a deformation behavior characterized by fiber alignment toward the loading direction and, as a consequence, strain-stiffening and large volume reduction under tensile loading [1]. The deformation mechanisms observed in these macroscopic experiments contribute to provide the skin with exceptional tear resistance and defect tolerance [2]. However, tests on the macroscale has consistently failed to predict the mechanical microenvironment of dermal cells, for which several orders of magnitude lower stiffness than on the macroscale has been reported [3]. Such a compliant cellular microenvironment has been shown in *in vitro* studies to promote physiological cell behavior, for example maintaining dermal fibroblast phenotype and gene expression profiles [4]. In general, measuring the stiffness of the skin remains challenging, as evidenced by reported Young's moduli ranging from 1 kPa [4] to tens of MPa [5], and an understanding of the differences, in particular between length scales, is lacking.

MATERIALS AND METHODS

Healthy skin biopsies from female donors undergoing surgery and providing signed informed consent are obtained and cut to yield samples for macroscopic uniaxial testing as previously described [1]. Adjacent tissue pieces are embedded in optimal cutting temperature compound and snap-frozen in liquid-nitrogen-cooled isopentane. Subsequently, through-thickness cryosections of 50 µm thickness are cut with a cryotome and collected on positively charged microscope slides. Atomic force microscope (AFM)-based indentation experiments are performed on skin sections hydrated in phosphate-buffered saline solution using a commercial AFM. The AFM is mounted on top of an inverted optical microscope, providing visual feedback to guide the cantilever over the skin cross-section and to clearly distinguish between epidermis and the papillary and reticular layers of the dermis (Fig. 1a). Each layer is independently probed using soft cantilevers (nominal spring constant 0.1 N m^{-1}) with a 6.1 µm diameter polystyrene colloidal particle attached to the cantilever tip. The local apparent modulus from each force–indentation curve is extracted by fitting the curve to the Hertzian contact solution for a rigid, spherical indenter and a flat, elastic half-space [6].

To rationalize the mechanical properties across length scales, a microstructural model of the human dermis is developed. The model consists of an assembly of discrete fiber elements, connected at cross-links to form a network, and coupled to a continuum representation of the surrounding non-fibrillar matrix [7]. Fibers are modeled as slender, nonlinear springs, with high stiffness in tension and low resistance to compression. Representative volume elements are generated for simulating macroscopic uniaxial tension experiments under affine-displacement boundary conditions, whereas microscale indentation is simulated by coupling fiber and continuum element nodes at the surface and modeling the interaction with a rigid sphere as hard, frictionless contact (Fig. 1d) [8].

RESULTS AND DISCUSSION

The extracted apparent moduli from AFM experiments (Fig. 1b) show a large heterogeneity (Fig. 1f), with values on the order of 1 kPa, consistent with a previous study [4]. The determined moduli from uniaxial tension tests are, however, roughly two orders of magnitude higher (Fig. 1c), in agreement with our previous data [1]. The differences observed between length scales can therefore not be attributed to natural variations between body locations or due to donor age, and additional tests on murine skin, following the same protocols, confirm the same order-of-magnitude discrepancy as observed for human skin.

*Corresponding author. E-mail: wahlsten@imes.mavt.ethz.ch

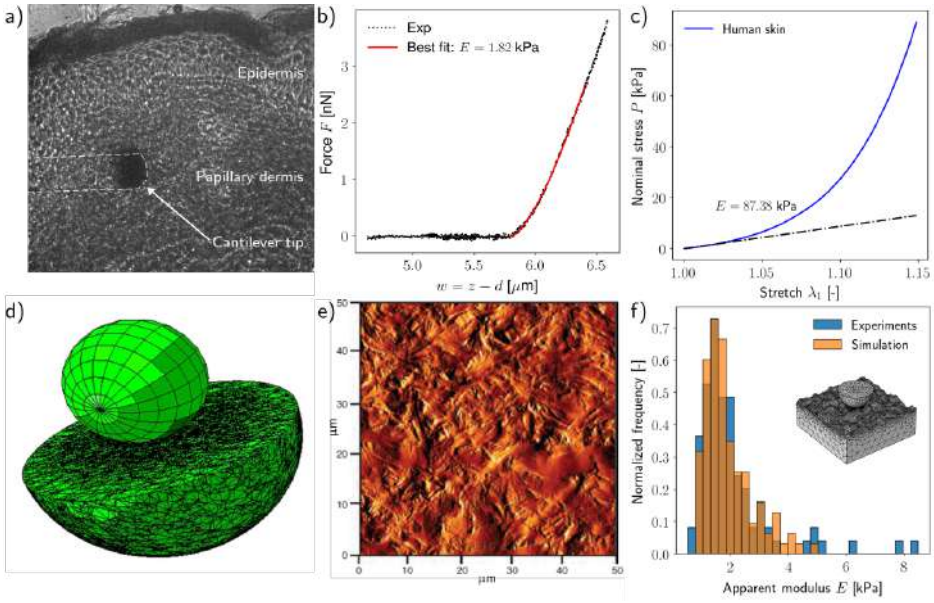

Figure 1: Multiscale measurements and modeling of skin stiffness. AFM indentation experiments were performed on through-thickness sections of human skin (a); a typical force–indentation curve is shown in (b). The macroscopic response in uniaxial tension is significantly stiffer (c). Indentation tests were simulated using a microstructure-based model of the human dermis (d). High-resolution AFM scan of a human skin cross-section showing topographical variations on the order of 1 µm (adapted from [4]). Incorporating realistic surface topographies reproduces the experimental results (f).

The AFM-based indentation experiments probe the local modulus on the length scale of 1 µm—of similar scale as the focal adhesions of a dermal fibroblast [9]—whereas the dimensions in macroscopic uniaxial tests are on the order of several millimeters. The collagen fibers in the papillary dermis form a network with fiber segment lengths of tens of micrometers [10], *i.e.* in between the length scales probed in the experiments. Our microstructural model shows that part of the stiffness difference originates from the network microstructure: the compliant response to indentation arises from the soft behavior of single, slender fibers and the non-fibrillar matrix, compared to a stiffer, collective response when homogenized. However, in disagreement with the AFM experiments, the microscale model predictions are stiffer and show only little variation between locations or the local network structure. These discrepancies can be rationalized in terms of significant variations in topography (Fig. 1e), which question the assumption of a locally flat surface in the analysis of AFM indentation data. Simulations of indentations on a rough surface, qualitatively similar to the measured topography, reproduce the experimental data of apparent moduli on the microscale (Fig. 1f).

CONCLUSIONS

An extensive experimental and numerical analysis of the scale-dependent stiffness of human skin was performed. The measured apparent moduli, differing by orders of magnitude depending on the length scale, were rationalized in terms of the heterogeneous microstructure of the dermis and the nanoscale topography. The analysis presented in this work provides a deeper understanding of skin mechanics across length scales, with implications for fundamental studies in cell mechanobiology and the design of tissue-equivalent materials.

References

[1] A. Wahlsten, M. Pensalfini, A. Stracuzzi, G. Restivo, R. Hopf, and E. Mazza. On the compressibility and poroelasticity of human and murine skin. *Biomech. Model. Mechanobiol.*, 18(4):1079–1093, 2019. doi: 10.1007/s10237-019-01129-1.
[2] W. Yang, V. R. Sherman, B. Gludovatz, E. Schaible, P. Stewart, R. O. Ritchie, and M. A. Meyers. On the tear resistance of skin. *Nat. Commun.*, 6:1–10, 2015. doi: 10.1038/ncomms7649.
[3] C. T. McKee, J. A. Last, P. Russell, and C. J. Murphy. Indentation versus tensile measurements of Young's modulus for soft biological tissues. *Tissue Eng. Part B Rev.*, 17(3):155–164, 2011. doi: 10.1089/ten.teb.2010.0520.
[4] V. F. Achterberg, L. Buscemi, H. Diekmann, J. Smith-Clerc, H. Schwengler, J. J. Meister, H. Wenck, S. Gallinat, and B. Hinz. The nano-scale mechanical properties of the extracellular matrix regulate dermal fibroblast function. *J. Invest. Dermatol.*, 134(7): 1862–1872, 2014. doi: 10.1038/jid.2014.90.
[5] M. L. Crichton, B. C. Donose, X. Chen, A. P. Raphael, H. Huang, and M. A. F. Kendall. The viscoelastic, hyperelastic and scale dependent behaviour of freshly excised individual skin layers. *Biomaterials*, 32(20):4670–4681, 2011. doi: 10.1016/j.biomaterials.2011.03.012.
[6] D. C. Lin, E. K. Dimitriadis, and F. Horkay. Robust strategies for automated AFM force curve analysis—I. Non-adhesive indentation of soft, inhomogeneous materials. *J. Biomech. Eng.*, 129(3):430, 2007. doi: 10.1115/1.2720924.
[7] A. Stracuzzi, A. Wahlsten, A. E. Ehret, and E. Mazza. *In preparation*, 2020.
[8] A. Wahlsten, A. Stracuzzi, I. Lüchtefeld, A. E. Ehret, and E. Mazza. *In preparation*, 2020.
[9] J. M. Goffin, P. Pittet, G. Csucs, J. W. Lussi, J. J. Meister, and B. Hinz. Focal adhesion size controls tension-dependent recruitment of α-smooth muscle actin to stress fibers. *J. Cell Biol.*, 172(2):259–268, 2006. doi: 10.1083/jcb.200506179.
[10] I. A. Brown. Scanning electron microscopy of human dermal fibrous tissue. *J. Anat.*, 113(Pt 2):159–168, 1972.

PROBING THE BIOPHYSICAL ENVIRONMENT OF CELLS *IN SILICO*

Alberto Stracuzzi*[1], Adam Wahlsten [1], Edoardo Mazza[1,2], and Alexander E. Ehret[1,2]
[1]ETH Zurich, Institute for Mechanical Systems, 8092 Zürich, Switzerland
[2]Empa, Swiss Federal Laboratories for Materials Science and Technology, 8600 Dübendorf, Switzerland

Summary In soft collagenous tissues, resident cells use their focal adhesions to mechanically probe their environment. They also adapt to changes in osmotic pressure of the interstitial fluid. In fact, both mechanical and chemical cues affect cell processes and functionality. Due to the presence of negatively charged macromolecules interconnected with the collagen network, a mechanical load always induces an osmotic stress, and *vice versa*, causing an interplay which affects the macro- and micro-scales to different extents. We developed a hybrid discrete-continuum model to investigate the spatial heterogeneity of the mechanical stiffness and the chemical signal at the cellular length scale, and we show that the tissue chemoactive components play a key role in establishing the cell environment.

MECHANICAL CUES AND CHEMOACTIVE COMPONENTS

The mechanical characteristics of tissue extracellular matrix (ECM) strongly affect the behaviour of resident cells. In fact, cells use specific transmembrane proteins in so called focal adhesions (FAs) to anchor and effectively probe the ECM scaffold, whose mechanical properties may influence cells' behaviour, *e.g.* by controlling their direction of motion in durotaxis [1], or by inducing proliferation [2] or tumorigenesis [3].

In soft collagenous tissues, the extracellular environment is highly diverse. Resident cells live and move within the pore space shaped by the 3D network-like arrangement of collagen fibres. Moreover, long chains of proteoglycans (PGs) are tightly interwoven with the collagen network and carry negatively charged groups of glycosaminoglycans (GAGs), which regulate tissue hydration and influence the concentration of ions diffused in the interstitial liquid.

Due to the difficulty to assess experimentally the ECM mechanical contributions at a cellular length scale, recent studies recognized the need to analyse the cell environment using dedicated multi-scale numerical frameworks, which mainly focused on the representation of the fibre skeleton by using discrete network approaches, without considering the presence of mobile and fixed ions. These studies reveal that cells feel a strongly heterogeneous mechanical signal in terms of local stiffnesses at the FAs, both in 3D disordered fibre networks [4] and on 2D fibrous substrates [5]. However, the presence of dissolved chemical species not only constitutes an important cellular cue *per se*, but also in its interaction with the chemoactive components, *i.e.* PGs and GAGs. In fact, applied mechanical loads may change locally the concentration of fixed charges and the corresponding osmotic pressure, thus inducing fast redistributions of mobile ions and gradients of chemical potential which slowly drive the fluid in or out, over the tissue boundaries. The resulting chemomechanical coupling has been identified to be relevant also for soft biomembranes when subjected to physiological tensile deformation states [6]. In this particular case, upon stretching, the collagen network contracts, the tissue volume decreases as a consequence of water outflow, and the internal osmotic pressure increases, thus modulating the internal state of stress.

In this contribution, we analyse the effects on both the mechanical and chemical characteristics of the cell environment determined by the presence of chemoactive components within the ECM, by developing a hybrid discrete-continuum approach, representative of a real biological tissue, and probing it *in silico* at the cell length scale (~$10\mu m$).

A HYBRID DISCRETE-CONTINUUM MODEL

The proposed model is a combination of a discrete network of trilinear axial connectors [6], which model the collagen fibre ensemble, and biphasic continuum elements [7], which provide a lumped representation of water, PGs and other ECM components. Cubic RVEs are seeded with a specified density of crosslinks (Fig.1). These are then connected according to prescribed length and orientation distributions, and constitute the starting set of nodes to mesh the RVE domain with a Delaunay triangulation scheme (Fig.1). While crosslinks at the RVE vertices are always included, a subset of the remaining crosslinks is selected for the triangulation algorithm. Hence, the resulting mesh size is correlated with the definition of a length scale of interactions (LsI), which represents an average length of the entanglements between collagen fibres and PGs, allowing for parametric studies.

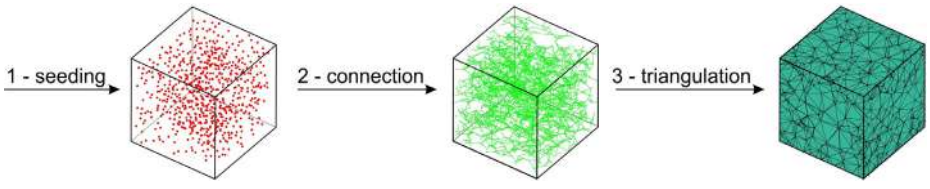

Figure 1: The three main steps of RVE generation.

*Corresponding author. E-mail: stracuzzi@imes.mavt.ethz.ch

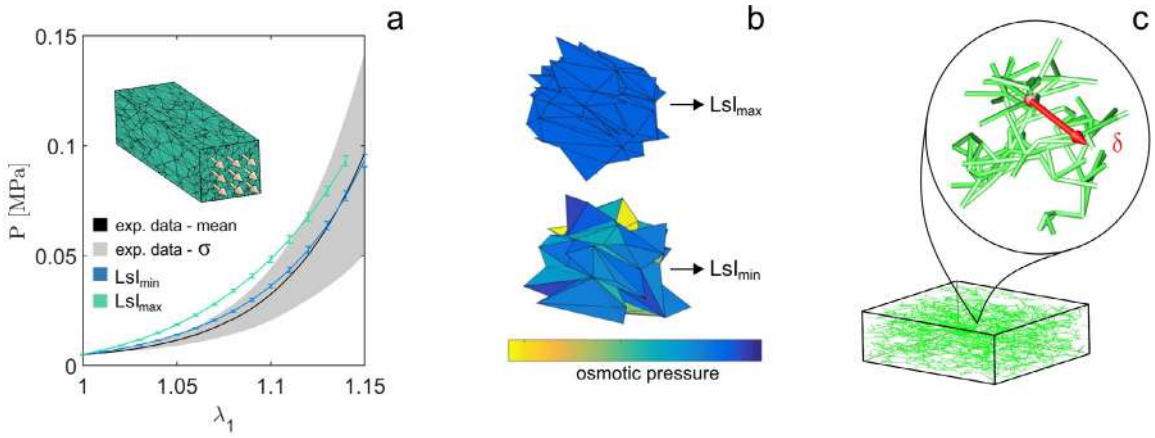

Figure 2: Macroscopic uniaxial response (a), osmotic pressure field of a subdomain of the RVE (b) and qualitative representation of a unit displacement of a crosslink for the determination of the local stiffness in a deformed RVE (c).

MULTI-SCALE NUMERICAL ANALYSES

In order to be representative of a biological tissue, most of the model parameters were derived from histological and morphological data of human dermis, and the macroscopic response of the RVE was then tuned according to uniaxial data of human skin [8]. The homogenised, macroscopic response showed good agreement with the experimental data, with minor dependence on the LsI (Fig.2a). In contrast to this, at cellular length scale, the chemical signal strongly depends on the LsI. In fact, the osmotic pressure passes from homogeneous to highly scattered when ranging from the highest to the lowest value of the LsI, respectively (Fig.2b). Further multi-scale simulations were performed to study the heterogeneity of the mechanical stiffness as perceived by resident cells. To this end, we applied a unit displacement to several random crosslinks (Fig.2c), and we extracted the local stiffness at the loaded points. While the general signature confirmed the broad spectrum of stiffnesses as found in previous studies [4], the resulting stiffness distributions revealed a marked dependence on the LsI. In addition to this large variability of the local mechanical stiffness, the calculations also show a long-range decay pattern for both forces and displacements over the crosslinks, especially if compared with corresponding homogeneous materials.

CONCLUSIONS

We present a hybrid discrete-continuum model which provides new insights on the mechanical and chemical signals experienced by cells in 3D collagenous tissues. In particular, the framework includes the osmotic contribution of the negatively charged PGs, thus providing access not only to the mechanical stimuli but also to the chemical signals and the way the latter influence cell mechanosensing.

References

[1] Lo C.M., Wang H.B., Dembo M., Wang Y.L. Cell movement is guided by the rigidity of the substrate. *Biophys. J.* **79**: 144-152, 2000.
[2] Segel M., Neumann B., Hill M.F.E. et al. Niche stiffness underlies the ageing of central nervous system progenitor cells. *Nature* **573**: 130-134, 2019.
[3] Chaudhuri O., Koshy S., Branco da Cunha C. et al. Extracellular matrix stiffness and composition jointly regulate the induction of malignant phenotypes in mammary epithelium. *Nature Mater.* **13**: 970-978, 2014.
[4] Beroz F., Jawerth L., Münster S. et al. Physical limits to biomechanical sensing in disordered fibre networks. *Nat. Commun.* **8**: 16096, 2017.
[5] Zündel M., Ehret A.E., Mazza E. The multiscale stiffness of electrospun substrates and aspects of their mechanical biocompatibility. *Acta Biomater.* **84**: 146-158, 2018.
[6] Ehret A.E., Bircher K., Stracuzzi A. et al. Inverse poroelasticity as a fundamental mechanism in biomechanics and mechanobiology. *Nat. Commun.* **8**: 1002, 2017.
[7] Stracuzzi A., Mazza E., Ehret A.E. Chemomechanical models for soft tissues based on the reconciliation of porous media and swelling polymer theories. *Z. Angew. Math. Mech.* **98**: 2135-2154, 2018.
[8] Wahlsten, A., Pensalfini, M., Stracuzzi, A. et al. On the compressibility and poroelasticity of human and murine skin. *Biomech. Model. Mechanobiol.* **18**: 1079-1093, 2019.

QUANTIFYING MECHANICAL STRAIN IN STEM CELL DERIVED CARDIOMYOCYTES IN A CPVT DISEASE MODEL

A. Stempien*[1,2], J. Notbohm[3], W.J. de Lange[4], J.J. Hernandez [4], J.C. Ralphe[4], W.C. Crone[1,2,3]
[1]Department of Biomedical Engineering,
[2]Wisconsin Institute for Discovery,
[3]Department of Engineering Physics, University of Wisconsin-Madison, Madison, WI, USA
[4]Department of Pediatrics, University of Wisconsin School of Medicine and Public Health, Madison, WI, USA

Summary: Cardiovascular disease continues to be leading cause of death worldwide; of particular concern are diseases which can lead to sudden death, such as in patients with Catecholaminergic Polymorphic Ventricular Tachycardia (CPVT). It is hypothesized that the amplitude of contractile strain can be utilized as a quantitative indicator of cardiomyocyte functionality and disease severity. Digital image correlation (DIC) allows for evaluation of strain across many cells acting in coordination by capturing displacement data throughout contraction events in collections of cardiomyocytes cultured *in vitro*. The technique is demonstrated using a disease model derived from a CPVT patient and a familial control, where we show statistically significant differences in maximum contractile strains between the disease and control conditions.

BACKGROUND

Cardiomyocytes are the contractile cell type of the heart and their coordinated contraction is required for proper pumping of blood throughout the body. Cardiovascular disease continues to be a leading cause of death worldwide motivating the need for models of cardiac function in both healthy and diseased states for both basic science and clinically translational research. Cardiomyocytes (CMs) derived from human induced pluripotent stem cells (hiPSCs) provide a source for developing *in vitro* cardiac models, however current *in vitro* analysis techniques provide only a portion of the necessary means to fully characterize functionality. Specifically, there is a need for additional techniques to quantify and understand the contractile behavior of CMs as the interact collectively with each other and their surroundings.

In these studies, a previously validated human stem-cell derived cardiomyocyte culture platform [1] was used. The platform is created by microcontact printing extracellular matrix (ECM) proteins onto a compliant polymeric substrate with physiologically relevant stiffness. This culture platform bridges the gap between single-cell and tissue studies, by allowing for measurement of contraction between multiple cells while including the structural detail of individual cells. Here we demonstrate the functionality of this platform and the application of digital image correlation (DIC) for analysis with a Catecholaminergic Polymorphic Ventricular Tachycardia (CPVT) disease model. Full-field displacements were measured using high contrast images of sample regions containing CMs [2]. From displacement, principal strains were calculated. Of particular interest is the second principal strain, which in these experiments represents the contractile strain along the major axis of the cardiomyocyte and was used as the quantitative indicator of functionality and disease severity.

RESEARCH METHODS

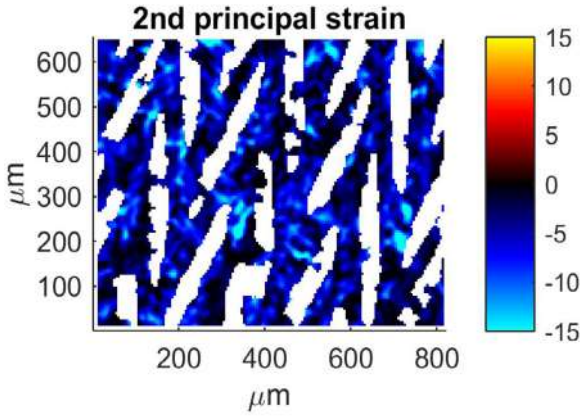

Figure 1: Full field contractile strain at peak contraction

The CPVT model was created using a patient-specific-derived iPSC line with RyR2-H2464D mutation and healthy control line from the patient's mother [3]. Cells were differentiated into cardiomyocytes using a modified version of the small molecule Wnt-agonist method [5], followed by a purification process to remove non-CM cell types.

CMs respond to substrate stiffness through focal adhesions, which enable connection between the cell's cytoskeleton and underlying ECM. Focal adhesions also play a role in formation and alignment of actin stress fibers and force transduction. Microcontact printing of ECM proteins was used to created patterned substrates on PDMS with a Young's modulus from 5-50 kPa, which spans the range of healthy to diseased myocardium [6]. The chevron pattern used was made up of narrow lanes connected by bridges. The lane width influences CM shape and sarcomere organization by providing defined

* Corresponding author. Email: astempien@wisc.edu

attachment regions, and the bridges increase connectivity which allows for synchronized contractions across a large array of CMs.

Videos of spontaneous contractions were captured using a Nikon Eclipse Ti microscope with a 10x objective and Nikon DS-QiMc camera at a capture rate of 11 frames per second and edited such that in the initial frame the CMs were in the relaxed state. Correlations between relaxed and subsequent frames during contraction of the cardiomyocytes were calculated for many spontaneous contractions and multiple biological replicates. The random high contrast pattern from the phase contrast of the cells is sufficient to allow tracking of displacements. The displacement fields in the horizontal and vertical directions for the entire pattern were calculated using the open source digital image correlation software, Fast Iterative Digital Image Correlation (FIDIC) [7] with input parameters of a target subset size of 32 pixels and subset spacing of 8 pixels. From the displacements, the strain tensor was calculated by taking the gradient of the displacement data. Principal strains and principal directions were then computed. Using the full field second principal strain (contractile strain), the average across all cells in the frame was taken and the maximum value over time, or peak strain, was used as the comparative measure between cell lines.

RESULTS

CPVT disease model experiments were performed using a range of PDMS substrate stiffnesses, and relative differences between patient and control varied based on stiffness. The maximum contractile strain of the patient line was 28% higher than the control line (p<.0001) when cultured on 30 kPa PDMS.

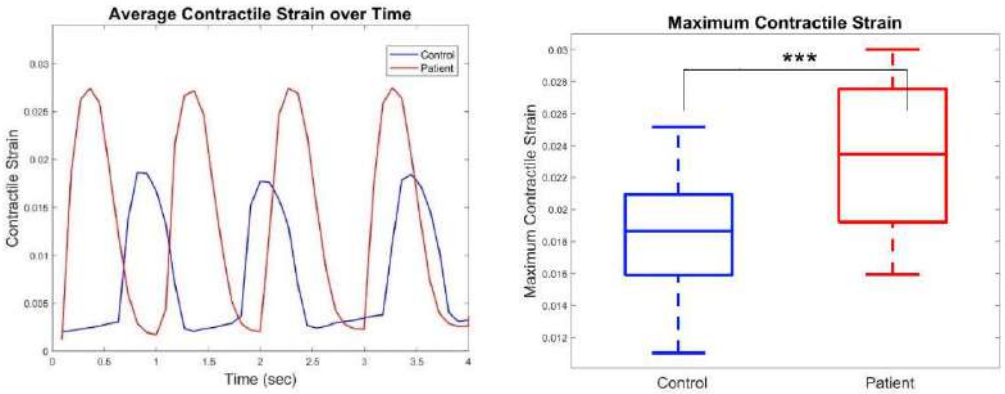

Figure 2: (A) Representative average contractile strains over time, and (B) maximum of average contractile strain over for CPVT cardiomyocytes cultured on 30 kPa PDMS. Patient data (n=19) is shown in red, and control (n=47) data is shown in blue. *** $p <$ .0001

CONCLUSION

DIC was used to investigate differences in mechanical function of human induced pluripotent stem cell derived cardiomyocytes cultured in a microcontact printed platform. A stem cell derived disease model for Catecholaminergic Polymorphic Ventricular Tachycardia (CPVT) was compared to a familial healthy control line to assess differences in contractile function. Mechanical strain was quantified, and in particular second principal strain was used as a functional readout. Statistically significant differences in maximum contractile strains between the disease and control conditions were observed, demonstrating the utility of this approach in quantifying mechanical function as an indicator of disease severity.

References

[1] Salick, M. R. *et al.* Micropattern width dependent sarcomere development in human ESC-derived cardiomyocytes. *Biomaterials* **35**, 4454–4464 (2014).

[2]Notbohm, J. *et al.* Two-Dimensional Culture Systems to Enable Mechanics-Based Assays for Stem Cell-Derived Cardiomyocytes. *Experimental Mechanics* 1–14 (2019).

[3] Hernández Jonathan J et al., Abstract 17750: A CPVT Mutation Confers Gain of Function to the Cardiac Ryanodine Receptor Channel. Characterization Using Cardiomyocytes Derived From Patient-Specific Ips Cells, *Circulation* 128, no. suppl_22 (November 26, 2013):

[4] Ralphe John C, *et al*. Abstract 16773: Ablation of Cardiac Myosin Binding Protein-C in Human iPSC- Engineered Cardiac Tissue Model Causes Increased Calcium Sensitivity and Accelerated Contractile Kinetics. *Circulation* **138**, A16773–A16773 (2018).

[5] Lian, X. *et al.* Robust cardiomyocyte differentiation from human pluripotent stem cells via temporal modulation of canonical Wnt signaling. *Proceedings of the National Academy of Sciences of the United States of America* **109**, E1848–E1857 (2012).

[6] B. Bhana *et al*., "Influence of Substrate Stiffness on the Phenotype of Heart Cells.," *Biotechnology and Bioengineering* 105, no. 6 (April 2010): 1148–60, https://doi.org/10.1002/bit.22647.

[7] Bar-Kochba, *et al*. A Fast Iterative Digital Volume Correlation Algorithm for Large Deformations. *Experimental Mechanics* **55**, 261–274 (2015).

THE VASCULAR ENDOTHELIAL GROWTH FACTOR RECEPTOR DYNAMICS DURING THE SPREADING OF ENDOTHELIAL CELLS:EXPERIMENTAL AND COMPUTATIONAL INVESTIGATIONS

Mattia Serpelloni*[1], Matteo Arricca[1], Elisabetta Grillo[2], Cosetta Ravelli[2], Stefania Mitola[2], and Alberto Salvadori[1]
[1]Department of Mechanical and Industrial Engineering (DIMI), University of Brescia, Brescia, 25123, Italy
[2]Department of Molecular and Translational Medicine (DMMT), University of Brescia, Brescia, 25123, Italy

Summary We propose a co-designed experimental and computational study of the Vascular Endothelial Growth Factor Receptors (VEGFR) dynamics during the spreading of Endothelial Cells (ECs), one of the key processes regulating tumor angiogenesis. The study combines evidence deduced from in vitro experiments on ECs plated on a substrate enriched of ligands with simulations of a predictive multi-physics model set up in the field of continuum thermodynamics. The work allows discerning the relevance of cell mechanics in tumor angiogenesis and realizing that predictive models could open unknown roads towards antiangiogenic strategies.

BIOLOGICAL BACKGROUND - MOTIVATIONS

A solid tumor, in order to survive and proliferate, exchanges nutrients and waste with the surroundings. The high metabolism of cancer cells leads to a rapid depletion of resources and simultaneously to a hypoxic state of the tissues nearby the tumor, compromising its survival. As a consequence, cancer cells release growth factors[1], specific proteins that act as signaling molecules. These immobilized factors, that are absorbed in the Extracellular Matrix (ECM), represent a persistent stimulus for the otherwise quiescent Endothelial Cells (ECs), eventually leading to tumor angiogenesis [1]. New blood vessels restore the exchange of nutrients and waste between cancer and the rest of the body and play a pivotal rule in metastasis of tumors, mostly at the very early stage.

At a molecular level, angiogenesis is triggered by the interaction between the growth factors and transmembrane proteins on the lipid membrane of ECs, called receptors[2]. Since the geometry of the membrane evolves in time, the mechanisms behind tumor angiogenesis are affected by the mechanical response of the ECs.

Vascular Endothelial Growth Factor Receptor-2 (VEGFR2) is one of the most relevant transmembrane proteins for tumor angiogenesis. Although the biochemical pathways that follow the activation of VEGFR2 are well established, investigations of the influence of cellular mechanics in angiogenic processes deserve further progresses.

The activation of VEGFR2 shall not be detached from the interaction between integrin (receptor) and fibronectin (ligand). This receptor-ligand interplay rules the continuous exchange of mechanical signals (mechanotransduction) between the ECM and bundles of actin that belong to the cytoskeleton, a dynamic network of proteins that organize themselves as a consequence of external stimuli and is responsible for the mechanical response of the ECs. An accurate description of the cytoskeleton evolution and of the receptor-ligand dynamics is thus pivotal in the modeling of tumor angiogenesis and is the goal of this work.

CO-DESIGNED EXPERIMENTS AND MODELS

Based on these premises, we developed a chemo-mechano-transport model to study the relocation and recruitment of VEGFR2 and integrin on the cell membrane during the spreading of an EC on a substrate enriched of VEGFA/Gremlin and fibronectin, which was concurrently experimentally investigated. The model accounts for the formation and reorganization of the cytoskeletal contractile machinery, in particular of the stress-fibers[3] (SFs).

The model formulation stems from three chemical reactions, two of which describe the ligand-receptor interactions that rule the mechano-transduction and the triggering of angiogenic stimuli, whereas the third describes the chemical interaction between the complex given by VEGFR2-VEGFA/Gremlin with integrin [2]. The affinity between the VEGFR2-Ligand complex and integrin makes the activation signal of the angiogenic stimulus more lasting and more robust.

Thermodynamically, the model can be seen as an instance of the framework presented in [3], in terms of Helmholtz free energies and constitutive relationships, enriched by models of the activation and reorganization of the cytoskeleton published in [4]. Coupling of the cytoskeleton evolution with the chemo-transport part of the model that accounts for the integrins diffusion and reaction, provides a description of the mechanotransduction apparatus in ECs.

*Corresponding author. E-mail: m.serpelloni002@unibs.it.

[1]Growth factors are also called ligands (e.g. the canonical ligand VEGFA or the non-canonical ligand Gremlin).

[2]Receptors are proteins that have an extra- and intra-cellular domain. This feature allows them to connect cells with their surroundings and makes the receptor-ligand interaction an optimal way for cell-ECM communication. For these reasons, several biological processes at the cellular level are modulated through the high degree of specificity of the chemical interaction between receptors and ligands.

[3]SFs are actin filaments connected to the ECM through integrins and focal adhesions. These actin bundles are among the entities responsible for contractile forces during EC adhesion on the substrate.

NUMERICAL SIMULATIONS

The governing equations have been rephrased in their weak form. Discretization and FEM numerical simulations are a further purpose of the present work. The implementation is carried out exploiting the high performance computing open source software library deal.ii (http://www.dealii.org). A picture of the evolution in time of the cell-substrate contact and spreading, as well as of VEGFR relocation and activation is shown in Fig. 1.

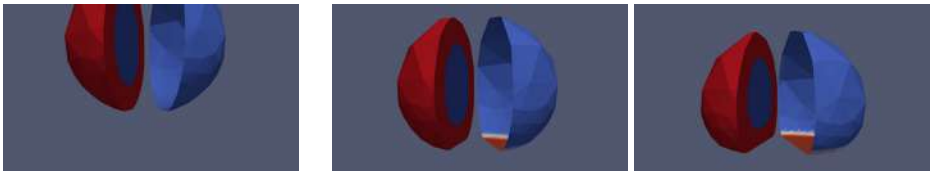

(a) (b) (c)

Figure 1: Time evolution of the cell-substrate contact dynamics. The cell is visually split in two halves: the left depicts the internal part of the EC (the nucleus in blue and the cytosol in red). The receptor relocation and the formation of the VEGFR2-Gremlin complex is shown on the right half.

The computational versus experimental time evolution of the concentrations of VEGFR2 and of its complex with Gremlin is shown in Fig. 2 [5], reprinted from a former publication [6] in which strong assumptions on cell mechanics were made. They have been removed in the present work. Modeling allowed finding a quantitative correlation between

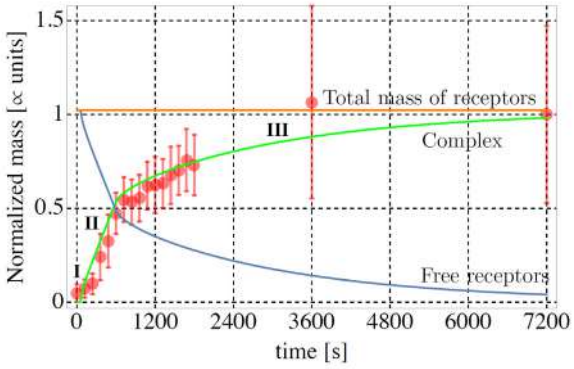

Figure 2: Evolution in time of the normalized concentrations of VEGFR2 and of its complex with Gremlin. The simulation outcomes are plot in continuous line, while the values of the experimental data are shown in dotted lines and error bars.

the phases of the recruitment of VEGFR2 (I, II, III in Fig. 2) and three distinct mechanisms: I) the cell-ligand contact, II) the chemo-mechanical evolution (until 600s) and III) the diffusive slow motion of the receptors.

CONCLUSIONS

Quantifying the influence of mechanical processes onto tumor angiogenesis can play a major role in the fight against cancer. For this sake, a mechanobiological study has been here proposed at a molecular level yet in a continuum mechanics framework. A mechano-chemo-transport model has been developed, capable of describing the relocation and recruitment of VEGFR2 and integrins on the lipid membrane during the mechanical spreading of an EC. The model describes the mechanical response of an EC during cell adhesion, accounting for the dynamic evolution of the cytoskeletal contractile machinery.

References

[1] Bergers G., Benjamin L. E. Tumorigenesis and the angiogenic switch. *Nat Rev Cancer.* **3(6)**: 401-10, 2003.

[2] Ravelli C., Grillo E., Corsini M., Coltrini D., Presta M., Mitola S. β_3 integrin promotes long-lasting activation and polarization of vascular endothelial growth factor receptor 2 by immobilized ligand. *ARTERIOSCL THROM VAS.* **35(10)**: 2161-2171, 2015

[3] Salvadori A., McMeeking R.M., Grazioli D., Magri M. A coupled model of transport-reaction-mechanics with trapping. Part I - small strain analysis. *J MECH PHYS SOLIDS.* **114**:1-30, 2018.

[4] Vigliotti A., Ronan W., Baaijens F.P.T., Deshpande V.S. A thermodynamically motivated model for stress-fiber reorganization. *BIOMECH MODEL MECHAN.* **15**: 761-789, 2015.

[5] Damioli V., Salvadori A., Beretta G.P., Ravelli C., Mitola S. Multi-physics interactions drive VEGFR2 relocation on endothelial cells. *SCI REP-UK.* **7(1)**:16700, 2017.

[6] Salvadori A., Damioli V., Ravelli C., Mitola S. Modeling and Simulation of VEGF Receptors Recruitment in Angiogenesis. *MATH PROBL ENG.* 2018.

MULTISCALE SIMULATION OF THE LEFT VENTRICLE MECHANICS WITHIN THE CARDIOVASCULAR SYSTEM

Fedor Semin*[1,2], Albina Khabibullina[3], Anna Osepyan[3], and Andrey Tsaturyan[1]
[1]Institute of Mechanics, Lomonosov Moscow State University, Moscow,Russia
[2]Peoples'Friendship University of Russi a(RUDNUniversity),Moscow,Russia
[3]Department of Mathematics and Mechanics, Lomonosov Moscow State University, Moscow, Russia

Summary The paper presents a mathematical model of circulation with a detailed description of the left ventricle (LV) mechanics. The model was applied for simulations of heart-beats in normal and pathological conditions. In particular, it was demonstrated how the LV multiscale model allows one to simulate local and global changes in contractile or regulatory properties of the LV myocardium and examine numerically the influence of these changes on the macroscopic strains and stress of the LV walls, and the systemic and pulmonary haemodynamics. The results of the simulations of impaired myocardial contractility and the effects of some cardiomyopathic mutations in the regulatory proteins of cardiac muscle including the accompanying LV remodelling are presented.

INTRODUCTION

Modelling of the heart electromechanics is a very promising and fast-developing field of biomechanics. Electrical processes in LV myocardium were described in details in a number of papers. LV passive mechanics was also examined thoroughly. However, the implementation of active mechanics of cardiac muscles in the heart models is often quite simplistic although its detailed description is important for correct reproduction and numerical investigation of the effects of cell-level cardiac disorders on the heart performance.

Earlier, we developed a model of myocardium mechanics with active stress depending on the kinetics of the contractile and regulatory proteins in the cardiac muscle cells [1]. The kinetic model was set by a system of ordinary differential equations (ODEs) that makes it computationally suitable for 2D-3D simulations. The myocardium model was applied for the simulation of the LV pumping function in the cardiovascular system [2]. Here we present some results of the simulations of various cell-level myocardium dysfunctions examining their effects on the LV performance.

MODEL AND METHODS

Model of the cardiovascular system

The cardiovascular system (CVS) was described by a lumped parameter model in which the LV pressure P_{LV} and volume V_{LV} were specified from our multiscale model of the LV mechanics. The LV was approximated by an axisymmetric body with walls consisting of cardiac muscle. Myocardium was supposed to be an incompressible transversely isotropic solid material. The axes of the anisotropy were defined by the orientation of muscle fibres, which was specified by a rule-based algorithm: the fibres were aligned with helices (the helix axis is the axis of rotation for the LV approximation), and helical angle with the horizontal plane was linearly changed through the LV wall [3].

The LV stress is assumed to be the sum of an isotropic passive stress tensor specified by a strain-energy function, Lagrange multiplier (hydrostatic pressure) caused by incompressibility and the anisotropic stress tensor describing forces acting along the cardiac fibres. These forces were the passive nonlinear elastic tension of the giant muscle protein titin and the active force generated by the interaction of contractile proteins of cardiac muscle. The active stress was set by our kinetic model of cardiac muscle contraction and its regulation [1]. In brief, the model of cardiac muscle was specified by a system of ordinary differential kinetic equations for several states of contractile and regulatory proteins. The active tension was determined by the formation of so-called cross-bridges – the globular parts of one of the contractile proteins, myosin, bound to another contractile protein, actin. The number of cross-bridges was determined by the normalized concentration of the complexes of a regular protein, troponin, with the Ca^{2+} ions (CaTnC). The transition rates of the contractile properties depended only on one average micro-level strain of contractile proteins in a structural muscle unit, sarcomere. The transition rates of the regulatory proteins depended on the Ca^{2+} concentration, sarcomere length and some other variables providing so-called activation cooperativity.

The right ventricle and the atria of the heart were considered being viscoelastic reservoirs with time-depended stiffness and viscosity specified by ODEs. The other parts of the vascular bed including aorta, systemic and pulmonary arteries, systemic and pulmonary veins were described as elastic reservoirs with variable pressures and volumes and constant compliances. The final lumped parameter model was set by a system of ODEs for the pressures and volumes of the reservoirs and the flows between them.

The complete problem set for the heart contraction was specified by the following equations: equilibrium equations for the LV (inertial terms were neglected), incompressibility equations for the LV myocardium, the ODEs of the kinetic model of cardiac muscle, the ODEs of the lumped parameter model for the haemodynamics. The problem was solved by a finite element method (FEM) using small increments approach: at each time step, the equilibrium and incompressibility equations for the LV were linearized for small unknown increments of nodal displacements of a FEM mesh, pressures, caused by incompressibility, and LV blood pressure. The model implementation was described in details earlier [2].

*Corresponding author. E-mail: f.syomin@imec.msu.ru.

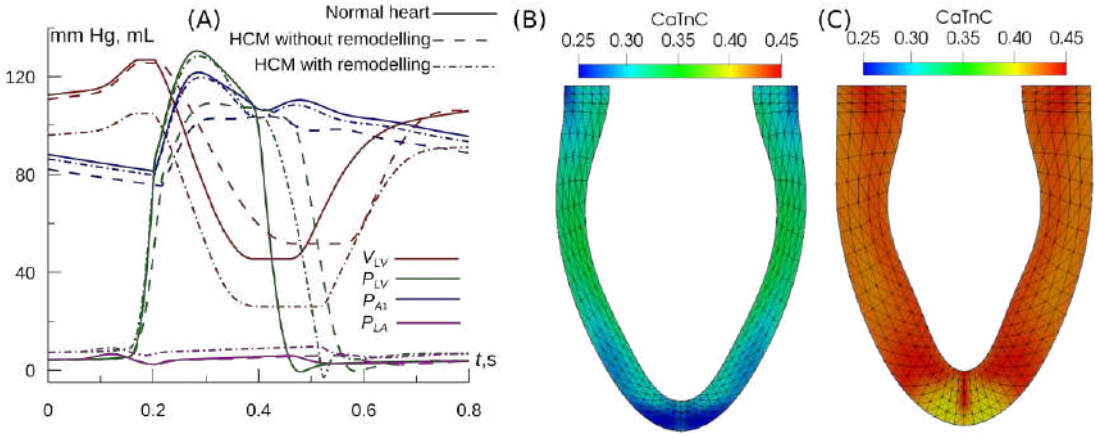

Figure 1: Simulated heart-beats with 'normal' and HCM LVs. (A) The LV, aortic and left atrial pressures (P_{LV}, P_{A1}, P_{LA}) and the LV volume (V_{LV}) for the simulation of a heart-beat with 'normal' LV myocardium (solid lines) and myocardium changed by a HCM mutation with either the 'normal' LV shape (dash lines) or with concentric hypertrophy (dash-dot lines). (B,C) The normalized concentration of Ca^{2+}-troponin complexes in the LV at the moment of the peak LV pressure in 'normal' (B) and hypertrophic (C) LVs.

Numerical experiments

Firstly, we simulated a heartbeat with model parameters corresponding to an average healthy human. Then we changed some cell-level parameters of the myocardium to investigate their effect on the heart performance. We simulated the regional decrease of myocardial contractility in the apical region of the LV (apical myocardial infarction) and a decrease of the maximal steady-state shortening velocity of the cardiac muscle, observed in some cases of cardiomyopathies. We also varied the cell-level parameters of calcium regulation of the muscle contraction reported for some mutations of a regulatory protein, tropomyosin, associated with the inherited hypertrophic and dilated cardiomyopathies. The remodelling accompanying the mutations – the LV wall thickening at the case of its concentric hypertrophy and an increase in the LV cavity volume at the case of its dilatation – was also accounted for.

RESULTS AND DISCUSSION

We showed previously, that resulting heamodynamic variables of the CVS and global and local strains of the LV in the case of the simulation of a 'healthy' heartbeat were in accordance with the data of medical observations [2]. The results of the numerical experiments reported here showed the decrease in the LV stroke volume upon apical infarction or the impairment of the force-velocity relationship for cardiac muscle. A decrease in the LV contractility estimated from the pressure-volume loops also took place. Figure 1 shows the results of the simulated effects of a mutation in a regulatory protein tropomyosin that causes hypertrophic cardiomyopathy (HCM). Despite an increase in Ca^{2+} sensitivity of troponin that results in an increase in the CaTnC concentration (Fig. 1B,C), the decreased maximal tension and length-dependence of Ca^{2+} activation, which are associated with the mutation [4], caused a significant decrease in aortic pressure, LV pressure and stroke volume (Fig. 1A). The remodelling compensated the impaired muscle contractility and regulation.

The model has certain limitations: we did not take into account the changes in passive properties of myocardium and redistribution of fibres orientation, which are often observed in animal and patients with cell-level myocardium disorders.

CONCLUSIONS

The model presented is able to reproduce the effects of such complex phenomena as apical myocardial infarction and cardiomyopathies caused by protein mutations due to the introduced model of myocardial mechanics. We believe that the model can be expanded for 3D patient-specific simulations of the heart.

The work was supported by grants No 18-31-00065 and No 17-00-00066 (a part of the complex project No 17-00-00071) of the Russian Foundation for Basic Research (RFBR).

References

[1] Syomin F. A., Tsaturyan A. K. A simple model of cardiac muscle for multiscale simulation: passive mechanics, crossbridge kinetics and calcium regulation. *J. Theor. Biol.* **420**: 105-116, 2017.

[2] Syomin F. A., Zberia M. V. Tsaturyan A. K. Multiscale simulation of the effects of atrioventricular block and valve diseases on heart performance. *Int. J. Numer. Methods Biomed. Eng.* **e3216**, 2019.

[3] Syomin F. A., Tsaturyan A. K. Mechanical model of the left ventricle of the heart approximated by axisymmetric geometry. *Russ. J. Numer. Anal. Math. Model.* **32**: 327-337, 2017.

[4] Sequeira V., Wijnker P. J., Nijenkamp L. L. et al. Perturbed length-dependent activation in human hypertrophic cardiomyopathy with missense sarcomeric gene mutations. *Circ. Res.* **112**: 1491-1505, 2013.

ON THE ROLE OF INTERSTITIAL FLOW IN HUMAN SKIN BIOMECHANICS

David Sachs[1], Bettina Müller [1], Fanny Enz [1], Adam Wahlsten[1]and Edoardo Mazza [1,2]
[1]ETH Zurich, Institute for Mechanical Systems, Zurich, Switzerland
[2]EMPA, Swiss Federal Laboratories for Materials Science and Technology, Dubendorf, Switzerland

Summary Recent experimental observations of human skin's response to tensile loading revealed large volume changes associated with interstitial fluid flow. In this contribution, we show that a histologically motivated layered biphasic model is capable of rationalizing a wide range of in-vivo and ex-vivo experimental observations. The model allows to investigate the layer specific deformation mechanisms governing tissue response in in-plane tensile as well as out-of-plane suction experiments. The importance of fluid motion for the in-vivo dissipative response of human skin in cyclic suction experiments is examined, with special consideration to their application for diagnosis.

HISTOLOGICAL AND MECHANICAL FEATURES OF HUMAN SKIN

Medical applications increasingly benefit from mechanical analyses of human skin [e.g. 1, 2]. Skin is a multiphasic multi-layered soft tissue composed of a keratinocyte-rich epidermis, a collagen-based dermis and an adipocyte cell built hypodermis, as depicted in figure 1. Resulting from differences in collagen content and orientation, the dermis is further divided into a papillary and a reticular layer. Fine type III collagen fibres characterize the papillary layer, whereas thicker type I collagen fibre bundles are present in the reticular layer. Skin is a multiphasic material composed of a solid and a fluid component as well as distributed fixed charges. Extensive ex-vivo experimental characterization in our lab revealed specific features of its mechanical behaviour [3]. First, skin exhibits a strong volume reduction upon monotonic tensile loading, caused by ejection of interstitial fluid. Second, an out-of-plane deflection of the epidermal surface is visible in uniaxial experiments. Third, uniaxial relaxation experiments reveal a strong tension decay within short time. In-vivo suction experiments induce an equibiaxial stress state resulting in a reduction of thickness. Moreover, application of a constant suction pressure causes skin to creep. Further experimental investigation of skin response to suction experiments suggested motion of interstitial fluid as a key contribution to the observed behaviour [4]. Attempts to rationalize all characteristics with a single-layer biphasic model of skin did not succeed. We therefore hypothesize that subdivision of skin into an epidermal, papillary, and reticular layer is necessary.

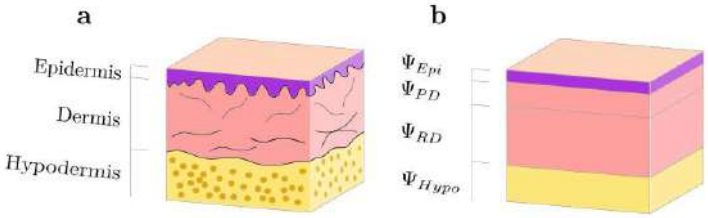

Figure 1. The biphasic mechanical model of human skin is motivated by experimental observations, the anatomy, and the histology of the tissue. We distinguish four layers: epidermis, papillary and reticular dermis, and hypodermis.

MODEL IMPLEMENTATION

A biphasic finite element model accounting for skin's layered structure was implemented in COMSOL [3]. The solid constituent was modelled with a Rubin-Bodner type strain energy function [5], with contributions from a compressible Neo-Hookean solid as well as elastic and dissipative fibre elements. The solid isotropic component represents the proteoglycan matrix (including fixed charges) and the fibres represent the contribution of the collagen network. The motions of the solid and fluid phases are coupled through the balance laws of a biphasic mixture [6], and the relative fluid motion is modelled using Darcy's law with a spatially isotropic deformation dependent permeability tensor. The osmotic pressure resulting from fixed charged groups attached to the solid matrix provides a contribution to the chemical potential, driving fluid flow [7].

RESULTS

The new multi-layered model rationalizes experimental results of in-vivo suction as well as ex-vivo uniaxial tensile experiments. Iterative optimization of the material model parameters yields a stiff and strongly anisotropic reticular dermis, a softer and less anisotropic papillary dermis, and a very soft and almost isotropic epidermis. Corresponding simulations show that for uniaxial tensile loading the reticular dermis is the main load-bearing layer of skin. In contrast, for suction experiments the influence of the upper layer increases for smaller probe openings. Furthermore, also the deformation state changes. For larger probe opening diameters an equibiaxial stress state dominates, whereas smaller probe openings cause a significant level of shear deformation. This results in a reduced dermal thickness for large probe openings and an increased thickness for small probe openings. Consequently, dissipative behaviour, i.e. creep and residual deformation after unloading, depends on the probe opening size. The layered model also quantitatively reproduces the

out-of-plane deflection in uniaxial tensile tests, as it is a direct result from the different mechanical properties in the dermal layers.

INFLUENCE OF INTERSTITIAL FLOW

Fluid mobility is essential for the response of each dermal layer to in-plane extension. It also determines the time scale of tension reduction in relaxation experiments. The model indicates that increased skin tension in-vivo generates conditions of increased hydrostatic and osmotic pressure, in particular in papillary and reticular dermis. The mechanical response to in-vivo suction experiments also depends strongly on the motion of the interstitial fluid. As depicted in figure 2(a) the maximum apex displacement increases with increasing permeability. The remaining apex displacement after one cycle, however, exhibits a non-monotonic relationship with the permeability. Both limiting cases of a very high and a very low permeability cause the residual apex displacement to vanish. This feature is enhanced for cyclic loading. As shown in figure 2(b), the residual apex displacement accumulates with each cycle, resulting in an overall creep-like behaviour. Analysis of extracellular fluid redistribution during suction experiments indicates that the dependence of the dissipative properties of skin on interstitial flow opens new possibilities for clinical applications. In fact, healthy skin, diseased skin as well as scars not only differ in their elastic but also in their dissipative properties, as results from their hindrance to interstitial fluid motion. Current investigations evaluate the possibility to characterize skin's viscoelasticity for an early diagnosis of fibrotic scar formation [7] or diseases (e.g. scleroderma [8]).

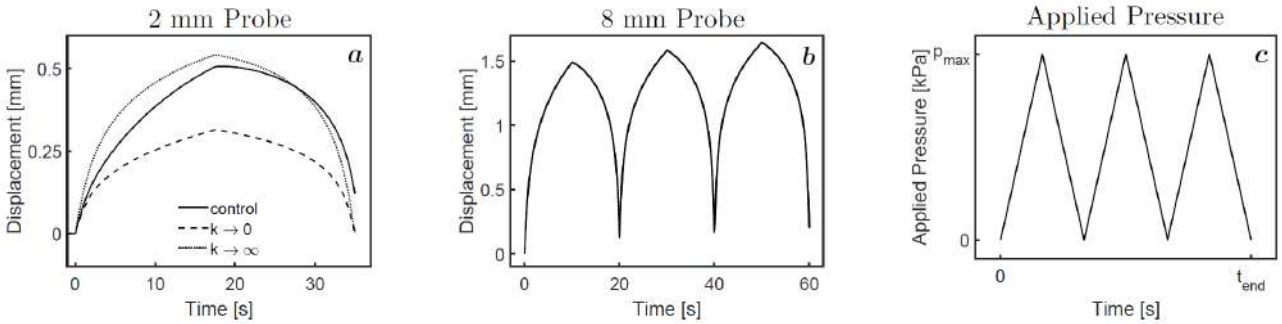

Figure 2. Suction response of human skin: Apex displacement for one cycle (a) and three consecutive cycles (b), the applied suction pressure is shown in (c).

CONCLUSIONS

The proposed multi-layered biphasic model of human skin contributes to a better understanding of the in-vivo as well as the ex-vivo response of human skin for various deformation modes. Thus, it represents a useful tool to investigate the clinical relevance of the assessment of specific mechanical properties of human skin. Future work will focus on the direct measurement of layer specific parameters including fixed charges density, permeability, hydration level, density and distribution of collagen fibres, as well as their variations in case of specific pathologies.

References

[1] Mollemans et al., Predicting soft tissue deformations for a maxillofacial surgery planning system: from computational strategies to a complete clinical validation. *Medical Imag. Analysis* ***11(3)***: 282 - 301, 2007.

[2] Buganza Tepole & Kuhl, Computational modeling of chemo-bio-mechanical coupling: a system biology approach toward wound healing, *Comp. Methods in Biomechanics and Biomedical Engineering* ***19***: 13 – 30, 2016.

[3] Wahlsten et al., On the compressibility and poroelasticity of human and murine skin, *Biomechanics and Modeling in Mechanobiology*. ***18***: 1079 – 1093, 2019.

[4] Pensalfini et al., Location-specific mechanical response and morphology of facial soft tissues, *Journal of the Mechanical Behavior of Biomedical Materials* ***78***: 108 – 115, 2018.

[5] Rubin & Bodner, A three-dimensional nonlinear model for dissipative response of soft tissue, *International Journal of Solids and Structures* ***39(19)***: 5081 – 5099, 2002.

[6] Ehlers et al., An extended biphasic model for charged hydrated tissues with application to the intervertebral disc, *Biomechanics and Modeling in Mechanobiology* ***8***: 233 – 251, 2009.

[7] Ehret et al., Inverse poroelasticity as a fundamental mechanism in biomechanics and mechanobiology, *Nature Communications* ***8***: 1002, 2017.

[8] Elrod et al., An effective procedure for skin stiffness measurement to improve Paediatric Burn Care, *Burns* ***45(5)***: 1102 - 1111, 2019.

[9] Muller et al., Investigative study on the ability of suction devices to detect skin involvement in patients with systemic sclerosis, *in preparation.*

NUMERICAL SIMULATION OF A TWO COMPARTMENTAL FRACTIONAL MODEL IN PHARMACOKINETICS AND PARAMETERS ESTIMATION

Yanli Qiao[1], Huanying Xu[1], and Haitao Qi*[1]
[1]School of Mathematics and Statistics, Shandong University, Weihai 264209, PR China

Summary Compartmental model is the most widely used approach to study the pharmacokinetics characterization of drug. Recently, fractional calculus is introduced to describe the time course of drugs in human body which follow the anomalous diffusion mechanism. To consider the different fractional order transmission process, the two compartmental fractional model has been proposed and studied. And, it will be of great significance to find out a simple and efficient numerical method to solve the model and estimate model parameters. This work investigates two numerical methods of the two compartmental fractional model using finite difference schemes, which are based on the shifted Grünwald-Letnikov approximate formula and $L1$ formula, respectively. The hybrid Nelder-Mead simplex search and particle swarm optimization, denoted as NMSS-PSO, is provided to estimate the fractional model parameters. Comparison between the numerical solutions and the solutions obtained by the numerical inverse Laplace transform establishes the validity of the developed numerical algorithms. Then, the influence of the order of fractional derivative on the drug amount in human body is also presented and discussed. Finally, the two compartmental fractional model is applied to fit the amiodarone pharmacokinetics data based on the NMSS-PSO algorithms. This work will be of importance for the development of fractional pharmacokinetics.

INTRODUCTION

Fractional calculus, which introduces integrals and derivatives of fractional order, has almost the same history as classical calculus. However, only in recent decades, fractional calculus becomes popular because of its successful applications in different fields, such as physics, electrochemistry, bioengineering and pharmacology [1, 2, 3, 4]. Now it is well known that fractional kinetics offers an elegant description of anomalous kinetics owing to its memory effect and the non-local property. So it is natural to adopt the theory of fractional calculus to improve compartmental analysis when modeling the uptake, distribution and elimination of drug in human body [5].

Compartmental analysis originated from the study of radioactive tracers and was used to simplify complex physiological systems. Now, fractional compartmental models have been proved to be useful and successfully applied to describing the absorption of drug in a living biological system. But with the development of fractional calculus in pharmacokinetics and other fields, a new problem how to analytically and numerically solve the fractional compartmental model appeared naturally. Unlike the integer differential equations, fractional differential equations with the specified initial conditions are difficult and even impossible to find their analytical solutions. Therefore, it is essential to build efficient numerical algorithms to solve these corresponding problems. Dokoumetzidis et al. applied the numerical inverse Laplace transform (NILT) method to solve the system they proposed [6], but the direct numerical simulation of the two compartmental fractional model was not considered in their studies. Based on the fact, we propose two numerical methods of the two compartmental fractional model by using the shifted GL approximate formula and $L1$ formula respectively and compare the numerical solutions with the semi-analytical solution by the NILT method. And we also know particle swarm optimization (PSO) is a random global optimization technology moving towards the best goal and the Nelder-Mead simplex search (NMSS) algorithm remove the worst. So we used the NMSS-PSO method to improve the accuracy of the parameter estimation. This method is proposed by Liu et al. and has been proven the effectiveness for the fractional dynamical models [7, 8, 9].

TWO COMPARTMENT FRACTIONAL MODEL

A two compartment fractional model in pharmacokinetics will be considered shown schematically in Fig. 1. Compartment 1 corresponds to general circulation and well perfused tissue while compartment 2 represents the target tissue. The system can be represented mathematically as [6, 5]:

$$\begin{aligned}\frac{\mathrm{d}q_1(t)}{\mathrm{d}t} &= -k_{10}\ {}_0^C D_t^{1-\alpha_{10}} q_1(t) - k_{12}\ {}_0^C D_t^{1-\alpha_{12}} q_1(t) + k_{21}\ {}_0^C D_t^{1-\alpha_{21}} q_2(t) + u_1(t),\\ \frac{\mathrm{d}q_2(t)}{\mathrm{d}t} &= -k_{20}\ {}_0^C D_t^{1-\alpha_{20}} q_2(t) - k_{21}\ {}_0^C D_t^{1-\alpha_{21}} q_2(t) + k_{12}\ {}_0^C D_t^{1-\alpha_{12}} q_1(t) + u_2(t),\end{aligned} \tag{1}$$

where $0 < \alpha_{ij} \leq 1$ and $q_i(t)$ is the mass of drug in the compartment i. k_{ij} represents the rate of elimination, distribution and uptake from compartment i to compartment j and has a dimension of $[\mathrm{time}]^{-\alpha_{ij}}$. $u_i(t)$ is the infusion rate in compartment i, which has a dimension of $[\mathrm{mass/time}]$ and may be zero, constants or time dependent. Initial value for $q_1(t)$ and $q_2(t)$ can be considered $q_1(0) = d$, $q_2(0) = 0$, respectively. For this non-zero initial conditions, we can convert it to a zero initial value problem by variable substitution ($q_1^*(t) = q_1(t) - q_1(0)$) and then solve it numerically by means of the relationship of Caputo derivative and GL derivative.

*Corresponding author. Tel./Fax: +86 631 5687309.

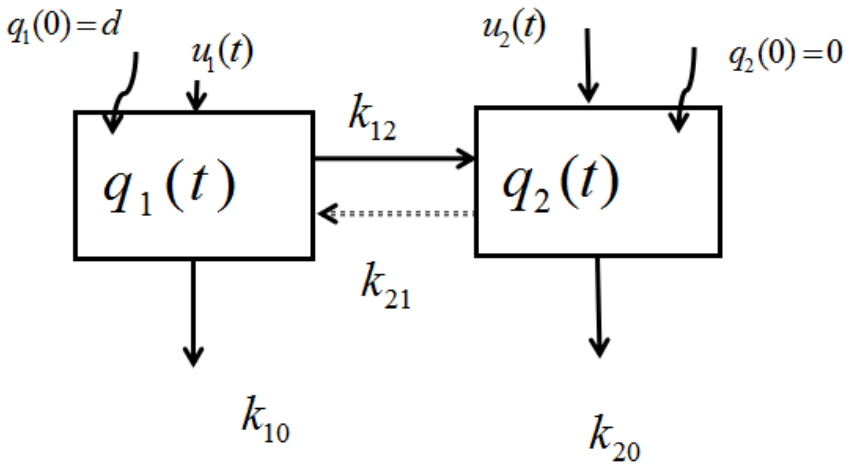

Figure 1: Schematic representation of a fractional two compartmental model. k_{ij} are constants that represent the rate of mass transfer from compartment i to compartment j , k_{i0} are elimination rates from compartment i and $u_i(t)$ denote infusion rates .

In this paper, we focus mainly on the following model including several processes of drug release in the body. One is the elimination from compartment 1, one is the distribution from compartment 1 to compartment 2 and the rest is the mass flux from compartment 2 to compartment 1. The first two processes are assumed to follow classic kinetics, while the last one is supposed to follow fractional kinetics. The system can be expressed in the following form

$$\begin{aligned} \frac{\mathrm{d}q_1(t)}{\mathrm{d}t} &= -(k_{12}+k_{10})\, q_1(t) + k_{21}\, {}_0^C D_t^{1-\alpha} q_2(t) + u_1(t), \\ \frac{\mathrm{d}q_2(t)}{\mathrm{d}t} &= k_{12}\, q_1(t) - k_{21}\, {}_0^C D_t^{1-\alpha} q_2(t), \end{aligned} \tag{2}$$

where $q_1(0) = d,\ q_2(0) = 0$ are initial conditions of the model. In this paper, we pay attention to the following two important cases of Eq. (2).

CONCLUSION

In this work, we consider the numerical simulation and parameters estimation of a two compartmental fractional model with different initial conditions, which consider the different transmission processes in pharmacokinetics. The finite difference algorithms based on the shifted GL approximate formula and the $L1$ formula of the Caputo derivative respectively are proposed. Meanwhile, we use the NMSS-PSO algorithm to achieve the parameters estimation and obtain the results we expected. Furthermore, we compare the numerical solutions with the semi-analytical solution and amiodarone data. The results indicate that two numerical methods are effective and available. And the influence of the order of fractional derivative on the drug amount in human body is also presented and discussed. The results show that the drug amounts of the compartment 1 resemble the power-law distribution and the amounts of compartment 2 fall more quickly with α increasing.

References

[1] Rudolf H. Applications of fractional calculus in physics. Singapore: River Edge, World Scientific, NJ 2000.
[2] Oldham KB. Fractional differential equations in electrochemistry. Adv Eng Softw. 41: 9-12, 2010.
[3] Magin RL. Fractional calculus in bioengineering. Redding: Begell House. 269-355, 2006.
[4] Băleanu D, Lopes AM. Handbook of Fractional Calculus with Applications. De Gruyter 2019.
[5] Sopasakis P, Sarimveis H, Macheras P, Dokoumetzidis A. Fractional calculus in pharmacokinetics. J Pharmacokinet Pharmacodyn. 45(1): 107-125, 2018.
[6] Dokoumetzidis A, Magin R, Macheras P. Fractional kinetics in multi-compartmental systems. J Pharmacokine Pharmacodyn. 37(5): 507-524, 2010.
[7] Liu F, Burrage K. Novel techniques in parameter estimation for fractional dynamical models arising from biological systems. Comput Math Appl, 62(3): 822-833, 2011.
[8] Liu F, Burrage K, Hamilton NA. Some novel techniques of parameter estimation for dynamical models in biological systems. Ima J Appl Math. 78(2): 235-260, 2013.
[9] Fan W, Liu F, Jiang X, Turner I. Some novel numerical techniques for an inverse problem of the multi-term time fractional partial differential equation. J Comput Appl Math, 336: 114-126. 2018.

A MULTISCALE MICROSTRUCTURAL APPROACH OF CROSS-LINK INTERACTION IN THE HUMAN CORNEA

Anna Pandolfi*[1], Alessio Gizzi[2], and Marcello Vasta[3]
[1]Department of Civil and Environmental Engineering, Politecnico di Milano, Milano, Italy
[2]Department of Engineering, University of Rome Campus Bio-Medico, Rome, Italy
[3]Dipartimento INGEO, Universit Chieti-Pescara, Viale Pindaro 42, Pescara, Italy

Summary We propose a multiscale micromechanical model of the collagen reinforcement of the human cornea. We focus on the structural function of the collagen lamellae embedded in the stroma and construct a structure made of collagen fibrils and transversal chemical bonds (crosslinks). The specific design chosen for describing inter-crosslink and intra-crosslink bonds relies on the fact that the cornea's ability to carry loads depends on the density and strength of crosslinks that confer intrinsic transversal and shear stiffness to the lamellae. We conduct an extensive numerical analysis of the mechanical response under the action of the intraocular pressure of the system, varying multiple mechanical properties of the structure. Our approach shows that the weakening of transversal crosslinks is associated with a marked increase of the deformability of the system, typically observed in keratoconus corneas.

INTRODUCTION

Cornea Biomechanics & Keratoconus

The cornea, the external lens of the eyeball, sustains the intraocular pressure (IOP) exerted by the filling fluids. From a structural viewpoint, the cornea is a spherical shell made of many parallel layers reinforced with collagen fibrils to accomplish a load carrying function. The preservation of a stable spherical shape is due to the complex architecture of the collagen fibrils, embedded in a homogeneous matrix of proteoglycans and elastin, and of transversal chemical bonds that confer the necessary stiffness to the stucture. The central part of the cornea shows a typical fibril arrangement with nasal-temporal (NT) and superior-inferior (SI) patterns whereas a circumferential and radial organization is observed along the limbus, i.e. the outer part [1].

Keratoconus is a progressive disorder of the cornea that alters dramatically its shape [2]: irregular astigmatism, strong myopia and a marked loss of vision usually occur. Macroscopically, keratoconic corneas present a non-physiological conical shape, with abrupt changes of curvature, and degenerative and irreversible changes in the organization of the collagen architecture have been documented. Albeit the aetiology of keratoconus has not been clarified yet, the particular microstructure of the stroma in keratoconus suggests that a weakening of the chemical bonds (cross-link) appears between the collagen fibrils [3].

Object of study

We aim at developing a physically based model of keratoconus that can potentially account for its onset and progression. In particular, we propose a structural model of the stroma collagen microstructure in the human cornea. The model consists of a trusswork including the two sets of fibrils and the associated cross-links.

MICROMECHANICAL MODEL OF STROMAL COLLAGEN

The microstructural model of the collagen reinforcement was constructed from patient-specific cornea geometry and the trusswork was directly derived from the finite-element discretization [4, 5, 6, 7]. The micromechanical architecture of the collagen fibrils was also constructed on the basis of the well-known ex vivo X-ray data [1] disregarding the variability of such structures across the thickness. The model accounts for five sets of trusses. The first two sets (F1 and F2) describe the collagen fibrils. The two sets are separated by a small amount corresponding to the cornea thickness, and the chosen discretization allows one to define the topology of a hexahedron which is considered as the basic unit cell (see Fig. 1(a)). The third and fourth networks, parallel to F1 and F2, model the inter-fibril connections (inter-cross-links C1 and C2) that allow the fibrils to organize themselves in parallel sheets (lamellae). They are designed as trusses connecting the fibrils of the same network with non-parallel side links. The fifth network (C12) describes the intra-fibrils connections (intra-cross-links) between the two sets of fibrils. These trusses connect the fibrils of the anterior and the posterior lamellae along sub-diagonal directions to provide mechanical stability of the system. A coarse structure of the cornea is shown in Fig. 1(b) to understand the connections.

The fine structural model used in the static calculations, $\mathbf{KU} = \mathbf{F}$, is shown in Fig. 1(c). Here, $\mathbf{K}$ is the stiffness matrix, $\mathbf{U}$ the unknown displacement array and $\mathbf{F}$ is the external load array that collects the point loads with IOP. Adopting the linearized truss theory, we consider an equivalent rigidity parameter $D_i = E_i A_i$, with E_i the Young modulus and A_i the cross section area, such that the truss stiffness is $k_i = D_i/h_i$.

Numerical simulations are conducted with an in-house software developed specifically for this study. The trusswork includes 48 sub-parallel fibrils for each set, 5000 nodal points and 28 600 trusses.

*Corresponding author. E-mail: ictam2020@aimgroup.eu.

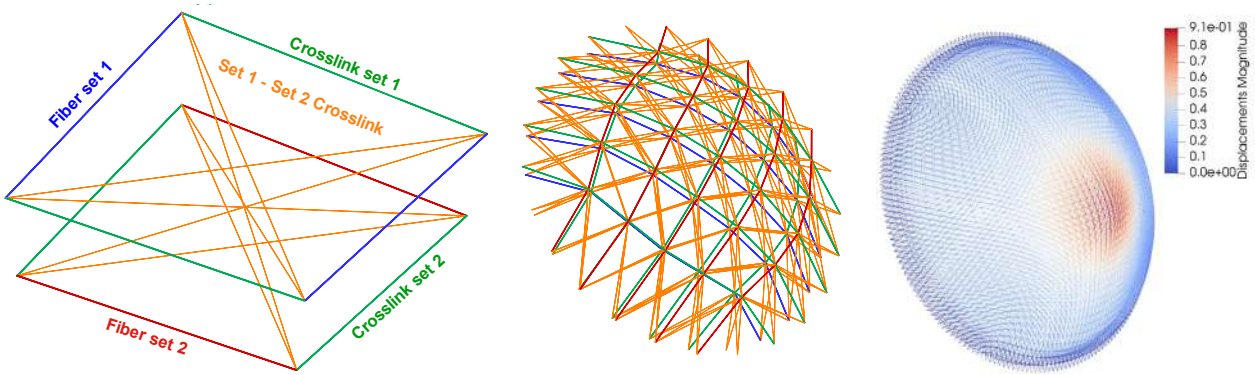

(a) (b) (c)

Figure 1: (a) Detail of the cross-links between the fibrils of the same set (inter-link, green) and of two different sets (intra-link orange). (b) Coarse model of the assembled trusswork including all fibril and cross-link trusses. (c) Example of output of the numerical calculations. Colours map the displacement field, for the cases of keratoconus cornea.

RESULTS

The stiffness of trusses representative of the fibrils was estimated as an equivalent measure derived by homogenizing the contribution of the fibrils over a reference area. In particular, we estimated the equivalent rigidity of a fibril truss as $D_F = E_f A_f = 0.009N$. The stiffness of the trusses representative of the intermolecular covalent cross-links that connect fibrils of the same or different families was estimated on the basis of experimental data. The stiffness of the components of the trusswork was finally normalized with respect to the stiffness of the fibril truss, obtaining the values $D_{F1} = D_{F2} = 1, D_{C1} = D_{C2} = 0.8, D_{C12} = 0.5$.

With such a model we simulate the structural response of healthy and keratokonic corneas. In the case of a healthy cornea, we assign a uniform rigidity to all the elements of the same set. To model keratoconus, we make the assumption that the stiffness of both fibrils and cross-links reduces smoothly in the radial direction from the limbus, where it reaches its maximum value, to the centre of the conus, where it reaches its minimum value. To reach such a distribution, we consider three functional forms of material stiffness variation: linear, quadratic and cubic, respectively.

Numerical simulations show that the smooth reduction of stiffness of the components allows one to model the protrusion of keratoconus.

We further conducted an intense programme of factorial experiments considering the variation of the stiffness of each group of components of the network (fibrils F_1 and F_2, inter-cross-link C_1 and C_2, and intra-cross-link C_{12}). The study includes 28 764 analyses. Numerical results reveal that, as far as the conical shape is concerned, the most influential parameter is the stiffness of the intra-cross-link stiffness C_{12}. The reduction of the stiffness of the fibrils without a corresponding reduction of the intra-cross-link stiffness does not lead to a conical shape. Moreover, a reduction of the inter-cross-link stiffness does not lead to any significant modification of the spherical shape.

CONCLUSIONS AND PERSPECTIVES

This study achieved two goals: (i) to understand the importance of the explicit description of the cross-links in a microstructural model of the human cornea; (ii) to identify the components of the network whose failure is connected to the bulging and keratoconus. In the future, we will improve the purely microstructural model accounting for the actual causes (chemical, mechanical and inflammatory) that trigger the disease.

References

[1] Meek K. M., Boote C. The use of X-ray scattering techniques to quantify the orientation and distribution of collagen in the corneal stroma. *Prog. Retin. Eye Res.* **28**, 369–392, 2009.

[2] Ambekar R., Toussaint K. C., Johnson A. W. The effect of keratoconus on the structural mechanical, and optical properties of the cornea. *J. Mech. Behav. Med. Biomater.* **4**, 223–236, 2011.

[3] Daxer A., Fratzl P. Collagen fibril orientation in the human corneal stroma and its implication in keratoconus. *Invest. Ophthalmol. Vis. Sci.* **38**, 121–129, 1997.

[4] Pandolfi A., Manganiello F. A material model for the human cornea. *Biomech. Model. Mechanobiol.* **5**: 237–246, 2006.

[5] Pandolfi A., Holzapfel G. A. Three-dimensional modelling and computational analysis of the human cornea considering distributed collagen fiber orientation. *J. Biomech. Eng.* **130**, 061006, 2008.

[6] Simonini I., Pandolfi A. Customized finite element modelling of the human cornea. *PLoS ONE* **10**, e0130426, 2015.

[7] Montanino A., Gizzi A., Vasta M., Pandolfi A. Modeling the biomechanics of the human cornea accounting for local variations of the collagen fibril architecture. *Z. Angew. Math. Mech.* **98**: 2122–2134, 2018.

[8] Pandolfi A., Gizzi A., Vasta M. A microstructural model of cross-link interaction between collagen fibrils in the human cornea. *Phil. Trans. R. Soc. A.* **377**: 20180079, 2019.

A BIOINSPIRED MECHANICAL MODEL OF THE ULTRASONIC CLICKS PRODUCED BY ERMINE MOTHS

Hernaldo Mendoza-Nava[1], Alberto Pirrera[1], Marc Holderied[2], and Rainer Groh *[1]
[1]Bristol Composites Institute (ACCIS), University of Bristol, Bristol, UK
[2]School of Biological Sciences, University of Bristol, Bristol, UK

Summary A recently discovered sound production system (Aeroelastic Tymbal) located at the base of the hindwings of ermine moths produces bursts of ultrasonic clicks. The sound is produced when a ridge area on the aeroelastic tymbal buckles. The resultant sound has similar characteristics to that produced by the tiger moth, which in a certain genus is capable of jamming a bat biosonar. The biomechanical function of the aeroelastic tymbal is idealised by a simplified one-dimensional compliant mechanism, and the stability of the structure is evaluated using the modified Riks method. The purpose of this research is to take inspiration from evolved biological structures found in insects, for the development of adaptive and well-behaved non-linear structures.

A tymbal organ, which is a well known sound production system found in cicadas [1], and also present in different moth species [1, 2], allows the production of sounds for social communication or defence purposes. A moth's tymbal organ consists of a cuticular membrane typically located at the tegula, thorax (muscular actuated tymbals) or wings (aeroelastic tymbal), and produces a high-frequency clicking sound when it buckles. Also, the tymbal's membrane can present a striated band on one side, leading to the production of bursts of ultrasonic clicks when buckled. It has previously been observed that ermine moths (*Yponomeuta*) continuously produce two sets of ultrasonic clicks while flying, and such sound production occurs during the rotational stages of the stroke cycle [3]. Furthermore, it is suggested that this species mimics the sound produced by toxic tiger moths; thus, warning their predators (bats) of potential danger. Experimental approaches such as the use of high-speed cameras have provided evidence on how a tymbal organ buckles [4]. However, far too little attention has been paid to the structural mechanics associated with such phenomena. An objective of this study is to investigate the aeroelastic tymbal actuation mechanism among ermine moths. The function is modelled using a one-dimensional compliant mechanism, analysed using the finite element method. This project provides an important opportunity to explore the feasibility of bio-inspired adaptive or morphing structures.

The aeroelastic tymbal is distinguished as a clear patch (due to the absence of scales) at the base of the hindwing (Figure 1A), located between the cubital (Cu) and postcubital (pCu) veins. A micro-computed tomography (micro-CT) shown in Figure 1B indicates the venation and parts of the aeroelastic tymbal. Individual ridges forming the striated band alongside the pCu vein are referred to as "microtymbals", the rest of the translucent patch is called the "window". Throughout the pCu axis, the membrane is folded through a steep angle, and this region is called the "wall". A set of micromanipulators on an ablated hindwing, and a bat detector (to detect ultrasound signals), allowed the identification of two conditions for the sound production. Folding and unfolding the crease along the pCu vein axis was found as the triggering mechanism. Both, the initial and buckled states are shown in Figure 1C, and the latter is characterised by the birefringence of the wing's membrane.

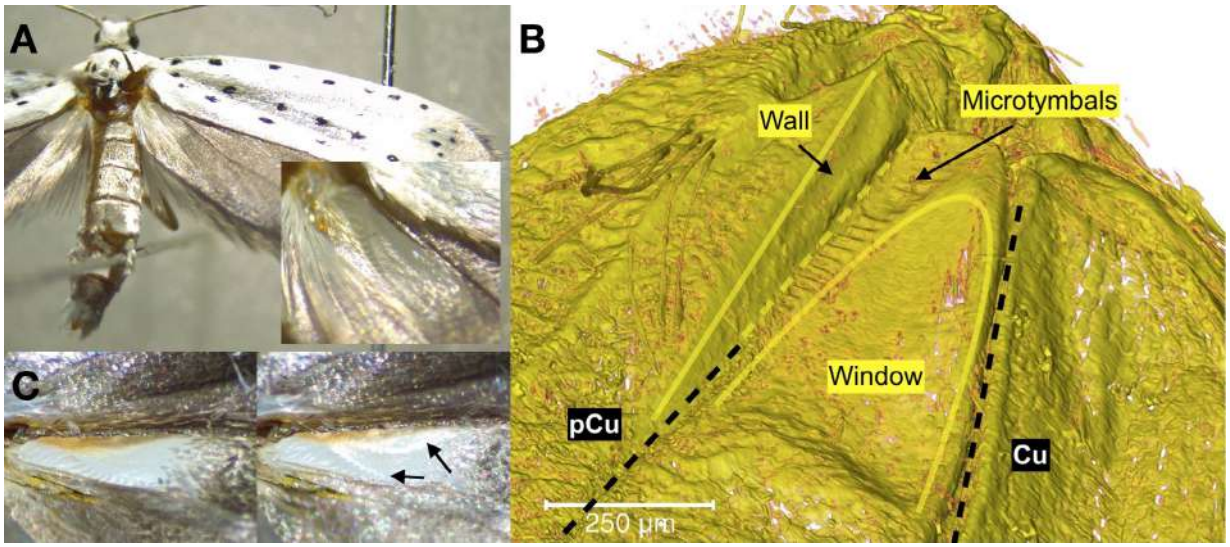

Figure 1: A. Ermine moth (*Y. malinellus*), with an enlarged image of the aeroelastic tymbal. B. Dorsal view of a micro-CT of the base of the hindwing (the yellow dotted line along the pCu indicates a folding region, also known as the claval furrow). C. Initial and buckled states of the aeroelastic tymbal (birefringance is indicated).

*Corresponding author. E-mail: rainer.groh@bristol.ac.uk.

From the micro-CT it can be observed that the tymbal is not a flat structure but a doubly curved membrane. The membrane's thickness was found to be less at the interface between the microtymbals and the window. Inspired from how the aeroelastic tymbal works, a simplified approach is undertaken. Taking a chordwise cross-section of the tymbal, the system can be represented by a curved compliant mechanism (Figure 2A). The stability response is then evaluated using the modified Riks method in the Abaqus commercial software package. Three design parameters (w_t/w_w: tymbal-to-window width ratio, t_t/t_{int}: tymbal-to-interface thickness ratio and the κ: tymbal's curvature), and the material properties (E: modulus of elasticity and v: Poisson's ratio) are considered, while the structure is simply actuated by a transverse force at the flexure hinge. Assuming the boundary condition (BC) at the Cu vein position is clamped and the BC at the pCu is simply-supported, the t_t/t_{int} ratio is the parameter driving the stability of the structure; which can be tuned to obtain a bistable or monostable behaviour. Assuming an even tymbal thickness, and a width ratio bounded to the tymbal-to-window dimensions, the tymbal response is characterised in terms of the thickness ratio. As a result, the Force-Displacement diagram in Figure 2B demonstrates that when a critical thickness value (t_{crit}) is achieved, the system behaves as a bistable structure.

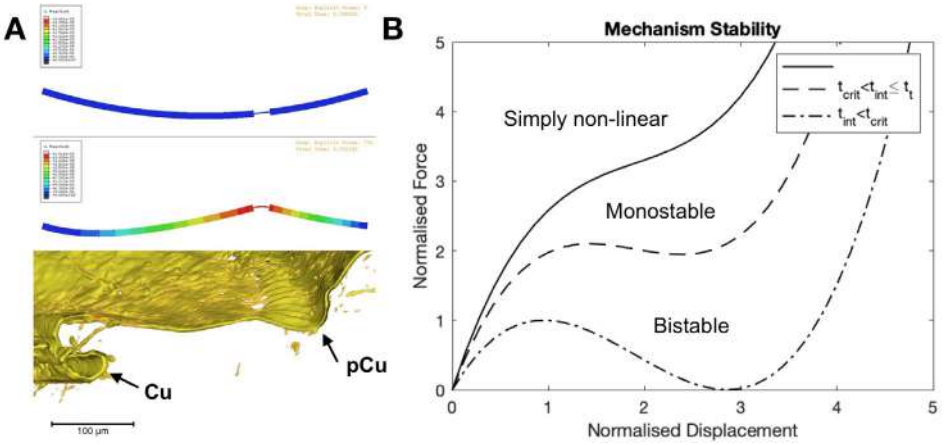

Figure 2: A. Compliant mechanism model taken from a cross-section of the aeroelastic tymbal. B. Force-displacement diagram of the stability behaviour of the compliant mechanism.

To gain insight into the acoustic response, a modal analysis is performed to obtain the fundamental frequency of the structure. This value can be tuned by modifying the elastic modulus to match the peak frequency obtained in acoustic recordings. The κ parameter determines the depth of the mechanism, controlling the maximum deflection attained from the initial to the secondary stable position. The transverse deflection of the structure is averaged and together with the resonant frequency, the sound pressure level can be calculated from a closed-form structural-acoustic model such as the baffled-piston [5], assuming the window as the sound radiator. However, this is only a representative result as the actual dynamic and acoustic response are influenced by the tymbal membrane's mass and the combined spanwise and chordwise constraints; added to the consideration that the baffled-piston model is a non conservative approach as it assumes an infinite baffle boundary.

CONCLUSIONS

The function of the aeroelastic tymbal was studied experimentally. Taking inspiration from this system, a curved compliant mechanism from a chordwise cross-section was designed. The stability, dynamics and acoustics of the one-dimensional structure were approached successfully to the extent of the assumptions. Further studies are undergoing on the design of a 2D shell structure to better address the function of the aeroelastic tymbal. This would improve the understading of the structural and acoustic response towards the design of larger scale adaptive structures.

Acknowledgements: Financial support by the Science and Technology National Council (CONACYT - Mexico, CVU/Studentship No. 530777/472285) is gratefully acknowledged. This research is funded by the Engineering and Physical Sciences Research Council through the EPSRC Centre for Doctoral Training in Advanced Composites for Innovation and Science (grant number EP/L0160208/1) and supported by the Royal Academy of Engineering under the Research Fellowship scheme (grant no. RF/201718/17178) and the UK Engineering and Physical Sciences Research Council (grant no. EP/M013170/1).This work was carried out using the computational facilities of the Advanced Computing Research Centre, University of Bristol (http://www.bristol.ac.uk/acrc/).

References

[1] J. W. S. Pringle. A physiological analysis of cicada song. *JEB*, 31(4):525560, 1954.
[2] W.E. Conner. un chant dappel amoureux: acoustic communication in moths. *JEB*, 202(13):17111723, 1999.
[3] Liam J. OReilly, David J. L. Agassiz, Thomas R. Neil, and Marc W. Holderied. Deaf moths employ acoustic müllerian mimicry against bats using wingbeat-powered tymbals. *Sci. Rep.*, 9(1):1444, 2019.
[4] Jesse R. Barber and William E. Conner. Acoustic mimicry in a predator-prey interaction. *PNAS*, 104(22):93319334, 2007.
[5] Lawrence E. Kinsler, Austin R. Frey, Alan B. Coppens, and James V. Sanders. Fundamentals of acoustics. Wiley, 4th edition, 2000.

FINITE ELEMENT ANALYSIS OF PERCUTANEOUS CORONARY INTERVENTION

Kiran Manjunatha*[1], Jan Frischkorn[2], and Stefanie Reese[1]
[1]Institute of Applied Mechanics, RWTH Aachen University, Aachen, Germany
[2]Volkswagen AG, Wolfsburg, Germany

Summary The aim of this work is to develop a computationally efficient simulation framework for percutaneous coronary intervention. In this regard, efficient finite element formulations to model filigree structures are investigated. Additionally, constitutive modeling of arterial wall is considered. Building upon the work presented here, models for plaque build up as well as vascular smooth muscle cell aggregation shall be arrived at.

INTRODUCTION

Constriction of the blood vessels in the heart arise due to plaque build up, which is a condition termed as atherosclerosis. Percutaneous coronary intervention (PCI) is a process of placing structures called stents within these constricted blood vessels to normalize the blood flow. The damage ensued in the vessel walls during PCI results in progressive narrowing of blood vessels due to an inflammatory response, the condition being termed in-stent restenosis. The overarching goal of this work is to setup a computationally efficient finite element framework to simulate PCI and thereby assist selection of stent materials and geometries, predict tissue damage during pre- and/or post-dilation and stent deployment, and finally arrive at optimal PCI conditions that reduce the risk of in-stent restenosis. Within the intended simulation framework, two important aspects are considered here: (a) Efficient modeling of stent deformation (b) Arterial wall and plaque mechanics.

EFFICIENT MODELING OF STENT DEFORMATION

Commercial stent configurations comprise of filigree constructions which render the three-dimensional finite element simulations of PCI computationally expensive due to the factors described in [1]. Additionally, the presence of multiple layers within the stent cross-sections (e.g. drug-eluting polymer layer, gold reinforce- ment layer for welds etc.) exacerbates the computational costs. The solid-beam finite element formulation (Q1STb) [1], serves as an efficient tool for simulating slender strut geometries of stents, while still inheriting the ease of handling contact interactions. However, the current focus will be on modeling drug-eluting stents, which possess a layer of drug-carrier vehicle on top of the metallic core of the struts. In this regard, to model the stent deployment mechanics, the solid-beam elements are to be used for the metallic core and the reduced integration hexahedrons (Q1SP), described in [2], shall be utilized for the drug-eluting polymeric layer. A critical section of a drug-eluting stent which repeats itself throughout the structure, is chosen for our investigations. Cross-section with just the metal core as well as that including the polymer layer are investigated under the boundary conditions shown below. Within the cross-section ($k-l-m-n$), the metal core is considered to be 0.8 mm wide and the polymer layer to be 0.08 mm thick. The sum of reaction forces at the point of application of displacement D is investigated and presented.
Abbreviations: NQT = number of quadrature points on the trasnverse plane at the center of beam axis, NEL = number of elements longitudinally along the radius, NET = number of elements across the thickness.

Table 1: Material parameters

Layer	Material model	E	ν	σ_y	H
Metal core	elasto-plasticity with linear isotropic hardening	200 GPa	0.3	370 MPa	7 GPa
Polymer	Neo-Hooke	1 GPa	0.49	-	-

It is observed that with just one element across both the layers, results comparable to those using fine discretizations of the strut with C3D8I and C3D8R elements (ABAQUS) are obtained.

ARTERIAL WALL AND PLAQUE MECHANICS

The arterial wall shall be simulated using a combination of the anisotropic hyperelastic models presented in [3] and [4], thereby considering dispersion of collagen fiber orientations as well as accurate incorporation of slight compressibility of soft tissues. The optical parameters required for the model shall be obtained from histological data via automated image processing techniques. The mechanical material parameters shall hence be fit to experimental data post fixation of optical parameters.

*Corresponding author. E-mail: manjunatha@ifam.rwth-aachen.de

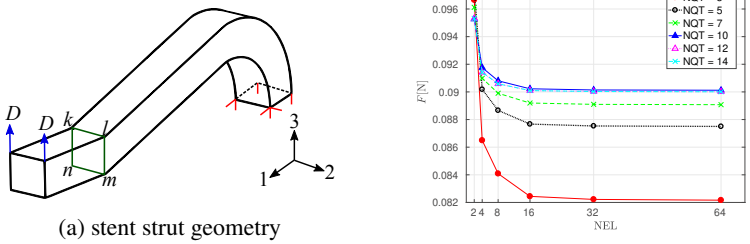

(a) stent strut geometry

(b) NEL convergence

Figure 1: bare-metal strut

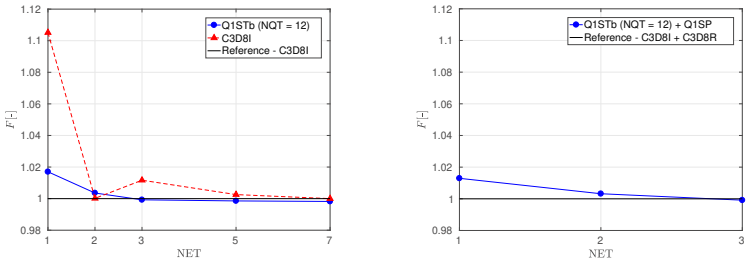

(a) bare-metal

(b) multi-layer

Figure 2: NET convergence

Uniaxial tensile tests were conducted in ABAQUS, using user material subroutines, on an arterial wall specimen with various collagen orientations γ and different degrees of dispersion κ, the results of which are shown below.

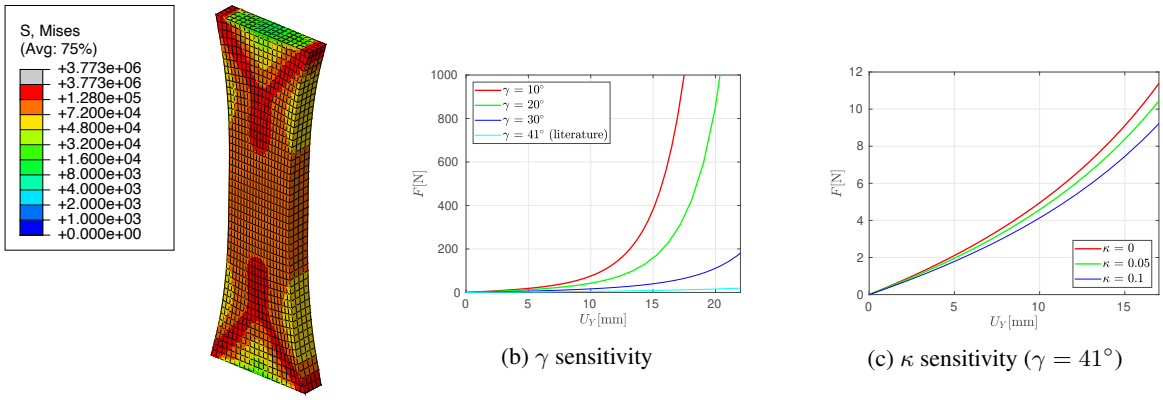

(a) von Mises stress

(b) γ sensitivity

(c) κ sensitivity ($\gamma = 41°$)

Figure 3: uniaxial tension tests on an arterial wall specimen

CONCLUSIONS

With minimal element count, stent structures are deemed to be characterized using the Q1STb and Q1SP elements. The arterial wall behaviour is highly sensitive to the collagen orientations and hence have to be accurately determined from histological data. Future work shall entail modeling of plaque growth modeling and vascular smooth muscle cell proliferetion.

References

[1] Frischkorn, J. and Reese, S. A solid-beam finite element and non-linear constitutive modelling. *Comput. Methods Appl. Mech. Engrg.* (2013) **265**:195-212.

[2] Reese, S. On a physically stabilized one point finite element formulation for three-dimensional finite elasto- plasticity. *Comput. Methods Appl. Mech. Engrg.* (2005) **194**:4685-4715.

[3] Gasser, T.C., Ogden, R.W. and Holzapfel, G.A. Hyperelastic modelling of arterial layers with distributed collagen fibre orientations. *J. R. Soc. Interface.* (2006) **3**:15-35.

[4] Nolan, D.R., Gower, A.L., Destrade, M., Ogden, R.W. and McGarry, J.P. A robust anisotropic hyperelastic formulation for the modelling of soft tissue. *Journal of the Mechanical Behaviour of Biomedical Materials.* (2014) **39**:48-60.

POROELASTIC PROPERTIES OF BIOLOGICAL TISSUES CHARACTERIZED USING AN IMPROVED INDENTATION THEORY FOR LARGE RELAXATION

Tian Jian Lu*[1,2], Ming Wang[3,4], Shaobao Liu[1,2], Zhimin Xu[5], Kai Qu[3,6], Moxiao Li[3,5], Qing Xue[3,5], Guy M. Genin[3,4,7], Feng Xu[3,4]
[1]State Key Laboratory of Mechanics and Control of Mechanical Structures, Nanjing University of Aeronautics and Astronautics, Nanjing 210016, P.R. China
[2]Nanjing Center for Multifunctional Lightweight Materials and Structures, Nanjing University of Aeronautics and Astronautics, Nanjing 21006, P.R. China
[3]The Key Laboratory of Biomedical Information Engineering of Ministry of Education,
School of Life Science and Technology, Xi'an Jiaotong University, Shaanxi, 710049, P.R. China
[4]Bioinspired Engineering & Biomechanics Center (BEBC), Xi'an Jiaotong University, Xi'an 710049, P.R. China
[5]State Key Laboratory for Strength and Vibration of Mechanical Structures, School of Aerospace, Xi'an Jiaotong University, Xi'an 710049, P.R. China
[6]Department of Hepatobiliary Surgery, The First Affiliated Hospital of Xi'an Jiaotong University, Xi'an 710061, China
[7]National Science Foundation Science and Technology Center for Engineering Mechanobiology, Washington University, St. Louis, MO 63130, USA

Summary Resistance of porous scaffold to fluid flow within biological tissues causes a size- and rate-dependent material behavior known as poroelasticity. Indentation has been widely used to characterize the poroelasticity of soft materials and a variety of theoretical models have been well established for cases of small strain and modest force relaxation. However, when the force on the indenter at a fixed depth at long-time scale drops to below half of the initially peak force (*i.e.*, $F(0)/F(\infty) > 2$), the existing models are inapplicable for large relaxation. For such cases of large relaxation, we built upon the Biot theory and the Hertz contact theory to develop an indentation theory by considering fluid flow in biological tissues during both the indentation and relaxation periods of an indentation test. We performed indentation tests for representative biological tissues (e.g., porcine liver, spleen, kidney, skin, apple, and human cirrhosis liver), and demonstrated that the proposed theory is suitable for biological tissues exhibiting both small and large relaxations.

INTRODUCTION

Biological tissues are mostly porous materials, where their poroelastic properties are associated with physiological functions and many diseases. Characterizing poroelasticity can provide insight into a great variety of physiological functions, and has been applied to pathological study and disease diagnosis in clinic. Indentation combined with theoretical analysis is often used to characterize the poroelasticity of soft materials [1-3]. However, existing theoretical models are typically established by neglecting liquid transport as induced by deformation during indentation process, which may be not suitable when force relaxation is substantial. For example, recent studies have reported negative Poisson ratios in hydrogels [4] when the force relaxes to below half of the peak indentation force. Therefore, there is still an unmet need for a more effective indentation method by considering fluid-flow-induced deformation during the indentation process for biological tissues with large relaxation.

MATERIALS AND METHODS

Large relaxation indentation theory

We developed an indentation theory by considering fluid flow during both the indentation and relaxation processes by combining the Biot theory [5, 6] with the Hertz contact theory. We considered the asymmetrical, small strain, large displacement problem of indentation in a semi-infinite space (**Fig. 1A**), and obtained:

$$F(t)=\begin{cases} F_{Hertz}(u(t),R)\left(\dfrac{1}{1-Aexp\left(-\dfrac{t}{\tau_p}\right)}\right), -t_0 \le t \le 0 \\ F_{Hertz}(\delta_{max},R)\left(\dfrac{1}{1-A\,exp\left(-\dfrac{t}{\tau_p}\right)}\right), t>0 \end{cases}$$

where $A \approx \exp(-t_0/\tau_p)$ is a coefficient that quantifies the effect of solvent diffusion during indentation ($-t_0 \le t \le 0$) on subsequent force relaxation ($t > 0$), and F_{Hertz} is the force for a displacement δ_{max} predicted for linear elasticity

*Corresponding author. E-mail: tjlu@nuaa.edu.cn.

by the Hertz contact model, and τ_p is the poroelastic relaxation time-scale. The force required to indent a poroelastic material increases with indentation depth, but decreases with solvent flowing away from the compressed region. Thereafter, as the indenter is held isometrically, the force needed to hold the indenter at a fixed depth relaxes over time with continued solvent flow (**Fig. 1A**), which can be well predicted by our model (**Fig. 1B**).

Indentation testing

Indentation experiments were performed on a Bose ElectroForce 3220 (Bose Corporation, Framingham, MA). Before performing displacement control tests, the indenter tip was first adjusted to a position slightly above the surface, and then proceeded with indentation to a fixed depth δ at a speed of 0.5 mm/s. The indenter was held isometrically for a time interval sufficient to enable relaxation, and the applied force on the indenter was recorded in the real time. Through fitting the measured indentation relaxation curve with the proposed theoretical model, we characterized the poroelastic properties of several biological tissues, specifically the shear modulus, the Poisson ratio, and the diffusion coefficient. Specifically, we performed indentation tests for porcine liver, spleen, kidney, skin, apple and human cirrhosis liver tissues, respectively.

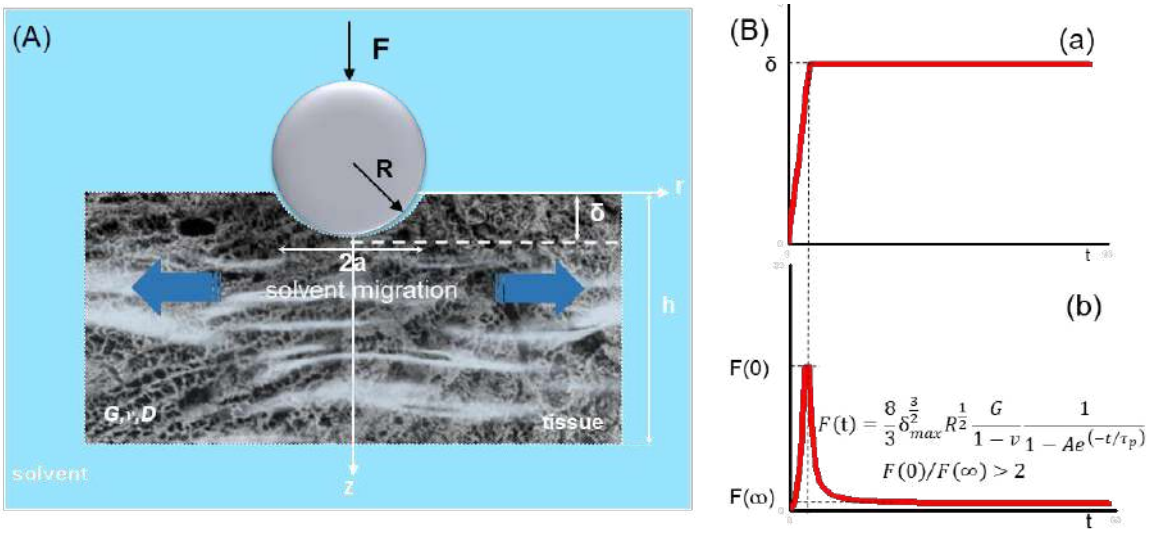

Figure 1. Indentation theory and test of biological tissue. (A) Asymmetrical problem of indentation in a semi-infinite space and cylindrical coordinates selected for theoretical modeling. The parameters G, ν and D are the Poisson ratio, shear modulus and diffusion coefficient of the biological tissue, respectively; a is the contact radius between the indenter and the tissue. (B) Force response of a poroelastic tissue in an indentation test. (a) The indenter is pressed into a liver tissue from zero to a fixed depth δ. (b) The solvent in tissue migrates, and the force on indenter in the indentation process is plotted as a function of time. $F(0)$, $F(\infty)$ are the maximal and minimum force on indenter during the relaxation process. δ_{max} is the maximal pressed displacement during the indentation. A is a modified coefficient, which reflects the liquid flow during the pressing process. $\tau_p = a^2/D$ is the poroelastic relaxation time-scale.

CONCLUSIONS

We proposed a method based on the modified spherical indentation model to characterize the poroelastic properties of biological tissues undergoing large relaxation by accounting for the effects of fluid flow in the tissue during loading. We demonstrated that this method is appropriate not only for biological tissues with small relaxation but also biological tissues with relaxation in large range ($1.6 < \frac{F(0)}{F(\infty)} < 3.9$). The modified theory provides substantially better estimates of Poisson ratio for cases of large relaxation in comparison with those estimated with existing models, while predicting diffusion coefficients and shear moduli on the order of existing results.

References

[1] Mow V.C., M.H. Holmes, W.M. Lai. Fluid transport and mechanical properties of articular cartilage: a review. *J. Biomech.* **17**(5): 377-394, 1984.
[2] Simon B.R. Multiphase poroelastic finite element models for soft tissue structures. *Appl. Mech. Rev.* **45**(6): 191-218, 1992.
[3] Cowin S.C. Bone poroelasticity. *J. Biomech.* **32**(3): 217-238, 1999.
[4] Wang Q.-M., et al. Separating viscoelasticity and poroelasticity of gels with different length and time scales. *Acta Mech. Sin.* **30**(1): 20-27, 2014.
[5] Biot M.A. General theory of three-dimensional consolidation. *J. Appl. Mech.* **12**(2): 155-164, 1941.
[6] Mow V.C., et al. Biphasic creep and stress relaxation of articular cartilage in compression? Theory and experiments. *J. Biomech. Eng.* **102**(1): 73-84, 1980.

O108014 - SM01 - Biomechanics and Biomaterials - Oral

A SNAP-THROUGH INSTABILITY GOVERNS THE ADHESION OF CELLSUNDER HYDROSTATIC PRESSURE

Shaobao Liu[1,2,3#], Haiqian Yang[1,3#], Guang-Kui Xu[4#], Ru Tao[2,3], Meng Wang[2,3], Rongyan He[2,3], Guy M. Genin[2,3,5], Tian Jian Lu[1], Feng Xu[*2,3]

[1]State Key Laboratory of Mechanics and Control of Mechanical Structures,Nanjing University o fAeronautics and Astronautics, Nanjing 210016, P.R.China

[2]The Key Laboratory of Biomedical Information Engineering of Ministry of Education, School of Life Science and Technology, Xi'an Jiaotong University, Xi'an 710049, P.R. China

[3]Bioinspired Engineering & Biomechanics Center (BEBC), Xi'an Jiaotong University, Shaanxi, 710049, P.R. China

[4]International Center for Applied Mechanics, State Key Laboratory for Strength and Vibration of Mechanical Structures, School of Aerospace, Xi'an Jiaotong University, Xi'an 710049, P.R. China

[5]National Science Foundation Science and Technology Center for Engineering Mechanobiology, Washington University, St. Louis, MO 63130, USA

#Authors contributed equally

Summary In this work, we hypothesized that the high hydrostatic pressure of the tumor environment can contribute to cell metastasis, and therefore studied the balance between responses to hydrostatic pressure and adhesion. To elucidate the critical points in this balance, we developed and validated a theoretical model to describe the change of morphology and volume of adherent cells under hydrostatic pressure. Cell morphologies exhibited bistability under hydrostatic pressure in the physiological range for relatively low adhesion energy density. Importantly, we found a snap-through instability under small adhesion energy density and intermediate hydrostatic pressure. The snap-through instability of adhesive cells suggests a potential mechanism by which elevated pressure within a tumor can contribute to cancer metastasis.

INTRODUCTION

In many cancers, the progression from Stage I to Stages II and III involves cells spontaneously losing of adhesion from the bulk of a tumor and migrating to new tissues, a process known as metastasis. The balance between hydrostatic pressure and adhesions governs the morphology and volume of animal cells, which strongly influences various cell behaviors, such as cancer metastasis. To elucidate the critical points in this balance, we developed and validated a theoretical model to describe the change of morphology and volume of adherent cells under hydrostatic pressure.

MATERIALS AND METHODS

Theoretical model. The snap-through behavior related to the morphological and volume change of adherent cells under hydrostatic pressure (Fig. 1) can be predicted by

$$p_{out}^{*}=f(\theta_0)\left[\frac{(1+\cos\theta_0)^{\frac{1}{2}}}{[\Gamma^{*}+(1-\sigma_a^{*})(1-\cos\theta_0)]}+\pi_{out}^{*}\right]\left[1+\left(\frac{\Gamma^{*}}{1-\cos\theta_0}+\sigma_a^{*}\right)\right]^{3}(1+\cos\theta_0)^{-3/2} \quad (1)$$

where $f(\theta_0)=(8+9\cos\theta_0-\cos 3\theta_0)/12$.

Cell culture under hydrostatic pressure. Human lung cancer cells (CL1-5) were cultured on a culture dish at a density of 10,000 cells/cm^2. After incubation for 24 h, CL1-5 cells were loaded with hydrostatic pressure of 0, 1, 2, 4, or 8 kPa above atmospheric pressure for 8 hours, and interval sufficient for a steady state in height and volume to be reached.

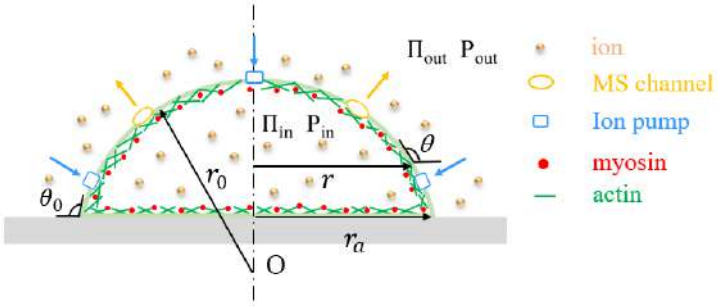

Figure 1 Schematic of the theoretical model:The adherent cell is enclosed by the actomyosin cortical layer and cell membrane

*Corresponding author. E-mail: fengxu@mail.xjtu.edu.cn

THEMATIC SESSION SM

RESULTS

The model predicted that the equilibrium contact angle decreases with the hydrostatic pressure, which may undergo a snap-through instability (Fig. 2). In this snap-through, cells suddenly jump up from the substratum in response to increasing hydrostatic pressure or down to the substratum in response to decreasing hydrostatic pressure. As the adhesion energy density decreases, this snap-through of contact angle is possible over a larger range of pressures.

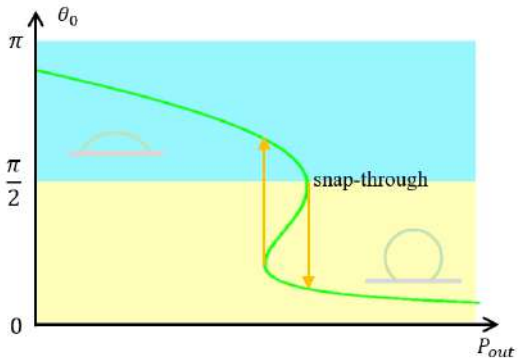

Figure 2 Snap-through instability of an adherent cell under hydrostatic

To further explore this instability phenomenon, we draw a phase diagram of normalized hydrostatic pressure and dimensionless adhesion energy density. This phase diagram revealed three different regions of cell adhesion, with a bistable region sandwiched between acute and obtuse contact angles.

DISCUSSION

We have many cures for many cancers, but, from the perspective of chemistry and genetics, nearly all cancers are different, and many remain untreatable. However, from the perspective of mechanobiology, a cure is possible. Death from cancer most often occurs not from a primary tumor, but from metastasis. From the mechanical view, metastasis could be interpreted as instability, where small changes of input lead to disastrous outcomes. Here, we demonstrate that how hydrostatic pressure could be the governing parameters inducing this instability. These findings provide new insights in controlling metastasis.

References

[1] Hui T.H., Zhou Z.L., Qian J., Lin Y., Ngan A.H.W. & Gao H. Volumetric deformation of live cells induced by pressure-activated cross-membrane ion transport. Phys. Rev. Lett., 113(11): 118101, 2014.
[2] Xie K., Yang Y., Jiang H. Controlling Cellular Volume via Mechanical and Physical Properties of Substrate. Biophy. J., 114(3): 675-687, 2018.

DETERMINING AND COMPARING THE TIMESCALES GOVERNING SINGLE CELL EVOLUTION

Alberto V. Ippolito*[1], Antonio DeSimone[2,3], Vikram S. Deshpande[1]
[1]Department of Engineering, Cambridge University, Cambridge CB2 1PZ, UK (ai318@cam.ac.uk)
[2]SISSA – International School for Advanced Studies, Trieste, Trieste, Italy
[3]The BioRobotics Institute, Scuola Superiore Sant'Anna, Pontedera, Pisa, Italy

Summary The aim of this theoretical work is to compare the timescales of the evolution of a range of observables of single adherent cells and to elucidate and explain the physical phenomena that set the different evolution rates in single cells. We report the response of myofibroblasts adhering to micropatterned substrates with varying widths of fibronectin stripes. These investigations are performed with a novel computational model, an overdamped Langevin equation, derived from the homeostatic ensemble. The study demonstrates two distinct timescales governing cell expansion and elongation. Additionally, we predict that confinement severely changes the evolution rates of cell observables. Remarkably, our investigation reveals that these biological timescales are primarily driven by the landscape of the cell free-energy hypersurface.

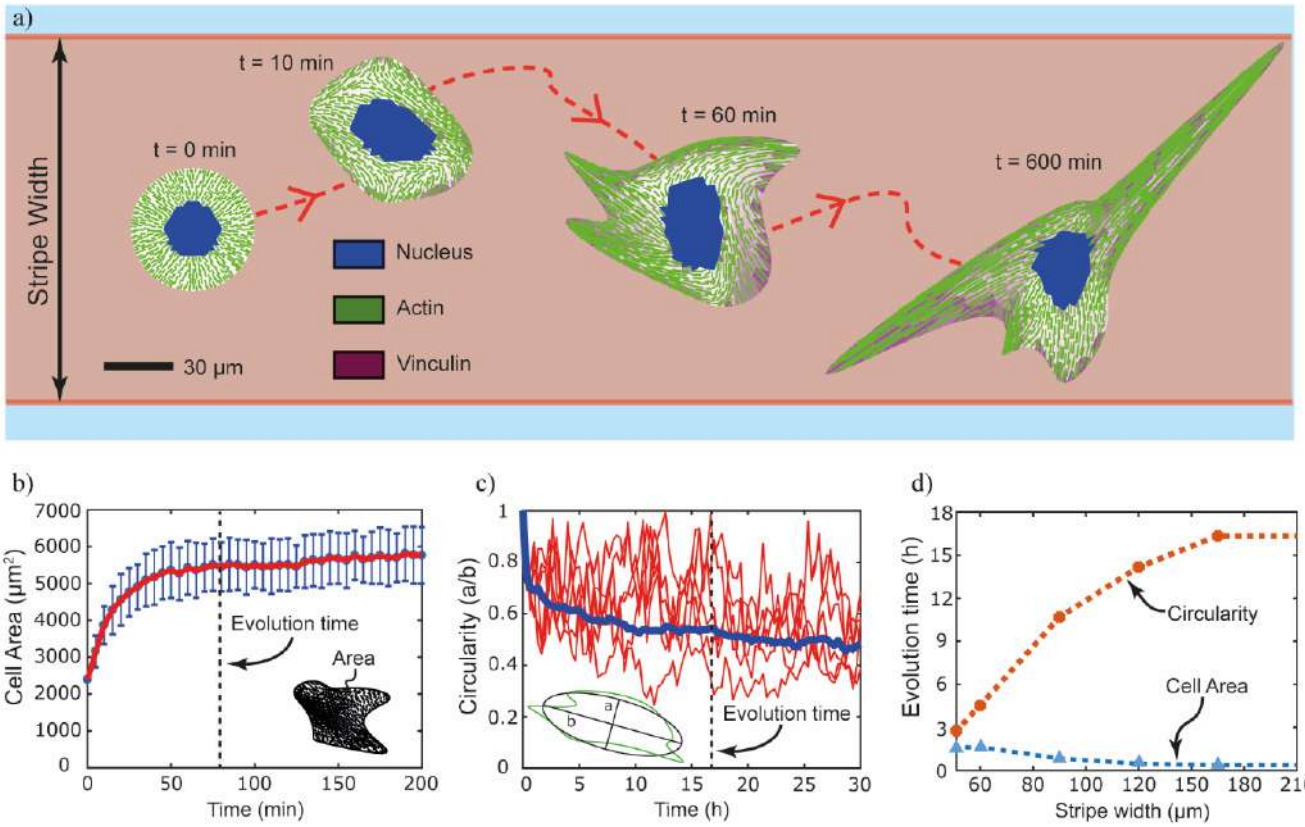

Fig. 1. Cell expansion and elongation on a patterned substrate. (a) Snapshot showing the temporal evolution of a fibroblast seeded from suspension on a fibronectin stripe of width 180 μm wide. In the early stages (t < 60 min), the cell expands and begins forming mature focal adhesions, as shown by the increase in vinculin density, but still does not form large protrusions. After several hours, the fibroblast becomes very elongated with large protrusions, several mature focal adhesions and long actin strands. **(b)** Temporal evolution of cell spread area on a wide adhesive stripe. The red line shows the average spread area measured from all simulations, while the variations over the $n = 100$ simulations are shown in blue. The evolution time of fibroblast area is taken to be 1.5 h. **(c)** Temporal evolution of cell circularity on a wide adhesive stripe. Blue line is the average behavior ($n = 100$) while each red line is the circularity variation for selected fibroblasts. The evolution time is 17 h. **(d)** The evolution times of cell area and circularity as a function of stripe width. As the stripe width reduces below 180 μm, the evolution time of the circularity decreases rapidly while the evolution time of the cell area increases slightly.

INTRODUCTION

Timescales and morphological transformations are critical in understanding living systems. For instance, during fetal development, the size and morphology of the embryo changes dramatically, also due to each organ forming and maturing at a different timescale. In fact, the brain forms at an earlier stage, but matures much later, than the fingers [1].

*Corresponding author. E-mail:ai318@cam.ac.uk

Since this very complex and fundamental process is characterized by vastly different timescales, it is sensible to think that the simpler evolutions of geometric observables of single cell spreading also may not occur concurrently. While the timescales of the evolution of some observables for single cells, such as expansion and elongation, have been reported in literature [2, 3] and are vastly different, the reason behind these timescale differences remains elusive. The aim of this theoretical work is to compare the timescales of the evolution of a range of observables of single adherent cells and to elucidate and explain the physical phenomena that set the different timescales in single cells. We report results for the response of single cells on substrates micropatterned with varying widths of fibronectin stripes.

METHODOLOGY

The evolution of single adherent cells on micropatterened fibronectin stripes is performed using a novel computational model: an overdamped Langevin equation derived from the homeostatic ensemble [4]. Briefly, the model describes the time evolution of the variables r_i, describing the shape of the cell, and is given by:

$$33333333333333333\dot{r}_i(t) = -\frac{1}{\gamma}\frac{\partial G}{\partial r_i} + \sqrt{\frac{2}{\zeta\gamma}}W(t), \tag{1}$$

where t is time, γ is the damping coefficient, G is the Gibbs free-energy of the configuration, $1/\zeta$ the homeostatic temperature [4] of the cell and $W(t)$ a Weiner process. The cell parameters are those of myofibroblasts [5], but the same study can be easily repeated for any cell type. A span-shot of the prediction of a simulated fibroblast in suspension seeded on a substrate patterned with a fibronectin stripe is shown in **Fig. 1a**.

RESULTS

- The simulations correctly demonstrate that, on an unpatterned substrate, cell area evolves with a much faster timescale than cell circularity, as shown in **Figs 1b and 1c** and also demonstrated in literature [2, 3] for fibroblasts.
- Our simulations suggest that confinement heavily influences the morphological evolution of single fibroblasts, see **Fig. 1d.** However, these changes only occur for stripe widths below 180 μm.
- Stripe widths smaller than 180 μm reduce the circularity evolution time, from 18h for 180 μm to about 3h for 60 μm, while only slightly increasing the evolution timescale of cell area; see **Fig. 1d.**

CONCLUSIONS

The study confirms that there are different timescales governing the evolution of single fibroblasts on a given substrate. The nature of the theoretical model used in this work, i.e. the overdamped Langevin equation based on the homeostatic ensemble [4], is such that the evolution of the cell is governed by energetic and entropic driving forces while maintaining a state of overall homeostasis. The analysis suggests that the evolution times of the morphological observables are dominated by the landscape of the of cell free-energy hypersurface. In particular, the gradients of the free-energy cause the fibroblast evolution path to choose a rapid initial cell spreading prior to the onset of cell elongation, i.e. a faster increase in cell area followed by a slower decrease in cell circularity. Confining the cell introduces barriers in the free-energy landscape which change the gradients of the free-energy, ultimately affecting the evolution path of the cell by enhancing the elongation rates while simultaneously reducing the rate of cell expansion.

References

[1] Bhattacharya, Niranjan, and Phillip G. Stubblefield, eds. *Human Fetal Growth and Development: First and Second Trimesters*. Springer, 2016.
[2] Greiner, Alexandra M., et al. "Cyclic tensile strain controls cell shape and directs actin stress fiber formation and focal adhesion alignment in spreading cells." *PloS one* 8.10 (2013): e77328.Nygus G. Numerical Analysis Using Finite Element Method. *PhD Thesis*, NTU Mech. Eng. Dept., Lagos, 1983.
[3] Kesavan, S. Vinjimore, et al. "High-throughput monitoring of major cell functions by means of lensfree video microscopy." *Scientific reports* 4 (2014): 5942.
[4] Shishvan, S. S., A. Vigliotti, and V. S. Deshpande. "The homeostatic ensemble for cells." *Biomechanics and modeling in mechanobiology* 17.6 (2018): 1631-16.
[5] Buskermolen, Antonetta BC, et al. "Entropic forces drive cellular contact guidance." Biophysical journal 116.10 (2019): 1994-2008.

PLANT CELL WALL GROWTH: FROM SOLID CONTINUUM MODEL TO MIXTURE THEORY MODEL

Ruoyu Huang*[1], Adib Becker[2] and Arthur Jones [2]
[1]Lightweight Manufacturing Centre (NMIS), Department of Design, Manufacturing and Engineering Management, University of Strathclyde, Glasgow, UK
[2]Department of Mechanical, Materials and Manufacturing Engineering, University of Nottingham, Nottingham, UK

Summary Plant cell wall growth has served as an interesting and important question inspiring, challenging and justifying different methodologies of growth modelling. In this work, a thorough study has been conducted to model the plant cell wall growth using both the single-phase solid continuum model and mixture theory model with fluid phase transporting through solid skeleton in typical direction taken into account. The present study not only established the integrative growth model to cover extensive features of cell wall growth in a consistent framework, but also deepen the understanding about the advantages and disadvantages of the different typical modelling methodologies.

INTRODUCTION

The very astonishing fact of growing plant cell is that the cell wall is living under high turgor pressure which may be up to five times higher than atmosphere (5 bars). The life of cell wall under pressure refers to a central question in plant developmental biology, i.e. whether and how mechanical forces serve as cues for cellular behavior and thereby regulate growth. (Hamant *et al*. 2008). For cells enclosed by a cell wall, growth is dependent on deposition of new wall materials driven by fluid transport coupled with turgor pressure to drive expansion of the cell in the longitudinal direction. Neither deposition of new wall materials nor turgor driven expansion is in itself sufficient to promote growth. Therefore, the well-known Lockart's equations stated that the growth of cell wall follows the rules in a parallel way as follows

$$r_g = \Phi(P - Y) \tag{1}$$

and

$$r_g = L_c \Delta\Psi \,, \tag{2}$$

where r_g is the (volumetric) growth strain rate which is either positive for $P > Y$ or zero for $P \le Y$, Φ is the extensibility of the cell wall, P is the turgor pressure and Y is the yield threshold, i.e. the minimum pressure required for growth, L_c is water conductance coefficient, and $\Delta\Psi$ is the water potential difference between protoplast and apoplast (Schopfer, 2006). The Lockart equations (1) and (2) indicates that the role of mechanics in cell wall growth can be subdivided into two intertwined parts: the role of stresses in the solid skeleton of cell wall and the role of fluid transport through the void space of cell wall.

Interestingly, it is noted that there are two key different methodologies to modelling growth, i.e. single-phase solid continuum model and mixture theory (see e.g. Taber (1995)). At the first glance, the mixture theory may naturally represent the aforementioned features of cell wall growth. However, it must need sufficient theoretical and numerical studies for understanding the advantages and disadvantages of the different typical modelling methodologies.

SINGLE PHASE CONTINUUM MODELLING

The typical single-phase continuum is proposed based on the decomposition of the total deformation gradient into two parts, i.e. the growth part and non-growth part. The growth part in principle is not subjected to geometric compatibility constraint which in finite strain theory can be represented by satisfying the vanishing condition of curvature tensor on a Riemannian manifold (so it is not the gradient of deformation). Thus, this part may be considered as the counterpart of plastic deformation gradient in plasticity theory. The growth part will follow a growth law which is mainly driven by stress, strain or energy with temperature effects. Unlike plasticity theory where the stress tensor plays a key role in the anisotropy of plastic deformation, most of the existing growth model has been focused on the anisotropy of materials, which did not reflect the bioscientists' hypothesis about anisotropic growth that there are the different growth mechanisms in the different directions. Our work presented the method to model the anisotropic growth by using the anisotropy of stress, which showed the good consistency with cell wall features where growth in wall thickness direction and wall longitudinal direction following the different laws as indicated in the Introduction. The non-growth part plays the role to piece together those incompatible local configurations of growth together for retaining the

*Corresponding author. E-mail: Ruoyu.huang@strath.ac.uk.

compatibility of the whole configuration. Based on this consideration, the finite strain fibre-reinforced viscoelasto-viscoplasticity-like growth models have been proposed to implement in Finite Element (FE) analysis is present work. Three components of the deformation of growing cell wall, i.e. elasticity, viscoelasticity, and viscoplasticity-like growth, are modelled within a consistent framework aiming to present an integrative growth model. The two key features of cell wall growth, i.e. turgor-driven creep and new material deposition, and the interplay between them are shown to be modelled by the typical concepts in solid continuum theory like yield function, flow rule, and hardening law.

MIXTURE MODEL

On the other hand, a cell wall growth model based on mixture theory has been established to be consistent with the Lockhart eqns. (1) and (2). To the authors' knowledge, it is the first time that the Lockhart eqns. (1) and (2) together are generalised to a 3D model. First, the kinematics and elasto-plastic decomposition are discussed. Secondly, governing equations including equilibrium equation, balance of mass, and inequality of entropy are presented. Thirdly, the elastic and inelastic responses of the mixture are proposed in a thermodynamics-consistent way and the crucial mechanisms of transport of new wall material in fluid are discussed. Numerical result of case studies with comparison with experimental data are shown to verify the model.

COMPARISON AND DISCUSSIONS

Above all, the present work demonstrated and verified that both single-phase continuum model and mixture theory model could cover the key features of the cell wall growth. However, for addressing the deposition of the new material on the surface of cell wall, the single component model of an open system may involve complicated higher order formulation which is not straightforward to implement in numerical study since the modified Cauchy stress and higher order derivative of displacement may cause the numerical difficulties for the convergence of solution. There are still some great challenges for the single component model to take into account mechanisms which in essence involves transport in a fluid. On the other hand, although it may describe the physical phenomena and underlying mechanisms in a more natural way, the general framework of growth modelling based on mixture theory itself still has some inherent open questions needed to be sorted out.

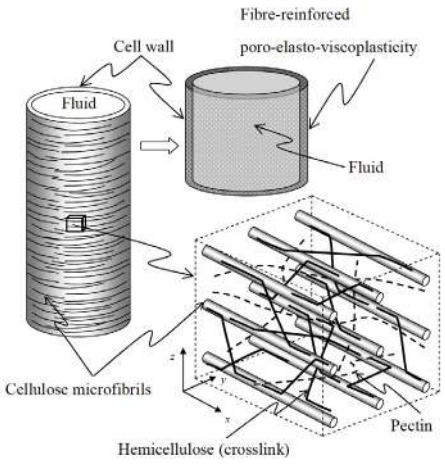

Figure 1. The hierarchy structure of cell wall.

CONCLUSIONS

By modelling the plant cell wall growth, the present work demonstrated and compared the effectiveness and limitations of the two key growth modelling methodologies: single-phase continuum model and mixture theory model. Both the key achievements and existing key challenges are discussed for inspiring the future work.

References

[1] Hamant, O., Heisler, M.G., Jönsson, H., Krupinski, P., Uyttewaal, M., Bokov, P., Corson, F., Sahlin, P., Boudaoud, A., Meyerowitz, E.M., Couder, Y., Traas J. Developmental patterning by mechanical signals in Arabidopsis, *Science* **322**: 1650-1655, 2008.
[2] Schopfer, P. Biomechanics of plant growth. *American Journal of Botany* **93**: 1415-1425, 2006.
[3] Taber, L.A. Biomechanics of growth, remodelling, and morphogenesis. *Appl Mech Rev* **48**: 488-545, 1995.

MORPHOELASTICITY OF LARGE BENDING DEFORMATIONS OF CELL SHEETS DURING DEVELOPMENT

Pierre A. Haas* and Raymond E. Goldstein†
Department of Applied Mathematics and Theoretical Physics, University of Cambridge, Cambridge, UK

Summary Deformations of cell sheets during morphogenesis are driven by developmental processes such as cell division and cell shape changes. In morphoelastic theories of development, these processes appear as variations of the intrinsic geometry of a thin elastic shell. However, morphogenesis often involves large bending deformations that are outside the formal range of validity of these shell theories. Here, by asymptotic expansion of three-dimensional incompressible morphoelasticity in the limit of a thin shell, we derive a shell theory for large intrinsic bending deformations and emphasise the elastic role of cell constriction. Taking the inversion of the green alga *Volvox* as a model developmental event, we reveal how the results of this model differ from those of a simpler shell theory which is not formally valid for large bending deformations.

BACKGROUND

During animal and plant development, cell division, cell shape changes, and related processes can drive deformations of cell sheets [1]. In elastic continuum theories of the development of the green alga *Volvox* [2, 3], tissue folding in *Drosophila* [4], or more general active surfaces [5], these driving processes appear as changes of the reference or intrinsic geometry of thin elastic shells. The elastic theories describing these shells have often been posited *ad hoc* in previous work, by replacing the elastic strains of classical shell theories [6] with measures of the difference of the intrinsic and deformed geometries of the shell. They therefore lack a formal derivation by asymptotic expansion of three-dimensional elasticity or *morphoelasticity* [7], the framework based on a multiplicative decomposition of the deformation gradient tensor into intrinsic and elastic deformations.

There is however one more serious limitation of these models: tissues in development undergo large bending deformations (Fig. 1) that are outside the formal range of validity of the thin shell theories underlying previous models. In particular, even if the ratio of the thickness of the cell sheet to its radius of curvature is small in the initial, undeformed state, the local value of this ratio may not be small in the deformed configuration. This is associated with cells contracting at one cell pole to splay and thereby bend the cell sheet (Fig. 1). Here, we derive a shell theory valid for these large bending deformations by asymptotic expansion of three-dimensional morphoelasticity.

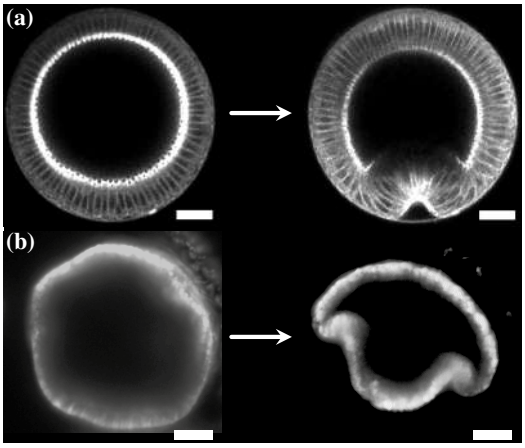

Figure 1: Large bending deformations during morphogenesis: even if the thickness of the cell sheet is small compared to the undeformed radius of curvature, it need not remain small compared to the local radius of curvature as the sheet deforms. (a) Cross section of ventral furrow formation in *Drosophila*, reproduced from Ref. [8]. (b) Midsagittal cross section of invagination in the spherical alga *Volvox globator*, reproduced from Ref. [3]. Scale bars: 20 µm.

ELASTIC MODEL

We consider an axisymmetric elastic shell of thickness h, made of an incompressible neo-Hookean material of elastic modulus E. (The restriction to axisymmetric shells avoids a bog of tensorial notation that arises in the general case.) The geometry of the undeformed shell is described by its arclength s and distance $r(s)$ from the axis of symmetry [Fig. 2(a)]. In the deformed configuration of the shell [Fig. 2(b)], arclength is $\tilde{s}(s)$, distance from the axis of symmetry is $\tilde{r}(s)$, and the tangent angle to the shell is $\tilde{\psi}(s)$. These quantities define the (meridional and circumferential) stretches and curvatures

$$f_s = \frac{\mathrm{d}\tilde{s}}{\mathrm{d}s}, \qquad f_\phi = \frac{\tilde{r}(s)}{r(s)}, \qquad \kappa_s = \frac{\mathrm{d}\tilde{\psi}}{\mathrm{d}\tilde{s}}, \qquad \kappa_\phi = \frac{\sin\tilde{\psi}(s)}{\tilde{r}(s)}.$$

The stretches relate the undeformed and deformed configurations of the shell. These stretches and curvatures differ in general from the intrinsic stretches f_s^0, f_ϕ^0 and intrinsic curvatures $\kappa_s^0, \kappa_\phi^0$ set by the underlying biological processes, such as cell shape changes. Deviations of the actual stretches and curvatures from their intrinsic values lead to elastic stresses.

We expand the three-dimensional elastic energy of the shell in its small thickness h. Large bending deformations are introduced by allowing $h\kappa_s^0$ to be an $O(1)$ quantity. After a long calculation, we find the leading-order expression for the elastic energy in the shell limit,

$$\mathcal{E} = \frac{\pi E}{6}\int \Big\{ h\left[\alpha_{ss}E_s^2 + (\alpha_{s\phi}+\alpha_{\phi s})E_sE_\phi + \alpha_{\phi\phi}E_\phi^2\right] + 2h^2\left[\beta_{ss}E_sK_s + \beta_{s\phi}E_sK_\phi + \beta_{\phi s}E_\phi K_s + \beta_{\phi\phi}E_\phi K_\phi\right] + h^3\left[\gamma_{ss}K_s^2 + (\gamma_{s\phi}+\gamma_{\phi s})K_sK_\phi + \gamma_{\phi\phi}K_\phi^2\right]\Big\}\,\mathrm{d}s, \qquad (*)$$

*P.A.Haas@damtp.cam.ac.uk; current address: Mathematical Institute, University of Oxford, Oxford, UK
†R.E.Goldstein@damtp.cam.ac.uk

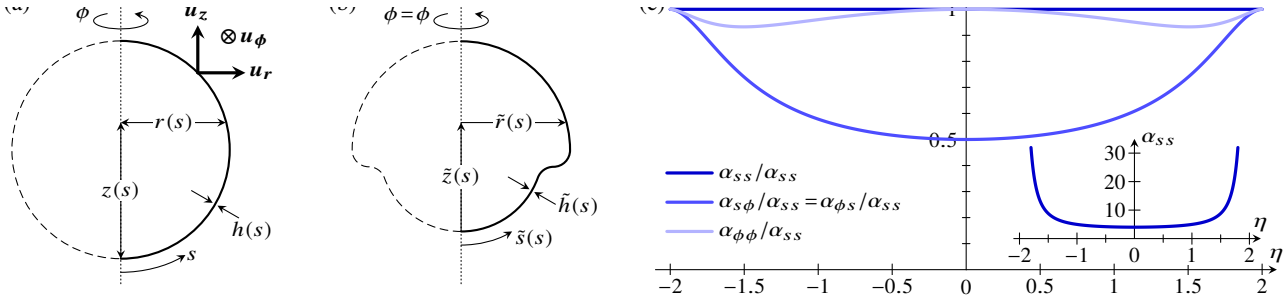

Figure 2: Elastic model: geometric setup and plot of some of the coefficient functions in Eq. (∗). (a) Undeformed geometry of an axisymmetric shell of thickness h, described by coordinates $r(s), z(s)$, where s is arclength, with respect to the basis $\{\boldsymbol{u_r}, \boldsymbol{u_\phi}, \boldsymbol{u_z}\}$ of cylindrical polars. (b) Deformed geometry of the shell: after a torsionless deformation, the shell has arclength $\tilde{s}$, and is described by coordinates $\tilde{r}(s), \tilde{z}(s)$ with respect to cylindrical polars. (c) Plot of the stretching coefficients $\alpha_{ss}, \alpha_{s\phi}, \alpha_{\phi s}, \alpha_{\phi\phi}$, scaled with α_{ss} to absorb the divergence as $\eta \to \pm 2$. Inset: unscaled plot of α_{ss} against η, showing divergence as $\eta \to \pm 2$.

wherein the shell strains and curvature strains are defined to be

$$E_s = \frac{f_s - f_s^0}{f_s^0}, \qquad E_\phi = \frac{f_\phi - f_\phi^0}{f_\phi^0}, \qquad K_s = \frac{f_s \kappa_s - f_s^0 \kappa_s^0}{\left(f_s^0\right)^2 f_\phi^0}, \qquad K_\phi = \frac{f_\phi \kappa_\phi - f_\phi^0 \kappa_\phi^0}{f_s^0 \left(f_\phi^0\right)^2},$$

and where the coefficients $\alpha_{ss}, \alpha_{s\phi} = \alpha_{\phi s}, \alpha_{\phi\phi}, \beta_{ss}, \beta_{s\phi}, \beta_{\phi s}, \beta_{\phi\phi}, \gamma_{ss}, \gamma_{s\phi} = \gamma_{\phi s}, \gamma_{\phi\phi}$ are functions of $\eta = h\kappa_s^0 / f_s^0 f_\phi^0$ only. We have obtained explicit expressions for these coefficients; the stretching coefficients $\alpha_{ss}, \alpha_{s\phi} = \alpha_{\phi s}, \alpha_{\phi\phi}$, for example, are plotted in Fig. 2(c). In the limit of small bending deformations, $\eta \to 0$, these coefficient functions limit to their well-known values from classical shell theories [6], $\alpha_{ss} = 2\alpha_{s\phi} = 2\alpha_{\phi s} = \alpha_{\phi\phi} = 1$, $\beta_{ss} = \beta_{s\phi} = \beta_{\phi s} = \beta_{\phi\phi} = 0$, $\gamma_{ss} = 2\gamma_{s_\phi} = 2\gamma_{\phi s} = \gamma_{\phi\phi} = 1/12$. For non-zero η, the values of the coefficients differ from their values in this small-bending limit. Hence the relative importance of the different deformation modes now depends on the amount of intrinsic bending. In particular, the coefficients diverge in the limit $\eta \to \pm 2$. This is the limit of constricted cells, i.e. wedge-shaped cells in which one surface of the cell sheet has contracted to a point. As the intrinsic configuration approaches this constricted limit somewhere, deviations from the intrinsic configuration become more and more expensive energetically there compared to other positions in the cell sheet.

EXAMPLE: *VOLVOX* INVERSION

The spherical embryos of the green alga *Volvox* turn themselves inside out during their development [2, 3]. At the start of this inversion [Fig. 1(a)], the cell sheet invaginates due to the formation of wedge-shaped cells near the equator, or, equivalently, a bend region of negative intrinsic curvature, $\kappa_s^0 < 0$, there, evolving quasi-statically. Fig. 3 shows shapes at two stages of invagination, respectively computed using Eq. (∗) and the classical theory (obtained from Eq. (∗) in the small bending limit $\eta \to 0$). The computed shapes differ the more the more constricted the cells in the bend region are (Fig. 3). Equivalently, model parameters inferred from strongly invaginated embryo shapes, as in Fig. 1(a), using the classical theory can be inaccurate.

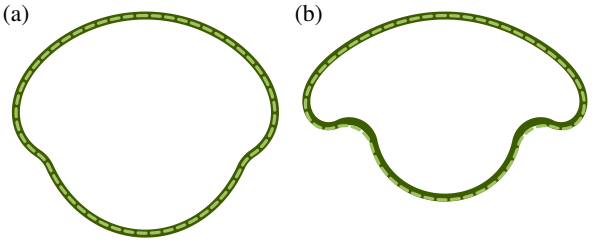

Figure 3: Invagination in *Volvox*. Midsagittal cross sections of computed shapes for (a) an early invagination stage, (b) a later stage in which the bend region near the equator is almost constricted ($\eta \approx -2$ there). Thick solid lines: Eq. (∗); dashed lines: classical model.

CONCLUSION

Here, we have derived, from first principles, an elastic shell theory for the large bending deformations that commonly arise in problems in morphogenesis (Fig. 1), illustrating the theory for invagination of a *Volvox* embryo. This example has in particular emphasised the elastic role of the geometric singularity of cell constriction.

References

[1] R. Keller and D. Shook, *BMC Biol.* **9**, 90 (2011).
[2] S. Höhn, A. R. Honerkamp-Smith, P. A. Haas, P. Khuc Trong, and R. E. Goldstein, *Phys. Rev. Lett.* **114**, 178101 (2015).
[3] P. A. Haas and R. E. Goldstein, *J. R. Soc. Interface* **12**, 20150671 (2015).
[4] N. C. Heer, P. W. Miller, S. Chanet, N. Stoop, J. Dunkel, and A. C. Martin, *Development* **144**, 1876 (2017).
[5] P. W. Miller, N. Stoop, and J. Dunkel, *Phys. Rev. Lett.* **120**, 268001 (2018).
[6] B. Audoly and Y. Pomeau, Elasticity and Geometry (Oxford University Press, Oxford, United Kingdom, 2010), Chap. 12, pp. 435–453.
[7] A. Goriely, The Mathematics and Mechanics of Biological Growth (Springer, Berlin, Germany, 2017), Chap. 11 & 12, pp. 261–373.
[8] V. Conte, F. Ulrich, B. Baum, J. Muñoz, J. Veldhuis, W. Brodland, and M. Miodownik, *PLoS One* **7**, e34473 (2012).

SIMULATIONS OF BUBBLE GATING IN HYDROPHOBIC NANOPORES

Alberto Giacomello*[1] and Antonio Tinti[1]
[1]Department of Mechanical and Aerospace Engineering, Sapienza Università di Roma, Roma, Italy

Biological ion channels are the gates of cells which allow the exchange of ions and molecules across cellular membranes. The typical size of the interior of biological channels is of the nanometer or below, often characterized by hydrophobic residues. Molecular dynamics simulations have reported [1] that, in some ion channels, such confined conditions promote the formation of a nanoscale vapor cavity which is capable of blocking the flux of ions – giving rise to the so-called hydrophobic gating mechanism [2]. In addition, bubble formation in solid-state or hybrid nanopores may be detrimental in several bioengineering applications, such as DNA sequencing [3]. While molecular dynamics has proven an invaluable tool to connect the structure of biological channels with their function, an open challenge for simulations concerns the timescales that can be afforded on current architectures, still far from the biologically relevant ones, typically in the millisecond range. An analogous limitation applies to gating in synthetic channels.

In this talk, the state of the art in the understanding of gating in nanopores is discussed [4], with particular regard to molecular dynamics simulations combined with specialized rare-event methods capable of disclosing the long timescales of the thermally activated formation of vapor cavities (Figure 1) in hydrophobic nanopores immersed in water [5]. The mechanism and the kinetics of bubble formation are investigated in simple pore geometries, reproducing some salient features of biological ion channels but which are also relevant to synthetic nanochannels (Figure 2). The effect of extreme confinement on the phase behavior of water is assessed, revealing the contributions of size, geometry, and hydrophobicity in accelerating the formation of nanoscale bubbles. The relevance of these results for hydrophobic gating in biological ion channels is discussed together with more technology-oriented applications to porous materials with controlled wetting properties [6].

The considered models, in their simplicity, disclose the dependence of hydrophobic gating on the geometry, size, and hydrophobicity of the confinement. In addition, the presented methods allow to tackle the timescales of gating, opening the way to a direct comparison of simulations with experiments in electrophysiology and in the nanochannels literature. Overall the results are promising both for understanding some important biological phenomena, including the action of general anesthetics, and as quantitative tools useful in the design of nanoporous materials with controlled wettability for technological applications.

ACKNOWLEDGEMENT
This project has received funding from the European Research Council (ERC) under the European Union's Horizon 2020 research and innovation programme (grant agreement No 803213).

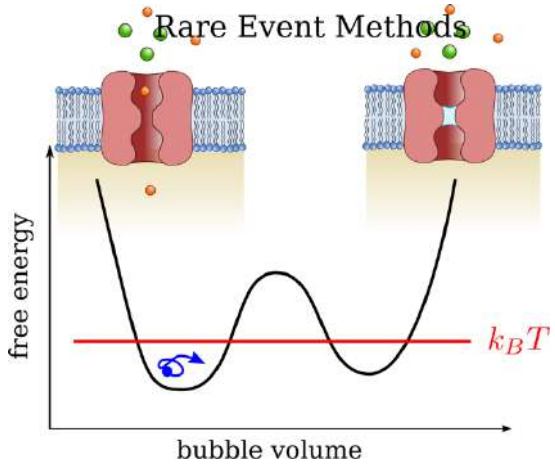

Figure 1. Illustration of the thermally activated formation of a nanoscale vapor cavity within a generic ion channel, giving rise to hydrophobic gating, in which the vapor cavity blocks ion currents. The free-energy profile shows that the bubble formation is a "rare event", i.e., it happens on timescales which are not amenable of brute force simulation.

*Corresponding author. E-mail: alberto.giacomello@uniroma1.it.

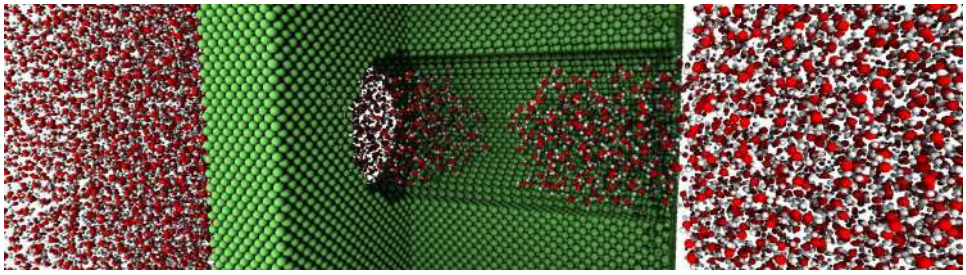

Figure 2. Model system – a hydrophobic cylindrical pore – used to investigate bubble formation within a hydrophobic nanopore via rare-event molecular dynamics simulations [5].

References

[1] Aryal, P., Sansom, M.S., Tucker, S.J. Hydrophobic gating in ion channels. *J. Mol. Bio.*, **427**:121, 2015.
[2] Roth, R., Gillespie, D., Nonner, W., Eisenberg, R.E. Bubbles, gating, and anesthetics in ion channels. *Biophys. J.,* **94**: 4282, 2008.
[3] Smeets, R. M., Keyser, U. F., Dekker, N. H., & Dekker, C. Noise in solid-state nanopores. *Proc. Natl. Acad. Sci. USA*, **105**:417-421, 2008.
[4] Giacomello, A., Roth, R. Bubble formation in nanopores: a matter of hydrophobicity, geometry, and size. Adv. Phys. X, **5**:1817780, 2020.
[5] Tinti, A., Giacomello, A., Grosu, Y., Casciola, C.M. Intrusion and extrusion of water in hydrophobic nanopores. *Proc. Natl. Acad. Sci. USA*, **114**:E10266, 2017.
[6] Amabili, M., Grosu, Y., Giacomello, A., et al. (2019). Pore Morphology Determines Spontaneous Liquid Extrusion from Nanopores. ACS Nano, **13**: 1728-1738, 2019

SELECTION AND PARAMETER INFERENCE OF MYOCARDIAL CONSTITUTIVE LAWS: FROM EX VIVO TO IN VIVO

Hao Gao[1], Debao Gaun [1], and Xiaoyu Luo [1]
[1]School of Mathematics and Statistics, University of Glasgow

Summary Personalized cardiac modelling can provide unique insights on heart function both physiologically and pathologically. Choosing an appropriate constitutive law and inferring its parameters from limited experimental data, however, still remain a great challenge. In this study, we firstly analysed the descriptive and predictive capability of a general 14-parameter constitutive law developed for myocardial passive response using ex vivo data. We then reduced the general laws using Akaike information criterion (AIC) for different experimental studies by maintaining its mechanical integrity whilst achieving minimal computational cost. To model active stress, we introduced a structural tensor into the contraction model for describing dispersed myofibres. Finally we inferred those unknown constitutive parameters using routine clinical data with the constitutive law determined from ex vivo human data. Our results suggest that a combined ex/in vivo experimental and modelling approach is important in selecting an appropriate constitutive law for predictive biomechanical models.

INTRODUCTION

Constitutive laws that describe the mechanical responses of cardiac tissue under loading hold the key to the accurate modelling of biomechanical behaviours of the heart. Determining the constitutive laws and their parameters from limited experimental data, however, still remain a great challenge for the cardiac modelling community. It is even more challenging to infer those constitutive parameters for real patients with routinely available clinical data. There have been ample choices of phenomenological constitutive laws derived from experiments for describing myocardial responses, such as the strain-invariant based Holzapfel-Ogden 2009 model [1], denoted as HO2009. To model active contraction, a most widely used approach is the active stress formulation in which the total stress tensor is additively decomposed into a passive ($\boldsymbol{\sigma}^{\text{pass}}$) and active ($\boldsymbol{\sigma}^{\text{act}}$) parts. To date, only very limited studies included myofibre dispersion in active contraction for myocardium using the active stress formulation. Currently, there are no established approaches which can relate ex vivo calibrated parameters to in vivo myocardial behaviours, imposing a major difficulty for translational studies. In this study, we propose an initial attempt to address this issue from ex vivo to in vivo towards personalized modelling.

MYOCARDIAL CONSTITUTIVE LAW FROM EX VIVO DATA

Three sets of experimental data were taken from ex vivo myocardial biomechanical studies: Dokos et al [4] investigating porcine myocardium; Sommer et al [5] investigating human myocardium; and, Ahmad et al [3] investigating neonatal porcine myocardium. To characterize the mechanical behaviours of myocardium, the general HO strain energy function [1] Ψ was considered here,

$$\Psi = \frac{a}{2b}\exp[b(I_1-3)] + \sum_{i=\text{f,s,n}} \frac{a_i}{2b_i}\{\exp[b_i(\max(I_{4i},1)-1)^2]-1\} + \sum_{ij=\text{fs,fn,sn}} \frac{a_{ij}}{2b_{ij}}[\exp(b_{ij}I_{8ij}^2)-1], \qquad (1)$$

where $a, b, a_i, b_i, a_{ij}, b_{ij}$ are the 14 material constants, $I_1 = \text{trace}(\mathbf{F}^T\mathbf{F})$, represents the overall squared stretch, $I_{4\text{f}}$, $I_{4\text{s}}$ and $I_{4\text{n}}$ are squared stretches along the myofibre direction ($\mathbf{f}$), sheet direction ($\mathbf{s}$) and sheet-normal ($\mathbf{n}$), respectively. $I_{8\text{fs}}$, $I_{8\text{fn}}$ and $I_{8\text{sn}}$ are invariants representing the coupling between two different directions. $\mathbf{F}$ is the deformation gradient. We first fitted the general HO model and HO2009 using all test data for each experimental study, and the unknown parameters were estimated using a non-linear least square minimization method. We found that the widely used simplified HO law (HO2009) failed to describe all experimental data, while the general HO model can fit all three experiments very well, as shown in Figure 1(a) for Sommer's data as an example. However, the general HO model has too many parameters, and determining unique values from limited experimental data be very challenging. To derive a simplified but competent strain energy function for a specific experiment, the Akaike information criterion (AIC) analysis was employed here to determine which term can be dropped in Eq.1. The importance of each strain invariant was ranked by the AIC value which was calculated by fitting the reduced constitutive law to experimental data without this strain invariant, the term with the least change (within 5%) was dropped. Figure 1 shows the associated AIC values of each strain invariant compared to the general HO model for the three experimental studies.

Experimental studies have shown that myofibres do not align perfectly along one direction at any location, but are dispersed [5]. We first adopted the structural tensor approach for calculating active stress by taking into account of myofibre dispersion following [6]. At any location, myofibre dispersion can be described as $\rho(\mathbf{M}) = \rho(\Theta,\Phi) = \rho_{\text{op}}(\Phi)\,\rho_{\text{in}}(\Theta)$, in which $\rho_{\text{op}}(\Phi)$ is the out-of-plane dispersion described by a π-periodic von Mises distribution, $\rho_{\text{in}}(\Theta)$ is the in-plane dispersion distribution. Φ and Θ are fibre angles in a Cartesian coordinate system ($\mathbf{e}_1$-$\mathbf{e}_2$-$\mathbf{e}_3$). The general structural tensor $\mathbb{H}$ can be defined over an unit sphere as $\mathbb{H} = \frac{1}{N}\int_0^{2\pi}\int_0^{\pi}\rho_{\text{op}}(\Phi)\,\rho_{\text{in}}(\Theta)\,\sin\Theta\mathbf{M}\otimes\mathbf{M}d\Theta d\Phi$, in which N is a normalization

[1]Corresponding author. E-mail: hao.gao@glasgow.ac.uk

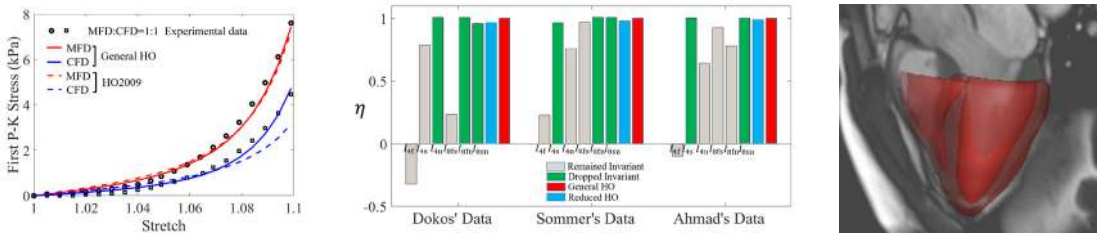

(a) (b) (c)

Figure 1: (a) fitting HO2009 and the general HO model to Sommer's study [5], MFD: mean fibre direction, CFD: cross-fibre direction; (b) normalized AIC with respect to the AIC from the general HO model; (c) predicted end-systolic shape using optimal constitutive parameters superimposed in a MR cine image at end systole.

factor. Without loss of generality, considering the mean fibre direction at reference state $\mathbf{f}_0$ aligns to $\mathbf{e}_3$, the mean sheet direction ($\mathbf{s}_0$) along $\mathbf{e}_1$ and the mean sheet normal ($\mathbf{n}_0$) along $\mathbf{e_2}$, then we can define a structural tensor for describing the active stress $\hat{\mathbb{H}}_a = \mathbb{H}_{11} I_{4\mathrm{s}}^{-1} \mathbf{s}_0 \otimes \mathbf{s}_0 + \mathbb{H}_{22} I_{4\mathrm{n}}^{-1} \mathbf{n}_0 \otimes \mathbf{n}_0 + \mathbb{H}_{33} I_{4\mathrm{f}}^{-1} \mathbf{f}_0 \otimes \mathbf{f}_0$. Thus the dispersed active stress is

$$\boldsymbol{\sigma}^{\mathrm{act}} = T_a \mathbf{F} \hat{\mathbb{H}}_a \mathbf{F}^T = T_a \left(\mathbb{H}_{11} \hat{\mathbf{s}} \otimes \hat{\mathbf{s}} + \mathbb{H}_{22} \hat{\mathbf{n}} \otimes \hat{\mathbf{n}} + \mathbb{H}_{33} \hat{\mathbf{f}} \otimes \hat{\mathbf{f}} \right) \tag{2}$$

in which T_a is the active stress generated by myocytes, and usually described by a set of ODE functions. Because of the significant difficulty of in vivo myofibre acquisition, rule-based myofibre structures are still commonly used in cardiac mechanics modelling, even in personalized models. In this study, we simulated a bi-ventricular porcine heart using a rule-based generated fibre structure with dispersed active stress derived in Eq.2, based on a diffusion-tensor magnetic resonance imaging (DT-MRI) dataset, and then compared the pump functions with a similar bi-ventricle but using the DT-MRI fibres. Our results show that by incorporating fibre dispersion using a structural tensor $\hat{\mathbb{H}}^{\mathrm{a}}$ in active contraction, rule-based method can be a good approximation of realistic myofibre structures.

FROM EX VIVO TO IN VIVO

Currently, there is no consistent way on how to adjust parameters derived from ex vivo experiments to in vivo models. Published studies have suggested passive parameters estimated from ex vivo experiments can over-estimate the stiffness in vivo. Thus in many published studies, parameters of in vivo myocardium are scaled from ex vivo experiments to match in vivo measurements. For active contraction, most parameters are calibrated through single cell experiments, and usually, the isometric contractility (T_{max}) is inversely determined by matching the stroke volume or ejection fraction. In this work, a bi-ventricle model of a healthy volunteer at early diastole was developed from routine clinical MR cine images. The constitutive law for human myocardium and its parameters were determined in the previous section based on ex vivo human experimental data [5]. Two stages were designed to calibrate constitutive parameters for this healthy volunteer. In the first stage, a linearly ramped pressure was applied to the ventricular endocardial surfaces to passively fill the ventricle without active contraction, that is the diastolic filling phase. Passive parameters were then inversely determined through a multi-step optimization procedure by matching the volume and strains at end diastole [7], three sub-steps were involved including (1) scaling ex vivo parameters to match end-diastolic volumes as in [7]; (2) matching measured strains by optimizing a_{f} and b_{f} using a gradient-based method; (3) updating a and b to match end-diastolic volumes again. In the second stage, the myocardium contracted simultaneously after the simulation reaching end diastole with optimized passive parameters from the first stage, T_{max} was inversely determined by matching the measured ejection fraction. Figure 1 (c) shows the simulated end-diastolic shape of the bi-ventricle model, which agrees well with the MR cine image at end systole.

CONCLUSIONS

In this study, we applied the AIC analysis to the general HO model to derive a suitable passive constitutive law for a given set of ex vivo experimental data, and further introduced a structural tensor in active stress modelling based on fibre dispersion, and finally simulated a personalized bi-ventricular dynamics in vivo. Our results show that a combined experimental and modelling approach is important in selecting an appropriate constitutive law for predictive models.

References

[1] Holzapfel GA, Ogden RW. Constitutive modelling of passive myocardium: a structurally based framework for material characterization. Philos. Trans. R. Soc. A, **367**: 3445–3475, 2009.
[2] Guan D, et al. On the AIC based model reduction for the general Holzapfel-Ogden myocardial constitutive law. BMMB **18**: 1213–1232, 2019.
[3] Ahmad F, et al Biomechanical properties and microstructure of neonatal porcine ventricles. JMBBM **88**:18–28, 2018
[4] Dokos S, et al, Shear properties of passive ventricular myocardium. AJP-Heart and Circulatory Physiology, **283**:H2650–H2659, 2002
[5] Sommer G, et al, Biomechanical properties and microstructure of human ventricular myocardium. Acta biomaterialia, **24**:172–192, 2015
[6] Gasser TC, et al. Hyperelastic modelling of arterial layers with distributed collagen fibre orientations. J. R. Soc. Interface **3**: 15–35., 2005
[7] Gao, H., et al. Parameter estimation in a Holzapfel–Ogden law for healthy myocardium. JEM, **95**: 231-248, 2015

MODELLING OF COMPLEX SIGNALS IN NERVES AND THE ANALYSIS OF COUPLING EFFECTS

Jüri Engelbrecht*, Kert Tamm, and Tanel Peets
Department of Cybernetics, Tallinn University of Technology, Tallinn, Estonia

Summary. In this talk a mathematical model which describes jointly electrical, mechanical, and thermal signals in axons is proposed and analysed. The model is based on the analysis of experimental results. The governing equations of single effects are united into a system with coupling forces. As a result, the numerical simulation demonstrates that an ensemble of waves will emerge following the predictions of experiments. The properties of this ensemble are analysed in detail.

INTRODUCTION

Recent studies have revealed the complex structure of nerve signals in axons. There is the experimental evidence that the propagation of an electrical signal (an action potential) is accompanied by mechanical and thermal effects. This calls for analysis at the interface of physiology, mechanics and mathematics taking into account the structure of an axon and possible processes in them. A nerve is actually a cylindrical tube with the wall made of lipid molecules (a biomembrane) inside of which is the axoplasmic (intracellular) fluid. The biomembrane has ion channels through which the ions can pass from the intracellular fluid to the extracellular fluid and vice versa. Experiments have demonstrated beside the action potential (AP) the existence of longitudinal (LW) and transverse (TW) displacements of the biomembrane, the pressure wave (PW) in the axoplasm and the temperature changes (Θ) accompanying the propagation of an AP. It is a challenge to build up a mathematical model able to describe all these effects as an ensemble. In this paper, such a model for unmyelinated axon is presented and analysed. This phenomenological model is based on the analysis of experimentally measured mechanisms of interactions between the single components of the ensemble which permit to propose hypotheses for building up the mathematical description of the whole process.

MODELLING

Based on classical understandings of axon physiology [1] the following basic assumptions are made: (i) electrical signals are the carriers of information and trigger all the other processes; (ii) the axoplasm can be modelled as a fluid where a pressure wave is generated due to the electrical signal [2]; (iii) the biomembrane is able to deform (stretch, bending) under mechanical impact [3]; (iv) the ion channels in biomembranes can be opened and closed under the influence of electrical signals as well as of the mechanical input. Such a description needs the existence of interaction forces between the single components. Three physical mechanisms responsible for coupling are:
(i) electric-biomembrane interaction resulting in a mechanical response (LW, variable U);
(ii) electric-fluid (axoplasm) interaction resulting in a mechanical response (PW, variable $\bar{P}$);
(iii) electric-fluid (axoplasm) interaction resulting in a thermal response (Θ).

The following hypotheses are made: (i) all mechanical waves in the axoplasm and the surrounding biomembrane together with the heat production are generated due to changes in electrical signals (AP or ion currents) that dictate the functional shape of coupling forces [5]; (ii) the formalism of internal variables is used for describing the exo- and endothermic processes of heat production [6]. In addition, not only the influence of an AP to other effects but also possible feedback is taken into account. The possible mechanisms of coupling are described by space or time derivatives of variables governing the AP (amplitude Z), the LW (amplitude U), PW (amplitude $\bar{P}$), temperature Θ. The transverse displacement of the biomembrane W is taken proportional to the gradient of U like in the theory or rods.

A block-scheme of modelling is shown in Fig. 1 (left).

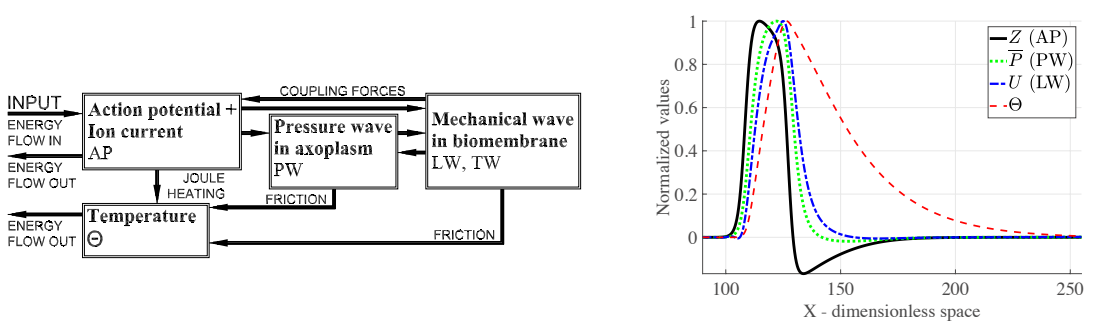

Figure 1. Block diagram of the model (left) and solutions of the dimensionless model equations (right).

* Corresponding author. E-mail: je@ioc.ee.

The governing equations in the dimensionless form are as follows. In the first approximation, the AP is modelled by the FitzHugh-Nagumo model [7]

$$Z_T = Z\big(Z - (a_1 + b_1)\big)(1 - Z) - J + DZ_{XX},$$
$$J_T = \varepsilon(-J + (a_2 + b_2)Z),$$

where Z is the voltage, J is an ion current, a_i, b_i, D and ε are constants. Indices T and X here and further indicate differentiation with respect to time and space, respectively.

Pressure wave (PW) in the axoplasm is governed by the 1D wave model with added viscosity term

$$\bar{P}_{TT} = c_f^2 \bar{P}_{XX} - \mu \bar{P}_T + F_1(Z, J),$$

where $\bar{P}$ is pressure, c_f – the velocity, μ – the viscosity constant and $F_1(Z)$ is a force from the AP.

The longitudinal wave (LW) in biomembrane is governed by the improved Heimburg-Jackson model [3,4]

$$U_{TT} = [(c_0^2 + PU + QU^2)U_X]_X - H_1 U_{XXXX} + H_2 U_{XXTT} + F_2(J, Z),$$

where $U = \Delta\rho_A/\rho_A$, ρ_A is the density, velocity c_0 corresponds to the unperturbed state, P, Q, H_1, H_2 are constants and $F_2(J, Z)$ is the force from the AP. Transverse wave (TW) in biomembrane, which is actually measured in experiments, can be modelled like in the theory of rods [4]

$$W = \kappa U_X,$$

where κ is a coefficient.

Temperature Θ is governed by the modified diffusion equation

$$\Theta_T = \alpha \Theta_{xx} + F_3(Z, J, U, \bar{P}),$$

where α is a coefficient and $F_3(Z, J, U, \bar{P})$ is the force from the AP, LW and PW.

The functional shapes of contact forces are proposed on the basis of several experimental studies taking into account the hypotheses introduced above. The specific mechanisms of coupling and feedback will be discussed in the talk. The heat transfer responsible for changes in temperature Θ is analyzed by introducing several possible physical mechanisms including the process with the internal variables [8]. Such an approach allows distinguishing, if needed, the role of various ion currents when replacing the FitzHugh-Nagumo model [7] with the Hodgkin-Huxley model [6].

The model equations presented above are solved in their dimensionless form by making use of the Fourier transform based pseudospectral method [4]. An example of an ensemble of waves is shown in Fig. 1 (right).

CONCLUSIONS

The model described above is actually the first attempt in order to couple all the measurable effects of the signal propagation in nerves (axons) into a system. This is an interdisciplinary approach at the interface of physiology, physics and mathematics. Clearly the signal propagation in nerves is a complex electro-mechano-thermo-physiological process spiced with molecular effects (opening and closing the ion channels) resulting in emergence of an ensemble of waves. Like demonstrated in various experiments, the components of the ensemble have synchronized velocities. The proposed mathematical model is robust following the trends in systems biology and also in the theory of complex systems. It permits easily modifications by taking more physiological effects into account, for example the Hodgkin-Huxley model [6] and endothermic reactions, etc. Several possible modifications will be discussed in the talk.

References

[1] Debanne, D., Campanac, E., Bialowas, A., Carlier, E., Alcaraz, G. Axon physiology. *Physiol. Rev.*, **91**(2), 555–602, 2011.
[2] Terakawa, S. Potential-dependent variations of the intracellular pressure in the intracellularly perfused squid giant axon. *J. Physiol.*, **369**(1), 229–248, 1985.
[3] Heimburg, T., Jackson, A. D. On soliton propagation in biomembranes and nerves. *Proc. Natl. Acad. Sci. USA*, **102**(28), 9790–9795, 2005.
[4] Engelbrecht, J., Tamm, K., Peets, T. Modeling of complex signals in nerve fibers. *Med. Hypotheses*, **120**, 90–95, 2018.
[5] Engelbrecht, J., Tamm, K., Peets, T. Internal variables used for describing the signal propagation in axons, (submitted).
[6] Hodgkin, A. L., Huxley, A. F. A quantitative description of membrane current and its application to conduction and excitation in nerve. *J. Physiol.*, **117**(4), 500–544, 1952.
[7] Nagumo, J., Arimoto, S., Yoshizawa, S. An active pulse transmission line simulating nerve axon. *Proc. IRE*, **50**(10), 2061–2070, 1962.
[8] Maugin, G. A., Muschik, W. Thermodynamics with internal variables. Part I, General concepts. *J. Non-Equilib. Thermodyn.* **19** (3), 217-249, 1994.

MICROPATTERNED PLATFORM WITH STRUCTURAL, MECHANICAL, AND ELECTRICAL READOUTS FOR CULTURE OF CARDIAC CELLS

W.C. Crone*[1,2,3], B.N. Napiwocki [2,3], D. Lang [4], A. Stempien [2,3], J. Zhang [4], R. Vaidyanathan [4], J.C. Makielski [4], L.L. Eckhardt [4], A.V. Glukhov [4], T.J. Kamp [4,5]

[1]Department of Engineering Physics,
[2]Department of Biomedical Engineering,
[3]Wisconsin Institute for Discovery,
[4]Department of Medicine, Division of Cardiovascular Medicine,
[5]Department of Cell and Regenerative Biology, University of Wisconsin-Madison,Madison,WI,USA

Summary The development of *in vitro* models for the study of cardiac cells is essential to the understanding of cardiomyocyte function in healthy and diseased states as well as changes in cell behavior as a result of exposure to drugs, toxins, or genomic editing. We provide a two-dimensional culture platform, amenable to a range of characterization assays, that emulates *in vivo* cardiac behavior through the use of patterned extracellular matrix and multiple cell types differentiated from human induced pluripotent stem cells. The utility of this platform is illustrated through functional readouts that span immunohistochemistry-assisted assessment of both extracellular and intracellular organization, optical mapping of calcium transients to measure critical parameters such as conduction velocity, and digital image correlation to assess strain output during contraction events.

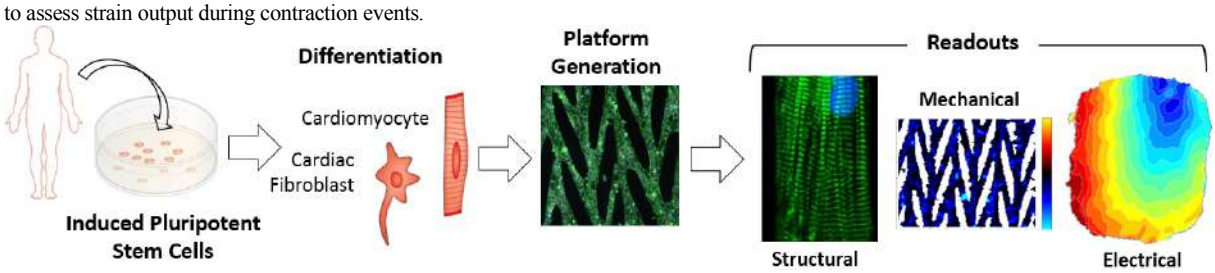

Figure 1. Human iPSCs are differentiated into cardiomyocytes and cardiac fibroblasts for timed introduction into the micropatterned platform for *in vitro* culture. At later time points, functional readouts are performed to determine extracellular and intracellular organization, mechanical strain measures, and electrophysiological outputs.

Human induced pluripotent stem cells (hiPSCs) are capable of being differentiated into all cell types present in the body including those of the heart. Prior work in the field has enabled the reliable differentiation of both cardiomyocytes, the muscle cells of the heart, and cardiac fibroblasts, the most prevalent support cell in the heart, at high levels of purity[1, 2]. These cells exhibit relevant cardiac electrical and mechanical function enabling the desired assays to be performed. Furthermore, they exhibit functional properties of the human heart, which are distinct from many common animal models including rodent models where calcium cycling and cellular electrophysiology exhibit important differences [3-5].

For *in vitro* experiments to be reliable, engineered systems must guide cells to create an organized internal structure similar to that of adult cardiomyocytes *in vivo.* This provides control over intracellular features and a means to design well-controlled, repeatable experiments. We have focused on a two-dimensional platform because it enables the observation of multicellular interconnected networks of cells and is more amenable to *in situ* characterization by optical methods. Additionally, two-dimensional constructs can be more readily manipulated given the lack of diffusion barriers present in three-dimensional constructs, can have its cellular composition and organization more readily adjusted, and are more readily scalable.

As illustrated in Figure 1, we have developed a repeatable, organized, integrated, multicellular culture platform that enables robust assessment of the major functional readouts for cardiomyocyte physiological behavior – structural, mechanical, and electrical - using advanced optical methods. This culture platform bridges the gap between single-cell studies, which do not account for critical mechanical and electrical coupling between cardiomyocytes nor interactions with other cell types, and engineered three-dimensional heart tissue studies, which are not as amenable to full optical characterization. Using multicellular aggregates in a defined micropattern offers the advantages of tissue-like connectivity and coordinated cell-cell functionality.

Cardiomyocytes (CMs) are differentiated from hiPSC using a modified version of the small molecule GSK3β inhibition / Wnt inhibition (GiWi) method [6] and then subjected to lactate purification [7]. Purified hiPSC-CM cultures are washed with PBS and a 10-15 minute exposure to TrypLE (Life Technologies) dissociates and singularizes CMs before seeding them onto micropatterned substrates in a 10% serum-containing media. Soft lithography techniques are used to create the platform on which 30-day differentiated cardiomyocytes and cardiac fibroblasts and seeded [8].

*Corresponding author. E-mail: crone@engr.wisc.edu

Micropatterned extracellular matrix (ECM) (Matrigel, BD Biosciences) promotes preferential cell attachment to the pattern upon seeding onto a PDMS substrate to model healthy (E = 10 kPa) and diseased (E = 30-50 kPa) tissue stiffnesses.

Digital image correlation (DIC) is used to measure full-field displacements and provide strain mapping. This allows characterization of maximum contractile strain and variability in contractility among CMs in the multicellular platform. To measure full-field displacements, we use Fast Iterative DIC (FIDIC) [9], along with a custom algorithm for strain analysis [8]. As illustrated by Figure 2, large data sets are generated for a contractile event and then analyzed to determine the full field principal contractile strain values as well as scalar measures for comparison between different experimental conditions. These results show how the detailed data maps can also be used to produce a scalar value so that quantitative comparisons can be made across different conditions, such as the substrate stiffness.

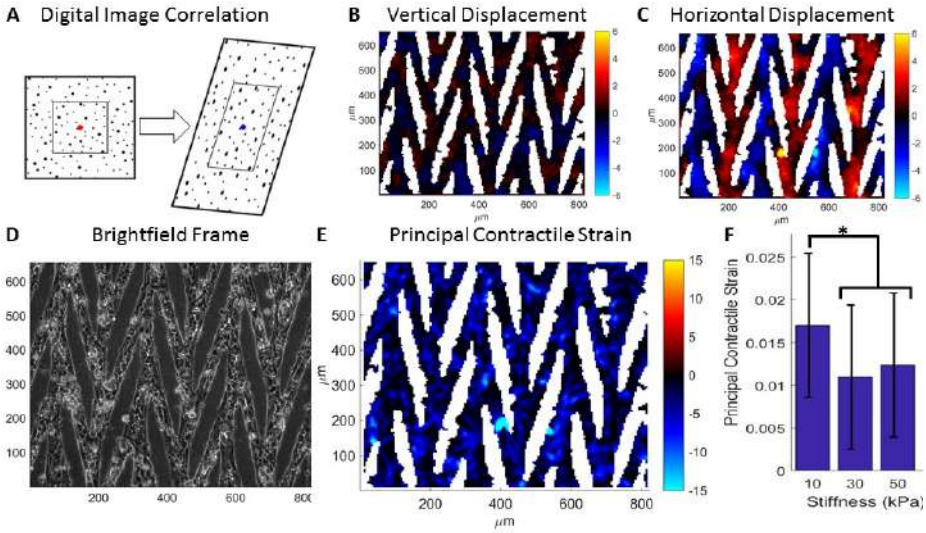

Figure 2. Conceptual sketch of the DIC method (A) used on every brightfield frame of video captured during a contractile event (e.g. D). Using a relaxed frame as reference, local displacements are calculated for each subsequent frame to create 2D maps (B-C). These displacements are then used to determine normal and shear strains at each location and then calculate the principal strains, of which the second principal strain is used as a measure of contractility for CM studies (E). The scalar value representing the median strain for the frame of peak contraction can be calculated and compared over many samples and conditions. Here we show how the maximum contractile strain is influenced by substrate stiffness (F). * $p < .05$

CONCLUSIONS

Stem cell differentiation techniques combined with this micropatterned platform enable precisely controlled seeding of desired cell types to generate reproducible highly organized and interconnected cardiomyocyte arrays, and in co-culture with other cell types such as cardiac fibroblasts, to produce a collection of cardiac cells mimicking the microenvironment in the heart. Experimental results using this culture platform have already demonstrated how micropatterning dimension influences intracellular alignment and cell-cell attachment; as well as mature functional status of cardiomyocyte contraction amplitude, calcium transient amplitude, and calcium release and sequestration upon exposure to beta-adrenergic stimulation [8]. Here we show changes in mechanical functionality of an *in vitro* cardiac syncytium through modification of the substrate stiffness between 10 kPa (healthy model) and 30-50 kPa (disease model). Our other recent findings also illustrate that this platform can control cardiac fibroblast migration and alignment of remodelled extracellular matrix; increased contractility when cardiomyocytes are cocultured with cardiac fibroblasts; and changes in strain production as a result of genomic editing.

References

[1] Zhang J, Tao R, Campbell KF, Carvalho JL, Ruiz EC, Kim GC, et al. Functional cardiac fibroblasts derived from human pluripotent stem cells via second heart field progenitors. Nature communications 2019;10:2238.
[2] Lian X, Zhang J, Azarin SM, Zhu K, Hazeltine LB, Bao X, et al. Directed cardiomyocyte differentiation from human pluripotent stem cells by modulating Wnt/β-catenin signaling under fully defined conditions. Nat Protoc 2013;8:162.
[3] Nerbonne JM, Kass RS. Molecular physiology of cardiac repolarization. Physiol Rev 2005;85:1205-53.
[4] Bers DM, Bassani JW, Bassani RA. Na-Ca exchange and Ca fluxes during contraction and relaxation in mammalian ventricular muscle. Ann N Y Acad Sci 1996;779:430-42.
[5] Milani-Nejad N, Janssen PM. Small and large animal models in cardiac contraction research: advantages and disadvantages. Pharmacol Ther 2014;141:235-49.
[6] Lian X, Hsiao C, Wilson G, Zhu K, Hazeltine LB, Azarin SM, et al. Robust cardiomyocyte differentiation from human pluripotent stem cells via temporal modulation of canonical Wnt signaling. Proceedings of the National Academy of Sciences 2012;109:E1848-E57.
[7] Tohyama S, Hattori F, Sano M, Hishiki T, Nagahata Y, Matsuura T, et al. Distinct metabolic flow enables large-scale purification of mouse and human pluripotent stem cell-derived cardiomyocytes. Cell stem cell 2013;12:127-37.
[8] Notbohm J, Napiwocki BN, deLange WJ, Stempien A, Saraswathibhatla A, Craven RJ, et al. Two-Dimensional Culture Systems to Enable Mechanics-Based Assays for Stem Cell-Derived Cardiomyocytes. Exp Mech;to appear.
[9] Bar-Kochba E, Toyjanova J, Andrews E, Kim KS, Franck C. A Fast Iterative Digital Volume Correlation Algorithm for Large Deformations. Exp Mech 2015;55:261-74.

AN APPROACH TO MODELING RECANALIZATION IN ACUTE ISCHEMIC STROKE THROUGH CYCLIC ASPIRATION

Francesco Costanzo*[1], Bryan Good[2], Scott Simon[3], and Keefe Manning[2]
[1]Department of Engineering Science and Mechanics, Penn State University, University Park, PA, USA
[2]Department of Biomedical Engineering, Penn State University, University Park, PA, USA
[3]Department of Neurosurgery, Penn State Hershey Medical Center, Hershey, PA, USA

Summary An acute ischemic stroke (AIS) occurs when a thrombus (blood clot) occludes a cerebral artery. AIS is the 2nd leading cause of death worldwide and 80% of patients eligible for a thrombectomy (clot removal) with current methods will either die or suffer major disability. Using *cyclic* aspiration in thrombectomies is a promising new approach to achieve better recanalization outcomes. We present a first study of this process using a nonlinear viscoelastic model for the thromboembolus and treating the thromboembolus–artery interface as a nonlinear viscoelastic cohesive zone (CZ) with damage accumulation. An initial experimental validation was conducted and the effect of the various CZ constitutive parameters was investigated computationally to determine the most prevalent effects.

INTRODUCTION

Stroke causes 6.5 million death each year [1]) and 87% of all stroke-related deaths are due to AIS [2]. Mechanical thrombectomy can achieve recanalization, typically in larger vessels or in patients with contraindications to systemic thrombolysis. Current devices, e.g., Solitaire (Medtronic) and Trevo (Stryker) stent retrievers and suction thrombectomy (Penumbra), typically achieve recanalization only in 85% of patients [3]. These devices could be improved by using *cyclic* aspiration instead of static suction. In a benchtop model [4] cyclic aspiration significantly outperformed static aspiration in removal speed, overall clearance, and with lower operating pressures. There are very few computational studies of aspiration in AIS. To our knowledge, there have been no experimental studies of AIS aspiration, and no computational models of cyclic aspiration in AIS. Here we present a first attempt to fill this gap by modeling the nonlinear viscoelastic behavior of the thrombus and the rate-dependent response of the thrombus-artery interface. The latter was modeled as a cohesive zone (CZ)[5] inspired by studies on coarsely ligated biofilms [6] and tearing in atherosclerotic plaques [7]. The computational solver was initially validated in an experimental flow chamber tracking a thromboembolus analog's surface motion. A range of simulations were then conducted to ascertains the most prevalent model parameters. The result we will present also include some calculations with physiological-relevant clot and interface CZ models [8].

MODELING FRAMEWORK

Our simplified axisymmetric system consists of a thrombus lodged in a cerebral artery (Fig. 1) subject to a uniform

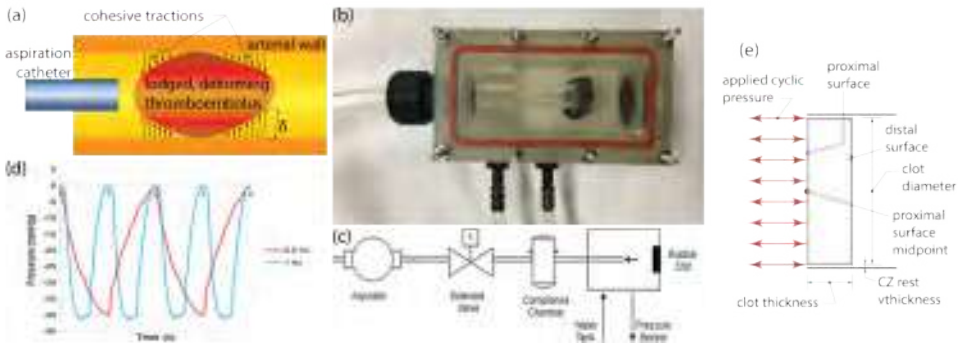

Figure 1: (a) A thromboembolus lodged in a cerebral artery: the shape is exaggerated to show the arterial wall/thrombus interface. (b,c) Experimental aspiration chamber with a neoprene clot analog. (d) Aspiration pressures and frequencies. (e) Clot and CZ reference and loading configurations used in the calculations.

pressure imposed on its proximal surface by a catheter. The distal surface is assumed to be traction-free. The thrombus is modeled via the theory of evolving natural reference configurations (see [8] for details) with a stress response given by

$$\sigma = -pI + \lambda_0(B - I) + \lambda_1(B_e - I) + 2\eta D \quad \text{and} \quad \dot{B}_e - LB_e - B_eL^T = \frac{1}{\tau}(I - B_e). \tag{1}$$

The dot is the material time derivative (time is t). σ is the Cauchy stress, p is a multiplier for enforcing incompressibility, I is the identity, $B = FF^T$ (F being the familiar deformation gradient), $D = (L + L^T)/2$, with $L = \nabla v$, namely the (Eulerian) gradient of the material velocity v, B_e is a symmetric 2nd order tensor analogous to B, but pertaining to a putative deformation allowing the current configuration to relax to its companion evolving natural reference configuration.

*Corresponding author. E-mail: fxc8@psu.edu.

The constant constitutive parameters λ_0 and λ_1 are elastic moduli, η is the dynamic viscosity, and τ is a relaxation time. This model recovers the Kelvin–Voigt (KV) solid for $\lambda_0 > 0$ and $\lambda_1 = 0$, and the Oldroyd-B (OB) fluid for $\lambda_1 > 0$ and $\lambda_0 = 0$. The KV model is also recovered for $\lambda_0 = 0$, $\lambda_1 > 0$ and $\tau \to \infty$. We note that the left-hand side of the 2nd of Eqs. (1) is the Oldroyd upper-convected time derivative of B_e. For the CZ we adopt a conceptually similar model:

$$\vec{s} = (k\delta_e + \eta_{cz}\dot{\delta})\,\vec{g} \quad \text{and} \quad \dot{\delta_e} = \dot{\delta} - \delta_e/\tau_{cz}, \tag{2}$$

where $\vec{s}$ is the cohesive traction, $\delta\,\vec{e}$ ($\|\vec{e}\| = 1$) the CZ opening displacement, δ_e the recoverable part of δ. The constant constitutive parameters k, η_{cz}, and τ_{cz} are the CZ stiffness, viscosity, and relaxation time, respectively. For $0 < \tau_{cz} < \infty$, and under loading conditions promoting opening, the CZ can open without restriction but without a well-defined failure condition. We model the CZ failure using a damage accumulation approach. We call $0 \le \phi \le 1$ the CZ (dimensionless) damage parameter and posit that the CZ stiffness $k = k_i(1-\phi)$, k_i being the initial stiffness and $k = 0$ identifying failure. We assume that $\phi = 0$ everywhere over the interface at $t = 0$. Then, $\phi = (\delta - \delta_{cr})/\ell$ whenever $\delta \ge \delta_{cr} + \bar{\phi}\ell$, $\bar{\phi}$ being the damage at the previous iteration step and δ_{cr} the opening displacement triggering damage accumulation. The governing equations consist of the balance of momentum (with inertia), the continuity equation, and the stated constitutive equations. We implemented our model in a large deformation Lagrangian finite element formulation with the geometry sketched in Fig. 1(e). The formulation was verified using the Method of Manufactured Solutions (see [8] for details).

RESULTS AND CONCLUSIONS

Once verified the correctness of our code, we proceeded to ascertain whether or not the model was adequate for the study of AIS. We created an experimental chamber to subject a neoprene clot analog (Fig. 1(b,c,d)) to a variety of loading conditions. The stress/strain and creep data were collected and fit to the KV and OB limit cases. Using the result of these tests, we predicted the deformation of the clot analog under cyclic loading with the wave forms in Fig. 1(d) but without the presence of a CZ. These predictions, consisting of the displacement of the entire proximal surface of the clot, were compared to corresponding experimentally measured deflections and we found excellent agreement (absolute worst discrepancy was to within 11% error) [8]. We then explored the response of the clot for various values of both the clot relaxation time τ and the various parameters defining the CZ displacement. We will present the full spectrum of the 24 cases we analyzed [8]. In this this extended abstract, we report only the sample shown in Fig. 2. These simulations

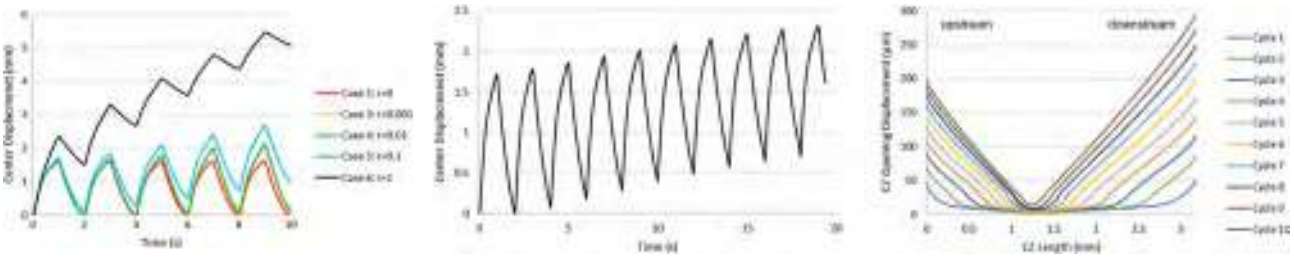

Figure 2: **Left:** Displacement of the clot's center point (cf. Fig. 1(e)) (b,c) under an applied cyclic pressure of 40 mmHg with 0.5 Hz frequency (cf. Fig. 1(d)) for a KV model with $\lambda_0 = 377$ MPa and $\eta = 3.6$ MPa·s for Case 1, and an OB model with $\lambda_1 = 377$ MPa, $\eta = 3.6$ MPa·s and τ are indicated (in seconds) for Cases 3–6. For these simulations no CZ was present and the clot's edges were fixed. **Center and right:** Simulation for a KV clot analog with $\lambda_0 = 377$ MPa and $\eta = 3.6$ MPa·s under an applied cyclic pressure of 40 mmHg with 0.5 Hz frequency, but with a CZ with $k_i = 2.7\,\text{kPa}/\mu\text{m}$, $\eta_{cz} = 10^{-9}\,\text{kPa·s}/\mu\text{m}$, $\ell = 10\,\mu$m, and $\delta_{cr} = 10\,\mu$m.

show that both the constitutive behavior of the clot and that of the interface can both strongly affect the overall system's response under to cyclic pressures. Furthermore, the simulations confirm that, under the assumption that the interface suffers damage accumulation, conditions for the clot removal can be achieved by cyclic loading with applied pressures that are physiologically acceptable. Some simulations seem to indicate that the damage accumulation is more prominent at the distal end of the clot, this being a somewhat surprising result that requires further investigation by properly modeling the deformability of the blood vessel. The results with parameters relevant to AIS used dimensions and mechanical properties of the internal carotid artery and removed thromboemboli [8]. In these AIS cases, more upstream CZ opening was observed compared to the clot analog cases and greater displacement was also achieved with the lower-frequency aspiration (0.5 Hz vs. 1 Hz).

References

[1] Benjamin EJ *et al.* (2017), *Circulation*, **135**(10):e146–e603.
[2] Go AS *et al.* (2014), *Circulation*, **129**(3):e28–e292.
[3] Grech R *et al.* (2015), *The Neuroradiology Journal*, **28**(2):152–171.
[4] Simon S *et al.* (2013), *Journal of NeuroInterventional Surgery*, **6**(9):677–683.
[5] Costanzo F (2001), *Mathematics and Mechanic of Solids*, **6**(2):149–173.
[6] Safari A *et al.* (2016), *Journal of the Mechanical Behavior of Biomedical Materials*, **54**:205–218.
[7] Leng X *et al.*, (2018), ArXiv preprint arXiv:1806.05013.
[8] Good B *et al.* (2019), *Biomechanics and Modeling In Mechanobiology*, electronic form ahead of publication: DOI: 10.1007/s10237-019-01247-w.

MICROSTRUCTURE OF HUMAN AORTIC TISSUE AT DIFFERENT SCALES IN RELATIONSHIP TO MECHANICAL PROPERTIES

Ivan D. Breslavsky*[1], Meisam Asgari[2], Francesco Giovaniello[1], and Marco Amabili[1]
[1]Department of Mechanical Engineering, McGill University, 817 Sherbrooke St. W, Montreal, Quebec, Canada
[2]Department of Mechanical Engineering, Northwestern University, 2145 Sheridan Road, Evanston, Illinois, USA

Summary Microscopic imaging of the three layers of several human descending thoracic aortas was performed by second harmonic generation, two-photon and atomic force microscopy to receive a better understanding of the collagen and elastin structure, distribution and role in the mechanical response of the aortic tissue. Results show a significant inhomogeneity of collagen fiber orientations taking samples of 300 μm in size. These differences are homogenized on larger images of 2 mm in size. This suggests a further refinement of hyperelastic material models currently used to take into account this feature.

METHODS

The mechanical strength and stiffness of biological tissues are governed by their constituting protein molecules that form fibrils with a hierarchical structure. The most contributing into mechanical response of the arterial tissue protein is collagen, often organized in fibrils and fibers. The entanglement of the fibrils is reflected in the tissue matrix that inherits its stiffness from the concentration and orientation of collagen strands.

Different microscopic imaging techniques were used on in order to obtain collagen structure in aortic tissues since couple of decades. In this work, we apply a combination of (i) second harmonic generation imaging (SHG) [1], (ii) two-photon microscopy, and (iii) atomic force microscopy (AFM) [2] to several samples of healthy human aortic tissue obtained from heart-beating donors (from Transplant Québec), in order to better visualise the structure and orientation of collagen and elastin fibers in the three layers. Since most aortic hyperelastic material models include the collagen fiber mean orientation and dispersion, the identification of these global parameters from local imaging is a primary goal of microscopy image processing. We used SHG to get the global picture of collagen distribution and AFM, which is able to deliver the image at much smaller scaler (see Figure 1(a)), to clarify the local structure. In parallel, two-photon images provide the elastin distribution, which can be superimposed to collagen in order to obtain the three-dimensional structure (see Figure 1(b)). Static and dynamic uniaxial tensile tests were performed on each layer and on the full aortic wall on strips taken in axial and circumferential directions. They allow for the hyperelastic and viscoelastic material characterization. Cameras were used to measure the strains orthogonal to the tensile direction.

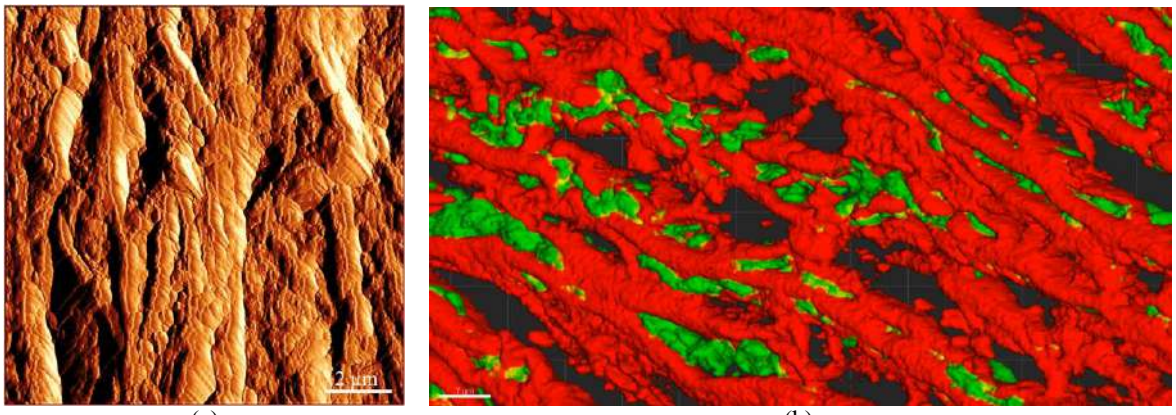

(a) (b)

Figure 1. (a) Microscopic image of the collagen fibers (adventitia, male patient, 39 years) obtained by AFM; (b) aorta microstructure obtained with two-photon and SHG imaging, (media, female, 40 years). Green – collagen, red – elastin.

RESULTS

A widely used assumption in the literature is that every layer (intima, media, adventitia) of aortic tissue has two families of collagen fibers with main angles that are symmetrical with respect to circumferential direction [3, 4]. The in-plane fiber dispersion is significant around these two angles, while the out-of-plane dispersion is small. Microscopic images show a more complex structure. Figure 2(a) shows a much more intricate distribution of fibers. As it can be observed, there are locations with two families of fibers, as well as with only one visible family. Moreover, the angles of the families are different for fibers in different zones. There is no certain structure peculiar to the layer as a whole. Figure 3(b) shows the histogram of the in-plane fiber distribution in four distinct zones of the image with dimension of the order of 300 μm, as well as for the whole image that is about 2 mm of size.

*Corresponding author. E-mail: ivan.breslavskyi@mcgill.ca

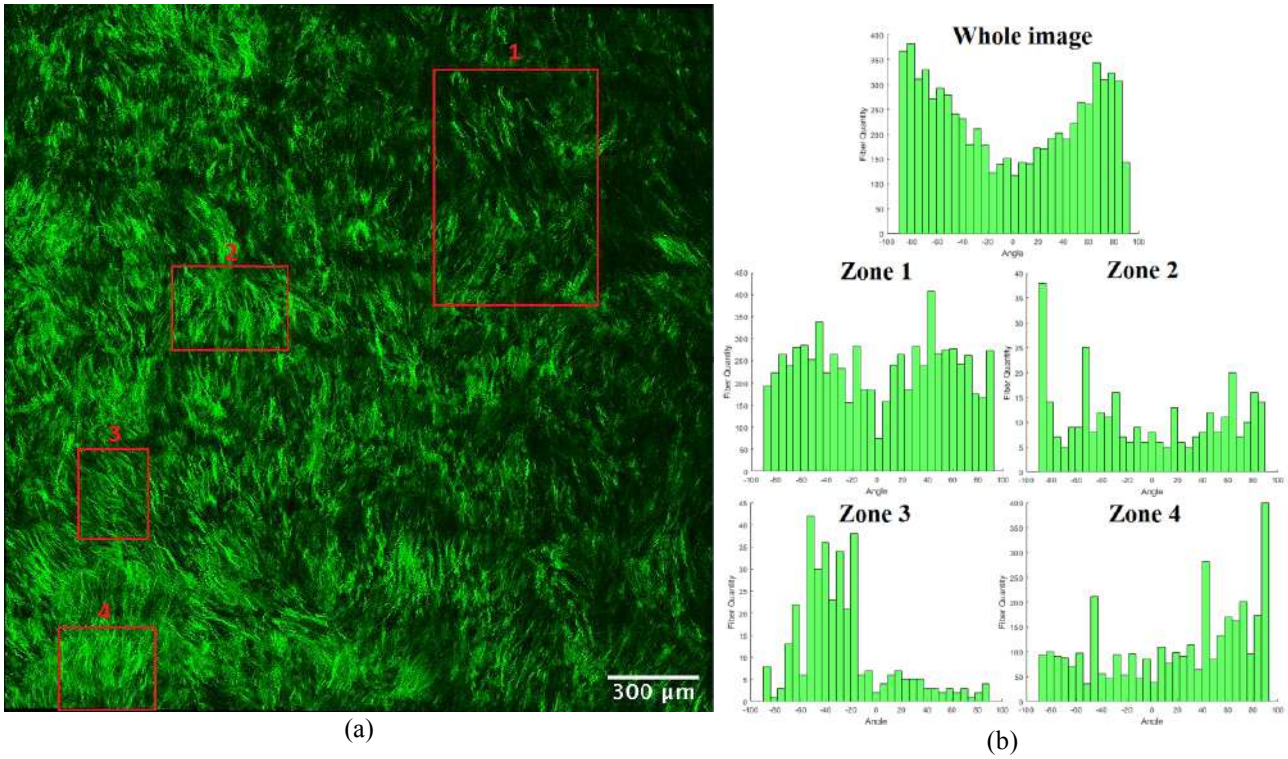

(a) (b)

Figure 2. Large-scale SHG image on media tissue (media, female patient, 42 years) showing different fiber structure at different zones (a) and histograms of the fiber distributions in these zones and over the whole image (b).

We observe that cases similar to the one in Figure 2 are common. Typical size of blood vessel tissue used for fiber recognition shown in the literature is 500 µm or less [5-8]. Several areas of similar size are marked out in Figure 2(a), giving completely different patterns. In any of them the fibers seems to be pretty organized, but assuming this organization to all the tissue is wrong.

Uniaxial tensile tests on axial and circumferential strips, together with the Holzapfel et al. material model [3], were used to characterize the hyperelastic behaviour of the three aorta layers for each donor. Uniaxial harmonic excitations at different frequency, superimposed to initial stretch values, were used to characterize the viscoelastic behaviour. The storage modulus and the loss factor were obtained for each layer in both directions for all the donors. The generalized Maxwell model, within the framework of nonlinear viscoelasticity with internal variables, was used to obtain the constitutive material parameters. The materials parameters were obtained by using unconventional real-valued genetic optimization algorithms [9]. Data for fiber distribution obtained from microscopy were used to fit the material model to the uniaxial tensile tests.

CONCLUSIONS

Large-size microscopic images are necessary in order to obtain average values of fiber orientations in aortic tissues. The fact that collagen fibers presents locally organized structures suggest the use of more refined material models based homogenization criteria to take into account for this inhomogeneity. In addition, the interaction of elastin and collagen can be used to develop advanced viscoelastic material models. The mechanical properties of healthy aortas significantly vary with age [10] and are fundamental to develop a new generation of mechanically compatible grafts for aortic repair.

References

[1] Campagnola P.J. et al. Three-Dimensional High-Resolution Second-Harmonic Generation Imaging of Endogenous Structural Proteins in Biological Tissues. *Biophys. J.* **82**: 493-508, 2002.
[2] Asgari M. et al. In Vitro Fibrillogenesis of Tropocollagen Type III in Collagen Type I Affects Its Relative Fibrillar Topology and Mechanics. *Sci. Rep.* **7**: 1392, 2017.
[3] Holzapfel G.A. et al. Modelling Non-Symmetric Collagen Fibre Dispersion in Arterial Walls. *J. Royal Soc. Interface* **12**: 20150188, 2015.
[4] Amabili M. Nonlinear Mechanics of Shells and Plates in Composite, Soft and Biological Materials. Cambridge University Press, NY 2018.
[5] Holzapfel G.A. Determination of Material Models for Arterial Walls from Uniaxial Extension Tests and Histological Structure. *J. Theor. Biol.* **238**: 290-302, 2006.
[6] Weisbecker H. et al. Layer-Specific Damage Experiments and Modeling of Human Thoracic and Abdominal Aortas with Non-Atherosclerotic Intimal Thickening. *J. Mech. Behav. Biomed. Mater.* **12**: 93-106, 2012.
[7] Kamenskiy A.V. et al. Biaxial Mechanical Properties of the Human Thoracic and Abdominal Aorta, Common Carotid, Subclavian, Renal and Common Iliac Arteries. *Biomech. Model. Mechanobiol.* **13**: 1341–1359, 2014.
[8] Sommer G. et al. Mechanical Response of Human Subclavian and Iliac Arteries to Extension, Inflation and Torsion. *Acta Biomater.* **75**: 235–252, 2018.
[9] Amabili M. et al. Layer-Specific Hyperelastic and Viscoelastic Characterization of Human Descending Thoracic Aortas. *J. Mech. Behav. Biomed. Mater.* **99**: 27-46, 2019.
[10] Amabili M. et al. Nonlinear Dynamics of Human Aortas for Material Characterization. *Phys. Rev. X*, in press.

ASSESSMENT OF SAINT-VENANT PRINCIPLE FOR BIOLOGICAL TISSUES: EXPONENTIAL DECAY OF INCREMENTAL END PERTURBATIONS

Neta Blum[1], David Durban *[1], and Baruch Karp [2]
[1]Department of Aerospace Engineering, Technion, Haifa, Israel
[2]Department of Mechanical Engineering, Ben-Gurion University of the Negev, Beer-Sheva, Israel

Summary The present research aims at an initial theoretical analysis of diffusion with distance of self-equilibrating incremental loads applied to bio-tissues. Setting follows the classical Fadle-Papkovich eigenfunction analysis, in plane linear elasticity, of a semi-infinite strip loaded by self-equilibrating end stresses. Thus, we attempt to determine exponential decay rates of incremental self-equilibrating loads imposed over the edge of an axially pre-stretched strip made of soft tissue. Exposing the nature of strain redistribution near local irregularities can help with understanding of local defects in arteries walls, onset of aneurysm, stents insertion, and membrane perforation that induce local self-equilibrating loads in bio-tissues. Likewise, evaluating applicability of SVP in an aorta could help in studying mechanics of cardiovascular pathologies, possibly improving treatments.

ABSTRACT

Saint-Venant Principle (SVP) is commonly accepted as a central and useful idea in structural mechanics. However, while considerable research on the validity of this principle is available for standard structural materials, only few studies have examined the validity of SVP for biological tissues. This is surprising since there are numerous situations, like presence of defects in arteries walls, onset of aneurysm, stent insertion, skin injuries and bio-membrane perforation, which impose local self-equilibrating loads on bio-tissues.

There appears to be a definite need to understand how localized stress and strain fields decay with distance from loaded zone. Unlike metals, bio-tissues admit large strains and become progressively convex as stretches increase. Earlier studies noted that decay of local effects depends on material orthotropic axes orientation. It has also been reported that decay length is higher in presence of anisotropy in bio-tissues. In a different direction, work by Humphrey and co-workers, on redistribution of localized stresses and strains near circular plane irregularities, indicates sensitivity to both anisotropy and initial stretch.

The present research aims at an initial theoretical analysis of diffusion with distance of self-equilibrating incremental loads applied to bio-tissues. Setting follows the classical Fadle-Papkovich eigenfunction analysis, in plane linear elasticity, of a semi-infinite strip loaded by self-equilibrating end stresses. Thus, we attempt to determine the exponential decay rates (and associated decay lengths) of incremental self-equilibrating loads imposed over the edge of an axially pre-stretched strip (including presence of transverse stretch) made of soft tissue.

Material response is assumed to be hyperelastic, incompressible, and isotropic in the unloaded reference state. Formulation is within the framework of finite strain continuum mechanics, employing laboratory verified hyperelastic constitutive relations for representative biological tissues like the aorta, brain, fat tissues, liver and skin.

We start with a long rectangular strip uniformly stretched in the axial direction, completely constrained in the transverse direction yet accounting for associated changes in thickness. Self-equilibrating incremental disturbances are then imposed over the end of the strip, inducing a set of exponentially decaying incremental eigen-fields. The validity of SVP is determined by the lowest axially decaying eigenfunction, as evaluated from the solution of the corresponding linear eigenvalue system.

Results, over a range of bio-tissues, reveal considerable sensitivity of exponential decay rates, in axial direction, as influenced by material properties and level of pre-stretch. it appears that presence of axial finite strain weakens the applicability of SVP, especially at large stretch levels. That sensitivity stands in marked contrast with the original linear elastic result obtained from the Fadle-Papkovich solution. Furthermore, in this setting the SVP validity is dictated by the first antisymmetric eigenfunction which is the lowest decaying component of the end disturbance. Another noteworthy observation is the direct connection between decay rates and convexity of strain energy function. In fact, our findings indicate that convexity tends to lower decay rates; an extreme example is the Gent tissue for which there is almost no decay near the critical stretch. Essential results have been evaluated numerically and supported by simple and accurate asymptotic expansions.

Next, we relax the transverse deformation constraint on the primary field, allowing for arbitrary pre-stretch in transverse direction. The configuration is now of a bi-axially stretched semi-infinite strip perturbed by a self-equilibrating end disturbance. Analysis is along the lines of previous case and the main conclusion is that presence of transverse stretch

*Corresponding author. E-mail: netab@campus.technion.ac.il.

(simulating aorta circumferential stretch induced by blood pressure) lowers the axial decay rate, again due to convexity of the strain energy function in bio tissues.

Important issues like soft tissues compressibility, anisotropy due to fibers distribution, multilayer structure and age deterioration, growth and remodeling, are not considered in this work. However, we believe that we have presented a start of systematic assessments of SVP validity and sensitivities in soft biological tissues.

Exposing the nature of strain redistribution near local irregularities can help with understanding of local defects in arteries walls, onset of aneurysm, stents insertion, skin injuries and membrane perforation that induce local self-equilibrating loads in bio-tissues. Likewise, evaluating applicability of SVP in an aorta could help in studying the mechanics of cardiovascular pathologies, possibly improving treatments. Research results can contribute also in fixing boundary conditions in experimental procedures.

As a practical by-product, the central observation of our research could be useful in structural health monitoring by providing a theoretical base for technologies aiming at detecting irregularities in living tissues and improving treatment. While this research is only an initial step in assessing the validity of Saint-Venant Principle in soft biological tissues, it provides new and challenging observations that call for further study on the applicability of that fundamental principle in biomechanics. In particular, the role of strain energy function convexity deserves a comprehensive investigation in context of SVP validity for soft biological tissues.

A SIMPLE ELASTIC-CONTINUUM MODEL TO EXPLAIN CELL REORIENTATION UNDER CYCLIC STRETCHING

Vageesh Singh Baghel and G. K. Ananthasuresh
Mechanical Engineering, Indian Institute of Science, Bengaluru, India

Summary We present a simple homogeneous, isotropic elastic-continuum model to explain the cell reorientation under cyclic stretching. Our hypothesis is that cells tend to minimize energy by re-arranging their focal adhesion points. By using topological derivative with Dirichlet boundary condition, the new locations of focal adhesion points can be found.

Introduction

It has been observed through experiments that cells reorient to specific angle relative to the stretch direction when subjected to cyclic stretching of the substrate [1]. The reorientation angle varies from 60° to 90° depending upon the type of cells as well as the frequency and magnitude of cyclic stretch [1-5]. There are models explaining such cell behaviours, e.g., zero strain model [1,3] and zero stress model [4]. Livne et al. [2] claimed that there is a clear difference between zero strain and zero stress models pertaining to the experimental results. They presented a relaxational dynamics model which suggests that the dissipative strain energy leads to change in cell orientation angle with time converging to the final angle [2]. It has also been shown that the focal adhesion alignment precedes cell reorientation [6]. By combining both the findings, we present here a simple elastic-continuum model to find the focal adhesion (FA) locations such that strain energy (SE) is minimized. Mathematically, by referring to Fig. 1, it can be expressed as an optimization problem:

$$\underset{\text{FA points}}{Min} \; SE = \frac{1}{2}\int_{\Omega} \varepsilon : \sigma \, d\Omega$$

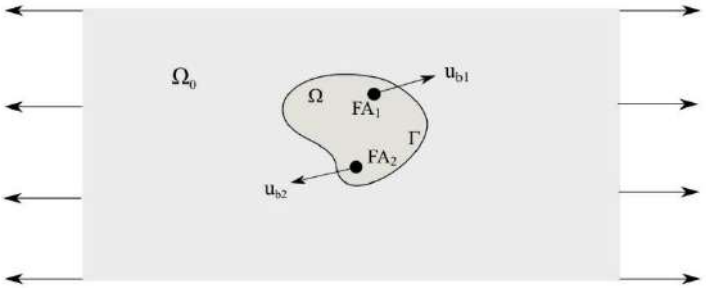

Figure 1: Schematic of cell attached to the background substrate through focal adhesions.

Here in Figure 1, we have a substrate with domain Ω_0 being uniaxially and cyclically stretched, cell with domain Ω and boundary Γ, and two focal adhesions (FA_1 and FA_2) with background displacements u_{b1} and u_{b2} as per the substrate stretching.

Methods

We know that the focal adhesion serves as an interactive interface between cell and substrate to communicate the mechanical changes and transmit the substrate displacement to the cell. As focal adhesion changes its location, the background displacement from substrate to cell also changes and we get different strain energies at different focal adhesion locations. We apply this approach to calculate strain energy exhaustively in the continuum domain of cell. Our interest here is to search for the focal adhesion locations with minimum strain energy.

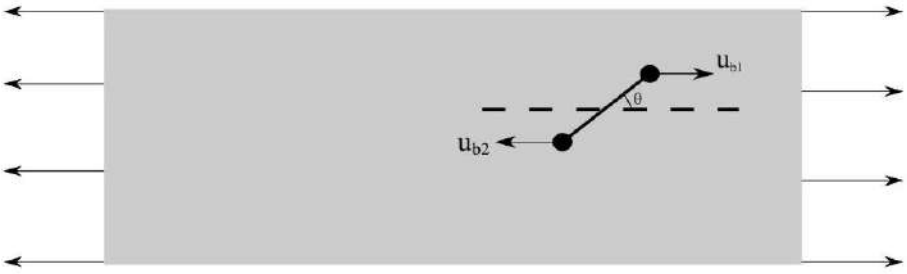

Figure 2: Schematic of stress fiber as dipole with focal adhesion at the end.

We investigate this first for 1D case where we assume stress fiber as a dipole with focal adhesions at the end of it [Figure 2] and calculate strain energy for every orientation of the stress fiber. Strain energy is minimum at 90° orientation angle [Figure 3].

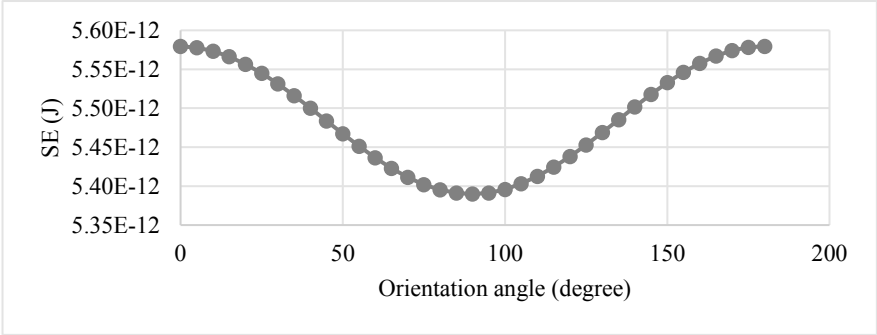

Figure 3: Plot between strain energy and orientation angle of stress fiber.

We use a similar approach to search for focal adhesion location in 2D circular domain with the boundary conditions shown in Figure 1. We found focal adhesions aligning in perpendicular direction relative to the stretch direction [Figure 4].

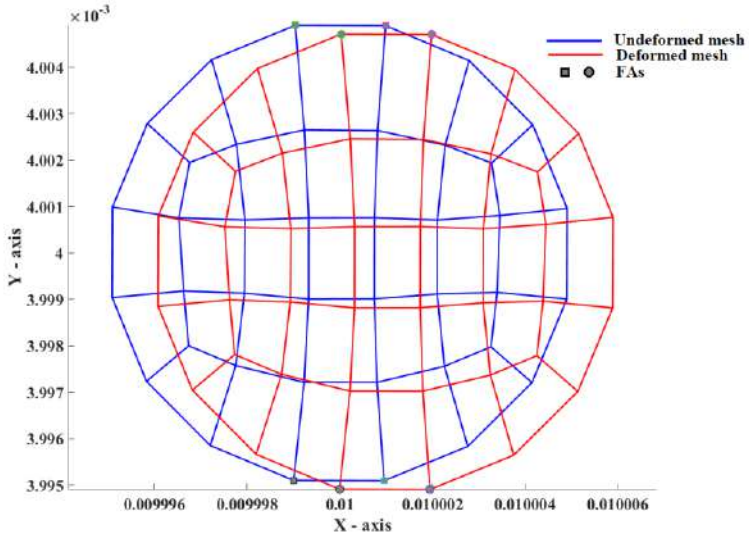

Figure 4: Cell's focal adhesions attaching to the point with minimum strain energy which is the perpendicular direction to the stretched direction.

We use topological derivative to put in more constraint such as focal adhesion area, cell polarity, etc. into our problem. Topological derivative is an analytical approach to measure the sensitivity of the performance functional with respect to an infinitesimal perturbation [7]. In our case, performance functional is strain energy and perturbations in the domain are focal adhesions. Topological derivative (T_D) expression for Dirichlet boundary condition is as follows:

$$T_D = 4\pi E \frac{(1-\nu)}{(1+\nu)(3-4\nu)} \left[\{u(x) - u_b(x)\} \cdot \{u(x) - u_b(x)\} \right]$$

Reference

[1] R.C. Buck, Reorientation response of cells to repeated stretch and recoil of the substratum, *Exp. Cell Res.*, **127** (1980), pp. 470-474

[2] A. Livne, E. Bouchbinder and E. Geiger, Cell reorientation under cyclic stretching thermometry, *Nature Communications* **5**, 3938 (2014).

[3] J. H.-C. Wang, Substrate Deformation Determines Actin Cytoskeleton Reorganization:A Mathematical Modeling and Experimental Study, *J. Theor. Biol.* **202**, 33–41 (2000)

[4] S. A. Safran, and R. De, Nonlinear dynamics of cell orientation *Phys. Rev. E* **80**, 060901 (2009)

[5] Qian J., Liu H., Gao H. A mechanochemical model of cell reorientation on substrates under cyclic stretch. PLoS One. (2013), 8: e65864

[6] Prager-Khoutorsky, M., Lichtenstein, A., Krishnan, R. *et al.* Fibroblast polarization is a matrix-rigidity-dependent process controlled by focal adhesion mechanosensing. *Nat Cell Biol* **13,** 1457–1465 (2011)

[7] A.A. Novotny and J. Sokolowski, Topological Derivatives in Shape Optimization, *Springer* (2013)

CONTRACTION OF ACTIVE GELS VIA MOLECULAR MOTOR ACTIVITY: A THEORY BASED ON TRANSIENT MICROSTRUCTURAL EVOLUTION

Mattia Bacca, Gwynn J Elfring, Albert Kong, Mehadi Hasan
Department of Mechanical Engineering, University of British Columbia, Vancouver, BC - Canada

Summary Active polymeric gels have been prototyped to recreate cytoskeletal contraction from in-vitro experiments. These gels are composed of a loose polymer network largely swollen by the presence of an aqueous solvent, which includes molecular motors and ATP (adenosine triphosphate). These motors bind to the chains of the polymer and catalyze ATP hydrolysis. Thanks to this reaction they create motion, which results in local polymer chain shortening and the consequent macroscopic contraction. To quantitatively describe this phenomenon, we propose a theory based on *transient microstructural evolution*, where the mechanical properties of the gel, described by chain density and average chain length, are subject to change due to molecular motor activity. We finally compare this theory with experiment and observe good agreement.

Introduction

Cytoskeletal gels are synthetic prototypes that mimic the active contractile behaviour of biological cells [1]. They are composed of a polymer network swollen by the absorption of an aqueous solvent containing molecular motors (MM) and their fuel, ATP (adenosine triphosphate). The mechanical behaviour of the gel is characterized by the stiffness of the polymer network and by the mobility of the solvent molecules inside the network. MM can alter the configuration of the polymer network by pulling its chains, therefore changing the stiffness of the gel. This evolution of the microstructure is transient since the motors will detach from the chains once the tension in the chains is sufficient to overcome the intermolecular bonds between chains and motors. Stiffness evolution is characterized by an evolution of chain density [2] and chain length [3], which then increments the osmotic pressure of the fluid, thereby motivating its flow. This finally creates macroscopic contraction in the gel.

Mechanical theory and results

We take chain density and chain length to be *microstructural variables* in the material. The energetic cost, per unit time and unit volume, p, for a transient evolution of the microstructure in the gel is

$$p = \frac{\partial \psi^{el}}{\partial \xi_i} \dot{\xi}_i \qquad (1)$$

where ψ^{el} is the gel free energy due to network elasticity, ξ_i the i-th microstructural variable, and $\dot{\xi}_i$ its rate of change, per unit time. An evolution of ξ_i increments gel stiffness, which increments its free energy. Gel stiffening therefore only occurs if $p > 0$ and this energetic cost is provided by the MM pulling the polymer chains.

The principal components of the Cauchy stress in the gel, homogenized from the stress sustained by the polymer network and the solvent, are

$$\sigma_i = \frac{NkT}{J}\left(\lambda_i{}^2 - 1\right) - \Pi 3 \qquad (2)$$

where N is the number of chains in the unit volume of the dry polymer (our reference state), before it swells by absorption of solvent molecules, k is Boltzmann's constant, T is the temperature, J is the swelling ratio of the polymer, λ_i is the i-th component of the principal stretch, and Π is the total pressure [2]. In Eq. (2) we describe the elastic behaviour of the gel via neo-Hookean elasticity, which implies the polymer chains are loose inside the gel and therefore in their Gaussian state. If no external loads are applied to the gel, it will only sustain the pressure of the solvent bath in which is embedded, which we call Π^{ext}. Hence $\sigma_i = -\Pi^{ext}$ for all principal directions. This, substituted into Eq. (2), implies $\lambda_i = J^{1/3}$ in all directions. The osmotic pressure in the solvent is therefore $\Pi^{osm} = \Pi - \Pi^{ext}$ with

$$\Pi^{osm} = NkT\left(J^{-1/3} - J^{-1}\right) \qquad (3)$$

This pressure is proportional to the tension sustained by the polymer chains due to swelling by solvent absorption and corresponds to the pressure sustained by the solvent inside the network. As long as the chemical potential of the solvent molecules, proportional to Π^{osm}, is equivalent to the chemical potential of the solvent molecules in the surroundings, the solvent will be in chemical equilibrium, hence will not flow. However, an evolution of the chemical potential can alter chemical equilibrium, *i.e.* when Π^{osm} increments due to an evolution of N, and this can prompt solvent flow. The evolution of N is due to the increment of crosslink density by MM binding to the polymer chains (dynamic crosslinks) and to the reduction of the mean spacing among crosslinks, which can be seen as an increment in chain density. This evolution is transient since the MM are attached to the polymer chains via intermolecular bonds and these will break once the chain will carry sufficient tension to prompt motor detachment. At this point, the microstructure of the gel will recover its initial state until the motors will bind to a new chain and will repeat the process.

Stiffness evolution in the gel can also be described more accurately by considering an evolution of the average chain density, *i.e.* of the average number of monomers n in each polymer chain. Considering again a Gaussian network, the probability associated with the i-th end-to-end chain vector, $\boldsymbol{r}_i$, is described by the function

$$f_n(\boldsymbol{r}_i) = \left(\frac{3}{2\pi 3na^2}\right)^{3/2} \exp\left(-\frac{33\boldsymbol{r}_i\cdot\boldsymbol{r}_i}{23na^2}\right)3 \qquad (4)$$

with a the average length of a chain monomer in the network. The elastic free energy of the Gaussian network is

$$\psi^{el} = -kT3\sum_{i=1}^{N} \ln\left(\frac{f_n(\boldsymbol{r}_i)}{f_{n_0}(\boldsymbol{r}_{0,i})}\right) \qquad (5)$$

with $\boldsymbol{r}_{0,i}$ and n_0 the i-th chain vector and the average number of monomer per chain, respectively, in the reference state. A change in network configuration due to affine deformation via stretching, which components in the principal directions are $\tilde{\lambda}_i$, will generate the stresses at Eq. (2), with $\lambda_i = \tilde{\lambda}_i$, if $n = n_0$, *i.e.* if the average number of monomers in the network is unchanged. Conversely, if $n < n_0$, associated with the shortening of a chain by MM activity, we will have

$$\lambda_i = \tilde{\lambda}_i/\lambda_m \text{ and } J = \tilde{J}/{\lambda_m}^3 \qquad (6)$$

with $\lambda_m = (n/n_0)^{1/2} < 1$ the *micro stretch* of the network due to chain length evolution. From Eq. (6) we can conclude that an evolution of λ_m with $\dot{\lambda}_m < 0$ will increment λ_i and J and result in an increment of Π^{osm} from Eq. (3). This will again create macroscopic contraction as previously discussed for an evolution of N.

Both the evolutions of N and λ_m occur due to energy transduction, as described by Eq. (1) with substitution of ξ_i with these quantities. We considered these two cases separately for simplicity.

In Figure 1*c* we report the results of dynamic contraction by solving the coupled problem of the evolution of N and solvent transport, for the case of uniaxial contraction and compare these results with experiments [1-2]. In Figure 1*d* we show the relation between the mechanical work provided by MM and gel stiffness for an evolution of N and for an evolution of λ_m [3]. Here we analyze two simplified cases for solvent diffusion. Solvent diffusivity $D = 0$, where no solvent flow can occur, and $D = \infty$, where solvent flow is instantaneous with respect to MM activity.

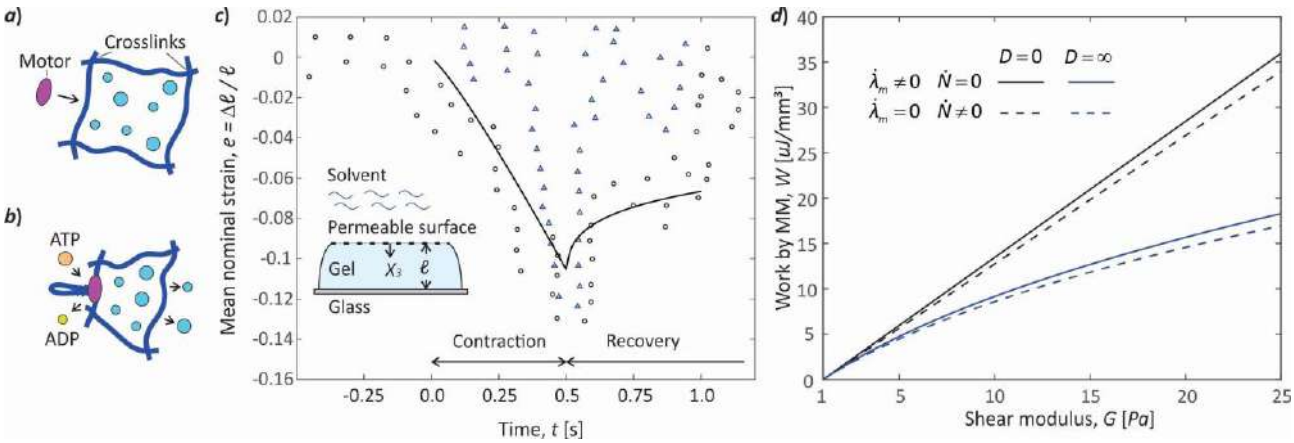

Figure 1: *a*) Gel structure; blue lines indicate the polymer chains while cyan circles indicate solvent molecules; *b*) Molecular motor (MM) activity involving chain shortening via ATP hydrolysis and local expulsion of solvent molecules to accommodate contraction; *c*) Comparison of our theoretical prediction with experiments [1-2]; *d*) Gel shear modulus versus mechanical work by MM [3].

Discussion and conclusions

Our prediction in Figure 1*c* shows good agreement with the experiments during the contraction phase, however, underestimates the rate of recovery. The experimental results are taken from 2 peaks of active contraction [1] since we consider the contraction to be periodic. We also consider all the motors to be synchronized during contraction and recovery (after the motors detach from the chains). This simplification is justified by the assumption of cascade detachment of all motors (see [2] for more details). This model can also be extended to describe the active mechanical behaviour of a real cytoskeleton, by considering the concurrent evolution of N and λ_m. The former can be associated mainly with actin polymerization while the latter can be associated with myosin contraction. In this case, however, Eq. (1) must be divided into two equations describing the energetic contribution of actin polymerization and myosin contraction as distinct phenomena. Figure 1*d* compares both phenomena energetically and can provide a good reference.

References

[1] Bertrand O. J. N., Fygenson D. K., Saleh O. A. Active, motor-driven mechanics in a DNA gel. *Proc. Natl. Acad. Sci. U.S.A.*, **109**: 17342-7, 2012.
[2] Bacca M., Saleh O. A., McMeeking R. M. Contraction of polymer gels created by the activity of molecular motors. *Soft Matter*, **15**:4467-4475, 2019.
[3] Hasan M., Kong A., Elfring G.J., Bacca M. Statistical mechanics of active gels contracting by molecular motor activity. *In preparation*

COMPUTATIONAL MODELING OF THE EFFECTS OF HEMODYNAMICS ALTERATION ON ANEURYSM GROWTH IN THE ASCENDING THORACIC AORTA

S. Jamaleddin Mousavi[1], Jayendiran Raja[1], Ataollah Ghavamian[1], and Stéphane Avril*[1]
[1]Mines Saint-Etienne, University of Lyon, University Jean Monnet, INSERM, Saint-Etienne, France

Summary In this work, we present a numerical framework combining computational fluid dynamics coupled with arterial growth and remodelling (G&R) to model the adaptation of patient-specific ascending thoracic aortas to altered hemodynamics during aneurysm development. A sensitivity study is conducted on the respective roles of smooth muscle cells (SMCs) and of matrix degradation in the aneurysm fate. Predictions of aneurysm growth and of stiffness evolution are in good agreement with experimental data on the same patient.

INTRODUCTION

The thoracic aorta is complex and susceptible to localized dilation, especially from the root of the ascending aorta to the aortic arch and it is referred to as ascending thoracic aortic aneurysms (ATAAs). Three aetiologies predominate in human ATAAs [1]: (i) genetic causes in heritable familial forms, (ii) an association with bicuspid aortic valves (BAV), and (iii) a sporadic degenerative form linked to the aortic aging process. In condition (ii) related to BAV, hemodynamics is altered and this is believed to induce damage in the aortic wall, the resulting aortic dilation potentially leading to dissection or rupture. In the hemodynamics assumption, changes of the local wall shear stress (WSS) distribution induce a cascade of signalling events leading to arterial weakening and further development of the aneurysm. Several mechanisms were proposed to explain arterial weakening: a first one is an increase in wall permeability leading to transmural advection of plasma proteins which could interact with matrix and cell components and induce elastin degradation; a second one is a decrease of the contractility of smooth muscle cells (SMCs) leading to deficient mechanosensing and mechanoregulation. Our objective is to evaluate these two assumptions in patient-specific models.
Different modeling frameworks were proposed to capture fundamental features of arterial growth and remodelling (G&R) responses to altered hemodynamics based on the constrained mixture theory [2-4]. However, existing models did not consider complex patient-specific geometries of ATAAs and they did not integrate the layer-specific properties in their models to distinguish the media and adventitia layers. Moreover, fluid-solid-growth simulations previously developed by different authors for cerebral or abdominal aneurysms did not fully couple G&R model with hemodynamics. Consequently, the objective of the present work is to fully couple a constrained mixture G&R model of ATAA with a computational fluid dynamics to study the effects of altered hemodynamics on ATAA growth.

MATERIALS AND METHODS

A 3D numerical model based on homogenized constrained mixture theory was implemented in ABAQUS through a coupled UEL to predict anisotropic G&R of arteries [4]. At the Gauss points level, the passive behavior was assumed hyperelastic and a strain energy function (SEF) was assumed for each constituent with decoupled contributions of the purely volumetric and isochoric parts. Although the same SEF was assumed for every element across the geometry of the artery, different material properties and mass fraction were applied at each layer. It was assumed that the arterial wall was composed of a constrained mixture of elastin, collagen fibers and SMC and included the *in situ* internal stresses existing in the reference configuration. Four families of collagen fibers with different mass fractions in the media and adventitia layers in the axial, circumferential and angular directions were considered. The contractility of SMC and turnover of collagen fibers were assumed to be stress-dependent.
Simulations were performed on a bilayer thick-wall geometry reconstructed from the CT scan of patients harboring an ascending thoracic aortic aneurysm (ATAA), subjected to boundary conditions in homeostatic conditions.
Two different mechanisms were considered for the initiation of aneurysm enlargement, namely loss of SMC contractility and elastin proteolytic injury. The regional distribution of these effects was related to local WSS distribution obtained from computer fluid dynamics [5]. Different gain parameters for collagen turnover were considered to account for possible variations of mechanosensitivity.

RESULTS

The G&R response of a patient-specific ATAA to localized elastin degradation is shown in Fig. 1. Due to change in shape, the stress distribution is in continuous adaptation and the largest stress values concentrate at the point of most intense remodelling (Fig 1a) where the WSS peak was located.
For all cases simulated, a transfer of stress was obtained from the media to the adventitia in the damaged region. Moreover, an increase in maximum principal stresses was obtained when increasing the elastin degradation rate. In Fig. 1b, the distribution of collagen mass density shows that most of the collagen was deposited in the media where elastin has been lost (recall that ~97% of the elastin is in media), causing finally a thickening of the arterial wall (Fig. 1c). It is noteworthy

*Corresponding author. E-mail: avril@emse.fr.

that the increase in gain parameter (modelling for instance a larger mechanosensitivity of SMCs or a larger concentration of growth factors) accelerates collagen deposition and consequently wall thickening.

DISCUSSION

Results obtained in this study showed that the typical shape of an ATAA can be obtained in regions of deranged hemodymanics either by localized elastin proteolysis or by localized deficiency of SMC contractility. This is the first time that computational G&R models are coupled with computer fluid dynamics to simulate realistic ATAA evolutions and to study the mechanobiological effects involved in these aortopathies. The most interesting result is that although the effects induced by deranged hemodynamics occur locally in the ATAA around the hotspot of WSS, the whole ATAA globally undergoes G&R due to redistribution of stresses, leading to ATAA dilatation. In our model, G&R is driven by the homeostasis principle, where collagen deposition tends to compensate the elastin loss to maintain stress metrics at constant values despite the change of morphology and composition.

CONCLUSIONS

A robust computational model based on the homogenized constrained mixture theory was presented and its potential was shown to predict ATAA evolution for a patient-specific aortic geometry, leading to results which are in agreement with a follow-up performed on the same patient. Therefore, the present model has the potential for clinical applications to predict G&R of patient-specific geometries and should be applied on a larger number of cases for further validation. The future work will focus on identifying patient-specific values for the rates of elastin loss, collagen deposition and SMC contractility as these parameters directly determine ATAA fate in a patient.

ACKNOWLEDGEMENTS

The authors are grateful to the European Research Council for Grant ERC-2014-CoG BIOLOCHANICS.

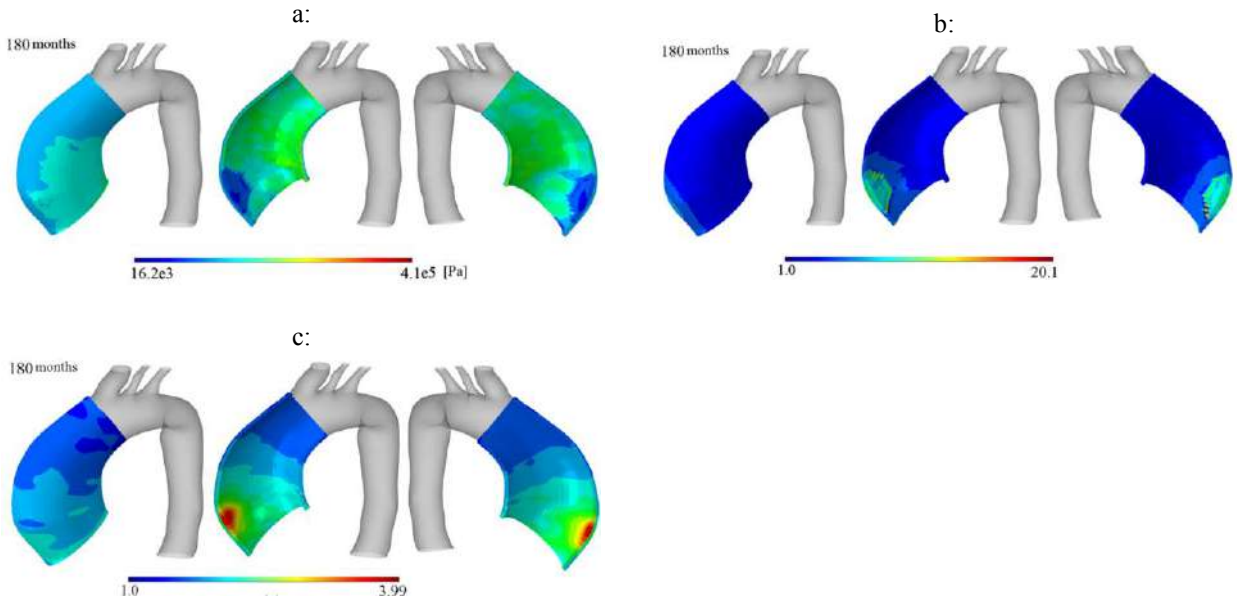

Figure 1. Distribution of the maximum principal stress (a), thickness (b) and normalized collagen mass density (c) in a two-layer patient-specific human ATAA responding to altered hemodynamics conditions provoking a localized elastin degradation.

References

[1] Michel J.B. et al. From genetics to response to injury: vascular smooth muscle cells in aneurysms and dissections of the ascending aorta. *Cardiovascular Research*, **114**:578–589, 2018.

[2] Braeu F.A et al. Homogenized constrained mixture models for anisotropic volumetric growth and remodeling. *Biomech. Model. Mechanobiol.* **16(3)**: 889-906, 2017.

[3] Valentin et al. A finite element-based constrained mixture implementation for arterial growth, remodeling, and adaptation: theory and numerical verification. *Int J Numer Method Biomed Eng*, **29(8)**:822–49, 2013.

[4] Mousavi S.J. et al. Patient-specific predictions of aneurysm growth and remodeling in the ascending thoracic aorta using the homogenized constrained mixture model. *Biomech. Model. Mechanobiol.* **In press**, 2020.

[5] Condemi F. et al. Relationship between ascending thoracic aortic aneurysms hemodynamics and biomechanical properties, *IEEE Trans. Biomed. Eng,* **In press**, 2020.

DYNAMIC CHARACTERIZATION OF HUMAN AORTAS TESTED ON A MOCK CIRCULATORY LOOP

Marco Amabili[1], Prabakaran Balasubramanian[1], Isabella Bozzo[2], Ivan D. Breslavsky[1], Giovanni Ferrari[1], Giulio Franchini[1], Francesco Giovanniello[1], and Chloe Pogue[1]

[1]Department of Mechanical Engineering, McGill University, 817 Sherbrooke St. W, Montreal, Quebec, Canada
[2]Faculty of Medicine, McGill University, 3605 de la Montagne, Montreal, Quebec, Canada, H3G 2M1

Summary This study presents the results obtained from eleven human thoracic aortas tested on a mock circulatory loop that was developed to simulate physiological pulsatile conditions. Results showed cyclic axisymmetric diameter changes, which satisfactorily compared to *in-vivo* measurements at a resting heart rate. Additionally, a large reduction of the cyclic diameter change during the heart pulsation at rest and a significant reduction of the energy dissipation was noted with age. Large damping was observed with increased age and at higher pulse rates due to the combined effects of fluid-structure interaction and viscoelasticity of the aortic wall. The findings expand upon new avenues in advanced materials, with the aim of creating mechanically compatible cardiovascular devices.

INTRODUCTION

An escalating interest in cardiovascular surgery is replacing widely used synthetic grafts, like Dacron, with innovative biomaterials or tissue engineering [2], as Dacron fails to correctly mimic the dynamic behaviour of the aorta. This negatively affects the local blood pressure and flow through a large reduction of the Windkessel effect [3-5]. Cardiomyopathies and replacement surgeries may ensue from prolonged usage of synthetic grafts, thus inciting research in understanding aortic tissue behavior to design mechanically compatible grafts [6]. This study aimed to characterize the nonlinear viscoelastic properties and the nonlinear dynamics of human descending thoracic aortas.

METHODS

The aortas of eleven different donors (VI-XXI), 51.5 ± 17.3 years, were obtained from Transplant Québec. All specimens were tested in the MCL within 24 hours to minimize necrosis. A custom MCL was built to study the nonlinear dynamics of human descending thoracic aortas was built including a Harvard Apparatus volumetric pump, expansion chamber, test section, second expansion chamber, pinch valve, atmospheric tank with thermal heater and temperature control. The loop was tuned to accurately reproduce physiological flow and pressure at different pulse rates, covering the full range of physiological heart rates. Four Polytec laser Doppler vibrometers (model OFV 505/PSV 500) equipped with displacement decoders, were installed at 90° to capture the bending and axisymmetric diameter changes at the center of the aorta. These were used to compute the storage modulus and the loss factors. The storage modulus of the aorta, E', was found as: $E' = \frac{3R_i^2 R_e}{2hR_m}\frac{dp}{d\,\Delta d}$, where p is the internal pressure, Δd is the diameter change of the aorta, R_i is the inner radius of the aorta, R_e is the external radius of the aorta, h is the thickness of the wall of the aorta, and R_m is the mean radius of the aortic wall. Then, the loss factor η was obtained by: $\eta = \frac{\Delta W_d}{2\pi W_s} = \frac{A_{inside\ loop}}{\pi(S_1+S_2)}$. The loss factor coincides with the loss tangent in case of linear viscoelasticity. A comparison of the mechanical properties of human descending thoracic aortas to commercial Dacron aortic grafts was also performed with the MCL. A Hemashield Platinum woven double velour straight graft, made by Maquet (model 175428P) for descending thoracic aorta replacement surgeries, with a nominal diameter of 28 mm, was tested in [5] at different pulse rates by using a MCL. The axial pre-stretch was 1.3 and the straight portion without branches was tested.

RESULTS

The correlation between age and the normalized cyclic diameter change, the loss factor, and the storage modulus at 60 bpm is given in Fig. 1. The maximum cyclic diameter change is shown to be inversely correlated with the age of the donor. For the older donors, the diameter exhibited smaller cyclic amplitude changes per pulsation. This result is consistent with *in-vivo* CT images at rest for fourteen individuals, comparing the average diameter change with age [7]. The experimental data obtained fell within the same bounds as [7], confirming that the MCL was capable of reproducing *in-vivo* conditions. The reduction of the diameter expansion with age gave a reduced Windkessel effect in the elderly. The dependence between age and the viscoelastic material properties was evaluated for all the donors. The loss factor was shown to decrease with age, Fig. 1(b), whereas the storage modulus increased, Fig. 1(c). At 60 bpm the loss factor can be mainly attributed to the dissipation by the aorta wall, while the fluid-structure interaction contribution dominated at larger heart rates. The loss factor seemed to show a dependency from the radial expansion of the aorta, such that the material internal damping capacity decreased with age. The larger storage moduli for older donors reflected the development of pathologies causing aortic tissue to stiffen, like atherosclerotic plaque. Increased aortic stiffness has a major effect on pulse pressure, wave reflections, and above all, cardiovascular disease risk [8].

The variation of relative diameter change, the loss factor and the storage modulus with the pulse rate is shown in Figs. 2(a-c). A modest increase in the diameter change (normalized with respect to the external central diameter at 30 mm Hg) is observed in Fig. 2(a) for the two highest pulse rates, 145 and 170 bpm, for all the three age groups, showing that dynamics play a role. From Fig. 2(b), as the pulse rate increased from 60 bpm to 170 bpm, the loss factor values more

*Corresponding author. E-mail: marco.amabili@mcgill.ca

than doubled. This trend impacted the younger donors more than the elder ones. At higher pulse rates the contribution of fluid-structure interaction on the loss factor was larger, and the reduced diameter change during pulsation seemed like the cause of the reduced dissipative effect of the flow for the elder group. On the other hand, the pulse rate had little impact on the storage modulus. As observed in Fig. 2(c), the variation of the storage modulus with increasing pulse rates was negligible. The storage modulus was dependent upon the age of the donors: the younger the donor, the smaller the storage modulus. Therefore, the stiffness of the aortas was intrinsic to the tissue, as the effect of the fluid-structure interaction was negligible in the physiological regime. Instead, a significant change of the storage modulus occurred from static to dynamic conditions. This reaffirmed the importance of a viscoelastic material characterization for the aorta, rather than a purely static one. Figure 2(d) presents the variation of relative diameter change with the pulse rate for the 60-85 years old group of aorta donors, which are the stiffest ones in the present study, versus the two similar Dacron aortic grafts subjected to different axial pre-stretches. The results show a major mismatch between the cyclic expansion of the human aorta for elder humans versus commercial Dacron grafts. This discrepancy is largely magnified for younger age groups, as seen by comparing Fig. 2(a) and Fig. 2(d). Figure 2(c) shows that the storage modulus of the tested human aortas was always below 3 MPa. This reaffirms that Dacron grafts are much stiffer in circumferential direction as compared to human aortas. Therefore, Dacron grafts provided no Windkessel effect, and altered the nonlinear dynamics of the aorta and the flow.

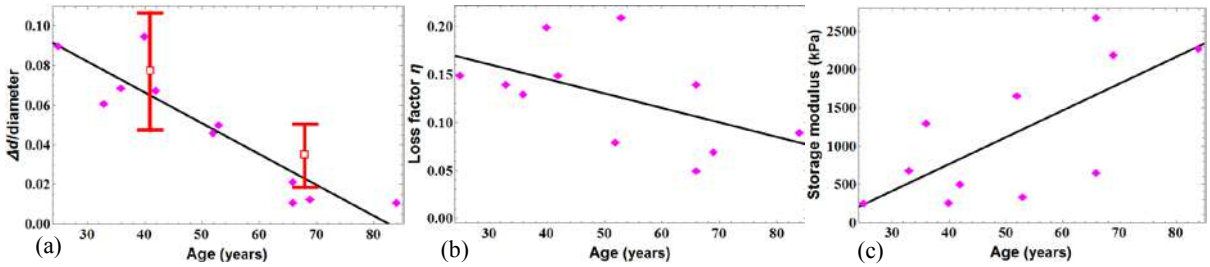

Figure 1. Correlation for cyclic diameter change and viscoelastic parameters with age at 60 bpm, for the eleven donors: (a) maximum diameter change at 60 bpm pulse rate normalized with respect to the diameter (Δd/diameter, experimental points ♦) with linear regression. The data was obtained as the average of diameter changes at the proximal and distal extremities of thoracic descending aortas from *in-vivo* CT images [7]; average values and standard deviations for two age groups of seven individuals each are given (two red error bars). (b) Loss factors with linear regression. (c) Storage modulus with linear regression.

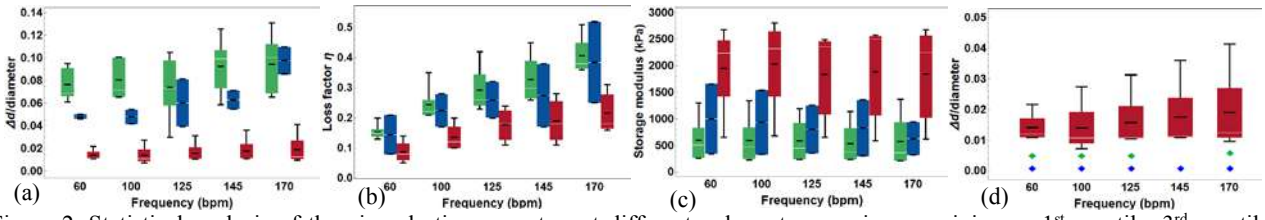

Figure 2. Statistical analysis of the viscoelastic parameters at different pulse rates; maximum, minimum, 1st quartile, 3rd quartile, average (black horizontal line inside the box) and median (white horizonal line in the box) are reported for 3 age groups, ——, 25-44 years old; ——, 45-59 years old; ——, 60-85 years old: (a) maximum relative diameter change; (b) loss factor; (c) storage modulus. (d) Comparison of the maximum relative diameter change for human aortas within the 60-85 years age group and woven Dacron aortic grafts at different pulse rates. ——, statistical analysis of the data for human aortas for the 60-85 years group; ♦, Dacron graft tested in [5] with an axial pre-stretch of 1.3; ♦, Dacron graft tested by the present authors with an axial pre-stretch of 1.33.

CONCLUSIONS

The aims of the experiment were successfully met: the viscoelastic material parameters for the human descending thoracic aorta were identified by using a MCL specifically conceived to reproduce physiological pulsatile flow. The dependency of the loss factor from age was never observed before. The dynamics and the material properties of the aorta obtained from these experiments are essential for advancing cardiovascular medical device designs and improving surgical outcomes [9].

References

[1] O. Khavjou, D. Phelps, and A. Leib, Projections of Cardiovascular Disease Prevalence and Costs: 2015–2035, Technical Report prepared for the American Heart Association (2016).
[2] E. S. Place, N. D. Evans, and M. M. Stevens, Complexity in biomaterials for tissue engineering, Nat. Mater. 8, 457 (2009).
[3] D. Wang, L. Vahala, Z. Hao, Radial and longitudinal motion of the arterial wall: Their relation to pulsatile pressure and flow in the artery, Phys. Rev. E 98, 032402 (2018).
[4] M. Amabili, P. Balasubramanian, I.D. Breslavsky, G. Ferrari, and E. Tubaldi, Viscoelastic characterization of woven Dacron for aortic grafts by using direction-dependent quasi-linear viscoelasticity, J. Mech. Behav. Biomed. Mater. 82, 282 (2018).
[5] G. Ferrari, P. Balasubramanian, E. Tubaldi, F. Giovanniello, and M. Amabili, Experiments on dynamic behaviour of a Dacron aortic graft in a mock circulatory loop, J. Biomech. 86, 132 (2019).
[6] E. Ehret, K. Bircher, A. Stracuzzi, V. Marina, M. Zündel, and E. Mazza, Inverse poroelasticity as a fundamental mechanism in biomechanics and mechanobiology, Nat. Commun. 8, 1002 (2017).
[7] T. M. Morrison, G. Choi, C. K. Zarins, and C. A. Taylor, Circumferential and longitudinal cyclic strain of the human thoracic aorta: age-related changes, J. Vasc. Surg. 49, 1029 (2009).
[8] M. E. Safar, Arterial stiffness as a risk factor for clinical hypertension, Nat. Rev. Cardiol. 15, 97 (2017).
[9] M. Amabili et al., Nonlinear dynamics of human aortas for material characterization, Phys.Rev X 10 (2020).

COMPUTATIONAL MODELLING OF THE MECHANICAL BEHAVIOUR OF TURTLE SHELLS

Benjamin Alheit*[1], B. Daya Reddy[2], and Swantje Bargmann[3]
[1]Department of Mechanical Engineering, University of Cape Town, Cape Town, South Africa
[2]Department of Mathematics and Applied Mathematics, University of Cape Town, Cape Town, South Africa
[3]Department of Mechanical Engineering, University of Wuppertal, Wuppertal, Germany

Summary The turtle shell is a highly effective bio-composite, with the sutures between adjacent plates playing a significant role. This work presents results of a computational investigation of the behaviour and influence of sutures having a geometry and material properties representative of that in turtle sutures. Both hyperelastic and viscoelastic behaviour are considered. Results presented here are in relation to the response to indentation of the shell; further results will focus on oscillatory and impact loading, the effects of viscoelastic modelling, and the effects of different fibre alignments.

INTRODUCTION

The turtle (or tortoise) shell exhibits impressive mechanical performance as a protective structure. As a result, there is interest in gaining an understanding of the geometrical and material features that enable tortoise shells to carry and distribute loading efficiently, with a view to assessing their feasibility as candidates for biomimetic design. Of particular interest are the sutures of interdigitating protrusions between adjacent ribs. As shown in Figure 1, these bone protrusions are bound together by a soft collagenous tissue, which also serves as a skin over the skeleton and is, in turn, coated by a hard keratinous tissue.

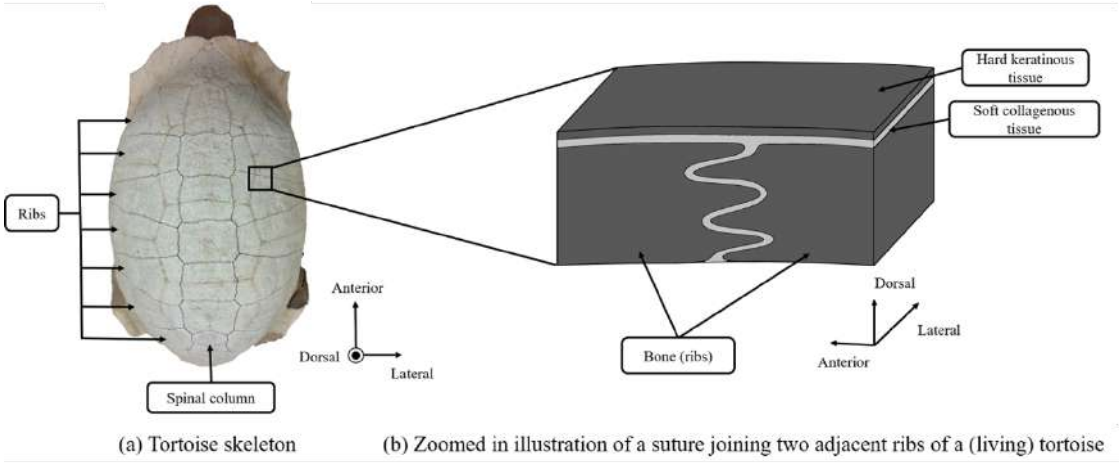

Figure 1: Display of the structure of a tortoise shell.

Numerous mechanical tests have been carried out on turtle shells to elucidate aspects of their properties. However, to the best of the authors' knowledge, there have been no detailed theoretical and computational studies of the mechanics of turtle shells, nor in particular of the role played by sutures in optimizing shell behaviour.

The aim of this work is to undertake a study of the mechanical behaviour of sutures, as components in a heterogeneous structure. For this purpose the model studied comprises a single interdigitated suture, located in a surrounding homogeneous bony structure, and with a geometry representative of that found in turtle shells. The response of the heterogenous structure to both static and dynamic loading are studied, using constitutive models appropriate to the relevant materials.

THE MODELS

The geometry is based on parameters such as protrusion length, soft tissue thickness, and degree of interdigitation, and is generated using the ABAQUS Python Application Programming Interface (API). A finite element mesh is then generated, using tetrahedral elements with piecewise quadratic approximation. The skin and hard keratinous tissue are modelled using triangular shell-type elements with piecewise quadratic approximation generated by copying the upper face of the base mesh. The resulting geometry and mesh are shown in Figure 2. Spring-type conditions are applied at relevant boundaries to account for adjacent material.

*Corresponding author. E-mail: alhben001@myuct.ac.za

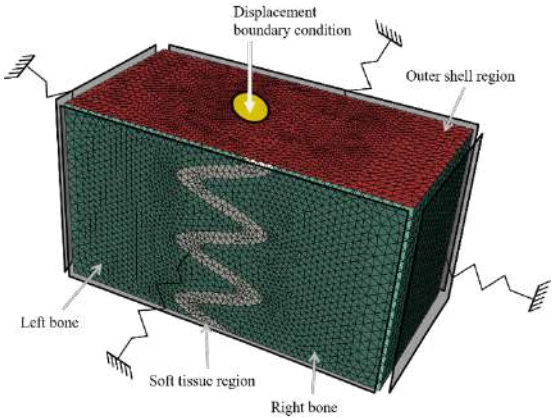

Figure 2: Diagram of ABAQUS model.

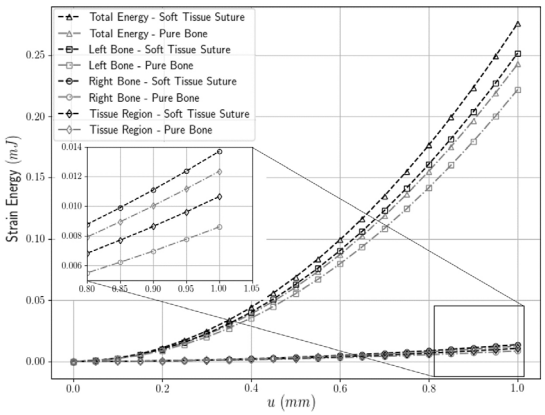

Figure 3: Strain energy vs indent displacement

Two material models are developed for the suture. The first, in which the material is assumed to be transversely isotropic and hyperelastic, is based on a model originally developed with reference to vascular structures [2], and the material constants are determined by means of nonlinear least squares fits to test data [1, 3]. The second is an extension of the hyperelastic model to make provision for viscoelastic behaviour.

It has been found that the fibres in the soft tissue of sutures tend to arrange themselves so that they are loaded in tension [4]. This is replicated by first running a setup simulation assuming isotropy. Another simulation is then run, with the degree of anisotropy set to the optimal value determined by the non-linear least squares fit. The fibre direction at each integration point is then set to be in the direction of the maximum principal stretch of the prior setup simulation.

The bone and hard keratinous tissue are modelled as linear elastic with material constants found from the literature [1].

SOME RESULTS

The results of various simulations, intended to replicate particular scenarios such as impact, oscillatory motion, or a predator attack, are presented. An example, given here, pertains to quasistatic indentation of a small region to represent the tooth of a predator. Figure 3 shows curves of strain energy against indentation, and gives an indication of the energy-absorbing ability of the suture, by comparing with results obtained for a pure bone model. It is observed that the energy-absorbing ability of the suture is due to a greater dispersion of stress throughout the suture region relative to the pure bone model.

Figure 4 shows that defining the fibre directions as described above does indeed lead to stretching of the fibres throughout the soft tissue.

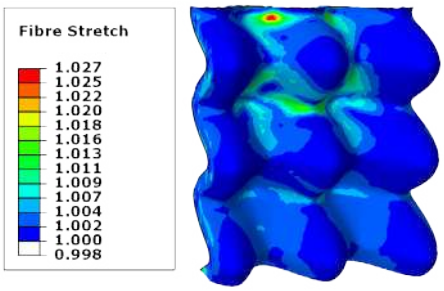

Figure 4: Fibre stretch during quasi-static indentation loading.

Further details in the presentation will include the results of investigations under conditions of oscillatory and impact loading, the effects of viscoelastic modelling, and the effects of different fibre alignments.

References

[1] Achrai B, Wagner HD, The turtle carapace as an optimized multi-scale biological composite armor A review, *J. Mech. Behav. Biomed. Mater.*, **73**, 50-67, 2017

[2] Gasser TC, Ogden RW and Holzapfel GA, Hyperelastic modelling of arterial layers with distributed collagen fibre orientations, *J. R. Soc. Interface*, **3**, 15-35, 2006

[3] Lanir Y, Fung YC, Two-dimensional mechanical properties of rabbit skin II. Experimental results, *J. Biomech*, **7**, 171-182, 1974

[4] Jasinoski SC, Reddy BD, Louw KK, Chinsamy A, Mechanics of cranial sutures using the finite element method, *J. Biomech.*, **43**, 3104-3111, 2010

MECHANO-CHEMISTRY OF ACTIVE SWELLING IN HYBRID GELS

Horacio Lopez Menendez *[1] and Francisco Monroy[1]
[1]Physical Chemistry Department, Complutense University of Madrid

Summary The fabrication of mechano-active hydrogels is dependent on the potency of internal actuators to exert localized stresses inside the polymer network. We describe a novel hybrid class of mechano-active extensile matter, based on a soft polycramide hydrogel matrix driven by the action of FtsZ, a genuine prokaryote cytokinetic protein able to form living filaments. Interestingly we found that after the GTP activation, the FtsZ filaments unexpectedly the pores of the microstructure soften and fluidize, showing an extensibility that enhances with protein concentration. Here we propose a theoretical model for the active hybrid gel where we consider that the active swelling effect is a consequence of the interplay between a mechanical instability, chemically promoted by the fluidization of the gel, due to the activation/polymerization of the FtsZ and the osmotic pressure.

INTRODUCTION

Mechano-active gels represents a new type of internally-driven active matter. Success in the fabrication of mechano-active hydrogels is dependent on the potency of internal actuators to exert localized stresses inside the polymer network. Often, nature uses reversibly polymerizing filaments fueled by metabolic energy, also named living polymers, as powerful molecular actuators to produce forces at different biological scales. We describe a novel hybrid class of mechano-active extensile matter, based on a soft polycramide hydrogel matrix driven by the action of FtsZ, a genuine prokaryote cytokinetic protein able to form living filaments. The FtsZ, is a cytoskeletal protein found in all bacteria, which assembles as dynamical filaments into a cytokinetic ring at the membrane during bacteria division by contributing to generate the force needed for membrane constriction. The FtsZ monomers can bundle together for strength and flexibility, but that can also reversibly depolymerize in a dynamical balance driven by the extent of GTP hydrolysis. This reversible polymerization, or living polymerization of FtsZ, happens under the hydrolysis of one GTP molecule by every FtsZ monomer bounded, requires the presence of Mg2+ as a catalyst, and occurs only above a critical concentration of the monomer [1]. Once the activation of the FtsZ filaments takes place the hybrid hydrogel fluidize, showing an extensibility that enhances with protein concentration. These new mechano-active metamaterials clearly can open an avenue of innovative applications in smart drug delivery and regenerative medicine, showing also promise in emerging fields such as soft robotics, and bionics.

Interestingly we found that after the GTP activation, the FtsZ filaments unexpectedly the pores of the microstructure soften and fluidize, showing an extensibility that enhances with protein concentration. In addition, to better understand the underlying mechanism rheological experiments the behavior of the passive gel in comparison with the hybrid gel with and without GTP activation, we found that the passive becomes stiffer as much as the concentration of FtsZ increases, but during the activation fluidize the structure towards values below the stiffness of the passive gel. Here we propose a theoretical model for the active hybrid gel where we consider that the active swelling effect is a consequence of the interplay between a mechanical instability, chemically promoted by the fluidization of the gel, due to the activation/polymerization of the FtsZ and the osmotic pressure.

THEORETICAL MODEL

In a first approximation we consider a Helmholtz free energy as follows:

$$\Psi(\mathbf{C},\Gamma,c) = \Psi_{mech}(\bar{\mathbf{C}},\Gamma) + \Psi_{mix}(\bar{\mathbf{C}},J) + \Psi_{int}(\chi,\Gamma) + \Psi_{chem}(\chi) + U(J), \tag{1}$$

This function accounts the elastic strain energy function associated with the elasticity of the hybrid gel, where its mechanical strain deformation is described by the Cauchy-Green tensor $\mathbf{C}$. The swelling effect is described by the energy Ψ_{mix} following the Flory-Rehner formalism. Also, an energy term associated with the interaction between passive and active components which is proportional to the chemical potential that allow us to define an interaction parameter (Γ). Finally the chemical energy associated with the active components and the volumetric part.

We describe the expansion effect produced by the hybrid gel as a mechanical instability induced by the activation of the FtsZ produced by the rise of the chemical potential above the critical value. Under these conditions the shells that made the pores of the hydrogel achieve a metastable state by which undergoes an expansion in a similar manner as during the inflation of a rubber ballon [3].

In order to capture the typical non-monotonic response we propose a model that takes as a starting point a neo-hookean elastic strain energy function where the stiffness scale as $G \sim Nk_BT$. Nevertheless, in this case we split $N = m + n$ where m describe the number of chains that contribute with the passive response and n the number of chains that soften due to the activation of the FtsZ. As $m > n$ due to the hybrid gel do not collapse the resultant response manifest a metastable response that allow to define a phase diagram showing a spinodal regime. The way in which we describe the functional form of N is described in the figure (see $[2-4]$ for details).

*Corresponding authors. E-mail: holopez@ucm.es; monroy@quim.ucm.es

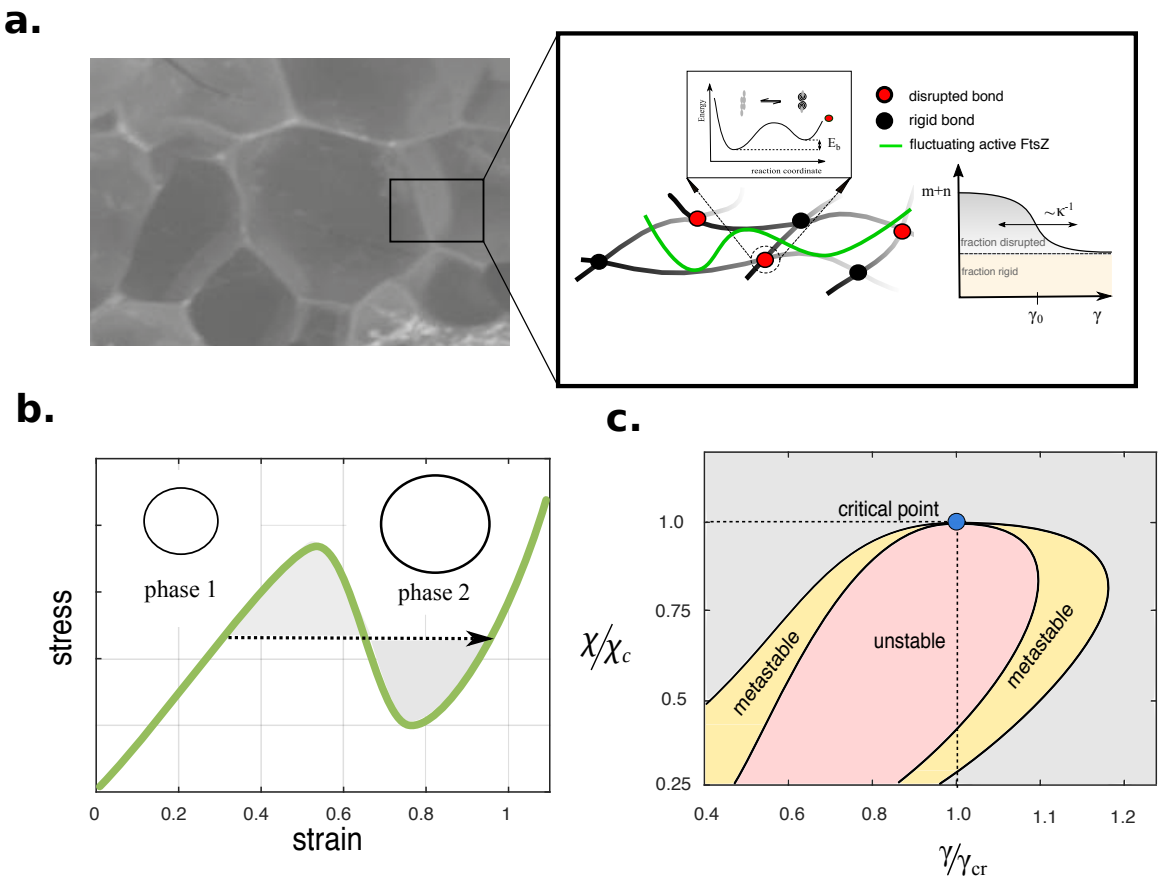

Figure 1: a. Cartoon describing the interaction between the passive and active polymers. b. Stress-strain relation that show the softerning-stiffening instability c. Phase diagram showing the spinodal region.

In addition we defines an interaction energy following the formalism of Landau for phenomenological phase transition where the interaction parameter emerge from a double well potential expressed as $\Psi_{int} \sim \alpha(\chi - \chi_{cr})\Gamma^2 + \beta\Gamma^4$. The model is able to capture the sort of interaction of stiffening or softening depending the activation or not of the living polymer is described by using concepts of phase transition, where we define an interaction parameter Γ that depends of a chemical potential χ that weights the level of GTP and the ratio of concentration between FtsZ and the passive gel. For values of $\chi < \chi_{cr}$ the living polymer is not active enough and the interaction between the two polymers increase the level of gelation and its stiffness increase, and the interaction parameter $\Gamma(\chi) > 0$. But once $\chi > \chi_{cr}$ the activation of the FtsZ is higher enough to allow the fluidization of the passive gel, the interaction parameter $\Gamma(\chi) > 0$ and the stiffness of the hybrid gel suddenly falls.

The characteristic time for the expansion involves the combination of at least to process that scale apparently in the same order. On the one hand the swelling time $\tau_{poroel} \sim L^2/D$ defined by the water permeation across the gel, where L is in the order of the radius and D is the poroelastic diffusion that depends of the solvent viscosity and the effective mesh-size. On the other hand the remodeling time that seems to be plausible to scale according with the reptation time τ_{rep} (if we consider that the chemical dynamics is very fast). In order to simplify the model at this stage we consider that $\tau_{proel} \sim \tau_{rep}$ and in this way we can describe the measurements for $G'(\omega, \Gamma; \chi)$ and $G''(\omega, \Gamma; \chi)$.

By considering the the associated energy terms and its time evolution we obtain the stress tensor and we can describe the ways to control the swelling dynamics of this novel hybrid biomaterial where soft and living matter meets.

References

[1] I. Lopez-Montero... F.Monroy *Biochimica et Biophysica Acta* **1828**: 687-698, 2013.
[2] H. Lopez-Menendez et al. *J. Mech. Phys. Solids* **127**: 208-220, 2019.
[3] J. Cheng et al et al. *J. Mech. Phys. Solids* **124**: 143-158, 2019.
[4] H. Lopez-Menendez ... F. Monroy under preparation.

PATIENT-SPECIFIC FEM/FBEM-BASED EVALUATION OF PERIPROSTHETIC FEMUR FRACTURE RISK IN TOTAL HIP ARTHROPLASTY

R. Zona*[1], L. Esposito[1], , P. Ferla[1], E. Ruocco[1], S. Palladino[1], E. Totaro[1] and V. Minutolo[1]
[1]Department of Engineering, Università della Campania "L. Vanvitelli", Aversa, Italy

Summary Total hip arthroplasty is one of the most used and successful orthopaedic surgeries. The incidence of intraoperative periprosthetic femur fractures in the case of cementless prosthesis, however rare they are, lead to revision surgery with high rates of morbidity and mortality. The study aims to support surgeons in the THA pre-operative decision making process, avoiding early perioperative fractures, by means of a numerical forecast of the effect of the implant on the surrounding bone tissue based on Field Boundary Element Method. The applied method has taken into account the variability of the mechanical properties of the spongy bone. The obtained results, expressed in terms of colour flag maps, provide a first aid tool to the surgeon for the assessment of intra-operative femur fracture risk.

ABSTRACT

Total hip arthroplasty (THA) is one of the most successful orthopedic procedures with effective results in terms of durability and improvement in the quality of life [1]. However, perioperative periprosthetic femur fractures (PPFs) after THA present high rates of morbidity and mortality and often seem to go unreported or unrecognized [2].
Typically, when a cementless stem is implanted, the fracture events occur during femoral canal broaching or implant insertion while trying to obtain a tight press fit [3]. Cracks in the proximal femur due to press-fit stem implantation are often recognized only after surgery when patients already have started to mechanically load their prosthesis [4]. Summing up, surgeons rely mainly on their experience without the support of quantitative measures for guiding their making-decision process, that is, "older and less-healthy" patients receive cemented implants while for "younger and healthier" are preferred un-cemented prostheses.
Hence, this study aims to pursue fracture risk maps [5,6], so to help the medical decision-making process, in particular with respect to the choice of adopting cemented or cementless implant. The numerical model is based on the 2D-Field Boundary Elements Method that is a procedure able to calculate heterogeneous elastic materials by means of boundary elements and field equations arising from heterogeneity [7]. The femur cross sections have been considered and approximated as circular Functionally Graded Material annuli, see Figure 1. The applied strategy allows highlighting the zones most subject to high stress and strain within patient-specific femur sections.
The evaluation of resistance is possible even by using a novel fem strategy based on discontinuous FEM calculation.
With this strategy, one can evaluate the stress state of a solid, in this case a human femur modeled as a poro-elastic material, using the maximum dissipation of strain energy theorems.
The results are resumed into maps (Figure 2) of fracture risk zones, expressed in term of traffic lights color code. The code consists of the comparison between the calculated actual strain and bone-dependent strain thresholds. The final result represents a tool for the surgeons to assess intra-operative femur fracture risk due to cementless implant.

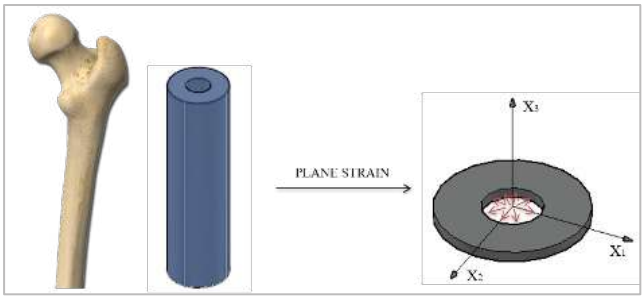

Figure 1. Aproximated femur model

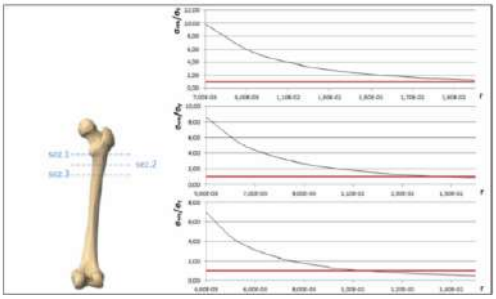
Figure 2. Result table

*Corresponding author. E-mail: renato.zona@unicampania.it.

References

[1] Ethgen O, Bruyere O, Richy F, Dardennes C, Reginster JY. Health-related quality of life in total hip and total knee arthroplasty: a qualitative and systematic review of the literature. *J Bone Joint Surg Am*. **86**: 963-74, 2004.

[2] Lopez M.. Intraoperative periprosthetic hip fractures. *Eur Orthop Traumatol*. **4**:1-4. 2013.

[3] Holley K, Zelken J, Padgett D, Chimento G, Yun A, Buly R.. Periprosthetic fractures of the femur after hip arthroplasty: an analysis of 99 patients *HSS J*. **3**:190-197. 2007.

[4] Savin L, Barharosie C, Botez P.. Periprosthetic femoral fractures-evaluation of risk factors. Rev Med Chir Soc Med Nat Iasi. 116:846-852. 2012.

[5] L. Esposito, P. Bifulco, P. Gargiulo, M.K. Gíslason, M. Cesarelli, L. Iuppariello, H. Jónsson, A. Cutolo & M. Fraldi. Towards a patient-specific estimation of intraoperative femoral fracture risk. *Computer methods in biomechanics and biomedical engineering*. **21(12)**: 663–672. 2012.

[6] V. Minutolo, L .Esposito, P. Gargiulo, M. Fraldi. Towards an app to estimate patient-specific perioperative femur fracture risk. *Computer methods in biomechanics and biomedical engineering*. Submitted.2018.

[7] E. Ruocco, V. Minutolo. 2012. Two-dimensional stress analysis of multiregion functionally graded materials using a field boundary element model. *Composites Part B: Engineering*. **43(2)**:663-672.

FEM ANALYSIS OF A DENTAL ARC WITH PERIODONTAL TEMPORARY RIGID SPLINT

L. Esposito[1], R. Zona*[1], P. Ferla[1], M. Musilli,G. Paolantoni and V. Minutolo[1]
[1]Department of Engineering, Università della Campania "L. Vanvitelli", Aversa, Italy

Summary In patients with periodontitis, in addition to satellite pathologies of inflammation, one of the consequences is increased teeth mobility. In this study, in order to practice a methodology for the treatment of periodontitis, a non-prosthetic device, a Periodontal Temporary Rigid Splint (PTR Splint), is tested. The proposed approach is aimed to reach the best shape of the device, the optimal material behaviour and the best adhesion to withstand stress and help patients to improve the prognosis and success of the therapy. Numerical analyses have been conducted through FEM simulation that takes place through a model of the dental arc, of the device and the adhesive material, reading results in terms of stress between the components and the displacements of the teeth under physiological loads.

ABSTRACT

Periodontal disease is considered an infectious pathology caused by the alteration of the balance between a predisposed host and bacterial factors present in the dental plaque. [1,2]. As a result of the inflammatory process, there is a disorganization of the periodontal fibres, destruction of the epithelial cells near the mesenchyme and ultimately the induction of bone resorption.

Occlusal forces also play an important role because they can exacerbate a pre-existing periodontal injury when they exceed the compromised resistance threshold of the system tooth - periodontal ligament – gingiva [3], affecting both the normal functioning of the microcirculation and the composition of the saprophytic microbiome, in opportunistic bacterial species more pathogenic [4].

In the presence of an anomalous load due to intensity and/or frequency, the time for adaptation of the periodontium may not be sufficient, and therefore give rise to a rearrangement of the deep support [5]. In the presence of a reduced periodontal link (rehabilitated or inflamed), it can result in increased migration and/or mobility of the teeth which consequently can increase the risk of creating altered occlusal relationships that hinder the normal trophism of the periodontal, the homeostasis between resorption and bone remodelling [6] and finally the reorganization of periodontal fibres [3].

Excessive mobility can also hinder the outcome of the periodontal therapeutic course in all the phases that make it up:

-in the Non-Surgical Periodontal Therapy (NSPT) phase it can hinder the normal performance of the patient's home hygiene manoeuvres, and alters the clot's stability during the early stages of wound healing induced by the above and below gingival debridement [7- 8];

- in regenerative therapy (GTR) and in its stages of organization of the clot that composes it, it does not allow the formation of a new link, by favouring the formation of an epithelial link less performing than the connective one [9,10].

Therefore, the treatment of tooth mobility in periodontal patients becomes essential to improve the prognosis and non-prosthetic devices which this mobility can be reduced with. A possible approach to this aim is the dental splinting.

The procedure known as dental splinting is used to treat teeth with increased mobility, by joining them together. The splint stabilizes teeth so that they are less likely to move, which can weaken teeth and cause them to loosen or even fall. It may be used for temporary stabilization of loose teeth, or to address ongoing issues.

In this study, a Periodontal Temporary Rigid Splint (PTR Splint), which has the function of compensating for periodontal problems in the treatment and healing phase, was FE modelled. The PTR Splint consists of a titanium bar glued to the 6 front teeth: 4 incisors and 2 canines. The FEM modelling involves the analysis of three bodies: titanium bar, glue and teeth., as shown in Figure 1. The three bodies are to be understood as sub-structures of a single overall structure which is the splinted dental arc.

The study is aimed at analysing the system in terms of absolute and relative displacements measured at the base of the teeth. A parametric elastic-linear analysis has been performed, as the dimensions of the splint, as the characteristics of the glue vary. As a result, the differences between the displacements induced by the loads in the presence and absence of the splint, as well as the stress at the interface between teeth and splint, have been evaluated.

The main objective of the present study consisted of the evaluation of the optimization of the shape of the splint to obtain the optimal stress distribution, in the splint-glue and glue-teeth interfaces, and minimal displacements of teeth over their support.

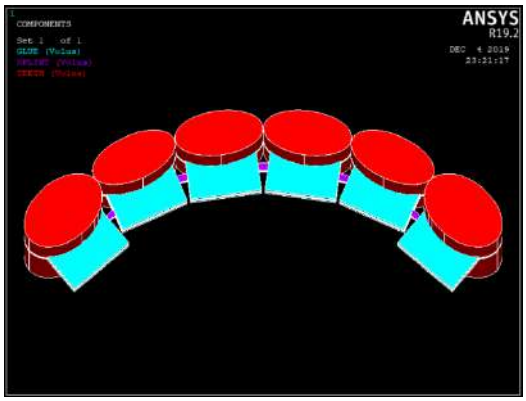

Figure 1. Splinted Dental Arch FEM model

References

[1] Davies SJ, Gray RJ, Linden GJ, James JA. Occlusal considerations in periodontics. *Br Dent J.* **191(11)**: 597– 604, 2001.

[2] Forabosco A, Grandi T, Cotti B. The importance of splinting of teeth in the therapy of periodontitis. *Minerva Stomatol*. **55(3)** :87–97, 2006.

[3] Serio FG, Hawley CE. Periodontal trauma and mobility diagnosis and treatment planning. *Dent Clin North Am*. **43(1)**:37–44, 1999.

[4] Meynardi, F and Biancotti, PP. Etiopathogenetic correlations between periodontal disease and occlusal trauma. *IAPNOR-International Academy of Posture and Neuromuscular Occlusion Research*. **13**, 2009.

[5] Serio FG. Clinical rationale for tooth stabilization and splinting. *Dent Clin North Am*. **43(1)**: 1–6. 2009.

[6] Oosterwyck HV, Sloten JV, Duyck J, Naer I. Bone loading and adaptation around oral implants. In: Las Casas EB, Pamplona DC, editors. *Computational Models in Biomechanics.* CIMNE Barcelona. 1–40. 2003.

[7] Giuseppe Polimeni, Andreas V. Xiropaidis & Ulf M. E. Wikesjo. *Biology and principles of periodontal wound healing/regeneration.* ¨ Periodontology **41**: 30–47. 2003.

[8] Botelho J, Machado V, Mascarenhas P, Alves R, Cavacas MA, Mendes JJ. Fine-tuning multilevel modeling of risk factors associated with nonsurgical periodontal treatment outcome. *Braz. Oral Res.*;**33**:70-81,2019

[9] Trejo PM, Weltman RL. Favourable periodontal regenerative outcomes from teeth with presurgical mobility: a retrospective study. *J Clin Periodontol*: **75:** 27-39, 2004.

[10] Clinical concepts for regenerative therapy in intrabony defects :PIERPAOLO CORTELLINI & MAURIZIO S. TONETTI :Periodontology 2000, Vol. **68**: 282–307, 2015.

SIZE-DEPENDENT TEMPERATURE EFFECT ON VIRAL DNA'S STIFFNESS

Cheng-Yin Zhang[1,2] and Neng-Hui Zhang*[1,2]
[1]School Mechanics and Engineering Science, Shanghai University, Shanghai 200444, China
[2]Shanghai Key Laboratory of Mechanics in Energy Engineering, Shanghai Institute of Applied Mathematics and Mechanics, Shanghai 200027, China

Summary The mobility of the packaged DNA is indispensable for virus infections. The paper is aimed to respond to a recent controversy on temperature-dependent mobility of viral DNA found in single-molecule experiments. We present a multi-scale correlation between the macroscopic stiffness of viral DNA and its microscopic structure, which is characterized by an alternative two-zone structural model with the temperature-dependency. Our model shows that thermal rise can enlarge the interchain spacing, which leads to the increase of the disordered zone volume, and these changes in DNA structure reduce its energy density accompanied with the weakness of its macroscopic stiffness. In addition, the size of the viral or phage capsid will impact the efficiency of temperature effect.

INTRODUCTION

Accompanied with deep insights into structural biology of proteins and nucleic acids related to gene regulation, delicate experiments by single molecule or other biophysics techniques have been carried out to probe the mechanical properties or dynamic processes of viruses and their genes. Typical activities of viruses are often associated with temperature variation. By using AFM to measure the stiffness of the packaged DNA of herpes simplex virus type 1 (HSV-1) and phage λ at a given temperature range, Evilevitch et al. found that the increasing temperatures resulted in a decline of the stiffness of the packaged DNA, especially at temperatures close to that of viral infection (37 °C) [1, 2]. Simultaneously, the area of the DNA scattering peak by small angle X-ray scattering (SAXS) undergoes a prominent decrease with the increasing temperature, which suggests a remarkable structural transition of the packaged DNA in capsid [1, 2]. Livolant et al. repeated the SAXS experiments on four bacteriophages, T5, λ, T7, and Φ29, however did not observe any significant evolution of the scattering area in the temperature range of 20−40℃, so they suggested the reconsideration of temperature effect on DNA organization [3]. In this paper, we aim to quantitatively reveal a multi-scale theoretical correlation between temperature-dependent microstructure and the resultant macroscopic stiffness of the packaged DNA in virus, thereout to elucidate the controversy in the academic community of virus.

MATHEMATICAL MODEL

First, different from the classical single inverse spool model [4], a two-zone model of packaged DNA structure is developed. In response to two distinct regions revealed in the cryo-EM experimental images, here the two zones, respectively, are termed as the ordered zone and disordered zone as shown in the inset of Fig. 1., which statistically represent different liquid crystal phases of the packaged DNA. This two-zone structural model can be described in terms of three undetermined structural variables: DNA length in the ordered zone L_{ord}, interchain spacing in the ordered zone d_{ord} and that in the disordered zone d_{dis}. The minimum energy theorem is applied to determine the microscopic structural variables in the ordered and disordered zones of viral DNA:

$$\frac{\partial(E_{\mathrm{ord}}(d_{\mathrm{ord}},d_{\mathrm{dis}},L_{\mathrm{ord}})+E_{\mathrm{dis}}(d_{\mathrm{ord}},d_{\mathrm{dis}},L_{\mathrm{ord}}))}{\partial(d_{\mathrm{ord}}\ \text{or}\ d_{\mathrm{ord}}\ \text{or}\ L_{\mathrm{ord}})}=0\cdot \tag{1}$$

Second, the energy model of viral DNA is expressed in terms of three structural parameters. Parsegian's mesoscopic potential energy model of DNA liquid crystals [5] is updated by using temperate-dependent persistence length of DNA chain and temperate-dependent Debye length of salt solution. The energy stored in the respective zone includes the interactional energy [5] and the elastic bending energy [4], expressed as

$$E_{\mathrm{ord}}=(G_0-\sqrt{3}A(\lambda_{\mathrm{A}}^2+\lambda_{\mathrm{A}}d_{\mathrm{ord}})e^{-d_{\mathrm{ord}}/\lambda_{\mathrm{A}}})L_{\mathrm{ord}}+\frac{2\pi k_{\mathrm{c}}}{\sqrt{3}d_{\mathrm{ord}}}f(L_{\mathrm{ord}},d_{\mathrm{ord}}),$$

$$E_{\mathrm{dis}}=(G_0+ck_BT\frac{\pi^{5/2}}{20\pi\sqrt{3}}k_{\mathrm{c}}^{-1/4}\sqrt[4]{\frac{\partial^2G_0}{\partial^2d_{\mathrm{dis}}}-\frac{1}{d_{\mathrm{dis}}}\frac{\partial G_0}{\partial d_{\mathrm{dis}}}})(L-L_{\mathrm{ord}})+\frac{2\pi k_{\mathrm{c}}}{\sqrt{3}d_{\mathrm{dis}}}f(L_{\mathrm{dis}},d_{\mathrm{dis}}),\tag{2}$$

$$G_0(d)=a\sqrt{\frac{\pi}{2}}\frac{e^{-d/\lambda_{\mathrm{H}}}}{\sqrt{d/\lambda_{\mathrm{H}}}}+b\sqrt{\frac{\pi}{2}}\frac{e^{-d/\lambda_{\mathrm{D}}}}{\sqrt{d/\lambda_{\mathrm{D}}}},$$

where the coefficients a, b, A are the hydrated, electrostatic and attractive amplitude coefficients, respectively, λ_{D} is the Debye length, λ_{H} and λ_{A} are the hydrated length and attractive decay length, respectively, $k_{\mathrm{c}}=\xi_{\mathrm{p}}k_{\mathrm{B}}T$ is the intrinsic bending stiffness of DNA, in which ξ_{p} is the persistence length of DNA, k_{B} is the Boltzmann constant, T is the environmental temperature. Note that the temperature as an external conditional variable is introduced via a modified persistence length of DNA and the Debye length of the solution.

*Corresponding author. E-mail: nhzhang@shu.edu.cn.

Finally, the stiffness caused by the confined DNA is obtained in terms of the above-mentioned DNA structural variables. The stiffness caused by DNA in capsid is contributed by two parts: the osmotic pressure and DNA bending elasticity energy, i.e.

$$k_{\mathrm{DNA}} = \Pi_{\mathrm{osmotic}} \frac{\pi R_{\mathrm{capsid}}}{2} + G_{\mathrm{bend}} \frac{\pi R_{\mathrm{capsid}}}{2}, \quad \Pi_{\mathrm{osmotic}} = \frac{\partial (E_{\mathrm{int\,chain}} / L)}{\sqrt{3} d \partial d}, \quad G_{\mathrm{bend}} = \frac{E_{\mathrm{bend}}}{V_{\mathrm{DNA}}}, \tag{3}$$

in which Π_{osmotic} is the osmotic pressure derived from DNA energy and G_{bend} is DNA elastic bending energy density.

NUMERICAL RESULTS

In computation, the parameters are taken as follows [6]: R_{capsid} = 47 nm, L_{DNA} = 51500 nm for HSV-1 , R_{capsid} = 29 nm, L_{DNA} = 16500 nm for λ phage and R_{capsid} = 22 nm, L_{DNA} = 14960 nm for T7 phage, $a = 1.1 \times 10^{-7}$ J/m, λ_{H} = 2.88 Å, $b = 0.41 \times 10^{-9}$ J/m, c = 0.8, A = 300005.168 J/m, λ_{A} = 4.8 Å, and the temperature rises from 298 K to 314 K. Substituting these parameters into Eqs. (1) and Eq. (2) yields the structural variables, then the two-zone volume ratio $V_{\mathrm{ord}}/V_{\mathrm{dis}}$ is calculated in Fig. 1 to reflect the global change of DNA structure. Obviously, the volume of the ordered zone in a larger capsid decrease dramatically than that in a smaller capsid. Because the virus with a larger capsid allow more space to fluctuate DNA structure when temperature rises. It's the size effect make previous researchers see different responses for viruses with different sizes [1−3]. Note that the size effect not only means capsid size, but also means DNA size, and they are in a complex coupling relationship. After determining structural variables, the stiffness change of the confined DNA is obtained from Eq. (3) as shown in Fig. 2, the results show that the stiffnesses of three viral DNAs decrease consistently as temperature rises, the downward trends agree well with the experiment [1]. However, the stiffness change of HSV-1 decreased more remarkably than the others. The difference of temperature-dependent stiffness for different viruses or phages is attributed to size effect on DNA structure.

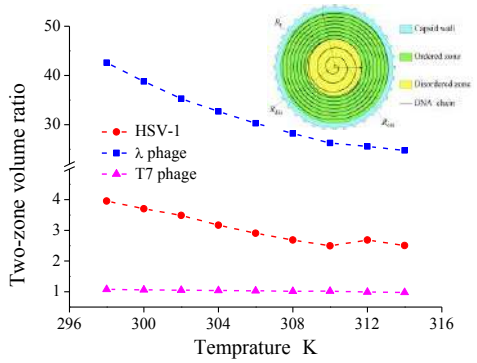

Fig. 1. Variation of two-zone volume ratio with temperature for three viruses (phages)

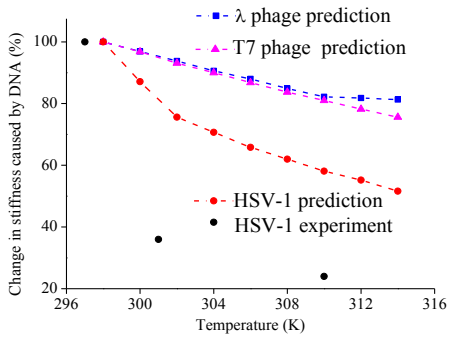

Fig. 2. Variation of DNA stiffness with temperature for three viruses (phages)

CONCLUSIONS

A two-zone structural model of viral DNA is presented in this paper to reveal a multi-scale correlation between temperature-dependent microscopic structure and the resultant macroscopic stiffness of viral DNA. The results show that the size effect makes the complex dependency of the macroscopic stiffness of viral DNA on temperature variation. In other words, we elucidate the controversy in previous literatures by our multi-scale model.

Acknowledgement

This research was supported by the National Natural Science Foundation of China (Nos. 11772182, 11272193, 10872121) and the Program of Shanghai Municipal Education Commission (No. 2019−01−07−00−09−E00018)

References

[1] Sae-Ueng U. Solid-to-fluid DNA Transition inside HSV-1 Capsid Close to the Temperature of Infection. *Nat. Chem. Biol.* **10**: 861−867, 2014.
[2] Liu T. Solid-to-fluid–like DNA Transition in Viruses Facilitates Infection. *Proc. Natl. Acad. Sci. USA.* **111**: 14675−14680, 2014.
[3] Frutos M. Can Changes in Temperature or Ionic Conditions Modify the DNA Organization in the Full Bacteriophage Capsid? *J. Phys. Chem. B.* **120**: 5975−5986, 2016.
[4] Purohit P. K. Force Steps during Viral DNA Packaging? *J. Mech. Phys. Solids*. **51**: 2239−2257, 2003.
[5] Strey H.H. Equation of State for DNA Liquid Crystals: Fluctuation Enhanced Electrostatic Double Layer Repulsion. *Phys. Rev. Lett.* **78**: 895−901, 1997.
[6] Zhang C. Y. Influence of Microscopic Interactions on the Flexible Mechanical Properties of Viral DNA. *Biophys. J.* **115**: 763−772, 2018.

AN EFFECTIVE PREDICTION FACTORS FOR DIAGNOSIS OF THE VERTEBRAL COLUMN PATHOLOGIES USING DATA MINING CLASSIFICATION TECHNIQUE

Malgorzata Zdrodowska*[1], and Agnieszka Dardzinska [1]
[1]Institute of Biomedical Engineering, Bialystok University of Technology, Bialystok, Poland

Summary Knowledge Discovery in Databases (KDD) is the process of discovering useful knowledge from a collection of data. The major phase of KDD process is Data Mining, which use the proper algorithm for finding dependencies and schemas in the prepared data set. Data mining techniques are developing very quickly and are more often used not only in typical fields such as customer relationship or management, but also in medicine, biomechanics, industry, materials sciences or mechanical engineering. The paper presents the use of data mining in biomechanics. The study analyzed the data of 310 patients using five known classification algorithms, which allowed to build an exploration model given with an accuracy of over 87%. Potential features of the occurrence of disk hernia and spondylolisthesis are also pointed out.

INTRODUCTION

Data Mining uses many different techniques that build specific types of knowledge. Depending on the purpose of the discovered knowledge, it can map classifications, regressions, clustering, characteristics, discrimination, associations, etc. The most popular Data Mining technique is classification. Classification is techniques that maps the data into the predefined classes and groups. It is used to predict group membership for data instances. There are many areas that adapt data mining techniques. For example, in the medical database, we found the rules that classify individual diseases, and then the diagnosing of subsequent patients can be carried out automatically using the found rules [1,3].

Due to the development of data mining techniques, it will achieve higher and higher popularity - not only in the typical areas (customer relationship, management), but also in others fields, like medicine, biomechanics, industry or mechanical engineering [4,5].

The aim of this study is to evaluate the effectiveness of selected data mining techniques for predicting the occurrence of disk hernia and spondylolisthesis, as well as to identify those features of the patient that have the greatest impact on the occurrence of those disabilities.

METHODOLOGY

For research we use public data set of human balance evaluations [2]. Our dataset contains data of 310 patients. Each patient is represented in the data set by 6 biomechanical attributes derived from the shape and orientation of the pelvis and lumbar spine: pelvic incidence, pelvic tilt, lumbar lordosis angle, sacral slope, pelvic radius and grade of spondylolisthesis, and classified into three groups: normal – healthy (100 patients) disk hernia (60 patients) and spondylolisthesis (150 patients). In addition, the data was divided into two separate data sets: a set of training data (80%) to build the model and a set of test data (20%) for model evaluation. In this work classification was made for two models: model 1 – all available variables (6 attributes) and model 2 – variables extracted by means of attributes selection – chi-square test (4 attributes: grade of spondylolisthesis, pelvic incidence, lumbar lordosis angle and pelvic radius). The data classification was made using WEKA software. Due to the high accuracy, for classification were used the following algorithms [1]: C4.5(J48), Random Forest, JRip, PART and Naive Bayes. The ACC (Total Accuracy) measure was used to assess the above classifiers. ACC is the total efficiency of the classifier, which determines the probability of correct classification, ie the ratio of correct classifications to all classifications.

RESULTS AND DISCUSSION

The results of classification for both models are presented in Figure 1. It was compared the results obtained on the test set, because it show us the correct accuracy and usefulness of the model.

As we can see in Fig. 1., the most accurate classification (87,10%) was obtained using the Random Forest and JRip algorithm for model 1, i.e. working on all available attributes. A slightly lower accuracy (85,48%) was obtained for the JRip algorithm and model 2, which contains only attributes extracted using the feature selection - the chi-square. We can also see, the small difference between accuracy for the model containing all features and for models after feature selection. In several cases, classifiers for models after feature selection give very similar accurancy as models in which all attributes are included. It shows the usefulness of using attributes selection, which not only saves time but also gives good predictive results.

*Corresponding author. E-mail: m.zdrodowska@pb.edu.pl.

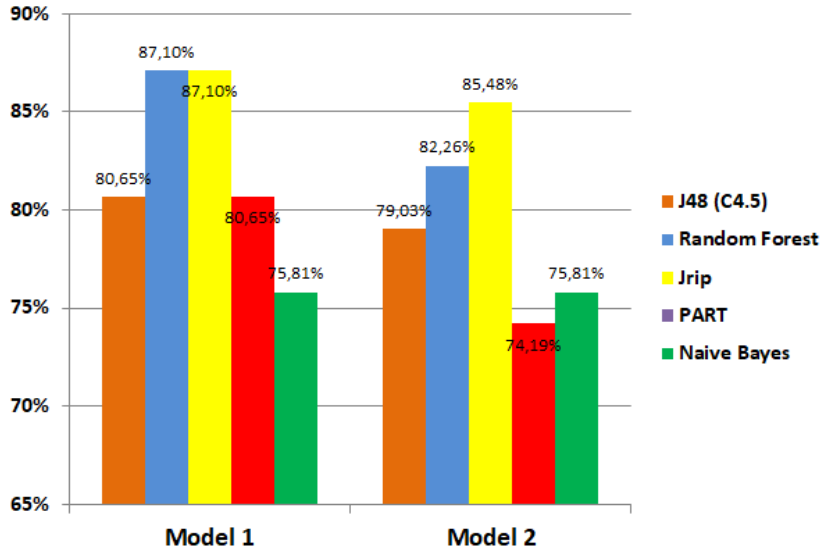

Figure 1. Comparison of correctly classified objects in individual models (for test set)

CONCLUSIONS

Discovering knowledge in databases is a dynamically developing field, whose rapid development is related to the growing number of databases and the size of information collected in them. Increasingly, data mining finds its application in engineering sciences. The analysis of classification algorithms carried out shows that they can be a very important tool supporting, e.g. vertebral column pathologies analysis. Detailed data analysis, proper preparation and proper classification allow achieving very accurate results. The research done with WEKA software also allowed to show the attributes most important in diagnosing of disk hernia and spondylolisthesis. Grade of spondylolisthesis, pelvic incidence, lumbar lordosis angle and pelvic radius proved to be important features.

References

[1] Aggarwal C.C. Data Classification Algorithms and Applications. Chapman & Hall/CRC. New York, 1–31 (1), 2015.
[2] Dua D., Graff, C. UCI Machine Learning Repository (**http://archive.ics.uci.edu/ml**), Irvine, CA, University of California, School of Information and Computer Science, 2019.
[3] Maimon O., Rokach L. (ed) Data mining and knowledge discovery handbook. Springer (10), 2010.
[4] Rogalewicz M., Sika R. Methodologies of Knowledge Discovery from Data and Data Mining Methods in Mechanical Engineering, *Management and Production Engineering Review*. **7(4)**: 97-108, 2016.
[5] Yoo I., Alafaireet P., Marinov M. Data mining in healtcare and biomedicine, A survey of the literature. *Journal of the medical systems*. **35(4):** 2431-2448, 2012.

BLOOD FLOW AND DRUG ELUTION IN COATED STENTS

Anna Maria Ranno[1] and Marek Behr[1]
[1]Chair for Computational Analysis of Technical Systems, RWTH Aachen University, 52056 Aachen, Germany,
{ranno,behr}@cats.rwth-aachen.de, www.cats.rwth-aachen.de

Summary The treatment of coronary artery disease largely involves coronary stents. The usage of stents often gives rise to in-stent restenosis, which can lead to long-term lesions or stent thrombosis. The analysis of blood flow microdynamics in stented arteries is carried out for both Newtonian and shear-thinning constitutive models. In order to help the healing process and reduce the risk of restenosis, stents are coated with a layer of drug, whose elution and deposition on the vessel wall is analyzed. Given the two different time scales required for the drug elution process and the blood microdynamics, a MOR technique is proposed.

BLOOD FLOW IN STENTED ARTERIES

Cardiovascular diseases are the most common cause of death worldwide, and more specifically, 30% of global mortality is due to coronary artery disease [1]. The treatment of such disease largely involves the implantation of coronary stents.

The usage of such devices often gives rise to in-stent restenosis or thrombosis. The critical areas where such side-effects occur highly depend on the shear stresses inside the artery. For this reason, the analysis of blood flow dynamics in stented arteries is of great interest. In-stent restenosis is due to the vessel inflammatory reaction after the implantation of the stent, which can lead to long-term lesions (40% occurance rate). Thrombus formation can be predicted by identifying the areas of rapid platelet aggregation.

The stent mainly considered here is the *Xience V* stent (shown in fig. 1). The mesh is obtained from a CAD geometry, using the commercial software Hypermesh. The Navier-Stokes equations serve as the mathematical model. The model is tested for both steady and unsteady scenarios. Pulsatile inflow boundary conditions aim at describing the flow in coronary arteries. Particular emphasis is given to the influence of stent struts on microdynamics: the analysis of streamlines show that recirculation areas and vortices are often located near the stent struts and that their geometry strongly influences them.

All the simulations are performed by means of finite element method and implemented in an in-house code.

Figure 1: Crimped geometry of the *Xience V* stent. The stent struts are highlighted in red.

Blood flow constitutive models

Blood is a suspension of red blood cells, white blood cells, and platelets, in a Newtonian fluid (plasma). In large arteries, blood can be approximated as a Newtonian fluid, without altering the overall flow. The choice of the blood constitutive model, in fact, mainly influences the local microdynamics and variables, e.g., the viscosity and the shear stress. The latter is of great importance, since coronary arteries are characterized by a specific healthy shear stress. Both lower and higher shear stress can lead to inflammation, restenosis, or platelets aggregation.

In order to investigate the local flow behavior, a generalized Newtonian model [2] is taken into consideration. In particular, a shear-thinning constitutive model takes into consideration the dependence of the blood viscosity with respect to the shear rate.

Both Newtonian and shear-thinning constitutive models are compared, with particular focus on wall shear stress, viscosity and shear rates. Shear rates and wall shear stress are analyzed as an indicator of the possible areas of inflammation and thrombosis.

DRUG ELUTION

To help the healing process and reduce the risk of restenosis, coated stents have a layer of drug that is slowly released into the blood stream.

The elution and deposition of the drug in the vessel wall is analyzed by means of an advection-diffusion equation and tailored boundary conditions. The convective field is obtained coupling the drug equation to the Navier-Stokes equation used to describe the blood flow. Once again, both the Newtonian and the shear-thinning consitutive models are compared: blood flow microdynamics can influence the drug deposition on walls. These scenarios are tested for both a test case, where a simplified one-strut stent geometry is used (see fig. 2), and for the *Xience V* stent (see fig. 3).

Figure 2: Drug elution in a cross-section of a one-strut simplified stent configuration.

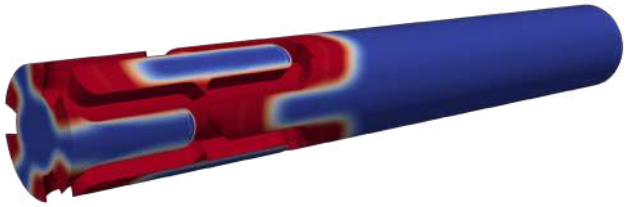

Figure 3: Drug elution in a cross-section of a *Xience V* stent. The figure shows a downstream clip of the stent.

Since the healing process spans a time frame of weeks, an appropriate time scale has to be considered and adapted to the boundary conditions. For example, starting from the Higuchi formula, a multiscale model with simplified Robin boundary conditions can be derived to simulate the drug release into the blood stream [3].

Coupling the blood flow, whose characteristic time scale is in the order of seconds, and the drug elution process, which can last up to three months, requires the usage of multiscale techniques. Here, a model order reduction (MOR) technique is proposed.

References

[1] N. Townsend, L. Wilson, P. Bhatbagar, K. Wickramasinghe, M. Rayner & M. Nichols, Cardiovascular disease in Europe: Epidemiological update 2016. *European Heart Journal*, **37**.42 (2016) 3232-3245.

[2] F. J. H. Gijsen, F. N. van de Fosse & J. Janssen, The influence of non-newtonian properties of blood on the flow in large arteries: Steady flow in a carotid bifurcation model. *Journal of Biomechanics*, **32** (1999) 601-608.

[3] P. Zunino, C. D'Angelo, L. Petrini, C. Vergara, C. Capelli & F. Migliavacca, Numerical simulation of drug eluting coronary stents: mechanics, fluid dynamics and drug release. *Computer Methods in Applied Mechanics and Engineering*, **198** (2009) 3633-3644.

MECHANICALMANIPULATION OF β -2INTERGRIN-INDUCED NEUTROPHIL RECRUITMENT IN HEPATIC SINUSOIDS

Chunfang Tong[1,2], Hao Yang[1,2], Yu Du[1,2], Peiwen Li[1,2], Ning Li[1,2], and Mian Long[1,2†]
[1]Center for Biomechanics and Bioengineering,Key Laboratory of Microgravity (National Microgravity Laboratory) and Beijing Key Laboratory of Engineered Construction and Mechanobiology, Institute of Mechanics, Chinese Academy of Sciences, Beijing 100190, China
[2]University of Chinese Academy of Sciences, Beijing 100049, China.
†E-mail: mlong@imech.ac.cn

Summary The regulating mechanisms of neutrophils (PMN) adhesion and crawling dynamics remain unclear in sinusoids. To address this issue, binding kinetics measurement and *in vitro* liver models were conducted to investigate the roles of distinct adhesive molecules and hepatic cellular interactions in the liver-specific PMN recruitment. Binding kinetics measurements showed that binding of hepatic or cerebral ICAM-1 to β2-integrin follows distinct kinetics. The 2D *in vitro* liver sinusoidal model demonstrated that LFA-1 dominates the static or shear resistant adhesion of PMNs while Mac-1 decelerates PMN crawling on LSEC monolayer. The 3D *in vitro* liver sinusoidal model suggested that each type of hepatic cells may contribute to PMN recruitment differently. Our data furthers the understandings in the distinct functions of β2 integrins in PMN accumulation within liver sinusoids and other tissues.

INTRODUCTION

Liver microcirculation is unique in human body due to the complicated structure of sinusoidal nodes, in which multiple types of hepatic and hemapoietic cells interact with each other under blood flow. The liver sinusoid is a specialized capillary network with narrow luminal diameter (7-15 μm), slow blood flow (0.1-1 dyn/cm^2), and consists of four major types of cells, including liver sinusoid endothelial cells (LSEC), liver resident macrophage Kupffer cells (KC), hepatic stellate cells (HSC), and hepatocytes (HC)[1-2]. Polymorphonuclear leukocytes (neutrophils, PMN) recruitment in the liver sinusoid is widely observed in almost all liver diseases and contributes to pathogen clearance or tissue damage. It is known that two β2 integrins lymphocyte function-associated antigen-1 (LFA-1) and macrophage-1 antigen (Mac-1) play distinct functions that LFA-1 initiates PMN slow rolling and firm adhesion but Mac-1 mediates cell crawling in PMN recruitment in the most of organ-specific microcirculations. In a liver sinusoid, however, Mac-1 seems to be predominant in PMN adhesion and crawling in localized inflammation while the role of LFA-1 is controversial [3]. The regulating mechanisms of PMN adhesion and crawling dynamics are still unclear from those *in vivo* studies. To address this issue, binding kinetics measurements were conducted to elucidate the biophysical characteristics of β2-integrin-intercellular adhesive molecule 1 (ICAM-1) in mediating PMN recruitment in liver and brain[4]. *In vitro* two-dimensional (2D) and 3D reconstructed sinusoidal models were developed to recapitulate key features of the liver microenvironment and to investigate the roles of distinct adhesive molecules and hepatic cellular interactions in the liver-specific PMN recruitment [5-6].

MATERIALS AND METHODS

PMNs, cerebral microvascular endothelial cells (BMEC) and hepatic cells were freshly isolated from the bone marrow, brain and liver of 8–12-week old male C57BL/6 mice. LSEC, HC, KC and HSC were isolated by a two-step collagenase perfusion of whole liver, a density gradient centrifugation and a cytometry sorting.

We used micropipette aspiration technique to compare the binding kinetics of LFA-1 and Mac-1 coupled on human red blood cells (RBC) to ICAM-1 expressing on BMEC or LSEC for comparing the distinct functions of β2 integrins in different tissues.

A 2D live-cell flow chamber system was established to perfuse PMNs under shear flow and record the interplay between PMN and LSEC alone or co-cultured with KC. PMN adhesion and crawling were quantified for fMLF-activated PMN on TNF-α-stimulated LSEC. Related molecular regulations of LFA-1, Mac-1, and CD44 and the impact of KC were also analyzed.

An *in vitro* 3D liver model was developed to further mimic liver microenvironment with well-organized cell composition and physical interactions. Two microfabricated polydimethylsiloxane (PDMS) layers were bonded together with a polyethylene (PE) porous membrane between them, forming two fluidic channels separated by a permeable membrane, which represents liver sinusoids with an endothelium separating microvenule and Disse Space. To replicate the physiological structure and cellular composition, the 3D microfluidic device was constructed by integrating LSEC monolayer with sparsely distributed KC and HSC on either side of extracellular matrix (ECM)-coated PE membrane into HC monolayer immobilized on lower PDMS substrate. Typical liver specific functions and multi-typed cell interactions in protein secretion, drug metabolism and immune responses were analyzed under shear flow. Moreover, the evolution dynamics of LSEC fenestrae was tested using total internal reflection fluorescence structured-illumination microscopy (TIRF-SIM) and atomic force microscopy (AFM).

RESULTS AND DISCUSSION

Binding kinetics measurements showed that binding of hepatic or cerebral ICAM-1 to β2-integrin follows distinct kinetics. ICAM-1 on murine LSECs binds to LFA-1 with higher on- and off-rates but lower effective affinity compared

with Mac-1, whereas ICAM-1 on BMECs binds to LFA-1 with higher on-rates, similar off-rates, and higher effective affinity compared with Mac-1.

The 2D *in vitro* liver sinusoid model demonstrated that LFA-1 dominates the static or shear resistant adhesion of PMNs while Mac-1 decelerates PMN crawling on LSEC monolayer. Any one of LFA-1, Mac-1, and CD44 molecules alone is not able to work effectively for mediating PMN transmigration across LSEC monolayer. The presence of KC only affects the randomness of PMN crawling.

The 3D *in vitro* liver sinusoid model suggested that shear flow fostered albumin secretion for HC alone or even higher when combining with nonparenchymal cell (NPC) co-culture, implying that co-culture and shear flow could work cooperatively. Shear flow enhanced dramatically CYP1A2 activity when HC were cultured alone or co-cultured with NPC, while co-culture with NPC alone had no effects on CYP activities. Under LPS stimulation, co-culture of LSEC with HSC, KC or HC, or all the three cell types increased PMN accumulation, implying that each type of hepatic cells may contribute to PMN recruitment differently. The fenestrae number decreased with culture time, which could be rescued by HC co-culture. PMN adhesion was reduced after fenestrae degeneration, suggesting an extra role of fenestrae in PMN recruitment.

CONCLUSIONS

Our results clarified the molecular mechanisms of PMN recruitment in the liver sinusoids using well-defined biophysical approaches, which provide a mechanistic insight into relating binding kinetics of hepatic sinusoidal and cerebral microvascular ICAM-1 to free PMN crawling, shear-induced PMN adhesion and crawling on primary LSEC, and the distinct impacts of each type of hepatic cells. Moreover, the 3D microfluidic device replicates the key architecture of liver sinusoids by integrating four major types of cells into two separated flow channels, which could serve as a functional platform to investigate the short-duration functional maintenance, hepatic cellular interplay, cytotoxic metabolism, and inflammatory cascade under physiologically-like microenvironment

ACKNOWLEDGEMENT

This work was supported by National Natural Science Foundation of China Grants 31661143044, 91642203, 31627804, 31230027 and 31870930, and Strategic Priority Research Program and Frontier Science Key Project of Chinese Academy of Sciences grants QYZDJ-SSW-JSC018 and XDB22040101.

References

[1] Dash A., Simmers M.B., Deering T.G., et al. Hemodynamic flow improves rat hepatocyte morphology, function, and metabolic activity in vitro. *Am J Physiol Cell Physiol*, 304(11):C1053-1063, 2013.

[2] Vollmar B., Menger M.D. The hepatic microcirculation: mechanistic contributions and therapeutic targets in liver injury and repair. *Physiol Rev*, 89(4):1269-1339, 2009.

[3] Menezes G.B., Lee W.-Y., Zhou H., et al. Selective down-regulation of neutrophil Mac-1 in endotoxemic hepatic microcirculation via IL-10. *J Immunol*, 183(11):7757-7568, 2009.

[4] Tong C.F., Zhang Y., Lü S.Q., et al. Binding of intercellular adhesion molecule 1 to β2-integrin regulates distinct cell adhesion processes on hepatic and cerebral endothelium. *Am J Physiol Cell Physiol*, 315:C409-421, 2018.

[5] Yang H., Li N., Du Y., et al. Neutrophil adhesion and crawling dynamics on liver sinusoidal endothelial cells under shear flow. *Exp Cell Res*, 351:91-99, 2017.

[6] Du Y., Li N., Yang H., et al. Mimicking liver sinusoidal structures and functions using a 3D-configured microfluidic chip. *Lab Chip*, 17(5):782-794, 2017.

STUDY OF MECHANICAL PROPERTIES OF A CHITOSAN-VANCOMYCIN- NANOCELLULOSE NANOPARTICLES COMPOSITE MATERIAL OF BACTERIAL ORIGIN TO CLOSE DURA MATER DEFECTS

Daniil Parshin[1,2*], Lipovka Anna[1,2], Alexey Kharchenko[3],
[1]Lavrentyev Institute of Hydrodynamics, Novosibirsk, Russia
[2]Novosibirsk State University, Novosibirsk, Russia
[3]Neurosurgical Department No. 1, Novosibirsk Research Institute of Traumatology and Orthopaedics, Novosibirsk, Russia

Summary In neurosurgical practice often arises the need for dura mater restoration. The lack of integrity of the dura mater leads to infectious complications: cerebrospinal fluid, meningitis, and meningoencephalitis which can lead to death of the patient. The restoration of the patient's meninges is not always possible precisely because of injuries. In such cases, it is imoirtant to synthesize membranes that would be universal in the sense of biocompatibility and antibacterial for the purpose of clinical use. The aim of this work is to investigate properties of a biopolymer analogue of the dura mater.

EXPERIMENTAL METHODS

Material synthesis:

Bacterial nanocellulose is a nanoscale biopolymer that has similar properties with collagen, obtained by culturing in a medium containing carbohydrate (glucose, fructose, sucrose, etc.) the bacteria Komagataeibacter xylinus under static conditions.

Bacterial cellulose is widely used as a material for the treatment of burns and cosmetology, as well as a scaffold, because various body cells grow well on it. There are experimental studies of the use of bacterial nanocellulose as a vascular prosthesis, menisci. Bacterial cellulose also shows good results in animal models during experimental restoration of a damaged peripheral nerve.

The thickness measurement was carried out on the device "laser complex for high-speed cutting of biological tissue." The thickness measurement sensor (LD200) of the biological material at the time of measurement produces a sinusoidal voltage of a certain value, the value of which is directly proportional to the thickness of this material. The measurement result is transmitted to a computer, where the data is processed by software. This method allows to accurately determine the thickness of the material. This installation also produces precise cutting of the material.

Mechanical Testing:

For mechanical testing a universal rupture machine Zwick&Roell is used. The dog-bone shaped specimen is cut from the sheet, its size is measured. Then the specimen is fastened in custom made (3d-printed) clamps (Pic. 1), which is placed in the jaws of the rupture machine. During the experiment the specimen is fully immersed into the sodium solution of normal body temperature (37C). The loading is divided into the several stages, with the preconditioning technique used at the initial stages.

RESULTS AND CONCLUSIONS

A prospective, randomized, double-blind, controlled clinical trial performed on the dura mater defect plastics registered on the ClinicalTrials.gov website under the number NCT00859508 showed that bacterial nanocell in the form of a SyntheCelproduct is not inferior to other implants.

Since after implantation into the patient's body the sample will experience certain mechanical stress, it is critically necessary to assess the mechanical properties of the samples depending on the parameters of their synthesis. Tests for more than 30 tissue samples with various parameters of its synthesis were conducted during this study.

After mechanical tests, differences in the strength characteristics of the samples were determined depending on the synthesis parameters of the material. A comparison was made with the cadaveric material of the dura mater.

Picture 1. The specimen after the experiment. (Visible rupture can be observed ad the middle)

References

[1] Iguchi, M., S. Yamanaka, and A. Budhiono. Journal of materials science 35.2 (2000): 261-270
[2] Scionti, Giuseppe. MS Thesis "Mechanical properties of bacterial cellulose implants." (2010).

A COLLAGEN RECRUITMENT MODEL OF FAILURE IN TENDONS AND LIGAMENTS

James Gregory*[1], Andrew L. Hazel[1], and Tom Shearer[1]
[1]Department of Mathematics, University of Manchester, UK

Summary Collagen fibrils are microstructural components of tendons and ligaments that we model as elastoplastic solids, assumed to be continuously distributed within the tissue. We compute the stress in the tendon by assuming that the yield stretch and rupture stretch of the collagen fibrils follow distributions, rather than being single-valued. This approach allows us to fit to a larger range of tendon stress-strain data than was previously possible using similar models, whilst only including parameters that can be measured experimentally.

INTRODUCTION

Tendons and ligaments, connecting bone to muscle and bone to bone, respectively, are vitally important soft tissues found in the body. When a tendon or ligament is subjected to unusually high loads, such as during strenuous activities like running and jumping, micro-tears can appear within the tissue. These micro-tears can be responsible for injuries varying in severity from tendinitis to catastrophic total rupture [1]. Mathematical models of soft tissue typically seek to model their mechanical response over the physiological range of strains observed during everyday motion. This means that the commonly used models are only applicable up to the initial onset of damage and they cannot be used to make predictions on how tendons or ligaments will behave under continued loading.

Tendons and ligaments have a complex hierarchical structure, the main mechanical component of which is collagen, making up 65-80% of the dry weight [2]. Collagen fibrils, made of mostly type-I collagen, are bound within fascicles which make up a tendon/ligament. The fibrils are crimped within the fascicle, with the amount of crimp varying between fibrils [2]. This varying amount of crimp is responsible for the gradual stiffening of tendons as more fibrils are recruited over the course of a deformation. When the applied strain goes beyond the physiological range (>4% for some positional tendons), damage is likely to occur. Injuries due to overloading are prevalent for strains in the region of 4-8%. When a strain of over 8% is applied, a combination of both yielding in the fibrils and shear failure in the matrix leads to tendon rupture. There are two main ways in which an unusually high load can cause damage to tendon microstructure, leading to a debate over the main mechanism leading to rupture. If fibrils are discontinuous then it is argued that the mechanism that leads to yielding is the breakdown of interfibrillar components and the subsequent slippage of fibrils past one another, whereas if fibrils are continuous, yielding in the tendon will occur due to yielding of the fibrils themselves [3].

THE MODEL

We assume that the tendon is composed of a family of parallel fibres embedded within a mechanically inactive matrix. Each fibril has a critical stretch λ_c, equal to the tendon stretch required to remove the slack in the fibril. Once a fibril is taut, it exhibits a linearly elastic response until it has been stretched by a factor of λ_Y, where it yields. The fibril then deforms plastically until it ruptures, after having been stretched by a factor of λ_R. The stress in a fibril σ_f is given by

$$\sigma_f(\lambda,\lambda_c,\lambda_Y,\lambda_R) = \begin{cases} E\left(\dfrac{\lambda}{\lambda_c}-1\right) & \lambda_c \le \lambda \le \lambda_c\lambda_Y, \\ p(\lambda,\lambda_c,\lambda_Y,\lambda_R), & \lambda_c\lambda_Y \le \lambda \le \lambda_c\lambda_R, \\ 0, & \text{otherwise}, \end{cases} \tag{1}$$

where $p(\lambda,\lambda_c,\lambda_Y,\lambda_R)$ is a function that describes the plastic behaviour of an individual collagen fibril. We assume that the critical stretch λ_c, the yield stretch λ_Y, and the rupture stretch λ_R, all follow a joint distribution given by $\Lambda(\lambda_c,\lambda_Y,\lambda_R)$. We then compute the stress in the tendon σ_T using

$$\sigma_T(\lambda) = \phi \int_{-\infty}^{\infty}\int_{-\infty}^{\infty}\int_{1}^{\lambda} \sigma_f(\lambda,\lambda_c,\lambda_Y,\lambda_R)\Lambda(\lambda_c,\lambda_Y,\lambda_R)\mathrm{d}\lambda_c\mathrm{d}\lambda_Y\mathrm{d}\lambda_R, \tag{2}$$

where λ is the applied tendon stretch, and ϕ is the collagen volume fraction. This model is similar to those of Hurschler et al. [4] and Hamedzadeh et al. [5], in that we exclude fibrils from the integral in equation (2) once they have been stretched by a factor of λ_R. We were able to fit these existing models to data from Goh et al. [6] in cases where there was a well-defined peak in the stress-strain curve, however, a significant proportion of the data contained features that could not be accounted for. These include plateaus instead of well-defined peaks, and step-like failure behaviour. By including distributions for the yield and rupture stretch, we can account for these features by adjusting the shape of these distributions, and how much they overlap.

*Corresponding author. E-mail: james.gregory@manchester.ac.uk

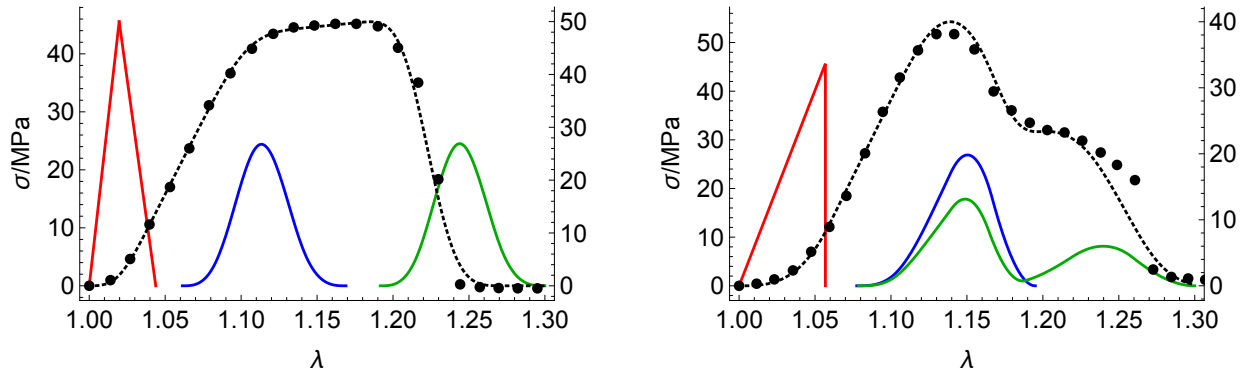

Figure 1: Our model (black dashed lines) fitted to data from Goh et al. [6] (black markers). The red curves show the distribution of critical stretch λ_c. The blue and green curves show the distributions of yield and rupture stretch, respectively, transformed to be in terms of tendon stretch. The right hand axis refers to these distributions. Both sets of data contain features that could not previously be accounted for using collagen recruitment models: (a) contains a plateau instead of a well-defined peak, and (b) contains step-like failure behaviour.

Figure 1 shows the model fitted to stress-strain data from Goh et al. [6], taken from mouse tail tendons stretched to failure. By modelling the fibrils as bilinear elastoplastic, it is possible to produce a macroscale stress-strain curve containing a second linear region/plateau by ensuring that there is no overlap between the yield and rupture stretch distributions, once they have been transformed to be in terms of tissue stretch. This means that all of the fibrils yield before any have ruptured. By allowing the transformed distributions to overlap, we can produce a more well-defined peak, as can be seen in Figure 1b. By using a bimodal distribution for the fibril rupture stretch, we can achieve step-like failure behaviour, also present in Figure 1b.

CONCLUSIONS

We have derived a general model of tendon failure, capable of fitting to a much wider array of stress-strain data than was previously possible using similar collagen recruitment models. By splitting the fibril stress into elastic and plastic parts, and by introducing distributions for the yield and rupture stretch, we are able to produce macroscale stress-strain curves that closely resemble those determined experimentally by Goh et al. [6]. There is a large amount of variability in the reported values of fibril yield and rupture strain, and so using distributions for these parameters, rather than single values, means that the microstructure is better represented. This model has the added benefit of only using parameters that can be measured experimentally. This means that if we know how a certain process, such as ageing or disease, affects the microstructure, we can use this model to predict how the macroscale tendon properties will be affected.

References

[1] Bass, E. Tendinopathy: why the difference between tendinitis and tendinosis matters. *International journal of therapeutic massage & bodywork.* 2012.
[2] Kannus, P. Structure of the tendon connective tissue. *Scandinavian journal of medicine & science in sports.* 2000.
[3] Hijazi, K. M., Singfield, K. L., & Veres, S. P. Ultrastructural response of tendon to excessive level or duration of tensile load supports that collagen fibrils are mechanically continuous. *Journal of the mechanical behavior of biomedical materials*. 2019.
[4] Hurschler, C., Loitz-Ramage, B., & Vanderby Jr, R. A structurally based stress-stretch relationship for tendon and ligament. 1997.
[5] Hamedzadeh, A., Gasser, T. C., & Federico, S. On the constitutive modelling of recruitment and damage of collagen fibres in soft biological tissues. *uropean Journal of Mechanics-A/Solids.* 2018.
[6] Goh, K. L., Holmes, D. F., Lu, Y. H., Kadler, K. E., & Purslow, P. P. ge-related dataset on the mechanical properties and collagen fibril structure of tendons from a murine model. *Scientific data.* 2018.

FLEXURE OF BIOLOGICAL GLASS FIBERS LEADS TO SAWTOOTH FORCE-DISPLACEMENT RESPONSES RELATED TO SLIP INSTABILITIES, NOT TOUGHNESS ENHANCEMENT

Wenqiang Fang[1], Haneesh Kesari *[1], Michael A. Monn[1], and Sayaka Kochiyama[1]
[1]School of Engineering, Brown University, Providence, RI, USA

Summary Layered architectures are prevalent in biological composites, such as nacre and bone. The skeletal elements—called spicules—from the sponge *Euplectella aspergillum* are another example of a biological composite with a layered architecture. We performed three-point bending tests on the spicules and also observed nonlinear force-displacement responses containing jagged, sawtooth shapes. However, based on the analysis of micrographs obtained during the tests, we found that the sawtooth pattern of the force-displacement response is actually a consequence of slipping interactions between the spicule and the test fixture, not from toughening mechanisms like crack arrest and crack deflection. We propose a nonlinear bending-sliding model to illustrate how is the sawtooth pattern related to the heterogeneous friction between the spicule and the test fixture.

INTRODUCTION

There are few engineering materials that are both strong and tough. However, some biological materials have been shown to possess both high strength and high toughness [1, 2, 3, 4]. For example, nacre—the iridescent portion of some mollusk shells—has a flexural strength similar to aluminum (around 280 MPa) and a specific fracture initiation toughness similar to nylon (around 2-5 MPa $\mathrm{m}^{1/2}$).

Often, these biological materials are composites that are made up of a combination of a brittle ceramic phase, such as calcium carbonate or hydroxyapatite, and a compliant protein phase, like collagen or chitin. It has been hypothesized that like nacre, the marine sponge *Euplectella aspergillum* (*Ea.*) anchor spicules' layered architecture enhances its fracture toughness [5, 6].

We investigated whether the sawtooth pattern in the *Ea.* spicules' mechanical response is connected to toughness enhancement by 1) performing flexural tests on the spicules and 2) analyzing this data and data obtained from previous three-point bending tests performed on the spicules [7]. Our analysis shows that the sawtooth pattern can arise as a consequence of the spicule slipping on the flexural test fixture. Therefore, the presence of the sawtooth pattern alone cannot be used as proof that the spicule's toughness is enhanced.

MATERIALS AND METHODS

In a conventional three-point bending test, a specimen is held/supported by a test fixture that consists of either two rollers or "knife edges" that are set a fixed distance apart. We performed three-point bending tests on a group of *Ea.* spicules using this type of test configuration, which we refer to as "simply supported". In this work, the test fixture supports consisted of the edges of a trench cut in a metal plate. We then measured the arc length of the spicule specimen between the trench edges at every stage displacement step from micrographs taken during the tests. We also conducted the same measurements on data previously presented in [7] for 33 additional *Ea.* specimens. From these measurements, we found that discontinuities in the F-w_0 response corresponded with discontinuous changes in the arc length of the specimen (see Figure 1 (D)–(F)).

We also present data from 12 experiments in which we glued the ends of the spicules to the test fixture to prevent them from sliding during the test. In this glued configuration, the spicules fail without any sawtooth pattern in their F-w_0 response. This suggests that the sawtooth pattern can be a pathology of the simply support test configuration and in a previous study [7], and not a characteristic of the spicule's failure process.

DISCUSSION AND CONCLUSIONS

We propose a nonlinear bending-sliding model, in which we assume that the deformation of the spicule is governed by Euler's Elastica theory in cooperation with kinetic friction between the spicule and the test fixture. We found that the fluctuation in frictional coefficient causes waviness in the equilibrium dimensionless force-displacement ($\hat{F}$-$\hat{w}_0$) curves. By considering the loading strategy, displacement controlled loading with finite machine compliance, we provide an explanation of discontinuities in the $\hat{F}$-$\hat{w}_0$ curves. We assume the frictional coefficient along the arc length of the spicule varying in a sinusoidal form and fit the parameters to experimental data. The best fitting parameters we choose to qualitatively capture the sawtooth pattern are in reasonable ranges for the tested samples. With the nonlinear bending-sliding model, we are able to explain the existence of the sawtooth pattern and how it is related to the heterogeneous friction between the spicule and the test fixture. This further supports our experimental observation that the sawtooth jumps in the $\hat{F}$-$\hat{w}_0$ response is mostly a consequence of sliding instead of crack growth.

*Corresponding author. E-mail: Haneesh_Kesari@brown.edu

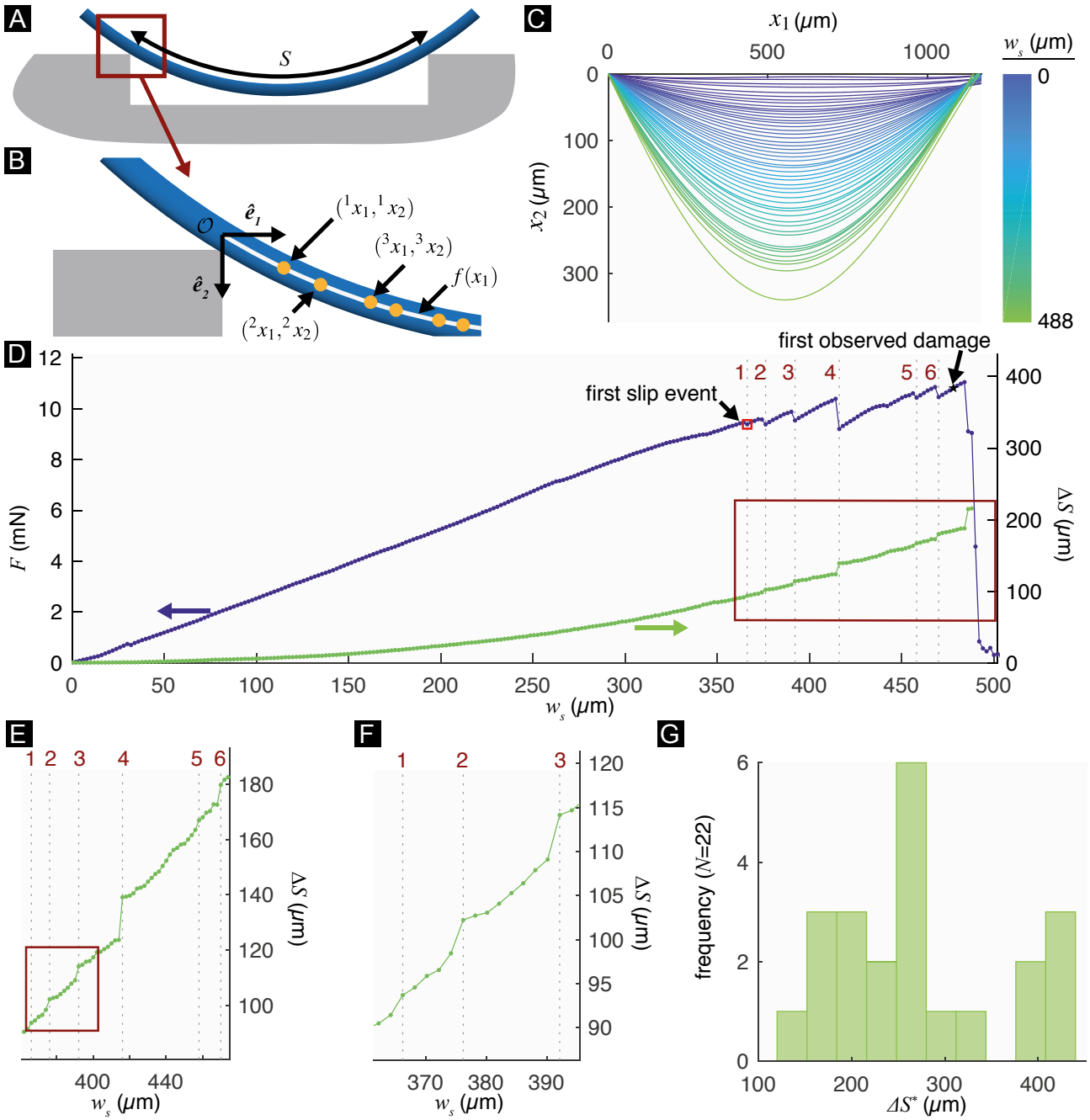

Figure 1: Correlation between the sawtooth pattern in the force-displacement response and discontinuous jumps in arc length. (A) A schematic of a spicule's deformed configuration in the simply supported tests showing the arc length S. (B) Magnified view of (A) showing the points $({}^ix_1, {}^ix_2)_{i=1\ldots n}$ identified along the spicule's longitudinal axis and the continuous representation of the longitudinal axis $f : [0, L] \to \mathbb{R}$. (C) A graph of the function f for a representative spicule computed for every fifth stage displacement increment. (D) The force, F, (left axis) as a function of stage displacement, w_s, for a representative spicule compared to the total change in arc length ΔS (right axis). The vertical, dashed lines indicate the w_s values at which we identified discontinuities (numbered 1–6) in the F-w_s response. (E) A zoomed in view of the plot region within the red rectangle in (D). (F) A zoomed in view of the plot region within the red rectangle in (E) highlighting the discontinuous changes in ΔS at locations 1–3. (G) A histogram of the total change in arc length at the initiation of failure ΔS^* for the 22 spicules exhibiting sawtooth patterns in their F-w_0 responses.

References

[1] John D Currey. How well are bones designed to resist fracture? *J. Bone Miner. Res.*, 18(4):591–598, 2003.

[2] RZ Wang, Z Suo, AG Evans, N Yao, and IA Aksay. Deformation mechanisms in nacre. *J. Mater. Res.*, 16(9):2485–2493, 2001.

[3] Reza Rabiei, Sacheen Bekah, and Francois Barthelat. Nacre from mollusk shells: Inspiration for high-performance nanocomposites. *Nat. Polym.*, 2:113–149, 2012.

[4] Francois Barthelat and Reza Rabiei. Toughness amplification in natural composites. *J. Mech. Phys. Solids.*, 59(4):829–840, 2011.

[5] SL Walter, BD Flinn, and G Mayer. Mechanisms of toughening of a natural rigid composite. *Mater. Sci. Eng: C*, 27(3):570–574, 2007.

[6] George Mayer. New toughening concepts for ceramic composites from rigid natural materials. *J. Mech. Behav. Biomed. Mater.*, 4(5):670–681, 2011.

[7] Michael A Monn and Haneesh Kesari. Enhanced bending failure strain in biological glass fibers due to internal lamellar architecture. *J. Mech. Behav. Biomed. Mater.*, 2017.

ANALYTICAL SOLUTIONS MIMICKING MORPHOLOGICAL EVOLUTIONS OF TWO MUSHROOMS-A. MUSCARIA AND M. CHLOROPHOS

Xiaoyi Chen[1] and Hui-Hui Dai *[2]
[1]Division of Science and Technology, BNU-HKBU United International College, Guangdong, China
[2]Department of Mathematics, City University of Hong Kong, Kowloon Tong, Hong Kong

Summary A theory for stress-free axisymmetric configurations induced by locally incompatible growth fields is developed. Through polar decomposition of the growth tensor and appropriate choice of base vectors, we derive two constraints on the growth functions and a system of equations for the current configuration and elastic rotation. Under a particular case, a family of analytical solutions are constructed, which can mimic the morphological evolutions of two mushrooms-A. muscaria and M. chlorophos with a turnup cap and a depressed cap respectively. The growth functions (heterogeneous and anisotropic) and explicit analytical results reveal clearly the relationship between parameters and growth patterns. It is also found that the slightly turnup cap and the depressed cap of the mushrooms are well captured by two parameters, which turn out to be driven by the circumferential growth function.

INTRODUCTION

The multiplicative decomposition model proposed by Rodriguez *et al.* [1] is widely used to understand pattern formations of biological tissues (algae, intestine, skull *etc*). When applying this model, the growth functions are usually taken to be constants and numerical methods are adopted. Only in some exceptional cases, analytical solutions were obtained. Here, within the framework of this growth theory, we intend to construct analytical solutions which can mimic the morphological evolutions of two mushrooms-A. muscaria and M. chlorophos, from which some insights are deduced.

A. muscaria is one of the most iconic toadstool species and is noted for its hallucinogenic and M. chlorophos is among the oldest bio-luminescent fungus and emits pale green light in the darkness. Both the two mushrooms initially have ellipsoidal cap and expand outward during the growth, but at the final stage, the former mushroom "chooses" to turn up the cap slightly while the latter one "chooses" to depress its cap in the central part. We will establish a theory for stress-free $3D$ axisymmetric configurations induced by growth, from which some special analytical solutions are obtained to describe the above-mentioned two processes. We point out that a theory for stress-free 2D configurations induced by growth is given in a previous work [2].

STRESS-FREE 3D AXISYMMETRIC DEFORMATION

We adopt the multiplicative decomposition method [1], according to which the deformation gradient $\mathbf{F}=\mathbf{AG}$ where $\mathbf{G}$ is the growth tensor and $\mathbf{A}$ is the accommodating elastic tensor. Our goal is to find appropriate forms of $\mathbf{A}$ and $\mathbf{G}$ so that the current configuration is 3D axisymmetric and stress-free under the condition $\nabla\times\mathbf{G}\neq\mathbf{0}$ (the growth tensor is locally incompatible [3]). Given the eigenvalues $(\mu_1^2,\mu_2^2,\mu_3^2)(\mu_i>0,i=1,2,3)$ and orthonormal eigenvectors $(\mathbf{p}^1,\mathbf{p}^2,\mathbf{p}^3)$ of the growth metric $\mathbf{M}=\mathbf{G}^T\mathbf{G}$, we have the polar decomposition (see [4]) of the growth tensor as

$$\mathbf{G}=\mu_1\mathbf{q}^1\otimes\mathbf{p}^1+\mu_2\mathbf{q}^2\otimes\mathbf{p}^2+\mu_3\mathbf{q}^3\otimes\mathbf{p}^3,\quad \mathbf{q}^i=\mathbf{Q}\mathbf{p}^i,\ i=1,2,3, \tag{1}$$

where $\mathbf{Q}$ is an orthogonal tensor. One key step of our derivation is the appropriate choice of the base vectors. Based on (1), the curvilinear coordinates $(\Theta^1,\Theta^2,\Theta^3)$ in the initial configuration R_0 (assumed to be Euclidean) are chosen such that the contra-variant base vectors are $\{\mathbf{g}^i=|\mathbf{g}^i|\mathbf{p}^i,i=1,2,3\}$, where $\mathbf{g}^i\cdot\mathbf{g}_j=\delta^i_j$, $\mathbf{g}_j=\partial\mathbf{X}/\partial\Theta^j$ and $\mathbf{X}=R(\Theta^1,\Theta^3)\mathbf{e}_R+Z(\Theta^1,\Theta^3)\mathbf{e}_Z$ is the initial position vector ($\{\mathbf{e}_R,\mathbf{e}_\Theta,\mathbf{e}_Z\}$ are the cylindrical base vectors with $\Theta^2=\Theta$). For the virtual state R_g ($\mathbf{G}$ is the defromation gradient from R_0 to R_g) and current configuration R_t, base vectors are chosen repectively to be $\{\mathbf{q}^i,i=1,2,3\}$ and $\{\mathbf{e}_R,\mathbf{e}_\Theta,\mathbf{e}_Z\}$.

To ensure the stress-free deformation of a hyperelastic material, we set $\mathbf{A}$ to be a locally rotation tensor (excluding rigid body rotations), and for an axisymmetric deformation we have $\mathbf{A}=\cos\alpha\mathbf{e}_R\otimes\mathbf{q}^1+\sin\alpha\mathbf{e}_R\otimes\mathbf{q}^3-\sin\alpha\mathbf{e}_Z\otimes\mathbf{q}^1+\cos\alpha\mathbf{e}_Z\otimes\mathbf{q}^3+\mathbf{e}_\Theta\otimes\mathbf{q}^2$. Then from $\mathbf{F}=\mathbf{AG}$ and $\mathbf{F}=\nabla\mathbf{x}$ where $\mathbf{x}=r(\Theta^1,\Theta^3)\mathbf{e}_R+z(\Theta^1,\Theta^3)\mathbf{e}_Z$ is the current position vector, we have equations for $\mathbf{x}$ and one constraint for the circumferential growth function

$$\frac{\partial z}{\partial\Theta^1}=-\lambda_1\sin\alpha,\quad \frac{\partial z}{\partial\Theta^3}=\lambda_3\cos\alpha,\quad \frac{\partial r}{\partial\Theta^1}=\lambda_1\cos\alpha,\quad \frac{\partial r}{\partial\Theta^1}=\lambda_3\sin\alpha,\quad r=\lambda_2, \tag{2}$$

where $\lambda_i=\mu_i/|\mathbf{g}^i|,i=1,2,3$. Then the compatibility conditions $\frac{\partial^2 z}{\partial\Theta^1\partial\Theta^3}=\frac{\partial^2 z}{\partial\Theta^3\partial\Theta^1}$, $\frac{\partial^2 r}{\partial\Theta^1\partial\Theta^3}=\frac{\partial^2 r}{\partial\Theta^3\partial\Theta^1}$ and $\frac{\partial^2\alpha}{\partial\Theta^1\partial\Theta^3}=\frac{\partial^2\alpha}{\partial\Theta^3\partial\Theta^1}$ lead to respectively the equations of α and the other constraint for growth functions

$$\frac{\partial\alpha}{\partial\Theta^1}=\frac{1}{\lambda_3}\frac{\partial\lambda_1}{\partial\Theta^3},\quad \frac{\partial\alpha}{\partial\Theta^3}=-\frac{1}{\lambda_1}\frac{\partial\lambda_3}{\partial\Theta^1},\quad \frac{\partial}{\partial\Theta^1}\left(-\frac{1}{\lambda_1}\frac{\partial\lambda_3}{\partial\Theta^1}\right)=\frac{\partial}{\partial\Theta^3}\left(\frac{1}{\lambda_3}\frac{\partial\lambda_1}{\partial\Theta^3}\right). \tag{3}$$

It is noted that $(3)_{1,2}$ can also be obtained from $\nabla\times\mathbf{F}=\mathbf{0}$ and $(3)_3$ can also be derived from $\mathcal{R}=\mathbf{0}$ where $\mathcal{R}$ is the Riemann curvature tensor associated with the growth metric $\mathbf{M}$.

*Corresponding author. E-mail: mahhdai@cityu.edu.hk

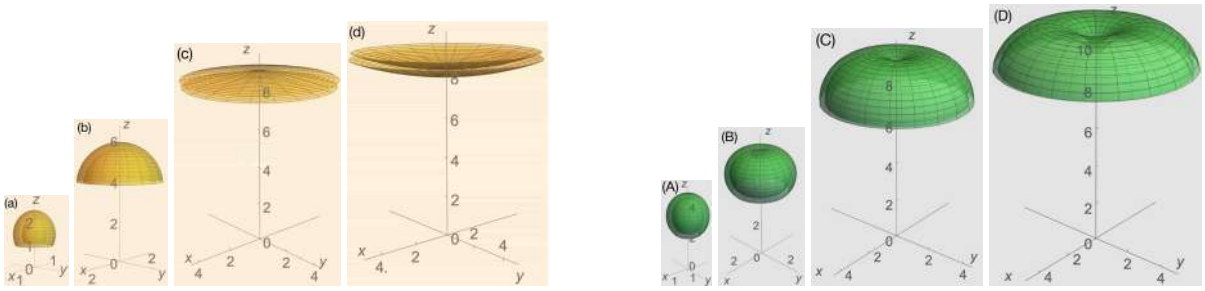

Figure 1: Simulation of growth patterns of A. muscaria (a-d) and M. chlorophos (A-D) based on the result of (4-5) together with the determination of C_1, C_2, α_0 and the properly chosen values of s, k, d_1.

A FAMILY OF ANALYTICAL SOLUTIONS

In this section, we construct analytical solutions to (2-3) for the particular case $\lambda_3 = \lambda_3(\Theta^3)$. We have from $(3)_3$ that $\lambda_1 = h_1(\Theta^1)\int \lambda_3(\Theta^3)\mathrm{d}\Theta^3 + h_2(\Theta^1)$, where $h_i(\cdot)(i = 1, 2)$ are two arbitrary functions. To further simplify the result, we consider $h_2 = d_0 \cdot h_1$ where d_0 is a constant. Then taking λ_1, λ_3 back to $(3)_{1,2}$ and $(2)_{1-5}$, α, (r, z) and λ_2 are obtained. In summary, we have

$$\begin{aligned} &\lambda_3 = \lambda_3(\Theta^3), \quad \lambda_1 = h_1(\Theta^1)\left[\int \lambda_3(\Theta^3)\mathrm{d}\Theta^3 + d_0\right], \quad \alpha = \int h_1(\Theta^1)\mathrm{d}\Theta^1 + \alpha_0, \\ &z = \cos\alpha\left[\int \lambda_3(\Theta^3)\mathrm{d}\Theta^3 + d_0\right] + C_1, \quad \lambda_2 = r = \sin\alpha\left[\int \lambda_3(\Theta^3)\mathrm{d}\Theta^3 + d_0\right] + C_2, \end{aligned} \tag{4}$$

with the trajectory of r and z being $(z - C_1)^2 + (r - C_2)^2 = [\zeta(\Theta^3)]^2$, $\zeta(\Theta^3) = \int \lambda_3(\Theta^3)\mathrm{d}\Theta^3$, and α_0, C_1, C_2 being integration constants. In order the current configuration is Euclidean, one also needs to impose the restriction that the mappings of $r(\Theta^1, \Theta^3)$ and $z(\Theta^1, \Theta^3)$ are invertible. Also, it is needed that $\lambda_1, \lambda_2, \lambda_3$ are all positive. In the following, to obtain biologically relevant solutions, we further let $\lambda_3 = s > 0$ (constant) and $h_1 = k \neq 0$ (constant).

MIMICKING THE GROWTH PATTERNS OF TWO MUSHROOMS

In this section, analytical solutions in (4) are applied to generate growth patterns. For the axisymmetric deformation, the initial configuration on the cross section in the $Z - R$ plane is set to be an elliptic strip $Z = c \cdot \cosh(\Theta^3)\cos(\Theta^1) + D_1$, $R = c \cdot \sinh(\Theta^3)\sin(\Theta^1) + D_2$, where $(\Theta^1, \Theta, \Theta^3)$ are orthogonal curvilinear coordinates and $0 < \Theta^1 \leq \eta_0 < \pi$, $0 \leq \Theta \leq 2\pi$, $\xi_0 \leq \Theta^3 \leq \xi_1$, and (D_1, D_2) is the center point and c is the distance between the foci and the center point. The principal directions of growth and growth functions are derived based on results of previous two sections

$$\begin{aligned} &\mathbf{g}^1 = \tfrac{2}{c}\cdot\tfrac{\sinh\Theta^3\cos\Theta^1}{\cosh 2\Theta^3 - \cos 2\Theta^1}\mathbf{e}_R - \tfrac{2}{c}\cdot\tfrac{\cosh\Theta^3\sin\Theta^1}{\cosh 2\Theta^3 - \cos 2\Theta^1}\mathbf{e}_Z, \ \mathbf{g}^2 = \tfrac{\mathbf{e}_\Theta}{R} = \tfrac{1}{c\cdot\sinh(\Theta^3)\sin(\Theta^1) + D_2}\mathbf{e}_\Theta, \\ &\mathbf{g}^3 = \tfrac{2}{c}\cdot\tfrac{\cos\Theta^3\sin\Theta^1}{\cosh 2\Theta^3 - \cos 2\Theta^1}\mathbf{e}_R + \tfrac{2}{c}\cdot\tfrac{\sinh\Theta^3\cos\Theta^1}{\cosh 2\Theta^3 - \cos 2\Theta^1}\mathbf{e}_Z, \ \mu_1 = \lambda_1\cdot|\mathbf{g}^1| = \tfrac{k\cdot s\,\Theta^3 + d_1}{c}\sqrt{\tfrac{2}{\cosh(2\Theta^3) - \cos(2\Theta^1)}}, \\ &\mu_2 = \lambda_2\cdot|\mathbf{g}^2| = \tfrac{r}{R} = \tfrac{(s\,\Theta^3 + d_1/k)\sin(k\Theta^1 + \alpha_0) + C_2}{c\cdot\sinh(\Theta^3)\sin(\Theta^1) + D_2}, \ \mu_3 = \lambda_3\cdot|\mathbf{g}^3| = \tfrac{s}{c}\sqrt{\tfrac{2}{\cosh(2\Theta^3) - \cos(2\Theta^1)}}, \end{aligned} \tag{5}$$

where $d_1 = k \cdot d_0$. The integration constants C_1, C_2, α_0 can be determined by introducing the resctriction that the point $(R, Z) = (D_2, c \cdot \cosh(\xi_1) + D_1)$ and the line $R = D_2$ in the initial configuration correspond respectively to $(r, z) = (P_{1r}, P_{1z})$ and the line inclined an angle γ with the z-axis in the current configuration. Then designating proper values for growth parameters s, k, d_1, the current configurations are obtained from (4). The results are shown in Fig. 1 (a-d) and (A-D) which respectively mimic the morphological evolutions of two mushrooms-A. muscaria and M. chlorophos.

From (4) and (5), we may derive the following insights. (i) The turnup of a cap (a-d) corresponds to the reverse of the sign of k and the formation of a depressed cap (A-D) corresponds to a positive and growing γ. (ii) Behaviors of μ_1, μ_3 for (a-d) and (A-D) are similar, and μ_2 is responsible for the behaviors of k and γ.

CONCLUSIONS

A theory for stress-free 3D axisymmetric configurations induced by locally incompatible growth functions is developed. Some special analytical solutions are constructed, which mimic the morphological evelutions of two types of mushrooms. Some interesting insights are deduced from the analytical results.

References

[1] Rodriguez, E. K., Hoger, A., McCulloch, A. D. Stress-dependent finite growth in soft elastic tissues. *J. Biomech.* **27**: 455-467, 1994.
[2] Chen X., Dai H.-H. Stress-free configurations induced by a family of locally incompatible growth functions. *J. Mech. Phys. Solids*, 2019. https://doi.org/10.1016/j.jmps.2019.103834.
[3] Yavari, A. Compatibility equations of nonlinear elasticity for non-simply-connected bodies. *Arch. Rational Mech. Anal.* **209**: 237-253, 2013.
[4] Ogden, R. Non-linear Elastic Deformations. Dover 1997.

THEORETICAL MODELING OF FORCED OSCILLATIONS OF HERBACEOUSPLANT INFLORESCENCE-INFLUENCE OF BRANCHINGANGLE

Andjelka Hedrih*[1], Djordje Jovanovic[1], and Katica (Stevanovié) Hedrih[1,2]
[1]Mathematical Institute of Serbian Academy of Sciences and Arts (MI SANU), Belgrade, Serbia
[2]Faculty of Mechanical Engineering, University of Nis, Serbia

Summary Using previously proposed mechanical oscillatory model of corymb type of inflorescence, in this paper we study the influence of different branching angle on amplitudes of forced oscillations for four different values of circular frequencies of external force. Oscillatory behavior of this complex system in horizontal plane under external force can be described by a system of linear differential equations using influence deflection coefficients and reduced inertia forces. Displacement influence coefficients were determined on the basis of equations of elastic line of cantilever load with unit force and unit momentum. Increasing the branching angle of inflorescence, amplitudes of oscillations change non-linearly or linearly depending on external force frequency values.

.

INTRODUCTION

Herbaceous plants that grow in nature, concretely in valleys, are exposed to different external forced conditions like wind, insects, animals etc. Under such circumstances plant stems that carry flowers or complex flowers called inflorescence oscillate. Oscillating behavior will depend on plants' structural and anatomical properties - type of inflorescence, number of flowers in it… Bending process of crops' stems are significantly influenced by crop species growing conditions, stem diameter and wall thickness [1]. Elastic properties of sunflower tissues [2] and stems of different herbaceous pants [3] are determined by other factors. Recently mechanical oscillatory model of corymb type of inflorescence [4] was proposed. We were interested how anatomical variations of stem branching of inflorescence (different branching angle) will affect the amplitudes of forced oscillations. Analyses were done for four different values of circular frequencies of external force.

Description of the mechanical oscillatory model of corymb type of inflorescence

Schematic representation of the mechanical oscillatory model of a corymb type of inflorescence is shown on Fig 1 [3]. Model is in in the form of complex light elastic cantilever fixed in point A at which unit force is applied. In cross-section 2 and 3, rigid rods with material particles at the end of the rods (corresponds to the lateral branches of the inflorescence) are rigidly fixed to the corresponding sections of the elastic cantilever. At the end of the elastic cantilever a material particle is attached (corresponds to the apical part of the inflorescence). This complex system belongs to the discrete complex oscillatory systems and have certain assumptions: lateral branches have negligible mass and are rigidly connected to the cantilever (corresponds to the main stem of herbaceous plant); oscillations of cantilever and system are small, tilts of deformed axis of banded cantilever are very small and negligible, tilts of cantilever cross-section during cantilever banding according to x and y axis of cross sections are very small and negligible. Nonlinearities are considered to be small, as well as the amplitude of the external excitation force and the bends of the base ideal elastic and light cantilever. The bending stiffness of the elastic cantilever is equal in horizontal and vertical plane; mass of the apical part of inflorescence is higher than the masses of lateral branches of inflorescence; displacements of material particles are equal to the displacements of points - the section of the cantilever in which each light rigid rod with neglected mass, that carries the material particle, is attached. Oscillatory behavior of this complex system in horizontal plane, can be described by a system of linear differential equations.

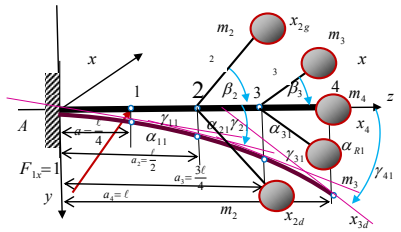

Figure 1. Mechanical oscillatory model of inflorescence. Oscillations in horizontal plane. $m_2 = m_3 < m_4$; $\beta_2 = \beta_3$-branching angles of lateral branches of inflorescence. x-coordinates in horizontal plane. Pint 1, 2, 3 and 4. points of which amplitudes of oscillations are analyzed; -length of the plants' stem.

For oscillations in horizontal plane:

$$x_i = \alpha_{i1}F_{01x}\sin\Omega_x t + \alpha_{i2}\left(-2m_2\ddot{x}_2\right) + \alpha_{i3}\left(-2m_3\ddot{x}_3\right) + \alpha_{i4}\left(-m_4\ddot{x}_4\right) + \\ + \delta_{i2}\left(-2m_2\ddot{x}_2\ell_2\sin\beta_2\right) + \delta_{i3}\left(-2m_3\ddot{x}_3\ell_3\sin\beta_3\right) \qquad i = 1\ldots4 \qquad (1)$$

Where α_{ik} and δ_{ik} are influence coefficients of deflection on cross section "i" under unit force $F_{k=1}$ and under unit

*Corresponding author. E-mail: handjelka@hm.co.rs

momentum. $M_{k=1}$ respectively, on section 'k'. For calculating the influence coefficients of deflection, the bending stiffness of the elastic console is needed and is equal to: $B_x = B_y = EI_x = EI_y = E\frac{r^4\pi}{4}$ where $I_x = I_y = \frac{r^4\pi}{4}$ is the axial moment of inertia for the surface of cross-sectional area for the corresponding central axis passing through the center of the circle. E is Young's module of elasticity, r is half a diameter of the cantilever- stem. We analyze influence of branching angle on amplitudes of horizontal forced oscillations at the certain points of the plant stem.
Numerical analysis was done for the plant *Sorghum halepense* [4], r=0,0016m, $_2 = _3 = 0.08m$, $=1m$:, E=7,7x10^{9}Pa, (average value for stem of grass plants taken from [4] , for inflorescence masses approximatively values of $m_2 = m_3 = 0,075kg$ $m_4 = 0,15kg$, were used. $\beta_2 = \beta_3$. For different branching angles (from $\frac{1}{12}\pi$ to $\frac{5}{12}\pi$) under each of the circular frequencies $\Omega_y = 5/s$, $\Omega_y = 10/s$; $\Omega_y = 15/s$, and for $\Omega_y = 20/s$ of external forces the amplitudes of forced oscillations were done in points 1, 2, 3 and 4 of the model.

RESULTS

Results of our numerical analyses are shown on Fig2. Some characteristic extreme values are present for branching angle near $\frac{4}{12}\pi$. For $\Omega_y = 15/s$ and for $\Omega_y = 20/s$ amplitudes in point 3 (second branching) show almost linear increasing character as branching angle in this point increases, while amplitudes in other points decrease.

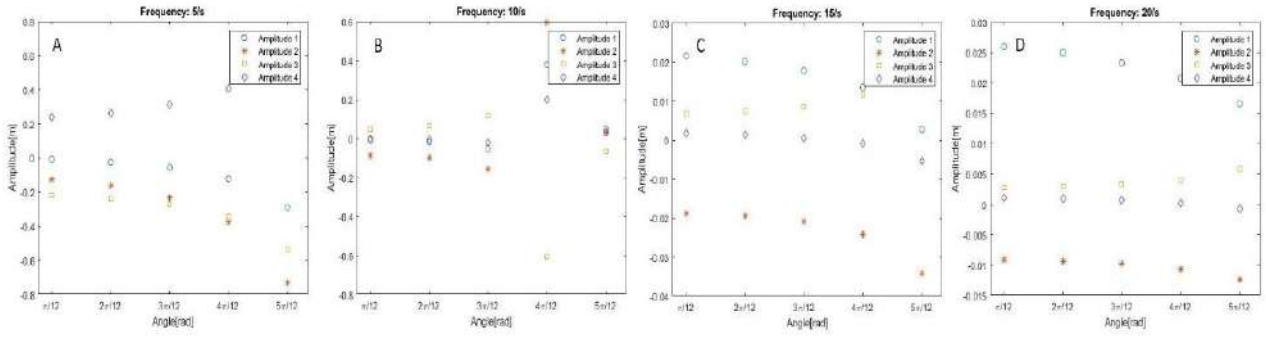

Figure 2. Amplitudes of forced horizontal oscillations for different external force circular frequencies values at different branching angles from $\frac{1}{12}\pi$ to $\frac{5}{12}\pi$. A. for $\Omega_y = 5/s$ .B. for $\Omega_y = 10/s$ C. for $\Omega_y = 15/s$. D. for $\Omega_y = 20/s$.

CONCLUSIONS

We study the influence of different branching angle on amplitudes of forced oscillations for four different values of circular frequencies of external force using previously proposed mechanical oscillatory model of corymb type of inflorescence. Our numerical results show that amplitudes of forced oscillations are frequency dependent, showing linear or non-linear character of amplitude oscillations depending on frequencies of external force excitation. Non-linear character of amplitudes changing have local minimums and maximums as value of branching angle increase. This model may be used for studying oscillations of different herbaceous plants which have corymb, or corymb-like type of inflorescence.

Acknowledgements: Parts of this research is supported by the Ministry of Sciences and Technology of Republic of Serbia through Mathematical Institute SASA, Belgrade.

References

[1] Leblicq T, Vanmaercke S, Ramon H, Saeys W. Mechanical analysis of the bending behaviour of plant stems. *Bios Eng.* 129: 87-99. 2015.
[2] Hejnowicz Z, Sievers A. Tissue stresses in organs of herbaceous plants III. Elastic properties of the tissues of sunflower hypocotyl and origin of tissue stresses. *J. Exp Bot.* 47(297): 519-528, 1996.
[3] Hedrih A, Atanasovska I and Jovanovic Dj. Inflorescence inspired complex oscillatory systems. In Booklet of Abstracts of Symposium "Nonlinear Dynamics –Scientific work of Prof. Dr Katica (Stevanović) Hedrih", Mathematical Institute of the Serbian Academy of Sciences and Arts, Belgrade, 04.-06. September 2019, Editors: Ivana Atanasovska, Anđelka Hedrih, Milan Cajić, Mathematical Institute of the Serbian Academy of Sciences and Arts, Belgrade (Sven, Niš), pp. 117-118, 2019.
[4] Evans L.S. Kahn-Jetter Z, Marks C, Harmoney K.R. Mechanical properties and anatomical components of stems of 42 grass species. *J. Tor Bot Soc*. 134(4):458–467, 2007.

KHALLWA: DESIGN OF AN AERIAL ROBOT FOR THE PREVENTING BIRD DAMAGE TO BLUEBERRY CROPS

Jason Valera[1]
[1]Department of Engineering, Pontificia Universidad Católica del Perú, Lima, Perú

Summary Preventing bird damage to crops has remained a top priority for farmers since the dawn of time. When poultry feeding is not mitigated, crop yields are greatly reduced, a major economic blow. Currently, in Peru, up to an eighth of crops are lost each year due in part to bird activity. When the birds are comfortable enough near an abundant source of food and a safe environment, then they begin to settle. Then nesting begins and then they produce more young that feed on the crops. However, by using Khallwa to impose a sense of predation on resident birds, nesting is prevented and populations are reduced.

INTEGRATED DESIGN

The system presented consists of an unmanned aerial vehicle of the bird type. This aerial robot is composed of a lightweight and resistant expanded polypropylene and carbon fiber structure. Its flap wing flight mechanism allows it to fly lightly and with maneuverability. The flight control will be carried out by an autopilot, in this way, the system will be able to have an autonomous flight and travel the indicated cultivation area.

The robot will begin its movement when through a Wi-Fi connection between the embedded system and the computer, the flight parameters such as coordinates of the start of the flight, average height, distance to be traveled and coordinates of the destination are delivered. Once the system is configured with the flight parameters, the next step is the flight of the aerial robot. Once the aerial robot finishes its journey or the battery sensor indicates that the LiPo battery does not have enough energy for it to continue moving, the system will fly to its destination point.

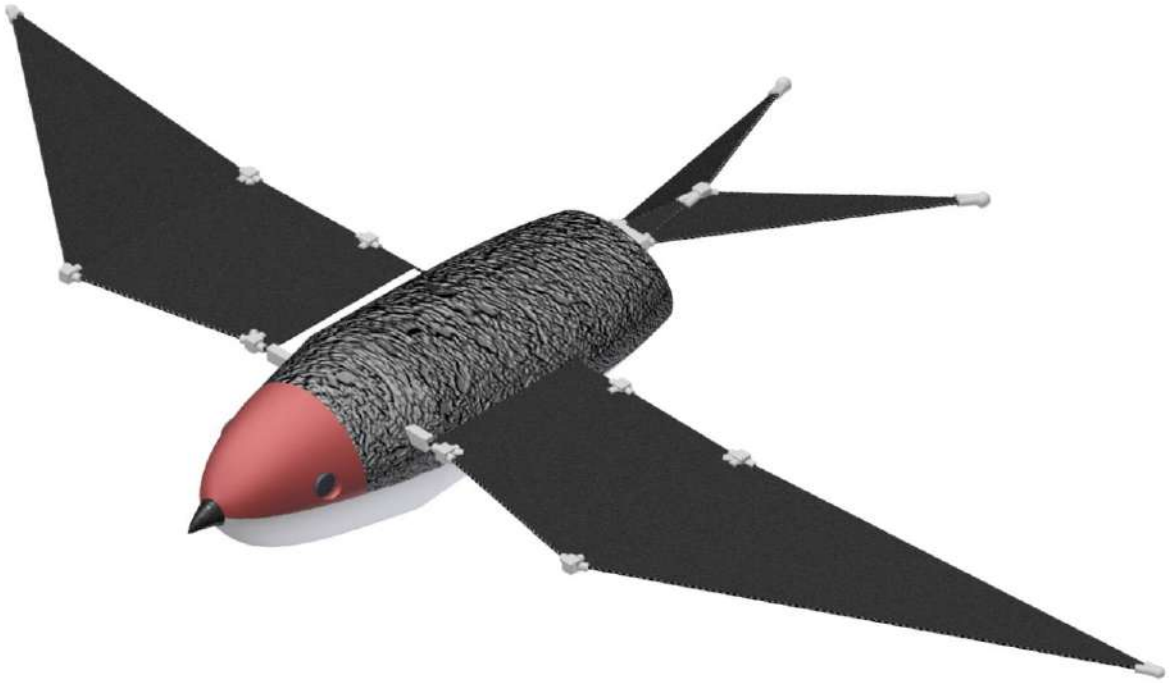

Figure 1. 3D Design (“Khallwa”)

Mechanical design

An unmanned aerial vehicle of the bird type is a flight vehicle that generates aerodynamic forces and moments to fly. The flexibility of the wings helps to gain sufficient lift and thrust. As a starting point you start with the main fundamental forces that must be balanced for flight. The lift force generated by the wings is equal to the weight of the system and the thrust generated by it is equal to the drag force or air resistance- This is so because the lift force occurs in a direction perpendicular to the of airflow, therefore, there is a component of lift force in the direction of horizontal flight. To achieve a high thrust effect, a high speed should be aimed. That means a high-impact wingbeat. As can be seen, with a noticeable "V" wing position, the main lift force, which is decisive for the model, is significantly less than the secondary lift force generated in the wing. Therefore, it is advisable to keep a small flap angle to generate lift; flap angles between ± 20 ° and ± 40 ° are considered adequate [1].

The flapping mechanism is the most critical part of the system, as it converts the electrical energy provided by the battery into the flapping motion of the wings. The design of the mechanism corresponds to a DC motor with a transverse

shaft that allows the double gear crank mechanism to perform the turning movement. The rotating gears and flapping wings are not in the same plane, so the connector rod must be able to rotate. The connector rod has ball joints to ensure the operation of the mechanism. The tail design is of the swing type, causing a swinging moment when swinging either side. The tilting tail works like a rudder, when tilted to the right it causes the system to turn to the right and vice versa. Also, lift can be added providing maneuverability and balance. The recommended starting angle for maneuverability is -20 ° [2].

Electronic design

The electronic design consists of the selection of the various electronic components. The power of the system is provided by the lithium-polymer (LiPo) battery, which will be connected to a power module that has a voltage and current sensor, which in turn will transmit the information on the state of the battery to the controller. Of flight. The flight controller is powered by the power module, feeds and communicates with a GPS module, allowing it to know its location at all times, it will also communicate with the electronic speed controller (ESC) to control the speed of the engine. DC. The servomotors are powered by the ESC voltage regulator and communicated with the flight controller.

CONCLUSIONS

A system was designed that allows navigating the blueberry field in such a realistic and unpredictable way that the birds perceive it as a true hunting bird of prey. Pilots can circle and dive, chasing birds off the ground, trees, and airspace over farmland.

References

[1] Silin D. Aerodynamics and Flight Performance of Flapping Wing Micro Air Vehicles. *PhD. Thesis*, University of Arizona, Arizona, US, 2017.
[2] Srigrarom S. and Chan W. L. Ornithopter Type Flapping Wings for Autonomous Micro Air Vehicles. *J. Aerospace*. pp. 235-278, 2015.

AN OSCILLATION-FREE FULLY STAGGERED ALGORITHM FOR THE NUMERICAL SIMULATION OF CARDIAC ACTIVE MECHANICS

Francesco Regazzoni*[1] and Alfio Quarteroni[1,2]
[1]MOX - Dipartimento di Matematica, Politecnico di Milano, P.zza Leonardo da Vinci 32, 20133 Milano, Italy
[2]Mathematics Institute,École Polytechnique Fédérale de Lausanne,Av. Piccard,CH-1015 Lausanne,Switzerland (Professor Emeritus)

Summary We address an unresolved problem in the numerical simulation of cardiac electromechanics, that is the onset of numerical oscillations due to the dependence of force generation models on the fibers shortening velocity. Despite these oscillations can be cured by resorting to monolithic schemes for the solution of the coupled problem of active-passive mechanics, staggered strategies (in which the submodels are solved sequentially) are preferable because of their reduced computational cost and low implementation effort. In this work we propose a cure for this issue, by introducing, with respect to the standard staggered scheme, a numerically consistent stabilization term. We prove that the proposed scheme is unconditionally absolutely stable, yet within a fully staggered framework, as we verify by means of 0D and 3D numerical tests.

INTRODUCTION

In silico models of cardiac electromechanics couple together mathematical models describing different physics. One instance is represented by the model describing the generation of active force, coupled with the one of tissue mechanics. For the numerical solution of the coupled model, partitioned schemes, that foresee the sequential solution of the two subproblems, are often used. However, this approach may be unstable. For this reason, the coupled model is commonly solved as a unique system using Newton type algorithms, at the price, however, of high computational costs. In light of this motivation, in this work we propose a new numerical scheme, that is numerically stable and accurate, yet within a fully partitioned (i.e. segregated) framework. A detailed derivation of the scheme and proofs of its stability properties can be found in [4].

THE STABILIZED-STAGGERED SCHEME

To derive our stabilized scheme, we move from energetic considerations on the coupling, at the microscale, between active and passive mechanics models. We show that instabilities are linked to the mismatch between macroscopic and microscopic strains, inconsistently expressed in Lagrangian and Eulerian coordinates, respectively. Hence, we formulate a novel scheme, in which all the variables are framed in a coherent fully Lagrangian reference system.

More precisely, in the standard staggered scheme, at each time step k one first updates the state variables of the force generation model (using an extrapolation from the previous time steps to account for the feedback of the mechanical model); then one updates the displacement variables, employing the updated active tension (that we denote by $T_{\mathrm{a}}^{(k)}$). Our proposed scheme only differs in this second step, in which one replaces the active tension $T_{\mathrm{a}}^{(k)}$ by the following term:

$$T_{\mathrm{a}}^{(k)} + K_{\mathrm{a}}^{(k)}(\lambda^{(k)} - \lambda^{(k-1)}), \tag{1}$$

where $K_{\mathrm{a}}^{(k)}$ denotes the *active stiffness* (i.e. the stiffness of all the attached molecular motors) and where λ is the tissue strain in the muscle fibers direction. The additional term can be regarded as a correction term, by which the active tension is not expressed as a constant anymore, rather it depends on the tissue strain in the fibers direction, more coherently with the microscopic phenomenon that generates the macroscopic force. We remark that such additional term is numerically consistent, as it is first order infinitesimal with respect to the time step size Δt. A formula for K_{a} can be based upon physical considerations, or can be derived formally from the force generation model, as the sensitivity of the rate of change of the tension with respect to the rate of change of the tissue strain, i.e. $K_{\mathrm{a}} = \frac{\partial \dot{T}_{\mathrm{a}}}{\partial \dot{\lambda}}$.

STABILITY ANALYSIS

Our stability analysis focuses on the eigenvalues of the transition matrices between two consecutive time steps. By considering a model problem of active mechanics, we show that the monolithic scheme is unconditionally absolutely stable. Conversely, when the active stiffness is larger than the passive stiffness in the fibers direction, the standard staggered scheme is only conditionally stable (i.e. stable for small enough Δt) and even unconditionally unstable in the case of quasistatic mechanics. Consequently, in the case of quasistatic mechanics the staggered scheme cannot be convergent when the active stiffness is larger than the passive stiffness in the fibers direction – as it happens during systole for realistic values of the parameters. We show that the stabilization term proposed in this paper brings all the eigenvalues of the transition matrix associated with the staggered scheme back into the unit circle, thus ensuring numerical stability.

*Corresponding author. E-mail: francesco.regazzoni@polimi.it

Figure 1: Computational mesh used for the 3D electromechanical simulation and reconstructed fibers fields.

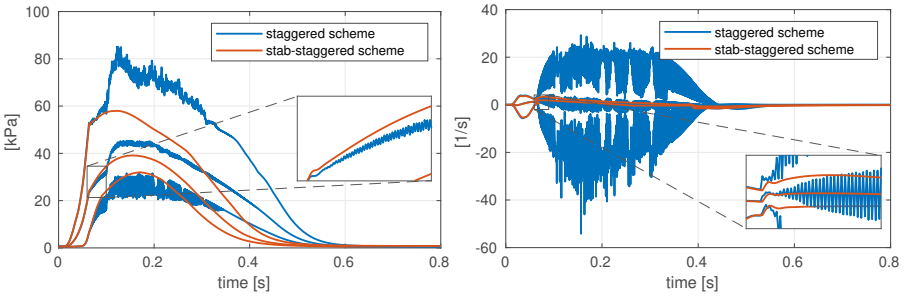

(a) Active tension (T_a).

(b) Fibers shortening velocity ($-\dot{\lambda}$).

Figure 2: Results of multiscale cardiac electromechanics simulations obtained with the staggered scheme (blue lines) and the stabilized-staggered scheme (red lines). The three lines refer to the minimum, average and maximum value over the computational domain.

NUMERICAL TESTS

We apply the proposed method to several force generation models available in the literature, namely the Niederer-Hunter-Smith model [2], the model of Land and coworkers [1] and the mean-field model that we proposed in [3]. We show, by means of several numerical tests, that the proposed stabilization term successfully removes the nonphysical numerical oscillations characterizing the non stabilized segregated scheme solution. This is verified in two different test cases, namely an isotonic twitch and a test case where a contracted fiber shortens as a consequence of a gradual decrease of the external load, similarly to what happens in the ejection phase of the heart cycle. We show that the new scheme preserves the first order convergence with respect to Δt of the non-stabilized staggered scheme. The numerical error is only slightly larger than the error obtained with the monolithic scheme and it tends to zero with the same rate. Finally, we apply the proposed scheme in the context of a three-dimensional multiscale electromechanical simulation of the left ventricle.

ACKNOWLEDGEMENTS

This project has received funding from the European Research Council (ERC) under the European Union's Horizon 2020 research and innovation programme (grant agreement No 740132, iHEART, P.I. Prof. A. Quarteroni).

References

[1] S. Land, S. Park-Holohan, N. Smith, C. dos Remedios, J. Kentish, and S. Niederer. "A model of cardiac contraction based on novel measurements of tension development in human cardiomyocytes". In: *Journal of Molecular and Cellular Cardiology* 106 (2017), pp. 68–83.

[2] S. A. Niederer, P. J. Hunter, and N. P. Smith. "A quantitative analysis of cardiac myocyte relaxation: a simulation study". In: *Biophysical Journal* 90.5 (2006), pp. 1697–1722.

[3] F. Regazzoni, L. Dedè, and A. Quarteroni. "Biophysically detailed mathematical models of multiscale cardiac active mechanics". In: *PLOS Computational Biology* 16.10 (2020), e1008294.

[4] F. Regazzoni and A. Quarteroni. "An oscillation-free fully partitioned scheme for the numerical modeling of cardiac active mechanics". In: *Computer Methods in Applied Mechanics and Engineering* 373 (2021), p. 113506.

EFFECTIVE ELASTIC PROPERTIES OF EXTRACELLULAR MATRIX SIMULATED AS A FIBER NETWORK

Daria Orlova*[1], Sadik Omairey [2], Ayelet Lesman [1], Igor Berinskii [1]
[1]School of Mechanical Engineering, Tel Aviv University, Tel Aviv, Israel
[2]Brunel Composites Centre, Brunel University London, London, United Kingdom

Summary In this work, we investigated the effective elastic properties of a fiber periodic network. The randomly distributed network of the linear elastic elements represents the extracellular matrix on a microscopic level. In order to measure how the local anisotropy is changed at the scale of a cell, the square network samples were stretched up to 50% and the homogenization was performed at each stretching step. This allowed calculating the effective anisotropy parameter of the sample and the network effective elastic properties. It was shown, that for uniaxial stretching the maximal effective constant C_{11} exists, and corresponds to 10-20% strain, whereas the maximal anisotropy occurs at 30%.

INTRODUCTION

Cells respond to the physical characteristics of their surrounding environment in a manner that strongly affects the formation and repair of tissues. Environment's stiffness, porosity, and fibrous connectivity are important characteristics in tissue engineering and regenerative medicine. Accordingly, computational and experimental studies help determine the role of physical characteristics in directing multiple cell activities, such as cell reorientation, signaling, and extracellular matrix (ECM) remodeling [1]. The ECM is a cross-linked biopolymer network in which cells are embedded and provides support for the growing tissue.

The ECM fibers are mechanically connected to the cells and respond to contractile forces applied by cells [2]. When cells contract, they deform the surrounding matrix, which leads to large displacements and anisotropy that can propagate to long-distances. The anisotropy, which is a structural change of ECM fibers under mechanical forces, plays a significant role in cell migration and communication. However, it remains unclear how the external stretching influences the local anisotropy of the ECM between contractile cells.

The purpose of this work is to study the local anisotropy generated due to cell contraction and how this would change the structure of the surrounding environment for the cell's own benefit. For this, numerical homogenization of a periodic fiber cell is performed, to estimate the effective elastic moduli of the material, which will be used to further study the behavior of the material under various tension steps.

DISCRETE FIBER SIMULATION

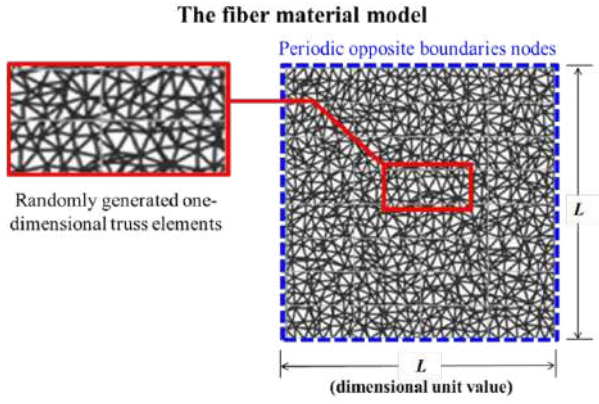

Figure 1. An illustration of fiber discrete periodic cell

A model of fiber material is developed to consider the response of the ECM to the external stretching induced by contractile cells. For the fiber periodic cell modelling we used Python program code, which was based on an algorithm that builds a triangular mesh using the Delaunay triangulation method. Then, the existing nodes were spatially displaced to simulate the random fibrous network of the ECM (Fig.1). The resulting model was transferred to ABAQUS CAE software for further tensile and homogenization calculations. Each fiber was modeled as a one-dimensional truss element, having an assumed cross-sectional area of 3.14E-05 μm. At this stage of the study, a linear mechanical model [2] is considered, with the fibers having an elastic moduli E = 0.0115 kPa, and Poisson's ratio $\nu = 0.475$

LINEAR HOMOGENISATION

In order to understand how the material responds to external forces, homogenization of the periodic cell was developed. For this purpose, EasyPBC plugin that implemented to the ABAQUS CAE software [3] is used. The plugin adopts the Representative Volume Element (RVE) homogenization method by, imposing periodic boundary conditions and external strains to calculate effective elastic properties of the randomly distributed fiber material model. As this numerical homogenization method assumes that the RVE is a part of periodic a material, the fiber model (Fig.1) is also modelled with periodic opposite boundary edges.

Five periodic fiber samples with different random distributions were considered. Each fiber sample was stretched up to 50% and considered for every 10% step along X-axis. It is assumed that the cells that stretch the matrix fibers are located

*Corresponding author. E-mail: dariaegorova@mail.tau.ac.il

on the X axis. During stretching, the fiber samples changed their shape to a rectangular one, so square regions of the same area were cut to satisfy the periodic boundary conditions for the following homogenization step.

Initially, the homogenized random fiber network has isotropic elastic properties. During tension, the effective material becomes anisotropic; namely, it reveals an orthotropic symmetry. The dimensionless parameter η was chosen, to measure the degree of anisotropy [4]:

$$\eta = 3\frac{2C_{66}}{C_{11}-C_{12}}$$

The value of the anisotropy parameter ranges from 0 to 1. The latter value corresponds to the isotropic case.

The elastic properties of the effective continuum corresponding to the studied fiber network. For each stage of stretching, a stiffness matrix was calculated for the two-dimensional material. The elastic constants (C11, C12, and C66) used to estimate the anisotropy parameter were calculated using the effective elastic properties estimated by the homogenization method and the stress-strain relation.

CONCLUSIONS

Using a finite element periodic cell, we explored how the external tension influences the local anisotropy. The fibrous material in the undeformed state was close to isotropy corresponding to the anisotropic parameter around 1. With an increase of uniaxial strain, the anisotropy parameter gradually decreased, indicating the appearance of local anisotropic properties. However, after deformation of 40%, the anisotropy parameter began to increase again (Fig.2 a). The maximum value of C_{11} is observed between 10-20% strain steps, making this configuration most preferable for cells to contact one another. On the other hand, a continues decrease in C_{11} is observed between 20-50% (Fig.2 b), which means that there is less material in the cut-out square of material during stretching. The graphs also show that the maximum of C_{11} does not coincide with the minimum of the anisotropy parameter.

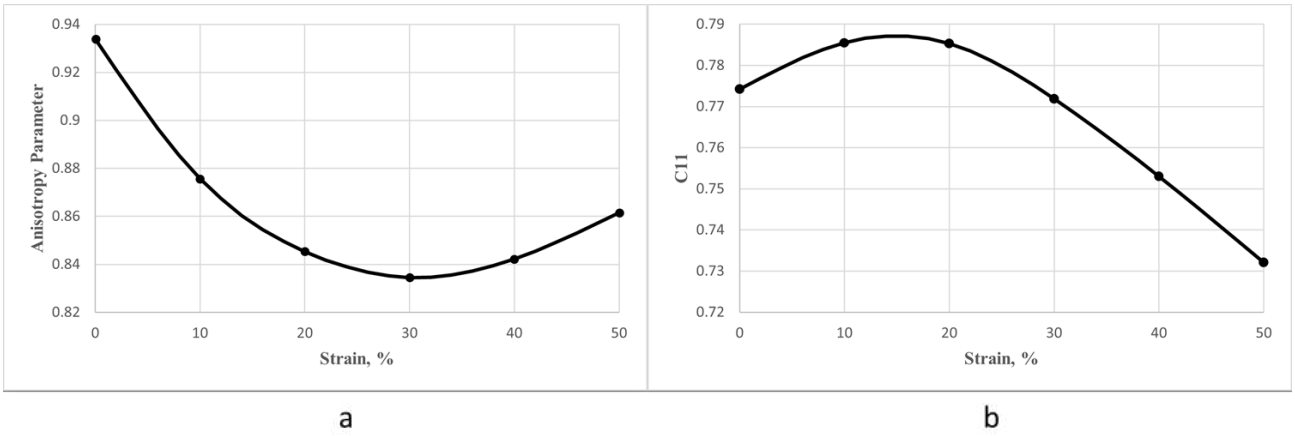

Figure 2. (a) – Average anisotropy parameter values versus the strain steps of 5 different randomly distributed periodic cells; (b) – Average C11 element value of the Stiffness matrix versus the strain steps of 5 different randomly distributed periodic cells.

The next step of our work is to perform homogenization using a nonlinear material model. The nonlinear characteristics of the material will help to study the local anisotropy between long-range cells. Additionally, using the obtained homogeneous material properties, the behavior of the nonlinear fiber material at the macro level can be investigated, which will significantly facilitate the study of fiber materials and allow considering large scale models.

ACKNOWLEDGMENETS

The authors gratefully acknowledge Mr. Yoni Koren and Dr.Artem Panchenko for their help with code development.

References

[1] Maziar Aghvami, Kristen L. Billiar, Edward A. Sander. Fiber Network Models Predict Enhanced Cell Mechanosensing on Fibrous Gels. *J of Biomechanical Engineering* ***138***, 2016

[2] Shahar Goren, Yoni Koren, Xinpeng Xu, Ayelet Lesman. Elastic Anisotropy Governs the Range of Cell-Induced Displacements. *Biophysical J.* ***118****: 1152-1164, 2020*

[3] Sadik L. Omairey, Peter D. Dunning, Srinivas Sriramula Development of an ABAQUS plugin tool for RVE homogenisation. *J. Engineering With Computers, 2018*

[4] A.M. Krivtsov. Theoretical Mechanics. Elastic properties of monatomic and diatomic crystals, SPBPU Publishing, Saint-Petersburg, 2009 (in Russian)

DEVELOPMENT AND IMPLEMENTATION OF A FINITE ELEMENT CODE TO SIMULATE THE CARDIOBAND® PROCEDURE FOR MITRAL VALVE REGURGITATION: FIRST HUMAN PLANNING CASES

Emanuele Gasparotti[1,2], Sergio Berti[3], and Simona Celi*[1]
[1]BioCardioLab, Bioengineering Unit, Heart Hospital, Fondazione Toscana Gabriele Monasterio, Massa, Italy
[2]Department of Information Engineering, University of Pisa, Pisa, Italy
[3]Adult Cardiology Unit, Heart Hospital, Fondazione Toscana Gabriele Monasterio, Massa, Italy

Summary The Mitral Valve (MV) regurgitation is a disease produced by the dilatation of the MV annulus ring. In recent years new techniques have been proposed to correct MV regurgitation. Among these, the Cardioband® system (Edwards Lifesciences, Irvine, USA) is a promising technique able to reduce the MV regurgitation by using a transcatheter approach. In this study we present an in-silico tool able to reproduce the Cardioband® procedure. Our tool is based on the integration of image processing and a finite element simulation. The specific aim of this study is to evaluate the accuracy of the tool by simulating the procedure of three different patients.

INTRODUCTION

Mitral valve regurgitation disease is one of the most common heart valve pathology [1]. Cardioband® system is a surgical-like direct annuloplasty adjustable device, implanted via transcatheter on beating heart [2]. This procedure consists by fixing the polyester sleeve (PS) of the device around the mitral annulus through specific metal anchors (about 12-17) and to contract the annulus by pulling a guide-wire (GW) sewed on the PS. Due to the complexity of the implant, this procedure requires skilled operators and an accurate planning phase. Currently, the implant size (anchors number) and the anchors position is defined on the base of the CT dataset by analysing the site of access and the annulus commissure to commissure length. In this study, for the first time in literature, we have developed an in-silico tool to fully reproduce the Cardioband® procedure starting from conventional medical images and the FE simulations. The accuracy of the tool was evaluated via simulation of the procedure performed on three different patients underwent to Cardioband® procedure.

WORKFLOW AND COMPUTATIONAL SET-UP

The considered patients' geometries include left atrium, mitral annulus, left ventricle and aortic root. These were obtained from a 3D segmentation of CT pre-procedural datasets, at maximal diastolic opening of the valve. A specific finite element routine was developed in Matlab® to simulate the biomechanical behaviour of the entire Cardioband® procedure. The routine applied the Cardioband® system equations (equilibrium and geometrical constrains) with the resolution of finite element equations of left heart mesh model. A 3D shell elements (Triangular 3-node 18 DOF [3]) was implemented and used to mesh the geometries. Different thickness and material properties were applied on the meshed domains to describe the different structures: the annulus ring, the left atrium, the aortic root and the ventricle were modelled with hyperelastic isotropic model [4]. The model was constrained with fixed nodal displacements in the interface areas between the right and the left ventricle. To simulate the force that anchor acts on the annulus, the relative node sub-selection was defined and then, the load interactions were imposed by compatibility equations. The behaviour of the Cardioband® device during the cinching phase of the guide wire was reproduced by the resolution of equation system. These equations govern the physics of a schematized model able to reproduce the interaction between the PS, the anchors and the GW. In particular, the GW was schematized as a 3D ideal inextensible cable with zero flexural and torsional rigidity. The cable can also slide through the sewn points during the cinching phase. The PS has the function to link the anchors to the GW. It is composed by a fabric able to transmit traction loads only. For this reason, in the simulation, the PS is considered as tie-rod structures connecting each anchor point to the corresponding sewn point of GW (Fig. 1a).

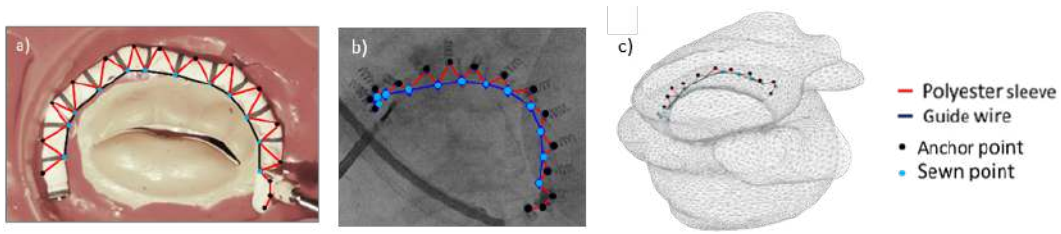

Figure 1: Cardioband® scheme (a), X-ray projection (b) and 3D Cardioband® models (c).

Three different patients were simulated. To evaluate the accuracy of the developed routine the initial device position was selected by the device projection, visible in the pre-cinching X-ray image (Fig. 1b). Fig. 1c depicts the initial

*Corresponding author. E-mail: s.celi@ftgm.it

configuration of the device, obtained by the registration between the 3D mesh of the left heart model and the X-ray projections. Finally, the resulting anchors and sewn point positions were compared with the corresponding ones found in the post procedure X-ray images.

RESULTS AND DISCUSSION

The simulation workflow, including medical images availability, the 3D geometries creation, the device positions definition and equations system resolution, was carried out with success through the developed tool. As regards the post-procedure, is it possible to observe a good overlapping between the patient's clinical procedure and the corresponding simulation in terms of the anchor positions and wire curves (Fig. 2a-f).

Tab. 1 summarizes the assessment of the accuracy by showing for each case, the position error was evaluated as the absolute distance between the simulated and actual final position of the anchor and the sewn points. These values are reported as the average ± the standard deviation. The average value error is less than 2 mm both anchor and sew positions.

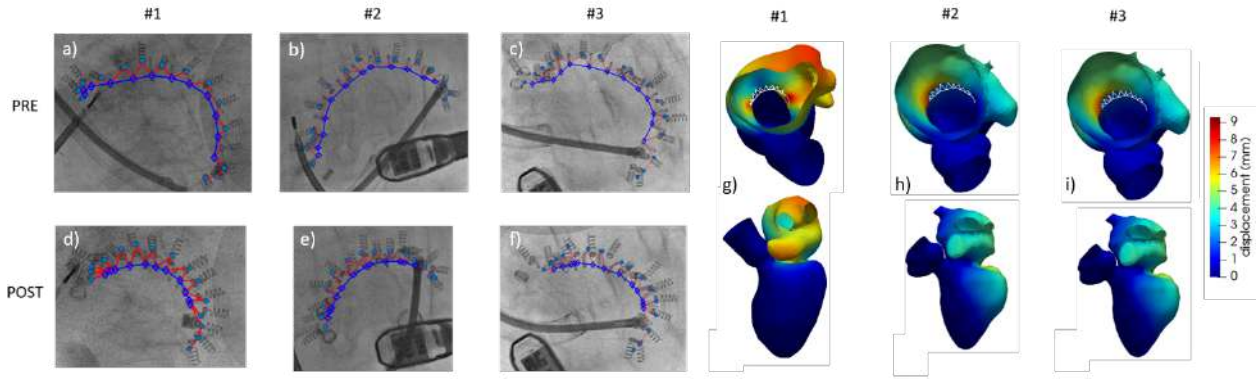

Figure 2: Cardioband® pre (a-c), post (d-f) procedure comparisons and left heart dispacements (g-i).

	#1	#2	#3
Anchors	1.6 ± 0.9	1.9 ± 1.3	1.8 ± 0.6
Sew points	1.9 ± 0.7	1.7 ± 0.9	1.9 ± 1.1

Table 1: Device position error comparison (mm).

Moreover, the results of simulations allow to evaluate the influence of the device procedure on the left heart chambers and vessels (Fig. 2g-i). For all simulated patients it is possible to observe a left atrium displacement along the anterior direction (maximum value: 20 mm) and a left ventricle compressive displacement (maximum value: 10 mm). The left ventricle apex does not undergo to any displacements as well as the aortic root. The work presented here confirms that the routine of the Cardioband® procedure can reproduce the clinical procedures with a good accuracy. It is worth to point out that, the error committed by the routine to predict the anchor and sewn positions, is mainly affected by the intrinsic errors of the segmentation and by the identification of the anchors in the x-ray projection. The variability of the cases' outcomes suggests that the Cardioband® device capability to reduce the MV regurgitation is highly dependent on the patient's geometries, on anchors' positions and on anchors' number. The routine permits to foresee the procedure outcomes in terms of annulus shape and geometrical displacements; it gives the possibility to better understand the influence of the anchors position on the final annulus shape to increase the device effectiveness in the reduction of mitral regurgitation during a pre-planning phase in a clinical environment.

References

[1] Virani, Salim S., et al. "Heart disease and stroke statistics—2020 update: a report from the American Heart Association." Circulation (2020): E139-E596.

[2] G. Nickenig, C. Hammerstingl, R. Schueler, et al, "Transcatheter Mitral Annuloplasty in Chronic Functional Mitral Regurgitation 6-Month Results With the Cardioband® Percutaneous Mitral Repair System," JACC: Cardiovascular Interventions, 2016, vol. 9, pp. 2039-2047.

[3] F. Caselli, P. Bisegna, A corotational flat triangular element for large strain analysis of thin shells with application to soft biological tissues,Computational Mechanics 54 (3) (2014) 847–864.

[4] G.M. Gunning, B. P. Murphy, "Determination of tensile mechanical properties of the segmented mitral valve annulus" J. of Biomech, 2014, vol 47, pp. 334-340

MODELLING MORPHOGENESIS OF SOFT CONNECTIVE TISSUES

Shuvrangsu Das*[1], Vikram S. Deshpande[1]
[1]Department of Engineering, Cambridge University, Cambridge CB2 1PZ, UK

Summary In this work, we develop a statistical mechanics framework for the stochastic interaction of cells with extracellular matrix (ECM) in a developing connective tissues. The resident cells fluctuate in their positions and morphologies as well as subcellular cytoskeletal protein distributions while exchanging nutrients with its surroundings and sensing their mechanical environment. We hypothesize that the cellular behaviour is determined by the fact that the whole system of the cells and ECM maintains a homeostatic equilibrium, which in turn requires that the cellular morphologies depend strongly on the ECM stiffness. In particular, while on average the cellular areas remain similar for a range of ECM stiffness, the cells become progressively more elongated with a decrease of the ECM stiffness, contrary to what has been observed in in vitro experiments for cells on Petri dish.

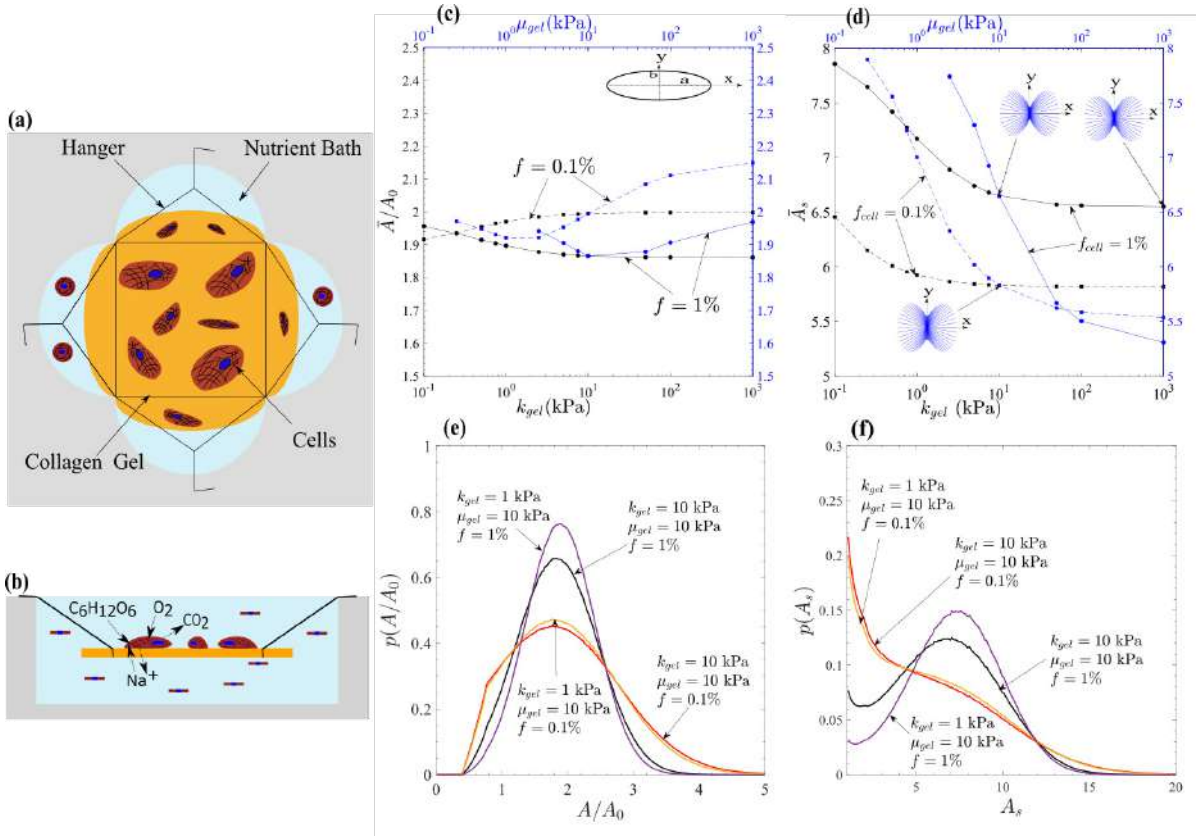

Fig 1. Cell expansion and elongation in a tissue construct. Sketch of the experimental setup: **(a)** top view **(b)** cross-sectional view. Collagenous gel, submersed in a nutrient bath, is seeded with cells to create a tissue construct, with its deformation is restricted by hangers on its edges. The cells exchange nutrients with the bath to maintain a homeostatic equilibrium. For simplicity, we present results only for the cases when cells are confined within the gel. **(c)** The ensemble averages of cellular areas $\bar{A}$, normalized by the area of undeformed cell A_0, for different substrate stiffness at seeding density of $f = 0.1\%$ and 1%. The cells are approximated by ellipses, with major and minor axes a and b, respectively, as shown in inset, such that each morphological area $A/A_0 = \pi ab$. The results are shown for varying bulk moduli of gel k_{gel} (kPa) for a constant gel shear modulus $\mu_{gel} = 10$ kPa, with the corresponding results are shown by black lines, and for varying μ_{gel} (kPa) for a constant $k_{gel} = 10$ kPa, with the corresponding results shown by blue lines. **(d)** The ensemble averages of cellular elongations $\bar{A}_s$, with elongation for each morphology $A_s = a/b$, are shown as well for varying k_{gel}, with $\mu_{gel} = 10$ kPa, and for varying μ_{gel}, with $k_{gel} = 10$ kPa. Insets show circular histogram for stress-fibre concentrations. **(e)** The probability density function for cellular areas $p(A/A_0)$. **(f)** The probability density function for cellular elongations $p(A_s)$.

* Corresponding author email address: sd909@cam.ac.uk

Introduction

Soft connective tissues maintain homeostatic equilibrium in its dynamic steady state. The resident cells, such as fibroblasts, exchange nutrients with its surroundings and generate proteins and other substances to develop ECM, thereby establishing the mechanical environment they live in. The cells, driven by intracellular biochemical processes, fluctuate their positions and morphologies and continuously assess their mechanical environment by exerting forces and deforming the ECM. On the other hand, the mechanical loads acting on tissues are supported by the ECM components, such as collagen, elastin, and transmitted to the subcellular structures, such as stress fibres, via focal adhesions. The ECM deformation also leads to long-range cell-cell interactions through substrate deformation [1], especially at relatively large seeding density of cells. However, most of the studies to unravel the interaction between the ECM and cells are performed by seeding cells with a low density on relatively stiff substrates [2], thus failing to account for the effects of substrate deformation. The aim of this work is to develop a statistical mechanics framework based on homeostatic equilibrium [3], including the cell-substrate interaction as well as cell-cell interaction through the substrate. We report the cellular morphologies for a range of the ECM stiffness for two different seeding densities of cells.

Methodology

We consider an in vitro experiment concerning a 2D tissue in a nutrient bath. Extending the concept for the homeostatic ensemble for cells [3] to tissues, the cellular migration, morphologies and interactions are hypothesized to be dictated by a probability distribution such that the entropy of the system of the tissue and bath is maximized under the constraint that the total number of cells in the tissue remain constant and the homeostatic condition for the tissue is satisfied. However, for simplicity, here we restrict ourselves to the cases when all cells reside on the tissue.

Results

To account for complex cell-cell interactions for a large number of cells, we approximate each cellular morphology by ellipses. Fig. 1 shows the ensemble averages and distribution of area and aspect ratio of elliptical cells. The collagenous gel is modelled as compressible Ogden material with bulk and shear modulus given by k_{gel} and μ_{gel} kPa, respectively. The results indicate that

- The average cell expansions depend weakly on substrate stiffness, at least for seeding density of $f = 0.1\%$ and 1%, as shown in Fig. 1**(c)**.
- Fig. 1**(d)** shows that the average aspect ratio depend strongly on the substrate stiffness, where the cell elongation increases with decreasing substrate stiffness. This can be argued to be originated from stronger cell-cell interactions at highly deforming substrate. Moreover, Fig. 1**(d)** shows that circular histograms for stress-fibres concentrations and they are predominantly concentrated along the major axis of the ellipse, where the concentrations along the major axis relative to the minor axis increase with cell elongations.
- The cell areas exhibit unimodal distributions with similar mean and modes, as shown in Fig. 1**(e)**. In addition, the distributions are increasing peaked with decreasing substrate stiffness and increasing cell density.
- Finally, Fig. 1**(f)** shows that the cell aspect ratios could exhibit unimodal distributions at low cell density, with mode and mean being very different. However, with an increase of cell density, at relatively low substrate stiffness, the distribution become bimodal.

Conclusion

This work demonstrates that the cell-cell interactions are strong when complaint substrates are seeded with a high density of cells. Our statistical framework captures these interactions as well as cell-ECM interactions by developing a homeostatic ensemble for cellular position and morphologies, which enables us to obtain the underlying distributions of cellular morphologies as well.

References

[1] Reinhart-King, C.A., Dembo, M. and Hammer, D.A., 2008. Cell-cell mechanical communication through compliant substrates. *Biophysical journal*, *95*(12), pp.6044-6051.

[2] Buskermolen, A.B., Suresh, H., Shishvan, S.S., Vigliotti, A., DeSimone, A., Kurniawan, N.A., Bouten, C.V. and Deshpande, V.S., 2019. Entropic forces drive cellular contact guidance. *Biophysical journal*, *116*(10), pp.1994-2008.

[3] Shishvan, S.S., Vigliotti, A. and Deshpande, V.S., 2018. The homeostatic ensemble for cells. *Biomechanics and Modeling in Mechanobiology*, *17*(6), pp.1631-1662.

IMPROVING THE RELIABILITY OF SKIN SUCTION FOR CLINICAL APPLICATIONS

Bettina Müller[1], Julia Elrod [2], Oliver Distler[3], Clemens Schiestl[2], and Edoardo Mazza[1,4]
[1]Department of Mechanical and Process Engineering, ETH Zürich, Zurich, Switzerland
[2]Department of Surgery, University Children's Hospital Zürich, Zurich, Switzerland
[3]Department of Rheumatology, University Hospital Zürich, Zurich, Switzerland
[4]Empa, Swiss Federal Laboratories for Materials Science and Technology, Dübendorf, Switzerland

Summary Mechanical characterization of human skin based on suction experiments was shown to be useful for detection of structural changes in the dermis, as it occurs in fibrotic tissue. Several suction devices are commercially available, however so far no one is used for a clinical assessment. This is mainly due to high inter- and intra-observer variability, but the cause of these problems is poorly understood. The present work provides a thorough analysis of the factors influencing the mechanical response of human skin to suction. The results are used to improve and optimize existing measurement protocols and to develop a more effective suction device.

MECHANICAL CHARACTERIZATION OF HEALTHY AND DISEASED SKIN

Human skin consists mainly of three layers, the epidermis, the dermis and the subcutaneous tissue layer. While the epidermis functions, inter alia, as a barrier for our body against environmental influence, the dermis provides the mechanical structure of the skin. Consisting of collagen, elastin, proteoglycans and ground substances, the interaction of these components determines a complex mechanical behaviour. Several skin diseases modify the microstructure of the dermis and therefore the mechanical behaviour of the skin. For example, in patients with systemic sclerosis (SSc) skin fibrosis leads to massive deposition of collagen fibres in the dermis [1] and therefore to a stiffer tissue behaviour compared to healthy skin. In hypertrophic scars, similar processes can be observed, where the structure of the dermis, mainly density and organisation of collagen fibres, is altered and therefore leads to higher stiffness of the scar tissue. Quantification of such alterations associated with skin diseases can be based on mechanical measurements. A suitable measurement principle is the suction method [2, 3], where a negative pressure draws the tissue into a geometrically defined probe opening while the elevation of the skin is measured. With such measurement tools, the elastic and viscoelastic deformation behaviour of the tissue can be captured. One specific mechanical parameter is the skin stiffness, based on the pressure needed for a certain tissue elevation. Suction is pain-free, non-invasive and thus a highly promising in-vivo measurement method. Unfortunately, existing devices show limitations in their handling, which lead to issues when operating in a clinical environment. The main limitation was shown to be related to the contact force between the aspiration probe and the skin surface while placing the probe [4, 5]. To improve existing measurement protocols and facilitate clinical application of suction devices, we aim at a better understanding of the measurement procedure and its impact on the investigated tissue. To this end, we used measurement outcomes of a load and a displacement controlled suction device.

METHODS

Skin mechanical characterization was performed with the Cutometer®, a commercially available device, and the *Nimble*, a novel suction device [5]. The Cutometer® operates load-controlled (Figure 1 A): a predefined negative pressure draws the skin into the probe opening. The light source tracks the tissue elevation through the entire measurement cycle. For calculation of the tissue stiffness, $k^{Cutometer}$, the maximum pressure in *mbar* is divided by the maximum reached elevation in *mm*. The *Nimble* operates displacement-controlled, where a negative pressure draws the skin into the probe opening until a defined height h is reached. The outcome measure is the pressure needed for the specific tissue elevation, and the tissue stiffness, k^{Nimble}, can be calculated as the ratio of this pressure in *mbar* and the elevation h in *mm* (Figure 1 B).

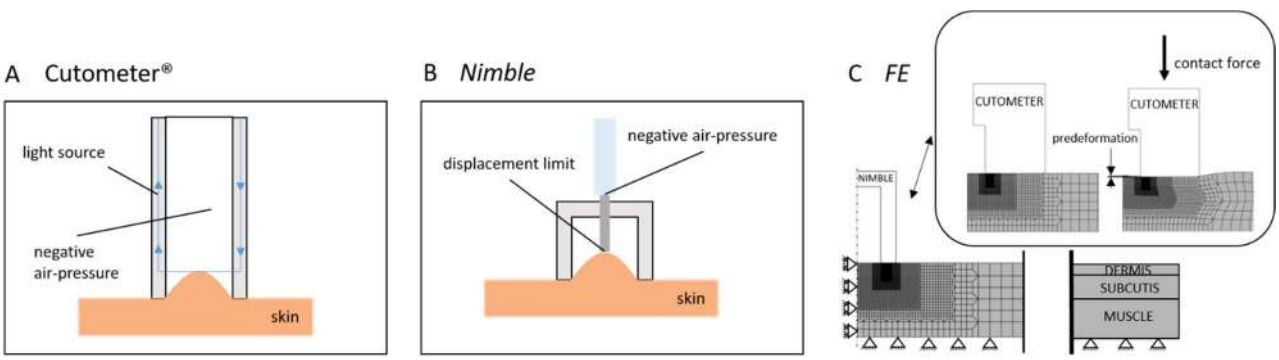

Figure 1. Schematic representation of the working principle of the suction devices Cutometer® (A) and *Nimble* (B). (C) *FE* models for the suction simulations of Cutometer® (top) and *Nimble* (bottom).

A data set from suction measurements with tightly controlled contact conditions on healthy skin and scar tissue was used for an *FE* based inverse analysis (Figure 1 C) determining the parameters of a hyperelastic viscoelastic model[6]. *FE* simulations with the calibrated material model helped to understand factors influencing the measurement procedure on healthy skin and scars.

RESULTS

Results from a clinical trial including 26 burn patients [7] to evaluate the potential of suction measurements for assessment of hypertrophic scar formation, and a clinical trial including 30 SSc patients [8] to investigate the diagnostic potential of the suction method, showed correspondences, but also clear differences between measurement outcomes of the two suction devices. One important deviation concerns the stiffness, which was systematically higher from Cutometer® measurements. The reason for this is the higher deformation level in Cutometer® measurements (Figure 2 A). Skin's response is nonlinear, leading to higher stiffness for larger tissue's elevation. The second observation is related to the effect of predeformation due to the contact force in suction measurements. Based on *FE* analyses it was possible to identify a correction procedure, minimizing the effect of the predeformation. *FE* simulations also enabled to rationalize the higher sensitivity of displacement- when compared to load-controlled suction measurements (Figure 2 B). Wider range parametric studies demonstrated that a displacement-controlled system with low elevations captures changes in tissue stiffness much better than a load-controlled system.

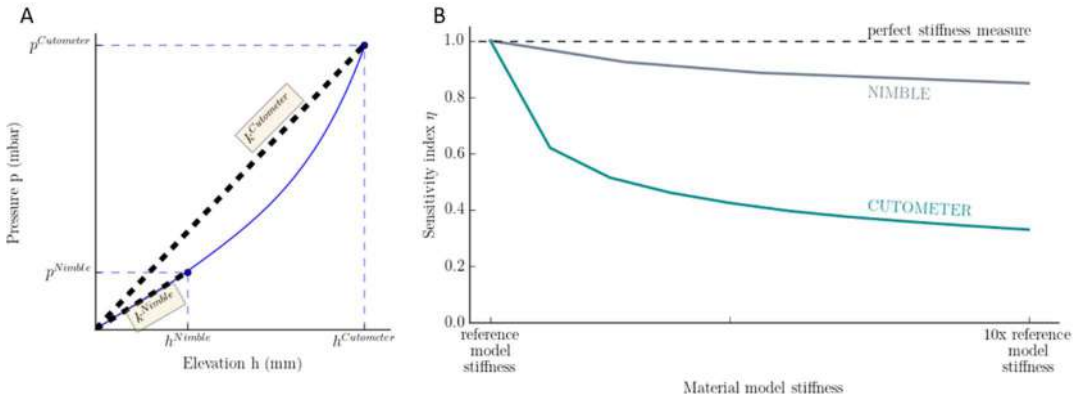

Figure 2. (A) Pressure - elevation curve of the fitted healthy skin model. Elevation and pressure measure of the two suction devices are indicated, and the evaluation of tissue stiffness measure k^{Nimble} and $k^{Cutometer}$ are shown. (B) Sensitivity index shows the different ability of the devices to capture variations of skin stiffness.

CONCLUSION

The suction method is suitable for characterization of human skin. It is a non-invasive in-vivo measurement method and can be applied for clinical assessment. However, clinical use is limited due to measurement uncertainties, the most important one being due to the contact force induced at probe placement. Our studies investigate different factors influencing suction measurements. *FE* based simulations of the suction response of healthy and fibrotic skin provided methods to improve data analysis towards higher reliability and sensitivity of suction measurements. More importantly, simulations indicated that lower level of deformations and a displacement controlled measurement procedure significantly enhance the ability of suction to detect clinically relevant tissue modifications. Current investigations focus on the diagnostic relevance of parameters associated with the dissipative tissue behaviour, which might be quantified in long duration suction or cyclically repeated measurements.

References

[1] Allanore Y et al., Systemic sclerosis. *Nat Rev Dis Prim* **1(1)**, 2015
[2] Dobrev HP, In vivo study of skin mechanical properties in patients with systemic sclerosis. *J Am Acad Dermatol* **40(3)**:436-442, 1999
[3] Verhaegen PDHM et al., Objective Scar Assessment Tools: A Clinimetric Appraisal. *Plast Reconstr Surg* **127(4)**:1561-1570, 2011
[4] Bonaparte JP et al., The effect of probe to skin contact force on Cutometer MPA 580 measurements. *J Med Eng Technol* **37(3)**:208-212, 2013
[5] Müller B, Elrod J et al., A novel ultra-light suction device for mechanical characterization of skin. *PLoS One* **13(8)**, 2018
[6] Rubin MB, Bodner SR. A three-dimensional nonlinear model for dissipative response of soft tissue. *Int J Solids Struct* **39(19)**:5081-5099, 2002
[7] Elrod J, Müller B et al., An effective procedure for skin stiffness measurement to improve Paediatric Burn Care. *Burns* **45(5)**:1102-1111, 2019
[8] Müller B, Ruby L, Jordan S et al., Investigative Study on the Ability of Suction Devices to Detect Skin Involvement in Patients with Systemic Sclerosis. *in preperation,* 2020.

THE INTERPLAY OF SOLID AND FLUID MECHANICS IN CONTACT INTERFACES AT THE ROUGHNESS SCALE

Vladislav A. Yastrebov*[1], Andrei G. Shvarts[2], Guillaume Anciaux[3], and Jean-François Molinaris[3]
[1]Centre des materiaux, MINES ParisTech, PSL University, UMR CNRS 7633, Evry, France
[2]James Watt School of Engineering, University of Glasgow, Glasgow, Scotland, United Kingdom
[3]Laboratoire de Simulation en Mécanique des Solides, EPFL, Lausanne, Switzerland

Summary Solid Mechanics SM02 Tribology - Contact and Friction

We study the normal contact between representative rough surfaces in presence of a fluid flow in the contact interface. Both one- and two-way couplings of fluid and solid equations are considered via the boundary and finite element methods as well as via the self-consistent homogenization scheme. Some general results are obtained for the transmissivity of rough contact interfaces for incompressible creeping fluid within the one- and two-way coupling frameworks. One of the main novelties is a careful account for fluid "lakes" representing pockets of fluid, which are trapped within non-simply connected contact zones. An appropriate non-linearly compressible liquid model is used there to ensure physically meaningful results. This framework enables us to study the effect of trapped fluid on the macroscopic static friction of the interface both for elastic and elasto-plastic material models.

INTRODUCTION

Contact and friction interactions play an essential role in many quotidian contexts, including those related to industry (e.g., tire-road and wheel-rail contacts, electric switches, bearings, and brake systems), everyday human activity (e.g., walking, handling, touching, and sitting) and natural phenomena (e.g., earthquakes, landslides, and glacier motion). Regardless of such prevalence, contact-related mechanisms (friction, adhesion, and wear) are still not fully understood and thus are among the most cutting-edge research topics in the mechanical community. This is explained by the fact that those processes are inherently of multi-scale and multi-physical nature and thus are very challenging to be modelled in their integrity. One of particular multi-physical problems related to contact and friction is the fluid flow through the contact interface which involves, from mathematical point of view, a concurrent resolution of fluid and solid equations which is further complicated by the non-smooth nature of contact constraints which have to be respected by the solution. The deformation of the solid constrained by the contact interaction determines the available paths for the fluid to flow, the flow pattern determines the repartition of the fluid pressure and shear tractions, which deform in its turn the contacting solid. At the roughness scale, in the first approximation, the interfacial flow of an incompressible creeping fluid can be accurately modelled using relatively simple Reynolds equation, which is further simplified when there is no tangential motion of the walls (normal contact). However, for complex surface geometries, such a random self-affine roughness, this simplest fluid-solid coupling problem has a particular difficulty related to the fact that the fluid can be trapped within non-simply connected contact clusters (zones). The "lakes" of trapped fluid add additional constraints to the problem and, being coupled to the surrounding contact, result in a strongly non-linear and computationally challenging problem. The laws governing creeping fluid flow and diffusion through contact interfaces between rough surfaces brought in contact are essential not only for sealing engineering but also for understanding mass transport through porous media consisting of networks of percolating cracks encountered in many geological materials.

The objective of this study is multi-fold. First, we make a link between the roughness characteristics of contacting surfaces and its mechanical characteristics, and further with the transmissivity of the contact interface for different externally applied pressures and fluid pressures. Second, we characterize various effects of the trapped fluid, notably, how they affect the macroscopic transmissivity of the interface and its static friction limit. Moreover, the possibility of hardly compressible fluids to escape from the contact trap is analysed. Finally, the necessity of the strong, two-way coupling between fluid and solid equations is investigated in detail in the present context.

METHODS

In the case of *one-way coupling*, we use a spectral-based boundary element method [4] to solve frictionless and non-adhesive normal contact between two elastic half-spaces with rough surfaces in the framework of infinitesimal deformations. Numerical simulations of contact are carried out on synthetic rough surfaces with controlled spectra. The study is focused on the analysis of the evolution of the true contact area and the free-volume field under increasing squeezing pressure, which together determine the transmissivity of the interface and could be used in the analytical self-consistent homogenization model. To improve the accuracy of the contact area simulations, we used a simple technique which is based on the estimation and correction of the discretization error [5]. This technique enables us to study rough surfaces within unprecedentedly *wide* range of parameters without loss of accuracy. Therefore, this analysis could be done using moderate computational grids of only 2048×2048 points on the surface. The fluid problem on the resulting free-volume

*Corresponding author. E-mail: vladislav.yastrebov@mines-paristech.fr

Figure 1: Left: weakly-coupled simulation of the fluid flow in rough contact interface, pockets of trapped fluid are shown in blue, contact area is shown in black, reddish colours correspond to the fluid flux; right: fully coupled finite element simulation of a creeping fluid flow in contact interface between a rigid wall (not shown) and an elasto-plastic substrate.

field is solved using the finite element method. A complete statistical study of (1) the contact area growth, (2) the force-separation evolution and (3) the change in transmissivity is carried out, the mean value and the standard deviation are estimated. A novel monolithic finite element formulation ensuring a strong coupling between fluid and solid equations is used to solve the two-way coupled problem for the creeping flow in the contact interface [3, 1]. Within this framework, based on the mortar-like contact discretization which relies on the monolithic augmented Lagrangian method to handle contact and friction, we successfully handle three types of interface elements: contact, fluid flow and trapped fluid, which are in permanent evolution and change, but the resulting scheme is shown to converge even in most challenging situations.

RESULTS

The obtained results can be split into two categories: first, related to the mechanical contact of rough surfaces and, second, related to the fluid flow in the interface. For the first category, we obtained relatively universal phenomenological equations for the evolution of the contact area with increasing applied pressure, which is valid for different spectral contents [6]. Moreover, we estimated the growth of the "conducting" area, i.e. the interface area excluding the contact area and the trapped area; this area can be used in the self-consisted homogenization model for the estimation of transmissivity. The force-separation curves are also obtained and compared to models available in the literature. Novel results on the asymptotics of the opening field near zero values are obtained analytically and compared with the simulations. For the case of incompressible and non-linearly compressible trapped fluid, we found analytically the external pressure needed to "untrap" the fluid. This theoretical possibility for the fluid's escape implies a decrease of the frictional resistance of the interface with the increasing pressure, which presents an interesting results. This case is analysed both for elastic and elasto-plastic material models; for the latter, an interplay of non-linear fluid compressibility and the plastic flow produces a non-monotonous change in the friction coefficient [2]. Finally, for the case of trapped fluid in frictional interface, using the linear elastic fracture mechanics we predict emergence of shear-stress peaks near the zone where the fluid penetrates in the contact under the increasing pressure; this results is important for the fatigue of contact interfaces subjected to a cyclic load. In what concerns the results for the fluid transmissivity, we obtain novel results making a link between roughness parameters, applied pressure, pressure drop in the fluid and the mean fluid pressure. A very accurate phenomenological model is constructed and generalized for the permeability of cracks with initially conformal geometry. A fine analysis is carried out to characterize the effect of trapped fluid, critical junctions and transitional regimes of the transmissivity, including the near-percolation asymptotics. The one- and two-way coupling strategies are compared.

References

[1] A. Shvarts, J. Vignollet, and V. Yastrebov. Computational framework for monolithic coupling for thin fluid flow in contact interfaces. *submitted*, 2020. Preprint is available at https://arxiv.org/abs/1912.11292.
[2] A. Shvarts and V. Yastrebov. Trapped fluid in contact interface. *J Mech Phys Solids*, 119:140 – 162, 2018.
[3] A. G. Shvarts and V. A. Yastrebov. Fluid flow across a wavy channel brought in contact. *Tribol Int*, 126:116 – 126, 2018.
[4] H. M. Stanley and T. Kato. An FFT-based method for rough surface contact. *J Tribol-T ASME*, 119:481–485, 1997.
[5] V. Yastrebov, G. Anciaux, and J. Molinari. On the accurate computation of the true contact-area in mechanical contact of random rough surfaces. *Tribol Int*, 114:161–171, 2017.
[6] V. Yastrebov, G. Anciaux, and J. Molinari. The role of the roughness spectral breadth in elastic contact of rough surfaces. *J Mech Phys Solids*, 107:469 – 493, 2017.

MULTIPHYSICAL FINITE ELEMENT MODEL FOR AIR FOIL THRUST BEARING OPTIMIZATION

Markus Rieken*[1], Pascal Zeise[1], Marcel Bauer[1], and Bernhard Schweizer[1]
[1]Institute of Applied Dynamics, Technical University Darmstadt, Darmstadt, Germany

Summary Air foil bearings are applicable in high speed turbomachinery and oil-free environments. Detailed thermo-elasto-hydrodynamic (TEHD) finite element models can be used to optimize bearing geometry. Results for an air foil thrust bearing (AFTB) are presented in this work. Deformations and temperatures of the foils and the rotor as well as the temperature and the pressure of the lubricating air film are calculated. Moreover, the rotation-induced laminar/turbulent flow on the backside of the runner disk is part of this multiphysics model. Results show the strong connection between the lubricating gap height and thus the pressure buildup with top foil sagging. Thermal bending of the runner disk is a key factor in performance reduction.

MULTIPHYSICS MODEL OUTLINE

For the modeling of an AFTB (see Fig. 1), physical equations from 3 disciplines are used, namely thermo-elasticity (deformations of the top and bump foils and of the rotor disk), hydrodynamics (pressure distribution in the air film and backside flow) and thermodynamics (temperature of top foil, air film, backside flow, radial gap, rotor and rotor disk). Figure 1 gives an overview over the bearing components. The governing partial differential equations (PDEs) are discretized using finite elements (FE). The resulting nonlinear FE model has approximately 425 000 degrees of freedom in 260 field equations for which stationary studies are carried out. The investigated rotor-bearing system has the following main parameters: rotor diameter $d_R = 27\,\mathrm{mm}$, disk radius $r_D = 31\,\mathrm{mm}$, disk thickness $t_D = 4\,\mathrm{mm}$, inner top foil radius $r_i = 15\,\mathrm{mm}$, outer top foil radius $r_o = 30\,\mathrm{mm}$ and maximum rotational speed $\Omega_{max} = 120\,\mathrm{krpm}$. In this study, only a single bearing pad (a single top foil with bump foil underneath) is investigated. While the base plate of Fig. 1 (blue) is treated as a rigid body, deformations of the thin bump and top foils (yellow/orange) due to pressure forces cannot be ignored. The governing equations used in the current model for the foil deformations originate from Reissner-Mindlin shell theory. The normal contact force between bump and top foil on the one hand and bump foil and base plate on the other hand are both implemented using a penalty formulation. The tangential behavior between top and bump foil is modeled via a stick-slip approach (regularized Coulomb friction). Using the generalized Reynolds equation of lubrication theory [1] combined with an averaging approach [2, 3] for the air temperature, a simplified Reynolds equation in 2D Cartesian coordinates is obtained to calculate the pressure distribution $p(x, y)$ in the lubricating gap with height profile $h(x, y)$. For the temperature calculation in the lubricating gap, the 3D energy equation (without external heat source terms) is solved. Radial and axial deformations of the rotor disk are calculated based on the Navier-Lamé equations with an account for thermal stresses. Temperatures of the rotor disk and the top foil are calculated using a 2D energy equation. At the backside of the rotor disk, the disk rotation causes an airflow. The velocity field consisting of the radial, the circumferential and the axial velocity is calculated from the boundary layer equations for steady incompressible axisymmetric flow (neglecting a radial pressure gradient), see Ref. [4].

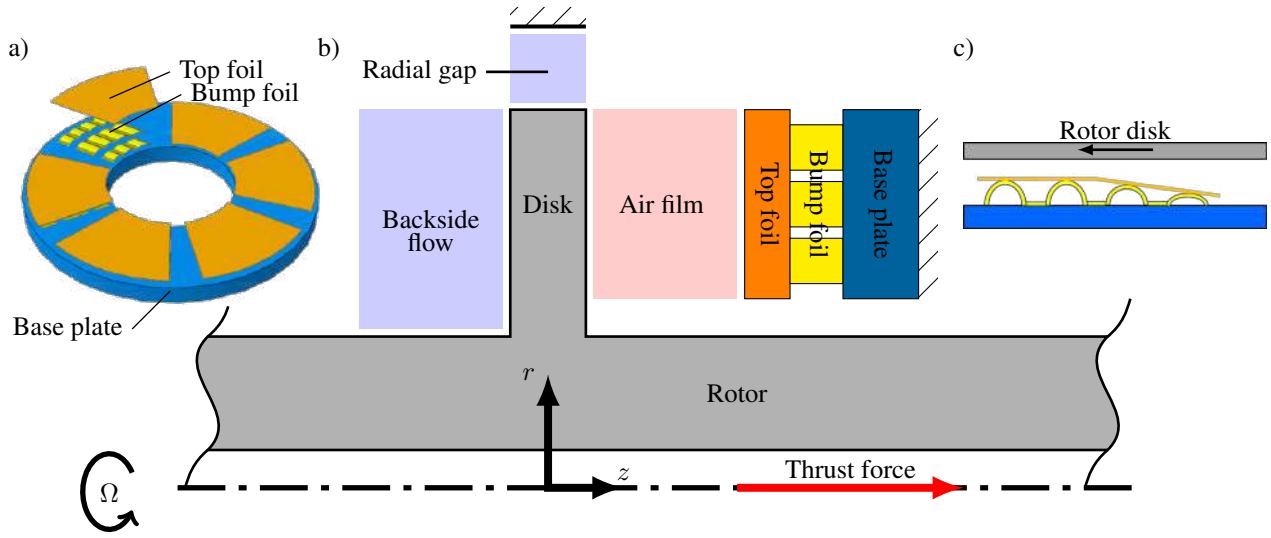

Figure 1: Overview over AFTB components (not to scale). a) Bearing with 6 identical pads, b) section view of bearing in assembly and c) converging gap between top foil (stationary) and rotor disk.

*Corresponding author. E-mail: rieken@ad.tu-darmstadt.de.

SIMULATION RESULTS

Fig. 2 shows simulation results for a stationary study at a rotational speed of $\Omega = \Omega_{max}$. Fig. 2 a) shows the lubricating gap height h which is a combination of the taper-land geometry through bump height variation as well as the top foil and rotor disk deflections. It is clearly visible that the top foil sags between its contact lines with the underlying bump foil (depicted in the line scheme at the bottom of Fig. 2 a)). Due to the thermally induced bending of the rotor disk away from the lubricating gap, gap height increases towards the outer radius of the pad. Therefore, the minimal gap height (in this case $5\,\mu$m) is found close to the trailing edge at the inner radius of the pad which is likely to be the first point of contact between top foil and runner disk in an overload scenario.
Fig. 2 b) shows the 2D pressure increase (with regard to ambient pressure) over a pad with two distinct pressure peaks near the trailing edge. These originate from the wavelike deflection of the top foil and occur at the contact lines of top and bump foil (cf. Fig. 2 a)).
Fig. 2 c) shows 3 slices through the 3D temperature field of the air film. At the top, a radial pattern results from the temperature distribution in the runner disk. Due to the more efficient heat transfer near the outer radius of the disk (on its backside), temperature drops despite higher velocities. At the bottom, the interface to the top foil is visible. While the temperature generally increases from leading to trailing edge, the pattern of contact lines clearly shows as colder spots. This is because most of the heat flux at this bottom interface is conducted through the bumps, cf. [5]. Thus, the hottest spots are not observed at the spot of the smallest gap height, but at the trailing edge and between the contact lines. As can be seen from the intermediate slice, this pattern eventually fades out when the interface to the disk is reached.

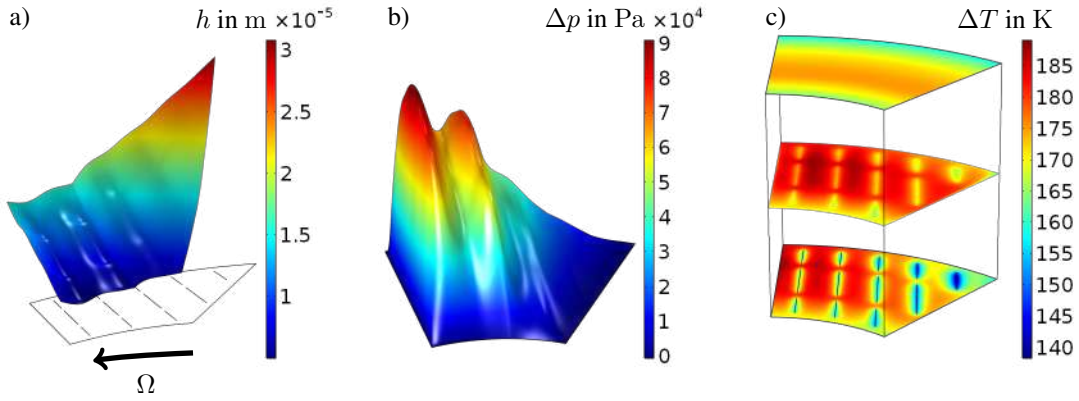

Figure 2: a) Gap height h, b) air pressure increase Δp and c) air temperature increase ΔT.

CONCLUSIONS

The performance of AFTBs is significantly influenced not only by the hydrodynamic, but also by the elastic and thermal behavior of its components. Pressure induced top foil sagging between the bump support lines and, more importantly, thermally induced rotor disk bending are two key contributors to a decrease in load capacity and can eventually lead to bearing and (consequently) machine failure.

References

[1] Dowson, D. A Generalized Reynolds Equation for Fluid-Film Lubrication. *International Journal of Mechanical Sciences* **4**(2): 159-170, 1962.
[2] Lee, D., and Kim, D. Three-Dimensional Thermohydrodynamic Analyses of Rayleigh Step Air Foil Thrust Bearing with Radially Arranged Bump Foils. *Tribology Transactions* **54**(3): 432-448, 2011.
[3] Mahner, M., Lehn, A., and Schweizer, B. Thermogas- and Thermohydrodynamic Simulation of Thrust and Slider Bearings: Convergence and Efficiency of Different Reduction Approaches. *Tribology International* **93**: 539-554, 2016.
[4] Cebeci, T., and Smith, A. Analysis of Turbulent Boundary Layers. Academic Press, NY 1975.
[5] Lehn, A. Air Foil Thrust Bearings: A Thermo-Elasto-Hydrodynamic Analysis. *PhD Thesis*, Technical University Darmstadt, Darmstadt, 2017.

ROTATIONAL INSTABILITY IN SUPERLUBRIC JOINTS†

Cangyu Qu[1,2,3], Songlin Shi[2,3], Ming Ma[3,4,5], Quanshui Zheng[1,2,3,‡]
[1]Institute of Superlubricity Technology, Research Institute of Tsinghua University in Shenzhen, Shenzhen, China
[2]Department of Engineering Mechanics, Tsinghua University, Beijing, China
[3]Center for Nano and Micro Mechanics, Tsinghua University, Beijing, China
[4]State Key Laboratory of Tribology, Tsinghua University, Beijing, China
[5]Department of Mechanical Engineering, Tsinghua University, Beijing, China

Summary Surface energy plays an important role in instability phenomena in liquids and soft matters, but rarely has similar effects in solids. Here, a novel mechanical instability controlled by surface energy is reported which is valid for a large class of solid materials, in particular two-dimensional layered materials. When sliding a top flake cleaved from a microscale graphite mesa by a probe through a point contact, we observe that the flake moves without rotation for a certain distance, and then suddenly rotates when a critical displacement is reached. The theoretical analysis is consistent with experiments and reveals that this instability is an interesting effect of superlubricity (a state of nearly zero friction). The uncovered mechanism provides useful knowledge for manipulating and controlling these sliding joints, and can guide the design of future superlubric devices.

INTRODUCTION

Surface energy plays an important role in a number of instability phenomena observed in liquids and soft matters, but rarely has similar effects in solids. For a micro/nano system, the surface-to-volume ratio is increased significantly, and thus surface energy is expected to have a greater effect. However, in sliding devices, this effect is usually overwhelmed by interfacial friction. In order to observe the effect of surface energy in these sliding joints, friction has to be ultralow. This is exactly the case in superlubric systems, where the incommensurability of the solid contact results in systematic cancellation of interfacial friction, thus the total friction of the contact is almost zero[1]. This fascinating phenomenon was theoretically predicted and then observed on nano-contacts[2–4]. Microscale superlubricity was later achieved on graphite mesa system, which contains pillar-like mesas fabricated on the surface of highly orientated pyrolytic graphite (HOPG) through micro-fabrication[5].

EXPERIMENTAL OBSERVATION

During the manipulation of graphite mesas, rotational instability was observed. The experimental setup is shown in Fig.1(a). The square shaped graphite mesa (with typical width 4 μm) is sheared by a tungsten tip quasi-statically under an optical microscope. As shown in Fig.1(b), when sheared by a nearly centric tip (centric loading), the top flake with side length of a, slides without rotation for a displacement up to a critical value. When the critical point is reached, the top flake suddenly rotates, showing a rotational instability. On the other hand, when shearing using an eccentric tip (eccentric loading) with eccentricity, e, one might expect the top flake to rotate immediately due to the eccentric loading. However, a different behavior was observed in fact. As shown in Fig.1(c), the top flake still slides without rotation for a considerable displacement, until similar rotational instability occurs at a critical displacement, which is smaller than that in centric loading case. This can be better seen from the curve of the top flake rotation angle θ vs. displacement δ. As shown in Fig.1(d), θ remains nearly zero before a discontinuity in the curve corresponding to the rotational instability.

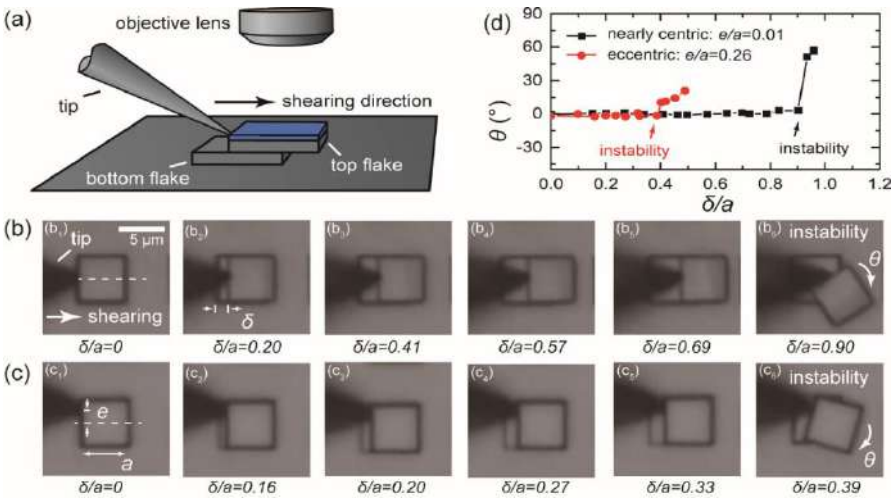

Figure 1. (a) Experimental setup. (b)(c) Images from top view for the case of centric loading and eccentric loading, respectively. Scale bar 53μm. (d) Top flake rotation angle θ vs shearing displacement δ. The sudden rotation (rotational instability) happens at a critical displacement, while before the instability, the top flake stays unrotated.

MECHANISM & APPLICATIONS

† This work has been published in Qu, C., Shi, S., Ma, M. & Zheng, Q. *Phys. Rev. Lett.* 122, 246101 (2019).
‡ Corresponding author. E-mail: zhengqs@tsinghua.edu.cn

The experimental observations can be rationalized by a kinematic model. We model the system as a fixed bottom flake and a rigid but movable top flake with two degrees of freedom, i.e. the displacement along with the tip δ, and the rotation around the tip contact point θ, as shown in Figs. 2(a)(b). For an arbitrary configuration (δ, θ), the total potential energy of the system[6] is $U = 2\gamma_{sa}(A - A_{ss}) + \sigma A_{ss}$, where γ_{sa} is the surface energy of graphite, σ is the interfacial energy of the incommensurate graphite-graphite interface, i.e. the overlapping area, A_{ss}, between the top and bottom flakes during sliding, and $A = a^2$, as shown in Fig. 2(b). By noting that $\Gamma = 2\gamma_{sa} - \sigma$ which is the cleavage energy of graphite, we have

$$U(\delta, \theta) = 2\gamma_{sa}a^2 - \Gamma A_{ss}(\delta, \theta). \quad (1)$$

By defining the normalized total excess potential $U^* = (U - 2\gamma_{sa}a^2)/(\Gamma a^2) = -A_{ss}/a^2$, the calculation of U^* comes down to the calculation of the overlapping area A_{ss}, which is conducted either analytically or with numerical algorithms. Neglecting kinematic energy, the equilibrium configuration of the system is determined by the potential minima in (δ, θ) space.

Figure 2(c) shows the calculated U^* as a function of θ in the case of perfectly centric tip loading ($e/a = 0$, left) and eccentric tip ($e/a = 0.225$, right), respectively. When the loading is centric, $\theta = 0$ is always a local energy minimum regardless of δ, thus un-rotated sliding is always stable/metastable. On the other hand, in the case of $e/a = 0.225$ (eccentric loading), an energy minimum is still found at $\theta = 0$, but only for $\delta < \delta_{cr} \approx 0.329a$. At δ_{cr}, such an this energy minimum vanishes, leading to the sudden rotation of the top flake.

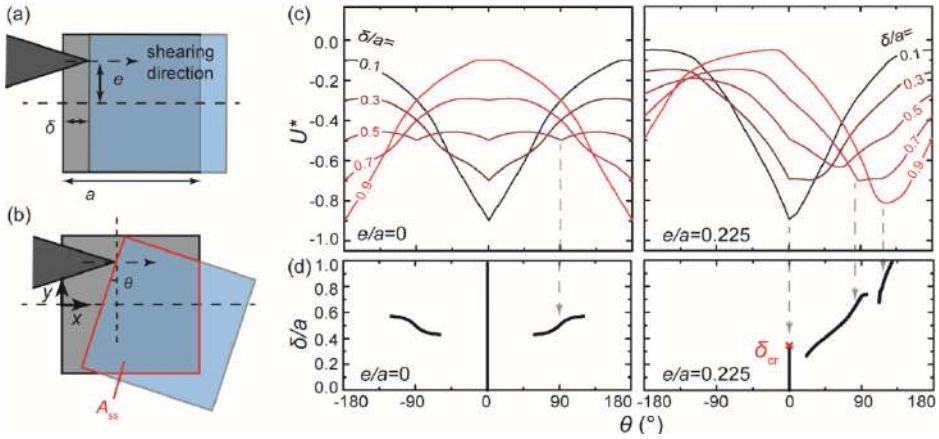

Figure.2 (a)(b) The kinematic model. The bottom flake is fixed and the top flake is a rigid but movable body with two degrees of freedom, i.e. the displacement δ, and the rotation around the tip contact point θ. (c) Calculated normalized total potentials (U^*) as functions of θ for centric loading ($e/a = 0$, left) and eccentric loading ($e/a = 0.225$, right), respectively. In the former case, an energy minimum is always found at $\theta = 0$. In the latter case, an energy minimum is found at $\theta = 0$ for $\delta < \delta_{cr} \approx 0.329a$. When δ_{cr} is reached, this energy minimum vanishes, leading to the sudden rotation. (d) Branches of stable/metastable points are indicated by the black lines that correspond to the left- and right-hand sides of (c) in (δ, θ) space where local energy minimum is met.

The mechanism behind the rotational instability provides an elegant idea for effectively constraining the relative rotation of a superlubric joint through surface energy. This is very important in the design of superlubric devices since one of the main challenges in superlubric devices is to control the sliding direction and constrain the relative rotation without introducing extra mechanical contacts (where friction cannot be avoided). Through simple geometric design, the superlubric joint can be made rotation-proof in certain range of parameters. For example, a case study performed on a superlubric slider sliding on a guide rail shows that the slider is expected to stay on track thanks to the constraining effect of surface energy[7,8].

CONCLUSIONS

In conclusion, a rotational instability was observed in microscale graphite sliding joints. The comparison between experimental observation and theoretical modelling reveals that such instability is controlled by the surface and interfacial energies of graphite. The result is independent of the specific material and is fully scalable. Thus, it is not limited to graphite, and is also applicable to other superlubric sliding systems. Our results provide useful knowledge for manipulating and controlling these sliding joints, especially for constraining relative rotation through interfacial energy and design of the device geometry.

References

1. Hod, O., Meyer, E., Zheng, Q. & Urbakh, M. Structural superlubricity and ultralow friction across the length scales. *Nature* **563**, 485–492 (2018).
2. Peyrard, M. & Aubry, S. Critical behaviour at the transition by breaking of analyticity in the discrete Frenkel-Kontorova model. *J. Phys. C Solid State Phys.* **16**, 1593–1608 (1983).
3. Hirano, M. & Shinjo, K. Atomistic locking and friction. *Phys. Rev. B* **41**, 11837–11851 (1990).
4. Dienwiebel, M. *et al.* Superlubricity of Graphite. *Phys. Rev. Lett.* **92**, 126101 (2004).
5. Liu, Z. *et al.* Observation of Microscale Superlubricity in Graphite. *Phys. Rev. Lett.* **108**, 205503 (2012).
6. Wang, W. *et al.* Measurement of the cleavage energy of graphite. *Nat. Commun.* **6**, 7853 (2015).
7. Qu, C., Shi, S., Ma, M. & Zheng, Q. Rotational Instability in Superlubric Joints. *Phys. Rev. Lett.* **122**, 246101 (2019).
8. Ball, P. A new twist on superlubricity. *Nat. Mater.* **18**, 774–774 (2019).

WHAT IS THE BENDING RIGIDITY OF A BOOK? MECHANICS OF STACKED PLATES COUPLED BY FRICTION

Samuel Poincloux*[1], Tian Chen[1], Basile Audoly[2], and Pedro Reis[1]
[1]Flexible Structures Laboratory,Ecole Polytechnique Fédérale de Lausanne(EPFL),Lausanne,Switzerland
[2]Laboratoire de Mécanique des Solides,Ecole Polytechnique,Palaiseau,France

Summary Multi-layered structures have long been exploited to design stiff and lightweight devices. When inter-layer sliding occurs, friction must also be considered, making this a challenging problem. Here, we focus on rationalizing the mechanical response of a stack of a large number ($n \sim 50$) of elastic plates interacting through dry friction; a system akin to a book. We ask: "What is the bending rigidity of this *book*?" We perform precision nonlinear bending tests to measure the mechanical response of our stacks. Our findings deviate from both the purely elastic case and the thick Timoshenko beam cases, with nontrivial stiffening effects and hysteretic behavior. Taking friction as a perturbation, we develop a reduced model involving the coupling between the geometric nonlinearities, elasticity, and friction that is in excellent agreement with experiments.

EXPERIMENTAL EVIDENCE OF INTER-PLATES FRICTIONAL INTERACTIONS

We study multi-layered systems in which, in contrast to classic sandwiched structures [1], the layers are not bonded together. In this case, the friction of the layers sliding against each other is crucial to understand their mechanical properties [2]. Conversely, by carefully tracking how the inter-layer interactions yield a mechanical response that is different from the purely elastic situation, it is possible to retrieve the tribological properties of the layers [3].

Here, we focus on stacked elastic plates interacting through friction and subjected to bending tests. The layers of this stack are $220 \times 30 \times 0.3\,\mathrm{mm}$ plates made of a thermoplastic polymer (PET), which behave elastically throughout the experimental tests, despite the large deformations imposed. Both surfaces of the plates are carefully scrapped with sandpaper to get as close as possible to the realm of so-called dry-friction [4]. The full stack is then subjected to a 3-point bending test (Fig. 1a), with an imposed displacement w_0, and the resulting vertical force Q is recorded during loading and unloading. In these experiments, the layers can slide freely against each other as they are not constrained laterally. The test is also carried out far into the non-linear regime, which highlights the hysteretic behavior of the mechanical response (Fig. 1b). Since we are interested primarily in the interaction between the layers, the external supports must not be dissipative: the two supports comprise two cylindrical steel shafts mounted onto air bearings, hence ensuring moment-free pins. Moreover, these shafts are coated with a thin ($\sim 100\,\mu\mathrm{m}$) layer of elastomer (VinylPolySiloxane) to prevent any sliding with the bottom plate of the stack. In this way, all the measured dissipation originates from the inter-layer frictional interactions within the stack.

The bending tests are performed on stacks composed of n layers, with n ranging from 1 to 70. As a first step to characterize how stacking the layers affects the mechanical behavior, the response curve $Q(w_0)$ is normalized by the number of layers (Fig. 1b). These curves would remain identical if the response of the stack were only the sum of the responses of the individual plates. Instead, while the overall shape of the measured load curve resembles what would be expected for a standard non-linear 3-point bending test, the behavior of our stacks exhibits significant quantitative differences. Specifically, the amplitude of the hysteresis increases, the maximal force also increases for both loading and unloading, and the initial slope of the curve (proportional to the bending stiffness) splits for the loading and unloading curves.

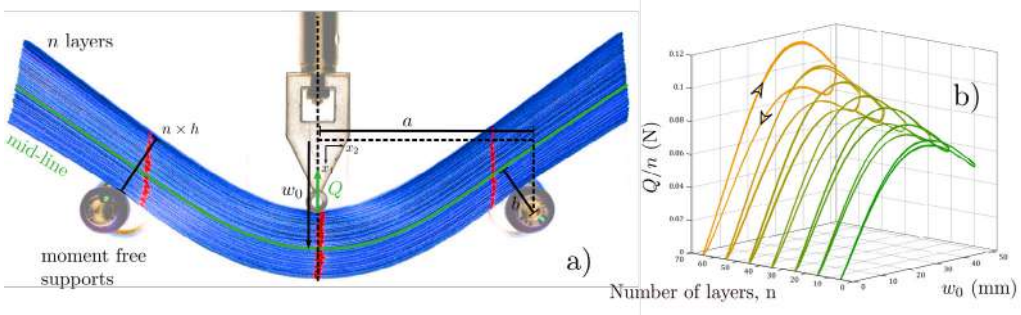

Figure 1: a) Front view of the experimental set-up. A stack of $n = 70$ plates (thickness $h = 0.3\,\mathrm{mm}$) is placed on moment-free supports separated by a distance $2a = 130\,\mathrm{mm}$. An indenter loads the stack in its center by imposing a displacement w_0 while recording the vertical force Q needed to deform the stack. To visualize the shear occurring inside the stack, vertical red lines are painted on the stack at rest. b) Loading and unloading force-displacement curves $Q(w_0)$ normalized by the number of layer in the stack n and plotted for selected values of n. The curves displayed are the superposition of several tests carried with the stack shuffled in-between and for 3 loading cycles, the good overlap of the curves demonstrates the reproducibility of the experiments.

*Corresponding author. E-mail: samuel.poincloux@epfl.ch.

PREDICTION OF THE EFFECTIVE BENDING STIFFNESS AND DISSIPATION IN THE STACK

We have developed a reduced model to rationalize the experimental measurements, in particular the change in bending stiffness (Fig. 2a), capturing the phenomenology of our observations. The inter-layer interactions are treated as a perturbation to the elastic deformation of the stack, meaning that the equilibrium shapes of the layers and the response force upon loading are first solved without taking friction into consideration. Subsequently, assuming a simple Amontons-Coulomb law between the layers, the energy dissipated by the frictional forces can be estimated from the known inter-layers displacements and normal forces. The dissipated energy is then added (loading) or subtracted (unloading) to the elastic energy. The resulting total energy is finally differentiated with respect to w_0 to retrieve the vertical force Q, which can now be compared to the experimental data. This force has an analytical solution if we restrict ourselves to linear deformation and assume that all the plates are simply supported and deformed similarly:

$$Q = \frac{6}{a^3} n B_0 \cdot \left(1 \pm \mu(n-1)\frac{3}{4}\frac{h}{a}\right) w_0, \tag{1}$$

where B_0 is the bending stiffness of a single plate, μ is the inter-layer kinetic friction coefficient, and the $+$ and $-$ signs correspond to loading and unloading, respectively. The effective bending stiffness of the stack, $B^{\pm} = nB_0\left(1 \pm \mu(n-1)\frac{3}{4}\frac{h}{a}\right)$, contains a correction factor from the purely elastic case that is a function of the friction μ and the slenderness of the plates $\frac{h}{a}$. While this reduced model captures the linear variations of $B^{\pm}(n)/n$, it misses the asymmetry between in the slopes for loading vs unloading observed experimentally (Fig. 2a).

To understand this asymmetry, it is necessary to consider how staking an increasing number of layers modifies the geometry of the problem. To address this, we have developed a homogenized model of the stack by reducing it to its mid-line. The curvature of all the plates is written with respect to this mid-line by assuming they are parallel and separated by their thickness h. The primary adjustment induced by the homogenized model turns out to be that the effective radii, b, of the supports in-between which the mid-plane is bent (Fig. 1a), increases with the number of plates n. As a result, even in the absence of friction, $B(n)/n$ increases linearly with n in a way (Fig. 2a, dashed) that lies in-between the loading and unloading experimental curves. Thus, with the symmetry restored, measuring $B^{\pm}(n)$ and using an adjusted version of Eq. 1 that takes into account the geometrical correction, provides a way to estimate the friction coefficient μ of the stacks by simply measuring the slope of the functions $B^{\pm}(n)/n$.

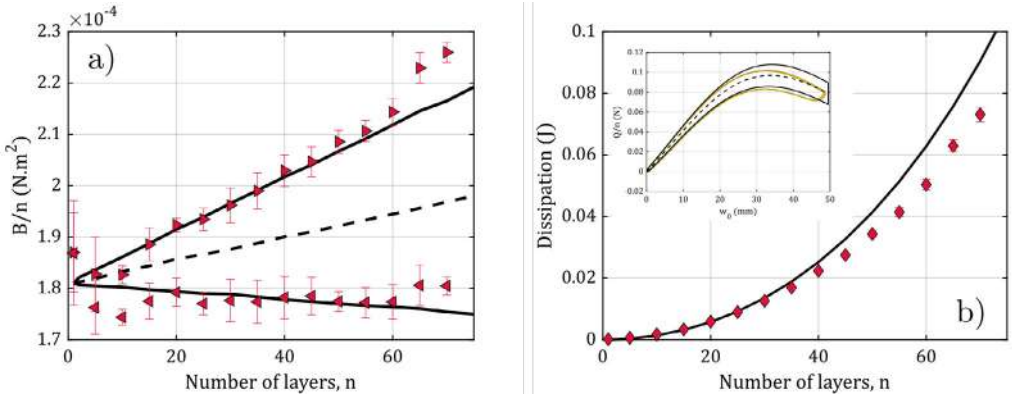

Figure 2: a) Normalized bending stiffness of the stack B/n as a function of the number of plates n for loading and unloading. The bending stiffness of a single plate is $B_0 = 1.8 \times 10^{-4}\,\mathrm{N.m}^{-2}$. Experimental data are the red triangles (loading $\triangleright$, unloading $\triangleleft$). The dashed lines is the result from the perturbative model without friction, the solid lines, with friction. b) Inset, Comparison between the experimental mechanical response (for $n = 50$) and the prediction using the perturbative model (dashed line without friction, solid lines, with). Energy dissipated by the stack upon one cycle, measured experimentally ($\Diamond$) and predicted (solid line). The error bars are the standard deviations over a multitude of tests made for the same set of parameters.

Finally, the estimated friction coefficient is introduced into the perturbative approach to compute the full non-linear mechanical response of the stack. The calculated response is in excellent agreement with the experimental data (Fig. 2b, inset), especially for the bending stiffness of the stack (Fig. 2a, solid lines). Our approach also enables us to predict the energy dissipated in the stack upon cycling far into the non-linear regime (Fig. 2b). We believe that our quantitative description for the mechanical response of a stack of frictional plates opens an exciting avenue to design optimized dampers that rely on the interplay between elasticity and frictional interactions in multilayered systems.

References

[1] Vinson J. R. The Behavior of Sandwich Structures of Isotropic and Composite Materials. Routledge, NY 2018.
[2] Asker H. K., Rongong J. A., Lord C. E. Dynamic properties of unbonded, multi-strand beams subjected to flexural loading. *Mechanical Systems and Signal Processing*, 101 (2018), 168-181
[3] Wang G. et al. Bending of Multilayer van der Waals Materials. *Physical Review Letters*, 123.11 (2019): 116101.
[4] Baumberger T., Caroli C. Solid friction from stick–slip down to pinning and aging, *Advances in Physics*, 55:3-4 (2006), 279-348

OPTIMAL CONTROL OF CROSS ROLL STRAIGHTENING PROCEDURE

Jindrich Petruska,*[1] and Tomas Navrat
Institute of Solid Mechanics, Mechatronics and Biomechanics, Faculty of Mechanical Engineering, Brno University of Technology,Brno, Czech Republic

Summary Cross roll straightening of bars with circular cross section on multi-roller straightening machines is described in the paper. First, a quick review of possible analytical approaches is described and the fast computational algorithm based on the Eulerian description of the material flow through the straightening machine is presented. The fast algorithm is used for analysis of a large number of straightening problems. These results serve in the next step as training data for a neural network, which provides an efficient tool for correct optimal adjusting of intermeshing rollers of the straightening machine to obtain acceptable output curvature of the straightened bar together with the residual stress and roller loading being as low as possible.

INTRODUCTION

The problem we try to solve is to find an optimal intermeshing w_C, w_E of the straightening machine with two bending sections according to Figure 1. By the term "optimal" we mean to obtain a final product with acceptable output curvature (typically 0.5 mm/m) with minimal loading od the working rollers to minimize their wear and minimal residual stress in the bar to keep the stability of its shape in the next technological steps. To solve this problem for different diameter, material and input curvature of the bar is not an easy task due to its inherent nonlinearity. Many approaches have already been applied to it, from classical analytical models based on simplified suggestions combined with empirical knowledge [1] up to fully nonlinear 3D Finite Element models. With the Finite Elements, many of the nonlinear effects can be now included, but the analysis is still rather a time-consuming procedure [2], [3]. It can be used for academic and research purpose, but hardly for a fast suggestion of possible intermeshing strategy of multi roller straightening machines in real industrial situations. To fill this gap, a fast algorithm of straightening problem analysis

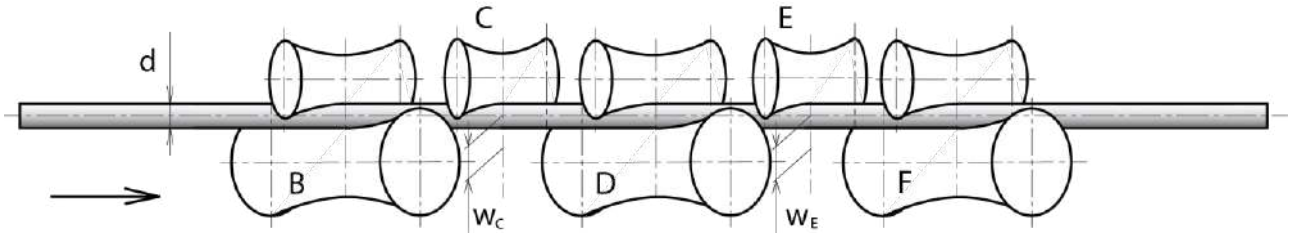

Figure 1. Straightening machine with two intermeshing rollers C, E.

was suggested and applied first to section and rail straightening processes [4]. The main idea of the algorithm is based on the Eulerian description of material flow through the axial direction of beam elements, which represent the position of the straightened long product within the leveling machine. The elements are fixed in axial direction, but their transversal displacements and slopes are described by a standard Lagrangean approach. Some of the simplifying assumptions are still adopted: the long product deflection and curvature can be described by a bending theory of beams with uniaxial state of stress, without the influence of shear force and planar deformation of the cross-section. The decisive nonlinear effect of material plasticity is modelled by a bilinear stress-strain diagram with linear plastic hardening and kinematic hardening rule. Adding the rotation of material around the longitudinal axis of the bar with circular cross section enabled the application of the algorithm to cross roll straightening of circular bars. Detailed description of this algorithm together with its validation and experimental verification was described in [5].

SELECTION OF OPTIMAL STRAIGHTENING PARAMETERS

The algorithm described above is very efficient in solution of straightening problems with two bending sections according to Figure 1, or even more of them. Nevertheless, we start the solution from known intermeshing of rollers C, E, which is not a typical problem to solve for the operators of straightening machine. They have to answer the inverse question: what intermeshing will lead to acceptable output curvature k_{OUT} less than 0.5mm/m, together with the sum of roller loading R and residual stress S being as low as possible? The initial known values for this task is the input curvature k_{IN}, diameter and material parameters of the bar.

In the following, we illustrate possible way of solving this inverse problem on the example of the bar with diameter 70 mm, yield stress 900 MPa and ultimate strength 1200 MPa. We suppose the input curvature of the bar can reach maximal value of 10 mm/m and maximal intermeshing of both adjustable rollers in Figure 1 can be 10 mm, too. Within these limits, repeated Monte Carlo simulations of the direct problem of straightening process were realized, with random distribution of the input parameters of w_C, w_E and k_{IN}. Discrete solutions of the Monte Carlo simulations were

*Corresponding author. E-mail: petruska@fme.vutbr.cz

then fitted by Neural Network. The sets of inputs (w_C, w_E and k_{IN}) and outputs (output curvature k_{OUT} [mm/m], roller loading R [kN] and residual stress in straightened product S [MPa]) were randomly divided into three sets. 70% were used for training, 15% for validation and last 15% for independent test of network generalization.

In Figure 2 we can see the results of acceptable output curvature (left) and response surfaces of roller loading (center) and residual stress (right). In the left figure we can clearly see that different intermeshing combinations can lead to acceptable output curvature results. This is well known from the industrial experience. The central picture proves the expected increase of roller loading with the growth of intermeshing values, whereas the residual stress response shows rather unpredictable shape for intermediate values of intermeshing.

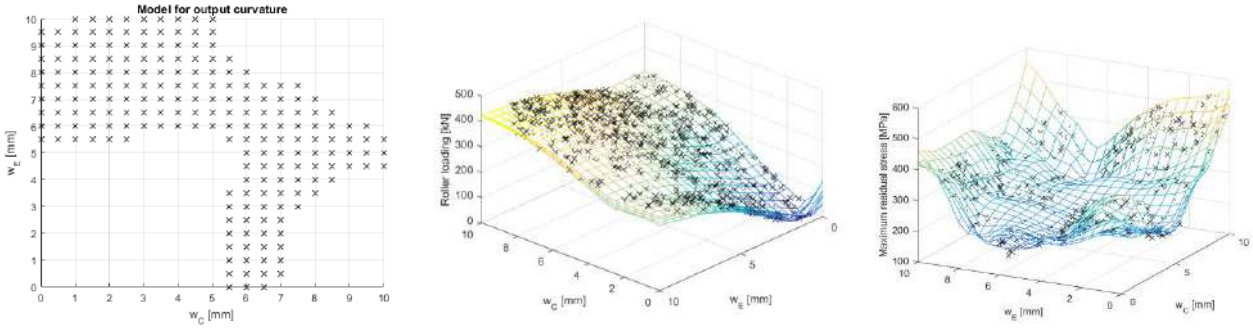

Figure 2. Intermeshing combinations with acceptable k_{OUT} (left) and response surfaces of roller loading and residual stress

To minimize both the output curvature k_{OUT}, roller loading R and residual stress S, all the values are normalized and a new weighted variable Z is formulated as

$$Z = \frac{1}{3}\left(\frac{k_{out}}{max(k_{out})} + \frac{S}{max(S)} + \frac{R}{max(R)}\right) .$$

Here the expression $max(\,)$ represents the maximal value reached by the appropriate variable in the domain $w_C - w_E$. Distribution of Z in Figure 3 then shows possible combinations of intermeshing w_C, w_E with minimal output curvature, roller loading and residual stress. The domain is limited strictly to acceptable results of $k_{OUT} <$ 0.5 mm/m.

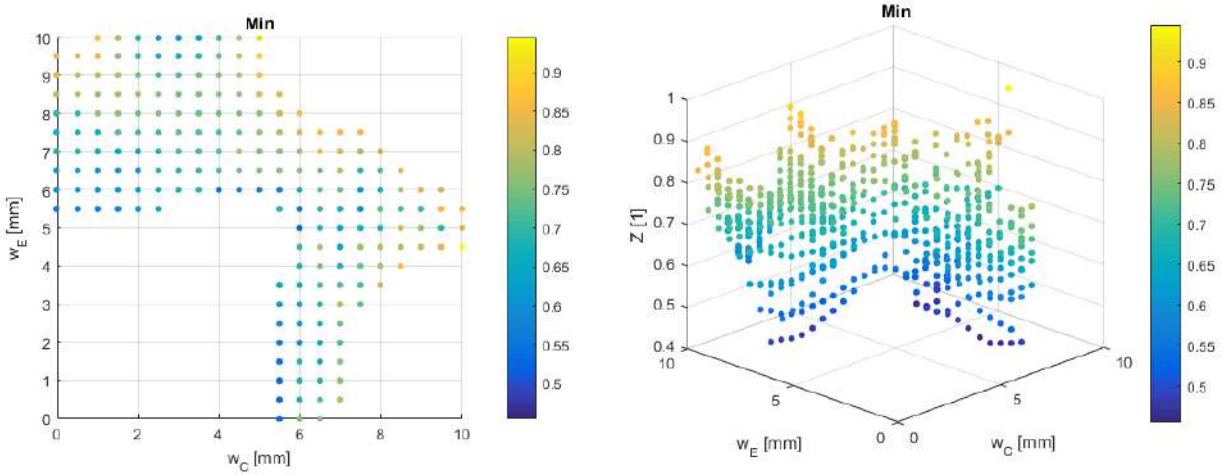

Figure 3. Possible combinations of intermeshing values with minimal response of normalized output variable Z.

CONCLUSIONS

Optimal adjusting of the cross roll machine intermeshing parameters was illustrated on the example of the two bending sections machine and selected material and diameter of the straightened bar. The results prove that there are more possible strategies of intermeshing (i.e. more combinations of adjusting of intermeshing rollers), which lead to similar and acceptable results of the procedure. This corresponds to known industrial experience. Possible generalization of presented method to other types of straightening problems will be the topic of the conference talk.

References

[1] Tokunaga, H., *Trans. Jpn. Soc. Mech. Eng.* ***26***: 1720–1726, 1960.
[2] Biempica, C.B., del Coz Díaz, J.J., García Nieto, P.J., Pe˜nuelas Sánchez, I., *Appl. Math. Model.* ***33***: 34–53, 2009.
[3] Huh, H., Heo, J.H., Lee, H.W., *Int. J. Mach.Tool Manuf.* ***43***: 345–350, 2003.
[4] Petruška, J., Návrat, T., Šebek, F., *Advanced Materials Research* ***586****:* 389-393, 2012.
[5] Petruška, J., Návrat, T., Šebek, F., *Journal of Materials Processing Technology* ***233:*** 53-67, 2016.

ON THE MOSSAKOVSKII METHOD FOR CONTACTS SUPPORTING A MOMENT

Matthew Moore*[1] and David Hills[2]
[1]Mathematical Institute, University of Oxford, Oxford, UK
[2]Department of Engineering Science, University of Oxford, Oxford, UK

Summary The Mossokovskii solution of the half-plane formulation for contacts between elastically-similar materials is extended to contacts supporting a moment. We reduce the Cauchy singular integral formulation of the problem to a non-symmetric Abel integral relating the indenter geometry to the applied normal force. We use the formulation to derive simple expressions the applied normal force and moment as functions of the contact extent and indenter tilt. We also for the coefficients of the square-root terms in the pressure expansion local to the ends of contact, which may be of use in asymptotic analyses of the partial-slip problem.

INTRODUCTION

The usual starting point for analysing contact problems is the Flamant solution for a force applied to the apex of a wedge, specialised to a half-plane, from which a Cauchy integral equation is derived where the primary unknown is the contact pressure distribution [2]. This approach works well for problems in which the normal load is established first, with the shearing force then developed as the normal force is held constant. However, if both the normal load and shearing force are simultaneously varying functions, an alternative incremental method originally formulated by [4] and extended by [3] is more suited. In this analysis, we adapt the method to contacts that support a moment and hence are, in general, non-symmetric.

PROBLEM FORMULATION

Consider the configuration illustrated in figure 1a for a general indenter with profile $y = g(x)$. We suppose the profile is tilted by an angle α with respect to the horizontal, and we shall assume α is known. Our aim will be to derive the necessary applied normal force and applied moment to sustain a contact over $-b < x < a$ with tilt angle α. We assume that the indenter and the material it is indenting are elastically similar and that a half-plane idealisation is suitable. The assumption of elastic similarity uncouples the normal and tangential displacement problems [3]; we shall concentrate on the normal displacement problem here, although the ideas readily extend to consider an applied tangential force and differential remote bulk stresses.

The standard relation between the relative normal displacement gradient and the contact pressure, $p(x)$, is

$$\frac{\mathrm{d}v}{\mathrm{d}x} = \frac{\kappa+1}{2\mu\pi}\fint_{-b(a)}^{a} \frac{p(s)}{s-x}\,\mathrm{d}s \text{ such that } v'(x) + g'(x) = 0 \text{ for } -b < x < a. \tag{1}$$

The integral above is interpreted in a Cauchy principal value sense, and can be inverted in the usual manner assuming the pressure is bounded at both ends of the contact set. This yields a consistency condition, which, along with the equilibrium condition to balance the applied normal force, yields two equations for the size of the contact set

$$0 = \int_{-b}^{a} \frac{v'(s)}{\sqrt{(a-s)(s+b(a))}}\,\mathrm{d}s, \quad P = \int_{-b}^{a} p(s)\,\mathrm{d}s. \tag{2a, b}$$

The form of the consistency condition (2a) allows us to say that, if we know a, we can derive $b(a)$. We can then utilise the equilibrium condition (2b) to find a, and hence b, as a function of P.

We can use the knowledge of the size of the contact set as a function of the applied normal force to avoid the difficulties associated with singular integrals by approximating the indenter using a series of rectangular punches as we increase P (and hence a), see figure 1b. The contact pressure is then given by

$$p(x,a) = \int_0^a F(s) m_0(x,s)\,\mathrm{d}s, \quad m_0(x,a) = \begin{cases} \dfrac{1}{\sqrt{(a-x)(x+b(a))}} & \text{for } -b(a) < x < a, \\ 0 & \text{otherwise} \end{cases}, \tag{3}$$

where $m_0(x,s)$ is the contact pressure induced by a flat punch of size $(-b(s), s)$ and $F(\cdot)$ is an unknown coefficient that encodes the geometry of the indenter. We utilise (1) to show that

$$\frac{2\mu g'(x)}{\kappa+1} = \int_0^x \frac{F(s)}{\sqrt{(x-s)(x+b(s))}}\,\mathrm{d}s \text{ for } 0 < x < a, \tag{4}$$

which is a non-symmetric Abel integral equation for $F(\cdot)$, and a direct analogue to the moment-free case considered in [3].

*Corresponding author. E-mail: moorem@maths.ox.ac.uk.

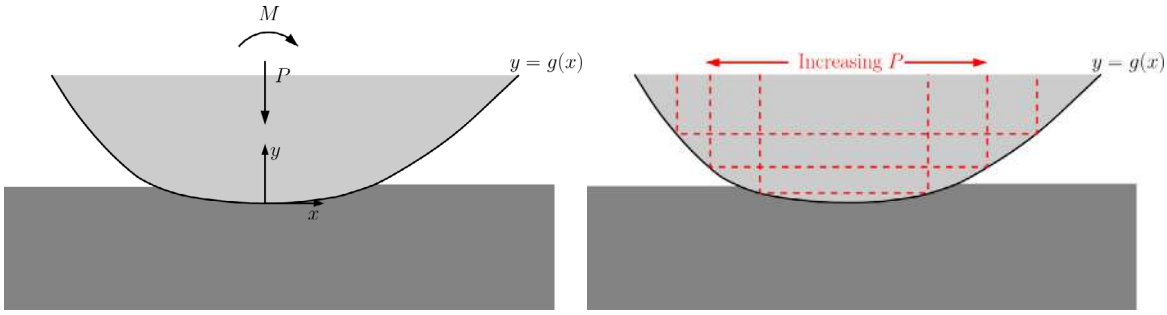

(a) a) (b) b)

Figure 1: a) An indenter of profile $y = g(x)$ contacts an elastically similar half-space under an applied normal force, P, and an applied moment, M. b) A schematic showing the Mossakovskii method. We approximate the contact by considering an infinite number of flat punches that conform to the geometry of the indenter, enforced by $(2a)$ and (4).

GENERAL RESULTS

For a general geometry, (4) must be tackled numerically. However, we can use (4) to derive a number of useful results that have applications in considerations of the partial slip problem for contacts where the applied normal and shearing forces are varying functions of time [3, 4].

Firstly, integrating (3) and, recalling the equilibrium condition $(2a)$, yields

$$P = \pi \int_0^a F(s)\,\mathrm{d}s, \text{ that is, } F(a) = \frac{1}{\pi}\frac{\mathrm{d}P}{\mathrm{d}a}, \tag{5}$$

so that we can remove $F(\cdot)$ from the problem entirely by replacing it with the applied normal force in (3)–(4). Secondly, the applied moment M necessary to sustain the contact is thus given by

$$M = \frac{1}{2}\left[P(a)(a - b(a)) - \int_0^a P(s)(1 - b'(s))\,\mathrm{d}s\right]. \tag{6}$$

Hence, given that the tilt angle was encoded in the original geometry, (4)–(6) can be viewed as a way to find P and M as functions of a and α (or vice versa).

Finally, we can expand the contact pressure solution (3) locally at the contact ends to find the coefficients of the square-root terms, $K_{n,a}$ and $K_{n,b}$, which gives

$$p = \frac{2}{\pi}\frac{P'(a)}{\sqrt{a + b(a)}}\sqrt{a - x} + o(\sqrt{a - x}) \text{ as } x \to a^-, \text{ so that } K_{n,a} = \frac{2}{\pi}\frac{P'(a)}{\sqrt{a + b(a)}}, \tag{7}$$

while

$$p = \frac{2}{\pi}\frac{P'(a)}{b'(a)\sqrt{a + b(a)}}\sqrt{b(a) + x} + o(\sqrt{b(a) + x}) \text{ as } x \to -b(a)^+, \text{ so that } K_{n,b} = \frac{2}{\pi}\frac{P'(a)}{b'(a)\sqrt{a + b(a)}}. \tag{8}$$

In particular, we note that $K_{n,b} = K_{n,a}/b'(a)$. Such simple relations for the K_n-coefficients are of use when considering asymptotic models of contacts for particular geometries, where we only consider one end of the contact and consider the tractions there. This has applications in problems where the differential bulk tensions are large enough to reverse the direction of slip at one end of the contact, so that the Ciavarella-Jäger theorem is no longer applicable [1].

CONCLUSION

We have extended the Mossakovskii method to half-plane contact problems that allow for an applied moment. The singular integral formulation is reduced to a non-symmetric Abel integral equation by assuming that the left-hand contact point is known as a function of the right-hand contact point using the standard consistency condition. The resulting solution has been used to derive general expressions for the K_n-coefficients in the contact pressure expansion local to the contact edges, as well as relating the applied normal force and moment, to the contact extent and tilt of indenter.

References

[1] Andresen, H., Hills, D. A. and Moore, M. R. The steady state partial slip problem for half plane contacts subject to a constant normal load using glide dislocations. Eur. J. Mech. / A Solids. **79**:103868
[2] Barber, J. R. Elasticity. Springer 2002.
[3] Hills, D. A., Davies, M. and Barber, J. R. An incremental formulation for half-plane contact problems subject to varying normal load, shear, and tension. J. Strain Anal. for Eng. Design **46**(6): 436–443, 2011.
[4] Mossakovskii, V. I. Application of the reciprocity theorem to the determination of the resultant forces and moments in three-dimensional contact problems. PMM **17**: 477–482, 1953.

ROLLING OF ELASTIC BODIES WITH SLIPPAGE IN THE PRESENCE OF AN INTERMEDIATE VISCOELASTIC LAYER

Almira Meshcheryakova[1,2]
[1]Moscow Institute of Physics and Technology (National Research University), Moscow,Russia
[2]Laboratory of Tribology, Ishlinsky Institute for Problems in Mechanics RAS, Moscow,Russia

Summary The three-dimensional problem of stationary rolling of an elastic body along a viscoelastic layer bonded to an elastic half-space is considered. The Coulomb friction law is used to describe friction in the slip subregion within the contact region. The relative slippage has longitudinal and lateral components. An algorithm based on a variational method is developed to calculate the shear stress and configuration of slip and stick subregions. The effect of relative slippage on the shear stress distribution and the shape and location of the stick and slip subregions is studied. The results calculated with developed algorithm are compared with known solutions for limiting cases.

INTRODUCTION

The exact solution for two-dimensional rolling problem for bodies with equal modulus of elasticity and the configuration of stick and slip subregions were obtained by Carter [1]. The variational approach to solve sliding and rolling contact problems was formulated and applied by Kalker. In rolling contact for a circular contact region, the location of stick and slip subregions for various combinations of creepage and spin were obtained with the variational theory based on virtual work [2]. The solution based on the variational method for rolling contact of two elastic bodies with an elliptic contact region was developed in [3]. The contact problem for the elastic cylinder rolling over the elastic half-space covered by the viscoelastic layer was studied in [4]. The results of an analysis of the viscoelastic layer effect in rolling contact were presented in [5].

In this study the variational method was developed to solve the rolling contact problem for elastic bodies with an elliptical contact area taking into account the intermediate layer.

PROBLEM FORMULATION AND METHOD OF SOLUTION

Problem formulation

The elastic body rolls over the layer bonded to the elastic half-space with friction. The body has a form of solid of revolution, and the axis of revolution is moving with the constant linear velocity V. When rolling, the contact region consists of stick and slip subregions, which boundaries are unknown in advance. In the slip subregion, the normal and shear stresses are related with Coulomb's law. In tangential direction the compliance of the layer is described by the Maxwell model.

$$s_l(x,y) = \frac{h}{VT_\tau E_l}\tau(x,y) - \frac{h}{E_l}\frac{\partial\tau(x,y)}{\partial x}, \tag{1}$$

where E_l is the modulus of elasticity of the layer's material, s_l is the vector function of derivative of the layer shear displacements, T_τ is the relaxation time of the layer's material, h is the thickness of the layer.

We consider the case when the modulus of elasticity of the rolling body and the half-space are equal, therefore the normal and shear stresses are calculated independently. We also assume that the layer compliance in normal direction is negligibly small.

Method of solution

The normal stress distribution for elliptic contact region is calculated according to Hertz contact theory:

$$p(x,y) = p_0\sqrt{1-\left(\frac{x}{a}\right)^2-\left(\frac{y}{b}\right)^2}, \quad \left(\frac{x}{a}\right)^2+\left(\frac{y}{b}\right)^2 \le 1, \tag{2}$$

where maximum normal stress p_0 and the semi-major a and semi-minor b axes of elliptical contact region depend on the geometry of the rolling body and the normal load.

To calculate the shear stress, the variational method is used. The problem of determining the vector function of shear stresses in the contact region of a sphere and a viscoelastic layer is considered equivalent to the problem of minimizing the following functional, when the boundary conditions are fulfilled [3]:

$$\min_{|\tau|\le\mu p}\left\{F[\tau, s(\tau)] = \iint_\Omega \left[\mu p|s(\tau)| - \langle\tau, s(\tau)\rangle\right]dxdy\right\} \tag{3}$$

where μ is the coefficient of sliding friction, τ (τ_x, τ_y) is the vector function of shear stresses, p is the normal stress, s (s_x, s_y) is the vector function of the slippage, Ω is the contact region. The gradient projection method [3] is used to calculate the shear stress vector function which minimizes the value of the functional in (3).

RESULTS AND DISCUSSION

In calculations we assume that there is no lateral slippage. The shear stress distribution within the elliptic contact region is illustrated in Figure 1 for various intermediate layer properties and also without layer.

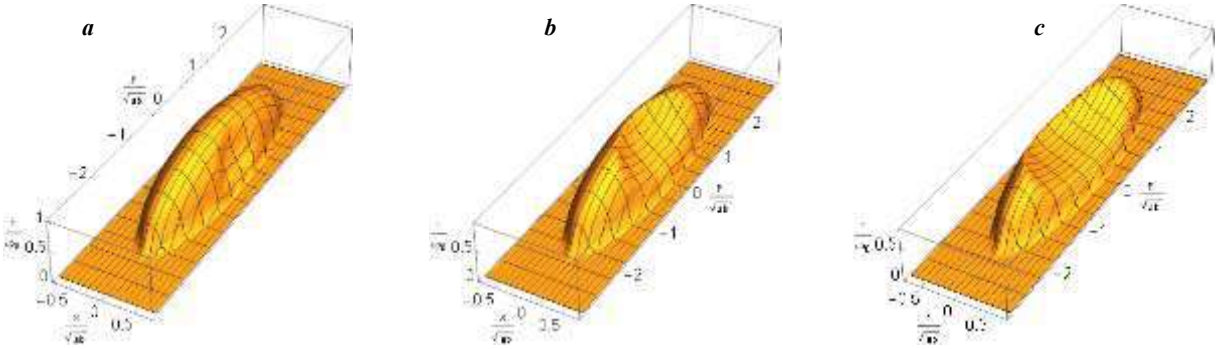

Figure 1. Shear stress distribution for $ab\omega/(2R_y v_{0x}) = 0.5$, $\mu p_0 V/(G v_{0x}) = 1$, $\alpha = h/(VT_\tau E v_{0x})$, $\sqrt{a/b} = 0.5$ and α = 0 (no layer) (*a*), α = 1 (*b*), α = 2 (*c*)

The results demonstrate that in rolling contact the contact region consists of the slip and stick subregions. The stick subregion is located closer to the front side of the contact region relatively to the rolling direction.

The configuration of stick and slip subregions for various layer parameters is shown in Figure 2.

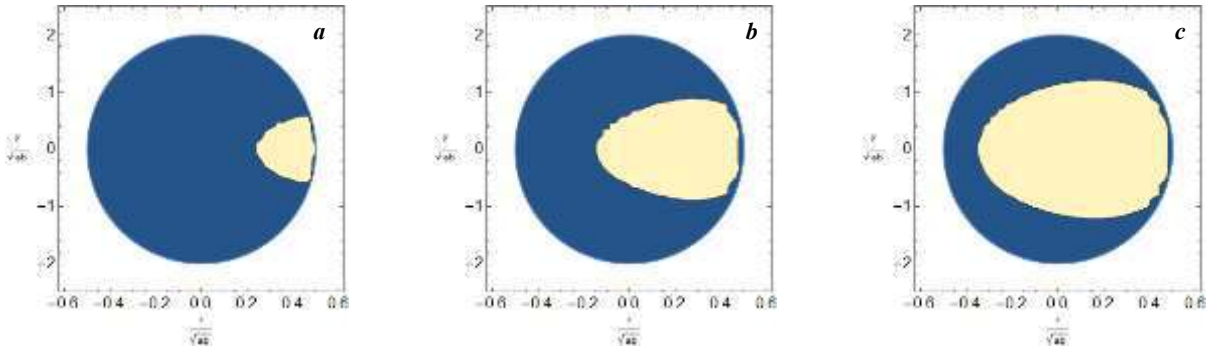

Figure 2. Configuration of stick and slip subregions for $ab\omega/(2R_y v_{0x}) = 0.5$, $\mu p_0 V/(G v_{0x}) = 1$, $\alpha = h/(VT_\tau E v_{0x})$, $\sqrt{a/b} = 0.5$ and α = 0 (no layer) (*a*), α = 1 (*b*), α = 2 (*c*)

Figure 2 illustrates that the stick subregion is prolonged in the rolling direction. The area of the stick subregion increases with the growth of the layer viscosity parameter α, which is inversely proportional to the relaxation time of the layer material.

CONCLUSIONS

The solution of the three-dimensional contact problem for the elastic body, rolling over the viscoelastic layer bonded to the elastic half-space is presented. It is based on the variational approach which allows us to obtain the shear stress distributions within the contact region taking into account slippage in the longitudinal and lateral directions with respect to the rolling direction of the body. The effect of a viscoelastic layer on the shear stresses and the configuration of stick and slip subregions in rolling contact has been studied. The dependence of the shear stress on the friction coefficient, characteristics of the interacting bodies material and the load can be used to determine a wear rate, a friction loss, an origin of cracks and the patterns of their propagation.

The reported study was funded by RFBR, project number 19 31 90015.

References

[1] Carter, F.W. On the Action of a Locomotive Driving Wheel. *Proceedings of the Royal Society A: Mathematical, Physical and Engineering Sciences*. **112(760)**: 151–157, 1926.

[2] Kalker J.J. Three-Dimensional Elastic Bodies in Rolling Contact. Dordrecht etc.: Kluwer. 314 p. 1990.

[3] Goldshtein R.V., Zazovskii A.F., Spektor A.A., Fedorenko R.P. Solution of three-dimensional contact problems of rolling with slip and adhesion by variational methods. *Advances in Mechanics*. **5**, **3/4**: 61-102, 1982.

[4] Goryacheva I.G., Sadeghi F. Contact characteristics of rolling/sliding cylinder and a viscoelastic layer bonded to an elastic substrate. *Wear*. **184**: 125-132, 1995.

[5] Goryacheva I.G., Miftakhova A.R. Modelling of the viscoelastic layer effect in rolling contact. *Wear*. **430**: 256-262, 2019.

ESTIMATING FRICTION PROPERTIES FROM LARGE-SCALE ROCK EXPERIMENTS

David S. Kammer*[1], Chun-Yu Ke[2], and Gregory C. McLaskey [2]
[1]Institute for Building Materials, ETH Zurich, Switzerland
[2]School of Civil and Environmental Engineering, Cornell University, Ithaca, USA

Summary We present result from two large-scale friction experiments. In both experimental setups, two rock blocks are placed side-by-side to form a frictional interface. External load is applied such that the interface is subjected to normal and shear stress, which can be controlled independently. The shear stress is slowly increased until local slip spontaneously occurs. The onset of sliding is rupture-like: it nucleates at a critical point and then propagates along the interface until it potentially arrests spontaneously. During this rupture propagation, we measure the strain at multiple locations close to the interface but slightly offset. We compare these measurements with analytical fracture mechanics theory for near-tip strain fields to determine local interface properties. Further, we analyze rupture arrest to provide a second independent measurement of these local friction properties.

INTRODUCTION

The macroscopic frictional strength of an interface between two solids depends on both instability-driven local failure mechanisms and local friction properties at various scales. For instance, the onset of frictional sliding, which is often described by the macroscopic static friction coefficient, is characterized by the nucleation and propagation of a shear-crack-like rupture front along the interface [1]. The nucleation of this rupture front, which is key for the overall strength of the interface, depends on local properties and stress distributions. The macroscopic static friction coefficient does not provide direct evidence of these local properties since it is an integrated quantity of a potentially non-uniform shear stress along the interface. Experimentally measuring local friction properties is therefore crucial for a better understanding of the macroscopic strength of an interface.

METHOD

In this work, we present experimental observations from two different large-scale rock experiments and develop a fracture-mechanics-based interpretation that provides estimates of important local friction properties [2,3]. In both experimental setups, two meter-scale rocks were brought into contact by a normal load. The interface was then slowly sheared until slip spontaneously nucleated and propagated dynamically along the interface.

In the first experimental system [2], the stress distribution along the interface is relatively uniform due to the applied loading configuration. Once a critical level of stress was exceeded at a given point, a slip instability was spontaneously nucleated and a frictional rupture front propagated along the interface. These rupture fronts eventually reached the edges of the interface, where they were reflected and propagated in the opposite direction as so-called secondary rupture fronts. We measured the dynamic strain evolution at multiple locations along the interface with strain gages that were installed slightly away from the interface.

In the second experimental system [3], the spatial distribution of stresses along the interface is non-uniform due to the structural compliance of the loading frame, and various loading procedures were used to generate a range of different spatial stress distributions. This led to a variety of different rupture phenomena. In some cases, unilateral contained ruptures nucleated near the loading end of the interface, propagated unilaterally toward the leading end, and arrested before reaching the edge. In other cases, bilateral contained ruptures nucleated close to the middle of the interface, propagated bilaterally, and arrested before reaching both edges. We used local slip measurements and static strain measurements along the interface to determine the nucleation and arrest location of these slip instabilities.

RESULTS

In the first experimental system [2], we use dynamic shear strain measurements from strain gages that are installed slightly away from the interface and apply analytical fracture mechanics theory for near-tip fields to determine local interface properties. These results show that the measurements at these offset strain gages do not resemble the stress evolution as expected along the interface (Figure 1) but provide a direct measurement of local friction properties when combined with fracture-mechanics theory.

In the second experimental setup [3], we use fracture-mechanics-based energy considerations to describe the arrest position [4]. Fundamentally, these rupture fronts propagate dynamically when the region with a rupture-favored stress state is larger than a critical nucleation length. Further, arrest occurs when the rupture reaches regions with more friction (specifically, higher fracture energy), or unfavorable stress states. The detailed fracture-mechanics-based models, as applied here, contain a single free parameter, which is the local fracture energy of the interface. By comparing the model with experimental observations, we can constrain the local fracture energy [3]. Finally, we compare our estimates with observations from experiments on other materials [5].

*Corresponding author. E-mail: **dkammer@ethz.ch**

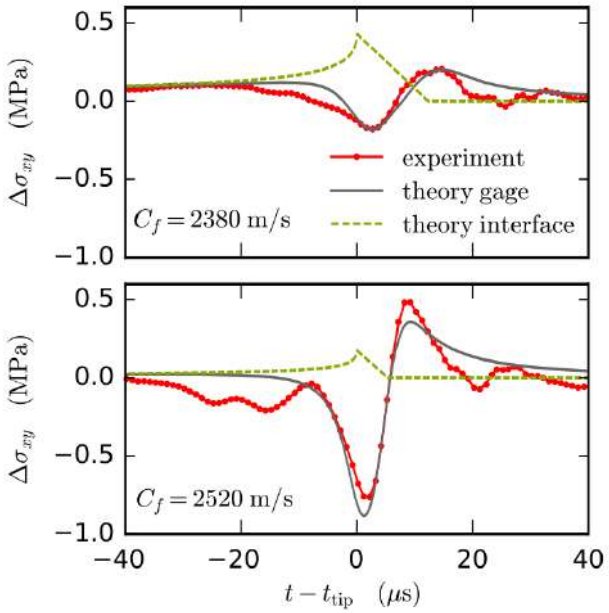

Figure 1. Examples of measured shear stress oscillations with comparison to fracture-mechanics based model. Two examples of experimentally measured shear stress evolution relative to rupture tip arrival with different oscillation amplitudes are shown in red. Fracture-mechanics based model that incorporates shape and position of strain gage pairs is depicted by grey curve. The associated shear stress evolution at the interface (y = 0) is shown in dashed green.

References

[1] I. Svetlizky and J. Fineberg. Classical shear cracks drive the onset of dry frictional motion, Nature, 509, 205, 2014.
[2] D.S. Kammer and G.C. McLaskey. Fracture energy estimates from large-scale laboratory earthquakes, Earth Planet. Sci. Lett., 551, 36-43, 2019.
[3] C.Y. Ke, G.C. McLaskey, and D.S. Kammer. Rupture Termination in Laboratory-Generated Earthquakes, Geophys. Res. Lett., 45(23), 784-12, 2018.
[4] D.S. Kammer, M. Radiguet, J.P. Ampuero, and J.F. Molinari. Linear elastic fracture mechanics predicts the propagation distance of frictional slip, Tribol. Lett., 57, 1-10, 2015.
[5] E. Bayart, I. Svetlizky, and J. Fineberg. Fracture mechanics determine the lengths of interface ruptures that mediate frictional motion, Nat. Phys., 12, 166-170, 2016.

WEAR AND SURFACE FRACTURE OF FIBER COMPOSITES IN FRICTIONAL INTERACTION

Irina Goryacheva*[1] and Yulia Makhovskaya[1]
[1]Ishlinsky Institute for Problems in Mechanics of the Russia Academy of Sciences, Moscow, Russia

Summary Wear of a fibrous composite material is theoretically studied based on two mechanisms – due to different wear rates of structural components of a composite and due to detachment of fibers during friction. An intermediate layer between the matrix and fibers is taken into account. The effect of the microstructure parameters of the composite on the worn surface shape, effective wear rate of the material, and local stress field near surface fibers is analyzed.

INTRODUCTION

Fiber composites are widely used in industry, e.g., in aviation brake systems consisting of carbon-carbon composite disks. Wear process in such composites depends on their microstructure (size and density of fibers, existence of intermediate layer between matrix and fibers, mechanical and thermal properties of all components). There exist only a few theoretical models in the literature, which relate wear of composites to their microstructure (e.g., [1,2]), they are focused on particular wear mechanisms under given friction conditions.

In the present study, based on the contact mechanics approaches presented in [3], two mechanisms of wear of fiber composites are considered. The first one is associated with different wear rates of the matrix, fibers, and intermediate layers. The second mechanism is due to surface fracture and detachment of fibers from the surface during friction.

MODELING STEADY-STATE WEAR OF A FIBER COMPOSITE

A model of wear process of a fiber composite is developed for steady-state conditions. The composite is modeled by an elastic half-space with a variable wear coefficient which has different values for the fibers (K_{w1}), matrix (K_{w3}), and intermediate layer (K_{w2}). A plane surface of a rigid counter body slides over the composite material surface with the constant velocity V and wears the composite material (Fig. 1).

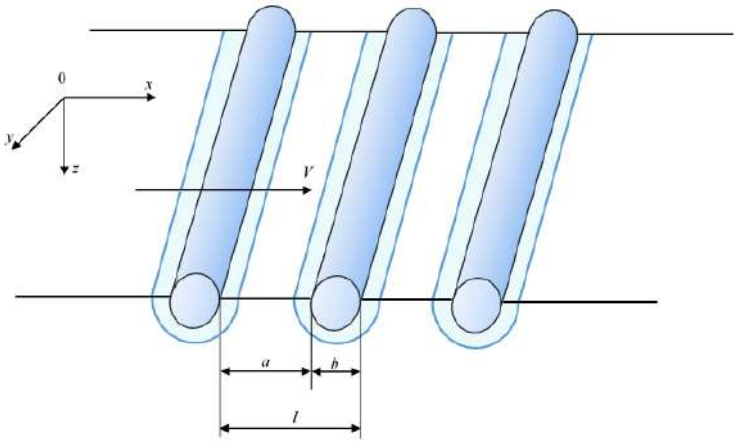

Figure 1. Surface structure of a fiber composite.

Analytic relations are obtained for the shape of the worn surface, the effective wear rate of the composite, and the magnitude of contact pressures acting on the fiber and matrix. These values are calculated as functions of the parameters of the composite microstructure. In particular, it is established that the worn surface of the composite strongly depends on the size and concentration of fibers, as well as on the ratio of the wear coefficients of fibers and intermediate layer to matrix ($m_1 = K_{w1}/K_{w3}$ and $m_2 = K_{w2}/K_{w3}$). The calculated shapes of the worn surface are compared to the results of surface profilometry (Fig. 2). It is shown that the effective wear rate as a function of the fiber concentration increases if the fibers are harder than the matrix and decreases in the opposite case. Results of the calculation and analysis of the pressures acting upon the fibers and matrix in the steady state wear process are used to model the stress state near a separate fiber during wear which is presented in the next section.

*Corresponding author. E-mail: goryache@ipmnet.ru.

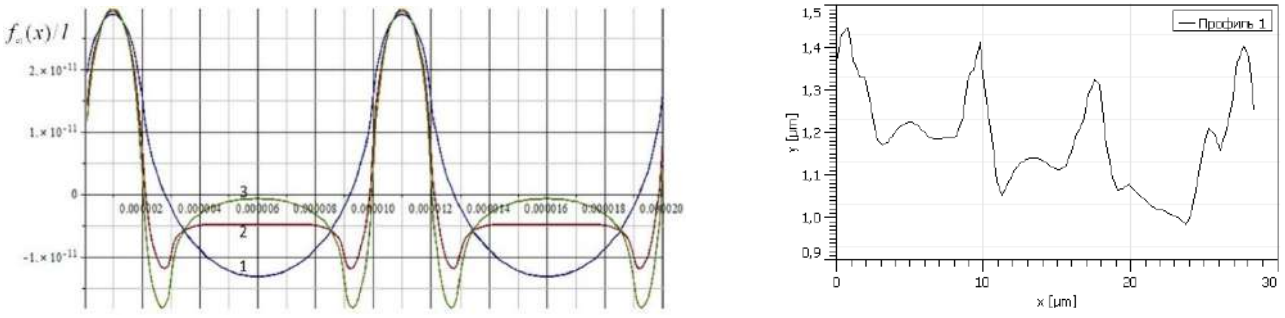

(a) (b)

Figure 2. (a) Calculated shape of the worn surface for $m_1 = 2$ with no intermediate layer (curve 1) and with an intermediate layer with $m_2 = 5$ and 10 (curves 2 and 3). (b) Measured profile for a carbon-carbon fiber composite worn surface

MODELING THE STRESS STATE NEAR A SEPARATE FIBER

The local stress field near a separate fiber embedded into the surface of the composite (Fig. 3,a) is analysed with and without an intermediate layer. The maximum tensile stresses (in Pa) in the matrix (solid lines) and fiber (dashed lines) as a function of the fiber concentration are presented in Fig. 3,b for the nominal contact pressure $p_0 = 0.5$ MPa, radial gap between the fiber and matrix $\varepsilon_0 = 0.1$ μm, fiber radius $R_2 = 5$ μm, the elastic characteristics $E_1 = 10$ GPa, $\nu_1 = 0.25$, $E_2 = 15$ GPa, $\nu_2 = 0.35$, and two different values of the ratio of the wear coefficient of fiber to matrix m_1. The results indicate that the maximum tensile stresses considerably increase with decreasing fiber concentration, especially when the wear coefficients of the fiber and matrix differ substantially from each other.

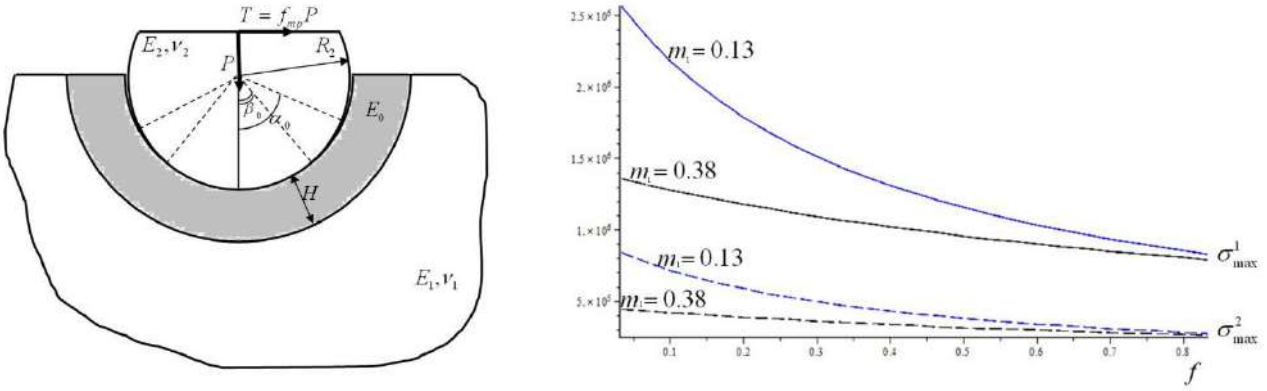

(a) (b)

Figure 3. (a) Sheme of contact of a separate fiber and the matrix in the presence of an intermediate layer. (b) Maximum tensile stresses in the fiber and matrix vs. the fiber concentration

Based on the stress field obtained, possibility of detachment of the fiber is analyzed, depending on the microstructure parameters as well as the nominal pressure and temperature on the friction surface. Note that the surface temperature itself is a function of the composite microstructure [4].

CONCLUSIONS

The theoretical study of a fiber composite wear is presented which makes it possible to analyse the influence of the microstructure parameters of the composite on the shape of the worn surface, the effective wear rate of the material, and the local stress field near surface fibers. The results obtained are used to predict the process of wear, including the possibility of fracture and detachment of fibers from the surface of the matrix.

The work was carried out under the financial support of the Russian Science Foundation (grant No. 19-19-00548).

References

[1] Lee G. Y. et al. A physically-based abrasive wear model for composite materials. *Wear*. **252**: 322-331, 2002.
[2] Zhao S. et al. Numerical simulation of wear in a C/C composite multidisc clutch. *Carbon*. **47** (9): 2219–2225, 2009.
[3] Goryacheva I.G. Contact Mechanics in Tribology. Springer, Dodrecht 1998.
[4] Makhovskaya Yu. Modeling frictional heating of fibrous composite brake disk. *J. Frict. Wear*. **36** (4): 286-292, 2015.

A FULLY COUPLED BEM FORMULATION FOR NORMAL AND TANGENTIAL CONTACT PROBLEMS

Jacopo Bonari* and Marco Paggi
IMT School for Advanced Studies Lucca, Lucca, Italy

Summary A boundary element formulation has been developed for solving contact problems between a rigid indenter and an elastic layer of finite thickness, under the hypotheses of linear elasticity and plane strain assumption, subject to imposed normal and tangential displacements. The normal contact problem is fully coupled with the tangential one, allowing for the study of an arbitrary sequence of loading. As a consequence, the application of a normal pressure causes not only vertical, but also in-plane displacements, providing a rigorous methodology to quantitatively investigate the effect of tangential and normal coupling with indenters of arbitrary shapes.

KERNEL FUNCTIONS

In the general case of a two-dimensional frictional contact problem involving a rigid indenter pressed against an elastic layer, the vertical and horizontal displacements of the elastic frontier can be described by u_z and u_x. These quantitities are linked to the relative components of surface tractions p_z and q_x by appropriate Green functions. If the discretisation of a selected portion of the boundary is introduced, the surface displacement, defined by an index i, can be expressed by the sum of the contribution of the tractions acting in the other points, multiplied by the respective influence coefficients. Thus, in matrix form, it is possible to write:

$$\begin{bmatrix} \mathbf{u}_z \\ \mathbf{u}_x \end{bmatrix} = \begin{bmatrix} \mathbf{H}_{zz} & \mathbf{H}_{zx} \\ \mathbf{H}_{xz} & \mathbf{H}_{xx} \end{bmatrix} \begin{bmatrix} \mathbf{p}_z \\ \mathbf{q}_x \end{bmatrix}$$

where the four $\mathbf{H}$ matrices collects the influence coefficients resulting from the discretisation of the Green functions. In the present work, they are relative to the application of a traction of uniform intensity over the length of a single element of the boundary, for an elastic layer of finite thickness in z direction and semi-indefinite in x direction. This framework has been chosen because semi-analytic solutions of the convolution integrals representing the four Green functions have been determined, guaranteeing a high level of accuracy and a fast computation of the influence coefficients.

SOLUTION ALGORITHM

The application of the classic Coulomb friction law over a two-dimensional domain leads to its partition in 4 different states, according to [1]: *(i)* a zone of *separation*, where contact does not occur; *(ii)* a zone of *stick*, with no relative tangential displacements between the indenter and the half plane; *(iii)* and *(iv)* zones of *backward* and *forward slip*, characterised by negative and positive relative tangential displacements, respectively. Since coupling is accounted for, tangential tractions affect the normal displacements, thus requiring an iterative solution of the normal contact problem. A fixed point iteration scheme has been implemented for evaluating contact tractions. At the initial step, all points are assumed to be in *separation* and the tangential tractions to be null. The normal contact problem is then solved and the states are updated, moving the point in contact to the *stick* domain. With the value obtained for $\mathbf{p_z}$, $\mathbf{q_x}$ in the *stick* domain is evaluated. At this point, a check is performed on the state of every node, and, if a violation of the friction law is encountered, the domain is updated accordingly, *e.g* if a point is in the stick domain, $|q_{x,i}| \leq \mu p_{z,i}$ must hold for that node: if it is not so, $q_{x,i}$ is set equal to $\mathrm{sgn}\,(q_{x,i})\mu p_{z,i}$ and the state is modified to *forward slip*. The procedure stops when the difference between the norm of the tractions for two consecutive steps lies below a certain threshold.

RESULTS

The classical ironing problem has been used as benchmark for testing the algorithm using two different indenters. The first is parabolic, while the second has a Weierstrass-Mandelbrot profile, made up, for the sake of representation, using only two terms, with a fractal dimension $D = 0.4$ and $\gamma = 15$. In Fig. 1a and 1b, the results are shown in terms of vertical tractions (black dashed lines) and horizontal tractions (red solid lines). The problem has been discretised using 10 time steps. In the first stage of loading, a vertical far field displacement is imposed on the indenter. It rises from 0 to $5 \times 10^{-3} b$, being b the thickness of the elastic layer. The first five inner concentric black lines correspond to the increasing vertical pressure. The five polarsimmetric overlapping red lines correspond to them, representing the horizontal tractions resulting from the application of the vertical load only. In the second stage of loading, the vertical far field displacement is held constant, while a horizontal imposed far field displacement linearly rises from 0 to $1 \times 10^{-2} b$. Since in this second phase the vertical load is constant, the vertical tractions almost overlap except for a slight difference, given by the effect of coupling. On the other hand, the horizontal tractions start shifting leftwards.

*Corresponding author. E-mail: jacopo.bonari@imtlucca.it.

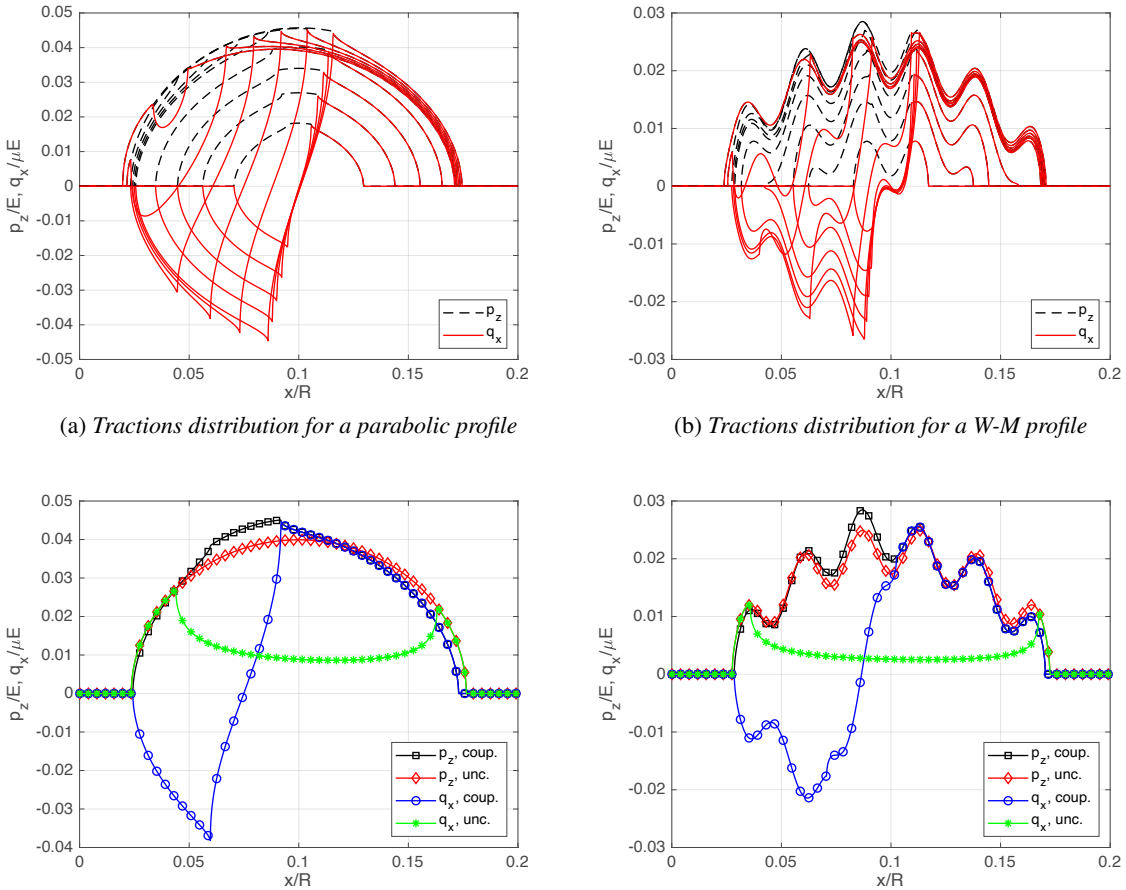

(a) *Tractions distribution for a parabolic profile*

(b) *Tractions distribution for a W-M profile*

(c) *Parabolic profile, coupled* vs *uncoupled tractions*

(d) *W-M profile, coupled* vs *uncoupled tractions*

Figure 1: Distribution of tractions for two different rigid indenters, with or without coupling

The horizontal tractions have been normalised with respect to the friction coefficient μ, in such a way that, in slip regime, they coincide with the vertical pressure when positive, and with its opposite when negative. Given that, the identification of the state of a node is straightforward. For example, in Fig. 1a, the solid lines overlapping with the dashed lines are in forward slip, the solid lines which follow the shape of the vertical pressure but with opposite sign in the third quadrant are in a state of backward slip, while the lines that link them are related to nodes which are still in a state of stick. As the horizontal load rises, the area of stick first shifts leftward and then start shrinking, representing the evolution of the system from a state of *partial* slip to one of *full* or *gross slip*.

In Fig. 1c and 1d, a comparison has been made, for a selected time step (the number 8), between the coupled and the uncoupled version of the same algorithm, simply obtained by zeroing the terms H_{xz} and H_{zx}. The first result obtained is the remarkable difference in the distribution of the horizontal tractions which, in the backward slip zone, reach their maximum when the horizontal load is yet to be applied. The same trend can be observed both for the parabolic and the W-M profiles. Non negligible differences can be noticed in the distribution of the vertical pressures as well: indeed, the coupled case presents vertical traction values higher, in the stick zone, than the ones predicted by the uncoupled model. Finally, the contact area is influenced as well, with a light shift towards, again, the stick zone.

CONCLUSION

A fully coupled boundary element algorithm for the evaluation of the surface tractions in a frictional contact problem has been presented. As a first preliminary result, significant differences have been found in terms of both vertical and horizontal tractions with respect to the uncoupled models usually found in literature, due to the non-negligibility of the terms in the coupling matrices H_{xz} and H_{zx}.

References

[1] Barber J. R. Response of frictional receding contact to cyclic loading. *IJMS* (**50**): 1519-1525, 2008.

[2] Bemporad A., Paggi M. Optimization algorithms for the solution of the frictionless normal contact between rough surfaces. *IJSOLSTR* (**69-70**): 94-105, 2015.

[3] Paggi M., Hills D. Modeling and Simulation of Tribological Problems in Technology. Springer, 2020.

INTERPLAY BETWEEN WALL SLIP AND SURFACE TEXTURING: A NOVEL ALGORITHM BASED ON VARIATIONAL INEQUALITIES

Luca Biancofiore*[1], Matteo Giacopini[2], and Daniele Dini[3]
[1]Department of Mechanical Engineering, Bilkent University 06800 Bilkent, Ankara, Turkey
[2]DIEF-Engineering Department Enzo Ferrari,Universitá degli Studi di Modena e Reggio Emilia,via Vivarelli 10, 41125, Modena, Italy
[3]Department of Mechanical Engineering, Imperial College London, Exhibition Road, London, SW7 2AZ, United Kingdom

Summary In this work we develop an innovative and accurate numerical model, based on complementary variables, to predict simultaneously the slip at the wall, by using the Tresca model, and the formation of cavitation, through a mass-conserving formulation. To show the flexibility of our model, several bearing geometries have been analysed, such as a cosine profile used to mimic a bearing, and a pocketed slider bearing employed to study the effect of surface texture. We observe that the lubrication performance (i.e. low friction coefficient) can be improved by using materials that promote slippage at the moving wall. The location of the slippage region can be optimised to find the lowest value of friction coefficient.

INTRODUCTION

Around 23% of the world's total energy consumption originates from tribological contacts, most of it used to overcome friction [1]. More and more efficiency savings must be made in mechanical systems, since stricter emissions standards are enforced. Particularly in the long term the implementation of advanced tribological technologies for friction reduction and wear protection, could bring in the long term to (i) saving about 8.7% of the total energy consumption (1.4% of the world GDP) and (ii) reduce the CO_2 emissions globally by as much as 1,460 MtCO2 (i.e. 450,000 million Euros cost savings) [1].

Experimental and theoretical studies have shown that, if properly optimised, both surface texturing and artificially induced slip can individually reduce the friction of a system. A fundamental aspect to consider in modelling contacts with surface texturing or slip at the walls is cavitation, which is usually referred to describe a complex thermodynamical process including nucleation, growth and implosion of vapour or gas bubbles within a liquid.

But is it possible to combine the effect of wall slip and surface textures? Several papers on the subject have showed that both surface texture and slip can theoretically cause a significant reduction in the friction coefficient, see the review by Senatore & Rao [2]. However still a careful optimisation of the surface parameters is needed before conducting expensive and time-demanding experiments. Particularly it is necessary to understand how - and if - it is possible to maximise the bearing performance while minimising the increase in manufacturing cost. The aim of the present work is to fill this gap by producing robust and innovative numerical schemes to enable researchers to explore a wide parameter space for the optimisation of patterned surfaces in the presence of micro-textures and oleophobic coatings.

BASIC EQUATIONS AND NUMERICAL METHOD

In this work we develop a 1D algorithm, based on a Finite Elements approach, to model the two intertwined problems (i.e. cavitation and slippage at the upper wall) in terms of complementarity. The flexibility of the complementary algorithm is fundamental to predict the behaviour of contact with extreme thickness gradients, typical of textured surfaces (such as dimple or pockets, for instance).

Following Giacopini *et al.* [3], we can write the complementary formulation related to the problem of cavitation in lubricant films in a compact functional form

$$p(x) = L_c r(x) + Q_c, \tag{1}$$

with $p(x) \geq 0$, $r(x) \geq 0$ and $p(x)r(x) = 0$, where the two complementary variables p and r, are, respectively, the pressure and the density ratio, i.e. $r(x) = 1 - \frac{\rho(x)}{\rho_0}$, $\rho(x)$ is the fluid density, ρ_0 is the density in the liquid region and x is the streamwise direction. The operators L_c and Q_c can be found from examining Ref. [3] but in our case they depend on the possible relative velocity of the fluid at the upper fixed surface U_s.

We use the Tresca model for the possible slippage at the wall. Briefly, if the shear stress at the upper wall τ is lower than the critical value τ_c no slippage occurs, and therefore $U_s = 0$. If τ reaches its critical upper bound τ_c, the fluid velocity can be higher than that of the upper boundary, $U_s \geq 0$. Particularly, following Strozzi *et al.* [4], we can arrive to the complementary formulation

$$M^{-1}U_s(x) + M^{-1}P = \tau_c(x) - \tau(x), \tag{2}$$

$(\tau_c(x) - \tau(x)) \geq 0$, $U_s(x) \geq 0$, and $U_s(x)(\tau_c(x) - \tau(x)) = 0$. Note that in our formulation the critical value $\tau_c(x)$ depends on the streamwise direction. The operators M and P can be found similarly to Ref. [4], but in our work they depend on the density ratio r.

Finally, we have validated our algorithm presented in this section with comparing our results to Bayada [5].

*Corresponding author. E-mail: luca@bilkent.edu.tr.

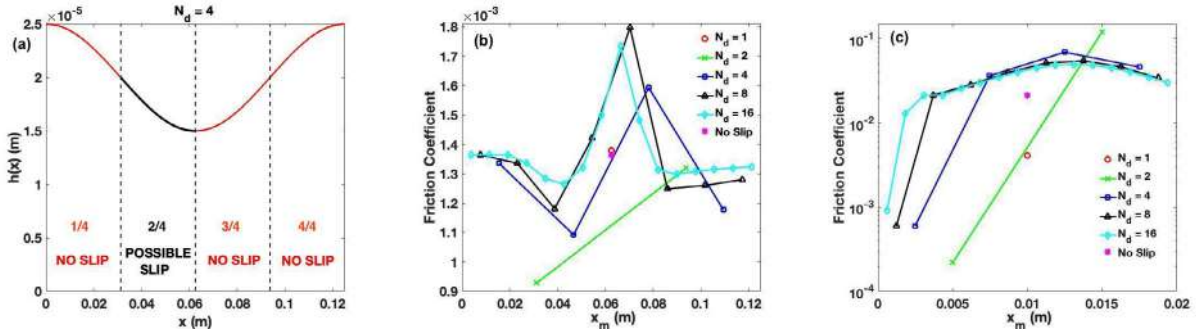

Figure 1: (a) The bearing modelled as a cosine profile. Note that the critical shear stress can be uniform or non-uniform. In particular, in this figure a specific non-uniform configuration ("$2/4$") is depicted. Friction coefficients (b) for the cosine profile for $\tau_c = 1$kPa and (c) for the pocketed slider for $\tau_c = 2$ kPa.

RESULTS AND DISCUSSIONS

Obtaining a slippage condition by using superoleophobic surfaces is expensive and not easy to be manufactured. For this reason it would be worthwhile to optimise the surface in order to reach good lubrication performance (i.e. low friction coefficient, defined as the ratio between friction and load) while minimising the superoleophobic region. For this reason a possibly non-uniform τ_c is considered. Particularly, the profile is divided in N_d equal parts and just in $1/N_d$-th of the profile a finite value of the critical shear stress is considered, while in the other parts a no-slip boundary condition is implemented, i.e. $\tau_c = \infty$. An example is shown in fig.1(a) where the black line depicts the possible slippage region. This configuration mimics the case in which just a partial surface of the bearing is superoleophobic. A specific notation is used to identify the area where slip can occur as exemplified below. For instance if we divide the profile in $N_d = 4$ parts and we apply the slippage in the second quarter only, we define this configuration as "$2/4$".

Bearing

In this section we model a bearing by using a cosine profile shown in figure 1(a). We illustrate in fig.1(b) the friction coefficient for several N_d and $\tau_c = 1$kPa. In particular every marker depicts a different configuration in which the slippage zone is on a different $1/N_d$-th of the profile. Note that each configuration is associated to the median abscissa of the slippage zone x_m. The fully slip (i.e. $N_d = 1$) and the purely no slip cases have a very similar value of the friction coefficient. Interestingly the lowest values of the friction coefficient are for super-oleophobic regions in the second quarter of the bearing. Particularly the case "$1/2$", "$2/4$", "$3/8$" and "$6/16$" are the configurations for each N_d in which the friction coefficient is minimal. They show a gain in friction coefficient with respect to both the no slip and fully slip cases of 31%, 20%, 13% and 7%, respectively, but having a significant shorter slippage zone.

Pocketed slider

We consider a pocketed slider already studied by Giacopini et al. [3], but implementing the possible slippage at the upper wall. This profile is analyzed to mimic a surface texture. Fig. 1(c) shows the value of the friction coefficient for several values of N_d and for $\tau_c = 2$ kPa, compared with the pure no slip case. If the slippage zone is located close to the entry of the domain the friction coefficient could decrease by one or two orders of magnitudes with respect to the uniform critical shear stress case, depending on the number of parts in which the domain is divided.

CONCLUSIONS

We have shown that the performance of bearings in which there is interplay between slip at the wall and cavitation can be significantly improved (up to two orders of magnitude reduction in the friction coefficient) while minimising the slippage region. This can reduce cost in manufacturing superoleophobic bearings since surface treatments can be confined to specific (small) regions to strongly improve bearings' performance. Furthermore, our model has showed that the values of the critical shear stress necessary to achieve a significant decrease of the friction coefficient are not prohibitively small and can be achieved using conventional processes, pointing out further the possibility of reduction in manufacturing cost.

References

[1] Holmberg, K. and Erdemir, A., *Friction* **5**: 263–284, 2017
[2] Senatore, A and Rao, T. V. V. L. N., *Journal of Tribology* **4**: 040801, 2018
[3] Giacopini, M. and Fowell, M. T. and Dini, D. and Strozzi, A., *Journal of Tribology* **132**: 041702, 2010.
[4] Strozzi, A. and Giacopini, M. and Bertocchi, E. and Dini, D., *Proceedings of the Institution of Mechanical Engineers, Part J: Journal of Engineering Tribology*, **228**: 1122–1135, 2014.
[5] Bayada G., *Tribology International* **118**: 71–88, 2018.

REDUCED NONLINEAR FEM-MODEL FOR BEAM-TYPE AIR FOIL BEARINGS: SIMULATION AND OPTIMIZATION OF BEARING HYSTERESIS CURVES

Marcel Bauer*[1], Marcel Mahner [1], Pascal Zeise [1], and Bernhard Schweizer [1]
[1]Department of Mechanical Engineering, Technical University of Darmstadt, Darmstadt, Germany

Summary A reduced two-dimensional nonlinear FEM-model of a beam-type air foil journal bearing including contact and stick-slip friction is presented. The main goal of the model is the investigation of the nonlinear force-deflection characteristic, which provides important insight into the stiffness and damping/friction behaviour of air foil bearings. The force-deflection curves (bearing hysteresis curves) of the developed 2D-model are compared with a detailed 3D-model. In addition, a test-rig for measuring hysteresis curves of air foil bearings is presented. Experimental results are compared with the 2D and 3D simulation results.

INTRODUCTION

In high-speed turbomachinery applications, air foil bearings are an interesting alternative to classical oil-lubricated bearings. Air foil bearings consist of a bearing housing, a compliant foil structure and a top foil. The purpose of the compliant foil structure is to compensate both manufacturing deviations and thermal and mechanical growth of the rotating shaft. It also defines the stiffness and damping behaviour of the whole bearing. The coated top foil, which is placed between the compliant foil and the shaft, provides the necessary surface for the pressure build-up of the air film.

The compliant foil structure can be designed in different ways. One design option is the bump foil, which is investigated numerically and experimentally in [1] and [2]. Another design option is the beam foil [3]. With static load-displacement measurements and comparisons between different foil designs, Shalash and Schiffmann experimentally showed the high robustness of beam-type bearings. Equivalent measurements for other beam foil designs are depicted in [4]. Despite the recent studies on beam-type bearings, there is still a lack of detailed models for the prediction of the nonlinear force-deflection characteristic. Numerical models can provide a deeper understanding of the physics of air foil bearing systems and may further be used for design optimizations.

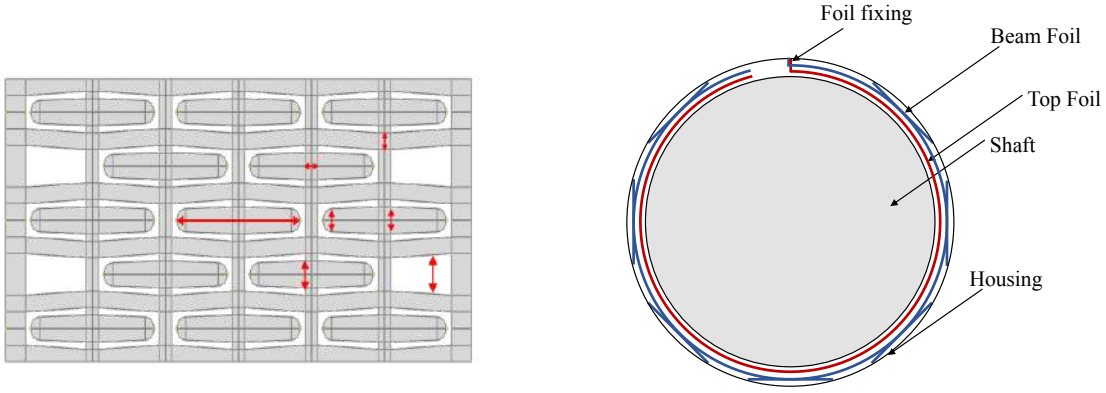

Figure 1. a) Beam foil, b) 2D-modell of a beam-type air foil bearing

STRUCTURAL FEM MODEL OF AIR FOIL BEARINGS

Firstly, a detailed three-dimensional structural FEM model is presented, which is used as a reference model. Although this model considers many important features (nonlinear deformations, contact and friction, etc.), its use is limited due to the high computational effort, especially with respect to structural optimization. A further drawback of the 3D-model lies in the difficulty to expand the model by further physical aspects (air film, temperature effects, etc.).

Secondly, a reduced 2D model is presented. The regular structure of the beam foil enables a straightforward reduction to a two-dimensional model. Here, both foils (top foil and beam foil) were described by a nonlinear beam theory according to Reissner [5]. The left picture in Figure 1 depicts a typical design of a beam foil. In its initial, stress-free configuration the beam foil is plane. When the beam foil is bent for the insertion into the bearing housing, the beams remain almost plane and are supported on the inner wall of the housing. In this position they act like leaf springs, see the right graphic in Figure 1.

Bearing dissipation is mainly caused by friction, which occurs during relative motions between the bearing components as a result of radial shaft deflections. In order to investigate the effect of friction, appropriate contact

*Corresponding author. E-mail: bauer@ad.tu-darmstadt.de.

conditions have to be formulated. The inequality constraints for the contacts are implemented with the augmented Lagrange method [6]. Friction is calculated by the Coulomb friction law.

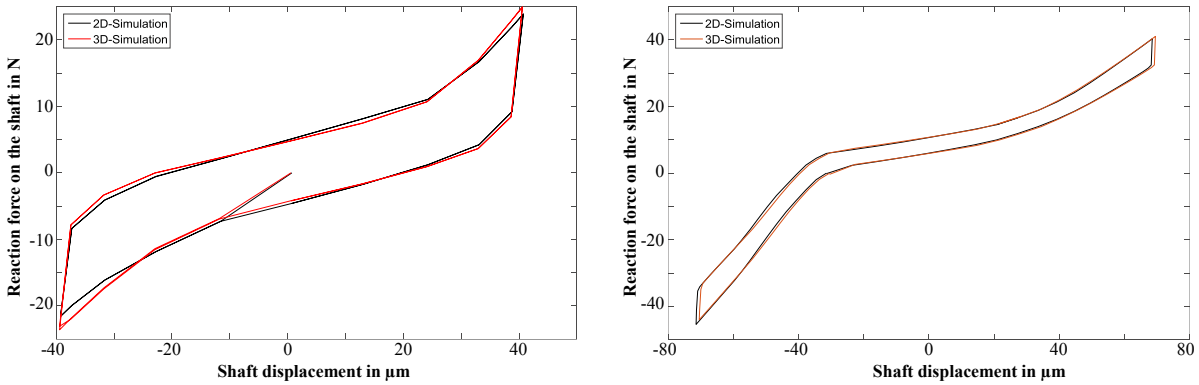

Figure 2. Load-displacement curve of a beam-type air foil bearing: a) horizontal, b) vertical displacement

RESULTS AND CONCLUSION

The simulated load-displacement curves generated with the two- and three-dimensional model are depicted in Figure 2. A hysteresis effect and a nonlinear stiffness behaviour can be clearly observed, which are both dependent on the direction of the shaft displacement. The results of the two-dimensional and three-dimensional model are in good agreement. The simulation time for the 3D model (approximately $3.7{\cdot}10^6$ DOF) is approx. 60 hours, while the computation time for the 2D model (approximately $30 \cdot 10^3$ DOF) is only 1 hour. The simulated hysteresis curves also show a good agreement with experimental results, which have been carried out on a special test rig for air foil bearings.

References

[1] Mahner M., et al. Numerical and Experimental Investigations on Preload Effects in Air Foil Journal Bearings. *Journal of Engineering for Gas Turbines and Power* 140.3: 032505, 2018.

[2] Mahner M., et al. An Experimental Investigation on the Influence of an Assembly Preload on the Hysteresis, the Drag Torque, the Lift-Off Speed and the Thermal Behavior of Three-Pad Air Foil Journal Bearings. *Tribology International* 137: 113-126, 2019.

[3] Shalash K., Schiffmann J. Comparative Evaluation of Foil Bearings with Different Compliant Structures for Improved Manufacturability. *ASME Turbo Expo 2017: Turbomachinery Technical Conference and Exposition*. American Society of Mechanical Engineers Digital Collection, 2017.

[4] Feng K., Zhao X., Guo Z. Design and Structural Performance Measurements of a Novel Multi-Cantilever Foil Bearing. *Proceedings of the Institution of Mechanical Engineers, Part C: Journal of Mechanical Engineering Science* 229.10: 1830-1838, 2015.

[5] Reissner E. On One-Dimensional Finite-Strain Beam Theory: the Plane Problem. *Zeitschrift für angewandte Mathematik und Physik ZAMP* 23.5: 795-804, 1972.

[6] Wriggers P. Computational Contact Mechanics. *Springer-Verlag*, 2004.

INFLUENCE OF DIFFERENT FITTING METHODS ON THE IDENTIFICATION OF THE SYNCHRONOUS DYNAMIC COEFFICIENTS OF TILTING PAD JOURNAL BEARINGS

Michele Barsanti*[1], Enrico Ciulli[1], Paola Forte[1], and Matteo Nuti[2]
[1]Dipartimento di Ingegneria Civile e Industriale, University of Pisa, Largo Lazzarino, 56122 Pisa, Italy
[2]AM Testing s.r.l., Pisa, Italy

Summary Tilting pad journal bearings (TPJB) are mechanical components of fundamental importance for the proper operation of turbomachinery and the knowledge of bearing stiffness and damping coefficients is essential for rotor design. A high performance test bench has been designed specifically to carry out the experimental activity necessary for their determination. The tests carried out show a dependence of the dynamic coefficients on the excitation frequency of the dynamic load. In this work, different data fitting methods for the identification of synchronous dynamic coefficients are compared in order to evaluate the corresponding error in the predictions.

INTRODUCTION

The stiffness and damping coefficients of TPJBs are computed by applying dynamic loads (at several excitation frequencies) to the bearing, measuring the rotor-stator relative displacement and processing results in the frequency domain [1, 2]. The dependence of dynamic coefficients on the excitation frequency shows a non-linear trend [2] which makes it difficult to determine the synchronous coefficients (at an excitation frequency equal to the rotor rotational frequency) usually obtained by interpolation among the coefficients corresponding to excitation frequencies slightly lower and higher than the synchronous frequency. In this work different fitting functions have been compared to investigate their influence on the results.

CLASSICAL EXPERIMENTAL IDENTIFICATION OF DYNAMIC COEFFICIENTS

Several tests were performed at the University of Pisa on a test bench specifically designed for large size journal bearings operating at high peripheral speeds and static loads [1]. The test rig is shown in Fig. 1 (a); a sketch of actuators and sensors is shown in Fig. 1 (b). Details on the experimental activity are reported in [3]. The linear model used for the

(a) 

(b) 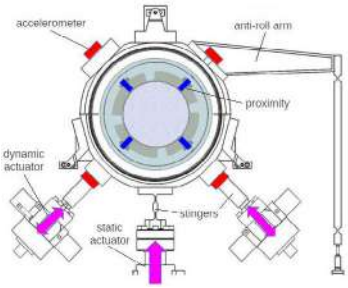

Figure 1: (a) Photo of the test rig. (b) Test section, showing actuators and sensors.

identification of the dynamic coefficients and described in [4] is based on the impedance matrix H that can be computed using

$$\begin{bmatrix} H_{xx} & H_{xy} \\ H_{yx} & H_{yy} \end{bmatrix} = \begin{bmatrix} F_{b1x} & F_{b2x} \\ F_{b1y} & F_{b2y} \end{bmatrix} \begin{bmatrix} X_1 & X_2 \\ Y_1 & Y_2 \end{bmatrix}^{-1} \text{ where } \begin{bmatrix} H_{xx} & H_{xy} \\ H_{yx} & H_{yy} \end{bmatrix} = \begin{bmatrix} k_{xx} & k_{xy} \\ k_{yx} & k_{yy} \end{bmatrix} + i\omega \begin{bmatrix} c_{xx} & c_{xy} \\ c_{yx} & c_{yy} \end{bmatrix}, \quad (1)$$

in which F indicates the amplitude of the force (acting on bearings) Fourier transform, X, Y indicate the amplitudes of the displacement Fourier transforms for the two perturbation tests respectively in horizontal (subscript 1) and vertical direction (subscript 2). The determination of the stiffness k and damping c coefficients at each of the excitation frequencies ω are obtained as respectively the real and the imaginary parts of the impedance direct and cross-coupled coefficients. The need to improve the accuracy and precision of the synchronous coefficients estimates leads to the development of increasingly elaborate models.

STATISTICAL PROCEDURE FOR DYNAMIC COEFFICIENTS IDENTIFICATION

A new identification procedure, based on a statistical approach, was developed in [4] to improve the classical identification procedure and to estimate the associated random uncertainties as well. The statistical model, adopted at each excitation frequency, has been generalized in this work analyzing simultaneously the measurements at all the excitation

*Corresponding author. E-mail: michele.barsanti@unipi.it.

frequencies and introducing a class of functions to fit the dependance of dynamic coefficients on the excitation frequency ω of the dynamic coefficients:

$$\begin{cases} \mathrm{Re}(F_{b1x}) = k_{xx}(\omega)\mathrm{Re}(X_1) - \omega c_{xx}(\omega)\mathrm{Im}(X_1) - \omega c_{xy}(\omega)\mathrm{Im}(Y_1) + k_{xy}(\omega)\mathrm{Re}(Y_1) \\ \mathrm{Im}(F_{b1x}) = k_{xx}(\omega)\mathrm{Im}(X_1) + k_{xy}(\omega)\mathrm{Im}(Y_1) + \omega c_{xx}(\omega)\mathrm{Re}(X_1) + \omega c_{xy}(\omega)\mathrm{Re}(Y_1) \\ \mathrm{Re}(F_{b2x}) = k_{xx}(\omega)\mathrm{Re}(X_2) - \omega c_{xx}(\omega)\mathrm{Im}(X_2) - \omega c_{xy}(\omega)\mathrm{Im}(Y_2) + k_{xy}(\omega)\mathrm{Re}(Y_2) \\ \mathrm{Im}(F_{b2x}) = k_{xx}(\omega)\mathrm{Im}(X_2) + k_{xy}(\omega)\mathrm{Im}(Y_2) + \omega c_{xx}(\omega)\mathrm{Re}(X_2) + \omega c_{xy}(\omega)\mathrm{Re}(Y_2) \\ \mathrm{Re}(F_{b1y}) = k_{yx}(\omega)\mathrm{Re}(X_1) - \omega c_{yx}(\omega)\mathrm{Im}(X_1) - \omega c_{yy}(\omega)\mathrm{Im}(Y_1) + k_{yy}(\omega)\mathrm{Re}(Y_1) \\ \mathrm{Im}(F_{b1y}) = k_{yx}(\omega)\mathrm{Im}(X_1) + k_{yy}(\omega)\mathrm{Im}(Y_1) + \omega c_{yx}(\omega)\mathrm{Re}(X_1) + \omega c_{yy}(\omega)\mathrm{Re}(Y_1) \\ \mathrm{Re}(F_{b2y}) = k_{yx}(\omega)\mathrm{Re}(X_2) - \omega c_{yx}(\omega)\mathrm{Im}(X_2) - \omega c_{yy}(\omega)\mathrm{Im}(Y_2) + k_{yy}(\omega)\mathrm{Re}(Y_2) \\ \mathrm{Im}(F_{b2y}) = k_{yx}(\omega)\mathrm{Im}(X_2) + k_{yy}(\omega)\mathrm{Im}(Y_2) + \omega c_{yx}(\omega)\mathrm{Re}(X_2) + \omega c_{yy}(\omega)\mathrm{Re}(Y_2) \end{cases} . \quad (2)$$

The relationship can be linear, polynomial or spline. In order to obtain the best estimates of all the quantities, a constrained minimum of the following weighted sum of squared residuals S as a function of the dynamic coefficients, displacements and forces is searched, in a similar way to what was already developed in [4]:

$$S = \sum_{i=1}^{N} \left[\left| \frac{\hat{X}_{1,i} - X_{1,i}}{\sigma_X} \right|^2 + \left| \frac{\hat{X}_{2,i} - X_{2,i}}{\sigma_X} \right|^2 + \left| \frac{\hat{Y}_{1,i} - Y_{1,i}}{\sigma_Y} \right|^2 + \left| \frac{\hat{Y}_{2,i} - Y_{2,i}}{\sigma_Y} \right|^2 + \left| \frac{\hat{F}_{b1x,i} - F_{b1x,i}}{\sigma_{Fx}} \right|^2 + \left| \frac{\hat{F}_{b2x,i} - F_{b2x,i}}{\sigma_{Fx}} \right|^2 + \left| \frac{\hat{F}_{b1y,i} - F_{b1y,i}}{\sigma_{Fy}} \right|^2 + \left| \frac{\hat{F}_{b2y,i} - F_{b2y,i}}{\sigma_{Fy}} \right|^2 \right] \quad (3)$$

in which N is the total number of measurements (at all the frequencies) and the relationships (among the hat variables) shown in equation (2) are the constraints. Standard deviations σ_X, σ_Y and σ_F have the same value for all the measured displacements and forces. This methodology can then be extended to determine an estimate of the random error as well.

RESULTS AND CONCLUSIONS

An example of preliminary result is shown in Figure 2. For given test conditions, the dynamic coefficients at various excitation frequencies (estimated using the conventional technique) [2] are reported in black dots, simply connected by segments. The coloured curves show the various predictions of the different modeling of the relationship between dynamic coefficients and excitation frequency: in blue quadratic models, in magenta cubic models. Polynomials are drawn in full lines, splines are reported using dashed lines. The black dashed line, drawn in correspondance of synchronous frequency, highlights that the prediction of the synchronous dynamic coefficients depends on the choice of the model. The difference among the various predictions can be of the same order of the random or systematic uncertainty [2, 4] and therefore these preliminary results indicate that the choice of the fit model can be critical.

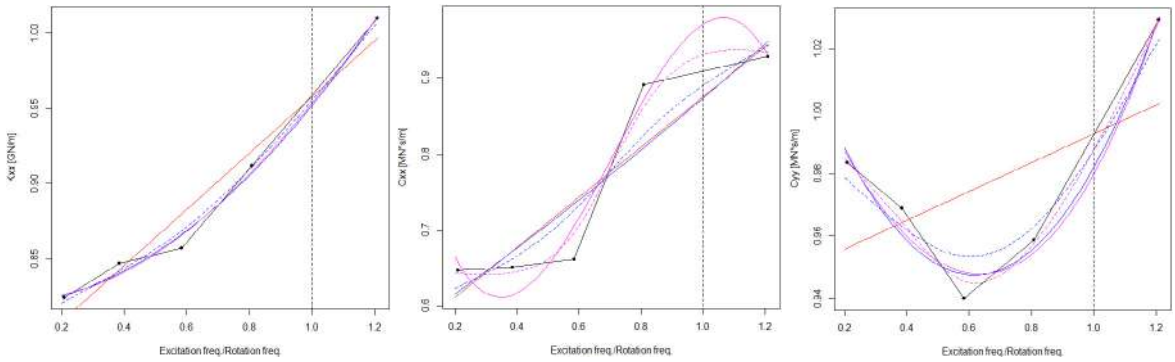

Figure 2: Examples of prediction of stiffness and damping coefficients as a function of the excitation frequency.

References

[1] Ciulli E., Forte P., Libraschi M., Nuti, M. Set-up of a novel test plant for high power turbomachinery tilting pad journal bearings. *Trib. Int.* **127**: 276-287, 2018.

[2] Barsanti M., Ciulli E., Forte P., Libraschi M., Strambi M. Error analysis in the determination of the dynamic coefficients of tilting pad journal bearings. *Procedia Structural Integrity* AIAS2019 - 48th Conference on Stress Analysis and Mechanical Engineering Design, Assisi (PG), Italy, 4-7 September 2019.

[3] Ferraro R., Innocenti A., Libraschi M., Barsanti M., Ciulli E., Forte P. Nuti M. Dynamic identification of large tilting pad journal bearings: test results and measurement uncertainties assessment of different technologies. Submitted to *ASME 2020 Turbomachinery Technical Conference and Exposition* GT2020

[4] Barsanti M., Ciulli E., Forte P. Random error propagation and uncertainty analysis in the dynamic characterization of Tilting Pad Journal Bearings. *Journal of Physics: Conference Series* **127**: 276–287, 2019.

RING BASED MODEL FOR COMPUTING POWER LOSS INLATERALLY COMPRESSED GEL-FILLED OPTICAL FIBERCABLES

Anshul Agrawal[*†], Shakti S. Gupta[†], Ishan Sharma[†], and Manoj Mittal[§]
[†]Department of Mechanical Engineering, IIT Kanpur, Kanpur - 208016, India
[§]Sterlite Technologies Limited, Dadra and Nagar Haveli - 396230, India

Summary We model a critical orientation of outer sheath and loose tubes of an optical cable as thin elastic rings. The laterally compressed sheath between two flat rigid plates circumscribes the diametrically placed vertical loose tubes, separated by a rigid core at the cable's center. Sheath-flat plate, sheath-loose tube, and loose tube-core interactions are modelled as point contacts transitioning to line contacts during deformation. The nonlinear equilibrium equations are solved satisfying deformation compatibility to compute fraction of applied load on the gel filled loose tubes. This is used to find the excess pressure in the tubes which eventually acts on the optical fibers in those. Using this pressure the field of refractive index over the cross-section of the fiber is computed employing stress-optic law which is further used in COMSOL to compute the power loss in the optical fiber.

INTRODUCTION

Optical fiber cable as shown in Fig. 1, consists of an outer sheath, an inner rigid core and loose tubes between them which carry optical fibers. Depending on situations these cables may come under constant external loads for example, crushing due to a heavy vehicle passing or a boulder falling over it. These external loads deform the components of the structure of the cable leading to excess pressure in the gel filled in the loose tubes. This excess pressure is exerted onto the optical fibers, stressing those which leads to the loss in signal transmission.

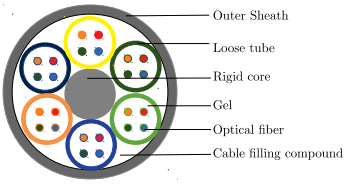

Figure 1: Schematic of the cross-section of an optical fiber cable and its components.

Problem formulation

Assuming plane strain state in the cable, a set of three elastic thin rings with one rigid circular core at the center, pressed between two rigid plates is shown in Fig. 2(a) is chosen as the critical orientation of the cable. This symmetric arrangement of rings is subjected to the externally applied distrubuted line load of P (N/m) perpendicular to the plane of the paper as shown in Fig. 2(a). The loose tubes and the sheath are denoted by the numbers 1 and 2, respectively. The rings are characterized by their constant bending stiffness D_i and unloaded radii of curvature ρ_i. It is also assumed that the rings are inextensible and the contact at various interfaces is frictionless.

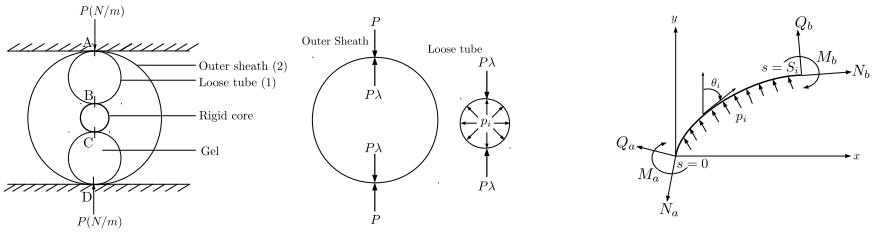

(a) (b) (c)

Figure 2: (a) Structural model of the cross-section of the cable, (b) FBD of the sheath and a loose tube, and (c) Forces and moments on an arc of the ring.

The static equilibrium equations for the outer and the inner rings can be written as follows [1]:

$$\frac{\partial Q_i}{\partial \theta_i} + N_i + p_i \rho_i = 0, \quad \frac{\partial M_i}{\partial \theta_i} + Q_i \rho_i = 0, \quad \frac{d\theta_i}{ds} = \frac{1}{\rho_0} + \frac{M_i}{D_i}, \tag{1}$$

*Corresponding author. E-mail: anshula@iitk.ac.in.

where θ_i is the local slope, s_i is the arc-length, N_i the membrane force, Q_i the shear force, M_i the bending moment, p_i the internal gel pressure, ρ_0 the original radius of curvature, ρ_c the raidius of curvature of core. Note that while writing the equilibrium of the sheath p_i will be set to zero.

While solving the above equations the inextensibility condition is enforced by maintaining the initial and the final arc-lengths equal. Additionally, at any step of deformation AB = AC + CD + DB is maintained (see Fig. 2(a)). These equilibrium equations are solved using elliptic integrals [3] to compute fractional load parameter λ.

To compute the gel pressure the equilibrium equations for the loose tube are written as below:

$$D_1 \frac{d^3\theta_1}{ds^3} - \frac{N_1}{\rho_1} - p_1 = 0, \quad \mu = \frac{-p_1}{(\Delta V/V)}, \tag{2}$$

where for unit depth of the loose tube we write the change in volume $\Delta V = \Delta A$, the change in cross-sectional area for unit length of cylinder, and the initial volume $V = A$, the initial area. Equation (2) is solved satisfying the constraint in Eq. (3) and the boundary conditions in Eq. (4) resulting in the deformed configuration of the ring.

$$\frac{P}{2D_1} - \sqrt{-\frac{k_L^4}{4} + \frac{2p_1k_L}{D_1} + c_1k_L^2 + c_2} = 0, \quad \frac{P}{2D_1} + \sqrt{-\frac{k_R^4}{4} + \frac{2p_1k_R}{D_1} + c_1k_R^2 + c_2} = 0, \quad k_L = \frac{d\theta_L}{ds}, \quad k_R = \frac{d\theta_R}{ds}, \tag{3}$$

L, R corresponds to $s = 0$, S_i, respectively.

$$\text{At} \quad s = 0, \quad \theta_i = \pi, \quad \text{At} \quad s = S_i, \quad \theta_i = 0, \tag{4}$$

For a given value of bulk modulus μ of gel, excess pressure p_1 is computed using the second of Eq. (2). This excess pressure is further used to compute the stress from the problem of a disk (optical fiber) under radial compression [5] ($\sigma_{rr} = -p_1, \sigma_{\theta\theta} = 0, \sigma_{r\theta} = 0$) and hence strain tensor using linear constitutive relation (σ = E ϵ) over the cross-section of the optical fiber.

Using the strain computed above and employing the stress-optic law [4] for an isotropic material the change in refractive index is given by

$$\Delta n_k = \frac{n_k^3}{2} \sum_{m=1}^{4} P_{km}\epsilon_m. \tag{5}$$

where Δn_k is the change in refractive index of the k^{th} component tensor in Voigt notation, ϵ_m are the four components of the strain tensor in Voigt notation, and P_{km} the photo-elastic constants comprising the photo-elastic tensor. Equation (5) is used to compute refractive index profile over the cross-section of the optical fiber which in turn is used in COMSOL to compute power loss in the cable.

RESULTS AND CONCLUSIONS

For the parameters $D_1 = 5.95 \times 10^{-5}\, Nm^2$, $D_2 = 1 \times 10^{-3}\, Nm^2$, $\rho_1 = 0.682\, mm$, $\rho_c = 1\, mm$, $\rho_2 = 2.6\, mm$.

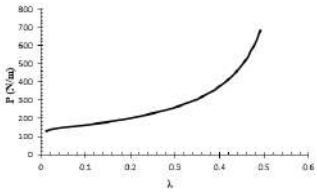

(a)

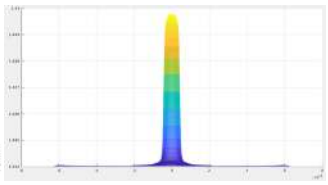

(b)

$P(N/m)$	$Powerloss(dB/mm)$
50	0.00014
80	0.00022
100	0.00028
150	0.0004198
200	0.000561

(c)

Figure 3: (a) Load (P) versus λ, (b) Modified refractive index profile, and (c) For Young's modulus of fiber = 21 GPa, wavelength = 1550 nm, fiber diameter = 125 μm.

Ring based model to compute optical power loss in optical cables is studied. The optical cable is modeled as an array of thin elastic rings. The fraction of total load (parameter λ) on the loose tube is computed solving governing nonlinear equations. This parameter is used to derminine the excess gel pressure inside loose tubes which is used to evaluate the field of refractive index change over the cross-section of the fiber employing stress-optic law. This is further used in COMSOL to compute the power loss in the optical fibers.

References

[1] Wu, C. H., & Plunkett, R. (1965). On the Contact Problem of Thin Circular Rings. *Journal of Applied Mechanics*, 32(1), 11-20.
[2] Flugge Wilhelm. (1960). *Stresses in shells*. Berlin, Gottingen, Heidelberg: Springer.
[3] Fay, R. F. (1962). *Flexible bars*. London: Butterworth.
[4] Nye, J. F. (2011). *Physical properties of crystals: their representation by tensors and matrices.* Oxford: Clarendon Press.
[5] Sadd, M. H. (2014). *Elasticity theory, applications, and numerics.* Amsterdam: Elsevier/Academic Press.

FROM A PERFECT JUNCTION TO A TILTED ASPERITY: EXPERIMENTAL, ANALYTICAL, AND NUMERICAL STUDIES

Mohammad Malekan*[1], Michal K. Budzik[1], and Ramin Aghababaei[1]
[1]Department of Engineering, Aarhus University, 8000 Aarhus C, Denmark

Summary Friction and wear of brittle materials during sliding contact are often associated with the fracture-induced failure of interlocking asperities under shear loading. This paper presents analytical, numerical and experimental studies of an idealized asperity under lateral load. The material under study was chosen as PMMA. Both experimental and numerical studies were done for different asperity base angle (θ), from 60 to 90 degrees. Maximum force to initiate the crack and also crack initiation angle were derived from analytical, numerical, and experimental investigations. The results showed that the maximum force went higher for smaller θ angle, along with good agreements between all the three approaches.

INTRODUCTION

Brittle fracture is a major mode of failure in cracked brittle materials like PMMA. In many practical applications related to brittle materials, such as material cutting processes and hydraulic fracturing, the fracture strength is an important material property. Moreover, for applying the crack growth retardation methods an estimate of the direction of the fracture initiation and early propagation is required. Hence, the investigation of the fracture trajectory is an interesting topic for researchers involved in the field of fracture mechanics of brittle and quasi-brittle materials. Under pure mode-I loading conditions, cracks sometimes grow along curvilinear paths and not necessarily along the direction of the initial cracks. This paper presents analytical, numerical and experimental studies of an idealized asperity under lateral load. The material under study was chosen as PMMA.

THEORETICAL MODEL

A theoretical model is derived here using general Euler-Bernoulli beam theory, aiming to determine the maximum loading magnitude that derives the crack initiation in the problem. The geometrical setup for our theoretical analysis is illustrated in Fig. 1. We assume that the asperity width (d_x) varies as a function of height, where d_0 is the base width (the asperity is prismatic when $d(x) = d_0$). We note a geometrical constraint that h should be smaller than the asperity height. A constant out-of-plane thickness t is considered in this study.

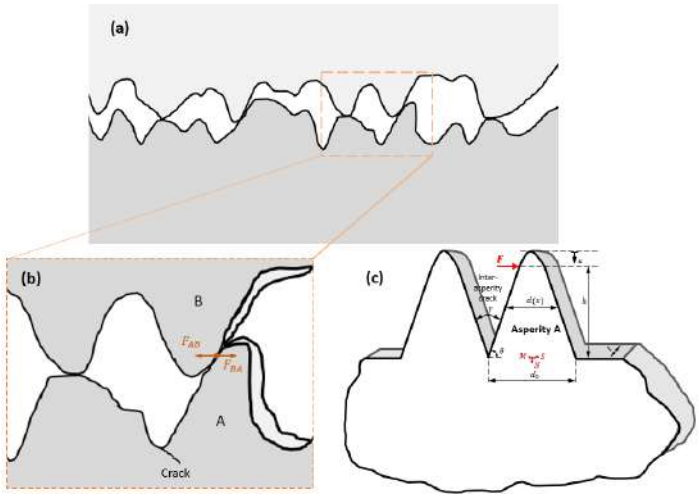

Figure 1: Schematic of the sliding contact between two rough solid surfaces at **(a)** multi-asperity and **(b)** single asperity levels. **(c)** an idealized asperity model used to develop the theoretical model.

Considering the case of two prismatic asperities [i.e. $d(x) = d_0$] with an interfacial sharp crack (i.e. $\gamma = 0$, $\theta = 90$), the energy release rate G can be obtained similar to the problem of interlaminar crack propagation in a double cantilever beam setup [1, 2], as

$$G = \frac{1}{Et^2 d_0}\left(N^2 + S^2 + \frac{12M^2}{d_0^2}\right) \tag{1}$$

where N, S and M represent the magnitude of the normal and shear forces and the bending moment at the asperity base and E is the elastic modulus. Our analysis shows that the energy release rate is only a function of the beam width at the location of the crack tip (d_0) and is independent of the asperity shape.

*Corresponding author. E-mail: m.malekan@eng.au.dk

Considering a contact force laterally applied to the asperity side, the crack tip forces and moment can be replaced by $M = Fh$, $S = F$ and $N = 0$ in Eq. (1). Accordingly, the critical force at the onset of crack propagation for non-zero crack opening angles ($0 \leq \gamma \leq \pi$) can be obtained as [3, 4, 5, 6]

$$\widetilde{F}_c = \frac{F_c}{K^*_{IC}\, t\, d_0^{1-\lambda(\gamma)}} = \frac{\alpha}{\sqrt{12+\alpha^2}} \tag{2}$$

where λ represents the degree of stress singularity at the crack tip which varies between $1/2$ (when a sharp crack and square-root stress singularity presents, i.e. $\gamma = 0$) and zero (when the stress singularity is absent, i.e. $\gamma = \pi$) and can be calculated from the following eigen-equation [5]

$$(1-\lambda)\sin(2\pi-\gamma) = \sin[(1-\lambda)(2\pi-\gamma)] \qquad K^*_{IC} = [1-\lambda(\gamma)]\,\sigma_{ult}\left(\frac{2K_{IC}}{\sigma_{ult}}\right)^{2\lambda(\gamma)} \tag{3}$$

As seen in Eq. (2), the normalized fracture force $\tilde{F}_c$ is independent of the asperity shape and is only a function of the ratio between the asperity width at its base and the height of the loaded part of the asperity.

EXPERIMENTAL AND NUMERICAL STUDIES

We study experimentally the fracture failure of tapered asperities made of PMMA (polymethylmethacrylate) using a set of in-situ experiments. Test specimens are cut from PMMA sheets of 1.8 mm thickness by laser cutting. Dictated by the minimum resolution of the cutting line, all base corners have a radius of curvature of about $100\mu m$. We fixed the height of the applied load ($h = 8$ mm) and the width of asperity tip (5 mm) and systematically varies the θ angle from 60^o to 90^o with 5^o increments. The asperity base width d and the aspect ratio α (i.e., d/h) change accordingly.

To study the evolution of deformation and failure, we also performed numerical simulations using the extended finite element method (XFEM) implemented in the Abaqus® commercial package. The geometrical model and boundary conditions are presented in Fig. 2. A fixed displacement and rotation are assumed at the asperity base where a displacement rate of 2 mm/min is applied at a fixed distance of 2mm from the asperity tip. A linear elastic material with brittle behavior and parameters corresponding to PMMA properties is assumed. FE model is discretized using plane stress CPS4 elements (4-node bilinear quadrilateral element) with an average size of $0.015 \sim 0.03$mm for the corner areas (i.e. crack nucleation site) and $0.075 \sim 0.1$mm for the rest of the domain.

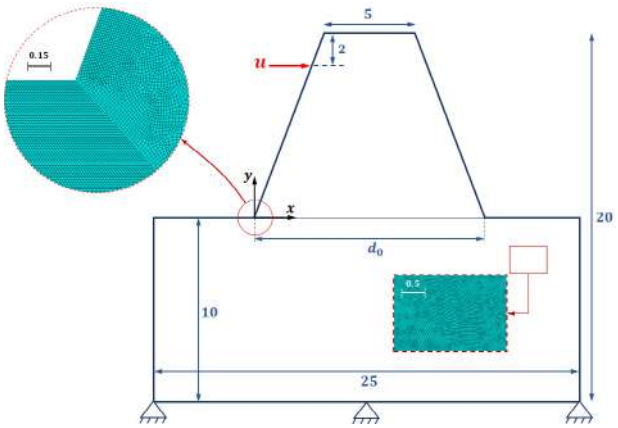

Figure 2: Geometry schematic of the problem under study along with mesh representation for different parts of the problem. All dimensions are in mm

CONCLUSIONS

The aim of this paper was to demonstrate a package of theoretical, experimental, and numerical studies of idealized asperities in order to investigate their fracture behavior, in terms of maximum force to fracture and also the crack initiation angle. The results will include comparison between all the three approaches and final goal is to propose a proven theoretical formulae that can be used for similar conditions.

References

[1] Suo Z, Hutchinson J. Interface crack between two elastic layers. *International Journal of Fracture* **43**:1–18, 1990.
[2] Jensen H, Thouless M. Effects of residual stresses in the blister test. *International Journal of Solids and Structures* **30(6)**:779–795, 1993.
[3] Williams M. Stress singularities resulting from various boundary conditions in angular corners of plates in extension. *Journal of Applied Mechanics* **19**:526–528, 1952.
[4] Carpinteri A. Stress-singularity and generalized fracture toughness at the vertex of re-entrant corners. *Engineering Fracture Mechanics* **26(1)**:143–155, 1987.
[5] Seweryn A. Brittle fracture criterion for structures with sharp notches. *Engineering Fracture Mechanics* **47(5)**:673–681, 1994.
[6] Carpinteri A, Pugno N, Sapora A, Taylor D. A finite fracture mechanics approach to structures with sharp v-notches. *Engineering Fracture Mechanics* **75(7)**:1736–1752, 2008.

INDENTATION OF A SPHERICAL PUNCH INTO A VISCOELASTIC BASE IN THE PRESENCE OF ADDITIONAL LOADING

Anastasiya Yakovenko*[1,2], Irina Goryacheva [1]
[1]Laboratory of Tribology, Ishlinsky Institute for Problems in Mechanics RAS, Moscow, Russia
[2]Phystech School of Aerospace Technology, Moscow Institute of Physics and Technology (National Research University), Moscow, Russia

Summary A numerical-analytical solution of the problem of indentation of a spherical punch into a viscoelastic base in the presence of additional loading outside a circle of a given radius is presented. The influence of the viscoelastic properties of the base on the dependence of the contact characteristics (radius of the contact area, contact pressure distribution) on time for the exponential creep function. The analysis of the dependence of the pressure distribution under the punch at different instants of time on the radius of the additional loading is also presented.

The effects of mutual influence of the microcontacts in contact interaction of the surfaces with irregularities are well studied for the elastic bodies. Many works have been devoted to modeling of an indentation of the surfaces with regular relief into elastic base. 2-D periodic contact problems were considered in [1], and 3-D discrete contact problems with limited and unlimited nominal contact region were studied in [2]. However, when analysing the indentation of rough bodies into the viscoelastic base, the effect of the mutual influence of microcontacts is poorly studied. To analyse the effect of the additional loading on the indentation of the punch into the viscoelastic base the model of the interaction of a punch with a viscoelastic base loaded outside the contact region is developed.

The indentation of an axisymmetric punch into viscoelastic half-space under the action of a given force P is considered. Simultaneously, the half-space is loaded by the uniform pressure $\bar{p}$ outside the circle of a given radius A. The shape of the indenter contact surface is described by the function $f(r)$. For spherical punch under the assumption of small indentation depth, we assume $f(r)=r^2/2R$, where R is the indenter radius of contacting surface curvature. Material of the base is linearly viscoelastic. The load P applied to the indenter is constant, so $P=P_0H(t)$ ($H(t)$ is the Heaviside function), while the value of the additional pressure $\bar{p}$ is also constant and it is expressed in terms of the load applied to the indenter as $\bar{p}=P/\pi A^2$.

To solve the problem of indentation of the axisymmetric punch into the half-space in the presence of the additional nominal pressure distributed over a given area, the superposition method is used, in other words, two problems are considered. The first problem is the determination of the displacement of the half-space boundary under the action of a nominal pressure outside the circle of a given radius. The second problem is the penetration of the spherical indenter into a curved half-space boundary. The solution of this problem for the elastic half-space has been developed in [2], and has the following form

$$\frac{a^3}{\arccos\frac{a}{A}+\frac{a}{A}\sqrt{1-\left(\frac{a}{A}\right)^2}}=\frac{3}{2\pi}\left(1-\nu^2\right)R\frac{P}{E}, \qquad (1)$$

$$p(r)=\frac{P}{\pi^2}\left(\frac{3}{a^2}\left(\arccos\frac{a}{A}+\frac{a}{A}\sqrt{1-\left(\frac{a}{A}\right)^2}\right)\sqrt{1-\frac{r^2}{a^2}}+\frac{2}{A^2}\arctan\sqrt{\frac{a^2-r^2}{A^2-a^2}}\right), \qquad (2)$$

$$D(t)=\frac{a(t)^2}{R}-2\frac{\left(1-\nu^2\right)\bar{p}(t)}{E}\sqrt{A^2-a(t)^2}, \qquad (2)$$

where a is the radius of the contact region, D is the additional displacement which is a difference between the displacement of the punch tip and the boundary of the half-space loaded by the nominal pressure $\bar{p}$ inside the circle of radius A, ν and E are the Poisson ratio and the Young's modulus of the base, respectively.

The analysis of Eqs.(1)-(3) shows that the contact region is monotonically increasing if the load P does not decrease. So the Volterra method [4] can be used to solve the contact problem for viscoelastic half-space in similar formulation. Assuming that the Poisson's coefficient is constant, we replace the elastic constants in formulas (1)-(3) with the integral operator. As the result we obtain

$$\frac{a(t)^3}{\arccos\left(\frac{a(t)}{A}\right)+\frac{a(t)}{A^2}\sqrt{A^2-a(t)^2}}=\frac{3R\left(1-\nu^2\right)P_0J(t)}{2\pi}, \qquad (4)$$

*Corresponding author. E-mail: anastasiya.yakovenko@phystech.edu.

$$p(r,t)=\frac{2}{\pi(1-\nu^2)}\int_0^t E(t-\tau)\frac{d}{d\tau}\left(\frac{\sqrt{a(\tau)^2-r^2}}{R}+\frac{P_0(1-\nu^2)}{\pi A^2}J(\tau)\arctan\left(\frac{\sqrt{a(\tau)^2-r^2}}{\sqrt{A^2-a(\tau)^2}}\right)\right)d\tau,\quad r\le a(t),\qquad(5)$$

$$d(t)=\frac{a(t)^2}{R}-\frac{2(1-\nu^2)P_0J(t)}{\pi A^2}\sqrt{A^2-a(t)^2},\qquad(6)$$

where $E(t)$ and $J(t)$ are the relaxation and creep functions, which describe the mechanical properties of the viscoelastic material. Here we consider the model of the standard viscoelastic body. The relaxation and creep functions of this model have the form [5]

$$E(t)=E_0\left(\frac{\beta-\alpha}{\beta}+\frac{\alpha}{\beta}e^{-\beta t}\right)\quad\text{and}\quad J(t)=\frac{1}{E_0(\beta-\alpha)}\left(\beta-\alpha e^{-(\beta-\alpha)t}\right),\qquad(7)$$

where $\alpha=1/T_\sigma-1/T_\varepsilon$, $\beta=1/T_\varepsilon$, T_σ and T_ε are the relaxation and creep times of the half-space. E_0 is the instantaneous modulus of elasticity, and $E_\infty=E_0(\beta-\alpha)/\beta$ corresponds to the long-term modulus of elasticity.

The expressions (4) and (7) allows us to calculate the value of the radius of the contact area in the indentation process. Then the contact pressure and the additional displacement are calculated from (5) and (6).

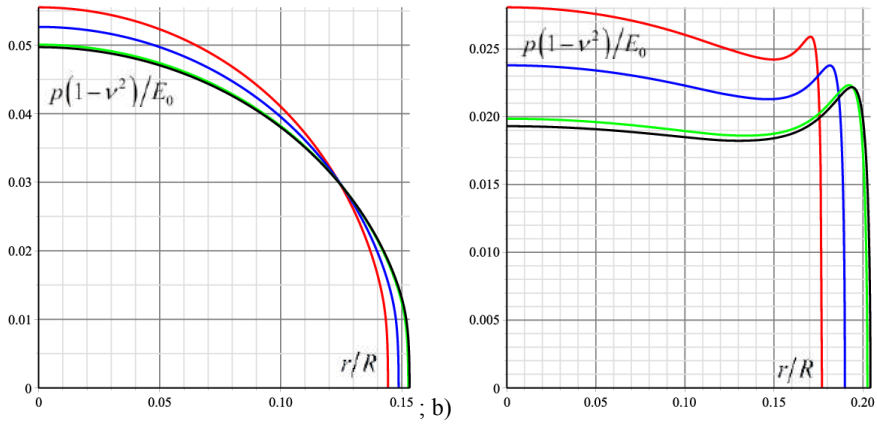

a) ; b)

Fig.1 Contact pressure distribution at $A=0.2$ (red line), $A=0.3$ (blue line), $A=0.5$ (green line), $A\to\infty$ (black line); $T=2$ (a) and $T=10$ (b)

The following dimensionless parameters are introduced: $r=r/R$, $t=\beta t$, $p=p(1-\nu^2)/E_0$, $A=A/R$, $P=P(1-\nu^2)/R^2E_0$, and $T=T_\varepsilon/T_\sigma=\beta/(\beta-\alpha)$. The results show that the contact characteristics are affected by three dimensionless parameters: the value of load P_0, the radius of the circle A outside of which the additional nominal pressure acts, and the viscoelastic coefficient T. Fig.1 presents graphs of the dimensionless contact pressure distribution for three values of the radius A and two values of the coefficient T at given instant of time ($t=5$) for the fixed value of the load $P_0=0.0025$. It follows from the results that the additional loading effect is more significant for materials with a higher coefficient T ($T=1$ corresponds to the elastic case). It is established for fixed time of loading that the larger is the coefficient T, the greater is the radius of the contact area and the less is the maximum contact pressure. It also follows from the results that if the additional pressure radius A decreases, the maximum contact pressure increases and the contact radius decreases. If $A\to\infty$, the pressure tends to the case of the indentation neglecting additional loading (black line).

Thus, based on the obtained solution of the problem of indentation of an axisymmetric indenter into a viscoelastic half-space in the presence of an additional load the influence of the loading parameters on the contact characteristics in indentation were studied. The results can be used to analyse the stress state of polymer materials under loading by rigid body with surface irregularities and to analyse the limits of applicability of simplified models, which do not take into account the mutual influence of microcontacts.

The work was supported by the Russian Foundation of Basic Research, grant 20-01-00400.

References

[1] Shtaerman I.Ja. Contact problem of elasticity theory. Gostekhizdat, Moscow-Leningrad, 1949. (in Russian)
[2] Goryacheva I.G.Contact Mechanics in Tribology. Kluwer, Dordrecht, 1998.
[3] Christensen R.M. Theory of Viscoelasticity: An Introduction. Academic Press, New York, 1971.
[4] Johnson K.L. Contact mechanics. Cambridge University Press, London, 1985.
[5] Rabotnov Y.N. Creep of Structure Elements. Nauka, Moscow, 1966. (in Russian)

EFFECT OF THE CONTOUR CONTACT AREA VARIATIONS ON THE TEMPERATURE DURING BRAKING

Aleksander Yevtushenko, Michal Kuciej and Katarzyna Topczewska*
Department of Mechanics and Computer Science, Faculty of Mechanical Engineering, Bialystok University of Technology, Bialystok, Poland

Summary In this study a new analytical model was proposed to determine temperature during single braking with exponential growth of contact pressure with account of time-dependent contour surface of friction. For this purpose, an initial problem of motion and a boundary-value problem of heat conduction were formulated and solved. Results obtained based on performed analysis were compared with corresponding data found without account of contour surface variations during process. This allowed to determine the effect of time-dependent contour contact area of the friction pair elements on the attained temperature distribution.

INTRODUCTION

Friction process in the braking systems takes place on the real disk–pad contact area. At the micro level, friction surfaces of the disc and pads are not perfectly flat and mutually matched. In fact, the real contact area is only a small part of the nominal surface of contact determined by the geometrical dimensions of frictional elements. Surface waviness causes the limitation of contact spots occurrence area by the so–called contact plateaus [1] that are located on the nominal friction surface. These plateaus form surface contours that determine the boundaries of the contact zone. The real contact area is composed of tiny contact spots between surface peaks and asperities within the friction contour surface [2]. Wear and deformations of surface asperities associated to the friction process, result in irregular fluctuations of the size and location of the contact points. Thus, the contact area of friction changes the space-time distribution, as well as the properties during braking [3]. This has a significant impact on the distribution of generated frictional heat and the tribological characteristics of the brake system.

DEVELOPMENT OF THE CALCULATION MODEL

The increase of contact pressure during braking causes more plateaus to be incorporated into the contour friction surface over time. In addition, it results in the growth of load on previously engaged plateaus and this leads to an increase of their contribution within the nominal friction surface. Therefore the actual contact area, as wells as the contour area increase during braking. Known from the literature review [4] analytical solutions to thermal friction problems, for determining the temperature and thermal stresses distributions, have been developed with the assumption that the contact area is constant during braking and equal to the nominal friction surface. In this study, a new analytical model was developed to predict the temperature achieved during braking on the friction surface, which area increases during the process. In order to determine the sliding velocity and friction power, the initial problem of motion was considered for the process of single braking with an exponential growth of pressure on the contour contact surface, which increases linearly over time. Such a function of changing the contour surface was proposed in the article [5] for a disc brake system with friction elements made of carbon composite. The obtained results allowed for the formulation of an appropriate one–dimensional, boundary–value problem of heat conduction for a system consists of two semi–spaces under the conditions of perfect thermal contact of friction. The solution to this problem was found analytically using the Duhamel's theorem. Based on achieved formula, the analysis was performed to investigate the effect of the contact area variations on the main tribological characteristics during braking, such as friction power and temperature distributions.

ACKNOWLEDGEMENTS

This paper is a part of the project no. 2017/27/B/ST8/01249 financed by the National Science Centre of Poland.

References

[1] Eriksson M., Bergman F., Jacobson S. On the nature of tribological contact in automotive brakes, *Wear* **252**, 1-2, 26–36, 2002.
[2] Varadi K., Neder Z., Friedrich K. Evaluation of the real contact areas, pressure distributions and contact temperatures during sliding contact between real metal surfaces. *Wear*, **200,** 1-2, 55-62, 1996.
[3] Qi H.S., Day A.J., Investigation of disc/pad interface temperatures in friction braking, *Wear*, **262**, 505–513, 2007.
[4] Yevtushenko A., Kuciej M., One-dimensional thermal problem of friction during braking: The history of development and actual state. *Int. J. Heat Mass Tran.* **55**, 4118–4153, 2012.
[5] Chichinadze A.V., Kozhemyakina V.D., Suvorov A.V., Method of temperature-field calculation in model ring specimens during bilateral friction in multidisc aircraft brakes with the IM-58-T2 new multipurpose friction machine, *J. Frict. Wear* **31**, 1, 23–32, 2010.

*Corresponding author. E-mail: k.topczewska@pb.edu.pl.

EXPERIMENTAL AND NUMERICAL INVESTIGATION OF FRETTING FATIGUE FAILURE IN LUG-BUSH JOINTS

Emine Burcin Ozen[1], Demirkan Coker*[1,2], and Yezdan Medet Korkmaz [1,3]
[1]Department of Aerospace Engineering, Middle East Technical University, Ankara, Turkey
[2]METU Center for Wind Energy, Middle East Technical University, Ankara, Turkey
[3]Turkish Aerospace Industries, Ankara, Turkey

Summary In aerospace industry, load transfer between two parts can be provided by several components. One example to these components is lug joints with interference-fitted bushes. This type of components fails due to fretting fatigue under small amplitude cyclic loadings due to relative motion at the contact surfaces of the lug and the bush. In this study, failure mechanism of lug-bush joints is investigated by macroscopic and microscopic evaluations and compared with the FEA results. Four different lug-bush joints are tested under high cycle tensile fatigue loading until failure. Investigation of the contact surfaces of lugs and bushes under SEM and conducting EDS analysis showed that tribolayers are formed at distinct regions of the contact surfaces. Fracture of the lug occurred at the vicinity of these tribolayer patches. FEA results showed good agreement with the experimental evidence.

INTRODUCTION

Fretting fatigue occurs between two contacting bodies under constant normal load and cyclic tangential load. For fretting to occur, the applied tangential load should not overcome the force required to create a bulk motion. However, at some regions of the contact surface the applied tangential load is at least equal or greater than the required force to create a bulk motion. Therefore, regional stick and slip zones form at the contact surface. For example, in the case of a spherical body and a flat surface contact, a central stick region and a slip annulus occur at the contact surface under constant normal load and cyclic tangential load according to the Hertz and Mindlin analytical solutions [1]. Periodical changes in the slip amplitude at these slip zones due to applied cyclic loads cause fretting fatigue [2].

Fretting fatigue failure is observed in lug joints with interference-fitted bushes which are used widely in aerospace industry, for example, at the rotor to body connections of the helicopters.

The objective of this study is to investigate the failure mechanism of different lug-bush joints. Investigated lug-bush joints are made of Ti and Al lugs with Al and steel bushes, as shown in Figure 1, and subjected to high-cycle tensile fatigue loading. Figure 1 also shows crack locations of the lugs.

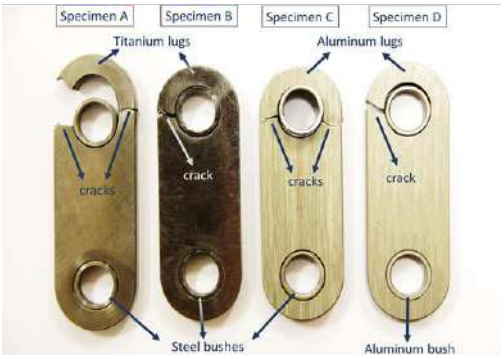

Figure 1. Investigated lug-bush joints consisting Ti and Al lugs combined with Al and steel bushes.

METHODOLOGY

Photographs of the failed lug-bush joints are taken using a camera with macro lenses. Black residues lying discontinuously in the direction of the cyclic loading are observed at the contacting surfaces of both lugs and bushes. Matching surfaces of the lugs and bushes are detected with the help of these pictures and residues. Using the matching residues on the lug and bush surfaces, the corresponding location of the cracks of lugs are identified on bush surfaces.

A digital microscope, Huvitz HDS 5800, is used to investigate the surfaces at high magnifications. In addition, scanning electron microscope (SEM) is used for further observations of the surface as well as the determination of the elemental composition, using energy dispersive spectroscopy (EDS) analysis.

RESULTS AND DISCUSSION

Experimental Results

Observations of the lug and bush mating surfaces using both camera and digital microscope revealed that the fracture of all lugs occurred near the boundary of an intense residue and a clean surface, as shown in Figure 2 for specimen A.

*Corresponding author. E-mail: coker@metu.edu.tr

The two distinct regions of black residues and clean parts raised the question of whether the residues are product of relative motion and the clean parts are product of sticking of the contacting surfaces.

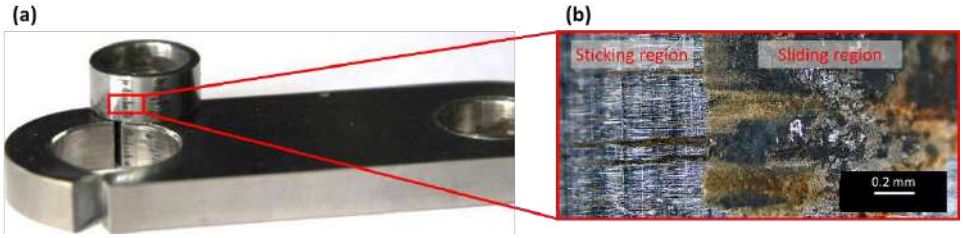

Figure 2. (a) Photograph of the matching lug-bush contacting surfaces and (b) boundary of the sticking and sliding regions on the steel bush surface of specimen A under digital microscope at 200x magnification.

In order to determine the differences between sticking and sliding regions in terms of elemental composition, EDS analysis is conducted under SEM. According to the results of the EDS analysis, sliding regions contain 20% of oxygen whereas the sticking regions do not have any oxygen content. These results indicate that at the sliding region, oxidation of wear debris occurred due to relative motion of the contacting bodies. The final product is called tribolayer which contains fine metallic particles from the two contacting surfaces and oxides [3].

Locations of fracture and sticking-sliding regions of these four members made of Ti and Al lugs with Al and steel bushes are mapped, as shown in Figure 3. The red lines in the maps represent the sliding regions where tribolayer is observed on the contacting lug and bush surfaces. Remaining surfaces were free from any residues and are represented with blue, indicating the sticking surfaces. All specimens are fractured at the vicinity of the boundary of sticking and sliding regions.

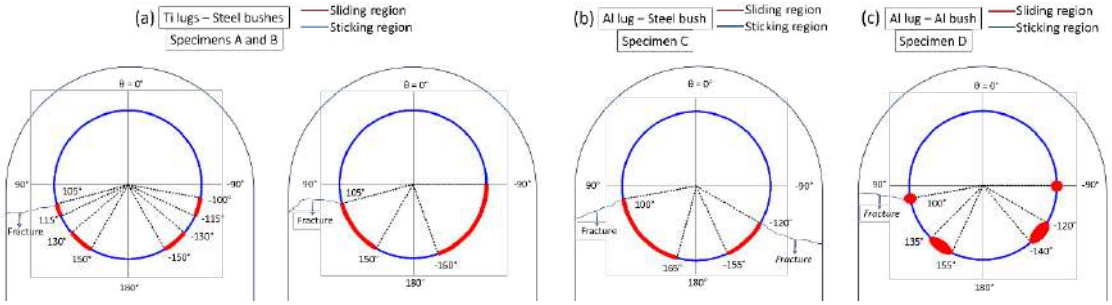

Figure 3. Locations of sticking and sliding regions of tested specimens.

Finite Element Analysis Results

3-D finite element model of statically loaded lug-bush assembly is generated using ABAQUS/Standard. Half of the lug and bush are modelled separately using their original dimensions, where the outer bush diameter is greater than the inner lug diameter. Both parts are discretized with 8-noded 3-D linear solid elements (C3D8 from ABAQUS library). In the analysis, the interface of the bush into the lug hole is defined prior to the application of a cosine pressure distribution to the bush. Master-slave algorithm is defined between the inner surface of the lug hole and the outer surface of the bush with a coefficient of friction of 1. The magnitudes of the maximum pressure and friction coefficient are defined by trial and error in order to differentiate the sticking and sliding regions clearly.

Relative slip amount between the lug and bush surfaces under the applied static loading is plotted around the bush. Slip amplitude reaches a peak value around ±115° for Ti lug and steel bush combination.

CONCLUSIONS

High cycle tensile fatigue loading of the lug-bush joints creates partial stick and slip zones at the contacting surface. In sliding regions, relative motion between contacting lug and bush surfaces create wear debris and oxidation of this debris leads to tribolayer formation. In the sticking regions, the surface remains clean due to lack of relative motion between contacting lug and bush surfaces. Fracture of all lugs occurred in the vicinity of these sticking and sliding region boundaries, approximately 100°. FEA results estimate the sticking and sliding region locations consistently with the experimental results. Peak locations of the slip amplitudes at the contact surfaces are included in the sliding regions of the tested specimens.

References

[1] Vingsbo, O. Fretting and Contact Fatigue Studied with the Aid of Fretting Maps, in Standardization of Fretting Fatigue Test Methods and Equipment. ASTM International, 1992.
[2] Goryacheva, I. G., Rajeev, P. T., Farris, T. N. Wear in partial slip contact. *Journal of Tribology*, **123**, 848-856, 2001.
[3] Blau, P. J. Friction Science and Technology, from Concepts to Applications. CRC Press/Taylor & Francis Group, Boca Raton, 2009.

ON THE STATISTICAL CHARACTERIZATION OF PLAIN GRINDING SURFACES

Xuan-Ming Liang[1], Wei-Ke Yuan [1], Yue Ding [1], and Gang-Feng Wang [*1]
[1]Department of Engineering Mechanics, SVL, Xi'an Jiaotong University, Xi'an, China

Summary In tribology, it is of importance to properly characterize the topography of rough surfaces. In this work, the three-dimensional topographies of plain grinding surfaces are measured through a white light interferometer, and their geometrical statistical features are analyzed. It is noticed that only when the total measured area is larger than a threshold value, is the statistical characterization reasonable and stable. For various plain grinding surfaces, the height of asperity-summit obeys a Gaussian distribution, and the equivalent curvature radius follows a modified *F*-distribution. These statistical characteristics are helpful to analyze the contact and friction behaviors of rough surfaces.

INTRODUCTION

Surface topography has a significant influence on the mechanical and physical performances of contacting bodies, such as friction, wear, lubrication, sealing, electricity transfer, heat transfer, etc. However, precisely characterizing the topography of rough surfaces is still a challenging task on account of the geometric complexity and randomness. There are several different theoretical models available for this issue and these can be grouped into two main categories: multi-asperity models and fractal models [1]. In addition to the theoretical models mainly based on assumptions and conjectures, experimental researches [2] on the accurate description of rough surfaces have also been conducted. Usually a two-dimensional profile is measured to extract the geometrical features of isotropic surfaces, in this study, the 3D topographies were measured to characterize anisotropic surfaces.

TECHNIQUES

Surface specimens were prepared by applying standard plain grinding processing on the 45 quality carbon structural steel (C45E4, ISO 683-18-1996). Six specimens with increasing roughness were produced, and their size is 20 mm × 8 mm. In this work, the 3D surface topography was recorded by using a white light interferometer (NanoMap-1000WLI, AEP) with a 50× interference objective lens. It should be pointed out that the scanned region in each operation is much smaller than the specimen size. To ensure the statistical and random nature, a randomized algorithm was utilized to choose multiple positions for scanning.

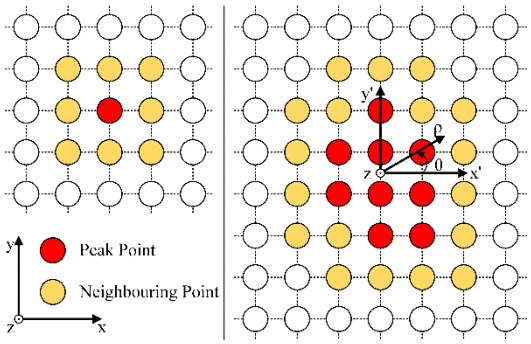

Figure 1. Identification of the asperity summits on 3D surfaces: left for 9-point rectangular asperity summit [2], right for an irregular asperity summit.

According to our scanning result, the peak of one asperity may consist of several points instead of one single point as shown in Fig. 1. For a summit with only one highest point, the 9-point rectangular approach [2] was widely used to calculate its curvature. However, for asperity-summits with a cluster of peak points, the 9-point rectangular approach is no longer applicable. Herein, we developed a new criterion using an elliptic paraboloid to approximate each asperity-summit and in the meantime calculate its height and principal curvature.

RESULTS

Before summarizing the statistic information of rough surface, a necessary preparation is conducted to check how large a scanned area is required. It is found that the specimen with higher surface roughness requires a larger area to achieve a stable surface statistic. Fig. 2a displays the distribution of summit height h. It is found that, for six specimens with different roughness, h follows a Gaussian distribution. In addition, it is found that most ratios of the principal curvature k_1/k_2 are smaller than 10. For an asperity-summit like this, it is appropriate using $R_g = (k_1k_2)^{-1}$ to account for the

*Corresponding author. E-mail: wanggf@mail.xjtu.edu.cn.

asperity radii [3]. The normalized equivalent radius R_g/p follows an F-distribution with degrees of freedom being (8.0, 2.2) as shown in Fig. 2b. The fitting parameters for six specimens are given in Table 1.

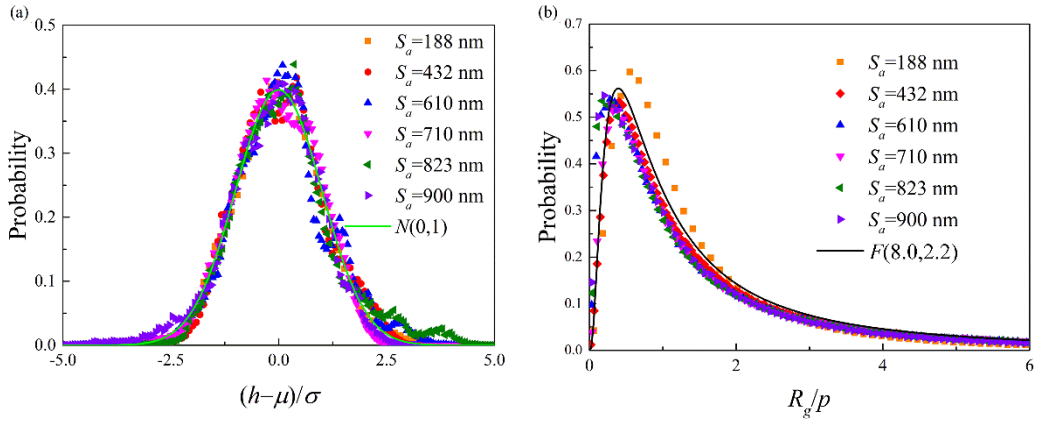

Figure 2. Probability density distribution of (a) normalized summit height $(h-\mu)/\sigma$, (b) normalized equivalent radius R_g/p.

Table 1. Fitting parameters of the probability density distributions of h and R_g (nm)

S_a	188	432	610	720	823	900
σ	227	542	727	921	937	1065
μ	72	37	75	187	-10	285
p	1632	4663	3204	2801	2871	2472

The joint probability density distribution of h and R_g, denoted as $p(h, R_g)$, can be obtained either numerically or by simply multiplying these two distribution function, $f(h)$ and $g(R_g)$. The distributions $f(h)\times g(R_g)$ and $p(h, R_g)$ of the specimen with S_a = 188 nm are shown in Fig. 3. For all these specimens measured, $f(h)\times g(R_g)$ shows little distinction from $p(h, R_g)$. This leads to the conclusion that $p(h, R_g) \approx f(h)\times g(R_g)$.

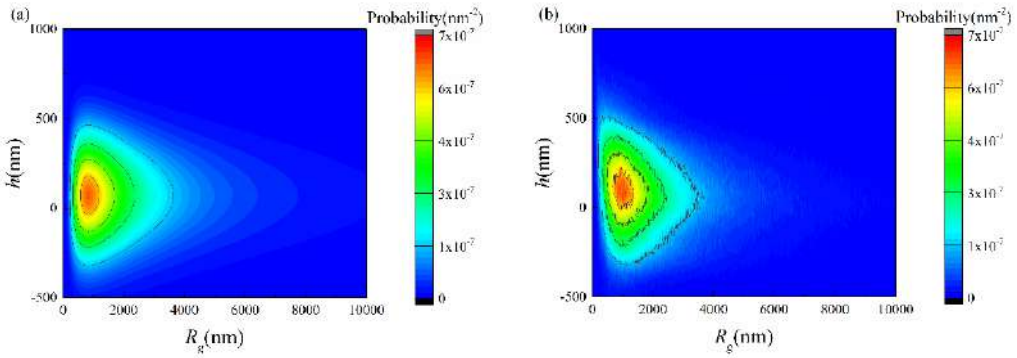

Figure 3. The joint probability density distribution of h and R_g (a) $f(h)\times g(R_g)$, (b) $p(h, R_g)$.

CONCLUSIONS

The three-dimensional topographies of plain grinding surfaces are characterized by combing the experimental measurement with statistical analyses. The results suggest that the statistical characterization of rough surfaces should be conducted on a sufficiently large sampling area. With a new asperity identification criterion employed, it is found that the height of asperity-summit follows a Gaussian distribution, while the equivalent radius of asperity-summit follows a modified F-distribution. Moreover, we demonstrate the height and equivalent radius of asperity-summit are nearly independent, and the joint probability density function is derived directly. These findings can be utilized for developing simplified contact models of anisotropic rough surfaces and provide a new perspective for the characterization of rough surfaces.

References

[1] Persson B.N.J. Contact Mechanics for Randomly Rough Surfaces. *Surf. Sci. Rep.* 61(4): 201-227, 2006.
[2] Kalin M., Pogačnik A. Criteria and properties of the asperity peaks on 3d engineering surfaces. *Wear* 308(1): 95–104, 2013.
[3] Greenwood J.A. A simplified elliptic model of rough surface contact. *Wear* 261(2): 191–200, 2006.

STUDY ON THE EFFECT OF TEMPERATURE ON THE FRICTIONAL CHARACTERISTICS OF RAILWAY DISC BRAKE PADS

Aleksander Yevtushenko[1], Michał Kuciej[*1], and Piotr Wasilewski[2]
[1]Faculty of Mechanical Engineering, Bialystok University of Technology (BUT), Białystok, Poland
[2]Research and Development Department, Frimatrail Frenoplast S.A., Majdan, Poland

Summary Characterisation of the temperature-dependent properties of the friction elements is crucial in the design of braking systems. In this study three types of railway disc brake pads were designed, manufactured and tested on a full-scale dynamometer. Two materials contained copper fibre in different concentration, third was a non-metallic material. Drag brake appllication was performed to determine how the coefficient of friction changes with the increase in temperature. It is concluded that copper fibre has beneficial effect on the frictional properties of railway disc brake pads by improving high-temperature stability of the friction coefficient.

INTRODUCTION

As operating speed of contemporary passenger rolling stock increases, braking systems are exposed to higher thermal loads. When kinetic energy is converted into heat during braking, it is dissipated to the elements of the friction pair leading to increase in their temperature, which has in turn influence on the coefficient of friction [1]. Characterisation of the temperature-dependent coefficient of friction is useful in FE-based calculations of temperature fields in brakes or clutches [2, 3].

The purpose of this study was to investigate the effect of temperature on the coefficient of friction of railway disc brake pads manufactured from three types of organic composite material.

EXPERIMENTAL

Formulations and prototypes

Three friction mixtures denoted Material A, Material B and Material C were manufactured for the purpose of the study. The mixtures were produced by adding certain amount of copper fibre and calcite to 70 kg of the premix (Table 1). The premix contained two binders, namely rubber and phenolic resin, mineral fibre to provide mechanical strength, graphite and antimony trisulfide (Sb_2S_3) as friction modifiers, calcite and curing agents. The formulations were designed to establish equal volume of the added fillers (total volume of added calcite and copper fibre, considering their specific density).

The prototypes were moulded from friction mixtures (Material A, B and C as described in Table 1) to a standard UIC200 shape designed for railway disc brake pads [4]. The parts were processed through thermal treatment to cure the thermosetting phenolic resin. The final stage of the manufacturing process was grinding of the brake pads to 35 mm thickness.

Table 1: Modification of the basic formulation.

Friction mixture	Filler	Specific density, kg/m^3	Amount added, kg
Material A	Calcite	2800	10.8
Material B	Copper fibre	8900	17.1
	Calcite	2800	5.4
Material C	Copper fibre	8900	34.2

Test conditions

Frictional characteristics of the prototype disc brake pads were determined in the course of the test performed on a full-scale dynamometer at Instytut Kolejnictwa (the Railway Institute) in Warsaw, Poland. Cast iron brake disc of 640 mm nominal outer diameter was the counterface element. A complete set of brake pads for testing consisted of two "right-hand" and two "left-hand" items. The test discussed in this study concerned a single drag brake application. To investigate solely the effect of temperature on the coefficient of friction, velocity and force exerted on the brake pads were maintained constant at 80 km/h and 10 kN respectively. The total time of brake application was 1200 s. Ventilation and cooling condtions of the friction pair were in compliance with the requirements presented in the railway standard [4]. In the course of the test instantaneous coefficient of friction was determined by measuring the braking torque related to the contact force. Temperature was measured by six K-type thermocouples embedded in the brake disc 1 mm below the contact surface, three per friction ring. Two of the thermocouples were installed at the equivalent braking radius (r_{eq}), two were positioned 40 mm outside r_{eq} and the remianing two 40 mm inside r_{eq}. The thermocouples were displaced 120° along the circumference.

*Corresponding author. E-mail: m.kuciej@pb.edu.pl.

DISCUSSION OF RESULTS

Change in the value of the friction coefficient with the increase in average temperature of the brake disc up to 300°C is presented on Fig. 1. Average brake disc temperature was calculated as the mean value from measurements by 6 thermocouples.

In general Material C is characterised by the highest coefficient of friction and the lowest value was exhibited by Material A. Final average brake disc temperature during the test of Material A (at t=1200 s) was below 300°C. It is explained by lower coefficient of friction of Material A – hence lower heat flux – but also due to the slower increase in temperature of the brake disc as compared to the other two tested materials.

Increase in the coefficient of friction up to approx. 150°C can be observed for each of the tested materials. After exceeding this temperature level, each of the materials exhibits slightly different characteristics: friction coefficient of Material A sharply drops, it steadily increases for Material B and it is quite stable for Material C up to approx. 280°C when it starts to decline.

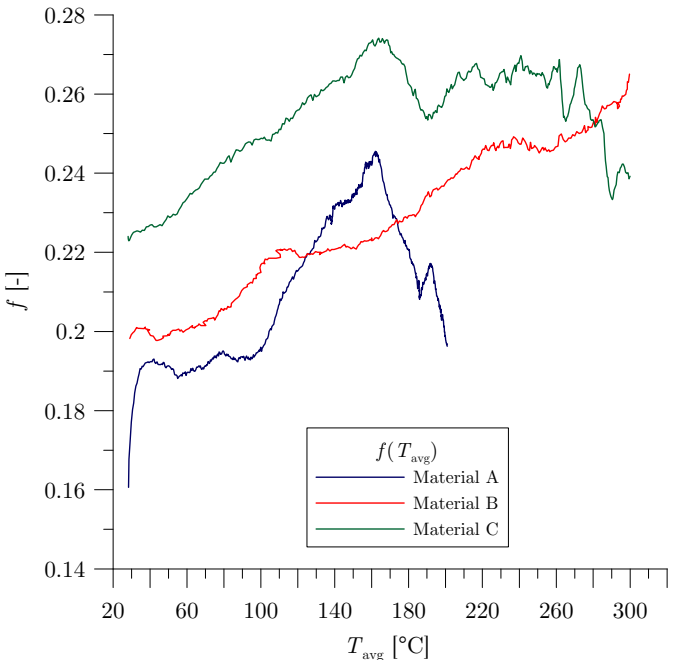

Figure 1: Temperature-dependence of the coefficient of friction.

CONCLUSIONS

Three friction material formulations were tested on a full-scale railway dynamometer to investigate effect of temperature on the coefficient of friction. It can be concluded that apart from enhancing high-temperature stability of the friction coefficient, introducing of the copper fibre to the formulation leads also to increase in its value. Further study will be focused on thermophysical properties of the materials discussed in this paper.

ACKNOWLEDGEMENTS

This article was supported by the National Science Centre of Poland (research project no. 2017/27/B/ST8/01249).

References

[1] Thuresson D. Influence of material properties on sliding contact braking applications. *Wear* **257(5-6)**: 451-460, 2004.

[2] Yevtushenko A. A., Grzes P. Axisymmetric FEA of temperature in a pad/disc brake system at temperature-dependent coefficients of friction and wear. *Int. Commun. Heat Mass* **39(8)**: 1045-1053, 2012.

[3] Pisaturo M., Senatore A. Simulation of engagement control in automotive dry-clutch and temperature field analysis through finite element model. *Appl. Therm. Eng.* **93**: 958-966, 2016.

[4] UIC Leaflet 541-3, Brakes – Disc brakes and their application – General conditions for the approval of brake pads, 8th edition, Union Internationale des Chemins de fer, Paris, 2017.

A NOVEL ROTATING BLADE-CASING RUBBING MODEL CONSIDERING ABRADABLE SEAL COATINGS

Yanhong Kang[123], Shuqian Cao *[123]
[1]Department of Mechanics, Tianjin University, Tianjin 300354, China
[2]Tianjin Key Laboratory of Nonlinear Dynamics and Control, Tianjin 300354, China
[3]National Demonstration Center for Experimental Mechanics Education, Tianjin University, Tianjin 300354, China

Summary Aiming at rubbing fault between the rotating blade and casing with abradable seal coatings, a new nonlinear rubbing model is established. In this paper, the blade is assumed to be a cantilever beam with an equal section under centrifugal load, the bending deformation of the blades, the elastic deformation of the casing, and the effects of abradable coatings are considered. Then, the influence of system parameters such as Young's modulus of the coating and the stiffness of the casing on the rubbing force model is analyzed. Finally, by comparing with the existing blade-casing rubbing model and experiment, the accuracy of the model is verified.

INTRODUCTION

To improve the efficiency of aero-engines, the clearance between the rotating blade and casing is designed to be smaller and smaller, resulting in an increased probability of rubbing fault. It is of great significance for the structural design of blades and the diagnosis of rub impact fault to establish a reasonable model of blade-casing rubbing model and predict the vibration response of the system under typical working conditions. For the rigid casing without coatings, Padovan [1] assumed that the blade was a cantilever beam and derived a rubbing model of normal contact force and blade deformation. Jiang [2] based on the model of Padovan and considered the centrifugal stiffness effect of the blade, a modified normal rubbing force model was obtained. Ma [3] considered the flexibility of the casing and the blade, and used the equivalent stiffness of the casing to describe the contact force between the casing and the blade, and proposed a new blade-casing rubbing model. Li [4] considered the rotating effect of the blade, and used a flexible ring with spring support to simulate the casing, and derived a new rubbing force model between the rotating blade and the flexible casing. However, as an important functional material, the abradable seal coatings often participate in aero-engine rubbing fault. When a rubbing fault occurs, the blade first contacts with the coating, and the impact of the coating on the rubbing mechanism and system vibration characteristics cannot be ignored. In this paper, the geometry of rotating blades is considered, and the blade-casing rubbing model with abradable coatings is established.

BLADE-CASING RUBBING MODEL CONSIDERING ABRADABLE COATINGS

The contact diagram of the blade-coated casing is shown in Fig. 1. Assuming that the blade is a cantilever beam of equal section. The blade is subjected to centrifugal force, normal contact force, and friction force. Taking the root of the blade as the coordinate origin and analyzing the moment balance of the beam at any cross-section, the radial displacement of the blade due to the bending of the blade is obtained. Based on the elastic compatibility conditions, considering the elastic deformation of the blade and the casing and the impact of the abradable coating, the expression of the rubbing force model is:

$$F_{\mathrm{n}}=\frac{5\Gamma L(\alpha\frac{\delta}{L}+3\frac{\Gamma}{K})-\sqrt{5}L\Gamma\sqrt{\frac{15\Gamma}{K}(\frac{3\Gamma}{K}-2\alpha\frac{\delta}{L})+12\frac{\delta}{L}\mu^2\cos^2\beta}}{-2\mu^2\cos^2\beta+10\alpha\frac{\Gamma}{K}+\frac{5}{6}\alpha^2\frac{\delta}{L}} \tag{1}$$

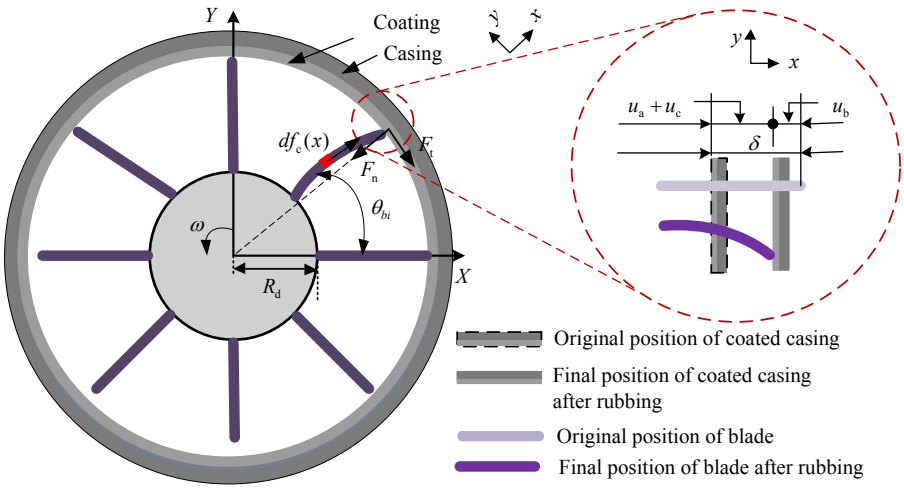

Fig 1. The contact diagram of the blade-coated casing

*Corresponding author. E-mail: sqcao@tju.edu.cn

Among them, $\alpha = \frac{L+3R_{\mathrm{d}}}{R_{\mathrm{d}}+L}$, $\Gamma = \frac{EI}{L^3} + \frac{1}{6}\rho A\omega^2(R_d + \frac{1}{4}L)$. Where ρ, ω, A, R_d, L are blade density, working speed, blade cross-sectional area, disk radius respectively and length of blade; K is the equivalent stiffness of the coated casing; u_b, u_c, u_a are bending deformation of the blades, the elastic deformation of the casing, and the deformation of abradable coatings.

VALIDATION OF THE MODEL

Under the condition of rotating speed $\omega = 2000\mathrm{r/min}$, the rubbing force model in this paper is compared with the existing rubbing model (see Fig.2 and Fig.3) [5]. It can be seen that the model without considering coating in this paper has the same overall change trend, the rubbing force of considering coating is lower than that without considering the influence of coating. Therefore, choosing an appropriate coating is of great significance to reduce the rubbing impact and protect the blade. Besides, the model is verified by the experimental bench in Fig.4.

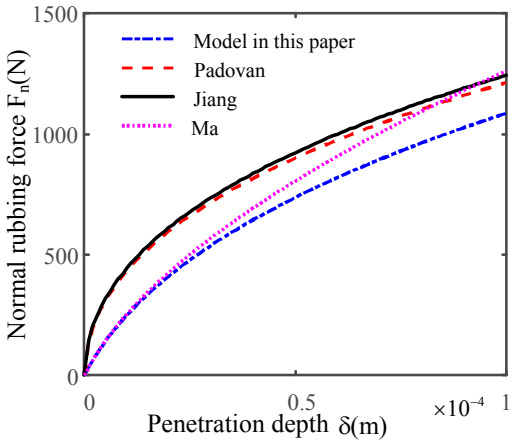

Figure 2. Comparison of rubbing model without coating

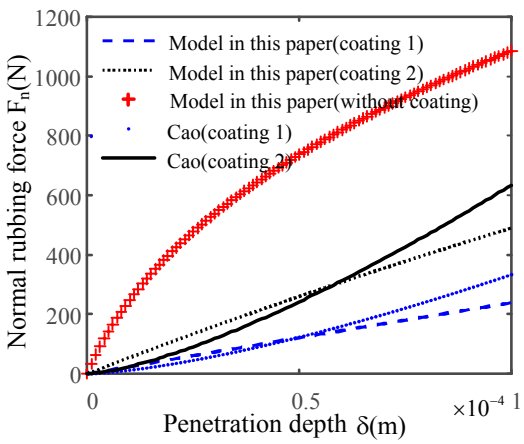

Figure 3. Comparison of rubbing model with coating

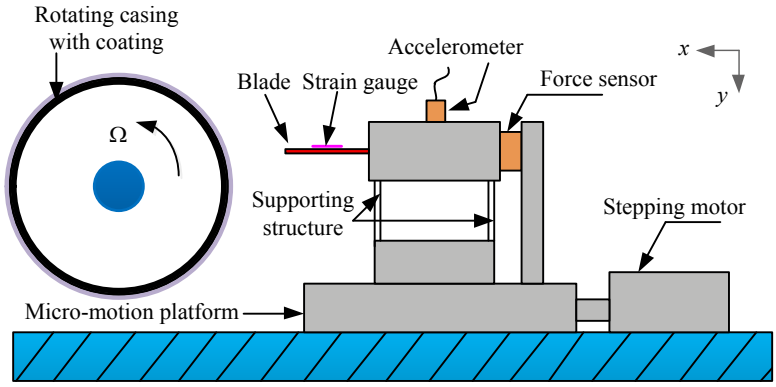

Figure 4. Schematic diagram of the test rig

CONCLUSIONS

The blade-casing rubbing model established in this paper can comprehensively consider the contact deformation of the coated casing and the blade geometry. By comparing with the existing blade-casing rubbing model and experiment, the accuracy of the model is verified.

Acknowledgments This work is financially supported by the National Natural Science Foundation of China (No.11672201) and National Science and Technology Major Project（2017-IV-0008-0045）

References

[1] Padovan J, Choy F K. Nonlinear dynamics of rotor/blade/case rub interactions. J Turbomach, 109: 527-534, 1987.
[2] Jiang J, Ahrens J, Ulbrich H, et al. A contact model of a rotating, rubbing blade. IFTOMN, Darmstadt, 1998.
[3] Ma H, Tai XY, Han QK, et al. A revised model for rubbing between rotating blade and elastic casing. J Sound Vib, 337:301-320, 2015.
[4] Li BQ, Ma H, Zeng J, et al. Rotating blade-casing rubbing simulation considering casing flexibility. Int J Mech Sci, 148: 118-134, 2018.
[5] Cao DQ, Yang Y, Chen HT, et al. A Novel Contact Force Model for the Impact Analysis of Structures with Coating and its Experimental Verification. Mech Syst Signal Pr, 70: 1056–72, 2016.

INFLUENCE OF THE METALLIC FIBRES OF THE MATERIAL OF THE LINING ON TEMPERATURE OF THE RAILWAY DISC BRAKE – EXPERIMENTAL STUDY AND NUMERICAL CALCULATIONS

Piotr Grześ*[1], Aleksander Yevtushenko [1], Michał Kuciej [1], and Piotr Wasilewski [2]
[1]Faculty of Mechanical Engineering, Bialystok University of Technology (BUT), 45C Wiejska Street, Bialystok 15-351, Poland
[2]Frimatrail Frenoplast S.A., Watykańska 15, 05-200 Majdan, Poland

Summary In this paper, numerical model of railway vehicle disc brake was proposed. The objective was to analyse the effect of metallic fibres in the brake pads material on temperature of the brake. The studies were carried for five different brake lining materials. The calculated temperature fields of the brake components were verified by temperature changes measured at specified points in the disc using the thermocouples on a full-scale dynamometer test rig. During the experimental studies the braking torque, velocity of the vehicle, clamping force acting on the brake pads, instantaneous friction coefficient, simulated mass per one brake disc and velocity of the airflow through the friction pair were recorded and selected parameters were incorporated in the computational model.

INTRODUCTION

Properties of brake pads and disc materials have an effect on the separation of heat and thermal state of the friction elements in sliding contact. Therefore when developing new materials it is essential to determine their properties and identify their influence on the friction characteristics of the brake. In this work, a computational model of railway vehicle disc brake was proposed to simulate changes in transient temperature fields of the disc and brake linings. The purpose of temperature calculations was to estimate the effect of material properties on the basis of five different formulations of the organic composite linings on the friction characteristics of the brake [1, 2].

EXPERIMENTAL STUDY

The brake pads used for experimental tests were manufactured from friction mixtures by moulding to comply with standard UIC200 shape of railway brake pads [3, 4]. Moulded parts underwent thermal treatment to ensure curing of the thermosetting phenolic resin. The basic formulation contained rubber, phenol-formaldehyde resin, vulcanizers and curing agents, mineral fibres, graphite, antimony sulphide and calcite.

To study the effect of the steel and copper fibres on the properties of the brake pad material, five mixtures denoted Recipe 1, Recipe 2, Recipe 3, Recipe 4 and Recipe 5, were manufactured by adding specified amount of filler to 70 kg of the basic formulation. The amounts of filler added were defined to ensure that their volume remains equal. In order to establish a reference case, non-metallic material (Recipe 1) was manufactured, where additional amount of calcite instead of metallic fibres was included. The dependence of the thermophysical properties of the developed materials (thermal diffusivity, thermal conductivity, specific heat capacity) on temperature were determined experimentally in the range between 25°C and 250°C (Fig. 2).

Parameters set in the test program were: mass of rail vehicle per brake disc (braking to stop); total pressure exerted on the brake pads; braking torque, braking speed and braking time per friction pair; diameter of the rail vehicle wheel; medium friction radius; braking start speed; average temperature of the friction surfaces of the brake disc at the beginning of braking; velocity of air ventilating friction pair; number of brakes; etc.

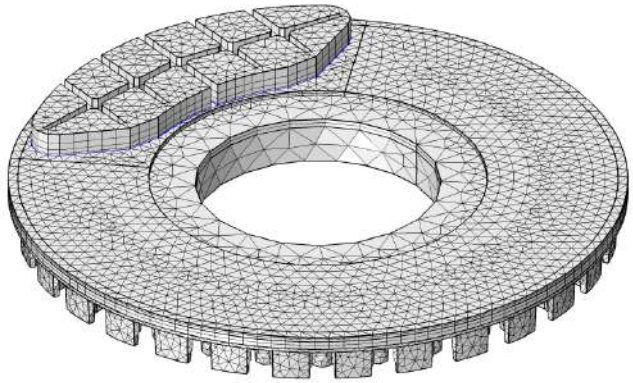

Figure 1. Finite element mesh of the analysed railway disc brake.

*Corresponding author. E-mail: p.grzes@pb.edu.pl.

During the tests the following parameters were recorded: the beginning of braking; the moment of reaching 95% of the nominal total brake lining pressure; angular and rotational speed of the wheel; vehicle linear speed for a given wheel diameter; braking distance; braking time; brake cylinder pressure; total clamping force; simulated mass per brake disc; temperatures at six points of the friction surfaces of the disc and their instantaneous average value; instantaneous friction coefficient; velocity of air ventilating friction pair; etc.

The measurements of brake disc temperature were carried out at the Rolling Stock Testing Laboratory of Railway Institute at the test bench for rail vehicle brake friction pairs (for testing disc and tread brake friction pairs) up to a maximum speed of 420 km/h. The UIC homologated BSI 640/350x110 brake disc was used for the tests. The subject of the research were 5 sets of organic brake linings by Frimatrail, in "UIC200" shape (4 pieces per set): Recipe 1, Recipe 2, Recipe 3, Recipe 4 and Recipe 5.

FINITE ELEMENT ANALYSIS

The numerical calculations of the spatial temperature fields of the railway disc brake were carried out in COMSOL Multiphysics® using the *Heat Transfer in Solids* and *Mathematics* modules [5]. Three conditions of friction contact were assumed: 1) perfect friction contact of brake components assuming that the temperature of points in contact is equal and the sum of heat fluxes directed to the linings and disc is equal to the friction power density; 2) contact taking into account thermal resistance; 3) the issue of separate heating of the disc and lining with the introduction of the heat flux distribution coefficient [6]. Out of the contact surface, convection according Newton's law of cooling was applied. In order to simulate sliding motion of the components of the brake it was assumed that the pads are stationary and the contact surface of the disc deforms according to its rotating motion (*Deformed Geometry* module) [2, 5]. The obtained temperature evolutions from the specific points of the region of the disc were compared with the temperature measured during the full-scale dynamometer tests.

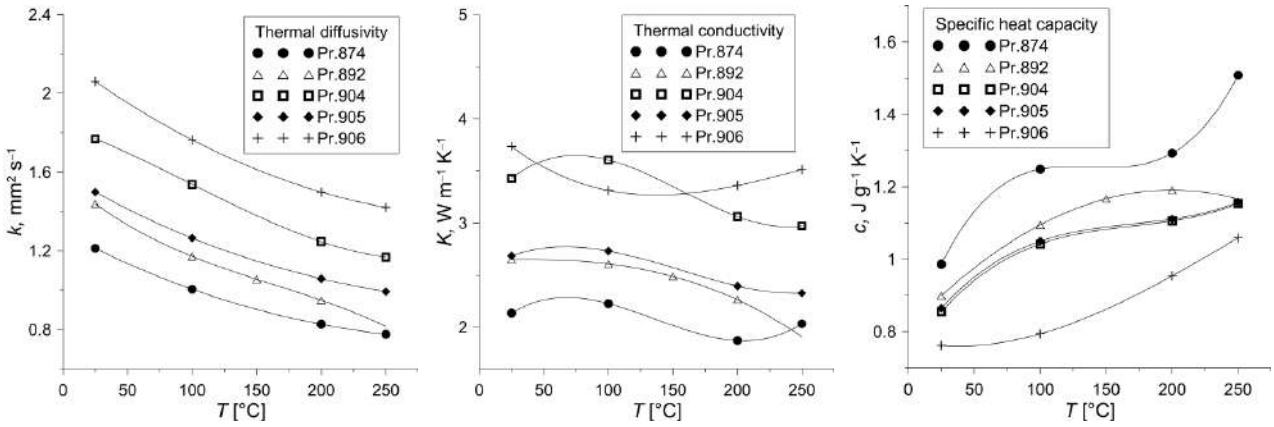

Figure 2. Experimental dependencies of thermal diffusivity, specific heat capacity and thermal conductivity on temperature of the five mixtures for pads materials approximated by third order polynomial function.

CONCLUSIONS

The calculations of changes in brake disc temperature using 3D finite element model of the brake and the corresponding values of temperature measured in six points of the disc region revealed good agreement. This allows to state that the proposed model can be used to determine thermal state of the railway disc brake when developing new linings materials.

Acknowledgements

This article was supported by the National Science Centre of Poland (Research project No. 2017/27/B/ST8/01249).

References

[1] Grzes P., Oliferuk W., Adamowicz A., Kochanowski K., Wasilewski P., Yevtushenko A.A. The numerical–experimental scheme for the analysis of temperature field in a pad-disc braking system of a railway vehicle at single braking. *Int. Commun. Heat Mass Transfer* **75**: 1-6, 2016.

[2] Yevtushenko A.A., Kuciej M., Grzes P., Wasilewski P. Temperature in the railway disc brake at a repetitive short-term mode of braking. *Int. Commun. Heat Mass Transfer*. 84, pp. 102-109, 2017.

[3] Wasilewski P. Frictional heating in railway brakes: A review of numerical models. *Arch. Computat. Methods Eng.* **27**: 45-58, 2020.

[4] Union Internationale des Chemins de fer, Paris, UIC Leaflet 541-3, Brakes – Disc brakes and their application – General conditions for the approval of brake pads, 8th Edition, 2017.

[5] COMSOL Multiphysics® v. 5.3. **www.comsol.com**. COMSOL AB, Stockholm, Sweden.

[6] Charron F. Partage de la chaleur entre deux corps frottants. *Publ. scient. et techn. Ministere air.*, **182**, 1943.

SOFT LUBRICATION IN PRESENCE OF VISCOELASTIC BODIES

Carmine Putignano[1] and Giuseppe Carbone [1]
[1]Department of Mechanics, Mathematics and Management, Polytechnic University of Bari, Italy.

Summary Soft materials often exhibit a viscoelastic time dependent behaviour, which determines dramatic deviations in comparison with classic elastic solutions. Specifically, in this work, we focus on what occurs when two viscoelastic bodies are in lubricated contacts: a new viscoelasto-hydrodynamic is defined. Numerical simulations, carried out by means of a coupled boundary element-finite difference approach, are corroborated by experimental outcomes.

Assessing the main peculiarities of lubrication between soft viscoelastic solids is a crucial issue that has only recently raised the attention of the lubrication science community. Indeed, in the last decades, massive research efforts have been dedicated to understand the role of non-Newtonian lubricants, but very little has been done to determine what occurs when the lubricated solids are not linearly elastic, and are instead characterized by a different rheology.
In this work, as shown in Figure 1, an innovative numerical methodology is presented to analyze the lubrication regimes between linear viscoelastic layers. In detail, an explicit finite difference scheme is coupled to a Boundary Element solver: this enables the study of the viscoelastic lubrication without any limitation in terms of material properties, geometry and viscosity. The results and, specifically, the film thickness, the contact pressure and, ultimately, the friction force show marked differences in comparison with classic lubrication theory. All this is validated by means of experiments specifically developed to deal with soft matter. In particular, to measure the film thickness, an innovative technique based on interferometry for soft solids [1] has been employed.

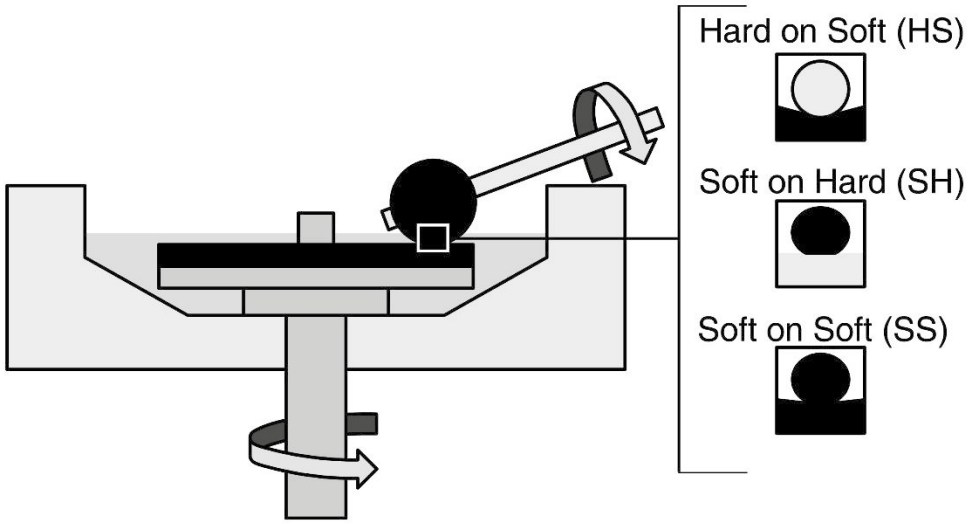

Figura 1: Schematic of a typical tribo-system involving soft materials. Three different configurationscan be considered: hard ball on soft disk (HS), soft ball on hard disk (SH) and soft ball onsoft disk (SS).

To point out the main features of the proposed numerical approach, it is possible to focus on a simple problem: this is the description of the physics governing the lubrication of a rigid sphere in pure rolling over a one-relaxation-time viscoelastic half-space. For very low values of the speed, the deformable solid is in the elastic rubbery region and behaves, consequently, as a soft elastic body: no viscoelastic effect is present. When looking at the lubricating film, as expected (see e.g. Ref. [3,4,5]), we observe an almost perfectly circular shape and, due to the flow conservation, a minimum at the fluid inlet can be observed. However, something different occurs when the speed is increased. Indeed, the contact zone gradually evolves towards a shape that is increasingly far from a circle and is affected by a sharp shrinkage at the fluid outlet. The contour plots of the fluid pressure clearly reveal a pressure peak that increases with the speed and produces, ultimately, a strong asymmetry towards the contact inlet. Such a trend is in agreement with analogous results in dry conditions [6] and marks the peculiarity of soft viscoelastic lubrication.

References

[1] Marx N, Guegan J, Spikes H A, A, *Trib. Int.*, 99, 267-277, 2016.
[2] Putignano C and Dini D. *ACS Applied Materials & Interfaces*, 9 (48), 42287-42295, 2017.
[3] Putignano C . *JMPS* 134, 103748, 2020.
[4] Venner C.H. , Lubrecht A.A., Multilevel Methods in Lubrication, Elsevier Tribology Series, Ed. D. Dowson et al., V. 37, 2000.
[5] Sadowski P., Stupkiewicz S., *Trib. Int.*, 129, 246-256, 2019.
[6] Carbone G., Putignano C., *JMPS*, 61 (8), 1822-1834, (2013).

THERMAL PROBLEM OF FRICTION DURING BRAKING FOR FUNCTIONALLY GRADED MATERIALS

Aleksander Yevtushenko, Katarzyna Topczewska* and Przemysław Zamojski
Department of Mechanics and Computer Science, Faculty of Mechanical Engineering, Bialystok University of Technology, Bialystok, Poland

Summary The aim of this study is to develop the analytical model of frictional heating during braking in a system consist of a pad and disc made of functionally graded materials. For this purpose, the one–dimensional heat conduction problem of friction for a semi–space/semi–space were formulated and solved. Obtained solutions allow to calculate temperature distribution on the contact surface and inside the friction elements. The influence of exponential variation of thermal properties along the thickness of friction elements on thermal behaviour of a brake system was investigated based on obtained results.

FUNCTIONALLY GRADED MATERIALS

Functionally graded materials (FGMs) are the group of nonhomogeneous materials with properties dependent on the spatial position. Expected distributions of FGMs properties are obtained by changing porosity, microstructure or composition across the volume of the material structure [1]. Mainly, functionally graded materials are composites where the contribution of the component materials changes so that a specific variation of the material properties is achieved. Many results proved that properly controlled gradients of thermo–mechanical properties in the FGM can significantly improve the resistance to contact deformation and damage [2]. FGMs are consider as advanced materials, resistance to wear and extreme temperature conditions. Often these materials are manufactured of the composition of two different materials. One is a ceramic to resist the severe thermal environment, and the other is a metal to maintain the structural rigidity. Due to their exceptional properties, functionally graded materials are widely used in lots of technology areas, including sliding systems under frictional heat loading, such as braking systems. Application of FGMs with thermal properties dependent on the distance from friction surface, allow to improve dissipation of generated heat, thus avoid overheating of the frictional elements and reduce the magnitude of thermal stresses. Therefore, thermoelastic contact behavior of functionally graded materials is an up–to–date scientific problem [1–4]. In considered models, changes of thermal and mechanical material properties are assumed to be expressed by appropriate functions. Typically, the exponential or power dependencies of FGMs properties on the spatial position are incorporated to the analysis [3].

DEVELOPMENT OF MODEL

In recent years, the thermal problems of friction during braking have been concerned by many researchers. Modeling of the temperature and thermal stress distributions in such heavy–loaded frictional system is essential. Most of obtained exact solutions, known in literature, have been found for a homogeneous materials properties, due to the complexity of the solution achievement in case of heterogeneous properties [5].

The purpose of this study is to investigate thermal behavior of pad/disc tribosystem made entirely of functionally graded materials during single braking. Proposed model is based on the one–dimensional boundary–value problem of heat conduction for two semi–infinite bodies with frictional heat generation on their contact surface. The perfect thermal contact conditions on the friction surface and uniform contact pressure during braking was assumed. Thermal properties of frictional materials are considered to be nonlinear with an exponential distribution along the thickness. In order to solve formulated problem, the Laplace transform technique was used. Exact solution was obtained in the analytical form involving the modified Bessel functions. Based on developed model, the influence of exponential variations of thermal conductivities and diffusivities of friction materials along the thickness of the elements on the transient temperature distributions in a pad/disc system during braking was investigated.

ACKNOWLEDGEMENTS

Investigation presented in this paper has a financial support from NAWA organisation as a part of the PROM project.

References

[1] Mahamood R.M., Akinlabi E.T. *Functionally Graded Materials*. Springer International Publishing. AG. 2017.
[2] Liu, Jing, Liao-Liang Ke, and Yue-Sheng Wang. Two–dimensional thermoelastic contact problem of functionally graded materials involving frictional heating. *International Journal of Solids and Structures* **48**, 18, 2536-2548, 2011.
[3] Noda N. Thermal stresses in functionally graded materials. *Journal of Thermal Stresses* **22**, 4-5, 477-512, 1999.
[4] Mao J.J., Ke L.L, Yang J., Kitipornchai S., Wang Y.S. Thermoelastic instability of functionally graded materials with interaction of frictional heat and contact resistance, *Mechanics Based Design of Structures and Machines*, **46**, 139-156, 2018.
[5] Yevtushenko A., Kuciej M., One–dimensional thermal problem of friction during braking: The history of development and actual state. *International Journal of Heat Mass Tran.* **55**, 4118–4153, 2012.

*Corresponding author. E-mail: k.topczewska@pb.edu.pl.

FLUID VISCOELASTICITY IN LUBRICATED CONTACTS IN THE PRESENCE OF CAVITATION

S. S. Gamaniel[1], D. Dini[2], and L. Biancofiore[1,2]
[1]Department of Mechanical Engineering, Bilkent University, Bilkent 06800, Ankara, Turkey.
[2]Department of Mechanical Engineering, Imperial College London, SW7 1AL, United Kingdom.

Summary The use of lubricants in machine components is essential in reducing wear and friction between solid surfaces in moving parts. Lubricants which contain polymer additives exhibit strong viscoelastic effects. A model is proposed to study the influence of fluid viscoelasticity on the performance of lubricated contacts in the presence of cavitation. The proposed model uses the Oldroyd-B constitutive relation to describe the effect of viscoelasticity. To properly define the presence of film cavitation, this model incorporates the mass-conserving Elrod-Adams algorithm. Studies are carried out for the flow of viscoelastic lubricants in: (i) a parabolic profile representing a journal bearing unwrapped geometry, (ii) a pocketed profile to model a textured surface, and (iii) the oscillatory squeeze motion of two flat surfaces. As viscoelastic effects increase, results indicate that: (i) in the parabolic slider there is an increase in the load carrying and a decrease in the cavitation region, (ii) the load capacity in the surface textured bearing depends on the location of the pocket, and (iii) there is a reduction in the load carrying capacity in the oscillatory squeeze motion.

INTRODUCTION

A technique to enhance the performance of lubricants is to add polymers to mineral oils. Lubricants with polymer additives can present viscoelastic effects and, generally, have been shown to exhibit superior lubrication properties when compared to lubricants without additives [1, 2]. Since viscoelastic lubricants possess different mechanical properties we need to make modifications to the classical lubrication theory.

The Navier-Stokes equations and the constitutive equations can be coupled linearly to account for the viscoelasticity of the lubricants. By using the Oldroyd-B constitutive model and assuming that the product between ϵ, i.e. the ratio of the vertical and horizontal length scales, and the Deborah number (De), i.e the ratio of the polymer relaxation time to the flow time scale, is small, a linearized set of the thin film equations can be achieved, similar to the approach pioneered by Tichy et. al. [3].

Several studies on viscoelastic lubricants have been conducted but have failed to account for the presence of cavitation. Cavitation describes the process of the formation of gaseous and vapor bubbles in a liquid due to rapid depressurization usually below the saturation pressure of the liquid. This study proposes a model for viscoelastic lubricants where the presence of cavitation is accounted for using the Elrod-Adams algorithm [4]. In addition, a new set of boundary conditions for the evolving rupture and reformation locations of the viscoelastic lubricant is introduced.

MODEL AND NUMERICAL METHOD

The non-dimensional thin film equations for the isothermal flow of a viscoelastic lubricant are

(i) Continuity equation

$$\frac{\partial \theta}{\partial t} + \nabla \cdot (\theta \mathbf{u}) = 0, \tag{1}$$

(ii) Momentum equation

$$\nabla p = \beta \nabla^2 \mathbf{u} + \nabla \cdot \tau, \tag{2}$$

(iii) Oldroyd-B constitutive equation

$$\tau + \epsilon De \left(\frac{\partial \tau}{\partial t} + \mathbf{u} \cdot \nabla \tau - (\nabla \mathbf{u}) \cdot \tau - \tau \cdot (\nabla \mathbf{u})^T \right) = (1-\beta) \left(\nabla \mathbf{u} + \nabla \mathbf{u} \right)^T, \tag{3}$$

where $\mathbf{u}(u_x, u_y)$ is the velocity vector, t is time, θ is the film fraction or non-dimensional density, p is the pressure, τ is the stress tensor, $\beta = \frac{\eta_s}{\eta}$ is the solvent concentration, $De = \lambda \frac{U_{ref}}{H_{max}}$, λ is the characteristic fluid relaxation time, H_{max} is the maximum film height, η_s is the solvent viscosity and η is the overall viscosity. Note that Eqs. 1-3 are obtained by assuming that the film height H_{max} is much smaller than the contact length L, making it possible then to apply the lubrication approximation.

The set of governing equations (Eqs. 1-3) can then be linearized by using ϵDe as the perturbation parameter. This results in a zeroth-order and first order set of governing equations. Solutions are obtained by applying the boundary conditions for (i) a pure sliding motion and (ii) the oscillatory squeeze flow cases. The solution to the zeroth-order equations corresponds to the Reynolds solution for Newtonian lubricants.

Viscoelasticity is expected to have an effect on the location of both the film rupture and reformation. To define the presence of cavitation in the viscoelastic lubricant we use the mass conserving Elrod-Adams computational scheme. A new set of boundary conditions capable of accurately capturing the transition from Newtonian to non-Newtonian for the cavitation region are introduced. The two possible cases of either (i) an expansion, or (ii) a shrinking of the cavitation region are both addressed by the model.

RESULTS

To understand the effect of fluid viscoelasticity when cavitation is present, an analysis is conducted using (i) a parabolic profile to mimic an unwrapped journal bearing, (ii) single and multiple pockets to represent textured surfaces, and (iii) an oscillatory squeeze flow between two flat plates.

Results for the parabolic profile configuration in Fig. 1a shows there is an increase in the maximum pressure and a decrease in the cavitation region as viscoelastic effects are increased (see Fig. 1b). This leads to an overall increase in the load capacity as the viscoelastic effects get stronger (see Fig. 1c).

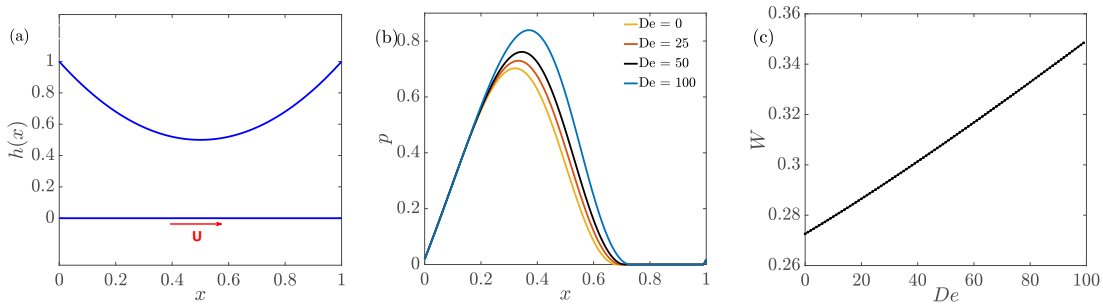

Figure 1: (a) A parabolic profile geometry representing an unwrapped journal bearing, (b) lubricant film pressure for the parabolic slider at several values of De, and (c) the load W for the parabolic slider over several values of De.

The lubrication performance in a surface textured bearing depends on the location of the pocket. The maximum pressure is observed to increase before the pocket location and decreases after the pocket. This suggests that the sign of dh/dx is important in determining the lubrication performance. The maximum increase in the load capacity with increasing viscoelastic effects is observed when the pocket is located at the rear section of the channel. It is also shown that viscoelastic effects do not have a detrimental effect on the lubricant friction.

In the oscillatory squeeze motion of two parallel plates, viscoelasticity reduces the maximum pressure in the lubricant (see Fig. 2a). There is also an observable delay in the reformation of the lubricant film, causing a larger cavitation region as viscoelastic effects become stronger. For very large values of De, the cavitation region widens, until reaching a value of De at which a full-film reformation does not occur after the initial film rupture as shown in Fig. 2b. The observed effects result in a reduction of the load capacity when De is increased (see Fig. 2c).

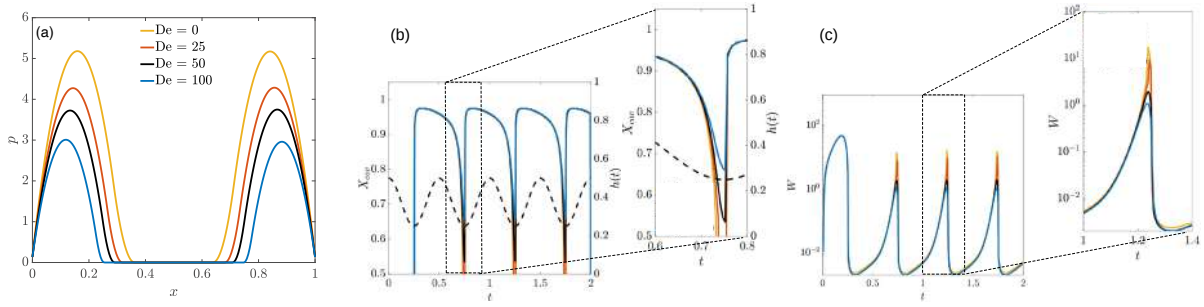

Figure 2: (a) Pressure at $t = 1.22$, (b) location of the right cavitation boundary X_{cav}, and (c) the load evolution for an oscillatory squeeze flow over several values of De. Note that the dashed line in (b) represents the position of the oscillating upper plate.

CONCLUSIONS

A model for viscoelastic lubricated contacts when cavitation is present has been proposed. Viscoelastic effects are modeled using the Oldroyd-B constitutive relation, whereas cavitation is described by using the mass conserving Elrod-Adams algorithm. Viscoelasticity increases the load capacity in a parabolic profile mimicking an unwrapped journal bearing. The lubrication performance in a surface textured profile is shown to depend on the location of the texture. Load capacity in an oscillatory squeeze film flow is observed to decrease with increasing viscoelastic effects due to the delay in the film reformation at larger values of De.

References

[1] Williamson, B. P., Walters, K., Bates, T. W., Coy, R. C., and Milton, A. L., Journal of Non-Newtonian Fluid Mechanics 73.1-2 (1997): 115-126.
[2] Davies, A. R., and Li, X. K., Journal of Non-Newtonian Fluid Mechanics 54 (1994): 331-350.
[3] Tichy, J. A., Journal of Tribology, 118.2, (1996), 344-348.
[4] Elrod, H. G., Cavitation and related phenomena in lubrication 37 (1974).

A NOVEL FINITE ELEMENT APPROACH FOR THE ANALYSIS OF NORMAL AND SLIDING CONTACTS

Jacopo Bonari* and Marco Paggi
IMT School for Advanced Studies Lucca, Lucca, Italy

Summary A finite element procedure is exposed, capable of tackling the challenging problem of the contact between an indenter characterised by an arbitrarily complex shape and a deformable layer, considering all the possible phases of contact, starting to simple normal load up to finite sliding displacements. The method relies on a novel interface discretisation method, that allows an accurate representation of the contacting geometries, yet significantly reducing the complexities related to contact detection and the difficulties and pitfalls proper of the representation of complex boundaries.

INTRODUCTION

The importance of considering accurate geometries at increasingly smaller length-scales in the context of mechanics of interacting surfaces in real life and industrial applications has considerably grown in the recent years, such that nowadays it is not possible anymore to treat surface features as waviness and roughness as simple side-effects. For this reason, computational frameworks capable of dealing with these characteristics in efficient yet accurate manner are gaining importance. In this contribution, a recently developed finite element procedure is presented, capable of addressing the problem of a deformable layer making contact with a rigid indenter characterised by an arbitrarily complex boundary surface, in presence of interface friction. The cornerstone of the method consists in considering a simplified equivalent geometry at the mesh level, while the exact original contact conditions are retrieved at the interface level thanks to a precise modification of the normal gap function.

CONTACT PROBLEM FORMULATION

The eMbedded Profile for Joint Roughness (MPJR) interface finite element presented in [1] and furtherly developed in [2,3] is exploited in the present contribution as a useful tool in the framework of the finite element method applied to contact mechanics. From the computational contact standpoint, the strategy relies on a node-to-node approach with penalty constraints. The strength of the method lies in its capability of re-casting the geometry of the contact problem into the simpler one of two equivalent surfaces undergoing conformal contact. This operation is performed at two different levels. At the mesh level, the actual shape of the indenter is replaced by a smooth profile, conformal with respect to the deformable boundary, in such a way that the interface can be easily discretised employing a standard approach with, for example, simple low-order linear elements. In function of the relative displacements of the two opposite sides composing the equivalent interface, a standard normal gap function can be defined. If a common abscissa is set along the interface,

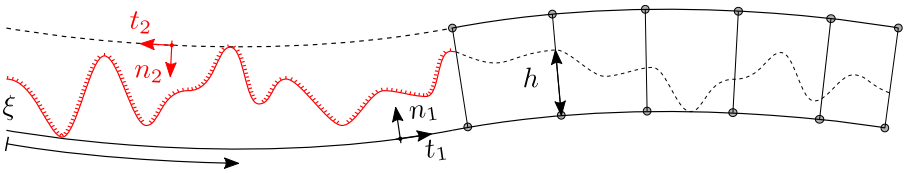

Figure 1: Contacting surfaces discretisation. Subscripts 1 refer to the lower body, while 2 to the upper rigid indenter

mapping both the normal gap and the actual profile elevation, the original contact condition can be restored adding the profile elevation to the gap function, and the contact problem solved using a standard approach. For example, if the deformable layer has a flat interface and a datum of zero elevation is set in correspondence of the point of first contact, the modified gap reads $g_z^*(x,t) = g_z(x) + h(x,t)$, where $h(x,t)$ maps the indenter's elevation field at position x and time t. It is important to remark that the elevation field can be given either as an analytic expression, like has been done in the example below, or, more relevantly for real applications, as a discrete heights field coming, for example, from profilometric data or AFM measurements, with the only requirement that the discretisation of the interface should be fine enough to properly capture the relevant geometric features of the profile. Once the definition of modified normal gap is issued, the interface tractions can be evaluated, and, given a penalty approach for normal tractions and a regularised Coulomb friction law for the tangential tractions, they read:

$$p_z = \begin{cases} \varepsilon_{\mathrm{n}} g_z^*, \text{ if } g_z^* < 0, \\ 0, \text{ if } g_z^* \geq 0, \end{cases} \qquad q_x = f p_z \tanh\left[\frac{\dot{g}_x(x,t)}{\dot{\varepsilon}_{\mathrm{t}}}\right] \tag{1a}$$

where p_z and q_x are the normal and tangential tractions, respectively, ε_{n} is the penalty parameter, f is the coefficient of friction, $\dot{g}_x(x,t)$ is the sliding velocity and finally $\dot{\varepsilon}_{\mathrm{t}}$ is a tangential regularisation parameter.

*Corresponding author. E-mail: jacopo.bonari@imtlucca.it.

APPLICATION TO VISCOELASTIC MATERIALS

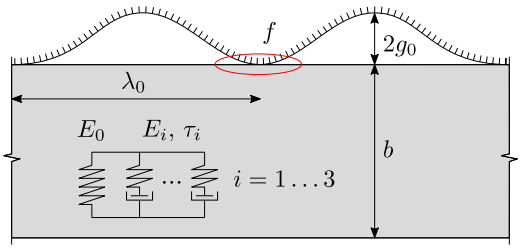

Figure 2: Sketch of the model geometry with $\lambda_0 = 1$, $b = \lambda_0$, $g_0 = 5 \times 10^{-4}\lambda_0$, a Maxwell model with three arms is employed for modelling viscoelasticity

To give an example of the variety of problems that can be addressed with the present formulation, the non-conformal partial contact problem of an indenter with harmonic profile sliding over a viscoelastic layer of finite thickness is presented. A sketch of the model is shown in Fig. 2, together with the geometric and mechanical parameters which are necessary for characterising the problem. In a first loading step, the indenter is pressed downward by an imposed vertical far field displacement, which is then held constant while a rightward shift with constant velocity is applied. All the relevant stages concerning the transient regime in which the transition from a state of *stick/slip*, proper to normal loading, to *full sliding* can be perfectly captured by the model, together with the features strictly related to viscoelasticity. Representative distributions of contact tractions are shown in Figs. 3a, 3b and 3c. In all the selected plots, different curves correspond to different time steps of the simulation. The first plot is related to the beginning of the horizontal loading. The red curve represents an anti-symmetric distribution of self-equilibrating tangential tractions, proper of a purely normal load condition. As the tangential load is applied, the tangential tractions rise in intensity until a condition of full slip is reached, in which they coincide with the vertical distribution of pressures scaled by the friction coefficient f, black curves. The transition is marked by a colour gradient that from red, shifts toward black. In the subsequent picture, the horizontal sliding proceeds. The tangential tractions coincide with the vertical ones scaled by f. Here the viscoelastic effect can be appreciated. If right after the end of the normal loading stage a certain degree of relaxation is observed, a recovery in stiffness takes place as virgin material is disturbed. Advancing in time, the last figure captures the overlapping of a new contact zone with a portion of the material which had already been excited, resulting in a appreciable decrease of the vertical reaction, which marks a clear difference with an elastic material lacking of memory effects.

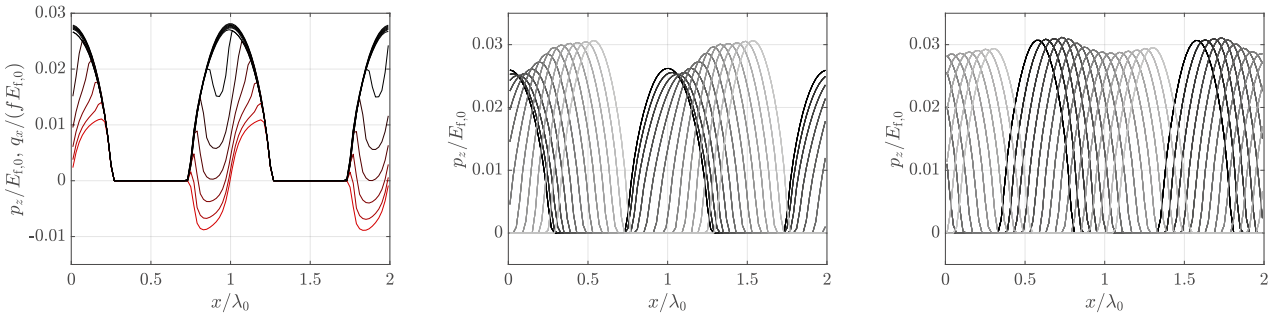

(a) From *stick/slip* to full sliding

(b) Relaxation and recovery in stiffness

(c) Material memory effect

Figure 3: Distribution of normal and vertical interface tractions for different time steps, scaled by the coefficient of friction f and a reference Young's Modulus $E_{f,0}$. As the simulation advances in time, different effects can be appreciated

CONCLUSION

The study proposes a finite element procedure capable of analysing all the different phases of the contact problem describing an indenter sliding over a deformable material. In particular, a viscoelastic material has been chosen as case study. The methodology offers a straightforward solution for a class of problems for which results would be difficult to be addressed using different techniques. The use of the finite element method overcomes the difficulties which are proper of different solutions schemes, dealing with mixed linear and nonlinear boundary value problems. On the top of that, the proposed interface interface finite element opens new perspectives thanks to its ability of taking into account arbitrarily complex contacting geometries, considering them either via their analytical expression or as the result of a real surface sampling with AFM or profilometer technology.

References

[1] Paggi M., Reinoso J. (2018) A variational approach with embedded roughness for adhesive contact problems. Mech Adv Mat Struct 20:1731-174
[2] Bonari J., Paggi M., Reinoso J. (2020) A framework for the analysis of fully coupled normal and tangential contact problems with complex interfaces. [Manuscript submitted for publication]
[3] Bonari J., Paggi M., (2020) Viscoelastic effects during tangential contact analyzed by a novel finite element approach with embedded interface profiles. [Manuscript submitted for publication]

LIPSCHITZ REGULARIZATION FOR SOFTENING ELASTIC AND PLASTIC MATERIAL MODELS: THE LIP-FIELD APPROACH

Nicolas Moës[1,2*] and Nicolas Chevaugeon [1]
[1]Ecole Centrale de Nantes, GeM Institute, UMR CNRS 6183, Nantes, France
[2]Institut Universitaire de France (IUF)

Summary *Softening material models are known to trigger spurious localizations. This may be shown theoretically by the existence of solutions with zero dissipation when localization occurs and numerically with spurious mesh dependency and localization in a single layer of elements. A new way to avoid spurious localization is presented. The idea is to enforce a Lipschitz regularity on the internal variable responsible for the material softening. The regularity constraint introduces the needed length scale in the material formulation. Bounds on the domain affected by the constraint may be a priori obtained. Several one- and two-dimensional examples will demonstrate the capabilities of the new Lip-field approach both for softening elasticity and softening plasticity.*

LIPSCHITZ REGULARITY

Consider a field d defined over a domain Ω. This field is said to be Lipschitz regular with constant 1/l if it satisfies

$$|d(\mathbf{x})-d(\mathbf{y})|\leq \mathrm{dist}(\mathbf{x},\mathbf{y})/l, \quad \forall \mathbf{x},\mathbf{y}\in\Omega \tag{1}$$

where dist indicates the length of the shortest path joining **x** and **y** inside Ω. The basic idea of the Lipschitz regularization for softening material models is to enforce the above condition on the field responsible for softening [1]. The condition, which is convex, introduces the length l inside the model.

MINIMIZATION OF THE INCREMENTAL VARIATIONAL ENERGY

As is classically done, [2], the mechanical model is formulated as the minimization of an incremental potential, (2). The variables are the displacement field u, the damage variable responsible for softening d and possible other internal variables α. Knowing the three fields at some step n, the fields at the next time step are giving by the global minimization (2). The potential F is assumed convex with respect to the pair (u, α) and with respect to d. It is however not necessarily convex with respect to all three variables (explaining the softening).

$$(\boldsymbol{u},\alpha,d)=\arg\min F(\boldsymbol{u},\alpha,d) \text{ under the constraints } (\boldsymbol{u},\alpha)\in U_n\times A_n \text{ and } d\in D_n\cap L \tag{2}$$

Convex constraints are also imposed on the unknown fields. They are linked to kinematics, U_n, and linked to internal variables, A_n. The set D_n enforces damage growth and bounded damage (below 1). Finally, the set L indicates the Lipschitz condition (1). Using the strategy developed for variational fracture, [3], the above is solved by alternate minimization leading to a sequence of convex minimization: finding the pair $(\boldsymbol{u},\alpha)$ for a given d field and finding d for a given pair $(\boldsymbol{u},\alpha)$. When solving the latter, once can show that a priori bounds on the domain over which L is active may be computed thus reducing dramatically the cost of the minimization over d. Moreover, the irreversibility condition on d is taken into account exacly and does not require any approximation of this constraint.

The presentation will compare the Lip-field approach to other existing approaches to alleviate spurious localization. It will also illustrate the capability of the approach on several one- and two-dimensional simulation examples. One such example is given below.

EXAMPLE OF A SOFTENING PLASTICITY MODEL

Figure 2 illustrates the response of a bar of length L under tension with a non-uniform body force. The left column gives the results for a local model whereas the right column gives the Lipschitz regularized response. The first row gives the load - average strain response. The second and last row give the damage and cumulative plasticity field, respectively. The local response suffers from spurious localization of the damage and plastic fields when the limit point is reached. On the contrary, the Lip-field approach ensures a non-zero dissipation in the post-peak response. Note that the local and Lip-regularized field are equal before the limit point.

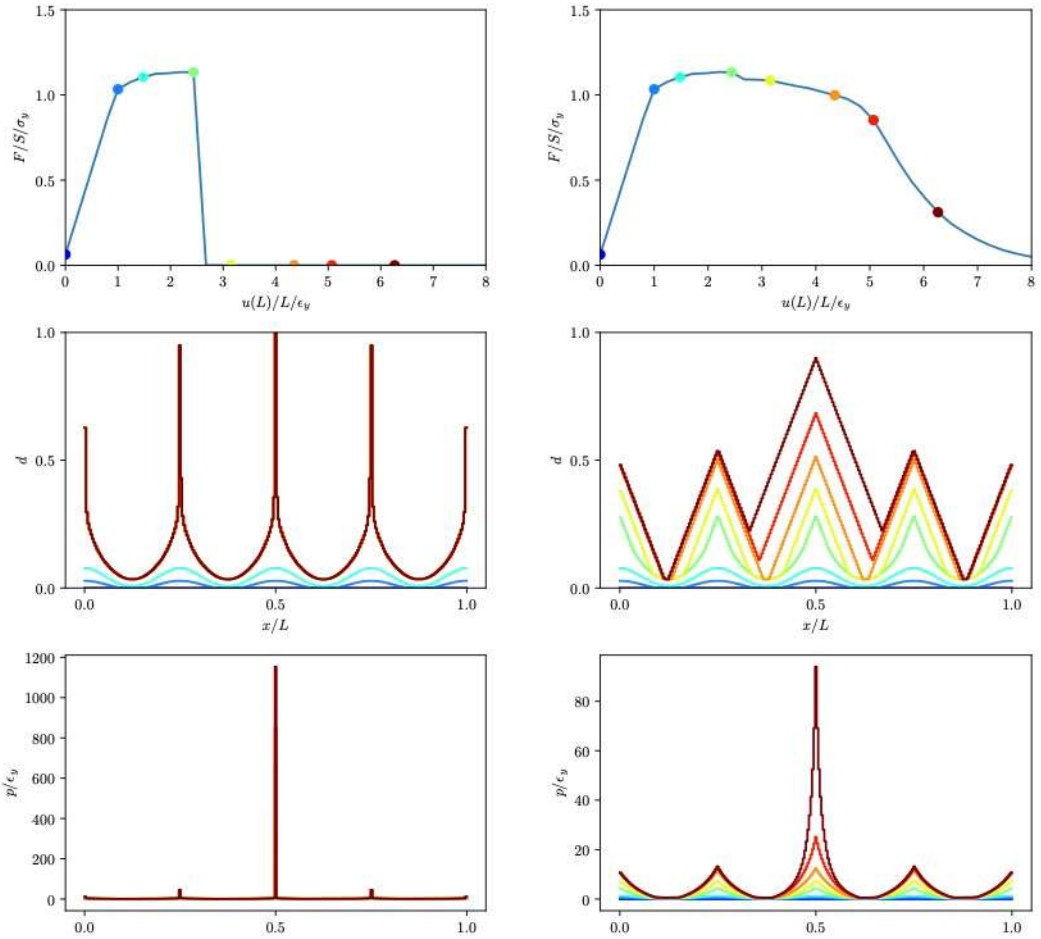

Figure 1. Local (left column) and Lip-regularized (right) response for a softening plasticity model. The bar is loaded with a non-uniform body force.

References

[1] Moës, N. and Chevaugeon, N. (2021). Lipschitz regularization for softening material models: the Lip-field approach. Comptes Rendus de l'Académie des sciences, Series IIB, Mechanics, (submitted).

[2] Ortiz M. and Stainier L. (1999), The variational formulation of viscoplastic constitutive updates, Computer Methods in Applied Mechanics and Engineering **171**, no. 3, p. 419 - 444.

[3] Bourdin, B., Francfort, G. a. A., & Marigo, J.-J. (2000). Numerical experiments in revisited brittle fracture. Journal of the Mechanics and Physics of Solids, 48(4), 797–826.

AN OVERVIEW OF THE MODELLING OF FRACTURE BY GRADIENT DAMAGE MODELS

Jean-Jacques Marigo
Laboratoire de Mécanique des Solides, École polytechnique, Palaiseau, France

The lecture is devoted to gradient damage models which allow us to describe all the process of degradation of a body including the nucleation of cracks and their propagation. The construction of such model follows the variational approach to fracture [2] and proceeds into two stages: (1) definition of the energy; (2) formulation of the damage evolution problem. The total energy of the body is defined in terms of the state variables which are the displacement field and the damage field in the case of quasi-brittle materials [5], whereas they contain also the plastic strain field in the case of ductile materials [1]. That energy contains in particular gradient damage terms in order to avoid too strong damage localizations. The formulation of the damage evolution problem is then based on the concepts of irreversibility, stability and energy balance, as well in quasi-static as in dynamic [4]. That allows us to construct homogeneous as well as localized damage solutions in a closed form and to illustrate the concepts of loss of stability, of scale effects, of damage localization, and of structural failure. Moreover, the variational formulation leads to a natural numerical method based on an alternate minimization algorithm. Several numerical examples will illustrate the ability of this approach to account for all the process of fracture including a 3D thermal shock problem where the crack evolution is very complex [3].

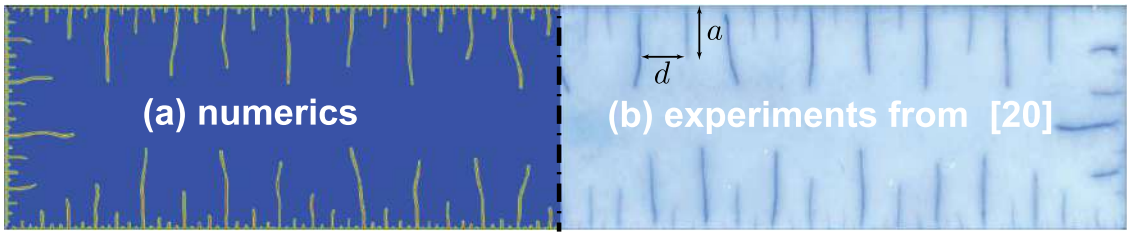

Figure 1: Numerical simulation of a ceramic slab submitted to a thermal shock by a gradient damage model (a) Computed damage field d (blue, d=0; red, d=1). (b) Experimental results from [20]: Y. Shao, Y. Zhang, X. Xu, Z. Zhou, W. Li, and B. Liu, J. Am. Ceram. Soc., 94: 2804 , 2011.

References

[1] R. Alessi, J.-J. Marigo, S. Vidoli. Gradient damage models coupled with plasticity: variational formulation and main properties. *Mechanics of Materials*, **80**:351–367, 2015.
[2] B. Bourdin, G. A. Francfort, J.-J. Marigo. The variational approach to fracture. *J. Elasticity*, **91(1–3)**:5–148, 2008.
[3] B. Bourdin, J.-J. Marigo, C. Maurini, and P. Sicsic. Morphogenesis and propagation of complex cracks induced by thermal shocks. *Phys. Rev. Lett.*, **112(1)**:014301, 2014.
[4] A. Geromel Fischer, J.-J. Marigo. Gradient damage models applied to dynamic fragmentation of brittle materials. *Int. J. Fracture*, **220**: 143–165, 2019.
[5] K. Pham, H. Amor, J.-J. Marigo, C. Maurini. Gradient damage models and their use to approximate brittle fracture. *International Journal of Damage Mechanics*, **20(4)**:618–652, 2011.

CHARACTERIZATION OF THE SOLUTION NON-UNIQUENESS IN PHASE-FIELD MODELING OF BRITTLE FRACTURE

Tymofiy Gerasimov*[1], Ulrich Römer[2], Hermann Matthies[3], and Laura De Lorenzis[1]
[1]Institute of Applied Mechanics, Technische Universität Braunschweig, Braunschweig, Germany
[2]Institute of Dynamics and Vibration, Technische Universität Braunschweig, Braunschweig, Germany
[2]Institute of Scientific Computing, Technische Universität Braunschweig, Braunschweig, Germany

Summary The variational phase-field formulation of brittle fracture [1, 2, 3] may have non-unique solutions, which is indicated by the non-convexity of the associated incremental minimization problem. In practice, only one representative of all possible solutions is computed numerically. In this contribution, we trigger non-uniqueness in a simple problem and characterize it by switch to a stochastic setting, using the Monte Carlo method.

INTRODUCTION

The phase-field approach to brittle fracture dates back to the seminal work of Francfort and Marigo [4] on the *variational formulation of quasi-static brittle fracture* and to the related *regularized formulation* of Bourdin et al. [1]. The former is the mathematical theory of quasi-static brittle fracture mechanics, which recasts Griffith's energy-based principle as the minimisation problem of an energy functional. The latter presents an approximation, in the sense of Γ-convergence, of the energy functional and is designed to enable the numerical treatment.

Non-uniqueness of the solution in phase-field modeling of brittle fracture is a result of the lack of convexity of the energy functional to be minimized, and has been occasionally reported in the literature. Possible triggers were found to be the finite element mesh, the numerical solution strategy and its parameters, and round-off errors. However, to the best of the authors' knowledge no attempt has been made so far to investigate and characterize the multiple solutions. This is our objective in this work.

We were inspired by [5, 6] in fluid mechanics, where the field problem was reformulated with Young measure-valued solutions and a Monte Carlo method was used to compute its mean and variance field, removing the solution non-uniqueness. We propose a similar numerical approach, but omit any interpretation in the sense of measure-valued solutions. Instead the reasoning here is based on the observation that assuming fixed values for input data is unrealistic. Hence, input data such as the geometry, boundary values or loading terms are modeled as random quantities. The solution may then be numerically much more difficult to obtain, however, it may carry more information as different crack patterns may be triggered during the simulation. The result of such an analysis are probabilities associated to each crack pattern which ideally display crack patterns of all possible types.

DETERMINISTIC AND PROBABILISTIC PHASE-FIELD MODELING OF BRITTLE FRACTURE

The model example is as follows. We consider a two-dimensional rectangular domain $(0, 2\mathtt{a}) \times (0, 2\mathtt{a})$ containing a slit along $\{\mathtt{a}\} \times (3\mathtt{a}/2, 2\mathtt{a})$ and a circular hole with center $(0.3\mathtt{a}, 0.3\mathtt{a})$ of radius $R = 0.2\mathtt{a}$. The incremental anti-plane shear displacement $\mp\bar{u}_n$, with $n \geq 1$ as the discrete pseudo-time step parameter, is applied on $\Gamma_D^- := (0, \mathtt{a}) \times \{2\mathtt{a}\}$ and $\Gamma_D^+ := (\mathtt{a}, 2\mathtt{a}) \times \{2\mathtt{a}\}$, respectively, see Figure 1. Following [1], the energy functional used in the incremental minimization problem reads:

$$\mathcal{E}(u, \alpha) = \int_\Omega \frac{1}{2}(1-\alpha)^2 \mu |\nabla u|^2 \, \mathrm{d}\mathbf{x} + \frac{G_c}{2} \int_\Omega \left(\frac{\alpha^2}{\ell} + \ell |\nabla \alpha|^2 \right) \mathrm{d}\mathbf{x} + \frac{\gamma}{2} \int_\Omega \langle \alpha - \alpha_{n-1} \rangle_-^2 \, \mathrm{d}\mathbf{x}, \tag{1}$$

where $u : \Omega \subset R^2 \to R$, $\nabla := (\frac{\partial}{\partial x}, \frac{\partial}{\partial y})$, μ is the second Lamé constant, and G_c is the material fracture toughness. The last term enforces the irreversibility constraint $\alpha \geq \alpha_{n-1}$ via penalization with $\langle y \rangle_- := \min(0, y)$ and $\gamma \in R_+$ as the penalty parameter, see [7]. In the computations, we set $\mathtt{a} = 1$, $\mu = 1$, $\ell = 2\mathtt{a}/50 = 0.04$, $G_c = 1$ and $\gamma = \frac{G_c}{\ell}\left(\frac{1}{\mathtt{TOL}_{\mathrm{ir}}^2} - 1\right)$ with $\mathtt{TOL}_{\mathrm{ir}} = 0.01$. The applied displacement is given by $\bar{u}_n = n\Delta\bar{u}$, $n = 1, ..., \frac{1.5}{\Delta\bar{u}}$ with $\Delta\bar{u} = 0.1$. For solving the coupled system of equations resulting from the (necessary) stationarity conditions of the energy functional we apply the so-called staggered solution algorithm which implies alternately fixing u and α and solving the corresponding equations until convergence. Both the displacement field u and the crack phase-field α are approximated using P_1-triangles. Perturbation of the minimal mesh size leads to a change in the final crack pattern, as depicted in Figure 2. From the energy-displacement curves (not shown here), we conclude that the Type 1 (nearly vertical) crack path is not energetically favorable in comparison with Types 2 and 3 (curved paths). Also, the latter ones seem to have almost identical energy levels.

*Corresponding author. E-mail: t.gerasimov@tu-braunschweig.de.

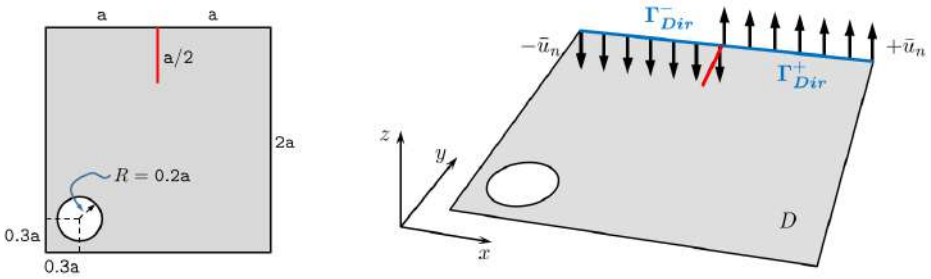

Figure 1: Geometry and loading setup for the anti-plane shear experiment.

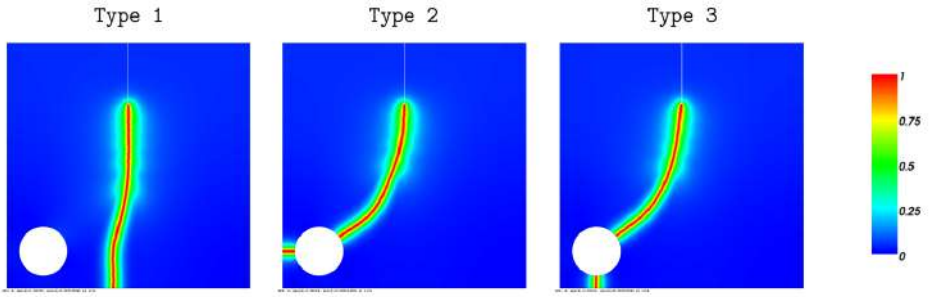

Figure 2: Three different fracture mechanisms as an examples of non-unique solutions (in terms of crack path) are computed on the perturbed meshes.

In view of the above, we use the Monte Carlo approach as a method to capture and characterize all possible solutions. We choose to randomly perturb the hole geometry of our specimen assuming that, in the polar coordinates (r, ϕ) with $\phi \in [0, 2\pi)$,

$$r(\theta, \varphi) = R + \varepsilon \sum_{j=1}^{J} c_j Y_{2j-1}(\theta) \cos(j\varphi) + s_j Y_{2j}(\theta) \sin(j\varphi), \tag{2}$$

where R refers to the unperturbed radius and c_j, s_j are deterministic coefficients which weigh the influence of the different harmonics, with $c_j = s_j = \frac{1}{j}$. Finally, $\theta \in \Theta$ and $Y_k : \Theta \to R, k = 1, \ldots, 2J$ are assumed to be uniformly distributed random variables on $[-1, 1]$.

In presence of a random geometry of the domain, the phase-field model turns into a stochastic partial differential equation. Hence, (u, α) represent random fields: $u : \Theta \times \Omega \to V_{\bar{u}_n}$, $\alpha : \Theta \times \Omega \to H^1(\Omega)$, for which we assume the existence of the mean value μ_z and variance. For $\mathbf{x} \in \Omega$ and $z \in \{u, \alpha\}$ they are defined as $E[z](\mathbf{x}) = \int_\Omega z(\theta, \mathbf{x}) \, \mathrm{d}P(\theta)$, $V[z](\mathbf{x}) = \int_\Omega (z(\theta, \mathbf{x}) - E[z](\mathbf{x}))^2 \, \mathrm{d}P(\theta)$, respectively. Moreover, as we distinguish between Type 1, 2 and 3 cracks, we can compute Monte Carlo approximations of the associated crack probabilities, which can be assumed to characterize the non-uniqueness of the solution.

CONCLUSIONS

The phase field approach to britte fracture delivers in general a non-unique solution. Through an illustrative test case, we have exposed this non-uniqueness due to competing energy levels of different crack paths. Resorting to a stochastic setting turned out to be a viable method to capture various crack paths at once. This was achieved in a standard Monte Carlo framework, which delivered approximate probabilities of occurrence of the different crack paths.

References

[1] Bourdin B., Francfort G.A., Marigo J.-J. The variational approach to fracture. *Journal of Elasticity* **91**: 5–148, 2008.

[2] Miehe C., Hofacker M., Welschinger F. A phase field model for rate-independent crack propagation: robust algorithmic implementation based on operator splits. *Comput. Methods Appl. Mech. Engrg.* **199**: 2765–2778, 2010.

[3] Ambati M., Gerasimov T., De Lorenzis L. A review on phase-field models of brittle fracture and a new fast hybrid formulation. *Computational Mechanics 55(2)*: 383–405, 2015.

[4] G.A. Francfort and J.-J. Marigo. Revisiting brittle fractures as an energy minimization problem. Journal of the Mechanics and Physics of Solids, 46:1319–1342, 1998.

[5] U. Fjordholm, S. Mishra, and E. Tadmor. On the computation of measure-valued solutions, Acta Numerica, 25: 567–679, 2016.

[6] U. Fjordholm, R. Käppeli, S. Mishra, and E. Tadmor. Construction of approximate entropy measure-valued solutions for hyperbolic systems of conservation laws, Foundations of computational mathematics, 17(3): 763–827, 2017.

[7] T. Gerasimov and L. De Lorenzis. On penalization in variational phase-field models of brittle fracture. Comput. Methods Appl. Mech. Engrg., 354:990–1026, 2019.

THE THERMO-CHEMO-MECHANICAL FAILURE MECHANISM OF THERMAL BARRIER COATINGS: APPLICATION TO CRACK PROPAGATION CAUSED BY CMAS CORROSION

Yichun Zhou*[1], Guangnan Xu[1]and Li Yang [1]
[1]Key Laboratory of Key Film Materials & Application for Equipment (Hunan province), School of Materials Science and Engineering, Xiangtan University, Xiangtan, Hunan 411105, China

Summary In this work, a mechanism-based constitutive theory is proposed for crack growth and CMAS corrosion process based on phase field method and thermodynamic laws. Stress distributions, infiltration of CMAS, dissolution of ceramic grain and crack growth in thermal barrier coatings (TBCs) are simulated simultaneously by finite element method. By variational operation of free energy we have the governing equation of field variables. The results obtained by theory model validate spalling phenomena thermal barrier coating by CMAS corrosion.

INTRODUCTION

A considerable amount of researches on corrosion issue of TBCs have been performed during the last decades. As reported by Shan (2016), during the process of CMAS corrosion in TBCs, ceramic coating generates swelling deformation by separating grain boundaries and exfoliating the t'-ZrO_2 grains. Compressive stress accumulates in the corrosion area with corroded ceramic coating being restricted by substrate and uncorroded coating. In addition, when CMAS reaches the bottom of ceramic coating, thermally grown oxide (TGO) caused by bond-coat oxidation will be corroded by CMAS, and reaction products like $CaAl_2Si_2O_8$ and $MgAl_2O_4$ appear. Cracks prefer to grow along the interface of $CaAl_2Si_2O_8/Al_2O_3$, $CaAl_2Si_2O_8$/MCrAlY and $MgAl_2O_4/Al_2O_3$ which can reduce interface adhesive strength (Chen et al., 2018). Consequently, compressive stress and interface defects induced by corrosion may cause coating spallation from interface.

The theory of phase field method for crack propagation was first proposed by Francfort and Marigo[25] in 1999, and further developed and improved by Bourdin (2000) to form a crack propagation criterion based on variational principle. The central idea is to introduce a continuous order parameter to represent the discontinuous crack. When the order parameter is equal to 1, it means that the material is damaged; When the order parameter is equal to 0, it means that the material is intact; Miehe (2014) obtained the evolution equation of crack propagation based on the variational principle from the perspective of thermodynamics, and simulated the crack by writing a finite element program. His work greatly promoted the development of phase field method in the treatment of cracks.

In this work, a thermodynamically-consistent constitutive theory of coupled infiltration, corrosion dissolution and deformation is presented for describing CMAS corrosion process in TBCs. The governing equations of crack order parameter is derived by the variational calculus of constructed free energy.

RESULTS AND DISCUSSION

As shown in figure 1, Spatial distribution of σ_{yy}(Pa) at different time is displayed. During the process of CMAS corrosion, stress concentration happens near the bottom of ceramic coating. The Maximum tensile stress appears at the interface under the corroded area. But out of the corroded area, compressive stress is induced accordingly. Spatial distribution of order parameter of crack d at different time is shown in figure 2.

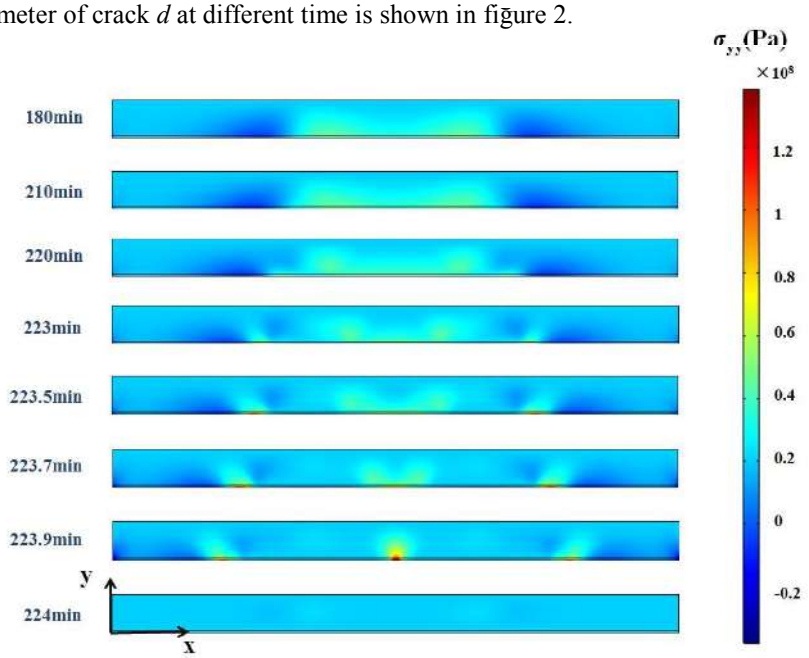

Fig. 1. Spatial distribution of σ_{yy}(Pa) at different time.

*Correspondingauthor. E-mail: zhouyc@xtu.edu.cn

Crack spreading on both sides of corroded area starts to happen at about 210min. At a short time, the cracks connect to each other and extend out to uncorroded area. Note that corresponding to the development of crack, the area of stress concentration starts to broke down at 220min. The stress value drops sharply in the region of crack propagation. But at the tip of crack, the stress value has a sudden increase. At last, the crack spreads throughout the whole interface of ceramic coating and the stress is completely released at 224min.

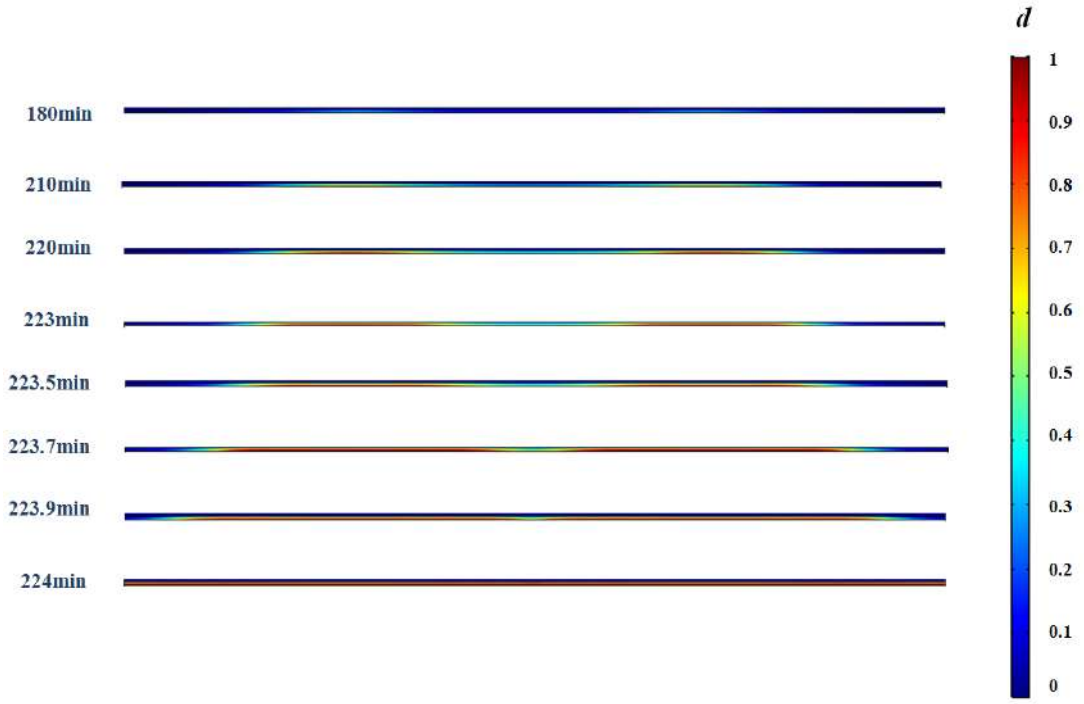

Fig. 2. Spatial distribution of order parameter of crack *d* at different time.

CONCLUSIONS

In this work, a thermodynamically-consistent constitutive theory combined with phase field method is presented for describing crack growth during CMAS corrosion process in TBCs. The main results can be summarized as follows: (1) During the process of CMAS corrosion, out-plane tensile stress is induced in the interface of corroded coating. (2) Induced stress is released in the region of crack propagation and the stress has sharp increase around the crack tip. (3) Cracks appear on both sides of corroded area and then connect with each other and extend out.

References

[1] Shan, X., Zou, Z., Gu, L., Yang, L., Guo, F., Zhao, X., Xiao, P., 2016. Buckling failure in air-plasma sprayed thermal barrier coatings induced by molten silicate attack. Scripta Materialia 113, 71-74.

[2] Chen, Z., Zheng, H., Li, G., Li, H., Peng, P., 2018. Mechanism of crack nucleation and growth in YSZ thermal barrier coatings corroded by CMAS at high temperatures: First-principles calculation. Corrosion Science 142, 258-265.NygusG. Numerical Analysis Using Finite Element Method. *PhD Thesis*, NTU Mech. Eng. Dept., Lagos, 1983.

[3] Bourdin, B., Francfort, G. A., Marigo, J-J. Numerical experiments in revisited brittle fracture[J]. Journal of the Mechanics and Physics of Solids, 2000,48(4): 797-826.

[4] Miehe, C., Schänzel, L-M. Phase field modeling of fracture in rubbery polymers. Part I: Finite elasticity coupled with brittle failure[J]. Journal of the Mechanics and Physics of Solids, 2014,65: 93-113.

HOMOGENIZATION-BASED ANALYSIS OF THE INFLUENCE OF MICROCRACKING ON THERMAL CONDUCTION AND THERMOELASTICITY

Hélène Welemane*, Sharan Raj Rangasamy Mahendren, Olivier Dalverny, and Amévi Tongne
Université de Toulouse; INP/ENIT; LGP; 47 Avenue d'Azereix, F-65016, Tarbes, France

Summary Microcracks are known to affect the behaviour of the materials and several modelling studies are devoted to finding their effective elasticity. This paper aims to extend such investigation to thermal properties, concerning both the steady-state conduction and the thermoelasticity. Accounting simultaneously for the anisotropy induced by microcracks orientation and for their unilateral effect (different behaviour whether they are open or closed) remains a difficult task. In this work, 3D homogenization-based approaches are developed to derive closed-form estimations of the effective thermal properties of a microcracked media with arbitrarily oriented microcracks, either open or closed.

INTRODUCTION

Effects of microcracks on the elastic properties have been extensively studied through experiments and modelling approaches. In the latter case, the homogenization (up-scaling) technique appears as an effective tool to provide the overall properties from the microstructural features of the Representative Volume Element (RVE) [1]. Especially for microcracks, main difficulties arise from: (i) the anisotropy induced by the oriented nature of defects, (ii) their ability to be open or closed (according to tension or compression stresses) and to influence differently the overall response of the material. Regarding the thermal steady-state conduction and thermoelastic properties of microcracked media, very few investigations of these effects have been done in the literature, even on the experimental point of view. Some micro-macro modelling works have been proposed to derive effective properties of a given RVE but they consider only the open state of microcracks [2]. This work aims at exploring homogenization-based approaches to derive anisotropic thermal conductivity and thermoelasticity accounting for unilateral effect.

MICROMECHANICAL FRAMEWORK

Assuming length scale separation, let us consider a 3D RVE composed of an isotropic matrix weakened by N number of randomly distributed families of parallel microcracks. Such media exhibits a matrix-inclusion topology in which each phase (matrix, microcracks) is homogeneous, allowing the use averaging techniques. Two conditions can be imposed on the outer boundary of the RVE, i.e. uniform macroscopic temperature gradient G (for the thermal conduction problem) and uniform macroscopic strain $\mathbf{E}$ with constant temperature difference ΔT over the RVE (for the thermoelastic problem). Under equilibrium condition, the macroscopic quantities $(G, \mathbf{E})$ correspond to the average value of their respective microscopic quantity $(g, \boldsymbol{\varepsilon})$ over the RVE, i.e. $G = \langle g \rangle$, $\mathbf{E} = \langle \boldsymbol{\varepsilon} \rangle$. The microscopic and macroscopic quantities can be linked linearly as $g = \mathbf{A} \cdot G$ and $\boldsymbol{\varepsilon} = \mathbb{A} : \mathbf{E}$, where $\mathbf{A}$ and $\mathbb{A}$ are the second-order gradient and fourth-order strain localization tensors, respectively. Regarding the steady-state heat conduction problem, the microscopic heat flux q is given by Fourier's law:

$$q = -\boldsymbol{\lambda} \cdot g \tag{1}$$

where $\boldsymbol{\lambda}$ is the symmetric second-order thermal conductivity tensor. On the other hand, thermoelasticity is classically described by the following linear constitutive equation:

$$\boldsymbol{\sigma} = \mathbb{C} : \boldsymbol{\varepsilon} - \boldsymbol{\kappa}\, \Delta T \tag{2}$$

where $\boldsymbol{\sigma}$ is the microscopic stress tensor, $\mathbb{C}$ is the fourth-order stiffness tensor and $\boldsymbol{\kappa} = \mathbb{C} : \boldsymbol{\alpha}$ is the second-order thermoelasticity tensor with $\boldsymbol{\alpha}$ being the thermal expansion tensor.

Based on the boundary conditions, the overall heat flux $Q = \langle q \rangle$ and stress $\boldsymbol{\Sigma} = \langle \boldsymbol{\sigma} \rangle$ of the RVE can be expressed as:

$$Q = -\boldsymbol{\lambda}_{hom} \cdot G \qquad \text{and} \qquad \boldsymbol{\Sigma} = \mathbb{C}_{hom} : \mathbf{E} - \boldsymbol{\kappa}_{hom}\, \Delta T \tag{3}$$

where $\boldsymbol{\lambda}_{hom}$, $\mathbb{C}_{hom}$, and $\boldsymbol{\kappa}_{hom}$ are the effective tensors related to the thermal conductivity, stiffness and thermoelasticity of the microcracked media, respectively. Taking all simplifications into account, the effective thermal properties $\boldsymbol{\lambda}_{hom}$ and $\boldsymbol{\kappa}_{hom}$ are given as:

$$\boldsymbol{\lambda}_{hom} = \boldsymbol{\lambda}_m + \sum_{i=1}^{N} f_{c,i}\, (\boldsymbol{\lambda}_{c,i} - \boldsymbol{\lambda}_m) \cdot \langle \mathbf{A} \rangle_{c,i} \qquad \text{and} \qquad \boldsymbol{\kappa}_{hom} = \boldsymbol{\kappa}_m + \sum_{i=1}^{N} f_{c,i} \big(\boldsymbol{\kappa}_{c,i} - \boldsymbol{\kappa}_m \big) : \langle \mathbb{A} \rangle_{c,i} \tag{4}$$

where $\boldsymbol{\lambda}_m$ (resp. $\boldsymbol{\lambda}_{c,i}$) and $\boldsymbol{\kappa}_m$ (resp. $\boldsymbol{\kappa}_{c,i}$) are the thermal conductivity and thermoelasticity tensors of the matrix (resp. of the i^{th} family of parallel cracks) and $f_{c,i}$ is the cracks volume fraction for the i^{th} family.

Estimations of localization tensors $\mathbf{A}$ and $\mathbb{A}$ can be obtained using the works of Eshelby on the single-inhomogeneity problem [3]. In line with the recent study of [4], each family of microcracks is modelled as a flat oblate ellipsoid with

*Corresponding author. E-mail: Helene.Welemane@enit.fr

unit normal $\mathbf{n}_i$, crack density d_i and aspect ratio $\omega_i \to 0$. We assume both the matrix and cracks are isotropic and their properties can be given by $\boldsymbol{\lambda}_r = \lambda_r\, \mathbf{I}$, $\boldsymbol{\kappa}_r = \kappa_r\, \mathbf{I}$ and $\mathbb{C}_r = 3k_r\, \mathbb{J} + 2\mu_r\, \mathbb{K}$ with $r = \{m; c, i\}$ (where λ_r and κ_r are scalars while k_r and μ_r are the bulk and shear moduli). The unilateral effect is taken into account via the $\lambda_{c,i}$ and $\kappa_{c,i}$. For open cracks, it is assumed adiabatic (for thermal conduction) and stress-free (for thermoelasticity) conditions on the microcracks lips, so $\lambda_{c,i} = 0$, $\mathbb{C}_{c,i} = \mathbb{O}$ ($k_{c,i} = 0, \mu_{c,i} = 0$) and $\kappa_{c,i} = 0$. Inspired by the works of Deudé *et al.* [5], the closed cracks (frictionless contact) are considered as a fictitious isotropic material such that $\lambda_{c,i} \neq 0$, $\kappa_{c,i} \neq 0$ and $\mathbb{C}_{c,i} = 3k_m\, \mathbb{J}$ ($k_{c,i} = k_m, \mu_{c,i} = 0$), which accounts for some heat (for conduction) and stress (for thermoelasticity) transfer continuity across the closed microcracks lips.

RESULTS

From these assumptions, closed-form expressions of the whole thermal properties (Eq (4)) are derived for dilute and Mori-Tanaka (MT) schemes and Ponte Castañeda-Willis (PCW) bound. For a single family of open microcracks, $\boldsymbol{\lambda}_{hom}$ is function of $d, \mathbf{n}, \boldsymbol{\lambda}_m$ and $\boldsymbol{\kappa}_{hom}$ is function of $d, \mathbf{n}, \boldsymbol{\kappa}_m$ and matrix Poisson ratio ν_m. Also the material shows a damage-induced anisotropy, irrespective of the estimation. To be precise, the effective thermal properties are transversely isotropic around the axis $\mathbf{n}$ of the crack. As an illustration, Fig. 1 presents the generalized scalar thermal conductivity $\lambda(\mathbf{v})$ and thermoelasticity $\kappa(\mathbf{v})$ in any direction of unit vector $\mathbf{v}$ defined by: $\lambda(\mathbf{v}) = \mathbf{v} \cdot \boldsymbol{\lambda}_{hom} \cdot \mathbf{v}$ and $\kappa(\mathbf{v}) = \mathbf{v} \cdot \boldsymbol{\kappa}_{hom} \cdot \mathbf{v}$ respectively. While both properties are mostly degraded along the direction $\mathbf{n}$ normal to the crack surface, the cracks influence is stronger on thermoelastic properties for a given cracks density. We should also note the differences for both properties according to the estimations, related to the account (MT and PCW) or not (dilute) of interactions between microcracks and, in the former case, to the considered spatial distribution of microcracks (ellipsoidal for MT and spherical for PCW).

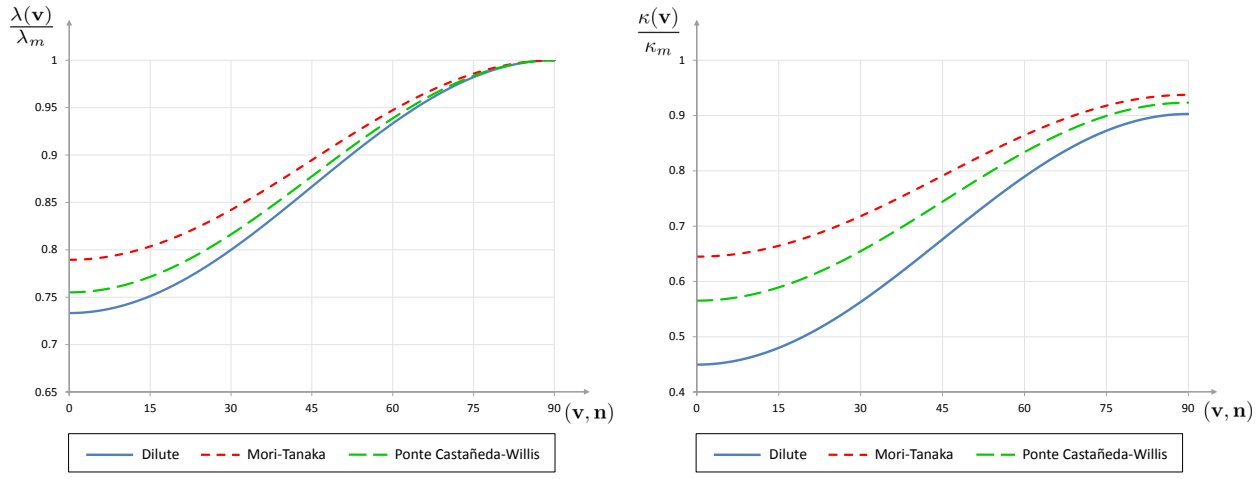

(a) $\dfrac{\lambda(\mathbf{v})}{\lambda_m}$ (b) $\dfrac{\kappa(\mathbf{v})}{\kappa_m}$

Figure 1: Generalized thermal conductivity $\lambda(\mathbf{v})$ and coefficient $\kappa(\mathbf{v})$ normalized by their initial values for a material weakened by a single family of parallel open microcracks of unit normal $\mathbf{n}$ (cracks density $d = 0.1$, matrix Poisson ratio $\nu_m = 0.15$).

On the other hand, it is demonstrated that closed cracks do not contribute to the degradation of the thermal conductivity or thermoelasticity. This result is irrespective of the estimation (dilute, MT, PCW), fictitious cracks properties or space direction, i.e. effective conductivity and thermoelasticity in any direction $\mathbf{v}$ recover their respective values for the virgin material: $\lambda(\mathbf{v}) = \lambda_m$ and $\kappa(\mathbf{v}) = \kappa_m$, $\forall\, \mathbf{v}$. While elastic properties are only fully recovered in the direction $\mathbf{n}$ normal to closed microcracks [6], we observe here a total deactivation of microcracking influence on thermal properties.

CONCLUSIONS

Using Eshelby approach, we have derived in this work several homogenization-based expressions for effective thermal properties of a microcracked media, both regarding steady-state conduction and thermoelasticity. Special attention has been paid to the unilateral effect and its consequences on the overall behaviour. This study provides some relevant information to further develop a fully coupled thermo-mechanical model with evolving damage.

References

[1] Nemat-Nasser S., Hori M., Micromechanics: overall properties of heterogeneous materials. Elsevier, Amsterdam 1993.
[2] Sevostianov I., Kachanov M., On the effective properties of polycrystals with intergranular cracks. *Int. J. Solids Struct.* **156–157**: 243–250, 2019.
[3] Eshelby J. D., The determination of the elastic field of an ellipsoidal inclusion, and related problems. *Proc. R. Soc. A.* **421**: 379–396, 1957.
[4] Rangasamy Mahendren S. R., Welemane H., Dalverny O., Tongne A., Thermal conduction properties of microcracked media: Accounting for the unilateral effect. *C. R. Mécanique*. **347**: 944–952, 2019.
[5] Deudé V., Dormieux L., Kondo D., Pensée V., Propriétés élastiques non linéaires d'un milieu mésofissuré. *C. R. Mécanique*. **330**: 587–592, 2002.
[6] Welemane H., Cormery F., Some remarks on the damage unilateral effect modelling for microcracked materials. *Int. J. Damage Mech.* **11**: 65–86, 2002.

COMPARATIVE ANALYSIS OF MODELLING TECHNIQUES TO PREDICT IMPACT DAMAGE IN THICK COMPOSITE STRUCTURES

N. van Hoorn*[1,2], C. Kassapoglou[2], S.R. Turteltaub[2], and W.M. van den Brink[1]
[1]Royal Netherlands Aerospace Centre, Aerospace Vehicles and Collaborative Engineering Systems, Voorsterweg 31, 8316 PR Marknesse, The Netherlands
[2]Delft University of Technology, Faculty of Aerospace Engineering, Aerospace Structures and Computational Mechanics, Kluyverweg 1, 2629 HS Delft, The Netherlands

Summary Predicting impact damage in composite structures is a challenging topic that has received a significant amount of attention. Only little effort, however, is directed toward thick composite structures (i.e., 20-50mm) that start to appear in aerospace applications. This work aims to provide accurate and efficient modelling techniques to predict impact damage in thick composite structures. Analytical and numerical methodologies are compared with experimental results and it is shown that each model shows potential for certain applications. Overall these methodologies improve the understanding of impact events on thick composite structures, could decrease uncertainties in the design process, and reduce cost by minimising the amount of tests required.

INTRODUCTION

Innovations in the aerospace sector are necessary to reduce the environmental impact of aviation. One approach is to reduce the weight by using composite structures in the latest generation aircraft. However, the theoretical benefits of composite materials are not utilised to their full extent because of uncertainties in damage tolerance predictions. In particular, risk associated to accidental impact events are critical in designing a damage tolerant composite structure. Despite significant effort focussed on predicting impact on composite structures with thickness in the range of a few millimetres, it is unclear if these methodologies are suitable for thick composites in the range of 20-50mm.

Thick composite structures are becoming more prevalent in aircraft, such as the landing gear and wing component illustrated in Figures 1 and 2. The challenges, especially regarding the trade-off between accuracy and efficiency, are even more evident for simulating impact events on these structures. Therefore, the goal of this contribution is to provide an efficient analytical and a detailed numerical methodology which are compared to each other and to experimental results.

EXPERIMENTS AND MODELLING TECHNIQUES

Due to the many variables involved in impact events, a simplified impact problem is defined, as shown in Figure 3. It concerns a perpendicular impact with a spherical steel impactor with a 16mm diameter on a 150×100mm specimen on a frame with a 125×75mm opening and clamped at four corners. This complies with the ASTM D7136/D7136M-15 standard used for impact experiments. One-dimensional (1D) and two-dimensional (2D) approximations allow for a more computationally efficient solution to the impact problem compared to a three-dimensional (3D) simulation.

Impact Experiments

Impact experiments that focus on thick composites are limited to a few studies in literature [2]. To ensure that the modelling techniques can be validated and compared to suitable experimental data, extensive experimental impact tests were conducted at Royal NLR. The specimens were produced with a quasi-UD 2/2 twill weave fabric, infused by a low viscosity toughened liquid epoxy resin and cured using Resin Transfer Moulding (RTM). As a result, multiple data points are available including 55 and 100J large-mass drop-tower and small-mass gas cannon impacts on 20 and 40mm thick specimens with two different layups. The impact response characteristics of each data point were obtained, such as contact force and impactor displacement histories, as well as absorbed energy and the characteristic damage state (i.e., dent depth and delaminated area, width, height, and depth obtained from C-scans, CT-scans, and visual inspection of cross-sections).

Figure 1: Demonstrator of a NH90 main landing gear trailing arm.

Figure 2: Gear rib of the Affordable Low Cost Aircraft Structures (ALCAS) airliner wing [1].

*Corresponding author. E-mail: niels.van.hoorn@nlr.nl.

Analytical Impact Response Prediction

An analytical impact response model, that represents the 1D approximation of the impact problem in Figure 3, is used to provide a computationally efficient solution. The model of Christoforou and Yigit [3] is used in combination with the Sun-Christoforou contact law proposed by Talagani [4]. This model is capable of predicting the impact response characteristics, such as, contact force and impactor displacement histories. However, due to a missing stress solution and implementation of failure criteria, no predictions of the characteristic damage state can be given.

Numerical Impact Response and Damage Prediction

A numerical model is developed in Abaqus/Explicit that uses a discrete cracking approach. Delaminations as well as in-ply failure (i.e., fibre breakage and transverse matrix cracks) are simulated by cohesive interface elements (i.e., COH2D4 or COH3D8). Properties of these cohesive elements have been carefully selected based on material characterisation data available and guidelines provided by Turon *et al.* [5, 6]. Contact definitions allow for these cohesive elements to be deleted once fully failed. The drop-tower impactor is modelled in full such that its eigenfrequencies are included in the simulation, while the gas cannon impactor (i.e., steel ball) can be assumed rigid. Behaviour analogous to an elasto-plastic response is included in the bulk material by Von Mises plasticity with isotropic hardening. In the full 3D numerical model, the bulk material is represented by solid elements (i.e., C3D8R and C3D6R) in a ply-oriented mesh. However, a 2D approximation in the xz-plane in Figure 3 gives a simplified model that is computationally more efficient. This model uses axisymmetric elements for a correct representation of the impactor.

COMPARATIVE ANALYSIS AND CONCLUSIONS

The analytical model and the 2D/3D numerical models are compared in terms of accuracy and computational efficiency. In terms of efficiency, the analytical model provides a solution in 10-100 seconds, while the 2D numerical model requires approximately two orders of magnitude longer time. The extension to 3D increases the computational time by another order of magnitude. The accuracy is assessed by comparison with experimental results. Preliminary results show that all three models are capable of a relatively accurate prediction of the impact response characteristics. Noteworthy is that the analytical impact response model in many cases gives the best prediction of force and displacement histories. At the time of writing this abstract, a thorough evaluation of the impact damage predictions is still on-going. Due to the computational efficiency of the analytical model an extensive sensitivity analysis of impact characteristics is possible in early stages of design. The 2D numerical model gives, in addition to the force and displacement histories, a relatively efficient prediction of the characteristic damage state. However, the only model that can give an accurate and realistic representation of the characteristic damage state including all damage types is the 3D numerical model.

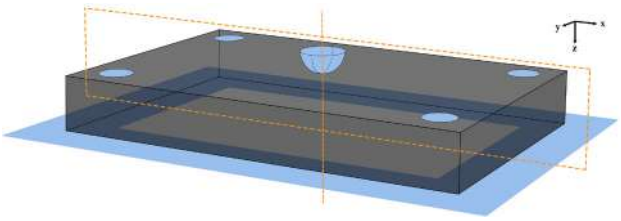

Figure 3: Illustration of the impact problem with a 1D approximation along the z-axis and 2D approximation in the xz-plane.

Figure 4: Example of the axisymmetric 2D numerical model simulating a 55J small-mass impact on a 20mm thick specimen.

References

[1] H. P. J. de Vries, Development of a main landing gear attachment fitting using composite material and resin transfer moulding, techreport NLR-TP-2009-732, NLR - Netherlands Aerospace Centre (Dec. 2010).

[2] R. J. C. Creemers, M. J. Smeets, Static and fatigue behaviour of impact damaged thick-walled composites, techreport NLR-TP-2013-511, NLR - Netherlands Aerospace Centre (Apr. 2014).

[3] A. P. Christoforou, A. S. Yigit, Transient response of a composite beam subject to elasto-plastic impact, Composites Engineering 5 (5) (1995) 459–470. doi:10.1016/0961-9526(95)00018-I.

[4] M. R. Talagani, Impact analysis of composite structures, Phd thesis, Delft University of Technology (Dec. 2014).
URL http://resolver.tudelft.nl/uuid:f576163e-3d28-4b76-b50e-2431622c1da5

[5] A. Turon, C. G. Dávila, P. P. Camanho, J. Costa, An engineering solution for mesh size effects in the simulation of delamination using cohesive zone models, Engineering Fracture Mechanics 74 (10) (2007) 1665–1682. doi:10.1016/j.engfracmech.2006.08.025.

[6] A. Turon, P. P. Camanho, J. Costa, J. Renart, Accurate simulation of delamination growth under mixed-mode loading using cohesive elements: definition of interlaminar strengths and elastic stiffness, Composite Structures 92 (8) (2010) 1857–1864.
URL http://www.sciencedirect.com/science/article/pii/S026382231000022X

MICRODAMAGE AND FRACTURE INITIATION IN THE MATERIALS SUBJECTED TO ION-IRRADIATION

Aneta Ustrzycka*[1] and Marcin Nowak[1]
[1]Institute of Fundamental Technological Research, Polish Academy of Sciences, Warsaw, Poland

Summary In this work defects induced by ion-irradiation in the elastic-plastic materials are investigated by using the nano-indentation technique. Radiation induced damage level is expressed in terms of displacements per atom (dpa), afterwards, the radiation induced damage is defined in the framework of Continuum Damage Mechanics (CDM) to solve the problem of further evolution of damage fields under mechanical loads. The new mathematical relation between radiation damage (dpa) and porosity parameter is proposed. Deformation process experienced by the ion irradiated materials during the indentation test is then simulated by Gurson–Tvergaard–Needleman (GTN) model. Moreover, a novel material model with radiation induced damage based on nonlocal peridynamic theory is proposed to study of ion-irradiated materials. The peridynamic theory based on integro-differential equations without spatial derivatives is a powerful tool for the modelling of materials involving discontinuities. The conditions of fracture, the onset and the propagation of macro-crack are investigated.

INTRODUCTION

In general, radiation induced damage causes profound changes of the macroscopic response, reflected by progressive material degradation. Radiation damage creates the threats for structural components working under mechanical loads. Moreover, damage evolution causes degradation of mechanical properties and severely compromises the lifetime of structural components. Radiation-induced defects serve as strong obstacles to dislocation motion. Irradiation invariably renders a metal less ductile and leads to drastic modifications of mechanical properties, e.g., growth of porosity, fracture toughness and increase in yield stress. Depending on the degree of irradiation, fracture can have the brittle or ductile characteristics. A microcrack can rapidly propagate across the entire component, or it can occur as result of stress and or large plastic deformation.

IRRADIATION INDUCED POROSITY

The irradiation of metals by high energy particles leads to the interaction of energetic incident particles with lattice atoms. The pair of interstitial atom and vacancy in irradiated crystalline solids is known as the Frenkel defect. After the end of the collisional phase (cascade) the point defects (vacancies and interstitials) may migrate in the material leading to the formation of various forms of defect clusters: e.g. clusters of voids. In this way, the process of damage initiation is created. To evaluate radiation damage, a damage variable that characterizes the material degradation is required. Radiation induced damage level is expressed in terms of displacements per atom (dpa) parameter. The nature of radiation induced damage is close to porosity because of formation of clusters of vacancies. The porosity ξ of the material expressed by dpa function takes the form

$$\xi = q_c \frac{4}{3}\pi C (dpa)^n$$

where q_c is the density of vacancy clusters caused by irradiation, C and n are material parameters. The processes of the defects formation and initial clustering as well as the interaction between point defects which are the basis of the fracture are considered.

ELASTIC-PLASTIC DEFORMATION DURING INDENTATION

In the irradiated ductile materials, the plastic deformation is based on similar mechanisms like in the virgin materials. In particular, the main mechanism of plastic flow is still slip. However, due to the presence of radiation induced defects, like the groups of interstitial atoms or vacancy clusters containing impurities, strong hardening is usually observed. The motion of dislocations within the easy slip planes is hindered by numerous types of obstacles, causing substantial increase of the flow stress. The experimental characterization of the deformation process of the ion irradiated materials during the nano-indentation test is carried out (Fig.1).

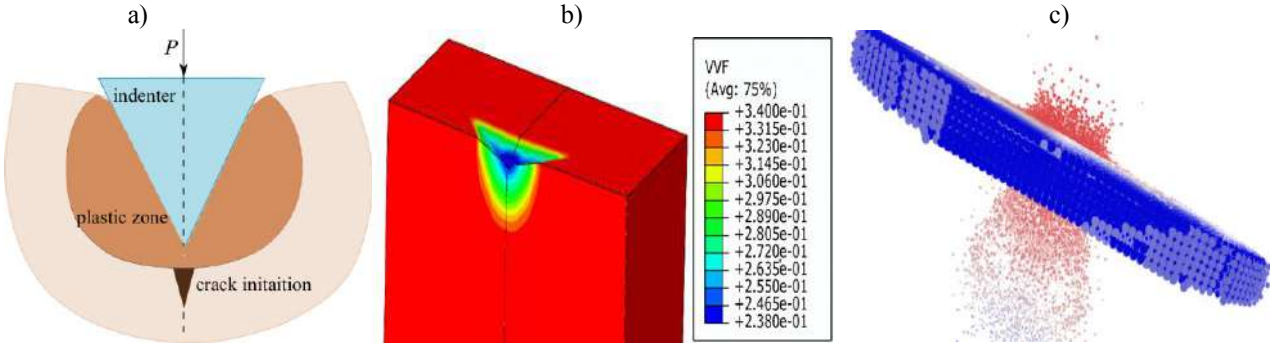

Figure 1. a) Indentation of an elastic-plastic solid by a rigid cone; b) Evolution of porosity in the damaged material subjected to indentation in the framework of CDM; c) Indentation test results of peridynamics simulation (PD)

*Corresponding author. E-mail: austrzyc@ippt.pan.pl

Afterwards, the radiation induced damage is defined in the framework of Continuum Damage Mechanics (CDM) and peridynamics theory (PD) to solve the problem of further evolution of damage fields under mechanical loads [1]. A novel material model based on nonlocal peridynamic theory is proposed to study of irradiated materials. The peridynamic theory is particularly powerful in modelling problems where spontaneous formation of discontinuities, like micro-damage, voids and cracks, occurs. Numerical simulation of indentation test results of PD is shown in Fig. 1c. Emphasis is placed on the macroscopic behaviour, like the evolution of damage and fracture through the plate.

ELASTIC-PLASTIC DAMAGE MODEL OF INDENTATION OF THE ION-IRRADIATED MATERIAL

The nature of radiation induced damage is close to porosity because of formation of clusters of vacancies and helium bubbles. For this reason, the models describing the porosity evolution appear most suitable. The kinetics of radiation induced damage involves essentially two models describing the evolution of porosity in the materials: the Gurson–Tvergaard–Needleman (GTN) model and - for comparison – the Rice and Tracey (R-T) model [2]. Both of them address the evolution of porosity in the form of spherical or ellipsoidal voids in a different way. GTN proposed a constitutive model of porous materials including the micro-voids. The porosity rate is controlled by the appropriate GTN yield function. Moreover, the GTN kinetics is accompanied by the yield surface that retracts in the course of increasing porosity. On the other hand, the R-T model predicts the evolution of radius of spherical void as a function of triaxiality and the plastic strain. The R-T model is expressed in the form of a differential equation and has, therefore, implicit character. Main drawback of the R-T model consists in the fact, that there is no full coupling between the plasticity and the damage. The reasons for which the GTN kinetics appears far better for the irradiated materials are as follows:

- the nature of radiation induced damage is close to porosity because of formation of clusters of voids, without generation of cracks,
- the GTN model represents a dilatational constitutive model based on the yield function formulated for a porous solid, with the volume fraction of voids reflecting randomly distributed spherical voids,
- the void growth in the GTN model is driven by the volumetric plastic strain rate, combined with type GTN yield surface,
- the current porosity value is computed and can be easily converted to damage parameter.

The numerically obtained loading-unloading curves were imposed on the experimental data in order to verify their consistence, both for the loading and for the unloading stages. The curves were corrected for the initial stage of the indentation process, where the indenter cuts through the surface layer and the hardware adjustment takes place (Fig. 2). Quite good agreement between the numerical and the experimental curves is obtained, which confirms validity of the GTN model.

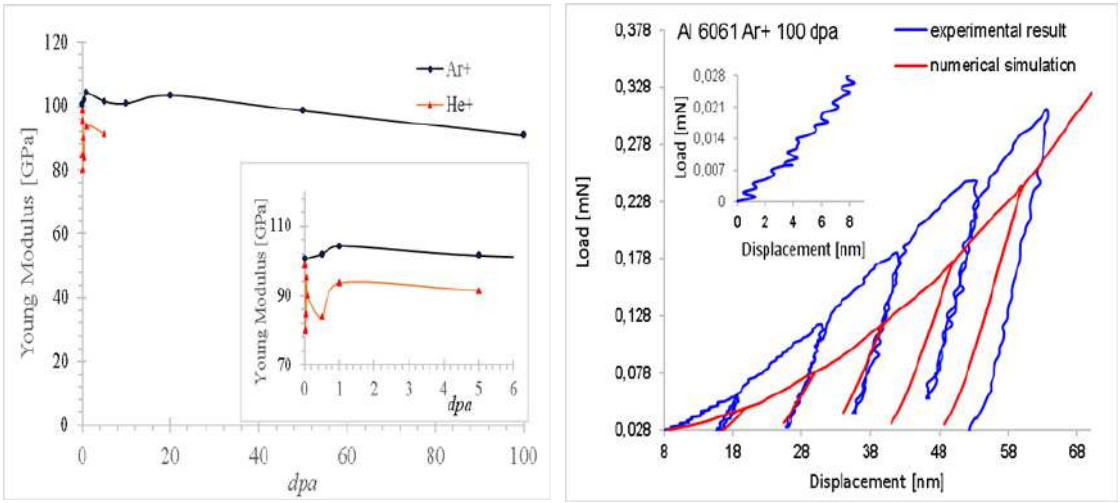

Figure 2. Young's modulus as a function of the irradiation dose; Load-indentation depth curves - experimental results and numerical simulations

THE ONSET OF FRACTURE AND THE MACROCRACK PROPAGATION

In view of the above model of irradiated elastic-plastic material, the conditions of fracture are to large extent determined by the radiation induced porosity. This phenomenon largely affects the conditions of the onset and the evolution of macrocrack, that depend on the level of irradiation (porosity). Therefore, the conditions of fracture, including the fracture toughness as well as the propagation of the micro-crack, are investigated. A criterion of the macro-crack initiation is proposed and implemented.

References

[1] Ustrzycka A., Skoczeń B,. Nowak M., Kurpaska Ł., Wyszkowska E., Jagielski J. Elastic-plastic-damage model of nanoindentation of the ion-irradiated 6061 aluminium alloy. *Int. J. Dam. Mech.* **29:** 1271-1305, 2020.

[2] Skoczeń B., Ustrzycka A. Kinetics of evolution of radiation induced micro-damage in ductile materials subjected to time-dependent stresses. *IJP*. **80**: 86-110, 2016.

A THREE-DIMENSIONAL CONTINUUM DAMAGE-HEALING MODEL FOR SELF-HEALING MATERIALS

Harini Subramanian[1] and Shantanu S. Mulay [*1]
[1]Department of Aerospace Engineering, Indian Institute of Technology Madras, India

Summary A three-dimensional continuum damage-healing mechanics (CDHM) model is proposed to study the behaviour of self-healing materials. The present work focuses on the class of materials undergoing self-healing at lower strain values, where the damaged surfaces wet each other and partially recover the bond strength. The concept of effective configuration is extended, defining a healing configuration to study the healing effects. The principle of strain equivalence and strain energy equivalence are adopted to establish the relation between stiffness moduli in current and healing configurations. The damage and healing variables evolve according to different evolution surfaces. The proposed model has been successfully validated under different types of strain histories. The developed model is employed to solve boundary value problems by ABAQUS through user material subroutines (UMAT).

INTRODUCTION

The ability of a material to recover/repair autonomously or with an external intervention upon the damage is called healing. Different types of materials, such as polymers, concrete, ceramics, and metals have unique self-healing mechanisms. The potential of self-healing materials to delay failure and increase a component's lifecycle warrants theoretical models of self-healing materials that are applicable under different loading conditions. The present work aims to model the self-healing behavior of materials during unloading and rest periods. The proposed model ensures a *kinetic* coupling between the damage and healing variables through the use of damage energy release rate Y in the damage evolution. The developed model is also applied to analyze the effect of healing in textile composites with a self-healing matrix. The model will be further extended in future to account for the viscoelastic effect of the polymer matrix and the effect of temperature on healing.

CONTINUUM DAMAGE-HEALING MODEL

An isotropic damage variable is defined based on continuum damage mechanics (CDM) to measure the material degradation due to damage under loading. An isotropic healing variable is also defined capturing the amount of damaged area that has undergone healing. The concept of effective configuration in CDM is extended, and a healing configuration is introduced eliminating damaged and unhealed area from the current configuration as shown in Figure 1 [1].

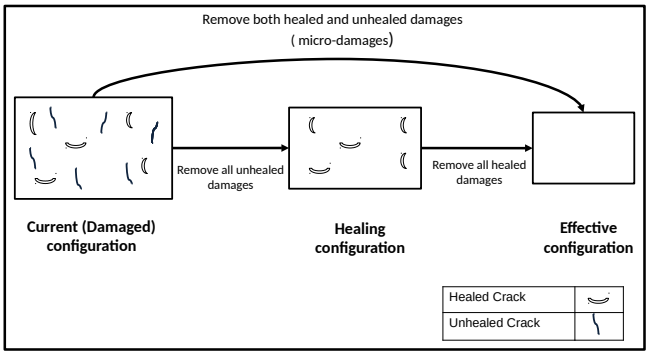

Figure 1: Schematic representation of the current-, healing-, and effective- configurations

The effective damage variable is defined as

$$\phi = D(1-h) \tag{1}$$

where D and h are damage and healing variables. The stress tensors in the current and healing configurations are related by the principle of mechanical equivalence as

$$\tilde{\tilde{\boldsymbol{\sigma}}} = \underline{\underline{\underline{\underline{\mathcal{Q}}}}}\ \boldsymbol{\sigma}, \quad \text{and} \quad \underline{\underline{\underline{\underline{\mathcal{Q}}}}} = \left[\underline{\underline{\underline{\underline{M}}}}^{-1} + \left(\underline{\underline{\underline{\underline{I^s}}}} - \underline{\underline{\underline{\underline{M}}}}^{-1}\right) \underline{\underline{\underline{\underline{H}}}}^{-1}\right] \tag{2}$$

where $\underline{\underline{\underline{\underline{\mathcal{Q}}}}}$ is the damage-healing effect tensor [2], and $\underline{\underline{\underline{\underline{M}}}}^{-1}$ is the inverse damage effect tensor defined as

$$M^{-1}_{ijkl} = I^s_{ijkl} - D_{ijkl}, \quad \text{and} \quad I^s_{ijkl} = \frac{1}{2}\left(\delta_{ik}\,\delta_{jl} + \delta_{il}\,\delta_{jk}\right) \tag{3}$$

*Corresponding author. E-mail: ssmulay@iitm.ac.in

where I^s_{ijkl} is the 4^{th}-order identity tensor. The energy-based damage criterion is employed [3], and extended to account for the healing effect on the evolution of damage. The damage evolution *during loading* is thus governed by the evolution of healing *during unloading and rest periods* ensuring *kinetic* coupling between the damage and healing variables. The damage evolution function is thus given as

$$f^D\left(D;\boldsymbol{\epsilon},h\right)=\left(1-D\right)^{m(D)}Y\left(\boldsymbol{\epsilon},h\right)-W\leq 0,\quad m\left(D\right)=m_1(1-D)^{m_2}+m_3 \tag{4}$$

where W is the damage initialization threshold energy $(\mathrm{J/m^3})$, $Y\left(\boldsymbol{\epsilon},h\right)$ is the damage energy release rate $(\mathrm{J/m^3})$, and $m(D)$ is the exponential material parameter controlling hardening and softening regions [3]. The phenomenological-based healing increment equation and the corresponding initiation condition are given as [1]

$$\dot{h}=\beta_h\left[\left(1-D\right)\left(1-h\right)\right]^p,\quad f^h=\boldsymbol{\epsilon}^h_{th}-\boldsymbol{\epsilon}_{eff}\leq 0 \tag{5}$$

where β_h is the healing viscosity parameter controlling the rate of healing and p is a material constant. f^h is the healing loading surface, $\boldsymbol{\epsilon}^h_{th}$ is the healing threshold strain, and $\boldsymbol{\epsilon}_{eff}$ is the effective strain.

RESULTS AND DISCUSSION

(a) (b)

Figure 2: (a) Strain input equal unloading-reloading with rest period (b) Stress vs strain response

(a) (b)

Figure 3: (a) Variation of effective damage with time (b) Variation of algorithmic tangent modulus with time

The model is demonstrated in one dimension for a cyclic loading strain input with unloading-reloading coupled with a rest period. The stress increases linearly with strain, and damage is initiated when $f^D \geq 0$. The algorithmic tangent modulus E^T remains constant (E_0) until damage initiates and then evolves with progressive damage. The healing process is initiated during unloading (phase 3) when the strain is lower than a threshold value, until which ϕ remains constant. The healing evolution in phase 3 results in a decrease of ϕ. The effect of healing is thus observed in the next loading cycle (phase 4), when E^T during reloading is higher than the corresponding value during unloading. The effective damage ϕ is thus found to decrease during the rest period and increases when further damage occurs.

CONCLUSION

A CDHM model has been formulated focussing on the class of materials undergoing self-healing at lower strain values, where the damaged surfaces wet each other and partially recover the bond strength.

References

[1] M.K. Darabi, R.K.A. Al-Rub, D.N. Little, International Journal of Solids and Structures **49**(3-4), 492 (2012)
[2] George Z Voyiadjis, Amir Shojaei, Guoqiang Li, and Peter I Kattan. A theory of anisotropic healing and damage mechanics of materials. *Proceedings of the Royal Society A: Mathematical, Physical and Engineering Sciences*, 468(2137):163–183, 2011.
[3] B. Nedjar, R. Le Roy, International Journal for Numerical and Analytical Methods in Geomechanics **37**(9), 1066 (2013)

A TWO-WAY COUPLED CHEMICAL-MECHANICAL MODEL FOR SULFURIC ACID CORROSION OF CONCRETE

Frits Rooyackers*[1], Emanuela Bosco[1], Akke Suiker[1], and Francois Clemens[2,3]
[1]Eindhoven University of Technology, Department of the Built Environment, Eindhoven, the Netherlands
[2]Delft University of Technology, Department of Civil Engineering and Geosciences, Delft, the Netherlands
3Deltares, Department of Hydraulic Engineering, Delft, the Netherlands

Summary A computational approach is proposed to describe the chemo-mechanical corrosion of concrete subjected to sulfuric acid. The framework is based on a set of coupled (diffusion-)reaction equations, two-way coupled with a continuum damage model by means of a staggered scheme. At each timestep, the chemical problem is solved first. As a result of phase transformation, a chemical strain is introduced, which triggers the deterioration of the material, and further increases the ionic transportation through concrete containing micro-cracks. This model is applied to a simple benchmark problem of a concrete cube submerged in a sulfuric acid solution. A parametric study is currently being performed, in parallel with an experimental program in order to calibrate the input parameters required for the numerical model.

INTRODUCTION

This work focuses on the numerical modeling of the degradation of concrete sewer pipes, due to sulfuric acid attack, and its implications on the residual load bearing capacity of the system. Sulfuric acid, which is produced by bacteria present in the sewage environment [1], may diffuse through the pore structure of the cement matrix of concrete. The chemical reaction of sulfuric acid with the calcium-hydroxide contained in the cement paste produces gypsum. This reaction product occupies a larger volume than the original cement paste and induces stresses and strains in the remaining cement matrix, leading to the formation of micro-cracks. The presence of micro-cracks promotes additional transport of sulfuric acid, thereby further accelerating the deterioration process.

METHODOLOGY

The modeling approach used in this study is based on the two-way coupling of a chemical model and a mechanical model, defined within a finite element setting. A staggered scheme is used. Several studies have already been proposed in the literature on the chemo-mechanical degradation process of cement as due to sulfate attacks [4, 5, 6]. This study aims to develop a model that extends earlier work from a chemical point of view by considering some additional complex chemical considerations occurring in the process, in order to determine the effect on the mechanical response. A summary of the adopted modeling strategy is given in the following.

The chemical process is described by means of a set of (diffusion-)reaction equations, which simulate the formation/dissolution of the relevant chemical species in the cement paste into their ionic components. The source and sink terms of these (diffusion-)reaction equations couple the equations and satisfy the mass balance of the system as a whole.

The chemical problem is solved first, providing the local concentrations of the chemical species. The coupling between the chemical and the mechanical models is achieved by:

- introducing a chemically-induced growth strain, proportional to the gypsum concentration, which quantifies the effect of gypsum formation on the stress field in the system,
- defining a chemical damage parameter, proportional to the concentration of calcium-silicate-hydrate, which quantifies the loss of structural integrity of the domain.

Finally, the mechanical problem, based on a continuum damage model, is solved. For this, a mechanical damage parameter is defined for which a regularisation method similar to that presented in [7] is used. This parameter represents the amount of micro-cracks in a region. The presence of damage accelerates additional transport of dissolved ions through the micro-cracks of the material. Therefore, the diffusion coefficient is assumed to degrade from the diffusion coefficient of the intact material as a function of mechanical damage. This makes the framework two-way coupled.

RESULTS

The proposed model is applied on a benchmark geometry, based on an ongoing experimental program. In the future, the model will be used to simulate realistic geometries of sewer systems. Figure 1 shows the formation of a corrosion front in a concrete block (from the exterior to the interior of the domain), which can be identified with respect to several key

*Corresponding author. E-mail: F.A.M.Rooyackers@tue.nl

parameters such as the gypsum concentration and mechanical damage. It can also be seen that stresses can only develop in the remaining intact concrete.

A parameter variation study is currently being performed in addition to an experimental campaign, which will be used in the future to calibrate the model.

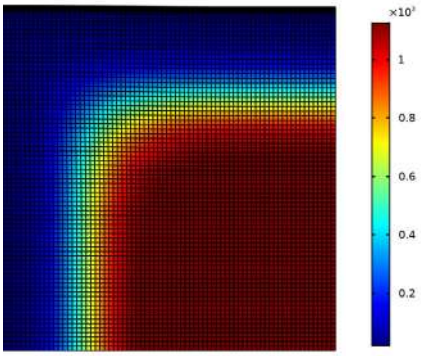

(a) CSH Solid concentrations

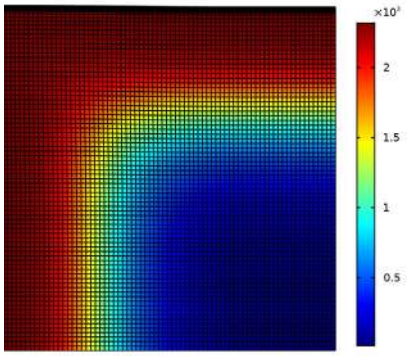

(b) $CaSO_4$ (gypsum) Solid concentrations

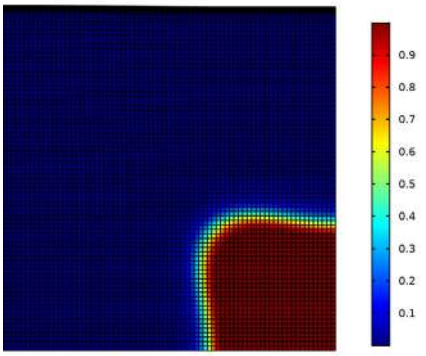

(c) Mechanical Damage Parameter

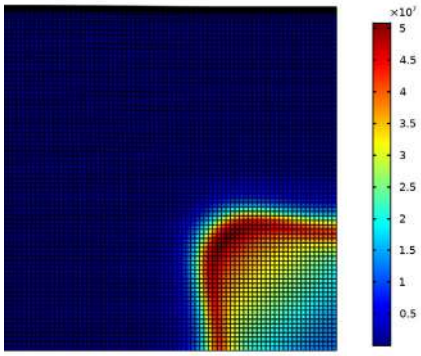

(d) Tresca Stress

Figure 1: Corrosion front (in terms of different relevant parameters) on a concrete domain subjected to a sulfuric acid solution of pH of 1, after a simulation time of 12 years. A square concrete block has been considered. Due to symmetry, only a fourth of it has been modeled.

CONCLUSIONS

In conclusion, the model presented in this study is capable of representing a corrosion front in concrete subjected to sulfuric acid attack, while accounting for the mechanical degradation of structural properties in the damaged zone. The proposed framework may be used in the future to improve the guidelines for the design of concrete sewer systems.

References

[1] Parker C. The corrosion of concrete. *Australian Journal of Experimental Biology and Medical Science*. **42**: 81-98, 1945.

[2] Le Bellgo C., Pijaudier-Cabot G., Grard B., Dub J., Molez L. Coupled Mechanical and Chemical Damage in Calcium Leached Cementitious Structures. *Journal of Engineering Mechanics*. **129**: 333-341, 2003.

[3] Johannsen K., Rademacher S. Modelling the Kinetics of Calcium Hydroxide Dissolution in Water. *Acta Hydrochimica et Hydrobiologica*. **27**: 72-78, 1999.

[4] Idiart A.E., Lopez C.M., and Carol I. Chemo-mechanical Analysis of Concrete Cracking and Degradation due to External Sulfate Attack: A Meso-scale Model. *Cement and Concrete Composites*.**33**: 411-423, 2010.

[5] Bary B. Simplified Coupled Chemo-Mechanical Modeling of Cement Pastes Behavior Subjected to Combined Leaching and External Sulfate Attack. *International Journal for Numerical and Analytical Methods in Geomechanics*.**32**: 1791-1816, 2008.

[6] Cefis N., Comi C. Chemo-mechanical Modelling of the External Sulfate Attack in Concrete. *Cement and Concrete Research*.**93**: 57-70, 2017.

[7] Cid Alfaro M.V., Suiker A.S.J., de Borst R., Remmers J.J.C. Analysis of fracture and delamination in laminates using 3D numerical modelling. *Engineering Fracture Mechanics*.**76**: 761-780, 2009.

COMPARISON OF CONSTITUTIVE MODELS DESCRIBING STRESS SOFTENING OF RUBBER MATERIALS

Alexander Ricker*[1,2], Nils Kröger[1], and Peter Wriggers[2]
[1]Deutsches Institut für Kautschuktechnologie e.V., Eupener Straße 33, 30519 Hannover, Germany
[2]Institute of Continuum Mechanics, Leibniz Universität Hannover, Appelstraße 11, 30167 Hannover, Germany

Summary Several authors presented benchmarks of hyperelastic models for rubberlike materials, see e.g. [4, 2]. This contribution continues these comparisons and analyzes nine softening models describing the well-known Mullins Effect. For this purpose, multi-hysteresis experiments in several loading modes were conducted. The softening models are combined with the most promising strain energy functions and fitted to this data. Besides the fitting quality and parameter correlation, theoretical background, thermodynamic aspects and numerical details are discussed.

INTRODUCTION AND SCOPE OF CONSIDERED MODELS

Earliest constitutive models for rubber materials which are suitable for large deformation in three-dimensional analyses date back to the 1940s, e.g. Mooney-Rivlin and Neo-Hooke model. These simple models reproduce nonlinear, but purely elastic behaviour applicable for unfilled rubber under moderate loads. Since then, many authors invested much time and effort in more realistic and sophisticated models reproducing the inelastic phenomenology of filled rubber, see [1].

One important branch of models includes those which describe the typical material softening of rubber, commonly called Mullins effect. This contribution reviews such softening models which reproduce the idealized Mullins effect, viz. neither permanent set nor equilibrium hysteresis nor continuous softening will be considered, see for instance Fig. 1 and the associated explanation in [5]. Further, the considered models can be combined with any basic strain energy function. They are classified into three groups depending on the type of the internal variable: 1. Virgin state variable (pseudo-elasticity), 2. Damage variable, 3. Amplification variable. All tested models are listed in Tab. 2. They are compared with respect to several benchmark assessment criteria like fitting quality, number of parameters and their correlation, run time, robustness and others.

No.	Literature	No. of param.	Fit to very last cycle RMSE [MPa]	Fit to very last cycle Avg. corr.	Fit to peaks of each amplitude RMSE [MPa]	Fit to peaks of each amplitude Avg. corr.
1	Amin et al. (2006)*	6	0.23548	0.53662	0.19855	0.57568
2	Klingbeil and Shield (1964)**	6	0.25061	0.34421	0.18382	0.28157
3	Kaliske and Heinrich (1999)*	4	0.31943	0.45335	0.28491	0.37898
4	Khiêm and Itskov (2016)	6	0.37975	0.75421	0.17837	0.69511
5	James et al. (1975)	5	0.34929	0.77488	0.22245	0.79059

Table 1: Considered hyperelastic models and fitting results. *slightly modified due to numerical reasons, **generalized

EXPERIMENTS AND CHOICE OF BASIC STRAIN ENERGY FUNCTION

The most important criterion is probably the fitting quality to experimental findings. For this purpose, quasi-static multihysteresis experiments with carbon black filled, sulphur-linked EPDM under uniaxial, planar (also pure shear) and equi-biaxial tension were conducted. Load amplitudes up to 400 %, 200 % and 70 %, respectively, were considered. See Fig. 1(left) for the test procedure in case of uniaxial loading.

The fitting quality depends crucially on the employed basic strain energy function. Therefore, a short list from the huge number of strain energy functions which can be found in literature (see e.g. [4]) is compiled in Tab. 1. On the one hand, these models are fitted simultaneously to the very last cycle of the multihysteresis experiments. On the other hand, the peaks of each load amplitude are extracted and considered for fitting. In both cases, the least-squares method is used to minimize the error sum regarding the absolute 2nd Piola-Kirchoff stress. The results are given in terms of the root mean square error and the average parameter correlation. Very good fits are obtained from the strain energy function proposed by Amin et al. (2006). Hence, this one serves as the basic strain function in the following section.

*Corresponding author. E-mail: alexander.ricker@dikautschuk.de.

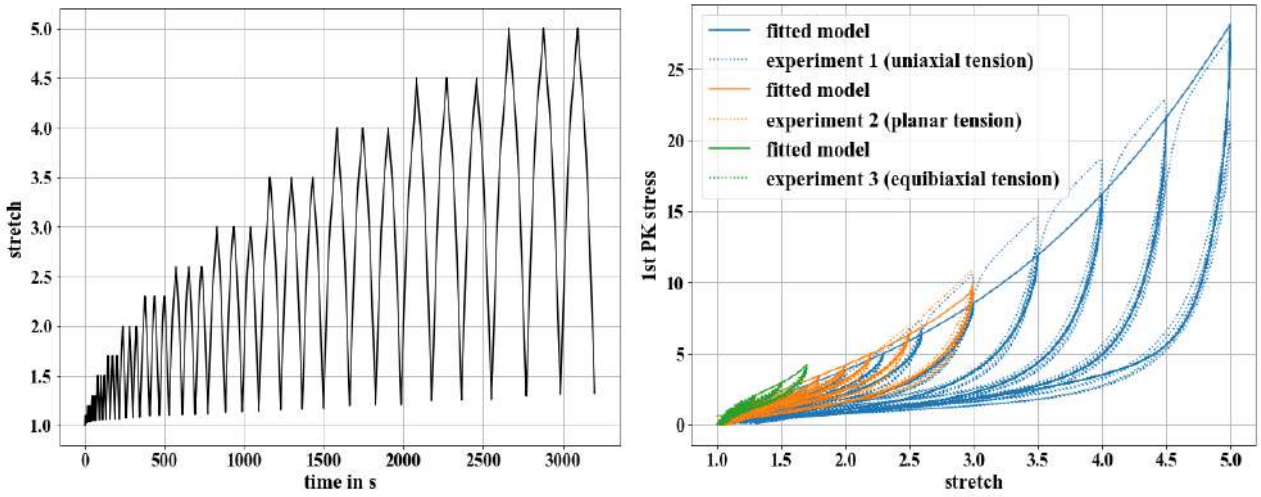

Figure 1: Quasi-static, uniaxial multihysteresis experiment.

PARAMETER FITTING OF SOFTENING MODELS AND CONCLUSION

Next, the softening models listed above are fitted to the experimental data. Instead of extracting particular cycles or data points, the whole experiments are considered now. The results are listed in Tab. 2. The class of softening models using a virgin state variable yields clearly the best results. Within this class, the model by Wrubleski and Marczak (2015) stands out from the rest. Even reducing its number of parameters by fixing $q = \frac{1}{2}$ leads to very good results with $\mathrm{RMSE} = 0.16335$ MPa and a comparatively low average parameter correlation of 0.3748969. The fitting quality is depicted in Fig. 1(right).

No.	Literature	No. of param.	Fit to whole experiments RMSE [MPa]	Avg. corr.
1.1	Wrubleski and Marczak (2015)	3	0.15862	0.33637
1.2	Dorfmann and Ogden (2003)	2	0.19440	0.37016
1.3	Ogden and Roxburgh (1999)	2	0.19922	0.37056
1.4	de Souza Neto et al. (1993)	3	0.30787	0.34938
2.1	Chagnon et al. (2004)	2	0.27923	0.44417
2.2	Miehe (1995)	2	0.29803	0.39989
2.3	Simo (1987)	2	0.31826	0.37481
2.4	Besdo and Ihlemann (2003)*	2	0.34481	0.39211
3.1	Plagge and Klüppel (2017)	3	0.33316	0.36886

Table 2: Considered softening models and fitting results. * slightly modified "basic stress".

OUTLOOK

Other relevant criteria for material models are their run time and robustness, viz. sensitivity to the mesh and time step size. For testing purposes, FE simulations of a rotating shear test with various spatial and temporal discretisations were carried out. To ensure similar test conditions for all models, the automatic code generation toolbox AceGen [3] is used guaranteeing fast codes and analytical material tangents. These results as well as theoretical background, thermodynamic aspects and numerical details will be discussed at the conference.

References

[1] Carleo F., Barbieri E., Whear R., Busfield J. J. C. Limitations of Viscoelastic Constitutive Models for Carbon-Black Reinforced Rubber in Medium Dynamic Strains and Medium Strain Rates. *Polymers* **10**: 988, 2018.

[2] Dal H., Badienia Y., Açikgz K., Aksu Denlï F. A comparative study on hyperelastic constitutive models on rubber: State of the art after 2006. *ECCMR XI*: 239-244, 2019.

[3] Korelc J., Wriggers P. Automation of Finite Element Methods. Springer International Publishing, Switzerland 2016.

[4] Marckmann G., Verron E. Comparison of Hyperelastic Models for Rubber-Like Materials. *Rubber Chem. Technol.* **79**: 835-858, 2006.

[5] Ogden R. W., Roxburgh, D. G. A pseudo-elastic model for the Mullins effect in filled rubber. *P. Roy. Soc. Lond. A Mat.* **455**: 2861-2877, 1999.

A MODEL APPROACH FOR THE FAILURE BEHAVIOR OF CERAMIC MATRIX COMPOSITES UNDER THERMAL AND MECHANICAL LOADING

Marie-Christine Reuvers*[1], Theron Guo[1], Shahed Rezaei[1], Tim Brepols[1], and Stefanie Reese[1]
[1]Institute of Applied Mechanics, RWTH Aachen University, Aachen, Germany

Summary Higher demands on material components in aerospace application result in extensive research for new materials to replace metallic engine parts. A well suited class of materials for this challenging environments are ceramic matrix composites (CMCs). Their fracture toughness compared to classical ceramics is increased by an additional fibrous reinforcement. Although the additional fibers are also of ceramic origin, the resulting composite improves in ductility, due to the interface manufacturing process. The result is a pseudo-plastic material response, similar to metal. This contribution focusses on the development of a thermomechanical model for the various failure mechanisms of CMCs. Therefore two damage formulations are combined: a continuum damage approach to account for brittle matrix failure and an interface model based on classical cohesive elements.

INTRODUCTION

Ceramic matrix composites (CMCs) or technical ceramics were developed as an enhancement of classical ceramic materials to overcome previous limitations such as for example low fracture toughness and brittle failure under mechanical or thermomechanocal loading. This enables this new class of materials for use in aerospace engines which are exposed to high temperatures, oxidizing environments and have to withstand numerous load cycles during their lifetime. Until now most engine components are made out of metal alloys, resulting in a rather short component lifespan. The use of CMCs in these kind of surroundings increases the temperature resistance and therefore allows for higher service temperatures leading to a better utilisation factor of the engine. In addition to the high temperature stability, their corrosion resistance as well as their low weight makes CMCs attractive for aerospace application. On the other hand ceramic materials are considered relatively brittle in comparison to metals. To counteract this phenomenon CMCs consist of ceramic fiber bundles, the so called tows embedded in a ceramic matrix, often in a woven manner. To achieve a plastic material response similar to metals, the interface of technical ceramics is designed to be weak. In the case of damage, a crack that develops in the matrix, evolves until it reaches the interface, there it deflects, leaving the fiber undamaged. This way the fibers can separate individually from the matrix and still carry load until the final damage state, the fiber sliding and rupture, is reached. There are two different ways to generate a weak interface. Either by using a highly porous matrix material or through an additional coating on the fibers with a lower fracture energy compared to the ceramic material. For our application, the latter method is more relevant. Still the coating interphase is neglected during simulation, its effect however is captured in the modelig of the inteface. [1, 2]

This work focusses on the development of a general modeling strategy for various CMC scales using multiple damage models. As can be seen in Fig.1 the delamination between several plies or the separation of the weak interface between matrix and tow is modeled using an interface model based on [3] which predicts cohesive behavior. The brittle matrix is repesented by an elastic gradient-extended damage formulation based on a more general model by [4, 5]. Both formulations are thermocoupled to realistically account for the material degradation under high thermal loading.

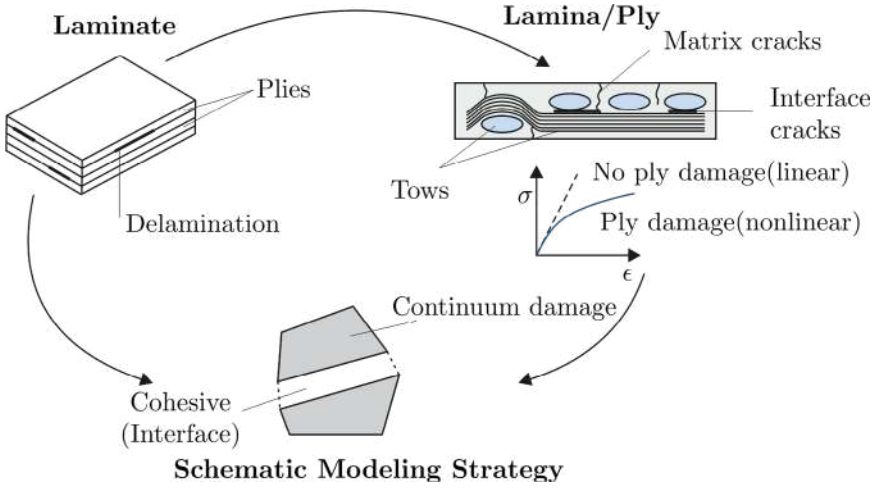

Figure 1: Schematic modeling strategy for different CMC scales using continuum damage and cohesive behavior.

*Corresponding author. E-mail: marie.reuvers@ifam.rwth-aachen.de.

INTERFACE BEHAVIOR

Based on the work of [3] and [4] a thermodynamically consistent interface formulation was derived, in accordance with the principals of [6]. The model predicts the separation in the interface of delaminating materials under thermal and mechanical loading. Taking the frictional behavior between the two components into account, also the subsequent failure mode after the interface separation is considered. The mechanical part of the Helmholtz free energy can be divided into four parts:

$$\psi = \psi_e(\boldsymbol{g}, D, \theta) + \psi_d(\xi_d, \theta) + \psi_g(\boldsymbol{g}) + \psi_f(\boldsymbol{g}^e).$$

The elastic part $\psi_e(\boldsymbol{g}, D, \theta) = (1-D)^b \, \frac{1}{2} \, \boldsymbol{g}^T \, \boldsymbol{K}^\theta \, \boldsymbol{g}$ depends on the damage variable D, as well as the damage exponent b. With the vector $\mathbf{g}$ the gap between the separating bodies is indicated, split into normal (N) and tangential (T) direction while the temperature dependent interface stiffness for both directions is embedded in $\mathbf{K}^\theta$. A nonlinear damage hardening $\psi_d(\xi_d) = \frac{r_i^\theta}{1-\exp(-s_i)} \left(\xi_d + \frac{\exp(-s_i \xi_d) - 1}{s_i} \right)$ is given through as a function of the interface material specific damage parameters r_i^θ and s_i. By $\psi_g(\boldsymbol{g}) = \frac{1}{2} K_p \langle -g_N \rangle$ a penalty term is given, that prevents penetration of the two bodies, depending on the opening in normal direction and the penalty stiffness K_p. To capture frictional behavior between the components a split of the gap in tangential direction in an elastic and a frictional part $g_T = g_T^e + g_T^f$ is proposed after [7]. With the use of the modified Coulomb's law of friction, the last part of the Helmholtz free energy follows to $\psi_f(\boldsymbol{g}^e) = H(-g_N) \left(\frac{1}{2} c_T \, (g_T^e)^2 \right)$, $H(-g_N) = \begin{cases} 1 & \text{if } g_N \leq 0 \\ 0 & \text{if } g_N > 0 \end{cases}$, depending on the initial stiffness c_T. In analogy to [8] the parameters $\mathbf{K}^\theta$, r_i^θ and the onset of damage Y_0^θ are dependent on the temperature to capture thermal effects. To complete the model equations a heat flow $q(g_\theta, D^\theta) = -((1-D^\theta)k_s + k_a) g_\theta$ based on [9] is introduced, depending on the thermal damage variable D^θ, the thermal conductivity of the solid k_s and the gaseous k_a phase as well as a temperature jump g_θ.

BRITTLE MATRIX DAMAGE

The damage in the matrix material is captured using an elastic gradient-extended damage formulation, based on a more general model by [4, 5]. Note that the plastic part of the model is neglected here, due to the brittle nature of the ceramic material. The free energy

$$\psi = (1-D)^2 \psi_e(\boldsymbol{\varepsilon}_e) + \psi_d(\xi_d) + \psi_{\bar{d}}(D - \bar{D}, \nabla \bar{D})$$

is split into an elastic part $\psi_e(\boldsymbol{\varepsilon}_e) = \frac{1}{2} \boldsymbol{\varepsilon}_e \cdot \mathbb{C} \, [\boldsymbol{\varepsilon}_e]$ and a damage hardening term $\psi_d(\xi_d) = r_m \left(\xi_d + \frac{\exp(-s_m \xi_d) - 1}{s_m} \right)$ depending on the matrix material specific damage parameters r_m and s_m. To conclude a micromorphic extension $\psi_{\bar{d}}(D - \bar{D}, \nabla \bar{D}) = \frac{A}{2} \nabla \bar{D} \cdot \nabla \bar{D} + \frac{H}{2} (D - \bar{D})^2$ is introduced as a function of the micromorphic damage $\bar{D}$ and its first gradient. To capture the thermal degradation of CMCs a thermocoupling of the respective elastic material parameters as well as the onset of damage is implied. In addition due to the high Young's modulus temperature differences in the material lead to high local stresses, which needs to be accounted for.

References

[1] Bansal N.P., Lamon J. Ceramic matrix composites: materials, modeling and technology. John Wiley & Sons, 2014.
[2] Chawla K.K. Ceramic matrix composites. Springer Science & Business, 2013.
[3] Rezaei S., Jaworek D., Mianroodi J.R., Wulfinghoff S., Reese S. Atomistically motivated interface model to account for coupled plasticity and damage at grain boundaries. *J Mech Phys Solids.* **124**: 325-349, 2019.
[4] Brepols T., Wulfinghoff S., Reese S. Gradient-extended two-surface damage-plasticity: micromorphic formulation and numerical aspects. *Int J Plasticity.* **97**: 64-106, 2007.
[5] Brepols T., Wulfinghoff S., Reese S. A micromorphic damage-plasticity model to counteract mesh dependence in finite element simulations involving material softening. Multiscale Modeling of Heterogeneous Structures. Springer, 2018.
[6] Gurtin M. E.Thermodynamics and the cohesive zone in fracture. *Z Angew Math Phys.* **30(6)**: 991-1003, 1979.
[7] Alfano G., Sacco E. Combining interface damage and friction in a cohesive-zone model. *Int J Numer Meth Eng.* **68(5)**: 542-582, 2006.
[8] Dandekar C.R., Shin Y.C. Molecular dynamics based cohesive zone law for describing Al-SiC interface mechanics. *Compos Part A-Appl S.* **42.4**: 355-363, 2011.
[9] Wu T., Wriggers P. Multiscale diffusion-thermal-mechanical cohesive zone model for concrete. *Comput Mech.* **55(5)**: 999-1016, 2015.

MECHANISTIC ORIGIN OF THE APPARENT SUBSTRUCTURE BOUNDARY SLIDING OF MARTENSITE IN HIGH-STRENGTH STEELS

Francesco Maresca*[1], Varvara Kouznetsova [2], William Curtin[3], and Marc Geers[2]
[1]Faculty of Science and Engineering, University of Groningen, Groningen, The Netherlands
[2]Department of Mechanical Engineering, Eindhoven University of Technology, Eindhoven, The Netherlands
[3]Institute of Mechanical Engineering,Ecole Polytechnique Fédérale de Lausanne,Lausanne,Switzerland

Summary Lath martensite is a key constituent phase in advanced high strength steels, providing the high strength. Furthermore, its combination with other phases, such as austenite and ferrite, enables to overcome the strength-ductility trade-off of conventional steels. Understanding the complex mechanical response of martensite in multi-phase steels is therefore essential to enable the control of the damage behaviour of steels. Experiments have shown that martensite has an extremely anisotropic deformation behaviour. The easiest deformation mode is the apparent sliding occurring at lath boundaries. By developing a multi-scale model that includes thin austenite films at lath boundaries, we show that the apparent boundary sliding can be rationalized by the dislocation-mediated plasticity and/or the phase transformation of the austenite, acting as a greasy layer on which the stiffer laths slide.

INTRODUCTION

New advanced high strength steels (AHSS) that are characterized by good strength and deformability are being constantly developed and improved in order to fulfill the growing demands for light-weight and safe materials. Lath martensite is a main constituent of such steels, since it provides the high strength and plays a key role in controlling the fracture behaviour. It is therefore essential to understand the fundamental mechanisms that control martensite plasticity and damage, in order to be able to improve the damage behaviour of high strength steels.

Lath martensite is characterized by a hierarchical microstructure [1], which originates from the symmetries of the martensitic transformation [2]. The body-centered-cubic (BCC) martensite crystals form after rapid quenching of the face-centered cubic (FCC) austenite, and organize into subgrains consisting of parallel stacks of elongated BCC (the laths) belonging to the same crystallographic variant – a fact that marks an important difference with the so-called "plate" martensite, where twin-related variants are found instead. Even in the presence of low alloying elements, which is the case of AHSS, all internal lath martensite boundaries can be decorated with thin, nanometer-sized films of retained austenite [3]. The hierarchical microstructure, containing subgrains with stacks of BCC martensite alternating with thin austenite film, is the focus of the modelling work presented here.

In the first part of the presentation, the lath martensite microstructure is modelled using continuum crystal plasticity, assuming dislocation-mediated plasticity to occur within the interlath retained austenite films [4]. In the second part of the presentation, the martensite microstructure with the austenite films is modelled by assuming that plasticity is carried by the phase transformation of the thin, retained austenite films [5]. Both cases lead to apparent grain boundary sliding, thus providing a mechanistic framework that rationalizes the recent observations of subgrain boundary sliding of martensite in low carbon steels [6].

LATH MARTENSITE WITH DISLOCATION SLIP IN THE AUSTENITE FILMS

One lath martensite sub-grain (called "sub-block", M) is modelled as a locally infinite laminate where both the overall deformation $\mathbf{F}^M$ and the (first Piola-Kirchhoff) stress $\mathbf{P}^M$ are the weighted averages (over the volume fraction f) of the austenite (A) and the lath (L) single-phase deformations and stresses, under the conditions of interface compatibility and equilibrium

$$\begin{aligned} &\mathbf{F}^M = f^A\mathbf{F}^A + f^L\mathbf{F}^L\,, && \mathbf{P}^M = f^A\mathbf{P}^A + f^L\mathbf{P}^L \\ &\mathbf{F}^A\cdot(\mathbf{I}-\mathbf{n}_0\otimes\mathbf{n}_0) = \mathbf{F}^L\cdot(\mathbf{I}-\mathbf{n}_0\otimes\mathbf{n}_0)\,, && \mathbf{P}^A\cdot\mathbf{n}_0 = \mathbf{P}^L\cdot\mathbf{n}_0 \end{aligned} \tag{1}$$

where $\mathbf{n}_0$ is the interface normal in the reference configuration, which is assumed parallel to a $\{111\}_A$ plane normal, thus about $\theta = 10°$ from the typical habit plane normal in FeC steels [2]. Slip in the austenite occurs parallel to such an interface. Both the austenite films and the laths are modelled using a continuum crystal plasticity framework respecting the experimental orientation relationship [4]. A rate-dependent, smeared-interface damage model is also used, that models failure at the A/L interface within the martensite [7]. Microstructural configurations with multiple sub-grains are then modelled, based on experimental micrographs, and simulated under quasi-static tensile loading conditions. Figure 1 shows the comparison between the simulation results and the experiments performed on such microstructures. The figure shows that the multi-scale model of lath martensite, including multiple sub-grains and dislocation-mediated plasticity in the thin interlath retained austenite films, can capture the stress-strain response and the global onset of necking of actual lath martensite microstructures.

*Corresponding author. E-mail: f.maresca@rug.nl

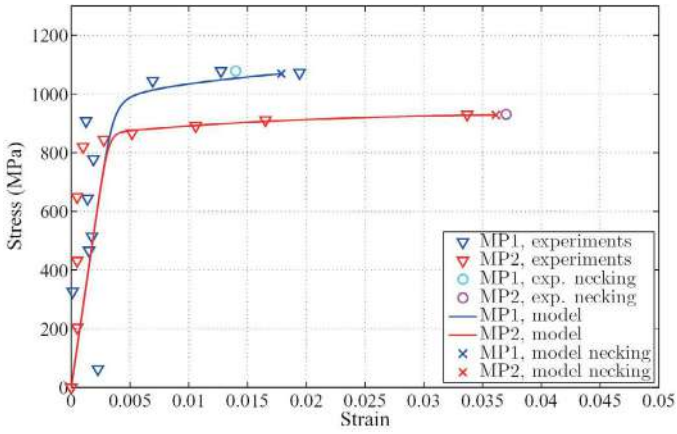

Figure 1: Comparison between simulations and experiments, reproduced from [7].

LATH MARTENSITE WITH TRANSFORMING RETAINED AUSTENITE FILMS

In low C, low-alloyed steels, the interlath austenite films can be so thin that they can hardly accommodate any dislocation plasticity. We have therefore performed detailed Molecular Dynamics (MD) simulations of the austenite-martensite interface, reproducing all the main features observed in experiments [2], see Figure 2.

A combination of crystallographic theory and atomistic modelling [2] shows that, even in absence of any dislocation in the thin retained austenite films, large deformations amounting to $\sim 90\%$ shear can be accommodated by phase transformation of the austenite, which is driven by interface migration.

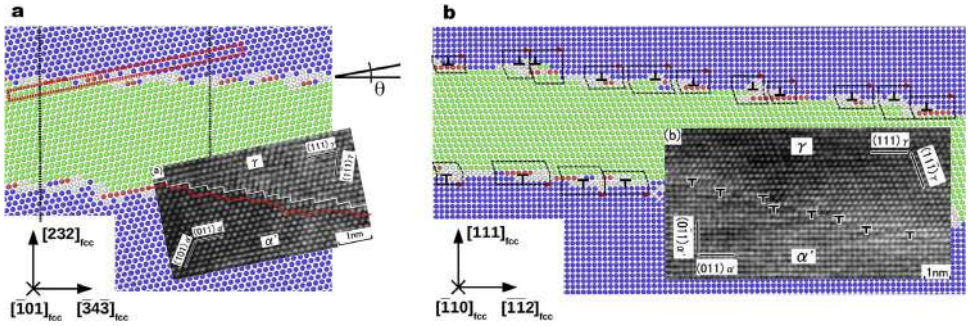

Figure 2: MD simulation of the FCC austenite/BCC martensite interface, compared with high-resolution transmission electron micrographs, viewed along **a** $[\bar{1}01]_A$ and **b** $[\bar{1}10]_A$ directions. Reproduced from [2].

CONCLUSIONS

The characteristic deformation mode of lath martensite is substructure boundary sliding at lath boundaries. We have shown, by means of multi-scale crystal plasticity and atomistic simulations, that the substructure boundary sliding can originate by the deformation of thin, nanoscale retained austenite films at lath boundaries. The austenite films can accommodate this deformation either by dislocation-mediated plasticity, or by phase transformation.

References

[1] S. Morito, H. Tanaka, R. Konishi, T. Furuhara, T. Maki, The morphology and crystallography of lath martensite in Fe-C alloys, *Acta Mater.* **51** (2003) 1789–1799.

[2] F. Maresca, W. A. Curtin, The austenite/lath martensite interface in steels: Structure, athermal motion, and in-situ transformation strain revealed by simulation and theory, *Acta Mater.* **134** (2017) 302–323.

[3] B. P. J. Sandvik, C. M. Wayman, Crystallography and substructure of lath martensite formed in carbon steels, *Metallography* **16** (1983) 199–227.

[4] F. Maresca, V. G. Kouznetsova, M. G. D. Geers, Subgrain lath martensite mechanics: A numerical-experimental analysis, *J. Mech. Phys. Solids* **73** (2014) 69–83.

[5] F. Maresca, V. G. Kouznetsova, M. G. D. Geers, W. A. Curtin, Contribution of austenite-martensite transformation to deformability of advanced high strength steels: From atomistic mechanisms to microstructural response, *Acta Mater.* **156** (2018) 463–478.

[6] C. Du, J. P. M. Hoefnagels, R. Vaes, M. G. D. Geers, Plasticity of lath martensite by sliding of substructure boundaries, *Scripta Mater.* **120** (2016) 37–40.

[7] F. Maresca, V. G. Kouznetsova, M. G. D. Geers, Predictive modeling of interfacial damage in substructured steels: application to martensitic microstructures, *Modelling Simul. Mater. Sci. Eng.* **24** (2016) 025006.

A ROBUST EXPLICIT ALGORITHM FOR PHASE-FIELD MODELING OF QUASI-BRITTLE FRACTURE

Alessandro Marengo*[1], Alessia Patton [2], Matteo Negri[3], Umberto Perego [1], and Alessandro Reali [2]
[1]Department of Civil and Environmental Engineering, Politecnico di Milano, Milano, Italy
[2]Department of Civil Engineering and Architecture, University of Pavia, Pavia, Italy 3Department of Mathematics, University of Pavia, Pavia, Italy

Summary The phase-field modeling of quasi-brittle fracture accounting for the irreversible growth of the regularization variable is considered. As a consequence of this irreversibility, the minimization problem turns into a variational inequality. A staggered solution scheme is employed to decouple the optimization algorithm. This leads to two sub-problems for the displacement and the phase field. The spatial discretization transforms the phase-field sub-problem into a symmetric linear complementarity problem. The present paper shows a robust and explicit algorithm to solve this problem.

INTRODUCTION

The phase-field model is used here for a variational approach to quasi-brittle fracture. The topology of a sharp crack is regularized or diffused into the bulk of the body with a transition function that can be interpreted as a damage variable (see [1]). A consistent thermodynamic formulation requires the damage to be a non-decreasing function during any transformation. This property is here referred to as *irreversibility* and acts as a constraint in the mechanical model.
The variational approach to fracture interprets the crack evolution within the elastic body as a minimization problem of a suitable energy functional. The irreverstibility makes the approach a constrained minimization problem and turns it into a variational inequality. This constraint is enforced in [2] with a monotonically growing driving force of the phase field (so-called history variable), while in [3] a penalty functional is introduced into the formulation to replace the constraint. Inspired by the work of [4], the current paper presents a robust and explicit iterative algorithm [5] to rigorously enforce the constraint and solve the variational inequality.

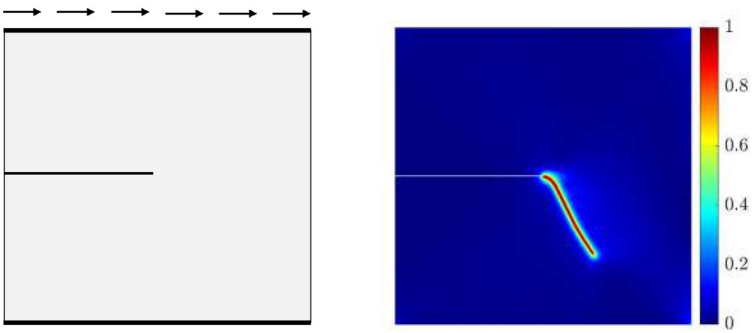

(a) *Static Scheme* (b) *Phase-Field*

Figure 1: Shear test on 2D square specimen in plane strain. The initial notch has length equal to half the domain side. The bottom edge is clamped, while the top edge undergoes a uniform horizontal displacement. The phase field ranges from $d = 0$ (undamaged material) to $d = 1$ (fully broken material).

MECHANICAL MODEL

The state variables are the displacement vector $\mathbf{u}$ and the scalar phase field d. Irreverstibility requires that $\dot{d} \geq 0$. The variational approach minimizes the total energy functional defined as follows:

$$\Pi(\mathbf{u}, d) = \mathcal{E}(\mathbf{u}, d) + \mathcal{D}(d, \nabla d) - \mathcal{W}(\mathbf{u}) \tag{1}$$

The internal energy functional $\mathcal{E}(\mathbf{u}, d) = \int_\Omega \psi(\mathbf{u}, d)\, \mathrm{d}\Omega$ measures the energy stored into the body, while the dissipation functional $\mathcal{D}(d, \nabla d) = \int_\Omega \phi(d, \nabla d)\, \mathrm{d}\Omega$ accounts for the energy dissipated due to crack propagation. The functions ψ and ϕ are respectively the free and dissipated energy per unit volume. The free energy of the unbroken material is split into its volumetric and deviatoric parts. The damage degrades the positive volumetric and the deviatoric parts only.
The dissipation functional $\mathcal{D}(d,\nabla d)$ depends on the phase field and its gradient (see [1]). The presence of the gradient term makes the constitutive behavior non-local, eliminating the pathological mesh-dependence of the softening models, at the cost of the introduction of a new field variable in the problem. Finally, the work of volume and surface actions resides

*E-mail: alessandro.marengo@polimi.it

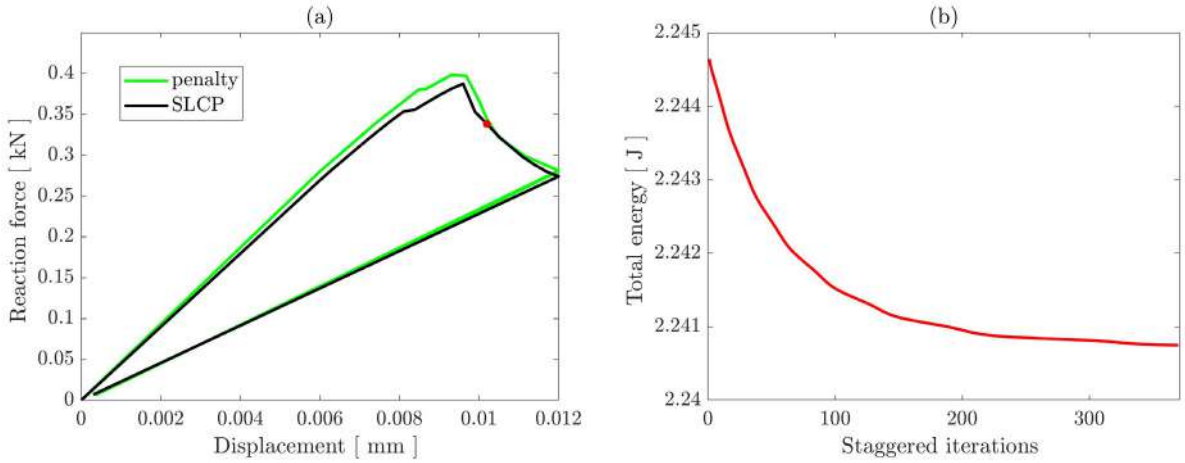

Figure 2: Loading-unloading shear test: (a) reaction force versus imposed displacement, (b) minimization of the total energy. The red marker denotes increment 15.

in the external work functional $\mathcal{W}(\mathbf{u})$.
Introducing the notation $\delta_x \Pi(x) := \Pi(x + \delta x) - \Pi(x)$, stationarity of (1) can be written as follows:

$$\delta_{\mathbf{u}} \Pi = 0 \tag{2a}$$

$$\delta_d \Pi = 0 \quad \text{with} \quad \dot{d} \geq 0 \tag{2b}$$

The irreversibility condition on the phase-field variable leads the optimization problem (2) to be a constrained minimization principle. While the stationarity with respect to the dispacement (2a) leads to a variational equation (i.e., the balance of linear momentum), the stationarity with respect to the constrained phase-field variable (2b) leads to a variational inequality (i.e., the well-known set of Kuhn-Tucker conditions).

NUMERICAL IMPLEMENTATION

Staggered Iterative Scheme A staggered scheme is adopted for the solution, since the non-convex total energy becomes convex whenever a state variable is kept fixed and the other is free. For each load increment the balance of linear momentum (2a) and the Kuhn-Tucker conditions (2b) are solved alternatively until a convergence criterion is met.

Symmetric Linear Complementarity Problem (SLCP) The spatial discretization turns the variational inequality (2b) into a so-called *Symmetric Linear Complementarity Problem*. Its standard form reads:

$$\mathbf{f}(\Delta \mathbf{d}) \cdot \Delta \mathbf{d} = 0 \quad , \quad \mathbf{f}(\Delta \mathbf{d}) \geq \mathbf{0} \quad , \quad \Delta \mathbf{d} \geq \mathbf{0} \tag{3}$$

where $\Delta \mathbf{d}$ is the vector of nodal phase-field increments; $\mathbf{f}(\Delta \mathbf{d}) := \mathbf{Q}\,\Delta \mathbf{d} + \mathbf{q}$ is the activation function; $\mathbf{Q}$ is a symmetric, positive definite matrix and $\mathbf{q}$ is a vector accounting for the driving force. The problem is *symmetric* due to the symmetry of matrix $\mathbf{Q}$ deriving from the variational nature of the approach and is *linear* because of the linearity of the activation function $\mathbf{f}(\Delta \mathbf{d})$ in the phase-field increment $\Delta \mathbf{d}$. In the current paper, (3) is solved using the explicit and iterative algorithm proposed by Mangasarian in [5], where the irreversibility constraint $\dot{d} \geq 0$ is rigorously enforced.

SIMULATIONS AND RESULTS

Numerical simulations are perfomed under the hypotesis of small displacements and quasi-statics. The phase-field profile of a loading-unloading shear test on a 2D specimen in plane strain is shown in Figure 1. In Figure 2(a) the reaction force is plotted versus the imposed displacement and is compared with the corresponding result in [3], while the evolution of the total energy during the staggered iterations for a typical load increment is reported in Figure 2(b).

References

[1] Miehe C., Welschinger F., Hofacker M., Thermodynamically-consistent phase field models of fracture: Variational principles and multi-field FE implementations. *Int. J. Num. Meth. Engng.* Vol. **83** : 1273–1311, 2010.
[2] Miehe C., Hofacker M., Welschinger F., A phase field model for rate-independent crack propagation: robust algorithmic implementation based on operator splits. *Comput. Methods Appl. Mech. Engrg* **199** : 2765–2778, 2010.
[3] Gerasimov T., De Lorenzis L., On penalization in variational phase-field models of brittle fracture. *Comput. Methods Appl. Mech. Engrg* **354** : 990–1026, 2019.
[4] Comi C., Perego U., A generalized variable formulation for gradient dependent softening plasticity. *Int. J. Num. Meth. Engng.* Vol. **39** : 3731–3755, 1996.
[5] Mangasarian O.L., Solution of symmetric linear complementarity problems by iterative methods. *J. Opt. Theor.* Appl. **22** : 465, 1977.

REGULARIZATIONAL APPROACH TO ANISOTROPIC DUCTILE DAMAGE: APPLICATION TO LOW-CYCLE-FATIGUE

Kai Langenfeld[1], Kerstin Möhring[2], Frank Walther[2], and Jörn Mosler[*1]
[1]Institute of Mechanics, TU Dortmund University, Dortmund, Germany
[2]Department of Materials Test Engineering, TU Dortmund University, Dortmund, Germany

Summary Low cycle fatigue is in general associated with large plastic strains accompanied by the formation and coalescence of pores. Considering continuum damage mechanics, there are many local constitutive models for ductile damage in the literature. These local models, that do not involve any length scale are ill-posed from a mathematical point of view. In order to regularize the resulting mesh dependency, the micromorphic approach will be applied. Within this talk, it will be shown that a straightforward implementation of the micromorphic approach is not suitable to regularize ductile damage models of Lemaitre-type. A modified version will be thus proposed and applied to an anisotropic model for ductile damage. This modified model will be adapted to low cycle fatigue and its capabilities are shown by illustrative examples.

KINEMATICS

Let $\boldsymbol{u}(\boldsymbol{X})$ be the displacement field of all points $\boldsymbol{X}$ of body $\mathcal{B}$. Then, the Hencky strain tensor follows as $\boldsymbol{\varepsilon} = \frac{1}{2}\ln(\boldsymbol{C})$ with $\boldsymbol{C}$ being the right Cauchy-Green tensor. The additive split of the Hencky strain tensor in an elastic part and a plastic part $\boldsymbol{\varepsilon} = \boldsymbol{\varepsilon}^{\mathrm{e}} + \boldsymbol{\varepsilon}^{\mathrm{p}}$, cf. [1], allows to extend linearized kinematics to finite strains while preserving the local constitutive framework.

CONSTITUTIVE MODEL

The constitutive model is adopted from [2, 3] and based on the principal of strain energy equivalence, cf. [4]. The gradient-enhanced Helmholtz energy reads

$$\psi = \psi^{\mathrm{e}}(\boldsymbol{\varepsilon},\, \boldsymbol{\varepsilon}^{\mathrm{p}},\, \boldsymbol{b}) + \psi^{\mathrm{p}}(\boldsymbol{a},\, \boldsymbol{k};\, \boldsymbol{b}) + \psi^{\mathrm{pen}}(\boldsymbol{b},\, \boldsymbol{\varphi_b}) + \psi^{\mathrm{grad}}(\nabla\boldsymbol{\varphi_b}) \tag{1}$$

with $\boldsymbol{a}$ and $\boldsymbol{k}$ being two second-order tensors associated with kinematic and isotropic hardening. The tensor $\boldsymbol{b}$ describes the integrity of material points, i.e., $\boldsymbol{b} = \boldsymbol{I}$ denotes intact material points and $\boldsymbol{b} \to \boldsymbol{0}$ fully damaged material points. Tensor $\boldsymbol{\varphi_b}$ is coupled to integrity tensor $\boldsymbol{b}$ in terms of the micromorphic regularization technique [5, 6]. The dual variables then follow as

$$\boldsymbol{\sigma} = \frac{\partial\psi}{\partial\boldsymbol{\varepsilon}},\quad \boldsymbol{\omega} = \frac{\partial\psi}{\partial\boldsymbol{\varphi_b}},\quad \boldsymbol{\alpha} = -\frac{\partial\psi}{\partial\boldsymbol{a}},\quad \boldsymbol{\kappa} = -\frac{\partial\psi}{\partial\boldsymbol{k}},\quad \boldsymbol{\beta} = -\frac{\partial\psi}{\partial\boldsymbol{b}}\,. \tag{2}$$

The model is completed in terms of evolution equations falling into the framework of Generalized Standard Materials, cf. [7], i.e., the dissipation inequality is automatically fulfilled. The corresponding plastic potential g reads

$$g = \Phi(\boldsymbol{\sigma}, \boldsymbol{\omega},\, \boldsymbol{\alpha},\, \boldsymbol{\kappa};\, \boldsymbol{b}) + \Gamma_{\boldsymbol{\alpha}}(\boldsymbol{\alpha};\, \boldsymbol{b}) + \Gamma_{\boldsymbol{\beta}}(\boldsymbol{\beta};\, \boldsymbol{b})\,, \tag{3}$$

and consists of the yield function Φ and the non-associative parts $\Gamma_{\boldsymbol{\alpha}}$ and $\Gamma_{\boldsymbol{\beta}}$. The aforementioned modification of the

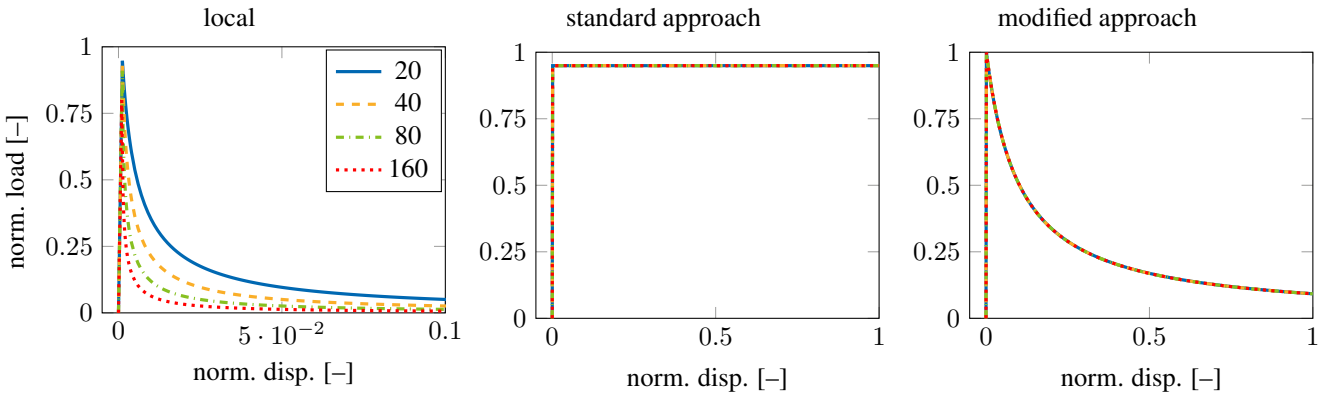

Figure 1: One-dimensional truss with an imperfection: Load-displacement diagrams predicted by: (left) the local model, (middle) the standard micromporphic model and (right) the modified micromorpic model for different finite element meshes (20, 40, 80 and 160 finite elements)

*Corresponding author. E-mail: joern.mosler@tu-dortmund.de.

micromorphic approach is the direct dependence of the yield function on ω, that can be rewritten as a gradient contribution, cf. [8].

Fig. 1 highlights this effect by the example of a one-dimensional truss with an imperfection. The left figure shows the typical localization effect when considering models without internal length scale. Contrary, both the standard micromorphic approach and the modified version yield mesh independent results. Yet, only the modified version shows a softening response. By considering two-dimensional boundary value problems, it is shown in [8] that the standard approach leads, similar to the local model, to mesh-dependent results.

EXTENSION TO LOW CYCLE FATIGUE

In order to adapt the model to low cycle fatigue, certain changes to the constitutive equations are introduced. To be more precise, the adapted model is able to simultaneously represent linear and non-linear isotropic hardening as well as non-linear kinematic hardening. Furthermore the damage evolution is triggered in dependence on the dissipated plastic work during deformation, i.e., the damage evolution starts as soon as the dissipated plastic work exceeds a material specific parameter as suggested by [9].

A first impression of the final model is given in Fig. 2, in which the model is calibrated with respect to a cyclic tensile test. The left plot shows the load-displacement diagram at 77 cycles and the right plot the load-displacement diagram

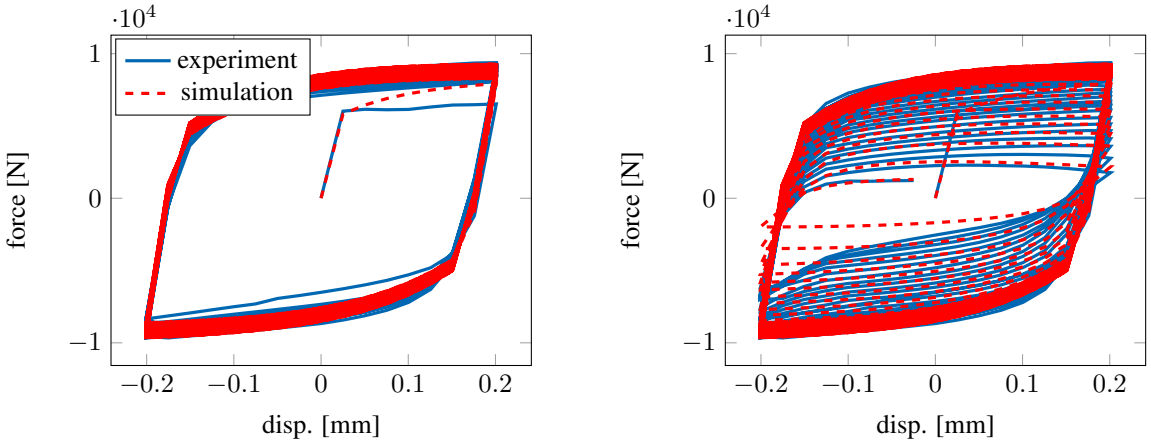

Figure 2: Cyclic tensile test – left: load-displacement diagram at 77 cycles; right: load-displacement diagram at 93 cycles (failure)

until failure after 93 cycles. It can be seen that the extended model is able to simulate the cyclic hardening as well as the material degradation in a mesh objective manner.

CONCLUSION

A constitutive model suitable for the analysis of ductile damage with respect to low cycle fatigue was presented. It is based on the local constitutive framework proposed in [2, 3] and it has been gradient-enhanced by means of the micromorphic regularization suggested in [5, 6]. It was shown, that a straightforward implementation of the micromorphic approach fails in regularizing the aforementioned model and an alternative method was thus elaborated. The resulting gradient-enhanced model was adapted to low cycle fatigue, i.e., the evolution equations for isotropic and kinematic hardening as well as the evolution equation for anisotropic ductile damage have been amended. It was shown that the final model indeed captures the low cycle fatigue behaviour observed in experiments – qualitatively as well as quantitatively.

References

[1] Papadopoulos P., Lu J., A general framework for the numerical solution of problems in finite elasto-plasticity. *Computer Methods in Applied Mechanics and Engineering* **159**: 1-18, 1998.
[2] Menzel A., Ekh M., Steinmann P., Runesson K., Anisotropic damage coupled to plasticity: Modelling based on the effective configuration concept. *International Journal for Numerical Methods in Engineering* **54**: 1409-1430, 2002.
[3] Ekh M., Menzel A.,Runesson K., Steinmann P., Anisotropic damage with the MCR effect coupled to plasticity. *International Journal of Engineering Science* **41**: 1535-1551, 2003.
[4] Steinmann P., Carol, A framework for geometrically nonlinear continuumdamage mechanics. *International Journal of Engineering Science* **36**: 1793–1814, 1998.
[5] Dimitrijevic B. J., Hackl K., A Method for Gradient Enhancement of Continuum Damage Models. *Technische Mechanik* **28**: 43-52, 2008.
[6] Forest S., Micromorphic approach for gradient elasticity, viscoplasticity, and damage. *Journal of Engineering and Mechanics* **135**: 117-131, 2009.
[7] Halphen B., Nguyen Q. S., Sur les matériaux standard généralisés. *Journal de Mécanique* **14**: 39-63, 1975.
[8] Langenfeld K., Mosler J., A micromorphic approach for gradient-enhanced anisotropic ductile damage. *Computer Methods in Applied Mechanics and Engineering* in press, 2019
[9] Lemaitre J., Desmorat R., Engineering Damage Mechanics. Springer, Berlin, Heidelberg 2005.

VARIATIONAL FORMULATIONS AND COMPARISON OF REGULARIZED DAMAGE MODELS

Patrick Kurzeja*[1], Kai Langenfeld[1], and JörnMosler[1]
[1]Institute of Mechanics, Technical University Dortmund, Dortmund, Germany

Summary Gradient-enhanced models and viscous regularization are two prominent and yet conceptually different examples for regularization approaches in fracture modeling. They implement a regularization length using a gradient or a viscosity combined with a characteristic loading time scale, respectively. This work aims at providing a comparison between these methods and the classical fracture energy concept by deriving and utilizing a variational formulation. This allows to evaluate the well posedness of the problem at hand and to analyse the capabilities to rigorously capture localization and regularization. A numerical example of crack propagation will demonstrate individual peculiarities of the different approaches by means of the evolving fracture energy.

REGULARIZATION APPROACHES

Predicting failure is crucial to determine the limitations and performance of mechanical components during their design, production and application processes. The variety of loading conditions (e.g., static/dynamic, mechanical/thermal, uniaxial/mulitaxial) can yield complex stress states and equally complex responses of the material of interest that drive the evolution of damage until failure. Several underlying microscopic mechanisms can interact, e.g., multiple slip planes in crystals or material discontinuities such as interfaces between the host matrix and inclusions that support the nucleation of micro cracks by stress amplification at high cycles. After potential elastic and/or plastic pre-deformation, failure can finally emerge in the form of cracks or shear bands showing strain localization [1]. The present work aims at the investigation of quasi-static crack propagation in the context of brittle damage evolution and its implementation into a finite-element framework. This evolution, however, can cause a drastic change in the set of the governing equations that breaks, amongst others, the well posedness of the mathematical problem by loss of ellipticity and the mesh independence of the numerical implementation.

Various modelling approaches have been developed to address crack propagation in brittle materials of which we can only review selected examples. Models for damage in brittle materials typically capture the interaction of void nucleation and growth, micro-cracking, micro-scale yielding, interface leakage and others leading to degradation of the material. Also the numerical implementation offers different approaches, e.g., the location of the displacement discontinuities within finite bulk elements or in the form of surface elements [2], not to mention phase field and elaborated X-FEM methods.

The fracture energy concept, e.g., according to the Griffith criterion [3], provides an explicit (surface-based) energy criterion with a dissipation potential that implicate a characteristic length scale. Crack growth is initiated by reaching a critical energy release rate with suitable constraints (irreversibility, energy bounds, non-interpenetration). Its advantages are a straight-forward interpretation of the associated energy related to the fracture domain and the availability of comprehensive analytical studies of benchmark problems and mathematical properties [4]. It will thus serve as a reference for comparison. Gradient-enhanced regularization serves as a well-known, representative candidate in the class of generalized continua that provide higher-order regularization (e.g., micromorphic) and fully non-local regularization (e.g., integral based) to introduce the necessary additional length scale [5]. Damage is usually coupled to an additional field variable by a penalty term, while the gradient of the variable allows to account for the non-local nature. Viscous regularization approaches, in contrast, employ an aritificial viscosity that is combined with a dynamic load, following the ideas of visco-plasticity [6]. They utilize a time derivative instead of a spatial derivative, introducing the additional length scale by coupling to a viscosity [7, 8, 9].

VARIATIONAL FORMULATION

Damage models can often be recast into a variational format. Based on a rate potential that is composed of the rate of the (damage-reduced) Helmholtz free energy and the dissipation potential, $\dot{\mathcal{I}} = \dot{\Psi} + \mathcal{D}$, we can briefly introduce an initial potential for body $\mathcal{B}$ under volumetric loading $\mathbf{b}$ and tractions $\mathbf{t}^*$ at its Neumann-boundary

$$\mathcal{E} = \int_{\mathcal{B}} \dot{\mathcal{I}} \, \mathrm{d}V - \int_{\mathcal{B}} \rho \, \mathbf{b} \cdot \dot{\mathbf{u}} \, \mathrm{d}V - \int_{\partial \mathcal{B}_{\mathrm{N}}} \mathbf{t}^* \cdot \dot{\mathbf{u}} \, \mathrm{d}A, \tag{1}$$

where $\mathbf{u}$ is the displacement field and ρ is the density. Starting from strain $\boldsymbol{\varepsilon}$ and internal variables $\boldsymbol{\alpha}$ for strain-softening, extensions like convexifications with artificial stiffness, artificial viscosity via relaxation or gradient-based extensions can be introduced to achieve different types of regularizing damage models [9]. The variational formulation (if available) is then beneficial to evaluate the models by the stationarity condition and its (first and second) variation with respect to:

- well posedness (existence, uniqueness, stability), convexity, localization, regularization.

*Corresponding author. E-mail: patrick.kurzeja@tu-dortmund.de.

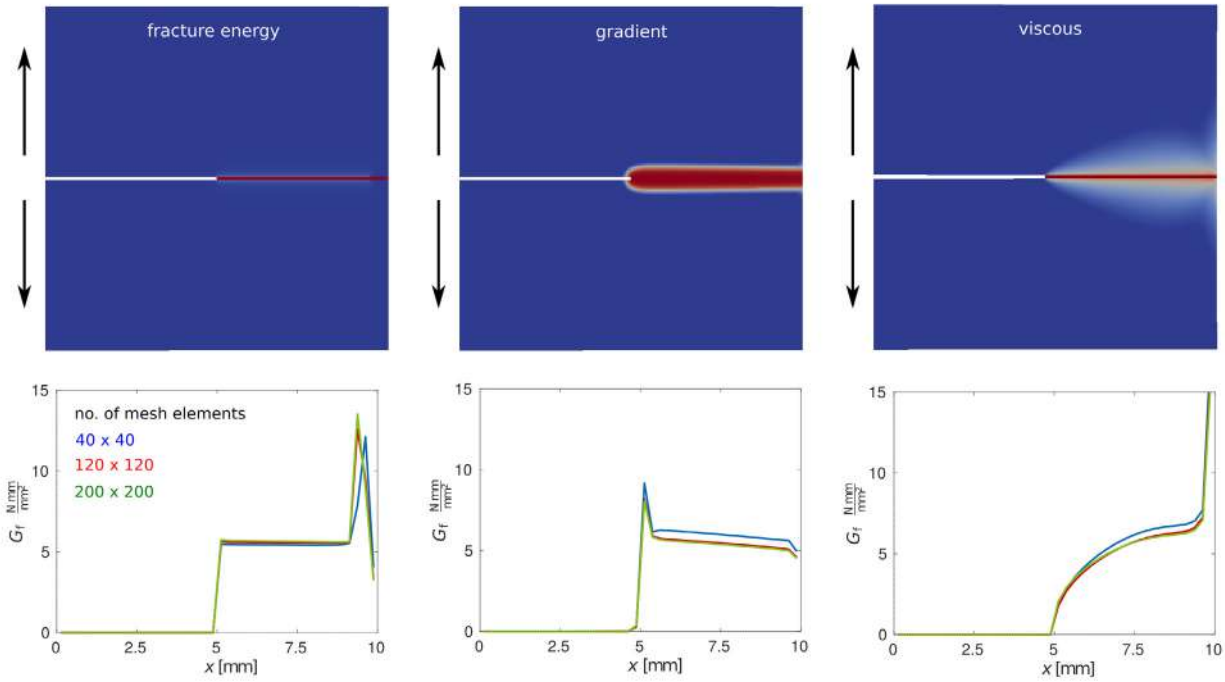

Figure 1: Numerical simulation of the fracture energy concept, a gradient-enhanced method and viscous regularization for a single propagating crack in a notched plate. Top row: damage field; bottom row: fracture energy integrated over vertical axis.

NUMERICAL EXAMPLE

In addition to the analytical investigation of the aforementioned modelling approaches, their numerical implementation and the study of more complex boundary value problems provide further interpretation of the physical behaviour. More specifically, the integrated fracture energy along the crack path can be studied and shows characteristic peaks depending on the regularizatoin technique, see Fig. 1. It peaks at the end of the crack path for the fracture-energy approach, strongly increases at the same location for the viscous approach and exhibits a less pronounced peak at the crack initiation tip for the gradient-enhanced model. A constant energy plateau is only observed for the fracture-energy and shows a strong incline for the viscous damage model. Accordingly, the damaged zone of the viscous regularization resembles the thin damage distribution of the fracture-energy approach with additional branching while the gradient-enhanced model predicts a distinct but broader damage zone. Mesh independence has been assured for all concepts.

CONCLUSION

Models for damage in brittle materials face various analytical and numerical challenges as they aim at predicting strain softening and guaranteeing mesh independence within a well-posed framework. Their variational formulation allows to compare their individual mathematical properties and to highlight differences. The present work highlights the gradient-enhanced and viscuous regularization against the background of the fracture-energy concept. The crack propagation of the numerical boundary value problem shows quantitative similarity with qualitative differences with respect to the evolution of the integrated fracture energy and the corresponding damage zones.

References

[1] Fohrmeister V., Díaz G., Mosler J. Classic crystal plasticity theory vs crystal plasticity theory based on strong discontinuities - Theoretical and algorithmic aspects. *Int. J. Numer. Methods Eng.* **117**: 1283-1303, 2019.
[2] Radulovic R., Bruhns O. T., Mosler J. Effective 3D failure simulations by combining the advantages of embedded Strong Discontinuity Approaches and classical interface elements. *Eng. Fracture Mech.* **78**: 2470-2485, 2011.
[3] Griffith A. The phenomena of rupture and flow in solids. *Philos. T. Roy. Soc. A* **CCXXI-A**: 163-198, 1920.
[4] Bourdin B., Francfort G. A., Marigo J.-J. The variational approach to fracture. *J. Elasticity* **91**: 5-148, 2008.
[5] Dimitrijevic B. J., Hackl K. A method for gradient enhancement of continuum damage models. *Technische Mechanik* **28**: 43-52, 2008.
[6] Duvaut G., Lions J.-L. Inequalities in Mechanics and Physics. Springer, Berlin 1976.
[7] Needleman A. Material rate dependence and mesh sensitivity in localization problems. *Comput. Methods Appl. Mech. Eng.* **67**: 69-85, 1988.
[8] Forest S., Lorentz E. Local Approach to Fracture. Presse des Mines, Paris 2004 (Ch. 11).
[9] Langenfeld K., Junker P., Mosler J. Quasi-brittle damage modeling based on incremental energy relaxation combined with a viscous-type regularization. *Continuum Mech. Thermodyn.* **30**: 1125-1144, 2018.

HYDROGEN-ASSISTED CRACKING OF ELASTIC-GRADIENT PLASTIC SOLIDS

Philip K. Kristensen[1], Christian F. Niordson[1], and Emilio Martínez-Pañeda [2*]
[1]Department of Mechanical Engineering, Technical University of Denmark, Kgs. Lyngby, Denmark
[2]Department of Civil and Environmental Engineering, Imperial College London, London, UK

Summary A novel framework for modelling hydrogen-assisted cracking (HAC) in elastic-plastic solids has been developed based on recent advances in solid mechanics. A stress-driven hydrogen transport model is utilized in conjunction with strain gradient plasticity, which is crucial for accurate crack-tip stress predictions. Initiation and propagation of cracks are captured using a novel phase field fracture model with a hydrogen dependent fracture energy. A quantum-mechanically informed approach is utilized for determining the relation between fracture energy and local hydrogen occupancy. The framework is shown to capture the quasi-cleavage fracture mode often observed in HAC failure at realistic material values when realistic hydrogen concentrations are present.

INTRODUCTION

The adverse influence of hydrogen on the fracture resistance of steels and other metals is an important issue in several industries. Hydrogen has been known to reduce the fracture toughness of modern high-strength steels by up towards 90%. The phenomenon spans multiple material scales and is highly interdisciplinary; predictive models that can capture crack initiation and growth at engineering scales have yet to be developed. A tool that has been gaining significant attention in recent years is the phase-field fracture model. Phase field provides a robust framework for capturing arbitrarily complex crack patterns, including initiation and branching of cracks. The framework has been applied to a wide variety of problems, including hydrogen embrittlement in elastic solids [1].
For elastic-plastic solids, crack tip stresses in the plastic zone are significantly reduced when geometrically necessary dislocations (GNDs) are not accounted for. The influence of GNDs as expressed in strain gradient plasticity (SGP) theories have been shown to have a critical effect on the propagation of sharp cracks [2]. In the case of HAC, accurate crack tip stresses are doubly important, as the diffusion of hydrogen in the metal lattice is known to depend on the stress field [3]. HAC models incorporating the role of plastic strain gradients have shown an unprecedented agreement with experiments [4]. However, a model able to explicitly capture crack growth, hydrogen transport and strain gradient plasticity has yet to be developed; this motivates the present work.

MATERIAL MODEL

An advanced material model is developed using four main elements. First, a phase field fracture model, which expresses material damage using a scalar field to approximate the Griffith criterion in a continuous manner. Second, a higher order SGP model based on [5], implemented using a viscoplastic law. Third, a mass transport model, based on an extended version of Fick's law, in which the gradient of the stress fields acts as a driving force for hydrogen diffusion. Fourth, A quantum-mechanically informed approach for coupling the fracture energy of the solid to the occupancy of hydrogen in a critical lattice plane, in the manner proposed in [6].
The material model is numerically implemented in a finite element framework, as described in [7]. A moving boundary condition prescribing the hydrogen concentration of the environment to the growing crack surface has also been implemented using a penalty approach. The model is applied to a series of small-scale yielding problems in plane strain where an infinite domain with a crack is approximated by a large semicircular domain. A remote K-field is applied to the far boundary, corresponding to pure mode I loading. The purpose of these simulations is to obtain a series of fracture resistance curves to determine the influence of important material and model parameters, as well as the influence of hydrogen.
In addition, to showcase the potential engineering applications of the model, the example of a pipeline which has suffered pitting corrosion damage has been considered. The problem has been emulated by modelling a quarter section of a pipe and prescribing a series of small pseudo-random pit-like defects to the inner surface. A combined load of tension and internal pressure is applied, leading to growth and coalescence of critical corrosion defects under the effect of an internal environment in the pipeline which is assumed to contain hydrogen.

NUMERICAL RESULTS

The application of this advanced deformation-diffusion-damage model to plane strain mode I fracture under small-scale yielding has provided a series of fracture resistance curves that show that the model complies with expected trends. Increases in plastic length scales relative to the plastic zone size lead to reduced fracture resistance, as would be expected due to the associated increased gradient hardening, which also increases. More importantly, the size of the length scale of the phase field model relative to the plastic zone size can be set such that the effective critical strength in the absence of hydrogen is on the order of the lattice strength (approximately 10 times the initial yield strength). At such an effective critical strength, it is shown that even for realistically small plastic length scales the presence of modest amounts of

*Corresponding author. E-mail: mail@empaneda.com.

hydrogen is sufficient to make crack propagation possible, as shown in figure 1a. The implication of this finding is that the quasi-cleavage fracture mode common to HAC specimens is rationalized by accounting for GNDs and the deleterious effect of hydrogen on the cohesive strength of the metal lattice.
In addition to capturing crucial features such as increased crack-tip stresses, sub-critical crack initiation and quasi-cleavage, diffusion-controlled crack growth where transport of hydrogen is the rate-limiting component of crack growth is also captured.
In the example of the damaged pipeline, an example crack pattern can be seen in figure 1b. The pipe has initially formed a radial tension-dominated crack, after which ongoing loading from internal pressure causes some defects to grow through the thickness and coalesce axially.

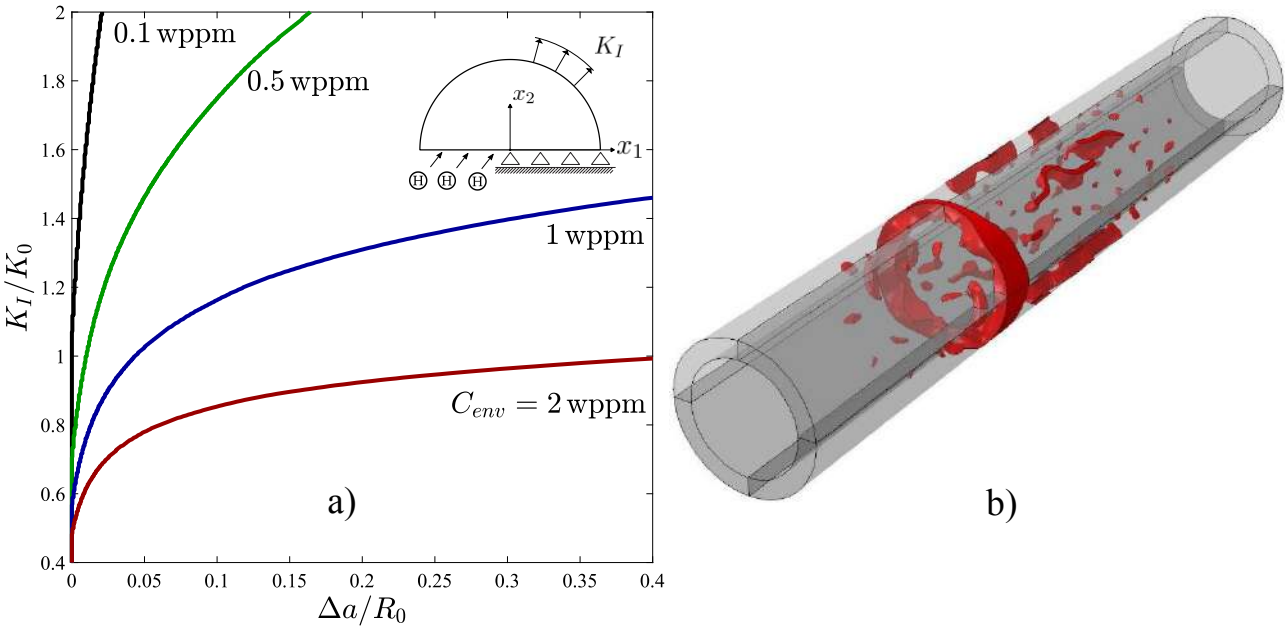

Figure 1. **a)** Representative results in small scale yielding. Increase in crack length Δa relative to initial plastic zone size R_0 at realistic material values for varied applied hydrogen concentrations. At an environment hydrogen concentration of 0.5 wppm or above, steady state fracture toughness tends towards a reasonable finite value. **b)** Damage caused by ongoing load by tension and internal pressure to a pipeline which has initially suffered pitting corrosion damage. Red areas signify damaged material. The small defects shown are representative of the size of all initial defects.

CONCLUSIONS

An advanced continuum model has been developed and implemented in a finite element framework. The model incorporates key elements necessary to capture the physics of hydrogen-assisted cracking, among which strain gradient plasticity is crucial. The increased crack tip stresses predicted by SGP in conjunction with the reduced fracture energy due to the effects of hydrogen jointly serve to rationalize the quasi-cleavage fracture mode, which is commonly observed in HAC failures. By virtue of being cast within a phase field fracture model, the framework can be applied to complex cracking problems as illustrated by the above pipeline example, making it a promising tool for engineering applications in the presence of hydrogen.

References

[1] Martínez-Pañeda, E., Golahmar, Niordson, C.F. A phase field formulation for hydrogen assisted cracking. *Comp. Methods Appl. Mech. Eng.* **342**: 742-761, 2018
[2] Martínez-Pañeda, E., Deshpande V.S., Niordson C.F., Fleck N.A. The role of strain gradients in the crack growth resistance of metals. *J. Mech. Phys. Solids* **126**: 136-150, 2019
[3] Lynch S., Hydrogen embrittlement phenomena and mechanisms. *Corrosion Reviews* **30**: 105-123, 2012.
[4] Martínez-Pañeda, E., Niordson C.F., Gangloff R.P. Strain gradient plasticity-based modeling of hydrogen environment assisted cracking. *Acta Mat.* **117**: 321-332, 2016
[5] Gudmundson, P. A unified treatment of strain gradient plasticity. *J. Mech. Phys. Solids* **52**: 1379-1406, 2004.
[6] Serebrinsky S., Carter E.A., Ortiz M. A quantum-mechanically informed continuum model of hydrogen embrittlement. *J. Mech. Phys. Solids* **52**: 2403-2430, 2004
[7] Kristensen P.K., Martínez-Pañeda, E., Niordson C.F. A phase field model for elastic-gradient-plastic solids undergoing hydrogen embrittlement. *(In review)*

AN INVESTIGATION INTO THE BEHAVIOUR OF THE KACHANOV-RABOTNOV TYPE CONTINUUM DAMAGE MODEL

Harm Askes[1], Juha Hartikainen[2], Kari Kolari[3], Reijo Kouhia[*2], Timo Saksala[2], and Jani Vilppo[2]
[1]Department of Civil and Structural Engineering, The University of Sheffield, Sheffield, UK
[2]Unit of Civil Engineering, Tampere University, Tampere, Finland
[3]VTT Technical Research Centre of Finland, Espoo, Finland

Summary In this paper the behaviour of the Kachanov-Rabotnov type continuum damage constitutive model are studied. Dispersion analysis as well as numerical finite element study of one-dimensional dynamic problem have been performed. In the case of non-gradient solid, it is found from numerical simulations that the width of the localisation zone is independent of the mesh size only if the loading rate is below a certain threshold value.

INTRODUCTION

In the late 1950's Kachanov and Rabotnov [4, 8] introduced a well known model to describe continuous degradation of a material. Originally they used the model to predict the creep rupture time. Since then, continuum damage mechanics has developed into an important and active field of continuum mechanics, see e.g. [5, 6, 7]. Progressing degradation of elastic properties will eventually lead to strain softening behaviour, which can result to ill-posedness of the underlying partial differential equation system. In numerical solution the ill-posedness caused by strain softening produces severe mesh size dependency. Several remedies have been proposed to alleviate or remove this deficiency: non-local integral constitutive models, adding spatial gradients, rate-dependency, etc. In the case of the Kachanov-Rabotnov continuum damage model, the evolution equation for damage has the following form

$$\dot{D} = \frac{1}{t_\mathrm{d}(1-D)^p}\left(\frac{Y}{Y_\mathrm{r}}\right)^r, \tag{1}$$

where $Y = -\rho\partial\psi/\partial D$ is the thermodynamic force dual to the damage rate $\dot{D}$, Y_r a freely chosen reference value for Y. Material parameters are p, r (dimensionless) and t_d, which has dimension of time. The most important parameters for stress-strain behaviour are r and t_d, while p effects to behaviour in the post-peak strain softening region.

Even though the Kachanov-Rabotnov damage model (1) involves rate-dependency, it does not completely resolve the pathological mesh sensitivity from the numerical solution. As it is shown in [2], to obtain a mesh independent numerical solution, the loading rate should be below a certain threshold. This is in contrast to numerical solutions in viscoplasticity.

GRADIENT ENHANCEMENT

One approach to obtain a well-posed model is to add gradient terms to the constitutive model. In damage mechanics the effect of higher-order strain gradients has been studied in [1]. Damage gradient is used in [3], however, their approach needs an additional balance equation. Here, the following gradient enhancement to the classical Kachanov-Rabotnov model is proposed:

$$\dot{D} = \frac{1}{t_\mathrm{d}(1-D)^p}\left(\frac{Y}{Y_\mathrm{r}}\right)^r \langle 1 + \ell^2\Delta D\rangle, \tag{2}$$

where Δ is the Laplace operator, ℓ is an additional material parameter having dimension of length and $\langle\bullet\rangle$ denotes the Macaulay brackets, i.e. the positive part of its argument.

To investigate the regularizing behaviour of the Kachanov-Rabotnov continuum damage model, a one-dimensional finite element and finite difference analyses are carried out. A bar fixed at $x = L$ and subjected at $x = 0$ to a linearly increasing displacement $u(0) = \eta\epsilon_\mathrm{r}L/t_\mathrm{d}$ ($L = c_\mathrm{e}t_\mathrm{d}$, where c_e is the elastic wave speed) has been analysed with different uniform mesh sizes [2]. A standard central difference scheme is used to integrate the equations of motion and in the gradient model the simple Euler forward method is used to integrate the evolution equation (2).

For the non-gradient damage model (1), the width of the localisation zone is shown as a function of the loading rate η in figure 1 for three different mesh sizes $h = L/100, L/1000$ and $L/10000$ and for the cases $r = 2, p = 1$, and $r = 4, p = 1$. As it can be seen, the width of the damage localisation zone is mesh-size independent if the loading rate satisfies $\eta \lessapprox 0.75$. Linearly interpolated finite elements for the spatial discretisation are used.

In figure 2 the damage profiles at time intervals $t_\mathrm{d}/100$ have been shown for the gradient model (2) when finite element and finite difference approach for the spatial discretisation is used. The additional material parameter has been $\ell = L/10$. Homogeneous natural boundary conditions have been used for the damage.

*Corresponding author. E-mail: reijo.kouhia@tuni.fi.

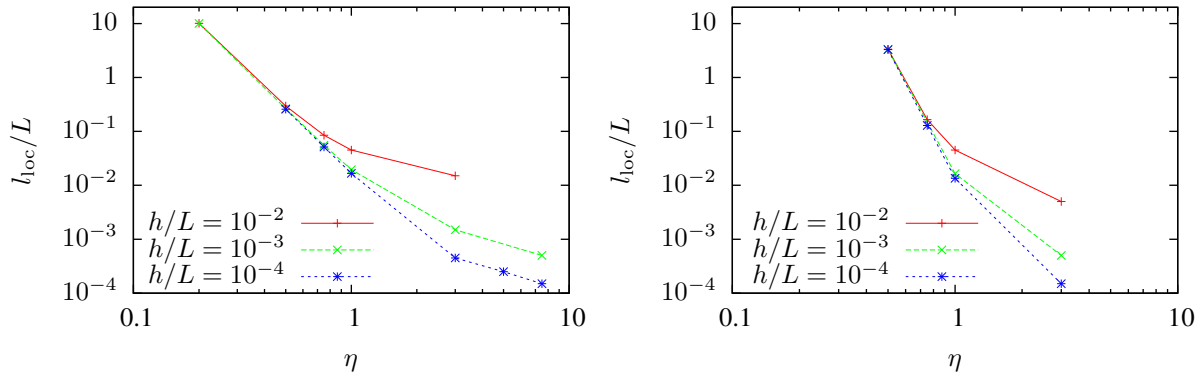

Figure 1: Damage localisation width as a function of the prescribed loading rate for the non-gradient model, $r = 2$ (lhs), $r = 4$ (rhs). In both cases $p = 1$.

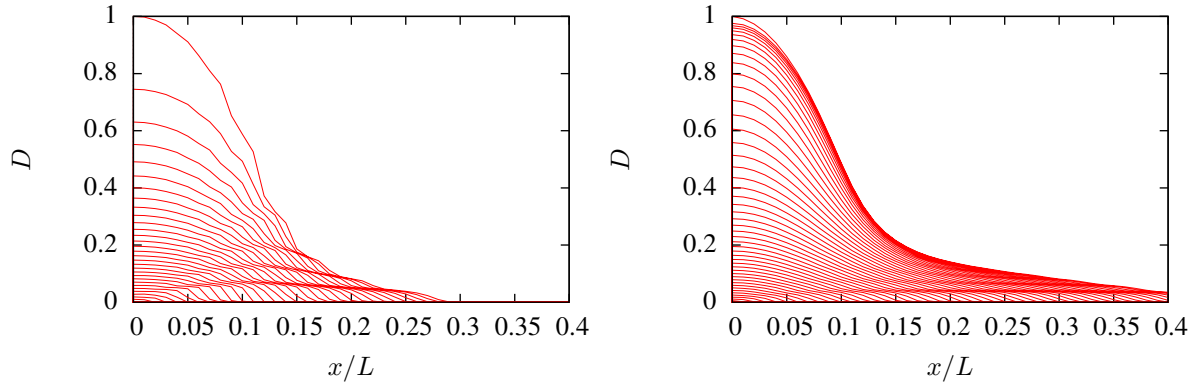

Figure 2: Damage profiles at different time instances for the gradient model, $h/L = 1/100$, $r = 4, p = 1, \ell = L/10$ and $\eta = 1$. Finite element (lhs) and finite difference solutions (rhs) shown.

CONCLUDING REMARKS

The classical Kachanov-Rabotnov continuum damage model has been shown to yield mesh-independent numerical solutions only if the loading rate is below a certain threshold. The dispersion analysis shows that the wave speeds of damaging material exceeds the elastic wave velocity. Based on a preliminary numerical study, addition of second-order derivatives to the damage evolution equation seems to result in mesh-independent solutions for a larger loading rate range. Further study will be focused on the dispersion analysis as well as on developing efficient numerical methods to solve the gradient enhanced model in 3D.

References

[1] Askes H., Sluys, L.J. Explicit and implicit gradient series in damage mechanics. *Eur. J. Mech. A/Solids*, **21**, 2002, 379–390.

[2] Askes H., Hartikainen J., Kolari K., Kouhia R., Saksala T., and Vilppo J. Manuscript, May 2019.

[3] Frémond M., Nedjar B. Damage, gradient of damage and principle of virtual power. *Int. J. Sol. Struct.*, **33**, 1996, 1083-1104.

[4] Kachanov L.M. On the creep fracture time. *Izv. Akad. Nauk SSSR. Otd. Tekhn. Nauk*, (8):26–31, 1958. (in Russian).

[5] Krajcinovic D. *Damage Mechanics*, volume 41 of *North-Holland series in Applied Mathematics and Mechanics*. Elsevier Science B.V., Amsterdam, 1996.

[6] Lemaitre J. *A Course on Damage Mechanics*. Springer-Verlag, Berlin, 1992.

[7] Murakami S. *Continuum Damage Mechanics*, volume 185 of *Solid Mechanics and Its Applications*. Springer Netherlands, 2012.

[8] Rabotnov Y.N. A mechanism of the long term fracture. *Voprosy prochnosti materialov i konstruktsii AN SSSR*, pages 5–7, 1959. (In Russian).

SOME NOVEL INSIGHTS ON THE DUCTILITY AND DAMAGE OF ADVANCED MULTI-PHASE STEELS

Marc G.D. Geers*[1], Lei Liu[1], Vahid Rezazadeh[1], Varvara Kouznetsova[1], Ron Peerlings[1], Francesco Maresca[2], and Johan Hoefnagels[1]
[1]Department of Mechanical Engineering, Eindhoven University of Technology, The Netherlands
[2]Faculty of Science and Engineering, Groningen University, The Netherlands

Summary Advanced high-strength steels are widely used in the automotive industry, as an adequate compromise between light-weight, strength and ductility. This contribution focuses on some mechanisms that affect the ductility of dual-phase steels. First, the underlying mechanisms controlling necking-driven global ductility and shear-driven local ductility are examined. The yield stress phase contrast and the strain hardening of martensite are thereby key parameters. Local shear-driven failure of martensite often occurs at the interface with ferrite. Martensite has a complex hierarchical morphology with multiple substructure boundaries. Interfacial damage initiation has been analysed for different interfacial morphologies using crystal plasticity simulations, revealing that substructure boundary sliding triggers plastic deformation localization in the near-interface ferrite matrix.

INTRODUCTION

Advanced high-strength multi-phase steels are of key importance in e.g. the automotive industry, where a compromise needs to be found between light-weight and high-strength. However, automotive steels also need to be ductile since this strongly affects the crash performance and accompanying energy dissipation. Such advanced steels typically consist of multiple phases. Two phases are typically present: ferrite as the soft ductile phase; martensite as the hard phase. The failure of these steels is largely governed by its multi-phase nature, whereby necking may be triggered by the soft phase, fracture by the hard phase, or decohesion by the interfaces. This presentation focuses on these mechanisms, providing some novel insights explaining the peculiar behaviour of these steels in edge cracking problems and on the martensite mechanisms that may induce interfacial decohesion.

EDGE CRACKING: GLOBAL VERSUS LOCAL DUCTILITY

Failure of sheet metal is typically initiated by either localized necking or shear fracture, also respectively termed as global and local ductility. Dual-phase steels outperform conventional steel grades (of comparable strength) in necking-controlled formability tests. They often reveal more strain hardening, leading to a high global ductility. This is not the case when they are subjected to a localized failure test where necking does not occur, e.g. in shear loading. They often reveal a poor performance in such a local ductility test. This apparent contradictory behaviour is known in the steel community as the edge cracking phenomenon (reflecting the higher tendency to damage initiation at a sheared edge) [1]. The literature attributes this phenomenon to the intrinsic incompatibilty between the properties of the constituing phases, but a precise explanation is still lacking. Therefore, an in-depth analysis was carried out on simplified dual-phase microstructures to unravel the edge cracking mechanism, reproducing observations reported in literature. Some of the results are presented in Figure 1. A higher global ductility (necking-driven) is obtained upon delaying the onset of martensite plasticity (higher

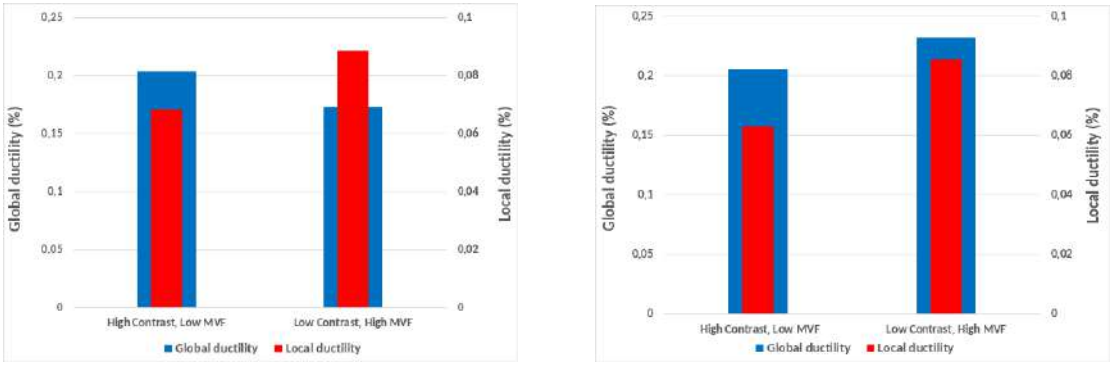

Figure 1: Influence of phase contrast and martensite volume fraction (left); Influence of a higher strain hardening in martensite (right)

yield stress). This entails an increased mechanical phase contrast (Figure 1, left) and more heterogeneous stress-strain distributions, through which one of the phases or interfaces will more rapidly reach its fracture limit in shear loading. Hence, local ductility decreases. In order to seek for a better compromise between global and local ductility, the strain hardening of martensite needs to be increased to a level that is comparable to that of ferrite (Figure 1, right).

*Corresponding author. E-mail: m.g.d.geers@tue.nl

INTERFACIAL FRACTURE IN DUAL-PHASE STEELS

The failure limit (stress or strain) of martensite is still a debated subject. Whereas martensite is commonly known as a brittle phase, it has a complex hierarchical structure, in which the substructures boundaries may slide due to the presence of very thin interlath austenitic films [2, 3, 4]. Since these films are fully embedded in the martensite phase, this triggers an apparent ductility of martensite for some load configurations activating glide in the substructure boundaries. A second important aspect is the morphology of the martensite-ferrite interface. Unlike the commonly accepted straight interfacial morphology, experimental evidence reveals that martensite forms sharp wedges instead, whereby substructure boundary sliding may already appear during phase transformation. The resulting morphology is a jagged martensite-ferrite interface. To study the role of the substructure boundary glide and the jagged morphology, four configurations are considered with one martensite island embedded in the ferrite matrix. Single variant martensitic laths are considered, stacked in the vertical direction and separated by the interlath retained austenite films enabling substructure boundary sliding. The four configurations, shown in Figure 2, only differ through the interfacial morphology and phase composition. Crystal plasticity simulations reveal that the interfacial damage is essentially triggered by substructure boundary sliding. Indeed the sliding in between the martensitic laths entails large stress concentrations at the interface, inducing plastic deformation localization as a precursor to damage. This observation holds regardless of the morphological shape of the interface, the phase contrast or the residual stress state.

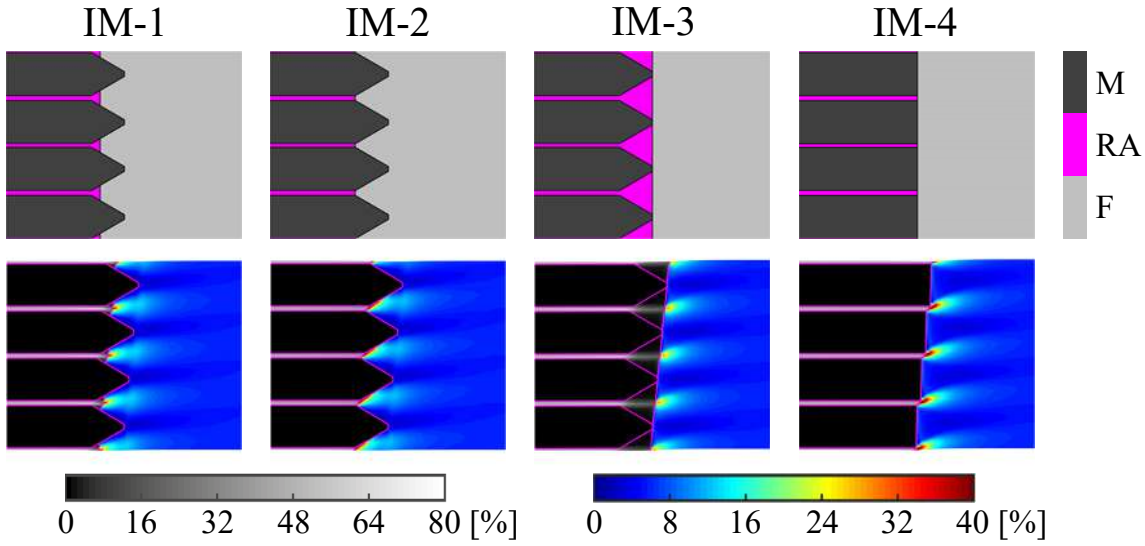

Figure 2: Local interfacial equivalent plastic strain fields for 4 different interface morphologies (IM), at a macroscopic shear strain of 5.7% (simple shear). The top row visualizes the different morphologies, with martensite (M), retained austenite (RA) and ferrite (F). The gray and jet colormaps are used for the martensite/austenite and the ferrite matrix, respectively.

CONCLUSIONS

The failure behaviour of advanced high-strength steels governs their ductility, which is of prime importance for applications exploiting energy dissipation. This contribution focused on the underlying mechanisms discerning necking-driven global ductility from shear-driven local ductility in dual-phase steels. The phase contrast and the strain hardening of martensite are thereby the governing parameters. The local failure of martensite often happens at the interface with ferrite. It has been shown that the substructure gliding triggers plastic deformation localization in the near-interface ferrite matrix, ultimately initiating damage.

References

[1] Teng Z.K., Chen X.M., Edge cracking mechanism in two dual-phase advanced high strength steels. *Mat. Sc. Eng. A* **618**: 645-653, 2014.
[2] Maresca F., Kouznetsova V.G., Geers M.G.D., Deformation behaviour of lath martensite in multi-phase steels. *Scripta Mat.* **110**: 74-77, 2016.
[3] Maresca F., Kouznetsova V.G., Geers M.G.D., Curtin W.A., Contribution of austenite-martensite transformation to deformability of advanced high strength steels: From atomistic mechanisms to microstructural response. *Acta Mat.* **156**: 463-478, 2018.
[4] Du C., Petrov R., Geers M.G.D., Hoefnagels J.P.M., Lath martensite plasticity enabled by apparent sliding of substructure boundaries. *Materials & Design* **172**: article 107646, 2019.

ON THE COUPLING OF DAMAGE AND SINGLE CRYSTAL PLASTICITY FOR DUCTILE POLYCRYSTALLINE MATERIALS

Bjørn Håkon Frodal*[1], Tore Børvik[1], and Odd Sture Hopperstad[1]
[1]Structural Impact Laboratory (SIMLab), Department of Structural Engineering, Norwegian University of Science and Technology (NTNU), Trondheim, Norway

Summary A crystal plasticity formulation accounting for damage evolution and failure in the single crystal due to the presence of voids or micro-cracks is developed. An efficient and robust rate-dependent single crystal plasticity implementation is used and extended to model the behaviour of a textured aluminium alloy. Tensile tests on axisymmetric smooth and notch specimens are modelled in Abaqus/Explicit. Prior to failure a significant damage induced softening is observed in the tests. Due to the crystallographic texture, distinct fracture surfaces are observed for the different specimens with each specimen having unique features.

INTRODUCTION

The thermo-mechanical processing of metals influences microstructural characteristics such as the grain structure and the crystallographic texture, and determines the plastic behaviour of these materials. The process of ductile fracture includes nucleation, growth and coalescence of microscopic voids at second-phase particles or inclusions, and depends markedly on the local stress state and microstructural characteristics. For typical metals such as aluminium, the second-phase particles and voids present within the material could be several orders of magnitude smaller than the grain size. Thus, in a single grain there can reside some thousand particles and voids. It then becomes apparent that the yielding and plastic flow of the single crystal around these smaller constituents are important for the ductile fracture process.

One of the advantages of the crystal plasticity theory is its intrinsic ability to predict the change of plastic anisotropy by evolving the crystallographic texture and rotation of the grains. In turn, this allows studying phenomena which are outside the scope of phenomenological plasticity models, like surface roughening, and their influence on ductility. In addition, the discrete representation of the crystallographic texture can evoke phenomena important for ductile failure, such as strain localization and shear banding [1].

MATERIAL AND CRYSTAL PLASTICITY

In this work, we introduce damage mechanics in the crystal plasticity formulation, accounting for damage evolution and failure in the single crystal due to the presence of voids or micro-cracks. Plastic deformation is assumed to occur by plastic slip on certain crystallographic slip systems, determined by the crystal structure. An efficient and robust rate-dependent single crystal plasticity implementation [2] is used and extended to model the behaviour of a polycrystalline aluminium alloy. The AlMgSi alloy investigated is from an extruded profile that has a recrystallized grain structure with a sharp cube texture and a minor Goss component. The strong crystallographic texture leads to a significant plastic anisotropy [2], which can also induce failure anisotropy [3], i.e., a variation in the failure strain with loading direction.

FINITE ELEMENT MODELLING

The coupled damage and rate-dependent crystal plasticity (RDCP) model described above is used in the following to model the response of the textured aluminium alloy. Tensile tests on axisymmetric smooth and notched specimens are modelled in Abaqus/Explicit. The initial diameter of the minimum cross section is 6 mm and 6.4 mm for the smooth and notched specimens, respectively. The notch radius is 3.6 mm for the notched specimen and the gauge length is 40 mm for the smooth specimen, see [2] for further details. The specimens were oriented and pulled along the transverse direction of the extruded profile. To reduce the computational time, only 1/8th of the specimens was modelled with symmetry boundary conditions on the appropriate planes. In the gauge area of the specimens, the element size is set to $100 \times 100 \times 100$ μm^3, and one grain is represented by an element. Each element is given an initial crystallographic orientation so that several elements will recreate the crystallographic texture of the textured aluminium alloy. Elements are eroded upon material failure, i.e., when a material integration point has reached a critical damage level.

RESULTS AND DISCUSSION

Figure 1 depicts the true stress versus logarithmic strain curves from the crystal plasticity finite element simulations of the axisymmetric smooth and notched specimens with and without damage and failure included. Due to the triaxial stress field created by the notch, the notched specimen experiences a higher stress level and has a lower failure strain than the smooth specimen. Prior to failure a significant damage induced softening is observed in the tests including damage.

*Corresponding author. E-mail: bjorn.h.frodal@ntnu.no

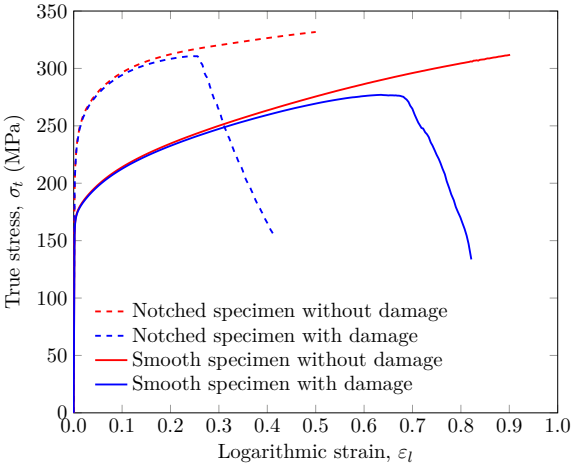

Figure 1: Stress - strain curves from the crystal plasticity finite element simulations of the tensile tests on smooth and notched specimens.

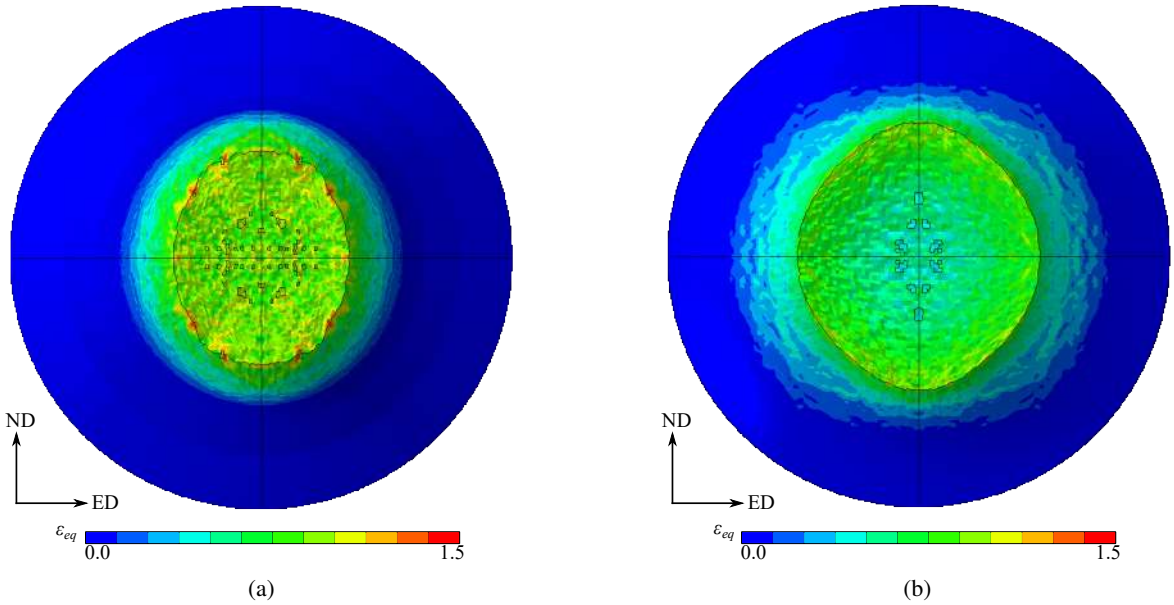

Figure 2: Fracture surfaces of the axisymmetric (a) smooth and (b) notched specimens predicted by the crystal plasticity finite element simulations. Contours of the plastic equivalent von Mises strain are shown.

Figure 2 shows the fracture surfaces predicted by the crystal plasticity finite element simulations of the axisymmetric smooth and notched specimens. Due to the strong crystallographic texture, distinct fracture surfaces are observed for the different specimens with each specimen having unique features. For the smooth specimen, a fracture surface that is somewhere between an ellipse and a rectangle is observed. In contrast, the notched specimen displays a more diamond-shaped fracture surface typically observed experimentally for aluminium alloys with this crystallographic texture and notched specimens [2]. Due to grain rotations during deformation, the outer surface of the specimens close to the fracture surface has developed a surface roughness, i.e., orange peel.

Acknowledgements

The authors gratefully appreciate the financial support from NTNU and the Research Council of Norway through the FRINATEK Programme, Project No. 250553 (FractAl).

References

[1] Khadyko, M., Marioara, C.D., Ringdalen, I.G., Dumoulin, S., Hopperstad, O.S., 2016. Deformation and strain localization in polycrystals with plastically heterogeneous grains. International Journal of Plasticity 86, 128-150.

[2] Frodal, B.H., Dæhli, L.E.B., Børvik, T., Hopperstad, O.S., 2019. Modelling and simulation of ductile failure in textured aluminium alloys subjected to compression-tension loading. International Journal of Plasticity 118, 36-69.

[3] Frodal, B.H., Morin, D., Børvik, T., Hopperstad, O.S., 2019. On the effect of plastic anisotropy, strength and work hardening on the tensile ductility of aluminium alloys. International Journal of Solids and Structures, https://doi.org/10.1016/j.ijsolstr.2019.10.003.

SIMULATION OF THERMAL SHOCK CRACKING IN THIN CYLINDRICAL SPECIMEN BY USING A PHASE FIELD MODEL

Marwa Dhahri*[1,2], Radhi Abdelmoula[1], Jia Li[1], and Yamen Maalej[2]
[1]Laboratory of Process and Materials Sciences, University of Paris 13, Villetaneuse, France
[2]Laboratory of Applied Mechanics and Engineering, National Engineering School of Tunis,Tunis, Tunisia

Summary In this work, we present a study on initiation and propagation of cracks in brittle materials under thermal shock. Based on the variational approach to fracture mechanics, a damage model was formulated and implemented into a finite element code. This damage model verifies the conditions of irreversibility, stability and conservation of total energy. By using this numerical model, the evolution of cracks in a thin cylindrical specimen quenched with cold water was simulated. The numerical simulations allow a presentation on whole the process of crack initiation and propagation. It has been shown that there are three phases during the evolution of the damage. First an elastic response without any damage, then a phase of homogeneous damage, followed by several bifurcations where cracks distributed periodically. We studied the influence of the material and loading parameters on the damage evolution. The present study leads to an understanding of the formation and evolution of thermal shock crack patterns in brittle materials such as ceramics.

INTRODUCTION

In this paper, a damage model based on the variational approach was used and implemented into a finite element code and then extended to simulate the evolution of cracks in ceramics exposed to a thermal shock. We perform numerical simulations of thermal shock cracking by using the phase field model where the cracks are replaced by high gradient damage areas. This damage model verifies the conditions of irreversibility, stability and conservation of total energy. The developed numerical model was used to simulate the evolution of cracks in a thin cylindrical specimen quenched in cold water. This numerical model allows predicting the periodic and hierarchical characteristics of the crack models with a satisfactory prediction. The numerical simulations successfully reproduce the cracking process of the quenched specimens in agreement with experiments[1].

CONTEXT OF THE GRADIENT DAMAGE MODEL

Numerical quenching experiments have been conducted in order to observe crack development in ceramic materials [1,2].For numerical simulation of cracking phenomena in solids, damage models are often used. Energy approaches based on a variation formulation provide a clear theoretical framework for determining the relationships between damage models [3,4] and fracture models [5]. The purpose of this paper is to illustrate, as part of the variational approach to fracture mechanics, the modelling and numerical simulation of brittle fracture phenomena under thermal shock. We consider a damage model whose quasi-static evolution is formulated as a problem of minimizing following under an irreversible constraint on the damage energy.

$$W\left((\varepsilon(\mathbf{u}^t)-\varepsilon^{th}(t)),\alpha^t,\nabla\alpha^t\right)=\frac{1}{2}a(\alpha^t)\mathsf{A}(\varepsilon(\mathbf{u}^t)-\varepsilon^{th}(t)).(\varepsilon(\mathbf{u}^t)-\varepsilon^{th}(t))+w(\alpha^t)+\frac{1}{2}w_1\ell^2\nabla\alpha^t.\nabla\alpha^t \tag{1}$$

Where $\mathbf{u}^t$ denoted the displacement field, α the damage field, $\varepsilon(\mathbf{u}^t)$ the linearized deformations, $\varepsilon^{th}(t)$ thermal deformation, A the undamaged elasticity tensor, G_c the toughness of the material, and ℓ a material parameter that has the physical dimension of a length. The functions $a(\alpha^t)$ and $w(\alpha^t)$ indicate the behaviour law of the damage model, representing the modulation of the rigidity and the bulk density of disspated energy, respectively. We study the quasi-static evolution of damage in a circular disc determined by the local minimization of (1) under the constraint of irreversibility, demonstrating that it is possible to account for the phenomena of crack initiation and propagation with complex morphologies without any additional assumption. We will show that the periodic and hierarchical evolution of crack models can be predicted with satisfactory accuracy.

THE THERMOELASTIC PROBLEM

A flat cylindrical specimen is assumed, to be composed of a homogeneous material without pre-stress in its initial state. In the experiments [1], a number of plates are piled together, heated uniformly to the temperature T_i, then they are deposited in a cold water bath in free fall thus inducing a temperature drop T_B on the lateral surfaces. The thermal shock in the structure generates a tensile stress in the edge of the disc, causing a complex pattern of cracks to appear. These cracks propagate inside the spicemens periodically and arrest in the vicinity of the center. The shrinkage of the material generated by thermal effects is determined by thermal deformations as a function of time in the form of :

$$\varepsilon^{th}(t)=\beta(T(t,r)-T_i)\mathbf{I}\qquad T(t,r)=T_B+\sum_{n=1}^{N}\frac{2\Delta T J_0(\lambda_n r)\exp(-k_c\lambda_n^2 t)}{\lambda_n R J_1(\lambda_n R)},\qquad \Delta T=T_i-T_B \tag{2}$$

*Corresponding author. E-mail: marwa.dhahri@lspm.cnrs.fr

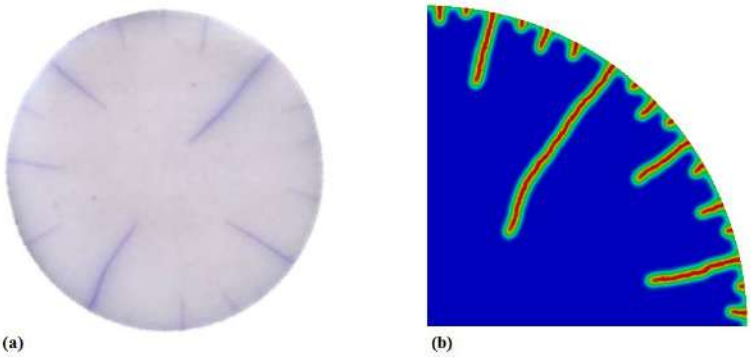

Figure 1: (a) Experimental tests in the specimens with initial temperatures $T_i = 250C$ and bordering temperature $T_B = 15C$, (b) The crack patterns obtained from numerical simulations for a quater of the specimen.

where β is the thermal expansion coeffcient, $T(t,r)$ is the temperature field in the cylindrical structure, and J_0, J_1 are the Bessel function of first unmodified species of order 0 and 1 respectevely, λ_n are the roots of $J_0(\lambda_n R) = 0$, k_c is the thermal diffusivity, and it is supposed that the evolution of damage does not influence the temperature field.

THE EVOLUTION OF CRACKS

It has been demonstrated analytically and verified numerically that there is a cracking threshold ΔT_c above which there is cracking:

$$\Delta T_c = \frac{\sigma_c}{E\beta\sqrt{\mathcal{S}(t=0, r=R, \nu)}} \tag{3}$$

Where $\mathcal{S}(t,r,\nu)$ is expressed by:

$$\mathcal{S}(t,r,\nu) = 8\sum_{n=1}^{N} \frac{\exp(-k_c\lambda_n^2 t)^2}{r\lambda_n^4 R^4 J_1(\lambda_n R)}\{(1-\nu)rJ_1(\lambda_n R) - (1+\nu)RJ_1(\lambda_n r) + \frac{J_1(\lambda_n r)(\nu + J_1(\lambda_n r))R^2}{rJ_1(\lambda_n R)} + \tag{4}$$
$$\frac{J_1(\lambda_n r)J_0(\lambda_n r)\lambda_n R^2}{J_1(\lambda_n R)}(1+\nu) \ -2\nu J_0(\lambda_n r)\lambda_n rR - R - J_1(\lambda_n r)R\}$$

Where σ_c presents the critical stress of the structure, E is the Young's module, R is the radius of specimen, and ν is the poisson coefficient. Therefore, for a thermal shock intensity $\Delta T < \Delta T_c$, we obtain a stable elastic solution at any time t in the entire structure. In the case when $\Delta T > \Delta T_c$ it is demonstrated that there are three phases during the evolution of the damage. First an axisymmetric damage phase presented by a formation of a homogeneous band of damage to the surface exposed to thermal shock, followed by several bifurcations, ie.the localization phase of damage and finally the propagation of the cracks by developing a periodic array of crack bands. These crack bands propagate with a phenomenon of period doubling. Figure (1) shows the evolution of cracks with thermal shock intensitie $\Delta T = 235K$. These crack patterns is compared with the image experimentally obtained. It can be observed that the crack model achieved from the numerical test is in good agreement with the experimental result.

CONCLUSIONS

In this work, we showed that the proposed numerical simulations can faithfully reproduce the crack patterns in the ceramic specimens [1]. The periodic and hierarchical form of the crack models were precisely predicted. From the numerical results, the spacing between the two consecutive cracks and the length of the cracks were well estimated. The obtained results agree qualitatively with the experiment.

References

[1] Y.X.Liu, X.F.Wu, Q.K.GUO, C.P.JIANG, F.SONG, J.LI , Experiments and numerical simulations of thermal shock crack patterns in thin circular ceramics pecimens, *Ceramic International*, **40**: 1107-1114, 2014.

[2] C.P. Jiang, X.F. Wu, J. Li , F. Song, Y.F. Shao, X.H. Xu, P. Yan, A study of the mechanism of formation and numerical simulations of crack patterns in ceramics subjected to thermal shock, *Acta Materialia*, **60**: 4540âĂŞ4550,2012.

[3] K. PHAM, J.-J. MARIGO et C. MAURINI. The issues of the uniqueness and the stability of the homogeneous response in uniaxial tests with gradient damage models. *Journal of the Mechanics and Physics of Solids* , **59**: 1163-1190, 2011.

[4] P. SICSIC et J.-J. MARIGO. From Gradient Damage Laws to GriffithâĂŹs Theory of Crack Propagation. *Journal of Elasticity*, 1-20, 2012.

[5] P. SICSIC, J.-J. MARIGO et C. MAURINI. Initiation of a periodic array of cracks in the thermal shock problem : A gradient damage modeling. *Journal of the Mechanics and Physics of Solids*, **63**: 256-284, 2014.

UNIFYING BREAKAGE MECHANICS WITH THE COSSERAT CONTINUUM TO PREDICT SHEAR BAND LOCALISATION

Nicholas Anton Collins-Craft[1,2], Ioannis Stefanou[2,3], Jean Sulem[2], and Itai Einav*[1]
[1]Particles and Grains Laboratory, The School of Civil Engineering, The University of Sydney, Sydney, Australia
[2]Laboratoire Navier,Ecole des Ponts Paris Tech,UPE,CNRS,Champs-sur-Marne,France
[3]GeM (Institute de Recherche en Genie Civile et Mécanique),Ecole Centrale de Nantes,Université de Nantes, CNRS, Nantes, France

Summary In this work, we present a combination of two previously separate continuum mechanical theories, Breakage Mechanics and Cosserat continuum mechanics. The Cosserat continuum is typically employed as a means of obtaining an internal length that serves to regularise the equations of continuum mechanics, which removes issues such as pathological mesh-dependence that frequently arise in constitutive models that feature softening or non-associated behaviour . Historically, Cosserat models for geomechanics have used internal lengths that are related to the mean grain size of the underlying distribution, and which are fixed properties of the system. We adopt the Breakage Mechanics family of models to take into account the evolution of the grain size distribution in a consistent and thermodynamic way, and include this more refined physics in an evolving internal length.

We start by providing an energetic upscaling method that is comparable with the original formulation of Breakage Mechanics [1, 2], extended to capture the energetic contribution of the elastic curvatures that arise as a result of the Cosserat continuum. Through the upscaling procedure, we define a new material constant θ_κ that acts in concert with the internal breakage variable B to include the contribution of the entire grain size distribution to the energy at the continuum level. Importantly, this material constant allows us to define a new internal length scale that includes the entire grain size distribution, and evolves as that distribution evolves towards an well-defined ultimate distribution.

In a similar fashion we also perform an upscaling of the rotational inertia to take into account the contributions of the entire grain size distribution, defining a second new material constant θ_I, for use in dynamic analysis.

The energetic upscaling provides a generic framework in which to specify Breakage Mechanics models. We then proceed to detail a model within the framework of rate-independent thermodynamic processes. This model is an extension of previous Breakage Mechanics models [3] into the Cosserat continuum. In order to achieve this extension, we define the second deviatoric stress invariant and the second deviatoric strain invariant in a manner consistent with [4], which serves to include both contributions from the stresses and the couple-stresses that arise as a consequence of the Cosserat continuum. The couple-stresses are made dimensionally consistent with the stresses through a length scale, which we select to be the length scale defined through our energetic upscaling.

We proceed to define certain relationships between the additional stiffnesses that arise in linear Cosserat elasticity, such that by measuring the classical bulk modulus K and shear modulus G, the additional Cosserat moduli G_c, H, H_c are also obtained. The result of this is that the new Cosserat model requires no additional calibration over the same model phrased in the classical continuum. All the remaining parameters have straightforward physical interpretations and can be obtained via standard geotechnical testing apparatus such as the triaxial test.

At this point, our model is fully specified and calibrated, and we move on to using it to study a system of interest, specifically shear under constant volume. This corresponds to fast undrained shear that occurs during seismic slip. We analyse our system using two techniques, linear stability analysis (LSA) and the finite element method (FEM).

We first apply LSA to determine which parts of the yield surface are capable of supporting localisation into shear bands under this load condition. We find that this localisation type occurs only on the lower confining pressure side of the yield surface, and the extent of this region depends on the value of the internal breakage variable B, and the system parameter ω, which allocates dissipation between grain crushing and plastic volumetric straining. In general, systems that have more crushed grains have a relatively smaller part of the yield surface that will support band localisation. Similarly, systems that favour grain crushing over plastic volumetric straining as a means of dissipation have smaller localisation regions than systems that favour plastic straining.

We then turn our attention to following individual load paths, and using LSA to obtain their predicted widths. In the case of changing values of ω, we find that systems with higher values (and hence "softer" behaviour localise at smaller values of strain and have thinner initial shear band widths, but also tend to grow more rapidly than bands in systems with lower values of ω.

*Corresponding author. E-mail: itai.einav@sydney.edu.au

Of particular interest to us is the effect of polydispersity on the width of shear bands. Classically it is considered that the width of shear bands scale as a function of mean grain size. However, the range of apparent scalings found in the literature [5, 6] suggest that this single grain size is insufficient to fully characterise the width. Using our model, we can vary the polydispersity in several different ways. Starting by changing only the ratio of minimum to maximum grain size (and thus changing our material parameter θ_κ, we find that normalisation by our evolving internal length scale collapses all the predicted shear band widths onto a single curve. However, when we adopt a more complex measure of polydispersity, by changing the initial value of the breakage variable B, no normalisation scheme is sufficient to collapse all the curves. We find that normalisation by the largest grain size d_{Max} is most indicative of the initial localisation width, while the evolving internal length scale causes different values of B to converge faster post-localisation at increasing shear. In all cases, the mean grain size (either initial or evolving) is the least effective normalisation, which may help to explain why no fixed scaling relationship between d_{50} and shear band width has been found.

Finally, by implementing our model using the FEM, we explain the formation of double-cataclastic shear bands in certain rock formations in the field. We observe that for values of ω favouring grain crushing, our system progresses from homogeneous to a single shear band, which is then followed by two shear bands at the edge of the initial band, before finally one of these bands becomes dominant and saturates.

CONCLUSIONS

By defining this Cosserat Breakage Mechanics model, we have added physical fidelity to the Cosserat modelling tradition and predictive power post-localisation to the Breakage Mechanics family, allowing us to gain insight into several physical phenomena that were previously unexplained.

References

[1] Einav I. Breakage Mechanics-Part I: Theory. *Journal of the Mechanics and Physics of Solids* **55**: 1274-1297, 2007.
[2] Einav I. Breakage Mechanics-Part II: Modelling granular materials. *Journal of the Mechanics and Physics of Solids* **55**: 1298-1320, 2007.
[3] Nguyen G. D, Einav I. The Energetics of Cataclasis Based on Breakage Mechanics. *Pure and Applied Geophysics* **166**: 1693-1724, 2009.
[4] Vardoulakis I. A., Sulem J. Bifurcation analysis in geomechanics. Blackie Academic & Professional, Glasgow, 1995.
[5] Mülhaus H. B, Vardoulakis I. A. The thickness of shear bands in granular materials. *Géotechnique* **37**: 271-283, 1987.
[6] Ord A., Vardoulakis I. A., Kajewski R. Shear band formation in Gosford Sandstone. *International Journal of Rock Mechanics and Mining Sciences* **28**: 397-409, 1991.

A CONTINUUM MECHANICAL FRAMEWORK FOR GRADIENT-EXTENDED DAMAGE COUPLED WITH PLASTICITY

Tim Brepols*[1], Stephan Wulfinghoff[2], and Stefanie Reese[1]
[1]Institute of Applied Mechanics, RWTH Aachen University, Aachen, Germany
[2]Institute for Materials Science, Computational Materials Science, Kiel University, Kiel, Germany

Summary A novel continuum mechanical framework is presented which is suitable for modeling gradient-extended damage coupled with plasticity. The geometrically nonlinear formulation is based on sound thermodynamic principles and applicable to arbitrarily large elastic and plastic deformations. Damage and plasticity are treated as truly independent yet coupled mechanisms by considering separate damage and plastic yield criteria as well as individual sets of loading / unloading conditions. Such a 'two-surface' approach makes the model formulation very flexible, as it can be applied in cases in which the material exhibits an either more brittle- or more ductile-like damaging behavior. An exemplary model derived on the basis of this framework is carefully examined in a structural finite element computation for its mesh-regularizing properties in case of large plastic strains and severe damage.

CONSTITUTIVE ASPECTS

The model framework presented in the following can be regarded as the geometrically nonlinear variant of a corresponding version for small strains, which was presented earlier by the same authors (see [1]).

General gradient-extended model framework for combined damage and plasticity

The gradient-extension of the model formulation is based on Samuel Forest's well-established micromorphic approach (see [2, 3]). As such, an additional global field variable $\bar{D}$ is introduced which is considered a primary unknown of the problem in addition to the displacements $\boldsymbol{u}$ and shall here be referred to as the 'micromorphic damage'. It can be interpreted as the 'nonlocal' counterpart of the 'local' internal damage variable D, the latter of which accounts for the rather complicated effects of damage in a material (e. g., occurrence and evolution of microcracks and microvoids during the deformation) in an averaged sense only. Via a micromorphic balance equation, which can be derived by applying an extended version of the principal of virtual work and which needs to be solved in addition to the classical balance of linear momentum, the spatial developments of D and $\bar{D}$ are linked.

The weak form of the problem is obtained by multiplying the balance of linear momentum and the just mentioned micromorphic balance equation by appropriate vectorial and scalar test functions $\delta\boldsymbol{u}$ and $\delta\bar{D}$, respectively, and by integrating over the reference domain B_0 of the body under consideration. This leads to:

$$g(\boldsymbol{u},\bar{D},\delta\boldsymbol{u}) := \int_{B_0} \mathbf{S}\cdot\delta\mathbf{E}\,\mathrm{d}V - \int_{B_0} \boldsymbol{f}_0\cdot\delta\boldsymbol{u}\,\mathrm{d}V - \int_{\partial B_{0_\mathrm{t}}} \boldsymbol{t}_0\cdot\delta\boldsymbol{u}\,\mathrm{d}A = 0 \qquad \forall\delta\boldsymbol{u} \tag{1}$$

$$h(\boldsymbol{u},\bar{D},\delta\bar{D}) := \int_{B_0} \left(H\left(D-\bar{D}\right)\delta\bar{D} - A\,\mathrm{Grad}\left(\bar{D}\right)\cdot\mathrm{Grad}\left(\delta\bar{D}\right)\right)\mathrm{d}V = 0 \qquad \forall\delta\bar{D} \tag{2}$$

Here, g is the weak form of the balance of linear momentum whereas h is the weak form of the micromorphic balance equation. Furthermore, $\mathbf{S}$ is the second Piola-Kirchhoff stress tensor, $\mathbf{E}$ is the Green-Lagrange strain tensor, $\boldsymbol{f}_0$ and $\boldsymbol{t}_0$ are volume distributed forces and prescribed tractions, respectively, and $\mathrm{Grad}(\bullet)$ denotes the gradient operator with respect to the coordinates in the reference configuration. Parameters A and H are the micromorphic moduli whose meaning will be described later. Since the the weak form (1) - (2) is generally nonlinear, it needs to be linearized with respect to the global unknowns $\boldsymbol{u}$ and $\bar{D}$ which in the end leads to a coupled set of equations that need to be solved iteratively for the increments $\Delta\boldsymbol{u}$ and $\Delta\bar{D}$. At that point, independent finite element approximations of the global field variables can be introduced, as usual. Further details are omitted here for brevity.

In accordance with a geometrically nonlinear theory of elastoplasticity, the deformation gradient $\mathbf{F}$ is assumed to be multiplicatively separable into an elastic ($\mathbf{F}_e$) and a plastic ($\mathbf{F}_p$) part, i. e. $\mathbf{F} = \mathbf{F}_e\,\mathbf{F}_p$. Furthermore, in order to consider nonlinear kinematic hardening, an additional physically-motivated split of the plastic part of the deformation gradient into recoverable ($\mathbf{F}_{p_e}$) and irrecoverable ($\mathbf{F}_{p_i}$) parts is presumed, leading to $\mathbf{F}_p = \mathbf{F}_{p_e}\,\mathbf{F}_{p_i}$. With this at hand, the following general form of the Helmholtz free energy per unit reference volume is assumed:

$$\psi = f_\mathrm{dam}(D)\left(\psi_e\left(\mathbf{C}_e\right) + \psi_p\left(\mathbf{C}_{p_e},\xi_p\right)\right) + \psi_d\left(\xi_d\right) + \psi_{\bar{d}}\left(D-\bar{D},\mathrm{Grad}\left(\bar{D}\right)\right) \tag{3}$$

Here, ψ_e is the elastic part of the free energy expressed in terms of $\mathbf{C}_e = \mathbf{F}_e^\mathrm{T}\,\mathbf{F}_e$. Furthermore, ψ_p denotes the plastic energy stored due to kinematic and isotropic hardening which depends on both $\mathbf{C}_{p_e} = \mathbf{F}_{p_e}^\mathrm{T}\,\mathbf{F}_{p_e}$ and ξ_p, the latter of which being the isotropic hardening variable. As indicated above, both ψ_e and ψ_p are affected by damage via a monotonically decreasing, but otherwise freely selectable, degradation function $f_\mathrm{dam}(D)$. Moreover, ψ_d accounts for stored energy due to damage hardening and depends on the damage hardening variable ξ_d, which plays a similar role as ξ_p in plasticity. Finally, $\psi_{\bar{d}}$ is the energy related to the micromorphic extension of the model. It depends on both the gradient of $\bar{D}$ and on the difference between the micromorphic and the local damage variable $D-\bar{D}$, thus enforcing a coupling between the two quantities in the formulation.

*Corresponding author. E-mail: tim.brepols@rwth-aachen.de

Particular gradient-extended 'two-surface' damage-plasticity model in this study

The above model framework is quite flexible and generally allows adaptation to a variety of conditions by an appropriate selection of the energetic components. For a meaningful discussion of the numerical results in the present paper, it is reasonable to make an exemplary selection at this point. A Neo-Hookean type format is chosen for the elastic part of the energy, i. e., $\psi_e := \mu/2\left(\operatorname{tr}\mathbf{C}_e - 3 - 2\ln\left(\sqrt{\det\mathbf{C}_e}\right)\right) + \Lambda/4\left(\det\mathbf{C}_e - 1 - 2\ln\left(\sqrt{\det\mathbf{C}_e}\right)\right)$ where Λ and μ are the Lamé constants. The plastic part of the energy reads $\psi_p := a/2\left(\operatorname{tr}\mathbf{C}_{p_e} - 3 - 2\ln\left(\sqrt{\det\mathbf{C}_{p_e}}\right)\right) + e\left(\xi_p + \left(\exp\left(-f\,\xi_p\right) - 1\right)/f\right)$ and is composed of two parts: the first is related to kinematic hardening, whereas the second accounts for nonlinear isotropic hardening of Voce type (a, e and f are corresponding plastic material parameters). A nonlinear damage hardening energy is chosen, i. e., $\psi_d := r\left(\xi_d + \left(\exp\left(-s\,\xi_d\right) - 1\right)/s\right)$ (r and s are damage related material parameters) and $\psi_{\bar{d}} := H/2\left(D - \bar{D}\right)^2 + A/2\,\mathrm{Grad}(\bar{D}) \cdot \mathrm{Grad}(\bar{D})$ represents the energy due to the micromorphic extension of the model: the first term penalizes the difference between D and $\bar{D}$ via parameter H, whereas parameter A controls the influence of the gradient term in the formulation. The damage degradation function is chosen as $f_{\mathrm{dam}}(D) := (1 - D)^2$. Following a 'two-surface' strategy, in which damage and plasticity are treated as individual dissipative mechanisms, separate damage and plastic yield criteria as well as individual loading / unloading conditions are defined.. Finally, thermodynamically consistent evolution equations for all strain-like internal variables are postulated (nonlinear kinematic hardening of Armstrong-Frederick type is considered in the model). Further details are omitted here for brevity and can be found in a paper which was very recently accepted for publication (see [4]).

NUMERICAL EXAMPLE

In order to demonstrate the mesh-regularizing properties of the gradient-extended damage-plasticity model introduced above, exemplary structural finite element computations of a 2D plane strain problem are considered in this study. More specifically, a uniaxial tensile test of a specimen which has two symmetrical notches in its middle is performed. The specimen is clamped at the bottom and pulled with a force F at the top (further details about the geometry and the setup of the boundary-value problem are omitted here for brevity). Simulations with different meshes ranging from 928 up to 70372 elements are carried out and compared to each other.

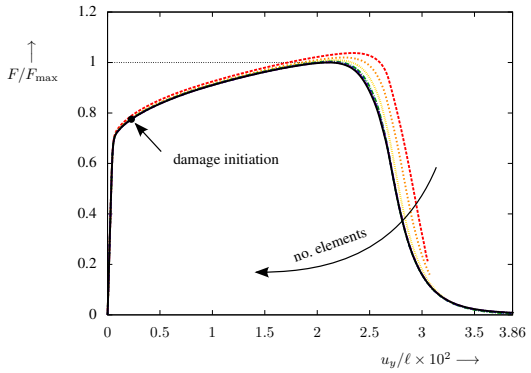

Figure 1: Normalized load-displacement curves.

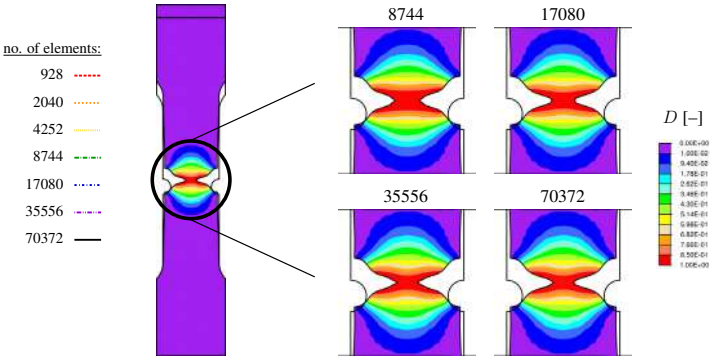

Figure 2: Damage contours D at end of process.

Fig. 1 shows the normalized load-displacement curves which are obtained in the simulations ($F_{\max}$ denotes here the load maximum, whereas u and ℓ are the displacement at the top and the original length of the specimen, respectively). Convergence towards a unique solution with a finite amount of energy dissipation during the damage process becomes clearly visible and the simulations can robustly be performed up to almost complete loss of load-bearing capacity of the specimen. A comparison of the damage contours D at the end of the process is shown in Fig. 2 for the four finest mesh discretizations. As can be seen, large plastic deformations and high damage occur in the middle area of the specimen and the results for the different discretizations agree very well. The numerical example therefore serves as a good first indicator that the proposed continuum mechanical framework for geometrically nonlinear gradient-extended damage-plasticity indeed works as desired: it leads to models which can adequately regularize the mesh size dependence of results in finite element simulations involving arbitrarily large plastic deformations and severe damage.

References

[1] Brepols T., Wulfinghoff S., and Reese S., Gradient-extended two-surface damage-plasticity: Micromorphic formulation and numerical aspects. *Int. J. Plast.* **97**, 64-106, 2017.
[2] Forest S., Micromorphic Approach for Gradient Elasticity, Viscoplasticity, and Damage. *J. Eng. Mech.* **135**, 117-131, 2016.
[3] Forest S., Nonlinear regularization operators as derived from the micromorphic approach to gradient elasticity, viscoplasticity and damage. *Proc. R. Soc. A* **472**, 20150755, 2016.
[4] Brepols T., Wulfinghoff S., and Reese S., A gradient-extended two-surface damage-plasticity model for large deformations, *Int. J. Plast.*, 2019 (in press).

EXPERIMENTAL INVESTIGATION OF DYNAMIC DELAMINATION UNDER IMPACT LOADING

Mirac Onur Bozkurt[1,2] and Demirkan Coker *[1,2]
[1]Department of Aerospace Engineering, Middle East Technical University, Ankara, Turkey
[2]METU Center for Wind Energy, Middle East Technical University, Ankara, Turkey

Summary The paper presents the experimental investigation of failure process in $[0/90]_s$ CFRP beams subjected to static and low-velocity impact (LVI) type flexural loadings. A drop-weight impact test setup is designed and built, and the same line load fixture is used in a static testing machine. During the experiments, failure events are captured with an ultra-high-speed (UHS) camera at frame rates up to half a million fps. Using the UHS pictures, in-situ damage characterization is performed and crack tip speeds during delamination propagation are measured. Digital image correlation analysis is carried out prior to failure to elucidate damage driving mechanisms. As a result, no distinct failure mechanisms exist for $[0/90]_s$ CFRP beams under static and LVI loadings. It is also shown that dynamic delamination propagation occurs at same speeds in this configuration independent of loading rate.

INTRODUCTION

In design of aerospace structures, composite laminates are stacked in order to fulfil some stiffness requirements with limited weight allowance. However, this might cause the laminate to be inefficient in terms of strength. Such weakness become prominent when the laminate is subjected to an out-of-plane impact load. Furthermore, static response of an impacted laminate may get dramatically worse especially under compressive loads. Thus, it is essential to understand impact damage very well to design damage tolerant structures.

In the literature, there are several experimental works dealing with parameters affecting and mechanisms of impact damage in composite laminates [1-5]. Results of the impact experiments conducted in such studies are used as benchmark for numerical simulations alongside of their use for understanding damage formation. In this study, we conduct in-situ line-load experiments with up-to-date experimental techniques to elucidate impact damage mechanisms. Moreover, we claim that crack tip speed during delamination propagation is a property that can be used in modelling of high-fidelity simulations.

EXPERIMENTAL METHOD

To conduct LVI tests, a non-standard drop-weight impact setup, shown in Figure 1, is designed and built. The flat beam specimen fixture, which consists of two couples of top and bottom rectangular steel plates placed on linear guideways, allows visualization of the damage process from the side of the beam specimen. Two ends of the specimen are sandwiched by the top and bottom plates and squeezed via bolt and nut fasteners passing through the holes located at corners of each plate. Impactor crosshead assembly consists of a steel crosshead, an in-line load cell and a hemi-cylindrical steel impactor located at the tip of the assembly and weighs 1865-g. Linear bearings are embedded at both ends of the crosshead and slide almost frictionless over two parallel guiding shafts. In static tests, the same boundary conditions are created by installing the impactor and the specimen fixture to 10-kN Shimadzu electromechanical testing machine.

The test matrix, given in Table 1, is constituted considering the number of specimens, parameters affecting the damage and the techniques used for better understanding of damage formation. In all impact and static tests, in-situ formation and progression of damage are captured at either 70,000 or 525,000 fps via the UHS camera system. In one static and one impact test, strain distribution on the specimen is computed during elastic loading using two-dimensional DIC method.

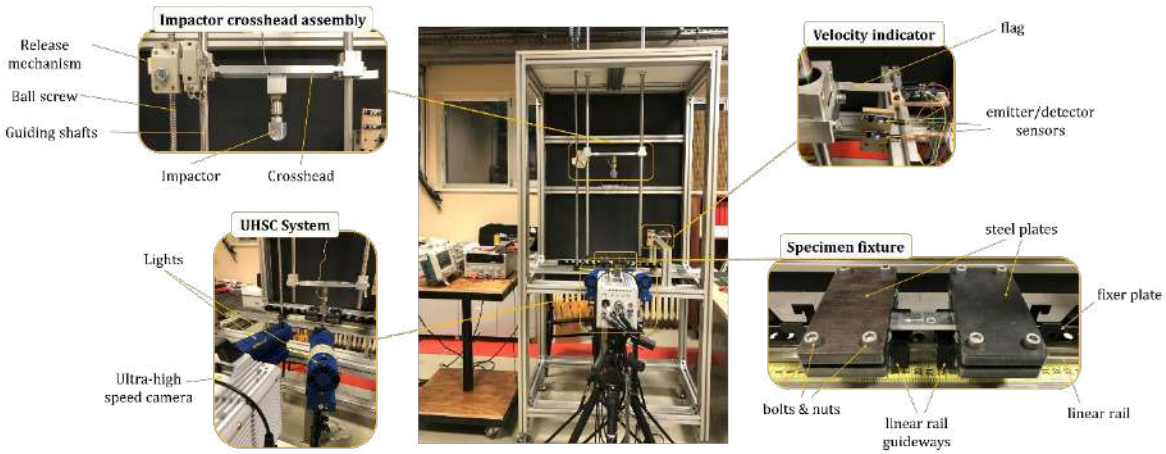

Figure 1. In-house low-velocity impact test setup with its sub-components.

*Corresponding author. E-mail: coker@metu.edu.tr

Table 1. Test matrix for impact and static loading of CFRP composite beams.

Layup	Specimen	Energy	UHSC capturing rate [fps]	DIC
$[0_5/90_3]_s$	Imp1	9.15 J	70,000	No
	Imp2	9.15 J	70,000	Yes
	Imp3	9.15 J	525,000	No
	Sta1	Static	525,000	No
	Sta2	Static	70,000	Yes

RESULTS AND CONCLUSIONS

Strain distributions on $[0/90]_s$ – Sta2 prior to failure on the left and right-hand sides of the specimen are obtained using DIC method and shown in Figure 2a. It is observed that initiation of diagonal matrix cracks occurs at the location of one of the hot ε_{xy} spots. Regarding to this coincidence and higher ε_{xy} magnitudes, it can be deduced that formation of these 'shear cracks' are controlled by the shear component of the strain in the case of these specimen and testing configurations. In addition to these observations, absolute ε_{xy} and ε_{yy} and concentrations at the delamination tips which point out the existence of opening and shearing modes exist in such fracture are observed.

UHS camera pictures showing the evolution of impact induced damage process in $[0/90]_s$ beam taken at 525,000 fps are presented in Figure 2b. The crack tip position data used in the first plot of Figure 2c are extracted from the UHSC pictures by visual assessment. Variation of the delamination crack tip speeds with crack length is also shown in Figure 2c. It is shown, under both static and impact loadings, that delaminations are not only dynamic but also reach the same speed plateau of 850 m/s. This concludes that the experimental data consisting of the crack tip positions and the crack tip speeds can be used as a benchmark for the simulations of the experiments conducted on $[0/90]_s$ beams.

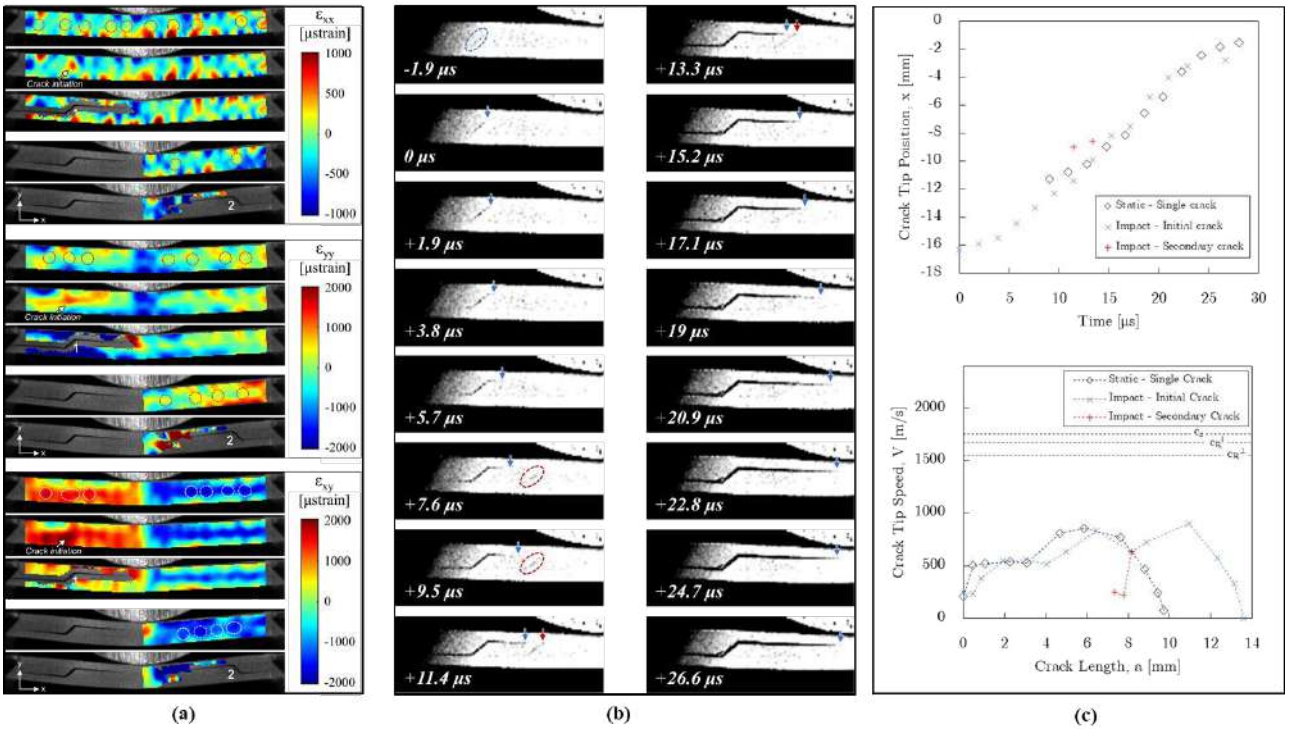

Figure 2. (a) Strain distributions prior to failures on the $[0/90]_s$ – Sta2 under static loading, (b) UHS camera pictures showing the evolution of the impact induced damage on the left half of $[0_5/90_3]_s$ – Imp3 taken at 525,000 fps, and (c) crack tip position vs. time and crack tip speed vs. crack length plots for one static and one impact test.

References

[1] Choi H.Y., Downs R.J., Chang F-K. A new approach toward understanding damage mechanisms and mechanics of laminated composites due to low-velocity impact: Part I-experiments. *J Compos Mater,* **25**: 992–1011, 1991.

[2] Liu D. Impact-induced delamination–a view of bending stiffness mismatching. *J Compos Mater*, **22**: 674–92, 1988.

[3] Abrate S. Impact on laminated composite materials. *Appl Mech Rev*, **44**: 155, 1991.

[4] Lopes C.S., Seresta O., Coquet Y., Gürdal Z., Camanho P.P. and Thuis B. Low-velocity impact damage on dispersed stacking sequence laminates. Part I: Experiments. *Compos Sci Technol*, **69**: 926-936, 2009.

[5] Topac O.T., Gozluklu B., Gurses E. and Coker D. Experimental and computational study of the damage process in CFRP composite beams under low-velocity impact. *Compos Part A-Appl S*, **92**: 167-182, 2017.

A NOVEL ANISOTROPIC ELASTOPLASTIC DAMAGE FE MODEL FOR WOOD

Elena Benvenuti*[1], Nicola Orlando[1], Michael Kaliske[2], and Clemens Gebhardt[2]
[1]Department of Engineering, University of Ferrara, Ferrara, Italy
[2]Technische Universität Dresden,Dresden,Germany

Summary We propose a novel constitutive model for wood based on a multi-surface failure criterion resulting from a set of plastic laws for compressive failure modes and orthotropic damage laws for tensile/shear failure modes. We show that the proposed formulation satisfactorily simulates compression and Mode I debonding tests until failure.

INTRODUCTION

Wood is increasingly being used for both restoration purposes and design of advanced wood-based materials. It is an inhomogeneous, anisotropic and porous material with moisture-, temperature- and time-dependent behaviour [1]. Common features of state-of-the-art FE-models for wood structures are the assumption of material orthotropy and the recognition that both structural behavior and failure modes change depending on direction and sign of the prevailing stress component [2].

The present study can be ascribed to the category of multi-surface anisotropic constitutive models for wood combining plasticity and damage. The plasticity constitutive law draws inspiration from the multi-surface plasticity model [3], while the orthotropic Continuum Damage Model model extends the approach in [4]. In the two-dimensional case, we introduce three damage variables d_θ associated with the directions $\theta = L, R, LR$ (Fig. 1a) and define five failure surfaces, three associated with damage and two with the plastic strain $\boldsymbol{\varepsilon}^p$ evolution. Given the sets $\mathcal{I}^p$ and $\mathcal{I}^d$ indexing the active failure functions f plastic and damaging type, respectively, we cast the generic i-th failure surface F_i $i \in \mathcal{I} = \mathcal{I}^p \cup \mathcal{I}^d$ and the equivalent-stress scalar $\bar{\tau}_i$ as

$$\bar{\tau}_i = \begin{cases} f_i(\boldsymbol{\sigma}) & i \in \mathcal{I}^p \\ f_i(\tilde{\boldsymbol{\sigma}}) & i \in \mathcal{I}^d \end{cases}, \quad F_i = \begin{cases} \bar{\tau}_i + q_i - 1 & i \in \mathcal{I}^p \\ \bar{\tau}_i - r_i & i \in \mathcal{I}^d \end{cases},$$

where r_i is a non-decreasing, history-dependent, state variable. We formulate the rate form of the evolution of damage and plasticity state variables in the compact form

$$\dot{\boldsymbol{\varepsilon}}^p = \sum_{i \in \mathcal{I}^p} \dot{\lambda}_i^p \frac{\partial F_i}{\partial \boldsymbol{\sigma}}, \qquad \dot{d}_\theta = \dot{\lambda}_{i_\theta}^d \dot{\bar{\tau}}_{i_\theta} \frac{\partial G_{i_\theta}(\bar{\tau}_{i_\theta})}{\partial \bar{\tau}_{i_\theta}}, \ \theta = L, R, LR,$$

where the loading/unloading conditions

$$\begin{aligned} &\dot{\lambda}_i^p \geq 0, \quad F_i \leq 0, \quad \dot{\lambda}_i^p F_i = 0, \quad i \in \mathcal{I}^p, \\ &\dot{\lambda}_i^d \geq 0, \quad F_i \leq 0, \quad \dot{\lambda}_i^d F_i = 0, \quad i \in \mathcal{I}^d, \end{aligned}$$

hold. The resulting failure domain is shown in Fig. 1b. Most available FE models for wood use cohesive elements to

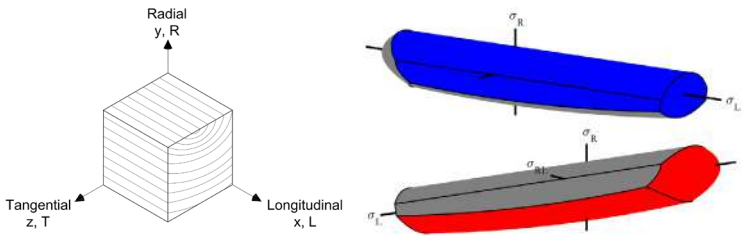

(a) (b)

Figure 1: a) Adopted reference system; b) Failure surface.

simulate tensile and shearing cracks. Cohesive elements require an explicit, mesh-dependent, representation of the crack geometry. Alternatively, the crack geometry can be implicitly represented by means of the extended finite element method (XFEM) [5], a mesh-independent tool for propagating cracks and discontinuities. While the number of applications of the XFEM to concrete and steel elements is, nowadays, countless, applications of the XFEM to timber mechanics are not so diffused. The regularized XFEM captures strain localization [6], and debonding along finite width interfaces [7]. In

*Corresponding author. E-mail: elena.benvenuti@unife.it

particular, let the displacement $\boldsymbol{u}$ jump across the surface Γ and $d_\Gamma(\boldsymbol{x})$ be the signed distance function of $\boldsymbol{x}$ from Γ. The regularized XFEM is based on the following discrete approximation of displacement $\boldsymbol{u}$ [6]

$$\boldsymbol{u}(\boldsymbol{x}) = \boldsymbol{N}(\boldsymbol{x})\boldsymbol{V} + \mathcal{H}_\rho(d_\Gamma(\boldsymbol{x}))\boldsymbol{N}\boldsymbol{A},$$

where $\mathcal{H}_\rho$ is a regularized Heaviside function depending on the length parameter ρ, $\boldsymbol{V}$ and $\boldsymbol{A}$ denote the vectors collecting the standard and enriched nodal degrees of freedom, respectively, and $\boldsymbol{N}$ are the standard FE shape functions. Since crack development in wood comes along with fiber-bridging, and fiber-bridging spreads the cracking process over a Fracture Process Zone (FPZ), in the present methodology, joints and interfaces are simulated by means of the regularized XFEM.

APPLICATIONS

Fig. 2a shows the load-displacement results obtained with different regularization lengths ρ for the double cantilever beam test [8]. The proposed model correctly reproduces wood behavior also at compressive loading. This is illustrated by Fig. 2b and Fig. 2c for the tests performed by Franke et al. [9], corresponding to compression along the radial and longitudinal direction, respectively.

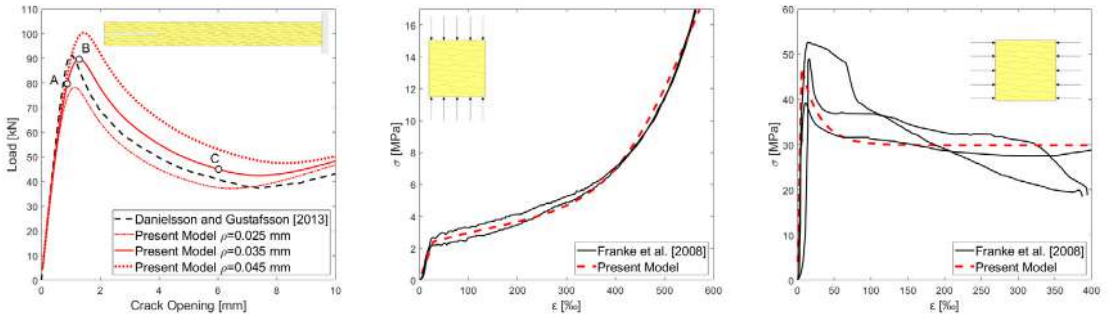

(a) (b) (c)

Figure 2: a) Load-displacement result for the DCB test [8]. Stress-strain results obtained for the test with compression along b) the radial and c) the longitudinal direction.

CONCLUSIONS

The proposed multi-surface orthotropic CDM model combined with the regularized XFEM correctly captures loading-directionality dependence, ductile failure induced by compressive stresses, as well as brittle failure associated with tensile stress states. The use of the regularized XFEM ensures a smooth continuous-discontinuous transition and reproduces a physically-consistent FPZ.

ACKNOWLEDGEMENT

The first two authors acknowledge the support of the research fund PRIN Prot. 2015LYYXA8.

References

[1] de Borst K., Jenkel C., Montero C., Colmars J., Gril J., Kaliske M., Eberhardsteiner J. Mechanical characterization of wood: An integrative approach ranging from nanoscale to structure. *Comp. & Struct.* **127**: 53-67, 2013.

[2] Schmidt J. and Kaliske M. Models for numerical failure analysis of wooden structures. *Engng. Struct.* **31**: 571-579, 2009.

[3] Mackenzie-Helnwein P., Eberhardsteiner J., Mang H. A. A multi-surface plasticity model for clear wood and its application to the finite element analysis of structural details. *Comp. Mech.* **31**: 204-218, 2003.

[4] Maimí P., Camanho P. P., Mayugo J. A., Dávila C. G. A continuum damage model for composite laminates: Part I - Constitutive model. *Mech. Mat.* **39**: 897-908, 2007.

[5] Moës N., Dolbow J., Belytschko T. A finite element method for crack growth without remeshing. *Int. J. Num. Meth. Engng.* **46**: 131–150, 1999.

[6] Benvenuti E. Mesh-size-objective XFEM for regularized continuous–discontinuous transition. *Finite Elements in Analysis and Design*, **47**: 1326-1336, 2011.

[7] Benvenuti E. and Orlando N. Intermediate flexural detachment in FRP-plated concrete beams through a 3D mechanism-based regularized eXtended Finite Element Method. *Comp. Part B: Engng.* **145**: 281-293, 2018.

[8] Danielsson H., Gustafsson, P. J. A three dimensional plasticity model for perpendicular to grain cohesive fracture in wood. *Engng. Fract. Mech.* **98**: 137-152, 2013.

[9] Franke S., Franke B., Schober K. U., Rautenstrauch K. The strength behavior of wood in experiment and simulations. Proceedings of the 10th World Conference on Timber Engineering (WCTE 2008), Miyazaki, Japan, 2008.

LUMPED DAMAGE MECHANICS FOR TWO AND THREE-DIMENSIONAL ANALYSIS

David L.N.F. Amorim[1], Ricardo Picón[2], Sergio P.B. Proença*[3], and Julio Flórez-López[4]
[1]Department of Civil Engineering, Federal University of Sergipe, Sergipe, Brazil
[2]Departament of Civil Engineering and Geology, Catholic University of Temuco, Araucanía, Chile
[3]Department of Structural Engineering, University of São Paulo, São Carlos, Brazil
[4]ILATIT, Federal University of Latin-American Integration, Foz do Iguaçu, Parana, Brazil

Summary Lumped Damage Mechanics (LDM) is a formulation that merges ideas of both fracture and damage mechanics with the concept of plastic localization zone. A typical finite element in LDM for analyses of framed structures is the assembly of an elastic beam-column with two inelastic hinges at the ends of the element. This paper proposes an innovative extension of this framework to two and three dimensional continuum. Accordingly, in a two-dimensional continuum a plastic hinge becomes a localization band and in a three-dimensional continuum it becomes a localization surface. The finite element hereby described for LDM-2D analysis is a four-node quadrilateral with bands of damage localization on its sides. Damage evolution laws are introduced for describing the constitutive behavior of each band. The element formulation can also be applied to three-node triangles and four-node tetrahedra. The feasibility of the resulting formulation is confirmed through numerical analyses, in particular showing the mesh-independence of the numerical results.

BACKGROUND INFORMATION

Classical Damage Mechanics (CDM), [1], evolved from the theory of plasticity including material deterioration in a continuous approach. The CDM constitutive models comprise a softening constitutive response associated to a homogeneous strain state. However, those models have failed in describing non-homogeneous strain states, leading to ill-posed problems and mesh-dependent numerical algorithms.

An alternative for circumventing the ill-posed issue was the introduction of a non-local approach, [2]. Next, a strong discontinuity framework was coined to directly account for localization phenomena, [3]. Furthermore, a finite element based scheme for describing a transition from damage to crack is also an important contribution to be mentioned [4].

However, the alternative form of damage mechanics addressed in this paper is radically different. Lumped Damage Mechanics (LDM) was proposed in the early nineties and has been developed since then, [5, 6]. The major assumption is that localization is a separate phenomenon that needs the introduction of specific state variables with their respective evolution laws. Unlike the classical damage mechanics, constitutive modeling in LDM does not use the concept of strain, or curvature as in beam models, but rather the inelastic elongation of the localization band, as hereby considered, or inelastic rotation of the hinge. Under this assumption, the derived models lead to mathematically objective results.

So far, LDM has been limited to the analysis of framed structures, in which both damage as well as plasticity are localized in zones of zero length: the inelastic hinges. This paper shows that LDM is a general framework that can be extended to the analysis of any continuum. Actually, in a two-dimensional continuum the inelastic hinge concept transforms into a localization band and in a tridimensional solid, into a localization surface.

ON THE LDM EXTENSION

Focusing on the referred extension, the localization of damage in a narrow band with a nil initial thickness, while the rest of the element remains elastic, is a major aspect to be accounted for. A hypothesis of elongation equivalence instead of strain equivalence as in CDM is then introduced. It means that the total elongation is composed by the elastic elongation plus a measure of the elongation of the damage localization band.

Aiming numerical simulations, an extension of LDM to plane analysis can be done firstly by revisiting the conventional four node bilinear quadrilateral element shown in Figure 1a. An important modification is to consider elongations instead of strains. The equivalent truss system conceived as shown in Figure 1b helps in this way. The element strains can then be related to the truss-bars elongations, and these to the nodal displacements of the element. Following such conception, the kinematic and equilibrium equations leading to the internal forces vector and stiffness matrix of the conventional quad-element may now involve an equivalent matrix of gradient operators expressed in terms of elongations.

Next, as damage variables are supposed to describe inelastic phenomena lumped on localization bands, four fixed localization bands of null volume are added at the sides of the revisited element (see Fig 1c). In order to apply a deformation equivalence hypothesis and to compute the elongations in each band, the elongation at the extremities of a localization band are related to the elongations of the equivalent truss-bars crossing those sections. Moreover, the nature of the shape functions of the element impose a linear variation of the elongation at any section across a band (see Fig 1d). The constitutive equations are then completed with eight damage functions, in correspondence to the two elongations at each node in reference directions of the element.

Finally the same kinematic and equilibrium equations of the revisited quadrilateral element may be used. An analogous procedure can be adopted to generate LDM three-node triangle elements and even LDM four-node tetrahedron aiming three-dimensional analysis.

*Corresponding author. E-mail: persival@sc.usp.br

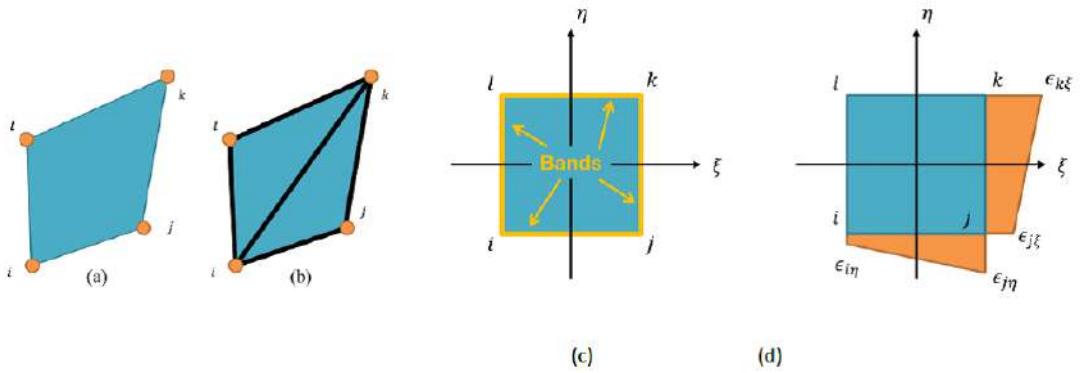

Figure 1: a) Quadrilateral element; b) Equivalent truss-system; c) Localization bands; d) Bands elongations.

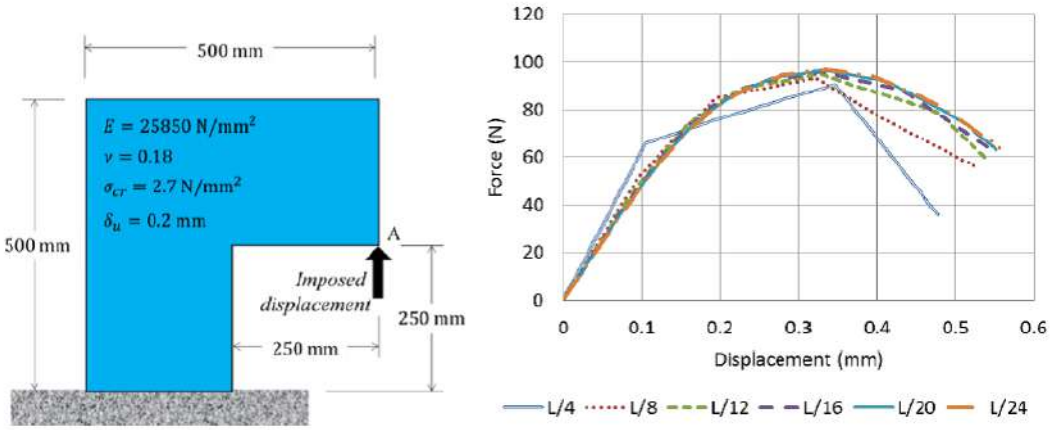

Figure 2: Left) L-shaped solid; Right) Displacement vs. force for several meshes.

CONCLUSIONS

Six meshes were used in the problem depicted in Figure 2. The finite elements present square shape, dividing the larger sides forming the L-shaped solid equally. For instance, for the mesh L/4 the larger sides were divided by 4 equal segments, leading to a total of 12 elements in the discretization. Also in Figure 2 the convergence of the global response with mesh refinement is shown .

The formulation hereby presented is remarkable for its simplicity and physical correctness, which are clear advantages with respect to other approaches.Regarding further efforts in this direction, for instance, a more complex formulation involving mode II too could be considered since the bands of the elements addressed in this paper are loaded on mode I. Additionally, outside the localization bands the elements do not need to have exclusively an elastic behavior. It can be elastic-plastic or even exhibit continuous damage. In this more general scenario, merging CDM modeling to LDM formulation can be envisaged.

Finally, the extension to the tridimensional case opens the possibilities for a significant number of new applications.

References

[1] Lemaitre J. A Course on Damage Mechanics. Spriger-Verlag, 1992.

[2] Bazant Z. P., Jirasek M. Nonlocal Integral Formulations of Plasticity and Damage: Survey of Progress. *J. Eng Mech.* **128**: 11, 2002.

[3] Borja R. A finite element model for strain localization analysis of strongly discontinuous fields based on standard Galerkin approximation. *Comput. Methods Appl. Mech. Engrg.***190**:1529-1549, 2000.

[4] Comi C., Mariani S., Perego U.An extended FE strategy for transition from continuum damage to mode I cohesive crack propagation. *Int. J. Numer. Anal. Meth. Geomech.* **31**: 2, 213-238, 2007.

[5] Flórez-López J., Marante M.E., Picón R.Fracture and Damage Mechanics for Structural Engineering of Frames: State-of-the-Art Industrial Application.Hershey, Pennsylvania, USA, IGI-GLOBAL, 2015.

[6] Amorim D.L.N.F. On the lumped damage mechanics for nonlinear structural analysis: new developments and applications. *PhD Thesis*, São Carlos School of Engineering, University of São Paulo, Brazil, 2016.

COMPARATIVE THERMODYNAMICS-BASED ANALYSIS OF TWO TYPES OF GRADIENT DAMAGE MODELS

Kossivi Kpotufe[1,3], Radhi Abdelmoula[2], Nadjime Pindra[1], and Djimédo Kondo*[3]
[1]Université de Lomé, Département de Mathématiques, Togo
[2]Université Paris 13, LSPM, Villetaneuse, France
[3]Sorbonne Université, Institut Jean le Rond d'Alembert, Paris, France

Summary The present study is devoted to a comparative analysis of two types of gradient damage models. To this end, we first rely on the Generalized Standard Materials framework recently overviewed by Nguyen [9] for gradient plasticity models and which includes the corresponding variational formulation. For the first class of gradient damage models, the regularization term enters in the dissipation potential, while in the second class it is in the form of a stored energy (then as the part of the material free energy). For comparison purpose, we performed various simulations among which those shown below for an elastic matrix containing a rigid inclusion. The numerical results allow to investigate the differences between the two types of models, notably from an energetic point of view.

A GENERALIZED STANDARD MATERIALS FRAMEWORK FOR GRADIENT DAMAGE MODELS

Due to induced stress softening, local damage models exhibit pathological sensibility to mesh size or orientation. A common way to regularize such damage models consists in adding gradient-damage based contribution which involves a length scale (see for instance [5]). An interesting aspect of such regularized damage models is their link to variational approach to fracture [2], as established by [10] (see also [8]) by relying to the so-called Drucker-Ilyushin postulate. Owing to the importance of the above cited works and their corresponding variational formulation, it can be hepful to provide their thermodynamics-based formulation in the context of Generalized Standard Materials. This will allow to clarify the place of the regularization terms in the free energy and/or the dissipation potential. Though, ideas of formulating the gradient damage models at the global level of a structure Ω can be found in [6], we refer here to the recent study [9]. With the condensed notation $U=(\underline{u},d)$, $\underline{u}$ being the displacement field and d the damage one in Ω, let us introduce the global free energy $\boldsymbol{W}(U)=\int_\Omega \rho w\big(\underline{\underline{\varepsilon}},d,\underline{\nabla} d\big)d\Omega$ and the overall dissipation potential $\boldsymbol{D}(\dot{U})=\int_\Omega \varphi\big(\underline{\dot{\underline{\varepsilon}}},\dot{d},\underline{\nabla}\dot{d}\big)d\Omega$.
By considering the so-called generalized Biot equations, $\boldsymbol{W}_{,U}+\boldsymbol{D}_{,\dot{U}}=0$ under quasi-static conditions, and the global normality rule, it can be shown (based on [9]) that for all t, the quasi-static response $U(t)$ of the solid submitted to a given displacement loading path satisfies the evolution variational inequality:

$$\forall \dot{U}^*,\quad \boldsymbol{W}_{,U}\cdot(\dot{U}^*-\dot{U})+\boldsymbol{D}(\dot{U}^*)-\boldsymbol{D}(\dot{U})\geqslant 0. \tag{1}$$

THE TWO CONSIDERED TYPES OF GRADIENT DAMAGE MODELS

We consider two types of time-independent gradient damage models whose main elements at a material point are:

- Dissipative model: $\rho w\big(\underline{\underline{\varepsilon}},d\big)=\frac{1}{2}\underline{\underline{\varepsilon}}:\mathbb{C}(d):\underline{\underline{\varepsilon}}$; $\quad\varphi(\dot{d},\underline{\nabla}\dot{d})=Y_c(d)\dot{d}+2w_1{l_D}^2(\underline{\nabla}d\cdot\underline{\nabla}\dot{d})+I_+(\dot{d}),\quad Y_c(d)>0.$
- Energetic model: $\rho w\big(\underline{\underline{\varepsilon}},d,\underline{\nabla}d\big)=\dfrac{1}{2}\underline{\underline{\varepsilon}}:\mathbb{C}(d):\underline{\underline{\varepsilon}}+E_0{l_E}^2\big|\big|\underline{\nabla}d\big|\big|^2$; $\quad\varphi(\dot{d})=Y_c(d)\dot{d}+I_+(\dot{d}),\quad Y_c(d)>0$

where, as usually, $I_+(\dot{d})$ stands for an irreversibility condition. l_D and l_E are the internal lengths in the dissipative and energetic models, respectively. Note that in φ the quantities d and $\underline{\nabla}d$ may be considered as (state) parameters.
First, by reporting the above expressions of ρw and φ in the global potentials and then in (1) one gets the rate form of the variational inequality. Then, owing to the particular homogeneity of degree one of the above dissipation potentials (see [3] for definition of "Simple Dissipative" systems), the later can be integrated in time. This results in a variational formulation consisting to minimize the following functionals with respect to the fieds $\underline{u}$ and d on the domain Ω:

- Dissipative model: $\xi\big(\underline{u},d\big)=\int_\Omega\left(\frac{1}{2}\underline{\underline{\varepsilon}}(\underline{u}):\mathbb{C}(d):\underline{\underline{\varepsilon}}(\underline{u})+w(d)+w_1{l_D}^2\big|\big|\underline{\nabla}d\big|\big|^2\right)d\Omega$
- Energetic model: $\xi\big(\underline{u},d\big)=\int_\Omega\left(\frac{1}{2}\underline{\underline{\varepsilon}}(\underline{u}):\mathbb{C}(d):\underline{\underline{\varepsilon}}(\underline{u})+E_0{l_E}^2\big|\big|\underline{\nabla}d\big|\big|^2+w(d)\right)d\Omega$

The above formulations have the form of the so-called Ambrosio-Tortorelli approximation introduced by [2] (see also [8]) for fracture mechanics problems. For comparison purpose, we consider $\mathbb{C}(d)=(1-d)^2\mathbb{C}_0$ in which $\mathbb{C}_0$ is the elastic stiffness of the sound material. Moreover, we choose for simulations $Y_c(d)=2w_1d,$, that is $w(d)=\int_0^d Y_c(\alpha)d\alpha=w_1d^2$.

*Corresponding author. E-mail: djimedo.kondo@sorbonne-universite.fr

APPLICATIONS AND COMPARATIVE ANALYSIS

Let us first note that models considered by [8] or [10] are dissipative ones, while those introduced in [5] or [7] belong the class of energetic models. As an example, we consider a model-problem adopted by a number of authors, such as [2], [1] and [4]. It consists in a traction experiment on a fiber-reinforced matrix. The studied domain is composed of a squared linear-elastic matrix of side $L = 300mm$ with a cylindrical rigid inclusion of radius $R = L/6$. The materials properties and the boundary conditions are the same as in [4]. In particular, the young modulus $E = 12000MPa$, the Poisson ratio $\nu = 0.25$, the characteristics length $l_D = 5mm$ and the fracture energy $G_c = 25.10^{-3}N/mm$ (equivalent to $w_1 = G_c/(2l_D) = 2,5.10^{-3}MPa$).

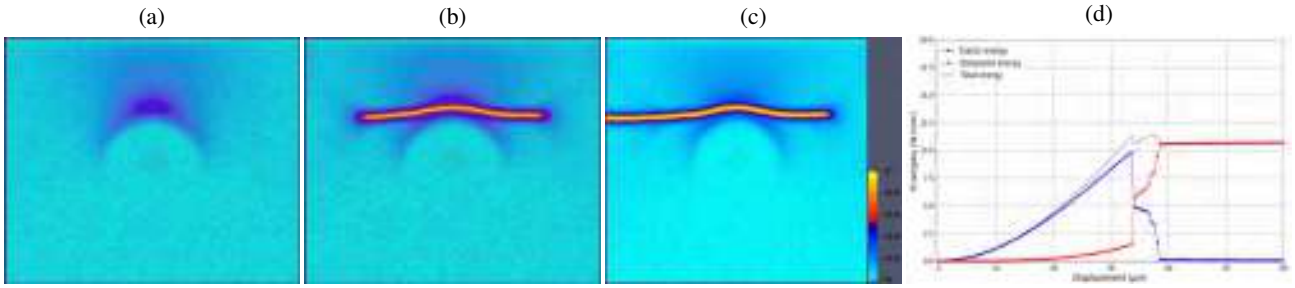

Figure 1: Elastic matrix reinforced by a rigid inclusion: evolution predicted by dissipative model. (a) $u = 31\mu m$, (b) $u = 34\mu m$, (c) $u = 38\mu m$, (d) evolution of the different energies

Fig.1 shows damage distribution and the different energies evolution predicted by the dissipative model. The damage starts early and concentrates at the bottom of the inclusion (see figure 1a); from a detailed examination of the numerical results, it appears that fracture starts for a displacement about $u = 33\mu m$ and the complete fracture is observed for $u = 39\mu m$. This is confirmed by the evolution of energies (see figure 1d)) whose overall trend is the same as in [4].

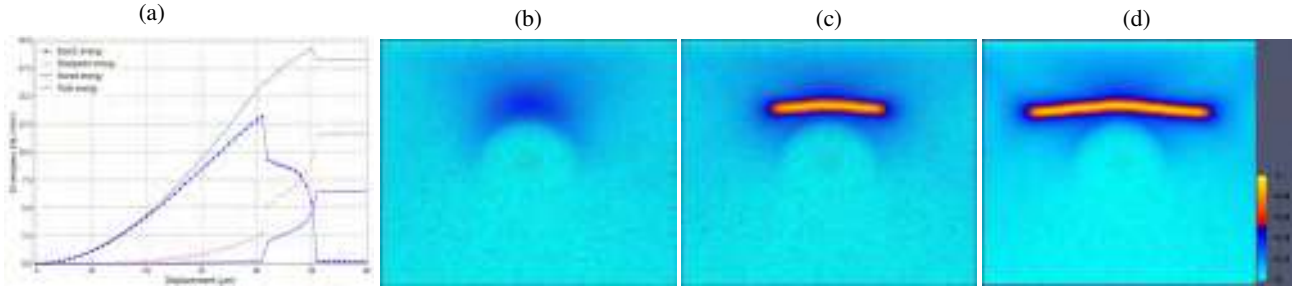

Figure 2: Elastic matrix reinforced by a rigid inclusion: evolution predicted by energetic model. (a) evolution of the different energies, (b) $u = 38\mu m$, (c) $u = 42\mu m$, (c) $u = 50\mu m$.

Let us come now to the energetic model for which one needs not only to consider the previous material parameters, but also E_0 which affects the amount of the stored energy. It must be emphasized that, a priori, the order of magnitude of E_0 is not that of the Young modulus E, but rather that of w_1. For the energetic model, the stored energy must not be taken into account in the interpretation of the fracture energy G_c. From the theoretical study of 1D bar, it can be shown that the internal length l_E is given by $l_E = 2l_D\sqrt{w_1/E_0} = G_c/\sqrt{E_0 w_1}$. For illustrative purpose, we choose $E_0 = w_1$. Fig.2 illustrates the evolutions of damage pattern and energies predicted by the energetic model. Though, the results are qualitative comparable to the those on fig.1, it is observed here that fracture occurs later ($u = 42\mu m$) and ends at $u = 51\mu m$. Moreover, it appears from Fig.2a that the stored energy is not negligible during fracture growth.

References

[1] Amor, H., Marigo, J.J., Maurini, C. Regularized formulation of the variation brittle fracture with unilater contact: numerical experiments. J. Mech. Phys. Solids, 57 (2009), 1209–1229.
[2] Bourdin, B., Francfort, G. A., Marigo, J-J. Numerical experiments in revisited brittle fracture. J. Mech. Phys. Solids, 48 (2000), 797–826.
[3] Ehrlacher A. and Fedelich B., Stability and bifurcation of simple dissipative systems: application to brutal damage " , in Strain Localisation and Size Effect Due to Cracking and Damage, pp.217-227, 1988
[4] Freddi, F. and Royer-Carfagni, G. Regularized Variational theories of fracture: A unified approach. J. Mech. Phys; Solids, 58 (2010) 1154-1174
[5] Fremond, M. and Nedjar, B. Damage, gradient of damage and principle of virtual power. Int. J. Solids Structures, 33 (1996), 1083-1103
[6] Lorentz, E. and Andrieux, S. A variational formulation for nonlocal damage models. International Journal of Plasticity 15 (1999) 119-138
[7] Lorentz, E. and Godard, V. Gradient damage models: Toward full-scale computations. Comp. Meth. Appl. Mech. Engrg. 200 (2011) 1927–1944
[8] Marigo, J-J., Maurini, C. and Pham K. An overview of the modelling of fracture by gradient damage models. Meccanica (2016) 51:3107–3128
[9] Nguyen Q.S. Quasi-static responses and variational principles in gradient plasticity. J. Mech. Phys. Solids, 97 (2016) 156–167
[10] Pham K. and Marigo, J-J. From the onset of damage to rupture: construction of responses with damage localization for a general class of gradient damage models. Continuum Mech. Thermodyn. (2013) 25:147–171.

IMPACT ABSORPTION IN AUXETIC DAMAGEABLE MATERIALS

David Faraci*[1] and Claudia Comi [1]
[1]Department of Civil and Environmental Engineering, Politecnico di Milano, Milano, Italy

Summary In this work we study the behaviour of elastic and quasi-brittle auxetic metamaterial under impact. Particular reference is made to the use of these structured materials for facial protector devices for sport activities. Impact analyses of a ball over an auxetic and a non-auxetic honeycomb material show the potential benefit of the densification mechanism occurring in the auxetic material below the impacted region. Moreover, when the bulk material is assumed to have a brittle behaviour, the auxetic lattice in compression develops a smaller damage with respect to the honeycomb, non-auxetic lattice. This can be another advantage in impact absorption applications.

AUXETIC AND NON-AUXETIC STRUCTURED MATERIALS

Auxetic metamaterials, i.e. micro-structured materials with the unusual negative Poisson's rate property, thanks to a significant densification mechanism occurring when they are compressed, have extremely good performances under impact, [1]. We consider two different periodic lattice materials, with two-dimensional (2D) and three-dimensional (3D) microstructures, that may exhibit an equivalent global auxetic behaviour and traditional (non-auxetic), behaviour. The lattices and the unit cells for the re-entrant honeycomb (RHC), originally proposed in [2], and the honeycomb (HC) structures are shown in Figs.1a,c and Figs.1b,d, respectively. For fixed geometries of these lattices, an equivalent density, ρ_{eq}, defined as the mass of the unit cell divided by the volume, can be easily computed.

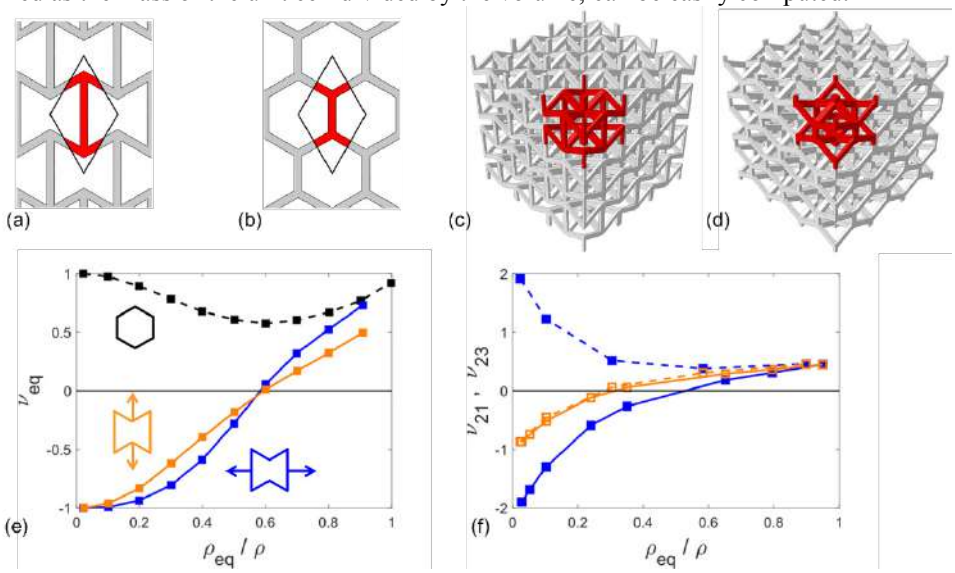

Figure 1. Lattice with unit cell in red of: (a) 2D RHC, (b) 2D HC, (c) 3D RHC, (d) 3D HC. Equivalent Poisson's ratios versus normalized equivalent mass density: (e) 2D lattices, plane strain conditions, (f) 3D lattices (dotted lines: HC, solid lines: RHC, ν_{21} in blue, ν_{23} in orange).

Elastic behaviour: equivalent Poisson's ratio

Several lattices, endowed with different thickness of the beam elements inside the cell, are considered and a linear-elastic analysis allows computing the equivalent Poisson's ratios. The results are shown in Figs. 1e and 1f in terms of equivalent Poisson's ratio versus normalized equivalent density. Note that the microstructure makes the homogenized or equivalent behaviour non-isotropic, with the exception of the 2D HC. For low values of the equivalent density, the 2D RHC lattice exhibits auxetic behaviour in both directions (orange and blu curves in Fig. 1e) and the same holds true for the 3D RHC lattice (solid lines in Fig. 1f). While in the 2D case the HC lattice always has a non-auxetic behaviour (black curve in Fig. 1e), the 3D HC lattice, which is transversally isotropic, can have an auxetic behaviour (i.e. $\nu_{23}<0$) in the horizontal plane of isotropy.

Damageable 2D-lattice micro-structured materials

With the aim to study the effect of damage on the different lattices, we consider the geometries shown in Fig. 1a with $\rho_{eq}=0.27\rho$ and in Fig. 1b with $\rho_{eq}=0.22\rho$ and we assume that the constituent bulk material is brittle, with a tensile strength of 10 MPa and a mode I fracture energy of 0.01 Nmm. In compression, the behaviour of the bulk material is assumed linear elastic. We numerically simulate the response of the two damageable metamaterials under compression. A specimen constituted by 5 x 5 cells is considered, a uniform displacement, inducing shortening, is imposed on the upper boundary and the global reaction is computed. A brittle-crack model is used in the finite element code, with the option of element deletion to avoid over distorted mesh. Figure 2 shows the obtained force vs displacement curves that

*Corresponding author. E-mail: david.faraci@polimi.it.

can be interpreted as uniaxial compression stress-strain curves of the structured materials. For comparison, the linear elastic response is also shown (dashed line). One can observe that the auxetic effect provides an additional strength mechanism in compression that results in a higher global force, with a reduced equivalent damage at equal global displacement. The equivalent damage at the peak of the force, estimated from the secant stiffness, is 0.23 for the RHC and 0.41 for the HC. The global behaviour is however quite brittle. The plots in Fig. 2 (right) show the failure patterns corresponding to the points marked in the global curves.

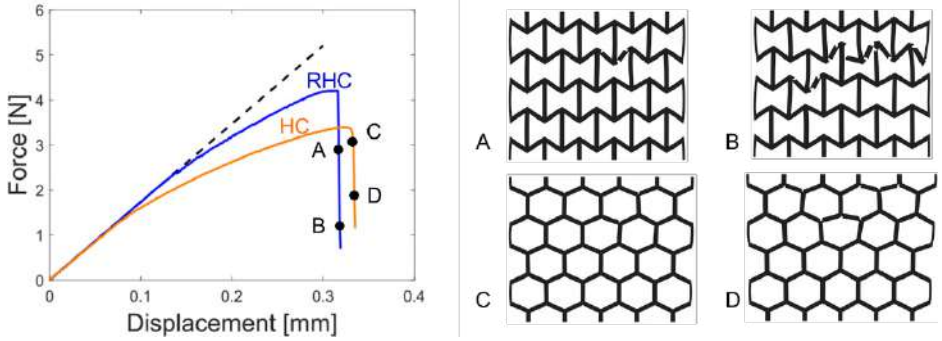

Figure 2. Force vs displacement of 2D-RHC (orange curve) and 2D-HC (blue curve) lattices in compression. Dashed line represents the linear elastic response, solid lines represent the response with a damage model. Failure patterns for RHC and HC materials.

IMPACT ON STRATIFIED MATERIALS WITH AUXETIC CORE

The problem considered is related to the choice of optimal materials for protector facial masks to be used by athletes. The real functional requirement sets a limit on the thickness of the device and a limit to the transmitted force in case of impact. In this context, [3] proposed a mask made of two layers of flexible and rigid ethylene vinyl acetate (EVA) and compared the stresses on the face in case of impact with and without the mask.

In [4], we proposed a different solution, with the inclusion of an intermediate layer of structured material, see Fig. 3a and analysed the impact of a rigid sphere on a small portion of the mask, assuming an elastic behaviour of the bulk material used to fabricate 3D HC and RHC lattices and large deformations. Figure 3b shows the results in terms of the time evolution of the reaction force transmitted to the internal surface. A more efficient impact absorption in obtained with the RHC lattice (lower value of the peak of transmitted force). This is due to the densification of the material in the impacted region, with activation of self-contact inside the highly deformed metamaterial.

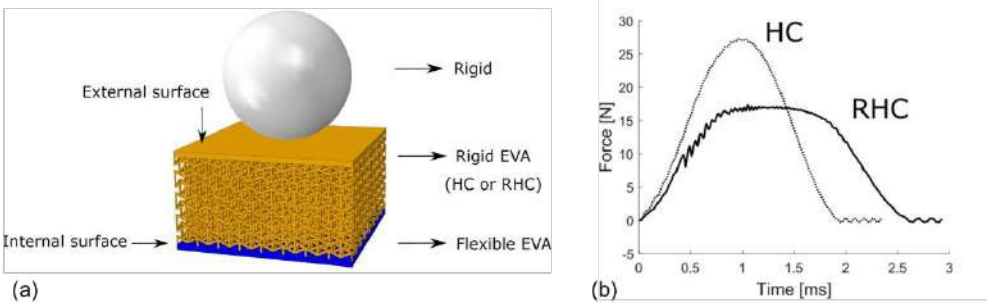

Figure 3. (a) Scheme of analyzed portion of mask. (b) Time evolution of reaction force at internal surface of protector device

To set the safefy margin of a real protector device one has to include also the non-linear behaviour of the bulk material. The effect of non-linear material behaviour, possibly with damage, has to be properly taken into account. As here shown, assuming small strain, the auxetic behaviour can induce additional strength mechanisms to prevent damage development, but can also result in a brittle final failure. The combined effect of large displacements and damage deserves further study and is currently under development.

CONCLUSIONS

The densification mechanism of auxetic material under compression can improve the impact absorption performance and modify the damage mechanism. This opens the way to possible application to protector devices for athletes. The real design of such devices however would require proper identification of the actual nonlinear behavior of the bulk material and the definition of homogenized constitutive law for the micro-structured materials.

References

[1] Lakes, R., Elms, K. Indentability of Conventional and Negative Poisson's Ratio Foams. *Journal of Composite Materials* **27**: 1193–1202, 1193.
[2] Almgren, R.F. An isotropic three-dimensional structure with Poisson'sratio = -1. *Journal of Elasticity* **15**: 427–430, 1985.
[3] Coto, N. P., Meira, J. B. C., Brito e Dias, R., Driemeier, L., de Oliveira Roveri, G., Noritomi, P. Y. Assessment of nose protector for sport activities: Finite element analysis. *Dental Traumatology* **28**: 108–113, 2012.
[4] Faraci, D., Driemeier, L., Comi, C. Bending-dominated auxetic materials for facial protector devices. *Submitted,* 2019.

MULTILE CRACK AND DEBONDING MECHANISMS IN QUASI-BRITTLE COATINGS

Guido Borino*[1] and Francesco Parrinello [1]
[1]Department of Engineering, University of Palermo, Palermo, Italy

Summary The mechanical failure of coatings is analyzed in its main features together with the proposal of new strengthening strategies. The quasi-brittle behavior of ceramic-type coatings is the source of the nucleation and propagation of tensile vertical cracks. A second type of weakness is given by the imperfect adhesion coating/substrate, which can produce decohesion and eventually spallation of the fragmented coating. The study is conducted mainly by a nonlinear computational approach based on finite elements with nonlocal damage and cohesive-frictional interface elements. Finally, new techniques of reinforcements are proposed and their effectiveness numerically verified.

THE MECHANICAL PROBLEM

There are many circumstances in which structural elements need a boundary surface protection from external agencies, such as high temperature variations, chemical aggressive environment, small particle impacts, extreme moisture environment and so on. The function of the coating is to protect the integrity and the functionality of the structural element but, however the coating has also to carry mechanical loads transmitted by the structural system without failure or suffering damage. Only minimal damage could be accepted provided that the coating maintains its overall function. It would also desirable an easy restoration which does not compromise the structural safe function.

Typically the structural element is constituted by a material with high mechanical performance, namely with high strength and stiffness, designed for giving an appropriate structural safe response to the external loadings. On the other hand, the coating layer is usually a quasi-brittle material with moderate strength and small ductility, but with high thermal and chemical resistant performances. For ensuring the high thermal insulation properties, the coating is usually realized by ceramic-type materials.

Two main weakness are therefore to be considered. The first it the quite small strength of the coating to sustain tensile stress and therefore the coating is prone to multiple tensile cracking localization. The second weakness is related to the adhesion between the coating and the structural stiff substrate. This means that a decohesion mechanism may develop along the interface between the coating layer and the substrate, which in turn can produce a spallation of the coating.

The present paper presents a computational approach to evaluate and optimize the mechanical efficiency of thermal coating with respect to the above mentioned possible failure weakens. In particular the substrate is treated as a linear elastic continuum, the coating behaves as a quasibrittle material and therefore is modelled by a nonlocal elastic-damage material model. The possible dechoesion is reproduced inserting a cohesive-frictional interface between the elastic substrate and the coating thin layer. The problem is analyzed by means of Finite Element simulations showing the qualitative and quantitative response and the main failure mechanisms which develops as function of the material property variation and of the thickness of the coating.

Finally, it will be shown how specific type of micro-reinforcements can effectively improve the mechanical performance of the coating.

MECHANICAL MODELLING

The problem analyzed consists of a plate formed with different layers subjected to uniform traction/bending and thermal variation through the thickness. The basic layers is the elastic high-performance substrate followed by a zero thickness interface which represents a potential dechoesion surface and finally on the top the quasibrittle coating film. The analyses are performed employing 2D nine-node finite element discretization for the substrate and for the coating and a six-node interface elements between substrate and coating. The constitutive assumption employed for the coating and the interface are briefly reported in the following subsections.

Nonlocal elastic-damage constitutive relations for the coating film

A symmetric thermodynamically consistent nonlocal damage formulation is adopted for modelling the quasi-brittle coating [1]. The nonlocality is obtained by employing a spatial integral operator applied to the damage variable and it require the introduction of an iternal lenght parameter ℓ. The nonlocal regularization allows to reproduce, in an objective way, the strain localization/diffusion. The stress - strain relation reads

$$\boldsymbol{\sigma}(\boldsymbol{x}) = \left(1 - \bar{\omega}(\boldsymbol{x})\right) \boldsymbol{E}\, \boldsymbol{\varepsilon}(\boldsymbol{x}) \tag{1}$$

where $\boldsymbol{\sigma}$ is the Cauchy stress tensor, $\boldsymbol{E}$ is the elastic moduli tensor, $\boldsymbol{\varepsilon}$ is the infinitesimal strain tensor and $\bar{\omega}$ is the scalar nonlocal measure of the isotropic damage ω, defined as

$$\bar{\omega}(\boldsymbol{x}) = \int_V W(\boldsymbol{x}, \boldsymbol{y})\, \omega(\boldsymbol{y})\, dV(\boldsymbol{y}) \tag{2}$$

*Corresponding author. E-mail: guido.borino@unipa.it

where $W(\boldsymbol{x},\boldsymbol{y})$ is an appropriate positive value spatial weight function in which the amplitude of the spatial interactions is governed by the value of the internal length parameter ℓ. For $\ell \to 0$ the weight function $W(\boldsymbol{x},\boldsymbol{y}) \to \delta(\boldsymbol{x},\boldsymbol{y})$, where δ is the Dirac's delta function and therefore eq. (2) becomes an identity, whereas eq. (1) collapses in the standard local elastic damage constitutive equation. See [2] for details on nonlocal damage formulations. The constitutive model requires a damage activation function of the type:

$$\phi_d(\bar{Y},\chi) = \bar{Y} - \chi - Y_0 \leq 0 \tag{3}$$

where $\bar{Y}$ is a nonlocal measure, obtained with the same integral averaging procedure of eq. (2), of the energy release rate $Y = 1/2\,\boldsymbol{\varepsilon}^T \boldsymbol{E}\,\boldsymbol{\varepsilon}$, χ is an internal variable which describes the post peak stress-strain softening law and Y_0 is the initial threshold for damage activation.

The constitutive relations are completed by associative damage flow rule and by loading/unloading conditions.

Cohesive-frictional interface constitutive model

The potential development of a delamination mechanism at the bounding plane between the elastic substrate and the quasi-brittle coating, is modeled by a zero thickness cohesive-frictional interface. The model adopted in this paper is a recent extension of the thermodynamically consistent mixed-mode model developed by the authors [3, 4, 5, 6]. The basic idea is that a unit interface element can be subdivided in two fractions. A cracked fraction $\omega_s\, dS$ and a sound fraction $(1-\omega_s)\, dS$. The traction vector transmitted by the interface $\boldsymbol{t}$ is therefore additively represented by the sum of the contribution of the two interface surface fractions $\boldsymbol{t} = \boldsymbol{t}_s + \boldsymbol{t}_c$. Each fraction has its own constitutive relation given as

$$\boldsymbol{t}_s = (1-\omega_s)\boldsymbol{K}_s\boldsymbol{\delta}_s^e; \qquad \boldsymbol{t}_c = \omega_s \boldsymbol{K}_c \boldsymbol{\delta}_c^e \tag{4}$$

$\boldsymbol{K}_s$ and $\boldsymbol{K}_c$ are diagonal stiffness matrices and $\boldsymbol{\delta}_s^e$ and $\boldsymbol{\delta}_c^e$ are the vector displacement jump of the two interface fractions.

For reproducing delamination and frictional sliding two activation functions are required. The first is:

$$\phi_d^s = Y_s - \chi_s - \tilde{Y}_{s0}(\boldsymbol{u}) - Y_{s0} \leq 0 \tag{5}$$

where Y_{s0} is the initial interface damage activation threshold, χ_s is the internal variable governing the interface softening law and $\tilde{Y}_{s0}(\boldsymbol{u})$ is a positive term which allows to drive fracture mixity. Y_s is the surface energy release rate defined $Y_s = \frac{1}{2}\boldsymbol{\delta}_s^{eT}\boldsymbol{K}_s\boldsymbol{\delta}_s^e - \frac{1}{2}\boldsymbol{\delta}_c^{eT}\boldsymbol{K}_c\boldsymbol{\delta}_c^e$.

The second activation function for the frictional sliding has the form of a Mohr-Coulomb law given as

$$\phi_p^s(\boldsymbol{t}_c) = |t_{ct}| + \alpha t_{cn} \leq 0 \tag{6}$$

where α is the frictional coefficient and t_{ct} and t_{cn} are the tangential and normal components of the traction vector $\boldsymbol{t}_c$ which acts on the damaged fraction.

The interface constitutive relations are completed by nonassociative (for dilatancy effects) flow rule and by loading/unloading conditions.

CONCLUSIONS

The formulation proposed is able to elucidate the main weakness of quasibrittle coating. The influence of the coating thickness is shown as a parameter that can discriminate different failure mechanisms. Once understood the mechanical features which promote the failure, possible new strategies for reinforcing are proposed and numerically verified. Namely, tensile cracking can be prevented by inserting a very thin ductile film, [5], whereas debonding can be combatted by micro-pin reinforcements.

Acknowledgments

The financial support of the Italian Ministry for University and Research (MIUR), under the grant PRIN-2015, project No. 2015LYYXA8. Multi-scale mechanical models for the design and optimization of micro-structured smart materials and metamaterials is gratefully acknowledged.

References

[1] Borino G., Failla B., Parrinello F., A Symmetric Nonlocal Damage Theory. *Int. J. Sol. Struct.* **46 (13)**: 2680-2692, 2003.

[2] Bažant Z.P., Jirásek M., Nonlocal integral formulations of plasticity and damage: Survey of progress, *J. Eng. Mech.*, **128 (11)**, 1119–1149, 2002.

[3] Parrinello F., Marannano G., Borino G., Pasta A., Frictional effect in mode II delamination: Experimental test and numerical simulation *Eng. Fract. Mech.* **110**: 258-269, 2013.

[4] Parrinello F., Marannano G., Borino G., A Thermodynamically Consistent Cohesive-Frictional Interface Model for Mixed Mode Delamination *Eng. Fract. Mech.* **153**: 61-79, 2016.

[5] Parrinello F., Borino G., Non-Associative Damage Interface Model for Mixed Mode Delamination and Frictional Contact *Eur. J Mech. A/Sol.* **76**: 108-122, 2019.

[6] Fan, X., Xu, R., Kikuchi, M. *J. Cent. South Univ.* **21 (7)**: 25792583, 2014.

EXPERIMENTAL EVIDENCE OF NON-LOCAL INTERACTIONS DURING THE COMPRESSIVE FAILURE OF ELASTO-DAMAGEABLE SOLIDS

Ashwij Mayya[1], Estelle Berthier[2], and Laurent Ponson *[1]
[1]Institut Jean le Rond d'Alembert,Sorbonne Université,CNRS,Paris,France
[2]Department of Physics, North Carolina State University, Raleigh, North Carolina, USA

Summary We study experimentally the compressive failure of cellular solids by damage accumulation and then localization. We observe that damage spreads by bursts separated by elastic phases before it localizes in a narrow band. We investigate the spatial organization of these bursts within the specimen and show that they are characterized by regions of size ξ where the damage increases cooperatively. As failure approaches, the non-local length ξ increases until it reaches the specimen size. Our results provide a detailed characterization of the non-local effects involved during damage growth and open new perspectives for the multi-scale modelling of compressive failure.

INTRODUCTION

Quasi-brittle materials such as rocks wood, mortar or ceramics under compression fail through the accumulation and then the localization of a large number of microcracks in interaction. These interactions affect the evolution of the damage within quasi-brittle solids, and ultimately, control their load-bearing capacity. However, damage mechanics relies on the introduction of a representative volume element, neglecting the long-range interactions between the material elements constituting a specimen [1]. Recently, it was shown that these non-local effects do impact the failure response of quasi-brittle solids like the inclination of localization band [2]. To capture these interactions, several non-local damage models have been proposed, but they all remain largely phenomenological [3]. In addition, there are very few quantitative investigations of the non-local effects during the spreading of damage that could be used to discriminate and feed competing non-local approaches. This study intends to fill this gap by exploring experimentally the non-local effects involved during the spreading of damage using compressive tests of 2D cellular solids. We evidence a growing length scale ξ that emerges from the cooperative evolution of the damage field within the specimen before localization. In addition, we show that ξ reaches the specimen size at the onset of failure. To interpret this behaviour, we develop a micro-mechanical model that takes into account both the long-range elastic interaction within the specimen and the disordered failure properties of the material. It successfully captures our experimental observations, thus challenging non-local damage models considering a constant (non-evolving) non-local length scale.

EXPERIMENTAL INVESTIGATION OF NON-LOCAL EFFECTS DURING DAMAGE SPREADING

The failure of elasto-damage solids is investigated through compressive tests carried on 2D cellular materials made of hollow cylinders (Fig. 1(a)). As the compressive load is slowly increased, the specimen shows a linear elastic response and then a softening behavior until the emergence of a localization band at peak load (Fig. 1(b) and (c)). The detailed investigation of the mechanical response of the specimen shows that damage accumulates through a series of failure bursts manifesting as load drops, as shown in the inset of Fig. 1(b). The energy S_{global} dissipated during each of these bursts is first estimated macroscopically, using the mechanical response of the specimen. It is shown to increase as the specimen is driven to failure (Fig. 1(d)). In parallel, using particle tracking from image analysis and coarse-graining techniques [4], we compute the evolution of the mechanical fields at the scale of the unit cell. This provides an independent measurement of the size S_{local} of the damage bursts that correlates with the value S_{global} obtained at the macroscopic scale (See Fig. 1(d)).

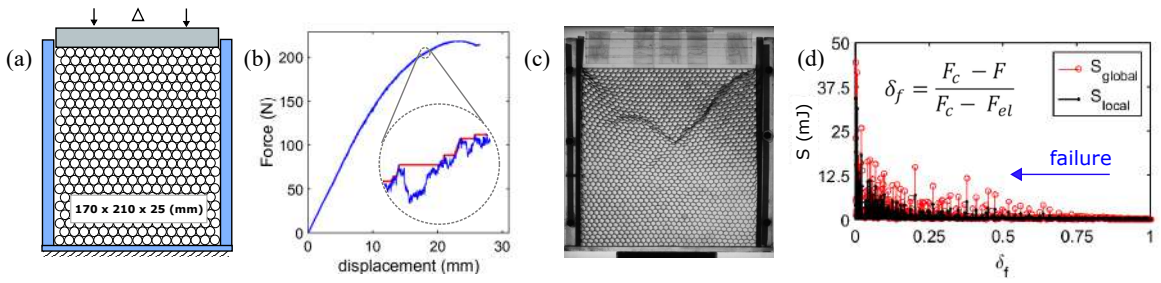

Figure 1: (a) Schematic representation of the compression test. (b) Force-displacement response. (c) Pattern of damage localization observed shortly after the peak. (d) Evolution of dissipated energy during each burst as obtained from global and local analysis.

Interestingly, this local analysis also provides the spatial organization of these bursts, i.e. the location of the local failure events within the specimen at a coarse-grained scale (Fig. 2(a)). This analysis reveals that each individual burst is

*Corresponding author. E-mail: laurent.ponson@upmc.fr.

actually composed of several clusters of characteristic size ξ that corresponds to regions of the specimen where damage grew cooperatively. ξ emerges from the spatio-temporal evolution of the damage field and is reminiscent of the elastic interactions between material elements. It is shown to grow as the specimen is driven close to failure, following the power law behaviour $\xi \sim 1/\delta^{1/2}$ (Fig. 2(b)). Changing the specimen size shows that the non-local length scale ξ reaches the specimen size at localization. Alternatively, the energy S dissipated during each individual burst is represented in Fig. 2(c) and is also shown to grow with a power law behaviour $S \sim 1/\delta^{1/2}$. This is consistent with the scaling relation $\xi \sim S$ between the correlation length of the damage bursts and their energy represented in inset of Fig. 2(c).

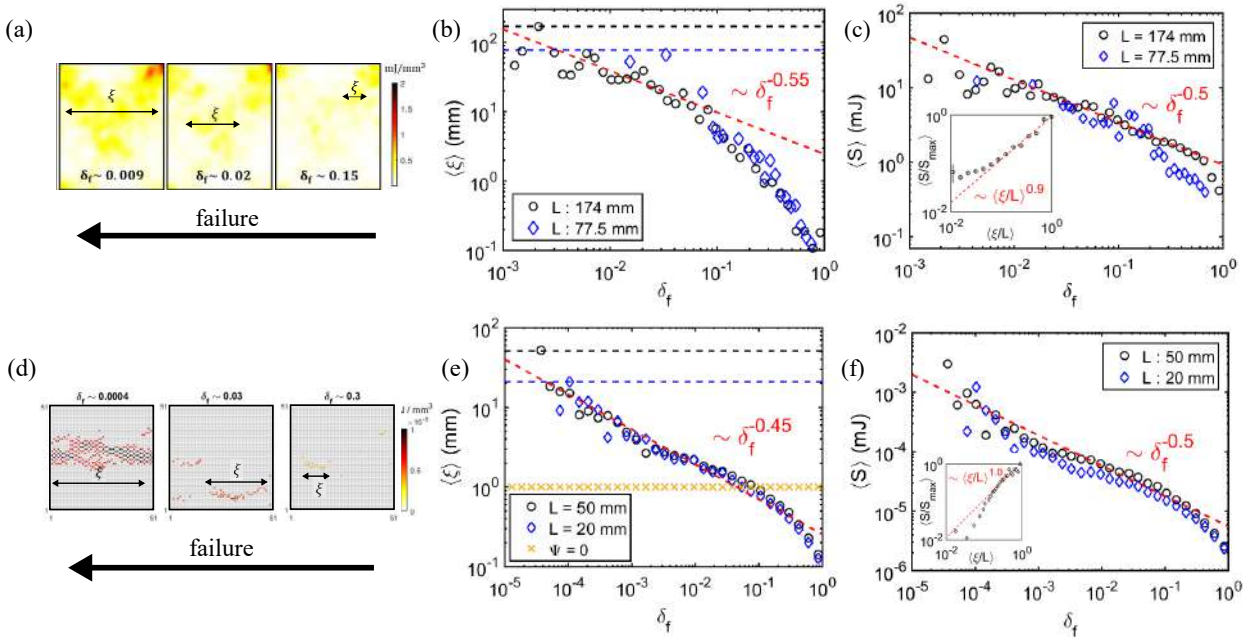

Figure 2: Spatial organization of damage bursts at different distances to failure (a - experiments, d - simulations). Variation of correlation length (b - experiments, e - simulations) and burst sizes with distance to failure (c - experiments, f - simulations). Insets in (c) and (f) : Scaling of correlation length with burst size.

How to interpret these observations? Figures 2(d)-(f) show numerical results drawn from a micro-mechanical model of damage spreading in 2D disordered elasto-damageable specimen. Our simulations rely on two main ingredients: (i) the critical stress at which damage takes place is heterogeneously distributed within the specimen; (ii) each individual damage event induces a local softening of the material. This leads to a redistribution of the stress through the specimen that in turn leads to other damage events through a domino effect. Here, the new mechanical fields are computed after each damage events using a Green function computed from damage mechanics [2]. This model leads to localization at peak load and captures fairly well the macroscopic response of the specimen. More interestingly, it also captures the increase of the length ξ and the size S of the bursts measured from the evolution of the damage field, as well as the associated scaling laws (Figs. 2(e) and (f)). Note that when the stress redistribution is shut down or if the material is homogeneous, the non-local length ξ remains constant (see Fig. 2(e)).

IMPLICATIONS AND PERSPECTIVES

What are the implications of our work? The cooperative spreading of damage in elasto-damageable solids is characterized by a length scale ξ that results from the interplay between the material disorder and the elastic interactions. This size ξ increases and even reaches the specimen size at localization. This evolution challenges current non-local damage models that assumes a finite and constant correlation length. As a perspective, I will discuss how the complex dynamics of damage growth in elasto-damage specimens can be harnessed to estimate and predict their residual life time.

References

[1] Rudnicki J., Rice J. Conditions for the localization of deformation in pressure-sensitive dilatant materials. *J. Mech. Phys. Solids* **23**: 371-394, 1975.
[2] Dansereau V., Démery V., Berthier E., Weiss J., Ponson L. Collective damage growth controls fault orientation in quasi-brittle compressive failure. *Phys. Rev. Lett.* **122(8)**: 085501, 2019.
[3] Pijaudier-Cabot G., Bazant Z. Non local damage theory. *J. Eng. Mech.* **113**: 1512-1533, 1987.
[4] Glasser B. J., Goldhirsch I. Scale dependence, correlations, and fluctuations of stresses in rapid granular flows. *Phys. Fluids* **13 (2)**: 407-420, 2001.

THE EFFECT MECHANISM OF PRESTRESS ON THE DEFORMATION OF METAL BEAMS SUBJECTED TO IMPULSIVE LOAD

Jian Zheng, Fangyun Lu*, Xiangyu Li, and Kefang Zhang
College of Liberal Arts and Sciences, National University of Defense Technology, Changsha, China

Summary During the service time of engineering structures, most structural members are under prestress conditions. In order to figure out the effect mechanism of prestress on the damage of metal beams subjected to impulsive loading, a series of numerical simulations with different prestress conditions and different impulse intensity are conducted. A prestress coefficient and a dimensionless impulsive loading, normalized by energy, are introduced to organised the results. A reasonable relationship between α, Φ and the residual central deformation is found, as well as a small counter-intuitive phenomenon. Because of the correspondence between deformation and internal energy, a simple analysis on the aspect of stress transition and energy absorption is performed and effectively explained the effect mechanism of prestress on the deformation on the mental beams subjected to impulsive loading.

BACKGROUND IMFORMATION

Metal beams are basic structural members, and the study of its damage mechanism to impulsive loading is an important issue in engineering. Since Menkes and Opat [1] published their findings on damage modes of beams in 1973, there follows lots of researches concerned about the deformation prediction and the damage modes segmentation of intensity loaded beams and plates. In these researches, prestress is a rarely talked topic. But in fact, while subjected to impulsive loading, these structural members have mostly been under prestress condition during their service time. In order to figure out the effect mechanism of prestress on the damage of metal beams subjected to impulsive loading, two typical prestress conditions are employed by axial and transverse pre-loading, as shown in figure 1, and only the inelastic deformation damage mode is concerned in this article.

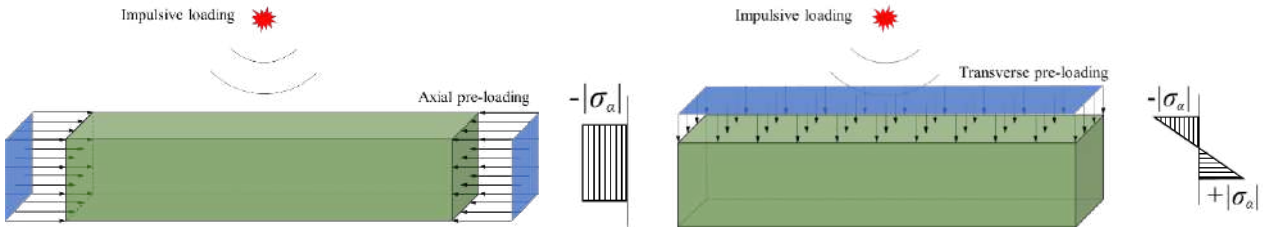

Figure 1. Fully clamped beams under impulsive loading with initial prestress condition.

In the axial pre-loading condition, the prestress can be described by the axial stress σ_α, which can be written as:

$$\sigma_\alpha = \alpha\sigma_0$$

where σ_0 is quasi static yield stress, α is prestress coefficient, $-1 \le \alpha \le 1$. The σ_α is positive when tension, negative when compression. While in the transverse pre-loading condition, the σ_α is the bending stress in the lowest end of section at the central beam.

METHODS

Numerical models were built to simulate plenty of conditions by AUTODYN software, and Aluminium beams with a width, thickness and length of 10mm, 10mm and 100mm were employed. In the axial pre-loading conditions, a series of constant stress boundary condition σ_α was applied to both ends of the beam to perform the axial prestress. In the transverse pre-loading conditions, a series of constant stress boundary condition q was applied to the upside of the beam to perform the transverse prestress, the relation of q and σ_α can be written as: $\sigma_\alpha = ql^2/4bh^2$, where b, h and l are the width, thickness and length of the beam. After the stress condition of the beam have been stabilized, the impulsive loading was performed by apply analytical blast boundary condition on the upside of the beam. The charge weight and coordinates of blast were accurately controlled in the analytical blast definition.

The dimensionless central deformation of the beam ($\delta = W/h$) is the main variable to analysis the effect of prestress. The impulsive loading is normalized by the energy theoretically induced by the charge and the maximum energy absorbed by the beam before yield, which can be calculated by:

$$\Phi = \sqrt{\frac{E_T}{bhl\sigma_0}} = \sqrt{\frac{3mE_m}{4\pi R^3\sigma_0}}$$

where E_T is the theoretical energy given by the charge, m is the charge weight, R is the blast distance. and E_m is the C-J energy per unit mass. The dimensionless impulsive loading Φ and prestress coefficient α are used to show the results of the deformation of the beam.

* Corresponding author. E-mail: **zhengjian14@nudt.edu.cn**

RESULTS AND CONCLUSIONS

Deformation results of two typical prestress conditions

The deformation data is organized by variables mentioned above, and the final results are shown in figure 2. Figure 2a) shows the residual central deformation of beams subjected to different impulsive intensity under axial pre-loading, while figure 2b) under transverse pre-loading. At all events, the deformation is obviously increased with the increasing Φ. In transverse prestress condition, a negative α always reduces the deformation while a positive α increasing the deformation. However, in axial prestress condition, opposite α doesn't always bring in opposite influence on the deformation (In figure 2a), the δ at α=0.6 are slightly higher than the left points).

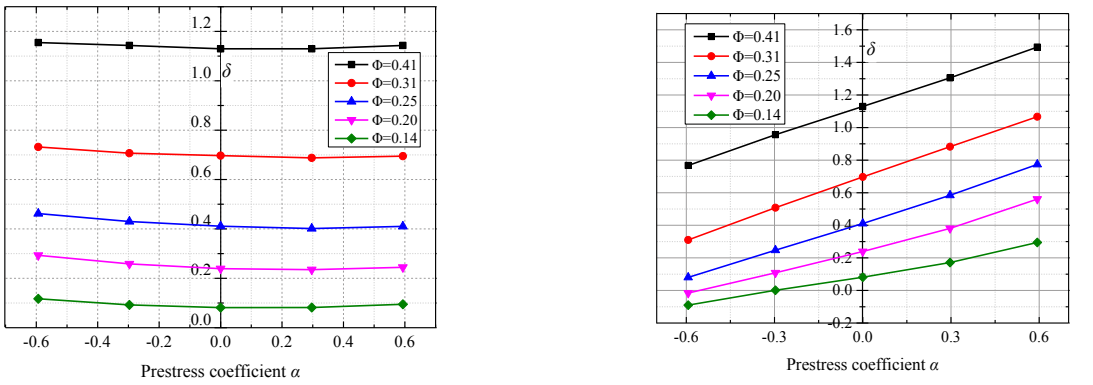

a) Results under axial prestress conditions

b) Results under transverse prestress conditions

Figure 2. The central deformation of beams under different prestress conditions subjected to different impulsive loadings.

Effect mechanism of the prestress on the energy absorption

To make clear the different effect mechanism of two prestress, a simplify analysis on the change of stress and a contrast of the energy absorption were performed, shown in figure 3. In the axial prestress condition, the impulsive loading made the stress of the beam section changing from the uniformly distributed elastic stress to the plastic stress, separated by the neutral axis, with one side of being positive and the other side negative. During this transition, the stress on one side of the neutral axis continues to increase, while the stress on the other side is released first and then increased. Therefore, the initial internal energy caused by axial prestress is not fully contributed to the final energy. In the transverse prestress condition, the stress changed from linearly distributed elastic stress to neutral-axis-separated plastic stress. The stress on both sides of the neutral axis change in the same pace, so the initial internal energy caused by transverse prestress is totally contributed to the final energy.

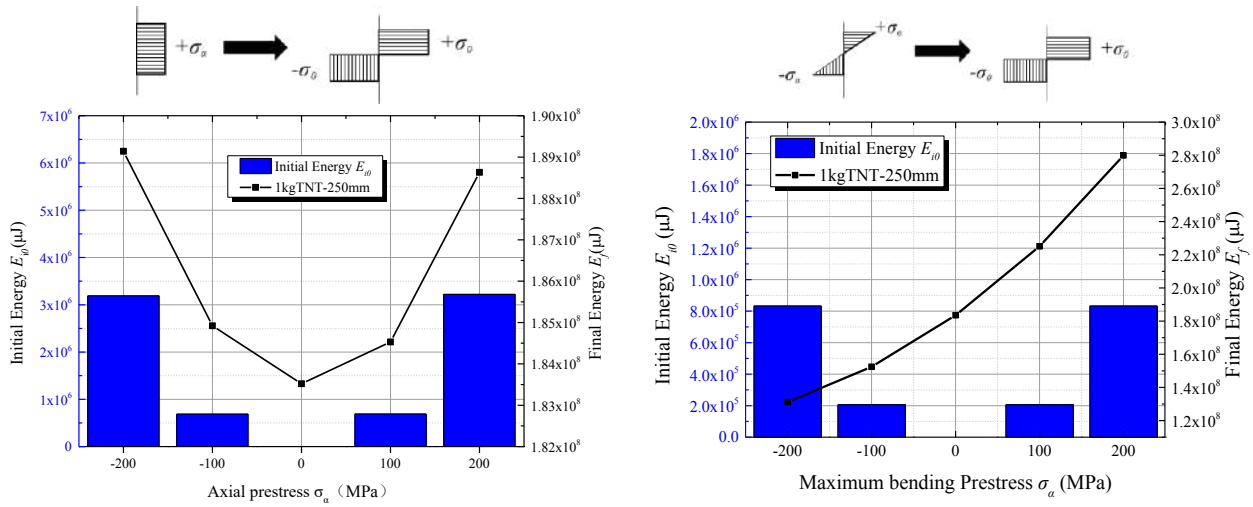

Figure 3. The transition of stress and energy in beams. Up: stress transition. Down: energy transition. The initial internal energy in axial $E_{i0} = \sigma_\alpha^2 bhl/2E$, and in transverse $E_{i0} = \sigma_\alpha^2 bhl/8E$

References

[1] Menkes S. B., Opat H. J. Broken beams. *Exp. Mech.* **13**: 480-486, 1973.

EFFECTS OF STRESS TRIAXIALITY ON DAMAGE BEHAVIOUR OF HDPE

Yi Zhang[1]*, Shifeng Xue[1]& P.-Y. Ben Jar[2]
Department of Engineering Mechanics, College of Pipeline and Civil Engineering, China University of Petroleum (East China), Qingdao, China
Department of Mechanical Engineering, University of Alberta, Edmonton, Alberta, Canada

Summary This paper examines the influence of stress triaxiality on damage behaviour of high-density polyethylene (HDPE) using notched round bar specimens with different notch radii. A two-stage test method was developed to quantitatively assess damage evolution under different stress triaxialities. The first-stage tests were to introduce damage by subjecting the specimens to different prestrain levels under monotonic tensile loading condition. Two months later, the second-stage tests apply monotonic tensile loading at a crosshead speed of 0.01 mm/min to characterize the change in mechanical properties. The results indicate that both yield stress and elastic modulus decrease with the increase of the prestrain. The results also suggest that the extent of decrease of yield stress and elastic modulus, and the damage evolution, strongly depend on the stress triaxality.

INTRODUCTION

Semi-crystalline polymers are increasingly used in a broad range of applications such as pressure tubing, pipeline systems and parts in nuclear power plant. Nowadays, majority of low-pressure natural gas pipes with a 50-year service life are made of polyethylene (PE). It is well-known that characteristics of damage and failure mechanisms depend on the stress state acting in a material point. Although a number of research work have been conducted to investigate effects of stress state on damage and fracture behaviour, majority of them were focused on metallic materials [1–5]. Very few studies have been conducted to reveal the influence of stress state on the damage and fracture behaviour of polymeric materials, let alone its influence on the damage evolution and undamaged constitutive equations [6–8]. Scarcity of information in this area provides motivation for the current study.

EXPERIMENTAL DETAILS

This study concerns a semi-crystalline polymer, high density polyethylene (HDPE). As shown in Figure 1, Notched round bar specimens with notch radii of 0.5, 2, 5 and 20mm are used in this study. The specimens are of the same minimum diameter of 6 mm in the gauge sections, the same diameter of 10 mm in the shoulder parts and the same length of 150 mm. The variation of the minimum diameter was measured using an extensometer.

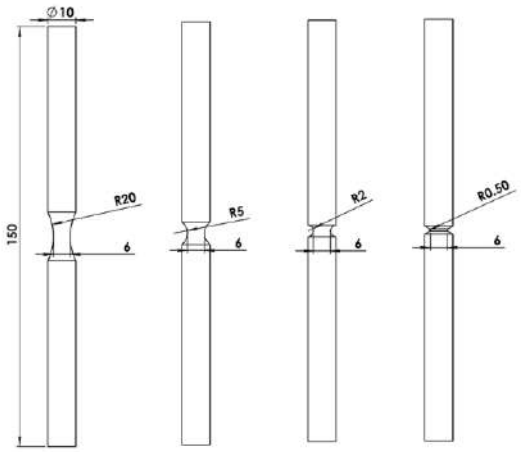

Figure 1 Notched round bar specimens with different notch radii

A two-stage test procedure was proposed to quantitatively determine damage evolution based on the degradation of elastic modulus. The first-stage tests were to apply monotonic tensile loading to five displacements (1.8, 2, 2.3, 2.5 and 2.7mm for specimen with radius of 0.5mm, 1.5, 2, 2.5, 3, 3.5 and 4mm for specimens with radius of 2mm, 1, 2, 3, 4 and 5mm for specimens with radius of 5mm, and 2, 3, 4, 5, 6 and 8mm for specimens with radius of 20mm) at a crosshead speed of 1 mm/min. In contrast, condition used for the second-stage test was monotonic tensile loading at the crosshead speed of 0.01mm/min. Yield stress and elastic modulus were determined from the second-stage tests, to evaluate influence of the prestrain level and stress triaxiality on variation of their values.

[a)] Corresponding author. Email: zhangyi@upc.edu.cn.

RESULTS AND DISCUSSION

Yield stress and elastic modulus determined from the second-stage tests are summarized in Fig. 2(a) and 2(b), respectively, as a function of prestrain introduced in the first-stage tests. The figures suggest that both yield stress and elastic modulus decrease with the increase of the prestrain. The degradation of yield stress and elastic modulus is more severe when the notch radius is reduced. Damage parameter (D) is determined based on the variation of elastic modulus, as shown below [6]:

$$D = 1 - \frac{E}{E_0} \tag{1}$$

where E and E_0 are elastic moduli of the specimens with and without the prestrain, respectively.

Fig. 2(c) presents variation of D value as a function of the prestrain introduced in the first-stage test. The figure also includes curves generated using Equation (2) [7], with values for A and B determined by fitting the curves to the trend of change of measured values. Fig. 2(c) indicates that both prestrain and stress state have a significant effect on the change of D values.

$$D = A\left[1 - \exp\left(-B\varepsilon\right)\right] \tag{2}$$

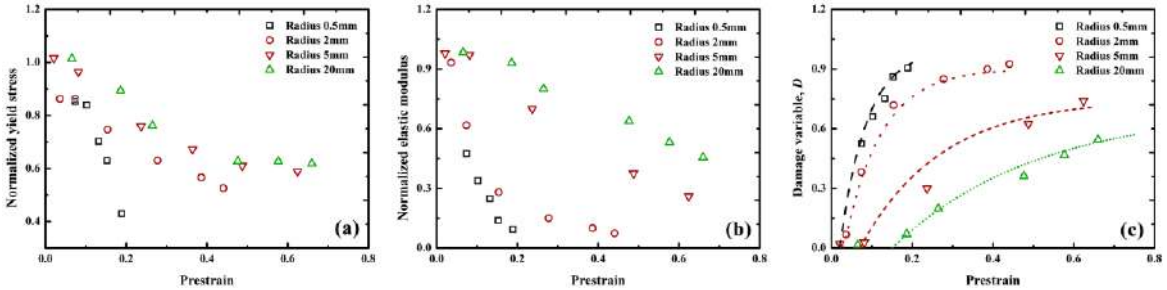

Figure 2 Effects of prestrain applied in the first test on the yield stress (a), elastic modulus (b) and the damage parameter *D* determined based on the variation of elastic modulus (c)

CONCLUSIONS

Effects of stress triaxiality on damage behaviour of HDPE have been assessed using the two-stage test method, on notched round bar specimens with different curvature radii. The results show that mechanical properties of HDPE are strongly affected by the stress state of specimens used in the first-stage test. In particular, elastic modulus from the second-stage test, measured at the strain of 0.5%, decreases significantly with the increase of prestrain applied in the first-stage test. Damage evolution in the first-stage test is established using a phenomenological damage model based on the variation of the elastic modulus measured from the second-stage test. The results suggest that increase of stress triaxiality, i.e., decrease of the curvature radii, causes acceleration of the damage evolution, thus increasing the extent of damage in the HDPE material. Further investigation will be conducted to evaluate effects of stress triaxiality on damage mechanism in HDPE from microscopic point of view, and the results will be presented in the conference.

ACKNOWLEDGEMENT

The authors acknowledge the financial support from National Natural Science Foundation of China (11802343) and the Fundamental Research Funds for the Central Universities (18CX02174A).

References

[1] M.S. Mirza, D.C. Barton, P., The effect of stress triaxiality and strain-rate on the fracture characteristics of ductile metals, J. Mater. Sci. 31 (1996) 453–461.
[2] N. Bonora, D. Gentile, A. Pirondi, G. Newaz, Ductile damage evolution under triaxial state of stress: theory and experiments, Int. J. Plast. 21 (2005) 981–1007.
[3] M. Brünig, O. Chyra, D. Albrecht, L. Driemeier, M. Alves, A ductile damage criterion at various stress triaxialities, Int. J. Plast. 24 (2008) 1731–1755.
[4] M. Brünig, S. Gerke, M. Schmidt, Damage and failure at negative stress triaxialities: Experiments, modeling and numerical simulations, Int. J. Plast. 102 (2018) 70–82.
[5] G.H. Majzoobi, M. Kashfi, N. Bonora, G. Iannitti, A. Ruggiero, E. Khademi, Damage characterization of aluminum 2024 thin sheet for different stress triaxialities, Arch. Civ. Mech. Eng. 18 (2018) 702–712.
[6] K. Hachour, L. Sadeg, D. Sersab, M. Aberkane, On the stress triaxiality sensitivity of high density polyethylene, in: ASME 2014 12th Bienn. Conf. Eng. Syst. Des. Anal., American Society of Mechanical Engineers Digital Collection, 2014.
[7] S. Olufsen, A.H. Clausen, O.S. Hopperstad, Influence of stress triaxiality and strain rate on stress-strain behaviour and dilation of mineral-filled PVC, Polym. Test. 75 (2019) 350–357.
[8] A.S. Ognedal, A.H. Clausen, A. Dahlen, O.S. Hopperstad, Behavior of PVC and HDPE under highly triaxial stress states: An experimental and numerical study, Mech. Mater. 72 (2014) 94–108.

STABILITY AND DAMAGE EVALUATION ON FULL-SCALED ASYMMETRIC SANDWICH PANELS UNDER COMPRESSION

Jian Deng*[1,2] and Tian Jian Lu[1,2]
[1]State Key Laboratory of Mechanics and Control of Mechanical Structures, Nanjing University of Aeronautics and Astronautics, Nanjing, China
[2]Nanjing Center for Multifunctional Lightweight Materials and Structures, Nanjing University of Aeronautics and Astronautics, Nanjing, China

Summary In practical applications, asymmetric sandwich panels (ASPs) with tapered and junction regions are frequently used. For structure safety consideration, it is necessary to systematically investigate the stability and damage behaviour of full-scaled asymmetric sandwich panels under uniaxial compression experimentally and numerically. Comparisons between numerical predictions and experimental measurements were conducted with a good agreement achieved. Results showed the tapered region intensified the asymmetry and introduced additional bending moments into ASPs and thus caused early local buckling. Large amounts of matrix cracking, fibre push-out and core-skin delamination were captured numerically and experimentally.

INTRODUCTION

One of the biggest challenges in modern times is how to create products that are lighter, faster and stronger, and a technical revolution to realize this goal is composite materials. Sandwich structures characterizing in light weight and high performance are universally introduced and continuing to be in demand in high-performance industries [1, 2]. Due to the asymmetry in nature, sandwich panels with junction regions are susceptible to buckle, that may cause damage and ultimate failure of sandwich panels. This intensifies the necessity of evaluation on stability and damage mechanism of asymmetric sandwich panels. This is the main objective of present study. Uniaxial compression tests and numerical modelling were conducted. Numerical predictions are compared to experimental results, and the findings are discussed.

EXPERIMENTS AND NUMERICAL MODELLING

The test specimens were foam-core sandwich panels skinned with carbon fibre reinforced plastics (U3160/5284). As illustrated in Fig. 1, the ASP can hypothetically be divided into three different regions, namely central region (pure sandwich), tapered region and junction region. The junction region composed of monolithic fibre-reinforced composites are functionally used to introduce loads to the central pure sandwich through the tapered region. It should be noted that the lower smooth skin is generally applied with thick laminates, named as working face-sheet (WFS). On the other hand, the upper fluctuant face serves as stabilizing skin with fewer layups, named as the stabilizing face-sheet (SFS). The core material is PMI foam, commonly used in aerospace industry.

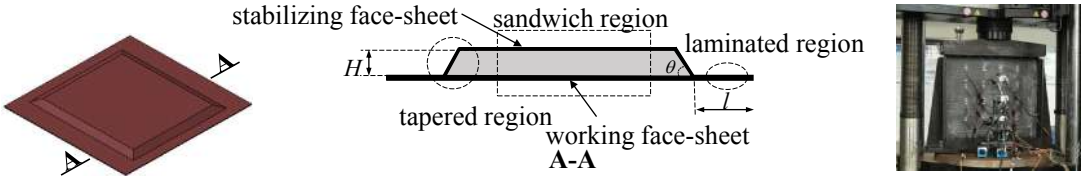

Figure 1: Schematic illustration of the asymmetric sandwich structure and test setup.

For sandwich panels subjected to compression, damage may initiate in the skins at intra-laminar level (i.e. fibre breakage and matrix cracking), in the core layer and at the interface between the core and skins. Cohesive zone model is applied to predict the core-skin interfacial damage initiation and evolution. The initiation of intra-laminar damage is determined with Hashin [3] and Puck criteria [4]. An energy-based smeared crack approach is then employed to simulate the damage evolution. The fracture energy release rate is assumed constant during the softening procedure. Numerical analysis are conducted in ABAQUS® coupled with a UMAT subroutine.

RESULTS AND DISCUSSION

A good agreement is achieved from the comparison between numerical predictions and experimental measurements regarding both linear-elastic and nonlinear responses of the load vs. end-shortening curves in Fig. 2(a). For axial strains, numerical results are embedded by the experimental measurements since the loading starts as shown in Fig. 2(b),. Discrepancies exist in experimental and numerical results. The possible reason is that the micro manufacturing defects cannot be completely taken into account in the FEM simulation. A quasi-linear response is found in the thicker WFS

*Corresponding author. E-mail: dengjian@nuaa.edu.cn

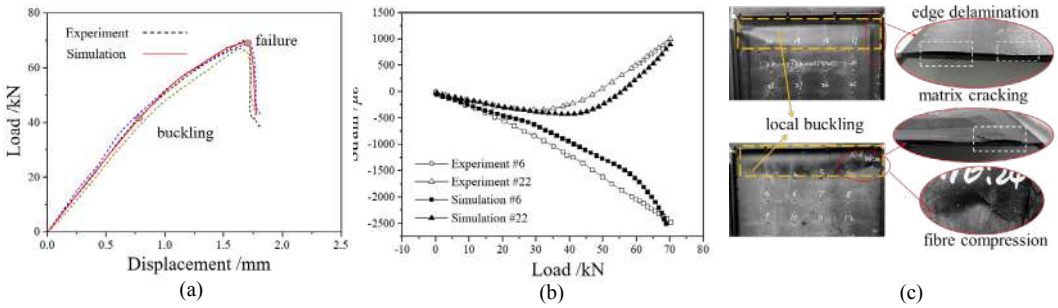

Figure 2: (a) Comparison of numerical and experimental results of end-load vs. end-shortening curves; (b) Comparison of numerical and experimental strains vs. end-load; (c) Typical failure modes in experiments.

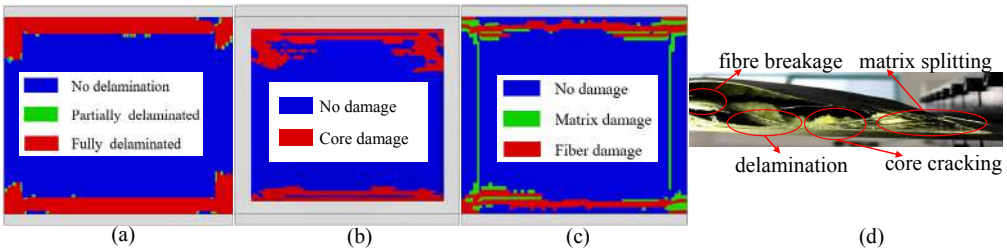

Figure 3: Damage patterns at the ultimate failure load: (a) Delamination at the WFS-core interface; (b) Core damage; (c) Intra-laminar damage in face-sheets; (d) Experimental observation of failure mechanisms.

while remarkable nonlinearity occurs in the SFS prior to ultimate failure. Prior to ultimate failure, the SFS remains in tension with strains at low levels while extreme compression occurs on WFS, causing more damage in WFS. Intermittent sounds occurred after buckling. As loading continued, the panel surface was locally bulged with a continuous cracking sound. Various types and amounts of damage observed across the width direction near the tapered region, including delamination, matrix cracking and fibre compression as shown in Fig. 2(c).

Fig. 3(a) illustrates the failure patterns of skin-core interfacial delamination. With delamination accumulating, the face-sheets are losing support from the core, and fibre and matrix damage initiates and propagates in the laminates while the foam core fails by shearing and compression. As shown in Fig. 3(b), large amount of damage accumulated in the core through width direction. The location of core cracking is quite identical to detailed experimental observation that validates the numerical accuracy of the FE model. Without the core support, critical fibre breakage and matrix splitting are dramatically developed in the face-sheets, further leading to ultimate failure of the sandwich panel as shown in Fig. 3(c). Compared to experimental results in Fig. 3(d), the proposed numerical model can feasibly predict the failure mechanisms.

CONCLUSIONS

Full-scaled asymmetric sandwich panels (ASPs) with tapered and junction regions under compression were investigated experimentally and numerically in this work, regarding stability, load capacity and damage mechanism. Results showed that the tapered region intensifies the asymmetry and introduces additional bending moments into ASPs, causing early local buckling. Large amounts of matrix cracking, fibre push-out and core-skin delamination occurred. Optimal parameters of the tapered region will be studied in the future.

ACKNOWLEDGMENT

This work was supported by the National Natural Science Foundation of China (11972185, 12002157); the China Postdoctoral Science Foundation Funded Project (2019M661818); the New Faculty Foundation of NUAA (1001-YAH19069); Science and Technology Innovation Project for Returned Overseas Scholars in Nanjing (2020); and the Priority Academic Program Development of Jiangsu Higher Education Institutions.

References

[1] Vinson J. *The behavior of sandwich structures of isotropic and composite materials*. Routledge, 2018.
[2] Yuan Z, Kardomateas GA and Frostig Y. Finite element formulation based on the extended high-order sandwich panel theory. *AIAA J.* 53(10): 3006–3015, 2015.
[3] Hashin Z. Fatigue failure criteria for unidirectional fiber composites. *J. Appl. Mech.* 48(4): 846–852, 1981.
[4] Knops M. Analysis of failure in fiber polymer laminates: the theory of Alfred Puck. Springer, 2008.

A SIMPLE EXPLICIT HOMOGENIZATION SOLUTION FOR THE MACROSCOPIC ELASTIC RESPONSE OF ISOTROPIC POROUS ELASTOMERS

Victor Lefèvre*[1], Bhavesh Shrimali[2], and Oscar Lopez-Pamies[2]
[1]Department of Mechanical Engineering, Northwestern University, USA
[2]Department of Civil and Environmental Engineering, University of Illinois at Urbana-Champaign, USA

Summary An approximate homogenization solution is put forth for the effective stored-energy function describing the macroscopic elastic response of isotropic porous elastomers comprised of incompressible non-Gaussian elastomers embedding equiaxed closed-cell vacuous pores. In spite of its generality, the solution is fully explicit and remarkably simple. Its key theoretical and practical features are discussed in detail and its accuracy is demonstrated by means of direct comparisons with novel computational solutions for porous elastomers with four classes of physically relevant isotropic microstructures wherein the underlying pores are: (i) infinitely polydisperse in size and of abstract shape, (ii) finitely polydisperse in size and spherical in shape, (iii) monodisperse in size and spherical in shape, and (iv) monodisperse in size and of oblate spheroidal shape.

A *fully explicit*, *remarkably simple*, and *accurate* approximate homogenization solution was recently put forth [1] for the effective stored-energy function describing the macroscopic elastic response of porous elastomers. More specifically, the solution pertains to isotropic porous elastomers comprised of incompressible non-Gaussian elastomers embedding non-percolative equiaxed — but of arbitrary shape otherwise — closed-cell vacuous pores with initial porosity f_0; see Fig. 1 for a schematic.

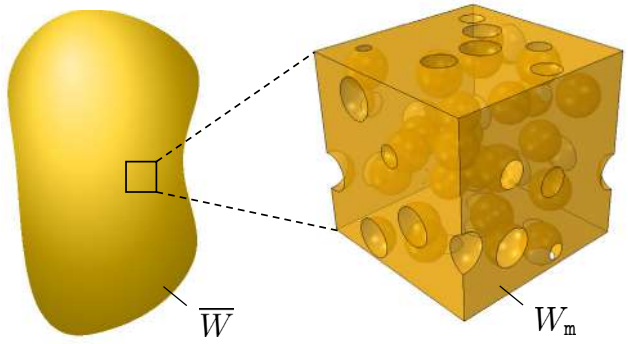

Figure 1: Schematic of a porous elastomer with initial porosity $f_0 = 0.15$ with spherical and monodisperse pores.

For an isotropic incompressible non-Gaussian elastomeric matrix with stored-energy function $W_{\rm m}$ of the form[1]

$$W_{\rm m}(\mathbf{F}) = \begin{cases} \Psi_{\rm m}(\mathbf{F}\cdot\mathbf{F}) & \text{if } \det\mathbf{F} = 1 \\ +\infty & \text{otherwise} \end{cases}$$

where $\mathbf{F}$ denotes the deformation gradient, the approximate homogenization solution for the effective stored-energy function $\overline{W}$ of the porous elastomer is given by

$$\begin{cases} \overline{W}(\overline{\mathbf{F}}, f_0) = (1-f_0)\,\Psi_{\rm m}\left(\dfrac{\mathcal{I}_1}{1-f_0}+3\right) & \text{with} \\ \mathcal{I}_1 = \dfrac{3(1-f_0)}{3+2f_0}\left[\overline{I}_1-3\right] + \dfrac{3}{\overline{J}^{1/3}}\left[2\overline{J}-1-\dfrac{(1-f_0)\,\overline{J}^{1/3}\left(3\overline{J}^{2/3}+2f_0\right)}{3+2f_0} - \dfrac{f_0^{1/3}\overline{J}^{1/3}\left(2\overline{J}+f_0-2\right)}{\left(\overline{J}-1+f_0\right)^{1/3}}\right] \end{cases}$$

in terms of the standard macroscopic principal invariants $\overline{I}_1 = \overline{\mathbf{F}}\cdot\overline{\mathbf{F}}$ and $\overline{J} = \det\overline{\mathbf{F}}$ of the macroscopic deformation gradient $\overline{\mathbf{F}}$. The above effective stored-energy function implies the simple explicit expression

$$\overline{\mathbf{S}} = \frac{6(1-f_0)}{3+2f_0}\Psi'_{\rm m}\left(\frac{\mathcal{I}_1}{1-f_0}+3\right)\overline{\mathbf{F}} + \left[\frac{3+6\overline{J}+2f_0(1+7\overline{J})}{(3+2f_0)\overline{J}^{1/3}} + \frac{f_0^{1/3}\overline{J}(4-5f_0-4\overline{J})}{(\overline{J}+f_0-1)^{4/3}}\right]\Psi'_{\rm m}\left(\frac{\mathcal{I}_1}{1-f_0}+3\right)\overline{\mathbf{F}}^{-T} \tag{1}$$

for the macroscopic stress $\overline{\mathbf{S}} \doteq \partial\overline{W}/\partial\overline{\mathbf{F}}$.

*Corresponding author. E-mail: victor.lefevre@northwestern.edu.
[1] $\Psi_{\rm m}$ is a non-negative function of choice satisfying the standard linearization and strong ellipticity conditions.

With the objective of illustrating the accuracy of the proposed simple explicit homogenization solution for arbitrary finite deformations, the general macroscopic stress-deformation response (1) is confronted to FE solutions for a porous elastomer comprising an elastomeric matrix characterized by the stored-energy function[2]

$$W_{\rm m}(\mathbf{F}) = \begin{cases} \Psi_{\rm m}(\mathbf{F}\cdot\mathbf{F}) = \displaystyle\sum_{r=1}^{2} \frac{3^{1-\alpha_r}}{2\alpha_r}\mu_r\left[(\mathbf{F}\cdot\mathbf{F})^{\alpha_r} - 3^{\alpha_r}\right] & \text{if } \det\mathbf{F} = 1 \\ +\infty & \text{otherwise} \end{cases}$$

and embedding pores that are monodisperse in size and spherical in shape. Figure 2 shows plots of the macroscopic stress-deformation response for the porous elastomer subjected to two types of loading conditions that are accessible by standard experimental techniques and three values of initial porosity, $f_0 = 0.05$, 0.15, and 0.25. Corresponding FE stress-deformation results for isotropic distributions of polydisperse spherical pores and monodisperse oblate spheroidal pores are virtually indistinguishable from those presented in Fig. 2 for monodisperse spherical pores.

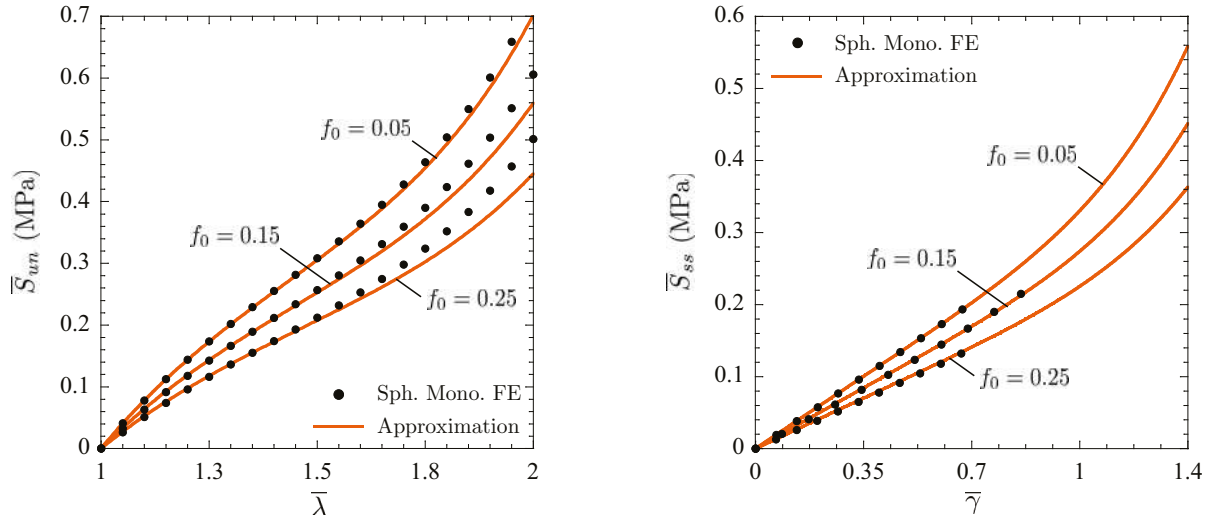

Figure 2: Macroscopic response of porous silicone elastomers with various values of initial porosity f_0 under: (a) uniaxial tension and (b) simple shear. Plots are shown for the appropriate component of the stress-deformation relation (1) — labeled "Approximation" and displayed as solid lines — together with corresponding FE solutions (solid circles) for isotropic distributions of pores of monodisperse size and spherical shape.

References

[1] Shrimali B., Lefèvre V., Lopez-Pamies O. A simple explicit homogenization solution for the macroscopic elastic response of isotropic porous elastomers. *J. Mech. Phys. Solids* **122**: 364-380, 2019.

[2]This particular choice of $W_{\rm m}$ with material parameters $\mu_1 = 0.26915$ MPa, $\mu_2 = 0.04406$ MPa, $\alpha_1 = 0.22743$, $\alpha_2 = 4.53944$ happens to describe the non-Gaussian response of a commercial silicone elastomer of popular use.

ESHELBY'S INCLUSION PROBLEM IN LARGE DEFORMATIONS

Mawafag F. Alhasadi and Salvatore Federico*
Department of Mechanical and Manufacturing Engineering, The University of Calgary, Calgary, AB, Canada

Summary In the framework of large deformations, we propose a multiplicative decomposition of the deformation gradients corresponding to the additive decomposition that Eshelby (1957, *Proc. Roy. Soc. Ser. A*, 241: 376-396) used to investigate the theory of inclusions in the case of infinitesimal deformations. We show that the proposed decomposition is a hybrid between the Bilby-Kröner-Lee and the Noll-Epstein-Maugin ones and encompasses those proposed by other Authors as particular cases.

INTRODUCTION

In a classical paper, Eshelby [3] studied the problem of a body in which a region (the inclusion) has a geometrical misfit with the surrounding material (the matrix). Eshelby represented the geometrical misfit in terms of a *transformation strain* (or *eigenstrain*) $\boldsymbol{\epsilon}_t$ (in our notation), transforming the shape of a cavity in a body into a different shape. In order to implant this misfitting inclusion into the original cavity, one first applies surface tractions causing a strain exactly equal to $-\boldsymbol{\epsilon}_t$ in the inclusion, then implants the inclusion, and finally releases the surface tractions, which causes a strain $\boldsymbol{\epsilon}_c$ (in our notation), called *constrained strain*, discontinuous at the interface between the inclusion and the matrix.

In the setting of large deformations, Eshelby's inclusion problem has been formulated in terms of a multiplicative decomposition $\boldsymbol{F} = \boldsymbol{F}^e\boldsymbol{F}^*$ of the deformation gradient (in the notation of [1]), where $\boldsymbol{F}^*$ and $\boldsymbol{F}^e$ correspond to Eshelby's $-\boldsymbol{\epsilon}_t$ and $\boldsymbol{\epsilon}_c$, respectively. This approach is based on the classical Bilby-Kröner-Lee (e.g., [4]) decomposition $\boldsymbol{F} = \boldsymbol{F}_e\boldsymbol{F}_a$, originally devised for plasticity, in which $\boldsymbol{F}_a$ is the anelastic deformation and $\boldsymbol{F}_e$ the purely elastic one, and both are generally *non-integrable*. In Noll's theory of material uniformity [5], Epstein and Maugin [2] defined the *implant* tensor $\boldsymbol{P}$ as the tensor mapping an *archetypal* point with tangent space $\mathcal{A}$ (a fixed vector space) into the body, causing a generally *non-integrable* distortion $\boldsymbol{F}_e$. In this formulation, the purely elastic deformation of the theory of plasticity reads $\boldsymbol{F}_e = \boldsymbol{F}\boldsymbol{P}$. Comparison with the Bilby-Kröner-Lee decomposition shows that, for the case of a uniform body, the implant tensor is the inverse of the plastic deformation, i.e., $\boldsymbol{P} = \boldsymbol{F}_a^{-1}$ (Figure 1).

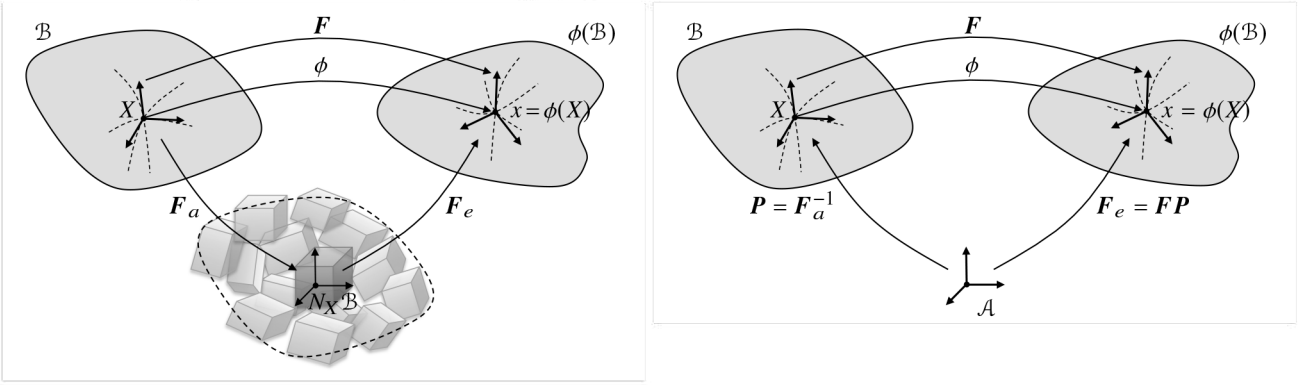

Figure 1: Left: Bilby-Kröner-Lee decomposition, with the generally incompatible collection of natural states $N\mathcal{B}$, disjoint union of the vector spaces $N_X\mathcal{B}$. Right: Implant tensor $\boldsymbol{P}$ in a uniform material, mapping, at every $X \in \mathcal{B}$, the archetype $\mathcal{A}$ into the tangent space $T_X\mathcal{B}$ and equivalence of the Bilby-Kröner-Lee and Noll-Epstein-Maugin decompositions, for the case of a uniform body.

Our goal is twofold. First, we show that Eshelby's inclusion problem admits a multiplicative decomposition of the deformation gradient that is *piecewise* (matrix/inclusion) compatible, i.e., each resulting deformation gradient is in fact the tangent map of a certain configuration map in the matrix or the inclusion. Second, we show that Eshelby's original additive decomposition of the infinitesimal strain [3] is most naturally represented, in large deformations, via a *mixed* formulation, in which the deformation corresponding to the transformation strain $\boldsymbol{\epsilon}_t$ is an $\boldsymbol{F}$-type tensor of the Bilby-Kröner-Lee (BKL) decomposition, while the deformation corresponding to the constrained strain $\boldsymbol{\epsilon}_c$ is a $\boldsymbol{P}$-type implant tensor of the Noll-Epstein-Maugin (NEM) decomposition.

ESHELBY'S PROCEDURE IN LARGE DEFORMATIONS

We build the body $\mathcal{B}$ with a homogeneous inclusion with reference to Figure 2 (left). We start from a body $\tilde{\mathcal{M}}$ with a cavity described by $\tilde{\mathcal{R}}$ and another body $\mathcal{D}^*$ which *does not fit* the cavity $\mathcal{R}$. The set $\mathcal{B}^* = \tilde{\mathcal{M}} \cup \mathcal{D}^*$ is an *incompatible* configuration of our body $\mathcal{B}$. In order to fit $\mathcal{D}^*$ into the cavity $\tilde{\mathcal{R}}$ of $\tilde{\mathcal{M}}$, we apply tractions on the boundary $\partial\mathcal{D}^*$ of the inclusion. As a result, the inclusion $\mathcal{D}^*$ undergoes a deformation described by

$$\varphi_t = \begin{cases} \varphi_t^{(i)} & : \mathcal{D}^* \to \tilde{\mathcal{D}}, \quad \text{in } \mathcal{D}^*, \\ \varphi_t^{(m)} \equiv \mathrm{Id} & : \tilde{\mathcal{M}} \to \tilde{\mathcal{M}}, \quad \text{in } \tilde{\mathcal{M}}, \end{cases} \qquad \boldsymbol{P}_t = \begin{cases} \boldsymbol{P}_t^{(i)} & : T\mathcal{D}^* \to T\tilde{\mathcal{D}}, \quad \text{in } \mathcal{D}^*, \\ \boldsymbol{P}_t^{(m)} \equiv \boldsymbol{I} & : T\tilde{\mathcal{M}} \to T\tilde{\mathcal{M}}, \quad \text{in } \tilde{\mathcal{M}}, \end{cases} \tag{1}$$

*Corresponding author. E-mail: salvatore.federico@ucalgary.ca

where the *transformation map* $\varphi_t^{(i)}$ in the inclusion transforms $\mathcal{D}^*$ precisely into $\tilde{\mathcal{D}} \equiv \tilde{\mathcal{R}}$ while the $\varphi_t^{(m)}$ is the identity map and leaves the matrix untouched, and thus the *transformation implant* $\boldsymbol{P}_t$ is integrable and defined *piecewise*, with $\boldsymbol{P}_t^{(i)}$ being a deformation and $\boldsymbol{P}_t^{(m)}$ being the identity tensor. We denote $\tilde{\mathcal{B}} = \tilde{\mathcal{M}} \cup \tilde{\mathcal{D}}$ the configuration in which the matrix $\tilde{\mathcal{M}}$ is still stress-free but the inclusion $\tilde{\mathcal{D}}$ is subjected to the stresses caused by the transformation map $\varphi_t^{(i)}$ and transformation implant $\boldsymbol{P}_t^{(i)}$. Once the transformed inclusion $\tilde{\mathcal{D}}$ has been fit into the cavity $\tilde{\mathcal{R}}$, we impose *perfect bonding* between matrix and inclusion and relax the surface tractions on $\partial\tilde{\mathcal{D}}$. This causes *both* $\tilde{\mathcal{D}}$ and $\tilde{\mathcal{M}}$ to relax elastically, according to

$$\varphi_c : \tilde{\mathcal{B}} \to \mathcal{B}, \qquad \boldsymbol{P}_c = \begin{cases} \boldsymbol{P}_c^{(i)} & : T\tilde{\mathcal{D}} \to T\mathcal{D}, \quad \text{in } \tilde{\mathcal{D}}, \\ \boldsymbol{P}_c^{(m)} & : T\tilde{\mathcal{M}} \to T\mathcal{M}, \quad \text{in } \tilde{\mathcal{M}}, \end{cases} \tag{2}$$

where the *constrained map* φ_c is everywhere continuous but is non-differentiable on $\partial\tilde{\mathcal{D}}$, i.e., its tangent map $\boldsymbol{P}_c \equiv T\varphi_c$ is not defined on $\partial\tilde{\mathcal{D}}$ and presents a *jump condition* on $\partial\tilde{\mathcal{D}}$. The resulting configuration $\mathcal{B}$ is the sought reference configuration of our body with a misfitting inclusion, and is subjected to *residual stresses*, which are *continuous* on the matrix-inclusion interface $\partial\mathcal{D}$. When $\mathcal{B}$ is subjected to a deformation described by the configuration map ϕ and its tangent map $\boldsymbol{F} = T\phi$, it attains the *current configuration* $\phi(\mathcal{B})$.

PROPOSED MULTIPLICATIVE DECOMPOSITION

Let us refer to Figure 2 (right). For the case of the BLK decomposition, we have $\boldsymbol{F} = \boldsymbol{F}_e\boldsymbol{F}_t\boldsymbol{F}_c$, where $\boldsymbol{F}_t\boldsymbol{F}_c$, given by the *transformation deformation gradient* $\boldsymbol{F}_t$ and the *constrained deformation gradient* $\boldsymbol{F}_c$, replaces the anelastic deformation $\boldsymbol{F}_a$ of the classical BLK decomposition $\boldsymbol{F} = \boldsymbol{F}_e\boldsymbol{F}_a$. For the case of the NEM multiplicative decomposition, we have $\boldsymbol{F}_e = \boldsymbol{F}\boldsymbol{P}_c\boldsymbol{P}_t$, where the implant tensor $\boldsymbol{P}$ has been replaced by the product $\boldsymbol{P}_c\boldsymbol{P}_t$ of the constrained implant $\boldsymbol{P}_c$ and transformation implant $\boldsymbol{P}_t$ described in Eqs. (1) and (2). Thus, we have that $\boldsymbol{P}_c = \boldsymbol{F}_c^{-1}$ and $\boldsymbol{P}_t = \boldsymbol{F}_t^{-1}$.

In order to match Eshelby's original additive decomposition of the infinitesimal strain, we propose a *mixed* BKL-NEM formulation, in which we consider as primary objects the transformation deformation $\boldsymbol{F}_t = \boldsymbol{P}_t^{-1}$ and the constrained implant $\boldsymbol{P}_c$, and write the decomposition as

$$\boldsymbol{F}_e = \boldsymbol{F}\boldsymbol{P}_c\boldsymbol{F}_t^{-1}, \tag{3}$$

in which we recall that $\boldsymbol{F}_t^{-1} = \boldsymbol{P}_t$ is defined *piecewise* in the matrix and in the inclusion, according to Eq. (1). Linearising, we see that Eq. (3) is the large-deformation counterpart of Eshelby's decomposition $\boldsymbol{\epsilon}_e = \boldsymbol{\epsilon} + \boldsymbol{\epsilon}_c - \boldsymbol{\epsilon}_t$ (in our notation).

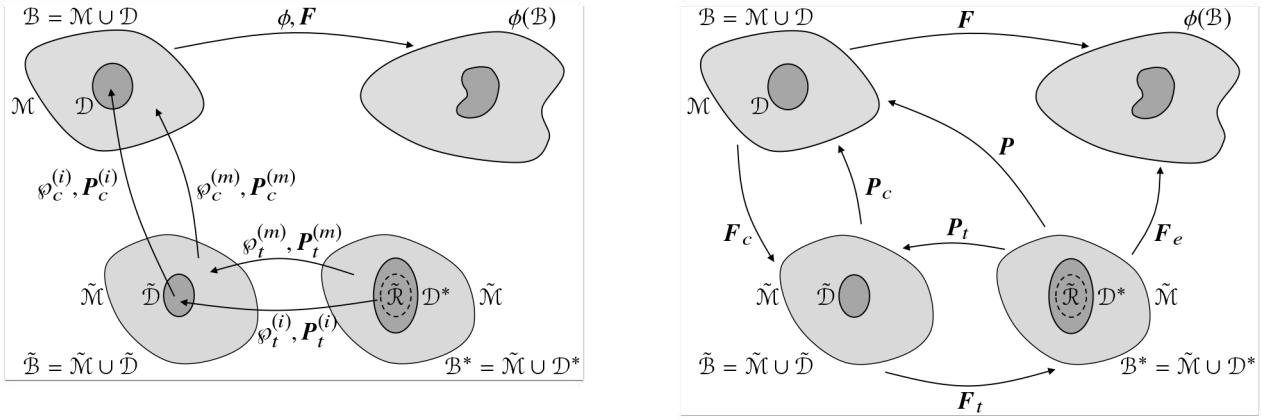

Figure 2: Left: Eshelby's procedure to *implant* an inclusion in a homogeneous matrix. Right: Mixed BKL-NEM decomposition for the inclusion problem in large deformations, corresponding to Eshelby's additive decomposition in in infinitesimal deformations.

REMARKS AND CONCLUSIONS

In his original presentation Eshelby [3] actually deformed the shape of the cavity $\tilde{\mathcal{R}}$ into the shape of the misfitting inclusion $\mathcal{D}^*$ by means of the transformation strain $\boldsymbol{\epsilon}_t$, corresponding, in our framework, to $\boldsymbol{F}_t = \boldsymbol{P}_t^{-1}$. Thus, Eq. (3) shows that Eshelby's formulation was in fact a *mixed* formulation, with the (*implant*) constrained strain $\boldsymbol{\epsilon}_c$, corresponding to our constrained implant $\boldsymbol{P}_c$, and the transformation strain $\boldsymbol{\epsilon}_t$, corresponding to our transformation deformation $\boldsymbol{F}_t$.

References

[1] Diani J.L., Parks D.M., Problem of an inclusion in an infinite body, approach in large deformation. *Mech. Mat.*, **32**: 43-55, 2000.
[2] Epstein M., Maugin G.A., The energy momentum tensor and material uniformity in finite elasticity. *Acta Mech.*, **83**: 127-133, 1990.
[3] Eshelby J.D., The determination of the elastic field of an ellipsoidal inclusion, and related problems. *Proc. Roy. Soc. Ser. A*, **241**: 376-396, 1957.
[4] Kröner E., Allgemeine Kontinuumstheorie der Versetzungen und Eigenspannungen. *Arch. Rat. Mech. Anal.*, **4**: 273-334, 1959.
[5] Noll W., Materially uniform bodies with inhomogeneities. *Arch. Rat. Mech. Anal.*, **27**: 1-32, 1967.

POLARIZATION RATIO OF RAYLEIGH WAVES IN VERTICALLY-INHOMOGENEOUS AND WEAKLY-ANISOTROPIC ELASTIC MEDIA

Kazumi Tanuma*[1], Chi-Sing Man[2], and Yue Chen[3]
[1]Department of Mathematics, Faculty of Science and Technology, Gunma University, Kiryu, Japan
[2]Department of Mathematics, University of Kentucky, Lexington, USA
[3]Department of Mathematics and Computer Science, Auburn University at Montgomery, Montgomery, USA

Summary The polarization ratio r_R of Rayleigh waves is defined as the ratio of the maximum longitudinal and maximum normal component of the displacements at the surface on which the Rayleigh waves propagate. Herein we present a procedure by which a high-frequency asymptotic formula can be derived for the polarization ratio of the Rayleigh waves that propagate along the free surface of a vertically-inhomogeneous, prestressed, and weakly-anisotropic elastic half-space. The vertical inhomogeneity of the half-space induces dispersion or frequency (f) dependence of r_R, for which the high-frequency formula can be used to obtain asymptotic approximations. We illustrate the procedure by using it to generate dispersion curves of $r_R(f)$ for Rayleigh waves that propagate in various directions along the surface of a prestressed thick-plate sample of an AA 7075-T651 aluminum alloy.

INTRODUCTION

There are simulation studies [1, 6] which indicate that for many materials the polarization ratio of Rayleigh waves could be a promising means for nondestructive evaluation of stress. As compared with Rayleigh-wave velocity, the polarization ratio r_R enjoys the advantages that it is more sensitive to the state of stress (up to an order of magnitude bigger per MPa shift in stress in various steels, CP titanium, etc.), less sensitive to uncertainties in third-order elastic constants, and independent of wave-path distance, the culprit that limits the accuracy in absolute velocity measurements. On the other hand, both the aforementioned studies pertain to *homogeneous* media.

In this paper we study dispersion of polarization ratio $r_R(f)$, where f is the frequency, for Rayleigh waves that propagate in various directions along the surface of a vertically-inhomogeneous, prestressed, and weakly-anisotropic elastic half-space. We present a procedure to derive a high-frequency asymptotic formula by which asymptotic approximations to $r_R(f)$ can be generated when all the relevant information on material constants and prestress are known.

THE DIRECT PROBLEM

In a Cartesian coordinate system let (x_1, x_2, x_3) be the Cartesian coordinates of place $\mathbf{x}$. We consider Rayleigh waves which propagate along the traction-free surface of the material half-space $x_3 \leq 0$. We assume that the material half-space carries a density $\rho(x_3)$ and prestress $\overset{\circ}{\boldsymbol{T}}(x_3)$, which are smooth functions[1] of x_3 and $\overset{\circ}{\boldsymbol{T}}$ satisfies the equation $\operatorname{div}\overset{\circ}{\boldsymbol{T}} = \mathbf{0}$. We assume also that the superimposed small elastic motion pertaining to the Rayleigh wave in question obeys the theory of linear elasticity with initial stress (cf. [2, 3]). In addition, we suppose that the incremental elasticity tensor $\mathbb{L}$ can be written as a sum of two terms: a principal part $\mathbb{C}^{\text{Iso}}$ which is *homogeneous* and isotropic, and a perturbative part $\mathbb{A} = \mathbb{A}(x_3)$ which is a smooth function of x_3 ($x_3 \leq 0$) and is generally anisotropic. Then $\mathbb{L}$ can be expressed as a fourth-order tensor on the infinitesimal strain $\boldsymbol{E}$ in the form

$$\mathbb{L}(x_3)[\boldsymbol{E}] = \mathbb{C}^{\text{Iso}}[\boldsymbol{E}] + \mathbb{A}(x_3)[\boldsymbol{E}] = \lambda(\operatorname{tr}\boldsymbol{E})\mathbf{I} + 2\mu\boldsymbol{E} + \mathbb{A}(x_3)[\boldsymbol{E}], \tag{1}$$

where $\mathbf{I}$ is the identity matrix, λ and μ are the Lamé constants that pertain to $\mathbb{C}^{\text{Iso}}$, and $\mathbb{A} = \mathbb{A}(x_3)$ has 21 generally independent components. Moreover, at the free surface $x_3 = 0$ of the material medium $\mathbb{A}(0)$ and $\overset{\circ}{\boldsymbol{T}}(0)$ are assumed to be sufficiently small as compared with $\mathbb{C}^{\text{Iso}}$ that for all expressions and formulas which depend on $\mathbb{A}(0)$ and $\overset{\circ}{\boldsymbol{T}}(0)$ it suffices to keep only those terms linear in the components of these tensors. See [7] for details about this constitutive assumption.

Let $\boldsymbol{u} = e^{ik(x_2 - v_R t)}\boldsymbol{a}(\mathbf{x}, v_R, k)$ be a time-harmonic solution to the elastic wave equations which describes the displacement at $\mathbf{x}$ and time t of the superimposed small elastic motion pertaining to the Rayleigh wave that propagates in the direction of the 2-axis with phase velocity v_R, where $k = \frac{2\pi f}{v_R}$ is the wave number. The polarization ratio r_R of Rayleigh waves on the surface $x_3 = 0$ is defined as the ratio of the maximum longitudinal component to the maximum normal component of the displacements on $x_3 = 0$ (see [1]):

$$r_R = \left|\frac{(\boldsymbol{a})_2}{(\boldsymbol{a})_3}\right|_{x_3=0},$$

where $(\boldsymbol{a})_i$ denotes the i-th component of the vector $\boldsymbol{a}$ and $|z|$ denotes the absolute value of a complex number z.

*Corresponding author. E-mail: tanuma@gunma-u.ac.jp

[1]Here by a smooth function of the coordinate x_3 ($x_3 \leq 0$) is meant an infinitely differentiable function all of whose derivatives are bounded and continuous.

Herein we present a procedure for obtaining a high-frequency asymptotic formula for r_R, more specifically, for expressing each term r_i $(i = 0, 1, 2, \cdots)$ in the asymptotic formula of the polarization ratio

$$r_R \,=\, r_R(k) \,=\, r_0 \,+\, r_1\, k^{-1} \,+\, r_2\, k^{-2} \,+\, r_3\, k^{-3} \,+\cdots \tag{2}$$

in terms of $\mathbb{C}^{\mathrm{Iso}}$ and $\mathbb{L}(x_3), \mathring{\boldsymbol{T}}(x_3), \rho(x_3)$ at $x_3 = 0$ and their first and higher-order x_3-derivatives at $x_3 = 0$.

Let $\mathbf{Z}(v) = \mathbf{Z}(v, k)$ be the 3×3 surface impedance matrix that expresses a linear relationship between the displacements at the free surface and the surface tractions needed to sustain them. In [4, 7] an algorithm is given by which each Hermitian matrix $\mathbf{Z}_i(v)$ $(i = 1, 2, 3, \cdots)$ of the asymptotic expansion

$$\mathbf{Z}(v) \,=\, k\,\mathbf{Z}_0(v) \,+\, \mathbf{Z}_1(v) \,+\, k^{-1}\,\mathbf{Z}_2(v) \,+\, k^{-2}\,\mathbf{Z}_3(v) \,+\cdots \tag{3}$$

can be computed iteratively through Lyapunov-type equations once $\mathbf{Z}_0(v)$ is determined. Note that $k\,\mathbf{Z}_0(v)$, which is also Hermitian, is the surface impedance matrix of the comparative homogeneous elastic half-space which has its incremental elasticity tensor, mass density, and initial stress equal to $\mathbb{L}(0)$, $\rho(0)$, and $\mathring{\boldsymbol{T}}(0)$, i.e., their value at the surface $x_3 = 0$, respectively. We keep terms up to those linear in $\mathring{\boldsymbol{T}}(0)$ and $\mathbb{A}(0)$ to write $k\,\mathbf{Z}_0(v) \,=\, k\,\mathbf{Z}_0^{\mathrm{Iso}}(v) + k\,\mathbf{Z}_0^{\mathrm{Ptb}}(v)$. Here $k\,\mathbf{Z}_0^{\mathrm{Iso}}(v)$, which is of zeroth order in $\mathring{\boldsymbol{T}}(0)$ and $\mathbb{A}(0)$, is the surface impedance matrix pertaining to the homogeneous isotropic elastic half-space with constitutive equation $\boldsymbol{S} = \mathbb{C}^{\mathrm{Iso}}[\boldsymbol{E}]$ and density $\rho = \rho(0)$, whereas $k\,\mathbf{Z}_0^{\mathrm{Ptb}}(v)$ is of first order in $\mathring{\boldsymbol{T}}(0)$ and $\mathbb{A}(0)$. The formulas of $\mathbf{Z}_0^{\mathrm{Iso}}(v)$ and $\mathbf{Z}_0^{\mathrm{Ptb}}(v)$ are given in Propositions 3.1 and 3.2 of [7], respectively.

From vanishing of the determinant of the right hand side of (3) at $v = v_R$, which leads us to an approximate secular equation, we have obtained in [4] a high-frequency asymptotic formula for v_R:

$$v_R = v_R(k) = v_0 \,+\, v_1\, k^{-1} \,+\, v_2\, k^{-2} \,+\, v_3\, k^{-3} \,+\, \cdots . \tag{4}$$

Rayleigh waves produce no traction on the free surface $x_3 = 0$, which implies that the polarization vector $\boldsymbol{a}|_{x_3=0}$ generates the null-space of $\mathbf{Z}(v_R)$. On the basis of this assertion we get

Proposition 1 *For $N = 1, 2, 3, \cdots$, an algorithm for computing the truncated sum of the asymptotic formula (2) up to the order k^{-N} is described as follows:*

1st step *Substitute (4) into $r_R = \dfrac{|N(v_R)|}{|D(v_R)|}$, where*

$$N(v) = \Big(\overline{\ell_{12}} + \sum_{n=1}^{N} k^{-n}\overline{(\mathbf{Z}_n)_{12}}\Big)\Big(\ell_{13} + \sum_{n=1}^{N} k^{-n}(\mathbf{Z}_n)_{13}\Big) - \Big(s_{11} + \ell_{11} + \sum_{n=1}^{N} k^{-n}(\mathbf{Z}_n)_{11}\Big)\Big(-is_{23} + \ell_{23} + \sum_{n=1}^{N} k^{-n}(\mathbf{Z}_n)_{23}\Big),$$

$$D(v) = \Big(s_{11} + \ell_{11} + \sum_{n=1}^{N} k^{-n}(\mathbf{Z}_n)_{11}\Big)\Big(s_{22} + \ell_{22} + \sum_{n=1}^{N} k^{-n}(\mathbf{Z}_n)_{22}\Big) - \Big|\Big(\ell_{12} + \sum_{n=1}^{N} k^{-n}(\mathbf{Z}_n)_{12}\Big)\Big|^2.$$

Here s_{11}, s_{22} and $-is_{23}$ denote the $(1,1), (2,2)$ and $(2,3)$ components of $\mathbf{Z}_0^{\mathrm{Iso}}(v)$, respectively, ℓ_{ij} the (i,j) component of $\mathbf{Z}_0^{\mathrm{Ptb}}(v)$, $\overline{z}$ the complex conjugate of a complex number z, and $(\mathbf{Z})_{ij}$ the (i,j) component of a matrix $\mathbf{Z}$.

2nd step *Expand the resulting form with respect to k^{-n} $(n = 0, 1, 2, \cdots, N)$.*

3rd step *In each coefficient of the order of k^{-n} $(n = 0, 1, 2, \cdots, N)$, we retain terms up to those linear in $\mathbb{A}(0)$ and $\mathring{\boldsymbol{T}}(0)$ and neglect the higher order terms, to obtain r_n $(n = 0, 1, 2, \cdots, N)$ in (2).*

The perturbation formulas for v_0 and that for r_0 of the comparative homogeneous half-space, which are correct to within terms linear in $\mathbb{A}(0)$ and $\mathring{\boldsymbol{T}}(0)$, are given in [5] and [6], respectively.

As illustration, Proposition 1 is applied to generate dispersion curves of Rayleigh-wave polarization ratio (i.e., graphs of the functions $r_R(f)$) for a thick-plate sample of an AA 7075-T651 aluminum alloy that carries a residual stress imparted by prior surface treatment of low plasticity burnishing.

References

[1] Junge M., Qu J., Jacobs L. J. Relationship between Rayleigh Wave Polarization and State of Stress. *Ultrasonics* **44**: 233–237, 2006.
[2] Man C.-S., Carlson D. E. On the Traction Problem of Dead Loading in Linear Elasticity with Initial Stress. *Arch. Rational Mech. Anal.* **128**: 223–247, 1994.
[3] Man C.-S., Lu W. Y. Towards an Acoustoelatic Theory for Measurement of Residual Stress. *J. Elasticity* **17**: 159–182, 1987.
[4] Man C.-S., Nakamura G., Tanuma K., Wang S. Dispersion of Rayleigh Waves in Vertically-Inhomogeneous Prestressed Elastic Media. *IMA. J. Appl. Math.* **80**: 47–84, 2015.
[5] Tanuma K., Man C.-S. Perturbation Formula for Phase Velocity of Rayleigh Waves in Prestressed Anisotropic Media. *J. Elasticity* **85**: 21–37, 2006.
[6] Tanuma K., Man C.-S. Perturbation Formulas for Polarization Ratio and Phase Shift of Rayleigh Waves in Prestressed Anisotropic Media. *J. Elasticity* **92**: 1–33, 2008.
[7] Tanuma K., Man C.-S., Chen Y. Dispersion of Rayleigh Waves in Weakly Anisotropic Media with Vertically-Inhomogeneous Initial Stress. *Int. J. Eng. Sci.* **92**: 63–82, 2015.

GEOMETRY OF THE NONLINEAR MECHANICS OF ACCRETION

Fabio Sozio*[1] and Arash Yavari[1,2]
[1]School of Civil and Environmental Engineering, Georgia Institute of Technology, Atlanta, GA 30332, USA
[2]The George W. Woodruff School of Mechanical Engineering, Georgia Institute ofTechnology, Atlanta, GA 30332, USA

Summary By accretion we mean the growth of a deformable solid by the gradual addition of material on its boundary. The result of such a process is the creation of a residually stressed solid. To this extent, accretion can be seen as the study of the formation of "non-Euclidean solids"—an expression coined by Poincaré [1]—through the continuous joining of infinitely many two-dimensional layers. Examples of accretion processes in Nature are the growth of biological tissues, crystal growth, the formation of rocks; in technology we mention additive manufacturing (3D printing), metal solidification, the build-up of concrete structures in successive layers. Our formulation of the nonlinear mechanics of accretion explicitly uses a Riemannian material manifold with an a priori unknown metric that describes this material structure. This work is based on references [2, 3, 4, 5].

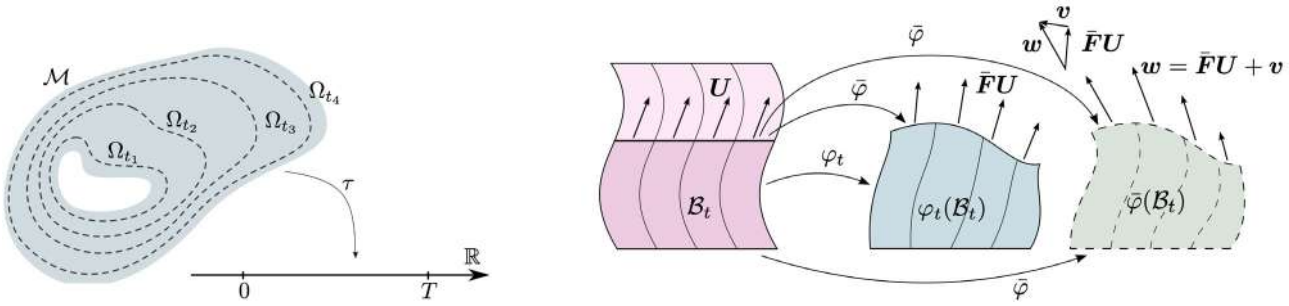

Figure 1: Left: The material manifold of an accreting body as a foliation. Right: Material and spatial kinematics of an accreting body.

THE MATERIAL MANIFOLD

An accreting body is represented by a foliated manifold, where every leaf is given by a two-dimensional level set of the function τ assigning to every point its time of attachment (see Fig. 1). This bundle of layers is in turn endowed with a material flow describing the way layers are added atop each other. The material motion is then combined with the standard spatial kinematics, to obtain the motion of the growing boundary (see Fig. 1). The novelty in our formulation is represented by the introduction of the accretion tensor $\mathbf{Q}$, expressing the local deformation gradient of a particle at a time immediately before its time of attachment (see Fig. 2). It can be proved that the accretion tensor depends on the deformation gradient at the time of attachment $\mathbf{F}(X, \tau(X))$, and on the rate and direction at which the new material is being added (the growth velocity $\mathbf{u}$). The fundamental assumption of our work is the following: For the addition of stress-free material, the accretion tensor represents a local isometry for the material manifold, so the material metric can be built by pulling back the ambient metric via $\mathbf{Q}$. Being built using the accretion tensor, the material metric in turn depends on the growth velocity and on the deformation of a particle at its time of attachment. In general, such deformation is unknown, and so is the material metric.

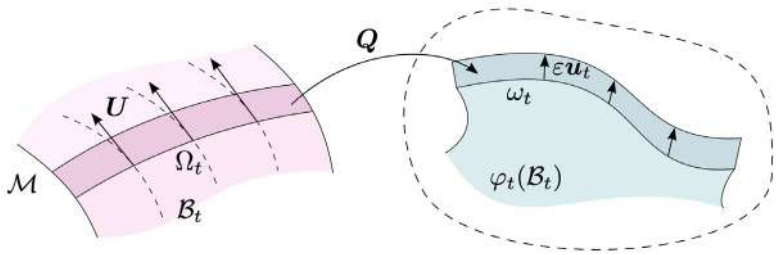

Figure 2: Addition of an infinitesimally thin layer to the boundary of a deforming body. The local deformation gradient is expressed by the two-point tensor $\mathbf{Q}$.

*E-mail: fsozio3@gatech.edu

THE CURVATURE TENSOR

As already mentioned, the Riemannian manifold is not necessarily Euclidean. A non-Euclidean solid is characterized by local natural distances (encoded in the material metric) that are not realizable in the three-dimensional ambient space. This implies the impossibility to minimize the energy at every point at the same time, leading to the presence of residual stress (see Fig. 3). It should be noted that a non-Euclidean manifold is the mathematical object that represents an anelastic solid. Anelasticity is usually modeled through the multiplicative decomposition of the deformation gradient. To this extent, the tensor $\mathbf{Q}$ can be seen as the plastic part of the deformation gradient in accretion-induced anelasticity. From a geometric perspective, the presence of residual stress is equivalent to the non-vanishing of the Riemann curvature tensor built on the material metric. In our framework, the partition into infinitely many layers with different times of attachment allows one to express the geometry of a deformable 3D body with respect to its layer-wise structure. The nonflat structure of an accreted solid is then studied using an approach similar to the ADM formalism of general relativity by Arnowitt et al. [6]. The Riemannian structure is first decomposed in layer and out-of plane quantities, allowing one to express the 3D geometry in terms of the geometry of each layer, and in terms of the tangent and normal components of the growth velocity. In some cases, when the geometry of the accreted body is know a priori, these expressions provide a useful tool for quantifying the lack of flatness of the material structure. In some other cases, one is first required to solve the accretion initial boundary value problem.

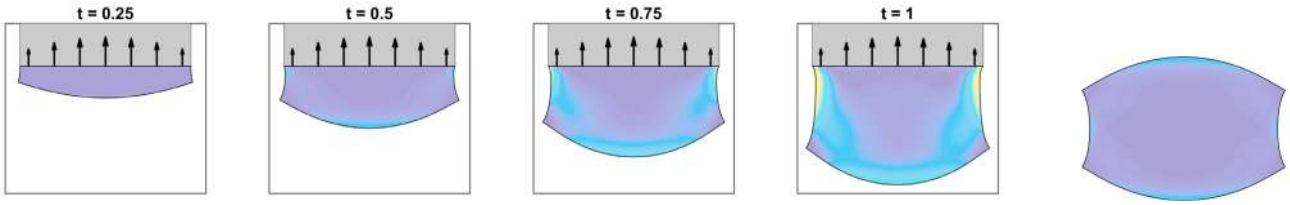

Figure 3: Growth through a fixed straight line. Left: The deformed configuration during accretion at four different dimensionless times. Right: The residually-stressed configuration.

NUMERICAL RESULTS

In order to solve examples and calculate the residual stresses (see Fig. 3), a pure accretion IBVP and a thermal accretion IBVP have been formulated. These are solved numerically using a two-step scheme based on a finite difference method (see Fig. 4). At each time step i, we start from the solution at the time step $i-1$ adding layer of hot material to the outer boundary of the accreting solid and updating the grid for this new geometry. In the first step, we solve the thermal problem discretizing the heat equation. In the second step, we use thermal data to solve the mechanical problem in a weak form. When we reach the final time, we remove the constraints, impose ambient temperature everywhere, and calculate the residually-stressed configuration through a load control procedure.

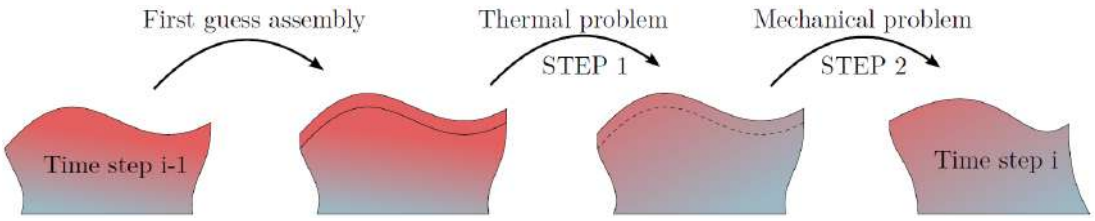

Figure 4: A two-step computational scheme for a layered manufacturing process.

References

[1] Poincaré, H. "Science and hypothesis". *Science Press* (1905).
[2] Sozio F., Yavari A."Nonlinear mechanics of surface growth for cylindrical and spherical elastic bodies." *Journal of the Mechanics and Physics of Solids* 98 (2017): 12-48.
[3] Sozio F., Yavari A. "Nonlinear mechanics of accretion." *Journal of Nonlinear Science* (2019): 1-51.
[4] Sozio F., Yavari A. "Riemannian and Euclidean Material Structures in Anelasticty." *Mathematics and Mechanics of Solids* (2020)
[5] Sozio F., Fagih-Shoajei M., Sadik S., Yavari A. "Nonlinear mechanics of thermoelastic accretion." (Under Review)
[6] Arnowitt R., Deser S., Misner C. W. "Dynamical structure and definition of energy in general relativity". *Physical Review* (1959): 116(5), 1322.

SMOOTH AND SINGULAR DISTRIBUTIONS OF DISLOCATIONS

Marcelo Epstein[1] and Reuven Segev *[2]
[1]Department of Mechanical and Manufacturing Engineering,Le University of Calgary,Calgary,Canada
[2]Department of Mechanical Engineering,Ben-GurionUniversity of the Negev,Beer-Sheva,Israel

Summary A continuum geometric theory for the representation of the distribution of dislocations in crystalline solids is presented. The theory applies to bodies represented by general n-dimensional manifolds and the distribution of dislocations may be either smooth or singular. For the smooth case the theory is based on calculus of differential forms on manifolds and for the singular case it is based on the notion of a de Rham current.

INTRODUCTION

We present below a mathematical framework for the description of the geometry of the distributions of dislocations from the continuum mechanics, macroscopic, point of view (see also [1, 2]). A material body is modeled by a general n-dimensional differentiable manifold $\mathcal{B}$ and the mathematical framework does not require that a Riemannian metric or a connection be specified on $\mathcal{B}$. Thus, the description is independent of any particular configuration of the body in the physical space and the distribution of dislocations is viewed as a part of the material structure of the body.

The distribution of each family of Bravais hyper-planes describes the crystalline structure of the body. We refer to such a family of Bravais hyper-planes as a *layering*. Dislocations occur when hyper-planes belonging to such a layering are not conserved, that is, hyper-planes are created or annihilated within the body. The distributions of hyper-planes and dislocations specified by a layering may be singular, and clearly, as a special case, they may be smooth. For example, one may consider the case where a singular half hyper-surface is removed from the body.

The point of view adopted here differs from some approaches to the continuum description of the geometry of dislocations by not considering any configuration, neither continuous nor discontinuous, of the body in space, and being independent of mechanical constitutive relations. Other works do consider purely geometric structures (such as a crystal basis at each point), but we consider the atomic planes as basic. Thus we assume, right from the start, that a distribution of a family of Bravais hyper-planes, specifying the material structure of the body, is given.

The next section considers the case of a smooth layering. Such a smooth distribution of hyper-planes is specified by a differential 1-form on the manifold $\mathcal{B}$. Then, we consider the more general singular case using the theory of de Rham currents (see [3]).

SMOOTH DISTRIBUTIONS OF DISLOCATIONS

In accordance with the paradigm described above, we consider a layering of the material body $\mathcal{B}$. This is done mathematically by a differential 1-form

$$\varphi : \mathcal{B} \longrightarrow T^*\mathcal{B}, \tag{1}$$

to which we refer as the *layering form*. Thus, at each body point $X \in \mathcal{B}$, $\varphi(X) : T_X\mathcal{B} \to \mathbb{R}$ is a linear mapping of tangent vectors to the real numbers. The solutions, v, of the linear equation $\varphi(X)(v) = a$, for the various constants $a \in \mathbb{R}$, describe the family of Bravais hyper-planes at X. The components of φ relative to any basis are related to the Miller indices of this family of hyper-planes. The particular number $\varphi(X)(v) = a$ may be interpreted as a measure of the quantity of hyper-planes penetrated by the vector v.

Absence of dislocations is indicated if for any close circuit $c : [0, 1] \to \mathcal{B}$, $c(0) = c(1)$, the total amount of hyper-planes penetrated by the tangent to the curve c, vanishes. Specifically, for a given circuit c, the total amount of hyper-planes penetrated is computed by

$$I_c := \int_{t=0}^{1} \varphi(c(t))(\dot{c}(t))\mathrm{d}t, \tag{2}$$

where $\dot{c}(t)$ denotes the tangent to the curve at $c(t)$. It is noted that the orientation of the penetration is taken into account by the sign of the evaluation $\varphi(c(t))(\dot{c}(t))$. Assuming $\dot{c}(t) \neq 0$ for all t, one may view the parameter t as a coordinate on the 1-dimensional manifold $\tilde{c} :=$ Image $c \subset \mathcal{B}$. Thus, we may write, using integration of differential forms,

$$I_c = \int_{\tilde{c}} \varphi. \tag{3}$$

Let $\mathcal{S}$ be a 2-dimensional submanifold with boundary of $\mathcal{B}$ such that $\partial\mathcal{S} = \tilde{c}$. Then, by Stokes's theorem,

$$I_c = \int_{\mathcal{S}} \mathrm{d}\varphi, \tag{4}$$

*Corresponding author. E-mail: rsegev@bgu.ac.il.

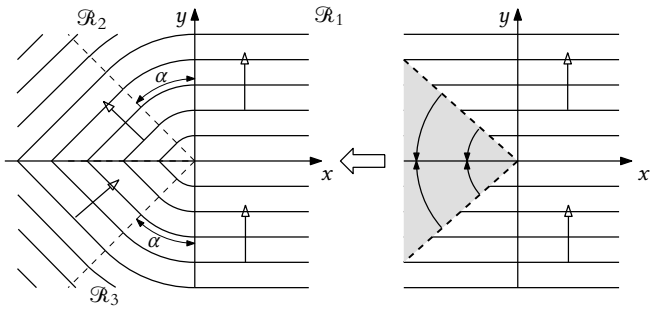

Figure 1: Example

where $\mathrm{d}\varphi$ is the exterior derivative of φ—a differential 2-form. Hence, the condition $\mathrm{d}\varphi = 0$, guarantees that for any circuit c, we have $I_c = 0$.

It is concluded that the exterior derivative $\mathrm{d}\varphi$ indicates the distribution of dislocations and its integration over a hyper-surface $\mathcal{S}$ indicates the total amount of planes created inside $\mathcal{S}$. If $\mathrm{d}\varphi = 0$, at least locally, there is a real valued function u so that $\varphi = \mathrm{d}u$. The function u is viewed as an enumeration of the Bravais hyper-surfaces. A 2-form $\psi = \mathrm{d}\varphi$ specifying the distribution of dislocations will be referred to as a *dislocation form*. It is recalled that for any differential form ω, $\mathrm{d}^2\omega = 0$. Thus, if ψ is a dislocation form, we have a compatibility condition $\mathrm{d}\psi = 0$.

SINGULAR DISTRIBUTIONS OF DISLOCATIONS

In order to adapt the foregoing paradigm to singular distributions of dislocations, we now view the differential 1-form φ as an object inducing a linear functional T_φ on the space of differential $(n-1)$-forms having compact supports in $\mathscr{B}$. Specifically,

$$T_\varphi(\omega) := \int_{\mathscr{B}} \varphi \wedge \omega, \tag{5}$$

for any $(n-1)$-form ω having a compact support. Here, $\wedge$ denotes the exterior product of forms so that $\varphi \wedge \omega$ is indeed an n-form that may be integrated over the body manifold. Such linear functionals on vector spaces of differential $(n-1)$-forms are referred to as $(n-1)$-*de Rham currents* (see [3]).

Thus, in order to generalize the foregoing to the singular case, we no longer consider only de Rham currents induced by smooth form as in (5) but admit any $(n-1)$-de Rham current T as a layering current. In contrast with a current induced by a smooth 1-form as above, one may consider a current $T_{\mathscr{V}}$ induced by an $(n-1)$-dimensional submanifold with boundary $\mathscr{V} \subset \mathscr{B}$ in the form

$$T_{\mathscr{V}}(\omega) = \int_{\mathscr{V}} \omega. \tag{6}$$

This current represents a singular layering which consists of the single layer $\mathscr{V}$. As a generalization of the exterior derivative as a measure of the dislocations, one uses now the *boundary* ∂T of the layering current T, an $(n-2)$-current defined by $\partial T(\alpha) := T(\mathrm{d}\alpha)$, for any $(n-2)$-form α of compact support in $\mathscr{B}$. Thus, in particular, for the current $T_{\mathscr{V}}$ defined above and any $(n-2)$-form α,

$$\partial T_{\mathscr{V}}(\alpha) = \int_{\mathscr{V}} \mathrm{d}\alpha = \int_{\partial\mathscr{V}} \alpha = T_{\partial\mathscr{V}}(\alpha). \tag{7}$$

Thus, the boundary of $T_{\mathscr{V}}$ is the current induced by the boundary $\partial\mathscr{V}$ as expected of a single hyper-surface $\mathscr{V}$ with boundary $\partial\mathscr{V}$ inside the body—an edge dislocation.

It is noted that the boundary operator for currents also generalizes the exterior derivative in analogy with the smooth case. Thus, for the current T_φ above, ∂T_φ acts by

$$\partial T_\varphi(\alpha) = \int_{\mathscr{B}} \varphi \wedge \mathrm{d}\alpha = -\int_{\mathscr{B}} \mathrm{d}(\varphi \wedge \alpha) + \int_{\mathscr{B}} \mathrm{d}\varphi \wedge \alpha = -\int_{\partial\mathscr{B}} \varphi \wedge \alpha + \int_{\mathscr{B}} \mathrm{d}\varphi \wedge \alpha = T_{\mathrm{d}\varphi}(\alpha), \tag{8}$$

where we have used the identity $\mathrm{d}(\varphi \wedge \alpha) = \mathrm{d}\varphi \wedge \alpha - \varphi \wedge \mathrm{d}\alpha$ and the fact that α vanishes on $\partial\mathscr{B}$.

The presentation will consider further aspects of singular dislocations and various examples such as illustrated in Figure 1.

References

[1] Epstein M., Segev R. Geometric aspects of singular dislocations. *Mathematics and Mechanics of Solids*, **19**:335–347, 2014.
[2] Epstein M., Segev R. On the geometry and kinematics of smoothly distributed and singular defects, in Differential Geometry and Continuum Mechanics, Chen, G.-Q.; Grinfeld, M. Knops, R. *(Eds.) Springer Proceedings in Mathematics and Statistics,* **137:** 203–234, Springer, 2015.
[3] de Rham G. Differentiable Manifolds, Springer, 1984.

SAINT-VENANT'S PRINCIPLE FOR GENERALIZED THERMOELASTICITY WITH MEMORY-DEPENDENT DERIVATIVE

Indranil Satrkar*[1]
[1]Indian Institute of Engineering Science and Technology, Shibpur

Summary The spatial behavior of the thermal signals related to the topic "Saint-Venant's principle" [1] in the generalized thermoelasticity theory is interesting from the both thermomechanical and mathematical viewpoints. The research is theoretically developed on two mathematical aspects in order to study the spatial behavior of the thermal signals in an isotropic, homogeneous, thermoelastic continuum in the context of a very recently proposed heat conduction model [2] with memory-dependent derivative (MDD). To prove the finite propagation speeds of thermal signals in the present model, a domain of influence theorem is established and to analyze the spatial propagation of thermal signals inside the domain of influence, a spatial decay theorem is established. As an immediate outcome from this theoretical analysis, a uniqueness theorem for the present model is also derived.

INTRODUCTION

The thermoelasticity theory is mainly focussed on dealing with the interaction between the mechanical and thermal field variables in the deformable bodies. As a result of the parabolic nature of the heat conduction equation in the classical dynamic thermoelasticity theory, based on the Fourier's heat conduction law, the impact of thermomechanical loading on an isotropic and homogeneous body reaches instantaneously to all points of the body from the point of application. In the case of coupled thermoelastic problems, it describes that the impact of thermomechanical loading influences the magnitude and pattern of the displacements, stresses and temperature distribution instantaneously everywhere in the solution domain. Its physical interpretation is that the thermal signals occupy the whole space for any time $t > 0$. i.e. the propagation speed for the thermal signals is infinite. This inconsistent behavior of the heat transfer mechanism contradicts physical phenomena. In order to overcome the mathematical inconsistency connected with the infinite speed propagation for the thermal signals, generalized thermoelasticity theories involving finite speed propagation for the thermal signals have been developed in the literature by several researchers. In recent decades memory-dependent derivative (MDD) proposed by Wang and Li [3] is at the height of popularity among the researchers due to its enormous applications in real world problems. The aim of the present contribution is to to establish the following **Saint-Venant's principle** of the proposed model for an isotropic, homogeneous body subjected to an external thermomechanical loading having a bounded support $\hat{\Delta}_T$, $\hat{\Delta}_T \subset \mathscr{D}$: (i) **Domain of influence theorem:** The entire thermoelastic disturbance or thermal signals vanishes beyond a well-defined bounded domain Δ_{vt}, $\hat{\Delta}_T \subset \Delta_{vt} \subset \bar{\mathscr{D}}$, $t \in [0, T]$, where v is a constant of velocity dimension, (ii) **Spatial decay theorem:** The suitable energetic measure $\mathscr{E}(r, t)$ related with the thermoelastic problem involving memory-dependent derivative (MDD) decays spatially along the distance r from the bounded support $\hat{\Delta}_T$ and the factor $1 - \frac{r}{vt}$ controls the decay rate. From the theoretical analysis of the article, a uniqueness theorem is also proved for the present model.

GOVERNING EQUATIONS

The governing equations for the present model model with MDD over a bounded regular region $\mathscr{D}$ in the Euclidean space are formulated as follows:
The kinematic relation:

$$\varepsilon_{ij} = \frac{(u_{i,j} + u_{j,i})}{2}, \tag{1}$$

The Hooke's law:

$$\sigma_{ij} = \lambda \varepsilon_{kk} \delta_{ij} + 2\mu \varepsilon_{ij} - \gamma \theta \delta_{ij}, \tag{2}$$

The equation of motion:

$$\sigma_{ij,j} + \rho f_i = \rho \ddot{u}_i, \tag{3}$$

The heat conduction equation of the proposed model with MDD:

$$\rho C_E \dot{\theta} + \gamma T_0 \dot{\varepsilon}_{k,k} - \rho Q = k\theta_{,ii} + k^* \nu_{,ii} + k^* \tau D_\omega \nu_{,i} + k^* \frac{\tau^2}{2} D_\omega^2 \nu_{,ii} \tag{4}$$

where, the memory-dependent derivative operator D_ω in association with the the time-delay parameter $\omega(\omega > 0)$ and the differentiable kernel function $K(t - \varsigma)$ over the delayed interval $[t - \omega, t]$ is defined in the article [2].
The adjoined initial-boundary conditions for the thermoelastic problem with MDD are $u_i(x, 0) = u_i^0(x)$, $\dot{u}_i(x, 0) = u_i^1(x)$, $\theta(x, 0) = \theta^0(x)$ for $x \in \bar{\mathscr{D}} = \mathscr{D} \cup \partial\mathscr{D}$, $u_i = \bar{u}_i$ on $\partial\mathscr{D}_1 \times [0, T]$, $\sigma_{ij} n_j = \bar{\sigma}_i$ on $\partial\mathscr{D}_1^c \times [0, T]$, $\theta = \bar{\theta}$ on $\partial\mathscr{D}_2 \times [0, T]$, $q = q_i n_i = \bar{q}$ on $\partial\mathscr{D}_2^c \times [0, T]$, where, $\partial\mathscr{D}_1 \cup \partial\mathscr{D}_1^c = \partial\mathscr{D}_2 \cup \partial\mathscr{D}_2^c = \partial\mathscr{D}$, $\partial\mathscr{D}_1 \cap \partial\mathscr{D}_1^c = \partial\mathscr{D}_2 \cap \partial\mathscr{D}_2^c = \emptyset$, $\emptyset$ denotes the empty set.

*Corresponding author. E-mail: is.30.687@gmail.com

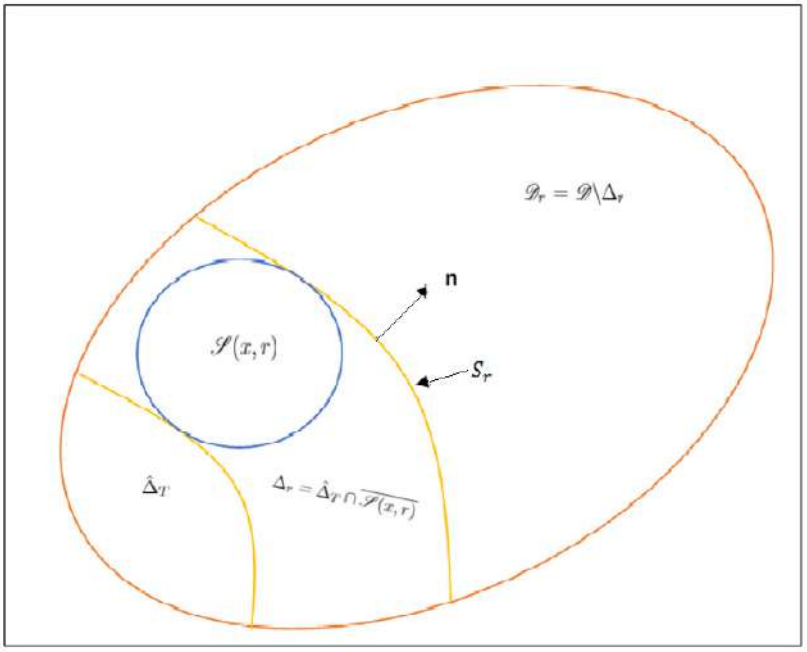

Figure 1: Schematic diagram of the considered sets

SPATIAL BEHAVIOR

For a fixed time $T > 0$, the support of the initial and boundary data of the initial-boundary value problem of generalized thermoelasticity with MDD on the time interval $[0, T]$ is defined by the set $\hat{\Delta}_T$, such that:
i. if $x \in \mathscr{D}$, then $u_i^0 \neq 0$ or $u_i^1 \neq 0$ or $\theta^0 \neq 0$ or $\exists\, t' \in [0, T]$ such that $f_i(x, t') \neq 0$ or $Q(x, t') \neq 0$, ii. if $x \in \partial\mathscr{D}_1$, then $\exists\, t' \in [0, T]$ such that $\bar{u}_i(x, t') \neq 0$, iii. if $x \in \partial\mathscr{D}_1^c$, then $\exists\, t' \in [0, T]$ such that $\bar{\sigma}_i(x, t') \neq 0$, iv. if $x \in \partial\mathscr{D}_2$, then $\exists\, t' \in [0, T]$ such that $\bar{\theta}(x, t') \neq 0$, v. if $x \in \partial\mathscr{D}_2^c$, then $\exists\, t' \in [0, T]$ such that $\bar{q}(x, t') \neq 0$. Then, the spatial behavior of the thermal signals in the present model is described by the **Saint-Venant's principle** and the proof is established by following the Lemmas:

Lemma 1

For each $t \in [0, T]$, $r \in [0, \mathscr{D}]$ $\mathscr{E}(r, t)$ is the nonincreasing function with respect to r on the interval $[0, \mathscr{D}]$.

Lemma 2

Let A_{ij} denote the components of a symmetric tensor, y_i denote the components of a vector, $(x) = (x_i) \in R^3$, $|x| = r$ and $i, j = 1, 2, 3$, then for any arbitrary parameter $p' > 0$, the following inequality holds: $\frac{A_{ij}x_iy_j}{r} \leq \frac{1}{2}[p'A_{ij}A_{ij} + \frac{1}{p'}y_iy_i]$.

UNIQUENESS

The thermoelastic mixed initial-boundary value problem with MDD subjected to the initial-boundary conditions posses a unique solution and it is established by proving associated problem subjected to the homogeneous initial-boundary conditions posses only the trivial solution.

CONCLUSIONS AND POSSIBLE FUTURE INSIGHTS

The thermal signals in generalized thermoelasticity theory with memory-dependent derivative (MDD) propagates with finite speeds which is deduced by proving domain of influence theorem [4] and decays inside the domain of influence. The analysis is considered for homogeneous and isotropic materials. Based on appropriate hypotheses upon the material coefficients, the results can also be extended to the class of anisotropic and inhomogeneous materials.

References

[1] Chiriţă, S. Saint-Venant's principle in linear thermoelasticity. *J Therm. Stresses* **18**: 485-496, 1995.
[2] Quintanilla R. Some solutions for a family of exact phase-lag heat conduction problems. *Mech. Res. Commu.* **38**: 355-360, 2011.
[3] Wang J.-L, Li H.-F. Surpassing the fractional derivative: Concept of the memory-dependent derivative. *Comp. Math. Apppl.* **62**: 1562-1567, 2011.
[4] Ignaczak J, Ostoja-Starzewski M. Thermoelasticity with Finite Wave Speeds. Oxford, 2010.

EFFECTIVE TRANSPORT PROPERTIES OF MULTI-PHASE FIBRE COMPOSITES

R. Guinovart-Díaz[1],Y. Espinosa-Almeyda[2],R. Rodríguez-Ramos[1],J. Bravo-Castillero[2],and F.J. Sabina[2]
[1]Facultad de Matemática y Computación.Universidad de La Habana,La Habana,Cuba
[2]Instituto de Investigaciones en Matemáticas Aplicadas y en Sistemas.Universidad Nacional Autónomade México, CDMX,México

Summary The two-scale asymptotic homogenization method (AHM) is used to find closed-form formulas for effective transport complex properties of periodic multi-phase fibre-reinforced composites (FRC). Examples for three- and four-phase composites with complex constituents and periodic parallelogram unit cells (PUCs) are considered. Numerical validations are carried out through comparisons with other methods. Good agreement is obtained. The formulas may be useful as benchmarks for checking experimental and numerical results.

INTRODUCTION

The knowledge of effective transport properties of composites is important in applications. Models have been developed for the study of multi-phase FRC in the wide field of transport problems [1–5]. The main aim of this work is the prediction of effective transport complex properties of periodic multi-phase FRC with complex constituents and PUCs with microstructure by AHM. Anisotropic interphase effects on effective properties quality in relation to complex shear and anisotropic conductivity of biological tissue comprising tubular cells, such as skeletal muscle, are studied as a multi-phase FRC. Validation and analysis of results are given and discussed.

STATEMENT OF THE PROBLEM AND METHOD OF SOLUTION

AHM is applied to obtain effective transport properties of periodic $n-$phase FRC. Phases are composed of transport materials belonging to crystal symmetry class 6*mm* along fibre $3-$direction with complex-valued properties. PUC is made up of a central circular core and its complement to the parallelogram. Former is occupied by phase 1 and later by circularly nested $n-1$ phases, as a generalization of results in [2, 3]. Hence, it yields simple closed-form formulas for three- and four-phase composites under perfect contact conditions across the interfaces. However, Hashin's imperfect interface analysis is carried out [6] wherever necessary. The porous material limit case is analyzed using a three-phase composite. The analytical formulae are also used in order to find the effective shear moduli, conductivity, permittivity and the like for three-phase FRC.

NUMERICAL ANALYSIS

The broad applicability and accuracy of results by AHM is determined by comparison with other methods reported earlier for three- and four-phase FRC where good agreement is found. From now on, let matrix properties be p_α, q_α (diagonal) and r_α (off-diagonal) entries of $\alpha-$phase; p, q and r are effective transport properties, respectively.

Shear. Fig. 1 shows interphase effect on effective shear for a four-phase FRC with either a hard or soft phase p_2. The effective shear moduli p/p_1, q/p_1 and r/p_1 as a function of p_3/p_1 are shown. PUC is defined by periods $(1,0), (\cos(\pi/4), \sin(\pi/4))$. Material properties are taken from [1]. In Fig. 1(a), effect on shear is very small for low p_3/p_1 values. In contrast, a strong anisotropic behaviour is displayed for high p_3/p_1 values, that is, the axial properties differ noticeably and $p_1 < p < q$, $r < 0$. The opposite occurs in Fig. 1(b). For low p_3/p_1 values, interphase effect induces a composite anisotropic behaviour and $p_1 < p < q$, $r < 0$ instead. When p_3/p_1 increases, then $p \approx q \approx p_1$ is attained. This radical change in the effective properties is due to the interphase property p_2 being softer in the composite of Fig. 1(b) than in Fig. 1(a), while a rest of parameter remain fixed.

Conductivity. Fig. 2 plots real and imaginary parts of normalized effective complex conductivity p/p_1 and q/p_1 versus dimensionless frequency $\Omega(=\omega C L/\sigma_m)$ for several periodic PUCs with periods $(1,0), (\cos\theta, \sin\theta)$, where L is composite microstructural dimension and σ_m is matrix conductivity, showing a comparison with results in [5] (red circles, BC) for isotropic composite with hexagonal cell $(p = q)$. Good agreement is obtained. Fig. 2(a) and (b) also display a composite orthotropic behavior when $\theta = 45^o$ and $\theta = 50^o$ due to $p \neq q$. In both PUCs, real and imaginary parts of p and q are different. The complex conductivities p, q and r of the biological tissue (skeletal muscle) with interfacial admittance K studied in [5] are determined here using the three-phase FRC with a thin interphase via [6], where $K = B + i\omega C$, $B(C)$ is conductance (capacitance) per unit area and ω is circular frequency. A thin interphase admittance caused by electric potential to jump across the interfaces can be referred to as an imperfect interface as well

as impedance interface [6]. The relationship between K and interphase property p_2 is $K = p_2 R_2 / h$ with $h = 10^{-4}$, as in [6].

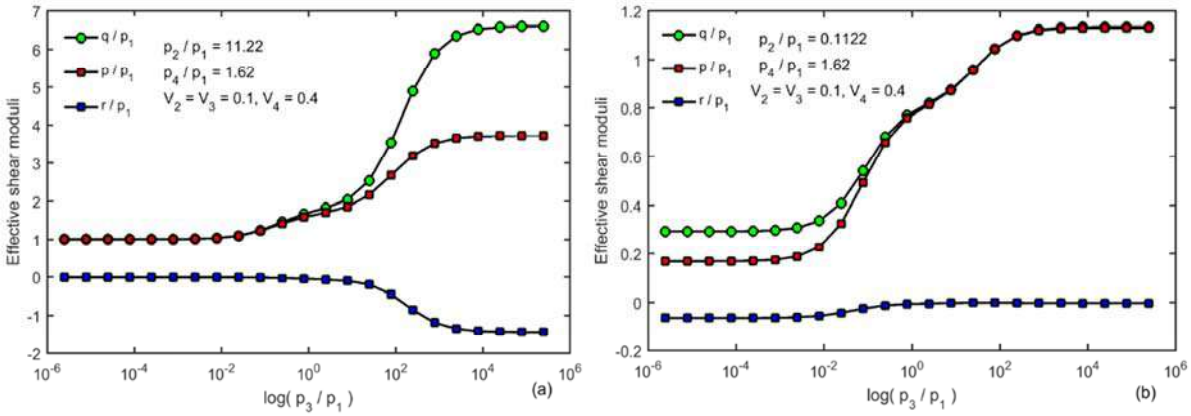

Fig. 1. Dimensionless effective shear moduli as function of p_3 / p_1 (a) p_2 hard phase, (b) p_2 soft phase.

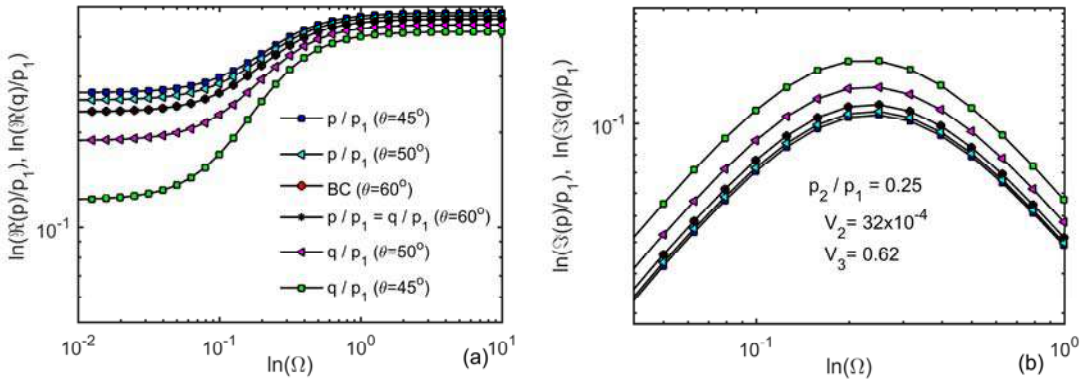

Fig. 2. Real and imaginary parts of normalized effective p and q versus dimensionless circular frequency for different PUCs.

CONCLUSIONS

Complex transport properties of periodic multi-phase FRC with different PUCs with microstructure are found by AHM. The general formulas of local problems and associated effective coefficients for transport problems are derived. Simple closed-forms formulas for three- and four-phase FRC are found. The broad applicability and efficiency of the model are tested against results obtained from other method for periodic multi-phases FRC. The formulas may be useful as benchmarks for checking experimental and numerical results. This model illustrates anisotropic interphase effects on effective complex shear properties quality and orthotropic conductivity of an idealized model of biological tissue with interfacial impedance (periodic tubular cells, such as skeletal muscle), in a proper way.

References

[1] Dasgupta, A., Bhandarkar, S. M. A generalized self-consistent Mori-Tanaka scheme for fiber-composites with multiple interphases. Mech. Mater. **14**: 67-82, 1992.

[2] Rodríguez-Ramos, R., Sabina, F. J., Guinovart-Díaz, R., Bravo-Castillero, J. Closed-form expressions for the effective coefficients of a fiber-reinforced composite with transversely isotropic constituents–I. Elastic and square symmetry. *Mech. Mater*. **33**: 223-235, 2001.

[3] Guinovart-Díaz, R., Bravo-Castillero, J., Rodríguez-Ramos, R., Sabina, F. J. Closed-form expressions for the effective coefficients of fibre-reinforced composite with transversely isotropic constituents. I: Elastic and hexagonal symmetry. *J. Mech. Phys. Solids* **49:**, 1445-1462, 2001.

[4] Bravo-Castillero, J., Ramírez-Torres, A., Sabina, F. J., García-Reimbert, C., Guinovart-Díaz, R., Rodríguez-Ramos, R. Analytical formulas for complex permittivity of periodic composites. Estimation of gain and loss enhancement in active and passive composites. *Waves Random Complex.* 2018. DOI: 10.1080/17455030.2018.1546063

[5] Bisegna, P., Caselli, F. A simple formula for the effective complex conductivity of periodic fibrous composites with interfacial impedance and applications to biological tissues. *J. Phys. D: Appl. Phys.* **41**: 115506, 2008.

[6] Hashin, Z. Thin interphase/imperfect interface in elasticity with application to coated fiber composites. *J. Mech. Phys. Solids* **50**: 2509 – 2537, 2002.

INSTABILITY-DRIVEN PATTERN FORMATIONS IN SOFT HETEROGENEOUS MATERIALS

Stephan Rudykh*[1], Jian Li [2], Viacheslav Slesarenko [3], and Pavel I. Galich [4]
[1]Department of Mechanical Engineering, University of Wisconsin-Madison, Madison, WI, USA
[2]Department of Civil and Environmental Engineering, Massachusetts Institute of Technology, Cambridge, MA
[3]Freiburg Institute for Advanced Studies, University of Freiburg, Freiburg, Germany
[4]Department of Materials Science and NanoEngineering, Rice University, Houston, TX, USA

Summary Elastic instability is a fascinating phenomenon playing an important role in pattern formations in soft biological systems. The phenomenon also has been actively used to design new (meta-) materials with switchable microstructures, properties, and functions. Here, we investigate the elastic instability phenomenon in soft heterogeneous materials. These deformable composites typically combine soft deformable matrix and stiffer phase (such as fibers or inclusions). We specifically focus on the influence of the geometrical microstructure parameters and material composition on the instability phenomenon giving rise to the microstructure switches.

INTRODUCTION

Soft materials have attracted significant attention in recent decades due to their ability to sustain extremely large deformations, thus, allowing us to actively alter their properties and functionalities. Potential applications of the wide class of materials include soft and human-interactive robotics, sensors and actuators, tunable acoustic devices, and noise and vibration canceling systems, among many others.

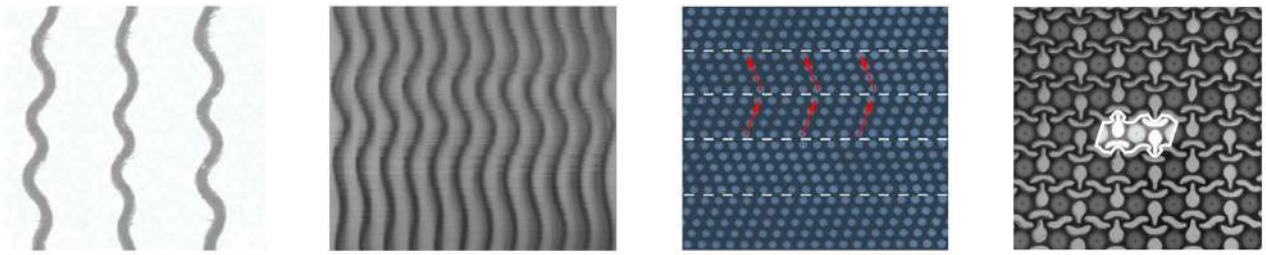

(a) Laminate (b) 3D fiber composite (c) Particulate composite (d) Multiphase composite

Figure 1. Instability-induced wavy patterns forming in (a) soft 3D printed laminates [2] and (b) 3D-fiber composites [4]; (c) twining pattern in particulate composites [8], and (d) auxetic microstructure transformations in inclusion-matrix-void soft systems [5,6].

The rich and complicated mechanical behavior of soft materials poses numerous challenges related to various intrinsic aspects of soft material mechanics and physics such as material and geometrical nonlinearities, characteristic inelastic behavior, and the fascinating instability phenomenon. The latter is of a specific interest due to the unusual behavior of the materials in the unstable or post-instability extreme regimes; for example, exotic properties such as negative Poisson's ratio, negative stiffness, and induced negative group velocities and band gaps in elastic waves are predicted and observed in a variety of instability transformed microstructured materials. Motivated by these predictions and observation, here, we specifically focus on the elastic instabilities in soft microstructured composites with a specific focus on utilizing the instability phenomenon for triggering reversible and controllable microstructure transformations.

RESULTS

To predict and analyze the stability behavior of soft heterogeneous materials we employ the so-called "small-on-large" framework, when incremental small deformations are super-imposed on the finitely deformed state. The corresponding linearized equilibrium equations in the deformed state yield the macroscopic stability condition through the effective tensor of elastic moduli; the condition is also referred to as the loss of ellipticity condition. This allows providing estimates for the onset of elastic instabilities for the longwave mode. However, many composites develop instabilities at smaller length scales comparable with their microstructure characteristic length. This microscopic type of instability is usually analyzed by employing the Bloch-Floquet analysis superimposed on finite deformations. We note that, for the specific case of wavenumber approaching zero value (the long wave mode), the Bloch-Floquet technique reproduces the predictions of the loss of ellipticity analysis, thus, establishing the connections between these distinct methods. While the analysis can be performed analytically for a limited set of microstructured (such as periodic laminates), typically the finite element (FE) method is used to examine the mechanical stability of soft materials and structures. Here, we employ the numerical analysis to perform a detailed study the elastic instability phenomenon in we perform a detailed study of the dependence of pattern formations on material properties and geometrical parameters of soft composites such as hyperelastic (i) periodic laminates [1,2], (ii) 3D transversely isotropic (TI) fiber composites [3,4],

*Corresponding author. E-mail: **rudykh@wisc.edu**

(iii) void-matrix-particles soft periodic systems [5,6], hexagonal stiff networks embedded in soft matrix [7], and, finally, (iv) periodic particulate soft composites [8]. Moreover, we employ the multi-material 3D printing to fabricate the periodic soft-stiff microstructured composites, and we further externally test these systems. For example, wavy patterns develop in layered materials upon achieving the critical compressive strain level. Moreover, we show that the buckled shapes in the relatively simple material system with rate-dependent constituents can be tuned and controlled by the applied strain-rate through inelastic rate-dependent behavior of the laminate constituents [2]. In laminates, the critical wavelength of the instability induced wavy patterns varies with the applied strain-rate. It is possible, however, to design composites, in which the critical wavelength remains the same independent of the applied strain rate, while the critical strain varies with a change in the strain-rate. Thus, a wider range of wavy patterns with various wavelengths and amplitudes can be archived through the combination of the instability and viscoelastic phenomena [2].

We expend the stability analysis to the 3D setting and examine the response of 3D transverse isotropic soft fiber composites in a fully 3D deformation setting. We find that the primary buckling mode in the fiber composites is determined by the fiber volume fraction and the contrast between elastic moduli of fibers and matrix [3]. We show that for composites with fiber volume fractions exceeding a threshold value (which depends on elastic modulus contrast) the primary buckling mode corresponds to the long wave or macroscopic instability. Composites with a lower amount of fibers, however, experience microscopic instabilities corresponding to either wavy or helical buckling shapes [3]. In addition, instability modes and critical wavelengths are shown to be highly tunable by material composition. The numerical results showed a good agreement with experimental observations in 3D printed soft composite [4].

Next, we explore the instability-induced pattern transformations in 3D-printed soft composites consisting of stiff inclusions and voids periodically distributed in a soft matrix. These soft auxetic composites are prone to elastic instabilities giving rise to negative Poisson's ratio (NPR) behavior [5,6]. Upon reaching the instability point, the composite microstructure rearranges into a new morphology attaining an NPR regime. Remarkably, identical composites can morph into distinct patterns depending on the loading direction. These fully determined instability-induced distinct patterns are characterized by significantly different NPR behaviors, thus, giving rise to enhanced tunability of the composite properties. In addition, we illustrate a potential application of these reversible pattern transformations as tunable acoustic-elastic metamaterials capable of selectively filtering low-frequency ranges controlled by deformation [5].

The idea of using the instability induced switches in materials microstructures has been further extended to a class of soft composites with stiff networks embedded in a soft matrix [7]. Two distinct types of instability patterns were observed, dependent on the geometry and the material combination. While Type I patterns retain the original periodicity (developing wrinkles in the network walls), Type II patterns transform the original periodicity. The elastic wave propagation analysis showed that a change in frequency band gaps is for both instability-induced pattern transformations, but differs for each type due to their dramatic difference in structure transformation (i.e. Type I wall wrinkling vs. Type II periodicity switching).

Finally, we report experimental observations of domain formations and pattern transitions in soft particulate composites under large deformations. We observe the formation of microstructures with anti-symmetric domains [7], and its geometrically tailored evolution into a variety of patterns of cooperative particle rearrangements. We show that these fully determined new patterns can be achieved by fine-tuning of the initial microstructure

CONCLUSIONS

In this work, we investigated the elastic instability phenomenon in soft heterogeneous materials. These deformable composites combine soft deformable matrix and stiffer phase (such as fibers or inclusions). Figure 1 shows the experimentally observed wavy patterns forming in (a) soft 3D printed laminates [2] and (b) 3D-fiber composites [4], (c) twining pattern in particulate composites [8], and (d) auxetic microstructure transformations in inclusion-matrix-void soft systems [5,6]. In this presentation, we will discuss the influence of the geometrical microstructure parameters and material composition on the instability phenomenon giving rise to the microstructure transformations.

References

[1] Li Y., Kaynia, N., Rudykh S., Boyce M.C. Wrinkling of Interfacial Layers in Stratified Composites *Adv. Eng. Mater*. **15**(10): 921-926, 2013.
[2] Slesarenko V., Rudykh S. Harnessing viscoelasticity and instabilities for tuning wavy patterns in soft layered composites. *Soft Matter* **12**: 3677-3682, 2016.
[3] Slesarenko V., Rudykh S. Microscopic and macroscopic instabilities in hyperelastic fiber composites. *J. Mech. Phys. Solids* **99**: 471-482, 2017.
[4] Li J., V. Slesarenko V., Galich, P.I., Rudykh, S. Instabilities and pattern formations in 3D-printed deformable fiber composites. *Comp. B* **148**: 114-122, 2018.
[5] Li J., Slesarenko V., Rudykh S. Auxetic multiphase soft composite material design through instabilities with application for acoustic metamaterials. *Soft Matter* **14**: 6171-6180, 2018.
[6] Li J., Rudykh S. Tunable microstructure transformations and auxetic behavior in 3D-printed multiphase composites: The role of inclusion distribution *Comp. B* **172**: 352-362 2019.
[7] Gao C., Slesarenko V., Boyce M.C., Rudykh S., Li Y. Instability-Induced Pattern Transformation in Soft Metamaterial with Hexagonal Networks for Tunable Wave Propagation. *Scientific Reports* **8**: 11834, 2018.
[8] Li J., Dora T., Slesarenko V., Goshkoderia A., Rudykh S. Domain formations and pattern transitions via instabilities in soft heterogeneous materials. *Advanced Materials* **31**: 1807309, 2019

EFFECT OF WALL LIQUID REDISTRIBUTION ON THE PRESSURE INFLATION RESPONSE OF A PORO-HYPERELASTIC SHELL

Vahid Zamani[1] and Thomas J. Pence*[1]
[1]Department of Mechanical Engineering, Michigan State University, East Lansing, MI, USA

Summary We consider a spherical shell composed of a poro-hyperelastic material in order to examine how the through-wall distribution of liquid affects the pressure-expansion response. It is shown that different through-thickness distributions of the same overall amount of liquid can significantly alter this response. Uniform liquid distributions give the most compliant structural response whereas sequestering liquid near either the inner or outer wall stiffens the overall behavior. Liquid redistribution can also alter the basic monotonicity properties of the resulting inflation graphs.

We consider an internally pressurized spherical shell with "gel-type" walls. That is to say that the walls consist of a liquid infused poro-hyperelastic material. The overall amount of liquid in the structure as a whole is fixed. However, this fixed liquid may redistribute itself within the cell wall. At issue is how the liquid distribution affects the amount of overall expansion that is due to an internal pressurization.

We follow a continuum mechanical treatment that tracks change in the local liquid content in terms of the associated material volume change [1]. Both the soft porous ground substance and the mobile liquid constituent are regarded as incompressible. Material swelling from a nominally dry reference state then correlates with the current local amount of liquid that is present. When liquid migration is active, a standard treatment is to invoke some form of Darcy's law to describe the liquid seepage [2]. For our purposes, attention is restricted to static distributions of liquid (i.e., all such migration has ceased) and to states for which the overall system is in mechanical equilibrium.

For the case of spherical symmetry this gives a boundary value problem that admits to a certain amount of direct analysis. The corresponding hyperelastic problem (no liquid and hence no swelling) is the classical nonlinear elastic spherical balloon – a much beloved problem that has been analyzed extensively [3]. The poro-hyperelastic problem with swelling due to a uniform distribution of liquid is examined in [4]. In the present work we specifically consider nonuniform liquid distributions where the goal is to contrast different distributions, all of which correspond to the same overall amount of liquid. Although usually acting on very different time scales, certain aspects of this mechanics treatment of swelling are closely related to problems in growth mechanics [5].

The technical approach makes use of a swelling field v where $v = 1$ is the nominally dry state (no mobile liquid being present). Swelling due to the presence of mobile liquid gives $v > 1$. Because of this, the usual incompressiblity condition of volume preservation is generalized to $\det\mathbf{F} = v$, where $\mathbf{F}$ is the deformation gradient. The poro-hyperelastic theory then generalizes the hyperelastic energy $W = W(\mathbf{F})$ so as to admit an additional dependence upon v. The particular constitutive model considered here takes the well known hyperelastic Mooney-Rivlin model and extends it to include the swelling effect via

$$W(I_1, I_2, v) = \frac{1}{2}\alpha\mu\Big(\frac{I_1}{v^{2/3}} - 3\Big) + \frac{1}{2}(1-\alpha)\mu\Big(\frac{I_2}{v^{4/3}} - 3\Big).$$

Here $\mu > 0$ is the infinitesimal shear modulus in the absence of swelling and α obeying $0 \le \alpha \le 1$ is the Mooney-Rivlin parameter that distinguishes between the I_1 and I_2 content of the material.

We consider a finite thickness spherical shell with inner radius $R_i > 0$ and outer radius $R_o > R_i$ prior to any loading or swelling. Attention is restricted to radially symmetric swelling $v = v(R)$. The total added volume due to the swelling

$$\Delta V = 4\pi \int_{R_i}^{R_o} (v(R) - 1) R^2 dR, \tag{1}$$

is thus identified with the total amount of mobile liquid in the system.

The surface loading consists of an internal pressurization ΔP. Spherical symmetry motivates the consideration of radial deformations such that the deformed radius location r is a function of reference radius R. The volumetric swelling constraint determines this $r(R)$ function in terms of the location of the deformed inner surface $r_i \equiv r(R_i)$, namely

$$r^3 = r_i^3 + 3\int_{R_i}^{R} v(\zeta)\,\zeta^2\,d\zeta.$$

Thus the "total loading input" on the structure consists of both the volumetric swelling field $v(R)$ and the surface pressurization ΔP. The "deformation output" is the single value r_i that characterizes the inflationary expansion.

We examine swelling fields of the form

$$v(R) = A/R + B, \tag{2}$$

where A and B are constants. This is a *harmonic swelling field*, because the form (2) provides the general spherically symmetric solution to $\nabla^2 v = 0$. We consider the range of harmonic swelling fields that distribute a fixed amount of liquid

*Corresponding author. E-mail: pence@egr.msu.edu

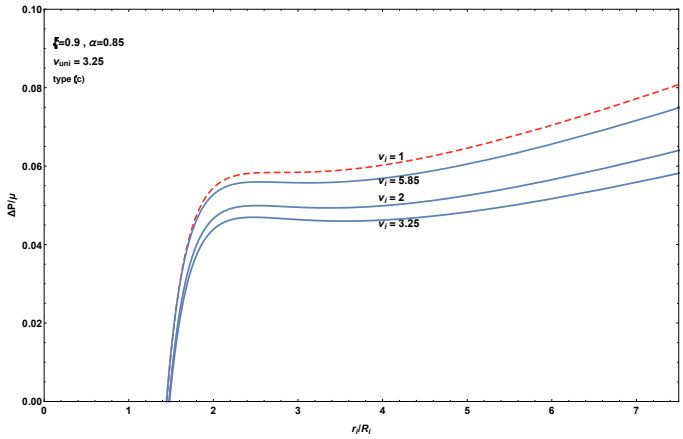

Figure 1: The family of inflation graphs for $\alpha = 0.85$, $\xi = 0.9$, $\Delta V/R_i^3 = 3.53$. This makes $v_i^{max} = 5.85$ and corresponds to a structure wall that is 70% mobile liquid.

ΔV throughout the structure wall in different ways. Thus A and B provide two degrees of freedom that are constrained by the single condition (1). Consequently, there will be a one degree of freedom – or one parameter family – of harmonic swelling fields that so redistribute the liquid. Letting $v_i = v(R_i)$ and $v_o = v(R_o)$, we may let either v_i or v_o parameterize this family. Choosing v_i as the parameter, it then follows that

$$A = \left[-\frac{3\Delta V}{2\pi R_i^3} \left(\frac{\xi^3}{2 - 3\xi + \xi^3} \right) + v_i \left(\frac{2(1-\xi^3)}{2 - 3\xi + \xi^3} \right) - \frac{2(1-\xi^3)}{2 - 3\xi + \xi^3} \right] R_i, \tag{3}$$

with a similar expression for B. Here $\xi = R_i/R_o$ so that $0 < \xi < 1$ with ξ close to one describing a thin shell and ξ close to zero describing a thick shell. In order for $v(R) \geq 1$ for all R it follows that the parameterization range for v_i is $1 \leq v_i \leq v_i^{max}$ where v_i^{max} is a function of the same parameters appearing in (3). Values v_i close to one correspond to liquid that is heavily concentrated near the outer wall. Values v_i close to v_i^{max} correspond to liquid that is heavily concentrated near the inner wall. An intermediate value corresponds to the uniform fluid distribution.

Integrating the stress equations of equilibrium leads to

$$\Delta P = 2\mu \int_{R_i}^{R_o} \frac{R}{r^2} \left[\alpha \left(\frac{r}{R v^{2/3}} - \frac{R^5 v^{4/3}}{r^5} \right) + (1-\alpha) \left(\frac{r^3}{R^3 v^{4/3}} - \frac{R^3 v^{2/3}}{r^3} \right) \right] dR,$$

which enables the construction and analysis of pressure-inflation graphs for the family of swelling fields. One such set of graphs is shown in Figure 1. The value $\alpha = 0.85$ is standard for hyperelastic modeling with the Mooney-Rivlin form. The thickness ratio $\xi = 0.9$ corresponds to a relatively thin shell. In the classical hyperelastic theory this gives a nonmonotone pressure-inflation graph. Each of the poro-hyperelastic graphs in the figure also exhibit such a nonmonotone behavior. Note that the overall structural stiffness is highly variable as seen in the range of heights to the various graphs. The stiffest response corresponds to the highest curve, in this case that for $v_i = 1$. The most compliant response corresponds to the lowest curve, for which the liquid distribution is essentially uniform. Changes in material (α), structural geometry (ξ) and total liquid content (ΔV) cause the overall family of harmonic swelling distributions to exhibit qualitative changes, sometimes within the same family. These behaviors can be organized in terms of phase diagrams in parameter spaces [6]. In fact, the set shown in Figure 1 is key to one such analysis as a slight increase in ΔV will cause the uppermost curve (that corresponding to $v_i = 1$) to become monotonic.

Acknowledgement: This work is made possible by NPRP grant nos. 4-1333-1-214 and 8-2424-1-477 from the Qatar National Research Fund (a member of Qatar Foundation). The statements made herein are solely the responsibility of the authors.

References

[1] H. Tsai, T. J. Pence, and E. Kirkinis. Swelling induced finite strain flexure in a rectangular block of an isotropic elastic material. *Journal of Elasticity*, 75(1):69–89, 2004.

[2] A. P. S. Selvadurai and A. P. Suvorov. On the development of instabilities in an annulus and a shell composed of a poro-hyperelastic material. *Proceedings of the Royal Society A - Mathematical Physical and Engineering Sciences*, 474(20180239), 2018.

[3] M. M. Carroll. Pressure maximum behavior in inflation of incompressible elastic hollow spheres and cylinders. *Quarterly of Applied Mathematics*, pages 141–154, 1987.

[4] V. Zamani and T. J. Pence. Swelling, inflation, and a swelling-burst instability in hyperelastic spherical shells. *International Journal of Solids and Structures*, 125:134–149, 2017.

[5] A. Goriely, D. E. Moulton, and R. Vandiver. Elastic cavitation, tube hollowing, and differential growth in plants and biological tissues. *EPL (Europhysics Letters)*, 91(1):18001, 2010.

[6] V. Zamani and T. J. Pence. Expansion-contraction behavior of a pressurized poro-hyperelastic spherical shell due to fluid redistribution within the structure wall. Accepted for publication in *Journal of Mechanics of Materials and Structures*, 2020.

ON THE MECHANICS OF NARROW ELASTIC RIBBONS

Roberto Paroni *[1]
[1]Dipartimento di Ingegneria Civile e Industriale,Università di Pisa,56122 Pisa,Italy

Summary The classical theory of ribbons, developed by Sadowsky and Wunderlich, has recently received renewed attention. Here, we re-examine the derivation of the limit energy of an inextensible elastic strip as the width goes to zero, without making any symmetry assumption. We further study the equilibrium configurations of a thin elastic strip subject to combined twist and traction and show that two types of equilibrium states are possible: the straight-helicoid and the spiral-ribbon.

Geometrically a ribbon is a body with three length scales: it is a parallelepiped whose length ℓ is much larger than the width ε, which, in turn, is much larger than the thickness h. That is, $\ell \gg \varepsilon \gg h$. Since two characteristic dimensions are much smaller than the length, ribbons can be efficiently modelled as a one-dimensional continuum.

The starting point for the study of elastic ribbons can be either the three-dimensional nonlinear theory of elasticity or, taking advantage that the thickness h is much smaller than the other two dimensions, a nonlinear theory for plates. Within the latter framework, since energetically stretching 'costs' much more than bending, one can further assume that the plate is inextensible.

The (bending) energy of an inextensible elastic strip $S_\varepsilon = (-\ell/2, \ell/2) \times (-\varepsilon/2, \varepsilon/2)$, is

$$u \mapsto \frac{1}{\varepsilon} \int_{S_\varepsilon} Q(A_u(x))\, dx, \tag{1}$$

where Q is the bending energy density and A_u denotes the second fundamental form of $u : S_\varepsilon \to \mathbb{R}^3$. For isotropic strips the energy density Q depends only on the determinant and the trace of A_u: the Gaussian curvature $K_u := \det A_u$ and the mean curvature $H_u := 1/2 \operatorname{tr} A_u$. Since inextensible, and hence developable, surfaces have null Gaussian curvature we have that Q only depends on H_u. By assuming the material to be isotropic and the energy density to be quadratic, the bending energy is proportional to

$$u \mapsto \frac{1}{\varepsilon} \int_{S_\varepsilon} |H_u(x)|^2\, dx. \tag{2}$$

In 1930, in a seminal paper, Sadowsky argued that as $\varepsilon \to 0$ the energy of the ribbon reduces to

$$y \mapsto \int_{-\ell/2}^{\ell/2} \frac{(\kappa^2 + \tau^2)^2}{\kappa^2}\, ds \tag{3}$$

where κ and τ are the curvature and the torsion, respectively, of the centerline y of the strip, and s is its arc length. This functional is now known as Sadowsky's functional. The model was formally justified in 1962 by Wunderlich.

Wunderlich's technique is quite ingenious, but it leads to a singular energy density, as (3) reveals. In this talk we shall briefly show what is the correct energy that is obtained by letting $\varepsilon \to 0$ in (2). We will also drop the isotropic assumption and deduce a one dimensional model for an anisotropic ribbon. We shall study the equilibrium configurations of a thin elastic strip subject to combined twist and traction and we shall recover two types of equilibrium states: the straight-helicoid and the spiral-ribbon. Finally, we will identify the critical value of the twist at which the transition from one state to another takes place for a prescribed traction.

The talk is based on joint works with R. Barsotti, L. Freddi, P. Hornung, M.G. Mora, and G. Tomassetti.

References

[1] L. Freddi, P. Hornung, M.G. Mora, R. Paroni. A corrected Sadowsky functional for inextensible elastic ribbons. *J. Elasticity* **123**: 125–136, 2016.
[2] L. Freddi, P. Hornung, M.G. Mora, R. Paroni. A variational model for anisotropic and naturally twisted ribbons. *SIAM Journal on Mathematical Analysis* **48**: 3883–3906, 2016.
[3] L. Freddi, P. Hornung, M.G. Mora, R. Paroni. One-dimensional von Kármán models for elastic ribbons. *Meccanica* **53**: 659–670, 2018.
[4] R. Paroni, G. Tomassetti. Macroscopic and microscopic behavior of narrow elastic ribbons. *J. Elasticity* **135**: 409–433, 2019.
[5] R. Barsotti, R. Paroni, G. Tomassetti. On the straight-helicoid to spiral-ribbon transition in thin elastic ribbons. *submitted 2019.*

*E-mail: roberto.paroni@unipi.it.

CONFIGURATIONAL FORCES ON 2-D ELASTIC LINE SINGULARITIES

Youjung Seo [1], Shubhada Garnaik[2], and Y. Eugene Pak[2]*
[1]Graduate School of Convergence Science and Technology, Seoul National University, Suwon, Republic of Korea
[2]Department of Mechanical Engineering, SUNY Korea, Incheon, Republic of Korea

Summary Configurational forces acting on two-dimensional (2-D) elastic line singularities are evaluated by path-independent J-, M-, and L-integrals in the framework of plane strain linear elasticity. The elastic line singularities considered in this study are the edge dislocation, the line force, the nuclei of strain, and the concentrated couple moment that are subjected to far-field loads. The interaction forces between two similar parallel elastic singularities are also calculated. Self-similar expansion force, M, evaluated for the line force shows that it is exactly the negative of the strain energy prelogarithmic factor as in the case for the well-known edge dislocation result. It is also shown that the M-integral result for the nuclei of strain and the L-integral result for the line force yield interesting nonzero expressions under certain circumstances.

INTRODUCTION

It is well known that the energy release rates or the configurational forces associated with translation, self-similar expansion, and rotation of cavities or defects are expressed by the path-independent integrals, J, M, and L, respectively [1–3]. These path-independent integrals are useful in characterizing various defects and elastic singularities in that they are related to the total energy change (change in strain energy plus work done by external loads) resulting from the configurational change of these defects and singularities; hence, the name energy release rate or configurational force [4].

To demonstrate the usefulness of these integrals in studying the configurational forces acting on elastic line singularities, we evaluated these integrals for the edge dislocation, the line force, the nuclei of strain, and the concentrated couple moment that are subjected to far-field mechanical loads. The interaction forces between two similar parallel elastic singularities are also calculated. Closed-form expressions for the configurational forces on each elastic singularity are obtained in the framework of two-dimensional (2-D) plane strain linear elasticity.

This concise work provides an interesting insight into the behavior of interacting elastic line singularities by evaluating particularly the less-utilized M-integrals that can give explicit expressions for self-similar expansion force. There have been similar studies on the in-plane and the out-of-plane line forces [5] as well as on 2-D and three-dimensional (3-D) nuclei of strain [4]. Here, we present some novel M-integral results for 2-D line singularities [6].

FORMULATIONS

Path-Independent Integrals Using Decomposed Energy Momentum Tensor

The path-independent J-, M-, and L-integrals for 2D linear elastic solid are

$$P_{ij} = \frac{1}{2}\sigma_{kl}\varepsilon_{kl}\delta_{ij} - \sigma_{i\gamma}u_{\gamma,j}$$

$$J_j = \int_c P_{ij}n_i dS$$

$$M = \int_c P_{ij}n_i x_i dS$$

$$L_k = \int_c e_{kij}P_{ij}n_i x_i dS$$

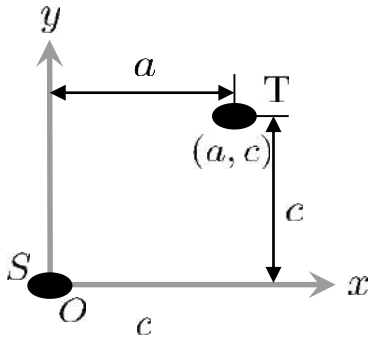

Figure 1. Elastic singularity T located at (a, c) interacting with singularity S at the origin.

These path-independent integrals for the interacting singularities S and T can be calculated by summing up the elastic fields generated by each singularity. Here, S denotes the elastic singularity at the origin of the coordinate system for which the configurational forces are calculated and T denotes other interacting singularities or far-field loads. The integrands of these integrals are then composed of the singular self-field and the regular field due to singularity T or the far-field loads. We calculated the above path-independent integrals on a contour C with vanishingly small radius that completely surrounds the singularity S at the origin. We can further simplify the calculations by assuming that the elastic field induced by T is constant along the contour C.

Forces Between Two Parallel Elastic Line Singularities

Interacting configurational forces between two similar parallel elastic singularities are evaluated by the path-independent integrals along the contour C surrounding the elastic singularity S (Table 1). It can be seen that the M-integral

*Corresponding author. E-mail: eugene.pak@sunykorea.ac.kr

expressions for the edge dislocation and the line force do not recognize other interacting fields, i.e., the elastic field due to singularity T, hence, only the self-field contributes to the M value. Interestingly, and perhaps for the first time, it is observed that the M-integral expression for the line force is identical to the negative of the prelogarithmic strain energy factor. This is analogous to the well-known dislocation result given by Rice [7]. Our result also shows that the self-similar expansion force, M, acting on the nuclei of strain exists only when the normal stresses are present. This is because the nuclei of strain, which equivalently model the misfitted cylinder in an infinite matrix, induces a state of pure shear in the matrix resulting in no volume or scale change. Only in the presence of volume changing normal stresses, the self-similarly expanding force is realized. A similar M-integral result was obtained for the case of a three-dimensional misfitted spherical inclusion embedded in an infinite solid [8]. Contrary to the line force, the M-integral for the nuclei of strain does not provide the coefficient of strain energy factor. At the same time, the M-integral result for the concentrated couple moment under far-field loads is interestingly zero.

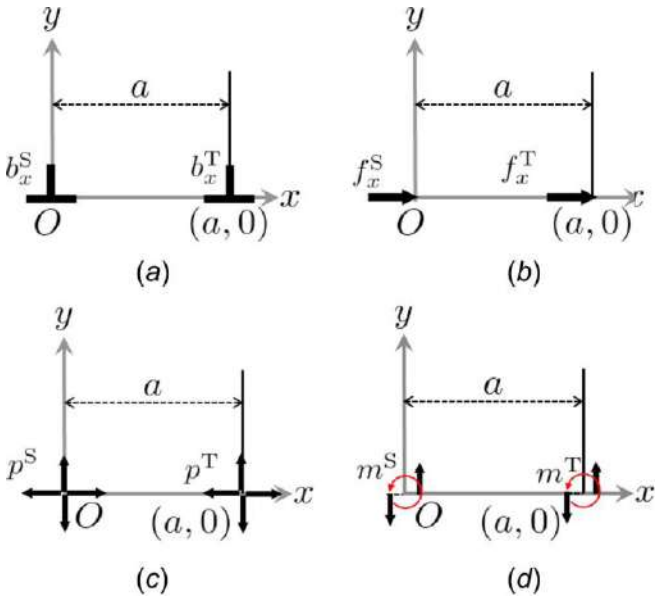

Figure 2. In-plane elastic singularities: (a) edge dislocation, (b) line force, (c) nuclei of strain, and (d) concentrated couple moment, interacting with identical parallel line singularities in an infinite medium.

Table 1. Configurational forces between two parallel elastic line singularities in the absence of far-field loads

	J_x	J_y	M	Prefactor	L
Edge Dislocation, b_x^S	$-\frac{b_x^S b_x^T \mu}{2\pi(1-\nu)a}$	0	$\frac{b_x^{S2}\mu}{4\pi(1-\nu)}$	$\frac{b_x^{S2}\mu}{4\pi(1-\nu)}$	0
Line Load, f_x^S	$\frac{f_x^S f_x^T(3-4\nu)}{8\pi\mu(1-\nu)a}$	0	$-\frac{f_x^{S2}(3-4\nu)}{16\pi\mu(1-\nu)}$	$\frac{f_x^{S2}(3-4\nu)}{16\pi\mu(1-\nu)}$	0
Nuclei of Strain, p^S	0	0	0	$\frac{p^{S2}(1-2\nu)^2}{8\pi\mu(1-\nu)^2}\left(\frac{r_{out}^2-r_{in}^2}{r_{in}^2 r_{out}^2}\right)$	0

Acknowledgement
The Korea National Research Foundation (Grant Nos. NRF 2014M1A3A3A02034928 and NRF 2016R1D1A1B03932553).

References

[1] Rice, J., 1968, "A Path Independent Integral and the Approximate Analysis of Strain Concentration by Notches and Cracks," ASME J. Appl. Mech., 35(2), pp. 379–386.
[2] Cherepanov, G., 1981, "Invariant Integrals," Eng. Fract. Mech., 14(1), pp. 39–58.
[3] Budiansky, B., and Rice, J. R., 1973, "Conservation Laws and Energy-Release Rates," ASME J. Appl. Mech., 40(1), pp. 201–203.
[4] Eshelby, J., 1951, "The Force on an Elastic Singularity," Philos. Trans. R. Soc. London, Ser. A, 244(877), pp. 87–112.
[5] Pak, Y. E., "Force on a Piezoelectric Screw Dislocation," ASME J. Appl. Mech., Vol. 57, No. 4, pp. 863-869, 1991
[6] Seo, S. Y. et al., 2018. Configurational Forces on Elastic Line Singularities. ASME J. Appl. Mech. 85, 034501.
[7] Rice, J. R., 1985, "Conserved and Integrals and Energetic Forces," Fundamentals of Deformation and Fracture, B. A. Bilby, K. J. Miller, and J. R. Willis, eds., Cambridge University Press, Cambridge, UK, pp. 33–56.
[8] Seo, S. Y., Mishra, D., Park, C. Y., and Pak, Y. E., 2015, "Energy Release Rates for a Misfitted Spherical Inclusion Under Far-Field Mechanical and Uniform Thermal Loads," Eur. J. Mech. A, 49, pp. 169–182.

GENERIC SEPARATING SETS FOR 3D ELASTICITY TENSORS

Marc Olive*[1], Rodrigue Desmorat [1], Nicolas Auffray[2], Boris Desmorat[3], and Boris Kolev[1]
[1]Université Paris-Saclay,ENSParis-Saclay,CNRS,LMT-Laboratoire de Mcanique et Technologie,94235,Cachan, France
[2]MSME , Univ Gustave Eiffel, UPEC , CNRS , F-77454, Marne -la- Valle , France
[3]Institut dAlembert,Sorbonne Université,CNRSUMR7190,F-7525 2Paris Cedex 05,France

Summary We define what is a *generic separating set* of invariant functions (a.k.a. a *weak functional basis*) for tensors. We produce then two generic separating sets for 3D elasticity tensors, one of them constituted of 21 polynomial invariants, the second comprising a minimal number of 18 rational invariants.

SEPARATING SETS OF ELASTIC MATERIALS

In the classical linear theory, the elastic behaviour of a material is described by a fourth-order tensor $\mathbf{E}$ having major and left/right minor indicial symmetries

$$E_{ijkl} = E_{ijlk} = E_{klij}.$$

In 3D, and with respect to a given basis, such a tensor is defined by 21 components. However, as pointed out for instance by Boehler–Kirilov–Onat [2], any other orientation of the material with respect to the reference basis, will define a new tensor $\overline{\mathbf{E}}$ given by

$$\overline{E}_{ijkl} = g_{ip}g_{jq}g_{kr}g_{ls}E_{pqrs} \quad \text{denoted} \quad \overline{\mathbf{E}} = g \star \mathbf{E} \tag{1}$$

where $g \in \mathrm{SO}(3)$ is some rotation of the space.

For anisotropic materials, there's no reason for $\mathbf{E}$ and $\overline{\mathbf{E}}$ to be the same: tensors' components do not characterize elastic materials independently of their spatial orientation. To give different names to different elastic materials require to define a finite set of $\mathrm{SO}(3)$-invariant *functions* $f_1, \dots, f_n$ such that

$$f_i(\mathbf{E}_1) = f_i(\mathbf{E}_2) \iff \mathbf{E}_2 = g \star \mathbf{E}_1.$$

A classical set of functions solving this problem is the *integrity basis* of the elasticity tensor, which is a finite set of polynomial invariants having the property of generating the algebra of *polynomial invariants*.

For instance, for a second order symmetric tensor $\mathbf{a}$, such an integrity basis is $\mathrm{tr}(\mathbf{a}), \mathrm{tr}(\mathbf{a}^2), \mathrm{tr}(\mathbf{a}^3)$. Nevertheless, for the elasticity tensor a minimum integrity basis includes 297 polynomial invariants [6], so it is not very usable. To have a basis of lower cardinality, it is possible to consider *rational invariants* instead of polynomial ones. The resulting set is known as a *weak separating set*, since it allows only to distinguish tensors in generic position. A weak separating set constituted of 39 polynomial invariants was already obtained by Boehler–Kirilov–Onat [2].

RATIONAL INVARIANTS AND WEAK SEPARATING SETS

The relation (1) defines a *linear representation* of the rotation group $\mathrm{SO}(3)$ on the real vector space $\mathbb{E}\mathrm{la}$ of elasticity tensors. In this specific case, any rational invariant r of an elasticity tensor can be written $r = p/q$, with p and q being polynomial invariants. From invariant theory [7], we know that the *field of rational invariants* is finitely generated by some family $s_1, \dots, s_k$.

A very important result [7, Lemma 2.2] indicates that such a family $s_1, \dots, s_k$ is a *weak separating set*: there exists an open dense set $\mathcal{Z}^c \subset \mathbb{E}\mathrm{la}$ such that

$$\forall \mathbf{E}_1, \mathbf{E}_2 \in \mathcal{Z}^c, \quad s_i(\mathbf{E}_1) = s_i(\mathbf{E}_2) \iff \exists g \in \mathrm{SO}(3), \quad \mathbf{E}_2 = g \star \mathbf{E}_1.$$

The open dense set $\mathcal{Z}^c$ defines a set of *generic tensors*, so that a random elasticity tensor belongs to $\mathcal{Z}^c$ almost surely.

In fact, this is a purely theoretical result, and two questions naturally arise :

1. What is the minimal number k of elements of a generating set ?
2. How to explicitly construct the rational invariants s_j?

In the case of the elasticity tensors, we answer both questions: the minimal number corresponds to the transcendence degree 18 (which is the dimension of $\mathbb{E}\mathrm{la}$ minus the dimension of $\mathrm{SO}(3)$). The effective computations are finally obtained using a strong relationship between the tensor space and the space of *binary forms* (homogeneous polynomials in two complex variables [5]).

*Corresponding author. E-mail: marc.olive@math.cnrs.fr

RESULTS

The first step is to consider an *harmonic decomposition* of elasticity tensors [1]. Any elasticity tensor can be expressed

$$\mathbf{E} = (\lambda, \mu, \mathbf{d}', \mathbf{v}', \mathbf{H}) \in \mathbb{H}^0 \oplus \mathbb{H}^0 \oplus \mathbb{H}^2 \oplus \mathbb{H}^2 \oplus \mathbb{H}^4, \quad d_{ij} := E_{kkij}, \quad v_{ij} := E_{kikj} \tag{2}$$

$$\lambda := \operatorname{tr}(\mathbf{d}), \quad \mu := \operatorname{tr}(\mathbf{v}), \quad \mathbf{d}' := \mathbf{d} - \frac{\lambda}{3}\mathbf{1}, \tag{3}$$

where $\mathbb{H}^n$ is the space of n-th order harmonic tensors (traceless and totally symmetric).

Before exhibiting a weak separating set of 18 rational invariants, a first (not minimal) weak separating set of 21 polynomial invariants will be considered. Our result are formulated using the following notation

$$(\mathbf{ab})^s := \frac{1}{2}(\mathbf{ab} + \mathbf{ba}), \quad [\mathbf{a}, \mathbf{b}] := \mathbf{ab} - \mathbf{ba}.$$

Theorem 1 *Let* $\mathbf{E} = (\lambda, \mu, \mathbf{d}', \mathbf{v}', \mathbf{H})$ *be an elasticity tensor,* $\mathbf{d}_2 = \operatorname{tr}_{13} \mathbf{H}^2$ *and* $\mathbf{d}_3 = \operatorname{tr}_{13} \mathbf{H}^3$.

Then, the following 21 polynomial invariants, $\lambda = \operatorname{tr} \mathbf{d}$, $\mu = \operatorname{tr} \mathbf{v}$,

$$I_2 := \operatorname{tr} \mathbf{d}_2, \quad I_3 := \operatorname{tr} \mathbf{d}_3, \quad I_4 := \operatorname{tr} \mathbf{d}_2^2, \quad I_5 := \operatorname{tr}(\mathbf{d}_2\mathbf{d}_3), \quad I_6 := \operatorname{tr} \mathbf{d}_2^3, \quad I_7 := \operatorname{tr}(\mathbf{d}_2^2\mathbf{d}_3)$$
$$I_8 := \operatorname{tr}(\mathbf{d}_2\mathbf{d}_3^2), \quad I_9 := \operatorname{tr} \mathbf{d}_3^3, \quad I_{10} := \operatorname{tr}(\mathbf{d}_2^2\mathbf{d}_3^2), \quad D_3 := \operatorname{tr}(\mathbf{d}'\mathbf{d}_2), \quad D_4 := \operatorname{tr}(\mathbf{d}'\mathbf{d}_3), \quad D_5 := \operatorname{tr}(\mathbf{d}'\mathbf{d}_2^2),$$
$$D_6 := \mathbf{d}' : (\mathbf{d}_2\mathbf{d}_3)^s, \quad D_{11} := \mathbf{d}' : [\mathbf{d}_2, \mathbf{d}_3]^2, \quad V_3 := \mathbf{v}' : \mathbf{d}_2, \quad V_4 := \mathbf{v}' : \mathbf{d}_3, \quad V_5 := \mathbf{v}' : \mathbf{d}_2^2,$$
$$V_6 := \mathbf{v}' : (\mathbf{d}_2\mathbf{d}_3)^s, \quad V_{11} := \mathbf{v}' : [\mathbf{d}_2, \mathbf{d}_3]^2,$$

separate generic tensors $\mathbf{E}$*, satisfying the following conditions:*
(1) the pair $(\mathbf{d}_2, \mathbf{d}_3)$ *is triclinic (i.e no common eigenvector), and (2)* $\mathbf{d}_2$ *is orthotropic (i.e three distinct eigenvalues).*

In this result, the 9 polynomial invariants I_k (introduced in [2]) are used to separate the fourth-order harmonic part $\mathbf{H}$ of (2). This set is completed by a family D_l, V_m of 10 polynomial invariants. The minimum separating set is then obtained by reducing the family $I_2, \ldots, I_{10}$ to a set of 6 rational invariants. This reduction is achieved by translating a result obtained by Maeda [4, 3] in the domain of *classical invariant theory* [5]. This gives us a set of 6 rational separating invariants for $\mathbb{H}^4$:

$$i_2, \quad i_3, \quad i_4, \quad k_4, \quad k_8, \quad k_9,$$

all defined with denominator being some power of the same polynomial invariant. We finally obtain:

Theorem 2 *The following 18 rational invariants*

$$\lambda, \quad \mu, \quad i_2, \quad i_3, \quad i_4, \quad k_4, \quad k_8, \quad k_9,$$
$$D_3, \quad D_4, \quad D_5, \quad D_6, \quad D_{11}, \quad V_3, \quad V_4, \quad V_5, \quad V_6, \quad V_{11}$$

separate generic tensors $\mathbf{E} = (\lambda, \mu, \mathbf{d}', \mathbf{v}', \mathbf{H})$*, satisfying the following conditions: (1) the pair* $(\mathbf{d}_2, \mathbf{d}_3)$ *is triclinic, and (2)* $\mathbf{d}_2$ *is orthotropic.*

CONCLUSIONS

To separate *generic elastic materials*, the notion of *weak separating set*, classical in invariant theory, has been used. A first weak generating set of 21 *polynomial invariants* is obtained, which is an improvement over the 39 polynomial invariants of Boehler–Kirilov–Onat in [2]. By exploiting the field of rational invariants and results from binary forms, a minimal weak generic separating set of 18 rational invariants is finally obtained. From this, we can even deduce a weak separating set of 19 *polynomial invariants* [3, Corolary 4.6], so to be as close as possible to the transcendence degree of the space of Elasticity tensors.

References

[1] Backus, G. (1970). A geometrical picture of anisotropic elastic tensors. Reviews of geophysics, 8(3), 633-671.
[2] Boehler, J. P., Kirillov, A. A., & Onat, E. T. (1994). On the polynomial invariants of the elasticity tensor. Journal of elasticity, 34(2), 97-110.
[3] Desmorat, R., Auffray, N., Desmorat, B., Kolev, B., & Olive, M. (2019). Generic separating sets for three-dimensional elasticity tensors. Proceedings of the Royal Society A, 475(2226), 20190056.
[4] Maeda, T. (1990). On the invariant field of binary octavics. Hiroshima Mathematical Journal, 20(3), 619-632.
[5] Olver, P. J. (1999). Classical invariant theory (Vol. 44). Cambridge University Press.
[6] Olive, M., Kolev, B., & Auffray, N. (2017). A minimal integrity basis for the elasticity tensor. Archive for Rational Mechanics and Analysis, 226(1), 1-31.
[7] Popov, V. L., & Vinberg, E. B. (1994). Invariant theory. In Algebraic geometry IV (pp. 123-278). Springer, Berlin, Heidelberg.

THREE-DIMENSIONAL SOLIDS AND STRUCTURES WITHIN STRAIN GRADIENT ELASTICITY: A CONFORMING ISOGEOMETRIC IMPLEMENTATION WITH MODEL COMPARISONS AND APPLICATIONS

Jarkko Niiranen[1] and Seyyed B. Hosseini[1]
[1]Department of Civil Engineering, Aalto University, Finland

Summary The three-dimensional theory of strain gradient elasticity is formulated as a weak formulation and discretized by isogeometric Galerkin methods. The formulation and its numerical implementation are compared to the corresponding dimension reduction models – beam, plate and shell models – and to the associated numerical methods with a set of benchmark problems and applications.

THEORETICAL MODELS

The three-dimensional theory of strain gradient elasticity is formulated as a weak formulation within an H^2 Sobolev space setting. The corresponding three-dimensional solid model is compared to the corresponding dimension reduction models: gradient-elastic beam, plate and shell models [1–4].

NUMERICAL METHODS

The formulation is discretized by adopting the framework of isogeometric NURBS-based Galerkin methods. This numerical approach is implemented and verified via a set of benchmark problems. The comparisons, accomplished with respect to the most essential – non-classical – features of the models, serve as a validation for the gradient-elastic dimension reduction models. The comparisons rely on the numerical results obtained with the isogeometric finite element implementations for both the structural models [1–4] and for three-dimensional solids. For lattice applications [5, 6], the strain gradient models are compared to the corresponding (unhomogenized or full-field) fine-scale models based on classical elasticity.

References

[1] J. Niiranen, V. Balobanov, J. Kiendl and S. B. Hosseini. Variational formulations, model comparisons and isogeometric analysis for Euler–Bernoulli micro- and nano-beam models of strain gradient elasticity. *Mathematics and Mechanics of Solids* **24**: 312–335, 2019.

[2] V. Balobanov and J. Niiranen. Locking-free variational formulations and isogeometric analysis for the Timoshenko beam models of strain gradient and classical elasticity. *Computer Methods in Applied Mechanics and Engineering* **339**: 137–159, 2018.

[3] J. Niiranen, J. Kiendl, A. H. Niemi and A. Reali. Isogeometric analysis for sixth-order boundary value problems of gradient-elastic Kirchhoff plates. *Computer Methods in Applied Mechanics and Engineering* **316**: 328–348, 2017.

[4] V. Balobanov, J. Kiendl, S. Khakalo and J. Niiranen. Kirchhoff–Love shells within strain gradient elasticity: weak and strong formulations and an H3-conforming isogeometric implementation. *Computer Methods in Applied Mechanics and Engineering* **344**: 837–857, 2019.

[5] S. Khakalo, V. Balobanov and J. Niiranen. Modelling size-dependent bending, buckling and vibrations of 2D triangular lattices by strain gradient elasticity models: applications to sandwich beams and auxetics. *International Journal of Engineering Science* **127**: 33–52, 2018.

[6] S. Khakalo and J. Niiranen. Anisotropic strain gradient thermoelasticity for cellular structures: plate models, homogenization and isogeometric analysis. *Journal of the Mechanics and Physics of Solids* **134**: 103728, 2019.

*Corresponding author. E-mail: jarkko.niiranen@aalto.fi.

GEOMETRICAL APPROACH ON KINEMATICS OF DEFECTED MATERIAL

Van Hoi Nguyen[1], Guy Casale[1], and Loïc Le Marrec *[1]
[1]Université deR ennes,CNRS,IRMAR-UMR6625,F-35000 Rennes,France

Summary In the present continuum mechanical model, the body is idealized as a collection of material points for which a frame is attached to illustrate the local lattice structure. Frames and points behave independently. Points transformation is governed by map ϕ and vector fields transformation is associated with Ψ. The motion is said inconsistent if $\Psi \neq D\phi$. This allows potential distribution of defects in the current medium. In the reference configuration the body is a material manifold $\mathcal{B} = (G, \nabla)$. The corresponding induced set $(\overline{g}, \overline{\nabla})$ as well as torsion are defined on the current state $\phi(\mathfrak{B})$. In a next step, strains associated to this general (large) transformations are introduced in terms of ϕ and Ψ. Equation of motion for infinitesimal transformation is briefly presented.

MATHEMATICAL MODEL

Let (G, ∇) be the metric and metric-compatible connection on $\mathfrak{B}$. We denote $\{X^A\}$, $\{E_A\}$, $\{dX^A\}$ and $T\mathfrak{B}$ (respectively $\{x^a\}$, $\{e_a\}$, $\{dx^a\}$ and $T\mathcal{S}$) the coordinates system, basis tangent, its dual and tangent bundle defined on $\mathfrak{B}$ (respectively $\mathcal{S}$). Here $\mathcal{S}$ is the ambient space with a metric g. A mechanical transformation is a bundle map

$$\Upsilon : T\mathfrak{B} \to T\mathcal{S},\ (X, W) \mapsto \big(x = \phi(X), \Psi(X)W\big), \quad \forall X \in \mathfrak{B}, \quad \forall W \in T_X\mathfrak{B}. \tag{1}$$

Where $\phi : \mathfrak{B} \to \mathcal{S}$ is C^1-regular. The vector transformation $\Psi : T_X\mathfrak{B} \to T_x\mathcal{S}$ is C^1 linear and satisfies $\det \Psi \neq 0$. The map Ψ can be expressed by $\Psi^a{}_A(X) e_a \otimes dX^A$. Its inverse $\Psi^{-1} : T_x\mathcal{S} \to T_X\mathfrak{B}$ can be written $\Psi^{-1} = \Psi^{-1B}_b(x) E_B \otimes dx^b$, with $\Psi^{-1B}_b \Psi^a{}_B = \delta^a_b$. The deformation gradient of ϕ is $\mathbf{F} = D\phi$ (or denoted by ϕ_*). It is a linear map from $T_X\mathfrak{B}$ into $T_x\mathcal{S}$. In terms of components, $\mathbf{F} = F^a{}_A(X) e_a \otimes dX^A$, where $F^a{}_A = \partial_A \phi^a$. Its inverse is $\phi^* = F^{-1A}_b(x) E_A \otimes dx^b$, with $F^{-1A}_b F^a{}_A = \delta^a_b$. Hereafter, the transformation is called consistent if $\Psi = \mathbf{F}$, in contrary it is called inconsistent: in physical terms, the micro-structure is not convected by the macro-scale transformation.

Let u, v be vector fields on $\phi(\mathfrak{B})$. A metric $\overline{g}$ and a connection $\overline{\nabla}$ are defined on $\phi(\mathfrak{B}) \subset \mathcal{S}$ following, [1]:

$$\begin{aligned} &\overline{g}(x)(u, v) = G(X)\big(\Psi^{-1}(x)u, \Psi^{-1}(x)v\big), && \overline{g}_{ab} = \Psi^{-1A}_a \Psi^{-1B}_b G_{AB}, \\ &\overline{\nabla}_v u = \Psi(X)\big(\nabla_{\phi^*(x)v} \Psi^{-1}(x)u\big), && \overline{\Gamma}^c{}_{ba} = \Psi^c{}_C F^{-1A}_b \big(\Psi^{-1B}_a \Gamma^C_{AB} + \partial_A \Psi^{-1C}_a\big). \end{aligned} \tag{2}$$

Such a connection is metric-compatible $\overline{\nabla}\overline{g} = 0$. For a perfect body and appropriate coordinates system $\Gamma^C_{AB} = 0$ and the induced connection becomes $\overline{\Gamma}^c{}_{ba} = \Psi^c{}_C \partial_b \Psi^{-1C}_a$.

The current torsion is related to the induced connection as $\overline{T}(u, v) = \overline{\nabla}_u v - \overline{\nabla}_v u - [u, v]$ or in components $\overline{T}^a{}_{bc} = \overline{\Gamma}^a{}_{bc} - \overline{\Gamma}^a{}_{cb}$. It must be emphasized that for a consistent transformation, $\overline{T}$ is related to the torsion T of $\mathfrak{B}$ by:

$$\overline{T}(u, v) = \phi_*\big(\nabla_{\phi^* u}\phi^* v - \nabla_{\phi^* v}\phi^* u - [\phi^* u, \phi^* v]\big) = \phi_* T(\phi^* u, \phi^* v). \tag{3}$$

The induced curvature tensor is defined by $\overline{R}(u, v)w = \overline{\nabla}_u \overline{\nabla}_v w - \overline{\nabla}_v \overline{\nabla}_u w - \overline{\nabla}_{[u,v]} w$, we have the following relation

$$\overline{R}(u, v)w = \Psi\Big(\nabla_{\phi^* u}\nabla_{\phi^* v}\Psi^{-1}w - \nabla_{\phi^* v}\nabla_{\phi^* u}\Psi^{-1}w - \nabla_{[\phi^* u, \phi^* v]}\Psi^{-1}w\Big) = \Psi R(U, V)W. \tag{4}$$

with $U = \phi^* u$, $V = \phi^* v$ and $W = \Psi^{-1} w$. It' straigth forward that the curvature $\overline{R}$ vanishes *iff* R is zero.

Let consider an initial state given without initial defect (for example $G = \delta$ and $T = 0$). For consistent transformation, (3) imposes $\overline{T} = 0$: the current state is defect free. However for an inconsistent transformation $\overline{T}$ is not necessary zero. This is illustrated by a classical example where the reference manifold supports no point-motion: $\mathbf{F} = \mathbb{I}$ but transformation is inconsistent as $\Psi \neq \mathbf{F}$ is given as follow:

$$\Psi^a{}_B = \begin{pmatrix} 1 & -\psi & 0 \\ 0 & 1 & 0 \\ 0 & 0 & 1 \end{pmatrix} \qquad \text{hence} \qquad \overline{g}_{ab} = \begin{pmatrix} 1 & \psi & 0 \\ \psi & 1+\psi^2 & 0 \\ 0 & 0 & 1 \end{pmatrix}, \tag{5}$$

In [2] $\psi : \mathfrak{B} \to \mathbb{R}$ is C^∞ and depends on X^2, here we consider a slightly more general case as $\psi(X^1, X^2, X^3)$. *A priori* non-zero connection coefficients are $\overline{\Gamma}^1{}_{b2} = \partial_b \psi$ yielding to *a priori* non-zero torsion component $\overline{T}^1{}_{\alpha 2} = \partial_\alpha \psi$ with $\alpha = 1$ or 3. In particular if $\psi \equiv \psi(X^2)$, the current state is defect free ($\overline{T} = 0$) but inconsistent ($\Psi \neq \mathbf{F}$). However, if $\psi \equiv \psi(X^1)$ we observe a density of edge dislocations: $\overline{T}^1{}_{12} \neq 0$ (see Fig.1). Last, for $\psi \equiv \psi(X^3)$, a density of screw type dislocations is created: $\overline{T}^1{}_{32} \neq 0$.

*Corresponding author. E-mail: loic.lemarrec@univ-rennes1.fr

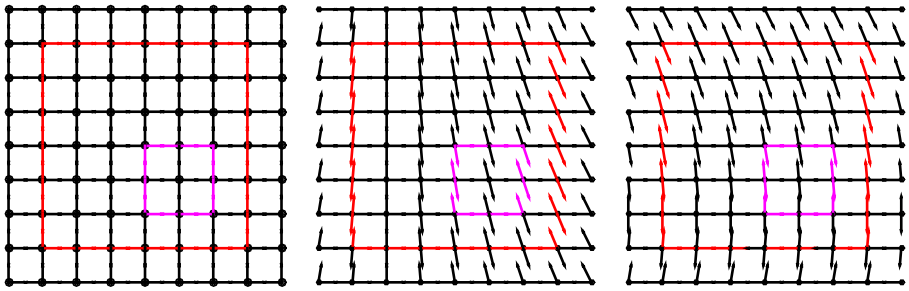

Figure 1: Left: material manifold $\mathcal{B}$ for which are depicted one horizontal and one vertical vector fields attached to each material point (dots). Center and left: current state for transformation with $\psi = X^1$ and $\psi = X^2$ respectively. For the two cases points are unchanged but vectors are transformed. Center: along any closed material loops (colored example) the total vectors gap is non-zero denoting the presence of screw-dislocation densities. This is not the case for the left figure for which the transformation is dislocation free.

STRAINS AND EQUATIONS OF MOTION

The classical strain $\mathbf{E} = (\phi^* g - G)/2$ refers to the macro-stretch of the body caused by the motion ϕ. It measures the change of the distance and angle between a material point and its neighborhood. As the motion is not defined only by ϕ, the strain $\mathbf{E}$ is not sufficient. A so-called consistent strain is given:

$$\mathcal{E}(U,V) = \frac{1}{2} g\big(\Psi - \mathbf{F})U, (\Psi - \mathbf{F})V\big), \qquad \forall U, V \in T_X\mathfrak{B}. \tag{6}$$

It measures the difference between the point and frame motion: it vanishes *iff* the transformation is consistent. This tensor defined on $T\mathfrak{B}$ and invariant under arbitrary body rotation. It is symmetric in contrary to the relative strain $\mathbf{F} - \Psi$ introduced in [3]. If $\mathcal{E} = 0$ no torsion is observed after transformation of a defect-free body but the converse is not true: see previous example for which the only non-zero component of $\mathcal{E}$ is $\mathcal{E}_{22} = \frac{1}{2}\psi^2$. In order to measure the non-homogeneity of Ψ and following [3, 4] a wryness tensor $\mathcal{M}$ is introduced with $\mathcal{M}^L{}_{KA} = \Psi^{-1L}_{\ \ l}\partial_A \Psi^l{}_K$.

Functional of the energy density Ξ per unit reference volume on $\mathfrak{B}$ is assumed to be of the form $\Xi(\mathbf{E}, \mathcal{E}, \mathcal{M})$. Accordingly, the set of stress tensors are defined as follows

$$\mathbf{S} = \frac{\partial \Xi}{\partial \mathbf{E}}, \qquad \mathfrak{S} = \frac{\partial \Xi}{\partial \mathcal{E}}, \qquad \mathfrak{T} = \frac{\partial \Xi}{\partial \mathcal{M}}. \tag{7}$$

The linear approximation for the stress, couple stress fields requires a quadratic approximation for the stored energy Ξ, in its variables. In terms of strain, $\mathbf{F} \simeq \mathbb{I} + \mathfrak{u}$, with $\mathfrak{u}_{ij} = u_{i,j}$ and u is displacement vector field. Similarly, $\Psi \simeq \mathbb{I} + \mathfrak{a}$, and $\Psi - \mathbf{F} \simeq \mathfrak{d} = \mathfrak{a} - \mathfrak{u}$. With these, the strain tensors are approximated by

$$\mathbf{E}_{AB} \simeq \varepsilon_{ab}\delta^a{}_A\delta^b{}_B\,, \qquad \mathcal{E}_{AB} \simeq \mathfrak{c}_{ab}\delta^a{}_A\delta^b{}_B\,, \qquad \mathcal{M}^K{}_{LM} \simeq \mathfrak{a}_{kl,m}\delta^k_K\delta^l_L\delta^m_M\,, \tag{8}$$

with $\varepsilon_{ab} = \frac{1}{2}(u_{a,b} + u_{b,a})$, $\mathfrak{c}_{ab} = \frac{1}{2}(\mathfrak{d}_{ab} + \mathfrak{d}_{ba})$ and $\mathfrak{a}_{mkl} = \partial_m \mathfrak{a}_{kl}$. For the homogeneous isotropic material, the linear constitutive equations for stresses read

$$\sigma_{ab} \simeq \frac{\partial \Xi}{\partial \varepsilon_{ab}}\,, \qquad \tau_{ab} \simeq \frac{\partial \Xi}{\partial \mathfrak{c}_{ab}}\,, \qquad \mu_{pqr} \simeq \frac{\partial \Xi}{\partial \mathfrak{a}_{pqr}}\,, \tag{9}$$

where σ and τ are both symmetric. In terms of inertia, the microacceleration reads $\Lambda^B_a = \mathcal{I}^{bb}\ddot{\mathfrak{a}}_{ab}\delta^b_B$ with $\mathcal{I}_{bb}$ is a constant. Then, for this material, the local equations of motion on $\mathfrak{a}$ and $\mathfrak{u}$ are given by

$$\mathfrak{b}_a + \sigma_{ab,b} - \tau_{ab,b} = \rho_0 \ddot{u}_a \tag{10a}$$

$$\mathfrak{Z}_{ab} - \tau_{ab} + \mu_{lab,l} = \rho_0 \mathcal{I}^{bb}\ddot{\mathfrak{a}}_{ab}. \tag{10b}$$

where $\mathfrak{b}$ is the body force per unit volume and $\mathfrak{Z}$ is interpreted as a double forces per unit volume.

References

[1] Marsden J.E., Hughes T.J.R. Mathematical Foundations of Elasticity. Dover, NY 1983.
[2] Yavari A., Goriely A. Riemann-Cartan Geometry of Nonlinear Dislocation Mechanics. *Arch. Rational Mech. Anal.* **205**.1, 2012
[3] Mindlin R.D. Micro-structure in linear elasticity. *Arch. Rational Mech. Anal.*. **16**, 1964.
[4] Eringen A.C Microcontinuum field theories: I. Foundations and solids. Springer, 2012.

CRACK TIP FIELDS IN A FIBER-REINFORCED NEO-HOOKEAN SHEET

Yin Liu[1], Brian Moran, Luca Di Stasio
Division of Physical Sciences and Engineering, King Abdullah University of Science and Technology, Thuwal, 23955-6900, Kingdom of Saudi Arabia

Summary The asymptotic crack tip fields in a fiber-reinforced neo-Hookean sheet are derived, where a strain energy function motivated by composite mechanics (Guo et al., 2006, 2007) is employed. The resulting asymptotic deformation and stress fields depend quantitatively on the degree of fiber reinforcement and orientation angle. For suitable choice of parameters, the asymptotic fields reduces to those obtained by Knowles and Sternberg (1983). Both asymptotic path-independent *J*-type integrals and interaction energy integrals are derived to evaluate the crack tip amplitude parameters. The analytical results agree well with the finite element results for a stretch long strip with an edge crack. The result obtained may prove useful in providing a framework for future exploration in modeling the mechanical behaviour near a slit or tear in soft biological tissue reinforced by collagen fibers.

INTRODUCTION

Mechanical anisotropy like fiber-like inclusions or specifically oriented microstructures plays a key role in achieving specific functions in muscles, cartilage and arteries [1]. It is important to understand the influence of material anisotropy on the fracture behaviors of soft solids and thus to provide a basis for guidance on the design of highly tough soft composites through introducing anisotropic microstructures.

In the present paper, we analyze the crack tip fields of an anisotropic hyperelastic sheet using the neo-Hookean fiber-reinforced neo-Hookean matrix material model developed in [2]. For the case of a thin sheet in which plane stress conditions hold, the asymptotic governing equations at the crack tip field for the fiber-reinforced material reduce to those obtained by Knowles and Sternberg [5] for a pure neo-Hookean material by a suitable scaling of the coordinate system. Furthermore, following the observation by Liu and Moran [3], where the asymptotic governing equations separate into two independent Laplace equations, we use the asymptotic path-independent integrals derived in that paper to evaluate the crack tip parameters. The analytical deformed coordinates and stress fields agree well with finite element results for different stretch levels, loading modes, and material parameters.

THE ASYMPTOTIC CRACK TIP FIELDS

We are interested in the crack tip fields of a material which consists of a neo-Hookean matrix reinforced by neo-Hookean fibers and for which the strain energy is given by [2,4]

$$W=\frac{\mu}{2}[(I_1-3)+\kappa(I_4+2I_4^{-1/2}-3)] \tag{1}$$

where μ is the shear modulus, κ is a material constant which represents the relative shear stiffness of the fiber to the matrix, $I_1=\mathrm{tr}\mathbf{C}$, $I_4=\mathbf{a}_o.\mathbf{C}.\mathbf{a}_o$, $\mathbf{C}=\mathbf{F}^{\mathrm{T}}.\mathbf{F}$, $\mathbf{F}$ is the deformation gradient and $\mathbf{a}_o$ denotes the orientation of the aligned fibers. Thus, the first Piola-Kirchhoff stress is given by $\mathbf{P}=\mu\mathbf{F}+\mu\kappa(1-I_4^{-3/2})\mathbf{F}.\mathbf{a}_o\otimes\mathbf{a}_o-p\mathbf{F}^{-\mathrm{T}}$, where p is a Lagrangian multiplier. The equilibrium equation and surface traction are expressed by

$$y_{\alpha,\beta\beta}+\kappa(1-\lambda_f^{-3})_{,\beta}y_{\alpha,u}a_u^oa_\beta^o+\kappa(1-\lambda_f^{-3})y_{\alpha,u\beta}a_u^oa_\beta^o-\lambda^3\varepsilon_{\beta u}\varepsilon_{\alpha v}y_{u,v\beta}-3\lambda^2\lambda_{,\beta}\varepsilon_{\beta u}\varepsilon_{\alpha v}y_{u,v\beta}=0 \tag{2}$$

$$t_\alpha=P_{\alpha\beta}n_\beta=\mu[y_{\alpha,\beta}n_\beta+\kappa(1-\lambda_f^{-3})y_{\alpha,v}a_v^oa_\beta^on_\beta-\lambda^3\varepsilon_{\beta u}\varepsilon_{\alpha v}y_{u,v}n_\beta] \tag{3}$$

where $I_4=\lambda_f^2$ and $\varepsilon_{\alpha\beta}$ is the two-dimensional alternating symbol.

The out of plane stretch exhibits the asymptotic form $\lambda=J^{-1}=O(r^q)$ as $r\to0,(-\pi\le\theta\le\pi)$ for some real $q>0$ [5], where (r,θ) are polar coordinates in the reference configuration centered at crack tip. This implies that the fiber stretch $\lambda_f\to\infty$ as $r\to0$ and consequently, the out of plane stretch $\lambda\to0$ as $r\to0$.Using these results, we can rewrite the governing equation and the traction free boundary conditions on the crack surfaces, i.e.,

$$c_{55}y_{\alpha,11}+2c_{45}y_{\alpha,12}+c_{44}y_{\alpha,22}=0,\quad c_{45}y_{\alpha,1}+c_{44}y_{\alpha,2}=0 \tag{4}$$

where $c_{44}=1+\kappa\cos^2\phi, c_{45}=\kappa\sin\phi\cos\phi, c_{55}=1+\kappa\sin^2\phi$.

Based on a linear transformation of the original coordinates $x_i,i=1,2$ to scaled coordinates $\eta_i,i=1,2$, that is $d\eta_i=A_{ij}dx_j,\ i,j=1,2$, where $A_{11}=\sqrt{c_{44}/(c_{44}c_{55}-c_{45}^2)},\ A_{12}=-c_{45}\omega_{11}/c_{44},\ A_{21}=0,\ A_{22}=\sqrt{1/c_{44}}$, the asymptotic governing equation is given by

$$\frac{\partial^2y_\alpha}{\partial\eta_1^2}+\frac{\partial^2y_\alpha}{\partial\eta_2^2}=0,\quad \text{as } \left(\eta_1^2+\eta_2^2\right)^{1/2}\to0 \text{ and } \frac{\partial y_\alpha}{\partial\eta_2}=0,\quad \text{on } \eta_1\le0,\ \eta_2=0 \tag{5}$$

[1]Corresponding author. E-mail: yin.liu@kaust.edu.sa

which has a general solution $v_m = p_m \sin(\frac{m}{2}\psi)$, when $m = 1,3,5,...$ and $q_m \cos(\frac{m}{2}\psi)$ when $m = 2,4,6,..$, where p_m and q_m are amplitude coefficients, $\rho^2 = r^2[(A_{11}\cos\theta + A_{12}\sin\theta)^2 + (A_{22}\sin\theta)^2]$, $\psi = \text{atan}(A_{22}\sin\theta/(A_{11}\cos\theta + A_{12}\sin\theta))$ and $x_1 = r\cos\theta$ and $x_2 = r\sin\theta$. Thus, the crack shape and the Cauchy stress can be described by

$$\begin{aligned} y_1 &\sim p_1\rho^{1/2}\sin\tfrac{\psi}{2} + q_1\rho\cos\psi \\ y_2 &\sim p_2\rho^{1/2}\sin\tfrac{\psi}{2} \end{aligned}, \qquad \begin{aligned} \sigma_{11}/\mu &\sim \tfrac{1}{4}p_1^2\rho^{-1} - p_1q_1\rho^{-1/2}\sin\tfrac{\psi}{2} + q_1^2 \\ \sigma_{22}/\mu &\sim \tfrac{1}{4}p_2^2\rho^{-1} \\ \sigma_{12}/\mu &\sim \tfrac{1}{4}p_1p_2\rho^{-1} - \tfrac{1}{2}\rho^{-1/2}p_2q_1\sin\tfrac{\psi}{2} \end{aligned} \tag{6}$$

Using the these results, the J-integral is given by $J = \frac{\mu\pi\sqrt{c_{44}}}{4}\left(p_1^2 + p_2^2\right)$. The asymptotic path-independent integrals developed in [3] can be used to extract the crack tip parameters

$$J^{y_\alpha} = \sqrt{c_{44}}J^{y_\alpha} = \frac{\mu\pi\sqrt{c_{44}}}{4}p_\alpha^2,\ \alpha = 1,2 \tag{7}$$

$$I_1^{y_\alpha} = \sqrt{c_{44}}I_1^{y_\alpha} = \frac{\sqrt{c_{44}}\pi\mu p_\alpha}{2},\ \alpha = 1,2,\ \text{for}\ y^{\text{aux}} = \rho^{1/2}\sin\tfrac{\psi}{2} \tag{8}$$

$$I_2^{y_\alpha} = \sqrt{c_{44}}I_2^{y_\alpha} = -2\sqrt{c_{44}}\pi\mu q_\alpha,\ \alpha = 1,2,\ \text{for}\ y^{\text{aux}} = \ln\rho \tag{9}$$

ANALYTICAL AND NUMERICAL RESULTS

To verify the theoretical results and compute the crack tip parameters, we use the finite element method to model the crack tip fields of a long cracked strip under combined stretch and shear (Fig. 1a). In this case, the J-integral evaluation along the contour shown in red and green gives $J_{\text{far}} = W(\mathbf{F}_s)H_0$. The J-integral (Fig. 1b) shows good agreement between the results by different calculation methods for several combinations of ϕ and κ. The deformed crack shape is not symmetric due to the anisotropic effects (Fig. 1c and d) and the analytical and finite element results for the crack shapes (Fig. 1d) agree with each other for different parameters, indicating the accuracy of the asymptotic solution (6) for characterizing the deformed shape of the crack. The angular variation of the stress components σ_{22} (Fig. 1e-g) also show good agreement for the analytical and the finite element results and follow periodic patterns with peaks related to the fiber orientations.

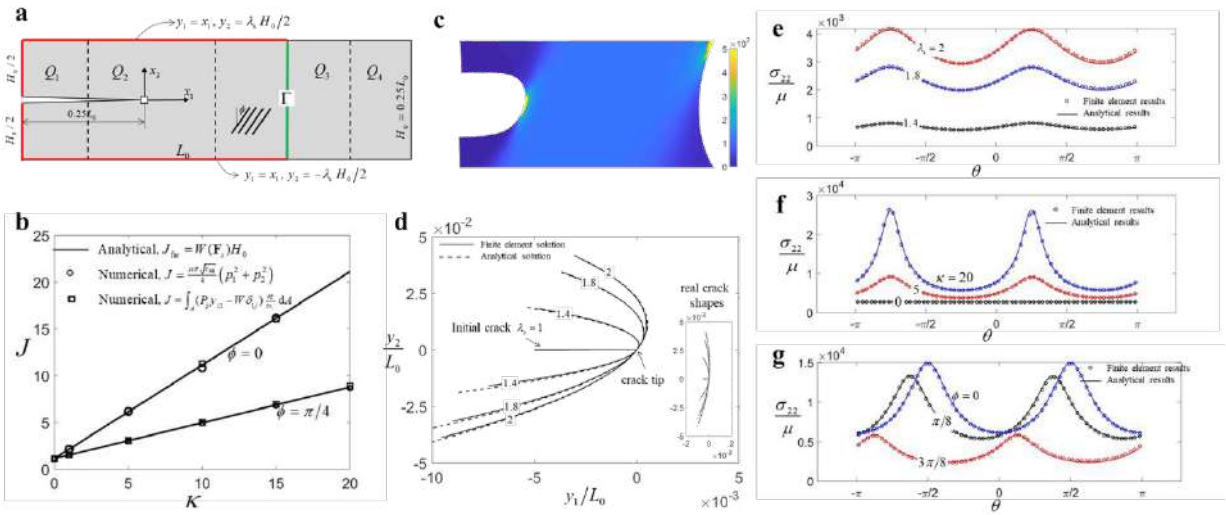

Figure 1. (a) Sketch of a long cracked strip and the finite element mesh near the crack tip. (b) Comparison of the J-integrals by the analytical and numerical methods for different ϕ and κ. (c) A presentative deformed crack shape for the parameters $\kappa = 1$, $\phi = \pi/4$ and $\lambda_s = 2.0$. (d) The crack shapes at different stretches $\lambda_s = 1.4, 1.8, 2.0$ within the range $r \in [0, 10^{-3}L_0]$. (e-g) Angular distributions of σ_{22} at the Gauss points $r_1 = 3.29\times10^{-5}L_0$ for different stretches, modulus ratios and fiber orientation angles, respectively.

References

[1] Holzapfel, G. A., Ogden, R. W., and Sherifova, S., 2019, "On Fibre Dispersion Modelling of Soft Biological Tissues: A Review," Proc. R. Soc. Math. Phys. Eng. Sci., **475**(2224), p. 20180736.

[2] Guo, Z., Peng, X., and Moran, B., 2007, "Mechanical Response of Neo-Hookean Fiber Reinforced Incompressible Nonlinearly Elastic Solids," Int. J. Solids Struct., **44**(6), pp. 1949–1969.

[3] Liu, Y., and Moran, B., 2019, "Asymptotic Path-Independent Integrals for the Evaluation of Crack-Tip Parameters in a Neo-Hookean Material," International Journal of Fracture, 224(1), 133-150.

[4] Guo, Z., Peng, X., and Moran, B., 2006, "A Composites-Based Hyperelastic Constitutive Model for Soft Tissue with Application to the Human Annulus Fibrosus," J. Mech. Phys. Solids, **54**(9), pp. 1952–1971.

[5] Knowles, J. K., and Sternberg, E., 1983, "Large Deformations near a Tip of an Interface-Crack between Two Neo-Hookean Sheets," J. Elast., **13**(3), pp. 257–293.

DIFFERENTIAL GEOMETRY AND STRESS FIELDS OF DISLOCATED MEDIUM

Shunsuke Kobayashi*[1] and Ryuichi Tarumi[1]
[1]Graduate School of Engineering Science, Osaka university, Osaka, Japan

Summary We conduct the stress fields analysis of dislocation in three-dimensional hyperelastic material. Our formulation is based on the theory of elasto-plasticity and differential geometry. Continuous distribution of dislocations is introduced into a Weitzenböck manifold using the equivalence between the dislocation density tensor and torsion of the Weitzenböck connection. Riemannian metric of the intermediate configuration is obtained from the integration of Cartan first structure equation by the homotopy operator. The variational problem is solved numerically using the isogeometric analysis. We conduct the numerical analysis for stress field around a dislocation loop. The result shows fair agreement with a prediction given by the classical elasticity. This result demonstrates that this framework is applicable for stress field analysis of less-symmetric configuration of dislocations.

INTRODUCTION

Stress fields around a dislocation play a central role in plastic deformation of crystalline solids. A pioneering work of the subject is conducted by Volterra. He reported the analytical expression of the stress fields of dislocation using the classical elasticity. Although this is a standard theory of dislocation in continuum mechanics, it fails to express the stress fields near the core of dislocation due to a failure of linear approximation. Kondo, Bilby and Kröner introduced the continuous distribution of dislocation and considered the problem on the basis of differential geometry. The key concept here is the equivalence between the dislocation density tensor and non-vanishing torsion of an affine connection of a differentiable manifold [1]. Recently, Yavari and Goriely employed the theory of geometrical elasto-plasticity and obtained some analytical expressions for nonlinear stress fields of dislocation [2]. Their analysis is, however, limited to highly symmetrical problems. In the present study, we implement the theory into numerical analysis so as to develop a framework for practical applications. After a brief review of the geometrical elasto-plasticity, we conduct the numerical analysis for the stress fields around a dislocation loop. The result verify the present formulation and numerical implementation.

MATHEMATICAL PRELIMINARIES OF GEOMETRICAL ELASTO-PLASTICITY

Let us introduce the initial, intermediate and current configurations denoted by $\overline{\mathcal{S}}$, $\mathcal{B}$ and $\mathcal{S}$, respectively. Here $\overline{\mathcal{S}}$ and $\mathcal{S}$ are simply connected open subsets in the Euclidean 3-space $\mathbb{R}^3$. It means that we have global coordinates for the two configurations; $(\overline{x}^1, \overline{x}^2, \overline{x}^3)$ and (x^1, x^2, x^3). Let $\overline{x}^i$ be the Cartesian coordinates and let x^i be a smooth curvilinear coordinates written as $x^i = x^i(\overline{x}^j)$. Then, the total deformation gradient is expressed by $F^i_j = \partial x^i / \partial \overline{x}^j$. Note that the deformation gradient defines the transformation of dual frames; $dx^i = F^i_j d\overline{x}^j$. Following to the standard theory of elasto-plasticity, we conduct the multiplicative decomposition of the deformation gradient in such a way that $F^i_j = (F_e)^i_k (F_p)^k_l$, where $(F_e)^i_k$ and $(F_p)^k_j$ are elastic and plastic parts of the deformation gradient, respectively. The intermediate configuration $\mathcal{B}$ is a 3-dimensional material manifold which equips a Riemannian metric g. It shows a plastically deformed configuration and, therefore, free from elastic stress. Let $\varphi \colon \mathcal{B} \to \mathcal{S} \subset \mathbb{R}^3$ be an embedding map of the material manifold to the Euclidean 3-space with the Euclidean metric h. Here the embedding map φ is nothing but the elastic deformation. We express the pullback of Euclidean metric h to the intermediate configuration by $\varphi^* h$. Then, the Green strain tensor is given by the difference between the induced metric $\varphi^* h$ and Riemannian metric g such that $E := (\varphi^* h - g)/2$. It is convenient to introduce the dual frame ϑ^i which is an orthonormal frame in $\mathcal{B}$ with respect to the metric g. Namely, $g = \delta_{ij} \vartheta^i \otimes \vartheta^j$ where δ_{ij} is the Kronecker delta. The plastic distorsion F_p, which is a matrix of C^∞ functions on $\overline{\mathcal{S}}$, is defined using the dual frame ϑ^i such that $\vartheta^i = (F_p)^i_j d\overline{x}^j$. In a local coordinate representation on $\overline{\mathcal{S}}$ we have

$$\overline{\varphi^* h} = \delta_{ij} F^i_k F^j_l \, d\overline{x}^k \otimes d\overline{x}^l, \quad \overline{E} = \delta_{ij} (F^i_k F^j_l - (F_p)^i_k (F_p)^j_l) d\overline{x}^k \otimes d\overline{x}^l. \tag{1}$$

In the present formulation, a continuous distribution of dislocations, which is included in F_p, induces elastic deformation. Hence, we need to relate the plastic distorsion F_p and dislocation density for a given distribution of dislocations. It is known that the dislocation density is equivalent to the torsion 2-form τ^i in differential geometry. Following to a previous study by Yavari and Goriely, we obtain the plastic distorsion from a geometric consideration on Weitzenböck manifold, that is, Cartan first structure equation. This equation relates the torsion 2-form τ^i and plastic distorsion F_p in the following way; $\tau^i = d\vartheta^i$, where d is the exterior derivative. Integration of the first structure equation yields F_p for a given τ^i. We employed the homotopy operator H and solved the first structure equation explicitly [3].

The coordinate function $x^i(\overline{x}^j)$ is determined by using the standard framework of nonlinear elasticity and the calculus of variations. To simplify the analysis we assume that the medium is St.Venant-Kirchhoff hyperelastic material. This material has a linear relation between the second Piola-Kirchhoff stress tensor S and the Green strain tensor E such that

*Corresponding author. E-mail: kobayashi@nlsm.me.es.osaka-u.ac.jp

$S = C(E)$ where C is the elastic stiffness tensor. We also assume that the material is free from external forces, *i.e.*, elastic deformation is induced solely by F_p. Then, the strain energy W becomes a functional of the coordinate of the current configuration; $W[x^1, x^2, x^3] := \int_{\mathcal{B}} S(E)/2\vartheta^1 \wedge \vartheta^2 \wedge \vartheta^3$. For the numerical analysis, it is useful to express $W[x^1, x^2, x^3]$ in the initial configuration:

$$\overline{W}[x^1, x^2, x^3] = \int_{\overline{\mathcal{S}}} \frac{1}{2}\overline{S}(\overline{E}) \det(F_p) d\overline{x}^1 \wedge d\overline{x}^2 \wedge d\overline{x}^3. \tag{2}$$

Weak form stress equilibrium equation is derived from a stationary condition to the functional (2) and which is solved numerically using the isogeometric analysis [4], *i.e.*, Galerkin method which uses non-uniform rational B-spline (NURBS) as the basis functions.

RESULTS AND DISCUSSION

We conduct stress field analysis around a dislocation loop using the framework of geometrical elasto-plasticity. To simplify the analysis, we employed a cubic shape initial configuration, $\overline{\mathcal{S}} = \{(\overline{x}^1, \overline{x}^2, \overline{x}^3) | -1/2 < \overline{x}^i < 1/2\}$, and set the shear modulus $\mu = 1$ and Poisson ratio $\nu = 0.3$. A circular dislocation loop is inserted into the center of the material with the radius of $\overline{r} = 0.125$. We assume that the dislocation loop generates a continuous distribution of dislocation density $f = f(\overline{r})$ which is reported by Lazar *et. al.* [5]. Magnitude of Burgers vector is $(b^1, b^2, b^3) = (0.01, 0, 0)$. Then the torsion 2-from of the dislocation loop is expressed by $\tau^i = f(r) b^i l^l \epsilon_{ljk}/2 d\overline{x}^j \wedge d\overline{x}^k$, where l^i denotes the tangent vector along the dislocation line. Figure 1 shows the result of stress field obtained by the isogeometric analysis. Here, (a) shows the distribution of 2nd Piola-Kirchhoff stress S_{13}. The shear stress component is highly localized near the core of the dislocation loop. A cross section of the stress fields is shown in (b). In this figure, a pair of two edge dislocations are located at $(\pm 0.0625, 0, 0)$. This result shows a fair agreement with the prediction given by the classical elasticity under the same configuration of dislocation. Another cross section is shown in (c), where two screw dislocations are located at $(0, \pm 0.0625, 0)$. Again, the stress field is close to the classical system. These results verify the present formulation as well as the numerical implementation to the isogeometric analysis.

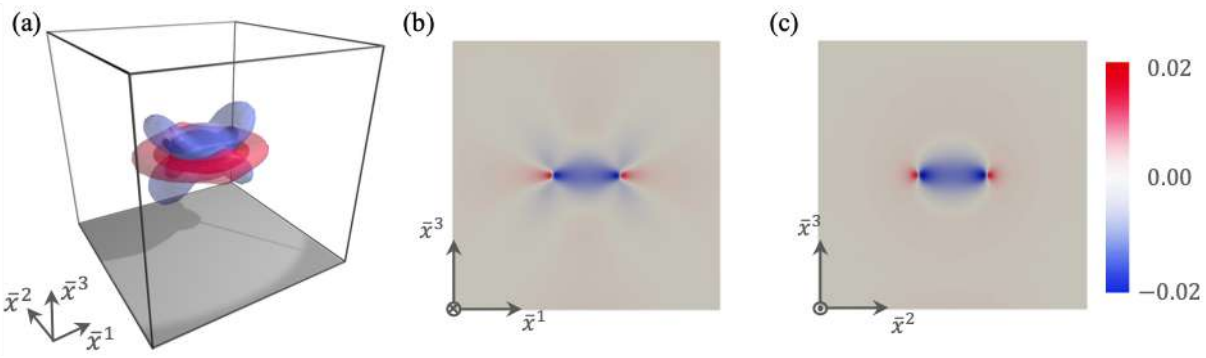

Figure 1: Distribution of the 2nd Piola-Kirchhoff stress component S_{13} with respect to the Cartesian coordinate system. (a) iso-surfaces of the shear stress S_{13}, (b) cross section of the stress distribution including two edge dislocations and (c) cross section of the stress distribution including two screw dislocations.

CONCLUSIONS

We conduct the stress field analysis around a dislocation loop on the basis of geometrical elasto-plasticity. Continuous distribution of dislocation density is converted into the torsion 2-form τ^i and plastic distorsion F_p is obtained from the integration of Cartan first structure equation by the homotopy operator. Embedding map of the Weitzenböck manifold to Euclidean 3-space is determined so as to minimize the strain energy functional. Numerical analysis for a dislocation loop revealed that the stress fields agree qualitatively well with the prediction given by the classical elasticity. This result demonstrates that the implementation of the geometrical elasto-plasticity theory enables us to analyze the stress fields for less-symmetric configuration of dislocations.

References

[1] Knodo K. Non-Riemannian geometry of imperfect crystals from a macroscopic viewpoint, *RAAG memoirs of the unifying study of basic problems in engineering and physical sciences by means of geometry*, Vol. 1, Division D-I (1955), Gakujutu Bunken Fukyu-kai, pp. 6–17.
[2] Yavari A., Goriely A. Riemann-Cartan Geometry of Nonlinear Dislocation Mechanics. *Arch. Raional Mech. Anal.* **205**: 59-118, 2012.
[3] Edelen D. G. B. Applied Exteriror Calculus. Dover, NY 2005.
[4] Cottrell J. A., Hughes T. J. R., Bazilevs Y. Isogeometric Analysis: Toward Integration of CAD and FEA. Wiley, Chichester 2009.
[5] Lazar M., Maugin G. A., Aifantis E. C. Dislocations in Second Strain Gradient Elasticity. *Int. J. Solids Structs.* **43**: 1787-1817, 2006.

IDENTIFICATION OF A MODEL OF NONLINEAR ELASTIC MATERIAL

Dmitrii Khristich*, Alexey Markin, Marina Sokolova, and Yuri Astapov
Department of Computational Mechanics and Mathematics, Tula State University, Tula, Russia

Summary The paper demonstrates how to determine the constants of a model of a nonlinear elastic body from experiment on inhomogeneous deformation. The formulation of the problem of finite strain of an elastic body, using a generalized model of Hencky material, is presented. A numerical model is constructed for taking into account the boundary conditions of the contact type in the interaction of an elastic body with absolutely rigid stamps. To solve the inverse problem of determining constants, an optimization algorithm is used. The material constants are determined from uniaxial compression test. The results of the numerical solution and the experimental data are in good agreement.

The reported study was partially funded by the grant from the President of the Russian Federation according to the Research Project MD-1803.2019.1 and by RFBR according to the Research Project No. 18-31-20053.

INTRODUCTION

Rubber-like materials are widely used to produce critical components of modern mechanisms. In most cases these materials can be described by a model of weakly compressible isotropic elastic medium. Such models are based on constitutive relations connecting stresses and strains in elastomers. Among the known materials in the nonlinear theory of elasticity, hypoelastic and hyperelastic models are distinguished, as well as various generalizations of Hooke's law to the case of finite strains. However, there are no unambiguous recommendations regarding the choice of a variant of constitutive relations adequately describing the mechanical behavior of elastomers at final elastic strains. The use of the Hencky logarithmic tensor as a measure of deformations makes it possible to simplify the description of materials with significantly different reactions to changes in volume and shape. The linear version of the relations associates the generalized stress tensor with energetically conjugated Hencky logarithmic strain measure. This model is similar to the Neo-Hookean model of material and contains two material constants too. A generalized nonlinear version of the constitutive relations is also obtained by keeping third-order terms in expansion for the specific potential strain energy.

Elastic constants are usually determined from experiments on uniaxial and biaxial tension, compression and bending. Recently, more and more researchers [1] use an indentation experiment to verify the reliability of numerical solutions. Processing of such experiments is reduced to the necessity of solving the initial-boundary-value problem with mixed contact-type boundary conditions. We present results of a comparison of the numerical solution of the problem of a spherical stamp indentation into a cylindrical sample with experimental data obtained on a designed test bench.

CONSTITUTIVE RELATIONS

It was shown in [2, 3] that in an isotropic material, the generalized "rotated" stress tensor $\mathbf{\Sigma_R} = e^{\theta}\mathbf{R}\cdot\mathbf{S}\cdot\mathbf{R}^{-1}$ and the Hencky logarithmic strain tensor $\mathbf{\Gamma}=\ln\mathbf{U}$, where $\mathbf{U}$ is the left a measure of distortion included in the polar decomposition of the strain gradient, are energetically conjugated. Assuming the potential strain energy by the analytic function of the Hencky strain tensor, we obtain a decomposition of the form

$$W = W_0 + \boldsymbol{A}\cdot\cdot\,\mathbf{\Gamma} + \frac{1}{2!}\boldsymbol{N}\cdot\cdot\cdot\cdot\,\mathbf{\Gamma\Gamma} + \frac{1}{3!}\boldsymbol{L}\cdot\cdot\cdot\cdot\cdot\cdot\,\mathbf{\Gamma\Gamma\Gamma} + \cdots,$$

where $W_0 = 0, \boldsymbol{A} = 0$ for the initial unstressed state, and the tensors $\mathbf{N}$ and $\mathbf{L}$ are the tensors of the elastic constants of the material. If we confine ourselves only to a second-order term with respect to the logarithmic strain tensor in the expansion for W and take into account the expression for the components of the tensor $\mathbf{N}$ in terms of the constants K and G in an isotropic material, we obtain a constitutive relation in the form:

$$\mathbf{\Sigma_R} = K\theta\boldsymbol{E} + 2G\,dev\mathbf{\Gamma}, \tag{1}$$

where $dev\mathbf{\Gamma} = \mathbf{\Gamma} - \frac{1}{3}\theta\mathbf{E}$ is the deviator of the Hencky tensor, $\theta = \mathrm{I}_1(\mathbf{\Gamma}) = \ln\left(\frac{dV}{dV_0}\right)$ is the first invariant of the Hencky tensor, K is the bulk modulus, and G is the shear modulus.

In the issue [4], a variant for generalizing the model of the Hencky material (1), obtained by keeping the third-order terms in the expansion for the specific potential strain energy:

$$\mathbf{\Sigma_R} = \sigma_0\boldsymbol{E} + \tau_e\,dev\mathbf{\Gamma} + \tau_q\,dev((dev\mathbf{\Gamma})^2), \tag{2}$$

was proposed. In the relation (2) $\sigma_0 = K\theta + \frac{C_1}{6\sqrt{3}}\theta^2 + \frac{C_2}{6\sqrt{3}}e^2$, $\tau_e = 2G + \frac{C_2}{3\sqrt{3}}\theta$, and $\tau_q = C_3$ are functions of the invariants of the strain measure: relative changes in the volume θ and intensity of the form change $e^2 = dev\mathbf{\Gamma}\cdot\cdot\,dev\mathbf{\Gamma}$. The model contains five elastic constants: K, G, C_1, C_2, C_3. If we assume a weak compressibility of the material, i.e., assume $\theta \approx 0$, then only two of them are subject to determination: G and C_3.

EXPERIMENTAL AND NUMERICAL SIMULATION RESULTS

The constants of model G and C_3 for natural rubber are determined from a series of uniaxial compression experiments of a set of cylindrical samples at a kinematic loading bench. The points in Fig. 1 show the results of the

* Corresponding author. E-mail: dmitrykhristich@rambler.ru.

compression experiments. For the problem of compression of a cylinder made of a material that obeys (2), an analytical solution is known, obtained under the assumption of homogeneity of the stress-strain state and allowing simple parameter fitting of the material. It is shown in the work that in real experiments it is possible to obtain only close to homogeneous states when using samples with a large radius to height ratio. In this case, the relative size of the inhomogeneity zone caused by friction with the support planes decreases. Therefore, it is possible to determine the model constants from the uniaxial compression experiment using an analytical solution, only if a sufficiently small slip coefficient of the sample with reference planes is provided.

It is required to consider the numerical implementation of the inverse problem, which is the problem of unconditional minimization. In this problem the target function is the standard deviation of the calculated curve $P(D)$ from the experimental data. The nature of the level surface of this function of two variables G and C_3 has been studied. It is found that it exhibits the character of a "ravine function" for which the gradient components at a certain point differ significantly. For such functions, it turns out to be difficult to achieve convergence using gradient methods, so the direct Hooke–Jeeves method of searching for unconditional minimum is chosen. The constructed computational procedure is applied to the problem of determining the elastic constants of models G and C_3 from experimental data obtained from a series of experiments on the indentation of natural rubber samples. Determined values of the constants are as follows: $G = 5 \cdot 10^5 Pa,\ C_3 = -2 \cdot 10^6 Pa$.

The determined values of the constants are used to verify the model in solving the problem of indentation a spherical stamp into an elastic plate. In the process of indentation, inhomogeneous stress and strain fields are observed in the deformable body. To determine them, an initial-boundary-value problem is solved, in which the constitutive relations are supplemented by the variational conditions of the equilibrium process flow [4], and by the initial and boundary conditions. The problem is solved numerically using finite element method and incremental loading method.

Tests are conducted to indent samples of natural rubber. The results are shown in Fig. 2 in the form of points reflecting the dependence of the force on the rod on the relative value of the draft. The red curve in Fig. 2 corresponds to the calculations according to relations (1), when $C_3 = 0$, that is, to the Hencky material model, and the black curve corresponds to the non-linear Hencky model (2). Comparison of calculated curves and indentation test data shows that the developed mathematical model of the process describes the experimental data with a sufficient degree of accuracy.

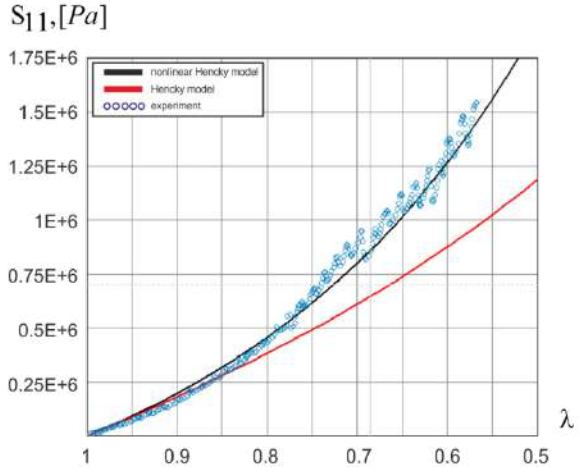

Figure 1. The dependence of the axial force on the ratio of elongation in the compression experiment

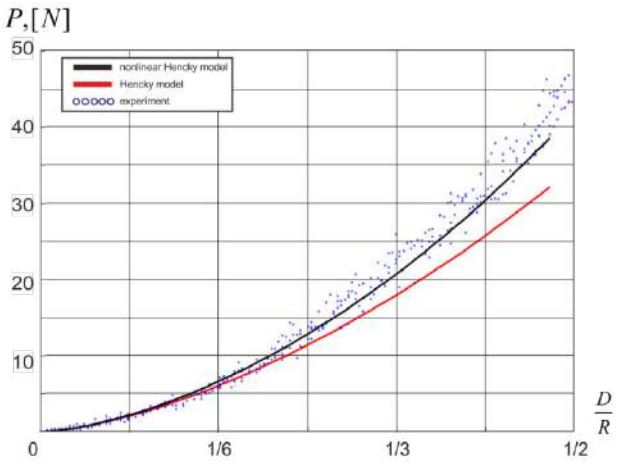

Figure 2. The dependence of the main vector of the acting force on the value of the relative depth in the indentation experiment

CONCLUSIONS

The article proposes a variant of the physically nonlinear Hencky model and its special case for weakly compressible materials. A series of experiments is carried out to determine the constants and to verify the proposed model. A numerical model of the process of indentation of a weakly compressible material with a hard rigid stamp of a spherical shape is developed. Comparison of experimental data and calculation results allows us to conclude that the proposed model is adequate. It describes the experimental data to deformations of the order of 50% with a sufficient degree of accuracy. The elastic constants of the model of a weakly compressible material can be determined from experiments on inhomogeneous deformation using the developed numerical model.

References

[1] Zhang M. G., Gao Y.P., Li G.Y., Feng X.Q. Spherical indentation method for determining the constitutive parameters of hyperelastic soft materials. *Biomech. Model. Mechanobiol.* **13**: 1-11, 2014.

[2] Hill R. On constitutive inequalities for simple materials–I. *J. Mech. Phys Solids*. **16(4)**: 229-242. 1968.

[3] Xiao H., Chen L.S. Hencky's Elasticity Model and Linear Stress-Strain Relations in Isotropic Finite Hyperelasticity. *Acta Mechanica*. **157**: 51-60, 2002.

[4] Markin A.A., Sokolova M.Yu. Thermomechanics of Elastoplastic Deformation. Cambridge International Science Publishing, Cambridge, UK 2015.

MODELING AND SIMULATION OF COSSERAT RODS BASED ON THE SPECIAL EUCLIDEAN ALGEBRA WITH APPLICATIONS TO THE ANALYSIS OF PIPES

Giulio G. Giusteri*[1], Edie Miglio[2], Nicola Parolini[2], Mattia Penati[2], and Raffaello Zambetti[2,3]
[1]Department of Mathematics,Università degli Studi di Padova,Padova,Italy
[2]Department of Mathematics, Politecnico di Milano, Milano, Italy
[3]Tenaris Dalmine, Dalmine, Italy

Summary We propose a method for the description and simulation of the nonlinear dynamics of slender beams that is based on interpreting the strains and the generalized velocities of the rigid cross sections as basic variables and elements of the special Euclidean algebra. The discretization of the corresponding equations for the three-dimensional motion of a Cosserat rod is performed, in space, by using a staggered grid that leads to a locking-free scheme. The time evolution can then be approximated with various semi-implicit methods. Within this approach we are able to include dissipative effects due to both the action of external forces and the presence of internal mechanical dissipation. Moreover, external constraints on the attainable configurations can be easily included via penalization schemes. All these features render this method effective for the mechanical analysis of long pipes.

BACKGROUND

The modeling and simulation of beams is of great importance in the engineering practice to analyze the configurations and stress distributions of a wide variety of mechanical structures, with sizes ranging from those of pipelines and cables to those of microactuators. When these structures are sufficiently slender or very flexible, they can undergo large displacements even in the small-strain and linear-response regime, and geometric nonlinearities must be taken into account to capture their mechanical behavior.

Since the seminal work by Simo and Vu-Quoc [1], the number of publications and the variety of numerical methods related to geometrically-exact beam models has been growing significantly. Nevertheless, given the variety of applications and the different features pertaining to each method, no universal standard is available for an efficient simulation of such models. On the other hand, it has become clear that the theory of Cosserat rods provides the optimal mathematical background to deal with slender structures, as it comprises all of the classical beam models as special cases.

Several discretization schemes represent the rod via the position and orientation of nodal cross sections. In this way, the computation of the strain and stresses associated with twist, bending, stretching, and shearing of the rod rely on interpolation procedures that introduce some important arbitrariness in the calculations [2]. Discretization methods that avoid the need for such an interpolation have been devised [3, 4, 5] and entail a piecewise constant approximation of the strains. Within those schemes, the strains are viewed as elements of the Lie algebra associated with the special Euclidean group of rigid body motions. Such a parametrization of the rod shape corresponds to a consistent finite-element approximation of the stresses, which is preferable to interpolation in the analysis of engineering structures.

Describing also the generalized velocity of the nodal cross sections in terms of the special Euclidean algebra allows to write the full Hamiltonian and Lagrangian functions of a moving rod using variables that live on a linear space, instead of a curved manifold, as pointed out by Simo *et al.* [6] and further clarified by Holm and Ivanov [7]. This has important advantages from the computational perspective, since numerical integration on manifolds would require much more sophisticated techniques.

THE COMPUTATIONAL MODEL

We propose a method for the description of the nonlinear dynamics of slender beams that is based on extensions of the $SE(3)$-strand equations described by Holm and Ivanov [7], with a suitable mechanical interpretation of stress and momenta as dual to strains and velocities. Within this approach we are able to include dissipative effects due to both the action of external forces and the presence of internal mechanical dissipation. Moreover, external constraints on the attainable configurations can be easily included via penalization schemes.

We view the rod as a collection of equally-shaped cross sections parametrized by a real variable $s \in [0, L]$, with L being the reference length of the rod. Differentiation with respect to s is indicated by a prime, while a superimposed dot denotes the time derivative. The twist density u_3, curvatures u_1, u_2, the stretching σ_3, and the shearing densities σ_1 and σ_2 are the six strains, function of s, that describe the shape of the rod. We will identify the collection of them with the six-component strain vector $U = (u_3, u_1, u_2, \sigma_3, \sigma_1, \sigma_2)$. The natural (relaxed) shape of the rod is given by fixing the strains $\bar{U}(s)$ for each value of s. Similarly, the generalized velocity of each cross section is given by three linear velocities v_i and three spins w_i $(i = 1, 2, 3)$. We will identify the collection of them with the generalized velocity vector $V = (w_3, w_1, w_2, v_3, v_1, v_2)$. We can now introduce the momentum and stress, P and Σ, as

$$P = \mathsf{M}V \qquad \text{and} \qquad \Sigma = \mathsf{A}(U - \bar{U}),$$

*Corresponding author. E-mail: giulio.giusteri@math.unipd.it.

where the diagonal matrices M and A represent, respectively, the rigid-body inertia (linear density) and the elastic stiffnesses at each cross section. The elastic response of the rod is thus modeled in a standard way as a linear function of the difference between the current strains and the relaxed ones. The field Σ represents torques and forces (tensions), while P is a linear density of angular and linear momenta.

We can introduce the Lie bracket $[U, V]$ between elements of the algebra and the adjoint-transpose operator ad^t defined by the pairing

$$\langle \mathrm{ad}^t_U \Sigma, Z\rangle = \langle \Sigma, \mathrm{ad}_U Z\rangle = \langle \Sigma, [U, Z]\rangle,$$

where $\langle \cdot, \cdot \rangle$ denotes the scalar product in $\mathbf{R}^6$. The evolution equations for the rod dynamics are

$$\dot{P} - \Sigma' = \mathrm{ad}^t_V P - \mathrm{ad}^t_U \Sigma - \mathsf{D}\dot{\Sigma} + F, \tag{1}$$

$$\dot{U} - V' = \mathrm{ad}_U V, \tag{2}$$

the second relation being a compatibility constraint between the rigid-body motion of each cross section and the fact that they should collectively move as a continuous rod. The six-component vector F represents external force and torque densities acting on each cross section, while the matrix D contains the damping coefficients associated with the internal mechanical dissipation.

We discretize the evolution equations using a standard semi-implicit time integration that linearizes the evolution operator. On the other hand, some care is in order when considering the spatial discretization. In fact, shear-locking phenomena can appear, partly enhanced by the presence of the constraint represented by equation (2). We avoided such complications by using finite differences on a staggered grid that mirrors the character of our variables: momenta and velocities are assigned to nodal cross sections, while stresses and strains are viewed as distributed on the intermediate segments.

Boundary conditions are imposed by adding ghost cells and nodes at the two ends of the rod. Within this method it is rather straightforward to drive or fix the motion of the rod ends or set free-end conditions.

MAIN FEATURES OF THIS APPROACH

Our target application is the structural analysis of long pipes and there are several features that make this approach an effective one. First of all, the theoretical setting based on concepts from differential geometry avoids, by means of a wise choice of the system variables, the need for interpolating between points on a curved manifolds (i.e. the group of rigid body motions) and, at the same time, links the computation directly to the quantities of practical interests, such as the distribution of mechanical stresses. Moreover, our very simple strain discretization produces rod segments of a general helical shape, such as those used by Borri and Bottasso [3], offering great flexibility in capturing non-straight constrained configurations. Secondly, the numerical discretization of the $SE(3)$-strand equations turns out to be advantageous if compared to discrete rod models (in which the mechanical structure is discretized in a multibody system) because it avoids the somewhat involved computation of nonlocal inertial terms [4, 5]. In fact the local nature of the evolution equations is reflected in a markedly banded structure of the discrete evolution matrix, which is at the heart of the computational efficiency of the scheme. Thanks to these features, we are able to simulate also long pipes, that require a comparatively large number of elements, in arbitrary three-dimensional configurations. Comparisons with benchmark data from earlier publications show the good performance of the scheme.

Acknowledgments

This research is supported by Tenaris Dalmine S.p.A..

References

[1] Simo J. C., Vu-Quoc L. A three-dimensional finite-strain rod model. Part II: computational aspects. *Comput. Methods Appl. Mech. Eng.* **58**: 79-116, 1986.

[2] Bauchau O. A., Han S. Interpolation of rotation and motion. *Multibody Syst. Dyn.* **31**: 339-370, 2014.

[3] Borri M., Bottasso C. An intrinsic beam model based on a helicoidal approximation—Part I: formulation. *Int. J. Numer. Methods Eng.* **37**: 2267-2289, 1994.

[4] Bertails F., Audoly B., Cani M.-P., Querleux B., Leroy F., Lévêque J.-L. Super-helices for predicting the dynamics of natural hair. *ACM Trans. Graph.* **25**: 1180-1187, 2006.

[5] Giusteri G. G., Fried E. Importance and effectiveness of representing the shapes of Cosserat rods and framed curves as paths in the special Euclidean algebra. *J. Elast.* **132**: 43-65, 2018.

[6] Simo J. C., Marsden J. E., Krishnaprasad P. S. The Hamiltonian structure of nonlinear elasticity: the material and convective representations of solids, rods, and plates. *Arch. Ration. Mech. Anal.* **104**: 125-183, 1988.

[7] Holm D. D., Ivanov R. I. Matrix G-strands. *Nonlinearity* **27**: 1445-1469, 2014.

2D INTEGRITY BASES WITH APPLICATIONS TO LINEAR MULTIPHYSICS COUPLING AND FABRIC TENSORS

Boris Desmorat*[1], Nicolas Auffray[2], Rodrigue Desmorat [3], Marc Olive[3], and Boris Kolev[3]
[1]Institut d'Alembert, Sorbonne Université, CNRSUMR7190, F-75252 Paris Cedex 05, France
[2]MSME, Univ Gustave Eiffel, UPEC, CNRS, F-77454, Marne-la-Vallée, France
[3]Université Paris-Saclay, ENS Paris-Saclay, CNRS, LMT-Laboratoire de Mécanique et Technologie, 94235, Cachan, France

Summary We describe in this work a general methodology to obtain a minimal polynomial integrity basis of any 2D linear constitutive law, represented by real valued tensors of any order. To do so, we need to consider $\mathrm{SO}(2)$ or $\mathrm{O}(2)$ linear representations on considered tensors, and then the computation is based i) on an explicit harmonic decomposition of tensors, ii) the introduction of complex numbers to rewrite polynomial invariants, and finally iii) the use of diophantine equation and a step-by-step algorithm to obtain minimality.

MECHANICAL MOTIVATIONS

Linear constitutive equations write as linear mappings between tensorial state variables via constitutive tensors. For instance, in the case of standard linear elasticity, Cauchy stress tensor (of order 2) is related to the strain tensor (of order 2) via the elasticity tensor (of order 4), while in the case of strain-gradient elasticity, the stress and hyper-stress tensors (of order 2 and 3) are related to the strain and strain-gradient tensors (of order 2 and 3) via three constitutive tensors of order 4, 5 and 6. Such linear constitutive equations are also present for multiphysics coupling. For instance, three constitutive tensors (of order 2, 3 and 4) are involved in piezo-electricity. However, constitutive tensors $\mathbf{T}_1, \ldots, \mathbf{T}_n$ do not characterize materials independently of their spatial orientation [1].

Any transformation $g \in \mathrm{SO}(2)$ or $\mathrm{O}(2)$ —where $\mathrm{O}(2)$ and $\mathrm{SO}(2)$ stand respectively for the orthogonal and the special orthogonal groups in 2D— define a new set of tensors using the standard action $\star$ (e.g. for a second order tensor, $\tilde{T}_{ij} = g_{ip} g_{jq} T_{pq}$):

$$(\tilde{\mathbf{T}}_1, \ldots, \tilde{\mathbf{T}}_n) = g \star (\mathbf{T}_1, \ldots, \mathbf{T}_n) = (g \star \mathbf{T}_1, \ldots, g \star \mathbf{T}_n),$$

representing the same material.

Thus, characterizing a material requires the definition of a finite set of $\mathrm{SO}(2)$ or $\mathrm{O}(2)$-invariant functions such that

$$f_i(\mathbf{T}'_1, ..., \mathbf{T}'_n) = f_i(\mathbf{T}_1, ..., \mathbf{T}_n) \Leftrightarrow (\mathbf{T}'_1, ..., \mathbf{T}'_n) = g \star (\mathbf{T}_1, ..., \mathbf{T}_n).$$

It is known [2] that an integrity basis (i.e. a finite set of polynomial invariants generating the algebra of polynomial invariants) provides such a set of functions (see [3] for 2D non polynomial separating invariants, see [4, 5] for polynomial separating sets for 3D fourth order tensors).

An integrity basis also allows for the explicit characterization of specific material behaviors, e.g. the explicit characterization of membership to a symmetry class [6]. An other classical example in elasticity is that the uncoupling of spherical and deviatoric parts of the elastic energy is given by setting the value of a particular invariant to zero [7].

We propose in this work a general methodology to compute an explicit 2D integrity basis for any real valued tensors of any orders (a similar procedure was used in [8] in the particular case of 2D elasticity).

$\mathrm{SO}(2)$ INTEGRITY BASIS

The first step is to perform an explicit harmonic decomposition of the tensors $(\mathbf{T}_1, \ldots, \mathbf{T}_n)$ involved in the constitutive equations. Such a procedure leads to an identification

$$(\mathbf{T}_1, \ldots, \mathbf{T}_n) \simeq (\lambda_1, \ldots, \lambda_m, \mathbf{H}_1, \ldots, \mathbf{H}_r)$$

with scalars invariants $\lambda_i \in \mathbb{H}^0$ and p_j^{th}-order 2D harmonic tensors $\mathbf{H}_j \in \mathbb{H}^{p_j}$. For any $p \geq 1$, $\mathbb{H}^p$ is isomorphic to $\mathbb{R}^2$, so we can consider *complex coordinates* $z_j, \overline{z}_j$ for harmonic tensors $\mathbf{H}_j$ (instead of $\mathrm{Re}(z_j)$ and $\mathrm{Im}(z_j)$), so that $\mathbf{H}_j \simeq (z_j, \overline{z}_j)$ with action given by $g \star \mathbf{H}_j \simeq e^{i\theta} \star (z_j, \overline{z}_j) = (e^{ip_j\theta} z_j, e^{-ip_j\theta} \overline{z}_j)$ for all $g \in \mathrm{SO}(2)$.

Since any polynomial splits into a sum of monomials $z_1^{\alpha_1} \ldots z_r^{\alpha_r} \overline{z}_1^{\beta_1} \ldots \overline{z}_r^{\beta_r}$ and

$$e^{i\theta} \star (z_1^{\alpha_1} \ldots z_r^{\alpha_r} \overline{z}_1^{\beta_1} \ldots \overline{z}_r^{\beta_r}) = z_1^{\alpha_1} \ldots z_r^{\alpha_r} \overline{z}_1^{\beta_1} \ldots \overline{z}_r^{\beta_r} e^{i\theta(p_1\alpha_1 + \ldots + p_r\alpha_r - p_1\beta_1 - \ldots - p_r\beta_r)},$$

invariants are generated by the monomials with exponents satisfying *Diophantine equation*:

$$p_1\alpha_1 + \ldots + p_r\alpha_r - p_1\beta_1 - \ldots - p_r\beta_r = 0.$$

The monomials constructed from the finite set of the irreducible solutions of this Diophantine equation are real polynomials $I_k = z_k \overline{z}_k$ and complex polynomials J_m. We finally have the

*Corresponding author. E-mail: boris.desmorat@sorbonne-universite.fr.

Theorem 1 *The set* $\{\lambda_i, I_k, Re(J_m), Im(J_m)\}$ *constitutes a minimal* $\mathrm{SO}(2)$ *integrity basis of the algebra of* $\mathrm{SO}(2)$ *polynomial invariants of the* n*-tuple of real valued tensors* $(\mathbf{T}_1, \ldots, \mathbf{T}_n)$.

The minimal integrity basis is obtained as a set of SO(2)-invariant polynomials of the components of the initial n-tuple of tensors. The tensorial expressions of such invariant polynomials can be straightforwardly recovered from the complex expressions.

$\mathrm{O}(2)$ INTEGRITY BASIS

In the $\mathrm{O}(2)$-case, the harmonic decomposition derives directly from the harmonic decomposition of the restriction of the action to $\mathrm{SO}(2)$. Indeed, the group $\mathrm{O}(2)$ is obtained from $\mathrm{SO}(2)$ by adding a mirror symmetry σ across a given line. For each $\mathrm{SO}(2)$-invariant scalar we have to check whether $\sigma \star \lambda_i = \lambda_i$ or $-\lambda_i$. In the case of negative sign, we will use the notion of pseudo-scalar invariant, and denote it $\mu_i \in \mathbb{H}^{-1}$. Note that, in 2D, the harmonic decomposition under O(2) does not involve any pseudo-tensors. We have the following result:

Theorem 2 *The set* $\{\lambda_i, I_k, \mu_{j_1}\mu_{j_2}, \mu_j Im(J_m), Re(J_m), Im(J_{m_1})Im(J_{m_2}),\}$ *constitutes a (non-minimal)* $\mathrm{O}(2)$ *integrity basis of the algebra of* $\mathrm{O}(2)$ *polynomial invariants of the n-tuple of real valued tensors* $(\mathbf{T}_1, \ldots, \mathbf{T}_n)$.

The last difficulty lies in the fact that some of the invariant polynomials $Im(J_i)Im(J_j)$ can be reduced, i.e. can be expressed as invariant polynomials of other invariant polynomials. In order to perform this reduction step, all the invariant polynomials $Re(J_k)$ and $Im(J_i)Im(J_j)$ are tested using a reduction algorithm similar to the one developed in [9]. Once the reduction step is performed, a minimal integrity basis is obtained, i.e. any strict subfamily is no longer a generating family. Again, the minimal integrity basis is obtained as a set of O(2)-invariant polynomials of the components of the initial tensors n-tuple. The tensorial expressions of such invariant polynomials can be straightforwardly recovered from the complex expressions.

RESULTS

We present here the number of elements of $\mathrm{SO}(2)$ and $\mathrm{O}(2)$ integrity bases of a few linear constitutive laws:

Third order tensor (including piezoelectricity tensor), $T_{ijk} \simeq 3\mathbb{H}^1 \oplus \mathbb{H}^3$

- SO(2)-integrity basis is composed of 30 elements,
- O(2)-integrity basis is composed of 17 elements (all invariants $Im(J_i)Im(J_j)$ are reduced).

Fourth order tensor (including elasticity tensor), $T_{ijkl} \simeq 3\mathbb{H}^{-1} \oplus 3\mathbb{H}^0 \oplus 4\mathbb{H}^2 \oplus \mathbb{H}^4$

- SO(2)-integrity basis is composed of 43 elements,
- O(2)-integrity basis is composed of 78 elements (all invariants $Im(J_i)Im(J_j)$ are reduced).

Totally symmetric tensor of order 12 (such as fabric tensors), $\mathbb{H}^0 \oplus \mathbb{H}^2 \oplus \mathbb{H}^4 \oplus \mathbb{H}^6 \oplus \mathbb{H}^8 \oplus \mathbb{H}^{10} \oplus \mathbb{H}^{12}$

- SO(2)-integrity basis is composed of 211 elements,
- O(2)-integrity basis is composed of 113 elements (not all invariants $Im(J_i)Im(J_j)$ are reduced).

Note that the case of the fabric tensors of order 2, 4, 6, 8 (and of course 12) that describe directional datas densities [10] are included as particular cases of totally symmetric tensor of order 12.

Elasticity / Piezo-electricity coupling, $(T^{(1)}_{(ij)|(kl)}, T^{(2)}_{(ij)k}, T^{(3)}_{ij}) \simeq 3\mathbb{H}^0 \oplus 2\mathbb{H}^1 \oplus 2\mathbb{H}^2 \oplus \mathbb{H}^3 \oplus \mathbb{H}^4$
(where (ij) stands for the indical symmetry $T_{ij} = T_{ji}$, and $ij|kl$ stands for the indicial symmetry $T_{ijkl} = T_{klij}$)

- SO(2)-integrity basis is composed of 121 elements,
- O(2)-integrity basis is composed of 71 elements (not all invariants $Im(J_i)Im(J_j)$ are reduced).

References

[1] Forte S.,Vianello M., Symmetry classes for elasticity tensors. J. Elasticity, 43(2):81–108, 1996.
[2] Abud M. and Sartori G., The geometry of spontaneous symmetry breaking, Annals of Physics, 150(2), 307–372, 1983.
[3] Vannucci P. and Verchery G., Anisotropy of plane complex elastic bodies, Int. J. Solids Struct., 47, 1154–1166, 2010.
[4] Boehler J. P., Kirillov A. A., Onat, E. T., On the polynomial invariants of the elasticity tensor, J. Elasticity, 34(2):97–110, 1994.
[5] Desmorat R., Auffray, N., Desmorat B., Kolev B., Olive, M., Generic separating sets for three-dimensional elasticity tensors, Proc. R. Soc. A, 475, 2019.
[6] Auffray N., Kolev B., Petitot M., On anisotropic polynomial relations for the elasticity tensor. J. Elas. 115(1), 77–103, 2014.
[7] Vannucci, P. , Plane Anisotropy by the Polar Method. Meccanica. 40, 437–454, 2005.
[8] Vianello M., An integrity basis for plane elasticity tensors. Arch. Mech. 49 (1), 197–208, 1997.
[9] Olive M., Kolev B., Auffray N., A minimal integrity basis for the elasticity tensor. Arch. for Rational Mechanics and Analysis, 226(1):1–31, 2017.
[10] Kanatani K. I., Distribution of directional data and fabric tensors, Int. J. of Engng Science, 22 (2), 149–164, 1984.

ADAPTIVE CONTROL OF UNSTEADY STRESS OSCILLATION IN FUNCTIONALLY GRADED MULTIFERROIC COMPOSITE THIN PLATE

Fumihiro Ashida*[1], Takuya Morimoto [1], and Ryo Kuwahara [2]
[1]Department of Mechanical, Electrical, and Electronic Engineering, Shimane University, Matsue, Japan
[2]Interdisciplinary Graduate School of Science and Engineering, Shimane University, Matsue, Japan

Summary When a functionally graded material thin plate is subjected to impact pressure, an unsteady oscillation of dynamic stress with tensile stress is induced. In this paper, adaptive control of the unsteady stress oscillation with piezoelectric sensing and magnetic actuation is investigated for a functionally graded multiferroic composite (FGMC) thin plate subjected to uniform impact pressure of unknown magnitude. One-dimensional electro-magneto-elastodynamic problems are analyzed by employing the method of characteristics. Numerical results demonstrate that the maximum amplitude of the controlled unsteady stress oscillation is suppressed to about a half of the uncontrolled one.

INTRODUCTION

Many papers dealt with dynamic problems in functionally graded material (FGM) solids subjected to harmonic loadings, but a few papers investigated stress oscillations induced in FGM solids by elastic wave propagations. The first author et al. analyzed a direct control problem of an unsteady stress oscillation in a functionally graded piezoelectric thin plate and revealed that the unsteady stress oscillation was completely cancelled by applying appropriate voltage [1].

In this paper, one-dimensional magneto-electro-elastodynamic problems in functionally graded multiferroic composite (FGMC) thin plates subjected to uniform impact pressure are analyzed by employing the method of characteristics. The material properties are assumed to vary in the thickness direction according to a power law distribution. First, a direct control problem is analyzed, when known uniform impact pressure acts on the FGMC thin plate. It is seen from obtained numerical results that the actuation magnetic potential difference for controlling the unsteady stress oscillation to the minimum is given as a linear function of a volume fraction exponent. Next, an adaptive control problem is analyzed, when uniform impact pressure of unknown magnitude acts on the FGMC thin plate of an unknown volume fraction exponent and the output voltage between both plate surfaces and its period are measured in the first cycle. The volume fraction exponent and the magnitude of impact pressure are inferred from the knowledge of the period and output voltage. The unsteady stress oscillation is controlled from the third cycle by applying the actuation magnetic potential difference calculated from the previous linear function.

PROBLEM STATEMENT

Let us consider an FGMC thin plate depicted in Fig. 1, in which case its material properties $P_i(z)$ vary in the thickness direction as follows:

$$P_i(z)=P_{MSi}\hat{V}_{MS}+P_{PEi}\hat{V}_{PE},\ \hat{V}_{MS}=1-\left(\frac{z}{l}\right)^{\frac{1}{n}},\ \hat{V}_{PE}=\left(\frac{z}{l}\right)^{\frac{1}{n}}\quad(0<n\le 1)\quad(1)$$

where P_{MSi} are material properties of a magnetostrictive material at the top surface, P_{PEi} are those of a piezoelectric material at the bottom surface, and n is a volume fraction exponent.

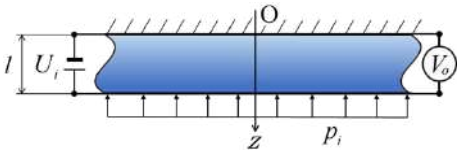

Figure 1. An FGMC thin plate.

The FGMC thin plate is considered to be initially in stress-free state. It is assumed that the bottom surface is subjected to uniform impact pressure p_i, the top surface is fixed to a flat rigid body, and an actuation magnetic potential difference U_i is applied between both surfaces. The initial and boundary conditions are then given by

$$u_z(z,0)=0,\ v_z(z,0)=0,\ \sigma_{zz}(z,0)=0,\ D_z(z,0)=0,\ B_z(z,0)=0 \quad (2)$$

$$u_z(0,t)=0,\ D_z(0,t)=0,\ \psi(0,t)=0,\ \sigma_{zz}(l,t)=-p_iH(t),\ D_z(l,t)=0,\ \psi(l,t)=U_iH(t-t_d) \quad (3)$$

where $v_z(z,t)=u_{z,t}(z,t)$, $u_z(z,t)$ is the displacement, $v_z(z,t)$ is the particle velocity, $\sigma_{zz}(z,t)$ is the stress, $D_z(z,t)$ is the dielectric flux density, $B_z(z,t)$ is the magnetic flux density, $\psi(z,t)$ is the magnetic potential, $H(t)$ is Heaviside's unit step function, t is time, t_d is the time delay, and a comma denotes partial differentiation.

The constitutive and governing equations for the elastic, electric, and magnetic fields are

$$\sigma_{zz}=c_{33}(z)u_{z,z}+e_3(z)\phi_{,z}+q_3(z)\psi_{,z},\ D_z=e_3(z)u_{z,z}-\eta_3(z)\phi_{,z}-\alpha_3(z)\psi_{,z},\ B_z=q_3(z)u_{z,z}-\alpha_3(z)\phi_{,z}-\mu_3(z)\psi_{,z} \quad (4)$$

$$\sigma_{zz,z}=\rho(z)v_{z,t},\ D_{z,z}=0,\ B_{z,z}=0 \quad (5)$$

where $\phi(z,t)$ is the electric potential, $c_{33}(z)$ is the elastic modulus, $e_3(z)$ is the piezoelectric constant, $q_3(z)$ is the piezo-magnetic coefficient, $\rho(z)$ is the density, $\eta_3(z)$ is the dielectric permittivity, $\alpha_3(z)$ is the magnetoelectric coefficient, and $\mu_3(z)$ is the magnetic permeability.

The output voltage $V_o(t)$ is induced between both plate surfaces by action of the mechanical and magnetic loads.

$$\phi(l,t)-\phi(0,t)=V_o(t) \quad (6)$$

*Corresponding author. E-mail:ashida@ecs.shimane-u.ac.jp.

Solving the constitutive and governing equations for the electric and magnetic fields under their initial and boundary conditions, the electric potential ϕ, dielectric flux density D_z, magnetic potential ψ, and magnetic flux density B_z are represented in terms of the particle velocity v_z and stress σ_{zz}. Finally, this problem is reduced to solving two coupled first-order partial differential equations. Employing the method of characteristics [1], the particle velocity and stress which satisfy their initial and boundary conditions are numerically obtained.

NUMERICAL RESULTS

For convenience in presentation of numerical results, the following dimensionless quantities are introduced:

$$\bar{z}=\frac{z}{l},\ \bar{t}=\frac{v_l t}{l},\ \bar{p}_i=\frac{p_i}{p_c},\ \bar{\sigma}_{zz}=\frac{\sigma_{zz}}{p_c},\ \bar{V}_o=\frac{d_3 Y_l V_o}{p_c l},\ \bar{U}_i=\frac{U_i}{p_c v_l d_3 l}$$

where p_c is a constant pressure and v_l, Y_l, and d_3 are respectively the velocity of elastic wave propagation, equivalent elastic modulus, and piezoelectric coefficient of a piezoelectric material at the bottom surface of the FGMC thin plate.

Numerical calculations have been carried out for the FGMC thin plate composed of barium titanite and cobalt ferrite [2].

Direct control of unsteady stress oscillation

Let us consider the FGMC thin plate subjected to the uniform impact pressure $\bar{p}_i=1$ and an actuation magnetic potential difference, simultaneously, namely the time delay is $\bar{t}_d=0$. The optimum actuation magnetic potential differences $\bar{U}_{io}(n)$ are determined for the cases of $n=1$, 0.75, 0.5, 0.25, and 0.1 by employing a trial-and-error approach in order to control the unsteady stress oscillation to the minimum. Obtained numerical results are illustrated in Fig. 2. It is seen from the figure that the optimum actuation magnetic potential difference is given as a linear function of the volume fraction exponent.

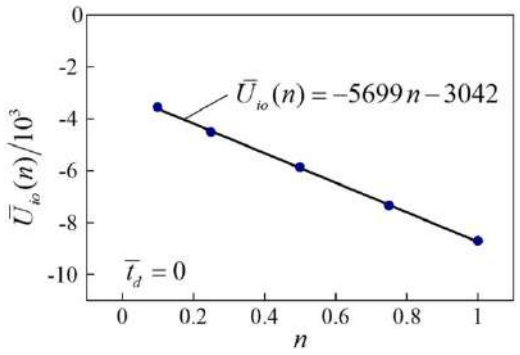

Figure 2. Optimum magnetic potential difference.

Adaptive control of unsteady stress oscillation

Let us consider a case where uniform impact pressure of unknown magnitude $\bar{p}_i$ acts on the FGMC thin plate of an unknown volume fraction exponent and the actuation magnetic potential difference is zero in the beginning. It is assumed that the output voltage $\bar{V}_o(\bar{t})$ and its period $2\bar{t}_p$ are measured in the first cycle, as shown in Fig. 3, in which case the period is $2\bar{t}_p=3.399$. The volume fraction exponent is calculated from the period as $n=0.5228$. The magnitude of the impact pressure is inferred from the knowledge of the output voltage, so that it is found to be $\bar{p}_i=1.3715$. For this case, the linear function given in Fig. 2 leads to $\bar{U}_{io}(0.5228)=-6022$ and thus the optimum actuation magnetic potential difference is $\bar{p}_i\cdot\bar{U}_{io}(0.5228)=-8259$. Applying it to the FGMC thin plate from the third cycle, namely $\bar{t}_d=4\bar{t}_p$, the unsteady stresss oscillation at $\bar{z}=0.5$ is controlled as illsutrated in Fig. 4. The maximum amplitude of the controlled unsteady stress oscillation is suppressed to 50.1 percent of the uncontrolled one.

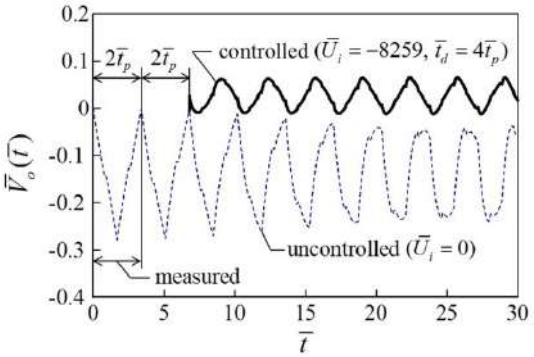

Figure 3. Time histories of output voltages.

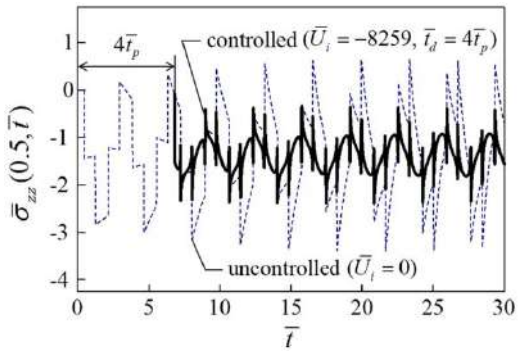

Figure 4. Time histories of stress oscillations.

CONCLUSIONS

This paper deals with adaptive control of the unsteady stress oscillation induced in the FGMC thin plate of an unknown volume fraction exponent by action of uniform impact pressure of unknown magnitude. The one-dimensional magneto-electro-elastodynamic problems are analyzed by employing the method of characteristics. Obtained numerical results demonstrate that the unsteady stress oscillation is adaptively controlled with piezoelectric sensing and magnetic actuation.

References

[1] Ashida, F., Morimoto, T., Ozaki, H. Active Cancellation of Unsteady Stress Oscillation in a Functionally Graded Piezoelectric Thin Plate Subjected to Impact Loading. *Eur J. Mech. A-Solid.* **67**: 84-91, 2018.

[2] Ramirez F., Paul R., Heyliger P.R., Pan E. Free Vibration Response of Two-dimensional Magneto-electro-elastic Laminated Plates. *J. Sound. Vib.* **292**: 626-644, 2006.

STATIC AND VIBRATIONAL ANALYSIS OF A CANTILEVERED THIN BEAM WITH A CREASED FOLD

Romeo Antier*[1], Benjamin Thiria[1], and Ramiro Godoy-Diana[1]
[1]PMMH Laboratory, ESPCI - PSL, CNRS, University of Paris, Sorbonne University, Paris, France

Summary Creases and folds confer rigidity to thin plates. We study experimentally the mechanical response of an elastic thin plate with a single crease subjected to external loading. The fold runs along the long symmetry axis of the slender plate, which has thus a V-shaped crosssection. Using quasi-static bending tests, vibration tests, and linear beam theory, we examine the strong correlation between the dynamical response of the system and its quasi-static mechanical behavior. In particular, we establish the role of the crease angle and its coupling with the bending rigidity on the bending and vibrational behaviors. Not surprisingly, the bending rigidity and thus the resonant frequency increases when the folding angle increases. However we bring evidence of a remarkable softening dynamics: the resonant frequency and thus the bending rigidity decreases when the amplitude of the external excitation increases in the vibration tests. We demonstrate that this softening is a consequence of the dynamical opening of the crease angle.

INTRODUCTION

A thin plate bends easily, and an interesting way to improve remarkably its rigidity is to fold it symetrically in the middle of its width. This capability is found in nature in the shape of a single blade of grass or of a single leaf of agave for plants, but also in the shape of insect wings where it seems to rigidify wings. For creased sheets with a long length compared to their width, those structures can be considered as cantilevered thin beams with a creased fold. The study of a single fold is at the foundation of the understanding of metamaterials inspired by nature.

Several works have been devoted to the study of creased sheets, origami, kirigami and miura ori. However the link between all of those structures, which is a single crease, remains not fully understood. Following the work of Lechenault et al. [1] and Jules et al. [2] who studied the mechanical response of a creased sheet in traction loadings, here we study the mechanical response of a creased thin elastic plate submitted to bending, then submitted to vibrations.

EXPERIMENTAL SETUP

We fabricated a series of creased plates by laser cutting sheets of $100\mu m$-thick Mylar and folding them by using 3D-printed molds, thus obtening a precise creased angle of the plate. The creased plates are set up on the test bench. All the experiments are carried out with one plate's end clamped to a fixed support, which is also 3D printed to fit to the plate. Two different tests are performed: a bending test to load periodically at different frequencies, and a vibrating test to study the effect of the frequency and of the input amplitude on the behavior of each creased plate of a specific folding angle.

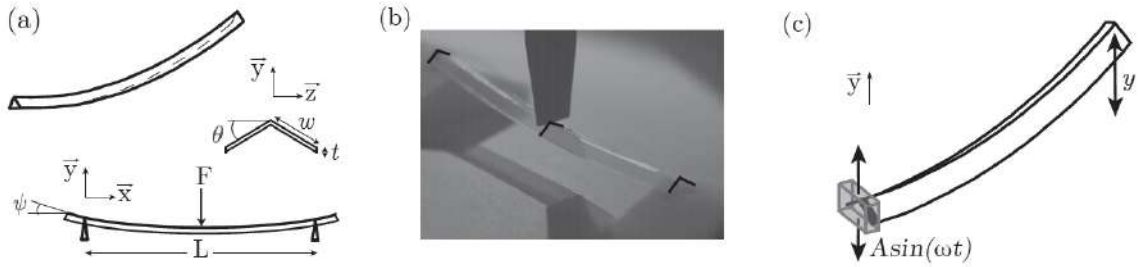

Figure 1: (a) Schematic of the creased sheet of thickness t, (b) Photograph of the three-points bending test highlighting the crease opening when the sheet undergoes a curvature, and (c) Schematic of the vibration experiments with a imposed forcing $A\sin(\omega t)$.

STATIC ANALYSIS

We characterize the bending rigidity of a controlled creased sheet and its dependence on geometrical and loading parameters. The narrower the folding angle, the higher the bending rigidity, for a same loading. This observation can be easily understood because the folding leads to increase the height of the flexural section that opposed to surface rotation while bending; entailing an increase in the moment of inertia and thus in the bending rigidity. A beam model allows to retrieved this conclusion in this case where the length of the thin plate is much higher than other dimensions. The moment of inertia is defined by:

$$I = \iint y^2 ds \approx t w^3 \sin^2\theta \cos\theta \left(\frac{2}{3} - \cos\theta + \frac{1}{2}\cos^2\theta\right) \quad (1)$$

*Corresponding author. E-mail: romeo.antier@espci.fr.

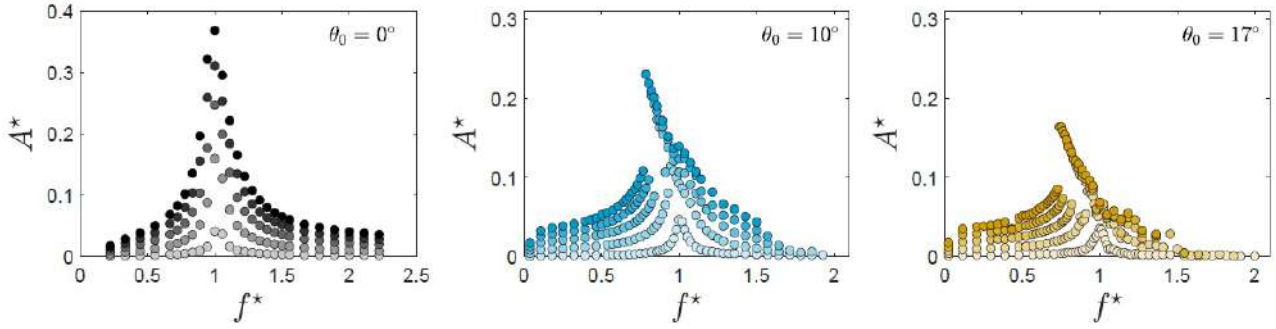

Figure 2: Upward sweep frequency response of creased sheets unfolded ($\theta = 0°$), and of crease angles θ of 10 and 17° from the unfolded reference, for forcing amplitude of $A_0 = 0.19$mm to $10 \times A0$ (from ligth to dark points). We define: $A^\star = y/L$ and $f^\star = f/f_0$ where f_0 is the linear resonance frequency.

Where I is the moment of inertia, t the thickness, w the half-width and θ the folding angle from the unfolding plate.

According to Jules et al [2], the geometrical conditions of our study leads to model the crease as a hinge spring where panels can not bend transversally. Thus one observes that for small curvatures, the folded sheet stretches and the crease angle opens from few degrees. It results from the competition between the longitudinal bending energy and the energy of the hinge. The bending tends to open the crease whereas the hinge tends to maintain the crease in its rest configuration. We found a relation linking the crease angle to the curvature for relatively small curvatures. When the bending displacement imposed to the structure is higher than a specific limit, the system changes suddenly its shape and snaps [3]. The snapping is accompanied by a quick opening of the crease until becoming totally flat. The snap causes the folded sheet to lose benefits of rigidity from the crease.

VIBRATION ANALYSIS

The vibration analysis aims characterizing the dynamical behavior of creased sheets determining the resonance frequencies of bending, which depend on experimental parameters. As expected from the bending analysis, resonance frequencies increase when the folding increases. Indeed, an increase in folding leads to an increase in the area moment of inertia, that leads to an increase in bending rigidity. However the sweep frequency response shows a non-linear behavior, likely to a Duffing oscillator, that is due to the non-linear geometry imposed by the fold; non-linear behaviors are the most noticeable for highest foldings. But the response is linear for small foldings or for very small input amplitudes of excitation.

For a given sample, a counter-intuitive phenomenon appears when the input amplitude of excitation is changed: the higher the input amplitude, the lower the bending resonance frequency, and thus the lower the bending rigidity; a creased sheet has a softening behavior. Experimental results are in agreement with numerical studies on geometrically non-linear plates charaterizing the behavior of such plates [4]. The softening is explained by the evolution of the crease angle when the beam vibrates near its resonance frequency. When the folded sheet vibrates close to its resonance, its curvature is no more small and its crease angle opens. During one cycle of vibration, the crease opens twice. We demonstrated the correlation between the crease angle evolution the softening behavior of folded sheets.

CONCLUSIONS

The intuive behavior of a simply folded sheet of paper, where the bending rigidity increases drasticaly when a fold appears, is retrieved and characterized in our work thanks to a well-controled creased elastic sheet. The more folded the thin plate, the higher its area moment of inertia, thus the higher the bending rigidity. The second conclusion, coming from the vibrational study, is that bending rigidity decreases when the loading increases, leading to a softening phenomenon: this softening is due to the opening of the plate angle. Competition between longitudinal bending and transverse hinge rigidity, that are coupled in such a struture, defines the behavior of a cantilevered thin beam with a creased fold.

References

[1] Lechenault F., Thiria B., Adda-Bedia M. Mechanical Response of a Creased Sheet. *Physical Review Letters* **112**: 244301, 2014.
[2] Jules T., Lechenault F., Adda-Bedia M. Local mechanical description of an elastic fold. *Soft Matter* **15**: 1619, 2019.
[3] Walker M. G., Seffen K. A. On the shape of bistable creased strips *Thin-Walled Structures* **124**: 538, 2018.
[4] Irie T., Yamada G., Kobayashi Y. Free vibration of a cantilever folded plate. *The Journal of the Acoustical Society of America* **76**: 1743, 1984.

EQUILIBRIUM OF A LINEARLY ELASTIC PERIDYNAMIC MATERIAL

Adair Aguiar *[1] and Alan B. Seitenfus[1]
[1]Department of Structural Engineering, University of São Paulo, São Carlos, SP, Brazil

Summary We investigate equilibrium solutions of an isotropic elastic material in the context of a state-based peridynamic theory. The response function of the material is derived from a quadratic free energy function that depends on measures of both length and relative angle changes and contains four material constants. For a particular class of polynomial displacement fields, differential equations found in this investigation become the classical equilibrium equations if two relations hold between the Lamé constants and the four peridynamic constants. These results are consistent with results of previous investigation that used energy-based arguments and homogeneous deformations. The determination of two peridynamic constants that are still arbitrary is the subject of ongoing investigation.

INTRODUCTION

The peridynamic theory is an extension of the classical continuum theory, in which a material point interacts directly with other material points separated from it by a finite distance. In parts of a body where the deformation is smooth, the peridynamic theory yields the same governing equations of the classical continuum theory in the limit of vanishing distances between material points. In this work, we consider small but not vanishing distances together with a class of second-degree polynomial displacements to show that the peridynamic and classical equations of equilibrium have similar forms for a linearly elastic peridynamic material with a free energy function that is quadratic in measures of both length and relative angle changes and depends on four peridynamic coefficients. The equations are the same provided that two relations hold between these coefficients and the Lamé constants. Two peridynamic coefficients are left undetermined, which seem to reflect the nonlocal nature of the theory. Relevant references are cited below.

PERIDYNAMIC EQUILIBRIUM EQUATION

Let $\mathcal{B} \subset \mathbb{E}^3$ be the undistorted reference configuration of an elastic solid body in its natural state and let $\boldsymbol{\chi}(\mathbf{x}, t)$ be the position of the particle $\mathbf{x} \in \mathcal{B}$ at time $t \geq 0$. Constitutive modeling within the peridynamic theory considers the collective deformation at each time t of all the material within a neighborhood of an arbitrary point $\mathbf{x}_0 \in \mathcal{B}$. We shall omit writing the time variable t. Here, this neighborhood is a sphere of radius δ centered at $\mathbf{x}_0$ and is denoted by $\mathcal{N}_\delta \subset \mathcal{B}$. For any $\mathbf{x} \in \mathcal{B}$ such that $|\mathbf{x} - \mathbf{x}_0| < \delta$, the vector $\boldsymbol{\xi} := \mathbf{x} - \mathbf{x}_0$ is called a bond to $\mathbf{x}_0$ and the collection of all bonds is denoted by $\mathcal{H}_\delta$. The displacement field $\mathbf{u}$ associated with the motion $\boldsymbol{\chi}$ at $\mathbf{x} \in \mathcal{B}$ is defined through $\mathbf{u}(\mathbf{x}) := \boldsymbol{\chi}(\mathbf{x}) - \mathbf{x}$. We also define the difference displacement state at $\mathbf{x}_0 \in \mathcal{B}$ as $\underline{\mathbf{u}}(\mathbf{x}_0)\langle\boldsymbol{\xi}\rangle := \mathbf{u}(\mathbf{x}) - \mathbf{u}(\mathbf{x}_0)$ for $\boldsymbol{\xi} = \mathbf{x} - \mathbf{x}_0 \in \mathcal{H}_\delta$.

Near a natural state of a body subjected to body force density $\mathbf{b}$, the peridynamic equation of equilibrium is given by

$$\mathbf{0} = \int_{N_\delta} [\underline{\mathbf{L}}(\mathbf{x}_0)\langle\mathbf{x} - \mathbf{x}_0\rangle - \underline{\mathbf{L}}(\mathbf{x})\langle\mathbf{x}_0 - \mathbf{x}\rangle]\, dv_x + \mathbf{b}(\mathbf{x}_0)\,, \qquad \mathbf{x}_0 \in \mathcal{B}\,, \tag{1}$$

where $\underline{\mathbf{L}}(\mathbf{x}_0)\langle\boldsymbol{\xi}\rangle$ is a linearized force vector state at $\mathbf{x}_0$ evaluated on bond $\boldsymbol{\xi}$. The integral equation (1) is analogous to the differential equilibrium equation from the classical linear theory. For a simple elastic material, $\underline{\mathbf{L}}(\mathbf{x}_0)\langle\boldsymbol{\xi}\rangle$ is given by

$$\underline{\mathbf{L}}(\mathbf{x}_0) = \underline{\widehat{\mathbf{L}}}_{\mathbf{x}_0}[\underline{\mathbf{h}}] \equiv \frac{\delta_{\underline{\mathbf{h}}} \widehat{W}_{\mathbf{x}_0}[\underline{\mathbf{h}}]}{|\underline{\mathbf{x}}|}, \tag{2}$$

where $\underline{\mathbf{h}} := \underline{\mathbf{u}}/|\underline{\mathbf{x}}|$ with $|\underline{\mathbf{h}}\langle\boldsymbol{\xi}\rangle|$ being small, $\underline{\mathbf{x}}\langle\boldsymbol{\xi}\rangle \equiv \boldsymbol{\xi}$, $\delta_{\underline{\mathbf{h}}}$ is the Fréchet derivative with respect to $\underline{\mathbf{h}}$ and, here, $\widehat{W}_{\mathbf{x}_0}$ is a quadratic free energy function given by

$$\widehat{W}_{\mathbf{x}_0}[\underline{\mathbf{h}}] = \int_{\mathcal{H}_\delta}\int_{\mathcal{H}_\delta} \omega(|\boldsymbol{\xi}|, |\boldsymbol{\eta}|)\Big[\frac{\alpha_1}{2}\big(\widehat{\underline{\varepsilon}}[\underline{\mathbf{h}}]\langle\boldsymbol{\xi}\rangle\big)^2 + \alpha_2\, \widehat{\underline{\varepsilon}}[\underline{\mathbf{h}}]\langle\boldsymbol{\xi}\rangle\, \widehat{\underline{\varepsilon}}[\underline{\mathbf{h}}]\langle\boldsymbol{\eta}\rangle + \frac{\alpha_3}{2}\big(\widehat{\underline{\gamma}}[\underline{\mathbf{h}}]\langle\boldsymbol{\xi},\boldsymbol{\eta}\rangle\big)^2 + \alpha_4\, \widehat{\underline{\gamma}}[\underline{\mathbf{h}}]\langle\boldsymbol{\xi},\boldsymbol{\eta}\rangle\, \widehat{\underline{\varepsilon}}[\underline{\mathbf{h}}]\langle\boldsymbol{\xi}\rangle\Big]\, dv_{\boldsymbol{\eta}}\, dv_{\boldsymbol{\xi}}\,. \tag{3}$$

In (3), $\omega(\cdot,\cdot)$ is a given weighting function satisfying $\omega(|\boldsymbol{\xi}|, |\boldsymbol{\eta}|) = \omega(|\boldsymbol{\eta}|, |\boldsymbol{\xi}|)$, α_i, $i = 1, \ldots, 4$, are peridynamic constants to be specified, $\widehat{\underline{\varepsilon}}[\underline{\mathbf{h}}]\langle\boldsymbol{\xi}\rangle := \underline{\mathbf{e}}\langle\boldsymbol{\xi}\rangle \cdot \underline{\mathbf{h}}\langle\boldsymbol{\xi}\rangle$ is an infinitesimal normal strain state with $\underline{\mathbf{e}}\langle\boldsymbol{\xi}\rangle := \boldsymbol{\xi}/|\boldsymbol{\xi}|$, and $\widehat{\underline{\gamma}}[\underline{\mathbf{h}}]\langle\boldsymbol{\xi},\boldsymbol{\eta}\rangle := \Big(\underline{\mathbf{e}}\langle\boldsymbol{\xi},\boldsymbol{\eta}\rangle \cdot \underline{\mathbf{h}}\langle\boldsymbol{\xi}\rangle + \underline{\mathbf{e}}\langle\boldsymbol{\eta},\boldsymbol{\xi}\rangle \cdot \underline{\mathbf{h}}\langle\boldsymbol{\eta}\rangle\Big)\Big/2$ is an infinitesimal shear strain state with $\underline{\mathbf{e}}\langle\boldsymbol{\xi},\boldsymbol{\eta}\rangle := \big(\underline{\mathbf{e}}\langle\boldsymbol{\eta}\rangle - \underline{\mathbf{e}}\langle\boldsymbol{\xi}\rangle \cos\alpha\big) / \sin\underline{\alpha}\langle\boldsymbol{\xi},\boldsymbol{\eta}\rangle$ and $\underline{\alpha}\langle\boldsymbol{\xi},\boldsymbol{\eta}\rangle$ being the smallest included angle between $\boldsymbol{\xi}$ and $\boldsymbol{\eta}$.

Introducing the decomposition $\underline{\mathbf{h}}\langle\boldsymbol{\xi}\rangle = \underline{\varphi}\langle\boldsymbol{\xi}\rangle\, \underline{\mathbf{e}}\langle\boldsymbol{\xi}\rangle + \underline{\mathbf{h}}_d\langle\boldsymbol{\xi}\rangle$, where $\underline{\mathbf{h}}_d$ satisfies $\underline{\mathbf{h}}_d\langle\boldsymbol{\xi}\rangle \cdot \underline{\mathbf{e}}\langle\boldsymbol{\xi}\rangle = 0$, we readily find that $\widehat{\underline{\varepsilon}}[\underline{\mathbf{h}}] = \underline{\varphi}$ and that $\widehat{\underline{\gamma}}\langle\boldsymbol{\xi},\boldsymbol{\eta}\rangle = \big(\underline{\mathbf{e}}\langle\boldsymbol{\eta}\rangle \cdot \underline{\mathbf{h}}_d\langle\boldsymbol{\xi}\rangle + \underline{\mathbf{e}}\langle\boldsymbol{\xi}\rangle \cdot \underline{\mathbf{h}}_d\langle\boldsymbol{\eta}\rangle\big) / \big(2\sin\underline{\alpha}\langle\boldsymbol{\xi},\boldsymbol{\eta}\rangle\big)$. Substituting these expressions into (3) and then the resulting expression into (2), we obtain the linear elastic response function state given by

*Corresponding author. E-mail: aguiarar@sc.usp.br.

$$\widehat{\underline{\mathbf{L}}}_{\mathbf{x}_0}[\underline{\mathbf{h}}]\langle\boldsymbol{\xi}\rangle = \int_{\mathcal{H}_\delta} \frac{\omega(|\boldsymbol{\xi}|,|\boldsymbol{\eta}|)}{|\boldsymbol{\xi}|}\Big\{\alpha_1\,\underline{\varphi}\langle\boldsymbol{\xi}\rangle\,\underline{\mathbf{e}}\langle\boldsymbol{\xi}\rangle + 2\,\alpha_2\underline{\varphi}\langle\boldsymbol{\eta}\rangle\,\underline{\mathbf{e}}\langle\boldsymbol{\xi}\rangle + \frac{\alpha_3}{2\,\sin\underline{\alpha}\langle\boldsymbol{\xi},\boldsymbol{\eta}\rangle}\Big(\underline{\mathbf{e}}\langle\boldsymbol{\eta}\rangle\cdot\underline{\mathbf{h}}_d\langle\boldsymbol{\xi}\rangle + \underline{\mathbf{e}}\langle\boldsymbol{\xi}\rangle\cdot\underline{\mathbf{h}}_d\langle\boldsymbol{\eta}\rangle\Big)\underline{\underline{\mathbf{e}}}\langle\boldsymbol{\xi},\boldsymbol{\eta}\rangle + \frac{\alpha_4}{2}\Big[\Big(\underline{\varphi}\langle\boldsymbol{\xi}\rangle + \underline{\varphi}\langle\boldsymbol{\eta}\rangle\Big)\underline{\underline{\mathbf{e}}}\langle\boldsymbol{\xi},\boldsymbol{\eta}\rangle + \frac{1}{\sin\underline{\underline{\alpha}}\langle\boldsymbol{\xi},\boldsymbol{\eta}\rangle}\Big(\underline{\mathbf{e}}\langle\boldsymbol{\eta}\rangle\cdot\underline{\mathbf{h}}_d\langle\boldsymbol{\xi}\rangle + \underline{\mathbf{e}}\langle\boldsymbol{\xi}\rangle\cdot\underline{\mathbf{h}}_d\langle\boldsymbol{\eta}\rangle\Big)\underline{\underline{\mathbf{e}}}\langle\boldsymbol{\xi}\rangle\Big]\Big\}\,dv_{\boldsymbol{\eta}}\,. \tag{4}$$

In [1] we show that (4) reduces to the linearized version of the force response function state proposed by Silling *et al.* [3] if $\alpha_3 = \alpha_4 = 0$ and $\omega(|\boldsymbol{\xi}|,|\boldsymbol{\eta}|) = \widetilde{\omega}(|\boldsymbol{\xi}|)\,\widetilde{\omega}(|\boldsymbol{\eta}|)|\boldsymbol{\xi}|^2|\boldsymbol{\eta}|^2$, where $\tilde{\omega}:\mathbb{R}\to\mathbb{R}$ is a known weighting function.

A CLASS OF POLYNOMIAL DISPLACEMENTS

In this work we consider the special class of displacement fields given by

$$\underline{\mathbf{h}}(\mathbf{x}_0)\langle\boldsymbol{\xi}\rangle = \frac{1}{|\boldsymbol{\xi}|}\left(\frac{\partial\,u_i(\mathbf{x}_0)}{\partial\alpha_j}\xi_j + \frac{1}{2}\frac{\partial^2\,u_i(\mathbf{x}_0)}{\partial\alpha_j\partial\alpha_k}\,\xi_j\,\xi_k\right)\mathbf{e}_i\,, \tag{5}$$

where $\alpha_i := \mathbf{x}\cdot\mathbf{e}_i$, $\xi_i := \boldsymbol{\xi}\cdot\mathbf{e}_i$, $u_i := \mathbf{u}\cdot\mathbf{e}_i$, and $\{\mathbf{e}_1,\mathbf{e}_2,\mathbf{e}_3\}$ is a fixed orthonormal basis in $\mathbb{E}^3$. The states $\underline{\varphi}$ and $\underline{\mathbf{h}}_d$ in the decomposition of $\underline{\mathbf{h}} = \underline{\varphi}\,\underline{\mathbf{e}} + \underline{\mathbf{h}}_d$ can then be determined from (5) and substituted into (4). A similar procedure also yields $\widehat{\underline{\mathbf{L}}}_{\mathbf{x}}[\underline{\mathbf{h}}]\langle-\boldsymbol{\xi}\rangle$, which together with $\widehat{\underline{\mathbf{L}}}_{\mathbf{x}_0}[\underline{\mathbf{h}}]\langle\boldsymbol{\xi}\rangle$ and $\boldsymbol{\xi} = \mathbf{x}-\mathbf{x}_0$ can be substituted in the integrand of the equation (1) with the help of (2). After integration and using $\omega_\delta := \pi^2\int_0^\delta\int_0^\delta \omega(\check{\rho},\hat{\rho})\check{\rho}^2\hat{\rho}^2 d\hat{\rho}\,d\check{\rho}$, the resulting equation becomes

$$\frac{8\,\omega_\delta}{45}\left[(20\,\alpha_2+\alpha_3+12\,\alpha_1)\,\frac{\partial^2 u_{j_{\mathbf{x}_0}}}{\partial\alpha_j\partial\alpha_i} + 3\,(\alpha_3+2\,\alpha_1)\,\frac{\partial^2 u_{i_{\mathbf{x}_0}}}{\partial\alpha_j\partial\alpha_j}\right] + b_i(\mathbf{x}_0) = 0\,,\quad b_i := \mathbf{b}\cdot\mathbf{e}_i\,,\quad i=1,2,3. \tag{6}$$

Seleson and Littlewood [2] have also used a class of second-degree polynomials to study equilibrium of the linearized model obtained from Silling *et al.* [3]. Because this linearized model is a particular case of the model considered in this work, they find differential equations that are particular cases of the equations in (6).

On the other hand, the equilibrium equations of classical linear elasticity theory at the point $\mathbf{x}_0\in\mathcal{B}$ are given by

$$(\lambda+\mu)\frac{\partial^2 u_j(\mathbf{x}_0)}{\partial\alpha_j\partial\alpha_i} + \mu\frac{\partial^2 u_i(\mathbf{x}_0)}{\partial\alpha_j\partial\alpha_j} + b_i(\mathbf{x}_0) = 0\,,\qquad i=1,2,3, \tag{7}$$

where λ and μ are the Lamé constants. The peridynamic equilibrium equations in (6) become the classical equilibrium equations in (7) provided that $3\,\lambda+2\,\mu = (\alpha_1+2\,\alpha_2)\,16\,\omega_\delta/15$, $(\lambda+\mu) = (2\,\alpha_1+\alpha_3)\,8\,\omega_\delta/15$. By using the relations $\mu = E/[2\,(1+\nu)]$, $\lambda = E\,\nu/[(1+\nu)(1-2\,\nu)]$, where E is the Young's modulus and ν is the Poisson's ratio, we find

$$\alpha_{11}+2\alpha_{12} = \frac{3\,E}{16\,(1-2\nu)\,\omega_\delta}\,,\qquad 2\alpha_{11}+\alpha_{33} = \frac{15\,E}{16\,(1+\nu)\,\omega_\delta}, \tag{8}$$

which were also found by Aguiar [1] using energy-based arguments together with homogeneous deformations. Differently from that work, here, we use the peridynamic equilibrium equation (1) together with the class of second-degree polynomial displacements given by (5). Observe from (8) that two constants remain undetermined. Aguiar [1] proposes an energy-based correspondence argument to determine these constants, which will be discussed at the meeting.

CONCLUSIONS

We have used a class of second-degree polynomial displacement fields to investigate equilibrium of a linearly elastic peridynamic material having a quadratic free energy function with four peridynamic constants. We have found equations for the second-order derivatives of the displacement fields that have the same form of the equilibrium equations from classical linear theory. By equating the coefficients of these differential equations, we have found two relations between the four peridynamic constants and the two Lamé constants, which are the same relations found in previous work through energy-based considerations. In addition of being consistent with the results found previously, the results of this work indicate that local equilibrium is not sufficient to determine the four peridynamic constants. The fact that two peridynamic constants are left undetermined reflects the nonlocal nature of the theory and is the subject of ongoing investigation.

ACKNOWLEDGEMENTS

Financial support provided by the National Council for Scientific and Technological Development (CNPq), # 420099/2018-2, and the State of São Paulo Research Foundation (FAPESP), # 2019/00428-7. are gratefully acknowledged.

References

[1] Aguiar A. R., 2016. On the Determination of a Peridynamic Constant in a Linear Constitutive Model. *J Elast*, **122**:27-39, 2016.
[2] Seleson P., Littlewood, D. J. Convergence Studies in Meshfree Peridynamic Simulations. *Comp Math Appl*, **71**:2432-2448, 2016.
[3] Silling S. A., Epton M., Weckner O., Xu J., Askari E. Peridynamic states and constitutive modeling. *J Elast*, **88**: 151-184, 2007.

EFFECTS OF MISFIT STRAIN ON QUANTUM MECHANICAL STATES OF SPHERICAL CORE/SHELL QUANTUM DOTS

Youjung Seo [1], Anh Tay Nguyen*[2], Seong-Hwan Park [3], and Y. Eugene Pak[2]
[1]Nano Science and Technology, Graduate School of Convergence Science and Technology, Seoul National University, Suwon 443-270, Republic of Korea
[2]Department of Mechanical Engineering, SUNY Korea, Incheon, Republic of Korea
[3]Department of Electronics Engineering, Catholic University of Daegu, Hayang, Kyeongbuk 712-702, Republic of Korea

Summary Effects of lattice-mismatched strain on optical properties of CdSe/CdS, CdSe/ZnSe, and CdSe/ZnS core/shell quantum dot nanostructures are investigated theoretically using simple continuum elasticity and effective mass models. This strain is calculated based on the spherically symmetric linear elasticity solution for a misfitted inclusion embedded in a finite matrix. The effective mass quantum mechanics model shows that the subband energy is blueshifted by the compressive strain in the core, whereas the corresponding tensile strain in the shell, albeit less influentially, shifts the conduction subband energy downward. It is also quantitatively shown that the shift in the subband energies is proportional to both the amount of lattice mismatch and the shell thickness.

INTRODUCTION

The core/shell nanostructure systems such as quantum dots (QDs) have been used extensively as stable light sources with color-tunable feature induced by their dimensional change. Lattice distortions induced by the structural lattice mismatch between the core and the shell give rise to an internal potential effect [1]. This leads to a shift of the conduction and valence subband energies in QD core/shell assembly by changing the interatomic distances, which alters the energy levels of the bonding electrons [2]. As a result, QD core/shell nanostructure can exhibit a large change in the emission properties because of the intrinsic strain fields.

Quantifying the strain effects that depend on the shell thickness and the core/shell lattice mismatch have not yet been theoretically analyzed in detail. Therefore, we developed the spherically-symmetric analytical model incorporating deformation potentials in the Hamilitonian to quantify the effects of strain on the energy states of light exciton confined in type I II-VI group semiconductors with spherical QDs core/shell structure. Assuming that the QD core/shell structure exhibits spherically hexagonal anisotropy, an exact solution is obtained through the eigenvalue decomposition method and the analytical expressions of the strain fields are found using appropriate boundary and continuity conditions [3]. To calculate the ground-state subband energies in the conduction and valence bands and the exciton binding energy that includes the strain effects in QD core/shell calculated previously, we used 1s hydrogenic-like wavefunctions, the variational method and the effective-mass approximation (EMA). Parametric studies on the ground-state subband and the binding energies considering variations in the hydrostatic strains and the parameters such as QD radius and shell thickness are also presented. Since the strains used in the analysis take into account of both QD size and shell thickness, this work can be useful for functional improvements by optimizing the geometries of the QD nanostructure. For future work, a closed-form solution for the strain field arising from lattice mismatch of the spherical QD core/shell structures with rectilinear material anisotropy embedded in an infinite matrix will be taken into account for a more realistic model [4].

FORMULATIONS

Let's consider a lattice-mismatched QD core/shell structure modelled as a size-mismatched, spherical inclusion embedded in a finite spherical matrix in the framework of linear elasticity [3], which satisfies the following assumptions:
1. Quantum dot core/shell assembly is regarded as a spherically symmetric concentric structure exhibiting spherically anisotropic material properties.
2. Linear elastic behavior is assumed in the quantum dot core/shell structure despite mismatch strain up to 4%.
3. Non-local nanoscale effects are not considered in this continuum model.

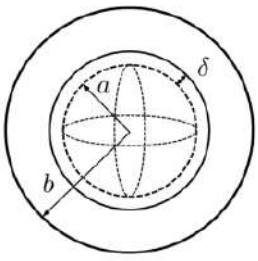

Figure 1. A spherical QD core/shell nanostructure with lattice-mismatched displacement, δ, and radii, a and b.

The constitutive equations relating elastic stresses, σ_{ij}, to strains, ε_{kl}, in a continuum body can be written as

$$\sigma_{ij} = C_{ijkl}\varepsilon_{kl} \quad (1)$$

where C_{ijkl} are the elastic constants. Due to the spherical symmetry of the QD structure, the displacement field, u_i, depends only on the radial direction ($u_\theta = u_\phi = 0$). The governing equation is then simplified as

$$\sigma_{ij,j} = \frac{d\sigma_{rr}}{dr} + \frac{2\sigma_{rr} - \sigma_{\theta\theta} - \sigma_{\phi\phi}}{2} = 0 \quad (2)$$

where σ_{rr}, $\sigma_{\theta\theta}$, $\sigma_{\phi\phi}$ are the stress components and C_{11} and C_{12} are cubic elastic constant. The general solution for Eq. (2) can be obtained as

*Corresponding author. E-mail: anh.nguyen.1@stonybrook.edu

$$u_r = Ar + \frac{B}{r^2} \tag{3}$$

By solving the boundary value problem for QD core/shell nanostructure subjected to a lattice-mismatched misfit strain, $\varepsilon_m = (l^C - l^S)/l^S$, where l^C and l^S are the lattice constants for the core and the shell, the radial displacement in the core, u_r^C, and in the shell, u_r^S, are found to be

$$u_r^C = \frac{2\delta}{D}(a^3 - b^3)\left(C_{11}^{S\,2} + C_{11}^S C_{12}^S - 2C_{12}^{S\,2}\right)\frac{r}{a}3$$
$$u_r^S = \frac{\delta}{D}(C_{11}^C + 2C_{12}^C)[b^3(C_{11}^S + 2C_{12}^S) + 2(C_{11}^C - C_{12}^C)r^3]\frac{a^2}{r^2}3 \tag{4}$$

where

$$D = 2a^3(C_{11}^S - C_{12}^S)(3C_{11}^C + 2C_{12}^C - C_{11}^S - 2C_{12}^S) + b^3(C_{11}^S + 2C_{12}^S)[C_{11}^C + 2(C_{12}^C + C_{11}^S - C_{12}^S)], \tag{5}$$

a is the core radius, b is the shell radius, and δ is the mismatch displacement created by the mismatched lattice at the interface. Subsequently, the closed-form expressions of the elastic strain distribution can be derived as

$$\varepsilon_{rr}^C = \varepsilon_{\theta\theta}^C = \varepsilon_{\phi\phi}^C = \frac{1}{D}\left[2(a^3 - b^3)\left(C_{11}^{S\,2} + C_{11}^S C_{12}^S - 2C_{12}^{S\,2}\right)\right]\frac{\delta}{a}$$
$$\varepsilon_{rr}^S = -\frac{2a^2}{D}(C_{11}^C + 2C_{12}^C)[b^3(C_{11}^S + 2C_{12}^S) - (C_{11}^S - C_{12}^S)r^3]\frac{\delta}{r^3} \tag{6}$$
$$\varepsilon_{\theta\theta}^S = \varepsilon_{\phi\phi}^S = \frac{a^2}{D}(C_{11}^C + 2C_{12}^C)[b^3(C_{11}^S + 2C_{12}^S) + 2(C_{11}^S - C_{12}^S)r^3]\frac{\delta}{r^3}$$

The dilatational strain, $\varepsilon_{ii} = \varepsilon_{rr} + \varepsilon_{\theta\theta} + \varepsilon_{\phi\phi}$, can be obtained as

$$\varepsilon_{kk}^C = \frac{6}{D}(a^3 - b^3)\left(C_{11}^{S\,2} + C_{11}^S C_{12}^S - 2C_{12}^{S\,2}\right)\frac{\delta}{a}$$
$$\varepsilon_{kk}^S = \frac{6a^2}{D}(C_{11}^C + 2C_{12}^C)(C_{11}^S - C_{12}^S)\frac{\delta}{a} \tag{7}$$

The QD core/shell nanostructure modeled as a single electron or a hole confined in a spherical finite potential well in the presence of a deformation potential yields the following transcendental equation solving for energy states E of the QD,

$$\sqrt{m_{(e,h)}^w(E - V_w)\frac{2m_o b^2}{\hbar^2}}\cot\left[a\sqrt{m_{(e,h)}^w(E - V_w)\frac{2m_o b^2}{\hbar^2}}\right]$$
$$= -\sqrt{m_{(e,h)}^b(V_b - E)\frac{2m_o b^2}{\hbar^2}} \tag{8}$$

where $\hbar$ is the Dirac constant, $m_{(e,h)}^w$ and $m_{(e,h)}^b$ are the effective masses for the core and the shell, respectively, normalized to the electron's true mass, m_o. The potential V corresponding to a mechanical deformation alters the band energy that is influenced by the strain field arising from the core/shell lattice misfit. The deformation potentials within the well, V_w, and within the potential barrier, V_b, are assumed to be influenced by the dilatational strains as follows

$$\text{for } r \le a \quad V_w = d_w^C(\varepsilon_{xx}^C + \varepsilon_{yy}^C + \varepsilon_{zz}^C),$$
$$\text{and for } r \ge a \quad V_b = \Delta E_{C,V} + d_w^S(\varepsilon_{xx}^S + \varepsilon_{yy}^S + \varepsilon_{zz}^S) \tag{9}$$

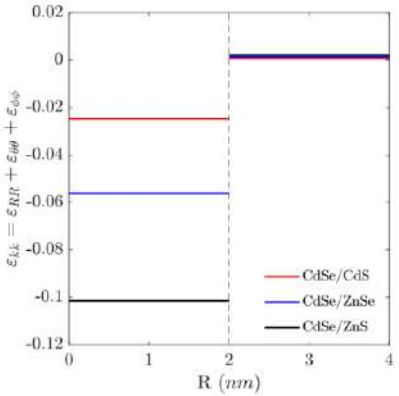

Figure 2. Dilatational strains as a function of radial dimension r, where a=2 nm and b=4 nm.

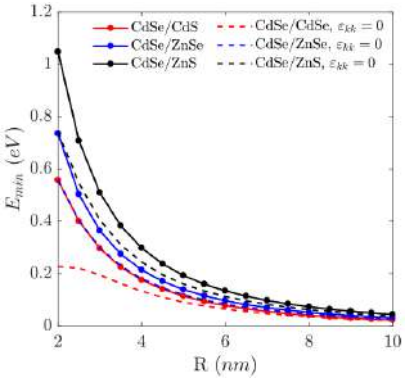

Figure 3. Ground-state energies, E_{min}, as a function of CdSe QD radius of various core/shell QD structures.

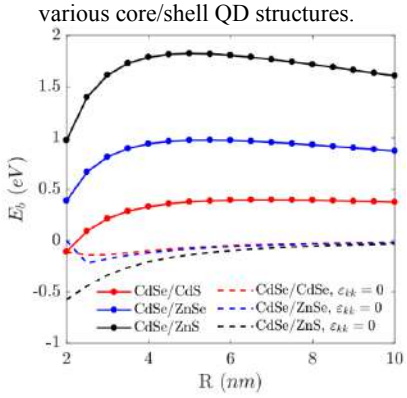

Figure 4. Binding energies, E_b, for an exciton in various core/shell QD structures with respect to QD radius, compared to those without the lattice-mismatch strain.

where ΔE_C and ΔE_V are the conduction and valence band offsets, and d_w^C and d_w^S are the deformation potential constants of the core and the shell, respectively. Eq. (8) will be solve numerically to find the eigenvalues corresponding to the respective energy states.

The ground-state binding energy for the exciton, E_b, is defined as

$$E_b = E_{1e} + E_{1h} - E(\alpha)_{min} = E_{1e} + E_{1h} + \bar{K} + \bar{V}_{conf} + \bar{V}_{e-h} \tag{10}$$

where E_{1e}, E_{1h}, and $E(\alpha)_{min}$ are the ground-state energies for the conduction and valence subbands and the exciton, and $\bar{K}$, $\bar{V}_{conf}$ and $\bar{V}_{e-h}$ are the kinetic energy, the confinement potential, and the coulomb interaction energy, which can be obtained using variational method. The numerical results are given in Figure 2-4.

References

[1] Lim, J., Jeong, B. G., Park, M., Kim, J. K., Pietryga, J. M., Park, Y.-S., … Bae, W. K. Influence of Shell Thickness on the Performance of Light-Emitting Devices Based on CdSe/Zn1-XCdXS Core/Shell Heterostructured Quantum Dots. *Adv. Mater.*, **26(47)**, 8034–8040, 2014.
[2] Smith, A. M., Mohs, A. M., Nie, S. Tuning the optical and electronic properties of colloidal nanocrystals by lattice strain. *Nat. Nanotechnol.*, **4(1)**, 56–63, 2008.
[3] Seo, S. Y., Yoo, S. S., Mishra, D., Park, S.-H., Pak, Y. E. Exact piezoelectric solution for misfitted inclusion in finite spherical matrix: Applications to quantum dot core/shell crystals. *Int J Solids Struct.*, **94-95**, 158–169, 2016.
[4] Eshelby, J.D., The determination of the elastic field of an ellipsoidal inclusion, and related problems. *Proc. R. Soc. A* **241**, 376, 1957

THERMODYNAMIC FOUNDATION OF GENERALIZED VARIATIONAL PRINCIPLE

Bo-Hua Sun[1]
[1]School of Civil Engineering & Institute of Mechanics and Technology, Xi'an University of Architecture and Technology, Xi'an 710055, China, http://imt.xauat.edu.cn, email: sunbohua@xauat.edu.cn

Summary One open question remains regarding the theory of the generalized variational principle, that is, why can the stress-strain relation still be derived from the generalized variational principle while the method of Lagrangian multiplier method is applied in vain? This study shows that the generalized variational principle can only be understood and implemented correctly within the framework of thermodynamics. As long as the functional has one of the combination $A(\epsilon_{ij})-\sigma_{ij}\epsilon_{ij}$ or $B(\sigma_{ij})-\sigma_{ij}\epsilon_{ij}$, its corresponding variational principle will produce the stress-strain relation without the need to introduce extra constraints by the Lagrangian multiplier method. It is proved herein that the Hu-Washizu functional $\Pi_{HW}[u_i,\epsilon_{ij},\sigma_{ij}]$ and Hu-Washizu variational principle comprise a real three-field functional.

INTRODUCTION

Generalized variational mechanics began in the 1950s with the breakthrough works of Reissner [1] on two-field variational principles for elasticity problems, in which the displacement u_i and stress σ_{ij} are considered independent fields. Reissner introduced a functional F that is defined in terms of 12 arguments: six stresses σ_{ij} and six strains ϵ_{ij}: $F=\sigma_{ij}\epsilon_{ij}-B(\sigma_{ij})$, where $B(\sigma_{ij})$ is the elastic complementary energy density. Reissner proved the following theorem: Among all states of stress and displacement that satisfy the boundary conditions of the prescribed surface displacement, the actually occurring state of stress and displacement is determined by the variational equation: $\delta\left\{\iiint_V F dV-\iint_{S_p}\bar{p}_i u_i dS\right\}=0$, where the symbol V indicates the volume of the elastic body and S_p indicates that the surface integrals are to be taken over that part of the surface only where the appropriate surface stress is prescribed.

In 1954, Hu published a paper [3] (its English version appeared in 1955 [4]) that borrowed the idea from Reissner [1] and successfully extended Reissner's two-field (displacement-stress) theory to a three-field (displacement-stress-strain) theory by introducing a functional H_U given by $H_U=A(\epsilon_{ij})-f_i u_i-\sigma_{ij}(\epsilon_{ij}-\frac{1}{2}u_{i,j}-\frac{1}{2}u_{j,i})$. Hu [4]) proved a theorem as follows:$\delta\left\{\iiint_V H_U dV-\iint_{S_\sigma}\bar{p}_i u_i dS-\iint_{S_u}\sigma_{ij}n_j(u_i-\bar{u}_i)dS\right\}=0$. In 1955, Washizu [5] independently proposed the same functional and proved the same theorems as Hu [3, 4].

Regarding the history of the generalized variational principle, Felippa [9] published a dedicated paper on the original publication of the generalized variational principle and showed that de Veubeke had developed a much more generalized variational principle in a report dated 1951 [2], in which four fields, namely, displacement, stress, strain, and surface force, were included. de Veubeke's four-field $(u_i,\sigma_{ij},\epsilon_{ij},t_i)$ theory can be presented as follows [9]: $\delta\Pi=0$, where the functional: $\Pi_V[u_i,\sigma_{ij},\epsilon_{ij},t_i]=\iiint_V[A(\epsilon_{ij})+\sigma_{ij}(\frac{1}{2}u_{i,j}-\frac{1}{2}u_{j,i}-\epsilon_{ij})-f_i u_i]dV-\iint_{S_\sigma}\bar{t}_i u_i dS-\iint_{S_u}t_i(u_i-\bar{u}_i)dS$. The three-field standard form is obtained by setting $t_i=\sigma_{ij}n_j$ on S_u a priori. Hence, Fellippa proposed that the canonical functional be called the de Veubeke-Hu-Washizu functional Π_{VHW}. This proposal has been confirmed by The History of the Theory of Structures Searching for Equilibrium [10].

In 1983, Chien [7], who was Hu's supervisor and communicated Hu's paper to both the Chinese Journal of Physics [3] and Science Sinica [4], pointed out that, regarding all publications and reports of Reissner [1], Hu [3, 4] and Washizu [5] did not give any information on how to construct the functional. The formulation of the generalized variational seems mystical, and thus Chien indicated that the trial-and-error method was used when Reissner, Hu, and Washizu formulated their functional [7, 8].

To derive the generalized functional in a systematic way, Chien proposed to formulate the functional by using the well-known method of Lagrangian multipliers [7]. With the help of the Lagrangian multipliers, in 1983 Chien [7] successfully reformulated the two-field functional, namely, $\Pi[u_i,\sigma_{ij}]$ and $\Pi[u_i,\epsilon_{ij}]$, which are called the Hellinger-Resissner functional [1] and De Veubeke functional [2], respectively. However, Chien [7] found that the constitutive relation between stress and strain cannot be included to form a three-field functional $\Pi[u_i,\epsilon_{ij},\sigma_{ij}]$ due to the zero crisis of corresponding Lagrangian multipliers, as it is known to be impossible to incorporate this condition of constraint into a functional whenever the corresponding Lagrange multiplier turns out to be zero. Therefore, Chien claimed that the functional H_U is not a three-field, but rather a two-field, functional. To address this point of view, Chien elegantly wrote a monograph on the generalized variational principle [8] and, to overcome the difficulty, he proposed a method of a higher-order Lagrange multiplier, a four-field functional Π_Q that is suggested to be expressed as follows: $\Pi_Q[u_i,\sigma_{ij},\epsilon_{ij},\lambda]=\iiint_V H_U dV-\iint_{S_\sigma}\bar{p}_i u_i dS-\iint_{S_u}\sigma_{ij}n_j(u_i-\bar{u}_i)dS+\iiint_V\lambda[A(\epsilon_{ij})+B(\sigma_{ij})-\sigma_{ij}\epsilon_{ij}]dV$. Chien proved that for no zero $\lambda\neq 0$, the $\delta\Pi_Q[u_i,\sigma_{ij},\epsilon_{ij},\lambda]=0$ will produce balance equations, strain-displacement relations, stress-strain relations, and corresponding boundary conditions. Owing to the arbitrary nature of the Lagrangian multiplier λ, there are an infinite number of functionals $\Pi_Q[u_i,\sigma_{ij},\epsilon_{ij};\lambda]$.

Regarding Chien's questioning [7, 8], no explanation from Hu, to the best of our knowledge, has been found in the literature. Because the formulation of the generalized variational principle has been recognized as a key contribution by a Chinese scholar to mechanics worldwide, and in particular, considering its importance in finite-element formulation, it is vital that Chien's question can be clearly answered. Otherwise, it will continue to cause confusion to both scholars and students. The task of answering this question has become a newcomer's responsibility.

THERMODYNAMIC FOUNDATION OF GENERALIZED VARIATIONAL PRINCIPLE

Since thermodynamics is foundation of material constitutive theory, to solve Chien's question, let's go back to the original point of thermodynamics of continuum. Combining the first law and second laws of thermodynamics leads to an equation defined in the current configuration as follows: $\rho(\dot{\phi}+\eta\dot{\theta})-\boldsymbol{\sigma}:\dot{\boldsymbol{\epsilon}}+\frac{1}{\theta}\boldsymbol{q}\cdot\boldsymbol{\nabla}\theta\leq 0$, where $\phi(\boldsymbol{\epsilon},\theta)$ is the Helmholtz free energy, $\eta(\boldsymbol{\epsilon},\theta)$ the entropy, θ the temperature, $\boldsymbol{\sigma}$ the stress tensor, $\dot{\boldsymbol{\epsilon}}$ the rate of deformation, and $\boldsymbol{q}$ the heat flux vector. Since $\dot{\phi}=\phi_{,\boldsymbol{\epsilon}}:\dot{\boldsymbol{\epsilon}}+\phi_{,\theta}\dot{\theta}=\phi_{,\boldsymbol{\epsilon}}:\dot{\boldsymbol{\epsilon}}+\phi_{,\theta}\dot{\theta}$, one can obtain $(\rho\frac{\partial\phi}{\partial\boldsymbol{\epsilon}}-\boldsymbol{\sigma}):\dot{\boldsymbol{\epsilon}}+\rho(\frac{\partial\phi}{\partial\theta}+\eta)\dot{\theta}+\frac{1}{\theta}\boldsymbol{q}\cdot\boldsymbol{\nabla}\theta\leq 0$. Note that the left-hand side of the inequality is a polynomial of degree 1 in $\dot{\boldsymbol{\epsilon}}$ and $\dot{\theta}$. Because the inequality must hold for all choices of $\dot{\boldsymbol{\epsilon}}$ and $\dot{\theta}$, it will therefore be violated unless $\boldsymbol{\sigma}=\rho\frac{\partial\phi}{\partial\boldsymbol{\epsilon}}\ and\eta=-\frac{\partial\phi}{\partial\theta}$, which are the constitutive equations of simple materials. The purpose of this brief review of the formulation of constitutive equations is to show that the thermodynamic relation, $\rho(\dot{\phi}+\eta\dot{\theta})-\boldsymbol{\sigma}:\dot{\boldsymbol{\epsilon}}+\frac{1}{\theta}\boldsymbol{q}\cdot\boldsymbol{\nabla}\theta\leq 0$, has already contained the constitutive relations. In other words, the thermodynamic relation, $\rho(\dot{\phi}+\eta\dot{\theta})-\boldsymbol{\sigma}:\dot{\boldsymbol{\epsilon}}+\frac{1}{\theta}\boldsymbol{q}\cdot\boldsymbol{\nabla}\theta\leq 0$, is an implicit form of constitutive equation.

For isothermal reversible thermodynamics, $\dot{\theta}=0$, one has $\rho\dot{\phi}-\boldsymbol{\sigma}:\dot{\boldsymbol{\epsilon}}=0$, which can further be reduced to $\rho d\phi-\boldsymbol{\sigma}:d\boldsymbol{\epsilon}=\rho d\phi-\sigma_{ij}\epsilon_{ij}=0$. If one replaces $\rho\phi$ by the potential energy density $A(\epsilon_{ij})$, we have $dA(\epsilon_{ij})-\sigma_{ij}d\epsilon_{ij}=0$, the equivalent form of which is the stress-strain relation: $\sigma_{ij}=\frac{\partial A(\epsilon_{ij})}{\partial\epsilon_{ij}}$. Similar to the above-mentioned general case, $dA(\epsilon_{ij})-\sigma_{ij}d\epsilon_{ij}=0$ implies the stress-strain relation.

Furthermore, since $dA(\epsilon_{ij})-\sigma_{ij}d\epsilon_{ij}=dA(\epsilon_{ij})-[d(\sigma_{ij}\epsilon_{ij})-\epsilon_{ij}d\sigma_{ij}]=0$, and denoting $dB=\epsilon_{ij}d\sigma_{ij}$, after integration one has $A(\epsilon_{ij})+B(\sigma_{ij})-\sigma_{ij}\epsilon_{ij}=C$. Applying conditions $A(0)=0$ and $B(0)=0$, thus $C=0$. Hence, $A(\epsilon_{ij})+B(\sigma_{ij})-\sigma_{ij}\epsilon_{ij}=0$, where $A(\epsilon_{ij})$ and $B(\sigma_{ij})$ are the potential and complementary energy density, respectively.

Following the above thinking, it is easy to know that a functional has included a stress-strain relation if it contains either the terms $[A(\epsilon_{ij})-\sigma_{ij}\epsilon_{ij}]$ or $[B(\sigma_{ij})-\sigma_{ij}\epsilon_{ij}]$. In other words, if the structure of the functional was in the following form: $\Pi[u_i,\epsilon_{ij},\sigma_{ij}]=\iiint_V\left[\underline{A(\epsilon_{ij})-\sigma_{ij}\epsilon_{ij}}+...\right]dV+\text{Boundary tems}$, which implies that the stress-strain relation $\sigma_{ij}=\frac{\partial A(\epsilon_{ij})}{\partial\epsilon_{ij}}$ is included, since its variational $\delta\Pi[u_i,\epsilon_{ij},\sigma_{ij}]=0$, leads to $\iiint_V\left\{[\frac{\partial A(\epsilon_{ij})}{\partial\epsilon_{ij}}-\sigma_{ij}]\delta\epsilon_{ij}+...\right\}dV+\delta(\text{Boundary tems})=0$, and due to the arbitrary variation $\delta\epsilon_{ij}$, one therefore has the following stress-strain relation: $\frac{\partial A(\epsilon_{ij})}{\partial\epsilon_{ij}}-\sigma_{ij}=0$. With this understanding, an examination of the following Hu-Washizu functional is necessary:

$$\Pi_{HW}[u_i,\epsilon_{ij},\sigma_{ij}]=\iiint_V\left\{\underline{A(\epsilon_{ij})}-f_iu_i-\underline{\sigma_{ij}[\epsilon_{ij}}-\frac{1}{2}(u_{i,j}+u_{j,i})]\right\}dV-\iint_{S_\sigma}\bar{p}_iu_idS-\iint_{S_u}\sigma_{ij}n_j(u_i-\bar{u}_i)dS.$$

The combination of the underlined terms in the above functional is exactly the term of $A(\epsilon_{ij})-\sigma_{ij}\epsilon_{ij}$. Therefore, the Hu-Washizu functional $\Pi_{HW}[u_i,\epsilon_{ij},\sigma_{ij}]$ has already included the stress-strain relation $\sigma_{ij}=\frac{\partial A(\epsilon_{ij})}{\partial\epsilon_{ij}}$. The Hu-Washizu functional $\Pi_{HW}[u_i,\epsilon_{ij},\sigma_{ij}]$ is a real three-field functional. This key point might not be understood by Hu [3, 4], Reissner [1], and de Veubeke [2] when they constructed their own generalized functional by the trial-and-error method.

CONCLUSIONS

This study shown that the generalized variational principle can only be correctly understood and implemented within the framework of thermodynamics. As long as the functional has any one of the combination $A(\epsilon_{ij})-\sigma_{ij}\epsilon_{ij}$ or $B(\sigma_{ij})-\sigma_{ij}\epsilon_{ij}$, its corresponding variational principle can produce the stress-strain relation without the need to introduce extra constraints by the Lagrangian multiplier method. Therefore, the Hu-Washizu functional $\Pi_{HW}[u_i,\epsilon_{ij},\sigma_{ij}]$ is a real three-field functional and the Hu-Washizu variational principle is a three-field variational principle. In addition, that Chien's functional $\Pi_Q[u_i,\epsilon_{ij},\sigma_{ij},\lambda]$ is a much more general three-field functional has been confirmed.

Acknowledgments: It is my privilege to dedicate this paper to the memories of Prof. Chien and Prof. Hu for their great contribution to the establishment of the generalized variational principle.

References

[1] Reissner, E., On a variational theorem in elasticity. *J. Math. & Phys.* **29**:90-95, (1950)
[2] Fraeijs de Veubeke, B. M., Diffusion des inconnues hyperstatiques dans les voilures á longeron couplés, Bull. Serv. Technique de L'Aéronautique No. 24, Imprimerie Marcel Hayez, Bruxelles, 56pp (1951)
[3] Hu, H.-C. On the variational princinples in the theory of elasticity and the plasticity. *Acta Physica Sinica*, **10**(3):259-290 (1954)
[4] Hu, H.-C., On some variational methods on the theory of elasticity and the theory of plasticity, *Scientia Sinica*, **4**:33-54(1955)
[5] Washizu, K., On the variational principles of elasticity and plasticity, Aeroelastic and Structures Research Lab, Tech. Rep. 25-18, MIT, Cambridge (1955)
[6] Washizu, K., Variational Methods in Elasticity and Plasticity, Pergamon Press, New York(1968)
[7] Chien, W.Z., Method of higher-order Lagrange multiplier and generalized variational principles of elasticity with more general forms, *Appl. Math. Mech.* **4**(2):143-157(1983)
[8] Chien, W.Z., Generalized Variational Princinples. Knowledge Publisher, Beijing (1985) (In Chinese).
[9] Felippa, C. A., On the original publication of the general canonical functional of linear elasticity, *J. Appl.Mech.* **67**(1):217-219, 2000.
[10] Kurrer,K.E. Thrift,P. and Ramm, E. The History of the Theory of Structures Searching for Equilibrium, Wilhelm Ernst & Sohn.,Berlin, Germany (2018)

METHOD OF IMAGE CHARGES FOR DESCRIBING SMALL DEFORMATIONS OF BOUNDED PLANAR SOLID STRUCTURES WITH HOLES AND INCLUSIONS

Matjaž Čebron*[1], Siddhartha Sarkar[2], Andrej Košmrlj[3], and Miha Brojan[1]
[1]Laboratory for Nonlinear Mechanics, University of Ljubljana, Ljubljana, Slovenia
[2]Department of Electrical Engineering, Princeton University, Princeton, NJ 08544, USA
[3]Department of Mechanical and Aerospace Engineering, Princeton University, Princeton, NJ 08544, USA

Understanding how deformation patterns of highly deformable structures form when an external load is applied is crucial for designing metamaterials with unique properties. Here, we present a method to predict the linear deformation of finite 2D solid structures with circular holes and inclusions, using analogies with image charges and induction in electrostatics. Charges in electrostatics induce image charges near the boundaries and an external electric field induces polarization of conductive and dielectric objects. Similarly, charges in elasticity induce image charges near boundaries and an external stress induces polarization inside holes and inclusions. In the presented method, the induced polarization is expanded into a series of multipoles and interactions of the inclusions with the external stress field, between them, and with their images is systematically taken into account.

ELASTIC MULTIPOLE METHOD

In mechanical metamaterials the geometry, topology and contrasting elastic properties of adherent materials are exploited to achieve exceptional functionalities such as negative thermal expansion and Poisson`s ratio, shape morphing, mechanical cloaking, tuneable phononic band gaps etc. At the heart of these functionalities are deformation patterns of such materials with holes and inclusions. In this contribution we illustrate a method of describing linear deformations of finite planar solid structures by employing similarities between electrostatics and elasticity.

Analogies between electrostatics and 2D linear elasticity can be recognized when the governing equations are formulated in terms of scalar functions, namely the electric potential U and the Airy stress function χ. The electric field $\boldsymbol{E}$ in electrostatics is obtained from the gradient of the electric potential: $\boldsymbol{E} = -\boldsymbol{\nabla} U$. Similarly, the stress tensor field σ_{ij} is obtained by taking spatial derivatives of the Airy stress function: $\sigma_{xx} = \partial^2\chi/\partial y^2$, $\sigma_{yy} = \partial^2\chi/\partial x^2$ and $\sigma_{xy} = -\partial^2\chi/\partial x\partial y$. The most compelling aspect of these formulations in terms of scalar functions is that Faraday`s law in electrostatics and the force balance equation in elasticity are automatically satisfied. Furthermore, the governing equations for these scalar functions take simple forms. For the electric potential we have the well-known Gauss`s law $\Delta U = -\rho_e/\varepsilon_e$, where ρ_e is the electric charge density and ε_e is the permittivity of the material. The analogous equation in elasticity $\Delta\Delta\chi = E\rho$ describes the strain (in)compatibility conditions, where E is the 2D Young`s modulus and ρ is the elastic charge density associated with defects that are the sources of incompatibility.

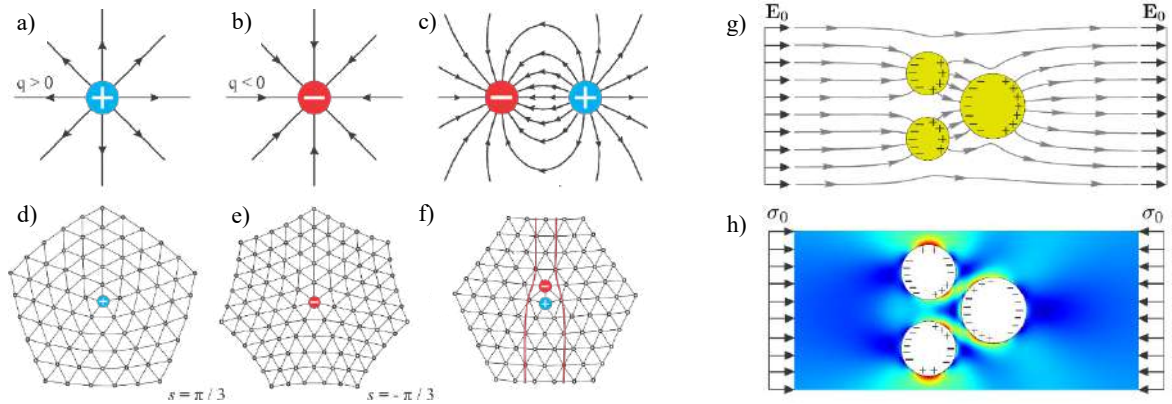

Figure 1. a) Positive electric monopole with charge q (arrows show the electric field), b) neg. electric monopole, c) electric dipole, d) positive elastic monopole (disclination) with $s = \pi/3$, e) negative elastic monopole ($s = -\pi/3$), f) elastic dipole (dislocation), g) induced polarization of conducting spheres (yellow), h) induced polarization due to external stress of holes in an elastic matrix.

In electrostatics a monopole is defined as the electric charge density distribution proportional to the Dirac delta function $\rho_e = q\delta(\boldsymbol{x} - \boldsymbol{x}_0)$ (Figs. 1a, 1b). Similarly, we can define a monopole in 2D elasticity, i.e. $\rho = s\delta(\boldsymbol{x} - \boldsymbol{x}_0)$ where s is the charge and $\boldsymbol{x}_0$ describes its position. The physical interpretation of monopoles in elasticity comes from condensed matter theory. When a wedge of angle s is cut from a 2D material and the newly formed boundaries are "glued" back together, a positive disclination defect (point elastic charge) of charge s is formed (Fig. 1d). The negative disclination with charge $s < 0$ corresponds to the insertion of a wedge with angle $|s|$ (Fig. 1e). An electrostatic dipole is formed by two opposite point charges $\pm q$ (Fig. 1c). Analogous elastic dipoles (Fig. 1f) consist of two elastic dipoles and are commonly known as dislocations. Similarly, higher order electric and elastic multipoles can be constructed. Elastic multipoles are closely related to the general solution of the biharmonic equation $\Delta\Delta\chi = 0$ due to Michell [1], since this solution contains the Airy stress functions of monopoles, dipoles and all higher order elastic multipoles.

*Corresponding author. E-mail: matjaz.cebron@fs.uni-lj.si.

An external electric field induces polarization in conducting and dielectric objects (Fig. 1g). Similarly, external stress with a stress function χ_{ext} induces elastic multipoles in holes and inclusions (Fig. 1h) which in turn interact with each other through their induced elastic multipoles. Let the induced stress function in the i-th inhomogeneity be χ_i. The total stress function in the material is then $\chi_{tot} = \chi_{ext} + \sum \chi_i$. The amplitudes of the induced elastic multipoles, i.e. the terms of the Michell solution, can then be determined from satisfying the boundary at the circumference of each of the inclusions. A detailed description of the elastic multipole method is given by the authors in [2].

Image charges

Image charges are commonly used in electrostatics to satisfy boundary conditions. For the same purpose image charges can also be introduced in 2D elasticity. Let us consider a 2D semi-infinite dielectric medium with permittivity ε_e filling half space $y < y_b$ with a monopole charge q at position $\boldsymbol{x}_0 = (x_0, y_0) = (x_0, y_b - h)$, which is at distance h from a perfectly conductive straight edge at $y = y_b$ (Fig. 2a). The electric potential for this case can be found by solving the governing equation $\Delta U = (-q/\varepsilon_e)\delta(\boldsymbol{x} - \boldsymbol{x}_0)$ subject to the boundary condition $E_x(x, y_b) = 0$. The solution for the governing equation in an infinite 2D medium is $U_m(\boldsymbol{x} - \boldsymbol{x}_0|q) = -(q/2\pi\varepsilon_e)\ln|\boldsymbol{x} - \boldsymbol{x}_0|$, however the resulting electric field does not satisfy the boundary conditions at the conducting edge. Boundary conditions can be satisfied by placing an image monopole charge $-q$ on the opposite side of the conducting edge at $\boldsymbol{x}_0^* = (x_0^*, y_0^*) = (x_0, y_b + h)$.

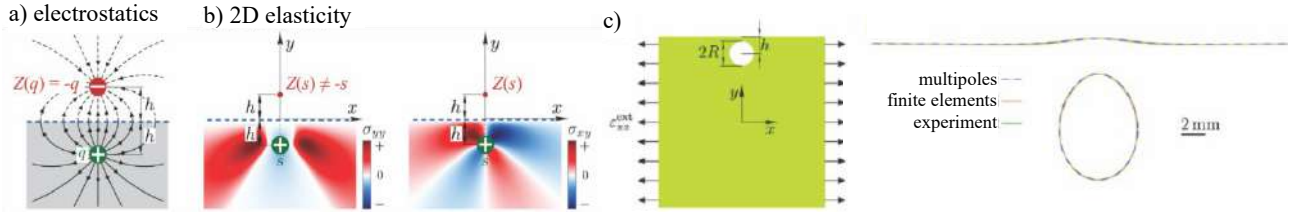

Figure 2. a) image charge of electric monopole b) image charge of disclination, c) contours of deformed hole and free edge obtained with elastic multipole method, finite elements and experiments ($2R = 8.113$mm, $h = 6.253$mm, $\varepsilon_{xx}^{ext} = -0.05$, 100x3x100 mm sample).

Let us look at a related problem in 2D elasticity for a semi-infinite elastic medium with Young`s modulus E with a monopole with charge s at $\boldsymbol{x}_0 = (x_0, y_b - h)$ which is at distance h from a traction free edge (Fig. 2b). The Airy stress function for this case can be found by solving the governing equation $\Delta\Delta\chi = Es\delta(\boldsymbol{x} - \boldsymbol{x}_0)$ subject to boundary conditions $\sigma_{xy}(x, y_b) = \sigma_{yy}(x, y_b) = 0$. Inspired by electrostatics we try placing an image disclination with charge $-s$ on the opposite side of the traction free edge. The resulting trial stress function satisfies only one boundary condition $\sigma_{yy}^{tr}(x, y_b) = 0$, while the other boundary condition is violated $\sigma_{xy}^{tr}(x, y_b) \neq 0$. This difference between electrostatics and elasticity stems from the fact that the electric potential is a harmonic function, while the Airy stress function is a biharmonic function. The additional multipoles needed for satisfying both boundary conditions can be found by calculating the Airy stress function that corresponds to the distributed tractions $f_y = -\sigma_{yy}^{tr}$ and $f_x = -\sigma_{xy}^{tr}$ along the free edge. This can be done with the help of the Boussinesq problem in 2D, where $\chi_B(\boldsymbol{x}|x', y_b)$ describes the stress function of a concentrated force $\boldsymbol{F} = (1,0)$ at point (x', y_b). The stress function of the additional image multipoles is obtained as $\chi^a(\boldsymbol{x}) = \int_{-\infty}^{\infty} \chi_B(\boldsymbol{x}|x', y_b) f_x(x') dx'$. The Airy stress function for the image of the disclination can then be used to systematically construct the Airy stress functions for the images of all other elastic multipoles [4]. The operator Z for constructing the Airy stress functions of images may be written in a compact form:

$$Z[\chi_0(x,y)] = -\chi_0(x, 2y_b - y) + 2(y_b - y)\frac{\partial \chi_0(x, 2y_b - y)}{\partial y} - (y_b - y)^2 \Delta\chi_0(x, 2y_b - y)$$

Similarly to electrostatics, the image of the image charge is the original charge $Z[Z[\chi_0]] = \chi_0$. For bounded structures, external load induces elastic multipoles at the centers of inclusions and holes, which further induce image multipoles in order to satisfy boundary condition at the edges. The amplitudes of induced multipoles are obtained from satisfying the boundary conditions at the interface between inhomogeneities and the elastic matrix.

CONCLUSIONS

In this contribution, we present how image charges and induction, commonly used in electrostatics, can be used for the analysis of linear deformations of bounded 2D elastic structures with inhomogeneities. The presented method shows good agreement with finite element calculations and experiments (Fig. 2c). While we focused on linear deformation, these concepts can also be extended to the nonlinear regime [3] and various geometries [4] thus the elastic multipole method has the potential to advance our understanding of deformation patterns in structures with holes and inclusions.

References

[1] J.H. Michell, On the direct determination of stress in an elastic solid, with application to the theory of plates, Proc. of the London Mat. Soc., 100-124, 1899.
[2] S. Sarkar, M. Čebron, M. Brojan, A. Košmrlj, Elastic multipole method for describing linear deformation of infinite 2D …, ArXiv:1910.01632, 2020.
[3] Y. Bar-Sinai, G. Librandi, K. Bertoldi, M. Moshe, Geometric charges and nonlinear elasticity of soft metamaterials, ArXiv:1910.01953, 2019.
[4] S. Sarkar, M. Čebron, M. Brojan, A. Košmrlj, Method of image charges for describing linear deformation of bounded 2D …, ArXiv:2004.01044, 2020.

IN-SITU STRENGTH EFFECT IN LONG FIBRE REINFORCED COMPOSITES: A MICRO-MECHANICAL ANALYSIS USING THE PHASE FIELD APPROACH OF FRACTURE

T. Guillen-Hernandez[1], A. Quintana-Corominas[2], I.G. Garcia[3], J. Reinoso[3], M. Paggi[*1], A. Turon[2]
[1]IMT School for Advanced Studies Lucca, Lucca, Italy
[2]AMADE, Polytechnic School, Universitat de Girona, Girona, Spain
[3]Elasticity and Strength of Materials Group, School of Engineering, Universidad de Sevilla, Seville, Spain

Summary Transverse intralaminar cracks in layers perpendicular to the main loading direction have a significant impact on the apparent ultimate strength of the corresponding laminate. This effect stems from the fact that such transverse cracks generally promote the occurrence of other failure mechanisms leading to specimen failure. A micro-mechanical analysis of cross-ply laminates is herein proposed for the onset and progression of transverse intralaminar cracking. Numerical simulations are carried out according to the recently proposed fracture mechanics approach coupling: (i) the phase field approach for matrix cracking, and the bilinear cohesive zone model for fibre-matrix decohesion. Relying on this framework, the influence of the transverse ply thickness on the onset and propagation of damage under tensile conditions is assessed and compared with experiments taken from the literature.

INTRODUCTION

Thin-ply laminate technologies in long fibre-reinforced composite materials (usually comprising carbon- and glass-reinforcements in polymeric-based matrix, i.e. CFRP and GFRP, respectively) has emerged as a potential alternative for the production of composite components due to their ability to preclude delamination and micro-cracking prior the corresponding collapsing points. However, there exist some unsolved issues associated with different mechanical effects in composite materials regarding their specific fracture responses. Associated with the analysis of transverse fracture response, the seminal work conducted by [1] on $[0/90]_s$ laminates showed that the reduction of the 90° layer thickness provokes an increase in the critical strain for transverse cracking initiation. Therefore, for sufficiently thin 90° layers, the actual strength response of the laminate would be that governed by the 0° supporting layers, this scenario being of crucial importance for the incorporation of thin and ultra-thin plies in composite structures. This characteristic behaviour is commonly denominated as *in-situ strength effect* in cross-ply composite laminates. Existing models in the literature [2-4] to interpret such a phenomenon differ from each other upon the fundamental hypotheses for their development. Therefore, from the authors' point of view, the physical soundness of such arguments should be revisited in a consistent manner, i.e. how cracks initiate and propagate within fibrous composites based on a micro-mechanical level of analysis.

METHODOLOGY AND BRIEF DESCRIPTION OF THE COMPUTATIONAL MODEL

This cracking sequence, i.e. the specific sequence of damage phenomena at the micro-mechanical level for this application, motivates the use of the coupling between the PF method for bulk fracture and the CZM for fibre-matrix decohesion proposed in [5,6], which can be denoted as PF-CZ technique. Specifically, the nonlocal PF method of fracture is considered in the current research for triggering matrix-cracking events, while a bi-linear CZM is implemented within interface finite elements to model decohesion at fibre-matrix interfaces.

The current FE model (Fig. 1) is generated through the adoption of a multi-scale embedded approach, with the aim at replicating the experimental configurations described in [7]. Tensile loading conditions in the specimen along the longitudinal direction experienced in the real tests is reproduced by transferring displacement conditions to the central portion of the specimen, providing the boundary conditions for the solution of the FE model.

MAIN RESULTS AND CONCLUSIONS

The analysis of the in-situ strength effect for the simulated specimens with different layer configurations led to predictions in very good agreement with the trend reported in [3] and with the experimental observations in [7], in terms of through-the-thickness fracture propagation pattern based on the thickness of the 90° central layer (see Fig. 2 for the $[0°_2/90°_4/0°_2]$ assembly configuration). The analysis of the numerical results shows the occurrence of a phenomenon of cracking propagation within the matrix significantly delayed by reducing the thickness of the specimen, which leads in its turn to an increase in the apparent critical strain for its development through-the-thickness. Nevertheless, current predictions presented deviations with respect to the strain levels at which these phenomena occurred. These differences are mainly attributed to possible 3D effects that haven not yet been taken into consideration in the present 2D modeling framework and that deserve further research.

ACKNOWLEDGEMENTS

The financial support of the Italian Ministry of Education, University and Research to the Research Project of National Interest (PRIN 2017: "XFAST-SIMS: Extra fast and accurate simulation of complex structural systems", CUP: D68D19001260001) is gratefully acknowledged.

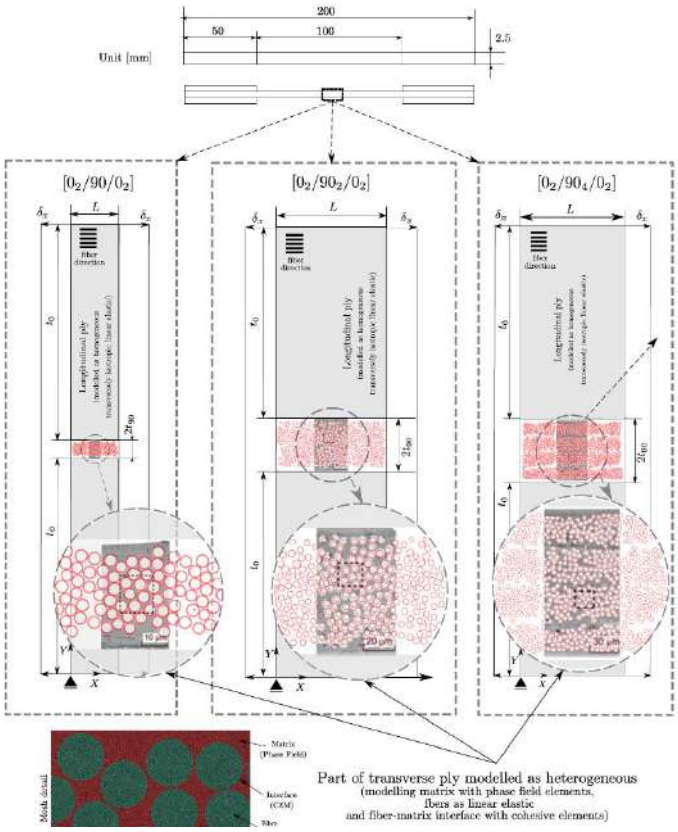

Figure 1. Details of the computational models generated to simulate the experiments in [7].

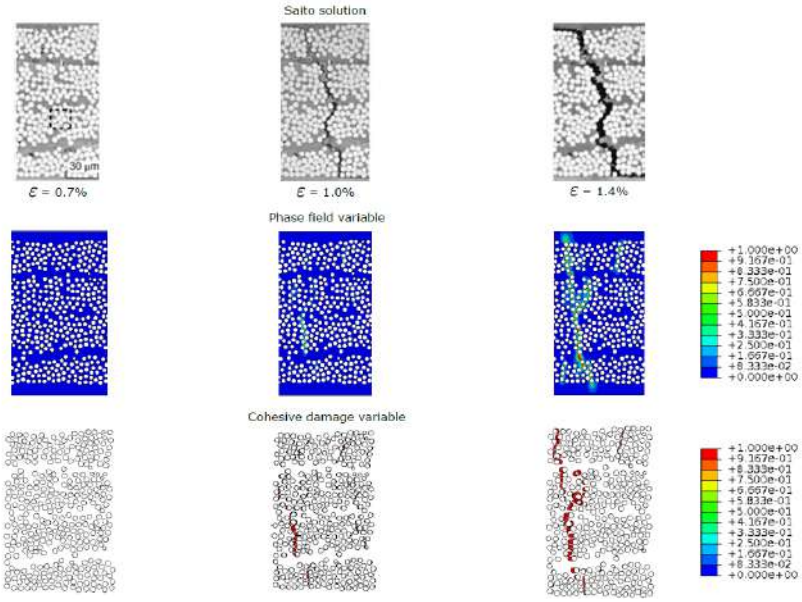

Figure 2. Phase field (matrix) and cohesive (interface) damage patterns, compared to experiments [7] for the assembly $[0°_2/90°_4/0°_2]$.

References

[1] Parvizi A., Garrett K., Bailey, J. Constrained cracking in glass fibre-reinforced epoxy cross-ply laminates. *J. Mat. Sci.* **13:**195-201, 1978.

[2] Camanho P.P., Davila C.G., Pinho S.T., Iannucci L., Robinson P. Prediction of in situ strengths and matrix cracking in composites under transverse tension and in-plane shear. *Comp. Part A* **37**:165-176, 2006.

[3] Dvorak G.J., Laws N. Analysis of first ply failure in composite laminates. *Engng. Fract. Mech.* **25**:763-770, 1986.

[4] Garcia I., Mantic V., Blazquez A., Paris F.Transverse crack onset and growth in cross-ply $[0/90]_s$ laminates under tension. Application of a coupled stress and energy criterion. *Int. J. Sol. Struct.* **51**:3844-3856, 2014.

[5] Paggi M., Reinoso J. Revisiting the problem of a crack impinging on an interface: a modeling framework for the interaction between the phase field approach for brittle fracture and the interface cohesive zone model. *Comp. Meth. Appl. Mech. Eng.* **321**:145-172, 2017.

[6] Guillen-Hernandez T., Garcia I.G., Reinoso J., Paggi M. A micromechanical analysis of inter-fiber failure in long reinforced composites based on the phase field approach of fracture combined with the cohesive zone model. *Int. J. Fracture*, 2019, doi:10.1007/s10704-019-00384-8

[7] Saito H., Takeuchi H., Kimpara I. Experimental evaluation of the damage growth restraining in 90 layer of thin-ply CFRP cross-ply laminates. *Advanced Composite Materials* **21**:57-66, 2012.

WHEN AND HOW FRACTURE NUCLEATES AND PROPAGATES IN RUBBER

Aditya Kumar and Oscar Lopez-Pamies*
Department of Civil and Environmental Engineering, University of Illinois Urbana–Champaign, USA

Summary In a recent contribution, Kumar et al. [1] have introduced a phase-field formulation aimed at modeling the nucleation and propagation of fracture and healing in elastomers undergoing arbitrarily large quasistatic deformations, phenomena that have come into clear focus thanks to new experiments carried out at high spatiotemporal resolution [2, 3]. In this work, we present a specific model within the general formulation for the prominent case of isotropic and nearly incompressible rubbers capable of describing, explaining, and predicting fracture nucleation at large, be it within the bulk, from large pre-existing cracks, small pre-existing cracks, or from smooth and non-smooth boundary points. With the primary object of explaining when and how fracture nucleates and propagates in rubber, we then make use of the proposed model to perform 3D simulations of several famed experiments.

Guided by the experimental results presented in [2, 3], Kumar et al. [1] have recently introduced a regularized theory of fracture — of phase-field type — that views the nucleation and propagation of fracture as well as the possibility of healing in elastomers as three intertwined parts of the same phenomenon. The theory can be thought of as a generalization of the celebrated phase-field regularization [4] of the variational theory of Francfort and Marigo [5] in that it modifies the former on two pivotal counts, one pertaining to nucleation, the other to healing.

Indeed, it is now well understood that the standard phase-field regularization introduced in [4] cannot properly describe fracture nucleation because it is a purely energetic formulation and as a result it cannot account for one essential ingredient that is not energetic, but rather stress-based: the strength of the material. Furthermore, such a formulation describes fracture as an irreversible and purely dissipative process ruling out thus the possibility of healing. Kumar et al. [1] proposed alterations that circumvent these limitations on nucleation and healing while keeping undisturbed the remarkable proven ability of the standard phase-field formulation to model crack propagation. Roughly speaking, the idea behind the phase-field framework proposed in Kumar et al. [1] amounts:

- to consider the Euler-Lagrange equations — and not the underlying variational principle — describing the evolution of the deformation field $\mathbf{y}(\mathbf{X}, \mathtt{t})$ and the phase field $z(\mathbf{X}, \mathtt{t})$ in the material as the primal model,
- to add an external driving force $c_{\mathrm{e}}(\mathbf{X}, \mathtt{t})$ in the Euler-Lagrange equation governing the evolution of the phase field z that represents the macroscopic manifestation of the presence of the inherent microscopic defects in the material and hence that brings into the model direct dependence on its strength, and
- to remove the irreversibility constraint on the phase field z by introducing a critical energy release rate or toughness with two branches, $k(\dot{z}) = k_{\mathrm{f}} = G_c$ if $\dot{z} \leq 0$ and k_{h} if $\dot{z} > 0$, one to describe $\mathtt{f}$racture (when $\dot{z} < 0$), the other to describe $\mathtt{h}$ealing (when $\dot{z} > 0$).

In their original work, aimed at explaining the nucleation of internal fracture observed in the experiments of Poulain et al. [2, 3] on various synthetic rubbers, Kumar et al. [1] also proposed a specific constitutive prescription for the external driving force c_{e} that restricted attention to accounting for the strength of the given rubber of interest only under hydrostatic stress. In this work, we introduce a complete constitutive prescription for c_{e} that accounts for the entire strength of the rubber under arbitrary stress states. The resulting phase-field model is thus one capable of describing fracture nucleation at large, be it within the bulk (under arbitrary states of stress, not just hydrostatic), from large pre-existing cracks, small pre-existing cracks, or from smooth and non-smooth boundary points. With the object of explaining when and how fracture nucleates and propagates in rubber, we then make use of the proposed model to perform 3D simulations of several famed experiments wherein fracture nucleates and propagates in very different and very complex manners. Specifically, we work out simulations on very short, short, and long rubber bands of initially circular cross section. The very short and short rubber bands correspond to the so-called poker-chip specimens studied experimentally by many. The long rubber bands, on the other hand, are representative of the celebrated specimens — invented by Stephen Perry in the 1840s — that most of us have used and played with since childhood.

By way of an example, we present below sample 3D simulations on very short (see Fig. 1) and long (see Fig. 2) rubber bands made of a soft silicone rubber. Specifically, we consider rubber bands of circular cross with initial diameter $d_0 = 2$ mm and two different initial lengths $l_0 = d_0/35 = 0.057$ mm and $l_0 = 20 \times d_0 = 40$ mm. The bands are stretched by bonding their top and bottom boundaries to rigid plates which are pulled apart by a prescribed displacement u. The corresponding force required to do so is denoted by P. For consistency with the experimental literature, the results below are presented in terms of the "global" stretch λ and the "global" nominal stress s, which are defined in terms of u and P by the relations $\lambda = 1 + u/l_0$ and $s = 4P/(\pi d_0^2)$.

Consistent with the experimental observations reported in the literature for thin poker-chip experiments, the key observation from Fig. 1 is that fracture occurs exclusively around the midplane of the band, entirely within its bulk, in a cascading sequence of crack nucleation events that originates from the center and proceeds radially outward as the applied

*Corresponding author. E-mail: pamies@illinois.edu.

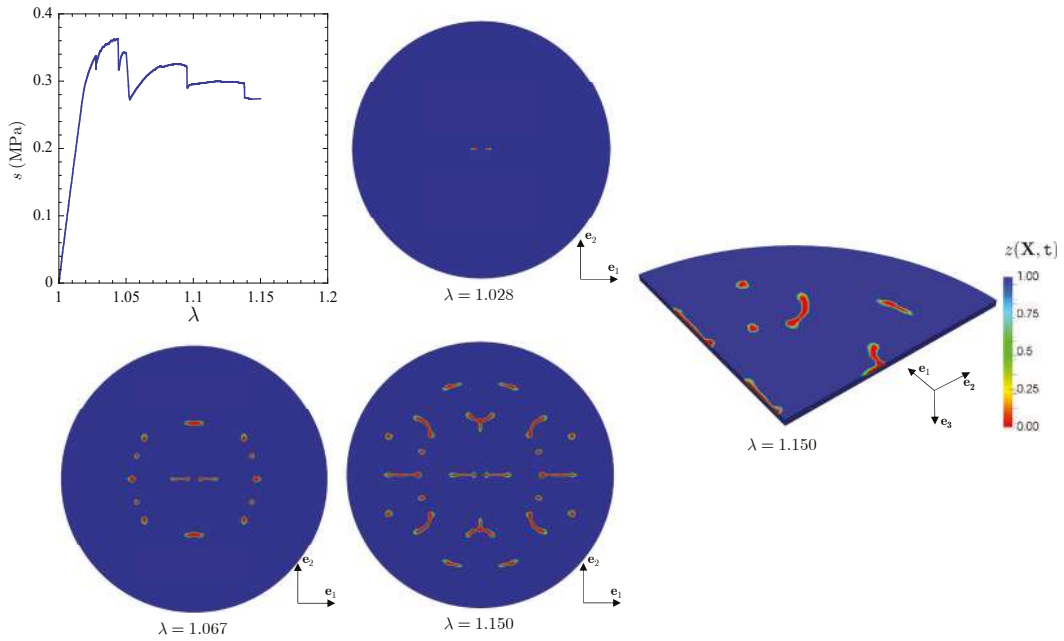

Figure 1: 3D simulation of a very short rubber band — or poker-chip specimen — under tension. The line plot shows the predicted stress s as a function of the applied stretch λ. The contour plots show the predicted phase field $z(\mathbf{X}, \mathtt{t})$ across the midplane of the band at three different applied stretches, $\lambda = 1.028, 1.067, 1.150$, and over an octant of the band at $\lambda = 1.150$.

stretch λ increases. Precisely, two cracks are first nucleated around the center of the band at a stretch of about $\lambda = 1.028$. As λ increases, more cracks are sequentially nucleated radially away from the center at random locations. At the stretch of about $\lambda = 1.150$, cracks are already present throughout the entire midplane of the band, save for a boundary layer around its lateral traction-free boundary. Once a crack is nucleated, it exhibits limited subsequent stable propagation, instead the nucleation of more cracks is preferred as λ increases.

In stark contrast with the preceding result, as expected from the experience of playing with rubber bands and consistent with the experimental observations reported in the literature on the tensile strength of elastomers, Fig. 2 shows that the long rubber band stretches uniformly — save for, of course, the localized heterogeneous stretching taking place near its top and bottom boundaries because of the bonding to rigid plates — until an applied stretch of about $\lambda = 4.01$, at which point a crack nucleates — in this case, near the bottom boundary — abruptly across the band severing it in two pieces.

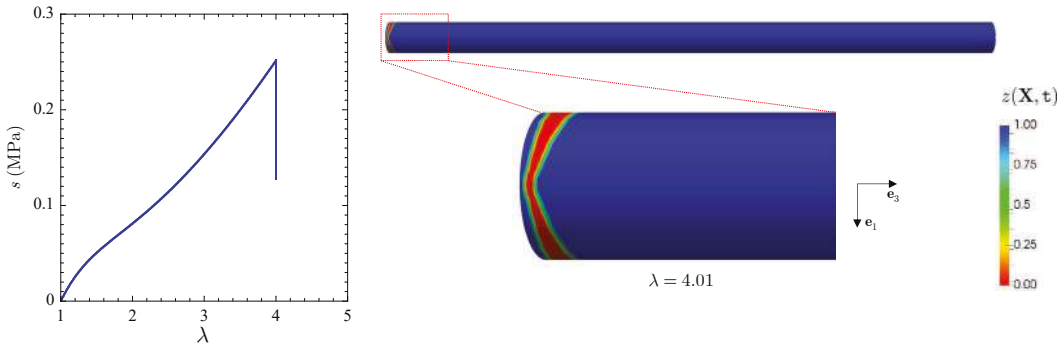

Figure 2: 3D simulation of a long rubber band under tension. The line plot shows the predicted stress s as a function of the applied stretch λ. The contour plot shows the predicted phase field $z(\mathbf{X}, \mathtt{t})$ over the entire band at $\lambda = 4.01$.

References

[1] Kumar A., Francfort G. A., Lopez-Pamies O. Fracture and healing of elastomers: A phase-transition theory and numerical implementation. *Journal of the Mechanics and Physics of Solids* **112**: 523–551, 2018.

[2] Poulain X., Lefèvre V., Lopez-Pamies O., Ravi-Chandar K. Damage in elastomers: Nucleation and growth of cavities, micro-cracks, and macro-cracks. *International Journal of Fracture* **205**: 1–21, 2017.

[3] Poulain X., Lopez-Pamies O., Ravi-Chandar K. Damage in elastomers: Healing of internally nucleated cavities and micro-cracks. *Soft Matter* **14**: 4633–4640, 2018.

[4] Bourdin B., Francfort G. A., Marigo J. J. The variational approach to fracture. *Journal of Elasticity* **91**: 5–148, 2008.

[5] Francfort G. A., Marigo, J. J. Revisiting brittle fracture as an energy minimization problem. *Journal of the Mechanics and Physics of Solids* **46**: 1319–1342, 1998.

HOW MOVING CRACKS IN BRITTLE SOLIDS CHOOSE THEIR PATH

Lital Rozen-Levy[1], John M. Kolinski[2], Gil Cohen[1] and Jay Fineberg[1]
[1]The Racah Institute of Physics, The Hebrew University of Jerusalem, Givat Ram, Jerusalem Israel.
[2]École Polytechnique Fédérale de Lausanne, Lausanne, 1015, Switzerland.

Summary While we have an excellent fundamental understanding of the dynamics and structure of cracks propagating in brittle solids, we do not fully understand how the path of a moving crack is determined. Here we experimentally study cracks that are propagating between 10-95% of their limiting velocity within a brittle material. We deflect these cracks by either allowing them to interact with sparsely implanted defects or driving them to undergo an intrinsic oscillatory instability in defect-free media. By dense measurements of the strain fields surrounding the crack tips via high speed imaging, we determine what governs a crack's direction when it is strongly deflected. We reveal that the paths selected by these rapid and strongly perturbed cracks are entirely governed by the direction of maximum strain energy density and not by local symmetry of the fields. This fundamentally important result may potentially be utilized to either direct or guide running cracks.

We experimentally probe the effects of both dilute rigidly embedded inclusions and intrinsic instability in an unperturbed medium on the dynamic path selection of cracks in otherwise perfect (homogeneous) brittle isotropic materials. To reduce crack speeds while retaining fully dynamic propagation, we utilize polyacrylamide (*1, 2*) hydrogels. These materials are representative of brittle materials that undergo brittle failure, as has been demonstrated through direct verification of the predictions of fracture mechanics to describing the dynamic fields near crack tips, energy balance and the equation of motion for brittle cracks moving at velocities ranging from nearly zero to nearly their limiting velocity, (*1*).

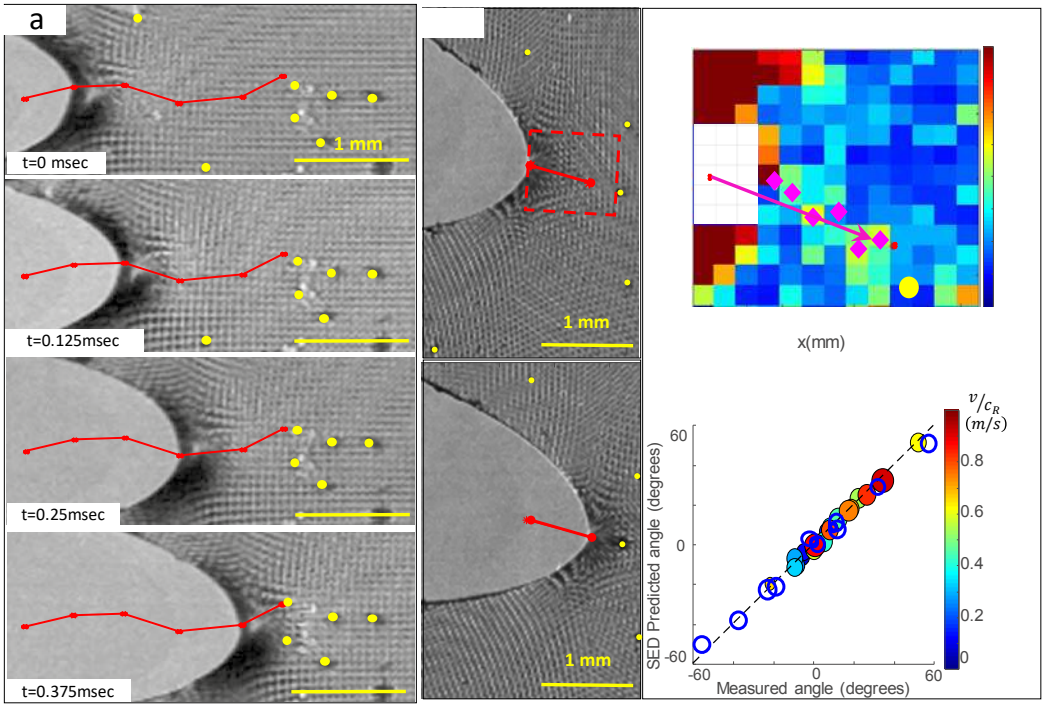

Figure 1: Comparing predictions of the crack propagation direction to maximum strain energy density. (a) A time series of images separated by 0.125 msec as a crack tip rapidly evolves while interacting with the particles (yellow dots) that it encounters. Its resulting path, denoted by the red line connecting successive crack tips (red dots), becomes tortuous. (b) 2 sequential images with the crack trajectory in red. (c) (top) Predicted crack directions in the reference frame for (b) using the maximal strain energy density (SED) criterion. The measured strain energy density (J/m^3) within the square section denoted in (b) diamonds denote the maximal SED for each x location. The purple arrow is a linear fit to these data. Crack tip locations in (b) are denoted by red points. (bottom) Predicted angles using the SED for 21 different experiments – each with significantly different ensembles of surrounding particles and propagation velocities, v. v of each point is indicated by the colors in the legend. Open symbols are additional experiments in homogeneous materials upon excitation of the oscillatory instability (See Fig. 2) The error bars are the size of the points.

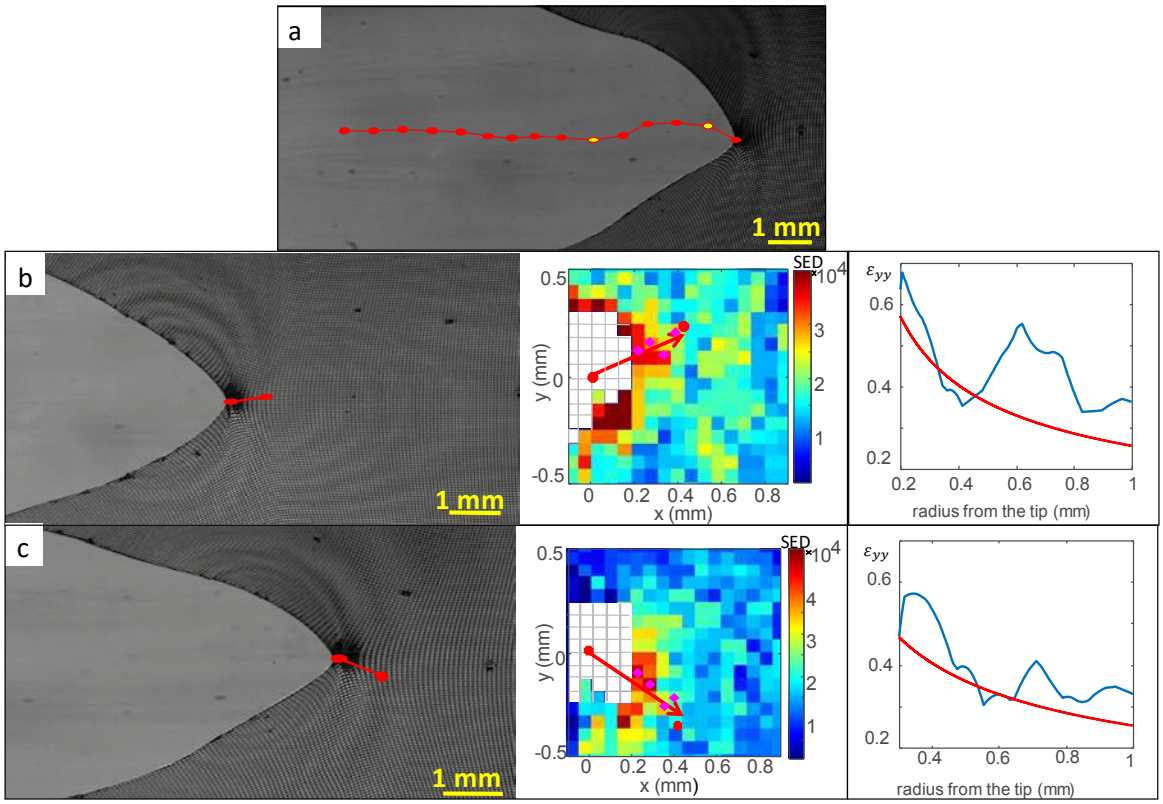

Figure 2 The local direction of oscillatory cracks are well-predicted by the maximum strain energy density (SED) condition. (a) The trajectory of a spontaneously oscillating crack propagating at approximately $0.9c_S$ at the onset of the oscillatory instability (*3, 4*). Shown is a snapshot of the vicinity of the tip of a crack undergoing this instability. The trajectory of successive crack tips leading to this instant is denoted in red. Note that this instability takes place spontaneously in a uniform medium, without the insertion of rigid particles. (b,c) Two typical instantaneous snapshots (left panels) of the crack tip at the locations denoted by the yellow dots in (a). The center panels demonstrate that the trajectory directions in both (b) and (c) are well-predicted by the SED criterion (SED units are in J/m^3). Predicted (measured) angles were $30°$ ($31°$) in (b) and were $-40°$ ($-36°$). The PLS predictions were, respectively were $4°$ and $3°$. (Right) Corresponding ε_{yy} as a function of the distance from the crack tip along the instantaneous direction of the crack tip.

Figure 1 shows that crack paths often become tortuous as a consequence of crack interactions with embedded inclusions. The near-tip strain fields of these rapidly propagating cracks reveal that nearby particles significantly affect the form and even existence of the singular fields predicted by Linear Elastic Fracture Mechanics (LEFM). When a crack approaches a particle, the stress fields surrounding its tip typically deviate from the singular, 'K-dominant' scaling predicted by LEFM (or its nonlinear extensions (*5-8*)) in homogeneous materials. Crack paths also deviate strongly when cracks become unstable to an oscillatory instability at high velocities (>0.9C_S where C_S is the material's shear wave speed), as presented in Fig. 2.

In all cases where a crack's path deviates, we find that its path is perfectly predicted by the direction of *maximum strain energy density* ahead of the crack tip, as demonstrated in both Figs. 1c and 2.

References

[1] T. Goldman, A. Livne, J. Fineberg, Acquisition of Inertia by a Moving Crack. *Physical Review Letters* **104**, 114301 (2010).
[2] A. Livne, G. Cohen, J. Fineberg, Universality and Hysteretic Dynamics in Rapid Fracture. *Physical Review Letters* **94**, 224301 (2005).
[3] A. Livne, O. Ben-David, J. Fineberg, Oscillations in Rapid Fracture. *Phys. Rev. Lett.* **98**, 124301 (2007).
[4] C. H. Chen, E. Bouchbinder, A. Karma, Instability in dynamic fracture and the failure of the classical theory of cracks. *Nature Physics* **13**, 1186-+ (2017).
[5] E. Bouchbinder, A. Livne, J. Fineberg, Weakly Nonlinear Theory of Dynamic Fracture. *Phys. Rev. Lett.* **101**, 264302 (2008).
[6] E. Bouchbinder, T. Goldman, J. Fineberg, The dynamics of rapid fracture: instabilities, nonlinearities and length scales. *Reports on Progress in Physics* **77**, 046501-046501 (2014).
[7] O. Ronsin, C. Caroli, T. Baumberger, Crack front echelon instability in mixed mode fracture of a strongly nonlinear elastic solid. *Epl* **105**, (2014).
[8] R. Long, C. Y. Hui, Crack tip fields in soft elastic solids subjected to large quasi-static deformation - A review. *Extreme Mechanics Letters* **4**, 131-155 (2015).

STRESS INTENSITY FACTORS FOR INTERACTING ARBITRARILY SHAPED 3D CRACKS - A SIMPLE, FAST AND ACCURATE FINITE ELEMENT-BASED METHOD

Mari Åman*[1], Kennie Berntsson [1]and Gary Marquis[1]
[1]Department of Mechanical Engineering, Aalto University, Espoo, Finland

Summary A finite element-based method for accurately determining stress intensity factors (SIF) for interacting arbitrarily shaped 3D cracks is proposed. The method utilizes the superposition principle and does not require fine meshes or singular elements. The foundation of the new method is that disturbances in an elastic stress field due to neighbouring cracks can be captured accurately by splitting the total stress at the crack tip element into two components, singular and non-singular terms. Computed results are in excellent agreement with the existing analytical solutions. In addition, novel SIF solutions for various crack geometries and configurations are presented and the conversion of size-independent solutions to the small crack model, $\sqrt{area}$ parameter model, is introduced. The proposed method can be applied to the SIF analysis for interacting cracks with various shapes often observed in additively manufactured (AM) components and the solutions will be useful for the standardization for such complicated defect configurations.

INTRODUCTION

Defect interaction has been a concern for fatigue experts for many decades. The need to understand defect interaction precisely has been recently underscored due to the significant reduction in fatigue strength of AM components due to defect interaction [1]. Current design rules rely on a British standard [2], which provides analytical interaction criteria based on the crack size, shape and proximity. Since fracture mechanic-based design criteria are often based on critical SIF values, it becomes important to be able to compute SIFs accurately. However, determination of SIFs for 3D cracks by FEM is typically time-consuming and the accuracy depends strongly on the mesh characteristics such as singular elements. It is easy to understand that SIFs for complex shaped cracks is even more difficult to obtain, and yet, the complexity increases when the interacting cracks are involved. This work provides an accurate tool for SIF analysis using the common FEM software ABAQUS. Previously, the method has been successfully applied to 2D cracks by Murakami [3]. The greatest advantages of the proposed method are that it does not require fine meshes, extrapolations or so-called singular elements. This work also presents novel SIFs for various crack geometries and configurations. Moreover, the conversion of size-independent solutions to the well-known small crack model, the $\sqrt{area}$ parameter model [4], is introduced. The solutions will be very useful for standardization of general rules for interacting defect guidelines.

PRINCIPLE OF THE METHOD

The new method utilizes the superposition principle that is applicable in linear-elastic problems, see Fig. 1. Although the SIF's for problems Fig. 1 (a) and (c) are the same, the stress distributions are different by the remote stress, as illustrated in Fig. 2. The total stress in a crack tip element can be divided into two components, a singular term and a non-singular term both of which are included, for example, in a constant stress element. The singular term is associated with the SIF whereas the non-singular term is obtained based on the stress which already exists at the same element by assuming that the crack does not exist. In FEM, the non-singular term is dominant and interferes with the accurate determination of SIF based on the singular term. Thus, the key of the method is to extract the non-singular term from the total stress, after which only the singular term remains. By comparing the two components with those of a basic single crack for which an exact SIF is known, the interaction factor is obtained. In the case of a single crack, the non-singular stress is equivalent to the remote stress. However, in the interacting crack problem, the neighbouring crack contributes to the non-singular stress field. In the problem of two cracks, first the non-singular term at the tip of an imaginary crack is calculated by solving the problem with only one crack. Secondly, the problem with two cracks is solved to obtain the total stress at the crack tip element. Finally, the non-singular term is subtracted from the total stress and only the singular term remains.

Traditionally, the stresses at the crack tip are obtained by using very fine meshed and singular elements. Since the exact stresses at the crack tip are unbounded, the SIF is obtained by extrapolating the results with different meshes until reasonable accuracy is obtained. Such analyses tend to be troublesome in interaction problems, because the two cracks *simultaneously* influence the stress distributions in the vicinity of other cracks. Thus, by traditional methods, it is impossible to separate the stress distribution caused by a crack itself and the magnification of the stress distribution caused by a neighbouring crack.

RESULTS

The results are in an excellent agreement with the known numerical solutions. Figure 3 shows the validation of some selected problems, for which SIF's are known. Body Force Method (BFM) solutions are from a previous work that focused on semi-elliptical cracks [5].

*Corresponding author. E-mail: mari.aman@aalto.fi.

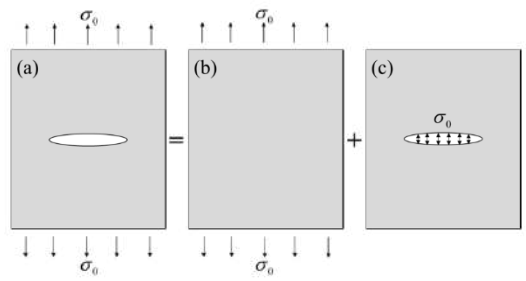

Figure 1. Superposition principle.

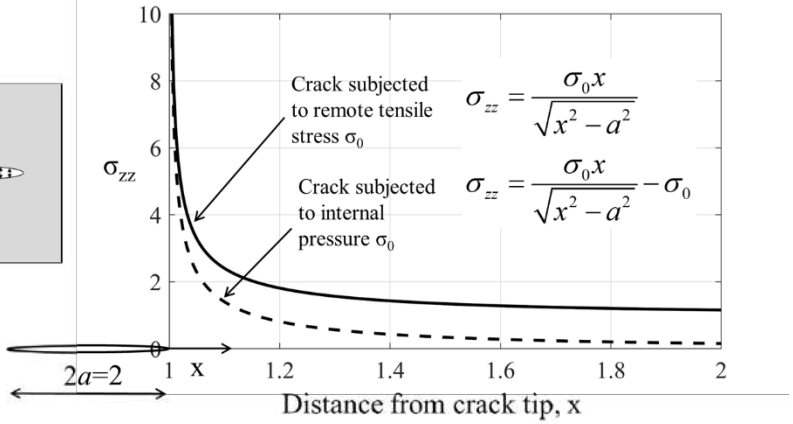

Figure 2. Stress distributions for problems in Fig. 1 (a) and (c).

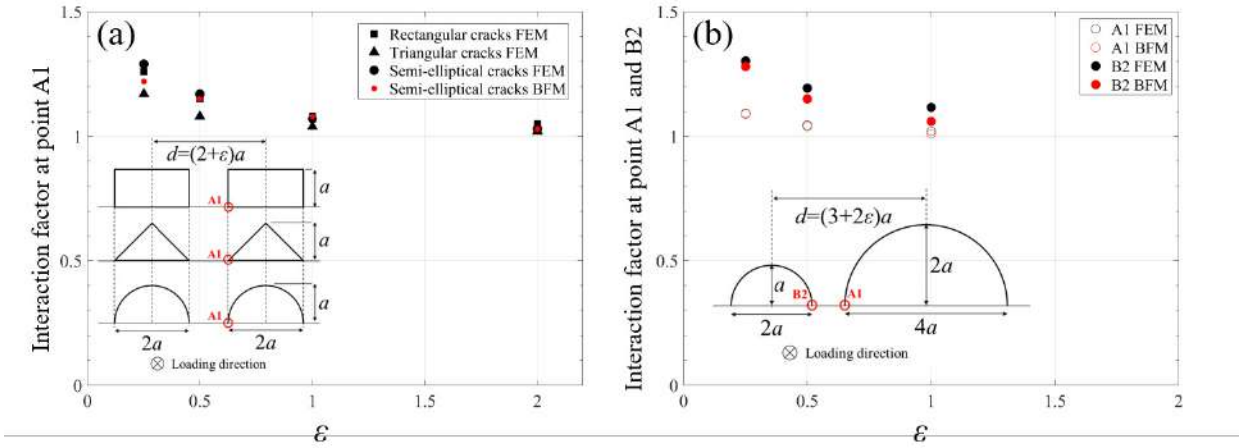

Figure 3. Validation of the new method and comparison with the known numerical solutions [5].

DISCUSSION & CONCLUSIONS

The SIF solutions for non-elliptical cracks can be obtained when the SIF for similar semi-elliptical crack and the stresses at the crack tip elements are known; $K_{\text{rectangle}} = \sigma_{\text{rectangle,tip}} * K_{\text{semi-ellipse}} / \sigma_{\text{semi-ellipse,tip}}$. Using the known solution $K_{\text{semi-ellipse}} = 0.730\sigma_0\sqrt{\pi a}$ [5], we obtain $K_{\text{rectangle}} = 0.809\sigma_0\sqrt{\pi a}$ and $K_{\text{triangle}} = 0.536\sigma_0\sqrt{\pi a}$ at A1 points. However, considering the size-dependency of small crack threshold SIF range, small cracks are commonly treated in a different manner than long cracks. Murakami [4] has established a well-known $\sqrt{area}$ parameter model for the fatigue limit evaluation of small cracks. Since the $\sqrt{area}$ parameter model literally uses the $\sqrt{area}$ of irregularly shaped defects, it is necessary to express SIF's in terms of the square root of the projected area of defects, $\sqrt{area}$. The solutions of the present method can be easily converted to corresponding values of the $\sqrt{area}$ even for interacting defects.

References

[1] Beretta, S., & Romano, S. (2017). A comparison of fatigue strength sensitivity to defects for materials manufactured by AM or traditional processes. International Journal of Fatigue, 94, 178-191.

[2] Standard, B. (2015). BS 7910: 2013+ A1: 2015 Guide to methods for assessing the acceptability of flaws in metallic structures. London, UK: BSI Stand Publ.

[3] Murakami, Y. (1976). A simple procedure for the accurate determination of stress intensity factors by finite element method, Engineering Fracture Mechanics, Volume 8, Issue 4, 643-655,

[4] Murakami, Y. & Endo, M. (1983). Quantitative evaluation of fatigue strength of metals containing various small defects or cracks. Engineering Fracture Mechanics, Volume 17, Issue 1, 1-15.

[5] Åman, M. (2015). Interacting three-dimensional surface cracks under tensile loading, Master's Thesis. (https://aaltodoc.aalto.fi/handle/123456789/16692)

A CHEMO-THERMO-MECHANICALLY CONSTITUTIVE THEORY FOR CRACK PROPAGATION WITH INTERFACIAL OXIDATION IN THERMAL BARRIER COATINGS

Li Yang* [1], and Yichun Zhou[1]

[1]Key Laboratory of Key Film Materials & Application for Equipment (Hunan province), School of Materials Science and Engineering, Xiangtan University, Xiangtan, Hunan 411105, China

Summary During service at high temperatures, the thermal barrier coating oxidizes at the ceramic/bonding layer interface, forming a dense layer of thermal growth oxide (TGO). In this paper, the thermal barrier coating interface oxidation model and the numerical solution method are established: order parameter is introduced for crack, and the contribution of thermoelastic energy, diffusion energy and chemical reaction energy in the coating is superimposed to give the free energy of the coating as a whole. It was found that the thermal barrier coating was prone to crack at the ceramic layer /TGO trough and the TGO/ bonding layer peak during the interface oxidation.

INTRODUCTION

With the upgrading of aero-engines, the bearing capacity of high-temperature components is continuously increasing. Thermal barrier coating (YSZ) as a key thermal protection material has greatly improved the temperature bearing capacity of high-temperature components of the engine. During the high-temperature service of the thermal barrier coating, oxygen in the air passes through the ceramic layer, and an oxidation reaction occurs with the Al element in the bond coating on the ceramic/bond coating interface, forming a dense thermally grown oxide (TGO)[1]. Further, TGO growth and stress evolution will induce coating flaking failure. Flaking failure is an important bottleneck which restricts the safety application of thermal barrier coatings in advanced aero-engines. Therefore, the establishment of the thermal barrier coating interfaces oxidative failure theory is crucial to the accurate understanding of the thermal barrier coating interface oxidative spalling failure[2].

The TGO growth process is a complex thermo-mechanical multi-field coupling phenomenon, and the coating peeling failure caused by it is a complex interface and bulk material coupling failure process. Based on the thermal-mechanical-chemical multi-field coupled growth model of the thermal barrier coating (TGO), a thermal-mechanical-coupled failure model and numerical solution method for the interface oxidation of the thermal barrier coating are established. The interface auxiliary field variable is introduced as the substitution of the ceramics layer and TGO interface, distinguishing interface failure from material failure. We define crack auxiliary field variable and construct free energy functions. The governing equation and constitutive relationship of each field in the material have been obtained according to the variational principle. The cohesive force model was used to simulate the failure of the interface between the ceramic layer and TGO. Finally, the crack propagation model caused by interface oxidation has been achieved.

RESULTS AND DISCUSSION

As shown in figure 1, in TGO trough, The maximum average compressive stress near the TC/TGO interface changes from 2.4 GPa at 0 h to 1.15 GPa at 1000 h. In BC crest, the maximum average tensile stress near the BC/TGO interface change from 0.48 GPa at 0 h to 0.42 GPa at 1000 h. Causing by stress concentration place crack is produced. After crack extending, the average tensile stress and compressive stress are reduced.

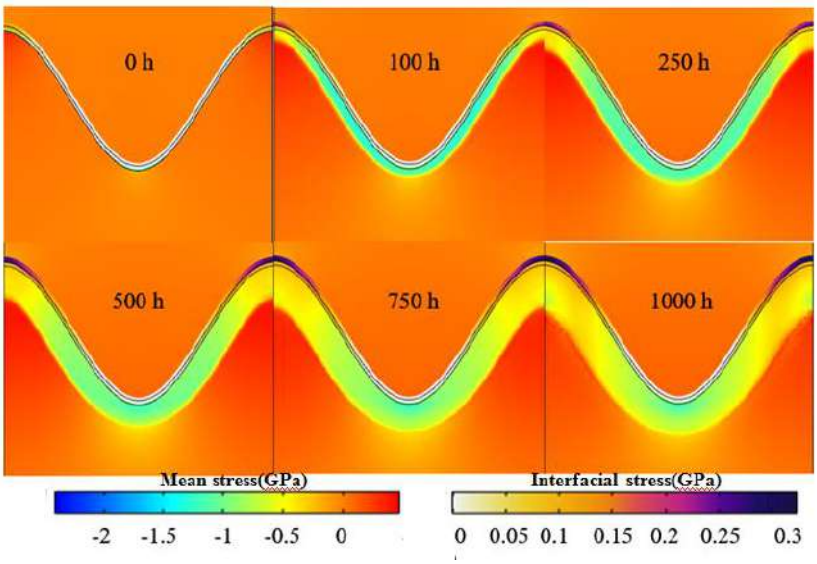

Figure 1. Average stress distribution of thermal barrier coating (bottom left) and interfacial stress distribution (bottom right)

*Correspondingauthor. E-mail: Lyang@xtu.edu.cn

As shown in Fig. 2, the thermal barrier coating will crack at the trough of the TC/TGO interface. When it is not completely disconnected, it will also crack at the peak of the TGO/BC interface.

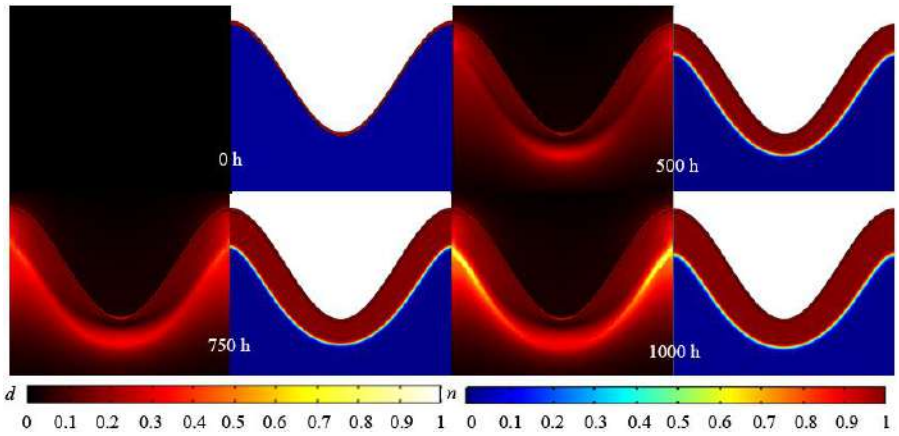

Figure 2. Thermal barrier coating crack (d) distribution over time (left) and TGO volume fraction (n) distribution over time (right)

CONCLUSIONS

In this work, combined with thermal growth model and phase field model, interface cohesion model is established for the crack growth causing by oxidation of interface in thermal barrier coating. The main results can be summarized as follows: (1) The thermal barrier coating at the trough of the TC/TGO interface produces the crack, but has not completely disconnect, in TGO/BC interface wave cracks can also produce, and gradually expand to the troughs. (2) At 1000 h, crack completely disconnect in TGO/BC interface wave, which will cause the coating reducing internal stress at the same time.

References

[1] P. Padture, M. Gell, E. H. Jordan. Thermal barrier coatings for gas-turbine engine applications[J]. Science, 2002,296(5566): 280-284.

[2] Q. Shen, L. Yang, Y. C. Zhou, et al. Effects of growth stress in finite-deformation thermally grown oxide on failure mechanism of thermal barrier coatings[J]. Mechanics of Materials, 2017,114: 228-242.

SIMULATION OF DUCTILE PLATE TEARING USING A STRAIN GRADIENT ENHANCED GURSON-TVERGAARD-NEEDLEMAN MODEL

Vishal Vishwakarma*[1] and Kim Lau Nielsen[1]
[1]Department of Mechanical Engineering, Solid Mechanics Section, Technical University of Denmark, DK-2800 Kgs Lyngby, Denmark

Summary The ductile failure process ahead of an advancing crack in a thin large scale plate subject to mode I loading is modeled using a newly proposed gradient enriched Gurson-Tvergaard-Needleman (GTN) material model that includes a constitutive length parameter to account for strain gradient hardening. The aim is to study the chronology of plate tearing from the first local thinning far ahead from the crack tip and until shear localization followed by slant fracture in the presence of strain gradient hardening. The details of the failure process are used to investigate the influence of the length scale on the fracture energy going into the tearing process as well as the forces involved.

ABSTRACT

The well known Gurson-Tvergaard-Needleman (GTN) model [1, 2, 3], incorporating the mechanics of void nucleation and growth to coalescence, is widely used in the assessment of structural integrity and the modeling of ductile failure. The complex void nucleation, growth and coalescence mechanisms takes place at the micron scale where strain gradient hardening can also play a significant role in the mechanical response. Essentially, the general trend is that "smaller is stronger" and a number of experiments on the micron scale have shown increased hardening and higher apparent yield stress at the small scale. The classical GTN model, however, only accounts for void volume fraction and, thus, cannot distinguish between length scales. But, since the fracture process zone ahead of the crack tip in a ductile specimen comprises of the micro-mechanisms outlined above, it is expected that the scale dependent hardening (coming from strain gradients) can have a significant effect on the fracture process during ductile tearing. The strain gradient effect is usually modeled by incorporating a length scale parameter in the constitutive law, and it is anticipated that the existing micro-mechanical material modeling techniques can substantially be improved by accounting for such effects. Recently, an effort was made to bring in the strain gradient effect in the void growth model of Gurson-Tvergaard (GT model) by introducing a constitutive length parameter in the yield function [4]. The gradient enriched GT model was later studied with analogous unit cell based calculations to show a strong influence of size effect on the rate of void growth and thus on hardening [5]. By incorporating the length parameter into the GT model, the door has opened to unravel the effect of microscale hardening on large scale plate tearing.

In this work, an investigation of the fracture process ahead of an advancing crack tip in a thin plate is conducted by adopting a two-dimensional plane strain finite element model along the lines of Nielsen and Hutchinson [6], but with the gradient enriched GTN material model describing the shear localization and failure process. A full three-dimensional FE model was employed by Andersen et al. [7], with the GTN model to study the plate tearing from crack initiation to steady-state crack growth. They observed a reasonably good agreement between a full 3D crack propagation simulation and the simplified 2D plane strain setup by Nielsen and Hutchinson [6] that mimics steady-state crack growth. The sequence of deformation steps ahead of the crack tip is shown in Fig. 1. The onset of necking and thinning starts far ahead of the crack tip, (i) & (ii), whereafter shear localization, (iii) sets in and controls slant fracture, (iv). The current study sticks to a 2D plane strain representation of this sequence. A slight development is made to the gradient enriched Gurson material model of Niordson and Tvergaard [4] in order to account for void coalescence. The gradient enriched void growth and coalescence model used here is as follows,

$$\Phi = \frac{\sigma_{eq}^2}{\sigma_y^2} + 2Q_1 q_1 f^\star \cosh\left(\frac{3Q_2 q_2}{2}\frac{\sigma_m}{\sigma_y}\right) - 1 - (Q_1 q_1 f^\star)^2$$

$$f^\star = \begin{cases} f, & \text{for } f \le f_C, \\ f_C + \dfrac{f_U^\star - f_C}{f_F - f_C}(f - f_C), \quad f_U^\star = \dfrac{1}{Q_1 q_1}, & \text{for } f > f_C \end{cases}$$

where, Q_1 and Q_2 are the gradient enriched factors that are functions of $\frac{L_D}{R_C}$. L_D and R_c are the constitutive length parameter and initial in-plane void distance respectively. (See [3, 4] for more details). It is worth mentioning that the enriched factor, Q_1, also enters into the expression for $f^\star$ controlling the void coalescence. Finite strain formulation of the enriched GTN model based on a total Lagrangian approach is used for solving the incremental boundary value problem shown in Fig. 2 (b). This is implemented into an in-house finite element code written in FORTRAN using MPI for parallel computing. The simulations performed here are motivated from Nielsen and Hutchinson [6], where they studied the sequence of ductile failure and characterized the cohesive zone using the shear modified Gurson model free from any length scale. Here, the primary focus is to investigate the strain gradient hardening effect on the fracture process.

*Corresponding author. E-mail: visvi@mek.dtu.dk

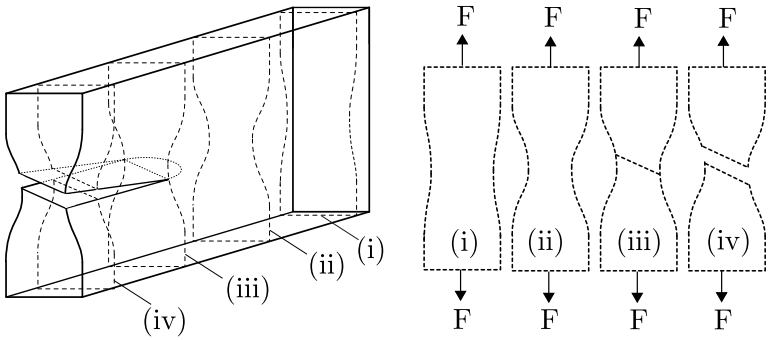

Figure 1: An illustration of the deformation sequence ahead of a mode I crack propagating at steady-state.

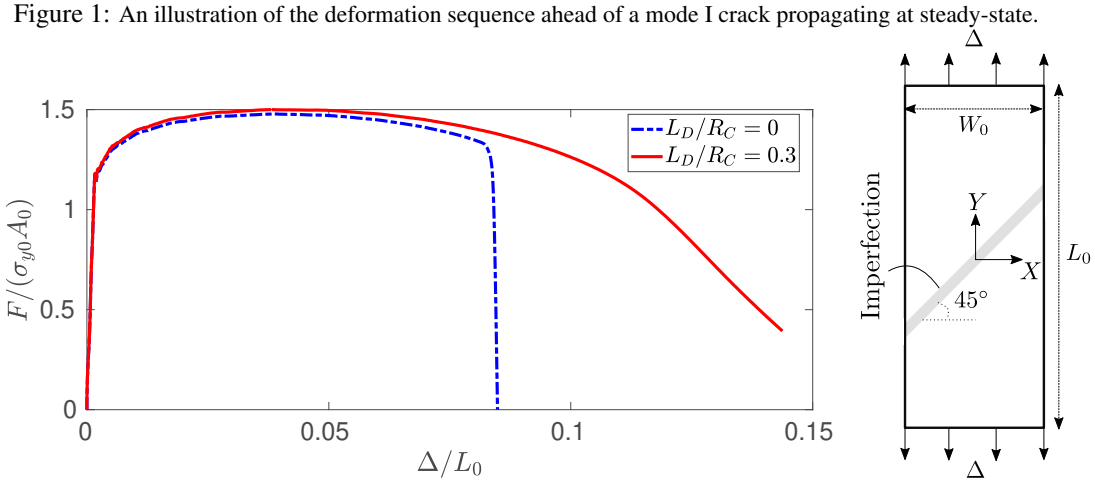

Figure 2: Load – Deflection curve obtained with (red) and without (blue) constitutive length scale parameter.

RESULTS

The sketch of the 2D plane strain problem considered here is shown in Fig. 2 (b), where the plate height to width ratio is taken as, $\frac{L_0}{W_0} = 3$. The section is subjected to a monotonically increasing displacement along the Y-axis as shown. The final fracture is triggered by introducing a small imperfection in the system by lowering the initial yield stress of the material along the 45° band by 2%. An assessment of the load-deflection behavior of the model for different values of the constitutive length parameter is made by considering two values of the length parameter: $\frac{L_D}{R_C} = 0$ representing the classical GTN model, and $\frac{L_D}{R_C} = 0.3$ representing the enriched GTN model. All other material parameters remain equal to those used by Nielsen and Hutchinson [6]. It is observed that with $\frac{L_D}{R_C} = 0.3$, the fracture is delayed significantly due to enhanced hardening in the material. In fact, shear localization is absent for such high values of $\frac{L_D}{R_C}$. The micro-mechanical unit cell calculations performed by Niordson and co-workers [4, 5] have shown a similar effect of $\frac{L_D}{R_C}$.

A detailed study showing the dependence of length parameter on response from the 2D plane strain section will be presented along with how this couple to the traction-separation relation and cohesive fracture energy related to ductile tearing. Moreover, the effect of having a length scale in the constitutive law on the mesh sensitivity will also be discussed.

ACKNOWLEDGEMENTS

The work is supported by the Danish Council for Independent Research in the project “Advanced Damage Models with InTrinsic Size Effects”, grant no. DFF-7017-00121.

References

[1] Gurson, Arthur L. Continuum theory of ductile rupture by void nucleation and growth: Part I—Yield criteria and flow rules for porous ductile media. *J. Eng. Mater. Technol.* **99**: 2-15, 1977.

[2] Tvergaard, V. Influence of voids on shear band instabilities under plane strain conditions. *International Journal of Fracture* **17**: 389-407, 1981.

[3] Tvergaard, V., Needleman, A. Analysis of the cup-cone fracture in a round tensile bar. *Acta Metallurgica* **32**: 157-169, 1984.

[4] C.F. Niordson, V. Tvergaard. A homogenized model for size-effects in porous metals. *J. Mech. Phys. Solids.* **123**: 222-233, 2019.

[5] I. Holte, C.F. Niordson, K.L. Nielsen. Investigation of a gradient enriched Gurson-Tvergaard model for porous strain hardening materials. *European Journal of Mechanics/A Solids* **75**: 472-484, 2019.

[6] Nielsen, K. L, Hutchinson, J. W. Cohesive traction-separation laws for tearing of ductile metal plates. *International Journal of Impact Engineering* **48**: 15-23, 2012.

[7] Andersen, R.G, Felter, C. L, Nielsen, K. L. Micro-mechanics based cohesive zone modeling of full scale ductile plate tearing: From initiation to steady-state. *International Journal of Solids and Structures* **160**: 265–275, 2019.

PHASE-FIELD APPROACH FOR FRACTURE USING REPRESENTATIVE CRACK ELEMENTS FOR GEOMETRICAL AND MATERIAL NON-LINEARITIES

Johannes Storm[1] and Michael Kaliske *[1]
[1]Institute for Structural Analysis, Technische Universität Dresden, Dresden, Germany

Summary The contribution addresses challenges of the kinematic consistency of phase-field models for fracture. The framework of Representative Crack Elements is introduced in order to derive consistent phase-field fracture models. Applications of this approach to geometrical and material non-linearities are derived. Finally, results of a self-consistency test and of illustrative examples are presented.

INTRODUCTION

The phase-field method for fracture has been rapidly developing over the past 10 years. The regularised description of discrete cracks in a variational framework allows to develop thermodynamically consistent models. A small number of fundamental assumptions (restrictions) and straight forward integration into standard Finite Element Method (FEM) yielded an active scientific community in this field and various promising developments and results. Even though, phase-field fracture has been applied to non-linear, rate-dependent and multi-physical material behaviour in many publications, focus on some fundamental challenges is necessary so that the method can become a standard tool in fracture mechanics. The critical convergence behaviour of these bi-convex problems, the consistent formulation and implementation of fracture irreversibility and the investigation of conditions for the numerical discretisation are key tasks for upcoming developments.

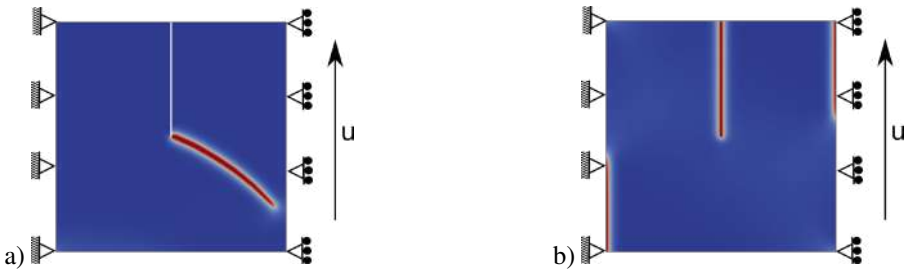

Figure 1: Comparison of crack propagation at a single-edge notch at shear load with a) a discrete initial crack and b) a phase-field initial crack applying phase-field fracture with the spectral strain split [1].

Another essential property for a fracture model is the realistic prediction of the kinematic mechanisms at the crack. Crack states, i.e. opening and closure, as well as material degradation, i.e. force transfer through and along crack surfaces, are considered by decomposition of the mechanical energy potential into a passive and an active portion

$$\psi^{\text{mech}} = \psi^{-} + g(s)\psi^{+}, \tag{1}$$

where $g(s)$ is the degradation function in dependence on the phase-field variable s. Various approximations for this decomposition are proposed in literature based on the deformation state [1, 2, 3, 4, 5, 6, 7, 8, 9, 10, 11, 12, 13], e.g. strain and deformation gradient, or stress state [14]. However, Strobel and Seelig [15] and Steinke and Kaliske [16] have shown that those approximations lead to misleading predictions for force transfer through the crack for quasi-static and dynamic problems, respectively. In Storm et al. [17], the authors have proposed to compare the predictions of phase-field fracture models to those of corresponding discrete crack models in order to validate the kinematic consistency. The crack propagation of a shear plate with an initial discrete and an initial phase-field crack is compared in Fig. 1, which demonstrates the effects of unrealistic force transfer through the crack surfaces.

CONCEPT OF REPRESENTATIVE CRACK ELEMENTS

Two approaches for a consistent crack kinematic in a strain based [15] and a stress based formulation [16] are published for phase-field fracture with isotropic, linear elastic material behaviour. The concept to derive kinematically consistent crack behaviour from a discrete crack model is adopted and generalised to the computational framework of phase-field fracture with Representative Crack Elements (RCE) in Storm et al. [17]. The overall deformation behaviour of the RCE is coupled to the phase-field model by means of the variational homogenisation principle of virtual multi-scale power

$$\bar{\boldsymbol{P}} : \delta\dot{\bar{\boldsymbol{H}}} - \bar{\boldsymbol{b}} \cdot \delta\dot{\bar{\boldsymbol{u}}} \overset{!}{=} \frac{1}{V}\left[\int_{\Omega} \boldsymbol{P} : \delta\dot{\boldsymbol{H}}\, \mathrm{d}V - \int_{\Omega} \boldsymbol{b} \cdot \delta\dot{\boldsymbol{u}}\, \mathrm{d}V\right] \tag{2}$$

*Corresponding author. E-mail: michael.kaliske@tu-dresden.de.

presented by Blanco et al. [18]. Analytical solutions for the embedded RCE problem, compare Fig. 2, are derived for isotropic and anisotropic elasticity and thermo-elasticity [17], for RCE with crack surface friction and finite rotations [19] and for linear visco-elasticity [20]. Thus, these phase-field models, derived with the RCE framework, have similar computational costs like phase-field models with kinematic approximations mentioned above.

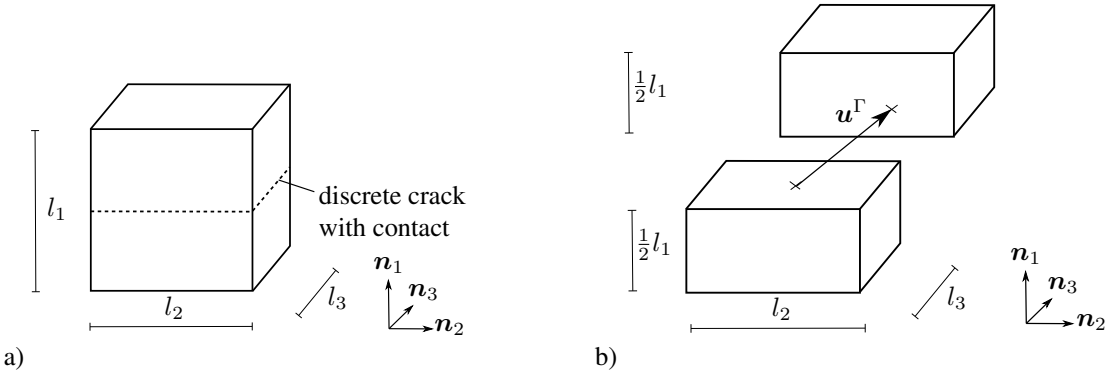

Figure 2: a) Sketch of the RCE with a discrete crack in local coordinates and b) definition of crack displacements and deformations.

In this contribution, the RCE framework is applied to geometrical and material non-linearities. A semi-analytical solution scheme for the embedded RCE problem

$$\Gamma_i(\bar{\boldsymbol{F}}, \boldsymbol{\chi}_{n+1}) = \arg\left\{ \min_{\Gamma_i \in \mathcal{R}} \; \hat{\psi}(\bar{\boldsymbol{F}}, \Gamma_i, \boldsymbol{\chi}_{n+1}) \right\}, \tag{3}$$

regarding the unknown crack deformations Γ_i, is derived, which preserves computational efficiency. The derived models are applied to self-consistency tests and representative examples are shown.

References

[1] C. Miehe, M. Hofacker, F. Welschinger: A phase field model for rate-independent crack propagation: Robust algorithmic implementation based on operator splits. *Computer Methods in Applied Mechanics and Engineering* **199** (2010) 2765-2778.
[2] H. Henry, H. Levine: Dynamic Instabilities of Fracture under Biaxial Strain Using a Phase Field Model. *Physical Review Letters* **93** (2004) 105504.
[3] H. Amor, J.-J. Marigo, C. Maurini: Regularized formulation of the variational brittle fracture with unilateral contact. *Numerical experiments, Journal of the Mechanics and Physics of Solids* **57** (2009) 1209-1229.
[4] F. Freddi, G. Royer-Carfagni: Variational Models for Cleavage and Shear Fractures. *in: Proceedings of the XIX AIMETA Symposium, Ancona, Italia* (2009) 715-716.
[5] G. Lancioni, G. Royer-Carfagni: The Variational Approach to Fracture Mechanics. A Practical Application to the French Panthon in Paris. *Journal of Elasticity* **95** (2009) 1-30.
[6] F. Freddi, G. Royer-Carfagni: Regularized variational theories of fracture: A unified approach. *Journal of the Mechanics and Physics of Solids* **58** (2010) 1154-1174.
[7] M. Ambati, T. Gerasimov, L. De Lorenzis: A review on phase-field models of brittle fracture and a new fast hybrid formulation. *Computational Mechanics* **55** (2015) 383-405.
[8] F. Zhang, W. Huang, X. Li, S. Zhang: A Study on Phase-Field Models for Brittle Fracture. *arXiv e-prints* (2018) arXiv:1805.07357.
[9] E. C. Bryant, W. Sun: A mixed-mode phase field fracture model in anisotropic rocks with consistent kinematics. *Computer Methods in Applied Mechanics and Engineering* **342** (2018) 561-584.
[10] V. I. Levitas, H. Jafarzadeh, G. H. Farrahi, M. Javanbakht: Thermodynamically consistent and scale-dependent phase field approach for crack propagation allowing for surface stresses. *International Journal of Plasticity* **111** (2018) 1-35.
[11] X. Zhang, S. W. Sloan, C. Vignes, D. Sheng: A modification of the phase-field model for mixed mode crack propagation in rock-like materials. *Computer Methods in Applied Mechanics and Engineering* **322** (2017) 123-136.
[12] M. J. Borden: Isogeometric analysis of phase-field models for dynamic brittle and ductile fracture. *Ph.D. thesis, University of Texas at Austin* (2012).
[13] C. Hesch, K. Weinberg: Thermodynamically consistent algorithms for a finite-deformation phase-field approach to fracture. *International Journal for Numerical Methods in Engineering* **99** (2014) 906-924.
[14] S. Teichtmeister, D. Kienle, F. Aldakheel, M.-A. Keip: Phase field modeling of fracture in anisotropic brittle solids. *International Journal of Non-Linear Mechanics* **97** (2017) 1-21.
[15] M. Strobl, T. Seelig: A novel treatment of crack boundary conditions in phase field models of fracture. *Proceedings in Applied Mathematics and Mechanics* **15** (2015) 155-156.
[16] C. Steinke, M. Kaliske: A phase-field crack model based on directional stress decomposition. *Computational Mechanics* **63** (2018) 1019-1046.
[17] J. Storm, D. Supriatna, M. Kaliske: The concept of representative crack elements for phasefield fracture: Anisotropic elasticity and thermoelasticity. *International Journal for Numerical Methods in Engineering* (2019) 1-27.
[18] P. J. Blanco, P. J. Snchez, E. A. Souza Neto, R. A. Feijo: Variational Foundations and Generalized Unified Theory of RVE-Based Multiscale Models. *Archives of Computational Methods in Engineering* **23** (2016) 1-63.
[19] J. Storm, D. Supriatna, M. Kaliske: Method of Representative Crack Elements for Phase-field Fracture with Finite Deformations and Dissipative Material Behaviour. *Talk at: VI International Conference on Computational Modeling of Fracture and Failure of Materials and Structures*, Braunschweig (2019).
[20] B. Yin, J. Storm, M. Kaliske: A Rate-dependent Phase-field Model based on the RCE Framework. *Talk at: 7th GAMM Workshop on Phase-field Modeling*, Kaiserslautern (2020).

HYDROGEN INDUCED FAST-FRACTURE IN HIGH STRENGTH STEELS

Siamak S. Shishvan*[1,2], Gábor Csányi[2], and Vikram S. Deshpande[2]
[1]Department of Structural Engineering, University of Tabriz, Tabriz, Iran
[2]Department of Engineering, University of Cambridge, Cambridge CB2 1PZ, UK

Summary One of the recurring anomalies in the hydrogen induced fracture of high strength steels is the apparent disconnect between their toughness and uniaxial tensile strength in identical hydrogen environments. Here we propose, supported by detailed atomistic and continuum (Finite element) calculations, that unlike macroscopic toughness, hydrogen-mediated tensile failure is a result of a fast-fracture mechanism. Specifically, we show that failure originates from the fast propagation of cleavage cracks that initiate from cavities that form around inclusions such as carbide particles. A host of well-established experimental observations of hydrogen embrittlement are accurately predicted using the proposed fast-fracture mechanism without recourse to fitting parameters.

INTRODUCTION

While the adverse effects of hydrogen ingress on the mechanical properties of metallic alloys have long been recognized the mechanism of hydrogen embrittlement (HE), especially in steels and ferrous alloys, remains a highly controversial issue with numerous mechanisms having been proposed, e.g. [1]. The two commonly invoked mechanisms are: (a) Hydrogen Enhanced DEcohesion (HEDE) and (b) Hydrogen Enhanced Localized Plasticity (HELP). However, there exist a number of experimental observations that are not only apparently inconsistent with each other but also cannot be rationalized by the commonly proposed embrittlement mechanisms. We proceed to discuss some of these observations in order to set the background of this study. For the sake of conciseness, we restrict the discussion to very low rates of loading where the observed embrittlement is most severe.

A detailed assessment of the embrittlement of high strength steels carried out by Ayas et al. [2] confirmed that: (i) the level of hydrogen embrittlement scales with the lattice hydrogen and (ii) is independent of the hydrogen trapped in dislocations, grain boundaries or carbide particles. This is now widely recognized in the literature, i.e. the level of embrittlement scales with the diffusible hydrogen [3]. With the experimental data suggesting that embrittlement in ferritic steels scales with lattice hydrogen that typically is less than 1 appm, the mechanism by which such low concentrations of hydrogen cause embrittlement remains unclear. The main aim of the current study is to present a coherent mechanism for understanding the dependence of the tensile strength of steels in a hydrogen environment and thereby rationalize the apparent contradictions exposed in the literature.

THE HYDROGEN EMBRITTLEMENT MODEL

Detailed atomistic calculations carried out here for the effect of hydrogen on a mode-I loaded crack with a crack plane (110) and crack front direction $[\bar{1}10]$ in BCC Fe demonstrate that, consistent with findings in [4], cleavage can occur due to the presence of a crack-tip hydride with a direct competition between the rate of formation of a crack-tip hydride (and consequently the rate of crack propagation by cleavage) and crack blunting by dislocation emission. An estimate of the minimum crack velocity $v_{\text{blunt}}^{\text{crit}}$ required for preventing blunting by dislocation emission leads to the key result that a cleavage crack velocity $v_c > v_{\text{blunt}}^{\text{crit}} \approx 5.43\text{ms}^{-1}$ is required to frustrate blunting of the crack-tip by dislocation emission and allow any reasonable level of crack extension. However, when the hydrogen required to form the hydride is supplied via diffusive flux from the specimen bulk, a hydrogen-assisted cleavage crack is estimated to propagate at a speed $v_{\text{d}}^{\text{crit}} \leq 1203\mu\text{m3s}^{-1}$. Such a slow growing cleavage crack will blunt by dislocation emission and arrest after a negligible amount of crack extension. We therefore conclude that for hydrogen-assisted cleavage to occur, a mechanism is needed to rapidly supply H to the crack-tip so as to maintain a cleavage crack velocity of at-least 5.43ms^{-1}. Diffusive flux from the lattice is unable to maintain such a fast crack growth and this understanding forms the basis of the new model proposed in [5].

The overall mechanism is illustrated in Fig. 1 and comprises two stages: a hydrogen-assisted crack growth stage-A and crack growth in the absence of hydrogen supply in stage-B. These two stages can be summarized as follows:

(i) Remote loading results in the formation and growth of small cavities. These cavities form either by the expansion of pre-existing flaws or more likely by debonding of inclusions such as carbides from the surrounding matrix (Fig. 1a). Hydrogen gas (H_2) fills these cavities via diffusive flux of H from the surrounding material (Fig. 1b). Under equilibrium conditions, the H_2 gas pressure in the cavity equals the pressure p_{H} of the external hydrogen atmosphere.

(ii) The loading induces stress concentrations ahead of nanoscopic cracks/notches (associated with surface roughness) on the cavity surface. Cracks oriented along the (110) plane are very potent in initiating hydrogen-assisted cleavage due to the formation of a hydride (FeH_y where $y \approx 1-3$) over a nanometer size region at the crack-tips (Fig. 1c).

(iii) Hydrogen to form these hydrides is provided from the H_2 gas in the cavity. This is because the large crack-tip stresses reduce the barriers for the entry of H from the cavity as well as for diffusion of H in a nanometer region

*Corresponding author. E-mail: sshishvan@tabrizu.ac.ir

around the crack-tip. This implies that the crack-tip hydrides can form rapidly allowing for a hydrogen-assisted cleavage crack speed $v_c > 1003\text{ms}^{-1}$ (Fig. 1d). The key here is that this H supply route can sustain a cleavage velocity $v_c > v_{\text{blunt}}^{\text{crit}}$ and this significantly limits blunting via dislocation emission thereby allowing hydrogen-assisted cleavage to continue until the hydrogen supply within the cavity is exhausted. This is the end of stage-A. Predictions of this hydrogen-assisted crack growth mechanism are supported by atomistic calculations of binding energies, mobility barriers and molecular dynamics calculations of the fracture process.

(iv) Hydrogen-assisted fast crack growth induces a high strain-rate at the crack-tip which not only maintains a sharp crack-tip but also limits plasticity in the bulk around the crack-tip. Here, we show via macroscopic continuum (FE) crack growth calculations in a rate dependent elastic-plastic solid with fracture modelled using a cohesive zone that cleavage is possible if the crack propagates fast enough. This is because strain-rates at the tips of fast propagating cracks are sufficiently high for the drag on the motion of dislocations resulting from phonon scattering to limit plasticity. This implies that given a sufficiently high remote applied stress σ^{∞}, fast and brittle crack-growth can continue over large distances in stage-B even after the hydrogen supply within the cavity is exhausted. It is this macroscopic fast crack growth that results in the final failure of the specimen (Fig. 1e).

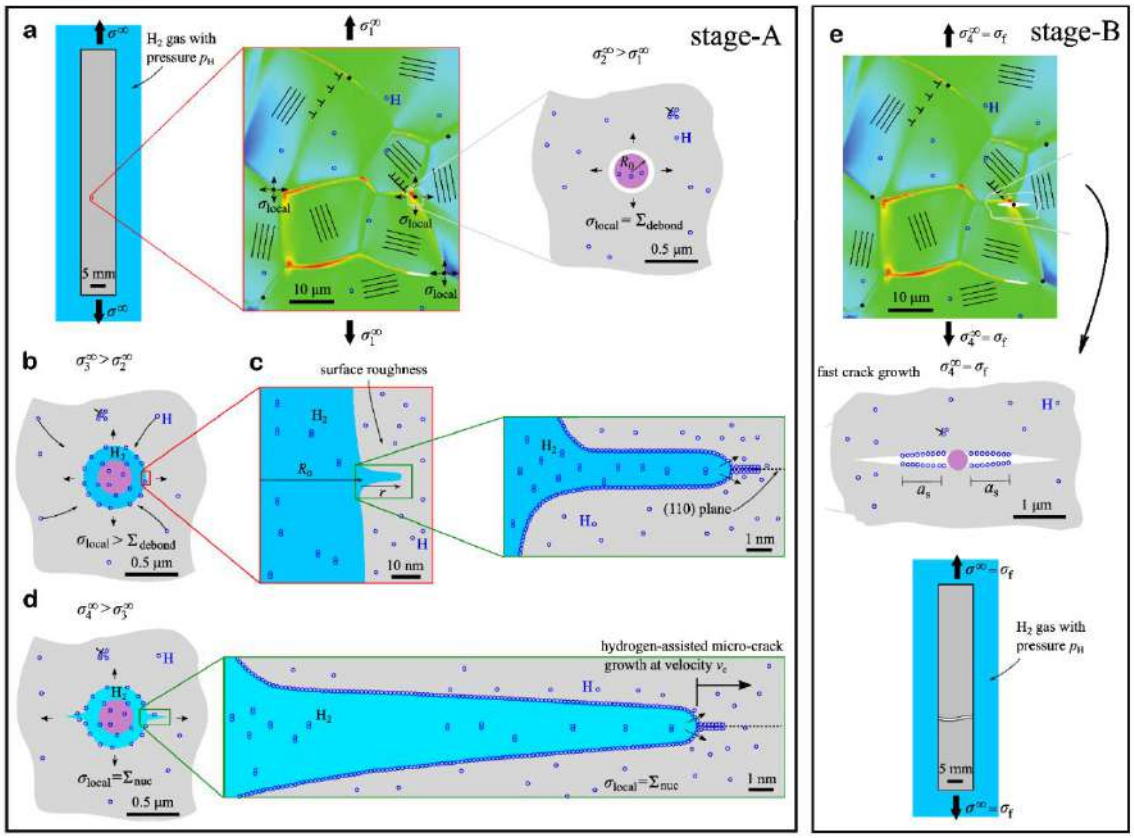

Figure 1. Summary of the overall mechanism for the tensile fracture of high strength steel in a hydrogen environment.

CONCLUDING REMARKS

The combined atomistic/continuum model developed here is used to explain a host of well-established experimental observations including (but not limited to): (i) the disconnect between the measured toughness and tensile strength of steels in identical hydrogen environments; (ii) the dependence of the level of embrittlement primarily on the lattice or diffusible hydrogen rather than trapped hydrogen; (iii) the extensive microcracking in addition to the final cleavage fracture event; and (iv) the higher susceptibility of high strength steels to hydrogen embrittlement. Moreover, our calculations point towards some critical experiments, with some counterintuitive expected findings, that have not been reported to-date: future experiments to confirm or refute these predictions will help gauge the validity of the model developed here.

References

[1] Dadfarnia M., Nagao A., Wang S., Martin M. L., Somerday B.P., Sofronis P. *Int. J. Fract.* **196**: 223–243, 2015.
[2] Ayas C., Deshpande V.S., Fleck N.A. *J. Mech. Phys. Solids* **63**: 80–93, 2014.
[3] Bhadeshia H.K.D.H. *ISIJ Int.* **56**: 24–36, 2016.
[4] Song J., Curtin W.A. *Nat. Mater.* **12**: 145–151, 2013.
[5] Shishvan S.S., Csányi G., Deshpande V.S. *J. Mech. Phys. Solids* **134**: 103740, 2020.

THE CLEAVAGE ENERGY OF BRITTLE CRYSTALS: FROM GRIFFITH BARRIER TO LATTICE TRAPPING

Dov Sherman
School of Mechanical Engineering, Tel-Aviv University, Tel-Aviv 69978, Israel

Summary The ranges of the quasi-static and dynamic cleavage energies, Γ_0 and Γ_{DM}, of silicon crystal along two low energy cleavage systems (LECSs), were evaluated by sets of cleavage fracture experiments. An important variable in this study was found to be the gradient of the energy release rate (ERR) per unit length of crack advance, dG_0/da, denoted Θ. For $\Theta \leq 0.5$, the cleavage energy is either the Griffith barrier of $2\gamma_s$ (γ_s is the free surface energy) or lower due to stress corrosion cracking mechanisms. For $\Theta \geq 0.7$, the cleavage energy increased up to the 'lattice trapping' value of about $3\gamma_s$ for $\Theta \sim 2$. We attribute this behaviour to the way the bonds along the crack front are breaking; being curved, the crack front is actually constructed from planner atomistic scale steps, or kinks. We suggest that the cleavage energy is related to the kinks breaking sequence and energies.

We have recently completed an experimental study of dynamic crack propagation in quasi-statically loaded silicon crystal specimens where the cracks were propagated on the two LECSs, (110)[$1\bar{1}0$] and (111)[$11\bar{2}$]. These specimens served as a model material for the behavior of long range order brittle materials. The experiments were performed using our Coefficient of Thermal Expansion Mismatch (CTEM) method [1-3], where silicon specimens were adhered by two layers of epoxy resin in the middle of a rectangular hole in an aluminum loading frame, see **Fig. 1a and b**. When heating up the assembly on top of an electrical heating stage by only few centigrade, the thermal expansion coefficients mismatch between the aluminum loading frame ($26 \cdot 10^{-6}/^0$C) and silicon specimen ($2.6 \cdot 10^{-6}/^0$C) generates the required driving force to initiate and propagate the crack. Since the ERR, $G_0(a)$, is a monotonic increasing function (**Fig. 1c**), the crack propagate unstably. A significant variable in our experiments was found to be the gradient of the energy release rate (ERR) for unit length of crack advance, dG_0/da we denote Θ (in units of J/m^2/mm), which is the slope of the calibration function, $G_0(a)$. Θ in our specimens was evaluated by FEA, and is shown schematically in **Fig. 1c** for long (blue lines) and short (red lines) precracks. In specimens with long precrack Θ is low, while short precrack brings to much higher value of Θ. We were able to manipulate the precrack length in order to control Θ.

The experimental energy-speed relationships [1,2] were compared with Freund equation of motion to extract the varying cleavage energies at initiation and during propagation, denoted here Γ_0 and Γ_{DM}, respectively. We show, at first, that $\Gamma_0 = \Gamma_{DM}$, and that both Γ_0 and Γ_{DM}, are Θ dependent, namely:

$$\Gamma_0 = \Gamma_0(\Theta). \qquad (1)$$

Surprisingly, $\Gamma_0(\Theta)$ *is* independent of crack speed. Considering Freund equation of motion:

$$G_D = G_0(1-V/C_R), \qquad (2)$$

the dynamical ERR, $G_D = \Gamma(\Theta)$ during propagation, and the kinetic ERR $G_K = G_0 V/C_R = G_K(V)$, V is the crack speed. As discuss bellow, the cleavage energy depends upon Θ through atomistic bond breaking energies along the crack front, while the kinetic energy is that of particles in the entire specimen, hence during crack propagation Eq. (2) is now revised:

$$\Gamma_0(\Theta) = G_0(1-V/C_R = G_0 - G_K(V) \qquad (3)$$

The cleavage energy $\Gamma_0 \leq 2\gamma_s$ when $\Theta \leq 0.5$ J/m^2/mm in air due to stress corrosion cracking **(Fig. 2a and b)**. It significantly increases when $\Theta > 0.7$ J/m^2/mm, where the SCC mechanisms vanish, and approaching the 'lattice trapping' value for $\Theta \sim 2$ J/m^2/mm **(Fig. 2a and b)** [1,2]. Our results explain the large scatter appearing in the literature for the cleavage energy of silicon crystals of both LECSs due to possible large variations in Θ during these experiments. Therefore, following our experiments, we advise that reporting the cleavage energies should be accompanied by reporting Θ.

An important macroscopic physical occurrence in our experiments is the curvature of the crack front, as shown by confocal microscope images in **Fig. 3a to f** for cracks propagating on the two LECSs. The only topological explanation to the curvature is that it constructed from atomistic scale planar steps, or, kinks. These propagate by two major mechanisms: kink advance and kink formation, with distinct energy of propagation between the two [4] (see **Fig. 3b**).

We suggest that the macroscopic crack front curvature and the cleavage energy, and the microscopic bond breaking mechanisms and sequence in the atomistic scale, depend on the ratio between the number of kink advance to kink formation mechanisms. All are governed by the macroscopic variable Θ. For low value of Θ, the crack front is curved, while for high Θ, it is straitening up to become a straight crack front. A simple model relating the macroscopic cleavage energy to the king advance and formation energies using the rule of mixtures: $\Gamma = (1-f)\,\Gamma_{adv} + f\,\Gamma_{form}$, f being the fraction of kink formation mechanisms. Assuming $\Gamma_{adv} \sim 2\gamma_s$ and $\Gamma_{form} \sim 3\gamma_s$ explains the experimental results, where $f \alpha \Theta$.

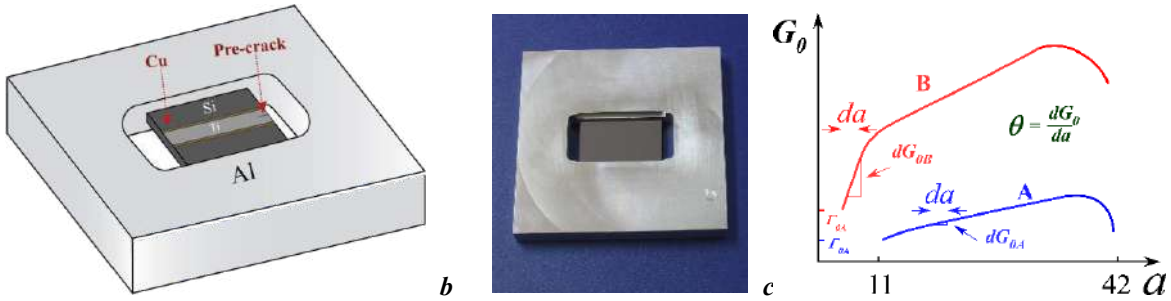

Fig. 1. ***a*** Optical picture of the loading frame and the adhered silicon specimen assembly, ***b*** schematic presentation of the assembly, and ***c*** G_0 vs. a, the calibration functions of the specimen for long precrack (blue-A) and short precrack (red-B) revealing $\Theta=dG_0/da$, the gradient of the ERR for unit length of crack advance in units of J/m^2/mm.

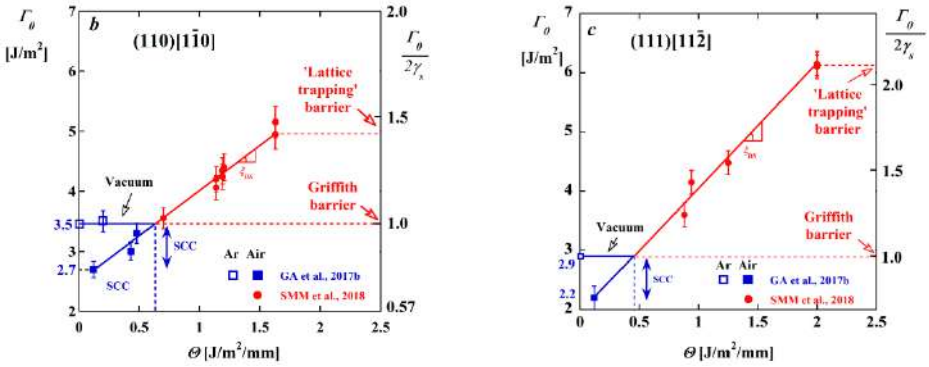

Fig. 2. The cleavage energy at initiation, Γ_0, as a function of Θ and environment for the two LECSs of silicon crystal, ***a*** (110)[1 $\bar{1}$ 0] and ***b***, the (111)[11 $\bar{2}$] [1,2]. A new material property: $\xi_{DS}=d\Gamma_0/d\Theta$ correlates the cleavage energy and the driving force.

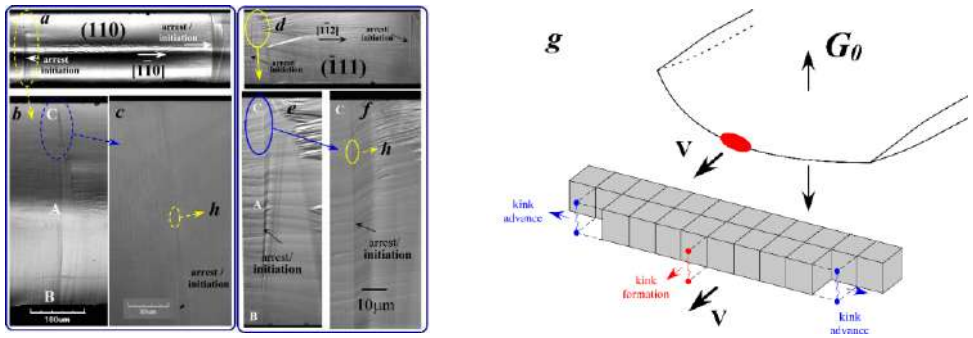

Fig. 3. Confocal optical microscope images of the fracture surfaces of silicon specimens fractured under Mode I during crack initiation, propagation, and arrest cycles: ***a-c*** The fracture surface of the (110) LECS between two initiation and arrest cycles whith varying magnifications; ***d-f*** same for the (111) LECS between two initiation and arrest cycles; ***g*** Schematic presentation of kinks: the grey cubes represents broken bonds along the crack front, while the red and blue bonds represent kink formation and kink advance mechanisms.

This investigation led to another, new material property, the dynamic free surface energy, γ_{ds}, which is considerably higher than the static one, γ_s, and is still free surface energy:

$$2\gamma_{ds}=2\gamma_{ds}(\Theta)=\Gamma_0(\Theta) \quad (4)$$

which is, in the atomistic scale, defined by the two kinking mechanisms energies: kink advance and kink formation [5].

References:

[1] Shaheen-Mualim M and Sherman D. The dynamic cleavage energy of brittle crystals. Journal of Engineering Science 129,111-128 (2018).

[2] Shaheen-Mualim M, Gleizer A. and Sherman D. Dynamic stress corrosion cracking in silicon crystal. Int. Journal of Fracture **219**, 161-174 (2019).

[3] Shaheen-Mualim M. and Sherman D. The effect of reflected stress wave on crack speed in silicon crystal. Engineering Fracture Mechanics **225**, 106196 (2020).

[4] Kermode J.R. et al., Low speed crack propagation via kink formation and advance on the silicon (110) cleavage plane. Phys. Rev. Let. **115**, 135501 (2015).

[5] Merna Shaheen Mualim, Guy Kovel, L. Ben-Bashat Bergman, Anna Gleizer, and Dov Sherman, Macro cleavage energy to atomistic bond breaking mechanisms-From Griffith barrier to Lattice Trapping barrier. Submitted, 2021.

A MICROMECHANICS-INFORMED PHASE FIELD APPROACH TO FRACTURE

Yongxing Shen*[1], Cheng Cheng [1], Yangyuanchen Liu [1]and Vahid Ziaei-Rad [1]
[1]University of Michigan – Shanghai Jiao Tong University Joint Institute, Shanghai Jiao Tong University, Shanghai, China

Summary The regularized variational theory of fracture [2], or so-called phase field approach to fracture, has gained popularity due to its ability to predict crack nucleation, propagation, and branching without extra criteria. This approach works by minimizing total energy functional with the displacement field and phase field as arguments, and eliminates the cumbersome geometric tracking. However, each of the prevailing models [4, 5] predicts a different crack path even under certain simple loadings. To obtain a new anisotropic phase field model for the unilateral constraint, we apply the homogenization theory on the representative volume element (RVE). The proposed model predicts reasonable crack paths for the three-point bending test and through-crack shear test. We will compare the prediction of our model with similar ones proposed by Strobl and Seelig [6, 7] and Steinke and Kaliske [8].

INTRODUCTION

The prediction of failure mechanisms due to crack initiation and propagation in solids is of great significance for engineering applications. Griffth's theory [1] provides a criterion for crack propagation but it is unable to predict crack initiation, merging, and branching. Based on the Griffth's theory [1], Francfort and Marigo [2] proposed a variational theory of fracture and Bourdin et al. [3] regularized this theory, the outcome of which is then the phase field approach to fracture. As is shown in Figure 1, this approach works by minimizing total energy functional with the displacement field and phase field (0=intact material, 1=crack) as arguments, and eliminates the cumbersome geometric tracking compared with traditional discrete crack methods such as the extended finite element method.

The phase field modeling of brittle fracture has shown its advantages on simulating complex fracture processes, see [3, 4, 5]. Nevertheless, the original model proposed in [3] adopts an isotropic response of the cracked solid, i.e., it assumes both tension and compression loads can contribute to cracking, leading to unphysical crack propagation under a compressive load. Early models that do distinguish tension vs. compression were those proposed in [4] and [5]. Amor et al. [4] built their model based on the volumetric-deviatoric split of the strain tensor, while Miehe et al. [5] based their model on the spectral decomposition of the strain tensor. Recently, more sophisticated models based on the local crack orientation were proposed. For example, in the model by Strobl and Seelig [6, 7], the crack orientation is assumed to coincide with the local gradient direction of the phase field, while in that by Steinke and Kaliske [8], a crack coordinate system is defined and is changeable, and the split is based on the decomposition of the stress tensor with respect to the crack orientation. Wu et al. [9] utilized a positive/negative projection based on the spectral decomposition to model the unilateral behavior, where the crack orientation is assumed to be the principal direction of the effective stress tensor.

In 2018, Cheng [10] and Cheng and Shen [11] proposed a phase field model with the tension-compression split and local crack orientations through the homogenization of cracked microstructures. Storm et al. [12] constructed a homogenization framework for their phase field model in a similar way.

In this work, we aim to construct a phase field strain energy density expression that is: (a) variationally consistent, (b) able to distinguish the loading as tension or compression and appropriately degrade the stress-strain response, and (c) is three-dimensional.

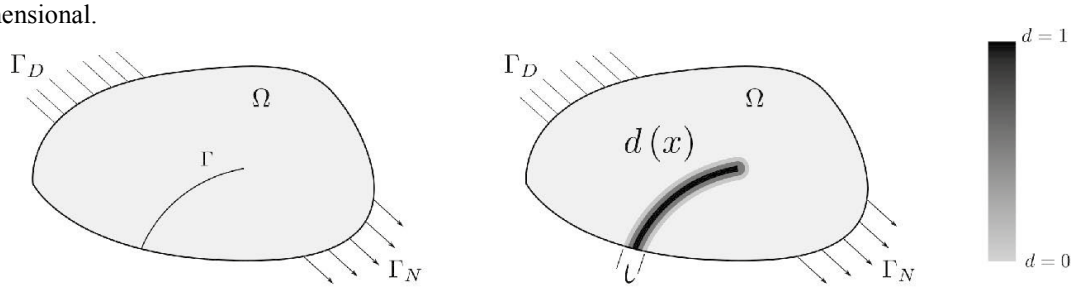

Figure 1. Comparison of a sharp crack and its phase field representation. The left figure illustrates the sharp crack model; the right figure shows the phase field representation of the crack through a smooth transition area, in which the phase field variable is between 0 and 1. The phase field is one of the arguments in the regularized variational theory of fracture, also named the phase eld approach to fracture.

*Corresponding author. E-mail: **yongxing.shen@sjtu.edu.cn** .

CONSTRUCTION OF THE PROPOSED PHASE FIELD MODEL

Essentially we model a possibly curvilinear crack as a collection of fictitious small straight cracks with a particular spatial distribution. More precisely, we assume that a portion of the solid can be divided into many cube-shaped subdomains (or in 2D square-shaped), at the center of each of which there exists a said small plane (or in 2D straight crack). The behavior of the macroscopic crack is then described by the collection of such small cracks, see Figure 2. Here we borrow a terminology of the homogenization theory and call each cube-shaped subdomain a representative volume element (RVE), and will apply standard homogenization techniques to extract its response subjected to mechanical loading.

In a nutshell, we will establish a one-to-one relation between the crack length in the RVE and the local phase field d. Then for any macroscopic input strain $\bar{\boldsymbol{\varepsilon}} \in \mathbb{R}^{\eta\times\eta}(\eta = 2,3)$ with standard homogenization technique, we calculate the average stress $\bar{\boldsymbol{\sigma}} \in \mathbb{R}^{\eta\times\eta}$, and then obtain $\mathbb{C} \in \mathbb{R}^{\eta\times\eta\times\eta\times\eta}$ such that $\bar{\boldsymbol{\sigma}}(\bar{\boldsymbol{\varepsilon}}, d) = \mathbb{C}(\bar{\boldsymbol{\varepsilon}}, d) : \bar{\boldsymbol{\varepsilon}}$, where $\mathbb{C}$ is the effective secant modulus. The expression of $\mathbb{C}(\bar{\boldsymbol{\varepsilon}}, d)$ can be obtained by comparing with analytical expressions or by numerical fitting. This way the strain energy density $\Psi(\bar{\boldsymbol{\varepsilon}}, d)$ can also be obtained.

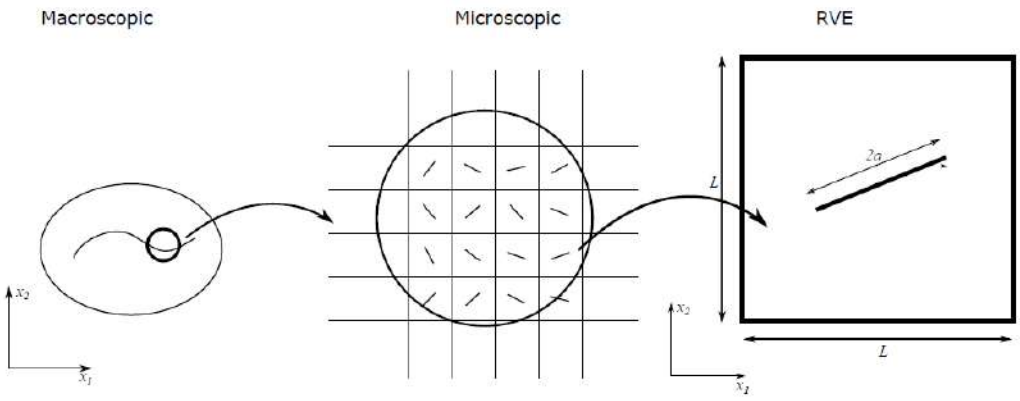

Figure 2. Modeling a macroscopic crack as a collection of fictitious small straight cracks, each in an RVE.

CONCLUSIONS

We have proposed a micromechanics-informed phase field model whose macroscopic constitutive relationship is fully determined by the fictitious microstructure. This model enjoys the following features:

1. The proposed model is the only that outputs a reasonable stiffness response and crack path among the models compared.
2. The performance is achieved via the introduction of a tension-compression discriminant that gives the correct behavior, namely whether the response should be degraded by the phase field.
3. The model can be expressed in terms of invariants and pseudo-invariants of the strain tensor, and hence easy to generalize to an arbitrary crack orientation and to three-dimensions.

References

[1] Griffith A. A., The phenomena of rupture and flow in solids. *Proc. R. Soc. Lond. A. Math. Phys. Sci.* **221**(582-593): 163-198, 1921.
[2] Francfort G. A., Marigo J.-J. Revisiting brittle fracture as an energy minimization problem. *J. Mech. Phys. Solids*. **46**(8): 1319-1342, 1998.
[3] Bourdin B., Francfort G. A. , Marigo J.-J. Numerical experiments in revisited brittle fracture. *J. Mech. Phys. Solids*. **48**(4): 797-826, 2000.
[4] Amor H., Marigo J.-J., Maurini C. Regularized formulation of the variational brittle fracture with unilateral contact: numerical experiments. *J. Mech. Phys. Solids*. **57**(8): 1209-1229, 2009.
[5] Miehe C., Hofacker M., Welschinger F. A phase field model for rate-independent crack propogation: Robust algorithmic implementation based on operator splits. *Comput. Methods. Appl. Mech. Eng.* **199**(4): 2765-2778, 2010.
[6] Strobl M., Seelig T. A novel treatment of crack boundary conditions in phase field models of fracture, *Proc. Appl. Math. Mech.* **15**(1): 155-156, 2015.
[7] Strobl M., Seelig T. On constitutive assumptions in phase field approaches to brittle fracture, *Procedia. Structural. Integrity.* **2**: 3705-3712, 2016.
[8] Steinke C., Kaliske M. A phase-field crack model based on directional stress decomposition. *Comput. Mech.* **63**(5): 1019-1046, 2019.
[9] Wu J.-Y., Nguyen V. P., Zhou H., Huang Y. A variational consistent phase-field anisotropic damage model for fracture. *Comput. Methods. Appl. Mech. Eng.* **358**: 112629, 2020.
[10] Cheng C. A micromechanics-based phase field approach to fracture. Master's thesis, Shanghai Jiao Tong University, 2018.
[11] Cheng C., Shen Y. A micromechanics-based phase field approach to fracture. In: The Third International Conference on Damage Mechanics, 2018.
[12] Storm J., Supriatna D., Kaliske M. The concept of representative crack elements for phase-field fracture: Anisotropic elasticity and thermo-elasticity. *Int J Numer Method Biomed Eng.* doi:10.1002/nme.6244.

FRACTURE TOUGHNESS OF SELF-SIMILAR HIERARCHICAL MATERIAL

Michael Ryvkin*[1], Puneet Kumar [1], and Leonid Kucherov [1]
[1]School of Mechanical Engineering Tel Aviv University, Tel Aviv, Israel

Summary The brittle fracture of the two-dimensional materials with a self-similar second-order hierarchy is considered. The microstructure with four-fold cubic symmetry is generated by a periodic system of macro- and microvoids in a homogeneous isotropic parent material. A semi-infinite crack terminates in a void, and the fracture toughness is determined in the framework of critical stress criterion. The analysis addresses a rectangular domain with hundreds of repetitive cells, which subjected to the K-field boundary conditions. The computationally expansive analysis of the domain is reduced to the multiple analysis of the single repetitive cell by the use of the discrete Fourier transform. A parametric study is carried out, and, in particular, the influence of parent material redistribution between the hierarchical levels is examined.

ANALYSIS

One of the design principles for the development of new materials with the desired mechanical properties is employing the structural hierarchy. The influence of the structural hierarchy on the bulk material properties has been much studied, while the fracture behavior of hierarchical materials is not entirely understood. A possible reason is serious computational difficulties arising in the modeling of a multiscale fracture phenomenon in a multiscale hierarchical material. The present work suggested a way to overcome these difficulties by employing the finite element method in conjunction with the representative cell approach based on the discrete Fourier transform.

Consider two-dimensional material with second-order self-similar hierarchical microstructure generated by periodic voids with the four-fold rotational symmetry. Two materials types are addressed. In material A macrovoids in a solid parent material filled with microvoided material generated from the same parent one, while in material B (see Fig. 1), the macrovoids are cavities surrounded by the microvoided material. The translational symmetry on the macro- and microscale is defined by the values L and l, respectively. The fracture toughness problem is formulated for a square

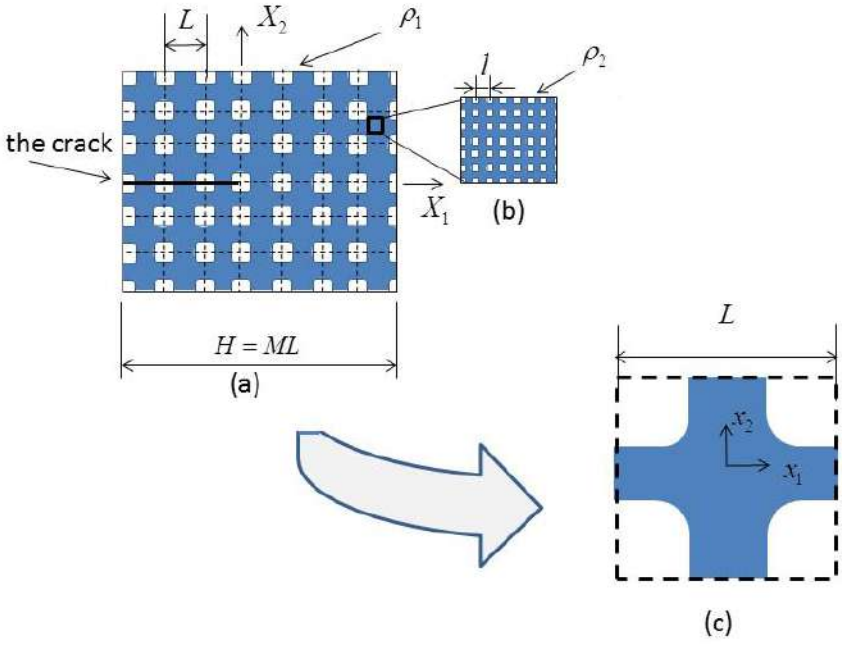

Figure 1: Analysis scheme for material B. (a) The analysis domain on a macrolevel with homogenaized microvoided constituent; (b) microvoides layout; (c) representative cell with the local coordinate system.

*Corresponding author. E-mail: ryvkin@tauex.tau.ac.il

domain $-H/2 \leq X_i \leq H/2, i = 1, 2$ with embedded crack subjected to K-field boundary conditions at its boundaries, and the critical maximal stress criterion for crack propagation is adopted. The number of repetitive cells in the domain must be sufficiently large so that the near tip stress field becomes insensitive to the domain size, and, consequently, corresponds to the case of a semi-infinite crack.

The remote K-field is calculated after evaluation of the effective elastic moduli of the hierarchical material, and then the problem where the microvoided material is replaced by the homogenized one is considered. It is resolved by the representative cell method [1,2]. To this end, the domain is viewed as an assemblage of repetitive cells, which perfectly bonded everywhere except the crack region. The finite discrete Fourier transform is applied, and the problem for the domain is reduced to the problem for the representative cell $-L/2 \leq x_i \leq L/2, i = 1, 2$ with the boundary conditions of Bloch-Floquet type. The numerical experiments have shown that in order to model a semi-infinite crack, one has to consider the domain including at least $M = 20$ cells along its boundary. Consequently, the number of degrees of freedom, which was addressed in the present analysis, is 400 times less than for the direct numerical simulation approach. After the solution of the representative cell problem by the finite element method, the displacements and stresses in any point of the domain are determined by the inverse discrete Fourier transform formula. Finally, the problem for the near tip zone with the actual microvoids layout is considered with the boundary conditions derived from the stress field obtained at the previous analysis step. The obtained maximal stress value yields the fracture toughness magnitude K_{IC} in terms of the critical rupture stress of the parent material σ_f.

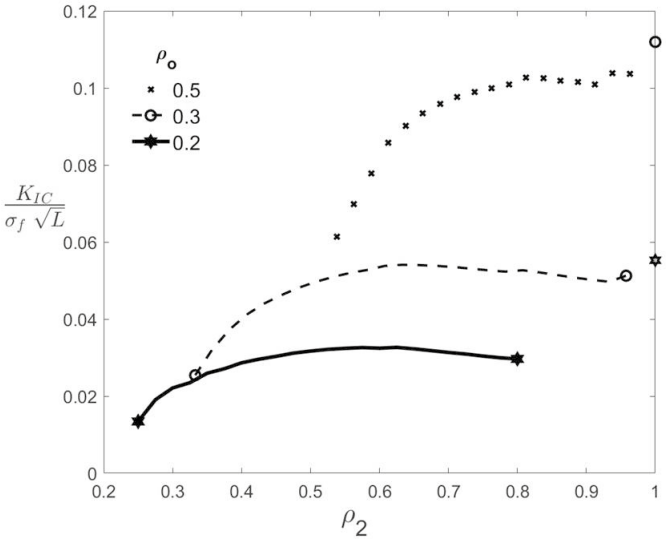

Figure 2: Dependence of the normalized fracture toughness upon the relative density on the microlevel ρ_2 for different values of the fixed total relative density $\rho_0 = \rho_1\rho_2$ (ρ_1 denotes macrolevel density - see Fig. 1). The values for the non-hierarchical voided materials with $\rho_2 = 1$ are shown for the reference.

RESULTS

The influence of parent material redistribution between the hierarchical levels on the fracture toughness was investigated. It was found that for material A growth of the relative density at the second hierarchical level (microdensity) accompanied by the macrovoids increase and microvoids decrease causes monotonic fracture toughness reducing, while for material B, the effect is opposite. It takes place for low and medium microdensity values, then the fracture toughness becomes insensitive to the material redistribution and depends upon the total relative density of hierarchical material only (see Fig. 2).

A comparison of the fracture toughness of the hierarchical and non-hierarchical voided materials of the same relative density shows that introducing hierarchy may have either a positive or negative effect. The final result is determined by the relation between two opposite tendencies: the toughness decrease due to the stress concentration in a material with more complicated microstructure and possible toughness increase due to an increase of the material periodicity length scale.

Acknowledgement The authors gratefully acknowledge support by Israel Science Foundation, Grant No, 1494/16.

References

[1] Ryvkin, M. and Nuller, B. Solution of Quasi-Periodic Fracture Problems by Representative Cell Method. *Comput. Mech.*, **20**: 145-149, 1997.
[2] Ryvkin, M. and Hadar, O. Employing of the discrete Fourier transform for evaluation of crack-tip field in periodic materials, *Int. J. Eng. Sci.* **86**: 10-19, 2015.

HETEROGENEOUS DYNAMIC FRACTURE: AMPLITUDE SCALING OF CRACK FRONT DEFORMATIONS

Thibault Roch[1] and Jean-François Molinari*[1]
[1]Civil Engineering Institute,Institute of Materials Science and Engineering,Ecole Polytechnique Fédérale de Lausanne (EPFL), Lausanne, Switzerland

Summary We study numerically the deformation of a dynamic crack propagating through a planar heterogeneous interface. We investigate the evolution of the front shape due to variations of fracture toughness, represented by weak and strong stripes parallel to the rupture direction. When going from homogeneous to heterogeneous properties, the crack enters a transient regime during which the front evolves from a straight configuration to a sinusoidal shape. This process is governed by crack front waves that decay with time. Following this regime, the front reaches a stationary shape whose amplitude is determined by the heterogeneity size, the toughness variation between heterogeneities, the relative contraction of the process zone, and the process zone elasticity. We propose a unique scaling relation for the front amplitude that we support with an extensive parametric study.

The slow propagation of cracks through homogeneous media is quite accurately described by the Linear Elastic Fracture Mechanics framework. Dynamic rupture propagation, however, and in particular its interaction with material heterogeneities, remains still overlooked. In this study, we focus on the crack front perturbation due to the presence of local variation of toughness for a planar crack under mode II loading. Previous studies on front distortion, using the Rice perturbation approach ([1]) which is based on the weight function theory introduced by [2], consider the crack front as a one-dimensional object. However recent results highlight the importance of the fracture process zone size (the length along which damage is spread ahead of the crack tip) and its variation with crack velocity for dynamic heterogeneous fracture. We therefore investigate the complete dynamics of a planar heterogenous fracture, by accurately modeling the crack as a two-dimensional object including the process zone. For this purpose, we take advantage of a spectral boundary integral method coupled with a cohesive model model, which allows us to model efficiently the full dynamics with a good resolution of the damage zone. The heterogeneous interface behaves following a standard slip weakening law. The variations of properties consist of an alternation of weak and strong (in terms of fracture toughness) stripes parallel to the crack propagation. When entering this heterogeneous field of toughness, the shape of the crack front is altered. It evolves from a straight line to a sinusoidal shape during a transient regime. We show evidence that this regime, which features oscillations of the crack front shape, is dominated by the propagation of crack front waves. These waves decay exponentially in time and the front tends toward an equilibrium shape after this initial regime. We show that the amplitude of this sinusoidal profile is directly controlled by the rupture properties as well as the interface and bulk parameters. More specifically, the deformation amplitude scales with the heterogeneity size, the contraction of the process zone related to dynamic crack propagation, the process zone elasticity, and the variation of toughness. We validate these relations by providing evidence of a collapse of measured amplitudes, computed for various set-up, into a master curve depending only on physical parameters, without the need for fitting variables. This scaling illustrates the relevance of the process zone size as one of the controlling parameters related to dynamic front distortion. Similarly to evidence from previous studies [3], [4] that heterogeneities in the direction of the crack propagation only matters if their dimension is comparable to the size of the process zone size, we show that for small heterogeneities compared to the size of the process zone, the front perturbation is negligible. Although the interface used in this study is a regular and simplified heterogeneous pattern, it offers new insights into the underlying physical mechanisms behind the deformation of a crack front.

References

[1] Rice, J. Weight Function Theory for Three-Dimensional Elastic Crack Analysis, in *Fracture Mechanics: Perspectives and Directions (Twentieth Symposium)*, edited by Wei, R. and Gangloff, R. (ASTM International). 29, 1989

[2] Bueckner, H.F. (1987). Weight Functions and Fundamental Fields for the Penny-Shaped and the Half-Plane Crack in Three-Space. *Int. J. Solids. Struct.* **23**(1):57-93, 1987.

[3] Barras, F., Geubelle, P. H., and Molinari, J.-F. Interplay Between Process Zone and Material Heterogeneities for Dynamic Cracks. *Phys. Rev. Lett.* **119**(14), 2017.

[4] Kammer, D.S., Pino Munõz, D. and Molinari J.-F. Length Scale of Interface Heterogeneities Selects Propagation Mechanism of Frictional Slip Fronts. *J. Mech. Phys. Solids* **88**:23-24, 2016

*Corresponding author. E-mail: jean-francois.molinari@epfl.ch .

COMPUTATIONAL FRACTURE MECHANICS ANALYSIS OF TRANSIENT CREEP-FATIGUE CRACK GROWTH IN NICKEL-BASE SUPERALLOYS

Joshua D. Pribe*[1], Thomas Siegmund[1], and Jamie J. Kruzic[2]
[1]School of Mechanical Engineering, Purdue University, West Lafayette, Indiana 47907, USA
[2]School of Mechanical and Manufacturing Engineering, UNSW Sydney, Sydney, NSW 2052, Australia

Summary Creep-fatigue crack growth is a key failure mechanism in nickel-base superalloys at high temperature. While many crack growth laws have been developed for constant-amplitude and hold-time loading, load transients such as overloads must also be considered. The crack growth rate after load transients at high temperature can depend on the material and active damage mechanisms in a more complex manner than at low temperatures. In this study, a computational fracture mechanics model is used to investigate creep-fatigue crack growth following overloads. The results indicate that the presence of a classical retardation effect after the overloads depends strongly on the extent of viscoplastic deformation in the bulk material. In some situations, retardation is nearly absent. Further, hardening due to plastic strain gradients is shown to be important in predicting post-overload behavior.

INTRODUCTION

Realistic load spectra for engineering components include load transients, such as overloads and multi-step block loading. The effect of these transients on subsequent crack growth rates must be considered when predicting component lifetimes. This is particularly true for components expected to operate in an environment where they cannot be readily accessed for testing or replacement, such as nuclear power plants.

The current study is motivated by high-temperature crack growth experiments on two nickel-base superalloys that show seemingly contradictory behavior in steady-state versus post-overload crack extension. First, alloy 718 is a legacy alloy that is widely used in aerospace and land-based gas turbine engines. It exhibits creep-brittle behavior during crack extension, which is associated with environmental attack ahead of the crack tip and high crack growth rates relative to the expansion of the plastic zone. However, the material responds in a more ductile fashion following overloads, with notable crack growth retardation [1]. Second, alloy 617 has been proposed for use in the intermediate heat exchanger in the very high temperature nuclear reactor design. It exhibits creep-ductile behavior, meaning that substantial viscoplastic deformation accompanies high-temperature crack growth. However, this alloy seems to exhibit more brittle behavior following overloads, as a single overload does not produce any measurable retardation. Blocks of ten or more overloads do produce retardation, but this becomes less significant at higher loads [2].

This apparent contradiction is investigated in this study using finite element computations that combine viscoplastic constitutive material models and a cohesive zone model. In the computations, creep-fatigue crack growth emerges as the outcome of interactions between these model components. Two key research questions are addressed using this computational fracture mechanics model. First, how can the concepts of creep-ductile and creep-brittle materials be applied when load transients like overloads occur? Second how does hardening due to plastic strain gradients affect these outcomes? The predicted crack growth rates and crack-tip fields before, during, and after overloads provide insight into the differing behaviors of each alloy.

MODEL APPROACH

A power law viscoplasticity model is used for the bulk material. The model accounts for both statistically-stored dislocations (SSDs, associated with strain hardening) and geometrically-necessary dislocations (GNDs, associated with plastic strain gradients) in the material flow stress. GNDs are neglected in classical plasticity models, but they can significantly enhance hardening in regions of highly nonuniform plastic deformation, such as the crack-tip plastic zone [3]. Crack propagation is modeled using an irreversible cohesive zone model. Damage evolution equations for fatigue and creep allow subcritical crack growth under cyclic and hold-time loading to occur.

The incremental finite element model used in this study allows arbitrary waveforms to be discretized into a series of load steps. In this way, the model captures the evolution of crack-tip fields under both steady-state and transient loading, with crack extension as an outcome of the boundary value problem. This approach goes beyond correlations with conventional fracture mechanics parameters, providing more insight into both the crack extension and bulk deformation processes.

RESULTS AND CONCLUSIONS

The computational fracture mechanics model is first calibrated to the constant-amplitude and hold-time crack growth experiments for both alloys to demonstrate suitability of the model. Then, a parametric study is undertaken to understand how the viscoplastic deformation in the bulk, under hold-time and block-loading waveforms.

*Corresponding author. E-mail: jpribe@purdue.edu

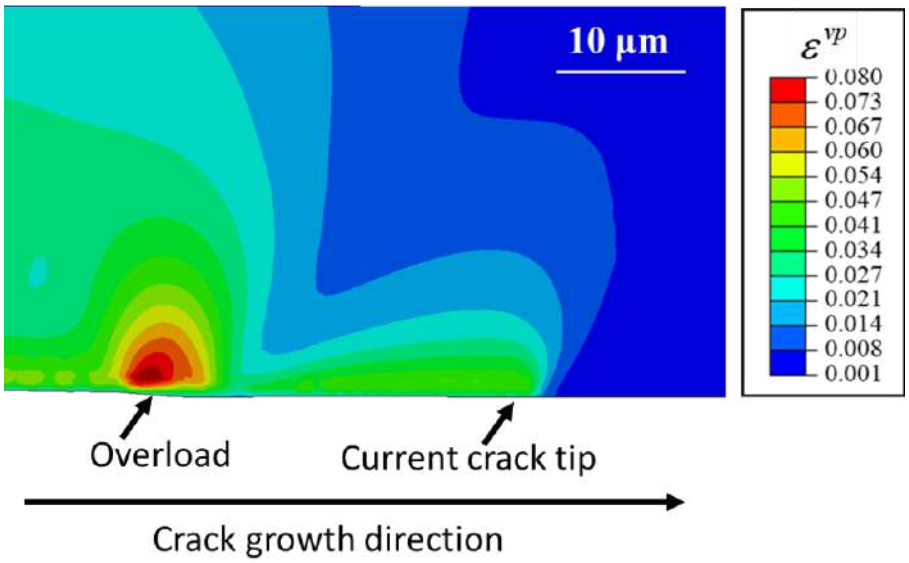

Figure 1: Equivalent viscoplastic strain contours for a computation of creep-fatigue crack growth in creep-brittle alloy 718 involving constant-amplitude cyclic loading interrupted by an overload. Due to symmetry, only half of the model is shown, with crack growth occurring along the symmetry line. Note the significant increase in viscoplastic strain near the location of the overload, followed by a region where crack growth retardation occurs while the steady-state plastic zone redevelops.

For creep-brittle materials like alloy 718, the small viscoplastic strains under constant-amplitude or hold-time loading do not significantly influence crack extension—energy dissipation associated with material separation dominates over the irreversible viscoplastic deformation in the bulk. However, overloads significantly increase the viscoplastic strain ahead of the crack tip, leading to compressive residual stresses that reduce the subsequent crack growth rate. The material separation process therefore becomes significantly affected by the overload-induced viscoplastic deformation, unlike in the steady-state crack growth regime. The differing viscoplastic strains during constant-amplitude loading and following an overload are shown in Figure 1.

On the other hand, for creep-ductile materials like alloy 617, a crack growing in steady state is embedded deep within an extensive plastic zone. Here, a single overload does not appreciably change the viscoplastic strain distribution ahead of the crack tip. This leads to the lack of crack growth retardation observed in the experiments. A larger number of overloads applied in a block does sufficiently increase the viscoplastic strains and thereby produces retardation.

Finally, hardening due to plastic strain gradients is also shown to play an important role in the development of the overload plastic zone, especially in the creep-brittle case. By restricting viscoplastic deformation, plastic strain gradients tend to mitigate crack closure and residual compressive stress ahead of the crack tip. The subsequent crack growth retardation is reduced compared with predictions using a classical plasticity model.

In summary, the key conclusions include the following. For creep-brittle materials, material separation dominates the response during steady-state crack growth, but interaction with viscoplasticity in the bulk material becomes important following overloads. For creep-ductile materials, there is significant viscoplastic deformation in the bulk material during steady-state crack growth, but a single overload does not sufficiently perturb the crack-tip fields to alter crack growth rates. Finally, neglecting plastic strain gradients renders the model predictions non-conservative, particularly during transient crack growth.

References

[1] Gustafsson D., Lundström E. High temperature fatigue crack growth behaviour of Inconel 718 under hold time and overload conditions. *Int. J. Fatigue* **48**: 178–86, 2013.

[2] Addison D. A., Tucker J. D., Siegmund T., Tomar V., Kruzic J. J. Cyclic and time-dependent crack growth mechanisms in Alloy 617 at 800°C. *Mater. Sci. Eng. A* **737**: 205–12, 2018.

[3] Huang Y., Qu S., Hwang K. C., Li M., Gao H. A conventional theory of mechanism-based strain gradient plasticity. *Int. J. Plast.* **20**: 753–82, 2004.

MODELLING OF MATERIALS SELF-HEALING AS CRACKS BRIDGED ZONES FORMATION

Mikhail Perelmuter *
Ishlinsky Institute for Problems in Mechanics RAS, Prospect Vernadskogo 101-1, 119526, Moscow, Russia

Summary The process of materials self-healing is considered as kinetic formation of bridged zones of cracks. In the crack bridged model it is assumed that the tractions that prevent a crack opening reduce the stress intensity factors, but the stress singularity at the crack tip is preserved. As the main characteristic of cracks self-healing efficiency is used the decreasing of the stress intensity factors as the crack bridged zone is formed . The mathematical background of the problem solution is based on the singular integral-differential equations. The analysis of the cracks self-healing processes at the different materials interface with the adhesive layer having the effect of self-healing is presented.

INTRODUCTION

Materials with self-healing properties can be used to avoid premature destruction of devices and to guarantee their stable long-term mechanical reliability. During the last decades wide range of self-healing materials (metals, polymers, ceramics, composites) have been developed. The analysis of various factors' influence on materials self-healing processes is necessary for increasing efficiency of these material application. In many cases the experimental investigations can be extremely long and labor-consuming. It is possible to mark out three basic stages of materials self-healing process: 1) formation and growth flaws/cracks under external loading; 2) activation of self-healing mechanisms; 3) healing of flaws/cracks with partial or total restoration of bonds between crack surfaces. Experimental results have been obtained at each of these stages, but physical-mechanical models and numerical techniques of cracks self-healing have only started to develop in the last decade. Known techniques are based, mostly, on the using of cohesive models in the framework of finite elements method. In this paper we use the bridged crack model (in this model it is assumed that the stress intensity factors do not vanish at the crack tip) for the efficiency evaluation of materials self-healing. The process of materials self-healing is considered as kinetic formation of bridged zones of cracks over time.

KINETIC MODEL OF BRIDGED ZONE FORMATION

Interface crack bridged model. It is assumed within of this model that [1]: 1) a zone of weakened bonds between materials is considered as an interfacial crack with distributed nonlinear spring-like bonds between the crack faces (bridged zone); 2) distributed bridging traction, which are functions of a crack opening, are imposed to the crack faces at the bridged zone; 3) materials ahead of the crack tips are considered as linearly-elastic; 4) the total stress intensity factor (due to the action of the external loading and the bridging tractions) is not zero; within the bridged model (in contrast to cohesive models) a stress singularity is accounted at the crack tip. To describe mathematically the interaction between the crack surfaces, we assume that the nonlinear deformation law of bonds between the surfaces of the crack at the bridging zone is given. The tractions appeared in the bonds between the interface crack surfaces under the external loads action have the normal q_n and tangential q_τ components, $\sigma = \sqrt{q_n^2 + q_\tau^2}$ is the modulus of the traction vector. The surfaces of the crack are loaded by the normal and tangential stresses, which are numerically equal to these components of the tractions. The relations between bonds tractions and displacements difference of the upper and lower crack surfaces at the crack bridged zone are used in the following generalized form [1] $u_{n,\tau}(x) = C_{n,\tau}(x,\sigma)\ q_{n,\tau}(x)$ where $u_{n,\tau}$ and $q_{n,\tau}$ are the components of traction vector and crack opening in the local coordinate system connected with the normal n and tangential τ directions to the crack surface and $C_{n,\tau}(x,\sigma)$ are the bonds compliances depending on the distance x from the crack tip, σ is the tractions vector modulus at the current point x.

Stresses analysis. The stresses at the interfacial crack bridged zone are analyzed for the given nonlinear bond deformation law and with accounting for bonds kinetic destruction (on the stage of a crack formation) or bonds kinetic restoration (on the stage of a crack self-healing). The bonds destruction kinetic model is the alliance of the Zhurkov's fluctuation model and the interface crack bridged model [2]. The kinetic model of bonds restoration is presented below, see also in [3]. The mathematical background of the bridged stresses analysis is the singular integral-differential equations (SIDE) [1] and the boundary element methods [4]. The stress intensity factors (SIF) for the bridged interfacial crack in 2D problem can be written due to the linearity of the problem in the following complex form as in [1]

$$K_{\rm I} + iK_{\rm II} = (K_{\rm I}^{ext} - K_{\rm I}^{\rm int}) + i(K_{\rm II}^{ext} - K_{\rm II}^{\rm int})\,, \quad K = \sqrt{K_I^2 + K_{II}^2}, \quad i^2 = -1; \tag{1}$$

where $K_{I,II}^{\rm ext}$ and $K_{I,II}^{\rm int}$ are the SIFs caused by the external loads and bonds stresses, K is SIFs modulus (MSIF). SIFs for an interface crack in (1) are calculated accounting the stresses ahead of the crack tip due to the external loads and the bonds stresses at the crack bridged zone. If the bonds properties dependent on time, then these SIFs also are time-dependent.

*Corresponding author. Email: perelm@ipmnet.ru

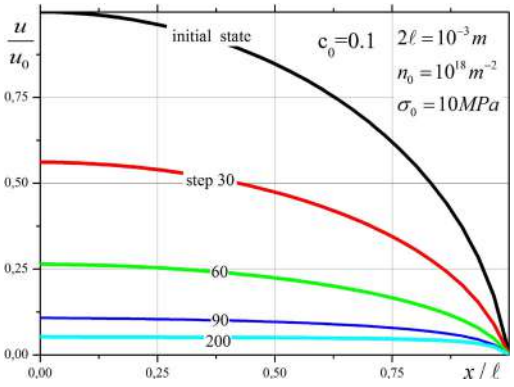

Figure 1: Decreasing of the crack opening during self-healing process, totally filling of a crack with a healing material, $d = \ell$.

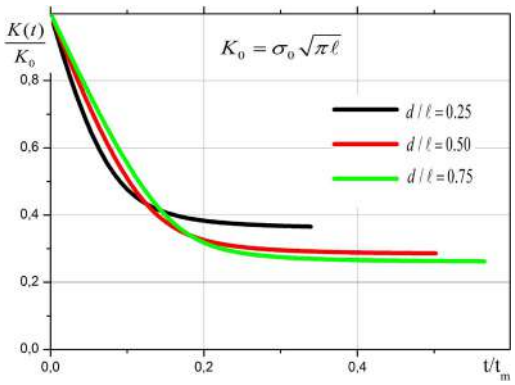

Figure 2: Bonds restoration effect. The relative MSIF versus time, different bridged zones sizes.

Kinetic of bonds restoration. The restoration of bonds inside of cracks (bridged zone formation) is considered on the basis of fluctuation kinetic model. We assume that the increasing in the density of bonds between the crack faces over time $n_h(x,t)$ is governed by the first-order kinetic equation [3]

$$\frac{dn_h(x,t)}{dt} = \frac{n_0 - n_h(x,t)}{\tau_h(x,\sigma)},\ \tau_h(x,\sigma) = \psi(x,\sigma)A(T),\ \psi(x,\sigma) = \frac{\sqrt{u_x^2(x,t) + u_y^2(x,t)}}{H},\ A(T) = \tau_0 \exp\left(\frac{U_h}{RT}\right), \tag{2}$$

Here n_0 is the maximum of bonds density between crack faces, τ_h is the characteristic time of bonds healing ($1/\tau_h$ is the healing rate) is defined by the Arrhenius type relation, $\tau_0 = \alpha h/kT$ is the characteristic time, h is Planck's constant, k is the Boltzmann constant, T is absolute temperature, α is a dimensionless coefficient depending on the material type (polymer, metal, or ceramics), U_h is the energy of bonds healing activation, R is the gas constant, H is a linear scale related to the thickness of the intermediate layer adjacent to the interface. Dimensionless function $\psi(x,\sigma)$ is introduced into (2) to define the dependence of bonds healing time on the distance to the crack tip and the external load. The solution of first equation in (2) (at the initial condition $n(x,0) = 0$) gives increasing bonds density between the crack faces over time [3]. The increasing in the bond density leads to the bonds compliance decreasing at the crack bridged zone. The crack bridged zone formation is modelling by means of bonds compliance variation over time. The system of SIDE is solved by the time-steps scheme as in [2]. The bond compliances at each time step depend on the density of bonds over the bridged zone. The decreasing of the stress intensity factors over time is used as the measure of the healing effect.

RESULTS OF MODELLING AND CLOSING

The proposed approach for cracks self-healing modelling has been used for several problems analysis. Specifically, a straight crack at the interface between different materials was considered. It was assumed that the adhesion layer between material has self-healing ability and at the initial time instant (when the crack surfaces are free of constraints) some healing process is activated inside of the crack, bonds between the crack surfaces are built (the crack bridged zone formation is started). The numerical calculations were performed for plane strain conditions and the elastic constants of the stainless steel-polymer junction, see details in [3]. During the self-healing process the initial crack opening without bonds considerably decreases due to bonds formation. For example, this decreasing is about $u/u_0 \approx 0.05$ at the crack center, for the restored bonds density up to $n(x,t) = 0.95n_0$ after 215 time-steps, see Fig. 1. The next part of calculations was performed for different lengths of crack parts filled with healing agent (bridged zones, d). If only the crack quarter length is involved in the self-healing process then the materials interface strengthening (decreasing of the MSIF) is reasonable in comparison with the cases $d/\ell = 0.5$ and $d/\ell = 0.75$, see Fig. 2.

The results of computations allow to estimate the MSIF decreasing due to bonds restoration over time. Since the computational parameters strongly depend on the initial data (which is caused by the exponential dependence in formula (2)), the comparative analysis of different self-healing methodology can be the major practical application in this model. The determination of the model parameters together with validation of the model will allow us to apply this model to analysis processes of self-healing in polymers, ceramics, metals and theirs joins.

Work was supported by the **Russian Science Foundation**, the project number is 19-19-00616.

References

[1] Goldstein, R.V., Perelmuter, M.N.: Modelling of bonding at an interface crack, *Int. J. of Fracture*, **99**: 53-79, 1999
[2] Goldstein R. V., Perelmuter M. N.: Kinetics of crack formation and growth on the material interface, *Mech. Solids* **47**, 4: 400-414, 2012
[3] Perelmuter M.: Modelling of materials self-healing for artery stents application, *Procedia Structural Integrity*, **15**, 60-66, 2019
[4] Perelmuter M.:Boundary element analysis of structures with bridged interfacial cracks, *Comput. Mechanics*, **51**, 4: 523-534, 2013

HIGH CYCLE FATIGE PROPERTIES OF MEDICAL IMPLANT GRADE NITINOL

Robert M. McMeeking*[1,2,3]
[1]Materials and Mechanical Engineering Departments, University of California, Santa Barbara CA 93106, USA
[2]School of Engineering, Aberdeen University, King's College, Aberdeen AB24 3UE, Scotland, UK
[3]INM – Leibniz Institute for New Materials, Campus D2 2, 66123 Saarbrücken, Germany

Summary It is claimed that increasing the mean strain *increases* the fatigue life of Nitinol. To investigate this, cyclic bending tests were carried out on medical grade Nitinol at 37°C up to 400 million cycles at various mean strains. A constant life model was developed having 90% reliability at 95% confidence. The result is monotonic yet nonlinear for lives of 400 million cycles. We find that the strain amplitude limit *at zero mean strain* is 0.52% for a 400 million cycle life; however, to achieve the same life for a 3% or more mean strain, *the required strain amplitude limit is decreased* to 0.16%. For mean strains from 3% to 7%, the strain amplitude limit that allows a 400 million cycle life is ~0.16%, and essentially independent of mean strain. We conclude that the debatable claim that an increase in the mean strain can increase the fatigue life of Nitinol is not supported by our data.

FATIGUE OF NITINOL MEDICAL IMPLANTS

Nitinol is an alloy of almost equal fractions of nickel and titanium that is a shape memory material, but, within a specific temperature range, also has superelastic properties, in which strain induced transformation from austenite to martensite and back leads to a hysteresis loop in the stress strain behavior. In medical implant grade Nitinol the austenite start and finish temperatures and the martensite start and finish temperatures are designed so that the resulting superelastic stress strain hysteresis loop is closed at body temperature upon straining beyond the hysteresis loop followed by return to zero strain [1]. This permits the superelastic properties to be exploited for transcatheter delivery of implants. For example, Nitinol vascular stents, prosthetic heart valves with tissue leaflets and a Nitinol annulus, and clot-trapping inferior vena cava filters made from Nitinol are all squeezed into narrow sheaths, delivered through a catheter to the implant location, and then pushed out to expand towards their design shapes, thereby firmly locating themselves in the vasculature [1]. In all of the implants mentioned, the metal component experiences cyclic strain after implantation. The expansion and contraction of the heart tends to bend coronary artery stents. The design of prosthetic heart valves typically involves bending of stent posts that support the leaflets when the valve is closed during diastole. The inferior vena cava is squeezed during breathing such that its width expands and contracts, doing so to a degree that has been measured to be as high as a 9 mm change for a 35 mm wide vein. As a consequence of all of these situations, the fatigue properties of medical implant grade Nitinol are of great significance. In 10 years, one breathes more than 80 million times, and one's heart beats over 300 million times, making implant fatigue durability imperative.

ENDURANCE LIMIT OF NITINOL

The endurance limit for medical implant grade Nitinol, defined as 10 million cycles of completely reversed strain cycling without fracture, has been measured as anywhere from 0.2% alternating strain to 0.8% alternating strain, although the latter figure is for electropolished material that is laser-cut from tubes [2]. (Fatigue properties of Nitinol are always quoted in alternating strain due to the strain induced austenite-martensite phase transformation that makes fatigue properties ambiguous when stated in terms of stress.) The austenite-martensite phase transformation in Nitinol is thought to cause the Goodman diagram, a plot of the alternating strain versus mean strain at a fixed lifetime, to be non-monotonic. In some ranges of mean strain the endurance limit in terms of alternating strain is thought to increase with mean strain, an effect that is attributed to martensite, being harder, and having better fatigue resistance than austenite. The outcome is that in the literature there are Goodman diagrams for Nitinol with multiple non-monotonic features [2]. The situation is further complicated by the fact that fatigue testing of medical implant grade Nitinol, other than by use of rotating bend specimens, is a challenge given the small diameter wire and thin tubular material that is used in devices. As a consequence, fatigue testing is often carried out through use of specimens that have configurations similar to the implants, such as the diamond shaped lattice units that are common features in vascular stents and heart valve rings [3]. Unfortunately, in the case of the diamond lattice unit cell specimen the strains being experienced by the material has to be analyzed and interpreted through finite element calculations. Even though state-of-the-art superelastic constitutive laws, such as that due to Auricchio and Taylor and improvements upon it, are used in these computations, inaccuracies in the estimates of strain occur. As a result, the fatigue properties of medical implant grade Nitinol that have been established are quite inaccurate.

*Corresponding author. E-mail: rmcm@ucsb.edu.

FATIGUE TESTS OF NITINOL

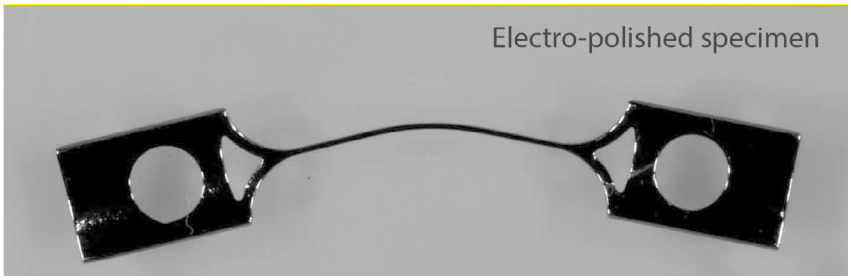

Figure 1. *C-shaped electro-polished Nitinol fatigue test specimen.*

Through use of a simpler, C-shaped specimen that enables the identification of strain levels more easily and more accurately, and via simpler finite element simulations that avoid the complex analysis necessary for specimens such as the diamond lattice unit cell, we have re-measured and re-evaluated fatigue data for medical implant grade Nitinol [4]. The C-shaped specimen is illustrated in Figure 1, and is deformed by compression of one end toward the other to establish a state of mean strain, followed by compression/extension deformation for up to 400 million cycles. In addition, prior to fatigue testing, the specimen is put through one severe cycle of compression and re-extension to simulate insertion into the delivery catheter. Every combination of mean and cyclic strain utilized in the fatigue tests is analyzed individually by finite element analysis to ensure as much accuracy as possible. In addition, the finite element solutions are validated by comparison with load deflection data for the C-specimen, augmented by measurements of strain by digital image correlation.

RESULTS

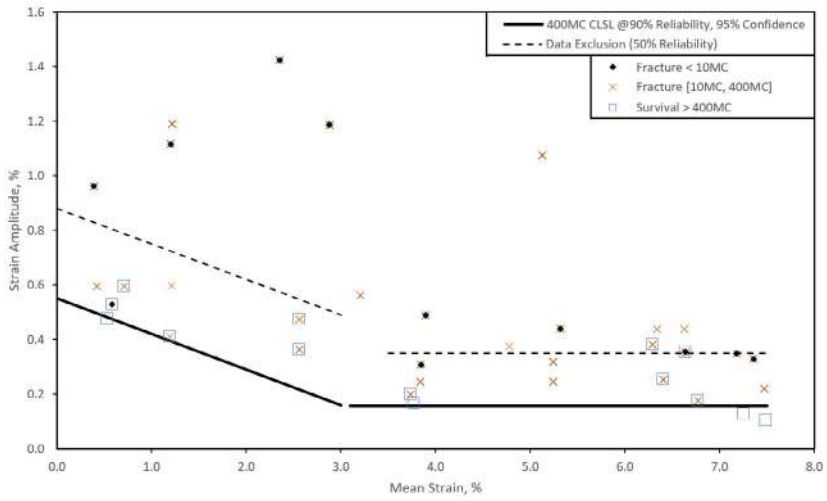

Figure 2. *Fracture diagram and constant life model for 400 x 10^6 cycles of straining. The cross symbols indicate that specimens fractured before reaching 400M cycles, the open square symbols indicate that specimens were runouts and the black diamonds represent specimens that fractured prior to 10 million cycles. Where there are multiple symbols plotted together, both or all of the specified events were experienced. The dashed lines are the constant life model at 400M cycles of straining with 50% reliability and 95% confidence. The solid lines are the constant life model at 400M cycles of straining with 90% reliability and 95% confidence.*

Our results for fatigue indicate that data from rotating bend specimens overestimate the endurance limit for material used at means strains typical of those prevailing in Nitinol medical implants [4]. We also deduce that the Goodman diagram for medical implant grade Nitinol, as shown in Figure 2, is monotonic, though nonlinear [4]. In addition, our Goodman diagram differs significantly from those already in the literature. Our Goodman diagram shows that the allowable alternating strain, at mean strains typical of Nitinol medical implants, is much less than the allowable at zero means strain, an important point, as many Nitinol implants are designed on the assumption that the endurance limit at zero mean strain is conservative [4]. As a result, the constraints on allowable alternating strains for medical implants made from Nitinol are tighter than has previously been believed. As a consequence, design limits on such Nitinol medical implants must be carefully reconsidered, and more conservative design allowables used than have previously been imposed for fatigue life.

References

[1] Duerig, T., Pelton, A., Stoeckel, D. An Overview of Nitinol Medical Applications. *Mater. Sci. Eng.* **A273-A275**: 149-160, 1999.

[2] Robertson, S.W., Pelton, A.R., Ritchie, R.O. Mechanical Fatigue and Fracture of Nitinol. *Int. Mater. Rev.* **57**: 1-36, 2012.

[3] Pelton, A.R., Schroeder, V., Mitchell, M.R., Gong, X.-Y., Barney, M., Robertson, S.W. Fatigue and Durability of Nitinol Stents. *J. Mech. Behav. Biomed. Mater.* **1**: 153-164, 2008.

[4] Cao, H., Wu, M.H., Zhou, F., McMeeking, R.M., Ritchie, R.O. The Influence of Mean Strain on the High-Cycle Fatigue of Nitinol with Application to Medical Devices. Submitted, 2019.

ON THE FRACTURE BEHAVIOR OF SOFT COLLAGENOUS TISSUES

Edoardo Mazza[1,2], Serjosha Robmann[1], Eleni Kahle[1], Vita Marina[1], Kevin Bircher[1], Adam Wahlsten[1], Alexander E. Ehret[1,2]
[1]Department of Mechanical and Process Engineering, ETH, Zurich, Switzerland
[2]Empa, Swiss Federal Laboratories for Materials Science and Technology, Dübendorf, Switzerland

Summary An efficient computational tool that combines a continuum representation of the far field with a discrete fibre network model of the crack near field is used to investigate the conditions leading to crack propagation in soft collagenous tissues, with a specific focus on human fetal membranes. Computational results are informed and validated through fracture experiments, including tests performed inside a multiphoton microscope. The results indicate that, for defect dimensions up to several mm, the analysis of fracture behaviour of soft biotissues cannot be based on conventional fracture mechanics approaches. The model helps rationalizing the influence of osmolarity, hydration level, as well as specific biochemical agents on the toughness of human fetal membranes.

INTRODUCTION

Soft collagenous tissues (SCT) are generally considered as highly defect tolerant [1,2], but a quantitative determination of the conditions leading to SCT fracture is relevant for medical applications involving tissue cutting, perforation or suturing. As an example, premature rupture of fetal membranes is a major reason for neonatal morbidity and death. Fetal membranes can fail as a consequence of perforation for amniocentesis, suturing during prenatal surgery, or "embrittlement" due to influence of biochemical agents [3, 4]. These problems motivated a wide range of biomechanical investigations aimed at an improved understanding of the deformation mechanisms and the fracture behaviour of human amnion (HA), the layer determining stiffness and strength of fetal membranes (e.g. [5]).

The multiaxial deformation behaviour of SCT was analysed in [8] showing that uniaxial tension causes very large lateral contraction associated with outflow of interstitial fluid. This mechanism is facilitated by the asymmetric stiffness of collagen fibers, which is very low in compression and high in tension. This leads to a strong compaction of the collagen fibres network in the nearfield of a defect, effectively avoiding propagation of cracks. This peculiar behaviour was analysed in [9] using a dedicated computational framework to rationalize experimental observations on the tearing energy of bovine liver capsule and collagen hydrogels, used as model systems for compliant collagenous membranes. Based on [6, 7], the present contribution extends previous experimental and computational methods to investigate HA and analyses relevant factors influencing its fracture behaviour.

METHODS

Figure 1 illustrates the collagen compaction and alignment in the defect nearfield in HA. Experiments were performed within a multiphoton microscope, which allows visualizing the collagen network through second harmonic generation, and the stained nuclei of epithelial cells. The latter can be used as markers to characterize the local kinematics. The data in Figure 1 demonstrate a rapid decay of collagen densification and nuclei deformation so that at about 200 μm from the notch tip the network and cells deformation corresponds to far-field conditions.

A dedicated computational approach was developed that allows reproducing the specific mechanisms observed in our experiments, which include strip biaxial mode I fracture tests and biaxial tension of membranes containing a crack-like defect. The model is based on a "hybrid" approach in that it combines a continuum (CM) with a discrete fibre network model (DNM) for the nearfield of the defect (Figure 2). The DNM represents collagen fibres as connectors embedded in an isotropic matrix able to bind and release water. While a continuum representation of the crack near field leads to a singularity, obviously also for the case of a non-linear analysis, the discrete model allows implementing a fiber-level failure criterion, which governs material failure. We performed corresponding parametric analyses and identified conditions promoting or resisting crack propagation, thus leading to either brittle or tough response. Model parameters for CM and DNM are selected to represent the behaviour in uniaxial and equibiaxial tension experiments, and the critical strain ε_c of the connectors is determined based on the failure stretch measured in uniaxial tests.

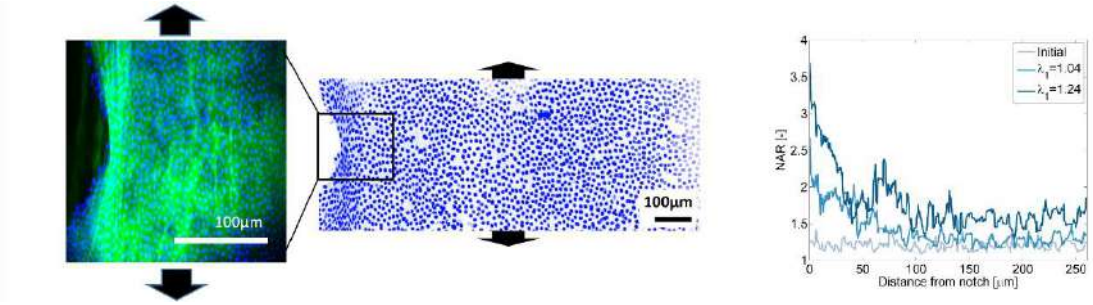

Figure 1. In-situ fracture experiments on HA within the multiphoton microscope. Collagen compaction in the nearfield of a notch in a mode I tear test is visualized through higher intensity of the second harmonic generation signal (green). Epithelial cell nuclei (stained in blue) deform to an elliptical shape. The corresponding aspect ratio of their main dimensions (NAR) is reported in the graph, demonstrating a rapid decay towards far field conditions.

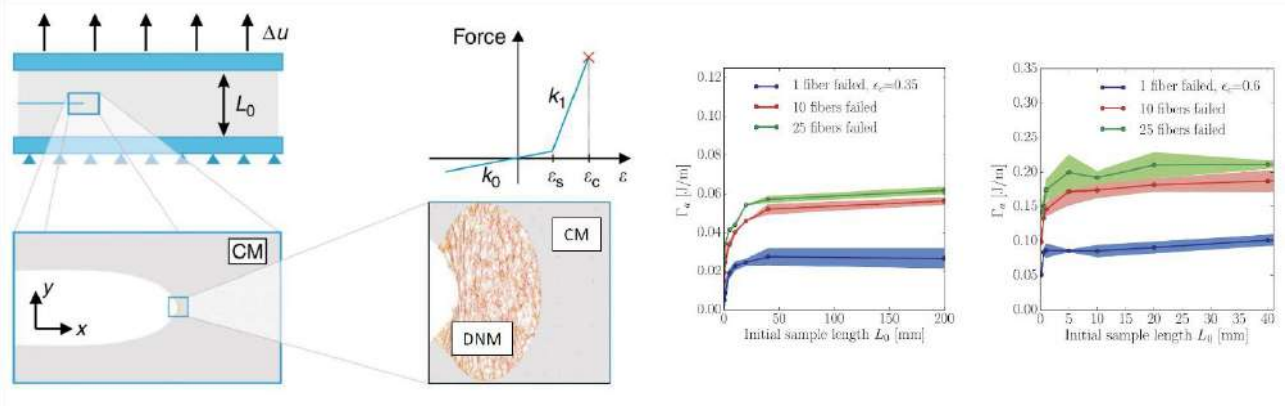

Figure 2. Left: Hybrid model for Mode I fracture experiments of SCT (adapted from [9]): the nearfield is represented through a discrete network model (DNM) and the farfield as a continuum (CM). The force-strain law of the connectors forming the DNM is shown. Right: Results of sample length dependence of the apparent tearing energy Γ_a, for different failure criteria (1, 10 and 25 failed fibers) and critical connector strain ε_c (0.35 and 0.6).

RESULTS AND DISCUSSION

As a consequence of the particular fiber compaction mechanism, the fracture process zone in HA (and in general for SCT) is very small, typically in the range of 100 µm, while the size of "short cracks" (i.e. cracks that are not governed by the material specific tearing energy Γ) is very large, i.e. >10 mm for HA. Biaxial tension experiments on defective membranes showed that the strength of HA is not significantly reduced when the defect size is <1 mm. Interestingly, a modification of the deformation law of the connectors in the DNM (with symmetric behavior for tension and compression) resolves this apparent contradiction and allows recovering the correspondence of process zone size and critical flaw size typically reported for synthetic materials.

Experimental and computational results show that the defect tolerance of SCT does not originate from major dissipative mechanisms on fibre or network scale. On the other hand, dissipative effects in the defect nearfield can increase the fracture toughness as indicated by our recent data on the loading rate-dependence of the apparent tearing energy Γ_a. The hybrid model was applied to analyse how network elastic deformation, brittle failure of collagen fibres and interstitial fluid flow interact towards the remarkable fracture properties of SCT. Specifically, the model is used to rationalize the influence of bath osmolarity, hydration level, as well as specific biochemical agents on the fracture behaviour of HA. The results contribute to a better understanding of the pathophysiology of premature rupture of fetal membranes, and to an optimization of surgical instruments and procedures in order to reduce the risk of iatrogenic preterm rupture.

CONCLUSIONS

The hybrid model was shown to provide results that are well in line with experimental observations both at macroscopic length scales and in the defect nearfield of SCT. The model was used for the analysis of factors influencing the defect tolerance of SCT. Experiments and computations demonstrate that fracture mechanics theories based on a continuum material representation might be inadequate to quantify and explain the remarkable defect tolerance of HA. In particular, the fracture mechanics concept of tearing energy fails in predicting rupture for small defects, as occurring naturally in HA [10], or iatrogenically induced when suturing in prenatal surgery or when puncturing the membranes for amniocentesis.

References

[1] Gordon JE., Structures or Why things don't fall down, Plenum Press, New York (1978)
[2] Yang W et al., "On the tear resistance of skin", Nat Commun, 6 (2015)
[3] Adzick, N.S. et al., "A randomized trial of prenatal versus postnatal repair of myelomeningocele.", N Engl J Med 364, 993-1004, (2011)
[4] Kumar D. et al., "The physiology of fetal membrane weakening and rupture: Insights gained from the determination of physical properties revisited". Placenta 42, 59–73, (2016)
[5] Mauri A et al., "Deformation mechanisms of amnion: Quantitative studies based on SHG microscopy". J Biomech 48, 1606–1613 (2015)
[6] Bircher K et al.,"On the defect tolerance of fetal membranes", Royal Soc Interface Focus, 9, 2019
[7] Bircher K et al., "Influence of osmolarity and hydration on the tear resistance of the human amniotic membrane", J Biomech 98, 109419 (2020)
[8] Ehret AE et al., "Inverse poroelasticity as a fundamental mechanism in biomechanics and mechanobiology", Nat Commun, 8 (2017)
[9] Bircher K et al., "Tear resistance of soft collagenous tissues", Nat Commun, 10, 792 (2019)
[10] Richardson LS et al., "Discovery and characterization of human amniochorionic membrane microfractures.", Am J Pathol 187, 2821-2830 (2017)

PARAMETER CHARACTERIZATION OF ONE-DIMENSIONAL THEORIES FOR SANDWICH COMPOSITES THROUGH BOUNDS AND ASYMPTOTIC MATCHING

Roberta Massabò*
Department of Civil, Chemical and Environmental Engineering, University of Genova, Genova, Italy

Summary Accurate upper and lower bounds are derived for the parameters of approximate structural theories used for fracture mechanics characterization of sandwich composites. The derivation takes advantage of novel 2D elasticity solutions for the decohesion of a thin layer from a half plane. The structural theories are the model of a beam on a Winkler elastic foundation and modified beam theory; they have been recently proposed to model the Single Cantilever Beam sandwich specimen, which is under consideration for possible standardization, and rely on the accurate definition of foundation modulus and crack length correction. A simple description of the transition from thick- to thin-core behaviour is obtained by asymptotic matching of the exact bounds. Results show important differences with respect to bounds derived for the description of other collapse mechanisms in sandwich composites.

INTRODUCTION

The model of a beam on a Winkler elastic foundation is used in various fields of engineering for its simplicity and accuracy in a large range of applications involving the interaction of beam type structures and elastic substrates. The action of the substrate on the beam is described by means of a distributed pressure which is related linearly to the beam deflection, u_{wf}, through a foundation modulus, k; the beam equilibrium equation is $\mathrm{d}^4u_{wf}/\mathrm{d}x^4 + ku_{wf}/K_\chi = 0$, with K_χ the flexural stiffness. The first application to fracture mechanics problems dates back to the work by Kanninen [1], where the model has been applied to describe the upper half of a homogeneous Double Cantilever Beam specimen of Young's modulus E, height $2h$ and width b; in the original model, the modulus $k = 2Eb/h$ describes the transverse stiffness of a uniformly stressed strip of material of thickness $h/2$ ahead of the crack tip. The definition of the foundation modulus has been recently improved in [2], by using the concept of root rotation and 2D fracture mechanics solutions in [3,4]; for a homogeneous isotropic material this accurate approach yields $k = 1.622Eb/h$. The Winkler foundation approximation has been applied to model various collapse mechanisms in sandwich composites, e.g. delamination fracture triggered by face wrinkling [5], face/core elastic/plastic indentation [6,7] and delamination fracture [8]. The foundation modulus has been defined by matching 2D elasticity solutions, e.g. [9], or case specific finite element results [8]. The dependence of the modulus on relative thickness and elastic mismatch of core and face-sheets has been highlighted in [5].

This work refers to recent applications of the Winkler foundation model to define the energy release rate in the Single Cantilever Beam sandwich specimen (Fig. 1a), which is currently under consideration for possible standardization [8]. In order to verify the accuracy of the approach and improve the description of the foundation modulus, which has been based on case specific finite element analyses only, reference is made to recently published 2D elasticity solutions for the decohesion of a thin layer from a half plane [10,11] and to 2D analytical and numerical solutions for a sandwich with a very thin core [12,13]. Matching the energy release of the approximate model to the exact solutions provides upper and lower bounds for the foundation modulus, which depend on the face/core elastic mismatch and can be used directly for composites with very thick or thin cores. The transition from thick- to thin-core behavior is described using asymptotic matching. The results are directly applicable to define the crack length correction of modified beam theory.

UPPER AND LOWER BOUNDS FOR THE MODEL PARAMETERS

The foundation modulus for the Single Cantilever Beam sandwich specimen in Fig. 1a,b, with isotropic core and face sheets and subjected to the force per unit width F/b, is defined as $k = \bar{E}_c b/\bar{h}$ and defines the transverse stiffness of an equivalent uniformly stressed strip of core material of thickness $\bar{h}$ which describes the actual non-uniformly stressed core/face material; $\bar{E}_c = E_c/(1-\nu_c^2)$ for plane strain. The energy release rate calculated using the model in Fig. 1b is [8]:

$$\mathcal{G}_F^{wf} = \frac{F^2}{2b^2}\left\{\frac{12}{\bar{E}_f h_f^3}\left(a+\frac{1}{\lambda}\right)^2\right\} \quad \text{with} \quad 1/\lambda = \sqrt[4]{\bar{E}_f b h_f^3/(3k)} \qquad [1]$$

The energy release rate of modified beam theory is given by Eq. 1 with $1/\lambda = \Delta$ the crack length correction. Matching Eq. 1 with the exact elasticity solution for the decohesion of a thin layer from a half plane [10]:

$$\mathcal{G}_F = \frac{6F^2}{\bar{E}_f b^2 h}\left[\left(\frac{a}{h}\right)^2 + 2\delta\left(\frac{a}{h}\right) + \left(\delta^2+\frac{1}{4}\right)\right] \quad , \qquad [2]$$

*Corresponding author. E-mail: roberta.massabo@unige.it.

where $\delta = \delta(\bar{E}_f / \bar{E}_c; \beta = 0)$ is given in closed form in [10] and shown in Fig. 1c for materials with second Dundurs' parameter $\beta = 0$, and using the results in [12,13], yield lower and upper bounds for foundation modulus and crack length correction, $k^{lb} = b\bar{E}_c / \bar{h}^{ub}$, $\Delta^{ub} = \delta h_f$, $k^{ub} = b\bar{E}_c / \bar{h}^{lb}$ and $\Delta^{lb} = 0.6h_f$ with $\bar{h}^{ub} / h_f = 3\delta^4 \bar{E}_c / \bar{E}_f$ and $\bar{h}^{lb} / h_f = 0.39$ [13]. Figure 1c shows upper and lower bounds for the crack length correction.

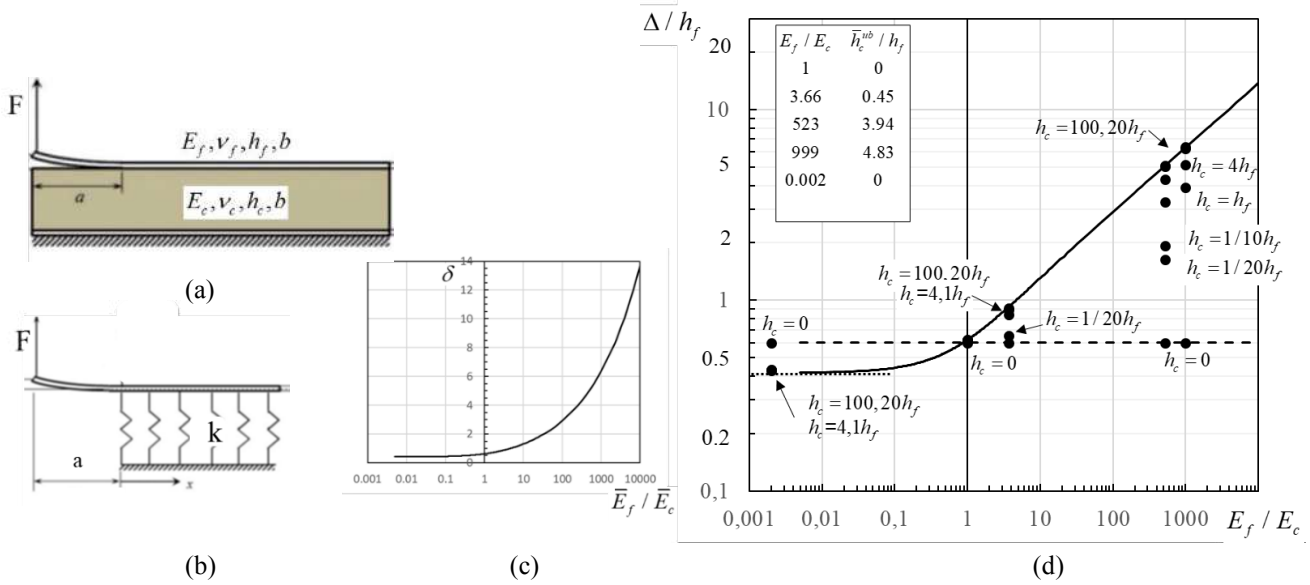

Figure 1. (a) Single Cantilever Beam sandwich specimen. (b) Beam on a Winkler foundation model. (c) Parameter $\delta = \delta(\bar{E}_f / \bar{E}_c)$ of the closed form solution in [10]. (d) Upper/lower bounds for the crack length correction (thick sold and dashed lines) and results obtained by matching finite element results for exemplary sandwich systems [13].

CONCLUSIONS

Upper and lower bounds have been derived for the elastic foundation modulus of the beam on a Winkler foundation model for fracture mechanics characterization of sandwich composites using the Single Cantilever Beam sandwich specimen. The results directly provide bounds for the crack length correction of modified beam theory. The derivation relies on novel 2D fracture mechanics solutions for the decohesion of a thin layer from a half plane [10,11]. The results show that bounds previously derived to describe face-sheet indentation/wrinkling are not applicable to the fracture problem. For face wrinkling [5], the upper bound modulus was found to correspond to an equivalent thickness equal to the core thickness while our results for fracture show that it can be much larger and correspond to an equivalent thickness equal to a fraction of the face thickness.

Acknowledgement – Support by the U.S. Office of Naval Research, grant no. N00014-17-1-2914, is gratefully acknowledged.

References

[1] Kanninen MF. An augmented double cantilever beam model for studying crack propagation and arrest. Int J Fract 9:83-92, 1973.
[2] Thouless MD. Shear forces, root rotations, phase angles and delamination of layered materials. Eng Fract Mech 191:153–67, 2018.
[3] Andrews MG, Massabò R. The effects of shear and near tip deformations on energy release rate and mode mixity of edge-cracked orthotropic layers. Eng Fract Mech 74:2700–20, 2007.
[4] Barbieri L, Massabò R, Berggreen C. The effects of shear and near tip deformations on interface fracture of symmetric sandwich beams. Eng Fract Mech 201:298–321, 2018.
[5] Bažant Z, Grassl P. Size effect of cohesive delamination fracture triggered by sandwich skin wrinkling. J Appl Mech Trans ASME 74:1134-1141, 2007
[6] Shuaeib FM, Soden PD. Indentation failure of composite sandwich beams. Compos Sci Technol 57:1249-1259, 1997.
[7] Steeves CA, Fleck NA. Collapse mechanisms of sandwich beams with composite faces and a foam core, loaded in three-point bending. Part I: Analytical models and minimum weight design. Int J Mech Sci 46:561-583, 2004.
[8] Saseendran V, Carlsson LA, Berggreen C. Shear and foundation effects on crack root rotation and mode-mixity in moment- and force-loaded single cantilever beam sandwich specimen. J Compos Mater 52:2537–47, 2018.
[9] Biot M. Bending of an infinite beam on an elastic foundation. J Appl Mech A1-A7, 1937.
[10] Ustinov K. On separation of a layer from the half-plane: Elastic fixation conditions for a plate equivalent to the layer. Mech Solids 50:62–80, 2015.
[11] Massabò R, Ustinov K, Barbieri L, Berggreen C. Fracture mechanics solutions for interfacial cracks between compressible thin layers and substrates. Coatings 152;9:1-19..
[12] Suo Z, Hutchinson JW. Sandwich test specimens for measuring interface crack toughness. Mater Sci Eng A107:145-153, 1989.
[13] Massabò, R., Upper and lower bounds for the parameters of one-dimensional theories for sandwich fracture specimens, submitted for consideration for possible publication, 2020.

COMPETITION BETWEEN ADHESIVE AND COHESIVE FAILURE: AN INVESTIGATION BASED ON THE PHASE FIELD APPROACH TO FRACTURE ANDTHE COHESIVE ZONEMODEL

Maria Rosaria Marulli*[1], Marco Paggi[1]and José Reinoso [2]
[1]IMT School for Advanced Studies Lucca, Lucca, Italy
[2]Group of Elasticity and Strength of Materials, School of Engineering, University of Seville, Seville, Spain

Summary The present study is concerned with the numerical simulation of the steady-state fracture of adhesively bonded joints in peel test configuration. The fracture process that takes place inside the adhesive layer is modelled using a phase field approach in order to investigate the influence of the mechanical and geometrical properties of the adhesive. The numerical framework is further developed using a combined phase field-cohesive zone model approach in order to capture the adhesive/cohesive failure of the joint by examining the competition between crack propagation within the adhesive layer and delamination along the interfaces between such adhesive layer and the adherents.

INTRODUCTION

Computing the ultimate strength of a structural adhesive layers on a given substrate is of great importance in many applications. Among the different experimental procedures developed to characterize the bond behaviour of adhesives, one of the most popular configurations is the so-called peel test. This test configuration consists of a strip bonded to a substrate which is pulled from it at a certain angle (*peel angle*) and characterizing the *peeling force* required to produce debonding. The failure of an adhesive joints is generally classified as *cohesive* when it takes place inside the adhesive layer or *adhesive* when it develops at the interface between the adhesive and the adherent. In the most general case, the failure involves the weakest link between the adhesive, the substrate and the bonded strip, or even a combination of them if the crack propagates at some spots in a cohesive and in others in an interfacial manner.

A prediction of the mechanical behaviour of peel tests can be achieved using different fracture mechanics approaches. Initial studies for the peel geometry treated the film as an elastic beam attached to an elastic foundation representing the interaction between the film and substrate [1]. Subsequently, the condition for fracture of an adhesive joint had been derived considering an energy-balance approach in [2], the exploitation of the Linear Elastic Fracture Mechanics (LEFM) approach was conducted in [3], while the cohesive zone model (CZM) has been extensively applied for peel test simulations in several contributions, as in [4].

In the related literature, up to now, a limited attention has been given to the simulation of the adhesive layer as a bulk where, in the case of cohesive failure, the crack nucleates and propagates, especially when the adhesive layer thickness is not negligible compared to the dimensions of the adherents. In the present contribution, the phase field approach has been used to investigate the influence of the adhesive geometrical and mechanical properties on the joint strength, with the major focus on the influence of the adhesive layer thickness, t_a, and of the mechanical quantities: the fracture energy, G_{IC}, and the internal length scale, l_0 (which is closely related to the critical strength, σ_c, according to [5]). Furthermore, a numerical framework combining the phase field approach for modelling the fracture inside the adhesive layer and a cohesive zone model for the adhesive-adherent interfaces debonding is herein proposed.

COHESIVE FAILURE OF THE ADHESIVE LAYER: PHASE FIELD APPROACH

The 90-degree peeling test has been simulated through a preliminary 2D finite elements model using the phase field approach implemented within linear elastic plain strain 4-nodes finite elements. The simulations show the effects of different fracture energy values (Fig. 1a), which mainly affect the steady-state peeling force, and of different internal length scales (Fig.1b) which has a major influence on the peak peeling force. The adhesive thickness effects on the peeling force is shown in Fig. 1c, together with the crack path evolutions shown in (Fig. 2). For thick adhesive layers ($t_a = 3\text{mm}; 1\text{mm}$), the simulations predict that the crack nucleates close to the upper interface and propagates downwards reaching a steady-state perfectly horizontal. Conversely, for the thinnest adhesive layer, ($t_a = 0.3\text{mm}$), the crack path develops at the same distance from the upper interface and propagates horizontally.

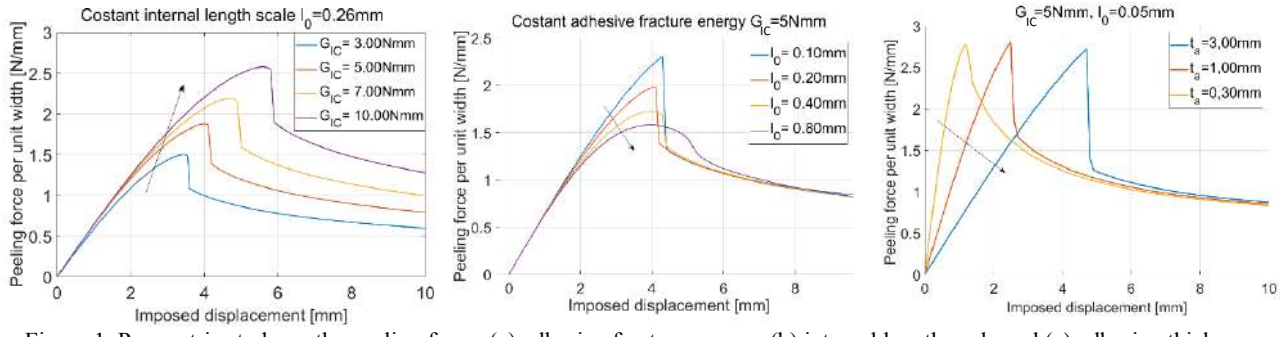

Figure 1. Parametric study on the peeling force: (a) adhesive fracture energy, (b) internal length scale and (c) adhesive thickness effects on the peeling force.

Figure 2. Details of the crack path evolution from the models with different thicknesses of the adhesive.

ADHESIVE/COHESIVE FAILURE OF THE ADHESIVE JOINT: COUPLED PHASE FIELD AND CZM

The previous numerical framework has been enhanced in order to consider the mechanical properties of the existing interfaces. The adhesive bond at the two interfaces (at the lower interface between the adhesive layer and the substrate, at the upper interface between the adhesive and the upper strip) has been modelled using zero-thickness interface finite elements compatible with the phase field model, developed in [6], using a tension cut-off cohesive zone model. A physical crack extension occurs at the interface when the fracture energy release rate reaches a critical value of the interface adhesive energy, G_a^i, which physically corresponds to the debonding of the adhesive layer from the substrate or the upper strip. The critical crack opening, g_0^i, represents also another parameter of the model that influences the adhesive/cohesive failure phenomenon of the joint. In order to capture the nucleation and propagation of the crack at the interface or inside the bulk layer and to better understand how the mechanical properties of the two interfaces influence the crack phenomena, different situations have been analysed: (i) via the consideration of the cohesive bond of the adhesive layer weaker than the interface adhesive bond or (ii) vice versa. Consistently, in the numerical model, the fracture energy of the adhesive bulk, G_{IC}, can be lower or higher than the interface adhesive energy which may also be different for the upper interface, $G_a^{i,up}$, and the upper one, $G_a^{i,low}$ (Fig. 3).

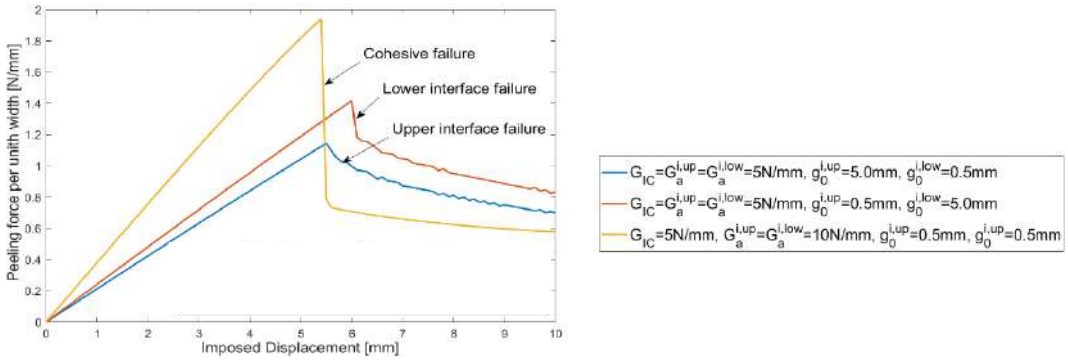

Figure 3. Adhesive/Cohesive failure: influence of fracture energy G_{IC}, adhesive interface energy G_a^i and critical opening g_0^i.

CONCLUSIONS

In this work, a novel numerical model has been proposed for the simulation of structural adhesive and, in particular, to reproduce the failure mechanisms of adhesive joints in 90-degree peeling test configuration. The phase field approach has been used for better understanding how the mechanical properties of the adhesive layer influence the peeling force and how the adhesive thickness affects the crack nucleation and propagation. Subsequently, a variational framework combining the phase field method of fracture and the cohesive zone model approach has been applied for modelling the competition between crack propagation in the adhesive layer and debonding at the interfaces. A tension cut-off cohesive zone model has been used to capture a brittle behavior of the adhesive bond at the two interfaces between the adhesive and the adherents.

The present simulations constitute a first step towards the generation of a more general model aiming at reproducing the different failure mechanisms at adhesive joints, i.e. adhesive and cohesive failures, that can arise in structural applications. This first analysis focuses on a linear elastic constitutive behavior for the adhesive, but a hyper elastic model will be introduced in a second step, in order to more accurately capture the non-linearity of a real system. The proposed framework can be further developed considering how the damage evolution inside the adhesive layer affects the mechanical properties of the interface. These aspects can also be analyzed in a 3D framework in order to capture with more details the failure of an adhesive join.

References

[1] Kendall K., The adhesion and surface energy of elastic solids, *J. Phys. D. Appl. Phys.*, **4**:320, 1971.
[2] Kinloch A. J., Lau C. C., and Williams J. G., The peeling of flexible laminates, *International Journal of Fracture* **66**: 45-70, 1994.
[3] Thouless M. D. and Jensen H. M., Elastic fracture mechanics of the peel-test geometry, *J. Adhes.*, **38**:185–197, 1992.
[4] Williams J. G. and Hadavinia H., Analytical solutions for cohesive zone models, *J. Mech. Phys. Solids*, **50**:809–825, 2002.
[5] Nguyen T. T. et al., On the choice of parameters in the phase field method for simulating crack initiation with experimental validation, *Int. J. Fract.*, **197:**213–226, 2016.
[6] Paggi M. and Reinoso J., Revisiting the problem of a crack impinging on an interface: A modeling framework for the interaction between the phase field approach for brittle fracture and the interface cohesive zone model, *Comput. Methods Appl. Mech. Eng.*, **321**:145–172, 2017.

DIC-BASED J-INTEGRAL FOR THE EVALUATION OF THE FRACTURE TOUGHNESS OF ADDITIVELY MANUFACTURED WALLS

Pierre Margerit[1,2], Krishnaswa Ravi-Chandar *[2], Daniel Weisz-Patrault[1], and Andrei Constantinescu[1]
[1]Laboratoire de mécanique des solides,CNRS,Ecole Polytechnique,Institut Polytechnique de Paris,France
[2]Department of Aerospace Engineering & Engineering Mechanics, The University of Texas at Austin, USA

Summary An experimental procedure is proposed to evaluate the fracture toughness of thin specimens by means of J-integral evaluation on Digital Image Correlation results. First, the DIC mesh is defined at the final stage, where the crack surface geometry is known. Second, the DIC is run backward, from the final stage to the initial stage; so that displacements and strains can be deduced. Third, the stresses are computed using an a-priori known constitutive law, and the J-integral evaluated. It is shown that even if the plastic zone is spread over the entire observed region, the strain energy is mostly confined near the crack, thus ensuring the path-independence of the J-integrals.

INTRODUCTION

In the past decade, additive manufacturing of metals has evolved from a rapid prototyping technique to a process suited for the production of fully functional parts [1]. In the same time, additive manufacturing processes received a strong interest from the scientific community, with a number of challenges still needed to be solved. These include the understanding of the effect of the process parameters (e.g heat source power, scanning path, powder flow) on the mechanical properties of the produced parts [2]. At the end, the chosen printing strategy has consequences at different scales: (i) at the microstructure scale, where the grain growth is driven by the temperature gradient, resulting in epitaxial grains with an orientation highly influenced by the heat source path [3]; (ii) at the *meso* scale, where the layering process as well as the lack-of-fusion defects result in a high surface roughness responsible for stress concentrations [4]; (iii) at the *macro* scale, where the residual stresses associated to heating/cooling cycles are responsible for part distortion [5]. As a result, a particular research effort is given on the experimental characterization of produced parts and materials, for the needs of process modeling and optimization.

The present work focuses on the characterization of the fracture toughness of structures printed using Direct Energy Deposition (DED) [6], a promising process suitable for applications ranging from functionally graded parts [7] to structural repair [8]. The powder used for the print is AISI 316L stainless steel, preferred for its welding capacity, its relatively high mechanical properties and for its high-temperature performance. In the case of the Selective Laser Melting process (SLM), it has been observed that additively manufactured 316L exhibits higher yield stress and ultimate tensile strength than conventionally manufactured 316L, whereas having a lower elongation to failure and fracture toughness [9]. More precisely, the DED process is well suited for the production of thin walled structures (approx. thickness 0.8 mm); in this particular case, Compact Tension Tests (CPT) specimens cannot be used to determine the fracture toughness as they would buckle under the compressile stresses developing in the bending region. In addition, as a consequence of the high ductility of the 316L, the large plastic zone surrounding the crack forbids the use of classical formulas based on Linear Elastic Fracture Mechanics to determine the fracture toughness.

The proposed alternative consists in the evaluation of the material toughness by J-integral evaluation on a notched specimen. It is found that even if the plastic zone is spread over the entire specimen, the J-integral remains path-independent as soon as the contour is chosen sufficiently far from the crack path. A justification of this observation is given by observing that most of the strain energy is confined near the crack surface.

MATERIALS AND METHODS

In order to keep the mechanical properties as uniform as possible over the specimens, the printed structure is chosen so that the process is as stationary as possible. This can be achieved by printing cylinders following a helical scanning path; aiming to obtain flat specimens, cylinders with a square section are printed for the present study. The specimens are then extracted from the cylinder walls by water-jet cutting.

Due to the low thickness of the produced walls, the side dimension of the square section of the cylinder has to be kept small to prevent in-process buckling as the result of residual stresses. Thus, only small specimens can be extracted (with a total length of the order of 40mm). Consequently, test are performed *in-situ* under a Keyence VHX-6000 microscope (X50 magnification). The load is applied monotonically up to failure with a small-scale tensile machine (MTI SEMTester-1000).

Strains are measured via Global Digital Image Correlation [10]. By opposition with classical methods implementing adaptive meshing to follow DIC domain changes associated to crack opening and propagation [11], it is chosen here to define the DIC mesh on the *final* loading stage, just before specimen failure (see Fig. 1a). At this particular stage, the

*Corresponding author. E-mail: ravi@utexas.edu

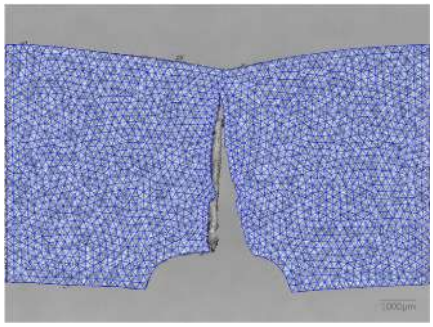

(a) DIC mesh defined at the intial loading stage.

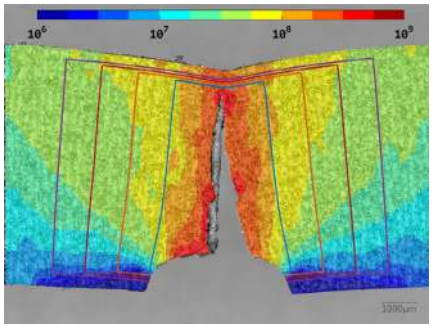

(b) Accumulated strain energy $\mathcal{W}$ and integral contour paths at the final stage.

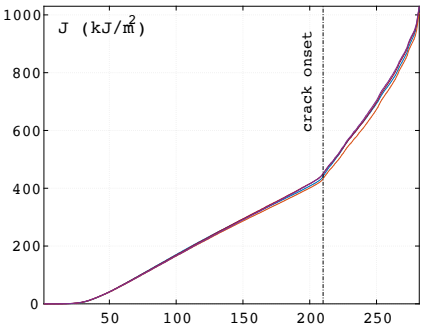

(c) J-values corresponding to the contour paths as a function of the stage number.

Figure 1: J-integral evaluation results.

crack geometry is well defined, and no DIC domain change is expected to happen. The DIC is then ran in the *backward* direction, from the final stage to the initial stage. At the end, displacements and strains are computed with respect to the *initial* configuration $\underline{\mathbf{X}}$.

Finally, the J-integral is evaluated by processing the DIC maps. Once the subsequent configurations $\underline{\mathbf{x}}$ have been identified by means of the proposed DIC procedure, the strains and thus the corresponding stresses can be computed using a given constitutive law. For any contour Γ enclosing the crack path, the following J-integral, expressed in the *current* configuration, can be evaluated:

$$J_d = \int_\Gamma \underline{\mathbf{e}}_d \cdot \left[\mathcal{W}\, \underline{\mathbf{n}} - \underline{\mathbf{t}} \cdot \frac{\partial \underline{\mathbf{u}}}{\partial \underline{\mathbf{x}}} \right] d\Gamma \tag{1}$$

with $\underline{\mathbf{e}}_d$ the crack direction, the strain energy density $\mathcal{W} = \int \underline{\underline{\boldsymbol{\sigma}}} : d\underline{\underline{\boldsymbol{\varepsilon}}}$, the normal to the contour $\underline{\mathbf{n}}$, the stress vector $\underline{\mathbf{t}} = \underline{\underline{\boldsymbol{\sigma}}} \cdot \underline{\mathbf{n}}$ and $\underline{\mathbf{u}} = \underline{\mathbf{x}} - \underline{\mathbf{X}}$ the displacement.

RESULTS

Beforehand, tensile tests are performed on dog-bone specimens of different orientations with regard to the print direction. The obtained stress-strain curves show that the material exhibit almost no anisotropy, with a true stress-true strain behavior that can be well approximated by an isotropic power hardening law ($E = 150$ GPa, $\nu = 0.4$, $\sigma_y = 320$ MPa, $K = 880$ MPa, $n = 0.67$).

The material fracture properties are evaluated using a pre-notched specimen, loaded up to failure. DIC results show that the plastic region (defined as $\varepsilon_{\text{eq}} > 0.2\%$) spread across the entire specimen in the early stages of the loading; such an observation would normally break the path-independence of a J-integral using a contour close to the crack surface. However, it is observed that most of the strain energy $\mathcal{W}$ is confined in the crack region (see Fig. 1b). Hence any J-integral evaluated *sufficiently far* from the crack path should be path-independent.

J-integrals are finally evaluated using different contour paths represented in figure 1b. The result of eq. (1) is plotted in Figure 1c for the different contours, as a function of the loading stage. It is observed that the J-curves are very close to each other, showing the relative path-independence of the proposed J-integral evaluation procedure.

References

[1] N. Guo, M.C. Leu. Additive manufacturing: technology, applications and research needs. *Front. Mech. Eng.* **8**: 215-243, 2013.
[2] Y. KoK & al. Anisotropy and heterogeneity of microstructure and mechanical properties in metal additive manufacturing: A critical review. *Materials & Design* **139**: 565-586, 2018.
[3] Y. Balit & al. Digital image correlation for microstructural analysis of deformation pattern in additively manufactured 316L thin walls. *Additive Manufacturing.* **31**: 100862, 2020.
[4] J. Pegues & al. Surface roughness effects on the fatigue strength of additively manufactured Ti-6Al-4V. *International Journal of Fatigue.* **116**: 543-552, 2018.
[5] J. Robinson & al. Determination of the effect of scan strategy on residual stress in laser powder bed fusion additive manufacturing. *Additive Manufacturing.* **3**: 13-24, 2018.
[6] ISO/ASTM 52900, Additive Manufacturing-General Principles-Terminology, Technical Report. *International Organization for Standardization.* 2015.
[7] T. Hwang & al. Functionally graded properties in directed-energy-deposition titanium parts. *Optics & Laser Technology* **105**: 80-88, 2018.
[8] J. M. Wilson & al. Remanufacturing of turbine blades by laser direct deposition with its energy and environmental impact analysis. *Journal of Cleaner Production* **80**: 170-178, 2014.
[9] J. Suryawanshi & al. Mechanical behavior of selective laser melted 316L stainless steel. *Materials Science and Engineering: A* **696**: 113-121, 2017.
[10] F. Hild, S. Roux. Comparison of local and global approaches to digital image correlation. *Experimental Mechanics* **52.9**: 1503-1519, 2012.
[11] J. Réthoré, F. Hild and S. Roux. Extended digital image correlation with crack shape optimization. *International Journal for Numerical Methods in Engineering* **73.2**: 248-272, 2008.

INSTABILITY IN DYNAMIC FRACTURE AND THE FAILURE OF THE CLASSICAL THEORY OFCRACKS

Yuri Lubomirsky*[1], Chih-Hung Chen[2], Aditya Vasudevan[2], Alain Karma[2], and Eran Bouchbinder†[1]
[1]Chemical and Biological Physics Department, Weizmann Institute of Science, Rehovot, Israel
[2]Department of Physics and Center for Interdisciplinary Research on Complex Systems, Northeastern University, Boston Massachusetts, USA

Summary Linear Elastic Fracture Mechanics (LEFM), the classical theory of cracks, is a powerful framework of great scientific and technological importance. Yet, it fails to account for various generic shape instabilities of propagating cracks, such as the micro-branching, the oscillatory and the tip-splitting instabilities. Using a new theoretical and computational framework, we show that the properties of the two-dimensional oscillatory instability, and in particular the oscillations wavelength, are controlled by small-scale elastic nonlinearity near the crack tip and the intrinsic lengthscale associated with it, signaling the failure of LEFM in strongly dynamic situations. We further show that the existence and properties of the oscillatory instability are largely independent of the form of the small-scale elastic nonlinearity near the crack tip.

Crack propagation is the main mode of materials failure. It has been a topic of intense research for decades because of its enormous practical importance and fundamental theoretical interest. The classical theory of brittle crack propagation, Linear Elastic Fracture Mechanics (LEFM), assumes that linear elastodynamics applies everywhere inside a stressed body except for a "process zone" near the crack tip. The latter is assumed to be negligible in size, only accounting for the dissipation associated with the fracture process, but is otherwise completely passive. A central prediction of this theory is that straight cracks smoothly accelerate to the Rayleigh wave-speed c_R. However, in practice cracks universally undergo symmetry-breaking instabilities before reaching their theoretical limiting velocity. Recent experiments in brittle gels have shown that, in thin "quasi 2D" system, cracks reaching ultra high propagation velocities ($v_c \approx 0.9c_s$) undergo an oscillatory instability, characterized by a well-defined intrinsic wavelength λ, which is independent of system geometry [1]. Such behavior cannot be explained by LEFM, even qualitatively, as it contains no lengthscales other than the external dimensions of the system.

To investigate dynamic fracture instabilities, we use the novel phase-field (PF) approach, which naturally incorporates two intrinsic length scales missing in LEFM: the size ξ of the microscopic dissipation zone around the tip, where elastic energy is dissipated while creating new fracture surfaces, and the size ℓ of the near-tip nonlinear zone, where linear

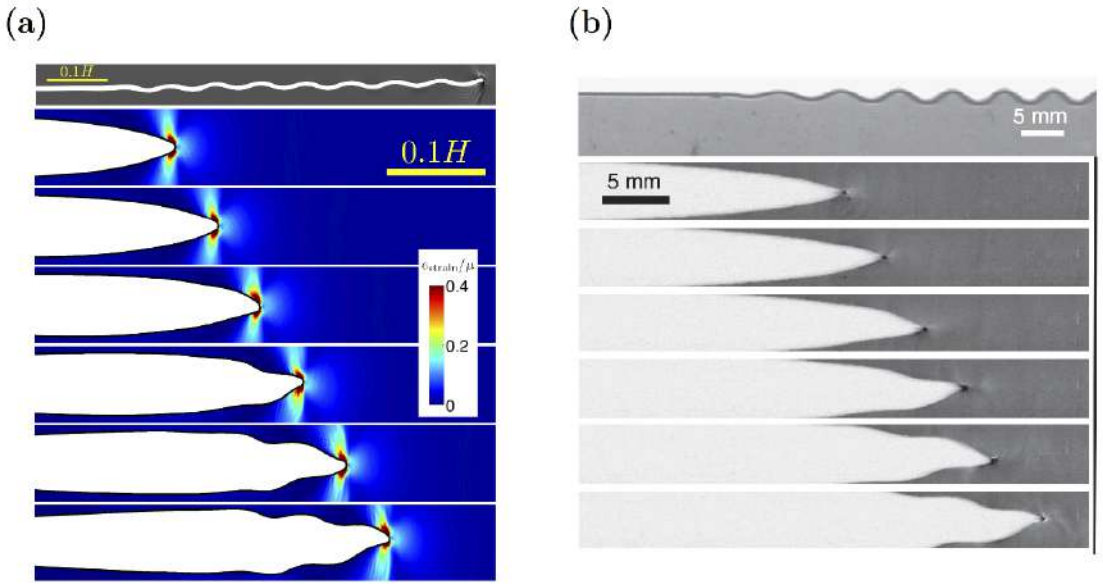

Figure 1: **Onset of the oscillatory instability.** (a) A zoom in on the 2D oscillatory instability in a phase-field simulation of brittle neo-Hookean (NH) materials under tensile (mode I) loading [2]. The color code corresponds to the normalized strain energy density. (b) The corresponding experimental observations in brittle gels (adapted from [1]).

*contact information: yuri.lubomirsky@weizmann.ac.il
†contact information: eran.bouchbinder@weizmann.ac.il

elasticity breaks down when strains become large. ℓ scales with the ratio, Γ/μ, the fracture energy to the shear modulus, but is generally much larger than Γ/μ and also depends on crack velocity. In Fig 1a we present results of large scale PF simulations, using the neo-Hookean elastic model, which represents generic elastic nonlinearities and quantitatively describes the experiments of [1]. An oscillatory instability, which is strikingly similar to the oscillatory instability observed experimentally (shown in Fig 1b), emerges. The wavelength of the emergent instability is independent of system size and linearly varies with nonlinear lengthscale Γ/μ. Moreover, the properties of the instability are in quantitative agrement with the experimental results [1].

Next, we seek to determine whether the oscillatory instability is universal, i.e. observed independently of the nature and form of near tip elastic nonlinearity. To that end, we consider the Saint-Venant Kirchhoff (SVK) elastic model, whose nonlinearity is geometric in origin and stems only from the nonlinear nature of deformation, while being constitutively linear. While materials typically feature constitutive nonlinearity in addition to geometric nonlinearity, they should at least feature the latter, and hence the SVK constitutes the minimal possible elastic nonlinearity. Simulations preformed using the SVK model produce a high velocity oscillatory instability, whose salient properties are qualitatively identical to those observed for the NH model. Moreover, the wavelength of the oscillations was found to be a model-independent, universal function, of the actual nonlinear lengthscale ℓ.

The success of the new PF model in quantitatively explaining the 2D oscillatory instability raises the question whether there are additional, previously undiscovered instabilities in 2D dynamic fracture. Indeed, simulations preformed with various loading conditions show that there exists a range of driving forces for which steady-state oscillatory cracks exist. However, with increasing loading level, once a certain critical threshold is surpassed, a tip-splitting instability emerges, either after oscillations set in (asymmetric tip-splitting) or directly from the straight crack state (symmetric tip-splitting). This ultra-high-velocity tip-splitting instability in 2D dynamic fracture appears to be different from the well-known low velocity tip-splitting in 2D simulations and from the micro-branching instability in 3D experiments. Remarkably, such oscillations followed by tip-splitting have been recently observed under strong loading conditions in brittle NH materials (Fig 2b).

Taken together, we were able to construct a comprehensive stability phase diagram of 2D fracture in terms of the loading level and $\ell/\xi \sim \Gamma/\mu\xi$, whose topology is universal, irrespective of the form of near tip nonlinearity.

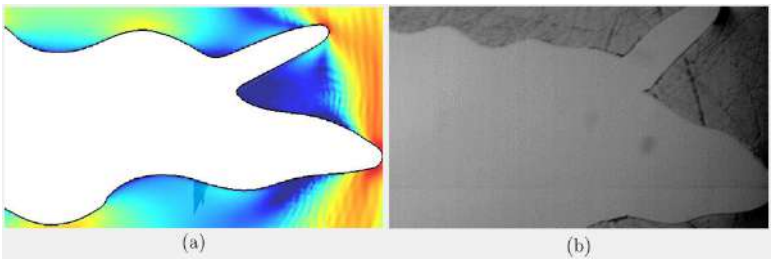

Figure 2: **Tip-splitting instability.** (a) Oscillations followed by tip-splitting in a phase-field simulation of NH materials under a large driving force. (b) The corresponding experimental observation (courtesy of Jay Fineberg). Adapted from [3].

CONCLUSIONS

In conclusion, we have shown that the properties 2D oscillatory instability, are determined by near tip nonlinearities, which are entirely absent is LFEM, hence demonstrating the failure of the classical theory fracture in explaining dynamic crack instabilities.

References

[1] Tamar Goldman, Roi Harpaz, Eran Bouchbinder, and Jay Fineberg. "Intrinsic nonlinear scale governs oscillations in rapid fracture." Physical review letters 108, no. 10 (2012): 104303.

[2] Chih-Hung Chen, Eran Bouchbinder, and Alain Karma. "Instability in dynamic fracture and the failure of the classical theory of cracks." Nature Physics 13, no. 12 (2017): 1186.

[3] Lubomirsky Yuri, Chih-Hung Chen, Alain Karma, and Eran Bouchbinder. "Universality and stability phase diagram of two-dimensional brittle fracture." Physical review letters 121, no. 13 (2018): 134301.

DIRECT EXTRACTION OF RATE-DEPENDENT COHESIVE LAWS AT ANY MODE-MIX

Tianhao Yang[1], Vatsa Gandhi [2], Rui Huang[1] and Kenneth M. Liechti[*1]
[1]Department of Aerospace Engineering and Engineering Mechanics, University of Texas, Austin, TX, USA
[2]GALCIT, California Institute of Technology, Pasadena, CA , USA

Summary The paper describes a novel approach for directly extracting the normal and shear components of the traction-separation relations for interfaces at any mode-mix. The approach is based on measuring the interactions between the contacting surfaces of two beams in a laminate that is clamped at one end with independently controlled displacements applied to the other end of each beam. Under certain conditions, the extraction of the normal and shear components of the traction-separation relations can be decoupled even if the interactions themselves are coupled. The efficacy of the approach is demonstrated for the interface between silicon and an epoxy by considering rate-dependent effects in addition to the influence of mode-mix on the interactions.

INTRODUCTION

Laminated materials have been used in a wide range of applications. A common failure mode has always been delamination between the layers. Thus, the adhesion between the layers has become crucial to the stability of such materials. Moreover, the loading/separation rate substantially influences the adhesion of interfaces involving polymers, which are commonly seen in transfer printing [1, 2] and transfer of 2D materials [3, 4]. The rate effect of polymeric interfaces has been addressed mostly for mode I fracture in previous studies. However, the loading conditions in real applications are more general, which brings the focus to the characterization of polymeric interfaces under mixed-mode fracture conditions.

EXPERIMENTAL

In the present work, a dual-actuator loading device was designed and used to provide the mixed-mode loading conditions to symmetric laminated beam specimens (Fig. 1) over a range of separation rates. Two load cells measure the reactive loads $(P_1, P)_2$ as the specimen is loaded in displacement control by each actuator. Digital image correlation was adopted to measure the rotations (θ_1, θ_2) and normal (Δ_1, Δ_2) and lateral displacements (U_1, U_2) at the loading points.

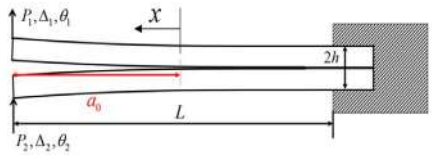

Figure 1. Silicon epoxy laminate under proportional displacement control $\Delta_2 = \alpha\Delta_1$.

As this is a balanced configuration [5], the normal and shear components of the J-integral are decoupled and are determined along with the associated crack tip openings based on the far field measurements. The normal and shear components of the traction-separation relations were then extracted by differentiating [6] each J-integral component with respect to its associated crack tip opening displacement.

RESULTS & DISCUSSION

The range of mode-mix that can be provided by the proportional loading is shown in Figure 2. Obtaining a full range of negative mode mixes is also possible. For this study, six mode-mixes were considered, each over five different separation rates.

The load-displacement data from a series of experiments at a global separation rate of 0.625 mm/are shown in Figure 3 for several proportional loading cases. The upper beam behaved in a similar way across all mode-mixes, with the force rising and reaching the peak when the crack started to grow, followed by a descending portion. The behavior of the lower beam was highly affected by the loading mode. When the mode II component dominated $\Delta_2/\Delta_1 = 0.95, 0.8$, the force still increased with the applied displacement. As more mode I component weighed in, the lower beam provided a "drag" force (e.g. $\Delta_2/\Delta_1 = 0.5$), even though the lower beam moved in the same direction as the upper beam. Space does not allow the corresponding rotation and lateral displacement data to be shown here, but in each case, along with the measured crack length, it was used to determine the normal and shear components of the crack tip displacements and J-integrals through

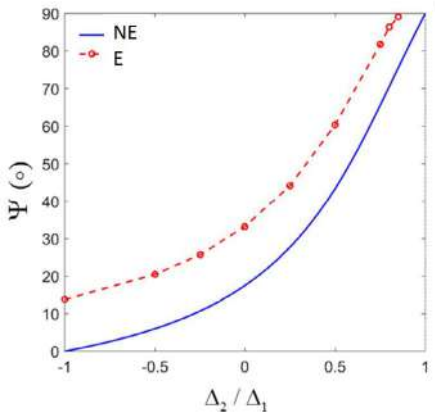

Figure 2. Achieving mode-mixes ranging from 0 to 90° by proportional separation paths. NE refers to an analysis that does not account for the presence of the epoxy, whereas E does.

$$\delta_n^* = \tilde{\Delta} + \frac{a^3}{6}\left(\frac{P_1}{D_1} - \frac{P_2}{D_2}\right) - a\left(\theta_1 - \theta_2\right),$$

$$\delta_t^* = \tilde{U} - \frac{\bar{P} h_1 a^2}{4 D_1}$$

$$J_1 = \frac{\hat{D}}{b}\left(\frac{P_1}{D_1} - \frac{P_2}{D_2}\right)\left(\theta_1 - \theta_2\right),$$

, where

$$J_2 = \frac{\hat{A} h_1}{2 D_1}\bar{P}\tilde{U}$$

$\tilde{\Delta} = \Delta_1 - \Delta_2$, $\tilde{U} = U_1 - U_2$, $\bar{P} = P_1 + P_2$,

$D_i = E_i I_i$, $\hat{D} = \left(\frac{1}{D_1} + \frac{1}{D_2}\right)^{-1}$ and

$\hat{A} = \left(\frac{1}{E_1 h_1} + \frac{1}{E_2 h_2} + \frac{b h_1^2}{4 D_1} + \frac{b h_2^2}{4 D_2}\right)^{-1}$ The normal and shear components of the traction-separation relation at any mode-mix is then obtained by taking the derivative of the corresponding components of J-integral and crack tip displacement.

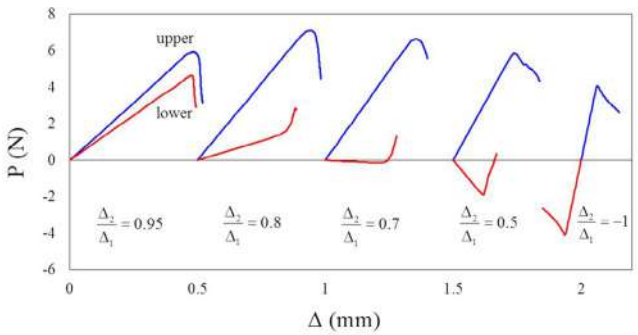

Figure 3. Force-displacement curves obtained at the upper (blue) and lower (red) beams, with different loading conditions but the same separation rate (0.625 mm/s) at the loading point.

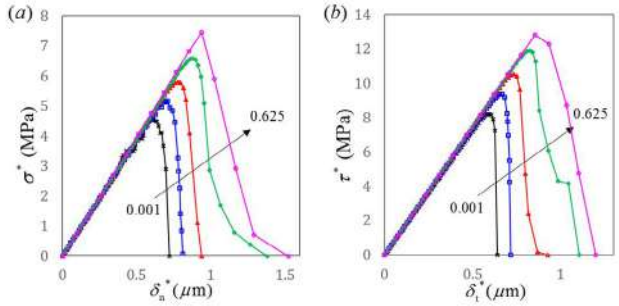

Figure 4. (a) Normal and (b) shear traction-separation relations, at the global separation rates: 0.001, 0.005, 0.025, 0.125, and 0.625 mm/s.

For purposes of illustration, we present the normal and shear components of the traction-separation relations at a displacement ratio of $\Delta_2 / \Delta_1 = 0.8$, or a nominal mode-mix of 65°, at different separation rates (Figure). In both cases, the steady state toughness, strength and range of the interactions increased with increasing separation rate. Similar results were obtained in a previous study [7] for the normal interactions. The rising portions of the two sets of data were very similar across the separation rates that were considered, but the shear stiffness was consistently higher. At each separation rate, the shear strengths were also higher than the normal ones. The interaction ranges of the normal traction-separation relations were longer than those experienced under shear. We will also present traction-separation relations as a function of mode-mix.

CONCLUSIONS

To conclude, a powerful and efficient approach has been developed for determining the traction-separation relations of interfaces at any mode-mix that has provided data that should stimulate the development of mechanistic models of crack growth at interfaces that go beyond potential or phenomenological damage based models.

REFERENCES

1. Meitl, M.A., et al., *Transfer printing by kinetic control of adhesion to an elastomeric stamp.* Nat Mater, 2006. **5**(1): p. 33-38.
2. Carlson, A., et al., *Shear-enhanced adhesiveless transfer printing for use in deterministic materials assembly.* Applied Physics Letters, 2011. **98**(26): p. 264104.
3. Na, S.R., et al., *Selective mechanical transfer of graphene from seed copper foil using rate effects.* ACS Nano, 2015. **9**(2): p. 1325-1335.
4. Na, S.R., et al., *Clean graphene interfaces by selective dry transfer for large area silicon integration.* Nanoscale, 2016. **8**: p. 7523-7533.
5. Wu, C., R. Huang, and K.M. Liechti, *Simultaneous extraction of tensile and shear interactions at interfaces.* Journal of the Mechanics and Physics of Solids, 2019. **125**: p. 225-254.
6. Sorensen, B.F. and P. Kirkegaard, *Determination of mixed mode cohesive laws.* Engineering Fracture Mechanics, 2006. **73**(17): p. 2642-2661.
7. Yang, T., et al., *Rate-dependent traction-separation relations for a silicon/epoxy interface informed by experiments and bond rupture kinetics.* Journal of the Mechanics and Physics of Solids, 2019. **131**: p. 1-19.

PHASE FIELD APPROACH TO TENSILE FRACTURE AND COMPRESSIVE CRUSHING IN BRITTLE MATERIALS

Pietro Lenarda[1] and Marco Paggi *[1]
[1]IMT School for Advanced Studies, Lucca, Italy

Summary In phase field constitutive models the splitting of the strain energy density into active and passive parts plays an important role to activate cracking only in tension. Here, two of the most used phase filed models, the spectral and the volumetric-deviatoric decompositions are enhanced to extend their capabilities in capturing complex fracture patterns emerging not only in tension but also in compression. A novel strain energy decomposition is therefore intruduced to consistently simulate loading scenarios involving both damage in tension leading to cracking, and damage in compression responsible for crushing.

INTRODUCTION

In recent years, fracture mechanics has seen an increasing interest in phase field models for the numerical simulation of crack growth in brittle materials [1]. In the phase field framework, the crack evolution is described by an internal variable s representing damage of the material in the bulk and ranging from 0 (undamaged) to unity (fully damaged). To activate damage only in tension, among the methods that have been proposed so far for the decomposition of the strain energy density, there are two which are widely used. One is the spectral decomposition by Miehe et al. [2], while the other is the deviatoric-volumetric split by Amor et al. [3]. The choice of the strain energy decomposition method significately affects the numerical results. It will be shown here that both models become ineffective when the driving damage mechanism requires an energy dissipation not only in tension but also in compression, associated to cracking and crushing failure modes, respectively.

VARIATIONAL FORMULATION

The strain $\boldsymbol{\varepsilon} = \frac{1}{2}\left(\nabla\mathbf{u} + (\nabla\mathbf{u})^{\mathrm{T}}\right)$ is decomposed into its positive and negative parts defined as $\boldsymbol{\varepsilon}_{\pm} = \mathrm{P}\Lambda_{\pm}\mathrm{P}^{\mathrm{T}}$, where $\Lambda_{\pm} = \mathrm{diag}\left(\langle\varepsilon_1\rangle_{\pm}, \ldots, \langle\varepsilon_{\mathrm{d}}\rangle_{\pm}\right)$ is the diagonal matrix containing the positive and negative parts of the eigenvalues of $\boldsymbol{\varepsilon}$ and P is a matrix whose columns are the normalized eigenvectors of the strain tensor, while $\mathrm{d} = 2, 3$ is the spatial dimension and $\langle\cdot\rangle_{\pm} = (\cdot \pm |\cdot|)/2$ denote the McCauley brakets. In the spectral model [2], the strain energy density is decomposed into an active and passive part as: $\Psi^{\mathrm{act}} = \frac{\lambda}{2}\langle\mathrm{tr}(\boldsymbol{\varepsilon})\rangle_+^2 + \mu\mathrm{tr}(\boldsymbol{\varepsilon}_+^2)$ and $\Psi^{\mathrm{pas}} = \frac{\lambda}{2}\langle\mathrm{tr}(\boldsymbol{\varepsilon})\rangle_-^2 + \mu\mathrm{tr}(\boldsymbol{\varepsilon}_-^2)$. The stress is also decomposed into positive and negative parts as: $\boldsymbol{\sigma}_{\pm} = \lambda\langle\mathrm{tr}(\boldsymbol{\varepsilon})\rangle_{\pm}\mathrm{I} + 2\mu\boldsymbol{\varepsilon}_{\pm}$. Notice that $\boldsymbol{\varepsilon}_+$ represents the tensile strain component that is involved in crack initiation and propagation, while $\boldsymbol{\varepsilon}_-$ represents the compression strain component that in the formulation [2] does not contribute to damage. In the volumetric-deviatoric model in [3], the strain energy density function is decomposed as: $\Psi^{\mathrm{act}} = \frac{K}{2}\langle\mathrm{tr}(\boldsymbol{\varepsilon})\rangle_+^2 + \mu\mathrm{tr}(\boldsymbol{\varepsilon}_{\mathrm{dev}}^2)$ and $\Psi^{\mathrm{pas}} = \frac{K}{2}\langle\mathrm{tr}(\boldsymbol{\varepsilon})\rangle_-^2$ and the corresponding positive and negative stresses are: $\boldsymbol{\sigma}_+ = K\langle\mathrm{tr}(\boldsymbol{\varepsilon})\rangle_+\mathbf{I} + 2\mu\boldsymbol{\varepsilon}_{\mathrm{dev}}$ and $\boldsymbol{\sigma}_- = K\langle\mathrm{tr}(\boldsymbol{\varepsilon})\rangle_+\mathbf{I}$, where $K = 2\lambda/\mathrm{d} + \mu$ is the bulk modulus, $(\mathrm{d} = 2, 3)$, and $\boldsymbol{\varepsilon}_{\mathrm{dev}}$ is deviatoric strain. In this model, both the expansive volumetric and the deviatoric strain energies are assumed to be responsible for the creation of new cracks, whereas the compressive volumetric strain energy does not. In both models, the total stress is defined as $\boldsymbol{\sigma} = \{(1-s)^2 + \mathrm{k}\}\boldsymbol{\sigma}_+ + \boldsymbol{\sigma}_-$. The variational problem is to find the displacement field $\mathbf{u}$ and the phase field variable s such that, for all $\delta\mathbf{u}$ and δs test functions satisfy the following system of equations:

$$\begin{aligned} -\int_\Omega \boldsymbol{\sigma} : \delta\boldsymbol{\varepsilon}\, \mathrm{d}\mathbf{x} = 0 \\ -\int_\Omega 2\mathrm{H}(1-s)\delta s\, \mathrm{d}\mathbf{x} + \int_\Omega \mathrm{G_c}\left(l_0 \nabla s \cdot \nabla(\delta s) + \frac{1}{l_0} s\, \delta s\right)\, \mathrm{d}\mathbf{x} = 0, \end{aligned} \tag{1}$$

where $\mathrm{H} = \max_{\tau\in[0,t]}\Psi^{\mathrm{act}}(t)$ is an history field to ensure irreversibility of the crack path, l_0 is the internal lenght scale and $\mathrm{G_c}$ is the fracture energy.
Here, to model also damage in compression caused by crushing it is introduced another damage variable, s_c, whose evolution is governed by another equation formally similar to Eq. (1b) but with a different internal lenght scale l_0 and crushing energy $\mathrm{G_c}$, which is usually one order of magnitude higher than the fracture energy [6]. Damage in compression then affects the so-called passive part of the strain enegry density of the material. The stress state in the material point is used to select one of the two damege mechanisms.

*Corresponding author. E-mail: marco.paggi@imtlucca.it.

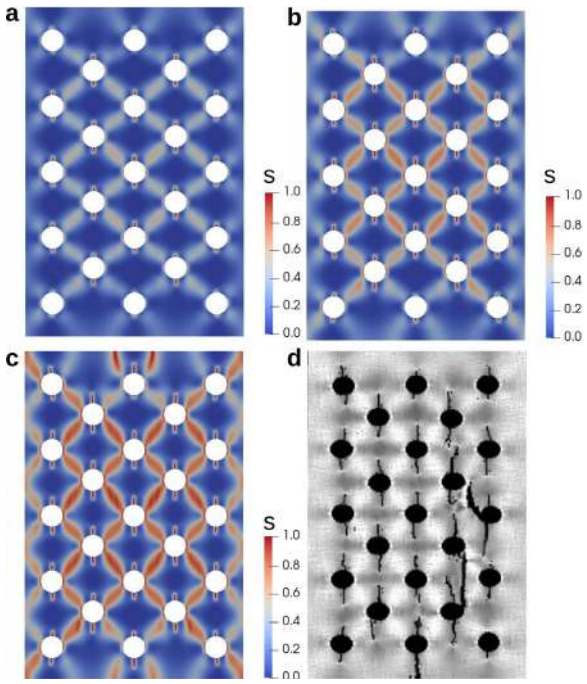

Figure 1: **(a, c)** Evolution of the phase field variable s in a compression test of a plate with regular distribution of holes. The displacement is imposed at the top side of the specimen. **(d)** Numerical results in [5].

NUMERICAL IMPLEMENTATION

A finite element procedure is adopted to solve numerically the system of equations in Eq. (1). The mechanical problem is solved first and then the displacement field is used to solve the phase field equation according to a staggered scheme. Despite the problem for the phase field is linear, this is not the case for the mechanical problem involving the calculation of eigenvalues and eigenvectors of the strain tensor and its positive and negative decomposition. To solve the eigenvalue problem for the strain, closed formulas are found to be very efficient both in $\mathrm{d} = 2$ and $\mathrm{d} = 3$ (Cardano and vector product formulas) compared to iterative solvers. The solution scheme has been implemented in FEniCS [7], which allows automatic symbolic computation of the Jacobian in the Newton's solver for the mechanical problem, which is very convenient to avoid lengthy calculations. In Figure 1. it is shown the evolution of the crack path in a plate with a regular distribution of holes subjected to compressive loading. The method in [1] is capable to simulate the correct vertical crack propagation which is experimentally observed. This test shows the capability of the method to nucleate cracks from undamaged microstructure.

CONCLUSIONS

The aim of the present work is to test and compare the capabilities of different models in capturing failure in materials under crushing or under combination of tension-compression loading. For this purpouse, it is required an extension of the existing formulations considering a modified decomposition of the strain energy density.

References

[1] Quintanas-Corominas A., Reinoso J., E. Casoni E., Paggi M., Turon A., Mayugo J.A., A phase field approach to simulate intralaminar and translaminar fracture in long fiber composite materials *Composite Structures* **220**: 899 - 911, 2019.

[2] Miehe C., Hofacker M., Welschinger F., A phase field model for rate-independent crack propagation: Robust algorithmic implementation based on operator splits *Computer Methods in Applied Mechanics and Engineering* **199**(45): 2765 - 2778, 2010.

[3] Amor H., Marigo J.J., Maurini C., Regularized formulation of the variational brittle fracture with unilateral contact: Numerical experiments *Journal of the Mechanics and Physics of Solids* **57**(8): 1209 - 1229, 2009.

[4] Freddi F., Royer-Carfagni G., Variational fracture mechanics to model compressive splitting of masonry-like materials *Ann. Solid Struct. Mech.* **2**: 5767, 2011

[5] Nguyen T.T., Yvonnet J., Qi-Zhi Zhu, Bornert M., Chateau C., A phase field method to simulate crack nucleation and propagation in strongly heterogeneous materials from direct imaging of their microstructure. *Engineering Fracture Mechanics* **139**: 18 - 39, 2015.

[6] Carpinteri A., Corrado M., Paggi M., Mancini, G., New Model for the Analysis of Size-Scale Effects on the Ductility of Reinforced Concrete Elements in Bending *Journal of Engineering Mechanics-asce - J ENG MECH-ASCE* **135**, 2009.

[7] Alnaes M.S., Blechta J., Hake J., Johansson A., Kehlet A., Logg A., Richardson C., Ring J., Rognes M.E. and Wells G.N., The FEniCS Project Version 1.5 *Archive of Numerical Software*, **3**, 2015

HOMOGENIZED TOUGHNESS PROPERTIES OF LARGE-SCALE DISORDERED BRITTLE SOLIDS

Mathias Lebihain*[1,2], Laurent Ponson[1], Djimédo Kondo[1], and Jean-Baptiste Leblond[1]
[1]Institut Jean Le Rond d'Alembert (SU/CNRS), Paris, France
[2]Laboratoire Navier (ENPC/IFSTTAR/CNRS), Marne-la-Vallée, France

Summary Homogenization theory constitutes nowadays a well-established theoretical framework to estimate the overall response of composite materials for a broad range of mechanical behaviors. However, such a framework is still lacking for brittle fracture properties. In this work, we propose a comprehensive theoretical framework inspired by micromechanics and statistical physics to predict the *intrinsic* effective toughness of large-scale disordered brittle composites, taking into account the decisive influence of both the *material disorder* and the *dissipative mechanisms* involved at the crack-tip. The theoretical predictions are successfully compared to the results of large-scale numerical simulations of crack propagation in composite materials displaying spatial variations of toughness.

EFFECTIVE TOUGHNESS OF LARGE-SCALE BRITTLE COMPOSITES

Being able to predict the macroscopic response of a material from the knowledge of its constituents at a microscopic scale has always been the Holy Grail pursued by material science, for it provides building bricks for the understanding of complex structures as well as for the development of tailor-made optimized materials. However, such a framework is still lacking for brittle fracture. In this work, we propose a homogenization framework for fracture properties of composite materials that builds on the specificities of brittle fracture, which is (i) a *dissipative evolution* problem that (ii) is related to a *structural one* and (iii) involves damage processes *localized at the crack tip*.

First, one has to model crack propagation in heterogeneous material to estimate the overall dissipation and deduce from it effective fracture properties. Recently, Lebihain et al. [1] proposed a semi-analytical method based on the perturbative approach of Linear Elastic Fracture Mechanics initiated by Rice [2] to model efficiently crack propagation under tensile Mode I loading in large-scale composites displaying local variations of toughness properties. The crack can interact with the tough inclusions through two mechanisms : a crossing one where it goes through the inclusion, and a by-pass one where it wanders out-of-plane and propagates along the inclusion/matrix interface (see Fig. 1.a). The numerical method allows to compute crack interaction with millions of inclusions in only few hours, and track the instantaneous macroscopic energy release rate G^∞ as well as the surface energy G_c^{frac} dissipated during material failure.

The proposed numerical method provides the core elements to investigate the effective fracture properties of large-scale disordered solids. However, no consensus has emerged yet to define the effective toughness of heterogeneous materials, which can be alternatively measured from the dissipation G_c^{frac} as the average surface energy dissipated during material failure $\langle G_c^{\text{frac}} \rangle$, or from the loading G^∞ as its maximal $G^\infty_{\max}$ or average G^∞_{mean} value. We show here that under the scale-separation condition :

$$\mathcal{L} = -G^\infty \Big/ \frac{\partial G^\infty}{\partial x} \gg d \tag{1}$$

all three definitions mentioned above converge towards a single value G_c^{eff} (see Fig. 1.b) that can be unambiguously referred to as the *intrinsic* effective toughness of the composite. The structural length $\mathcal{L}$ is related to the boundary conditions and the specimen geometry, while d is the heterogeneity characteristic size. This condition has strong implications on the experimental set-ups as well as on the numerical boundary conditions one has to use to measure intrinsic effective fracture properties.

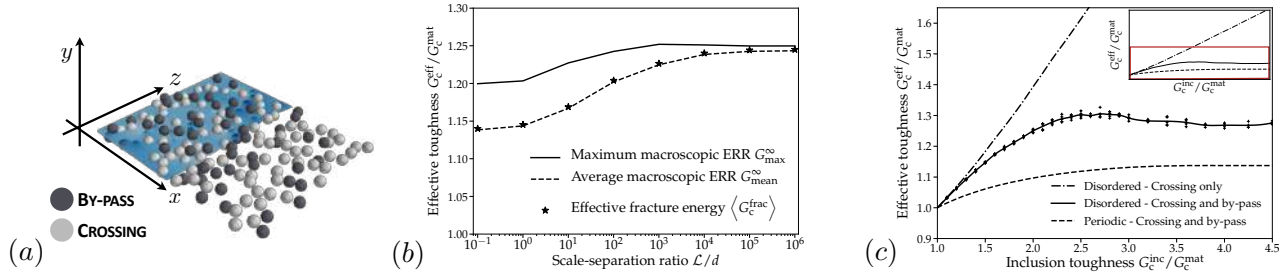

Figure 1: (a) Perturbative LEFM approach for crack propagation in disordered material displaying spatial variations of toughness properties under a macroscopic loading G^∞ : the crack can either cross (in light grey) or by-pass (in dark grey) the inclusion when interacting with it. (b) Scale-separation condition for effective toughness measurements : the structural length $\mathcal{L}$ has to be far larger than the heterogeneity size d to define an *intrinsic* effective toughness G_c^{eff}. (c) Influence of the inclusion toughness G_c^{inc} on the effective toughness G_c^{eff}, stressing out the decisive importance of the material disorder and the interaction mechanisms.

*Corresponding author. E-mail: mathias.lebihain@enpc.fr

We can then investigate the influence of microstructural features on the effective toughness G_c^{eff} and start with the inclusion toughness G_c^{inc} (see Fig. 1.c). By comparing the results with simulations of coplanar crack propagation in disordered materials where the sole crossing mechanism is modeled, and ones where the inclusions are positioned in a periodic ordered manner, we observe that both the material disorder and the interaction mechanisms localized at the crack tip play a decisive influence on the overall toughness of the composite.

HOMOGENIZING FRACTURE PROPERTIES OF DISORDERED SOLIDS

The influence of material disorder has already been studied by Démery et al. [3] using tools inspired by statistical physics in the case of coplanar crack propagation where the influence of the mechanisms of interaction is ignored. The effective toughness G_c^{eff} of the composite can be predicted from 4 statistical features of the local toughness field : its average value $\langle G_c \rangle$, its standard deviation σ, and its correlation lengths ξ_z and ξ_x in both the front and the propagation direction. We propose here a three-step homogenization procedure (see Fig. 2.a) that reconstructs the toughness field the crack actually experiences during its interaction with material heterogeneities.

First, we break down the full problem of the propagation of a crack in a disordered distribution of inclusions into multiple simpler problems, referred to as *fractured elementary volumes* (FEVs), considering all the possible ways a crack interacts with a single inclusion and its respective probability. This decomposition relies on the absence of interaction during the out-of-plane by-pass of neighboring inclusions and is referred to as the *non-collective mechanisms* hypothesis. Second, the three-dimensional cell problems provide equivalent coplanar ones, called *coplanar equivalent coplanar elements* (ECEs), which derive from the way the crack interacts with the single inclusion (crossing or by-pass). Third, the superposition of all the coplanar cell problems allows to get back to an equivalent coplanar toughness distribution, from which the statistical features $(\langle G_c \rangle, \sigma, \xi_z, \xi_x)$ can be inferred under the *ergodic assumption*. It ultimately allows to estimate the effective toughness of three-dimensional heterogeneous brittle materials using Démery et al.'s coplanar theory [3].

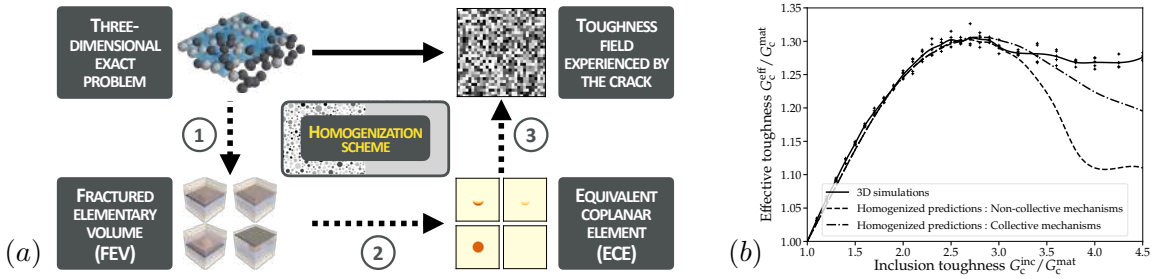

Figure 2: (a) Three-step homogenization procedure to predict the impact of microstructural features on the overall toughness of the brittle composite. (b) Application to the influence of the inclusion toughness on the effective toughness. Average numerical results (in solid lines) are compared to homogenized predictions (in dashed and dashed-dotted lines).

Predictions of the homogenized toughness are shown to be in perfect agreement with numerical results (see Fig. 2.b) as long as the *non-collective mechanisms* hypothesis is valid (i.e. inclusions 3 times tougher than the matrix). An alternate procedure can be derived from the one proposed here to take into account the collectivity in the mechanisms of interaction and thus improve the quality of the theoretical predictions. Such a framework paves the way to investigate the influence of the microstructural features (e.g. inclusion shape or density) on the homogenized toughness and design brittle composites with tailored fracture properties.

CONCLUSIONS

We proposed here a comprehensive homogenization framework that predicts the influence of microstructural features on the intrinsic effective toughness of large-scale disordered composites, taking into account the decisive impact of both the material disorder and the mechanisms of interaction localized at the crack tip. It has been shown to successfully match the results of large-scale LEFM-based simulations of a crack interacting with spatial heterogeneities of toughness. The proposed approach aims nonetheless at predicting the effective toughness in presence of a broader class of heterogeneities. For example, the case of elastic inclusions or pores could be addressed using much more adapted computational tools (e.g. phase-field models) in a periodic setting to estimate the mechanisms involved during the crack-inclusion interaction (FEV) as well as their individual contribution (ECE). The influence of the material disorder would then be taken into account using tools borrowed from statistical physics.

References

[1] Lebihain M., Leblond J.B., and Ponson L. Effective toughness of periodic heterogeneous materials: the effect of out-of-plane excursions of cracks. *J. Mech. Phys. Solids* 2020.
[2] Rice J.R. First-Order Variation in Elastic Fields Due to Variation in Location of a Planar Crack Front *J. Appl. Mech* **52**, 571–579, 1985.
[3] Démery, V. and Rosso, A. and Ponson, L. From microstructural features to effective toughness in disordered brittle solids *EPL* **105**, 34003, 2014.

GRADIENT ENHANCED DAMAGE GROWTH MODELLING OF DUCTILE FRACTURE

Ragnar Larsson*[1] and Ahmet S. Erturk [1]
[1]Division of Materials and Computational Mechanics, Department of Industrial and Materials Science,
Chalmers University of Technology,SE-41296 Göteborg,Sweden

Summary A gradient enhanced damage model for ductile fracture modeling describing the material response including damage induced degradation is presented. The continuum damage evolution of Lemaitre type is focusing the degradation of the shear response eventually leading to shear induced ductile failure. The major incentive of the present paper is to examine the convergence and stability properties of both damage rate and gradient dependence in the fracture area production. In fact, this model can partly remove the pathological mesh dependence and have a stable behavior without the additional gradient effect. A major concern in this development is the choice of a nonlocal criterion for elastoplastic damage onset. The application in mind of the damage modeling is the modeling of impact problems, like split Hopkinson tests and machining process simulations.

INTRODUCTION

The micro-mechanics of fracture processes involve void nucleation/micro-crack development, coalescing, first on a micro-structural level, eventually forming a macroscopic crack or a diffuse damage zone on the macro-scale. Since ductile fracture is a frequently phenomenon in all fields of engineering, e.g. machining [1], it is of vital importance to efficiently and accurately control the fracture process to optimize the design and to reduce the weight of new components. From the key work of Gurson [2], ductile damage is attributed to the growth of micro voids, whose evolution are often formulated in (local) Gurson type plasticity models coupled to void volume growth. In the FE-application, the void formation is assumed to coalesce into fracture surfaces corresponding to localized deformation that is highly mesh dependent. As a remedy to the highly mesh dependent behavior, nonlocal extensions of the Gurson model have been proposed, [3, 4].

Another way to represent ductile fracture is to generalize recent developments of continuum phase field models for brittle fracture processes into the corresponding one for ductile fracture, e.g. [5, 6]. In Miehe et al. [6], the proposed phase field modeling is introduced into a thermoplasticity framework in conjunction with a nonlocal damage model. It has been argued that viscous regularization of the continuum material model coupled to damage via visco-plasticity may remove the pathological mesh dependence [7]. In a recent paper [8], rate dependent scalar damage for ductile fracture processes was proposed to overcome mesh dependence without gradient damage enhancement. Recent developments using the phase field approach to ductile fracture also indicates removed mesh dependence, even for highly refined meshes [5, 6]. Ductile fracture may also be modelled by extending continuum phase field models for brittle fracture processes so that ductile fracture characteristics are included [5, 6].

A SCALAR DAMAGE MODEL FOR DUCTILE FRACTURE

The present contribution extends the developments in [8] to include the effect of nonlocal damage for ductile failure. The main prototype for the effective material is the Johnson-Cook model, accounting for deformation and strain rate hardening and temperature degrading effects. In the damage modeling we are concerned with:

1. the energy dissipation rate describing a damage coupled to plasticity driving dissipation to the fracture area production process [8].

2. the description of energy dissipation due to fracture area production, involving area production due to “damage convection” and “damage nucleation” in the temporal evolution of the damage field [9]. In addition, a “gradient” fracture area production effect is obtained due to spatial growth of the damage field.

3. the formulation of nonlocal condition for onset of the plasticity driven damage evolution.

Thereby, the model constitute a novel control of the ductile failure process. In fact, this model can partly remove the pathological mesh dependence and have a stable behavior without the additional gradient effect [8, 9]. A major incentive of the present investigation is to consider the convergence and stability properties in the FE-application considering both damage rate and gradient dependence in the fracture area production.

In line with Lemaitre concept for continuum damage evolution, the model is formulated so that the damage evolution is driven by the stored free shear energy and plastic work of the effective material. This effect is described by degrading the isochoric portion of the free energy in terms of the scalar damage variable $0 \leq \alpha \leq 1$. In order to enhance the ductile failure modeling capability, an initiation criterion is introduced to monitor the contribution of the plastic work to damage force. As to the nonlocal damage evolution model, the global fracture area functional defines the total fracture

*Corresponding author. E-mail: ragnar@chalmers.se

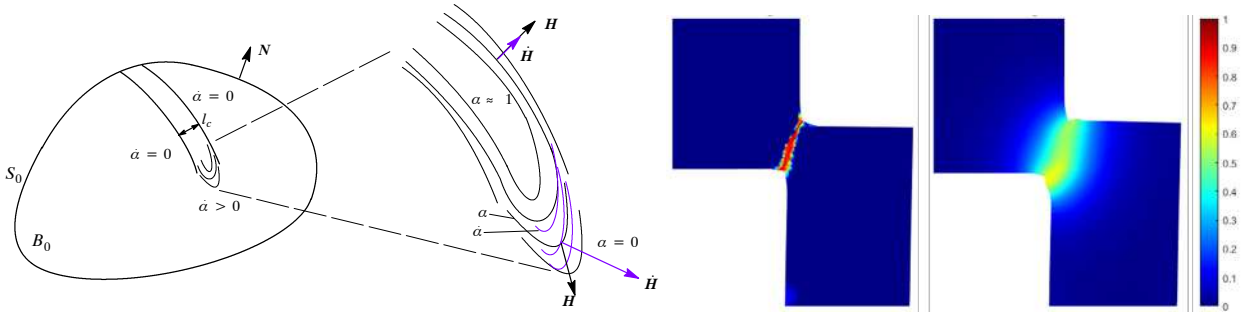

Figure 1: a) Localized damage progression zone of internal width l_c in the solid region B_0 with external boundary S_0 and with unit normal $\boldsymbol{N}$. The close-up shows shematic isolines for the damage field (black) and the damage evolution field (mangenta). The damage flux vectors show the directional dependence of the nonlocal damage contribution to the evolution of fracture area. b) Resulting localized damage fields for Split Hopkinson test analysed by the rate sensitive local and nonlocal damage evolution models.

area through the fracture area density γ [9], which takes on values based on damage state, the rate of damage and gradient damage.

$$\dot{\gamma} = \frac{1}{l_c}\left(\alpha\dot{\alpha} + \boldsymbol{H}\cdot\dot{\boldsymbol{H}}\right) + \frac{1}{v^*}\dot{\alpha}^2 \geq 0 \tag{1}$$

where the parameters involved are the internal length parameter l_c and the fracture area progression speed parameter v^*, controlling the damage evolution. The interpretation is shown in Figure 1a, considering schematic isolevels of the damage state and evolution. Note the directional dependence of the nonlocal damage through the damage flux vectors $\boldsymbol{H}$ and $\dot{\boldsymbol{H}}$. From Eq.(1) there are three mechanisms governing the fracture area evolution: The first two mechanisms, $\alpha\dot{\alpha}/l_c$ and the gradient damage term $\boldsymbol{H}\cdot\dot{\boldsymbol{H}}/l_c$, are due to growth (or convection) of existing damage induced voids, whereas the term $\dot{\alpha}^2/v^*$ represents void nucleation [8]. Clearly, the conventional completely rate independent fracture area evolution is obtained when the damage propagation speed parameter $v^* \to \infty$ [8, 9].

Split Hopkinson tests are considered to show the predictive capabilities of the model [10]. Figure 1b shows our preliminary results of the localized deformation patterns for the rate sensitive damage evolution model [8] and the combined damage rate and gradient dependent damage model. Clearly, in the present case of shear failure the gradient damage effects becomes pronounced due to the extreme localization when considering the local rate dependent model.

References

[1] S. Razanica, A. Malakizadi, R. Larsson, S. Cedergren, B. L. Josefson, Fe modeling and simulation of machining alloy 718 based on ductile continuum damage, *International Journal of Mechanical Sciences* 171 (doi: 10.1016/j.ijmecsci.2019.105375) (2020).

[2] A. L. Gurson, Continuum theory of ductile rupture by void nucleation and growth: Part i - yield criteria and flow rules for porous ductile media, *Journal of Engineering Materials and Technology* 99 (1) (1977) 14 (1977).

[3] V. Tvergaard, A. Needleman, Nonlocal effects on localization in a void-sheet, *International Journal of Solids and Structures* 34 (18) (1997) 2221–2238 (1997).

[4] F. Reusch, B. Svendsen, D. Klingbeil, Local and non-local gurson-based ductile damage and failure modelling at large deformation, *European Journal of Mechanics - A/Solids* 22 (2003) 779–792 (2003).

[5] M. Ambati, T. Gerasimov, L. De Lorenzis, Phase-field modeling of ductile fracture, *Computational Mechanics* 55 (5) (2015) 1017–1040 (2015).

[6] C. Miehe, M. Hofacker, L. Schanzel, F. Aldakheel, Phase field modeling of fracture in multi-physics problems. part ii. coupled brittle-to-ductile failure criteria and crack propagation in thermo-elastic–plastic solids, Comput Methods Appl Mech Engrg 294 (2015) 486–522 (2015).

[7] M. Niazi, H. Wisselink, T. Meinders, Viscoplastic regularization of local damage models: revisited, *Computational Mechanics* 51 (2) (2013) 203–216 (2013).

[8] S. Razanica, R. Larsson, B. L. Josefson, A ductile fracture model based on continuum thermodynamics and damage, *Mechanics of Materials* 139 (2019) (2019). doi:10.1016/j.mechmat.2019.103197.

[9] R. Larsson, R. Gutkin, M. Rouhi, Damage growth and strain localization in compressive loaded fiber reinforced composites, *Mechanics of Materials* 127 (2018) 77–90 (2018).

[10] J. Johansson, C. Persson, H. Lai, Microstructural examination of shear localisation during high-strain-rate deformation of alloy 718, *Materials Science Engineering A: Structural Materials: Properties, Microstructure and Processing* 662 (2016) 363–372 (2016).

SOME RECENT PROGRESS ON PHASE-FIELD MODELING: FATIGUE, R-CURVES, AND LARGE STRUCTURES

Chad M. Landis[1,2], Yu-Sheng Lo[1], Amin Anvari[1], K. Ravi-Chandar[1], Thomas J.R. Hughes[1,2], and Michael J. Borden[3]
[1]Aerospace Engineering and Engineering Mechanics, University of Texas at Austin, Austin, TX USA
[2]Institute for Computational Engineering and Science, University of Texas at Austin, Austin, TX USA 3Coreform, Orem, UT USA

Summary Phase-field modeling approaches for fatigue crack growth, R-curve behavior, and large-scale structures are presented. For fatigue, a modified J-integral is developed to demonstrate how the phase-field approach can be used to generate Paris-Law type crack growth rates. A steady-state finite element method is then applied to generate fits of the phase-field theory to measured crack growth rate data. Full transient simulations are performed and compared to experimental measurements on samples where crack turning is induced by the presence of a hole in the vicinity of the crack. To model R-curve behavior plasticity is introduced into the formulation and adaptive refinement is used to capture different length scales. Finally, modifications to the damage functions are introduced to allow for the analysis of large-scale structures and some issues are identified and discussed.

PHASE-FIELD MODELING OF HIGH CYCLE FATIGUE

The most well-known phenomenological relationship between fatigue crack growth and mechanical loading is the so-called Paris-law. Paris et al. [1] found that the fatigue crack growth per cycle, da/dN, is governed by the stress intensity factor range, ΔK, that is, $da/dN = f(\Delta K)$, and it can often be assumed to follow a simple power-law relation called the Paris-law: $da/dN = C(\Delta K)^n$ in which C and n are material constants. Since the Paris-law is a phenomenological description based on linear elastic fracture mechanics, it is possible to enhance phase-field methods for brittle fracture to allow for fatigue crack growth without the need to include the complications of plastic deformation around crack tips. Hence, the primary goal of this work is to extend the phase-field approach to reproduce the macroscopic fatigue crack growth behavior that is either driven by cyclic loading or monotonic loading, i.e. static fatigue. Cyclic fatigue conjures notions of applied forces or displacements that are increased from zero to some maximum value and then decreased to some minimum value, with such a cycle repeating as the crack grows and the sample eventually fails. The present model *does not* require the full time integration of the details of individual cycles that would track the full history of loading and unloading. For high cycle fatigue this would require explicit solutions for millions of cycles. Instead, we regard the Paris-law as a *kinetic law* governing the relationship between the crack growth driving force and the crack growth rate. Hence, instead of applying cyclic loads explicitly within the model, the loading is applied *statically* as ΔK and the crack trajectory evolves according to the partial differential equations of the phase-field model, suitably modified to reproduce the correct $da/dN = f(\Delta K)$ behavior. We use the J-integral to aid in determining the relationship between the phase-field kinetic law and the Paris law and we then apply the theory within the finite element method to predict the crack growth [2]. One example of the results of the theory compared to an experimentally measured fatigue crack path is shown in Figure 1.

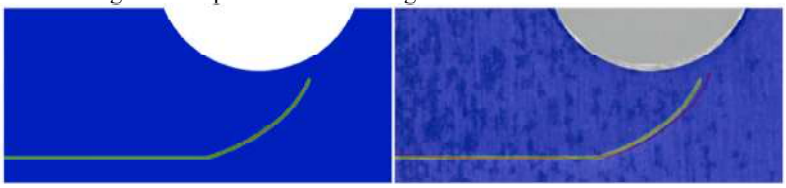

(a) (b)

Figure 1. The crack path from (a) the phase-field simulation and (b) an overlay of the results for the crack path with the experimental observation.

PHASE-FIELD MODELING OF R-CURVE BEHAVIOR

The modeling of R-curve behavior using the phase-field approach was performed to compare to the results obtained for the R-curve behavior predicted with cohesive zone models. Here, the bulk material behavior is modeled with isotropic hardening J_2 plasticity, and the phase-field evolution equation is driven by the elastic stored energy in the material. A new adaptive mesh refinement scheme was developed in order to resolve the disparate length scales associated with the large elastic region required to model small-scale yielding, the size of the plastic zone, and the size of the phase-field region surrounding the crack. Figure 2 shows the results for a R-curve for a specific set of material parameters, and Figure 3 shows the evolution of the plastic zone up until steady state crack growth is achieved.

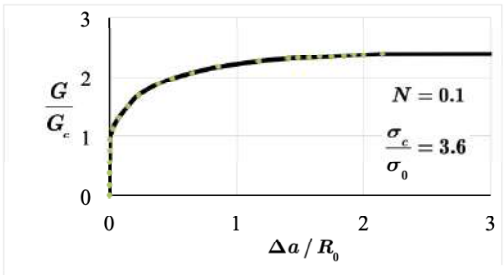

Figure 2. R-curve bahavior predicted by the phase-field approach with plasticity and phase-field driven by elastic energy.

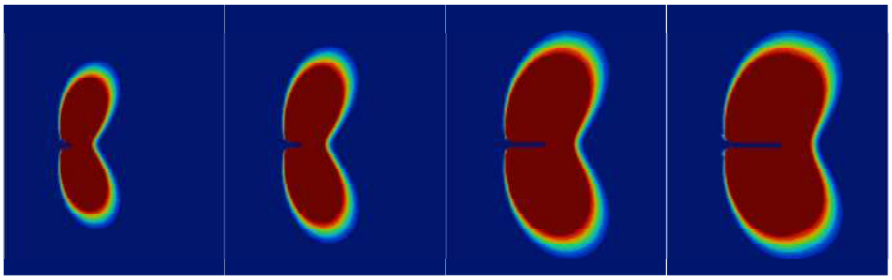

Figure 3. The evolution of the plastic zone associated with the R-curve behavior shown in Figure 2.

PHASE-FIELD MODELING OF LARGE STRUCTURES

Phase-field fracture theories contain a small length-scale interface region around the cracks. In fact, this length-scale, ℓ_0, is set by the material properties, specifically the peak stress, σ_c, and fracture toughness, G_c, such that $\ell_0 = 3G_cE/8\sigma_c^2$. Unfortunately, this length-scale can be very small. In a brittle material it can be on the order of nanometers, and for a ductile material it can be on the order of a fraction of a millimeter. Furthermore, the numerical solution of the phase-field equations requires that the discretization of the model can resolve this length scale. Clearly, such resolution makes the application of the phase-field theory to meter-sized structures difficult in two dimensions and prohibitive in three dimensions. Hence, all of the attractive features of the phase-field formulation are for naught if it cannot be applied to the analysis relevant large scale structures. Most of the academic research so far has focused on the generality and the accuracy of results, rather than computational cost. It is on this avenue of inquiry that we focus this study. The insight that we have uncovered is that the very small process zone length-scale that is set by the material properties can be decoupled from the phase-field length scale that must be numerically resolved within the calculations by the appropriate choice of the function that degrades the elastic load carrying capacity of the material. Specifically, the function used is the exponential form introduced in [3]. Furthermore, as is relevant for improving the computational cost, the phase-field length scale can be made orders of magnitude *larger* than the material length scale. We will present new results for this approach and explain the limitations on how far the decoupling can be pushed on a given mesh discretization. Figure 4 shows results for this new approach.

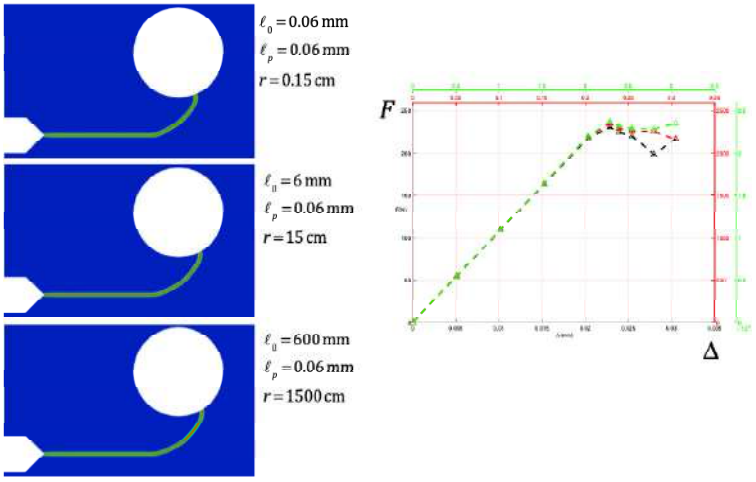

Figure 4. Simulations on increasingly larger compact tension specimens with a hole. In all cases the material process zone length scale is taken as a physically reasonable value of 0.06mm, but the phase-field length scale is allowed to vary such that the mesh density required to resolve the fields around the hole can also be used to resolve the phasse-field distribution around the cracks, which is 1, 100, and 10,000 times as large as the process zone length-scale going from top to bottom. Both the crack path agreement and the scaling of the load deflection curves are in agreement with the requirements of linear elastic fracture mechanics.

References

[1] Paris P.C., Gomez M.P., Anderson W.E., A rational analytic theory of fatigue, *Trend Eng.* **13**, 9-14, 1961.
[2] Lo Y.S., Borden M.J., Ravi-Chandar K., Landis, C.M. A Phase-field Model for Fatigue Crack Growth. *J. Mech. Phys. Solids* **132**, 103684, 2019.
[3] Wilson Z.A., Borden M.J., Landis C.M., A phase-field model for fracture in piezoelectric ceramics, *Int. J. Fract.* **183** 135–153, 2013.

SYSTEMATIC INVESTIGATION OF FRACTURE BEHAVIOR OF COMPOSITES IN THE VICINITY OF TOUGH-BRITTILE TRANSITION

Uttam S. Kachhwah*[1] and Sivasambu Mahesh[1]
[1]Department of Aerospace Engineering, Indian Institute of Technology Madras, Chennai 600036 India

Summary The Monte Carlo simulation plane transverse to the composite direction has been studied for various parameters such as patch size, variability of fibre strength, and the stress transfer coefficient. Limitation of patch size is overcome by FFT algorithm used by Ankit Gupta *et al*. and hence it has been possible to explore the tough-brittle transition existence marked by previous researchers. Patch size and other constraints imposed on simulation have shown different trends during cluster analysis and a counter fitting model respectively, which has helped take an assertive decision to scan peaks on moments ratio vs stress transfer coefficient plots. Two-parameter based probabilistic tight cluster growth model is developed to capture the empirical strength distribution and also extrapolated to map the survival probability.

INTRODUCTION

Composite structures are light in weight and high in strength due to which it has been widely used in aerospace applications as well as ground structures (e.g. Composite flywheel material design for high-speed energy storage) where anisotropicity in strength is our primary concern. Increasing demand of high strength and reliable composite in the market has narrowed down the probability failure tolerence. Keeping this into mind, studies based on cluster formation statistics (unstable cluser growth) and model fitting parameters are carried in the present study. Final rupture of materials depends upon how crack grows and interact each other. The correlation of crack growth depends on many factors such as fibre strength variability (weibull moduli), ρ, stress transfer coefficient, β, and patch size, N. Smaller weibull moduli corresponds to the formation of scattered breaks whereas strong correlation in cluster formation is observed for higher weibull moduli. Another factor, β decides the intensity of load shared amongst intact fibres. Two load sharing extremum which exists are, first: equal load sharing (ELS) where aditional load is borne by all the intact fibres equally, second: local load sharing (LLS) wherein only neighbors share additional load dropped by a broken fibre. All remaining set of β, between these two limits, have also been explored in order to comment on the point where fracture mode changes suddenly. In breif, two modes of failure, tough and brittle mode is separated by a point calculated by R.C. Hidalgo *et al* [3] and S. Pradhan *et al* [4] using the method of moment for cluster analysis and is given at around $\beta = 2.2 \pm 0.1$ and its equivalent value by [4], respectively. In this paper, empirical distribution results, model fit based on tight cluster growth, and cluster moment analysis results are presented. Empirical data is obtained from two-parameter based weibull distributed fibre strength formula,

$$F(\sigma) = 1 - exp(-\sigma^{\rho}) \tag{1}$$

where σ is normalized strength per fibre and F is failure probability. Re-writing Eq. 1 for strength expression,

$$\sigma = [-log(1 - F(\sigma))]^{1/\rho} \tag{2}$$

PROBABILISTIC MODELS

Probablistic model and weakest-link analysis on weibull plot are explaind in two subsections explaining tough and brittle fracture mode.

Tough mode - This mode is generally observed for high variability of fibre strength; uncorrelated crack growth is the main cause. A relatively larger bundle of loose threads is considered as ELS patch and can be captured exactly by gaussian distribution done by Daniels [5] whereas for smaller patch size McCartney and Smith [6] have developed a recursion formula, discussed in [1]. Final failure of tough composite does not occur by a single running crack but due to the coalesence of small cracks into a comparitively big well-rounded fissure which makes the composite weaker for higher loads. One way of defining tough regime is cluster calculation which will be discussed in the result section.

Brittle mode - It's imprudent to explain brittle fracture mode alone in a single way however, qualitatively one can say that a crack formation which leads to the final rupture of composite with no additional load application possible is termed as brittle failure. Brittle failure in composites occur with no apparent deformation before fracture like other materials. Most likely cases where brittle mode dominates are due to selection of parameters from the higher $\beta - \rho$ plane. The existence of critical cluster or weakest-link, used interchangeably, can be seen pictorially on weibull paper where all curves collapse into a single curve. When a patch comprises a critical cluster whose size is less than the size of the patch itself, the failure under this mode can be regarded as the weakest-link phenomenon which becomes independent of the number of fibres. These two modes are quantified using cluster statistics calculation and few questions are also raised on interpretation on genesis of peaks during the method of moment application analysis.

*Corresponding author. E-mail: kachhwahbais@gmail.com

RESULTS AND DISCUSSION

Strength distribution of intermediate β fibre bundles are discussed for three different N, shown in Fig.1. A best fit for each β distribution is obtained by running the model based on tight cluster formation [6]. Variability in fibre strength plays significant role on the selection of ELS bundle size, M, taken as model fitting parameter. For higher ρ, crack grows in a tight cluster manner $\forall\ \beta > 2.0$, whereas for lower ρ, in order to make them grow in the same fashion entire patch needs to be divided into N/M number of ELS-bundle [2] of size M where $1 \leq M \leq N$. To esnure the minimum amount of overload on neighboring ELS bundle, appropriate value of M has been opted with in given limit. M increases with decreasing ρ and increaing patch size untill it reaches to the critical cluster size. $N_{sim} = 256$, Monte Carlo simulation have been performed for each set of $N \in \{2^{14}, 2^{16}, 2^{18}, 2^{20}\}$, $\beta \in \{2.0, 2.1, 2.2, 2.3, 2.4, 2.5\}$, and $\rho = 2.0$. Fig.1(a, b, c), do not show any sudden jump near $\beta = 2.1$, whereas Fig.1(d), has shown a clear peak at $\beta = 2.2 \pm 0.1$. As we can see that the gap between curves are changing gradually from $\beta = 2.0$ to 2.5 unlike peaks observed during cluster analysis; this just contradicts the previous study on tough-brittle transition point. Our empirical strength distribution has considered mutual break interaction thus making simulation realistic unlike others however, change in stress concentration has just altered the failure probability (not presented in this article).

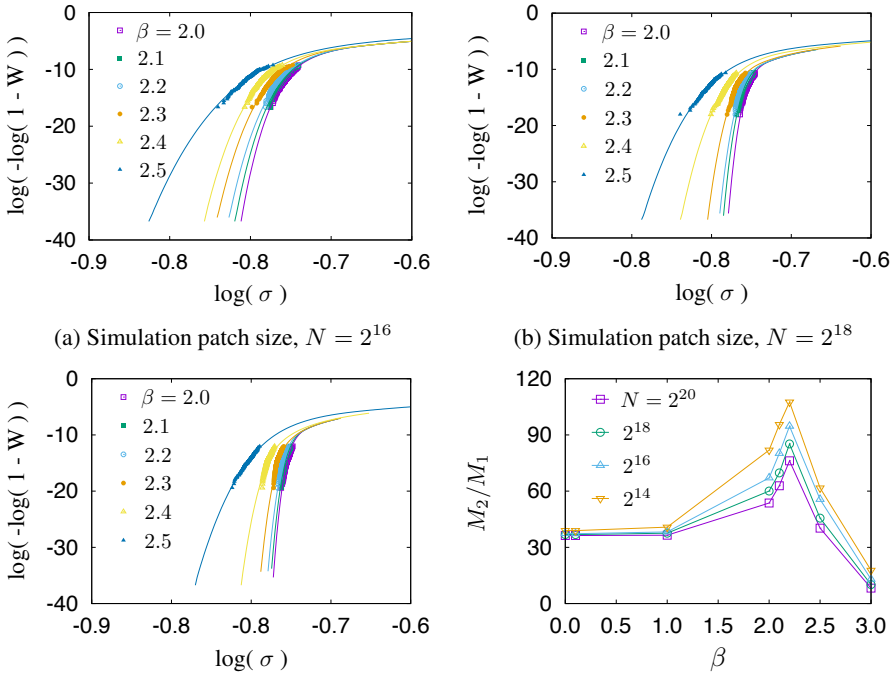

(a) Simulation patch size, $N = 2^{16}$

(b) Simulation patch size, $N = 2^{18}$

(c) Simulation patch size, $N = 2^{20}$

(d) Variation of the cluster moment ratio

Figure 1: (a), (b), and (c) are weakest-link plot on weibull paper for various β and $\rho = 2.0$. A gradual change in empirical distribution can be clearly seen unlike sudden jump nearby $\beta = 2.1$. Model fits exactly well to the empirical distribution following monotonicity in M across β and ρ. (d) is the varaition of ratio of second and first cluster moment (M_2/M_1) over the desired range of β.

CONCLUSIONS

Monte Carlo simulations have been performed thoroughly for various β coefficeints and $\rho = 2.0$. Brittle region of fracture mode is still unclear for other varaibility of fibre strength, which is also an important parameter to be considered in the simulation part. Our next goal is to set a model which can capture the lower probability of failure perfectly and analyse thoroughly for various ρ values. From the Fig.1(a, b, c), it's clear that, for any arbitrary $\beta > 2.0$ and $\rho = 2.0$ in the limit of $N \to \infty$ mode of failure is brittle fracture.

References

[1] Gupta, A., Mahesh, S. and Keralavarma, S.M., 2017. A fast algorithm for the elastic fields due to a single fiber break in a periodic fiber-reinforced composite. International Journal of Fracture, 204(1), pp.121-127.
[2] Mahesh, S., Gupta, A., Kachhwah, U.S. and Sheikh, N., 2019. A fast algorithm to simulate the failure of a periodic elastic fibre composite. International Journal of Fracture, pp.1-9.
[3] Hidalgo, R.C., Moreno, Y., Kun, F. and Herrmann, H.J., 2002. Fracture model with variable range of interaction. Physical review E, 65(4), p.046148.98+69+8
[4] Pradhan, S., Chakrabarti, B.K. and Hansen, A., 2005. Crossover behavior in a mixed-mode fiber bundle model. Physical Review E, 71(3), p.036149.
[5] Daniels, H.E., 1945. The statistical theory of the strength of bundles of threads. I. Proceedings of the Royal Society of London. Series A. Mathematical and Physical Sciences, 183(995), pp.405-435.
[6] McCartney, L.N. and Smith, R.L., 1983. Statistical theory of the strength of fiber bundles.

POROELASTIC EFFECTS ON TIME AND RATE DEPENDENT FRACTURE OF GELS

Yalin Yu[1], Nikolaos Bouklas[2], Chad M. Landis[1], and Rui Huang[1]*
[1]Department of Aerospace Engineering and Engineering Mechanics, University of Texas, Austin, TX 78712, USA
[2]Sibley School of Mechanical and Aerospace Engineering, Cornell University, Ithaca, NY 14853, USA

Summary Fracture of polymer gels is often time and rate dependent. The underlying mechanisms include local fracture processes, viscoelasticity, and solvent diffusion (poroelasticity). This paper focuses on the effects of poroelasticity, for which a modified J-integral is adopted to define the crack-tip energy release rate for crack growth in gels. For a stationary crack, the energy release rate is time dependent, with which delayed fracture can be predicted based on a Griffith-like fracture criterion. For steady-state crack growth in a long-strip specimen, the energy release rate is a function of the crack speed, with rate-dependent poroelastic toughening. With a poroelastic cohesive zone model, solvent diffusion within the cohesive zone leads to significantly enhanced poroelastic toughening as the crack speed increases. We present numerical results and discuss implications for experiments.

INTRODUCTION

Recently, polymer gels have been exploited as a class of soft active materials with potential applications in soft machines and soft robotics. These applications have motivated development of smart and tough gels. However, it remains a challenge to accurately measure the fracture toughness of polymer gels [1], and fundamental understanding of the fracture mechanisms in gels is still lacking. In particular, fracture of polymer gels is often time and rate dependent. For example, in an experimental study on steady-state crack growth in gelatin gels, Baumberger et al. [2] found that the effective fracture energy was rate dependent and increased with the crack speed (so-called "velocity toughening"). Recently, Tang et al. [3] conducted fracture experiments of polyacrylamide hydrogels under monotonic, static, and cyclic loads; they observed time-dependent, delayed fracture below the critical load for fast fracture but above a threshold load. In this paper, we present a set of theoretical and numerical results concerning the poroelastic effects on the time and rate dependent fracture of polymer gels, including both delayed fracture and steady-state crack growth.

J-INTEGRAL AND ENERGY RELEASE RATE

Based on a nonlinear poroelastic theory of polymer gels, a modified J-integral was derived by Bouklas et al. [4] to calculate the energy release rate for crack growth in poroelastic gels, where the energy dissipation by solvent diffusion was subtracted from the classical J-integral. It was shown that the modified J-integral is path independent for both transient and steady-state crack growth in poroelastic gels [4-8]. With the modified J-integral as the crack-tip energy release rate, a Griffith-like fracture criterion is proposed. In the case of a stationary crack, the modified J-integral is time dependent [4,5], and the onset of crack growth may be predicted when the modified J-integral reaches a critical value, namely, $J^*(t) = \Gamma_{c0}$, where Γ_{c0} is the fracture energy for initiation of crack growth. For steady-state crack growth, the modified J-integral is a function of crack speed $\dot{a}$ [6-8] and must be equal to the fracture energy at the same crack speed, namely, $J^*(\dot{a}) = \Gamma_{SS}(\dot{a})$, where $\Gamma_{SS}(\dot{a})$ is the rate-dependent steady-state fracture energy.

DELAYED FRACTURE

Consider a specimen with a stationary center crack (Fig. 1a), subject to uniaxial tension by either displacement or load (traction) controlled step loading under plane strain conditions. The initial state of the gel is assumed to be stress free and homogeneously swollen. The specimen may be immersed in an external solution so that all of the boundaries (including the crack faces) are in contact with the external solution where the chemical potential $\mu = 0$ is assumed. Alternatively, if the specimen is not immersed, we assume that all of the boundaries are impermeable to solvent diffusion. For simplicity, only the results from the linear poroelastic analysis [5] are discussed here, whereas the nonlinear results [4] are qualitatively similar.

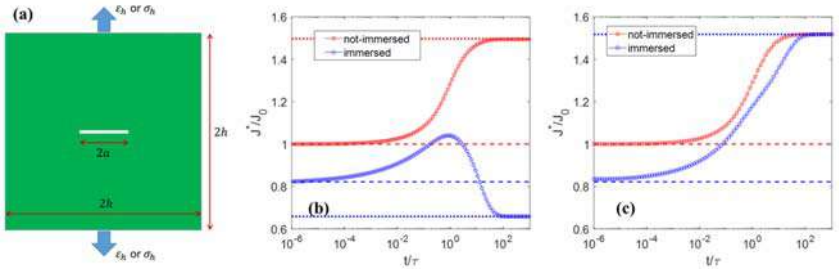

Fig. 1: (**a**) Schematic of a stationary center-crack model. (**b-c**) Normalized energy release rate versus the normalized time under displacement and load control, respectively. The horizontal dashed and dotted lines are the short-time and long-time limits.

By dimensional considerations, the energy release rate can be written as

$$\frac{J^*}{J_0} = \Lambda\left(\frac{t}{\tau}, \frac{h}{a}, \nu\right), \tag{1}$$

where $J_0 = \frac{K_{I0}^2}{4G}$, $\tau = a^2/D^*$ is the characteristic diffusion time with an effective diffusivity D^*, and ν is Poisson's ratio (drained). The dimensionless function on the right-hand side is determined numerically by a finite element method, as shown in Fig. 1. For linearly poroelastic materials, analytical solutions for the energy release rate were found at the short- and long-time limits [5].

According to Fig. 1, except for the immersed case under displacement-controlled loading, the energy release rate (J^*) increases monotonically over time. In these cases, the crack would grow immediately if the short-time limit of the energy release rate is greater than the fracture toughness, but would never grow if the long-time limit is lower than the fracture toughness; in between, delayed crack growth is predicted. Taking J_0 as the applied loading parameter, the delay time is predicted when $0.66\Gamma_{c0} < J_0 < \Gamma_{c0}$ for the not-immersed case and when $0.66\Gamma_{c0} < J_0 < 1.22\Gamma_{c0}$ for the immersed case under load control. The numerical results are qualitatively consistent with recent experiments by Tang et al. [3], who observed delayed fracture of polyacrylamide hydrogels when the applied energy release rate (J_0) was below the critical load for fast fracture and above a threshold value.

STEADY STATE CRACK GROWTH

For steady-state crack growth, an infinitely long strip specimen with a semi-infinite crack was considered, first under plane strain conditions [7] and then under plane stress conditions [8]. The steady-state crack model has two relevant length scales: the specimen half-width h and the steady-state diffusion length $l_{ss} = D^*/\dot{a}$. The ratio between the two length scales defines a dimensionless number, $\mathrm{Pe} = \frac{\dot{a}h}{D^*}$, called the Péclet number. For a linearly poroelastic long-strip specimen, the normalized energy release rate for the steady-state crack growth can be written as

$$\frac{J^*}{J_e} = \Lambda_{ss}(\mathrm{Pe}, \nu). \tag{2}$$

where $J_e = 4G\varepsilon_\infty^2 h$. The dimensionless function on the right-hand side was determined numerically, as shown in Fig. 2. Analytical solutions for the steady-state energy release rate were found at the slow and fast crack limits [7,8]. In all cases, the crack-tip energy release rate is smaller than the classical J-integral applied at the remote boundary ($J^* < J_e$), because part of the supplied energy has been dissipated by solvent diffusion in the poroelastic specimen. The poroelastic toughening depends on the normalized crack speed.

A cohesive zone model was developed to partly account for the rate-dependent fracture processes in gels [6,8]. For the immersed case, significantly enhanced poroelastic toughening is predicted (Fig. 2c) for relatively fast crack growth ($\mathrm{Pe} > 100$), due to solvent diffusion within the cohesive zone. This is consistent with "velocity toughening" observed in experiments [2]. On the other hand, for the not-immersed case, with no solvent diffusion in the cohesive zone, the effect of poroelastic toughening decreases as the normalized crack speed increases.

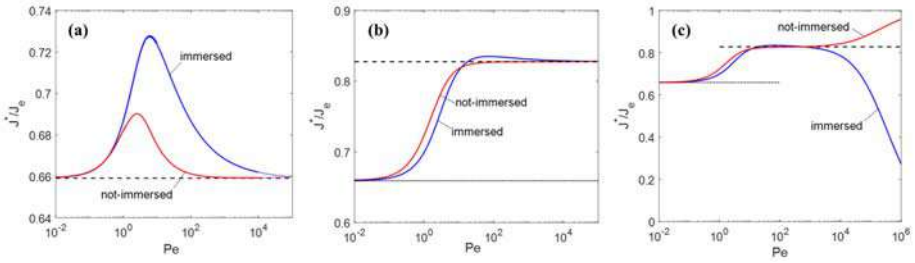

Fig. 2: (**a-b**) Normalized energy release rate versus the normalized crack speed ($\mathrm{Pe} = \dot{a}h/D^*$) for steady-state crack growth under plane strain and plane stress conditions, respectively. The dotted and dashed lines are the slow and fast crack limits. (**c**) Plane stress results with the cohesive zone model.

CONCLUSIONS

A modified J-integral method is developed for calculating the crack-tip energy release rate for fracture in poroelastic gels, with which Griffith-like fracture criteria are proposed for delayed fracture with a stationary crack and for rate-dependent steady-state crack growth. While the method is generally applicable for linear and nonlinear poroelasticity, analytical and numerical results are presented here based on linear poroelasticity only. Future studies may extend to nonlinear poroelasticity with large deformation.

References

[1] Long, R., and Hui, C. Y., Fracture toughness of hydrogels: measurement and interpretation. *Soft Matter* **12**: 8069-8086, 2016
[2] Baumberger, T., Caroli, C., and Martina, D., Solvent control of crack dynamics in a reversible hydrogel. *Nature Materials* **5**: 552-555, 2006.
[3] Tang, J., Li, J., Vlassak, J. J., and Suo, Z., Fatigue fracture of hydrogels. *Extreme Mechanics Letters* **10**: 24-31, 2017.
[4] Bouklas, N., Landis, C. M., and Huang, R., Effect of solvent diffusion on crack-tip fields and driving force for fracture of hydrogels. *J. Appl. Mech.* **82**: 081007, 2015.
[5] Yu, Y., Bouklas, N., Landis, C.M., Huang, R., A Linear Poroelastic Analysis of Time-Dependent Crack-Tip Fields in Polymer Gels. *J. Appl. Mech.* **85**: 111011, 2018.
[6] Noselli, G., Lucantonio, A., McMeeking, R. M., and DeSimone, A., Poroelastic toughening in polymer gels: A theoretical and numerical study. *J. Mech. Phys. Solids* **94**: 33-46, 2016.
[7] Yu, Y., Landis, C.M., Huang, R., Steady-state crack growth in polymer gels: a linear poroelastic analysis. *J. Mech. Phys. Solids* **118**: 15-39, 2018.
[8] Yu, Y., Landis, C.M., Huang, R., Poroelastic effects on steady state crack growth in polymer gels under plane stress. *Mechanics of Materials*, submitted.

FRACTURE STRENGTH OF LATTICE MATERIALS

Shengzhi Luan[1], Enze Chen[1], and Stavros Gaitanaros [*1]
[1]Department of Civil and Systems Engineering, Johns Hopkins University, Baltimore, USA

Summary This work focuses on the fracture strength of brittle lattice materials under tensile loads. We design three-dimensional lattices with controlled morphological characteristics and synthesize them using stereolithography. We perform tensile experiments to failure and connect the measured strength to key microstructural features. Micromechanical numerical models are used to simulate the experiments and estimate the effect of base material properties and loading conditions to the macroscopic strength. Finally, we propose an energy-based method for analysing the fracture mechanics of lattice materials. We show that using this approach does not require any assumptions on the stress and displacement fields near the crack tip. The accuracy of the method is illustrated by predicting the strength of 2D lattices and comparing the estimated critical stresses with direct numerical simulations.

INTRODUCTION

Cellular solids have excellent mechanical, thermal and acoustic properties and have thus been widely used in a variety of engineering applications including thermal shielding, acoustic insulation and shock absorption [1]. Recent advances in additive manufacturing have enabled the synthesis of novel cellular materials and micro-lattices with unprecedented properties. While there has been a large volume of work focusing on the nonlinear mechanics associated with the compressive behavior of these materials, their fracture properties under tension remain relatively unexamined [2-3]. The design of new materials with superior combinations of strength and toughness, by manipulating material architecture, requires a strong understanding of the connection between key microstructural characteristics and fracture properties. Here, we combine additive manufacturing, characterization and modelling of 3D-lattice materials in order to measure their fracture strength and establish its connection to the underlying microstructures. We finally present an energy-based method to calculate the critical load in lattices that have a crack. We examine the accuracy of our method by comparing analytical estimates of critical stresses to numerical simulations.

TENSILE FRACTURE OF 3D BRITTLE LATTICE MATERIALS

In this work we focus on 3D lattices with different average node-connectivities leading to their mechanical behavior varying from bending- to stretching-dominated. Kelvin, octet and BCC lattice specimens are synthesized in a stereolithography-based printer with 50μm layer thickness using a high-temp photocurable resin (see Fig. 1a). The strength of the base material is measured using micro-tensile tests in struts. The results show a typical brittle polymer behavior with an average tensile strength of 63 MPa and a corresponding failure strain close to 3%. A series of uniaxial tension experiments are conducted on all lattices with relative densities ranging from 3% to 15%. A typical response of a Kelvin lattice with two relative densities (6% and 12%) is shown in Fig. 1. One notices that the response becomes nonlinear for nominal strains larger than 1%. The material stiffness is gradually decreasing and at a critical load damage initiates at some area within the domain and then instantaneously propagates through the whole specimen. The corresponding macroscopic stress drops to zero and all elastic strain energy is released. Several experiments are used to establish strength as a function of key microstructural characteristics for all lattices. Numerical models are developed that are able to capture the lattice materials' strength and are then used to examine the effect (a) topology, (b) material distribution and (c) base material behavior to the macroscopic lattice strength.

a 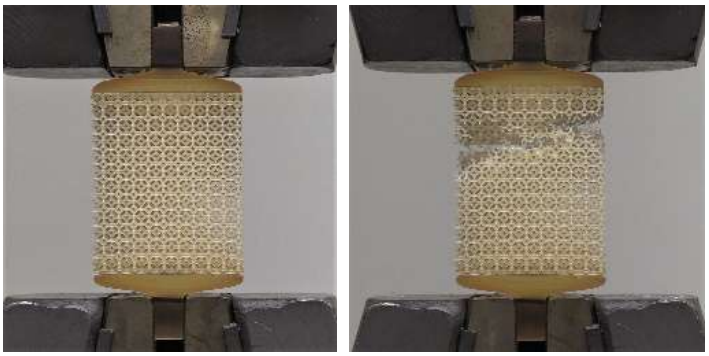 b 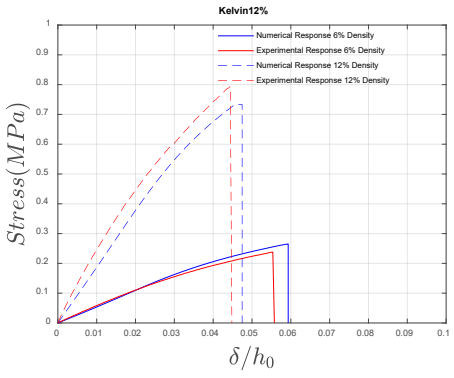

Figure 1. a) Synthesis and testing to failure of a 3D-printed Kelvin lattice with 6% relative density. Image on the right shows the fractured specimen. b) Comparison between experimental and numerical tensile responses for Kelvin lattices with 6% and 12% relative densities.

*Corresponding author. E-mail: stavrosg@jhu.edu.

ENERGY-BASED FRACTURE MECHANICS FOR LATTICES

We next consider lattices materials with pre-existing cracks and try to predict their fracture strength under macroscopic loads. In this case, the failure mechanism is greatly affected by the behavior of the lattice material around the crack region. In contrast to traditional fracture mechanics of monolithic solids, where the stress and displacement fields are described by the stress intensity factors, defining the corresponding fields in lattice materials remains an open challenge. The complex microstructure can strongly alter the stress behavior ahead of an existing crack as well as its propagation under external loads. Here we propose an energy-based method that combines modelling and theory in order to predict the critical macroscopic failure stress. For simplicity, we focus first on a 2D triangular lattice (see Fig. 2a) under mode I loading conditions and made of a perfectly-brittle material. We measure the strain energy difference $U = E_1 - E_2$ between the cracked and the intact lattice. The calculation of the elastic strain energy stored in the cracked model requires the measurement of the crack profile $\delta(x)$ (see Fig. 2b). Hence, the energy release rate $G(\sigma_0, E^*, \rho^*, \alpha) = \partial(E_1 - E_2)/\partial\alpha$ can then be formulated as a function of remote stress, lattice material properties and crack length.

The fracture energy $\Gamma = \Gamma(\sigma_f, E, \rho^*, \alpha)$ is a function of the base solid properties, the lattice microstructure and the crack length and can be measured using the energy of the broken ligaments as the crack propagates. The criterion for crack propagation corresponds to the energy release rate being equal to the fracture energy $G(\sigma_0, E^*, \rho^*, A) = \Gamma(\sigma_0, E, \rho^*, A)$. Using this equality the critical macroscopic stress $\sigma_c = \sigma_c(\sigma_f, \rho^*, \alpha)$ can then be estimated. We note here that the stiffness of the underlying solid in this case does not affect the fracture strength. The accuracy of the method is verified against numerical calculations. In the numerical model, all struts are discretized with beam elements and the crack propagates once the stress in any element ahead of the crack reaches the base material strength σ_f. Both central-crack and single-edge-notch models are examined and the results are shown in Fig. 2c. The theory seems to agree well with the simulation for a range of different densities and crack lengths. We will show that contrary to other techniques that assume an infinite lattice material [4], the current methodology remains accurate even for finite size domains. It does require however, as in the case for classical continuum fracture mechanics, an a priori knowledge of the crack propagation direction.

Finally, we use our energy-based approach to estimate the critical fracture strength of different materials and connected it to their macrostructure. We will present results from both stretching- and bending-dominated lattices under general loading conditions.

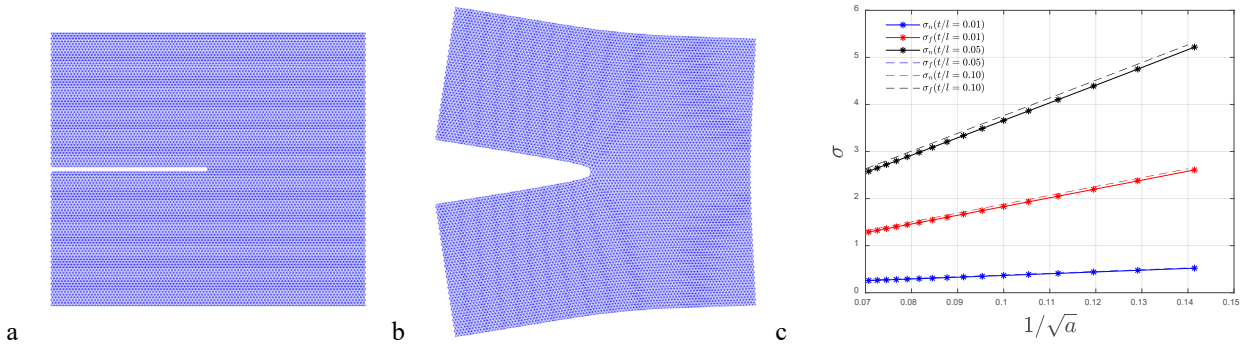

Figure 2. a) A triangular lattice with a single-edge crack. b) Deformed configuration of triangular lattice with single-edge crack under mode I loading conditions. c) Comparison between analytical and numerically estimated critical stresses under mode I for different relative densities and crack lengths.

References

[1] Gibson L.J., Ashby M.F. Cellular solids: structure and properties. Cambridge university press, 1999.
[2] Fleck N.A. and Qiu, X. The damage tolerance of elastic–brittle, two-dimensional isotropic lattices. *J. Mech Phys Slds*, 55(3), pp.562-588, 2007.
[3] Quintana-Alonso, I. and Fleck, N.A. Fracture of brittle lattice materials: A review. In Major accomplishments in composite materials and sandwich structures (pp. 799-816). Springer, Dordrecht, 2009.
[4] Lipperman, F., Ryvkin, M. and Fuchs, M.B. Nucleation of cracks in two-dimensional periodic cellular materials. *Computational Mechanics*, 39(2), pp.127-139, 2007.

A PHASE FIELD FRACTURE MODEL FOR POROUS ROCKS

Ralf Denzer*[1] and Alex Spetz [2]
[1]Division of Solid Mechanics, Lund University, Lund, Sweden
[2]Department of Construction Science, Geotechnical Engineering, Lund University, Lund, Sweden

Summary In this contribution, we present a modified phase-field model for simulating the evolution of mixed mode fractures and compression bands in porous rocks and the comparison to experimental results. For the purpose of validation, the behaviour of samples of artificial rock, with either a single or double saw cuts, under uniaxial plane strain compression has been numerically simulated. The simulated results are compared to experimental data, both qualitatively and quantitatively. It is shown that the proposed model is able to capture the commonly observed propagation pattern of wing cracks emergence followed by secondary compaction bands driven by compressive stresses. Additionally, the typical types of complex crack patterns observed in experimental tests are successfully reproduced, as well as the critical loads.

INTRODUCTION

Numerical phase-field fracture models have the appealing numerical property that a crack can propagate at least in principle arbitrarily through a mesh without being restricted to mesh lines, e.g. when using cohesive zone interface elements, or using enrichment techniques in cracked elements such as the extended finite element method. In phase-field fracture models, a crack is indicated by a scalar order parameter, which is coupled to the material properties in order to model the change in stiffness between broken and undamaged material.

Quasi-static brittle fracture mechanics can be formulated in a variational setting [2]. A numerical implementation of the regularized approximation of the variational formulation was first described in [1]. In [4] the interpretation of the phase-field parameter in the context of a gradient damage model was presented. The phase-field fracture model has since been extended in a number of directions, e.g., including dynamic fracture, coupled thermo-mechanical-driven, high-order phase-field approaches.

However, these contributions assume that the critical energy release rate for different fracture modes are the same, which is not the case for rocks and rock like materials [7]. In fact, in rock-like materials, the critical energy release rate for Mode I and Mode II can differ significantly. In [8] a phase-field fracture model that distinguish between the critical release rates for Mode I and Mode II is proposed. Moreover, porous rocks, e.g. sandstone and volcanic rock often displays fractures in compression, referred to as compaction bands [6].

PHASE-FIELD FRACTURE MODEL FOR POROUS ROCKS

Following [3], the phase-field fracture model is characterised by a coupled set of local equations,

$$\mathbf{0} = \mathrm{div}\boldsymbol{\sigma} + \boldsymbol{f} \tag{1}$$

$$0 = \frac{\dot{d}}{M\mathcal{G}_c} + 2d[1-\eta]\frac{\mathcal{H}}{\mathcal{G}_c} + \frac{1}{2\ell_0}[d-1] + 2\ell_0\Delta d \tag{2}$$

where $\mathcal{G}_c$ is the critical energy release rate, $\mathcal{H}$ represents the crack driving part of the elastic energy density and the kinetic coefficient or mobility parameter M is a non-negative scalar function $M = M(\boldsymbol{\varepsilon}, d, \nabla d, \dot{d})$ introduced to control the crack velocity. The most simple assumption, $M =$ constant lead to the standard Ginzburg-Landau evolution equation.

To take different critical energy release rates for Mode I and Mode II as well as formation of compaction bands into account we propose a generalisation to the ratio $\frac{\mathcal{H}}{\mathcal{G}_c}$ in the evolution equation (2) to

$$\frac{\mathcal{H}}{\mathcal{G}_c} = \frac{\mathcal{H}_I^+}{\mathcal{G}_{cI}} + \frac{\mathcal{H}_{II}^+}{\mathcal{G}_{cII}} + \frac{\mathcal{H}^-}{\mathcal{G}_{band}} \tag{3}$$

with $\mathcal{H}_I^+ = \frac{1}{2}K\langle \mathrm{tr}[\boldsymbol{\varepsilon}]\rangle^2 H(\mathrm{tr}[\boldsymbol{\varepsilon}])$, $\mathcal{H}_{II}^+ = \mu \mathrm{tr}[(\boldsymbol{\varepsilon}_d^+)^2]H(\mathrm{tr}[\boldsymbol{\varepsilon}])$ and $\mathcal{H}^- = \frac{1}{2}K[\mathrm{tr}[\boldsymbol{\varepsilon}] - \langle \mathrm{tr}[\boldsymbol{\varepsilon}]\rangle]^2 + \mu \mathrm{tr}[(\boldsymbol{\varepsilon}_d^-)^2][1 - H(\mathrm{tr}[\boldsymbol{\varepsilon}])]$. Where the parameters $\mathcal{G}_{cI}$, $\mathcal{G}_{cII}$ are the critical energy release rates for Mode I and Mode II respectively and $\mathcal{G}_{band}$ the energy release rate for compaction bands forming due to compressive stresses. H is the Heavyside function and ε_d is the deviatoric part of the linearized strain tensor. the definition of $\varepsilon^{\pm}$ are given in [3].

The spatial discretisation of the weak forms of eqn. 1 and 2 is performed by means of the Galerkin method, using C^1-continuous NURBS basis functions as the finite dimensional approximations to the function spaces. We utilise a staggered scheme to solve the displacements and phase-field separately. The staggered approach allows for robust solution of the incremental update of both the displacement and phase fields. An implicit Euler backward method is used for the numerical time integration of the evolution equation of the phase-field parameter d.

*Corresponding author. E-mail: ralf.denzer@solid.lth.se

NUMERICAL RESULTS

As an example we study an rectangular sample made out of an artificial porous rock under uniaxial compressive load under plane strain conditions. Figure 1a)-c), see [5], depicts evolution of the crack pattern. Note, that the sample has an initial saw cut inclined under 45°, indicated by the blue line in the pictures. In comparison we show in Figure 1d)-f) the evolution of the phase-field parameter d from the numerical simulation for the corresponding load states. We observe a very good agreement of the simulated crack patterns and the experimentally observed ones.

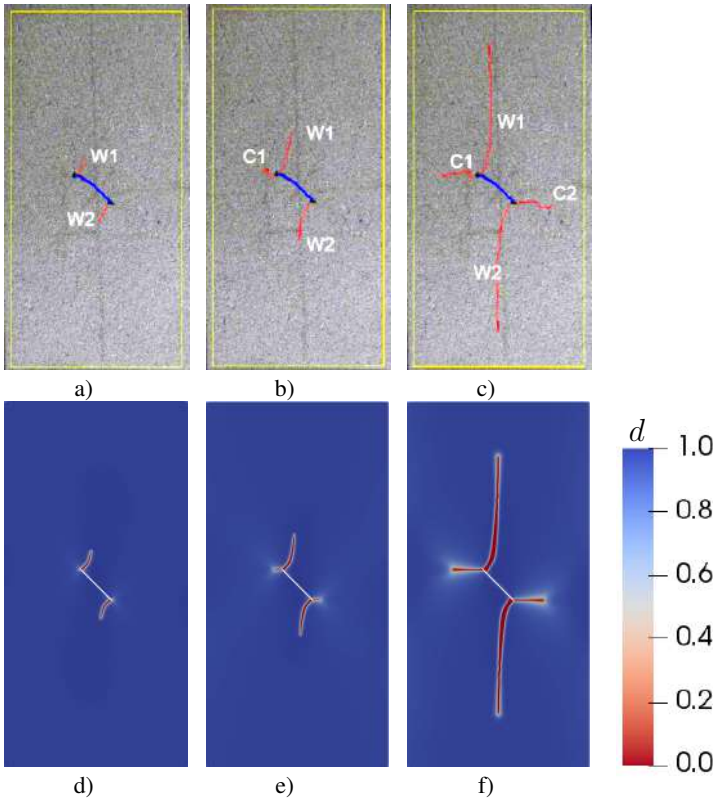

Figure 1: Comparison of experimental results a)-c) of the crack pattern at and d)-f) the phase-field parameter from the numerical simulation for the corresponding load states.

In our contribution we will discuss more details of the proposed phase-field fracture model, show further numerical results for samples with two saw cut and also Meuwissen samples having two U-notches with an vertical offset. Additionally, we discuss also the quantitative comparison between simulated and experimental load-deflection curves.

References

[1] B. Bourdin. Numerical implementation of the variational formulation for quasi-static brittle fracture. *Interfaces and Free Boundaries*, 9(3):411–430, 2007.

[2] G. A. Francfort and J.-J. Marigo. Revisiting brittle fracture as an energy minimization problem. *Journal of the Mechanics and Physics of Solids*, 46(8):1319–1342, 1998.

[3] C. Miehe, M. Hofacker, and F. Welschinger. A phase field model for rate-independent crack propagation: Robust algorithmic implementation based on operator splits. *Computer Methods in Applied Mechanics and Engineering*, 199(45-48):2765–2778, 2010.

[4] C. Miehe, F. Welschinger, and M. Hofacker. Thermodynamically consistent phase-field models of fracture: Variational principles and multi-field FE implementations. *International Journal for Numerical Methods in Engineering*, 83(10):1273–1311, 2010.

[5] T. L. Nguyen. *Endommagement localisé dans les roches tendres. Expérimentation par mesure de champs*. PhD thesis, Université de Grenoble, 2011.

[6] J. W. Rudnicki. Compaction bands in porous rock. In J. F. Labuz and A. Drescher, editors, *Bifurcations and Instabilities in Geomechanics*, pages 29–39. CRC Press, June 2003.

[7] B. Shen and O. Stephansson. Modification of the G-criterion for crack propagation subjected to compression. *Engineering Fracture Mechanics*, 47(2):177–189, 1994.

[8] X. Zhang, S. W. Sloan, C. Vignes, and D. Sheng. A modification of the phase-field model for mixed mode crack propagation in rock-like materials. *Computer Methods in Applied Mechanics and Engineering*, 322:123–136, 2017.

LATTICE TRAPPING AND FRACTURE TOUGHESS SELECTION IN BRITTLE CRYSTALS

Daniel Bonamy[1] and Thuy Nguyen[1,2]
[1]Université Paris-Saclay, CNRS, CEA, SPEC, 91191, Gif-sur-Yvette, France
[2]Université Paris-Seine, EISTI, Avenue du Parc, 95000 Cergy Pontoise Cedex, France

Summary Predicting the resistance-to-failure from the solid structure at the atomistic scale remains unsolved, even in the simplest situations of perfectly brittle fracture. By examining numerically crack growth in electrical analogues of brittle crystals, we shed a new light on this question: Fracture toughness is found to be significantly higher than expected from Griffith's relationship between fracture and specific surface energy. This discrepancy finds its origin in the matching between the continuum displacement field at the engineering scale and the discrete lattice of solids at the atomic scale. We will show how to use the specific asymptotic form taken by this field near crack tip to infer this matching, and subsequently to predict toughness from the atomistic parameters. The implications will be discussed.

INTRODUCTION

Predicting when rupture occurs is central to many industrial, societal and geophysical fields. For brittle solids under tension, the problem reduces to the destabilization of a pre-existing crack. Material's resistance-to-failure is then defined by two dependent material constants (one is proportional to the square of the other): fracture energy and fracture toughness. Nowadays, there exists well-established standard test methods allowing the accurate experimental determination of these material constants. Conversely, their relation with the atomistic parameters of the considered solid remains unsolved, even in perfectly brittle situations where fracture occurs via successive bond breaking, without involving further elements of dissipation. The cornerstone in this context was provided by Griffith [1], which identifies the fracture energy with the free surface energy (energy of the chemical bonds crossed by a fracture surface of unit area). Unfortunately, this conjecture does not fit with the observations: Fracture energy is always measured to be anomalously high, even in perfectly brittle crystals (silicon or mica for instance, see. e.g. [2]). The study reported here aimed at uncovering the origin of this discrepancy.

METHOD & RESULTS TO BE PRESENTED

We examined numerically how crack propagates in a two-dimensional lattice of fuses arranged periodically (triangular, square or honeycomb geometry, see e.g. figure 1A). Such model digital materials, indeed, (i) possess fully prescribed and tuneable "atomic bonds"; (ii) break in a perfectly brittle manner, by the successive breakdown of fuses, and (iii) satisfy isotropic linear elasticity under antiplane deformation at the continuum scale [3]. Fracture energy was determined in these digital materials and, as in real elastic solids, it was found to be significantly larger than Griffith specific surface energy, by a factor depending on the lattice geometry.

To understand the origin of this discrepancy, we looked at the spatial distribution of the displacements within the digital materials (Figure 1B). At the continuum-level scale, the displacement field displays a mathematical singularity at the crack tip. As such, it takes a generic asymptotic form [4], referred to as Williams' series expansion. The difficulty is to position the singularity origin properly in the discrete lattice at the atomic scale. As an illustration, placing it at the center of the next bond to break (O_{guess} in figure 1A) makes the Williams's series expansion describe the measured field fairly well, except in the very vicinity of the crack tip [figure 1C]. Unfortunately, this near-tip zone is precisely the one setting whether or not the next bond breaks!

However, as we will see in the presentation, it is possible to make use of the Williams' form taken by the displacement field near crack tip to infer accurately the singularity positioning in the discrete lattice, and then to predict fracture toughness from the atomistic parameters [5]. It is then possible to derive an analytical method to predict fracture toughness and fracture energy in our digital materials and the obtained values coincide exactly to those obtained numerically. We will discuss how to extend the analysis to genuine elastic (plane stress) crack problems and predict toughness in 2D and 3D materials. Implication will be finally discussed.

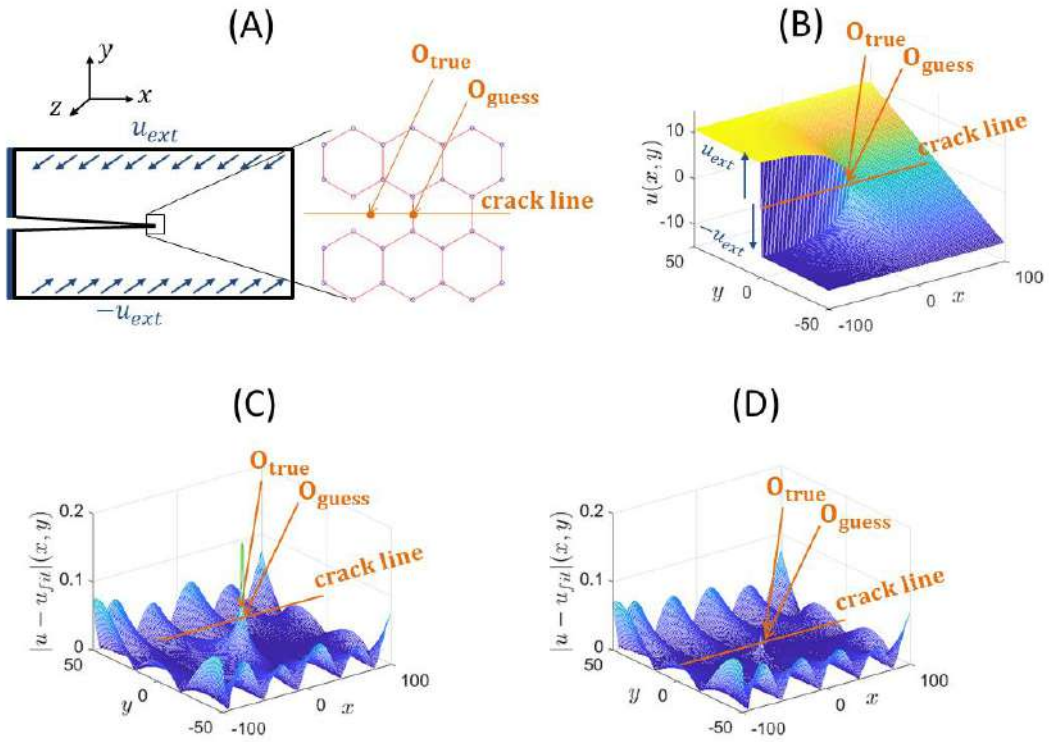

Figure 1, panel A: Sketch and notation: A crack is introduced into a two-dimensional electric crystal (here honeycomb lattice). The crack is parallel to x-axis, lies in the middle of the crystal ($y3 = 30$) and stops in the center. The cracked crystal is loaded by imposing a constant potential u_{ext} (opposite signs) to the left/ top and left/bottom edges. Panel B: measured displacement field. This should obey Williams asymptotic singular form. The difficulty is to place the singularity properly in the discrete lattice. Panel C: Absolute difference between the displacement field $u(x,y)$ measured in panel B and Williams asymptotic form, $u_{fit}(x,y)$ obtained after having placed the singularity at the center of the next bond to break (O_{guess} in panel A). The fit is very good everywhere, except in the vicinity of the crack tip. Panel D: $|u_{fit} - u(x,y)|$ after having corrected the singularity position (now at O_{true} in panel A). The fit is now good everywhere, including in the very vicinity of the crack tip.

References

[1] A. A. Griffith, The phenomena of rupture and flow in solids, *Phil. Trans. R. Soc. A* **221**, 163 (1921).
[2] R. Pérez and P. Gumbsch, Directional Anisotropy in the Cleavage Fracture of Silicon, *Phys. Rev. Lett.* **84**, 5347 (2000)
[3] M. J. Alava, P. K. V. V. Nukala, and S. Zapperi, Statistical models of fracture, *Adv. Phys*. **55**, 349 (2006).
[4] M. L. Williams, Stress singularities resulting from various boundary conditions in angular corners of plates in extension, *J. Appl. Mech*. **19**, 526 (1952).
[5] T. Nguyen and D. Bonamy, Role of the Crystal Lattice Structure in Predicting Fracture Toughness, *Phys. Rev. Lett*. **123**, 205503 (2019).

A PERIDYNAMIC FRAMEWORK FOR SIMULATING DUCTILE FRACTURE

Masoud Behzadinasab*[1], John T. Foster[2], and Yuri Bazilevs[1]
[1]School of Engineering, Brown University, 184 Hope St., Providence, RI 02912, USA
[2]Hildebrand Department of Petroleum & Geosystems Engineering, The University of Texas at Austin, 200 E. Dean Keeton St., Austin, TX 78712, USA

Summary A semi-Lagrangian constitutive correspondence framework has been recently developed for peridynamics as a remedy for shortcomings of the theory in modeling large deformation. In the new formulation, peridynamic material point interactions depend only on the current properties in the deformed configuration. A bond-associated approach is introduced, which enhances stability and enables localization of damage. We show that the new model is more reliable in simulating ductile fracture, through a Sandia Fracture Challenge study. A novel, convenient approach for incorporating natural boundary conditions in peridynamics is also presented. Application of the new framework to other extreme events (e.g. air-blast simulation) is discussed.

PERIDYNAMIC MODELING OF DUCTILE FRACTURE

Prediction of ductile fracture, which is a prevalent failure mode in most engineering structures, is vital to numerous industries. Despite significant advancements in fracture mechanics, ductile fracture modeling has remained a challenging task and a continuing area of research. Peridynamics [1, 2], a nonlocal theory based on integration instead of partial differentiation, has attracted broad interest in recent years, mostly for its natural capabilities in handling material discontinuity (e.g. cracks). While peridynamics has been largely utilized to simulate cracking events in brittle materials, its ability in predicting ductile failure remains unclear.

An investigation into the capabilities of peridynamics in simulating ductile fracture in metallic alloys was recently conducted [3]. The third Sandia Fracture Challenge (SFC3) [4], as a true blind prediction challenge, was employed in the examination, where the state of the art of peridynamic modeling of ductile fracture was implemented to predict deformations and failure of an additively manufactured metal, with a complex geometry, under the dynamic tensile experiments performed by Sandia National Laboratories. While the peridynamic approach led to qualitatively good results, it underpredicted the load-carrying capacity of the structure and simulated an early fracture. Post-experiment analysis identified the main sources of error to be (1) material instabilities associated with the finite deformation peridynamic model [5] and (2) unreliability of a Lagrangian peridynamic framework in solving large distortion problems.

A bond-associated, semi-Lagrangian, constitutive correspondence model

Due to the involvement of a mapping between the deformed and reference configurations, the Lagrangian framework (which is the foundation of most previous developments of peridynamics) can become unsuitable under extremely large deformations, i.e., the Lagrangian kinematic variables (e.g. the peridynamic deformation gradient [2]) become non-physical (e.g. have non-positive determinants). With the motivation of simulating extreme events, a semi-Lagrangian constitutive correspondence framework for peridynamics has been recently developed [6]. In the semi-Lagrangian theory, while the material points are still tracked in motion (the Lagrangian view), an updated kernel is used to determine the degree of interactions between material points (the Eulerian view).

The local balance of linear momentum in the semi-Lagrangian model is given by

$$\rho \frac{\mathrm{D}\dot{\mathbf{x}}}{\mathrm{D}t} = \int_{\mathcal{H}(\mathbf{x})} \left[\underline{\mathbf{t}}(\mathbf{x})\langle \boldsymbol{\eta} \rangle - \underline{\mathbf{t}}(\mathbf{x}+\boldsymbol{\eta})\langle -\boldsymbol{\eta} \rangle\right] \mathrm{d}\boldsymbol{\eta} + \rho \mathbf{b}, \tag{1}$$

in which $\mathbf{x}$ is a material point in the current domain of peridynamic body $\mathcal{B}$ with density ρ. $\mathbf{b}$ is an applied body force density field. $\mathcal{H}(\mathbf{x})$ is the neighbor set of $\mathbf{x}$, defined in the deformed configuration, i.e.,

$$\mathcal{H}(\mathbf{x}) = \{\mathbf{x}+\boldsymbol{\eta} \mid \mathbf{x}+\boldsymbol{\eta} \in \mathcal{B},\, 0 < |\boldsymbol{\eta}| \leq \delta\}\,. \tag{2}$$

$\boldsymbol{\eta}$ denotes a peridynamic *bond* in the current domain, and δ is called the *horizon*. $\underline{\mathbf{t}}$ is the force vector state operating in the deformed frame, analogous to the Cauchy stress. Following an energy balance analysis [6]

$$\dot{\mathrm{u}}(\mathbf{x}) = \int_{\mathcal{H}(\mathbf{x})} \underline{\mathbf{t}}(\mathbf{x})\langle \boldsymbol{\eta} \rangle \cdot \dot{\boldsymbol{\eta}}\, \mathrm{d}\boldsymbol{\eta}, \tag{3}$$

where u is the strain energy density function. The classical (local) theory postulates that the strain power density is the power conjugate of the velocity gradient and Cauchy stress tensors. A bond-associated velocity gradient is given by

$$\underline{\mathbf{L}}(\mathbf{x})\langle \boldsymbol{\eta} \rangle = \frac{\bar{\mathbf{L}}(\mathbf{x}) + \bar{\mathbf{L}}(\mathbf{x}+\boldsymbol{\eta})}{2} + \left(\dot{\boldsymbol{\eta}} - \frac{\bar{\mathbf{L}}(\mathbf{x}) + \bar{\mathbf{L}}(\mathbf{x}+\boldsymbol{\eta})}{2} \cdot \boldsymbol{\eta}\right) \otimes \frac{\boldsymbol{\eta}}{|\boldsymbol{\eta}|^2}, \tag{4}$$

*Corresponding author. E-mail: masoud_behzadinasab@brown.edu.

which maps a bond (vector) to a velocity gradient (tensor). $\bar{\mathbf{L}}(\mathbf{x})$ is the nodal velocity gradient at $\mathbf{x}$ that accounts for the collective deformation of the neighborhood, i.e.,

$$\bar{\mathbf{L}}(\mathbf{x}) = \left(\int_{\mathcal{H}(\mathbf{x})} \underline{\omega}\langle \boldsymbol{\eta} \rangle \, \dot{\boldsymbol{\eta}} \otimes \boldsymbol{\eta} \, \mathrm{d}\boldsymbol{\eta} \right) \mathbf{M}^{-1}(\mathbf{x}), \quad \mathbf{M}(\mathbf{x}) = \int_{\mathcal{H}(\mathbf{x})} \underline{\omega}\langle \boldsymbol{\eta} \rangle \, \boldsymbol{\eta} \otimes \boldsymbol{\eta} \, \mathrm{d}\boldsymbol{\eta}. \tag{5}$$

$\underline{\mathbf{L}}$ is used as an intermediate kinematic variable in determining the (bond-associated) Cauchy stress (using local theories) and evaluating the force state [6]. A bond-associated damage correspondence framework is also developed in [6] by incorporating local fracture models using the bond-associated properties (i.e., deformation, stress, strain, etc.), which enables the modeler to localize failure and avoids loss of a finite amount of material in numerical simulations.

REVISITING SANDIA FRACTURE CHALLENGE 2017

The bond-associated, semi-Lagrangian formulation is employed to revisit SFC3. To effectively assess the applicability of the new theory to modeling large deformation and ductile fracture (in the context of SFC3), minimal changes to the initial attempt in solving the challenge problem were made. Therefore, only the material and damage models were adopted using the new framework. To achieve a blind-prediction setting, experimental data from the challenge main objective is masked during the model calibration. Fig. 1 compares the simulation results with the experiments. The correct crack path is resulted from the simulation. The new model significantly improves the load-displacement predictions of the structure, in addition to a better capturing of the crack propagation speed.

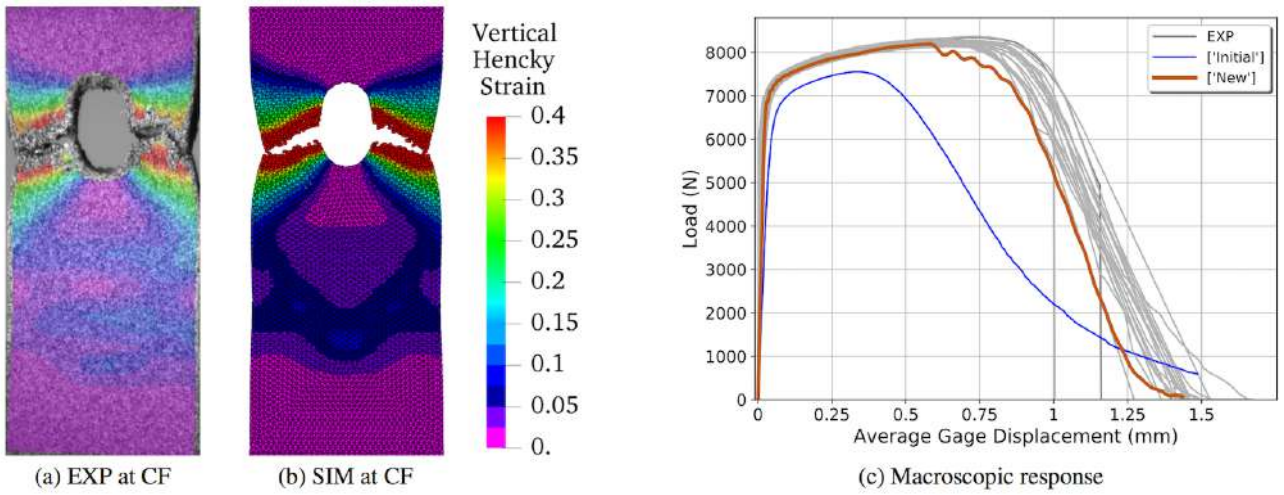

(a) EXP at CF (b) SIM at CF (c) Macroscopic response

Figure 1: Vertical Hencky strains compared between the experimental DIC measurements (EXP) and the new simulations (SIM) at complete failure (CF) (a–b). The new approach has significantly improved the bulk response predictions (c).

ADDITIONAL DISCUSSIONS

We introduce a novel approach for incorporating natural boundary conditions within peridynamics (both Lagrangian and semi-Lagrangian models). The proposed method would be helpful in local-nonlocal coupling to conveniently model traction/stress conditions on boundaries/interfaces. We also present applications of the semi-Lagrangian formulation to other extreme events, such as air-blast-structure interactions (ABSI), using an immersed isogeometric-peridynamic framework for ABSI modeling.

References

[1] Silling S. Reformulation of elasticity theory for discontinuities and long-range forces. *J. Mech. Phys. Solids* **48**(1): 175–209, 2000.
[2] Silling S. Peridynamic states and constitutive modeling. *J. Elasticity* **88**(2): 151–184, 2007.
[3] Behzadinasab M., Foster J. T. The third Sandia Fracture Challenge: peridynamic blind prediction of ductile fracture characterization in additively manufactured metal. *Int. J. Fract.* **218**: 97–109, 2019.
[4] Kramer S. L. B., *et al.* The third Sandia Fracture Challenge: predictions of ductile fracture in additively manufactured metal. *Int. J. Fract.* **218**: 5–61, 2019.
[5] Behzadinasab M., Foster J. T. On the stability of the generalized, finite deformation correspondence model of peridynamics. *Int. J. Solids. Struct.* **182**: 64–76, 2020.
[6] Behzadinasab M., Foster J. T. A semi-Lagrangian, constitutive correspondence framework for peridynamics. *J. Mech. Phys. Solids* 103862, 2020.

A PHASE-FIELD MODEL FOR FATIGUE CRACK GROWTH AND LIFETIME ESTIMATION

Md Mehedi Hasan and Theocharis Baxevanis*
Department of Mechanical Engineering, University of Houston, USA

Summary A phenomenological, phase-field, continuum model for lifetime estimation and fatigue crack formation and growth in brittle materials is proposed. Additionally to the classical elastic stiffness degradation in the phase-field approach to overload fracture, a fracture toughness degradation through a suitably defined fatigue history variable is introduced. The model's ability to estimate the lifetime of smooth specimen under uniaxial constant cycling loading, *i.e.*, to predict Wöhler curves and 1D critical plane models, such as the Smith-Watson-Topper parameter, as well as to reproduce the Paris law with exponents characteristic of brittle fatigue crack growth is demonstrated. The numerical implementation of the model in a staggered scheme is described and its ability to handle complex geometries and loading conditions demonstrated.

INTRODUCTION

In the phase-field approach to fracture, also known as variational approach to fracture, proposed in the pioneering works of Francfort and Marigo [1] and Bourdin et al [2], the solution to the fracture problem is found as the minimizer of a global energy functional that includes a surface term associated with the energy required to create a unit area of fracture surface. The major advantage of the phase-field approach over the complexity of discrete fracture models stems from the regularization of the sharp crack surface topology by a diffusive crack zone governed by a scalar auxiliary variable, a phase field, which interpolates between the unbroken and the broken state of the material. An alternative to the aforementioned formal and mathematically demanding formulation, based on continuum mechanics and thermodynamic arguments, was presented by Miehe et al [3, 4]. The proposed work builds on a growing body of recent phase-field approaches to fatigue of brittle materials that aim at linking regularized overload fracture to fatigue crack growth [5, 6] based on a proposed degradation of the surface term associated with the energy required to create a unit area of fracture surface, *i.e.*, the fracture toughness, through a suitably defined fatigue history variable.

PHASE-FIELD MODEL FOR FATIGUE

The proposed phase-field model for fatigue is derived for isothermal quasistatic proccesses, *i.e.*, neglecting inertia, wave propagation, and thermal effects, under the small-strain assumption. The model formulation is based on postulating a microforce balance. The resulted strong-form, boundary-value problem of the constitutive response reads as

Mechanical Equilibrium. –

$$\nabla \cdot \boldsymbol{\sigma} = 0, \tag{1}$$

Microforce Balance. –

$$\frac{2\mathcal{G}_c^0 \ell}{\rho} \nabla \cdot \nabla c = g'(c)\mathcal{H}\left[1 + a(\tilde{\mathcal{H}} - \mathcal{H})^b\right] + \frac{\mathcal{G}_c^0}{2\ell} c, \tag{2}$$

Constitutive equation. –

$$\boldsymbol{\sigma} = g(c)\left[\lambda\langle \mathrm{tr}\,\boldsymbol{\varepsilon}\rangle \boldsymbol{\delta} + 2\mu\boldsymbol{\varepsilon}^+\right] + \left[\lambda\left(\mathrm{tr}\,\boldsymbol{\varepsilon} - \langle \mathrm{tr}\,\boldsymbol{\varepsilon}\rangle\right)\boldsymbol{\delta} + 2\mu\boldsymbol{\varepsilon}^-\right]. \tag{3}$$

with appropriate boundary conditions that are omitted here due to space limitations.

In the above, $\boldsymbol{\sigma}$ stands for the stress tensor, $\boldsymbol{\varepsilon}$ for the strain tensor, c is the phase field variable, $\ell > 0$ is a model length parameter that controls the width of the smooth approximation of the cracks, $\mathcal{G}_c^0$ stands for the fracture toughness of the material in its reference state, $W^+ = \frac{1}{2}\lambda\langle \mathrm{tr}\,\varepsilon\rangle^2 + \mu \mathrm{tr}\left[(\varepsilon^+)^2\right]$ and $W^- = \frac{1}{2}\lambda\left(\mathrm{tr}\,\varepsilon - \langle \mathrm{tr}\,\varepsilon\rangle\right)^2 + \mu \mathrm{tr}\left[(\varepsilon - \varepsilon^+)^2\right]$ are the strain energies computed from the positive and negative components of the strain tensor defined through its spectral decomposition [3, 4], λ and μ are the Lamé constants, $\mathcal{H}$ satisfies the Kuhn-Tucker conditions for loading and unloading

$$W^+ - \mathcal{H} \leq 0, \quad \dot{\mathcal{H}} \geq 0, \quad \dot{\mathcal{H}}\left(W^+ - \mathcal{H}\right) = 0, \tag{4}$$

$\tilde{\mathcal{H}}$ is an accumulated strain energy history functional, which evolves only for increasing driving force, $\dot{W}^+ > 0$, and for $W^+ > W_e^+$, where W_e^+ is the endurance limit, *i.e.*, the lowest energetic barrier again fatigue damage,

$$\dot{\tilde{\mathcal{H}}} = H\left(W^+ - W_e^+\right)\langle \dot{W}^+ \rangle, \tag{5}$$

$H(x)$ is the Heaviside function, $\boldsymbol{\delta}$ is the Kronecker's delta, $g(c) = (1-c)^2$and a and b are positive material constants that should be calibrated by appropriate experimental data.

RESULTS & DISCUSSION

*Corresponding author. E-mail: tbaxevanis@gmail.com

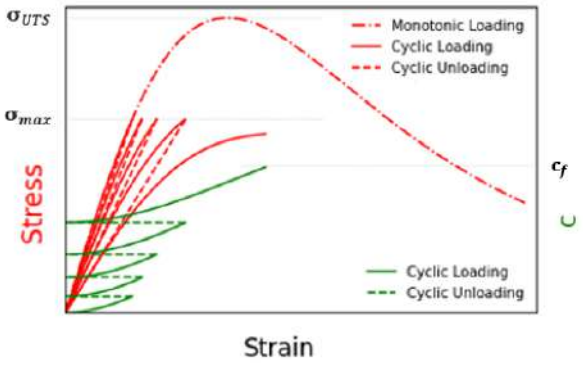

Figure 1: Stress–strain response and phase field evolution (inset) at uniaxial (constant) stress-controlled cyclic loading with maximum applied load σ_{max} and load ratio $R = 0$.

Presuming a homogeneous stress state within test specimens, the numerical model reduces essentially to a single material point and the deformation response may be tracked in closed form or with low numerical effort even for large numbers of cycles. The general response of the model under uniaxial homogeneous (constant) stress-controlled cyclic loading is shown in Figure 1. The maximum attainable traction, σ_{UTS} (ultimate tensile strength) successively reduces until it falls below the external applied load level and final failure occurs.

Experimental S–N or Wöhler curves showing stress amplitude vs. fatigue life N_f have been simulated. In Figure 2, the model estimation of lifetime for an epoxy glass composite subjected to an stress-controlled cycling of a load ratio $R = 0$ is depicted. Ignoring the endurance limit, the model reduces to the following equation

$$\frac{\sigma_{max}^2}{2E} + a(N_f - 1)^b \left(\frac{\sigma_{max}^2}{2E}\right)^{b+1} = -\frac{\mathcal{G}_c^0}{2\ell g'(c_f)} c_f \tag{6}$$

where N_f is the number of cycles at failure, and c_f and σ_{max} (the latter being the experimental maximum applied stress level) correspond to the values of c and the stress, respectively, obtained at $\partial\sigma/\partial\varepsilon = 0$, *i.e.*, σ_{max} equals the maximum attainable traction at N_f and c_f is the corresponding value of the phase field parameter. A least square fit is then performed over the experimental data that allows for the calibration of the model parameters $a = 0.0017$ and $b = 3.545$.

The efficiency of the numerical implementation of the model is verified by crack growth simulations in complex geometries and loading conditions. The fatigue crack growth path in a Compact Tension (CT) specimen with a hole in the vicinity of the initial crack tip subjected to cyclic tensile loading is shown in Figure 3. Isotropy and plane strain conditions are assumed and a sufficiently fine mesh is used to resolve the process zone properly. The model predicts crack turning observed in experiments recently performed in aluminum alloy AL2024-T351 [7].

Moreover, a systematic analysis of the mean load effect and load sequence on the uniaxial fatigue life prediction as well as of the correlation between the model parameters and the global fatigue crack growth characteristics (Paris law) is performed. The model calibration for the latter case is discussed and the physical meaning of the parameter ℓ in both the uniaxial lifetime and crack growth cases is explored.

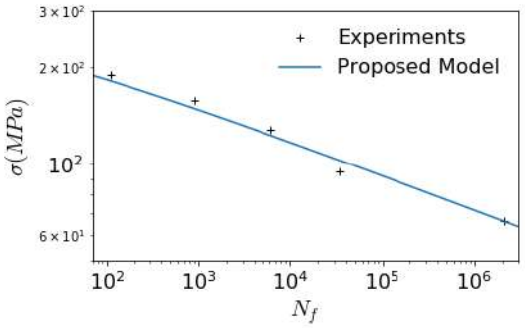

Figure 2: Model predictions vs experimental lifetime for an epoxy glass composite subjected to an $R = 0$ stress-controlled cycling.

Figure 3: Phase field simulations showing the path of fatigue crack growth in a CT specimen with a hole in the vicinity of the initial crack tip subjected to cyclic tensile loading.

References

[1] Francfort, G., Marigo, J.J., 1998. Revisiting brittle fracture as an energy minimization problem. J. Mech. Phys. Solids 46, 1319-1342.
[2] Bourdin, B., Francfort, G., Marigo, J.J., 2000. Numerical experiments in revisited brittle fracture. J. Mech. Phys. Solids 48, 797-826.
[3] Miehe, C., Hofacker, M., Welschinger, F., 2010a. A phase-field model for rate-independent crack propagation: Robust algorithmic implementation based on operator splits. Comp. Methods Appl. Mech. Engng. 199, 2765-2778.
[4] Miehe, C., Welschinger, F., Hofacker, M., 2010b. Thermodynamically consistent phase-field models of fracture: Variational principles and multi-field FE implementations. Int. J. Num. Methods Engng. 83, 1273-1311.
[5] Carrara, P., Ambati, M., Alessi, R., De Lorenzis, L., 2019. A novel framework to model the fatigue behavior of brittle materials based on a variational phase-field approach. arXiv:1811.02244 [cond-mat].
[6] Mesgarnejad, A., Imanian, A., Karma, A., 2019. Phase-field models for fatigue crack growth. arXiv:1901.00757 [cond- mat].
[7] Lo, Y-C., and Borden, J.M., Ravi-Chandar, K., Landis, C.M., 2019. A phase-field model for fatigue crack growth. J. Mech. Phys. Solids 132, 103684.

FAILURE CRITERIA FOR INTERFACE CRACKS

Leslie Banks-Sills*
Dreszer Fracture Mechanics Laboratory, School of Mechanical Engineering,Tel Aviv University, Ramat Aviv, Israel

Summary A crack along an interface between two dissimilar linear elastic, homogeneous and isotropic materials is considered. Failure criteria for this case have been presented in the literature. Criteria have been based upon the stress intensity factors K_1 and K_2 or the interface energy release rate $\mathcal{G}_i$ together with a mode mixity phase angle ψ. Thus, two parameters are required to predict failure. Several criteria will be presented. The parameter $\mathcal{G}_i$ is an invariant and does not depend on a length scale; the parameter ψ does depend upon a length scale. Recently, a second invariant parameter L_1 has been defined. This investigation will examine use of the the two invariant parameters in a failure criterion.

INTRODUCTION

Interface fracture mechanics is a well established discipline. The failure of an interface is treated here. Results from an interface crack between glass and epoxy were considered. Tests were carried out on this material pair and presented in [1]. The results from the tests were reanalyzed and given in [2]. These results were used here to examine two failure criteria.

Various failure criteria were presented in [3, 4]. The best criterion for this data, as well as for an interface crack between two ceramic clays [5] is given by

$$\mathcal{G}_{ic} = \overline{\mathcal{G}}_{1c}\left(1+\tan^2\hat{\psi}\right) \ . \tag{1}$$

In eq. (1), $\mathcal{G}_{ic}$ and $\overline{\mathcal{G}}_{1c}$ are the critical interface and mode 1 energy release rates, respectively; the phase angle $\hat{\psi}$ is

$$\hat{\psi} = \tan^{-1}\left(\frac{\hat{K}_2}{\hat{K}_1}\right) \tag{2}$$

where

$$\hat{K} = K\hat{L}^{i\varepsilon}. \tag{3}$$

In eq. (3), the complex stress intensity factor

$$K = K_1 + iK_2 \tag{4}$$

where K_1 and K_2 are real and are the modes 1 and 2 stress intensity factors and $i=\sqrt{-1}$; $\hat{L}$ is a length scale which is used to fit the failure data to the failure curve and ε is the oscillatory parameter and related to the mechanical properties of the two materials on either side of the interface. In eq. (1),

$$\overline{\mathcal{G}}_{1c} = \text{avg}\left(\frac{\hat{K}_1^2}{H}\right) \tag{5}$$

where avg is the average of the quantity in parentheses, values of $\hat{K}_1$ are calculated from eq. (3) for each specimen and H is related to the mechanical parameters of the materials. It should be emphasized that choosing $\hat{L}$ properly leads to a good fit between the failure curve in eq. (1) and the failure data. The failure criterion in eq. (1) was also found to fit the data for a carbon/epoxy laminate with an interface between two plies, one with fibers in the $0°$- direction and the other with fibers in the $90°$- direction [6].

In [7], invariant parameters which do not depend on $\hat{L}$ were presented. The interface energy release rate given by

$$\mathcal{G}_i = \frac{1}{H}\left(K_1^2+K_2^2\right) = \frac{1}{H}\left(\hat{K}_1^2+\hat{K}_2^2\right) \tag{6}$$

is known to be an invariant. A second, new invariant is defined as

$$L_1 = \hat{L}\exp\left(-\frac{\hat{\psi}}{\varepsilon}\right) \ . \tag{7}$$

It turns out that the combination of $\hat{L}$ and $\hat{\psi}$ in eq. (7) causes L_1 to be independent of $\hat{L}$.

In the next section, the criterion in eq. (1) and a criterion related to the parameter L_1 will be presented for a crack along the interface between glass and epoxy. Conclusions are made in the last section.

*Corresponding author. E-mail: banks@tau.ac.il

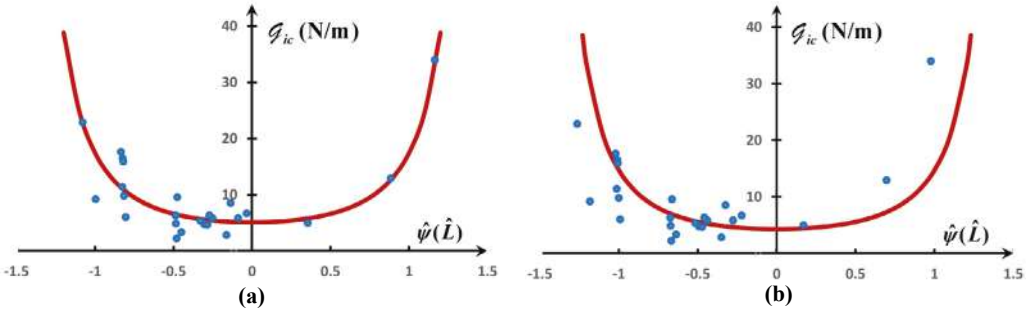

Figure 1: Failure curves for glass/epoxy interface using eq. (1) with (a) $\hat{L} = 1.2$ mm and (b) $\hat{L} = 10$ mm.

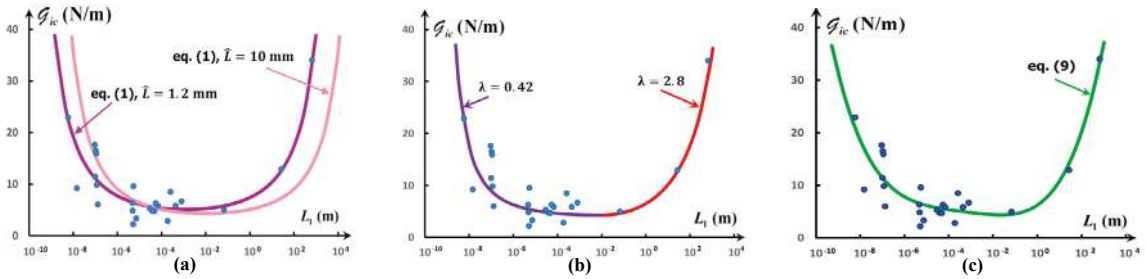

Figure 2: Failure curves for glass/epoxy interface using the invariants in eqs. (6) and (7). The data and failure curves from (a) eqs. (1), (b) (8) and (c) (9).

FAILURE CRITERIA FOR GLASS/EPOXY

Tests on Brazilian disk specimens fabricated from glass and epoxy were presented in [1]. The data presented here was taken from [2] where analyses were improved. For the glass/epoxy pair considered here, the oscillatory parameter is $\varepsilon = -0.0881$ and the modulus $H = 6.56$ GPa. By choosing $\hat{L} = 1.2$ mm, the failure curve in eq. (1) fits the data well as shown in Fig. 1a. Note that $\mathcal{G}_{1c} = 5.09$ N/m. If $\hat{L} = 10$ mm, then the failure curve does not fit the data well, as may be observed in Fig. 1b, where $\mathcal{G}_{1c} = 4.31$ N/m.

Next, the data is plotted in a $(\mathcal{G}_{ic}, L_1)$-plane in Fig. 2a. The failure curve in eq. (1) for $\hat{L} = 1.2$ mm fits the data well. But for $\hat{L} = 10$ mm, the failure curve does not fit the data well. Various failure curves were examined with the data in Fig. 2. One possibility is to write

$$\mathcal{G}_{ic} = \overline{\mathcal{G}}_{1c}\left(1 + \lambda \tan^2 \hat{\psi}\right) \ . \tag{8}$$

To test this curve, $\hat{L} = 10$ mm was chosen, so that $\mathcal{G}_{1c} = 4.31$ N/m. With $\lambda = 0.42$ and 1.28, it is possible to fit that data as seen in Fig. 2b. Another option is to use brute force with curve fitting applied to obtain a quartic equation given by

$$\mathcal{G}_{ic} = 6.27 + 2.84\log(L_1) + 1.44[\log(L_1)]^2 + 0.28[\log(L_1)]^3 + 0.02[\log(L_1)]^4 \tag{9}$$

with the coefficient of determination $R^2 = 0.81$ as shown in Fig. 2c.

CONCLUSIONS

Although the invariants are attractive, the failure curve using these quantities was found here by curve fitting. The failure curve in eq. (1) was determined from first principles [4]. Of course, for this criterion, a proper choice of $\hat{L}$ is required.

References

[1] Bank-Sills L., Travitzky N., Ashkenazi D., Eliasi R. A Methodology for Measuring Interface Fracture Properties of Ccomposite Materials. *Int. J. Fract.* **99**: 143-161, 1999.
[2] Banks-Sills L., Konovalov N., Fliesher A. Comparison of Two and Three-Dimensional Analyses of Interface Fracture Data Obtained from Brazilian Disk Specimens. *Int. J. Struct. Integr.* **1**: 20-42, 2010.
[3] Hutchinson J. W., Suo Z. Mixed Mode Cracking in Layered Materials. In: *Advances in Applied Mechanics*, eds. Hutchinson J. W., Wu T. Y. **29**: 63-191, 1991.
[4] Banks-Sills L., Ashkenazi D. A Note on Fracture Criteria for Interface Fracture. *Int. J. Fract.* **103**: 177-188, 2000.
[5] Banks-Sills L., Travitzky N., Ashkenazi D. Interface Fracture Properties of a Bimaterial Ceramic Composite. *Mech. Mater.* **32**: 711-722, 2000.
[6] Banks-Sills L., Boniface V., Eliasi R. Development of a Methodology for Determination of Interface Fracture Toughness of Laminate Composites—the $0°/90°$ Pair. *Int. J. Solids Struct.* **42**: 663-680, 2005.
[7] Zhao J-M., Wang H-L., Liu B. Two Objective and Independent Fracture Parameters for Interface Cracks. *J. Appl. Mech.* **84**: 041006, 2017.

MECHANICS OF FAILURE OF BONDED JOINTS

Sina Askarinejad*[1], Emilio Martínez-Pañeda[2], Ivan Cuesta[3], and Norman Fleck[1]
[1]Engineering Department, University of Cambridge, Cambridge, UK
[2]Department of Civil and Environmental Engineering, Imperial College London, London SW7 2AZ, UK
[3]Universidad de Burgos, Escuela Politécnica Superior, 09006 Burgos, Spain

Summary Adhesive joints have potential structural application in ships in joining a composite superstructure to the steel hull, but joint reliability is a concern. The purpose of this study is to develop a mechanics model for the adhesive fracture of lap joints under shear loading. An MMA-based adhesive is being considered for use in the ship-building industry. Modified Thick-Adherend-Shear-Test (TAST) joints are designed and fabricated. The cracking response of these joints are measured and monitored by Digital Image Correlation (DIC). A cohesive zone model is able to predict the average shear strain across the adhesive layer both at crack initiation and at peak load. However, the as-calibrated model is less successful at predicting the degree of crack growth as a function of shear strain across the adhesive layer.

INTRODUCTION

Historically, mechanical joints such as bolts and rivets were used in ship building, however, bonded joints offer benefit such as reduced weight, reduced through life maintenance, and reduction of the stress concentrations. A limitation in advancing this technology is the lack of acceptance of adhesive by the qualifying agencies. Although the adhesive joint is subjected to shear loading, mode II fracture of adhesives has received limited attention in the literature [1, 2]. Our aim is to investigate the effect of geometry and material parameters upon the shear strength of an adhesive joint.

EXPERIMENTS

The shear strength of a pre-cracked specimen is measured as a function of adhesive layer thickness, h, and pre-crack length, a_0. The adhesive is the MMA-based Scigrip-300, and the substrates are low carbon steel. The Young's modulus of this adhesive is 322 $\pm$ 33 MPa, its ultimate strength is 14.2 $\pm$ 1.8 MPa, and the tensile failure strain is 0.26 $\pm$ 0.06. In order to evaluate the mechanical properties of adhesive under shear and adhesive/steel interface fracture properties, a modified Thick-Adherend-Shear-Test (TAST) joint is designed and manufactured (see Fig. 1(a)). Pre-cracks of length a_0 are placed at each end of the adhesive layer, as shown in Fig. 1(a). Samples with selected adhesive layer thickness h = 3, 5, 8, 10, 13 mm, and pre-crack length a_0 = 0, 10, 20 mm are manufactured and tested. The aim of the study is to measure the fracture response of the joint including the degree of crack extension versus shear displacement across the adhesive layer.

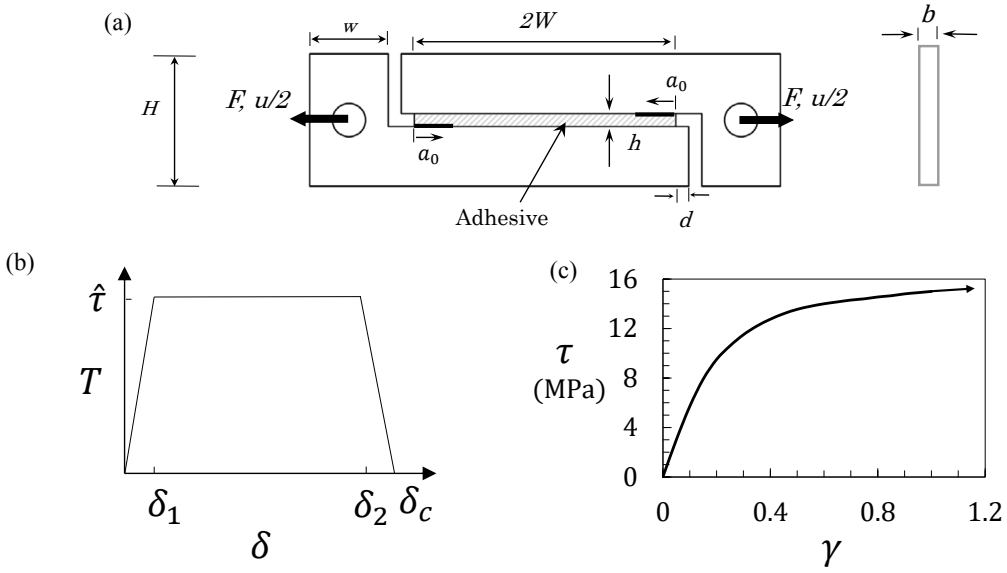

Figure 1: (a) Sketch of modified TAST joint ($2W$ = 100 mm, h = 3, 5, 8, 10, 13 mm, H = 50.4 mm, w = 30 mm, a_0 = 0, 10, 20 mm, d = 5 mm, b = 6.35 mm), (b) Shear cohesive zone law assumed in this study ($\hat{\tau}$ = 13 MPa, δ_1 = 0.05 δ_c, and δ_2 = 0.95 δ_c, δ_c = 1.3 mm), (c) The measured shear stress-strain for the adhesive ($\dot{u}/h = 5 \times 10^{-4}\ s^{-1}$).

*Corresponding author. E-mail: sa898@cam.ac.uk

COHESIVE ZONE MODELLING

Crack advance is predicted by the progressive failure of a shear cohesive zone, placed at the interface between adhesive and substrates (see Fig. 1(b)). The cohesive zone is implemented into the Finite Element (FE) model by means of cohesive elements [3]. A mesh sensitivity study is chosen to ensure that the cohesive zone is resolved. The shear response of the cohesive zone law is given in Fig. 1(b) in the form of a shear traction T versus shear displacement δ. The value of $\hat{\tau}$ is chosen to fit the experimental peak load for the case of $h = 3$ mm ($\hat{\tau}$ = 13 MPa) and DIC is used to measure the displacement jump between the adhesive and the substrate at the crack tip (δ_c = 1.3 mm). The shear stress strain curve of the adhesive is used in the FE simulations.

RESULTS AND DISCUSSIONS

Take representative case of $h = 8$ mm and a_0 = 10 mm. Fig. 2(a) compares the numerical and experimental results for average shear stress ($F/2Wb$) versus shear strain (u/h) across the adhesive layer. Crack extensions of 1 mm, 5 mm and 10 mm are included. The FE simulation has a limited ability to predict the degree of crack extension, see Fig. 2(b), but is able to predict the initiation of crack extension and the displacement jump u across the adhesive layer at peak load, see Fig. 2(c).

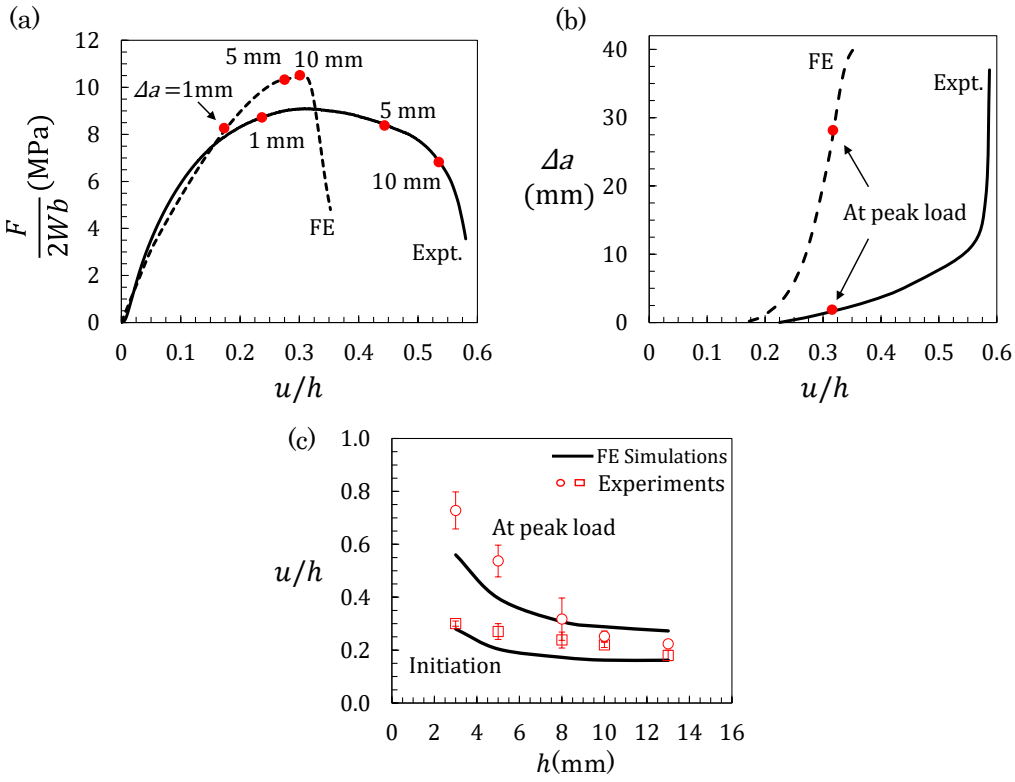

Figure 2: (a) Average shear stress versus shear strain across the adhesive layer in finite element simulation and experiment for the case of $h = 8$ mm and $a_0 = 10$ mm. (b) Interface crack extension as a function of shear strain across the adhesive layer for the case of $h = 8$ mm and $a_0 = 10$ mm. Shear strain across the adhesive layer at crack initiation and peak load as a function of adhesive layer thickness for the case of $a_0 = 10$ mm.

CONCLUSIONS

A numerical and experimental study on Mode II fracture of a ductile adhesive joint is reported. The geometry of TAST setup is considered. The capability of cohesive zone modelling with trapezoidal shear cohesive zone law in predicting failure of these joints is evaluated. The shear cohesive zone model is capable of predicting the fracture strength and average shear strain at crack initiation and peak load.It is less accurate in predicting the details of crack extension.

References

[1] Q. D. Yang, M. D. Thouless, S. M. Ward. Elastic-plastic mode-II fracture of adhesive joints. *Int. J. Solids Struct.* **38**: 3251–3262, 2001.
[2] E. Martínez-Pañeda, I. I. Cuesta, N. A. Fleck, Mode II fracture of an elastic-plastic sandwich layer, *J. Appl. Mech.* **87 (3)** 031001, 2020.
[3] S. del Busto, C. Betegón, E. Martínez-Pañeda, A cohesive zone framework for environmentally assisted fatigue, *Eng. Fract. Mech.* **185** 210-226, 2017.

MODELING FATIGUE EFFECTS IN BRITTLE MATERIALS WITH A VARIATIONAL PHASE-FIELD APPROACH

Roberto Alessi*[1], Jacopo Ciambella[2], and Giovanni Lancioni[3]
[1]Department of Civil and Industrial Engineering, Università di Pisa, Pisa, Italy
[2]Department of Structural and Geotechnical Engineering, Sapienza Università di Roma, Roma, Italy
[3]Department of Construction, Civil Engineering and Architecture, Università Politecnica delle Marche, Ancona, Italy

Summary Fatigue is a key material degradation phenomenon in mechanics, since it is largely responsible for most structural failures. Yet, the prediction of fatigue failures still represents an open challenge for modelling and simulation at the cutting edge of mechanics. Indeed, most existing fatigue theories are based on empirical laws that lack of generality and predictive capabilities. Moreover, a unified framework that links the mechanics of monotonic fracture and the fatigue behavior reproducing, for instance, the Wöhler curve and the Paris law together with the transition between low- and high-cycle fatigue is still missing. The present work aims at discussing some novel ideas for the development of a unified framework to model fatigue effects in brittle materials in both small and large strain regimes, taking advantage of the variational phase-field approach to fracture.

Fatigue degradation phenomena are responsible for most of structural failures. Despite the significance of the problem, most existing fatigue theories are based on empirical lawsthat lack of generality and predictive capabilities. Current available fatigue analysis tools are characterised by some limitations since they are often based on empirical laws and strongly rely on expensive experimental tests. Furthermore, they describe each fatigue failure stage (initiation, stable fatigue crack propagation and abrupt failure) separately. As a consequence, they lack generality and are not sufficiently flexible to describe complicated fatigue crack scenarios. In this work, new ideas for the development of unified framework to model fatigue effects in brittle materials, built on top of the variational phase-field approach to fracture, are presented.

The phase-field approach to fracture [1, 2] has demonstrated to be an effective tool for the description of fracture phenomena and has recently gained a lot of attention, see [3] for a review. Its main advantage is the possibility of capturing complicated crack patterns through the solution of a minimization problem. In the recent years, the phase-field approach to brittle fracture has been extended to simulate also ductile and cohesive fracture phenomena, as well as coupled problems such as thermal- and diffusion-induced cracking, to mention a few. Nevertheless, the majority of these models are restricted to the case of monotonic loading without the capability to capture cyclic effects.

The common underlying theoretical framework for the development of all these phase-field models is the Energetic Formulation for rate-independent systems [4], which has been successfully applied to the modelling of many problems of non-smooth evolution and material instability induced by strain localization. According to this energetic approach and within the theory of Generalised Standard Materials [5], once the state variables, the potential energy, the dissipation potential and the work of external actions have been specified, the entire evolution is governed by solely three energetic requirements, which are a stability condition, an energy balance and a dissipation inequality. Compared to standard theories, the energetic formulation owns the advantage of being completely derivative-free, admitting discontinuities both in space and in time. Such a feature, in addition to evolution governing principles, allows for a natural and straightforward numerical implementation based on incremental energy minimization schemes, which is a valuable alternative to the integration of differential evolution equations. It is worth to remark that in the phase-field approach to brittle fracture, the dissipated work turns out to be a state function and therefore, a total internal energy is introduced instead of the internal potential energy and the dissipation potential.

As first introduced in [6], the basic idea to include fatigue effects within phase-field models is that not only the stiffness degrades due to damage, but also the apparent fracture energy (or fracture toughness) decreases as a suitable history variable increases, describing the material "mileage". Such fracture energy reduction, which promotes the occurrence of a macroscopic crack, may be caused by a multitude of different microscopic degradation mechanisms. In order to model such feature, a state dependent dissipated work energy functional cannot be prescribed anymore and a dissipation potential (dissipated power) must be introduced instead. In summary, the additional ingredients that we include in the phase-field approach to brittle fracture to capture fatigue effects are: A fatigue history variable, as the accumulated elastic energy; A fatigue degradation function, that reduces the fracture toughness as the fatigue history variable increases; An explicit dissipation potential. The two-dimensional numerical analyses performed in [7] have demonstrated that this fatigue model is capable to contemporary describe fatigue crack initiation, according to typical Wöhler curves, and fatigue crack propagation, in agreement with Paris law. Despite such result, the model has limited capabilities in tuning separately the fatigue crack initiation and fatigue crack propagation features, therefore not allowing for a real material parameters identification.

In this work, we further develop such a model under many points of view. First, we provide an analytical model within Griffith's theory of brittle fracture. To the author's knowledge, fatigue effects have been considered in cohesive models [8], by using the accumulated crack opening variable as fatigue history variable, but never within Griffith's brittle fracture

*Corresponding author. E-mail: roberto.alessi@unipi.it

model. Then, the phase-field approach to brittle fracture is again considered and an updated fatigue model considered, based on the analytical estimates, in order to overcome the limits emerged in [7] and to separately describe, with a unique model, independent fatigue crack initiation and fatigue crack propagation behaviours. Finally, the extension to finite strain elasticity is discussed. The capability of the model to describe the three typical fatigue fracture regimes, namely the elastic stage, the stable fatigue crack propagation phase and the final abrupt fracture, is highlighted. In addition, mean strain/stress effects as well as different energy split, are discussed. For both the small and large strain theory, an effective numerical implementation is proposed and the model validated against experimental results taken from the literature.

References

[1] Bourdin B, Francfort GA, Marigo J-J. *J. Elast.* **91**:5-148, 2008.
[2] Marigo J-J, Maurini C, Pham K. *Meccanica* **51**:3107-3128, 2016.
[3] Ambati M, Gerasimov T, De Lorenzis L. *Comput. Mech.* **55**:383-405, 2015.
[4] Mielke A, Roubíček T. Rate-Independent Systems: Theory and Application. Springer, 2015.
[5] Halphen B, Nguyen QS. *J. Mcanique* **14**:39-63, 1975.
[6] Alessi R, Vidoli S, De Lorenzis L. *Eng. Fract. Mech.* **190**:53-73, 2018.
[7] Carrara P, Ambati M, Alessi R, De Lorenzis L. *Comput. Methods. Appl. Mech. Eng.* in press, 2019.
[8] Abdelmoula R, Marigo J-J, Weller T. *Comptes Rendus Mec.* **337**:166-172, 2009.

STATISTICAL FRACTOGRAPHY: A NEW TOOL FOR QUANTIFYING THE DAMAGE MECHANISMS CONTROLLING THE TOUGHNESS OF MATERIALS

Laurent Ponson*[1,2]
[1]Institut Jean le Rond d'Alembert, CNRS – Sorbonne Université, Paris, France
[2]Tortoise, Paris, France

Summary The roughness of fracture surfaces is the fingerprint of the interaction of cracks with the microstructure of materials. During this presentation, I will show how their statistical features can help us to characterize the dissipation processes accompanying failure, and ultimately, reveal the basic mechanisms controlling the toughness of materials. I will also discuss some applications of these findings by illustrating how the statistical analysis of fracture surfaces can now be used to characterize and measure the failure properties of materials at multiple scales, overcoming the characterization achieved by standard mechanical tests.

INTRODUCTION

Crack propagation is the main mechanism leading to material failure. However, the processes controlling the resistance of materials to crack growth are far from being fully understood. The main challenge lies in the multiscale nature of failure problems: The macroscopic behavior of materials (like their toughness) is governed by damage processes localized at the crack tip vicinity at the microstructural scale. These are then extremely difficult to investigate in real time during fracture experiments and they might also not be amenable to a theoretical treatment by standard methods of continuum mechanics. Another challenge lies in the seemingly wide variety of damage mechanisms as one explores different types of material, so that formulating a generic description of the dissipative processes driving crack growth resistance seems nearly impossible. Here, we address this challenge by adopting an original strategy: our approach consists in investigating the fingerprints left by dissipative failure processes on fracture surfaces. We show that it resolves these both difficulties at once: the roughness of fracture surfaces can then be investigated post-mortem at the microscale and it reveals that cracks proceed through nucleation, growth and coalescence of damage, irrespective of the material considered. This crack growth mechanism is characterized by a length scale ξ, specific to each material, that can be extracted from the statistical analysis of the roughness of fracture surfaces. Last but not least, this length scale correlates with the toughness of materials, opening new perspectives in material characterization and structural failure analysis.

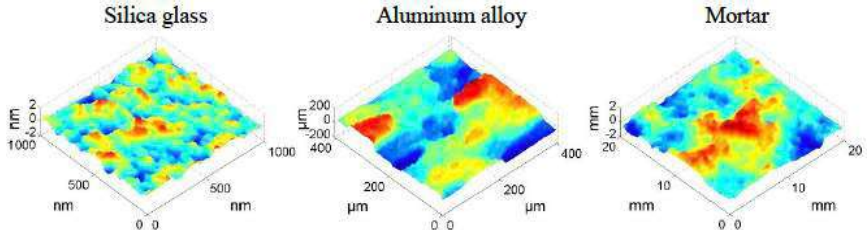

Figure 1. Three fracture surfaces of three very different materials. Despite their apparent diversity, their roughness shares similar fractal statistical properties signature of a common mechanism of crack growth by damage coalescence [1,2].

STATISTICAL FRACTOGRAPHY: FROM ROUGHNESS TO TOUGHNESS

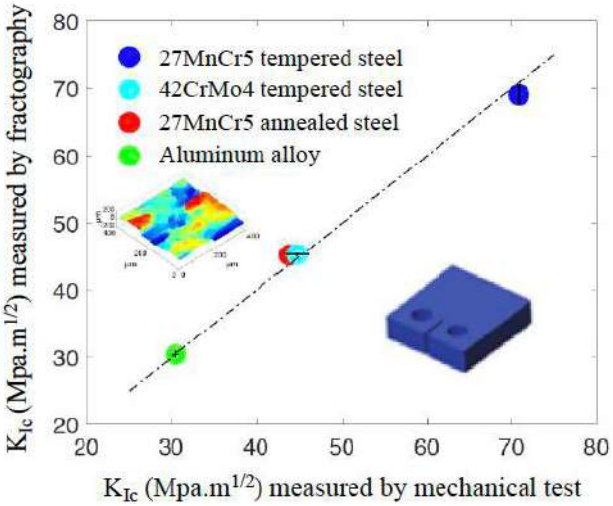

Figure 2. Comparison of the toughness measured by mechanical test and by statistical fractography on four different metallic alloys [6]. Both measurements are carried out independently.

Since the seminal work of B. Mandelbrot et al. [1] in the 80's, the investigation of the statistical features of the roughness of fracture surfaces has drawn a lot of attention (see Ref. [2] for a recent review). Until recently, the main motivation has been to understand the origin of the common properties observed on a large range of materials (Fig. 1), and more specifically the seemingly universal value of the fractal exponent characterizing the scale invariant properties of fracture surfaces [3]. But these last few years, this research field has taken another turn with the measurement of a material dependant length-scale ξ embedded in the statistical properties of the roughness of cracks [4]. In this work, we go one step further, and show on experimental examples that this length scale correlates with the toughness of materials, in line with previous numerical observations [5]. As a result, the toughness of materials can now be measured from the statistical analysis of fracture surfaces (see Fig. 2 for the application of this approach to metallic alloys [6]).

*E-mail: laurent.ponson@upmc.fr.

APPLICATION TO MATERIAL CHARACTERIZATION AND STRUCTURAL FAILURE ANALYSIS

In this presentation, I will review these recent findings and discuss their implications for the characterization of materials and the analysis of structural failure [7,8]. As a matter of fact, characterizing the failure properties of materials without resorting to a mechanical test, but from the analysis of a scan of its fracture surface, greatly simplifies the mechanical characterization of materials. But it also enables to reach new information that were not accessible before, beyond the average material toughness obtained by standard mechanical tests. Like a microscope to mechanical properties, statistical fractography also provides the field of toughness of a material within its fracture plane with a resolution of a few hundred of micro-meters (see Fig. 3e). Beyond the detailed characterization of the fracture properties of materials, it also provides new means to analyse a failed part to determine the root causes of failure (initiation region, amplitude and nature of the mechanical loading at failure...), thus enabling the redesign of safer parts (Fig. 3).

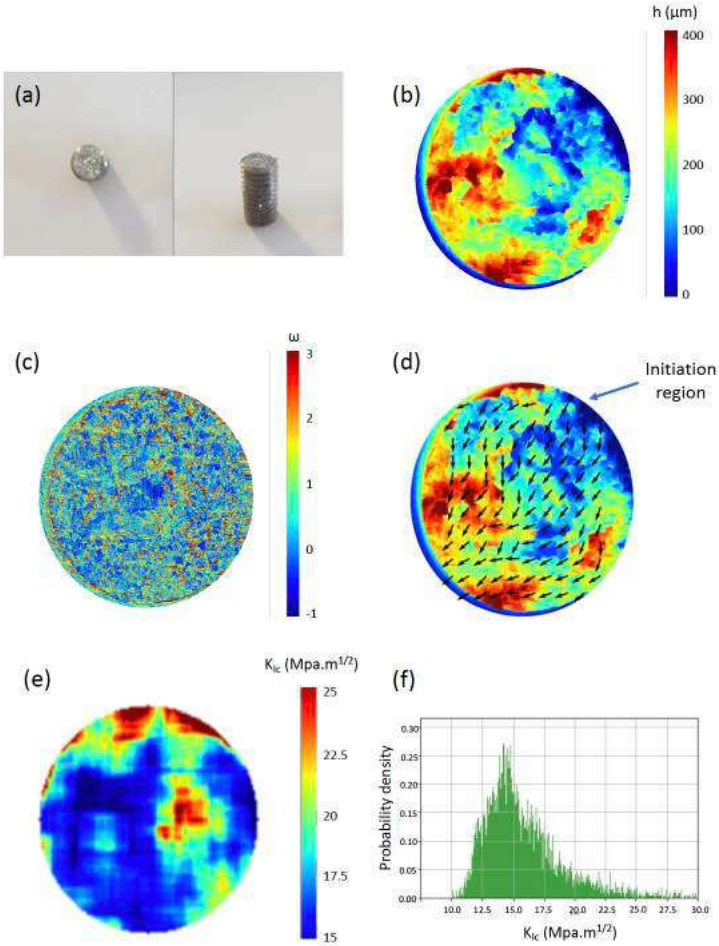

Figure 3. Example of data extracted from a statistical fractographic analysis performed on a broken screw (a). The topographic map (b) of the fracture surface is used as input data. It is first used to compute the field ω of local slopes (c) that is reminiscent of the damage coalescence processes. The anisotropy of ω allows the determination of the crack propagation direction and its sense (d). The cliffs visible on the field ω allow the measurement of the length ξ and ultimately, the toughness field (e) of the specimen within its fracture plane. Figure (f) finally provides the dispersion of the local toughness values, thereby quantifying the degree of homogeneity of the material.

CONCLUSIONS

In summary, the recent advances in the statistical analysis of the topography of fracture surface reinvents classical fractography, by changing it into a quantitative technique. This new tool may assist scientists in the development of predictive multi-scale models of failure that will provide a microscopic understanding of the crack growth resistance of materials. It also opens new perspectives for analysing structural failures to assist the design of safer structures and materials.

References

[1] Mandelbrot B.B., Passoja D.E., Paullay A.J. Fractal character of fracture surfaces of metals. *Nature* **308**: 721–722, 1984.
[2] Ponson L. Statistical aspects in crack growth phenomena: How the fluctuations reveal the failure mechanisms. *Int. J. Frac.* **201**, 11-27, 2016.
[3] Bouchaud E., Lapasset G., Planès J. Fractal dimension of fractured surfaces: A universal value? *Europhysics Letter* **13**: 73–79, 1990.
[4] Vernède S., Ponson L., Bouchaud J.P. Turbulent fracture surfaces: A footprint of damage percolation? *Phys. Rev. Lett.* **114**: 215501, 2015.
[5] Srivastava A., Ponson L., Osovski S., Bouchaud E., Tvergaard V., Needleman A. Effect of inclusion density on ductile fracture toughness and roughness. *J. Mech. Phys. Solids* **63**, 62-79, 2014.
[6] Delgado J. Statistical fractography: a comparative study. CETIM report 147440, 2018.
[7] Vernède S., Ponson L. Method for characterizing the cracking mechanism of a material from the fracture surface thereof. *European patent* 15778244 and *US patent* 10254205, 2014.
[8] Auvray N., Negi N. Trancart S., Ponson L., L'analyse statistique des faciès de rupture : la science de la donnée au service de l'analyse de défaillances, *Traitements & Matériaux* **459** : 47-50, 2019.

FRACTURE PROPAGATION AS A STANDARD DISSIPATIVE PROCESS: APPLICATION TO HYDRAULIC FRACTURES

Alberto Salvadori*[1] and Francesca Fantoni[2]
[1]DIMI, University of Brescia, Brescia, 25123, Italy 2DICATAM, University of Brescia, Brescia, 25123, Italy

Summary We propose a novel set of differential equations to model hydraulic fracture processes. Current formulations are affected by an inherent difficulty brought by the moving boundary nature of the problem, since the fronts velocitiesdo not appear explicitly in the governing equations, which makes recourse to standard computational methods for front tracking (as level sets) not possible. The formulation here proposed is capable to model the evolution of the lag and of the crack advancing in a straightforward way and can be easily extended to account for fractures pressurized by gas or other substances.

BACKGROUND AND MOTIVATIONS

Recent publications framed the problem of three-dimensional quasi-static crack propagation in brittle materials into the theory of standard dissipative processes [1]. Variational formulations, stated therein, characterize the three dimensional crack front quasi-static velocity as the minimizer of constrained quadratic functionals. An implicit in time crack tracking algorithm, that computationally handles the constraint via the penalty method algorithm, was developed and implemented in [2].

Although the theoretical setting is sound, the derived crack tracking methods suffered from a major drawback that limited the interest in the method to its theoretical content. Specifically, the need of still currently unavailable accurate approximations for weight functions made the approach of minor interest from the numerical standpoint. Such a drawback was overcome in [3], where a viscous regularization of the fracture propagation in brittle materials as a standard dissipative process was formulated. Rate-dependency provided a simple and accurate approximation of the crack front velocity, thus allowing to formulate effective crack tracking algorithms, as depicted in Fig. 1.

NUMERICAL SIMULATIONS

As well known, three-dimensional crack propagation in brittle materials still presents unresolved issues, pertaining to *when* and *how* crack elongates. For this sake, we focus in this paper on pressurized cracks that propagate in their own plane in a state of pure mode I at every point of $\mathscr{F}(t)$. Hence, at any location of $\mathscr{F}(t)$ the evolution in time of the crack path generates a smooth curve in the normal plane, at least of class C^1.

Figure 1, reprinted from [3] , depicts an example that falls out of these assumptions with the mere aim to show the potential of the algorithm devised in [3] in generic configurations when dealing with real-life, three-dimensional applications.

Consider a penny-shape crack with radius $r(t) \geq r(0) > 0$ embedded in an unbounded continuum body, loaded by two point-loads $\vec{P} = -\kappa(t)\left[\vec{n} + 0.2\vec{t}\right]$ acting on the upper and lower crack surfaces, which are directed away from the crack faces, thus opening the crack.

To cause non-planar crack growth, a shear component was added to normal point forces. The magnitude of the shear component was 20% of the normal, and the forces were applied at a location 10% of the distance from the center to the radius of the initial crack.

Because the normal and shear loads were increased proportionally, as the crack extends it shall asymptotically approach a state of planar crack growth, where resultant direction of the applied normal and shear forces is perpendicular to the growth plane.

Figure 1 shows three different views of the predicted final crack shape and the interim converged crack fronts. Six load steps are depicted: the magnitude of the applied forces were increased by 20% for each crack step (both normal and shear proportionally). It is clearly seen that the crack front rapidly approaches the plane normal to the applied load.

HYDRAULIC FRACTURES

That idea is further developed here to model hydraulic fracture processes. Current formulations are affected by an inherent difficulty brought by the moving boundary nature of the problem, since the fronts velocitiesdo not appear explicitly in the governing equations, which makes recourse to standard computational methods for front tracking (as level sets) not possible. The main novelty of the formulation stands in its ability to explicitly account for the evolution of the lag and of the crack advancing in the differential governing equations.

The problem under investigation is the penny-shaped hydraulic fracture in impermeable rock described in [4], subjected to a point-wise injection at its center of magnitude $Q(t)$. The infinite domain in which the crack is defined shows a

*Corresponding author. E-mail: alberto.salvadori@unibs.it.

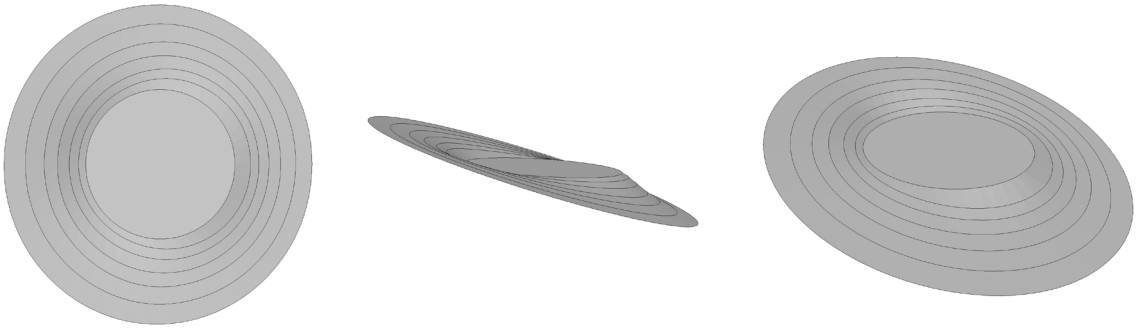

(a) (b) (c)

Figure 1: Penny shaped crack of radius equal to $10\,\mu$m in an unbounded linear elastic medium, subject to two point-loads $\vec{P} = -\kappa(t)\left[\vec{n}+0.2\vec{t}\right]$ at a distance $1\,\mu$m from the center. $\vec{n}$ stands for the outer normal, whereas $\vec{t}$ is a unit vector that spans the radial direction. Top view (a), side view (b), perspective view (c).

linear elastic behavior with no limitation in stress and strain magnitudes. The problem is formulated in the realm of small strains, as usual for linear elastic fracture mechanics.

We can idealize a process in this form. At time $t = 0$ a crack of radius $a(0)$ is given, without any fluid in it. A (sufficiently smooth in time) injection of magnitude $Q(t)$ takes place. It develops a fluid flow, and the zone occupied by the fluid is also axis-symmetric of radius $\ell(t) \leq a(t)$. The fluid lag is denoted with $\lambda(t) = a(t) - \ell(t)$.

The fluid in the crack experiences a pressure $p(r,t)$ that opens the crack of the amount $w(r,t)$. Both p and w are assumed to be smooth in time.

The set of governing equations stem from the viscous regularized formulation described in [3] for capturing the crack advancing, on the mass balance to describe the fluid front advancing, to linear elasticity theory to account for the response of the rock, and on the so-called lubrication equation (Reynold's form of the fluid transport equation) to model the fluid response, connecting the crack opening to the fluid pressure.

CONCLUSIONS

Although limited to a penny shaped crack benchmark, the novel set of differential equations that are here proposed are capable to model the evolution of the lag and of the crack advancing in a straightforward way. The formulation can be easily extended to account for fractures pressurized by gas or other substances.

References

[1] A. Salvadori. A plasticity framework for (linear elastic) fracture mechanics. *J MECH PHYS SOLIDS*, 56:2092–2116, 2008.

[2] A. Salvadori and F. Fantoni. Fracture propagation in brittle materials as a standard dissipative process: general theorems and crack tracking algorithms. *J MECH PHYS SOLIDS*, 95:681–696, 2016.

[3] A. Salvadori, P.A. Wawrzynek, and F. Fantoni. Fracture propagation in brittle materials as a standard dissipative process: Effective crack tracking algorithms based on a viscous regularization. *J MECH PHYS SOLIDS*, 127:221–238, 2019.

[4] E. Detournay. Mechanics of hydraulic fractures. *ANNU REV FLUID MECH*, 48:311–339, 2016.

I-INTEGRAL METHOD FOR FRACTURE OF MULTI-INTERFACE MATERIALS

Hongjun Yu*[1]
[1]Department of Astronautic Science and Mechanics, Harbin Institute of Technology, Harbin 150001, China

Summary The interaction integral (I-integral) has been widely used to extract the stress intensity factors of homogeneous and nonhomogeneous materials. The I-integral is the cross terms of the J-integral through superimposing an auxiliary field on the actual field. Due to the designability of the auxiliary field, the I-integral was developed to solve the SIFs and the T-stress of nonhomogeneous materials with continuous and discontinuous properties. This paper introduces a new I-integral which is independent of integration domain size, regardless of the existence of thermo-mechanical interfaces. The new I-integral is thus effective for the materials with complex interfaces.

INTRODUCTION

Most of composite materials, such as particulate and granular composites, contain complex interfaces which usually act as the source of cracks and holes, due to deformation mismatch during the manufacturing process. These composite materials are prone to fracture than homogeneous materials and the residual thermal stresses often act as the driving forces of crack growth. In order to decouple mixed-mode SIFs, Stern et al. [1] proposed the I-integral method through substituting a composition of an auxiliary field and the actual field into the J-integral. Subsequently, the I-integral method was developed to solve the T-stress [2]. In the early 2000s, the I-integral was expanded to extract the SIFs of a crack in functionally graded materials which possess continuously differentiable material properties [3]. For isotropic and orthotropic FGMs, Kim and Paulino [4] proposed three alternative auxiliary fields and gave a summary on how to extract the SIFs and the T-stress. The domain-independent I-integral (DII-integral) developed by Yu et al. [5, 6] is independent of the size of the integral domain, regardless of the existence of material interfaces. The DII-integral shows its superiority in dealing with the materials with complex interfaces. As thermal loading is applied, the I-integral becomes domain-dependence for the interfaces across which the coefficients of thermal expansion jump [7]. To overcome this difficult, a new auxiliary field was proposed and the new DII-integral was established [8, 9]. This paper will discuss the influences of the auxiliary fields on the DII-integral.

DOMAIN-INDEPENDENT I-INTEGRAL

As shown in Figure 1, the standard J-integral for thermo-elasticity is given by

$$J=\lim_{\Gamma_\varepsilon\to 0}\int_{\Gamma_\varepsilon}\left(\frac{1}{2}\sigma_{jk}\varepsilon^m_{jk}\delta_{1i}-\sigma_{ij}u_{j,1}\right)n_i d\Gamma \tag{1}$$

where σ_{jk} is the stress tensor, $\varepsilon^m_{ij}=\varepsilon_{ij}-\varepsilon^T_{ij}$ is the mechanical strain tensor, $u_{j,1}$ is the derivative of the displacement u_j with respect to the coordinate x_1, n_i is the unit outward normal vector to the contour Γ_ε and Γ_ε is the integral path from the lower surface to the upper surface of the crack. The thermal strain is given by $\varepsilon^T_{ij}=\alpha(T-T_0)\delta_{ij}$, where α is the coefficient of thermal expansion, T and T_0 are the current and initial temperatures, respectively, and δ_{ij} is the Kronecker delta. Extracting the interaction terms from the J-integral for the superposition of the actual field and an auxiliary field, one can obtain the I-integral as

$$I=\lim_{\Gamma_\varepsilon\to 0}\int_{\Gamma_\varepsilon}\left(\frac{1}{2}(\sigma^{aux}_{jk}\varepsilon^m_{jk}+\sigma_{ij}\varepsilon^{aux}_{jk})\delta_{1i}-\sigma^{aux}_{ij}u_{j,1}-\sigma_{ij}u^{aux}_{j,1}\right)n_i d\Gamma \tag{2}$$

The auxiliary fields marked by the superscript "*aux*" are given by

$$u^{aux}_i=\frac{K^{aux}_I f^I_i(\theta)+K^{aux}_{II}f^{II}_i(\theta)}{\mu_{tip}}\sqrt{\frac{r}{2\pi}},\quad \sigma^{aux}_{ij}=\frac{K^{aux}_I g^I_{ij}(\theta)+K^{aux}_{II}g^{II}_{ij}(\theta)}{\sqrt{2\pi r}},\quad \varepsilon^{aux}_{ij}=S^{(\mathbf{x})}_{ijkl}\sigma^{aux}_{kl} \tag{3}$$

where K^{aux}_I and K^{aux}_{II} are the mode-I and mode-II auxiliary SIFs, respectively, and $S_{ijkl}(\mathbf{x})$ is compliance tensor. In numerical calculations, the I-integral is generally converted into a domain form. As shown in Fig. 1, if the angular functions $f^I_i(\theta)$, $f^{II}_i(\theta)$, $g^I_{ij}(\theta)$ and $g^{II}_{ij}(\theta)$ are taken to be those of the asymptotic solutions of the crack-tip fields [4], the I-integral can be simplified as [8]

$$I=\int_A(\sigma_{ij}u^{aux}_{j,1}+\sigma^{aux}_{ij}u_{j,1}-\sigma^{aux}_{jk}\varepsilon^m_{jk}\delta_{1i})q_{,i}d\Gamma-\int_A\sigma_{ij}(S^{(\mathbf{x})}_{ijkl}-S^{(0)}_{ijkl})\sigma^{aux}_{kl,1}qd\Gamma+\int_{A_1+A_2}\sigma^{aux}_{ii}[\alpha(T-T_0)]_{,1}qdA+I_{\Gamma_I} \tag{4}$$

The last term is a non-zero line integral along the interface Γ_I. If the zero-mean-stress auxiliary field [8] is adopted, i.e., $-f^I_1=f^{II}_2=\cos\frac{\theta}{2}$, $f^{II}_1=f^I_2=\sin\frac{\theta}{2}$, $-g^I_{11}=g^I_{22}=g^{II}_{12}=\cos\frac{\theta}{2}$ and $-g^{II}_{11}=g^{II}_{22}=-g^I_{12}=\sin\frac{\theta}{2}$, the interface integral vanishes and the I-integral can be simplified as

$$I=\int_A(\sigma_{ij}u^{aux}_{j,1}+\sigma^{aux}_{ij}u_{j,1}-\sigma^{aux}_{jk}\varepsilon^m_{jk}\delta_{1i})q_{,i}d\Gamma-\int_A\sigma_{ij}(S^{(\mathbf{x})}_{ijkl}-S^{(0)}_{ijkl})\sigma^{aux}_{kl,1}qd\Gamma+\int_{C^+ +C^-}\sigma^{aux}_{2j}u_{j,1}qd\Gamma \tag{5}$$

*Corresponding author. E-mail: **yuhongjun@hit.edu.cn**. This study was supported by the NSFC (No. 11772105).

Compared with the I-integral in Eq. (4), Eq. (5) eliminates the area integral with respect to the thermal property gradient, including the gradient of the thermal expansion coefficient and the gradient of temperature. Moreover, Eq. (5) does not contain any terms related to the thermal properties. These features facilitate the practical implementation of the I-integral in dealing with the materials with complex thermo-mechanical interfaces.

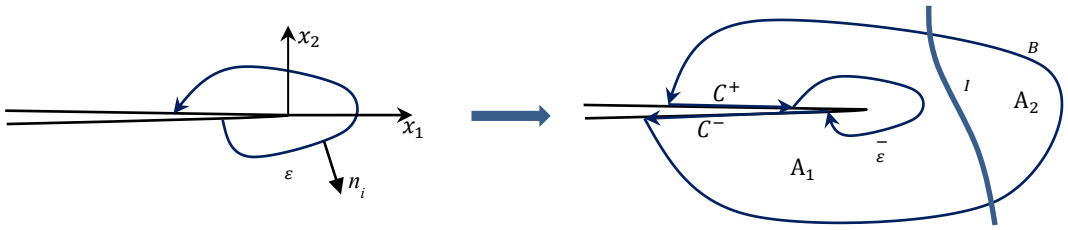

Figure 1. Integral contours around a crack tip

A REPRESENTATIVE EXAMPLE

As shown in Figure 2, a square plate of length $2W = 100$ contains a central crack of length $2a = 40$ and a particle of radius $R = 16$. The top and bottom edges are fixed and adiabatic. The left and right edges are traction-free, and the temperatures on the edges are prescribed to be $T_1 = 0$ °C and $T_2 = -20$ °C, respectively, with initial temperature $T_0 = 0$ °C. The relations between material constants of the particle and those of the matrix are as follows: $E_p = 4E_m$, $\nu_p = \nu_m$, $\alpha_p = 4\alpha_m$. Numerical results show that the interface affects the DII-integral in Eq. (4) greatly as the integration domains contain interfaces but has no influence to the new DII-integral in Eq. (5). It implies that the new I-integral in Eq. (5) can facilitate the calculation of the SIFs of multi-interface materials.

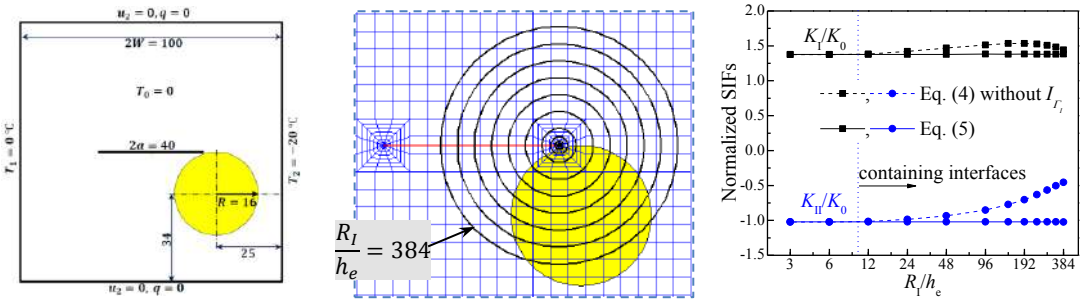

Figure 2. A particle-reinforced plate: model, integration areas of radius R_I, and normalized SIFs (h_e: edge length of the tip element).

CONCLUSIONS

In comparison with the I-integral using the classical solutions of the crack-tip fields, the I-integral applying a zero-mean-stress auxiliary field is domain-independent for the interfaces across which the coefficient of thermal expansion is discontinuous. The new I-integral is devoid of the calculation of the interface integrals and the gradient of the thermal expansion coefficient, which facilitates the practical implementation on the extraction of the SIFs for the materials with complex interfaces.

References

[1] Stern M., Becker E.B., Dunham R.S. A contour integral computation of mixed-mode stress intensity factors. *Int. J. Fract.* **12**(3): 359-368, 1976.
[2] Kfouri A.P. Some evaluations of the elastic T-term using Eshelby's method. *Int. J. Fract.* **30**: 301-315, 1986.
[3] Dolbow J.E., Gosz M. On the computation of mixed-mode stress intensity factors in functionally graded materials. *Int. J. Solids Struct.* **39**: 2557-2574, 2002.
[4] Kim J.H., Paulino G.H. Consistent formulations of the interaction integral method for fracture of functionally graded materials. *J. Appl. Mech.* **72**: 351-364, 2005.
[5] Yu H.J., Wu L.Z., Guo L.C., Du S.Y., He Q.L. Investigation of mixed-mode stress intensity factors for nonhomogeneous materials using an interaction integral method. *Int. J. Solids Struct.* **46**: 3710-3724, 2009.
[6] Yu H.J., Wu L.Z., Guo L.C., Wu H.P., Du S.Y. An interaction integral method for 3D curved cracks in nonhomogeneous materials with complex interfaces. *Int. J. Solids Struct.* **47**: 2178-2189, 2010.
[7] Guo L.C, Guo F.N., Yu H.J. An interaction energy integral method for nonhomogeneous materials with interfaces under thermal loading. *Int. J. Solids Struct.* **49**: 355-365, 2012.
[8] Yu H.J., Kitamura T. A new domain-independent interaction integral for solving the stress intensity factors of the materials with complex thermo-mechanical interfaces. *Eur. J. Mech. A-Solids* **49**: 500-509, 2015.
[9] Yu H.J., Sumigawa T., Wu, L.Z., Kitamura, T. Generalized domain-independent interaction integral for solving the stress intensity factors of nonhomogeneous materials. *Int. J. Solids Struct.* **67-68**: 151-168, 2015.

REVIEW ON FINITE ELEMENT ANALYSIS AND FRACTURE MECHANICS FOR COMPUTING INTENSITY FACTORS FOR NOTCHES CRACKS

José Airton Neiva Alves da Silva Brasil, Jorge Luiz de Almeida Ferreira *1
[1]Department Mechanical Engineering, Universidade de Brasília, Brasília, Brazil

Summary This paper presents the theory of the finite element analysis for fracture mechanics and a method for calculating the stress intensity factor for cracks emanating from notches. The results of the finite element analysis results will be compared with data from literature to demonstrate the accuracy of the method.

INTRODUCTION

For a fracture mechanics analysis, it is important to observe the interplay between the initial state of the component (no crack was present), the initial crack and its growing, especially in situations where notches are present, which occurs in most of real engineering situations. The difficult behind this analysis is that for every geometry, crack size and load condition the stress intensity assumes a different formulation, but can be expressed in general for by:

$$K = \sqrt{JE'} = F\sigma\sqrt{\pi a} \quad (1)$$

For actual engineering analysis the finite element method has become common to use as procedure to fracture problems. The use of finite elements in fracture predictions requires considerations: the crack tip singularity modelling and the displacement and stress fields throughout the cracked solid.

The objective of this work is to review the theory for the determination of the stress intensity factor K, apply it together with a finite element code, and compare the results with the results of different geometries with the results of others authors.

REVIEW OF J-INTEGRAL

Moran and Shih [n1], developed a formulation for the calculation of the J-integral by applying the integral method over the energy domain. Fakkoussi Et al [1], discretized this formulation, in the formula presented in Equation (2).

$$J = \sum_{A*}^{n} \sum_{p=1} \left\{ \left[\left(\sigma_{ij} \frac{\partial u_j}{\partial x} - w\delta_{1i} \right) \frac{\partial q}{\partial x_i} \right] \det \left(\frac{\partial x_j}{\partial x_{\xi_k}} \right) \right\} w_p \quad (2)$$

Where A^* is the area of the surface between the contours, q is parameter of the smoothed function, n_p is the number of Gauss points, w_p the integration weight and ξ_k the coordinates of elements in local landmarks.

The J-integral is equivalent to the rate of the energy restitution under a single mode. The integral J is used to calculate the stress intensity factor for mechanical case with linear elastic rupture.

REVIEW OF FINITE ELEMENT IN LINEAR ELASTIC FRACTURE MECHANICS

For a line integral path with multiple integral contours, which will enclose the crack tip and the initial and end points lies on the crack faces, this is show in Figure 1. The integral quantity is path independent when taken along any path which satisfies the condition represented by Equation (2).

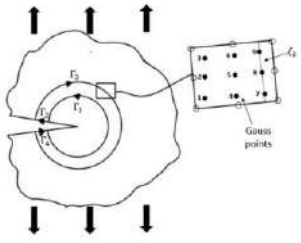

Figure 1. Closed contour path for J-integral evaluation

The J-integral estimates from different contours may vary because of nature of the finite element solution. Strong variation in the estimates indicates an error of contour dependence. Gradual variation indicates that finer mesh is needed.

*Corresponding author. E-mail: airton.bra@gmail.com.

The first contour integral is defined specifying the nodes at the crack tip, the first few contours tends to be inaccurate, so the study is made increasing the number of contours until the results converges.

FRACTURE ANALYSIS

To test the accuracy of the finite element analysis, some different of notched specimen will be compared using data of obtained from Tada, Paris and Irwin [6] compilation, and the results of the simulations. The geometric configuration, mesh, boundary conditions and results for 5 mm crack can be seen in Figure 2.

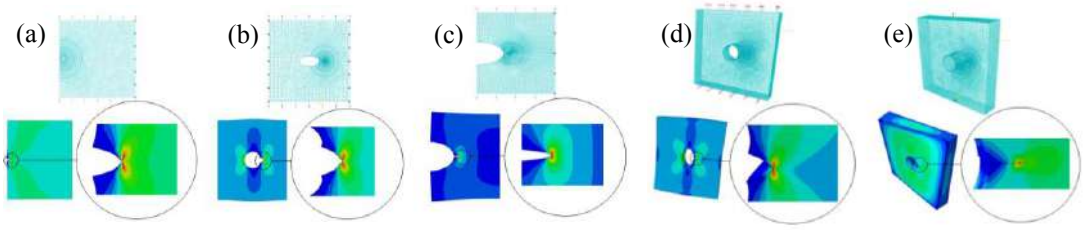

Figure 2. Simulation conditions and results. (a) 2D model of specimen without notch subjected to normal stresses, (b) 2D model of specimen with central ellipse hole subjected to normal stresses, (c) 2D model of specimen with lateral ellipse hole subjected to normal stresses, (d) 3D model of specimen with circular hole subjected to normal stresses, (e) 3D model of specimen with circular hole subjected to shear stresses

The results and the comparison between the data and the simulation for the tested notches, will be presented relating the generalized crack size and the correlation function, to avoid the characterization of the crack size and remote stress, applying the found correlation function in Eq. 1 the stress intensity factor could be calculated. The results could be seen in Figure 3.

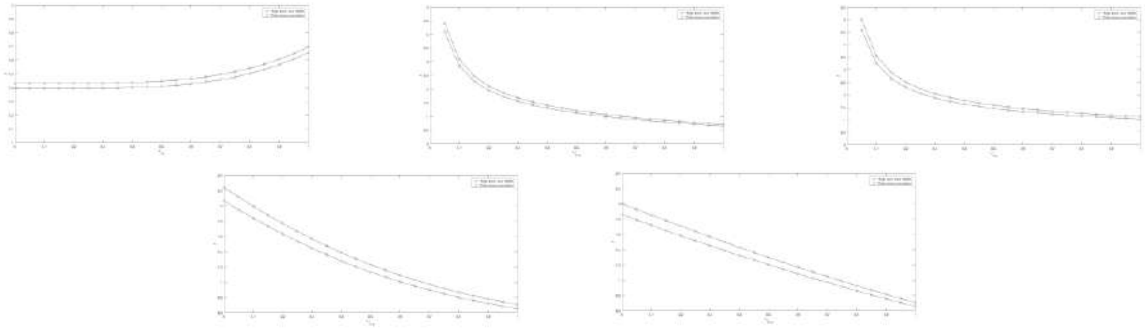

Figure 3. Comparation between the data of Tada and Irwin (2000), and the data from finite element simulation. (a) 2D model of specimen without notch subjected to normal stresses, (b) 2D model of specimen with central ellipse hole subjected to normal stresses, (c) 2D model of specimen with lateral ellipse hole subjected to normal stresses, (d) 3D model of specimen with circular hole subjected to normal stresses, (e) 3D model of specimen with circular hole subjected to shear stresses

The simulation without notch had a mean error of 2,20% and the simulations with notches had a mean error of 7,73 % between they and the data.

CONCLUSION

To test the accuracy of the finite element analysis, some different geometries were compared with already established data, proving that the FEA method can be used having relatively low error, so this model can be used for complex geometries, especially in real component cases where testing has a high cost and has technical difficulties.

References

[1] Fakkoussi S., Moustabchir H., Elkhalfi A., Pruncu C. I., Computation of the stress intensity factor KI for external longitudinal semi-elliptic cracks in the pipelines by FEM and XFEM methods. *International Journal on Interactive Design and Manufacturing (IjIDeM)*. **13**: 545-555, 2019.

[2] Jones R., Peng D., A simple method for computing the stress intensity factors for cracks at notches. *Engineering Failure Analysis*, **9**, 683-702, 2002.

[3] Moran, B., Shih, C.F.: A general treatment of crack tip contour integrals. Int. J. Fract. **35**, 295–310, 1987.

[4] Owen D. R, Fawkes A. J., **Engineering Fracture Mechanics: Numerical Methods and Application**. Pineridge Press Ltd., Swansea, 1983.

[5] Rice, J.R., et al.: A path independent integral and the approximate analysis of strain concentration by notches and cracks. *J. Appl. Mech*. **35**, 379–386, 1968.

[6] Tada H., Paris P. C., Irwin, G. R, **The Stress Analysis of Cracks Handbook**. ASME Press, New York, 2000.

DISLOCATION INTERACTING WITH A CRACK IN A SEMI-INFINITE PLANE

Xiaodong He[1], Wenjiao Dan *[1], and Weigang Zhang[1]
[1]School of Naval Architecture, Ocean and Civil Engineering,Shanghai Jiao Tong University, Shanghai, China

Summary The pre-existing edge dislocation interacting with a sharp crack under Mode I loading is examined by atomistic simulations using a semi-infinite crack model. The simulation results show that, an edge dislocation generates more shielding when approaching the crack tip along the crack propagation direction. When placed orienting at an angle in respect of crack plane, the effect produced by an edge dislocation on crack tip, shielding or anti-shielding, depends on both the angle and distance of its location defined in the polar coordinate located at crack tip. The results presented here also broaden the application of semi-infinite crack model in fracture mechanics.

INTRODUCTION

It has been recognized that discrete dislocations near crack-tip field generate shielding or anti-shielding effect on crack-tip behaviors which are associated with materials' brittle-ductile transition[2]. In the present letter, we perform direct "K-test" simulations[3] to exhibit the effect produced by discrete edge dislocations on crack tip.

SIMULATION METHOD

We perform molecular statics simulations using LAMMPS[4], in which a semi-infinite crack with a discrete edge dislocation existed under plane strain condition is introduced. The whole dimensions of the system are approximately $30\times30\times1$ nm. The dislocation is constructed by displacing the atoms according to the anisotropic displacements[1](as shown in Fig. 1a). The crack is loaded incrementally by anisotropic displacements based on linear elastic fracture mechanics[5] and after each increment of displacement, atoms within boundary (blue atoms in Fig. 1a) are held fixed during energy minimization process.

We first investigate the effect of a discrete edge dislocation located at the plane with θ=0, then dislocations placed at the same distance away from crack tip with different angles are considered. Finally, we simulate the dislocations with the same angle but at different distances from crack tip. The simulation is terminated when crack-tip cleavage occurs(see Fig. 1b and Fig. 1c).

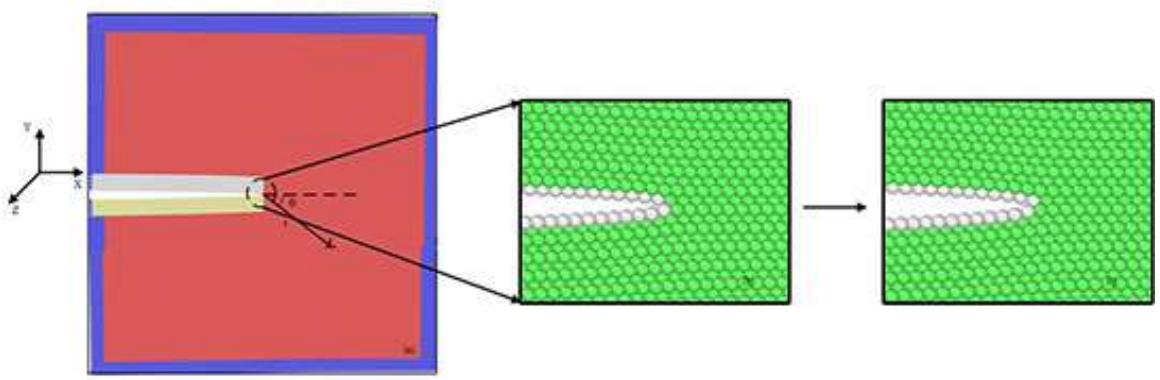

Figure 1: Illustration of atomistic simulation model:(a) a semi-infinite crack model with an edge dislocation; (b) crack tip geometry before cleavage; (c) crack tip geometry at cleavage (FCC atoms are shown in green colour and white coloured atoms represent surface atoms).

RESULTS

Fig. 2 exhibits the results of critical stress intensity factor K_{Ic} for crack-tip cleavage accompanied by the dislocation-induced shielding effect at crack tip. With the distance between crack tip and a discrete edge dislocation increasing, the shielding effect on crack tip is decreasing.

It is shown in Fig. 3a that when an edge dislocation is inserted at a distance 9 nm from crack tip, it anti-shields the crack tip first, and then shileds it with the increment of the value of θ.

Fig. 3b presents the results of K_{Ic} with dislocations at $\theta = -35.26°$ but at differnet distances away from crack tip. At this given angle, anti-shielding effect is apparent to find while minor difference is detected.

*Corresponding author. E-mail: wjdan@sjtu.edu.cn.

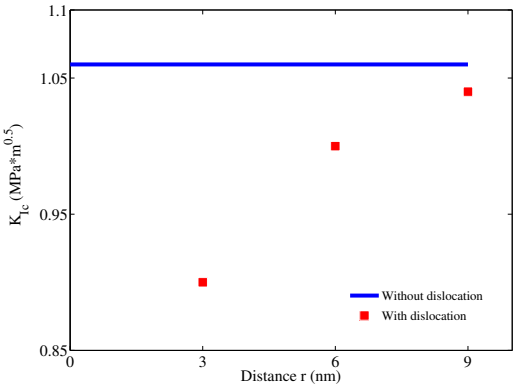

Figure 2: Critical stress intensity factor K_{Ic} for crack tip cleavage with an edge dislocation placed at different distances away from crack tip along the crack propagation direction. Blue line: K_{Ic} acquired without dislocation, Red squares: K_{Ic} obtained with dislocation.

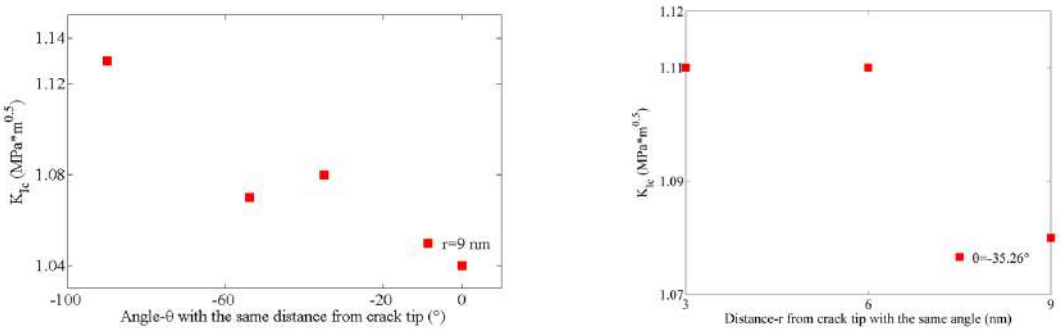

Figure 3: Results of K_{Ic} with dislocations inserted at $\theta < 0$. Fig. 3a shows the variation of K_{Ic} with dislocations at the same distance with different angles from crack tip; Fig. 3b presents the results of K_{Ic} with dislocations at different distances with the same angle.

CONCLUSIONS

The dislocation-induced effect on crack tip, whether shielding or anti-shielding, decreases with the increment of the distacne between the edge dislocation and crack tip. When the crack propagation direction is coincidence with pre-existing dislocations' Burgers vector direction, the shielding effect becomes predominant. The interaction between crack tip and an edge dislocation is mainly through changing crack tip local stress state which can be measured and viewed directly in atomistic simulations.

References

[1] Hirth J P, Lothe J. Theory of Dislocations. *Wiley, New York.* **1982**.
[2] Zhang T Y, Tong P, Ouyang H, et al. Interaction of an edge dislocation with a wedge crack. *Journal of applied physics.*, **1995, 78(8): 4873-4880**.
[3] Andric P, Curtin W A. Atomistic modeling of fracture. *Modelling and Simulation in Materials Science and Engineering*, **2018, 27(1): 013001**.
[4] Plimpton S. Fast parallel algorithms for short-range molecular dynamics.*Journal of computational physics*, **1995, 117(1): 1-19**.
[5] C.T. Sun and Z.-H. Jin. Fracture Mechanics.*Academic Press,Boston*, **2012**.

EFFECT OF STRAIN RATE ON FRACTURE IN ROUNDED V-NOTCHED SPECIMENS UNDER COMPRESSION

Elżbieta Bura*[1] and Andrzej Seweryn[1]
[1]Faculty of Mechanical Engineering, Bialystok University of Technology, Bialystok, Poland

Summary The paper presents the results of experimental compression tests (with unloading) of Poly(methyl methacrylate) (PMMA) notched specimens. Elements with V-notches with root radius equal to 1 mm were used. Three measurement base shortening levels u_{max} were implemented. The effect of strain rate on the fracture process was investigated, by asking three different velocities of the measurement base shortening v. The occurring deformation and fracture processes were recorded with the PHANTOM high-speed camera – different locations of crack initiation were indicated. Two types of cracks were observed and the causes and moments of their formation were diagnosed.

INTRODUCTION

Fracture is a complex process, which depends on many factors. Material, operating and environmental parameters have a strong influence on this phenomenon. It becomes particularly dangerous in the presence of notches. This makes all structural materials subject to fracture tests. Nowadays, polymers such as PMMA have become particularly popular. The interest in Plexiglas is mainly due to its good optical and impact properties, but its big disadvantage is its susceptibility to brittle or quasi-brittle fracture. Both in the case of PMMA and other materials, it is particularly important to build tools for predicting fracture processes, i.e. determining the points and moments of crack initiation. The basis for formulating fracture criteria is experimental testing. Components made of PMMA were analyzed during experimental tests of tensile [1], compressive [2], three-point bending [3], torsion [4] and complex states [5]. A large group of works concerns the fracture tests during uniaxial compression of specimens in the form of Brazilian discs weakened by rhombus-shaped notch [6], key-hole [7] and many others. It has been observed that thin elements, weakened by sharp notches or with small root radius, were subjected to fracture during compression. These actions made it possible to obtain linear characteristics and thus to predict processes using the brittle fracture criteria. There were no studies on fracture during compression with unloading stage. The influence of strain rate on the fracture process was not analyzed in most of the studies.

SPECIMENS AND TESTING STAND

The subject of the study was Poly(methyl methacrylate). Flat elements (9.7 mm thick) were weakened with double-sided V-notches with the root radius $R \sim 1$ mm and opening angle equal to 90°. Monotonic compression tests (with unloading) were carried out on a MTS 809.10 biaxial testing machine. The tests were carried out under displacement control using an INSTRON 2620.601 axial extensometer with a measuring base of 25 ± 5 mm. In order to investigate the influence of the strain rate on the fracture process, three velocities of the measurement base shortening v were used: (a) 0.02 mm/s – 0.2 mm/s, (b) 0.1 mm/s – 1 mm/s and (c) 0.5 mm/s – 5 mm/s. Unloading stage was realized respectively 10 times faster than loading. In addition, three levels of the maximum base shortening u_{max} were used. Fracture processes were observed in real time, thanks to the PHANTOM v1610 monochromatic camera.

RESULTS

As a result of experimental research, load curves as a function of measurement base shortening were obtained (Fig. 1). With the increase in the base shortening, a gentle increase in the maximum compressive force is observed. The increase of base shortening velocity v causes the increase of the maximum compressive force value. For the shortening of $u_{max} = 3$ mm, the maximum compressive force at $v = 0.02$ mm/s was about 24.75 kN. With a five-fold increase in the base shortening velocity to $v = 0.1$ mm/s, an increase in the maximum compressive force of approximately 17.5% was recorded. Another increase to $v = 0.5$ mm/s was associated with an increase in the maximum compressive force by about 10.3%. Similar trends were noted for the remaining u_{max} values. The load curve is characterized by a visible step, which regardless of the base shortening velocity v, always occurs for a shortening at $u \approx 3.25$ mm. The analysis of recordings from the PHANTOM camera, allows to conclude that the visible offset of the graph is related to the start of notch closing process. It should be noted that regardless of the preset shortening speed v, after unloading, a similar level of base shortening was obtained.

Two types of cracks were observed. The first one is formed in the result of contact stress during the notch closure (crack type A – Fig. 1). The crack initiates from the edge of the contact surface and takes the form of a butterfly wing. For the base shortening velocity $v = 0.02$ mm/s and 0.1 mm/s, the first crack initiation was recorded for $u \approx 5.85$ mm. It was only the increase in velocity v to 0.5 mm/s that accelerated the destruction process. The first crack initiation was recorded for $u \approx 4.38$ mm. The second crack type is initiated during the unloading stage (crack type B – Fig. 1). As the

*Corresponding author. E-mail: e.bura@doktoranci.pb.edu.pl

level of maximum base shortening u_{max} increases when loading the specimen, the critical force responsible for the crack initiation decreases. An increase in the base shortening velocity v accelerates the destruction process. The higher the rate of deformation, the higher the compressive force at which the crack initiation was recorded. It was found that for u_{max} = 3 mm, the crack initiates at 29%, 31% and 33% of the maximum compressive force value – respectively for base displacement velocity (unloading) 0.2, 1 and 5 mm/s. And for u_{max} = 7 mm, the crack initiation corresponds to a load of 6.7%, 6.9% and 7.7% of the maximum compressive force for the base shortening velocity (unloading) 0.2, 1 and 5 mm/s respectively. The higher the level of base shortening the differences resulting from different velocities v become less visible.

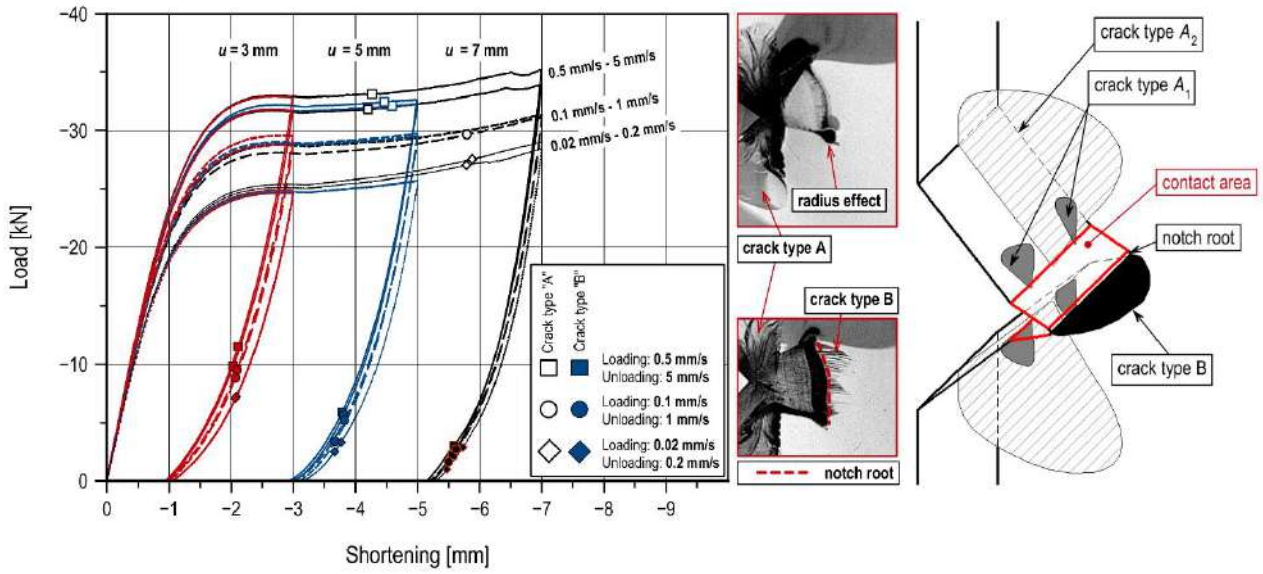

Figure 1. Compression curves with fracture initiation points for specimens with rounded V-notches.

CONCLUSIONS

The paper presents the results of experimental fracture tests of PMMA flat specimens, weakened by rounded V-notches. The phenomenon was analyzed during the loading and unloading stages, taking into account such parameters as: maximum shortening of the measurement base u_{max} and the velocity of base shortening v. Two types of cracks were observed. The first of them was formed during the loading stage as a result of contact stress. The second one was initiated at the notch root, during the unloading. The influence of the base shortening velocity on the moment of crack initiation was observed. The contact cracks initiated for a similar value of base shortening u, with base shortening velocity v = 0.02 and v = 0.1 mm/s. Significant acceleration of the destruction process was observed only at a velocity equal to v = 0.5 mm/s. An increase in the deformation velocity led to an earlier (at a lower value of the base shortening) initiation of the crack from the contact surface. In the case of cracks created by residual stresses, the influence of the strain rate on the moment of crack initiation was also found. For a given maximum level of base shortening u_{max}, it can be stated that the higher the strain rate, the fracture process occurs at higher force values. Thus, the greater the base shortening u_{max}, the differences resulting from the change in base shortening velocity v become less significant.

References

[1] Bura E., Seweryn A. Mode I fracture in PMMA specimens with notches – Experimental and numerical studies. *Theor. App. Fract. Mech*. **97**:140-155, 2018.
[2] Bura E., Derpeński Ł., Seweryn A. Fracture in PMMA notched specimens under compression – Experimental study. *Polym. Test.* **77**: 105923, 2019.
[3] Gomez F. J., Elices M., Planas J. The cohesive crack concept: application to PMMA at −60 °C. *Eng. Fract. Mech*. **72(8)**:1268-1285, 2005.
[4] Berto F., Elices M., Lazzarin P., Zappalorto M. Fracture behaviour of notched round bars made of PMMA subjected to torsion at room temperature. *Eng. Fract. Mech*. **90**:143-160, 2012.
[5] Ayatollahi M. R., Aliha M. R. M. Analysis of a new specimen for mixed mode fracture tests on brittle materials. *Eng. Fract. Mech*. **76(11)**:1563-1573, 2009.
[6] Torabi A. R., Bahrami B., Ayatollahi M. R. Mixed mode I/II brittle fracture in V-notched brazilian disk specimens under negative mode I conditions. *Phys. Mesomech*. **19(3)**:332-348, 2016.
[7] Torabi A. R. , Abedinasab S. M. Brittle fracture in key-hole notches under mixed mode loading: Experimental study and theoretical predictions. *Eng. Fract. Mech*. **134**:35-53, 2015.

A UNIFIED MICROSTRUCTURE-BASED APPROACH FOR DUCTILE AND BRITTLE FRACTURE OF A MORPHOUS GLASSY POLYMERS

Osman Gültekin*[1], Fabian Welschinger[2], and Hüsnü Dal[3]
[1,3]Department of Mechanical Engineering, Middle East Technical University, Ankara, Turkey
[2]Corporate Sector Research and Advance Engineering, Applied Material and Manufacturing Technologies for Metals and Polymers, Robert Bosch GmbH, Renningen, Germany

Summary Amorphous glassy polymers exhibit *shear yielding* and *crazing* associated with *ductile* and *brittle* fracture responses, respectively, under certain internal and external conditions. This study presents a microstructure-based approach to model both responses by incorporating the local evolution equations and failure criteria into staggered solution of mechanical problem that involves the total, plastic and crazing strains and the phase–field problem governing the non-local evolution of the crack phase–field. Finally, the numerical performance of the model is demonstrated through a benchmark boundary value problem in regard to the onset and growth of plastic and crazing strains inducing the ultimate rupture in the material.

INTRODUCTION

Amorphous glassy polymers, such as polymethylmethacrylate (PMMA) and polystyrene (PS), have broad end-use applications in automobile, construction and aerospace industry. They exhibit *shear yielding* under *low strain-rate*, relatively *high temperature* (around glass transition temperature θ_g) levels and *high entanglement density*, see Berger & Kramer [4], accompanied by volume-preserving inelastic deformations leading to *ductile* response. The well-accepted double-kink theory proposed by Argon [2] explains the ductile response of the glassy polymers. Constitutive models accounting for the finite viscoplastic behavior of glassy polymers can be found among others in [1, 8]. The development of *crazes* the amorphous polymers is favored by *high strain-rate*, relatively *low temperature* levels, and *low entanglement density* under tension dominated straining due the existence of flaws or grooves in the material leading to *brittle* response, see Berger & Kramer [4]. Craze development can be investigated in three stages, namely, the nucleation, growth, and failure. The growth is well explained by the interface convolution mechanism, i.e. the meniscus instability, see Argon [3]. The most widely used failure criteria for the breakdown of craze are the critical craze tip opening displacement, e.g., [10], the critical inelastic strain criterion, e.g., [6]. Although such properties of thermoplastics are separately treated in the literature, a unique research which treats thermal, mechanical and failure aspects concurrently is lacking.

THEORY

Let $\mathcal{B}$ and $\mathcal{S} \subset \mathcal{R}^3$ be the reference and the spatial configuration of the body of interest at time t_0 and $t \in \mathcal{T} \subset \mathcal{R}_+$, respectively. Then, we introduce the nonlinear *deformation map*, the covariant *Lagrangian inelastic metrics* for the shear-yielding and crazing processes, and the *crack phase–field* based on Miehe et al. [9] as follows,

$$\boldsymbol{\varphi} : \left\{ \begin{array}{ccc} \mathcal{B}\times\mathcal{T} & \rightarrow & \mathcal{S}\in\mathcal{R}^3 \\ (\boldsymbol{X},t) & \mapsto & \boldsymbol{x}=\boldsymbol{\varphi}(\boldsymbol{X},t) \end{array} \right. \qquad \boldsymbol{G}^{p,c} : \left\{ \begin{array}{ccc} \mathcal{B}\times\mathcal{T} & \rightarrow & \mathcal{R}^6 \\ (\boldsymbol{X},t) & \mapsto & \boldsymbol{G}^{p,c}(\boldsymbol{X},t) \end{array} \right. \qquad d : \left\{ \begin{array}{l} \mathcal{B}\times\mathcal{T}\rightarrow[0,1] \\ (\boldsymbol{X},t)\mapsto d(\boldsymbol{X},t) \end{array} \right. \tag{1}$$

Focusing on the kinematics, one can define the Hencky-type total, plastic and crazing strains in the sense of Miehe et al. [7], i.e.

$$\boldsymbol{\varepsilon} := \frac{1}{2}\ln \boldsymbol{C}\,, \qquad \boldsymbol{\varepsilon}^p := \frac{1}{2}\ln \boldsymbol{G}^p \qquad \text{and} \qquad \boldsymbol{\varepsilon}^c := \frac{1}{2}\ln \boldsymbol{G}^c \tag{2}$$

in the logarithmic strain space, which enables the use of additive decomposition of the strain measures, i.e. $\boldsymbol{\varepsilon} = \boldsymbol{\varepsilon}^e + \boldsymbol{\varepsilon}^p + \boldsymbol{\varepsilon}^c$, akin to the small strain context. Next, postulating stronger conditions on the reduced form of the Clausius–Planck inequality, the inelastic processes read

$$\boldsymbol{\pi}^p : \dot{\boldsymbol{\varepsilon}}^p \geq 0\,, \qquad \boldsymbol{\pi}^c : \dot{\boldsymbol{\varepsilon}}^c \geq 0 \qquad \text{and} \qquad \pi^d : \dot{d} \geq 0 \tag{3}$$

where $\boldsymbol{\pi}^p$, $\boldsymbol{\pi}^c$, and π^d are driving thermodynamic logarithmic stress tensors and scalar associated with shear yielding, crazing and phase-field of damage, respectively. An isotropic, volume-preserving viscoplastic flow in the direction of the deviatoric stress $\mathrm{dev}(\boldsymbol{\pi}^p)$ and another flow in the direction of the maximum effective stress $\boldsymbol{\pi}_0$ drive the shear yielding and crazing, i.e.

$$\dot{\boldsymbol{\varepsilon}}^p := \dot{\gamma}^p \frac{\mathrm{dev}(\boldsymbol{\pi}^p)}{||\,\mathrm{dev}(\boldsymbol{\pi}^p)||} \qquad \text{and} \qquad \dot{\boldsymbol{\varepsilon}}^c := \dot{\gamma}^c \boldsymbol{e}_{max}\otimes\boldsymbol{e}_{max} \tag{4}$$

*Corresponding author. E-mail: osmang@metu.edu.tr

in terms of the scalar flow functions $\dot{\gamma}^p$ and $\dot{\gamma}^c$ in the sense of Boyce et al. [5] and Gearing & Anand [6], respectively. In the sequel, we postulate two serial viscoplastic dashpots along with a one-way switch function for craze initiation

$$\mathcal{F}_c(\boldsymbol{\pi}) : \begin{cases} f_c(\boldsymbol{\pi}) \leq 0 & \vee \quad \pi_{max} \leq 0 \quad \vee \quad \pi_{vol} \leq 0 \quad \longrightarrow \quad \text{shear yielding} \\ f_c(\boldsymbol{\pi}) > 0 & \wedge \quad \pi_{max} > 0 \quad \wedge \quad \pi_{vol} > 0 \quad \longrightarrow \quad \text{crazing} \end{cases} \tag{5}$$

where the mean normal stress reads $\pi_{vol} = \mathrm{tr}(\boldsymbol{\pi})/3$ in the logarithmic strain space. A slightly modified version of that stated in Gearing & Anand [6] is adopted for the craze nucleation criterion $f_c(\boldsymbol{\pi})$. Considering the quasi-static conditions, the fundamental balance laws that serve as the basic axioms of the thermomechanics are the balance of linear and angular momentum, i.e.

$$J\,\mathrm{div}(\boldsymbol{\tau}/J) + \rho_0 \boldsymbol{\gamma} = \boldsymbol{0} \quad \text{and} \quad \boldsymbol{\tau} = \boldsymbol{\tau}^T\,, \tag{6}$$

where $\boldsymbol{\tau}$, ρ_0 and $\boldsymbol{\gamma}$ represent the Kirchhoff stress, the material density and the prescribed body force, respectively. Next, we write down the balance equation for the fracture process

$$\frac{1}{l}(d - l^2\Delta d) = 2(1-d)\mathcal{H}\,, \tag{7}$$

that governs the non-local evolution of the crack phase-field. l indicates the length-scale parameter inherent in the phase-field theory, while a monotonically increasing specific crack driving source term $\mathcal{H}$ drives the phase-field from intact to ruptured state, i.e. $d \to 1$, of the solid. On the spatial side, a canonical Galerkin-type finite element procedure, together with a standard discretization, yields the algebraic counterparts of the weighted residual expressions and the symmetric tangent matrices from (6) and (7). Subsequently, the partition of the monolithic solution scheme on the temporal side successively updates the history fields, the deformation and the crack phase-field . During the non-local update of the deformation field, the local updates associated with the shear yielding and crazing are also performed.

RESULTS

We perform a tension test on a micro-structure plate with a hole in the center made of PMMA. The lower edge is fixed in horizontal and vertical directions, while the upper edge is only fixed in the horizontal direction. The specimen is loaded monotonically in the vertical direction. The simulation results are shown in terms of the maximum principal stress π_{max}, the amount of plastic strain $||\boldsymbol{\varepsilon}^p||$ due to the shear yielding, and the amount of plastic strain ϵ^c due to crazing. When the applied stresses reach the yield stress, plastic deformations due to shear yielding occurs. Until the onset of crazing, a full-fledged shear band is evident whose development is later terminated by the initiation of the craze, see Fig. 1(i). Plastic strains due to crazing continue to accumulate and as soon as ϵ^c exceeds the threshold $\overline{\epsilon^c}$, the crack phase-field develops. The crack phase-field fully grows at the intersection of the circular hole with the mid-plane leading to the first visible crack. Figure 1(ii) shows stresses, plastic strains due to shear yielding and plastic strains due to crazing at the onset of crack, respectively. Figure 1(iii) depicts the stress concentration at the crack front, plastic strains due to shear yielding and crazing as the crack advances in the horizontal direction. Finally, in Fig. 1(iv), the fully ruptured specimen is visualized. Due to excessive plastic deformations, the specimen cannot recover its initial unloaded shape.

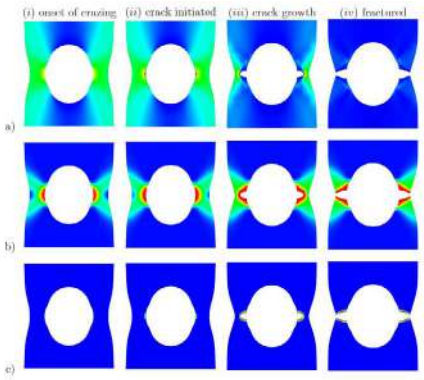

Figure 1: Contour plots of a) actual driving stress π_{max}, b) amount of plastic shear yielding strain $||\boldsymbol{\varepsilon}^p||$ and c) crazing strain ϵ^c at the (i) onset of crazing, (ii) the initiation of the crack, (ii) while the crack grows, and (iv) when the fracture occurs.

References

[1] Anand L., Gurtin M. E. A theory of amorphous solids undergoing large deformations with application to polymeric glasses. *Int. J. Solids Struct.*, **40**:1465-1487, 2003.
[2] Argon A. S. A theory for the low-temperature plastic deformation of glassy polymers. *Philos. Mag.*, **28**: 839-865, 1973.
[3] Argon A. S. Role of heterogeneities in the crazing of glassy polymers. *Pure and Appl. Chem.*, **43**:247-272, 1975.
[4] Berger L., Kramer E. Chain disentanglement during High-temperature crazing of polystyrene. *Macromolecules*, **20**:1980-1985, 1987.
[5] Boyce, M. C., Parks, D. M., Argon, A. S. Large inelastic deformation of glassy polymers. Part I: Rate dependent constitutive model. *Mech. Mat.*, **7**:15-33, 1988.
[6] Gearing B. P., Anand L. On modeling the deformation and fracture response of glassy polymers due to shear-yielding and crazing. *Int. J. Solids Struct.*, **41**: 3125-3150, 2004.
[7] Miehe C., Apel N., Lambrecht M. Anisotropic additive plasticity in the logarithmic strain space: modular kinematic formulation and implementation based on incremental minimization principles for standard materials. *Comput. Meth. Appl. Mech. Eng.*, **191**:5385-5425, 2002.
[8] Miehe C., Göktepe S., Mendez J. Finite viscoplasticity of amorphous glassy polymers in the logarithmic strain space. *Int. J. Solids Structures*, **46**:181-202, 2009.
[9] Miehe, C., Welschinger, F., Hofacker, M. Thermodynamically consistent phase-field models of fracture: Variational principles and multi-field FE implementations. *Int. J. Numer. Meth. Engng.*, **83**:1273–1311, 2010.
[10] Tijssens M., van der Giessen E., Sluys L. Modeling of crazing using a cohesive surface methodology. *Mech. Mat.*, **32**: 19-35, 2000.

PHASE FIELD MODELLING OF ENVIRONMENTALLY ASSISTED FATIGUE

Alireza Golahmar*[1], Emilio Martínez-Pañeda [2], Christian F. Niordson[1]
[1]Department of Civil and Environmental Engineering, Imperial College London, London SW7 2AZ, UK
[2]Department of Mechanical Engineering, Technical University of Denmark, Kgs. Lyngby DK-2800, Denmark

Summary A novel variational approach to assess environmentally assisted fatigue in structural steels is presented. A coupled deformation-diffusion-phase field scheme has been developed in the framework of the finite element method. The model builds upon a hydrogen-dependent surface energy degradation law based on Density Functional Theory that adequately characterizes the sensitivity of the fracture energy to atomic hydrogen concentration. The results demonstrate the capability of the model to appropriately capture the main trends observed in laboratory experiments; namely, the sensitivity of fatigue crack growth rates to (i) the hydrogen content and (ii) the loading frequency.

INTRODUCTION

The phase field fracture model has recently emerged as a promising computational method for addressing crack initiation and propagation in solids. The model builds upon Griffith's thermodynamics framework and enables predicting complex cracking features such as crack nucleation, branching, kinking or merging in arbitrary geometries and dimensions, on the original finite element mesh, and without convergence problems [1]. The method has very recently been extended to fatigue damage [2, 3], showing that features such as fatigue crack growth rate curves or S-N curves can be predicted without any prior assumption. However, most failures often occur due to the combination of environmental effects and mechanical fatigue loading. One of the most relevant environmental effects is the role of what is generally referred to as hydrogen embrittlement. Hydrogen has been known, for over a hundred years, to cause catastrophic failure in many engineering alloys such as high strength steels [4]. Hydrogen atoms enter the material, migrate through the crystal lattice and degrade the mechanical properties of the material, reducing (by up to 90%) the fracture toughness and augmenting fatigue crack growth rates.

In this work, the phase field formulation is extended to predict environmentally assisted fatigue. The modelling framework builds upon the success of recent phase field fracture formulations for environmentally assisted cracking under static loads [5, 6]. Of interest are hydrogenous environments and capturing the synergy between corrosion fatigue and hydrogen embrittlement. The model is first used to gain fundamental insight and provide a mechanistic rationale for the trends observed in the experiments; namely, the sensitivity of fatigue crack growth rates to the hydrogen content and the loading frequency. Secondly, the model is employed to predict the impact of the environment on fatigue crack growth rate curves, in several 2D and 3D case studies of technological interest, enabling optimising design and maintenance through *Virtual Testing*, as well as planning efficient and targeted experimental campaigns.

STRESS-ASSISTED HYDROGEN DIFFUSION COUPLED WITH PHASE FIELD FATIGUE

Hydrogen transport towards the fracture process zone and subsequent cracking are studied through a coupled mechanical-diffusion-phase field finite element (FE) formulation. The model builds upon: (i) a phase field formulation of fatigue cracking, (ii) a coupled mechanical-diffusion response, driven by chemical potential gradients, as an extension of Fick's law for mass diffusion, and (iii) a hydrogen-dependent surface energy degradation law grounded on Density Functional Theory (DFT). The response of a material point, in terms of displacements $\boldsymbol{u}$, phase field order parameter ϕ and hydrogen concentration C, is governed by a set of three equilibrium equations on a bulk domain Ω along with the corresponding set of boundary conditions on its external surface $\partial\Omega$ of outward normal $\boldsymbol{n}$,

$$\begin{aligned} &\nabla\cdot\boldsymbol{\sigma}=\boldsymbol{0} \\ &\nabla\cdot\boldsymbol{\zeta}-\omega=0 \\ &\frac{\mathrm{d}C}{\mathrm{d}t}+\nabla\cdot\boldsymbol{J}=0 \end{aligned} \quad \text{on } \Omega \qquad \begin{aligned} &\boldsymbol{h}=\boldsymbol{\sigma}\cdot\boldsymbol{n} \\ &p=\boldsymbol{\zeta}\cdot\boldsymbol{n} \\ &q=\boldsymbol{J}\cdot\boldsymbol{n} \end{aligned} \quad \text{on } \partial\Omega \tag{1}$$

where $\boldsymbol{\sigma}$ is the symmetric Cauchy stress tensor, ω and $\boldsymbol{\zeta}$ the microstress quantities work conjugates to the phase field ϕ and its gradient $\nabla\phi$, respectively, $\boldsymbol{J}$ the hydrogen flux, $\boldsymbol{h}$ the prescribed boundary traction, p the phase field fracture microtraction and q the concentration flux entering the body across its external surface. The deformation, diffusion and phase field fracture problems are weakly coupled. First, mechanical deformation affects hydrogen diffusion through the stress field by governing the hydrostatic stress dependence of the bulk chemical potential. Secondly, mass transport impacts the fracture resistance via hydrogen accumulation at the fracture process zone, lowering the critical energy release rate. Thirdly, the hydrogen-sensitive phase field variable degrades the strain energy density of the solid.

NUMERICAL RESULTS: PROPAGATING CRACKS IN THE PRESENCE OF HYDROGEN

The modelling framework is implemented in the commercial finite element (FE) package Abaqus using user-defined subroutines. The coupled deformation-diffusion-phase field FE equations are solved in an implicit time integration scheme by means of a residual control-based staggered algorithm [7]. A remote mode I K-field is prescribed and both crack initiation and crack growth are considered. Dimensional analysis shows that the hydrogen concentration ahead of a stationary crack can be quantified by the interplay between loading frequency f and hydrogen diffusion coefficient D via $\bar{f} = fR_0^2/D$ where R_0 is a measure of the gradients close to the crack tip: $R_0 = K_{\text{mean}}^2/E^2$. Fig. 1(a) demonstrates, in agreement with experimental observations, that the sensitivity of a material to hydrogen embrittlement is bounded between two limiting cases: (a) slow tests, where the test time significantly exceeds the characteristic diffusion time of hydrogen throughout the specimen – very low value of $\bar{f}$, and (b) fast tests, where the test time is much less than the characteristic hydrogen diffusion time – very high value of $\bar{f}$. Subsequently, the effect of hydrogen embrittlement on the stable crack growth behaviour (Paris law regime) is demonstrated in Fig1(b). By applying the well-known Paris equation $\mathrm{d}a/\mathrm{d}N = C\Delta K^m$, one can readily observe that C increases with the hydrogen content, in agreement with the experimental trends. On the other hand, results yield a Paris' exponent that demonstrates less sensitivity to the hydrogen content ($m3 \approx 3.2$), lying in all the cases in the experimentally reported range of 2 to 4 for metals in inert environments. For higher values of ΔK, the red curve (1 wt ppm) starts deviating from the linear behaviour, demonstrating a transition phase between the stable (Paris' regime) and unstable crack propagation regions. A reference stress intensity factor is defined as $K_0 = \sqrt{G_c(C)E/(1-\nu^2)}$ for $C = 13\text{wt}3\text{ppm}$. Other problem parameters are $f = 1\text{Hz}, R = 0.1, D = 0.0127\text{mm}^2/\text{s}, E = 210\text{GPa}, \nu = 0.3, \text{and}3G_c = 2.73\text{kJ/m}^2$.

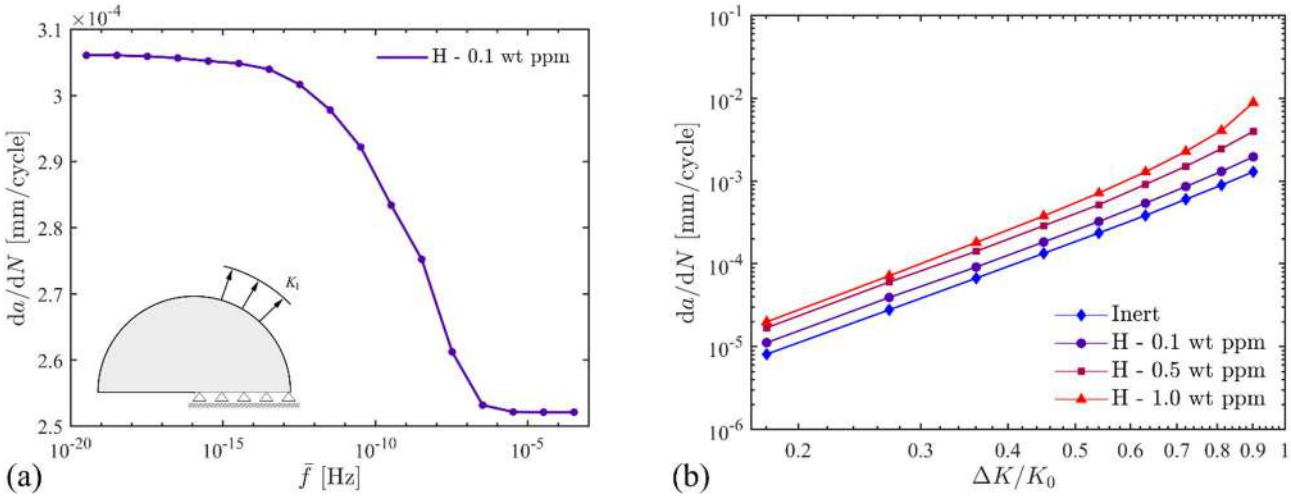

Figure 1. Hydrogen embrittlement effects on propagating cracks: (a) Sensitivity of crack growth rate to the loading frequency (relative to the diffusion coefficient) for $\Delta K/K_0 = 0.543$(b) Impact of environment on Paris curves.

CONCLUSIONS

We have presented a phase field formulation for the long-standing problem of environmentally assisted fatigue. A coupled mechanical-diffusion-phase field scheme has been developed in the context of finite element method using Abaqus user-defined subroutines. We show that the model can appropriately capture the main experimental observations: (i) the impact of environment on fatigue crack growth rates, (ii) the effect of loading frequency/testing time on the crack growth rate of a fracturing solid undergoing hydrogen embrittlement.

References

[1] Bourdin, B., Francfort, G. A., Marigo, J.-J. The Variational Approach to Fracture. *J. Elast.* **91**: 5–148, 2008.
[2] Carrara, P., Ambati, M., Alessi, R., De Lorenzis, L. A framework to model the fatigue behavior of brittle materials based on a variational phase-field approach. *Comput. Methods Appl. Mech. Eng.* **361**: 112731, 2020.
[3] Kristensen, P. K., Martínez-Pañeda, E. Phase field fracture modelling using quasi-Newton methods and a new adaptive step scheme. *Theor. Appl. Fract. Mech.* 102446, 2019.
[4] Gangloff, R. P. Hydrogen assisted cracking of high strength alloys. *Compr. Struct. Integr.* **6**: 31–101, 2003.
[5] Martínez-Pañeda, E., Golahmar, A., Niordson, C. F. A phase field formulation for hydrogen assisted cracking. *Comput. Methods Appl. Mech. Eng.* **342**: 742–761, 2018.
[6] Kristensen, P. K., Niordson, C. F., Martínez-Pañeda, E. A phase field model for elastic-gradient-plastic solids undergoing hydrogen embrittlement. *J. Mech. Phys. Solids*. **143**: 104093, 2020.
[7] Seleš, K., Lesičar, T., Tonković, Z., Sorić, J. A residual control staggered solution scheme for the phase-field modeling of brittle fracture. *Eng. Fract. Mech.*, 2019.

CRACK FRONT SHAPE EFFECT ON LIFETIME PREDICTIONS

Louis David*[1,2] and Véronique Lazarus[1]
[1]IMSIA, CNRS, EDF, CEA, ENSTA Paris, Institut Polytechnique de Paris, 828bd des Maréchaux, 91762 Palaise au cedex, France
[2]Safran Aircraft Engines, site de Villaroche, Rond-point René Ravaud-Réau, 77550 Moissy-Cramayel, France

Summary Accurate fatigue lifetime prediction is a central element in many industries. Often, a damage tolerant approach is used to ensure that some given imperfection are safe. However, these lifetime predictions are frequently made using simplified crack geometries (circular or straight cracks), leading to costly conservatism. Using an iterative perturbation method, we simulate the fatigue growth of many complexly shaped cracks, and find a metric of crack size whose evolution with the number of loading cycles does not depend on the actual shape of the crack, namely the cracked surface.

INTRODUCTION

Damage tolerant design of mechanical part assumes the presence of a known defect in the media and ensures that the crack propagation caused by this defect will not lead to catastrophic consequences before the next inspection or reparation. Such defects can have complex shapes as shown by initial observation or postmortem fractography, however, their lifetimes are often predicted using massively simplified geometries : circular or straight cracks, for example. This simplification leads to costly conservatism since the simple cracks used for lifetime assessment are bigger (for example totally enclose the original crack) than the original crack to prevent overly optimistic predictions. The aim here is to focus on the influence of the shape on lifetime predictions, and to find a way to use less conservative circular cracks to assess the lifetime of defects in damage tolerant design. Hence, we consider a planar crack embedded in an infinite, linear elastic isotropic material, loaded by a uniform and constant cyclic tensile mode I stress. We assume the crack advances following a simple Paris's law. In this way, the sole complexity comes from a possible distorted crack front, avoiding any additional effect such as free boundary conditions, mode mixity, material anisotropy or non-linearity, complex loading condition and history, or sophisticated advance law.

ITERATIVE PERTURBATION METHOD USED TO STUDY THE CRACK EVOLUTION

The perturbative method based on the weight-function theory initially developed by Bueckner-Rice [1, 2, 3], allows the computation of the variation of the stress intensity factor (SIF) along a given plane crack caused by some small perturbation of the crack front, knowing the SIF K along the original front and an influence function W derived from the weight function. Using it iteratively, we can simulate any propagation of a crack front if we know the initial K and W. Moreover, we can compute K and W for any crack front by perturbing a circle, for which they are known ($W = 1$, and $K = 2\sqrt{r/\pi}$, r being the radius). Therefore, the iterative perturbation method can be used to simulate the propagation and predict the lifetime of a crack of any shape subject to uniform remote tensile stress in an infinite media in two steps: (i) Starting from a circle and perturb it in order to get the desired shape (initialisation step, fig 1b); (ii) Apply perturbations that correspond to the advance of the crack given by a Paris's law or any fatigue propagation law (propagation step, fig 1c). Details of the method and its implementation can be found in [4].

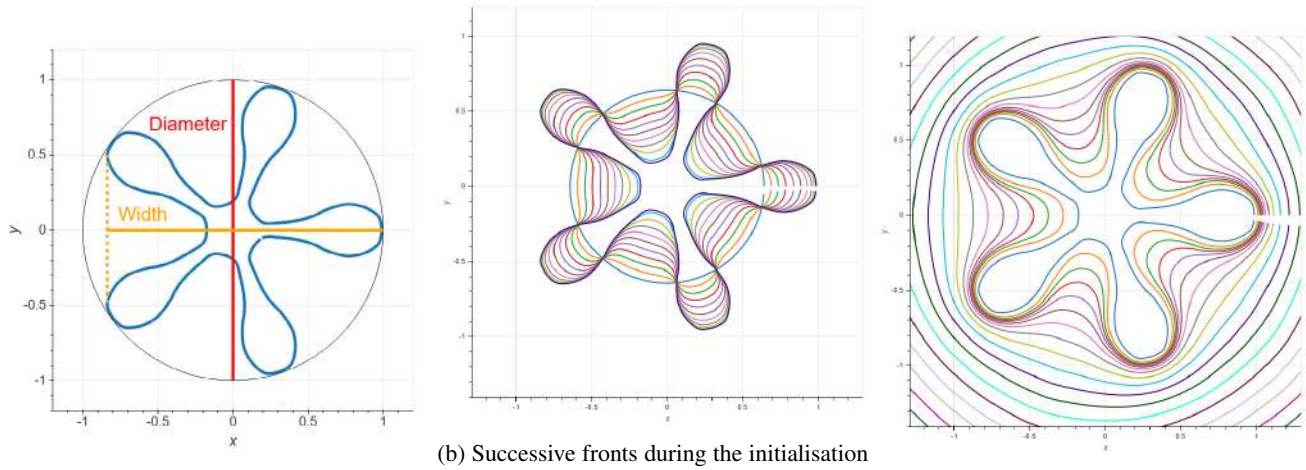

(a) Definition of the crack width and diameter step

(b) Successive fronts during the initialisation

(c) Successive fronts in propagation

Figure 1: Example of flower shaped crack with five petals used in this study

For a given planar crack front (see figure 1), several metrics can be chosen to describe its size a: diameter, width, area, and perimeter. For each of them, the iterative perturbation method can be used to get the dimensionless crack size a/a_0 as a function of the

*Corresponding author. E-mail: louis.david@ensta-paris.fr.

dimensionless number of loading cycles $NC\,(\Delta\sigma)^n\,a_0^{n/2-1}$, $\Delta\sigma$ being the amplitude of the applied stress, C, n Paris parameters, a_0 the initial crack size.

Here, two metrics are chosen as representative cases: the external diameter and the surface area. The figure 2 shows for both metrics, the evolution of the crack size with the number of loading cycle for 450 cracks different crack growth simulations. Each curve represents a single crack growth simulation and a given value of n ($n = 1$ being the slowest growing bundle and $n = 5$ the fastest). We observe that, while the curves are dispersed for choice 1, they are grouped in five bundles corresponding to the five values of n when the surface area is chosen as metric. It shows that this evolution does not depend on the crack shape provided that the crack area is chosen. This is the main result that can be directly implemented in damage tolerant methodologies : given an arbitrarily shaped crack, its lifetime can be predicted with acceptable precision as if it was a circular crack of the same initial area (under the hypotheses listed earlier). The precision of this approximation is quite good since the bundles are rather tight.

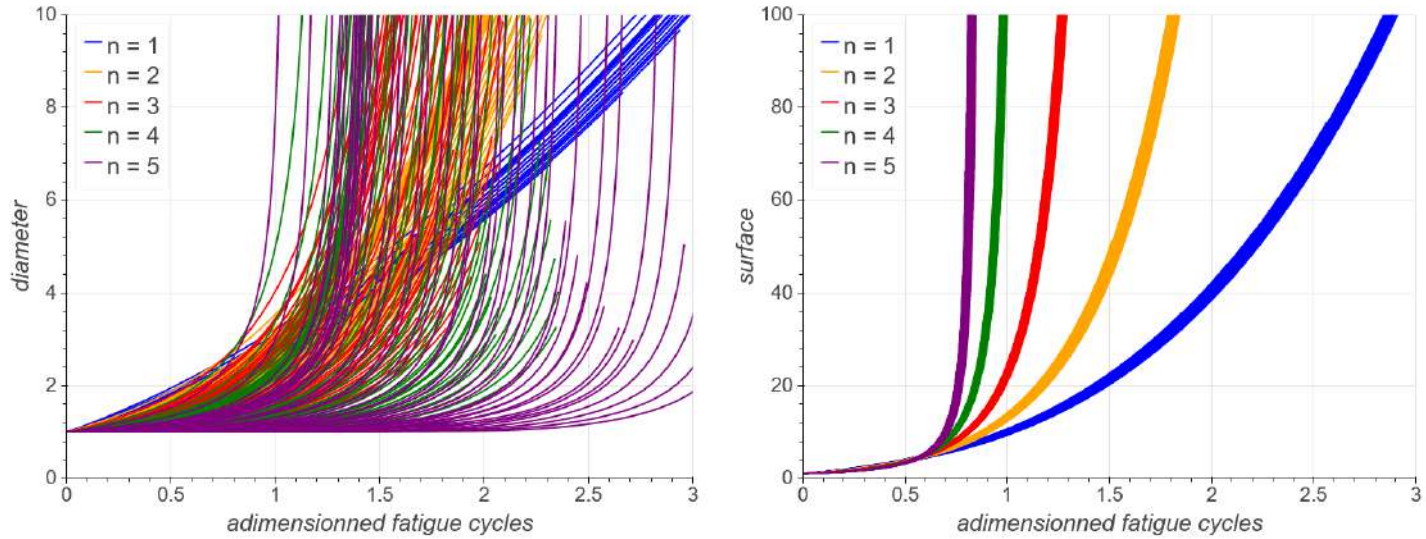

(a) adimensionned cracked diameter

(b) Adimensionned cracked surface

Figure 2: Evolution two different crack size metrics versus the dimensionless number of loading cycles for large bunch of different crack shapes and values of the parameter n of the Paris's law

CONCLUSIONS

Using an iterative perturbative method whose main advantage is to restrict the meshing operations to that of the initial crack front, we show that under the hypotheses of a plane crack uniformly loaded in mode I only in an infinite media :

1. The evolution of a cracks' surface area due to its propagation in fatigue is not dependent on the shape of the crack.
2. Using the fact that cracks of equal area have therefore similar lifetimes in fatigue, it is possible to avoid some conservatism in damage tolerant design by using simpler cracks (in our case circular) with an area equal to that of the original crack, instead of cracks enclosing the original crack, for example.
3. It is possible to keep using analytical tools requiring simple crack shapes to assess the lifetime of a crack while taking into account the real shape of defect more accurately: only the choice of equivalent circular crack is changed.

References

[1] H. F. Bueckner, Weight functions and fundamental fields for the penny-shaped and the half-plane crack in three-space, International Journal of Solids and Structures 23 (1987) 57–93.

[2] J. R. Rice, Weight function theory for three-dimensional elastic crack analysis, in: R. P. Wei, R. P. Gangloff (Eds.), Fracture Mechanics : Perspectives and Directions (Twentieth Symposium), American Society for Testing and Materials STP 1020, Philadelphia, USA, 1989, pp. 29–57.

[3] V. Lazarus, Perturbation approaches of a planar crack in linear elastic fracture mechanics: a review, Journal of the Mechanics and Physics of Solids 59 (2011) 121–144. doi:10.1016/j.jmps.2010.12.006.

[4] V. Lazarus, Brittle fracture and fatigue propagation paths of 3D plane cracks under uniform remote tensile loading, International Journal of Fracture 122 (2003) 23–46. doi:10.1023/B:FRAC.0000005373.73286.5d.

[5] N. Fleck, K. Kang, M. Ashby, Overview no. 112: The cyclic properties of engineering materials, Acta Metallurgica et Materialia 42 (1994) 365 – 381. doi:10.1016/0956-7151(94)90493-6.

IS THERE A UNIFIED RULE FOR POLYGONAL CRACKING IN COOLED LAVA SURFACE?

Yuri Akiba, Aika Takashima, and Hiroyuki Shima*[1]
Department of Environmental Sciences, University of Yamanashi, Yamanashi, Japan

Summary An orderly polygonal crack pattern is often found on the exposed surface of columnar joints, which are geological structures engendered from cooled lava flow. In the present work, field measurements of columnar joints at four sites with different lithologies in Japan were performed to explore the unified law that regulates the statistical fluctuation in the geometry of polygonal cracks. Drone shooting and digital image analysis were fully utilized to examine the geometric attributes of constituent polygons and their statistics with high accuracy. The investigation established that the geometric fluctuation is regulated by the Gumbel distribution, a special class of distribution curve that is widely used when analyzing deterioration phenomena over time and accidental fracture phenomena. A possible relevance of the present result to the desiccation-based crack network is also discussed.

INTRODUCTION

Polygonal cracking is a typical quasi-regular pattern that occurs spontaneously in nature. It includes cracks on dried soil surface and those in old paintings; a further example is found on the planetary surface [1]. In polygonal crack systems, the entire surface of the fractured medium is divided into numerous polygonal cells in which hexagons, pentagons, and heptagons dominate with irregularity in terms of edge lengths and cell domain area. The most important observation is that the geometry of the polygonal patterns is preserved over many systems despite considerable differences in chemical composition and spatial length scale. This strongly suggests the existence of a common rule for polygonal crack networks, although it has not yet been clarified which mechanism governs this spontaneous formation.

To elucidate the unified rule, the statistical fluctuations in the crack pattern geometry observed at the exposed surface of the columnar joint were investigated in this study. A columnar joint is a spectacular geological structure composed of an array of well-ordered prismatic columns with polygonal sections. The quasi-regularity in the column's cross section is a consequence of inward penetration of cracks driven by thermal contraction of the original hot lava flow. In principle, the typical column diameter depends on the cooling rate of lava, whereby slower cooling rates produce large-diameter columns and vice-versa. In addition, a previous argument based on the least-work principle led to a conjecture [2] that each polygon tends to be a cyclic polygon, that is, a polygon with vertices upon which a circle can be circumscribed. However, it should be noted that the cracking process is intrinsically stochastic; thus, in real columnar joints, the section geometry should deviate from cyclic polygons in both size and shape. The two competing effects, preference to and deviation from cyclic polygons, will regulate the degree of geometric fluctuation in the columnar section. If it is true, then a unified rule regarding the fluctuation in polygonal cracking at the surface can be established. In order to test this hypothesis, field surveys of several columnar joints in Japan were conducted in this study. At each locality, the columnar joint exposed surface was photographed from above by a drone, followed by image analysis to study the geometric fluctuation in polygonal cracking.

METHODS

Japan is one of the world's most volcanically active countries, with many volcanoes distributed along the subduction zones of four tectonic plates. When flowing lavas cool and contract, this may result in formation of fractures and jointing called columnar jointing. Consequently, various columnar joints with diverse lithological characters and columnar cross-section sizes are distributed at more than 60 locations in Japan. Among the choices, four specific sites were investigated as presented in Figure 1. Three sites (O, Sm, and Sz) are positioned along the seacoast and the remaining site (Y) is situated inland. It was necessary to choose field survey sites that did not have significant obstructions, such as buildings or overgrown tree branches, to obtain sufficiently clear image analysis photographs.

Aerial images of the localities were taken using a drone. From a height of 10 m above, it was directed to take an elevated view of the site using the hovering mode. Next, the drone was sequentially moved slightly parallel to the ground such that additional overlapping photos could be acquired. An example of the aerial photos taken from O-site is shown in Figure 2. Several hundred photos that were taken at each site were merged into a single large-scale image, which was then converted into polygonal patterns using an analytic software called ArcGIS. The resulting data set contains geometric information about the coordinates of the polygon vertices and the topology of the line segments between the vertices. The total number of polygons acquired was 1069 from O-site, 894 from Y-site, 1012 from Sm-site, and 3987 from Sz-site.

Once the numeric data were processed, the geometric deviation of constituent polygons from a cyclic counterpart was quantified. Given an n-sided polygon, any three vertices that make up the polygon were selected to form a triangle connecting each vertex. Then the coordinates of the center of the circle that passes through these three points were calculated; see Figure 3. This procedure was repeated for all ${}_nC_3$ triangles in order to obtain a point set of ${}_nC_3$ circumcenters, designated by $\boldsymbol{R}_i$ $(1 \leq i \leq {}_nC_3)$. Then the geometric center of the point set, designated by $\boldsymbol{G}$, and distances given by $r_i = |\boldsymbol{R}_i - \boldsymbol{G}|$ were evaluated. Finally, μ was defined by the standard deviation of r_i divided by the

*Corresponding author. E-mail: hshima@yamanashi.ac.jp.

average of r_i; $\mu = 1$ if the *n*-gon inscribed a circle, while $\mu \gg 1$ if the *n*-gon was considerably distorted compared with a cyclic polygon.

RESULTS & DISCUSSION

Figure 4 shows the probability distribution of the μ value for each of the four investigation sites. All the distributions are upward convex with asymmetry, which are slightly slanted to the left. After the fitting procedure, it was found that all the data are well collapsed onto a special class of distribution curve called the Gumbel distribution, independent of the size, shape, or investigation sites. The Gumbel distribution is a probability distribution that is widely used to statistically describe the strength of brittle materials and is also used to analyze deterioration phenomena over time and accidental fracture phenomena. The study's finding implies that the geometric fluctuation in polygonal cracking at columnar joints is regulated by the Gumbel distribution.

An interesting problem related to the present finding is whether the Gumbel distribution is universal over other types of polygonal cracking. For instance, the polygonal prismatic shape of columnar joints can be reproduced by numerous table-top analog experiments as have been successfully demonstrated earlier. Most of these experiments were based on desiccation cracks of starch–water mixtures [3] and calcium carbonate–water mixtures [4]. These mixtures consist of solid grains and pore spaces filled with either liquid or air bubbles. Upon drying, the liquid content evaporates, causing volumetric shrinkage of the mixture. Subsequently, cracks occur at the surface and develop toward the interior of the mixture. As a result, these materials exhibit a regular array of tiny polygonal prisms reminiscent of columnar joints. Considering the similarity in the cracking mechanism, it is expected that the Gumbel distribution also governs analog-experiment systems. Regarding the issue, we have not yet obtained a conclusion at the time of writing this Abstract. The experimental results will be presented at the conference venue.

ACKNOWLEDGEMENT

This research was supported by the Japanese Society for the Promotion of Science Grants-in-Aid for Scientific Research (JSPS KAKENHI, Grant nos. 18H03818, 19K03766, and 20J10344).

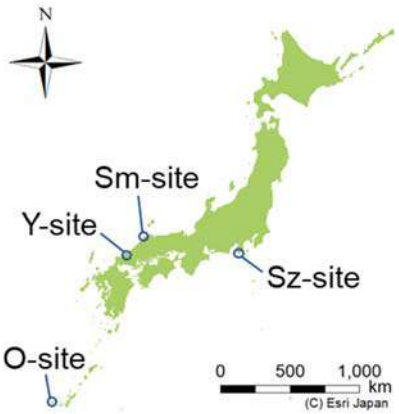

Figure 1. Location map of the four investigation sites.

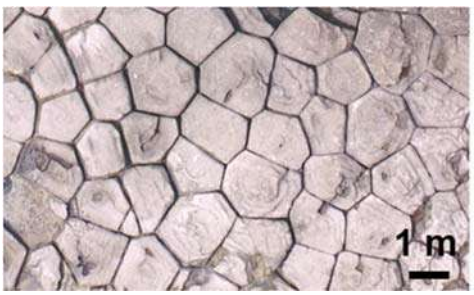

Figure 2. Overview of columnar joint surface at O-site.

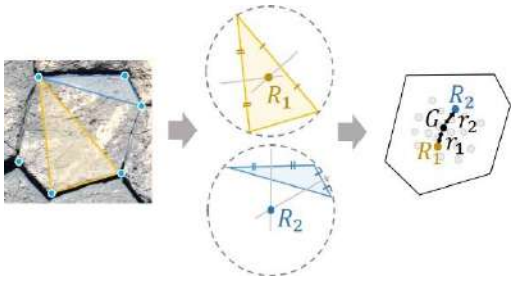

Figure 3. Diagram for calculation of the circumcenters $\boldsymbol{R}_i$ $(1 \leq i \leq {}_nC_3)$ for a given n-sided polygon.

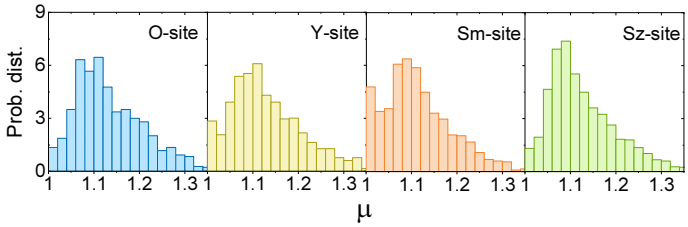

Figure 4. Probability distribution of μ, the degree of deviation in the vertex configuration from cyclic polygon geometry.

References

[1] Pieri D. C. Lineament and polygon patterns on Europa. *Nature* **289**: 17-21, 1981.
[2] Hewes L. I. A Theory of Surface Cracks in Mud and Lava and Resulting Geometrical Relations. *Am. J. Sci.* **246**: 138-149, 1948.
[3] Akiba Y., Magome J., Kobayashi H., Shima H. Morphometric analysis of polygonal cracking patterns in desiccated starch slurries. *Phys. Rev. E* **96**: 023003, 2017.
[4] Akiba Y., Shima H. Flow-Velocity-Dependent Transition of Anisotropic Crack Patterns in $CaCO_3$ Paste. *J. Phys. Soc. Jpn.* **88**: 024001, 2019.

CONSTITUTIVE MODELLING: UP- AND DOWN-SCALING (MICRO TO MACRO AND BETWEEN)

Stefan Luding[1]
[1]Multiscale Mechanics, Engineering Technology, University of Twente, Enschede, Netherlands

Summary The behavior of particles is of interest in a wide range of industries and nature. These materials are dissipative and disordered with a wide distribution of particle sizes and materials or mixtures, and can behave both solid- or fluid-like. The related mechanisms and processes are active at multiple scales (from nanometers to meters) and understanding them is an essential challenge for both science and application, as well as the theoretical description of all the transitions between the different states. The step from micro-mechanics(particle simulations) to large-scale flow applications, due to their enormous particle numbers, has to be addressed by so-called micro-macro transition methods that translate particle positions, velocities and forces into density-, stress-, and strain-fields, compatible with the conservation equations for mass, momentum and energy of continuum mechanics.

OVERVIEW

The behavior of particles such as powders and granular matter is of considerable interest in a wide range of industries and nature. These materials are intrinsically dissipative and disordered; often they come with a wide distribution of particle sizes and materials or mixtures, and can behave both solid- or fluid-like. The related mechanisms and processes in particle systems are active at multiple scales (from nanometers to meters) and understanding them is an essential challenge for both science and application, as well as the theoretical description of all the transitions between the different states.

In order to understand the fundamental micro-mechanics one can use particle simulation methods [1-6]. However, large-scale flow applications (due to their enormous particle numbers) have to be addressed by coarse-grained models [1,3,6] or by rheology and continuum theory [1,5,6]. In order to bridge the gap between the scales, so-called micro-macro transition methods are necessary, which translate particle positions, velocities and forces [2,3,4] into density-, stress-, and strain-fields, which all must be compatible with the conservation equations for mass, momentum and energy of continuum mechanics.

References

[1] A. Singh, K. Saitoh, V. Magnanimo, S. Luding, Role of gravity/confining pressure contact stiffness in granular rheology, New J. Phys. 17, 043028, 2015
[2] A. Singh, V. Magnanimo, K. Saitoh, S. Luding, Effect of cohesion on shear banding in quasi-static granular material, Phys. Rev. E 90(2), 022202, 2014
[3] N. Kumar, S. Luding, V. Magnanimo, Macroscopic model with anisotropy based on micro-macro informations, Acta Mechanica 225(8), 2319, 2014
[4] N. Kumar and S. Luding, Memory of jamming -- multiscale models for soft and granular matter, Granular Matter 18, 58, 2016
[5] D. Vescovi and S. Luding, Merging fluid and solid granular behavior, Soft Matter 12, 8616, 2016
[6] S. Roy, S. Luding, and T. Weinhart, A general(ized) local rheology for wet granular materials, New J. Phys. 19, 043014, 2017

THERMO-HYDRO-MECHANICAL BEHAVIOUR OF FROZEN SOILS: TESTING AND MODELLING

Francesca Casini[1]
[1]Department of Civil Engineering and Computer Science Engineering, Universit degli Studi di Roma Tor Vergata, Roma, Italy

Summary Artificial Ground Freezing (AGF) is often used as temporary supporting technique for excavation in granular materials below the water table . The ability to predict the effects induced by AGF on granular materials is therefore crucial to assessing construction time and cost and to optimising the method. In this keynote, the thermo-hydro-mechanical behaviour of frozen soil is presented and discussed. Then, the experimental results obtained using an advanced triaxial apparatus (FROZEN) working under temperature and stress path controlled shown.
Finally, the experimental results are interpreted using a constitutive model that encompasses frozen and unfrozen behaviour within a unified effective-stress-based framework. It makes use of a combination of ice pressure, liquid water pressure and total stress as state variables.

INTRODUCTION

The control of displacements is crucial to the viability of urban tunnelling in soft ground as ground movements transmit to adjacent structures as settlements, rotations and distortions of their foundations, which can, in turn, induce damage affecting or function, and, in the most severe cases, stability of the structure. Therefore, is necessary to adopt controllable method as support of excavation to mitigate damage on the building surrounding.

The thermo-hydro-mechanical (THM) processes induced by freezing and thawing of pore fluid within soils are complex and can have significant mutual interaction [1]. As the temperature decreases, the ice content of the soil increases; the ice becomes a bonding agent between soil particles or blocks of rock, increasing the strength of the soil/rock mass and modifying the pore water pressures and the effective stress on the soil skeleton, which, in turn, induces mechanical deformation. At the same time, any changes in the hydraulic and mechanical boundary conditions can affect the thermal processes by advection and changes of ice and water contents [1].

The experimental behaviour of frozen soils are first summarized based on the available literature data. Then, some recent advances in the development of new apparatus are presented and a set of experimental results discussed. Finally, the ability of new fully coupled THM framework developed to describe the behaviour of frozen soils is validated against experimental data ([2], [3]).

Mechanical behaviour of frozen soils

The experimental results obtained with FROZEN on a sand with silt retrieved from Cesano (RM, Italy). The e

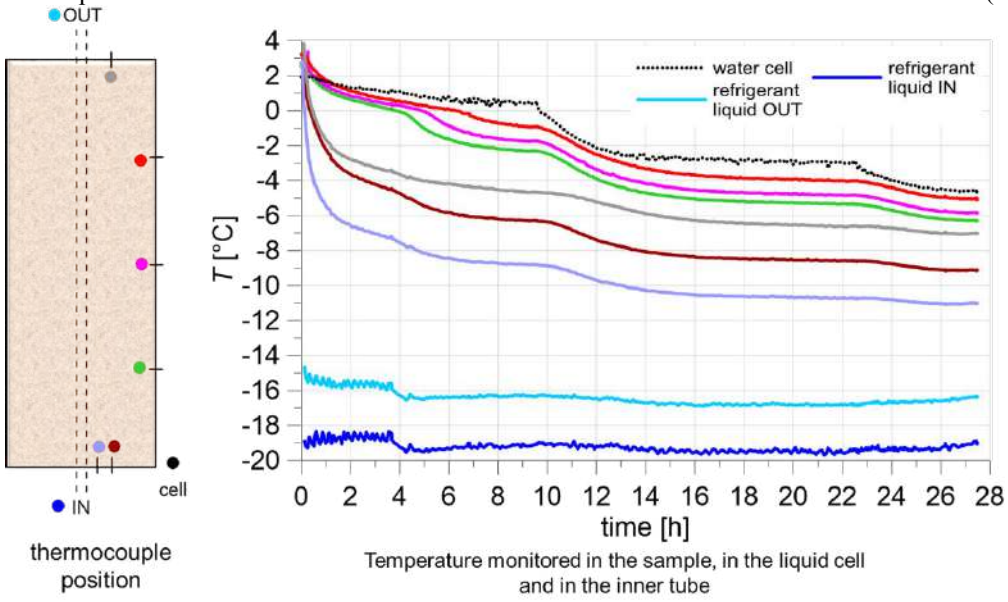

Figure 1 Temperature evolution in a sample upon freezing

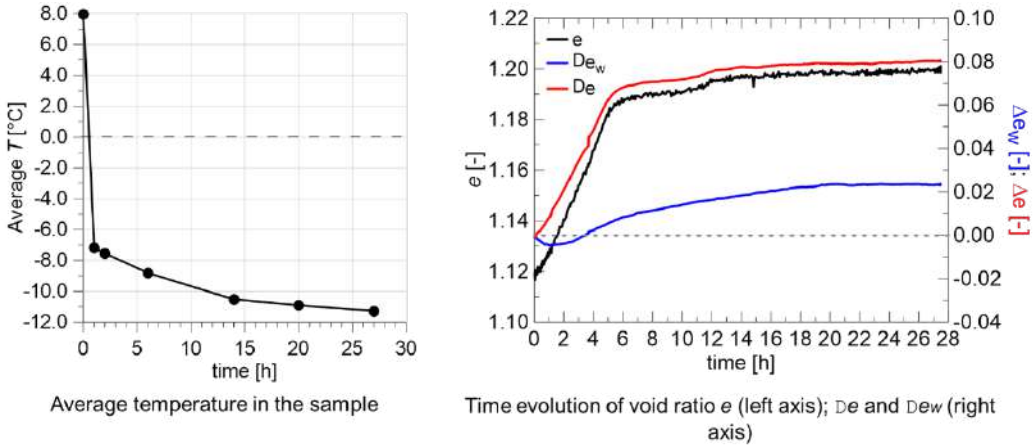

Average temperature in the sample

Time evolution of void ratio *e* (left axis); De and Dew (right axis)

Figure 2 Evolution with time: (a) average temperature in the sample; (b) void ratio; Δe and Δe_w

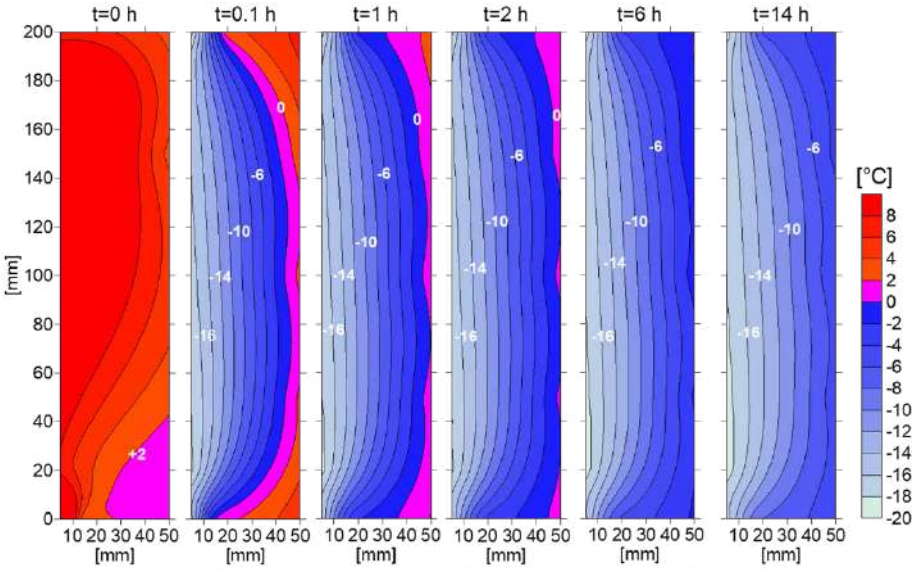

Temperature contours evolution inside specimen with a ΔT=2 °

Figure 3 Temperature contour at different time step.

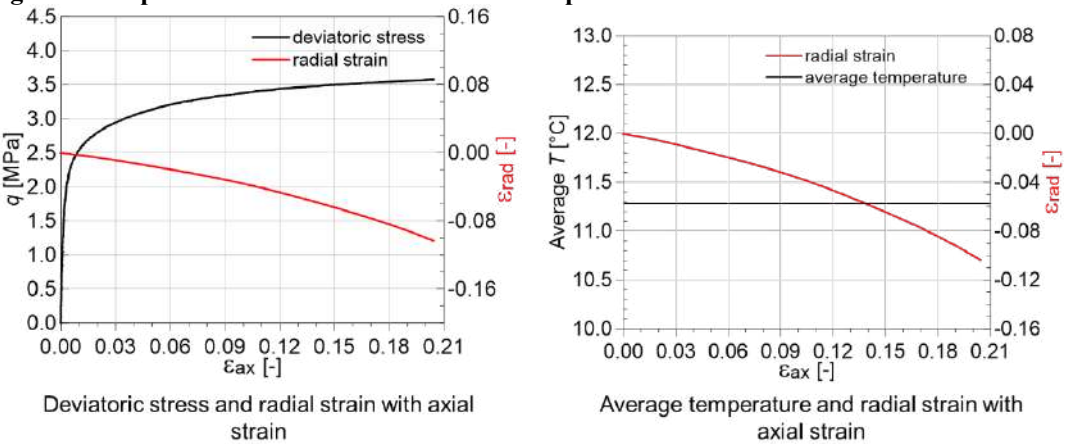

Deviatoric stress and radial strain with axial strain

Average temperature and radial strain with axial strain

Figure 4 Axial loading at controlled velocity v=0,33 mm/min T=-11°C (sc=700 kPa; pw0=500 kPa)

References

[1] Casini F, Gens A, Olivella S, Viggiani GMB (2016) Artificial ground freezing of a volcanic ash: laboratory tests and modelling. Enviromental Geotechnics 3(3), 141-154

[2] Bartoli M, , Casini F Grossi Y (2019) Geotechnical characterization of an artificially frozen soil with an advanced triaxial apparatus. In: Tunnels and Underground Cities. Engineering and Innovation Meet Archaeology, Architecture and Art, 646-54

[3] Ferrigno A (2019). Comportamento termo-idro-meccanico dei terreni artificialmente congelati: studio sperimentale e numerico. Master Thesis in Civil Engineering, Università degli Studi di Roma Tor Vergata (IT).

SIMULATION OF UNDRAINED BEHAVIOR OF SAND-SILT MIXTURES USING GENERALIZED PLASTICITY MODEL WITH STATE PARAMETER

Fu-Hsuan Yeh*[1], Min-Chien Chu[1], Louis Ge[1], and Chi-Chin Tsai[2]
[1]Department of Civil Engineering, National Taiwan University, Taipei, Taiwan
[2]Department of Civil Engineering, National Chung Hsing University, Taichung, Taiwan

Summary Recent findings have shown that sands with a high amount of fines, non-plastic and/or low plastic silt exhibit a complex stress-strain-volume change behavior. From past research, one of the factors affecting the behavior of granular material is effective mean stresses. The effect of fines content (FC) on critical state, including effective mean stresses (p') and void ratio, is considered to simplify a constitutive model in order to present the complexity of geomaterial. From a series of triaxial test results, the void ratio was found to be presented in terms of FC and p'. Therefore, the aim of the research is to numerically perform monotonic undrained triaxial tests within the framework of a generalized plasticity model, where a state parameter was incorporated. In summary, the proposed model is capable of mimicking the stress-strain-volume change behavior of sand-silt mixtures.

INTRODUCTION

The concept of generalized plasticity theory was first introduced by Pastor and Zienkiewicz in 1985 [1]. Unlike conventional elastoplastic hardening models, the developed model with an explicit form provides an analytical geometrical interpretation to formulate stress-strain behavior through the plastic flow rule, loading direction, and plastic modulus. The theory of generalized plasticity incorporating the state parameter is adopted herein to describe the constitutive behavior of the sand-silt mixtures. Within this framework, the fines content (FC) in the state parameter has to be considered to improve the accuracy of the model.

GENERALIZED PLASTICITY MODEL

Generalized plasticity theory incorporating a state parameter

The model incorporates the deformation characteristics of sand and sand-silt mixtures into generalized plasticity by subsequently defining nonlinear elasticity, dilatancy, and plastic modulus. In recent years, a number of models based on this theory have been developed to simulate the specific soil materials ([2]-[7]). This model has the advantage that the yield and potential surfaces are not directly defined, but only the scalar functions for plastic modulus $H_{L/U}$, direction tensors $\mathbf{n}$, and $\mathbf{n}_g$, are required.

For conventional elastoplastic behavior of any materials. The total strain increment can be divided into elastic and plastic components as follows:

$$d\boldsymbol{\varepsilon} = d\boldsymbol{\varepsilon}^e + d\boldsymbol{\varepsilon}^p \tag{1}$$

where $d\boldsymbol{\varepsilon}$, $d\boldsymbol{\varepsilon}^e$, and $d\boldsymbol{\varepsilon}^p$ are the increments of total, elastic, and plastic strain tensors, respectively.

The increments of elastic and plastic strain can be calculated as below:

$$d\boldsymbol{\varepsilon}^e = \mathbf{C}^e : d\boldsymbol{\sigma} \tag{2}$$

, and

$$d\boldsymbol{\varepsilon}^p = d\lambda \mathbf{n}_g = \frac{1}{H_{L/U}} \left(\mathbf{n}_{gL/U} \otimes \mathbf{n} \right) : d\boldsymbol{\sigma} \tag{3}$$

where $\mathbf{C}^e$ is the elastic constitutive tensor, $d\boldsymbol{\sigma}$ is the increment of the stress tensor, $\mathbf{n}_g$ is the unit tensor defining the plastic flow direction, $\mathbf{n}$ represents the loading-direction tensor, $d\lambda$ is a plastic scalar, and $H_{L/U}$ is the plastic modulus, which can be assumed directly without introducing a hardening rule. Subscripts L and U indicate loading and unloading, respectively.

In this study, the definition of the elastic matrix, flow rule, plastic modulus is based on Manzanal et al. [6], whereas the state parameter is extended in following chapter.

STATE PARAMETER AND CRITICAL STATE

In a series of monotonic tests, the results show that the void ratios are affected by the fines content and effective mean stresses. The correlations, including the 3D curved surface and projected fitting curves at a critical state, are shown in Figure 1. The void ratio e_{cs} at the critical state is the function of fines content and effective mean stress, which is defined as

$$e_{cs} = f(\mathrm{FC}, p') = a + b \times \mathrm{FC} + c \times \mathrm{FC}^2 + d / p' \tag{4}$$

where a, b, c, and d are model constants, FC is fines contents, and p' is effective mean stress. These model constants are determined by fitting the laboratory test data.

Moreover, in the proposed model, the state parameter ψ is followed by Been and Jefferies [8] as:

$$\psi = e - e_{cs} \tag{5}$$

where e is the void ratio varying at the loading stage.

*Corresponding author. E-mail: d06521001@ntu.edu.tw

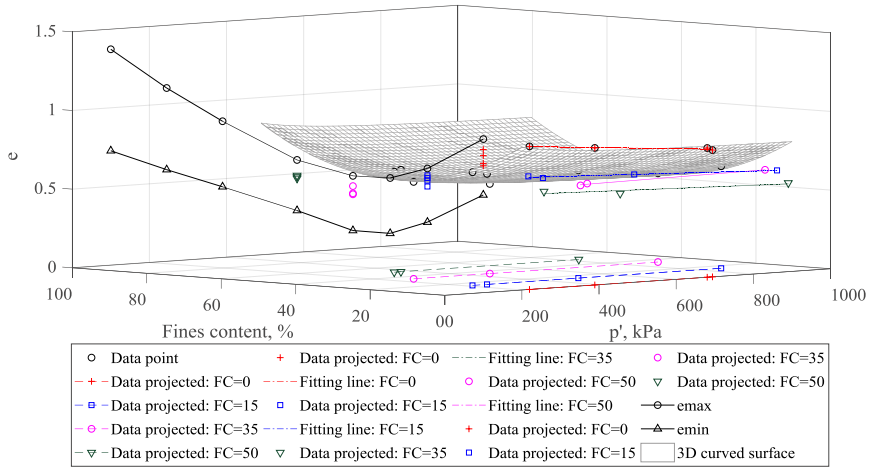

Figure 1. Illustration of critical state surface in effective mean stress (p') and fines content (FC)

MODEL VALIDATION AND SIMULATION

In order to consider the different percentages of fines content under varies effective mean stresses, the state parameter incorporating fines content is involved so that these parameters can be determined meaningfully. Figure 2 displays the simulation results of the stress paths, the deviatoric stress versus axial strain response, and pore pressure verse axial strain behavior under different fine aggregates, and shows that the model can fit the laboratory test data.

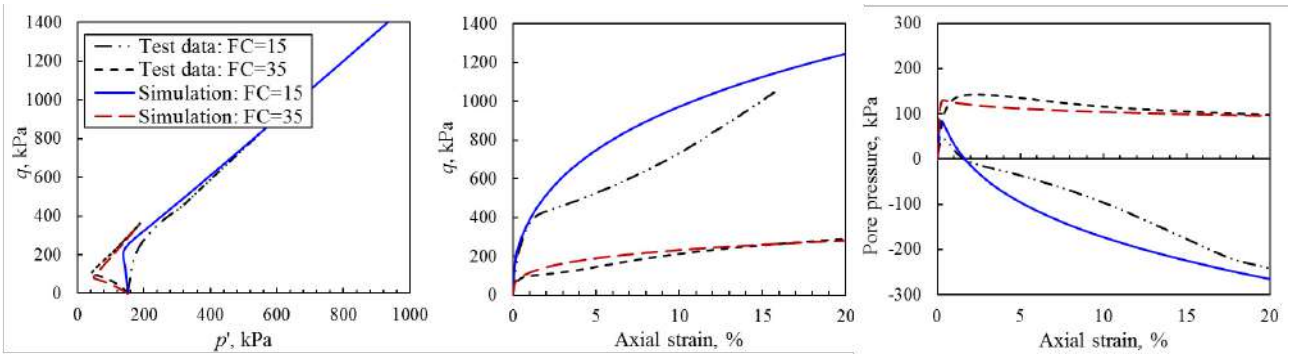

Figure 2. Undrained triaxial compression tests on sand-silt mixtures

CONCLUSIONS

The proposed model with a state parameter incorporating fines content has been shown to predict the undrained behavior of sand-silt mixtures. Also, the generalized plasticity model has been recognized as an effective framework to describe soil behavior. Through the study, a series of monotonic triaxial tests were successfully simulated by the proposed model. The results show that the stress-strain response of sand-silt mixtures can be captured by this model.

ACKNOWLEDGEMENT

The partial financial support provided by the Earthquake Engineering Research Centre in the College of Engineering, National Taiwan University, Taiwan, is greatly acknowledged.

References

[1] Pastor, M., Zienkiewicz, O. C., and Leung, K. H. Simple model for transient soil loading in earthquake analysis. II. Non- associative model for sands. *Int. J. Numer. Anal. Methods Geomech.*, **9**: 477–498, 1985.

[2] Pastor, M, and Zienkiewicz, O.C. Generalized plasticity and the modelling of soil behavior. *Int. J. Numer. Anal. Methods Geomech.,* **14**: 151–190, 1990.

[3] Ling, H.I., and Liu, H. Pressure-level dependency and densification behavior of sand through generalized plasticity model. *J. Eng. Mech.*, **129**(8):851-860, 2003.

[4] Ling, H.I., and Yang S.T. Unified sand model based on the critical state and generalized plasticity. *J. Eng. Mech.*, **132** (12): 1380-1391, 2006.

[5] Liu, Yang, Chang, C.S., and Wu, S.C. A simple one-scale constitutive model for static liquefaction of sand-silt mixtures. *Lat. Am. J. Solids Struct.*, **13**, 2190-2218, 2016.

[6] Manzanal, D., Fernández Merodo, J. A., and Pastor, M. (2011). Generalized plasticity state parameter-based model for saturated and unsaturated soils. Part 1: Saturated state. *Int. J. Numer. Anal. Methods Geomech.*, **35**: 1347-1362, 2011.

[7] Cen, W. J., Luo, J. R., Bauer, E., and Zhang, W. D. Generalized plasticity model for sand with enhanced state parameters. *J. Eng. Mech.*, **144**(12): 04018108, 2018.

[8] Been, K., and Jefferies, M. G. A state parameter for sand. *Géotechnique*, **35**(2): 99-112, 1985.

ON THE BEHAVIOUR OF FINE-GRAINED SOILS IN LABORATORY TESTS AND CONSTITUTIVE MODELING

Merita Tafili*[1] and Theodoros Triantafyllidis[1]
[1]Institute of Soil Mechanics and Rock Mechanics, Karlsruhe Institute of Technology, Karlsruhe, Germany

Summary The complex behaviour of clays is described with a new constitutive model and by experimental observations. Hereby, a new experimental study performed on Lower Rhine Clay (LRC) is presented. Based on the dilatancy rule presented by Taylor (1984), a state dependent dilatancy relation for clays is proposed. A new model neither afflicted with the intergranular strain nor with the fabric-dilatancy tensor is proposed. This model introduces an evolving and rotating historiotropic flow surface, which accounts i.a. for the induced anisotropy and for the degradation of shear modulus. Simulations of LRC are shown to be in good agreement with experimental results, whereby also the 8-shaped hysteresis in the stress space under undrained cyclic loading has been described well. The validation of the model is performed simulating some boundary value problems with ABAQUS.

PROBLEM DEFINITION

Worldwide, more and more areas with soils of low bearing capacity and low stiffness, as in the case of cohesive soils, have to be accessed. Reasons for this include, for example urban expansion or infrastructure projects. Investigations of the ultimate limit state and in particular the serviceability of geotechnical structures on soft soils by means of numerical methods require the use of sophisticated material models which accurately reproduce the specific material behaviour of these soils. Different types of loading have to be considered. A static (or monotonic) loading results from the construction of buildings or a groundwater drawdown, while a cyclic loading is caused by traffic due to cars, trucks and trains. A well documented example is the Metro Line No. 4 in Shanghai [1] where up to 16 cm cumulative settlement within the first four years of operation has been recorded (Fig. 1a). These settlements were mainly caused by the cyclic loading due to the passing trains in the tunnel and resulted in soil subsidence of the surface where buildings suffered cracks and damage. Due to the plasticity of the subsoil, time-dependent settlements have been observed as well.

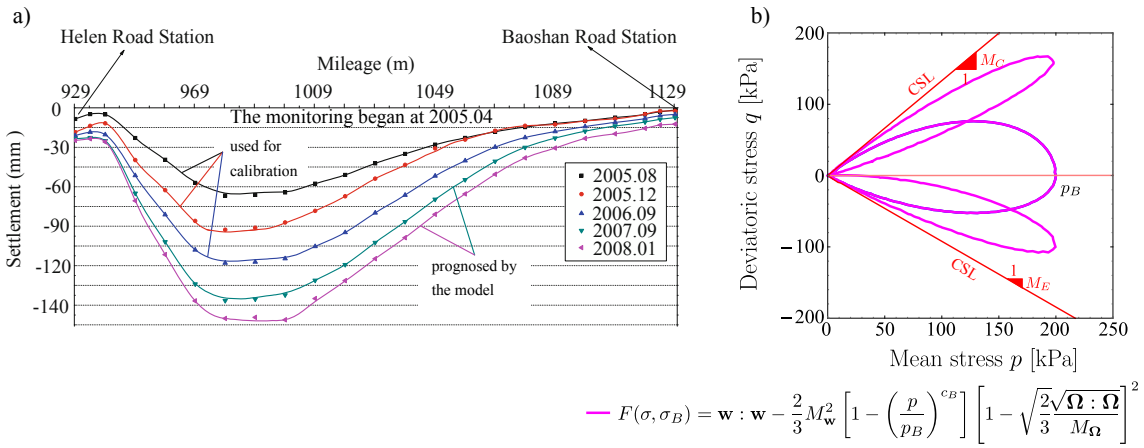

Figure 1: a) Monitoring data (symbols) and prediction with the model (solid lines) of tunnel settlement of Metro Line 4. b) Historiotropic surface for different values of the deviatoric structural tensor $\mathbf{\Omega}$.

To enable the development of constitutive models for the purpose of improving the forecast capabilities of the practical problems addressed above, a new experimental series on the highly plastic LRC ($I_P = 34\,\%$) has been performed at the Institute of Soil Mechanics and Rock Mechanics (IBF) at KIT. Due to the high plasticity of LRC, the realisation of these experiments takes a comparatively very long time. The study comprises tests on normally as well as overconsolidated samples under monotonic and cyclic loading. The loading velocity has been varied in order to evaluate the strain rate dependency of the LRC behaviour. Based on these laboratory tests a new constitutive model with anamnesis function is developed. This model is neither afflicted with the intergranular strain nor with the fabric-dilatancy tensor. It introduces an evolving (in magnitude) and rotating (anisotropic) historiotropic flow surface (Fig. 1b), which accounts i.a. for the induced anisotropy (preloading history of the soil) and for the degradation of shear modulus. The validation of the model was accomplished with the forecast of the accumulated deformations due to cyclic loading of Metro Line No. 4.

RESULTS AND CONCLUSIONS

The experimental study on LRC comprises oedometric tests as well as triaxial tests on normally and overconsolidated samples under monotonic and cyclic loading with variation of initial mean pressure, displacement rate, initial overconsolidation ratio OCR_0 and deviatoric stress amplitude. The effective stress paths of initially normally consolidated samples

*Corresponding author. E-mail: merita.tafili@outlook.de.

reflect a contractant behaviour after an initial isobaric increase of the deviatoric stress. The shear strength increases with increasing initial mean pressure. For initially overconsolidated samples $OCR_0 > 2$ the material behaviour is rendered dilatant and the undrained shear strength increases with OCR_0. The well-known decrease of the undrained shear strength with decreasing displacement rate has also been confirmed with these experiments, see Fig. 2a. Isotropic consolidation with variation of cyclic deviatoric stress amplitude lead to a failure due to large strain accumulation with eight-shaped effective stress paths in the final phase of the tests, Fig. 2b. The inherent anisotropy has been additionally evaluated using samples cut out in either the vertical or the horizontal direction.

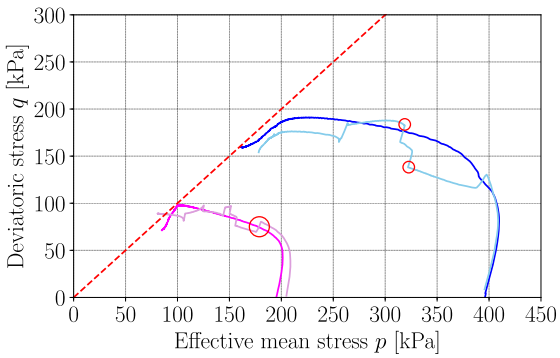

(a) Monotonic undrained triaxial tests with variation of displacement rate $\dot{s}$ on initially normally consolidated samples.

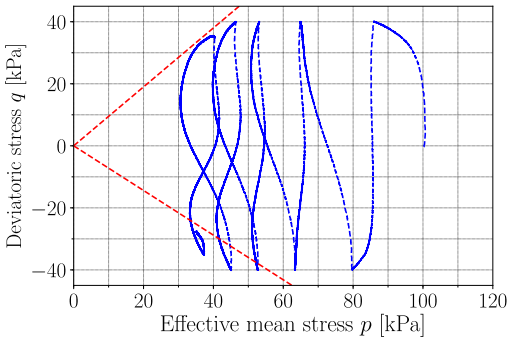

(b) Cyclic undrained triaxial test with $q^{ampl} = 40$ kPa and $\dot{s} = 0.02$ mm/min.

Figure 2: Results of some laboratory tests on LRC.

The new constitutive model with anamnesis function has been used to simulate the experiments. Besides the introduction of inherent and induced anisotropy through the historiotropic surface shown in Fig. 1b, a state-dependent dilatancy rule for clays (depending also on the straining direction) has been proposed:

$$\tan\psi = \beta \left(\overrightarrow{\boldsymbol{\sigma}}^{*} : \overrightarrow{\dot{\boldsymbol{\varepsilon}}}^{*} \tan\varphi_m - \tan\varphi_c \left(\frac{e}{e_c} \right)^{n_{PTL}} \right). \tag{1}$$

Three strain rate components consisting of: total $\dot{\boldsymbol{\varepsilon}}$, hypoplastic $\dot{\boldsymbol{\varepsilon}}^{hp}$ and viscous $\dot{\boldsymbol{\varepsilon}}^{vis}$ strain rates are introduced into the model. Therefore, also rate- and time-dependent phenomena can be described. Even the eight-shaped stress hysteresis at cyclic mobility is reproduced well with this model, see Fig. 3.
In addition the model has been used to predict the monitored settlements of Metro Line No. 4 (symbols in Fig. 1a). Thereby, the three monitoring data sets from August 2005, December 2005 and September 2006 have been used to calibrate the material parameters of the constitutive anamnesis model (solid lines in Fig. 1a). These parameters are used to calculate the subsequent settlements in September 2007 and January 2008 showing a perfect agreement between the model and the monitored data (solid lines in Fig. 1a).

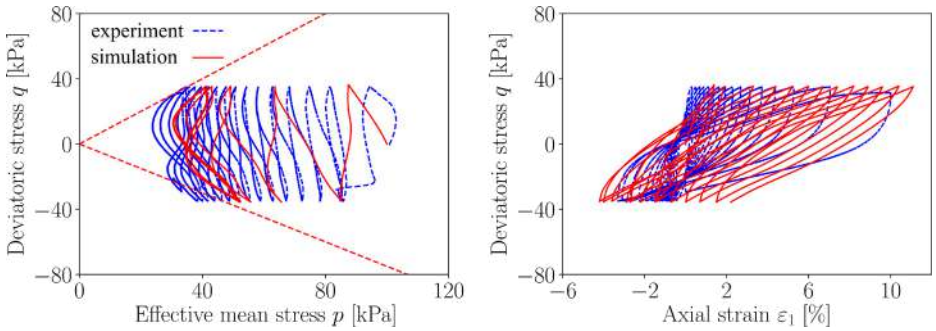

Figure 3: Effective stress path and deviatoric stress - axial strain relations for an undrained cyclic test on LRC with $q^{ampl} = 35$ kPa.

References

[1] Ren X. W., Qun T., Li J., Yang Q. A prediction method using grey model for cumulative plastic deformation under cyclic loads. *Nat Hazards* **64**: 441-457, 2012.
[2] Tafili M., Fuentes W., Triantafyllidis T. A comparative study of different model families for the constitutive simulation of viscous clays. *Int J Numer Anal Methods Geomech* **1**: 1-35, 2020.
[3] Tafili M. On the Behaviour of Cohesive Soils: Constitutive Description and Experimental Observations. *PhD Thesis*, Institute of Soil Mechanics and Rock Mechanics, Karlsruhe, Germany, 2019.

HYBRID FEM/PD SIMULATION OF FORERUNNING OF A DYNAMIC FRACTURE IN DRY AND FULLY SATURATED POROUS SOLIDS

Tao Ni[1], Ugo Galvanetto[1], Francesco Pesavento[2], Mirco Zaccariotto[1], and Bernhard A. Schrefler*[2]
[1]Industrial Engineering Department, University of Padova, Padova, Italy
[2]Department of Civil, Environmental and Architectural Engineering, University of Padova, Padova, Italy

Summary In this paper, a novel hybrid FEM and Peridynamic modelling approach is used to predict the forerunning fracture behavior in dry and saturated porous solids. Fracturing in a rectangular structure with a central initial crack is simulated both under mechanical loading and fluid-driven conditions. In the mechanical loading fracture case, fixed concentrated forces are applied on the upper and lower surfaces of the initial crack at the central position to force its opening. In the fluid-driven fracture case, a fixed fluid injection rate is adopted. Under the action of the applied concentrated force and fluid injection, forerunning of the fracture is observed.

INTRODUCTION

According to some experimental and numerical evidences [1-2], the dynamic fracture propagation in dry and fully saturated porous solids is not always smooth and continuous. The stepwise fracture tip advancement has duly been documented with experiments and geophysical observations [3]. A special type of stepwise tip advancement is forerunning observed in dynamics [4-6]. In particular Tvergaard and Needleman [4] observe in case of a dynamic crack growth in a ductile porous medium that "sometimes a secondary crack develops ahead of the main crack and subsequently links up with it. This leads to a situation where the crack appears to be stationary for a relatively long time and then grows rather abruptly". Inspired by [6], which evidences that the action of high-amplitude incident sinusoidal waves could lead to forerunning mode of fracture, Peridynamic-based numerical approach is used to investigate the possibility of forerunning fracture behavior in a rectangular structure with a central initial crack under different loading conditions. A novel hybrid FEM and Peridynamic modelling approach, based on Hybrid Mixture Theory [7] and proposed in [8], is adopted to simulate the hydro-mechanical coupled fracturing process in saturated porous media. Under the action of the applied concentrated force and fluid injection, forerunning fracture behavior is observed in the structure.

MATERIALS AND METHODS

Governing equations

In the whole domain Ω of the porous medium, the solid phase is governed by the ordinary state-based peridyanmic equation:

$$\rho\ddot{\boldsymbol{u}}\left(\boldsymbol{x},t\right)=\int_{\mathcal{H}_x}\left\{\underline{\mathbf{T}}\left[\boldsymbol{x},p,t\right]\left\langle\boldsymbol{\xi}\right\rangle-\underline{\mathbf{T}}\left[\boldsymbol{x}',p',t\right]\left\langle-\boldsymbol{\xi}\right\rangle\right\}dV_{x'}+\boldsymbol{b}\left(\boldsymbol{x},t\right)\tag{1}$$

and the flow field in the saturated porous medium is described by Darcy's law, resulting in a mass conservation equation of the fluid as:

$$\rho s\frac{\partial p}{\partial t}+\rho\alpha\frac{\partial\varepsilon_v}{\partial t}+\rho\nabla\cdot\left[\frac{k}{\mu^w}\left(\nabla p+\rho g\right)\right]=q\tag{2}$$

Discretization and numerical algorithm

In a plane discretization, the solid portion is discretized by PD nodes and the fluid portion is discretized by 4-node FE elements. PD nodes and FE nodes share the same node coordinates. A 'staggered approach' is used to solve the coupled system. The peridynamic and FEM equations are solved sequentially, and the previously solved results of $\boldsymbol{u}$ and $\boldsymbol{p}$ are used to evaluate the fluid volumetric source terms or nodal forces for the next solving sequence.

NUMERICAL RESULTS

The geometry and constraints of the considered rectangular structure are shown in Figure 1. The mechanical and fluid parameters used in the calculation are, Young's modulus: $E=10GPa$, Poisson's ratio: $\upsilon=0.2$, critical energy release rate: $G_c=1J/m^2$, porosity: $n_r=0.002$, mass density: $\rho_r=\rho_f=1000kg/m^3$, Biot constant: $\alpha=1$, bulk modulus and viscosity coefficient of the fluid: $K_w=2.2GPa$ and $\mu_w=10^{-3}Pa\cdot s$, permeability coefficient of the reservoir domain: $k_r=10^{-12}m^2$.

Two different loading conditions, mechanical loading and fluid injection, are adopted. In the mechanical loading case, concentrated forces, $25000N$, are applied on the upper and lower surfaces of the initial crack at the central position to force its opening, and both dry and saturated condition are considered. In the fluid injection case, the injection rate is adopted as $Q=5\times10^{-2}m^2/s$. In the simulation, the forerunning of the fracture, see Figures 2a to 2c, is observed. As shown in Figures 3a-3d, the wave propagation of pore pressure is also observed in the saturated structures both under the action of mechanical loading and fluid injection conditions.

*Corresponding author. E-mail: bernhard.schrefler@dicea.unipd.it.

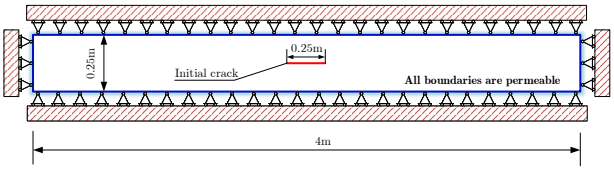

Figure 1: Geometry and constraints of the rectangular structure with a central initial crack.

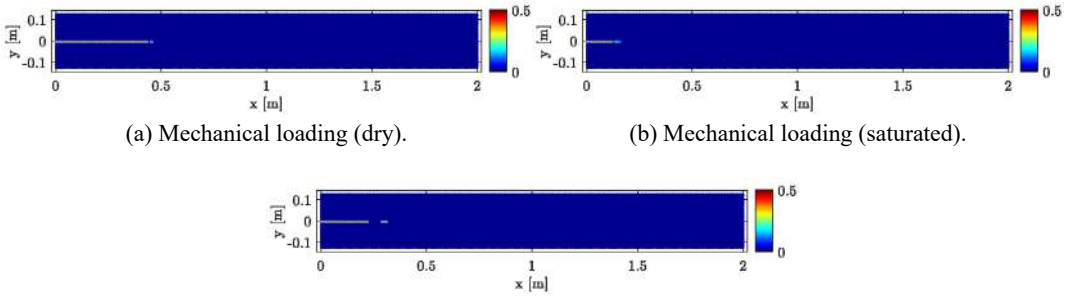

(a) Mechanical loading (dry).

(b) Mechanical loading (saturated).

(c) Fluid injection (saturated).

Figure 2: Forerunning fracture in the front of the crack tip.

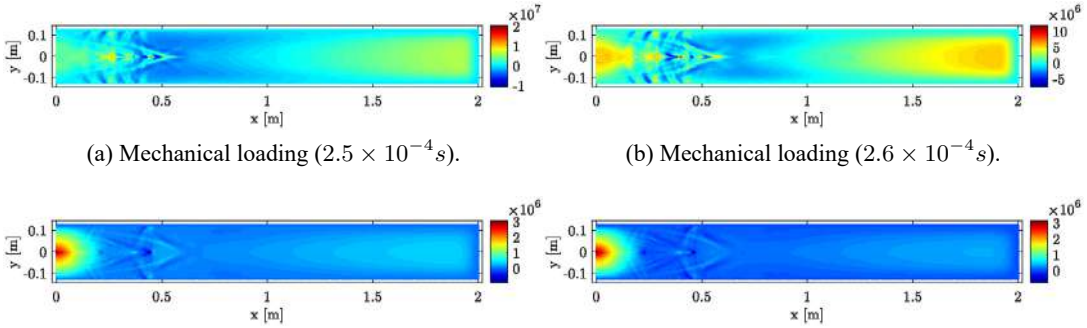

(a) Mechanical loading ($2.5 \times 10^{-4}s$).

(b) Mechanical loading ($2.6 \times 10^{-4}s$).

(c) Fluid injection ($4.5 \times 10^{-4}s$).

(d) Fluid injection ($4.6 \times 10^{-4}s$).

Figure 3: Wave propagation of pore pressure in the saturated structures.

CONCLUSIONS

The hybrid FEM and Peridynamic modelling approach is applied in the simulation of dynamic fracture propagation in dry and fully saturated porous media. In the simulations, forerunning fracture events, a phenomenon that has been observed experimentally in geomaterials [5], occur in the studied structures. Besides of the mechanical wave, the pressure waves have also been numerically confirmed to exist in saturated structures. The interaction between mechanical waves and pressure waves makes dynamic fracturing in saturated media more complicated, influencing also the forerunning episodes.

References

[1] Peruzzo C, Cao D T, Milanese E, et al. Dynamics of fracturing saturated porous media and self-organization of rupture. ***EUR. J. MECH. A-SOLID***, **74**: 471-484, 2019.

[2] Cao T D, Hussain F, Schrefler B A. Porous media fracturing dynamics: stepwise crack advancement and fluid pressure oscillations. ***J. MECH. PHYS. SOLIDS***, **111**: 113-133, 2018.

[3] Peruzzo C., Simoni L., Schrefler B. A. On stepwise advancement of fractures and pressure oscillations in saturated porous media. ***ENG. FRACT. MECH.***, **215**: 246-250, 2019.

[4] Tvergaard V., Needleman A. An analysis of the brittle-ductile transition in dynamic crack growth. ***INT. J. FRACT.***, **59**: 53-67, 1993.

[5] Sammonds PR, Meredith PG, Ayling MR, Jones C, Murrell SAF. Acoustic measurements during fracture of triaxially deformed rock, from Fracture of Concrete and Rock: recent developments. In: Shah S, Swartz SE, Barr S, editors, eBook, Boca Raton, FL : ***CRC Press***, 2014.

[6] Slepyan L., Ayzenberg-Stepanenko M., Mishuris G.. Forerunning mode transition in a continuous waveguide. ***J. MECH. PHYS. SOLIDS***, **78**: 32-45, 2015.

[7] R. W. Lewis and B. A. Schrefler, The Finite element method in the static and dynamic deformation and consolidation of porous media. ***John Wiley***, 1998.

[8] Tao Ni, Francesco Pesavento, Mirco Zaccariotto, Ugo Galvanetto, Qizhi Zhu, Bernhard A. Schrefler. Hybrid FEM and Peridynamic simulation of hydraulic fracture propagation in saturated porous media. **COMPUT. METHOD. APPL. M.**, **366**, 113101, 2020.

3D DEM INVESTIGATION OF THE MECHANICAL PROCESSES OCCURING IN DRY GRANULAR MASSES DURING IMPACTS

Irene Redaelli*[1], Claudio di Prisco[1], and Francesco Calvetti [2]
[1]Department of Civil and Environmental Engineering, Politecnico di Milano, Milano, Italy
[2]Department of Architecture, Built Environment and Construction Engineering Politecnico di Milano, Milano, Italy

Summary In this work, the authors will investigate the physical and mechanical processes occurring during impacts between rigid bodies and coarse granular materials. Two different configurations will be considered: (i) impact between a granular flowing mass and a rigid body at rest, (ii) impact between a boulder and a granular material at rest. The impact process will be numerically simulated by employing the Discrete Element Method (DEM) since this is capable of automatically take into account the discrete nature of the granular material and allows to correlate the macroscopic quantities, such as the impact force, with local information.

INTRODUCTION

Dry granular materials can be involved in impacts phenomena either when a flow like landslide interacts with structures or during rockfall events, when a boulder impacts against the coarse granular stratum placed along a slope. In the first case, the granular mass is characterized by an initial geometry, velocity and porosity and impacts against a fixed rigid body; in the second case, the collision involves a rigid boulder, characterized by an initial velocity and mass, and the granular material, which is at rest.
In both cases, due to the dynamicity of the impact process, different phenomena occur in the granular materials, such as shock wave propagation, wave reflections, bouncing, force chains buckling effects and phase transition. These processes are strongly influenced by either the energy content of the impact, the granular mass packing, and particle size distribution. The purpose of this work is to investigate the physical mechanisms governing the dynamic interaction of a dry granular mass and a rigid body. The Discrete Element Method is employed and the dry granular mass involved in the impact process is represented as an assembly of polydisperse spherical particles. The contact force among grains is computed by employing a linear model along the normal direction and a linear model in series with a slider obeying the Coulomb failure criterion, along the tangential direction. The parameter employed in [1, 2, 3] have been imposed and damage or fragmentation of soil particles is not considered. In order to reproduce the response of a real granular material with non-spherical particles, particles rotation is not allowed [1]. The DEM allows to correlate the macroscopic quantities, such as time evolution of the impact force, with local information (contact forces, particle velocities, coordination number, energy propagation) and to highlight the physical and mechanical processes responsible for the macroscopic behavior [1,2].

NUMERICAL MODELS AND RESULTS

Dry granular masses impacting against a rigid obstacle

The impacting granular mass has been generated just in front of a vertical wall with a prescribed geometry and initial conditions (Fig 1a) [1, 2, 3]. The geometry of the impacting mass is characterized by the length L and height h. The front of the sliding mass is assumed to be planar and inclined of an angle a. Plain strain conditions are imposed by confining the flow between two smooth lateral walls. The flow width is chosen in order to avoid boundary effects [3]. The mass flows on a frictional horizontal wall, wheras the obstacle is modelled as a frictional vertical rigid and massless wall.
After the impact, different concurring and competiting processes are observed within the granular media [2, 4]: the increase in the contact area between the mass and the obstacle, the propagation of compression and no-tension waves and internal buckling. The last two mechanisms cause a continuous fluidification and resolidification of the granular material, due to the disruption and regeneration of force chains. All these processes are governed by the geometry of the sliding mass (length, width and flow height, inclination of the front) by the initial mass velocity and porosity. Basing on the correlation between physical observations and the shape of the force-time curve, a formula to be used as an input for the dynamic design of sheltering structures has been proposed.

Rigid boulder impacting against dry granular masses

The soil cushion is modelled as an assembly of polydisperse spherical particles [5, 6]. This cushion is generated by employing the pluviation method and is confined by four lateral walls and one wall at the bottom (Fig 1b). The size of the domain has been chosen in order to eliminate lateral boundaries disturbances. Inclined layers are generated by quasi-statically rotating the model of a prescribed angle. The spherical impacting block is generated on the top of the granular layer with an initial incident translational velocity (vertical or inclined). After the impact, an energy exchange between the block and the granular mass is observed. This results in the propagation of a shock wave in the mass and the the

*Corresponding author. E-mail: irene.redaelli@polimi.it

subsequent fluidification and resolidification of the material arount the impacting point. All these processes are governed by the energy content of the impact, by the ratio between impacting bolder radius and mean radius of the particles of the soil layer, by the soil properties (porosity, granular size distribution), by the geometrical and kinematic properties of the impacting boulder (velocity modulus and direction) and by the distance of the bottom wall (representing the bedrock below the scree).

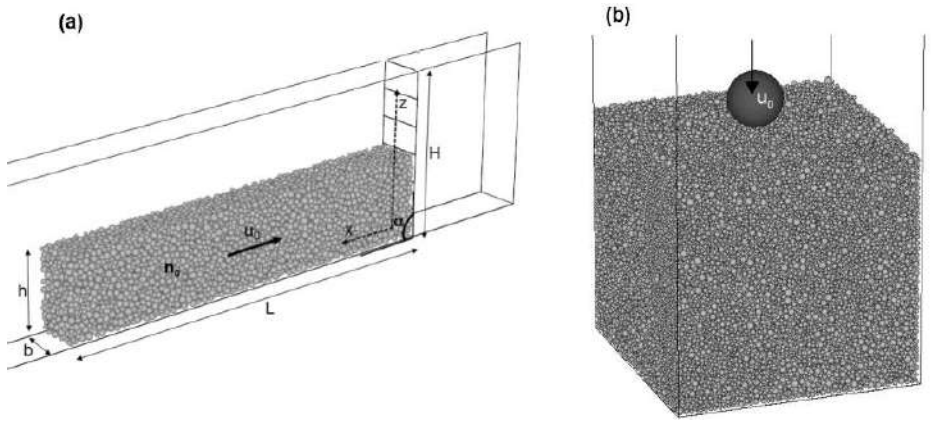

Figure 1. Numerical DEM models: (a) impact of a landslide against a rigid wall (b) impact of a boulder against a granular stratum.

CONCLUSIONS

The impact process between a rigid body and a deformable granular mass is very complex since the dynamicity of the process may induce waves propagation, damage of particles and fluidification within the granular media.
In this study the DEM has been employed to put in evidence all these processes either when a dry granular mass impact a rigid wall or when a spherical boulder impacts against a granular layer. The DEM can in fact automatically take into account local variation of porosity and internal microstructure, the dependence of the material response on strain rate and packing as well as all the dissipation mechanisms characterizing the granular materials such as inelastic collisions and frictional processes occurring between contacting grains. The results have been employed to interpret the macroscopic observation, such as time evolution of interaction force between soil and rigid body (Fig.2). This represent an important information which can be employed for the dynamic design of sheltering structures.

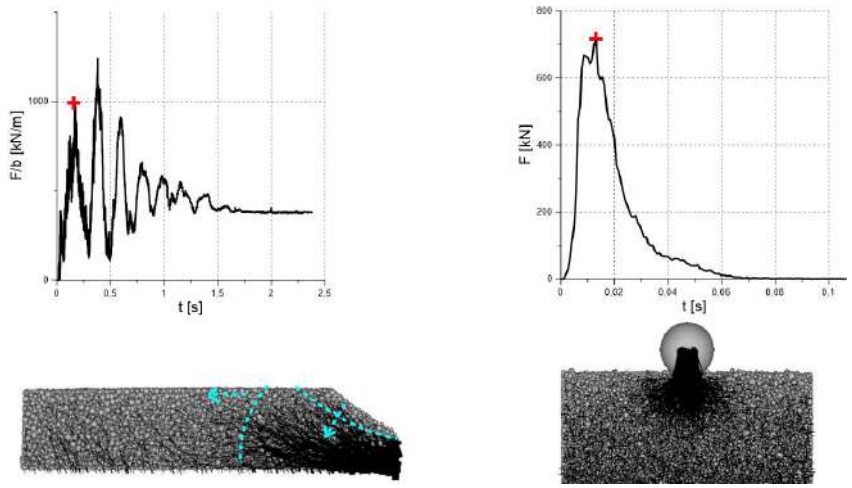

Figure 2. Force time curve and force chains at the peak in case of (a) impact of a landslide against a rigid wall (b) impact of a boulder against a granular stratum.

References

[1] Calvetti, F., di Prisco, C, Redaelli, I, Sganzerla, A, Vairaktaris E. Mechanical interpretation of dry granular masses impacting on rigid obstackes. *Acta Geotech*. 1-17, 2019.
[2] Calvetti, et. al. DEM assessment of impact forces of dry granular masses on rigid barriers. *Acta Geotech*, *12*(1), 129-144, 2017
[3] Ceccato, F., Redaelli, I., di Prisco, C., & Simonini, P. Impact forces of granular flows on rigid structures: comparison between discontinuous (DEM) and continuous (MPM) numerical approaches. *Comput and Geotech*, *103*, 201-217, 2018.
[4] Redaelli, I., di Prisco, C., & Calvetti, F. (2019, July). Temporal Evolution of the Force Exerted by Dry Granular Masses Impacting on Rigid Sheltering Structures. In *National Conference of the Researchers of Geotechnical Engineering* (pp. 13-22). Springer, Cham.
[5] Calvetti, F. Rockfall shelters covered by granular layers: Experiments and design approach. *Eur J Environ Civ En*, *15*(sup1), 73-100, 2011
[6] Bourrier, F., Nicot, F., & Darve, F. Physical processes within a 2D granular layer during an impact. *Granular Matter*, *10*(6), 415-437, 2008.

CONSTITUTIVE MODELLING OF SATURATED GRANULAR MATERIALS UNDER STEADY CONDITIONS

Pietro Marveggio[1*], Dalila Vescovi[1], Irene Redaelli [1]and Claudio di Prisco [1]
[1]Department of Civil and Environmental Engineering, Politecnico di Milano, Milano, Italy

Summary The authors introduce a new constitutive model capable of capturing the transition from solid-to-fluid like conditions of dry and saturated granular materials on the base of the mixture theory, according to which granular and liquid phases are considered separately. As far as the granular contribution is concerned, the authors employ an already conceived constitutive model where the critical state concept and the kinetic theory of granular gases are merged, and in which the granular temperature plays the role of state variable for the material. Under saturated conditions, the new model accounts for granular-liquid coupling effects. In fact, the liquid viscosity results to be a function of granular concentration, whereas the evolution of granular temperature is influenced by the liquid molecular viscosity. The model is validated against numerical results and critically discussed.

INTRODUCTION

Flow-slides are commonly numerically simulated tackling separately the inception and the propagation of gravitational movements, since a constitutive model capable of simulating the transition of the material behaviour from solid- to fluid-like conditions and vice versa is still an open challenge. Such a transition takes place when force chains disappear and the energy is mainly dissipated by collisions among grains. From an energetic point of view, under solid conditions the elastic contribution is dominant, whereas under fluid-like conditions the kinetic term (associated with grain agitation) prevails.
Recently, the authors have proposed a constitutive approach to describe the mechanical behaviour of dry granular materials in both regimes (quasi-static and collisional) [6,7]. To extend the proposed framework to saturated conditions, additional dissipation mechanisms associated with the liquid phase have been accounted for.

CONSTITUTIVE APPROACH

The theoretical approach conceived by the authors to describe the mechanical behavior of both dry and saturated granular materials under steady conditions is based on the description of the physics of the grain-grain and grain-water interaction, assuming that: (i) the granular material can be either dry or saturated by water (unsaturated conditions are not taken into account), (ii) solid fraction is made of an assembly of ideal, monodisperse, frictional, deformable and uncrushable spheres.
As far as the granular solid fraction is concerned, the authors employ an already conceived constitutive approach capable of describing, at the same time, the mechanical behaviour of agitated granular flows (fluid-like regime) and solid-like granular systems. The approach followed by the authors is based on the introduction of an additional state variable, the granular temperature [2], describing the system agitation, and on the assumption that the critical state [8,11,12] for highly concentrated granular materials is the limit of steady state conditions for shear strain rates going to zero. Under dry conditions, the energy dissipation may be due either to frictional contacts belonging to force chains, or to instantaneous collisions, these latter dominating in case of small values of concentration and large values of shear rates.
Under saturated conditions, additional dissipation contributions arise in the liquid phase. These are associated with the following effects: (i) deviation of the liquid streamlines due to the presence of particles, behaving as obstacles; (ii) lubrication; (iii) liquid velocity fluctuations due to grain agitation.
These dissipation contributions involve the liquid phase. According to the approach proposed by the authors, the liquid viscosity depends on the concentration according to a suitably calibrated function [10]. On the other hand, the presence of water plays a damping role in reducing the fluctuating energy of the granular phase. This damping effect is associated with an increase in the liquid pressure (dynamic contributions).
The energy balance is used by the authors to describe the coupling between the two phases. In fact, the granular temperature results to be influenced by the liquid phase molecular viscosity and governs the fluid- to solid-like transition and vice versa in the material response.

VALIDATION AND DISCUSSION

The new constitutive approach is validated against DEM numerical simulations for steady conditions and discussed in the framework of the μ-e-I [3,4] and μ-e-K [1,9] rheology for dry and saturated conditions, respectively. For dry materials, DEM simulations by Redaelli et al. [7] are considered, while numerical data by Ness and Sun [5] are simulated by saturated conditions. These simulations have been performed by replacing the liquid phase with some long-range lubrication forces acting at the contact among particles. Concerning saturated conditions the proposed framework is capable of correctly reproducing the reality by capturing: (i) for sufficiently small values of concentration, the transition from Newtonian to Bagnoldian regimes, when the shear rate is increased; (ii) the independence of the shear mechanical behaviour of the mixture when the concentration is sufficiently high and the material behaves like a solid.

*Corresponding author. E-mail: pietro.marveggio@polimi.it.

CONCLUSIONS

The authors presented an innovative approach capable of capturing the transition from solid-to-fluid like conditions, in dry or saturated granular materials, validated under steady conditions against DEM numerical results and the well-known μ rheology for both dry (μ-e-I) and saturated conditions (μ-e-K). The formulation proposed by the authors has been shown to be capable of satisfactorily simulate the mechanical behavior of granular materials (under dry and saturated conditions), in both fluid and solid regimes and to put clearly in evidence the limitations of the commonly employed constitutive approaches not considering separately solid and liquid phases.

This work has been supported by Fondazione Cariplo, grant n. 2016-0769.

References

[1] F. Boyer, E. Guazzelli, and O. Pouliquen, "Unifying suspension and granular rheology," Physical Review Letters, vol. 107, 2011.
[2] Garzó, V. & Dufty, J. W. (1999). Dense fluid transport for inelastic hard spheres., Physical. Re-view. E. 59(5): 5895-5911.
[3] Jop, P., Forterre, Y., & Pouliquen, O. (2006). A constitutive law for dense granular flows. Na-ture, 441(7094), 727.
[4] MiDi, G. D. R. (2004). On dense granular flows. The European Physical Journal E, 14(4), 341-365.
[5] Ness, C. & Sun, J. (2015). Flow regime transitions in dense non-Brownian suspensions: Rheology, microstructural characterization, and constitutive modeling Physical Review E, American Physical Society (APS), 91
[6] Redaelli, I., di Prisco, C. & Vescovi, D. (2016). A visco-elasto-plastic model for granular materials under simple shear conditions. International Journal for Numerical and Analytical Methods in Geomechanics. 40(1): 80–104.
[7] Redaelli, I., di Prisco, C. (2019). Three dimensional steady-state locus for dry monodisperse gran-ular materials: DEM numerical results and theoretical modelling. International Journal for Numerical and Analytical Methods in Geomechanics. 43(16): 2525-2550.
[8] Sun, J., & Sundaresan, S. (2011). A constitutive model with microstructure evolution for flow of rate-independent granular materials. Journal of Fluid Mechanics, 682, 590-616.
[9] M. Trulsson, B. Andreotti, and P. Claudin, "Transition from the Viscous to Inertial Regime in Dense Suspensions," Physical Review Letters, vol. 109, p. 118305, Sept. 2012
[10] Vescovi D., Marveggio P. & di Prisco C. (2019). Saturated granular flows: constitutive modelling under steady simple shear conditions. Géotechnique. Ahead of print, 10.1680/jgeot.19.P.023.
[11] Xiao, Y., Liu, H., Sun, Y., Liu, H., & Chen, Y. (2015). Stress–dilatancy behaviors of coarse granular soils in three-dimensional stress space. Engineering Geology, 195, 104-110.
[12] Zhao, J., & Guo, N. (2013). Unique critical state characteristics in granular media considering fabric anisotropy. Géotechnique, 63(8), 695.

CHANGE IN CURVATURE OF PORE WATER IN PARTIALLY SATURATED SAND AND ITS INFLUENCE ON DEVIATOR STRESS UNDER TRIAXIAL COMPRESSION

Ryunosuke Kido*[1] and Yosuke Higo [2]
[1]Department of Civil and Earth Resources Engineering, Kyoto University, Kyoto, Japan
[2]Department of Urban Management, Kyoto University, Kyoto, Japan

Summary Two triaxial compression tests on partially saturated silica sand specimens are conducted under drained and undrained conditions for water. In these tests, microscopic deformation of the specimens focusing on shear bands are visualized using x-ray micro tomography and the change in the curvature of pore water, i.e., suction, is investigated using image analyses. It is found that the curvature of pore water under drained condition for water is higher than that under undrained condition for water, and hence the deviator stress of the specimen under drained condition for water is higher than that under undrained condition for water.

INTRODUCTION

Partially saturated soil comprises soil particle, pore water and pore air. Mechanical behaviors of the partially saturated soil strongly depend on suction at capillary bridges. The suction works as inter-particle force, resulting in higher stiffness of partially saturated soil than fully saturated soil. On the other hand, partially saturated soil exhibits more brittle modes of failure with clearer shear band than fully saturated soil [1]. This is related to the loss of suction due to variations in bulk density and degree of saturation caused by water infiltration and shearing, causing a reduction in the stiffness and the strength of partially saturated soil. It is important, therefore, to measure the variation in suction during deformation of partially saturated soil with shear bands in order to reveal the failure mechanism of partially saturated soil.

In the present study, x-ray micro tomography focusing on shear bands is applied at different stages of deformation during triaxial compression tests on partially saturated sand specimens under two conditions: drained conditions for air and water, and a drained condition for air and an undrained condition for water. Deviator stress-axial strain relationships of the specimens are observed and then the development of shear bands is visualized. A segmentation technique for the soil particle, the pore water and the pore air, i.e., trinarization, is applied to the tomographic volumes obtained in the tests. Principal curvatures of pore water in the trinarized volumes are measured using an image processing technique. It is found that the curvature of pore water under drained condition for water is higher than that under undrained condition for water, and hence the residual stress of the specimen under drained condition for water is higher than that under undrained condition for water.

EXPERIMENTAL METHODS

The material used in the present study was silica sand #5. The physical properties of the silica sand include a soil density of 2.64 g/cm^3, a maximum void ratio of 1.013, a minimum void ratio of 0.694, a D_{50} of 456 μm, a uniformity coefficient of 1.3 and a fines content of 0.1 %. The silica sand is advantageous for visualizing individual soil particles and distributions of pore water and pore air with high spatial resolution because of the large grain size. On the other hand, the water retention capability of the silica sand is relatively low; the level of suction lower than 10 kPa gives the residual degree of saturation of about 20%. Two triaxial specimens were prepared by a water pluviation technique. Once the water-saturated specimens had been prepared, they were desaturated by a water head difference.

The x-ray micro tomography facility used in the present study is KYOTOGEO-μXCT (TOSCANER-32250μhdk, TOSHIBA IT and Control Systems Corporation) [2]. At the different loading stages of the triaxial compression, the local region of interest focusing on shear bands in the specimens was visualized. Axial loading was suspended during x-ray tomography for around two hours, after which it was resumed.

Triaxial tests were performed under two conditions, namely, drained conditions for both air and water, and a drained condition for air and an undrained condition for water. The former condition assumes that partially saturated soil deforms without any excess pore water pressure due to slow shearing or the high permeability of the soil, while the latter condition assumes that partially saturated soil deforms with excess pore water pressure due to relatively fast shearing or low permeability, respectively. Namely, the level of suction in the former condition is kept constant, while that in the latter condition is varied.

IMAGE PROCESSING TECHNIQUES

A minimum unit of CT images is called as voxel. Each voxel in CT images shows a certain CT value depending on the material density. CT images scanning partially saturated sand include voxels for the soil particle phase, the pore water phase and the pore air phase. In the present study, a segmentation technique of the three phases, i.e., trinarization [3], is applied to the CT volumes obtained during the triaxial compression tests. The 3D image analysis software VGstudioMax3.1 (Volume Graphics GmbH) is used for the trinarization. Voxels in the trinarized volumes show three kinds of CT value corresponding to the soil particle phase, the pore water phase and the pore air phase. Therefore, local void ratios and local degrees of saturation in the trinarized volumes can be calculated by counting the number of voxels

*Corresponding author. E-mail: kido.ryunosuke.2m@kyoto-u.ac.jp

for the three phases. The trinarization technique was validated by confirming that the void ratio and the degree of saturation of a specimen and those calculated by the trinarization technique were quite similar to each other.

Interfaces between the pore water phase and the pore air phase were extracted from the trinarized volumes as shown in Figure 1. Maximum principal curvatures whose inverted values are closer to the radius of a sphere locally fitting the interface are calculated as the principal curvatures of pore water. Suction can be estimated by a surface tension of water and principal curvature of water $1/r_1$ as shown in Figure 1.

RESULTS

Two triaxial specimens show the peak deviator stress followed by the strain softening and finally the residual stress is observed. It is found from the CT images that the specimens exhibit shear bands. Trinarization reveals that the void ratio is increased and then the degree of saturation is decreased due to the development of shear bands. The residual stress under drained condition for water is higher than that under undrained condition for water, and then the curvature of pore water, i.e., suction, under drained condition for water is higher than that under undrained condition for water as shown in Figure 2.

CONCLUSIONS

A Principal curvature of pore water in partially saturated sand is lower during the triaxial compression under an undrained condition for water than under a drained condition for water at the residual state, resulting in the lower deviator stress under an undrained condition for water than under a drained condition for water.

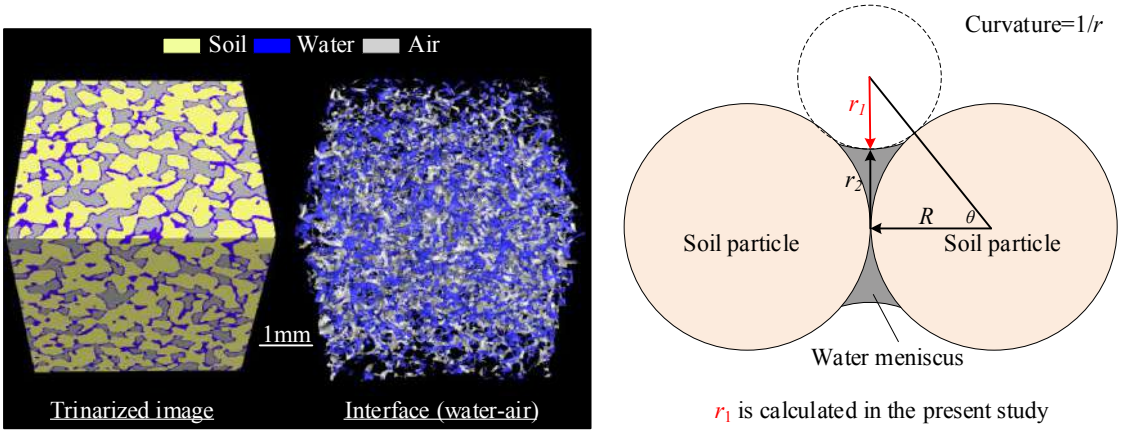

Figure 1. Interface between water and air extracted from trinarized image and principal curvature of pore water between soil particles

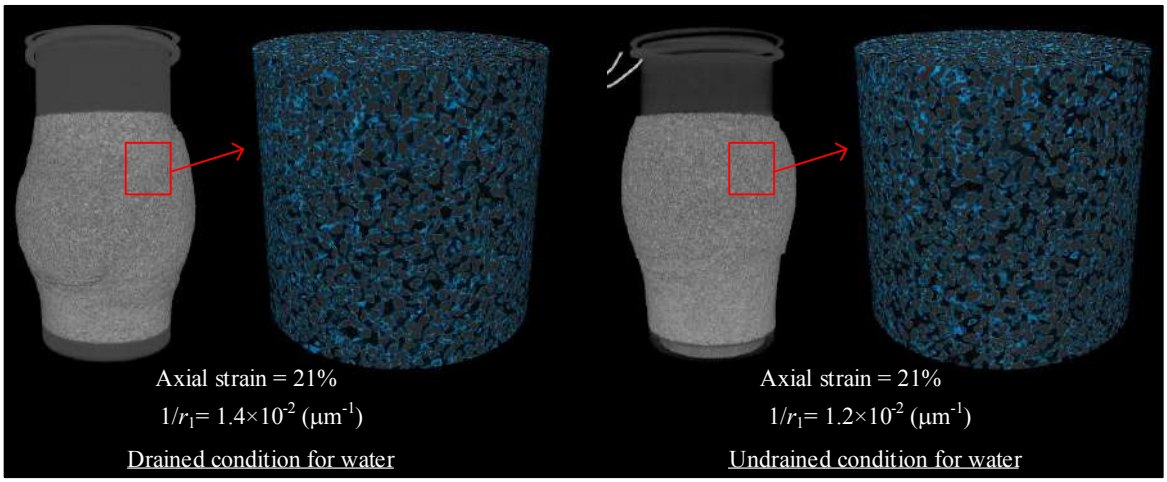

Figure 2. Application of image analysis techniques to CT images obtained in triaxial compression tests.

References

[1] Cunningham M. R. The mechanical behavior of a reconstituted unsaturated silty clay. *Geotechnique*. **53**: 183-194, 2003.
[2] Y., Oka F., Kimoto S., Sanagawa T., Matsushima Y. Study of strain localization and microstructural changes in partially saturated sand during triaxial tests using microfocus X-ray CT. *Soils and Foundations*. **51**: 95-111, 2011.
[3] Kido R., Higo Y. Evaluation of distribution of void ratio and degree of saturation in partially saturated triaxial sand specimen using micro x-ray tomography. JGS special publication. **5**:22-27, 2017.

MULTIPLE MULTI-SCALE INSTABILITIES IN THE PROCESS OF DRYING OF GRANULAR MATERIALS

B. Mielniczuk[1], S.M. El-Youssoufi[2], Shu Yang[1], A. Guevel[1], M. Veveakis[1] and T. Hueckel[1]
[1] Department of Civil and Environmental Engineering, Duke University, Durham, NC, USA;
[2] Department of Mechanics and Civil Engineering, University of Montpellier, France

Summary Drying granular materials transition between forms of water that are classified as capillary, funicular and pendant bridges. These transitions are controlled either by a slow evaporation induced displacement of the liquid/gas interface, or an unstable reconfigurations of the interface, called correspondingly *isons*, and *rheons*. Some of the above phenomena have been known for long time, but their understanding and quantitative descriptions are lacking. We present results of experiments and their interpretation at three different geometrical scales: a micro-scale of assemblies of several grains, a meso-scale of large assemblies of hundreds of grains, and at a macro-scale of a continuum. At each scale the fluid (water) plays the role of a cohesive medium that transmits forces between the grains, with different characteristics and different repercussion for the other scale.

INTRODUCTION

Transition between various forms of capillary water that are classified as capillary bridges, funicular and pendant bridges are primary events in granular materials undergoing drying. The transitions are due to either a slow evaporation induced displacement of the liquid/gas interface, or an ultra-fast and unstable reconfigurations of the interface, called correspondingly *isons*, and *rheons*. Dynamic manifestations of rheons have been known as Haines jumps. Although some of the characteristics of the above phenomena have been known for long time, their understanding and quantitative descriptions are lacking.

In the paper we present the experiments and their interpretation at three different geometrical scales: a micro-scale of assemblies of several grains, a meso-scale of large assemblies of hundreds to thousands of grains, and finally at a macro-scale of a continuum of grains. At each scale the fluid (water) plays the role of a cohesive medium that transmits forces between the grains, with different characteristics and different consequences for the other scale.

The variables characterizing the evolution during evaporation of capillary bridge between the grains are analyzed. The grains investigated are spheres of different materials, such as glass, Teflon and clay clusters, and are of the same kind and size.

MICRO-SCALE PHYSICAL MODELING

Experimental results for drying micro-scale granular assemblies

The variables at the micro-scale include: average Laplace pressure, forces resulting from pressure, surface tension forces and the resultant total capillary force calculated based on the previously reported geometrical variables using Young-Laplace law. This is the first time to our knowledge that Laplace pressure is calculated from the measured curvatures of the interface between liquid and gas phase, along the process of evaporation and compared to experimental measurement data. A comparison with the experimental data from analogous capillary bridge extension tests is also shown and discussed. The measurements are possible through the image processing for pendular bridges, which constitute the last phase of the evaporation process, prior to loss of cohesion of the medium.

The behavior of evaporating liquid bridges is seen as strongly dependent on the grain separation. Initial negative Laplace pressure at small separations in pendular bridges is seen to significantly augment during an advanced stage of evaporation, but to invert the tendency and become positive pressure, after an instability toward the end of the process, and prior to rupture. At larger separations the pressure is positive all the time, changing a little, but rupturing early. Rupture in all cases occurs at positive pressure. However, because of the evolution of the surface area of contact, the resultant total capillary forces are always tensile, and decreasing toward zero in all cases. Comparison between measured total resultant capillary forces and those calculated from the Young-Laplace law is very good, except for some discrepancies at very small separations (below 50 μm). Up to four consecutive instabilities of capillary bridge are seen developing at some sphere separations. They are: re-pinning-induced suction (pressure) instability; Rayleigh nodoid/catenoid/unduloid unstable transition, associated with zero-pressure; Rayleigh unduloid/cylinder unstable transition, associated with the formation of a liquid-wire; and lastly, a pinching instability of the liquid-wire, associated with the bridge rupture. Rupture of the bridges is seen at large separations to occur quite early, at only 1/4–1/3 of the initial water volume evaporated. At smallest separations, rupture occurs in a seemingly unstable way when water evaporates from the bridge thinnest section of the neck.

At a sub-microscopic scale of a single bridge capillary bridges between two glass spheres show that the bridge gorge radius decreases much faster than the contact radius, distorting the original constant mean curvature bridge shape. In addition, the Laplace pressure calculated from local principal curvatures exhibits high gradients along the bridge moving

external surface, most commonly with a high suction near the triple phase contact and positive pressure near the gorge. The high suction results from a negative external curvature at contact. Numerical dynamic simulations with a moving evaporating interface do not currently allow for reproducing a negative external curvature at contact. A series of static approximation simulations are shown based on a representation of an experimentally observed interface, which does include the negative curvature at contact. The resulting Laplace pressure distribution is close to the experimental ones. Most importantly, the pressure gradients induce a consistent flow of liquid from the central area of the bridge, axially toward the solid contact, and then along the solid interface toward the contact area. The flow is believed to contribute to contact pinning. Pinning is viewed as one of the precursors of capillary bridge rupture.

For larger assemblies of 3, 5 and 8 grains the unstable transition between different water configurations takes the form of air entry episode that correspond to Haines jumps observed at meso-scale. The adhesion-force of a cluster initially grows at most to three times the original value before decreasing to zero by the end of evaporation. The adhesion-force is composed of capillary pressure force acting over the liquid/solid contact surface area, and surface tension forces acting over the three-phase contact perimeter length. This is in contrast with most macro-scale phenomenological models, in which the only desaturation process variables affecting strength are suction and saturation. Both the contact surface area and contact perimeter length are reduced to zero upon complete liquid evaporation. The morphology of an evaporating water body evolves through slow flow controlled by evaporation rate, interrupted by various modes of fast air entry, which are non-equilibrium jumps of liquid/gas interfaces. The instabilities involve large adhesion force discontinuities and substantial water mass reconfiguration with water flow in an extremely short time, which makes the process transient. The reconfigurations can reduce the original multi-grain water clusters to four-, three- and two-grain clusters by way of three different instability modes: of thin-sheet instability, or meniscus snap-through instability, depending on the sign of the Gauss curvature of the liquid surface, or finally, for two-grain bridges only, a liquid wire pinch-off. For larger meso-scale assemblies, however, the global adhesion force evolution is little affected by the jumps. The air entries are potential sites for drying cracks. The (approximately) calculated capillary pressure for two- and three-grain clusters, in no cases is seen to reach high values, predicted from water retention curves.

MACRO-SCALE CONSIDERATIONS

At the macro-scale of a granular continuum modeling of desiccation cracking via macroscopic approach suffers from a major handicap. Consideration of a 1D drying of a constrained saturated granular body easily shows that a modest total stress is generated in reaction to the constraints and that it is tensile, whereas the values of suction induced by the evaporation flux are significant. Consequently, the resulting effective stress appears to be compressive. This is counterintuitive, as drying failure evidently occurs through tensile cracking.

To address this paradox Scherer (1992) postulated a scenario suggesting that desiccation cracking is necessarily triggered through crack propagation from a tip of a pre-existing structural flaw, at which a substantial total stress concentration occurs. As a result, the remote total stress is substantially magnified through the stress concentration and becomes larger in absolute terms than the elevated suction. In turn, the local effective stress becomes tensile, and hence prone to reach the tensile strength of the material. Based on the presented results we postulate that a non-symmetric finger of an air entry, as described above, constitutes a sufficient imperfection (flaw) in the drying granular body to produce a concentration of total stress induced by the kinematic restraints to the drying shrinkage around the tip of the flaw, to generate crack propagation. In this spirit we consider an air finger (flaw) with the given depth and curvature radius at the finger tip at the soil surface, which is surrounded by the micro-tubes pore system. Using the principles of linear fracture mechanics, the stress at the external boundary of the tubes which are placed near the flaw tip can be calculated. Following the methodology by Scherer (1992), the far-field (macro-scale) stress at crack initiation can be found as tensile, easily becoming larger than macroscopic tensile strength of soil.

CONCLUSIONS

The presented data indicate that the abrupt phenomena of air entry inducing adhesion force discontinuities are not seen as discontinuous at a macro-scale. However, they trigger instabilities at a macro-scale that may lead to macro-scale drying crack formation and propagation.

References

[1] Scherer, G.W., 1992, Crack-tip stress in gels, J. Non-Cryst. Solids 144 , 210-216

BI-DISPERSE MIXTURES: STUDY OF DENSITY, COMPRESSIBILITY AND CRUSHING

Giulia Guida*[1], Gianluca Salvatori[2], and Francesca Casini[2]
[1]Department of Civil and Environmental Engineering, Politecnico di Milano, Milan, Italy
[2]Department of Civil and Computer Engineering,Università degli Studi di Roma Tor Vergata,Rome,Italy

Summary This work aims to investigate different type of bi-disperse grain size distributions in terms of minimum/maximum density, compressibility and crushing. The material adopted is the Light Expanded Clay Aggregate (LECA), an artificial granular material characterized by light, porous and crushable grains. The bi-disperse grading are firstly analysed in terms of packing efficiency, measuring experimentally the minimum and the maximum void ratios for different combination of fractions and proportions. Then, some selected mixtures are subjected to one-dimensional compression tests up to high pressures. Evolution of grain size due to grain crushing phenomena and compressibility are therefore measured and interpreted. Finally a theoretical model is adopted in order to predict the mechanical material behaviour accounting grain crushing and granular microstructure. The comparison is satisfactory.

PACKING EFFICIENCY

Bi-disperse distributions are composed by two distinct sizes, namely d_1 and d_2 where $d_1 > d_2$. The quantitative proportion of the two volume fraction is expressed by the coefficient $V = V_1/V_{tot}$, where $V_{tot} = V_1 + V_2$ and V_1, V_2 are the percentage by volume of fractions d_1 and d_2 respectively. The choice to express the fraction proportion by volume is due to the material adopted, the light expanded clay aggregate (LECA), which has a unit weight that increases with decreasing particle diameter [1] due to the presence fo intra-porosity [2]. Figure 1 shows experimental measurements of maximum and minimum void ratio for different type of bi-disperse grading, characterised by a ratio between diameters $R = d_1/d_2$ and fractions proportions V. The experimental evidences coming from Figure 1 highlight how, especially for grater R, the material reaches a more efficient packing, both for the maximum and minimum densities, in correspondence of $V \sim 70\%$ in accordance to several theoretical and experimental studies [2, 3, 10]. Note that in the case of mono-disperse distribution, when $V = 0$ or $V = 1$, the void ratios limits assume different values based on the size, higher for smaller grains and *vice versa*. A morphological analysis of grains proved that the shape of the smaller fractions is more irregular than the bigger, and a greater morphology irregularity lead to an increase of maximum and minimum void ratios in accordance with [7, 6].

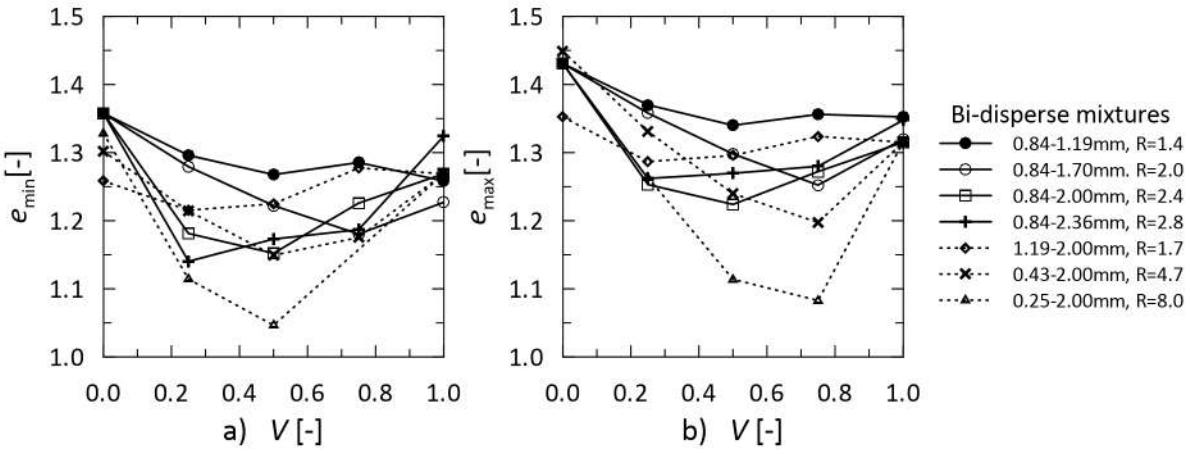

Figure 1: Measures of (a) minimum and (b) maximum void ratios for bi-disperse mixtures with different R and V.

ONE-DIMENSIONAL COMPRESSION TEST

Some selected bi-disperse grain size distributions (*e.g.* in Figure 2 characterised by $d_1 = 2.00$ mm, $d_2 = 0.43$ mm, $R = 4.7$ and $V = 0.6$) are subjected to one-dimensional compression tests up to the maximum vertical pressure of 54 MPa. The results are compared to the mono-disperse gradings relative to the single two constitutive fractions , MONO_{d1} and MONO_{d2}. Samples are prepared by dry pluviation, getting the minimum density configuration state. Figure 2 shows the experimental results in terms of (a) evolution of cumulative grain size distributions (CGSD) obtained by sieving and (b) the compressibility curves. Note that the bi-disperse CGSD at the final maximum vertical stress evolves due to crushing similarly to MONO_{d1} for $d \geq 0.43$mm, and similarly to MONO_{d2} for $d < 0.43$mm. Overall the constitutive fractions start to crush at low pressures applied, with the tendency to assume a fractal configuration [11]. The compressibility

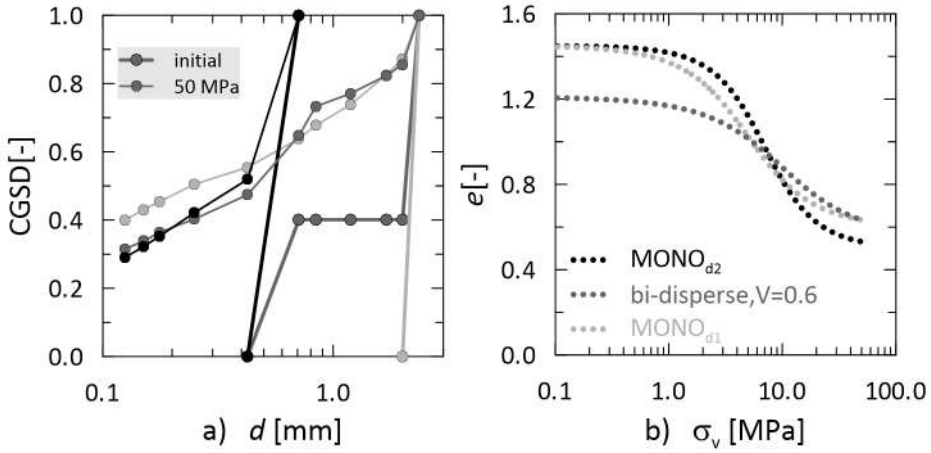

Figure 2: (a) Evolution of cumulative grain size distributions for a bi-disperse grading compared to its relative monodisperse ones; (b) Compressibility curves.

curve of the bi-disperse GSD (Figure 2) has initial stiffness close to that of MONO$_{d1}$, while after yielding it behaves such MONO$_{d2}$. The initial void ratio of the bi-disperse grading, as seen in Figure 1, assumes lower values than monodisperse.

The model developed by [5] is used to predict the compressibility of the mixture. In particular the model links the variation of porosity $\dot{n}$ to the variation of the maximum and the minimum void ratio:

$$\dot{n} = \tau_n \dot{n}_{max} + (1 - \tau_n)\dot{n}_{min}, \tag{1}$$

where τ_n is the auxiliary porosity index such that when $\tau_n = 1$, $n = n_{min}$ and when $\tau_n = 0$, $n = n_{max}$ [8, 9]. The intrinsic values of $n_{max/min}$ are defined as function of GSD polydispersity quantified by the index of grading I_{Gr}:

$$n_{max/min} = n^{MONO}_{max/min} I_{Gr}^{-\alpha}, \tag{2}$$

where $n^{MONO}_{max/min}$ are the minimum and maximum porosity at zero stress of a mono-disperse grading and α is a dimensionless model parameter. The index of grading I_{Gr} is defined as the geometric standard deviation of the particle size distribution of normalized sizes, it is dimensionless and describes the spread of GSD about its geometric mean.

CONCLUSIONS

The experimental results show that bi-disperse mixtures explicate a greater packing efficiency than mono-disperse grading, an evolution of cumulative grain size distribution and a compressibility behaviour in between those of the two mono-disperse constitutive fractions. Finally, those interesting experimental evidences are used to validate a compressibility model for granular material with crushable grains recently developed.

References

[1] Casini F., Viggiani, G. M. B. Experimental investigation of the evolution of grading of an artificial material with crushable grains under different loading conditions. In *Proceedings of the 5th international symposium on deformation characteristics of geomaterials*, Seoul, Korea. 957–964, 2011.

[2] Cubrinovski M., Ishihara K. Maximum and minimum void ratio characteristics of sands. *Soils and foundations*. **42**(6), 65–78, 2002.

[3] Farr R. S., Grooth R. D. Close packing density of polydisperse hard spheres. *The Journal of chemical physics*. **131**(24), 244104, 2009.

[4] Guida G., Casini F., Viggiani G. M. B., Andò E., Viggiani, G. Breakage mechanisms of highly porous particles in 1d compression revealed by x-ray tomography. *Géotechnique Letters* **8**(2) 155–160, 2018.

[5] Guida G., Einav, I., Marks, B. and Casini, F. Linking micro grainsize polydispersity to macro porosity. *International Journal of Solids and Structures*. URL: http://dx.doi.org/10.1016/j.ijsolstr.2018.11.032, 2018.

[6] Guida G., Sebastiani D., Casini F., Miliziano S., Grain morphology and strengthdilatancy of sands. *Géotechnique Letters*. URL: http://dx.doi.org/10.1680/jgele.18.00199, 2019

[7] Miura K., Maeda K., Furukawa M. and Toki S. Physical characteristics of sands with different primary properties. *Soils and Foundations*. **37**(3), 53–64, 1997

[8] Rubin M., Einav, I. A large deformation breakage model of granular materials including porosity and inelastic distortional deformation rate. *International Journal of Engineering Science*. **49**(10), 1151–1169, 2011

[9] Tengattini A., Das A., Einav, I. A constitutive modelling framework predicting critical state in sand undergoing crushing and dilation. *Géotechnique*. **66**(9), 695–710, 2016

[10] Wood D. M., Maeda, K. Changing grading of soil: effect on critical states. *Acta Geotechnica*. **3**(1), 3, 2008

[11] Zhang X., Baudet B. A., The multi-fractal nature of soil particle size distribution. In Geomechanics from Micro to Macro, Taylor & Francis Group London, 1183–1188, 2015

*Corresponding author. E-mail: giulia.guida@polimi.it.

INSTABILITY IN ELASTIC-VISCOPLASTIC MEDIA: FROM MICRO TO MACRO

Luca Flessati*[1] and Claudio di Prisco [1]
[1]Department of Civil and Environmental Engineering, Politecnico di Milano, Milano, Italy

Summary In landslide risk assessment, the justification of unexpected collapses involving creeping landslides is considered to be very crucial. In this paper, the authors consider the case of an infinite long slope constituted of an elastic-viscoplastic material and, by employing the controllability theory, directly applied on the representative elementary volume and here tailored to interpret the global system response, observe that increments in slope acceleration are anticipated by a local increase in strain rate along the shear band. This implies that the observation of inclinometer data may in principle allow to foresee the slope collapse.

INTRODUCTION

In the scientific literature, many authors reported the occurrence of unexpected collapses in creeping landslides. This transition is, in many cases, associated with a phenomenon called "progressive failure", which mainly takes place in geomaterials characterized by a high level of fragility, such as cemented geomaterials. In these materials, at the microscopic scale, the cracks present in both grains and intergranular bonds propagate with time ("subcritical crack growth" [1]). This crack propagation induces a spatial rearrangement of the microstructure which is associated with both an accumulation with time of irreversible strains and a reduction in the material strength. At the global (landslide) scale, this local behaviour causes a spatial propagation of the damaged zone, which, in some cases, may be associated with a rapid increase in the displacement rate in the unstable soil/rock mass.
By taking into consideration an infinite slope resting on a rigid bedrock, the authors intend to illustrate that, by following a suitably defined upscaling procedure, the controllability theory ([2]) employed to analyse the (local) onset of instability at the representative elementary volume scale may also be extended to analyse boundary value problems. Moreover, the employment of controllability theory at both local and global scales allows to put in evidence that the local instability is a precursor of the slope collapse.

LOCAL ONSET OF INSTABILITY

In the case of an infinite long slope (Fig. 1a), if both the hydro-mechanical coupling and dynamic effects are disregarded, the response of every layer is analogous to the one of a representative elementary volume under simple shear conditions. The controlled stress ($\dot{\boldsymbol{\sigma}}'_\alpha$)/strain ($\dot{\boldsymbol{\varepsilon}}_\beta$) variables are:

$$\dot{\boldsymbol{\sigma}}'_\alpha = [\dot{\sigma}'_n \quad \dot{\tau}_{tn}]^T \qquad \dot{\boldsymbol{\varepsilon}}_\beta = [\dot{\varepsilon}_t \quad \dot{\varepsilon}_y]^T, \tag{1}$$

whereas the corresponding response strain ($\dot{\boldsymbol{\varepsilon}}_\alpha$)/stress ($\dot{\boldsymbol{\sigma}}'_\beta$) variables are:

$$\dot{\boldsymbol{\sigma}}'_\beta = [\dot{\varepsilon}_n \quad \dot{\gamma}_{tn}]^T \qquad \dot{\boldsymbol{\varepsilon}}_\alpha = [\dot{\sigma}'_t \quad \dot{\sigma}'_y]^T, \tag{2}$$

where the coordinates *t* and *n* are defined in Fig.1a, while the coordinate *y* represents the out of plane direction.
In case of an elastic-viscoplastic material ([3]) the total, the elastic ($\dot{\boldsymbol{\varepsilon}}^{el}$) and the viscoplastic ($\dot{\boldsymbol{\varepsilon}}^{vp}$) strain rate vectors may be suitably partitioned to put in evidence the controlled and the response variables:

$$\begin{bmatrix}\dot{\boldsymbol{\varepsilon}}_\alpha \\ \dot{\boldsymbol{\varepsilon}}_\beta\end{bmatrix} = \begin{bmatrix}\dot{\boldsymbol{\varepsilon}}^{el}_\alpha \\ \dot{\boldsymbol{\varepsilon}}^{el}_\beta\end{bmatrix} + \begin{bmatrix}\dot{\boldsymbol{\varepsilon}}^{vp}_\alpha \\ \dot{\boldsymbol{\varepsilon}}^{vp}_\beta\end{bmatrix} = \begin{bmatrix}\boldsymbol{C}^{el}_{\alpha\alpha} & \boldsymbol{C}^{el}_{\alpha\beta} \\ \boldsymbol{C}^{el}_{\beta\alpha} & \boldsymbol{C}^{el}_{\beta\beta}\end{bmatrix}\begin{bmatrix}\dot{\boldsymbol{\sigma}}'_\alpha \\ \dot{\boldsymbol{\sigma}}'_\beta\end{bmatrix} + \Phi\begin{bmatrix}\frac{\partial g}{\partial \boldsymbol{\sigma}'_\alpha} \\ \frac{\partial g}{\partial \boldsymbol{\sigma}'_\beta}\end{bmatrix}, \tag{3}$$

being $\boldsymbol{C}^{el}$ the elastic compliance matrix, Φ the viscous nucleus and g the plastic potential. According to [4], Equation 3 may be derived with respect to time and rearranged to put in evidence the relationship between the response variables $\boldsymbol{X} = \left[\dot{\boldsymbol{\varepsilon}}_\alpha \quad \dot{\boldsymbol{\sigma}}'_\beta\right]^T$ and their time derivative $\dot{\boldsymbol{X}} = \left[\ddot{\boldsymbol{\varepsilon}}_\alpha \quad \ddot{\boldsymbol{\sigma}}'_\beta\right]^T$. This relationship is linear and may be expressed as it follows:

$$\dot{\boldsymbol{X}} = \boldsymbol{A}\boldsymbol{X} + \boldsymbol{F}, \tag{4}$$

being **F** a "forcing" term related to the controlled variables, whereas the matrix **A** depends on both the constitutive relationship and the controlled variables. In case of "generalized creep tests" ($\dot{\boldsymbol{\sigma}}'_\alpha = \ddot{\boldsymbol{\sigma}}'_\alpha = \dot{\boldsymbol{\varepsilon}}_\beta = \ddot{\boldsymbol{\varepsilon}}_\beta = \boldsymbol{0}$), **F=0** and **A** only depends on the constitutive relationship. Under simple shear conditions ([5]), the non-nil terms of the constitutive matrix **A** may be expressed as

$$A_{11} = A_{22} = -\frac{\partial \Phi}{\partial f}(H - H_\chi),\ A_{33} = A_{44} = -\frac{\partial \Phi}{\partial f}(H - H_\chi) - \Phi\frac{E}{1-\nu^2}\frac{\partial^2 g}{\partial \sigma'^2_t},\ A_{13} = \Phi\left(\frac{\partial^2 g}{\partial \sigma'_n \partial \sigma'_t} - \frac{\nu}{1-\nu}\frac{\partial^2 g}{\partial \sigma'^2_t}\right) \text{ and } A_{23} = \Phi\frac{\partial^2 g}{\partial \tau_{tn} \partial \sigma'_t}, \tag{5}$$

being f the yield function, E the Young modulus, ν the Poisson's ratio, H the hardening modulus and H_χ the controllability modulus:

$$H_\chi = -\frac{\partial f}{\partial \sigma'_t}\frac{E}{1-\nu^2}\frac{\partial g}{\partial \sigma'_t} \tag{6}$$

According to [6], for **F=0**, a stable response is obtained in case all the eigenvalues of **A** are negative. In other words, instability takes place when at least one eigenvalue of **A** becomes non-negative. Eigenvalues λ_i (with i=1,4) can be expressed as:

*Corresponding author. E-mail: luca.flessati@polimi.it

$$\lambda_1 = \lambda_2 = A_{11} = A_{22} \qquad \lambda_3 = \lambda_4 = A_{33} = A_{44} = A_{11} - \Phi \frac{E}{1-\nu^2} \frac{\partial^2 g}{\partial \sigma_t'^2}. \tag{7}$$

Since E, Φ and $\partial\Phi/\partial f$ are positive, in case g is convex in the stress space, $\lambda_1 \geq \lambda_3$. The instability condition is obtained when $\lambda_1 \geq 0$, i.e. when $H - H_\chi \leq 0$.

GLOBAL ONSET OF INSTABILITY

When the global response of the slope is taken into account, it is convenient the introduction of the following global response variables:

$$\boldsymbol{X} = \left[\dot{u}_n \quad \dot{u}_t \quad \dot{\Sigma}_t \quad \dot{\Sigma}_y\right]^T = \left[\int_0^h \dot{\varepsilon}_n\, dz \quad \int_0^h \dot{\gamma}_{tn}\, dz \quad \int_0^h \dot{\sigma}'_t\, dz \quad \int_0^h \dot{\sigma}'_t\, dz\right]^T \tag{9a}$$

$$\dot{\boldsymbol{X}} = \left[\ddot{u}_n \quad \ddot{u}_t \quad \ddot{\Sigma}_t \quad \dot{\Sigma}_y\right]^T = \left[\int_0^h \ddot{\varepsilon}_n\, dz \quad \int_0^h \ddot{\gamma}_{tn}\, dz \quad \int_0^h \ddot{\sigma}'_t\, dz \quad \int_0^h \ddot{\sigma}'_t\, dz\right]^T \tag{9b}$$

In case of generalized creep tests, by combining Equations 4, 9a and 9b the relationship between $\boldsymbol{X}$ and $\dot{\boldsymbol{X}}$ may be obtained:

$$\dot{\boldsymbol{X}} = \boldsymbol{A}^g \boldsymbol{X} = (\boldsymbol{A}^{max} - \boldsymbol{\Omega})\boldsymbol{X}, \tag{10}$$

where $A_{ij}^{max} = \max\{A_{ij}\}$ in the spatial domain, while the non-nil terms of $\boldsymbol{\Omega}$ are:

$$\Omega_{11} = \frac{\int_0^h (A_{11}^{max} - A_{11})\dot{\varepsilon}_n dz}{\int_0^h \dot{\varepsilon}_n dz}, \quad \Omega_{13} = \frac{\int_0^h (A_{13}^{max} - A_{13})\dot{\sigma}'_t dz}{\int_0^h \dot{\sigma}'_t dz}, \quad \Omega_{22} = \frac{\int_0^h (A_{22}^{max} - A_{22})\dot{\gamma}_{tn} dz}{\int_0^h \dot{\gamma}_{tn} dz}, \quad \Omega_{23} = \frac{\int_0^h (A_{23}^{max} - A_{23})\dot{\sigma}'_t dz}{\int_0^h \dot{\sigma}'_t dz},$$

$$\Omega_{33} = \frac{\int_0^h (A_{33}^{max} - A_{33})\dot{\sigma}'_t dz}{\int_0^h \dot{\sigma}'_t dz}, \quad \Omega_{44} = \frac{\int_0^h (A_{44}^{max} - A_{44})\dot{\sigma}'_y dz}{\int_0^h \dot{\sigma}'_y dz}. \tag{11}$$

By definition, $\lambda_i(\boldsymbol{A}^g)$ are smaller than $\lambda_i(\boldsymbol{A}^{max})$, since $\lambda_i(\boldsymbol{\Omega})$ are always non negative. As a consequence, when local instability takes place (i.e. when one eigenvalue of the local constitutive matrix $\boldsymbol{A}$ and, consequently, one eigenvalue of $\boldsymbol{A}^{max}$ become non-negative) $\boldsymbol{A}^g$ is not necessarily non-negative. Therefore, the first local and the global instability are not simultaneous. In other words, a time lag between the first local and the global instability exists and the first local instability always anticipates the onset of the global one. This is testified in Fig. 1b where the evolution in time (t) of slope displacements (u_t) numerically obtained by considering an infinite slope constituted of a strain softening elastic-viscoplastic material (a Mohr-Coulomb type yield function is employed) and resting on a rigid bedrock subject to an instantaneous increase in the water table level is considered. Point A corresponds to $\ddot{u}_t$=0 (global onset of instability), whereas point B to the first local onset of instability ($\ddot{\gamma}_{tn} = 0$). As is evident, the local instability severely anticipates the global one.

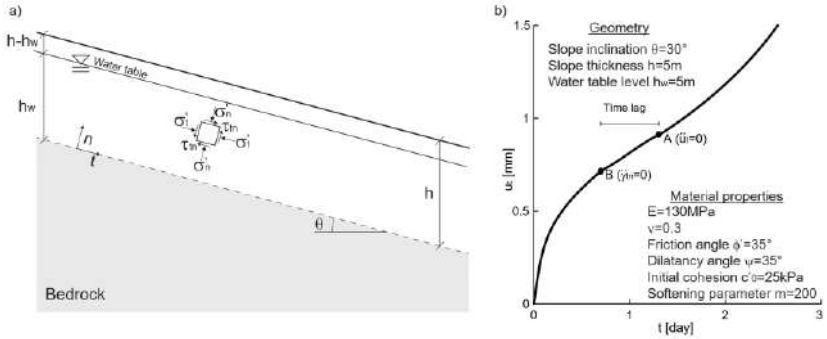

Figure 1. a) Geometrical scheme of the infinite slope and b) evolution in time of the slope displacements [5

CONCLUSIONS

The authors take into consideration the case of progressive failure in slopes constituted of elastic-viscoplastic materials. For the sake of simplicity, the case of an infinite long slope is taken into account. By employing the controllability theory, applied both on representative elementary volumes and on the global slope response, the authors conclude that: (i) the first local instability anticipates the global one, (ii) the occurrence of local instability is necessary condition for the global instability to take place and (iii) local instability is a precursor of the global one.

References

[1] Wiederhorn, S. M., Fuller, E. R., & Thomson, R. (1980). Micromechanisms of crack growth in ceramics and glasses in corrosive environments. Metal science, 14(8-9), 450-458.

[2] Nova, R. (1994). Controllability of the incremental response of soil specimens subjected to arbitrary loading programmes. Journal of the Mechanical behavior of Materials, 5(2), 193-202.Icer D.F., Adams J.A. Mathematical Elements for Computer Simulation. McGraw Hill, NY 1977.

[3] Perzyna, P. (1963). The constitutive equations for rate sensitive plastic materials. Quarterly of applied mathematics, 20(4), 321-332

[4] Pisanò, F., & di Prisco, C. (2016). A stability criterion for elasto - viscoplastic constitutive relationships. International Journal for Numerical and Analytical Methods in Geomechanics, 40(1), 141-156.

[5] di Prisco, C. & Flessati, L. (2019) Progressive failure in elastic-viscoplastic media: from theory to practice Géotechnique, In Press DOI https://doi.org/10.1680/jgeot.19.p.045

[6] Lyapunov, A. M. (1892) The general problem of motion stability. Kharkovskoye Matematicheskoe Obshchestvo, 11

FRACTURE PROPAGATION ALONG A FAULT – STRESS HYSTERESIS EFFECT

Clément Cardon[1] and Pierre Cerasi*[2]
[1]Ecole Polytechnique, Palaiseau, France
[2]Petroleum Department, SINTEF Industry, Trondheim, Norway

Summary A bespoke fracturing software combining finite and discrete elements is used to assess the leakage risk along a fault adjacent to a CO_2 storage reservoir. A 25 m large process zone containing pre-existing fractures is modelled, with idealized fracture patterns of a typical deformation zone. Simulations are performed to compare a storage reservoir as hanging wall versus footwall. Two stress path scenarios are looked at, depletion of the reservoir with subsequent re-pressurization, and injection into a normally pressured reservoir. Results show that hanging wall reservoirs undergoing depletion are the most at risk of developing continuous fracture paths, potentially leading to leakage to shallower permeable layers. Sensitivity analysis is also performed, showing that shallower reservoirs are more at risk, in that less depletion is supported prior to fracture propagation along the fault. Although simple, the model suggests that care should be taken when selecting depleted gas reservoirs for CO_2 storage, to avoid leakage along faults.

INTRODUCTION

According to the 2018 Intergovernmental Panel on Climate Change (IPCC) report, to keep temperature rise under 1.5 °C compared to pre-industrial level, no credible emission scenario can be considered without Carbon Dioxide Removal (CDR), CCS and afforestation being the only two solutions available. CCS on the scale of hundreds of gigatons of CO_2 will be needed to reach these goals, with tens of thousands of suitable reservoirs to be found and exploited to store CO_2. Two main types of geological formations are considered for storage: deep saline aquifers with thick sealing caprock and depleted oil or gas fields, already proven natural reservoirs. Several demonstration facilities have already proved feasibility of CO_2 storage. However, storing carbon dioxide underground may not be as safe as producing oil and gas in the long term, as it is mainly about increasing pressure in a reservoir rather than decreasing it. Therefore, when purely considering pore pressure change scenarios, depleted oil and gas reservoirs are the preferred storage choice, since one can limit the pressure increase to reach back the original pressure in place when the reservoir was discovered. This pressure had been maintained over geological time without any leakage of the pore fluid and should therefore be ideal to store CO_2. Another argument in favour of depleted reservoirs is the presence of existing infrastructure in place, which could probably be used with minor modifications, compared to virgin aquifer targets. On the other hand, the very presence of wells penetrating the underground dramatically increases the risks of leakage, principally along these wells, where many of them could be old and in poor condition.

These considerations about depleted oil and gas fields do not however take into account non-elastic associated effects in the proposed pore pressure rebound scenario. These effects are translated into stress hysteresis and stress concentration, which could exceed the strength of the formations in and around the proposed reservoir. Many oil and gas reservoirs are compartmentalised in pressure cells bound by sealing caprock and lateral faults. Stress changes accompanying depletion when the reservoir was in production mode may not be evenly distributed but concentrate on the bounding faults. Hysteresis related to plastic yielding (non-recoverable deformation) may also aggravate the solicitation of the faults upon CO_2 injection into the reservoir and lead to reactivation of the faults and hence leakage out of the intended reservoir.

In this paper, we implement a simple scenario looking at a fault on the side of a sandstone reservoir and simulate a depletion and recharge of the reservoir while monitoring stress evolution on the fault. A process zone around the fault core is explicitly implemented in the simulations, by assigning the zone weaker mechanical properties as compared to intact rock and placing in the zone pre-existing fractures.

NUMERICAL METHOD

An in-house explicit fracturing code is used for the fault reactivation simulations [1]. Reactivation is looked at here in more detail, as the fault has a given thickness, 25 m, with pre-existing fractures modelled in different patterns, such that these may further propagate and link to new fractures. The goal of the simulations was to investigate under which conditions (which reservoir pore pressure change history), fractures in the fault's process zone may form a percolating pathway along the fault to shallower layers, which would then be interpreted as a significant leakage risk from the reservoir. The software used was developed at SINTEF and combines finite element and discrete element methods. The simulation domain is initially discretized into triangular finite elements, with linear elastic behaviour, until local stress conditions exceed either tensile or compressive shear conditions. At that point, the discretisation scheme is changed to discrete elements, defined by the failed interfaces of the original finite elements. Fluid flow can be simulated by coupling the code to a CFD code such as TOUGH2 or SINTEF's MRST reservoir simulator. Fractures are monitored in terms of opening mode (tensile or shear) with accompanying permeability related to opening degree.

The simulation domain was assigned different properties for the reservoir sandstone and surrounding shale, consistent with typical values for North Sea sedimentary formations analysed in geomechanical testing. The top boundary was then lowered until the desired stress state was accomplished in the domain, compatible with offshore depth of target reservoirs (Figure 1). A half reservoir was simulated, where reflection of the fault about the centre vertical line provided two cases, one (shown in Figure 1) where the reservoir is in the footwall of the fault, and the other when the reservoir is in the

hanging wall. Simulations consisted in lowering the pore pressure in the reservoir to simulate depletion and monitor stresses at the fault and potential fracturing there. A depletion of up to 10 MPa was applied, in steps of 1 MPa. Pore pressure was then increased back by up to 15 MPa, simulating the injection of CO_2 inside the reservoir, and further evolution at the fault was monitored.

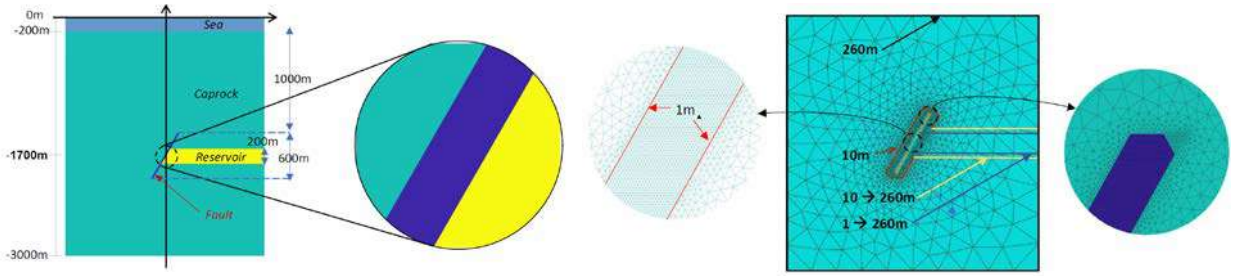

Figure 1. Left: Schematic representation of the sandstone reservoir, in yellow surrounded by shale (green) and bound by a fault (blue). Right: adaptative meshing ranging from 1 m triangle side in the fault to 260 m at the boundaries.

RESULTS

All cases of reactivation of the fault occurred as stepwise propagation of fractures in the fault, not wholescale failure of the fault as is customary in simulations with no fault structure. All cases of fracturing occurred during the **depletion** phase, **none during pressurisation**, confirming previous initial work [2]. Reducing the **stiffness** in the fault zone led to earlier fracturing in terms of depletion magnitude; this corresponds to a high shale gouge ratio in terms of our chosen stiffnesses for sandstone and shale. The **presence of fractures** in the fault zone led to **later** fracturing when these were aligned with the fault, simulating a weak fault core, as compared to cross patterns and horizontal fractures at the reservoir to fault border. Fractures were seen to propagate upwards (to shallower levels) in the **hanging wall** case, while downwards for the **footwall** case (Figure 2).

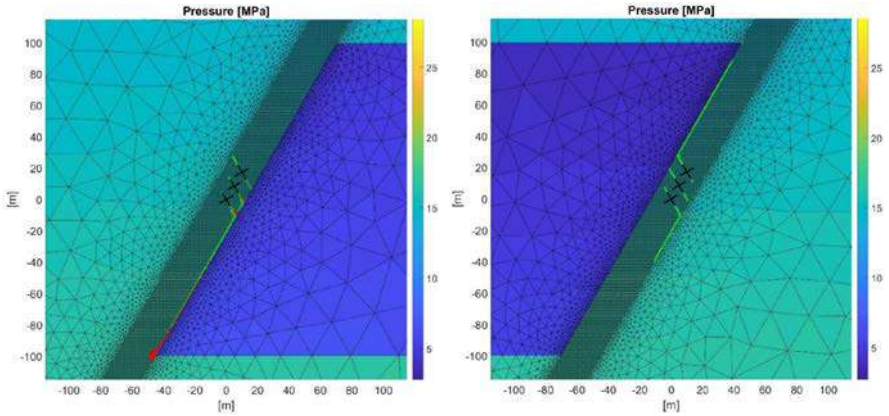

Figure 2. Fracture propagation along the fault for a reservoir is in the footwall (left) and hanging wall (right). Red and light green lines visualize shear and tensile failure, respectively. The depletion is 11 MPa in both cases.

CONCLUSIONS

Modelling fault reactivation taking into account the structure of the fault, even in a greatly simplified manner, shows that this process is not a simple on/off event. The results can be taken to imply that depleted reservoirs may be more leakage-prone than normally pressured aquifers; however, the depletion modelled was very large while fracture propagation not extreme, provided no other high-permeability layers juxtapose the fault.

Acknowledgments

This research was funded by the Research Council of Norway in the framework of the SPHINCSS—Stress Path and Hysteresis effects on Integrity of CO_2 Storage Site Researcher Project, grant number 268445 and with support from the NCCS Centre, performed under the Norwegian research program Centres for Environment-friendly Energy Research (FME). The authors acknowledge the following partners for their contributions: Aker Solutions, Ansaldo Energia, CoorsTek Membrane Sciences, Emgs, Equinor, Gassco, Krohne, Larvik Shipping, Norcem, Norwegian Oil and Gas, Quad Geometrics, Shell, Total, Vår Energi, and the Research Council of Norway (257579/E20).

References

[1] Alassi, H.T.I.; Li, L.; Holt, R.M. Discrete Element Modeling of Stress and Strain Evolution Within and Outside a Depleting Reservoir. *Pure Appl. Geophys*. 2006, **163**, 1131–1151.

[2] Rongved, M., & Cerasi, P. (2019). Simulation of Stress Hysteresis Effect on Permeability Increase Risk Along A Fault. *Energies*, **12**(18), 3458.

CONVECTIVELY COUPLED EQUATORIAL KELVIN WAVES IN THE UPPER TROPOSPHERE NEAR SUMATRA AND THEIR INTERACTIONS WITH LOCAL DIURNAL CYCLE

Wojciech Szkolka, Dariusz B. Baranowski
[1]Institute of Geophysics, Polish Academy of Sciences

Summary This research have proved that Equatorial Kelvin waves are present in the upper troposphere over Indian Ocean. Various methods of data analysis were used, especially calculating filtered anomalies and EOF-analysis. We have used data from reanalysis ERA-5 as well as Equatorial Atmospheric Radar on Sumatra. The huge impact of Kelvin waves on the atmosphere dynamics over Sumatra and diurnal cycle in Maritime Continent is easily visible.

The Earth's atmosphere is characterized by weather phenomena, which occur at various spatial scales – from a small (about 1mm) to a large (about 10 000km) scale. Therefore, the nature of a phenomenon of interest determines scales that should be considered. Hence, different approximations can be used to describe dynamics of specific events.
One of typical approximate models for large-scale dynamics is based on shallow water approximation to governing equations. When such model is applied in equatorial zone, the Matsuno model can be derived, and wave solutions can be obtained. One of the important types of these solutions are equatorial Kelvin waves. Although it is a theoretical solution of an approximate model, it can be shown that such waves really exist in the atmosphere. Using appropriate methods of data analysis applied to meteorological data, we may find structures resembling theoretical structure of Kelvin waves.

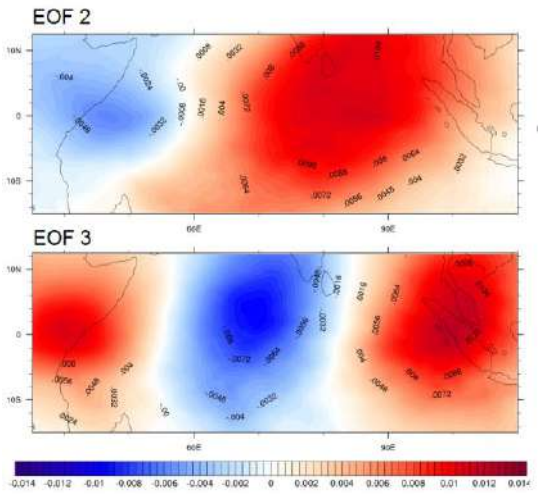

Fig. 1. Results of EOF-analysis on filtered anomalies of wind data ERA-5 over Indian Ocean.

This research focuses on occurrence of atmospheric convectively coupled Kelvin waves (CCKWs) in the upper troposphere (200mb) over Indian Ocean. The analysis is based on 2000-2018 ERA-5 upper level (200mb) wind data and techniques, which allow extraction of specific modes of variability, such as temporal and spatial filtering, and EOF analysis. Spatio-temporal evolution of 2-20 day band pass filtered anomalies of upper level zonal wind matches theoretical structure of Kelvin waves. (Fig. 1)

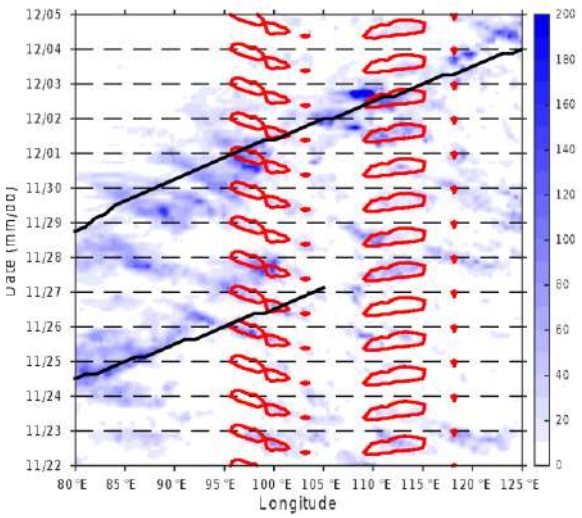

Fig. 2 Hovmoller diagram of total precipitation rate (mm day^{-1}) for the period 22 November to 5 December 2011. The two black lines indicate the propagation of the two CCKWs embedded in an MJO event. The red lines show the 12.5 mm day^{-1} contour from the mean diurnal cycle [from Baranowski et al. (2016)].

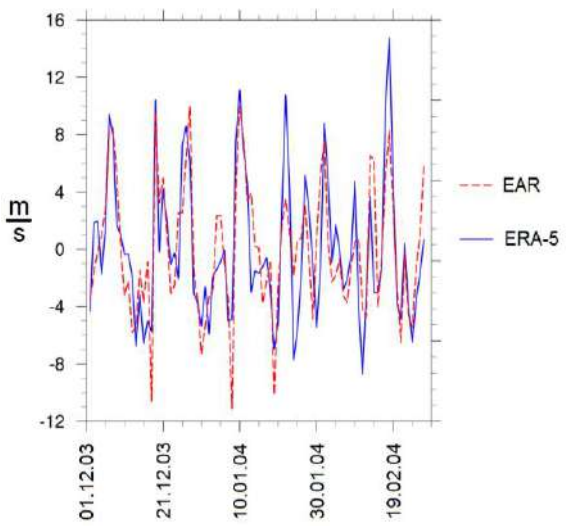

Fig. 3 Comparison between filtered anomalies of ERA-5 data and Equatorial Atmospheric Radar.

THEMATIC SESSION SM

The CCKW upper level anomalies from ERA-5 were augmented with independent upper level wind data measured by Equatorial Atmospheric Radar (EAR), located at the equator, near the west coast of Sumatra, Indonesia. The diurnal cycle of zonal winds at different levels was extracted from EAR data. It is shown that propagation of upper level anomalies associated with CCKWs not only correlate with zonal wind variability over Sumatra, but impact diurnal evolution of the dynamical field across atmospheric column. These results indicate dynamical coupling between larger scale propagating phenomenon (CCKWs) and local processes (diurnal cycle).

To further investigate dynamical feedback between local diurnal cycle and large scale variability, CCKWs trajectories were utilized. The trajectories are based on TRMM, a satellite-based precipitation estimation and allow tracking CCKWs in space and time. Results indicate that CCKW events which propagate across the island of Sumatra (and Maritime Continent) have stronger coupling than those that dissipate within the region.

References

[1] Matsuno, T. (1966). Quasi-Geostrophic Motions in the Equatorial Area. *Journal of the Meteorological Society of Japan. Ser. II*, *44*(1), 25–43. https://doi.org/citeulike-article-id:12719588
[2] Kiladis, G. N., Wheeler, M. C., Haertel, P. T., Straub, K. H., and Roundy, P. E. (2009). Convectively Coupled Equatorial Waves. *Reviews of Geophysics*, *47*. https://doi.org/10.1029/2008rg000266
[3] Baranowski, D. B., Flatau, M. K., Flatau, P. J., and Matthews, A. J. (2016b). Phase locking between atmospheric convectively coupled equatorial Kelvin waves and the diurnal cycle of precipitation over the Maritime Continent. *Geophysical Research Letters*, *43*(15), 8269–8276. https://doi.org/10.1002/2016GL069602

INTERROGATION OF CRACK TIP FIELDS AND FRICTION THROUGH ULTRAHIGH-SPEED DIGITAL IMAGE CORRLEATION

Vito Rubino*[1], Ares J. Rosakis[1], and Nadia Lapusta [2,3]
[1]Graduate Aerospace Laboratory, California Institute of Technology, Pasadena, CA, USA
[2]Department of Mechanical and Civil Engineering, California Institute of Technology, Pasadena, CA, USA
[3]Division of Geological and Planetary Sciences, California Institute of Technology, Pasadena, CA, USA

Summary Dynamic shear ruptures are characterized by highly variable spatiotemporal features. Understanding the behaviour of dynamic ruptures and the frictional processes controlling their propagation is relevant to various fields, such as fracture mechanics and earthquake physics. Until recently, it was not possible to quantify experimentally the full-field behaviour of dynamic ruptures due to metrological limitations. In this study, we present our recent advances in investigating the near-tip fields of dynamic ruptures and elucidate the frictional processes governing their propagation. Our experimental measurements, based on ultrahigh-speed digital image correlation technique, reveal the intricate structure of sub-Rayleigh and supershear ruptures improving our understanding of the physics of rupture propagation with important implications for evaluating earthquake hazard.

INTRODUCTION

Understanding the behaviour of dynamic shear ruptures is important for applications ranging from the failure of composite structures, to car brakes and earthquake physics. Capturing the temporal evolution of propagating dynamic ruptures poses a metrological challenge, as ruptures propagate at speeds close to the Rayleigh wave speed or even exceed the shear wave speed. Recently, we have been able to quantify the full-field structure of dynamic frictional ruptures by combing digital image correlation [1] and ultrahigh-speed photography [2-7]. Here, we focus on the description of near-field features and the evolution of dynamic friction, in various experimental configurations.

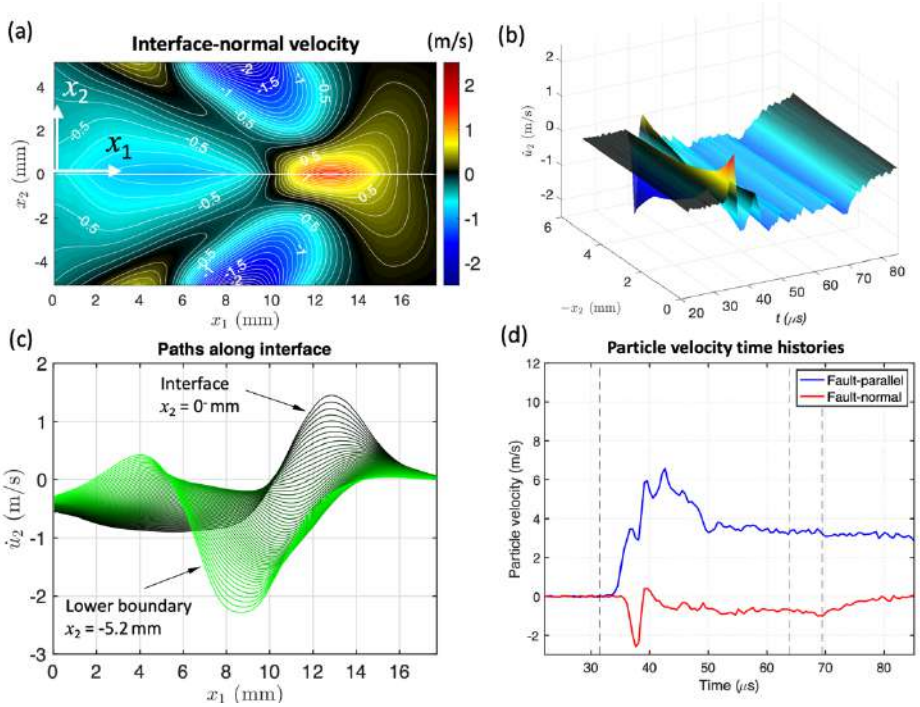

Figure 1. Capturing the near-field structure of shear cracks showing the interface-normal particle velocity. (a) Full-field map, (b) spatiotemporal plot, the fault-normal velocity is plotted vs. time and vs. distance from the interface, (c) interface-normal velocity along the interface plotted at various distances from the interface, (c) particle velocity time history for both the interface-parallel (blue) and interface-normal (red) components. Modified from [7].

EXPERIMENTAL APPROACH

Dynamic shear cracks, representative of earthquake ruptures, are produced in our laboratory setup as frictional ruptures propagating along the inclined interface of two quadrilateral plates of Homalite-100 [6,8]. Ruptures are nucleated by the small burst of a NiCr wire placed across the interface, and once nucleated they propagate under the

*Corresponding author. E-mail: vito.rubino@caltech.edu

applied level of static normal and shear pre-stress levels. A ultrahigh-speed camera records a sequence of images of the propagating ruptures on a portion of the specimen covered by a characteristic pattern, at 1-2 million frames/second (200 ns exposure time). The images are analysed with the digital image correlation method to infer the time evolution of full-field displacements, particle velocities, and strains [4]. Stress fields are computed from the strain fields assuming linear elastic constitutive models, friction is then obtained as the ratio of shear to normal stress along the interface [2].

QUANTIFYING RUPTURE BEHAVIOR AND FRICTION EVOLUTION

We have characterized the behavior of dynamic ruptures ranging from sub-Rayleigh to supershear speeds and comprising both cracks and pulses. The sequence of full-field displacements and particle velocity reveal the complex dynamics at a unique level of detail. In this presentation, we concentrate on describing the near-field spatiotemporal features obtained by dedicated experiments performed with a field of view focusing in the near-tip region. The interface-parallel velocity component of supershear ruptures are characterized by pronounced shear motion and by marked shock fronts extending into the far field [7]. The interface-normal velocity presents a complex behavior with an initial (upward) positive motion followed by a negative (downward) motion along the interface (Figure 1). These features are very distinctive in the near-tip field but attenuate very quickly with distance from the interface. Two wedge regions, characterized by negative (downward) motion, radiate away from the crack tip and are parallel to the shock fronts displayed by the interface-parallel velocity and maximum shear stress. By contrast, these features propagate into the far-field regions (Figure 1a and 2b). We will present our findings for sub-Rayleigh ruptures as well as our current work on quantifying the decay of the fields away from the interface..

Friction is a key process controlling rupture propagation and how earthquake ruptures release waves that cause destructive shaking. Nonetheless, it is one of the least constrained ingredients in earthquake physics. Our measurements allow us to infer the local evolution of friction associated with spontaneously propagating ruptures [2] and to characterize the evolution of frictional resistance in response to rapid normal stress variations [9], which we have done for analog materials. However, earthquake ruptures in mature faults propagate in gouge, which is a powdered rock material. In order to better study the rheology of natural faults in the Earth's crust, we have been performing dynamic rupture experiments using a hybrid configuration featuring quartz gouge embedded along the interface of a Homalite specimen. This configuration enables to use the advantage of smaller nucleation length scales provided by Homalite, while capturing the evolution of friction in quartz gouge. We will report our current observations of rapid and pronounced dynamic weakening as well as dynamic triggering in this configuration.

CONCLUSIONS

Our highly instrumented experiments allow us to quantify dynamic rupture behaviour of sub-Rayleigh and supershear ruptures and to infer the local evolution of the friction coefficient for a wide range of loading conditions. A new configuration featuring quartz gouge embedded in a Homalite specimen reveals a much more complex rupture behavior controlled by the gouge rheology, which we simultaneously measure and characterize. These results contribute to our understanding of dynamic rupture propagation and friction evolution with important implications for earthquake physics.

References

[1] Sutton, M. A., Orteu J.-J., Schreier H. W.: Image Correlation for Shape, Motion, and Deformation Measurements. Springer, 2007.

[2] Rubino, V., Rosakis A. J., Lapusta N. Understanding dynamic friction through spontaneously evolving laboratory earthquakes. *Nat. Commun.* 8:15991, DOI 10.1038/ncomms15991, 2017.

[3] Gori, M., Rubino, V., Rosakis A. J., Lapusta N. Pressure shock fronts formed by ultra-fast shear cracks in viscoelastic materials. *Nat. Commun.* 9:4754, DOI: 10.1038/s41467-018-07139-4, 2018.

[4] Rubino, V., Rosakis A. J., Lapusta N. Full-field ultrahigh-speed quantification of dynamic shear ruptures using digital image correlation. *Exp. Mech.* **59**(5), 551-582, 2019.

[5] Tal, Y., Rubino, V., Rosakis A. J., Lapusta N. Enhanced digital image correlation analysis of ruptures with enforced traction continuity conditions along interfaces. *Appl. Sci.* **9** (8), 1625, 2019.

[6] Rosakis A. J., Rubino, V., Lapusta N. Recent milestones in unravelling the full-field structure of dynamic shear cracks and fault ruptures in real-time: From Photoelasticity to ultrahigh-speed digital image correlation. *J. Appl. Mech.* **87**(3): 030801, 2020.

[7] Rubino, V., Rosakis A. J., Lapusta N. Spatiotemporal properties of sub-Rayleigh and supershear ruptures inferred from full-field dynamic imaging of laboratory experiments. *J. Geophys. Res.* 125, e2019JB01892, DOI:10.1029/2019JB018922, 2020.

[8] Xia, K., Rosakis A. J., Kanamori H.: Laboratory Earthquakes. The Sub-Rayleigh-to-Supershear Rupture Transition. *Science* **303**: 1859-1861, 2004.

[9] Tal, Y., Rubino, V., Rosakis A. J., Lapusta N. Illuminating the physics of dynamic friction through laboratory earthquakes on thrust faults. *Proc. Natl. Acad, Sci. U.S.A.* **117**(35), 21095-2100, 2020.

DYNAMIC STRENGTH OF MATERIALS AT HIGH STRAIN RATES AND PRESSURES

Guruswami Ravichandran
Division of Engineering and Applied Science, California Institute of Technology, Pasadena, California, USA

Summary Impact, blast, and other dynamic loading events can result in extreme loading conditions of high strain-rates and pressures in materials. The work described here focusses on measuring the dynamic strength of materials using plate impact techniques at strain rates of up to ~10^7/s and pressures of up to ~50 GPa. Recent advances in extending the pressure shear plate impact technique to measure the strength of materials and characterizing their constitutive response at high pressures are discussed. Results are presented for a variety of materials, including copper, magnesium, and soda lime glass. The work presented here was performed at Caltech by Christian Kettenbeil, Zev Lovinger, Suraj Ravindran, Vatsa Gandhi, and Michael Mello.

INTRODUCTION

Dynamic events such as impact and blast of materials and structures involve the propagation of stress waves in solids, which results in high pressures and high strain rates [1]. Knowledge of the response of solids at high strain rates and pressures would help advance our fundamental understanding of material behavior under extreme conditions. Experimental data obtained by studying the response of solids at high pressures and strain rates are needed for validating constitutive and failure models. Such models would aid in the design and analysis of structures subjected to transient loading. Investigating the response of materials at high strain rates and pressures is an active field of research. Experimental techniques for direct measurement of dynamic strength of materials include the split Hopkinson (Kolsky) bar (SHPB) [2] and the pressure shear plate impact (PSPI) technique [3,4]. These techniques rely on a relatively thin sample of interest sandwiched between rods/plates, which remain elastic during the dynamic deformation of the sample. The SHPB typically uses a cylindrical sample, which is nominally in a state of uniaxial stress. The PSPI technique uses a thin disk as the sample, which is subjected to combined normal and shear loading. The gage section in a shear compression specimen (SCS) used in an SHPB is subjected to multiaxial loading [5]. The state of stress and strain in the deforming sample in SHPB and PSPI are inferred based on the analysis of elastic waves propagating in bars/plates. Typical pressures and strain rates that are currently achievable are <1 GPa and 10^4/s in the SHPB and ~10 GPa and ~10^6/s in PSPI. The need for strength measurements at higher pressures is motivated by applications such as inertial confinement fusion [6], earth and planetary interiors [7], and defense and security [1]. The current work focusses on extending the range of the PSPI technique to higher pressures (~50 GPa) and strain rates (~10^7/s).

EXPERIMENTAL

In the pressure shear plate impact experiments, a thin disc of the material of interest is sandwiched between hard anvil plates. It is impacted at an oblique angle by a hard flyer plate, and the normal and transverse particle velocities are measured on the rear free surface [3,4]. PSPI experiments are typically conducted using single-stage gas guns, which limit the pressures that can be achieved. In this work, PSPI experiments are extended to higher pressures, approaching 50 GPa by employing higher impact velocities. The impact facility consists of a single-stage powder gun, with a 38.7 mm in diameter and 3 m long barrel with a keyway, capable of launching projectiles at velocities in the range of 200-2,000 m/s.

The high-pressure and high-velocity impact regimes pose several challenges for measurement and interpretation of the free surface velocities. At high pressures (above the Hugoniot Elastic Limit, HEL), the anvils yield and undergo inelastic deformation, which precludes traditional elastic analysis from extracting the normal stress and material's strength from the measured free surface particle velocity signals [3]. The higher impact velocities also require accurate measurement of the transverse velocities at large normal displacements, resulting from the higher impact velocities. An all fiber-optic heterodyne velocity interferometer system has been developed to simultaneously measure both normal and transverse velocities at high impact velocities [8]. Higher pressures in PSPI experiments are achieved by increasing the velocity of the flyer plate impacting standard anvil materials such as tungsten carbide and tool steel, which can undergo significant inelastic deformation at pressures beyond the HEL.

A new hybrid numerical/experimental approach has been developed to extract the strength of the material of interest when the anvil and flyer plates no longer remain elastic. The inelastic response of anvil plates of interest is characterized by conducting symmetric pressure shear plate experiments at pressures of interest. A material model for describing the inelastic response of the anvil material is calibrated by comparing numerical simulation results with the experimentally measured free surface velocity signals. Requiring the simultaneous matching of both the normal and the transverse signals between experiments and simulations provides a strong constraint in calibrating the constitutive model for the anvil material. Once the constitutive model for the inelastic high-pressure response of the anvil material is established, sandwich configuration PSPI experiments are conducted wherein the material of interest is sandwiched between the anvil plates. Finally, the strength of the material of interest is extracted by simulating the sandwich configuration experiments and matching the normal and transverse velocity measurements from the PSPI experiments with the simulation results. Since the anvil material model has been calibrated previously, only the strength model for the material of interest remains to be calibrated. The pressure and strain rate in the sample are computed as part of the numerical simulations. For a given impact velocity, the pressure is relatively unaffected by the presence of the material of interest in the sandwich

configuration. The hybrid procedure has been used to determine the high-pressure strength of copper with tool steel anvils, magnesium with tool steel anvils [9], and soda lime glass with tungsten carbide anvils [10].

CONCLUSIONS

A new hybrid methodology based on PSPI experiments and numerical simulations has been developed for the extraction of material strength at high pressures and strain rates. The method relies on the ability to account for the inelastic response of the flyer and anvil plates at pressures exceeding their HEL. The successful implementation of the high-pressure PSPI technique to extract the strength of materials at high pressures of up to ~50 GPa and strain rates of up to 10^7/s has been demonstrated for quasi-brittle and ductile materials.

ACKNOWLEDGMENTS

The authors are grateful for support from the Office of Naval Research (Award No. N00014-16-1-2839) for the development of the PSPI capability at high pressures and the Air Force Office of Scientific Research and the Air Force Research Laboratory (Award No. FA955012-1-0091) for development of the PDV-HTV interferometer system. The PSPI work on magnesium was supported by the Army Research Laboratory and was accomplished under Cooperative Agreement No. W911NF-12-2-0022. The authors thank Professor R. J. Clifton and Dr. T. Jiao of Brown University for many helpful discussions and assistance in developing the high-pressure PSPI experimental capability by generously sharing their vast experience.

References

[1] Meyers M.A. Dynamic Behavior of Materials. John Wiley, NY 1994.
[2] Chen W., Song B. Split Hopkinson (Kolsky) Bar. Springer, NY 2010.
[3] Clifton R.J., Klopp R.W. Pressure-shear plate impact testing. *ASM Metals Handbook.* **8**: 230-239, 1985.
[4] Grunschel S.E., Clifton R.J. Dynamic plastic response of aluminum at temperatures approaching melt. *Met. Mat. Trans. A.* **38**: 2885-2890, 2007.
[5] Rittel D., Ravichandran G., Lee, S. Large strain constitutive behavior of OFHC copper over a wide range of strain rates using the shear compression specimen, *Mech. Mat.* **34**: 627-642, 2002.
[6] Pickworth L.A., et al. Measurement of hydrodynamic growth near peak velocity in an inertial confinement fusion capsule implosion using a self-radiography technique. *Phys. Rev. Lett.* **117**: 035001, 2016.
[7] Millot M., et al. Shock compression of stishovite and melting of silica at planetary interior conditions. *Science* **347**: 418-420, 2015.
[8] Kettenbeil C., Mello M., Bischann M., Ravichandran G. Heterodyne transverse velocimetry for pressure-shear plate impact experiments. *J. App. Phys*. **123**: 125902, 2018.
[9] Ravindran S., Lovinger Z., Kettenbeil C., Mello M., Ravichandran G. Pressure shear plate impact experiments of magnesium at high pressures. *Proceedings of the 21st APS-SCCM Conference*, Portland, OR 2019.
[10] Kettenbeil C. Dynamic strength of silica glasses at high pressures and strain rates. *PhD Dissertation*, California Institute of Technology, Pasadena, 2019.

STABILITY OF THE TIME DOMAIN BOUNDARY INTEGRAL EQUATION FOR ACOUSTICS AND ELASTICITY REVISITED

Ryota Misawa[1], Kazuki Niino[2], Toru Takahashi[3], and Naoshi Nishimura*[2]
[1]Graduate School of Science and Engineering, Saitama University, Saitama, Japan
[2]Graduate School of Informatics, Kyoto University, Kyoto, Japan
[3]Graduate School of Engineering, Nagoya University, Nagoya, Japan

Summary This study considers the stability of the traditional time domain collocation BIEMs (boundary integral equation methods) for acoustics and elasticity. We show that the question of stability of time domain BIEMs is reduced to a nonlinear eigenvalue problem related to frequency domain integral equations. We propose to solve this eigenvalue problem numerically with the Sakurai-Sugiura method (SSM). The proposed approach is validated numerically with standard BIEs for exterior and transmission problems for the wave equation and the Navier-Cauchy equation for elastodynamics. We also investigate fast methods for solving boundary integral equations for acoustics based on the interpolation technique.

INTRODUCTION

It is unfortunate that the stability issues of the collocation boundary integral equation methods (BIEMs) for the wave equation in time domain have remained unsolved for decades. Although recent developments of CQM by Lubich[1] provided a partial solution to this instability problem, there still remain demands for simpler traditional methods. In examining the stability of the traditional collocation BIEM, however, one has few effective alternatives than to solve large eigenvalue problems for the space-time discretised system matrices. The situation becomes even worse in 2D problems in which such eigenvalue problems become huge because of the infinite "tail" of the fundamental solution in time domain.

In view of this, we have proposed to carry out the required stability analyses in frequency domain rather than in time domain[3]. This approach converts the stability analysis for BIEMs in the wave equation to a non-linear eigenvalue problem similar to those for the Helmholtz equation and solves it with the Sakurai Sugiura method (SSM)[2]. In addition, this approach makes the relation between eigenvalues of the integral operators in frequency domain and the stability of the time domain BIEM clearer thus providing insights into the choice of accurate and stable formulations. In the proposed presentation, we use the proposed technique to investigate stability of various time domain integral equations for exterior and transmission problems of acoustics and elasticity. We also discuss fast methods using stable formulations thus obtained.

STABILITY ANALYSIS

Theory

We consider the following integral equation with respect to the time variable t:

$$f(t) = \int_0^t K(t-s)v(s)\,ds \tag{1}$$

obtained typically by discretising the time domain BIEs for the wave equation in the spatial direction using N collocation points, where K is a given $N \times N$ matrix, f is a given N-vector and v is an unknown N-vector function. Discretising the unknown function $v(s)$ in (1) using time interpolation functions $\phi_m(s)$ as $v(s) \approx \sum_m \phi_m(s) v_m$ ($v_m \in \mathbb{R}^N$), we obtain the following algebraic equation:

$$f(l\Delta t) = \sum_{m=1}^{l} \int_0^{l\Delta t} K(l\Delta t - s)\phi_m(s)\,ds\, v_m \qquad l = 1, 2, \cdots \tag{2}$$

where $\phi_m(s) = \phi_{\Delta t}(s - m\Delta t)$ and $\phi_{\Delta t}(t)$ is a basis function which satisfies $\phi_{\Delta t}(k\Delta t) = \delta_{k0}$ (where δ_{ij} is the Kronecker delta), respectively. One shows that the question of the stability of the scheme in (2) is now reduced to the following non-linear eigenvalue problem: find $\Omega \in \mathbb{C}$ with which the following equation

$$0 = \sum_{m=-\infty}^{\infty} \frac{1}{\Delta t} \hat{K}(\Omega_m)\hat{\phi}_{\Delta t}(\Omega_m)\, v \tag{3}$$

has a non-trivial solution $v \in \mathbb{C}^N$, where $\Omega_m = \Omega - \frac{2m\pi}{\Delta t}$ and $\hat{}$ stands for the Fourier transform with respect to time. One shows that the scheme in (2) is stable (unstable) if $\mathrm{Im}\,\Omega \le 0$ ($\mathrm{Im}\,\Omega > 0$) holds for all the eigenvalues (an eigenvalue) of (3). One may use solvers of non-linear eigenvalue problems such as the Sakurai-Sugiura method (SSM) in the solution of the problem in (3). In the special case where the boundary of the domain is a unit circle Γ, one may simplify (1) using the Fourier series with respect to the angular variable. See Fukuhara et al.[3] for further details.

*Corresponding author. E-mail: nishimura.naoshi.8r@kyoto-u.jp

Numerical experiments

We now carry out numerical experiments to see if the stability analysis given in the previous section can predict the behaviour of the time domain BIEM correctly. We consider an elastodynamic scattering problem in 2D in which an incident plane wave u^{inc} impinges upon a fixed circular scatterer Γ. The radius of this scatterer is 1 (arbitrary unit). One may reduce this problem to the solution of the following time domain integral equation of the Burton-Miller (BM) type:

$$\left(B\left(a+\frac{\partial}{\partial t}\right)+T^{-}\right)Sq(t,x)=\left(B\left(a+\frac{\partial}{\partial t}\right)+T\right)u^{\mathrm{inc}}(t,x)\qquad x\in\Gamma \tag{4}$$

where Sq, T, $^{-}$, a and B, respectively, stand for the single layer potential for elastodynamics with the unknown traction q on the boundary, traction operator, limit from the interior of the scatterer, a constant and the matrix given by

$$B=\rho(c_L n\otimes n+c_T(1-n\otimes n)),\qquad \rho:\ \text{density},\quad c_L:\ \text{P wave velocity},\quad c_T:\ \text{S wave velocity}. \tag{5}$$

Note that our stability analysis[3] shows that a non-zero a in (4) improves the accuracy of the solution. We use piecewise constant boundary elements, piecewise linear time elements and the collocation method to discretise the BIE in (4).

Fig.1 (a) shows the plot of the magnitude of q at a certain point on the boundary obtained with time domain BIE vs time step. We see that (4) leads to stability, which is consistent with the distribution of the eigenvalues given in Fig.1 (b).

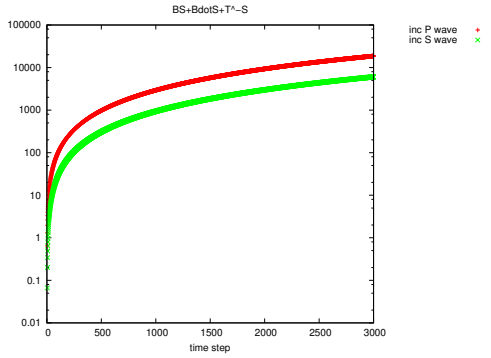

(a) q vs time step

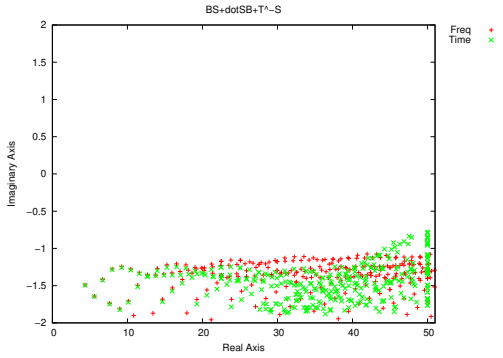

(b) green: eigenvalues of (3), red: eigenvalues of the frequency domain BIEM ($m=0$ term in (3))

Figure 1: Stability of time domain BIEM for elastodynamics in 2D. $\rho=\lambda=\mu=1$ (arbitrary unit), 100 boundary elements, $\Delta t=\pi/50$, $a=1$.

Motivated by the stability of the BM type formulation for the exterior Dirichlet problems in 2D shown above, we have tested a similar approach in acoustics in 3D using an interpolation based fast multipole method (FMM) in time domain proposed in [4]. We consider a spherical sound soft scatterer having a unit diameter subjected to a plane incident wave. This problem is solved with a conventional BIEM and an interpolation based FMM using the BM type formulation. Fig. 2 shows the time history of $\partial u/\partial n$ at a certain point on the boundary. It is seen that the numerical results agree with the analytical solution. It is also seen that the FMM solutions remain stable regardless of the degrees of the spatial interpolation (p) in spite of sporadic disturbances caused inevitably by the interpolation used in this approach. These numerical results clearly show the effectiveness of the proposed stability analysis.

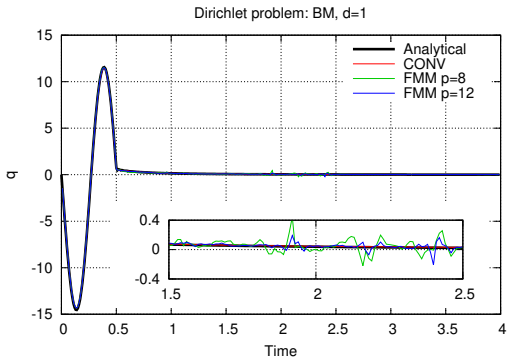

Figure 2: $\partial u/\partial n$ on boundary of a sound soft scatterer in 3D vs t. 5120 elements, $\Delta t=0.01$, 400 time steps

References

[1] Lubich C. On the Multistep Time Discretization of Linear Initial- Boundary Value Problems and their Boundary Integral Equations. *Num. Math.* **67**: 365–389, 1994.

[2] Asakura J, Sakurai T., Tadano H., Ikegami T., Kimura K. A Numerical Method for Nonlinear Eigenvalue Problems Using Contour Integrals. *JSIAM Letters* **1**: 52–55, 2009.

[3] Fukuhara M., Misawa R., Niino K., Nishimura N. Stability of Boundary Element Methods for the Two Dimensional Wave Equation in Time Domain Revisited. *Eng. Anal. with Boundary Elements* **108**: 321–338, 2019.

[4] Takahashi, T. An Interpolation-Based Fast-Multipole Accelerated Boundary Integral Equation Method for the Three-Dimensional Wave Equation. *J. Comput. Phys.* **258**: 809–832, 2014.

EMERGENCE OF CRACKLIKE BEHAVIOR OF FRICTIONAL RUPTURE

Fabian Barras[1], Michael Aldam[2], Thibault Roch[1], Efim Brener[3,4], Eran Bouchbinder[2], and Jean-Francois Molinari[*1]
[1]Civil Engineering Institute, Materials Science and Engineering Institute, Ecole Polytechnique Fédérale de Lausanne, Station 18,CH-1015 Lausanne, Switzerland
[2]Chemical and Biological Physics Department, Weizmann Institute of Science, Rehovot 7610001, Israel
[3]Peter Grünberg Institut,Forschungszentrum Jülich,D-52425 Jülich, Germany
[4]Institute for Energyand Climate Research,Forschungszentrum Jülich,D-52425Jülich,Germany

Summary We provide a comprehensive theoretical and numerical framework to understand the emergence of cracklike behaviour of frictional rupture. We discuss the origin of stress drop behind the slip front and show that, in the presence of such a stress drop, energy balance controls slip front propagation for generic rate and state friction laws.

ABSTRACT

The process of frictional rupture, i.e., the failure of frictional systems, abounds in the technological and natural world around us, ranging from squealing car brake pads to earthquakes along geological faults. A general framework for understanding and interpreting frictional rupture commonly involves an analogy to ordinary crack propagation, with far-reaching implications for various disciplines from engineering tribology to geophysics. An important feature of the analogy to cracks is the existence of a reduction in the stress-bearing capacity of the ruptured interface, i.e., of a drop from the applied stress, realized far ahead of a propagating rupture, to the residual stress left behind it. Yet, how and under what conditions such finite and well-defined stress drops emerge from basic physics are not well understood.

In the first part of this talk, we show that for a rapid rupture a stress drop is directly related to wave radiation from the frictional interface to the bodies surrounding it and to long-range bulk elastodynamics and not exclusively to the physics of the contact interface. Furthermore, we show that the emergence of a stress drop is a transient effect, affected by the wave travel time in finite systems and by the decay of long-range elastic interactions. Finally, we supplement our results for rapid rupture with predictions for a slow rupture. All of the theoretical predictions are supported by available experimental data and by extensive computations.

In the second part, we show that for generic and realistic frictional constitutive relations, and once the necessary conditions for the emergence of an effective crack-like behavior are met, frictional rupture dynamics are approximately described by a crack-like, fracture mechanics energy balance equation. This is achieved by independently calculating the intensity of the crack-like singularity along with its associated elastic energy flux into the rupture edge region, and the frictional dissipation in the edge region. We further show that while the fracture mechanics energy balance equation provides an approximate, yet quantitative, description of frictional rupture dynamics, interesting deviations from the ordinary crack-like framework — associated with non-edge-localized dissipation — exist. Together with the results about the emergence of stress drops in frictional rupture, this work offers a comprehensive and basic understanding of why, how and to what extent frictional rupture might be viewed as an ordinary fracture process [1,2].

References

[1] Barras F., Aldam A., Roch T., Brener E.A., Bouchbinder E., Molinari J.F., The emergence of crack-like behavior of frictional rupture: The origin of stress drops, *Physical Review X* **9**, 041043, 2019.
[2] Barras F., Aldam M., Roch T., Brener E.A., Bouchbinder E., Molinari J.F., The emergence of crack-like behavior of frictional rupture: Edge singularity and energy balance, *Earth and Planetary Science Letters*, 115978, 2019.

MODELLING OF DYNAMIC BEHAVIOUR OF INHOMOGENEOUS ELASTIC MEDIA

Chen Wang, Zhengwei Li, and Xiaodong Wang*
Department of Mechanical Engineering, University of Alberta, Edmonton, Canada

Summary The dynamic response of periodic elastic materials with multiple interaction is discussed to explore the relation between the local property of the material in the representative volume elements (RVEs) and the overall effective properties when dynamic loads are applied. Attention is paid to the modelling and numerical simulation of the dynamic behaviour of such materials when a large number of inhomogeneities are involved. Using the general idea of Pseudo-incident wave method to deal with the multiple interaction the effective material properties are calculated. The results are validated by comparing the result from homogenization with that obtained directly by using RVE with periodic boundary conditions. It is shown that the current method is effective in analyzing the dynamic behaviour of periodic materials.

INTRODUCTION

The understanding of the elastic wave propagation in heterogeneous materials is essential for their applications in a variety of engineering structures involving dynamic loading. More recently, the artificially structured metamaterials have attracted extensive attention because of their exotic dynamic properties. The modelling of their elastodynamic behaviour plays a significant role in their design and optimization. Because of the substantial separation of scales, the pure numerical simulation becomes prohibitive when both the local and global responses are important. Therefore, for material systems with complex structures in various scales, it is usually necessary to use multiscale models in which local structures are replaced by homogeneous materials with effective properties.

For dynamic problems of periodic materials, models based on Bloch waves are admitted as the solution for wave propagation problems. In recent studies on phononic crystals, the periodicity of the local structures and the waveforms are assumed inherently, and various numerical techniques have been developed to determine the resulting dispersion relations. In these studies since the works are mainly focused on the band structures [1,2], the Bloch wave vector is prescribed and the frequency of the incident wave is computed as the eigenvalue. In addition, the Bloch wave vector is usually limited to the boundary of the irreducible Brillouin zone. So the existing methods are inefficient to determine the effective wave fields under prescribed incident waves. This paper presents a computational framework for the elastodynamic homogenization of heterogeneous materials based on the optimization of boundary integrals of explicitly computed wave fields.

MODELLING OF THE PERIODIC ELASTIC MEDIA

To illustrate the current method, consider the dynamic behaviour of a periodic elastic medium subjected to a general incident wave, as shown in Fig. 1. The properties of macroscopically homogeneous materials can be approximated by those of their representative volume elements (RVE). For the periodic heterogeneous material, a repeating volume composed of one or multiple unit cells can be considered as a RVE, as shown by the boxes in Fig. 1. A RVE with one unit cell is shown in Fig. 2. With defined RVEs, the response of the heterogeneous material can then be treated by considering the interactions among multiple RVEs under the prescribed loads. Since the RVEs interact with each other only through the surfaces, the mechanical behaviour of a RVE can be encapsulated by its boundary response, which can be represented by the relation between the surface displacement and the traction. For example for antiplane problems with multiple inhomogeneities the property of the RVE selected will be determined by the antiplane displacement w.

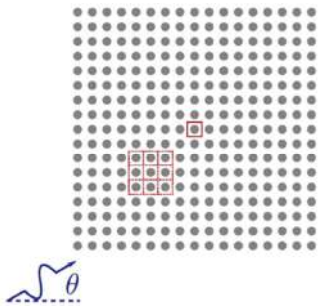

Figure 1 Periodic material subjected to an incident wave.

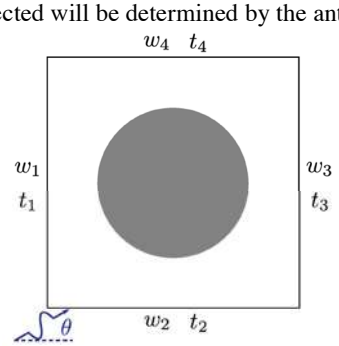

Figure 2 Unit cell under periodic boundary condition

EFFECTIVE PROPERTY OF THE RVE

The wave field in RVE subjected to typical incident waves are determined by using a Pseudo-incident wave method [3]. The resulting wave field is then used to evaluate the dynamic effective property of the RVE. If the RVE is modelled

*Corresponding author. E-mail: xiaodong.wang@ualberta.ca.

as a homogeneous effective medium, the relation between the boundary displacement w and the traction t can be expressed by the boundary integral equation, as

$$c(\boldsymbol{x})w(\boldsymbol{x}) + \int_S \frac{\partial G(\boldsymbol{x},\boldsymbol{y})}{\partial \boldsymbol{n}(\boldsymbol{y})} w(\boldsymbol{y}) ds(\boldsymbol{y}) = \int_S G(\boldsymbol{x},\boldsymbol{y}) t(\boldsymbol{y}) ds(\boldsymbol{y}) \tag{1}$$

where S is the boundary of the RVE with $\boldsymbol{n}$ being the outward normal vector. $c(\boldsymbol{x})$ depends on the geometry of the boundary at position $\boldsymbol{x}$. $G(\boldsymbol{x},\boldsymbol{y})$ is the Green's function of the effective medium.

For homogeneous media, the solution from (1) will be exactly same as that from the solution by Pseudo-incident wave method. But for the current periodic media, since the RVE is not composed of the homogeneous material with the same properties upon which the Green's function is determined, the solution will be different and will be described by a residue function. The magnitude of the residual function depends on the material properties of the effective medium. The minimum residue occurs when the material properties of the fictitious homogeneous effective medium can best represent the boundary response of the RVE. Accordingly, the effective properties of the heterogeneous material are determined by adjusting the effective properties to minimize the residual function. In the numerical implementation, the boundary is discretized into segments, and the boundary integrals are computed by using Gaussian quadrature.

RESULTS AND DISCUSSION

This section will present the verification and the evaluation of the accuracy of the developed homogenization algorithm, and the application of the algorithm to general examples. The homogenization results are verified by comparing the direct numerical simulation results of the wave fields of interacting inhomogeneities with that based on the effective properties obtained by the proposed procedures. As shown in Fig. 3, the multiple scattering model is composed of *20X20* identical circular inhomogeneities arranged in a rectangular lattice. The radius of the inhomogeneities is *6 mm* and the size of a cell is *20 mm*. The density and shear modulus of the matrix are *7670 kg/m*^{3} and *84.3GPa*, and the corresponding values for the inhomogeneities are *11400 kg/m*^{3} and *8.43GPa*.

The normalized amplitude of the displacement along the horizontal line marked in Fig. 3 is plotted in Fig. 4, where w^0 represents the displacement caused by the original incident wave. From the comparison of the results, it can be observed that the displacement matches well outside the region of inhomogeneities ($-10 < x < 10$). Inside the region, deviation is observed but the results still agree reasonably well. The use of homogenized model in simulating the multiple scattering in larger scale is also conducted and validated by the comparison between the numerical simulations of the two models. Excellent agreement of the predicted wave is also observed for both displacement and stress fields.

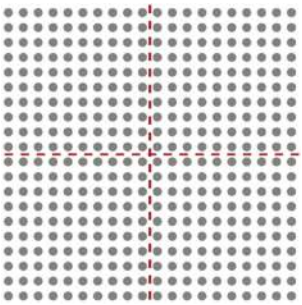

Figure 3 Multiple scattering model

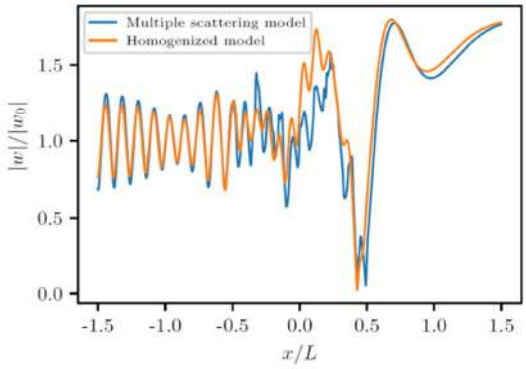

Figure 4 Normalized displacement amplitude

CONCLUSIONS

A computational homogenization method is presented to evaluate the dynamic effective properties of periodic elastic media. The method makes use of the optimization of the boundary integral of the RVEs with periodic boundary conditions based on the explicitly solved multiple scattering wave fields. The residue function, which indicates the mismatch between the boundary responses of the RVE and the homogenized substitution, is defined as the objective function to be minimized over the material properties. Similar simulations conducted indicate that for difficult frequencies the periodic material will show pass-band or stop-band, as well understood for other similar structures. The RVE is defined as multiple unit cells surrounded by a number of identical cells for approximating the ambient wave field in infinitely periodic structure. The approximation is validated by comparing the homogenization results with the ones obtained by using RVE with periodic boundary conditions. The results indicate that the current method is effective in determining the dynamic effective properties of periodic elastic materials.

References

[1] Parnell W.J. and Abrahams I.D. Dynamic homogenization in periodic fibre reinforced media: quasi-static limit for SH waves. Wave Motion, **43**: 474–498, 2006.

[2] Liu Z.Y., Chan C.T., and Sheng P. Three-component elastic wave bandgap material. Physical Review B, **65:** 165116, 2002.

[3] Wang C. and Wang X.D. Modeling and simulation of wave scattering of multiple inhomogeneities in composite media. Composites B: Engineering, **90**, 341-350, 2016.

STUDY ON THE PENETRATION OF A JACKETED ROD INTO SEMI-INFINITE TARGET

Jinxiang Wang*, Kui Tang
National Key Laboratory of Transient Physics, Nanjing University of Science and Technology, Nanjing, China

Summary A combined experimental, numerical and theoretical study is conducted herein on the penetration of semi-infinite targets by jacketed rods with two types of jacket materials. Specially, the damage mode of the 93W/1060Al jacketed rod changed from "bi-erosion" to "co-erosion" at a striking velocity of 936 m/s. While, for other striking velocities, only "co-erosion" damage was observed. Two kinds of jacketed rods presented completely different damage mechanisms for striking velocity less than 2.0 km/s, due to the differences in material properties of the jacket. For striking velocity lager than 2.0 km/s, the penetration performance of the two types of jacketed rods is the same as that of the unitary 93W rod. Meanwhile, the kinetic energy and the strength of the jacket have a significant effect on the penetration performance of the jacketed rod. Based on the detailed analysis of the damage mode and the failure mechanism of the jacketed rod by combining the experimental and numerical results, the analytical model for penetration depth was modified, and the predicted results of the modified model were in good agreement with the experimental results.

Jacketed projectile is usually consists of a central high-density rod surrounded by a low-density jacket. Recently, a series of numerical simulations[1-5] and experiments[1,2,5-7] have been performed to examine the ballistic performance of the jacketed rod. And, Wen et al.[4] have developed an analytical model to predict the penetration depth of jacketed rod into semi-infinite target. However, almost all these experiments carried out above had controlled the striking velocity around 1.6 km/s and 2.5 km/s. In addition, only a few types of jacket materials are used in these tests. Therefore, we carried out series of experimental and numerical study on the penetration of two types of jacketed rods into semi-infinite 4340 steel targets, in which the striking velocity was extended to 0.9-3.3 km/s and two kinds of new jacket materials were considered. And, the penetration depth model presented by Wen et al.[4] was modified.

EXPERIMENTAL PROCEDURE

In this study, 93W4.9Ni2.1Fe (93W) is used as the central core, as to jacket material, 1060 aluminum and TC4 titanium alloy are considered. The total length (L), the diameters of the core (d) and the jacket (D) of the jacketed rods tested are 70 mm, 5 mm and 7 mm, respectively. In addition, the homogeneous 93W rod with the same shape and size as that of the jacketed rod is tested. And, 4340 steel target is used. The striking velocity was during 0.9-3.3 km/s.

NUMERICAL SIMULATION

To supply sufficient data for the analysis of the damage mechanism and the penetration performance of the unitary 93W projectiles and jacketed projectiles, AUTODYN was adopted to simulate the penetration process. The Smoothed Particle Hydrodynamics method (SPH) was employed for the projectile. And, the Lagrange solver was employed for the target to improve computing efficiency. Fig. 1 shows the comparison of experimental and numerical simulation results under one of the conditions. It is evident that the numerical results are in good agreement with the experimental results.

DAMAGE MECHANISM

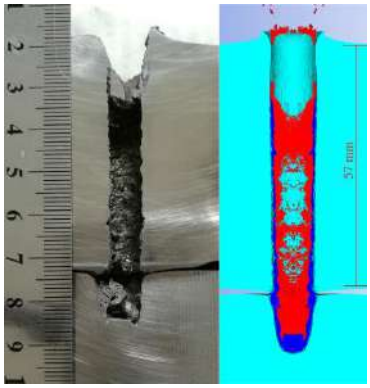

Fig. 1 Comparisons of experimental and simulated results of Shot 1-6

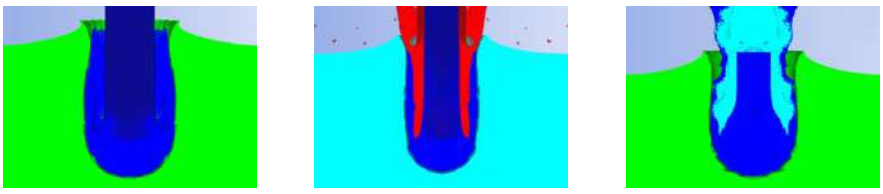

(a) 93W rod, 949m/s (b) 93W/1060Al rod, 936m/s (c) 93W/TC4 rod, 930m/s

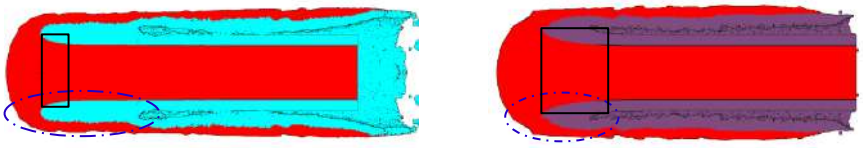

(d) 93W/1060Al rod, 1654m/s (e) 93W/TC4 rod, 1521m/s

Fig. 2 Morphology of 93W and jacketed rods

The typical morphology of the unitary 93W rod and the jacketed rods under different striking velocity is shown in Fig. 2. It can be found that the unitary 93W rod formed a "mushroom head" during penetration. Specially, the damage mode of the 93W/1060Al jacketed rod change from turns from "bi-erosion"[4] at early penetration stage to "co-erosion" [4] at late penetration stage at a striking velocity of 936 m/s. While, typical "co-erosion" damage mode was observed in other cases for two types of jacketed rods. In addition, there are significant differences in the damage mechanisms of the two kinds of jacketed rods, the core of the 93W/TC4 jacketed rod formed an obvious bulges between the rigid tail and the head as shown in Fig. 2 (c), while it was not observed in Fig. 2 (b). As shown in Fig. 2 (d) and (e), the deformation of the core for 93W/TC4 jacketed rod in the box is still larger than that of the 93W/1060Al jacketed rod. Meanwhile, the jacket of the 93W/1060Al jacketed rod is more serious and the deformation area is much bigger than that of the

* Corresponding author. E-mail: wjx@njust.edu.cn

93W/TC4 jacketed rod. However, the difference in the damage mechanisms of the jacket and core of the jacketed rod decreases with increasing incident velocity.

PENETRATION PERFORMANCE

It was found that the penetration performance of the two types of jacketed rods is less than that of the unitary 93W rod for striking velocity lower than 1.65 km/s, while it is the same for striking velocity larger than 2.0 km/s. As a typical kinetic energy penetrator, the kinetic energy has a great effect on the penetration performance of the jacketed rod. For example, the penetration performance of the 93W/1060Al jacketed rod is about 43.5% higher than that of the unitary 93W rod at an initial incident kinetic energy of 36.55 kJ. But, this advantage gradually decreases as the incident kinetic energy increases. The strength of the jacket has a significant effect on the penetration performance of the jacketed rod, compared to the density of the jacket. The lower the strength of the jacket, the better the penetration performance is.

ANALYTICAL MODEL FOR PENETRATION DEPTH

In the case of "co-erosion" penetration, assume that at time t, the length and velocity of the rigid body of the jacketed rod are l and v, respectively. And the penetration velocity is u. Wen et al.[4] have developed an analytical model to predict the penetration depth of jacketed rod into semi-infinite target as follow.

The momentum balance of the rigid part of the rod gives: $Y_c A_{c0} + Y_j A_{j0} = -\left(\rho_c A_{c0} + \rho_j A_{j0}\right) l \mathrm{d}v / \mathrm{d}t$ (1)

Let $\lambda = A_{j0} / A_{c0}$, and divide both ends of equation (1) by (1+λ), then it can be rewritten as: $Y_{eq} = -\rho_{eq} l \mathrm{d}v / \mathrm{d}t$.

The rod erodes as: $\mathrm{d}l / \mathrm{d}t = -(v-u)$ (2)

The v~u relationship is given as: $\rho_{eq}(v-u)^2/2 + Y_{eq} = \rho_t u^2/2 + R_t$ (3)

where, the R_t is defined as a piecewise function by Wen et al.[4], herein, a continuous function R_t=7$Y_t$ln(α)/3 that given by Walker and Anderson[8] is used, which agree better with the experimental results. Thus, the penetration depth is

$$P = \frac{\rho_{eq}}{Y_{eq}} \int_{V_c}^{V_0} u l \mathrm{d}v = \frac{\rho_{eq} L_0}{Y_{eq}} \int_{V_c}^{V_0} u \exp\left[\int_{V_0}^{v} \frac{\rho_{eq}}{Y_{eq}} (v-u) \mathrm{d}v\right] \mathrm{d}v \quad (4)$$

The prediction results obtained by the above model are shown in Fig. 3 as dotted lines. It can be seen that there is a large error between the theoretical prediction result and the experimental result. Therefore, equation (1) was modified by us based on the numerical simulation results. The modified equation is: $Y_c A_{c0} + Y_j A_j = -\left(\rho_c A_{c0} + \rho_j A_j\right) l \mathrm{d}v / \mathrm{d}t$, where A_j is an effective area of the jacket during penetration, it is given as: $A_j = \frac{Y_j \rho_j}{Y_c \rho_c} A_{j0}$ (5)

After modification, the predicted results are given in Fig. 3 as solid lines, it can be found that good agreement between the theoretical prediction result and the experimental result are obtained.

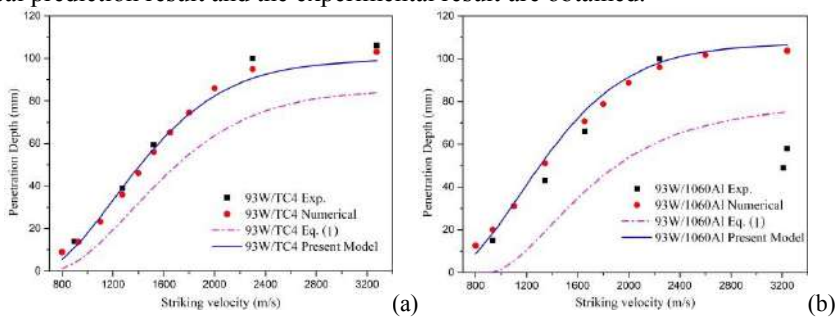

Fig. 3 Comparison of the predicted penetration depth with experimental data for (a) 93W/TC4 and (b) 93W/1060Al jacketed rods

CONCLUSIONS

Two types of jacketed rods presented typical "co-erosion" damage for striking velocity at 0.9-3.3 km/s, except for the 93W/1060Al jacketed rod at a striking velocity of 936 m/s. Due to the differences in material properties of the jacket, the core and the jacket of the jacketed rod show different damage mechanisms. Under the same initial kinetic energy, penetration performance of the jacketed rod is significantly better than that of the unitary 93W rod, but this advantage decreases as the incident kinetic energy increases. Compared to the density of the jacket, the strength of the jacket has a more significant effect on the penetration performance of the jacketed rod. The analytical model for penetration depth of the jacketed rod was modified, and good agreement between the predicted and experimental results are obtained.

References

[1] Andersson O., Ottosson J. High velocity jacketed long rod projectiles hitting oblique steel plates. *Proc. of the 19th Int. Symp. on Ballistics*, Interlaken, Switzerland, 7-11 May, pp: 1241-1247, 2001.

[2] Pedersen B.A., Bless S.J., Cazamias J.U. Hypervelocity jacketed penetrators. *Int. J. Impact Eng*. 26: 603-611, 2001.

[3] Sorensen B.R., Kimsey K.D., Zukas J.A., Frank K. Numerical analysis and modelling of jacketed rod penetration. *Int. J. Impact Eng*. 22: 71-91, 1999.

[4] Wen H.M., He Y., Lan B. A combined numerical and theoretical study on the penetration of a jacketed rod into semi-infinite targets. *Int. J. Impact Eng*. 38: 1001-1010, 2011.

[5] Cullis I.G., Lynch N.J. Hydrocode and experimental analysis of scale size jacketed KE projectiles. *Proc. of the 14th Int. Symp. on Ballistics*, Quebec, Canada, 26-29 Sep., pp: 271-280, 1993.

[6] Ernst H.J., Lanz W., Wolf T. Penetration comparison of L/D=20 and 30 mono-block penetrators with L/D=40 jacketed penetrators in different target materials. *Proc. of the 19th Int. Symp. on Ballistics*, Interlaken, Switzerland, 7-11 May, pp: 1151-1158, 2001.

[7] Lehr H.F., Wollman E., Koerber G. Experiments with jacketed rods of high fineness ratio. *Int. J. Impact Eng*. 17: 517-526, 1995.

[8] Walker J.D., Anderson C.E. A time-dependent model for long-rod penetration. *Int. J. Impact Eng*. 16: 19-48, 1995.

DYNAMIC STRESS EVALUATION DUE TO HYPERVELOCITY IMPACT USING TIME GATED RAMAN SPECTROSCOPY

Abhijeet Dhiman[1] and Vikas Tomar[1]
[1]School of Aeronautics and Astronautics, Purdue University, West Lafayette, IN, 47907, USA

Summary In this work, an experimental setup based on time-gated Raman spectroscopy for impact-induced local stress evolution measurements is presented. The setup is used to obtain local Raman shift variation as a function of time at strain rates approaching 10^6 s-1. Based on an analytical expression, stress evolution as a function of time under dynamic impact loading is presented. The setup is shown to be able to measure the local in-situ evolution of dynamic stress in a Hydroxyl-terminated polybutadiene (HTPB) sample induced by an impact from 250 micron-sized microsphere using a pulse laser.

INTRODUCTION

Application such as Armor design and meteor impact resistant structure design require high-performance composite materials resistant to impact failure. Under impact, stress-wave interacts with the material interfaces and defects that play an important role in determining the material performance. Material behavior under shock is entirely different from materials behavior under static loading. Understanding of material behavior in-situ under shock can lead to important new advances in material development not currently possible. It is, therefore, important to investigate the dynamic behavior of materials under shock at fundamental interface level in an in-situ manner. One aspect of such an understanding is stress-strain behavior at a local microscale material length scale under hypervelocity (> 1 km/sec) impact-induced shock. This work presents real-time measurements of stress evolution under impact shock loading at micron length scale.

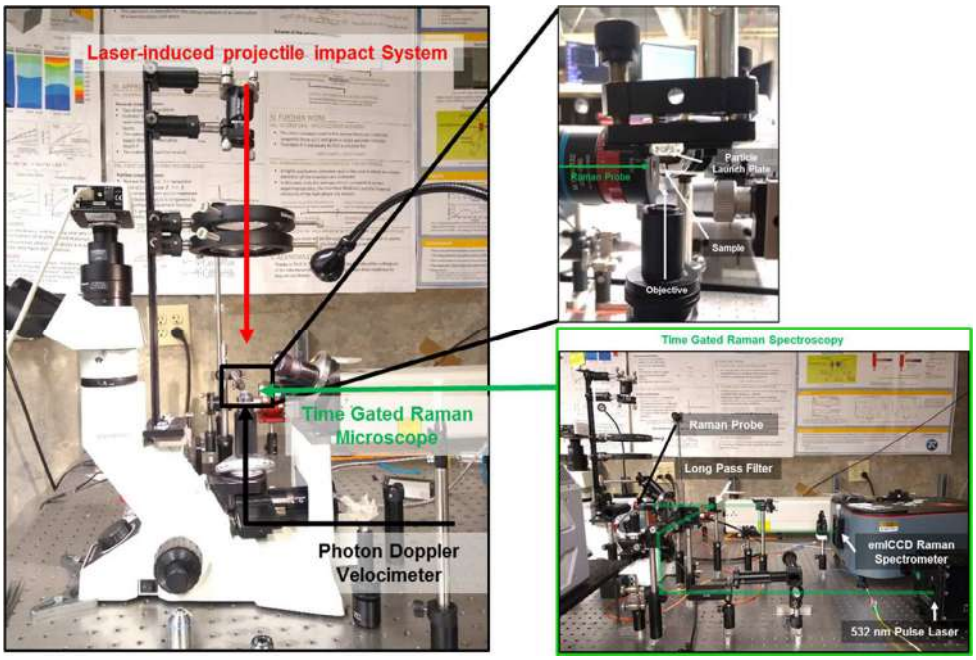

Figure 1: Micro-particle impact Raman microscope

There are several experimental tests that have been used to characterize a material's response to an impact or shock loading. Drop weight test, light gas gun-based Taylor Impact test, Split Hopkinson Bar test are some of the specialized experimental techniques that are primarily used. The outcome of such tests are the deformation and strain as well as strain rates which can be used to obtain strain rate dependent material constitutive behavior [1]. The measurement techniques used in these experiments involve strain gauges, digital image correlation, Xray diffraction (XRD), Photonic Doppler Velocimetry (PDV) or the electron diffraction based methods. These methods are either of insufficient time and length resolution (strain gauge etc.) or are based on large-scale facilities (XRD, phase contrast imaging, etc.)[2]. Also, these methods can only measure strains directly and stress is a derived quantity [3] using the constitutive models of the respective materials. Currently the only laboratory method available, which can directly measure stresses in the material without using a constitutive model, is mechanical Raman spectroscopy (MRS) developed by Tomar and co-workers [4, 5]. Several previous works [4, 5] have established the robustness and repeatability of MRS for stress measurement without constitutive models under quasi-static loading conditions in different materials by comparing the results with constitutive model based predictions. However, when it comes to the direct stress measurement at microscale under hyper-velocity impact conditions, there are no established experimental techniques available. In this work, time gated Raman

spectroscopy is extended for direct in-situ measurement of stress evolution at microscale under hyper-velocity particle impact loading using a MRS setup developed earlier [6]. Figure 1 shows the experimental setup developed to preform dynamic stress evolution under shock loading.

KEY RESULTS

The particle launch system with 250 μm zirconia microspheres and 75 μm aluminum layer was used to induce shock in Hydroxyl-terminated polybutadiene (HTPB) samples with impact velocities of 543.52 ± 6.74 m/s. The impact behavior of HTPB due to impact was recorded using high speed camera with frame rate of 900 kHz. Figure 2(a) shows Raman spectra of HTPB for CH_2 stretching and peak fitting using Lorentz curve for 2848.95 cm^{-1} peaks corresponding to CH_2 stretching accumulated over 40 impacts.

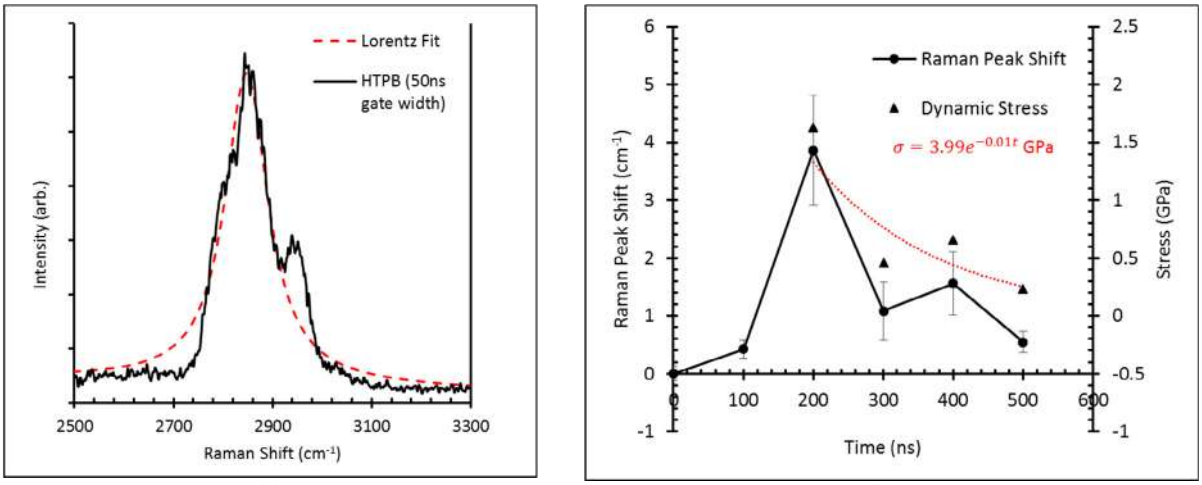

(a) (b)

Figure 2: (a) Raman spectra of HTPB collected over 40 accumulations (b) Raman peak shift and dynamic stress evolution over impact time history.

The analytical solution for 1D longitudinal stress propagation in a rod due to spherical ball impact is given by [7]:

$$\sigma_{\max} = \rho U_s u_{p\_\max} \tag{1}$$

Raman shift due to 543.52 ± 6.74 m/s impact using 250 μm microsphere can be calibrated as

$$\sigma = 0.44\Delta w[GPa] \tag{2}$$

Figure 2(b) shows the change in Raman peak due to shock loading which lasts for less than 100 ns. Similar results have been observed by other researchers . Based the Raman shift at different impact time history, the stress evolution after the impact is given by exponential fitting as:

$$\sigma(t) = 3.99e^{-0.01t}[GPa] \tag{3}$$

CONCLUSION

In this work, the stress evolution due to shock-induced by microparticle impact on Hydroxyl-terminated polybutadiene was characterized using time-gated Raman spectroscopy. The current works provide further opportunities to evaluate stress using Raman shift under different loading scenarios. Future work will involve increasing the impact velocities for bigger size microspheres and integrating Photon Doppler Velocimetry system to obtain time-resolved deformation on the sample.

References

[1] Ruan, D., M.A. Kariem, and I.G. Crouch 2017. "High strain rate and specialised testing." Woodhead Publ Mater: 581-637 (10.1016/B978-0-08-100704-4.00010-4).

[2] Dieing, T., O. Hollricher, and J. Toporski, *Confocal Raman microscopy*. Springer series in optical sciences,2010, Heidelberg Germany ; New York: Springer. xv, 289 p.

[3] Johnson, Q., L. Evans, and A.C. Mitchell 1972. "X-Ray-Diffraction Study of Single-Crystals Undergoing Shock-Wave Compression." Appl Phys Lett **21**(1): 29-& (Doi 10.1063/1.1654205).

[4] Prakash, C., I.E. Gunduz, and V. Tomar 2019. "Simulation guided experimental interface shock viscosity measurement in an energetic material." Model Simul Mater Sc **27**(8) (Artn 08500310.1088/1361-651x/Ab4148).

[5] Gan, M., V. Samvedi, and V. Tomar 2015. "Raman Spectroscopy-Based Investigation of Thermal Conductivity of Stressed Silicon Microcantilevers." J Thermophys Heat Tr **29**(4): 845-857 (10.2514/1.T4491).

[6] Gan, M. and V. Tomar 2014. "An in situ platform for the investigation of Raman shift in micro-scale silicon structures as a function of mechanical stress and temperature increase." Review of scientific Instruments **85**(1) (Artn 01390210.1063/1.4861201).

[7] Millett, J.C.F., N.K. Bourne, and J. Akhavan 2004. "The response of hydroxy-terminated polybutadiene to one-dimensional shock loading." J Appl Phys **95**(9): 4722-4727 (10.1063/1.1689758).

2D DISCRETE SPECTRAL ANALYSIS — A TOOL FOR EXAMINING OF COMPLEX WAVE STRUCTURES

Andrus Salupere*[1] and Mart Ratas [1]
[1]Department of Cybernetics, School of Science, Tallinn University of Technology, Estonia

Summary In the present paper we demonstrate application of 2D spectral characteristics for examining of space-time behaviour of complex wave structures that can be formed from different initial pulses. Temporal periodicity and temporal symmetry of the solution as well as recurrence phenomenon will be discussed in case of 2D wave propagation.

INTRODUCTION AND STATEMENT OF THE PROBLEM

We have demonstrated earlier that in case of 1D models of wave propagation the discrete spectral analysis is very helpful tool in order to analyse the space-time behaviour of different wave structures [1, 2]. Here the method is generalised to 2D case and we demonstrate application of 2D spectral characteristics for analysis of time-space behaviour of complex wave structures. In the present short paper we consider the KPI equation

$$(u_t + \alpha_1 u u_x + \alpha_2 u_{xxx})_x - \alpha_3 u_{yy} = 0, \tag{1}$$

as a model equation. Here α_1, α_2 and α_3 can be called as the nonlinear coefficient, the dispersion coefficient and the transverse perturbation coefficient, respectively. In order to generate a complex wave structure the initial wave is given in form of bended sinusoid:

$$u(x, y, 0) = \sin(a_x x + \beta \cos(a_y y)), \tag{2}$$

where a_x and a_y define the number of periods per 2π, and β is arbitrary parameter. For numerical integration the pseudospectral method is applied. Details of the numerical scheme and some results on the application of 2D discrete spectral analysis can be found in [3]. Temporal periodicity, temporal symmetry, and recurrence phenomenon will be discussed in the presentation.

DISCUSSION

An example of the initial bended sinusoidal wave and the emerged complex wave structure that consist of several interacting solitary waves is presented in Fig. 1. In the present case, (i) soliton trains (similar to the KdV solitons) are propagating along x axis, and (ii) breather like solitonic structures are formed along y axis.

The solution of Eq. (1) has form $u(x, y, t)$ and spectral amplitudes $a_k(y, t)$ are defined as follows:

$$\begin{aligned} a_k(y,t) &= \frac{2|U(k,y,t)|}{N}, \quad k = 1, 2, ..., \frac{N}{2} - 1, \\ a_k(y,t) &= \frac{|U(k,y,t)|}{N}, \quad k = 0, \frac{N}{2}. \end{aligned} \tag{3}$$

Here $U(k, y, t) = F_x(u(x, y, t))$ and F_x denotes the Fourier transform with respect to space variable x.

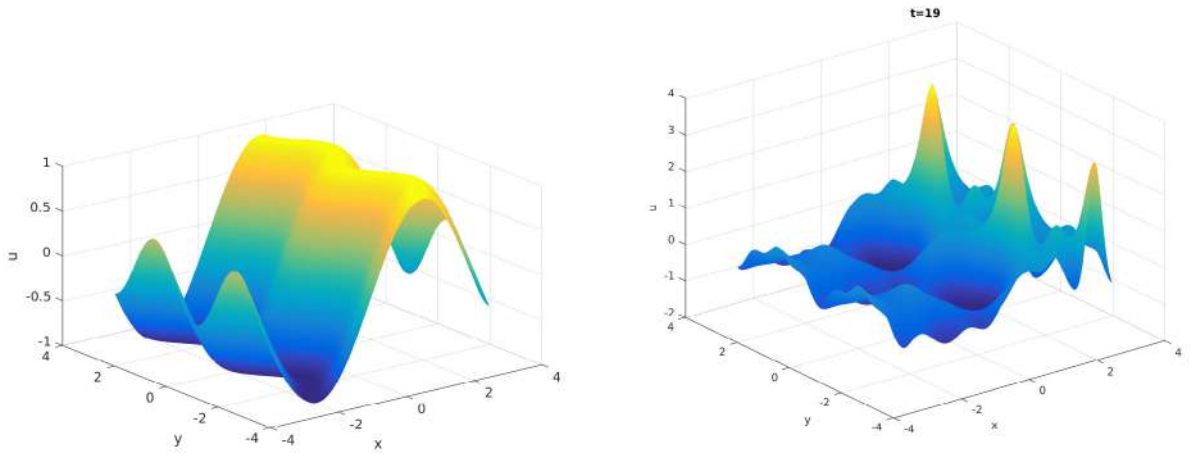

Figure 1: Initial bended sinusoid (the left panel) and solution at $t = 19$ (the right panel); $a_x = 1$, $\beta = 0.4$, $a_y = 2$ and $d_l = 1.4$

.

*Corresponding author. E-mail: salupere@ioc.ee.

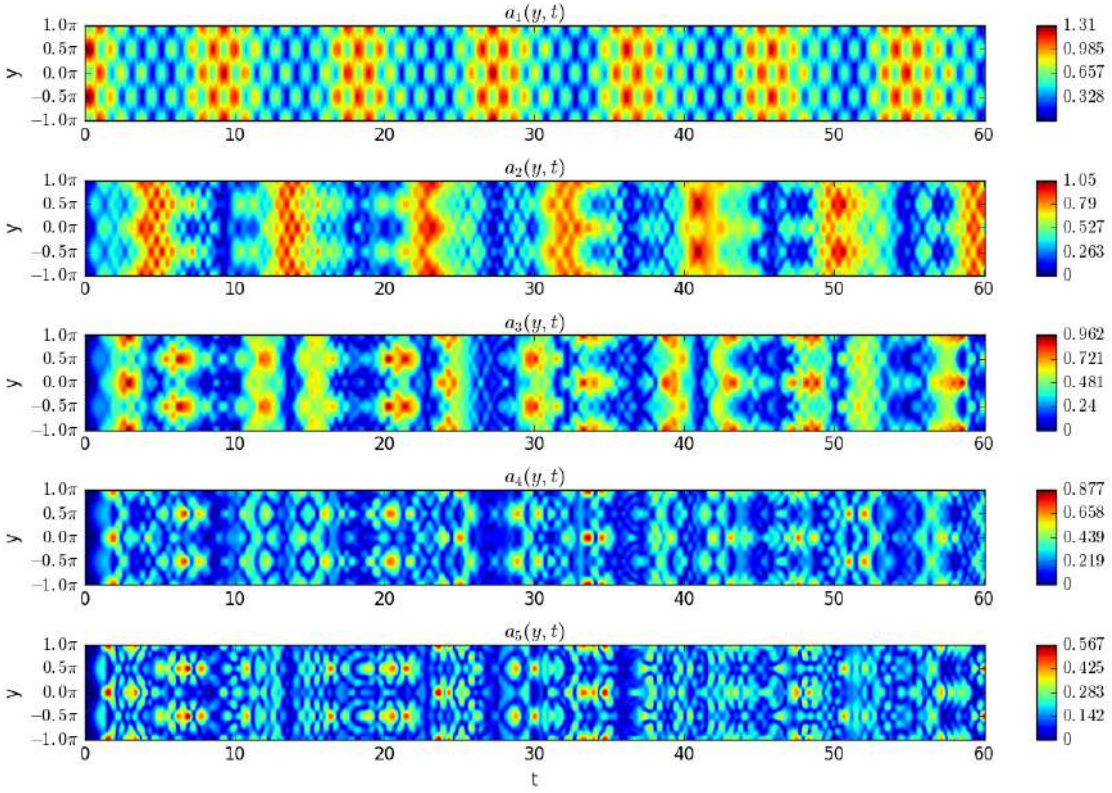

Figure 2: Spectral amplitudes $a_1(y,t) \ldots a_5(y,t)$ for $a_x = 1$, $\beta = 0.4$, $a_y = 2$ and $d_l = 1.3$.

In the case of 1D waves spectral amplitudes depend only on time variable t and therefore plotting all of them in one 2D figure is very easy. However, in the case of 2D waves spectral amplitudes (3) depend on two variables: t and y. Therefore we had to work out a different technique for plotting of them. We are using 3D pseudocolor plots for this reason – a 3D pseudocolor plot is formed for each spectral amplitude. An example of such a depiction is given in Fig. 2, where the horizontal axis refers to time t while the vertical axis refers to the spatial variable y. Image of this kind shows how different 2D spectral amplitudes behave in the considered time interval.

In the presentation we will analyse several numerical examples and demonstrate how to use spectral amplitude plots for estimating whether or not the solution has (quasi)periodic behaviour, and how to find temporal symmetries of solutions. In addition, we will demonstrate that for detection of recurrence phenomenon it is useful to average the individual spectral amplitudes over y, i.e. to introduce averaged spectral amplitudes.

CONCLUSIONS

Similarly to the 1D waves the 2D spectral characteristics carry additional information about the internal structure of 2D waves. Therefore, the 2D discrete spectral analysis is a helpful tool for analysing spatio-temporal behaviour of 2D waves.

Acknowledgment

The research was supported by the Estonian Research Council (IUT3324).

References

[1] A. Salupere, The pseudospectral method and discrete spectral analysis. In *Applied Wave Mathematics: Selected Topics in Solids, Fluids, and Mathematical Methods*, E. Quak, T. Soomere (eds.), Springer, Heidelberg, 301–333, 2009.

[2] A. Salupere, M. Lints, J. Engelbrecht, On solitons in media modelled by the KdV equation. *Arch. Appl. Mech.*, **84**: 1583–1593, 2014.

[3] A. Salupere, M. Ratas, On the application of 2D discrete spectral analysis in case of the KP equation. *Arch. Appl. Mech.*, **93**: 141–147, 2018.

NUMERICAL INVESTIGATION REVEALING KEY FACTORS ASSOCIATED WITH INSTABILITIES IN GRANULAR MATERIALS DURING IMPACT

Benoit Revil-Baudard*[1] and Oana Cazacu[1]
[1]Department of Mechanical& Aerospace Engineering, University of Florida/REEF, 1350 N. Poquito Rd., Shalimar, Fl 32579, USA

Summary In general, elastic/plastic models for granular materials have been developed for geotechnical applications, and as such the constitutive laws are defined and calibrated from tests at low confining pressures (of the order of kPa). Dynamic applications such as penetration and impact in granular media require models valid for very high pressures (of the order of GPa) and very high strain rates. This leads to the need to provide constitutive laws valid for this pressure range, and require the development of new numerical strategies that could account for the pronounced precompaction that occurs at the beginning of the penetration event. In this paper, we investigate the effect of dynamic precompaction on the development of instabilities in soils. For this purpose, the Lade [1] model for soils has been revisited and modifications have been implemented such as to account for high-pressures and high-strain rates. Moreover, the model was implemented using a F.E. implicit procedure and most importantly, a new precompaction procedure involving the shift of the yield surface and the plastic potential has been integrated to allow the simulation of the influence of dynamic precompaction on the inception of instabilities. A sample of the results of this investigation are presented in the following.

KEY RESULTS ON THE EFFECTS OF INITIAL PRECOMPACTION ON LOCALIZATION DURING PENETRATION INTO SAND

Highlights of key findings revealed by the high-rate virtual tests are presented in the following. Fig.1 presents high-rate densification simulations that show the paramount influence of the initial state (precompaction level) on wave propagation. Note that for the same imposed velocity depending on the initial precompaction level (0.5 MPa vs. 10 MPa), the shape of the wave through the specimen is completely different (see Figure 1(c)). While for a higher initial confining pressure, the wave front is "smooth", for a low initial confining pressure, the wave front is very sharp. Due to the sharp front wave, oscillations of all field variables occur. Because of the different nature of the wave that propagates inside the specimens, the density map is totally different. For 10 MPa precompaction, the wave is smooth and leads to a "continuous" variation of density (see Figure 1(a)). In contrast, for 0.5 MPa precompaction, there are jumps in density. Almost two-third of the specimen is highly compacted, (densification of 13%) while in the other third of the specimen the density is unchanged (density= 2000 kg/m^3), there are also small oscillations of the density at the back of the front wave (see Figure 1(b)).

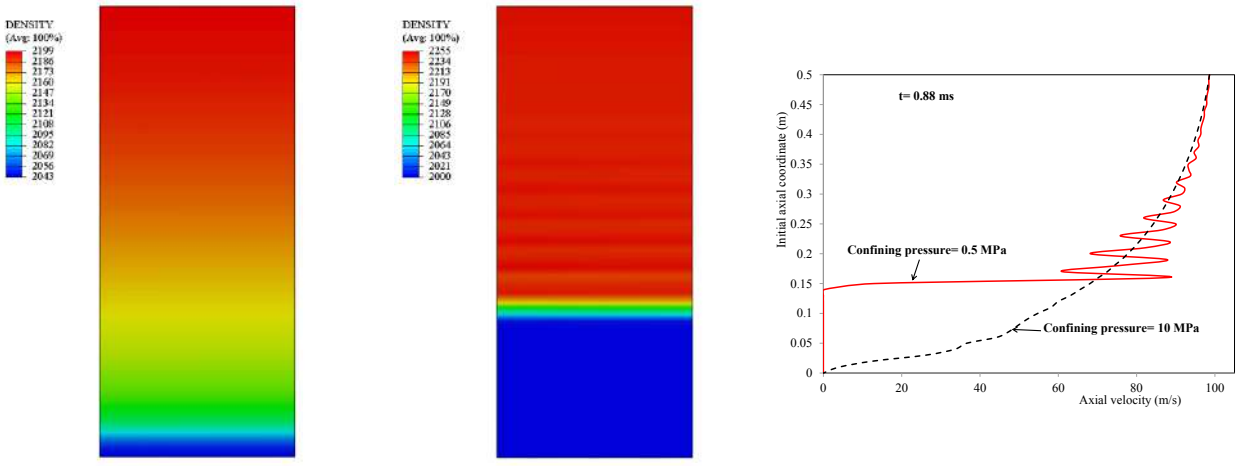

(a) Confining pressure: 10 MPa (b) Confining pressure: 0.5MPa (c) Velocity profile

Figure 1. Isocontours of the density (initial density = 2000 kg/m3) for loading with Vmax =100 m/s at t = 0.88ms: (a) Initial confining pressure of 10 MPa; (b) Initial confining pressure of 0.5 MPa; (c) Distribution of the axial velocity in the sand specimen at a given time for an imposed velocity Vmax = 100m/s

A sample of the results of the F.E. simulations of impact of a rigid object into a Sacramento River sand are presented in Fig.2. The impact velocity is 50 m/s. Simulations were run for the case of sand targets of different initial states: one target precompacted at 0.5 MPa, the other at 20 MPa. Our main goal being the assessment of the influence of the precompaction level of the sand on its subsequent plastic dissipation and densification, only the initial phase of the penetration event is analyzed. Isocontours of the plastic dissipation at 35μs after the impact are shown in Figure 2. For a loose sand (precompacted at 0.5 MPa), it is worth noting that multiple localization bands develop, while if the same material has a higher initial density (same material precompacted at 20 MPa), only a primary localization band develops

*Corresponding author. E-mail: revil@ufl.edu.

at a later stage (35ms after impact), which is followed by secondary localization bands. These results indicate that the initial confinement pressure has a very strong influence on the inception and nature of the localization bands that develop. Also, note that the less precompacted is the material, the slower is the wave, and the sharper is the wave front.

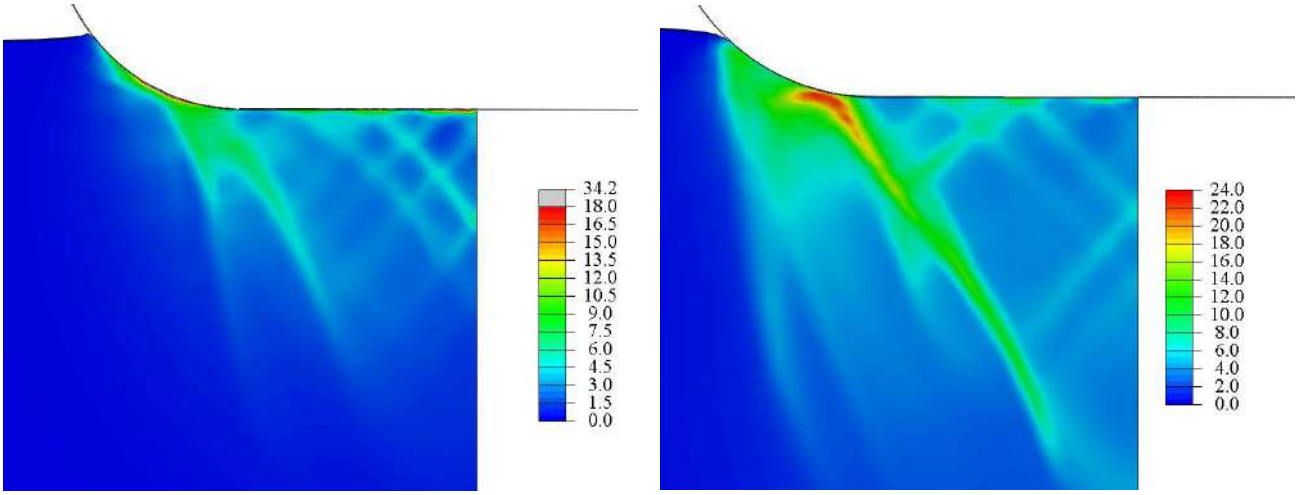

(a) Loose sand (b) Dense sand

Figure 2. Plastic dissipation isocontours at 35 ms after impact (velocity: 50m/s): (a) loose sand; (b) dense sand

References

[1] Lade P.V. Elasto-plastic stress-strain theory for cohesionless soil with curved yield surfaces. *Int. J. Solids and Struct*. **13**: 1019-1035, 1977

[2] Jakobsen K. P., Lade, P. V. Implementation algorithm for a single hardening constitutive model for frictional materials. *Int. J. Numer. Anal. Methods Geomech.* **26**: 661-681, 2002

[3] Revil-Baudard B., Cazacu O. High-strain rate applications for granular materials. (submitted *Mech Research Communications*).

STRAIN BASED HAMILTONIAN FORMULATION AND APPLICATION TO SUPERSHEAR CRACK PROPAGATION

Maddegedara Lalith*[1], Lionel Quaranta[2], Tomoo Okinaka[3], Muneo Hori[4], Tsuyoshi Ichimura[1], and Kohei Fujita[1]
[1]Earthquake Research Institute, The University of Tokyo, Tokyo, Japan
[2]Department of Civil Engineering, The University of Tokyo, Tokyo, Japan
[3]Department of Civil and Environmental Engineering, Kindai University, Osaka, Japan
[4]Japan Agency of Marine Earth Science and Technology, Yokohama, Japan

Summary We derived momentum-strain ($p-\epsilon$) form of the Hamiltonian equations for elastic solids, and applied to simulate supershear rupture of earthquake faults. We prove that the $p-\epsilon$ form is symplectic, even though its conjugate variables do not introduce equal number of dimensions to the corresponding phase space, and the Hamiltonian equations do not possess the typical antisymmetric structure. Numerical implementation is validated by comparing the speed and the stress field of crack tip with those of high speed (1Mfps) phtoelastic observations of a propagating mode-I crack. We simulate the super-shear earthquake rupture, modeling the contact at the fault surface by a linear slip weakening friction law. The Burridge-Andrews mechanism naturally appears in the simulations, making the crack front jump from the sub-Rayleigh regime to the intersonic regime.

INTRODUCTION

Simulating extreme events occurring in large domains, such as supershear earthquakes, is a challenging task due to the presence of cracks propagating at intersonic speeds, shock waves, etc. Due to high computational demand, widely used implicit time integration techniques like Newmark-β are not attractive choices for long period simulations of large-scale domains. We seek to utilize large pool of explicit symplectic algorithms available in Hamiltonian mechanics, which are higher order accurate, momentum conserving, suitable for steep potentials, and stable in long period time integration. Instead of the standard $p-u$ form of the Hamiltonian equation for wave propagation in solids, we derived $p-\epsilon$ form to directly compute strain[1], which is one of the main variable of interest in crack propagation problems. The $p-\epsilon$ form requires some investigations since it does not have the structure of typical Hamiltonian equations, especially in proving its symplecticity.

MOMENTUM-STRAIN FORM OF HAMILTONIAN EQUATIONS

Starting with the density of the Hamiltonian for an elastic solid continuum $h(p,\epsilon) = p.\dot{u} - l(\dot{u},\epsilon)$, where the density of the Lagrangian $l(\dot{u},\epsilon) = \frac{1}{2}(\rho\dot{u}^2 - \epsilon : C : \epsilon)$ and momentum $p = {}^{\partial l}/_{\partial \dot{u}}$, and applying the Hamilton's principle (i.e. $\delta \int_{t,V} p.\dot{u} - h(p,\epsilon)\mathrm{d}V\,\mathrm{d}t = 0$), the $p-\epsilon$ form of the Hamiltonian equations can be obtained as

$$\begin{cases} \dot{p} = \nabla.\frac{\partial h}{\partial \epsilon} \\ \dot{\epsilon} = sym\{\nabla \frac{\partial h}{\partial p}\} \end{cases} \tag{1}$$

Compared to typical $p-u$ form of Hamiltonian equations, the above form has several differences. ϵ contributes three time more dimensions to the corresponding phase-space than its conjugate variable p, whereas the conjugate variables of a typical Hamiltonian equations introduce equal number of dimensions to the corresponding phase space. Instead of the standard antisymmetric structure, the right hand side of the $p-\epsilon$ form consists of linear combinations of partial derivatives with respect to spatial coordinates (i.e. ${}^{\partial}/_{\partial x}$). These differences raise the question whether the $p-\epsilon$ form is symplectic. We demonstrated the symplecticity of this non-standard form by proving that the Jacobian of its phase space flow is independent of time.

NUMERICAL IMPLEMENTATION AND SIMULATION OF SUPER-SHEAR EARTHQUAKES

A symplectic algorithm equivalent to the classical Stomer-Verlet scheme and a bi-symplectic algorithm[2], which is suitable for problems with steep potentials, are derived for the $p-\epsilon$ form and implemented in PDS-FEM[3]. PDS-FEM is a finite element method which uses characteristic function of the elements of conjugate tessellations for approximating displacement and strain. The numerous discontinuities in the approximated displacement field, which are introduced by the use of characteristic functions, can be utilized to numerically efficiently model propagating cracks.

To validate the implemented time integration schemes, simulated crack tip stress field and propagation speed of a mode-I crack are compared with the photoelastic observations of a mode-I crack recorded with a high-speed camera (1Mfps). Figure 2 shows photoelastic fringe patters from the experiment and the simulation, at two stages. We use

*Corresponding author. E-mail: lalith@eri.u-tokyo.ac.jp.

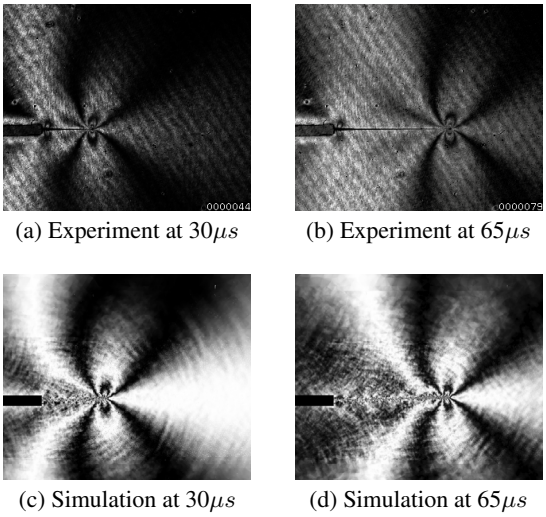

(a) Experiment at $30\mu s$ (b) Experiment at $65\mu s$

(c) Simulation at $30\mu s$ (d) Simulation at $65\mu s$

Figure 1: Comparison between experiment and simulation. Each fringe corresponds to an increase of 3.95 MPa

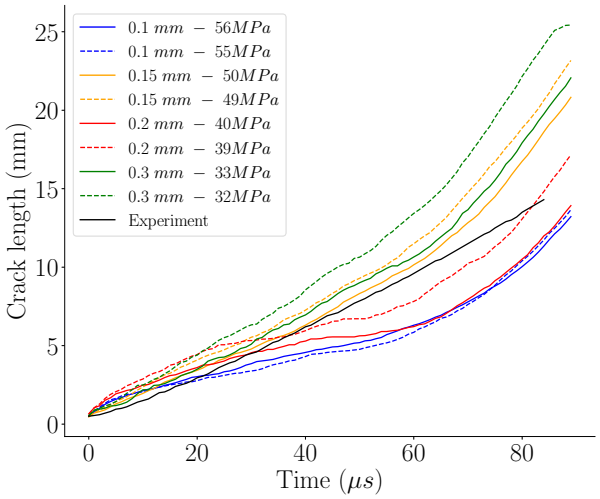

Figure 2: Time history of crack lengths with different mesh refinements and the corresponding σ_c.

the maximum principal stress criterion since the evaluation of J-integral in parallel computing environments introduces significant load imbalances to CPUs. In order to control the dependency of crack speed on mesh size, the average tensile strength of an element is estimated as $\sigma_c \approx {}^{K_c\sqrt{2}}/_{\sqrt{\pi l}}$, where l is the element size and K_c is the critical stress intensity factor. Figure 2 shows the time history of the crack length with different mesh sizes. These results indicate that the numerical implementation can reproduce crack tip stress field and the speed to a reasonable accuracy. Further, comparing with the photoeastic observation of a shear crack with frictional interface, we validated that the numerical implementation can accurately reproduce stress field around pre-existing shear cracks[4].

Simulation of supershear earthquake rupture

In order to demonstrate that the developed system can reproduce supershear earthquake rupture, we simulate the rupture along a straight fault plane in a crust layer of dimensions 10 km $\times$ 4 km $\times$ 0.1 km. The fault is assumed to be homogeneous and a linear slip weakening law is used. The simulations naturally reproduced the Burridge-Andrews mechanism[5], which classically explain the transition from the initial sub-Rayleigh propagation to supershear rupture in a homogeneous materials, making the crack front jump from the sub-Rayleigh regime to the intersonic regime, and propagate producing shear Mach cones. This further validates the implemented $p-\epsilon$ based time integration scheme. Further, we simulated the supershear rupture earthquake along the Palu-Koro fault, which produced a supershear earthquake in 2018, in Sulawesi, Indonesia.

CONCLUSIONS

We derived a momentum-strain form of Hamiltonian equations for elastic continuum, and implemented symplectic time integration algorithms in PDS-FEM framework to conduct large scale simulations of dynamic crack propagation. Good agreement with high speed photoelastic observations, and the natural emergence of Burridge-Andrews demonstrate that the implemented numerical scheme has reasonably high accuracy for simulating extreme events involving high speed crack propagation and shockwaves.

References

[1] Hori M., Wijerathne L., Riaz R., and Ichimura T. Rigorous derivation of Hamiltonian from Lagrangian for solid continuum. *J. of JSCE* **6(1)**: 1-11, 2018.

[2] Casetti L. Efficient symplectic algorithm for numerical simulation of Hamiltonian flows, *Physica scripta* **51**: 29-34, 1994.

[3] Wijerathne M. L. L., Oguni K., Hori M. Numerical analysis of growing crack problems using particle discretization scheme. *Int. J. Numer. Meth. in Eng.* **80(1)**: 46-73, 2009.

[4] Quaranta L., Maddegedara L., and Hori M., Interaction of horizontally aligned coplanar 3D penny cracks under compression. *J. of the Mech. and Phy. of Solids* **131**: 180-203, 2019.

[5] Andrews D. J. Rupture velocity of plane strain shear cracks. *J. of Geophysical Research*, **81(32)**: 5679-5687, 1976.

AN IMPACT HAMMER AS A DECISION SUPPORT SYSTEM FOR SURGEONS DURING OSTEOTOMY

Léo Lamassoure[1], Giuseppe Rosi[1], Justine Giunta[2], Romain Bosc[2], and Guillaume Haïat*[1]
[1]CNRS, Laboratoire Modélisation et Simulation Multi Echelle (MSME UMR 8208 CNRS), Université Paris-Est, 94010 Créteil Cedex, France
[2]Hôpital Henri Mondor, Plastic, Reconstructive, Aesthetic and Maxillofacial Surgery Department, 94000 Créteil, France

Summary Osteotomies are used to cut cartilage and bone tissues using a surgical mallet and a bone chisel (osteotome). However, it is still difficult to assess the properties of the osteotomy site during the procedure. This study aims at investigating whether an instrumented hammer could be used to retrieve information on the tissue located around the osteotome. A first study used plates of composite materials and evidenced that this device can be used to predict the material of a plate and to estimate its thickness. The second study was performed *ex vivo* on an animal model and suggests that this device is sensitive to the displacement of the osteotome and to the transitions between different materials (e.g., between the nasal and frontal bones). This study paves the way for the development of a medical device aiming providing a decision support system to surgeons performing an osteotomy.

INTRODUCTION

An osteotomy is a surgical procedure used to cut and reshape cartilage and bone tissues. Osteotomy is commonly performed using a surgical mallet and a chisel-like tool called osteotome, in various fields such as orthopaedic and maxillofacial surgery [1,2]. They are delicate interventions, during which the surgeon usually has no visibility of the osteotomy site. Therefore, the procedure remains mostly based on the surgeon proprioception, and a mispositioning of the osteotome or too strong impacts may lead to uncontrolled bone fractures, which may have dramatic consequences [3,4]. The objective of this study is to determine whether a hammer instrumented with a piezoelectric force sensor can be used to retrieve information on the mechanical properties of the tissue located around the tip of the osteotome.

METHODS

In a first study [5], 100 samples made of different composite materials and of different thicknesses were impacted with the instrumented hammer. The time dependence of the force applied to the osteotome was measured for each impact of the instrumented hammer with the sensor mentioned above, leading to a signal $s(t)$. A dedicated signal processing technique was applied to $s(t)$ using information derived from the different peaks obtained in the signal. The first two peaks of $s(t)$ were approximated using a Gaussian function. The data was analysed using the two following indicators. The first one, τ, is the difference between the times of the second and first peaks of $s(t)$, referred to as the *second peak time* in what follows. The second one, λ, is the ratio of the second peak integral I_2 on the first peak integral I_1 and is referred to as the *impulse ratio* in what follows.

Support Vector Machines (SVM) learning techniques [6] were applied to our dataset. Considering the two dimensional space (τ, λ), each plate sample #i was characterized by an averaged pair of coordinates (τ_i , λ_i) derived from the 30 impacts. SVM compute hyperplanes separating the space into regions of interest corresponding to the different material classes. The data were partitioned into five disjoint folds of 20 samples chosen randomly. Four folds were used iteratively as training data to determine the boundaries while the last fold was retained as the validation data. The model was tested on the validation data to estimate the prediction performances of the algorithm.

In a second study, a model closer to clinical conditions was considered. Four heads of New Zealand white rabbits were collected from the National Veterinary School of Alfort (Maisons-Alfort, France). This animal model is widely used to simulate rhinoplasty because of its convenience and of the similarities with the human anatomy [7]. The aim of this study was to determine whether it was possible to assess the displacement of the osteotome as well as changes of bone properties located around the osteotome. Therefore, the osteotomy path was set to begin at the frontal end of the nasal bone and to end when the osteotome reached the nasofrontal suture (i.e., the transition between the nasal and frontal bones). The same instrumented hammer as the one used in the first study was used to perform osteotomies on each nasal bone of the rabbit heads, and a video was recorded to track the progression of the osteotome. The same signal processing as the one employed in the first study was employed. A parameter Δ (referred to as *displacement*) was defined and corresponds to the absolute distance travelled by the tip of the osteotome with each impact, and its values were measured using the Tracker software and the video recordings of the experiments.

RESULTS

The results from the first study shows that the material type has a significant effect on both the second peak time τ and the impulse ratio λ, which is confirmed by ANOVA (p-values for τ : $p < 10^{-42}$ and λ: $p < 10^{-35}$). It was possible to predict the material of a sample impacted by the osteotome with an estimated 89% prediction performance, and to estimate its thickness with an error below 10% [5].

The results obtained in the second study shows that when the osteotome arrives at the frontal bone, the second peak time undergoes a significant decrease and reaches values below a threshold equal to 0.65 ms, as shown on Figure 1. Moreover, the second peak time is correlated with the displacement of the osteotome Δ (with typical R^2 values comprised between 0,6 and 0,8).

* Corresponding Author. E-mail: guillaume.haiat@cnrs.fr

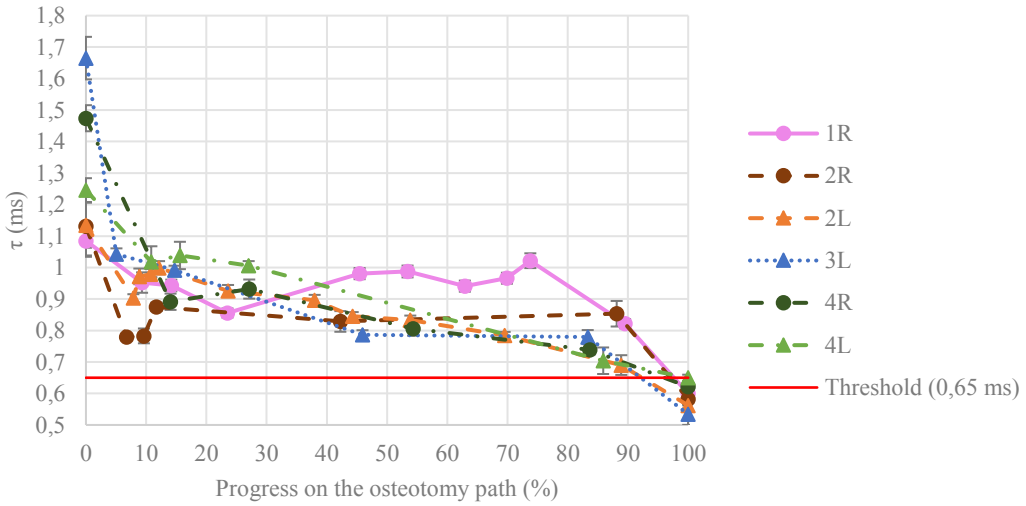

Figure 1. Variation of τ while progressing on the osteotomy path, from the frontal end of the nasal bone (0%) to the nasofrontal suture (100%). For each osteotomy, the lowest values of τ are reached at the nasofrontal suture, below a threshold of 0,65 ms.

DISCUSSION

The mechanical behavior of the osteotome could be modeled using an analytical model considering a damped system oscillating between the sample and the hammer. The second peak time τ could be approximated by its period of oscillation T_o. The results show that τ increases when the Young's modulus of the materials increases, confirming that the second peak time is a relevant indicator to assess the dynamic behavior of the system. The impulse ratio is the ratio of the energy exchanged during the second and first contacts, which is related to the material viscoelasticity. Therefore, λ was used in combination with the second peak time τ to classify the different materials.

The second study confirmed that the instrumented hammer could be used to detect the moment when the osteotome reaches the frontal bone. The frontal bone being stronger than the nasal bones (for both rabbits and humans), the mechanical properties of the environment around the tip of the osteotome suddenly change at the frontonasal suture, hence explaining the change obtained for the values of τ. Nonetheless, this animal model presented some limitations. First, the rabbit nasal bones are softer than the ones of humans (especially for the elderly where they tend to be particularly brittle), which explains why we did not observe the apparition of cracks as expected. Therefore, this part of the study will require further research with a better model. Second, due to the complexity of the architecture of the rabbit's nasal cavity (especially the presence of the nasal conchae), it was impossible to estimate bone thickness during the osteotomies.

CONCLUSION

This study paves the way for the development of an instrumented hammer to perform biomechanical measurements during an osteotomy. Future experiments on anatomical subjects will be determinant to confirm the results obtained on the animal model, as well as to study crack initiation and propagation. From the results, navigation and decision-support systems could be developed based on this approach to allow surgeons to adapt their surgical strategy in a patient-specific manner.

References

[1] Siemionow M. Z., and Eisenmann-Klein M. Plastic and reconstructive surgery, ch. Nasal Reconstruction and aesthetic rhinoplasty. Springer, 2010.
[2] Daniel R. K. Mastering rhinoplasty: a comprehensive atlas of surgical techniques with integrated video clips. Springer Science & Business Media, 2010.
[3] Dobratz E.J., Hilger P.A. Osteotomies. *Clinics in plastic surgery*, vol. 37, no. 2, pp. 301–311, 2010.
[4] Duron J.B., Jallut Y., Nguyen P., Aiach G., Bardot J. Ostéotomies en rhinoplastie. *Annales de Chirurgie Plastique Esthétique*, vol. 59, pp. 418–423, Elsevier, 2014.
[5] Hubert A., Rosi G., Bosc R., Haiat G. Using an impact hammer to estimate elastic modulus and thickness of a sample during an osteotomy. *J Biomech Eng*, in press.
[6] Dietterich T.G., Bakiri G. Solving multiclass learning problems via errorcorrecting output codes. *Journal of artificial intelligence research*, vol. 2, pp. 263–286, 1995.
[7] Badran K.W., Chang J.C., Kuan E.C., Wong B.J.F. Anatomy and surgical approches to the rabbit nasal septum. *JAMA Facial Plastic Surgery*, Vol. 19(5), pp. 386-391, 2017.

BLAST LOADING OF CONCRETE PIPES - EXPERIMENTS AND SIMULATIONS

Martin Kristoffersen*[1], Arianna Minoretti[2], Knut Ove Hauge[3], and Tore Børvik[1]
[1]Structural Impact Laboratory, Norwegian University of Science and Technology, Trondheim, Norway
[2]Norwegian Public Roads Administration (NPRA), Trondheim, Norway
[3]Norwegian Defence Estates Agency (NDEA), Oslo, Norway

Summary Blast loading of concrete structures like columns and plates has been studied extensively in the open literature. Tubular structures are studied to a much lesser extent, so the goal of this work was to establish a large experimental database for blast loading of concrete pipes. Different charge positions were used, (i) centre of the pipe, (ii) contact inside, (iii) contact outside. Position (ii) was the most harmful. The pressure measured inside the pipe was considerably higher than immediately outside, suggesting major confinement effects. Reinforcement greatly improved the pipes' performance as expected. Material tests on both the reinforcement bars and the concrete were used to calibrate material models for use with finite element simulations. The blast load was described by a particle-based method. The structural response from the simulations showed good agreement with the tests.

INTRODUCTION

The E39 coastal highway route in Norway is envisioned a future without ferries. Some fjord crossings are too wide and deep for conventional bridges or underwater rock tunnels. A possible solution to crossing these fjords is a submerged floating tube bridge (SFTB) in concrete [1]. Blast loading against SFTBs could have disastrous consequences and has only been studied numerically [2]. Full-scale testing of a detonation in an SFTB is not a feasible option, thus physical testing must be carried out on smaller samples. This study examined tubular concrete structures (plain and reinforced) subjected to blast loading. The first goal was to build a large experimental database for this topic [3], and the second was to investigate whether state-of-the-art finite element (FE) simulations could reproduce some key experimental results. The explicit FE code IMPETUS AFEA Solver [4] was used for all simulations herein, providing good overall results.

MATERIAL TESTING AND CALIBRATION OF CONSTITUTIVE RELATIONS

Cylinders and cubes were cut from the concrete pipes for cylinder compression (Fig. 1(a)), cube compression, and tensile splitting tests. The uniaxial compressive and tensile strengths were f_c = 76.1 MPa and f_t = 3.2 MPa, respectively. A load cell measured the force and digital image correlation (DIC) measured the axial strain (Fig. 1(b) and (c)). This data was used to establish engineering stress-engineering strain curves (Fig. 1(d)), which in turn were used as target curves for the calibration of the IMPETUS concrete model [4]. An LS-OPT procedure was set up to obtain the material parameters by inverse modelling. Since no dynamic material data was available, default strain rate parameters were used.

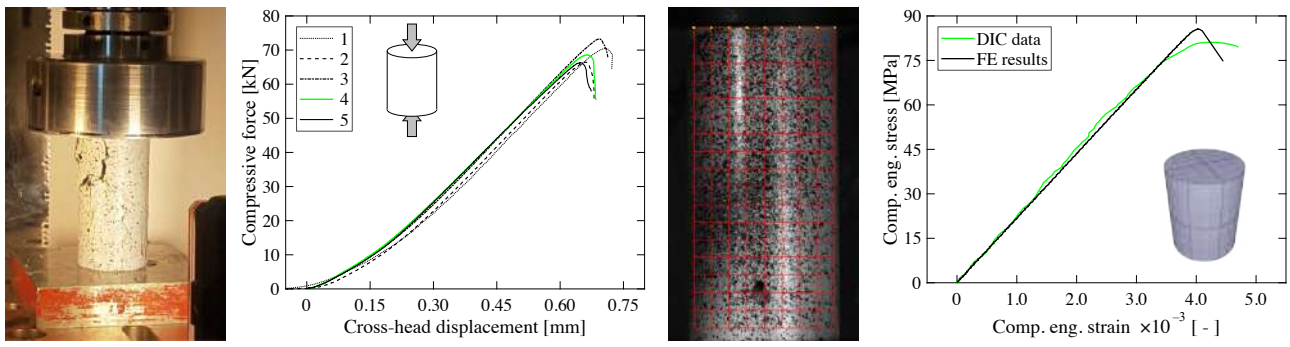

(a) Experiment (b) Force-diplacement curves (c) DIC (d) Model calibration

Figure 1: Material calibration procedure from (a) compression test and (b) force-displacement curves to (c) DIC and (d) FE model.

Smooth axisymmetric specimens were machined from both the hoop (D_{hoop} = 6 mm) and longitudinal (D_{long} = 8 mm) reinforcement bars for quasi-static tension testing. The longitudinal bars had a yield stress of 417.1 MPa, and the hoop bars 517.3 MPa. Lasers were used to measure the minimum diameters in two perpendicular directions. The minimum diameters were measured continuously throughout the tests, thereby providing true stress-true strain curves beyond necking all the way to failure. A modified Johnson-Cook J_2 plasticity model was calibrated by a least squares fitting.

BLAST TESTING OF CONCRETE PIPES

Description of concrete pipes and test setup

The test components were standard off-the-shelf concrete pipes intended for drainage. Using mass produced pipes ensures consistent material properties and geometry. Pipes with internal diameter D_i = 200 mm and 400 mm were used, with respective lengths 1560 mm and 2350 mm. The wall thicknesses were 41 mm and 85 mm. Each end of the pipe had

*Corresponding author. E-mail: martin.kristoffersen@ntnu.no.

flanges which enabled connecting the pipes to form a continuous pipeline. The smaller of the two geometries was without reinforcement and was used to investigate the effect of charge placement; (i) centre of the pipe, (ii) contact inside, (iii) contact outside as sketched in Fig 2(a). The larger was tested both with and without reinforcement, but only from position (i). The charges used were composition C-4 detonated by an electrically ignited blasting cap. Two high-speed cameras filmed the tests, while pressure sensors monitored the pressure both inside and outside the pipe (see Fig 2(b)).

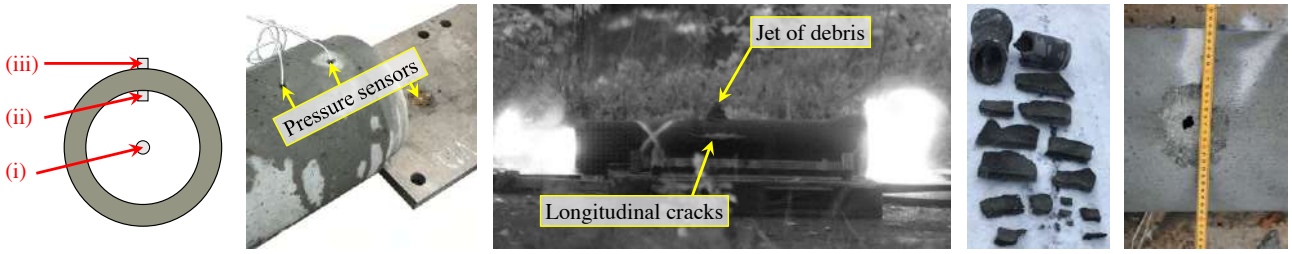

(a) Charge positions (b) Pipe and sensors (c) High-speed image from position (ii) (d) Fragments (e) Crater/hole

Figure 2: Summary and illustrations of component test setup and results.

Results

From position (i), the D_i = 200 mm plain concrete pipes first suffered longitudinal cracking before oblong fragments formed (illustrated in Fig. 2(c) and (d)). Larger charge sizes produced more and smaller fragments. The same behaviour was observed when detonating from position (ii) with the addition of a jet of debris from where the charge was placed (Fig. 2(c)). Charges placed at position (iii) simply produced cratering and spalling at the charge position without any fragmentation as seen in Fig. 2(e). Position (ii) was by far the most destructive, because only half the explosive amount was needed to breach the pipe compared with the other two positions.

The D_i = 400 mm plain concrete pipes generally behaved similarly to the 200 mm pipes. The reinforced 400 mm pipes had a substantially larger capacity as expected. It was interesting to note that the connecting flange broke off as shown close to the arrows in Fig. 3, likely due to reflecting stress waves in the thickness transition area. The pressure data showed that the pressure dropped orders of magnitude just outside the pipe, confirming the confinement effect.

(a) Plain concrete test (b) Plain concrete sim. (c) Reinforced concrete test (d) Reinforced concrete sim.

Figure 3: Images of tests and simulations of D_i = 400 mm pipe 10 ms after detonating a 150 g C-4 charge at position (i).

FINITE ELEMENT SIMULATIONS

The IMPETUS code [4] offers GPU acceleration, fully integrated higher order Lagrangian volume elements, and node splitting for describing fracture. Higher order elements represent the curved surfaces of the cylinder and pipe accurately. A particle-based method was used to emulate the blast load. The particles were able to account for the confinement and captured the results from the contact charges well. The damage patterns were recreated nicely by the node splitting technique as shown in Fig. 3. Setting all strain rate parameters to zero increased the damage to unrealistic extents, which shows the importance of including strain rate sensitivity.

CONCLUDING REMARKS

The blast tests showed that there is a significant confinement effect arising from detonating the charge inside the pipe, both in terms of structural response and pressure magnitude. This is important when designing structures like SFTBs. The concrete model in IMPETUS was calibrated to fit experimental data and provided good results in the FE simulations of the blast experiments. Particles proved to be a robust and powerful way of accounting for contact charges and confinement. Obtaining material data at elevated strain rates and performing a proper load characterisation are important future tasks.

ACKNOWLEDGEMENTS

We thank the NPRA for funding through the E39 Coastal Highway Route project, the NDEA for providing equipment for conducting the tests, and the Norwegian Research Council for funding through CASA by project number 237885.

References

[1] Tveit P. Submerged floating tunnels (SFTs) for Norwegian fjords. *Proc. Eng.* **4**:135-143, 2010.
[2] Kristoffersen M., Minoretti A., Børvik T. On the internal blast loading of submerged floating tunnels in concrete with circular and rectangular cross-sections. *Eng. Fail. Anal.* **103**: 462-480, 2019.
[3] Kristoffersen M., Hauge K.O., Minoretti A., Børvik T. Experimental and numerical studies of tubular concrete structures subjected to blast loading. *Eng. Struct.* Under review, 2020.
[4] IMPETUS Afea AB. *IMPETUS Afea Solver command manual v. 5.0.* Website **http://www.impetus-afea.com/support/manual/**

WAVE PACKET ENRICHED FINITE ELEMENT FOR AXISYMMETRIC ELECTROTHERMOELASTIC WAVE PROPAGATION PROBLEMS

Santosh Kapuria*[1,2] and Amit Kumar[3]
[1]CSIR-Structural Engineering Research Centre, Chennai 600113, India
[2]Department of Applied Mechanics, Indian Institute of Technology Delhi, New Delhi 110016, India
[3]CSIR-Central Mechanical Engineering Research Institute, Durgapur 713209, India

Summary An enriched finite element (FE) is developed to solve axisymmetric wave propagation problems of generalized piezothermoelasticity. The FE equations for the extended Lord–Schulman (L–S) theory are derived, wherein the interpolation functions for temperature, potential and displacement fields are enriched with element domain spatial sinusoidal functions and solved using direct time integration. The problem of axisymmetric thermal shock waves in a piezoelectric hollow cylinder is studied. The finite speed propagation of temperature and the associated sharp wavefronts are shown to be captured accurately by the enriched FE solution.

INTRODUCTION

Generalized piezothermoelasticity theories [1, 2] have been proposed to overcome the limitation of the classical theory predicting heat transport at infinite speed. The one dimensional (1D) thermal shock problems in piezoelectric media have been investigated using the L–S theory [3] and two-temperature theory [2], by employing the Laplace transform and the state space method. A hybrid FE-Laplace transform technique has been employed for solving the 1D problem of axisymmetric thermal shock in functionally graded piezoelectric cylinder using the L–S theory [4]. Accurate numerical evaluation of inverse Laplace transforms required for these solutions is computationally intensive and often unsteady. No solutions for the 2D problems of axisymmetric thermal shock based on the generalized piezothermoelasticity can be found in literature. The authors [5] have recently presented a novel enriched FE formulation for generalized thermoelasticity, which accurately captured the discontinuities at the wavefronts for thermal shock problems, using direct time integration. In this paper, an enriched FE formulation based on the L–S theory of generalized piezothermoelasticity is presented for accurate solution of 2D axisymmetric electrothermal shock wave propagation problems in piezoelectric media.

ENRICHED FE FORMULATION

The extended Hamilton's principle for the L–S theory of generalized piezothermoelasticity in absence of body forces, internal heat source and free charge can be written as

$$\int_{t_1}^{t_2}\Big[\int_\Omega\Big(\delta\mathbf{u}^{\mathrm{T}}\rho\ddot{\mathbf{u}}+\delta\boldsymbol{\varepsilon}^{\mathrm{T}}\boldsymbol{\sigma}+\delta\boldsymbol{\theta}'^{\mathrm{T}}(\mathbf{q}+\tau_0\dot{\mathbf{q}})-\delta\theta\rho T_0(\dot{\eta}+\tau_0\ddot{\eta})-\delta\mathbf{E}^{\mathrm{T}}\mathbf{D}\Big)\,\mathrm{d}V-\int_{S_\sigma}\delta\bar{\mathbf{u}}^{\mathrm{T}}\bar{\mathbf{f}}_{\mathbf{s}}\,\mathrm{d}S-\int_{S_q}\delta\theta^{\mathrm{T}}\bar{\mathbf{q}}.\bar{\mathbf{n}}\,\mathrm{d}S$$
$$-\int_{S_\phi}\delta\phi^{\mathrm{T}}\bar{D}_n\,\mathrm{d}S\Big]\,\mathrm{d}t=0\quad\text{for}\;\forall\,\delta\mathbf{u},\delta\theta,\delta\phi\mid\delta\mathbf{u}(t_1)=\delta\mathbf{u}(t_2)=\delta\theta(t_1)=\delta\theta(t_2)=\delta\phi(t_1)=\delta\phi(t_2)=0 \tag{1}$$

where $\mathbf{u}$, $\boldsymbol{\sigma}$, ε, $\mathbf{q}$, $\mathbf{D}$ and $\mathbf{E}$ denote displacement, stress, strain, heat flux, electric displacement and electric field intensity vectors, respectively. η, ϕ and ρ denote, respectively, the entropy density, electric potential and mass density. θ is the temperature rise above the stress-free reference temperature T_0 such that the absolute temperature $T=T_0+\theta$. τ_0 is the first order time delay. $\bar{\mathbf{f}}_{\mathbf{s}}$ is the traction vector prescribed over surface S_σ, $\bar{\mathbf{q}}$ and $\bar{\mathbf{n}}$ are the prescribed heat flux vector and unit normal vector, respectively, over boundary S_q, and, $\bar{D}_n$ is the prescribed charge density normal to the surface S_ϕ.

To obtain the FE formulation, the axisymmetric domain is discretized into quadrilateral finite elements within which the displacement components u, w, potential ϕ and temperature θ are related to the corresponding nodal values u^e, w^e, ϕ^e and θ^e by interpolation functions. In the enriched FE presented here, the interpolation functions are extrinsically enriched with sinusoidal functions. A typical solution variable ϑ in a four-node enriched element is interpolated as

$$\vartheta=\sum_{i=1}^{4}\Big[N_i\vartheta_i+\sum_{j=1}^{N_{F_r}}\Big(N_{ij}^{\xi c}\vartheta_{ij}^{\xi c}+N_{ij}^{\xi s}\vartheta_{ij}^{\xi s}\Big)+\sum_{k=1}^{N_{F_z}}\big(N_{ik}^{\eta c}\vartheta_{ik}^{\eta c}+N_{ik}^{\eta s}\vartheta_{ik}^{\eta s}\big)$$
$$+\sum_{j=1}^{N_{F_r}}\sum_{k=1}^{N_{F_z}}\Big(N_{ijk}^{c+}\vartheta_{ijk}^{c+}+N_{ijk}^{s+}\vartheta_{ijk}^{s+}+N_{ijk}^{c-}\vartheta_{ijk}^{c-}+N_{ijk}^{s-}\vartheta_{ijk}^{s-}\Big)\Big] \tag{2}$$

where

$$N_i=N_i^\xi N_i^\eta,\quad N_i^\xi=\frac{1}{2}(1+\xi_i\xi),\quad N_i^\eta=\frac{1}{2}(1+\eta_i\eta)$$
$$N_{ij}^{\xi c}=N_i[\cos(\bar{k}_{j_r}N_i^\xi)-\cos(\bar{k}_{j_r})]\qquad N_{ij}^{\xi s}=N_i[\sin(\bar{k}_{j_r}N_i^\xi)-\sin(\bar{k}_{j_r})]$$
$$N_{ik}^{\eta c}=N_i[\cos(\bar{k}_{k_z}N_i^\eta)-\cos(\bar{k}_{k_z})]\qquad N_{ik}^{\eta s}=N_i[\sin(\bar{k}_{k_z}N_i^\eta)-\sin(\bar{k}_{k_z})] \tag{3}$$
$$N_{ijk}^{c+}=N_i[\cos(\bar{k}_{j_r}N_i^\xi+\bar{k}_{k_z}N_i^\eta))-\cos(\bar{k}_{j_r}+\bar{k}_{k_z})]\qquad N_{ijk}^{s+}=N_i[\sin(\bar{k}_{j_r}N_i^\xi+\bar{k}_{k_z}N_i^\eta))-\sin(\bar{k}_{j_r}+\bar{k}_{k_z})]$$
$$N_{ijk}^{c-}=N_i[\cos(\bar{k}_{j_r}N_i^\xi-\bar{k}_{k_z}N_i^\eta)-\cos(\bar{k}_{j_r}-\bar{k}_{k_z})]\qquad N_{ijk}^{s-}=N_i[\sin(\bar{k}_{j_r}N_i^\xi-\bar{k}_{k_z}N_i^\eta)-\sin(\bar{k}_{j_r}-\bar{k}_{k_z})]$$

*Corresponding author. E-mail: kapuria@am.iitd.ac.in

N_i is the Lagrangian shape function and (ξ_i, η_i) are the normalized coordinates of ith node. N_{F_r} and N_{F_z} denote the number of harmonics in ξ and η directions, respectively. $\bar{k}_{j_r} = 2\pi j \nu_r$ and $\bar{k}_{k_z} = 2\pi k \nu_z$, ν_r and ν_z being constant enrichment parameters. Substituting the approximations and summing up the contributions from all n_e number of elements, the discretized form of the variational equation (1) is obtained as

$$\sum_{e=1}^{n_e} \left(\begin{bmatrix} \mathbf{M}^e_{\sigma\sigma} & \mathbf{0} & \mathbf{0} \\ \mathbf{M}^e_{\theta\sigma} & \mathbf{M}^e_{\theta\theta} & -\mathbf{M}^e_{\theta\phi} \\ \mathbf{0} & \mathbf{0} & \mathbf{0} \end{bmatrix} \begin{Bmatrix} \ddot{\mathbf{u}}^e \\ \ddot{\boldsymbol{\theta}}^e \\ \ddot{\boldsymbol{\Phi}}^e \end{Bmatrix} + \begin{bmatrix} \mathbf{0} & -\mathbf{C}^e_{\sigma\theta} & \mathbf{0} \\ \mathbf{C}^e_{\theta\sigma} & \mathbf{C}^e_{\theta\theta} & -\mathbf{C}^e_{\theta\phi} \\ \mathbf{0} & \mathbf{C}_{\phi\theta} & \mathbf{0} \end{bmatrix} \begin{Bmatrix} \dot{\mathbf{u}}^e \\ \dot{\boldsymbol{\theta}}^e \\ \dot{\boldsymbol{\Phi}}^e \end{Bmatrix} + \begin{bmatrix} \mathbf{K}^e_{\sigma\sigma} & -\mathbf{K}^e_{\sigma\theta} & \mathbf{K}_{\sigma\phi} \\ \mathbf{0} & \mathbf{K}^e_{\theta\theta} & \mathbf{0} \\ \mathbf{K}^e_{\phi\sigma} & \mathbf{K}^e_{\phi\theta} & \mathbf{K}^e_{\phi\phi} \end{bmatrix} \begin{Bmatrix} \mathbf{u}^e \\ \boldsymbol{\theta}^e \\ \boldsymbol{\Phi}^e \end{Bmatrix} = \begin{Bmatrix} \mathbf{F}^e_{\sigma} \\ -\mathbf{F}^e_{\theta} \\ \mathbf{F}^e_{\phi} \end{Bmatrix} \right) \tag{4}$$

The FE equations are obtained in non-dimensionalized form and solved using Newmark-β direct time integration.

NUMERICAL STUDY AND CONCLUSIONS

Consider a radially polarised thick hollow cylinder of Cadmium Selenide subjected to thermal shock in the form of $\theta(t) = H(z-a)H(t)$ imposed on the inner circumferential surface, $H(t)$ being the Heaviside unit function. For the FE solution, a symmetric zone OABC with $r_i = 0.5, r_o = 1.5$ and OA$= 1$ is considered. The L-S theory solution is obtained using $\tau_0 = 0.5$ and $a = 0.3$. The enrichment parameters are taken as $\nu_r = \nu_z == 0.3, N_{F_r} = N_{F_z} = 1$ for displacement, potential and temperature fields. The distributions of temperature rise, hoop stress, radial electric field along OC obtained using the present enriched FE are compared with the conventional FE solution in Figs. 2(a), (b) and (c). The total number of DOFs for enriched and conventional FE are 34596 and 40804, respectively. The present solution captures the second sound effect clearly showing the jumps at the thermal wavefront in temperature, stress and electric field distributions. Whereas the conventional FE solution shows quite extensive spurious oscillations at the wavefronts in these distributions, the enriched FE solution removes the oscillations thereby giving the accurate estimates of the location and magnitude of the jumps at wavefronts. The change in jumps at the wavefronts as they propagate is shown in Figs. 2(d) and (e). The amplitude of jumps at both wavefronts reduces with time. The effect of pyroelectric constant p_3 on the potential distribution is shown in Fig. 2(f). The induced potential is higher in presence of the pyroelectric effect.

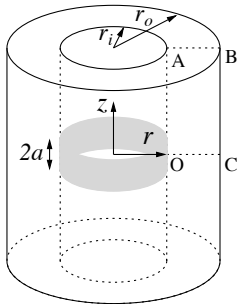

Figure 1: Hollow piezoelectric cylinder subjected to thermal shock

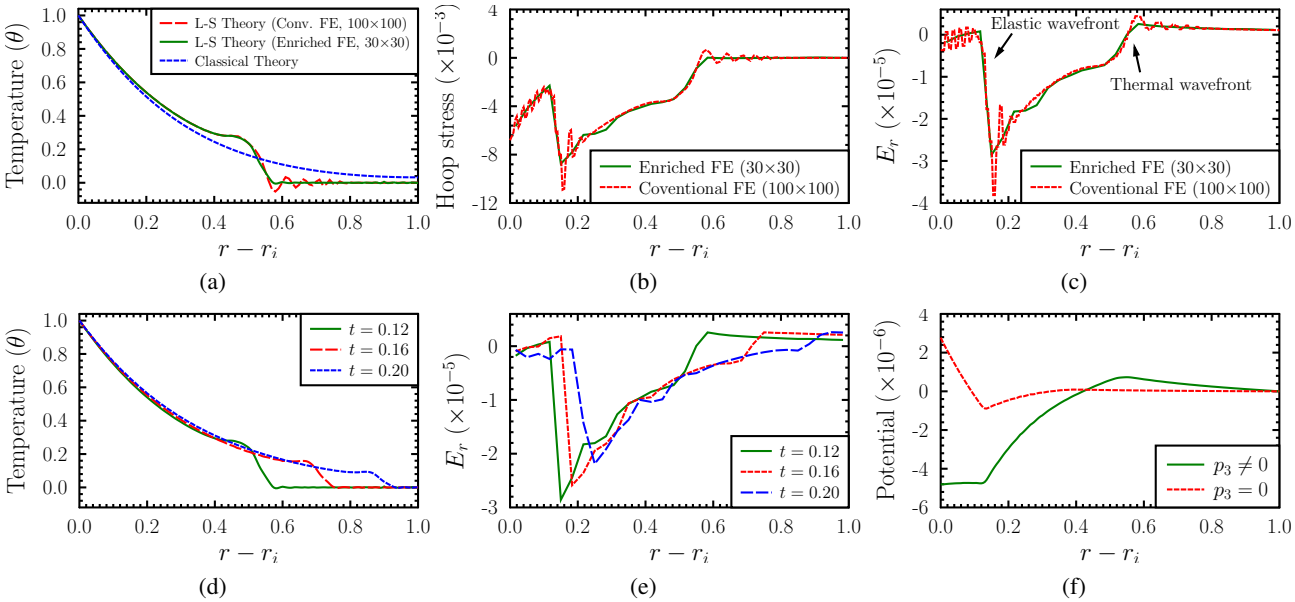

Figure 2: Distributions of temperature, hoop stress, radial electric field and potential along OC. $t = 0.12$ if not mentioned otherwise.

References

[1] Chandrasekharaiah D. A generalized linear thermoelasticity theory for piezoelectric media. *Acta Mechanica*, **71**: 39–49, 1988.
[2] Youssef H. M., Bassiouny E. Two-temperature generalized thermopiezoelasticity for one dimensional problems. *Comput. methods Sci. Tech.* **14**: 55–64, 2008.
[3] He T., Tian X., Shen Y. P. State space approach to one-dimensional thermal shock problem for a semi-infinite piezoelectric rod. *Int. J. Eng. Sci.* **40**: 1081–1097, 2002.
[4] Babaei M. H., Chen Z. T. The transient coupled thermo-piezoelectric response of a functionally graded piezoelectric hollow cylinder to dynamic loadings. *Proc. Roy. Society A: Mathematical, Physical and Engineering Sciences,* **466**: 1077–1091, 2010.
[5] Kumar A., Kapuria S. Wave packet enriched finite element for generalized thermoelasticity theories for thermal shock wave problems. *J. Therm. Stresses,* **41**: 1080–1099, 2018.

TRANSIENT DYNAMIC RESPONSES OF A PLATE SUBJECTED TO IMPACT LOADINGS WITH FLUID STRUCTURE INTERACTION

Ming Ji[1] and Kazuaki Inaba*[2]
[1]Sch. of Engineering, Tokyo Institute of Technology, Tokyo, Japan
[2]Sch. of Environment and Society, Tokyo Institute of Technology, Tokyo, Japan

Summary This talk addresses an analytical approach and an effective finite element method for transient dynamic responses of a circular plate subjected to impact loadings. The mode superposition method is used. The method is available for various types of impact loadings. The Mindlin plate theory is used to calculate the natural frequencies and mode shapes of the plate. Considering a small oscillating induced by the plate vibration in fluid, velocity potential function is used to describe the fluid motion. To validate the analytical results, an efficient and flexible MATLAB finite element procedure using fully vectorized codes is developed. MITC4 element is used to simulate the plate, and the acoustic pressure element is used to simulate the fluid. The results are compared with the transient responses for displacement and natural frequencies.

RESEARCH OBJECTIVE AND MOTIVATION

Plates are widely used for structural members in all branches of engineering such as automotive, civil, naval, etc.. Lyon [1] and Pretlove [2] first gave the analytical solutions for a flexible plate coupled with a fluid containing cavity under weak coupling assumption. Soedel [3] presented a closed form solution of the natural frequencies and modes of the plate-liquid combination for a simply supported rectangular plate, carrying liquid with reservoir conditions at its edges. The harmonic response of the plate-liquid system to a dynamic pressure distribution (and also point load) on the plate is expressed in terms of the orthogonal plate-liquid modes. Cho et al. [4] developed a procedure to solve the free and forced vibration analysis. The procedure is based on the assumed mode method for free vibration calculation and mode superposition method for forced vibration analysis. Zienkiewicz and Newton [5] solved the coupled vibrations of the fluid-structure interaction system using the finite element method. For the structural field, the variable considered was displacement. For the fluid field, the unknown variable was in the form of pressure. Under the same assumption, Craggs [6] used the plate and acoustic finite elements to simulate the behaviour of a window-room system. In his paper, the equations were solved for a simple window-room system being excited by a sonic boom. Olson and Bathe [7] presented a symmetric finite element method for solving fluid–structure interaction problem based on the fluid velocity potential. Several tests cases showed that the approach worked well for static, transient, and frequency analyses. Wang and Bathe [8] presented reliable finite element discretization based on displacement/pressure interpolations for the analysis of acoustic fluid-structure interaction problems. They showed that with their analysis procedure no spurious non-zero frequencies are encountered. Ohayon [9] reviewed several reduced order models for linear vibration analysis of bounded fluid–structure systems for low modal density situations. These methods were based on the Ritz-Galerkin projection using appropriate Ritz vectors. He constructed reduced models expressed in terms of physical displacement vector field u in the structure, and generalized co-ordinates vector r describing the behaviour of the fluid.

Despite a variety of the abovementioned methods, there is a strong need in analytical methods applicable for transient responses of a plate coupled with fluid subjected to impact loadings. This talk addresses an analytical approach for transient dynamic responses of a circular plate subjected to impact loadings. The normal mode method is used to investigate the dynamic transient response of a plate coupled with fluid subjected to impact loadings. The method is available for various types of impact loadings such as concentrated force and surface pressure. The Mindlin plate theory is used to calculate the natural frequencies and mode shapes of the plate. Considering a small oscillating induced by the plate vibration in fluid, velocity potential function is used to describe the fluid motion. To validate the analytical results, an efficient and flexible MATLAB finite element procedure using fully vectorized codes is developed. MITC4 element is used to simulate the plate, and the acoustic pressure element is used to simulate the fluid. At last, the drop test of a plate coupled with fluid is conducted. The results are compared with the transient responses for displacement and natural frequencies.

FORMULATION OF THE PROBLEM AND THE SOLUTION TECHNIQUE

A circular plate with the radius a and the thickness h and a cylindrical cavity with the height H are considered. The walls of the cavity are rigid except for the top, on which a flexible plate is placed. The plate is completely clamped. The Mindlin plate theory is used to obtain the natural frequencies and mode shapes. The fluid is assumed to be compressible, inviscid and irrotational. Due to the effect of added mass, there is no the orthogonality of wet modes. Wet modes mean the modes of the plate coupled with fluid. The wet mode is assumed to be the superposition of the modes of the dry modes. The dry modes mean the modes of the plate in air. The forced vibration of the plate coupled with fluid is assumed to be the superposition of the wet modes. The solutions of the coupled system can be obtained by applying the orthogonality of dry modes.

To validate the results obtained by the analytical method, an efficient and flexible MATLAB finite element procedure using fully vectorized codes is developed. Time performance of FEM assembly in MATLAB is comparable with other techniques for purely elastic stiffness matrices [10]. The technique is proved to be effective and flexible. The 4-node

*Corresponding author. E-mail: inaba.k.ag@m.titech.ac.jp

MITC4 element is used to simulate the plate without the shear locking problem, and the 8-node acoustic pressure element is used to simulate the fluid. The coupled system can be written in the following form.

$$\begin{bmatrix} M_S & 0 \\ \rho_0 c_0^2 H_{SF}^T & M_F \end{bmatrix} \begin{bmatrix} d_S \\ p_F \end{bmatrix} + \begin{bmatrix} K_S & -H_{SF} \\ 0 & K_F \end{bmatrix} \begin{bmatrix} d_S \\ p_F \end{bmatrix} = \begin{bmatrix} F_S \\ F_F \end{bmatrix}$$

Here M_S and K_S are the mass and stiffness matrix of the plate using MITC4 plate element. M_F and K_F are the mass and stiffness matrix of the fluid. H_{SF} is the coupling matrix of the system. F_S and F_F are the external forces applied on the plate and the fluid, respectively. d_S and p_F are the unknown displacements of the plate and the unknown pressure of the fluid, respectively. The Newmark's method is used to solve the coupled system. In the example, a circular plate with radius 0.1 m and thickness 0.002 m is made of the material with density 1200 kg/m^3, Young's modulus 2 GPa and Poisson ratio 0.37. The height of the fluid with density 1200 kg/m^3 and sound speed 1500 m/s is 0.1 m. A rectangular pulse with amplitude 15 N and period 70 μs is applied downwards at the centre of the plate. The displacement history of the point which is 0.02 m away from the centre is shown in Figure 1. It is reasonable to use the analytical method and the numerical method to predict the transient response of a plate coupled with fluid.

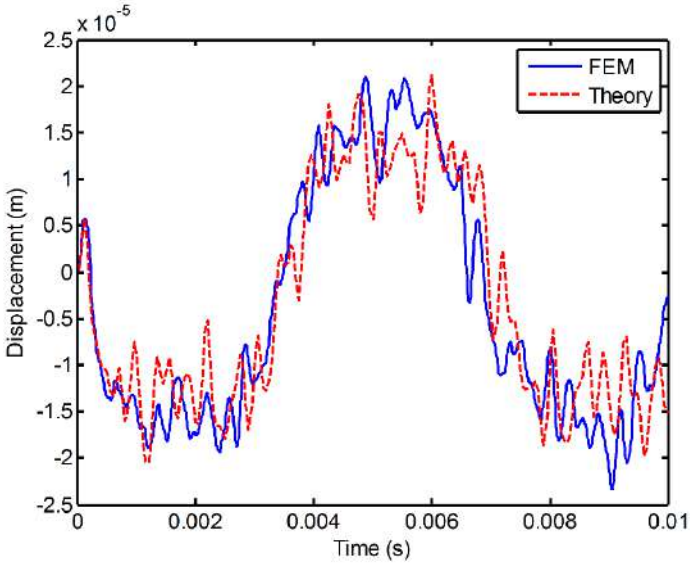

Figure 1. Displacement histories vs. time. The blue solid line is the FEM result, and the dashed red line is the theoretical result.

CONCLUSIONS

An analytical approach and an effective finite element method for transient dynamic responses of a circular plate subjected to impact loadings are proposed. The analytical method can solve the transient fluid-structure interaction problem for various types of impact loadings. It is valid for not only the thin plates but also the thick plates. The effect of the thickness of the plate on the transient responses is discussed. The developed FEM procedure is proved to be effective and flexible.

References

[1] Lyon R.H., Noise reduction of rectangular enclosures with one flexible wall, *J. Acoust. Soc. Am.*, **35**(11): 1791-1797, 1963.
[2] Pretlove A.J., Free vibrations of a rectangular panel backed by a closed rectangular cavity by a closed rectangular cavity, *J Sound Vib*, **2**(3): 197-209, 1965.
[3] Soedel S.M., Soedel W., On the free and forced vibration of a plate supporting a freely sloshing surface liquid, *J Sound Vib*, **171**(2): 159-171, 1994.
[4] Cho D S, Kim B H, Kim J H, et al. Frequency response of rectangular plate structures in contact with fluid subjected to harmonic point excitation force, *Thin Wall Struct*, **95**: 276-286, 2015.
[5] Zienkiewicz O.C., Coupled vibrations of a structure submerged in a compressible fluid, Proc. of Symposium on Finite Element Techniques Held at the University of Stuttgart, 1969.
[6] Craggs, A., The transient response of a coupled plate–acoustic system using plate and acoustic finite elements, *J Sound Vib*, **15**(4): 509-528, 1971.
[7] Olson L.G., Bathe K.J., Analysis of fluid–structure interactions. A direct symmetric coupled formulation based on the fluid velocity potential, *Comput Struct*, **21**(1-2): 21-32, 1985.
[8] Wang X.D., Bathe K.J., Displacement/pressure based mixed finite element formulations for acoustic fluid–structure interaction problems, *Int J Numer Methods Eng*, **40**(11): 2001-2017, 1997.
[9] Ohayon R., Reduced models for fluid–structure interaction problems, *nt J Numer Methods Eng*, 60(1): 139-152, 2004.
[10] Čermák M., Sysala S., Valdman J., Efficient and flexible MATLAB implementation of 2D and 3D elastoplastic problems, *Appl Math Comput*, **355**: 595-614, 2019.

IMPACTS OF BI-LAYERED PROJECTILES

Christophe D'Angelo*[1], Christophe Raufaste[1] and Franck Celestini [1]
[1]Institut de Physique de Nice, Université Côte d'Azur, Nice, France

Summary We investigate the impact of bi-layered elastic projectiles made of a soft layer standing on top of a rigid one. Taken separately these two layers bounce relatively well on a substrate and have a coefficient of restitution (COR) close to 1. We study the COR as a function of the soft material proportion for low velocity to prevent irreversible deformation (elastic regime). We observe that the COR is significantly smaller than the one of the homogeneous projectiles. A part of kinetic energy is transferred to the deformation modes of the projectile. The trend of the restitution as a function of the soft material proportion is complex and exhibits a minimum around 0.2. We also highlight the presence of multiple bounces during the impact and a theoretical model recovers the features observed experimentally. It shows that the deformation waves inside the material are of paramount importance.

CONTEXT OF THE STUDY

In the context of contact mechanics, the study of the impact of heterogeneous projectiles is complex. It is a problem with a large number of unknowns, exacerbating geometrical effects [1], very often coupled with a high degree of disorder [2].

These particularities play a role in the study of the coefficient of restitution of a heterogeneous projectile on a substrate. In the elastic limit, if we can neglect the deformation of the substrate [3, 4, 5, 6], we can expect the dynamics of the projectile to exhibit different time scales and some energy to be trapped in the deformation modes of the projectile [7, 8]. Such effects have not been studied experimentally.

Here we investigate both experimentally and theoretically the impact between a bi-layered elastic projectile and a substrate. The study reveals how the contact dynamics is affected by the two-time scales inherent to the coupling between the rigid and soft layers.

EXPERIMENTAL METHOD

Our projectiles are made of two parts: a soft layer on top of a rigid one. The rigid layer is made of a rigid plastic. By varying the nature of the material, the Young modulus is varied in the range 10 MPa- 4 GPa and the COR between 0.4 and 0.9. The shape of this layer is spherical at the contact point to control the nature of the Hertz-like contact. The soft layer is a cylinder to ensure a good contact with the rigid layer, made of hydrogel or PU (Polyurethane) with the Young modulus in the range 50 kPa - 1 MPa.

The typical length of the projectiles is 50 mm. Velocities before and after the impact are recorded with a highspeed camera (up to 16 000 fps) and the bounce is characterized by its global coefficient of restitution. We study the restitution as a function of the soft material proportion.

RESULTS AND DISCUSSION

Figures 1 and 2 present the results for a bi-layered projectile with a soft part made of hydrogel and a rigid one made of Peek (Polyetheretherketone). Taken separately, these two layers bounce relatively well and have a restitution close to one. We clearly see that the proportion of soft part as an effect on restitution (Fig.1 Left). The COR as a function of soft material proportion p exhibits a complex trend (Fig.2). A minimum restitution of 0.2 is found for p=42. Several local extrema are observed as well.

We also highlight the unexpected occurrence of multiple micro-bounces at the impact (Fig.1.Right). During a macro-bounce (defined as the time spent between the first contact and the final take-off) we have observed that the rigid layer can leave the substrate and reconnect several times before the final take-off. These micro-bounces are due to the elastic force of the soft layer that push back the rigid layer toward the substrate.

In this case it is relevant to note that there are two characteristic times. On the one hand, the time of contact of the rigid layer and, on the other hand, the wave propagation time in the soft layer.

A theoretical model is also proposed. It considers two aspects of the dynamics. The first one is the coefficient of restitution and the time of contact of the rigid layer. The second one is the elastic force, due to the wave propagation, related to the deformation of the soft layer at the contact area between the two layers.

*Corresponding author. E-mail: christophe.dangelo@unice.fr

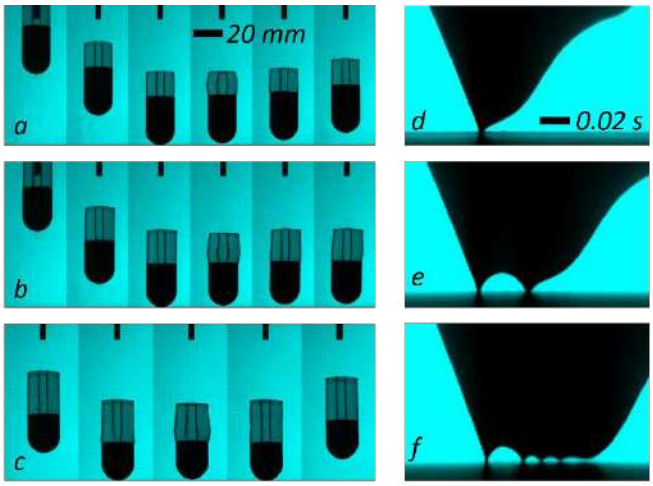

Figure 1. Image sequences (left) and space-time diagrams (right) ($\Delta t = 0.01s$) (zoom centred around the contact zone) of an impact and a bounce of our projectiles with a proportion of soft material p=34% (a, d), p=52 % (b, e) and 60% (c, f). We clearly see the effect of the proportion on the height of the bounce and with the multiple bounces in cases e and f.

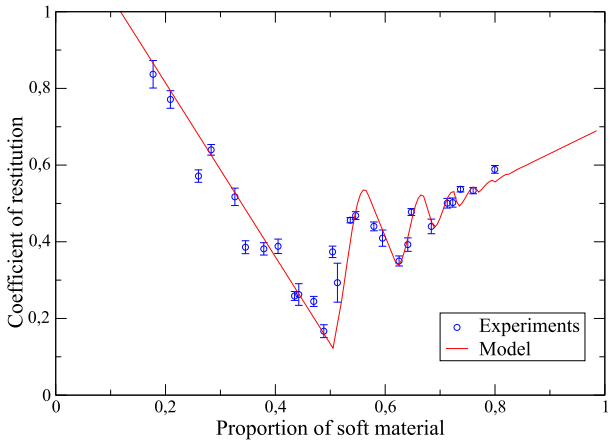

Figure 2. Coefficient of restitution as function of the proportion of soft material. Comparison between experiments and model.

CONCLUSIONS

In our experimental system we combine two elastic materials and by tuning the proportion we are able to control the restitution. The restitution is smaller than the one expected by Hertz theory because a significant part of the initial kinetic energy is transferred to the vibration modes. This study shows that the elastic waves inside the material are of paramount importance for the energy restitution.

References

[1] Falcon E., Laroche C., Fauve S., Coste C., Collision of a 1-D column of beads with a wall. *The European Physical Journal B-Condensed Matter and Complex Systems* **5.1**: 111-131,1998.
[2] Pacheco-Vázquez F., Dorbolo S., Rebound of a confined granular material: combination of a bouncing ball and a granular damper. *Sci Rep* **3**, 2158, 2013.
[3] Tillett J. P. A., A Study of the Impact of Spheres on Plates. *Proceedings of the Physical Society*. **Section B 67, no 9**: 677–688, 1954.
[4] Zener C., The Intrinsic Inelasticity of Large Plates. *Physical Review*. **59(8)**: 669 73, 1941.
[5] Hunter S. C., Energy absorbed by elastic waves during impact. *Journal of the Mechanics and Physics of Solids*. **5(3)**:162 71,1957.
[6] Reed J., Energy Losses Due to Elastic Wave Propagation during an Elastic Impact. *Journal of Physics D: Applied Physics*. **18(12)**:2329 37,1985.
[7] Basile A. G., Dumont R. S., Coefficient of restitution for one-dimensional harmonic solids. *Physical Review E*, **61(2)**,2000.
[8] Nagahiro S., Yoshinori H., Collision of one-dimensional nonlinear chains. *Physical Review E* **67(3)**:036609,2003.

THE LOW VELOCITY IMPACT RESISTANCE OF THERMOPLASTIC COMPOSITE CORRUGATED SANDWICH PANELS

Xin Pan[1,2], Liming Chen [*1,2], Shiwei Peng [1,2]
[1]College of Aerospace Engineering, Chongqing University, Chongqing 400030, China
[2]Chongqing Key Laboratory of Heterogeneous Material Mechanics, Chongqing University,Chongqing 400030, China

Summary The impact behavior of thermoplastic composite corrugated sandwich panels under low velocity loadings is investigated by experimentally and numerically. The face-sheets and the corrugated cores are both fabricated from glass fiber reinforced polypropylene prepregs by hot-pressing method. The dynamic response process, load-carrying capacity and energy absorption capacity of corrugated sandwich panels with three different kinds of core configurations namely regularly-arranged (REG), symmetrically-arranged (SYM) and perpendicularly-arranged (PER) under different impact energies were compared. The results showed that thermoplastic corrugated sandwich panels spring back after the impact, maintaining a good structural integrity. The core configuration has a certain influence on its dynamic properties. Among them, the perpendicular one has the biggest peak impact force, while most impact energy is absorbed by the symmetrical one.

INTRODUCTION

The corrugated sandwich panel (CSP) as a typical sandwich structure, has better deformation resistance and energy absorption ability. Thermoplastic composites (TPC) have attracted more and more attention for they have the property advantages of reforming and repeated processing that thermosetting composites do not have, which makes it easy to recycle and reduce the cost. The corrugated sandwich panels made of thermoplastic composites combine the advantages of functional characteristics of light materials and excellent structure performance [1]. In practical application, these composite structures, as the external components of aircraft or ship devices, will inevitably be affected by impact loads [2]. A substantial number of works on exploring the impact resistance of the sandwich panels and composites laminates have been done at present. But the work in area of the CSP made of fiber-reinforced thermoplastic thermoplastic composites under impact loadings is still at the stage of basic research. Therefore, it is necessary to carry out more in-depth researches in this area. The aim of this paper is to analyze the dynamic mechanical behavior of the glass fiber reinforced polypropylene (GF/PP) corrugated sandwich panels under low velocity impact loadings. The effects of loading intensity and the arrangement of two corrugated cores were carried out to identify and quantify the failure mode, and energy absorption efficiency of sandwich structures.

METHODS

The face-sheets and cores of corrugated sandwich panels are both fabricated from glass fiber reinforced polypropylene prepregs by hot-pressing method and bonded by hot-melting bonding technique. The stacking sequence of the face-sheet and corrugated core is $[0/90/0/90/0/90]_s$.

The JSL-3000 drop-weight impact testing machine, shown in Fig 1, is used in the experimental investigation to carry out the low-velocity impact tests. The total mass of the impactor remains constant as 35.4 kg, different impact energies can be adjusted via changing the drop height of the impactor.

The finite element calculation software, ABAQUS/Explicit, is used in this investigation. The REG CSP model shown in the Fig 2, as an example of finite element models for the simulation. In order to reflect typical mechanical features of thermoplastic composites, the 3D-Hashin failure criteria [3-4] are adopted to analyse the damage initiation of CSPs like tensile and compressive failure of fiber and matrix by a user-defined subroutine VUMAT in ABAQUS.

Figure. 1 The impact testing machine

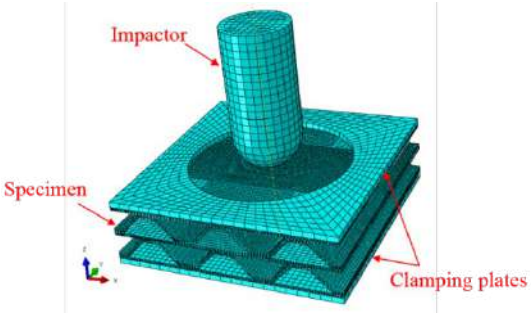

Figure. 2 The FE model

*Corresponding author. E-mail: clm07@cqu.edu.cn.

RESULTS AND DISCUSSION

As can be seen from Fig 3, the impact damage of CSPs are mainly as follows: cracks occur in the polypropylene matrix of the face-sheets and cores, a pit is formed in the impact center area of the top face-sheet, and partial debonding between the face-sheets and cores occurs. With the increase of impact energy, the damage to the structure is intensified. The fracture of the top face-sheet is increased and the crack traverses the entire face-sheet, the central area of the upper core is depressed inward, and the whole lower core is collapsed. The specimens all spring back after the impact. Among the sandwich panels with three configurations, the impact loading causes relatively serious damage to the REG and SYM CSPs, while the PER CSP can rely on the configuration characteristics to unload impact loading through the whole structure and so the local damage of components is reduced.

Fig 4 shows the force-time curves of the specimens under 400J impact energy in the experimental results. It illustrates that the PER one has the biggest peak impact force. This is also verified in other experiments and finite element simulation results.Thermoplastic composite corrugated sandwich panels have large elastic strain energy due to the advantages of material and the structural characteristics. The polypropylene matrix has good ductility and can absorb energy better. As shown in Fig 5, the energy absorbed by all specimens increases with the increase of impact energy. The SYM one has the best energy absorption effect, with the energy absorption efficiency of 61-75%. There is not much difference in energy absorption between the REG and PER CSPs, and energy absorption efficiency of the two is between 56-66%.

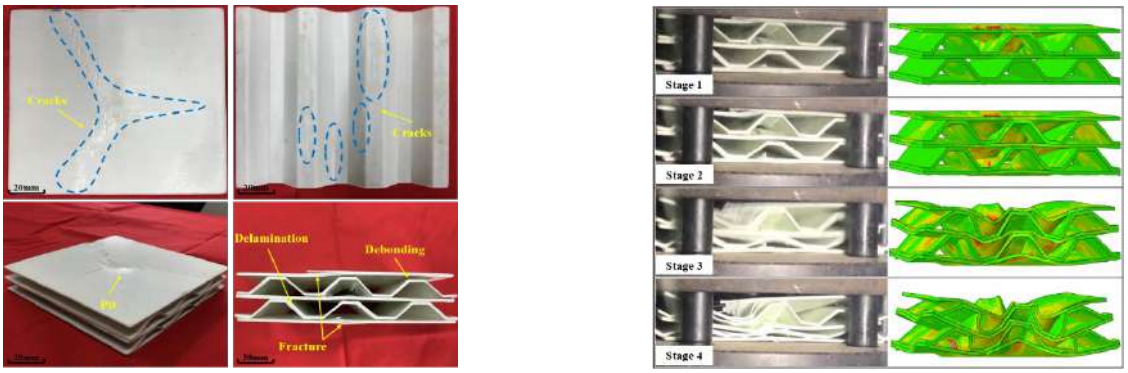

(a) (b)

Figure. 3 The (a) impact damage and (b) response process of REG CSP under the impact energy of 400 J

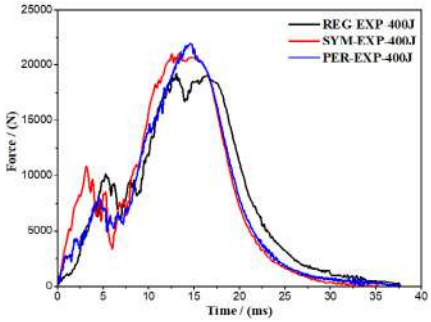

Figure. 4 Force-time curves of sandwich panels with different configurations subjected to 400J impact energy

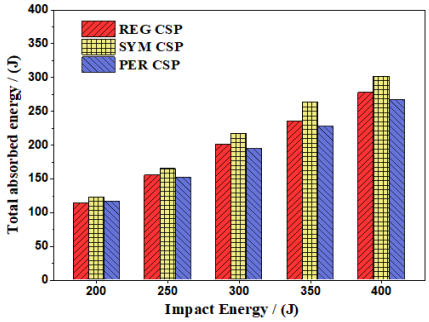

Figure. 5 Energy absorption comparison of CSPs with different configurations under different impact energies

CONCLUSIONS

Thermoplastic composite corrugated sandwich panels have certain resilience, maintaining a good structural integrity. Under impact loadings, local damages mainly occur in the top face-sheet and the upper core of TPC-CSPs, while the lower core collapses as a whole. The thermoplastic matrix has good ductility and can absorb more energy than the thermosetting one. The impact peak force and the absorbed energy keep increasing with the increase of impact energy. Among three configurations, the PER one suffers the least damage and has the optimal impact load-carrying capacity, while the SYM one suffers most severe impact damage but can absorb up to about 75% of the impact energy.

References

[1] Du B, Chen L M, Zhou H, et al. Fabrication and Flatwise Compression Property of Glass Fiber-Reinforced Polypropylene Corrugated Sandwich Panel. *International Journal of Applied Mechanics*,2017, 9(08): 1750110.
[2] Dogan A, Arikan V. Low-velocity impact response of E-glass reinforced thermoset and thermoplastic based sandwich composites. *Composites Part B: Engineering*, 2017, 127: 63-69.
[3] Hashin Z. Failure criteria for unidirectional fiber composites. *Journal of applied mechanics*, 1980,47(2): 329-334.
[4] Liu P F, Liao B B, Jia L Y, et al. Finite element analysis of dynamic progressive failure of carbon fiber composite laminates under low velocity impact. *Composite Structures*, 2016, 149: 408-422.

EFFECTS OF THERMAL SOFTENING AND STRESS STATE ON THE FORMATION OF ADIABATIC SHEAR BAND

Shengxin Zhu[1], Yazhou Guo[2], Haosen Chen[*1], and Daining Fang[1]
[1]Institute of Advanced Structure Technology, Beijing Institute of Technology, Beijing 100081, China
[2]School of Aeronautics, Northwestern Polytechnical University, Xi'an 710072, China

Summary Adiabatic shear band (ASB) is an important type of failure under dynamic loading conditions. However, clear knowledge regarding the true mechanisms is still lacking and experimental research is especially needed. A novel in-situ experimental setup was developed to observe the deformation localization and temperature evolution of the ASB simultaneously, by using the high-speed photography and high-speed infrared radiation. The effect of the temperature increase and stress state on the initiation of the ASB was studied. It is found that before the initiation of the ASB, the temperature of the deformed region does not increase rapidly. Rather, it might be the result of adiabatic shear localization. And the critical shear strains for ASB initiation was different. Micro-geometrical imperfection could be regarded as the softening mechanism, which leads to the initiation of ASB.

EFFECTS OF THERMAL SOFTENING AND STRESS STATE ON THE FORMATION OF ADIABATIC SHEAR BAND

It is well known that adiabatic shear localization (ASL) is an important type of failure mode for materials under impact loading. ASL normally leads to catastrophic failure of a structure with sudden loss of bearing capacity, and thus, attracts considerable interest within the scientific community[1–3]. It was widely believed that both the thermal softening[4] and stress state exert great influence on the initiation of the ASB. Many researchers tried to clarify the role of thermal softening or stress state[5] in the process of ASB by determining the temperature rise itself or different loading method. For thermal softening, all this experimental evidence seems to have shown that temperature rise and ASB formation occur simultaneously (or almost simultaneously), but they did not provide clear evidence of their causal relationship. For stress state, many experimental results indicated that the stress state has an impact on the initiation of ASB formation, while most experiments could not provide a proper instability moment of ASB and stress state quantitatively.

Combining high-speed photography and temperature measurement into one mechanical test is very helpful toward this purpose. Modified shear-compression[6], shear-tension[7] and thin-walled tubular are designed for analysing the effect of the thermal softening and stress state on ASB. The formation of the shear band was observed by taking a series of high-speed photographs of specimens with grids previously deposited on the surfaces. Simultaneously, the temperature increase during the ASL process was determined. By examining the deformation, temperature increase, and ASB initiation, the causal relationship between the temperature increase and the formation of the ASB was clarified. The critical shear strain is obtained by analysing the evolution of prefabricated grids on the surface of the gauge section. A phenomenological model for ASB initiation with dependence on stress triaxiality and Lode parameter is proposed using a hybrid experimental–numerical method.

EXPERIMENTAL RESULTS

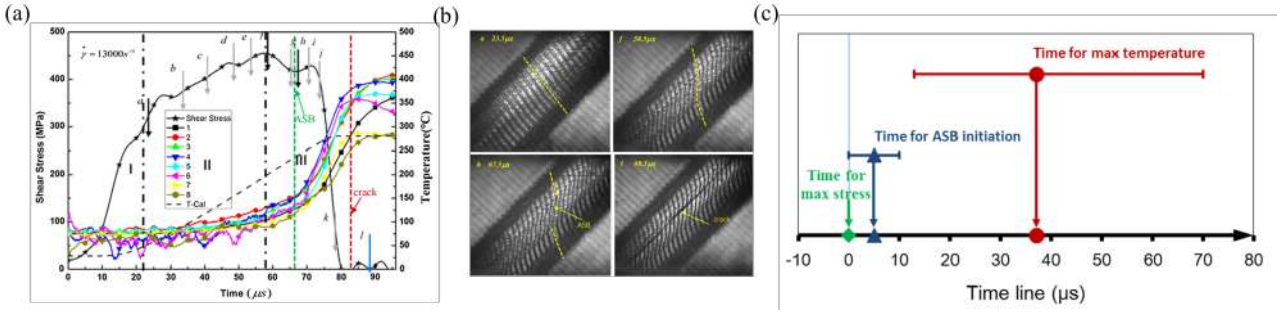

Figure 1. Effect of thermal softening on the formation of ASB, (a) deformation history of a shear-compression specimen, showing the time, shear stress, and temperature, (b) our representative high-speed photographic snapshots to show the deformation of a shear-compression specimen under dynamic loading, (c) Occurrence of important events in dynamic shear failure process. The time for maximum stress was set to be zero and the scatter of the data was also presented.

The shear stress and temperature evolution with respect to time are presented in Figure 1(a). The deformation of the shear-compression specimen could be divided into three stages, i.e., (i) uniform deformation, (ii) nonuniform deformation, and (iii) shear localization. The characteristics of deformation at these different stages are given in Figure 2(b). Severe shear localization is identified by examining the discontinuity of the strips or the grid lines. It should be pointed out that no visible discontinuity of the strips (or ASB) was observed at the maximum stress, which indicates that ASB should initiate after the peak stress. The temperature rise was measured before and after intense shear localization, as shown in Figure 1(a). The times for ASB initiation, maximum stress and maximum temperature are recorded by a synchronized system of photography, temperature and dynamic loading measurements. A summary of the measured time sequences is displayed in Figure 1(c). It is obvious that ASB initiates after the stress peak. What causes the stress drop? In our opinion, there are two potential reasons: thermal softening and large strain-induced damage. The experimental results in the present

*Corresponding author. E-mail: chenhs@bit.edu.cn

work show that temperature rise at the peak stress is only about 50–90 °C. Thermal softening itself is not sufficient for the stress drop or ASB initiation. Moreover, about 37 μs after the stress collapse, the maximum temperature rise was measured. The accelerated temperature elevation corresponds to the formation and propagation of ASB. If we rank these events chronologically, it should be: stress collapse, ASB initiation, ASB evolution and temperature elevation, maximum temperature and macro crack formation. The observed evidence that temperature rise is quite behind ASB initiation indicates that it should not be the trigger of ASB. The other candidate of softening mechanism, i.e., ASB initiation induced by the micro damage.

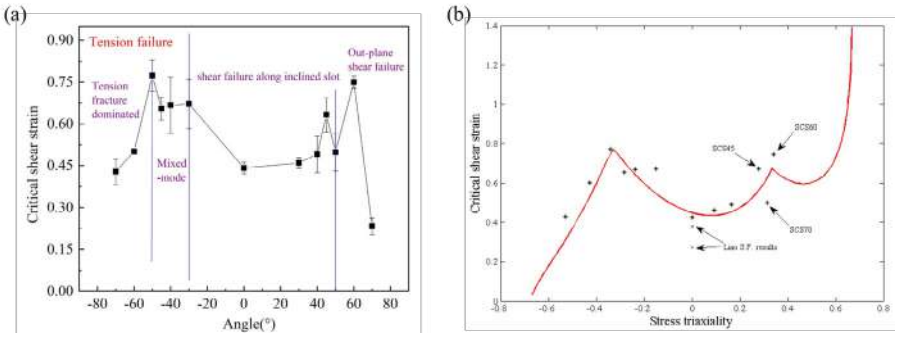

Figure 2. Effect of stress state on the formation of ASB, (a) failure-mode phase diagram and the critical shear strain with respect to different slot angles., (b) comparison of the critical shear strain constructed by a new criterion to experimental results as a function of stress triaxiality under plane stress condition

The micro damage could be the softening mechanism inducing ASB initiation, which was also proposed by some researchers[8,9]. If thermal softening is the only mechanism of ASB initiation, the critical shear strain should not sensitive to the stress state, which is contrary to our experimental observations. The failure-mode phase diagram showing the critical shear strain as a function of slope angle is obtained and presented in Figure 2(a). The different zones can be decided by using the high-speed photography as well as the fracture morphology of the specimens after tests. A positive value of the angle indicates shear-compression tests, while a negative value indicates shear-tension tests and zero degrees indicates torsion test. Obviously, due to the change in angles (or stress state), the failure mode of the specimen is different, and the critical shear strain is not a constant value. To the best of our knowledge, the present criteria for ASB initiation, such as Culver criterion[10], cannot describe the change in critical shear strain with respect to stress state. We have presented a phenomenological criteria model[11] based on our experimental results by using a hybrid experimental–numerical method. Figure 2(b) provides a comparison between the predicted shear failure strain and the experimental results in the space of stress triaxiality for the plane stress condition, which can describe the change in failure behaviours in SCS and STS

CONCLUSIONS

A novel in-situ experimental setup was developed to observe the deformation localization and temperature evolution of the ASB simultaneously, by using the high-speed photography and high-speed infrared radiation. The effect of the temperature increase and stress state on the initiation of the ASB was studied with the modified shear-compression/tension specimens of different degrees. It is found that before the initiation of the ASB, the temperature of the deformed region does not increase rapidly. Rather, it might be the result of adiabatic shear localization. A phenomenological criteria model was proposed based on our experimental results by using a hybrid experimental–numerical method.

References

1. Antolovich, S. & Armstrong, R. Plastic strain localization in metals: origins and consequences. *Prog Mater Sci* **59**, 1 160 (2014).
2. Bai, Y. & Dodd, B. Adiabatic shear localization: occurrence, theories, and applications. *Oxford* (1992).
3. Xu, Y., Zhang, J., Bai, Y. & Meyers, M. Shear Localization in Dynamic Deformation: Microstructural Evolution. *Metallurgical Mater Transactions* **39**, 811 843 (2008).
4. Wright, T. The physics and mathematics of adiabatic shear bands. *Cambridge University Press* (2002).
5. Peirs, J., Verleysen, P., Degrieck, J. & Coghe, F. The use of hat-shaped specimens to study the high strain rate shear behaviour of Ti-6Al-4V. *Int J Impact Eng* **37**, 703 714 (2010).
6. Dorogoy, A., Rittel, D. & Godinger, A. Modification of the Shear-Compression Specimen for Large Strain Testing. *Exp Mech* **55**, 1627 1639 (2015).
7. Dorogoy, A., Rittel, D. & Godinger, A. A Shear-Tension Specimen for Large Strain Testing. *Exp Mech* **56**, 437 449 (2016).
8. Dodd, B. & Atkins, A. G. Flow localization in shear deformation of void-containing and void-free solids. *Acta Metall Mater* **31**, 9–15 (1983).
9. Microvoid Formation during Shear Deformation of Ultrahigh Strength Steels. *Metallurgical Transactions* **20**, 1 11 (2007).
10. Culver, R. Thermal instability strain in dynamic plastic deformation. 519 530 (1973).
11. Zhu, S., Guo, Y., Chen, H., Li, Y. & Fang, D. Formation of adiabatic shear band within Ti–6Al–4V: Effects of stress state. *Mech Mater* **137**, 103102 (2019).

IMPACT OF HANGING CABLES AND POWER TRANSMISSION LINES BY MIXED FLOWING/POWDER SNOW AVALANCHES

Perry Bartelt*[1], Andrin Caviezel[1], Marc Christen[1], and Othmar Buser[2]
[1]WSL Institute for Snow and Avalanche Research, SLF, Davos, Switzerland 2Meierhof, Davos, Switzerland

Summary Hydroelectric power is generated at high elevation pumping stations and then transported over land by a network of towers and conductors often through dangerous avalanche terrain. We derive and solve a system of partial differential equations describing the impact of hanging cables by snow avalanches. At impact the avalanche air-blast causes cables to vibrate, producing elastic deformation waves that travel back and forth between the cable-supporting towers. We show that the forces associated with these energy waves can be large causing the towers to collapse. Especially dangerous is the fact that the frequency of the applied cable loading is often near the natural vibration frequency of the towers making tall, cable-supporting structures particularly venerable to snow avalanche impact.

INTRODUCTION

Avalanche engineers are often confronted with the problem of finding safe locations for power transmission towers (Fig. 1). Direct avalanche impact of these tall, lightweight towers usually leads to immediate collapse, with the consequence that entire valleys can be cut-off from power for weeks [1]. To avoid tower impacts, the engineers often apply numerical simulation programs to model the behaviour of snow avalanches in three-dimensional terrain (Fig. 1). With these programs it is possible to identify safe tower locations,outside the reach of the core or powder air-blast [2, 3]. However, a particularly difficult problem still remains: the engineers need to quantify the effects of an avalanche-conductor impact. The conductors typically cross the avalanche track (Fig. 2) and, depending on the conductor sag, are exposed to the air-blast which can reach at least 50m above the ground. The simulation programs provide the force of the avalanche air-blast as a function of the terrain as well as the avalanche size and snow properties.

The avalanche air-blast deforms the cables and induces transverse elastic waves that propagate back and forth between the towers. Experiments conducted in the 1980s at the Norwegian Ryggfonn test site [4] indicate that the magnitude of the forces associated with the wave propagation are large–up to 100kN. In the following we develop a model of avalanche impact and transverse wave propagation in a hanging conductor that allows the engineers to both understand and quantify the cable pull and collapse forces acting on transmission towers.

AVALANCHE IMPACT AND TRANSVERSE WAVE PROPAGATION

The problem of avalanche impact of a hanging cable is analogous to the problem of "plucking" a vibrating string. However, there are three important differences. The first is that the initial cable tension T_0 is given by the cable self-weight, as well as the elevation of the mountain terrain. Secondly, the cable deformations are large and subsequently small-deformation theory cannot be directly applied to model the dynamic forces [5]. Finally, the applied avalanche loading is multi-directional; primarily in the transverse y (slope parallel) $f_y(x,t)$ and upward z (slope perpendicular) $f_z(x,t)$ directions. These functions are derived from avalanche dynamics simulations (Fig. 1)

The problem statement leads to a system of three partial differential equations in the cable x (displacement u), avalanche y (displacement v) and slope perpendicular z (displacement w) directions,

$$\frac{\partial^2 u}{\partial t^2} = c_l^2 \frac{\partial^2 u}{\partial x^2} + \frac{c_l^2}{2}\frac{\partial}{\partial x}\left[\left(\frac{\partial v}{\partial x}\right)^2 + \left(\frac{\partial w}{\partial x}\right)^2\right] \qquad \frac{\partial^2 v}{\partial t^2} = c_t^2 \frac{\partial^2 v}{\partial z^2} + f_y(x,t) \qquad \frac{\partial^2 w}{\partial t^2} = c_t^2 \frac{\partial^2 w}{\partial z^2} + f_z(x,t). \tag{1}$$

Appropriate boundary and initial conditions corresponding to the tower position and support are needed to close the problem. The quantities c_l and c_t represent the longitudinal and transverse wave speeds which are a function of the cable elasticity E, cross-sectional area A, initial tension T_0 and mass per unit length m,

$$c_l = \sqrt{\frac{EA}{m}} \qquad c_t = \sqrt{\frac{T_0(x,t)}{m}}. \tag{2}$$

*Corresponding author. E-mail: bartelt@slf.ch.

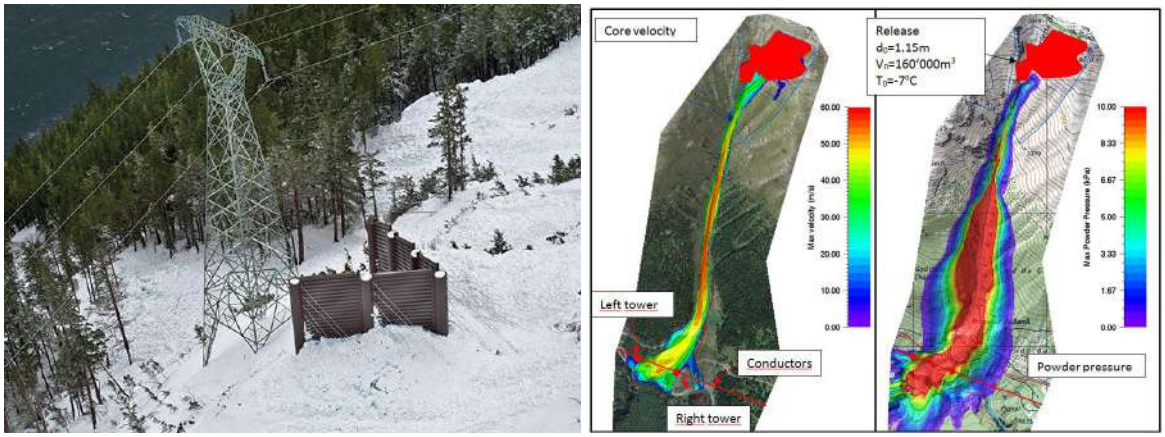

Figure 1: Left: Example of power transmission lines in avalanche terrain. Juneau, Alaska. The tower is part of the Snettisham transmission line [1]. The tranmission line was destroyed by avalanches in 2008. Right: Numerical avalanche dynamics models are used to calculate the motion of the core and cloud in general three-dimensional terrain. Example of a mixed flowing/powder avalanche calculation for an avalanche track near Zernez, Switzerland.

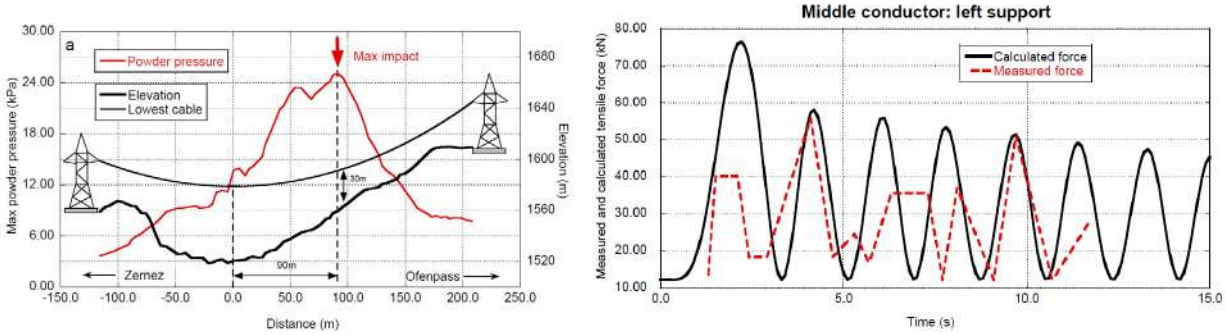

Figure 2: Left: Example of a power transmission line in avalanche terrain, Zernez, Switzerland. The towers are located over 300m apart. Note the position of maximum avalanche impact. Right: Example comparing measured and calculated avalanche forces in a 182m long conductor at the Ryggfonn test site [4].

NUMERICAL RESULTS

The partial differential equations are solved for a specific avalanche loadings. The duration of the impact usually lasts no more than 10s. Short duration blasts of only a few seconds are possible, depending on the location where the cable crosses the avalanche path. Again, depending on the particular avalanche track, the spatial distribution of the air-blast pressure can be localized (acting only over a specific cable length) or spread over the entire cable from tower to tower. Typical impact pressure values vary between 3kPa to 10kPa. In summary, we find two important results: (1) the magnitude of the forces matches the experimental observations, but is also surprisingly large, especially for low tension cables and (2) the frequency of the transverse waves matches the first bending mode resonance frequencies (1Hz - 5Hz) of many tubular steel and lattice-type tower constructions.

CONCLUSIONS

Although much effort has been made to place towers out of the reach of snow avalanches, power transmission lines and cableways must often traverse dangerous avalanche paths. When powder snow avalanche air-blasts impact hanging cables they can induce pull (cable direction) and collapse (downward) forces on the supporting structures reaching up to 10 tons. Furthermore, the frequency of the applied loading matches the natural vibration frequency of many tall, cable-supporting structures. Dynamic magnification effects clearly increase the vulnerability of the transmission line to avalanches.

References

[1] Eriksen, E. The Next Avalanche, *Transmission and Distribution World Magazine* Sept 26, 2016.
[2] Christen M., Kowalski J., Bartelt P. RAMMS: numerical simulation of dense snow avalanches in three-dimensional terrain, *Cold Regions Science and Technology*, 63(1-2), 1-14.
[3] Bartelt P., Buser O., Vera Valero C., Büehler Y. Configurational energy and the formation of mixed flowing/powder snow and ice avalanches, *Annals of Glaciology*, 57(71), 179-188. 2016.
[4] Norem H., Kristensen K., Tronstad K. The Ryggfonn Project: Avalanche Data from the 1986/1987 Winter, *NGI Report 58120-11*, 1988.
[5] Morse P. Theoretical Acoustics, McGraw Hill, NY 1968.

MATHEMATICAL STUDY OF WAVE REFLECTION AND REFRACTION PHENOMENON AT THE INTERFACE OF TWO DISSIMILAR PIEZOELECTRIC FIBER-REINFORCED COMPOSITE HALF-SPACES

Sayantan Guha*[1] and Abhishek Kumar Singh[1]
[1]Department of Mathematics and Computing, Indian Institute of Technology (Indian School of Mines) Dhanbad, Jharkhand-826004, India

Summary The phenomenon of wave reflection/refraction at the interface surface of two dissimilar piezoelectric fiber-reinforced composite half-spaces is studied. The PFRCs are composed of piezoelectric fibers & piezoelectrically inactive matrix & have been modeled using the Strength of Materials technique & rule of mixtures approach. Some electro-mechanical advantages of PFRC over monolithic piezoelectric materials are graphically demonstrated. Due to the incidence of a qP wave, three reflected & refracted waves viz. qP, qSV, & EA waves are generated in the PFRCs. The closed-form expressions of amplitude ratios of all reflected/refracted waves are derived using appropriate electro-mechanical boundary conditions. The expressions of energy ratios of all reflected/refracted waves & interaction energy are derived & graphically illustrated, and the Law of Conservation of Energy is established.

INTRODUCTION

Several piezoelectric materials are widely available and have countless applications like manufacture of SAW devices, sensors, actuators, etc. Some notable works related to wave reflection/transmission in smart composite structures have been performed by Guo and Wei [1] and Pang et al. [2]. However, these piezoelectric materials are, by nature, brittle and mechanically stiff, and hence quite vulnerable to accidental breakage during handling and bonding procedures. In order to overcome these inhibitions & obtain improvised effective electro-mechanical properties in comparison to monolithic piezoelectric materials, PFRC materials have come to be of widespread use. The micromechanics model for PFRC has been developed by techniques like strength of materials, continuum mechanics approach etc. by Kumar and Chakraborty [3], Ray [4] and others. PFRC are at the forefront of being utilized in a multitude of engineering fields due to their superior mechanical and electrical properties can be achieved by systematically adapting the most profitable properties of the constituents of composite materials. They are also lightweight and flexible, thus being able to provide strength to materials. Not much mathematical work was conducted previously dealing with the phenomenon of wave reflection/refraction in such complex composite structures - this served as one of the prime sources of motivation which led to the findings of the present study.

GOVERNING EQUATIONS

The constitutive equations for piezoelectric fibers are given as

$$\left\{\tau^{f}\right\}=[c^{f}]\left\{s^{f}\right\}-[e^{f}]^{T}\left\{E^{f}\right\},\qquad \left\{D^{f}\right\}=[e^{f}]\left\{s^{f}\right\}+[\varepsilon^{f}]\left\{E^{f}\right\}, \tag{1}$$

and the constitutive equations for piezoelectrically inactive matrix are given as

$$\left\{\tau^{m}\right\}=[c^{m}]\left\{s^{m}\right\},\qquad \left\{D^{m}\right\}=[\varepsilon^{m}]\left\{E^{m}\right\}, \tag{2}$$

where the superscripts f and m depict the components of the fiber and matrix respectively.
The expressions of the material constants in the constitutive equations of the PFRC are derived, following some assumptions, using the Strength of Materials technique along with the Rule of Mixtures approach.

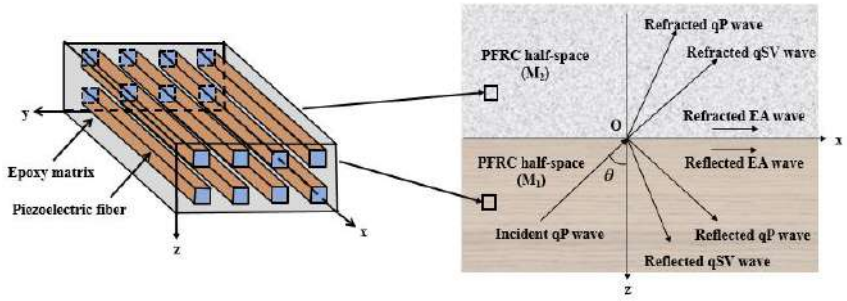

Fig.1. Geometry showing the micromechanics of PFRC and incident wave along with all reflected/refracted waves

The constitutive equations for the PFRC in the absence of body forces and electric forces are:

$$\sigma_{ij,j}=\rho u_{i,}\qquad D_{i,i}=0. \tag{3}$$

*Corresponding author. E-mail: **sayantanguha.maths@gmail.com**.

Using Equations (1)-(3) followed by proper boundary conditions, we derive the angles of reflected/refracted waves w.r.t. the angle of incidence of qP wave and also, the amplitude ratios of reflected/refracted waves. Using these, the expressions of energy ratios of all reflected/refracted waves & interaction energy are derived.

AMPLITUDE RATIOS

To obtain the amplitude ratios for incident qP wave, generalized Snell's law has been taken into account. After utilization of the boundary conditions, the finalized system of equations has been provided in matrix form as

$$\left[a_{ij}\right]_{6\times 6}=\left[\frac{A_1^{(1)}}{A_2^{(1)}}\quad \frac{A_3^{(1)}}{A_2^{(1)}}\quad \frac{A_5^{(1)}}{A_2^{(1)}}\quad \frac{A_2^{(2)}}{A_2^{(1)}}\quad \frac{A_4^{(2)}}{A_2^{(1)}}\quad \frac{A_6^{(2)}}{A_2^{(1)}}\right]^{T}=\left[b_{11}\quad b_{21}\quad b_{31}\quad b_{41}\quad b_{51}\quad b_{61}\right]^{T}, \tag{4}$$

The expressions of amplitude ratios for reflected/refracted waves are obtained using Cramer's rule from Equation (4) which exhibit their dependency on the various affecting parameters and incident angle.

ENERGY RATIOS

The energy shared among the incident wave and all reflected/refracted waves is evaluated across a unit area surface element of infinitesimal thickness on the interface (z = 0). Following Guo and Wei [1], the averaged energy flux across unit surface area and the general expression of energy ratios are

$$P_{\alpha\beta}^{(m)}=k^2c[D_{1\alpha}^{(m)}\overline{W_\beta^{(m)}}A_\alpha^{(m)}\overline{A_\beta^{(m)}}+D_{2\alpha}^{(m)}A_\alpha^{(m)}\overline{A_\beta^{(m)}}+\overline{D_{3\alpha}^{(m)}}\Phi_\beta^{(m)}\overline{A_\alpha^{(m)}}A_\beta^{(m)}]/2,\qquad E_{\alpha\beta}^{(m)}=P_{\alpha\beta}^{(m)}/P_{22}^{(1)}. \tag{5}$$

The expression of complete interaction energy considering incident wave & all reflected/refracted waves is

$$E_{int}=\sum_{\alpha=1,3,5}(E_{2\alpha}^{(1)}+E_{\alpha 2}^{(1)})+\sum_{\alpha=1,3,5}(\sum_{\beta=1,3,5}E_{\alpha\beta}^{(1)}-E_{\alpha\alpha}^{(1)})+\sum_{\alpha=2,4,6}(\sum_{\beta=2,4,6}E_{\alpha\beta}^{(2)}-E_{\alpha\alpha}^{(2)}), \tag{6}$$

and according to the Law of Conservation of Energy, we must have $\sum_{\alpha=1,3,5}E_{\alpha\alpha}^{(1)}+\sum_{\alpha=2,4,6}E_{\alpha\alpha}^{(2)}+E_{int}=1.$

CONCLUSIONS

- For the variation of angle of incidence of qP wave from $0<\theta<90$, the angle of reflection of qP wave has the same variation which shows that angle of incidence is equal to angle of reflection. The variation of angle of reflection for qSV wave is $0<\theta<24.7$, which proves the fact that reflected qSV wave travels with a lower velocity as compared to reflected qP wave. Reflected EA wave, being an evanescent surface wave, propagates along the interface.
- For the variation of angle of incidence of qP wave from $0<\theta<90$, the angle of refraction of qP and qSV waves range between $0<\theta<55.03$ and $0<\theta<24.08$ respectively, which shows that the refracted qP wave travels with a greater velocity as compared to refracted qSV wave. Refracted EA wave, also being an evanescent surface wave, propagates along the interface.
- The angle vs angle graphs demonstrate that that there is no critical angle when qP wave is incident in PZT-5A/epoxy composite. However, if qP is incident in CdSe/epoxy composite, a critical angle appears at 60.
- For the case of normal incidence $(\theta=0)$ of qP wave, no waves are reflected and only qP wave is refracted.
- For the case of grazing incidence $(\theta=90)$ of qP wave, no waves are refracted and only qP wave is reflected.
- Among all reflected and refracted waves, the energy ratios of reflected and refracted qP waves attain greatest magnitude.
- Throughout the entire range of the angle of incidence, the energy ratio of refracted qSV wave attains greater magnitude than the energy ratio of reflected qSV wave.
- The magnitudes of the energy ratios of reflected/refracted EA waves and the interacting energy are negligible.

References

[1] X. Guo, P. Wei, Effects of initial stress on the reflection and transmission of waves at the interface between two piezoelectric half spaces, Int. J. Solids. Struct. 51 (2014) 3735{3751. doi:10.1016/j.ijsolstr.2014.07.008.
[2] Pang, Y., Wang, Y. S., Liu, J. X., & Fang, D. N. (2008). Reflection and refraction of plane waves at the interface between piezoelectric and piezomagnetic media. *International Journal of Engineering Science*, *46*(11), 1098-1110.
[3] Kumar, A., & Chakraborty, D. (2009). Effective properties of thermo-electro-mechanically coupled piezoelectric fiber reinforced composites. *Materials & Design*, *30*(4), 1216-1222.
[4] Ray, M. C. (2006). Micromechanics of piezoelectric composites with improved effective piezoelectric constant. *International Journal of Mechanics and Materials in Design*, *3*(4), 361-371.

GENERALIZATION AND VALIDITY OF MOTT'S WAVE CONCEPT

Don-Pierre Zappa*[1], Gilles Damamme[1], and Helmut Klöcker [2]
[1]CEA, DAM, CEA-GRAMAT, F-46500, Gramat, France
[2]EMSE, F-42023, Saint Etienne, France

Summary: Predicting fragment size is mandatory when analyzing possible consequences of explosions. Mott offered the first physically based fragmentation model. He considered strain rate discontinuities propagating in a straight bar. Tank or reservoir explosions may lead to strain rates up to 10^4 s^{-1} or $10^5 s^{-1}$. Under these particular loadings, due to experimental difficulties, neither the material behavior, nor possible strain rate discontinuities are easily analyzed. Present work offers a new analysis of ring fragmentation in 2 dimensions without any particular assumption concerning the ring geometry.

INTRODUCTION

In 1943, Mott and Linfoot extended Lienau's (1936) purely mathematical line break-up model. Soon after, Mott made a conceptual breakthrough by highlighting two main physical phenomena which control ring fragmentation. First, Mott introduced a probability distribution of initial defects which were activated as long as plastic strain was growing. Secondly, Mott introduced stress relaxation waves, which are now named in his honor. Mott waves are one of the keystones needed to predict fragmentation debris size because unloaded parts are prevented from further crack nucleation. Unfortunately, Mott needed to simplify wave propagation by neglecting curvature effects and strain rate evolution, given one of the computational limits of the 1940s.

Grady introduced an ad hoc correction (Grady 1982, 2006) considering non instantaneous failure. Damamme et al. (2019) reformulated fragmentation based on energy balance (Damamme 2019). To the best of our knowledge, curvature or strain rate effects on Mott's wave existence and propagation have not been analyzed.

ORIGINAL MOTT'S MODEL

Mott described fragmentations of long cylinders by ring breakup. He assumed instantaneous through thickness crack propagation. After through thickness crack propagation an unloading wave propagates. Mott assumed that curvature was negligible so that governing equations were reduced to the case of an extending straight bar. Moreover, he supposed constant strain rate during the fragmentation process. Supposing a rigid plastic metal behavior, the conservation of momentum on rigidified bar (rod) allows determining the wave front position X as a function of time t:

$$X^2 = \frac{2\sigma_0}{\rho\dot{\varepsilon}}t.$$

σ_0, ρ and $\dot{\varepsilon}$ represent respectively the yield stress, material density and strain rate (constant during the wave propagation). Based on a simple energy balance, Damamme et al. [4] showed that Mott's approach leads to an upper bound for the wave front position, i.e. in a straight bar, the discontinuity propagates always slower than predicted by Mott. In the following, we analyzed the influence of curvature on possible strain rate discontinuities.

CONDITIONS OF EXISTENCE

Considering a weighted string $\mathcal{C}$ moving in a plane, the system of governing equation is established, considering finite strains. Physical values considered are velocity vector, strain and rotation and independent variables are cumulated mass and time (Wilkins 1963). The string is supposed to be extending therefore shocks or discontinuities of physical values are not considered, but discontinuities of their derivatives are possible.

Admissible discontinuities are analyzed with no specific assumption on material behavior. Specific jump relations are then established. These relations generalize the Mott's wave as the propagation of strain rate jump, for which the propagation could differ from Mott's parabola.

MOTT'S WAVE DOMAIN OF VALIDITY

Governing equations are numerically solved with a specific elastic-plastic code developed for the sake. Code results are analyzed with a dedicated algorithm that tracks strain rate jump. The time evolution of the position of the strain rate jump is then compared with original Mott's wave. Curvature and finite length effect are analyzed through the evolution corrective terms relatively to Mott's original governing equation.

Present work, firstly proves the existence of strain rate discontinuities independently of the material behavior and particular geometry. Secondly, it constitutes the bases for analyzing the validity of dynamic fragmentation, especially ring expansion, experiments.

References

*Corresponding author. E-mail: don-pierre.zappa@cea.fr

[1] Lienau Random fracture of brittle solids. J. Franklin Inst. 221 (6), 485-494, 674-686, 769-787, 1936
[2] Mott NF A Theory of the Fragmentation of Shells and Bombs. Ministry of Supply, A.C.4035, 1943
[3] Grady D.E. Fragmentation of rings and shells: the legacy of N. F. Mott. Springer, Berlin 2006
[4] Damamme G. New Fragmentation Model Considering Mott's Wave Arrests . J. Mech. Phys. Solids 128 (2019) 21-31
[5] Mark Wilkins. Calculation of elastic-plastic flow, technical report UCRL-7322, Lawrence Radiation Laboratory Livermore, California 1963.

THERMOMECHANICAL CONSTITUTIVE RESPONSE OF A NEAR α TITANIUM ALLOY OVER A WIDE RANGE OF STRAIN RATES

Longhui Zhang[1*], Antonio Pellegrino[1], David Townsend[1]and Nik Petrinic [1]
[1]Department of Engineering Science, University of Oxford, Oxford, OX1 3PJ, United Kingdom

Summary The constitutive behaviour of a near α Ti3Al2.5V alloy is characterized at strain rates ranging from 10^{-3} s^{-1} to 10^{6} s^{-1} by using the cylindrical compression specimen and Shear Compression Specimen (SCS). The adiabatic heating effect from medium to high rates is evaluated experimentally. Digital Image Correction (DIC) technique is used to measure strain from recorded images. The Ti3Al2.5V alloy presents noticeable strain rate sensitivity. The experimental results are used to determine the material parameters of a simple constitutive model, which is incorporated in the ABAQUS/explicit code for numerical simulations of the Taylor impact tests. The model predicts the deformed specimen shapes from Taylor impact experiments with good agreement.

INTRODUCTION

Titanium alloys with excellent high strength to weight ratio have been used widely in aerospace engineering applications which are unavoidably subjected to impact loading. It is important to understand the mechanical response under dynamic deformation. At high strain rates, the adiabatic temperature rise is likely to affect the mechanical response of the material by causing thermal softening [1]. The traditional Hopkinson bar technique has been used to characterize the mechanical behaviour up to strain rate of several 10^{3} s^{-1}. However, this strain rate is an order of magnitude lower than those commonly encountered during severe high velocity impact such as bird strike on an engine blade, impact of debris or blast loading. A better understating of response over a wide range of strain rate can provide the guidance for tougher engineering structure design.

EXPERIMENTAL SETUPS

The Ti3Al2.5V alloy is used as a model material in the present study. The SCS specimen [2] was employed to investigate the high strain rate behavior at the level of 10^{4} s^{-1}. The quasi-static and medium rate compressive experiments were conducted using a screw-driven Zwick mechanical test machine and a hydraulic Instron machine 8850 respectively. The strain measurements were obtained via DIC analysis. Intermediate (500 s^{-1}) and high rate experiments were carried out using a bespoke developed Hopkinson compression bar synchronized with a Kirana camera. To monitoring the temperature at medium rate, a K-type thermocouple was spot wielded on the centre surface of the specimen. The high rate temperature evolution was monitored by Zhang et al. [3] using a non-contact infrared thermometry technique. Additional high strain rate tests at 100 °C and 200 °C were also performed by using an environmental chamber on the Hopkinson bar system to evaluate the (environmental) temperature effect on the mechanical behaviour. The Taylor tests were completed using a nitrogen 12mm bore gas gun synchronized with the Kirana camera.

EXPERIMENTAL RESULTS

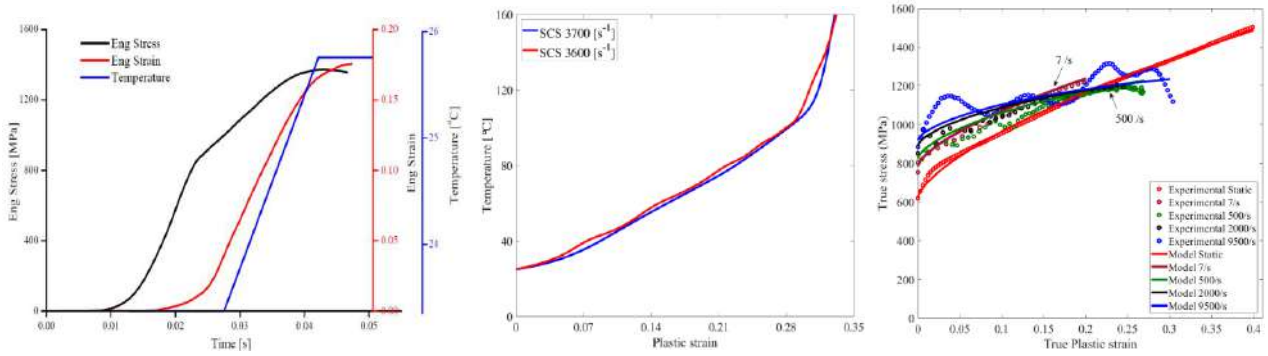

Figure 1. Temperature monitoring at medium rate 7 s^{-1}. (b) Temperature rise vs. plastic strain for Ti3Al2.5V at high strain rate 3600 s^{-1} (c) Comparison between the constitutive model and experimental data

The typical temperature recording at medium rate 7 s^{-1} (Figure 1a) shows a modest increasing temperature of the specimen, which cannot cause any thermal softening effects of the titanium alloy. Figure 1b presents the temperature vs plastic strain at strain rate of 3600 s^{-1}. The temperature rise increases to around 100 °C and ultimately soars up to several hundred degrees due to the strain localization, indicating the adiabatic heating characteristic at high strain rates. Figure 1c shows the stress-strain curves of Ti3Al2.5V at the various strain rates.

*Corresponding author. E-mail: longhui.zhang@eng.ox.ac.uk

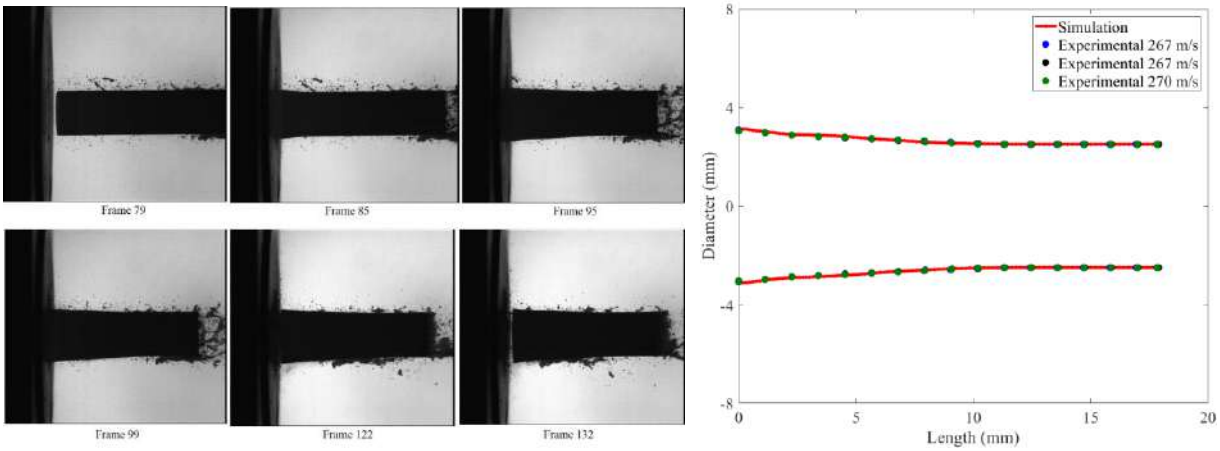

(a) (b)

Figure 2. (a) A montage of experimental images of the impact at 270 m/s with frame rate $1x10^6$ fps (b) Comparison between the experimental and numerical residual shape of the specimen impacted at 267 m/s.

Figure 2a shows photographs recorded at various stages during a Taylor test at 270 m/s. The deformation results in a high radial deformation at the impact end. The Combined advantages of Johnson-cook [4] and KHL model [5], namely CJK model, is designed to describe the strain rate and temperature dependent mechanical behaviour. A comparison between the experimental data and the calibrated model descriptions for Ti3Al2.5V is given in Figure 1c. Figure 2b shows a comparison of the experimentally observed residual shape with that predicted by the numerical simulations of the rod specimens impacted at around 267 m/s. The finite element model accurately predicts the overall geometry, including the final shortened length and the diameter along the length.

CONCLUSIONS

A wide range of strain rates is conveniently explored by using cylindrical and SCS specimens. A simple constitutive model with limited constants is employed to characterize the response under wide ranges of strain rates. The numerical predictions are made for the Taylor impact tests; good agreement is found between predicted and measured deformed shapes.

References

[1] M.A. Meyers, Dynamic behavior of materials, John Wiley & Sons, 1994.
[2] A. Dorogoy, D. Rittel, A. Godinger, Exp. Mech, (2015) 1-13.
[3] L. Zhang, D. Rittel, S. Osovski, Mater. Sci. Eng. A, 729 (2018) 94-101.
[4] G.R. Johnson, W.H. Cook, Eng. Fract. Mech, 21 (1985) 31-48.
[5] A.S. Khan, Y. Sung Suh, R. Kazmi, Int. J. Plasticity, 20 (2004) 2233-2248.

NONLINEAR ONE-WAY TWO-WAVE MIXING IN A MEDIA WITH RATE INDEPENDENT HYSTERESIS

Pravinkumar Ghodake[1], Saurabh Biswas[2]
[1]Department of Mechanical Engineering, Indian Institute of Technology Bombay, Mumbai, India
[2]Department of Mechanical Engineering, Indian Institute of Technology Jammu, Jammu,India

Summary One dimensional nonlinear one-way two-wave mixing in a media with rate-independent hysteresis models like Bouc-Wen and Two-states is presented systematically. In frequency response, sum and difference harmonics along with the original odd harmonics are accurately captured by both the hysteretic models. Both the hysteresis models captured minor, intermediate, and major loops in hysteresis curves effectively for Gaussian pulse as an incident wave. Various mixing studies are carried out for different combinations of amplitudes and frequencies of the incident wave to get an insight into the nonlinear wave mixing phenomenon in hysteretic material models.

INTRODUCTION

Interaction of single frequency wave with early-stage damages (micro-cracks, grains, dislocations, etc.) distorts the wave resulting in the generation of higher harmonics. Traditionally, the nonlinear wave propagation in damaged solids is described by modeling damages as quadratic, cubic, and hysteretic nonlinear materials. The theoretical and numerical studies show that the interaction of single frequency wave with Preisach-Mayergoyz [1-3] hysteretic nonlinearity generates only odd harmonics. Here in this wave propagation study, we are implementing the famous Bouc-Wen model [4,5] and a relatively new two-states hysteresis model [6]. To get more insight into the damage levels and damage mechanisms a one-way two-wave mixing is preferred due to some advantages like eliminating system harmonics etc. In mixing, a single wave with two different frequencies is sent pulse distorts and generates sum and difference frequencies as seen in quadratic and cubic nonlinear material models. Mixing in hysteretic material is explored systematically in this study.

NUMERICAL MODELS

To model one-dimensional wave propagation in a media, a long spring-chain with hysteresis elements is considered as shown in Figure 1(a). The hysteresis elements in a long spring-mass chain are modeled using the Bouc-Wen model and the two-state model. Input displacements u at is given at the left end of chain firstly as Gaussian pulse with a single input frequency (Figure 1(b)) and secondly as Gaussian pulse with two input frequencies (Figure 1(c)).

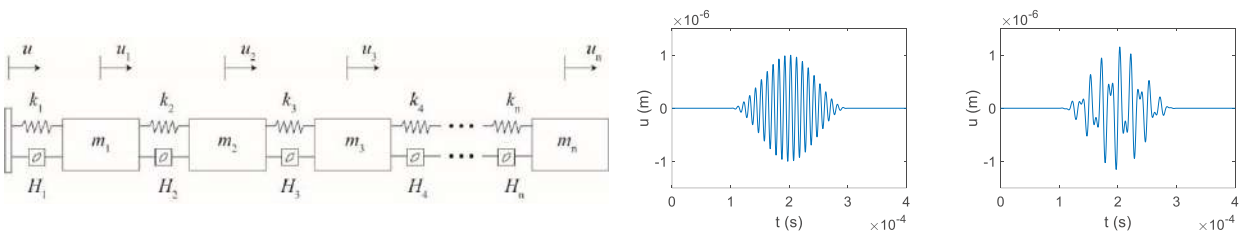

a) b) c)

Figure 1. (a) A spring-mass chain system, (b) Single-frequency (0.1 MHz) and (c) two frequency (0.06 and 0.1 MHz) Gaussian input pulses as two different input pulses (u) for a long spring-mass chain.

The original Bouc-Wen model is a scalar rate-independent hysteresis model with four free parameters. In the Bouc-Wen model, the hysteretic part of the force is given by a variable z driven by an input displacement u, as in

$$\dot{z} = \dot{u}(A - \alpha 3\mathrm{gn}(\dot{u}z)|z|^n - \beta|z|^n),$$

where the parameters satisfy

$$A > 0, \alpha > 0, \beta 3\epsilon 3[-\alpha, \alpha], n > 0.$$

Being a scalar model, the Bouc-Wen model is computationally simple and works fairly well for systems with single-frequency input. However, the model cannot capture small minor loops due to short loading-unloading within a larger load cycle, mainly in structural vibration applications where amplitudes of input signals are large and input frequencies are low as compared to the wave propagation studies.

The above drawback was addressed in the paper by Biswas and Chatterjee [6] and the authors there developed a new two-state hysteresis model that gives a more practical response than the Bouc-Wen model under multi-frequency inputs. The two-state model was originally developed from the famous Iwan model [7]. The model has system matrices $A3(23\times 32), 3\bar{K}\ (23\times 32), \bar{b}(23\times 32), 3$and the input u. The internal state vector is $q3(23\times 32)$. For the given parameters and the given input, an intermediate quantity is computed first,

$$\dot{s} = \left[\frac{\eta^T \bar{b}}{\eta^T \bar{K} \eta}\dot{u} - y|\dot{u}|\right].\{y \le 0\}.$$

Then finally,

$$\dot{q} = \eta \dot{s}.\{\dot{s} > 0\}.$$

Here, η is the slip direction. The hysteretic force is given by

$$f = u - q^T \bar{b}.$$

Where $\dot{s}$ is the slip rate and η can be found by solving a 4×4 eigenvalue problem [6]. We used both the models in our present study to generate a response of the one-way two-wave mixing in a media with rate-independent hysteresis.

SIMULATION RESULTS AND DISCUSSION

For a single frequency input pulse, both the models show the generation of only odd harmonics in their frequency responses (Figure 2(a) and Figure 3(a)). The corresponding hysteresis curves are captured nicely with increasing loop size from zero to a maximum and again back to zero as the amplitude of Gaussian pulse increases from zero to maximum amplitude and then coming back to zero (Figure 1(b)).

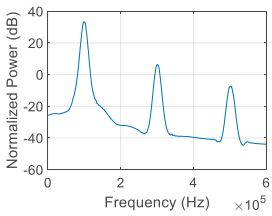

a) Single-frequency Gaussian input pulse frequency response

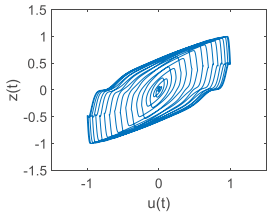

b) Single-frequency Gaussian input pulse hysteresis curves

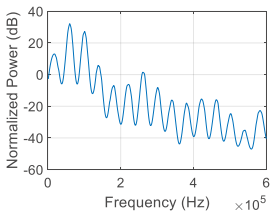

c) Two frequency Gaussian input pulse frequency response

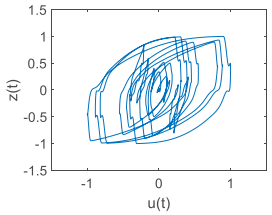

d) Two frequency Gaussian input pulse hysteresis curves

Figure 2. Nonlinear wave propagation in media with Bouc-Wen hysteresis model

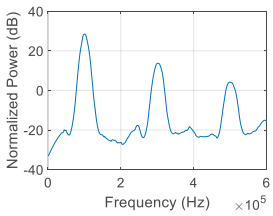

a) Single-frequency Gaussian input pulse frequency response

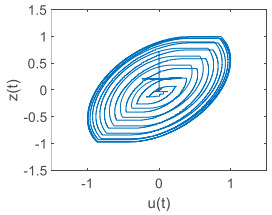

b) Single-frequency Gaussian input pulse hysteresis curves

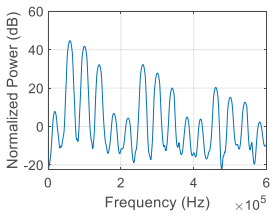

c) Two frequency Gaussian input pulse frequency response

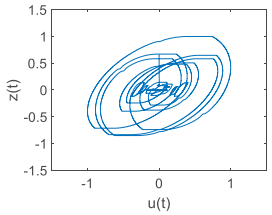

d) Two frequency Gaussian input pulse hysteresis curves

Figure 3. Nonlinear wave propagation in media with Two-State hysteresis model

Due to mixing, sum and difference frequencies (other than f_1 = 0.06 and f_2 = 0.1 MHz input frequencies) are observed by both the models (Figure 2(c) and Figure 3(c)). Both the models captured a wide range of possible mixing frequencies generated due to various combinations of input frequencies ($2f_1+f_2$, $2f_1-f_2$, f_1+2f_2, f_1-2f_2, $4f_1+f_2$, ..., *etc.*) excellently. From Figure 2(d) and Figure 3(d), at the low amplitude of Gaussian pulse, both models excellently captured minor loops that turns around and intersects with itself. Interestingly as the amplitude of Gaussian pulse increases (loops getting bigger), the medium size minor loops captured using the Bouc-Wen model are translated horizontally which is not the case in Two-States models where the medium size loops are observed within the big major loop. Both the models captured all possible minor and major loops effectively. To gain a detailed understanding of wave mixing studies, different practically possible combinations of input frequencies and amplitudes are also explored through several examples.

CONCLUSIONS

The Bouc-Wen and Two-states hysteresis models are successfully implemented for nonlinear wave mixing study. Both the models captured sum and difference frequencies along with original odd frequencies and all possible minor, intermediate, and major loops effectively. This study can be extended to understand wave mixing in a material with local hysteretic damage.

References

[1] McCall K & Guyer R, Equation of state and wave propagation in hysteretic nonlinear elastic materials, J. Geophys. Res., 99: 23,887-23,897, 1994.
[2] Van Den Abeele K, Johnson P, Guyer R, & McCall K, On the quasi-analytic treatment of hysteretic nonlinear response in elastic wave propagation, J. Acoust. Soc. Am., 101:1885–1898, 1997.
[3] Vanaverbeke S & Van Den Abeele K, Two-dimensional modeling of wave propagation in materials with hysteretic nonlinearity, J. Acoust. Soc. Am., 122:58–72, 2007.
[4] Bouc R, Forced vibrations of mechanical systems with hysteresis. Proc. the Fourth Conf. on Nonlinear Oscillation, Prague. p. 315. 1967.
[5] Wen Y. K: Method for random vibration of hysteretic systems. J. Eng. Mech. Div., ASCE, 102:2, 249-263. 1976.
[6] Biswas S & Chatterjee A, A two-state hysteresis model from high-dimensional friction. R. Soc. Open Sci. 2: 150188. 2015.
[7] Iwan W. D, A distributed-element model for hysteresis and its steady-state dynamic response. J. Appl. Mech., 33:4, 893-900. 1966.

MICROMECHANICS ANALYSIS OF COMPOSITES VIA CARRERA UNIFIED FORMULATION AND NASA MULTISCALE ANALYSIS TOOL

Marco Petrolo*[1], Erasmo Carrera[1], Ibrahim Kaleel[2], Evan J. Pineda[3], Trenton M. Ricks[3], Brett A. Bednarcyk[3], and Steven M. Arnold[3]
[1]Department of Mechanical and Aerospace Engineering, Politecnico di Torino, Torino, Italy
[2]DLR, Institute of Test and Simulation for Gas Turbines, Augsburg, Germany
[3]NASA Glenn Research Center, Cleveland, United States of America

Summary This paper presents numerical analyses concerning the micromechanics of composite structures. The results stem from the synergistic use of the Carrera Unified Formulation (CUF) and NASA Multiscale Analysis Tool (NASMAT). CUF provides the structural theories to model the representative volume elements (RVE) via 1D finite elements with improved kinematics. NASMAT is the new state of the art multiscale framework developed at the NASA Glenn Research Center for high-performance computing systems. The numerical assessments focus on various RVE architecture with increasing complexity and including wovens. The accuracy and numerical efficiency are discussed for homogenization and localization of the entire 3D stress field. As multifold improvements in the computational time are obtained, extensions to nonlinear multiscale analyses are plausible and attractive.

INTRODUCTION

The multiscale nature of composites unleashes several challenges concerning the numerical modeling. Depending on the structural response of interest, various strategies are available. Unfortunately, the direct numerical simulation of a composite structure accounting for all scales concurrently is still not feasible, and choices are necessary to minimize the computational costs with acceptable accuracy penalties. For instance, the proper evaluation of free-edge effects requires layer-wise modeling in which each layer's structural behavior is directly modeled. [1]. On the other hand, the proper numerical prediction of matrix/fiber failure onset and propagation requires the modeling of the microscale characteristics [2]. The use of micromechanics is helpful to model a volume of the structure, including a representative description of the microscale architecture of the constituents, e.g., fibers, matrix, honeycomb packing, voids, defects. The aim is to provide homogenized material properties for the upper scales starting from the constituent properties; then, via localization, provide stress and strain fields at the microscale for a given macroscale load. The main challenge is to develop a model having accurate homogenization and localization while keeping the computational cost low to favor multiscale and nonlinear analyses. Several features of composites may increase the difficulties, e.g., the use of complex 3D woven architectures [3, 4].

OVERVIEW OF NUMERICAL FRAMEWORK AND RESULTS

This work presents a full numerical method based on advanced 1D structural theories and finite elements. The structural modeling adopts CUF to generate governing equations and FE arrays. In the 1D version of CUF, the displacement field may be written as follows [5]:

$$\mathbf{u}(x,y,z) = F_\tau(x,z)\,\mathbf{u}_\tau(y) \qquad \tau = 1,\ldots,M \tag{1}$$

where $\mathbf{u}$ is the generic displacement vector, F_τ is the cross-section expansion function of the beam defined over the plane $x-z$ with M terms, and Einstein notation acts on τ. The class of function adopted as F_τ determines the theory of structure. This work adopts Lagrange-based polynomials. Examples of advantages of the adopted 1D approach are to have pure displacement unknowns and the possibility of keeping the material and geometrical characteristics of individual constituents as depicted in Fig. 1. Also, the use of 1D models instead of 3D leads to superior localization and computational cost performances.
The modeling approach based on CUF is integrated with a fully into NASMAT using the NASMAT Micro API. An Abaqus GUI generates CUF meshes, whereas the NASMAT input file defines loading, material properties, material models, output, and the like. NASMAT can combine CUF models with any material model available in its libraries. Furthermore, a library of predefined CUF architectures is under implementation in NASMAT. Figure 2 shows an example of localization via NASMAT. The High fidelity Generalized Method of Cell serves as the verification tool as it another method available in NASMAT. Numerical results on more complex architectures are expected to lead to some The use of CUF led to some 5-10 times reductions in computational time as compared to 3D FE.

*Corresponding author. E-mail: marco.petrolo@polito.it.

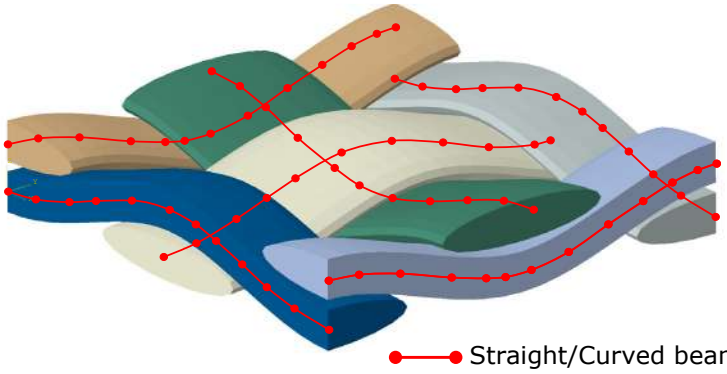

Figure 1: Example of modeling approach for a textile weave composite using 1D CUF.

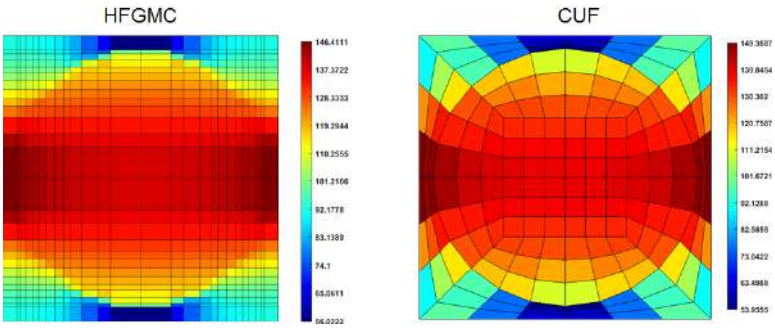

Figure 2: Localization of transverse stress fields under transverse loading conditions.

References

[1] de Miguel, A.G., Kaleel, I., Nagaraj, M.H., Pagani, A., Petrolo, M., Carrera, E. Accurate evaluation of failure indices of composite layered structures via various FE models. *Composite Science and Technology* **167**: 174-189, 2018.

[2] Kaleel, I., Petrolo, M., Carrera, E. Computationally efficient concurrent multiscale framework for the nonlinear analysis of composite structures. *AIAA Journal* **57**(9): 174-189, 2019.

[3] Bednarcyk, B.A., and Arnold, S.M. Micromechanics-Based Modeling of Woven Polymer Matrix Composites. *AIAA Journal* **41**(9): 1788-1796, 2003.

[4] Ricks, T.M., Farrokh, B., Bednarcyk, B.A., and Pineda, E.J. A Comparison of Different Modeling Strategies for Predicting Effective Properties of 3D Woven Composites. *SCITECH Forum* https://arc.aiaa.org/doi/abs/10. 2514/6.2019-0692, 2019.

[5] Carrera, E., Cinefra, M., Petrolo, M., Zappino, E. Finite Element Analysis of Structures Through Unified Formulation. Wiley, 2014.

[6] Aboudi, J., Pindera, M.J., Arnold S. M. Linear Thermoelastic Higher-Order Theory for Periodic Multiphase Materials. *Journal of Applied Mechanics*, **57**: 697-707, 2001.

VOID GROWTH IN A LITHIUM SOLID STATE BATTERY

Norman A Fleck*[1] and Alan Cocks [2]
[1]Cambridge University Engineering Dept., Trumpington St., Cambridge, CB2 1PZ, UK
[2]Department of Engineering Science, University of Oxford, Parks Rd., Oxford, OX1 3PJ , UK

Summary. Recent experimental studies in the literature reveal that the electrical performance of Li ion solid state batteries is limited by the development of micron-sized voids at the interface between the Li anode and the solid state electrolyte. The voids grow by the increased rate of Li stripping adjacent to the voids, and the current mitigation strategy is the imposition of a mechanical pressure on the interface. A mechanics analysis is presented of void growth by diffusional flow of Li atoms along the void surface and then along the interface. The main non-dimensional groups are identified that dictate whether void growth or void shrinkage occurs, and the significance of the interface electrical resistance is highlighted. The results are useful for steering the development of Li ion batteries to mitigate against this degradation mode.

INTRODUCTION

There is a major worldwide demand for increasing the performance and reliability of lithium (Li) ion batteries. A promising development is the Solid State Battery (SSB), comprising a Li anode, a ceramic electrolyte and a ceramic cathode. However, cell discharge at high currents leads to the formation of voids at the interface between the Li anode and the underlying ceramic electrolyte, see Fig. 1 and [1]. The voids degrade performance and promote the formation of Li dendrites within the adjacent electrolyte, thereby short-circuiting the cell. It is thought that void growth is by surface diffusion, such that a volumetric flux j of Li atoms migrate along the surface of the void, then along the interface between Li anode and electrolyte, and thence into the electrolyte in the form of Li cations. Void formation and growth can be prevented by imposing a sufficiently high pressure p on the interface. A mechanics analysis is developed for void growth, and the dominant non-dimensional groups are identified that control the process. The significance of the interfacial electrical resistance between Li anode and electrolyte is emphasised.

ANALYSIS

Assume that a representative void exists as a spherical cap of base radius a, and contact angle ω, such that local equilibrium of the interfacial energy γ_I, surface energy γ_S of the void and surface energy of the Li/air interface γ_I demands $\gamma_I = \gamma_C + \gamma_S \cos\omega$. The voids have a spacing of $2L$ and this configuration is idealised by the axisymmetric geometry of Fig 1. Continuity demands that the volumetric flux j along the interface between the Li anode and electrolyte is a function of the radius r from the axis of symmetry; j is related to the stripping velocity $v_E(r)$ of the Li into the electrolyte and to the rate of change of thickness of Li anode H according to

$$\frac{1}{r}\frac{\partial(rj)}{\partial r} + H + v_E = 0 \qquad (1)$$

Now, the velocity $v_E(r)$ into the electrolyte is aligned with the unit normal n_i to the surface of the electrolyte and is directly related to the normal component $n_i J_i$ of the ionic current density J_i of Li+ within the electrolyte, such that $v_E = -J_i n_i \Omega / F$ where Ω is the molar volume of Li and F is Faraday's constant. The current density J_i within the electrolyte is related to the electrical potential gradient $\phi_{,i}$ and to the conductivity κ of the electrolyte according to $J_i = -\kappa\phi_{,i}$. Charge neutrality within the electrolyte demands that $\nabla^2\phi = 0$. The finite interface resistance Z at the boundary between Li anode and electrolyte is sensitive to the processing conditions of the interface and provides the necessary boundary condition at the surfaces of the electrolyte. Following common experimental practice, we assume that the discharge current I_0 from anode to cathode of the unit cell is held constant. Consequently, as the void grows or shrinks, there is a small change in the voltage drop $\phi_2 - \phi_1$ between the electrodes.

Upon solving for $\phi(x_i)$ within the electrolyte from the governing Laplace's equation $\nabla^2\phi = 0$, the stripping velocity $v_E(r)$ is known and hence the flux $j(r)$ in terms of H by integration of (1). Additionally, growth of the void provides an expression for the volumetric diffusive flux $j(r=a)$ at the edge of the void, and we can thereby obtain a in terms of H. It remains to determine H. This is achieved by invoking the Cocks-Suo variational principle [2] as follows.

First, assume that dissipation occurs only at the interface between Li anode and electrolyte as a result of diffusion of Li along the interface, and write a dissipation potential in the form

$$\Psi(H) = \frac{1}{2D_S}\int_a^L 2\pi r j^2 dr \qquad (2)$$

where D_s is an effective interface diffusivity. Second, write the free energy of the unit cell as

$$G(H) = \pi L^2 Hp + S_V\gamma_S + \pi a^2\gamma_C + \pi\left(L^2 - a^2\right)\gamma_I \qquad (3)$$

We proceed to determine $G(H)$ and determine H from the stationary condition

$$\delta\Psi + \delta G = 0$$

This delivers H and in turn the void growth rate a

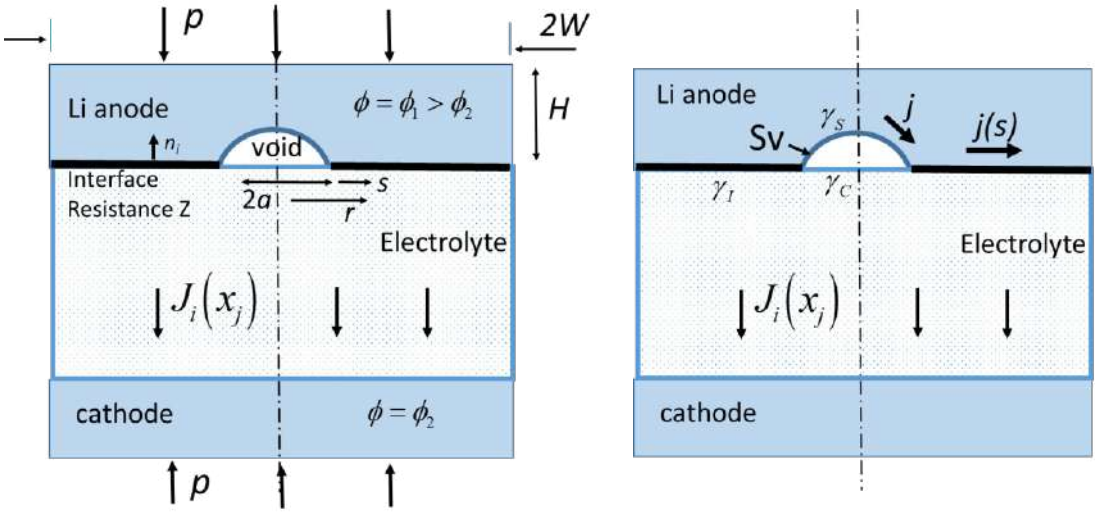

Figure 1. The voided Li anode, geometry and diffusion pathway.

RESULTS

The problem reduces to a determination of the void growth rate a due to the imposed current I_0, with void shrinkage driven by the surface energy γ_S and by the imposed pressure p. It is instructive to write the form of the solution in non-dimensional form

$$\frac{aL^3F}{aI_0\Omega} = f\left(\frac{a}{L}, \frac{Z\kappa}{a}, \frac{pa}{\gamma_S}, \frac{I_0 a}{FD_S\gamma_S}, \omega\right) \qquad (4)$$

Numerical solutions of the form (4) will be presented, and the sensitivity to parameters such as $Z\kappa/a$ will be highlighted. For example, a small value of $Z\kappa/a$ leads to an increased flux adjacent to the edge of the void and hence to enhanced void growth. The study provides insight into the sensitivity of void growth to parameters such as the pressure p on the cell: a threshold value of p is required in order to prevent void growth, which is a function of the imposed current I_0.

CONCLUSIONS

The study highlights the role of Li surface and interface diffusion in void growth within the Li anode of a solid state Li ion battery; this is an important degradation mechanism. A mechanism of void growth has been identified and the accompanying analysis quantifies the effects of imposed current and interface resistance on void growth and explains the physical basis of the mitigation pressure: the pressure required to arrest void growth. Additional deformation mechanisms remain to be analysed: bulk diffusion and power law creep within the Li anode.

References

[1] Kasemchainan J., Zekoll S., Spencer Jolly D., Ning Z., Hartley G.O., Marrow, J. and Bruce, P.G. Critical stripping current leads to dendrite formation on plating in lithium anode solid electrolyte cells. *Nature Materials* **18:** 1105–1111, 2019. https://doi.org/10.1038/s41563-019-0438-9.
[2] Cocks ACF, Gill SPA, Pan J. In: van der Giessen E, Wu TY, editors. Advances in applied mechanics, vol. 36. New York (NY): Academic Press; 1999. p. 82.

COMPLIANT AND LOW-EXPANSION COMPOSITE ELECTRODES FOR A SOLID-STATE BATTERY

Ying Zhao*[1,2] and Norman Fleck[2]
[1]School of Aerospace Engineering and Applied Mechanics, Tongji University, Shanghai, China
[2]Department of Engineering, University of Cambridge, Cambridge, United Kingdom

Summary We propose a hierarchical lattice cathode for a solid-state lithium-ion battery. Due to the stiff and brittle nature of the ceramic electrolyte and ceramic active material of the cathode, the proposed composite cathode structure should ideally accommodate high actuation strains of the active material without macroscopic expansion, during lithiation and delithiation. Also, the composite cathode should have high macroscopic compliance to maintain conformal contact with other parts of the battery without stress-induced fracture. Furthermore, we optimize the structure for both electrical and mechanical performance in order to achieve: (i) high energy density, (ii) high power density, (iii) high ionic conductivity and high electronic conductivity, and (iv) minimise the risk of fracture due to cyclic charge and discharge.

INTRODUCTION

Inorganic solid electrolytes are promising alternatives to liquid electrolytes in next-generation lithium-ion batteries because they don't leak, are not flammable and are mechanically and thermally stable [1]. However, most solid electrolyte materials—stiff oxides and compliant sulfides alike—are brittle.

Recent developments of next-generation cathode materials focus mainly on the improvement of specific/volumetric energy density, but the accompanied changes of lattice parameters during cycling pose an additional challenge to be solved, especially in all-solid-state batteries. As shown in Figure 1(a), lithium nickel cobalt aluminium oxide (NCA) and lithium nickel manganese cobalt oxide (NMC) of various composition can possess a specific energy density as high as $200\,\mathrm{mA\,h\,g^{-1}}$ and their volume change reaches $5\,\%$ [3], which increases with increasing capacity. Cathode materials such as olivines, spinels and tavorites have a lower capacity but also swell significantly upon lithiation.

In order for materials of high capacity but poor mechanical properties to be used as the cathode in an all-solid-state battery, we explored various structured composite cathodes. In particular, we propose the structure shown in Figure 1(b). The solid electrolyte forms the scaffold and ionic pathways of the cathode, while the active material is embedded inside the scaffold.

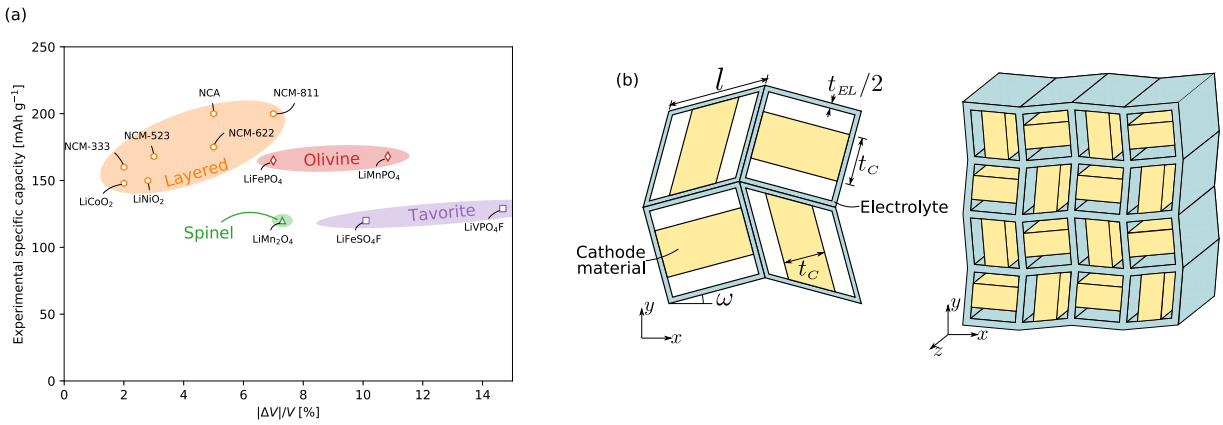

Figure 1: (a) The experimental capacity and volume change of some typical cathode materials (Refs: [6, 4, 3, 2]. NCM-333: $\mathrm{LiNi_{1/3}Co_{1/3}Mn_{1/3}O_2}$, NCM-523: $\mathrm{LiNi_{0.5}Co_{0.2}Mn_{0.3}O_2}$, NCM-622: $\mathrm{LiNi_{0.6}Co_{0.2}Mn_{0.2}O_2}$, NCM-811: $\mathrm{LiNi_{0.8}Co_{0.1}Mn_{0.1}O_2}$, NCA: $\mathrm{LiNi_{0.8}Co_{0.15}Al_{0.05}O_2}$.) (b) Proposed hierarchical composite structure.

METHOD

Electrical performance

We follow the methodology of [5], and consider a 1D model of a battery cell, which is composed of a lithium metal anode, a separator, a composite cathode and a current collector. Under galvanostatic discharge, the internal resistance of the battery cell compared with that with a traditional composite cathode is expressed as

$$R_{\mathrm{int}}^{\mathrm{rel}} = \frac{Z_a + w\chi^{-1} + W\left[2f_C\left(\chi f_{EL} + \chi_c f_C\right)\right]^{-1} + \lambda\left(\chi_c f_C\right)^{-1}}{Z_a + w\chi^{-1} + W\left(2\chi_c\right)^{-1} + \lambda\chi_c^{-1}}. \tag{1}$$

*Corresponding author. E-mail: 19531@tongji.edu.cn

In Equation (1), we denote Z_a as the interface resistance between Li-metal and electrolyte, χ as the conductivity and w as the thickness of the separator, W as the thickness of composite cathode, f_C as the volume fraction of active material and f_{EL} as the volume fraction of solid electrolyte in the structured cathode. λ is a characteristic length scale for the lithium intercalation reaction at the interface between the cathode material and the electrolyte.

Mechanical aspect

An analysis of the structure in Figure 1(b) by Euler beam theory shows that macroscopically the material is orthotropic in the xOy plane. Write E as Youngs modulus, t as the strut thickness and l as the strut length, consistent with Figure 1(b). Also, denote the electrolyte by the subscript EL and the cathode by the subscript C. Then, by making use of Euler beam theory, we may express the in-plane bulk modulus $\bar{K}$ and shear modulus $\bar{G}$ as

$$\frac{\bar{K}}{E_{EL}\bar{t}_{EL}^3} = \frac{4\,(1+2r)}{(8+3r)\sin^2\omega}, \qquad \frac{\bar{G}}{E_{EL}\bar{t}_{EL}^3} = \frac{2(2+7r)}{(8+3r)\cos^2\omega} \qquad \text{where} \qquad \bar{t}_{EL} = \frac{t_{EL}}{l}, \qquad r = \frac{E_C I_C}{E_{EL} I_{EL}}. \tag{2}$$

RESULTS

Based on the above calculations, we can plot a design map for the composite cathode for the choice $\omega = 20°$, see Figure 2. In order to achieve a high storage capacity and low internal resistance, the porosity should be minimized and the cathode volume fraction should be increased, as indicated in Figure 2(a). Mechanical failure can occur by exceeding the bend strength of the struts made from electrolyte. The degree of macroscopic swelling is minimised by the use of a small amount of active material. Two regimes can be identified on the map that deliver useful battery properties, as shown in fig. 2(b). Structures in region I exhibit a minor volumetric expansion upon lithiation of active material, and the structure also a high compliance and fracture-resistant. However, the storage capacity is low and the internal resistance is high. Structures in Region II exhibit high capacity, a low internal resistance but display a significant swell and are vulnerable to fracture. Thus, design is a compromise, and the optimal design is dependent upon the relative weighting of the above performance and failure metrics.

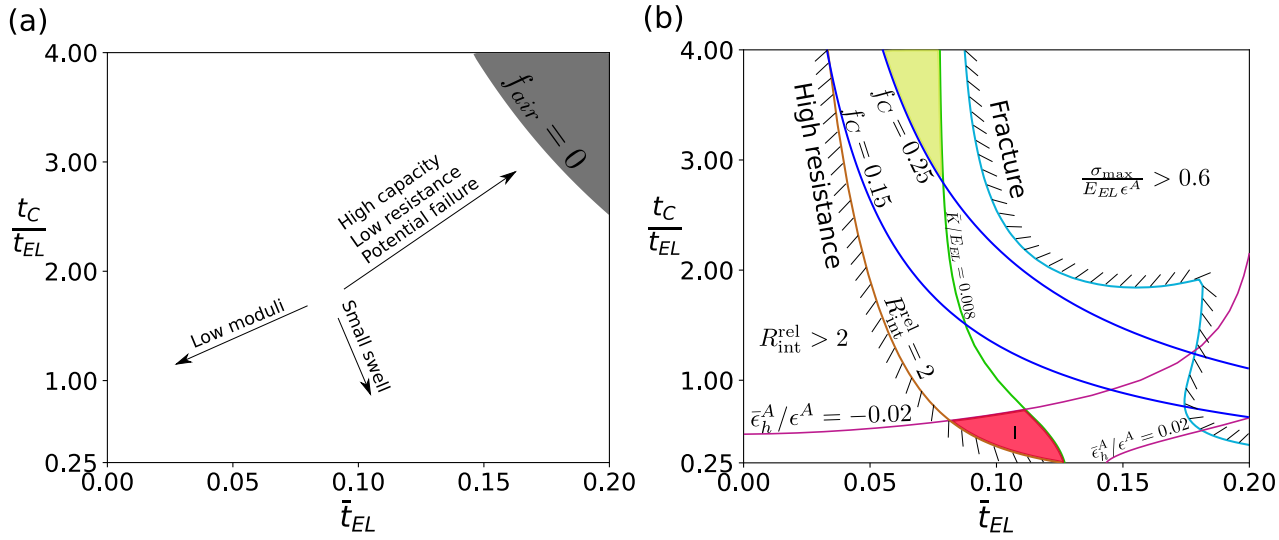

Figure 2: (a) The design map. (b) Predictions of composite cathodes for $\omega = 20°$.

CONCLUSIONS

A design map has been constructed for the composite cathode of a Li ion cell, in order to identify a geometry that delivers a satisfactory electrical and mechanical performance. The composite cathode exploits a lattice topology of high macroscopic compliance and low macroscopic volumetric strain associated with the expansion of the active material during lithiation.

References

[1] Theodosios Famprikis, Pieremanuele Canepa, James A. Dawson, M. Saiful Islam, and Christian Masquelier. *Nature Materials*, 1–14, August 2019.
[2] William H. Woodford, W. Craig Carter, and Yet-Ming Chiang. *Energy & Environmental Science*, 5(7):8014–8024, 2012.
[3] Raimund Koerver, Wenbo Zhang, Lea de Biasi, Simon Schweidler, Aleksandr O. Kondrakov, Stefan Kolling, Torsten Brezesinski, Pascal Hartmann, Wolfgang G. Zeier, and Jürgen Janek. *Energy & Environmental Science*, 11(8):2142–2158, August 2018.
[4] Y. Koyama, T. E. Chin, U. Rhyner, R. K. Holman, S. R. Hall, and Y.-M. Chiang. *Advanced Functional Materials*, 16(4):492–498, 2006.
[5] M. Mykhaylov, M. Ganser, M. Klinsmann, F. E. Hildebrand, I. Guz, and R. M. McMeeking. *Journal of the Mechanics and Physics of Solids*, 123:207–221, February 2019.
[6] Naoki Nitta, Feixiang Wu, Jung Tae Lee, and Gleb Yushin. *Materials Today*, 18(5):252–264, June 2015.

PIEZORESISTIVE RESPONSE OF GRAPHENE RUBBER COMPOSITES CONSIDERING TUNNELING EFFECT

Heng Yang[1], XueFeng Yao*[2], and DaiNing Fang [1]
[1]Institute of Advanced Structure Technology, Beijing Institute of Technology, Beijing, PR China
[2]Department of Engineering Mechanics, Tsinghua University, Beijing, PR China

Summary The piezoresistive behavior of graphene polymer composites is the key performance as the smart sensing materials. In this paper, the numerical method for predicting the piezoresistive properties of graphene rubber composites is established considering the quantum tunneling effect by user subroutines. A representative volume element with randomly distributed graphene has been constructed considering the large deformation characteristics of matrix, which predicted the electrical and mechanical properties and indicated a good agreement with the experimental results. Meanwhile, the strain sensing behavior of graphene rubber composites is calculated, and the influences of the curved graphene configuration, tunneling effect and nanoparticle distributions on the piezoresistive response have been discussed. These results play an important role in evaluating and designing smart rubber composites.

INTRODUCTION

Graphene conductive rubber composites have received more and more attention due to their excellent strain sensing performance and good repeatability. The piezoresistive response (i.e. strain resistance effect) of graphene rubber composites lays a theoretical foundation for the design and application of graphene rubber composites as intelligent sensors, which are mainly concentrated on experimental investigations. Though some literatures indicate that the resistance of graphene polymer composites is approximately linear with the strain(Park et al., 2015; Yan et al., 2018), more results confirm that there are obviously nonlinear relationship (Al-solamy et al., 2012; Lin et al., 2016; Yang et al., 2019), especially in the case of large strain. The nonlinear piezoresistive relationship is mainly attributed to the influence of tunnelling (Boland et al., 2014; Zheng et al., 2017). In addition, both the content and the conductive network structure of nanofillers also affect the strain sensing behavior of conductive rubber nanocomposites(Liu et al., 2016; Yang et al., 2018b), but the mechanism of the piezoresistive response remains to be deeply investigated. On the other hand, the research on the simulation of the piezoresistive response for conductive polymer composites is mainly concentrated in the carbon nanotube composites, and it is generally assumed that the carbon nanotubes are in the one-dimensional contact condition. The contact area between two dimensional graphene sheets in the polymer composites is more complicated, and the tunneling conduction area is often three-dimensional. Meanwhile, in view of the geometrical differences of different conductive particles (zero-dimensional carbon black, one-dimensional carbon nanotubes and two-dimensional graphene), it is necessary to establish a general numerical calculation program based on user-defined material subroutine for the piezoresistive properties of conductive polymer nanocomposites suitable for different dimensional nanofillers.

PIEZORESISTIVE MODEL

Geometric representative volume element (RVE) model

The piezoresistive response of graphene rubber composites is calculated by the RVE model, which consists of a cubic rubber matrix with a side length of L_1 and two-dimensional graphene sheets with random distribution. In the RVE model of graphene rubber composites, graphene is randomly and uniformly distributed. The process for establishing periodic geometric model of the RVE is shown in Fig. 1.

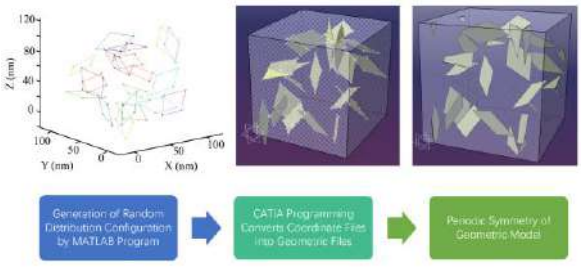

Fig. 1 The generation process of the RVE model for graphene rubber composites.

Electrical model and tunneling effect

Following the identical approach in CNT-polymer composites (Matos et al., 2018), the electrical model considering the tunneling effect is discussed here. The current of graphene and rubber in composites can be obtained according to Ohm's law, and the current density $\boldsymbol{J}$ can be written in term of homogenized values:

$$\bar{J}_i = \bar{\kappa}_{ij}\bar{E}_j = \overline{\kappa_{ij}\left(\frac{\partial V}{\partial x_j}\right)} \tag{1}$$

where κ_{ij} is the electrical conductivity tensor, $s(\boldsymbol{x})$ represents the position vector, E and V_e are the electric field and potential (voltage), respectively.

The tunneling effect should be considered in detail for conductivity calculation of conductive polymer composites. For two adjacent graphene sheets separated by polymer, the tunnel current density can be expressed as the function of the distance between graphene sheets(Simmons, 1963). Based on the distance function s, the current density model of the polymer matrix in the RVE model is calculated as follows.

$$\boldsymbol{J}=\begin{cases}\boldsymbol{k}_R\boldsymbol{E} & s>d_{cut-off}\\ J_T(\boldsymbol{E},s)\dfrac{\boldsymbol{E}}{|\boldsymbol{E}|} & s\le d_{cut-off}\end{cases} \tag{2}$$

Both the electrical constitutive model and the heat transfer constitutive model are similar(Lu et al., 2017). The ABAQUS steady-state thermo-mechanical coupling analysis module is used to analyze the mechanical and electrical properties of graphene rubber composites. The electrical model of rubber is realized by user-defined material thermal behavior subroutine UMATHT, which can calculate distance function and corresponding tunnel current density.

RESULTS AND DISCUSSIONS

Electrical and mechanical properties

The numerical model predicts a percolation thresholdof 1.76% (in Fig. 2 (a)), which is 5.9% smaller than the test result(Yang et al., 2018b), indicating a good agreement and the effectiveness of the proposed prediction method. The homogenized elastic modulus of rubber composites with different content of graphene has been presented in Fig. 2 (b). The predicted values of modulus agree with the experimental results

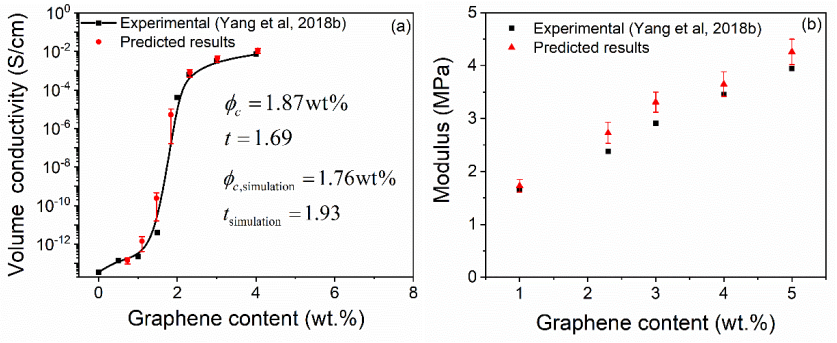

Fig. 2 Predicted conductivity (a) and elastic modulus (b) as a function of graphene content for composites.

Strain sensing behavior

The piezoresistive behaviors of the 2.3 wt.% and 3.0 wt.% graphene rubber composites are predicted. Fig. 3 (a) and (b) show that the predicted resistance response by the RVE model agrees with the test data in the previous paper(Yang et al., 2018b), which can effectively characterize the linear and nonlinear response characteristics in the experimental results.

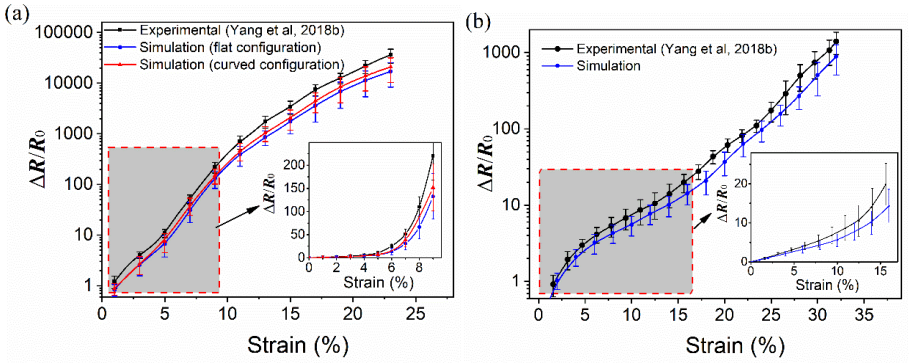

Fig. 3 Comparisons between predicted piezoresistive behavior and experimental results for the 2.3 wt.% (a) and 3.0 wt.% (b) graphene rubber composites.

In order to investigate the effect of non-planar configuration, the RVE model with the curved graphene sheet has also been established. The results indicate that there is a slight increase in conductivity for the graphene rubber composites considering the curved graphene configuration. Further, the strain sensing characteristics of the 2.3 wt.% graphene rubber composite was also predicted with the curved configuration at 15°. The resistance response between the flat and the curved configuration in the linear stage is basically consistent, but the conductivity of the curved configuration changes larger than that of the flat configuration in the nonlinear stage.

References

[1] Matos, M.A., Tagarielli, V.L., Baiz-Villafranca, P.M., Pinho, S.T. Predictions of the electro-mechanical response of conductive CNT-polymer composites. *J. Mech. Phys. Solids* 114:84-96,2018.

[2] Yang, H., Yao, X., Zheng, Z., Gong, L., Yuan, L., Yuan, Y., Liu, Y. Highly sensitive and stretchable graphene-silicone rubber composites for strain sensing. *Compos. Sci. Technol.* 167:371-378,2018b.

[3] Simmons, J.G. Generalized formula for the electric tunnel effect between similar electrodes separated by a thin insulating film. J. Appl. Phys. 34: 1793-1803, 1963.

NONLINEAR DYNAMIC BEHAVIOUR OF A NANOCOMPOSITE: EPOXY REINFORCED WITH FUMED SILICA NANOPARTICLES

Mertol Tüfekci*[1], Tom Mace[1], Burak Özkal[2], John P. Dear[1], Christoph Schwingshackl[1], and Loïc Salles[1]
[1]Department of Mechanical Engineering, Imperial College London, London, United Kingdom
[2]Department of Metallurgical and Materials Engineering, Istanbul Technical University, Istanbul, Turkey

Summary This study focuses on identification and modelling of vibration characteristics of a nanocomposite; an epoxy resin as the matrix and fumed silica as the reinforcement. The resin alone is manufactured and characterised. Using the same methodology, the manufacturing and characterisation of the silica-reinforced nanocomposite are performed. Following the manufacturing and the experimental characterisation process, a nonlinear model is built to represent characterised behaviour. The model is validated by a separate test case which is also an experimental technique to extract the damping characteristics of a structure.

INTRODUCTION

In comparison to the mechanical properties of their individual components, the nanocomposites display dramatically different characteristics [1]. A significant improvement in strength and dynamic behaviour can be achieved by tailoring the right nanocomposite. Tailoring can be done by controlling the manufacturing process as well as the matrix-reinforcement combinations [2]. This study investigates the effects of addition of a small mass fraction of nano-silica particles on the damped vibration characteristics of epoxy. Using the gathered knowledge, a model is built to predict the behaviour of the structures made of that nanocomposite [3].

MATERIAL PREPARATION, CHARACTERISATION AND MODELLING

Material Preparation and Manufacturing

First, epoxy samples without any nanoparticle addition are manufactured. Therefore, laminating resin MGS® L 285 Hardener MGS® 285 from Hexion are used. Both components are mixed slowly and moulded in vacuum. After an hour in vacuum, the samples are taken to ambient pressure and temperature for 24 hours. Then, post-curing is done at 70°C for 15 hours. Next, the silica particulate reinforced epoxy samples are manufactured with a similar process to eliminate the effects of manufacturing steps on the mechanics of the materials. As nanoparticles, fumed nano-silica (HDK® N20 Pyrogenic Silica - Fumed Silica from Wacker Silicones) is used. Also, the same epoxy resin, (Laminating resin MGS® L 285 Hardener MGS® 285 from Hexion) is used. Before starting, 0.49 g silica which was held in the furnace at 60°C for 8 hours to minimise the humidity, is dispersed in 66.79 g of epoxy resin without adding the hardener with at a high speed of 2000 rpm for 3 hours. Following mixing the silica resin mixture is put into a vacuum chamber for degassing 3 hours. Later on, 26.52 g hardener is added and mixed slowly for 10 minutes. Then the blend is cast into the mould for curing at room temperature in vacuum. The same post-curing process is followed [4].

Experimental Characterisation: Dynamic Mechanical Analysis (DMA) and Vibration Test

As one of the most widely used methods, Dynamic Mechanical Analysis (DMA) is employed to characterise the dynamic behaviour of the epoxy and epoxy-silica nanocomposites [1]. For this purpose, DMA Q800 of TA Instruments is utilised to perform the necessary tests. The epoxy samples and the nanocomposite samples with the mass fraction of 0.5% silica inclusion are put through the DMA with the dual cantilever fixture. The samples are rectangular prisms. The sizes of the samples are approximately 60 mm by 14 mm by 3.5 mm. The excitation is chosen as harmonic with frequencies 1, 2, 3, 4, 5, 10, 15, 20 and 25 Hz, while the vibration amplitudes are picked so that the maximum strain values are between 0.0002 and 0.0008 with 0.0001 incrementations. The temperature is kept constant at 20°C for this first step to avoid the effect of any temperature change on mechanical properties.

A vibration test is also conducted to understand the behaviour of a beam made of the nanocomposite material. The specimen used has the dimensions of 280 mm by 24 mm by 4 mm. The experimental setup consists of the specimen with two tip masses attached and suspended from a light steel cable at the tip masses. It is crucial that only the energy dissipation contribution of the material is measured. The masses are held in place via a frictional contact, enforced by a rounded profile to reduce specimen damage whilst minimising extraneous frictional dissipation. The tip masses ensure that the system demonstrates a 'simply-supported' mode shape for the first flexural mode, placing the nodal locations of this mode at the tips of the specimen, and ensuring that the cable moves only in rotation, minimising energy dissipation of interactions between the suspension and specimen. The specimen is excited mono-harmonically to its first flexural resonance (in this case 26.9 Hz) with a shaker which attaches to the specimen using a c-bracket and contacting surface on a single side. This allows the shaker arm to be displaced from the specimen using an input signal offset initiating a free decay, allowing the calculation of the loss factor using a curve fitting method. The vibration of the specimen is measured using a Polytech LDV system.

Both, DMA and the vibration test setups are displayed in Figure 1.

*Corresponding author. E-mail: tufekcime@itu.edu.tr.

Figure 1: DMA and the vibration experiment setups

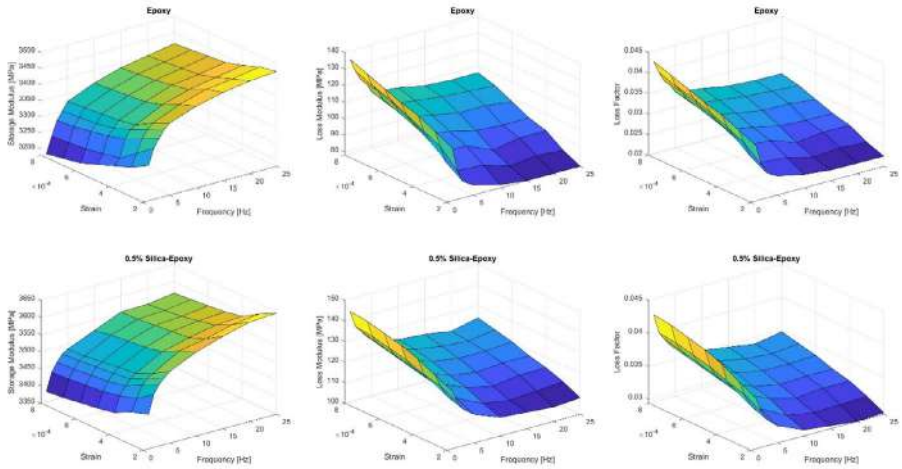

Figure 2: DMA results of epoxy and nanocomposite samples

Modelling of a Single Degree of Freedom (SDOF) System

The system, on which the vibration test is performed, is here considered as a single degree of freedom (SDOF) system. For a simply supported beam the equivalent stiffness is known as $k_{eq} = 48EI/L^3$ whereas the equivalent mass is $m_{eq} = m_{beam}/2$. The Young's modulus E is assumed to be complex. The storage and loss moduli, that are defined as functions of strain and strain rate by curve-fitting the results of DMA, are used as the real and imaginary parts respectively.

RESULTS AND CONCLUSIONS

The results of DMA are plotted in Figure 2 which display a considerable nonlinear behaviour from both materials. The variation of storage modulus of epoxy is found to be around 10% within the investigated range of amplitude and frequency. However, the damping is affected more dramatically. The change is found to be around 65%. For the nanocomposite, the storage modulus shows a similar trend by changing approximately 10%, whereas the damping is affected by around 45%. The addition of 0.5% mass of silica stiffened the material approximately by 5% whereas it increased the damping capabilities by up to 20%. This increase in damping is related to the effect of the interfaces created between the matrix and the nanoparticles. Meanwhile, in loss factor, both materials have almost the same trends as well as values. The vibration test with 0.0003 maximum strain and 26.9 Hz frequency, the loss factor is calculated as 2% whereas the SDOF model predicts the loss factor around 2.25% with an error around 12.5%. It is also important to note that the frequency of the vibration test is out of range of the DMA tests. Therefore, a direct comparison between those two tests are not done, instead, the vibration test results are compared to the results of the model which is built by using the results of the DMA.

ACKNOWLEDGEMENTS

The authors would like to acknowledge the support of Scientific and Technological Research Council of Turkey (TUBITAK) that makes this research possible.

References

[1] Mai Y. W., Yu Z. Z. (Eds.). (2006). Polymer Nanocomposites. CRC Press., Cambridge 2006
[2] Hussain F., Hojjati M., Okamoto M., Gorga R. E. Polymer-matrix Nanocomposites, Processing, Manufacturing, and Application: An Overview. *J. Comp. Mat.* **40(17)**, 1511–1575, 2006
[3] Valavala P. K., Odegard G. M. Modeling Techniques for Determination of Mechanical Properties of Polymer Nanocomposites. *Rev. Adv. Mater. Sci* **9**, 34–44, 2005
[4] Tian J., Tan Y., Wang X., Gao L., Zhang, Z., Tang, B. Investigation on Mechanical Properties and Reinforced Mechanisms of Hyperbranched Polyesters Functionalized Nano-silica Modified Epoxy Composites. *Mat. Res. Exp.* **6(8)**, 1–13, 2019.

THE ELECTROCHEMICAL AND MECHANICAL PROPERTIES OF CARBON NANOTUBE MAT-POLYANILINE COMPOSITES

Wei Tan*[1,2], Changshin Jo[2], Joe C. Stallard[2], Michael F. L. De Volder[2], Norman A. Fleck[2]
[1]Department of Engineering and Materials Science, Queen Mary University London, London, UK
[2]Department of Engineering, University of Cambridge, Cambridge,UK

Summary Composite electrodes of direct-spun carbon nanotube (CNT) mats and polyaniline (PANI) are manufactured and tested to determine their electrochemical and mechanical properties, and to investigate their degradation behaviour upon cycling and overcharging. Electrodes are manufactured by electrodeposition of a PANI layer on the CNT bundles within CNT mat. The PANI content is varied widely by suitable control of the electrodeposition time at a constant current density. The in-plane uniaxial stress-strain response and capacitance of the electrodes are determined as a function of the electrode composition, the PANI state of charge, after 1000 charge/discharge cycles, and after overcharging. The electrodes exhibit an elastic-plastic stress-strain response under uniaxial tension; their modulus and strength depend upon the volume fraction of CNT bundles. Electrode capacitance increases with increasing PANI volume fraction. A micromechanical model is proposed to relate the macroscopic modulus and yield strength of a CNT-PANI composite to the microstructure.

CARBON NANOTUBE MAT-POLYANILINE COMPOSITE ELECTRODES

The high power density, capacitance and cyclic stability of supercapacitors have attracted considerable attention from the research community [1]. A typical configuration of a supercapacitor is sketched in Fig.1a; it comprises two current collectors, each coated with an electrode material. The CNT mat microstructure comprises an interconnected network of carbon nanotube bundles. Upon coating with a suitable electrode material, the resultant porous electrode may be immersed in a liquid electrolyte, forming a psuedocapacitor. The electrode microstructure of PANI-coated CNT bundles is sketched in Fig.1b. The PANI uniformly coats the CNT bundle network, see the scanning electron microscopy (SEM) in Fig.1c. Studies of CNT-PANI composite electrodes have reported specific capacitances as high as 1030 F/g [1], much above the performance of many other capacitor materials. The reported electrode tensile strength of up to 135 MPa and Young's modulus of 5 GPa makes them promising candidate materials for structural energy storage devices. As yet, the influence of charge and discharge rate, electrode composition and state of charge upon the mechanical and electrochemical properties of these novel electrode composites remains unclear, as do the mechanisms of degradation upon cycling. These topics are the focus of this study.

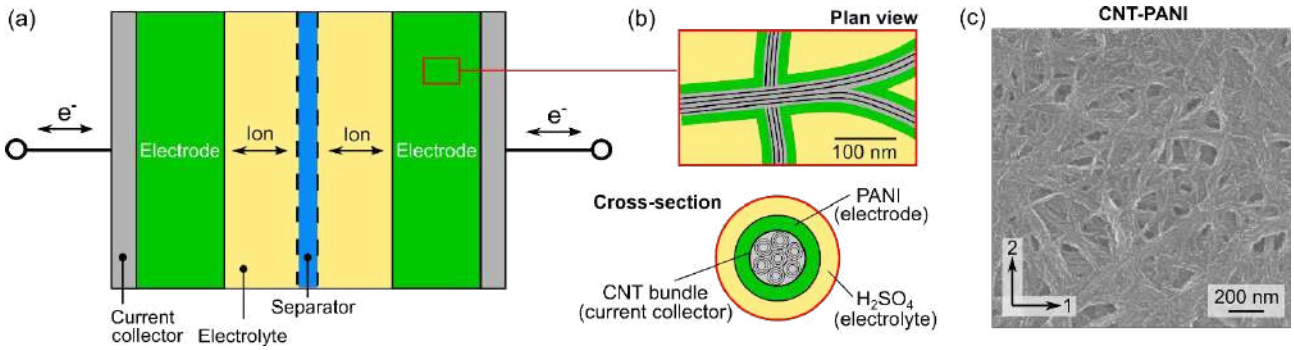

Figure 1. (a) Typical configuration of a supercapacitor. (b) Sketch and (c) SEM image of carbon nanotube-polyaniline (PANI) composite electrode microstructure.

MANUFACTURING AND CHARACTERISATION OF CNT-PANI COMPOSITE ELECTRODES

The CNT mat samples were coated with PANI through electrodeposition at a constant current of 5 mA with a potentiostat. The deposition time ranges from 5 minutes to 60 minutes. Cyclic voltammetry and linear sweep to voltage ranging from -0.2 V to 1 V were used to characterise the electrochemical properties of CNT-PANI electrodes. Tensile tests were performed on the CNT mat and CNT-PANI composites using a screw-driven machine at a strain rate of $\dot{\epsilon} = 10^{-4}\,s^{-1}$.

ELECTROCHEMICAL PROPERTIES OF CNT-PANI COMPOSITE ELECTRODES

A stable charge capacity after the application of multiple charge/discharge cycles are important property for the successful application of capacitor chemistries as energy storage devices. Consider the measured electrochemical properties of the CNT-PANI electrode after the application of 1000 charge/discharge cycles during. For these electrodes, peaks corresponding to Faradic reactions in the cyclic voltammetry response of Fig.2a are less prominent, but still present. The capacitance of a CNT-PANI-T20 electrode and CNT mat electrode absent PANI recorded over the application of 1000 charge/discharge cycles is plotted in Fig.2b, normalised to its value at the start of the test. For the CNT-PANI electrode, the rate of capacitance reduction decreases towards the end of the test, and the final measurement of capacitance

*Corresponding author. E-mail: wei.tan@qmul.ac.uk

is approximately 84% that recorded before cycling. Regardless of composition or charge/discharge history, the capacitance of these plotted CNT-PANI electrodes varies almost linearly with the ratio f_P/f_B, see Fig.2c. The PANI volume fraction is reduced by cycling or overcharging. The capacitance of the CNT-PANI-T20 samples measured after overcharging or cycling lies close to those of samples manufactured with similar ratios of f_P/f_B. Thus, the reduced PANI volume fraction is sufficient to account for the reduction in electrode capacitance upon cycling or overcharging.

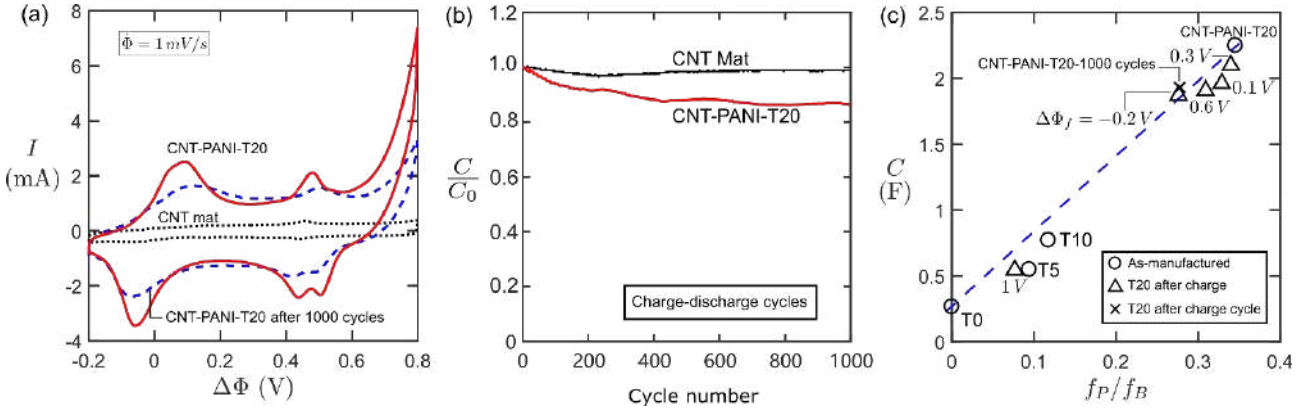

Figure 2. (a) Measured current versus voltage $\Delta\Phi$ relationship (b) The evolution of capacitance of CNT mat and CNT-PANI-T20 electrode over 1000 charge-discharge cycles. (c) Electrical capacitance versus the volume fraction ratio of PANI to CNT.

MECHANICAL PROPERTIES OF CNT-PANI COMPOSITE ELECTRODES

A micromechanical model is developed, based on the characterisation of the underlying CNT mat and CNT-PANI electrode microstructure, to predict the electrode modulus and strength. The CNT-PANI is idealized as a periodic, planar hexagonal honeycomb model, where the struts are formed from interconnected CNT bundles and PANI [2,3], as sketched in Fig.3a. Hill's anisotropic yield criterion is used here to represent the post-yield behaviour of the CNT bundles. The measured modulus and strength both lie close to values predicted by the model, see Fig.3b. The predicted modulus and strength based upon the CNT bundle honeycomb model with PANI volume fraction $f_p = 0$ and $f_p = 0.3$ is also included in Fig.3c. Note the predicted influence of the PANI content is minor compared to that of the bundle volume fraction for electrodes of the compositions studied herein. The measured modulus and strength both lie close to values predicted by the model. Hence, bundle volume fraction appears sufficient in predicting the modulus of the CNT-PANI electrodes.

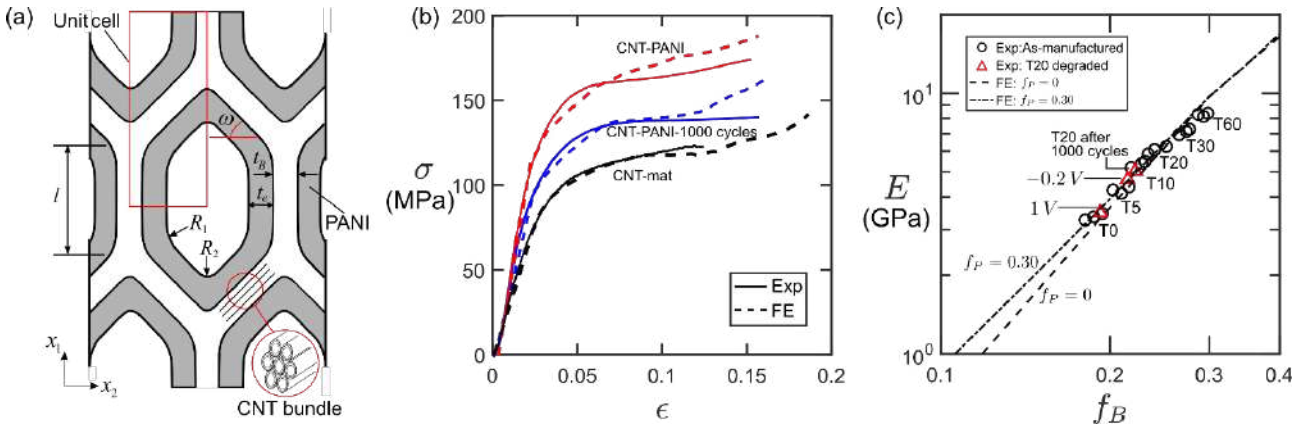

Figure 3. (a) Measured current versus voltage $\Delta\Phi$ relationship (b) The evolution of capacitance of CNT mat and CNT-PANI-T20 electrode over 1000 charge-discharge cycles. (c) Electrical capacitance versus the volume fraction ratio of PANI to CNT.

CONCLUSIONS

The electrochemical and mechanical properties of CNT-PANI were characterised. The reduction in capacitance after repeated cycling or overcharging is attributed to a decreases in PANI volume fraction. The decrease in modulus and strength is attributed to the reduction in CNT volume fraction, which is also captured by the micromechanical model.

References

[1] C. Breitkopf, K. Swider-Lyons, Springer handbook of electrochemical energy, Springer, 2016.
[2] J.C. Stallard, W. Tan, F.R. Smail, T.S. Gspann, A.M. Boies, N.A. Fleck, The mechanical and electrical properties of direct-spun carbon nanotube mats, Extrem. Mech. Lett. 21 (2018) 65–75.
[3] W. Tan, J.C. Stallard, F.R. Smail, A.M. Boies, N.A. Fleck, The mechanical and electrical properties of direct-spun carbon nanotube mat-epoxy composites, Carbon N. Y. 150 (2019) 489–504.

CUF-BASED FINITE ELEMENTS FOR THE FREE-EDGE STRESS CONCENTRATION ANALYSIS OF COMPOSITE COUPONS AND STRUCTURES

Alfonso Pagani*[1], Tommaso Cavallo[1], Enrico Zappino[1], and Erasmo Carrera[1]
[1]Mul2, Department of Mechanical and Aerospace Engineering, Politecnico di Torino, Turin, Italy

Summary Based on the Carrera Unified Formulation (CUF), the present study proposes refined finite elements for the free-edge stress concentration analysis of composite structures. CUF makes use of a hierarchical and scalar procedure to approximate the 3D elasticity problem with 1D or 2D theories. In detail, the displacements are expressed as an arbitrary expansions of the generalized unknowns by using generic expansion functions, which determines the theory approximation. In this manner, the theory accuracy can be refined with ease close to critical regions, e.g. at the free-edge, which remains an unresolved problem and for which analytical solutions are limited to a few cases. We demonstrate the high versatility of this approach, which can be indistinctly used at the coupon scale up to the size of a final composite assembly, such as a composite wing or a tape spring for space applications.

INTRODUCTION

Free-edge effects arise in laminates at the interfaces between dissimilar layers in the vicinity of discontinuities in the structure. This phenomenon has been demonstrated to be a crucial actor in damage initiation in composite structures. Nevertheless, current numerical methodologies for the analysis of composites lack in accuracy and efficiency, and the evaluation of stress fields close to free edges may be prohibitive in industrial practise. As a matter of fact, classical laminate theories cannot provide any useful information of the free-edge effects and active interest is still focused nowadays in the development of accurate tools for their evaluation in real composite applications [1].

This work introduces a numerical approach based on higher-order models for the free edge analysis of composite laminates. The Carrera Unified Formulation (CUF) [2] is employed to generate a theory of structure which makes use of displacements as only variables and Lagrangian polynomials as cross-sectional assumptions, named as Lagrange expansion (LE). This theory of structures was first introduced by Carrera and Petrolo [3] and has proven to be a powerful tool for the accurate stress analysis of composite structures in many works, see [4, 5, 6]. The use of a distribution of mathematical expansion domains to assume the deformation of the cross-section of the laminated beam enables the model to capture 3D-like stress distributions at the ply level. Moreover, it also allows the user to refine the cross-section domain in the zones of interest, such as the free-edges. The accuracy and robustness of the proposed method to represent the free-edge effects in generic composite beams is presented in the present work and particular emphasis is given to the scalable nature of CUF, which allows to study indistinctly composite coupon samples under traction/compression and complex assemblies under general loadings and boundary conditions.

LAYERWISE LAMINATED THEORIES BASED ON CUF

Many displacement-based theories of structure have been introduced in the past decades for the study of the mechanical response of laminated structures. Among the others, the layerwise (LW) models make use of independent assumptions for each layer and provide more information of the meso-scale effects by accounting for the deformation of each ply independently. Furthermore, by taking displacement assumptions at the ply-level, LW models are able to capture the zig-zag effect of the displacements in the thickness direction, which is strongly related to the complex distribution of transverse stresses in composite laminates.

In the framework of CUF for beam theories, the LW displacement field of the composite beam is written as:

$$\mathbf{u}(x,y,z) = F_\tau(x,z)\mathbf{u}_\tau^k(y) \quad \tau = 1,2,...,M \tag{1}$$

where $\mathbf{u}(x,y,z)$ is the three-dimensional displacement field, $\mathbf{u}_\tau(y)$ is the vector of generalized displacements that depends on the longitudinal coordinate y and $F_\tau(x,z)$ are the expansion functions of the cross-sectional domain. The class and number of expansion functions is arbitrary, being M the maximum number of expansions, which is a user defined parameter. Repeating indexes denote summation.

The LE beam theory, introduced by Carrera and Petrolo [3], is based on the use of interpolating Lagrange polynomials as expansion functions F_τ of the cross-sectional coordinates. In this manner, the cross-section of the composite beam can be discretized with an arbitrary number of Lagrangian domains, which are used to represent the surfaces of each layer. Since LE beam models make use of displacement unknowns as degrees of freedom, they represent a useful tool for the efficient stress analysis of beam-like structural components. Moreover, LE are in particular interesting to generate LW models since the displacement compatibility at the interfaces between plies is automatically satisfied with no need of numerical artifacts.

*Corresponding author. E-mail: alfonso.pagani@polito.it.

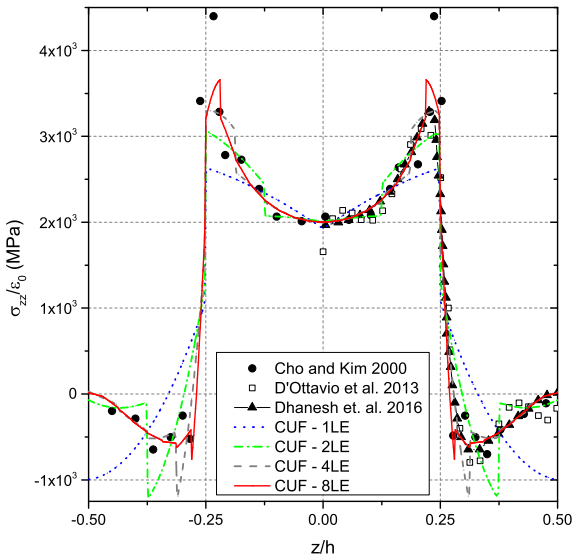

Figure 1: Transverse stresses along z of the $[0,90]_s$ laminate under extension at $x = b/2$.

COMPOSITE COUPON UNDER TRACTION

For representative purpose, we propose here the free-edge analysis of a composite coupon subjected to unitary axial strain, $\varepsilon_0 = 1$. The material and geometry are equivalent to that of the pioneering work of Pipes and Pagano [7], who considered a symmetric cross-ply with four layers of equal thickness, $t = h/4$.

The model generated for the present assessment consists of 6 cubic 1D elements along the beam axis and a distribution of quadratic LE over the cross-section domain which in all cases consists of 10 LE in the x-axis with a graded distribution towards both the free edges. A convergence study regarding the number of mathematical layers in the direction of the stacking sequence is perform, accounting from one LE per layer up to eight LE per layer. The total number of degrees of freedom goes from 10,431 for the coarsest model, to 77,805 for the finest. All the stress solutions reported in the following are obtained at half-length of the beam, $y = L/2$.

Fig. 1 shows the transverse normal stresses, σ_{zz}, across the thickness at the free-edge for an increasing number of mathematical layers per ply, from one (CUF - 1LE) to eight (CUF - 8LE). The convergence study proves that highly refined kinematics are required to compute accurate free-edge stresses by means of LW theories. Since the only unknowns are displacements and no recovery of the 3D stress fields is performed, the trasnverse stress solutions may show some discontinuities between the expansion domains (corresponding to the vertical lines in the graphs), which are more pronounced in the vicinities of the interfaces between layers due to the high stress gradients. By increasing the number of mathematical layers in the beam model, the stress distributions tend to those obtained from the exact theories, approximating well both the stress-free boundary conditions and the interlaminar continuity.

CONCLUSIONS

This paper has introduced the use of CUF to study free-edge stress concentrations of composite structures. Preliminary results demonstrate that LW models may provide accurate and efficient results at coupon scale. Further analyses will show that the method can be successfully employed for the study of complex composite structural assemblies, in a global/local sense. Particular attention will be given to, but not limited to, the analysis of composite wings and composite truss structures for space applications.

References

[1] C. Mittelstedt and W. Becker. Interlaminar stress concentrations in layered structures: Part i - a selective literature survey on the free-edge effect since 1967. *Journal of Composite Materials*, 38(12):1037–1062, 2004.

[2] E. Carrera, M. Cinefra, E. Zappino, and M. Petrolo. *Finite Element Analysis of Structures Through Unified Formulation*. John Wiley and Sons, Ltd, 2014.

[3] E. Carrera and M. Petrolo. Refined beam elements with only displacement variables and plate/shell capabilities. *Meccanica*, 47(3):537–556, 2012.

[4] E. Carrera and M. Petrolo. Refined one-dimensional formulations for laminated structure analysis. *AIAA Journal*, 50(1):176–189, 2012.

[5] A.G. de Miguel, A. Pagani and E. Carrera. Component-wise analysis of laminated anisotropic composites. *International Journal of Solids and Structures*, 49(13):1839 – 1851, 2012.

[6] E. Carrera, M. Filippi, P.K. Mahato, and A. Pagani. Free-edge stress fields in generic laminated structures: solutions and benchmarking via higher-order kinematics *Composites Part B*, 168:375 – 386, 2019.

[7] R.B. Pipes and N.J. Pagano. Interlaminar stresses in composite laminates under uniform axial extension. *Journal of Composite Materials*, 4(4):538–548, 1970.

MORPHING HEXAGONAL LATTICES

Matthew P. O'Donnell*[1], Madeleine Towes [2], Rainer M. J. Groh [1], and Isaac V. Chenchiah[2]
[1]Bristol Composites Institute (ACCIS), University of Bristol, Bristol UK.
[2]School of Mathematics, University of Bristol, Bristol UK.

Summary Non-linear structural responses present the opportunity for a paradigm change in the design of transformative (meta)-materials. Designers are presented with the opportunity to create truly bespoke elastic responses. However, design complexity, such as complex topological forms, is often a consequence, which leads to a reliance on non-intuitive computational simulation. Alternatively, through judicious selection of structural architecture, it is possible to harness structural non-linearity robustly to produce an algorithmic tailoring method that retains insight. Herein we extend this physical insight-driven approach to analysis to explore the behaviour of space-filling lattices constructed of bistable elements. By embedding non-linearity within each element we are able to produce highly adaptive multi-stable lattice frameworks with a simple topology.

INTRODUCTION

The increased use of compliant structures to facilitate adaptivity is indicative of the paradigm shift away from the purely-linear design philosophy. These structures oftentimes exploit large deformations facilitated by snapping between stable configurations to achieve desirable performance. Although structural topology can be tailored to obtain desirable transfomative properties, see, e.g. [1–3], it often relies upon costly computational analysis. Indeed, harnessing structural instabilities alone is not without its own challenges, see e.g. Champneys et al. [4] who outline recent advances in the field. In particular these limitations affect the (meta)-material community that is actively developing novel material systems constructed from multi-scale arrangements of mechanically multi-stable snapping components, e.g. [5]. As the size of the system increases, so the number of possible equilibrium states scales geometrically, making analysis challenging [6].

To avoid the difficulty of complex topology, non-linearity can be subsumed into a well understood 1D non-linear spring whose behaviour may be readily tuned [7]. By employing these structural response mechanisms at sufficiently small length scales, a desirable macroscopic continuum response can be achieved [8, 9]. When used in combination, they permit an algorithmic tuning process that can match, to an arbitrary precision, any energetic function up to a constant [10]. This approach permits an analytical exploration of the behaviour, retaining physical insight. Herein, we propose a new approach for creating novel material behaviour from a hierarchy of non-linear elements; namely, rather than utilising complex topologies to achieve the desired non-linear behaviour, we can subsume this complexity into well understood non-linear "springs" acting as base-units of a hierarchical design.

ANALYSIS APPROACH

Following the approach of Dixon et al. [10] we are able to construct a 1D bistable element that is tuned to possess two energetic minima at lengths l_0 and 1, and one maximum at the midpoint, see figure 1a. We are able to construct the first hierarchical form, the triangular lattice, from three identical elements, see Figure 1b. The lattice's total energy is described by specifying the lengths of each element permitting an analytical exploration of transitions between stable configurations using a parametric sweep of the cubic design space, see Figure 1c. In doing so we are able to identify the stability diagram and the energetic barrier to actuation.

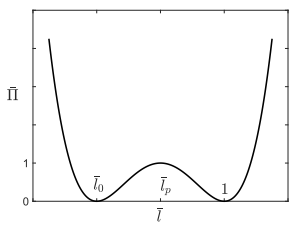

(a) Bistable energy function, Π, as a function of element extension l. Constructed from a fourth-order polynomial specifying the location of two minima and one maximum and the energy associated with each.

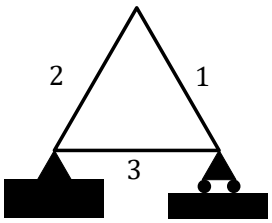

(b) Example of a system composed of three independently-extendable elements to create the first hierarchical form.

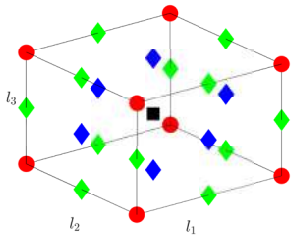

(c) Stability diagram for element lengths restricted to $[l_0, 1]$. The global maximum is denoted by a black square, global minima by red circles, and saddle points by diamonds with green indicating an energy of 1 and blue an energy of 2.

Figure 1: Representative analysis of a simple three element framework

*Corresponding author. E-mail: Matt.ODonnell@Bristol.ac.uk

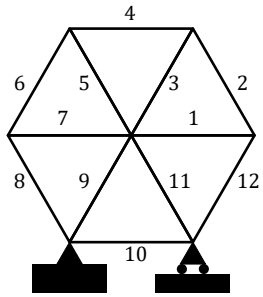

(a) Example of a regular hexagonal lattice composed of 12 bistable elements.

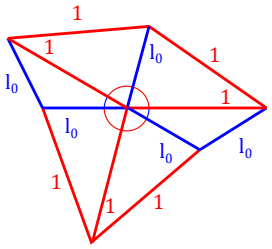

(b) Example of a non-regular hexagonal lattice in a stable configuration. The side lengths of each sub-triangle determines the interior angles which governs the existence of stable configuration for given lengths l_0.

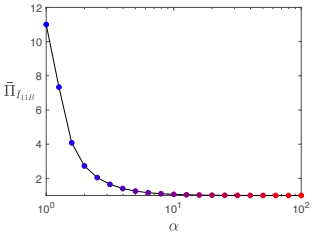

(c) Exploration of the energetic barrier to actuation between stable configurations obtained via a parametric path sweep.

Figure 2: Representative analysis of a hexagonal lattice framework.

The analysis is subsequently extended to the second hierarchy, the hexagonal lattice, see Figure 2a. In doing so we identify the geometric constraints, arising from the inability to independently modify all elements' length. We present constraints on the relative lengths of the stable configuration, i.e. permissible l_0, that determine the existence of non-regular hexagonal configurations that are also global energetic minima, see Figure 2b. A parametric sweep of the hypercube that defines the design space is used to identify the energetic barrier to actuation Figure 2c. Using our approach we are able to characterise the transition behaviour of hexagonal lattices and in doing so identified that sequential activation sequences minimise the energetic barrier.

CONCLUSIONS

We present the analysis of multi-stable space-filling lattices composed of bistable one-dimensional elements as an initial foray into the analysis of generalised space-filling lattices. We utilise an analytical description of the system's energy in order to characterise the behaviour of triangular and hexagonal lattices. In particular we identify the actuation path that minimises the energetic barrier, indicating the structures' preferred response mode, and explore the geometric constraints that govern the existence of global minima of hexagonal systems. Using our semi-analytical approach we retain physical insight into the system's behaviour and avoid the use of computationally-expensive analysis.

References

[1] K.-J. Lu and S. Kota. "Design of Compliant Mechanisms for Morphing Structural Shapes". In: *Journal of Intelligent Material Systems and Structures* 14.6 (2003), pp. 379–391.

[2] C. V. Jutte and S. Kota. "Design of Nonlinear Springs for Prescribed Load-Displacement Functions". In: *Journal of Mechanical Design* 130.8 (2008), p. 081403.

[3] G. Krishnan, C. Kim, and S. Kota. "A Kinetostatic Formulation for Load-Flow Visualization in Compliant Mechanisms". In: *Journal of Mechanisms and Robotics* 5.2 (Apr. 2013). 021007. ISSN: 1942-4302.

[4] A. R. Champneys et al. "Happy Catastrophe: Recent Progress in Analysis and Exploitation of Elastic Instability". In: *Frontiers in Applied Mathematics and Statistics* 5 (2019), p. 34. ISSN: 2297-4687.

[5] A. Rafsanjani et al. "Propagation of Pop-ups in Kirigami Shells". In: *Proceedings of the National Academy of Sciences* 116 (17 2019), pp. 8200–8205.

[6] G. W. Hunt and T. J. Dodwell. "Complexity in phase transforming pin-jointed auxetic lattices". In: *Proceedings of the Royal Society A: Mathematical, Physical and Engineering Sciences* 475.2224 (2019), p. 20180720.

[7] A. Pirrera et al. "Multi-stable cylindrical lattices". In: *Journal of Mechanics Physics of Solids* 61 (Nov. 2013), pp. 2087–2107.

[8] M. O'Donnell, P. Weaver, and A. Pirrera. "Can tailored non-linearity of hierarchical structures inform future material development?" In: *Extreme Mechanics Letters* 7 (2016), pp. 1–9.

[9] M. P. O'Donnell et al. "Multiscale tailoring of helical lattice systems for bespoke thermoelasticity". In: *Journal of the Mechanics and Physics of Solids* 133 (2019), p. 103704. ISSN: 0022-5096.

[10] M. Dixon et al. "Bespoke Extensional Elasticity Through Helical Lattice Systems". In: *Proceedings of the Royal Society A: Mathematical, Physical and Engineering Sciences* (Sept. 2019). ISSN: 0960-764X.

EFFECT OF BOUNDARY CONDITIONS, CONSTRAINTS AND IMPERFECTIONS ON THE SNAP-THROUGH PERFORMANCE OF BISTABLE LAMINATES

Aghna Mukherjee*[1], Shaikh Faruque Ali[1], and A Arockiarajan[1]
[1]Department of Applied Mechanics, Indian Institute of Technology Madras, India

Summary In this work, an analytical model is developed to predict the equilibrium shapes and the snap-through load for a class of hybrid symmetric bistable laminates (HBSL) with cantilever boundary conditions. Additionally, the snap-through behavior of HBSL is analyzed in detail to understand the effects of different loading conditions, clamp conditions, and imperfections using FEA (ABAQUS) and experiments. It has been shown that the snap-through behavior is highly complex and extremely sensitive to the parameters as mentioned above. The observations from the analysis are subsequently used to design an actuation system using a solid-state actuator.

INTRODUCTION

Bistable laminates are a class of composite structures exhibiting two stable equilibrium configurations. Since their discovery, there have been many attempts to understand the mechanics of bistability and snap-through (1). Several analytical models exist in the literature that predicts the equilibrium shapes and the snap-through loads of such laminates. However, all these attempts have been restricted to a free-free boundary condition. In this work, a model is developed that predicts the stable configurations and the snap-through loads for a class of HBSL with cantilever boundary conditions. It is possible to use FEA to study the behavior of these laminates in boundary conditions other than free-free; however, the FE models are computationally expensive and hence not suitable for the design space analysis. The developed model has been used to analyze the design space. Subsequently, a detailed numerical (using ABAQUS) and experimental study have been carried out to understand the effect of clamping, load configurations, and imperfections.

Analytical Model

To model the curing process, the total potential energy of the laminate system is written in terms of the assumed displacement field. The total potential energy function is then minimized with respect to the assumed coefficients to obtain the equilibrium shapes of the laminate. The potential energy function of the laminate is given as:

$$U_{tot} = \int_V \left(\begin{bmatrix} \epsilon^o \\ \kappa^o \end{bmatrix}^T \begin{bmatrix} A & B \\ B & D \end{bmatrix} \begin{bmatrix} \epsilon^o \\ \kappa^o \end{bmatrix} - \begin{bmatrix} \epsilon^o \\ \kappa^o \end{bmatrix}^T \begin{bmatrix} N_T \\ M_T \end{bmatrix} \right) dV - W_{ext} \tag{1}$$

In the formulation, von Karman nonlinear strains have been assumed (2). The novelty of the model is that the continuity requirements of multi-sectioned layup (shown in Fig. 1 (a)) and the boundary conditions are satisfied within the approximated displacement fields using the following constraints:

$$u^o_{in}(x,y^{ab}) = u^o_{out}(x,y^{ab}); \quad u^o_{in}(x,y^{cd}) = u^o_{out}(x,y^{cd}); \quad v^o_{in}(x,y^{ab}) = v^o_{out}(x,y^{ab}); \quad v^o_{in}(x,y^{cd}) = v^o_{out}(x,y^{cd})$$

$$w^o_{inner}(x,y^{ab}) = w^o_{outer}(x,y^{ab}); \quad w^o_{inner}(x,y^{cd}) = w^o_{outer}(x,y^{cd}); \quad \frac{\partial w^o_{in}}{\partial x}(x,y^{ab}) = \frac{\partial w^o_{out}}{\partial x}(x,y^{ab})$$

$$\frac{\partial w^o_{in}}{\partial x}(x,y^{cd}) = \frac{\partial w^o_{out}}{\partial x}(x,y^{cd}); \quad \frac{\partial w^o_{in}}{\partial y}(x,y^{ab}) = \frac{\partial w^o_{out}}{\partial y}(x,y^{ab}); \quad \frac{\partial w^o_{in}}{\partial y}(x,y^{cd}) = \frac{\partial w^o_{out}}{\partial y}(x,y^{cd})$$

Effect of point of application of load and clamping configurations

The equilibrium shapes obtained using the analytical model, FEA, and experiments are shown in Fig. 1(b). To understand the behavior of these laminates subjected to different clamping configurations and loading, two sets of numerical and experimental studies are done: a) The snap-through is obtained by applying the load at different distances from the clamped edge. b) The laminate is clamped at different lengths at the cantilevered edge. It is seen from the numerical simulations and experiments that, on loading the bistable laminate at different distances from the free edge, the laminate snaps to an intermediate state, as shown in Fig. 1(c). However, on the application of a small perturbation at the free end, the laminate snaps to the cylindrical shape initially predicted by the analytical scheme. In the second study, the load-displacement diagrams are plotted for the laminate clamped at different distances at the cantilever edge, while a concentrated load is applied at the center of the free edge. It can be seen from Fig. 1(d) that for an increase in the clamping distance, the area under the load-displacement hysteresis plot decreases, while the snapping load remains almost the same.

Effect of imperfections

To study the effect of imperfections, the relative thickness of the aluminum layers and the central $[0]$ laminae are varied. Using FE simulations in ABAQUS and experiments, it is observed that introducing an imperfection by changing the thickness of the $[0]$ laminae, from 0.3 mm to 0.25 mm while keeping the thickness of aluminum layer 0.3 mm, the load-displacement characteristics changes substantially, as shown in Fig.1(e). Introducing an asymmetry in the structure leads to an asymmetry in the load-displacement plot i.e., the load-displacement plot loses its symmetry about the x-axis.

*Corresponding author. E-mail: aghna11@gmail.com

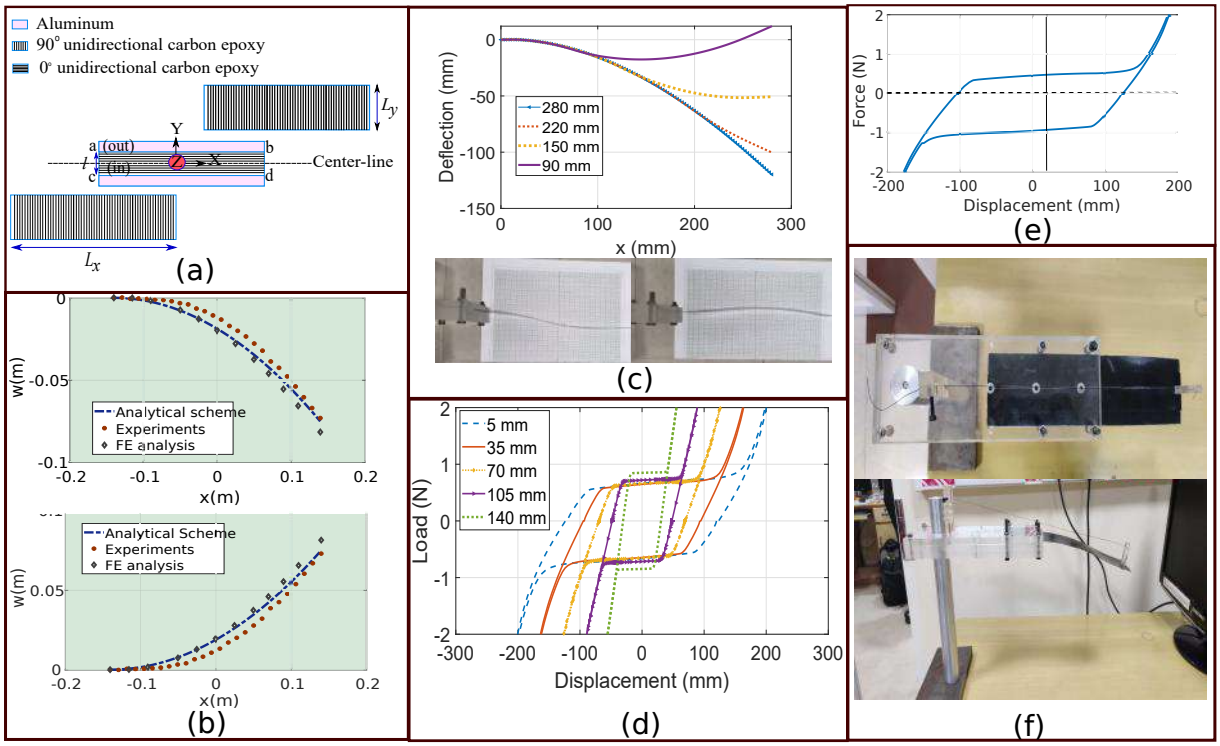

Figure 1: (a) Schematic of the HBSL. (b) Equilibrium shapes obtained using the analytical scheme, FEA and experiments. (c) Intermediate equilibrium states obtained against the position of application of load. (d) Load-displacement plots of the laminate clamped at different distances. (e) Effect of imperfections. (f) Snap through of the HBSL using SMA wire actuator.

Actuation by solid state actuator

The solid-state actuators available currently have certain limitations. For instance, SMA wires can be actuated at a maximum strain of 5-7%. From the analysis, it has been shown that for a complete snap-through, a continuous force over a large displacement is required. To analyze the efficacy of actuation, an SMA wire is attached to the bistable laminate at an eccentricity, as shown in Fig.1(f). The eccentricity has been kept at minimum, and the SMA wire is actuated at its full capacity. From the experiments, it is observed that a complete snap-through occurs only when the distance of clamping is more than 90 mm. The same set of experiments are repeated for a laminate with imperfection. It was observed that by virtue of imperfection, the forward snapping could be achieved with a clamping distance of 35 mm.

CONCLUSIONS

In conclusion, the developed analytical model accurately predicts the behavior of HBSL with cantilever boundary conditions, thus extending state of the art. From the numerical and experimental study, it is concluded that to achieve a complete snap-through, the position of application of load is critical. A force constraint, in addition to a boundary condition, can lead to an intermediate stable state which has higher energy than the configurations predicted by the analytical model. Furthermore, it is observed that clamping at different distances substantially reduces the area under the load-displacement hysteresis curve. This information has been subsequently used to design an actuation system using SMA wire. It is shown that SMA wire strained at 3% achieves complete snap-through when the laminate is clamped at 80 mm distance at the fixed end. Finally, the effect of imperfection has been analyzed, and it is shown that, while a small imperfection with respect to the relative thicknesses of the individual laminae does not have much effect on the equilibrium shapes, it substantially alters the load-displacement behavior.

Acknowledgment: The authors hereby acknowledges the funding obtained from DRDO (DRDO/DFTM/04/3304/PC/02/776/D(R&D)) through CoPT and ARDB (ARDB/01/1051810/M/I) project.

References

[1] Dano, M.L. and Hyer, M.W., 1996. The response of unsymmetric laminates to simple applied forces. *Mechanics of Composite Material And Structures*

[2] Li, H., Dai, F., Weaver, P.M. and Du, S., 2014. Bistable hybrid symmetric laminates. *Composite Structures*, *116*, pp.782-792. , *3(1)*, pp.65-80.

PERIODIC MATERIALS WITH RESONANT CAVITIES FOR ENERGY LOCALIZATION

Marco Moscatelli*[1,2], Claudia Comi[1], and Jean-Jacques Marigo[2]
[2]Laboratoire de Mécanique des Solides, École Polytechnique, Palaiseau, France
[1]Department of Civil and Environmental Engineering, Politecnico di Milano, Milano, Italy

Summary Composite periodic materials, made by a regular repetition of a unit cell with two or more components, can exhibit an "unusual" dynamic behavior. In particular, the propagation of elastic and/or acoustic waves of frequency within specific intervals can be attenuated. This peculiarity makes them feasible for controlling the mechanical energy flow carried by the traveling waves, guiding it into some demarcated regions where it can be localized.

RESONANT CAVITY IN THREE COMPONENT PERIODIC MATERIALS

In this contribution, we consider periodic continua whose unit cell contains an heavy and stiff inclusion with a soft coating, embedded in a stiff matrix, see Figure 1a . This particular internal structure is typical of the so-called "Locally Resonant Materials" (LRMs): the very compliant material used for the coating allows for the presence of local resonances inside each cell generating the so-called band-gaps, i.e. intervals of frequencies in the dispersion plot corresponding to a complex wavenumber and, thus, to attenuated propagating waves, as shown for instance in [1]. Here we analyze the possibility of focusing the mechanical energy of anti-plane elastic waves inside an homogeneous cavity (part Ω_3 in Figure 1a) placed between two barriers (Ω_2 and Ω_4) made of three-components LRMs. The described system resembles a Fabry-Pérot interferometer [2]; the dimensions along axis x_2 and x_3 (out-of-plane axis) are comparable and both very large with respect to the size of the unit cells composing the LRMs. The incoming wave, traveling through the homogeneous part Ω_1 with a fixed angular frequency ω inside a band-gap of the LRM and a wave front perpendicular to the x_1 axis, reaches the first barrier Ω_2 where it experiences both reflection and attenuation; once inside the cavity Ω_3, due to the presence of the two barriers, the wave is rebounded back and forward several times before leaving that region and reaching part Ω_5. The propagating elastic wave can hence be trapped inside the cavity, obtaining an accumulation and a focusing of its mechanical energy in that specific region.

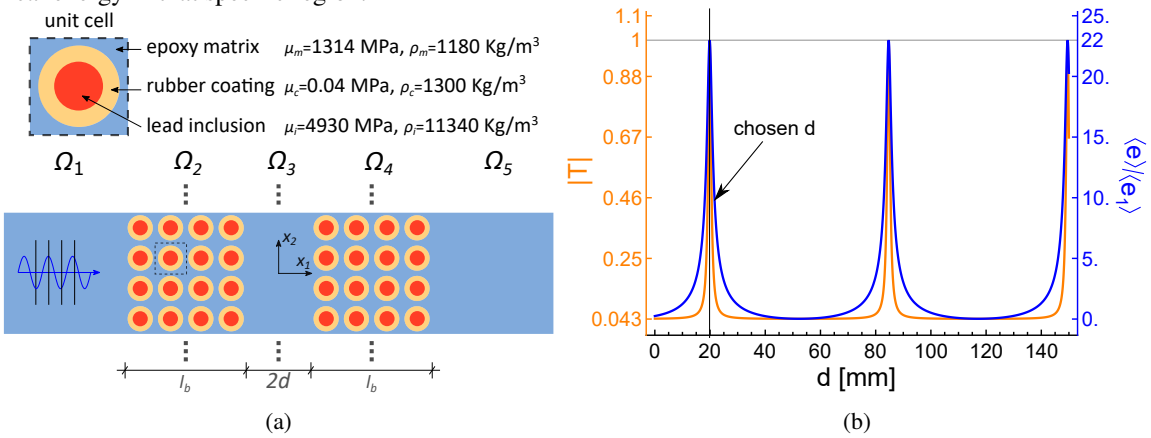

Figure 1: (a) Unit cell of the LRM with material properties and general scheme of the analyzed system: composite with resonant cavity; (b) modulus of wave amplitude $|\mathrm{T}| = 1$ (Orange, left axis) and cavity energy density $\langle e_3 \rangle$ normalized with input energy density $\langle e_1 \rangle$ (Blue, right axis) versus cavity width d.

Homogenized properties and bandgaps of LRM

The problem is characterized by two different length scales: a scale corresponding to the size a of the unit cell of the LRM and a scale L of the wave length of the considered wave propagating in the matrix. When $a/L = \epsilon << 1$, a two-scale asymptotic analysis could be applied for obtaining a macroscopic equivalent description of the behavior of the heterogeneous medium (see e.g. [3]). The unknown displacement field u can be expressed by asymptotic expansion, in powers of ϵ. By approximating the solution at the first order of the expansion, both an effective shear modulus μ_{eff} and an effective mass density ρ_{eff} can be derived. More in details, μ_{eff} is a function only of the elastic properties and the geometry of the LRM unit cells, whereas ρ_{eff} depends also on the frequency and can become negative. This latter peculiarity may occur only if $\mu_c/\mu_m = \mathcal{O}\left(\epsilon^2\right)$, where μ_c and μ_m are the shear moduli respectively of the coating and of the matrix materials. As shown in [4], the effective mass is negative for frequencies corresponding to a band-gap and becomes unbounded at the resonance frequencies of the internal inclusions. Considering the geometry of the unit cell shown in figure 1a, ρ_{eff} can be analytically derived, hence the effective motion of the two barriers becomes completely known in closed form, with the only exception of μ_{eff}, which can be computed numerically and remains constant for all the frequencies.

*Corresponding author. E-mail: marco.moscatelli@polimi.it

Optimization of the cavity

For a specific chosen LRM, the wave motion in the system of Figure 1a depends only on 3 parameters, namely the frequency (ω), the width of the barriers (l_b) and the width of the internal cavity ($2d$). For any fixed value of ω inside the band-gap and any fixed number of unit cells (i.e. for any l_b) the mechanical energy which is trapped inside the cavity is averaged in time over the period and optimized with respect to d. The problem can be entirely solved analytically and a sequence of optimal dimensions of the cavity are obtained. The maximization of $\langle e_3 \rangle$ (average energy density inside part Ω_3) provides the same optimal d of the maximization of the amplitude T of the transmitted wave propagating in part Ω_5. When $|\mathrm{T}| = 1$ (complete transmission), the energy reaches its maximum value, see Figure 1b.

ANALYTICAL AND NUMERICAL RESULTS

We have applied the analytical procedure previously described to an example problem, comparing the results with a finite element analysis. The analyzed composite is constituted by square unit cells,1mm×1mm, as specified in Figure 1a. Notice that the ratio $\mu_c/\mu_m << 1$, respecting the condition which guarantees the presence of band-gaps. The two barriers are made up of forty unit cells in the x_1 direction. The energy $\langle e_3 \rangle$ has been maximized considering a traveling wave with a frequency of $\omega = 4068$ Hz (value taken in the middle of the lowest band-gap). From the set of optimal cavity widths, the first value $d = 19.9$mm has been chosen, see Figure 1b. Note that a change of the frequency or a scaling of the unit cells geometry would imply a new optimal set of d.

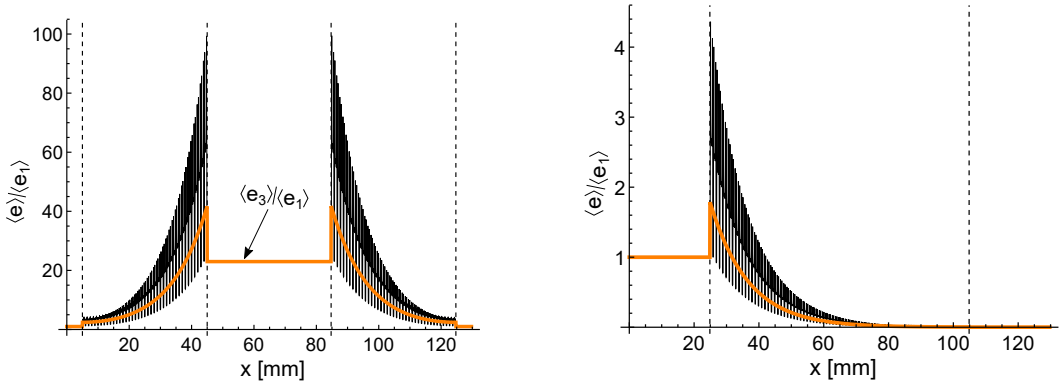

(a) (b)

Figure 2: Normalized mechanical energy density for ω=4087 Hz in the different parts of the analysed systems: (a) system with the optimal cavity (d = 19.9 mm), (b) system without the cavity. Orange curves: analytical results, black curves: numerical results.

In Figure 2a we report the average mechanical energy density generated by the motion caused by the propagating wave, normalized with respect to the energy of the incoming wave $\langle e_1 \rangle$. The analytical results (in orange) are in good agreement with the numerical one (in black), attaining for both cases a value of energy $\langle e_3 \rangle$ inside the cavity twenty-two times bigger than the value of the incoming wave in part Ω_1. In the LRM barriers the analytical solution, based on the homogenized material, does not describe the oscillations due to the inclusions which are evidenced by the numerical analysis. For comparison, Figure 2b shows the results obtained in a system without a resonant cavity (i.e. with d=0). One can see that in this latter case the LRM as expected attenuates the energy of the incoming wave and no energy localization occurs.

CONCLUSIONS

With the aim of focusing the vibration mechanical energy in a confined region, we analysed a system made with a composite material with a resonant cavity. By applying a two-scale asymptotic technique we computed the band-gap of the composite material and we derived the optimized cavity dimension to maximize the energy localization. Since $|\mathrm{T}| = 1$ when the energy inside the cavity is maximum, the system could also be employed for selecting some specific frequencies within a packet of waves which are traveling at a frequency situated inside a band-gap.

References

[1] Moscatelli M., Ardito R., Driemeier L., Comi C. Band-gap structure in two- and three-dimensional cellular locally resonant materials. *J. Sound and Vibration*, **454**: 73-84, 2019.

[2] C. Fabry, A. Pérot, Théorie et applications d'une nouvelle méthode de spectroscopie interférentielle. *Annales de Chimie et de Physique*, **16**(7), 115, 1899.

[3] Auriault J.-L., Boutin C., Geindreau C. Homogenization of Coupled Phenomena in Heterogenous Media. ISTE Ltd and John Wiley & Sons, GB 2009.

[4] Comi C., Marigo J-J. Homogenization approach and Bloch-Floquet theory for band-gap prediction in 2D locally resonant metamaterials. *J. Elast.* 2019 https://doi.org/10.1007/s10659-019-09743-x.

DAMPING OF VIBRATIONS OF SMART-STRUCTURES BASED ON PIEZOELECTRIC ELEMENTS AND GRAPHENE COMPOSITES

Valerii Matveenko*[1], Dmitrii Oshmarin[1], and Nataliia Iurlova [1]
[1]Institute of Continuous Media Mechanics Ural Branch of RAS, Perm, Russia

Summary In this paper a variant of a smart-structure, which is piecewise-homogeneous body composed of elastic and viscoelastic materials and also piezoelectric elements connected to shunting electric circuits with the aid of its electrodes, is considered. The content of the paper is connected with an option of a shunting circuit where a graphene composite is used as a resistor instead of classic one. In this case a graphene composite in smart-structure is not only a deformable solid but also acts as a resistor. The results of numerical experiments show the applicability of graphene-based composites for additional damping of vibrations in smart structures based on piezoelectric elements.

In general case smart-materials fix their parameters and change their properties taking into account information about their condition. Realization of these problems is reached when smart-materials or, to be more precise, smart-structures contain elements which serve a function of sensors, actuators and processors, which set up specified connections between sensors and actuators. Among the manifold of smart-structures there are a lot of possible variants where these elements are combined in different ways and partially perform the functions mentioned above.

In this paper smart-structures based on application of piezoelectric elements are considered. It should be noted that hardware basis for such smart-structures develops rapidly. Nowadays there are known more than fifteen hundred materials having a property of piezoelectric effect. An additional possibility of structural behavior control emerges for piezoelectric-based smart-structures, is in connection of shunting electric circuits, comprised of resistive, inductive and capacitive elements, across the electrodes of piezoelectric elements.

Analysis of the information about graphene composites allows concluding that elements made of these materials may acts as resistive elements simultaneously with realizing their mechanical properties. The main content of the current paper is devoted to proposition of application of graphene composites as resistors in piezoelectric-based smart-structures and mathematical modeling of dissipative properties of such systems.

The variational equation of motion of deformable solid having the elements which exhibit piezoelectric effect is used for mathematical formulation of a problem of vibrations of deformable solids with elements made of piezoelectric materials and resistors [1-4]. A piecewise-homogeneous body occupying the volume $V = V_1 + V_2$ is considered as the object under study. Here the volume V_1 is made of homogeneous elastic or viscoelastic elements and the volume V_2 is the volume of the element with piezoelectric properties.

Within the frameworks of the problem under consideration specific elements of the volume V_1 can be performed of graphene composites which have the property of electric conductivity along with conventional mechanical properties, and consequently they can additionally act as a resistor. In this case if piezoelectric element (V_2) and graphene-based element have electrodes, the latter will perform functions of resistor in addition to deformable properties. And if a conductor is placed across the electrodes of piezoelectric element and graphene composite such a system can be treated as electrodeformable body made of elastic and viscoelastic elements with a resistor.

An assessment of dissipative properties for the systems under study is carried out on the basis of quantities of amplitude values of displacements in resonant modes in case of steady-state vibrations or on the basis of decay rate of a corresponding mode in case of free vibrations. The procedures of finite element method are used for numerical realization of problems on natural vibrations and steady-state vibrations formulated for electro-viscoelastic body with electric circuits comprised of resistor, inductors and capacitors.

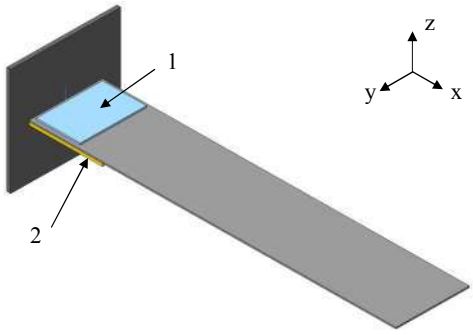

Figure 1. Plate with the piezoelectric element (1) and the element made of graphene composite (2).

The numerical demonstration of the problem under consideration is performed on the example of a plate having the dimensions 500x100x1 mm and presented at fig.1. Piezoelectric element is attached to the one of the surfaces of the

*Corresponding author. E-mail: mvp@icmm.ru.

plated and element made of graphene composite is attached to another side. The material of the plate is aluminum. Piezoelectric element (dimensions are 60x90x1.3 mm) is made of PKR7 piezoelectric ceramics. In the performed numerical calculations there was considered a variant of a graphene composite on the basis of PMMA. In the case when this element was modeled within the frameworks of the elastic model the following material properties was settled: shear modulus G=2.29·10^8 Pa, bulk modulus B=5.96·10^8 Pa, specific density ρ=1190 kg/m^3. For the case when viscoelastic model was used the complex shear modulus $G = G^R + iG^I$ and elastic bulk modulus was established as follows $G^R = 2.29 \cdot 10^8$ Pa, $G^I = 5.73 \cdot 10^7$ Pa, $B = 5.96 \cdot 10^8$ Pa.

For the problem of steady-state vibrations it is accepted that the clamped end of the plate performs the vibrations which can be described using the following relations: $x = 0$, $u_x = u_y = 0$, $u_z = U_0 e^{ipt}$. Figure 2 shows the frequency response plots of the component u_z of the displacement vector for the free end of the plate in the vicinity of the first and the second resonances for the following calculation cases:

1. Only elastic properties of the element made of graphene composite are taken into account (dashed line);
2. Graphene composite material is elastic and performs functions of a resistor (dot-dashed line);
3. Graphene composite material is viscoelastic and performs functions of a resistor (solid line).

The values of complex natural vibration frequencies for all these cases were also obtained and presented in table 1.

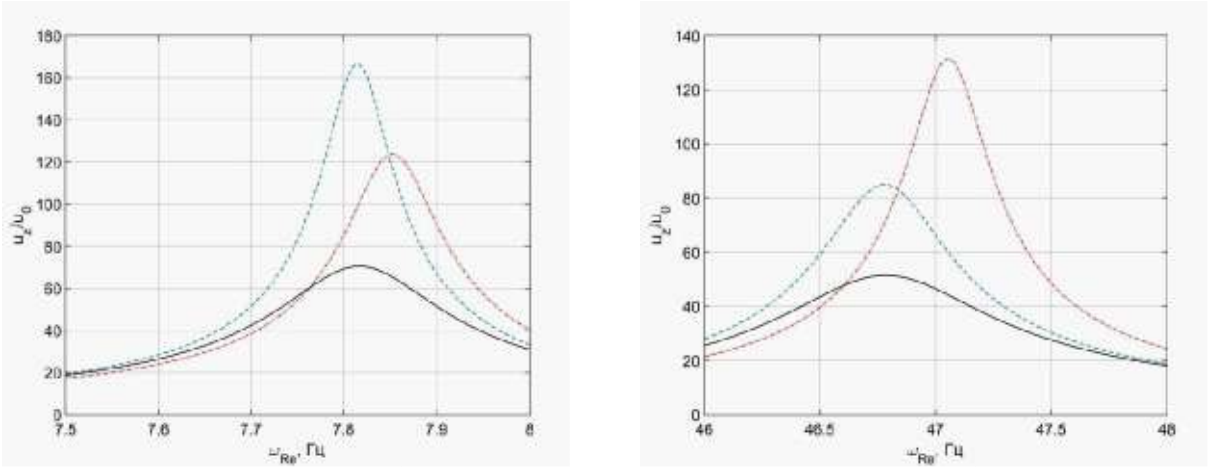

(a) (b)

Figure 2. Frequency response plots for the u_z component in the vicinity of the first resonance (a) and in the vicinity of the second resonance (b).

Table 1. The values of complex natural vibration frequencies for the first and the second vibration mode

Calculation case	$\omega = \omega_R + i\omega_I$	
	The first vibration mode	The second vibration mode
1	7.81597 – i 0.04401	46.33836 – i 0.16603
2	7.78116 – i 0.03360	46.10908 – i 0.22177
3	7.78344 – i 0.07784	46.11665 – i 0.38729

The analysis of the results presented at figure 2 and obtained values of complex natural vibration frequencies presented in table 1 shows that exploitation of property of electric conductivity of graphene composite in smart materials based on the application of piezoelectric elements gives additional possibilities for damping of vibrations.

The work was supported by RFBR (project № 19-51-10003-KO_a).

References

[1] Washizu. K. Variational Methods in Elasticity and Plasticity. Pergamon Press. London. 1982.
[2] V.Z. Parton and B.A. Kudryavtsev, Electromagnetoelasticity of piezoelectric and electro-conductive bodies, Nauka, Moscow, (1988).
[3] V.G. Karnaukhov and I.F. Kirichok, Electrothermal viscoelasticity, Nauk. Dumka, Kiev, (1988).
[4] Matveenko, V.P., Oshmarin, D.A., Sevodina, N.V. and Iurlova, N.A. Natural vibration problem for electroviscoelstic body with external electric circuits and finite-element relations for its numerical implementation. *Comp. Cont. Mech.* **9**(4): 476-485, 2016.

TEMPERATURE DEPENDENT PAYNE EFFECT OF FILLED RUBBER

Wenbo Luo*[1,2], Youjian Huang [2], Xiaoling Hu [2], and Boyuan Yin [3]
[1]Hunan Key Laboratory of Geomechanics and Engineering Safety, Xiangtan University, Xiangtan, China
[2]College of Civil Engineering and Mechanics, Xiangtan University, Xiangtan, China
[3]School of Civil Engineering, Hunan University of Science and Technology, Xiangtan, China

Summary The focus of this paper lies on the modelling of the temperature dependent complex modulus of filled rubber. The strain amplitude sweep DMA tests were conducted at various temperatures ranging from -30℃ to 50℃ on carbon-black filled rubber samples to obtain the variations of the storage and loss moduli with the dynamic strain amplitude, which swept from 0.1% to 5% by steps of 0.1%. A quantitative description of the Payne effect is presented by the Kraus model at a reference temperature of 20℃, and the effect of temperature on the Payne effect is evaluated by a reduced factor, by which the logarithmic storage and logarithmic loss modulus vs. strain amplitude curves at different temperatures can be overlapped by a vertical shift.

INTRODUCTION

The Payne effect is known to be a particular nonlinear characteristic of the mechanical behaviour of carbon black filled rubbers. It is manifested as a strain amplitude dependence of the dynamic viscoelasticity. Above approximately 0.1% strain amplitude, the dynamic storage modulus decreases gradually with the increase of strain amplitude and approaches to an asymptotic value, while the dynamic loss modulus increases first and then decreases, showing a maximum in the region where the storage modulus decreases[1]. The Payne effect and its frequency and temperature dependence are closely related to the damping characteristics of filled rubbers when they are used as vibration absorption and seismic isolation components. Therefore, modelling the temperature and frequency dependence of the Payne effect has attracted much attention in the last decades.

DYNAMIC VISCOELASTICITY MEASUREMENTS

Material

The material for Dynamic Mechanical Analysis (DMA) is carbon black filled natural rubber, and was generously provided by the Zhuzhou Times New Material Technology Co., Ltd. in China. The main formulation of the rubber compound was as follows: 100 phr NR (Thailand RSS3), 56 phr carbon black (N330), 5 phr ZnO, 2 phr antioxidant, 2.2 phr sulfur, 2 phr stearic acid, 0.8 phr vulcanization activator. Rubber sheet samples were prepared by platen vulcanizing press in according to the ASTM D3182.

Strain sweep DMA tests

In order to investigate the dynamic viscoelasticity and the Payne effect of the CB filled rubber, the DMA tests were conducted with a *Gabo Eplexor 500N* working in the tensile mode at a frequency of 5Hz and at various temperatures ranging from -30℃ to 50℃. All specimens were mechanically preconditioned to eliminate the Mullins effect. Afterward isothermal strain sweep measurements for a given prestrain of 0.1 were performed to obtain the variations of the storage and loss moduli with the dynamic strain amplitude, which swept from 0.001 to 0.05 by steps of 0.001. The test results are shown in Fig.1. It is indicated that when the strain amplitude (Δ) increases, the storage modulus (E') decreases with the increasing Δ, while the loss modulus (E'') shows a maximum in the region where the storage modulus decreases rapidly. This is referred as the Payne effect.

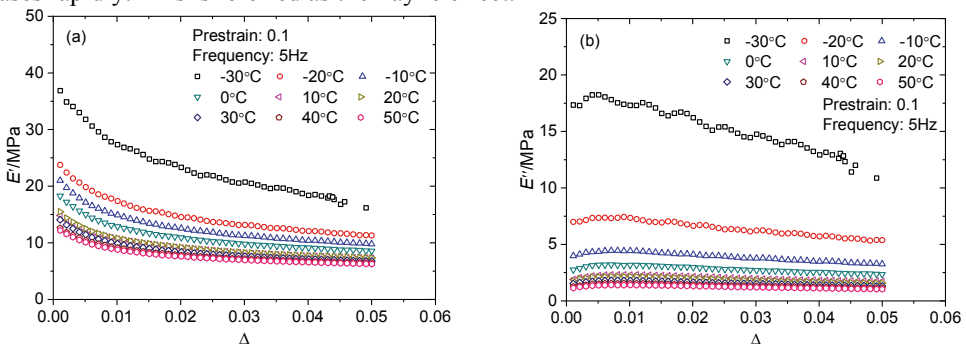

Fig.1 Variation of storage modulus (E') and loss modulus (E'') with strain amplitude at various temperatures

MODELLING OF THE PAYNE EFFECT

The Payne effect can be attributed to the deformation-induced breakage and reforming of the weak physical bonds between the filler aggregates in filled rubber. The Kraus model is the first phenomenological model to represent the Payne effect based on the mechanism of de-agglomeration and re-agglomeration of the filler clusters, it describes rather

*Corresponding author. E-mail: luowenbo@xtu.edu.cn.

well the experimental data using the following equations [2]:

$$E'(\Delta) = E'_{\infty} + \frac{E'_0 - E'_{\infty}}{1+(\Delta/\Delta_c)^{2m}} \tag{1}$$

$$E''(\Delta) = E''_{\infty} + \frac{2(E''_{\mathrm{m}} - E''_{\infty})(\Delta/\Delta_c)^{m}}{1+(\Delta/\Delta_c)^{2m}} \tag{2}$$

Δ_c is the characteristic value of the strain amplitude, at which the loss modulus reaches its maximum value E''_{m}, E'_0 is the storage modulus for small strain amplitudes (usually < 0.0001), E'_{∞} and E''_{∞} are the asymptotic plateau values of the storage and loss moduli at large strain amplitudes respectively, m is a non-negative phenomenological exponent to fit the experimental data. It was reported in the literatures that the exponent m is nearly independent of temperature and carbon black loading [3], but decreases slightly with increasing frequency [4]. In many cases $E''_{\infty} = 0$, thus Eq.(2) reduces to $E''(\Delta) = 2E''_{\mathrm{m}}(\Delta/\Delta_c)^{m}/1+(\Delta/\Delta_c)^{2m}$, the model parameters can be determined by fitting the test data in Fig. 1(b) with Eq.(3). Fig.2 shows the model fit curves in log-log scale. $\Delta_c = 0.006$, m=0.4, only the parameter E''_{m} is temperature dependent. Setting $E''_{\mathrm{m}}(T) = \phi(T)\cdot E''_{\mathrm{m}}(T_0)$, then the temperature dependent loss modulus can be written by

$$E''(\Delta,T) = \phi(T)\cdot E''(\Delta,T_0) \tag{3}$$

It is revealed that the $\log E''(\Delta,T) \sim \Delta$ curves at different temperatures are parallel to each other and can be overlapped by a vertical shift. The resultant shift factors with a reference temperature of 20°C are given in Fig.3, and are fitted by a WLF equation with C_1=-0.55 and C_2=80°C. A similar analysis can also be performed for the storage modulus in Fig.1(a), and the Kraus model fit and the corresponding temperature shift factors for storage modulus are shown in Fig.4 and Fig.5.

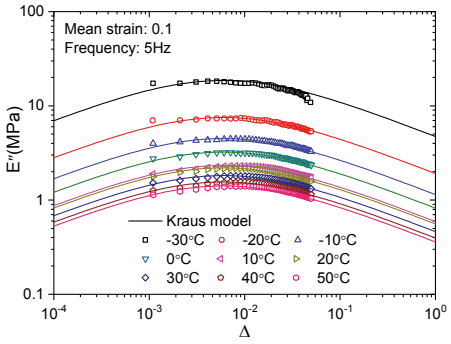

Fig.2 Kraus model fit vs. test data for loss modulus

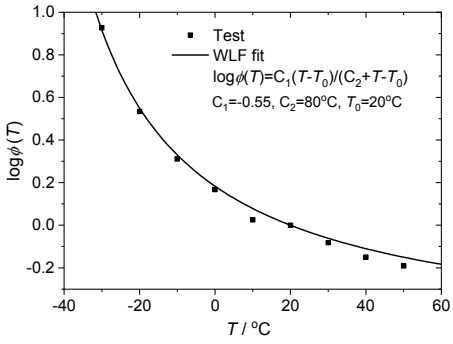

Fig.3 Temperature shift factors of loss modulus for T_0=20°C

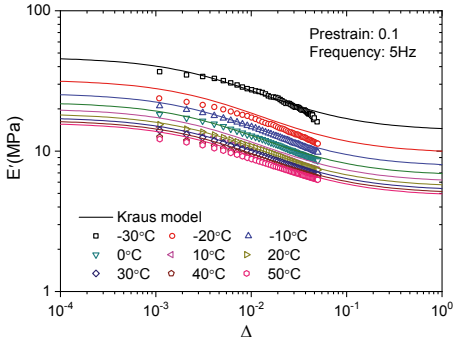

Fig.4 Kraus model fit vs. test data for storage modulus

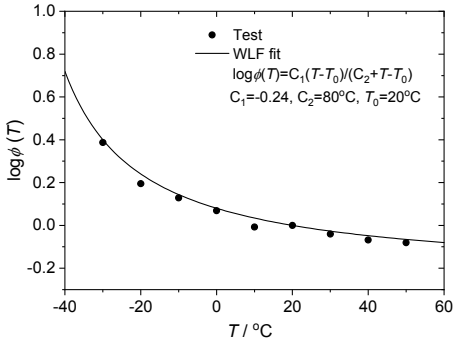

Fig.5 Temperature shift factors of storage modulus for T_0=20°C

CONCLUSIONS

The temperature dependent Payne effect of the carbon-black filled rubber is experimentally investigated and described by the Kraus model with a temperature shift factor. The logarithmic loss modulus vs. strain amplitude curves at various temperatures can be shifted vertically to overlap, and the temperature shift factor satisfies the WLF equation.

Acknowledgement: This work was supported by the National Natural Science Foundation of China (No.11572275)

References

[1] Payne A.R. The dynamic properties of carbon black-loaded natural rubber vulcanizates. Part I. *J. Appl. Polym. Sci.* 6(19): 57-63, 1962.
[2] Kraus G.J. Mechanical losses in carbon-black-filled rubbers. *Appl. Polym. Symp.* 39:75-92, 1984.
[3] Lion A., Kardelky C. The Payne effect in finite viscoelasticity: constitutive modelling based on fractional derivatives and intrinsic time scales. *Int. J. Plasticity*. 20:1313-1345, 2004.
[4] Luo W., Hu X., Wang C., Li Q. Frequency and strain amplitude dependent dynamical mechanical properties and hysteresis loss of CB-filled vulcanized natural rubber. *Int. J. Mech. Sci.* 52(2):168-174, 2010.

THE INTERFACIAL THERMAL RESISTANCE IN COMPOSITES ACCOUNTED BY THE REITERATED HOMOGENIZATION AND FINITE ELEMENT METHODS

Ernesto Iglesias-Rodríguez *[1], Julián Bravo-Castillero[1], Manuel E. Cruz[2], José A. Mesejo-Chiong[3], and Federico J. Sabina[1]
[1]Instituto de Investigaciones en Matemáticas Aplicadas y en Sistemas, Universidad Nacional Autónoma de México, CDMX, Mexico
[2]Departamento de Engenharia Mecânica, Politécnica/COPPE, Universid ade Federal de Rio de Janeiro, Rio do Janeiro-RJ, Brazil
[3]Facultad de Matemática y Computación, Universidad de La Habana, La Habana, Cuba

Summary The reiterated homogenization method is applied to investigate macroscopic behavior of fibrous and particulates conductive composites with a thermal barrier at the interface. Two micro-structural levels (nano- and micro- scales) are considered. The homogenization method provides a methodology for obtaining the effective coefficients through the solution of local problems corresponding to each level. Such problems involve partial differential equations on the periodic cells with imperfect conditions at the interfaces. The combination of finite element and domain decomposition methods is implemented to solve the local problems. The numerical results is calibrated by comparisons with known analytical formulas. This contribution could be useful for nanofibers and nanofluids applications.

INTRODUCTION

The Reiterated Homogenization Method (RHM) is a rigorous mathematical technique for investigating the macroscopic behavior of periodic composites with different microstructural levels. The application of RHM to the partial differential equations modeling such media leads to new PDE for each microscopic scale, called local problems. The macroscopic or effective coefficients in each higher scale can be calculated solving the local problem in the previous one.

Analytical solution of such problems can only be achieved for composites with specific geometries, and it is necessary to apply numerical methods, e.g. Finite Element Method (FEM). For instance, in [1] FEM is combined with RHM to investigate macroscopic behavior of heat transfer problems in 2D composites considering perfect thermal contact though the interfaces. In [2] an Ad-hoc homogenization model was developed to analyze the role of aggregation processes and interfacial thermal resistance on the effective thermal conductivity of nanofluids and nanocomposites. Aggregation relates directly with multiple spatial scales, and a significantly enhancement of the overall thermal conductivity was founded.

There is an increasing interest in the influence of imperfect contact, [3, 4] find variational bounds and analytical solutions for simple geometries respectively, but this feature adds difficulties in the implementation of numerical methods. The Domain Decomposition Method (DDM) developed in [5] showed to be efficient in the case of imperfect contact due to the natural characterization of the domains and its ability to manage several conditions in said interface. The combination of FEM and DDM [6] was used to obtain the effective coefficients in simple homogenization with imperfect contact.

METHODOLOGY AND RESULTS

The RHM is applied to a strong-form Fourier heat conduction problem on a composite formed by a matrix and an inclusion (fiber or particulate). With this asymptotic method we obtain a local problem for each microscopic scale consisting in to find the Ω^α-periodic local function u^α such that:

$$\begin{cases} \nabla \cdot (K^\alpha(\nabla u^\alpha + x)) &= 0, & \text{in} \quad \Omega^\alpha, \\ [\![K^\alpha(\nabla u^\alpha + x)]\!] \cdot n^\alpha &= 0, & \text{on} \quad \Gamma^\alpha, \\ K^\alpha(\nabla u^\alpha + x) \cdot n^\alpha &= \beta\,[\![u^\alpha]\!], & \text{on} \quad \Gamma^\alpha. \end{cases} \tag{1}$$

The supra-index α represent the micro-structural level for which the local problem was stated. Ω^α is the periodic cell, $x \in \Omega^\alpha$ is the local (fast) variable, and Γ^α is the interface, which determines the inner and outer region in Ω^α filled with the inclusion and the matrix, respectively. Here n^α is a normal unit vector to Γ^α and $[\![u^\alpha]\!]$ is the jump of the function u^α across the interface. The effective coefficients in each scale can be calculated by solving the local problem in the previous scale according to

$$K^1 = \left\langle K^2(\nabla u^2 + x) \right\rangle, \qquad \text{and} \qquad \hat{K} = \left\langle K^1(\nabla u^1 + x) \right\rangle, \tag{2}$$

where the angular brackets denotes the average over a periodic cell.

To solve (1) numerically we will apply the Schwarz scheme of DDM in a FEM framework [7], i.e. solving in the inner and outer region alternatively and using it in the boundaries condition. Applying this methodology twice we obtain the macroscopic effective coefficient (2). Finally, we compare the result for spherical cross section fibers and spherical particles with the analytical known results [8]. We compare also with [7] for circular fibers obtaining the same solutions.

*Corresponding author. E-mail: ernesto.iglesias@iimas.unam.mx.

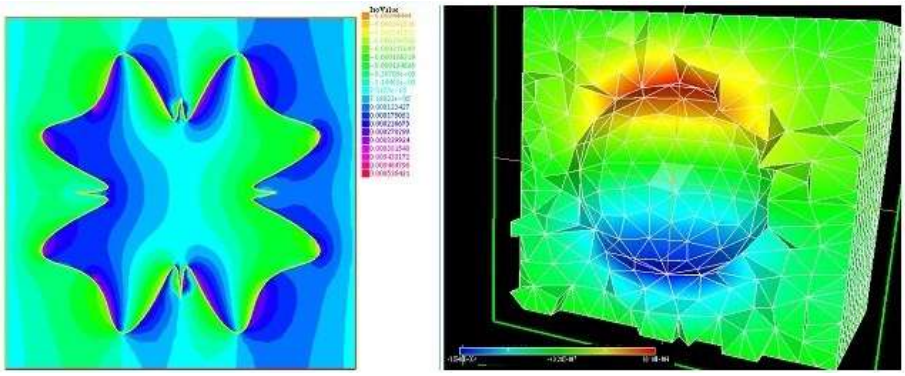

Figure 1: First component of the solution for a local problem in fibrous 2D (left) and particulate 3D (right) medium.

Figure 1 show the solutions of a local problem for a fiber (with an arbitrary cross section) and an spherical particle. All the computations were done with the software FreeFEM++ (under GNU Lesser General Public License: LGPL). In Table we compare our DDM approach with two scales with known results for different Biot numbers ($Biot = 10^k$) and concentrations (ϕ). We consider only the case of fibers with circular cross section, for our calculation we assume an aggregation ratio of 0.25. The fields marked in red is out of the theoretical admissible range [3].

Table 1: Comparison with known results in the case of circular fibers.

Biot	ϕ	**Lower Bound**[3]	**1 scale (DDM)**[7]	**2 scales (analytical)**[8]	**2 scales (DDM)**	**Upper Bound**[3]
10^{-3}	0.3	0.5378	0.5381	0.524177	0.547486	0.7003
1	0.3	0.679	0.7721	0.843996	0.696063	0.9
10^3	0.3	1.2194	1.221	1.24359	1.27085	1.2988
10^{-3}	0.75	0.0702	0.0793	*0.0413238*	0.205932	0.2507
1	0.75	0.4908	0.5003	0.674059	0.533934	0.75
10^3	0.75	1.624	1.6715	*1.86681*	1.71103	1.747

CONCLUSIONS

We combine DDM and FEM to solve numerically the local problems, for fibers and spherical inclusions arising from the RHM. This allow us to address the problem for a composite considering a thermal barrier at the interface and to obtain the effective conductive properties of composites with these feature. The novelty of the present work lies in the shapes considered for calculations, and in the fact that two micro level were taken in account to calculate the effective conductivities in a medium with two scales (it is justified via reiterated homogenization). In this way, the effective properties obtained on one scale are used to find these same properties on the next one. The results obtained are in agreement with analytical ones appearing in the literature.

ACKNOWLEDGMENT

E. Iglesias-Rodríguez would like to thank CONACYT for support his PhD studies at UNAM. Prof. M. E. Cruz is grateful to CNPq-Brazilian Council for Development of Science and Technology for Grant PQ-301715/2017-3. Project PAPIIT DGAPA UNAM IA100919 is also recognized.

References

[1] Mattos, L. P., Cruz, M. E., Bravo-Castillero, J. Finite element computation of the effective thermal conductivity of two-dimensional multi-scale heterogeneous media. *Eng Computations*. **35**: 2107–2123, 2018.

[2] Evans, W., Prasher, R., Fish, J., Meakin, P.,Phelan, P., Keblinski, P. Effect of aggregation and interfacial thermal resistance on thermal conductivity of nanocomposites and colloidal nanofluids. *Int J Heat & Mass Transf*. **51**: 1431–1438, 2008.

[3] López-Ruiz, G., Bravo-Castillero, J., Brenner, R., Cruz, M. E., Guinovart-Díaz, R., Pérez-Fernández, L. D. and Rodríguez-Rámos, R. Variational bounds in composites with nonuniform interfacial thermal resistance. *Applied Mathematical Modelling* **39**: 7266–7276, 2015.

[4] Álvares F. E.,Bravo-Castillero, J., Cruz M. E., Sabina F. J. Reiterated homogenization of a laminate with imperfect contact: gain-enhancement of effective properties. *App Math Mech*. **39**: 1119–1146, 2018.

[5] Lions, P. L. On the Schwarz alternating method. III: a variant for nonoverlapping subdomains, *Proceedings of the Third International Symposium on Domain Decomposition Methods for Partial Differential Equations*.**1989**: 202-223, 1990.

[6] Calabrò, F. Numerical Treatment of Elliptic Problems Nonlinearly Coupled Through the Interface. *J Sci Comput* **57**: 300–312, 2013.

[7] León-Mecías A., Mesejo-Chiong A., Pérez-Fernández L. D., Bravo-Castillero J. Computation of the Effective Conductivity of Fibrous Composites with Imperfect Thermal Contact by Combination of Asymptotic Homogenization, Domain Decomposition and Finite Elements Methods. *Defect and Diffusion Forum*. **372**: 60-69, 2016.

[8] Hasselman, D. P. H. and Johnson, L. F. Effective Thermal Conductivity of Composites with Interfacial Thermal Contact Resistance. *10th Annual Conference on Composites and Advanced Ceramic Materials: Ceramic Engineering and Science Proceedings*. **7**: 1011–1013, 1987.

ANISOTROPIC VISCOELASTIC MODELS FOR CREEP OF CONTINUOUSLY AND DISCONTINUOUSLY FIBER REINFORCED THERMOPLASTICS

Sascha Fliegener [1], and Jörg Hohe [*1]
[1]Fraunhofer Institute for Mechanics of Materials IWM, Freiburg, Germany

Summary The present contribution is concerned with the definition of anisotropic creep material models for different types of fiber reinforced plastics, considering both, continuous and discontinuous (chopped) fibers. For these materials, anisotropic three-term Kelvin-Voigt models are developed. The parameters are determined in tensile creep experiments at different temperatures and load levels. The formulation is validated in a structural experiment concerning a fastener support structure for a sandwich plate consisting of face sheets made from unidirectionally fiber reinforced thermoplastic tape laminates with a foam core. The load point support structure is made from a discontinuously long fiber reinforced thermoplastic, also forming an additional ply to the face sheets. The numerical prediction is found in a rather good agreement with experimental data obtained in breadboard tests.

INTRODUCTION

In lightweight construction, fiber reinforced materials with thermoplastic matrix become increasingly popular, especially in technological fields characterized by industrial scale mass production such as the automotive sector. Both, continuous and discontinuous (chopped) fiber reinforcements are used. Their advantages are their high load carrying capacity and especially the short manufacturing cycle times. On the other hand, neat thermoplastic materials - due to the missing crosslinking of the molecules - are subject to distinct creep deformation under long term loads. For fiber reinforced materials less extreme but still pronounced creep effects are encountered. Due to the anisotropy of the fiber reinforcement, anisotropic creep models are requires for the assessment of structures consisting of such materials.

MATERIAL MODEL AND NUMERICAL IMPLEMENTATION

Starting point of the development of the anisotropic creep models presented in the present contribution is the isotropic three-parameter Kelvin-Voigt formulation. Thus, the stress increments are defined by

$$\mathrm{d}\sigma_{ij} = 2\bar{G}(t)\left(\mathrm{d}\varepsilon'_{ij} - \sum_{q=1}^{3}\left(1-e^{-\frac{dt}{\tau^{(q)}}}\right)\varepsilon_{ij}^{is(q)}(t-dt)\right) + 3\bar{\kappa}(t)\left(\mathrm{d}\varepsilon^{v} - \sum_{q=1}^{3}\left(1-e^{-\frac{dt}{\tau^{(q)}}}\right)\varepsilon_{ij}^{iv(q)}(t-dt)\right)\delta_{ij}$$

with the time-dependent shear and bulk stiffness functions:

$$\bar{G}(t) = \left(\frac{1}{G^{(0)}} + \sum_{q=1}^{3}\frac{1}{G^{(q)}}\left(1-\frac{\tau^{(q)}}{dt}\left(1-e^{-\frac{dt}{\tau^{(q)}}}\right)\right)\right)^{-1}, \qquad G^{(q)} = \frac{E^{(q)}}{2(1+\upsilon)}, \qquad q = 0,1,2,3$$

$$\bar{\kappa}(t) = \left(\frac{1}{\kappa^{(0)}} + \sum_{q=1}^{3}\frac{1}{\kappa^{(q)}}\left(1-\frac{\tau^{(q)}}{dt}\left(1-e^{-\frac{dt}{\tau^{(q)}}}\right)\right)\right)^{-1}, \qquad \kappa^{(q)} = \frac{E^{(q)}}{3(1-2\upsilon)}, \qquad q = 0,1,2,3$$

The model is generalized to nonlinear viscoelasticity in the Schapery [3] sense by substituting the elastic moduli $E^{(q)}$ with stress dependent functions. In order to account for the anisotropy of fiber reinforced materials, two routes are employed. For moderately anisotropic materials as discontinuously long fiber reinforced thermoplastics (LFT) with a single, flow dependent preference orientation, anisotropic weight parameters for the individual stress components are introduced. For highly anisotropic unidirectionally (UD) fiber reinforced materials, the isotropic viscoelastic model is superimposed with the anisotropic Hooke's law. In this context, the isotropic viscoelastic part represents the response of the polymeric matrix whereas the anisotropic linear elastic part represents the response of the fibers. The anisotropic viscoelastic models are implemented as material subroutines into a finite element program.

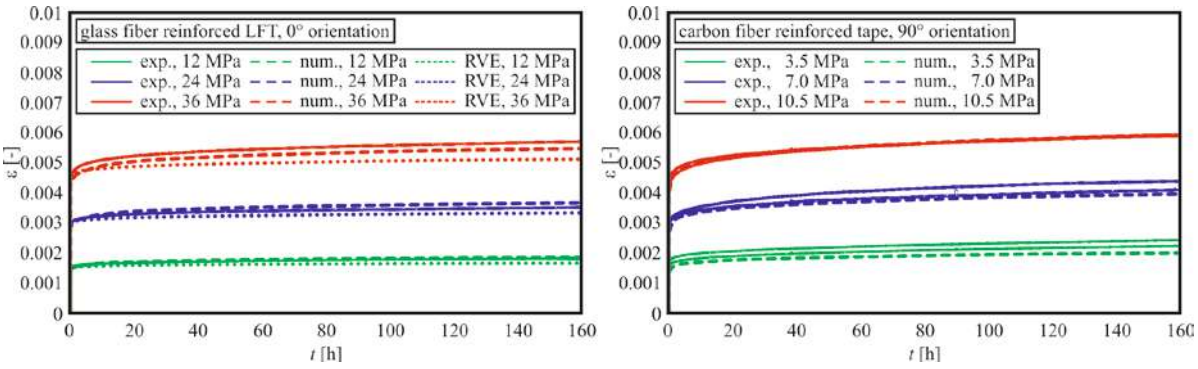

Figure 1: Coupon experiments for parameter identification and validation.

*Corresponding author. E-mail: joerg.hohe@iwm.fraunhofer.de.

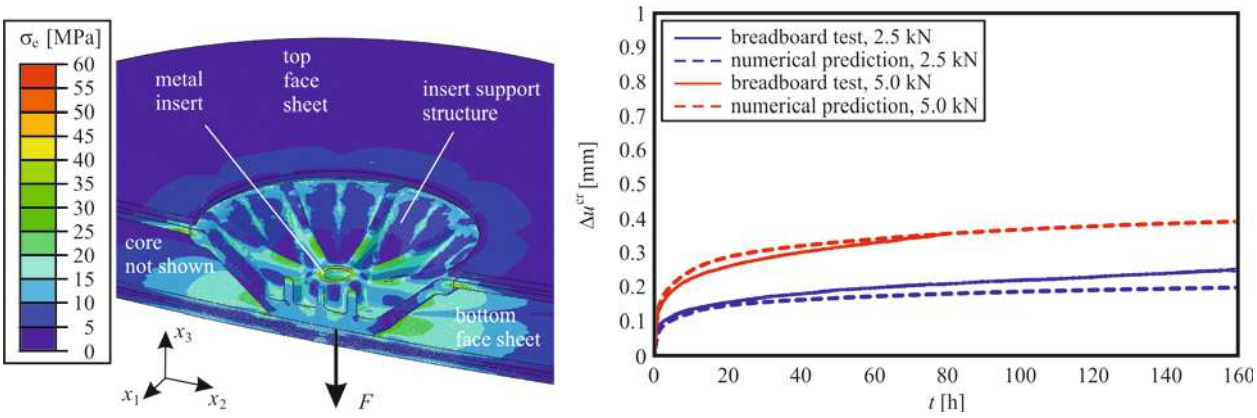

Figure 2: Breadboard test and simulation.

PARAMETER IDENTIFICATION

For determination of the material parameters and for a first validation of the proposed anisotropic creep models, an experimental study on coupon level is performed, considering continuously (UD) and discontinuously fiber reinforced thermoplastics (LFT) as well as neat matrix material. In all cases, PA6 is employed as matrix material Standard specimens are machined from plane plates. Creep experiments are performed at different constant load levels applied for 160 h. For the LFT materials, both carbon and glass fiber reinforced materials are tested within (0°) and perpendicular (90°) to the flow direction. The unidirectionally carbon fiber reinforced material is tested within and perpendicular as well as under 45° to the fiber direction.

As an example for the variety of experiments and simulation, the creep curves for glass fiber reinforced LFT and carbon fiber reinforced UD material, both tested at ambient temperature, are presented in Figure 1. For the LFT material, creep curves obtained in a microstructural analysis considering a representative volume element (RVE) for the LFT microstructure using the creep model and parameters for the neat matrix material are presented in addition to the experimental curves and the numerical prediction based on the model proposed in the previous section. In all cases, the experimental results and the numerical prediction as well as the prediction based on the microstructural (RVE) analysis are found in a good agreement. Similar results are obtained for the other test directions and temperatures.

BREADBOARD EXPERIMENTS AND VALIDATION

For a further validation, the creep modes together with the parameters determined in the previous section are applied to the numerical simulation of breadboard experiments on the long-term response of sandwich fastener support structures designed and tested in a previous contribution [2]. The breadboards consist of two circular laminated face sheets of unidirectionally carbon fiber reinforced plies with an additional co-moulded LFT ply, separated by a 20 mm thick PU foam core. In the centre of the sandwich plate, a fastener with a ribbed LFT support structure according to Figure 2 is positioned. The breadboards are loaded by a constant normal force of 2.5 kN and 5.0 kN applied to the metal insert for 160 h to 80 h. The creep experimental creep curves are presented in Figure 2 together with the numerical predictions. For both load levels, a rather good agreement is obtained.

CONCLUSIONS

Within the present study, an anisotropic creep model for different kinds of fiber reinforced polymers has been formulated and implemented. In a validation against an experimental data base of coupon experiments as well as more complex breadboard structures involving different types of FRP materials, the model provides accurate predictions.

ACKNOWLEDGEMENT

The work on the present contribution has been funded by the German Federal Department of Education and Research (BMBF) under grant no. 03X3041P as part of the “SMiLE” project. The authors are fully responsible for the contents of this contribution. The financial support is gratefully acknowledged.

References

[1] Fliegener, S., Hohe, J., Gumbsch, P. The creep behavior of long fiber reinforced thermoplastics examined by microstructural simulation, *Compos. Sci. Tech.* **131**: 1-11, 2016.

[2] Fliegener S., Rausch, J., Hohe, J. Loading points for industrial scale sandwich structures – a numerical and experimental design study. *Compos. Struct.* **236**: 111278, 2019.

[3] Schapery, R.A. On the characterization of nonlinear viscoelastic materials, *Pol. Eng. Sci.* **9**: 295-310, 1969.

GAUSSIAN PROCESS HOMOGENISATION AND DESIGN OF TECHNICAL TEXTILES

Sumudu Herath Mudiyanselage[1] and Fehmi Cirak *[1]
[1]Department of Engineering, University of Cambridge, Trumpington Street, Cambridge CB2 1PZ, U.K.

Summary A method for computational homogenisation of thin membranes is proposed to assist in the mechanical analysis of technical textiles. Conventional computational homogenisation schemes have a limited scope in analysing the complex nonlinear behaviour of textiles where the interlooped or interlaced fibres undergo large deformations. Also, the higher computational cost of the existing homogenisation schemes inspires the inception of a data-driven multiscale computational homogenisation scheme. In this paper, the efficient integration of statistical learning in computational homogenisation is proved not only to result in the efficient mechanical analysis but also to open avenues in material design of knitted and woven technical textiles.

MICROSCALE ANALYSIS

Finite deformation rod analysis

An isogeometric finite deformation rod model is developed to simulate the large deformations of interlooped and interlaced yarns of knitted and woven textiles, respectively. Base vectors of the rod centrelines ($\boldsymbol{X}$ and $\boldsymbol{x}$) are given by[1],

$$\boldsymbol{A}_1 = \frac{\mathrm{d}\boldsymbol{X}}{\mathrm{d}\theta^1}\,, \quad \boldsymbol{a}_1 = \frac{\mathrm{d}\boldsymbol{x}}{\mathrm{d}\theta^1} \qquad \text{and} \qquad \boldsymbol{a}_\omega = \boldsymbol{\Lambda}\boldsymbol{A}_\omega\,. \tag{1}$$

where θ^1 is a convected parameter and $\omega = 2, 3$. Base vectors $\boldsymbol{A}_\omega$ and $\boldsymbol{a}_\omega$ are chosen as unit vectors and are aligned with the principal directions of the rod cross-section. The rotation map $\boldsymbol{\Lambda}$ in Equation (1) is composed by two distinct rotations, $\boldsymbol{\Lambda}_1$ and $\boldsymbol{\Lambda}_2$, given by,

$$\boldsymbol{a}_\omega = \boldsymbol{\Lambda}_2(\boldsymbol{a}_1)\boldsymbol{\Lambda}_1(\vartheta)\boldsymbol{A}_\omega\,. \tag{2}$$

We use Rodrigues' rotation formula [2] for the rotation $\boldsymbol{\Lambda}_1$ where rotation axis is given by the undeformed normalised tangent vector $\boldsymbol{A}_1/||\boldsymbol{A}_1||$ and torsional rotation ϑ. Also, we use the smallest rotation formula [3] for the rotation $\boldsymbol{\Lambda}_2$.

$$\boldsymbol{\Lambda}_1(\vartheta) = \mathbf{I} + \sin\vartheta\mathbf{K} + (1-\cos\vartheta)\mathbf{K}\mathbf{K}\,, \quad \boldsymbol{\Lambda}_2(\boldsymbol{a}_1) = \mathbf{I} - \frac{(\boldsymbol{A}_{1u}+\boldsymbol{a}_{1u})\otimes\boldsymbol{a}_{1u}}{1+\boldsymbol{a}_{1u}\cdot\boldsymbol{A}_{1u}} \qquad \text{where} \qquad \boldsymbol{a}_{1u} = \frac{\boldsymbol{a}_1}{||\boldsymbol{a}_1||}. \tag{3}$$

Rod internal forces are formulated based on a St. Venant-Kirchhoff hyperelastic rod model and discretised using cubic B-spline basis functions. Also, the linearised algebraic system is solved iteratively using a Newton-Raphson scheme [2, 3].

Homogenised response validation

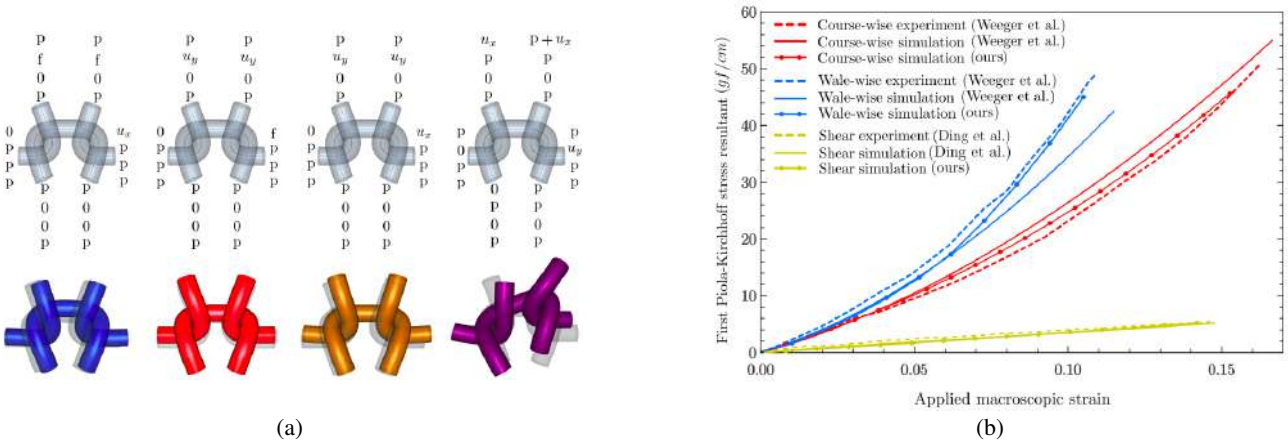

(a) (b)

Figure 1: Boundary value problem definitions for (a) weft-knitted textiles using periodic boundary conditions. At every boundary node, four characters denote the constraint enforcement to each degree of freedom at the respective boundary node. u_i refers to the applied displacements in the i direction. Moreover, $p, f, 0$ refer to *p*eriodic, *f*ree and *zero*-displacement constraints respectively. (b) Microscale homogenised response validation.

We formulate boundary value problems on characteristic weft-knitted and plain-woven textile RVEs. Homogenised responses of RVEs are validated against similar results from the literature to verify our microscale simulations [4, 5]. Figure 1 illustrates the boundary value definitions and result validation for weft-knitted textile RVEs. Though not presented, plain-woven textile RVEs are analysed and validated following a similar manner.

*Corresponding author. E-mail: fc286@cam.ac.uk
[1]Quantities in the reference and deformed configurations are denoted using uppercase and lowercase letters, respectively.

DATA-DRIVEN COMPUTATIONAL HOMOGENISATION

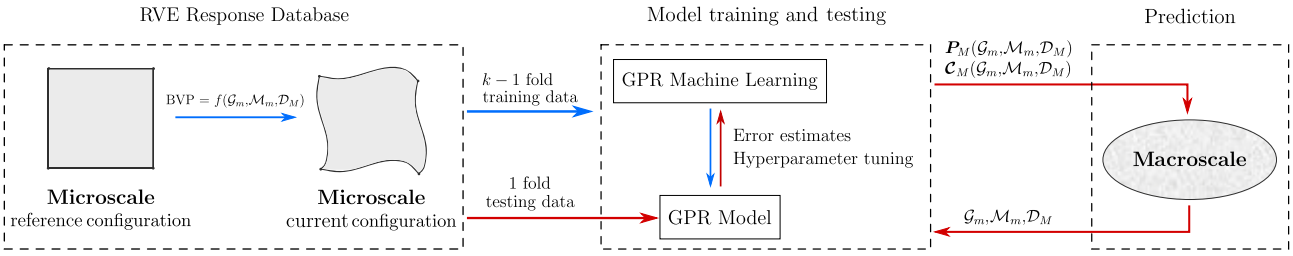

Figure 2: Data-driven computational homogenisation and textile material designing framework using GPR.

Homogenised responses of RVEs are stored in a response database with inputs: Green-Lagrange strains ($\mathcal{D}_M$), material ($\mathcal{M}_m$) and geometric ($\mathcal{G}_m$) parameters. Also, strain energy densities (ψ) are taken as outputs and stored in the same response database. Hence, the i^{th} data point in the response database is succinctly written as $(\mathbf{Z}_i, y_i)$. We also distinguish the test data points using subscript $(\bullet)_*$. The proposed data-driven homogenisation framework is presented in Figure 2.

Gaussian process regression (GPR)

The joint distribution of training and test outputs are written as a zero mean multivariate Gaussian distribution [1],

$$\begin{bmatrix} \boldsymbol{y} \\ \boldsymbol{y}_* \end{bmatrix} \sim \mathcal{N}\left(\mathbf{0}, \begin{bmatrix} \mathbf{K}(\mathbf{Z},\mathbf{Z}) & \mathbf{K}(\mathbf{Z},\mathbf{Z}_*) \\ \mathbf{K}(\mathbf{Z}_*,\mathbf{Z}) & \mathbf{K}(\mathbf{Z}_*,\mathbf{Z}_*) \end{bmatrix}\right) . \tag{4}$$

Predictions based on the conditioning of the joint Gaussian distribution on the observations and test inputs takes the form,

$$\boldsymbol{y}_*|\mathbf{Z}_*,\mathbf{Z},\boldsymbol{y} \sim \mathcal{N}(\mathbf{K}(\mathbf{Z}_*,\mathbf{Z})\mathbf{K}(\mathbf{Z},\mathbf{Z})^{-1}\boldsymbol{y}, \mathbf{K}(\mathbf{Z}_*,\mathbf{Z}_*) - \mathbf{K}(\mathbf{Z}_*,\mathbf{Z})\mathbf{K}(\mathbf{Z},\mathbf{Z})^{-1}\mathbf{K}(\mathbf{Z},\mathbf{Z}_*)) . \tag{5}$$

Gaussian process homogenisation

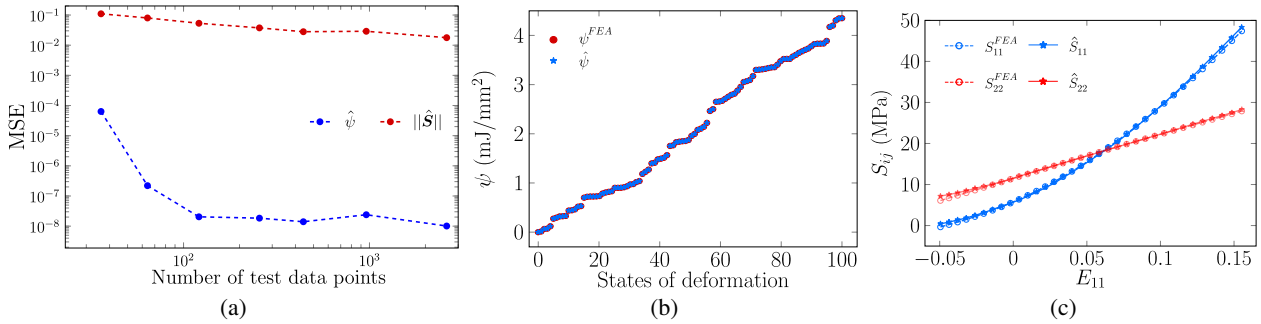

Figure 3: (a) GPR prediction mean squared errors. GPR predictions of (b) strain energy density (sorted by ascending potential) and (c) stress components for a biaxial strain state of $E_{11} = [0.\%, 15\%]$, $E_{22} = 8\%$ and $E_{12} = 0\%$.

CONCLUSIONS

Large deformations prevalent in technical textiles are accurately captured by the finite deformable rod model and validated against experimental and numerical results. Incorporating GPR in computational homogenisation circumvents the need for element-wise microscale simulations, thus yields significant computational savings. Also, the inclusion of design parameters were shown to open avenues for textile material designs.

References

[1] Rasmussen, Carl Edward. and Williams, Christopher K. I. Gaussian processes for machine learning, MIT Press 2006.
[2] Meier C., Popp A. and Wall W. A. An objective 3D large deformation finite element formulation for geometrically exact curved Kirchhoff rods *Computer Methods in Applied Mechanics and Engineering*
[3] Meier C., Popp A. and Wall W. A. A finite element approach for the line-to-line contact interaction of thin beams with arbitrary orientation *Computer Methods in Applied Mechanics and Engineering*
[4] Nadler B., and Papadopoulos P. and Steigmann D. J. Multiscale constitutive modelling and numerical simulation of fabric material *International Journal of Solids and Structures*
[5] Weeger, O. et al. Nonlinear MultiScale Modelling, Simulation and Validation of 3D Knitted Textiles *Applied Composite Materials*

DAMAGE PROGRESSION IN CURVED CFRP LAMINATES UNDER STATIC AND FATIGUE LOADING

Ahmet Çevik[1], Burcu Taşdemir[2], and Demirkan Çöker*[1,3]
[1]Dept. of Aerospace Engineering, Middle East Technical University, Ankara, Turkey
[2]Dept. of Engineering Science, University of Oxford, Oxford, United Kingdom
[3]METU Center for Wind Energy, Middle East Technical University, Ankara, Turkey

Summary In this paper, experimentally investigation of the progression of fatigue and static damage in L-shaped CFRP laminates is presented. Curved beam specimens having lay-up configurations $[0_3/90_3/0_3/90_3/0_3]_s$ were manufactured. To observe the fatigue and static damage progression, in-situ strain field of the specimens was obtained with Digital Image Correlation (DIC) method. In static experiments, deformed states of the specimens were taken at 3 Hz frequency while in fatigue experiments, those were taken at peak load of each cycle. Our results show that main failure mode of the specimens is delamination driven by the interlaminar stresses in the curved region [1-3]. It is shown that the static test specimens failed from the first 0/90 interface while fatigue test specimens failed from the second 0/90 interface.

INTRODUCTION

Advances in composite manufacturing technologies enable to produce complex parts such as curved beam section. These curved composite parts are used in aerospace industry, especially in spar flanges, shear webs and ribs. During their life time, these parts are experienced both static and fatigue loading. Due to applied loadings, interlaminar tensile and shear stresses develop in the curved region of that parts, and delamination type failure which is driven by these interlaminar stresses occurs [1-3]. This study is carried out to understand the damage mechanism in these L-shaped composite part under static and fatigue loading. Static and fatigue experiments were carried out on specimens having stacking sequence $[0_3/90_3/0_3/90_3/0_3]_s$.

EXPERIMENTAL METHOD

Static and fatigue experiments were conducted with the setup shown in Figure 1. Curved specimens were mounted to MTS servo-hydraulic test machine with test fixture. In static experiments, test speed was chosen as 1 mm/min. By using results of the static experiments, the load condition applied to specimens in fatigue experiment was determined as 2 Hz cycling load under displacement control with a displacement range 2 - 4 mm. ARAMIS DIC test setup is used to obtain in-situ strain field. In addition to experiment which were conducted with DIC method, some static tests were recorded at 100000 fps with Photron high speed camera to investigate the initiation and propagation of the delamination in detail.

Figure 1: Test setup used in the experiments.

*Corresponding author. E-mail: coker@metu.edu.tr.

RESULTS

High speed camera pictures show the sequence of dynamic damage progression under static loading. The damage progression under fatigue loading is shown with DIC pictures taken at specified number of cycles. These pictures show a difference between fatigue & static loading in terms of sequence and location of damage. Load displacement curve which was obtained from static test specimen is shown in Figure 2a. Mises strain field obtained at the half failure load and just before the failure load is shown in Figure 2b and Figure 2c, respectively.

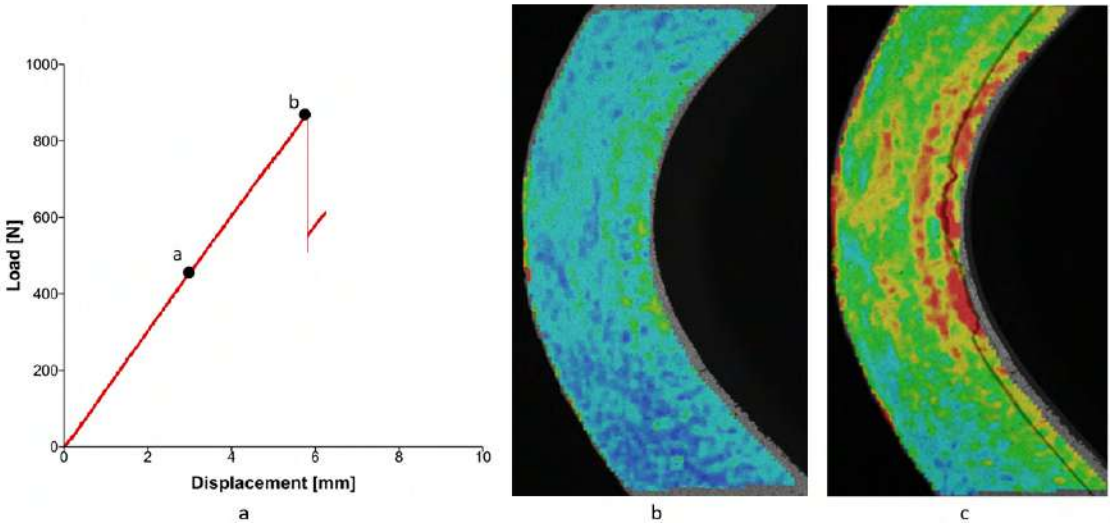

Figure 2: (a) Load - displacement curve of static test specimen, mises strain field (b) at point a (c) at point b on load displacement curve.

Under static loading, matrix cracks initiate in the first 90° grouped plies, then these cracks propagate to the 0/90 interface by making 45 - 50° kink as shown in Figure 3a. Under fatigue loading, microcracks in second 90° grouped plies grow, and connection of these microcracks leads to failure of the specimens shown in Figure 3b.

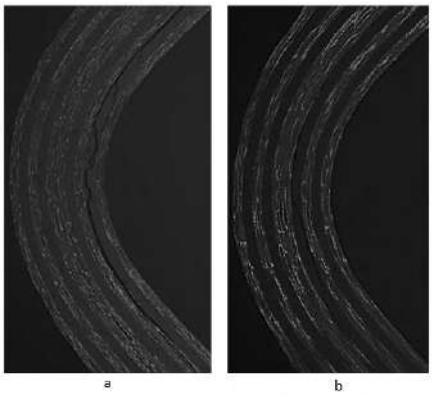

Figure 3: Failure location of curved beam specimens under (a) static loading and (b) fatigue loading.

CONCLUSIONS

In this study, fatigue and static experiments were conducted on curved beam specimens. These experiments show that failure mechanism and location of curved beam specimen under fatigue loading are different than that under static loading. In fatigue failure, growing microcracks under cyclic loading leads to failure so fatigue life of the curved beam specimens highly depends on manufacturing quality.

References

[1] Chang F and Springer GS. The strength of fiber reinforced composite bends. Journal of composite materials 1986;20:30-45.
[2] Sun, C.T. and S.R. Kelly. "Failure Analysis of Composite Angle Structures," in Developments in the Science and Technology of Composite Materials, Proc. of the First European Conference on Composite Materials and Exhibition, Bordeaux, France, pp. 277-284 (1985)
[3] Martin RH and Jackson WC. Damage prediction in cross-plied curved composite laminates. Composite materials: Fatigue and Fracture, ASTM STP 1156, W. W. Stinchcomb and N. E. Ashbaugh, Eds., American Society for Testing and Materials, Phledelphia, 1993;4:105 – 126.

NONLOCAL MICROMECHANICS OF COMPOSITES OF BOTH RANDOM AND PERIODIC STRUCTURES

Valeriy A. Buryachenko*
Micromechanics & Composites LLC, Cincinnati, OH 45202, USA

Summary The basic concepts and directions of locally elastic micromechanics of composites materials are generalized to the nonlocal micromechanics (so-called strongly nonlocal ones by Eringen and peridynamics by Silling). It was established formal similarity of the operator forms of the new general integral equations (forming the second background of micromechanics) for both locally elastic CMs and nonlocal ones that opens the opportunities for straightforward generalization of their solutions for locally elastic CMs to their nonlocal counterparts. Background principles for CMs with both random and periodic structures are proposed. New notions of both the micropolarization tensor and the average local polarization tensor as well as the volumetric periodic boundary conditions are introduced. Variational principle and generalized Hill's bounds of peristatic composites are proposed.

In locally elastic theory, the numerous methods of micromechanicsof random structure composite materials (CMs), inspired by Eshelby, can be classified, according to Willis, into four broad categories (see for Refs. [1]): perturbation methods, self-consistent methods of truncation of a hierarchy, variational methods, and the model methods among which there are no rigorous boundaries. In parallel with micromechanics of random structures, conceptually different methods of micromechanics of periodic structure composites can be subdivided on two-scale expansion methods (apparently coined by Babuska) and the methods of computational homogenization inspired by Suquet. We will demonstrate that the mentioned basic directions of locally elastic micromechanics are generalized to the nonlocal micromechanics (so-called strongly nonlocal ones by Eringen and peridynamics by Silling [2]).

In contrast to these classical local and nonlocal theories, the peridynamic equation of motion introduced by Silling [2] is free of any spatial derivatives of displacements. Wide expansion of the methods of locally elastic micromechanics into nonlocal phenomena [3, 4] was supported by a critical generalization of micromechanics. Namely, the author (see for Refs. [5, 6]) proposed the general integral equation GIE of microinhomogeneous media forming the second background of micromechanics (the first one is based on the effective field hypothesis, EFH, proposed by Faraday, Poisson, Mossotti, Clausius, and Maxwell (1830-1880), see for Refs. [1]). The critical features of the new GIE [5, 6] are the absent of a direct dependence of GIE on both the Green function and the constitutive law (either local or nonlocal) without restrictions of the conventional micromechanics (such as, e.g., acceptance of the EFH and ellipsoidal symmetry of microtopology) that offers opportunities for a fundamental jump in multiscale and multiphysics researches with drastically improved accuracy of local field estimations (even to the point of correction of a sign, see [6]). It was established formal similarity of the operator forms of GIEs for both locally elastic CMs and nonlocal ones (in the senses of either Eringen [7, 8] or Silling [9-12]) that opens the opportunities to straightforward generalization of their solutions for locally elastic CMs [1] to their nonlocal counterparts.

For statistically homogeneous thermoperistatic media subjected to homogeneous volumetric macro boundary loading, one proposed the background principles [10, 12] in the framework of the bond-based approach considered. The general results establishing the links between the effective properties (effective elastic moduli, effective thermal expansion) and the corresponding mechanical and transformation influence functions (do not miss with the influence functions in peridynamics) are obtained by the use of both the decomposition of local fields into the load and residual fields as well as extraction from the material properties a constituent of the matrix properties. The energetic definition of effective elastic moduli is proposed. A detected similarity of results for both the locally elastic (and so-called strongly nonlocal) and peristaltic composites is explained by the fundamental reasons because the methods used for obtaining of the mentioned results widely exploit the Hill's condition proved and the self-adjointness of the peristatic operator.

Effective moduli are expressed through the introduced new notions of both the micropolarization tensor and the average local polarization tensor (although the local polarization tensor is not defined) [10, 12]. The average is accomplished over the surface of the extended inclusion phase (that was performed by a straightforward generalization of interphase integral technique proposed by the author in locally elastic micromechanics [13-15]) rather than over an entire space. Any spatial derivatives of local displacement fields are not required. The basic hypotheses of locally elastic micromechanics (in the version of the second background of micromechanics [5, 6]) are generalized to their peristatic counterparts [16-18] as the generalized dilute approximation, Mori-Tanaka, and the effective field methods. In so doing, the classical EFH is relaxed, and the hypothesis of the ellipsoidal symmetry of the random structure of CMs is not used. Effective nonlocal properties of statistically homogeneous peristatic CMs subjected to arbitrary self-equilibrated strongly inhomogeneous body-force density are estimated as a straightforward generalization of locally elastic micromechanics (see Chapter 12 in [1]).

The variational methods proposed are based on introduction of the admissible displacement and force fields are defined in [19]. The theorem of work and energy, Betti's reciprocal theorem, and the theorem of virtual work are proved. Principles of minimum of both potential energy and complimentary energy are generalized. The strain energy bounds are estimated for both the displacement and force homogeneous volumetric boundary conditions. Generalized Hill's bounds

*Corresponding author. E-mail: buryach@yahoo.com.

on the effective elastic moduli of peridynamic random structure composites are obtained. In contrast to the classical Hill's bounds, in the new bounds, comparable scales of the inclusion size and horizon are taken into account that lead to dependance of the bounds on both the size and shape of the inclusions. Generalized Hashin-Shtrikman variational principle and bounds can be obtained as a straightforward combination of variational principles proposed and the new version of Hashin-Shtrikman bounds [20] obtained by the author in locally elastic micromechanics of CM with noncanonical shape of inclusions in the framework of the EFH.

The background principles of computational homogenization (initiated by Suquet for locally elastic micromechanics) of micromechanics of periodic structure CMs with the peristatic mechanical properties of constituents are proposed [21-23]. One introduces new volumetric periodic boundary conditions (PBC, [21, 23]) at the interaction boundary of a representative unite cell (UC) whose local limit implies the known locally elastic periodic boundary conditions. The classical representations of effective elastic moduli through the mechanical influence functions for elastic CM are generalized to the case of peristatics, and the energetic definition of effective elastic moduli is proposed. A generalization of the Hill's equality to peristatic composites is proved analogously to the theory for the peristatic random structure CM. Due to the volumetric displacement periodicity the special traction boundary condition is not required for establishment of the micro-to-macro displacement relationship although this classical antiperiodic traction condition at the geometrical boundary of the UC is needed for estimations of both the overall stresses and effective moduli. The discretization of the equilibrium equation acts as a macro-to-micro transition of the deformation-driven type, where the overall deformation is controlled. One shows numerically the convergence of the effective moduli estimations by the peristatic model to their locally elastic counterpart. Estimation of effective moduli of the medium with periodically distributed damage (i.e. with the broken bonds) is considered [22]. Asymptotic exactness of Kachanov formula is proved for uniformly damaged peridynamic medium. Proposal of the new volumetric Bloch conditions opens the opportunities for analyses of a wide class of wave propagation in periodic peridynamic composites (e.g. metamaterials and phononic crystals).

CONCLUSIONS

Background, opportunities, and prospective on nonlocal micromechanics are presented. The mentioned problems are considered for the bond-based approaches, which can be easy generalized to the linear state-based approaches in a straightforward manner. Linear solutions are used as the basic elements in analyses of wide classes of dynamic, nonlinear, and coupled problems in the framework of the second background micromechanics proposed by the author (see for Refs. [5, 6]).

Acknowledgements

The author acknowledges Dr. Stewart A. Silling for both the fruitful personal discussions, indispensable idea exchanges, encouragements, helpful comments, and suggestions.

References

[1] Buryachenko V. A. Micromechanics of Heterogeneous Materials. Springer, NY 2007.
[2] Silling S. Reformulation of elasticity theory for discontinuities and long-range forces. *J. Mech. Physics of Solids* **48**: 175-209, 2000.
[3] Buryachenko V. Nonlocal micromechanics of composites of both random and periodic structures (background, opportunities and prospects) (web site of mechanics and mechanicians; http://imechanica.org/node/20664. Posted 12.15.2019, 700 visitors on 01.08.2020
[4] Buryachenko V. Random structure composites with nonlocal thermoelastic properties of constituents. *24th ICTAM*, Montreal, Canada, 2016.
[5] Buryachenko V. A. General integral equations of micromechanics of heterogeneous mater. *Int. J. Multiscale Comput. Enging.* **13**: 11-53, 2015.
[6] Buryachenko V. A. Solution of general integral equations of micromechanics of heterogen. materials. *Int. J. Solids Struct.* **51**: 3823-3843, 2014.
[7] Buryachenko V. A. On thermoelastostatics of composites with nonlocal properties of constituents. I. *Int. J. Solids Struct.* **48**: 1818-1828, 2011.
[8] Buryachenko V. A. On thermoelastostatics of composites with nonlocal properties of constituents. II. *Int. J. Solids Struct.* **48**: 1829-1845, 2011.
[9] Buryachenko V. A. Effective elastic modulus of heterogeneous peristatic bar of random structure. *Int. J. Solids Struct.* **51**: 2940-2948, 2014.
[10] Buryachenko V. A. Some general representations in termoperistatics of random structure compos. *Int. J. Multisc. Comput. Eng.* **12**: 331-350, 2014.
[11] Buryachenko V. A. Effective thermoelastic properties of heterogeneous thermoperistatic bar of random structure. *Ibid.* **12**: 55–71, 2015.
[12] Buryachenko V. A. Effective properties of thermoperistatic random compos.: some background principles. *Math. Mech. Solids.* **22**: 366-386, 2017
[13] Buryachenko V. A. Statistical average of residual stresses in elastically homogeneous medium. *Comput. Structures* **187**: 24-34, 2017
[14] Buryachenko V. A. Method of fundamental solutions in micromechanics of elastic random composites. *Int. J. Solids Struct.* **124**, 135-150, 2017
[15] Buryachenko V. A. Interface integral technique in thermoelasticity of random structure composites. *Math. Mech. Solids.* **24**, 2785-2813, 2018
[16] Buryachenko V. A. Generalized Mori-Tanaka approach in micromech. of peristatic composites. *J. Peridyn. Nonlocal Modeling.* **2**, (in press), 2020
[17] Buryachenko V. A. Modeling of one inclusion in the infinite peristatic medium. *J. Peridynamics and Nonlocal Modeling.* **1**: 75-87, 2019
[18] Buryachenko V. A. Generalized effective field method in micromechanics of peristatic random structure composites. *Submitted.*, 2020
[19] Buryachenko V. A. Variational principals and generalized Hill's bounds of peristatic composites. *Math. Mech. Solids*, **25**: 682–704, 2020.
[20] Buryachenko V. A. Effective field hypothesis in Hashin-Shtrikman bounds estimations on effective moduli of composites with noncanonical inhomogeneous inclusions. *Mechanics of Materials*, **119**: 16–24, 2018.
[21] Buryachenko V. A. Effective elastic modulus of heterogeneous peristatic bar of periodic structure. *Computers and Structures*, **202**: 129-139, 2018.
[22] Buryachenko V. A. Effective elastic modulus of damaged peristatic bar of periodic structure. *J. Multiscale Comput. Enging*, **16**: 101-118, 2018.
[23] Buryachenko V. A. Computational homogenization in linear elasticity of peristatic periodic structure composites. *Math. Mech. Solids*, **24**, 2497-2525, 2018.

FINITE-ELEMENT MODELLING OF ACTIVE COMPOSITE MATERIALS TAKING INTO ACCOUNT INTERNAL STRUCTURE AND INTERFACE EFFECTS IN ANSYS AND ACELAN–COMPOS PACKAGES

Andrey Nasedkin*
Institute of Mathematics, Mechanics and Computer Science, Southern Federal University, Rostov-on-Don, Russia

Summary This research deals with computer modelling in finite element software ANSYS and ACELAN-COMPOS of multiscale two-phase piezoelectric or magnetoelectric (piezomagnetoelectric) bulk composites of irregular structures. The proposed technique is based on the models of micro- and nanoscale materials with interface or surface effects, the effective moduli method, the modelling of representative volumes, and the use of finite element technologies for solving the problems in the representative volumes.

In this short article, as active materials we will understand the materials in which sufficiently noticeable deformations can be caused by external nonmechanical influences. Such materials are piezoelectric, magnetoelectric, pyroelectric and other materials with coupling between mechanical fields and fields of a different nature: electric, magnetic or thermal. These materials are widely used in modern engineering as active elements of transducers, sensors, actuators and other devices. Recently, new materials with improved characteristics are being intensively developed to improve the efficiency of these devices. Especially important are the problems of developing active composite materials consisting of materials of different phases. Methods of mathematical and computer modelling help us to predict the effective properties of composite materials depending on the characteristics of the initial phases, their percentage ratio and the peculiarities of the internal structure.

The problems of determining effective properties, also called homogenization problems, can be solved on the basis of various approaches known in the mechanics of composite materials. For active materials whose behavior is described by a sufficiently complicated system of differential equations, it is convenient to use the method of effective moduli. For example, for piezoelectric composites according to this method, it is necessary to solve a set of boundary-value problems of piezoelectricity (electroelasticity) with special boundary conditions providing for homogeneous materials the exact solutions with constant field gradients (strains, stresses, electric field and electrical induction). In a non-uniform representative volume, these gradients, naturally, will not be constant, but their averaged integral characteristics will permit to determine the effective moduli of the composite material [1, 2].

For nanostructured composites, in which inclusions or pores have nanodimensions, the nanoscale effect can be taken into account in the framework of the Gurtin–Murdoch theory of surface stresses and its generalizations to the problems with coupling fields. In the theory of surface stresses for the interfaces of materials with different phases, the special equations are written that relate stress jumps in volumes with fields for surface stresses. Finally, in recent years, the technologies have been proposed for creating the new materials composed of piezoelectric matrix and of inclusions from other materials or pores, on which interface boundaries the particles of third type materials are deposited.

To solve the homogenization problems for all active composites described in this article, the specialized software was developed, which is based on the finite element solution of boundary problems in representative volumes and takes into account the main features of the internal structure of composites.

Namely, the program systems written in the APDL ANSYS language were created, which allow in the automated mode to solve in the ANSYS package the homogenization problems for active composites of various types and determining their effective moduli. To generate the structures of representative volumes in addition to the simple random ANSYS algorithm, external programs that implement various algorithms were created [1, 2, 3]: 3–x algorithm, supporting the connectivity of finite elements of the first phase, up to 90 % of inclusions of the second phase; 3–0 algorithm with a regular structure of connectivity of the first phase in three axial directions and with a closed structure of the elements of the second phase; cluster algorithms (Witten-Sander method, cluster of the second phase method; method of ”growth out of the plane”; method of initial concentration, etc.)

For the case of porous piezoceramic materials with metalized pore surfaces and nonuniform polarization we used the following approaches. The metallization of the pores we modelled by the boundary conditions of free electrodes and elastic shells [4]. Next, we simulated nonuniform by intensity and direction polarization field around the pores. For this we previously solved the electrostatic problem for the dielectric composite by finite element method. Further, according to founded electric field, the polarization field have been finding. After that every volumetric finite element of a representative volume was associated with a new coordinate system so that the third axis was chosen codirectional to the element polarization vector. The material properties for each finite element were also recalculated in accordance with the found intensities of the polarization field. As a result, we had a representative volume with inhomogeneous properties of piezoceramic matrix [5].

However, in the ANSYS package there were no basic means for solving the problems of magnetoelectricity and there were no piezoelectric and magnetoelectric shell finite elements. In this regard, at the Department of Mathematical

*E-mail: nasedkin@math.sfedu.ru.

Modelling of Southern Federal University, a specialized finite element package ACELAN–COMPOS was developed. The ACELAN–COMPOS package is focused on solving the homogenization problems with coupled mechanical and electromagnetic fields. In this package, implemented new algorithms 3–3 connectivity [6, 9], supporting the connectivity of the two phases; algorithm 3–0 connectivity, creating the granular structures [7, 9]; and algorithm 1–3 connectivity, creating the structures with rod elements in a matrix [8, 9].

For all these models of representative volumes, the algorithms have been developed for the automated search for finite elements located at the interphase boundaries and placing shell elements on them that simulate the presence of surface effects for nanoscale inclusions or pores. For transversely isotropic materials, an algorithm was additionally implemented for the plate surface elements, parallel to the coordinate axes, with the material properties that inherit the anisotropy structure of the neighboring volume elements.

Other means of ACELAN-COMPOS and a more detailed presentation of models, algorithms and results are presented in [4, 5, 6, 7, 8, 9, 10], et al.

Author acknowledges the support of the Government of the Russian Federation (contract No. 075-15-2019-1928).

References

[1] Nasedkin A. V., Shevtsova, M. S. Improved Finite Element Approaches for Modeling of Porous Piezocomposite Materials with Different Connectivity. In: *Ferroelectrics and Superconductors: Properties and Applications*. Ed. I.A. Parinov. Nova Science Publ., 2011, 231–254.

[2] Nasedkin A. V., Shevtsova M. S. Multiscale Computer Simulation of Piezoelectric Devices with Elements from Porous Piezoceramics. In: *Physics and Mechanics of New Materials and their Applications*. Eds. I.A. Parinov and S.-H. Chang. Nova Science Publ., 2013, 185–202.

[3] Nasedkin A. V., Nasedkina A. A., Remizov V. V. Finite Element Modeling of Porous Thermoelastic Composites with Account for Their Microstructure. *Vychisl. Mekh. Splosh. Sred - Computational Continuum Mechanics.* **7**(1): 100–109, 2014.

[4] Nasedkin A., Nasedkina A., Rybyanets A. Finite Element Simulation of Effective Properties of Microporous Piezoceramic Material with Metallized Pore Surfaces. *Ferroelectrics.* **508**: 100–107, 2017.

[5] Gerasimenko T. E., Kurbatova N. V., Nadolin D. K., Nasedkin A. V., Nasedkina A. A., Oganesyan P. A., Skaliukh A. S., Soloviev A. N. Homogenization of piezoelectric composites with internal structure and inhomogeneous polarization in ACELAN–COMPOS finite element package. In: *Wave Dynamics, Mechanics and Physics of Microstructured Metamaterials*. Ser. *Advanced Structured Materials*. vol. 109. Ed. M.A. Sumbatyan. Springer, Singapore, 2019, 113–131.

[6] Kudimova A. B., Nadolin D. K., Nasedkin A. V., Nasedkina A. A., Oganesyan P. A., Soloviev A. N. Models of Porous Piezocomposites with 3–3 Connectivity Type in ACELAN Finite Element Package. *Mater. Phys. Mech.* **37**: 16–24, 2018.

[7] Kudimova A. B., Nadolin D. K., Nasedkin A. V., Oganesyan P. A., Soloviev A. N. Finite Element Homogenization Models of Bulk Mixed Piezocomposites with Granular Elastic Inclusions in ACELAN Package. *Mater. Phys. Mech.* **37**: 25–33, 2018.

[8] Kurbatova N. V., Nadolin D. K., Nasedkin A. V., Nasedkina A. A., Oganesyan P. A., Skaliukh A. S., Soloviev A. N. Models of Active Bulk Composites and New Opportunities of ACELAN Finite Element Package. In: *Wave Dynamics and Composite Mechanics for Microstructured Materials and Metamaterials*. Ser. *Advanced Structured Materials*. vol. 59, Ed. M.A. Sumbatyan. Springer, Singapore, 2017, 133–158.

[9] Kurbatova N. V., Nadolin D. K., Nasedkin A. V., Oganesyan P. A., Soloviev A. N. Finite Element Approach for Composite Magneto–Piezoelectric Materials Modeling in ACELAN-COMPOS Package. In: *Analysis and Modelling of Advanced Structures and Smart Systems*. Ser. *Advanced Structured Materials*. vol. 81, Eds. H. Altenbach, E. Carrera, G. Kulikov. Springer, Singapore, 2018, 69–88.

[10] Kudimova A. B., Mikhayluts I. V., Nadolin D. K., Nasedkin A. V., Nasedkina A. A., Oganesyan P. A., Soloviev A. N. Computer Design of Porous and Ceramic Piezocomposites in the Finite Element Package ACELAN. *Procedia Structural Integrity.* **6**: 301–308, 2017.

COMPRESSIVE STRENGTH OF SOIL ECO-BLOCKS REINFORCED WITH PET FLAKES AND TREATED *LUFFA CYLINDRICA* PARTICLES

Maria-Belen Martinez-Pavetti*[1,2] and Magna Monteiro[1]
[1]Polytechnic Faculty, National University of Asuncion, San Lorenzo, Paraguay
[2]Research Center in Mathematics, Asuncion, Paraguay

Summary Influence of the addition of *Luffa cylindrica* (LC) particles in the compressive strength (CS) of eco-friendly soil blocks reinforced with PET flakes was studied. Samples of the composite blocks were manufactured; their matrix was a mixture of red soil, cement and water, in constant volume fractions. Volume fractions of total aggregate (PET+LC) were kept constant, but different PET:LC ratios were tried. The addition of LC to the composite was done in three conditions: natural, surface-treated with a boiling solution of sodium hydroxide, and with boiling water. Aiming to evaluate CS of the blocks, Paraguayan standards were applied, NP 131 for the compressive test conditions, and NP 17 027 077 to define the minimum CS of traditional ceramic bricks which is 5 MPa. No one of the samples reinforced with LC accomplished this requirement. Causes for low performance are still under discussion.

INTRODUCTION

The development of viable options to introduce alternative materials, as recycled waste and natural fibers, in the construction industry is one of the targets of eco-building. Since a very basic form of construction material is a brick, this work focuses on blocks, whose main structural function is to bear compressive stress (CS). As aggregate material, recycled PET is attractive for being inexpensive, lightweight, durable, and for having good mechanical properties. Regarding natural materials, one exhibiting good potential to be used as an aggregate in blocks is the sponge gourd *luffa cylindrica* (LC) [1].

Beneficial behavior when introducing reinforcements into a matrix can be achieved only if the interface between matrix and reinforcement has a good contact area [2]. This induces to considerate treatments to increase the surface area of the reinforcement. In this work, there were manufactured PET-LC reinforced soil bricks. In order to study the CS of the PET-LC soil b composite, apart from trying various dosifications, we added LC in three different states. It was intended to determine the influence of surface-treated LC in the CS of PET-reinforced soil blocks. These LC states were chosen for the low cost of acquisition of treating agents and ease of treatment application.

MATERIALS AND METHODS

The eco-blocks studied were composites, with a matrix of red soil (RS), Portland cement (PC) and water (W), and aggregates of PET flakes and LC particles. Raw materials underwent through different processes, in order to be prepared for the composite mixture. Red soil was processed with a grinder and then sieved. Portland cement was sieved. PET flakes were obtained from PET bottles, which were cleaned, got their labels and caps removed, were grinded into flakes and sieved. Flakes of 2,4 mm^2 approximately were used. LC particles were obtained by cutting the LC sponge with scissors into cubes of 1 cm^3, approximately. Skin and seeds were removed. Figure 1 shows the aggregate materials after conditioning.

(a) (b)

Figure 1. Reinforcement of the composite studied: (a) PET flakes, (b) LC particles.

Surface treatments on *Luffa cylindrica*

Luffa cylindrica particles in three states were used as aggregates, in order to produce different matrix-LC interfaces. One of these states consists of untreated LC particles, referred to as natural LC (LN). The other two states correspond to the treated LC, applying two surface modifying media, as explained as follows.

On one side, LC was treated with a basic solution of sodium hydroxide, in concentration 0,1 mol/L, dissolved in deionized water. Conversely, LC was treated with tap water. LC treated with sodium hydroxide is referred to as LS, and LC treated with tap water as LW. In both cases, LC was introduced to the vessel containing the treatment solution, and heat was supplied by a burner until boiling point, where LC was kept for 20 min. The mixture was constantly stirred throughout this process. LS was then washed with deionized water and LW with tap water. Right after, both of them were dried in a stove at 50°C until they reached a constant weight. The treatment procedures were adapted from [1;3].

Composite dosification

Seven kinds of composite soil eco-blocks, were manufactured, keeping the matrix materials ratio constant. The volume fractions of the matrix components RS:PC:W were 0,7:0,1:0,1, respectively. Volume fractions of aggregates, on the other hand, were considered in three different ratios, but

Table I. Identification code of different samples and their volume composition.

Sample Code(*)	RS (%)	PC (%)	W (%)	PET (%)	LC (%)
10P0LC	70	10	10	10	0
7P3LN	70	10	10	7	3
7P3LS	70	10	10	7	3
7P3LW	70	10	10	7	3
3P7LN	70	10	10	3	7
3P7LS	70	10	10	3	7
2P7LW	70	10	10	3	7

(*) **Nomenclature of samples**: ***X*P*Y*L**
X=volumen fraction of PET (%)
Y=volumen fraction of LC (%).
LN=LC as natural, **LS**=sodium hydroxide-trated LC, **LW**=tap water-treated LC.

*Corresponding author. E-mail: bmartinez.py@gmail.com.

total aggregate volume fraction (PET+LC) was kept constant in 0,1. The identification code of the different samples and their respective volume composition relation and are summarized in Table I.

Composite manufacturing

Manufacturing of bricks was done in volume fractions according to Table I. Samples were produced in triplicate. After conditioning of raw materials, and treatment of LC, matrix materials and aggregates were mixed homogeneously. The mixture was molded into blocks by a manual press, as shown in Figure 2 (a) and (b). The resulting dimensions of the bricks are, on average, 24cm x 12cm x 5,5 cm. After unmolding, soft bricks underwent the curing process, by manual spray wetting twice a day, for seven days. After 28 days from manufacturing, the final product was ready, as shown in Figure 2 (c), and compressive strength tests were performed.

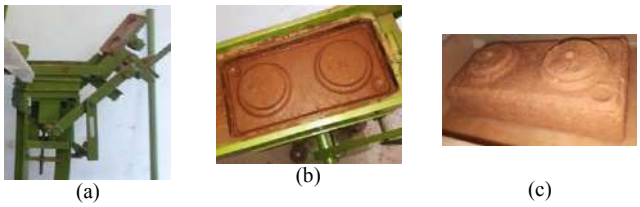

(a) (b) (c)

Figure 2. Moulding of blocks: (a) manual press, (b) molded soft block, (c) finished product.

Compressive strength test

The performance of samples manufactured with aggregates of PET and LC, in different volume fractions, was compared with that of samples manufactured with PET as only aggregate. Samples for the compressive tests were prepared according to Paraguayan standard NP 131 [4]. The minimum CS requirement for solid blocks in Paraguay is established by the standard NP 17 027 77 [5]; CS shall at least be 5 MPa.

(a) (b)

Figure 3. Compressive test: (a) specimens, (b) failure due to uniform compressive load.

The specimens for the compressive tests were prepared as described next. First, blocks were cut in halves, perpendicularly to their longest dimension, and the biggest faces were joined with a mortar layer, and mortar layers were also added at upper and lower faces, as shown in Figure 3 (a). Once mortar was hard, specimens were submitted to uniform compression through a universal testing machine, until failure, as shown in Figure 3 (b).

RESULTS

The results of the compressive tests are presented in Figure 4.

For the sample 10P0LC containing only PET, a good performance was observed, with CS = 7,12 MPa > 5 MPa, meeting the Paraguayan standard, which was reported on previous work.

Conversely, for all the samples containing LC, it can be observed that, CS < 5 MPa. The best performance was obtained for the sample 3P7LN, with 3% v/v PET and 7% v/v of LC as natural, exhibiting a CS = 3,56 MPa. However, this value is not enough to meet the requirement of the applicable Paraguayan standard.

The unexpected low CS values reached could be due to an inappropriate specimen manufacture, an excessive degradation of the LC fibers during the surface treatments, or a non-beneficial interface between the soil matrix and the LC fibers.

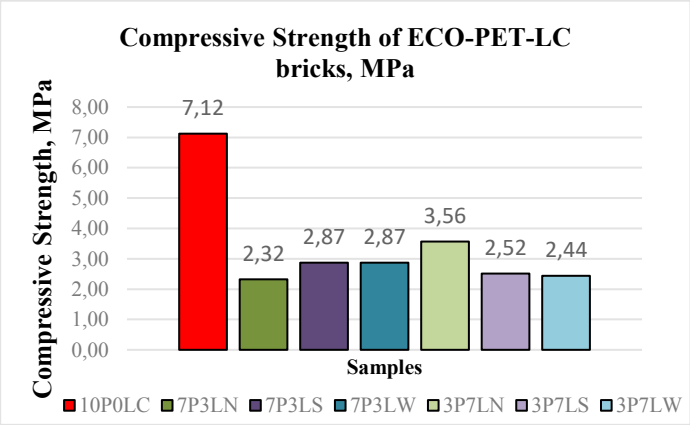

Figure 4. Results of compressive test.

CONCLUSIONS

Apparently, the inclusion of LC as aggregate in a PET reinforced soil composite reduced its CS for the conditions applied. Even worse, LC reinforced blocks do not meet the minimum requirement of 5 MPa of the Paraguayan standard. In order to determine if LC truly weakens the PET-soil composite studied, the same tests shall be performed again.

References

[1] Dias N. A., Xavier M. P. C., Malaquias N. G., Santos E. P., and da Silva M. L. C. P., Isolamento da celulose de bucha vegetal (*luffa cylindrica*) via diferentes tratamentos químicos para geração de material de reforço, in: *Anais do XX Congresso Brasileiro de Engenharia Quimica– COBEQ 2014, Blucher Chemical Engineering Proceedings, Sao Paulo: Blucher*: v. 1, n.2, p. 1436 9-14376. 2015.
[2] Chawla, K.K, Composite Materials: Science and Engineering, 3rd Edition, Springer Science & Business Media, p. 280, 2012.
[3] De Souza J. D. G. T., Motta L. A. de C., Pasquini D., Vieira J. G., and Pires C., Modificação química superficial de fibras de bucha vegetal visando compatibilização e aplicação como reforço em matriz cimentícia, in: *Ambiente Construído*: vol. 17, n. 2, , p. 269-28. Porto Alegre: ANTAC, abr./jun. 2017, Available: http://dx.doi.org/10.1590/s1678-86212017000200157
[4] Norma Paraguaya NP 131, Ladrillos macizos de barro cocido para albañilería, INTN. 1976.
[5] Norma Paraguaya NP 17 027 77 “Ladrillos cerámicos macizos – Requisitos Generales”. INTN. 2016.

MATHEMATICAL MODELING OF A SIMPLE SANDWICH COMPOSITE FOR THE CALIBRATION OF ULTRASOUND DEVICES FOR MEDICAL PURPOSES

Julián Bravo-Castillero*[1], Rogelio O. Caballero-Pérez[1], Ana P. Haro Álvarez[2], Francisco J. Heredia López[3], Nidiyare Hevia-Montiel[1], María del Carmen Jorge[1], Rubén A. Medina-Esquivel[4], Erik Molino-Minero-Re[1], José A. Neme Castillo[1], Jorge L. Pérez-González[1], Joel H. Sánchez-Paz[3], and Caridad Vales-Pinzón[4]

[1]*Instituto de Investigaciones en Matemáticas Aplicadas y en Sistemas, Universidad Nacional Autónoma de México, Unidad Académica del IIMAS en Yucatán, Mérida, Mexico*

[2]*CONACYT-Centro de Investigaciones Regionales "Dr. Hideyo Noguchi" Universidad Autónoma de Yucatán, Mérida, Yucatán, Mexico*

[3]*Centro de Investigaciones Regionales "Dr. Hideyo Noguchi", Universidad Autónoma de Yucatán, Mérida, Yucatán, Mexico*

[4]*Facultad de Ingeniería, Universidad Autónoma de Yucatán, Mérida, Yucatán, Mexico*

Summary The present study aims to develop a methodology to calibrate ultrasound devices for medical purposes. As a first step, a simple sandwich composite made of agar at different densities is modeled to estimate which thickness values of each layer produce a macroscopic response that guarantees a low acoustic impedance and an average attenuation coefficient. Each layer is considered homogeneous, isotropic, and with a complex elastic modulus. Analytical expressions for the corresponding effective properties such as the real and imaginary parts of the elastic modulus, and the mass density, which depends on the thickness, densities and elastic properties of each sheet, are derived. Next, the acoustic impedance and acoustic attenuation effective properties are obtained as a function of effective properties and, consequently, of the thickness of each sheet. Numerical experiments are performed using data reported in recent literature and it is shown how the proposed mathematical model could contribute to the design of a suitable prototype for the calibration of ultrasound devices. Model feedback is planned through experimental tests.

INTRODUCTION

The authors form a multidisciplinary research group interested in studies related to biomedical applications. One of the problems of its interest is to calibrate ultrasound equipments. For this purpose, it is necessary to design prototypes represented by composite materials in which the dimensions and geometric characteristics of their constituents are known. The components of these materials must be durable and have properties that allow waves to travel and return; additive manufacturing is being considered as a versatile and low-cost alternative to produce these prototypes. A first step in the mathematical modeling of these prototypes is to find which parameters should be optimized. For example, they must have a macroscopic behavior such that their acoustic impedance is low to avoid loss of energy at the transducer-prototype interface; as well as an attenuation coefficient of the average wave that allows the wave travels and not fade; and preferably a curvilinear shape to decrease dispersion effects and simulate geometric shapes similar to those of real organs. In this work, a methodology is described for modeling a simple sandwich composite made of Agar with different densities. The methodology is based on homogenization results reported in [1]. Each layer of the sandwich is assumed linear elastic, isotropic and homogeneous material. The problem is to estimate a variation range for the layers thickness to obtain a macroscopic response guarantying a low acoustic impedance and an intermediate wave attenuation. The procedure is presented by an example that suggests the best combination according to the parameters selected for the design.

METHODOLOGY AND RESULTS

We consider a simple sandwich composite wherein the top and the bottom layers has a shear elastic modulus $E^T = E^T_{Re} + iE^T_{Im}$, a mass density ρ^T, and a thickness l. The properties corresponding to the core layer are $E^C = E^C_{Re} + iE^C_{Im}$, ρ^C and $1-2l$, respectively, where $i^2 = -1$ and the sub-indexes Re and Im mean the real and imaginary parts of the elastic moduli. The elastic effective coefficients can be calculate by using the formulas (41) and (42) of [1], whereas the effective mass density is obtained by the mixtures rule, as follows

$$\overline{E}_{Re} = \left\langle \frac{E_{Re}(x)}{\tau(x)} \right\rangle \left(\left\langle \frac{E_{Re}(x)}{\tau(x)} \right\rangle^2 + \left\langle \frac{E_{Im}(x)}{\tau(x)} \right\rangle^2 \right)^{-1}, \tag{1}$$

$$\overline{E}_{Im} = \left\langle \frac{E_{Im}(x)}{\tau(x)} \right\rangle \left\langle \frac{E_{Re}(x)}{\tau(x)} \right\rangle^{-1} \overline{E}_{Re}, \tag{2}$$

$$\overline{\rho} = \langle \rho \rangle, \tag{3}$$

where $\langle P \rangle = 2lP^T + (1-2l)P^C$, with $l \in (0, 0.5)$, is the average on $[0,1]$ of a property P, $\tau(x) = E^2_{Re}(x) + E^2_{Im}(x)$, $E_{Re}(x) = E^T_{Re}\chi_T(x) + E^C_{Re}\chi_C(x)$ with χ_T and χ_C denote the characteristic function of the top layers and the core

*Corresponding author. E-mail: julian@mym.iimas.unam.mx.

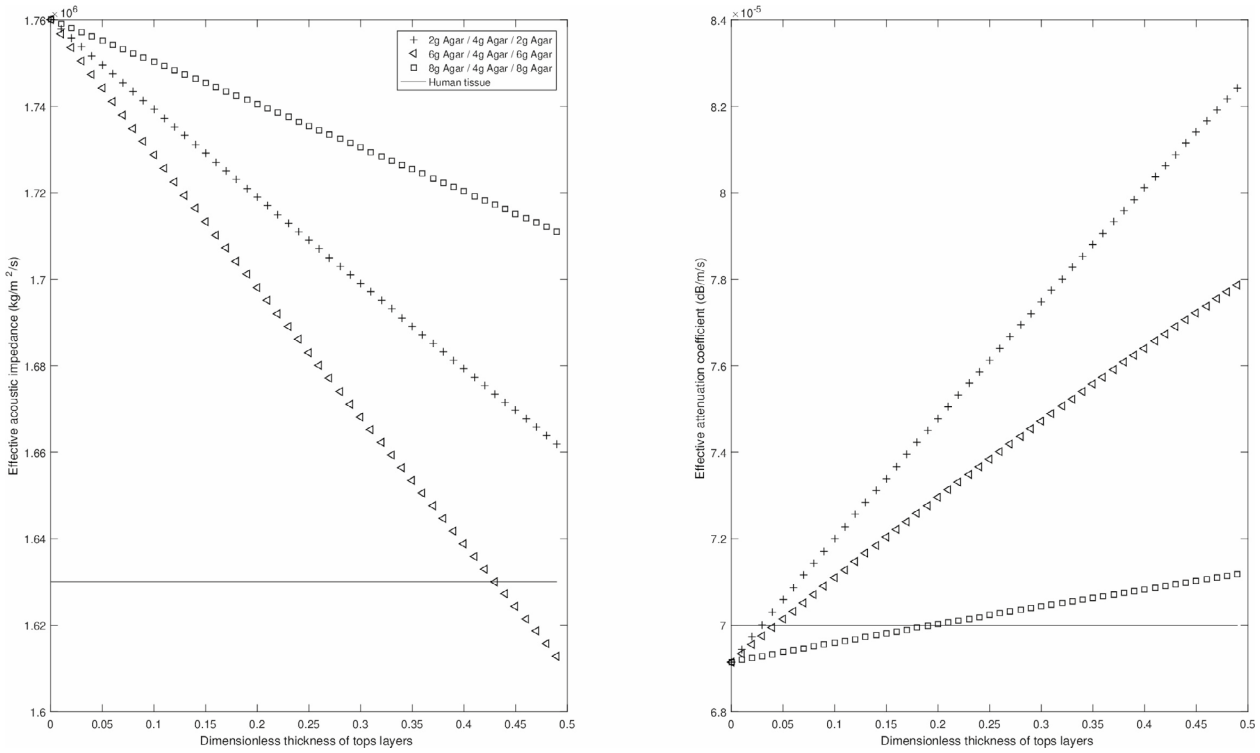

Figure 1: Effective acoustic impedance (left) and effective attenuation coefficient (right) as a function of dimensionless thickness of the top layers. Three simple sandwich composites made of Agar with different densities were considered.

layer, respectively. Using (1)-(3) it is possible to compute the effective acoustic impedance $\overline{Z}$ and the effective attenuation coefficient $\overline{\alpha}$ by means of the following formulas:

$$\overline{Z} = \sqrt{\overline{\rho}\overline{E}_{Re}}, \qquad \overline{\alpha} = 8.686\pi \frac{\overline{\rho}\overline{E}_{Im}\overline{f}}{\overline{Z}\overline{E}_{Re}}, \tag{4}$$

where $\overline{f} = \langle f \rangle$ is the average of the frequency. Formula for $\overline{\alpha}$ is a valid approximation for small loss factor $\frac{\overline{E}_{Im}}{\overline{E}_{Re}}$ [2]. The data used in the calculations, shown in Figure 1, were taken from Table 1 of [3]. As can be seen from the Figure, the sandwich "$6gAgar/4gAgar/6gAgar$" has the lowest acoustic impedance and an attenuation intermediate for all the variation range of the dimensionless thickness of top layers. Therefore, among the composites studied this would be the recommended combination for a dimensionless thickness l about 0.45.

CONCLUSIONS

A simple example is analyzed in order to show a modeling methodology for composite materials that could be used as prototypes for calibration of ultrasound devices. Sandwich models are useful for calibrating ultrasound equipment for imaging diagnosis. The current plan is to have model feedback by means of experiments to improve it. Mathematical and computational modeling of laminated media in curvilinear coordinates and composite materials with more complex geometries is envisaged. The manufacture of prototypes for the calibration of ultrasound equipment is of great social relevance and as far as we know the methodology proposed here is new.

ACKNOWLEDGMENT

ROC would like to thank CONACYT for financial support during his Ph.D. studies at UNAM. Project partially supported by CONACYT PDCPN 2015-102.The project PAPIIT-DGAPA-UNAM IA100910 is also recognized.

References

[1] Bravo-Castillero J., Ramírez-Torres A., Sabina F.J., García-Reimbert C., Guinovart-Díaz R., Rodríguez-Ramos R. Analytical formulas for complex permittivity of periodic composites. Estimation of gain and loss enhancement in active and passive composites. *Waves in Random and Complex Media* https://doi.org/10.1080/17455030.2018.1546063, 2018.

[2] Hartman, B. Relation of Polymer Chemical Composition to Acoustic Damping, Chapter 2 in *Sound and Vibration Damping with Polymers; Corsaro, R., et al.; A.C.S. Symposium Series; American Chemical Society: Washington, D.C.* **Ch 2**: 23–45, 1990.

[3] Manickam, K., Machireddy, M.R., Seshadri, S. Characterization of biomechanical properties of agar-based tissue mimicking phantoms for ultrasound stiffness imaging techniques. *journal of the mechanical behavior of biomedical materials*. **35**: 132–143, 2014.

THEORETICAL PREDICTION FOR THE STRAIN HARDENING OF ARTIFICIAL NACRE

Yi Yan[1], Zi-Long Zhao, and Xi-Qiao Feng*[1]
[1]Department of Engineering Mechanics, Tsinghua University, Beijing, China

Strain-hardening contributes to the high strength and toughness of nacre. Understanding the inner mechanisms of strain-hardening is vital to design biomimetic nacre-like composites. In this study, we provide a unit-cell theoretical model to predict the stress–strain response of nacre. We give two thresholds to predict the occurrence of strain-hardening and platelet failure. The analytical expressions of the strength of nacre are given based on three failure modes. Two parametric studies with regard to the aspect ratio and interfacial stiffness are presented.

Introduction

Owing to the simple mortar–brick microstructure and the outstanding strength and toughness, nacre becomes an important biomimetic resource of artificial composites [1]. To guide such biomimetic designation, we need to understand the inner relationships between the macroscopic properties of nacre and the microscopic properties of the mortar–brick structure. Strain-hardening is an important phenomenon that contributes to the high strength and toughness of materials. However, the designation of nacre-like composites with strain-hardening, thus, still lacks a theoretical guidance. In this study, we provide a unit-cell theoretical model to predict the stress–strain response of nacre. We give two thresholds to predict the occurrence of strain-hardening and platelet failure. Two parametric studies with respect to the aspect ratio and interfacial stiffness are presented.

Theoretical Model

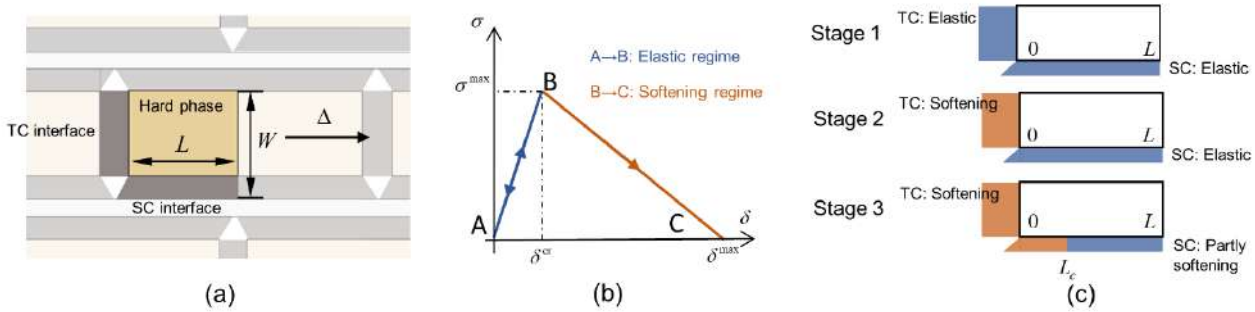

Figure 1. Schematic of the theoretical model. (a) A one-dimensional unit cell. (b) Bilinear cohesive law on the TC and SC interfaces. (c) Gradual softening of the TC and SC interfaces during the tensile deformation [4].

This study follows the classic Tensile–Shear–Chain (TSC) model developed by [2]. A uniaxial tensile displacement load Δ is imposed on the unit-cell model (Fig.1a). The unit-cell comprises three parts: the hard phase, tensile cohesive (TC) interface, and shear cohesive (SC) interface.

The tensile stress of the hard phase is write as the integrate from the tractions on the TC and SC interfaces

$$\sigma_{\text{hard}}(x_1)=\sigma_{\text{TC}}+\frac{1}{W}\int_0^{x_1}\sigma_{\text{SC}}(\xi)\,\mathrm{d}\xi,\ 0\le x_1\le L. \tag{1}$$

where W is the width of the hard phase platelet, and L denote the half length of the platelet.

The tangential moduli corresponding to the three stages are expressed as

$$E_1=\frac{\sigma_{\text{TC}}^{\max}L}{\delta_{\text{TC}}^{\text{cr}}}+\frac{L^2\sigma_{\text{SC}}^{\max}}{12W\delta_{\text{SC}}^{\text{cr}}},\quad E_2=\frac{\sigma_{\text{TC}}^{\max}L}{\delta_{\text{TC}}^{\text{cr}}-\delta_{\text{TC}}^{\max}}+\frac{L^2\sigma_{\text{SC}}^{\max}}{12W\delta_{\text{SC}}^{\text{cr}}},\quad E_3=\frac{\sigma_{\text{TC}}^{\max}L}{\delta_{\text{TC}}^{\text{cr}}-\delta_{\text{TC}}^{\max}}+\frac{L^2\sigma_{\text{SC}}^{\max}L_c}{12W\delta_{\text{SC}}^{\text{cr}}L}+\frac{L^2\sigma_{\text{SC}}^{\max}(L-L_c)}{12W\left(\delta_{\text{SC}}^{\text{cr}}-\delta_{\text{SC}}^{\max}\right)L}. \tag{2}$$

The critical strain can be solved based on the ellipticity condition of instability $E(\varepsilon_{\text{cr}})=0$.

Threshold 1: Occurrence of strain-hardening

When the TC interface steps into the softening stage, the SC interface still provides a positive modulus to the unit-cell, thus forming the strain-hardening stage. Accordingly, the occurrence of the strain-hardening stage is given as $E_2>0$.

Threshold 2: Failure of the platelet

We give the condition of platelet failure as $\sigma_{\text{norm}}>\sigma_{\text{platelet}}$, where σ_{platelet} is a material parameter of the fracture strength of the hard phase.

According to the two thresholds, we give the analytical prediction of the strength of nacre σ_{th} as: Mode 1: Platelet failure, Mode 2: Interface failure, with strain hardening, and Mode 3: Interface failure, without strain hardening.

Result

Figure 2 shows the stress–strain curves calculated from the unit-cell theoretical model and the finite element model in a larger representative volume element. In Fig. 2a, we can observe the TC interface softening first, and a gradual softening on the SC interface. In Fig. 2b, the softening of TC interface introduces crack initiation immediately. The contribution of the SC interface cannot be observed.

The effect of aspect ratio on the mechanical response of nacre is shown in Fig. 3. Our result reveals a preferred zone

*Corresponding author. E-mail: fengxq@mail.tsinghua.edu.cn

(green) of aspect ratio in which the model fails in Mode 2. It is shown that natural nacre chooses the strategy of high strength, which is coherent with its biological function (protect the shell from impact load) [4].

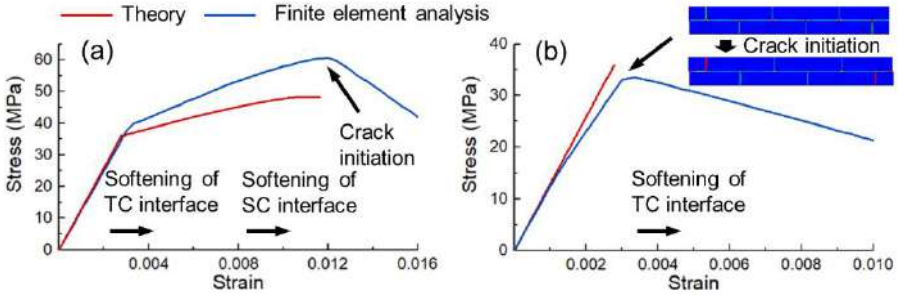

Figure 2. Theoretical prediction of the stress strain curve compared to finite element simulation result. (a) Interfacial failure with strain hardening (Mode 2), $\sigma_{SC}^{max} = 30$ MPa. (b) Interfacial failure without strain hardening (Mode 3), $\sigma_{SC}^{max} = 3$ MPa.

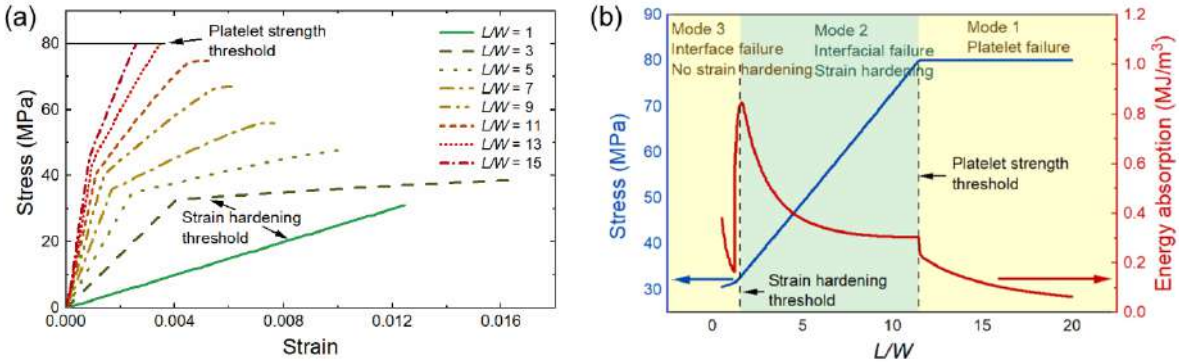

Figure 3. Effect of aspect ratio on the stress strain curve (a), strength, and toughness (b).

The interfacial stiffness is another important design parameter. There are variety of polymers as the candidate of the soft phase in artificial nacre. A basic but vital problem is to choose whether a stiff polymer such as PMMA, or a softer material like PLMA [5]. Our result shows that a softer interface is benefit to the toughness, which is consistent with the earlier analytical result [6]. However, if the interface is too soft, we can observe the occurrence of failure Mode 3 (no strain-hardening).

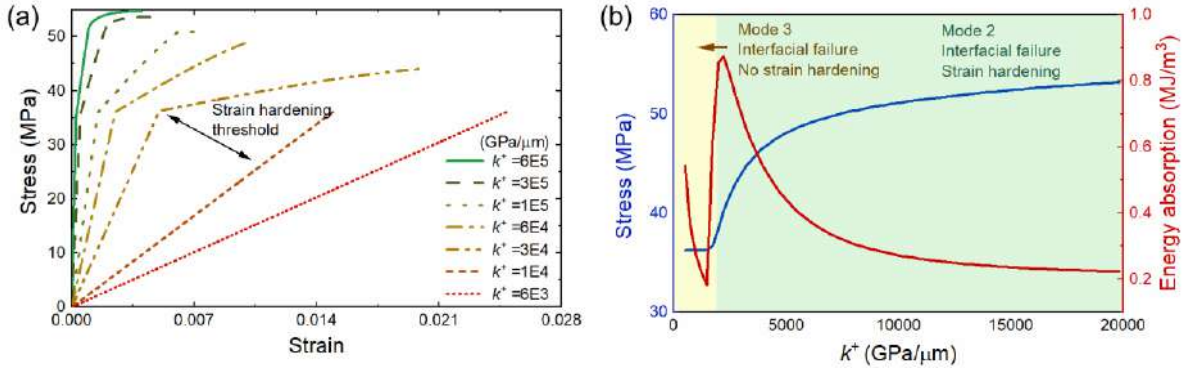

Figure 4. Effect of interfacial stiffness on the stress strain curve (a), strength, and toughness (b).

CONCLUSIONS

In this study we developed a unit-cell theoretical model to calculate the mechanical response of nacre. Two important thresholds are presented to predict the occurrence of strain-hardening and platelet failure. The results give a preferred range of aspect ratio and interfacial stiffness to achieve high strength and toughness. The strategy of structural design of natural nacre can be well explained, indicating the potential of this model as the guidance of the designation of artificial nacre.

References

[1] Yao HB, Tan ZH, Fang HY, Yu SH. Artificial nacre-like bionanocomposite films from the self-assembly of chitosan-montmorillonite hybrid building blocks. *Angew. Chemie.* **49**: 10127–31, 2010.
[2] Jäger I, Fratzl P. Mineralized collagen fibrils: a mechanical model with a staggered arrangement of mineral particles. *Biophys. J.* **79**: 1737–46, 2000.
[3] Askarinejad S, Rahbar N. Toughening mechanisms in bioinspired multilayered materials. *J. R. Soc. Interface.* **12**: 201408552015, 2015.
[4] Gould SJ. A natural history of shells. *Trends Ecol. Evol.* **9**: 410, 1994.
[5] Niebel TP, Bouville F, Kokkinis D, Studart AR. Role of the polymer phase in the mechanics of nacre-like composites. *J. Mech. Phys. Solids.* **96**: 133–46, 2016.
[6] Okumura K, De Gennes PG. Why is nacre strong? Elastic theory and fracture mechanics for biocomposites with stratified structures. *Eur. Phys. J. E.* **4**: 121–7, 2001.

MECHANICAL PROPERTIES OF FIBERBOARD COMPOSITE BONDED WITH POLYMER MATRIX COMPUTED BY MEAN-FIELD HOMOGENIZATION METHODS

Janka Kovacikova[*1], Martin Kroon[1], Sheikh Ali Ahmed [2], Reza Hosseinpourpia[2], and Stergios Adamopoulos[2,3]
[1]Department of Mechanical Engineering, Faculty of Technology, Linnaeus University, Växjö, Sweden
[2]Department of Forestry and Wood Technology, Faculty of Technology, Linnaeus University, Växjö, Sweden
[3]Department of Forest Biomaterials and Technology, Swedish University of Agricultural Sciences, Uppsala, Sweden

Summary Nowadays, the design of composite materials considering sustainability and the environmental impact of the production is conspicuous. Therefore, in this work, we focus on investigating the mechanical behaviour and structure of a new green wood-based fibrous composite material bonded with a novel polymer matrix. The constitutive prediction models employing the material and structure design approaches simultaneously are proposed here to describe the material's microstructure. The goal is speeding up trials and reducing experiments expenses by replacing tests with computer simulations. Additionally, the relationship between material behaviour and structure is established and will be later used to generate Representative Volume Elements (RVEs) for finite element analysis (FEA).

INTRODUCTION

Employment of a multiscale concurrent design approach while developing a new composite material compared to a conventional material and structural design executed separately has multiple advantages (from saving resources needed for conducting experiments to easing the environmental impact of production). Therefore, in this work, we focus on developing mean-field homogenization models of a composite material predicting a material's performance. Ultimately, we will couple these models with the macro-scale models to perform the complex structural analysis. The studied composite material is wood fibre-reinforced composite with a polymer matrix. We used *Digimat 2020.0* modelling platform and the mean-field homogenization (MFH) methods. The results are the homogenized micro-mechanical material models that consider the heterogeneous nature of component materials and predict the composite material properties and performance under uniaxial loading.

MATERIAL AND METHODS

Studied composite material belongs to the category of polymer-matrix composites (PMC) [1, 2] with short fibres. We consider that material is homogeneous, and it consists of two constituents: inclusion and matrix. The inclusion is wood fibres from Pinus sylvestris, and the matrix is polyurethane from isocyanates and dextrin. Both the inclusion and the matrix are products obtained from biomass; thus, they are biodegradable. The values used to describe the mechanical properties of constituents in the micromechanical models are in table 1 and compiled from [3-6].

Table 1. Input material parameters of constituents

Phase (compound)	Density [kg/mm^3]	Young's Modulus [MPa]	Ultimate Stress [MPa]	Ultimate Strain [%]	Poisson's ratio [-]
Matrix (PU)	9.88E-007	1554	46	5	0.4
Fibres (*Pinus Sylvestris*)	4.2E-007	9000	49	2	0.3

We executed a static analysis of elastoplastic brittle material with monotonic uniaxial loading applied and with no failure indicator. The microstructure consists of a mass fraction of 40% and an aspect ratio of 22. It is a single generic type microstructure.

We employed the mean-field homogenization (MFH) models to estimate the stress and stains regions, both at the macro scale level as well as microscale level. Namely, Mori-Tanaka (M-T) [7] using two available techniques: first and second-order homogenization. Material for each compound is calculated assuming an accurate material model of the phase and volume average of the strain field is computed in the phase, in first-order homogenization. To define comparison materials using second-order homogenization, we also employ second statistical moments of the strain field [8]: Double Inclusion (D-I) models [9]. Ultimately, we create a representative volume element (RVE) using the mentioned methods. Moreover, in our models, we assume that the composite is the RVE of composite consists of a matrix of uniform stiffness C0 in which the many inclusions (I) of uniform stiffness C1 are nested. At the same time, strain ε is constrained on the boundary.

In the Mori-Tanaka model, the strain concentration tensor expressing the strains' volume average over all inclusion to the mean matrix is presumed ad follows:

$$\mathbf{B}^{\varepsilon} = \mathbf{H}^{\varepsilon}(I, C_0, C_1) \quad (1)$$

*Janka Kovacikova. E-mail: janka.kovacikova@lnu.se.

Where $\mathbf{B}^{\varepsilon}$ is mean strain matrix, $\mathbf{H}^{\varepsilon}$ is the single inclusion's concentration tensor.

In the Double inclusion (D-I) model, each inclusion (I) of C_I stiffness assumes to be encircled by the material matrix of stiffness C_0. Additionally, a reference medium of stiffness C_r is introduced in the close area between inclusion and matrix.

In this case, the strain concentration tensor to the mean matrix is defined as follows:

$$\mathbf{B}^{\varepsilon} = \left[(1-\xi(v_1))(\mathbf{B}_l^{\varepsilon})^{-1} + \xi(v_1)(\mathbf{B}_u^{\varepsilon})^{-1}\right]^{-1} \quad (2)$$

Where v_1 is volume fraction and $\xi(v_1) = \frac{1}{2}\, v_1(1+v_1)$ is a smooth quadratic interpolation function.

RESULTS AND DISCUSSION

The engineering constants computed via M-T and D-I models for the macroscopic representation of RVE are in Table 2. Here, E_{11} (x-axis) is an axial modulus of elasticity, E_{22} (y-axis), E_{33} (z-axis) are transverse moduli of elasticity; υ_{12}, υ_{21}, υ_{13}, υ_{31}, υ_{23}, υ_{32} are macroscopic Poisson's ratios; G_{12}, G_{13}, G_{23}: macroscopic shear moduli.

Table 2. The engineering constants computed using MFH methods

Constant Model	E_{11} [MPa]	E_{22} [MPa]	E_{33} [MPa]	υ_{12} [-]	υ_{21} [-]	υ_{13} [-]	υ_{31} [-]	υ_{23} [-]	υ_{32} [-]	G_{12} [MPa]	G_{13} [MPa]	G^{23} [MPa]	Global Density [kg/mm^3]
M-T	5991	3953	3953	0.338	0.223	0.338	0.223	0.446	0.446	1438	1438	1367	6.41E-07
D-I	6043	4330	4330	0.334	0.239	0.334	0.239	0.418	0.418	1631	1631	1527	6.41E-07

The macroscopic stress-strain diagrams for M-T 1st order, M-T 2nd order and D-I models are shown in Figure 1 (a). Additionally, stress-strain diagrams for matrices, inclusions and macro are shown in Figure 1 (b-d).

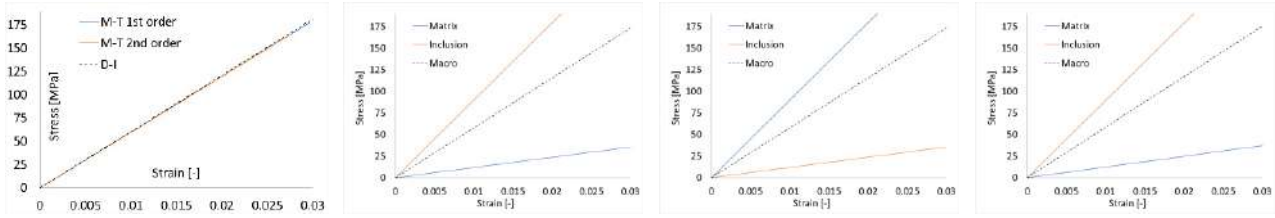

(a) (b) (c) (d)

Figure 1. Stress-strain diagrams: (a) comparison of all used models; matrix vs inclusion vs macro for (b) Mori-Tanaka 1st order, (c) Mori-Tanaka 2nd order, (d) Double inclusion models

We can see that there is no significant difference between the obtained engineering constants and stress-strain diagrams comparing the used methods. Thus, all methods are employable in the case of the studied composite.

CONCLUSIONS

The used methods are suitable to solve the studied problem and will be further developed into more sophisticated models. Specifically, we will consider mechano-sorptive creep models that will be described via the material's viscoelastic properties. The additional model using the direct finite element method (FEM) at the microscopical level will also be developed. These will be later compared to the experimental work submitted for publishing and the work presented in [10].

References

[1] Barbero, E. (2018). Introduction to Composite Materials Design. Boca Raton: CRC Press, https://doi.org/10.1201/9781315296494

[2] Aboudi, J., Arnold, S. M., & Bednarcyk, B. A. (2016). Micromechanics of composite materials: A generalized multiscale analysis approach. ISBN: 9780128101278

[3] Konieczny, J.; Loos, K. Green Polyurethanes from Renewable Isocyanates and Biobased White Dextrins. *Polymers* 2019, *11*,

[4] Page, D.H., El-Hosseiny, F., Winkler, K. and Lancaster, A.P.S. (1977). Elastic Modulus of Single Wood Pulp Fibres, Tappi, 60(4): 114 – 117.

[5] Wei, Jinguang, Fei Rao, Y. Huang, Y. Zhang, Y. Qi, Wenji Yu and C. Hse. "Structure, Mechanical Performance, and Dimensional Stability of Radiata Pine (Pinus radiata D. Don) Scrimbers." *Advances in Polymer Technology* 2019 (2019): 1-8.

[6] Pauzi, N., R. A. Majid, Mohd Haziq Dzulkifli and M. Yahya. "Development of rigid bio-based polyurethane foam reinforced with nano clay. "*Composites Part B-engineering* 67 (2014): 521-526.

[7] T. Mori and K. Tanaka. Average stress in the matrix and average elastic energy of materials with misfitting inclusions. Acta Metall. Mater., 21:571–574, 1973.

[8] Digimat_manual. Digimat -MF

[9] S. Nemat-Nasser and M. Hori. Micromechanics: overall properties of heterogeneous solids. Elsevier Science, 1993.

[10] Hosseinpourpia, R., Adamopoulos, S., Mai, C., Taghiyari, H.R. (2019). Properties of medium-density fibreboards bonded with dextrin-based wood adhesive. Wood research. 64. 185-194.

SELF-ASSEMBLY OF GRANULAR PARTICLES FOR INVERSE OPAL MANUFACTURE

Ivan Grega*, Angkur Shaikeea, and Vikram S. Deshpande
Department of Engineering, Cambridge University, Cambridge CB2 1PZ, UK

Summary Self-assembly is a scalable and cheaper method for the manufacture of certain architected solids compared to additive manufacturing methods. Here, via a combination of large-scale numerical simulations of granular assemblies and associated experiments, we investigate the use of vibration schemes to promote crystalline assemblies. The effect of vibrations type, seeding layer and height of assembly on both the kinetics and equilibrium of the assemblies is investigated.

INTRODUCTION

The motivation of this work is to improve the manufacture of inverse opal metamaterials, which exhibit superior mechanical properties [1]. Self-assembly of opal template followed by deposition of main material should bring improvements over additive manufacturing in terms of scalability, speed, and cost. The first step is to assemble opaline crystal without stacking defects such as vacancies, grain boundaries, dislocations, regions of low packing density, and misorientations of grains. Traditionally, inverse opal crystals were manufactured on a microscopic scale for their optical properties (photonic bandgap) [2]. Constituent spheres of diameters below 2 μm were often synthesised in a solution [3]. It was discovered that it is possible to achieve dense crystalline packing by slow evaporation of the solvent. The disadvantages of this approach are the limited thickness of opaline layers which can be produced, low control over the process, and the presence of numerous stacking defects [4]. On solvent drying, stresses can develop in the assembly which are high enough to initiate cracking of the sample [5]. In this work we take a top-down approach. Starting on a macroscale, we investigate the potential for achieving a defect-free crystalline granular assembly from random packing without resorting to colloidal solution.

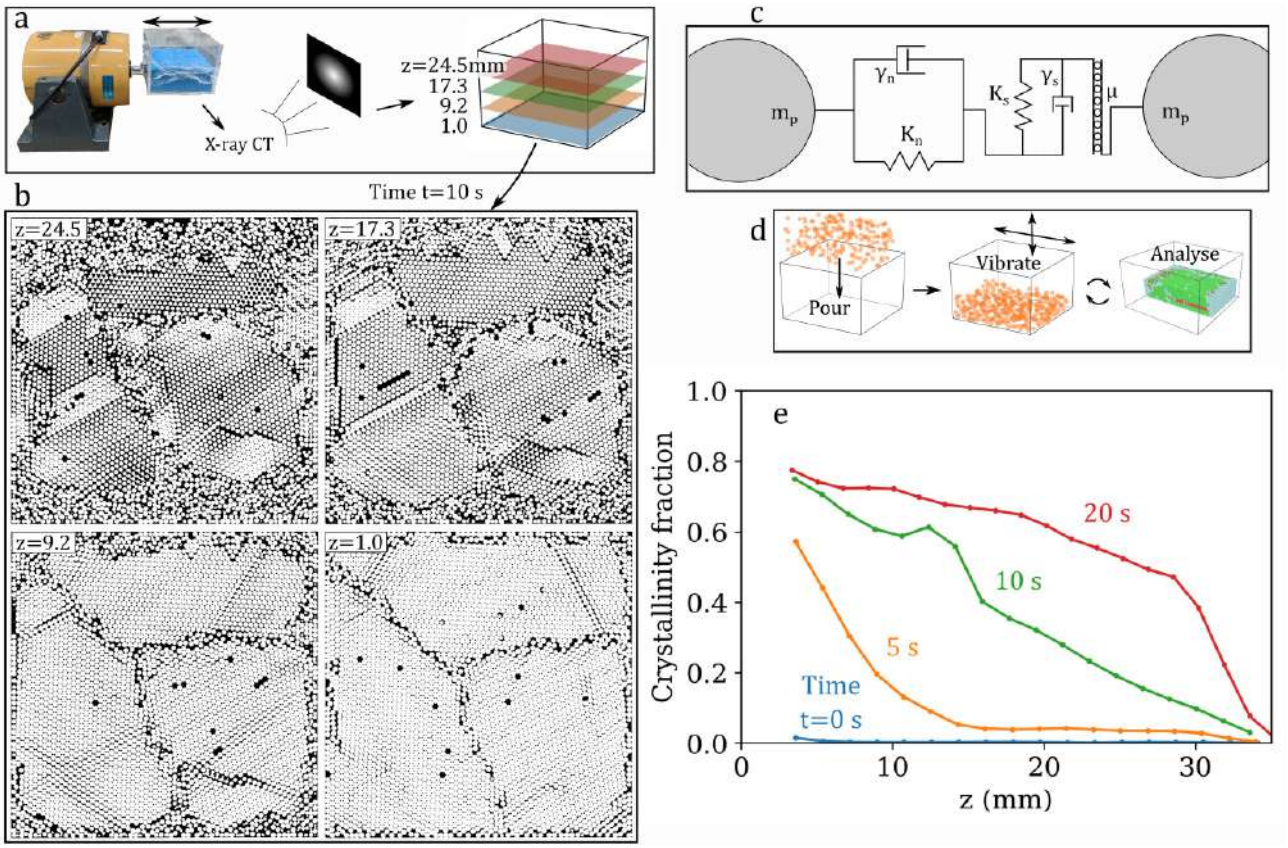

Figure 1 Development of crystallinity is captured by soft-sphere model
a) Experimental setup: enclosed box with cellulose acetate spheres (⌀2mm) connected to linear shaker. After vibration phase, sample is analysed using X-ray CT. b) Cross-sectional slices at representative heights *z* after 10s of horizontal vibration: lower layers have denser packing. c) Soft-sphere model is used to model particle interactions. d) Conceptual workflow in simulations: spherical particles are poured into simulation box, horizontal or vertical vibration is applied, and resulting packing is analysed using PTM [6]. e) Crystallinity varies with time *t* and height *z*, increasing from the bottom upwards.

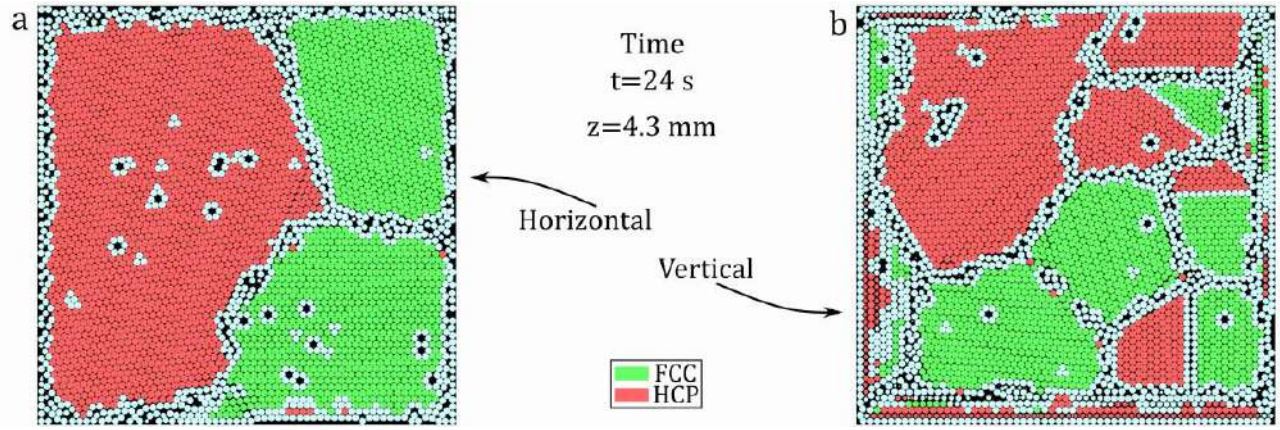

Figure 2 Horizontal vibration improves growth of single grain over vertical vibration
Cross-sections at *z=4.3mm* after *t=24s* of vibration at *16Hz*. Increased shearing motion resulting from horizontal vibration improves merging of grains

METHODOLOGY

In our experiments, the granular assembly was comprised of 75'000 precision cellulose acetate spheres with 2 mm diameter inside a transparent acrylic box with 120x120 mm planform. The box was placed on rollers and attached to a linear shaker to induce horizontal vibrations. Positions of particles were measured from X-ray CT cross-sectional images (Fig 1a). Numerical simulations were carried out using LAMMPS and its package *granular*. To model particle interactions, we used soft-sphere model (Fig. 1c) with parameters determined from experiments. Information about crystallinity of packing was obtained using polyhedral template matching (PTM) algorithm [6].

RESULTS

Agreement between results of numerical simulations and experiments was established. The soft-sphere model can capture the behaviour exhibited by experiments (Fig. 1). We found it possible to convert the bulk of granular assembly from random packing to grains of close-packed FCC and HCP by various vibration schemes.

- Horizontal vibration and associated shearing motion are more efficient at dissipating grain boundaries than vertical vibration. In vertical vibration it takes more time for various grains to coalesce (Fig. 2)
- The rate at which crystallinity is established and the quality of packing can be strongly influenced by the introduction of a *seeding* layer (with packing corresponding to FCC 100- or 111-planes). Seeding layer accelerates crystal growth and imposes matching lattice orientations to all grains.
- The total height of random assembly influences kinetics of crystal growth. When sample height is bigger, overall crystallinity increases more slowly. Secondly, while for smaller height crystal growth always starts from the bottom and propagates upwards, nucleation for taller samples initiates mainly at the vertical walls.

CONCLUSIONS

In the presented study, we show that granular assembly of spheres in random packing can be transformed to crystalline assembly using vibrations. We also demonstrate the rate and quality of this process can be largely influenced by several factors such as directionality of applied vibrations, presence of ordered seeding layer and total height of the granular assembly. It has been experimentally shown that line defects can be eliminated with sufficient time of vibration. By improving quality and eliminating the need for colloidal dispersant, this process has a potential to improve the manufacture of inverse opals.

References

[1] Pikul J.H., Özerinç S., Liu B. et al. High strength metallic wood from nanostructured nickel inverse opal materials. *Sci Rep* 9, 2019.
[2] Vlasov Y., Bo XZ., Sturm J. et al. On-chip natural assembly of silicon photonic bandgap crystals. *Nature* 414, 2001.
[3] Stöber W., Fink A., Bohn E. Controlled growth of monodisperse silica spheres in the micron size range. *J. Colloid Interface Sci.* 26, 1968.
[4] Holland B.T., Blanford C.F., Stein A. Synthesis of Macroporous Minerals with Highly Ordered Three-Dimensional Arrays of Spheroidal Voids. *Science* 281, 1998.
[5] Velev O.D., Lenhoff A.M., Colloidal crystals as templates for porous materials. *Current Opinion in Colloid & Interface Science* 5, 2000.
[6] Larsen P.M., Schmidt S., Schiotz J. Robust structural identification via polyhedral template matching. *Model. Simul. Mater. Sci. Eng.* 24, 2016.

SELF-ASSEMBLY BEHAVIOR OF BLOCK COPOLYMER BLEND THIN FILMS

Suwon Bae[1] and Kevin G. Yager *[1]
[1]Center for Functional Nanomaterials, Brookhaven National Laboratory, Upton, NY, USA 11973

Summary Block copolymer blend thin films have potential as patterning materials. Here, a molecular dynamics approach is used to investigate the variation in morphologies formed by block copolymer blends in a thin film geometry. It is shown that blends of cylinder- and lamella-forming block copolymers in a thin film geometry form patterns of dots and lines coexisting in separate regions, which is not observed in single component block copolymer thin films. Blending one with another block copolymer diversifies nanostructure registry and facilitates the use of block copolymer as patterning materials.

INTRODUCTION

Block copolymers (BCPs) are a class of self-assembling material that segregates on nanometer length scale. BCPs are as the name indicates are composed of two or more blocks which are chemically distinct and incompatible with each other. This chemical incompatibility drives BCPs to phase separation and self-assembly. Having a covalent bond between blocks prevents macrophase separation of otherwise free, distinct homopolymers. BCPs therefore microphase separate and self-assemble into nanoperiodic structure. The nanostructure shape and size can be controlled by the underlying BCP chain architecture such as molecular weight, chemical incompatibility, and relative fraction of blocks. BCPs in thin film geometries include applications in nanopatterning, nanoporous membranes, nanorods, etc. The patterns formed by BCP thin films can be diversified through blending, which further facilitates the use of block copolymer as patterning materials. We study the morphologies formed by blends of cylinder- and lamella-forming diblock copolymes in a thin film geometry by means of molecular dynamics simulations.

METHODS

We use a Kremer-Grest bead-spring model to describe our representative A-d-B diblock copolymer chain. For both cylinder- and lamella-forming BCP chains, denoted by C and L chains, the number of beads per chain is set to 20. f_A is set to 0.25 and 0.5 for C and L chains, respectively, meaning a C chain is composed of 5 A beads and 15 B beads. Mass of each bead is $1.0m$ regardless of type, where m is Lennard-Jones (LJ) unit for mass. The interactions between beads are governed by FENE and LJ potentials, widely used to describe the behavior of polymer melts. The LJ potential is responsible for non-bonded interactions and it normally describes repulsive interaction alone. We choose $r_c = 2.5\sigma$, where $sigma$ is LJ unit for distance, which enables attractive interactions between BCP chain beads. Thin films of representative BCP chains are constructed by using a self-avoiding random walk algorithm. The total number of chains is 2400, which yields $0.7L_0^*$ thin films, where L_0^* is the domain/repeat spacing of line patterns formed by pure L chains, which will be discussed in results. The films is placed on top of a substrate, which is located on the bottom surface of a simulation bocs. The substrate is modeled with a single layer of beads (type S) aligned and fixed on the 111 plane of an FCC lattice. The substrate beads interact only with BCP chain beads in the pairwise (non-bonded) manner. The pairwise interactions are captured by an LJ potential, enabling the BCP film to stand on the substrate with attractive interactions between the BCP chain beads and the substrate beads. The substrate interfacial energies are precisely tailored so that the substrate can behave as a "neutral" substrate, which promotes morphologies aligned perpendicular to it. With periodic boundary conditions imposed along the plane, MD simulations are performed using LAMMPS. Individual films are subjected to annealing and cooling, which are carried out using *NVT* ensemble with Nosé-Hoover thermostat. We define $f_C = n^C/(n^C + n^L)$, which is fractional number of C chains of individual blend thin films, and use it to quantify blending ratio.

RESULTS AND DISCUSSION

BCP blend thin films are studied as a function of f_C. At $f_C = 0$, pure L chains form vertical lamellae, visualized as a line pattern in a SEM-like top-down view image (Figure 1-a) generated by using BCP chain trajectories. The morphologies formed in the films studied here span the whole thickness. At $f_C = 1.0$, pure C chains self-assemble into vertical cylinders, visualized as a dot pattern in Figures 1-c and 2. We applied a Fast Fourier Transform (FFT) to determine domain spacing. Pure L and C chains exhibit $16\sigma(= L_0^*)$ and 13σ, respectively. Dual component thin films created by blending L chains with C chains show a pattern of dots and lines coexisting in separate regions (Figure 1-b). The dots are aligned as if each one has a guided line extended from the lines, which is confirmed by the domain spacing analysis of the pattern that the dots and lines share a single characteristic domain spacing. This provides more favorable environments to C and L chains at the boundaries between regions. The response of individual BCP chains is also studied by identifying which chain constructs which object. L chains in the blends does not nearly change in terms of R_g, radius of gyration, compared to the state at $f_C = 0$ while C chains in the blends experience chain stretching when blended with L chains to form line patterns.

*Corresponding author. E-mail: kyager@bnl.gov.

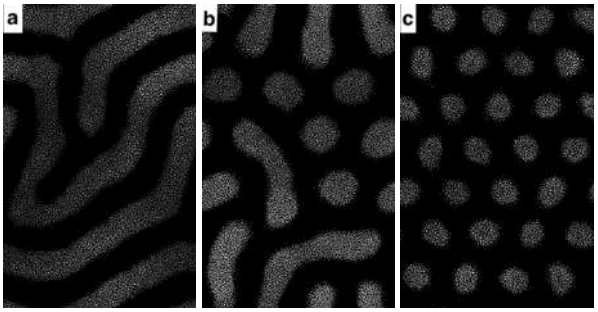

Figure 1: SEM-like top-down view images of patterns formed by (a) pure L chains at $f_C = 0$, (b) blends of C and L chains at $f_C = 0.55$, and (c) pure C chains at $f_C = 1$. Minority blocks (A blocks) remain with majority blocks (B blocks) removed.

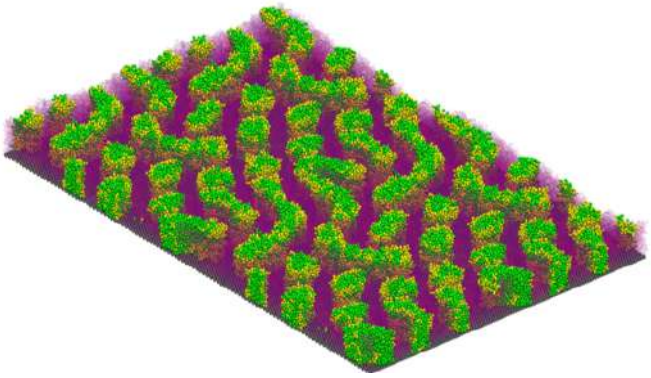

Figure 2: Perspective view image of patterns formed by blends of C and L chains at $f_C = 0.55$. Periodic images were copied and pasted in order to clearly show patterns over periodic boundary conditions. Yellow and green beads are A blocks constructing C and L chains, respectively, and purple and magenta beads are B blocks constructing C and L chains, respectively. B blocks, majority blocks, are slightly transparent to highlight vertical morphologies.

CONCLUSIONS

We built MD simulation models of BCPs in a thin film geometry with attractive interactions included. The neutral substrate was implemented in MD simulation and used to form vertical morphologies in BCP thin films. Since we focus on BCPs as patterning materials, films are thin (thickness of about $0.7L_0$) and all morphologies span the whole thickness. Pure L and C chains form undulating lines and an array of dots, respectively, and the dual component BCP thin films exhibit patterns of lines and dots coexisting in separate regions in a single film. Blending diversifies nanostructure registry and can further facilitates the use of BCPs as patterning materials.

References

[1] Yager, K.G., Lai, E. Black, C.T. *ACS Nano* **8**, 10: 10582-10588, 2014.
[2] Forrey, C., Yager, K.G., Broadaway, S. *ACS Nano* **5**, 4: 2895-2907, 2011.

A GUI-ASSISTED COMPUTATION OF LATH MARTENSITE VARIANTS

Thomas Antretter*, Manuel Petersmann, and Alexander Sannikov
Institute of Mechanics, Montanuniversitaet Leoben, Leoben, Austria

Summary Industrially relevant martensitic steels exhibit a complex morphology of martensite variants appearing as laths grouped into blocks and packets. The martensite is typically highly dislocated in order to ensure compatibility with the parent austenite matrix during formation. A graphical user interface is presented that predicts those variants that are most likely to appear in lath martensite. Knowledge of the deformation gradients accompanying the mechanisms of martensitic phase transformation in combination with shear along well defined slip planes is crucial for micromechanical full field models as illustrated by an example provided in the current work.

INTRODUCTION

In most industrially relevant martensitic steels the martensite forms at sufficiently high temperatures to make dislocation glide energetically favourable in comparison to twinning mechanisms. As has thoroughly been discussed in [1] the martensite morphology is hierarchical, with individual variants forming laths grouped in blocks, which, in turn, form packets. The position of those variants relative to the lattice of the parent phase is dictated by crystallographic compatibility conditions expressed in terms of an Invariant Plane Strain (IPS) condition. From a continuum-mechanical point of view martensite is commonly described by the classical phenomenolocial theory of martensite crystallography (PTMC). It allows calculating the deformation gradients accompanying the formation of individual martensite variants. Compatibility of those variants or ensembles thereof with the parent lattice requires $\lambda_2 = 1$ where λ_2 is the middle eigenvalue of the deformation gradient mathematically representing a transformed domain. In steels this can usually only be accomplished by applying an additional lattice invariant shear, which - on the atomic scale – is bound to discrete slip planes determined by the lattice. The latter rotates in the course of progressing deformation – a fact that is neglected by the classical PTMC. In [2] Petersmann et al. propose a concept that (i) accounts for the lattice rotation and updates it incrementally, (ii) applies an incremental amount of shear that guarantees the validity of the compatibility conditions at any time and any stage of transformation. As expected, the solution is not unique, i.e., there is a large number of eligible slip systems all ensuring the IPS condition. The number of solutions can be narrowed down by providing physically reasonable bounds dictated by crystallography-microstructure relationships reported in the literature, see e.g. [1,3,4].
The mathematical description of martensite variants is highly valuable in materials science. E.g., it is useful for inversely determining the morphology of prior austenite grains if only the martensite morphology is available from electron backscatter diffraction (EBSD) characterization, see also [5]. As another example any micromechanical model that resolves individual variants can take advantage of the presented algorithm.

THE GRAPHICAL USER INTERFACE

The theory described above has been coded into a graphical user interface (GUI) that allows computing a selection of most probable martensite variants along with their associated deformation gradients given the crystallographic features of the parent and the product lattice. Aside from lattice parameters and the lattice correspondence (defined by the Bain strain) the user must also specify the slip system families in the austenite and, if applicable, in the martensite. By default the algorithm then computes all possible deformation gradients satisfying the IPS condition. Without any additional constraint this would yield a large number of solutions where some are more likely to appear than others.

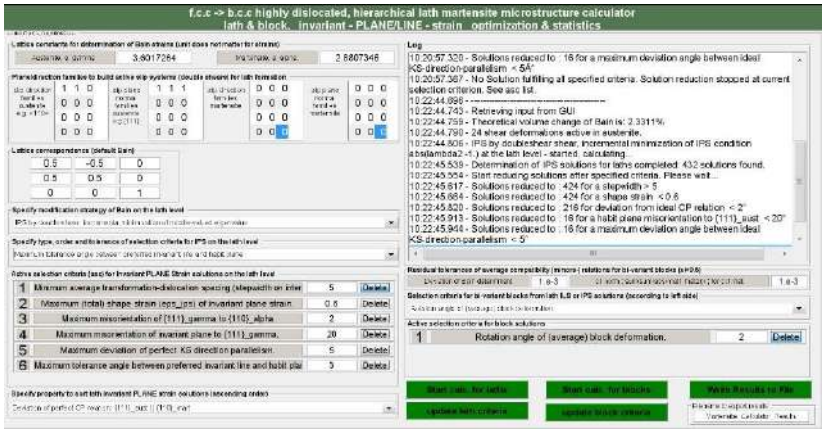

Figure 1. Graphical User Interface for calculating variants in lath martensite

The user may decide to prune the solution space by prescribing physically reasonable constraints of crystallography-microstructure relations entered in the lower left section of the GUI, see the example shown in Figure 1. In the particular case shown in this figure, the maximum misorientation angle between the {111} γ-plane and the {110} α'-plane has been set to 2°. The other constraints shown in the figure follow reasonable bounds found in the literature. Given these constraints the algorithm eventually reduces the number of solutions to a mere 16, see the upper right log window of the GUI. The so-determined solutions constitute bi-variant blocks which, in turn, are subject to selection criteria and constraints that can be defined in the lower right section of the GUI. The deformation gradients passing all filters set by the user are written to a results file for further use. The GUI is freely available at [6].

APPLICATION TO MICROMECHANICAL MODELS

The phenomena ensuing phase transformations in solids are frequently studied by means of representative volume elements (RVE), where the evolution of the morphology is monitored by phase field approaches, see e.g. [7]. The focus of this work is on studying the evolution of internal stresses and strains under the influence of an external stress. By contrast, here the thermodynamics of the phase formation is not considered. Therefore, it is admissible to prescribe the volume fraction of the product phase as a function of temperature without having to solve the phase field equations. The information of the transformation strains is obtainable from the deformation gradients calculated by the GUI presented above. The RVE is discretized by 32 x 32 x 32 finite elements, see Figure 2. Starting from a randomly chosen nucleation site an element is toggled from austenite to martensite by imposing the transformation strains from the list generated by the GUI. The direction of further growth of the variant is governed by the same arguments of austenite to martensite compatibility that defines the eligible transformation strains. The shape of the growing martensite domain is assumed ellipsoidal. It is further assumed that a martensite lath grows rapidly until it hits an obstacle such as an already existing variant or the domain boundary as represented by the faces of the RVE, see Figure 2. Such models can subsequently be used to calibrate mean-field models accounting for the consequences of martensitic transformation in industrially relevant steels.

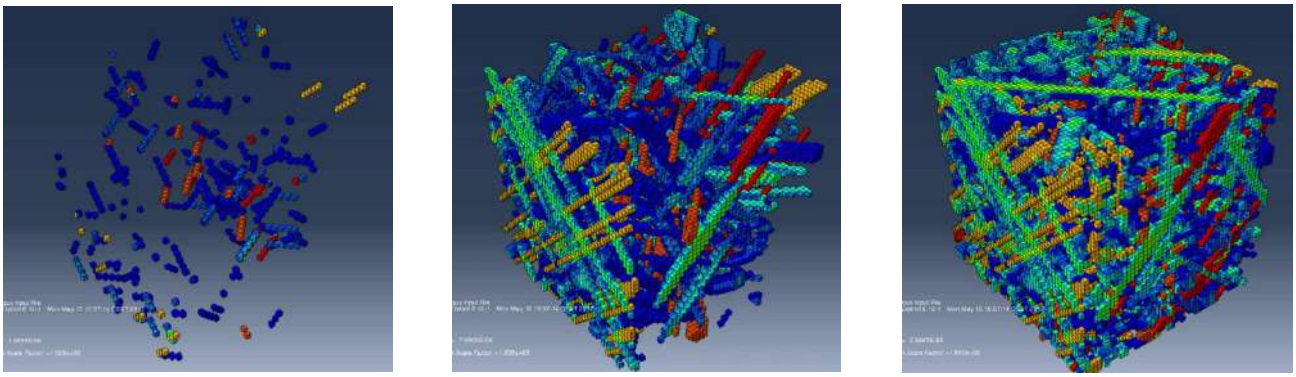

Figure 2. a) Representative volume element. The martensite fraction increases from left to right from 5% to 40% and 70%. The color coding indicates the reference to the habit plane. The elements representing the austenite are not shown.

CONCLUSIONS

A GUI-assisted implementation of the phenomenological theory of martensite enhanced by an incremental lattice orientation update produces the most probable set of transformation tensors of lath martensite variants. This information has been inserted into a RVE-based micromechanical model that allows the calculation of phase-specific stress and strain fields which can be used for the calibration of macroscopic models for materials undergoing martensitic transformation.

References

[1] Morito, S., Huang, X., Furuhara, T., Maki, T., Hansen, N. The morphology and crystallography of lath martensite in alloy steels. *Acta Mater.* **54**: 5323–5331, 2006.

[2] Petersman M., Antretter T., Sannikov A., Ehlenbröker U., Fischer F.D. Unification of the non-linear geometric transformation theory of martensite and crystal plasticity - application to dislocated lath martensite in steels. *Int. J. Plasticity* **119**: 140-155, 2019.

[3] Maresca, F., Curtin, W. The austenite/lath martensite interface in steels: structure, athermal motion, and in-situ transformation strain revealed by simulation and theory. *Acta Mater.* **134**: 302–323, 2017.

[4] Khachaturyan, A. Theory of Structural Transformations in Solids. Dover Publications Inc., Mineola, New York 1983.

[5] Cayron, C., Artaud, B., Briottet, L. Reconstruction of parent grains from EBSD data. *Mater. Char.* **57**: 386–401, 2006.

[6] https://github.com/ManuelPetersmann/Martensite_Calculator

[7] Levitas, V.I. Phase field approach for stress- and temperature-induced phase transformations that satisfies lattice instability conditions. part i. general theory. *Int. J. Plasticity* **106**: 164–185, 2018.

VARIATIONAL MODELING OF THE INFLUENCE OF CYCLIC THERMAL AND MECHANICAL LOADING ON THE PHASE TRANSFORMATION IN SHAPE MEMORY ALLOYS

Johanna Waimann*[1], Stefanie Reese[1], and Philipp Junker [2]
[1]Institute of Applied Mechanics, RWTH Aachen University, Aachen, Germany
[2]Institute of Continuum Mechanics, Ruhr-University Bochum, Bochum, Germany

Summary The phase transformation in shape memory alloys is induced by thermal as well as mechanical loading. The resulting special material properties can be summarized in the one-way and two-way effect as well as in the name giving shape memory effect. Under cyclic loading the material behaviour and thus the start of the phase transformation is influenced by the so-called effect of functional fatigue. We will present a material model which is based on the principle of the minimum of the dissipation potential and enables us to display the complex microstructural behaviour. In addition, we will show the model's implementation within a finite element scheme. Our results - on the material point level as well as on the finite element level show - the model's functionality.

INTRODUCTION

The microstructure of shape memory alloys (SMA) is highly influenced by the diffusionless phase transformation between austenite and several martensitic variants. Compared to classical steel, the transformation process is not only induced by thermal but also by mechanical loads. Due to this special microstructural evolution, SMA are very attractive for the industry, but their applicability is still limited by the so-called effect of functional fatigue. This effect comes along with the cyclic loading of the class of materials and results in a changed start of the transformation until convergence. During cyclic mechanical loading, the transformation from austenite to martensite is favoured and the reverse transformation is delayed. The transformation is accompanied by the accumulation of a remaining strain. The cyclic thermal loading leads to the opposite effect on the transformation behaviour: the transformation from austenite to martensite is delayed and the reverse transformation favoured [1].
Compared to our former works, we will present a material model which is able to show not only the material behaviour during mechanical but also during thermal cycling. In addition, we will present its finite element implementation and several numerical results.

INTERNAL VARIABLES AND VARIATIONAL CONCEPT

We use three internal variables to describe the complex microstructure: $\boldsymbol{\Lambda} = \{\boldsymbol{\lambda}, \rho, \boldsymbol{\alpha}\}$. The volume fraction of the austenite and the martensites $\boldsymbol{\lambda}$ describes the phase transformation. The transformation history variable ρ accounts for the fatigue effects. Based on [2], to additionally consider the polycrystalline structure of the material and thus the different oriented grains, a set of three Euler angles $\boldsymbol{\alpha}$ is used. The Euler angles describe the averaged orientation of the transformation which is taking place and thus, enable a faster computation than a grain-wise calculation of the phase transformations.
A first description of the model is presented in [3] and is based on the classical form of the principle of the minimum of the dissipation potential (PMDP) [4]. In its original form the PMDP is only applicable for isothermal problems. In [5], the method's extension for non-isothermal processes is given, which is also the base for the presented approach. The main idea of the PMDP is the minimization of a Lagrange function, which is an energetic term that describes the microstructure and its evolution of the observed material, with respect to the used internal variables' rates $\dot{\boldsymbol{\Lambda}}$. For non-isothermal processes the PMDP is formulated by

$$\mathcal{L} = \overline{\mathcal{D}} - \mathcal{D} \rightarrow \min_{\dot{\boldsymbol{\Lambda}}, \boldsymbol{q}} .$$

Therein, $\overline{\mathcal{D}}$ is a dissipation function which describes the energy which is necessary for the microstructural evolution. The variable $\mathcal{D}$ is the well-known dissipation. Compared to the classical PMDP the minimization is not only performed with respect to the rates of the internal variables but also with respect to the heat flux $\boldsymbol{q}$. The minimization automatically results in evolution equations for $\boldsymbol{\Lambda}$ and a modified form of the classical heat balance equation.
Finally, we will perform a Legendre transformation, which leads to a yield function for the phase transformation and the related Karush-Kuhn-Tucker conditions.

FINITE ELEMENT IMPLEMENTATION AND NUMERICAL RESULTS

After the derivation of the evolution equations, we will present the implementation of our model within a finite element algorithm. Therefore, we use an explicit scheme in form of a broken Taylor series.

*Corresponding author. E-mail: waimann@ifam.rwth-aachen.de.

The numerical results for a prescribed strain tensor and changing temperature [see Figure 1], show the functionality of our variational approach: The favouring transformation from austenite to martensite during the mechanical cycling (*left*) as well as the decrease of the transformation temperatures during thermal cycling (*right*). The presentation of first finite element results for the thermo-mechanically coupled variational material model, will show the applicability for more realistic problems.

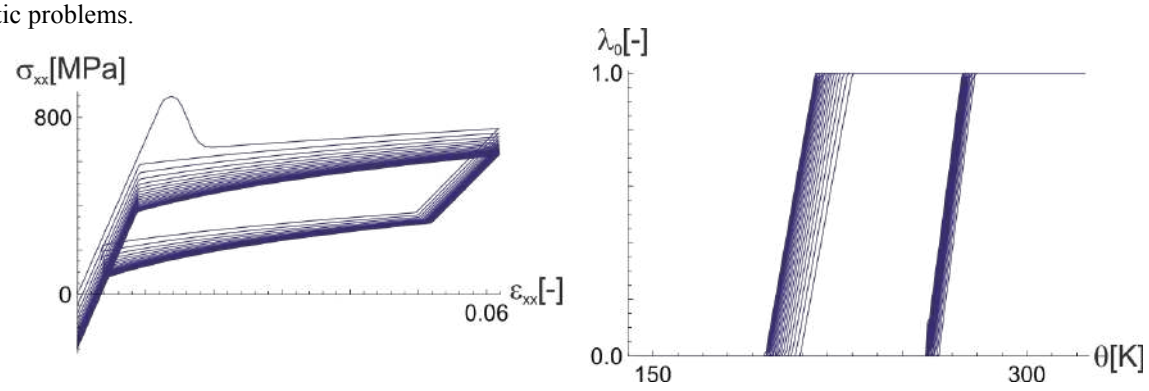

Figure 1. Simulations of cyclic mechanical loading (*left*): stress/strain-diagram; cyclic thermal loading (*right*): evolution of the austenite, see also [3].

CONCLUSIONS

In our talk, we will present the variational material model for thermal and mechanical cycling of shape memory alloys. Compared to our earlier works, we will use the principle of the minimum of the dissipation potential for non-isothermal problems and show the implementation within a finite element algorithm. The later numerical results show the models ability to display the complex material behaviour.

References

[1] Burow J. *PhD Thesis*, Ruhr-University Bochum, 2010.
[2] Junker P. Int. J. Numer. Meth. Eng. 98(11): 799–818, 2014.
[3] Waimann J. *PhD Thesis*, Ruhr-University Bochum, 2018.
[4] Carstensen C., Hackl K., Mielke A. P. Roy. Soc. Lond. A. Mat., 2002.
[5] Junker P., Makowski J., Hackl K. Continuum Mech. Therm., 2014.

PHASE-FIELD MODELLING OF NANO-INDENTATION IN SHAPE MEMORY ALLOYS: MICROSTRUCTURE AND SIZE EFFECTS

Mohsen Rezaee-Hajidehi[1], Karel Tůma[2], and Stanisław Stupkiewicz*[1]
[1]Institute of Fundamental Technological Research (IPPT), Warsaw, Poland
[2]Faculty of Mathematics and Physics, Charles University, Prague, Czech Republic

Summary A finite-strain phase-field model has been developed for the analysis of multivariant martensitic transformation in shape memory alloys (SMAs). The complete evolution problem is formulated within the incremental energy minimization framework, and its computational treatment is based on the finite-element method. The model has been applied to study the stress-induced martensitic transformation during nano-indentation. The study has revealed several interesting effects such as the pop-in effect associated with the martensite nucleation event and the energy-lowering breakdown of the symmetry of microstructure.

INTRODUCTION

Instrumented micro- and nano-indentation is a powerful and popular experimental technique, and thus it has been the subject of extensive computational modelling. This concerns also numerical simulations of indentation in SMAs. However, the studies reported in the available literature are limited to the macro- and meso-scales where either macroscopic phenomenological models or micromechanical crystal-plasticity-like models are used, which does not allow direct simulation of microstructure formation and evolution. On the other hand, atomistic simulations that employ the molecular dynamics (MD) models are limited to very small spatial and temporal scales. Apparently, continuum modelling of spatially-resolved martensitic microstructures in SMAs during nano-indentation is missing. Accordingly, our aim has been to fill this gap, and the phase-field method, which is a suitable approach at the relevant scales, has been adopted in this work. The respective model and the results of preliminary 2D simulations have already been published [1], while 3D simulations are the subject of ongoing work.

FINITE-STRAIN MULTIPHASE-FIELD MODEL

The model is an extension of our recent finite-strain phase-field model [2]. In particular, the multiphase double-obstacle potential [3] has been employed with the order parameters representing the volume fractions of the phases or martensite variants. The complete evolution problem is formulated as a constrained minimization problem for the global incremental potential that comprises the increments in potential energy and dissipation, the latter of the viscous type. The inequality constraints imposed on the order parameters as well as the unilateral contact constraints are then regularized using the penalty method, which leads to a straightforward finite-element implementation. Interestingly, a parametric study has shown that the penalty method performs surprisingly well for the problem at hand, also in the case of large-scale problems (with several million unknowns) solved using iterative solvers. In fact, simulation of multivariant transformations in 3D inevitably leads to large-scale problems. This is because the global unknowns comprise the nodal displacements and several order parameters and a uniform fine mesh is needed to accurately resolve the evolving diffuse interfaces.

MICROSTRUCTURE AND SIZE EFFECTS IN NANO-INDENTATION

Selected results of phase-field simulations of nano-indentation in pseudoelastic SMAs are shown in Figs. 1–3 and are briefly commented below. Preliminary studies have been carried out for a model problem of the square-to-parallelogram transformation in 2D with four variants of martensite. Fig. 1 shows the respective stress-induced microstructures for the indenter radius R varied between 25 nm and 100 nm. The colours in Fig. 1 indicate the domains occupied by the individual martensite variants according to the legend included in Fig. 1. The three microstructures in Fig. 1 correspond to the same normalized indentation depth $h/R = 0.6$, and the differences in shape and size result from the substantial effect of the interfacial energy which delivers a size-dependent contribution to the total free energy. It can also be seen that the microstructure corresponding to $R = 100$ nm is non-symmetric. It has been checked that the non-symmetric microstructure is energetically more favourable than the symmetric one, and it is not a numerical artifact.

Size effects are also illustrated in Fig. 2a which shows the normalized load P/R as a function of the normalized indentation depth h/R for three indenter radii R. The initial elastic response is size independent, however, the load at which martensite nucleates (which is associated with a load drop that leads to the characterisitc pop-in effect) and the subsequent response visibly depend on the indenter radius. Specifically, the normalized load needed to achieve a specified normalized indentation depth is higher for a smaller indenter radius. This is also visible in Fig. 2b which shows the dependence of the hardness on the indenter radius. Here, the hardness is determined for the fixed ratio of $h/R = 0.5$ and exhibits the usual indentation size effect (‘smaller is stronger’).

*Corresponding author. E-mail: sstupkie@ippt.pan.pl.

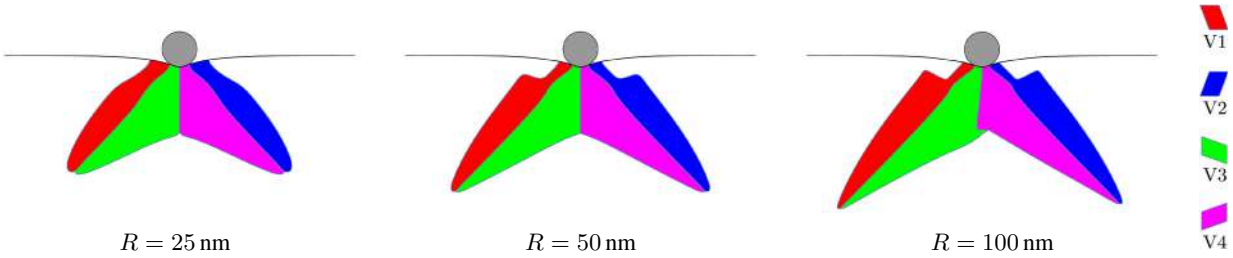

Figure 1: The effect of the indenter radius R on the microstructure for the square-to-parallelogram transformation in 2D [1].

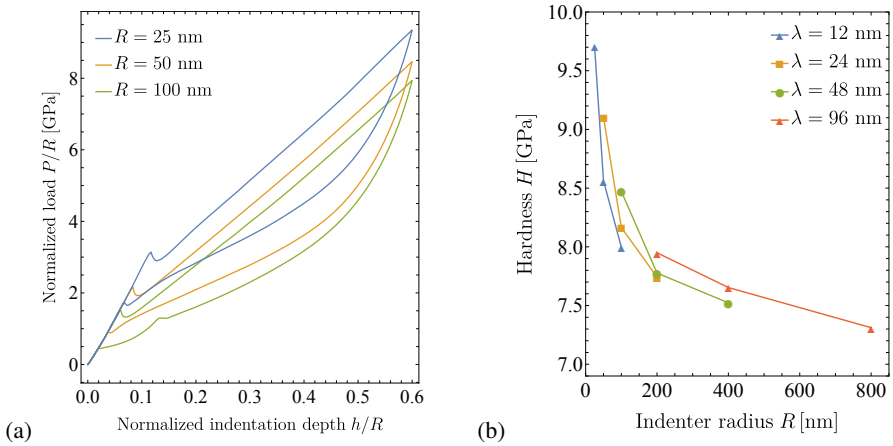

Figure 2: Size effects in nano-indentation: (a) normalized P–h curve; (b) dependence of the hardness on the indenter radius [1].

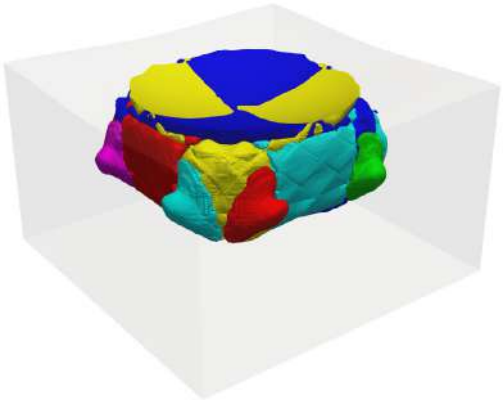

Figure 3: Stress-induced cubic-to-orthorhombic transformation in CuAlNi in nano-indentation, indenter radius $R = 200\,\text{nm}$.

Fig. 3 shows a 3D microstructure predicted for the cubic-to-orthorhombic transformation in a CuAlNi alloy for the indenter radius $R = 200\,\text{nm}$ and indentation depth $h = 28\,\text{nm}$ (the colours indicate the individual martensite variants, the austenite is transparent, the domain size is $280\times280\times160\,\text{nm}^3$). Note that there are six variants of martensite in this transformation, and thus six order parameters are needed in the respective phase-field model. The complete computational model involves thus nine global unknown fields that leads to a large-scale problem with about 10 million unknowns.

CONCLUSIONS

A finite-strain phase-field model has been developed for the analysis of multivariant martensitic transformation in SMAs. The model has been implemented in the finite-element code and successfully applied to simulate spatially-resolved microstructure evolution during nano-indentation revealing a number of important qualitative effects, including the size effects that are governed by the interfacial energy of phase boundaries.

References

[1] Rezaee-Hajidehi M., Stupkiewicz S. Phase-field modeling of multivariant martensitic microstructures and size effects in nano-indentation. *Mech. Mater.* **141**: 103267, 2020.

[2] Tůma K., Stupkiewicz S., Petryk H. Size effects in martensitic microstructures: Finite-strain phase field model versus sharp-interface approach. *J. Mech. Phys. Solids* **95**: 284-307, 2016.

[3] Steinbach I. Phase-field models in materials science. *Modell. Simul. Mat. Sci. Engng.* **17**: 073001, 2009.

THERMO-MECHANICALLY COUPLED MODEL FOR PHASE TRANSITION IN AUSTENITIC STEELS FOR LOW TEMPERATURE APPLICATIONS

Mrityunjay Kothari[1], Sijun Niu[2], and Vikas Srivastava *[2]
[1]Department of Civil & Environmental Engineering, Massachusetts Institute of Technology, Cambridge, MA, USA
[2]School of Engineering, Brown University, Providence, RI, USA

Summary. Metastable austenitic steels show plastic strain driven transformation to martensite at low temperatures. We have developed a finite-strain coupled thermo-mechanical continuum theory to model this austenite-martensite phase transition and implemented the model in ABAQUS through a user material subroutine. Our simulation-based predictions show good agreement with full scale experiments on corrugated-pipe in the range of room temperature to cryogenic temperature.

INTRODUCTION/MOTIVATION

The mechanical properties of austenitic steels make them desirable for a wide range of applications ranging from automobile industry to extreme temperature applications [1-4]. Metastable austenitic steels with γ phase and face-centered cubic (FCC) crystal structure show *plastic strain driven phase transformation* to α'-martensite phase with body-centered cubic (BCC) structure and this effect becomes more prominent at cryogenic temperatures. In applications such as transport of liquefied natural gas (LNG) through flexible, pre-strained austenitic steel pipes, understanding the response of steel to complex thermomechanical loading is crucial to ensure the proper design and safety. Since the martensite phase is harder than the austenite phase, this transition results in a *second strain-hardening in the stress-strain* response. Following Olson's and Cohen's seminal contribution [5,6], we assumed the intersection of shear bands as nucleation sites for martensite embryos and modeled the temperature dependent evolution of martensite volume fraction. In this paper, we address an important gap by presenting a fully-coupled, finite-strain, continuum thermo-mechanical model for phase transitioning austenitic steels. Our model is capable of simulating complex thermomechanical loadings and loading histories that are typical in real applications. We implement our model in finite element software ABAQUS through a user material subroutine and validated the predictions by comparison with full scale experiments on corrugated pipes at both room and cryogenic temperatures.

KEY HIGHLIGHTS OF THE MODEL

Free Energy

$$\boldsymbol{F} = \boldsymbol{F}_{\gamma}^{e}\boldsymbol{F}_{\gamma}^{p} = \boldsymbol{F}_{\alpha'}^{e}\boldsymbol{F}_{\alpha'}^{p} \qquad \text{(Kröner – Lee Decomposition)}$$

$$\psi = \phi_{\gamma}\psi_{\gamma} + \phi_{\alpha'}\psi_{\alpha'} \qquad \text{(Voigt – type Composite)}$$

$$\psi_{\gamma} = G_{\gamma}\left|\boldsymbol{E}_{\gamma}^{e}\right|^{2} + \lambda_{\gamma}\boldsymbol{tr}\left(\boldsymbol{E}_{\gamma}^{e}\right)^{2} - \alpha_{th}\left(2G_{\gamma} + 3\lambda_{\gamma}\right)(\theta - \theta_{0})\boldsymbol{tr}\left(\boldsymbol{E}_{\gamma}^{e}\right) - \frac{C_{\gamma}}{2\theta_{0}}(\theta - \theta_{0})^{2} \qquad \text{(Free Energy Density)}$$

where $\boldsymbol{F}$ is the deformation gradient, $\boldsymbol{F^e}$ is the elastic part, $\boldsymbol{F^p}$ is the plastic part, subscripts γ, α' denote the phase. ψ denotes the free energy density, ϕ denotes the volume fraction of the phase, $\boldsymbol{E}$ is the Lagrange strain tensor, G is the shear modulus, λ is the Lamé constant, θ is the temperature, θ_0 is a particular reference temperature, α_{th} is the coefficient of thermal expansion, C is the heat capacity. Mathematical form for free energy expression for martensite is same as what is shown for austenite.

Stress

$$\boldsymbol{T} = \phi_{\gamma}\boldsymbol{T}_{\gamma} + \phi_{\alpha'}\boldsymbol{T}_{\alpha'} \qquad \text{(Cauchy Stress)}$$

$$\boldsymbol{T}_{\gamma} = J^{-1}\boldsymbol{F}_{\gamma}^{e}\frac{\partial\psi_{\gamma}}{\partial\boldsymbol{E}_{\gamma}^{e}}\boldsymbol{F}_{\gamma}^{e\,T} \text{ and } \boldsymbol{T}_{\alpha'} = J^{-1}\boldsymbol{F}_{\alpha'}^{e}\frac{\partial\psi_{\alpha'}}{\partial\boldsymbol{E}_{\alpha'}^{e}}\boldsymbol{F}_{\alpha'}^{e\,T};\ J = \det\boldsymbol{F}$$

where $\boldsymbol{T}$ is the Cauchy stress.

Flow Rule

$$\sqrt{3/2}\boldsymbol{M}_{\boldsymbol{0}}^{\boldsymbol{e}} = \left\{\phi_{\gamma}Y_{\gamma}\left(\bar{\epsilon}_{p}\right) + \phi_{\alpha'}Y_{\alpha'}\left(\bar{\epsilon}_{p}\right)\right\}\boldsymbol{N^p}$$

where $\boldsymbol{M}$ is the Mandel stress, Y is yield function, $\boldsymbol{N^p}$ is the direction of plastic flow.

Balance of Energy

$$C\dot{\theta} = -Div\,\boldsymbol{q} + \omega\left(\phi_{\gamma}\bar{\sigma}_{\gamma}\dot{\bar{\epsilon}}_{p\gamma} + \phi_{\alpha'}\bar{\sigma}_{\alpha'}\dot{\bar{\epsilon}}_{p\alpha'}\right) - l\dot{\phi}_{\alpha'}$$

where $\boldsymbol{q}$ is the heat flux, ω is the fraction of plastic work converted to heat, l is the latent heat due to martensitic phase transformation.

Hardening Behavior

$$\bar{\sigma}_{\gamma} = \bar{\sigma}_{Y\gamma} + K_{\gamma}\bar{\epsilon}_{p}^{m} \quad \text{and} \quad \bar{\sigma}_{\alpha'} = \bar{\sigma}_{Y\alpha'} + K_{\alpha'}\bar{\epsilon}_{p}^{n} \qquad \text{(Power – law hardening)}$$

where $\bar{\epsilon}_p$ is the equivalent plastic strain, $\bar{\sigma}$ is the equivalent tensile stress, and K, m, n are temperature-dependent strain-hardening parameters.

*Corresponding author. E-mail: vikas_srivastava@brown.edu.

Kinetics of Martensite Evolution

$$\dot{\phi}_{\alpha'} = (1-\phi_{\alpha'})\beta\dot{\phi}_{sb}^{a} \text{ and } \dot{\phi}_{sb} = (1-\phi_{sb})\alpha\dot{\epsilon}_{p} \quad \text{(From [5])}$$

where ϕ_{sb} and $\phi_{\alpha'}$ denote the volume fraction of shear bands and martensite respectively. α, β and a are parameters of the model that are obtained by fitting the predictions of the model to the experimental data.

RESULTS AND DISCUSSIONS

The parameters for the thermomechanical model were obtained from uniaxial tensile test data [7]. Figure 1 shows the fits and highlights the stark difference in stress-strain response and evolution of martensite volume fractions between the two temperatures. While there is no significant martensite formed at the room temperature, considerable martensite is produced at cryogenic temperature. Note the second strain hardening is well-captured in this model.

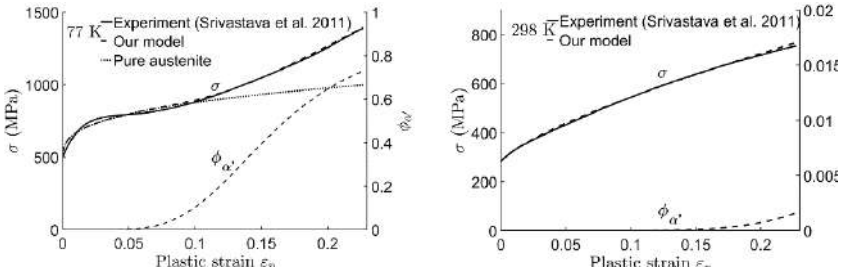

Figure 1. Model fit for 316L steel uniaxial tensile tests on flat dog-bone specimen at (a) room and (b) cryogenic temperatures. Left-axis: stress-strain curves. Right-axis: martensite evolution prediction by the model

Next, we evaluated the predictive capabilities of our model by carrying out tensile and compressive simulations of a full-scale C-pipe resulting in inhomogeneous local deformation and comparing the model predictions with experimental results. We replicated the steps involved in formation of the C-pipe as described in Figure 2. These steps were followed by tensile/compressive simulation and the results were compared with experiments. Figure 3 shows the force vs global strain response for tensile and compressive tests at both room and cryogenic temperatures. At 77 K, plastic straining produces a significant amount of martensite which makes the pipe stiffer than at 298 K. The figure shows good agreement between simulation predictions and experimental results.

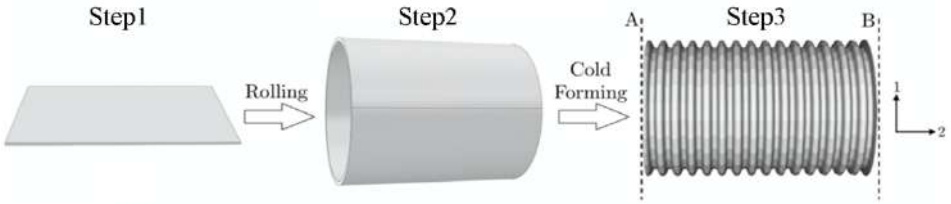

Figure 2. The steps involved in the manufacturing of the corrugated pipe.

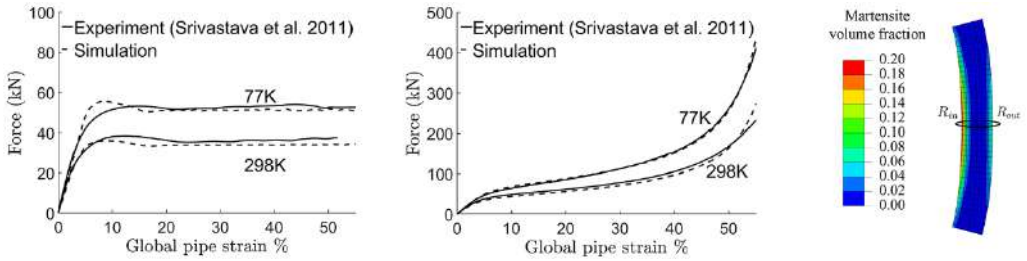

Figure 3. Force versus global pipe strain of a room temperature preformed C-pipe under (a) tensile load and (b) compressive load, (c) formed martensite across wall thickness of pipe corrugation under tension. In (a) and (b), simulation results (dotted lines) are plotted against experiments (solid lines) for room and cryogenic temperature.

References

[1] P. Jacques, Q. Furn´emont, F. Lani, T. Pardoen, F. Delannay, Multiscale mechanics of TRIP-assisted multiphase steels: I. Characterization and mechanical testing, *Acta Materialia* 55 (2007) 3681–3693.
[2] W. Bleck, I. Schael, Determination of crash-relevant material parameters by dynamic tensile tests, *Steel Research* 71 (2000) 173–178.
[3] V. Srivastava, J. Buitrago, S. T. Slocum, Stress analysis of a cryogenic corrugated pipe, *Proceedings of the ASME 2011 30th International Conference on Ocean, Offshore and Arctic Engineering*: Volume 3, American Society of Mechanical Engineers (2011) 411–422.
[4] A. Tyshchenko, W. Theisen, A. Oppenkowski, S. Siebert, O. Razumov, A. Skoblik, V. Sirosh, Y. N. Petrov, V. Gavriljuk, Low-temperature martensitic transformation and deep cryogenic treatment of a tool steel, *Materials Science and Engineering*: A 527 (2010) 7027–7039.
[5] G. B. Olson, M. Cohen, Kinetics of strain-induced martensitic nucleation, *Metallurgical Transactions* A 6 (1975) 791–795.
[6] T. Narutani, G. B. Olson, M. Cohen, Constitutive Flow Relations for Austenitic Steels during Strain Induced Martensitic Transformation, *Le Journal de Physique Colloques* (1982).
[7] M. Kothari, S. Niu, V. Srivastava, A thermo-mechanically coupled finite strain model for phase-transitioning austenitic steels in ambient to cryogenic temperature range, *Journal of the Mechanics and Physics of Solids* 133 (2019) 103729

PHENOMENOLOGICAL MODELING OF THE TWO-WAY SHAPE MEMORY EFFECT IN SHAPE MEMORY ALLOYS

Giulia Scalet*[1], Fabrizio Niccoli[2], Cedric Garion[2], Paolo Chiggiato[2], Carmine Maletta[3], and Ferdinando Auricchio[1]
[1]DICAr, University of Pavia - Italian Interuniversity Consortium on Materials Science and Technology (INSTM), Unit of Pavia, Pavia, Italy
[2]CERN-European Organization for Nuclear Research, Geneva, Switzerland
[3]Department of Mechanical, Energy and Management Engineering, University of Calabria, Rende (CS), Italy

Summary This work presents a three-dimensional phenomenological constitutive model considering plastic deformation and the two-way shape memory effect in severely pre-strained NiTi-based SMAs. A discussion about model calibration and implementation procedure within a finite element framework is addressed. Numerical responses for several loading conditions are compared against experimental results to validate the proposed modeling capabilities and to discuss the effect of plastic deformation on the one-way and two-way shape memory effect as well as on transformation temperatures.

INTRODUCTION

Shape Memory Alloys (SMAs) are smart materials possessing unique strain recovery capabilities due to reversible solid-state microstructural transitions, induced either by temperature changes or by mechanical loads, between a parent body-centered cubic phase (austenite) and a product monoclinic phase (martensite). Particularly, the two-way shape memory effect (SME) describes the ability of the SMA to change its shape reversibly during subsequent thermal cycles between its transformation temperatures under zero mechanical load. Such an effect is particularly exploited for the realization of dismountable and thermally-stable connection systems, operating without biasing elements [1].

The two-way SME is not a natural SMA feature, but can be induced in the material through a specific thermo-mechanical cyclic treatment (known as 'training' process) or a one-time martensite deformation. The latter treatment consists in deforming the SMA in the martensitic phase, unloading the material, and then in thermal cycling. Such a method generally causes two-way SME strains of limited magnitude; however, it has been shown by Liu et al. [2] that the two-way SME strains can be increased by imposing severe martensitic deformations, e.g., causing plastic yielding.

Differently from the two-way SME induced by training, the behavior induced by the one-time martensite deformation treatment has been less studied. In fact, to the authors' knowledge, no works from the current literature address the modeling of the effect of plastic deformation, occurring during severe martensitic pre-strain and possible subsequent constrained thermal cycles, on the two-way SME and on transformation temperatures.

The aim of the present work is to experimentally and numerically investigate plastic yielding and two-way SME in severely pre-strained SMAs. To this purpose, a three-dimensional constitutive model will be proposed and validated on experimental data from a performed experimental campaign. The assisted-design of fasteners and couplers will be presented and discussed.

METHODOLOGY

This work proposes to extend the three-dimensional small strain macroscopic phenomenological model by Souza et al. [3] to describe the response of severely pre-strained NiTi alloys.

Accordingly, in the framework of continuum thermodynamics with internal variables under small strain, two tensorial internal variables, i.e. the transformation strain and the plastic strain, are introduced to describe the macroscopic strain associated, respectively, to thermally-induced or stress-induced martensitic transformations and to plastic effects in SMAs. Constitutive equations and evolution laws are then written in a thermodynamically-consistent framework and a physical interpretation of model parameters is provided. Model equations are implemented within a finite element framework allowing for solving different boundary value problems. For the numerical implementation, the so-called Fischer–Burmeister complementarity function [4] is used since it allows to handle, in an easy way, complementarity inequality conditions deriving from physical constraints on internal variables and from the adopted yield surface-based formulation.

In order to calibrate and validate the model, an experimental campaign on a Ni rich NiTi alloy (50.8Ni-49.2Ti % at.) is performed. Uniaxial stress-free as well as constrained thermal recovery tests are carried out after mechanical pre-strain to measure both the transformation temperatures and shape recovery capabilities of the alloy, in terms of, e.g., one-way and two-way shape memory strains and recovery stresses.

*Corresponding author. E-mail: giulia.scalet@unipv.it.

RESULTS AND DISCUSSION

Several numerical simulations are performed, including uniaxial stress-free and constrained thermal recovery tests as well as finite element analyses for the assisted-design of a ring-shaped coupler and a C-shaped fastener (see Figure 1). Results from numerical simulations of uniaxial isothermal tests as well as free and constrained thermal recovery are validated through experimental data showing good agreement. Transformation temperatures as well as the two-way shape memory strain are shown to depend on the amount of plastic deformation obtained during pre-strain and unloading steps. Additionally, various aspects of SMA behavior, in particular low-stress phase transformations, phase-dependent material properties, and thermal strains, are also shown to affect the two-way SME.

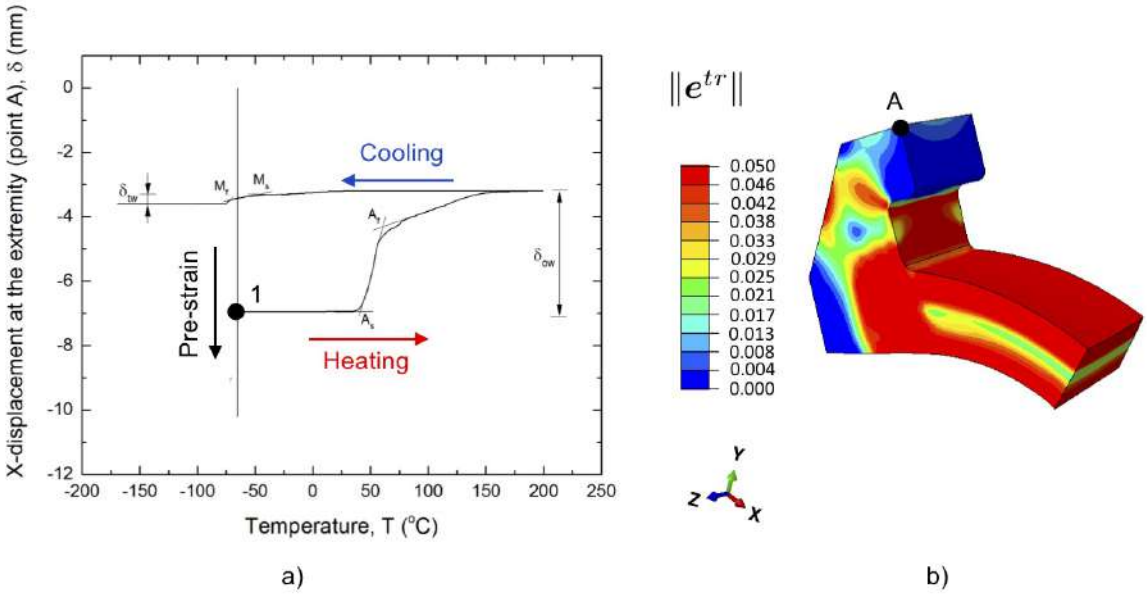

Figure 1: Finite element analysis of a C-shaped fastener. (a) Temperature-displacement diagram obtained after martensitic pre-strain, unloading, and subsequent stress-free heating and cooling cycle; (b) deformed mesh of half of the C-shape fastener after martensitic pre-strain and unloading with the contour plot of the norm of the transformation strain.

CONCLUSIONS

This paper has investigated the two-way SME and plastic effects in severely pre-strained SMA materials by formulating an extended three-dimensional macroscopic model. The achieved results demonstrate the possibility of using the model for the design of components under such a complex SMA material behavior.

ACKNOWLEDGMENTS

This work was partially supported by the project ”Nuovi materiali e approcci computazionali per stampa 4D” of INSTM Consortium.

References

[1] Jani, J., Leary, M., Subic, A., Gibson, M., A review of shape memory alloy research, applications and opportunities, *Materials & Design*, **56**:1078-1113, 2014.

[2] Liu Y., Liu Y., Van Humbeeck J., Two-way shape memory effect developed by martensite deformation in NiTi, *Acta Materialia*, **47**(1): 199-209, 1998.

[3] Souza, A., Mamiya, E., Zouain, N., Three-dimensional model for solids undergoing stress-induced phase transformations, *Eur. J. Mech. A/Solids*, **17**:789-806, 1998.

[4] Fischer, A., A special Newton-type optimization method, *Optimization*, **24**:269-284, 1992.

THERMODYNAMICALLY CONSISTENT JOHNSON-COOK-LIKE MATERIAL MODEL IN COSSERAT MEDIA UNDER LARGE DEFORMATIONS FOR FUTURE MANUFACTURING SIMULATION

Raffaele Russo[1], Franck Girot Mata *[1,2], and Samuel Forest †[3]
[1]Department of Mechanical Engineering, Faculty of Engineering of Bilbao, University of the Basque Country, Bilbao, Spain.
[2]IKERBASQUE, Basque Foundation for Science, Bilbao, Spain.
[3]CentresdesMatériaux,MINESParisTech,PSLUniversity,Evry,France.

Summary Simulations of manufacturing techniques involving metals deserve proper attention when material softening occurs. It is, in fact, well known that the classical set of equations governing the equilibrium yields to non-unique solutions when the material experiences softening. In this article we make use of the Cosserat theory as a possible solution to this problem. We present a Cosserat theory under a large deformation framework, enriched with a thermodynamically-consistent Johnson-Cook-like description of the material behavior. The theory has been used to simulate localization phenomena in a Hat-Shaped Specimen test.

MOTIVATIONS

Most metal transformation processes, such as machining, friction stir welding and superplastic forming, induce large deformations and high deformation rates in the material. In some cases, at high strain rate, and for specific metals, the deformation localizes into adiabatic shear bands, i.e. zones in which the material exothermically deforms, mostly by shear. At this location, the heat production rate due to plastic deformation may result larger than the heat diffusion rate, thus inducing the material to locally retain high temperature and to subsequently experience thermal softening.

Under these circumstances, the classical models used in Continuum Mechanics result to be inadequate to predict the deformation of the media and material behavior, and the causes lie in the loss of hyperbolicity of the *Partial Differential Equations* (PDE) governing the equilibrium [De Borst and Mühlhaus 1992]. This inadequacy appears as mesh dependency if these PDEs were to be discretized through *Finite Element Methods* (FEMs). The set of PDEs therefore requires a regularization method. One possible solution involves the introduction of non-local quantities at the constitutive law level (gradient-enhanced models). Among many other possible candidates, in the current work we decided to employ a Cosserat description of the media to solve the problem.

The Cosserat description of the media is a generalization of the classical continuum mechanical model, in the specific, the Cosserat brothers [E. Cosserat and F. Cosserat 1909] provided a model in which the microstructural rotation is decoupled from the material rotation. In the classical models instead, by adopting the point of view of the Cosserats, the microstructure rotation follows inertially the material rotation.

Within our scopes, the Cosserat model would allow us to enlarge the domain in which the ellipticity of the PDEs is retained, thus avoiding problems related to non-uniqueness of the solution and mesh dependency when metal manufacturing processes ought to be simulated. This is achieved through the adoption of the gradient of the microrotation as an additional deformation measure, consequently introducing a characteristic length in the model.

Another fundamental feature introduced by the adoption of the Cosserat model is that we are able to characterize the material response with more sophisticated models. The microstructural rotation and its gradient are used as additional deformation measures, thus contributing in defining the constitutive behavior of the material.

MODEL DESCRIPTION

The hyper-elastic version of the Cosserat model can be initially described by explicitly stating the definition of the internal power $p^{(i)}$ as:

$$p^{(i)} = \underset{\sim}{\sigma} : (\underline{\mathbf{v}} \otimes \underline{\nabla} - \underset{\sim}{\omega}) + \underset{\sim}{\mathbf{m}} : \left(\overset{\times}{\underline{\omega}} \otimes \underline{\nabla}\right); \tag{1}$$

where $\underset{\sim}{\sigma}$ is the non-symmetric stress tensor, $(\underline{\mathbf{v}} \otimes \underline{\nabla} - \underset{\sim}{\omega})$ is the Cosserat strain rate, $\underset{\sim}{\omega}$ is the skew-symmetric matrix created from the pseudo-vector of the microstructure rotation velocity, $\underset{\sim}{\mathbf{m}}$ is the couple stress tensor and $\left(\overset{\times}{\underline{\omega}} \otimes \underline{\nabla}\right)$ is the Cosserat wryness rate.

The Cosserat deformations, indicated with a sharp sign, can be written according to the Lagrangian description as:

$$^{\sharp}\mathbf{F} = \underset{\sim}{\mathbf{R}}^T \cdot \underset{\sim}{\mathbf{F}}; \tag{2}$$

$$^{\sharp}\mathbf{\Gamma} = \underset{\sim}{\mathbf{R}}^T \cdot \underset{\sim}{\Gamma}; \tag{3}$$

*Corresponding author. E-mail: frank.girot@ehu.eus.
†Corresponding author. E-mail: samuel.forest@mines-paristech.fr.

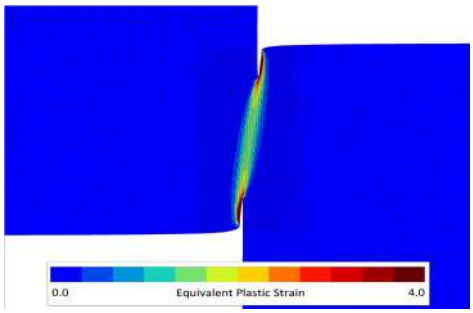

(a)

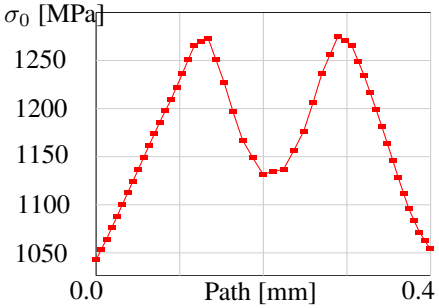

(b)

Figure 1: Equivalent plastic strain distribution at the localization band during Hat-Shaped specimen test under compression **(a)** and flow stress distribution along the cross section passing through the shear band**(b)**.

where $\underset{\sim}{\mathbf{F}}$ is the deformation gradient, $\underset{\sim}{\mathbf{R}}$ is the rotation matrix describing the microstructure rotation and $\underset{\sim}{\mathbf{\Gamma}}$ is the Cosserat wryness. To provide a robust material characterization, the constitutive response of the hyper-elastic model is derived from the Helmholtz free energy, which we defined as:

$$\rho\psi\left({}^{\sharp}\underset{\sim}{\mathbf{F}}, {}^{\sharp}\underset{\sim}{\mathbf{\Gamma}}\right) = \frac{\lambda}{2}\left(\mathrm{J}-1\right)^2 + \mu||\mathrm{sym}\left({}^{\sharp}\underset{\sim}{\mathbf{F}}\right) - \underset{\sim}{\mathbf{I}}||^2 + \mu_c||\mathrm{skew}\left({}^{\sharp}\underset{\sim}{\mathbf{F}} - \underset{\sim}{\mathbf{I}}\right)||^2 + \frac{\beta}{2}||\,{}^{\sharp}\underset{\sim}{\mathbf{\Gamma}}||^2; \tag{4}$$

Work has already been done on a thermodynamically-consistent visco-plastic material model in the small deformation framework. A Johnson-Cook-like model has been implemented in the Cosserat theory where the thermal variation is evaluated through a robust thermodynamic approach. The Taylor-Quinney coefficient, built on assumptions that are not valid anymore for our applications, has been replaced with an explicit evaluation of the contribution of the plastic work to the thermal variation:

$$\dot{T} = \frac{\left(\underset{\sim}{\boldsymbol{\sigma}} : \dot{\underset{\sim}{\mathbf{e}}}^p + \underset{\sim}{\boldsymbol{\mu}} : \dot{\underset{\sim}{\mathbf{k}}}^p - \frac{\partial\psi_\alpha}{\partial p}\dot{p}\right)}{\rho\left[C_\varepsilon + \frac{\partial C_\varepsilon}{\partial T}\left(T - T_0\right)\right]}; \tag{5}$$

The Equations of the hyper-elastic model above have been first simplified such that only one rotation is allowed (bi-dimensional rotation) while keeping a full three dimensional displacement field, and then they have been discretized such as to be implemented in a Finite Element solver. Finally, the thermodynamically-consistent Johnson-Cook-like model has been implemented in the theory.

RESULTS

By simulating the compression of a Hat-Shaped Specimen [Peirs et al. 2010], it has been shown that the Cosserat theory is a possible solution to the mesh dependency problem (Figure 1a), but, more importantly, it has also been shown that the theory can simultaneously predict material viscous hardening and thermal softening (Figure 1b).

The results of the on-going work will be presented at the ICTAM in August. In particular, a similar thermodynamically consistent visco-plastic model will be implemented in the large deformation framework, and it will be subsequently calibrated through the Hat-Shaped specimen test, in which it will also be possible to identify the effect of the characteristic length of the model.

Acknowledgments

This project has received funding from the European Union's Marie Skłodowska-Curie Action (MSCA) Innovative Training Network (ITN) H2020-MCSA-ITN-2017 under the grant agreement N° 764979.

References

Cosserat, Eugene and Francoise Cosserat (1909). *Theorie des corps deformables*. A. Hermann et fils.

De Borst, René and Hans-Bernd Mühlhaus (Aug. 1992). "Gradient-dependent plasticity: Formulation and algorithmic aspects". In: *International Journal for Numerical Methods in Engineering* 35.3, pp. 521–539. DOI: 10.1002/nme.1620350307.

Peirs, J., P. Verleysen, J. Degrieck, and F. Coghe (2010). "The use of hat-shaped specimens to study the high strain rate shear behaviour of Ti-6Al-4V". In: *International Journal of Impact Engineering* 37.6, pp. 703–714. DOI: 10.1016/j.ijimpeng.2009.08.002.

THEORETICAL AND EXPERIMENTAL STUDIES OF CU-SN INTERMETALLIC GROWTH DURING HIGH TEMPERATURE STORAGE TEST

Aleksandr Morozov*[1,2], Alexander B. Freidin[2], Victor Klinkov[3], Alexander Semencha[3], and WolfgangH.Müller[1]
[1]Institute of Mechanics, Berlin Institute of Technology, Berlin, Germany
[2]Institute for Problems in Mechanical Engineering of Russian Academy of Sciences, Saint-Petersburg, Russia
[3]Peter the Great Saint-Petersburg Polytechnic University, Saint-Petersburg, Russia

Summary The growth of the intermetallic compound of copper and tin in tin-based solders is modeled based on the chemical affinity tensor, which determines the configurational force driving the growth. The influence of temperature and mechanical stresses arising during operation of the soldered parts on the growth kinetics is studied. A high temperature storage experiment with microprocessor chips containing tin solder is carried out. The results of numerical modeling are compared with the obtained experimental data.

INTRODUCTION

The present work is devoted to the study of IMC (Intermetallic Compound) formation of tin (Sn) and copper (Cu) in tin-based solders, which are widely used in the microelectronic industry. These intermetallic phases are more brittle in comparison with pure metals. Therefore, during cyclic temperature loading, due to the difference in the coefficients of thermal expansion and elastic moduli, defect nucleation and destruction may arise. Predicting the growth kinetics of the intermetallic phase, in particular under temperature loading, mainly allows to determine the life of microelectronic elements.

The formation of intermetallic compounds is the result of diffusion and chemical processes [1]. Morphological changes during the formation of the intermetallic phase are accompanied by transformation strains, which, together with the change of temperature, cause mechanical stresses. In addition, during use of the microelectronic component, soldered joints are also subjected to shear stresses [2] due to different coefficients of thermal expansion of the substrate and the microchip. Thus, the growth of intermetallic compounds occurs under conditions of varying temperatures, varying thermal stresses, and cyclic external shear loads. Such complex loading affects the kinetics of the intermetallic compounds growth.

In the present work, the influence of mechanical stresses on the copper and tin intermetallic phase growth kinetics is modelled using the chemical affinity tensor concept [3, 4, 5]. A set of problems with various loading scenarios is modeled numerically and analytically. The effect of temperature loading on the kinetics of the IMC transformation front is studied. A quantitative evaluation of the proposed model was carried out according to the experimental results [6] obtained by heat treatment of the microchips with solder bumps at a constant high temperature [7].

THE KINETICS OF IMC FORMATION FRONT

The growth of the intermetallic phase is determined by by two chemical reactions taking place at two propagating reaction fronts:

$$6\ \mathrm{Cu} + 5\ \mathrm{Sn} \longrightarrow \mathrm{Cu_6Sn_5}, \qquad 3\ \mathrm{Cu} + \mathrm{Sn} \longrightarrow \mathrm{Cu_3Sn}. \tag{1}$$

The influence of mechanical stresses on the reaction front velocity are modelled using the chemical affinity tensor concept. According to this concept, the chemical reaction occurs at the sharp interface on the oriented surface element with the reaction rate expressed by

$$\omega = k_* c \left(1 - \exp\left(-\frac{\mathrm{A_{NN}}}{RT}\right)\right), \tag{2}$$

where k_* is the kinetic parameter of the chemical reaction, c is the concentration of the diffusing component (copper or tin atoms, depending on the chemical reaction under consideration) at the front of the chemical reaction, R is the universal gas constant, T is the temperature, $\mathrm{A_{NN}}$ is the normal component of the chemical affinity tensor, which in turn is a linear combination of chemical potentials. The normal component of the chemical affinity tensor can be expressed in terms of stresses and strains at the reaction front [4, 5, 8]:

$$\mathrm{A_{NN}} = \frac{n_- M_-}{\rho_-}\left(\gamma - [\![W]\!] + \mathbf{P}_-^{\mathrm{T}} : [\![\mathbf{F}]\!]\right) + n_* RT \ln\frac{c}{c_*}, \tag{3}$$

where M_- and ρ_- are the molar mass and mass density of the initial phase, n_- is a stoichiometric coefficient from (1), W is a Helmholtz free energy of the solid constituent, $\mathbf{P}$ is a first Piola-Kirchhoff stress tensor, $\mathbf{F}$ is a deformation gradient. In (3), the indices $-$, $+$ and $*$ refer to the initial solid phase, the final reaction product and the diffusive component (e.g.,

*Corresponding author. E-mail: morozov@tu-berlin.de.

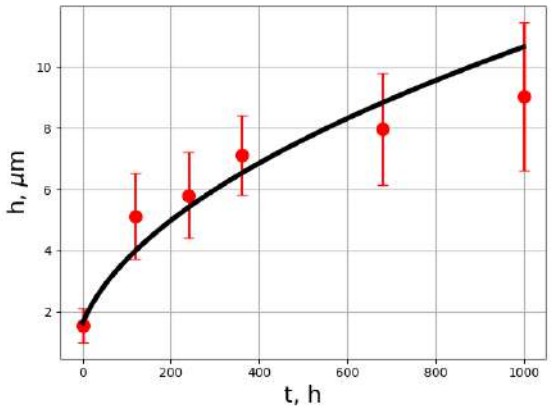

Figure 1: Cu_6Sn_5 phase growth kinetics. Comparison of the analytical (solid line) and experimental (dots with error bars) results.

Sn, Cu_6Sn_5 and Cu, respectively, for the reaction occurring at the boundary between IMC and tin). Square brackets denote the jump of a value across the reaction front $[\![\phi]\!] = \phi_+ - \phi_-$.

The simple problem for planar interface and linear elastic solid reactants was solved in order to validate material, diffusion and chemical reaction parameters used in (2)-(3) quantitatively. Comparison of theoretical and analytical thickness of the IMC layer during the high temperature storage test is shown in Fig. 1.

The numerical procedure for modeling the moving interface is based on the finite element method, which is used to determine the stresses, strains and the corresponding concentration at the reaction front. The propagation of the chemical interface is realized with a remeshing technique, similarly to [8, 9].

CONCLUSIONS

The growth of the Cu_6Sn_5 intermetallic compound was modeled analytically and numerically for various loading scenarios. The effects of high temperature during the storage test and temperature cycling on the IMC growths kinetics were studied. It has been shown experimentally that the intermetallic phase growth occurs non-uniformly along the interface of materials. The developed experimental method allows to measure the local change of layer thickness, which in turn leads to the evaluation of the kinetics of intermetallic growth in a specific area of the sample. The experimental results were used to determine the kinetic parameters in the chemical affinity tensor model for the first time.

ACKNOWLEDGEMENTS

The authors acknowledge the financial support from the Russian Science Foundation (RSF Grant 19-19-00552).

References

[1] Paul A. The Kirkendall Effect in Solid State Diffusion, *PhD Thesis*,Technische Universiteit Eindhoven, Eindhoven, 2004
[2] Kwak J. B., Yu D. , Nguyen T. T., Park S. In: *ASME 2011 Pacific Rim Technical Conference and Exhibition on Packaging and Integration of Electronic and Photonic Systems.* **2011**: 307316, 2011
[3] Freidin A.B., Vilchevskaya E.N. In: H. Altenbach and A. Öchsner, Encyclopedia of Continuum Mechanics, Springer, Berlin, Heidelberg, 2019
[4] Freidin A.B., Vilchevskaya E.N., Korolev I. *International Journal of Engineering Science.* **83**: 57-75, 2014
[5] Freidin A.B. *Mechanics of Solids.* **50**(3): 260-285, 2015
[6] Morozov A.V., Freidin A.B., Klinkov V.A. et al. *Journal of Electronic Materials*, 2020
[7] Standard JESD22-A103C, High Temperature Storage Life, 2004
[8] Freidin A.B., Korolev I.K., Aleshchenko S.P., Vilchevskaya E.N. *International journal of Fracture.***202**: 245259, 2016
[9] Morozov A.V., Khakalo S.S., Balobanov V.V. et al. *Technische Mechanik.* **38**(1): 73-90, 2018

MICROMECHANICAL MODELLING AND MAGNETOMECHANICALLY COUPLED FINITE-ELEMENT-BASED SIMULATION OF MAGNETIC SHAPE MEMORY ALLOY BEHAVIOUR

Thorsten Bartel[1], Bjoern Kiefer[2], and Andreas Menzel*[1,3]
[1]Institute of Mechanics, Department of Mechanical Engineering, TU Dortmund, Dortmund, Germany
[2]Institute of Mechanics and Fluid Dynamics, TU Bergakademie Freiberg, Freiberg, Germany
[3]Division of Solid Mechanics, Lund University, Lund, Sweden

Summary The macroscopic behaviour of ferroic functional materials such as magnetic shape memory alloys (MSMA) is highly affected by mechanisms at the microscale which drive the formation and further evolution of microstructures. The following mechanisms shall be taken into account within this contribution: (i) domain wall motion in terms of evolving domain volume fractions, (ii) local spontaneous magnetisation vectors (in each domain) that may rotate away from their respective easy axis, and (iii) variant switching in terms of evolving variant volume fractions. The material model is embedded into a fully magnetomechanically coupled finite element framework. This particularly allows the numerical analysis of the behaviour of arbitrarily shaped MSMA specimen where the demagnetisation tensor concept is no longer applicable, respectively valid.

VARIATIONAL FRAMEWORK

The material model is embedded into a variational framework, where the underlying field variables are the displacements $\boldsymbol{u}$, the magnetic field strength $\boldsymbol{h}$, and the magnetisation $\boldsymbol{m}$. The magnetic field strength $\boldsymbol{h} = \overline{\boldsymbol{h}} + \widetilde{\boldsymbol{h}}$ is decomposed into a prescribed contribution $\overline{\boldsymbol{h}}$ and a part referred to as the demagnetisation field $\widetilde{\boldsymbol{h}}$. Furthermore, the latter contribution is related to a scalar-valued magnetic potential $\widetilde{\phi}$ in terms of a gradient field, namely $\widetilde{\boldsymbol{h}} := -\nabla_{\boldsymbol{x}}\widetilde{\phi}$. In the present modelling approach, the magnetisation $\boldsymbol{m}$ does not appear as independent variable but shall be parametrised by state variables introduced in general form as $\boldsymbol{p}$, so that $\boldsymbol{m} = \widehat{\boldsymbol{m}}(\boldsymbol{p})$. Hence, the field variables used in the proposed framework are $\boldsymbol{u}$, $\widetilde{\phi}$, and $\boldsymbol{p}$. As a basis for the forthcoming finite element formulation, the micromagnetics-inspired energy-enthalpy function

$$\mathit{\Pi} := \int_{\mathcal{B}} \psi(\nabla_{\boldsymbol{x}}\boldsymbol{u}, \boldsymbol{p}) \, \mathrm{d}V - \frac{\mu_0}{2} \int_{\mathbb{R}^3} \|\nabla_{\boldsymbol{x}}\widetilde{\phi}\|^2 \, \mathrm{d}V - \mu_0 \int_{\mathcal{B}} \left[\overline{\boldsymbol{h}} - \nabla_{\boldsymbol{x}}\widetilde{\phi}\right] \cdot \boldsymbol{m}(\boldsymbol{p}) \, \mathrm{d}V - \int_{\partial\mathcal{B}} \overline{\boldsymbol{t}} \cdot \boldsymbol{u} \, \mathrm{d}S \tag{1}$$

is utilised. To take dissipation into account, this function is embedded into the power-type potential

$$\mathcal{L} := \dot{\mathit{\Pi}} + \int_{\mathcal{B}} \zeta(\dot{\boldsymbol{p}}, \boldsymbol{p}) \, \mathrm{d}V \, , \tag{2}$$

wherein $\zeta(\dot{\boldsymbol{p}}, \boldsymbol{p})$ represents the dissipation function and $\dot{\bullet}$ denotes the time derivative. Applying the stationarity principle

$$\left\{\dot{\boldsymbol{u}}, \dot{\widetilde{\phi}}, \dot{\boldsymbol{p}}\right\} = \arg\left[\min_{\dot{\boldsymbol{u}}} \max_{\dot{\widetilde{\phi}}} \min_{\dot{\boldsymbol{p}}} \{\mathcal{L}\}\right] \tag{3}$$

enables us to derive the localised balance equations, Neumann-type boundary conditions as well as the Biot-type evolution equations for $\boldsymbol{p}$. The first variation of the potential $\mathcal{L}$ with respect to the rates $\dot{\boldsymbol{u}}$, $\dot{\widetilde{\phi}}$, and $\dot{\boldsymbol{p}}$ is the basis for the subsequent finite element formulation, since the related set of equations corresponds to the weak form of the balance equations.

CONSTITUTIVE FRAMEWORK

The material model is governed by the definition of the energy density ψ, which generally depends on the displacement gradient and the magnetisation, and which is designed to capture the behaviour of an MSMA single crystal with tetragonal martensite variants. Therefore, variant volume fractions ξ_i with $i = 1, \ldots, 3$ as well as domain volume fractions α_j with $j = 1, \ldots, 6$ are introduced. For each domain, a specific energy density

$$\psi_j := \tfrac{1}{2}\left[\boldsymbol{\varepsilon}_j - \boldsymbol{\varepsilon}_j^{\mathrm{tr}}\right] : \mathbf{E}_j : \left[\boldsymbol{\varepsilon}_j - \boldsymbol{\varepsilon}_j^{\mathrm{tr}}\right] + K\left[1 - \left[\frac{1}{m_s}\boldsymbol{m}_j^{\mathrm{dom}} \cdot \boldsymbol{n}_j^{\mathrm{ea}}\right]^2\right] , \quad j = 1, \ldots, 6 \, , \tag{4}$$

is defined, which consists of an elastic contribution and a part related to the magnetocrystalline anisotropy energy. Here, $\boldsymbol{\varepsilon}_j$ denotes the total strain in each domain, $\boldsymbol{\varepsilon}_j^{\mathrm{tr}}$ is the Bain strain for each martensite variant, $\mathbf{E}_j$ the fourth order elasticity tensor, K is a material constant related to the magnetocrystalline anisotropy energy, and m_s is the saturation magnetisation. The vector $\boldsymbol{m}_j^{\mathrm{dom}}$ with $\|\boldsymbol{m}_j^{\mathrm{dom}}\| = m_s$ denotes the local spontaneous magnetisation in each domain being initially aligned with the so-called easy axis $\boldsymbol{n}_j^{\mathrm{ea}}$. In this regard, the second term in (4) can be interpreted as a penalisation for the

*Corresponding author. E-mail: andreas.menzel@udo.edu

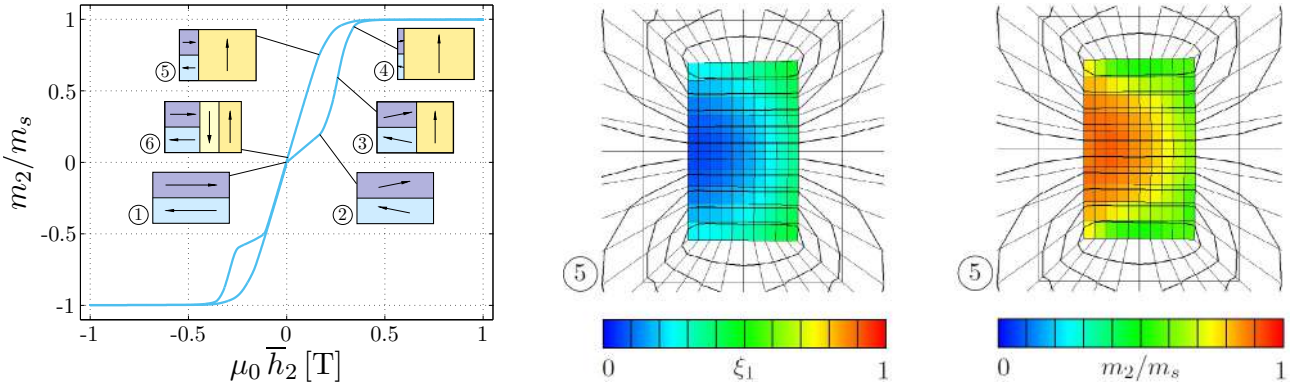

Figure 1: Effective response of a rectangular specimen under constant tractions in horizontal direction and varying prescribed magnetic field $\overline{h}_2(t)$ in vertical direction. Left: Averaged magnetisation response of the specimen with sketches of the parametrised microstructure at different load states (1 to 6) illustrating the domain volume fractions and orientations of local magnetisation vectors. Middle: Spatial distribution of martensite variant 1 at load state 5. Right: Spatial distribution of the effective magnetisation m_2/m_s in vertical direction at load state 5. The additional lines reflect isolines of the magnetic potential ϕ.

magnetisation when rotating away from the respective easy axis. It is remarked that the quantities referring to the first energy term are identical for each martensite variant, i.e. $\varepsilon_1 \equiv \varepsilon_2$, $\varepsilon_3 \equiv \varepsilon_4$, $\varepsilon_5 \equiv \varepsilon_6$, which analogously holds for the related Bain strains and elasticity tensors.

The total linearised strains for each variant generally differ from each other. The precise relations among them is governed by a specific homogenisation assumption, where we follow two different methods, namely (i) an approach based on first order laminates, and (ii) an approach based on convexification. In general, a mixture rule according to

$$\psi := \sum_{j=1}^{6} \alpha_j \, \psi_j \tag{5}$$

is applied in order to define the energy density. To complete the constitutive framework, the magnetisation has to be specified as a function of $\boldsymbol{p}$ which is chosen as

$$\boldsymbol{m}(\boldsymbol{p}) := \sum_{j=1}^{6} \alpha_j \, \boldsymbol{m}_j^{\mathrm{dom}} \, . \tag{6}$$

FINITE ELEMENT IMPLEMENTATION

The magnetomechanically fully coupled constitutive framework does not allow a condensation of certain variables to integration points. Thus, all state variables, i.e. the variant and domain volume fractions as well as the local magnetisation vectors (in case of the convexification approach), have to be treated as global fields in addition to $\boldsymbol{u}$ and $\widetilde{\phi}$. In this regard, it is noteworthy that shape functions with different polynomial order have to be used to avoid oscillations in the solutions of the resulting fields. Furthermore, different degrees of freedom are present in the material body and the surrounding free space which also affects the finite element formulation. Another important aspects is exemplified in the fact, that the evolution of state variables is subjected to several equality and inequality constraints. Hence, the associated Karush-Kuhn-Tucker system has to be solved at each node of the finite element mesh.

Results

The overall magnetomechanically fully coupled framework is capable of analysing inhomogeneous problems — which mainly refer to arbitrarily shaped specimens — and predicting the spatial distributions of, e.g., the magnetisation and martensite variants, as well as the averaged sample response in terms of, e.g., strains and magnetisation, cf. Fig. 1.

References

[1] Bartel T., Kiefer B., Buckmann K., Menzel A. An energy-relaxation-based framework for the modelling of magnetic shape memory alloys - Simulation of key response features under homogeneous loading conditions. Int. J. Sol. Struct. **182-183**:162-178, 2020.

[2] Buckmann K., Kiefer B., Bartel T., Menzel A. Simulation of magnetised microstructure evolution based on a micromagnetics-inspired FE framework: application to magnetic shape memory behaviour. Arch. Appl. Mech. **89**:1085-1102, 2019.

THERMOMECHANICAL DEGRADATION RESISTANT THERMAL BARRIER COATING SYESTEMS WITH STRAIN TOLERANT STRUCTURES

Bowen Lv[1], Robert Vaßen [2], Tiejun Wang[3*], and Daining Fang[1*]
[1]Institute of Advanced Structure Technology, Beijing Institute of Technology, Beijing, PR China
[2]Materials Synthesis and Processing (IEK-1), Institute of Energy and Climate Research, Forschungszentrum Jülich GmbH, Jülich, Germany
[3]State Key Laboratory for Strength and Vibration of Mechanical Structures, School of Aerospace Engineering, Xi'an Jiaotong University, Xi'an, PR China

Summary Sintering is a thermomechanical degradation process driven by surface and grain boundary energy. During extended exposure to elevated temperature in gas turbines, thermal barrier coating systems go through such process, resulting in losses of strain tolerance and thermal protection capacity. To counteract the thermomechanical degradation, strain tolerant structures were proposed and implemented in conventional lamellar-structured coating. In-situ bending tests at 1200 °C indicated improvements in both compliance and sintering resistance. A mass diffusion-based constitutive model was further formulated by variational principle and integrated in finite element analysis through user defined subroutines, confirming the significance of strain tolerant structures. This work shed light on the concept of structure design for the progress of coating technology.

BACKGROUND

Thermal barrier coating systems (TBCs) represent the cutting-edge thermal protection techniques in advanced gas turbines. With the increase of inlet gas temperature for thermal efficiency improvement, accelerated mass diffusion driven by surface and grain boundary energy leads to healing of microcracks and densification of porous structure, which deprives strain tolerance towards thermal shock and thermal insulation to hot gas. This thermomechanical degradation process, also known as sintering, is especially detrimental to conventional plasma-sprayed TBCs with limited strain tolerance due to the nature of lamellar microstructure. Rare-earth elements have been doped to improve sintering resistance at high costs. Alternatively, structure design has been proved to be an efficient way to counteract sintering induced thermomechanical degradation, as noted in our previous work [1].

Sintering of TBCs has been addressed by experimental characterizations of microstructure and property evolutions. The state-of-the-art method integrates bending or indentation test in high temperature field for in-situ evaluation of mechanical properties during sintering. In addition, a few mechanism-based sintering models have been proposed for lamellar-structured TBCs. Employing variational method, Clyne's group obtained structural and thermal conductivity evolutions [2], while constitutive models were proposed by Cocks and Fleck [3]. Nevertheless, in-depth analyses of the sintering behaviour of TBCs with strain tolerant structures require the integration of experimental, theoretical and numerical methods, which is the main purpose of this work.

METHODS AND MODELS

Four types of TBC samples with different strain tolerant structures were prepared via air plasma spray (APS) and suspension plasma spray (SPS) approaches, including micro-cracked APS TBC (Mc. APS), segmented APS TBC (Sg. APS), columnar structured SPS TBC (CS SPS), and vertically cracked SPS TBC (VC SPS). After the deposition of TBC on bond-coated substrate, samples were laser cut into millimetre-scaled rectangular bars at high precision and electrochemically etched to obtain free-standing TBC eliminating damage to strain tolerant structures during detaching. Confocal white light inspection system was utilized for high-resolution characterizations of dimension and interfacial topography, while microstructure examinations of polished and fractured cross-sections were performed by scanning electron microscopy (SEM) with image analyses. Thermo-mechanical analysis (TMA) was conducted by in-situ three-point bending test equipped with graphite furnace at 1200 °C. More details can be found in ref [4].

A constitutive model was developed for VC SPS TBC by variational principle through the derivation of system energy functional, considering sintering induced mass diffusion on free surface and grain boundary. Based on experimentally observed microstructure features (Figure 1(e)), rectangular grains were assumed with microcracks in between and partially connected by sintering necks, composing large lamellar structures with circular pores at boundary due to the layer-by-layer deposition of liquid feedstock made of nanopowders, as illustrated in Figure 1(f). Taking two separated grains as the reference energy state, the introduction of a single sintering neck, under a prescribed force f across the neck with the height of w, leads to an increase in the free energy G,

$$G = \int \gamma_{SUR} \mathrm{d}A_{SUR} + \int \gamma_G \mathrm{d}A_G - fw \tag{1}$$

where γ_{SUR} and γ_G are surface and grain boundary energy, respectively, with A_{SUR} and A_G being the corresponding area. For the energy dissipation due to mass diffusion, the potential Ψ is expressed in terms of mass fluxes J_{SUR} and J_G,

$$\Psi = \int J_{SUR}^2 / 2D_{SUR} \mathrm{d}A_{SUR} + \int J_G^2 / 2D_G \mathrm{d}A_G \tag{2}$$

where D_{SUR} and D_G are surface and grain boundary diffusion coefficients, respectively. During sintering, the system evolves so as to minimize the functional $\Omega(\dot{w}) = \dot{G} + \Psi$, where the point denotes time differentiation. The minimization

*Corresponding author. E-mail: wangtj@mail.xjtu.edu.cn (Tiejun Wang), fangdn@bit.edu.cn (Daining Fang)

relates the prescribed force f to neck deformation rate $\dot{w}$ and sintering force $f_{SIN(1)}$, satisfying mass conservation. Local deformation and force are converted to global strain and stress by consistency conditions. Taking account of the sintering stress contribution by circular pores $\sigma_{(2)}^{SIN}$, the constitutive relation reads

$$\{\varepsilon\}=[C]\{\sigma\}+[\Lambda]^{-1}\{\sigma\}-[\Lambda]^{-1}\left(\{\sigma_{(1)}^{SIN}\}+\{\sigma_{(2)}^{SIN}\}\right) \quad (3)$$

with [C] being the compliance matrix, [Λ] the viscous matrix, $\dot{\varepsilon}$ the strain rate and $\dot{\sigma}$ the stress rate. Subscripts (1) and (2) refer to the two domains without and with pores, respectively. Eq. (3) is rewritten in incremental form and implemented in finite element analysis (FEA) by programing user defined subroutines. Through-thickness vertical cracks of VC SPS were modelled in FEA, as shown in Figure 1(g).

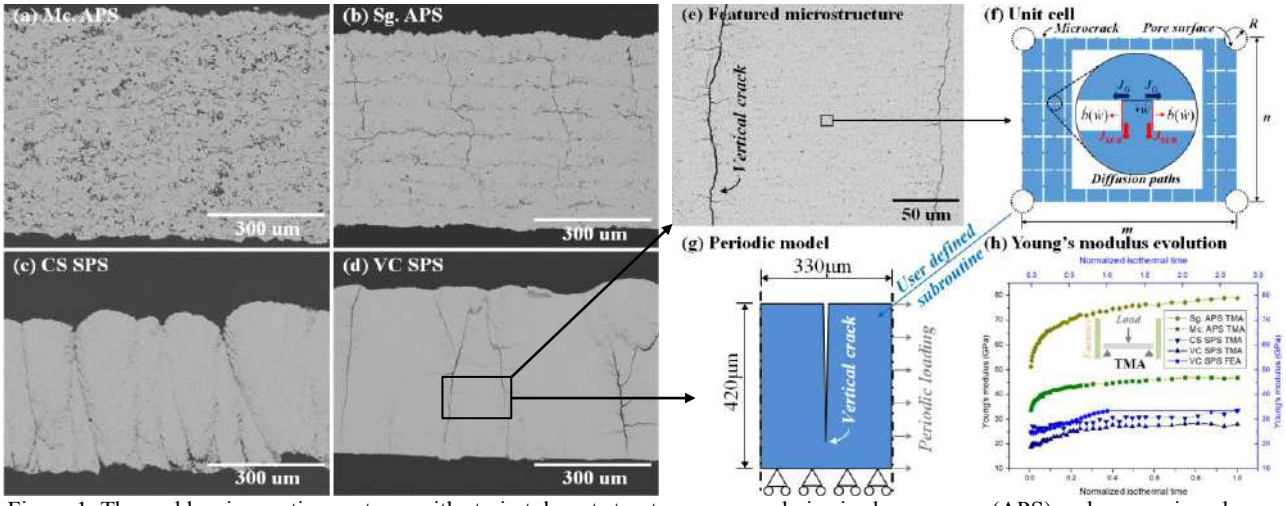

Figure 1. Thermal barrier coating systems with strain tolerant structures prepared via air plasma spray (APS) and suspension plasma spray (SPS) approaches: (a) micro-cracked (Mc.) APS; (b) segmented (Sg.) APS; (c) columnar structured (CS) SPS; (d) vertically cracked (VC) SPS; (e) featured microstructure of VC SPS; (f) unit cell with mass diffusion paths; (g) periodic model for finite element analysis (FEA); (h) sintering induced Young's modulus evolution obtained by thermomechanical analysis (TMA) and FEA.

MAIN RESULTS

TBCs with inter-columnar gaps and vertical cracks (Figure 1(c) and (d)) exhibited simultaneously improved strain tolerance and sintering resistance, according to experimental (TMA) and numerical (FEA) results. Young's modulus level was reduced by around 50% due to the introduction of strain tolerant structures, comparing the TMA results of CS and VC SPS with those of Mc. APS (Figure 1(h)). Significant reduction in Young's modulus level was confirmed by FEA with and without vertical cracks. Although the coating structure between two adjacent cracks/gaps had lower porosity level than the conventional coating (e.g. ~3% for VC SPS and ~12% for Mc. APS), relatively high crack/gap density (4 mm^{-1} for VC SPS and 7 mm^{-1} for CS SPS) provided extra strain tolerance by crack/gap opening. Regardless of coating structure, sintering induced stiffening of all the four TBCs well followed a power law, $E=E^{*}\cdot t^{S}$, with E being Young's modulus, E^{*} being characteristic modulus, t being isothermal sintering time and S being stiffening index. The stiffening index S is simple and elegant with clear physical interpretation as the slope of Young's modulus curve in log-log plot. It is proposed as a new evaluation parameter of sintering resistance for scientific and engineering applications.

In addition to stiffening induced by sintering, multi-scale structure evolution was elucidated by FEA. Mass diffusion driven by surface and grain boundary energy resulted in two-staged flattening of sintering neck and microcrack healing due to transversely anisotropic grain geometry at microscopic scale. Consequently, different coating shrinkage behaviours were predicted in horizontal and vertical directions at macroscopic scale. In brief, the two-staged neck flattening was responsible for non-uniform coating densification.

CONCLUSIONS

A new approach of structure design was proposed and examined to counteract thermomechanical in-service degradation of lamellar-structured TBCs at elevated temperature. Strain tolerance and sintering resistance were improved by introducing through-thickness vertical cracks and inter-columnar gaps, indicated by both in-situ bending tests and mass diffusion-based numerical analyses. Neck flattening driven by mass diffusion resulted in non-uniform densification and stiffening that followed power law. Furthermore, a new parameter, stiffening index S, was proposed for the evaluation of sintering resistance of TBCs.

References

[1] Lv B.W., Fan X.L., Wang T.J., et al. *J. Eur. Ceram. Soc.* **38**: 1946-1956, 2018.
[2] Cipitria A., Golosnoy I.O., Clyne T.W. *Acta Mater.* **57**: 980-92, 2009.
[3] Cocks A., Fleck N., Lampenscherf S. *J. Mech. Phys. Solids* **63**: 412-31, 2014.
[4] Lv B.W., Mücke R., Vaßen R., et al. *J. Eur. Ceram. Soc.* **38**: 5092-5100, 2018.

A GENERAL VARIATIONAL FRAMEWORK FOR THE THERMOMECHANICS OF GRADIENT-TYPE DISSIPATIVE SOLIDS INCLUDING STABILITY ANALYSIS

Marc-André Keip *[1] and Stephan Teichtmeister[1]
[1]Institute of Applied Mechanics (CE), Chair I, University of Stuttgart, Stuttgart, Germany

Summary We present a variational framework for the thermomechanical coupling in gradient-extended dissipative solids at large deformations. Such intrinsically symmetric formulations provide an elegant way to couple different macro- as well as microscopic fields. The key of the discussed formulation is the identification of the entropy as well as the entropy rate as the canonical variables on the energetic and dissipative side, respectively. By rigorous treatment of dual variables, extended variational formulations can be derived that are attractive for a numerical treatment by the finite element method. As model problem we consider additive thermo-gradient-plasticity and show representative numerical examples that are related to classical shear band formations. We further discuss the stability of homogeneous thermoplastic solutions in a one-dimensional tensile bar undergoing small deformations.

GENERAL MOTIVATION

Beside energy storage, the dissipation of mechanical work into heat is the fundamental process in solid materials. This energy conversion stems from kinematic changes in the material's microstructure such as the movement of dislocations which manifests oneself in plastic deformations or the irreversible growth of micropores resulting in damage. To model the physical coupling of different micro- as well as macroscopic quantities, incremental variational formulations provide a very elegant way. If such are available, implementations into typical finite element codes essentially require first and second derivatives of the underlying potential density with respect to the state variables resulting into *symmetric* algebraic systems. In this talk, we present a general variational framework for the thermomechanics of *gradient-extended* dissipative solids undergoing large deformations. It is an extension of the isothermal theory presented in [1] towards the evolution of thermal states in the solid with non-local effects based on length scales.

VARIATIONAL FORMULATION OF THERMOMECHANICS IN GRADIENT-TYPE SOLIDS

Point of departure is the the definition of two constitutive functions, namely the internal energy function formulated in terms of the entropy and a canonical dissipation potential function that is assumed to depend on the entropy rate. Then, the evolution of the macro- and micromotion fields $\boldsymbol{\varphi}$ and $\mathfrak{q}$ as well as the evolution of the entropy η are governed by a *canonical minimization principle*. However, since the explicit forms of the introduced internal energy and dissipation potential functions are in general unknown an extended formulation with the temperature (dual to the entropy) and a thermal driving force (dual to the entropy rate) as additional fields is introduced via generalized Legendre transformations. The obtained time-continuous saddle point principle is in line with the seminal work [2] on the variational treatment of local thermoplasticity.

By construction of consistent time integration algorithms, variational formulations valid for the time increment under consideration are obtained. In especially, we point out a procedure that renders the algorithmically correct form of the mechanical dissipation. All thermomechanical fields at current time are then determined by the incremental variational statement

$$\inf_{\boldsymbol{\varphi},\mathfrak{q},\eta} \sup_{\theta,T} \{ \int_{\mathcal{B}_0} \widehat{\pi}^\tau(\mathfrak{c},\eta,\theta,T,\nabla T)\, dV - P^\tau_{ext}(\boldsymbol{\varphi},T) \} \tag{1}$$

that yields as necessary condition all coupled field equations. Note, that the evolution of the entropy is additionally driven by mechanical gradient-type dissipative effects. Extended settings that include mechanical driving forces dual to the micromotions are highly attractive for numerical treatment by the finite element method, see [3]. However, finding finite element formulations that satisfy the LBB-condition is a non-trivial and difficult task, see [4].

THERMO-GRADIENT-PLASTICITY AND ITS STABILITY ANALYSIS

The presented framework is very versatile and can be applied to fully coupled non-isothermal theories of e.g. gradient-type damage and plasticity or phase transitions. As a model problem we consider an additive approach to the kinematics of plasticity and specify the array of micromotions to (i) the Lagrangian plastic Hencky strain tensor that is defined as the logarithm of an evolving plastic metric and (ii) a scalar hardening variable together with its first gradient. Due to plastic heating, a temperature-induced softening behavior is at hand and typical mesh-dependencies of finite element solutions of local theories can be circumvented by gradient extensions. With this regard, we present numerical examples that are typically related to the formation of shear bands with large plastic deformations.

*Corresponding author. E-mail: marc-andre.keip@mechbau.uni-stuttgart.de.

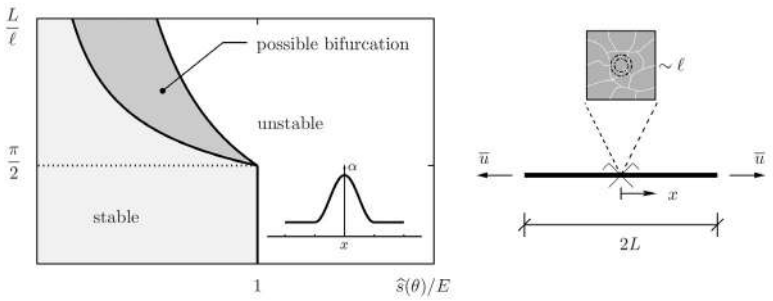

Figure 1: Stability analysis of homogeneous plastic solutions of a one-dimensional bar under tension. Depending on the temperature the solution may be stable, instable or even show bifurcations.

Furthermore, we discuss the *stability* of homogeneous plastic solutions with regard to its localization behavior by considering a simple one-dimensional bar under tension that undergoes small deformations. In contrast to (1), the temperature within this analysis will be treated as an external variable. Then, a second-order incremental stability condition results in a typical Rayleigh quotient minimization problem, see [5] as well as Figure 1 for a graphical illustration.

Our attention is also caught by the stability of homogeneous solutions obtained by the micromorphic plasticity approach in the sense of [6]. Within this theory, sharp elastic-plastic boundaries are regularized by the introduction of a micromorphic and a local hardening variable that are connected via a penalty term that requires an additional (material) parameter, see [7] for the application in phase field modeling of ductile fracturing and [8] for the application in variational thermomechanics of multiplicative gradient-type plasticity.

References

[1] Miehe C. A multi-field incremental variational framework for gradient-extended standard dissipative solids. *J Mech Phys Solids* **59(4)**: 898-923, 2011.

[2] Yang Q., Stainier L., Ortiz M. A variational formulation of the coupled thermo-mechanical boundary-value problem for general dissipative solids. *J Mech Phys Solids* **54(2)**: 401-424, 2006.

[3] Miehe C., Aldakheel F., Mauthe S. Mixed variational principles and robust finite element implementations of gradient plasticity at small strains. *Int J Numer Meth Eng* **94(11)**: 1037-1074, 2013.

[4] Krischok A., Linder C. A generalized inf-sup test for multi-field mixed-variational methods. *Comput Method Appl M* **357**:112497, 2020.

[5] Pham K., Marigo J.-J., Maurini C. The issues of the uniqueness and the stability of the homogeneous response in uniaxial tests with gradient damage models. *J Mech Phys Solids* **59(6)**: 1163-1190, 2011.

[6] Forest S. Micromorphic approach for gradient elasticity, viscoplasticity, and damage. *J Eng Mech-ASCE* **135(3)**: 117-131, 2009.

[7] Miehe C., Teichtmeister S., Aldakheel F. Phase-field modelling of ductile fracture: a variational gradient-extended plasticity-damage theory and its micromorphic regularization. *Philos T Roy Soc A* **374**: 20150170, 2016.

[8] Fohrmeister V., Bartels A., Mosler J. Variational updates for thermomechanically coupled gradient-enhanced elastoplasticityimplementation based on hyper-dual numbers. *Comput Meth Appl M* **339**: 239-261, 2018.

THE KINETICS OF POLARIZATION SWITCHING IN SINGLE CRYSTAL FERROELECTRICS

Vignesh Kannan*[1] and Dennis M. Kochmann[1]
[1]Department of Mechanical and Process Engineering, ETH Zürich

Summary We present an experimental study on polarization switching in ferroelectric crystals and the resulting mechanical deformation using barium titanate as a model material. An in-situ experimental technique, developed in-house, is used to apply time-varying electric fields to millimeter-scale cantilever beams made of single crystal barium titanate. The evolution of the resulting polarization is measured at different rates of electrical loading. Finally, these macroscopic switching kinetics are interpreted using data collected from ex-situ microscopy techniques like piezoresponse force microscopy and electron microscopy.

INTRODUCTION

Ferroelectric crystals are characterized by permanent polarization due to a non-centrosymmetric crystal structure. Reversal of this polarization begins to occur on application of large electric fields in the direction opposite to the existing state of polarization. This reversal is often termed 'spontaneous', although physically, it is governed by the kinetics of nucleation and growth of individual domains within the crystal. These domains are characterized by a different local polarization state than the parent crystal.

During this talk, we will discuss the kinetics of domain switching using a combination of an in-house experimental setup named Broadband Electromechanical Spectroscopy (BES) and post-mortem microscopy. Using the BES experiment, we apply large time-varying electric fields to cantilever beam samples made of barium titanate crystals. In-situ measurements of macroscopic polarization within the sample and strain fields on the sample surface offer insight into the electrical hysteresis and the coupled mechanical deformation of the crystal. Microscale domains are imaged ex-situ using piezoresponse force microscopy. The resulting phenomenological connection between macroscopic polarization and microscale domain patterns pave way for a physically robust kinetic law to describe polarization switching in ferroelectric crystals.

MATERIALS AND METHODS

Measuring macroscopic kinetics: Broadband Electromechanical Spectroscopy

Broadband Electromechanical Spectroscopy [1,2] is an experimental technique that allows for application of large time-varying electric fields to bulk ferroelectric materials while measuring their macroscopic polarization and coupled mechanical response in-situ. A schematic of the experiment is shown in Figure 1(a). A cantilever beam of dimensions 40 mm x 3 mm x 1 mm, made of a ferroelectric material, is held between two grips coated with conductive copper tape. The sample is sputter-coated with a thin conductive layer of nickel or gold film. High time-varying voltages of the order of ± 1.5 kV are applied across the samples via the conductive grips. The effective polarization in the sample is measured in-situ using a Sawyer-Tower circuit [3]. Strain fields on the sample surface due to polarization switching are measured using a 3-dimensional digital image correlation system (not shown in figure). A pair of Helmholtz coils in combination with a 5 mW Helium-Neon laser source and a 2D position sensing detector allow for measurements of the bending (and shear) modulus and corresponding loss tangent in-situ across a large mechanical frequency range, however these measurements will not be discussed in the current study. Figure 1(b) shows an example measurement of the electrical hysteresis curve during electrical cycling of a polycrystalline lead zirconate titanate ceramic sample at 1 Hz. The polycrystalline ceramic was used as a test material for the measurement system.

Material: Single crystal Barium Titanate

Single crystal barium titanate samples are used as a model material to maintain consistent and controllable initial and boundary conditions in the experiment. Moreover, the tetragonal crystal structure of barium titanate restricts the number of potential polarization directions to six unlike in lead zirconate titanate where additional rhombohedral phases are also present. Figure 1(c) shows a schematic of the sample geometry with the coordinate axes indicating crystallographic orientations. Electrodes are deposited on the 40 mm x 3 mm face, hence electric field is applied along the [001] direction.

Post-mortem microscopy

The micro-scale distribution of polarized domains are then measured using an ex-situ scanning probe technique called piezoresponse force microscopy (PFM) [4]. PFM data provides spatially resolved distribution of polarization vectors in the sample that, in conjunction with macro-scale data, offers insight into the multi-scale effects of polarization kinetics in ferroelectric crystals. The technique has been demonstrated in polycrystalline ceramic samples as well.

*Corresponding author. E-mail: kannanvi@ethz.ch

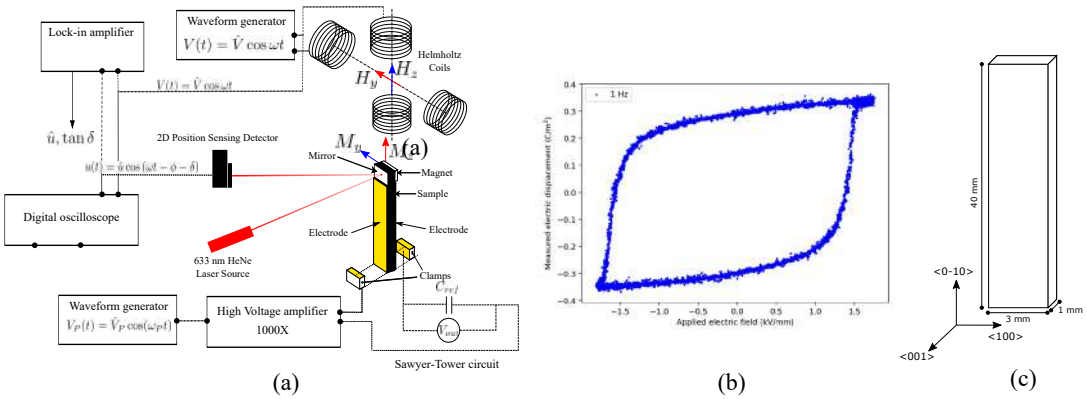

Figure 1: (a) Schematic of the Broadband Electromechanical Spectroscopy apparatus; (b) P-E switching curves for *polycrystalline* PZT samples; (c) Single crystal sample schematic, coordinate axes indicate crystallographic orientation relative to sample configuration

CONCLUSION

The broadband electromechanical spectroscopy experiment was developed to measure the kinetics of macroscopic polarization switching and the coupled mechanical response in millimeter-scale cantilever beams made of ferroelectric materials. The technique is applied to single crystal barium titanate samples at different rates of applied electric field. The measured macroscopic polarization kinetics are then interpreted in conjunction with post-mortem ex-situ measurements of the spatial distribution of micro-scale polarized domains. The resulting experimental data provide deeper insight into the kinetic laws that govern nucleation and growth of microscopic polarized domains and their effect on ferroelectric switching in these crystals.

References

[1] D. M. Kochmann, C. S. Wojnar and J-B. Graverend, *U. S. Patent* US 2014/0298918 A1, 2014
[2] J-B. le Graverend, C. S. Wojnar and D. M. Kochmann, *J. Mater. Sci.* **50**: 3656-3685, 2015
[3] C. B. Sawyer and C. H. Tower, *Phys. Rev.* **35(3)**: 269, 1930
[4] A. Kholkin et al., in *Scanning Probe Microscopy: Electrical and Electromechanical Phenomena at the Nanoscale*, Chapter I.6

A PHASE-FIELD MODEL FOR FERROELECTRICS WITH GENERAL DOMAIN WALL KINETICS

Laurent Guin*[1] and Dennis M. Kochmann[1]
[1]Mechanics&Materials, Department of Mechanical and Process Engineering, ETH Zürich, Zürich 8092, Switzerland

Summary In existing phase-field models for ferroelectric switching, the evolution equation for the polarization is governed by the Allen-Cahn equation. Such models help understanding the evolution of domain patterns and the macroscopic response of ferroelectrics under slow enough electromechanical loadings. However, they do not embed the complex kinetics of 180° and 90° domain walls, which is expected to have a strong influence on the response to high rate loadings. To address this issue, we propose an enhanced phase-field model for ferroelectrics where the kinetic relations for 180° and 90° domain walls can be independently prescribed. In addition, in the new formulation, these kinetic relations are extended to nonlinear functions which, in particular, allows us to account for the effect of pinning at low electric fields.

DOMAIN WALL KINETICS UNDERLYING THE ALLEN-CAHN EQUATION

For over two decades, phase-field models have been used to simulate the ferroelectric switching process, whereby the application of an electromechanical loading changes the electric polarization from one state to another. With a focus on ferroelectric perovskite ceramics (e.g., materials such as PZT, PTO, $BaTiO_3$), phase-field models have the advantage of properly accounting for the local electric and mechanical interactions between domains. With these assets, they have been particularly successful in predicting the shape of the electric and strain hystereses curves under slow electromechanical loading (see e.g. [1]).

These models are typically based on an electromechanical free-energy of the ferroelectrics that depends on an order parameter related to the polarization state of the ferroelectrics. An example of these models is the one proposed in Ref. [2], where the chosen order parameter is the spontaneous polarization $\boldsymbol{p}^s(\boldsymbol{x},t)$ (i.e., the electric polarization minus its piezoelectric and dielectric components). Denoting by $\boldsymbol{\varepsilon}(\boldsymbol{x},t)$ the small-strain tensor and $\boldsymbol{e}(\boldsymbol{x},t)$ the electric field, the phase-field formulation of Ref. [2] is based on the electric enthalpy

$$W(\boldsymbol{\varepsilon},\boldsymbol{e},\boldsymbol{p}^s,\nabla\boldsymbol{p}^s)=\Psi(\boldsymbol{\varepsilon},\boldsymbol{e},\boldsymbol{p}^s)+\Psi_{inter}(\nabla\boldsymbol{p}^s), \tag{1}$$

where Ψ_{inter} is a regularizing interface energy density and Ψ can be decomposed as

$$\Psi(\boldsymbol{\varepsilon},\boldsymbol{e},\boldsymbol{p}^s)=\Psi_{mech}(\boldsymbol{\varepsilon},\boldsymbol{p}^s)+\Psi_{piezo}(\boldsymbol{\varepsilon},\boldsymbol{e},\boldsymbol{p}^s)+\Psi_{diel}(\boldsymbol{e})-\boldsymbol{e}\cdot\boldsymbol{p}^s+\Psi_{sep}(\boldsymbol{p}^s). \tag{2}$$

Here the first three terms denote the mechanical (elastic strain) energy density, the piezoelectric-coupling energy density, and the dielectric energy density respectively, while the last one is a six-well potential energy density with equal minima at the six spontaneous polarization states associated with the tetragonal variants of the ferroelectric perovskite. In this formulation—as in all phase-field models for ferroelectrics, as far as we are aware—the phase field $\boldsymbol{p}^s$ is assumed to be governed by the Allen-Cahn equation:

$$\eta\dot{\boldsymbol{p}^s}=-\frac{\partial W}{\partial\boldsymbol{p}^s}+\operatorname{div}\left(\frac{\partial W}{\partial\nabla\boldsymbol{p}^s}\right), \tag{3}$$

where the superimposed dot denotes the time derivative and $\eta>0$ is a drag coefficient.

We see the phase-field model as a regularization of a sharp-interface interface model where a domain wall is represented by a surface $\mathcal{S}$ of discontinuity for $\boldsymbol{\varepsilon}$, $\boldsymbol{e}$, and $\boldsymbol{p}^s$. Denoting by $\boldsymbol{n}(\boldsymbol{x},t)$ the unit normal vector to $\mathcal{S}$, and by $v_n(\boldsymbol{x},t)$ its normal velocity, the above formulation is tantamount to assuming a linear kinetic relation between v_n and the driving force f:

$$v_n=cf, \tag{4}$$

where c is a non-negative constant and f is given by

$$f=\boldsymbol{n}\cdot[\![\boldsymbol{\Psi}\mathbb{1}-(\nabla\boldsymbol{u})^{\mathbf{T}}\cdot\boldsymbol{\sigma}+\boldsymbol{e}\otimes\boldsymbol{d}]\!]\boldsymbol{n}+\gamma\kappa, \tag{5}$$

where $\boldsymbol{u}(\boldsymbol{x},t)$ and $\boldsymbol{\sigma}(\boldsymbol{x},t)$ denote the displacement and stress fields, respectively; $\boldsymbol{d}(\boldsymbol{x},t)$ is the electric displacement, γ is the surface energy of the interface and $\kappa(\boldsymbol{x},t)$ is twice its mean curvature (taken positive when the center of curvature lies in the side of $\boldsymbol{n}$). The notation $[\![\phi]\!]=\phi(x^+,t)-\phi(x^-,t)$ denotes the jump at $x\in\mathcal{S}$ for any field $\phi(\boldsymbol{x},t)$ with the $+$ side corresponding to the one where $\boldsymbol{n}$ is pointing.

With such a perspective, it appears that the use of an Allen-Cahn equation in the phase-field model amounts to assuming a unique kinetics for 180° and 90° domain walls, which takes the form of a linear kinetic relation. The identity of the kinetics of the two types of domain walls seems physically unlikely and the linearity of the kinetic relation is only an approximation. Indeed, experimental measurements of the velocity of domain walls rather suggests a stick-slip type kinetic relation [3]. Note that these observations hold for phase-field models using the total polarization $\boldsymbol{p}(x,t)$ as the principal order parameter such as in Ref. [1].

*Corresponding author. E-mail: laguin@ethz.ch.

A PHASE-FIELD FORMULATION WITH GENERAL KINETICS

To address the limitations of the Allen-Cahn formulation that we have pointed out, we propose a new phase-field model with the following features:

- The order parameter is a vector $\boldsymbol{\varphi} \in \mathbb{R}^6$ such that each of the six polarization states (corresponding to the six variants of the tetragonal phase in perovskite ferroelectrics) is associated with $\varphi_i = 1$ for a particular $i \in 1, .., 6$ and $\varphi_j = 0$ for all $j \neq i$.
- The electric enthalpy $\tilde{W}(\boldsymbol{\varepsilon}, \boldsymbol{e}, \boldsymbol{\varphi}, \nabla\boldsymbol{\varphi})$ that we introduce is built upon $W(\boldsymbol{\varepsilon}, \boldsymbol{e}, \boldsymbol{p}^s, \nabla\boldsymbol{p}^s)$ in (1) from Ref. [2].
- The evolution equation for $\boldsymbol{\varphi}$ is inspired from the so-called hybrid model of Ref. [4] (see also Ref. [5]) which allows us to depart from the restriction of a linear kinetic relation between the driving force f and the domain wall normal velocity v_n. In addition, we extend the evolution equation proposed in Refs. [4] and [5] by generalizing it to the case of multiple phases and prescribe different kinetics for 180° and 90° domain walls. Indeed, the normal velocity of domain walls follows, in the proposed model, from the relations

$$\begin{aligned} v_n &= G_{180}(f) \quad \text{for } 180^\circ \text{ domain walls,} \\ v_n &= G_{90}(f) \quad \text{for } 90^\circ \text{ domain walls,} \end{aligned} \tag{6}$$

  where G_{180} and G_{90} are two arbitrary functions that map $\mathbb{R}$ into itself and satisfy $G_{180/90}(x) \cdot x \geq 0$ for all $x \in \mathbb{R}$.

The proposed formulation, when seen as the regularization of a corresponding sharp-interface model yields independent kinetic relations for the 180° and 90° domain walls, which, in addition, take very arbitrary functional dependence (allowing us to prescribe, for instance, the stick-slip behavior above mentioned). In conclusion, it allows us to address the shortcoming pointed out with regards to the treatment of the kinetics of ferroelectric switching in existing phase-field models.

References

[1] Vidyasagar A., Tan W.L., Kochmann D.M., Predicting the effective response of bulk polycrystalline ferroelectric ceramics via improved spectral phase field methods. *Journal of the Mechanics and Physics of Solids.* **106**: 133-151, 2017.
[2] Schrade D., Muller R., Gross D., On the physical interpretation of material parameters in phase field models for ferroelectrics. *Archive of Applied Mechanics*. **83(10)**: 1393-1413, 2013.
[3] Flippen R. B., Domain wall dynamics in ferroelectric/ferroelastic molybdates. *Journal of Applied Physics*. **46(3)**: 1068-1071, 1975.
[4] Alber H.-D., Zhu P., Comparison of a Rapidely Converging Phase Field Model for Interfaces in Solids with the Allen-Cahn Model. *Journal of Elasticity*. **111**: 153-221, 2013.
[5] Agrawal V., Dayal K., A dynamic phase-field model for structural transformations and twinning: Regularized interfaces with transparent prescription of complex kinetics and nucleation. Part I: Formulation and one-dimensional characterization. *Journal of the Mechanics and Physics of Solids.* **85**: 270-290, 2015.

THERMOMECHANICAL MODEL FOR NITI-BASED SHAPE MEMORY ALLOYS COVERING MACROSCOPIC LOCALIZATION OF MARTENSITIC TRANSFORMATION

Miroslav Frost*[1], Barbora Benešová[2], Petr Šittner[3], and Petr Sedlák[1]
[1]Institute of Thermomechanics, Czech Academy of Sciences, Prague, Czech Republic
[2]Department of Mathematical Analysis, Charles University, Prague, Czech Republic
[3]Institute of Physics, Czech Academy of Sciences, Prague, Czech Republic

Summary We present an extended thermomechanical model for polycrystalline NiTi-based shape memory alloys covering the deformation mode-dependent localization of the martensitic transformation. This is thanks to the introduction of a new austenite-martensite interaction term responsible for the strain-softening of the material. A time-discrete approximation of the constitutive model is proposed and used for numerical implementation to the finite-element method software Abaqus. Model performance is illustrated on several numerical simulations; some of them are compared with available experimental data.

INTRODUCTION

NiTi-based shape memory alloys (SMA) are usually utilized in the form of thin structures, e.g., wires, strips, tubes, or plates. In such samples, the stress-induced martensitic transformation tends to occur in a spatially inhomogeneous manner on the macroscopic scale: localized "martensitic bands" appear within the austenitic sample and the transformation propagates by their growth or multiplication. They can be visualized by various experimental means, and their occurrence and particular geometric form depend on many aspects, mainly on composition of the alloy, its texture, applied deformation mode, or deformation rate [1].

Because the localization gives rise to high gradients of strain concentrated in small volumes of material, it is supposed to be a critical factor for the fatigue lifetime. Hence, good understanding and effective modeling of the phenomenon would have direct practical impacts. Although several macroscopic (continuum) models incorporating localization have been developed recently, they either disregard the deformation mode-dependence of localization [2, 3] or include it purely heuristically [4]. In this contribution, we extend a well-established constitutive model for NiTi SMA by a specific internal energy term, which deals with this feature more formally and allows for applicability in general loading scenarios. Moreover, the chosen approach motivates a rigorous mathematical regularization of the complete model.

MODELING

We extend the continuum mechanics-based rate-independent constitutive model introduced in [5, 6], which is particularly suitable for simulations of the mechanical response of NiTi-based SMA components in complex loading modes. It has been formulated within the *generalized standard solids* thermodynamic framework, within the small-strain realm. The core of the original model consists of two material functions: one captures the energy stored in the material at a given thermodynamic state (free energy), the other defines the energy released during irreversible processes, and it is often called the dissipation function. The irreversible processes are related to changes of the microstructure of the material – crystallographic changes as phase transformations and reorientation – via a set of internal variables. Namely, we introduce a scalar variable, ξ, representing the volume fraction of martensite and a tensorial variable, $\varepsilon^{\mathrm{tr}}$, representing the mean macroscopic transformation strain. Specific constraints on these variables allow taking into account the (crystallographically) limited transformation strains, the isochoric nature of the transformation, and the tension-compression asymmetry [5].

The constitutive response in a material point is then determined via the so-called *principle of minimum dissipation potential*, which is an alternative to common definitions of domain(s) of admissible force(s) complemented by flow rule(s):

$$\text{Minimize}\,\{f_k + d_k + r_k\}\,\text{subject to}\,(\varepsilon^{\mathrm{tr}}, \xi). \tag{1}$$

Subscript $_k$ denotes a suitable numerical time-discretization of the free energy, f, dissipation, d and regularization, r, functions. The regularization function encompasses the numerical treatment of constraints imposed on internal variables. The alternative minimization technique is then employed for numerical implementation of the model into Abaqus FEA software (via UMAT subroutine) as thoroughly described in [6].

The experimental investigations suggest that the localization phenomena are rooted in the microstructural interactions between martensite and austenite phases on the level of grains forming the pollycrystaline material. The competition of the energy contribution stemming from interaction of differently oriented neighboring grains during phase transition (tending towards strain-hardening response in the conventional sense) and the interaction energy related to the growth of martensite inclusions within austenitic matrix inside grains (leading to strain-softening type of response) might lead either to homogeneous transformation response or to the localized one.

*Corresponding author. E-mail: mfrost@it.cas.cz.

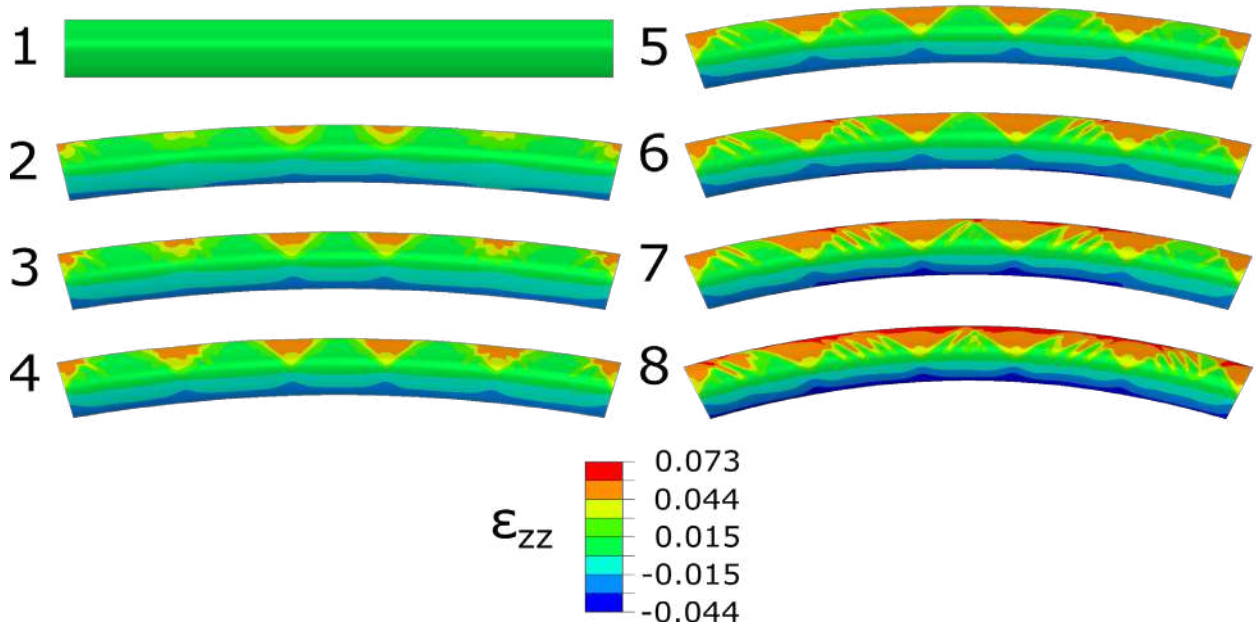

Figure 1: Snapshots from a three-dimensional numerical simulation of bending of a thin-walled NiTi tube plotted with the distribution of the axial component of strain (in the reference configuration) in color. Several common features of the localization patterning are reproduced: the appearance of isolated wedge-shaped regions of high strain, their growth and multiplication via crisscrossing and coalescence of martensitic "needles", which finally cover most of the (upper) tube surface undergoing predominantly tensile straining. Note that a homogeneous deformation develops on the (lower) tube surface that undergoes predominantly compressive straining.

Derivation of the elastic energy per unit volume of the specimen containing elliptical inclusions with transformation strain $\varepsilon^{\mathrm{tr}}$, as performed by Mori and Tanaka, motivates the new interaction term, which enables a strain-softening material response:

$$E^{\mathrm{int}} = C^{\mathrm{int}}_{\mathrm{MA}}\xi(1-\xi)^2\|\varepsilon^{\mathrm{tr}}\|^2 + C^{\mathrm{int}}_{\mathrm{AM}}\xi^2(1-\xi)\|\varepsilon^{\mathrm{tr}}\|^2, \tag{2}$$

where $C^{\mathrm{int}}_{\mathrm{MA}}, C^{\mathrm{int}}_{\mathrm{AM}}$ are suitable material parameters. By tuning these parameters and the parameters of the dissipation function, which incorporates the strain-hardening in the model, we can reach strain-softening in uniaxial tension and, simultaneously, strain-hardening in uniaxial compression as often observed in experiments. Since the localization contribution energy E^{int} makes the overall energy non-convex, a proper regularization treatment is needed. A possible solution is the non-local integral regularization approach proposed in [7]. Figure 1 shows a numerical simulation of a bending deformation of a NiTi thin-walled tube performed in Abaqus FEA software with our own-developed UMAT subroutine as an illustration of the capability of the complete model.

CONCLUSIONS

We extended a well-established constitutive model tailored for NiTi-based SMA by an interaction energy term, which is motivated by the Mori-Tanaka method and enables us to capture the localization effects. Thanks to two independent constants appearing in Eq. (2), we gained more freedom to adjust the strain-softening constitutive law to available experimental measurements. Thanks to the factor $\|\varepsilon^{\mathrm{tr}}\|^2$ in E^{int}, we reached the deformation mode-dependency of the response as observed in experiments. The motivation stemming from the Mori-Tanaka approach also provided a hint for a physically plausible regularization of the inherently non-convex model.

References

[1] Šittner, P., Liu, Y., and Novák, V. (2005) On the origin of Lüders-like deformation of NiTi shape memory alloys. *J. Mech. Phys. Solids,* **53**, 1719–46.

[2] Armattoe, K., Haboussi, M., and Ben Zineb, T. (2014) A 2D finite element based on a nonlocal constitutive model describing localization and propagation of phase transformation in shape memory alloy thin structures. *Int. J. Solids Struct.,* **51**(6), 1208–1220.

[3] Razaee-Hajidehi, M., Tůma, K., and Stupkiewicz, S. (2019) Gradient-enhanced thermomechanical 3D model for simulation of transformation patterns in pseudoelastic shape memory alloys. *Int. J. Plast.,* p. in press.

[4] Jiang, D., Kyriakides, S., Bechle, N. J., and Landis, C. M. (2017) Bending of pseudoelastic NiTi tubes. *Int. J. Solids Struct.,* **124**, 192–214.

[5] Sedlák, P., Frost, M., Benešová, B., Šittner, P., and Ben Zineb, T. (2012) Thermomechanical model for NiTi-based shape memory alloys including R-phase and material anisotropy under multi-axial loadings. *Int. J. Plast.,* **39**, 132–151.

[6] Frost, M., Benešová, B., and Sedlák, P. (2016) A microscopically motivated constitutive model for shape memory alloys: formulation, analysis and computations. *Math. Mech. Solids,* **21**(3), 358–382.

[7] Bobinski, J. and Tejchman, J. (2004) Numerical simulations of localization of deformation in quasi-brittle materials within non-local softening plasticity. *Comp. Concrete,* **1**(4), 433–455.

PROPAGATION AND STABILITY OF STRESS-AFFECTED CHEMICAL REACTION FRONTS IN SOLIDS

Alexander B. Freidin*[1],Aleksandr Morozov[1,2],Wolfgang H. Müller[2],Mikhail Poluektov[3],and Igor K. Korolev[1]
[1]Institute for Problems in Mechanical Engineering of the Russian Academy of Sciences, St. Petersburg, Russia
[2]Institute of Mechanics, Faculty of Mechanical Engineering, Berlin Institute of Technology, Berlin, Germany
[3]International Institute for Nanocomposites Manufacturing, WMG, University of Warwick, UK

Summary Localized stress-affected chemical reactions between solid and diffusing reactants are studied on the basis of the chemical affinity tensor. A kinetic equation in a form of the dependence of the chemical reaction front velocity on the normal component of the chemical affinity tensor is formulated and used for solving coupled boundary value problems "diffusion–chemistry–mechanics". It is shown that mechanical stresses can accelerate, retard and block the front propagation, and the reaction front can be stable or unstable in the blocking position. Then it is studied how the front converges to the stable and unstable blocking positions, and the competition between global and local kinetics of the front propagation is discussed in the context of the stability analysis. Finally it is studied how the unsteadiness of the diffusion may affect the front propagation.

INTRODUCTION

Interconnections between chemical reactions and mechanical stresses has been recognized and intensively studied during last decades, see e.g. the reference represented in [1]. Oxidation of silicon in integrated-circuit technologies, oxidation and fracture processes in polycrystalline silicon microscale parts of MEMS, lithiation of silicon in Li-ion batteries, formation of intermetallic phases in lead-free solders are among important examples of stress-affected chemical reactions. In all cases one deal with a reaction between diffusive and solid constituents which is accompanied by transformation strain, and mechanical properties including rheological behaviour change due to the reaction. It may be questionable whether the front propagation is controlled by the diffusion or by the reaction rate itself (see e.g. [2]). We consider the case for which the velocity of the reaction front is controlled rather by the reaction rate than by the diffusion (see e.g. [4, 3] and reference therein) and study a reaction front propagation within the frames of the mechanics of configurational forces.

As it was derived and approbated during last years (see [1] and reference therein), the configurational force driving the reaction font is determined by the normal component of a chemical affinity tensor. Then a kinetic equation can be formulated in the form of the dependence of the reaction front on the normal component of the affinity tensor. The chemical affinity tensor, in turn, depends on stresses and strains, and this quantifies how stresses and strains affect the chemical reaction rate and reaction front velocity. Note that the expression of the affinity tensor was derived from fundamental laws and entropy inequality for solid constituents of arbitrary rheology [5, 6]) (see also [7]).

Theory built on the chemical affinity tensor has been applied to a number of problems for the cases of linear elastic solid constituents, for finite strains of nonlinear viscoelasic solid constituents with applications to two-phase lithiation of Si particles, for the case a collection of interacting particles embedded into inelastic matrix, for intermetallic compound formations (see, e.g., the reference in [1, 8]). It was shown that stresses can accelerate, retard and even block the reaction front propagation, and forbidden regions were constructed in the strain space formed by strains at which the reaction cannot go [10].

Now we present results on the reaction front propagation and stability analysis, including numerical simulations of the front propagation validated by the comparison with analytical solutions. We develop a procedure of the stability analysis and study how the front converges to a blocking position if this position is stable or unstable. Then we study the front kinetics for various cases.

CHEMICAL AFFINITY TENSOR AND KINETIC EQUATION

We consider a chemical reaction between solid and diffusive constituents of the type $n_- B_- + n_* B_* \to n_+ B_+$ where B_-, B_* and B_+ are the chemical formulae of an initial solid constituent, a diffusive constituent and a transformed solid constituent, $n_\pm$ and n_* are stoichiometric coefficients. The reaction is localized at the reaction front and sustained by the diffusion of the gaseous constituent. It can be derived that the the energy dissipation per unit area of the propagating reaction front takes the form

$$D_g = \omega_N A_{NN} \geq 0$$

where ω_N is the reaction rate at the surface element with the normal $\mathbf{N}$, $A_{NN} = \mathbf{N} \cdot \mathbf{A} \cdot \mathbf{N}$ is the normal component of the chemical affinity tensor

$$\mathbf{A} = n_- M_- \mathbf{M}_- + n_* M_* \mu_* \mathbf{I} - n_+ M_+ \mathbf{M}_+ + \{\text{dynamical terms}\},$$

*Corresponding author. E-mail: alexander.freidin@gmail.com

THEMATIC SESSION SM

$\mathbf{M}_-$ and $\mathbf{M}_+$ are the chemical potential tensors of the solid constituents (the Eshelby stress tensors divided by the referential mass densities), μ_* is the chemical potential of the diffusing constituent. To find $\mathbf{M}_\pm$ and μ_* one has to find stresses and strains at the reaction front and to solve the diffusion problem.

Substituting A_{NN} instead of the scalar chemical affinity into the classical formula leads to a kinetic relationships which define the reaction rate and the normal component of the reaction front velocity W by the formulas

$$\omega_N = k_* c \left\{ 1 - \exp\left(-\frac{A_{NN}}{RT} \right) \right\}, \quad W = \frac{n_+ M_+}{\rho_+} k_* c \left\{ 1 - \exp\left(-\frac{A_{NN}}{RT} \right) \right\}.$$

where k_* is the kinetic constant, ρ_+ is the referential mass density of B_+, c is the concentration of the diffusive constituent.

KINETICS AND STABILITY OF THE REACTION FRONT

We study the stability of the reaction front in a blocking position following [9] and developing the procedure of so-called kinetic stability analysis and say that the front is unstable if interface perturbations grow due to the kinetic equations. We also relate strains at the equilibrium reaction front with strains belonging to the boundary of forbidden zone [10] which coincides with the phase transition zone (e.g., [11]) in the case of stress-induced phase transformation. This gives necessary stability conditions. Considering simplest problems for linear elastic solid reactants, we analyze analytically the stability of the reaction fronts and study how material parameters and stress state affect the stability.

After that we develop a FEM procedure for numerical simulations of the reaction front propagation. We study how the front propagates if the blocking position is stable or unstable. We demonstrate that in both cases the interface may propagate in the direction of the blocking position, but the interface converges smoothly to the blocking position in the stable case, and the initially smooth interfaces becomes unstable with the tendency to finger-type instabilities prior to reaching the blocking position if the position is unstable. We explain such a behavior by the competition between global kinetics of the front propagation and local kinetics of the interface perturbations. We study stress concentrations induced by the front instabilities and note that instabilities developing due to the front retardation and blocking may be the source of further intensive plastic deformations, damage and fracture. We also give example of the reaction front propagation in the vicinity of stress-concentrations like inhomogeneities. Finally, we study the unsteadiness of the diffusion may affect the front propagation.

CONCLUSIONS

An approach to study the influence of stresses on the chemical reaction front propagation was developed based on the chemical affinity tensor and implemented in a numerical procedure. Effects of the front retardation and blocking were explained within the framework of the theory developed. Stability analysis of the reaction front in a blocking position was done and stable and unstable reaction front propagations were simulated numerically. Stresses induced by the growth of the instability amplitudes were analyzed. The front propagation in the vicinity of stress concentrators was studied. Various diffusion regimes were discussed in the context of the front propagation.

ACKNOWLEDGEMENTS

The financial support from the Russian Science Foundation (RSF Grant 19-19-00552) is acknowledged.

References

[1] Freidin A.B., Vilchevskaya E.N. Chemical affinity tensor in coupled problems of mechanochemistry. In: Altenbach H., Öchsner A. (eds) Encyclopedia of Continuum Mechanics. Springer, Berlin, Heidelberg, 2020.

[2] Cui Z., Gao F., Qu J. Interface-reaction controlled diffusion in binary solids with applications to lithiation of silicon in lithium-ion batteries. *J. Mech. Phys. Solids*, **61**: 293-310, 2013.

[3] Jia Z., Li T. Stress-modulated driving force for lithiation reaction in hollow nano-anodes. *J. Power Sources*, **275**: 866–876, 2015.

[4] Zhao K., Pharr M., Wan Q., Wang W., Kaxiras E., Vlassak J., Suo Z. Concurrent reaction and plasticity during initial lithiation of crystalline silicon in lithium-ion batteries. *J. Electrochemical Society*, **159**: A238-A243, 2012.

[5] Freidin A. Chemical affinity tensor and stress-assist chemical reactions front propagation in solids. In: *ASME 2013 International Mechanical Engineering Congress and Exposition, San Diego, California, USA*. V. 9: Paper No. IMECE2013–64957, V009T10A102, 2013.

[6] Freidin A. On a chemical affinity tensor for chemical reactions in deformable solids. *Mechanics of Solids* **50**(3): 260–285, 2015.

[7] Freidin A.B., Vilchevskaya E.N., Korolev I. Stress-assist chemical reactions front propagation in deformable solids. *Int. J. Eng. Sci.* **83**: 57-75, 2014.

[8] Morozov A.V., Freidin A.B., Klinkov V.A. et al. Experimental and theoretical studies of Cu-Sn intermetallic phase growth during high-temperature storage of eutectic SnAg interconnects. *J. Electronic materials*, 2020, https://doi.org/10.1007/s11664-020-08433-y

[9] Morozov A.V., Freidin A.B., Müller W.H. Stability of chemical reaction fronts in the vicinity of a blocking state. *PNRPU Mechanics Bulletin*, 3: 58-64, 2019.

[10] Freidin A.B., Sharipova L.L. Forbidden strains and stresses in mechanochemistry of chemical reaction fronts. In: Altenbach H. et al (eds), Generalized Models and Non-classical Approaches in Complex Materials 1. Advanced Structured Materials, **89**, Springer, 335-348, 2018.

[11] Morozov N.F., Freidin A.B. Phase transition zones and phase transformations of elastic solids under different stress states. *Proc. of the Steklov Institute of Mathematics*, **223**: 220–232, 1998.

A THERMODYNAMICALLY CONSISTENT PHASE-FIELD THEORY FOR COUPLED DEFORMATION-DIFFUSION-REACTIONS IN SOLIDS: APPLICATION TO CONVERSION-TYPE ELECTRODES

Claudio V. Di Leo*[1] and Arman Afshar[1]
[1]School of Aerospace Engineering, Georgia Institute of Technology, Atlanta, USA

Summary We developed a thermodynamically consistent framework for materials undergoing large deformations coupled to deformation-diffusion-reaction phenomena with sharp interfaces. Our framework captures phenomena involving both diffusion- and reaction-controlled sharp interfaces. In addition, we present a novel decomposition of the deformation gradient to account for possible macroscopically stress free inelasticity due to incompatibilities at the microstructure. We apply our framework to modeling the experimentally relevant reaction of FeS_2 crystals with Li and Na ions and demonstrate that differences in the sharp interface morphologies are driven by stress effects on the thermodynamic reaction driving force. We conclude by studying the range of diffusion-reaction properties which enhance electrode performance and the role of mechanical stress in this relationship.

INTRODUCTION

Current state of the art lithium-ion batteries make use of active particles, such as graphite and cobalt oxide, whose primary mechanism of lithium storage is intercalation. Alternatively, next generation electrode materials made of transition metal oxides which store charge carrying ions via chemical conversion mechanism have recently been given attention as their theoretical capacity dwarfs that of intercalation based electrodes. The conversion reaction, however, is accompanied by *structural and chemical phase transformations* of the host material.[1] Recently, researchers have found that reaction of FeS_2 crystals with ions (Li^+, Na^+, and K^+) resulting in different volume changes drastically impacts the reaction morphology and susceptibility to fracture.[2] In order to understand this phenomena one must capture the complex coupled physics between diffusion, sharp interface reactions, and large deformations occurring in these materials.

SUMMARY OF THE THEORETICAL FRAMEWORK

Consider a general reaction of the form $A + B \to C$, as shown on the figure to the right. We characterize this system through a phase-field variable ξ which physically represents the volume fraction of reacted phase γ to unreacted phase α in a representative volume element (RVE), and through a molar concentration c of the diffusing species moving through the system. We employ a decomposition of the deformation gradient of the form

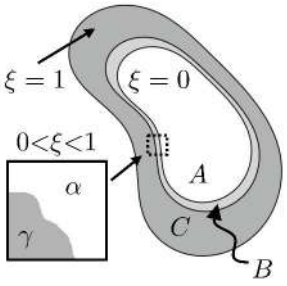

$$\mathbf{F} = \mathbf{F}^{\text{mech}}\mathbf{F}^{\text{chem}}, \quad \text{with velocity gradient} \quad \mathbf{L} = \mathbf{L}^{\text{mech}} + \mathbf{F}^{\text{mech}}\mathbf{L}^{\text{chem}}(\mathbf{F}^{\text{mech}})^{-1}. \tag{1}$$

Here, $\mathbf{F}^{\text{chem}}$ accounts for the combined distortions due to all chemical processes (diffusion and reaction), while $\mathbf{F}^{\text{mech}}$ accounts for subsequent stretching and rotations which may be elastic or inelastic in nature. The chemical velocity gradient is further decomposed into

$$\mathbf{L}^{\text{chem}} = (1-\xi)\mathbf{L}^{\alpha} + \xi\mathbf{L}^{\gamma} + \xi(1-\xi)\mathbf{L}^{\text{acc}}, \quad \text{with} \quad \mathbf{L}^{\alpha} = \dot{c}\mathbf{N}^{\alpha}, \quad \mathbf{L}^{\gamma} = \dot{\xi}\mathbf{N}^{\gamma}, \quad \text{and} \quad \mathbf{L}^{\text{acc}} = \dot{\kappa}\mathbf{N}^{\text{acc}}. \tag{2}$$

Here, $\mathbf{L}^{\alpha}$ and $\mathbf{L}^{\gamma}$ represent incompatible deformations associated with the diffusing species and the reaction induced phase transformations respectively. $\mathbf{L}^{\text{acc}}$ is then an accommodation deformation necessary to make the total deformation compatible. Importantly, through $\mathbf{L}^{\text{acc}}$ it is possible to have inelastic deformations which are macroscopically stress free, i.e. chemically induced inelastic deformation. In this abstract, for conciseness, we will not specify $\mathbf{L}^{\text{acc}}$ any further, we will assume $\mathbf{N}^{\alpha}$ and $\mathbf{N}^{\gamma}$ to be compatible, and will focus on the diffusion-reaction behavior.

The diffusing species is governed by a diffusion-reaction equation of the form

$$\begin{aligned} &\dot{c} = -J(\operatorname{div}\mathbf{j} - \dot{\bar{\xi}}), \quad \mathbf{j} = -m\nabla\mu, \quad \text{and} \\ &\mu = (1-\xi)\mu_0^{\text{UR}} + \xi\mu_0^{\text{R}} + R\vartheta\ln\left(\frac{\bar{c}}{1-\bar{c}}\right) - J^{\text{chem}}(1-\xi)\mathbf{M}^e : \mathbf{N}^{\alpha} \end{aligned} \tag{3}$$

Here $\mathbf{j}$ is the spatial flux of the mobile species, m is the mobility, μ the chemical of the diffusing species which is both concentration and stress dependent through the Mandel stress $\mathbf{M}^e$. Further, $J = \det\mathbf{F}$, $J^{\text{chem}} = \det\mathbf{F}^{\text{chem}}$, $\bar{\xi} = \xi c_{\text{max}}^{\text{react}}$ is a dimensional reaction coordinate, $\bar{c} = c/c_{\text{max}}^{\text{unreact}}$ is a dimensionless concentration, R is the gas constant, ϑ is the absolute temperature, μ^{UR} and μ^{R} are reference potentials for the unreacted and reacted phases respectively.

We employ a linear relationship between the reaction rate and the thermodynamic force $\mathcal{F}$ of the form

$$\dot{\bar{\xi}} = R_0\mathcal{F}, \quad \mathcal{F} = \mu^{\xi} - \mu, \quad \text{and} \quad \mu^{\xi} = \frac{\partial\psi}{\partial\bar{\xi}} - J^{\text{chem}}\bar{\xi}\,\mathbf{M}^e : \mathbf{N}^{\gamma} + \operatorname{div}(\lambda\nabla\bar{\xi}). \tag{4}$$

Here μ^{ξ} is the chemical potential of the species in the reacted phase which is also both concentration dependent through the free energy ψ, and stress dependent. The term $\operatorname{div}(\lambda\nabla\bar{\xi})$ is introduced for numerical reasons and arises from the free energy as a penalty on sharp interfaces such that we may treat them as diffuse. Combining μ from (3) and μ^{ξ} from (4) and neglecting the gradient term, we may write the thermodynamic driving force $\mathcal{F}$ as:

*Corresponding author. E-mail: cvdileo@gatech.edu

$$\mathcal{F} = \underbrace{\Big(\bar{c} + (1-\xi)\Big)(\mu_0^{\mathrm{R}} - \mu_0^{\mathrm{UR}}) + \frac{d\psi^R(\bar{\xi})}{d\bar{\xi}}}_{\text{energetic}} - \underbrace{R\vartheta \ln\left(\frac{\bar{c}^{\mathrm{C}}}{1-\bar{c}^{\mathrm{C}}}\right)}_{\text{entropic}} + \underbrace{J^{\mathrm{chem}}\mathbf{M}^e : \Big((1-\xi)\mathbf{N}^\alpha - \xi\mathbf{N}^\gamma\Big)}_{\text{mechanical}} \tag{5}$$

with $\psi^R(\bar{\xi}) = \beta\bar{\xi}^2(1-\bar{\xi}^2)$ a double-welled reaction free-energy giving rise to an energy barrier for the chemical reaction characterized through the parameter β which is on the order of $20 \cdot R\vartheta$.[3] The reaction driving force $\mathcal{F}$ is thus driven by: i) an energetic component which has both a global driving force (proportional to $(1-\xi)$) which drives the reaction forward, and a local driving force (related to $d\psi^R/d\bar{\xi}$) which serves as an energy barrier, ii) an entropic component, and iii) a mechanical term which can serve to enhance or supress the reaction.

For the mechanical behavior of the material we consider a simple isotropic elastic-plastic constitutive behavior with the Mandel stress given by $\mathbf{M}^e = 2G\mathbf{E}^e + (K - (2/3)G)\mathrm{tr}\mathbf{E}^e)\mathbf{1}$, with G and K phase dependent elastic moduli. The plastic behavior is elastic-perfectly plastic.

KINETIC VS. THERMODYNAMIC SHARP INTERFACES

We first demonstrate the manner in which our framework can capture both kinetically (diffusion controlled) and thermodynamically (reaction controlled) driven sharp interfaces. The figure to the right shows contours of reaction coordinate ξ for two sets of simulations (colorbar on the bottom figure). The top row shows simulations as we increase the reaction rate R_0 in relation to the diffusivity D_0 which in turn leads to a sharp interface as all diffusing species is quickly consumed, this sharp interface is hence driven by the kinetics of the system. However, some sharp interface reactions of relevance (cf. [2, 3]) have sluggish reaction kinetics (i.e. R_0 is not much larger than D_0). The second row of simulations shown on the right demonstrates our ability to capture a sharp interface by increase the energy barrier through an increase of β to a few times the thermal energy. This is critical as experiments (cf. [2]) show an anisotropic interface due to anisotropy in R_0 and can only be modeled if one simulates a thermodynamically driven sharp interface.

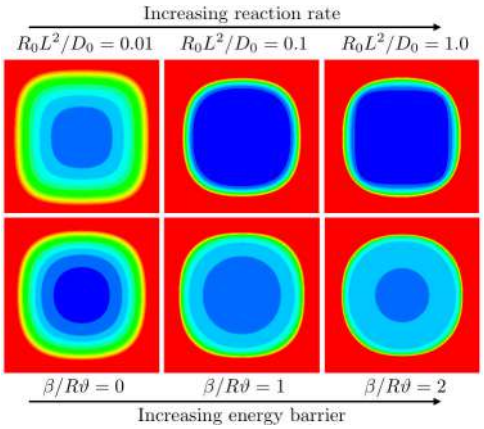

CHEMO-MECHANICS OF CONVERSION BATTERY MATERIALS

In this talk we will also present an in-depth study on the role of mechanics in the reaction of FeS_2 crystals with Li^+, Na^+, and K^+ ions each of which results in a different volume change and a different sharp interface morphology.[2] For conciseness of this abstract the results presented here assume that $\mathbf{L}^\alpha = \mathbf{L}^{\mathrm{acc}} = \mathbf{0}$, and we choose $\mathbf{N}^\gamma$ such that $\mathbf{F}^{\mathrm{chem}} = (1 + \Omega\bar{\xi})^{(1/3)}\mathbf{1}$ which leads to an isotropic reaction induced deformation characterized by Ω. The reaction rate R_0 is anisotropic with reactions being 30% faster in the horizontal and vertical directions, $R_0L^2/D_0 = 0.005$ and $\beta/R\vartheta = 20$. As shown on the bottom row in the figure to the right, when changing the reaction of FeS_2 from Li to Na ions, the interface goes from a concave sharp interface to a convex interface.[2] The top row on the figure shows the corresponding simulations using our model where we note that the *only parameter varied between the two simulations is the partial volume* Ω (the dashed lines show the undeformed configuration). The simulations recover the observed experimental behavior whereby chemical reactions with larger induced volume changes lead to concave reaction fronts and significantly lower stresses. This unintuitive result is critical, as it can be demonstrated that reactions with larger induced volume changes do not always result in higher stresses and larger degrees of damage and fracture.

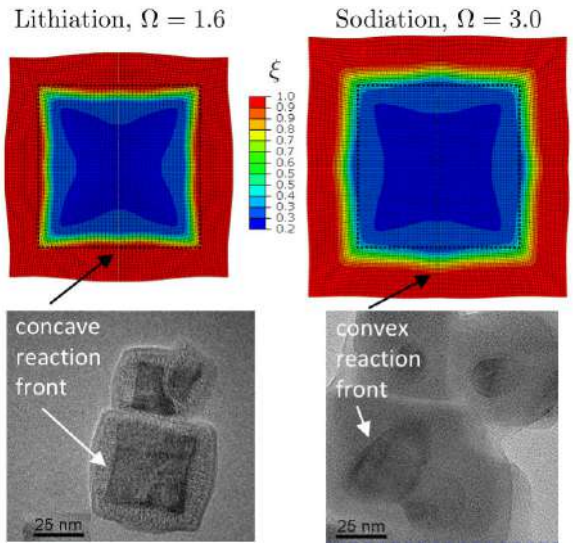

SUMMARY

We developed a thermodynamically consistent framework for materials undergoing large deformations coupled to deformation-diffusion-reaction phenomena with sharp interfaces. During this talk we will present the theoretical framework as well as its application to modeling conversion-type electrodes with suitable comparison to experiments. We will discuss the importance of mechanics in capturing the reaction-diffusion behavior of these systems as well as the reaction induced inelastic deformations during phase transformations of the host material.

References

[1] Wang, F., Yu, H. C., Chen, M. H., Wu, L., Pereira, N., Thornton, K., ... & Graetz, J. *Nature comm.* **3**:1201, 2012.
[2] Boebinger, M. G., Yeh, D., Xu, M., Miles, B. C., Wang, B., Papakyriakou, M., ... & Sang, X. *Joule*, **2(9)**:1783-1799, 2018.
[3] Zhang, X., Lee, S. W., Lee, H. W., Cui, Y., & Linder, C. *Extreme Mech. Lett.*, **4**:61-75, 2015

MATHEMATICAL MODELS AND IDEAS FOR DISCLINATIONS

Pierluigi Cesana *[1]
[1]Institute of Mathematics for Industry, Kyushu University, Japan

Summary In this talk, we describe some recent results on the modeling of self-similar martensitic microstructure and on the modeling of rotational mismatches at the level of a crystal lattice, two phenomena which appear to be strongly interconnected.

First, we present a probabilistic model for the description of martensitic microstructure as an avalanche process. A martensitic phase-transformation is a first-order diffusionless transition occurring in elastic crystals and characterized by an abrupt change of shape of the underlying crystal lattice. It is the basic activation mechanism for the Shape-Memory effect. Our approach to the analysis of the model is based on an associated general branching random walk process. Comparisons are reported for numerical and analytical solutions and experimental observations. This is a joint project with John M. Ball and Ben Hambly (Oxford).

Then, we introduce an energy functional defined over a triangular lattice accounting for nearest-neighbor interactions. We design special rotational-type boundary value problems on the lattice so that the minimizers necessarily exhibit non-homogeneous rotations. We are interested in the asymptotics of the energy minima and minimizers as the lattice spacing vanishes which we compute exactly with Gamma-convergence. We perform some numerical calculations for the discrete model and show that both the shape of the solutions as well as the values of the energies are in agreement with classical results for positive and negative disclinations. This is a collaboration with P. van Meurs (Kanazawa).

MARTENSITIC AVALANCHES

The austenite-to-martensite phase-transformation is a first-order diffusionless transition observed in elastic crystals and characterized by an abrupt change of shape of the underlying crystal lattice [3]. It manifests itself to what in materials science is called a martensitic microstructure, an intricate highly inhomogeneous pattern populated by sharp interfaces that separate thin plates composed of mixtures of different martensitic phases (i.e., rotated copies of a low symmetry lattice) possibly rich in defects and lattice mismatches. In the first part of this talk we review some results on the modeling of self-similar martensitic microstructure, a phenomenology observed in various experiments [6], [7].

Inspired by Bak's cellular automaton model for sand piles [1], we introduce a conceptual model for a martensitic phase transition and analyze the properties of the patterns obtained. Nucleation and evolution of martensitic variants are modeled as a fragmentation process in which the microstructure evolves via formation of thin plates of martensite embedded in a medium representing the austenite. While the orientation and direction of propagation of the interfaces separating the plates is determined by kinematic compatibility of the crystal phases, their nucleation sites are inevitably influenced by defects and disorder, which are encoded in the model by means of random variables.

To sketch our model, we consider a single crystal which transforms from austenite into martensite along a negative temperature gradient. In the simplest version of the model, martensite evolves over a unit square via nucleation of segments (representing thin martensitic plates which are parallel to their habit planes) that evolve until they encounter the boundary of the domain or an existing plate. We initially consider only two possible habit plane directions, which are taken to be, without loss of generality, horizontal and vertical. A point with coordinates measured by two uniform random variables is chosen in the unit square. The propagation of an interface is chosen to be vertical with probability p or horizontal with probability $1-p$, with $0 < p < 1$. After the first step the square is divided into two rectangles. Then, a new nucleation point is selected in one of the two rectangles and, starting from the chosen rectangle, another fragmentation process is activated as in step one. As this process is iterated, successive fragmentations result in formation of smaller and smaller rectangles. A realization of a microstructure obtained according to this fragmentation model is displayed in Fig. 1-left for 3000 interfaces and $p = \frac{1}{2}$. Extensions of the 2-direction model are obtained by allowing for additional habit planes. In Fig. 1-center we show a microstructure obtained according to a fragmentation model with 3 directions, that are, horizontal, vertical and $\frac{\pi}{4}$ (chosen with an equal probability) and composed of 3000 interfaces. In Fig. 1-right we show another microstructure composed of 3000 interfaces and obtained according to a fragmentation model with 4 directions (again, selected with an equal probability), which are, horizontal, vertical and $\pm\frac{\pi}{4}$.

We investigate distribution of the lengths of the interfaces in the pattern and establish limit theorems for some of the asymptotics of the interface profile. In particular, we prove that the density of the length of the interfaces generated corresponds to a power law for which we compute the exponent exactly [2]. We also show that the density of the rectangles generated during the fragmentation process are described by [4]

$$f(x,y) = \begin{cases} \sqrt{1-(2p-1)^2}\sqrt{1-(x-y)^2} + (1-2p)(x-y) & x+y=1, \\ -\infty & x+y \neq 1, \end{cases}$$

where $0 \leq x, y \leq 1$ are variables that parametrize the coordinates of the rectangles. We also discuss numerical realizations of microstructures according to these fragmentation models, describe computations of the density profile and power laws and present comparisons with experimental data. These results are from a collaboration with J.M. Ball and B. Hambly (Oxford).

*Corresponding author. E-mail: cesana@math.kyushu.u.ac.jp

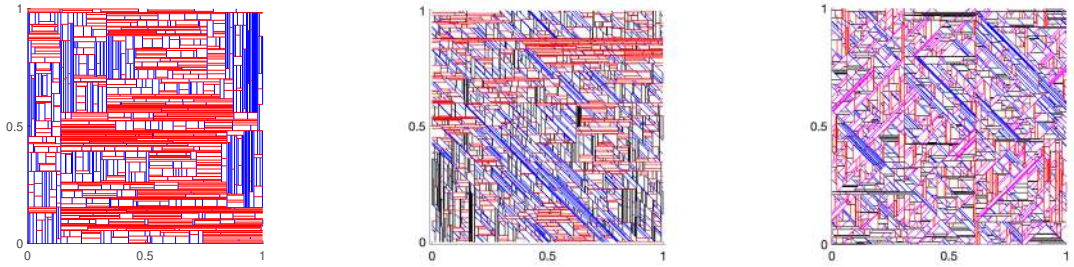

Figure 1: Realizations of microstructure as a fragmentation process with 2 (Left), 3 (Center) or 4 (Right) possible directions.

DISCRETE MODELS FOR PLANAR WEDGE DISCLINATIONS

In the second part of the talk we describe some recent results on the mathematical modeling of wedge disclinations. These are rotational defects caused by angular mismatch at the level of the crystalline lattice that were predicted by Volterra in his celebrated 1907 paper [8]. Unlike dislocations, which have received considerable attention since the 1930s, disclinations have received disproportionally less interest. However, disclinations are not uncommon as they accompany, as a relevant example, rotated and nested interfaces separating (almost) kinematically compatible variants as in martensitic avalanche experiments.

Our approach consists of an atomistic model measuring nearest-neighbor interactions over a triangular lattice. We describe the asymptotic behavior of the energy as the spacing of the lattice vanishes (continuum limit) via Gamma-convergence and we compute some numerical solutions of boundary value problems. Comparisons with data from literature on disclinations are also discussed. Some of these results are from a collaboration P. Van Meurs (Kanazawa) [5].

References

[1] Bak P., Tang C., Wiesenfeld K., Self-organized criticality: An explanation of the $1/f$ noise, *Phys. Rev. Lett.* **59**, 381, 1987
[2] Ball J.M., Cesana P., Hambly B.M. A probabilistic model for martensitic avalanches, *MATEC Web of Conferences* **33**: 02008, 2015.
[3] Bhattacharya K., Microstructure of Martensite, *Oxford University Press*, 2003.
[4] Cesana P., Hambly B.M. A probabilistic model for interfaces in a martensitic phase transition, *under review*.
[5] Cesana P., P. van Meurs, Discrete-to-continuum limits for planar disclinations, *in preparation*.
[6] Planes A., Manosa L., Vives E., Acoustic emission in martensitic transformations, *Journal of Alloys and Compounds* **577**, Supplement 1, S699-S704, 2013.
[7] Salje E.K.H., Koppensteiner J., Reinecker M., Schranz W., Planes A., Jerky elasticity: Avalanches and the martensitic transition in $Cu_{74.08}Al_{23.13}Be_{2.79}$ shape-memory alloy, *Appl. Phys. Lett.* **95**, 231908, 2009.
[8] Volterra V., Sur l'équilibre des corps élastiques multiplement connexes, Annales scientifiques de l'École Normale Supérieure **24**, 401-517, 1907.

NON LOCAL AND THERMAL EFFECTS IN NANOWIRES PHASE TRANSITION

Luca Bellino*[1], Giuseppe Florio[1], Stefano Giordano[2], and Giuseppe Puglisi[3]
[1]Department of Mechanics, Mathematics and Management, Polytechnic University of Bari, Bari, Italy
[2]Institute of Electronics, Microelectronics and Nanotechnology - UMR 8520, Univ. Lille, CNRS, France
[3]Department of Civil and Environmental Engineering, Polytechnic University of Bari, Bari, Italy

Summary Interface energy and thermal effects are comparable when micro dimensional scales are considered, leading to a temperature dependent phase transition strategy that, from a macroscopic point of view, often leads to the presence of a stress-peak characterizing the nucleation stress and the size of the first phase from the propagation ones. To account for these phenomena, in a Statistical Mechanics framework, we consider next to nearest neighbor (NNN) interactions on a chain of bi-stable elements, and we obtain fully analytical result describing the aforementioned effects on the thermo-mechanical response of the system. Moreover, we validate our model by comparing it with the temperature dependent phase transition behavior experimentally observed on memory shape nanowires.

Effective, microstructure based models have been shown to be able to describe the thermo-mechanical response of different materials undergoing phase transitions (*e.g.* new bio-inspired materials [1] or shape memory alloys, SMA [2]). Here, by extending [3, 4], we consider a prototypical example constituted by a chain of elements with bistable potentials, describing a material with two distinct phases (i.e folded→unfolded configuration in a macromolecule or austenitic and martensitic phases in SMA [2]). As in the continuous analogue of higher order gradient theories [5], here we describe the important role of interfacial energy by considering NNN interactions (see Figure 1). The zero temperature behavior of this system was described in [6, 3, 4]. Here we consider the role of temperature analyzing the behavior of the bistable chain with non local NNN interactions in the framework of equilibrium Statistical Mechanics [7, 8, 9].

The energy function –adimensionalized with respect to lk, where k is the stiffness and l the reference length in the first phase– for a chain of n bistable oscillators is (see Figure 1a)

$$\varphi(\{S_j\},\{\varepsilon_j\}) = \varphi_{NN}+\varphi_{NNN} = \frac{1}{2}\sum_{j=1}^{n}\left[(\varepsilon_j+\varepsilon_0)^2\frac{(1-S_j)}{2}+\Big(\zeta(\varepsilon_j-\varepsilon_0)^2+2\eta\Big)\frac{(1+S_j)}{2}\right]+\frac{1}{2}\sum_{j=1}^{n-1}\alpha(\varepsilon_j+\varepsilon_{j+1})^2, \quad (1)$$

where ε_j is the strain of $j-$th domain, $\pm\varepsilon_0$ is the reference strain of the two configurations, respectively. Here ζ is the relative stiffness between the two wells, η is the relative transition energy and $\alpha < 0$ (ferromagnetic interaction) is the reference stiffness of the NNN harmonic springs. We have also introduced the *"spin"* variable S_j that can assume the value ±1 depending on the phase of the bi-stable oscillator, as shown in figure 1b.

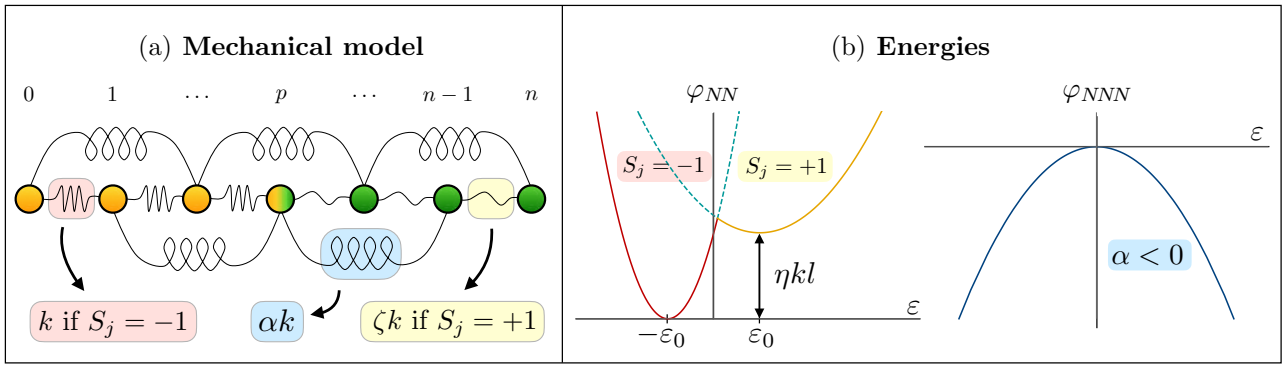

Figure 1: (a) Scheme of the chain with bistable units and NNN interactions. (b) NN and NNN energies.

To obtain fully analytical results, the NNN interaction is introduced in a perturbative framework (*i.e.* $|\alpha| \ll 1$) and the two parabolas modeling the NN energy terms are extended beyond the spinodal point [10, 8, 9] (see Fig 1b). We study the system in thermal equilibrium in the regimes of both soft (Gibbs ensemble) and hard (Helmholtz ensemble) devices, when a constant force σ or a fixed displacement δ are applied, respectively [11]. In the former case we obtain the expressions for the stress strain relation and the expectation values of both number of interfaces and nucleated phase fraction:

$$\langle\bar{\varepsilon}\rangle = (1-4\alpha)\Big[2\varepsilon_0\langle\chi\rangle_{\mathcal{G}}+(\sigma-\varepsilon_0)\Big], \quad \langle\chi\rangle_{\mathcal{G}} = \frac{\sum_{p=0}^{n}\sum_{i=0}^{n-1}\mathcal{W}_{p,i}\,\chi\,e^{\Gamma_{p,i}(\sigma)}}{\sum_{p=0}^{n}\sum_{i=0}^{n-1}\mathcal{W}_{p,i}\,e^{\Gamma_{p,i}(\sigma)}}, \quad \langle i\rangle_{\mathcal{G}} = \frac{\sum_{p=0}^{n}\sum_{i=0}^{n-1}\mathcal{W}_{p,i}\,i\,e^{\Gamma_{p,i}(\sigma)}}{\sum_{p=0}^{n}\sum_{i=0}^{n-1}\mathcal{W}_{p,i}\,e^{\Gamma_{p,i}(\sigma)}}, \quad (2)$$

*Corresponding author. E-mail: luca.bellino@poliba.it

where p is the number of elements in phase 2, i is the number of interfaces and $\beta = \frac{1}{k_B T}$, with k_B the Boltzmann constant and T the absolute temperature ($\zeta = 1$ for simplicity of the expression), $\mathcal{W}_{p,i}$ is a combinatorial counting coefficient and $\Gamma_{p,i}(\sigma)$ is a characteristic function for the Gibbs ensemble (see [11] for details).

On the other hand, at fixed displacement δ, we obtain

$$\langle\sigma\rangle = \frac{\left[\bar{\varepsilon} - (1-4\alpha)\big(2\langle\chi\rangle_{\mathscr{H}} - 1\big)\varepsilon_0\right]}{\left(1 - \dfrac{4\alpha}{n}(n-1)\right)}, \quad \langle\chi\rangle_{\mathscr{H}} = \frac{\sum_{p=0}^{n}\sum_{i=0}^{n-1}\mathcal{W}_{p,i}\,\chi\, e^{\Omega_{p,i}(\delta)}}{\sum_{p=0}^{n}\sum_{i=0}^{n-1}\mathcal{W}_{p,i}\, e^{\Omega_{p,i}(\delta)}}, \quad \langle i\rangle_{\mathscr{H}} = \frac{\sum_{p=0}^{n}\sum_{i=0}^{n-1}\mathcal{W}_{p,i}\, i\, e^{\Omega_{p,i}(\delta)}}{\sum_{p=0}^{n}\sum_{i=0}^{n-1}\mathcal{W}_{p,i}\, e^{\Omega_{p,i}(\delta)}}, \tag{3}$$

where $\Omega_{p,i}(\delta)$ is a characteristic function for the Helmholtz ensemble (see [11] for details).

In figure 2 we show the theoretical results obtained with our model (Fig. (a)) and the comparisons with the experimental data of Molecular Dynamic simulations performed by Lu at al [12] (Fig. (b)) and Wu [13] (Fig. (c)). In the first row of figure 2, can be observed that as the discreetness of the system increases, the nucleation (peak) stress becomes higher with respect to propagation one. On the other hand, as the temperature increases the stress peak decreases while the regime is opposite for increasing interfacial energy, showing a direct competition between the two energies during the transition process. In the second row of figure 2 we present the comparison of our analytical results with two different molecular dynamic simulations, obtaining an excellent agreement among the data.

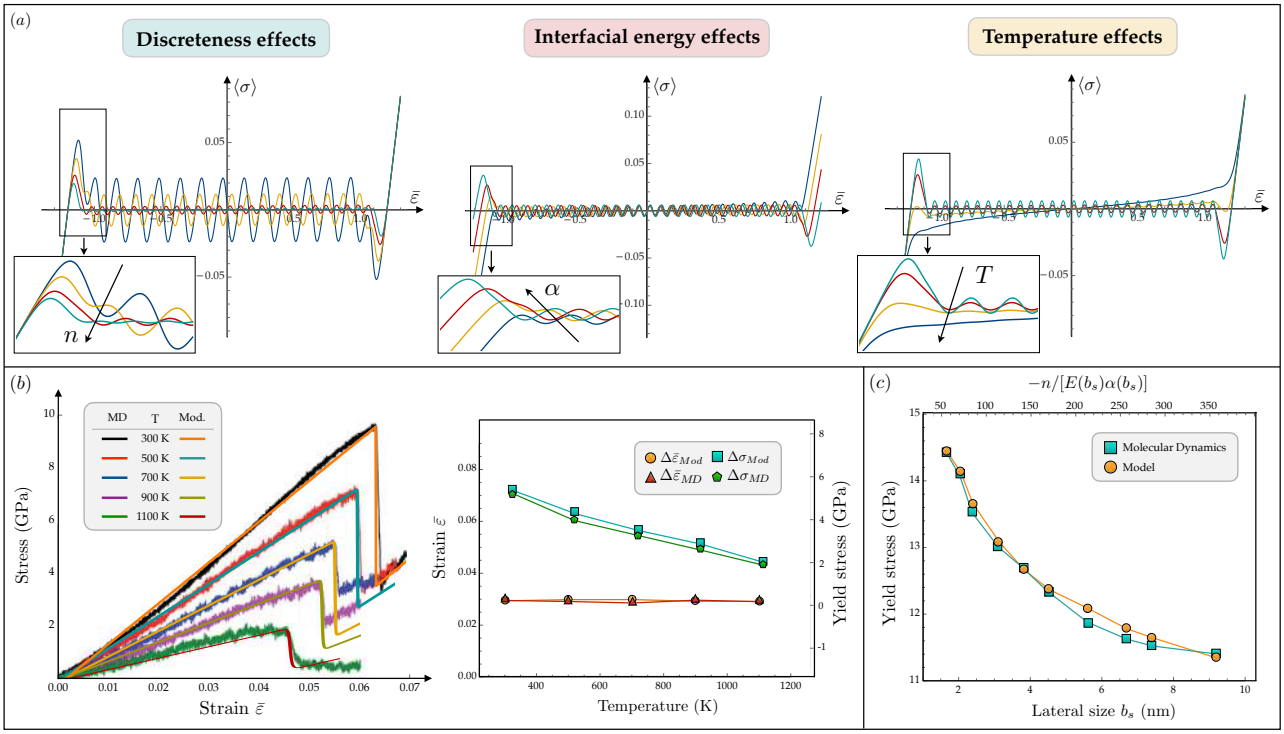

Figure 2: First row: theoretical results showing the effects of the discreteness of the system, of the interfacial energy and of the temperature in the case of applied displacement. Bottom row: comparison with the Molecular Dynamic simulations of memory shape nanowires of Lu et al. in figure (b) [12] and of Wu in (c) [13].

References

[1] Goriely A. The mathematics and mechanics of biological growth. *Springer*, 2017.
[2] Shaw J. A., Kyriakides S. On the nucleation and propagation of phase transformation fronts in NiTi alloy. *Acta mater.*, **45**, 2, 683-700, 1997.
[3] Puglisi G. Hysteresis in multi-stable lattices with non-local interactions. *JMPS*, **54**, 2060-2088, 2006.
[4] Puglisi G. Nucleation and phase propagation in a multistable lattice with weak nonlocal interactions. *Cont. Mech. Thermodyn*, **19**, 299-319, 2007.
[5] Triantafyllidis N., Bardenhagen S. J. Elasticity 33, 259-293, 1993.
[6] Truskinovsky L., Vainchtein A. The origin of nucleation peak in transformation plasticity. *JMPS*, **52**, 1421-1446, 2004.
[7] Manca F., Giordano S., Palla P. L., Cleri F., Colombo L. Two-state theory of single-molecule stretching experiments. *PRE*, **87**, 032705, 2013.
[8] Florio G., Puglisi G. Unveiling the influence of device stiffness in single macromolecule unfolding. *Scientific Reports*, **9**, 4997, 2019.
[9] Bellino L., Florio G., Puglisi G. The influence of device handles in single molecule experiments. *Soft Matter* **15** (43) 8680-8690, 2019.
[10] Efendiev R. Y., Truskinovsky L. Thermalization of a driven bi-stable FPU chain. *Continuum Mech. Thermodyn.* **22** 679-698, 2010.
[11] Bellino L., Florio G., Giordano S., Puglisi G. On the competition between interface energy and temperature in phase transition phenomena. *Applications in Engineering Science* **2** 100009, 2020.
[12] Lu, X., Yang, P., Luo, J., Ren, J., Xue, H., Ding, Y. Tensile mechanical performance of Ni-Co alloy nanowires by molecular dynamics simulation. *RSC Adv.* **(44)**, 25817- 25828, 2019.
[13] Wu, H. Molecular dynamics study on mechanics of metal nanowire. *Mech. Res. Commun.* **33**, (1) 9-16, 2006.

A COUPLED ELECTRO-CHEMO-MECHANICAL MODEL FOR ALL-SOLID-STATE THIN FILM LI-ION BATTERIES

Fenghui Wang*, Xu Song, Yongjun Lu, and Xiang Zhao
Bio-inspired and Advanced Energy Research Center, School of Mechanics, Civil Engineering and Architecture, Northwestern Polytechnical University, Xi'an 210129, PR, China

Summary For all-solid-state thin film batteries (TFBs) with high requirements for mechanical flexibility, stable electrochemical output and mechanical reliability are very important. Recently, mechanical-related problems in TFBs have drawn considerable attention. Herein, a fully coupled electro-chemo-mechanical theoretical model in continuum-scale for TFBs is proposed considering three main processes in the battery. The diffusion of lithium in electrode phase; the diffusion and migration of lithium in solid-state electrolyte phase; the interfacial transport reaction kinetics. This model provides an effective way for studying the TFBs respect different initial states, materials combination, and structural parameters.

MODEL DESCRIPTION

A TFB with non-porous anode, non-porous cathode, non-porous solid-state electrolyte, and perfectly bonded interfaces are considered in present work. The component in the system present are regarded as homogeneous isotropic linear elastic solids in which the deformation is infinitesimal. The Li transport process during charging is shown in fig. 1, the Li in the cathode released as a Li ion via an oxidation reaction taken place at the interface; the Li ion then arrive at the interface between anode and solid-state electrolyte and taken-up by anode as Li via a reduction reaction.

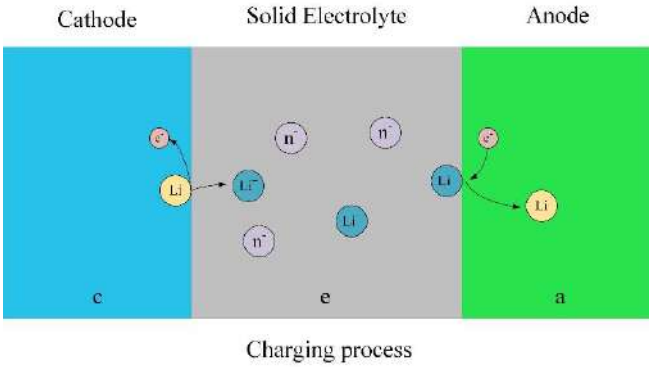

Figure 1. Schematic diagram of Li transport

Diffusion process of Li in electrode phase

The electrode material was considered as ideal intercalation storage materials, with lithium, vacancy and immobile host. We follow the frame work of Bohn. et al. to describe the diffusion process in electrode phase by an equation deduced from basic thermodynamics and statistical physics [1]. The Li-Li interactions are ignored in present work then the equation is given by

$$\frac{\partial c}{\partial t} - \nabla \cdot D\left[\nabla c - (1 - c/c^{\mathrm{m}})\frac{\Omega}{RT} c \nabla \sigma_{\mathrm{h}}\right] = 0, \tag{1}$$

where c, Li concentration; t, time; D, the diffusion coefficient; Ω, the partial molar volume; R, universal gas constant; T, temperature; $\sigma_{\mathrm{h}} = \frac{1}{3}\sigma_{kk}$, the hydrostatic stress; c^{m}, the maximum Li concentration.

Diffusion and migration in binary solid-state electrolyte

Several theoretical researches have been carried out to describe the diffusion and migration process of Li ion in solid-state phase. Here, a binary solid polymer electrolyte of particular interest is considered in which the electrolyte molecule dissociates into a monovalent cation and a monovalent anion. The coupled stress and ionic transport within solid polymer electrolyte are modeled following the framework of Grazioli et al. A charge balance equation is given by

$$\nabla \cdot \left[-F(D_+ - D_-)\nabla c - \frac{F^2(D_+ + D_-)}{RT} c \nabla \Phi + \frac{F(D_+\Omega_+ - D_-\Omega_-)}{RT} c \nabla \sigma_{\mathrm{h}}\right] = 0, \tag{2}$$

the subscripts $+$ and $-$ represent the corresponding variables of cation and anion in solid-state electrolyte; F, Faraday's constant; Φ, electric potential. In addition, a mass balance equation in solid-state phase is given by

$$\frac{\partial c}{\partial t} + \nabla \cdot \left(-D\nabla c + \frac{D\Omega}{2RT} c \nabla \sigma_{\mathrm{h}}\right) = 0. \tag{3}$$

Electrode-electrolyte interface chemical reaction kinetics

For the interface in a solid-state battery where the stress fields are inevitably involved, the reaction kinetics at interfaces are expected to be altered with stresses of adjacent region [2-4]. An extended Butler-Volmer equation including the effects of stress in electrode phase is presented to describe the interface reaction,

$$i = i_0 \left[\exp\left(\frac{(1-\beta)}{RT}F\eta\right) - \exp\left(-\frac{\beta}{RT}F\beta\right)\right], \tag{4}$$

where the exchange current density is given by

$$i_0 = Fk(c_{\mathrm{ed}})^{\beta}[c_{\mathrm{el}}(c_{\mathrm{ed}}^{\mathrm{m}} - c_{\mathrm{ed}})]^{1-\beta} \exp\left(\frac{(\alpha-\beta)}{RT}\left(\Omega_{\mathrm{ed}}\sigma_{\mathrm{h,ed}} - \Omega_{\mathrm{el}}\sigma_{\mathrm{h,el}}\right)\right), \tag{5}$$

the subscripts ed and el represent the corresponding variables in electrode and electrolyte phase; i, current density; β, symmetry factor; α, mechanically symmetry factor; η, overpotential; k, rate constant. An equilibrium potential at interface is given as

$$(\Phi_{\mathrm{ed}} - \Phi_{\mathrm{el}})^{\mathrm{eq}} = \Phi_{\mathrm{ref}} + \frac{RT}{F}\ln\left(\frac{c_{\mathrm{el}}(c_{\mathrm{ed}}^{m} - c_{\mathrm{ed}})}{c_{\mathrm{el}}^{\mathrm{ref}} c_{\mathrm{ed}}}\right) + \frac{1}{F}\left(\Omega_{\mathrm{ed}}\sigma_{\mathrm{h,ed}} - \Omega_{\mathrm{el}}\sigma_{\mathrm{h,el}}\right), \tag{6}$$

the overpotential can be expressed as

$$\eta = \Phi_{\mathrm{ed}} - \Phi_{\mathrm{el}} - (\Phi_{\mathrm{ed}} - \Phi_{\mathrm{el}})^{\mathrm{eq}}, \tag{7}$$

Mechanics

The stress under the assumption of infinitesimal strain can be expressed as

$$\sigma_{ij} = C_{ijkl}\left[\varepsilon_{kl} - \frac{1}{3}\Omega(c - c_0)\delta_{kl}\right], \tag{8}$$

where the elastic modulus tensor, $C_{ijkl} = \frac{E}{2(1-v)}\left(\delta_{il}\delta_{jk} + \delta_{ik}\delta_{jl}\right) + \frac{Ev}{(1+v)(1-2v)}\delta_{ij}\delta_{kl}$; strain tensor, $\varepsilon_{ij} = (u_{i,j} + u_{j,i})$; u, displacement; c_0, initial concentration; E, elastic modulus; v, Poisson's ratio.

Cell potential

The potential drops in electrode phase are ignored, then the cell potential is given as

$$V_{\mathrm{cell}} = \Phi_{\mathrm{c}} - \Phi_{\mathrm{a}}, \tag{9}$$

the subscripts a and c represent the corresponding variables in anode and cathode.

CONCLUSIONS

In view of the fact that there are few full-cell models to describe the electro-chemo-mechanical coupling behavior for TFBs, while the mechanical problems in TFBs have attracted considerable attentions [5, 6]. Based on the original electrochemical model of all-solid-state batteries, the mechanical effects are introduced into the model to establish a fully coupled electro-chemo-mechanical model. The model can be used to investigate the effects of external loads on battery performance.

References

[1] Bohn E., Eckl T., Kamlah M., McMeeking R. An Extended Formulation of Butler-Volmer Electrochemical Reaction Kinetics Including the Influence of Mechanics. *J. Electrochem. Soc.* **160**: A1638-A1652, 2013.

[2] Wu B., Lu W. A consistently coupled multiscale mechanical-electrochemical battery model with particle interaction and its validation. *J. Mech. Phys. Solids* **125**: 89-111, 2019.

[3] Lu Y.J., Zhang P.L., Wang F.H., Zhang K., Zhao X. Reaction-diffusion-stress coupling model for Li-ion batteries: The role of surface effects on electrochemical performance. *Electrochim. Acta* **274**: 359-369, 2018.

[4] Ganser M., Hildebrand F.E., Klinsmann M., Hanauer M., Kamlah M., McMeeking R.M. An Extended Formulation of Butler-Volmer Electrochemical Reaction Kinetics Including the Influence of Mechanics. *J. Electrochem. Soc.* **166**: H167-H176, 2019.

[5] Famprikis T., Canepa P., Dawson J.A., Islam M.S., Masquelier C. Fundamentals of inorganic solid-state electrolytes for batteries. *Nat. Mater.* **18**: 1278-1291, 2019.

[6] Janek J., Zeier W.G. Fundamentals of inorganic solid-state electrolytes for batteries. *Nat. Energy* **1**: 4, 2016.

ON CORROSION OF A PIPE WITH THE REDUCTION IN THE STRENGTH TAKING INTO ACCOUNT

Yulia Pronina[1*], Marina Elaeva [1]
[1]Department of Computational Methods in Continuum Mechanics, Saint-Petersburg State University, Saint-Petersburg, Russian Federation

Summary The paper concerns modelling the stress-assisted general corrosion of a pressurised pipe accompanied by the reduction in the strength of the pipe material. Analytical solution of the problem is obtained. Problems of optimal design are also considered with taking into account the presence of protective coatings on the pipe surfaces. The effect of the nonuniform temperature field on the synergistic growth of mechanical stress and corrosion rate is discussed in comparison with the effect of the elastic stress component.

INTRODUCTION

Most structures are exploited while being subjected to both mechanical loads and operating environments. Such conditions may activate the process of mechanochemical corrosion, which is more severe than the corrosion independent of stress. A lot of experimental data show a linear dependence of general corrosion rate on the effective stress [1]. Moreover, corrosion can degrade the useful properties of materials and structures including their strength [1].

When corrosion rate depends on stress, and stress, in turn, depends on changing – due to corrosion – geometry of an element, we have to consider initial boundary value problems with unknown evolving boundaries. Such problems are mostly studied by numerical methods. However, a number of analytical solutions have been found for uniform mechanochemical dissolution of structural elements, e.g. by the authors of [2, 3]; previous solutions for pressurised vessels have been built for the cases when the effective stresses on their inner and outer surfaces were assumed to be equal to each other. Authors could find analytical solutions for such problems taking into account the change in the effective stress through the shell thickness, as well as a possible inhibition of corrosion [4, 5]. The present paper also takes into consideration the reduction in the strength of the pipe material and the presence of protective coatings on the pipe surfaces. The effect of the thermal stresses on the durability of the pipe under the mechanochemical corrosion conditions is also discussed in comparison with the effect of the elastic stresses. The problems of optimal design are investigated on the base of the obtained solution.

FORMULATION OF THE PROBLEM

Consider an elastic circular pipe subjected to internal p_r and external p_R pressure of aggressive media that may have different temperatures T_r and T_R, correspondingly. Electrochemical reaction with these environments causes general dissolution of the pipe material and degrades its strength. The rates of corrosion inside (v_r) and outside (v_R) are linear functions of the maximum in absolute-value principal stress, σ_r and σ_R, at the corresponding surface [1, 2, 5]:

$$v_r = \frac{\mathrm{d}r}{\mathrm{d}t} = [a_r + m_r \sigma_r(r,R)]\exp(\beta_r[T_r - T_r^o]) \text{ at } t \ge t_r^c, \quad (1)$$

$$v_R = -\frac{\mathrm{d}R}{\mathrm{d}t} = [a_R + m_R \sigma_R(r,R)]\exp(\beta_R[T_R - T_R^o]) \text{ at } t \ge t_R^c. \quad (2)$$

Here $a_r, a_R, m_r, m_R, \beta_r, \beta_R, T_r^o, T_R^o$ are empirically determined constants of corrosion kinetics; t_r^c and t_R^c are the lives of the protective coatings on the inner and outer surfaces; r and R are the variable inner and outer radii of the pipe; t is time. If $T_r \le T_r^o$ and/or $T_R \le T_R^o$, then $\beta_r = 0$ and/or $\beta_R = 0$. The strength limit, $\sigma^* = \sigma^*(t)$, of the pipe material is supposed to decrease with time linearly or tending to a certain constant level.

It is required to analyse the effect of the strength degradation and other parameters on the durability of the pipe. Contribution of the elastic and thermal stress components in the mechanochemical effect is also compared.

The problem of optimal design is formulated in two senses: to find an initial thickness of the pipe wall which provides (I) a specified service life of the pipe and a minimum material consumption or (II) a minimum material consumption per the unit of the pipe life; the pipe capacity being given.

*Corresponding author. E-mail: y.pronina@spbu.ru

RESULTS

First, we found the conditions when the circumferential stress can serve as the effective stress in the corrosion kinetic equations. The stresses are determined by the sum of the elastic and thermal components. Although stresses σ_r and σ_R on the inner and outer surfaces depend on both evolving radii r and R, we could find analytical solution of the system of basic differential equations (1)–(2) at arbitrary coatings lives t_r^c and t_R^c. It has been revealed that despite the fact that the thermal stress can noticeably increase the absolute value of the mechanical stress in the pressurized vessel, thermal component does not have such a strong effect on the stress enhanced acceleration of corrosion process, as the elastic component.

The problem (I) of optimal design has a unique solution corresponding to the case when the maximum allowable stress is reached at the end of a specified service life of the pipe. In problem (II), it is necessary to find the minimum of the objective function proportional to the ratio of the initial mass of the pipe to its life. As one can see from Fig. 1, difference in the coating lives can noticeably change the behaviour of the objective function, other parameters being equal. The results were generalised with taking into account reduction in the strength of the pipe material.

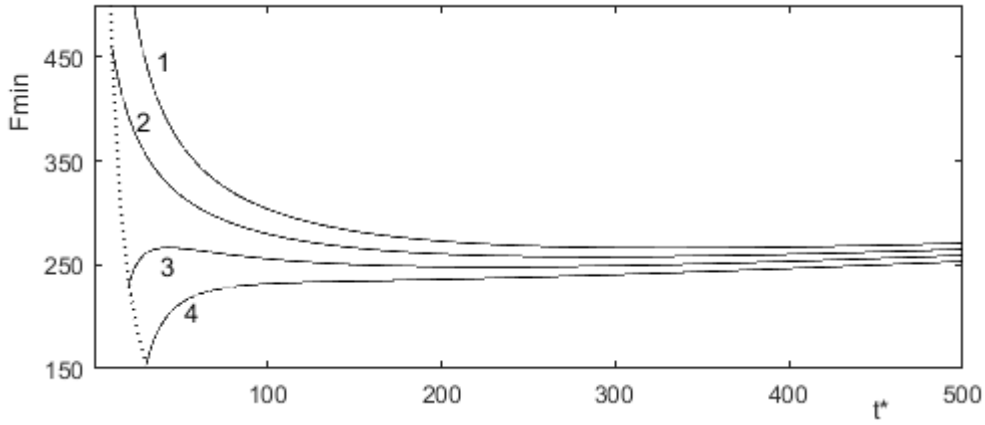

Figure 1. Objective function vs life of the pipe (in conventional units of time) for different coating lives t_R^c: 0 (line 1), 10 (line 2), 20 (line 3) and 30 (line 4) .

The obtained solutions can serve as benchmarks for numerical analysis and for design purposes.

References

[1] Zainullin R. S. Generalized equation of mechanochemical damageability of metals. *Oil and Gas Business*. **13**(3): 119–123, 2015.

[2] Elishakoff I., Ghyselinck G., Miglis Y. Durability of an elastic bar under tension with linear or nonlinear relationship between corrosion rate and stress. *J. Appl. Mech., Trans. ASME* **79**(2): 021013, 2012.

[3] Gutman E., Bergman R., Levitsky S. Influence of internal uniform corrosion on stability loss of a thin-walled spherical shell subjected to external pressure. *Corr. Sci.* **111**: 212–215, 2016.

[4] Pronina Y.G. Analytical solution for the general mechanochemical corrosion of an ideal elastic-plastic thick-walled tube under pressure. *Int. J. Solids and Struct.* **50**: 3626-3633, 2013.

[5] Pronina Y., Sedova O., Grekov M., Sergeeva T. On corrosion of a thin-walled spherical vessel under pressure. *Int. J. Eng. Sci.* **130**: 115-128, 2018.

APPLICATION OF MECHANOCHEMISTRY MODEL TO OXIDATION OF PURE NICKEL SPHERES

Svetlana Petrenko*[1], Eric Charkaluk [1], Alexandre Tanguy[1], and Cecile Davoine[2]
[1]Laboratory of Solid Mechanics, Ecole Polytechnique, Palaiseau, France
[2]ONERA, The French Aerospace Lab, Chatillon, France

Summary In this work, we study the two-phase chemical reactions on the example of the oxidation of nickel. We have carried out an experiment of high-temperature oxidation of nickel balls, and obtained the experimental data for the growth of the oxide layer over time. To select the best analytical solution we consider three different rheology for the oxide of nickel: elastic, elastoplastic and viscoelastic. We compare the solution for each rheological model with experimental data.

INTRODUCTION

In this contribution we discuss an extension of a microscopic model of oxidation to macro scale. In particular, we sketch a protocol of experimental validation of it based on measurements for (approximately) spherically-symmetric samples.

Stress-assisted chemical reactions are relevant in various industrial and medical applications and in modern technologies. It is enough to mention for instance batteries charging/discharging cycles: along with the introduction of silicon instead of carbon the issue of the dramatic change of volume in the active material is observed, which results in massive cracking when inappropriately handled [2]. In MEMS the oxidation process is responsible for rapid fatigue effects [3]. For composite material meant for high temperature resistance, the metallic inclusions being heated up and oxidized, expand and induce internal strain to the matrix [4, 5]. All these and a lot of other processes can be described using the two-phase reaction model, it is thus important to be able to handle it efficiently. The model however relies heavily on the rheological properties of the involved materials, which are in general to be defined. Here we present a procedure of identification of a proper model, based on few experimental data.

First we recall the general theoretical model, and some steps to reduce it to analytically tractable problem. Then we describe the available experimental data and some features to be taken into account during its acquisition. We conclude by some preliminary analysis of the experiment, the details of which will be described in [1].

TWO-PHASE REACTION MODEL

To describe the two-phase chemical reactions such as oxidation processes or charging/discharging of batteries, we consider the following model. We have some initial solid, we can set the geometrical parameters, boundary conditions and the mechanical properties of the body. There is a diffusion of some chemical, for example, it can be oxygen in the case of the oxidation or lithium in the case of the lithiation of silicon (charging of batteries), etc. A chemical reaction between the initial solid body and some diffusive constituent is of the following type: it begins from the outer surface of the initial solid, localized on the interface between initial and transformed material and maintained by the diffusion of the diffusive constituent through the transformed material.

To obtain the equation for the chemical reaction front propagation, taking into account the effect of the stress-strain state in the body, we use the classical kinetic equation ([8]) from the chemical thermodynamics. We substitute the normal component of the chemical affinity tensor A_{NN} ([9]) instead of scalar chemical affinity A in the equation for the reaction rate, hence we obtain the kinetic equation for the surface element of reaction front with the normal $\mathbf{N}$:

$$\omega_N = \frac{\nu_- M_-}{\rho_-} k_* c \left(1 - exp\left(-\frac{A_{NN}}{RT}\right)\right) = 0 \tag{1}$$

where ν_- is the stoichiometric coefficient, M_- is the molar mass and ρ_- is the mass density of the initial solid; k_* is the reaction constant; c is the molar concentration of the diffusive constituent; A is the chemical affinity; R is the universal gas constant; T is the temperature. And the normal component of the chemical affinity tensor in the case of the small deformations is defined ([9]) as follows :

$$A_{NN} = \frac{n_- M_-}{\rho_-}\left\{\gamma(T) + \frac{1}{2}\boldsymbol{\sigma}_- : \left(\boldsymbol{\varepsilon}_- - \boldsymbol{\varepsilon}_-^{ch}\right) - \frac{1}{2}\boldsymbol{\sigma}_+ : \left(\boldsymbol{\varepsilon}_+ - \boldsymbol{\varepsilon}_+^{ch}\right) + \boldsymbol{\sigma}_- : [\![\boldsymbol{\varepsilon}]\!]\right\} + \nu_* RT \ln\frac{c}{c_*} \tag{2}$$

where γ is the temperature-dependent parameter of the reaction; $\boldsymbol{\sigma}_\pm$ and $\boldsymbol{\varepsilon}_\pm$ are the stress and strain tensors for the transformed and initial material, respectively; $\boldsymbol{\varepsilon}_\pm^{ch}$ are the strain tensors which define the volumetric change due to the chemical transformation; ν_* is the stoichiometric coefficient of the diffusive constituent; c_* is the solubility of the diffusive constituent in the transformed material.

*Corresponding author. E-mail: svetlana.petrenko@polytechnique.edu

EXPERIMENTAL SETUP

In the current work we consider the oxidation of nickel balls. Nickel oxide nano-particles and nickel are widely used in heavy industries [6, 7]. To obtain the kinetic equation we have to choose the rheological model for the transformed material (initial material is elastic) and solve the mechanical problem in the spherical coordinates. To get the best analytical solution for this experiment we will consider three different rheology for the transformed material: elastic, viscoelastic and elastoplastic. For each rheological model we obtain the specific solution and the kinetic equation. This permits to spell-out the solutions to be compared with experimental data.

Several balls were oxidized in the air at temperature 800^{o}C for up to 500h: each ball was oxidized for a different amount of time: the first one for 100h, the second for 200h, ... and the fifth for 500h. After that, each ball was cut in halves, polished, and the outer layer was captured in the electronic microscope.

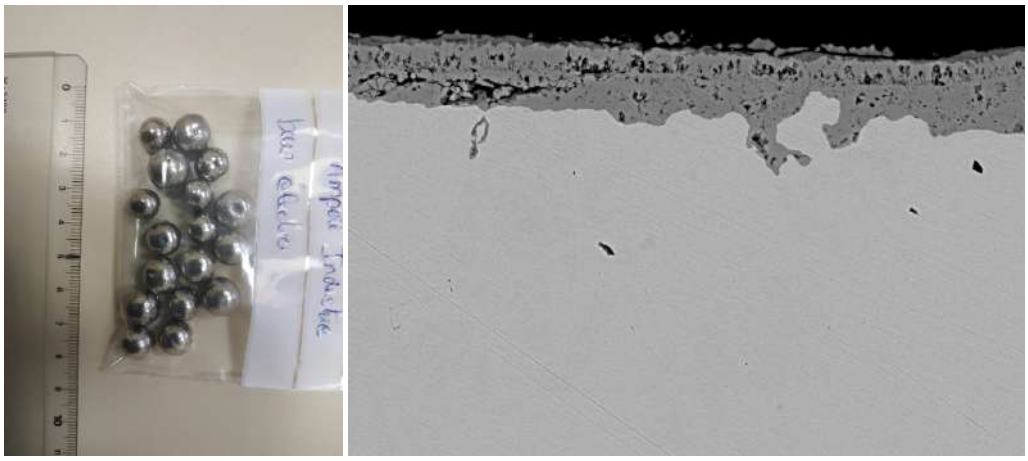

Figure 1: Experiments. Available samples (left) to be chosen for oxidation. Measurement results (right) – TEM imaging.

PRELIMINARY CONCLUSIONS AND PERSPECTIVES

Several remarks about the experiment are in place here. First, nikel oxide has a very fragile structure, however NiO is much stiffer than pure nickel. That makes the process of polishing hard: debris of NiO tend to scratch the pure metallic surface. It is thus very complicated to obtain precise mechanical properties of the oxide layer close to the interface. Second, with transmission electron microscopy we make the chemical analysis, study the morphology of the oxide, get the grain boundaries and measure the oxide thickness. However the balls used for different times of oxidation are slightly different in size and are not of perfectly spherical shape. Hence, measuring of the thickness of the oxide layer for each ball has to be relative to the initial radius of the ball. Here it is important to note, that the experiment confirms the validity of small deformations hypothesis. It means that the linearized model 2 is valid, and the time-dependence of the averaged renormalised thickness of the oxide layer is relevant.

Having analysed the dependence of the thickness of the oxide layer on time, we can say the best guess for the rheological properties would be elastoplastic. We will give proper details about this conclusion in a longer article ([1]). In the same paper we will also comment on the processing of images obtained by microscopy: renormalisation, reassembling and segmentation.

References

[1] Petrenko S., Charkaluk E., Tanguy A., Davoine C., Identification of rheology of the resulting material in two-phase reactions, in preparation, 2020.
[2] Beaulieu L., Eberman K., Turner R., Krause L., Dahn J. Colossal reversible volume changes in lithium alloys. Electrochem. Solid-State Lett.4: 137–140, 2001.
[3] Muhlstein C., Ritchie R. High-cycle fatigue of micro-scale polycrystalline silicon films: fracture mechanics analyses of the role of the silica/silicon interface. Int. J. Fracture 119/120, 2003.
[4] Nanko M. High-temperature oxidtaion of ceramic matrix composites dispersed with metallic particles. Science and Technology of Advanced Materials, 6, 2015.
[5] Jacobson N., Opilab E, Lee K. Oxidation and corrosion of ceramics and ceramic matrix composites. Current Opinion in Solid State and Materials Science, 5, 2001.
[6] Karmhag R., Tesfamichael T., Wackelgard E., Niklasson G., Nygren M. Oxidation kinetics of nickel particles: comparison between free particles and particles in an oxide matrix. Solar Energy 68, 4, 2000.
[7] Johnson, S. C., Todd Davidson, F., Rhodes, J. D., Coleman, J. L., Bragg-Sitton, S. M., Dufek, E. J., & Webber, M. E. Selecting Favorable Energy Storage Technologies for Nuclear Power. Storage and Hybridization of Nuclear Energy, 119–175, 2019.
[8] Glansdorff P., Prigogine I. Thermodynamic theory of structure, stability and fluctuations, Wiley, New York, 1971.
[9] Freidin A. On a chemical affinity tensor for chemical reactions in deformable materials. Mechanics of Solids, 50, 2015.

THERMODYNAMIC DISLOCATION THEORY

Le, Khanh Chau[1,2]*
[1]Materials Mechanics Research Group, Ton Duc Thang University, Ho Chi Minh City, Vietnam
[2]Faculty of Civil Engineering, Ton Duc Thang University, Ho Chi Minh City, Vietnam

Extended Abstract

This paper proposes the thermodynamic dislocation theory for uniform and non-uniform plastic deformations, which takes into account the effective disorder temperature. The latter occurs as the dynamic state variable characterizing the disorder of the configurational subsystem that contains degrees of freedom associated with the rearrangement of atoms during the motion of dislocations. We verify two laws for plastic flows of face-centered cubic crystals that deform at constant strain rates and fixed ambient temperatures. The first law relates steady-state flow stress to ambient temperature and strain rate. The second law requires an increase of configurational entropy towards a maximum reached in the steady state. The large-scale least squares analysis is provided which allows the physics-based parameters of the dislocation mediated plasticity proposed by Langer, Bouchbinder, and Lookman [1] to be identified in accordance with these laws [2]. The system of equations of LBL-theory has been extended based on the first and second laws of thermodynamics for the configurational and kinetic-vibrational subsystems to take into account the change of kinetic-vibrational temperature and the non-redundant dislocations. We then use it to simulate the stress-strain curves for single and polycrystals of copper, aluminum, and steel alloys that are subjected to simple shear, tension/compression tests, and torsion and compare them with the experimental results (see [3-12]). The theory can predict the stress-strain curves in a wide range of temperature and strain rates. We show the size and the Bauschinger effects due to the non-redundant dislocations, as well as the strain rate sensitivity and the thermal softening due to the redundant dislocations. Finally, we make a simple model of a weak notch-like disturbances that, when driven hard enough, triggers shear banding instabilities that are quantitatively comparable to those of Marchand and Duffy's experiments.

References

* Email: lekhanhchau@tdtu.edu.vn

[1] Langer, J.S., Bouchbinder, E. and Lookman, T., 2010. Thermodynamic theory of dislocation-mediated plasticity. *Acta Materialia*, *58*(10), pp.3718-3732.
[2] Langer, J.S., Le, K.C., 2020. Scaling confirmation of the thermodynamic dislocation theory. *Proceedings of the National Academy of Sciences USA*.
[3] Le, K.C., Tran, T.M. and Langer, J.S., 2017. Thermodynamic dislocation theory of high-temperature deformation in aluminum and steel. *Physical Review E*, *96*(1), p.013004.
[4] Le, K.C. and Tran, T.M., 2017. Dislocation mediated plastic flow in aluminum: comparison between theory and experiment. *International Journal of Engineering Science*, *119*, pp.50-54.
[5] Le, K.C., 2018. Thermodynamic dislocation theory for non-uniform plastic deformations. *Journal of the Mechanics and Physics of Solids*, *111*, pp.157-169.
[6] Le, K.C., Tran, T.M. and Langer, J.S., 2018. Thermodynamic dislocation theory of adiabatic shear banding in steel. *Scripta Materialia*, *149*, pp.62-65.
[7] Le, K.C. and Tran, T.M., 2018. Thermodynamic dislocation theory: Bauschinger effect. *Physical Review E*, *97*(4), p.043002.
[8] Le, K.C., Piao, Y. and Tran, T.M., 2018. Thermodynamic dislocation theory: Torsion of bars. *Physical Review E*, *98*(6), p.063006.
[9] Le, K.C. and Piao, Y., 2019. Thermodynamic dislocation theory: Size effect in torsion. *International Journal of Plasticity*, *115*, pp.56-70.
[10] Le, K.C. and Piao, Y., 2019. Thermal softening during high-temperature torsional deformation of aluminum bars. *International Journal of Engineering Science*, *137*, pp.1-7.
[11] Le, K.C. and Piao, Y., 2019. Non-uniform plastic deformations of crystals undergoing anti-plane constrained shear. *Archive of Applied Mechanics*, *89*(3), pp.467-483.
[12] Le, K.C., 2019. Thermodynamic dislocation theory: Finite deformations. *International Journal of Engineering Science*, *139*, pp.1-10.

IN SITU NANO-THERMO-MECHANICAL EXPERIMENT REVEALS BRITTLE TO DUCTILE TRANSITION IN SI NANOWIRES

Guangming Cheng[1], Yin Zhang[2], Tzu-Hsuan Chang[1], Qunfeng Liu[2], Lin Chen[3], Wei D. Lu[3], Ting Zhu[2*], and Yong Zhu[1*]
[1]Department of Mechanical and Aerospace Engineering, North Carolina State University, Raleigh, NC 27695, USA
[2]Woodruff School of Mechanical Engineering, Georgia Institute of Technology, Atlanta, GA 30332, USA
[3]Department of Electric Engineering and Computer Science, University of Michigan, Ann Arbor, MI 48109, USA

Abstract Silicon (Si) nanostructures are widely used in microelectronics and nanotechnology. Brittle to ductile transition in nanoscale Si is of great scientific and technological interest, but this phenomenon and its underlying mechanism remain elusive. By conducting in situ temperature-controlled nanomechanical testing inside a transmission electron microscope (TEM), here we show that the crystalline Si nanowires under tension are brittle at room temperature, but exhibit ductile behavior with dislocation-mediated plasticity at elevated temperatures. We find that reducing the nanowire diameter promotes the dislocation-mediated responses, as shown by 78 Si nanowires tested between room temperature and 600 K. In situ high resolution TEM imaging and atomistic reaction pathway modeling reveal that the unconventional ½⟨110⟩{001} dislocations become highly active with increasing temperature and thus play a critical role in the formation of deformation bands, leading to transition from brittle fracture to dislocation-mediated failure in Si nanowires at elevated temperatures. This study provides quantitative characterization and mechanistic insight for the brittle to ductile transition in Si nanostructures.

Introduction

Silicon nanostructures have been used extensively in modern microelectronics. The ever-increasing integration density in microelectronic chips inevitably leads to a marked temperature rise of Si nanostructures, which are required to withstand large thermal stresses for maintaining their proper functions. Si nanostructures are also the building blocks for many novel nanotechnology applications, including energy harvesting and storage, flexible and stretchable electronics, sensors and nanoelectromechanical systems.[1] The reliability concerns of these applications call for a fundamental understanding of the mechanical behavior of Si nanostructures at elevated temperatures. Here we report the *in situ* tensile testing of single crystal Si NWs in the temperature range of RT to 600 K.[2] We employ a newly developed microelectromechanical system (MEMS) for conducting the nano-thermo-mechanical testing inside a transmission electron microscope (TEM). This platform allows stress-strain measurement with simultaneous TEM imaging of atomic-scale deformation at different temperatures.[2,3] An on-chip heater is built into the MEMS-based platform, allowing the controlled heating of the specimen.

Results

Single crystal Si NWs were synthesized by chemical evaporation deposition through the vapor-liquid-solid mechanism. The Si NWs used for mechanical testing are ⟨112⟩-oriented and have a central {111} twin boundary running parallel to the axial direction of the NW. *In situ* TEM tensile testing of individual Si NWs was performed at temperatures ranging from 295 to 600 K. In Fig. 1, we compare the brittle response at RT (295 K) with the moderate ductile behavior at 600 K for Si NWs with similar diameters. Figure 1a shows the stress-strain curve of a Si NW with a diameter of 61 nm at 295 K. This NW initially exhibited a linear elastic response. As the tensile strain increased to 7.4% and the corresponding tensile stress to 11.5 GPa, brittle fracture occurred. The inset in Fig. 1a shows a TEM image of the sharp {111} cleavage surfaces, which are known to have the lowest surface energy and also typically observed during brittle fracture of bulk Si crystals.[4] The two fracture surfaces in the upper and lower twin variants are symmetric and tilted at ~70° with respect to the axial direction.

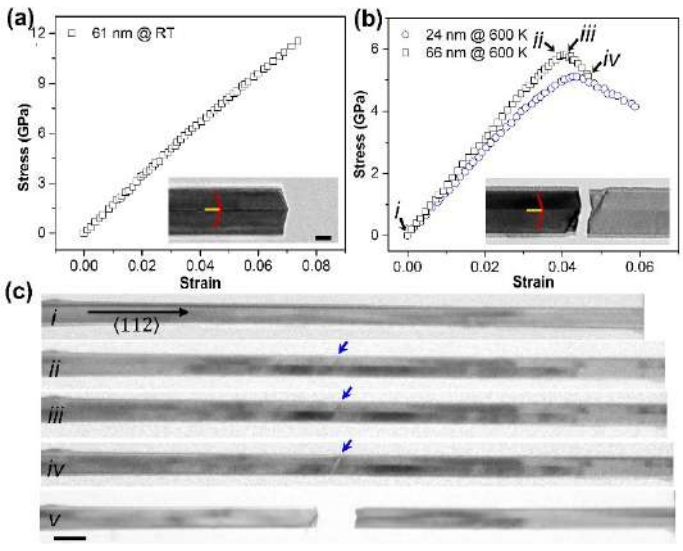

Figure 1. *In situ* MEMS-based measurement and TEM observation of mechanical behavior of individual Si NWs under uniaxial tension at room and elevated temperatures.

In contrast, the Si NW with a diameter of 66 nm at 600 K exhibited moderate ductile behavior. As shown in Fig. 1b, the tensile stress-strain curve was initially linear and became slightly nonlinear with increasing stress, until the maximum stress of 5.8 GPa was reached at the critical strain of 4.0%. Subsequently, the stress decreased with increasing strain, and this softening response continued until fracture occurred at the strain of 4.7%. The inset in Fig. 1b shows the TEM image of fracture surfaces, which exhibit the features of ductile failure such as localized necking, deformation bands and rough fracture planes. Figure 1c shows the TEM snapshots during *in situ* tensile testing at 600 K, and the corresponding stress/strain for each snapshot is marked in Fig. 1b. It is seen that the maximum stress and ensuing softening response can be associated with surface nucleation and migration of dislocations as well as dislocation interactions with the twin boundary, as marked

by blue arrows in Fig. 1c *ii-iv*. These continued dislocation processes resulted in large plastic strains in Si NWs at elevated temperatures. Overall, Fig. 1 reveals that the Si NWs under tension are brittle at RT, but exhibit pronounced plastic deformation followed by fracture at elevated temperatures (e.g., 600 K).

We found that a decrease in the NW diameter can lead to enhanced plastic deformation. Figure 1b also includes the tensile stress-strain curve of a thinner Si NW with a diameter of 24 nm at 600 K, which is qualitatively similar to the Si NW with a diameter of 66 nm at 600 K. However, in this thinner NW, a lower maximum stress of 5.1 GPa was attained at a smaller critical strain of 4.3%, signifying a stronger tendency to plastic deformation. Moreover, the subsequent softening response was sustained over a strain range of 1.6% until the fracture strain ϵ_f of 5.9%; this strain range is defined as plastic strain ϵ_p. Hence, both ϵ_p and ϵ_f measured for the thinner Si NW are larger than the corresponding ϵ_p of 0.7% and ϵ_f of 4.7% for the thicker Si NW (Fig. 1b). The more extensive plasticity in the thinner Si NW was manifested by the formation of a number of deformation bands that are uniformly distributed throughout the entire NW, which contrasts with fewer deformation bands in the thicker NW (Fig. 1c).

Our *in situ* HRTEM experiments [2] at elevated temperatures indicated that the formation of deformation bands originates from the dominant operation of ½⟨110⟩{001} full dislocations, which were observed in all Si NWs tested at elevated temperatures, irrespective of existence of a central twin boundary. This stands in contrast with the dominant activities of ½⟨110⟩{111} full dislocations or 1/6⟨112⟩{111} partials during plastic deformation of bulk Si structures [5]. Atomistic simulations suggested that the surface nucleation of ½⟨110⟩{1$\bar{1}$1} dislocations is less favorable than ½⟨110⟩{001} dislocations in <112>-oriented Si NWs under tension at elevated temperatures. The higher primary barrier of surface nucleation of the ½⟨110⟩{1$\bar{1}$1} loop can be partly attributed to the relatively small Schmid factor of 0.41 under axial loading, as opposed to 0.47 for the ½⟨110⟩{001} loop. In addition, differences in surface ledge energy and dislocation line tension can also affect the primary energy barriers for the two competing dislocation modes. It should be noted that the lack of (or substantially weaker) secondary barriers for nucleation of a ½⟨110⟩{1$\bar{1}$1} loop can be attributed to the close-packed {1$\bar{1}$1} slip planes in diamond cubic Si, which facilitate dislocation glide by eliminating (or largely reducing) the secondary barriers at high loads. Hence, ½⟨110⟩{1$\bar{1}$1} dislocations could become active at RT, when the primary energy barrier is sufficiently reduced by increasing load, provided that the tensile stress component on the potential cleavage planes is sufficiently low for averting brittle fracture.

To further understand the size and temperature dependence of dislocation-mediated plasticity and fracture, we tested 78 Si NWs with the diameter range of 24-160 nm and in the temperature range of 295-600 K. As shown in Fig. 2a, the plastic strain ϵ_p increases with decreasing NW diameter. For example, at 600 K, ϵ_p increases from 0.27 to 1.6%, as the NW diameter decreases from 160 to 24 nm. For the same diameter, ϵ_p increases with temperature. The results of the 78 Si NWs tested are summarized in a deformation mechanism map of Fig. 2b. In this map, green circles represent Si NWs with dislocation-mediated failure, while black squares Si NWs with brittle cleavage fracture. A transition line, as defined by a critical ϵ_p of 0.1%, is drawn to separate the regimes of brittle and dislocation-mediated responses. The map also reveals that as the NW diameter decreases, the critical temperature associated with dislocation-mediated plastic deformation decreases. For example, the Si NW with diameter of 110 nm showed brittle fracture at 398 K, while the NW with diameter of 30 nm exhibited plastic deformation with dislocation activities even at 362 K. Hence, Fig. 2b indicates that both the increase of temperature and the decrease of NW diameter can promote plastic deformation in Si NWs, leading to dislocation-mediated failure.

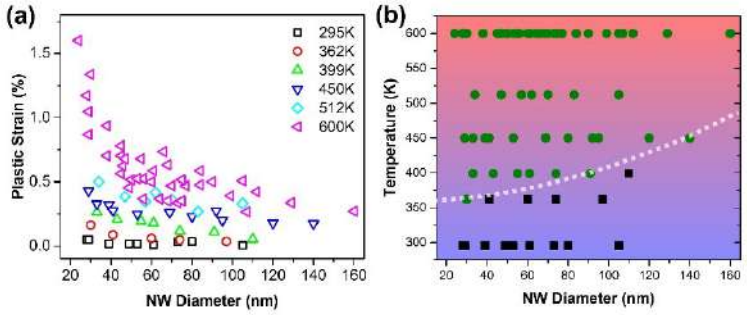

Figure 2. Size and temperature dependence of brittle versus ductile behaviors of 78 Si NWs tested in the temperature range of 295 to 600 K.

References

[1] F. Xu, W. Lu, and Y. Zhu, Acs Nano **5**, 672 (2011).
[2] G. Cheng, Y. Zhang, T.-H. Chang, Q. Liu, L. Chen, W. D. Lu, T. Zhu, and Y. Zhu, Nano Letters **19**, 5327 (2019).
[3] T.-H. Chang and Y. Zhu, Applied Physics Letters **103**, 263114 (2013).
[4] R. F. Cook, Journal of Materials Science **41**, 841 (2006).
[5] W. Cai, V. V. Bulatov, J. P. Chang, J. Li, and S. Yip, in *Dislocations in Solids* edited by F. R. N. Nabarro, and J. P. Hirth (Elsevier, Amsterdam, 2004), pp. 1.

STRAIN GRADIENT COUPLED CHEMO-MECHANICAL MODELLING OF HETEROGENEOUS CATHODE

Avtar Singh[1] and Siladitya Pal[1]
[1]Department of Mechanical and Industrial Engineering, IIT Roorkee, Roorkee, India

Summary Next generation electrodes for lithium-ion battery (LIB) are composite systems composed of heterogeneous microstructure. During charging and discharging process the electrodes are subjected to stress field due to misfit strain associated with diffusion of lithium ions in the host electrode. The attendant stress field further alters the phase kinetics of lithium. When the spatial dimension is reduced to nano-meter length, size effect plays significant role; thus, it may considerably influence coupled phenomena. Therefore, the size effect must be accounted to describe the chemo-mechanical behaviour. In order to accommodate the effect of strain gradient, we employ previously developed staggered strain gradient theory in which an intermediate displacement field utilized. In this study we developed novel multi-field numerical framework to take into account the effect of strain gradient.

FORMULATION

The mass-conservation equation for lithium ions is governed by

$$\frac{\partial c}{\partial t} + \nabla \cdot \mathbf{J} = 0 \tag{1}$$

in which flux **J**, chemical potential μ and concentration dependent mobility $M(c)$ are expressed as

$$\mathbf{J} = -M(c)\nabla\mu, \quad \mu = RT\left[\chi(1-2\tilde{c}) + \ln\frac{\tilde{c}}{1-\tilde{c}}\right] - \beta\sigma_h \quad \text{and} \quad M(c) = \frac{D}{RT}c(1-\tilde{c}) \tag{2}$$

where $\tilde{c}$ defines the normalized concentration field ($\tilde{c} = c/c_{\max}$), whereas $c_{\max}$ is the solubility limit of the intercalated lithium ions, D/RT represents the mobility of the dilute solution with D being the diffusivity of lithium ions in host material.

During the insertion/extraction of the lithium ions, host material expands or contracts and if it is constrained then stress results due to eigen strain. In order to account the effect of strain gradient, we employ previously developed staggered strain gradient theory in which additional computational complexities is avoided arising from higher order continuity requirement of regular displacement field by introducing the intermediate set of kinematic and kinetic variables, $\bar{\boldsymbol{u}}$, $\bar{\varepsilon}$ and $\bar{\sigma}$ as

$$\bar{\boldsymbol{u}} = \boldsymbol{u} - l_c^2\nabla\cdot\nabla\boldsymbol{u}, \quad \bar{\varepsilon} = \frac{1}{2}\left(\nabla\bar{\boldsymbol{u}} + \nabla\bar{\boldsymbol{u}}^T\right) \quad \text{and,} \quad \bar{\boldsymbol{\sigma}} = \boldsymbol{C} : \bar{\varepsilon}^e \tag{3}$$

where $\boldsymbol{C}$ is the fourth order elasticity tensor, $\bar{\varepsilon}^e = \beta(c - c_0)\boldsymbol{I}$ is the elastic strain in which β defines the expansion tensor and c_0 is the reference concentration, and l_c material length parameter associated with the strain gradient. The resulting diffusion induced stress in the electrode material must satisfy, $\nabla\cdot\bar{\sigma} = 0$ with traction boundary condition as $\mathbf{t}^p = \bar{\boldsymbol{\sigma}}\cdot\boldsymbol{n}$. After, the essential displacement boundary condition, $\bar{\boldsymbol{u}} = \boldsymbol{u}^p$ along with equilibrium equation, Eq. $(3)_3$ yields the standard equations of elasticity in terms of intermediate displacement field $\bar{\boldsymbol{u}}$. Finally, the gradient enriched displacement field, $\boldsymbol{u}$ can be obtained by solving the Helmholtz equation i.e., Eq. $(3)_1$ as follows

$$\boldsymbol{u} - l_c^2\nabla\cdot\nabla\boldsymbol{u} = \bar{\boldsymbol{u}}$$

with essential and natural boundary conditions as $\boldsymbol{u} = \boldsymbol{u}^p$, and $\partial_n\boldsymbol{u} = \tilde{\boldsymbol{u}}^p$, respectively.

VALIDATION

For the purpose of validation, two separate problems have been considered. One dimensional uniaxial bar is considered to validate the strain gradient theory and cylindrical particle for the coupled chemo-mechanical model.

One dimensional uniaxial bar: Fig. 1(a) depicts the inhomogeneous uniaxial bar made of two materials with different Young's modulus, $E_1/E_2 = 5$, $L = 10$ *mm* and $\bar{u} = 0.1$ *mm* respectively, while the length parameter, l_c is the same for both materials. It has been seen numerically predicted results are in good agreement with analytical (Askes et. al., 2008) model for different values of length scale parameter as shown in Fig. 1(b).

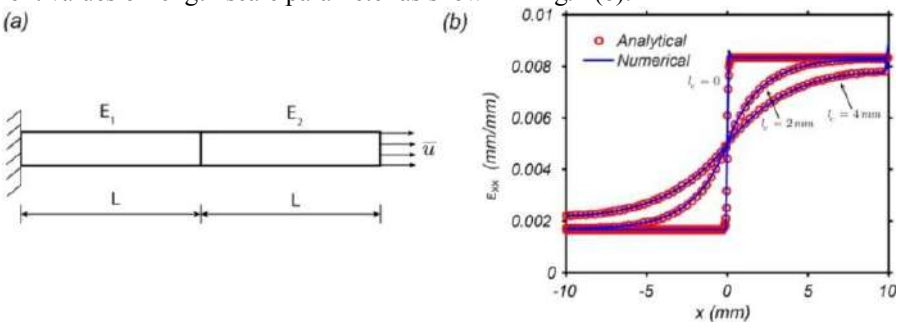

*Corresponding author. E-mail: avtarsinghh1991@gmail.com

Figure 1. (a) Schematic diagram inhomogeneous uniaxial bar and (b) distribution of axial strain along the length of uniaxial bar with different values of length parameter (l_c = *0, 2 and 4 mm*).

Cylindrical particle for coupled diffusion: A cylindrical particle of radius R_0 is considered to verify the coupled chemo-mechanical model subjected to galvanostatic loading with properties taken from Singh et. al., 2020 (Fig. 2(a)). It has been observed that the concentration and von-Mises stress profiles i.e., Fig. 2(a) and (b) obtained FEM is exactly overlaps the semi-analytical model.

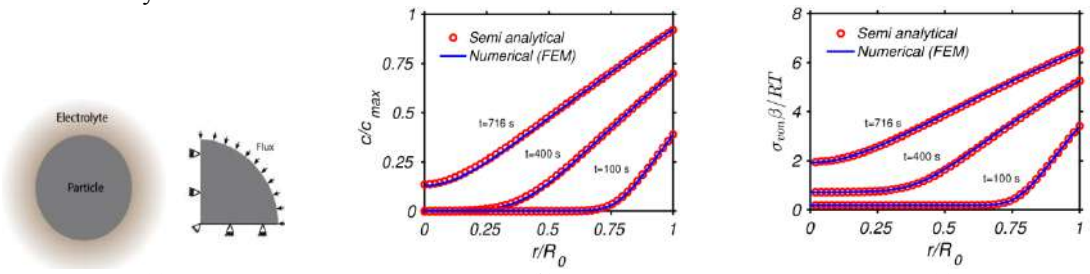

(a) (b) (c)

Figure 2. (a) Schematic diagram of cylindrical particle. (b) Normalised concentration profiles, and (c) von-Mises stress profiles obtained from both semi-analytical and FEM framework under fully coupled chemo-mechanical environment.

RESULTS AND DISCUSSION

In the present study, the $LiMn_2O_4$ cathode having a inclined junction is employed to simulate the effect of strain gradient as shown in Fig. 3(a). Further, the contour plots of concentration and von-Mises stress for with and without considering the size effect are provided in Fig. 3(b). It has been observed in Fig. 3(b) that the concentration and von-Mises stress fields are uniform for without size effect simulation. On the contrarily, size effect drives the lithium-ions into the domain and sharp gradient in the concentration field likely to be seen. We have also seen that as the charging continues, the size effect tends to hold and enhance the gradient within the concentration field. It is due to the fact that for $\bar{l}_c$=*0*, the hydrostatic pressure field is high which drives the lithium ion within the domain and diminishes the effect of interaction parameter. However, for $\bar{l}_c$=*0.2* the size effect plays significant role which reduces the order of hydrostatic stresses and strengthens the effect of interaction parameter. Likewise, the attendant von-Mises stress fields show similar behavior. Accordingly, the evolution of surface concentration with time is plotted in Fig. 3(c) for normalised length scale parameters, $\bar{l}_c$=*0* and $\bar{l}_c$=*0.2*.

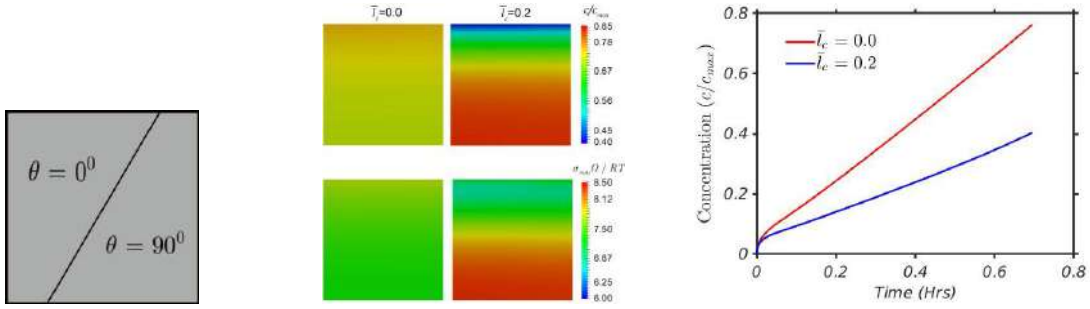

(a) (b) (c)

3. (a) Schematic diagram cathode having an inclined interface. (b) Contour plot for (a) concentration and (b) von-Mises stress distribution without ($\bar{l}_c$=*0*) and with ($\bar{l}_c$=*0.2*) considering the size effect.

CONCLUSIONS

Strain gradient significantly alters the distribution of Li-ions as well as stress field. Subsequently, the mechanical integrity will be influenced by the attendant stress field. Additionally, the voltage profile will also be altered in the presence of gradient.

References

[1] Askes Harm, Morata Irene, Aifantic Elias C., Finite element analysis with staggered gradient elasticity. 86: 1266-1279, 2008.
[2] Singh Avtar, Pal Siladitya, Coupled chemo-mechanical modeling of fracture in polycrystalline cathode for lithium-ion battery. 2019 (In press)

MULTISCALE DISCRETE DISLOCATION DYNAMICS SIMULATION OF GRADIENT NANO-GRAINED MATERIAL

Songjiang Lu[1], Xu Zhang*[1], Guozheng Kang [1], Qianhua Kan [1]
[1]School of Mechanics and Engineering, Southwest Jiaotong University, Chengdu, China

Summary Gradient nanostructured materials have synergetic strength and ductility. Multiscale discrete dislocation dynamics (DDD) method can track the evolution of dislocation microstructures and thus can help reveal the underlying mechanisms for curtain plastic behavior. However, the DDD investigations on gradient nano-grained metals are few due to the lack of a reasonable grain boundary (GB) model. In the present study, we first introduce a penetrable GB model, which is suit for arbitrary GB types, to the DDD framework. Then we conduct the DDD simulation to investigate the uni-axial compression of gradient nano-grained (GNG) polycrystals. The simulated results show that the dislocations initially activate and multiplicate in the larger grains, then propagating to the smaller grains gradually. The flow stress and strain hardening rate of the GNG samples are higher than the value calculated by the rule of mixtures. It turns out that the extract hardening of gradient nano-grained materials may come from the back stress induced by GNDs accumulation in front of GBs.

MULTISCALE DISCRETE DISLOCATION DYNAMICS FRAMEWORK

In present study, we use a three dimensional (3-D) hybrid model [1-3], which couples discrete dislocation dynamics (DDD) with finite element method (FEM), to conduct simulations on gradient nano-grained (GNG) face-centered cubic metals.

GRAIN BOUNDARY MODEL

So far, the GB models in 3-D DDD framework are still limited, especially for high-angle non-symmetrical GBs. In current study, we establish a GB model that is suit for a variety of GB types. In our GB model, two GB-dislocation interaction mechanisms, i.e. dislocation absorption at GBs and dislocation re-emission from GBs, are considered. By using the "coarse-graining" method, we can deal with the process of dislocation absorption and re-emission for arbitrary GB types.

SIMULATION MODEL

The gradient nano-grained (GNG) polycrystalline model with three grain sizes for multiscale DDD simulations is shown in Figure 1. The bottom surface of the sample is totally constrained and the top surface is uniaxially compressed along X-axis in a displacement-controlled mode.

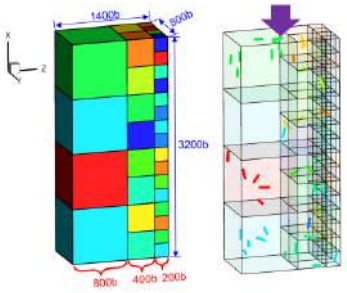

(a) (b)

Figure 1. (a) Gradient nano-grained (GNG) polycrystalline model with three grain sizes; (b) initial dislocation network.

RESULTS AND DISCUSSION

From the dislocation structures evolution shown in Figure 2a, we can see that the dislocations initially activate and multiplicate in the larger grains, then gradually propagating to the smaller grains. Besides, as shown in the stress-strain curve in Figure 2a, the apparent yield point (point II in the figure) does not occur until the amount of dislocation movement in the grain interior is large enough, which is different from that of single crystals. Figure 2b presents the distributions of equivalent stress and plastic strain along gradient orientation at various strains. It can be observed that the equivalent stress in the larger gains is lower than that of smaller ones, while the equivalent plastic strain has an opposite trend in relative to equivalent stress. Figure 3a shows the variations of stress and dislocation density as a function of strain for GNG material and three polycrystals with homogeneous grains, the flow stress calculated by the rule of mixtures is also shown in the figure. It can be seen that the flow stress and strain hardening rate of the GNG samples are higher than the value obtained by the rule of mixtures.

Furthermore, we also conduct compressive simulation on the GNG material with four grain sizes. Figure 3b displays the geometrically necessary dislocation (GND) density along gradient orientation. It shows that the GND density

*Corresponding author. E-mail: xzhang@swjtu.edu.cn

increases as the strain increases. Besides, it also can be seen that there are significant GND pile-ups between grains with different sizes. The extra hardening of GNG material shown in Figure 3a may come from the back stress induced by GNDs accumulation in front of GBs.

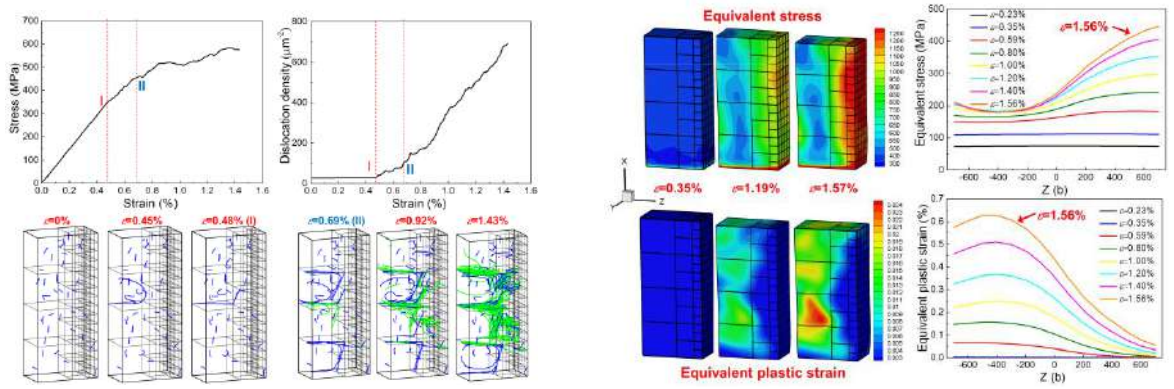

(a) (b)

Figure 2. (a) A representative result of compressive GNG aluminum, including stress-strain curve, dislocation density versus strain and dislocation structures at various strains (blue lines represent the dislocations in the grain interior, while the green ones are the dislocations emitted from GBs). (b) Equivalent stress and plastic strain distribute along gradient orientation at various strains, note that this result is obtained by averaging five realizations.

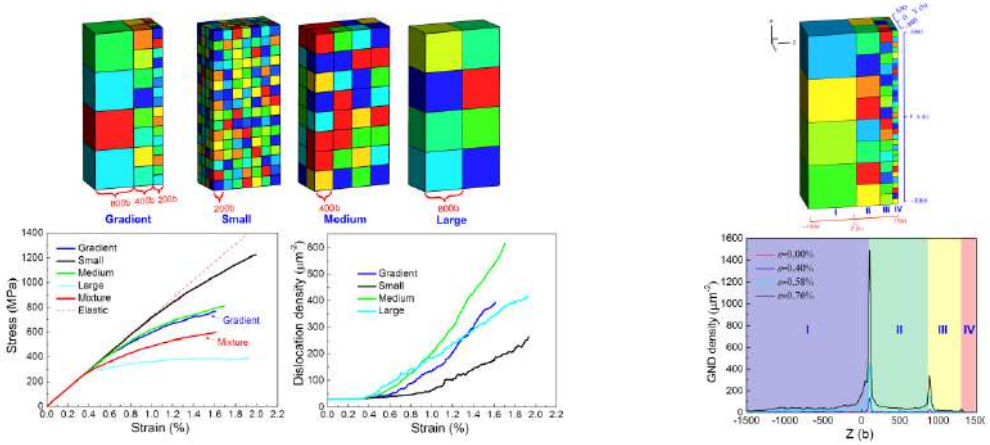

(a) (b)

Figure 3. (a) Stress-strain and dislocation density-strain curves of GNG material and corresponding homogenous grain material, the flow stress obtained by the rule of mixtures is also shown in the figure; (b) the geometrically necessary dislocation density along Z-axis for the GNG model with four different grain sizes. Note the above results are obtained by averaging five realizations.

CONCLUSIONS

The main conclusions for present study can be summarized as follows: (1) A GB model that can describe the interaction between dislocations for any GB types has been proposed and implemented in the multiscale DDD framework to conduct simulations on GNG material under uniaxial compression; (2) the dislocations initially activate and multiplicate in the larger grains, then gradually propagating to the smaller grains; (3) the extra hardening of GNG materials may come from the back stress induced by GNDs accumulation in front of GBs.

References

[1] M. Huang, S. Liang, Z. Li, An extended 3D discrete-continuous model and its application on single- and bi-crystal micropillars, Model. Simul. Mater. Sc 25 (2017).

[2] S. Lu, B. Zhang, X. Li, J. Zhao, M. Zaiser, H. Fan, X. Zhang, Grain boundary effect on nanoindentation: A multiscale discrete dislocation dynamics model, J. Mech. Phys. Solids. 126 (2019) 117-135.

[3] H.M. Zbib, T. Diaz de la Rubia, A multiscale model of plasticity, Int. J. Plasticity. 18(9) (2002) 1133-1163.

COMPUTATIONAL MODELING OF SIZE-EFFECTS IN POLYMER NANO-COMPOSITES

Paras Kumar*[1,2] and Julia Mergheim[1]
[1]Institute of Applied Mechanics, Friedrich-Alexander Universität Erlangen-Nürnberg (FAU), Germany
[2]Central Institute for Scientific Computing, Friedrich-Alexander Universität Erlangen-Nürnberg (FAU), Germany

Summary Nano-sized filler particles have been found to be much efficient reinforcements for improving the mechanical properties of polymers in comparison to their micro-sized counterparts. Standard first-order computational homogenization lacks the length scale necessary to capture this size effect. An enhanced computation homogenization scheme based on the concept of *interface energetics* has been considered in this work and a thorough evaluation of its suitability for modeling polymer nano-composites has been carried out by means of systematic numerical experimentation. The method is more suited for modeling size effects in case of weaker inclusions in a stiff matrix than stiffer filler particles in a weak matrix.

INTRODUCTION

The positive impact of reduced filler particle size in terms of improvement of the overall mechanical behavior of polymer composites has been extensively corroborated by experimental studies [2]. This *smaller is stronger* size-effect is usually attributed to the formation of an *interphase layer* around the filler particles, which is pronounced in case of nano-sized reinforcements owing to their much higher specific surface area (SSA) [3]. The standard first-order computational homogenization scheme, commonly employed for modeling overall behavior of heterogeneous materials, by virtue of lack of necessary length scale, is unable to encapsulate the aforementioned size effect.

This work explores the Interface-Energetics-Enhanced Computational Homogenization (IECH) approach, wherein the standard scheme is enhanced by means of equipping the material interface with its own energetic structure. For details about the underlying formulations and other relevant aspects we refer the reader to [1] and the references therein.

NUMERICAL EXPERIMENTATION & DISCUSSION

In order to conduct a thorough evaluation of the IECH approach, we consider a series of representative volume elements (RVEs) such as one shown in Figure 1. Furthermore, two different filler materials, i.e. silica ($\mu_S = 34\,188\,\text{MPa}, \nu_S = 0.17$) and rubber ($\mu_R = 0.67\,\text{MPa}, \nu_R = 0.49$) are considered in an epoxy matrix ($\mu_E = 1185\,\text{MPa}, \nu_E = 0.35$). The model is tested for three different loading conditions: (i) uni-axial tension, (ii) shear and (iii) volumetric loading.

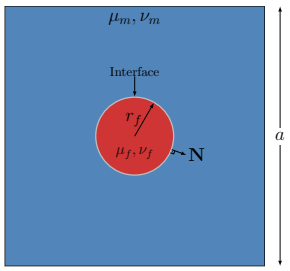

Figure 1: A 2D RVE consisting of a circular filler particle (red) of radius r_f embedded in a matrix material (blue). The subscripts m and f here refer to the matrix and the filler regions, respectively.

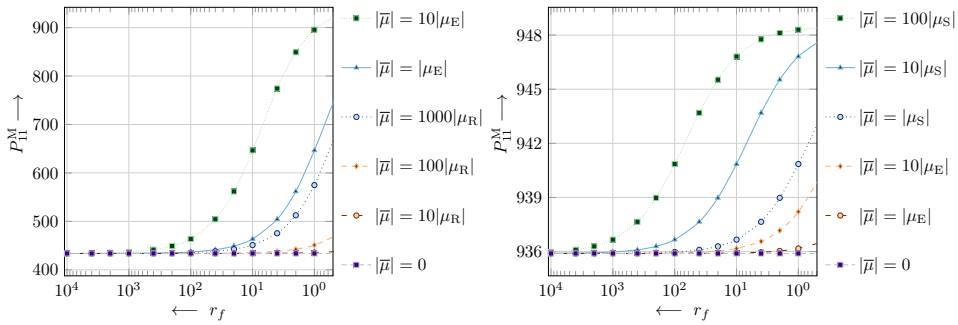

(a) Rubber inclusions in epoxy matrix.

(b) Silica inclusions in epoxy matrix.

Figure 2: Variation of the macroscopic Piola stress with filler particle radius for volumetric loading scenario.

Let the RVE having a given edge length a and filler particle radius r_f, cf. Figure 1, be scaled down by given factor K such that the particle size reduces while the filler volume fraction is left unchanged. Figure 2 depicts the variation of the macroscopic Piola stress w.r.t the filler particle radius r_f for different values of the interface shear modulus $\overline{\mu}$[1]. For the sake of brevity, only the results for volumetric loading have been presented here. A similar pattern has been observed for other loading scenarios as well. The curves for $|\overline{\mu}| = 0$ represent a *perfect interface*, which is observed in case of standard homogenization approach.

The overall response of the RVE becomes stiffer as the filler particles become smaller, especially, with increasing stiffness of the interface, cf. Figure 2a for instance. The observed size effect becomes pre-eminent for the cases where

*Corresponding author. E-mail: paras.kumar@fau.de.

[1]For a 2D RVE, the interface is actually a curve, i.e. a one-dimensional entity, thus a single material parameter suffices for the interface

$|\overline{\mu}| \geq \max\{|\mu_{\mathrm{m}}|, |\mu_{\mathrm{f}}|\}$. A saturation of the size effect w.r.t. the reducing filler particle radius is observed, particularly for the case of silica inclusions as shown in Figure 2b. The degree of stiffening achieved by means of the energetic interface is highly sensitive to the relative stiffness between the matrix and the filler material, cf. Figure 2a and Figure 2b respectively. In contrast to the softer rubber particles, a minimal improvement in the overall stiffness is achieved with much stiffer silica particles. This behavior can be attributed to the fact that, for the elastic interface considered in this study, the deformation of the interface depends on that of the particle. The appropriateness of the current approach is thereby restricted to the case of weaker filler particles in a stiffer matrix.

The applicability of the IECH approach to weaker filler particles is partially limited due to the occurrence of instabilities in the form of *kinks*, under shear loading conditions as depicted in Figure 3. Such behavior is more prominent for smaller particle sizes and higher interface stiffness. It is noteworthy that the instabilities are not of numerical nature, and are therefore observed for different finite element meshes. These instabilities are indeed caused due to the buckling of the stiff interface under excessive compression, which is observed on the top-right and bottom-left corners of the RVE during shear loading, cf. 3b. This bucking of the interface could be attributed to the lack of resistance from the surrounding filler material having almost negligible stiffness in comparison to the interface. On the contrary, no such instabilities are observed in the case of silica particles owing to the much larger stiffness of the filler particles. Thus, an energetic elastic interface can only sustain limited compressive loads.

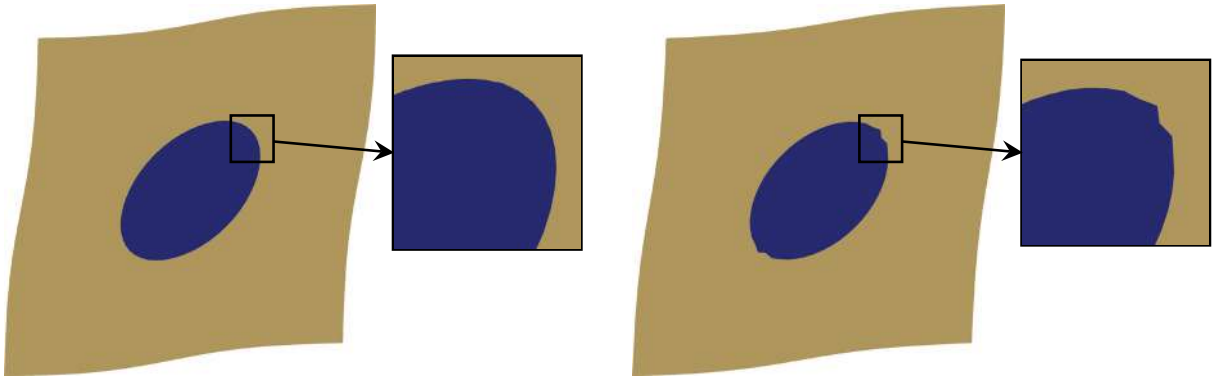

(a) Deformation contour for perfect interface($|\overline{\mu}| = 0$). (b) Deformation contour for active interface ($|\overline{\mu}| = 10|\overline{\mu}|$).

Figure 3: Comparison of deformation contours for rubber filler case with fixed RVE size under the shear loading scenario

OUTLOOK

The above discussion reveals the limitation of the interface energetics based approach in modeling size effects in case of polymer nano-composites containing stiffer filler particles in a weak matrix. An alternative approach involving explicit modeling of a finite thickness *interphase* around the filler particles is being developed. Herein, a continuously graded interphase region with material properties varying between those of the filler and the matrix is modeled.

References

[1] Kumar P., Mergheim J., Size Effects in Computational Homogenization of Polymer Nano-Composites. *Proceedings in Applied Mathematics and Mechanics* **Submitted**:2020.

[2] Cho J., Joshi M.S., Effect of inclusion size on mechanical properties of polymeric composites with micro and nano particles. *Composites Science and Technology* **66**:1941-1952, 2006.

[3] Schmidt D., Shah D., Giannelis E. P. New advances in polymer/layered silicate nanocomposites. *Current Opinion in Solid State and Materials Science* **6**:205-212, 2002.

EXTENSION OF ANISOTROPIC CORE-SHELL MODEL TO HCP NANOCRYSTALLINE METALS

Katarzyna Kowalczyk-Gajewska*[1] and Marcin Maździarz[1]
[1]Institute of Fundamental Technological Research, Polish Academy of Sciences, Warsaw, Poland

Summary Anisotropic core-shell model of a nano-grained polycrystal is extended to estimate the effective elastic stiffness of several metals of hexagonal crystal lattice symmetry. In the approach the bulk nanocrystalline metal is described as a two-phase medium with different properties for a grain boundary zone and a grain core. While the grain core is anisotropic, the boundary zone is isotropic andthe shell has a thickness defined by the *cutoff radius* of a corresponding atomistic potential for the considered metal. The predictions of the proposed mean-field model are verified with respect to simulations performed with the use of the Large-scale Atomic/Molecular Massively Parallel Simulator, the Embedded Atom Model, and the molecular statics method. The effect of the grain size on the overall elastic moduli of nanocrystalline material with random distribution of orientations is analysed.

INTRODUCTION

A class of nanostructured material is considered that is composed of equiaxed nanometre-sized building blocks - crystallites of the same chemical composition and with a characteristic dimension smaller than 100 nm, which differ only by the crystallographic orientation. In such nanostructured material two main phases are distinguished: the grain core and the grain boundaries. The effect of grain boundary zone on the overall properties of a bulk polycrystal is the more significant the smaller is a grain size. Usually at the macroscale level the stress-strain response of nanocrystalline metals is governed by the continuum mechanics theory, and the mean-field estimates are still in use for assessing the bulk properties of nanocrystalline metals. Because of different properties of a grain boundary zone and the grain core, for nano-grained polycrystals two-phase or multi-phase mean-field frameworks are formulated (see [1] for an extensive review).

MODEL FORMULATION

In [1] a two-phase model of elastic nanocrystalline material was formulated in two variants called the Mori-Tanaka(MT) and self-consistent (SC) core-shell model, respectively. As inspired by earlier works [2], an additional phase that forms an *isotropic* coating around the *anisotropic* grain core is introduced. The smaller is the grain this transient zone influences more on the effective properties of polycrystal (Fig. 1). The estimates of overall stiffness by a two-phase model presented in the next section are obtained under the assumption that representative volume element contains infinite set of orientations of random uniform distribution. Under such assumption the overall stiffness tensor $\bar{\mathbf{C}}$ is isotropic and specified by an overall bulk modulus $\bar{K}$ and a shear modulus $\bar{G}$. The effective stiffness $\bar{\mathbf{C}}$ is calculated by embedding the coated grain in the infinite medium of the stiffness $\mathbf{C}_\mathrm{m}$ and next using the procedure of the double-inclusion model, namely

$$\bar{\mathbf{C}} = \left[f_0\mathbf{C}_\mathrm{s}\mathbf{A}_\mathrm{s} + (1-f_0)\left\langle \mathbf{C}(\phi^c)\mathbf{A}(\phi^c)\right\rangle_{\mathcal{O}}\right]\left[f_0\mathbf{A}_\mathrm{s} + (1-f_0)\left\langle \mathbf{A}(\phi^c)\right\rangle_{\mathcal{O}}\right]^{-1} \tag{1}$$

where

$$\mathbf{A}(\phi^c) = (\mathbf{C}(\phi^c) + \mathbf{C}_*(\mathbf{C}_\mathrm{m}))^{-1}(\mathbf{C}_\mathrm{m} + \mathbf{C}_*(\mathbf{C}_\mathrm{m}))\,, \quad \mathbf{A}_\mathrm{s} = (\mathbf{C}_\mathrm{s} + \mathbf{C}_*(\mathbf{C}_\mathrm{m}))^{-1}(\mathbf{C}_\mathrm{m} + \mathbf{C}_*(\mathbf{C}_\mathrm{m}))\,, \tag{2}$$

$\langle . \rangle_{\mathcal{O}}$ denotes averaging over the orientation space and $\mathbf{C}_*(\mathbf{C}_\mathrm{m})$ is the Hill tensor depending on the stiffness $\mathbf{C}_\mathrm{m}$ of infinite matrix and the shape of the coated grain, which is assumed as spherical in the present study. For the MT variant of the core-shell model $\mathbf{C}_\mathrm{m} = \mathbf{C}_\mathrm{s}$ is assumed, while for the SC variant $\mathbf{C}_\mathrm{m} = \bar{\mathbf{C}}$. In formula (1) f_0 is the volume fraction of the transient zone. Assuming the spherical shape of coated grains and denoting by Δ the coating thickness, f_0 is calculated by the formula

$$f_0 = 1 - \left(1 - \frac{2\Delta}{d}\right)^3\,, \tag{3}$$

where d is an averaged grain diameter. The parameter Δ introduces the size effect to the model. In [1] it was demonstrated that Δ can be taken as equal to the *cutoff radius* of the atomistic potential valid for the considered metal. Tensor $\mathbf{C}(\phi^c)$ is the anisotropic local elastic stiffness tensor for the single and depends on the crystal orientation. For cubic crystals studied in [1, 3] it is given by three material parameters For the considered hcp crystals it exhibits transverse isotropy and is specified by 5 independent components, which are the material-specific constants.

*Corresponding author. E-mail: kkowalcz@ippt.pan.pl

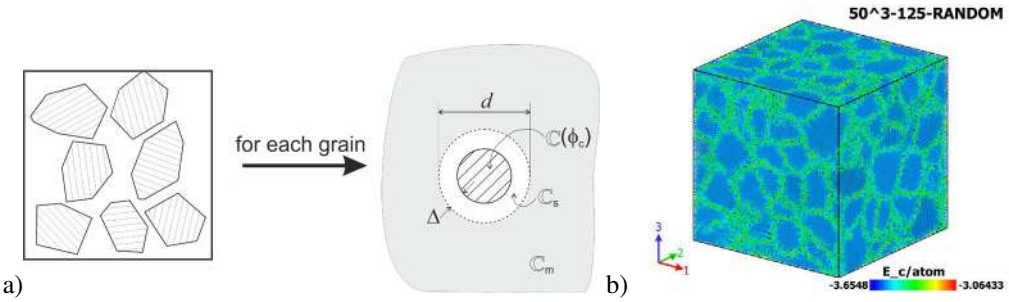

Figure 1: (a) Schematic of a core-shell model, (b) the example of a nanocrystalline sample considered in atomistic simulations.

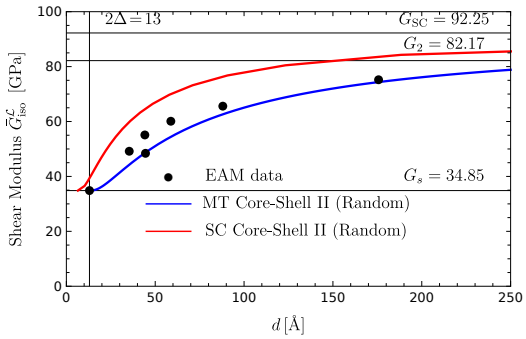

Figure 2: Effective shear modulus - $\bar{G}^{\mathcal{L}}_{\text{iso}}$ as a function of the average grain diameter d obtained by the two variants of the core-shell model - comparison with the results of atomistic simulations for Co.

RESULTS

Predictions of the mean field core-shell model will be compared with the results of atomistic simulations for 6 metals of hexagonal (hcp) lattice symmetry: Co, Zr, Mg, Re, Ti and Ru. The results are obtained by molecular statics using the corresponding EAM potentials taken from the literature [4] and then are analysed and visualized with the Open Visualization Tool OVITO [5]. The methodology for generating polycrystal samples by the Voronoi tessellation method, their pre-relaxation and numerical simulations were described in [1]. In particular, the samples with a different number of atoms per grain are generated, enabling to study the effect of grain size on the elastic stiffness. 21 components of stiffness tensor, of all pre-relaxed structures were computed by the stress-strain method with the maximum strain amplitude set to be 10^{-4}. Using the Log-Euclidean norm the closest isotropic approximation of the obtained tensor is found [1].

There is a known problem at the nano level with how to assume local effective material parameters for the boundary zone between atomistic layers in the local continuum approach (here, K_s and G_s values). Following [3], it is here proposed that elastic properties for the shells themselves are obtained by reducing the size of some generated polycrystal samples, so that the fraction of transient shell atoms is close to unity, $f_0 \to 1$.

Fig. 2 presents the preliminary results obtained for Co nanocrystalline bulk material. Elastic shear moduli obtained by the atomistic simulations and the core-shell model are compared. Good accordance of both predictions, especially fo rthe MT variant, is seen.

CONCLUSIONS

The two-phase core-shell model could provide reliable predictions of elastic properties of nanorystalline metals of hexagonal lattice symmetry. Variation of elastic bulk and shear modulus of polycrystals with random orientation distribution with a grain size is well reproduced as compared to the results of atomistic simulations.

Acknowledgements: The research was partially supported by the project No. 2016/23/B/ST8/03418 of the National Science Centre,Poland.

References

[1] Kowalczyk-Gajewska K., Maździarz M., Atomistic and mean-field estimates of effective stiffness tensor of nanocrystalline copper. *Int. J. Eng. Sci.* **129**:47-62, 2018.
[2] Jiang B., Weng G.J., A generalized self-consistent polycrystal model for the yield strength of nanocrystalline materials. *J. Mech. Phys. Solids* **52**:1125-1149, 2004.
[3] Kowalczyk-Gajewska K., Maździarz M., Effective stiffness tensor of nanocrystalline materials of cubic symmetry: The core-shell model and atomistic estimates. *Int. J. Eng. Sci.* **144**:103134-1-24, 2019.
[4] Plimpton, S., Fast Parallel Algorithms for Short-Range Molecular Dynamics. *Journal of Computational Physics* **117**:1-19, 1995.
[5] Stukowski, A., Visualization and analysis of atomistic simulation data with OVITO - the Open Visualization Tool (http://ovito.org). *Modelling Simul. Mater. Sci. Eng.* **18**:015012, 2010.

COMPOSITE MATERIALS WITH HEXAGONAL MICROSTRUCTURE ANALYZED WITH A MICROPOLAR MODEL

Nicholas Fantuzzi*[1] and Patrizia Trovalusci[2]
[1]Department of Civil, Chemical, Environmental and Materials Engineering, University of Bologna, Bologna, Italy
[2]Department of Structural and Geotechnical Engineering, Sapienza University of Rome, Rome, Italy

Summary The present work demonstrate the advantages of micropolar model with respect to classical continuum (e.g. Cauchy of Grade 1) and nonlocal couple stress model (continua with internal constraints) in studying composite materials with an internal microstructure. In particular, composite materials with hexagonal microstructure will be modeled and investigated when concentrated loads are applied to a sample structure. Homogenized material properties have different behavior according to the selected particle geometry such as orthotetragonal, auxetic and chiral. It is shown that when chiral and auxetic material behavior are considered a micropolar model allows to predict features that are unpredictable by other material models.

INTRODUCTION

Composite materials can be studied by modeling interactions among their constituents or by homogenizing an equivalent continuum. Homogenization is an efficient approach but its effectiveness is strongly related to the continuum theory used and the homogenization method adopted to convert the physical particle/matrix system into an equivalent continuum (see [1]). When classical kinematics is enriched with extra degrees of freedom, homogenization procedures have been shown to provide more reliable models than in the case of classical local continua. In particular, micropolar theory introduces as degree of freedom the microrotation, that is an additional kinematic feature of the material point, different from the local rigid rotation (the classical macrorotation), the rotational feature of the infinitesimal neighborhood, and their effects have been widely investigated by [2, 3, 4] for masonry–like materials. Note that these rotations coincide in the couple–stress theory, as well as in the classical theory (see [5], Appendix). Micro-polar effects widely analyzed in the literature [1] as have been recently compared to other non-local effects analyzed in [6, 7] in the presence of geometrical or load singularities, such as concentrated loads, voids or material inclusions. In the present work three particular assemblies of regular and irregular hexagonal particles are considered as RVE material models. Discussion on material behavior made of these assemblies is throughly discussed when solids are subjected to concentrated loads.

MICROPOLAR CONTINUUM

In the present theory, a microrotation is considered as independent kinematic parameter. In a 2D framework there are two displacements and one rotation so that $\{u\}^T = \{u_1\ u_2\ \omega\}$ applies. The strain displacement vector is represented as: $\{\varepsilon\}^T = \{\{\varepsilon_{11}\ \varepsilon_{22}\ k_1\ k_2\}\ \{\varepsilon_{12}\ \varepsilon_{21}\}\}$, where ε_{ij}, for $i,j = 1,2$ are the in-plane normal and shear strains and k_1, k_2 are the micropolar curvatures. Note that the strain components are not reciprocal, $\varepsilon_{12} \neq \varepsilon_{21}$, The kinematic compatibility relations can be written as: $\{\varepsilon_1\} = [D_1]\{u\}$ and $\{\varepsilon_2\} = [D_2]\{u\}$ where $[D_1]$ and $[D_2]$ can be found in [8]. As strain measure of the micropolar model we have the relative rotation, defined as the difference between the microrotation ω and the skew-symmetric part of the gradient of displacement, θ. The focus of this work is on such a peculiar strain measure $\theta - \omega$ of the micropolarity of the model under study. Analogously, the work-conjugated stress measures of the micropolar model are represented in the vector: $\{\sigma\}^T = \{\{\sigma_{11}\ \sigma_{22}\ \mu_1\ \mu_2\}\ \{\sigma_{12}\ \sigma_{21}\}\}$ where σ_{ij} for $i,j = 1,2$ represent the classical normal and shear stress components, and μ_1, μ_2 are the microcouples. From the virtual work principle without introducing the constitutive equations, described below, equilibrium equations in terms of stresses and microcouples can be carried out as $\delta U + \delta V = 0$. So that:

$$\delta U + \delta V = \{\delta u\}^T \left\{ h \int_{\mathcal{A}} \left([D_1]^T \{\sigma_1\} + [D_2]^T \{\sigma_2\} \right) d\mathcal{A} - \left(\int_{\mathcal{V}} \{f\} d\mathcal{V} + \int_{\mathcal{S}} \{p\} d\mathcal{S} \right) \right\} = 0 \tag{1}$$

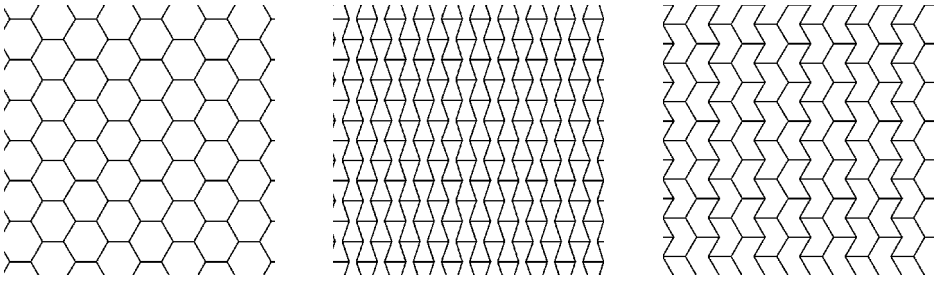

Figure 1: Hexagonal patterns given by geometric parameters $\alpha_1 = 0°$, $l_r = \frac{100}{1/\sqrt{3}+1}$: regular $\alpha_2 = \alpha_3 = 30°$, auxetic $\alpha_2 = \alpha_3 = -20°$ and asymmetric $-\alpha_2 = \alpha_3 = 30°$, from left to right.

*Corresponding author. E-mail: nicholas.fantuzzi@unibo.it

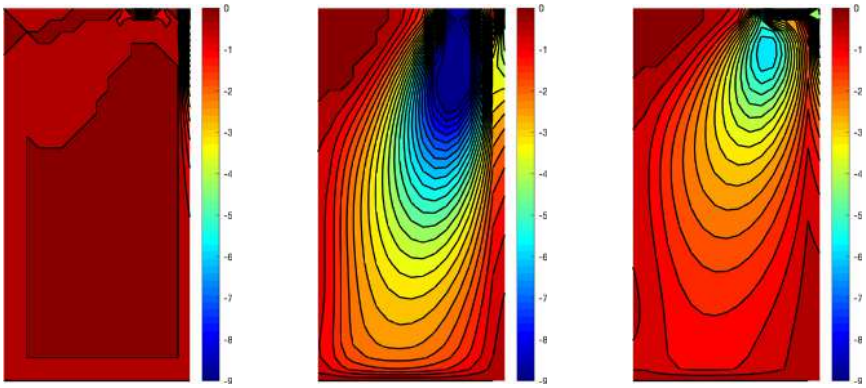

Figure 2: Relative rotation $\theta - \omega$ for regular, auxetic and chiral hexagonal patterns from left to right respectively.

h being the thickness of the 2D domain which can be considered as unitary for plane strain case. $\{f\}$ and $\{p\}$ are the vectors of body forces and boundary tractions, respectively. The micropolar constitutive equations take the form $\{\sigma\} = \mathbb{C}\{\varepsilon\}$ where $\mathbb{C}$ can be found in [8]. In the following, the finite element approximation will be applied directly to the variational principle in order to carry out the approximate solution of the problem.

RESULTS

The present irregular hexagonal geometry is defined by four parameters: three angles α_1, α_2, α_3, relative length, l_r. Using simple geometric formulae the RVE can be defined by translations and mirroring of tiles [8]. By changing the geometric parameters listed above several patterns can be obtained as the ones depicted in Figure 1 which are termed for future reference: regular, hourglass and asymmetric, respectively. They have been obtained by setting a equilateral geometry (all the sides have the same length) with $\alpha_1 = 0°$, $l_r = \frac{100}{1/\sqrt{3}+1} \cong 63.3975$ and by varying α_2 and α_3 angles as listed in Figure 1 caption. The solution of the problem is carried out using a finite element implementation [8]. A comparison in terms of relative rotation $\theta - \omega$ is shown in Figure 2 where it is clear that regular hexagons have a very small micropolar effect, whereas the other configurations have strong effect due to the present micropolar modelling.

CONCLUSIONS

The three selected patterns show peculiarities and outcomes related to the micropolar behavior. Assemblies of regular hexagons have an orthotetragonal behavior and it has been shown that their homogenized behavior is close to the behavior of classical elastic bodies. On the contrary, the other configurations showed strong nonlocal effects, related to the internal material size, which brought a larger stress diffusion within the body and reduced displacements. All these aspects could be underlined mostly because a micropolar continuum has extra rotational degrees of freedom with respect to classical continuum.

ACKNOWLEDGMENTS

This research was supported by the Italian Ministry of University and Research, P.R.I.N. 2017 No. 20172017HFPKZY (cup: B86J16002300001).

References

[1] Trovalusci P., Molecular Approaches for Multifield Continua: origins and current developments. Springer Vienna, 211–278, 2014.
[2] Trovalusci P., Masiani R., Non-linear micropolar and classical continua for anisotropic discontinuous materials, *Int. J. Solids Struct.*, **40**:1281-1297, 2003.
[3] Trovalusci P., Masiani R., A multifield model for blocky materials based on multiscale description, *Int. J. Solids Struct.*, **42**:5778-5794, 2005.
[4] Fantuzzi N., Trovalusci P., Dharasura S., Mechanical behavior of anisotropic composite materials as micropolar continua, *Front Mater* **6**:59, 2019.
[5] Masiani R., Trovalusci P., Cosserat and Cauchy materials as continuum models of brick masonry, Meccanica **31**:421-432, 1996.
[6] Tuna M., Kirca M. Trovalusci P., Deformation of atomic models and their equivalent continuum counterparts using Eringen's two-phase local/nonlocal model, Mech. Res. Commun. **97**:26-32, 2019.
[7] Tuna M., Trovalusci P., Scale dependent continuum approaches for discontinuous assemblies: explicit and implicit non-local models, Mech. Res. Commun., https://doi.org/10.1007/s11012-019-01091-3(0123456789().,-volV() 0123458697().,-volV) 2019.
[8] Fantuzzi N., Trovalusci P., Luciano R., Multiscale analysis of anisotropic materials with hexagonal microstructure as micro-polar continua, *Int. J. Multiscale Comput. Eng.*, In Press, 2019.
[9] Leonetti L., Fantuzzi N., Trovalusci P., Tornabene, F., Scale effects in orthotropic composite assemblies as micropolar continua: A comparison between weak- and strong-form finite element solutions, *Materials* **12**:5, 2019.

MODELLING THE CYCLIC TORSION OF POLYCRYSTALLINE MICRON-SIZED COPPER WIRES BY DISTORTION GRADIENT PLASTICITY

Lorenzo Bardella*[1] and Andrea Panteghini[1]
[1]Department of Civil, Environmental, Architectural Engineering and Mathematics, University of Brescia, Brescia, Italy

Summary Towards the modelling of the irreversible behaviour of micron-scale metals under non-proportional loading, we demonstrate that the distortion gradient plasticity recently proposed by our group [1] can predict the experimental data of Liu et al. [2] on the cyclic torsion of copper wires of diameter ranging from 18 to 42 micrometres. To reach our goal we plug the constitutive proposal of [1] in the model that we have previously developed for the torsion problem [3], which is based on the pivotal higher-order framework established by Gurtin [4], relying on Nye's dislocation density tensor to describe size effects in micron-scale metal plasticity. We implement the new model in a finite element (FE) code and identify its parameters by resorting to the Coliny evolutionary algorithm implemented in Dakota [5].

INTRODUCTION

This contribution focuses on modelling typical size effects in micron-scale metal plasticity [6, 7] by using a phenomenological theory of strain gradient plasticity. Here, the adjective phenomenological denotes theories neglecting metal crystallography. Specifically, we build on the 2004 Gurtin theory [4], here referred to as a distortion gradient plasticity (DGP) theory because it constitutively prescribes laws for the evolution of both the plastic strain and the plastic spin, i.e., the symmetric and skew-symmetric parts of the plastic distortion, respectively. This natural need ensues from the comparison with strain gradient *crystal* plasticity [8] along with the fundamental hypothesis that the primal higher-order (HO) kinematic variable characterising the theory is Nye's dislocation density tensor $\boldsymbol{\alpha}$ [9], that is the curl of the plastic distortion. Hence, $\boldsymbol{\alpha}$ is work-conjugate to a HO stress that, in the purely recoverable HO contribution proposed by Gurtin [4], is denoted as the defect stress, whose potential is the so-called defect energy, the latter being a function of $\boldsymbol{\alpha}$ entering the Helmholtz free energy density.

In particular, we consider the torsion of thin metal wires, for which, in [3], we have established that Gurtin theory [4] can accurately predict the experimental data under *monotonic* loading of Fleck et al. [6]. This is possible if one defines the defect energy as the sum of two regularised logarithmic contributions, each being a function of a distinct invariant of $\boldsymbol{\alpha}$, namely its trace (which represents the overall amount of pure densities of geometrically necessary screw dislocations) and the second invariant of its deviatoric part. Here, there are two crucial aspects that deserve to be briefly underlined. First, the logarithmic defect energy [10], beside resulting from statistical dislocation mechanics [11], is a *less-than-quadratic* defect energy, thus delivering some (energetic) strengthening with diminishing size, which is an increase in the yield point that characterises the experimental data in torsion [6, 2]. Second, in the torsion problem the first invariant of $\boldsymbol{\alpha}$ (i.e., its trace) depends on the plastic spin only [3] and its use as independent kinematic variable offers a natural and much richer description of the problem than that provided by the many phenomenological theories neglecting the plastic spin.

Unfortunately, the use of less-than-quadratic defect energies has a noticeable drawback, as highlighted in [3]: the predictions under cyclic loading are unreliable within polycrystal plasticity, as they exhibit questionable changes of concavity in the normalised stress-strain curves that are absent in experimental data [2]. In order to address this issue, in [1] we have proposed the use of a HO plastic potential, involving both recoverable and dissipative contributions, in the place of Gurtin's defect energy. Specifically, such HO plastic potential is the sum of M quadratic functions of the chosen primal HO variable (here, $\boldsymbol{\alpha}$), each of these M quadratic contributions being characterised by a different length scale parameter and being limited by a *pseudo*-yield surface of suitable size. Each contribution participates to dissipation when $\boldsymbol{\alpha}$ is larger than its maximum recoverable value, as governed by the *pseudo*-yield surface of the contribution. This technique is inspired by established laws within conventional nonlinear kinematic hardening [12]. This HO potential is particularly useful in the modelling as it can approximate (under monotonic loading) any less-than-quadratic defect energy, by suitably identifying the length scale parameters and the *pseudo*-yield surface limits of a relatively small number of quadratic contributions [1]. In passing, we note that this proposal, by establishing a thermodynamically consistent HO dissipation for HO strain gradient plasticity in general, also offers a way to address the issue concerned with the so-called "elastic gaps" affecting the predictions of *non-incremental* dissipative strain gradient plasticity theories under non-proportional loading [13].

Hence, the objective of this work is the accurate modelling of the experimental data on the cyclic torsion of thin metal wires by using the new HO potential proposed in [1] within the DGP applied to the torsion problem presented in [3]. To this purpose, we focus on the experimental results of Liu et al. [2] on polycrystalline copper wires of diameter ranging from 18 to 42 micrometres, whose grains have size variable from 5 to 9 micrometres, almost independently of the wire diameter.

*Corresponding author. E-mail: lorenzo.bardella@ing.unibs.it.

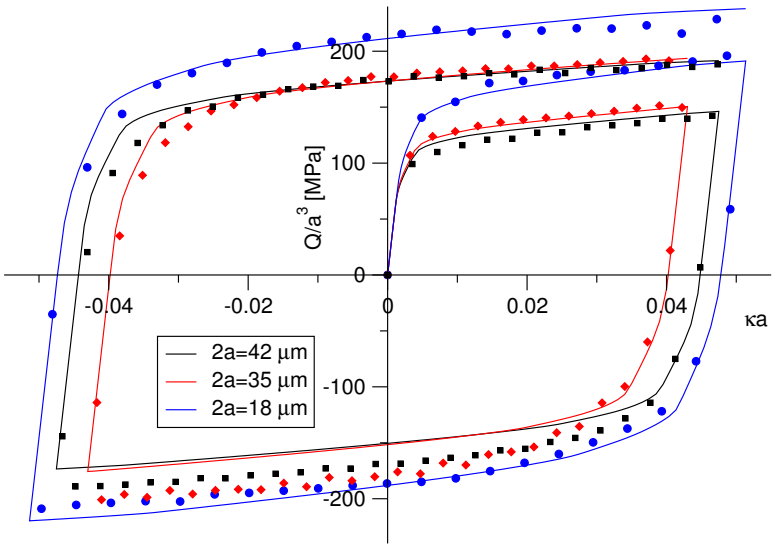

Figure 1: Comparison between the experimental data of Liu et al. [2] (discrete symbols) and theoretical predictions (continuous curves): normalised torque vs. nondimensional twist per unit length (from [15]).

METHOD, RESULTS, AND PERSPECTIVES

The DGP model for torsion is implemented in a user element subroutine for the FE code ABAQUS as detailed in [3], except that the constitutive laws of [3] concerned with the HO contributions are substituted with the HO potential proposed in [1], whose implementation straightforwardly follows the algorithm provided in [1]. Moreover, with respect to the model presented in [3], we have added a conventional kinematic hardening needed, in our phenomenological framework, to account for the polycrystalline microstructure, whereby the grain size is almost independent of the wire diameter (such that, the Hall-Petch size effect should be negligible).

The material parameters are identified by implementing a literature procedure originally developed for nonlinear kinematic hardening [14] and by resorting to the Coliny evolutionary algorithm implemented in Dakota [5]. The results, summarised in Fig. 1, show unprecedented good agreement between experimental data and model predictions [15].

We further demonstrate that once one selects a less-than quadratic defect energy predicting a certain behaviour under proportional loading, the number M of quadratic contributions in the new HO potential is only a matter of discretisation, as, for not-too-small M, it does not influence the results under any loading histories. This ensues from an analytical convergence result, by the way establishing that the parameters to be identified are solely those of a reference defect energy.

To assess our results, more experimental data should be analysed, such as the very recent ones of Guo et al. [16].

References

[1] Panteghini A., Bardella L., Niordson C. F. A Potential for Higher-Order Phenomenological Strain Gradient Plasticity to Predict Reliable Response under Non-Proportional Loading. *Proc. R. Soc. A* **475**: 20190258, 2019.
[2] Liu D., He Y., Dunstan D. J., Zhang B., Gan Z., Hu P., Ding H. Anomalous Plasticity in Cyclic Torsion of Micron Scale Metallic Wires. *Phys. Rev. Lett.* **110**: 244301, 2013.
[3] Bardella L., Panteghini A. Modelling the Torsion of Thin Metal Wires by Distortion Gradient Plasticity. *J. Mech. Phys. Solids* **78**: 467-492, 2015.
[4] Gurtin M. E. A Gradient Theory of Small-Deformation Isotropic Plasticity that Accounts for the Burgers Vector and for Dissipation Due to Plastic Spin. *J. Mech. Phys. Solids* **52**: 2545-2568, 2004.
[5] Dakota, web site **https://dakota.sandia.gov/sites/default/files/docs/6.0/html-ref/topic-package_coliny.html**.
[6] Fleck N. A., Muller G. M., Ashby M. F., Hutchinson J. W. Strain Gradient Plasticity: Theory and Experiments. *Acta Metall. Mater.* **42**: 475-487, 1994.
[7] Fleck N. A., Hutchinson J. W. Strain Gradient Plasticity. *Adv. Appl. Mech.* **33** :295-361, 1997.
[8] Bardella L. A Comparison between Crystal and Isotropic Strain Gradient Plasticity Theories with Accent on the Role of the Plastic Spin. *Eur. J. Mech. A-Solid.* **28** :638-646, 2009.
[9] Nye J. F. Some Geometrical Relations in Dislocated Crystals. *Acta Metall.* **1**: 153-162, 1953.
[10] Forest S., Guéninchault N. Inspection of Free Energy Functions in Gradient Crystal Plasticity. *Acta Mech. Sinica* **29**: 763-772, 2013.
[11] Groma I., Györgyi G., Kocsis, B. Dynamics of Coarse Grained Dislocation Densities from an Effective Free Energy. *Philos. Mag.* **97**: 1185-1199, 2007.
[12] Ohno N. A Constitutive Model of Cyclic Plasticity with a Non-Hardening Strain Region. *J. Appl. Mech.-T ASME* **49**: 721-727, 1982.
[13] Fleck N. A., Hutchinson J. W., Willis J. R. Strain Gradient Plasticity under Non-Proportional Loading. *Proc. R. Soc. A* **470**: 20140267, 2014.
[14] Abdel-Karim M., Ohno N. Kinematic Hardening Model Suitable for Ratchetting with Steady-State. *Int. J. Plasticity* **16**: 225-240, 2000.
[15] Panteghini A., Bardella L. Modelling the cyclic torsion of polycrystalline micron-sized copper wires by distortion gradient plasticity. *Philos. Mag.* **100**: 2352-2364, 2020.
[16] Guo S., He Y., Tian M., Liu D., Li Z., Lei J., Han S. Size effect in cyclic torsion of micron-scale polycrystalline copper wires. *Mater. Sci. Eng./A* **792**: 139671, 2020.

SIZE SCALING OF YIELD STRENGTH IN COPPER THIN LAYERS UNDERGOING SIMPLE SHEAR: A DISCRETE DISLOCATION DYNAMICS ANALYSIS BY THE METHOD OF MONOPOLES

Pilar Ariza*[1] and Michael Ortiz[2]
[1]Escuela Técnica Superior de Ingeniería, Universidad de Sevilla, Sevilla, Spain.
[2]Division of Engineering and Applied Science, California Institute of Technology, Pasadena, USA.

Summary We develop an approximation scheme for three-dimensional dislocation dynamics in which the dislocation line density is concentrated at points, or *monopoles*. Every monopole carries a Burgers vector and an element of line. The monopoles move according to mobility kinetics driven by elastic and applied forces. The divergence constraint, expressing the requirement that the monopoles approximate a boundary, is enforced weakly. The fundamental difference with traditional approximation schemes based on segments is that in the present approach an explicit linear connectivity, or 'sequence', between the monopoles need not be defined. Instead, the monopoles move as an unstructured point set subject to the weak divergence constraint. In this sense, the new paradigm is 'line-free', i. e., it sidesteps the need to track dislocation lines. This attribute offers significant computational advantages in terms of simplicity, robustness and efficiency, as demonstrated by means of selected numerical examples. We specifically assess the ability of discrete dislocation dynamics to reproduce the scaling laws and size effects uncovered by the recent experiments of Mu *et al.* (2014, 2016, 2017) on copper thin layers undergoing plastically constrained simple shear.

SIZE-SCALING OF YIELD STRESS IN SIMPLE SHEAR

There is at present ample experimental evidence that plastic deformation is scale dependent. Generally, as some measure of size related to a plastically deforming material decreases, the strength increases. Since the pioneering work of Hall [4] and Petch [5], a large number of experiments have been reported that reveal a size dependence of the yield stress of the form

$$\sigma_{\rm y} = \sigma_0 \left[1 + \left(\frac{\ell}{h}\right)^{\alpha}\right], \tag{1}$$

where ℓ is a constant constitutive length scale, h is an appropriate measure of the size of the plastically deforming region and α is an scaling exponent. Recently, an experimental protocol has been developed by Mu *et al.* [1, 2, 3] consisting of a thin layer of ductile copper sandwiched between stiff and brittle ceramic coatings (CrN and Si). Simple shear conditions can be induced in the metal by means of micro-pillar compression of the layered ceramic/metal/ceramic with the layers oriented at 45 degrees to the load axis. As the thickness of the copper layer is decreased, the shear stress required for large-scale plastic flow is increased. When fitting the yield stress in shear to a power law function of the inverse layer thickness, Mu *et al.* [1, 2, 3] found exponents α of the order of 0.2 in the as-deposited state. Hutchinson *et al.* have noted [2, 3] that conventional strain-gradient plasticity [6, 7, 8] tends to predict an scaling exponent $\alpha = 1$ and thus is fundamentally at odds with experiment. In a phenomenological vein, Dahlberg and Ortiz [9] have shown that the discrepancy can be removed if the theory is relaxed to allow for fractional plastic-strain gradients, i. e., by recourse to fractional strain-gradient plasticity [11, 10, 12].

THE METHOD OF MONOPOLES IN DISCRETE DISLOCATION DYNAMICS

In this work, we investigate whether the size scaling of yield stress in simple shear arises from discrete dislocation dynamics effects, including boundary pile-ups and other dislocation structures. To that end, we employ an approximation scheme for three-dimensional dislocation dynamics in which the dislocation line density is concentrated at points, or monopoles [13]. Every monopole carries a Burgers vector and an element of line. The monopoles move according to mobility kinetics driven by elastic and applied forces. The divergence constraint, expressing the requirement that the monopoles approximate a boundary, is enforced weakly. The fundamental difference with traditional approximation schemes based on segments is that in the present approach an explicit linear connectivity, or 'sequence', between the monopoles need not be defined. Instead, the monopoles move as an unstructured point set subject to the weak divergence constraint. In this sense, the new paradigm is 'line-free', i.e., it sidesteps the need to track dislocation lines. This attribute offers significant computational advantages in terms of simplicity, robustness and efficiency. Following concepts from optimal transportation theory (cf. [14]), we discretize the dislocation transport problem in time by introducing incremental transport maps. These maps push forward the dislocation density from one configuration to the next. Further adapting concepts from optimal transportation theory [15], we formulate an incremental minimum principle for the transport map, that encodes the energetics and mobility kinetics of the system. In particular, the motion of the monopoles is the result of a competition between energy, which drives the monopoles to low-energy configurations, and mobility, which opposes motion. Finally, the requisite interpolation of the transport maps is effected by means of mesh-free max-ent interpolation. The satisfaction of the requisite null-divergence constraint is ensured by the geometric exactness of the incremental updates. In addition, the monopoles tend to align 'head-to-toe' spontaneously in order to minimize the elastic energy (Figure 1a).

*Corresponding author. E-mail: mpariza@us.es.

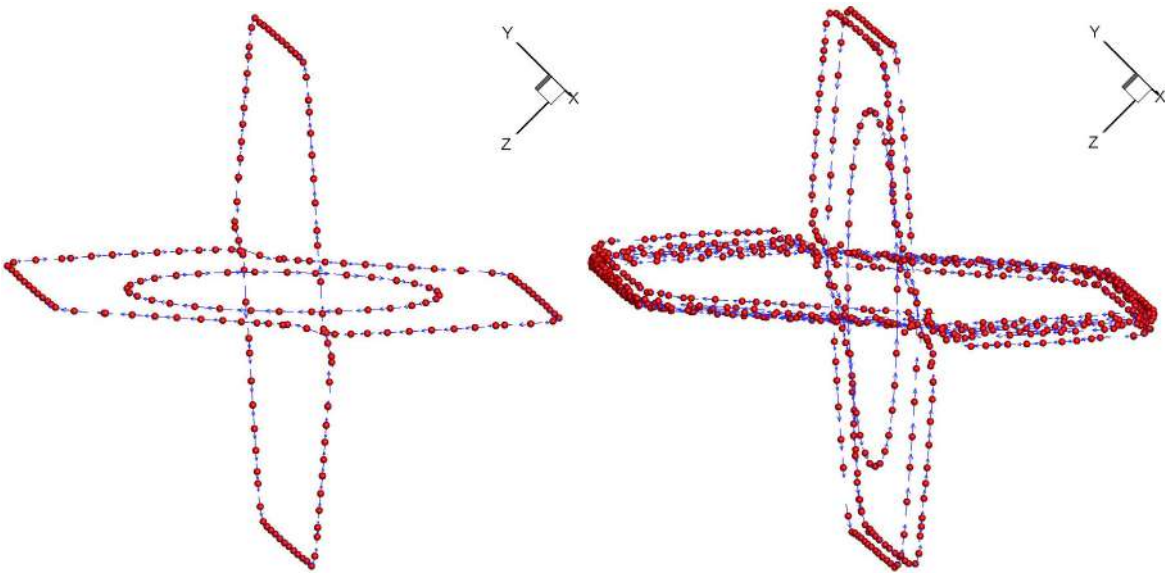

(a) (b)

Figure 1: Snapshots of single loop nucleating from a randomly-located source and expanding under the action of an applied uniaxial stress. BCC grain in elastic matrix.

CONCLUSIONS

Our calculations exhibit the expected size-scaling of the yield stress in simple shear and provide a physical explanation of the experimentally observed scaling relations [1, 2]. The calculations also attest to the remarkable robustness of the method of monopoles [13] and, in particular, to its ability to negotiate complex dislocation dynamics including nucleation, close-range interactions, pileups, intersections and other mechanisms (Figure 1b). Finally, the calculations shed light on possible phenomenological approaches to size-aware plasticity, including fractional strain-gradient plasticity.

References

[1] Y. Mu, K. Chen, and W. J. Meng. Thickness dependence of flow stress of Cu thin films in confined shear plastic flow. *MRS Communications Research Letters*, 4:126–133, 2014.

[2] Y. Mu, X. Zhang, J. W. Hutchinson, and W. J. Meng. Dependence of confined plastic flow of polycrystalline Cu thin films on microstructure. *MRS Communications Research Letters*, 20:1–6, 2016.

[3] Y. Mu, X. Zhang, J. W. Hutchinson, and W. J. Meng. Measuring critical stress for shear failure of interfacial regions in coating/interlayer/substrate systems through a micro-pillar testing protocol. *Journal of Materials Research*, 32(8):1421–1431, 2017.

[4] E. O. Hall. The Deformation and Ageing of Mild Steel: III Discussion of Results. *Proceedings of the Physical Society. Section B*, 64(9):747–753, 1951.

[5] N. J. Petch. The cleavage strength of polycrystals. *The Journal of the Iron and Steel Institute*, 174:25–28, 1953.

[6] E. C. Aifantis. The physics of plastic deformation. *International Journal of Plasticity*, 3:211–247, 1987.

[7] N. A. Fleck and J. W. Hutchinson. Strain Gradient Plasticity. In J W Hutchinson and T Y Wu, editors, *Advances in Applied Mechanics*, 33:295–361, 1997.

[8] W. D. Nix and H. Gao. Indentation size effects in crystalline material: A law for strain gradient plasticity. *Journal of the Mechanics and Physics of Solids*, 46:411–425, 1998.

[9] Dahlberg, C. F. O., Ortiz, M. Fractional strain-gradient plasticity. *European Journal of Mechanics A/Solids* 75:348–354, 2019.

[10] Heyden, S., Conti, S., Ortiz, M. A nonlocal model of fracture by crazing in polymers. *Mechanics of Materials* 90, 131–139, 2015.

[11] Heyden, S., Li, B., Weinberg, K., Conti, S., Ortiz, M. A micromechanical damage and fracture model for polymers based on fractional strain-gradient elasticity. *Journal of the Mechanics and Physics of Solids* 74, 175–195, 2015.

[12] Conti, M., Ortiz, M. Optimal scaling in solids undergoing ductile fracture by crazing. *Arch. Rational Mech. Anal.* 219, 607–636, 2016.

[13] A. Deffo, M.P. Ariza and M. Ortiz, A Line-free Method of Monopoles for 3D Dislocation Dynamics. *Journal of the Mechanics and Physics of Solids* 122: 56589, 2019.

[14] Villani, C. Topics in Optimal Transportation Theory. Volume 58 of Graduate Studies in Mathematics. American Mathematical Society, Providence, Rhode Island, USA 2003.

[15] Jordan, R., Kinderlehrer, D., Otto, F. The variational formulation of the Fokker-Planck equation. *SIAM Journal on Mathematical Analysis* 29:117, 1998.

ELECTRO-ELASTICITYFOR A MICROSTRETCHCONTINUUMMODEL AND ITS APPLICATION TO PLANE WAVES

Maurizio Romeo*
Department of Mathematics Università di Genova, Genova,Italy

Summary A general micromorphic model of a dielectric continuum is developed accounting for microrotation and microstretch of the material particle. The electro-elastic coupling is based on an effective connection of electric multipoles with the microdeformation tensor. The set of balance equations for this model is rewritten in a linearized form and applied to a plane wave problem. A set of dispersion equations for electro-acoustic modes are obtained where microstructural parameters as microinertia, electric susceptibility and electric quadrupole play a relevant role.

MICROMORPHIC ELECTRO-ELASTIC MODEL

The continuum models of electro-elastic coupling require the description of polarization effects connected to mechanical deformation. In classical continuum theories this is usually realized by including the electromagnetic field in the constitutive model, accounting for the Maxwell's equations.
The mechanical micromorphic continuum theory, introduced to model material responses characterized by its microstructure (see [1]), can be extended to electromagneto-elasticity by a constitutive approach similar to the classical one [1], [2]. An alternative analysis of this coupling is based on the connection of mass and charge microdensities so that polarization and magnetization are explicitly obtained from electric multipoles of the microstructure [3], coherently with the derivation of Maxwell's equations from its microscopic formulation [4]. Here we are interested in dielectric solids so that magnetization and conducting properties are not considered. A simple micromorphic model, the so-called "micropolar" theory, accounts for a rotational microdeformation. Its application to dielectric media, allows to describe electro-acoustic modes of wave propagation [5] comparable with polarization modes obtained from phenomenological theories of electroelasticity [6]. If in addition to microrotations we also consider micro-expansions/contractions, we deal with a "microstretch" theory.

In this presentation we consider a microstretch model where the microdeformation tensor is introduced as a polar decomposition into a rotation and a biaxial stretch along and orthogonal to the variable axis of rotation. Electric multipoles, up to the second order, are written in terms of the microdeformation to obtain the electric polarization. A similar representation is given for the microinertia tensor. The governing equations for the mechanical displacement, the electric field (referred to an electric potential) and the microvariables of stretch and rotation, include the balance laws of momentum and couple, together with the Gauss' law for a not conducting material. Then a set of linearized equations are obtained in both cases of compressible or incompressible dielectric materials [7].

APPLICATION TO PLANE WAVES

The successive step of this analysis concerns the study of plane wave solutions to the linearized problem. The dispersion equations within two geometrical configurations for the orientation of the axis of rotation, in presence of an applied electric field, are obtained. Beside classical longitudinal and transverse elastic modes, a set of coupled modes involving electro-microelastic fields are found for the two geometrical configurations. These results show that microstructural parameters such as microinertia, electric susceptibility and quadrupoles, together with the orientational configuration and the applied electric field, modulate the wavenumber range for the existence of modes, the frequency band gaps of some modes and the asymptotic behaviour of phase speed.

References

[1] Eringen, A.C., Microcontinuum Field Theories I - Foundations and Solids, Springer-Verlag, New York (1999).
[2] Lee, J.D., Chen, Y., Eskandarian, A., A micromorphic electromagnetic theory, Int. J. Solids Struct. **41**, 2099-2110 (2004).
[3] Romeo, M., Micromorphic continuum model for electromagnetoelastic solids, Z.A.M.P., **62**, 513-527 (2011).
[4] Romeo, M., A microstructure continuum approach to electromagneto-elastic conductors, Continuum Mech. Thermodyn. **28**, 1807-1820 (2016).
[5] Romeo, M., Electroelastic waves in dielectrics modeled as polarizable continua, Wave Motion **60**, 121-134 (2016).
[6] Pouget, J., Maugin, G.A., Coupled acousto-optic modes in deformable ferroelectrics, J. Acoust. Soc. Am. **68**, 588-601 (1980).
[7] Romeo, M., A Microstretch description of electroelastic solids with application to plane waves, Math. Mech. Solids **24**(7), 2181-2196 (2019).

*Corresponding author. E-mail: maurizio.romeo@unige.it

SIZE-SCALE EFFECTS ON MECHANICAL PROPERTIES OF AN ALUMINUM ALLOY

Vagish D. Mishra[1], Balkrishna C. Rao[2], and H. Murthy [*1]
[1]Dept. of Aerospace Engg., Indian Institute of Technology Madras, Chennai, 600036, India
[2]Engineering Design, Indian Institute of Technology Madras, Chennai, 600036, India

Summary: Aluminum and its alloys are widely used in many sectors to produce lightweight components for aircrafts, ships, satellites, etc. Moreover, such parts are also getting smaller by the day to address environmental issues while ensuring accuracy and working range. Size of some components is smaller than mentioned in the standard for experiments necessary to understand material behavior. Prior researches show size-effect below a critical size. In the present effort, uniaxial tension tests were conducted on Al6061 alloy samples, where size of the samples is ranging from ASTM standard to substandard size. Digital image correlation, a non-contact strain measurement method, was used to measure full-field strains during tests. Tests were conducted for samples of varying gauge lengths and it was found that strengths and ductility decrease with increasing gauge length in contrast to Young's modulus.

INTRODUCTION

Machines are designed and subsequently made-up of large and miniature parts of various materials for some functionality within safe working limits. Accurate mechanical properties of these miniature parts are accordingly required which can be measured by suitable testing procedures and by considering possible size scale-effects. ASTM standard [1] is created for relatively large sized samples and cannot be used for miniature ones thereby necessitating standards for miniature samples. Prior researches [2-4] have reported on the size scale-effects of mechanical properties of miniature samples with accurate measurements of properties being achieved by conducting experiments on nearly same size samples.

Standard and miniature sized dog-bone samples were prepared from Al6061 alloy plates by varying gauge length and cross-sectional dimensions. An appropriate universal testing machine (UTM), Zwick/Roell Z0.5, having a capacity of 500N was used for miniature samples while Zwick/Roell Z100 of capacity 100kN was used for standard sized samples. In the present effort, two-dimensional digital image correlation (2-D DIC) which is suitable for miniature samples [4, 5], was used to determine full-field strains for standard and miniature samples during uniaxial tension tests.

EXPERIMENTAL DETAILS

Standard and miniature samples were prepared where miniature samples are a scaled-down version of standard samples mentioned in ASTM [1]. The cross-sectional dimensions of the standard sized samples and smallest samples were 12.7mm x 7mm and 0.85mm x 0.85mm respectively but the gauge length of samples was kept in multiples of sample width (w) ranging from 6 to 20 times of width. The standard and miniature dog-bone samples for uniaxial tension tests were prepared by cutting by wire *electrical discharge machining* (EDM) with brass coated copper wire (diameter = 0.25 mm) to achieve accurate dimensions and minimal material wastage. Spark erosion marks on sample surface during EDM cutting created a gray colored surface texture, which was used as natural speckles for DIC to avoid any alteration of results of miniature samples [4]. Dog-bone shaped samples were tested at a displacement rate of 0.5 mm/minute at room temperature (25ºC). A pair of *high definition charged coupled device* (HD CCD) cameras i.e., Prosilica GX 1910 (2 Megapixel), were used to capture images by using the image capturing software called Vic-Snap-2010, Correlated Solutions at 20 frames per second and post-processing software, Vic-2D-2009 by Correlated Solutions, was used to determine full-field strains for tested samples. Samples were examined before conducting uniaxial tension tests and five samples of all dimensions were tested and the average value with standard deviation is reported in the present report**.**

RESULTS

ASTM standard-sized samples of cross-sectional dimensions 12.7mm x 7mm, 6.34mm x 6.34mm with gauge lengths of 4w (where w = sample gauge width) were tested and results are as follows: Young's modulus (E) = 68.8 ± 0.7 GPa, yield strength = 293 ± 3 MPa, ultimate tensile strength (UTS) = 321 ± 2 MPa, and ductility = 15 ± 0.7%. All miniature samples of square and rectangle cross-section with gauge length varying from 6w to 20w were tested and results were compared. Uniaxial tension test results of rectangular cross-section dimension (1mm x 0.4mm, 0.81mm x 0.44mm) and square cross-section (0.85mm x 0.85mm) samples are reported in Fig. 1. The mechanical properties (Young's modulus (E), yield strength, UTS, and ductility) for the miniature samples having rectangular and square cross-section are reduced when compared to standard-sized samples. Young's modulus of 1mm x 0.4mm sample with gauge length 20w was decreased by ~ 5% when compared to the one with gauge length of 6w, which can be seen in Fig. 1(a). Yield strength, ultimate tensile strength (UTS), and ductility for 1mm x 0.4mm sample were increased by

[*]Corresponding author. E-mail: mhsn@ae.iitm.ac.in

~10%, 11%, and 115% respectively by decreasing the gauge length from 20w to 6w which can be seen in Fig. 1(b, c, & d). Other miniature samples of the cross-section of 0.81mm x 0.44 and 0.85mm x 0.85mm show the same variation of mechanical properties as 1mm x 0.4mm, see Fig. 1.

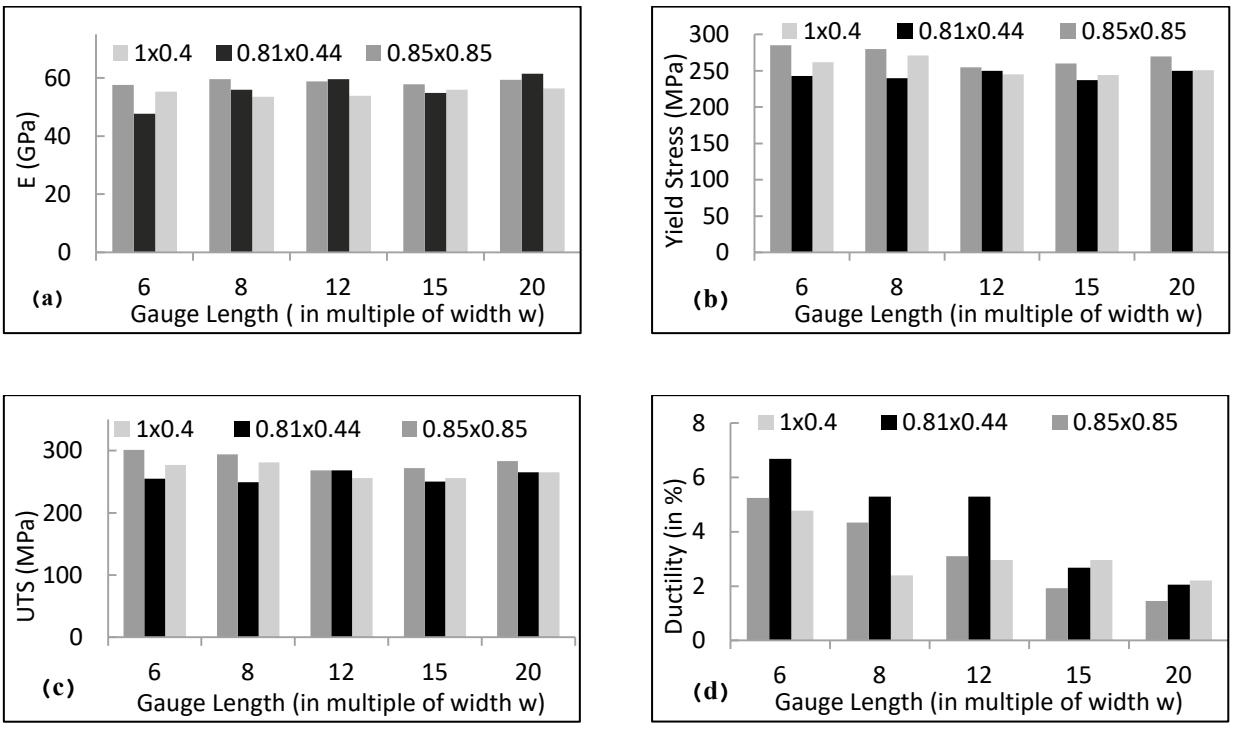

Figure 1: Variation of (a) Young's modulus (E, in GPa), (b) Yield strength (in MPa), (c) Ultimate tensile strength (UTS, in MPa), and (d) Ductility (in %), with gauge length for rectangle and square cross-sectional samples. E decreased with decrease in gauge length but other mechanical properties increased with decrease in gauge length for all the tested samples. (All dimensions are in mm)

CONCLUSIONS

Comparison of uniaxial tension test results for standard sized and miniature samples show reduced values of mechanical properties i.e. Young's modulus (E), yield strength, ultimate tensile strength, and ductility for miniature samples, which indicate presence of size-scale effects. Results of uniaxial tension tests of miniature samples with varying gauge length show a decreasing length resulting in increasing yield strength, ultimate tensile strength, and ductility for both rectangular and square cross-sections except for the Young's modulus. Further studies are required to find reason and relationship between sample geometry and mechanical properties for miniature samples.

References

[1] *ASTM B577*. "Standard Test Methods for Tension Testing Wrought and Cast Aluminum and Magnesium-Alloy Products".

[2] Ghangrekar, P. S., R. Banjare, Balkrishna C. Rao, and H. Murthy: "Tensile testing of Al6061-T6 microspecimens with ultrafine grained structure derived from machining-based SPD process". *J. Mater Res* 29(11) (2014): 1278-1287.

[3] A. V. Sergueeva, J. Zhou, B. E. Meacham, D. J. Branagan: "Gage length and sample size effect on measured properties during tensile testing". *Materials Science and Engineering* A526 (2009), 79–83.

[4] S. Venkatachalam, R. Banjare, H. Murthy, B. C. Rao: "Mechanical Testing of Micro-specimens of Al6061-T6 Using DIC for Strain Measurement". *Experimental Techniques* 43 (2019), 125–135.

[5] F. H. Akbary, M. J. Santofimia and J. Sietsma: "Elastic Strain Measurement of Miniature Tensile Specimens". *Experimental Mechanics* 54 (2014), 165–173.

ATOMISTIC SIMULATIONS OF PRECIPITATE/TWIN INTERACTIONS IN MG-AL-ZN ALLOYS

Anxin Ma*[1], Esteban Manzanares, Gustavo[1], and Javier Llorca[1]
[1]IMDEA materials institute, Tecnogetafe, Calle Eric Kandel, 2, 28906 Getafe, Madrid, Spain

Summary: Precipitate strengthening on twin migration is critical for controlling the mechanical properties and formability of Mg alloys, while our knowledge about this mechanism is not enough. In order to understand the twin-precipitate interaction, it is urgently needed to use molecular dynamics simulations with well validated Mg-Al-Zn potential to study the details of twin propagation and growth, when β-$Mg_{17}Al_{12}$ precipitate or Laves phase $MgZn_2$ precipitate exists inside a Mg matrix. This presentation reports the current MD simulations of the twin-precipitate interaction. At first, based on the Dickel-2019 MEAM potential for Mg-Al-Zn alloys, a strategy was developed to insert precipitates, e.g. lozenge-shaped $Mg_{17}Al_{12}$ precipitate with Burgers orientation relationship, or rode-shaped $MgZn_2$ precipitate with elliptical-cross-section obeying $(11\text{-}20)_{MgZn2}$ // $(0001)_{Mg}$ and $(1\text{-}100)_{MgZn2}$ // $(1\text{-}100)_{Mg}$, into a Mg matrix containing a (1-102) flat twin. The current approach ensures that the matrix/precipitate interfaces are close to the minimum energy configurations. In the next step, the influences of precipitate crystal lattice structure, precipitate geometry and orientation relation as well as temperature on the motion of (1-102) twin are investigated. It was found that the twin motion is mainly controlled by the formation of 2-atom-layer-steps, or twin dislocations. Depends on the temperatures and microstructures, the precipitate-matrix interface may retard or stimulate twin dislocation formation, see Figure 1. For both of Mg-Al and Mg-Zn alloys, precipitate produces pronounced hardening on twin migration at high temperature (>400K). Additionally, the Lavas phase precipitate, $MgZn_2$, produces better hardening than $Mg_{17}Al_{12}$ in the wide temperature region.

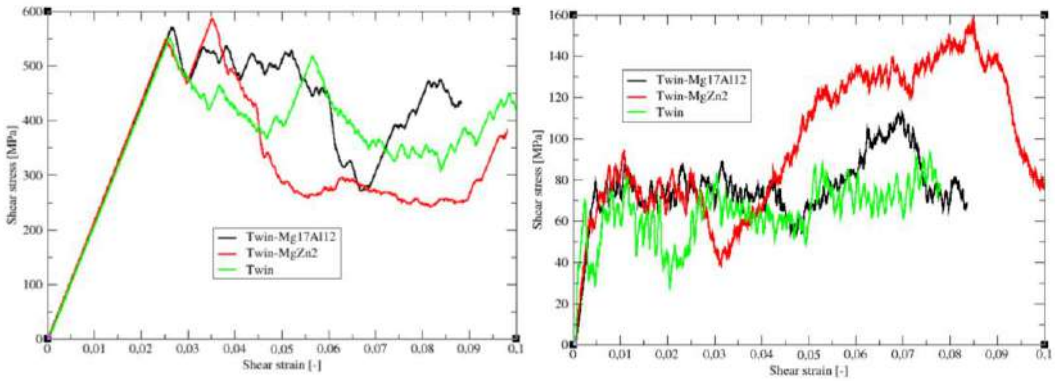

Figure 1. Stress strain curves as a (1,0,-1,2) twin passing a precipitate at 100K, left, and at 400K, right. The stress strain curve of a pure twin was also shown for comparison.

References

[1] Dickel D.E., Baskes M.I., Aslam I., and Barrett C.D. *Modelling and Simulation in Materials Science and Engineering*. **26(4)**: 45010, 2018.
[2] Manzanares G. E., Ma A., Papadimitriou I., Martínez E., LLorca J. *Modelling and Simulation in Materials Science and Engineering*. **27(7)**: 075003, 2019.

*Corresponding author. E-mail: anxin.ma@imdea.org.

SIZE-DEPENDENT FRACTURE TOUGHNESS AND ITS EFFACT ON DAMAGE OF COATINGS

Lihong Liang*[1], H Long[2], and Y Wei [2]
[1]Department College of Mechanical and Electrical Engineering, Beijing University of Chemical Technology, Beijing, China
[2]College of Engineering, Peking University, Beijing 100871, China

Summary Size effect of mechanical properties of nanomaterials attract great attention, especially toughness and strength affect mechanical behaviour of materials. Fracture toughness on the damage of coatings bonded on substrates is studied based on finite element methods by applying a four-point bending loading and introducing cohesive elements in the coatings. The simulation results show that the damage, defined by crack length evolution, is slower for the coatings with larger toughness. Furthermore, size effect of fracture toughness of nanocrystalline coatings is estimated theoretically, and the fracture toughness of nanocrytalline coatings was found to decrease compared with those of conventional coatings. Combining the theory with the simulation results, it can be deduced that the damage of nanocrystalline coatings is faster, agreeing with the previous experimental results.

INTRODUCTION

Nanomaterials, including nanoparticles, nanowires, nanofilms, and nanostructured materials, often show different mechanical properties from the corresponding bulk materials. For example, elastic modulus of nanofilms is size-dependent when the thickness of films is thinner than about 20 nm [1], yield strength of nanocrystals obeys the Hall-Petch relation [2], etc. Size effect of fracture toughness has still to be discovered.

Recently, the experimental study on damage rate (reflected by crack evolution) of thin ceramic coatings, bonded on the alloy substrates under three-point tests, found that average damage rate of nanostructured coatings is larger than that of conventional coatings with the microstructure in micron scale [3], i.e., the evolution rate of transverse cracks in nanostructured coatings is faster. According to the theoretical expression of damage rate [4], damage rate is inversely proportional to fracture toughness of the coatings. Combining with the experiments and the theory, it can be predicted that the fracture toughness of nanostructured coatings is different from that of the conventional coating. To understand size effect of fracture toughness and its effect on damage and fracture behaviour, fracture toughness effect on damage of coatings is studied systematically based on finite element method by adjusting toughness parameter, and the corresponding size-dependent fracture toughness is proposed to compare with the experimental results.

FINITE ELEMENT SIMULATION OF COATING CRACKING

Methods

Ceramic coating/alloy substrate models are considered in order to compare with and understand the previous experiments, and the models are assumed to be under the plane strain condition and the 2D FEM analysis is carried out using the commercial software ABAQUS. The model includes two layers: the substrate with thickness h_s of 1.2 mm and the ceramic coating with thickness h_c of 400 μm. The span length is 24 mm. The vertical loading displacement w is applied on the substrate. The ceramic coating is considered as the linear elastic material with Young's modulus E_c and Poisson's ratio v_c [5]. The alloy substrate is assumed to be the elastic-plastic material with Young's modulus E_s, Poisson's ratio v_s and yield strength σ_Y, and its constitutive relation can be referred to Ref. [5]. The four-node plane strain reduced integration elements (CPE4R) are selected to mesh substrates and coatings.

Cohesive elements, based on interface cohesive zone model, are inserted regularly into the coating, the mesh is dense enough between two neighbor cohesive elements. The four-node cohesive elements (COH2D4) are applied. The strength σ^0 and toughness Γ of the cohesive elements refer to actual coating strength and fracture toughness, respectively, the detailed forms of strength and toughness, as functions of the crack displacement δ, and the damage and fracture criterion can be referred to Ref. [5]. Coating strength σ^0_n is 80 MPa here with the subscript n represent normal direction. Fracture toughness Γ_n are about 20 J/m^2, and the toughness of cohesive elements varies in the range while others remain unchanged to consider influence of fracture toughness.

Results

The cracking mode of ceramic coating is showed in Fig. 1(a), the failure mode is naturally coating transverse cracking, agreeing with the experimental results [6] as showed in Fig. 1(b). The fracture toughness effects on damage behavior of coatings are summarized as Table 1. It can be seen that the crack length decreases with increasing coating toughness and cracking occurs later, too, i.e., damage defined by a total crack length is slower for coatings with higher toughness, which is consistent with the theory that damage rate is inversely proportional to the fracture toughness [4]. On the other hand, the displacement at crack initial and total crack length was observed for different coating thicknesses. The results show that crack initiates earlier and crack length is longer for the thicker coatings. At the same time, the crack length of thick coatings increases faster, which implies that the damage of the thick coatings is faster, agreeing with the experimental results [3].

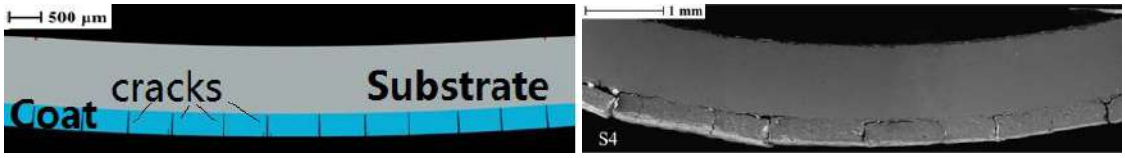

Figure 1. (a) Transverse cracks occur in the coat bonded on the substrate under 4-point bending simulation and (b) similar experimental results [6].

Table 1. Toughness effect on damage (crack length) of coatings.

Γ (J/m^2)	10	20	50
Crack initial displacement (mm)	0.36	0.5	1.27
Crack length at same displacement (mm)	5.89	4.8	1.72

SIZE EFFECT OF INTERFACE FRACTURE ENERGY

Table 1 indicates that the lower fracture toughness corresponds the larger damage rate, as demonstrated in the experiments for nanostructured coatings [3], which implies a size effect of intrinsic fracture energy of coatings. The studies have shown that both cohesive energy and surface energy decrease for nanocrystalline materials compared to corresponding bulk materials [7-8], the fracture energy of materials should also be size-dependent since it equals two times of surface energy [8] when interface energy of the same material is neglected. Therefore, size-dependent fracture toughness can be expressed as $\frac{\Gamma_n(d)}{\Gamma_b} = \exp\left(-\frac{Sl}{3Rd}\right)$ when the grain diameter d of nanocrystalline coatings is much larger than a critical size of the corresponding crystals related to the average bond length l, where $\Gamma_n(d)$ and Γ_b denote size-dependent fracture toughness of nanocrystalline coatings and the corresponding bulk value, respectively. $S = U/T_0$ is the entropy of solid-vapor transition with the cohesive energy U and boiling point T_0 of the corresponding crystals, and R is the ideal gas constant.

For zirconium oxide coatings, Γ_n/Γ_b is about 1/3 based on above expression with the parameter referring to the previous work [8]. According to the experimental results [3], the ratio of average damage coefficient of conventional coatings to that of nanostructured ones is about 0.7, which is roughly in agreement with the above discussion that damage rate is inversely proportional to the fracture toughness.

CONCLUSIONS

In summary, toughness effect of damage coatings was studied based on finite element method by introducing interface cohesive zone model. The results indicate that cracking is later and damage is slow for coating with large fracture toughness, agreeing with the theoretical prediction and experimental results. Size-dependent toughness is calculated and it is effective to characterize fracture behavior of nanocrystalline coatings.

References

[1] Dingreville R., Qu J.M., Cherkaoui M. Surface free energy and its effect on the elastic behaviour of nano-sized particles, wires and films. *J. Mech. Phys. Solid.* **53**: 1827-1854, 2005.
[2] Aifantis K.E., Konstantinidis A.A. Hall-Petch revisited at the nanoscale, *Mater. Sci. Eng. B* **163**: 139-144, 2009.
[3] Liang L.H., Li, X.N., Liu H.Y., Wang Y.B., Wei Y.G. Power-law characteristics of damage and failure of ceramic coating systems under three-point bending. *Surf. Coat. Technol.* **285**: 113–119, 2016.
[4] Liu H.Y., Wei Y.G., Liang L.H., Liu X.H., Wang Y.B., Ma H.S. Damage characterization model of ceramic coating systems based on energy analysis and bending tests. *Ceram. Int.* **44**: 4807–4813, 2018.
[5] Li X.N., Liang L.H., Xie J.J., Chen L., Wei Y.G. Thickness-dependent fracture characteristics of ceramic coatings bonded on the alloy substrates. *Surf. Coat. Technol.* **258**: 1039–1047, 2014.
[6] Liu H.Y., Liang L.H., Wang Y.B., Wei Y.G. Fracture characteristics and damage evolution of coating systems under four-point bending. *Int. J. Appl. Ceram. Technol.* **13**: 1043-1052, 2016.
[7] Jiang Q., Li J.C., Chi B.Q. *Chem. Phys. Lett.* **366**: 551-554, 2002.
[8] Liang L.H., Wei H., Li X.N., Wei Y.G. Size-dependent interface adhesive energy and enhanced interface strength of nanostructured systems. *Surf. Coat. Technol.* **236**: 525-530, 2013.

ATOMISTIC STUDY OF EQUILIBRIUM PRESSURE OF HELIUM BUBBLE IN FCC IRRADIATED COPPER AND ITS ABNORMAL SIZE EFFECT

Lv Chenyangtao, Huang Xinlong, Chu Haijian*
School of Mechanics and Engineering Science, Shanghai University, Shanghai, China

Summary Helium management is of prime concern for materials in future fusion and fast fission reactors. The helium density inside helium bubble and its corresponding internal pressure have a significant influence on the mechanical properties of materials with radiation-induced helium bubble. In this work, the equilibrium pressure, size effect, temperature effect and stress field of FCC copper containing helium bubble are systematically explored by means of molecular simulations in this paper. Based on energy principle and stress criterion, the method to determine the equilibrium internal pressure is proposed and applied. An abnormal effect of the bubble size on the equilibrium pressure is found. In addition, a method to reduce the effect of thermal disturbance or fluctuation on the stress field is proposed by means of the superposition of time-domain average and regional average.

EQUILIBRIUM PRESSURE OF THE HELIUM BUBBLE AND SIZE EFFECT

When the bubble is vacuum or its internal pressure is quite small, radial tensile stress can be generated in the matrix due to the contribution of the surface tension, whereas a radial compressive stress will be generated when the bubble pressure is large enough. Therefore, there must be a critical equilibrium pressure that generates the minimum stress in the matrix. In terms of energy, the system is in the minimum energy state under the effect of equilibrium pressure. Therefore, the equilibrium pressures of He bubbles are analyzed based on the criterion of energy equilibrium and mechanical equilibrium in this work. Configurations of helium bubble with different size and its surrounding atoms under equilibrium internal pressure are shown in Fig. 1(left). The size effect of bubbles on the equilibrium pressure at different temperatures is given in Fig. 1(right).

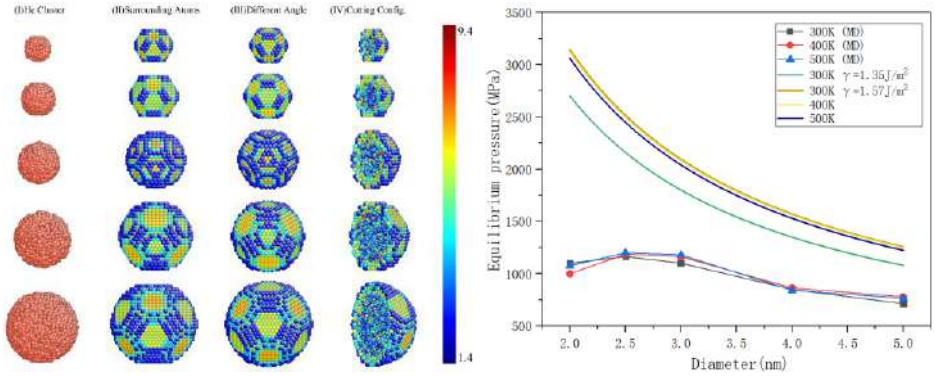

Fig.1 Configurations of helium bubble with different size under balance pressure after relaxation (from the top to bottom, bubble size 2, 2.5, 3, 4, 5nm) (left), and equilibrium internal pressure of the He bubble versus its diameter under different temperatures (right)

STRESS FIELD INTRODUCED BY HE BUBBLE

The atomic Virial stress tensors are processed by the method of time average and region average, Fig 2. shows the stress distribution on {111} plane due to the action of internal pressure of the bubble with respect to different bubble sizes. Stress concentrations at the Cu-He interface region are revealed on both contours of Mises equivalent stress and Shear stress. Fig. 3 shows the radial stress distribution along the $[1\bar{1}0]$ direction in helium bubble model.

* Corresponding author. E-mail: hjchu@shu.edu.cn

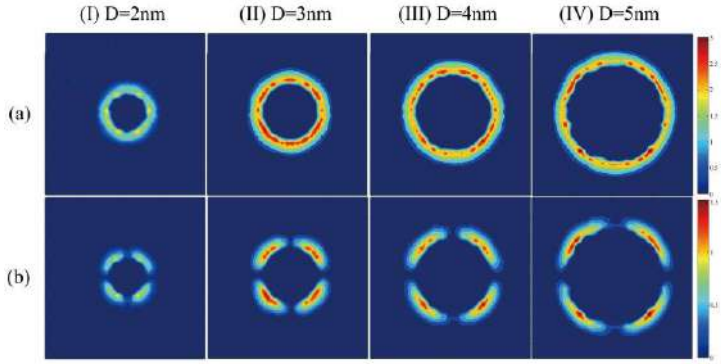

Fig.2 Stress distribution on the plane {111}. (a) Mises equivalent stress σ_M ; (b) Shear stress τ_n

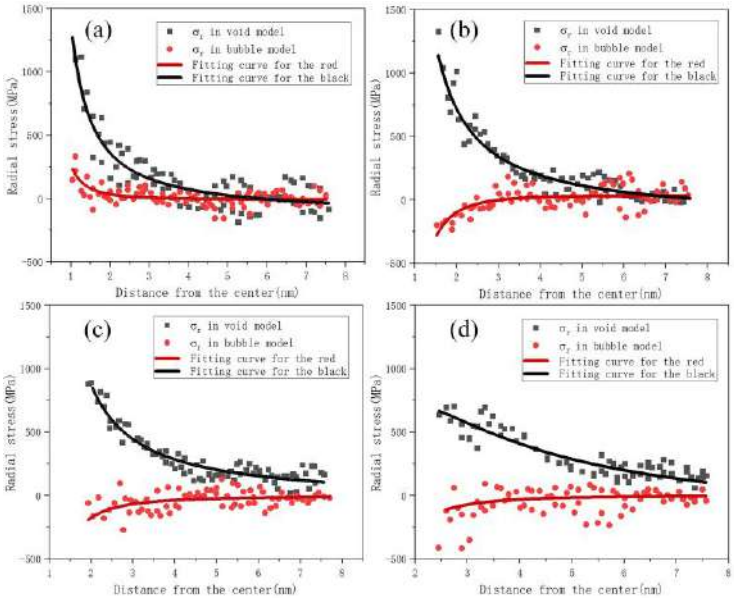

Fig.3 Helium bubble induced radial stress under equilibrium pressure along [$1\bar{1}0$]. (a) 2nm; (b) 3nm; (c) 4nm; (d) 5nm

CONCLUSION AND DISCUSSION

As a summary, the equilibrium pressure of He bubbles in FCC copper and its size effect are studied. The major contributions are included as follows:

1) The equilibrium pressures of the bubble obtained by means of the criterion of the minimum energy principle and stress criterion are self-consistent. Compared with simulation results of molecular simulation, the traditional theoretical formula based on spherical holes to estimate the equilibrium pressure seriously overestimates the results of helium bubbles, and the error increases significantly with the decrease of the size of helium bubbles. For instance, when the aperture is 3nm, the error exceeds 63%.

2) A critical size is firstly found. When the size of He bubble less than the critical one, the abnormal size effect arises, i.e. when the helium bubble diameter is less than 3 nm, the pressure does not increase obviously with the decrease of the aperture, whereas even reduce.

3) Due to the characteristics of the microscopic polyhedron of the hole and the anisotropy of the material, even under the action of the equilibrium pressure of helium bubble, there is still a certain stress in the surrounding copper matrix, which demonstrates a local feature and decreases rapidly as the increase of the distance from the center of the bubble.

The supports of NSFC(11872237) and NSFS(18ZR1414600) are acknowledged.

HIGHER-GRADE ELASTIC BEAMS TO PROBE SCALING EFFECTS IN SOLIDS

Fabien Amiot*[1]
[1]Department of Applied Mechanics,Univ. Bourgogne Franche-Comté,Institut FEMTO-ST,CNRS/UFC/ENSMM/UTBM,Besançon,France

Summary The mechanical behavior of micrometer-sized structures differs from that of usual macroscopic objects. Their surface plays a key role in the overall behavior of the structure. Higher-grade elasticity, and especially second-strain gradient elasticity seems particularly suited to describe the observed size effects, and in particular the strong surface couplings at stake. These frameworks however involve a large number of constitutive parameters whose experimental identification seems today far from attainable. This contribution thus targets the development of robust beam equations for materials featuring higher-grade elasticity, which solve the deficiencies of the available theories, provides solutions involving on a limited number of parameters, and paves the way to the experimental identification of higher-grade elasticity parameters.

INTRODUCTION

Because of their high surface over volume ratio, the mechanical behavior of micrometer-sized structures differs from that of usual macroscopic objects. Two main families of mechanical size effects are observed for solids :

- a material parameter (for instance a stiffness) depends on the specimen size [1] ;
- strong surface couplings are observed. Their surface plays a key role, and this property has been proposed to devise micromechanical sensors of environmental changes [2]. In particular, a significant effort has been put on the development of biological sensors, based on cantilevers operated in static mode (see Fig. 1), and the published results are highlighting the need for a more basic understanding of coupled surface phenomena [3].

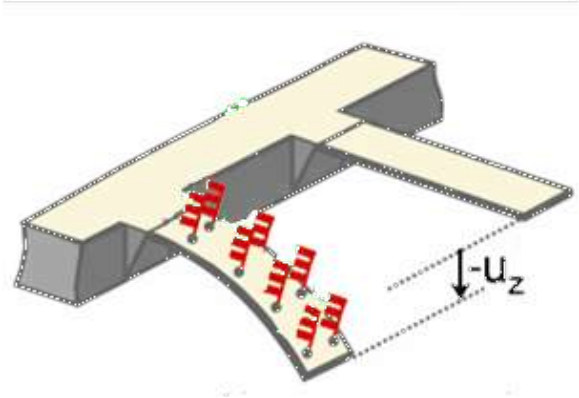

Figure 1: Principle of a cantilever-based sensor : a surface chemical modification induces a mechanical deformation (adapted from [2]).

It has been shown that the use of second strain gradient elasticity may provide a framework describing both these size effects, at the cost of additional modeling parameters which are yet to be identified [4]. Focusing on beams allows to simultaneously encompass most of the reported experimental results and to lower the complexity. The available higher-order beam theories are however only based on kinematic assumptions, so that they cannot render Poisson effect for instance [5]. The correct beam stiffness for vanishing higher-order elasticity parameters is sometimes recovered in a somehow arbitrary way, so that the consistency with the usual Cauchy material-based beam theory is questionable [6]. Refined higher-grade beam theories are therefore desirable, keeping their complexity as low as possible.

HIGHER-GRADE BEAM EQUATIONS

A method is proposed herein to build beam equations for materials featuring higher-grade elasticity. The proposed approach is based on the minimization of the constitutive equation gap in order to simultaneously satisfy kinematic and static conditions, including higher-order static admissibility conditions. It is shown that the resulting beam equations are consistent with the usual ones obtained with Cauchy materials when the dimensions are large enough and are yet tractable. The (few) driving parameters are obtained as closed-form expressions of the parameters of the three-dimensional constitutive law.

*Corresponding author. E-mail: fabien.amiot@femto-st.fr.

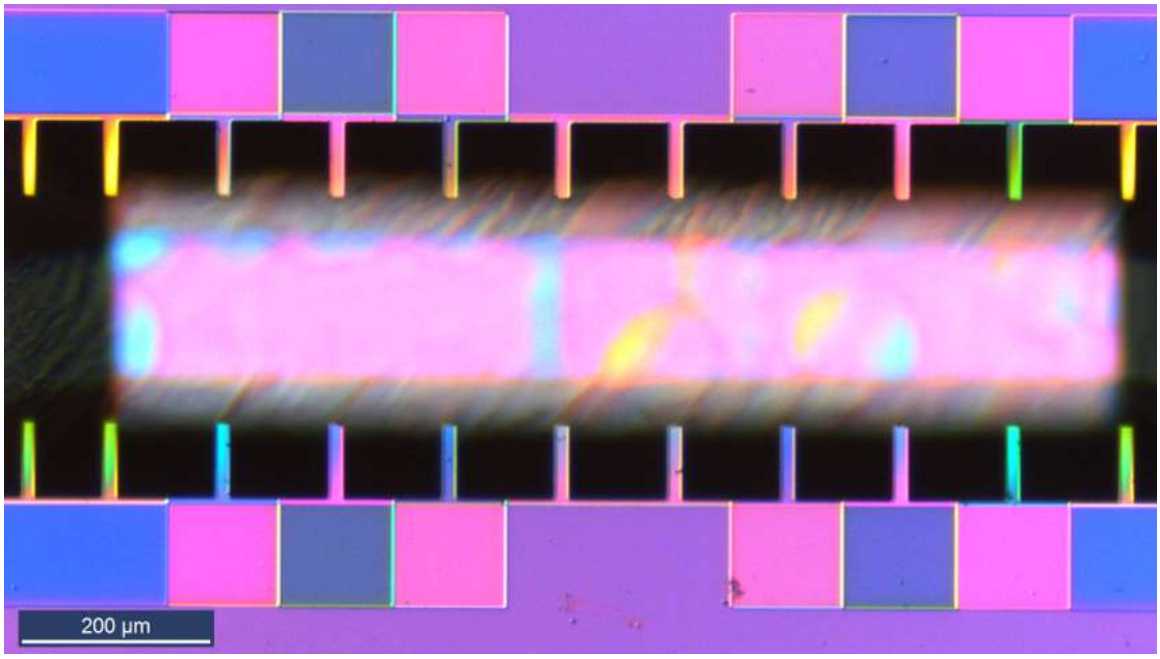

Figure 2: Optical view of a silicon nitride cantilevers array featuring different thicknesses (ranging from 230 to 550 nm).

For second-strain gradient elasticity, the resulting beam equations are found to be non-local : the non-local kernel results from the stationarity condition, and the involved length parameter is again expressed as a simple function of the parameters of the three-dimensional law. The differences with first-strain gradient theories and the usual (kinematic) second-strain gradient approach are highlighted for several representative load cases, so that the scale range such refined theory is required is identified. The obtained solutions can also be compared to those obtained from asymptotic analysis [7] or from a Gurtin-Murdoch like approach [8], and the obtained results are used to define bulk-driven and surface-driven (ecto-elastic) elasticity regimes.

Additionally spanning the range of thermodynamically admissible materials, the role of Mindlin's cohesion modulus is exemplified and it is shown that the predicted behaviors cluster in few, rather different, families, depending on the higher-grade elastic parameters. This could trigger the development of innovative MEMS devices and paves the way for the experimental approach of these higher-grade materials.

EXPERIMENTAL IDENTIFICATION

Based on the above-described framework and making use of arrays of silicon nitride cantilevers featuring different thicknesses (see Fig. 2), indications for the robust experimental identification of the involved higher-grade elastic parameters will be given.

References

[1] Cuenot S., Frétigny C., Demoustier-Champagne S., Nysten B. Surface tension effect on the mechanical properties of nanomaterials measured by atomic force microscopy. *Phys. Rev. B*, **69**: 165410, 2004.

[2] Fritz J., Baller M.K., Lang H.P., Rothuizen H., Vettiger P., Meyer E., Güntherodt H., Gerber C., Gimzewski J.K. Translating biomolecular recognition into nanomechanics. *Science*, **288**: 316-318, 2000.

[3] Boisen A., Dohn S., Keller S.S., Schmid S., Tenje M. Cantilever-like micromechanical sensors. *Reports on Progress in Physics* **74(3)**: 036101, 2011.

[4] Mindlin R.D. Second gradient of strain and surface tension in linear elasticity. *Int. Journal Solids Struct.* **1**: 417-438, 1965.

[5] Dehrouyeh-Semnani A.M., Nikkah-Bahrami M. A discussion on incorporating the Poisson effect in microbeam models based on modified couple stress theory. *Int. J. Engineering Science* **86**: 20-25, 2015.

[6] Amiot F. An Euler-Bernoulli second-strain gradient beam theory for cantilever sensors. *Phil Mag Letters* **93(4)**: 204-212, 2013.

[7] Amiot F. A model for chemically-induced mechanical loading on MEMS. *J. Mechanics of Materials and Structures* **2(9)**: 1787-1803, 2007.

[8] Begley M. R., Utz M. Multiscale modeling of adsorbed molecules on freestanding microfabricated structures. *Journal of Applied Mechanics-Transactions of the ASME* **75(2)**: 021008, 2008.

LOW ORDER NON-STANDARD CONTINUALIZATION OF A BEAM LATTICE. ENHANCED PREDICTION OF DISPERSIVE BEHAVIOUR

F. Gómez-Silva*[1] and R. Zaera[1]
[1]Department of Continuum Mechanics and Structural Analysis, University Carlos III of Madrid, Avda. de la Universidad,30.28911Leganés,Madrid,Spain

Summary In this work, standard and non-standard continualization techniques are applied to a beam lattice, consisting of a chain of masses and linear rotational springs. The study focuses on the reliability of the new continuous equations when capturing the dispersive behaviour of the discrete system, considered as a reference. Besides, their physical consistency is examined, and low order continuous equations are pursued, in order to avoid the need of extra boundary conditions when finite solids problems are solved. The performance of the new equations is evaluated through vibration analyses with the best performance being shown by the new novel models, obtained by means of techniques, applied here for the first time to a discrete system such as the one considered in this work.

INTRODUCTION

The formulation of classical continuum models fails when size effects are present, due to the discreteness of the matter. To eliminate this problem, Molecular Dynamics and Lattice Dynamics approaches appear as an alternative to these models. Although these approaches enable to capture scale effects in a precise way, they imply high computational costs. This is why, since the 19th century, great efforts have been focused on the development of non-classical continuum models, which accurately reproduce the dispersive behaviour of discrete media. The first attempts date back to the 1960s with works by Mindlin or Eringen, among others. These models are considered axiomatic and depend on non-classical parameters, which require experimental results to be calibrated. Therefore, as an alternative, models based on the continualization of discrete systems appear. These systems are made up of cells which repeat periodically. In this way, it is possible to relate the scale parameters of the new non-classical models to the mechanical and geometric characteristics of the system.

In this work, the dynamic behaviour of a linear beam lattice, made up of masses and linear rotational springs, is studied. Different continualization methods are proposed (both standard and non-standard), some of which have been applied here for the first time to this kind of system. The different non-standard continuum models obtained are evaluated by comparing their dispersion relations with those of the discrete one. The new continuous governing equations are intended to be of low order, to avoid the need of extra boundary conditions when applied to bounded solids. The regularization approach proposed by Baigalupo and Gambarotta [1], and applied by them to lattice systems different from the one presented in this paper, is the one showing the best performance. In short, this work presents an in-depth study on the appropriateness of the different non-standard continuity methods to be implemented, and on their ability to reflect the dynamic behaviour of a beam lattice.

DISCRETE MODEL

The discrete beam model (Fig. 1), which is taken as a reference, consists of a chain of length L, made up of N straight segments of length $d = L/N$, regarded as a characteristic length. These segments are joined by linear rotational elastic springs of rigidity C. This model also includes $N + 1$ particles with mass m, connected by the segments. The horizontal position of an arbitrary particle n is described by $x_n = nd, n = 0, ..., N$ and the vertical position is described by its vertical displacement $v_n(t)$, $n = 0, ..., N$.

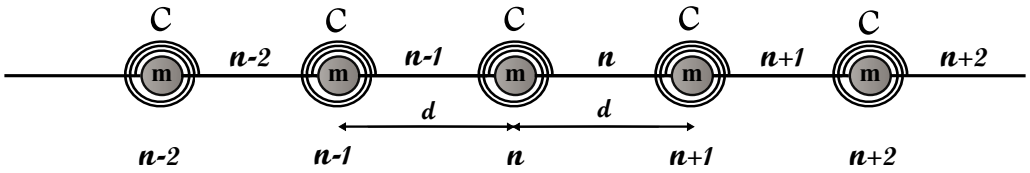

Figure 1: Discrete beam model.

*Corresponding author. E-mail: frgomezs@ing.uc3m.es.

NON-CLASSICAL CONTINUUM MODELS

As mentioned above, standard and non-standard continualization methods are applied to the discrete model in this work. Two standard continualization methods, using Taylor's series, are employed. One of them consists in expanding displacements in the governing equation of the discrete model, while in the other, displacements are expanded in the Lagrangian. Moreover, different non-standard procedures (employing pseudo-differential operators) are presented. The first one applies the pseudo-differential operator in the discrete governing equation, latter using Taylor's series and Padé approximants to expand it, as proposed by Hache et al. in [2]. This method is used also to obtain a new governing equation, including one additional scale parameter. In the second one, the shift operator is also introduced in the discrete governing equation, but in this case, only Padé approximants are used to expand it. Thirdly, a model with Enriched Kinetic Energy (EKE) is proposed, the shift operator applying to the Lagrangian of the system. Finally, the Regularization method is applied to the discrete governing equation. The last four procedures mentioned are applied here for the first time to this kind of system, leading to original governing equations. To summarise the results obtained, the following dimensionless general governing equation is derived

$$\overline{v}_{\overline{xxxx}} - a_1 \overline{v}_{\overline{xxxxxx}} + \overline{v}_{\overline{tt}} - a_2 \overline{v}_{\overline{xxtt}} + a_3 \overline{v}_{\overline{xxxxtt}} = 0, \tag{1}$$

which depends on the scale parameters a_1, a_2 and a_3, shown for each model in Table 1.

Table 1: Values of the parameters for the continuum models.

	Classic	Standard I	Standard II	Taylor-Padé I	Taylor-Padé II	Padé	EKE	Regularization
$\mathbf{a_1}$	0	-1/6	1/2	0	0	0	0	0
$\mathbf{a_2}$	0	0	0	1/6	1/6	1/6	1/12	1/6
$\mathbf{a_3}$	0	0	0	0	1/144	11/720	49/720	7/360

RESULTS AND MAIN CONCLUSION

In order to present some of the results obtained, the dimensionless dispersion curves of all models are shown near their corresponding errors in the Fig. 2. As can be proved, the four novel models show the best performance, the Regularization method having the smallest error. Furthermore, this model has no physical inconsistencies and does not require extra boundary conditions to be solved.

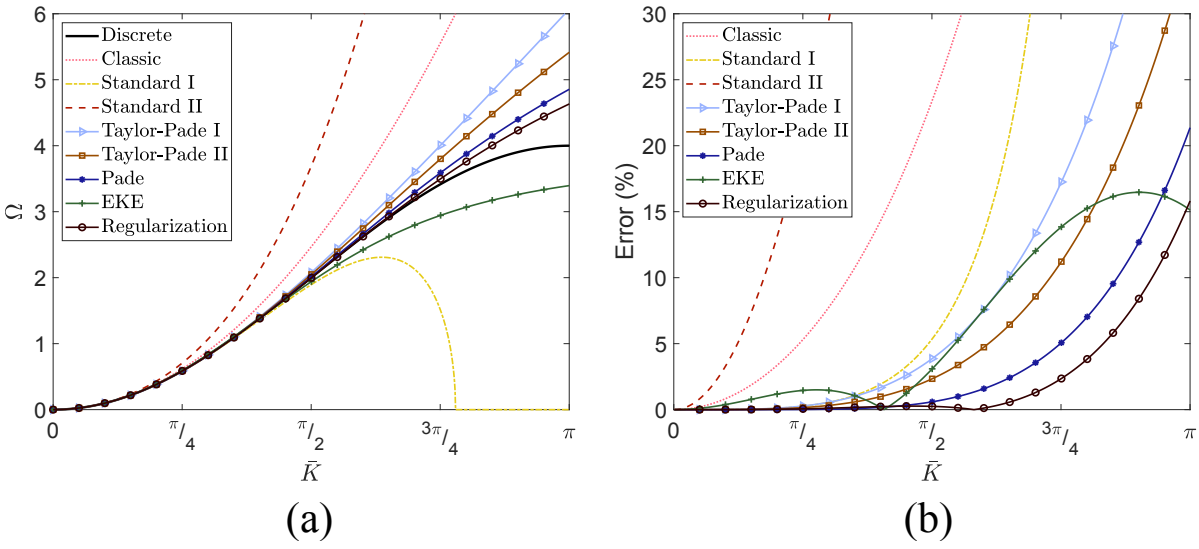

Figure 2: Comparison of the continuum models with the discrete model. (a) Dispersion curves; (b) Errors.

References

[1] Bacigalupo A., Gambarotta L., Generalized micropolar continualization of 1D beam lattices. *International Journal of Mechanical Sciences* **155**: 554-570, 2019.

[2] Hache F., Challamel N., Elishakoff I., Wang C., Comparison of nonlocal continualization schemes for lattice beams and plates.*Archive of Applied Mechanics* **87**: 1105-1138, 2017.

LOAD DEPENDENT STRUCTURE BORNE SOUND EXCITATION IN RAIL VEHICLE DRIVE TRAINS: SIMULATION APPROACH AND EXPERIMENTAL INSIGHT

Johannes Woller, Sascha Noack and Michael Beitelschmidt
Professorship of dynamics and mechanism design, Technische Universität Dresden

Summary The structure-borne noise input from the drive system largely characterizes the perceived interior noise of modern rail vehicles. In the development process, this sound component is still difficult to predict. In the present work, a simulation methodology based on the elastic multi-body simulation in the time-domain is outlined, which is suitable to enable a prediction of the drive-related (gearing excitation) structure-borne noise component in a frequency range up to 1 kHz. For the verification of the developed calculation methodology, vibration measurements on a test rig are evaluated over the operating field of the powertrain. A comparison with measurement data shows, that the model is able to reproduce the load dependency of the modelled drive and calculate comparable vibration levels and resonances.

INTRODUCTION

The acoustic requirements of new railway vehicles are rising steadily. Not only the exterior noise but also the interior sound is an important target for the development process. On this basis a research project, funded by BOMBARDIER TRANSPORTATION, deals with computational models of drive trains for rail vehicles. The objective of the project is the development of a calculation methodology for the source mechanisms and the transmission of structure borne (SB) sound in a driven running gear of a rail vehicle. A new approach for SB sound calculations is the use of elastic multi-body simulation (EMBS) in the acoustic frequency range. In railway industry, EMBS models are commonly used for calculation of the vehicle dynamics, dealing with safety against derailment, track loading calculations and ride comfort. The frequencies of interest are therefore in a range up to 20 Hz. In this publication, the modelling approach for the extension of that frequency range is outlined and first results of an experimental validation are shown. The investigation was carried out using a currently developed regional train built by BOMBARDIER TRANSPORTATION. Similar approaches can be found in literature e.g. for the passenger cars and wind energy systems [1].

EXPERIMENTAL INVESTIGATIONS

Measuring the interior sound in the vehicle, the tooth meshing frequencies of the gearboxes as well as the excitation due to the time-variant electromagnetic field of the traction motor were identified as dominant SB sound sources. In the interior, the traction-based noise components are of great importance, especially during acceleration and braking. The measurements reveal that the highest interior sound levels are dominated by SB noise transmission, especially in the range below 1000 Hz. A second measurement campaign was carried out on a powertrain test rig. Rotational speed and torque of the output shaft were measured. In addition, accelerations on the surfaces of powertrain components were recorded. From the known mechanical performance parameters of the powertrain, 98 representative performance points were selected and measured in stationary runs of 20 sec. Using the measured operating points, an operation map can be created (Figure 1) to determine the vibrational critical points. Detailed results from the experimental investigations at the test rig are published in [2].

MODELLING APPROACH

The powertrain model is built in the commercial software environment SIMPACK using a bottom-up methodology. To extend the validity to the acoustic frequency range, the structural dynamic behaviour of components involved into the transmission of SB noise must be considered. This is done by integrating flexible bodies. In SIMPACK the floating frame of reference (FFRF) method is used for this purpose. In the FFRF the deformation is made up of a large non-linear rigid body motion and a small linearized elastic local deformation. To reduce the high degree of freedom of elastic bodies, which are built by the finite element method (FEM), a Model Order Reduction (Component Mode Synthesis) is performed. Following the recommendation in [3], no constraint equation is used for the assembly of the system. All bodies are free, and the kinematics are handled via binding force elements (e.g. roller bearings, tooth contact etc.). The structure of the EMBS thus corresponds to a dynamically substructured system with an assembly on the right side of the equation of motion. The upper frequency limit for the validity of the model was set to 1000 Hz. All bodies have modal coordinates in a frequency range up to 2000 Hz. The housing of the powertrain, as the main elastic body, was validated by an experimental modal analysis. All shafts are modeled by means of beam elements (Timoshenko approach). For the elastomer bearings a linear stiffness approximation was used. The rolling bearings are modeled via point to point force law (3D including torque) using the ROLLERBEARING algorithm of SIMPACK consisting of nonlinear analytical formula. The gear contact and the related stiffness is calculated using the GEARPAIR 225 algorithm of SIMPACK [4]. This algorithm performs an analytical contact calculation and uses gear stiffness definitions according to DIN 3990. The model can calculate the dynamic tooth contact problem in the time domain even at high rotational speeds. The gear geometries include flank shape corrections. To take dynamic changes in the contact pattern into account, a width (115mm) discretization of the tooth is carried out. The tooth contact calculation takes place at 100 slices across the tooth width.

NONLINEAR SYSTEM BEHAVIOUR

Excitation mechanisms in gears are influenced by the relative position of the gear wheels. Consequently, the deformations of the gear wheels, the shafts, the bearings and the surrounding housing under load are of great importance for the gearing excitation. As the load torque increases, the stiffness of the tooth contacts varies due to changes in the contact pattern and the stiffness of the roller bearings changes. This leads to significant changes in system response across the operating field. Since the investigated drive is used in both directions of travel, two fundamental different excitation behaviors can be seen by changing the direction of rotation (positive and negative acting torque).

COMPARISON OF MEASUREMENT AND SIMULATION

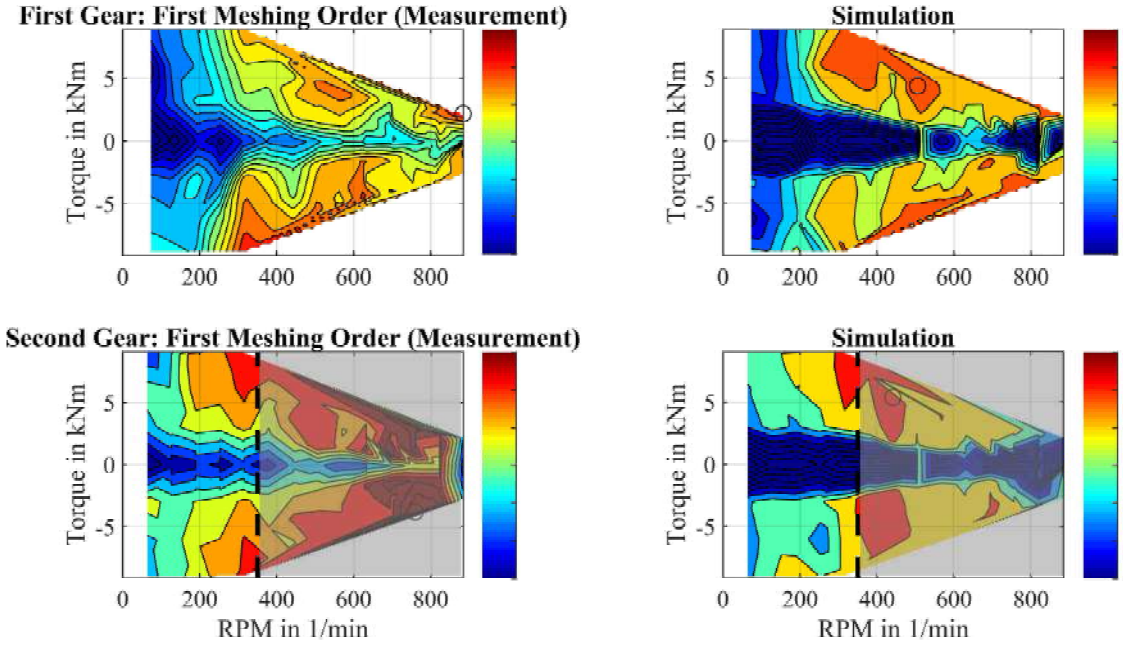

Figure 1: Linear interpolation surface based on the acceleration level (RMS) of the gear-related excitation frequencies at an important measuring point (MP2 in the Z direction) for measurement and simulation. The circle marks the highest level in each diagram. The dashed line indicates the frequency range > 1000 Hz based on the excitation order shown. Areas in gray exceed the model validity.

Figure 1 shows the comparison between measurement and simulation for the stationary acceleration levels at an important connection point of the powertrain. Similar resonance phenomena can be identified in measurement and simulation but not always at the same rotation velocity. The vibration level is comparable in wide speed ranges. The difference between traction and braking operation is clearly recognizable in both measurement and simulation. However, there are significant qualitative and quantitative deviations especially above 1000 Hz (thus outside the intended frequency scope). To calculate this operating field (98 stationary points), a calculation time of approx. 30 h was required on a standard workstation.

CONCLUSION

In this article, a calculation model for structure-borne noise from a rail vehicle powertrain was outlined. A systematic comparison between measurement and calculation is achieved by evaluating the entire operating field. The comparison of the gear-related orders between measurement and calculation reveals a globally qualitative and quantitative agreement at the shown measurement point. Nevertheless, there are significant deviations in detail and for individual operating points. Better agreement can potentially be achieved by eliminating model uncertainties in terms of parameters and a more suitable representation of modeling elements (e.g. bearing model, gear contact model).

References

[1] F. Vanhollebeke, “Dynamic analysis of a wind turbine gearbox”, KU Leuven, 2015.

[2] J. Woller and M. Beitelschmidt, “Structure-borne noise excitation from the drive train of a rail vehicle”, in Proceedings of the 1st International Railway Symposium Aachen, 2017.

[3] H. J. Weidemann, “Schwingungsanalyse in der Antriebstechnik“, Berlin: Springer-Verlag, 2003.

[4] “Simpack Assistent 2019”, Dassault Systèmes Simulia Corp., 2019.

TRANSFER MATRIX METHOD FORMULATION FOR ELASTIC BODY DYNAMICS WITH LARGE MOTION

Qinbo Zhou*[1,2], Jörg Fehr[1], Peter Eberhard[1], and Xiaoting Rui[2]
[1]Institute of Engineering and Computational Mechanics, University of Stuttgart, Stuttgart, Germany
[2]School of Energy and Power Engineering, Nanjing University of Science and Technology, PR China

Summary The transfer matrix method for multibody systems (MSTMM) is a multibody dynamics method developed in the last 25 years. It has been widely used in both science research and engineering and is capable of performing very fast calculations of the dynamics of complex multibody systems. This work extends the theory of MSTMM by formulating the transfer equation of an elastic body of general shape. The favorable ideas from the floating frame of reference method that (i) the overall motion is split into a large rigid body motion and a small elastic deformation, (ii) use of general shape are possible by calculating the standard input data, are transfered into the MSTMM formulation.

INTRODUCTION

The *transfer matrix method for multibody systems* (MSTMM) [1] is used for time-variant multibody dynamics with large nonlinear described overall motion. In the MSTMM, a system is decomposed into elements, including bodies and hinges. Kinematic and kinetic quantities at joint definition points are summarized as *state vectors* that are related by the characteristic of the element in between. This characteristic is described by linear *transfer equations* from one joint definition point to the other, which are called the *input and output points* I and O of the element, see Figure 1. For a specific system, by simple matrix operations, the element transfer equations are assembled into the *overall transfer equation*, which can be solved for given boundary states at the endpoints of the system.

The MSTMM has shown its strength in fast computation without establishing the global dynamics equation of the system and always keeping low order of system matrices independently from the degree of freedom, which makes MSTMM especially interesting in real-time applications or usage in embedded systems. With high-performance and high-precision demands on complex mechanical systems, high flexibility and large scale have emerged as essential trends to be covered by appropriate multibody simulation tools. However, the element transfer equation for elastic bodies has not been developed so far for the MSTMM. This work aims to bridge this gap by showing the framework of developing the transfer equation of a single elastic body described in the *floating frame of reference formulation* (FFRF).

DYNAMICS OF AN ELASTIC BODY

To model flexible bodies with elastic deformation and large rigid body motion, the FFRF is chosen. In this formulation, the motion of a free flexible body is separated into a nonlinear described overall motion of the reference frame K_R, see Figure 1, and a linear elastic deformation with respect to K_R. The small elastic deformations are further discretized using the Ritz approach ${}^R\boldsymbol{u}_P({}^R\boldsymbol{R}_{RP}, t) = \boldsymbol{\Phi}_P({}^R\boldsymbol{R}_{RP})\boldsymbol{q}(t)$ which is often handled by the finite element method. The dynamics equation of a flexible body is represented by a second order differential equation [2]

$$\boldsymbol{M}\dot{\boldsymbol{\eta}} = \boldsymbol{h}_a \quad \text{with} \quad \boldsymbol{\eta} = \left[{}^I\dot{\boldsymbol{r}}_{IR}^{\mathrm{T}} \quad {}^I\boldsymbol{\omega}_{IR}^{\mathrm{T}} \quad \dot{\boldsymbol{q}}^{\mathrm{T}}\right]^{\mathrm{T}}, \tag{1}$$

where $\boldsymbol{M}$ is the time-variant mass matrix, $\boldsymbol{\eta}$ is the generalized velocity and $\boldsymbol{h}_a$ is the generalized force. It is important to mention that the velocity ${}^I\dot{\boldsymbol{r}}_{IR}$ and angular velocity ${}^I\boldsymbol{\omega}_{IR}$ of K_R are herein expressed in the global inertial frame K_I. Consider two adjacent elements by connecting output O of an element j with input I of another element k. Then, in the MSTMM, it will greatly facilitate the transfer of state vectors from O of j to I of k, if these state vectors are projected onto a common coordinate system that is K_I.

One essential step for an efficient simulation is, to reduce the linear, time-invariant part corresponding to the linear FE model embedded in the nonlinear ODE (1). This is achieved by approximating elastic coordinates $\boldsymbol{q} \in \mathbb{R}^{n_q}$ using $\boldsymbol{q} \approx \boldsymbol{V}\bar{\boldsymbol{q}}$ with reduced elastic coordinates $\bar{\boldsymbol{q}} \in \mathbb{R}^{n_{\bar{q}}}$ ($n_{\bar{q}} \ll n_q$) and the projection matrix $\boldsymbol{V} \in \mathbb{R}^{n_q \times n_{\bar{q}}}$. Further, a second projection matrix $\boldsymbol{W} \in \mathbb{R}^{n_q \times n_{\bar{q}}}$ is selected such that $\mathcal{W} = \mathrm{span}(\boldsymbol{W})$ is orthogonal to the residual corresponding to the linear FE model. Finally, using the reduced ansatz space $\mathcal{V} = \mathrm{span}(\boldsymbol{V})$ and $\mathcal{W} = \mathrm{span}(\boldsymbol{W})$, Eq. (1) becomes

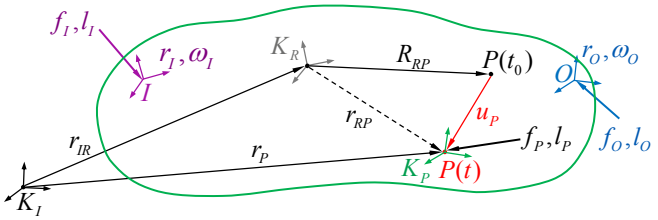

Figure 1: A single flexible body

$$\bar{\boldsymbol{M}}\dot{\bar{\boldsymbol{\eta}}} = \bar{\boldsymbol{h}}_a \quad \text{with} \quad \bar{\boldsymbol{\eta}} = \left[{}^I\dot{\boldsymbol{r}}_{IR}^{\mathrm{T}} \quad {}^I\boldsymbol{\omega}_{IR}^{\mathrm{T}} \quad \dot{\bar{\boldsymbol{q}}}^{\mathrm{T}}\right]^{\mathrm{T}}. \tag{2}$$

One can find the meaning of $\bar{\boldsymbol{M}}$ and $\bar{\boldsymbol{h}}_a$ in [3].

*Corresponding author. E-mail: zqb912_new@163.com

TRANSFER EQUATION OF AN ELASTIC BODY

The classical way of handling an elastic body can be now transferred into the MSTMM concept. In Figure 1, the kinematics on acceleration level for the translation and rotation at I and O can be expressed using $\dot{\hat{\boldsymbol{\eta}}}$ as

$$ {}^{I}\ddot{\boldsymbol{r}}_I = {}^{v}\boldsymbol{L}_{TI}\dot{\hat{\boldsymbol{\eta}}} + \boldsymbol{\zeta}_{TI}, \quad {}^{I}\ddot{\boldsymbol{r}}_O = {}^{v}\boldsymbol{L}_{TO}\dot{\hat{\boldsymbol{\eta}}} + \boldsymbol{\zeta}_{TO}, \quad {}^{I}\dot{\boldsymbol{\omega}}_I = {}^{v}\boldsymbol{L}_{RI}\dot{\hat{\boldsymbol{\eta}}} + \boldsymbol{\zeta}_{RI}, \quad {}^{I}\dot{\boldsymbol{\omega}}_O = {}^{v}\boldsymbol{L}_{RO}\dot{\hat{\boldsymbol{\eta}}} + \boldsymbol{\zeta}_{RO}, \tag{3} $$

respectively, where for point $P \in \{I, O\}$ there is

$$ \begin{aligned} {}^{v}\boldsymbol{L}_{TP} &= \begin{bmatrix} \boldsymbol{I}_3 & -{}^{I}\tilde{\boldsymbol{r}}_{RP} & \boldsymbol{A}^{IR}\boldsymbol{\Phi}_P\boldsymbol{V} \end{bmatrix}, \qquad {}^{v}\boldsymbol{L}_{RP} = \begin{bmatrix} \boldsymbol{O}_{3\times3} & \boldsymbol{I}_3 & \boldsymbol{A}^{IR}\boldsymbol{\Psi}_P\boldsymbol{V} \end{bmatrix}, \\ \boldsymbol{\zeta}_{TP} &= {}^{I}\tilde{\boldsymbol{\omega}}_{IR}{}^{I}\tilde{\boldsymbol{\omega}}_{IR}{}^{I}\boldsymbol{r}_{RP} + 2{}^{I}\tilde{\boldsymbol{\omega}}_{IR}\boldsymbol{A}^{IRR}\dot{\boldsymbol{u}}_P, \quad \boldsymbol{\zeta}_{RP} = {}^{I}\tilde{\boldsymbol{\omega}}_{IR}\boldsymbol{A}^{IRR}\boldsymbol{\omega}_{RP}. \end{aligned} \tag{4} $$

It should be mentioned that $\boldsymbol{\Psi}_P$ in Eq. (4) is the rotational shape function such that the infinitesimal rotation vector at point P is ${}^{R}\boldsymbol{\theta}_P({}^{R}\boldsymbol{R}_{RP}, t) = \boldsymbol{\Psi}_P({}^{R}\boldsymbol{R}_{RP})\boldsymbol{q}(t)$. The reconstruction of $\boldsymbol{\Psi}_P$ from $\boldsymbol{\Phi}_P$ can be found in [4].

To consider reaction forces $\vec{f}_I$, $\vec{f}_O$ and torques $\vec{l}_I$, $\vec{l}_O$ acting on I and O, see Figure 1, they are purposely extracted from the generalized force $\bar{\boldsymbol{h}}_a$ in Eq. (2). This yields the re-written equation of motion

$$ \bar{\boldsymbol{M}}\dot{\hat{\boldsymbol{\eta}}} = \bar{\boldsymbol{h}}_a + {}^{w}\boldsymbol{L}_{TI}^{\mathrm{T}}{}^{I}\boldsymbol{f}_I + {}^{w}\boldsymbol{L}_{TO}^{\mathrm{T}}{}^{I}\boldsymbol{f}_O + {}^{w}\boldsymbol{L}_{RI}^{\mathrm{T}}{}^{I}\boldsymbol{l}_I + {}^{w}\boldsymbol{L}_{RO}^{\mathrm{T}}{}^{I}\boldsymbol{l}_O, \tag{5} $$

where for point $P \in \{I, O\}$ there is ${}^{w}\boldsymbol{L}_{TP} = \begin{bmatrix} \boldsymbol{I}_3 & -{}^{I}\tilde{\boldsymbol{r}}_{RP} & \boldsymbol{A}^{IR}\boldsymbol{\Phi}_P\boldsymbol{W} \end{bmatrix}$ and ${}^{w}\boldsymbol{L}_{RP} = \begin{bmatrix} \boldsymbol{O}_{3\times3} & \boldsymbol{I}_3 & \boldsymbol{A}^{IR}\boldsymbol{\Psi}_P\boldsymbol{W} \end{bmatrix}$.

Then, the transfer equation of an elastic body can be deduced by relating O quantities ${}^{I}\ddot{\boldsymbol{r}}_O$, ${}^{I}\dot{\omega}_O$, ${}^{I}\boldsymbol{l}_O$, ${}^{I}\boldsymbol{f}_O$ (blue in Figure 1) with I quantities ${}^{I}\ddot{\boldsymbol{r}}_I$, ${}^{I}\dot{\omega}_I$, ${}^{I}\boldsymbol{l}_I$, ${}^{I}\boldsymbol{f}_I$ (purple in Figure 1). This can be achieved by eliminating $\dot{\hat{\boldsymbol{\eta}}}$ in Eq. (3) according to Eq. (5) where the generalized velocity $\dot{\hat{\boldsymbol{\eta}}}$ can be explicitly expressed as

$$ \dot{\hat{\boldsymbol{\eta}}} = \bar{\boldsymbol{M}}^{-1}\bar{\boldsymbol{h}}_a + \bar{\boldsymbol{M}}^{-1}{}^{w}\boldsymbol{L}_{TI}^{\mathrm{T}}{}^{I}\boldsymbol{f}_I + \bar{\boldsymbol{M}}^{-1}{}^{w}\boldsymbol{L}_{TO}^{\mathrm{T}}{}^{I}\boldsymbol{f}_O + \bar{\boldsymbol{M}}^{-1}{}^{w}\boldsymbol{L}_{RI}^{\mathrm{T}}{}^{I}\boldsymbol{l}_I + \bar{\boldsymbol{M}}^{-1}{}^{w}\boldsymbol{L}_{RO}^{\mathrm{T}}{}^{I}\boldsymbol{l}_O. \tag{6} $$

Equation (6) is substituted into Eq. (3) so that $\dot{\hat{\boldsymbol{\eta}}}$ vanishes, yielding the following equation in matrix form

$$ \begin{aligned} &\underbrace{\begin{bmatrix} \boldsymbol{I}_3 & \boldsymbol{O}_{3\times3} & {}^{v}\boldsymbol{L}_{TO}\bar{\boldsymbol{M}}^{-1}{}^{w}\boldsymbol{L}_{RO}^{\mathrm{T}} & {}^{v}\boldsymbol{L}_{TO}\bar{\boldsymbol{M}}^{-1}{}^{w}\boldsymbol{L}_{TO}^{\mathrm{T}} & \boldsymbol{0}_{3\times1} \\ \boldsymbol{O}_{3\times3} & \boldsymbol{I}_3 & {}^{v}\boldsymbol{L}_{RO}\bar{\boldsymbol{M}}^{-1}{}^{w}\boldsymbol{L}_{RO}^{\mathrm{T}} & {}^{v}\boldsymbol{L}_{RO}\bar{\boldsymbol{M}}^{-1}{}^{w}\boldsymbol{L}_{TO}^{\mathrm{T}} & \boldsymbol{0}_{3\times1} \\ \boldsymbol{O}_{3\times3} & \boldsymbol{O}_{3\times3} & {}^{v}\boldsymbol{L}_{TI}\bar{\boldsymbol{M}}^{-1}{}^{w}\boldsymbol{L}_{RO}^{\mathrm{T}} & {}^{v}\boldsymbol{L}_{TI}\bar{\boldsymbol{M}}^{-1}{}^{w}\boldsymbol{L}_{TO}^{\mathrm{T}} & \boldsymbol{0}_{3\times1} \\ \boldsymbol{O}_{3\times3} & \boldsymbol{O}_{3\times3} & {}^{v}\boldsymbol{L}_{RI}\bar{\boldsymbol{M}}^{-1}{}^{w}\boldsymbol{L}_{RO}^{\mathrm{T}} & {}^{v}\boldsymbol{L}_{RI}\bar{\boldsymbol{M}}^{-1}{}^{w}\boldsymbol{L}_{TO}^{\mathrm{T}} & \boldsymbol{0}_{3\times1} \\ \boldsymbol{0}_{1\times3} & \boldsymbol{0}_{1\times3} & \boldsymbol{0}_{1\times3} & \boldsymbol{0}_{1\times3} & 1 \end{bmatrix}}_{\boldsymbol{E}_1} \underbrace{\begin{bmatrix} {}^{I}\ddot{\boldsymbol{r}}_O \\ {}^{I}\dot{\boldsymbol{\omega}}_O \\ -{}^{I}\boldsymbol{l}_O \\ -{}^{I}\boldsymbol{f}_O \\ 1 \end{bmatrix}}_{\boldsymbol{z}_O} \\ &= \underbrace{\begin{bmatrix} \boldsymbol{O}_{3\times3} & \boldsymbol{O}_{3\times3} & {}^{v}\boldsymbol{L}_{TO}\bar{\boldsymbol{M}}^{-1}{}^{w}\boldsymbol{L}_{RI}^{\mathrm{T}} & {}^{v}\boldsymbol{L}_{TO}\bar{\boldsymbol{M}}^{-1}{}^{w}\boldsymbol{L}_{TI}^{\mathrm{T}} & {}^{v}\boldsymbol{L}_{TO}\bar{\boldsymbol{M}}^{-1}\bar{\boldsymbol{h}}_a + \boldsymbol{\zeta}_{TO} \\ \boldsymbol{O}_{3\times3} & \boldsymbol{O}_{3\times3} & {}^{v}\boldsymbol{L}_{RO}\bar{\boldsymbol{M}}^{-1}{}^{w}\boldsymbol{L}_{RI}^{\mathrm{T}} & {}^{v}\boldsymbol{L}_{RO}\bar{\boldsymbol{M}}^{-1}{}^{w}\boldsymbol{L}_{TI}^{\mathrm{T}} & {}^{v}\boldsymbol{L}_{RO}\bar{\boldsymbol{M}}^{-1}\bar{\boldsymbol{h}}_a + \boldsymbol{\zeta}_{RO} \\ -\boldsymbol{I}_3 & \boldsymbol{O}_{3\times3} & {}^{v}\boldsymbol{L}_{TI}\bar{\boldsymbol{M}}^{-1}{}^{w}\boldsymbol{L}_{RI}^{\mathrm{T}} & {}^{v}\boldsymbol{L}_{TI}\bar{\boldsymbol{M}}^{-1}{}^{w}\boldsymbol{L}_{TI}^{\mathrm{T}} & {}^{v}\boldsymbol{L}_{TI}\bar{\boldsymbol{M}}^{-1}\bar{\boldsymbol{h}}_a + \boldsymbol{\zeta}_{TI} \\ \boldsymbol{O}_{3\times3} & -\boldsymbol{I}_3 & {}^{v}\boldsymbol{L}_{RI}\bar{\boldsymbol{M}}^{-1}{}^{w}\boldsymbol{L}_{RI}^{\mathrm{T}} & {}^{v}\boldsymbol{L}_{RI}\bar{\boldsymbol{M}}^{-1}{}^{w}\boldsymbol{L}_{TI}^{\mathrm{T}} & {}^{v}\boldsymbol{L}_{RI}\bar{\boldsymbol{M}}^{-1}\bar{\boldsymbol{h}}_a + \boldsymbol{\zeta}_{RI} \\ \boldsymbol{0}_{1\times3} & \boldsymbol{0}_{1\times3} & \boldsymbol{0}_{1\times3} & \boldsymbol{0}_{1\times3} & 1 \end{bmatrix}}_{\boldsymbol{E}_2} \underbrace{\begin{bmatrix} {}^{I}\ddot{\boldsymbol{r}}_I \\ {}^{I}\dot{\boldsymbol{\omega}}_I \\ {}^{I}\boldsymbol{l}_I \\ {}^{I}\boldsymbol{f}_I \\ 1 \end{bmatrix}}_{\boldsymbol{z}_I}, \end{aligned} \tag{7} $$

where O and I quantities are summarized as state vectors $\boldsymbol{z}_O$ and $\boldsymbol{z}_I$ of output and input ends of the elastic body, respectively. The transfer equation of an elastic body is then obtained as

$$ \boldsymbol{z}_O = \boldsymbol{E}_1^{-1}\boldsymbol{E}_2\boldsymbol{z}_I =: \boldsymbol{U}\boldsymbol{z}_I, \tag{8} $$

where $\boldsymbol{U} = \boldsymbol{E}_1^{-1}\boldsymbol{E}_2$ is the transfer matrix. The deduced transfer matrix is also validated by simulation and compared with classical methods in the proposed talk.

CONCLUSIONS

The transfer matrix of an elastic body with a single input and a single output end moving in 3D space is derived. The deduced transfer matrix can be used as a building block plugged into a multibody system composed of other bodies and hinges in the context of the MSTMM. Note that there is no limitation of the meshing during the discretization process, the method is applicable for an elastic body with irregular shape. This is a major improvement compared to the previous investigations on flexible members using the transfer matrix method, which are restricted to strip-like meshing only.

References

[1] Rui X, Bestle D, Zhang J, Zhou Q. A new Version of Transfer Matrix Method for Multibody Systems. *Multibody System Dynamics*, **38**(2): 137-156, 2016.
[2] Schwertassek R, Wallrapp O. Dynamik flexibler Mehrkörpersysteme. Springer Fachmedien Wiesbaden, Wiesbaden 1999.
[3] Fehr J, Grunert D, Holzwarth P, Fröhlich B, Walker N, Eberhard P. Morembs - a Model Order Reduction Package for Elastic Multibody Systems and Beyond. In W. Keiper et al. (Eds.) Reduced-Order Modeling (ROM) for Simulation and Optimization. Springer, Cham 2018.
[4] Lehner M. Modellreduktion in elastischen Mehrkörpersystemen. *Dissertation*, ITM, Universität Stuttgart, Band 10. Shaker, Aachen 2007.

THE DYNAMICS OF A MOBILE ROBOT WITH FOUR MECANUM WHEELS AS A PROBLEM OF NON-HOLONOMIC MECHANICS

Igor Zeidis*[1] and Klaus Zimmermann[1]
[1]Department of Mechanical Engineering, Technische Universität Ilmenau, Thuringia, Germany

Summary For a mobile robot with four Mecanum wheels the kinematical rolling conditions lead to non-holonomic constraints. By solving the constraint equations for a part of generalized velocities by using a pseudoinverse matrix, the mechanical system is transformed to another system that is not equivalent to the original system. For certain special types of motions, e.g., translational motion of the robot or its rotation relative to the center of mass, with appropriate constraints being imposed on the torques applied to the wheels, the solution obtained by means of the pseudoinverse matrix coincides with the exact solution. In these cases, the constraints imposed on the system become holonomic constraints, which justifies using Lagrange's equations of the second kind. Using the methods of non-holonomic mechanics, a broader class of trajectories can be covered.

INTRODUCTION

This paper relates to mechanics of wheeled locomotion. Along with biologically inspired forms of locomotion like crawling, flying or swimming, the wheeled locomotion is still in the focus of research. The demand of mobile platforms working in complex environments or personal robots with high maneuverability for handicapped people has led to the invention of new kinds of wheels, especially in the last fifty years. A key issue of an efficient application of these wheels and an optimal control of the whole mobile system is the understanding of the physical interaction between the wheels and the environment. For this reason, mechanics of wheeled locomotion draws attention of mechanical engineers, see, e.g., [1], [2]. The authors of the cited papers mainly use methods of analytical mechanics to obtain the equations of motion. In many cases, Lagrange's equations of second kind are selected, which is correct, in general, for holonomic systems, see e.g. [3]. In this article, we consider the classical kinematic constraint implying point contact and rolling without slipping. The purpose of the present work is to analyze the method that is widely used in robotics. This method involves the approximate solution of the constraint equations with respect to part of the generalized velocities using a pseudoinverse matrix and subsequent derivation of Lagrange's equations of the second kind. We call this method approximate method. These equations are compared with the equations obtained by using non-holonomic mechanics methods. We will call the non-holonomic mechanics methods exact methods.

FORMULATION OF THE MECHANICAL PROBLEM

The dynamics of a four-wheeled robot with Mecanum wheels arranged on two parallel axles (Fig. 1) are studied. The robot moves so that all its wheels have permanent contact with the underlying plane. The body of the robot has a mass of m_0, its center of mass lies on the longitudinal axis of symmetry of the body. The distance from the center of mass C of the robot to each of its wheel axles is ρ, the distance between the centers of the wheels is $2l$. The coordinates of the center of mass in a fixed coordinate system XOY are x_c, y_c , the angle formed by the longitudinal axis of symmetry of the body with axis OX is ψ, each wheel has a mass of m_1. The angles of rotation of the wheels relative to the axes that are perpendicular to the planes of the respective wheels and pass through their centers are φ_i, and the torques applied to the wheels are M_i $(i = 1, \dots, 4)$.

A Mecanum wheel is a wheel with rollers fixed on its outer rim. The axis of each of the rollers forms the same angle δ $(0^\circ < \delta \leq 90^\circ)$ with the plane of the wheel. As a rule, the angle δ_i $(i = 1, \dots, 4)$ is equal to 45°. Each roller may rotate freely about its axis, while the wheel may roll on the roller. We will model a Mecanum wheel by a thin disk of radius R ; the velocity of the point of contact of the disk with the supporting plane is orthogonal to the axis of the roller. Such a design provides additional kinematic advantages for the Mecanum wheels in comparison with the conventional wheels and leads to non-holonomic constraints. For this reason, a full non-holonomic approach is used to describe the dynamics of a mobile robot with four Mecanum wheels.

Introduce a robot-attached coordinate system $\xi\eta\zeta$ with origin at the center of mass C of the cart. We point axis $C\xi$ along the longitudinal symmetry axis of the cart, axis $C\eta$ along the lateral symmetry axis, and axis $C\zeta$ vertically upward. Denote by $V_{C\xi}$ and $V_{C\eta}$ the projections of the velocity of the center of mass onto the movable axes $C\xi$ and $C\eta$, respectively. From four kinematic constraint equations two are non-holonomic:

$$V_{C\xi} = \frac{R}{2}(\dot\varphi_1 + \dot\varphi_2), \qquad V_{C\eta} = \frac{R}{2}(\dot\varphi_3 - \dot\varphi_1). \tag{1}$$

The other two equations are holonomic and can be integrated

$$\psi = \frac{R}{2(\rho + l)}(\varphi_2 - \varphi_3) + C_1, \qquad \varphi_4 = \varphi_1 + \varphi_2 - \varphi_3 + C_2, \tag{2}$$

where C_1, and C_2 are constants.

*Corresponding author. E-mail: igor.zeidis@tu-ilmenau.de

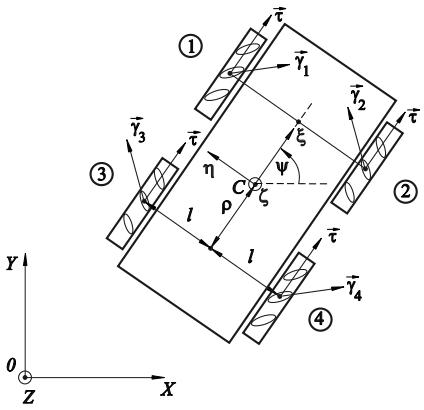

Figure 1: Four wheeled mobile robot with Mecanum wheels.

EQUATIONS OF MOTION OF THE SYSTEM

The system under consideration is called Chaplygin system, it can be described by Chaplygin's equations for non-holonomic systems. The equations of motion for such a mechanical system can be represented as follows [4]:

$$\frac{d}{dt}\left(\frac{\partial T^*}{\partial \dot{\varphi}_s}\right) - \frac{\partial T^*}{\partial \varphi_s} + P_s = Q_s, \quad s = 1, 2, 3. \tag{3}$$

Here, T^* is the function of the kinetic energy of the system from which the velocities $V_{C\xi}$, $V_{C\eta}$ have been eliminated using equations for non-holonomic constrains, Q_s are the generalized forces. The additional (as compared with Lagrange's equations of the second kind) terms P_s are accounted for by non-holonomic constraints and vanish if the constraints are holonomic.

In robotics, researchers often consider kinematic constraints as a system of four linear equations for three unknowns, $V_{C\xi}$, V_{C_η}, and $\dot{\psi}$. This system is overdetermined and does not have a solution for arbitrary values of $\dot{\varphi}_1$, $\dot{\varphi}_2$, $\dot{\varphi}_3$, and $\dot{\varphi}_4$. This system may have a solution only if the equations are linearly dependent. In this case, an approximate solution is obtained by means of the pseudoinverse matrix. The solution found in such a way do not satisfy the system of constraint equations for arbitrary $\dot{\varphi}_1$, $\dot{\varphi}_2$, $\dot{\varphi}_3$, $\dot{\varphi}_4$. However, of all possible triples of quantities $V_{C\xi}$, $V_{C\eta}$, $\dot{\psi}$, this triple provides a minimum for the sum of the squared discrepancies, i.e., the sum of the squared differences of the left-hand and right-hand sides of the equations.

CONCLUSIONS

To describe the dynamics of a robot with four Mecanum wheels one should use the equations of motion that are appropriate for mechanical systems with non-holonomic constraints. Apparently, for Chaplygin systems, Chaplygin's equations should be preferred, since in this case, the dynamic equations form a closed system with respect to the generalized velocities treated as independent variables. In the general case, solving the constraint equations for a part of the generalized velocities by using the pseudoinverse matrix reduces the mechanical system under consideration to a system that is not equivalent to the original system, because the number of degrees of freedom of the reduced system is larger than the number of degrees of freedom of the original system. However, if we confine our consideration to certain special types of motions, e.g., translational motion of the robot or its rotation relative to the center of mass, and impose appropriate constraints on the torques applied to the wheels, the solution obtained by means of the pseudoinverse matrix will coincide with the exact solution. In these cases, the constraints imposed on the system become holonomic constraints, which justifies using Lagrange's equations of the second kind. In the general case, the mathematical methods of non-holonomic mechanics should be used.

References

[1] Muir P. F., Neumann C. P. Kinematic modeling for feedback control of an omnidirectional wheeled mobile robot. Autonomous Robot Vehicles. Springer, NY 1990.

[2] Zimmermann K., Zeidis I., Abdelrahman M. Dynamics of Mechanical Systems with Mecanum Wheels. *Applied Non-Linear Dynamical Systems*: 269–279, 2014.

[3] Hendzel Z., Rykala L. Modelling of dynamics of a wheeled mobile robots with Mecanum wheels with the use of Lagrange equations of the second kind. *Int. J. Appl. Mech. Eng.* **22(1)**: 81-89, 2017.

[4] Zimmermann K., Zeidis I., Behn C. Mechanics of terrestrial locomotion with a focus on nonpedal motion systems. Springer, NY 2009.

INVESTIGATIONS INTO MODEL TUNING OF FLEXIBLE MULTI-BODY SYSTEMS WITHIN THE UDWADIA-KALABA FRAMEWORK

Edward J. H. Yap, D. Rezgui, M.H. Lowenberg, S.A. Neild and K. Rahman
CAME School, University of Bristol, Queens Building, Bristol, BS8 1TR, UK BAE Systems, Rochester, Kent, ME1 2XX, UK

Summary: The study of Multi-Body Dynamic (MBD) modelling approaches is integral to the analysis of mechanical systems that feature joints which govern the range of kinematic motion and display large displacements and geometric non-linearities. Further complexity is introduced if one or more system components is considered deformable due to inherent flexibility. This paper presents an investigation into modelling a flexible crank-slider mechanism within the Udwadia-Kalaba MBD framework by idealising the flexible links using a lumped parameter approach. Through time history simulations, frequency response characteristics are obtained which are compared against those from an alternative flexible mechanism model produced within MATLAB's MBD toolkit Simscape. Tuning studies are conducted to explore the capabilities and limitations of the lumped parameter approach for flexibility within the Udwadia-Kalaba framework whilst also assessing the feasibility of scaling this approach to larger systems of increased complexity.

THE UDWADIA-KALABA MBD MODELLING APPROACH

The Udwadia-Kalaba[1] equations of motion as presented in Eq.(1) are proposed for use in this work as they specifically address the modelling of multibody mechanical systems subjected to kinematical constraints. The formulations reduce the system to a corresponding system of rigid bodies with the system's physical geometrical constraints included as a separate entity.

$$\ddot{\mathbf{x}} = \mathbf{a} + \boldsymbol{M}^{-\frac{1}{2}}\left(\boldsymbol{A}\boldsymbol{M}^{-\frac{1}{2}}\right)^{+}(\boldsymbol{b} - \boldsymbol{A}\mathbf{a}) \tag{1}$$

$\ddot{\mathbf{x}}$ refers to the vector of true accelerations of the multibody system under the influence of geometric constraints. $\mathbf{a}$ refers to the vector of external accelerations due to impressed forces acting on the system. $\boldsymbol{M}$ is the mass matrix of the system and with $\boldsymbol{A}$ and $\boldsymbol{b}$ being matrices both arising from the differentiation of the system's geometric constraints twice with respect to time. The + symbol represents the Moore-Penrose generalized pseudoinverse function[2]. This dynamic modelling approach has also previously been investigated by Nielson et al[3], Li et al[4] and Xu et al[5] who all found convincing agreement of simulated system dynamic results with reference data. In these studies, the application of the Udwadia-Kalaba modelling approach was restrained to rigid-body systems. The scope of this paper is to further explore the application of this modelling approach to consider the inherent flexibility of multibody systems. In a comparison with alternative modelling methodologies, Udwadia and Phohomsiri[6] observed that this modelling approach provided for the first time an explicit set of equations for general constrained systems. The equations of motion obtained may be numerically solved; requiring only the system's mass matrix, acceleration vector due to impressed forces and geometric constraint equations expressed as differential algebraic equations,

In 2019, Yap *et al*[7] provided an application study of the Udwadia-Kalaba modelling approach to a rigid nonlinear planar crank-slider linkage mechanism (Figure 1). The dynamic behaviour of this mechanism under the influence of an externally applied sinusoidal force was assessed with results shown to match responses from alternatively-formulated models produced within MATLAB's MBD toolkit Simscape[8] and a reduced coordinate Lagrangian method. Results from the study validated the system responses produced from the Udwadia-Kalaba modelling approach against the other modelling methods[7] and demonstrated the applicability of the Udwadia-Kalaba approach to dynamically model generic multibody systems subjected to kinematical constraints that may also display nonlinearity. Simscape provides a useful alternative modelling framework as physical system models are created through connections of components that are represented through block diagrams.

THE CRANK-SLIDER MECHANISM

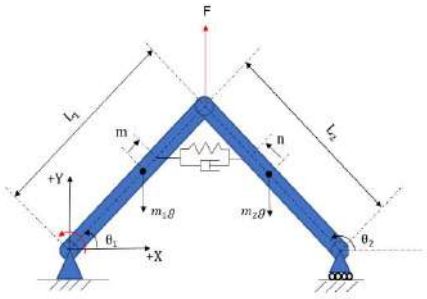

Figure 1: The crank-slider mechanism with rigid links

The crank-slider is a nonlinear planar mechanism consisting of two bars initially assumed to be rigid connected via a revolute joint as seen in Figure 1. One end of bar 1 is attached to the ground through a revolute joint whilst the end of bar 2 is attached to the ground via a translational/ revolute joint which permits horizontal translational displacement. A spring-dashpot connecting bars 1 and 2 provide means of translational resistance and energy dissipation.

The mechanism with both links initially assumed rigid can be described using six geometric positional states x_1, y_1, θ_1, x_2, y_2, θ_2 with subscripts 1 and 2 denoting the bars. x_i, y_i denote bar centre of gravity translations whilst θ_i represents bar rotations relative to the horizontal.

SCOPE OF THE FULL PAPER

The intended scope of this paper is to further develop the work on the crank-slider mechanism by now representing the dynamics of flexibility through the incorporation of linkage compliance. The flexibility is idealised by lumped masses and stiffnesses within the Udwadia-Kalaba framework, which has been shown to be applicable for generic multibody systems subjected to kinematical constraints. Frequency response characteristics are obtained which are compared against those from a a flexible crank-slider mechanism constructed within Simscape. The model tuning studies that ensue will explore the capabilities and limitations of adopting the lumped parameter approach for flexibility within the Udwadia-Kalaba framework whilst also assessing the feasibility to scale this approach to larger systems of increased complexity.

Since the underlying principle of the Udwadia-Kalaba formulation is to reduce the physical system to a corresponding system of rigid bodies, the flexible links are represented by a series of rigid elements connected by a set of springs. The determination of the appropriate mass and stiffness values is done through matching the dynamics of the discretised link to the original one. This approach is illustrated in Figure 2 where within the crank-slider mechanism, bar 1 which is now assumed to be deformable, is represented by a series of rigid elements connected with springs. M_i represents the mass of individual rigid elements and K_{T_i} represents individual spring stiffnesses where i is the number of rigid elements. Due to the planar motion of the mechanism in two-dimensional space, only three positional states x_i, y_i, θ_i, are required to describe the configuration of each rigid element.

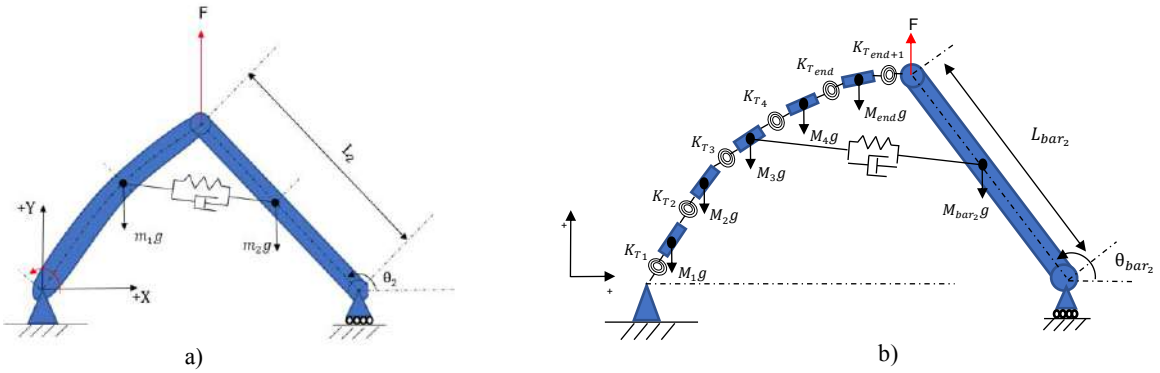

a) b)

Figure 2: The crank-slider mechanism a) bar 1 replaced with a flexible link, b) idealisation of the flexible link as a series of rigid elements connected with springs under the lumped parameter approach.

CONCLUSIONS

The Udwadia-Kalaba modelling approach has previously been demonstrated to be applicable for modelling generic multibody systems subjected to kinematical constraints that also display nonlinear behaviour. An application study of this modelling approach was conducted on a rigid nonlinear crank-slider mechanism and validated. This paper tackles the increasing of complexity through representing the dynamics of deformable links through the incorporation of linkage flexibilities. For this a lumped-parameter approach is adopted within the Udwadia-Kalaba framework. Frequency response characteristics are obtained which are compared against those from a flexible crank-slider mechanism constructed within Simscape. The model tuning studies that ensue will explore the capabilities and limitations of adopting the lumped parameter flexibility approach within the Udwadia-Kalaba framework whilst also assessing the feasibility to scale this approach to larger systems of increased complexity.

ACKNOWLEDGEMENT

The research presented is funded by EPSRC and BAE Systems Plc through an Industrial CASE award (no. 17000065).

References

[1] F.E. Udwadia, R.E. Kalaba, *Analytical Dynamics A New Approach*; Cambridge University Press: Cambridge,1996.
[2] Moore-Penrose pseudoinverse documentation, MathWorks, https://www.mathworks.com/help/matlab/ref/pinv.html, [retrieved 23 December 2019]
[3] M.C. Nielson, O.A. Eidsvik, M. Blanke, I. Schjolberg, *Validation of Multi-Body Modelling Methodology for Reconfigurable Underwater Robots*. Presented in the OCEANS 2016 MTS/IEEE Monterey conference, IEEE, Sept, 2016.
[4] C. Li, H. Zhao, S. Zhen, H. Sun, K. Shao, *Udwadia-Kalaba theory for the control of bulldozer link lever*, Advances in Mechanical Engineering, Vol. 10(6), pp1-15, 2018
[5] Y. Xu, R. Liu, *Dynamic modeling of SCARA robot based on Udwadia-Kalaba theory,* Advances in Mechanical Engineering, Vol. 9(10), pp1-12, 2017
[6] F.E.Udwadia, P.Phohomsiri, *Explicit Poincaré equations of motion for general constrained systems. Part I. Analytical results* 463: pp1421–1434 Proceedings of the Royal Society A: Mathematical, Physical and Engineering Science, 2007
[7] Yap, EJH, Rezgui, D, Lowenberg, MH, Neild, SA & Rahman, K, 'Resonant frequency tuning of a nonlinear helicopter inceptor model: a sensitivity analysis'. in: *Proceedings of the 45th European Rotorcraft Forum*., Warsaw, Poland, pp. 1-14, 2019
[8] Simscape documentation, MathWorks, https://uk.mathworks.com/products/simscape.html, [retrieved 23 December 2019]

SYMMETRY AND RELATIVE EQUILIBRIA OF A BICYCLE SYSTEM

Jiaming Xiong[1], Caishan Liu *[1]
[1]State Key Laboratory for Turbulence and Complex Systems, College of Engineering, Peking University, Beijing, China

Summary In this paper, we study the symmetries of a bicycle moving on a horizontal plane and a revolution surface, respectively. In each case, we obtain the reduced system on the reduced constraint space, i.e., the quotient manifold of the constraint distribution under the action of the symmetry group. We investigate the relative equilibria of the reduced system, which correspond to the bicycle's uniform upright straight motion, uniform circular motion or static equilibrium states. In general, these relative equilibria are not isolated, but rather form a series of one-parameter solution families. Finally, we analyze the Lyapunov stability of the relative equilibria and prove that they cannot be asymptotically stable, but may be stable under certain conditions.

INTRODUCTION

A bicycle is a typical nonholonomic system whose motion needs to be described using more coordinates than the dimensions of its velocity space [1]. Studies on bicycle dynamics started at the end of the 19th century. Since then the stability of the bicycle's upright straight motion and circular motion has been investigated widely [2-5], especially in the case of horizontal ground. However, the existing studies had little to say about the symmetry of the bicycle system, which is the key to reduction of bicycle dynamics. In this paper, we will systematically analyze the symmetries of a bicycle moving on a horizontal plane and a revolution surface, respectively. The connection between these two cases is that the symmetry group in the latter case is a Lie subgroup of that in the former case.

WHIPPLE BICYCLE AND ITS CONFIGURATION SPACE

As shown in Fig. 1, a Whipple bicycle consists of four rigid bodies including a rear wheel, a rear frame, a front frame and a front wheel [2]. The two frames have lateral symmetries in their shape and mass distributions. The two wheels are circular symmetric and make ideal knife-edge rolling contact with the ground. The effects of structural compliance, joint friction and rolling friction are assumed to be negligible.

The configuration space of the Whipple bicycle moving on the ground is a seven-dimensional manifold, $Q = S^1 \times S^1 \times S^1 \times \mathrm{SE}(2) \times S^1$ (strictly speaking, Q is an open submanifold of this manifold), whose components of product represent the lean motion of the rear frame, steer motion, rotation of the rear wheel, rigid body motion of the rear frame in the horizontal plane (including horizontal translation and yaw motion) and rotation of the front wheel, respectively. In addition, the bicycle is subjected to four nonholonomic constraints due to the non-slipping contact between its two wheels and the ground. Thus, at each point $q \in Q$, the set $\mathcal{D}_q$ of all possible velocities satisfying these constraints is a three-dimensional subspace of the tangent space T_qQ. The collection of these $\mathcal{D}_q$ form a constraint distribution on Q, $\mathcal{D} = \bigcup_{q\in Q} \mathcal{D}_q$, which is a ten-dimensional submanifold of the tangent bundle TQ.

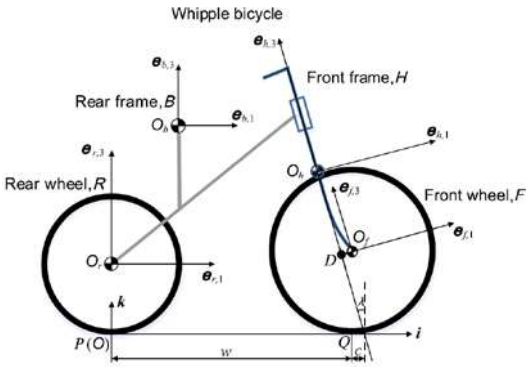

Figure 1. Whipple bicycle (in upright configuration).

BICYCLE SYSTEM ON A HORIZONTAL PLANE

Symmetry of the bicycle system

Denoting by $R = S^1 \times S^1$ the base space, and by $G = S^1 \times \mathrm{SE}(2) \times S^1$ the structure group, we know that the configuration space $Q = R \times G$ is a trivial principal fiber bundle. We introduce the left action of G on Q as follows, $hq = (r, hg), \forall h \in G, \forall q = (r, g) \in Q$. Under this action, the bicycle system has the following two invariances [1]:

(1) The Lagrangian is invariant, i.e., $L(q, \dot{q}) = L(gq, g\dot{q}), \forall (q, \dot{q}) \in TQ, \forall g \in G$.

*Corresponding author. E-mail: liucs@pku.edu.cn

(2) The constraint distribution is invariant, i.e., $g\mathcal{D}_q = \mathcal{D}_{gq}, \forall g \in G, \forall q \in Q$.

Therefore, the dynamic system on $\mathcal{D}$ induces a well-defined reduced system on the quotient manifold $\mathcal{D}/G$, which is called the reduced constraint space [1]. A local representative of this reduced system can be obtained using the Gibbs-Appell equations [4].

Relative equilibria

The equilibrium points of the reduced system on $\mathcal{D}/G$ are called relative equilibria [1]. We prove that these relative equilibria, under a regular condition, are not isolated, but rather form a series of one-parameter solution families. For the bicycle with benchmark parameters [2], we find that there a total of five one-parameter solution families of relative equilibria. Among them, one family corresponds to the uniform upright straight motion of the bicycle, and the other four families correspond to the bicycle's uniform circular motion.

The non-isolation property makes these relative equilibria non-hyperbolic. Thus, their Lyapunov stability cannot be directly determined via the linearized system around them [4]. To deal with this problem, we note that the conserved total energy of the bicycle system, under the Lagrangian and constraint distribution invariances, induces a well-defined reduced constrained energy on $\mathcal{D}/G$. It is a first integral of the reduced system, and equivalently, its level sets are invariant manifolds. Using these invariant manifolds, we prove that if all the eigenvalues of the linearized system, except a zero eigenvalue, have negative real parts, then a relative equilibrium is stable, but is not asymptotically stable. However, the restriction of the reduced system on an invariant manifold, may have an isolated asymptotically stable equilibrium point.

BICYCLE SYSTEM ON A REVOLUTION SURFACE

Symmetry of the bicycle system

When the bicycle moves on a revolution surface, its configuration space and constraint distribution take the same forms as those in the former case. However, a symmetry breaking occurs in this case since the ground no longer has horizontal translation symmetry. The symmetry group is $H = S^1 \times S^1 \times S^1$, where the three components of product represent the rotation of the rear wheel, rotation of the rear frame in the horizontal plane (i.e., yaw motion) and rotation of the front wheel, respectively. Clearly, H is a Lie subgroup of G. The quotient manifold $\mathcal{D}/H$ is a seven-dimensional manifold, and the reduced dynamic system induced on it can be implicitly obtained using the Lagrangian equations of the first type [5].

Relative equilibria

As in the case of horizontal ground, we prove that under a regular condition, the relative equilibria of the bicycle dynamics on the revolution surface also form a series of one-parameter solution families. We numerically investigate several cases where the grounds are specified as paraboloids of revolution. In each case, we find four solution families which correspond to the uniform circular motion of the bicycle, and one solution family corresponding to the bicycle's static equilibrium states. The Lyapunov stability of these relative equilibria can be analyzed in the same way as the case of horizontal ground. Under the condition that all the eigenvalues of the linearized system, except a zero eigenvalue, have negative real parts, a relative equilibrium is stable, but is not asymptotically stable.

CONCLUSIONS

In this paper, we study the symmetries of bicycle systems on the horizontal plane and revolution surface, respectively. Although the symmetry groups are different, the relative equilibria in these two cases have the same properties. Under a regular condition, these relative equilibria are not isolated, but rather form a series of one-parameter solution families. Furthermore, if all the eigenvalues of the linearized system around a relative equilibrium, except a zero eigenvalue, have negative real parts, then this relative equilibrium is Lyapunov stable, but is not asymptotically stable. However, the restriction of the reduced system on an invariant manifold, which is a level set of the reduced constrained energy, may have an isolated asymptotically stable equilibrium point.

References

[1] Bloch A. M. Nonholonomic Mechanics and Control. Springer, New York 2003.

[2] Meijaard J. P., Papadopoulos J. M., Ruina A., et al. Linearized Dynamics Equations for the Balance and Steer of a Bicycle: A Benchmark and Review. *Proc. R. Soc. A Math. Phys. Eng. Sci.* **463**: 1955–1982, 2007.

[3] Basu-Mandal P., Chatterjee A., Papadopoulos J. M. Hands-free Circular Motions of a Benchmark Bicycle. *Proc. R. Soc. A Math. Phys. Eng. Sci.* **463**: 1983–2003, 2007.

[4] Xiong J., Wang N., Liu C. Stability Analysis for the Whipple Bicycle Dynamics. *Multibody Syst. Dyn.* 2019. https://doi.org/10.1007/s11044-019-09707-y

[5] Xiong J., Wang N., Liu C. Bicycle Dynamics and Its Circular Solution on a Revolution Surface. *Acta Mech. Sin.* 2019. https://doi.org/10.1007/s10409-019-00914-6

EVOLUTION OF WHEEL-RAIL KINEMATIC COUPLING DUE TO RCF AND NATURAL & MAINTENANCE-INDUCED WEAR USING VEHICLE DYNAMIC SIMULATIONS

Visakh V Krishna*[1], Saeed Hossein-Nia[1], Carlos Casanueva[1], and Sebastian Stichel[1]
[1]Department of Engineering Mechanics, KTH Royal Institute of Technology, Stockholm, Sweden

Summary The wheel-rail interaction constitutes a complex kinematic coupling that evolves over time due to various factors such as wear, rolling contact fatigue and periodic maintenance activities, that determine the rail service life. The state of the rail surface after a specified traffic and tonnage passing reflects the track-friendliness of the vehicles. This is particularly helpful in guiding track access pricing strategies for different vehicle designs based on the amount of damage they cause to the track. A complex and highly non-linear multi-body simulation environment is set up and iterative vehicle dynamics calculations are performed, along with the implementation of recently developed wheel-rail contact models, damage models and maintenance procedures over a 100 MGT tonnage period.

INTRODUCTION

In a bid to increase the competitiveness of the European rail freight sector, there is a demand for increased rail freight traffic volumes with longer trains and heavier axle loads. Considering that 40% of the track-maintenance costs is accounted to rail surface damage in the form of wear and rolling contact fatigue, the long-term evolution of the rail surface can indicate the track-friendly nature of a given bogie-design. In this paper the authors utilize multi-body simulations to simulate the evolution of the wheel-rail kinematic coupling due to rolling contact fatigue on rails, the resulting maintenance-induced wear and the wear caused by the vehicles themselves.

FRAMEWORK

The overall framework is depicted in Figure 1. The methodology follows the iterative simulation framework described in [1] for wheel life prediction. A matrix of simulation inputs modelled according to the operation on the Swedish iron-ore line has been considered to simulate the rail surface over a tonnage passing corresponding to about 4 years of operation (100 MGT). The simulation module carries out three-dimensional multi-body simulations by generating wheel-rail geometry functions for the given set of profiles to provide the contact forces and creepages on the contact patch. The contact stresses are then calculated using the *Hertz* theory for normal contact and the recently developed *FaStrip* [1] for the tangential contact respectively. These are then implemented in a stress-based wear prediction model to calculate the vehicle-induced wear on the rail surface ($\mathbf{w_{nV}}$).

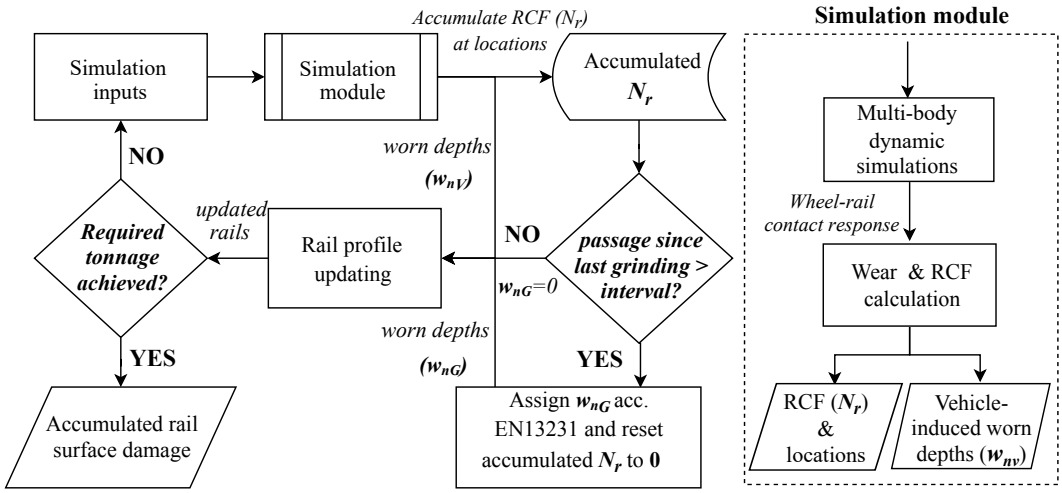

Figure 1: Simulation framework

In addition to wear, cracks arising due to RCF (Rolling Contact Fatigue) is a major driver of rail surface damage and can lead to fracture of the rail cross section if not mitigated on time. Based on the shakedown theory and the Tresca criterion for full slip, the RCF risk is calculated by counting the number of axle passes ($\mathbf{N_r}$) with a risk of exceeding the material yield limit in shear on individual mesh points on the contact patch. Further, to account for the effect of wear on RCF, an energy-dissipation based model that calculates local energy thresholds to scale $\mathbf{N_r}$ is implemented as described in [1].

*Corresponding author. E-mail: visakh@kth.se

Rolling Contact Fatigue and the mitigating maintenance interventions

Several works such as [2] and [3] recommend mitigation measures in the form of cyclic grinding actions removing surface cracks at regular intervals, modelled based on the principle of *gauge corner relief*. This alters the rail profile in such a way that the high RCF-prone gauge regions are relieved from wheel-rail contact, pushing the contact regions towards the centre of the rail. These actions drastically change the wheel-rail kinematic coupling and hence need to be considered while calculating long term evolution of rail profiles. A 15 MGT grinding interval and a moderate gauge corner relief has been considered in the methodology for curved track sections according to [3], corresponding to six maintenance interventions, each introducing an artifical grinding-induced wear ($\mathbf{w_{nG}}$). This depends on the location of cracks on the rail surface at the end of each grinding cycle and therefore for the ith grinding intervention, the grinding depths is calculated to

$$\mathbf{w_{nG_i}} = f\left(\sum_{\mathbf{i-1}}^{\mathbf{i}} \mathbf{N_r(y)}\right) \tag{1}$$

For each passing wearstep (loop), the rail head geometry is updated with the wear depths up to the required tonnage as:

$$\mathbf{W_n} = \sum_{j=0}^{100\ MGT} \mathbf{w_{nV_j}} + \mathbf{w_{nG_j}};\ \mathbf{w_{nG_j}} \neq 0 \in j \bmod 15\ \text{MGT} = 0 \tag{2}$$

For every instance of grinding intervention (i.e. j mod 15 MGT=0), the $\mathbf{N_r}$ concentrations are reset to zero, signifying the removal of cracks entirely on the affected regions.

EVOLUTION OF THE RAIL SURFACE

The evolution of the rail surface for the outer rail on a 600 m radius curve is depicted by Figure 2 for a standard Y25 bogie. Figure 2a depicts the evolving normal depths on the rail surface with the $\mathbf{w_{nV}}$ peaks along each wearstep marked by green squares. These are juxtaposed with the RCF ($\mathbf{N_r}$) concentrations for the tonnage passing in Figure 2b. There is a gradual shift and spread of vehicle-induced wear $\mathbf{w_{nV}}$ while the RCF concentrations become less dense after the first grinding intervention. This changes the wheel-rail kinematic coupling significantly since the contact point slides away from the gauge region with increasing tonnage. Also, this varies with vehicle suspension since it determines the radial steering performance of the wheelsets during curve negotiation.

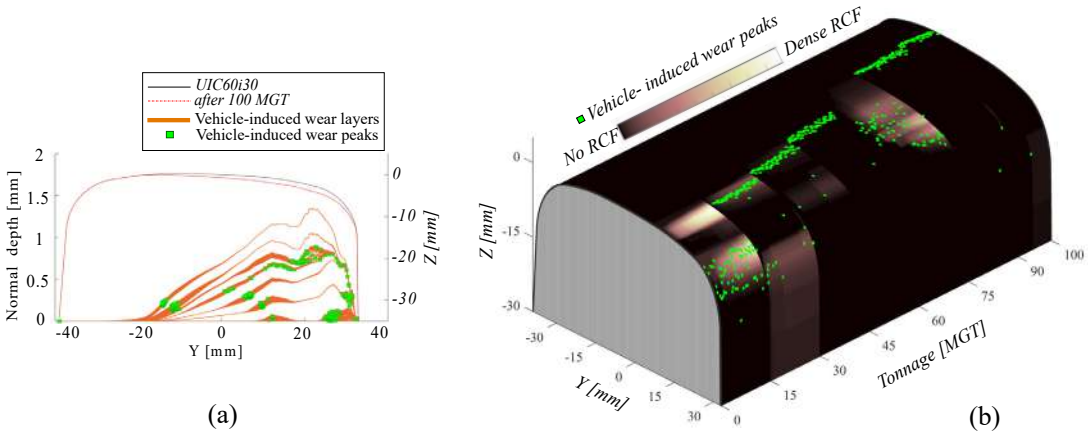

Figure 2: Mapping the evolving wheel-rail kinematic coupling and the associated migration of different damage regions over 100 MGT: (a) Normal wear- $\mathbf{W_n}$ (orange- $\mathbf{w_{nV}}$ and white- $\mathbf{w_{nG}}$) (b) RCF risk- $\mathbf{N_r}$; Radius= 600 m, Outer rail, Bogie: Standard Y25

CONCLUSIONS

The evolution of wheel-rail kinematic coupling over a long period of tonnage due to various damage modes and maintenance interventions has been modelled using an iterative multibody simulation framework and the migration of contacting points and the resulting damage regions is observed. This knowledge can be used to suggest predictive maintenance strategies w.r.t the vehicle dynamics of the train traffic on a given track section.

References

[1] Hossein-Nia S., Sichani S., Stichel S., and Casanueva C., Wheel life prediction model - an alternative to the FASTSIM algorithm for RCF, *Vehicle System Dynamics*, **56:7**: 1051-1071, 2018.
[2] Heyder R. and Brehmer M., Empirical studies of head check propagation on the DB network, *Wear*, **314:1**: 36-43, 2014.
[3] European Committee for Standardization, EN 13231-5:2018 – Procedures for rail reprofiling in plain line, switches, crossings and expansion devices, *European Norms*, 2019.

UPRIGHT PIANO ACTION: EXPERIMENTAL CHARACTERIZATION AND MULTIBODY MODELING

Sébastien Timmermans*[1], François Leroy[1], Anne-Emmanuelle Ceulemans[2], and Paul Fisette[1]
[1]Institute of Mechanics, Materials and Civil Engineering, Université catholique de Louvain, Belgium
[2]Faculté de philosophie, arts et lettres, Université catholique de Louvain, Belgium

Summary In this work, a multibody model of an upright piano action is presented, that has been experimentally validated via high speed camera. The model takes all the bodies into account as well as specific felt force laws and body geometries to deal with intermittent contacts. In addition, experimental tunings of model parameters have been undertaken. Simulations of the model allow, among others, to estimate the maximal playing frequency and a minimal input force on the key to produce a sound. More specifically, the bridle strap and butt spring usefulness are discussed, showing the interest of the multibody modeling approach for studying piano actions.

INTRODUCTION

In pianos, the sound is produced by the impact between the hammer and the strings. A mechanism – called piano action – propels the hammer according to the key motion which is controlled by the pianist. Upright pianos contain an action which differs from that of the grand piano. Both complex, these two actions can be modelled through multibody methods to analyse their behaviour over different impulses and to help understanding their functioning.

The multibody model is based on a demonstrator action, see Fig. 1. The latter has been used for both physical parameters estimation and experimental validation. An equivalent CAD replica of that action has been carried out.

PREVIOUS MODELS

Whereas many publications developed models of the grand piano action, very few focus on the upright piano ones. A first noticeable attempt by Oledzki presents a dynamic model containing only two masses and a nonlinear spring based on experimental observations [1]. After that, several publications of Ramin Masoudi, John McPhee and Stephen Birkett led to the most complete vertical action dynamic model so far. Using the graph theory, they modelled the physical interactions between the five main bodies of the action [2]. Their simulations already allowed to explore the model behaviour under different impulses. Five new features (bridle strap and butt spring, flexibility of some parts, new felt contact model, etc.) were introduced in [3] to enhance the model fidelity and an experimental validation is presented in [4].

In line with the upper modeling works, we propose to build an action multibody model, thanks to the symbolic Robotran multibody software [5], while going deeper in the parameters identification through well-targeted experimentations.

UPRIGHT MULTIBODY MODEL

Based on the action of Fig. 1, the model consists of five mobile bodies, several stops and springs shown in Fig. 2, all moving in a vertical plane. The model considers only rigid bodies, no backlash in the joints and simplified contact geometries: the corresponding bodies shapes are approximated by circular arcs or line segments to find the contact patch location and to compute the reaction forces resulting from felts laws characteristics. Fig. 3 illustrates the case of the hammer-jack contact geometry.

Figure 1: Upright piano action demonstrator and its equivalent CAD replica.

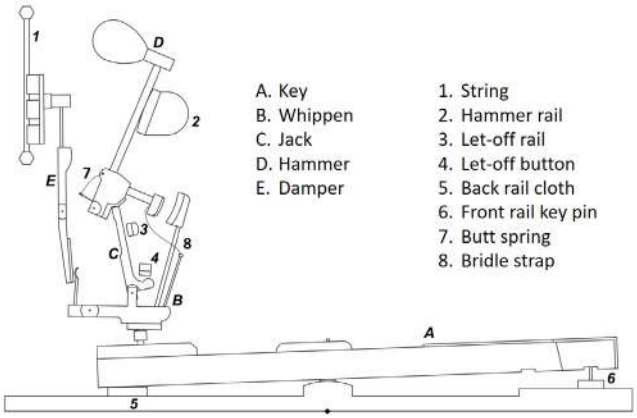

Figure 2: Multibody model main components: mobile bodies (resp. other elements) are indicated by letters (resp. numbers).

*Corresponding author. E-mail: sebastien.timmermans@uclouvain.be.

Parameters experimental characterization

Experimentations conducted on subparts of the model have allowed us to identify forces laws coefficients. For example, the friction of the hammer rotating joint has been characterized by identification between simulations and experiments, depicted in Fig. 4, using high speed camera tracking at 2000 fps. Whereas, with a 1-kg mass as input, the model reacts similarly as the demonstrator for the pre-impact phase [0;0.1] s, the imposed key motion causes the hammer to hit the string a bit too early, around 0.1 s in Fig. 5, but in a quite satisfactory manner, given the modeling parameters uncertainties.

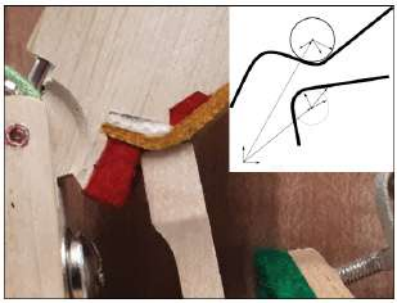

Figure 3: Modeling of the hammer-jack contact geometry.

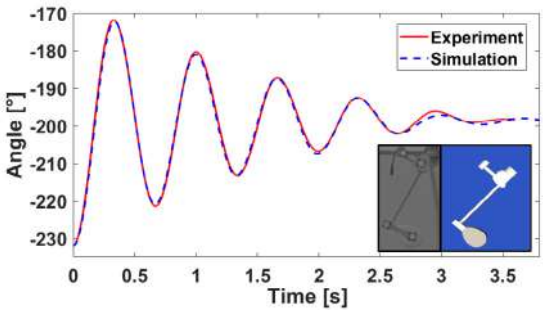

Figure 4: Hammer rotation time history: Sim. vs Exp.

Model advanced simulations

Exploration of the model response to an increasing frequency of key force inputs shows that the hammer is unable to hit the string from around 11 Hz. Therefore, 10 Hz can be considered as the maximal playability frequency of the model. Actuate experimentally the action with an external actuator provides a value between 11 and 12 Hz. The minimal force so that the hammer reaches the string and produce a sound is around 1.2 N, which correspond approximately to the experimentally measured values between 1.12 and 1.21 N. More importantly, the importance of the bridle strap and butt spring – see Fig. 2 – is illustrated in Fig. 6: they both help the hammer to travel back faster to its rest position so that key strokes can be repeated faster. This result is original since it refers to specific elements whose role is not clearly explained, even by piano tuners.

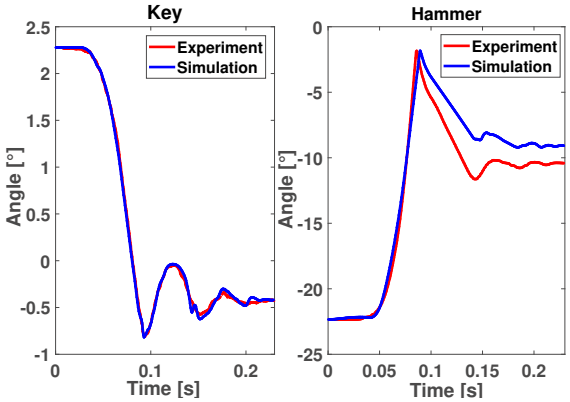

Figure 5: 1-kg input simulation.

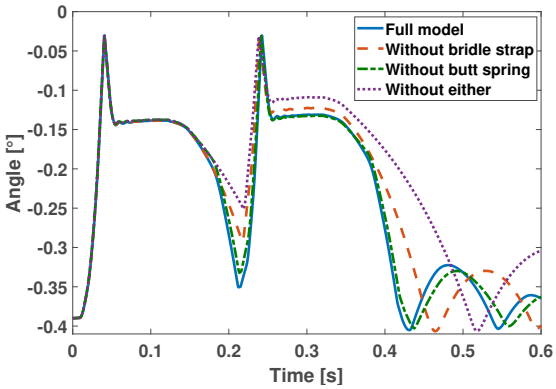

Figure 6: Hammer angular position for a double blow.

CONCLUSIONS

A multibody model of an upright piano has been carried out and has shown reasonable agreement with experimentations. Additional simulations have helped us to quantify and analyse the action performances, in particular for the bridle strap and butt spring whose role is important in fast dynamics. Improvement of the parameters identification would enhance the model fidelity for the next future, having in mind that it could be used in real-time to enhance the haptic feedback touch of numerical pianos, as we are currently developing for a grand piano action [6].

References

[1] Oledzki A. Dynamics of piano mechanisms. *Mechanism and Machine Theory.* **7**: 373385, 1972.
[2] Masoudi R., Birkett S., McPhee J. Dynamic Model of a Vertical Piano Action Mechanism. *Proceedings of the ASME IDETC/CIE, DETC2009-87680, San Diego, CA*: 389-398, 2009.
[3] Masoudi R., Birkett S., McPhee J. A Mechanistic Multibody Model For Simulating the Dynamics of a Vertical Piano Action. *ASME J. Comput. Nonlinear Dyn* **9**(3): 10 pp, 2014.
[4] Masoudi R., Birkett S. Experimental Validation of a Mechanistic Multibody Model of a Vertical Piano Action. *J. Comput. Nonlinear Dyn* **10**(6): 2015.
[5] Samin J.-C., Fisette P. Symbolic Modeling of Multibody Systems. Springer, Dordrecht, Netherlands, 2003.
[6] Timmermans S., Ceulemans A.-E., Dehez B., Fisette P. Real-Time Validation of a Haptic Piano Key based on a Multibody Model. *ECCOMAS Thematic Conference on Multibody Dynamics*, Duisburg, Germany, 2019.

HYBRID THIN SHELL TRIANGLE ELEMENT FOR MULTI-FLEXIBLE-BODY DYNAMICS

Alessandro Tasora, Dario Mangoni, Simone Benatti, Dario Fusai
Department of Engineering and Architecture, University of Parma, Italy

Summary In this work we discuss an efficient finite element for thin shells to be used in multi-flexible-body simulations involving large displacements and material nonlinearities. The formulation is based on the BST element, from whom it inherits the idea of rotation-less nodes and the computation of curvature from the state of the neighbouring triangles; additionally, in sake of performance, we added the possibility of de-activating the tangent stiffness matrix for the bending components in case of extreme flexural compliance, thus leading to hybrid implicit-explicit integration schemes. The element has been implemented in our open-source ProjectChrono multi physics simulation library.

INTRODUCTION

Triangular shell finite elements have been studied extensively in literature because, if compared to their quadrilateral counterparts, they provide an immediate way to mesh complex CAD surfaces with arbitrary topology. In particular, among the various formulations, the DKT-CST shell element [1] proved to be efficient and reliable, although at the cost of introducing rotational degrees of freedom at each node. The BST element presented in [2] circumvents this complication by using only translational degrees at each node, hence leading to a very straightforward and robust implementation – although limited to Kirchhoff-Love thin shells. Further research showed that the BST element can handle complex kinked shells with large displacements, such as those studied in inflatable structures, crash tests, etc. [3]. Because of these attractive features we developed a triangle shell on the basis of the BST element and we added it to our ProjectChrono multibody library [4]. In this context the thin-shell assumption was not a major issue because the library already contains alternative finite elements for Mindlin–Reissner thick shells; on the other hand, the thin shell triangle proved to be very efficient for problems involving objects such as foldable tissues, sails, etc., where shear effects are negligible. In order to improve the computational efficiency with implicit integrators, we investigated the possibility of discarding the terms that, in the tangent stiffness matrix, account for the bending stiffness; this leads to hybrid implicit/explicit time stepping schemes where the bending forces are handled like in explicit integrators, and the membrane effects are dealt by the implicit part: since bending forces are way less stiff then membrane counterparts, this results in methods that are almost as stable as the original implicit methods, but with less overhead in solving the linear systems requested at each iteration. We performed benchmarks with both geometric and material non-linearity, showing the efficiency of the discussed implementation.

IMPLEMENTATION

The BST finite element uses six nodes, as shown in Fig.1, and each node has only three degrees of freedom, as node rotation is not needed. Curvature $\boldsymbol{\kappa}$ is computed from the tilting of the neighbouring triangles, subtracted initial bending if any, and strain $\boldsymbol{\varepsilon}$ is assumed constant through the triangle as in CST elements.

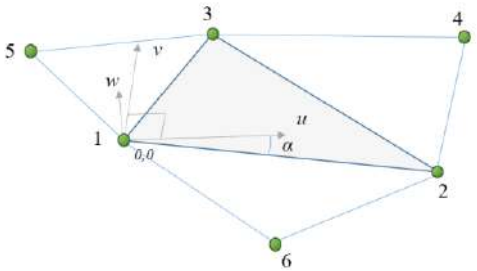

Figure 1. The six-node triangle shell element. Material coordinates can be rotated respect to the 2-1 direction via the α angle, for instance when using orthotropic layered materials. Nodes 4,5,6 are optional, if the triangle is on a boundary.

From the knowledge of $\boldsymbol{\kappa}$ and $\boldsymbol{\varepsilon}$, generalized stresses $\{\boldsymbol{m},\boldsymbol{n}\}$ are computed using through-the-thickness quadrature, thus supporting multi-layered materials via the Classical Laminate Theory. We exploited object oriented paradigms such as polymorphism and inheritance in order to provide an expandable material system; in this way one can reuse predefined constitutive equations for isotropic/orthotropic/generic elasticity at each layer, or one can provide its own custom material model using C++ programming, incurring in zero performance penalty.

After Gauss quadrature, internal forces and tangent stiffness matrices can be easily computed and inserted in the global system. Our multibody software supports systems made with arbitrary number of motors, constraints, parts, finite elements, even with frictional contact, as described in [5,6], resulting in a system of Differential Algebraic Equations (DAE) or a Differential Variational Inequality (DVI). The dynamical simulation is performed using an implicit integrator,

specifically an HHT method or, for faster and less precise tests, an implicit Euler with clamped iteration number. The latter also provide support for DVI non-smooth dynamics.

As in most implicit integrators, most CPU time is spent in solving a large system matrix that has the sparsity pattern of a KKT saddle-point matrix when constraints, contacts or motors are added. Aiming at higher performance, we provide the option of neglecting the bending components of the tangent stiffness matrices, resulting in a system matrix with higher sparsity and faster solution. This is possible only if the bending forces are not stiff compared to membrane forces, and this happens for example when simulating tissues and clothes.

NUMERICAL TESTS

For benchmarks where the shear effect is not relevant, the BST finite element provided comparable results with the two other shell elements implemented in our library (namely an ANCF shell quadrilateral element and a geometrically-exact quadrilateral element), but at a fraction of the computational overhead. It is fair to add that the quadrilateral elements are both capable of capturing Mindlin-Reissner thick shell effects, whereas the BST shell uses the Kirchhoff-Love hypothesis. Nevertheless, the thin shell assumption fits well with many engineering problems involving, for example, tissues or comparable materials, such as in the case of the simulation of sails, airbags, paper processing equipment, etc.

In Fig.2 we show a benchmark where a 1m x 1m sheet is dropped on a square support. Under the effect of the gravity, the sheet deforms and creates wrinkles. In Fig.1, left, Young modulus is $E=6\cdot10^4$, Poisson ratio is $\mu=0$, and thickness is 0.06m. In Fig.1, right, the thickness is 0.01m. In the latter case, given the fact that bending forces are not stiff from the integration point of view, we experienced that removing the bending components of the stiffness matrices decreased the computational effort for solving the linear system almost by a factor of two.

For solving the linear system in the HHT iterations we tested both the direct-parallel MKL Pardiso solver, and a GMRES Krylov solver with warm-starting and AVX vectorization.

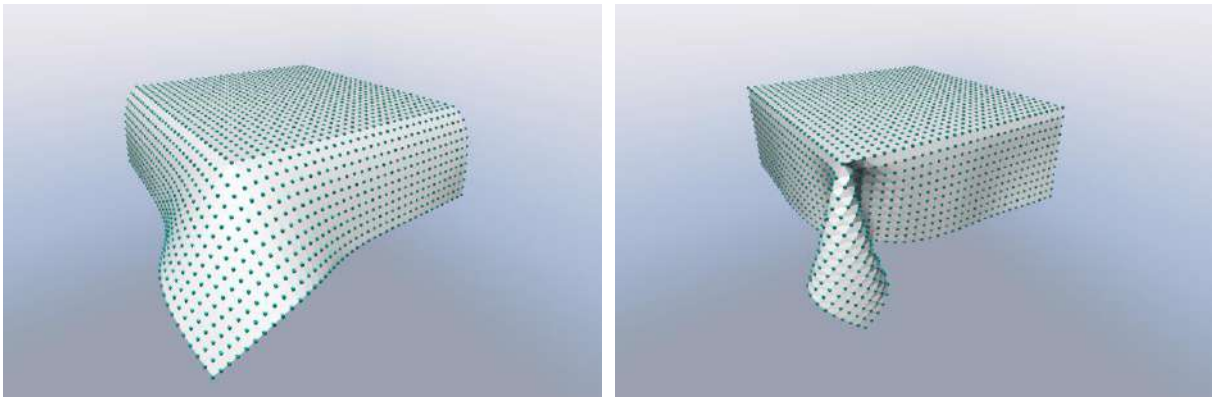

Figure 2. Left: a case where the bending component of tangent stiffness matrix is relevant, hence a conventional implicit integration is used. Right: for small bending stiffness, the tangent stiffness matrix can be simplified, for a hybrid implicit (membrane) / explicit (plate) integration scheme.

CONCLUSIONS

A rotation-free, triangular finite element for thin shells has been implemented within the ProjectChrono open source multibody library. Custom optimizations have been studied in order to increase the computational efficiency, in detail this element supports hybrid implicit/explicit integration in sake of coarser stiffness matrices. Object-oriented programming has been used in order to provide a modular and expandable material model; the predefined materials classes provide support for isotropic/orthotropic/generic elasticity, plasticity, structural damping, all reusable in a laminated multi-layer setting; further material models can be implemented by class inheritance and polymorphism.

References

[1] Belytschko T, Stolarski H, Carpenter N. A C^0 triangular plate element with one point quadrature. *Int. J. Numer. Meth. Engng.*1984; **20**:787–802.
[2] Oñate, E., Zarate, F. Rotation-free triangular plate and shell elements. *Int. J. Numer. Meth. Engng.* **47**, 557–603, 2000.
[3] Flores, F.G., Oñate, E. A rotation-free shell triangle for the analysis of kinked and branching shells. *Int. J. Numer. Meth. Engng.* **69**:1521–1551, 2007.
[4] ProjectChrono, web site **http://www.projectchrono.org**.
[5] Negrut, D., Serban, R., Tasora, A. Posing Multibody Dynamics with Friction and Contact as a Differential Complementarity Problem. *J. Comput. Nonlinear Dynam.* **13**(1): 014503, 2018.
[6] Tasora, A., Anitescu, M. A matrix-free cone complementarity approach for solving large-scale, nonsmooth, rigid body dynamics. *Comput. Method. Appl. M.* **200**(5–8), 439-453, 2011.

BIOMECHANICS AND MECHATRONICS FOR THE DESIGN OF INTEGRAL VEHICLE SAFETY SYSTEMS

Jörg Fehr*[1], Fabian Kempter[1], Jan Riethmüller[1], and Werner Schiehlen[1]
[1]Institute of Engineering and Computational Mechanics, University of Stuttgart, Germany

Summary The risks of injury or fatality in traffic accidents have declined significantly in recent years. Increasing emphasis for achieving further improvements in vehicle safety will be placed on integral safety systems. Integral safety involves a concerted strategy of interlinking sensors and actuators of active and passive safety. After a review on vehicle safety systems the Driver-in-the-Loop (DiL) Simulator at the University of Stuttgart, Germany, will be presented. This DiL is used to validate active human body models. In a test series with 17 test persons and three different warning signs, each of the occupants' behavior is further analysed, i.e. looking at the muscle stiffness to show the possibilities of further reduction of severe casualties.

INTRODUCTION

Today's cars feature different active and passive safety components to protect the occupants and other road users. If one combines advanced driver assistance systems (ADAS) with passive safety, we speak about integral safety concepts. In integral safety concepts, the countermeasures for accident damage minimization can react before the actual crash, i.e. through occupant alarming, repositioning to more beneficial postures, airbag firing and belts tightening. In contrast to classical crash scenarios, the investigation of such integral safety concepts requires new simulation methods. Prior to the crash the accelerations are much lower, enabling the occupants to change their posture by muscle contraction. At those smaller loads, dummies (ATD) and passive human body models (HBM) no longer adequately represent human occupants, as muscle activity must be included in the surrogate models. Furthermore, only with virtual tests, the full range of possible impact scenarios can be tested without any risk for human lives.

Therefore, the active human body models (AHBM) are now essential engineering tools to provide further biomechanical knowledge about the effects of human behavior on injury risks and others in wide range of possible scenarios. Two types of muscle activated human body models are available: (i) costly nonlinear finite element models for injury mechanics research down to the tissue level, see e.g. [1], and (ii) multibody models well suited for rather long simulations of pre-crash maneuvers to predict the overall motions of the human in such situations. For the development of AHBM, validation and calibration processes of the simulation models with advanced mechatronic testing devices are uttermost important [2]. Different types of validation setups differing in complexity, data acquisition, transferability to real driving scenarios, adjustability, reproducibility and safety issues are reported in the literature. In this work, a DiL approach is used to study the influence of warning signals on the driver's action to prepare himself for the virtual impact by muscle stiffening, see [3]. Therefore, a user study based on the ethical requirements was conducted with our DiL Simulator.

DiL SIMULATOR

Advantages of Driver-in-the-Loop simulators are: (i) the safe and replicable environment, (ii) kinematic feedback in all six degrees of freedom reducing the risk of motion sickness, (iii) in addition to classical sled tests, multi-directional trajectories can be performed, (iv) the visual feedback of a virtual driving environment, e.g. by using head-mounted displays, (v) the excellent accessibility for measurements and, (vi) the fast application and testing of early alert systems. The DiL simulator is depicted in Figure 1 and explained in [4]. The system consists of a 6-DOF motion platform, a force-feedback wheel and a bass-shaker at the back of the driving seat. The work-flow is based on a Matlab-Simulink-model, provided by Prescan, with multibody vehicle models, visualization of the designed scenario and logical operations to ensure reproducible crash scenarios.

To analyze the driver's behavior in the simulator during Pre-Crash situations, motions as well as muscle activation can be monitored. The subjects are tracked by a motion capture system from Optitrack using computer stereo vision with reflexive infrared markers. Furthermore, a force sensor mounted at the steering wheel allows measuring the support of the driver applied on the steering wheel [5]. This force can be considered as an indication of the amount and timing of pre-stressing in an emergency braking situation.

Two separate PCs are used to coordinate the real-time simulation, control of the motion platform and the acquisition of measured data. The workflow of the mechatronic system is depicted in Figure 2. The simulation PC is in charge of running the simulation and providing visual feedback to the driver at the same time. A 10 degree of freedom vehicle dynamics model [6] is used to simulate in real-time the behavior of the vehicle. The measurement PC controls the motion of the platform with the software package SimCorDX. For a more realistic driving experience motion cueing algorithms-[7] are applied. This PC also ensures the synchronized data acquisition of the kinematic measurement via the Optitrack system, the signals from the force sensor recorded with a digital oscilloscope and signals of the virtual simulation, i.e. steering motion. Synchronization of the measurement is done using TCP/IP communication and a small Arduino system.

The motion of the head and the arms are tracked with 200 Hz, furthermore the driving wheel angle and braking pedal state is saved. It is important, that all measurement systems, e.g. motions, EMG signals and support force on the driving wheel, are synchronized, automatically labeled and semiautonomous evaluated. A kinematic resimulation of the experimental results can be used to compare different motions of test persons without violating the General Data Protection Regulation.

*Corresponding author. E-mail: joerg.fehr@itm.uni-stuttgart.de.

Figure 1. Setup of the presented Driver-in-the-Loop (DiL) simulator with a Porsche racing simulator, a Stewart motion platform and an Optitrack motion capture system consisting of four cameras attached to the ceiling.

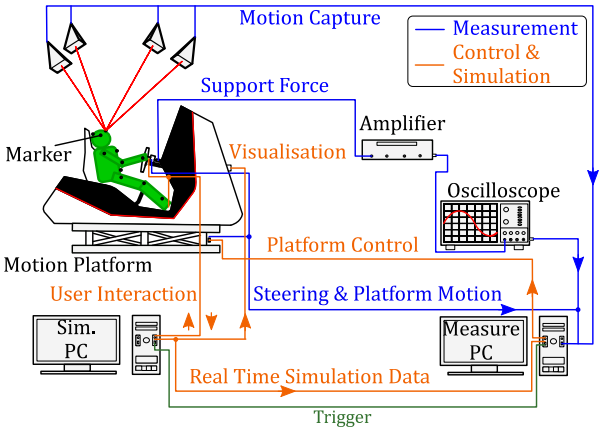

Figure 2. Overview of the data transfer between simulation and measurement PC to control the DiL simulator with motion platform and steering wheel (red) and collect synchronized measurements (blue) of the human driver (green) sitting inside the simulator.

TEST SERIES WITH 17 PERSONS AND 2 WARNING SIGNALS

To get a better understanding of the human behavior in those pre-crash situations and understand the prestressing, a preliminary test series with 17 persons (age 49.5+- 31.5) with a driving experience of 32+-31 years was conducted. The participants were driving in the simulator for some time to get comfortable with the system and were asked to drive with a constant velocity of 50 km/h. After a specific time, the crash scenario was initiated once per subject. The vehicle “ego” controlled by the subject hits the opponent car “bullet” approaching from the left. The participants performed a manual emergency braking when realizing the need for an intervention. To invest the effects of different warning signals, two randomly selected groups of the participants received a warning signal 20 m, respectively 0.5 s before the crash. They received either an acoustic signal of the sound system of the DiL or haptic feedback in the form of vibrations performed by the force-feedback steering wheel. The third control group didn`t receive any warning signal. The results of this study are shown in [5] and summarized in the following.

Without a warning signal, data shows more variance. While some people hit the braking pedal quite early, some made substantial effort much later. Both warning signals decreased the (mean) reaction times of the drivers. Furthermore, the group of participants with haptic feedback applied larger braking forces and a more significant support force on the driving wheel than the other two groups. This indicates that the warning with haptic feedback is an excellent possibility to prepare occupants for a potential impact and is better suited than the audio warning system. The study showed that measurements of the support force on the driving wheel during braking events could serve as an indicator of the level of alertness of the driver.

CONCLUSIONS

On the way towards autonomous transport, virtual testing of automated driving functionalities is inevitable to proof the safety of these systems. To strive for a higher level of road safety and thus to work towards the goal of Vision Zero, more effort is needed and a greater variety of critical scenarios must be considered, see e.g. [8]. Such a large variety of critical situations can only be tested virtually; therefore, the development of reliable biofidelic simulation models is important. Active HBM, validated for Pre-Crash simulations, can serve as a tool for enhancing integral safety systems and clear the way for automated traffic with improved real-world safety. The validation of active human body models is difficult as volunteers are needed. The proposed Driver-in-the-Loop simulator allows investigations of driver behavior in Pre-Crash scenarios, with and without the interaction of driver assistance systems. In further studies, muscle activity is recorded to get a better understanding of which muscle control strategy in the models is better suited to represent human behavior in pre-crash scenarios. Due to the small number of participants and the number of possible influences, i.e. actual velocity, on the investigated signals, the results should be considered as trends, needed to be examined in more extensive studies on high-end driver simulators.

References

[1] Kleinbach, C.: Simulation of Occupant Kinematics using Active Human Body Models. Dissertation, Schriften aus dem Institut für Technische und Numerische Mechanik der Universität Stuttgart, Vol. 60. Aachen: Shaker Verlag, 2019.

[2] Kempter, F.; Bechler, F.; Fehr, J.: Calibration Approach for Muscle Activated Human Models in Pre-Crash Maneuvers with a Driver-in-the-Loop Simulator. Advances in Transdisciplinary Engineering, Vol. 11, pp. 227 – 236, 2020.

[3] Virtual human-body models supplement crash-test dummies. Fraunhofer-Institut für Kurzzeitmechanik, Ernst-Mach-Institut, EMI, Freiburg, Germany, 2019. https://www.fraunhofer.de/content/dam/zv/en/press-media/2019/may/emi-virtual-human-models-supplement-crash-test-dummies.pdf.

[4] Kempter, F.; Fehr, J.; Stutzig, N.; Siebert, T.: On the Validation of Human Body Models with a Driver-in-the-Loop Simulator. In The 5th Joint Int. Conference on Multibody System Dynamics (IMSD 2018), Lisboa, Portugal, 2018.

[5] Riethmüller, J.: Einfluss der Muskelsteifigkeit bei der Notbremsung mit Hilfe eines Driver-in-the-Loop Prüfstands. BSC-114, Institute of Engineering and Computational Mechanics, University Stuttgart, 2019.

[6] Popp, K.; Schiehlen, W.: Ground Vehicle Dynamics. Berlin: Springer, 2010. ISBN 978-3-540-24038-9 (Print), ISBN 978-3-540-68553-1 (Online).

[7] Kempter, F.; Fehr, J.: Layout of a Driver-in-the-Loop Simulator for Validation of Human Body Models. In Proceedings in Applied Mathemathics and Mechanics, 2018.

[8] https://www.dekra-vision-zero.com accessed 2020/01/10

COLLISION DETECTION FOR RIGID SUPERELLIPSOIDS USING THE NORMAL PARAMETERIZATION

Ulrich J. Römer*[1]
[1]Institute of Engineering Mechanics, Karlsruhe Institute of Technology, Karlsruhe, Germany

Summary The normal parameterization as an approach to describe geometries is introduced. The advantages of this description – as compared to other parameterizations or implicit functions – in the context of collision detection are: the possibility to explicitly calculate axis aligned bounding boxes for any convex geometry, an efficient iterative algorithm for collision detection between objects with arbitrary geometry that does not require any (analytical) derivatives. A system of several rigid superellipsoids is used to demonstrate the application and performance of the proposed approach in a multibody simulation.

MOTIVATION

Collision detection is an essential task in multibody models with unilateral contacts. While the geometry of complicated objects can be approximated using mesh-based approaches, good approximations require a high number of vertices, which in turn increases the computational effort and computation times. These approaches are widely used because they are very flexible and efficient collision detection algorithms are available for mesh-based geometry descriptions [1].

Alternative approaches use smooth representations based on implicit functions or some parameterization. This typically requires far fewer parameters than high-accuracy mesh approximations, however, it is more difficult to describe or approximate arbitrary geometries. A possible remedy to mitigate this drawback is to use unions of several objects. In this context, ellipsoids, superellisoids and superovoids are popular geometries for the approximation of objects such as particles in granular media [2], rigid foot models [3], robot fingers or human teeth [4], to name but a few examples.

Collision detection for objects with smooth geometry representations can be performed based on the common normal concept: the outer normal vector at the (potential) contact points on the boundaries of two objects are (anti)parallel. There are few explicit solutions for this problem, e. g. detecting collisions between two spheres. In general, efficient algorithms based on Newton iterations are proposed in the literature [4, 5]. For these collision detection problems, significant improvements in computation times compared to mesh-based approaches with high-accuracy are reported [4].

The necessity for iterative methods arises from the geometry representation by the commonly used parameterizations or by implicit functions. Any representation based on implicit functions requires an iterative solution to even determine points on a boundary surface; the calculation of two points on opposing boundaries with parallel normal vectors must therefore also be solved iteratively. Parameterizations, on the other hand, are based on a formula for the explicit calculation of all points on the boundary surface of an object, which also allows an explicit calculation of the corresponding normals. However, the inverse relationship, the calculation of a point on the boundary for a given normal direction, generally yields an implicit relationship which again must be solved iteratively.

With the aims to improve current approaches for collision detection problem between smooth objects and to contribute to the derivation of explicit solutions, we propose a new parameterization for convex objects which we call the *normal parameterization* which is based on [6]. A useful property is the possibility to calculate axis aligned bounding boxes explicitly for any geometry described in this way. To illustrate further properties and the possible use in collision detection applications, we demonstrate its use by means of a simulation with several rigid superellipsoids. Two collision detection algorithms, one based on a Newton iteration with analytic Jacobian and one based on a fixed-point iteration without the need of any derivatives, are presented. A transient time simulation with several rigid superellipsoids and multiple collisions is used to compare these algorithms to approaches from literature.

METHOD

Given a normal direction $\mathbf{n}$ in spherical coordinates $(\varphi,\theta) \in \mathbb{S}^2$, the normal parameterization gives the position $\mathbf{r}(\varphi,\theta) : \mathbb{S}^2 \to \mathbb{R}^3$ of the corresponding point P on the object's boundary relative to a body-fixed point B. In general, the normal parameterization of a strictly convex object follows from the *generating potential* $g(\varphi,\theta) : \mathbb{S}^2 \to \mathbb{R}$ as

$$\mathbf{r}(\varphi,\theta) = \begin{cases} \frac{\partial g(\varphi,\theta)}{\partial \varphi}\mathbf{e}_\varphi + (\sin\varphi)^{-1}\frac{\partial g(\varphi,\theta)}{\partial \theta}\mathbf{e}_\theta + g(\varphi,\theta)\mathbf{e}_\mathrm{n}\,, & \text{if } \varphi \in (0,\pi)\,, \\ \frac{\partial g(\varphi,\theta)}{\partial \varphi}\mathbf{e}_\varphi + (\cos\varphi)^{-1}\frac{\partial^2 g(\varphi,\theta)}{\partial \varphi \partial \theta}\mathbf{e}_\theta + g(\varphi,\theta)\mathbf{e}_\mathrm{n}\,, & \text{if } \varphi \in \{0,\pi\}\,, \end{cases}$$

where the normal direction $\mathbf{e}_\mathrm{n} = \mathbf{n}$ and the tangent directions $\mathbf{e}_\varphi, \mathbf{e}_\theta$ are rotated with respect to a body-fixed reference frame $\{\mathbf{b}_\mathrm{x}, \mathbf{b}_\mathrm{y}, \mathbf{b}_\mathrm{z}\}$ by

$$\begin{aligned} \mathbf{e}_\varphi &= \cos\varphi\cos\theta\,\mathbf{b}_\mathrm{x} + \cos\varphi\sin\theta\,\mathbf{b}_\mathrm{y} - \sin\varphi\,\mathbf{b}_\mathrm{z}\,, \\ \mathbf{e}_\theta &= \quad -\sin\theta\,\mathbf{b}_\mathrm{x} + \quad \cos\theta\,\mathbf{b}_\mathrm{y}\,, \\ \mathbf{e}_\mathrm{n} &= \sin\varphi\cos\theta\,\mathbf{b}_\mathrm{x} + \sin\varphi\sin\theta\,\mathbf{b}_\mathrm{y} + \cos\varphi\,\mathbf{b}_\mathrm{z}\,, \end{aligned}$$

*Corresponding author. E-mail: ulrich.roemer@kit.edu.

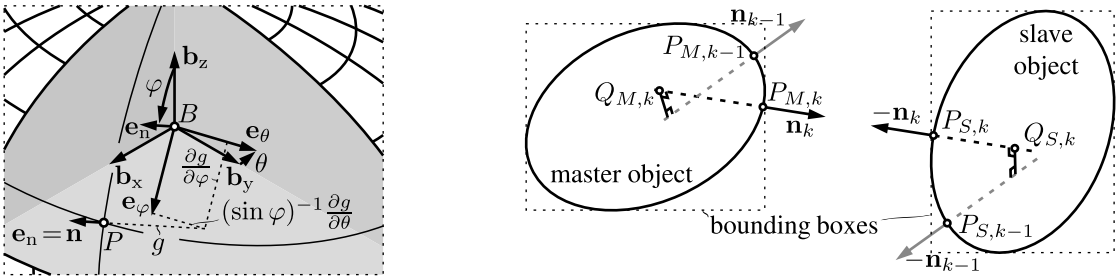

Figure 1: (a) Reference frames for the definition of the normal parameterization; (b) collision detection between two objects.

cf. figure 1a. Superellipsoids follow from the generating potential

$$g(\varphi,\theta) = \left(\left(\left(a^2 \sin^2\varphi \cos^2\theta\right)^{\frac{\delta}{2(\delta-1)}} + \left(b^2 \sin^2\varphi \sin^2\theta\right)^{\frac{\delta}{2(\delta-1)}} \right)^{\frac{\epsilon(\delta-1)}{\delta(\epsilon-1)}} \left(c^2\cos^2\varphi\right)^{\frac{\epsilon}{2(\epsilon-1)}} \right)^{\frac{\epsilon-1}{\epsilon}}$$

with $a, b, c, \delta, \epsilon \in \mathbb{R}$, $a, b, c > 0$ and $\delta, \epsilon > 1$. With this, the parameterization fulfills the implicit equation

$$\left(\left((x/a)^2\right)^{\delta/2} + \left((y/b)^2\right)^{\delta/2} \right)^{\epsilon/\delta} + \left((z/c)^2\right)^{\epsilon/2} = 1\,.$$

Collision detection is performed in two steps: first, axis aligned bounding boxes are used to quickly check whether two objects may overlap; if this test does not rule out a possible collision, one of two iterative procedures is employed for accurate collision detection. The calculation of an axis aligned bounding box for any object with arbitrary orientation with respect to an inertial frame $\{\mathbf{i}_x, \mathbf{i}_y, \mathbf{i}_z\}$ is simple. To determine the distance of the bounding box from the body-fixed point B in any direction $\{\pm\mathbf{i}_x, \pm\mathbf{i}_y, \pm\mathbf{i}_z\}$, calculate (φ, θ) from $\mathbf{e}_n$ for the respective direction and evaluate $g(\varphi, \theta)$. If the bounding boxes of two objects do not overlap, there can be no collision.

If there is an overlap of the bounding boxes, two iterative algorithms for accurate collision detection based on the common normal concept between two objects with arbitrary position and orientation are considered. For both algorithms, chose one object as master object with index M and the other as slave with index S. Let $\mathbf{n}_k = x_k\mathbf{i}_x + y_k\mathbf{i}_y + z_k\mathbf{i}_z$ with $x_k^2 + y_k^2 + z_k^2 = 1$ be the normal direction for the master object in the k-th iteration step. Determine the corresponding coordinates $(\varphi_{M,k}, \theta_{M,k})$ from $\mathbf{e}_{n,M,k} = \mathbf{n}_k$ and the coordinates $(\varphi_{S,k}, \theta_{S,k})$ from $\mathbf{e}_{n,S,k} = -\mathbf{n}_k$ due to the common normal concept. Evaluate the normal parameterization to determine the points $P_{M,k}$ and $P_{S,k}$ on the objects' boundaries, cf. figure 1b.

Algorithm I is based on a Newton iteration with analytic Jacobian and is adapted from [5]. Let $\mathbf{d}_{MS,k}$ be the vector from $P_{M,k}$ to $P_{S,k}$ and calculate a Newton step to zero the two tangential components $\mathbf{d}_{MS,k} \cdot \mathbf{e}_{\varphi,M,k}$ and $\mathbf{d}_{MS,k} \cdot \mathbf{e}_{\theta,M,k}$ and determine $\mathbf{n}_{k+1}$. Algorithm II is based on a fixed-point iteration for $\mathbf{n}$, which is designed such that no derivatives are required. Determine $Q_{M,k}$ as the point on the line given by $P_{M,k}$ and $\mathbf{e}_{n,M,k}$ which is closest to the same line from the previous iteration $k-1$ (cf. figure 1b). $Q_{M,k}$ is an approximation the center of curvature; $Q_{S,k}$ is determined analogously. The next iterate $\mathbf{n}_{k+1}$ is then taken as the unit vector pointing from $Q_{M,k}$ into the direction of $Q_{S,k}$.

RESULTS AND CONCLUSIONS

The collision detection approach is applied to a multibody system with several rigid superellipsoids. The investigated example systems show that the proposed approach works for rigid body simulations. Algorithm II which is based on a fixed-point iteration shows better robustness but slower convergence than algorithm I. The ability to explicitly calculate axis aligned bounding boxes is an advantage of the proposed normal parameterization, as is the possibility for an accurate and robust collision detection procedure which does not require any derivatives.

References

[1] Gilbert E. G., Johnson D. W., Keerthi S. S. A fast procedure for computing the distance between complex objects in three-dimensional space. *IEEE J. Robotics Autom.*, **4**(2): 193–203, 1988.

[2] Lu G., Third J. R., Müller C. R. Discrete element models for non-spherical particle systems: From theoretical developments to applications. *Chem. Eng. Sci.*, **127**: 425–465, 2015.

[3] Lopes D. S., Neptune R. R., Ambrósio J. A., Silva M. T. A superellipsoid-plane model for simulating foot-ground contact during human gait. *Comp. Meth. Biomech. Biomed. Eng.* **19**(9): 954–963, 2016.

[4] Gonçalves A. A., Bernardino A., Jorge J., Lopes D. S. A benchmark study on accuracy-controlled distance calculation between superellipsoid and superovoid contact geometries. *Mech. Mach. Theory* **115**: 77–96, 2017.

[5] Lopes D. S., Silva M. T., Ambrósio J. A., Flores P. A mathematical framework for rigid contact detection between quadric and superquadric surfaces. *Multibody Syst. Dyn.* **24**(3): 255–280, 2010.

[6] Römer U. J., Fidlin A., Seemann W. Explicit analytical solutions for two-dimensional contact detection problems between almost arbitrary geometries and straight or circular counterparts. *Mech. Mach. Theory*, **128**: 205–224, 2018.

FLIPPING THE WALKING ROBOT TO THE WORKING POSITION

Yury Golubev[1,2], Victor Koryanov[2] and Elena Melkumova[*1]
[1]Moscow State University, Moscow, Russia
[2]Keldysh Institute of Applied Mathematics, RAS, Moscow, Russia

Summary It is shown that the autonomous rescue of a six-legged machine from an emergency position "upside down" is possible with the help of cyclic movement of the legs, if the body has an upper shell in the form of a truncated cylinder. A method is proposed of rocking the body, which provides a flipping of the body and the return of the robot to the operating position. An analytical study and computer simulation of the full dynamics of the robot were fulfilled which confirmed the effectiveness of the developed technique for restore the functional capability of the robot. The results of numerical experiments and corresponding video materials are presented. The work was supported by the Russian Foundation for Basic Research (grant No. 19-01-00123 A).

INTRODUCTION

Except for hardware failures, the worst of emergencies is the case when the robot turns out to be in the upside down position when its body lies on the supporting plane with its legs upwards. If the robot is equipped with sensors that help it get its bearings in space and determine the direction of gravitational force, the upside down position of the body can cause the robot to lose orientation in space. To find a way out in such an emergency situation, the robot should have means to recover the normal position of its body. To facilitate the execution of this task, resonance effects that occur at a certain shape of the body due to special motion of the legs can be used.

ROCKING THE BODY WHEN LYING ON THE BACK

To facilitate the overturn, the robot's body in the working position can have the shape of convex (upward) part of a cylinder cut by a plane parallel to the cylinder's axis. Consider the model problem. Assume that a homogeneous segment of a circle of mass M lies on the horizontal supporting straight line. The segment is bounded by an arc of the circle of radius R and a chord that is at the distance h from the circle center. The circle arc touches the supporting line at the point A. The segment can roll without slippage on the supporting line rotating about the circle center at the angle φ measured from the vertical radius connecting the circle center with the point A at which the segment touches the supporting line. If $\varphi = 0$, then the segment lies such that its chord is parallel to the supporting line (Fig. 1).

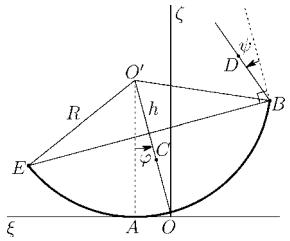

Figure 1. Upside down position of the robot.

To investigate the dynamic effects under the planar motion of the body and the legs that increase the oscillation amplitude as the body rocks itself in emergency situation, we assume that the parameters of the system are such that the upside down position of the robot is stable for all values of the angle ψ. Then, we can try to make the robot to turn over to normal position by cyclically varying ψ, thus making the robot's body to oscillate with increasing amplitude. To analytically describe the process of rocking, we use the theorem on changes of the system angular momentum about a moving point A [1, 2].

The robot design basically coincides with the one described in [3, 4]. The rigid body of the robot is composed of two truncated right cylinders put together by their common plane rectangular cut. Six identical two-link legs are symmetrically attached at the sides of the rectangular intersection of the cylinders. The leg attachment points on each side are equally spaced. In distinction from [3, 4], each part of the body and feet may touch the supporting surface and surrounding objects. The legs may not mutually cross during motion.

Suppose that as a result of an accident the robot turned over and lies on its back on the supporting horizontal plane with its legs up. It must choose the side of its body over which it will turn to the normal position with its back upwards (Fig. 3a). The rescue operations are performed in three phases.

Phase 1. The legs the attachment points of which are at the side chosen for turning over will be inactive. They must be straightened and arranged in such a way that they do not impede the turn over operation. The example of such arrangement is presented in figures with fragments of simulation of motion below.

*Corresponding author. E-mail: elena_v_m@mail.ru.

Phase 2. The legs on the other side of the body should be straightened, and they will be active. They start rocking the body due to direct control of their joint angles. All three legs move synchronously in the plane perpendicular to the longitudinal axis of the body at a fixed knee angle. For them, only the angles ψ between the leg and the body vary. To achieve unbounded body rocking, the function $\psi(t)$ cannot be periodic because the period of body oscillations depends on the amplitude. Fig. 2 contains the plot of the fragment of $\psi(t)$ corresponding to the typical oscillation.

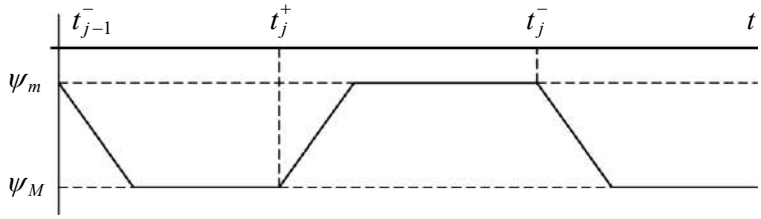

Figure 2. Control by angle ψ .

Here ψ_M, ψ_m are the values of ψ at which the active legs are closest to the attachment points of the passive legs (ψ_M), and at the greatest feasible deviation from these points (ψ_m) during the desired motion of the active legs. The sequence $\{t_j^+, t_j^-,\ j = 1, 2, \ldots\}$ marks time instants at which the height of the attachment points of the active (index +) and passive (index –) legs above the supporting plane is minimal. The time interval of transition from one constant value of ψ to the other is fixed. Fig. 3b, 3c shows the positions corresponding to time instants t_j^+, t_j^- of one of the oscillations.

Phase 3. After the turnover, the robot rests its active legs upon the supporting plane (Fig. 3d), and it must get on its feet. This can be done by sequentially transferring triples of legs with the leveling of the body [1, 2].

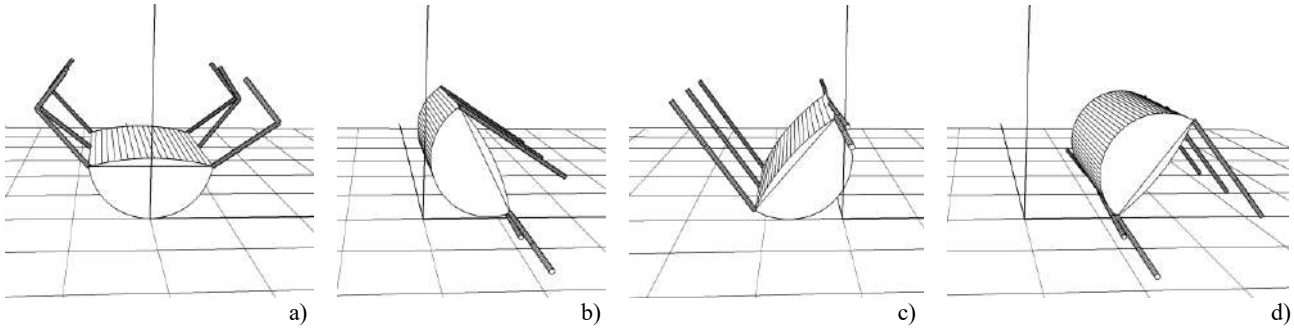

Figure 3. Initial position (a), typical swing in the direction of passive legs (b), its reverse swing (c), completion of rocking (d)

The computer simulation was performed by using the *Universal Mechanism* software package [5].

CONCLUSIONS

The new problem of rescuing an autonomous insectomorphic robot residing in the abnormal upside down position on the supporting plane is solved. To make the rescuing operation possible, a special shape of the robot's body consisting of two truncated right circular cylinders put together by their common plane rectangular cut is proposed. An algorithm for rocking the robot in the neighborhood of its emergency equilibrium position is developed. This algorithm uses the robot's kinematic and dynamic capabilities to bring the robot to normal position without outside assistance. The validity of the algorithm is proved analytically [1, 2]. A stable resonance motion of the system that turns the robot over to normal working position is designed.

References

[1] Golubev Yu. F., Koryanov V. V., Melkumova E. V. Flipping the Walking Robot to the Working Position from the Emergency "Upside Down". KIAM Preprint, No. 48, Keldysh Institute of Applied Mathematics, RAS, Moscow 2019, DOI: 10.20948/prepr-2019-48. (In Russian).

[2] Golubev Yu. F., Koryanov V.V., Melkumova E.V. Bringing an Insectomorphic Robot to Normal Position from the Abnormal Upside Down Position. *J. Computer and Systems Sciences International.* Vol. **58**, No. 6, 2019.

[3] Golubev Yu. F., Koryanov V. V. Extreme Locomotion Capabilities of Insectomorphic Robots. Keldysh Institute of Applied Mathematics, RAS, Moscow 2018. (In Russian).

[4] Golubev Yu. F., Koryanov V.V. Crossing a Small Body of Water by an Insectomorphic Robot on a Raft. *J. Computer and Systems Sciences International.* **56**: 1037-1058, 2017.

[5] Universal Mechanism. Modelling the dynamics of mechanical systems. URL: http://www.umlab.ru (accessed: 06/18/2015).

TAPE SPRING MODELLING AND DYNAMICS

J. P. Meijaard *[1]
[1]Olton Engineering Consultancy, Enschede, The Netherlands

Summary A beam model for the large deflections of a tape spring, which may be accompanied by significant distortion of its cross-section, is proposed. Besides the variables that describe a classical thin-walled beam, additional variables are introduced that describe the variable shape of the cross-section. A finite element based on this model is developed, which uses assumed strain fields and discrete deformation quantities. The element is applied to some static and dynamic test problems.

PROBLEM STATEMENT

In classical beam theory, it is assumed that changes in the shape of the cross-section are negligible. In the absolute nodal coordinate formulation, some deformations of the cross-section can be taken into account, but the distortion remains small. This assumption may no longer hold for some beams with a thin-walled cross-section. In particular, tape springs, which have a cross-section in the shape of a shallow arch, can develop folds in which the cross-section becomes almost flat. Also end-effects such as the constrained anticlastic curvature at clamped ends can influence the overall stiffness, especially for beams that are short in comparison with their cross-sectional dimensions.

Tape springs have been modelled by simple analytical expressions, where several effects are neglected [1, 2] and dynamics is not included, or by detailed finite element models with shell or solid elements [3]. Here, a beam model with some additional degrees of freedom to model the deformation of the cross-section is proposed. A similar approach has been pursued in [4]. The main contribution here is that the cross-sectional quantities are formulated in terms of known quantities, such as the position of the shear centre and the warping constant, with a few additional quantities specific to the condition of a varying cross-section over the length of the beam. Furthermore, a finite element based on this theory is developed.

BEAM MODEL

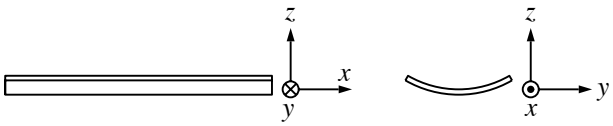

Figure 1: Beam with a shallow cross-section.

A prismatic beam with a thin-walled curved cross-section as shown in Fig. 1 is considered. The configuration and strains of the beam are related to the line of centroids. The axial strain and the shear strain in the xy-plane are included, but the shear strain in the xz-plane is neglected. The three curvatures, the torsion and the two bending curvatures, are defined in the usual way. The warping is connected to the torsion deformation, which can be constrained at clamped ends or give a contribution if variable torsion is present or the shape of the cross-section changes over the length of the beam. In addition to these classical aspects, the initial shape and the change of the shape of the cross-section is determined by two additional variables, which define a symmetric quartic curve. These changes of the shape make that the cross-sectional quantities such as the moments of inertia, the position of the shear centre and the warping function change over the length of the beam and in time. The difference between the centre of shear and the centroid of the cross-section gives rise to a contribution of the torsion to the shear measured at the line of centroids.

The shear stress in the cross-section is determined by the torsion and the shear force in the usual way. The axial stress distribution is more complicated and contains contributions due to the axial strain at the line of centroids, the bending in the two directions, the change in the torsion, large values of the torsion, the change in the warping function over the length of the beam and the change of the shape of the cross-section itself.

The mass distribution is modelled in a standard way with the distributed mass per unit of length and the moments of inertia of the cross-section. In addition, the change in the shape of the cross-section gives rise to mass coupled to the variables describing these changes. No additional mass has to be attached to the warping deformation of the cross-section.

*Corresponding author. E-mail: j.p.meijaard@olton.nl.

SOLUTION TECHNIQUES

Based on the above assumptions, a two-node beam element is developed based on assumed strains fields, the so-called generalized strains. The nodal coordinates are three displacements and rotations and also the value of the warping and the values of the two variables that describe the shape of the cross-section. The strain fields are linear for the bending, cubic for the torsion, and the shear is directly related to the bending and torsion strains. In addition, there are linearly varying variables for the shape of the cross-section. These assumptions on the strains give the elastic energy of the element, which determines its stiffness properties.

The mass properties are obtained from an interpolation of the position of the line of centroids with a distributed line mass. The mass moments of inertia are lumped to the nodes. The mass contribution from the variables for the shape of the cross-section is directly connected to these variables and coupling with the moments of inertia is neglected.

The element can be used in a multibody dynamics simulation context. Static problems, where a load path is followed by an arc continuation method, as well as dynamic simulations can be made, where explicit time integration methods are used.

SOME APPLICATIONS

A set of test problems for an initially flat strip is analysed. Large deflections caused by final bending moments are considered. Due to the suppression of the anticlastic curvature at large curvatures, the effective stiffness increases. The results compare well with the analytical solutions given by Ashwell [5]. Also the influence of the constrained anticlastic curvature at clamped ends can be fairly accurately described for the driving stiffness of a parallel leaf spring guidance [6]. In many cases, the static behaviour of a leaf spring can be modelled by a single element, with errors in the stiffness values below ten percent [7].

The bending of a tape spring in the xz-plane depends strongly on the direction of the bending moment. Loading a cantilevered beam in the positive z-direction, which gives rise to a mid-plane surface with a positive curvature, with increasing loads first leads to bending-torsional buckling with a stable post-buckling load path, which eventually becomes unstable in a snap-through instability. This contrasts with the behaviour of a tape spring loaded by end moments as reported in the literature [2]. Loading in the opposite direction gives rise to a snap-through instability.

The dynamic behaviour and the transfer of energy to modes with a higher frequency can be demonstrated by performing a simulation starting from an undeformed initial state.

Also the spatial behaviour if the cantilevered tape spring is loaded in the xy-plane can be described. There is no clear case of lateral buckling, because the shear centre and the centre of mass of the cross-section are not the same.

CONCLUSIONS

The proposed beam model for a tape spring can be used to make static and dynamic calculations in a multibody dynamics environment with fairly good accuracy of the results, which can be compared with experiments.

The approach is given in a general form, so more accurate models can easily be obtained by including more terms for the deformation of the cross-section and more elaborate interpolations of the strains in the finite element formulation.

References

[1] Mansfield E. H. Large-Deflection Torsion and Flexure of Initially Curved Strips. *Proc. Roy. Soc. Lond. A* **334**: 279–298, 1973.

[2] Seffen K. A., Pellegrino S. Deployment Dynamics of Tape Springs. *Proc. Roy. Soc. Lond. A* **455**: 1003–1048 1999.

[3] Hoffait S., Brüls O., Granville D., Cugnon F., Kerschen G. Dynamic Analysis of the Self-Locking Phenomenon in Tape-Spring Hinges. *Acta Astronaut.* **66**: 1125–1132, 2010.

[4] Picault E., Bourgeois S., Cochelin B., Guinot F. A Rod Model with Thin-Walled Flexible Cross-Section: Extension to 3D Motions and Application to 3D Foldings of Tape Springs. *Int. J. Solids Struct.* **84**: 64–81, 2016.

[5] Ashwell D. G. The Anticlastic Curvature of Rectangular Beams and Plates. *J. Roy. Aeronaut. Soc.* **54**: 708–715, 1950.

[6] Brouwer D. M., Meijaard J. P., Jonker J. B. Large Deflection Stiffness Analysis of Parallel Prismatic Leaf-Spring Flexures. *Precision Eng.* **37**: 505–521, 2013.

[7] Nijenhuis M., Meijaard J. P., Mariappan D., Herder J. L., Brouwer D. M., Awtar S. An Analytical Formulation for the Lateral Support Stiffness of a Spatial Flexure Strip. *ASME J. Mech. Des.* **139**: 051401-1-051401-11, 2017.

CONSTRAINTS THAT CONNECT FINITE ELEMENTS AND MULTIBODY MODELS - A CASE OF A DOUBLE PENDULUM THAT SLIDES ON AN ELASTIC BEAM

Krzysztof Lipinski[1]
[1]Mechanical Department, Gdansk University of Technology, Gdańsk, Poland

Summary The paper focuses on constraints between a multibody system and a finite elements model. It combines a set of some structurally different relations. The multibody part is composed of non-deformable bodies and joints. Joints' relative displacements are taken as the generalised coordinates (considered as significant). Non-constant mass matrix (displacements dependent), as well as the centrifugal/Coriolis/gyroscopic effects, are considered. Finite elements are used for the beam. Displacements of their nodes are taken as the generalised coordinates (considered as small). For other points, shape functions and the nodal displacements are used. Resulting dynamics equations are linear to the kinematic parameters of the nodes'. Proposed constraint equations are holonomo/scleronomic. In dynamics, Lagrange multipliers are used and the generalised coordinates are partitioned on dependent and independent ones. Classical method [1] is modified to fit to the actual case. Finally, an exemplary system is introduced, and results of its numerical simulations are presented.

INTRODUCTION

The paper focuses on a point-contact constraint that is present between a multibody system and an elastic deformable structure. The non-homogenous form of the considered model implies a set of consequences critical in formulation of the contact equations, mainly as a set of multibody relations has to be joined with kinematics of the finite elements. In the paper, in case of the multibody part, classical multibody modelling [2, 3] is considered. The model is composed of non-deformable bodies and mobile joints. Joints' displacements are assumed as the generalised coordinates of this sub-model. Their magnitudes are significant. The body associated orientation matrices, $\boldsymbol{T}^i$, are calculated as dependent on joints' rotation, and vectors of the mass centres, $\vec{x}^i$, are calculated form lengths of the elements of the chin. When differentiated twice, they result in velocity and acceleration formulas. For dynamics, free body diagrams are constructed for all the bodies (the joints are cut and replaced by joint interactions). Next, the Newton/Euler equations of dynamics are used, combined with the kinematics formulas, and projected onto the joint mobility directions. Resulting formulas are written in the standard matrix form [2, 3, 5]:

$$\boldsymbol{M_b}(\boldsymbol{q_b})\cdot\ddot{\boldsymbol{q}}_b + \boldsymbol{F_b}(\dot{\boldsymbol{q}}_b,\boldsymbol{q_b}) = \boldsymbol{Q}(\dot{\boldsymbol{q}}_b,\boldsymbol{q_b},\boldsymbol{f_e},\boldsymbol{t_e},t)\ , \tag{1}$$

where: $\boldsymbol{M_b}$– mass matrix; $\boldsymbol{q_b}$ – vector of the sub-system's coordinates, $\boldsymbol{F_b}$ – vector of inertial effects; $\boldsymbol{Q_b}$ – vector of the sub-system generalized forces; $\boldsymbol{f_e}$, $\boldsymbol{t_e}$ – external forces and torques, t - time.

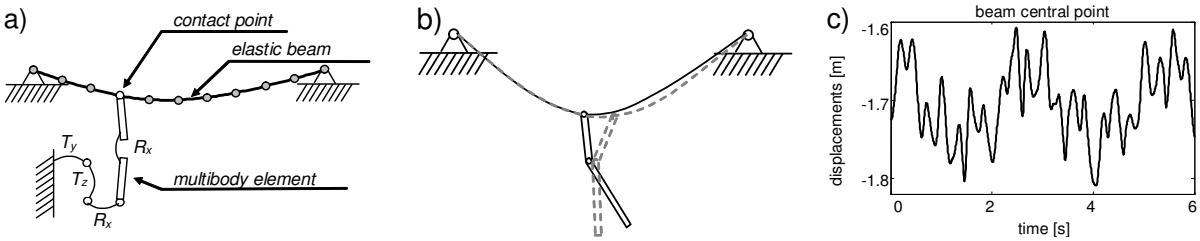

Figure 1: Draft of the system (a); selected slides of simulation (b); motion of the central node (c)

The matrix $\boldsymbol{M_b}$ depends on coordinates (i.e., it is a not constant one) and the vector $\boldsymbol{F_b}$ (understand as a column matrix) collects all the nonlinear inertial effects as: centrifugal accelerations, Coriolis accelerations, gyroscopic torques.

The finite elements part is composed of short segments, and it represents a stationary located elastic structure (its drift motion is absent). To express its pose, at a set of points is selected (called nodes) and displacements of these points are used (considered as the sub-system's coordinates and collected in $\boldsymbol{q_c}$ column matrix). Recalled displacements are assumed as small. When other point is considered, its displacements are described by so-called shape functions [4]:

$$\boldsymbol{q} = \boldsymbol{N_e}\cdot\boldsymbol{q_e}\ , \qquad \widehat{\boldsymbol{N}}_{be}(\zeta) = \begin{bmatrix} 2\zeta^3-3\zeta^2+1 & l_e(\zeta^3-2\zeta^2+\zeta) & -2\zeta^3+3\zeta^2 & l_e(\zeta^3-\zeta^2) \\ \dfrac{6(\zeta^2-\zeta)}{l_e} & 3\zeta^2-4\zeta+1 & \dfrac{6(-\zeta^2+\zeta)}{l_e} & 3\zeta^2-2\zeta \end{bmatrix}, \tag{2}$$

where: $\zeta = \hat{x}_1/l_e$ - relative position of the considered point in respect to its reference node.

To obtain equations of the model's dynamics, a method proposed in [4,5] is employed. Resulting equations are linear in respect to displacements, velocities and accelerations of the nodes, i.e. the mass, dissipation and stiffness matrices are considered as constant for this model. It can be expressed as [4]:

$$\boldsymbol{A_c}\cdot\ddot{\boldsymbol{q}}_c + \boldsymbol{B_c}\cdot\dot{\boldsymbol{q}}_c + \boldsymbol{C_c}\cdot\boldsymbol{q_c} = \boldsymbol{P_c}\ . \tag{3}$$

where: $\boldsymbol{M_c}$ – mass matrix; $\boldsymbol{D_c}$ - damping matrix; $\boldsymbol{K_c}$ - stiffness matrix; $\boldsymbol{P_c}$ - vector of nodal forces.

CONSTRAINTS FORMULAS AND DYNAMICS OF THE CONSTRAINED SYSTEM

The main zoom of the paper is set on the constraint equations. With the presence of the constraint, the previously obtained differential equations of dynamics of the sub-models are converted into a single set of differentially-algebraic equations (*DAE form*) [3,5]:

$$\begin{aligned} &\boldsymbol{M}_b(\boldsymbol{q}_b)\cdot\ddot{\boldsymbol{q}}_b+\boldsymbol{F}_b(\dot{\boldsymbol{q}}_b,\boldsymbol{q}_b)+\boldsymbol{J}_b^T(\boldsymbol{q}_b)\cdot\lambda=\boldsymbol{Q}_b(\dot{\boldsymbol{q}}_b,\boldsymbol{q}_b,\boldsymbol{f_e},\boldsymbol{t_e},t)\ ; \quad \boldsymbol{M}_c\cdot\ddot{\boldsymbol{q}}_c+\boldsymbol{D}_c\cdot\dot{\boldsymbol{q}}_c+\boldsymbol{K}_c\cdot\boldsymbol{q}_c+\boldsymbol{J}_c^T\cdot\lambda=\boldsymbol{P}_c\ ; \\ &\boldsymbol{\Phi}(\boldsymbol{q}_c,\boldsymbol{q}_b)=\boldsymbol{N}\cdot\boldsymbol{q}_c-p_n(\boldsymbol{q}_b)=0\ ; \quad \boldsymbol{J}_b=\tfrac{\partial}{\partial\boldsymbol{q}_b}\boldsymbol{\Phi}\ ; \quad \boldsymbol{J}_c=\tfrac{\partial}{\partial\boldsymbol{q}_c}\boldsymbol{\Phi}\ , \end{aligned} \tag{4}$$

where: $p_n(\boldsymbol{q_b})$ – vertical position of the contact point at the multibody sub-model.

To eliminate the dependent velocities and accelerations, derivatives of the constraint equations are necessary. Our intention is to write them as [3,5]:

$$\begin{aligned} &\boldsymbol{N}\cdot\dot{\boldsymbol{q}}_c+\dot{\xi}\cdot\boldsymbol{N}_\xi\cdot\boldsymbol{q}_c-\boldsymbol{J}\cdot\dot{\boldsymbol{q}}_b=0\ ; \quad \boldsymbol{N}\cdot\ddot{\boldsymbol{q}}_c+\ddot{\xi}\cdot\boldsymbol{N}_\xi\cdot\boldsymbol{q}_c+2\dot{\xi}\cdot\boldsymbol{N}_\xi\cdot\dot{\boldsymbol{q}}_c+\dot{\xi}^2\cdot\boldsymbol{N}_{\xi\xi}\cdot\boldsymbol{q}_c-\left(\boldsymbol{J}\cdot\dot{\boldsymbol{q}}_b\right)_q\cdot\dot{\boldsymbol{q}}_b-\boldsymbol{J}\cdot\ddot{\boldsymbol{q}}_b=0\ ; \\ &\boldsymbol{N}_\xi=\tfrac{\partial}{\partial\xi}\boldsymbol{N}\ ; \quad \boldsymbol{N}_{\xi\xi}=\tfrac{\partial^2}{\partial\xi^2}\boldsymbol{N}\ ; \quad \left(\boldsymbol{J}\cdot\dot{\boldsymbol{q}}_b\right)_q=\tfrac{\partial}{\partial\boldsymbol{q}_b}\left(\boldsymbol{J}\cdot\dot{\boldsymbol{q}}_b\right)\ ; \quad \boldsymbol{J}_c=\boldsymbol{N}\ ; \\ &\boldsymbol{J}=\tfrac{\partial}{\partial\boldsymbol{q}_b}p_n=-\boldsymbol{J}_b\ ; \quad \dot{\xi}=v_t(\dot{\boldsymbol{q}}_b,\boldsymbol{q}_b)/l\ ; \quad \ddot{\xi}=a_t(\ddot{\boldsymbol{q}}_b,\dot{\boldsymbol{q}}_b,\boldsymbol{q}_b)/l\ , \end{aligned} \tag{5}$$

where: v_t – horizontal speed of the contact point; a_t – horizontal acceleration of the contact point.

Of course, the horizontal kinematics of the contact point depends on the kinematics of the multibody part, thus [3,5]:

$$\begin{aligned} &\boldsymbol{N}\cdot\dot{\boldsymbol{q}}_c+\boldsymbol{J}_R\cdot\dot{\boldsymbol{q}}_b=0\ ; \quad \boldsymbol{N}\cdot\ddot{\boldsymbol{q}}_c+\boldsymbol{J}_R\cdot\ddot{\boldsymbol{q}}_b+2\dot{\xi}\cdot\boldsymbol{N}_\xi\cdot\dot{\boldsymbol{q}}_c+\dot{\xi}^2\cdot\boldsymbol{N}_{\xi\xi}\cdot\boldsymbol{q}_c+(1/l)\boldsymbol{N}_\xi\cdot\boldsymbol{q}_c\cdot\gamma_T-\gamma=0\ : \\ &\boldsymbol{J}_t=\tfrac{\partial}{\partial\boldsymbol{q}_b}p_t\ ; \quad \boldsymbol{J}_R=(1/l)\cdot\boldsymbol{N}_\xi\cdot\boldsymbol{q}_c\cdot\boldsymbol{J}_t-\boldsymbol{J}\ ; \quad \gamma_t=\left(\boldsymbol{J}_t\cdot\dot{\boldsymbol{q}}_b\right)_q\cdot\dot{\boldsymbol{q}}_b\ ; \quad \gamma=\left(\boldsymbol{J}\cdot\dot{\boldsymbol{q}}_b\right)_q\cdot\dot{\boldsymbol{q}}_b\ , \end{aligned} \tag{6}$$

where: $\boldsymbol{J}_t$ – matrix of partial derivatives of the horizontal position of the contact point.

Then, coordinates of the multibody structure, $\boldsymbol{q_b}$, are partitioned onto dependent, $\boldsymbol{v}$, and independent, $\boldsymbol{u}$, ones. As a consequence, the dynamic equation can be written, and $\boldsymbol{\lambda}$ can be evaluated:

$$\begin{aligned} &\boldsymbol{M}_{buu}\cdot\ddot{\boldsymbol{u}}+\boldsymbol{M}_{buv}\cdot\ddot{\boldsymbol{v}}+\boldsymbol{F}_{bu}+\boldsymbol{J}_{bu}^T\cdot\boldsymbol{\lambda}=\boldsymbol{Q}_{bu} \quad\Rightarrow\quad \boldsymbol{\lambda}=-\boldsymbol{J}_{bu}^{-T}\cdot\boldsymbol{M}_{buu}\cdot\ddot{\boldsymbol{u}}-\boldsymbol{J}_{bu}^{-T}\cdot\boldsymbol{M}_{buv}\cdot\ddot{\boldsymbol{v}}-\boldsymbol{J}_{bu}^{-T}\cdot\boldsymbol{F}_{bu}+\boldsymbol{J}_{bu}^{-T}\cdot\boldsymbol{Q}_{bu} \\ &\boldsymbol{M}_{bvu}\cdot\ddot{\boldsymbol{u}}+\boldsymbol{M}_{bvv}\cdot\ddot{\boldsymbol{v}}+\boldsymbol{F}_{bv}+\boldsymbol{J}_{bv}^T\cdot\boldsymbol{\lambda}=\boldsymbol{Q}_{bv}\ . \end{aligned} \tag{7}$$

Obtained $\boldsymbol{\lambda}$ is eliminated from the dynamics. Next, the constraint equations (at the acceleration level) are partitioned also, and the dependent accelerations are eliminated from the dynamics. They can be written in the standard way [3,5]:

$$\begin{aligned} &\boldsymbol{M}_{11}\cdot\ddot{\boldsymbol{u}}+\boldsymbol{M}_{11}\cdot\ddot{\boldsymbol{q}}_c+\boldsymbol{F}_1=\boldsymbol{Q}_1 \\ &\boldsymbol{M}_{21}\cdot\ddot{\boldsymbol{u}}+\boldsymbol{M}_{22}\cdot\ddot{\boldsymbol{q}}_c+\boldsymbol{D}_2\cdot\dot{\boldsymbol{q}}_c+\boldsymbol{K}_2\cdot\boldsymbol{q}_c+\boldsymbol{F}_2=\boldsymbol{P}_2 \end{aligned} \tag{8}$$

where:

$$\begin{aligned} &\boldsymbol{M}_{11}=\boldsymbol{M}_{bvu}-\boldsymbol{J}_{bv}^T\cdot\boldsymbol{J}_{bu}^{-T}\cdot\boldsymbol{M}_{buu}-\boldsymbol{M}_{bvv}\cdot\boldsymbol{J}_{Rv}^{-1}\cdot\boldsymbol{J}_{Ru}+\boldsymbol{J}_{bv}^T\cdot\boldsymbol{J}_{bu}^{-T}\cdot\boldsymbol{M}_{buv}\cdot\boldsymbol{J}_{Rv}^{-1}\cdot\boldsymbol{J}_{Ru} \\ &\boldsymbol{M}_{12}=-\boldsymbol{M}_{bvv}\cdot\boldsymbol{J}_{Rv}^{-1}\cdot\boldsymbol{N}+\boldsymbol{J}_{bv}^T\cdot\boldsymbol{J}_{bu}^{-T}\cdot\boldsymbol{M}_{buv}\cdot\boldsymbol{J}_{Rv}^{-1}\cdot\boldsymbol{N}\ ; \qquad \boldsymbol{Q}_1=\boldsymbol{Q}_{bv}-\boldsymbol{J}_{bv}^T\cdot\boldsymbol{J}_{bu}^{-T}\cdot\boldsymbol{Q}_{bu} \\ &\boldsymbol{F}_1=\boldsymbol{F}_{bv}-\boldsymbol{J}_{bv}^T\cdot\boldsymbol{J}_{bu}^{-T}\cdot\boldsymbol{F}_{bu}-\left(\boldsymbol{M}_{bvv}-\boldsymbol{J}_{bv}^T\cdot\boldsymbol{J}_{bu}^{-T}\cdot\boldsymbol{M}_{buv}\right)\cdot\boldsymbol{J}_{Rv}^{-1}\cdot\left(2\dot{\xi}\cdot\boldsymbol{N}_\xi\cdot\dot{\boldsymbol{q}}_c+\dot{\xi}^2\cdot\boldsymbol{N}_{\xi\xi}\cdot\boldsymbol{q}_c+(1/l)\cdot\boldsymbol{N}_\xi\cdot\boldsymbol{q}_c\cdot\gamma_T-\gamma\right) \\ &\boldsymbol{M}_{21}=-\boldsymbol{J}_c^T\cdot\boldsymbol{J}_{bu}^{-T}\cdot\boldsymbol{M}_{buu}+\boldsymbol{J}_c^T\cdot\boldsymbol{J}_{bu}^{-T}\cdot\boldsymbol{M}_{buv}\cdot\boldsymbol{J}_{Rv}^{-1}\cdot\boldsymbol{J}_{Ru}\ ; \qquad \boldsymbol{M}_{21}=\boldsymbol{M}_c+\boldsymbol{J}_c^T\cdot\boldsymbol{J}_{bu}^{-T}\cdot\boldsymbol{M}_{buv}\cdot\boldsymbol{J}_{Rv}^{-1}\cdot\boldsymbol{N} \\ &\boldsymbol{D}_2=\boldsymbol{D}_c+\boldsymbol{J}_c^T\cdot\boldsymbol{J}_{bu}^{-T}\cdot\boldsymbol{M}_{buv}\cdot\boldsymbol{J}_{Rv}^{-1}\cdot2\dot{\xi}\cdot\boldsymbol{N}_\xi\ ; \qquad \boldsymbol{K}_2=\boldsymbol{K}_c+\boldsymbol{J}_c^T\cdot\boldsymbol{J}_{bu}^{-T}\cdot\boldsymbol{M}_{buv}\cdot\boldsymbol{J}_{Rv}^{-1}\cdot\dot{\xi}^2\cdot\boldsymbol{N}_{\xi\xi}+ \\ &\boldsymbol{F}_2=-\boldsymbol{J}_c^T\cdot\boldsymbol{J}_{bu}^{-T}\cdot\boldsymbol{F}_{bu}+\boldsymbol{J}_c^T\cdot\boldsymbol{J}_{bu}^{-T}\cdot\boldsymbol{M}_{buv}\cdot\boldsymbol{J}_{Rv}^{-1}\cdot\left((1/l)\cdot\boldsymbol{N}_\xi\cdot\boldsymbol{q}_c\cdot\gamma_T-\gamma\right)\ ; \qquad \boldsymbol{P}_2=\boldsymbol{P}_c-\boldsymbol{J}_c^T\cdot\boldsymbol{J}_{bu}^{-T}\cdot\boldsymbol{Q}_{bu} \end{aligned} \tag{9}$$

CONSIDERED SYSTEM

The used exemplary model corresponds to a planar beam connected with a double pendulum that oscillates and slides on the beam (Fig.1a). The beam is modeled with use of 50 finite elements. Corresponding constraint equations are introduced as they are presented in the work, as well as the above method is used for the coordinate partitioning and for the elimination. Finally, obtained equations are tested numerically (Fig. 1bc).

References

[1] Haug E.J., Yen J. Gener. Coord.Partit.Meth. for Num.Integ. *NATO ASI Series*, **69**, 97–114, 1990.
[2] Fisette P., Samin J.C.. Symbolic Modeling of Multibody System, Kluwer Acad. Pub., 2003.
[3] Lipiński, K.: Multibody Systems with Unilateral Constraints in Application to Modelling of Complex Mechanical Systems. Monografie 123, Wydawnictwo P.G., Gdańsk (2012) (in Polish).
[4] Zienkiewicz O.C. Taylor R.C., The finite element method, 6th Edition, Elsevier, 2005.
[5] Lipiński K.: Multibody system in a contact with a model composed of finite elements, Proceedings of the ECCOMAS Thematic Conference in Multibody Dynamics, Warszawa, 2009.

ORBITAL MOTION DYNAMICS FOR ASTEROID APOPHIS ARTIFICIAL SATELLITE

Vyacheslav V. Ivashkin*[1,2], Anqi Lang [2,3], Peng Guo [1]
[1]Department of Mechanics of Space flight and Motion Control,M.V. Keldysh Institute of Applied Mathematics, RAS, Moscow,Russia
[2]Department of Dynamics and Control of Rockets and Spacecraft Motions,N.E. Bauman Moscow State Technical University, Moscow,Russia
[3]School of Aerospace, Xi'an Jiaotong University, Xi'an, Shaanxi, P.R. China

Summary Orbital motion of the satellite of the asteroid Apophis is studied taking into account main perturbations - from the attraction of main celestial bodies - the Sun, Earth, Moon, Venus, Jupiter, the non-sphericity of the asteroid and the solar radiation pressure. Two asteroid models are considered - a prolate spheroid and a triaxial ellipsoid. It is found the existence of stable orbits of the asteroid satellite, allowing for several years before the approach of the asteroid to the Earth in 2029 to realize the spacecraft motion near the asteroid. This makes it possible, in principle, to carry out radio measurements of satellite motion parameters from ground-based stations and to improve significantly our knowledge of the Apophis orbit.

INTRODUCTION. STATEMENT OF THE PROBLEM

The organization of an expedition to asteroids, in particular, to the Near-Earth ones, is an important problem of modern cosmonautics. In the paper, in frame of analysis of the characteristics of a possible expedition to the asteroid Apophis, the investigation of the orbital motion of the spacecraft (SC) around the asteroid is performed. In accordance with the considered mission scheme [1], we believe that after the main spacecraft arrives to the asteroid, a special mini-spacecraft is inserted in some orbit of the asteroid satellite, so that after the main spacecraft departs to the Earth, the mini-spacecraft will for a long time, ~ several years, continue to fly near the asteroid and some ground-based stations will measure the satellite motion parameters and it gives the possibility to know better the Apophis orbit. The purpose of the study is to investigate whether it is possible to choose the orbit of this mini-spacecraft so that it will passively move around the Apophis for several years without corrections. The analysis showed that we can create the stable mini-satellite orbit with motion of the satellite near the asteroid for several years till the close approach of the asteroid to the Earth in 2029.

MODEL OF SPACECRAFT MOTION. MODEL OF ASTEROID

In an investigation of the spacecraft motion relative to the asteroid Apophis, we took into account three types of perturbations: the attraction of distant celestial bodies (the Sun, Earth, Moon, Venus, Jupiter, etc.), the non-sphericity of the Apophis, and the solar radiation pressure (SRP). For this complicated field, we used a numerical method of the analysis based on the numerical integration of the equations of the spacecraft motion relative to the asteroid:

$$d\mathbf{r}/dt = \mathbf{V}; d\mathbf{V}/dt = \mathbf{a}_0 + \mathbf{a}_1 + \mathbf{a}_2 + \mathbf{a}_3.$$

Here: $\mathbf{r}$ (x, y, z), $\mathbf{V}$ (V_x, V_y, V_z) is the position vector and velocity vector of the spacecraft in the asteroid-centric non-rotating rectangular coordinate system OXYZ, $\mathbf{a}_0 = -\mu_A \mathbf{r}/r^3$ is the central acceleration, $r = |\mathbf{r}|$; μ_A is the gravitational parameter of the asteroid Apophis; $\mathbf{a}_1$, $\mathbf{a}_2$, $\mathbf{a}_3$ – perturbation accelerations: from the attraction of distant celestial bodies, from the non-sphericity of Apophis and from the solar radiation pressure. In the analysis, the position vectors of celestial bodies relative to the Sun were taken from Ephemeris DE421; Apophis position vector is defined on the corresponding JPL site or by the numerical integration. The Apophis gravitational parameter is taken in the range μ_A = 1.8-2.86 m^3/s^2 (for the Apophis mass 2.7-4.3·10^{10} kg). The average Apophis radius was taken equal to R_A = 160 m. The initial orbit of the spacecraft was taken circular with a radius r_0 in the range 0.5-2 km (with orbital velocity of 6-3 cm/s, orbital period ~ 15-116 hours for μ_A = 1.8 m^3/s^2).

Two models of asteroid were used to analyze the effect of asteroid's non-sphericity. This is, firstly, an approximate model of a homogeneous prolate spheroid, that is two-axial prolate ellipsoid of rotation [2]. Observations of the asteroid Apophis [3] showed that the asteroid is geometrically and dynamically close to this variant. Thus, an estimate of the ratios of the principal axes of a dynamically equivalent homogeneous ellipsoid yielded $b_A/a_A \approx 1.06$ (±0.02), $c_A/a_A \approx 1.5$ (±0.2), here a_A, b_A, c_A are the small, medium, and major semiaxes of the ellipsoid for Apophis. In addition, a variant of a homogeneous triaxial ellipsoid with shown values of the semiaxes is considered [4].

Moreover, at this stage of the analysis, the case of uniaxial rotation of an asteroid around the small axis a_A was considered, and it was assumed that this axis of rotation has a constant orientation in space along the vector of kinetic moment $\mathbf{K}_A$ specified in the ecliptic coordinate system by the longitude $\lambda \approx 250°$ and the latitude $\beta \approx -75°$ [1-3].

When calculating the acceleration from SRP, $\mathbf{a}_3$, it was assumed for a mini-satellite that it has the shape of a ball with a diameter of D = 40 cm, mass m = 10 kg, and for it the reflection coefficient is C_{SC} = 1.4-1.5.

*Corresponding author. E-mail: ivashkin@keldysh.ru

For these models, a numerical analysis of the spacecraft motion in the close vicinity of the Apophis asteroid was performed. The starting date t_0 was selected on April 23, 2020 [1, 2], in accordance with the analysis of the trajectories of the Earth-asteroid-Earth mission.

First, an analysis was made for the SC motion under the influence of partial perturbations. This analysis showed the importance of the SRP. It was revealed that if the orbital plane is not very successful, when the direction from the Sun to the asteroid is close to the orbital plane, then the SRP will greatly affect the size of the EC orbit. In this case, the distance in the orbit apocenter increases at one half of the revolution, and the distance at the orbit pericenter decreases at the its other half, the eccentricity of the orbit increases, and the spacecraft can quickly collide with the asteroid surface or fly away from it. More acceptable is the initial choice of the satellite's orbital plane approximately perpendicular to the direction of the solar light. In this case, the SRP causes a precession of the SC orbit, a rotation of the SC orbit plane, so that the normal to the SC orbit plane remains close to the direction to the sun. In this case, it is possible to ensure the SC long-term motion near the asteroid.

Then, the main analysis was performed, where the combined influence of all disturbances was taken into account. The importance of the SRP as the main disturbance remains. Moreover, the influence of this pressure increases with increasing radius of the orbit. Therefore, for orbits close to the surface of the asteroid, the main perturbation will be the influence of non-sphericity, and for orbits with a large radius, the solar radiation pressure becomes the main one.

From the point of view of the qualitative features of the SC motion near the asteroid, the most important will be the effect of nonlinearity due to the correlation between the influence of the non-sphericity of the asteroid and the SRP. The total change in the SC orbit is not obtained by summing the partial variations. As a result, under the joint action of perturbations, the situation can be greatly worse than in the variants of partial perturbations.

Another interesting and important from a practical point of view qualitative result was the detection of an “optimal” initial radius r_0 of the SC orbit, for which, with the correct choice of the initial orbit orientation (approximately perpendicular to the sun's light), the total perturbations in the linear dimensions of the orbit will be small enough, and the spacecraft remains in the close vicinity of the asteroid for a rather long time.

For the considered mini-spacecraft, the initial radius r_0 ~ 1.5 km is optimal, and then the mini-spacecraft moves near Apophis for ~9 years, before approaching the Earth in 2029. With this approach, the Earth’s gravity becomes the main and very large perturbation, and the spacecraft flies away from the asteroid. The figure below shows a typical dependence of the spacecraft altitude H (km) above the asteroid surface for t-t_0 ~9 years, until 2029.

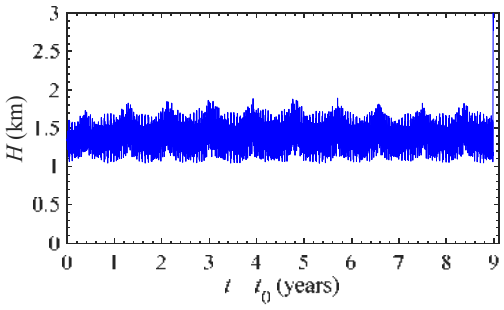

Figure 1. The evolution of the mini-spacecraft altitude above the surface of the asteroid Apophis

CONCLUSIONS

The analysis performed has shown the existence of the asteroid satellite’s stable orbits, which allow the motion of spacecraft near the asteroid for several years before the asteroid approaches the Earth in 2029. This provides an opportunity to realize radio measurements of satellite motion parameters by ground measurement stations and to define better the Apophis orbit.

References

[1] Ivashkin V.V., Lang A. Optimum Trajectories for an Earth-Asteroid-Earth Mission with a High Thrust Flight. *Doklady Physics*. 64, N 1: *14-19*, 2019.
[2] Ivashkin V.V., Lang A. Analysis of Spacecraft Orbital Motion around the Asteroid Apophis. *Doklady Physics*, 61, N 6: 288-292, 2016.
[3] Pravec P., Scheirich P., Durech J. et al. The tumbling spin state of (99942) Apophis. Icarus 233: 48-60, 2014.
[4] Guo P., Ivashkin V.V. Methods for calculating the gravitational potential of a homogenous triaxial ellipsoid and their application to the analysis of asteroid’s satellite dynamics. Preprints of M.V. Keldysh IAM. 2018. № 94, 32 p. doi: 10.20948/prepr-2018-94. URL: **http://library.keldysh.ru/preprint.asp?id=2018-94**

MULTIBODY DYNAMICS AND CONTROL OF ELECTRIC SCOOTERS

Daniel García-Vallejo*[1], Werner Schiehlen[2], and Alfonso García-Agúndez[1]
[1]Universidad de Sevilla, 41004 Seville, Spain
[2]University of Stuttgart, 70550 Stuttgart, Germany

Summary Everyday more and more companies are joining the business of electric single-passenger vehicles for urban micro-mobility. These single-person vehicles are usually based on the use of small diameter wheels as a rolling element. The modeling and computational analysis of their dynamics, as well as the study of their stability and, therefore, of the physical parameters that decisively influence it, are the object of this project. The theoretical results for bicycle lateral stability analysis are used for escooters. The knowledge of how the main parameters of the model affect its stability and control will allow design modifications that may lead to safer vehicles and may result in the reduction of accidents in urban mobility through these vehicles.

LATERAL STABILITY AND CONTROL

The lateral motion is related to the balancing required for two-wheelers. In particular, the bicycle research reported in [1, 2] resulted in a validated benchmark. The equations of lateral motion can be reduced to two degrees of freedom subject to 25 parameters. The equations of motion linearized to riding straight ahead read as

$$\boldsymbol{M}\ddot{\boldsymbol{q}} + v\boldsymbol{C}_1\dot{\boldsymbol{q}} + \left[g\boldsymbol{K}_0 + v^2\boldsymbol{K}_2\right] = \boldsymbol{f} \tag{1}$$

where the vector of generalized coordinates $\boldsymbol{q} = [\phi(t)\ \ \delta(t)]^T$ represents lean or roll motion, and the steering angle. The generalized torques $\boldsymbol{f} = [T_\phi(t)\ T_\delta(t)]^T$ describe lean disturbances and steering torques by the rider. The constant matrices $\boldsymbol{M}$, $\boldsymbol{C}_1$, $\boldsymbol{K}_0$ and $\boldsymbol{K}_2$ represent inertia, velocity dependent damping, gravitational stiffness as well as gyroscopic and centrifugal effects.

Computing the eigenvalues of the linearized equations to check the lateral stability, see Ref. [1, 2], it turns out that the benchmark bicycle is statically unstable at low speeds, asymptotic stable for medium speeds (4-6 m/s) and oscillatory unstable at high speeds. However, the self-stability is weak.

In this project, the SEAT eXS Kickscooter ES2 powered by Segway-Ninebot is used. Detailed information is available in the user manual [3]. The corresponding 25 parameters of the escooter were recently computationally evaluated and documented in Ref. [4, 5]. Now, it turns out that the benchmark escooter is completely unstable, it can't be ridden freehanded at all, Fig. 1a). However, for bicycles at low and high speeds as well as for escooters at all speeds stable riding is achieved by steering torques controlled by the experience of the rider.

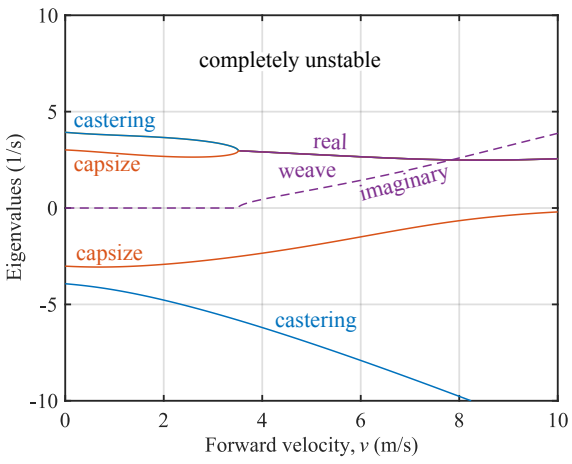

a)

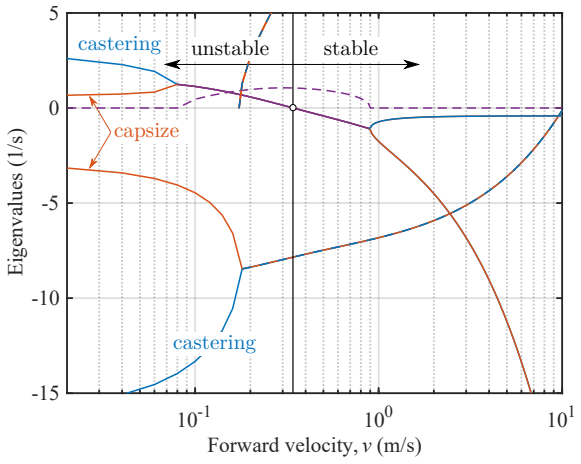

b)

Figure 1: a) Eigenvalues from the linearized speed analysis for the benchmark eXS KickScooter [4] without control;
Figure 1: b) Eigenvalues from the linearized speed analysis for the controled kickscooter in a semi logarithmic speed scale.

In 2014 Lipp [6], utilized different strategies to stabilize the lateral motion of the benchmark bicycle [1] based on instantaneous and delayed feedback. In principle, the idea of the controller is to generate a steering torque to compensate the lean of the bicycle. This leads to the following steering torque control law:

$$T_\delta = k_p\phi + k_d\dot{\phi}, \tag{2}$$

*Corresponding author. E-mail: dgvallejo@us.es.

where k_p and k_d are two gains that needs to be fixed. It makes sense to explore the use the same controller model (with instantaneous feedback) to stabilize the lateral motions of a kickscooter, too, in upward advance at constant velocity.

Figure 1b) shows the stability diagram of a controlled kickscooter in a logarithmic x-axis to better show the behaviour at low speed. The gain values were larger than those used for the bicycle benchmark controller in Lipp's Thesis (k_p = 0.2 Nm/rad and k_d = 20 Nm/rad/s) [6]. The stability diagram for the kickscooter in Fig. 1b) has been obtained with gains k_p = 85 Nm/rad and k_d = 205 Nm/rad/s. It is interesting that the stability is always lost for low enough speeds. According to the behaviour shown by the system, the controller behaves in such a way that the proportional gain, k_p, has larger influence for low speed while the derivative gain, k_d, has larger influence for high speeds.

MULTIBODY MODEL OF THE ESCOOTER AND THE DRIVER

A three dimensional multibody model of the escooter with the driver is developed, see Fig. 2a) where lean and steer angles are also represented. The model consists of five main bodies: the two wheels, the footboard, the handlebar and the driver, which is assumed to be connected by a spherical joint to the foot board. The wheels are modeled both as ring shaped and toroid shaped wheels, with the ground contact modeled as rolling without slipping. The escooter and the driver are constructed in an open kinematic chain with 6 coordinates for the footboard, 1 for the handle bar, 2 for the wheel rotations and 3 for the driver. A set of 4 (ring wheels) or 6 (toroidal wheels) holonomic plus 4 non-holonomic constraints arise from the contact with the flat ground. In a subsequent step, the stiffness and damping of the two suspensions are included in the model, by adding the required suspension dofs. In order to find the stiffness and damping constants, some test have been carried out in the laboratory of Mechanical Engineering of the University of Seville, see Fig. 2b) and Fig. 2c), where static and dynamic harmonic tests were conducted. Details of the results of the analysis can be found in Ref. [4].

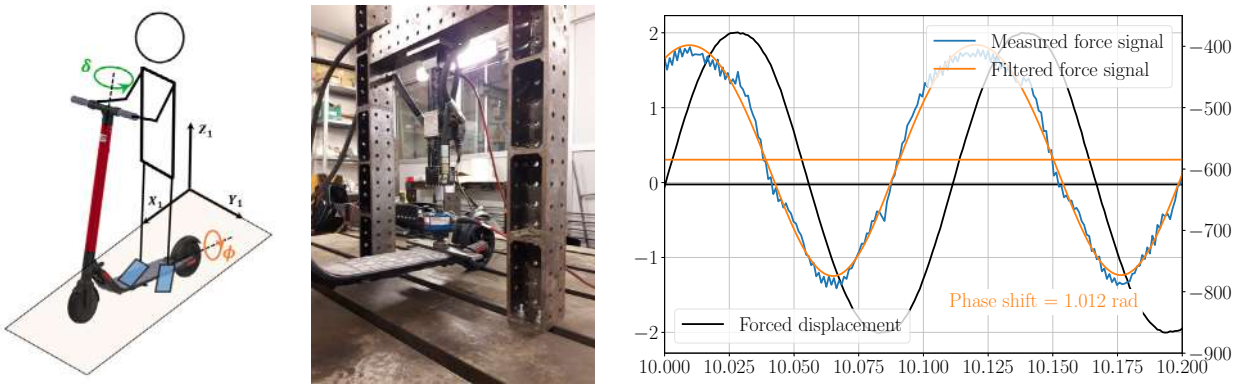

a) b) c)

Figure 2: a) Model of the Kickscooter, considering the rider; b) picture of the kickscooter during the tests for stiffness and damping estimation; and c) results of the dynamic tests for damping parameter estimation: measured and filtered load signals together with displacement with the load applied close to rear axis at a frequency of 9 Hz.

SIMULATION RESULTS

Numerical simulations of the multibody model were carried out to validate the stability behaviour of the linearized model described in Fig. 1. In addition, simulations are used to study the accuracy and efficiency of the ring shaped and torus shaped wheel models. The driver action is approximated by adding a harmonic relative motion between the driver modeled as an inverted pendulum and the footboard.

References

[1] Meijaard, J.P., Papadopoulos, Jim M., Ruina, A. and Schwab, A.L.: Linearized dynamics equations for the balance and steer of a bicycle: a benchmark and review. *Proc. R. Soc. A* **463**, 1955–1982, 2007.

[2] Kooijman J.D.G., Schwab A.L. and Meijaard, J.P.: Experimental validation of a model of an uncontrolled bicycle. *Multibody System Dynamics* **19**, 115–132, 2008.

[3] Segway product instructions manuals: Website, `http://eu-en.seway.com/support-instructions`, last accessed 2020/10/18.

[4] García-Vallejo, D., Schiehlen, W. and García-Agúndez-Blanco, A. *eXS KickScooter Benchmark Documents*. Institute Report **66**. Institute Eng. Comp. Mechanics, Stuttgart 2020.

[5] García-Vallejo, D., Schiehlen, W. and García-Agúndez-Blanco, A. *Dynamics, Control and Stability of Motion of Electric Scooters*. Advances in Dynamics of Vehicles on Roads and Tracks, Lecture Notes in Mechanical Engineering. Proceedings of the 26th Symposium of the International Association of Vehicle System Dynamics, IAVSD 2019, August 12-16, 2019, Gothenburg, Sweden. Springer, Cham, 1199-1209, 2020.

[6] Lipp, G.M.: *Single-track Vehicle Dynamics and Stability*, `https://www.semanticscholar.org/author/Genevieve-M.-Lipp/50854588?sort=influence&pdf=true/2014/`, last assessed 2020/10/18.

HOW HUMAN SITTING ON THE SWING PUMPS IT

Alexander Formalskii*, Liubov Klimina
Institute of Mechanics, Lomonosov Moscow State University, Moscow, Russia

Summary The three-link hinged mechanism as a model of person sitting on the swing is considered. In the knee- and hip-joints of this model, the control torques limited in absolute value are applied. Problem of generation of oscillations/rotations about the suspension joint is studied. First, the double-link mechanism is analyzed as auxiliary (simplified) model of a person sitting on the swing. For this auxiliary model, the autonomous feedback control strategy is designed in order to maximize the amplitude of the swing at the end of each semi-oscillation. Then it is shown that the similar strategy allows solving the named above problem for the three-link hinged mechanism. Designed control torques depend on the angle and angular speed of the swing. Numerical simulation is performed.

INTRODUCTION

It is possible to find in the literature many papers devoted to the swing pumped by human standing or sitting on it (see, for example, [1-5]). Here we study a rigid swing with a sitting human. Most authors consider double-link models of a person on the swing while here three-link hinged model is investigated. The quasi-optimal feedback strategy of the swing pumping is found with respect to the rate of increasing of amplitude. It is shown by numerical simulation that this strategy can pump the swing to oscillations with constant amplitude (if a viscous friction at the suspension joint is taken into account) as well as to rotations. This strategy is close to anthropomorphic one.

SIMPLIFIED MODEL: STATEMENT AND SOLUTION OF THE PROBLEM

Let us consider the double-link mechanism as an auxiliary model of a person sitting on the swing (see figure 1). In this model, a human is substituted by a single rigid body. Angle θ is a limited control input: $\theta_{\min} \le \theta \le \theta_{\max}$. The angle of rotation of the swing is denoted as φ.

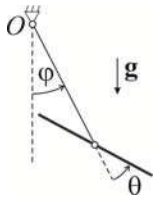

Figure 1: The scheme of the simplified double-link mechanism.

The quasi-optimal control strategy is designed in order to pump the swing with large as possible amplitude. In other words, we maximize the swing deviation from the vertical at the end of each semi-oscillation. The designed control strategy is presented by the picture in figure 2.

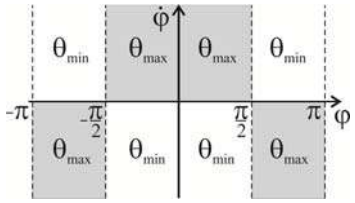

Figure 2. Dependence of control input θ on angle φ and angular speed $\dot{\varphi}$.

The following relay-type function $\theta(\varphi, \dot{\varphi})$ corresponds to the program law shown in figure 2:

$$\theta(\varphi, \dot{\varphi}) = \begin{cases} \theta_{\max}, & \text{if} \quad \dot{\varphi}\cos\varphi \ge 0, \\ \theta_{\min}, & \text{if} \quad \dot{\varphi}\cos\varphi < 0. \end{cases} \tag{1}$$

PLANAR THREE-LINK HINGED MECHANISM

The three-link mechanism is shown in figure 3. Link *HP* models a body, link *PK* – both thighs, and link *KF* – both shins. The inter-link hinge *K* models two knee-joints, the hinge *P* – two hip-joints. Link *PK* is rigidly joined to the swing (the rigid rod) pivotally attached to the suspension joint *O*. The viscous friction torque at axis *O* with coefficient *c* is taken into account.

*Corresponding author. E-mail: formal@imec.msu.ru.

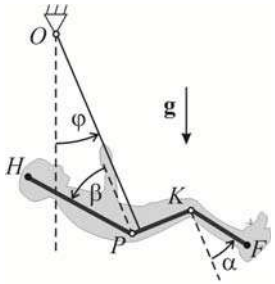

Figure 3. Three-link hinged mechanism as a model of human sitting on the swing.

Two limited control torques are applied at inter-link joints K and P. Thus, the system has three degrees of freedom, but only two control torques are applied. So, this system is under-actuated one. Angles α in joint K and β in joint P are limited: $\alpha_{\min} \le \alpha \le \alpha_{\max}$, $\beta_{\min} \le \beta \le \beta_{\max}$. The limitation upon these angles is modeled via relatively strong single-side spiral springs in joints K and P which ensure that angles α and β do not leave the prescribed domains. These springs model ligaments and tendons. The goal of the control is to pump the swing to the largest amplitude taking into account the restrictions imposed on the control. In this paper, the solution that is "close to optimal" is proposed. Function (1) is used as the program function in the initial problem for the three-link mechanism (substituting α or β instead of θ). Control torques are designed as combinations of linear feedbacks with respect to the differences between the current and program angles and their derivatives. Efficiency of this control strategy is illustrated by numerical simulation with anthropomorphic parameters of the mathematical model. This simulation shows that if friction coefficient c is rather large, then oscillations of the swing tend (if time t grows) to a stationary oscillatory mode (see figure 4a) corresponding to a cycle in the configuration space. But if friction coefficient c is sufficiently small, then the swing is pumped to a stationary rotation (see figure 4b) corresponding to the cycle in the configuration space $(\varphi \bmod 2\pi, \alpha, \beta)$. These cycles are attracting ones.

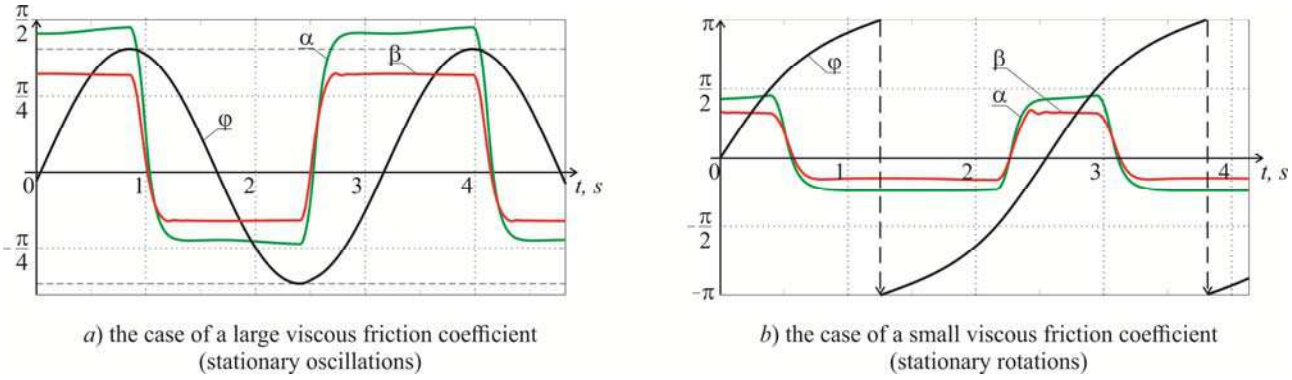

a) the case of a large viscous friction coefficient (stationary oscillations)

b) the case of a small viscous friction coefficient (stationary rotations)

Figure 4: Stationary oscillations and rotations of the swing.

CONCLUSIONS

The designed control maintains oscillations in wide range of amplitudes as well as rotations with a constant period depending on the restrictions upon angles α, β and on the viscous friction coefficient c.

References

[1] Case W.B., Swanson M.A. (1990) The pumping of a swing from the seated position. *American J. of Physics* **58**(5): 463-467.
[2] Wirkus S., Rand R., Ruina A. (1998) How to pump a swing. *The College Mathematics J.* **29**(4): 266-275.
[3] Roura P., González J.A. (2010) Towards a more realistic description of swing pumping due to the exchange of angular momentum. *European J. of Physics* **31**(5): 1195.
[4] Linge S.O. (2012) An assessment of swinger techniques for the playground swing oscillatory motion. *Computer methods in biomechanics and biomedical engineering* **15**(10): 1103-1109.
[5] Nikolov S., Zaharieva D. (2017) Dynamics of swing oscillatory motion in Hamiltonian formalism. *Mechanics, Transport, Communications* **15**(3): VII-7-VII-12.

INTEGRATED SIMULATION OF DYNAMICAL-OPTICAL SYSTEMS USING MULTIBODY APPROACHES

Peter Eberhard* and Luzia Hahn
Institute of Engineering and Computational Mechanics, University of Stuttgart, Stuttgart, Germany

Summary In this work, methods and procedures are investigated for the simulation of the dynamical behavior of high-performance optics like lithography objectives or mirror telescopes. Flexible multibody systems in combination with model order reduction methods and optical system analyses are used for transient simulations of the dynamical behavior of optical systems at low computational cost. In addition, the influence of temperature changes in optical lenses on the dynamical-optical systems will be analyzed using the proposed method.

INTRODUCTION AND MODELING

High-performance optical instruments like lithographic objectives or astronomical telescopes, are high resolution optical systems consisting of precise mirrors or lenses. The optical elements are mounted with high accuracy and they are very sensitive with respect to mechanical vibrations and temperature changes. In order to produce wavers, scanning systems use lithography objectives to project structures for a certain time onto the wafers. During the operation time, even small mechanical disturbances of the mirrors or lenses can be sufficient to produce aberrated images. Sources of these small vibrations can be minimal excitations at the objective frame, e.g., from noise of coolers or influences of the wafer motion system. The power of the used lasers in the scanning systems rises due to ever-growing demand of throughput [1]. This heats up the lenses or mirrors and can result in thermal aberrations. The thermo mechanical behavior of the optical systems can be described by a combination of rigid body motion, small deformations, the related stresses, and the temperature distribution. In order to investigate the overall dynamical-thermal-optical behavior, multi-disciplinary methods and software tools with suitable interfaces have to be used and combined as also shown in [2] and [3]. Here, a method is proposed for simulating the performance of dynamical-optical systems and a method for the additional analysis of thermal effects in these systems. An exemplary dynamical-optical system with a controlled adaptive optics is presented.

In order to simulate the dynamical-optical system behavior, a generalized workflow for such simulations using cooperating software packages according to Fig. 1 can be used. The first step in the dynamical-optical simulation is, to model the sensitive optical components of the system separately as elastic bodies using a finite element software like ANSYS. The system matrices and the node coordinates leading to the equations of motion can then be extracted using a software like MatMorembs. Additionally, the mode shapes are extracted and can be used in a model order reduction (MOR) in order to reduce the number of degrees of freedom and to speed up the mechanical simulations. For the assembly of the system and the mechanical simulation, a multibody software like Neweul-M2 is effective. It is able to import and to join several rigid and elastic bodies into a flexible multibody system [4]. The movements and deformations of the dynamical-optical system are resulting from a numerical time integration.

For the calculation of the optical aberrations of deformed surfaces, the mode shapes of a reduced body have to be approximated accurately, e.g., using a minimal set of Zernike polynomials. Furthermore, an optical simulation yields the related wavefront aberration (WFA). For this task, the program OM-Sim is developed, where ray tracing and Fourier optical methods are implemented. Since the deformation of a dynamically excited surface results from the superposition

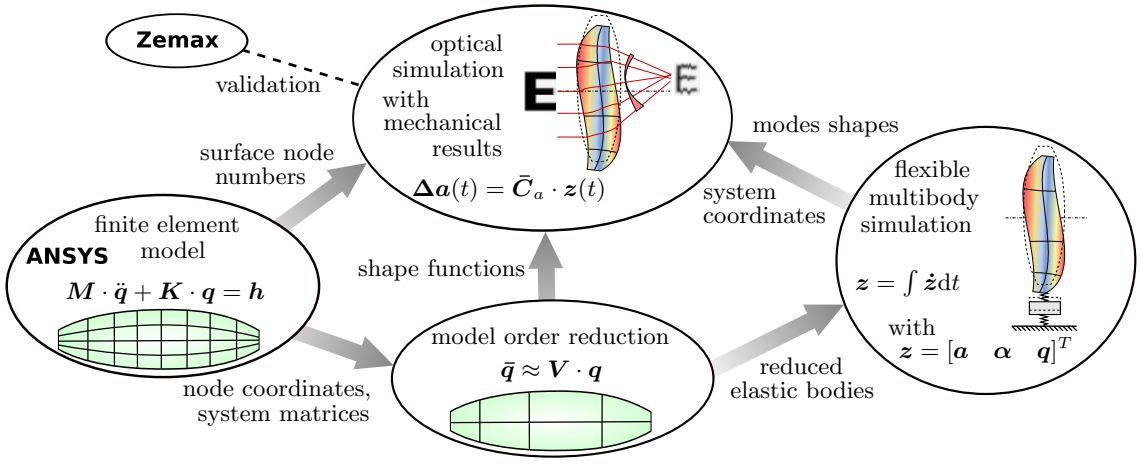

Figure 1: Workflow of the described dynamical-optical system simulation.

*Corresponding author. E-mail: peter.eberhard@itm.uni-stuttgart.de.

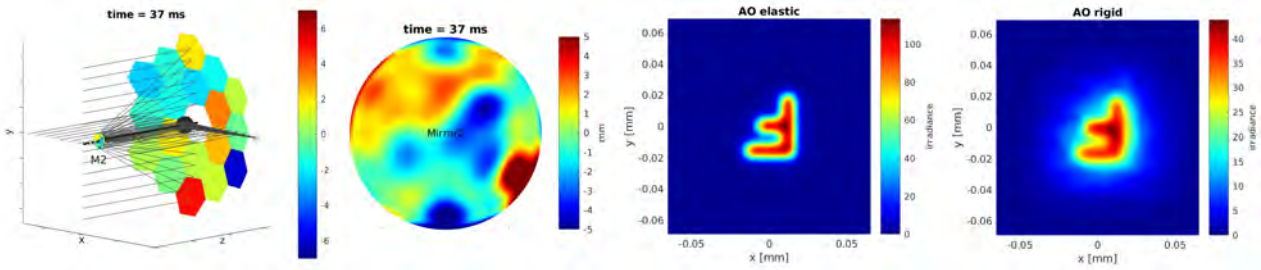

(a) ray tracing (b) deformation of M2 (c) image simulation with controlled deformation of M2 (d) image simulation with rigid M2

Figure 2: Snapshot of the dynamical-optical simulation of a segmented mirror with a controlled deformation of the second mirror (a), (b) and the resulting images after an exposure duration of 100 ms with the shape of the letter 'F' with a controlled deformation of M2 (c) and without the deformation of M2 (d).

of the mode shapes, the corresponding WFA can also be superposed if the mechanical disturbances are small enough to ensure diffraction limitation for the optical behavior. This case is mostly given in our applications and thereby, the overall integrated model considering the mechanical-optical behavior can even be regarded as a linear system [3].

Dynamical-Thermal-Optical System Analysis

Additional to mechanical disturbances, high resolution optical systems are sensitive to thermal influences. The refraction index changes with the temperature. Thus, the heating of the lens caused by the passing light or environmental influences can lead to thermal aberrations. For the additional analysis of transient thermal effects in dynamical-optical systems a thermal analysis of the optical elements has to be performed using FE-Methods. In order to consider the temperature dependency of the refraction index in the ray tracing, the discrete node temperatures must be described analytically, i.e. with polynomials. Cylindrical polynomials are well suited, especially for circular lenses. The combination of Zernike polynomials for the circular area with any one-dimensional polynomial like Chebyshev polynomials for the height portion is useful. In that way, the refraction index changes within an optical element due to temperature changes can be considered during the ray tracing and thermal WFA can be calculated. The superposition of the thermal WFA and the dynamical WFA makes the simulation and analysis of the transient behavior of dynamical-thermal-optical systems possible.

EXAMPLE AND CONCLUSIONS

As an example of the performance of an integrated dynamical-optical system simulation a segmented mirror with an adaptive optic (AO) is presented in Fig. 2. The mirror segments are mechanically disturbed in the z-direction using a predefined movement. The task of the AO unit is to control the deformation of the elastic mirror M2 such that the current aberration is compensated. This ensures an undisturbed space observation or perfect image exposure. The lightweight structures of a telescope mirror are sensitive with respect to deformations and dynamical disturbances. During the astronomical observation, e.g., dynamic wind loads, the AO unit, or other motion systems can unintentionally excite the whole system. In order to compensate for the resulting mechanical vibrations, they can be detected in real-time, e.g., using Laser Doppler vibrometers or they can be estimated by a model-based state observer. Based on this, the reconstruction of the mechanical mirror deformation can be performed [5]. Thus, the resulting optical aberrations can be compensated with a controlled deformation of the second mirror. The improvement of the image simulation with the controlled M2 in Fig. 2 (c) in comparison to the image simulation with the rigid mirror M2 in Fig. 2 (d) illustrates this compensation.

References

[1] Zhao, L.; Dong, L.; Yu, X.; Li, P.; Qiao, P.: Active lens for thermal aberration compensation in lithography lens. Applied Optics, Volume 57(29), pp. 8654-8663, 2018.

[2] Wengert, N.: Gekoppelte dynamisch-optische Simulation von Hochleistungsobjektiven. (in German), Dissertation, Schriften aus dem Institut für Technische und Numerische Mechanik der Universität Stuttgart, Vol. 40, Shaker Verlag, Aachen, 2015.

[3] Störkle, J.: Dynamic simulation and control of optical systems. Dissertation, Institut für Technische und Numerische Mechanik der Universität Stuttgart, Vol. 58, Shaker Verlag, Aachen 2018.

[4] Schwertassek, R.; Wallrapp, O.: Dynamik flexibler Mehrkörpersysteme. (in German), Vieweg, Braunschweig, 1999.

[5] Störkle, J.; Hahn, L.; Eberhard, P.: Simulation of Segmented Mirrors with Adaptive Optics. Advanced Optical Technologies, Volume 8(2), pp. 119-127, 2019.

MULTI-ROBOT OBJECT TRANSPORTATION WITH OPTIMIZED MANIPULATION KINEMATICS

Henrik Ebel*, Wei Luo, and Peter Eberhard
Institute of Engineering and Computational Mechanics, University of Stuttgart, Germany

Summary Employing multiple, cooperating robots for object manipulation can increase flexibility, robustness, and efficiency of operation. However, it introduces challenges regarding the coordination of the motion of the involved robots. With the cooperative transportation of arbitrary polygonal objects by mobile robots, this contribution focuses on a challenging subtask in multi-robot object manipulation. The contribution shows how the kinematic requirements of a successful transportation can be cast into an optimization problem, considering a robustness measure to reduce the time spent on reorganization. Furthermore, it is shown how the resulting non-convex problem can be solved by means of distributed optimization. Applying a distributed control scheme, challenging simulation results and insights from hardware experiments show the capabilities and applicability of the transportation strategy.

In recent times, the application of autonomous robotic systems has lead to efficiency gains in manufacturing, logistics, and transportation. In many applications, improved capabilities with regard to the manipulation and transportation of objects have contributed to this development. Further potential for progress may be found in the application of multi-robot systems, since they may increase flexibility, robustness, and efficiency of operation by means of a closely coordinated cooperation between multiple robots. Additional robots may join if larger or heavier objects need to be handled, and the robots may be able to reconfigure and continue task solution in case of hardware failures of individual robots. On the flipside, however, a successful coordination of the motion of the involved robots may be challenging and strongly depends on the type of object handled, with the multi-robot system ideally adapting self-reliantly to different scenarios. In light of these considerations, this contribution looks at a class of cooperative transportation problems as a model task in the area of multi-robot object manipulation. This kind of task has been studied extensively in scientific research, with the proposed approaches varying greatly with respect to the methods used, types of objects transported, robot dynamics considered, and the type of physical connection to the object [1]. In some approaches, the robots attach rigidly to the object, e.g. by means of suitably designed grippers, while in others, the robots merely push the object yielding unilateral constraints. This contribution studies the latter case, because it allows for a swift reorganization around the transported object. Dynamics-wise, the robots are assumed to not be subject to any non-holonomic constraints. An illustration of the task can be seen on the left-hand side of Figure 1, whereas the right-hand side shows a group of real-world robots that meet the dynamic requirements and that have been purpose-built at the ITM for this contribution's task.

Existing approaches are usually limited to different subclasses of object shapes that can be handled, often enough restricting themselves to convex shapes [2], or even cuboid or ellipsoidal shapes [1, 3, 4]. In contrast, by means of a distributed optimization taking into account the kinematic requirements of a successful transportation, this contribution's scheme can deal with any kind of polygonal shape, including non-convex ones. The intricacies of the formulation of the underlying optimization problem are discussed in detail. On the one hand, the robots need to be able to compensate the current translational and rotational errors of the object. Therefore, for instance, the translational error must be representable as a conic combination of the inner normal vectors at the contact points. On the other hand, configurations shall be preferred that do not necessitate immediate reorganizations if the desired transportation direction changes. To that end, a robustness measure is proposed that allows the evaluation of the robustness of a given configuration towards changes of

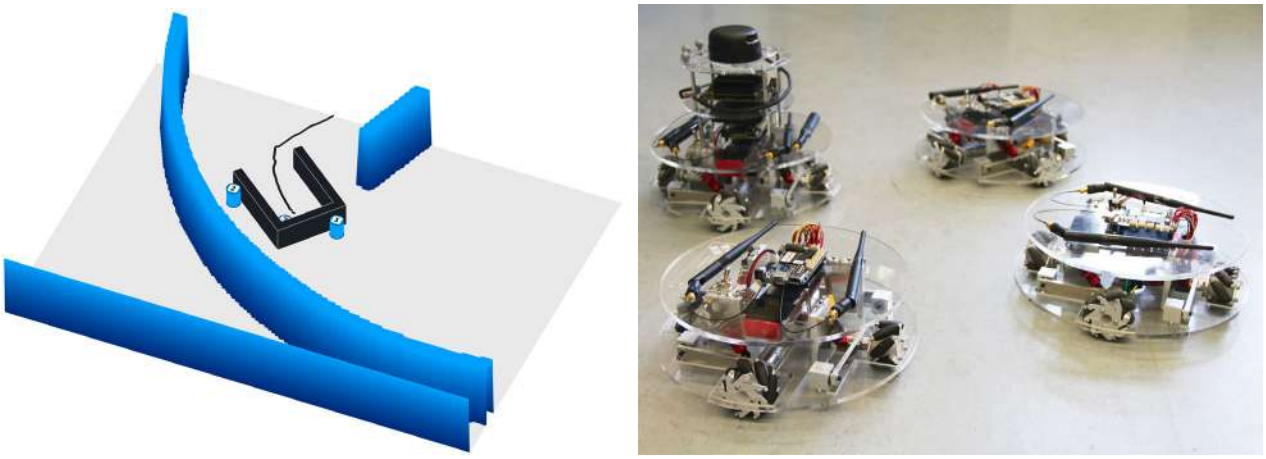

Figure 1: The left-hand side illustrates a transportation scenario in which three robots transport a U-shaped object through a narrow passageway, whereas the right-hand side shows robots tailor-made for such a transportation task, see www.itm.uni-stuttgart.de.

*Corresponding author. E-mail: henrik.ebel@itm.uni-stuttgart.de.

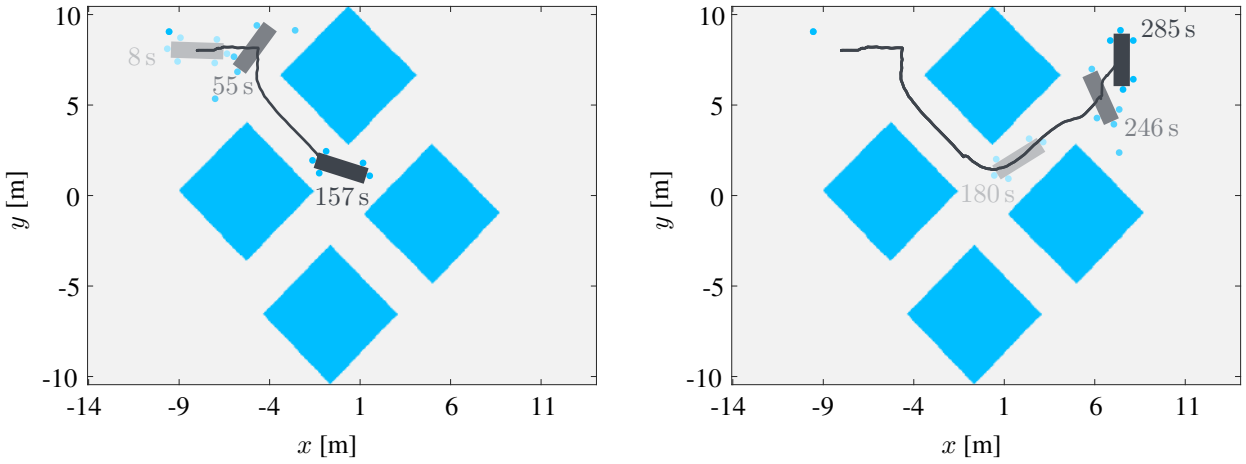

Figure 2: Simulation result with up to 6 robots transporting an object through an only partly known environment. The upper obstacle is discovered during system runtime, and robots are joining and leaving the transportation process in the course of the simulation.

the transportation direction. Incorporating this measure into the optimization problem enables a more efficient transportation process with less time spent on reorganization. It is shown that the resulting optimization problem is non-convex, with potentially multiple local minima. Due to its properties, the problem is solved with a custom, distributed version of an augmented Lagrangian particle swarm optimization algorithm [5].

While this aspect is in the focus of the contribution, the challenges posed by the task, and henceforth discussed in the contribution, are manifold. Ranging from the modeling of the robots and objects for simulation and for control synthesis purposes, to distributed control design, and to the navigation through obstacle-ridden environments, all major subaspects are discussed. Building upon our previous work [6, 7], having found a kinematically suitable configuration around the object, the task is treated as a formation control task. The resulting formation control problem is solved by means of distributed model predictive control. The latter is an optimization-based control approach, in which, in each time step, an optimal control problem is solved over a finite time horizon to obtain the control input, allowing to explicitly incorporate constraints in the optimization problem [8]. In this contribution's distributed setting, each robot solves its own optimization problem concurrently to the other robots, considering communicated information to allow for cooperative behavior [9].

Having introduced the transportation strategy and the underlying methods, the contribution intently analyzes the properties and performance of the multi-robot system in a variety of challenging and large-scale simulation scenarios, with different kinds of objects, requiring different transportation configurations. This includes scenarios that require reorganization, with robots dropping out of and rejoining the transportation process. Furthermore, scenarios are considered in which also unknown obstacles complicate the transportation process, requiring a careful planning and replanning of the object motion. Figure 2 provides an example of such a scenario, with one of the four obstacles in the environment being discovered during the transportation. The contribution concludes with insights from experiments in which the proposed transportation strategy is employed to real-world robotic hardware, suggesting that the strategy translates well from simulations to experiments.

References

[1] Tuci E., Alkilabi M. H. M., Akanyeti O. Cooperative Object Transport in Multi-Robot Systems: A Review of the State-of-the-Art. *Frontiers in Robotics and AI* **5**, 2018.

[2] Chen J., Gauci M., Li W., Kolling A., Groß R. Occlusion-Based Cooperative Transport with a Swarm of Miniature Mobile Robots. *IEEE Transactions on Robotics* **31(2)**: 307-321, 2015.

[3] Yamada S., Saito J. Adaptive Action Selection Without Explicit Communication for Multirobot Box-Pushing. *IEEE Transactions on Systems, Man, and Cybernetics, Part C (Applications and Reviews)* **31(3)**: 398-404, 2001.

[4] Gerkey B. P., Matarić M. J. Pusher-Watcher: An Approach to Fault-Tolerant Tightly-Coupled Robot Coordination. In *Proceedings of the 2002 IEEE International Conference on Robotics and Automation*, 464-469, Washington, D.C., 2002.

[5] Sedlaczek K., Eberhard P. Using Augmented Lagrangian Particle Swarm Optimization for Constrained Problems in Engineering. *Structural and Multidisciplinary Optimization* **32(4)**: 277-286, 2006.

[6] Ebel H., Eberhard P. Distributed Decision Making and Control for Cooperative Transportation Using Mobile Robots. In *Advances in Swarm Intelligence: 9th International Conference, ICSI 2018, Shanghai*, Eds. Tan Y., Shi Y., Tang Q. Springer International Publishing, Cham, 2018.

[7] Ebel H., Eberhard P. Optimization-Driven Control and Organization of a Robot Swarm for Cooperative Transportation. In *Proceedings of the 8th IFAC Symposium on Mechatronic Systems (MECHATRONICS 2019)*, Vienna, 2019.

[8] Rawlings J. B., Mayne D. Q., Diehl M. M. Model Predictive Control: Theory, Computation, and Design, 2nd Edition. Nob Hill Publishing, Santa Barbara, 2017.

[9] Ferramosca A., Limon D., Alvarado I., Camacho E. Cooperative Distributed MPC for Tracking. *Automatica* **49(4)**: 906-914, 2013.

MICRO-SLIP CONTROL OF WET DUAL CLUTCH TRANSMISSION BASED ON MODEL PREDICTIVE CONTROL METHOD

Xiwen Wang[1], Tongli Lu*[1], Leila Bridgeman [2]
[1]School of Mechanical Engineering, Shanghai Jiao Tong University, Shanghai, P.R. China
[2]Department of Mechanical Engineering and Materials Science, Duke University, Durham, USA

Summary In order to attenuate the vibration of the powertrain and improve the performance of wet dual clutch transmission, micro-slip control based on model predictive control is proposed. The vehicle powertrain with a hydraulic actuator model is modelled in MATLAB/Simulink. After verifying the feasibility and stability of the control algorithm with a simplified control-oriented model by applying appropriate terminal set and terminal cost, the model predictive controller is applied to enable a desired micro-slip on the clutches. The controller is validated by simulation works and the numerical results indicate that the proposed control strategy can reduce the gearshift time, improve the driveability and fuel economy of wet dual clutch transmission.

INTRODUCTION

Due to the high efficiency and quick gearshift response without power interruption, dual clutch transmissions (DCTs) are gradually favoured by vehicle manufactures. Nowadays, traditional control strategies keep the clutches locked after launch or gearshift, resulting in engine torque fluctuations to be transmitted through transmission, thus reducing drive comfort to some extent. An innovative control strategy based on model predictive control (MPC) is proposed to keep an appropriate micro-slip between the clutches to improve the performance of wet DCT. This article mainly includes the following aspects:

1. The dynamic system of the powertrain of wet DCT vehicle is established in MATLAB/Simulink including a hydraulic actuator model.

2. The main shifting processes of wet DCT is accurately analysed and divided to two phases: torque and inertia phase while the micro-slip control is also applied before and after gearshift. The simplified model of different stages based on the dynamic driveline model mentioned earlier is applied to reduce the complexity of the control algorithm. In order to verify the feasibility and stability of the model predictive controller, the terminal set and terminal cost are discussed and selected appropriately. Besides, the terminal set is the significant factor to ensure successful switching between all phases.

3. After sufficient and reasonable certification of the controller, it is applied to the entire driveline model with wet DCT. Simulation results of MPC strategy and lockup strategy are compared to demonstrate the necessity of micro-slip control in the wet DCT system. And the simulation results will indicate the effectiveness of the proposed model predictive controller.

DRIVELINE MODEL

A DCT-based driveline is shown in Figure 1. A DCT is consisted of two clutches, two input shafts, two output shafts and several gears. Specifically, the odd shift gears are controlled by clutch 1 and the even shift gears are controlled by clutch 2. Smooth shifting without power interruption can be achieved by disengaging one clutch while engaging the other one during the gear shift. The whole powertrain with a hydraulic actuator model is modelled in MATLAB/Simulink with Simscape block to properly express the clutch and other component in the driveline.

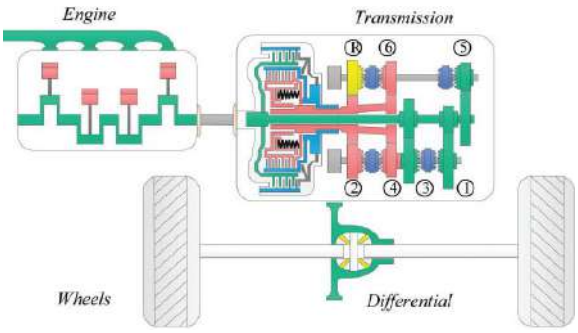

Figure 1. Configuration of a DCT-based drive

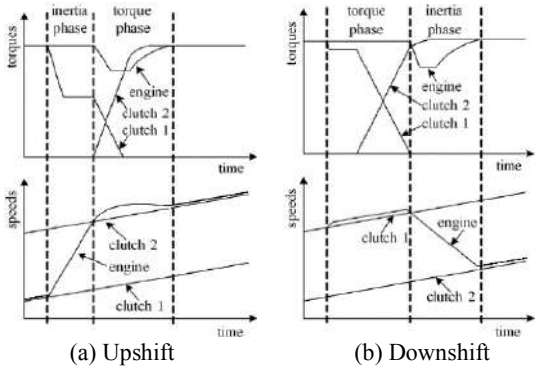

(a) Upshift (b) Downshift

Figure 2. Control strategy in gearshift

MICRO-SLIP CONTROL PRINCIPLE

There are two main phases during gearshift: torque phase and inertia phase. The power switching is achieved in the torque phase and in the inertia phase, the engine speed is changed to synchronize with the target clutch. During the upshift, the torque phase precedes the inertia phase, while the order is reversed in the downshift phase.

*Corresponding author. E-mail: **tllu@sjtu.edu.cn**
This work was supported by National Science Fund of China (Grant No. 51675326).

Micro-slip control can be applied in both torque phase and inertia phase of upshift and down shift. In torque phase, the micro-slip on the current clutch should be maintained so that the undesirable stick slip transition can be avoided. While in inertia phase, the micro-slip control can also be used to decrease the speed difference between the engine and the target clutch and keep the slip at a stable value. As a result, the simplified model of each stage in the gearshift process needs to be constructed, thereby reducing the complexity of the control algorithm.

MODEL PREDICTIVE CONTROLLER

In micro-slip control of wet DCT, the speed difference between engine and clutch, and the torque of engine and clutch are selected as states, and the variations of torque are selected as inputs. The purpose of this state selection is to keep a desired micro-slip between the engine and the clutch, and meanwhile achieve the torque switching in the torque phase or maintain the torque value in the inertia phase.

At each sample time, a constrained finite time optimization problem formed in Formulae (1) is solved to obtain the optimal control vector U_0. In this optimization, the constraints of states and inputs (X and U) are expressed in the form of polyhedron. According to the related control theory, terminal set X_f and terminal cost P are the vital factors to ensure the feasibility and stability of the control problem. Specific theories, proofs and calculation results of terminal set and terminal cost will be explained in the full text.

$$\begin{aligned} J_0^*(x(t)) = \min_{U_0} \quad & J_0(x(t),U_0) = x_N^{\mathrm{T}} P x_N + \sum_{k=0}^{N-1} x_k^{\mathrm{T}} Q x_k + u_k^{\mathrm{T}} R u_k \\ \text{subj. to} \quad & x_{k+1} = Ax_k + Bu_k,\ k = 0, \quad ,N-1 \\ & x_k \in X,\ u_k \in U,\ k = 0, \quad ,N-1 \\ & x_N \in X_f \\ & x_0 = x(t) \end{aligned} \tag{1}$$

Due to the different motion equations and constraints in different phases, a corresponding model predictive controller is constructed for each stage. And then all phases are integrated together to achieve the micro-slip control of the gearshift process for the wet DCT. Take the upshift from gear 1 to gear 2 as an example. The simulation results of micro-slip control and lockup control are compared in Figure 3.

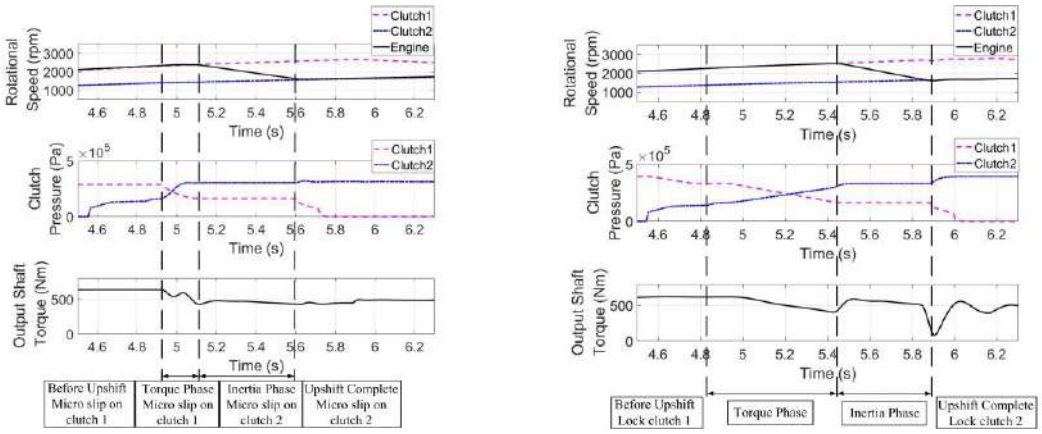

(a) Micro-slip control based on MPC (b) Lock up control

Figure 3. Numerical results of transient responses in upshift.

In the micro-slip control, the upshift process can be divided into two main stages. Before the upshift begins, the micro-slip on clutch 1 is stabilized at around 20 rpm by the model predictive controller and it is also maintained in the torque phase to avoid the undesirable stick slip transition. In the inertia phase, the micro-slip control is transferred to clutch 2. Engine speed is decreased by reducing the engine torque until it can be synchronized with clutch 2. After the upshift is complete, the micro-slip control is still on the clutch 2 to reduce the transmission of the engine torsional vibration. The whole upshift can be completed in about 0.7s and there is smaller torque fluctuation of the transmission of the transmission output shaft. While in the lockup control strategy, the torque fluctuation is larger especially in inertia phase which will reduce the shift smoothness. Besides, it takes longer time to complete the upshift in lockup controller. Therefore, the proposed micro-slip control based on MPC can achieve better shift performance. Other working conditions such as downshift are also discussed to provide a more comprehensive support.

CONCLUSIONS

The dynamic system of the vehicle powertrain is basically modelled, including a hydraulic actuator model. The micro-slip control based on model predictive control is then proposed to improve the shift quality of wet dual clutch transmission. The feasibility and stability of the control algorithm is verified and the model predictive controllers for each stage of gearshift is established to achieve micro-slip control during the entire gearshift. Simulation results are obtained by the present dynamic system and the proposed control strategy is validated to have better performance compared to the lockup control.

EVALUATING THE UDWADIA-KALABA APPROACH FOR MODELLING MULTIBODY ROTORCRAFT MECHANISMS

Aravind Kumar Kamaraj*[1], Djamel Rezgui [1], and Branislav Titurus [1]
[1]School of Civil, Aerospace and Mechanical Engineering, University of Bristol, Bristol, UK

Summary Udwadia-Kalaba (UK) approach allows for the construction of the equations of motion of a constrained multibody system as a set of ordinary differential equations (ODEs) even when redundant coordinates are employed. The approach utilizes the concept of Moore-Penrose generalized inverse of non-square matrices to calculate constraint forces that account for the holonomic and non-holonomic constraints present in the system. Thus, UK approach can improve the ease of implementation of the multibody simulation engine as a computer program and allows for the use of explicit time integration schemes. In this work, the accuracy of UK method is first explored considering the example of a double four bar mechanism for which the results have been compared against existing techniques such as minimal coordinates approach and augmented Lagrangian formulation.

INTRODUCTION

In most of the exisitng multibody dynamics software, redundant coordinates approach is adopted and the constraints are enforced with the help of Lagrange's multipliers. This results in the equations of motion of a system being formulated as a set of differential algebraic equations (DAEs). The solution of DAEs require specialized implicit numerical methods for time integration and are often tedious to implement in a computer program. Further, the accuracy of the numerical integration decreases with increase in the index of DAEs that are solved. As the engineering problems solved by these multibody dynamics software become increasingly complicated, various techniques such as index reduction techniques, constraint violation stabilization techniques and constraint violation elimination techniques have been developed to improve the accuracy of DAE solvers [1]. While most of the modern multibody dynamics software employ such improvised DAE solution algorithms, there is a huge potential for improvement in this area.

Udwadia and Kalaba, in 1992, proposed a new formulation of the equations of motion for a system of constrained rigid bodies wherein the equations of motion could be reduced to a set of ordinary differential equations (ODEs) even when redundant coordinates are used [2]. Furthermore, the formulation also treats both schleronomic and rheonomic constraints in the same way. These features make the Udwadia - Kalaba (UK) approach attractive for implementation in a computer program. We intend to develop a multibody dynamics code for the analysis of rotorcraft systems based on the UK approach. To this end, a simpler exploratory example of double four bar mechanism has been modelled using the UK approach and the accuracy of the obtained results is compared with that of those available in [3].

DOUBLE FOUR BAR MECHANISM

In [3], a collection of benchmark problems in multibody dynamics have been provided, amongst which a double four bar mechanism has been chosen for this study. This particular benchmark problem has been chosen as multiple published results based on different formulations such as augmented Lagrangian and minimal coordinates approach are available and could be used for comparison against the results obtained from this study. The initial configuration of the double four bar mechanism, with all the links having a length of 1 m and a uniform mass distribution of 1 kg/m, is indicated in Fig. 1. For each link, three coordinates have been assigned, two corresponding to the global x and y coordinates and the other corresponding to the angle subtended by the link with respect to the global x-axis. Consequently, a total of fifteen redundant coordinates and fouteen constraints have been used for the formulation.

Let the redundant coordinates be denoted as $\mathbf{q}$. If the equations of motion of the unconstrained system are represented as $\mathbf{M}\ddot{\mathbf{q}} = \mathbf{Q}(\mathbf{q}, \dot{\mathbf{q}}, t)$ and the holonmic constraints are differentiated twice and represented as $\mathbf{A}(\mathbf{q}, \dot{\mathbf{q}}, t)\ddot{\mathbf{q}} = \mathbf{b}(\mathbf{q}, \dot{\mathbf{q}}, t)$, then the equations of motion of the constrained system can be formulated based on the UK approach as follows [2]:

$$\mathbf{M}\ddot{\mathbf{q}} = \mathbf{Q} + \mathbf{M}^{1/2}\left(\mathbf{A}\mathbf{M}^{-1/2}\right)^{+}\left(\mathbf{b} - \mathbf{A}\mathbf{M}^{-1}\mathbf{Q}\right) \tag{1}$$

where the superscript $+$ denotes the Moore-Penrose generalized inverse. For the double four bar mechanism, using the UK approach leads to a set of fifteen second order ODEs as the final equations of motion. In comparison, the Lagrange multipliers method yields a set of DAEs consisting of 15 second order ODEs and 14 algebraic constraints.

RESULTS AND DISCUSSION

In [3], the time histories of the x-coordinate of displacement and velocity at joint 1 and the drift in the total energy with respect to that of the intial condition were reported by employing various formulations and ODE (or) DAE solvers. In this work, UK approach was adopted for formulating the problem and the in-built explicit ODE solver in MATLAB, *ode45*, was used for time integration. For the solver configuration, the relative tolreance was set as 10^{-5} and the other

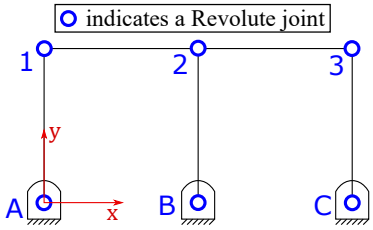

Figure 1: Schematic representation of the double fourbar mechanism.

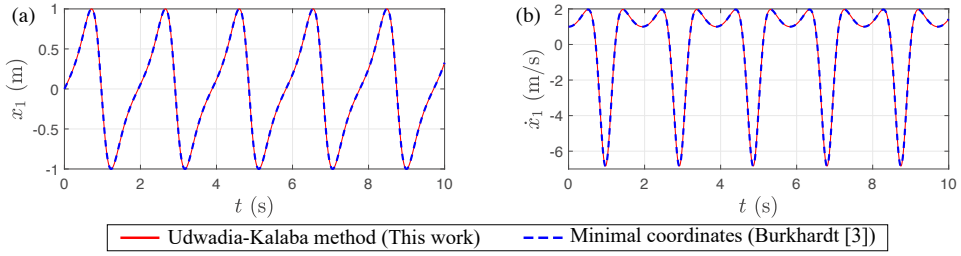

Figure 2: Time histories of the x-coordinate of the displacement and velocity at joint 1.

Table 1: Comparison of the accuracies obtained using different multibody dynamics formulations.

Researcher	**Formulation adopted**	**Solver**	**Time step (s)**	**Accuracy**
This work	Udwadia-Kalaba	ode45 (Explicit)	Variable	0.005
Roland Pastorino, Francesco Cosco	ALF with Penalty factor: 8E8 (OpenMBS)	Implicit Trapezoidal rule with Newton-Raphson iteration	Fixed: 0.01	0.0877
Javier Cuadrado	ALF with Penalty factor: 1E9	Implicit Trapezoidal rule with Newton-Raphson iteration	Fixed: 0.01	0.0917
Francisco Mouzo	ALF with Penalty factor: 1E15	Implicit Trapezoidal rule with Newton-Raphson iteration	Fixed: 0.01	0.029
Pierangelo Masarati	Lagrange multipliers based (MBDyn)	Implicit A/L stable multistep integration scheme	Fixed: 0.008	0.09
Markus Burkhardt	Non-recursive Newton-Euler formalism - minimal coordinates (Neweul-M^2)	ode45 (Explicit)	Variable	0.0015
*ALF indicates Index-3 Augmented Lagrangian Formulation with projections of velocities and accelerations				

parameters were left with default values. The simulated results corresponding to the x-displacement of joint 1 is shown in Fig. 2 (a) and that of velocity is shown in Fig. 2 (b).

In [3], the maximum drift in the total energy, $E_d(t) = E(t) - E(t_0)$, has been taken as a measure of accuracy. Hence, a lower drift in energy indicates a better accuracy. The accuracy, expressed as $\max(E_d(t))$, obtained using the UK approach is reported in Table 1 and compared aginst the results reported by other researchers in [3]. It could be seen that the UK approach provides an order of magnitude improvement in accuracy over the augmented Lagrangian method while the best accuracy is obtained with the minimal coordinates approach. This highlights the potential of UK approach as a promising candidate for the implementation of multibody dynamics formulation as a computer program.

CONCLUSIONS

The remarkable improvement in accuracy along with the ease of handling constraints in the UK approach has encouraged its implementation in the multibody dynamics suite that we intend to develop for rotorcraft applications. Further investigations regarding the applicability of UK approach to mechanisms that are of interest to the rotorcraft community will be performed and the results will be presented at the conference.

References

[1] Bauchau O. A. Flexible Multibody Dynamics. Springer, Dordrecht, 2011.
[2] Udwadia F. E., Kalaba R. E. A New Perspective on Constrained Motion. *Proc. R. Soc. Lond. A* **439**: 407-410, 1992.
[3] Library of Computational Benchmark Problems, web site **https://www.iftomm-multibody.org/benchmark/**.

*Corresponding author. E-mail: aravind.kamaraj@bristol.ac.uk

UNCERTAINTY ANALYSIS OF MECHANICAL DYNAMIC USING HHT AND LMD

Jiang Cui[1], Zhihua Zhao [*1], Jiawei Liu [1], Xuanbo Shu [1], and Gexue Ren [1]
[1]Department of Engineering Mechanics, Tsinghua University, Beijing, China

Summary For time-dependent uncertainty analysis, the response surface (RS) method suffers from a problem that the accuracy decays with time increasing. This study proposes two methods: RS method incorporated Hilbert-Huang transform (RS-HHT) and RS method incorporated local mean decomposition (RS-LMD) to solve the problem. The main steps are that firstly HHT or LMD is used to decompose the original signal into several monocomponent signals, and then the instantaneous amplitude and phase of each monocomponent are fitted with the uncertainty parameters. Two examples, the single pendulum and the slider crank mechanism, are used to show the effectiveness of the proposed methods. Both of RS-HHT and RS-LMD can get tighter bound than RS method. Furthermore, RS-LMD is a litter better than RS-HHT. When the response is monotonous, RS-HHT and RS-LMD are degenerated to RS method.

INTRODUCTION

The effect of uncertainty is significant in the engineering, because the important uncertainty factor should not be neglected [1]. One important purpose of solving the interval uncertainty dynamic problem where the uncertainty parameter is interval type rather than probabilistic type to get the upper bound (UB) and lower bound (LB), as is shown in Figure 1. The conventional response surface (RS) method is widely used to obtain the time bound and the main idea of RS method is to develop surrogate models at each time instant. The conventional RS method faces a serious problem that the accuracy deteriorates at long time instants. Many methods [2, 3] have been proposed to overcome the problem that conventional RS method possesses but did not solve the problem completely. There remains a strong need for an efficient method that can overcome the shortcoming of RS method. To this end, this paper proposes two methods: RS method incorporated Hilbert-Huang transform (RS-HHT) and RS method incorporated local mean decomposition (RS-LMD).

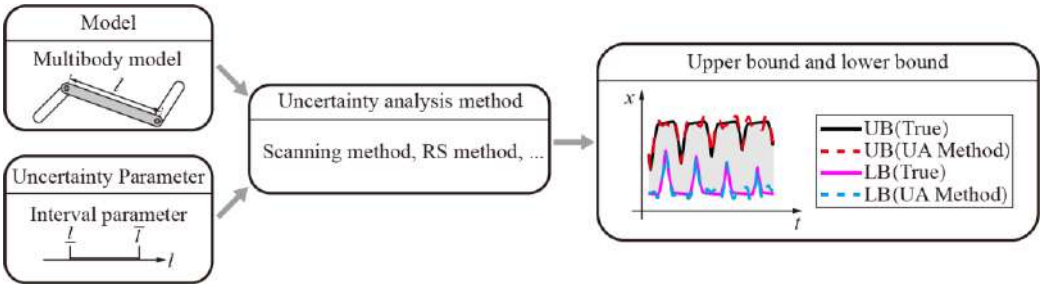

Figure 1. A schematic of the interval uncertainty analysis (UA) method for the dynamic problem.

PROBLEMS AND METHODS

The conventional response surface (RS) method shown in Figure 2(b) encounters the greatest challenge that the accuracy decreases with the increment of time. The linear single-degree-of-freedom (1DOF) model shown in Figure 2(a) is used as an example to illustrate the problem of the conventional RS method, in which the surrogate model of RS method is trained by three samples and corresponding responses. A quadratic polynomial surrogate model $P(\omega,t)$ is used to approximate the relationship between the response x and the uncertain frequency ω through three obtained points at each time instant, as is shown in Figure 2(b). When the time becomes large, RS method fails to approximate the real relationship, thus the upper and lower bound calculated from the maximum and minimum of each RS model are not accurate.

The above problem of 1DOF model can be overcome by the method shown in Figure 2(c), in which the amplitude a and phase φ are fitted with the uncertain parameter ω using the quadratic polynomial model. The relationship between the amplitude/phase and the parameter is simple and is nearly linear with time. The proposed surrogate model is

$$\text{given } t: x(\omega,t) \approx \hat{a}(\omega,t)\cos\left(\hat{\varphi}(\omega,t)\right) \tag{1}$$

where $\hat{a}$ is the amplitude surrogate model and $\hat{\varphi}$ the phase surrogate model. Therefore, the relationship is correctly approximated no matter t is small or large, and the upper and lower bound are accurate.

For the multicomponent response, the signal decomposition should be implemented before conducting surrogate models, thus RS-HHT and RS-LMD are proposed. A mechanic response is always a multicomponent signal which contains several monocomponent signals. Hilbert-Huang transform (HHT) and local mean decomposition (LMD) are two well-understood adaptive signal decomposition methods. With HHT or LMD technique, any multicomponent signal can be decomposed into a set of monocomponent signals, and every monocomponent signal can be written as $a(t)\cos\varphi(t)$ form no matter it is non-linear or linear, non-steady or steady. Combined with HHT or LMD, a new surrogate model is proposed as

*Corresponding author. E-mail: zhaozh@tsinghua.edu.cn.

$$\text{given } t: x(\mathbf{b},t) \approx \sum_{i}^{m} \hat{a}_i(\mathbf{b},t)\cos\left(\hat{\varphi}_i(\mathbf{b},t)\right) + \hat{r}(\mathbf{b},t) \tag{2}$$

where m is number of the monocomponent signals, $\mathbf{b}$ the uncertainty parameter vector, $\hat{a}_i$ the amplitude surrogate model of each monocomponent, $\hat{\varphi}_i$ the phase surrogate model of each monocomponent, and r is the residual. The surrogate model is a new surrogate type, and the non-linearity degree of the proposed surrogate model is improving with time increasing. RS method incorporated Hilbert-Huang transform is named RS-HHT, and RS method incorporated local mean decomposition is named RS-LMD.

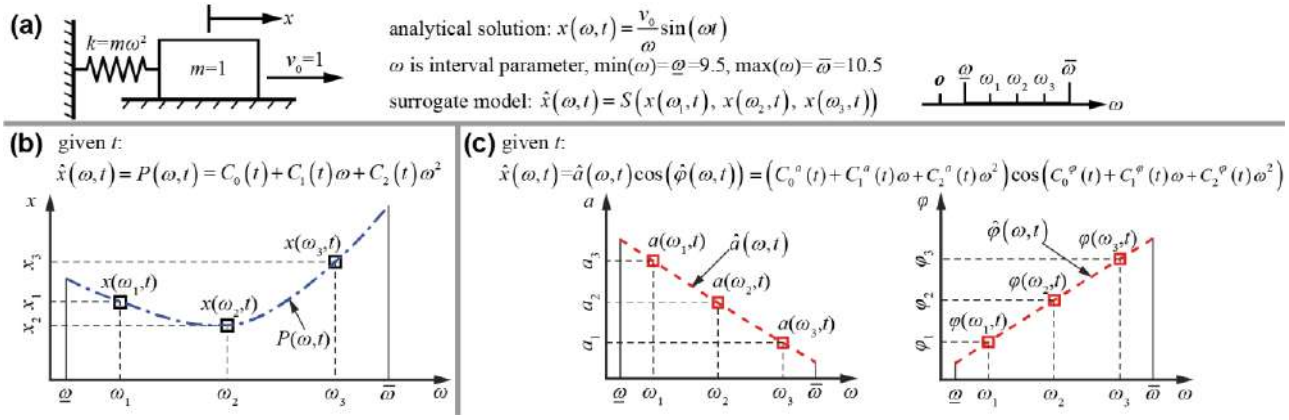

Figure 2. The problem of the conventional method and the main idea of the proposed method: (a) 1DOF model with an uncertainty parameter ω. (b) The surrogate model of the conventional method. (c) The surrogate model of the proposed method.

APPLICATIONS

A rigid slider crank mechanism is used to show the effectiveness of the proposed methods. Figure 3(a) is a rigid slider crank model with two uncertainty parameters, the crank length l_1 and the torque τ. The scanning method, conventional RS method, RS-HHT, RS-LMD are used to get the bounds of the slider displacement x_3. The scanning method is to scan the original equation to get precise bounds as a reference result using 50×50 samples. 12 samples and corresponding responses are used to train the surrogate model of RS, RS-HHT, RS-LMD method. From Figure 3(b), RS method cannot get a reasonable result, but RS-HHT and RS-LMD can approximate the real solution. From Figure 3(c), RS-HHT and RS-LMD can get high-accuracy bounds. Furthermore, RS-LMD has a little better performance than RS-HHT. RS-HHT and RS-LMD can also be effective in the flexible slider crank and flexible pendulum model.

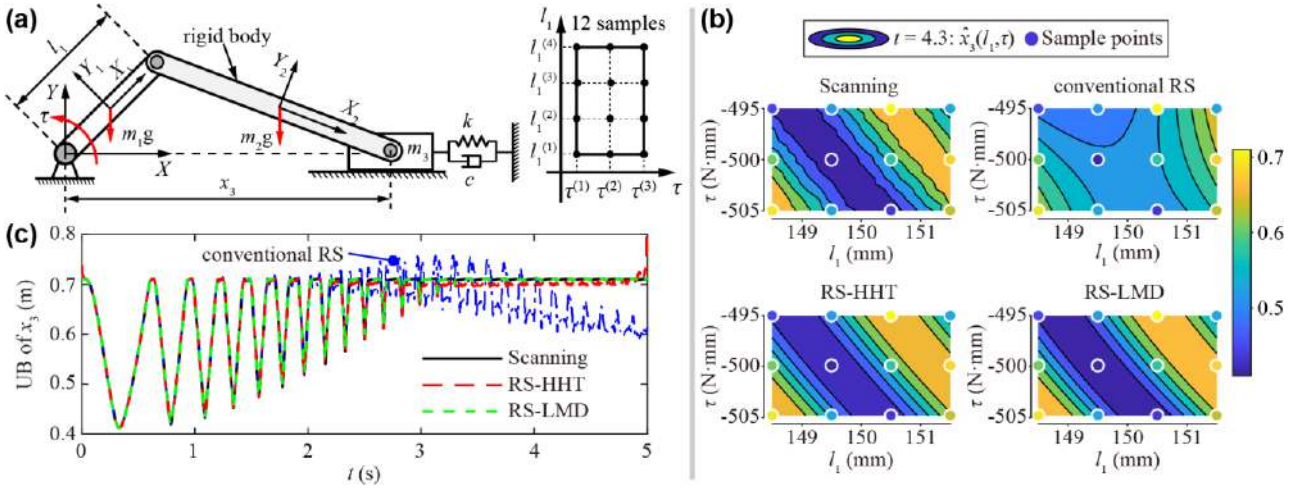

Figure 3. Uncertainty analysis of a rigid slider crank model: (a) The rigid slider crank model with 2 uncertainty parameters. (b) The surrogate models by scanning, RS, RS-HHT, RS-LMD method at t = 4.3s. (c) The upper bound (UB) of x_3 by different methods.

References

[1] D. Bonetti, G. De Zaiacomo, et al, Exomars 2016: Schiaparelli coasting, entry and descent post flight mission analysis, *Acta Astronautica* 149 (2018) 93-105.

[2] C. V. Mai, B. Sudret, Surrogate models for oscillatory systems using sparse polynomial chaos expansions and stochastic time warping, *SIAM/ASA Journal on Uncertainty Quantification* 5 (1) (2017) 540–571

[3] Z. Wang, Q. Tian, H. Hu, Dynamics of spatial rigid–flexible multibody systems with uncertain interval parameters, *Nonlinear Dynamics* 84 (2) (2016) 527–548.

SIMULATION OF ROAD SURFACES PROFILES BY A STOCHASTIC PARAMETRICAL MODEL OF SECOND ORDER

Alfons Ams
Institute of Mechanic and Fluiddynamic, Technical University of Freiberg, Freiberg, Germany

Summary Road irregularities have an important influence on the dynamic behavior of vehicles. Knowledge of their characteristics and magnitude is essential for the design of the vehicle. The problem of interest is the simulation of road surfaces profiles because modern test facilities and computer simulations of vehicle dynamics needs driving excitations. An import issue is the power spectral densities and the approximation by analytical formulas. In the paper a stochastic parametrical nonlinear model of second order with bounded amplitudes will be discussed. Some analytical and numerical results will be shown.

Road Surface Profiles

The road surface profiles are defined by ISO8608 Mechanical vibration – Road surface profiles – Reporting of measured data [1]. Figure 1 shows an example of a measured road.

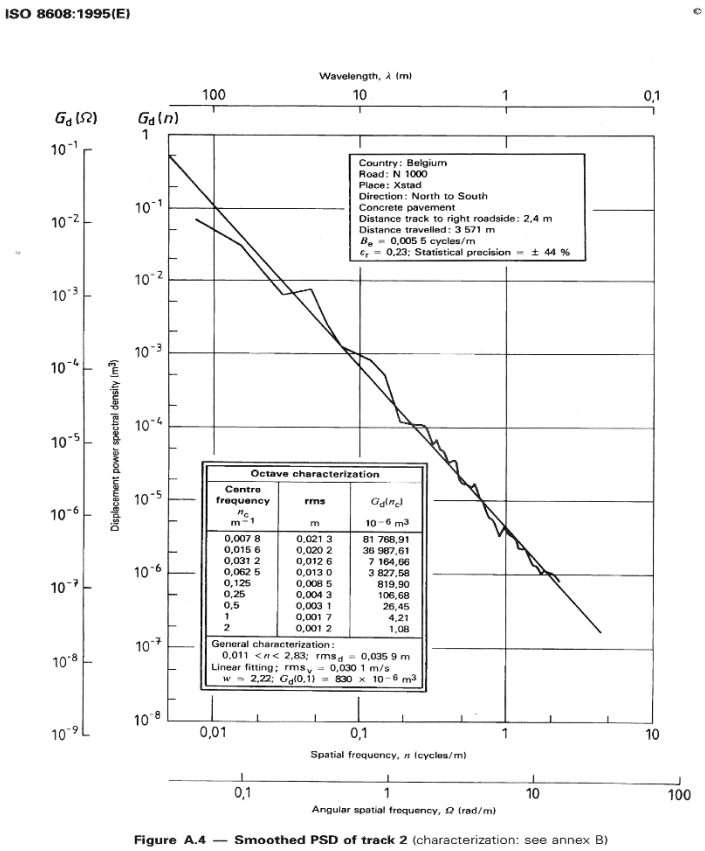

Figure A.4 — Smoothed PSD of track 2 (characterization: see annex B)

Figure 1: Measured road surface profile [1]

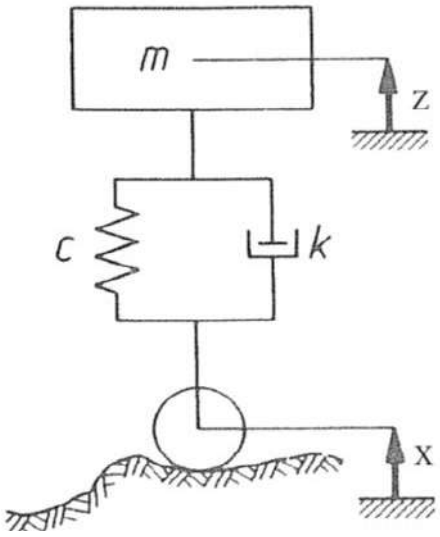

Figure 2: A quarter car (1 DOF) with road surface profile X_t

Stochastic Parametrical Model of Second Order

The stochastic parametrical nonlinear model of second order

$$\ddot{X}_t + 2\vartheta\omega_0\dot{X}_t + \omega_0^2 X_t - \frac{\sigma^2}{2}(X_0^2 - X_t^2)\dot{X}_t + \sigma\sqrt{(X_0^2 - X_t^2)(\dot{X}_0^2 - \dot{X}_t^2)}\,\dot{W}_t = 0$$

With the parameters σ intensity of white noise, ω_0 the corner frequency, ϑ the damping coefficient (Lehr), X_0 and $\dot{X}_0$ are the maximum values of the amplitudes $|X_t| \le X_0, |\dot{X}_t| \le \dot{X}_0$ and W_t the Wiener process with the mean value $\mathrm{E}\{dW_t\} = 0$ and the variance $E\{dW_t^2\} = dt$. With the coordinates of state space $X_{1t} = X_t$ and $X_{2t} = \dot{X}_t$ the stochastic differential equations (Ito) are

$$\mathrm{d}X_{1t} = X_{2t}dt$$

$$\mathrm{d}X_{2t} = (-2\vartheta\omega_0 X_{2t} - \omega_0^2 X_{1t})dt - \sigma\sqrt{(X_0^2 - X_{1t}^2)(\dot{X}_0^2 - X_{2t}^2)}\,dW_t \qquad \text{with} \quad |X_{1t}| \le X_0, |X_{2t}| \le \dot{X}_0$$

The Fokker Planck equation of the probability density function $p(x_1, x_2)$ is

$$\frac{\partial \mathrm{p}}{\partial \mathrm{t}} + x_2 \frac{\partial \mathrm{p}}{\partial x_1} - \frac{\partial}{\partial x_2}(2\vartheta\omega_0 x_2 + \omega_0^2 x_1)p - \frac{\sigma^2}{2}\frac{\partial^2}{\partial x_2^2}(X_0^2 - x_1^2)(\dot{X}_0^2 - x_2^2)p = 0$$

Examples: Probability density function $p(x_1, x_2)$

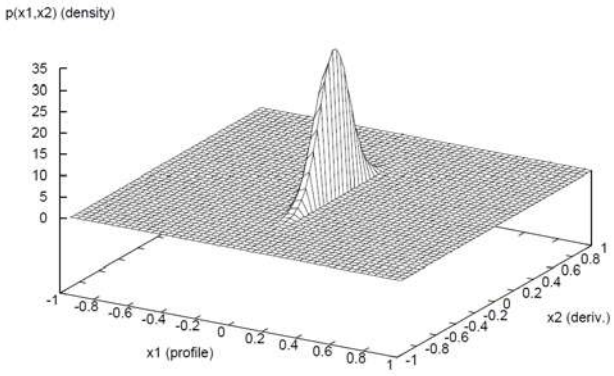

Figure 3: $\vartheta = 50, \omega_0 = 10, \sigma = 5, X_0 = 1, \dot{X}_0 = 1$

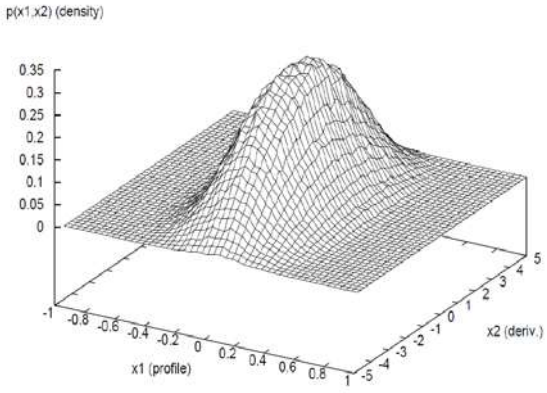

Figure 4: $\vartheta = 3, \omega_0 = 10, \sigma = 5, X_0 = 1, \dot{X}_0 = 5$

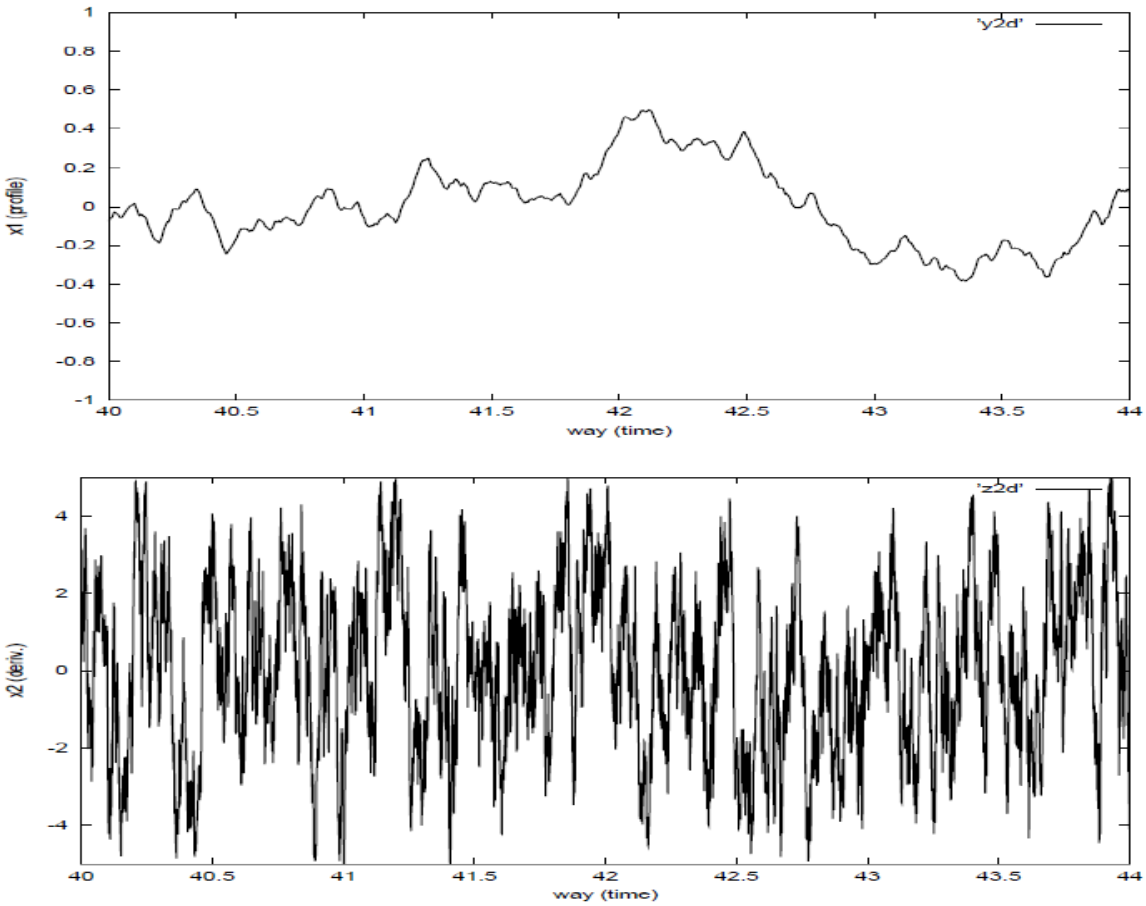

Figure 5: Numerical simulation of X_t and $\dot{X}_t$ for $\vartheta = 3, \omega_0 = 10, \sigma = 5, X_0 = 1, \dot{X}_0 = 5$

References

[1] ISO 8608:1995(E), Mechanical vibration - Road surface profiles - Reporting of measured data.
[2] Wedig W.: Dynamics of Cars Driving on Stochastic Roads, In: Spanos P., Deodatis G. (Eds), CSM-4., Rotterdam, Millpress, p. 647 - 654, 2003.
[3] Doods C. J., Robson J. D.: The Description of Road Surface Roughness, Journal Sound and Vibration, 31, p. 175 - 183, 1973.
[4] Arnold L.: *Stochastic Differential Equations*. New York, Wiley, 1974

3-D STABLE MOTION AND STABILITY ANALYSIS OF UNDERWATER GLIDERS

Bo Wang[1], Caishan Liu *1
[1]State Key Laboratory for Turbulence and Complex Systems, College of Engineering, Peking University, Beijing, China

Summary This paper focuses on the study of the equilibrium solution and the stability for the 3-D motion of underwater gliders. Equilibrium solution is critical because it represents the working pattern of an underwater glider and has essential dynamic features embedded. This stable 3-D motion, spiral mode motion, given by the equilibrium solution is the gliding mode of the underwater glider during the designated sea area observation. In order to facilitate analysis, we establish a reduced-dynamics model of the underwater glider based on symmetry reduction, and we can utilize the physical quantities projected into the quotient space to characterize the motion of the glider. We further analyse the stability characteristics of the equilibrium solution and conclude that the equilibrium solution is asymptotically stable.

INTRODUCTION

Since Stommel [1] first proposed the concept of the underwater glider, as a movable underwater measurement platform, the underwater glider has great application potential in the observation and characterization of marine ecosystems, underwater detection and seabed exploration. It glides downwards and upwards in the ocean by controlling its buoyancy to make itself negatively and positively buoyant, and it adjusts attitude by moving the location of the battery pack. The research on the motion performance of the underwater glider starts from the establishment of dynamic equations. Many scholars have contributed to the dynamic model of underwater gliders and investigated the characteristics of the stable motion [2,3]. However, these models ignore the problem of motion arbitrariness in the process of solving the equilibrium solution and the stability of the underwater glider under 3-D motion is rarely studied, which is the main motion of the observation of the designated sea area.

DYNAMICS MODELING OF UNDERWATER GLIDER

Configuration space and dynamic equation

As shown in the Figure 1, we regard the shell, the counterweight, the antenna, and the buoyancy adjustment device (gasbag) as a rigid body, and its mass is represented by m_b. The attitude adjustment system (battery pack) is served by a movable battery pack, whose mass is represented by m_c. To facilitate the description of the dynamic model of the underwater glider, we define a inertial coordinate frame $E-xyz$ and a body-fixed coordinate frame $B-XYZ$. The configuration space of the underwater glider is a six-dimensional manifold,

$$Q=\underbrace{(-\pi/2,\pi/2)\times(-\pi/2,\pi/2)}_{R}\times\underbrace{\mathrm{SE}(2)\times\ ^{1}}_{G}, \tag{1}$$

with the coordinates $\boldsymbol{q}=(\varphi,\theta,(z,x,\psi),y)$, where (x,y,z) are the coordinates of the glider buoyancy centre in $E-xyz$, and (φ,θ,ψ) are three Euler angles. In the body-fixed coordinate frame, we use $\boldsymbol{r}_b$ to represent the position vector between the gasbag buoyancy centre and the glider buoyancy centre, and use $\boldsymbol{r}_t=(l_t,e_r\cos\phi,e_r\sin\phi)$ to represent the position vector between the centre of mass of the battery pack and the floating centre, where l_t is the position of the centre of the battery pack along the X-axis, e_r is the rotation radius about the X-axis, and ϕ is the rotation angle.

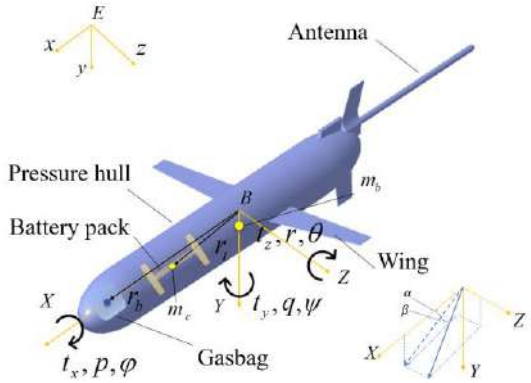

Figure 1. Schematic diagram of underwater glider structure and coordinate system.

Denote by $L:TQ\to\mathbb{R}$ the modified Lagrangian of the underwater glider system with the effect of the inertial hydrodynamics taken into account, and by $\boldsymbol{F}:TQ\to T^*Q$ the force field including gravity, buoyancy and viscous hydrodynamics. In coordinates, $\boldsymbol{F}$ takes the form $\boldsymbol{F}(\boldsymbol{q},\dot{\boldsymbol{q}})=F_i(\boldsymbol{q},\dot{\boldsymbol{q}})\mathrm{d}q^i$. The dynamic equations with six-degree-of-freedom can be established using the Euler-Lagrangian equation [3]:

$$\frac{\mathrm{d}}{\mathrm{d}t}\frac{\partial T}{\partial \dot{q}^i}-\frac{\partial T}{\partial q^i}=F_i,(i=1,\quad,6), \tag{2}$$

*Corresponding author. E-mail: liucs@pku.edu.cn

Symmetry and reduced system

Noting the decomposition $Q = R \times G$ shown in (1), we define the action of the Lie group G on Q as follows: $\forall \boldsymbol{h} \in G, \forall \boldsymbol{q} = (\boldsymbol{r}, \boldsymbol{g}) \in Q$, where $\boldsymbol{r} \in R$, $\boldsymbol{g} \in G$, we have $\boldsymbol{\Phi_h}(\boldsymbol{q}) := \boldsymbol{hq} = (\boldsymbol{r}, \boldsymbol{hg})$. More specifically, for $\boldsymbol{h} = ((a, b, \alpha), c)$, $\boldsymbol{r} = (\varphi, \theta)$ and $\boldsymbol{g} = ((z, x, \psi), y)$, we have $\boldsymbol{hq} = (\varphi, \theta, (z\cos\alpha - x\sin\alpha + a, z\sin\alpha + x\cos\alpha + b, \psi + \alpha), y + c)$. We claim that the underwater glider system has the following two symmetries:

(1) The Lagrangian is invariant, i.e., $L(\boldsymbol{q}, \dot{\boldsymbol{q}}) = L(\boldsymbol{hq}, \boldsymbol{h}_*\dot{\boldsymbol{q}}), \forall (\boldsymbol{q}, \dot{\boldsymbol{q}}) \in TQ, \forall \boldsymbol{h} \in G$, where $\boldsymbol{h}_*: TQ \to TQ$ represents the tangent map induced by the action of $\boldsymbol{h}$ on Q.

(2) The force field is invariant, i.e., $\boldsymbol{h}^*\boldsymbol{F}(\boldsymbol{hq}, \boldsymbol{h}_*\dot{\boldsymbol{q}}) = \boldsymbol{F}(\boldsymbol{q}, \dot{\boldsymbol{q}}), \forall (\boldsymbol{q}, \dot{\boldsymbol{q}}) \in TQ, \forall \boldsymbol{h} \in G$, where $\boldsymbol{h}^*: T^*Q \to T^*Q$ represents the cotangent map induced by the action of $\boldsymbol{h}$ on Q.

Therefore, we can define a reduced Lagrangian l on the quotient manifold $TQ/G \cong TR \times \mathfrak{g}$, where $\mathfrak{g}$ is the Lie algebra of G. A set of coordinates of TQ/G is given by $\boldsymbol{u} = (\boldsymbol{r}, \dot{\boldsymbol{r}}, \boldsymbol{\xi})$, where $\boldsymbol{\xi} \in \mathfrak{g}$. We have the following theorem:

Theorem 1 For a curve $\boldsymbol{q}(t) = (\boldsymbol{r}(t), \boldsymbol{g}(t)) \in Q$, $t \in [a, b]$, let $\boldsymbol{\xi}(t) = ((\boldsymbol{g}(t))^{-1})_*\dot{\boldsymbol{g}}(t)$. If $\boldsymbol{q}(t)$ satisfies the Euler-Lagrange equations (2), then $\boldsymbol{u}(t) = (\boldsymbol{r}(t), \dot{\boldsymbol{r}}(t), \boldsymbol{\xi}(t)), t \in [a, b]$ satisfies the following reduced equations:

$$\begin{cases} \dfrac{\mathrm{d}}{\mathrm{d}t}\dfrac{\partial l}{\partial \dot{r}^\alpha} - \dfrac{\partial l}{\partial r^\alpha} = f_\alpha^R, \alpha = 1, 2, \\ \dfrac{\mathrm{d}}{\mathrm{d}t}\dfrac{\partial l}{\partial \xi^a} - C_{ba}^c \xi^b \dfrac{\partial l}{\partial \xi^c} = f_a^G, a = 1, \quad, 4, \end{cases} \tag{3}$$

where $\xi^1, \cdots, \xi^4$ are the components of $\boldsymbol{\xi}$ decomposed in a basis $\{\boldsymbol{e}_a \mid a = 1, \cdots, 4\}$ of $\mathfrak{g}$, $f_\alpha^R, \alpha = 1,2$ and $f_a^G, a = 1, \cdots, 4$ are the components of $\boldsymbol{F}$ pulled back to T^*Q/G, and $C_{ab}^c, a, b, c = 1, \cdots, 4$ are the structure constants of $\mathfrak{g}$ defined by $[\boldsymbol{e}_a, \boldsymbol{e}_b] = C_{ab}^c \boldsymbol{e}_c$.

Equation (3) determines a reduced dynamic system on TQ/G:

$$\dot{\boldsymbol{u}} = \boldsymbol{Y}(\boldsymbol{u}), \tag{4}$$

where $\boldsymbol{Y}$ is a tangent vector field on TQ/G that can be obtained by transforming (3) into first-order forms.

EQUILIBRIUM SOLUTION AND STABILITY ANALYSIS

In the reduced dynamics system, we analyse the descending process in 3-D motion. We use the axis translation and circumferential rotation of the battery pack as the input conditions. Then we can get $\boldsymbol{u}_0 = [\varphi_0, \theta_0, \dot{\varphi}_0, \dot{\theta}_0, \xi_0^1, \xi_0^2, \xi_0^3, \xi_0^4]$ at each equilibrium point. In the reduced dynamic system, we can obviously transform the time-related physical quantities into time-independent physical quantities in the equilibrium solution. Under this transformation, in the equilibrium solution, $\dot{\varphi} = 0$, $\dot{\theta} = 0$. We can get equilibrium solution by changing the input pitch control and roll control of the battery pack, which do not show here due to space limitation.

For dynamic systems, we usually use the Lyapunov stability theory for analysing the stability characteristics near the equilibrium solution of the system. For the equilibrium solution $\boldsymbol{u}_0$ of the reduced dynamic system, its Lyapunov stability characteristic is determined by the eigenvalue of the Jacobi matrix of the system at this point. And the Jacobi matrix is defined as, $\boldsymbol{J}(\boldsymbol{u}_0) = \partial \boldsymbol{Y}/\partial \boldsymbol{u}$.

We choose six different positions of the battery pack as inputs, while the net buoyancy is 3N. According to the meaning of Lyapunov stability judgment conditions, we calculate the eigenvalues of the $\boldsymbol{J}$ matrix in these cases, the real parts of which are shown in Table.1. Obviously, these equilibrium solutions are all asymptotically stable.

Table.1 Stability of different working conditions

$\boldsymbol{r}_t$	The real part of the eigenvalues							
(0.02, 0.016, 0)	-1.1332	-1.1332	-0.5962	-0.0367	-0.0367	-0.0853	-0.1744	-0.1744
(0.02, 0.015, 0.005)	-1.1365	-1.1365	-0.5980	-0.0370	-0.0370	-0.0856	-0.1751	-0.1751
(0.02, 0.013, 0.009)	-1.1462	-1.1462	-0.6034	-0.0378	-0.0378	-0.0865	-0.1772	-0.1772
(0.02, 0.009, 0.013)	-1.1618	-1.1618	-0.6123	-0.0389	-0.0389	-0.0880	-0.1809	-0.1809
(0.02, 0.005, 0.015)	-1.1827	-1.1827	-0.6244	-0.0404	-0.0404	-0.0899	-0.1864	-0.1864
(0.02, 0, 0.016)	-1.2076	-1.2076	-0.6392	-0.0419	-0.0419	-0.0923	-0.1942	-0.1942

CONCLUSIONS

The paper introduces the reduced dynamics model of the underwater glider, which based on the symmetry of the configuration space. And the reduced dynamics model in quotient space eliminates the arbitrariness of motion, allowing us to more clearly focus on the essential physical quantities in the 3-D spiral motion of the underwater glider. Besed on the reduced dynamics model, we have processed the equations to obtain the equilibrium solutions of its motion. Moreover, we have investigated the asymptotic stability of the equilibrium solution by linearizing the reduced equation.

References

[1] HM Stommel. The Slocum Mission. *Oceanougraphy*. **32(4)**:93–96,1989.
[2] Rudnick and L. Daniel. Ocean research enabled by underwater gliders. *Ann Rev Mar Sci.* **8(1)**:519, 2016.
[3] Fossen T I and Fjellstad O E. Nonlinear modelling of marine vehicles in 6 degrees of freedom. *Mathematical Modelling of Systems.* **1(1)**:17–27,1991.

FAST MOTION PLANNING OF AUTOMATED VEHICLES WITH MULTIPLE CLOTHOIDS

Sanghoon Oh[1], Linjun Zhang[2], Eric Tseng[2], Lu Xu[2], and Gábor Orosz[*1,3]
[1]Department of Mechanical Engineering, University of Michigan, Ann Arbor, MI, USA
[2]Ford Motor Company, Dearborn, MI, USA
[3]Department of Civil and Environmental Engineering, University of Michigan, Ann Arbor, MI, USA

Summary A motion planning method for automated vehicles in structured road scenarios is considered. Utilizing a Hermite interpolation method with three consecutive clothoids, it is shown that real time generation of feasible trajectories for automated vehicles is possible. Separate path generation and consecutive optimal velocity planning is considered. The path is generated by solving nonlinear equations of the spline using Newton's method. Optimal velocity planning includes forward, backward and joint iteration processes and additional smoothing steps. Multiple plans that are all feasible are generated and one can be chosen based on criteria of choice of the passenger. A left turn in an intersection scenario is used as an illustrative example.

INTRODUCTION

Interpolating curve planning methods for automated vehicles can generate smooth solutions for a given set of waypoints, and clothoid curves have the advantage of making smooth transitions between straight lines and curved arcs [1]. A G^2 Hermite interpolation proposed in [2] to generate curves that consists of three consecutive clothoids, are second order smooth and satisfy boundary conditions of arbitrary initial and final position, angle, and curvature. To apply such a path generation method to automated vehicles, feasibility of the path should be validated using a kinematic vehicle model. In this paper, we formulate the problem of motion planning in two consecutive parts: fFirst, path generation and second, velocity planning. Since the proposed method is computationally cheap, a set of multiple plans can be computed in real time. The motion planner can be applied to automated vehicles in urban road situations to perform a large set if different maneuvers. A left turn at an intersection will be used below as an illustrative example.

MOTION PLANNING STRATEGY

Problem description and flow chart

Figure 1 shows the configuration of the motion planning problem. The initial is at the origin, and final position and tangent are given from the global waypoint. For simplicity, it is assumed that both initial and final curvatures are zero. The motion planner should generate a path (a curve of drawn between the initial and final point) and desired velocity which is given as a function of traveled distance along the path. The generated path should be second order continuous, that means the curvature should be continuous. The desired velocity should meet the input constraints of the vehicle.

Figure 2 describes the flow chart of the motion planner. The planning problem is divided into two parts: lateral planning and longitudinal planning. First, in the lateral planning, the geometric feasibility of the given global waypoint is verified. Then, for multiple spline generated, the parameter space of the curve is truncated to the region where any parameters generate feasible paths. In the longitudinal planning level, the desired path is given from the lateral planning. Based on the idea of linear time optimal velocity planner proposed in [3], a desired speed profile that considers constraints is generated for each path.

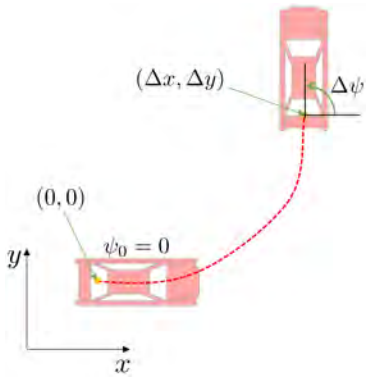

Figure 1: Motion planning configuration for a 90 degree left turn.

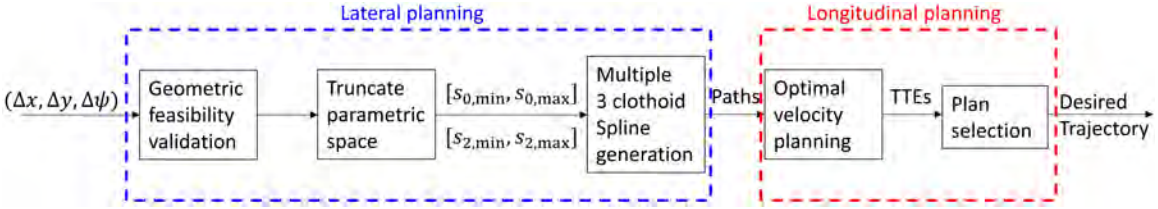

Figure 2: Flow chart of motion planner: Lateral planning and longitudinal planning is done sequentially. The input of the motion planner is the relative position and tangent of the waypoints. The output is the path and desired velocity along the path.

*Corresponding author. E-mail: orosz@umich.edu.

Lateral planning

The first step of lateral planning is validation of the geometric feasibility of the final position and tangent given by the waypoint. In this step, using 3-D lookup table that is computed offline is used to verify if the given waypoint id feasible. Next, the existence of G^2 Hermite interpolating curve with 3 clothoids is proven using the method presented in [2]. The interpolation problem has 10 unknowns and 8 equations, therefore two free variables can be used as parameters. We choose the length of the first arc s_0 and the length of the third arc s_2 as these two parameters. They can be initially assigned to certain values. Geometric feasibility validation is the process of finding the existence of the interpolating spline that satisfies the curvature constraint which comes from the maximum steering angle of the vehicle. In the truncation step, we numerically identify the region in the (s_0, s_2) parameter space where they admit feasible solutions. All the remaining constraints that are related to time derivatives of vehicle's state is handled in the consecutive longitudinal planning.

Longitudinal planning

The longitudinal planning problem is presented in equation (1). For ride comfort, lateral acceleration should be limited to some given level. Moreover, the the speed at which the steering angle can be turned is also limited. The velocity constraint $v_{\text{const}}(s)$ is chosen as the minimum value between the ride comfort or steering angle rate constraints. From generated path, limiting the lateral acceleration can be translated to limiting the velocity: $a_{\text{lat}} = \kappa(s)v(s)^2 < a_{\text{lat,max}}$. Since the steering angle rate constraint contains time information, it can also be translated to velocity constraint. We solve equation (1) as proposed in [3]. Thus, the longitudinal planning consists of 3 steps: 1) Forward iteration, 2) Backward iteration, 3) Joint iteration. Forward iteration is forward propagation using a_{max}, backward iteration is backward propagation using a_{min}, and joint iteration is choosing minimum value between the two on each point. Such iteration method can generate optimal velocity profile under given constraint with minimal computational burden since the computation time is linear to the number of steps [3]. Finally, combining multiple lateral desired paths from the lateral planning and desired velocity profile corresponding to each path, a set of different desired trajectories that are all feasible is generated. One may select one of these trajectories based on his/her own preferences.

$$\begin{aligned} &\min_{v(s)} t_f \\ &\text{such that} \\ &\dot{s} = v, \\ &\dot{v} = a, \\ &s(t_f) = s_{\text{fin}}, \\ &a_{\text{min}} \le a \le a_{\text{max}}, \\ &0 \le v(s) \le v_{\text{const}}(s) \end{aligned} \tag{1}$$

RESULTS

Example result of motion planning is shown in Figure 3. The waypoint is that of a left turn in an intersection with $(\Delta x, \Delta y, \Delta\theta) = (10\text{m}, 10\text{m}, \pi/2)$. Multiple different feasible paths are generated, and for the selected one the velocity profile and steering angle profile are depicted.

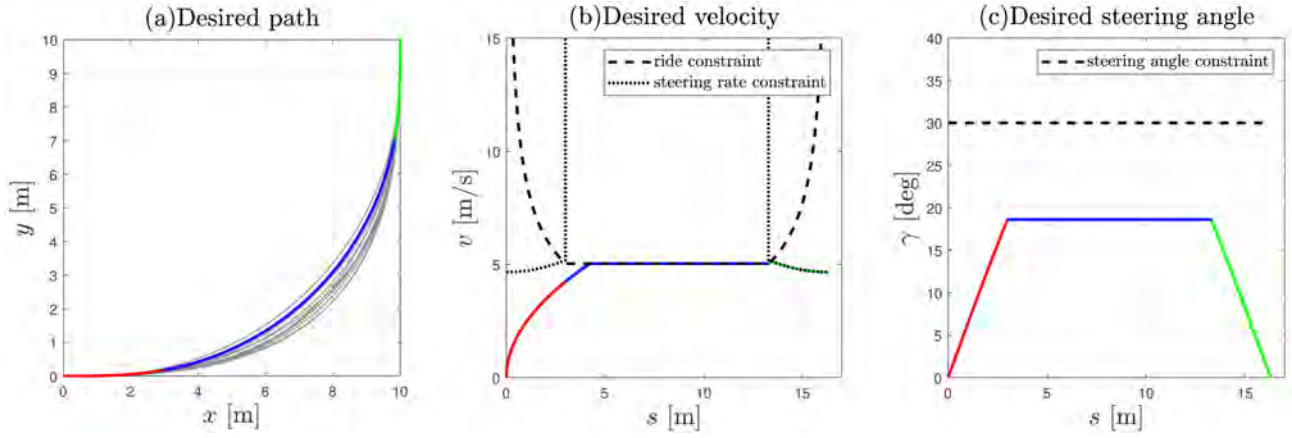

Figure 3: Motion planning results for a left turn. (a) Multiple feasible paths are colored gray and three segments of the selected one are colored red, blue, and green. (b) Velocity satisfying the constraints along the chosen path. (c) Steering angle satisfying the constraint along the chosen path.

References

[1] D. González, J. Pérez, V. Milanés, and F. Nashashibi, "A review of motion planning techniques for automated vehicles," *IEEE Transactions on Intelligent Transportation Systems*, vol. 17, no. 4, pp. 1135–1145, 2015.

[2] E. Bertolazzi and M. Frego, "On the g^2 hermite interpolation problem with clothoids," *Journal of Computational and Applied Mathematics*, vol. 341, pp. 99–116, 2018.

[3] L. Consolini, M. Locatelli, A. Minari, and A. Piazzi, "A linear-time algorithm for minimum-time velocity planning of autonomous vehicles," in *24th Mediterranean Conference on Control and Automation*. IEEE, 2016, pp. 490–495.

UNLOCKING DYNAMICS OF LOW-SHOCK SEGMENTED NUT DEVICE

Juncheng Lin[1], Caishan Liu[1]
[1]State Key Laboratory for Turbulence and Complex Systems, College of Engineering, Peking University, Beijing 100871, People's Republic of China

Summary Low-shock segmented nut (LSN), a typical explosive separation device, consisting of three parts: connecter, actuator and separator. In this paper, a complete mechanical model including connection and unlocking stages is established for LSN device. Actuating is realized by pyrotechnics and separation is achieved by relative movement of internal parts. Dynamic equation of LSN is established in first order impulse form where LZB theory is introduced to deal with the coupling of multi-point contacts. The velocity of internal parts has sudden changes originated from outer impulses and subsequent internal collisions. Separation time are also obtained by numerical calculation. Parametric analysis is held to find out the influence of friction coefficient, restitution coefficient and other geometrical design.

INTRODUCTION

In aerospace engineering, separation devices are usually used between two adjacent sections of rocket [1]. Separation devices have three characteristics in common: 1) effective connection, 2) enough actuation power, and 3) reliable separation design. Thread fastener is a typical structure to enhance the link between neighbour sections. Bolt and connected parts are assembled precedingly to ensure enough connecting force. The screw connection, however, is a non-linear problem stems from its complex geometry, and is sensitive to preloading process and preload level. Pyrotechnics, such as zirconium potassium perchlorate (ZPP), have the capability to generate explosive pulse in milliseconds [2]. And huge shock aroused by explosion may up to 10000G, which will cause malfunction to electro-devices assembled on the connected part. Nowadays, new actuators are designed and applied to reduce the structure shock, such as SMA or Cool-air actuator. And advanced connection types are also showed up such as low shock separation nuts device (LSN).

In this paper, complete mechanical model of LSN system is established. Static contact model will provide initial contact conditions for subsequent dynamic process. During the unlocking procedure, kinetic equation should be integrated to impulse equations to avoid multi-scale problem. LZB method is introduced to solve the impulse equations, so that the configuration state of the system can be determined.

LSN MODEL AND UNLOCKING PROCEDURE

The whole process of separation consists of four typical stages: 1) bolt pre-tightening on earth, 2) actuator operates to generate high pressure gas at scheduled location, 3) ring constraint moves until full unlocked to free nuts, and 4) nuts expand along radial direction to free bolt. When bolt started to release, the whole unlocking procedure ends, which lasts within several milliseconds. The design is so subtle that making it unnecessary for bolt to unscrew. After the separation among bolt and nuts, the bolt begins to freefall with initial velocity which we do not focused on.

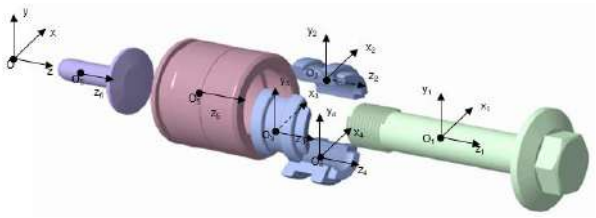

Figure 1. The geometry of LSN.

CONTACT MODEL OF THREAD FASTENER

Contact forces between threads originate in preload of thread fastener, consequently spread to other interfaces. To determine the initial stress state, the level of preload in bolt should be ascertained. Torque method is adopted to get preload in most cases which is originated from classical torque-preload equations mentioned by Motosh at 1976[3]. In this paper, simplified equation $M = k_M \cdot F$ is adopted, and preload F is set as static axial force on top side of bolt [4,5]. The component can be expressed in global system as

$$F = \begin{bmatrix} f^{\tau 1} \\ f^{\tau 2} \\ f^{n} \end{bmatrix} = \begin{bmatrix} (\cos\theta\cos\beta - \sin\theta\sin\alpha\sin\beta) f^{\tau 1} - \sin\theta\cos\alpha f^{\tau 2} + (\cos\theta\sin\beta + \sin\theta\sin\alpha\cos\beta) f^{n} \\ (\sin\theta\cos\beta + \cos\theta\sin\alpha\sin\beta) f^{\tau 1} + \cos\theta\cos\alpha f^{\tau 2} + (\sin\theta\sin\beta - \cos\theta\sin\alpha\cos\beta) f^{n} \\ -\cos\alpha\sin\beta f^{\tau 1} + \sin\alpha f^{\tau 2} + \cos\alpha\cos\beta f^{n} \end{bmatrix}$$

Supposing that contact forces are focused on the middle of threads, the equivalent axial contact stiffness and the contact force is equal to the stress of bolt in the axial direction. Setting a force on the top plane of the bolt and free on the bottom, the deformation u in equilibrium equation will be solved, and contact force can be expressed as

$$f^n = \frac{-F\omega}{\cot\alpha\cos\beta(e^{\omega l} - e^{-\omega l})}(e^{\omega z} + e^{-\omega z})$$

Contact forces on other contact region can be calculated as well, which will provide initial stress status to unlocking process together.

DYNAMIC MODEL FOR LSN IN UNLOCKING PROCESS

There exist collisions during unlocking process, provoking intensive interactions among contact couples within several milliseconds [6,7]. The second order differential equation should be integrated into

$$Mdq = dP + N_1 dP^{\tau 1} + N_2 dP^{\tau 2} + WdP^n + dP^i$$

Results calculated by numerical method mentioned in this paper are shown as follows. The kinetic energy experienced three major stages as seen in Fig. 2(a). Stage 1 has a relatively high peak at the beginning, which indicates the influence of initial impulse. Stage 2 includes the whole unlocking process of ring constraint, and there exists a continuous decline after a sharp peak. While in the final stage, potential energy is almost transferred to kinetic energy, and support base undertakes the main potential energy of the whole system after unlocking process seen in Fig. 2(b).

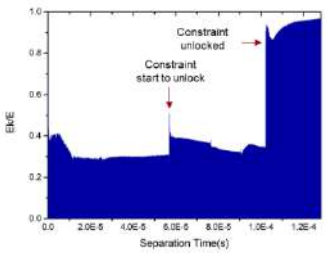

(a)kinetic energy during unlocking process

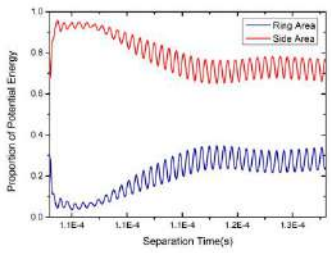

(b)potential energy of support base

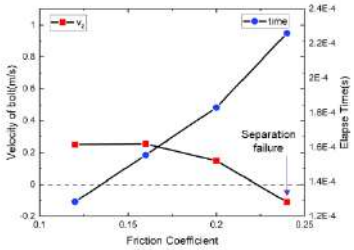

(c)parametric analysis

Figure 2. Numerical results.

Parametric analysis is held for separation prediction. As shown in Fig. 2(c), separation time is sensitive to coefficient of friction, which is doubled at the case of μ=0.24 compared with that of μ=0.12. The final axial velocity of bolt is stable when μ varies around 0.15, which is the most commonly status. However, there occurs a potential separation failure in the case of μ=0.24. In this special case, the axial velocity of bolt after unlocking process is below zero, which means the motion direction of bolt is reversed to the preconfigured one.

CONCLUSIONS

The whole mechanical model of LSN device is set up in this paper, and high effective and accurate algorithm and program are also established. Separation prediction can be easily held to find out crucial parameters of the system, which makes great contribution to parametric design.

References

[1] Brauer K O. Handbook of Pyrotechnics[M] Handbook of pyrotechnics. Chemical Publishing Co. 1974.
[2] S.-G. Jang, H.-N. Lee, J.-Y. Oh, Performance modelling of a pyrotechnically actuated pin puller, International Journal of Aeronautical and Space Sciences 15 (1) (2014)102–111.
[3] Motosh, N. Development of Design Charts for Bolts Preloaded up to the Plastic Range[J]. Journal of Engineering for Industry, 1976, 98(3):849.
[4] Nassar S A, Elkhiamy H, Barber G C, et al. An Experimental Study of Bearing and Thread Friction in Fasteners[J]. Journal of Tribology, 2005, 127(2):1097-1114.
[5] Yamatoto A. The theory and computation of threads connection[J]. Youkendo, Tokyo, 1980: 39-54.
[6] Caishan Liu, Zhen Zhao, Bernard Brogliato. Frictionless multiple impacts in multibody systems: Part I Theoretical Framework. Proceedings of Royal Society A, 2008, 464 (2100): 3193-3211.
[7] Caishan Liu, Zhen Zhao, Bernard Brogliato. Frictionless multiple impacts in multibody systems: Part II Numerical algorithm and simulation results. Proceedings of Royal Society A, 2009, 465 (2101): 1-23.

MEMS CORIOLIS VIBRATORY GYROSCOPES: A PERFECT PLAYGROUND FOR NONLINEARITY ENTHUSIASTS

Carlo Valzasina[1*], Gabriele Gattere [1], Luca Guerinoni[1], Patrick Fedeli[1] and Luca Falorni [1]
[1]Analog, MEMS and Sensors (AMS) Group R&D, STMicroelectronics, Cornaredo, Italy

Summary Coriolis Vibratory Gyroscopes (CVG) realized in MEMS technology represent a unique playground for nonlinearity enthusiasts. During development of high-volume MEMS CVG sensors, a strong effort is put on avoiding or minimizing all possible nonlinear effects, nevertheless the small physical dimensions and the complexity of structures increase the probability to introduce nonlinearities in the system, posing strong challenges to the system designer.
In this paper we report several case studies of MEMS CVG sensors realized by STMicroelectronics, in which nonlinear behaviour was observed and studied. We describe sensors showing hardening and softening mechanical nonlinearity [1], internal resonance, parametric resonance. We also report for each case study the best-known method to us for assessing, preventing or dealing with the effect.

NONLINEAR EFFECTS IN MEMS CAPACITIVE GYROSCOPES

MEMS sensors, and in particular Capacitive CVG, are widely studied as systems exhibiting nonlinear behaviour [2], because they are more prone than macroscopic systems to operate far from linear conditions. The main causes for this peculiarity are the small dimension of CVG MEMS structures and the complexity of the system.

Small dimensions of CVG conflicts with the need of high displacement in the drive motion to achieve decent Signal-To-Noise Ratio (SNR) [3] and to minimize effects of external vibrations [4]. Mechanical deformation could achieve a relevant amount of the characteristics dimensions, potentially introducing in the system hardening, softening effects and parametric resonance, as described below.

MEMS CVG are usually described in textbooks as two Degree-of-Freedom mechanical elements [3], but the technology and design constrains such as space limitation, minimum width of flexible elements, and multiple-axis operation usually force the MEMS designer to increase the complexity of the mechanical system. This can be easily understood by comparing the design of first capacitive MEMS CVG by DRAPER [5] to current 3-axis consumer CVG [6]. The complexity of the mechanical structure introduces a high number of low-frequency undesired vibration modes, usually referred as spurious vibration modes, prone to excitation by superharmonics generated in the drive motion through internal resonance.

The small dimensions of flexible elements make the effort of dealing with spurious modes even worse, by increasing the variability of eigenfrequencies due to dimensional process control and increasing the probability of mode-crossing in some process corner or operative conditions.

MEMS system design is targeted to provide reliable, repeatable and robust structures capable of performing within specified limits in all process corners and applicative conditions. This goal may be jeopardized by the presence of nonlinear effects, with small deviations in the operative or process conditions resulting in strong change in system output. In the following section, it is presented a selection of case-studies among STMicroelectronics MEMS CVG sensors development experience, in which nonlinear behaviour appeared.

CASE-STUDIES OF MEMS CVG WITH NONLINEAR EFFECTS

Mechanical Hardening or Softening

Hardening effects for large deformation of CVG flexures are well reported in literature: the spring constant deviates from linear term due to participation of axial strength to the main flexural deformation of the spring. This is modelled by adding a quadratic and positive cubic term to the conventional Hook law [3]. In less common cases, mechanical deformation of the spring may induce a softening effect, i.e. the reduction of stiffness with increasing displacement. This has been reported in Zega et. Al. [1] due to reduction of cross-section moment of inertia of the spring during deformation.

Assessment method is based on static FEM simulation where input displacement is given to the mechanical structure in order to reproduce the spring deformation during normal operation and the force-displacement relation is extracted and fit with polynomial law. Other methods to simulate these effects are reported in Putnik et. al. [7].

The presence of hardening or softening effects in drive dynamics of CVG has the main effects of increasing the temperature dependence of closed-loop drive oscillator frequency and of generating superharmonics potentially interacting with high-order spurious modes. Therefore, nonlinearity of CVG drive mode should be minimized during design phase.

Internal Resonance

Internal resonance is the process of excitation of secondary vibration modes due to energy coupling with a primary, forced vibration mode [8]. In CVG this effect can occur, as reported in Fig. 2, when drive mode couples with a spurious mode in presence of: 1. Spurious mode being at an exact multiple frequency of drive mode, 2. Drive mode exhibiting

*Corresponding author. E-mail: carlo.valzasina@st.com

nonlinear terms capable of generating superharmonics, 3. Drive motion induced force has a nonzero Lagrangian component on secondary mode.

In order to assess potential internal resonance, the three conditions above should be checked by: selection of critical modes potentially crossing drive harmonics through modal analysis in corner conditions, simulation of drive nonlinearity (as per paragraph above), harmonic FEM at multiples of drive frequency. Other methods to simulate these effects are reported in Frangi et. al. [2].

Avoiding any crossing of spurious modes with drive harmonics may be very challenging, due to the presence of several spurious modes located near to the first few drive harmonics. In addition to this, spurious mode eigenfrequency variation in process corner and across operative conditions (temperature, packaging, external stress) should be taken into account too. Main effect on system, observed and reported in Fig. 1, is the CVG sensor output change when mode-crossing occurs, due to a change in drive-sense phase relation.

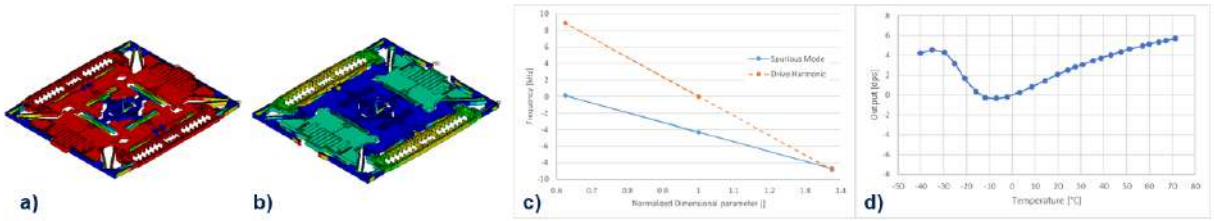

Figure 1. Example of internal resonance effect. a) Drive mode FEM simulation, b) Spurious mode FEM simulation, c) Frequency relation of Drive and Spurious mode vs. process variations, d) Effect of mode-crossing on gyroscope output.

Parametric Resonance

As per hardening or softening, a variation of spring stiffness modulated by drive motion can occur in CVG in case of large deformations. This is modelled by adding an additional, time-varying stiffness term in the system equation of motion of the secondary mode.

This is reported in Fig 3. where a modulation appears in the secondary mode transfer function, represented by the generation of two sidebands around sense resonance peak at ω_s.

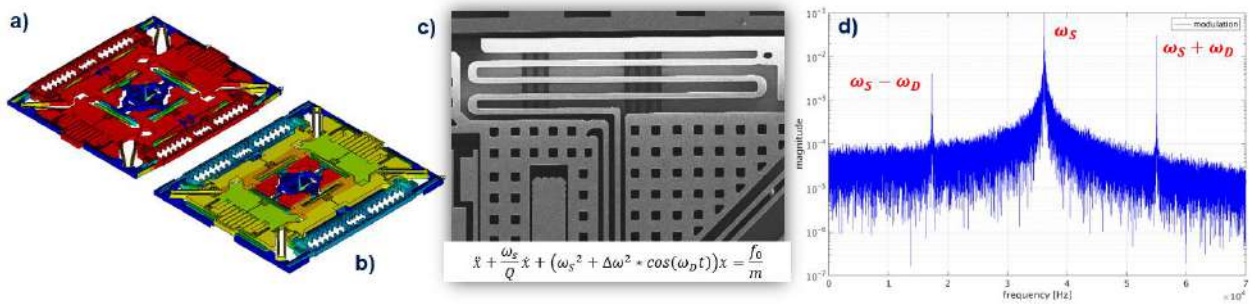

Figure 2. Example of parametric resonance. a) Drive mode simulation, b) Secondary mode simulation, c) SEM image of the spring and oscillator equation for including parametric resonance term. d) Effect of dive motion on secondary mode transfer function.

CONCLUSIONS

The reported case-studies on mechanical hardening, softening, internal and parametric resonance show how MEMS CVG represent a perfect playground for nonlinearity enthusiast, since pure linear models are not enough to describe the mechanical system on all process and operative conditions.

References

[1] Zega et. al., Hardening, Softening, and Linear Behavior of Elastic Beams in MEMS: An Analytical Approach, J. Microelectromech. Syst., vol. 28, no. 2, pp. 189 - 198, Apr. 2019.
[2] Frangi A., Gobat G., Reduced order modelling of the non-linear stiffness in MEMS resonators, International Journal of Non-Linear Mechanics 116 (2019) 211–218
[3] Inertial MEMS - Principles and Practice, V. Kempe, Cambridge University Press, 2010.
[4] Gaffuri Pagani L. et. al., Vibration Robustness and Noise in Automotive Gyroscope with Large Drive Motion and Levered Sense Mode, IEEE MEMS 2019
[5] Bernstein J. et. al., A micromachined comb-drive tuning fork rate gyroscope, IEEE MEMS 1993
[6] Prandi L., et al., "A Low-Power 3-Axis Digital-Output MEMS Gyroscope with Single Drive and Multiplexed Angular Rate Readout," ISSCC, pp. 104-106, 2011
[7] Putnik M. et. al., Predicting the Resonance Frequencies in Geometric Nonlinear Actuated MEMS, J. Microelectromech. Syst., vol. 27, no. 6, Apr. 2018.

NONLINEAR MODAL INTERACTIONS IN MICRO/NANOELECTROMECHANICAL SYSTEMS

Ashwin A. Seshia[1]
[1]Department of Engineering, University of Cambridge, Cambridge, UK

Summary Modal interactions in micro/nanoelectromechanical structures are commonplace. Nonlinear modal interactions evidenced also by autoparametric / internal resonances have been studied for many decades at macroscopic length scales but the engineering of these effects has only recently been explored as a route to enhanced device performance at the microscale. An increasing body of literature has emerged around the theme of tuning and control of nonlinear modal interactions in micro/nanoelectromechanical systems to address specific device features and performance attributes. This paper summarizes work in this area and discusses applications to inertial sensors, vibration energy harvesting, and frequency synthesis.

INTRODUCTION

Nonlinear effects are widely observed in micro/nanoelectromechanical systems (M/NEMS) [1]. Device nonlinearities can be detrimental to system performance but they can also be harnessed to provide features or performance benefits not conventionally possible through linear approaches alone. Common examples of engineered nonlinearity for practical device benefit include nonlinear suspensions as highly compliant, yet robust spring elements for inertial sensors [2], and nonlinear resonators providing features including increased parametric sensitivity [3], noise suppression [4] and temperature immunity [5]. The sources of nonlinearity may be geometric, inertial, material, or damping related or a combination thereof, and the associated nonlinear parameters can be tailored through design. Further, the integration of such devices with nonlinear transducers (e.g. parallel-plate electrostatic transducers [6]) and the precise control of driving conditions using external circuits provide further knobs, enabling electronic tunability of nonlinear effects.

This paper summarises relevant recent studies with a focus on practical device applications that could exploit engineered nonlinearity, specifically nonlinear modal coupling [7, 8]. Recent relevant device case studies include autoparametric excitation in the context of MEMS energy harvesters, micromachined devices describing phononic frequency combs, and the manipulation of the nonlinear modal coupling in micro/nanoelectromechanical gyroscopic resonators using electrostatic fields.

DEVICE APPLICATIONS

MEMS technology has been widely applied to the development of miniaturized sensors, vibration energy harvesters, frequency references and radio frequency signal processing (filters). Nonlinear effects have not been extensively exploited in first generation devices, and are often studied in this context only to set design boundaries and limits to achievable performance. However, in recent years, operation in the nonlinear regime with a view towards enhancing performance is being revisited and a number of studies (particularly over the past decade) have demonstrated advances arising from a thorough understanding of these effects applied to practical device engineering. This paper summarises research addressing three applications exploiting nonlinear modal coupling in MEMS/NEMS with application to inertial sensors, vibration energy harvesters and radio frequency comb synthesis.

Vibration Energy Harvesters: Vibration energy harvesters offer a means of converting ambient vibrations to electrical energy [9]. There has been much interest in the design of MEMS vibration energy harvesters due to their potential for enabling compact, chip-scale, self-powered sensors [10]. However, the vast majority of initial approaches have been based on employing a single-degree-of-freedom linear or Duffing resonators for this purpose. Power scalability for MEMS is poor unless the resonances are precisely tuned to the frequency of a stable periodic source (e.g. steady vibrations on a continuously operated motor or pump). Vibration energy harvesters employing two coupled modes (e.g. with frequencies in a 2:1 ratio) have been recently proposed where a second mode is autoparametrically excited through coupling to a directly excited primary mode. Mechanical amplification resulting from the autoparametric excitation of the second mode can lead to amplitude build-up even at low vibration levels. A prototype piezoelectric MEMS vibration energy harvester based on a coupled cantilever topology demonstrated an output power of 180 μW and a power density per acceleration squared metric, nearly an order of magnitude higher than the equivalent state-of-the-art [11].

Phononic frequency combs: The excitation of multiple modes in a standalone piezoelectric MEMS resonator using a single drive tone, as well as different combinations of modes by varying the drive parameters has been previously demonstrated [12] in a series of studies on autoparametric excitation / internal resonances in MEMS. Under specific driving conditions in such devices, nonlinear mixing of the resulting multimode responses can lead to the formation of phononic frequency combs [13] – a response defined by a set of equispaced discrete frequencies in the radio frequency domain. These phononic frequency combs (the mechanical analogue of optical frequency combs) are a direct result of nonlinear modal coupling within a composite resonator device. The response of such a device can be tracked continuously

without recourse to a feedback oscillator for e.g. by replacing the drive by a stable frequency source with well-defined characteristics [14]. The comb features of such devices can be tuned, demonstrating either high temperature sensitivity or relative insensitivity to temperature effects [15]. Applications include device elements for sensors and RF signal processing.

Resonant inertial sensors: Vibratory MEMS rate gyroscopes operate on the principle of coupling two orthogonal modes via the Coriolis effect and, therefore, modelling modal coupling accurately is integral to the design of these sensors [16]. Micromachined disk resonator gyroscopes have demonstrated near-navigation performance [17] and are based on Coriolis coupling of two elliptical modes within a single disk resonator structure. The modes of interest can be excited using electrostatic fields generated by parallel-plate transducers situated around the disk periphery. Recently, excitation of multiple internal resonances has been demonstrated in such devices. This can enable self-induced parametric amplification due to nonlinear elastic coupling between degenerate orthogonal vibratory modes resulting in an increase in rate sensitivity [19]. Additionally, by tailoring the electrostatic fields it is also possible to dynamically tune the modes of interest towards mode matching, and utilise nonlinear electrostatic fields to couple otherwise uncoupled modes to a driven primary mode [18]. Furthermore, a related parametric pumping scheme can enable dynamic tuning of the sensitivity of mode-localized sensors [20].

SUMMARY

The engineering of nonlinear modal coupling has been studied in M/NEMS demonstrating the potential for significant practical benefit. Three case studies are specifically highlighted including (1) the generation of elevated power output levels for MEMS inertial energy harvesters, (2) resonator devices demonstrating frequency comb response with application to the tracking of slow variations in parameters, and (3) the ability of dynamically tune modal interactions using nonlinear electrostatic fields for mode tuning in gyroscope devices or for tuning the coupling strength in coupled resonator micro/nanostructures including mode-localized accelerometers resulting in over an order of magnitude increase in parametric sensitivity and a consequent experimentally demonstrated reduction in noise floor.

Acknowledgments: The author acknowledges contributions by his former PhD students and academic colleagues with particular thanks to Yu Jia, Sijun Du, Adarsh Ganesan, Xin Zhou, and Chun Zhao. This work was supported by grants from Innovate UK, the Engineering and Physical Sciences Research Council, the Natural Environment Research Council and the Cambridge Trusts.

References

[1] Lifshitz, R. and Cross, M. C., Nonlinear dynamics of nanomechanical and micromechanical resonators, in *Review of Nonlinear Dynamics and Complexity*, **1**, 1, 1-52, Wiley-VCH 2008.
[2] Tang, S., *et al*., A high-sensitivity MEMS gravimeter with a large dynamic range, *Microsyst Nanoeng*., **5**, 45, 2019.
[3] Alridge, G. S. and Cleland A. N., Noise-enabled precision measurements of a Duffing nanomechanical resonator, *Phys. Rev. Lett*., **94**, 156403, 2005.
[4] Sobreviela, G. *et al*., Parametric noise reduction in a high-order nonlinear MEMS resonator utilizing its bifurcation points, *J. Microelectromech. Syst*.,**26**:6, 1189-1195, 2017.
[5] Defoort, M., Taheri-Tehrani, P., and Horsley, D., Exploiting nonlinear amplitude-frequency dependence for temperature compensation in silicon micromechanical resonators, *Appl. Phys. Lett*., **109**, 153502, 2016.
[6] Trusov, A. A. and Shkel, A. M., Parallel-plate capacitive detection of large amplitude motion in MEMS, in *Proc. Transducers'07*, Lyon, France, 1693-1696, 2007.
[7] Balachandran, B. and Nayfeh, A., Modal interactions in dynamical and structural systems, *Appl. Mech. Rev*., **42**:11, Part 2, 1989.
[8] Wenstra, H. J. R. *et al*., Nonlinear modal interactions in clamped-clamped mechanical resonators, *Phys Rev Lett*., **105**, 117205, 2010.
[9] Jia, Y., and Seshia A. A., Power optimization by mass tuning for MEMS piezoelectric cantilever vibration energy harvesting, *J. Microelectromech. Syst*., 25:1, 108-117, 2016.
[10] Du, S., *et al*., MEMS piezoelectric energy harvester driven wireless sensor module driven by noisy base excitation, in Proc. *Transducers '19 and Eurosensors XXXIII*, Berlin, Germany, 350-353, 2019.
[11] Jia, Y., Du, S., Arroyo, E., and Seshia A. A., Autoparametric resonance in a piezoelectric MEMS vibration energy harvester, in *Proc. IEEE MEMS*, Belfast, UK, 2018, pp. 226-229.
[12] Ganesan,A. and Seshia A. A., Coexistence of multiple multimode nonlinear mixing regimes in a microelectromechanical device, *Appl. Phys. Lett.*, **112**: 8, 084102, 2018.
[13] Ganesan. A., Do. C. and Seshia A. A., Phononic frequency combs via intrinsic three-wave mixing. *Phys. Rev. Lett*., **118**:3. 033903, 2017.
[14] Ganesan, A. and Seshia A. A, Resonance tracking in a micromechanical device using phononic frequency combs, *Sci. Rep*., **9**:9452, 1-7, 2019.
[15] Ganesan, A., Gorman, J. J., and Seshia A. A., Phononic frequency combs for engineering MEMS/NEMS devices with tunable sensitivity, in *Proc. IEEE Sensors*, Montreal, Canada, 1-4, 2019.
[16] Phani, A. S. *et al*., Modal coupling in micromechanical vibratory rate gyroscopes, *IEEE Sensors J*., **6**:5, 1144-1152, 2006.
[17] Li, Q. *et al*., 0.04 degree-per-hour MEMS disk resonator gyroscope with high-quality factor (510 k) and long decaying time constant (74.9 s), *Microsyst Nanoeng*., **4**, 32, 2018.
[18] Zhou X., *et al*., Dynamic modulation of modal coupling in microelectromechanical gyroscopic disk resonators, *Nat. Comm*., **10**: 1-9, 2019.
[19] Nitzan, S. H., *et al*., Self-induced parametric amplification arising from nonlinear elastic coupling in a micromechanical resonating disk gyroscope, *Sci. Rep.*, 5, 9036, 2015.
[20] Zhao C., *et al*., Toward high-resolution inertial sensors employing parametric modulation in coupled micromechanical resonators, *Phys. Rev. Appl*., 12(4), 044005, 2019.

SUCTION CUPS IN LIQUID AT MICRO SCALE

Yue Yang[1], M Taher A Saif[*1], [2]and Eduard Arzt [*1,3]
[1]INM – Leibniz Institute for New Materials, Saarbrücken, Germany
[2]Mechanical Science and Engineering, University of Illinois at Urbana-Champaign, Urbana, Illinois, USA
[3]Department of Materials Science and Engineering, Saarland University, Saarbrücken, Germany

Summary Dry suction cups are extensively used for attachment to substrates without any chemical glue. Van der Waals forces and air suction provide the adhesion. However, suction cups inundated in liquids are not commonly used, even though octopus and other aquatic animals use them gracefully at multiple size scales for locomotion (Fig 1). The precise mechanism of operation of suction cups in liquid remains elusive to date. Here we hypothesize a physical mechanism for suction cups in liquids, develop a mathematical model implementing the mechanism, and test the hypothesis by carrying out experiments with suction cups at micro scale.

INTRODUCTION

Suction cups in liquids are counter intuitive, particularly when the surfaces are hydrophilic. Here, the liquid wets the surfaces and the hydro dynamic lubrication layer between the cup and the substrate prevents them from coming in contact. Hence, the cups must employ suction pressure alone to adhere. In order to gain insight on the mechanism of operation, we explored (1) the process by which suction pressure evolves with time and (2) modes of failure, i.e., the detachment of the cup from the substrate. We start with the following working hypothesis.

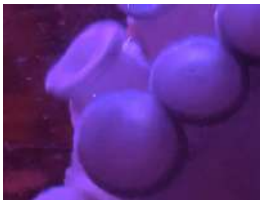

Figure 1. Suction cups of an octopus.

PROPOSED HYPOTHESIS

On suction pressure

A typical cup has a stalk and a compliant rim. The cup deforms elastically when pressed against a surface, while liquid is pushed out reducing the volume of the cup. Upon release, the cup tends to return to its original configuration immediately. This fast demand for increasing volume cannot be met by the slow flow of liquid from outside through the narrow gap between the rim and the substrate. This lag between demand and supply results in a suction pressure inside the cup and further reduces the gap in a positive feed forward way. If the stalk is retracted by applying a force, then suction increases even more, increasing the holding force. Faster the rate of retraction, higher is the suction pressure.

On modes of detachment (failure)

If the stalk is held fixed, or no external force is applied to retract, suction pressure decreases over time due to liquid seepage from outside, and the cup detaches. Under a prescribed rate of retraction, there can be two modes of failure. Mode 1: the applied force on the rim exceeds the suction force it experiences. Here, the rim opens as a crack from its inner boundary. Mode 2: During stalk retraction, the rim slides radially inward by hydro-plating. It undergoes a transition from circumferential tension to compression (Fig 2) which may lead to out-of-plane buckling of the rim along the outermost perimeter. The buckling waves create channels for flow from outside, relaxing the pressure leading to the detachment of the cup.

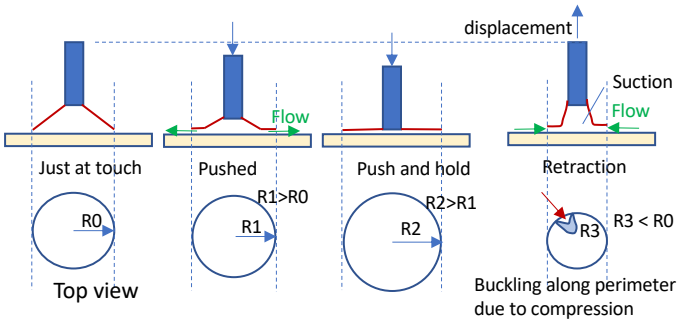

Figure 2. Proposed working principle of a suction cup in liquids and a possible failure mechanism by peripheral buckling of the rim.

MATHEMATICAL MODEL

A simple mechanical analogue of a suction cup consists of a cylindrical chamber with a rim (Fig 3). The spring K1 represents the compliance of the cup without any fluid. In the presence of an incompressible fluid, the deformation of the cup is constrained and its compliance decreases. This is accounted by a second chamber connected to the rigid substrate. Its spring constant is K2. If the rim is sealed and no liquid is allowed to flow inwards, the effective stiffness of the cup is K1 + K2. The gap, d, between the rim and the substrate decreases with increasing suction pressure. However, due to asperity contacts, the decrease in gap with suction is non-linear which we model with an exponential function: d = d0 Exp[-p/p0], where d0 is the initial gap, and p0 is a reference pressure. *Initial condition:* At time t=0, the stalk is pushed towards the substrate when the chamber volume decreases by pushing fluid out. Now, the suction pressure is zero, p(0)=0, i.e., pressures inside and outside are balanced.

*Corresponding author. saif@illinois.edu, Eduard.Arzt@leibniz-inm.de

Mass conservation

Upon release of the cup, with or without a prescribed retraction velocity, the volume of the chamber increases. The increased volume is balanced by inflow of liquid under pressure gradient through the gap d. This mass balance gives the governing equation for the suction pressure, p(t), with the initial condition, p(0)=0.

Failure criteria

During a constant rate of retraction, the spring force increases linearly with time (Fig 3) while the rim slides inward. Failure initiates due to earlier of the two events: spring force from K1 exceeding the suction force on the rim, or the sliding rim buckling along the periphery.

Experimental verification: hypothesis testing

Micro scale suction cups are fabricated with polyurethane elastomer and 3D printing (Fig. 4). The cups are inundated in water and pressed against a glass surface. The stalk is then retracted with a constant prescribed velocity until failure, while the mode of failure is observed. Force evolution with time shows a trend similar to that predicted by the model (Fig 3, right). Failure is preceded by the rim sliding radially inward followed by spontaneous buckling along the periphery. One of the buckling waves increases in amplitude resulting in a radial channel. This allows water to flow inwards causing failure of the cup, positively testing the hypothesis on failure mode 2.

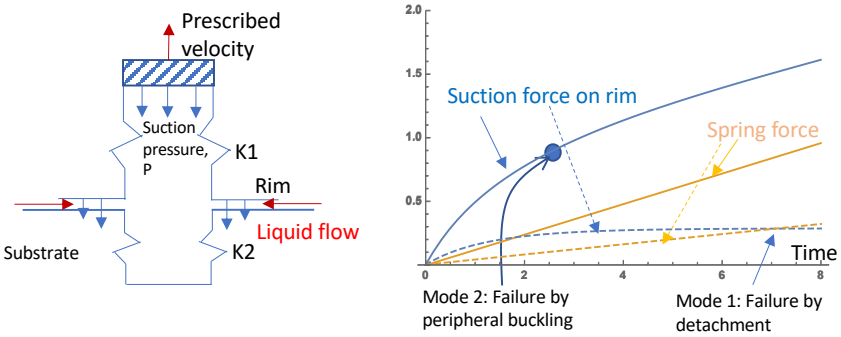

Figure 3. (left) Mechanical model of a suction cup in liquid. The cup is retracted to detach. (Right) The evolution of force on the rim due to suction between the rim and the substrate compared to the spring force. Two modes of failure are shown.

CONCLUSIONS

Here we proposed and tested a hypothesis on the mechanism of attachment of suction cups in liquids, and their failure modes. The mechanism was implemented in a mathematical model. Experiments with micro scale suction cups were used to test the hypothesis. The model predictions match experimental observations qualitatively. The work lays the foundation for designing and developing suction cups for a wide range of underwater applications.

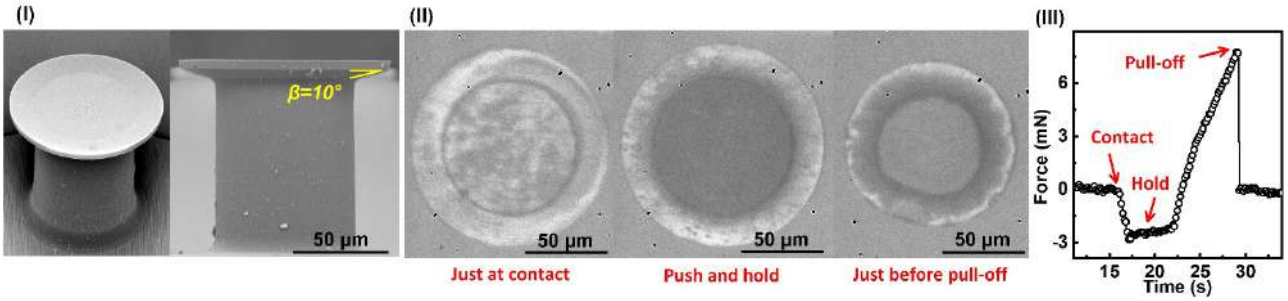

Figure 4. (i) Image of a suction cup in water contacting a glass surface. (ii) The three images show the rim in contact with substrate as the stalk is retracted. The last image is prior to detachment showing buckling from the periphery. Also, the rim diameter is much smaller indicating circumferential compressive stress initiating buckling. (iii) Force of retraction as a function of time. Retraction velocity: 10 um/s.

COARSE–GRAINED MODEL FOR SINGLE LAYER MOS_2. RIGID GRAINS APPROACH.

Artem Panchenko*[1], Ekaterina Podolskaya [2,3], and Igor Berinskii[1]
[1]School of Mechanical Engineering, Tel Aviv University, Israel
[2]Higher School of Theoretical Mechanics, Peter the Great St. Petersburg Polytechnical University, Russia
[3]Institute for Problems in Mechanical Engineering of Russian Academy of Sciences, Russia

Summary Single–layer molybdenum disulfide ($SLMoS_2$) is a promising two–dimensional material with a wide range of possible applications in NEMS. We develop a coarse–grained model combining the atoms of crystal lattice into rigid 'grains'. The interaction between the grains is based on Stillinger–Weber potential with parameters recalculated to fulfill the elastic properties of the original lattice. The model is applied to calculate the phonon spectrum and for the nanoindentation problem. It is shown that in the case of small strains the model is as accurate as regular MD simulations, but uses much less interatomic interactions; hence, it is much more time–efficient.

INTRODUCTION

Traditional molecular dynamics (MD) simulations of $SLMoS_2$ are very time–consuming and cannot be applied to the real microscopic–level systems. We propose another way to simulate the atomistic structure using the coarse-grained (CG) modeling: combining atoms of the lattice into 'grains'. The grain combines three unit cells of the $SLMoS_2$ hexagonal close-packed (HCP) structure, which is infinite in the plane of transverse isotropy and has only three layers in the orthogonal direction. As a result, they form a two-dimensional triangular lattice. We consider them as the rigid bodies, taking their rotational degrees of freedom into account. In this case, a specific potential has to be developed to add torques arising between the grains to the forces of interaction. Such type of potential was used before for the original $SLMoS_2$ crystal lattice [1], but not for the CG structure.

SIMULATION TECHNIQUE

Dynamics of the grains

The main idea of the simulations method is close to the discrete [2] and distinct [3] element methods and other generalizations of classical molecular dynamics. The position and rotation of a specific grain is determined by the solution of the following equations of motion:

$$m_i\ddot{\mathbf{u}} = \sum_\alpha \mathbf{F}_\alpha, \qquad \boldsymbol{\Theta}\cdot(\boldsymbol{\omega})^{\cdot} = \sum_\alpha \mathbf{M}_\alpha, \tag{1}$$

where $\mathbf{u}$ is displacement, $\boldsymbol{\omega}$ is an angular velocity $\mathbf{F}_\alpha$, $\mathbf{M}_\alpha$, sum of forces and torques caused by interaction between atoms of neighboring grains. We apply the quaternions formalism [4] to calculate a new orientation of the grain.

Elasticity of the CG–lattice

As the grains are rigid, the overall stiffness of the lattice increased and we cannot use the original SW potential. Instead we need to redefine its parameters. In order to determine the components of stiffness tensor we need to solve a set of problems in which the material is subject to homogeneous strain field $\varepsilon_{ij} = \pm 10^{-5}$ with one non-zero component. We write the Hooke's law in the form:

$$\frac{\Delta\sigma_{kl}}{\Delta\varepsilon_{ij}} = \frac{1}{2}\left(C_{klij} + C_{ijkl}\right), \qquad i,j,k,l = x,y, \qquad \boldsymbol{\sigma} = \frac{1}{2V_0}\sum_\alpha \mathbf{a}_\alpha\mathbf{F}_\alpha, \tag{2}$$

where ε_{ij} and σ_{kl} are the components of strain and Cauchy stress ($\boldsymbol{\sigma}$) tensors respectively, and C_{ijkl} are the components of stiffness tensor, V_0 is the unit cell volume, $\mathbf{F}_\alpha$ are the respective intergrain forces, and $\mathbf{a}_\alpha$ are the vectors connecting the given grain with its neighbors. The boundary effects in the plane of isotropy are eliminated by introduction of periodic boundary conditions, whereas the upper and lower boundaries are free.

A Simulated Annealing (SA) algorithm [5] was used to determine the parameters of the SW potential using the known values of the stiffness tensor. The highest relative error was obtained for C_{xxyy} and is 11%.

The corrected SW potential parameters for coarse–grained model are given in Table 1.

PHONON SPECTRUM

A phonon spectrum determination can be used to validate the system dynamics. Phonon spectrum of the coarse–grained lattice is measured using an approach based on molecular dynamics simulations [6].

Even though we consider the phonon spectrum of grains instead of atoms, we obtain a good agreement with the experimental results. The lower and upper curves give a good approximation of experimental data from [7]. The middle curve varies significantly from the experimental data in case of long waves, but the difference decreases at higher values of the wave vector.

*Corresponding author. E-mail: artemp@mail.tau.ac.il

	ε, eV	σ, Å	a	B	λ	γ	$\cos(\Theta_0)$
$Mo-Mo$	2.4436	0.6097	7.54817	119.751	0	0	0
$S-S$	4.1082	0.6501	6.06338	103.629	0	0	0
$Mo-S-S$	3.0014	0.7590	4.38728	37.8703	1.02384	0.872786	0.1525

Table 1: Re–calibrated Stillinger–Weber potential parameters.

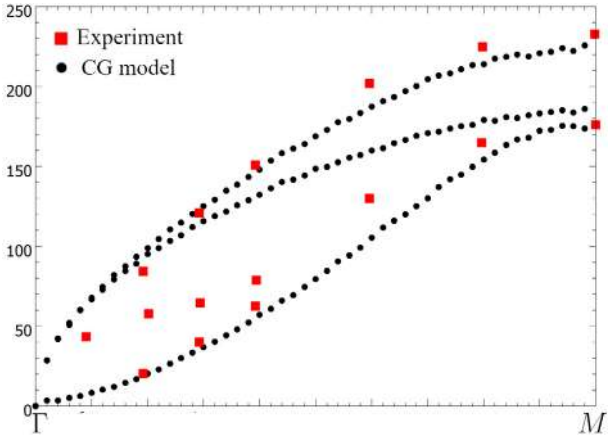

Figure 1: Phonon spectrum for grain–structured $SLMoS_2$ with the new parameters

CONCLUSIONS

We developed a coarse–grained model of $SLMoS_2$ with the grains considered as rigid bodies. For this specific study, the interactions between the grains were based on Stillinger–Weber potential with the parameters re-calibrated to fulfill the elastic properties of the original lattice. Note, that the same approach can be used with any other potential of interaction. The phonon spectrum was calculated, and it shows a good correspondence to the acoustic waves of the original lattice.

In this work, we considered the minimal possible grains. In this case, the number of interaction reduces almost twice. The larger grains with the same geometry can be used for the higher increase of the calculation speed.

The major advantage of the model is an opportunity to combine the coarse–grained and the original lattices in one model. For example, the original lattice can be considered near the stress concentration points in the tasks of nanoindentation or crack initiation, and the CG–lattice can be merged with the original on the relatively far distance from such points.

The drawback of the model yields from its main feature: the rigid grains 'freeze' part of the interactions. As a result, the bonds between the grains are highly elongated in comparison with the ones in the original lattice at the same strain, which lead to higher stresses in the CG–lattice. This effect limits the application of the model for problems with large deformations. However, in the small strain cases such as elastic wave propagation, thermal problems, and others the model can be used successfully. A possible solution to the aforementioned disadvantage may be considered by using elastic grains instead of rigid ones, which is a topic of further investigation.

References

[1] Berinskii I.E., Panchenko A.Yu., Podolskaya E.A. Application of the pair torque interaction potential to simulate the elastic behavior of $SLMoS_2$. *Modelling Simul. Mater. Sci. Eng.* **24(4)**: 045003, 2016.

[2] Cundall P.A. and Strack O.D.L. A discrete numerical model for granular assemblies. *Geotechnique* **29(1)**: 47-65, 1979.

[3] Ostanin I., Ballarini R., Potyondy D., Dumitrică T. A distinct element method for large scale simulations of carbon nanotube assemblies. *J. Mech. Phys. Solids* **61(3)**: 762-782, 2013.

[4] Altmann S.L. Rotations, Quaternions, and Double Groups. larendon Press, Oxford, 1986.

[5] Černỳ, V. Thermodynamical approach to the traveling salesman problem: An efficient simulation algorithm. *Journal of optimization theory and applications* **45(1)**: 41-51, 1985.

[6] Kong, L.T. Phonon dispersion measured directly from molecular dynamics simulations. *Computer Physics Communications* **182**: 2201–2207, 2011.

[7] Wakabayashi N., Smith H.G., Nicklow R.M. Lattice dynamics of hexagonal MoS_2 studied by neutron scattering. *Physical Review B* **12(2)**: 659-663, 1975.

NONLINEAR PIEZOELECTRIC BEHAVIOR OF PZT THIN FILMS: MODELING AND EXPERIMENTAL VALIDATION

Andrea Opreni*[1], Nicolò Boni[2], Patrick Fedeli[2], Roberto Carminati[2], Massimiliano Merli[2], Gianluca Mendicino[2], and Attilio Frangi[1]
[1] Department of Civil and Environmental Engineering, Politecnico di Milano, Milan, Italy
[2] Analog and MEMS Group, STMicroelectronics, Milan, Italy

Summary Piezoelectric materials in Micro-Electro-Mechanical Systems provide an enhanced linear response and lower actuation voltages compared to their capacitive counterparts. In this work, we propose a material model for thin films of piezoelectric materials derived from the Landau-Devonshire theory of ferroelectrics. The proposed model is validated with tests conducted on a cantilever made of monocrystalline silicon actuated with a PZT patch in quasi-static conditions in both unipolar and bipolar cycles.

INTRODUCTION

Piezoelectric Micro-Electro-Mechanical Systems (MEMS) represent an important class of devices both for actuation and sensing and they are often preferred to capacitive MEMS for their improved linearity and more reliable operation.

Most modeling procedures for the design of piezoelectric MEMS proposed in literature exploit a linear material model. Nevertheless, in application as micromirrors, the piezoelectric materials used for actuation are subjected to voltage biases of the order of tens of Volts, generating electric fields with maximum values that exceed the linear range of the piezoelectric material. As a consequence material nonlinearities are observed.

Extensive research has been performed to model the nonlinear electromechanical behavior of piezoelectric MEMS. First nonlinear models date to the work by Guyomar [1] during the analysis of Langevin transducers. Subsequent works developed constitutive models starting from a nonlinear electric enthalpy density function from which the constitutive model is derived. Most recent works included also terms to mimic the hysteretic behavior of the piezoelectric material [2].

Only in recent years intensive effort has been put to develop models for ferroelectric materials in MEMS considering the meso- and microscopic structure of the material itself. The Phase field approach [3] has emerged as the most effective tool to account for the irreversible part of the material polarization by simulating the process of domain reorientation in the piezoelectric material. The aim of this investigation is to formulate a macroscopic material model based on the theory of ferroelectrics developed by Landau-Devonshire [4]. The model does not introduce any semi-empirical constant and only the polarization history of the piezoelectric material during device operation is required. Our proposal is here validated on silicon cantilevers fabricated by STMicroelectronics actuated with a Lead-Zirconate-Titanate (PZT) patch.

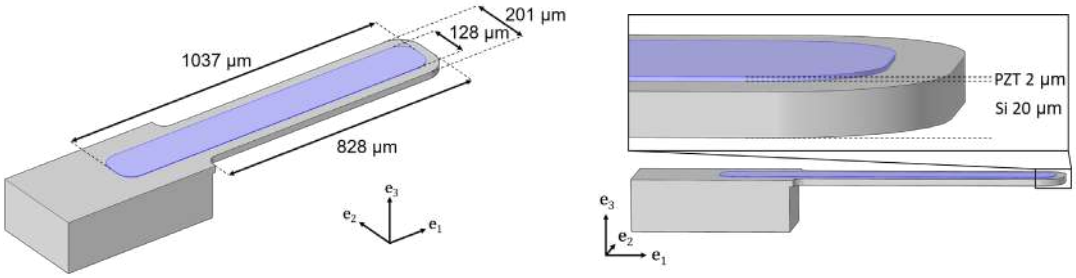

Figure 1: Cantilever geometry. Silicon appears in grey color. PZT is highlighted in light purple.

MODEL

Landau-Devonshire theory states that the polarization vector $\boldsymbol{P}$ induces inelastic strains ε^P associated to the deformation of the elementary cells of the piezoelectric crystal due to spontaneous polarization below the Curie temperature. Inelastic strains contribute to the Cauchy stresses $\boldsymbol{\sigma}$ according to the linearized theory of elasticity:

$$\boldsymbol{\sigma} = \boldsymbol{\sigma}^{\varepsilon}[\boldsymbol{u}] - \boldsymbol{\sigma}^{P}[\boldsymbol{P}] \qquad (1)$$
$$\boldsymbol{\sigma}^{\varepsilon}[\boldsymbol{u}] := \mathcal{C} : \varepsilon[\boldsymbol{u}], \quad \boldsymbol{\sigma}^{P}[\boldsymbol{P}] := \mathcal{C} : \varepsilon^{P}[\boldsymbol{P}]$$

*Corresponding author. E-mail: andrea.opreni@polimi.it.

where $\boldsymbol{\varepsilon}$ is the infinitesimal strain tensor, $\mathcal{C}$ is the fourth-order elasticity tensor, and the superscripts $(\cdot)^{\varepsilon}$ and $(\cdot)^{P}$ define elastic and inelastic quantities. We now impose linear momentum conservation of the system in its weak form neglecting active forces, and assuming that inertia forces are negligible:

$$\int_{\Omega} (\boldsymbol{\sigma}^{\varepsilon} - \boldsymbol{\sigma}^{P}) : \boldsymbol{\varepsilon}[\boldsymbol{w}] \, \mathrm{d}\Omega = 0 \tag{2}$$

where $\boldsymbol{\varepsilon}[\boldsymbol{w}]$ is the strain associated to the virtual displacement. If the film is deposited along the $\boldsymbol{e}_1\boldsymbol{e}_2$ plane, then the electric field is reasonably approximated as $\boldsymbol{E} = E\boldsymbol{e}_3$. If the dielectric behavior is isotropic, then the polarization has the form $\boldsymbol{P} = P\boldsymbol{e}_3$. Therefore, from Equation (1) we derive that inelastic shear stress components are zero and Equation (2) becomes:

$$\int_{\Omega} \boldsymbol{\sigma}^{\varepsilon} : \boldsymbol{\varepsilon}[\boldsymbol{w}] \, \mathrm{d}\Omega = P^2 \int_{\Omega_P} \Big[c_{13} \left(\varepsilon_{11}[\boldsymbol{w}] + \varepsilon_{22}[\boldsymbol{w}] \right) + c_{33} \varepsilon_{33}[\boldsymbol{w}] \Big] \, \mathrm{d}\Omega \tag{3}$$

where c_{ij} are constants that embed ferroelectric and mechanical properties of the piezoelectric material, and Ω_P is the volume occupied by the piezoelectric film.

NUMERICAL RESULTS AND EXPERIMENTAL VALIDATION

The model was validated on monocrystalline silicon cantilevers with (100) orientation actuated in quasi-static condition with a PZT patch. The geometry of the cantilever is reported in Figure 1. The cantilever was actuated by applying either unipolar or bipolar sinusoidal potential histories. In the former, the potential oscillated within 0 and $+V_0$, while in the latter it ranged between $-V_0$ and $+V_0$. The comparison between the tip displacement predicted from the proposed model and the values measured from experiments for $V_0 = 35$ V are reported in Figure 2. The charts report a remarkable agreement in both unipolar and bipolar measures.

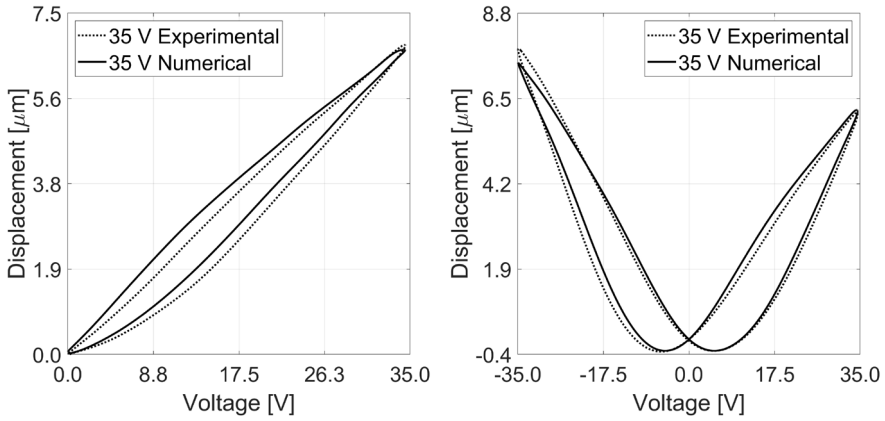

Figure 2: Comparison between proposed model and experimental data in unipolar (a) and bipolar (b) measures.

CONCLUSIONS

We have proposed a model to predict the nonlinear ferroelectric behavior of PZT thin films in MEMS. The model is based on first principles of ferroelectric materials theory, and it does not introduce parameters that require calibration. Furthermore, the presented model can be implemented in finite element codes for the design of realistic piezo MEMS.

References

[1] D. Guyomar, N. Aurelle, C. Richard, P. Gonnard, L. Eyraud. Nonlinearities in Langevin transducers. *IEEE Ultrasonics Symposium*, vol. 2, pp. 925–928, 1994

[2] S. Leadenham, and A. Erturk. Unified nonlinear electroelastic dynamics of a bimorph piezoelectric cantilever for energy harvesting, sensing, and actuation. *Nonlinear Dynamics*, 79(3):1727–1743, 2015.

[3] Fedeli, P., Kamlah, M., Frangi, A. Phase-field modeling of domain evolution in ferroelectric materials in the presence of defects, Smart Materials and Structures, v. 28, Issue 3, 5 February 2019, Article number 035021

[4] A. F. Devonshire. Theory of ferroelectrics. *Advances in Physics*, 3(10):85–130, 1954.

REDUCED ORDER MODEL FOR IN-WATER LARGE ARRAY OF PMUTS ANALYSIS

Gianluca Massimino*[1], Attilio Frangi[1], Raffaele Ardito[1], Fabio Quaglia[2], and Alberto Corigliano[1]
[1]Department of Civil and Environmental Engineering, Politecnico di Milano, Milano, Italy
[2]Analog, MEMS & Sensors Group, ST Microelectronics, Cornaredo, Italy

Summary In this work a multiphysics ROM for the electro-mechanical-acoustic problem is presented. The solution strategy consists of two main stages. The former is devoted to the determination of the electro-mechanical eigenmodes of a representative PMUT. Then, the acoustic-structure interface of each transducer is mapped onto the fluid domain boundary. In the latter stage, the electro-mechanical-acoustic problem is solved by means of a staggered algorithm, considering the PMUTs vibration as a combination of few selected modes. The numerical comparison with the COMSOL 5.2 full order FE model is reported in terms of pressure maps and histories at the PMUT center.

INTRODUCTION

Piezoelectric materials in smart microsystems [1] are widespread, in view of some recent techniques that allow for the fabrication of layered structures with thin films of piezoelectric material, namely lead zirconate titanate (PZT) or aluminium nitride (AlN). Piezoelectric micromachined ultrasonic transducers (PMUTs) are layered plates with a piezoelectric active layer for emitting and receiving ultrasonic waves [2]. Several applications involve the use of such piezo vibrating diaphragms; medical acoustic imaging [3] and hydrophones exploit the in-water wave propagation of ultrasonic pulses. The primary focus of the present work is to show the novel reduced order model (ROM) for electro-mechanical-acoustic analyses and the corresponding simulation performance related to the study of beamforming and interaction problems, involving several transducers. The presented model has been implemented into a Fortran code and represents a suitable tool to carry out pressure propagation analyses in which the transducers are independently driven. Furthermore, the acoustic interaction among multiple vibrating transducers, in the near field, is taken into account by means of the full order FEM approach for the acoustic problem [4], in spite of the order reduction of the PMUTs dynamic behaviour. Hence, the interference phenomena during the wave propagation is properly simulate.

METHODOLOGY

The generic piezoelectric transducer has a circular geometry with a radius of 115 μm and an overall thickness of 8 μm, so the diameter over thickness aspect ratio is 28.75. It consists of several layers with different elastic properties and thicknesses. The structural layer is made of silicon, while the active layer is made of PZT. It has thickness equal to 2 μm and is in a circular hat configuration with radius of 80.5 μm, coaxial with the plate. The transducers interaction surfaces belong to the flat fluid domain boundary while a hemisphere of water has been considered (see a detail in Figure 1).

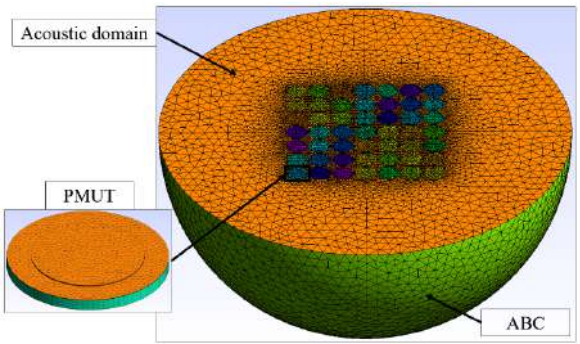

Figure 1: FE model: PMUT mesh detail (left), fluid domain mesh detail with 7x7 mapped PMUT interaction surfaces (right).

The solution strategy consists of two main stages. In the former one, the eigenvalue piezoelectric problem is solved, for the complete stack of a representative PMUT, by means of the Arnoldi method and few selected modes are extracted. Then, the acoustic-structure interaction surface of each transducer is mapped onto the fluid boundary. In the latter stage, the in-time domain piezo-acoustic problem is solved through a staggered procedure in which the electro-mechanical dynamic behaviour is obtained by a combination of the selected modes, reducing each transducer to few DOFs, while for the full order acoustic problem the solution is computed by means of the finite element method. The described procedure allows one to simulate in an exact manner the acoustic-structure interaction as the transducers are vibrating according to the selected modes. Moreover, the involved computational burden is basically related only to the pressure DOFs and depends on the size of the fluid domain in which the propagation wave pattern is simulated without any order reduction.

*Corresponding author. E-mail: gianluca.massimino@polimi.it.

RESULTS

The benchmark case study is reported in which the comparison between the reduced order model implemented in the custom code and the COMSOL 5.2 full order model is shown. The analyzed system consists of a single central vibrating transducer interacting with a hemispherical water domain with radius equal to $3\lambda = 1092.2$ μm where $\lambda = \nu_s/f_0 = 364.06$ μm is the wavelength, $\nu_s = 1481$ μm/μs is the speed of sound in water and $f_0 = 4.068$ MHz is the fundamental electro-mechanical frequency of the PMUT. The adopted excitation voltage is equal to 15 sinusoidal cycles at the fundamental frequency with 1 V amplitude. The considered common discretization, is characterized by the 15 elements in the PMUT radius, 4 elements through the thickness for the PZT and the silicon layers, while the other layers are discretized with 1 element through the thickness. Indeed, a maximum elements size of $\lambda/10$ is adopted for the fluid mesh. The numerical comparison, considering a ROM generated by the fundamental mode, in terms of pressure maps, at the final computation time $t = 3.69$ μs, on a cut plane passing through the transducer diameter is shown in Figure 2, while the corresponding pressure time histories, at the PMUT center, are reported in Figure 3.

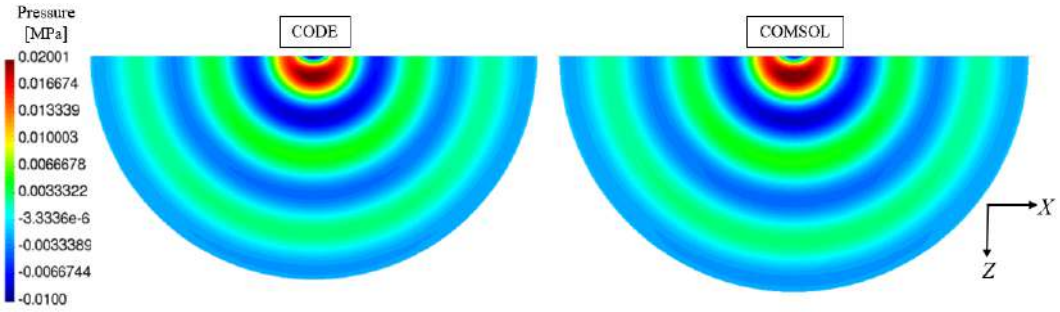

Figure 2: Pressure maps at $t = 3.69$ μs.

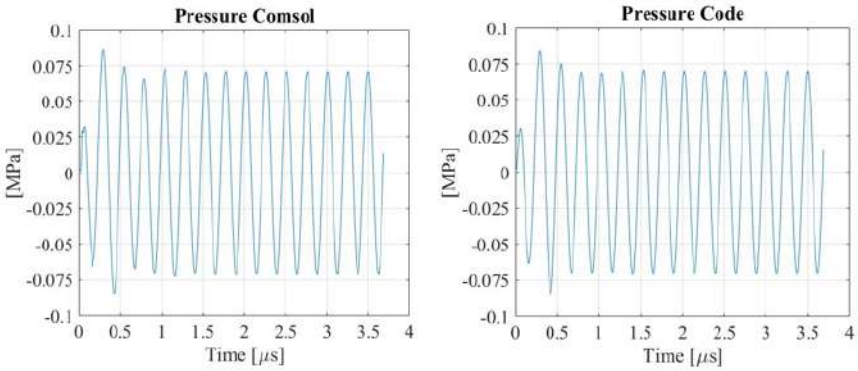

Figure 3: Pressure time histories at the PMUT center.

It is worth noting that the reduced order model predicts the same pressure history and propagation map of the COMSOL 5.2 model. Furthermore, the ROM computational time is about 8 mins while the corresponding one involved in the full-order finite elements model, built with the commercial code, is about 1 h 20 mins, running on the same machine with 6 Xeon CPU cores @3.6 GHz and 64 GB RAM.

CONCLUSION

The proposed ROM shows faster computational time than the standard procedure and the results are in good agreements with the full order finite element ones. Indeed, the novel approach represents a suitable tool to study the transmission and reception problems involving several PMUTs.

References

[1] Corigliano A., Ardito R., Comi C., Frangi A., Ghisi A., Mariani S. Mechanics of Microsystems. John Wiley & Sons, 2018.
[2] Massimino G., Colombo A., D'Alessandro L., Procopio F., Ardito R., Ferrera M., Corigliano A. Multiphysics Modelling and Experimental Validation of an Air-Coupled Array of PMUTs with Residual Stresses. J. of Micromech. and Microeng., 2018.
[3] Lu Y., Tang H., Fung S., Boser B. E., Horsley D. A. Short-range and high-resolution ultrasound imaging using an 8 MHz aluminum nitride PMUT array. 28th IEEE Inter. Conf. on Mic. Elec. Mech. Sys. (MEMS), 2015.
[4] Citarella R., Federico L. Advances in Vibroacoustics and Aeroacustics of Aerospace and Automotive Systems. Multidisciplinary Digital Publishing Institute, 2018.

MODELLING MICRO-PLATES IN VISCOUS FLUIDS WITH THE FUNDAMENTAL SOLUTIONS METHOD

Andre Loch Gesing*[1], Daniel Platz[1], and Ulrich Schmid[1]
[1]Institute of Sensor and Actuator Systems, TU Wien, Gußhausstraße 27, 1040 Vienna, Austria

Summary Micro-plates exhibit low losses in viscous fluids when vibrating in roof tile-shaped modes. Roof tile modes are often not considered for micro-sensors due to the lack of methods to predict the viscous losses of micro-plates vibrating in fluids. We develop a numerical method to predict the displacement of micro-plates in viscous fluids based on the Kirchhoff-Love plate equation - which we solve with the interior penalty method - with the method of fundamental solutions for the linearized Navier-Stokes equations for incompressible fluids. We show-case our method with the analysis of a silicon micro-plate in water. With our method it is straight forward to categorize peaks correspondent to flexural bending, torsional and roof tile modes and calculate the fluid flow associated to each mode. Our method provides a crucial understanding of the dynamics of micro-plates in viscous fluids.

INTRODUCTION

Micro electro-mechanical systems (MEMS) devices exploit as key building block the Euler-Bernoulli (EB) bending modes of narrow beams. These modes are chosen because methods to predict dynamic response and thermal calibration of narrow beams in viscous fluids are well established and straightforwardly implemented [1]. Higher order bending modes of beams in viscous fluids are subject to high viscous losses, while high order roof tile-shaped modes of micro-plates exhibit extraordinarily low losses in viscous fluids [2]. However numerical methods for the prediction of viscous losses of micro-plates oscillating in roof tile shaped modes are missing. A method for the prediction of the dynamic response of micro-plates in fluids is of utmost importance.

NUMERICAL METHOD

We solve the Kirchhoff-Love (KL) plate equation combined with the method of fundamental solutions for the linearized Navier-Stokes (LNS) equations. KL plate theory is based on a fourth order partial differential equation (PDE), which can't be solved with out-of-the-box Finite Element Method (FEM). We solve the KL PDE with a continuous / discontinuous method called interior penalty (IP). IP method enables us to use Lagrange-type continuous elements (C0 continuous) while minimizing discontinuities in first order derivatives (obtaining thus C1 continuity) and weakly enforcing clamped and free-end boundary conditions. For comparison purposes we also implemented the IP method for the EB beam equation. To model the fluid-structure interaction, we assume the non-slip condition at the plate's surface, and assume that the fluid velocity in the longitudinal direction of the plate is small in comparison to the other components. With this latter assumption, there is a fundamental solution for the LNS that relates pressure at the plate surface and the plate's transverse displacement at each cross-section [3]. Evaluation of the fundamental solution at top and bottom surfaces of the plate results in a pressure jump over the plate which is linearly and non-locally dependent on the plate's transverse displacement.

RESULTS

As an application example we consider a $300 \times 300 \times 5\ \mu\mathrm{m}^3$ silicon micro-plate immersed in water. The micro-plate is clamped on one side and free on the three others, and is excited by an external force at one of the free corners. Fig. 1 shows the displacement spectrum per unit excitation force ϕ/F of the free corner of the plate where the force is applied. Note that some of the peaks in the displacement spectrum are predicted by both KL and EB models. These peaks correspond, evidently, to flexural bending modes predicted both by EB and KL equations. The second peak in KL displacement spectrum corresponds to the first torsional mode. First beam bending mode and first torsional mode are shown in Figs. 2a and 2b, respectively. Roof tile modes for this micro-plate in water occur at frequencies equal to 237.4 kHz and 651.8 kHz and are shown in Figs. 2c and 2d. Evidently, these modes are predicted only with the KL method. Once the plate spectral displacement is calculated, we can reconstruct the velocity field at any point of the fluid domain by applying once again the fundamental solutions for the LNS. Velocity field associated with the first bending mode in Fig. 3a exhibits two vortices at the edges of the plate's cross section with opposite directions, and the fluid velocity near the center of the cross section is dominated by a normal component. For the first torsional mode we see in Fig. 3b that the vortices at the edges exhibit opposite directions, and the fluid moves across the plate's surface dominated by a tangential component. For roof tile modes in Figs. 3c and 3d the fluid moves back and forth across the plate's surface with a pattern that varies with the number of nodal lines of the vibrating mode. Note also that for roof tile modes the velocity field can reach higher velocities near the middle of the plate than at its edges. Vortices at the edge therefore are less dominant with increasing roof tile mode number, which could help explain the reduction in viscous losses with increasing mode number.

*Corresponding author. E-mail: andre.gesing@tuwien.ac.at

CONCLUSIONS

We showed that with the KL method we can model micro-plates vibrating in roof tile modes in viscous fluids. What is more, we are able to calculate the fluid flow associated to each vibrational mode, and better understand the viscous losses mechanism of micro-plates in fluids. Our numerical method can specially enable the use of roof tile modes in viscous fluids as novel strategies to further decrease energy losses of micro-sensors to the fluid. Future developments include implement 3D fundamental solutions for the LNS, comparison to experimental data and calculation of the thermal calibration.

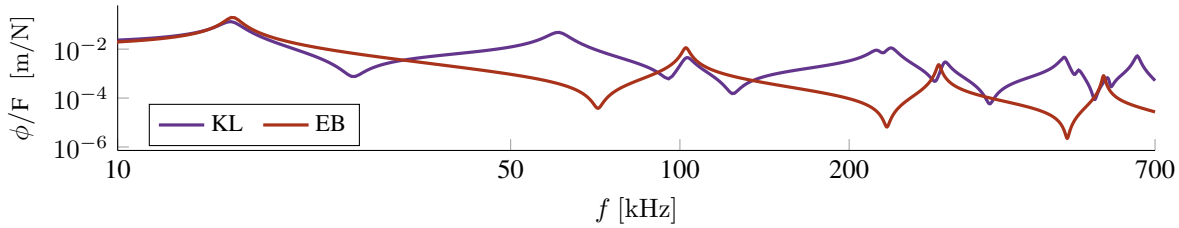

Figure 1: Displacement of a corner of the plate per unit excitation force calculated with KL and EB methods.

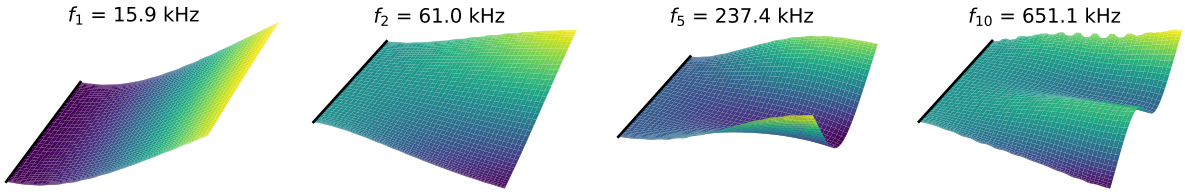

Figure 2: (a) First flexural, (b) first torsional, (c) first and (d) second roof tile-shaped vibrating modes.

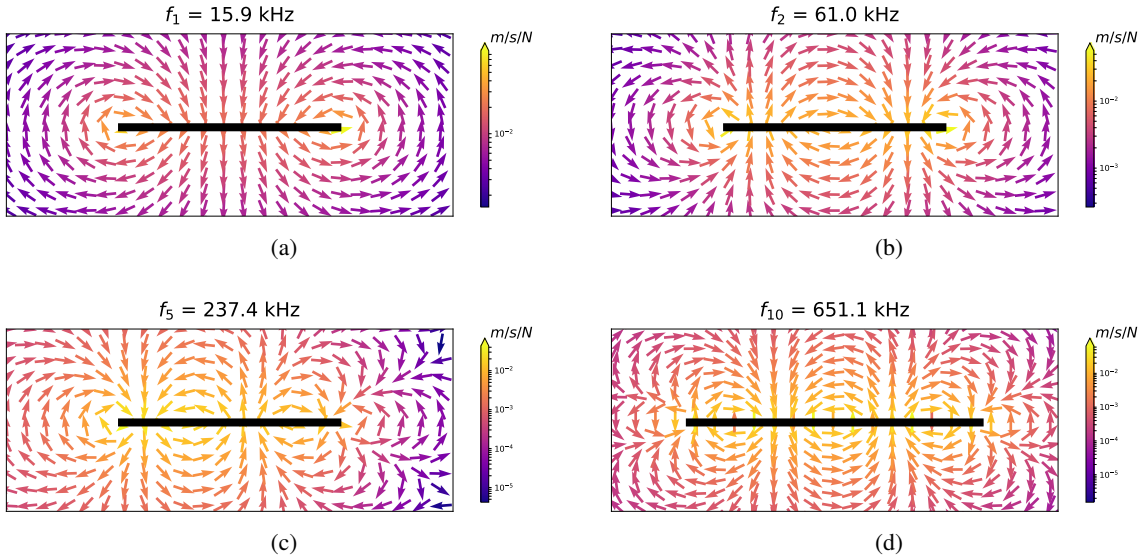

Figure 3: Fluid flow associated to the plate's different mode shapes.

References

[1] Sader J. E. Frequency response of cantilever beams immersed in viscous fluids with applications to the atomic force microscope. *J. of Applied Physics*, **84**: 64-76, 1998.

[2] Kucera M. et al. Characterisation of multi roof tile-shaped out-of-plane vibrational modes in aluminium-nitride-actuated self-sensing micro-resonators in liquid media. *Applied Physics L.* **107**: 1-5, 2015.

[3] Tuck E. O. Calculation of unsteady flows due to small motions of cylinders in a viscous fluid. *J. of Engineering Mathematics* **3**: 29-44, 1969.

O107411 - SM12 - Nanostructures and MEMS - Oral

ANALYSIS OF MECHANICAL AND GEOMETRIC PROPERTIES OF HIERARCHICAL LATTICE DEFECTS IN LOW-DIMENSIONAL CARBON NANO-MATERIALS

Xiao-Wen Lei*[1], Ako Kihara[1], and Yoshitada Tomioka[1]
[1]Department of Mechanical Engineering, University of Fukui, Fukui, Japan

Summary Low-dimensional carbon nano-materials have attracted significant attentions for its unique functional material properties, and graphene sheet (GS) is well-known as a fundamental 2D carbon nano-material. In this study, we focus on the mechanical and geometrical properties of GS with introduced hierarchical lattice defects for designing and controlling curved GS with out-of-plane deformation. According to the origami approach, we build atomic models of GS with different hierarchical lattice defects and perform their shape deformations with the molecular dynamic method. For GS, the out-of-plane deformation caused by the spontaneous curvature from lattice defects are often observed, so we consider such effects as well as the in-plane interaction, and discuss the relationship between the site potential energy, the mean curvature, and the Gauss curvature in details. In addition, we propose a general methodology for designing curved GS.

ANALYSIS MODEL OF GS WITH LATTICE DEFECTS

The lattice defects often cause remarkable out-of-plane deformation, which is a unique characteristic observed in low-dimensional carbon nano-materials [1]. For graphene sheet (GS) generally composed by hexagonal arrays of carbon atoms, according to the local variation of mechanical properties, pentagon defect can be considered as a positive disclination, whereas heptagon defect can be considered as a negative disclination. In this study, we define the hierarchical lattice defects as a combination of the positive disclination and the negative disclination that includes isolated disclination, isolated dislocation, dislocation dipole, dislocation array, and so on. Moreover, we use the technology of traditional Japanese paper craft art called "origami" to obtain the atomic position with complex out-of-plane deformation caused by the isolated disclination, dislocation, and dislocation array in GS. The initial atomic models are relaxed to the equilibrium states using the conjugate gradient method in molecular dynamics simulation to obtain the stable curved structures of GS.

MEAN CURVATURE AND GAUSS CURVATURE

To investigate the out-of-plane deformation of GS from plane to curved surfaces, we proposed a mathematical method to calculate the curvature tensor using the atomistic configuration. During the compression process, each GS initially modeled as 2D plane deforms to different 3D curved surfaces owing to the out-of-plane deformation [2], and this 2D–3D transition may generate folds and kink deformation. We introduce the mean curvature defined by the atomic configuration, such that we can characterize the out-of-plane deformation with quantification. Perfect GS has a hexagonal lattice structure, in which each atom is connected to three adjacent atoms via C–C covalent bond. As shown in Fig. 1, three neighboring atoms I, J, and K are connected to the carbon atom O. We consider these four carbon atoms O, I, J, and K span a curved surface $\boldsymbol{S}$. It would be a good approximation when the normal vector $\vec{\boldsymbol{n}}$ is defined as the normal vector of the plane I–J–K. Then, we establish a local Cartesian coordinates O–uvw, where the direction of w is parallel to the normal vector $\vec{\boldsymbol{n}}$. Thus, the curved surface S can be expressed as:

$$\kappa_{11}u^2 + 2\kappa_{12}uv + \kappa_{22}v^2 + w = 0, \tag{1}$$

where κ_{11}, κ_{12}, and κ_{22} are the components of curvature tensor $\boldsymbol{\kappa}$.

The mean curvature H is the average value of the principal curvature components κ_{11}^{P} and κ_{22}^{P}, and the Gauss curvature K is the product of the two principal curvature components that are given as:

$$H = \frac{\kappa_{11}^{\mathrm{P}} + \kappa_{22}^{\mathrm{P}}}{2}, \quad K = \frac{\kappa_{11}^{\mathrm{P}}\kappa_{22}^{\mathrm{P}}}{2} \tag{2}$$

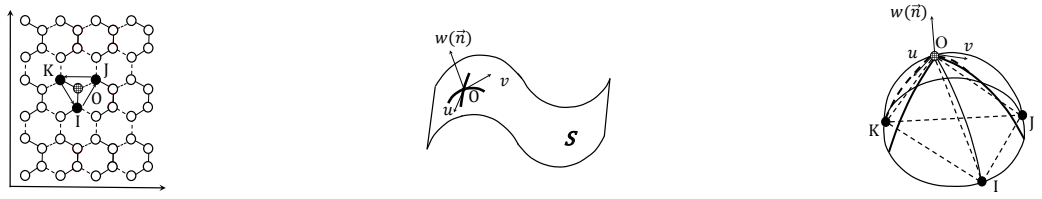

(a) Discrete lattice structure (b) Approximation of continuous surface (c) Curvature calculation

Figure 1: Schematic of mean curvature defined by atomic configuration.

*Corresponding author. E-mail: lei@u-fukui.ac.jp

RESULTS AND DISCUSSION

Figure 2 shows the distribution of potential energy, the mean curvature, and Gauss curvatre of the structure of GS with the isolated positive disclination. It can be seen that noticeable changes occur concentrically around the disclination core, and each distribution shows a concentric circle, respectively. It means the distribution values only depend on the distance from disclination corn, and do not depend on the angle. Furthermore, the Gauss curvature almost vanishes to 0 except for the part of the disclination. This phenomenon implies that the curved GS with isolated positive disclination has sufficient possibility to be regarded as a developable surface in mathematics.

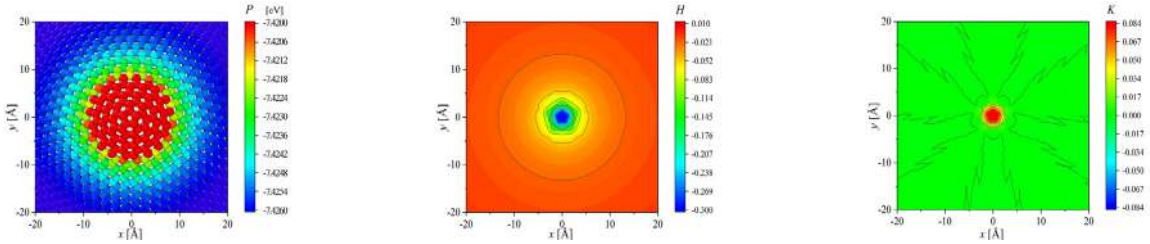

(a) Distribution of potential energy (b) Distribution of mean curvature (c) Distribution of Gauss curvature

Figure 2: Mechanical and geometrical properties of positive disclination.

Figures 3 and 4 show the analytical results of GS with positive dislocation array. We consider different densities of dislocation array, which is represented by the numbers of unit hexagon cell n between the adjacent dislocations. GS with dislocation array shows a periodic curved surface of mountain-valley-mountain-valley. From the distribution of potential energy, the periodical distribution has the largest value in pentagon defect and the smallest value in the heptagon defect. The distribution of the mean curvature shows that the entire model has nonzero curvature owing to out-of-plane deformation caused by the lattice defects, where the parts around the dislocation array own the largest absolute curvature and the absolute mean curvature decreases as the distance from dislocation array increases. In addition, as the dislocation density increases, the interval between contour lines increases. The same as Fig. 2(c), the Gasuss curvature is almost 0 except for the parts of dislocation array, which shows that a semi-developable curved surface can be obtained.

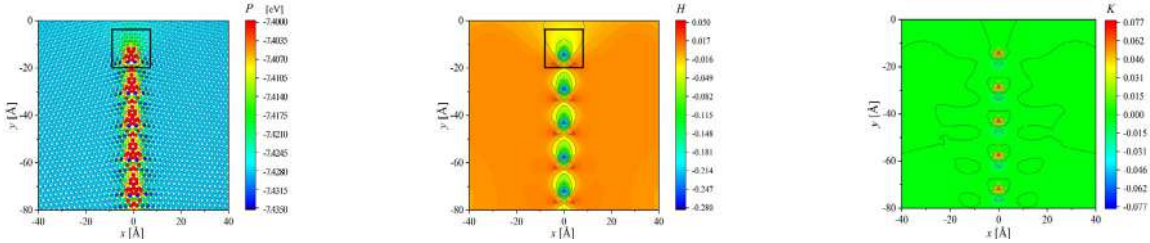

(a) Distribution of potential energy (b) Distribution of mean curvature (c) Distribution of Gauss curvature

Figure 3: Mechanical and geometrical properties of positive dislocation array with $n = 2$.

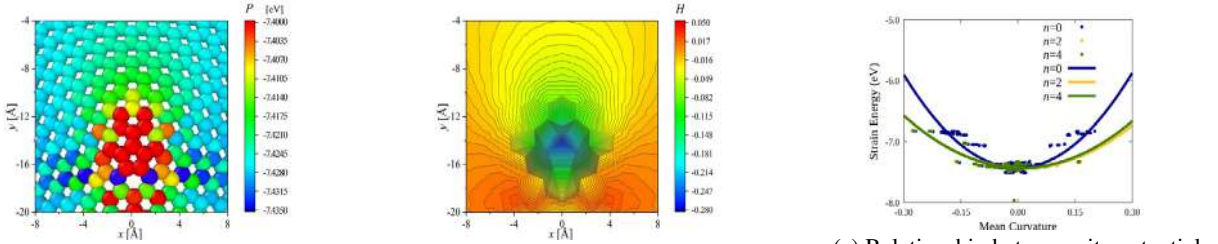

(a) Enlarged view of distribution of potential energy (b) Enlarged view of distribution of mean curvature (c) Relationship between site potential energy and mean curvature with different densities of dislocation

Figure 4: Relationship of mechanical and geometrical properties of positive dislocation array.

The relationship between the mean curvature and the site potential energy of the positive dislocation array is shown in Fig. 4(c). Because the mechanical properties near the dislocation and the free edge of GS are strongly affected by lattice defects, the potential energy distribution does not always correspond to the distribution of the mean curvature and the dispersion value is relatively large. However, the site potential energy can be universally expressed as a function of mean curvature regardless of the density of dislocation array. It indicates that the bending strain energy function can be defined using the mean curvature, so we can obtain the bending stiffness. In this way, the curved surface of GS with the intrinsic curvature caused by different arrangement of lattice defect will be predictable and controllable.

Acknowledgement: This work was supported by JSPS KAKENHI Grant Numbers 17K14145.

References

[1] Zhang T., Li X. and Gao H. Defects controlled wrinkling and topological design in graphene. *J. Mech. Phys. Solids*. **67:** 2-13, 2014.
[2] Yazyev O. V., Chen U. P. Polycrystalline graphene and other two-dimensional materials. *Nature Nanotech.* **9:** 755-767, 2014.

SHANNON ENTROPY IN STOCHASTIC ANALYSIS OF MEMS

Marcin Kamiński[1] and Alberto Corigliano [2]
[1]Department Structural Mechanics, Łódź University of Technology, Łódź, Poland
[2]Department of Civil and Environmental Engineering, Politecnico di Milano, Italy

Summary This work is focused on the numerical determination of Shannon probabilistic entropy for MEMS devices exhibiting some uncertainty in their structural response. This entropy is a universal measure of statistical or stochastic disorder in static deformation or dynamic vibrations of engineering systems and is available for both continuous and discrete distributions functions of structural parameters. Interval algorithm using Monte-Carlo simulation and polynomial structural response recovery have been implemented to demonstrate uncertainty propagation of forced vibrations in MEMS devices. Computational example includes stochastic nonlinear vibrations described by the Duffing equation calibrated for some micro-resonator, whose damping is adopted as the Gaussian input uncertainty source.

INTRODUCTION

Probabilistic entropy is a mathematical extension of its thermodynamic origin invented by Boltzmann and serves now as a universal measure of disorder (uncertainty) in the given engineering system. Various theories and formulas existing in this area have been initiated by Shannon in 1948, continued by Renyi, Tsallis [1] or Kolmogorov [2], Sinai and Kullback [3], and are available for both discrete and continuous probability distributions of the stochastic response of a given system. The main numerical difficulty in probabilistic entropy calculation is the necessity of final probability density function availability. This makes many of the stochastic computer techniques like Karhunen-Loeve, polynomial chaos or stochastic perturbation technique simply inapplicable and this is why the traditional Monte-Carlo simulation scheme may be preferred in this context.

The main aim of this study is the determination of probabilistic entropy fluctuations in some micro-resonator forced vibration problems with uncertainty described by the Duffing equations [4]; its understanding seems to be necessary for further more general numerical analyses of the disorder propagation in nonlinear vibrations of various MEMS devices [5]. The damping coefficient of this micro-devices is chosen as the input uncertainty source, because this parameter decisively affects its dynamic response, and its probability distribution is modelled using alternatively uniform, triangular, Gaussian as well as lognormal functions; all these distributions are based on the same upper and lower bounds for the uncertainty interval. The deterministic vibrations spectrum is obtained numerically using the Runge-Kutta-Fehlenberg algorithm implemented in the computer algebra system MAPLE and this is the basis for polynomial Least Squares Method approximation of the micro-resonator displacements with respect to this damping coefficient. Further part programmed in the same system includes Monte-Carlo sampling (MCS) of the damping parameter and the same sampling of the dynamic response and final Shannon entropy calculation using a formula adjacent to the interval representation of the statistical data. The approach proposed in this work may be used for more advanced MEMS analyses using commercial Finite Element Method codes like COMSOL or ABAQUS, for computer simulation of inelastic deformation in solids, for disorder propagation analysis in various computational fluid mechanics problems.

PRELIMINARY RESULTS

Let us consider further a continuous random variable b with its probability density function $g_b(x)$ discretized by a set of subintervals of the same length δ having the following representation within each ith subinterval:

$$g_b(x_i) = \frac{1}{\delta} \int_{i\delta}^{(i+1)\delta} g_b(x)\, dx \,. \tag{1}$$

Next, the quantized random variable $\hat{x}$ is defined as $\hat{x} = x_i \;\; for \; i\delta \le \hat{x} \le (i+1)\delta$, whose probability equals to

$$p_i = \int_{i\delta}^{(i+1)\delta} g_b(x)\, dx = \delta\, g_b(x_i) \,. \tag{2}$$

Shannon entropy corresponding to a partition of $g_b(x)$ into n equal subintervals can be rewritten as

$$H(\hat{x}) = -\sum_{i=1}^{n} p_i \log(p_i) = -\sum_{i=1}^{n} \delta g_b(x_i) \log(g_b(x_i)) - \log(\delta). \tag{3}$$

Determination of this entropy for the given MEMS device proceeds directly thanks to determination and partition of the probability distribution function of its structural response and is obtained in this work as the iterative solution to the following Duffing equation:

$$m\ddot{x}_{(j)}(t)+c_{(j)}\dot{x}_{(j)}(t)+k_1x_{(j)}(t)+k_2x^2_{(j)}(t)+k_3x^3_{(j)}(t)=F\sin(\omega t), \tag{4}$$

where m denotes the mass of the vibrating structure, $c_{(j)}$ stands for the damping coefficients discrete values, k_1, k_2 and k_3 are first, second, and third order stiffness coefficients related to various physical fields and sources, F and ω are the amplitude and frequency of the forcing signal. Since the damping coefficient is taken as the Gaussian input variable with the expectation and standard deviation equal to $E[c]$ and $\sigma(c)$, respectively, its discrete realizations are obtained via equidistant partition of the interval $[E[c]\text{-}3\sigma(c), E[c]+3\sigma(c)]$. These discrete solutions substituted to the Least Squares Method fitting procedure enable to determine structural response as a polynomial of its damping, and order of this polynomial is optimized using minimization of the fitting variance and RMS error as well as maximization of the correlation factor of the approximating polynomial to the fitting dataset. Having determined response polynomial, one may apply classical MCS strategy make a histogram of this response, whose further processing results in Shannon entropy value; such an algorithm enables for application of non-Gaussian parameters or even a couple of various uncertainties at the same time. Numerical simulation provided here has been completed with the input data adopted after [4] and it has been preceded with initial verification of Shannon entropy sensitivity to a partition of the input histogram. Left diagram of Fig. 1 shows convergence of this entropy together with an increasing partitioning of this histogram for the Gaussian random variable having expectation equal to 10 and the few standard deviations. Determination of satisfactory partition of both input and output uncertainty guarantees efficient estimation of probabilistic entropy, which can be evaluated when coefficient of variation reaches its extreme value. Shannon entropy is expected to be more efficient in uncertainty evaluation while periodic or quasi-periodic vibrations are analyzed, because of enormously large increase of coefficient of variation, when the expected value tends to 0 (cf. Fig. 1). Application of this technique to large scale MEMS system is possible with replacing of Eqn. (4) with its matrix counterpart and determination of the optimal polynomial responses in local manner – for each degree of freedom separately.

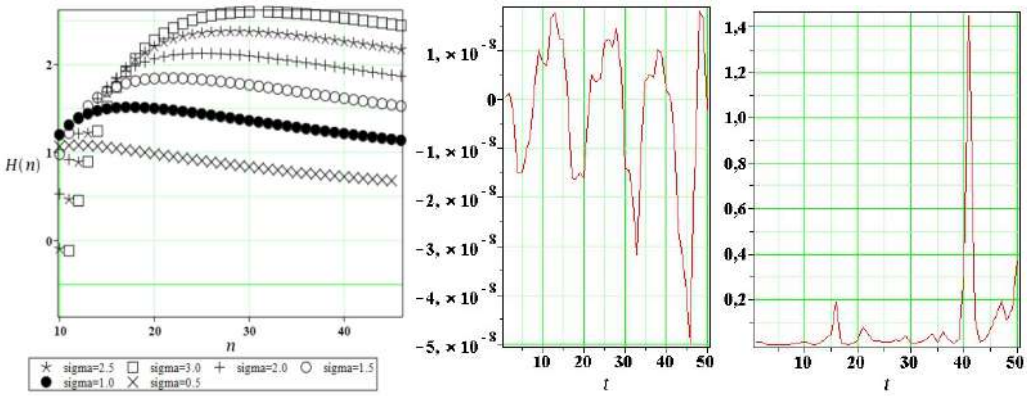

Figure 1. Convergence rate for the interval entropy computations (left) and expected values of MEMS device vibration (middle) and its coefficient of variation (right).

CONCLUDING REMARKS

Interval representation of the given probability density function applied together with Monte-Carlo simulation scheme of the structural response enables for reliable and relatively fast computation of probabilistic entropy propagation in many engineering systems including MEMS devices. As it was demonstrated, it does not demand large effort in discretization of the resulting probability distribution. In particular, one can model non-Gaussian distribution of any physical, material or geometrical parameters. It can be done both using some analytical solutions provided with the computer algebra systems like MAPLE as well as thanks to its common application with some Finite Element Method system.

References

[1] Kamiński M., Tsallis entropy in dual homogenization of random composites using the stochastic finite element method. *Int. J. Num. Meth. Engng*. **113**: 834-857, 2018.
[2] Cornfeld I.P., Fomin S.F., Sinai Y.A., Ergodic Theory. Springer-Verlag, Berlin-Heidelberg, 1981.
[3] Kullback S., Leibler, R.A., On information and sufficiency. *Ann. Math. Statist*. **22**: 79-86, 1951.
[4] Kamiński M., Corigliano A., Numerical solution of the Duffing equation with random coefficients. *Meccanica* **50**(7): 834-857, 2015.
[5] Corigliano A., Ardito R., Comi C., Frangi A., Ghisi A., Mariani S.. Mechanics of Microsystems, Wiley, ISBN 978-1-119-05383-5, 2018.

HOMOGENIZATION OF HETEROGENEOUS PIEZOELECTRIC MATERIALS FOR VIBRATIONAL ENERGY HARVESTING

Denis Aubry and Ann-Lenaig Hamon*
Université Paris-Saclay,Centrale Supélec,CNRS,
Laboratoire de Mécanique des Sols,Structures et Matériaux,91190,Gif-sur-Yvette,France

Summary We study here energy harvesting systems derived from solid vibrations. They require an efficient tranduce which can be made of piezoelectric, ferroelectric or triboelectric materials, or a combination of these. Heterogeneous structures designed with materials with various electromechanical properties are thus good candidates but require a homogenization process of their properties.

We propose to describe the multiphysic homogenization procedure of the electromechanical properties of piezoelectric nano-architectures, used to feed the complete harvester model, and then to describe the electromechanical behaviour of a harvester using MEMS.

Keywords: MEMS, Vibrational energy harvesting, Autonomous microsensors

INTRODUCTION

With the increasing use of IoT, the need for smart, integrated, miniaturized and low-energy wireless devices is boosted. In parallel, a wide range of needs for autonomous microsensors emerges, among which the health monitoring of civil engineering structures (bridges, dams), railway tracks, or transport vehicles (terrestrial, maritime, aeronautics), but also biomedical applications (autonomous pacemaker, smart garments).

We propose here to consider energy harvesting derived from solid vibrations. Indeed, they are an ubiquitous and constant source of energy which requires an efficient tranducer in order to harvest electric charges which are then stored in a capacitor before use. These transducers can be made of piezoelectric, ferroelectric or triboelectric materials, or a combination of these.

Heterogeneous structures designed with materials with various electromechanical properties are thus good candidates but require a homogenization process of their properties.

We propose to describe the multiphysic homogenization procedure of the electromechanical properties of piezoelectric nano-architectures, used to feed the complete harvester model and then to describe the electromechanical behaviour of a harvester using MEMS.

HOMOGENIZATION OF THE HETEROGENEOUS TRANSDUCER

The homogenization procedure involves an asymptotic strategy with respect to a scaling factor ξ proposed originally by Sanchez-Palancia [1] and recently by De Bellis [2] for an electromechanical coupling. The displacement $\boldsymbol{u}$ and voltage v^e fields are sought as:

$$\boldsymbol{u}\left(\boldsymbol{x},\boldsymbol{y}\right) = \sum_{k\geq 0} \xi_k \boldsymbol{u_k}\left(\boldsymbol{x},\boldsymbol{y}\right) \qquad \text{and} \qquad v^e\left(\boldsymbol{x},\boldsymbol{y}\right) = \sum_{k\geq 0} \xi_k v_k^e\left(\boldsymbol{x},\boldsymbol{y}\right)$$

where $\boldsymbol{x}$ is the macroscopic and $\boldsymbol{y}$ the microscopic space variables, considered as independent.

The coupled equations to solve are

$$\begin{cases} \textbf{Div}\left\{\boldsymbol{C}\left[\boldsymbol{\epsilon}\left(\boldsymbol{u}\right)+\boldsymbol{D^e}\boldsymbol{\nabla} v^e\right]\right\} = \boldsymbol{0} \\ \text{div}\left[-\boldsymbol{D^e}^T\boldsymbol{\epsilon}\left(\boldsymbol{u}\right)+\boldsymbol{d^e}\boldsymbol{\nabla} v^e\right] = 0 \end{cases}$$

where $\boldsymbol{C}$ is the 4^{th}-order elastic tensor, $\boldsymbol{\epsilon}$ the small strain tensor, $\boldsymbol{D^e}$ the 3^{rd}-order piezoelectric tensor, and $\boldsymbol{d^e} = \epsilon_0\boldsymbol{\epsilon_r}$ the 2^{nd}-order absolute local permittivity tensor.

We can prove that $\boldsymbol{u_0}$ and v_0^e only depend on $\boldsymbol{x}$, and that there exist three tensors $\boldsymbol{A}$, $\boldsymbol{B^e}$ and $\boldsymbol{b^e}$ functions of the $\boldsymbol{y}$ variable, and such that the 1^{st}-order microscopic strain and electric fields are given by:

$$\begin{cases} \boldsymbol{\epsilon_y}\left(\boldsymbol{u_1}\right) = \boldsymbol{A}\boldsymbol{\epsilon_x}\left(\boldsymbol{u_0}\right)+\boldsymbol{B^e}\boldsymbol{\nabla_x} v_0^e \\ \boldsymbol{\nabla_y} v_1^2 = -\boldsymbol{B^e}^T\boldsymbol{\epsilon_x}\left(\boldsymbol{u_0}\right)+\boldsymbol{b^e}\boldsymbol{\nabla_x} v_0^e \end{cases}$$

$\boldsymbol{A}$, $\boldsymbol{B^e}$ and $\boldsymbol{b^e}$ are determined with nine carefully chosen problems solved on the representative periodic cell and from which are infered the homogenized tensors $\tilde{\boldsymbol{C}}$, $\tilde{\boldsymbol{D}}^{\boldsymbol{e}}$ and $\tilde{\boldsymbol{d}}^{\boldsymbol{e}}$. The computational solution is sought using finite elements and requires to take into account the specific symmetry of the representative cell with specific boundary conditions. The chosen test materials are GaN [3] or ZnO [4] nanowires embedded in PVDF [5], ferroelectric nanoparticles [6] or triboelectric composites [7]. Their individual anisotropy is taken into account.

*Corresponding author. E-mail: ann-lenaig.hamon@centralesupelec.fr.

HARVESTER ARCHITECTURE

The complete structure of the harvesting device can be decomposed into three stages, which has already proven effective for an autonomous pacemaker using interdigitated electrostatic combs as the transducer device ([8],[9]) as shown in Fig. 1.

First, the vibrational input sets into motion a seismic mass. The input signal frequency is not necessarily in the range of the transducing material and the storage circuit efficiency. Thus, bistable prebuckled beams are used in order to apply vibrations in the proper frequency range to the transducer. Secondly, the transducer can be modelled using the homogenized properties calculated as shown above. Thirdly, an electrical circuit with non linear diodes allows the storage into a capacitor of an electric charge which must be optimized.

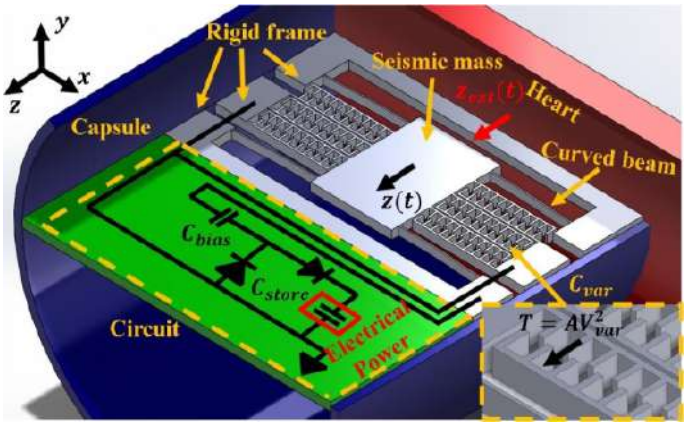

Figure 1: Typical architecture for a pacemaker: the transducing device consists in interdigitated electrostatic combs [10].

CONCLUSIONS

The homogenization process allows to exhibit the novel properties of the transducer and to select the most effective types of materials. Moreover, it allows to model the complete behaviour of a harvester and to size all of its components.

At last, let us note that specific attention must be paid to the different characteristic times involved, typically the vibration period versus the relaxation time of the electrical circuit.

ACKNOWLEDGEMENTS

This work is carried out within the NanoVIBES project supported by the NanoSaclay Labex and involving six academic partners of University Paris-Saclay.

References

[1] Sanchez-Palancia É. Homogenization method for the study of composite media *in* Asymptotic analysis II (Springer), *Lecture notes in mathematics* **985**: 192214, 1983.

[2] De Bellis M.L., Bacigalupo A., Zavarise G. Characterization of hybrid piezoelectric nanogenerators through asymptotic homogenization, *Comput. Methods Appl. Mech. Engrg.* **355**: 11481186, 2019.

[3] Morassi M., Largeau L., Oehler F., Song H.-G., Travers L., Julien F.H., Harmand J.-C., Cho Y.-H., Frank Glas F., Tchernycheva M., Gogneau N. Morphology tailoring and growth mechanism of indium-rich InGaN/GaN axial nanowire heterostructures by plasma-assisted molecular beam epitaxy, *Cryst. Growth Des* **18**(4): 2545 – 2554, 2018.

[4] Amiri G., Souissi A., Hanche N., Vilar C., Lusson A., Sallet V., Galtier P. Synthesis and characterization of coreshell ZnO/ZnSe nanowires grown by MOCVD, *Phys. Status Solidi* B**250**(10): 2132 – 2136, 2013.

[5] Melilli G., Lairez D., Gorse D., Garcia-Caurel E., Peinado A., Cavani O., Boizot B., Clochard M.-C. Conservation of the piezoelectric response of PVDF films under irradiation, *Rad. Phys. Chem.* **142**: 54 – 59, 2018.

[6] Bogicevic C., Thorner G., Karolak F., Haghi-Ashtiani P., Kiat J.-M. Morphogenesis mechanisms in the solvothermal synthesis of $BaTiO_3$ from titanate nanorods and nanotubes, *Nanoscale* **8**: 3594 – 3603, 2015.

[7] Feng S., Zhang H., He D., Xu Y., Zhang A., Liu Y., Bai J. Synergistic effects of $BaTiO_3$/multiwall carbon nanotube as fillers on the electrical performance of triboelectric nanogenerator based on polydimethylsiloxane composite films, *Energy technology* **7**(3): 1900101, 2019.

[8] Vysotskyi B., Aubry D., Gaucher P., Le Roux X., Parrain F., Lefeuvre É. Non linear electrostatic energy harvester using compensational springs in gravity field, *J. Micromech. Microreng.* **28**: 074004, 2018.

[9] Vysotskyi B., Parrain F., Aubry D., Gaucher P., Le Roux X., Lefeuvre É. Engineering the structural non linearity using multimodal-shaped springs in MEMS, *J. of microelectromechanical systems* **27**(1): 40 – 46, 2018.

[10] Vysotskyi B. Electrostatic MEMS vibrational energy harvester with large bandwidth for biomedical applications. *PhD Thesis*, Université Paris-Saclay, France, 2018.

NON-LINEARITIES MAPPING FOR MODEL ORDER REDUCTION IN MEMS

Giorgio Gobat*[1], Valentina Zega[1], and Attilio Frangi[1]
[1]Department of Civil and Environmental Engineering, Politecnico di Milano, Milano, Italy

Summary A numerical procedure able to simulate Micro-Electro-Mechanical-Systems (MEMS) resonant devices in presence of electrostatic and geometric non-linearities is proposed. The main idea is to represent MEMS devices as a collection of stiff components (e.g. moving mass or shuttle), compliant elements (e.g folded springs) and electrodes, thus reducing the original device to a model with the degrees of freedom (dof) of the stiff components. The non-linear elastic and electrostatic forces are evaluated through a mapping procedure starting from numerically precomputed tables. The method is applied to the analysis of a MEMS quad-mass structure and validated with experimental data.

INTRODUCTION

Micro-Electro-Mechanical-Systems are experiencing an explosive growth and pose new challenges also from the numerical simulation point of view. The increasing request of more sophisticated and smaller devices, in fact, often implies to consider many non-linear effects that can be strictly related to the mechanical response or to coupled electro-mechanical phenomena. Moreover, the high resonant frequencies (in the order of kHz-GHz) and the in-vacuum encapsulation (quality factors in the order of thousands) of such devices can result in difficulties in terms of computational effort.

The Finite Element Method (FEM) represents the most popular simulation tool employed so far to simulate the dynamic response of MEMS devices both in the linear and nonlinear regimes. It generates a second order differential system of equations that for complex mechanical structures (e.g. gyroscopes) can reach big dimensions and consequently require long computational times. There is then the need to find alternative methods able to simulate more efficiently the complex behaviours of MEMS devices. One possibility is represented by the Reduced Order Models (ROM).

In this work we propose a ROM procedure inspired by the lumped parameter ([1, 2]) and pseudo-rigid ([3, 4]) models. It consists in the reduction of the complex mechanical structure of the MEMS device in a simplified system made by rigid bodies connected one to the others and to the substrate through compliant elements. In this way it is possible to reduce the number of degrees of freedom to the ones of the identified rigid bodies and to evaluate the elastic and electrostatic forces from pre-computed tables, thus significantly reducing the computational time.

METHODOLOGY

The quad-mass MEMS structure proposed in [5] is considered in the following. It consists of four masses connected one to the others and to the substrate through folded beams and able to translate in-plane according to the beating-heart mode shown in Figure 1a. Comb fingers are also present in the four masses to allow for electrostatic actuation and readout.

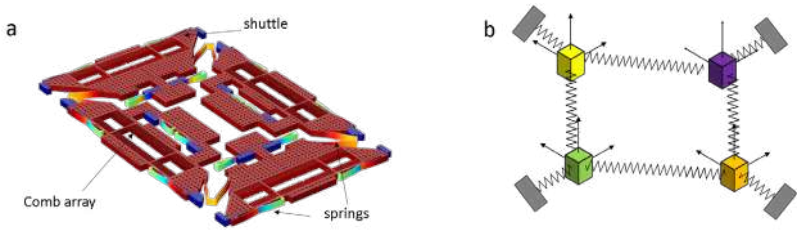

Figure 1: (a) Beating-heart mode of the quad-mass structure proposed in [5]. The contour of the displacement magnitude is shown in color. (b) Schematic view of the quad-mass structure employed in the proposed Reduced Order Model.

According to the proposed MOR procedure, we identify the stiff components with each moving mass (or shuttle) and the compliant elements with the folded springs (see Figure 1b). In order to apply the proposed ROM procedure, the stiff components are modelled as rigid bodies endowed with 6 dof each (colored cubes in Figure 1b), while compliant elements (zig-zag lines in Figure 1b) are simulated through nonlinear static FEM analyses to build the necessary pre-computed tables for the elastic nonlinear forces. To compute such tables, an admissible range for displacement and rotation amplitudes is evaluated a-priori according to the real quad-mass structure (i.e. maximum displacement to avoid contact between mechanical components or unstable phenomena such as pull-in). An increasing displacement and rotation amplitudes (in the admissible range before identified) are then applied to each compliant element and the corresponding reaction forces are computed and tabulated. The overall nonlinear elastic forces $\mathbf{F}_s$ acting on the rigid bodies can be then reconstructed through a numerical fitting of the tabulated discrete values.

*Corresponding author. E-mail: giorgio.gobat@polimi.it

A similar approach is adopted for the estimation of the nonlinear electrostatic forces acting on the rigid bodies. Each comb finger is subjected to a given increasing displacement (in the admissible range above identified) and the electrostatic forces are computed through a code based on integral equations and tabulated. The overall nonlinear electrostatic force $\mathbf{F}_e$ acting on the rigid bodies can be then reconstructed through a numerical fitting of the tabulated discrete values.

The equations of motion then read:

$$\mathbf{M}\,\ddot{\mathbf{q}} + \mathbf{F}_s(\mathbf{q}) = \mathbf{F}_e(t, \mathbf{q}) \tag{1}$$

where $\mathbf{M}$ is the mass matrix of the rigid bodies, $\mathbf{q}$ is motion parameters vector, $\mathbf{F}_s$ is the function describing the nonlinear elastic forces and $\mathbf{F}_e$ is the function describing the nonlinear electrostatic forces. In eq. (1) the number of differential equation to solve is dictated by the number of rigid bodies present in the ROM (e.g. 6 rigid motions x 4 bodies = 24 dof for the quad-mass structure under study) thus showing a great advantage with respect to a standard FEM approach that would discretize the full 3D geometry obtaining thousands of differential equations to solve.

EXPERIMENTS

To validate the proposed ROM procedure, we compare the numerical results with experimental data obtained on a quad-mass structure fabricated through the Thelma© surface micromachining process of STMicroelectronics [5].

A constant Direct Current (DC) voltage $V_{DC} = 10V$ is applied to the structure, while a Alternated Current (AC) voltage is applied on the driving electrodes located on the masses. The frequency of the AC voltage is swept from low to high frequencies (upward) and viceversa (downward) and the capacitance variation is measured on the readout electrodes located on the four masses. In Figure 2, the experimental frequency response of the quad-mass structure is reported in red dots for two amplitudes of the AC voltage. Note that the displacement amplitude is obtained from the capacitance measurements through standard relations [2] and the frequencies on the x-axis are normalized with respect to the natural frequency of the beating-heart mode ω_0 computed through a modal analysis.

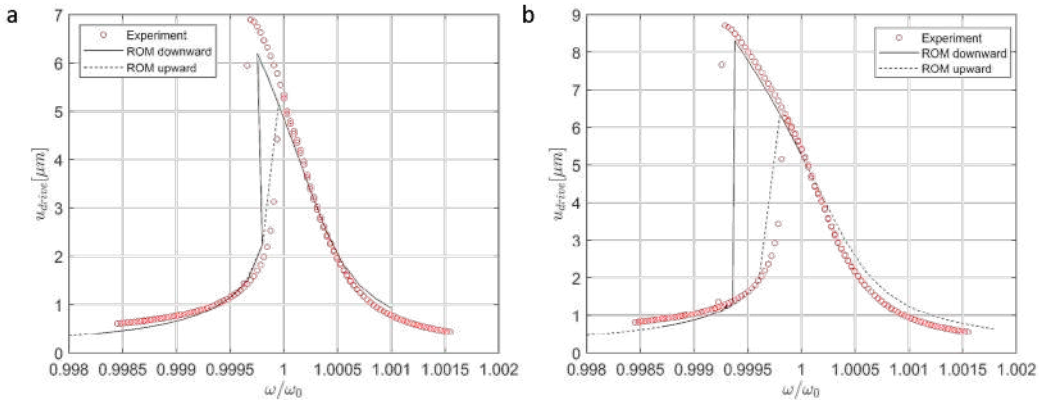

Figure 2: Frequency response of the quad-mass structure (beating-heart mode): experimental data vs ROM numerical prediction for (a) $V_{AC} = 1.5$ V and (b)$V_{AC} = 2$ V.

In Figure 2, the frequency response computed through the proposed ROM procedure is superimposed to the experimental data (black lines) and a good agreement is found. The nonlinear (softening) behaviour of the quad-mass structure is in fact well catched by the proposed model.

CONCLUSIONS

A ROM procedure able to simulate the linear and nonlinear dynamic response of a complex MEMS structure is here proposed. The proposed procedure is validated on a test structure and a good agreement between experiments and numerical predictions is found also in the nonlinear regime.

References

[1] Tilmans, Harrie AC. "Equivalent circuit representation of electromechanical transducers: I. Lumped-parameter systems." Journal of Micromechanics and Microengineering 6.1 (1996): 157.

[2] Senturia, Stephen D. Microsystem design. Springer Science & Business Media, 2007.

[3] Howell, Larry L. Compliant mechanisms. John Wiley & Sons, 2001.

[4] Ando, Bruno, et al. "Investigation on mechanically bistable MEMS devices for energy harvesting from vibrations." Journal of Microelectromechanical Systems 21.4 (2012): 779-790.

[5] Zega, Valentina, et al. "Hardening, Softening, and Linear Behavior of Elastic Beams in MEMS: An Analytical Approach." Journal of Microelectromechanical Systems 28.2 (2019): 189-198.

ON THE FAILURE OF SILICON THIN MEMBRANES DURING FREE FALL TESTS FOR MEMS MICROPHONES

Aldo Ghisi*[1], David Faraci[1], Silvia Adorno[2], and Alberto Corigliano [2]
[1]Department of Civil and Environmental Engineering, Politecnico di Milano, Milano, Italy
[2]ST Microelectronics, via Tolomeo 1, Cornaredo (MI), Italy

Summary *The effect of the impact against hard surfaces on MEMS thin membranes attached to dummy devices, as observed through guided free fall (GFF) tests, is investigated through three-dimensional, finite element numerical simulations. Accounting for the different scales involved, a multiscale top-down approach is followed, and first both purely fluid-dynamics and purely solid-mechanics macro-scale simulations are carried out, to provide fluid pressure histories and anchor displacements as input for the silicon thin membranes. Then, a micro-scale mechanical analysis is carried out to judge whether possible failures arise in a given GFF test for each membrane. It is shown that in some cases possible failures actually depend from the combination of the fluid-induced and of the solid-induced input transferred to the MEMS membrane, and not from a single domain-induced loading condition.*

INTRODUCTION

Accidental drops of mobile phones or other consumer electronics devices containing MEMS structures can induce severe loadings to micro-sensors [1]. In particular, MEMS microphones [2] feature silicon thin membranes that are connected with the outside environment through narrow ducts, where the fluid (air) can flow freely. Unfortunately, through the same passages sudden fluid pressure rises, such as the ones generated during the last instants before the impact against a target surface (i.e. a rigid floor), are also transferred to the thin membranes, making them prone to fail to this extreme (and not easily-to-estimate) loading condition.

In the industry, the effect of impact against hard surfaces on these thin silicon MEMS membranes can be inspected experimentally through guided free fall tests. In the latter, MEMS microphones are set on an exemplary device, such as a dummy smartphone also known as "jig", that is driven downwards and then left to fall and collide against a rigid floor. Impact waves travelling inside the solid domain combine with the aforementioned pressure rise in the fluid (air) surrounding the membrane; henceforth, strongly varying loading conditions during the contact and the following bounce are present and it becomes difficult to predict eventual failures of the thin structures, justifying an accurate study.

MULTI-SCALE PROBLEM FORMULATION

Macro-scale analysis

To judge the goodness of the design choices on the impact resistance for the thin membrane, here we impose the displacement histories of the falling jig, captured by a high-speed camera, as input for a macro-scale fluid-dynamic numerical simulation. In the latter, only the air surrounding the jig is modelled and the jig surfaces are treated as movable walls, displacing in accordance to the aforementioned experimental measurements. While the jig surfaces are moving, a remeshing has to occur in the fluid domain surrounding it. Consequently, we can calculate the (transient) pressure histories at the inlet of the narrow ducts (on the jig surface, see Figure 1a) leading into the chamber where the MEMS membranes are placed on the jig (see Figure 1b).

Because of the difference in the scales involved, ranging from about ten centimetres for the jig to the one-micrometre membrane thickness, a multiscale top-down approach is needed: the macro-scale fluid pressure history during the impact transitory is transferred as input at the micro-scale, where only the silicon membrane is modelled (see Figure 1c). A second macro-scale analysis is also carried out, accounting for a purely mechanical domain for the jig (i.e. neglecting air): in this second macro-scale analysis, the displacement time-histories of the membrane anchor points are registered and, similarly to the fluid-dynamic case, they are then transferred as input to the micro-scale membrane model.

Micro-scale analysis

At this scale, with the aforementioned fluid pressure and displacement transient histories at the anchor points as input, the silicon membrane is analysed through an implicit dynamics, mechanical analysis, allowing for large displacements and contact, and the status of the membrane is checked for possible failures. Particular attention has been devoted to the synchronization of the input signals with respect to the first impact. Since each jig can accommodate four microphones, i.e. four silicon membranes, and each membrane feature four vertices, a total of sixteen displacement signals are at hand for each free fall test. A fluid-structure interaction analysis of the air duct and membrane showed that the pressure at the inlet, obtained at the macro-scale, is transferred almost unchanged to the chamber where the membrane is placed: therefore, only one time-varying pressure signal is imposed at the membrane. The membrane itself can enter into contact with an upper and lower surface delimiting the internal chamber: these boundary conditions are taken into account during the micro-scale analysis.

*Corresponding author. E-mail: aldo.ghisi@polimi.it

RESULTS AND DISCUSSION

Experimental repetition of the tests (for a total of 25 guided free fall tests) showed that eventual failures are hardly predictable from nominally equal initial conditions; local observations of the impact history are hence necessary to clarify the failure behaviour, provided the accurate numerical analyses described above are carried out. The stress levels inside the membrane are inspected in terms of the envelopes of maximum and minimum principal stresses (see Figure 2) and checked versus a Rankine-like criterion in the tensile regime and versus a resistance domain defined as in [3] in the other regimes. Crack patterns due to the impact with the lower and upper surfaces are eventually observed.
It is also obtained that, in some cases, the failure is not simply pressure-induced (i.e. caused by pressure rise/decrease) or simply solid-induced (i.e. caused by the waves propagating in the solid jig and reaching the membranes), but it is the combination of the two phenomena to count.

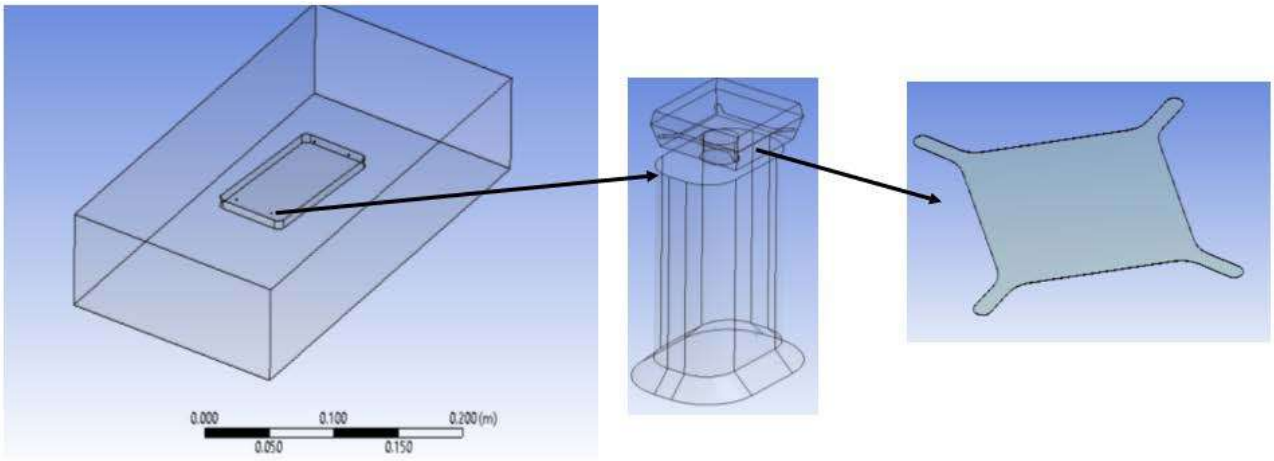

Figure 1. (a) macro-scale, fluid-dynamics model, (b) air duct and membrane chamber, and (c) thin silicon membrane.

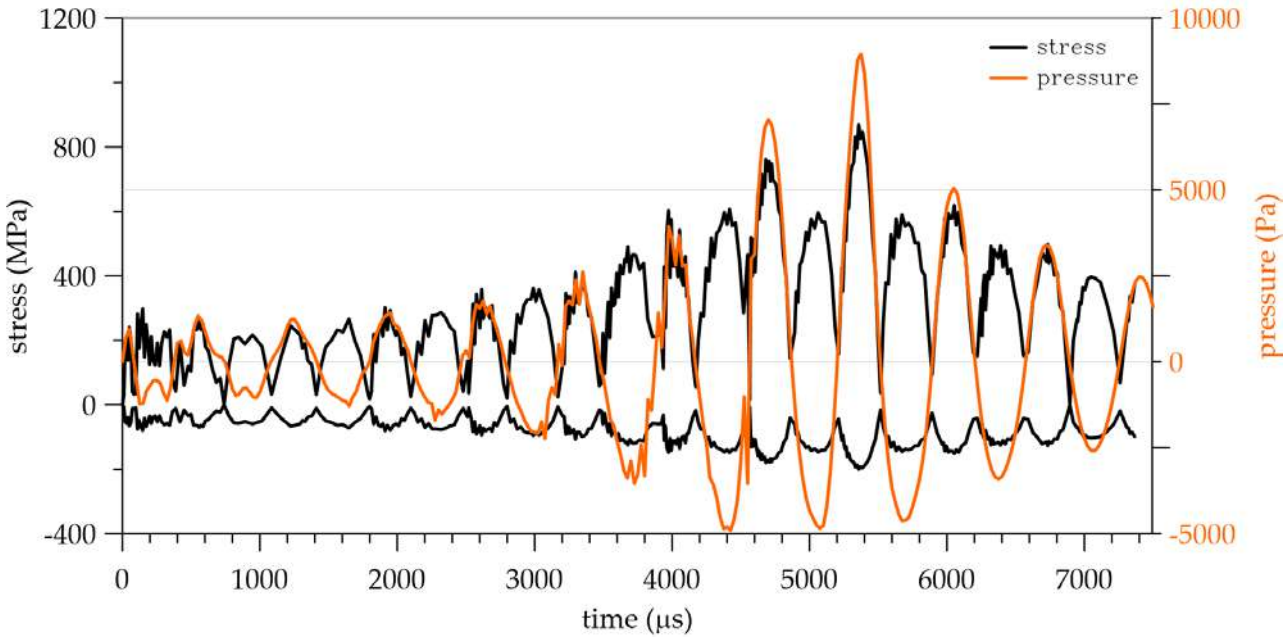

Figure 2. Time evolution of the envelopes of maximum principal stresses in the thin silicon membrane synchronized with the pressure signal in one sensor.

References

[1] Mariani S., Ghisi A., Corigliano A., Zerbini S. Multi-scale Analysis of MEMS Sensors Subject to Drop Impacts. *Sensors*, **7**:1817-1833, 2007.
[2] Nicollini G. Devecchi D. MEMS Capacitive Microphones: Acoustical, Electrical, and Hidden Thermal-Related Issues. *IEEE Sensors Journal*, **18**:5386-5394, 2018.
[3] Mariani S., Martini R., Corigliano A., Beghi M. Overall elastic domain of thin polysilicon films. *Comp. Mat. Sc.*, **50**:2993-3004, 2011.

A PROTOTYPE FOR VIBRATION ISOLATION AT THE MICROSCALE THROUGH TWO-PHOTON POLYMERIZATION

Claudia Comi*[1], Luca Pertoldi[2], Valentina Zega[1], Tommaso Zandrini[2], Roberto Osellame[2,3], Alberto Corigliano [1]
[1]Department of Civil and Environmental Engineering, Politecnico di Milano, Milano, Italy
[2]Institute for Photonics and Nanotechnologies, CNR, Milano, Italy
[3]Department of Physics, Politecnico di Milano, Milano, Italy

Summary The correct functioning of many micro-electromechanical devices requires the isolation from accidental vibration. Metamaterials, presenting band-gaps in the dispersion spectrum, i.e. interval of frequency in which propagating waves are attenuated, can provide an effective solution for isolation at the microscale. In the research work here presented we design, analyse and fabricate a prototype of an isolator made with a metamaterial fabricated through the two-photon polymerization process. The experimental validation is currently under development.

INTRODUCTION

Phononic crystals are periodic structures with properly conceived designs in terms of geometry and elastic properties of the constituent materials, that exhibit exceptional dynamic behaviours, such as frequency bandgaps formation. The presence of bandgaps in these structures, also called metamaterials, makes them very appealing for applications such as vibration shielding at different scales and this demonstrates the increasing interest of the scientific community on the topic. Several examples of macroscale vibration isolators made by phononic crystals are available in the literature [1], no much work has been done so far at the microscale where the complexity of the optimal geometry of the unit cell often makes difficult or impossible the fabrication process.

In the present work, we design through numerical simulations a 3D phononic crystal with a micrometric unit cell able to work as vibration isolator for a micro system. We then exploit the recently developed technique of the two-photon polymerization (2PP) [2, 3] to realize a prototype of the isolated system. Experiments are currently under development.

PHONONIC CRYSTAL: MECHANICAL DESIGN AND SIMULATIONS

The phononic crystal designed in this work is similar to the one proposed in [4]; it is constituted by a periodic repetition of cubic cells with nearly spherical masses suspended by slender beams mutually orthogonal (Figure 1a). This particular arrangement, thanks to an internal resonant mechanism [5], allows obtaining very peculiar dynamic properties (i.e. wide complete bandgap). Two 3D numerical simulations are performed in COMSOL-Multiphysics to demonstrate the dynamic behaviour of the proposed metamaterial and to identify the bandgap frequency interval. In particular, the Bloch-Floquet analysis conducted on the unit cell represented in Figure 1a, shows that the dispersion diagram exhibits very large complete band-gaps: waves of frequencies inside this interval cannot propagate without attenuation. For the case of a cell of 27 μm side, a bandgap from 4.5 MHz and 28 MHz is obtained as shown in Figure 1b.

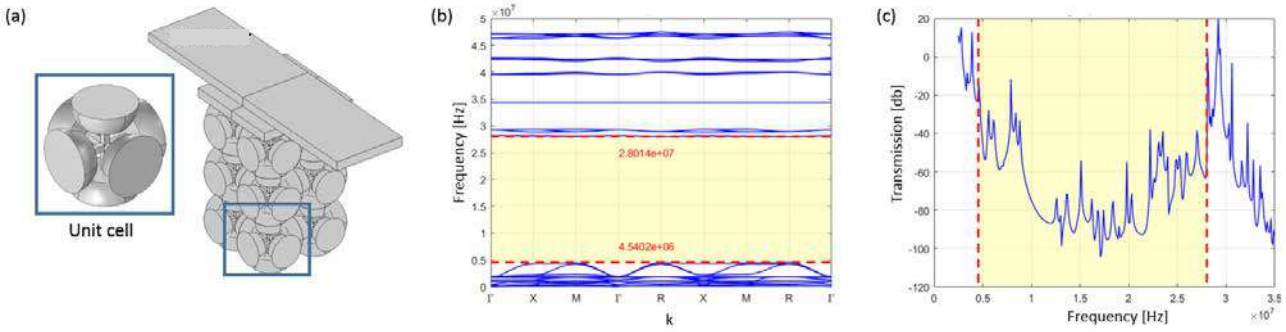

Figure 1. (a) Geometry of the proposed phononic crystal: a close-up view of the unit cell is also shown. (b) Dispersion and (c) transmission diagrams computed in COMSOL-Multiphysics.

In Figure 1c we report the transmission through the system made of the substrate and the 2 x 2 x 3 cells phononic crystal as a function of the frequency of the input waves. A prescribed sinusoidal displacement along the vertical direction is applied on the bottom substrate of the metamaterial and the resultant displacement on the top of the metamaterial is computed to show the attenuation properties of the proposed phononic crystal. From Figure 1c one can observe that, within the bandgap, shaded in the plot, a significant attenuation is obtained with 3 cells only. Note that the transmission diagram is reported only for the vertical direction because of the chosen configuration of the periodic cells (2 x 2 x 3) dictated by the application we want to prove as vibration isolator for the micro-beam.

With the aim of demonstrating the potentiality of this micro-structured material in vibration shielding of micro systems, we consider a beam that can oscillate in bending, and we isolate it from the support through the proposed metamaterial, see Figure 1a. The beam is designed to have the second bending resonant frequency inside the bandgap of the metamaterial.

FABRICATION BY TWO PHOTON POLYMERIZATION

Two-photon polymerization is a direct laser writing technology that allows the fabrication of fully 3D structures with sub-micron resolution. It is a technique based on two processes: two-photon absorption (2PA) and polymerization. The peculiar feature of 2PP with respect to conventional 3D laser printing is the sub-diffraction limit resolution. This feature is obtained thanks to the presence of two competing processes in the focal volume of the laser beam, polymerization and quenching, that tends to stop the polymerization. In fact, only the small region, called voxel, where the density of radicals is higher than a certain threshold value determined by the different quenching channels, is polymerized. The structures fabricated with 2PP strongly depend on the voxel characteristics that in turn depend on many factors, such as wavelength, pulse duration, repetition rate, numerical aperture, laser source polarization, laser power, writing speed and distance between lines.

The photoresist used in this work is called SZ2080 and it is a hybrid organic-inorganic negative sol-gel photoresist specifically developed for 2PP. It is made of two components: methacryloxypropil trimethoxysylane (MAPTMS) and zirconium propoxide (ZPO). A particular photoinitiator, called Irgacure 369 (IRG), is also added to enhance the 2PP effect. Compared to other photoresists, SZ2080 presents excellent mechanical properties [6], it is non-toxic and it shows negligible shrinkage after solvent washing.

To fabricate the structure one has first to prepare a bulky sample by drop-deposition, drop-casting and baking at 105°C, then the complex geometry of the micro-structure is realized within the sample through laser irradiation and finally the development process removes the non-irradiated zones of the drop and makes structures emerge.

In this work, we used a frequency-doubled erbium-doped fiber laser with wavelength of 780 nm, pulse duration of about 100 fs, and repetition rate of 80 MHz. The direct laser fabrication setup used is composed by a laser source, optical and optomechanical components to deliver, control, block, and focus the laser beam, a translation device to move the sample with respect to the laser beam focus, and a machine vision system for real-time monitoring of the fabrication process, as shown in Figure 2a.

Figure 2b shows the SEM image of the fabricated simple microstructure constituted by a beam clamped in the central part to the substrate without the presence of the metamaterial, while Figure 2c shows the prototype for vibration isolation of the micro beam, with a block of 2 x 2 x 3 cells of the metamaterial. The 2PP fabrication technique proved to be suitable to realize the very complex geometry of the metamaterial at the microscale.

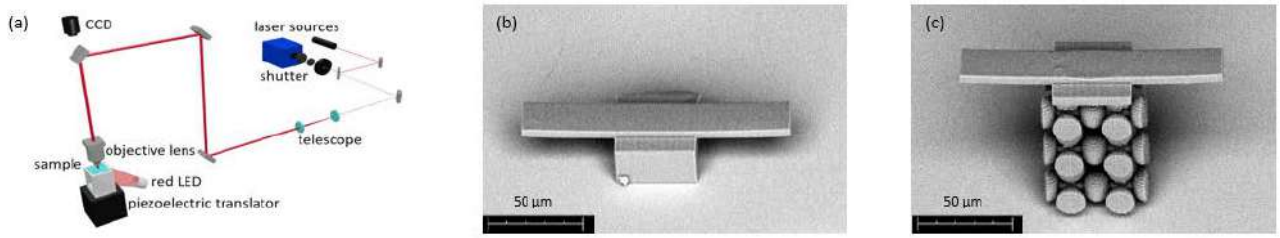

Figure 2. (a) Fabrication set-up. SEM images of the fabricated structures without (b) and with (c) an isolating phononic crystal.

The effectiveness of the proposed isolating system will be experimentally checked. Both structures will be excited at the resonant frequency of the beams by a piezoelectric actuator placed below the substrate. An optical system will allow to detect the oscillation of the beams which is expected to be attenuated by the presence of the metamaterial. This latter experimental apparatus is currently under development.

CONCLUSIONS

A vibration isolator for micro-systems has been designed through numerical simulations and a first prototype has been fabricated through the 2PP process. This represents an important step towards a new class of vibration isolators at the microscale that can be employed for example in microelectromechanical systems.

References

[1] Jia, Z., Chen, Y., Yang, H., Wang, L. Designing phononic crystals with wide and robust band gaps. *Ph. Rew. Applied* **9**: 044021, 2018.

[2] Kawata, S., Sun, H., Tanaka, T. et al. Finer features for functional microdevices. *Nature* **412**: 697–698, 2001.

[3] Raimondi, M. T., Eaton, S. M., Nava, M. M. , Laganà, M. , Cerullo, G., Osellame, R. Two-photon laser polymerization: from fundamentals to biomedical application in tissue engineering and regenerative medicine. *J Appl Biomater Function Mater,* **10** (1): 56-66, 2012.

[4] D'Alessandro, L., Belloni, E., Ardito, R., Corigliano, A., Braghin, F. Modeling and experimental verification of an ultra-wide bandgap in 3D phononic crystal. *Applied Physics Letters* **109**: 221907, 2016.

[5] Moscatelli, M., Ardito, R., Driemeier, L., Comi, C. Band-gap structure in two- and three-dimensional cellular locally resonant materials, *Journal of Sound and Vibration* **454**:73-84, 2019.

[6] Pertoldi, L., Zega, V., Comi, C., Osellame, R. Dynamic mechanical characterization of a two-photon-polymerized SZ2080 photoresist, *Journal of Applied Physics* **128** (17), 2020.

INTELLIGENT DESIGN OF NEW 2D NANO-MATERIALS

Tadeusz Burczyński[1a], Wacław Kuś[2], Marcin Maździarz[1]and Adam Mrozek[3]
[1]Institute of Fundamental Technological Research, Polish Academy of Sciences, Warsaw, Poland
[2]Institute of Computational Mechanics and Engineering, University of Technology, Gliwice, Poland
[3]AGH University of Science and Technology, Cracow, Poland

Summary New stable atomic arrangements in 2D nanostructures based on carbon (C) and as well as on molybdenum (Mo) using a memetic algorithm and the density functional theory (DFT) are presented. The semiconducting carbon allotrope as graphene-like material and the Single-Layered Molybdenum Disulfide ($SLMoS_2$) heterostructures with desired mechanical properties are created.

INTRODUCTION

2D materials play important role in modern materials science. Apart from materials based on carbon, e.g. graphene, there is possible to create new 2D materials based on molybdenum. New graphen-like materials X and Y created by hybrid intelligent approach [1, 2] represent the first class of materials. One of the most prominent 2D material based on molybdenum is the molybdenum disulfide (MoS_2), which reveals polymorphism at the nanolevel.

Optimal design technique enabling to obtain new 2D semiconducting carbon allotrope as graphene-like material and $SLMoS_2$ heterostructures with desired mechanical properties is presented. The proposed method is based on the memetic global optimization of the potential energy of the nanostructure. The behaviour and energy of the atoms is determined by the AEROBO potential in the case of graphene and the REAX-FF potential in the case of molybdenum. Examples of such semiconducting carbon allotrope and periodic $SLMoS_2$ 2H/1T heterostructure are presented with corresponding mechanical properties.

INTELLIGENT DESIGN BASED ON MEMETIC COMPUTING

The memetic algorithm, proposed and presented in this work, combines the parallel **E**volutionary **A**lgorithm (EA) prepared by the authors, and the classical **C**onjugated-**G**radient (CG) minimization of the total potential energy of the optimized atomic system. Since the processed structure is considered as a discrete atomic model, the behavior and the potential energy of carbon atoms are determined using the **A**daptive **I**ntermolecular **R**eactive **E**mpirical **B**ond **O**rder (AIREBO) in the case nanostructures based on carbon and REAAX-FF in the case of nanostructures based on molybdenum.

A chromosome represents design variables in the form of real-valued Cartesian coordinates of each atom in the considered unit cell of the newly created atomic lattice. Each chromosome represents a certain spatial arrangement of atoms. In the initial population, atoms have randomly generated coordinates and are placed in the area of the unit cell with periodic boundaries. Dimensions, the rectangular or triclinic type of the unit cell, as well as the number of atoms, are part of a set of parameters of the simulation. Such an approach enables controlling the value of atomic density of the newly-created structure. The periodicity of the atomic structure significantly reduces the number of design variables.

The fitness function is formulated as the total potential energy of the considered atomic system, i.e., the total sum of all potential energies of particular atomic interactions.

The periodicity of the newly-created structure is also achieved in this step by proper boundary conditions, imposed on the unit cell. After the CG minimization of the potential energy, the objective function is computed for each individual in the population. The CG optimization is the most time-consuming part of the algorithm. To overcome this problem, the authors decided to parallelize the proposed algorithm and make it suitable for running on multiprocessor computers. Thus, the population is scattered into certain number of parts using the MPI library. In the next step, each part is further processed in the parallel way.

DESIGNING OF NEW 2D SEMICONDUCTING CARBON ALLOTROPE

A new, single-atom thick semiconducting 2D-graphene-like material, called Anisotropic-Cyclicgraphene, is generated by the two stage searching strategy linking molecular and *ab initio* approaches. The candidate is derived from the memetic based algorithm and molecular simulations and next is profoundly analysed using the first-principles density functional theory from the structural, mechanical, phonon, and electronic properties point of view.

The structure of the 2D-graphene-like material is considered as a discrete atomic model, with imposed periodic boundaries. The behavior of such a system is investigated using one of the molecular methods. The potential energy of carbon atoms, the forces acting between them and the overall behavior is determined by the AIREBO potential, especially developed for hydrocarbons.

The goal is to discover an atomic structure with stable configuration, predefined number of atoms and elastic material properties. The elastic properties are computed based on the molecular analysis of a structure with applied small strains. The atomic structures with orthotropic elastic material properties are taken into account. The objective function depends on the norm of differences between of prescribed and computed elastic properties [3].

First-principles calculations with the use of the density functional theory (DFT) within the pseudopotential, plane-wave

approximation (PP-PW) are made using the Cambridge Serial Total Energy Package (CASTEP). For structural, mechanical and phonon calculations the modified Perdew-Burke-Ernzerhof generalized gradient approximation for solids is applied as an exchange-correlation functional whereas for band structure computations the hybrid exchange-correlation functional HSE06.
The material derived from the first stage is then profoundly analyzed using the first-principles density functional theory from the structural, mechanical, phonon and electronic properties point of view. The proposed Anisotropic-Cyclicgraphene is mechanically, dynamically and thermally stable and can be semiconducting-like with a direct band gap of 0.829 eV [4].

DESIGNING OF NEW 2D MATERIALS BASED ON MOLYBDENUM

One of the most prominent 2D material based on molybdenum is the Single-Layered Molybdenum Disulfide ($SLMoS_2$), which reveals polymorphism at the nanolevel.
The 2H phase has semiconducting properties and approx. Young's modulus equals to 130 N/m, while the 1T polymorph reveals metallic or ferroelectric properties and two times lower stiffness [2]. Both phases of MoS_2 can exist simultaneously [3].
Intelligent designing $SLMoS_2$ heterostructures (a 2H lattice with Δ-shape 1T inclusion) with desired mechanical properties is presented. The memetic optimization approach enabling to obtain MoS_2 heterostructures with desired mechanical properties is applied. The behaviour and energy of the atoms is determined by the REAX-FF potential [5]. Examples of such periodic $SLMoS_2$ 2H/1T heterostructures are presented in the paper with corresponding mechanical properties.

CONCLUSIONS

The presented approach is applied to design of 2D nano-materials based on carbon as well as molybdenum.
The process of designing nano-material based carbon consists of two stages. In the first molecular stage the optimization problem is solved using the memetic algorithm. The second stage based on the first-principles density functional theory is used to examine results from the previous step. The proposed polymorph of graphene is mechanically, dynamically, and thermally stable and can be semiconducting with a direct band gap of 0.829 eV.
The intelligent optimization technique is also applied to obtain nano-structures based on molybdenum – $SLMoS_2$ heterostructures with desired mechanical properties.
Some results in this paper are unique and we trust will be verified by other works. The synthesis of the proposed structure is a separate task and goes beyond the area of this work.

ACKNOWLEDGMENTS
This work was supported by the National Science Centre (NCN – Poland) Research Project: UMO-2016/21/B/ST8/02450.

References

[1] A. Mrozek, W. Kuś, T. T. T. Burczyński, Nano level optimization of graphene allotropes by means of a hybrid parallel evolutionary algorithm. *Computational Materials Science*, 106: 161-169, 2015.
[2] M. Maździarz , A.Mrozek, W. Kuś, T. Burczyński, First-principles study of new X-graphene and Y-graphene polymorphs generated by the two stage strategy. *Materials Chemistry and Physics*, 202: 7-14, 2017.
[3] A.Mrozek, W. Kuś, T. Burczyński, Method for determining structures on new carbon-based 2D materials with predefined mechanical properties. *International Journal for Multiscale Computational Engineering,* Vol. **15** (5): 379-394, 2017.
[4] M. Maździarz, A. Mrozek, W. Kuś, T. Burczyński, Anisotropic-cyclicgraphene: A new two-dimensional semiconducting carbon allotrope. *Materials,* Vol. **11** (3): 432-444, 2018.
[5] A. Mrozek. Basic mechanical properties of 2H and 1T single-layer molybdenum disulfide polymorphs. A short comparison of various atomic potentials. *Int. J. Multiscale Computational. Engineering,* Vol **17**(3): 339-359, 2019.

ON THE ROLE OF SURFACE TENSION IN MODELS OF NANO-PLATE BENDING

Anatolii Bochkarev*
Faculty Of Applied Mathematics And Control Processes, Saint Petersburg State University, 7/9 Universitetskaya nab., St. Petersburg, 199804 Russia

Summary A von Kármán-type model of nano-plate bending is formulated taken into account the Gurtin–Murdoch surface elasticity and basing on the Kirchhoff hypothesis. Unlike than most of previous related theories, surface tension, usually omitted in the conjugation condition of Young–Laplace law in the transverse direction, is incorporated in 2D motion equations and constitutive relations for membrane forces together with quadratic terms equal of the von Kármán-type strains. A influence of the accounting surface tension is illustrated in comparison with other models on an example of non-linear bending, free transverse vibration, and compressive postbuckling of a strip-like nano-film with simply supported and clamped edges.

INTRODUCTION

The two-dimensional models of plates and shells with allowance for surface stresses, proposed by Gurtin and Murdoch (GM) [1] and supported by the results of atomistic modeling [2], are widely used in problems of nano-mechanics. An integral part of these models is the conjunction condition in the form of Young–Laplace's law, which ensures equilibrium of a negligibly thin surface layer and bulk phase. The work [3] on the non-linear bending of nano-plates was the first one taking into account the GM surface elasticity and identified the basic elements for following related models: effective membrane forces and bending moments, constitutive relations for them, et al. In the same time, this model has an obvious flaw: the conjunction condition of Young–Laplace in the transverse direction, expressed through surface tension, was not considered. Usually it is customary to satisfy this omitted condition through non-zero σ_{33} in Hooke's law. However, the results of [4] showed that this refinement leads to the negligible size effect, thereby confirming the basic principles of plate theory, where σ_{33} is zero. So, most authors prevailed the view that surface stresses affect bending mainly due to the difference in the values of the surface and bulk elastic moduli, and not by surface tension. It was shown in [5, 6] that this is not the case, and surface tension can significantly correct the mechanical properties.

Present study is devoted to the role of surface tension with non-linear terms or without in nano-plate bending. For this purpose, the built in [5] model is considered. It incorporates the conjunction condition of Young–Laplace law in the 2D governing equations in full and takes into account the von Kármán-type non-linearity of surface tension. The solved examples show the effect of surface tension on non-linear bending, transverse free vibration, and compressive postbuckling of a strip-like nano-film with simply supported and clamped edges in comparison with other models.

PROBLEM FORMULATION

An elastic nano-plate is considered, on the top $(+)$ and bottom $(-)$ faces of which there are surface stresses $\boldsymbol{\tau}^{\pm}$ obeying the GM constitutive relations [1]

$$\boldsymbol{\tau}^{\pm} = \tau_0^{\pm}\mathbf{A}^{\pm} + 2(\mu_{\mathrm{s}}^{\pm} - \tau_0^{\pm})\boldsymbol{\epsilon}^{\pm} + (\lambda_{\mathrm{s}}^{\pm} + \tau_0^{\pm})\mathrm{tr}\boldsymbol{\epsilon}^{\pm}\mathbf{A}^{\pm} + \tau_0^{\pm}\nabla_{\mathrm{s}}^{\pm}\mathbf{u}^{\pm} \tag{1}$$

Bulk elastic stresses $\boldsymbol{\sigma}^{\pm}$ on the faces are balanced with surface stresses $\boldsymbol{\tau}^{\pm}$ according to Young–Laplace law [1]

$$\nabla_{\mathrm{s}}^{\pm}\cdot\boldsymbol{\tau}^{\pm} + \boldsymbol{\varphi}^{\pm} = \rho_0^{\pm}\ddot{\mathbf{u}}^{\pm} \pm \mathbf{n}\cdot\boldsymbol{\sigma}^{\pm} \tag{2}$$

Here $\mathbf{u}^{\pm}$ is the displacement, $\nabla_{\mathrm{s}}^{\pm}$ is the nabla-operator, $\boldsymbol{\epsilon}^{\pm} = \mathbf{A}^{\pm}\cdot\boldsymbol{\varepsilon}^{\pm}\cdot\mathbf{A}^{\pm}$ is the surface projection of strain tensor $\boldsymbol{\varepsilon}$, $\mathbf{A}^{\pm}$ is the surface unit tensor, $\lambda_{\mathrm{s}}^{\pm}$ and $\mu_{\mathrm{s}}^{\pm}$ are surface Lame's parameters, $\tau_0^{\pm}$ is the residual surface tension, $\rho_0^{\pm}$ is the surface density, $\boldsymbol{\varphi}^{\pm}$ is the external load – all on the top $(+)$ and bottom $(-)$ faces; $\mathbf{n}$ is a normal to the middle surface of a plate.

The 2D Kirchhoff model for complex bending of nano-plates with taking into account the GM surface stresses (1), incorporating the conjunction condition of Young–Laplace law on nano-plate faces (2) in full, and also considering non-linearity of surface tension, was proposed in [5]. Under the equal surface behaviours of faces, it can be expressed as the von Kármán set

$$\begin{cases} I^*\ddot{u}_\gamma^0 = T^*_{\beta\alpha,\alpha} - \tau_0(w^2_{,\alpha})_{,\beta} + P^*_\beta \\ J^*\ddot{w}_{,\alpha\alpha} - I^*\ddot{w} = D^*\nabla_{\mathrm{s}}^2\nabla_{\mathrm{s}}^2 w - 2\tau_0\nabla_{\mathrm{s}}^2 w - T^*_{\beta\alpha}w_{,\beta\alpha} - m^*_{\alpha,\alpha} - P^*_3 \end{cases} \tag{3}$$

with the constitutive relation for the effective membrane forces

$$T^*_{\beta\alpha} = 2\tau_0\delta_{\beta\alpha} + 2\tau_0(\nabla_{\mathrm{s}}u^0)_{\beta\alpha} + C^*\left((1-\nu_{\mathrm{t}}^*)\varepsilon^0_{\beta\alpha} + \nu_{\mathrm{t}}^*\delta_{\beta\alpha}\varepsilon^0_{\gamma\gamma}\right) \tag{4}$$

where the in-plane strain $\boldsymbol{\varepsilon}^0$ and surface tension $\tau_0(\nabla_{\mathrm{s}}\mathbf{u}^0)$ are expressed through the in-plane displacement of midplane $\mathbf{u}^0$ and together with the first Eq. (3) have the von Kármán-type quadratic non-linearity of deflection w

$$\varepsilon^0_{\beta\alpha} = \frac{1}{2}\left(u^0_{\beta,\alpha} + u^0_{\alpha,\beta} + w_{,\alpha}w_{,\beta}\right),\ \tau_0(\nabla_{\mathrm{s}}u^0)_{\beta\alpha} = \tau_0(u^0_{\beta,\alpha} - ww_{,\beta\alpha}),\ \tau_0(\nabla_{\mathrm{s}}w)_\alpha = \tau_0(w_{,\alpha} + u^0_\beta w_{,\beta\alpha}) \tag{5}$$

Here $D^*, C^*, \nu_{\mathrm{t}}^*, P_i^*, m_\beta^*, I^*, J^*$ are effective flexural and tangential stiffnesses, Poisson's ratio, external forces and moments, static and inertia moment respectively.

*Corresponding author. E-mail: a.bochkarev@spbu.ru

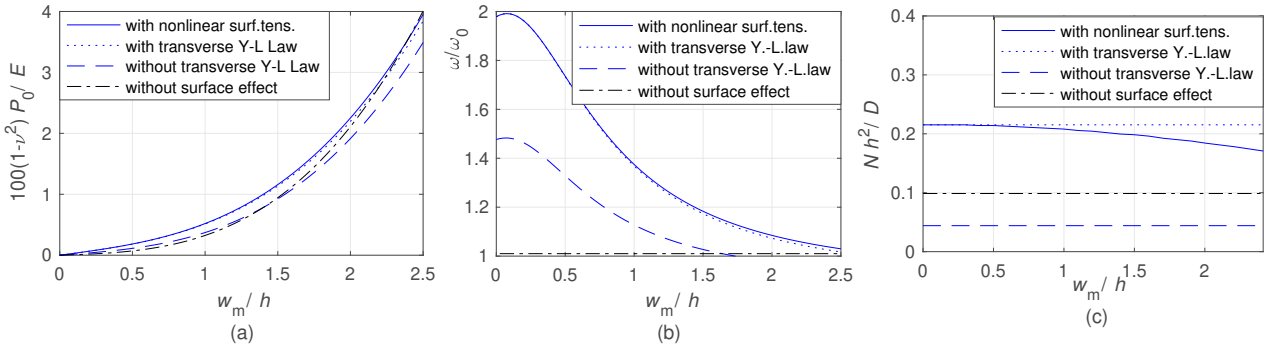

Figure 1: Nano-film with simply supported edges and the thickness $h = 1$ nm: (a) load-deflection ratio under cylindrical bending, (b) frequency-amplitude ratio of free vibration, (c) load-deflection ratio under compressive postbuckling

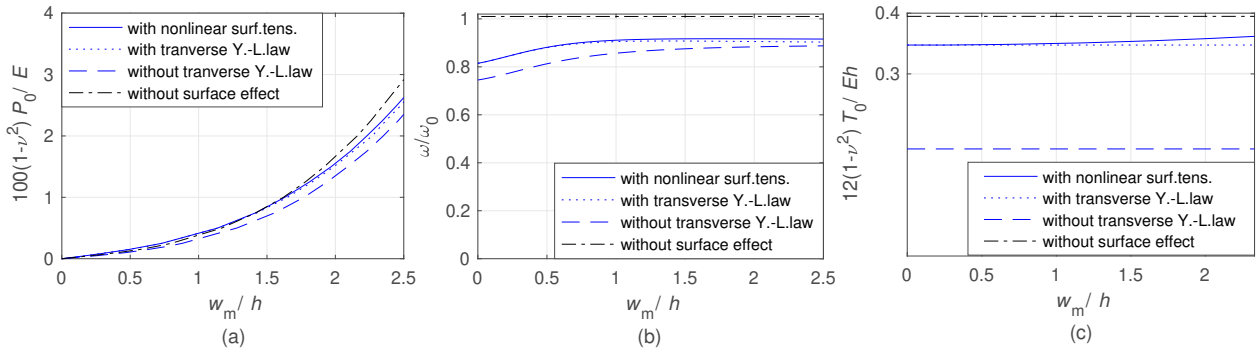

Figure 2: Nano-film with clamped edges and the thickness $h = 1$ nm: (a) load-deflection ratio under cylindrical bending, (b) frequency-amplitude ratio of free vibration, (c) load-deflection ratio under compressive postbuckling

CASE STUDY

Influence of the present surface tension on non-linear cylindrical bending, free transverse vibration and compressive postbuckling of a strip-like nano-film from Al[100] [2] is illustrated in Fig. 1 for simply supported edges and in Fig. 2 for clamped edges in comparison with other models. The considered examples show different directionality of size effect for simply supported and clamped edges. As can see, the 3rd Young–Laplace condition incorporated in the governing equation can significant enhance the size effect in comparison with accounting surface elasticity only as in [3]. Accounting non-linear terms of surface tension gives slight refinement, noticeable at a relative deflection of more than 2 under non-linear bending and free vibration. However, in the 3rd example, accounting linear part of surface tension allows only to find the critical Euler force, whereas accounting its non-linearity allows to consider deformation after the bifurcation point.

CONCLUSIONS

The plate theory proposed by [3] was further developed as an extension of von Kármám non-linear theory of elastic plates incorporated the GM surface elasticity including the non-linearity of surface tension and the conjugation condition of the Young–Laplace law in the transverse direction. As follows from the above examples, accounting surface tension reflects more properly the size effect, and accounting its non-linearity – also previously not described effects.

Acknowledgements

This research was supported by the Russian Foundation for Basic Research, grant No 18-01-00468.

References

[1] Gurtin M. E., Murdoch A. I. Surface stress in solids. *Int. J. Solids Struct.* **14**: 431–440, 1978.
[2] Miller R. E., Shenoy V. B. Size-dependent elastic properties of nanosized structural elements. *Nanotechnology* **11**: 139–147, 2000.
[3] Lim C.W., He L.H. Size-dependent nonlinear response of thin elastic films with nano-scale thickness. *Int. J. Mech. Sci.* **46**: 1715–1726, 2004.
[4] Huang D.W. Size-Dependent Response of Ultra-Thin Films with Surface Effects. *Int. J. Solids Struct.* **45**: 568–579, 2008.
[5] Bochkarev A.O. On taking into account surface tension in models of nano-plate bending. *Mech. Res. Comm.* **106**: 103521, 2020.
[6] Bochkarev A.O. Comment on ”On taking into account surface tension in models of nano-plate bending”. *Mech. Res. Comm.* **108**: 103578, 2020.

DISCRETE APPROACH TO MODEL AND TO SIMULATE THE ELASTIC PROPERTIES OF LATTICE MATERIALS

Igor Berinskii *[1]
[1]School of Mechanical Engineering, Tel Aviv University, Tel Aviv, Israel

Summary Elastic properties of two–dimensional cellular lattice materials are studied using a discrete model. The model is based on a representation of the lattice as a set of interacting nodes. A potential of interaction between the nodes is calibrated such that to simulate elastic linking. The analytical homogenization based on Cauchy–Born rule allows determining the elastic properties of the effective continuum corresponding to the specific lattice. On the other hand, the same properties can be found from the numerical simulations based on particle dynamics. It is shown that both ways lead to the same values of elastic components. Hence, particle–based numerical simulations can be used to design various applications of lattice materials including MEMS.

INTRODUCTION

Cellular materials attract the attention of researchers due to their outstanding stiffness and strength as well as enhanced absorption of mechanical energy at relatively small density. Artificial periodic cellular structures can be relatively easy fabricated using modern additive technologies. Due to this, nowadays they are extensively used in MEMS as well as in aerospace, sport, medical, fashion, and other industries. In a high variety of the cellular materials there are such of them, that expand in one or more directions at stretching along the other direction. These materials are called “auxetics”, and their unusual properties are explained by the negative value of Poisson’s ratio along one or several directions.

Computer simulations can help to choose the best cell topology, a number of cells, geometry of struts, material properties. Usually, FEM is used for simulations, however, in some cases, discrete models seem to be more applicable. For instance, such problems include big deformations, buckling, and fracture of cellular materials.

In this work, we consider two auxetic materials with reentrant double arrowheads (DAH), and semi–reentrant honeycombs (SREH) lattices (Fig.1). These lattices are based on the unit cells containing more than one node: such structures are referred to as multilattices. Following the approach proposed in [1] the lattice is represented as a set of particles having both translational and rotational degrees of freedom. Consequently, the interaction between the particles includes both forces and torques. This idea is used both for the theoretical analysis of the elastic properties of the effective continua corresponding to the lattices, and to determine these properties from computational simulations.

ANALYTICAL HOMOGENIZATION

The proposed homogenization procedure is described in [2] and allows finding the components of the stiffness tensor of the effective continuum analytically. The procedure is based on the Cauchy-Born rule: the strain energy of the lattice unit cell is assumed to be equal to the strain energy of the representative volume of the corresponding effective solid material. It is assumed that the nodes in a lattice have elastic connections. In general case, the axial, shear and torsional stiffness constants of these connections can be independent. As a result, the in-plane effective properties of the lattices can be found as the functions of the cells’ geometry and the stiffness constants of the bond. In the specific case considered here, the constants are fitted to simulate the connection by the Euler–Bernoulli rods with the rectangular section. As a result, the axial, torsional, shear and bending stiffness constants are not independent anymore and can be determined through the geometric and elastic parameters of the rod. In turn, these constants and the angles between the rods determine the elastic properties of the effective continuum.

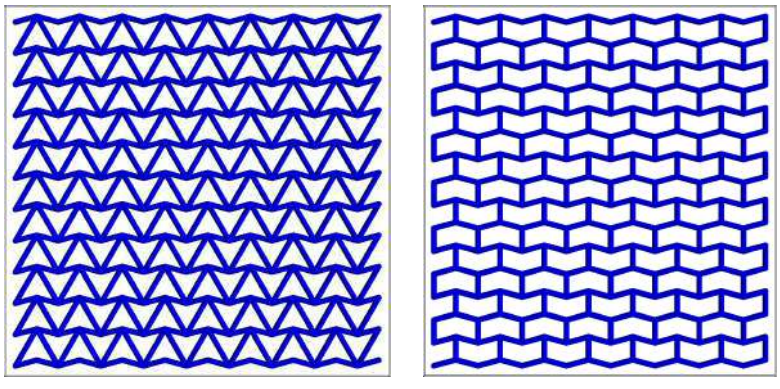

(a) (b)

Figure 1: Cellular multilattices. DAH (a), and SREH (b)

*Corresponding author. E-mail: igorbr@tauex.tau.ac.il.

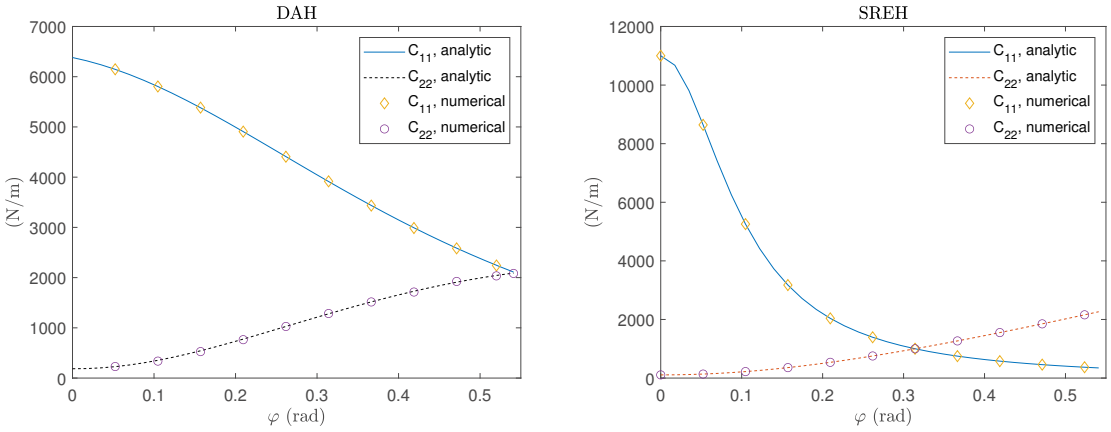

(a) (b)

Figure 2: Effective properties of DAH (a) and SREH (b) lattices (N/m) vs angle φ (rad). The results obtained from analytic results are shown with solid (C_{11}) and dashed (C_{22}) lines. The results obtained from numerical calculations are shown with diamonds (C_{11}) and circles (C_{22})

SIMULATIONS

The simulations are provided using particle dynamics. Each particle simulates a node of the lattice. The potential of interaction between the nodes is derived such that to represent the linking with Euler–Bernoulli beams. Initially, the uniform strains are applied to the elements of lattices. Then, the boundary conditions are set. The equations of motion for the translational and rotational degrees of freedom are solved using the Velocity Verlet algorithm. The equilibrium of the system is provided using the Langevin thermostat. As a result, the uniform stress field is obtained in a lattice and the necessary elastic properties can be determined. The components of stress tensor are calculated in two ways. The first way is to find the stress per one node considering the forces acting to the given node from its nearest neighbors. The second approach is to make an imaginary section in the lattice, sum the forces in the links crossing the section and divide the result to the section length. It is shown that both ways give the same or very close results.

RESULTS

The elastic properties of the lattices were determined both analytically and numerically. It was shown that the simulations with fixed boundary conditions may lead to a significant discrepancy between the analytic and numerical results. At the same time, periodic boundary conditions allow reaching a full coincidence (Fig. 2). It was shown, that the lattices can demonstrate highly anisotropic behavior, and due to this, the stiffness in different directions can vary up to several orders. The most typical cases from the practical point of view were considered and the corresponding parameters such as relative thickness, Young's moduli, and Poisson's ratios were calculated. The results were reported in [3].

From a numerical point of view, a case considered in this paper is the most basic. First, only the planar motion of the nodes was taken into account. Second, the linear elastic interaction between the nodes was considered. Also, the small displacement and rotations are presumed. However, the big advantage of the proposed method is its ability for generalization. First of all, much more complicated kinematics corresponding to the large displacements and rotations in three-dimensional motion can be considered. Second, the more complicated constitutive equations can be considered. In the case of large displacements, it seems more reasonable to use non–linear models to simulate hyperelastic materials, soft materials, and others.

References

[1] Ivanova, E.A. On the Use of the Continuum Mechanics Method for Describing Interactions in Discrete Systems with Rotational Degrees of Freedom. *Journal of Elasticity*, **133(2)**, 155-199, 2018.
[2] Berinskii, I.E. In-plane elastic properties of auxetic multilattices. *Smart Materials and Structures*, **27(7)**, 075012, 2018.
[3] Berinskii, I. Elastic in–plane properties of cellular materials: discrete approach. *Mechanics of Materials*, 103501, 2020.

NONLINEAR PULL-IN STUDIES OF COUPLED CARBON NANOTUBE RESONATORS: MOLECULAR DYNAMICS SIMULATIONS AND EQUIVALENT CONTINUUM MODELS

Aningi Mokhalingam *[1], Indranil S Dalal[2], and Shakti S Gupta[1]
[1]Department of Mechanical Engineering, IIT Kanpur, Kanpur - 208016, India
[2]Department of Chemical Engineering, IIT Kanpur, Kanpur - 208016, India

Summary In this paper, the static and dynamic pull-in of two coupled single-walled carbon nanotube (SWCNT) resonator is studied using molecular dynamics (MD) and an equivalent continuum model. The SWCNTs are coupled electrostatically and through van der Waals forces. The ReaxFF potential is employed in MD simulations. The distribution of charges due to the externally applied voltage is calculated using the charge equilibrium scheme within the ReaxFF. The SWCNTs are modeled using the Euler−Bernoulli beam theory incorporating the geometric nonlinearities. The Galerkin approach is used to discretize the governing equations of motion. The results from the beam model are in good agreement with the MD simulations within an error of 2%.

INTRODUCTION

Single-walled carbon nanotubes (SWCNTs) are potential candidates for designing nano-electro-mechanical systems (NEMSs), for applications in sensing mass, strain, and pressure/temperature. The SWCNT based resonators consist of either a single or multiple elements. In the single element resonator, the shift in the resonant frequency is measured to identify the perturbations in the system. However, in the multiple-element resonators, which are coupled with either electrically or mechanically, the change in the resonator response amplitudes can be up to three times higher than the shift in the resonant frequency [1]. For the safe operation of such resonators, knowledge of the pull-in voltage is very important. At this pull-in voltage, the elastic forces of the two SWCNTs are overcome by the electrostatic and vdW forces, leading to the collapse of one SWCNT onto the other. Dequesnes et al. [2] studied the static and dynamic pull-in instability of SWCNT based switch using MD simulations and the Euler beam model. In their MD simulations, continuum formulations are used to define the electrostatic and vdW forces. Ouakad and Younis [3] studied the pull-in instability of SWCNT resonator using the Euler-Bernoulli beam model. In this study, the pull-in instability of a SWCNT coupled-resonator is studied using MD simulations and an equivalent continuum model. In the MD simulations, environment-dependent charges are calculated at each time step using the charge equilibrium (QEq) scheme within the ReaxFF [4].

MOLECULAR SIMULATIONS AND CONTINUUM MODEL

In this study, we consider two parallel SWCNTs of (7,7) chirality with length to diameter ($2R$) ratio = 15 separated by $r + 2R$. The atomic interactions between the carbon atoms are defined using the ReaxFF forcefield [4]. The external voltage (V) is applied to the system by providing an offset electronegativity. The two SWCNTs are applied with the electronegativities of $\chi_0 + V/2$ and $\chi_0 - V/2$, where $\chi_0 = 5.7254$ eV is the standard potential parameter for Carbon. To check the accuracy of charge calculations in our simulations, charge distribution in a SWCNT of (5,5) chirality and length of 1.2 nm in infinite space is computed. For a total applied charge of 10 e, the charge distribution computed from the MD simulations is in good agreement with that obtained from earlier DFT calculations [5], within an error of $\approx 6\%$ (see Fig. 1(a)). After the initial setup, the system is brought to a minimum energy configuration using the Polak-Ribiere's conjugate gradient method. Next, the system is thermally equilibrated at 1 K. The natural frequencies are determined by allowing the system to vibrate in the NVE ensemble and using the FFT of the time history of the transverse displacement of the atoms at mid-length of a SWCNT.

In the continuum model, the two SWCNTs are modeled as Euler−Bernoulli beams. The equations of motion of electrostatically charged and closely spaced nanoscale beams of length L and cross-sectional area A, are given as [3]

$$EIu_i'''' + \rho A\ddot{u}_i = EA/2L \int_0^L (u_i')^2 dx\, u_i'' - (-1)^i (F_{elec} + F_{vdW}) \,, \tag{1}$$

where u_i (i=1 and 2) are the transverse deflections (along y-direction) of the two SWCNTs, E and I are Young's modulus and the second moment of area, respectively, and ρ is the density. The electrostatic force between the two SWCNTs is calculated from the capacitance model [6]. The electrostatic energy is given as $E_{\text{elec}} = \frac{1}{2}C(r)V^2$, where $C(r) = \pi\epsilon_0/(acosh(1 + (r - u_1 + u_2)/2R))$ is the capacitance per unit length, ϵ_0 is the permittivity of vacuum and V is the applied voltage. The electrostatic force per unit length is given by $F_{\text{elec}} = -dE_{\text{elec}}/dr$. The standard Lennard-Jones (LJ) potential is used to define the vdW interactions between the two SWCNTs. The vdW energy per unit length between two parallel SWCNTs is then given by [7] $E_{\text{vdW}} = 1.5\pi\epsilon{\rho_1}^2\sigma^6 R^{-3}[(21/32)A_{12}\sigma^6 R^{-6}((r - u_1 + u_2)/R)^{-9.5} - A_6((r - u_1 + u_2))/R)^{-3.5}]$, where ρ_1 is the areal density, determined as $4/(3\sqrt{3}l_0^2)$, with l_0 as C-C bond length (=

*Corresponding author. E-mail: aningi@iitk.ac.in

0.142 nm), $A_{12} = 0.4735$ and $A_6 = 1.3090$. The LJ parameters for Carbon are $\epsilon = 0.00239$ eV and $\sigma = 0.34$ nm. The vdW force per unit length is given by $F_{\text{vdW}} = -dE_{\text{vdW}}/dr$. The static pull-in instability is calculated by neglecting the inertia term in Eq. (1). The solution for the static problem is approximated as $u_1(x) = \sum_{i=1}^{m} a_i\phi_i(x)$ and $u_2(x) = \sum_{j=1}^{m} b_j\phi_j(x)$, where ϕ_i are the normalized linear undamped mode shapes of the beam and a_i is a scalar constant. The solution is then obtained by substituting the assumed solution into the static governing equation and multiplying with ϕ_n and thereafter integrating within the domain of beams. For calculating the linear frequencies about the static equilibrium position, the solutions of Eq. (1) is assumed as $u(x,t) = u_s(x,0) + u_d(x,t)$ [3], where u_s is the static solution and u_d is the dynamic part. The assumed solution is substituted in Eq. (1) and the nonlinear terms in u_d are neglected. The resulting linear equations are solved to obtain the natural frequencies.

NUMERICAL RESULTS

Here, we compare the pull-in voltages found from MD simulations and solving the continuum model for static and dynamic cases using definition and vanishing first mode frequency criteria, respectively. Also, the results from linear and nonlinear continuum models are compared to highlight the importance of nonlinearity. Figure 1(b) shows the variation of the midplane deflection of SWCNT-1 with the applied voltage for an initial gap of $r = 2$ nm. The estimated pull-in voltages are 10.2 V and 10.1 V from the MD and the nonlinear beam model, respectively. The same, predicted by the linear model is 9.45 V which produces an error of $\approx 7.5\%$ relative to the MD simulations. Thus, the inclusion of stretching nonlinearity is essential in the pull-in voltage calculations. Figure 1(c) shows the variation of first frequency, normalized with the frequency at zero applied voltage, of the SWCNT-1 with the applied voltage. The results from the MD simulations agree well with those determined from the nonlinear beam model within an error of $\approx 2\%$. At $t = 0$ ps, the charge distribution over the two SWCNTs is uniform. However, as the two SWCNTs deflects towards each other, the charge distribution shows higher concentration at the mid-span. At the pull-in state, the charge accumulates about 220% more at the midpoint than the uniform distribution. Also, the atoms, which are in contact with the second SWCNT at the pull-in state, have the charge 150% more than the atoms at the ends (see Fig 1d).

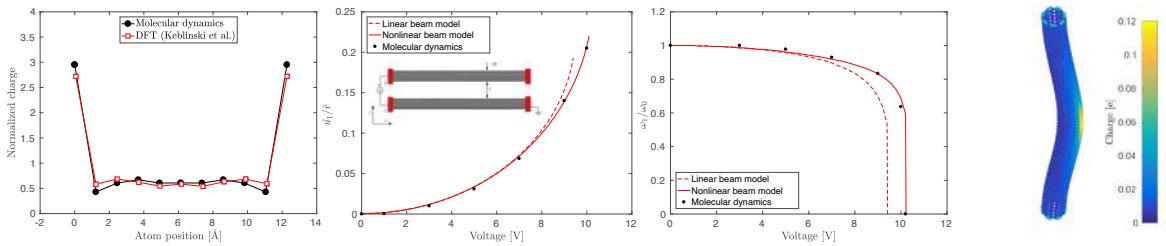

(a) (b) (c) (d)

Figure 1: (a) Comparison between charge distribution obtained from DFT and MD simulations for a CNT (5,5). The normalized charge distribution is defined as the ratio of charge per atom to the average charge. Variation of midpoint deflection and the first mode frequency with the applied voltage in panels (b) and (c), respectively. The charge distribution at the pull-in voltage = 10.2 V is shown in (d).

CONCLUSIONS

The nonlinear static and dynamic pull-in analysis of SWCNT coupled-resonator are studied using MD simulations and an equivalent continuum model based on the Euler-Bernoulli beam theory. Deflection and the fundamental frequency of vibration of the SWCNTs at different voltages from both approaches are found to agree well within an error of less than 2% when geometric nonlinearity is included in the continuum model.

References

[1] Thiruvenkatanathan P., Yan J., Woodhouse J., and Seshia A.A. Enhancing parametric sensitivity using mode localization in electrically coupled mems resonators. *J. Microelectromech. Syst.*, **18**(5):1077–1086, 2009.

[2] Dequesnes M., Tang Z., and Aluru N.R. Static and Dynamic Analysis of Carbon Nanotube-Based Switches . *J. Eng. Mater. Technol.*, **126**(3):230–237, 2004.

[3] Ouakad H.M. and Younis M.I. Nonlinear Dynamics of Electrically Actuated Carbon Nanotube Resonators. *J. Comput. Nonlin. Dyn.*, **5**(1), 2009.

[4] Strachan A., van Duin A.C.T., Chakraborty D., Dasgupta S., and Goddard W.A. Shock waves in high-energy materials: The initial chemical events in nitramine RDX. *Phys. Rev. Lett.*, **91**:098301, 2003.

[5] Keblinski P., Nayak S.K., Zapol P., and Ajayan P.M. Charge distribution and stability of charged carbon nanotubes. *Phys. Rev. Lett.*, **89**:255503, 2002.

[6] Hayt W.H. *Engineering electromagnetics*. McGraw-Hill, 1981.

[7] Anderson T. A multiscale methodology for modeling carbon nanotube mechanics with discrete element method. *MS thesis, Mech. Eng. Dept.,University of Minnesota, Minneapolis, MN*, 2010.

TOWARD A FLOW VELOCITY GRADIENT SENSOR USING A SINGLE MICROBEAM SENSING ELEMENT

Yoav Kessler, Alex Liberzon and Slava Krylov
School of Mechanical Engineering, Tel Aviv University, Israel

Summary In this work we present a novel micro flow sensor, based on a curved microbeam, capable of sensing two distinct locations in space with solely one sensing element. We exploit the critical snap-through (ST) and snap-back (SB) buckling phenomena of the electrostatic actuated and Joule's heated bistable structure, to conduct the measurement. In each cycle of the electrostatic signal, the beam encounters ST during the voltage rise and SB at the voltage drop. Airflow affects these critical points through the convective cooling and the direct aerodynamic forcing. Empirical results demonstrate supreme sensitivity of the device, which potentially could replace currently used larger and more complex multi hot wire based sensors.

INTRODUCTION

Due to an everlasting growing demand for more accurate flow sensors in advanced engineering and scientific systems, a large variety of flow microsensors have been reported in recent years [1,2]. Most of which are based on one of two disciplines; 1. Thermo-resistive heated film or wire, cooled by the forced convection caused by the airflow, or 2. A suspended structure free to deflect by direct lift/drag forcing. Despite a huge effort devoted to miniaturizing "macro" based flow sensors through micro-fabrication technology, it appears to reach a limit in the trade-off between performance and down-scaling. Thus, the next step is to develop and investigate new sensing paradigms, utilizing MEMS (and NEMS) prospects. Recently, a new flow sensing approach, based on the coupling between the flow, electrothermal heating, and the mechanical characteristics of bistable microstructures was introduced [3]. Flow sensing based on stability boundaries monitoring in initially straight beams undergoing static buckling due to thermal stress and cooled by airflow was first demonstrated in [3,4]. Using electrostatically actuated and Joule's heated curved beams, the flow velocity was measured by monitoring critical ST characteristics [5,6]. In this work, we demonstrate two-points flow sensing based on monitoring both the ST and SB events in a bistable microbeam. While ST based sensing was implemented in numerous applications, as far as we know, this is the first demonstration of the ST and SB as the basis of an applicative two-point sensing technique.

Operational principle

The device incorporates an initially curved bistable microbeam positioned within an airflow, Fig. 1. The beam is actuated electrostatically, by an electrode, and electrothermally, by Joule's heating. Competing effects of the Joule's heating and cooling by the airflow along with the direct aerodynamic forcing affect both ST and SB critical voltages, V_{ST} and V_{SB}, which can be therefore related to the flow velocity u. During the operation, the heating voltage V_{ET} is constant, while the actuating voltage V_{ES} is slowly increased up to a value above V_{ST} and then decreased below V_{SB}. For each u, the ST and SB events are identified, the voltages V_{ST} and V_{SB} are registered and the calibration (scale factor) curve relating the critical voltages and u is built.

RESULTS

Two equilibrium curves (built using image processing) corresponding to two different *u* are shown in Fig. 2 (a), (b), respectively. The inset shows the dependence between V_{ST} and V_{SB}, and *u* (the scale factor curve). The dynamics of the beam was also investigated using a reduced order model. The role of the air flow and heating/cooling was studied, and possible performance of the sensor was estimated using the model. Experimental results demonstrate high sensitivity for both critical voltages to the flow. Above a certain value of *u*, V_{SB} becomes higher than V_{ST}. This result is attributed to an interplay between the mechanical, drag force related, and the thermal stress within the beam. The suggested simple and compact device allows measurement of the flow in two closely positioned locations (and therefore of the flow velocity gradient) - the task which is difficult to accomplish using conventional sensors incorporating multiple hot wire assemblies [7].

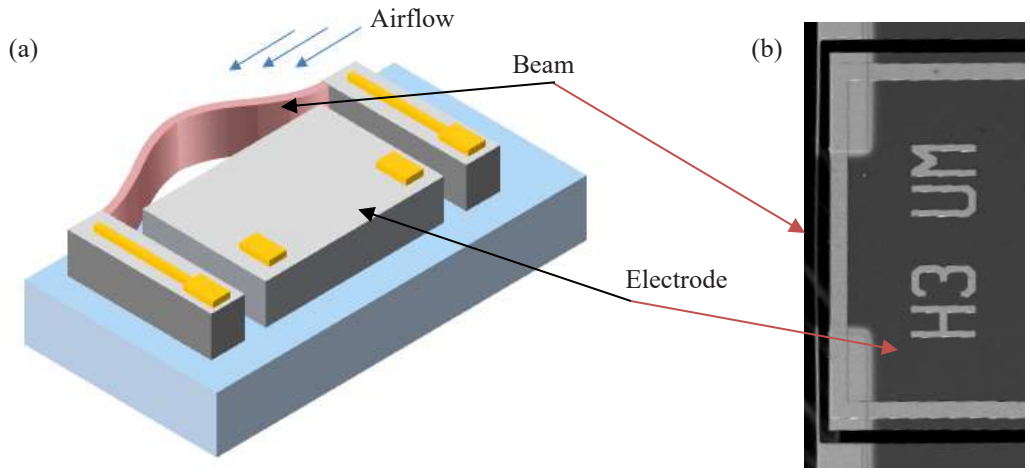

Figure 1: (a) Schematics of the flow sensor. The double-clamped curved microbeam is shown in its initial curved configuration. (b) SEM micrograph of one of the costumed fabricated devices.

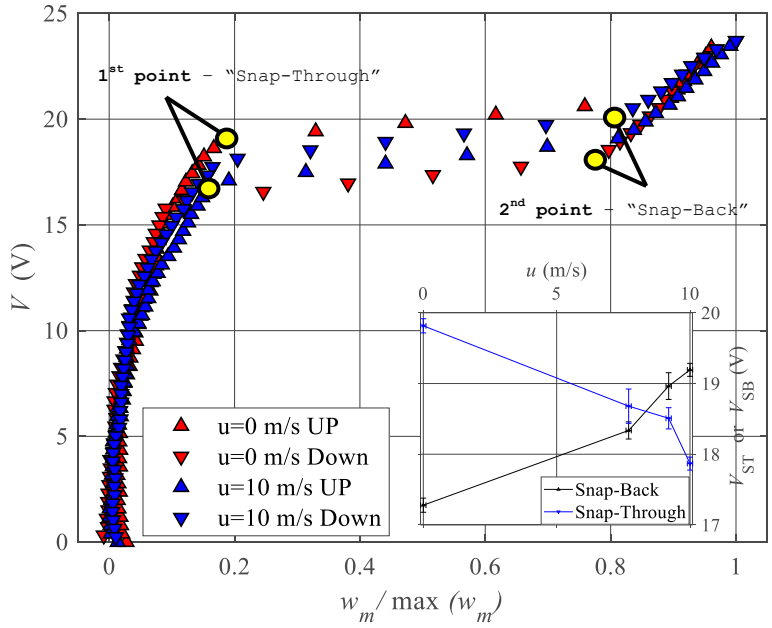

Figure 2: Experimental equilibrium curves of the bistable beam corresponding to two flow velocities (zero and 10 m/s, red and blue markers, respectively), in terms of the ES voltage V_{ES} and the midpoint deflection normalized by the maximal deflection adopted in the experiment. Triangle markers pointing up corresponds to the response to increasing voltages while triangles pointing down are for the decreasing part of the electrical signal. The inset depicts the scale factor curves - snap-through V_{ST} and snap-back V_{SB} voltages versus the air velocity. Error-bars represent the one standard deviation from the mean value at each velocity.

REFERENCES:

1. Y. Fan, G. Arwatz, T. Van Buren, D. Hoffman, and M. Hultmark Experiments in Fluids, 56 (7), 2015, pp. 138.
2. T. W. Kuo, L. Yu and E. Meng, Micromachines, 3, 2012, pp. 550-573.
3. Y. Kessler, A. Liberzon and S. Krylov, Proc. 2016 IEEE SENSORS.
4. Y. Kessler, S. Krylov and A. Liberzon, Appl. Phys. Lett, 109 (08), 2016 pp. 083503.
5. Y. Kessler, S. Krylov and A. Liberzon, J. Microelectromech. Syst, 27 (6), 2018, pp. 945-947.
6. S. Krylov, Y. Kessler, E. Benjamin, B. Torteman and A. Liberzon, Proc. 2018 IEEE SENSORS.
7. Y. Borisenkov, et al, J. Microelectromech. Syst, 24 (5), 2015 pp. 1503-1509.

DESCRIBTION OF THE DEFORMATIONS OF GRAPHENE AND GRAPHENE - REINFORCED COMPOSITES IN THE FRAMEWORK OF MOMENT THEORIES

S.H. Sargsyan
Department of Mathematics, Physics and Information Technologies, Shirak State University, Gyumri, Armenia

Summary The paper demonstrates the construction of the discrete and continuum (beam) moment models of the linear atomic chain. Based on the beam model discrete-continuum model of the graphene is constructed. By limit passage the following models are constructed: the model of deformation of graphene in plane as a plane stress state of the moment theory with free rotation; the model of bending-deformation out of plane as a model of bending of the moment theory of elasticity based on the 'shear plus free rotation' principle.

INTRODUCTION

Currently the construction and analysis of mathematical models describing the static and dynamic deformations of nanomaterials, such as graphene or carbon nanotubes is one of the topical problems. In the construction of these models the main focus is on the development of the basic principles of structuring such models, which are in reality most appropriate to their deformations (in the end, the construction of their discrete and continuum models).

If we pay attention only to the existence of graphene or a single-layered carbon nanotube, it is easy to justify that between the atoms of these materials there are not only force but also moment interactions, whereas, force interactions are non-axial. The moment interactions between the atoms of these nanomaterials indicate that their atoms should not be considered as physical points (as in the classical case), but it is necessary to consider them as bodies with small but finite sizes (in this case, as spherical bodies). This implies that atoms, in this case, will possess not only mass, but also moment inertia, as well as not only translational, but also rotational degrees of freedom. Thus, the reasoning of this approach leads to the idea that the moment theories can be taken as basis in constructing both the discrete and continuum models of graphene when describing their deformations.

To construct discrete and continuum models of graphene, a holistic program is implemented in the work, the content of which is stated in the following sections.

CONSTRUCTION OF DISCRETE AND CONTINUUM MODELS OF A LINEAR ATOMIC CHAIN

A linear chain of atoms is considered in the initial undeformed state oriented along axis x. It is assumed that each atom interacts only with its nearest neighbors and its additive energy is the sum of the interaction energies with the left and right neighbors. Small deviations of atoms from the equilibrium position are considered.

Differential equations of equilibrium (or motion) for each atom (which determine the discrete model of a linear chain of atoms) are written in the framework of Euler mechanics (i.e., for a solid, assuming that the chain undergoes deformations of general type). It is assumed that both force and moment interactions of atoms can be energetically described by harmonic (power-law) potentials (this means that the coefficients of these potentials are second order derivatives of the potential function) for the corresponding chain deformations (strain-compression, shift-bending in two perpendicular planes xy, xz and torsion around axis x.). For a discrete model of a linear chain, the corresponding functionals are also compiled (the principle of possible displacements — in the case of statics, or the Lagrangian — in the case of dynamics), on the basis of which the discrete model of a linear chain of atoms in the general case of its deformation is also presented in a variational form. By limit passage in these variational functionals (when $a \to 0$, where $a-$ is the distance between the atoms of the chain), the functionals (of possible displacements in the case of statics or Lagrangian in the case of dynamics) are obtained for the continuum model of a linear chain of atoms. It is established that the continuum model of a linear chain of atoms (both in the case of statics and in the case of dynamics) coincides with the model of a micropolar beam with free displacement and rotation fields. According to this model the motion of a micropolar elastic beam is characterized by the following: a strain-compression scheme; bendings: "shear plus free rotation" in planes xz, yz; torsion around axis x. In a particular plane case, such a model of a micropolar beam was previously constructed (using the asymptotic method of integrating the plane stress state problem of the micropolar theory of elasticity in a thin rectangular region) in [1].

CONSTRUCTION OF DISCRETE-CONTINUUM AND CONTINUUM MODELS FOR THE GENERAL CASE OF DEFORMATIONS OF GRAPHENE

It is assumed that each graphene atom interacts with three nearest neighbors (which are located on three straight lines originating from the point under consideration at angles at 120^0). The elastic interactions between the atom in question and the indicated neighbors are replaced by elastic micropolar beams (the model of which is constructed in section 1). Imagining that the graphene region under consideration is covered by such a beam system that replaces its atomic structure, the model constructed in this way will be a discrete-continuum model of graphene in the general case of its deformation.

On the indicated periodic lattice of graphene, by averaging the total sum (of three terms) of the functionals of elastic micropolar beams (total potential deformation energy in the case of statics or Lagrangian in the case of dynamics), after, by limit passage, the corresponding functionals of the continuum model of statics or dynamics of graphene are constructed. The constructed continuum graphene model is decomposed into two independent models: a) a continuum model of graphene for deformations in plane, b) a continuum model of graphene for the bending deformation out of plane. Both continuum models respectively coincide with the model of plane stress state and the model of bending deformation of the plate (shear plus free rotation), previously constructed in [2]. From general energy considerations, the relationships between the elastic parameters of the discrete model of graphene and the elastic physical constants of the indicated micropolar (moment) elasticity theories are determined.

Generalizing approaches (1), (2), based on moment theories, it is possible to construct discrete and continuum models for other nanomaterials too (nanotubes, fullerenes, etc.). Construction of a discrete-continuum model of nanocomposite (layered) elastic media, obtained by reinforcing a certain elastic medium with two-dimensional graphene-like elements of high strength is demonstrated. In the case, when the number of layers is sufficiently large, a continuum model for the indicated nanocomposite elastic media is constructed by limit passage. Versions of the finite element method for the numerical study of the constructed phased models are developed.

CONCLUSIONS

To sum up, by limit passage from discrete-moment model, a moment beam model of the linear atomic chain is constructed. By substituting atomic interactions of graphene by the constructed model, a discrete-continuum model is constructed. By limit passage a continual-moment model of graphene is constructed as: 1) deformations in plane; 2) bending out of plane. The first model is a plane stress state of the moment theory of elasticity with free rotation, the second theory is the bending based of the moment theory of elasticity based on the ‘shear plus free rotation’ principle. Discrete-continuum and continuum-moment models of graphene reinforced layered nanocomposite are constructed.

References

[1] Sargsyan S.H. Applied One-dimensional Theory of Beams Based on the Asymmetric Theory of Elasticity. *Physical Mesomechanics* V. 11. N5: 41-54, 2008.

[2] Sargsyan S.H. Boundary-Value Problems of Asymmetric Theory of Elasticity for Thin Plates. *Journal of Applied Mathematics and Mechanics*. Vol. 72. N1: 77-86, 2008.

EXACT FINITE ELEMENT FORMULATION FOR OUT-OF-PLANE STATIC ANALYSIS OF A CURVED NANOBEAM

Hilal KOC[1]*, Omer Ekim GENEL [1], and Ekrem TUFEKCI[1]
[1]Faculty of Mechanical Engineering, Istanbul Technical University, Istanbul, Turkey

Summary In this study, a new finite element formulation is developed for out of plane static behaviour of curved nanobeams by using nonlocal theory of elasticity. In the formulation, displacement functions that are the results of the exact analytical solution are utilized to formulate the stiffness matrix with the direct method. The exact analytical solution includes effects of small scale, shear deformation and nonlocal effects of shear forces, bending and torsional moments. A static example is handled and compared with similar studies in the literature. With that analysis, a circular nanobeam having uniform cross-section is investigated. The usage of a novel formulation which uses exact analytical solution as shape function does not exist in the literature. This is the first study that is investigated out of plane static behaviour of curved nanobeam with finite element formulation.

INTRODUCTION

Since having superior properties in terms of stiffness, strength, conductivity and low density, nanobeams have been utilised in a wide range of engineering applications. Because of manufacturing imperfections and excessive axial loadings, it is very hard to produce perfect straight nanobeam. [1] states that although most of the studies are about nanobeams having straight axes, in fact, they have curved axes due to their geometrical imprecisions.

In order to be able to model interactions between atoms or molecules properly with interparticle spaces taken into account, in nanostructures, there are some well-known methods. One of them is the molecular dynamics (MD) simulation method. However, compared to molecular dynamics (MD) simulations, high order continuum mechanics-based models are much more computationally cost-effective. Those high order continuum approaches are developed in order to determine the mechanical behaviour of micro/nano-scaled materials while offering simpler and more clear formulations. In nanoscale, effects of gaps between atoms cannot be neglected and a well-developed continuum model should consider these effects as well. Unlike the local theory of elasticity, the nonlocal theory of elasticity approach, which is developed by [2], concerns these effects on structural behaviour.

In the literature, there are numerous analytical studies on static behaviours of nanobeams by using the nonlocal theory of elasticity. In these studies, [3-5] obtained the exact analytical solution of curved nanobeams employing the nonlocal continuum theory. [5] presented a study on out-of-plane static behaviours of curved nanobeams by using the nonlocal theory of elasticity. In addition to analytical studies, there are few studies which investigate static behaviours of nanobeams by combining finite element method and nonlocal theory of elasticity [6-9].

In the present study, a nonlocal finite element formulation based on the exact analytical solution is developed for out-of-plane static behaviour of curved nanobeams. This formulation takes the effects of shear deformation into consideration and obtained results are compared with the literature. To the authors' knowledge, this formulation is the first study in the literature with the scope of mentioned content.

FORMULATION

The exact analytical solution of governing equations for the out of plane behaviour of curved nanobeams with varying curvature and cross-section are obtained in [5]. Effects of shear deformation and bending are taken into account and the solution can be represented as follow:

$$\mathbf{y}(\theta) = \mathbf{Y}(\theta, 0)\mathbf{y}_0 \tag{1}$$

Here, $\mathbf{y}(\theta)$, $\mathbf{Y}(\theta, 0)$ and $\mathbf{y}_0$ are the vector of variables, fundamental matrix and the vector of initial values, respectively. Elements of the fundamental matrix can be found in [5] for constant curvature and uniform cross-section case.

To obtain the stiffness matrix, elements of the fundamental matrix are grouped and expressed as submatrices. Therefore, Equation (1) becomes:

$$\begin{Bmatrix} \boldsymbol{X} \\ \boldsymbol{F} \end{Bmatrix} = \begin{bmatrix} \boldsymbol{A}(\theta_e) & \boldsymbol{B}(\theta_e) \\ \boldsymbol{C}(\theta_e) & \boldsymbol{D}(\theta_e) \end{bmatrix} \begin{Bmatrix} \boldsymbol{X_0} \\ \boldsymbol{F_0} \end{Bmatrix} \tag{2}$$

θ_e is the opening angle of a finite element. After utilising the direct method, the element stiffness matrix is obtained as below:

$$\boldsymbol{K^e} = \begin{bmatrix} \boldsymbol{B}(\theta_e) & \mathbf{0} \\ \boldsymbol{D}(\theta_e) & \mathbf{I} \end{bmatrix}^{-1} \begin{bmatrix} \boldsymbol{A}(\theta_e) & -\mathbf{I} \\ \boldsymbol{C}(\theta_e) & \mathbf{0} \end{bmatrix} \tag{3}$$

NUMERICAL EXAMPLE

The developed finite element formulation is validated with a numerical example and comparison with the literature. In the example, boundary conditions are clamped-free and nonlocal parameter (γ), Young's modulus (E), Poisson ratio

*Corresponding author. E-mail: koch16@itu.edu.tr

(v) values are taken as 1.56 nm, 1 TPa and 0.3, respectively. The opening angle (θ_T) and the factor of shear deformation (k_n) are $\pi/2$ and 6/5, respectively. Slenderness ratio is defined as: $\lambda = R\,\theta_T/\sqrt{I_n/A}$. Here, R is the curvature of the beam; I_n is the area moment of inertia about the normal axis; A is the cross-section area of the beam. In this example, the static analysis of a quarter cantilever beam is performed, Figure 1. Here, the slenderness ratio and curvature values are taken 20 and 5γ, respectively. The magnitude of the binormal force is taken 0.3 nN.

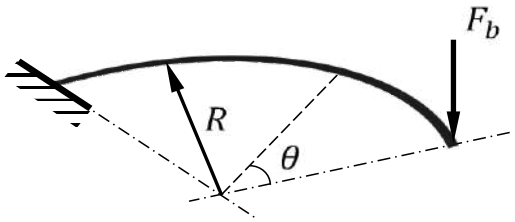

Fig. 1: A circular cantilever beam with uniform cross-section under a binormal force.

Analytical results of the analytical expression from [5] are compared with the ones from the finite element procedure. Due to having a single region, the problem is solved with one curved beam element as defined. The results are presented in Table 1 and it can be seen that finite element and analytical results are in agreement. Here, v is the binormal displacement; Ω_n and Ω_t are the rotation angles about normal and tangential axes, respectively.

Table 1: Comparison of the analytical approach and the finite element formulation

Displacement components	[5]	This study
v [nm]	0.226052	0.226052
Ω_n [rad]	-0.029816	-0.029816
Ω_t [rad]	-0.004049	-0.004049

CONCLUSIONS

In this study, the nonlocal theory of elasticity and initial value method are employed to derive a new finite element formulation in order to investigate out-of-plane static behaviour of curved nanobeams. Effects of small scale parameter, shear deformation, nonlocal effects of bending, torsional moments and shear forces are included in the exact analytical solution of governing equations. While almost all the studies in the literature use some approximate functions as the displacement functions, exact analytical solutions are dealt with as shape functions in the present study. To obtain the stiffness matrix, the direct method is used. To the authors' knowledge, this study is the first because of using exact analytical displacement functions as shape functions and finite element formulation for out of plane static behaviour of curved nanobeams. It is expected that the analysis of complicated nanobeam structures can be simplified with that solution. Thus, it will be possible that complicated nanosystem designs can be truer, more confidential and achieved in a shorter time.

ACKNOWLEDGEMENTS

The work described in this paper is supported by Istanbul Technical University Scientific Research Office (Project no. MGA-2018-41546).

References

[1] Joshi, A. Y., Sharma, S. C. and Harsha, S. P. Dynamic analysis of a clamped wavy single walled carbon nanotube based nanomechanical sensors. *Journal of Nanotechnology in Engineering and Medicine*, **1**, 031007-7, 2010.

[2] Eringen, A. C. Linear theory of nonlocal elasticity and dispersion of plane waves. *International Journal of Engineering Science*, **10 (3)**, 425-435, 1972.

[3] Tufekci, E., Aya, S. A., Oldac, O. A unified formulation for static behavior of nonlocal curved beams. *Structural Engineering Mechanics*, **59 (3)**, 475-502, 2016.

[4] Tufekci, E., Aya, S. A., Oldac, O. In-plane static analysis of nonlocal curved beams with varying curvature and cross-section. *International Journal of Applied Mechanics*, **8 (1)**, 1650010, 2016.

[5] Tufekci, E. & Aya, S. A. A nonlocal beam model for out-of-plane static analysis of circular nanobeams. *Mechanics Research Communications*, **76**, 11-23, 2016.

[6] Mahmoud, F. F., Eltaher, M. A., Alshorbagy, A. E. and Meletis, E.I. Static analysis of nanobeams including surface effects by nonlocal finite elements. *Journal of Mechanical Science and Technology*, **26**, 3555-3563, 2012.

[7] Alshorbagy, A.E., Eltaher, M.A., Mahmoud, F.F. Static analysis of nanobeams using nonlocal FEM. *Journal of Mechanical Science and Technology*, **27(7)**, 2035-2014, 2013.

[8] De Sciarra, F. M. Finite element modelling of nonlocal beams. *Physica E*, **59**, 144-149, 2014.

[9] Taghizadegh, M., Oversy, H.R., Ghannadpour, S.A.M. Nonlocal integral elasticity analysis of beam bending by using finite element method. *Structural Engineering and Mechanics*, **54 (4)**, 755-769, 2015.

A HIGHER ORDER SHEAR DEFORMATION BEAM MODEL FOR FREE VIBRATION PROBLEMS OF SMART NANOSTRUCTURES

Piotr Jankowski[1], Krzysztof Kamil Żur*[1], and Jinseok Kim[2]
[1]Faculty of Mechanical Engineering, Bialystok University of Technology, Bialystok 15-351, Poland
[2]Department of Mechanical and Aerospace Engineering, Western Michigan University, Kalamazoo, MI 49008-5343, USA

Summary In present study, a model for free vibration problems of elastically supported smart nanobeams made of functionally graded porous material is presented. Reddy third-order shear deformation theory that accounts for a nonlocal strain gradient theory, a power-law distribution for the variation of two material constituents through the nanobeam thickness, and three different porosity distributions as forms of cosine functions is used to develop piezoelectric functionally graded porous nanobeam model. The equations of motion are derived using the dynamic version of Hamilton's principle. The final nonlocal equations of motion are expressed by the displacements.

ABSTRACT

Consider a nanobeam of total thickness $H = h + 2h_p$, where h is the thickness of functionally graded porous nano-core and $2h_p$ is the total thickness of two piezoelectric layers [1-3] (Fig. 1). The nanobeam resting on Pasternak foundation, where K_w is spring stiffness and K_s is shear stiffness.

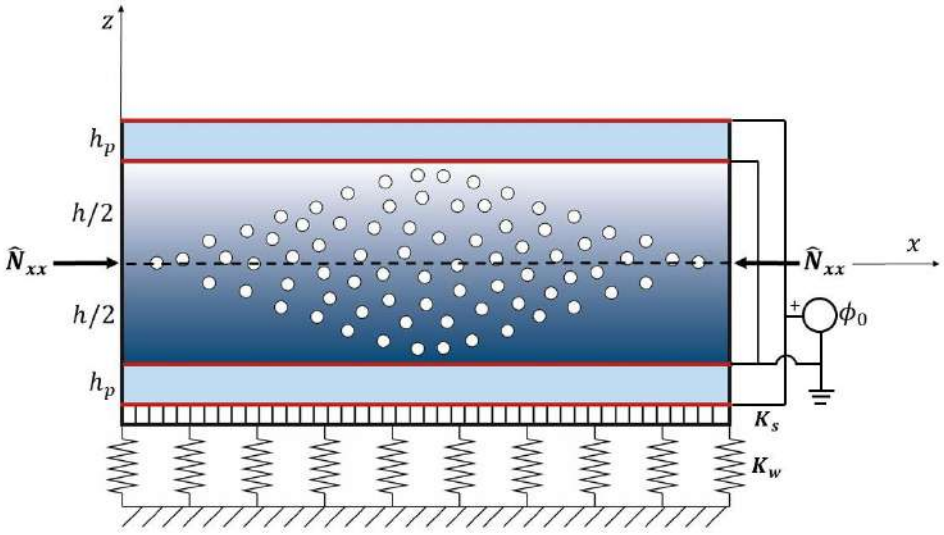

Figure 1. The cross-section and coordinate system of the electro-elastic FGM porous nanobeam subjected to in-plane forces.

The displacement field for the nanobeam under consideration is expressed on the basis on Reddy third-order beam theory [4]:

$$u_x(x,z,t) = u_0(x,t) + z\varphi_x(x,t) - \mathrm{c}_1 z^3\left(\varphi_x(x,t) + \frac{\partial w_0(x,t)}{\partial x}\right), \quad (1a)$$

$$u_z(x,t) = w_0(x,t), \quad (1b)$$

where $\mathrm{c}_1 = \frac{4}{3h^2}$, u_0 is the axial displacement, w_0 is the transverse displacement and φ_x is the rotation of a point on the centroidal axis x of the beam.

Assume that material properties of the FGM nano-core varies through the thickness h according to formula [5]:

$$E(z) = \left[(E_t - E_b)\left(\frac{z}{h} + \frac{1}{2}\right)^g + E_b\right][1 - \Upsilon(z,\vartheta)], \quad (2)$$

where E_t and E_b are Young's modulus values at the top and bottom surface, respectively. The constant g is the power-law index. Moreover, in the study three types of porosity distribution are defined by

$$\text{Type 1: } \Upsilon(\hat{z},\vartheta) = \vartheta cos\left(\frac{\pi z}{h}\right),$$

$$\text{Type 2: } \Upsilon(\hat{z},\vartheta) = \vartheta cos\left[\frac{\pi}{2}\left(\frac{z}{h} - \frac{1}{2}\right)\right], \quad (3)$$

$$\text{Type 3: } \Upsilon(\hat{z},\vartheta) = \vartheta cos\left[\frac{\pi}{2}\left(\frac{z}{h} + \frac{1}{2}\right)\right],$$

where ϑ is porosity coefficient, and $\hat{z} = z/h$ is normalized thickness of the nanobeam.

Figure 2 shows an example of effect of power-law index g, porosity coefficient ϑ, and porosity distribution types Υ on the variation of Young's modulus.

*Corresponding author. E-mail: k.zur@pb.edu.pl.

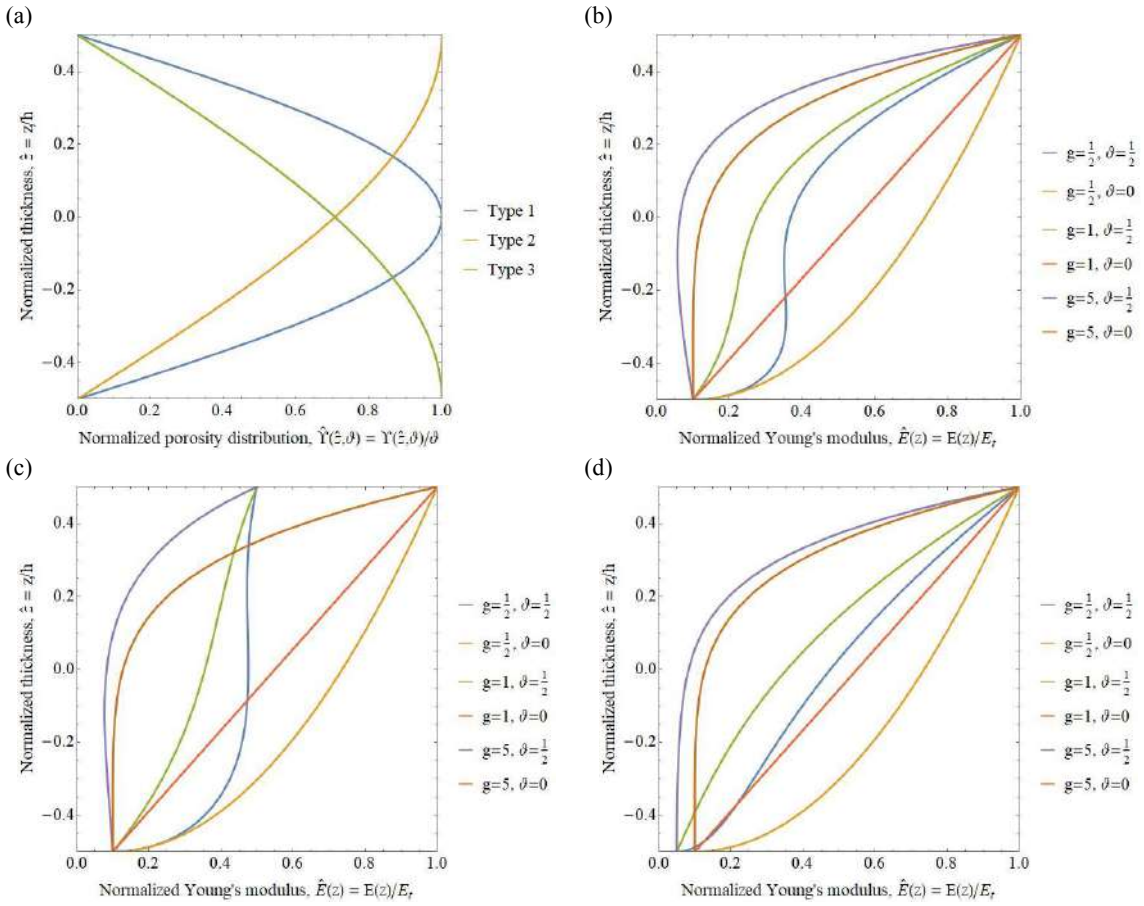

Figure 2. The variations of material properties through the nanobeam thickness, where: (a) normalized porosity distribution, (b) normalized Young's modulus from Type 1 distribution, (c) from Type 2 distribution, and (d) from Type 3 distribution.

References

[1] Mitchell J.A., Reddy J.N., A refined hybrid plate theory for composite laminates with piezoelectric laminae. International Journal of Solids and Structures. **32**: 2345-2367, 1995.

[2] Kim J., Reddy J.N., Modeling of functionally graded smart plates with gradient elasticity effects. Mechanics of Advanced Materials and Structures. **24**:437-447, 2017.

[3] Żur K.K., Arefi M., Kim J., Reddy J.N., Free vibration and buckling analyses of magneto-electro-elastic FGM nanoplates based on nonlocal modified higher-order sinusoidal shear deformation theory. Composite Part B: Engineering. **182**:107601, 2020.

[4] Reddy J.N., Energy principles and variational methods in applied mechanics. Third Edition, John Wiley & Sons, 2017.

[5] Kim J., Żur K.K., Reddy J.N., Bending, free vibration, and buckling of modified couples stress-based functionally graded porous micro-plates. Composite Structures. **209**:879-888, 2019.

VIBRATIONAL ANALYSIS OF DEFECTED CIRCULAR SINGLE-LAYERED SILICENE SHEETS UNDER PRE-STRAINS

S. Kamal. Jalali*[1], M.J. Beigrezaee[2], and Nicola Maria Pugno[1,3,4]
[1]Laboratory of Bio-Inspired & Graphene Nanomechanics, Department of Civil, Environmental and Mechanical Engineering, Università di Trento, via Mesiano, 77, I-38123 Trento, Italy
[2]Department of Mechanical Engineering, Kermanshah University of Technology, Kermanshah, Iran
[3]School of Engineering and Materials Science, Queen Mary University of London, Mile End Road, London E1 4NS, UK
[4]Fondazione E. Amaldi, Ket Lab, Via del Politecnico snc, 00133 Rome, Italy

Summary This paper investigates the effect of pre-strains in presence of vacancies as the structural defects on the vibration of circular single-layered silicene sheets (SLSSs) by the use of molecular dynamic (MD) simulations. The Stillinger-Weber potential is used for atomic interactions. The initial velocity is applied to impose the fundamental mode shape of sheets. The results show that increasing the percentage of vacancies decreases the fundamental frequency. Furthermore, increasing the pre-strains and the initial velocity both have increasing effects on the frequencies, however, pre-strain plays a significant role. The results can be considered for tuning the frequency response of silicene, powerfully.

INTRODUCTION

Two-dimensional (2D) materials, consisting of a single layer of atoms on a crystalline lattice, have received many attractions in the last decade thanks to their admirable potentials in the semiconductor, electronics, high resolution sensing, batteries, and composite materials applications. Graphene, as the first 2D material, was isolated in 2004. Thereafter many others were identified e.g. silicene, germanene, stanene, and plumbene in 2012, 2014, 2015, and 2018, respectively [1]. Investigation of the mechanical properties and the responses of these new-born materials is highly cited by the community. Due to the sensing and actuating possibility of 2D materials especially in the dynamic mode, their vibrational behavior have been addressed by the researchers. As the experimental efforts are expensive and challenging, the numerical approaches such as *ab initio*, Monte Carlo, and MD simulations are widely implemented. The mechanical properties of single-layered silicene sheets were investigated by Roman and Cranford [2]. Mahmoudinezhad and Ansari [3] analyzed the vibrational behaviour of the circular single-layered graphene sheets. Jalali et al. [4] studied the capability of tuning the frequency response of graphene sheets by use of out-of-plane defects and calibrated the nonlocal elasticity solution to the MD results. In another work, Jalali et al. [5] explored the effect of porosities on the vibrational behavior of square single-layered graphene sheets by finite element-based molecular structural mechanics. In the present study, the influence of the vacancies and the imposing velocity on the frequency responses of pre-strained circular SLSSs has been investigated by MD simulations.

METHODOLOGY

MD simulations is performed by implementing the well-known open source LAMMP software. The Stillinger-Weber potential is used for interactions between atoms in the circular SLSSs of the radius R. Vacancies are added to the system by uniform removing the atoms from the lattice. The peripheral atoms, the red ones in figure 1, are moved in the radial direction to apply the pre-strain and afterward all the degrees of freedom of the edge are fixed and the system is leaving to be relaxed at the temperature of 1 K. To impose the free vibration, an initial velocity in the form of $V(r) = V_0\cos(\pi r/2R)$ is applied to the atoms for actuating the fundamental mode shape and the system is allowed to vibrate considering an NVE ensemble. After that, using the FTT procedure the fundamental natural frequency of the system is extracted from the transverse displacement of the central atom.

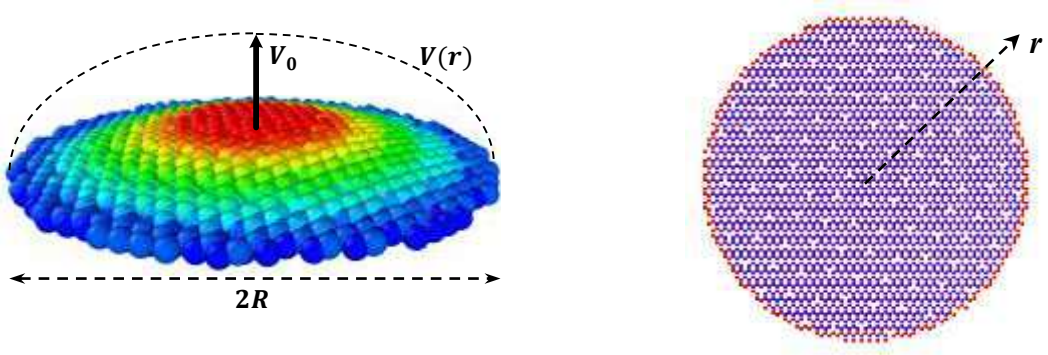

Figure 1. The definitions of the problem and methodology.

*Corresponding author. E-mail: seyed.kamal.jalali@gmail.com.

RESULTS AND DISCUSSION

In order to assess the sensitivity of the natural frequencies of the circular SLSSs, three influencing parameters i.e. the percentage of vacancies, the pre-strain, and the maximum initial velocity, V_0, have been taken into consideration. The percentage of vacancies is defined as the number of omitted atoms dived by the number of total atoms. The maximum initial velocity is increased in such a way that the sheets resist the tensions during the vibration and no fracture happens. The effect of all the mentioned parameters are explored in details. Figure 2 shows the fundamental natural frequency of the circular SLSSs with respect to the percentage of the vacancies for various initial velocities. As seen the frequencies reduces by increasing the value of vacancies. It means that the reduction in stiffness is higher than the reduction in the total mass due to omitting the atoms from the lattice structure however, this effect decreases by increasing the number of omitted atoms. Besides, raising the initial velocity increases the fundamental frequency for all the percentage of vacancies, which is known as the hardening effect in the classical nonlinear vibration of structures. From the results presented in Figure 3, the pre-strain has a significant increasing influence on the frequency response and by increasing the pre-strain the effect of increasing initial velocity is almost vanished. These results can be proved that the combination of considered parameters can be applied as a powerful tool for tuning the frequency response of silicene as a two-dimensional material.

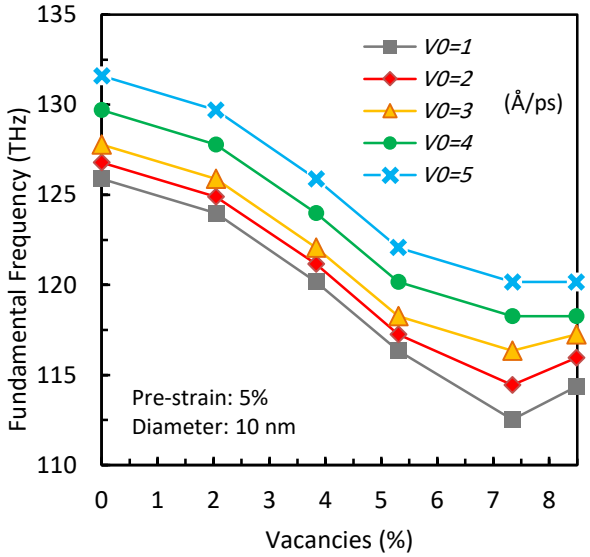

Figure 2. The effect of percentage of vacancies on the fundamental frequency of circular SLSSs for different initial velocities.

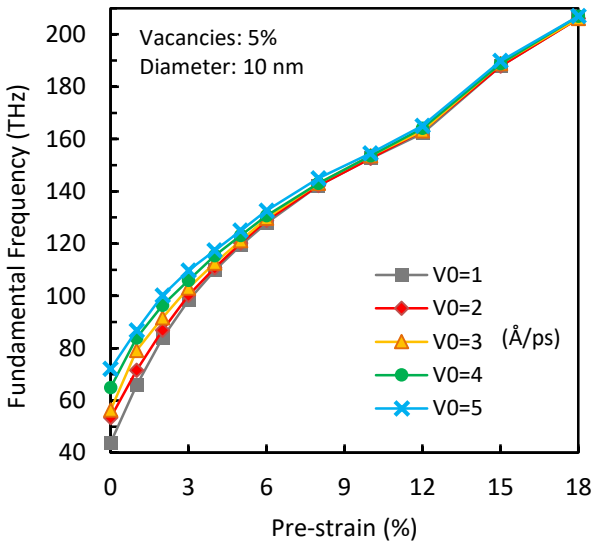

Figure 3. The effect of pre-strain on the fundamental frequency of circular SLSSs for different initial velocities.

CONCLUSIONS

By use of the MD simulations, the vibrational behavior of pre-strained defected circular SLSSs has been explored through an FFT procedure. The percentage of vacancies, the pre-strain, and the initial velocity have been presumed as the influencing parameters. The natural frequency decreases by increasing the percentages of vacancies. In addition, increasing the initial velocity and the pre-strain both lead to significant raising in the frequency of all sheets. It is concluded that by mixing the mentioned parameters, it is possible to tune the frequency response of SLSSs as optimal design.

References

[1] He, J.D.; Sun, J.S.; Jiang, J.W. Nanomechanical resonators based on group IV element monolayers. *Nanotechnology* ***29***: 2018.
[2] Roman, R.E.; Cranford, S.W. Mechanical properties of silicene. *Comput. Mater. Sci.* ***82***: 50–55, 2014.
[3] Mahmoudinezhad, E.; Ansari, R. Vibration analysis of circular and square single-layered graphene sheets: An accurate spring mass model. *Phys. E Low-Dimensional Syst. Nanostructures* ***47***: 12–16, 2013.
[4] Jalali, S.K.; Jomehzadeh, E.; Pugno, N.M. Influence of out-of-plane defects on vibration analysis of graphene: Molecular Dynamics and Non-local Elasticity approaches. *Superlattices Microstruct.* ***91***: 331–344, 2016.
[5] Jalali, S.K.; Beigrezaee, M.J.; Hayati, S. How does porosity affect the free vibration of single-layered graphene sheets? *Superlattices Microstruct.* ***128***: 221–242, 2019.

EXACT FINITE ELEMENT FORMULATION FOR IN-PLANE STATIC ANALYSIS OF A CURVED NANOBEAM

Omer Ekim GENEL [1]*, Hilal KOC[1], and Ekrem TUFEKCI[1]
[1]Faculty of Mechanical Engineering, Istanbul Technical University, Istanbul, Turkey

Summary In this study, a new, exact finite element formulation is proposed for in-plane static analysis of planar curved nanobeams. The shape functions are obtained from exact analytical solutions based on the nonlocal theory of elasticity. The effects of axial extension and shear deformation are taken into account. The stiffness matrix is obtained by using the direct method. The static behaviour of a quarter circular nanobeam having uniform cross-section under normal tip force is analysed and the results are compared with those in the literature.

INTRODUCTION

Nanobeams have a wide range of applications in engineering due to their improved material properties. Mainly, three approaches are employed to investigate the behaviour of nanobeams: molecular dynamics (MD) simulations, hybrid theory and continuum mechanics. The last approach has a less computational cost and is considered as the more effective field in comparison to other approaches. While classical continuum mechanics theory neglects the effect of interatomic gaps, the nonlocal theory of elasticity which is proposed by Eringen [1] takes into consideration this effect and gives reliable results in nanobeam applications.

In the literature, there are numerous studies which investigate in-plane static behaviours of nanobeams by using analytical approaches using the nonlocal theory of elasticity. In analytical studies, the static behaviour of curved nanobeams is investigated and obtained exact analytical solutions by using initial values method [2-4]. The in-plane behaviour of curved nanobeams is investigated and obtained exact analytical solutions by using initial values method [2,3]. In both papers, axial extension and shear deformation are taken into consideration. Compared to analytical studies, the studies which investigate the static behaviour of nanobeams with the finite element method are quite limited [5-8]. For design purposes and considering manufacturing limitations, nanobeams with curved axes are utilised in some applications; therefore, mechanical modelling and analysis of curved nanobeams are crucial in nanoscale engineering applications.

In the presented paper, in order to be able to investigate in-plane static behaviour of curved nanobeams, a finite element formulation, which is used exact analytical solutions based on the nonlocal theory of elasticity as shape functions, is developed. In the formulation, effects of axial extension and shear deformation are taken into consideration. To the best of the authors' knowledge, within the scope of mentioned content, this formulation is considered as the first study in that area in the literature.

FORMULATION

For the in-plane case, governing differential equations of curved nanobeams are given in [2]. The solution of this differential equation system can be expressed as follows:

$$\mathbf{y}(\theta) = \mathbf{Y}(\theta, 0)\mathbf{y}_0 \tag{1}$$

Here, $\mathbf{y}(\theta)$, $\mathbf{Y}(\theta, 0)$ and $\mathbf{y}_0$ are the vector of variables, fundamental matrix and the vector of initial values, respectively. For constant curvature and uniform cross-section case, elements of the fundamental matrix can be found in [2].

To obtain the stiffness matrix, elements of the fundamental matrix are grouped and expressed as submatrices. Therefore, Equation (1) becomes:

$$\begin{Bmatrix} \boldsymbol{X} \\ \boldsymbol{F} \end{Bmatrix} = \begin{bmatrix} \boldsymbol{A}(\theta_e) & \boldsymbol{B}(\theta_e) \\ \boldsymbol{C}(\theta_e) & \boldsymbol{D}(\theta_e) \end{bmatrix} \begin{Bmatrix} \boldsymbol{X_0} \\ \boldsymbol{F_0} \end{Bmatrix} \tag{2}$$

Here, θ_e as the opening angle of a finite element. After application of the direct method, the element stiffness matrix is obtained as below:

$$\boldsymbol{K^e} = \begin{bmatrix} \boldsymbol{B}(\theta_e) & \mathbf{0} \\ \boldsymbol{D}(\theta_e) & \mathbf{I} \end{bmatrix}^{-1} \begin{bmatrix} \boldsymbol{A}(\theta_e) & -\mathbf{I} \\ \boldsymbol{C}(\theta_e) & \mathbf{0} \end{bmatrix} \tag{3}$$

NUMERICAL EXAMPLE

In order to investigate in-plane static behaviour of nanobeams by using finite element method, a quarter circular beam with a uniform cross-section with a force at the tip is analysed. In the example, the nonlocal parameter (γ), Young's Modulus (E) and Poisson's ratio (v) values are taken as 1.56 nm, 1 TPa and 0.3, respectively. The opening angle (θ_T) of the beam is $\pi/2$ and the factor of shear deformation (k_n) is taken as 6/5 for rectangular cross-section. Also, the slenderness ratio is calculated $\lambda = R\theta_T/\sqrt{I_b/A}$. Here, R is the curvature of the beam; I_b is the area moment of inertia about binormal axis; A is the cross-section area of the beam. In the example, static analysis of a quarter circular beam

*Corresponding author. E-mail: genelo@itu.edu.tr

which has uniform cross-section is carried out, Figure 1. Slenderness ratio and curvature are taken as 20 and 5γ, respectively. The external force is taken as 1 nN at normal direction under clamped-free boundary conditions.

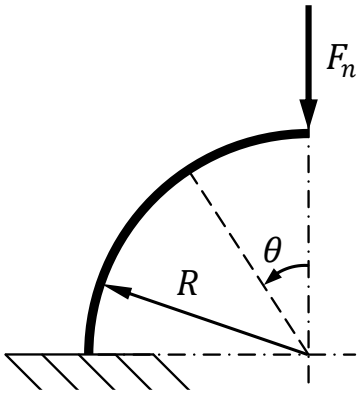

Fig. 1: Quarter circular beam under a tip force.

Due to having only one region, the problem is solved by using one element. Obtained results are compared with [2] and presented in Table 1. As can be seen from Table 1, results which are obtained from finite element formulation are in good agreement with analytical results. Here, w and u are tangential and normal displacements, respectively; Ω_b is the rotation angle about binormal axis.

Table 1: Comparison of the analytical approach and the finite element formulation

Displacement components	[2]	This study
w [nm]	0.213448	0.213448
u [nm]	0.339527	0.339527
Ω_b [rad]	0.053995	0.053995

CONCLUSIONS

In this study, a finite element formulation which uses exact analytical solutions as shape functions is developed for curved nanobeams. These exact analytical solutions are obtained by applying the nonlocal theory of elasticity. In the formulation, effects of axial extension and shear deformation are also considered. The stiffness matrix is constructed by using the direct method. It can be seen from the static example, results which are obtained from developed finite element formulation are in good agreement with the literature. To the authors' knowledge, no study which has abovementioned content has hitherto been published. It is thought that due to taking into account axial extension and shear deformation effects and using exact analytical solutions as shape functions, the presented formulation can be used to develop reliable complex curved nanobeam systems.

ACKNOWLEDGEMENTS

The authors would like to acknowledge the support of Istanbul Technical University, Scientific Research Office (Project no. MGA-2018-41546) that makes this research possible.

References

[1] Eringen, A. C. Linear theory of nonlocal elasticity and dispersion of plane waves. *International Journal of Engineering Science*, **10(3)**, 425–435, 1972.
[2] Tufekci, E., Aya, S. A., Oldac, O. A unified formulation for static behavior of nonlocal curved beams. *Structural Engineering Mechanics*, **59(3)**, 475-502, 2016.
[3] Tufekci, E., Aya, S. A., Oldac, O. In-plane static analysis of nonlocal curved beams with varying curvature and cross-section. *International Journal of Applied Mechanics*, **8(1)**, 1650010, 2016.
[4] Tufekci, E., Aya, S. A. A nonlocal beam model for out-of-plane static analysis of circular nanobeams. *Mechanics Research Communications*, **76**, 11-23, 2016.
[5] Phadikar, J.K., Pradhan, S.C. Variational formulation and finite element analysis for nonlocal elastic nanobeams and nanoplates. *Computational Materials Science*, **49**, 492-499, 2010.
[6] Mahmoud, F.F., Eltaher, M.A., Alshorbagy, A.E., Meletis, E.I. Static analysis of nanobeams including surface effects by nonlocal finite element. *Journal of Mechanical Science and Technology*, **26(11)**, 3555-3563, 2012.
[7] Alshorbagy, A.E., Eltaher, M.A., Mahmoud, F.F. Static analysis of nanobeams using nonlocal FEM. *Journal of Mechanical Science and Technology*, **27(7)**, 2035-2014, 2013.
[8] De Sciarra, F.M. Finite element modelling of nonlocal beams. *Physica E*, **59**, 144-149, 2014.

MICRO-RESONATORS MAGNETIC SENSOR

Nouha Alcheikh, Sofiane Ben Mbarek, and Mohammad I. Younis *[1]
[1]King Abdullah University of Science and Technology - KAUST, Thuwal, Saudi Arabia

Summary We present a Lorentz-force magnetic sensor based on electrothermally heated resonators operating in air at atmospheric pressure. The sensing mechanism is based on detecting the resonance frequency shift of micro-beams resonators due to the effect of Lorentz forces generated from a magnetic field. By operating near the buckling point of the straight micro-beam, the measured sensitivity, which is controllable by the bias current load, is shown around 1.63/T. To alleviate the dip in frequency near the buckling instability, another sensor is demonstrated based on an initially curved micro-beam, which shows a sensitivity of 0.19/T.

MANUSCRIPT

In recent years, miniaturized sensitive magnetic sensors based on Lorentz-force resonant sensing have received increasing attention[1]. Microelectromechanical Systems (MEMS) magnetic sensors have been explored for various applications, such as biomedical, inertial navigation systems, electronic compasses, telecommunications, and non-destructive testing[2]. They generally rely on two classes of readouts to detect the magnetic field: amplitude modulation (AM) and frequency modulation (FM)[3]. Compared to AM readout, tracking the frequency shift yields high accuracy, high outstanding stability, high sensitivity, low power consumption, and immunity to noise.

In this work, we explore two different kinds of Lorentz-force magnetic sensors, straight and curved micro-beams. The schematic of the micro-sensor is shown in Fig 1(a). The micro-sensors are fabricated from a highly conductive silicon device layer of silicon-on-insulator (SOI) wafer from MEMSCAP. They have a length (L) of 800 µm, a width (b) of 25 µm, and a thickness (h) of 2 µm. The curved micro-beam has a 2.5 µm initial rise (b_0). To generate a DC magnetic field in z-axis, we placed a permanent magnet above the sensor. Under the same value of magentic field +B (+z-axis), we measured the frequency responses of the micro-beam by changing I_{Th}. We repeated the same procedure by applying another direction of -B (-z-axis). As shown in Fig. 1(a), the presence of a permanent magnetic field (B) and with a bias current I_{Th}, which flows through the resonators, generates Lorentz-force in the y-axis. Upon changing I_{Th}, the resonance frequency of the curved micro-beam increases while for the straight beam it continuously decreases until reaching the buckling limit. After buckling, the resonance frequency increases, Figs 1(b,c). Figs 1(d,e) show the measured resonance frequency of the resonators for different values of B. As shown in Fig 1(d), the minimum detectable magnetic field in air at atmospheric pressure is ∓45 mT. Lower values of magnetic field can be detectable by reducing the damping effect by operating the micro-sensor at lower pressure. In addition, the measured results of curved micro-beam show excellent linearity. The insets show the measured frequency shift versus input magnetic field (B) for a constant current (d) and versus various bias currents for a constant B (e). As shown in the figure, for both resonators, the frequency shift for +B is higher compared to –B. The sensitivity of the magnetic sensor is calculated as the relative change in the resonant frequency ($\Delta f/f_0$) over the input magnetic field (B), where f_0 is the frequency of the micro-beams at B=0 T. As shown in the inset of Fig. 1(d), the sensitivities of the curved micro-beam, which is controllable by bias current load, is shown near S= 0.145/T (-B) and S= 0.19/T (+B) at I_{Th} =3 mA. These values of sensitivity are much higher than the values reported in the literature. As can be seen in the inset of Fig. 1(f) and at the buckling point I_{Th} =0.25 mA, the sensitivity increases with the magnetic field, S= 1.63/T (-B). It is expected that the straight beam around buckling is more sensitive than the curved micro-beam. This originates from the high sensitivity of the beam to a small variation of its stiffness in that region. However, it is sometimes desirable to avoid the dip in frequency near the buckling instability; and hence an arch in this case is advantageous. Also, one should note that the performance of the device is dependent on the applied bias current. The sensors show extremely low power consumption of about 2.1 mW and 14.5 µW, for curved and straight micro-beams, respectively. In addition to high sensitivity, the straight micro-beam shows more promising results for low power consumption.

CONCLUSIONS

In conclusion, we proposed highly sensitive Lorentz-force magnetic micro-sensors based on electrothermally heated straight and curved micro-beams. We show that a straight beam operated near the buckling threshold leads to the maximum sensitivity of the device. To alleviate the dip in frequency near the buckling instability, another sensor was demonstrated based on a curved micro-beam, which shows High sensitivity. The micro-sensor demonstrates high sensitivity compared to reported magnetic sensors. The advantages of the proposed sensor are the simplicity of fabrication, lower power consumption, and also scalability.

*Corresponding author. E-mail: nouha.alcheikh@kaust.edu.sa.

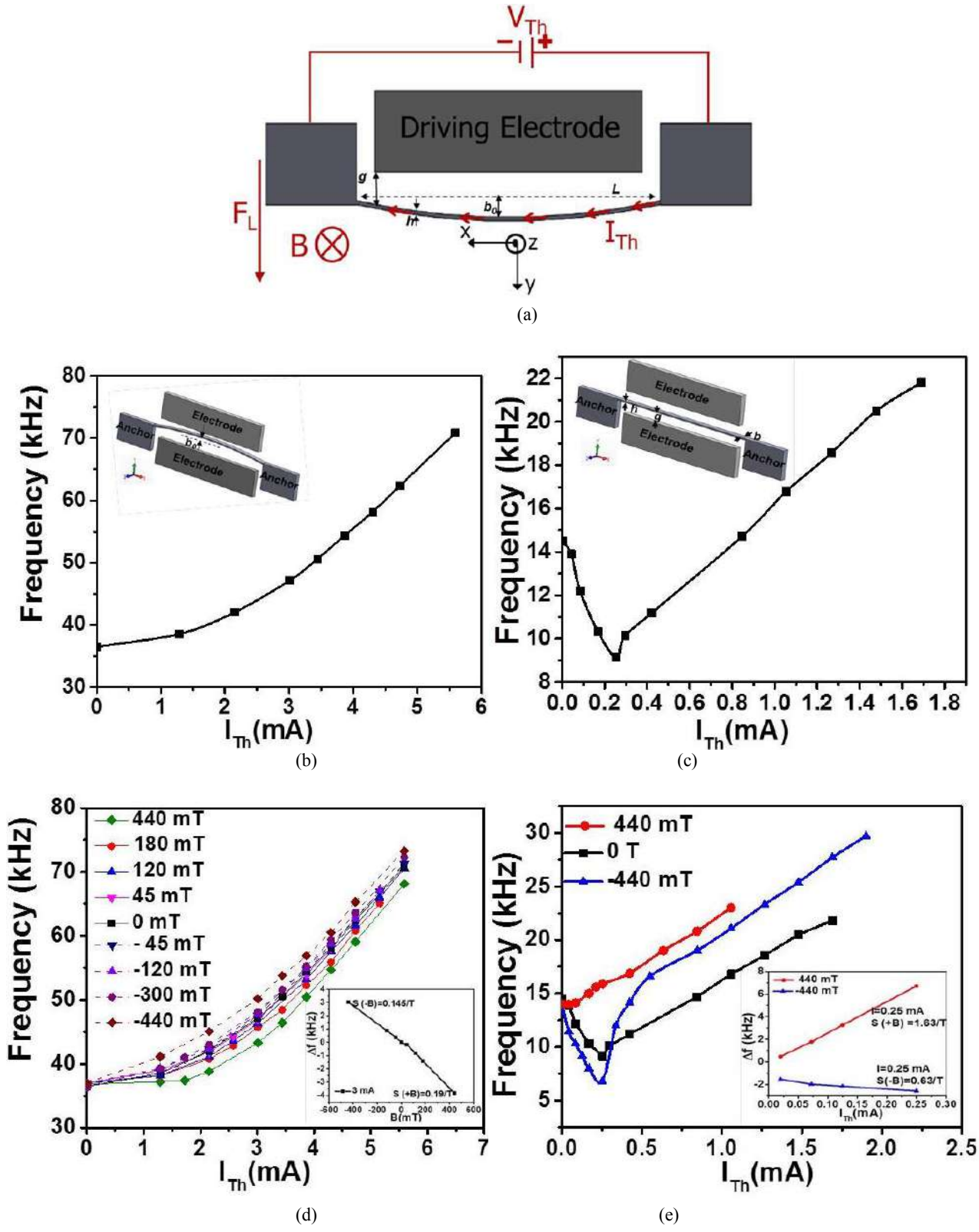

Figure 1. (a) Schematic of the working principle of the Lorentz-force magnetic sensors based on in-plane curved micro-beam electrothermally actuated. Experimental results of the variation of the resonance frequency of (b) the curved micro-beam and (c) straight micro-beam for various bias currents (I_{Th}). The insets show a schematic of the curved and straight micro-beams. (d),(e): Measured frequency variation of the sensors with bias current by applying z-axis magnetic fields; (d) for the arch micro-beam, and (e) for the straight. The insets show the measured frequency shift versus input magnetic field (B) for a constant current (d) and versus various bias currents for a constant B (e).

References

[1] Ding J., Huang L., Luo G., Lu D. , Wang J., Zhao L., Jiang J., J. *Micromech. Microeng.* **29**: 065010, 2019.
[2] Allen J. M., Taylor & Francis: Boca Raton, FL, USA, 2005.
[3] Li M., Nitzan S., Horsley D. A., *IEEE Elec. Dev. Lett.*, **36**:62-4, 2014.

REMOTE-CONTROLLED SPIN-FLIP PROCESS IN RHOMBIC GRAPHENE NANOFLAKES

Yi Ming Zhang[1], Jing Liu[2], Chun Li *[1,3], Wei Jin[4], Georgios Lefkidis[2,1], and Wolfgang Hübner[2]
[1]School of Mechanics, Civil Engineering and Architecture, Northwestern Polytechnical University, Xi'an 710072, China
[2]Department of Physics and Research Center OPTIMAS, University of Kaiserslautern, PO Box 3049, 67653 Kaiserslautern, Germany
[3]Department of Mechanical Engineering, University of Manitoba, Winnipeg MB R3T 5V6, Canada
[4]School of Physics and Information Technology, Shaanxi Normal University, Xi'an 710119, China

Summary We present the configurations and stability of the rhombic graphene nanoflakes (GNFs) with two Ni atoms attached its boundary (Ni_2&GNF) using strict and elaborate geometric modeling. It is shown that the spin-flip process on Ni_2&GNF is highly favored by work of the involved magnetic element and applied strain. The first-principles tensile test predicts that the variation of the C-Ni bond length plays an important role in the spin density distribution, especially for the low-lying magnetic states, and can therefore dominate the spin-flip processes. Furthermore, since the spin is localized on the right Ni atom, when the tensile strain along the right C-Ni bond is applied, the spin processes do not change much with the increasing strain, however, the L-type (strain along the left C-Ni bond) strain strongly influences the local spin-flip process on Ni_R atom. Such phenomenon demonstrates a remote-controlled spin-flip process, which could increase the functionality and the flexibility of the intergated spin-logic in real straintronic devices.

STRUCTURE OPTIMIZATION AND STRAIN MODEL

For simplicity and without loss of generality, in our present work we focus on rhombic graphene nanoflakes with two nickel atoms attached to the boundary of GNFs (Ni_2&GNF). Four initial structures are fully optimized to obtain the equilibrium geometry. The stability of each structure is confirmed after the calculations of normal mode with the absence of imaginary frequencies. After optimization, the GNF with two Ni atoms connected to the adjacent carbon atoms is further studied [Fig. 1(b)]. And Fig. 1(c) shows the strain model we applied, that is, the strain is applied along the left C-Ni bond (L type) and right C-Ni bond (R type).

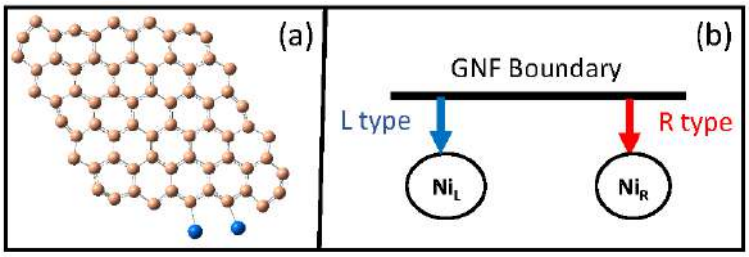

Figure 1: Ni_2&GNF structures and the strain model. (a) Optimized equilibrium structure; (b) Stretching along the C-Ni bonds, noted as L type (left bond) and R type (right bond), respectively.

REMOTE-CONTROLLED SPIN-FLIP PROCESS

Based on the Λ process[1, 2, 3, 4] theoretical model, we need to identify the adequate states with localized spin density, which could be the initial and final states of the spin-flip processes. To this end, we calculate the spin density on each many-body state using a Mulliken population analysis. It is noteworthy that this analysis only gives an estimate of the spin distribution in our structures, while it is enough to detect which atoms and states carry the spin. In our present calculation, the total spin density of the system is around 2, while in the initial structrue and the distorted structures, the Ni_R atom carris about 1.8 on the ground triplet state. It is obvious that the spin density is strongly localized on the Ni_R atom on the ground triplet state (even with the tensile strains). For the purpose of experimental implementation, the initial and final states should be as low as possible in energy, under the prerequisite of its realizability, the $|\downarrow\rangle$ (spin-down) and $|\uparrow\rangle$ (spin-up) states stem from the ground triplet state are chosen as the initial and final states for spin-flip processes. Therefore, the spin-flip processes we mentioned here are actually localized on Ni_R.

Fig. 2 shows the population transfer between the initial and final states via some intermediated states for the ultrafast spin-flip processes achieved on the distorted Ni_2&GNF structures with altering the C-Ni bond length. It is shown that the spin dynamics at the distorted structures can be strongly influenced with the tensile strain along the C-Ni bond. It is obvious that the manipulation scenarios of the two strain types are not identical. For the L-type strain, when 5.0% tensile strain is applied, the fidelity decreases to 81.4%, while the populations of final state under 2.5% and 7.5% strains

*Corresponding author. E-mail: lichun@nwpu.edu.cn

are 98.0% and 96.2%, respectively, indicating that the increasing L-type strain can strongly influence the local spin-flip processes. As for the R-type strain [Figs. 2(d-f)], one can see that the spin-flip processes do not change much with the increasing R-type strain. With the R-type strain increasing from 2.5% to 7.5%, the fidelity increase from 96.1% to 97.7%, while the Rabi oscillation cycles, the number and the occupation of involved intermediate states stay as is. Briefly, L-type strain strongly influences the local spin-flip process on Ni_R atom, while the R-type strain, which is directly applied on the Ni_R atom, seems having no obvious effect. Such phenomenon demonstrates a remote-controlled spin-flip process, which indicates that we can remotely controll the spin information by applying the tensile strain or external field to manipulate the local geometry and electronic properties of the system.

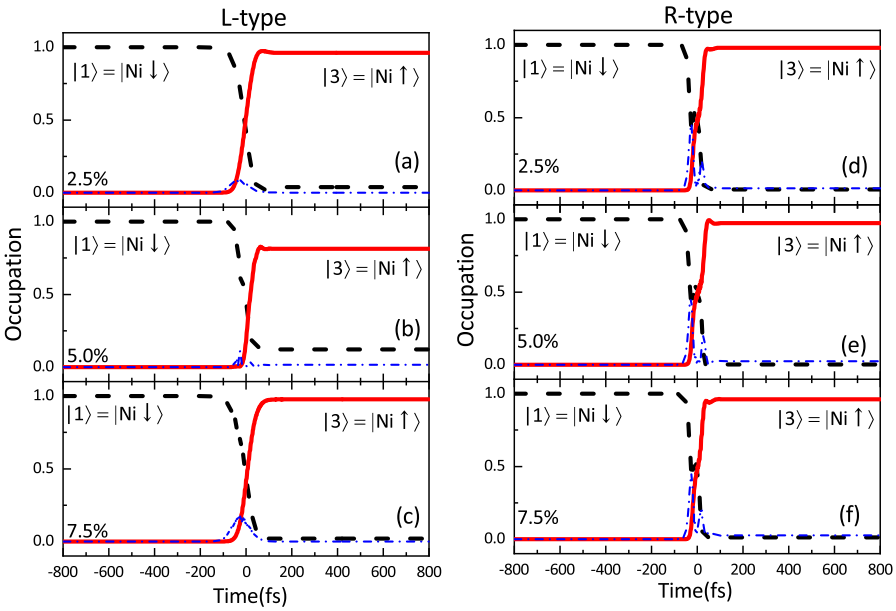

Figure 2: Spin-flip processes achieved in the distorted Ni_2&GNF structures with L-type (left panel) and R-type (right panel) strains, respectively. Time evolutions of the occupations of the initial (dashed black), final (solid red), and intermediate (dash-dotted) states for each spin-flip process are exhibited. Within each panel, the situations for 2.5%, 5.0%, and 7.5% tensile strains along the corresponding C-Ni bond are shown, respectively.

CONCLUSIONS

In summary, the laser-induced ultrafast spin flip on the Ni_2&GNF is investigated using Λ-process-based theoretical model and *ab initio* calculations. In Ni_2&GNF structures, the spin flip process can be modulated by the local strain along the C-Ni bond, and the increasing L-type strain can strongly influence the local spin-flip processes. Since the spin is localized on the right Ni atom, when the tensile strain along the right C-Ni bond is applied, the spin-flip processes do not change much with the increasing strain, however, the L-type (strain along the left C-Ni bond) strain strongly influences the local spin-flip process on Ni_R atom. This phenomenon indicates a remote controlled spin-flip process. Our results reveal the great potential of using the synergistic effect of strain, magnetic field, and laser pulse for active spin control, which could lead to more flexibility for romote spin control and hence functionalization in future carbon-based spintronic devices.

References

[1] Liu J., Zhang Y. M., Li C., Jin W., Lefkidis G., Hübner W. Magneto-straintronics on a Co-coordinating metalloboronfullerene. *Phys. Rev. B* **102** 024416, 2020.

[2] Li C., Liu J., Lefkidis G., Hübner W. Reversible ultrafast spin switching on Ni@B_{80} endohedral fullerene. *Phys. Chem. Chem. Phys.* **19**: 673-680, 2017

[3] Li C., Liu J., Zhang S. B., Lefkidis G., Hübner W. Strain assisted ultrafast spin switching on Co_2@C_{60} endohedral fullerenes. *Carbon* **87**: 153-162, 2015

[4] Li C., Zhang S. B., Jin W., Lefkidis G., Hübner W. Controllable spin-dynamics cycles and ERASE functionality on quasilinear molecular ions. *Phys. Rev. B* **87**: 184404, 2014

K107622 - SM13 - Plasticity, Viscoplasticity and Creep - Keynote

VARIATIONAL PROBLEMS IN PLASTICITY AND BRITTLE FRACTURE OF HETEROGENEOUS MATERIALS

Pierre Suquet*[1] and Jean-Claude Michel[1]
[1]LMA, Aix Marseille Univ, CNRS, Centrale Marseille, Marseille, France

Summary Homogenization results for limit load problems are recalled first. In anti-plane situations the resulting variational principle reduces to finding a minimal cut. This observation makes the link with Schneider's definition of the effective fracture energy of heterogeneous materials. It allows us to use, in the context of brittle materials, the same analytical and computational tools developed to determine the extremal surfaces of ideally plastic heterogeneous materials.

LIMIT LOADS AND MAXIMAL FLOWS

Consider a solid body Ω subjected to body forces $\lambda \boldsymbol{f}$ and surface tractions $\lambda \boldsymbol{F}$ on a part $\partial\Omega_F$ of its boundary, proportional to a load parameter λ,

$$\mathrm{div}\boldsymbol{\sigma} + \lambda \boldsymbol{f} = \boldsymbol{0} \quad \text{in } \Omega, \quad \boldsymbol{\sigma}.\boldsymbol{n} = \lambda \boldsymbol{F} \text{ on } \partial\Omega_F. \tag{1}$$

The body is comprised of a material, possibly heterogeneous, with a limited strength characterized by a *strength* domain $P(\boldsymbol{x})$ (convex set containing $\boldsymbol{0}$ in its interior)

$$\boldsymbol{\sigma}(\boldsymbol{x}) \in P(\boldsymbol{x}) \quad \text{in } \Omega. \tag{2}$$

The limit load is the maximal value of λ for which the two requirements (1) and (2) are compatible. In the above formulation, $\boldsymbol{\sigma}$ is a field of second-order symmetric tensors. Strang [11] noticed that the same formulation applies to the problem of maximal flow through a domain, $\boldsymbol{\sigma}$ being in that case a vector field.

This *static* definition of the limit load (in term of stress fields) admits an equivalent mixed formulation (saddle-point property) and a kinematic formulation (minimum principle)

$$\overline{\lambda} = \sup_{\lambda} \{\exists\, \boldsymbol{\sigma} \text{ satisfying (1) and (2)}\} = \inf_{\boldsymbol{u}} \sup_{\boldsymbol{\sigma} \in P} \frac{\int_\Omega \boldsymbol{\sigma} : \boldsymbol{\nabla u}\, d\boldsymbol{x}}{\int_\Omega \boldsymbol{f}.\boldsymbol{u}\, d\boldsymbol{x} + \int_{\partial\Omega_F} \boldsymbol{F}.\boldsymbol{u}\, ds} = \inf_{\boldsymbol{u}} \frac{\int_\Omega \pi(\boldsymbol{\nabla u})\, d\boldsymbol{x}}{L(\boldsymbol{u})}, \tag{3}$$

with

$$\pi(\boldsymbol{x}, \boldsymbol{e}) = \sup_{\boldsymbol{\sigma} \in P(\boldsymbol{x})} \boldsymbol{\sigma} : \boldsymbol{e}, \quad L(\boldsymbol{u}) = \int_\Omega \boldsymbol{f}.\boldsymbol{u}\, d\boldsymbol{x} + \int_{\partial\Omega_F} \boldsymbol{F}.\boldsymbol{u}\, ds. \tag{4}$$

In the limit load problem $\boldsymbol{u}$ is a vector field, $\boldsymbol{\nabla u}$ is the symmetric part of the gradient of $\boldsymbol{u}$. In the maximal flow problem u is a scalar field and $\boldsymbol{\nabla} u$ is the usual gradient of u. Although limit load analysis is often associated in the literature with plasticity, there is no such restriction in the above formulation which therefore applies to a wide variety of materials, ranging from brittle materials to ideally plastic ones (Salençon [9]). It is therefore not surprising that plasticity and brittle fracture bear common features.

Appropriate numerical schemes have been developed to solve the limit load problem (3) using the static, kinematic or saddle-point formulation (Christiansen [3] among others).

HETEROGENEOUS MEDIA.

Consider now that the body under consideration is highly heterogeneous, characterized by a small parameter ε measuring the size of the heterogeneities. For simplicity only the periodic case will be considered here. Bouchitté and Suquet [1] have shown that the limit as $\varepsilon \to 0$ of the limit load problem is again a limit load problem with two significant differences with respect to the usual homogenization results for convex energies with sufficient growth (here the function π is convex but has only linear growth):

$$\overline{\lambda} = \lim_{\varepsilon \to 0} \lambda^\varepsilon = \mathrm{Sup}\{\lambda \text{ such that } \exists\, \boldsymbol{\Sigma} \text{ satisfying (1)}, \ \boldsymbol{\Sigma} \in P^{hom} \text{ in } \Omega, \ \boldsymbol{\Sigma}.\boldsymbol{n} \in C^{hom} \text{ on } \partial\Omega_F\}, \tag{5}$$

where the homogenized stress domain C^{hom} on the boundary is not directly deduced from the strength domain P^{hom} in the bulk of the body. The discrepancy between the behavior in bulk and on the boundary is uncommon in homogenization.[1]

*Corresponding author. E-mail: suquet@lma.cnrs-mrs.fr

[1]The other noticeable difference, uncommon in homogenization, is that all boundary conditions on the boundary of the volume element are not equivalent in the limit of a large volume element. The periodicity conditions and prescribed affine displacement conditions lead to the same homogenized properties in the limit, but not the conditions of uniform stress on the boundary.

Concentrating on the bulk behavior, the homogenized strength domain is determined by solving a limit load problem on a unit-cell Q,

$$P^{hom} = \{\boldsymbol{\Sigma} \text{ such that } \exists\, \boldsymbol{\sigma},\ \text{such that } \langle \boldsymbol{\sigma} \rangle = \boldsymbol{\Sigma},\ \text{div}\boldsymbol{\sigma} = \mathbf{0} \text{ and } \boldsymbol{\sigma}(\boldsymbol{x}) \in P(\boldsymbol{x}) \text{ in } Q,\ + \text{periodicity conditions}\}, \quad (6)$$

where $\langle . \rangle$ stands for the volume average over a unit-cell (or volume element) V. By duality $P^{hom} = \{\boldsymbol{\Sigma} \text{ such that } \boldsymbol{\Sigma} : \boldsymbol{E} \leq \Pi^{hom}(\boldsymbol{E}) \text{ for all } \boldsymbol{E}\}$, where

$$\Pi^{hom}(\boldsymbol{E}) = \text{Inf} \quad \langle \pi(\boldsymbol{\nabla u}) \rangle, \quad \boldsymbol{u} = \boldsymbol{E}.\boldsymbol{x} + \boldsymbol{u}^*,\ \boldsymbol{u}^* \text{ periodic}. \quad (7)$$

Anti-plane problem. Consider now a unit-cell problem where both the geometry and the material properties are invariant along the direction $\boldsymbol{e}_3$ subjected to anti-plane shear along the directions $(1,3)$ and $(2,3)$. The strength domain$P(\boldsymbol{x})$ is defined by a von Mises criterion $\sigma_{\text{eq}} \leq \sigma_0(\boldsymbol{x})$. Then the variational problem (7) reduces to

$$\text{Inf } \langle \sigma_0 \, |\boldsymbol{\nabla} u| \rangle, \quad u = \boldsymbol{E}.\boldsymbol{x} + u^*,\ u^* \text{ periodic}, \quad (8)$$

where $u(x_1, x_2)$ is now a scalar field (component of the displacement field along $\boldsymbol{e}_3$), $\boldsymbol{E}$ is a vector with 2 components and $\langle . \rangle$ is the average over any cross section of the cylindrical unit-cell. Functions of bounded variation are admissible fields in the variational problem (8). Strang [11, 12] has shown in a similar, but different, problem that the solutions of his similar variational problem are characteristic functions (his problem involves a constraint on $\langle u \rangle$ instead of a constraint on $\langle \boldsymbol{\nabla} u \rangle$). Assuming that the same property holds true in the present problem, (8) is equivalent to the *minimal cut* problem:

$$\text{Inf} \int_S \sigma_0(\boldsymbol{x})\, ds, \quad S \subset V, \int_S \boldsymbol{n}\, ds = \boldsymbol{E}. \quad (9)$$

LINK WITH SCHNEIDER'S DEFINITION OF FRACTURE ENERGY OF BRITTLE MATERIALS [10]

Extrapolating a mathematical homogenization result of Braides *et al* [2], Schneider [10] suggested that the energy required to fracture a volume element of a heterogeneous brittle material is given in any dimension ($N = 2$ or 3) by the variational problem (9). How this definition is related to the *effective toughness* of Roux and Hild [8] or Hossain *et al* [4] remains to be clarified (it is probably only relevant in the weak pinning regime of [8]). Then, again at the expense of extrapolating Strang's result, this effective surface energy can be determined by solving the variational problem (8).

In this framework, it is therefore clear that the effective fracture energy can be determined by the very same computational schemes used to determine the effective strength domain (or extremal surface [13]) of an ideally plastic material, or more generally of materials with limited strength. Different algorithms can be used to that end, in particular those developed a number of years ago by Michel *et al* [5, 6]. Similarly, analytical upper bounds from this fracture energy can be deduced either from direct investigation of minimal surfaces through (9) (see for instance Willot [14]) or from nonlinear homogenization techniques based on linear comparison composites (Ponte Castañeda and Suquet [7]).

References

[1] G. Bouchitte and P. Suquet. Homogenization, Plasticity and Yield design. In G. Dal Maso and G.F. Dell'Antonio, editors, *Composite Media and Homogenization Theory*, pages 107–133. Birkhaüser, Boston, 1991.
[2] A. Braides, A. Defranceschi, and E. Vitali. Homogenization of free discontinuity problems. *Arch. Rational Mech. Anal.*, **135**:297–356, 1996.
[3] E. Christiansen. Computations of limit loads. *International Journal for Numerical Methods in Engineering*, **17**:1547–1570, 1981.
[4] M.Z. Hossain, C.-J. Hsueh, B. Bourdin, and K. Bhattacharya. Effective toughness of heterogeneous media. *Journal of the Mechanics and Physics of Solids*, 71:15 – 32, 2014.
[5] J.C. Michel, H. Moulinec, and P. Suquet. Effective properties of composite materials with periodic microstructure: a computational approach. *Comp. Meth. Appl. Mech. Engng.*, **172**:109–143, 1999.
[6] JC. Michel, H. Moulinec, and P. Suquet. A computational scheme for linear and non-linear composites with arbitrary phase contrast. *Int. J. Numer. Meth. Engng*, **52**:139–160, 2001.
[7] P. Ponte Castañeda and P. Suquet. Nonlinear composites. In E. Van der Giessen and T.Y. Wu, editors, *Advances in Applied Mechanics*, volume **34**, pages 171–302. Academic Press, New York, 1997.
[8] S. Roux, D. Vandembroucq, and F. Hild. Effective toughness of heterogeneous brittle materials. *European Journal of Mechanics - A/Solids*, **22**:743–749, 2005.
[9] J. Salençon. *Yield Design*. ISTE. John Wiley, 2013.
[10] M. Schneider. An FFT-based method for computing weighted minimal surfaces in microstructures with applications to the computational homogenization of brittle fracture. *International Journal for Numerical Methods in Engineering*, 2019. https://onlinelibrary.wiley.com/doi/abs/10.1002/nme.6270.
[11] G. Strang. Maximal flow through a domain. *Mathematical Programming*, **26**:123–143, 1983.
[12] G. Strang. Maximum flows and minimum cuts in the plane. *Journal of Global Optimization*, **47**:527–535, 2010.
[13] P. Suquet. Overall potentials and extremal surfaces of power law or ideally plastic materials. *J. Mech. Phys. Solids*, **41**:981–1002, 1993.
[14] F. Willot. The power laws of geodesics in some random sets with dilute concentration of inclusions. In J.A. Benediktsson, J. Chanussot, L. Najman, and H. Talbot, editors, *Mathematical Morphology and Its Applications to Signal and Image Processing*, Lecture Notes in Computer Science, pages 535–546. Springer Verlag, New York, 2015.

DUCTILE FAILURE MECHANISMS IN PURE METALS AND ALLOYS

Jianing Xie[1], Kyuminl Eom[1], and Krishnaswamy Ravi-Chandar*[1]
[1]Department of Aerospace Engineering and Engineering Mechanics, University of Texas, Austin, USA

Summary Ductile failure in structural materials has been a problem of longstanding interest, both from the fundamental scientific and applied technological perspectives. While different failure models – ranging from phenomenological to computational models to mechanism based micromechanical models – have been proposed and used, there is still an active debate concerning the predictive capabilities of these models. In this work, we describe the results of a multiscale, multimodal experiments utilizing interrupted testing protocol, quantitative optical and scanning electron microscopy, and x-ray tomography to identify and quantify the deformation and failure mechanisms that are at the root of ductile behaviour in both high purity metals and in engineered alloys. This investigation reveals that very large deformations occur without observable damage at scales above about one micron and above.

INTRODUCTION

Modeling of the inelastic response of metallic materials, such as the commercial alloy Al 6061-T6, is of significant interest in numerous applications in the aerospace, automobile, and naval industries. These models must encompass the early stages of deformation as well as the later stages leading up to failure. Typical models are based on phenomenological descriptions of the constitutive response during the early stages of deformation, and on micromechanical models of damage nucleation and growth (such as the Gurson model) during the later stages that generate softening of the material response triggered by the damage. Calibration of these models is typically based on measurements of the macroscopic response of the material and is an inherently non-unique process. While there are numerous investigations that implement such models in simulations, there are very few investigations that provide an experimental evaluation, both of the calibration of the models and of their use in predicting the deformation and failure in structural applications. In this work we seek to determine the mechanisms relating to the deformation and failure of pure metals as well as alloys that include second phase particles as impurities through a multiscale, multimodal investigation prior to engaging in the selection and calibration of models of the deformation and failure behavior. Interrupted testing protocol is used for macroscale observations and x-ray tomography, and *in situ* loading in a scanning electron microscope are used for continuous and noninvasive monitoring of surface deformation and interior damage. The presence of mechanisms leading to material softening become apparent with these observations, as well as the strain range over which such mechanisms initiate and evolve.

MATERIALS AND METHODS

Oxygen-free high-conductivity (OHFC) copper, pure tantalum, Al 6061-O and Al 6061-T6 are used as examples of high purity metals, materials with different strain hardening characteristics, and materials with second phase particles, spanning a range of fcc and bcc metals. Tests were performed under uniaxial tension, pure shear, and compact tension geometries to explore a range of macroscopic states of stress or constraint. Thus, nominal triaxialities in the range of zero to about three can be explored in these tests; it should be noted that the triaxiality is a local field and could only be estimated through a proper calculation of the stress field through finite element analysis of the nonhomogeneous deformation fields. Two types of interrupted tests were performed. In the first type, the test was halted at specific points along the loading path, and the specimen was the examined in an x-ray tomography system to identify and characterize potential interior damage in the form of voids or cracks at a spatial resolution of about 5 microns. The specimens were then returned to the test machine and subjected to further loading along the original load path and subjected to further x-ray tomographic inspection at selected deformation levels until final failure. In the second type of tests, the specimen recovered at a specific deformation level was sectioned across the thickness and polished for metallographic inspection; these images of the grain structure were used to identify the local strain levels using the procedure indicated in Ghahremaninezhad and Ravi-Chandar [1]. This metallographic inspection permits the observation of damage as well, but with a lower resolution than the x-ray tomography. Interpretation of the experimental observations in terms of constitutive model and damage evolution requires an inverse modeling approach that couples the experiments with finite element simulations. The simulations were performed in a hybrid experimental-computational procedure using MATLAB optimization tools and ABAQUS finite element software for modeling the response of the specimen.

RESULTS

Two different mechanisms of failure are observed in the different materials considered in this work. In the polycrystalline alloys that include a dispersion of second phase particles, we confirm through a combination of microscopy and x-ray tomography, that such particles act as nucleation sites for eventual failure [2]. The progression of these nuclei into a collection of growing and coalescing voids is traced to explore how such growth leads to a localization of the damage over a spatial extent of only about 10 microns (see Figure 1). In polycrystalline materials of high purity

* Corresponding author: ravi@utexas.edu

such as the OHFC copper [4] and pure tantalum [5], the absence of such second phase impurities deprives the material of the mechanism of void nucleation to evolve towards failure; in this case, failure occurs predominantly by the alternating slip mechanism identified for single crystals by Orowan [6] and in polycrystals by Ghahremaninezhad and Ravi-Chandar [3]. Secondary damage in the form of voids at the grain boundaries is also observed [4]. These results indicate that plastic flow is the failure mechanism!

The implication of these observations is that all deformation mechanisms (and damage processes, if any) occur at length scales smaller than a micron, and could/should be captured through a homogenized model, embedded in the stress-strain relation. The experiments also indicate that a robust strain-based failure criterion for the onset of fracture could be quite efficient in modelling ductile failure. The presentation will demonstrate such modeling through a hybrid experimental-computational procedure for constitutive and damage modeling.

Figure 1. X-ray absorption image of an aluminium alloy specimen indicating the localization of damage into an interior microcrack.

CONCLUSIONS

The onset of deformation and damage mechanisms is examined in two high purity metals OFHC copper and tantalum, and in two structural alloys Al-6061-O and Al 6061-T6. Interrupted and in situ tests were performed to assess the evolution of damage under conditions of different triaxiality. Muliscale, multimodal evaluation of damage was assessed using optical and scanning electron microscopy in the destructive tests and x-ray tomography for non-destructive assessment of the geometry of damage. Two different mechanisms of damage – void nucleation, growth and coalescence as well as alternating slip mechanism – were identified in materials with second phase particles and pure metals, respectively. Calibration of a constitutive model and a strain-based failure model based on these measurements of the local strain levels is shown to be an effective way to model ductile failure.

Acknowledgements
This work was funded by the US National Science Foundation through grant #171035. This support is gratefully acknowledged.

References

[1] Ghahremaninezhad A, Ravi-Chandar K. *Int J. Frac.* **174**: 177-202, 2012.
[2] Xie J, Eom K, Ravi-Chandar K, X-ray tomographic evaluation of failure in aluminium alloys, in preparation, 2020.
[3] Ghahremaninezhad A, Ravi-Chandar K. *Int J. Solids and Struct.* **48**: 3299-3311, 2011.
[4] Xie J, Eom K, Ravi-Chandar K, X-ray tomographic evaluation of failure in high purity OFHC copper, in preparation, 2020.
[5] Xie J, Eom K, Ravi-Chandar K, Evaluation of failure through slip in pure tantalum, in preparation, 2020.
[6] Orowan E. *Report on Progress in Physics*, **12**:185–232, 1948.

HOW IS DUCTILITY ACHIEVED IN MG ALLOYS ?

W. A. Curtin[1], Rasool Ahmad[1], Binglun Yin[1], and Zhaoxuan Wu[2]
[1]Institute of Mechanical Engineering, EPFL, Lausanne Switzerland
[2]Department of Materials Science and Engineering, City University of Hong Kong,Hong Kong,China

Summary The ductility of an alloy is usually determined at the continuum level with phenomenological flow and hardening rules. Pure Mg has a very low ductility yet certain dilute solid-solution alloys can have much larger ductility, making such alloys suitable for structural applications. Here, the mechanism of low-ductility in pure Mg is first identified, a mechanism for enhancing ductility by changing the fundamental behaviour of dislocations in the hcp metal is then proposed, and the dependence of operation of the mechanism on solute type is determined. The theory, using inputs from first principles, then predicts solutes and concentrations necessary for high ductility, and good agreement is found for essentially all alloys studied to date. The theory is then used to identify entirely new multi-component alloy compositions that are predicted to be ductile and do not involve the Rare-Earth Elements (Y, Ce, Nd, Gd, …) that are most frequently found to enhance ductility. This work highlights the role of sub-continuum level modelling that is essential in guiding design of new alloys.

BACKGROUND

For accurate modeling of polycrystalline metals, it is essential to understand the dislocation-based mechanisms that control the plastic flow on the different slip systems in metal alloys. Current approaches fit standard crystal plasticity models to experimental data [1]. Such models implicitly assumes that all plasticity occurs by normal glide and hardening mechanisms, and addresses only differences in crystallographic slip systems. Such approaches may thus misrepresent the underlying dislocation phenomena that operate in a given material. Crystal plasticity parameters can be fit to experimental data on any given alloy, but provide no insight into how to change the material to achieve different, and improved, performance.

Pure Mg is a hexagonally-close-packed metal with a number of different slip systems having different critical Burgers vectors and different stresses for activation (basal (<a>, prismatic <a>, pyramidal I and II <c+a>), where a and c are the lattice vectors for the hcp structure and <...> indicates the Burgers vector. Pure Mg has a very high hardening rate and low ductility (a few %). This has now been identified as mainly due to a thermodynamically favorable transition of the <c+a> pyramidal II dislocations to an immobile structure that is dissociated on the basal plane [2] (Fig. 1a). This behavior is typically represented indirectly in crystal plasticity by using a high critical resolved shear stress for <c+a> slip, and does not reflect the underlying dislocation process. Alloying generally improves ductility considerably; for instance, Mg-1at%RE (RE=Y, Tb, Dy, Ho, Er) alloys show high ductility (20-30%) [3], as compared to most commercial Mg-Al-Zn alloys at similar grain size. Again, crystal plasticity can be fit to the measured behavior, but the mechanisms that change the material from low-ductility to high-ductility at alloying levels as low as 0.03% for Ce, are not identified. Prevailing concepts for ductility in alloys include the reduction of plastic anisotropy due to solute strengthening, the nucleation of <c+a> from basal I1 stacking faults, the prevention of the detrimental <c+a> transformation to sessile structures, and the weakening of strong basal texture by some solute/particle mechanisms. Experiments and modeling do not strongly support any of these concepts, however. Thus, the achievement of high ductility in Mg alloys relies on some new phenomenon.

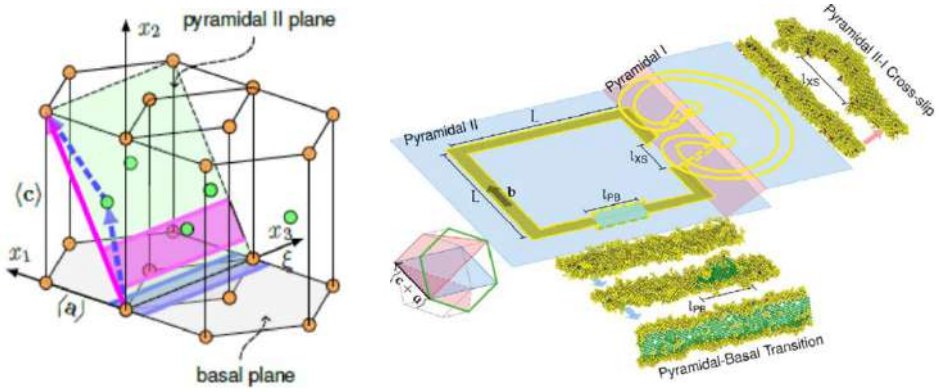

Figure 1. (a) Schematic of the hcp lattice showing the Pyramidal II plane in green, the Burgers vector for the Pyr. II <c+a> dislocation (pink arrow), the easy-glide dissociated Pyr. II <c+a> edge dislocation lying on the Pyr. II plane (pink), and the lower-energy basal-dissociated Pyr. II <c+a> edge dislocation (purple). (b) Schematic of the two competing processes: the undesireable Pyramidal to Basal transition along Pyr. II <c+a> edge segments and the desirable cross-slip of the Pyr. II <c+a> screw segments onto the (higher energy) Pyr. I plane followed by cross-slip back on to the Pyr. II plane, leading to isolation of the Pyr. II edge segments and multiplication of Pyr. II <c+a> dislocations; from Ref. 4, reprinted with permission from AAAS.

DUCTILITY IN Mg ALLOYS

We have recently introduced a new mechanism for achieving high ductility in Mg alloys [4]. The mechanism is that of pyramidal cross-slip of dislocations from the lower-energy Pyr. II plane to the higher energy Pyr. I plane (Fig. 1b). This process accelerates pyramidal dislocation multiplication and limits the undesirable transition of the Pyr. II dislocation to an immobile dislocation, enabling dislocation motion of the mobile pyramidal dislocations, and associated plastic strain. This process essentially turns Mg into a more-normal metal with sufficiently easy slip and multiplication on at least 5 slip systems as required for global plastic strain. The process does not operate effectively in pure Mg because the energy barrier for the cross-slip is much larger than that for the transition to the immobile structure. The process only becomes operative if its rate can sufficiently exceed the rate of the undesirable transition, which requires a reduction of the energy barrier for the cross-slip.

An analytical theory for the cross-slip energy barrier was developed [4]. The dominant role of the solutes was postulated to be in changing the Pyramidal I and II stacking fault energies, which then changes the relative energies of the Pyr. I and II dislocations. Solutes that reduce this energy difference will reduce the barrier and facilitate cross-slip. First-principles calculations reveal that the Rare Earth Elements are by far the most effective in reducing the cross-slip barrier, and hence are predicted to enhance ductility at low concentrations. The particular role of Ce is identified, with the model predictions showing ductility being achievable at the low Ce concentrations observed in experiments. Equally important is the finding that several other solutes, particularly Ca, Mn, and K, can be effective for enabling high ductility while the common solutes Al and Zn are unable to reduce the barrier sufficiently to achieve the ductility condition.

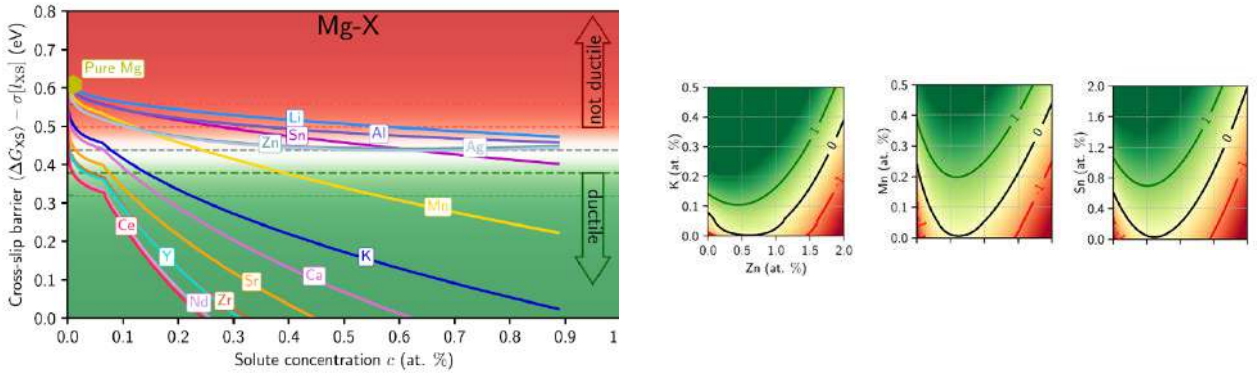

Figure 2. (a) Cross-slip barrier (predicted) as a function of solute type and concentration for binary Mg alloys. Ductility is predicted if the cross-slip barrier falls below ~0.38 (indicated by the heavy dashed green line). The Rare Earth solutes, Ca, K, Mn, and Zr can ductilize Mg at very low concentrations (<0.3%) whereas the common alloying elements Zn and Al cannot reach the necessary condition at any concentration. (b) Example predictions of ductility for ternary Mg-Zn-X alloys (X=K, Mn, Sn), where green shading indicates the ductile regime of compositions. The theory predicts that, while Zn is unfavorably in general, an addition of 0.5at% enables ductility in multicomponent alloys at lower concentration of the third element X. Zn at 0.5% is commonly used in existing alloys. Adapted from Ref. 5 with Permission of Elsevier.

The theory has been extended to multiple dilute solutes, e.g. ternary Mg-X-Y and quarternary Mg-X-Y-Z alloys, enabling validation of other experimental trends (Fig. 2b). In particular, ductility can be achieved at very low levels of K, Mn, and Sn with a small addition of ~0.5% Zn. The ductility of other alloys, especially Al-Ca-Mn alloys recently studied, is predicted in good agreement with experiments. Extensive details of the model and applications, and further predictions on a wide range of ternary and quarternary alloys without Rare Earth elements can be found in Ref. 5.

CONCLUSIONS

Achieving ductility in Mg involves the study of dislocation-level phenomena at scales well below typical continuum level models for polycrystalline alloys. Attaining quantitative results then requires modelling at the level of first-principles to determine the role of specific alloy chemistry in controlling the dislocation-scale phenomena. The ductility in Mg alloys is, furthermore, related to rate-dependent thermally-activated processes, that requires additional understanding of the energy barriers for the relevant processes. This example demonstrates the importance of sub-continuum modelling to drive the design of new alloys with desired plastic flow properties.

References

[1] V. Herrera-Solaz, J. Segurado and J. LLorca, Eur. J. Mech. – A/Solids ***53****, 220-228 (2015).*
[2] Z. Wu and W.A. Curtin, Nature ***526****, 62-67 (2015).*
[3] S. Sandlobes, et al., Acta Mater. ***59****, 429-439 (2011);* ***70****, 92–104 (2014).*
[4] Z. Wu, R. Ahmad, B. Yin, S. Sandlobes, and W. A. Curtin, Science ***359****, 447-452 (2018).*
[5] R. Ahmad, B. Yin, Z. X. Wu, and W. A. Curtin, Acta Materialia 172, 161-184 (2019).

PREDICTING THE VISCOPLASTIC BEHAVIOUR OF GLASSY POLYMERS VIA SHEAR TRANSFORMATION ZONE DYNAMICS

Frederik Van Loock[1], Jérémy Chevalier[2], Laurence Brassart[3], and Thomas Pardoen[1]
[1]Institute of Mechanics, Materials and Civil Engineering (iMMC), UCLouvain, Place Sainte Barbe 2, Louvain-la-Neuve 1348, Belgium
[2]Solvay, Rue de Ransbeek 310, Neder-Over-Heembeek 1120, Belgium
[3]Department of Engineering Science, University of Oxford, Parks Road, Oxford OX1 3PJ, United Kingdom

Summary The large deformation response of polymeric glasses is predicted by making use of shear transformation zone (STZ) theory. The STZ model requires the calibration of only five parameters to predict the complete uniaxial stress-strain response of glassy polymers, including the yield, softening, and hardening regime. Due to the simulated heterogeneous nature of the inelastic deformation, the framework also provides insight into the origin of micro shear band formation and of macroscopically observed phenomena such as non-linear unloading behaviour, Bauschinger and anisotropy effects, and rejuvenation/ageing evolutions. Future avenues involving the response of polymeric glasses at small and intermediate length scales are outlined.

INTRODUCTION

The deformation and failure behaviour of glassy polymers is complex. When deformed in uniaxial compression or tension at a temperature below the glass transition temperature, the measured stress-strain curve of a polymeric glass typically has, in the absence of failure, an initial linear, (visco-)elastic regime, followed by yield, strain softening, plastic flow, and strain hardening. In addition, the deformation response is sensitive to temperature and rate of deformation, physical ageing, and processing and/or deformation history. Other phenomena include pressure-dependent yield, the Bauschinger effect, and the Kohlrausch (or rate-reversal) effect upon unloading [1]. Sophisticated three-dimensional (visco)elastic-(visco)plastic continuum constitutive models have been developed to predict the large deformation response of glassy polymers [2-5]. Most of these frameworks are based on the one-dimensional constitutive model of Haward and Thackray [6], who decomposed the post-yield stress into a viscous intermolecular resistance and an entropic intramolecular resistance. These large deformation models generally give excellent fits to measured uniaxial stress-strain curves, but they rely on a large number of (often phenomenological) calibration parameters and do not allow the prediction of the inherently heterogeneous nature of inelastic deformation which is thought to be responsible for more complex phenomena such as the non-linear unloading behaviour and the Bauschinger effect. Molecular dynamics (MD) simulations have been used to elucidate the discrete molecular deformation mechanisms leading to the heterogeneous inelastic behaviour of polymeric glasses. The results of MD calculations suggest that plastic deformation of polymeric glasses is caused by thermally activated molecular rearrangements and conformational changes of a collection of polymer chains parts. Given the inherent restrictions in time and length scale of atomistic simulations, the practical use of MD methods is however limited when attempting to predict intermediate scale deformation phenomena such as micron-sized shear bands which may be observed in thin adhesive joints or fibre-reinforced polymer (FRP) composites.

The use of a mesoscale numerical model based on shear transformation zone (STZs) dynamics offers a practical avenue to bridge the state-of-the-art continuum and atomistic simulation approaches. The STZ framework was originally developed by Argon [7] to predict the deformation behaviour of metallic glasses. We have used the implementation by Homer and Schuh [8] of Argon's theory to develop a mesoscale finite element model for polymeric glasses. A first version of the model was presented by Chevalier *et al*. [1]. The scope of this contribution is twofold. We first discuss the effect of some modifications of the framework. In addition, we explore the use of the model when predicting the viscoplastic response of polymeric glasses in more complex loading scenarios and at small length scales. The paper is structured as follows. We first summarise the key ingredients of the STZ framework. Then, we briefly outline the implementation in Abaqus and the calibration of the finite element model to experimental results. We conclude by identifying some cases of interest for future work.

THE STZ FRAMEWORK

It is assumed that the elementary deformation mechanism giving rise to macroscopic plastic deformation in a polymeric glass is a pure shear deformation of an STZ. This STZ may correspond to part of a molecular chain or an assembly of such chain parts. Although we do not need to detail the nature of the collection of molecular changes leading to the shear transformation, one may think of these as conformational molecular changes including slipping of chains, dihedral twists and flips of chain parts. Inelastic deformation is a result of transformation of STZs due to these conformational changes and the elastic interaction of these transformations with the surrounding matrix. Following Argon's theory, we assume that shear zone transformations are thermally-activated. The activation attempt rate is governed by the competition between the free Helmholtz energy barrier ΔF for deformation of the STZ and the available mechanical energy given the STZ's stress state. The magnitude of the energy barrier may be calculated via Eshelby's inclusion theory, it comprises: (1) the transformation strain due to constrained shearing of the

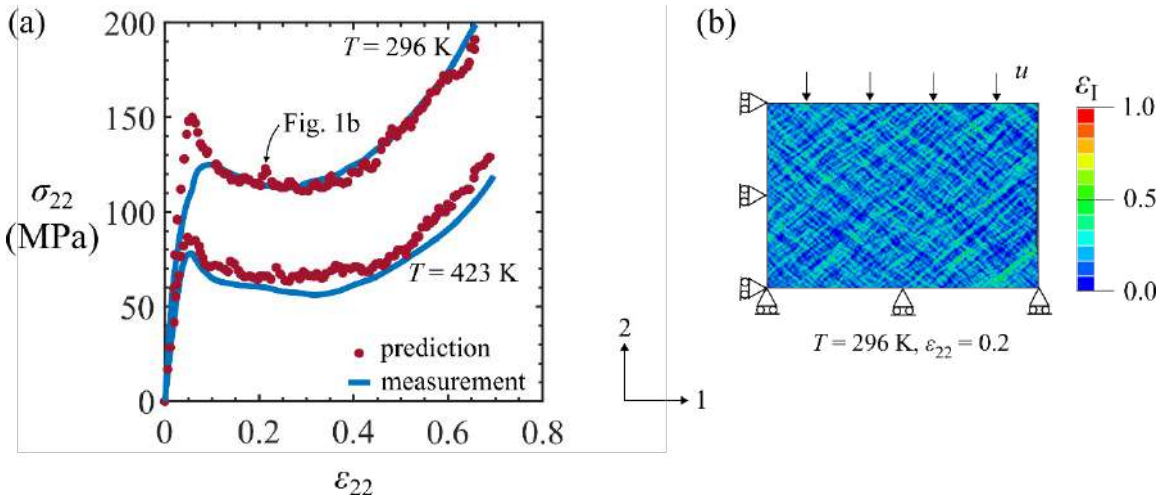

Figure 1. Predictions made by the STZ-based finite element model: (a) Calculated stress-strain versus measured stress-strain curves of an RTM6 epoxy in uniaxial compression at a strain rate equal to 10^{-2} s^{-1} at two testing temperatures. (b) Predicted maximum principal strain field for the $T = 296$ K response shown in (a) at $\varepsilon_{22} = 0.2$. Simulations are conducted for a square model geometry with boundary conditions shown in (b), details on the measurements are included in the work of Chevalier *et al*. [1].

STZ in the surrounding matrix, (2) the strain energy in the matrix and the inclusion due to the temporarily dilation of the STZ and (3) the intermolecular potential energy for shearing the STZ freely. The last two components are assumed to be sensitive to a local chain mobility parameter, which is a measure for the local excess energy for molecular conformational changes. A fourth energy component is added to the energy barrier to account for the finite extensibility of the polymer chains between the crosslinks; the energy contribution for stretching the STZ 'network' is computed by making use of a hyperelastic material model.

We have implemented the STZ framework in a commercial finite element (FE) software package (Abaqus) via a series of user subroutines. The glassy continuum is discretised by means of plane strain quadratic triangular elements. We assume that every element gives rise to one STZ, and that an STZ is comprised of this central element and its neighbouring (node-sharing) elements. Uniaxial compression tests were conducted on an RTM6 epoxy at different testing temperatures ($296\ \text{K} \leqslant T \leqslant 423\ \text{K}$) below the glass transition temperature at a true strain rate equal to 10^{-2} s^{-1}. The measured stress-strain curves for $T = 296$ K and $T = 423$ K are shown in Fig. 1a. The five fitting parameters of the FE model were calibrated to the measured strain-strain curves at different testing temperatures; the predicted response for $T = 296$ K and $T = 423$ K at a strain rate equal to 10^{-2} s^{-1} is included in Fig. 1a. The predicted curves are in good agreement with the measured ones. Interaction of individual STZ transformations at yield leads to the formation of shear bands. The nucleated shear bands start to propagate upon continued macroscopic deformation, resulting in the predicted softening response beyond the yield point. It is emphasised that the simulated heterogeneous stress and strain distributions in the deformed polymeric glass results in the prediction of anisotropic effects.

CONCLUDING REMARKS AND FUTURE AVENUES

The STZ model provides insight into the relation between the heterogeneous nature of viscoplastic flow in polymeric glasses and complex macroscopically observed deformation phenomena. In addition, it is anticipated to be a useful tool to study the deformation and failure of glassy polymers at intermediate length scales (in the order of 0.1 to 10 μm). Future work will therefore include (i) the use of the model to predict constrained plastic deformation at the crack tip in a thin adhesive joint, (ii) the use of the model to predict the stress (re)distribution in a polymer matrix close to a broken fibre in an FRP. More fundamental changes to the framework are also explored in order to predict the effect of physical ageing and mechanical rejuvenation on the viscoplastic response.

References

[1] Chevalier J, Brassart L, Lani F, Bailly C, Pardoen T, Morelle XP. Unveiling the nanoscale heterogeneity controlled deformation of thermosets. *J. Mech. Phys. Solids* **121**:432–446, 2018.
[2] Boyce M, Parks D, Argon A. Large inelastic deformation of glassy polymers. I: rate dependent constitutive model. *Mech.. Mater.* **7**:15–33, 1988.
[3] Buckley CP, Jones DC. Glass-rubber constitutive model for amorphous polymers near the glass transition. *Polymer (Guildf).* **36**:3301–3312, 1995.
[4] Klompen ETJ, Engels TAP, Govaert LE, Meijer HEH. Modeling of the postyield response of glassy polymers: Influence of thermomechanical history. *Macromolecules* **38**:6997–7008, 2005.
[5] Johnsen J, Clausen AH, Grytten F, Benallal A, Hopperstad OS. A thermo-elasto-viscoplastic constitutive model for polymers. *J. Mech. Phys. Solids* **124**:681–701, 2019.
[6] Haward RN, Thackray G. The use of a mathematical model to describe isothermal stress-strain curves in glassy thermoplastics. *Proc. R. Soc. A Math. Phys. Eng. Sci.* **302**:453–472, 1968.
[7] Argon AS, Shi LT. Development of visco-plastic deformation in metallic glasses. *Acta Metall,* **27**:47-58, 1983.
[8] Homer ER, Schuh CA. Mesoscale modeling of amorphous metals by shear transformation zone dynamics. *Acta Mater.* **57**: 2823–2833, 2009.

ENRICHED COMPUTATIONAL LIMIT ANALYSIS IMPLEMENTATION FOR LARGE-SCALE 3D TRUSS-FRAME STRUCTURES

Rosalba Ferrari[1], Giuseppe Cocchetti[2], and Egidio Rizzi *[1]
[1]Università degli studi di Bergamo,Dipartimento di Ingegneria e Scienze Applicate viale G. Marconi 5, I-24044 Dalmine (BG), Italy
[2]Politecnico di Milano, Dipartimento di Ingegneria Civile e Ambientale piazza L. da Vinci 32, I-20133 Milano, Italy

Summary The present short note compactly presents some new developments of recently proposed algorithms toward the computational Limit Analysis of 3D truss-frame structures. They concern the definition of the interaction yield domain in the space of the static generalized variables of the plastic joint, where localized plastic activations may take place. First results on a steel frame are presented, showing the enriched computational tools to reveal rather effective, toward structural optimization and form finding purposes.

Keywords: Computational Limit Analysis; evolutive elastoplastic response; kinematic (upper-bound) theorem; collapse load multiplier; plastic collapse mechanism; truss-frame structures; interaction domain.

INTRODUCTION

Two new algorithms of computational Limit Analysis (LA) have been recently proposed by the authors toward achieving an effective description of elastoplastic material non-linearity at the cross-section level, within large-scale 3D truss-frame structures [1-5]. The first LA algorithm is apt to trace a fully exact evolutive piece-wise linear elastoplastic response of the structure, up to plastic collapse, by reconstructing the true sequence of activation of made-available plastic joints (as a generalization of plastic hinges), within the true spirit of LA [1-2,4-5]. The second LA algorithm develops an independent kinematic iterative approach apt to directly determine the plastic collapse state, in terms of collapse load multiplier and plastic mechanism, based on the upper-bound theorem of LA [3,5].

The two LA algorithms are found to much effectively run and perform, even for computational models of quite a large size (for multi-storey reinforced concrete frames and a monumental historic bridge, in its structural parts or whole structure), by achieving good corresponding matches in terms of the estimate of the load-bearing capacity and of the collapse characteristics of the structure. Moreover, the kinematic algorithm displays a rather dramatic effective performance, as a "direct method" of LA, in truly precipitating from above onto the collapse load multiplier and in rapidly adjusting to the collapse mode, in very few iterations, by a considerable saving of computational time, with respect to the complete evolutive elastoplastic analysis, though of course without attempting to reconstruct the whole load-displacement response curve.

ENRICHED COMPUTATIONAL PROCEDURE

In the considered implementations, the algorithms so far adopted a simple boxed-form Rankine-type interaction domain in the space of the generalized static variables, to characterize the yield domain of the plastic cross-section joint. In the present work, the above-mentioned algorithms for the LA analysis of 3D truss-frame structures are enriched by dedicated additional computational features. In particular, the procedures are adapted to deal with more general forms of the yield domain of the plastic joint (see e.g. of the Orbison type), as a multi-facet linearized yield surface or by approximating the latter through appropriate ellipsoids, thus combining axial force and bending moments interaction (and possibly couple also other generalized variable internal actions), in this way further enlarging the potentialities of the LA algorithms, especially toward describing the response of truss-frames in practical terms and toward real application scenarios.

Specifically, in the present work focus is placed on the formulated kinematic approach [3,5], as it shall deserve a particular attention for its both straightforward implementation and elevated speed of convergence, being now enriched with computational features allowing for axial force and bending moment interaction. In particular, a six-story space frame adopted in [3] has been here re-considered as a benchmark case study, and preliminary analyses have been conducted so far by considering the yield domain of the plastic joint of the frame to be modelled through an ellipsoid.

NUMERICAL TESTS

As often assumed in elastoplastic frame analysis, in the considered implementation the permanent kinematic discontinuities in each beam element, commonly referred to as "generalized plastic strains", are assumed to be concentrated in so-called "plastic joints", located at the beam finite element edges. These consist of the axial and the transverse relative rotations, and the axial relative displacement for each joint, totalling to 8 plastic kinematic variables for each beam element. Accordingly, the internal actions activating the plastic strains at each plastic joint are axial force, torque and

*Corresponding author. E-mail: egidio.rizzi@unibg.it

two bending moments (shear effects are assumed to be negligible). The (hyper-)ellipsoid that defines the activation of the limit plastic behaviour is herein considered to be tangent to each couple of planes orthogonal to the axis of one static variable (i.e. it is considered to be strictly inscribed into a box describing a Rankine-type domain, as earlier considered in the references above, see Fig. 1(a)).

The considered six-story frame is depicted in Fig. 1(a). The structure is subjected to a uniform vertical floor pressure of 4.8 kN/m^2, leading to a uniform distributed load of 64.2 kN/m along the spandrel beams and of 128.4 kN/m along the central beams. Wind load is represented by horizontal forces of 26.7 kN acting in the y-direction at every beam-column joint of the front elevation. All loads are affected by common load multiplier μ_c. Material yield limits are taken as $\sigma_y = 250$ MPa and $\tau_y = \sigma_y/\sqrt{3} = 144.3$ MPa; the plastic section moduli for the determination of the yield limits defining the principal axes of the ellipsoid refer to the AISC structural steel shapes reported in Fig. 1(a) itself.

The obtained numerical results in terms of collapse load multiplier and associated collapse mechanism are reported in Fig. 1(b). Such results may be compared to those obtained by the same direct kinematic approach, by considering a Rankine-type boxed-form yield domain, actually leading to a higher though quite similar collapse load multiplier [3]. This shall mean that the considered interaction is not much activated, at least for the devised loading condition. The dramatic convergence curve on the collapse load multiplier is also plotted in Fig. 1(c), showing that few iterations are sufficient for the prediction of the collapse state.

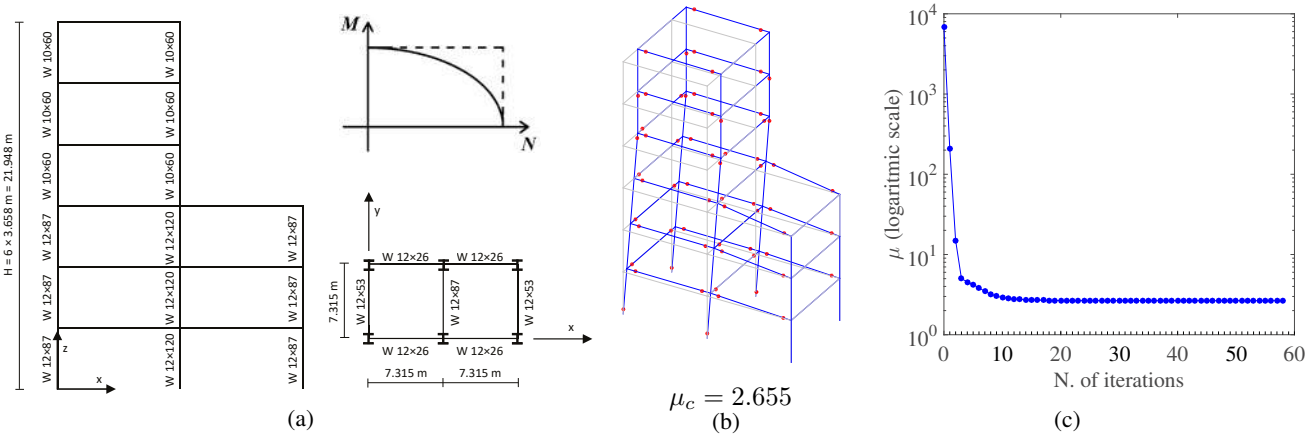

Figure 1: (a) six-story frame and N-M ellipsoidal interaction domain; (b) collapse mechanism and (c) relevant convergence curve.

Also in this case, the algorithm has confirmed to display a quick and easy convergence (Fig. 1(c)). In fact, it took just 58 iteration to get to the solution, demanding less that 1.5 s of computing time, thus showing a very similar computational performance as compared to that pointed out in [3], despite for the added complexity in the description of the yield domain. Moreover, only about 10 iterations are already enough to achieve a good estimate of the collapse load multiplier (Fig. 1(c)). The algorithm has been implemented and run as a non-compiled code within a MATLAB®environment, under a Windows 10 operating system, on a Dell laptop endowed with an Intel Core i7-6500U Processor, clock at 2.50 GHz and 16 GB RAM.

CONCLUSIONS

The present contribution shall much widen out the scopes of the present line of research and additionally open up the way for a further adoption of such advanced computational LA tools, with LA aiming at regaining a new momentum within modern and effective optimization analyses of structural design and form-finding problems.

References

[1] Ferrari R, Cocchetti G, Rizzi E (2016) Limit Analysis of a historical iron arch bridge. Formulation and computational implementation. *Computers and Structures*, 175(15 October 2016):184–196, doi: 10.1016/j.compstruc.2016.05.007.

[2] Ferrari R, Cocchetti G, Rizzi E (2017) Computational elastoplastic Limit Analysis of the Paderno d'Adda bridge (Italy, 1889). *Archives of Civil and Mechanical Engineering*, 18(1):291–310, doi:10.1016/j.acme.2017.05.002.

[3] Ferrari R, Cocchetti G, Rizzi E (2018) Effective iterative algorithm for the Limit Analysis of truss-frame structures by a kinematic approach. *Computers and Structures*, 197(15 February 2018):28–41, doi:10.1016/j.compstruc.2017.11.018.

[4] Ferrari R, Cocchetti G, Rizzi E (2019) Reference structural investigation on a 19th-century arch iron bridge loyal to design-stage conditions. *International Journal of Architectural Heritage*, Published online: 05 Jul 2019, doi.org/10.1080/15583058.2019.1613453.

[5] Ferrari R, Cocchetti G, Rizzi E (2019) Evolutive and kinematic Limit Analysis algorithms for large-scale 3D truss-frame structures: comparison application to historic iron bridge arch. *International Journal of Computational Methods*, Accepted 18 August 2019, Online Ready: 5 November 2019, 1940020 (18 pages), doi.org/10.1142/S0219876219400206.

SHOCK-INDUCED GRADIENT NANO-GRAINED MICROSTRUCTURES IN SILVER

Mauricio Ponga*[1] and David Funes Rojas[2]
[1]Department of Mechanical Engineering, University of British Columbia, Vancouver, Canada

Summary We study the dynamic recrystallization of Silver single crystals nanocubes subject to supersonic impact velocities. Our study shows that upon the impact, a rich, architected microstructure develops in the nanocubes due to the severe plastic deformation imposed by the impact. The resulting microstructure, called gradient nano grained structure, has shown to provide excellent mechanical properties. By doing systematic numerical experiments, we provide a pathway to control the recrystallization by impacting the particles in preferred orientations.

INTRODUCTION

Architecting materials from its microstructural features is one path to achieve extraordinary mechanical properties. Recently, heterogeneous microstructure has been receiving much attention. In a heterogeneous microstructure, the features (grains) exhibit large gradients in their sizes in different parts of the specimens. Materials exhibiting heterogeneous architectures can combine properties that otherwise would be mutually exclusive. This type of architecture is ubiquitous in many materials, including bones, shells, and cellulose materials. However, this type of architecture has not been explored in structural materials until recently. Examples of heterogeneous structure in structural materials have been developed in Copper using the mechanical surface grinding [1, 2], in Copper and other metallic materials using chemical deposition [3], and in semiconductors using shock loading [4]. Controlling the microstructure of crystalline structural materials represents a pivotal milestone to unlock the combination of different properties, *a priori* opposed to each other.

One type of architected microstructure that has been promising in improving the mechanical properties of structural materials is based on gradient-nano-grained structure (GNG). The microstructure of GNG materials is characterized by a smooth transition in the grain size. The grain sizes usually vary from the nano-to-micro scale. However, a key distinctive feature in GNG materials is that this change in grain size happens smoothly and, thus, elastic mismatching is reduced in comparison with other nano-architected microstructures. As a result, GNG materials have shown to combine traditionally mutually exclusive properties such as high-yield stress with high ductility [1, 4, 5]. Thus, GNG materials have areas of traditional strain hardening (micro grains) combined with areas of strain-softening (nanograins). This combination has shown to achieve strength levels compared with nano grained materials, while retaining the ductility of coarse materials [1, 4, 5]. GNG materials offer tremendous opportunities to exploit the properties of metal and push the envelope of structural materials.

Despite the tremendous efforts made to develop and control the microstructure of GNG materials, a fundamental understanding of the parameters that play a critical role remains unclear. This lack of understanding is especially true in the context of GNG materials made through severe plastic deformation and shock loading. Interesting experimental work carried out by Thevamaran *et al.* [5, 6] subjected Silver (Ag) single crystal micro-cubes of different sizes to supersonic impacts. Upon the impact, an extreme plastic deformation generated dynamic recrystallization of the micro-cube, showing the development of a GNG structure. Interestingly, Thevamaran *et al.* [6] have shown that upon the impact, the material transition into a martensitic phase-transformation from 3C face-centered cube (FCC) structure to a 4H hexagonal closed packed structure (HCP). Following the work of Thevamaran *et al.* [6], we systematically investigate through atomistic simulations the key factors that drive the dynamic recrystallization in micro-cubes under high-velocity impacts. Our goal is to better understand the deformation mechanisms in order to be able to control and manipulate the production of an optimized GNG structure.

METHODOLOGY

We perform a set of molecular dynamics (MD) simulations were we impacted single-crystal nanocubes made of 3C FCC silver at different speeds against an impenetrable target. We model the material using the interatomic potential developed by [7]. For all the cases, the impact occurs along the crystallographic direction [100]. The nanocubes size was 65 nm in the side and containing around 16 millions of atoms. The cubes were first stabilized at $T = 300$ K using an NVT ensemble for 30 ps. Next, the cubes were given an initial velocity in the range of $v_i = 200 - 600$ m·s^{-1}. The cubes impacted into an impenetrable wall that modeled with a Lennard-Jones potential. The spatial-temporal evolution of the stress and temperature was tracked down, to understand the shock behavior of the impact. In order to predict the evolution of dislocation density, we also developed a dynamic recrystallization model that was calibrated to our MD simulations. The model takes into account the wave propagation behavior of the shock load and treats the mobile and immobile dislocation densities.

*Corresponding author. E-mail: mponga@ubc.ca

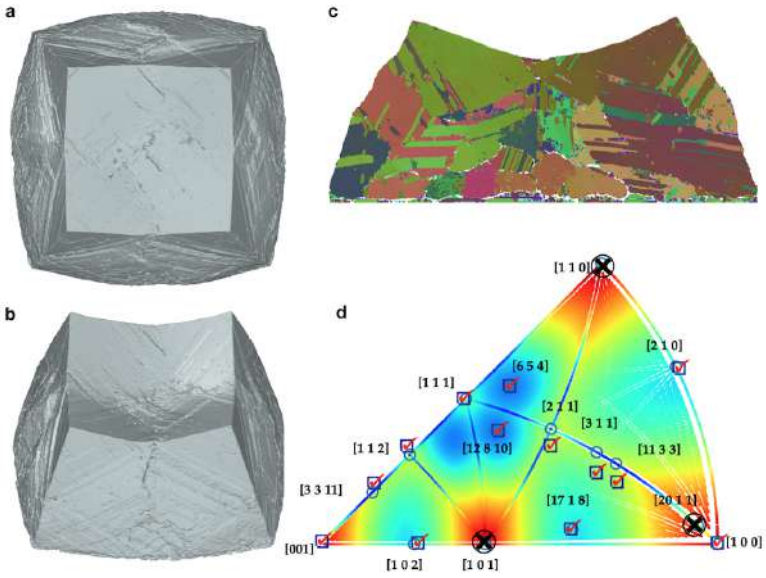

Figure 1: View of the nano-cubes after the impact. a) and b) external view. c) View of the grains. d) Stere0graphic projection for an fcc lattice. Locations with checkmarks indicate a high probability of GNG transformation.

RESULTS

Our simulations revealed that the nano-cubes recrystallize after the impact due to dislocation emission, and the plastic deformation generated during the collision. This is shown in Figure 1(a) and (b). The new grains formed in a sub-nanosecond scale, an illustration of high dynamic effects, where the stresses achieved values up to 20 GPa in compression. The resulting microstructure possesses geometrical features similar to the experiments, where small -nanosized- grains are placed in the impacted surface and with larger grains as one moves away from the impacted surface, as shown in Figure 1(c). Our simulations revealed that in order to obtain dynamic recrystallization, simultaneous activation of slip systems is required. Based on the numerical results, we concluded that at least eight slip systems need to be equally activated. The simultaneous activation occurs when the Schmid's factor of the eight slip systems are similar to each other, with a standard deviation smaller than 0.10. Figure 1(d) shows a stereographic projection with the orientations that produce a GNG recrystallization (indicated with a checkmark) in an fcc lattice for Ag.

The exact grain-size and grain-distribution of the resulting GNG structure strongly depend on the type of metal and the impact velocity. Our analysis shows that the ratio of kinetic energy transformed into temperature, and the ratio of kinetic energy transformed into plastic deformation are strongly dependent on the melting temperature and the stacking-fault energy. Melting is an unwanted effect, as it would degrade the rich microstructure. For each metal, there is an impact speed that produces a maximum density of dislocations and, therefore, the more exotic microstructures without reaching the melting temperature.

CONCLUSIONS

We have systematically investigated the high-velocity impact of Ag nanocubes. Our simulations showed that upon the impact, an avalanche of dislocation was emitted, and the single-crystal recrystallized. This process happened on a sub-nanosecond scale, due to the tremendous high strain rate of the shock load. We showed how the recrystallization depends on the orientation before the impact. For some preferred orientations, the GNG transformation was more likely. Thus, our simulations offer a pathway to control microstructure in metallic materials during high-velocity impact. Our results are relevant in manufacturing methods, such as cold spray.

References

[1] Fang, T., *et al.*, (2011). Revealing extraordinary intrinsic tensile plasticity in gradient nano-grained copper. *Science*, **331 (6024)**, 1587-1590.
[2] Fang, T. H. *et al.*, (2014). Tension-induced softening and hardening in gradient nanograined surface layer in copper. *Scripta Materialia*, **77**, 17-20.
[3] Zhao, C. *et al.*, Extra strengthening and work hardening in gradient nanotwinned metals, *Science*, **362, (6414)**, 0036-8075.
[4] Zhao, S. *et al.*, Generating gradient germanium nanostructures by shock-induced amorphization and crystallization, *PNAS*, **114(37)**, 9791–9796.
[5] Thevamaran, R. *et al.*, (2016). Dynamic creation and evolution of gradient nanostructure in single-crystal metallic microcubes. *Science*, **354 (6310)**, 312-316.
[6] Thevamaran, R., *et al.*, (2020). Dynamic martensitic phase transformation in single-crystal silver microcubes. *Acta Materialia*, **182**, 131-143.
[7] P L Williams and Y Mishin and J C Hamilton, (2006) An embedded-atom potential for the Cu–Ag system, Modelling and Simulation in Materials Science and Engineering, **14(5)**, 817–833.

A HOMOGENIZATION-BASED DAMAGE MODEL FOR STIFFNESS LOSS IN DUCTILE METAL-MATRIX COMPOSITES

K. Dorhmi[1], L. Morin*[1], K. Derrien[1], Z. Hadjem-Hamouche[1], and J.-P. Chevalier[1]
[1]PIMM, Arts et Metiers Institute of Technology, CNRS, Cnam, Paris, France

Summary A homogenized model that describes the progressive loss of stiffness observed experimentally on ductile metal-matrix composites is derived. Damage is supposed to be driven by plastic deformation using a Gurson-type model accounting for the nucleation and growth of voids. Completed by appropriate evolution equations of the microstructure, this model of plasticity is used to update the elastic properties that are described by a mean-field homogenization scheme. The complete incremental model is implemented numerically and applied to the prediction of stiffness loss. The model predictions are in very good agreement with experimental results on Al-SiC composites, cast irons and steel composites.

INTRODUCTION

Metal-matrix composites are attractive materials due to their enhanced mechanical properties; in structural applications, a classical property that is aimed at is the specific modulus, which is defined as the ratio between the elastic modulus E and the density ρ (E/ρ). However, structural metal-matrix composites are limited in real applications because they may lose their improved elastic properties when they are processed by plastic deformation (such as metal forming and rolling). Indeed, the presence of particles with high volume fraction promotes the nucleation of damage in the form of particle cracking and interface decohesion on the metal matrix, which may lead to a decrease of the elastic modulus.

The aim of this work is to derive a micromechanical model for ductile metal-matrix composites that is able to describe the progressive loss of stiffness observed during plastic straining, based on microstructure changes.

A TWO-STEP HOMOGENIZED MODEL FOR ELASTIC-PLASTIC METAL-MATRIX COMPOSITES

In metal-matrix composites, damage nucleation can arise from three sources [1]: (i) the decohesion of the interface between reinforcements (primary particles) and the matrix, (ii) the cracking of reinforcements and (iii) the nucleation within the matrix on second-phase particles. In this work, damage is supposed to be driven only by plastic deformation so no microstructure modifications are induced by elastic strains. The elastic behavior is thus supposed to depend on the microstructure (distribution and volume fraction of various phases) at a given instant while the plastic behavior is supposed to induce damage through the nucleation and growth of voids due to plastic straining .

Homogenization of elastic properties The macroscopic elastic properties are derived using the mean-field scheme of Mori-Tanaka. We investigate the overall behavior of a 3-phase composite made of an isotropic matrix characterized by its shear and bulk moduli μ_m and κ_m, reinforced by isotropic spherical particles characterized by its shear and bulk moduli μ_p and κ_p, and containing spherical voids. The volume fractions of the matrix, particles and voids are respectively denoted by f^m, f^p and f^v, where $f^m + f^p + f^v = 1$. The bulk modulus $\overline{\kappa}$ and shear modulus $\overline{\mu}$ of the composite are given by

$$\left\{\begin{array}{ll} \overline{\kappa} & = \kappa_m \dfrac{f^m(\kappa_m + \alpha_m(\kappa_p - \kappa_m)) + f^p\kappa_p}{f^m(\kappa_m + \alpha_m(\kappa_p - \kappa_m)) + f^p\kappa_m + \dfrac{f^v}{1-\alpha_m}(\kappa_m + \alpha_m(\kappa_p - \kappa_m))} \\ \overline{\mu} & = \mu_m \dfrac{f^m(\mu_m + \beta_m(\mu_p - \mu_m)) + f^p\mu_p}{f^m(\mu_m + \beta_m(\mu_p - \mu_m)) + f^p\mu_m + \dfrac{f^v}{1-\beta_m}(\mu_m + \beta_m(\mu_p - \mu_m))} \end{array}\right. , \left\{\begin{array}{ll} \alpha_m & = \dfrac{3\kappa_m}{3\kappa_m + 4\mu_m} \\ \beta_m & = \dfrac{6}{5}\dfrac{\kappa_m + 2\mu_m}{3\kappa_m + 4\mu_m} \end{array}\right. \quad (1)$$

Homogenization of plastic properties We consider Gurson's macroscopic yield criterion [2]

$$\Phi(\boldsymbol{\Sigma}) = \frac{\Sigma_{eq}^2}{\sigma_0^2} + 2q_1 f^v \cosh\left(\frac{3q_2\Sigma_m}{2\sigma_0}\right) - 1 - q_3(f^v)^2 \leq 0, \quad (2)$$

where Σ_{eq} is the macroscopic equivalent von Mises stress, Σ_m is the macroscopic mean stress and σ_0 is the yield stress of the matrix. The evolution equation of the porosity corresponding to void growth is classically deduced from the incompressibility of the matrix:

$$\dot{f}_{\text{growth}} = (1 - f^v)\,\text{tr}\,\mathbf{D}^p, \quad (3)$$

where $\mathbf{D}^{\text{p}}$ is the plastic Eulerian strain rate. Nucleation of voids is supposed to follow a strain-controlled model:

$$\dot{f}_{\text{nucleation}} = \frac{f_N}{s_N\sqrt{2\pi}}\exp\left[-\frac{1}{2}\left(\frac{\overline{\epsilon} - \epsilon_N}{s_N}\right)^2\right] \times \dot{\overline{\epsilon}} \quad (4)$$

where f_N, ϵ_N and s_N respectively represent the volume fraction, average nucleation strain and standard deviation [3].

*Corresponding author. E-mail: leo.morin@ensam.eu.

Evolution of the microstructure The evolution laws of the microstructure parameters are supposed of the form

$$\begin{cases} \dot{f}_v &= \dot{f}_{\text{growth}} + \dot{f}_{\text{nucleation}} \\ \dot{f}_p &= -\theta \dot{f}_{\text{nucleation}} \\ \dot{f}_m &= -\dot{f}_{\text{growth}} - (1-\theta)\dot{f}_{\text{nucleation}}, \end{cases} \tag{5}$$

where θ corresponds to the overall nucleation ratio that permits to distinguish nucleation within the matrix and the particles. In the case of decohesion of matrix/particles interfaces, the overall nucleation ratio takes the value $\theta = 1$, while in the case of second-phase particles nucleation, the overall nucleation ratio takes the value $\theta = 0$. In the case of a combination of several mechanisms, the parameter θ will take a value between 0 and 1.

APPLICATION TO STIFFNESS LOSS DURING PLASTIC DEFORMATION

The model's predictions are investigated in problems involving loss of stiffness. Experimental tension tests results from the literature are considered for several heterogeneous materials including Al-SiC composites, cast irons and Fe-TiB_2 composites. Model predictions are investigated with a single (homogeneous) element subjected to an axisymmetric proportional loading with major axial stress Σ_{33}, under conditions of fixed stress triaxiality $T = \Sigma_m/\Sigma_{eq} = 1/3$ (since tensile tests are considered). Two quantities are studied: (i) the evolution of the axial stress Σ_{33} versus the axial strain ε_{33} (the stress-strain curve) and (ii) the evolution of the macroscopic Young's modulus $\overline{E}$ versus the axial strain ε_{33} (the loss of stiffness) (see Figure 1 for Al-SiC composites with a volume fraction of particles of 15 %). In all cases considered, the model, calibrated with physical values of internal parameters, is in very good agreement with experimental data of the literature and permits to predict the influence of progressive damage on elastic modulus.

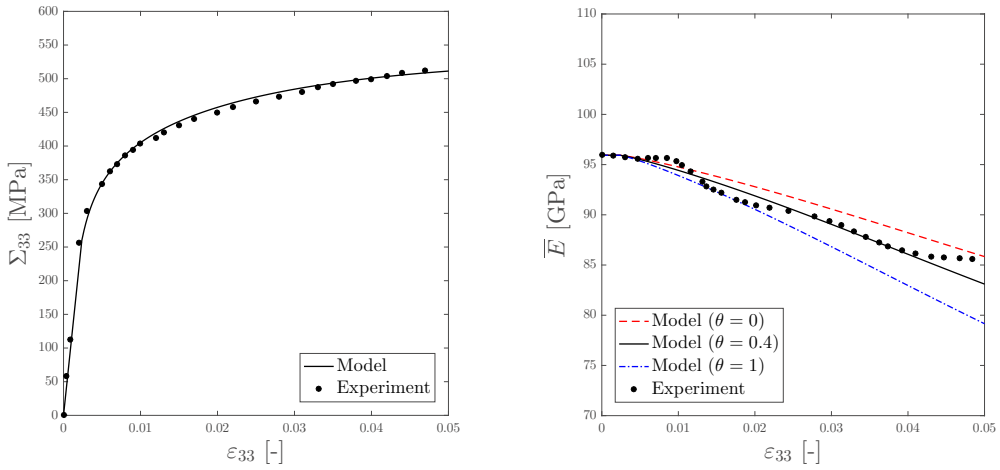

(a) (b)

Figure 1: Comparisons between experimental and model's predictions in the case of a 15%-SiC Al-SiC composite: (a) stress-strain curves and (b) stiffness loss.

CONCLUSION

A new micromechanical model for prediction stiffness loss in metal-matrix composites is presented. The elastic properties depends on the volume fraction of the present phases (matrix, particles and voids) which may evolve during plastic straining due to void nucleation and growth. Applied to several materials (Al-SiC, cast irons and Fe-TiB_2) the model has permitted to reproduce loss of stiffness in tensile tests.

References

[1] Babout, L. , Maire, E. , Fougeres, R. Damage initiation in model metallic materials: X-ray tomography and modelling. *Acta Mater.* **52**: 2475–2487, 2004.

[2] Gurson A.L. Continuum theory of ductile rupture by void nucleation and growth: Part I–Yield criteria and flow rules for porous ductile media. *ASME J. Eng. Mater. Technol.* **99**: 2–15, 1977.

[3] Chu, C.C. , Needleman, A. A. Void nucleation effects in biaxially stretched sheets. *J. Eng. Mater. Technol.* **102**: 249–256, 1980.

A MICROSTRUCTURALLY AND EXPERIMENTALLY MOTIVATED DISTORTIONAL HARDENING PLASTICITY MODEL

Knut Andreas Meyer*[1], Andreas Menzel[2,3], Johan Ahlström[1], and Magnus Ekh[1]
[1]Industrial and Materials Science, Chalmers, Gothenburg, Sweden
[2]Institute of Mechanics, TU Dortmund, Dortmund, Germany
[3]Solid Mechanics, Lund University, Lund, Sweden

Summary Plastic deformations cause yield surface distortion in most metals. Consequently, many models have been developed to capture this phenomenon. Starting from simulations of physical mechanisms at the microscale, we discuss the different modeling components of such models. The behaviors of models with those components are then compared to experimental observations of yield surface evolution due to large shear strains in pearlitic steel. By combining the observations from simulations of physical mechanisms with experimental results, a new model formulation is suggested. In contrast to several models in the literature, it guarantees a convex yield surface. Finally, we propose a novel experiment that enables a straight forward calibration procedure for the anisotropy parameters.

INTRODUCTION

Different mechanisms on the microstructural level give a material its macroscopic behavior. In this contribution, we study some mechanisms that influence anisotropy. The goal is to advance our understanding of both the physical mechanisms and which model components that are important to account for to accurately describe the macroscopic behavior.

We first consider a material consisting of isotropically hardening phases, with different initial yield strengths. In line with the Masing-model [1], the yield surface of this material translates. But it does not distort. Hence, standard kinematic hardening can describe this simple stress partitioning very well. Another explanation for the Bauschinger effect is the polarization of the dislocations [2]. This mechanism can be simulated by crystal plasticity with a back-stress on each slip system. It turns out that after a small predeformation, a high curvature of the yield surface in the loading direction is present. This result is in accordance with experimental findings in the literature, see e.g. Hu et al. [3].

A common motivation for distortional hardening is that the microstructure aligns with the deformation. This substructure evolution is often modeled as a strain-driven process, potentially also including the notion of plastic spin. We first show that for elastic inclusions to influence the yielding anisotropy, the behavior of the interface between the matrix and inclusions is essential. Additionally, the realignment of crystal grains also affects the yield surface shape.

EVALUATION OF SUBSTRUCTURE EVOLUTION

Based on the analysis in the previous section, it seems natural to propose a model in which the substructure evolution governs the distortional hardening. Fully pearlitic steels are well-suited materials to evaluate this approach, as they consist of hard cementite lamellas embedded in a softer ferrite matrix. The model by Larijani et al. [4] directly models the evolution of the yield criterion by considering areal affine reorientation of the cementite lamellas. In Figure 1, we compare the results with this model to our experimental results. But this strain-driven evolution cannot capture the experimentally observed yield surface evolution. Hence, a purely strain-driven evolution seems to be insufficient, and a different modeling strategy is required.

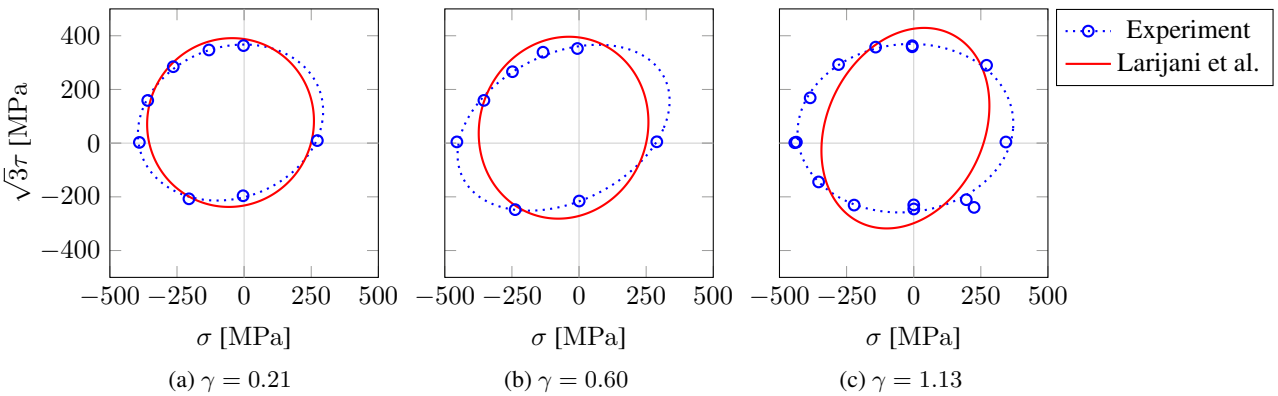

(a) $\gamma = 0.21$ (b) $\gamma = 0.60$ (c) $\gamma = 1.13$

Figure 1: Comparison of yield surface evolution between our experiments and the model by Larijani et al. [4]. γ is the predeformation shear strain.

*Corresponding author. E-mail: knut.andreas.meyer@chalmers.se

NEW MODEL FORMULATION

An alternative approach to the strain-driven evolution discussed in the previous section is a stress-driven evolution. This approach has proven successful in several studies and is chosen for the present model. We use the idea of a transformed stress state from Karafillis and Boyce [5], which guarantees a convex yield surface. Combined with a von Mises yield criterion, this approach results in a quadratic, Hill-type, yield surface, as in Shi et al. [6], but with ensured convexity. Furthermore, following Qin et al. [7], we introduce a second isotropic hardening stress. This component replaces the dynamic hardening in e.g. [6], making it easier to determine parameter bounds. Finally, we modify the flow rule to simplify the parameter identification procedure.

Model formulation

In this section, we present the key features of the model but omit many details due to space constraints. The yield function Φ is formulated by transforming the Mandel stress $\boldsymbol{M}$:

$$\Phi = \sqrt{\boldsymbol{M}_{\text{red}} : \hat{\mathbf{C}} : \boldsymbol{M}_{\text{red}}} - Y \leq 0, \quad \boldsymbol{M}_{\text{red}} = \boldsymbol{M} - \sum_{i=1}^{N_{\text{back}}} \boldsymbol{M}_{\text{kin},i}, \quad \hat{\mathbf{C}} = \frac{3}{2}\mathbf{C}^{\text{T}} : [\boldsymbol{I} \underline{\otimes} \boldsymbol{I}] : \mathbf{C} \tag{1}$$

where Y is the isotropic yield limit that evolves with plastic deformation. The evolution of $\mathbf{C}$, controlled by the material parameters b and c, is perpendicular to the loading direction $\boldsymbol{N}$ ($\dot{\lambda}$ is the plastic multiplier):

$$\mathbf{C} = \left[[1-b]\mathbf{I}^{\text{dev}} + b\mathbf{C}_{\text{l}}\right], \quad \dot{\mathbf{C}}_{\text{l}} = -c\dot{\lambda}\left[\mathbf{N}_{\perp}^{\text{T}} :: \mathbf{C}_{\text{l}}\right]\mathbf{N}_{\perp}, \quad \mathbf{N}_{\perp} = \mathbf{I}^{\text{dev}} - \boldsymbol{N} \otimes \boldsymbol{N}^{\text{t}}, \quad \boldsymbol{N} = \boldsymbol{M}_{\text{red}}^{\text{t}} / \left|\left|\boldsymbol{M}_{\text{red}}\right|\right| \tag{2}$$

Experimental calibration

Proportional loading, which is described by $\boldsymbol{N} = \pm\boldsymbol{N}_1$, leads to a constant $\mathbf{N}_{\perp}$. For this case, an analytical solution to the evolution of $\mathbf{C}$ exists:

$$\mathbf{C}(t) = \mathbf{I}^{\text{dev}} + \frac{b}{7}\left[\exp\left(-7c\lambda(t)\right) - 1\right]\mathbf{N}_{\perp,1}, \quad \lambda(t) = \int_0^t \dot{\lambda}\mathrm{d}t' \tag{3}$$

The yield limit, Y_2, in the loading direction $\boldsymbol{N}_2$, perpendicular to $\boldsymbol{N}_1$, is then

$$Y_2 = Y\left[1 - \frac{b}{7}\left[1 - \exp\left(-7c\lambda(t)\right)\right]\right]^{-1} \tag{4}$$

where Y is the yield limit in the $\boldsymbol{N}_1$ direction. Y_2 can be measured during a proportional loading experiment. By using a normalized flow rule, i.e. $\boldsymbol{L}_{\text{p}} = \dot{\lambda}\left(\partial\Phi/\partial\boldsymbol{M}\right) / \left|\left|\partial\Phi/\partial\boldsymbol{M}\right|\right|$, $\lambda(t)$ can be obtained from the experiment. The parameters b and c can then be identified directly, without the need for an inverse modeling optimization procedure.

Equation (4) shows that the cross hardening in the present model does not differentiate between monotonic and cyclic proportional loading. This feature is shared with other stress-driven models in the literature. To investigate the validity of this modeling assumption, an experiment comparing the cross-hardening during monotonic and cyclic proportional loading could shed new light on our understanding of distortional hardening. Such experiments will be conducted and presented at the conference.

CONCLUSIONS

A new model for distortional hardening has been developed. It is based on simulations of the physical mechanisms at the microscale, as well as on experimental findings. With the current understanding, a stress-driven approach seems to be the best option. However, results from proposed experiments, which we will present at the conference, will further advance our understanding of this subject.

References

[1] Masing, G. Eigenspannungen und Verfestigung beim Messing. In *2nd International Congress of Applied Mechanics*, 332–335 (1926).
[2] Kocks, U. F. & Mecking, H. Physics and phenomenology of strain hardening: The FCC case. *Progress in Materials Science* **48**, 171–273 (2003).
[3] Hu, G., Zhang, K., Huang, S. & Ju, J.-W. W. Yield surfaces and plastic flow of 45 steel under tension-torsion loading paths. *Acta Mechanica Solida Sinica* **25**, 348–360 (2012).
[4] Larijani, N., Johansson, G. & Ekh, M. Hybrid micro-macromechanical modeling of anisotropy evolution in pearlitic steel. *European Journal of Mechanics - A/Solids* **38**, 38–47 (2013).
[5] Karafillis, A. & Boyce, M. A general anisotropic yield criterion using bounds and a transformation weighting tensor. *Journal of the Mechanics and Physics of Solids* **41**, 1859–1886 (1993).
[6] Shi, B., Bartels, A. & Mosler, J. On the thermodynamically consistent modeling of distortional hardening: A novel generalized framework. *International Journal of Plasticity* **63**, 170–182 (2014).
[7] Qin, J., Holmedal, B. & Hopperstad, O. S. A combined isotropic, kinematic and distortional hardening model for aluminum and steels under complex strain-path changes. *International Journal of Plasticity* **101**, 156–169 (2018).

MESOSCALE LATTICE CONTINUUM: DIFFUSION, CREEP AND PLASTICITY

Sinisa Dj Mesarovic and Sasa Kovacevic,
School of Mechanical and Materials Engineering, Washington State University, Pullman, WA 99164-2920, USA

Summary At high temperatures, the interior of each grain in a polycrystal suffers: (1) dislocation glide, (2) climb, and (3) diffusion of vacancies. Grain boundaries undergo: (4) growth/disappearance, as a result of vacancy diffusion, and, (5) crystallographic reorientation/mismatch, as a result of dislocations arriving to the boundaries either by glide or by climb. All the above deformation mechanisms are naturally described in the lattice continuum framework, whereby the lattice represents the material. Climbing edge dislocations are lattice sink/source which must be reflected in the continuity equation and the transport theorem. The transport theorem for grains with lattice growing or disappearing lattice at different grain boundary faces results in the direct formulation of the boundary condition for vacancy diffusion flux in terms of the boundary velocity (different from the lattice velocity). The field equations for each grain are derived by means of the principle of virtual power. The resulting polycrystal initial/boundary value problem consists of elasticity-plasticity-diffusion field equations in each crystalline domain with moving boundaries, coupled through the boundary conditions.

KINEMATICS OF THE LATTICE CONTINUUM

We consider isothermal process in a single crystal with conserved mass, a single species of atoms and vacancies, without interstitials. The lattice velocity field is an Eulerian variable $\mathbf{v}(\mathbf{x},t)$, and the lattice velocity gradient $\mathbf{L}$ $\mathbf{v}$ is defined. The velocity field characterizing the continuum carries with itself the lattice density N, so that, in contrast to the standard mass continuum and its material derivative, we define the *lattice derivative* as the time derivative following the lattice. Similarly, the transport theorem takes the specific form [1-3].

In addition the lattice density N, the lattice point currently located at $\mathbf{x}$, carries the vacancy concentration c and the deformation gradient $\mathbf{F}$, which evolves as $D\mathbf{F}/Dt$ $\mathbf{L}$ $\mathbf{F}$. Deformation gradient in a newly grown lattice being thus defined, the reference position $\mathbf{X}$ of a newly grown lattice point is formally defined by integrating dX $\mathbf{F}^{-1}$ $d\mathbf{x}$.

Let N_0 be the number of lattice point per unit volume of the undeformed lattice. Then the number of lattice points per unit volume of the deformed lattice is N N_0/F; F $\det\mathbf{F}$.

The deformation gradient tensor can be decomposed into the plastic deformation gradient $\mathbf{F}^p$ and the elastic-compositional deformation gradient $\mathbf{F}^*$. The decomposition is multiplicative and formally identical to the standard (glide-only) elastic-plastic decomposition: $\mathbf{F}$ $\mathbf{F}^*$ $\mathbf{F}^p$. We envision a sequential application of the two gradients (Figure 1). First, the plastic deformation gradient is applied to the reference configuration to produce the intermediate (isoclinic) configuration $\mathbf{F}^p:\mathbf{X}$ $\mathbf{x}$. In contrast to standard crystal plasticity based on dislocation glide, here F^p $\det\mathbf{F}^p$ 1; lattice planes are lost/created, resulting in the translational motion of the parts of the lattice, but lattice symmetries and orientation are preserved. The elastic-compositional deformation gradients accounts for lattice stretching (compositional and elastic strains) and rotation, but the connectivity of lattice points is preserved.

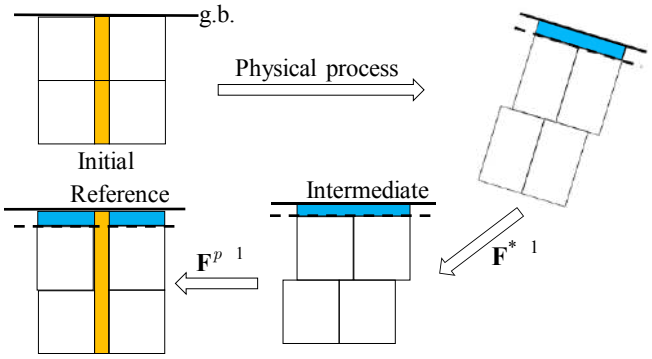

Figure 1. Illustration of elastic-plastic decomposition when the reference configuration is not the initial configuration. The initial element (upper left) at the grain boundary (g.b.) is transformed into the current configuration (upper right). The physical deformation process includes: loss of lattice planes through dislocation climb (yellow), dislocation glide along the horizontal pane, creation of new lattice planes at the boundary (blue), elastic-compositional lattice stretching, and, rotation.

The Eulerian deformation rates are additive:

$$\mathbf{L}\quad\mathbf{L}^*\quad\mathbf{L}^p\quad\mathbf{F}^*\ \mathbf{F}^{*\ -1}\quad\mathbf{F}^*\ \mathbf{L}^p\ \mathbf{F}^{*\ -1};\quad\mathbf{L}^p\quad\mathbf{F}^p\ \mathbf{F}^{p\ -1}. \tag{1}$$

The slip system is described by a triad of unit orthogonal vectors: the slip direction $\mathbf{s}$ $\mathbf{b}/|\mathbf{b}|$, the slip plane normal $\mathbf{m}$, and $\mathbf{t}$ $\mathbf{s}$ $\mathbf{m}$. The plastic velocity gradient on intermediate configuration $\mathbf{L}^p$ accounts for changes in lattice topology and is defined from the elementary slip system state variables: true slip rates $\hat{}$ and climb rates s :

$$\tilde{\mathbf{L}}^p\quad\sum\ \hat{}\ \mathbf{s}\ \mathbf{m}\quad\sum\ s\ \mathbf{s}\ \mathbf{s};\quad\mathrm{tr}\tilde{\mathbf{L}}^p\quad s\quad\sum\ s\ . \tag{2}$$

The boundaries of the crystal serve as vacancy sources and sinks. Upon defining the vacancy flux **J**, *relative to the lattice*, we obtain the diffusion equation for vacancy concentration as

$$Dc/Dt \quad F^* \quad \mathbf{J} \quad (1 \quad c)s \tag{3}$$

The *boundary velocity* **V** is defined on the boundary and is independent of the lattice velocity field, with the normal component V_n **V n**. Then, the boundary lattice growth rate is g V^n **n v**. For a variable crystal domain, with lattice growing/vanishing at the boundary, the local mass conservation condition implies absence of boundary diffusion by requiring that lattice growth/disappearance at the boundary be directly related to the normal atomic flux. The *creep velocity gradient* is the rank-2 tensor, constant within the domain Ω, and defined on the basis of the difference between the boundary velocity **V**, and the lattice velocity at the boundary:

$$\mathbf{C} \quad \frac{1}{} \quad \frac{F^* J_n}{1 \quad c} \mathbf{nn} d \quad ; \quad F^* \quad \det \mathbf{F}^*; \quad c \quad \text{vacancy concentration} . \tag{4}$$

GOVERNING EQUATIONS AND ANALYSIS

Upon defining the compositional strain as eigenstrain and the strain energy density (c), we formulate the power balance with linear dissipation. Then, application of the principle of virtual power yields the governing equations. In addition to the standard stress (quasi-) equilibrium and velocity or traction boundary conditions, we obtain coupled, moving-boundary diffusion problem with an unusual boundary condition on the moving boundaries:

$$\frac{Dc}{Dt} = BF^* \nabla^2 \frac{\partial \Phi}{\partial c} - (1-c)s \quad \text{in } \Omega(t) ; \quad \frac{1-c}{F^*} g = B\mathbf{n} \cdot \nabla \frac{\partial \Phi}{\partial c} = H \frac{F^* t_n}{1-c} - \frac{\partial \Phi}{\partial c} \quad \text{on } \partial\Omega(t) , \tag{5}$$

where B and H are bulk and boundary mobility coefficients.

Several approximations and asymptotic solutions are developed in [1], including linearized elasticity and periodic gran arrangements. Specifically, for small elastic deformation, small departures from equilibrium vacancy concentration and linear (Vegard's law) eigenstrain, the diffusion equations take the simplified form:

$$\frac{c}{t} = B\nabla^2 \frac{}{c} \quad \text{in } \Omega(t); \quad B\mathbf{n} \cdot \nabla \frac{}{c} = V_n = H \; t_n \quad \frac{}{c} \quad \text{on } \partial\Omega(t) , \tag{6}$$

where / c 3 p $(c \quad c_0)$, p is the pressure, t_n is normal traction, is the Vegard's law coefficient and c_0 is the equilibrium vacancy concentration at the given temperature. The following can be deduced:

- The secondary creep rate estimate corresponds to the standard Nabarro-Herring model.
- The volumetric creep is small.
- Equilibrium under deviatoric stresses is not possible without the inclusion of surface energy and then, only for grains with high aspect ratio.
- The main features of the primary creep are qualitatively understood.

In this paper we present numerical simulations of Nabarro-Herring model with emphasis of stress evolution along the grain boundaries which, although subjected the microscopically uniform tractions, exhibit stress concentrations as the result of non-uniform vacancy concentration.

CONCLUSIONS

The lattice continuum theory developed in [1 , 2, 3] represents natural and intuitive framework for analysis of diffusion in crystals and lattice growth/loss at the boundaries. The formulation includes the definition of the Lagrangean reference configuration for the newly created lattice, transport theorem and mass conservation. The latter connects the creep rate tensor, constant within a crystal, to the normal diffusional flux at the boundaries. Dislocation plasticity, including climb and glide is readily accommodated through the decomposition into elastic-compositional and plastic deformation pseudo-gradients. The special case of Nabarro-Herring creep under isothermal conditions has been analyzed. The governing equations are developed with coupled diffusion and elasticity.

The list of unresolved issues and directions for future research include:

- Inclusion of surface energy and surface stresses.
- Inclusion of boundary diffusion for Coble creep.
- Related to the above issues is the question of vacancy nucleation without subsequent absorption by the lattice. The activation energy of such process will be much higher than the one characterizing the nucleation with lattice absorption. A dependence of surface energy of the vacancy content (excess volume) appears to be the key component of such process.

References

[1] Mesarovic, S.Dj. 2016 Lattice continuum and diffusional creep. *Proc. R. Soc. A* **472**, 20160039.
[2] Mesarovic, S.Dj. 2017 Dislocation creep: Climb and glide in the lattice continuum. *Crystals* **7**(8).
[3] Mesarovic, S.Dj. 2019 Physical foundations of mesoscale continua. In *Mesoscale models: From micro-physics to macro-interpretation.* Eds. S.Dj. Mesarovic, S. Forest & H.M. Zbib. Springer.

AN INCREMENTAL VARIATIONAL PROCEDURE FOR ELASTO-PLASTIC COMPOSITES WITH COMBINED ISOTROPIC AND KINEMATIC HARDENING

Antoine Lucchetta*[1], François Auslender[2], Michel Bornert[3], and Djimédo Kondo[1]
[1]Université Pierre et Marie Curie, Institut Jean le Rond d'Alembert, Paris, France
[2]Université Clermont Auvergne, Institut Pascal, Clermont-Ferrand, France
[3]Université Paris-Est, Laboratoire Navier, Marne-la-Vallée, France

Summary In this study, we first investigate the nonlinear behavior of elasto-plastic composites with isotropic and linear (or nonlinear) kinematic hardening. To this end, we rely on the incremental variational principles introduced by Lahellec and Suquet [4]. We also take advantage of the formulation recently proposed by Agoras et al. [1]. The proposed model, named *Double Incremental Variational* procedure (DIV), consists in a double application of the variational procedure (VP) of Ponte Castañeda [8]. These two applications of the VP lead to a thermo-elastic Linear Comparison Composite (LCC) with an homogeneous polarization inside the phases. The effective behavior can then be estimated by the classical linear homogenization schemes. New theoretical results are also provided and they are in good agreement with numerical computations at both local and macroscopic scales.

ELASTO-PLASTIC COMPOSITES WITH ISOTROPIC AND KINEMATIC HARDENING

We consider a Representative Volume Element Ω of a composite material made of N phases $(r = 1, \ldots, N)$ with volume fraction $c^{(r)}$. The phases are generalized standard materials (GSM) having an elasto-plastic local behavior described by the conventional J_2 theory of plasticity combined with both linear kinematic hardening and isotropic hardening. This corresponds to a material with internal variables $\boldsymbol{\alpha} = (\boldsymbol{\varepsilon}^p, p)$ describing the irreversible phenomena, where $\boldsymbol{\varepsilon}^p$ is the plastic strain and p the cumulated plastic strain, and with two convex potentials whose expressions are detailed in [6]:

- The free-energy density $w^{(r)}(\boldsymbol{\varepsilon}, \boldsymbol{\varepsilon}^p, p)$ where $\boldsymbol{\varepsilon}$ denotes the local strain
- The dissipation potential $\varphi^{(r)}(\dot{\boldsymbol{\varepsilon}}^p, \dot{p})$ which depends on the indicator function of the convex $\mathcal{C} = \{(\dot{\boldsymbol{\varepsilon}}^p, \dot{p}) / g(\dot{\boldsymbol{\varepsilon}}^p, \dot{p}) = \dot{\varepsilon}^p_{eq} - \dot{p} \leq 0\}$.

Following Lahellec and Suquet [4], an incremental approximation of the constitutive equations for a classical GSM is obtained by using an implicit Euler-scheme at all time increments of duration Δt of a prescribed loading history. Then, two local potentials are introduced: first the incremental potential $J^{(r)}$ defined as $J^{(r)} = w^{(r)} + \Delta t\, \varphi^{(r)}$ which is nonuniform per phase. Second, the condensed free-energy $w^{(r)}_\Delta$ which is defined as the infimum of $J^{(r)}$ with respect to $\boldsymbol{\alpha}$ and leads to the expression $\boldsymbol{\sigma} = \partial w^{(r)}_\Delta / \partial \boldsymbol{\varepsilon}$ for the local stress field in phase r. Finally, the condensed effective free-energy $\tilde{w}_\Delta$ is defined in variational form as $\tilde{w}_\Delta(\boldsymbol{E}) = \inf_{\boldsymbol{\varepsilon} / \langle \boldsymbol{\varepsilon} \rangle = \boldsymbol{E}} \langle w_\Delta(\boldsymbol{\varepsilon}) \rangle$. Thanks to previous relation and using Hill's macro-homogeneity condition, the macroscopic stress $\boldsymbol{\Sigma} = \langle \boldsymbol{\sigma} \rangle$ is obtained as $\boldsymbol{\Sigma} = \partial \tilde{w}_\Delta / \partial \boldsymbol{E}$ (see [4]).

As the dissipation potential is non quadratic, a linearized incremental potential $J^{(r)}_L$ is introduced which depends on a set of per-phase uniform viscosities $\eta^{(r)}_{\varepsilon^p}$ one for each phase r. The application of the VP of Ponte Castañeda [8] provides an approximation of $\tilde{w}_\Delta$ associated with stationarity conditions. The resolution of these conditions leads to an expression for these unknows and to the definition of a thermo-elastic LCC with intraphase heterogeneous properties. Thanks to the VP introduced by Lahellec et al. [3], this heterogeneous LCC is approached by a homogeneous one.

This model has been further extended to an elastoplastic matrix with combined nonlinear kinematic and isotropic hardening. To develop the DIV formulation to nonlinear kinematic hardening, we considered for the matrix phase the Chaboche model which is a regularization of the Armstrong-Frederick one [2] in the framework of GSM (see [7]). In this case, the dissipation potential depends on the state variable, in addtion to their rates. This required to reformulate the incremental variational principles introduced by Lahellec and Suquet [4].

APPLICATIONS AND DISCUSSIONS

We applied this procedure to the case of a composite comprised of an elasto-plastic matrix exhibiting both types of hardenings and reinforced by elastic spherical particles. Both phases are supposed isotropic. The Hashin-Shtrikman lower bound is used to homogenize the LCC with per-phase homogeneous properties, assuming an isotropic phase distribution. As an example of application, let us consider composite materials composed of an elastoplastic matrix with isotropic and linear (or nonlinear) kinematic hardening reinforced by elastic spherical inclusions. These composites are submitted to a uniaxial cyclic isochoric extension along axial direction e_3, such that the macroscopic strain tensor reads $\boldsymbol{E}(t) = E_{33}(t)(-\frac{1}{2}(\boldsymbol{e}_1 \otimes \boldsymbol{e}_1 + \boldsymbol{e}_2 \otimes \boldsymbol{e}_2) + \boldsymbol{e}_3 \otimes \boldsymbol{e}_3)$. The materials mechanical parameters are as in [5].

*Corresponding author. E-mail: antoine.lucchetta@upmc.fr

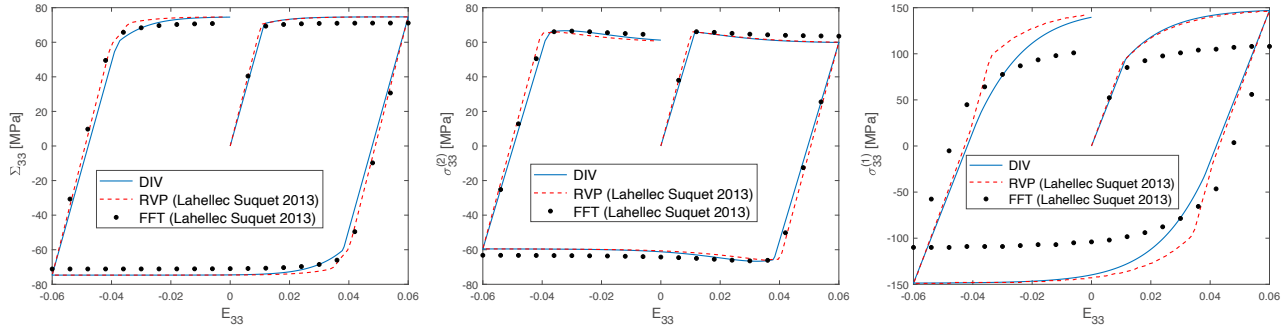

(a) (b) (c)

Figure 1: Elastically reinforced composite with an ideally-plastic matrix. $c^{(1)} = 0.17$. (a) Macroscopic axial stress, (b) Average axial stress in the matrix, (c) Average axial stress in the inclusion.

Fig.1 compares the predictions of the DIV formulation to that of RVP (*Rate Variational Procedure*) by Lahellec et Suquet [5], to FFT simulations for a composite comprised of an ideally-plastic matrix. Firstly, RVP and DIV predictions are very close and both of them provide accurate results for of the macroscopic stress and the average stress in the matrix. Moreover, they capture the Bauschinger effect. Is is also noted that although the DIV and RVP approaches qualitatively reproduce the trends of the FFT simulations, they overestimate the average stress in the inclusion. We note that the model has been similarly validated for composites comprised of a matrix with isotropic or linear kinematic hardening (see [6]).

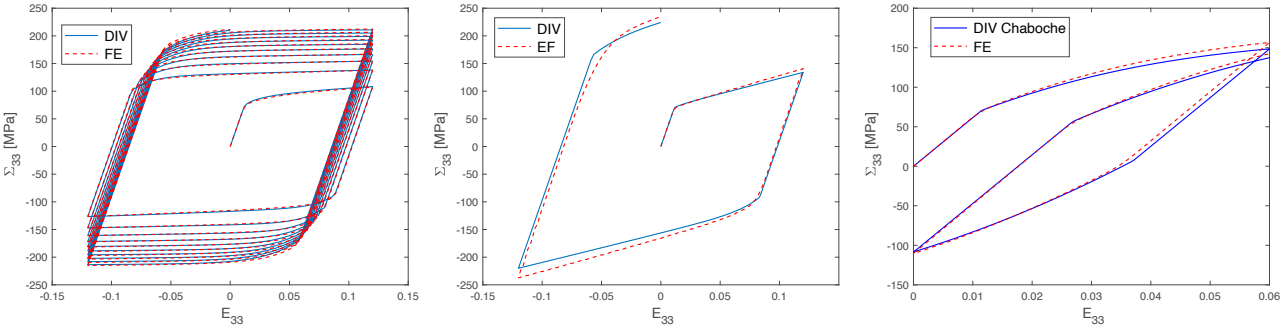

(a) (b) (c)

Figure 2: Macroscopic axial stress of elastically reinforced composites comprised of an elastoplastic matrix with (a) Isotropic hardening submitted to 10 radial loading cycles, (b) Isotropic and linear kinematic hardening, (c) Isotropic and nonlinear kinematic hardening.

We finally provide some results for composites with a matrix exhibiting combined hardening. Fig.2 represents the variation of the macroscopic stress of composite comprised of a matrix with (a) isotropic hardening,(b) isotropic and linear kinematic hardening and (c) isotropic and nonlinear kinematic hardening. In these three cases a close agreement is observed between the DIV approach and FE simulations. It is noted that the proposed models also capture the Bauschinger effect. In particular for isotropic hardening, the model reproduces this effect at each cycle. Moreover, we observe that in general the average stress in the matrix is in good agreement with the FE simulations and the predicted average stress in the inclusion reproduces qualitatively the FE simulations (see [6] and [7]).

References

[1] Agoras M., Avazmohammadi R., Ponte Castañeda P. Incremental variational procedure for elasto-viscoplastic composites and application to polymer- and metal-matrix composites reinforced by spheroidal elastic particles. *Int. J. Solids Struct.* **97-98**: 668-686, 2016.

[2] Armstrong P. J., Frederick C.O. A Mathematical Representation of the Multiaxial Bauschinger Effect. *CEGB Report RD/B/N731*, 1966.

[3] Lahellec N., Ponte Castañeda P., Suquet P. Variational estimates for the effective response and field statistics in thermoelastic composites with intra-phase property fluctuations. *Proc. R. Soc. A* **447**: 2224–2246, 2011.

[4] Lahellec N., Suquet P. On the effective behaviour of nonlinear inelastic composite: I. incremental variational principles. *J. Mech. Phys. Solids* **55**: 1932-1963, 2007.

[5] Lahellec N., Suquet P. Effective response and field statistic in elasto-plastic and elasto-viscoplastic composites under radial and non-radial loading. *Int. J. Plast.* **42**: 1-30, 2013.

[6] Lucchetta A., Auslender F., Bornert M., Kondo D. A double incremental variational procedure for elastoplastic composites with combined isotropic and linear kinematic hardening. *Int. J. Solids Struct.* **158**: 243-267, 2019.

[7] Lucchetta A. Homogénéisation de composites élasto-viscoplastiques écrouissables par une double procédure variationnelle incrémentale. *Ph.D. thesis*, 2019.

[8] Ponte Castañeda P. The effective mechanical properties of nonlinear isotropic composites. *J. Mech. Phys. Solids* **39**: 45-71, 1991.

RATE-DEPENDENT ANISOTROPIC PLASTICITY MODEL OF TITANIUM ALLOY FOR AEROSPACE APPLICATIONS

Miguel Ruiz de Sotto[1,2,3], Patrice Longère[1]*, Véronique Doquet[2], and Jessica Papasidero[3]
[1]ICA, Université de Toulouse, ISAE-SUPAERO, MINES ALBI, UPS, INSA, CNRS, 31000 Toulouse, France
[2]Laboratoire de Mécanique des Solides, CNRS UMR 7649, Ecole Polytechnique, 91128 Palaiseau, France
[3]Safran Aircraft Engines, Rond-point René Ravaud, 77550 Réau,France

Summary Following an extensive experimental campaign carried out on a cold-rolled Ti-6Al-4V titanium alloy grade within a wide range of (low and high) strain rate, temperature and loading cases (tension, compression, shear), an advanced constitutive model is built within the irreversible thermodynamics framework following the internal variable procedure. Some key aspects such as texture-induced anisotropy (which manifests through orthotropy, kinematic hardening and tension/compression asymmetry), rate dependence, strain hardening and thermal softening are consistently accounted for. Material constants are calibrated using the software Zset and the model has been implemented in the commercial finite element computation code LS-DYNA. The latter has been employed to conduct numerical simulations at the structural scale for evaluating the predictive performances of the numerical version of the model.

INTRODUCTION

Due to their high specific impact resistance, Ti-6Al-4V titanium alloys are widely used as protection material for ballistic applications. In aircraft engine fan, they accordingly constitute promising candidates for the leading edge of multi-component blades regarding bird ingestion. During the latter, impacted blades undergo complex loading path and history involving notably large strain, high strain rate and load reversal. In the context of aerospace structure engineering-oriented numerical simulation-aided design, an advanced constitutive model able to account for all the above mentioned parameters is therefore required.

We are here interested in a Ti-6Al-4V titanium alloy grade provided in the form of cold-rolled plate. An extensive experimental campaign has been carried out on it within a wide range of (low and high) strain rate, temperature and loading cases (tension, compression, shear). Experimental results have evidenced that its behaviour is strongly dependent on orientation, rate and temperature, and is subject to isotropic and kinematic hardening as well as tension-compression asymmetry, see Figs.1-2.

In view of describing the above mentioned effects, an advanced constitutive model is built within the irreversible thermodynamics framework following the internal variable procedure. In particular, some key aspects such as texture-induced anisotropy (which manifests through orthotropy, kinematic hardening and tension/compression asymmetry), rate dependence, strain hardening and thermal softening are consistently accounted for. Material constants are calibrated using the software Zset and the model has been implemented in the commercial finite element computation code LS-DYNA. The latter has been employed to conduct numerical simulations at the structural scale for evaluating the predictive performances of the numerical version of the model.

The salient features of the constitutive model will be presented, in particular those related to anisotropic plasticity and rate dependence, as will be shown some numerical simulations involving complex loading cases.

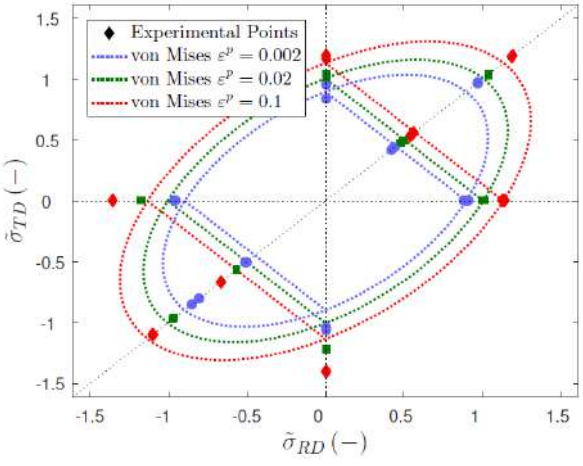

Fig.1: Yield locus in the rolling direction (RD)-transverse direction (TD) dimensionless stress plane. Superimposition of experimental results (dots) and Mises approximation (dotted lines). Uniaxial loading at room temperature and low strain rate.

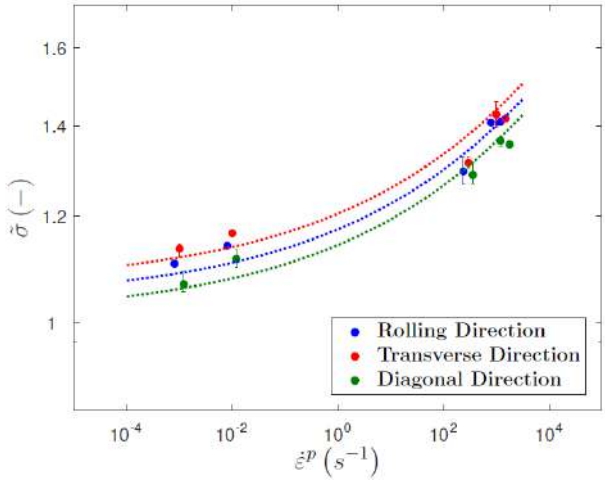

Fig.2: Dimensionless equivalent stress at 0.2% plastic strain vs. plastic strain rate. Superimposition of experimental results (dots) and numerical modelling results (dotted lines). Tension loading at room temperature.

*Corresponding author. E-mail: patrice.longere@isae.fr.

CONSTITUTIVE MODELLING

As mentioned previously, the internal variable procedure is herein applied within the irreversible thermodynamics framework to model the thermo-mechanical behaviour of the Ti-6Al-4V grade under consideration. Plastic anisotropy involves a loss of collinearity between the plastic strain rate and the stress deviator. As the plastic strain rate is derived from the transformed equivalent stress according to the normality rule in the context of non-associate plasticity adopted herein, plastic anisotropy effects are accounted for in the expression of the transformed equivalent stress. Yield function $f\left(\hat{\underline{\underline{\Sigma}}},r\right)$ and plastic potential $F\left(\hat{\underline{\underline{\Sigma}}},r\right)$ accordingly read

$$(1) \qquad f\left(\hat{\underline{\underline{\Sigma}}},R\right)=\sigma_{eq}\left(\hat{\underline{\underline{\Sigma}}}\right)-R\left(\kappa,T\right)=\sigma_{v}\left(\kappa\right)\geq 0 \;\; ; \;\; F\left(\hat{\underline{\underline{\Sigma}}},R\right)=f\left(\hat{\underline{\underline{\Sigma}}},R\right)+g\left(\underline{\underline{X}}\right)$$

where $\hat{\underline{\underline{\Sigma}}}$ and $R\left(\kappa,T\right)$ represent the transformed stress and radius of the elasticity domain subject to isotropic hardening and thermal softening, κ and T the isotropic hardening variable (or accumulate plastic strain) and temperature, and $g\left(\underline{\underline{X}}\right)$ a function of the kinematic hardening force $\underline{\underline{X}}$. $\sigma_{eq}\left(\hat{\underline{\underline{\Sigma}}}\right)$ and $\sigma_{v}\left(\kappa\right)$ are the transformed equivalent stress and strain rate induced over stress (or viscous stress).
It is reminded that in the present case plastic anisotropy manifests through (i) loading direction dependence, (ii) kinematic hardening, and (iii) strength differential. Combining Karafillis and Boyce [1] and Cazacu et al. [2] approaches for orthotropy coupled with kinematic hardening on the one hand and orthotropy coupled with strength asymmetry on the other hand, the expression of the transformed equivalent stress $\sigma_{eq}\left(\hat{\underline{\underline{\Sigma}}}\right)$ is of the form

$$(2) \qquad \sigma_{eq}^{a}\left(\hat{\underline{\underline{\Sigma}}}\right)=\frac{1}{m_{0}^{a}}\left[\left(\left|\hat{\Sigma}_{1}\right|-k\hat{\Sigma}_{1}\right)^{a}+\left(\left|\hat{\Sigma}_{2}\right|-k\hat{\Sigma}_{2}\right)^{a}+\left(\left|\hat{\Sigma}_{3}\right|-k\hat{\Sigma}_{3}\right)^{a}\right] \;\; ; \;\; \hat{\Sigma}_{i}=eig\left(\hat{\underline{\underline{\Sigma}}}\right) \;\; ; \;\; \hat{\underline{\underline{\Sigma}}}=\underline{\underline{\underline{\underline{A}}}}:\left(\underline{\underline{s}}-\underline{\underline{X}}\right)$$

where $\underline{\underline{s}}$ is the Cauchy stress deviator and $\underline{\underline{\underline{\underline{A}}}}$ the orthotropy tensor. eig stands for eigenvalue. a is a positive constant and k takes positive or negative values depending on the strength asymmetry. In addition to involving nonlinear kinematic hardening, function $g\left(\underline{\underline{X}}\right)$ is coupled with $R\left(\kappa,T\right)$ via common materials constants to better describe loading paths with load reversals, see e.g. [3].
Material constants have been calibrated using the software Zset, see Fig.2 for loading direction and strain rate effects. The above outlined advanced model has then been implemented into the commercial finite element computation code LS-DYNA to conduct numerical simulations at the structural scale. The predictive performances of the numerical version of the model have been shown.

CONCLUDING REMARKS

Following an extensive experimental campaign carried out on a cold-rolled Ti-6Al-4V titanium alloy grade within a wide range of (low and high) strain rate, temperature and loading cases (tension, compression, shear), an advanced constitutive model has been built within the irreversible thermodynamics framework following the internal variable procedure. It accounts for texture-induced anisotropy (which manifests through orthotropy, kinematic hardening and tension/compression asymmetry), rate dependence, strain hardening and thermal softening, and is expected to apply to a wide class of strongly nonlinear metals and alloys.

References

[1] A. Karafillis, M. Boyce, A general anisotropic yield criterion using bounds and a transformation weighting tensor, Journal of the Mechanics and Physics of Solids 41 (12) (1993)
[2] O. Cazacu, B. Plunkett, F. Barlat, Orthotropic yield criterion for hexagonal closed packed metals, International Journal of Plasticity 22 (7) (2006)
[3] J. Carbonnière, S. Thuillier, F. Sabourin, M. Brunet, P. Y. Manach, Comparison of the work hardening of metallic sheets in bending-unbending and simple shear, International Journal of Mechanical Sciences 51 (2) (2009)

MODELLING PRIMARY CREEP REGENERATION IN A MARTENSITIC 10%CR STEEL

Xiaolong Li[1,2], Stuart Holdsworth[1], Edoardo Mazza[1,2], and Ehsan Hosseini[*1]
[1]Empa, Swiss Federal Laboratories for Material Science and Technology, Dübendorf, Switzerland
[2]Department of Mechanical and Process Engineering, ETH Zürich, Zürich, Switzerland

Summary Primary creep regeneration is an important phenomenon observed for some materials loaded under stress-varying creep conditions. A Chaboche-type unified viscoplastic constitutive model has been developed in this study for representation of the PCR behaviour of a 10%Cr martensitic steel at 600 °C. It has been shown that the developed model can well represent the experimental observations from a comprehensive stress-varying creep testing program and successfully describe the sensitivity of the PCR response to various loading parameters.

INTRODUCTION

For some materials under creep loading, a stress reversal might clear the previous strain hardening memory and lead to regeneration of the primary creep stage upon reloading, i.e. creep re-priming or primary creep regeneration (PCR). PCR significantly increases the accumulated inelastic strain for components operating under cyclic creep loading conditions, and therefore might strongly affect their predicted lifetimes by the strain-based ductility exhaustion method [1]. Different approaches have been employed for consideration of the PCR in mechanical integrity assessment of high-temperature components. As an example, [2-4] assumed that the accumulation of a minimum of 0.01% reverse inelastic strain clears the previous strain hardening history and therefore results in re-occurrence of the primary creep stage upon reloading. The recently generated experimental records from a set of stress-varying creep experiments for two high-temperature steels [5-7] indicated that such simple representations cannot realistically describe the PCR phenomenon. For example, it has been experimentally shown that, depending on the reverse loading conditions, the strain-hardening memory might only partially be cleared or the creep rate after a load reversal might be even higher than that of the primary creep stage. This study presents a new variant of the Chaboche viscoplastic constitutive model, devised from [8, 9], for realistic representation of the PCR response of a 10%Cr steel under different loading conditions at 600 °C.

EXPERIMENTAL DETAILS

Ten stress-varying and two constant-load creep tests were designed to study the PCR behaviour of the 10%Cr steel and its sensitivity to different loading parameters at 600 °C. Fig. 1 shows an example of the loading profile and readers are referred to [6] for more details.

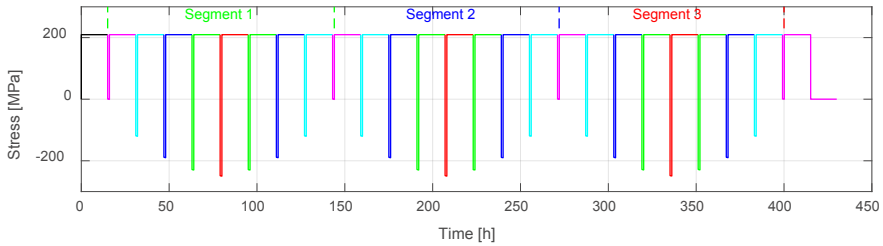

Figure 1. An example of the applied loading profiles for stress-varying creep tests.

MODEL DESCRIPTION AND RESULTS

The following presents the 1D representation of the developed unified viscoplastic constitutive model:

$$\dot{\varepsilon}_{vp} = \sum_{i=1}^{2} A_i \left(\left|\sigma - \Sigma X\right| / D\right)^{n_i} sign\left(\sigma - \Sigma X\right), \quad \Sigma X = \sum_{i=1}^{3} X_i \tag{1}$$

$$\dot{X}_i = C_i \dot{\varepsilon}_{vp} - \gamma_i \left|\dot{\varepsilon}_{vp}\right| X_i - K_i X_i, \quad X_i\big|_{t=0} = 0, \quad \gamma_i = \gamma_{i,\infty} + \left(\gamma_{i,0} - \gamma_{i,\infty}\right)\exp\left(-w_i \left|\varepsilon_{vp}\right|\right), \quad i = 1-3 \tag{2}$$

$$\dot{D} = C' \left|\dot{\varepsilon}_{vp}\right| - \gamma' D \left|\dot{\varepsilon}_{vp}\right| - K' D, \; D\big|_{t=0} = D_0, \quad \gamma' = \gamma'_{\infty} + \left(\gamma'_0 - \gamma'_{\infty}\right)\exp\left(-w' \varepsilon_{vp}^{eq}\right) \tag{3}$$

where σ, X and D are the applied stress, back stress and drag stress, respectively, $\dot{\varepsilon}_{vp}$ is the viscoplastic strain rate, and ε_{vp}^{eq} is the accumulated viscoplstic strain. Calibration of the model and determination of the material parameters (e.g. A_i, n_i, C_i, γ_i) were based on the experimental observations from the twelve conducted experiments.

Fig. 2 compares the experimental and model represented strain evolutions for two of the examined stress profiles, which demonstrates the capability of the developed model for describing different levels of PCR depending on the parameters of the stress profile.

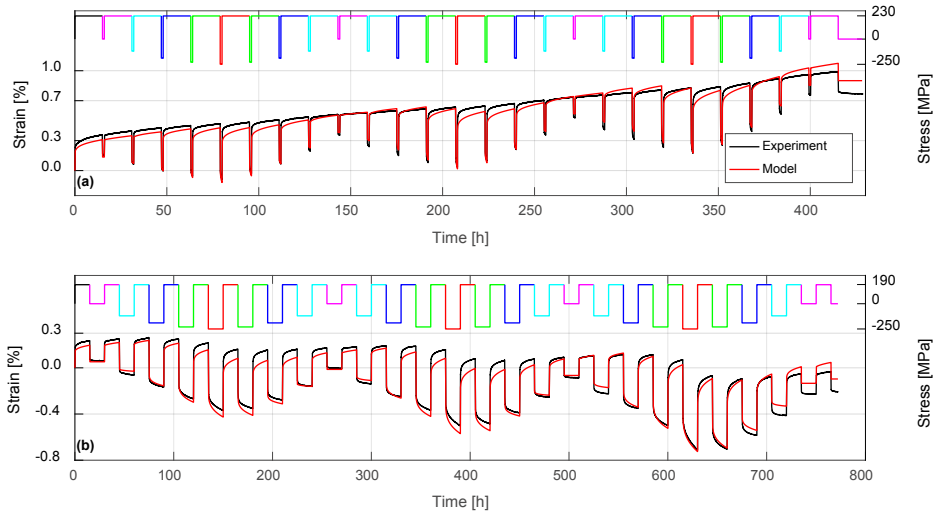

Figure 2. Comparison of the experimental and model represented strain evolutions for two of the examined stress profiles for the 10%Cr steel at 600 °C.

The model was then employed for prediction of the strain evolution for an independent benchmark test for the 10%Cr steel at 600 °C. The satisfactory consistency of the modelling and experimental strain profiles, shown in Fig. 3, demonstrates the predictive capability of the developed model formulation.

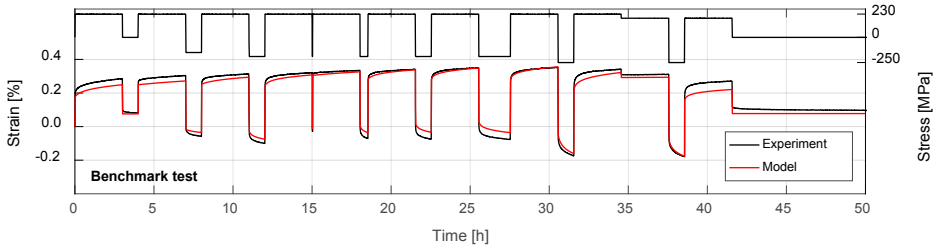

Figure 3. Comparison of the experimental and model-predicted strain evolutions for the conducted independent benchmark test for the 10%Cr steel at 600 °C.

CONCLUSIONS

A unified viscoplatic constitutive model has been developed for representation of the creep behaviour of a 10%Cr steel under stress-varying creep loading conditions at 600 °C. It has been demonstrated that the model can well represent the PCR phenomenon and its sensitivity to parameters of the loading profile.

References

1. R5: Assessment procedure for the high temperature response of structures. Issue 3, Revision 002, EDF Energy, Gloucester, UK, 2014.
2. Hosseini, E., S. Holdsworth, and E. Mazza, Advanced constitutive modelling for creep-fatigue assessment of high temperature components. Materials at High Temperatures, 2018. 35(6): p. 504-512.
3. Radosavljevic, M., Creep-fatigue assessment of high temperature steam turbine rotors (Diss ETH No. 19880). PhD thesis, ETHZ University, Zürich, Switzerland, 2011.
4. ElAgha, F., D. Tanner, and D. Knowles, Comparison of Predicted Cyclic Creep Damage From a Multi-Material Weldment FEA Model and the Traditional R5 Volume 2/3 Weldment Approach. ASME 2018 Pressure Vessels and Piping Conference. American Society of Mechanical Engineers Digital Collection, 2018.
5. Li, X., et al., Creep behaviour of AISI 316H stainless steel under stress-varying creep loading conditions: primary creep regeneration. Materials at High Temperatures, 2019. 36(3): p. 240-252.
6. Li, X., et al., Creep behaviour of a high chromium martensitic steel under stress varying creep loading conditions: primary creep regeneration (PCR). Under review, 2019.
7. Li, X., et al., Comparison of primary creep regeneration and anealstic recovery behaviour of 316H austenitic and 10%Cr martensitic steel. Under review, 2019.
8. Chaboche, J.-L., A review of some plasticity and viscoplasticity constitutive theories. International journal of plasticity, 2008. 24(10): p. 1642-1693.
9. Metzger, M. and T. Seifert, On the exploitation of Armstrong-Frederik type nonlinear kinematic hardening in the numerical integration and finite-element implementation of pressure dependent plasticity models. Computational Mechanics, 2013. 52(3): p. 515-524.

MICROSTRUCTURE-SENSITIVE FFT-BASED MODEL OF CREEP OF POLYCRYSTALLINE METALS

Ricardo Lebensohn*[1], M. Arul Kumar[1], Nathan Bieberdorf[1], and Laurent Capolungo[1]
[1]Los Alamos National Laboratory, Los Alamos, NM, USA

Summary We present a physics-based model to predict creep in polycrystalline metals, with application to steels. The model is an extension of the dislocation glide-based elasto-viscoplastic (EVP) Fast Fourier Transform (FFT) full-field crystal plasticity formulation, to consider other deformation mechanisms (dislocation climb, diffusion, diffusion- and plasticity-mediated cavitation) at temperatures and stresses relevant to in-service conditions of steels parts in thermal power plants. Upon calibration to reproduce the temperature and stress dependencies of primary, secondary, and tertiary creep for different steels, the model can be used to generate material response across a wide range of operating conditions.

INTRODUCTION

The development of high-strength steels has for decades improved the efficiency and safety of thermal power plants operating under more demanding in-service conditions. Safely employing these materials requires some a priori knowledge of their lifespan. In the case of the thermal creep, however, experimentally verifying the material's time-to-rupture is not always feasible, as operating conditions are generally chosen to produce lifespans on the order of years and decades. Instead, experimental campaigns are conducted at artificially elevated stresses and temperatures, and empirical relations are used to correlate the resultant short time-to-rupture to more realistic operating conditions. But, as temperature and stress are lowered, a different set of deformation mechanisms are expected to dominate the material's behavior. As a consequence, these empirical extrapolated lifetime predictors lack physical basis to predict performance outside of the deformation regime for which they were calibrated.

As a contribution to improve modelling and simulation tools available for engineering analysis and material design, we present a physics-based model to predict thermal creep of steels with sensitivity to the material's microstructure. The model is an extension of an efficient full-field crystal plasticity formulation for dislocation glide, to other relevant deformation regimes. Upon calibration to reproduce the temperature and stress dependencies of primary, secondary, and tertiary creep, the model can be used to generate material response across a wide range of operating conditions.

MODEL

FFT-based methods were developed in the 1990's by Moulinec and Suquet and initially applied to composite materials [1], in which the source of heterogeneity is related to the spatial distribution of phases with different mechanical properties. Later, this methodology was adapted to polycrystals [2], where the heterogeneity is related to the spatial distribution of crystals with anisotropic mechanical properties. This extension exploits the superior numerical performance of crystal plasticity (CP) solved by FFT-based methods, compared with CP Finite Elements. The CP-FFT implementation showed a large reduction of the computational time and the feasibility of solving complex and detailed polycrystalline unit cells. Since then, numerous numerical implementations of the FFT-based method for polycrystals have been developed, for different constitutive descriptions of the behavior of each single crystal material point, including elasto-viscoplasticity [3]. However, in the latter EVPFFT implementation, single-crystal plasticity is considered to occur by dislocation glide only, and the constitutive relation describing the contribution of individual slip systems to plastic strain-rate is given by a power-law relating the ratio between the resolved shear stress on each slip system (given by the projection of the applied stress on the Schmid dyadic tensor), and a critical stress that implicitly contains the dependencies with temperature, strain-rate and deformation history, i.e. strain hardening. This semi-phenomenological constitutive description is insufficient to capture temperature dependence explicitly, and other deformation mechanisms that become relevant, and, at sufficiently lower stresses and higher temperatures, even dominant, during thermal creep. For the ranges of stresses and temperatures of interest, these mechanisms are [4]: for primary and secondary creep, dislocation climb and grain boundary diffusion, and diffusion- and plasticity-mediated damage at grain boundaries in the tertiary creep regime.

In order to overcome these limitations, the EVPFFT formulation and its numerical implementation have been extended to consider: a) crystallographic dislocation climb, using the model of Lebensohn et al. [5], based on the consideration of a newly-defined dyadic climb tensor, which contracted with the applied stress gives the driving force for climb; b) Wen et al. [6]'s model crystal plasticity model, to consider explicit temperature-dependent and microstructure-sensitive dislocation mobility and dislocation density evolution in the climb-and-glide regime; c) a space-resolved constitutive description of Coble creep to model the vacancy-mediated plasticity at grain boundaries. Consideration and proper calibration of all these mechanisms provide a physics-based, temperature-dependent and microstructure-sensitive description of the behavior of steels in the primary and secondary creep regimes, as illustrated in the Results section.

In order to describe the material's behavior in the tertiary creep regime, void nucleation and growth by coupled viscoplastic and diffusive processes driven by local stresses generated in the secondary creep regime are considered. At local (grain boundary voxel) level, the interplay between porosity on local slip activity is accounted for using

homogeneized analytical expressions obtained for a voided rate-sensitive, single crystal matrix [7] and the interplay between porosity on local diffusion kinetics is described using rate-sensitive isotropic dilatational plasticity homogenization [8].

RESULTS

In the primary and secondary creep regimes, Figure 1 shows calibration/validation cases, for different temperatures and applied uniaxial stresses. All calculations were performed on a 32x32x32 polycrystalline unit cell with random texture and austenite single crystal elastic and plastic properties. For the different temperatures, we used one or two stresses for calibration of the single crystal properties and the solid curves for the other two stresses are predictions of the model for primary and secondary creep, which are compared with the corresponding dash lines representing the steady-state secondary creep rate, after [9] for 650C (Fig. 1a), [10] for 700C (Fig. 1b), and [11] for 750C (Fig. 1c).

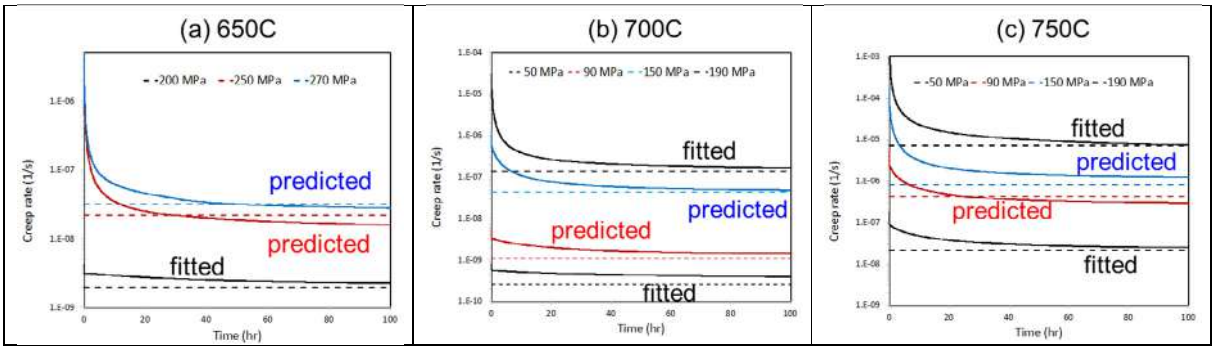

Figure 1: Calibration/validation of the constitutive model parameters to reproduce existing primary and secondary creep experiments of 347 steel for different temperatures and uniaxial stress states.

References

[1] Moulinec H., Suquet P. Numerical method for computing the overall response of nonlinear composites with complex microstructure. *Comput. Methods Appl. Mech. Engrg.* **157**:69-94, 1998.

[2] Lebensohn R.A. N-site modelling of a 3D viscoplastic polycrystal using Fast Fourier Transform. *Acta Mater.* **49**: 2723-2737, 2001.

[3] Lebensohn R.A, Kanjarla A.K, Eisenlohr P. An elasto-viscoplastic formulation based on fast Fourier transforms for the prediction of micromechanical fields in polycrystalline materials. *Int. J. Plast.* **32-33**: 59-69, 2012.

[4] Frost H.J., Ashby M.F. Deformation-Mechanism Maps: The Plasticity and Creep of Metals and Ceramics. Pergamon Press, 1982.

[5] Lebensohn R.A., Hartley C.S., Tomé C.N., Castelnau O. Modelling the mechanical response of polycrystals deforming by climb and glide. *Phil. Mag.* **90**: 567-583, 2010.

[6] Wen W., Capolungo L., Patra A., Tomé C.N. A physics-based crystallographic modeling framework for describing the thermal creep behavior of Fe-Cr alloys. *Metall. Mat. Trans. A* **48**, 2603-2617, 2017.

[7] Mbiakop A., Constantinescu A., Danas K., An analytical model for porous single crystals with ellipsoidal voids. *J. Mech. Phys. Solids* **84**, 436-467, 2015.

[8] Leblond J.B., Perrin G., Suquet P. Exact results and approximate models for porous viscoplastic solids. *Int. J. Plast.* **10**, 213-235, 1994.

[9] Nassour A., Bose W.W., Spinelli D. Creep properties of austenitic stainless-steel weld metals. *J. Mater. Eng. Perform.* **10**, 693, 2001.

[10] Osman H., Borhana A., Tamin M.N. Material parameters for creep rupture of austenitic stainless steel foils. *J. Mater. Eng. Perform.* **23**, 2858, 2014.

[11] Osman H., Nor F.M., Hamdan Y.M., Tamin M.N. Creep ruptures of AISI 347 austenitic stainless steel foils at elevated temperature of 750C. *Proc IMechE Part L* **231**, 516, 2015.

MODEL REDUCTION FOR DISSIPATIVE COMPOSITES BASED ON MEAN-FIELD HOMOGENIZATION

Martin Idiart*[1], Noel Lahellec*[2], Hervé Moulinec[2], and Pierre Suquet[2]
[1]Departamento de Aeronáutica,Facultad de Ingeniería,Universidad Nacional de La Plata,,Avda.1esq.47S/N, La Plata B1900TAG, Argentina.
[2]Aix Marseille Univ, CNRS, Centrale Marseille, LMA, Marseille, France

Summary This work provides an alternative derivation of the homogenization scheme for viscoelastic composites proposed by Lahellec and Suquet, see [1]. This derivation clearly shows that the scheme can be interpreted as a model reduction in the sense that the final estimate preserve the two-potential structure providing a macroscopic free energy and dissipation potential involving a finite number of internal variables (the per phase average and the fluctuations of the internal variable local field).

FRAMEWORK

Inelastic composites exhibiting short-memory effects at the microscale display long-memory effects at the macroscale. Consequently, microscopic constitutive descriptions based on finite sets of internal variables give rise to macroscopic constitutive descriptions with an infinity of internal variables, see [2]. This can be shown in the case of material described in the framework of generalized standard materials by the constitutive relations on the form :

$$\boldsymbol{\sigma} = \frac{\partial w}{\partial \boldsymbol{\varepsilon}}(\boldsymbol{x}, \boldsymbol{\varepsilon}, \boldsymbol{\alpha}), \quad \frac{\partial w}{\partial \boldsymbol{\alpha}}(\boldsymbol{x}, \boldsymbol{\varepsilon}, \boldsymbol{\alpha}) + \frac{\partial \varphi}{\partial \dot{\boldsymbol{\alpha}}}(\boldsymbol{x}, \dot{\boldsymbol{\alpha}}) = 0, \tag{1}$$

where $\boldsymbol{\varepsilon}$ and $\boldsymbol{\alpha}$ denote the infinitesimal and inelastic strains relative to a stress-free reference configuration, $\boldsymbol{\sigma}$ denotes the Cauchy stress, the dot over a variable denotes a time derivative, and the potential functions w and φ are, respectively, the Helmholtz free-energy density and the dissipation potential of the solid. The homogenized response relates the macroscopic stress $\overline{\boldsymbol{\sigma}}$ to the macroscopic strain $\overline{\boldsymbol{\varepsilon}}$, which are the averages of the local stress and strain fields over the representative volume element. This relation can be written in terms of the macroscopic free-energy density and dissipation potential as (e.g., [2])

$$\overline{\boldsymbol{\sigma}} = \frac{\delta \overline{w}}{\delta \overline{\boldsymbol{\varepsilon}}}(\overline{\boldsymbol{\varepsilon}}, \boldsymbol{\alpha}), \quad \frac{\delta \overline{w}}{\delta \boldsymbol{\alpha}}(\overline{\boldsymbol{\varepsilon}}, \boldsymbol{\alpha}) + \frac{\delta \overline{\varphi}}{\delta \dot{\boldsymbol{\alpha}}}(\dot{\boldsymbol{\alpha}}) = 0, \tag{2}$$

where

$$\overline{w}(\overline{\boldsymbol{\varepsilon}}, \boldsymbol{\alpha}) = \min_{\boldsymbol{\varepsilon} \in \mathcal{K}(\overline{\boldsymbol{\varepsilon}})} \langle w(\boldsymbol{x}, \boldsymbol{\varepsilon}, \boldsymbol{\alpha}) \rangle \quad \text{and} \quad \overline{\varphi}(\dot{\boldsymbol{\alpha}}) = \langle \varphi(\boldsymbol{x}, \dot{\boldsymbol{\alpha}}) \rangle \,. \tag{3}$$

In these expressions, $\mathcal{K}(\overline{\boldsymbol{\varepsilon}})$ is the set of kinematically admissible strain fields with average $\overline{\boldsymbol{\varepsilon}}$, $\langle . \rangle$ denotes volume averaging over the representative volume element, and the δ operator denotes a functional derivative. Expression (2) shows that the effective behavior of the composite material is defined by an infinity of internal variables which are the local internal variables of each material point.

This fact has motivated several attempts to generate approximate macroscopic descriptions based on reduced sets of effective internal variables that provide a partial but hopefully accurate characterization of the evolving microscopic state of the composite. One of the earliest attempts consisted in assuming that the inelastic strain within each phase of the composite is uniform and therefore expressible in terms of a finite set of internal variables, see [3]. While attractively simple, it is known that this approximate scheme, commonly referred to as "transformation field analysis", can be severly inaccurate when the local fields exhibit strong spatial fluctuations (e.g., [4]). In view of this observation, Michel and Suquet, see [4] and [5], refined the approximation by assuming non-uniform inelastic strain fields that can be expressed as a linear combination of a finite number of predefined fields, so that the amplitudes constitute a finite set of internal variables for which evolution laws can be provided. This refinement significantly improves the accuracy of the approximation but introduces the need to carry out full-field numerical computations. In this work we proposed an other way of improvement of the TFA method which relies on mean-field homogenization.

EFFECTIVE INTERNAL VARIABLE FORMULATION

To ease the exposition, we restrict attention to viscoelastic phases characterized by Maxwell potentials of the form (for the phase r)

$$w^{(r)}(\boldsymbol{\varepsilon}, \boldsymbol{\alpha}) = \frac{1}{2} (\boldsymbol{\varepsilon} - \boldsymbol{\alpha}) . \boldsymbol{L}^{(r)} (\boldsymbol{\varepsilon} - \boldsymbol{\alpha}) \quad \text{and} \quad \varphi^{(r)}(\dot{\boldsymbol{\alpha}}) = \eta^{(r)} \dot{\boldsymbol{\alpha}} . \dot{\boldsymbol{\alpha}}, \tag{4}$$

*Corresponding authors. E-mail: martin.idiart@ing.unlp.edu.ar, lahellec@lma.cnrs-mrs.fr

where $\boldsymbol{L}^{(r)}$ is positive-definite tensor of elastic moduli and $\eta^{(r)}$ the viscous modulus. Upon an implicit Euler scheme time discretisation, [1] shown that the evolution law $(2)_2$, in view of the convexity of the macroscopic potential, is equivalent to [1]

$$\min_{\boldsymbol{\alpha}} \left[\overline{w}(\overline{\boldsymbol{\varepsilon}}, \boldsymbol{\alpha}) + \Delta t \overline{\varphi}(\frac{\boldsymbol{\alpha} - \boldsymbol{\alpha}_n}{\Delta t}) \right] \tag{5}$$

The estimate is derived by bounding the macroscopic dissipation potential $\overline{\varphi}$ by two potentials $\overline{\varphi}^+$ and $\overline{\varphi}^-$ who only depend on the inelastic strain field $\boldsymbol{\alpha}(\boldsymbol{x})$ through their phase averages $\langle \boldsymbol{\alpha} \rangle^{(r)}$ and the square root of the intraphase fluctuations $\tilde{\alpha}^{(r)} = \left\langle (\boldsymbol{\alpha} - \langle \boldsymbol{\alpha} \rangle^{(r)}).(\boldsymbol{\alpha} - \langle \boldsymbol{\alpha} \rangle^{(r)}) \right\rangle^{(r)^{1/2}}$ of each phases :

$$\overline{\varphi}^{\pm} \left(\frac{\langle \boldsymbol{\alpha} \rangle^{(1)} - \langle \boldsymbol{\alpha}_n \rangle^{(1)}}{\Delta t}, ..., \frac{\tilde{\alpha}^{(1)} \pm \tilde{\alpha}_n^{(1)}}{\Delta t}, ... \right) = \sum_{r=1}^{N} c^{(r)} \eta^{(r)} \left[\frac{\langle \boldsymbol{\alpha} \rangle^{(r)} - \langle \boldsymbol{\alpha}_n \rangle^{(r)}}{\Delta t} . \frac{\langle \boldsymbol{\alpha} \rangle^{(r)} - \langle \boldsymbol{\alpha}_n \rangle^{(r)}}{\Delta t} + \left(\frac{\tilde{\alpha}^{(r)} \pm \tilde{\alpha}_n^{(r)}}{\Delta t} \right)^2 \right] \tag{6}$$

It is not shown here but these reduce potentials are found with the Cauchy-Schwartz inequality which gives bounds for $\left\langle (\boldsymbol{\alpha} - \langle \boldsymbol{\alpha} \rangle^{(r)}).(\boldsymbol{\alpha}_n - \langle \boldsymbol{\alpha}_n \rangle^{(r)}) \right\rangle^{(r)}$. It appears that two different estimates can be derived by switching the sign $\pm$. The form (6) suggests that the bound corresponding to the negative sign should be adopted to be consistent with the time continuous limit $\Delta t \to 0$, so that the last term could be seen as the discretised time derivative of $\tilde{\alpha}^{(r)}$. Choosing the sign $-$, we finally found the following estimate for the effective constitutive relations :

$$\overline{\boldsymbol{\sigma}} = \frac{\partial \hat{w}}{\partial \overline{\boldsymbol{\varepsilon}}} \left(\overline{\boldsymbol{\varepsilon}}, \overline{\boldsymbol{\alpha}}^{(1)}, ..., \tilde{\alpha}^{(1)}, ... \right), \quad \min_{\substack{\overline{\boldsymbol{\alpha}}^{(r)} \\ \tilde{\alpha}^{(r)}}} \left[\hat{w} \left(\overline{\boldsymbol{\varepsilon}}, \overline{\boldsymbol{\alpha}}^{(1)}, ..., \tilde{\alpha}^{(1)}, ... \right) + \Delta t \overline{\varphi}^{-} \left(\frac{\langle \boldsymbol{\alpha} \rangle^{(1)} - \langle \boldsymbol{\alpha}_n \rangle^{(1)}}{\Delta t}, ..., \frac{\tilde{\alpha}^{(1)} - \tilde{\alpha}_n^{(1)}}{\Delta t}, ... \right) \right]. \tag{7}$$

The above formulae simplify considerably when the composite is made up of isotropic phases. In this case, the tensors of elastic moduli are given by $\boldsymbol{L}^{(r)} = 3\kappa^{(r)}\boldsymbol{J} + 2\mu^{(r)}\boldsymbol{K}$ where $\boldsymbol{J}$ and $\boldsymbol{K}$ are the standard fourth-order isotropic bulk and shear projection tensors, $\kappa^{(r)}$ and $\mu^{(r)}$ are the bulk and shear moduli. We obtain the reduced expression for the macroscopic free-energy density which can be estimated by the classical mean field homogenization method :

$$\hat{w} \left(\overline{\boldsymbol{\varepsilon}}, \overline{\boldsymbol{\alpha}}^{(1)}, ..., \tilde{\alpha}^{(1)}, ... \right) = \min_{\in \mathcal{K}(\overline{\boldsymbol{\varepsilon}})} \sum_{r=1}^{N} c^{(r)} \left[\frac{9}{2} \kappa^{(r)} \left\langle \varepsilon_m^2 \right\rangle^{(r)} + \mu^{(r)} \left[\left(\left\langle \boldsymbol{\varepsilon}_d \right\rangle^{(r)} - \overline{\boldsymbol{\alpha}}^{(r)} \right) . \left(\left\langle \boldsymbol{\varepsilon}_d \right\rangle^{(r)} - \overline{\boldsymbol{\alpha}}^{(r)} \right) + \left(\left(\left\langle \boldsymbol{\varepsilon}_d^2 \right\rangle^{(r)} - \left\langle \boldsymbol{\varepsilon}_d \right\rangle^{(r)} . \left\langle \boldsymbol{\varepsilon}_d \right\rangle^{(r)} \right)^{1/2} - \tilde{\alpha}^{(r)} \right)^2 \right] \right] \tag{8}$$

where $\varepsilon_m = \mathrm{tr}\boldsymbol{\varepsilon}/3$ and $\boldsymbol{\varepsilon}_d = \boldsymbol{\varepsilon} - \varepsilon_m$. $\boldsymbol{I}$ denote the mean and deviatoric parts of the strain, respectively, $\boldsymbol{I}$ denotes the second-order identity tensor, and $\mathrm{tr}\boldsymbol{\alpha}^{(r)} = 0$.

CONCLUSIONS

In this paper we give an alternative derivation of the EIV estimate proposed by [1]. These new derivation has several advantages including : (i) it clearly shows the structure of the effective constitutive relation and the set of internal variables used to describe it ($\overline{\boldsymbol{\alpha}}^{(r)}$ and $\tilde{\alpha}^{(r)}$ for each phases). (ii) it gives some criterion to choose between the different roots arising when using the EIV estimate. The proposed method is sufficiently general to be used to derive the RVP estimate, firstly proposed by [6] then by [7], which is based on a dual formulation of equations (1).

References

[1] Lahellec, N. and Suquet, P. Effective behavior of linear viscoelastic composites: a time-integration approach. *International Journal of Solids and Structures*, 46, pp. 507–529, 2007.

[2] Suquet, P. Local and global aspects in the mathematical theory of plasticity. *Plasticity Today: Modelling, Methods and Applications*. In: Sawczuk, A., Bianchi, G.(Eds.), Elsevier, London, pp. 279–310, 1985.

[3] Dvorak, G. Transformation field analysis of inelastic composite materials. *Proc. R. Soc. Lond*, 437, pp. 311–327, 1992.

[4] Michel, J.C., Suquet, P. Nonuniform transformation field analysis. *Int. J. Solids Struct*, 40, pp. 6937–6955, 2003.

[5] Michel, J.C., Suquet, P. A model-reduction approach in micromechanics of materials preserving the variational structure of constitutive relations. *J. Mech. Phys. Solids*, 90, pp. 254-–285, 2016.

[6] Lahellec, N., Suquet, P. Effective response and field statistics in elasto-plastic and elastoviscoplastic composites under radial and non-radial loadings. *Int. J. Plasticity* 42, pp. 1–30, 2013.

[7] Agoras, M. , Avazmohammadi, R. , Ponte Castañeda, P. Incremental variational pro- cedure for elasto-viscoplastic composites and application to polymer- and met- al-matrix composites reinforced by spheroidal elastic particles. *Int. J. Solids Struct*. pp. 97–98, 2016.

[1] To simplify the notation, in all the following the subscript $n+1$ related for the field at time t_{n+1} will be omitted. $\overline{\boldsymbol{\varepsilon}}_{n+1}$, $\boldsymbol{\varepsilon}_{n+1}$ and $\boldsymbol{\alpha}_{n+1}$ will be simply noted $\overline{\boldsymbol{\varepsilon}}$, $\boldsymbol{\varepsilon}$ and $\boldsymbol{\alpha}$.

NUMERICAL STUDY OF INFLUENCE OF THERMAL RECOVERY ON THE RESIDUAL STRESS STATE AFTER MELTING AND SOLIDIFICATION

Martin Kroon*[1] and MB Rubin[2]
[1]Department of Mechanical Engineering, Linnaeus University, Vaxjo, Sweden
[2]Faculty of Mechanical Engineering, Technion, Haifa, Israel

Summary A thermomechanically consistent Eulerian plasticity model with work hardening is adopted for studying the residual mechanical state resulting from loading at elevated temperatures. The isotropic plasticity model includes the standard effect of work hardening as well as thermal recovery. The results indicate the importance of modeling thermal recovery for accurate prediction of residual stresses for problems dealing with melting and solidification.

INTRODUCTION

Controlling welding and 3D printing processes requires models for melting and solidification which include volumetric expansion and contraction. Melting during heating causes the material to loose resistance to distortional deformation with the melted material behaving more like a fluid than a solid. Solidification during cooling causes the material to regain resistance to distortional deformation with inhomogeneous shrinkage developing undesirable residual stresses. This paper discusses a thermodynamically consistent phenomenological model that is developed using an Eulerian formulation based on the work of Eckart [1] and Leonov [2] who proposed an evolution equation for elastic deformation directly.

THEORETICAL FRAMEWORK

The velocity is $\mathbf{v} = \dot{\mathbf{x}}$, with $\mathbf{x}$ being the position vector in the current configuration, and the velocity gradient $\mathbf{L}$ and the rate of deformation tensor $\mathbf{D}$ are defined in standard ways. Moreover, within the context of the Eulerian formulation of viscoplasticity developed in Rubin [3], the elastic dilatation is $J_{\rm e}$. Also, the elastic distortional deformation is determined by the symmetric, positive definite, unimodular tensor $\bar{\mathbf{B}}_{\rm e}$, which is determined by the evolution equation

$$\dot{\bar{\mathbf{B}}}_{\rm e} = \mathbf{L}\bar{\mathbf{B}}_{\rm e} + \bar{\mathbf{B}}_{\rm e}\mathbf{L}^{\rm T} - \frac{2}{3}(\mathbf{D}:\mathbf{I})\bar{\mathbf{B}}_{\rm e} - \Gamma\bar{\mathbf{A}}_{\rm p}, \quad \Gamma \geq 0, \tag{1}$$

where $\mathbf{I}$ is the second order unit tensor. In these equations, Γ is a non-negative function, and the direction of inelasticity is determined by the tensor $\bar{\mathbf{A}}_{\rm p}$, defined by

$$\bar{\mathbf{A}}_{\rm p} = \bar{\mathbf{B}}_{\rm e} - \left(\frac{3}{\bar{\mathbf{B}}_{\rm e}^{-1}:\mathbf{I}}\right)\mathbf{I}. \tag{2}$$

For an elastically isotropic material, the Helmholtz free energy is taken in the form

$$\psi = \psi(J_{\rm e}, \alpha_1, \theta), \quad \alpha_1 = \bar{\mathbf{B}}_{\rm e}:\mathbf{I}, \tag{3}$$

where α_1 is a scalar pure measure of elastic distortional deformation, and θ is the absolute temperature.

An overstress model is used to characterize the rate-dependent inelastic response with the inelastic distortional deformation rate controlled by the function Γ which is specified by the overstress form

$$\Gamma = a_1 \langle g \rangle, \quad a_1 \geq 0, \tag{4}$$

where a_1 is a temperature-dependent function that controls rate-dependence, and $\langle g \rangle$ denotes the Macaulay brackets. The yield function g is specified by

$$g = 1 - \frac{R_{\rm h}\kappa}{\gamma_{\rm e}}, \quad R_{\rm h}(\theta) \geq 0, \tag{5}$$

where $R_{\rm h}$ is a function of the temperature that influences the temperature dependence of the yield strength, and $\gamma_{\rm e}$ is a measure of effective elastic distortional deformation. Let κ be a scalar measure of hardening determined by the evolution equation

$$\dot{\kappa} = m_1\Gamma(\kappa_s - \kappa) - m_2(\kappa - \kappa_a), \quad m_1 \geq 0, \quad m_2 \geq 0, \quad \kappa_s > \kappa_a > 0, \tag{6}$$

where m_1 controls work hardening, m_2 controls thermal recovery, and $\kappa_{\rm a}$ is a constant that controls the minimum annealed value of κ.

*Corresponding author. E-mail: martin.kroon@lnu.se

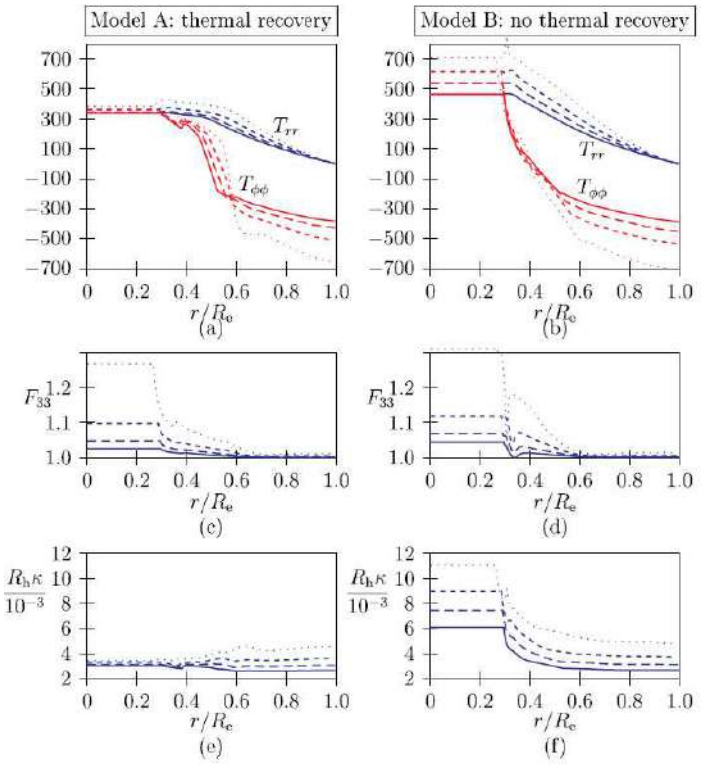

Figure 1: Solutions to the disk problem for different numbers of heating cycles: 1 cycle (solid lines), 2 cycles (dashed lines), 4 cycles (short dashed lines), and 10 cycles (dotted lines). Solution is shown in terms of stress components (T_{rr} and $T_{\phi\phi}$), relative thickness change (F_{33}), and material hardening ($R_h\kappa$). Comparison between the standard case with thermal recovery (a,c,e) and a solution for the simplified model without thermal recovery (b,d,f).

NUMERICAL EXAMPLE

Consider a thin, circular disk. The disk has an initially uniform thickness and consists of two parts: an inner part with radius R_i and an outer part with external radius R_e. The disk is modelled as a 2D structure, and a state of generalized plane stress is assumed. No external forces are acting on the disk, and all mechanical processes in the disk are driven by an inhomogeneous temperature distribution in the disk. The initial temperature distribution at time $t = 0$ is a uniform temperature, $T(R) = T_0 = 20°C$. During the analysis, the temperature in the disk first increases linearly with time, such that at $t = t_c$, the central part of the disk has reached a melted state at the temperature $T = T_m$, where T_m is the melting temperature of the material. At this point in time, the rim of the disk has increased to a lower temperature T_e with the temperature decreasing linearly from T_m at $R = R_i$ to T_e at $R = R_e$. After the maximum temperature distribution has been reached, the temperature field is decreased along the same temperature path, and at the end of the analysis, the disk has the same uniform temperature distribution as in the beginning of the analysis, i.e. $T(R) = T_0$.

Fig. 1 explores the influence of several consecutive heating cycles, each with $t_c = 10s$. Solutions are shown for 1 (solid lines), 2 (dashed lines), 4 (short dashed lines), and 10 (dotted lines) heating cycles. Results are shown in terms of the radial and hoop Cauchy stress components, the thickness component of the deformation gradient, and the accumulated hardening.

For Model A (with thermal recovery), the residual stresses in the inner part of the disk are of the order of 350-400MPa, and these stresses are negligibly affected by an increasing number of heating cycles. The residual hoop stress shows the strongest sensitivity to the number of cycles with its magnitude near the outer edge of the disk increases from about 400MPa to almost 700MPa from 1 to 10 heating cycles.

The predictions of Model B (with no thermal recovery) indicate that the residual stresses continue to increase with each cycle both in the inner region and along the outer edge of the disk. For 10 cycles, the residual stresses are of the order of 700MPa in both the inner part of the disk and along its outer edge. The huge difference in stress levels between the cases with and without thermal recovery is explained by the big differences in accumulated hardening shown in figures (e) and (f).

References

[1] Eckart, C. The thermodynamics of irreversible processes iv. The theory of elasticity and anelasticity. *Phys. Rev.* **73**:373-382, 1948.
[2] Leonov, A.I., Nonequilibrium thermodynamics and rheology of viscoelastic polymer media. *Rheological Acta* **15**:85-98, 1976.
[3] Rubin, M.B., Attia, A.V. Calculation of hyperelastic response of finitely deformed elastic-viscoplastic materials. *Int. J. Numer. Meth. Eng.* **39**:309320, 1996.

STABLE PHENOMENOLOGICAL DESCRIPTIONS OF ELECTROMECHANICAL CREEPING IN POLYCRYSTALLINE FERROCERAMICS

Martín I.Idiart*[1,2] and Cristian J. Bottero[1]
[1]Centro Tecnológico Aeroespacial/Departamento de Aeronáutica,Facultad de Ingeniería,Universidad Nacional de La Plata, La Plata,Argentina
[2]Consejo Nacional de Investigaciones Científicas y Técnicas (CONICET),Argentina

Summary Ferroceramics display nonlinear creep effects under both electrical and mechanical loadings at room temperature. These effects have been described by certain phenomenological theories that additively decompose the strain and the dipole density into reversible parts associated with elasticity and dipole perturbations, and irreversible parts associated with dipole switching, and generate constitutive relations from suitably chosen free-energy densities and dissipation potentials. It is shown in this work that the creeping responses predicted by those theories can be unstable, and it is argued that these instabilities are unphysical artifacts of the theories arising from the use of non-convex free-energy densities. Motivated by these findings, a novel class of convex free-energy densities is proposed and employed to generate stable responses reproducing the essential features of ferroelectric creeping.

Ferroceramics display nonlinear creep effects under both electrical and mechanical loadings at room temperature [7, 5]. Various phenomenological theories with the capacity to describe such effects have been proposed.

A particularly attractive class of multiaxial theories hinges upon an additive decomposition of the deformation and the electric polarization into reversible contributions from elasticity and molecular polarizability, on the one hand, and irreversible contributions from ferroelectric switching, on the other hand [6, 8, 9]. The measures of irreversible deformation and irreversible polarization are thus identified as internal variables, and corresponding evolution laws are derived from postulated thermodynamic potentials in accordance with the framework of generalized standard materials. The resulting laws are able to reproduce essential features of ferroelectric responses such as electric hysteresis loops, nonlinear stress-strain curves, butterfly loops, and dipole rotation, and are amenable to numerical implementation into efficient finite-element codes [9]. Rate effects are introduced by assuming dissipation potentials of degree greater than one in the internal rates. It has been recently recognized, however, that the free energies often employed in these theories are non-convex functions of the internal variables and that, consequently, the predicted responses can exhibit unrealistic material instabilities even for simple loading histories such as electric cycling under colinear mechanical tractions [1]. The offending non-convexity is always introduced —perhaps inadvertently— in the attempt to capture the expected contribution of switching to straining via an algebraic connection between the deformation and the irreversible polarization. Some of these theories have also been found to produce evolution equations with no solution [10]. The first part of this work provides predictions for the evolution of polarization and deformation in unpoled specimens subject to uniaxial electric and mechanical step loadings. The evolution laws are numerically integrated in time following an implicit Euler scheme. The resulting polarization and deformation are found to develop an appreciable misalignment relative to the applied loading, which confirms the issues alluded to above.

Motivated by these findings, a novel class of convex free-energy densities is proposed in the second part of the work. For conciseness, we restrict attention to ceramic systems with tetragonal perovskite structure below their Curie temperature and subject to isothermal electromechanical loadings such that the influence of inertia, magnetism and the potential presence of mobile charges can be neglected. It is further assumed that the polycrystalline microstructures are untextured. The theoretical framework borrows ideas from the various microelectromechanical and hybrid theories for polycrystalline ferroceramics already available in the literature (e.g., [3, 11]). These theories consider the switching process as a phase transformation between ferroelectric domain variants, and thus identify the volume fractions of the multiple variants as internal variables. The measures of deformation and polarization are then related indirectly via these volume fractions, whose evolution is dictated by suitably chosen thermodynamic potentials. Realistic predictions can be generated by considering some hundreds of variants, albeit with an equally large number of internal variables. A similar constitutive framework is employed here. Thus, the internal state of the material is initially characterized by an infinite-dimensional internal variable representing the orientation distribution function of ferroelectric domains. A class of convex thermodynamic potentials in terms of this internal variable is then posited, and constitutive relations within the framework of generalized standard materials are derived. However, the functional form of the dissipation is selected in such a way that it effects an order reduction of the constitutive description whereby the infinite-dimensional internal variable is reduced to finite-dimensional internal variables representing irreversible polarization and irreversible deformation due to ferroelectric switching, preserving at the same time the generalized standard structure of the theory. Existance and stability of the predicted material response are thus ensured [2]. As a result of this order reduction, an integral —rather than algebraic— connection between the deformation and polarization due to switching is obtained. Predictions for the evolution of polarization and deformation in unpoled specimens subject to uniaxial electric and mechanical step loadings are reported. Once again, the evolution laws are numerically integrated in time following an implicit Euler scheme. In contrast to the previous predictions, the resulting polarization and deformation are found to remain aligned with the applied loading for the entire history, in agreement with physical expectations.

*Corresponding author. E-mail: martin.idiart@ing.unlp.edu.ar.

References

[1] Bottero, C.J., Idiart, M.I. An evaluation of a class of phenomenological theories of ferroelectricity in polycrystalline ceramics. *J. Eng. Math.* **113**, 13–22, 2018.

[2] Germain, P., Nguyen, Q.S., Suquet, P., Continuum Thermodynamics. *J. App. Mech.* **50**, 1010–1020, 1983.

[3] Huber, J.E., Fleck, N.A., Landis, C.M., McMeeking, R.M. A constitutive model for ferroelectric polycrystals. *J. Mech. Phys. Solids* **47**, 1663–1697, 1999.

[4] Idiart, M.I., Bottero, C.J. A phenomenological constitutive theory for polycrystalline ferroelectric ceramics based on orientation distribution functions. *Submitted*.

[5] Kamlah, M., Zhou, D. Room-temperature creep of soft PZT under static electrical and compressive stress loading. *Acta Mater.* **54**, 1389–1396, 2006.

[6] Landis, C.M. Fully coupled, multi-axial, symmetric constitutive laws for polycrystalline ferroelectric ceramics. *J. Mech. Phys. Solids* **50**, 127–152, 2002.

[7] Liu, Q.D. Investigation into the creeping polarization and strain in PZT-855 under combined mechanical and electrical loadings. *Acta Mech.* **220**, 1–14, 2011.

[8] McMeeking, R.M., Landis, C.M. A phenomenological multi-axial constitutive law for switching in polycrystalline ferroelectric ceramics. *Int. J. Engrg. Sci.* **40**, 1553–1577, 2002.

[9] Miehe, C., Rosato, D. A rate-dependent incremental variational formulation of ferroelectricity. *Int. J. Engrg. Sci.* **49**, 466–496, 2011.

[10] Stark, S., Neumeister, P., Balke, H. Some aspects of macroscopic phenomenological material models for ferroelectroelastic ceramics. *Int. J. Solids Struct.* **80**, 359–367, 2016.

[11] Tan, W.L., Kochmann, D., An effective constitutive model for polycrystalline ferroelectric ceramics: Theoretical framework and numerical examples. **Comp. Mater. Sci.** *136*, 223-237, 2017.

LINEAR AND NONLINEAR ELASTIC-VISCOELASTIC MODELING OF HIGHLY POROUS POLYMERS

Zahra Hooshmand Ahoor and Kostas Danas *
LMS, Ecole Polytechnique, Institut Polytechnique de Paris, Palaiseau, 91128, France

Summary In this study, a modification of the random sequential adsorption (RSA) algorithm is proposed to generate virtual microstructures with random distributions of non-overlapping elliptical voids in two-dimensions. Due to polydispersity, we can reach very high porosities up to 90vol%. The calculation of the effective elastic and viscoelastic response of the porous unit cells is performed through the finite element (FE) analysis with periodic boundary conditions. We compare the elastic results with the corresponding Hashin-Shtrikman (HS) bounds and study in detail the effect of viscoelasticity upon the nonlinear response of the porous materials. Such materials can be readily 3D-printed and used as designed in applications.

INTRODUCTION

In this work, we study numerically and whenever possible analytically the effective elastic and nonlinear elastic-viscoelastic response of two-dimensional (plane-strain) porous materials. Emphasis is put on voids with circular cross-section but very different sizes (i.e., polydisperse distributions). This allows us to reach extremely large porosities in the range of 90%. The converged unit cells may be readily 3D-printed [1] and tested experimentally.

In the present study, the RSA algorithm [2] is modified accordingly in the two-dimensional case allowing to generate random distributions of mono and polydisperse non-overlapping elliptical inclusions/voids with arbitrary shape, size, and orientation. The center and orientation of the ellipses are set randomly with a uniform probability distribution. The final in-plane (i.e. surface fraction) porosity, denoted here with f, is controlled exactly in the context of monodisperse voids and up to a small tolerance in the context of polydisperse ones. In the latter case, that tolerance is defined by the smallest void radius used in the RSA process. Subsequently, the numerical computation of the effective elastic and nonlinear elastic-viscoelastic properties is carried out using the FE method together with periodic boundary conditions. The number and size ratio of the largest to smallest voids are gradually increased to have a converged response. The following results focus on voids with a circular cross-section, whereas a study of voids with elliptical cross-section is left for the future.

LINEAR ELASTICITY: FINITE ELEMENT VERSUS HASHIN-SHTRIKMAN BOUNDS

The elastic properties of the matrix phase are assumed to be isotropic with Young's modulus $E = 1$GPa and Poisson's ratio $\nu = 0.3$. We first analyze the effect of the different number of families, i.e. different void sizes: 1, 3, 5, etc. One family of inclusions refers to the monodisperse size of voids whereas more than two induces a polydisperse void distribution. Since the voids have a circular shape, the polydispersity is only in size and not shape but the general algorithm can deal with the latter case too but increases the parameters of the study substantially and is not pursued here. It follows from the numerical calculations that in the context of monodisperse voids, the increase of the porosity makes the addition of new voids progressively more challenging. In contrast, in the case of polydisperse voids, by allowing gradually smaller void sizes, one can easily reach a substantially higher porosity even up to 90%, as shown in figure 1.

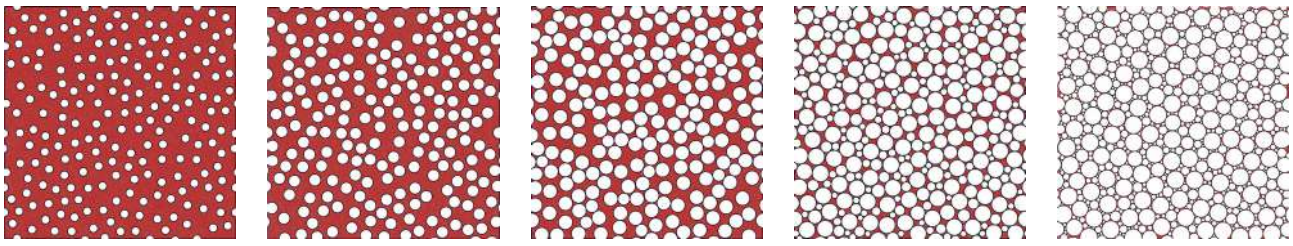

(a) f=20% (b) f=40% (c) f=60% (d) f=80% (e) f=90%

Figure 1: Realizations of microstructures at different porosities with (a)-(b):Monodisperse and (c)-(e):Polydisperse distribution

The final porosity that may be reached depends on the different parameters such as the number of families, offsets, properties of each phase, and more importantly the mesh size required to analyze the final unit cell or the minimum void size that is attainable by the 3D-printing process. In the case of monodisperse distributions with 200 voids, this numerically saturating value corresponds to $f_{sat} = 55\%$. To be able to reach higher porosities even up to $f = 90\%$, the addition of different void sizes is added to the RSA algorithm via an auto-generated rule. This allows for the automatic reduction of the void size by a prescribed percentage (e.g. 1%) once a large number of attempts (e.g. 1000) to introduce a given void size is done and fails. Figure 1 shows such representative microstructures in the case of monodisperse and polydisperse distributions.

*Corresponding author. E-mail: konstantinos.danas@polytechnique.edu.

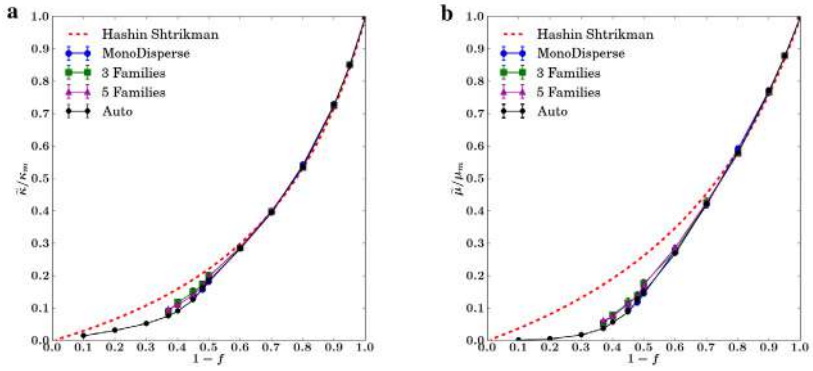

Figure 2: Numerical FE versus HS bounds for monodisperse and polydisperse distributions with 3 and 5 families as well as auto-generated distributions. (a) bulk modulus $\widetilde{\kappa}/\kappa_m$ and (b) shear modulus $\widetilde{\mu}/\mu_m$, where subscript m denotes the matrix phase.

Figure 2 shows comparisons between the numerical FE estimates and the analytical HS bounds for monodisperse and polydisperse voids (with a different number of families) for the effective bulk and shear moduli. The FE results remain very close to the HS estimates for porosities up to 50% for the bulk and 30% for the shear modulus. In turn, they start quickly diverging from those optimal bounds at larger porosities. The differences are much more pronounced for the shear modulus than for the bulk modulus. An attempt to further improve the FE estimates with respect to the HS bounds is made by manually designing the family choices and maximum to minimum void radii but is not shown here due to lack of space.

EFFECTIVE NONLINEAR ELASTIC-VISCOELASTIC RESPONSE

The elastomers exhibit more often than not a nonlinear elastic-viscoelastic response, particularly those resulting from 3D-printing. We present here briefly numerical FE estimates of the nonlinear elastic-viscoelastic behavior of porous polymers for different porosities and strain rates. For simplicity, we use the constitutive laws and parameters proposed in [3]. Figures 3(a) and 3(b) display plots of the stress-stretch response of the Nitrile rubber at constant stretch rate of 0.025 s^{-1} and for different strain rates at constant porosity $f = 20\%$, respectively. Interestingly, we see in figure 3(a) that the porosity leads to a reduction of the overall stress in the unit-cell but does not alter the final stretch after unloading and before relaxation. For completeness, in figure 3(c) we show the effect of porosity upon the overall volume change in the material as measured by the determinant average deformation gradient $\overline{J}$ at constant stretch rate 0.025 s^{-1}.

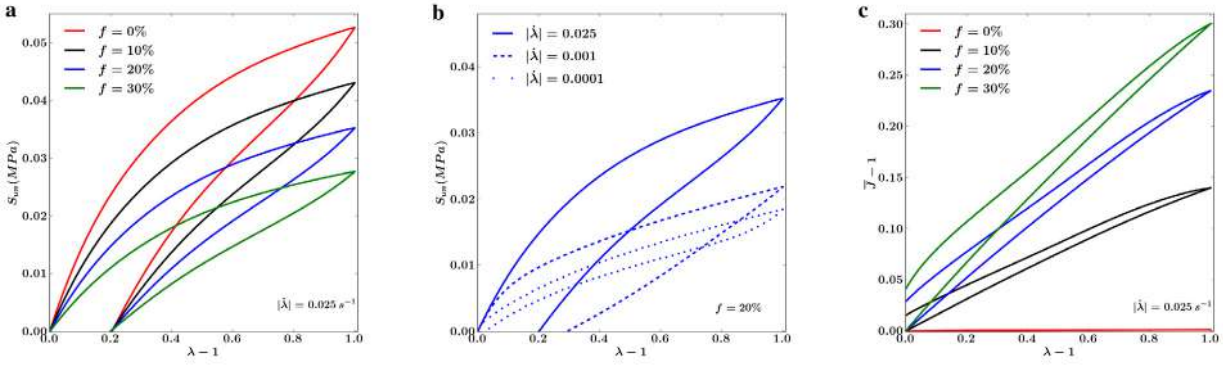

Figure 3: Stress-stretch effective response of porous Nitrile rubber at (a) different porosities and constant stretch rate 0.025 s^{-1} and (b) different stretch rates and porosity $f = 20\%$. (c) Determinant of the average deformation gradient $\overline{J}$ in terms of stretch at different porosities and constant stretch rate of 0.025 s^{-1}.

References

[1] M.G. Tarantino, O. Zerhouni, and K. Danas. Random 3D-printed isotropic composites with high volume fraction of pore-like polydisperse inclusions and near-optimal elastic stiffness. *Acta Materialia*, 175:331–340, 2019.

[2] K. Anoukou, R. Brenner, F. Hong, M. Pellerin, and K. Danas. Random distribution of polydisperse ellipsoidal inclusions and homogenization estimates for porous elastic materials. *Comp. Struct.*, 210:87 – 101, 2018.

[3] Aditya Kumar and Oscar Lopez-Pamies. On the two-potential constitutive modeling of rubber viscoelastic materials. *Comptes Rendus Mécanique*, 344(2):102–112, feb 2016.

A NEW METHOD TO MODEL DISLOCATION SELF-CLIMB DOMINATED BY CORE DIFFUSION

Fengxian Liu[1], Alan C.F. Cocks*[2], and Edmund Tarleton[2,1]
[1]Department of Materials, University of Oxford, Parks Road, Oxford OX1 3PH, UK
[2]Department of Engineering Science, University of Oxford, Parks Road, Oxford OX1 3PJ, UK

Summary Fast atomic transport along a dislocation core allows the dislocation to climb (referred to as dislocation self-climb) and is of particular importance in low-temperature creep and post-irradiation annealing. A variational principle is presented for problems in which this is the dominant mechanism of material redistribution. Studies of emergent dislocation behaviour involving both self-climb and glide are presented, in which the huge time scale separation between climb and glide is bridged by an adaptive time-stepping scheme. Loop coarsening of parallel prismatic loops is modelled. Excellent agreement is obtained with published experimental results. The formation of prismatic loops from the break-up of an edge dislocation dipole is also investigated. We demonstrate that edge dipoles sequentially pinch-off prismatic loops, rather than spontaneously breaking-up into a string of loops.

INTRODUCTION

The mobility of atoms in dislocation core regions is many orders of magnitude faster than in the surrounding lattice, resulting in a dislocation climb motion referred to as self-climb. In self-climb, atoms are rapidly rearranged in the dislocation core region to balance the difference of chemical potential along the dislocation line, which is more energetically favorable than mass exchange with the surrounding lattice (bulk diffusion), particularly at low temperatures where bulk diffusion is effectively frozen out. The rapid atomic diffusion along dislocations represents in itself an interesting physical phenomenon and plays a significant role in a wide variety of material behaviors, such as creep, loop or particle coarsening, precipitation and phase transformations, dynamic strain aging, and solute segregation. A systematic investigation of core diffusion and the corresponding self-climb process is therefore essential.

METHODOLOGY

The variational principle, as proposed by Needleman and Rice [1] and generalised by Cocks et al. [2] and Suo [3], has been widely used to solve mass diffusion or migration processes in which the rate of evolution of a system is given by the stationary value of the functional. That is,

$$\Pi = \Psi + \dot{G} \tag{1}$$

where Ψ is a rate potential, which contains contributions from all of the different kinetic and dissipative processes in the system and $\dot{G}$ is the rate of change of Gibbs free energy, which is the origin of the thermodynamic driving forces. It is the combination of thermodynamics and kinetics that determines the actual evolution path and the final state. Here, the

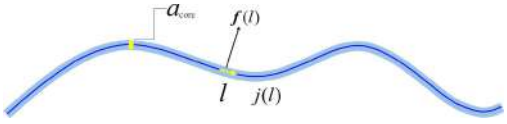

Figure 1: A system of an arbitrarily shaped dislocation line under $\mathbf{f}(\mathbf{l})$.

one-dimensional core diffusion-controlled self-climb process,as schematically shown in 1, is investigated. In which Ψ is caused by core diffusion, and $\dot{G}$ is the rate of change of Gibbs free energy during the self-climb motion. So that,

$$\Psi = \int_L \frac{j^2(l)}{2D(l)} dl, \qquad \dot{G} = -\int_L f_c(l) \mathrm{v}_c(l) dl \tag{2}$$

where $j(l) = -D\frac{\partial \mu}{\partial l}$ is the volumetric flux, which follows the Fick's law. $D(l) = \frac{D_{core}\Omega}{kT}$ is the effective diffusivity. f_c is the components of the Peach-Kohler force $\mathbf{f}$ in the climb direction. Additionally, during the self-climb process, mass conservation requires that the climb velocity is balanced by the variation of the flux,

$$\frac{dj(l)}{dl} + \mathrm{v}_c(l) b \sin\theta = 0 \tag{3}$$

The variational functional of the system can then be developed by subscribing Eq.2 into Eq.1. It can further be shown that, of all classes of assumed compatible flux and velocity fields, the actual motion renders Π stationary. So we can obtain the governing equations for the diffusion process from $\delta\Pi = 0$, which gives the climb velocities of the dislocations. We then implement the variational principle by discretizing the core diffusion formulation into the nodal based 3D-DDD framework to simulate the self-climb process.

*Corresponding author. E-mail: alan.cocks@eng.ox.ac.uk

VALIDATION AND APPLICATIONS

In this section, applications are presented to simulate dislocation evolution in engineering materials. The examples described in the following are chosen to illustrate the proposed method, and to demonstrate that it produces accurate results by comparison with available experimental observations. Addional examples are given in [6, 7] .

Loop coarsening during post-irradiation annealing: Dislocation self-climb has been proved to be the primary mechanism in the post-irradiation annealing process. The coarsening process of prismatic loops after irradiation by a glide and self-climb mechanism is then investigated based on the self-climb model. Two interstitial prismatic loops with $\mathbf{b} = \mathbf{a}/\mathbf{2}\langle\mathbf{111}\rangle$ and different radii, $R_1 = 12$ nm, $R_2 = 20$ nm, were introduced as the initial configuration. The results of a discrete dislocation simulation are shown in Fig.2 (a)-(d), experimental results for a similar coarsening process reported by [4] is reproduced in Fig.2 (e). The excellent consistency in both the dislocation configuration and time scale validates the new method and indicates the leading role played by self-climb during the post-irradiation annealing process.

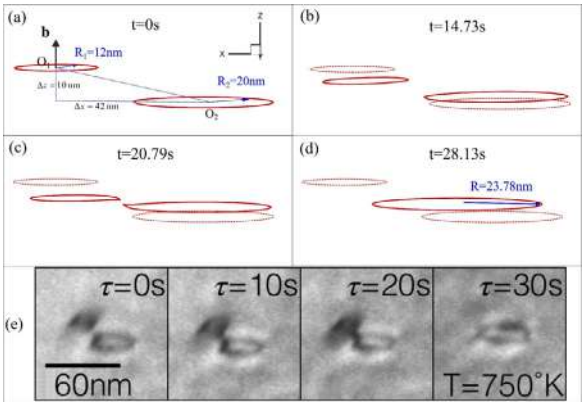

Figure 2: (a)-(d), DD simulation about loop coarsening over a time period, a movie is available in the supplementary S2, (e) Experimental results about the evolution of loop coarsening [4]

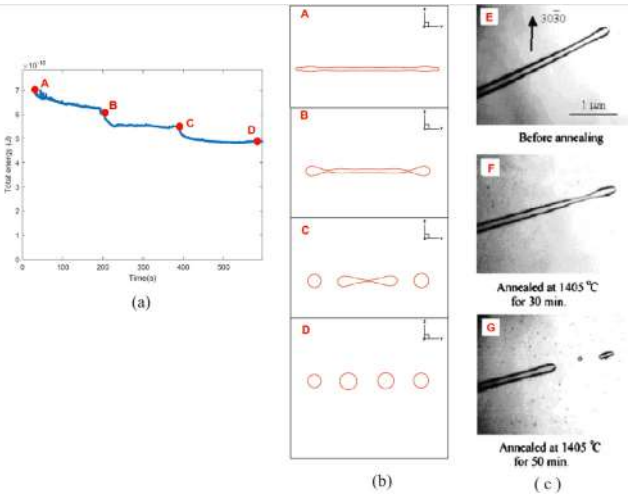

Figure 3: Prismatic loops forms from pinch-off of an edge dipole. (a) The energy evolution over time; (b) Dislocation profiles corresponding to the marked points A-D in (a); (c) Experimental observations from [5]

Formation of prismatic loops from pinch-off of a closed-end edge dipole : At high temperature or during annealing of deformed crystal, dislocation dipoles can annihilate and break up into prismatic loops by a conservative dislocation climb mechanism, which is primarily controlled by core diffusion along the dislocation line. An elongated edge dislocation dipole formed by jog dragging is introduced as the initial configuration, as shown in Fig. 3 (a). The results show that loops are pinched-off sequentially from the tip of the dipole rather than the dipole spontaneously breaking-up into a string of loops.

CONCLUSIONS

In the present work, a new methodology has been proposed for describing the core diffusion dominated dislocation self-climb process, which allows traditional DDD modeling to be extended to a new clan of physical problem. Applications in modeling the post-irradiation prismatic loop annealing and pinch-off of edge dislocation dipoles are conducted and compared with available experimental results.

References

[1] Needleman A, Rice J R. Plastic creep flow effects in the diffusive cavitation of grain boundaries, Perspectives in Creep Fracture. Pergamon, 1983: 107-124.
[2] Cocks, Alan CF, Simon PA Gill, and Jingzhe Pan. Modeling microstructure evolution in engineering materials. Adv. Appl. Mech., Vol. 36. Elsevier, 1998. 81-162.
[3] Suo Z., Motions of microscopic surfaces. Adv. Appl. Mech., 1997, 33: 193-294.
[4] Swinburne T D, Arakawa K, Mori H, et al. Fast, vacancy-free climb of prismatic dislocation loops in bcc metals. Sci. Rep., 2016, 6: 30596.
[5] Tang X, Lagerlöf K P D, Heuer A H. Determination of pipe diffusion coefficients in undoped and magnesia-doped sapphire:A study based on annihilation of dislocation dipoles. J. Am. Ceram. Soc., 2003, 86(4): 560-65.
[6] Liu F, Cocks A C F, Tarleton E., A new method to model dislocation self-climb dominated by core diffusion. J. Mech. Phys. Solids, 2020, 135: 103783.
[7] Liu F, Cocks A C F, Simon PA Gill, Tarleton E, An improved method to model dislocation self-climb, manuscript submitted for publication.

PREDICTION OF THE EFFECT OF INDIVIDUAL TEXTURE COMPONENTS ON THE PLASTIC ANISOTROPY OF POLYCRYSTALLINE METALLIC SHEETS

Oana Cazacu[1a)], Nitin Chandola[1], Benoit Revil-Baudard[1]
[1]Department of Mechanical &Aerospace Engineering, University of Florida/REEF, Shalimar, Fl, U.S.A

Summary In this study, the recent polycrystal model [1] is used to predict the influence of individual texture components on the macroscopic plastic properties of textured polycrystalline sheets. The constituent grain behaviour is described using the single-crystal yield criterion [2]. First, we present the predictions of plastic anisotropy in mechanical properties for metallic sheets containing a single texture component (e.g. Goss, cube, brass, copper) specified in terms of a Gaussian distribution of misorientations with scatter width ranging from 0º (i.e. ideal texture) up to 45º around the respective ideal texture component (i.e. close to random texture). Irrespective of the number of grains considered, the predicted Lankford coefficients have finite values for all loading orientations. When more than one ideal texture component exists in the material, it is shown that the polycrystal model captures the effect of each texture components on the overall plastic anisotropy of the polycrystal.

In this paper, using the yield criterion [2] for description of the plastic behaviour of single crystals, we study the effect of individual texture components on the plastic anisotropy of polycrystalline metallic sheets. Specifically, we predict the anisotropy in uniaxial yield stresses and Lankford coefficients (r-values) in metallic sheets containing the following texture components that are commonly observed experimentally: cube, Goss, Brass and Copper. First, results are presented for sheets having one texture component specified in terms of a Gaussian distribution of misorientations with scatter width ranging from 0º (i.e. ideal texture) up to 35º around the respective ideal texture component. It is shown that for ideal textures, using the single-crystal criterion [2] the directional dependence of the yield stress and Lankford coefficients can be obtained in closed-form. For the case of strongly textured sheets containing a spread about the ideal texture components, the polycrystalline response is calculated numerically using the polycrystal model [1]. It is shown that irrespective of the tensile loading direction the predicted r-values have finite values for all loading orientations. As an example, in Fig.2 are shown the predicted variations of macroscopic plastic properties with the loading orientation for a polycrystalline sheet for which the {111} pole figures are shown in Fig.1. Note the effect of the spread with respect to the ideal Goss texture on the directional dependence of the yield stresses and plastic strain ratios. For a spread of $\omega = 25º$ around the ideal Goss orientation, the numerical predictions of the yield stresses and r-values of the polycrystalline sheet are very close to those obtained for $\omega = 35º$. On the other hand, the anisotropy in $\sigma(\alpha)/\sigma(0)$ vs. α and $r(\alpha)$ vs. α variations are much less pronounced than the respective curves for the ideal Goss texture For example, for a spread $\omega = 35º$, the value of r(90º) is about five times smaller than the corresponding r-value of the ideal Goss texture. Nevertheless, the nature of the r-values variation is similar irrespective of the spread, with a point of inflection at around 55^0 from the reference direction (see Fig. 2).

(a) (b)

Figure 1: {111} pole figures for Goss texture corresponding to a series of Gaussian distributions of increasing scatter width : (a) $\omega=25^0$ and (b) $\omega=35^0$.

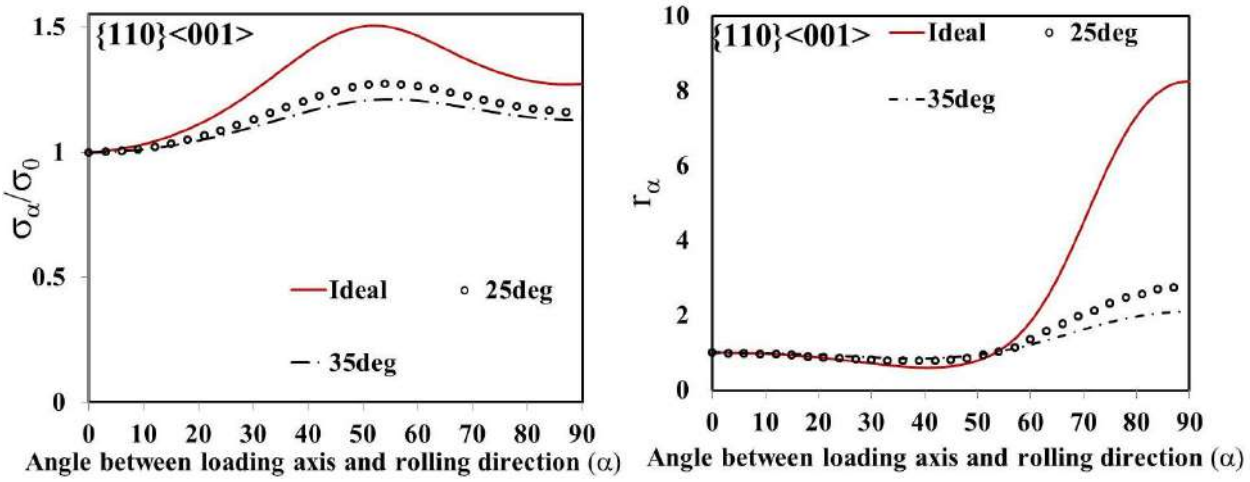

(a) (b)

Figure 2: Predictions obtained with the polycrystal model [1] of the directionality in: (a) yield stress ratio $\sigma(\alpha)/\sigma(0)$, and (b) plastic strain-rate ratio r(α) in the plane of the {110}<001> textured polycrystalline sheet. The textures for different scatter width are shown in Fig. 1. The results for ideal texture were obtained with analytical formulas in conjunction with the single-crystal model [2].

Next, an example is given for a polycrystalline sheet with dominant Goss texture component (70% volume fraction) and a minor $\{\bar{2}1\,\bar{1}\}<011>$ component (30% volume fraction). It is predicted that the $\{\bar{2}1\,\bar{1}\}<011>$ component contributes to a significant decrease in anisotropy of the material. Indeed, the predicted *r*-value in the transverse direction is significantly lower than that predicted for the ideal Goss component (compare results in Fig. 3(b) with the r-values variation shown in Fig. 2(b) for the ideal Goss component).

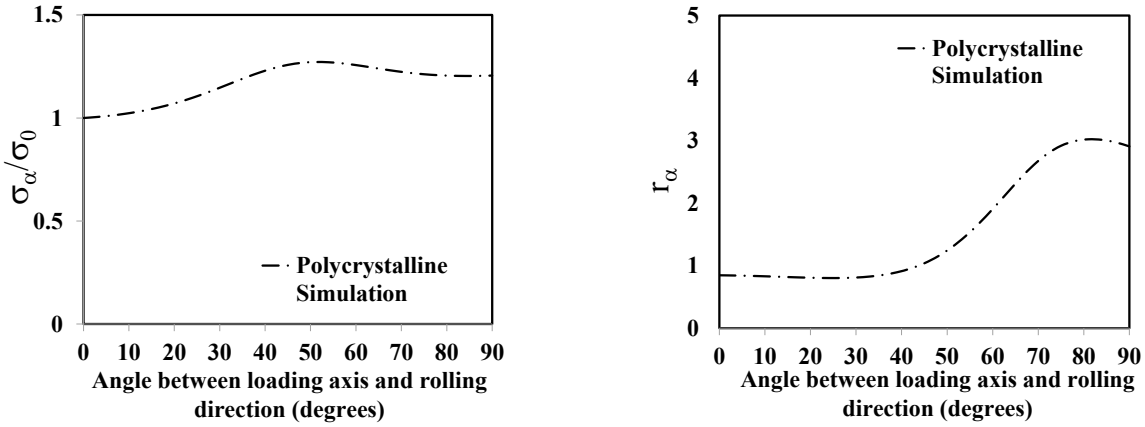

(a) (b)

Figure 3: Predictions of anisotropy in (a) yield stress ratio and (b) plastic strain-rate ratio in the plane of the polycrystalline sheet predicted with the polycrystal model [1] for a strongly textured polycrystal with components spread around the $\{\bar{2}1\bar{1}\}<011>$(30%) and ideal Goss (70%) orientation.

CONCLUSIONS

When more than one ideal texture component exists in the material, the polycrystalline simulations based on the new description of the plastic behavior of the constituent grains capture the influence of individual texture components on the overall plastic anisotropy of the polycrystal. The examples presented demonstrate the predictive capabilities of the model

References

[1] Chandola N., Cazacu O., Revil-Baudard B. *Mech. Research Communications* 84:98–101, 2017.
[2] Cazacu O., Revil-Baudard B., Chandola N. *Int. J. Solids Structures* 151:9–19, 2018.

RECIPROCAL RELATIONS IN DISLOCATION-MEDIATED PLASTICITY

Victor L. Berdichevsky
Department of Mechanical Engineering, Wayne State University, Detroit, USA

Summary Reciprocal relations are established for nonlinear driven dissipative systems. A consequence of these relations for dislocation-mediated viscoplasticity is the potentiality of constitutive equations in the limit of small and large stresses. Implications for double slip in single crystals are discussed.

Almost a century ago Onsager found a universal feature of all dissipative systems describing approach to thermodynamic equilibrium, the reciprocal relations. They hold for linear differential equations describing an evolution of macrovariables in vicinity of equilibrium states. The derivation assumed implicitly that underlying microdynamics is Hamiltonian and ergodic. There are many situations which are not covered by these assumptions. Such are the cases where macrovariables, which are the slow parameters of microdynamics, describe, in fact, the mesoscopic phenomena. Thus, an additional course graining is to be done to get the equations of macroscopic theory. In particular, this pertains to the problems of dislocation-mediated plasticity, where elimination of atomic degrees of freedom yields dislocation dynamics, and an additional averaging is needed to obtain the equations of macroscopic plasticity. This averaging problem is qualitatively different from the classical problems of nonequilibrium statistical thermodynamics because the equations to be averaged are not Hamiltonian, they are dissipative. However, the basic question remains the same: Are there universal relations which macroscopic equations must respect? In this talk, a positive answer to this question is given. Though the major focus of this work is on dislocation viscoplasticity, the results are formulated in quite general form. Let a mesoscopic process be described by a system of ODE with thermal noise,

$$B_{ij}\dot{x}_j = F_i - \frac{\partial H(x)}{\partial x_i} + \alpha_{ij}\dot{w}_j. \tag{1}$$

Here B_{ij} are drag coefficients, i,j run through the values $1,\dots,n$, summation over repeated indices is implied, F_i external force, $H(x)$ interaction energy which is either periodic or quasi-periodic function of x_i, $\dot{w}_i$ independent white noises, α_{ij} their intensities. The system coordinates x_i drift with some average velocities V_i which are functions of external forces F_i. The major result of this work is: In the limit of small and large forces, there exists a dissipative potential $D(F)$ such that

$$V_i(F) = \frac{\partial D(F)}{\partial F_i}. \tag{2}$$

Moreover, in the limit of small forces the dissipative potential is determined from the variational principle

$$D(F) = \frac{1}{\langle e^{-H/T}\rangle}\min\langle \frac{1}{2}B_{ij}^{-1}e^{-H/T}\left(F_i - \frac{\partial u}{\partial x_i}\right)\left(F_j - \frac{\partial u}{\partial x_j}\right)\rangle \tag{3}$$

where in periodic case $\langle\cdot\rangle$ is the cell average and minimum is sought over periodic functions $u(x)$, while in quasi-periodic case $\langle\cdot\rangle$ is the space average, and minimization is done over quasi-periodic functions $u(x)$; B_{ij}^{-1} is inverse tensor to B_{ij}, T temperature. In the limit of large forces, the dissipative potential is computed analytically for periodic structures,

$$D = \frac{1}{2B}F_iF_i - \frac{1}{B\epsilon^2}\sum_{k\in\mathbb{Z}_n'}|k|^2\,|H_k|^2\ln\left[|k|^2 + \left(\frac{\epsilon}{T}F\cdot k\right)^2\right].$$

Here the periodic cell is supposed to be an n −dimensional cube with the size ϵ, H_k are Fourier coefficients of energy $H(x/\epsilon)$, $\mathbb{Z}_n'$ is the orthogonal lattice in R_n with the size 2π and the excluded origin $k=0$, tensor B_{ij} is spherical $\left(B_{ij} = B\delta_{ij}\right)$, $F\cdot k$ is the scalar product of vectors F and k. The dissipative potential is a convex function of force F. The result formulated is based on homogenization theory of parabolic equations with minor terms developed by Jikov, Kozlov and Oleinik in their monograph [1].

For small forces, equations (2), (3) yield the relations which look similar to Onsager relations,

$$V_i = A_{ij}F_j, \quad D = \frac{1}{2}A_{ij}F_iF_j, \quad A_{ij} = A_{ji}. \tag{4}$$

However, the origin of the reciprocity relations (4) is quite different: they are caused by driven dissipative dynamics.

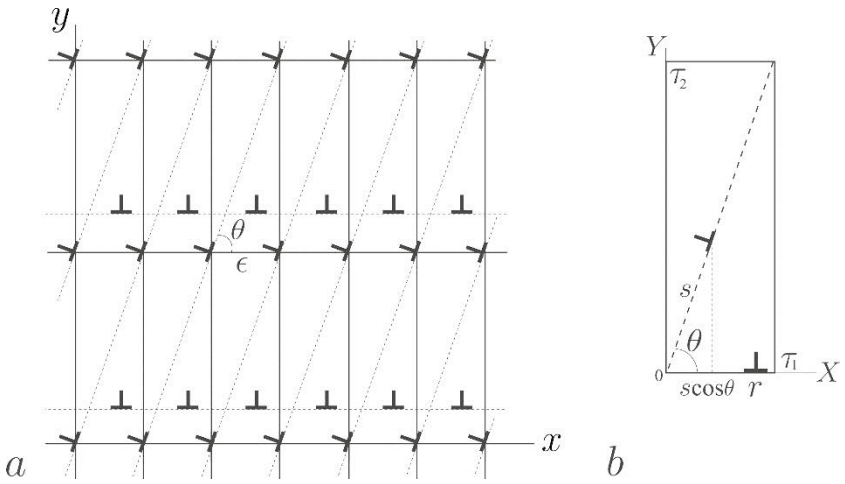

Fig. 1

As an application of (2), (3), we study the dislocation viscoplasticity in two interacting slip systems of a single crystal with cubic symmetry. Slip systems are in planes (111) and (-1-11). Dislocation microstructure is periodic (Fig. 1a), and dislocations in each slip systems move as a rigid body, so the flow has two degrees of freedom, *r* and *s* (Fig. 1b). Interaction energy for such dislocation systems was found in [2]. Typical values of dimensionless inverse temperature $\lambda = 5\mu b^3/(\pi(1-\upsilon)T)$ (μ, υ, b being shear modulus, Poisson's coefficient, and Burgers vector, respectively) are large. Therefore, we study asymptotics of variational problem (3) as *H/T* tends to infinity. General results for such type asymptotic problem were obtained by Kozlov [3, 4]. In the case under consideration the asymptotics is:

$$D = \frac{1}{2}A_{11}^2F_1^2 + A_{12}F_1\ F_2\ + \frac{1}{2}A_{22}F_2^2$$

$$A_{11} = 0.003\lambda e^{-0.001\lambda}B^{-1},\quad A_{22} = 0.16\lambda e^{-0.125\lambda}B^{-1}$$

$$A_{12} = 2A_{22}$$

These formulas reveal quite nontrivial interactions between two slip systems. If the slip systems were not interacting, then A_{11} and A_{22} would be equal to B^{-1}. In fact, A_{11} and A_{22} are exponentially smaller than B^{-1} due to interactions. Besides, A_{12} turns out to be equal $2A_{22}$. It is interesting and hard to foresee that A_{22} is much smaller than A_{11} (indices 1 and 2 mark horizontal and inclined slip systems, respectively). Physically, this means that dislocations of the second slip system are barely moving and rather play a role of a set of static obstacles for dislocations of the horizontal slip system. Apparently, this is caused by quite special non-symmetric geometry of the microstructure. In a special case of tension/compression by stress σ in the x-direction, F_1 vanishes, and both slip systems operate with extremely slow velocities, $V_1 = 2A_{22}F_2,\ V_2 = A_{22}F_2,\ F_2 = b\sigma\sin\theta\cos\theta$. Interestingly, V_1 is still larger than V_2, in fact, twice larger. All these intrinsic "reciprocities" are beyond of reciprocal relations (4) and came from the variational principle (3).

Dislocation dynamics equations can be cast in form (1) both in two-dimensional [2] and three-dimensional [5] cases. Thus, an immediate consequence of (2) and Orowan formula for dislocation-mediated viscoplasticity is the existence of a function of stresses σ_{ij}, $\mathbb{D}(\sigma_{ij})$, such that plastic strain rate $\dot{\varepsilon}_{ij}^{(p)}$ is linked to stresses by the constitutive equations,

$$\dot{\varepsilon}_{ij}^{(p)} = \frac{\partial\mathbb{D}(\sigma_{ij})}{\partial\sigma_{ij}}. \tag{5}$$

Equations (5) hold in the limit of small and large stresses. The validity of (5) in an intermediate range of stresses remains unclear.

References:

1. V.V. Jikov, S.M. Kozlov, and O.A. Oleinik, Homogenization of differential operators and integral functionals Springer-Verlag, Berlin, 1994.
2. V.L. Berdichevsky, A continuum theory of edge dislocations, J. Mech. Phys. Solids 106, 95-132, 2017.
3. S.M. Kozlov, Geometric aspects of averaging, Usp. Mat. Nayk 44, 79-121, 1989.
4. S.M. Kozlov, Asymptotics of Laplace-Dirichlet integrals, Funct. Anal. Appl. 24, 37-49, 1990.
5. V.L. Berdichevsky, Beyond classical thermodynamics: Dislocation-mediated plasticity, J. Mech. Phys. Solids 129, 83-118, 2019.

CRYSTAL PLASTICITY LIKE THEORY OF DUCTILE FRACTURE

Amine Benzerga*[1] and R Vigneshwaran[1]
[1]Department of Aerospace Engineering, Texas A & M University, College Station, USA

Summary A constitutive framework is developed to describe damage accumulation to failure in ductile materials by void growth and coalescence. A multi-surface representation of effective yielding is adopted to represent the competition between a single mechanism of nominally homogeneous yielding and a finite number of systems for inhomogeneous yielding. Homogeneous yielding represents the usual void growth mechanism whereas inhomogeneous yielding aims to capture void coalesence under tension-dominated loading or mere void distorsion under shear-dominated loading. The theory bears some connections to continuum crystal theories of plasticity with some notable differences. Simple examples are provided for one or two localization systems to illustrate the potentially large scatter in ductility obtained when void distributions are clustered.

INTRODUCTION

Constitutive relations for porous plastic solids have historically been obtained by considering elementary cells subjected to *homogeneous* deformation, along with limit analysis theory [1, 2]. By definition, such boundary conditions preclude strain concentrations within the cell. This essential limitation of Gurson-like models can be relaxed by employing boundary conditions that allow for mesoscopically *inhomogeneous* deformation. This is precisely what has been achieved in e.g. [3, 4]. This new class of models represents the potentially inhomogeneous yielding of porous solids.

With that as basis, a general multisurface constitutive framework is outlined so as to accommodate homogeneous yielding as well as various mechanisms of inhomogeneous yielding. The latter rests on the notion of localization systems akin to slip systems in crystal plasticity.

THEORY

The constitutive framework is one for a material with distributed porosity. The porosity may have resulted from prior cavitation, say at second phases and brittle interfaces, or processing-induced. The plastic part of the rate of deformation is written as:

$$\mathbf{D}^p = \underbrace{\dot{\lambda}^{\mathrm{H}} \frac{\partial \Phi^{\mathrm{H}}}{\partial \boldsymbol{\sigma}}}_{\text{Hill–Mandel}} + \underbrace{\sum_{\alpha=1}^{N_{\mathrm{loc}}} \dot{\lambda}^{\alpha} \frac{\partial \phi^{\alpha}}{\partial \boldsymbol{\sigma}}}_{\text{localized}} \tag{1}$$

with Φ^{H} corresponding to homogeneous yielding. If yielding is inhomogeneous at some appropriate scale, then there may be various localization systems, each being associated with a threshold condition of the type $\phi^{\alpha} = 0$ in the rate-independent limit.

In general, the porosity may be described by the void volume fraction, f, the void axes, and parameters that describe the spatial distribution of voids. To illustrate the main ideas, let us focus on axially symmetric voids, say spheroidal or (finite-height) cylindrical. For homogeneous yielding, proper descriptors of the internal state are the porosity f, void aspect ratio and orientation, so that

$$\Phi^{\mathrm{H}}(\boldsymbol{\sigma}; f, w, \mathbf{n}^{(3)}) = 0 \tag{2}$$

An example of this type of yielding was developed in [5].

For inhomogeneous yielding, the spatial distribution of voids matters, here represented by scalar W^{α} and director $\mathbf{n}^{\alpha}$:

$$\phi^{\alpha}(\boldsymbol{\sigma}; f, w, W, \mathbf{n}^{(3)}, \mathbf{n}^{\alpha}) = 0 \tag{3}$$

Here, $\mathbf{n}^{\alpha}$ denotes the normal to the localization plane, or in some cases the direction of localization itself (column coalescence). Examples of this type of model may be found in [6, 4].

DISCUSSION AND RESULTS

Localization systems are for the proposed theory what slip systems represent for crystal plasticity. In particular, the theory does not predict localization systems. Instead, they are provided as input based on the assumed toplogy of the void aggregate. Voids, unlike atoms, are generally not orderly distributed. For periodic void distributions, localization systems may be defined on the basis of nearest-neighbour topology. However, for clustered void distributions, as expected in practice, it is postulated that there is a *finite* number of potential localization systems, Fig. 1a. In the limit of an inifinite number of such systems, the distribution is random, and a statistically isotropic behavior is retrieved.

*Corresponding author. E-mail: benzerga@tamu.edu.

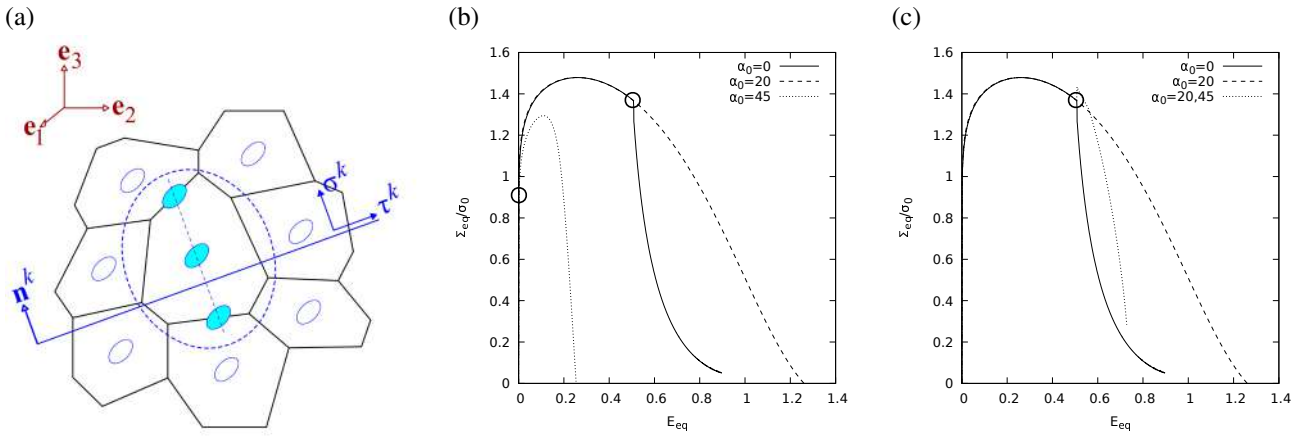

Figure 1: (a) Relative spacing in a void cluster. (b) Response and ductility for various orientations of a single localization system at fixed initial structure. (c) One versus two systems of localization.

For illustration, Fig. 1b shows a typical dependence of the response upon the orientation of the localization system. Here, plane strain was assumed with an imposed stress triaxiality $T = 1$. The variation of ductility between the various cases shown is indicative of the scatter in multiple realizations since various local void orientations may be encountered in a physical specimen.

Fig. 1b shows the effect of the number of localization systems on the response. A parallel with crystal plasticity is obvious, but with some key differences: (i) dependence upon the normal stress in addition to the shear stress (generalized normality holds); (ii) the constitutive relations are obtained through scale transition operations, thus involving no ad hoc parameters.

CONCLUSION

A crystal-plasticity like theory of ductile fracture is constructed on the basis of recent models of inhomogeneous yielding in porous plastic solids. The theory enables seemless transitions from void growth to void coalescence, tension-dominated to shear-dominated loadings and allows for scatter in ductility to be rationalized and quantified. In addition, the constitutive framework may be used in conjunction with the theory of strain localization (in the macroscopic sense) [7] in order to discriminate fracture by void impingement versus failure by instability.

References

[1] A. L. Gurson. Continuum Theory of Ductile Rupture by Void Nucleation and Growth: Part I– Yield Criteria and Flow Rules for Porous Ductile Media. *Journal of Engineering Materials and Technology*, 99:2–15, 1977.

[2] A. A. Benzerga and J.-B. Leblond. Ductile fracture by void growth to coalescence. *Advances in Applied Mechanics*, 44:169–305, 2010.

[3] A. A. Benzerga and J.-B. Leblond. Effective Yield Criterion Accounting for Microvoid Coalescence. *Journal of Applied Mechanics*, 81(3):031009, 2014.

[4] S. M. Keralavarma and S. Chockalingam. A criterion for void coalescence in anisotropic ductile materials. *International Journal of Plasticity*, 82:159–176, 2016.

[5] S. M. Keralavarma and A. A. Benzerga. A constitutive model for plastically anisotropic solids with non-spherical voids. *Journal of the Mechanics and Physics of Solids*, 58:874–901, 2010.

[6] M. E. Torki, A. A. Benzerga, and J.-B. Leblond. On Void Coalescence under Combined Tension and Shear. *Journal of Applied Mechanics*, 82(7):071005, 2015.

[7] J. R. Rice. The localization of plastic deformation. In W. T. Koiter, editor, *14th int. cong. Theoretical and Applied Mechanics*, pages 207–220. North–Holland, Amsterdam, 1976.

CREEP BEHAVIOUR OF METALLIC GLASSES AND EVOLUTION OF MATERIAL INHOMOGENEITY

Xiaoding Wei*[1,2], Wenqing Zhu [1]
[1]State Key Laboratory for Turbulence and Complex System, Department of Mechanics and Engineering Science, College of Engineering, Peking University, Beijing 100871, China
[2]Beijing Innovation Center for Engineering Science and Advanced Technology, Peking University, Beijing 100871, China

Summary In this work, a chemo-mechanical continuum theory based on a thermodynamically consistent framework is proposed to describe the creep behaviour of metallic glasses. In our theory, the inherent material inhomogeneity in metallic glasses at the nano- and micro-scale is taken into account. Visco-plastic deformation is described as the outcome of the atomic diffusion driven by the chemical potential gradient. Scenarios of microstructural evolutions under both stable and unstable creep are reproduced by finite element simulations. Different scaling of the steady-state creep strain rate and stress for the regimes below and above a critical stress are captured and consistent with the former studies.

Lack of dislocations and grain boundaries, metallic glasses (MGs) also known as amorphous metals, have distinct mechanical properties than their crystalline counterparts. Creep tests have been carried out on MGs at a variety of stress, temperature and sample size to study their unique plastic deformation mechanisms [1-3]. Particularly, when subjected to a high stress, the creep becomes unstable and the strain localization with shear band instability takes place [4, 5]. So far, theoretical studies on the creep of MGs have been studied mostly at the nanoscale (<100nm) using molecular dynamic simulations [6]. To overcome the limitations of system sizes and time scales in molecular simulations, a continuum theory that reflects the microscopic mechanisms of creep deformation in metallic glasses MGs is necessary to study the creep behaviors on large scale and at low temperature. In this study, we develop a chemo-mechanical continuum theory within a thermodynamically consistent framework that established earlier by Gurtin [7], and later developed by Anand [8] and Miehe et al. [9]. In this theory, the atomic diffusion is correlated with the inelastic deformation of MGs, as shown in Figure 1. Multiplicative decomposition of the deformation gradient assumes $\mathbf{F} = \mathbf{F}_e\mathbf{F}_p\mathbf{F}_c$ where $\mathbf{F}_e$ is the elastic deformation gradient, and $\mathbf{F}_p$ and $\mathbf{F}_c$ are two rate-dependent inelastic eigen deformation gradients. $\mathbf{F}_p$ is the plastic deformation gradient with $\det(\mathbf{F}_p)= 1$ due to the incompressibility of the plastic deformation. $\mathbf{F}_c = J_c^{1/3}\mathbf{I}$ is the dilatation deformation gradient where $J_c=\det(\mathbf{F}_c)$.

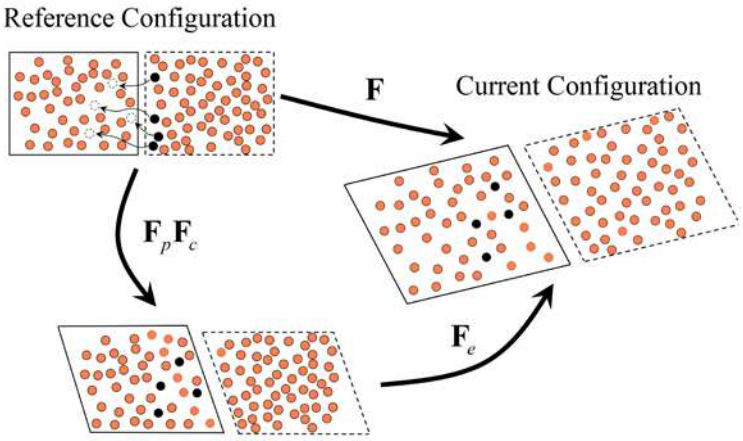

Figure 1. Illustration of decomposition of the total deformation.

The creep behavior of Cu-Zr MG is investigated at two stress levels ($\tilde{\sigma} = 1.93$ and 9.66), where the non-dimensional stress is $\tilde{\sigma} = \sigma\Omega^* / (k_B\theta)$. Note that Ω^* is the atomic volume, k_B is the Boltzmann constant, and θ is the temperature. The strain evolution trends under two stresses are summarized in **Figure 2**. Under the low stress ($\tilde{\sigma} = 1.93$), there is a steady-state creep stage (at a constant creep strain rate, manifested by the slope of 1) following a transient creep stage (decreasing creep strain rate). Under the high stress ($\tilde{\sigma} = 9.66$), however, a tertiary creep stage takes place following transient and steady-state creep, where the creep strain rate is rapidly increasing and the material fails eventually with mechanical instability.

*Corresponding author. E-mail: xdwei@pku.edu.cn

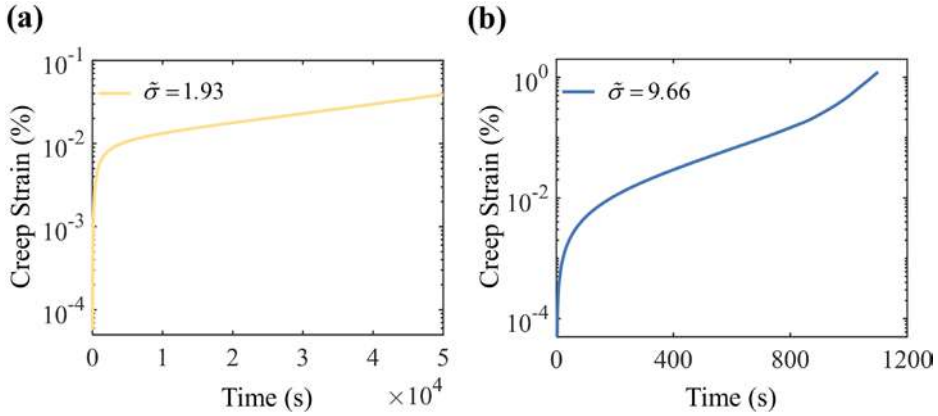

Figure 2. Creep history under (a) low ($\tilde{\sigma}=1.93$) and (b) high ($\tilde{\sigma}=9.66$) stresses.

Further, inspection of the free volume and von Mises stress evolutions under the low stress reveals that at transient creep stage interior atoms flow from low-free-volume regions to high-free-volume regions. As a result, the material becomes more homogeneous. Then, atoms on the free surfaces start to flow inside and thus free volume is accumulated on the free surfaces. The same phenomena in metallic glasses have been found in previous molecular dynamic simulations [10]. However, in the case of the high stress, we found that atoms flow from high-free-volume regions to low-free-volume regions so that the spatial heterogeneity becomes more prominent with the average free-volume gradient continuously increasing. With the time going, cavitation and voids nucleate and coalesce inside the material forming thin shear bands and leading to the strain localizations and mechanical instability. This finding is consistent with the void formation in shear bands recently observed through high-resolution electronic microscopy [11].

CONCLUSIONS

In summary, this work introduces a thermodynamically consistent chemo-mechanical theory to describe the atomic diffusion and resulting inelastic deformation in metallic glasses. The theory is implemented into a finite element code to simulate the creep responses varying imposed stress and temperature. Microscopic characteristics such as surface diffusion for stable creep and strain localization for unstable creep are successfully captured. An abrupt change of scaling at critical stress is found which is verified the existing experiments and molecular simulations.

References

[1] Qiao JC, Pelletier JM, Yao Y. Creep in bulk metallic glasses. Transition from linear to non linear regime. Materials Science and Engineering: A. 2019;743:185-9.
[2] Zhu F, Song S, Reddy KM, Hirata A, Chen M. Spatial heterogeneity as the structure feature for structure-property relationship of metallic glasses. Nat Commun. 2018;9:3965.
[3] Yoo B-G, Kim J-Y, Kim Y-J, Choi I-C, Shim S, Tsui TY, et al. Increased time-dependent room temperature plasticity in metallic glass nanopillars and its size-dependency. International Journal of Plasticity. 2012;37:108-18.
[4] Budrikis Z, Castellanos DF, Sandfeld S, Zaiser M, Zapperi S. Universal features of amorphous plasticity. Nat Commun. 2017;8:15928.
[5] Castellanos DF, Zaiser M. Avalanche Behavior in Creep Failure of Disordered Materials. Phys Rev Lett. 2018;121:125501.
[6] Cao P, Short MP, Yip S. Understanding the mechanisms of amorphous creep through molecular simulation. Proc Natl Acad Sci U S A. 2017;114:13631-6.
[7] Gurtin ME. Generalized Ginzburg-Landau and Cahn-Hilliard equations based on a microforce balance. Physica D: Nonlinear Phenomena. 1996;92:178-92.
[8] Anand L. A Cahn–Hilliard-type theory for species diffusion coupled with large elastic–plastic deformations. Journal of the Mechanics and Physics of Solids. 2012;60:1983-2002.
[9] Miehe C, Hildebrand FE, Boger L. Mixed variational potentials and inherent symmetries of the Cahn-Hilliard theory of diffusive phase separation. Proc R Soc A. 2014;470:20130641.
[10] Wei Y, Bower AF, Gao H. Analytical model and molecular dynamics simulations of the size dependence of flow stress in amorphous intermetallic nanowires at temperatures near the glass transition. Physical Review B. 2010;81.
[11] Shao Y, Yang G-N, Yao K-F, Liu X. Direct experimental evidence of nano-voids formation and coalescence within shear bands. Applied Physics Letters. 2014;105.

NUMERICAL DESCRIPTION OF SCREW DISLOCATION IN DILUTE AND HIGHLY-CONCENRATED BCC ALLOYS

Tomohito Tsuru[1,2,3]
[1]Nuclear Science and Engineering Center, Japan Atomic Energy Agency, 2-4 Shirakata, Tokai-mura, Ibaraki, Japan
[2]Elements Strategy Initiative for Structural Materials (ESISM), Kyoto University, Yoshida, Honmachi, Sakyo-ku, Kyoto, Japan
[3]PRESTO, Japan Science and Technology Agency, P4-1-8 Honcho, Kawaguchi, Saitama, Japan

Summary Plastic deformation of BCC alloys is generally achieved by the fundamental motion of screw dislocations via kink process of dislocation. We evaluated solid solution softening/strengthening behavior of various solutes in dilute and highly-concentrated BCC alloys by the first-principles calculations in combination with classical theory of dislocations. We identified a clear trend in interactions between a solute and a screw dislocation and found that the change in the energy barrier to kink nucleation is related to the interaction energy. These two properties are the main effects contributing to solid solution softening/strengthening. We proposed new analytical models describing kink process of screw dislocations, in which the fundamental properties are evaluated by the electronic structure calculations. The model found to reproduce reasonably well the complex solid solution behavior as a function of temperature and solute concentration. This specific balance of the interactive and repulsive interactions is the origin of macroscopic solid solution behavior.

MANUSCRIPT PREPARATION

Dislocation have been regarded as the most important lattice defects in plastic deformation, especially in metallic materials. The fundamental properties of the dislocation core have a dominant influence on the intrinsic ductility or brittleness of materials. The interaction between dislocations and other crystal defects plays a critical role in determining the mechanical properties of metals. The classical strengthening mechanism was developed by this major premise, and the mechanical properties of metals have been developed by under-standing and controlling the dislocation behavior. While continuum theory expresses an excellently long-ranged elastic field of a dislocation, it breaks down owing to the singularity near the dislocation core. With improvements in computer technology, atomic scale simulations such as molecular dynamics have been implemented to explore the relation between the dynamic behavior of defects and the mechanical response. Recently, a dislocation core structure can be captured directly by first principles calculations.

Especially, plastic deformation in BCC metals is achieved by a fundamental motion of screw dislocations through a kink mechanism. The first-principles calculations have been widely applied to directly calculate the dislocation core of various metals. The fundamental glide motion and the core structure of a dislocation in pure BCC metals and the effects of solutes on core structure have been investigated by the first-principles calculations. We have aimed to achieve a comprehensive understanding of solid solution softening/strengthening in BCC metals. The effects of various solutes in BCC metals have also been comprehensively investigated by the first-principles calculations through a solid solution model. In the present study, we performed the first-principles calculations of the dislocation core and examined the interaction energy between a screw dislocation and solute and the change in energy barrier for dislocation motion, where a quadrupolar configuration was used to evaluate the effects of solute on dislocation motion. These energy factors were applied to non-empirical evaluation of a solid solution model to elucidate the fundamental nature of solid solution softening and strengthening, which can be generalized for various kinds of dilute BCC alloys.

ANARYSIS METHODS

We constructed the core structure using the following procedure. The introduction of dislocations within our periodic cell was accomplished through application of a continuum linear elastic theory solution for the periodic dislocation dipole array [1]. The distortion field caused by periodic distribution of dislocations is expressed as a Fourier series:

$$\underline{\underline{\Delta}}(\mathbf{r}) = \sum_{\mathbf{G}} \underline{\underline{\tilde{\Delta}}}(\mathbf{G}) \exp(i\mathbf{G}\cdot\mathbf{r}), \tag{1}$$

Where $\underline{\underline{\Delta}}(\mathbf{r})$ is the distortion tensor at point **r**, **G** are the reciprocal lattice vectors, and $\underline{\underline{\tilde{\Delta}}}(\mathbf{G})$ is the Fourier coefficient describing the distortion tensor. The elastic energy per unit length of the supercell can be expressed in terms of the $\underline{\underline{\tilde{\Delta}}}(\mathbf{G})$ s as

$$E_{elastic} = \frac{1}{2} A_c c_{ijkl} \sum_{\mathbf{G}} \tilde{\Delta}_{ij}(\mathbf{G}) \tilde{\Delta}^{*}_{kl}(\mathbf{G}), \tag{2}$$

where A_c is the area of the supercell containing the dislocation dipole and c_{ijlk} represents the elastic constants of the material. The distortion field was then selected to minimize the total elastic energy subject to the topological constraints imposed by the screw dislocations. The predicted displacement at the atomic positions was determined by applying a line integral starting from a reference coordinate.

The interaction energies between the various solutes and the screw dislocation dipole were then evaluated. In the calculations of the solute-dislocation interaction energy, we used the supercell containing two sets of dislocations defined

above and solute atoms. The interaction energy is defined as the energy difference between two states: the solutes are substituted close to and far from the dislocation. First-principles electronic structure calculations were performed within the DFT framework using the Vienna Ab-initio Simulation Package (VASP) [2,3] We ensured that the total energy converged to within 10−6 eV for all calculations. The relaxed configurations were obtained by the conjugate gradient method, and the search was terminated when the force on all atoms had reduced to 0.02 eV/Å.

RESULTS AND DISCUSSION

The most stable configuration, the so-called easy-core, of a screw dislocation core was calculated by the first-principles calculations. A straight dislocation can move on two-dimensional configuration space perpendicular to direction. We evaluated the Peierls potential surface. Figure 1 shows the examples of energy barrier for the motion of strain screw dislocation along <112> direction. The core structures of easy-core saddle point configuration are given, where the core structure of the screw dislocation was visualized using a differential displacement (DD) vector [4]. Subsequently, we evaluated the effect of solute atoms on the solid solution behavior. The interaction energy between a solute and a screw dislocation is one of the main properties for solid solution softening/strengthening behavior through the pinning effect during the kink migration process. In our previous study, we investigated the interaction energy between the 5d solutes and the screw dislocation with the solutes being substituted around the dislocation core and found that trends the type of solute existed, which depended on the solute element. In the present study, we explored the interaction energy between wider range of solutes, including all 3d to 5d elements and a dislocation, to enable a more universal discussion of these findings. The interaction energies after full atomic relaxation are shown in Figure 2 for typical and transition metal elements, respectively. Finally, we applied these fundamental features of dislocation around solutes to the analytical model [5]. The solid solution model can reproduce the macroscopic softening/strengthening behavior. In the present study, the new model based on three-dimensional line tension model is also developed to reproduce the temperature-dependent kink process for dilute and highly-concentrated alloys.

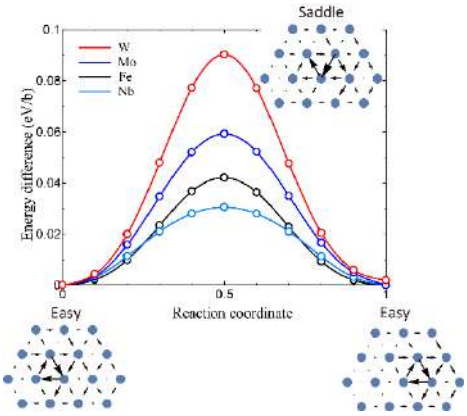

Figure 1. Energy barrier for dislocation motion.

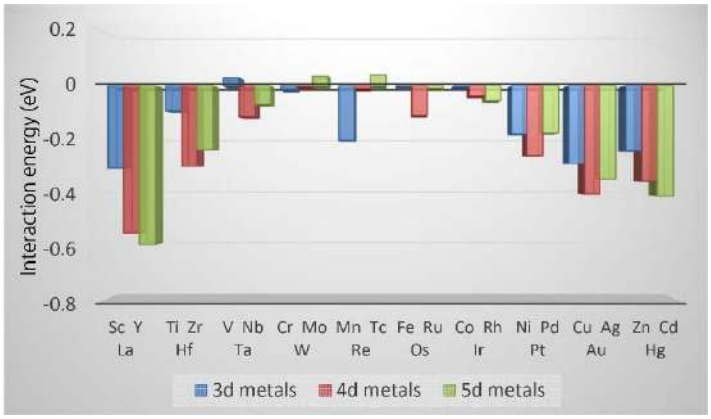

Figure 2. Interaction energies between 3d-5d solutes and a screw dislocation.

CONCLUSIONS

We evaluated softening/strengthening behavior of dilute and highly-concentrated BCC alloys by the first-principles calculations. We identified a clear trend in interactions between a solute and a screw dislocation and found that the change in the energy barrier to kink nucleation is related to the interaction energy. These two properties are the main effects contributing to solid solution behavior. The fundamental properties are efficiently applied to the analytical model such as solid solution model and line-tension model, reproducing macroscopic solid solution softening/strengthening depending on the temperature.

References

[1] M. S. Daw, Elasticity effects in electronic structure calculations with periodic boundary conditions. *Comp. Mater. Sci.* **38**, 293-297, 2006.
[2] G. Kresse, J. Hafner, Ab initio molecular dynamics for liquid metals. *Phys. Rev. B* **47**, 558-561, 1993.
[3] G. Kresse, J. Furthmuller, Efficient iterative schemes for ab initio total-energy calculations using a plane-wave basis set. *Phys. Rev. B* **54**, 11169-11186, 1996.
[4] V. Vitek, R. C. Perrin, D. K. Bowen, The core structure of ½(111) screw dislocations in b.c.c. crystals. *Philos. Mag.* **21**, 1049-1073, 1970.
[5] T. Tsuru, M. Wakeda, T. Suzudo, M. Itakura, S. Ogata, Anomalous solution softening by unique energy balance mediated by kink mechanism in tungsten-rhenium alloys. *J. Appl. Phys.* accepted.

EFFECT OF RATE OF LOADING AND CREEP CHARACTERISTICS OF EPOXY POLYAMIDE BLENDS

Chethana P Rao*1, Utkarsh Srivastava, Ramakrishna P A and H Murthy
Department of Aerospace Engineering, Indian Institute of Technology of Madras, Chennai, India

Summary Epoxy resins have been extensively used in composite industries due to their high strength, less shrinkage post curing and strong adhesion between fibres and matrix. However, their brittle nature has limited their usage in many industrial applications and thus are modified to increase plastic strain. Conventional additives increase the stiffness as well as brittleness in the material. Thereby, an alternative method is to change the curing agent. Polyamides is one such curing agent which naturally increases the toughness in epoxy. The current study focuses on acquiring material properties of epoxy and polyamide blends at different loading rate and its creep characteristics, for extending the material usage germane to sustain high impact load.

INTRODUCTION

Epoxy resins are toughened with additives to overcome their inherent brittle nature so that they can be used in industrial applications. However, rigid additives enhance stiffness and decrease the flexibility. Applications pertaining to sustenance of high impact loads require material with higher toughness. High toughness in epoxy resin can be achieved by curing it with polyamide resin [1, 2]. The present study aims on investigating the effect of rate of loading and creep behaviour at various stress levels for epoxy polyamide blends.

EXPERIMENT DETAILS

The material used for the study is epoxy (CY 230-1) with modified polyamide (XY 54) as hardener. The samples were prepared as per ASTM D 638 for uniaxial tensile test and ASTM D2990 for creep test and the tests were conducted on 0.5kN Universal Testing Machine. The uniaxial tensile tests were conducted at three different displacement rates of 5, 10 and 50 mm/min. The Creep tests were conducted at 50% and 35% of failure stress of the material. Strain for both the cases was obtained from digital image correlation (DIC) technique.

RESULTS AND DISCUSSION

Uniaxial test results: For each of the three displacement rates, three samples were tested. The typical stress strain curves are shown in Fig 1.

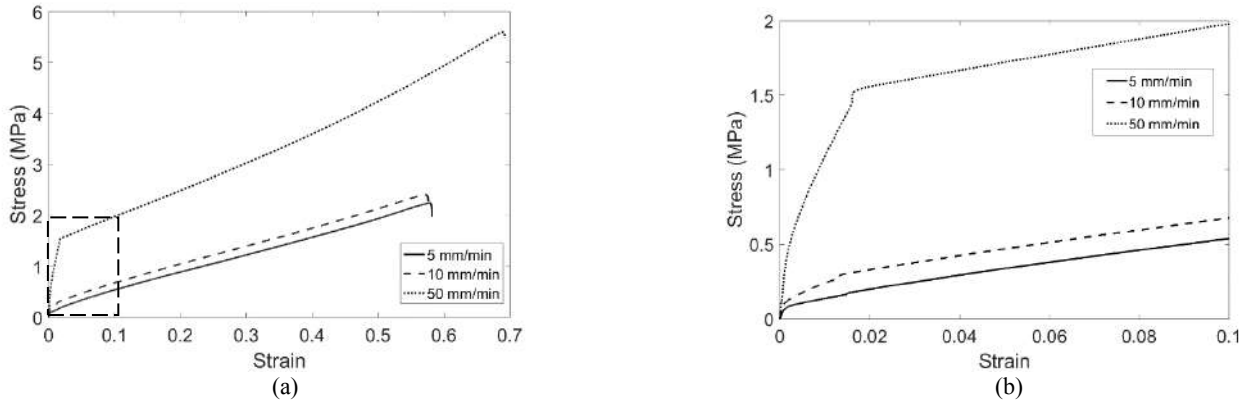

Figure 1 (a) Stress strain curves at different strain rate and (b) Magnified view of the region boxed in (a).

Fig.1 depicts that with increase in rate of loading, the tensile strength, the elastic modulus and the strain at failure increase. The material response from these stress strain curves consists of two major parts: the initial linear region followed by strain hardening. With the increase in rate of loading, the linear region becomes predominant and is distinct. The increased rate of loading decreases the strain hardening region. From these curves, it can be inferred that toughness of the material is very high even with an increase in rate of loading.

Fig 2 illustrates that tensile strength, stiffness and strain at failure increase with the rate of loading. The Tensile strength and the slope of initial linear region increased by seven and twelve times respectively in case of 50mm/min as

*Corresponding author. E-mail: ae13d209@smail.iitm.ac.in

compared to that of 5mm/min displacement rate. The strain at failure did not significantly change for higher rates. Results for the tensile test are summarised in Table. 1.

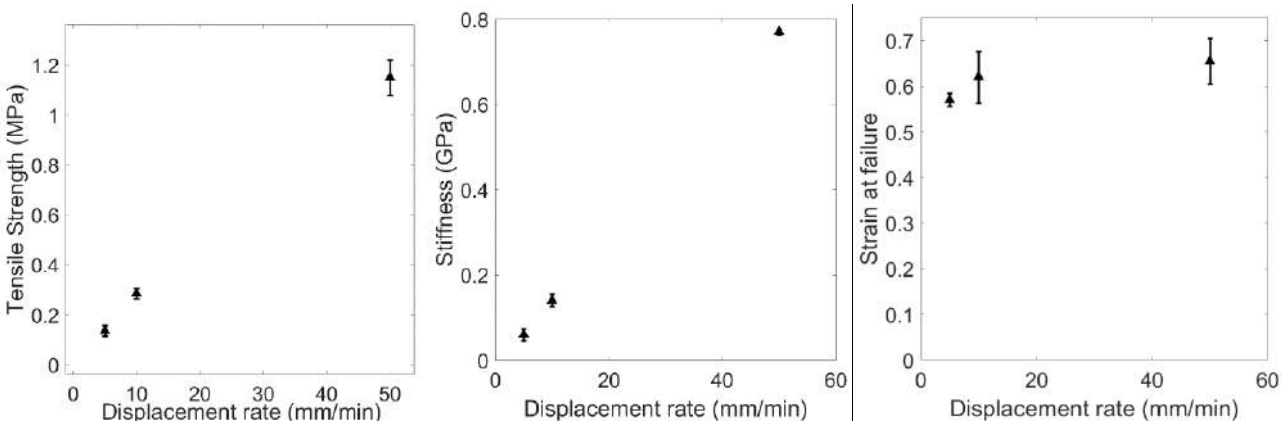

(a) (b) (c)

Figure 2 Effect of rate of loading on material properties

Table 1. Uniaxial tensile test results

Sl. No	Displacement rate (mm/min)	Tensile Strength (MPa)	Elastic modulus (GPa)	Strain at failure
1	05	0.14 ± 0.01	0.06 ± 0.01	0.57 ± 0.01
2	10	0.29 ± 0.02	0.14 ± 0.04	0.62 ± 0.06
3	50	1.15 ± 0.10	0.77 ± 0.01	0.66 ± 0.05

Creep test results: The creep tests were conducted at 50% and 35% of failure strength of the material at a loading rate of 10mm/min. The test was initially planned for two hours under constant stress and one hour of relaxation. However, the material failed within an hour of testing. The creep tests failed prematurely as the stress levels were out of the linear region. It can be observed that the material fails relatively quickly at even 35% of its failure stress. This shows that the creep fracture loads are very low for epoxy/polyamide blends.

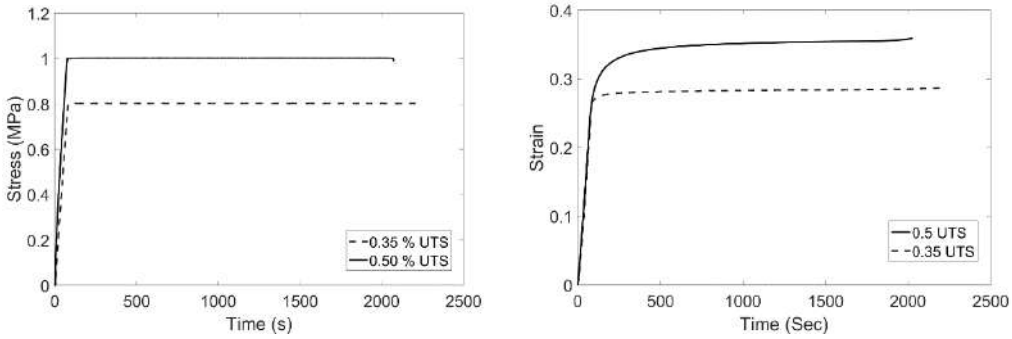

(a) (b)

Figure 3 Creep tests conducted at 35% and 50% stress levels

CONCLUSION

The study revealed that the material is highly deformable and nonlinear. With the increase in rate of loading, the tensile strength, modulus of elasticity and strain at failure increased. It is observed from these tests that polyamide blends performed better than tertiary blends in terms of fracture toughness and the strain at failure was seven times larger. Complete comparative study of all these tests with tertiary amines will be presented in the conference.

References

[1] Floyd D.E, Peerman D.E and Wittcoff: H, Characteristics of the polyamide-epoxy resin system. Journal of Chemical Technology and Biotechnology. 7(5), pp 250–260, 1957. .

[2] Lee H., Neville K., Epoxy resins: their application and technology. Mcgraw-Hill Book Company, 1957.

USING THRUST LINES TO CALCULATE BOTH STATIC AND KINEMATIC COLLAPSE MULTIPLIERS OF MASONRY ARCH BRIDGES

Giuseppe Stagnitto*[1] Massimiliano Ghioni [2]
[1]Department of Civil Engineering and Architecture, University of Pavia, Pavia, Italy
[2]Anastasi & Partners S.A., Locarno, Switzerland

Summary This paper presents an exhaustive exposition of the collapse multiplier calculation methods for arch bridges based on two recent limit analysis theorems. Starting with Jacques Heyman's ideas, originally expressed in terms of bending moments, the application has been extended to the bending and compression structures in no-tension material. Mechanical interpretations of static and kinematic collapse multiplier are derived using thrust lines. In the applicative field, the two multipliers' numerical correspondence can be made precise to the required degree.

SINGLE-SPAN BRIDGES

In limit analysis domain, the structural safety of a masonry arch bridge is usually assessed using the so-called kinematic approach. In the present paper, the adoption of the dual static method it is proved to be more convenient, since a recent theorem - Minimum Equilibrated Compression (M.E.C.) theorem [1] - makes its application straightforward for any kind of arch, including the case of multi-span bridges. The theorem identifies the collapse configuration in the equilibrated solution associated with the minimum compressive stress under the assumption of uniform stress distribution. The theorem starts from a key idea by Jacques Heyman [2], which was originally expressed in terms of bending moments and was then transposed to the stress field due to axial and flexural forces. The theorem has the following mechanical interpretation: "the collapse thrust line is the geometric axis of the inner arch with minimum uniform compression".

Computations are checked via kinematic method, by locating the plastic hinges (as many as needed to form a collapse mechanism) in the sections with maximum compression stress. Thanks to the Consecutive Plastic Hinges theorem (C.P.H.) [3], the kinematic multiplier may then be evaluated, using familiar moments of forces, without computing the virtual displacements due to the vertical and horizontal loads acting on the arch.

The theorem allows to calculate the virtual work as the sum of the products of the moments of the forces, that "precede" the plastic hinges, times the virtual rotations of hinges themselves. The name of the theorem is due the fact that the virtual displacement field associated with the single-degree-of-freedom mechanism, in which all the hinges rotate at the same time, can alternatively be obtained by allowing subsequent rotations of one hinge at a time (once the constraints are neglected). Even the consecutive plastic hinges theorem extends to the bending and compression case an original idea by J. Heyman [4], i.e. the possibility of expressing the virtual work of the external forces applied to a bending structure in form of the virtual work generated by "any system of bending moments", which equilibrates such forces.

Similarly, the Consecutive Plastic Hinges (C.P.H) theorem can use "any thrust line", balancing the forces themselves, in order to obtain virtual work through the moments of applied force resultant with respect to the plastic hinges, without computing the virtual displacements [5]. If the thrust line runs through three of the four plastic hinges of the arch, the virtual work of all the vertical and horizontal forces can be written as a simple single product.

Assuming infinite compressive strength, the further simplification of zero virtual internal work is obtained. Hence, if the resistance is infinite, the kinematic collapse multiplier has been obtained not only without calculating any displacement, but even without calculating any rotation.

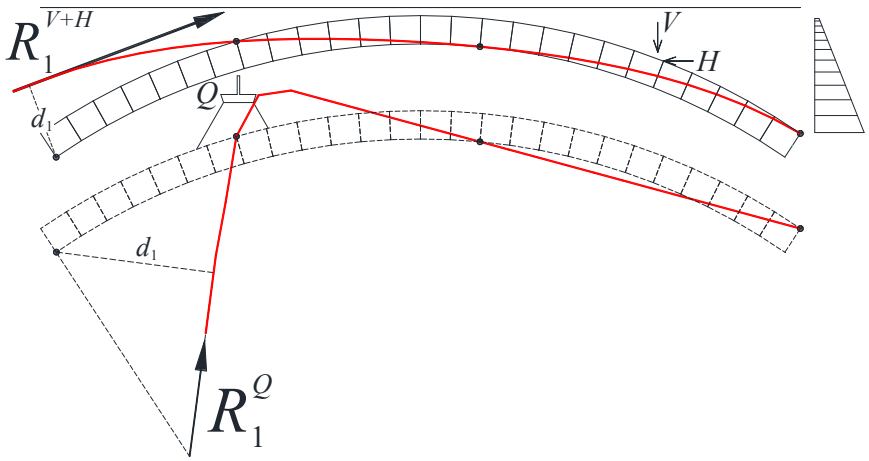

Figure 1. Virtual works using thrust lines.

*Corresponding author. E-mail: giuseppe.stagnitto@unipv.it

The paper focuses on masonry arch bridges (see Fig.1) and the thrust lines are obtained – separately for dead loads (V+H) and for live load Q – through three of the four plastic hinges. The kinematic collapse multiplier is given by the ratio between the moments of the resulting thrust force R_1 , due to permanent loads V+H, and the one due to live loads Q, with respect to the remaining hinge (hinge 1 in the Fig.1):

$$\lambda_Q = -\frac{(L_V + L_H)}{L_Q} = -\frac{(R_1 \cdot d_1)^{V+H}}{(R_1 \cdot d_1)^{Q}}$$

MULTI-SPAN BRIDGES

Even in the case of a collapse mechanism involving successive arches, the C.P.H. theorem allows one to calculate the kinematic multiplier without determining any virtual displacements. At first, the Minimum Equilibrated Compression theorem is used to obtain the static collapse multiplier for any compressive strength value [6] (even, at the asymptote, for infinite strength). This multiplier is checked via the kinematic method by drawing thrust lines (separately for the dead and live forces) through all the plastic hinges except the first one (see Fig.2).

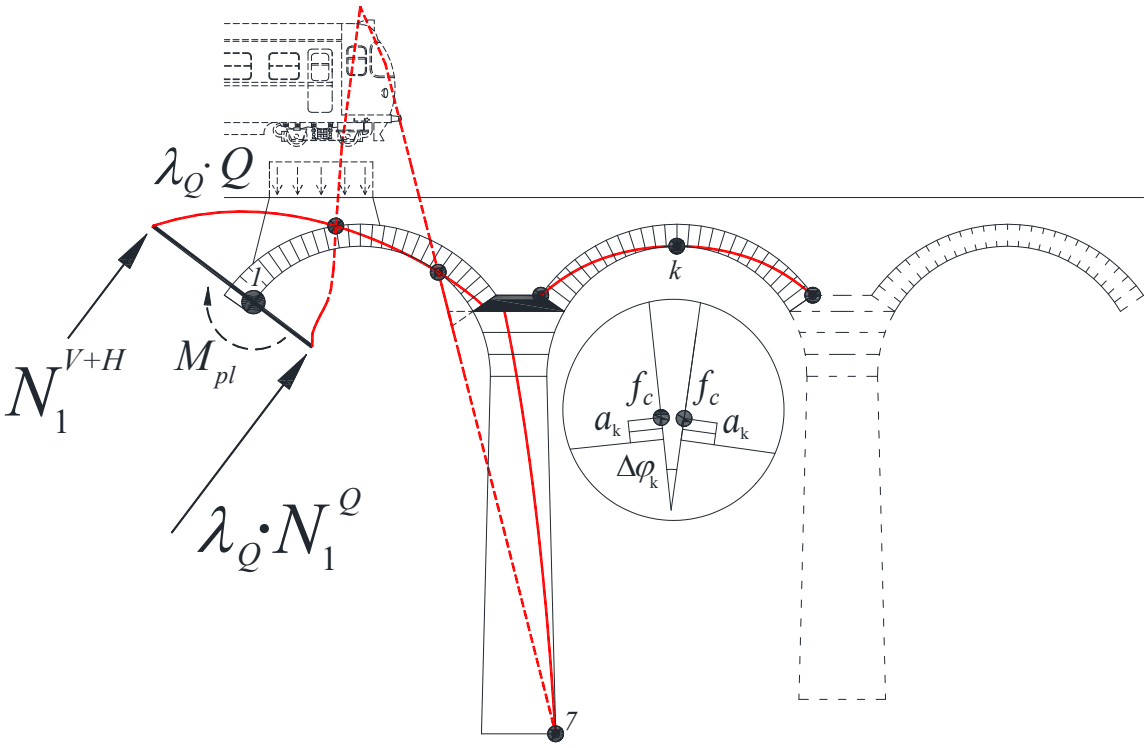

Figure 2. Mechanical interpretation of the kinematic multiplier

To automate the process, it is easier to calculate the moment using the axial action. The kinematic multiplier is simply "the multiplicative coefficient that must be applied to the axial force of the live forces to have the moment balance around the hinge 1".
If the compressive strength is not infinite, the balance equation should also account for the moment M_{pl} that is responsible for the effect of the rotations of all plastic hinges.

References

[1] Stagnitto G.,The Minimum Equilibrated Compression theorem. Calculation of the collapse multiplier of no tension arches, University of Pavia, 2016.
[2] Heyman J., The Safety of Masonry Arches, Int. J. Mech. Sci. 1969, 11(4): 363-385
[3] Stagnitto G., The Consecutive Plastic Hinges theorem. Calculation of the multiplier of collapse of no tension arches, University of Pavia, Pavia, 2017
[4] Heyman J., Elements of the theory of structures, Cambridge University Press,1996.
[5] A Stagnitto G., Pederzani A., Using thrust lines to calculate the kinematic collapse multiplier for retrofitting masonry arch bridges, Proceedings of ARCH 2019 October – 9th International Conference on Arch Bridges, Springer Nature Switzerland, pp. 349 – 357, 2019.
[6] Stagnitto G., Pederzani A., An innovative approach for the assessment of masonry bridges based on two new limit analysis theorems, IABSE Conference Guimaraes March, pp.176-183 27-29, Guimarães, 2019.

EFFECTIVE DUCTILITY MODEL BASED ON RANDOM MICROSTRUCTURE SIMULATIONS

Clement Cadet[1,2], Jacques Besson[2], Sylvain Flouriot[1], Samuel Forest *[1], Pierre Kerfriden[2], and Victor de Rancourt[1]
[1]CEA Valduc, Is-sur-Tille, France
[2]MINES ParisTech, PSL University,MAT - Centre des Materiaux, CNRS UMR 7633, BP 87, 91003 Evry, France

Summary In order to investigate ductile fracture behavior and validate damage models, computational experiments on unit cells have been widely used. Such experiments, consisting in simulating the response of a plastic matrix embedding a single void, oversimplify the interaction between defects. In order to better analyze the influence of this interaction on ductile fracture, this work proposes to simulate the response of microstructures containing randomly distributed voids. The dependence of the failure behavior on the stress state and the dispersion of results are quantified. The simulations on random microstructures are then used to calibrate an effective model of ductile behavior, taking into account the effects of the stress state and of the random distribution of voids. This model should be able to represent both extension (coalescence) and shear failure modes.

INTRODUCTION AND GOALS

Accurately predicting ductile fracture is still an open problem due to the diversity of phenomena taking place at a small scale and their dependency on the stress state. In order to represent these local phenomena and explicitly take into account local small scale plasticity, two main approaches have been undertaken. Analytic models such as Gurson's [1] have been and continue to be developed. They require to hypothesize plastic flows but they can easily be applied for engineering applications. On the other hand, computational methods which simulate the response of a matrix containing voids to some loading conditions, can provide insight on failure phenomena but they are numerically too expensive for applications.

Moreover, most numerical studies focus on unit cells, in which the matrix contains a single void. Even with periodic boundary conditions, using unit cells oversimplifies the interaction between voids, which behave as if they were arranged on a lattice. Some studies did however consider microstructures with a random distribution of defects. The response of such microstructures was simulated up to yield [2] and even coalescence [3]. The authors of these studies were able to fit a Gurson-Tvergaard-Needlemann-type model [4]. However both these studies only considered simple axisymmetric loading, and are therefore not able to represent all stress states.

We propose here to extend their method to general stress states, characterized by stress triaxiality T and Lode parameter L. We investigate the dependency of failure behavior on stress state and the dispersion due to the randomness of the microstructures. Moreover we use these results to calibrate an effective plasticity and ductile fracture model of materials with a random population of voids.

FINITE ELEMENT SIMULATIONS OF RANDOM MICROSTRUCTURES UP TO COALESCENCE

With a Poisson point process, a random distribution of identical non-overlapping spherical defects is inserted in a cubic matrix. A random microstructure is thus obtained and meshed (example in figure 1a). For the matrix, two material behavior models are compared: a perfect von Mises elastoplastic model, and a more realistic one, with hardening and damaging (represented by a GTN-type model). A corotational formulation is used to accommodate large strains. Periodic boundary conditions are applied on the faces of the microstructure. Finally a special macroscopic element is used to control five components of the macroscopic Cauchy stress tensor and an axial deformation component, so that the macroscopic stress triaxiality and the Lode parameter remain constant throughout the simulation. The random microstructure can then be proportionally loaded in a FEM simulation using Z-set software [5].

RESULTS AND DEVELOPMENT OF AN EFFECTIVE MODEL

Typical results for a perfectly plastic model are shown in figure 1. A sudden stress drop is present on the stress strain curves and can be interpreted as the failure of the cell. The cumulative plastic strain field after this failure shows the complex path of the strain localization band. Such a simulation can be repeated with various loading conditions (figure 1d shows for instance the dependence of failure strain on stress triaxiality). Contrary to unit cells, the randomly distributed voids entail a dispersion of results.

A response surface of the porosity at coalescence depending on the triaxiality and Lode parameter can be obtained with enough simulations. In order to decrease the computational cost, a kriging method is used to combine results from unit cells and random microstructures to compute the critical porosity response surface: numerous unit cell computations allow to recover the general form of the response surface, whereas the statistical distributions of failure quantities can be deduced

*Corresponding author. E-mail: samuel.forest@mines-paristech.fr

from simulations on random microstructures. Moreover the beginning of each simulation defines the yielding behavior of the random microstructure, following the method from [2, 3].

Combining the yielding behavior and the critical porosity response surface allows us to build and calibrate effective models, representing yield and possible failure modes, and accounting for the effect of T and L. Dispersion can also be taken into account in the response surface by specifying a risk threshold. Several forms of effective models are investigated: a GTN-type one whose critical porosity is given by the failure porosity response surface obtained from the simulations, and a more realistic multimechanism model representing growth and coalescence under tension and shear. These effective models are finally validated in more complex loading conditions.

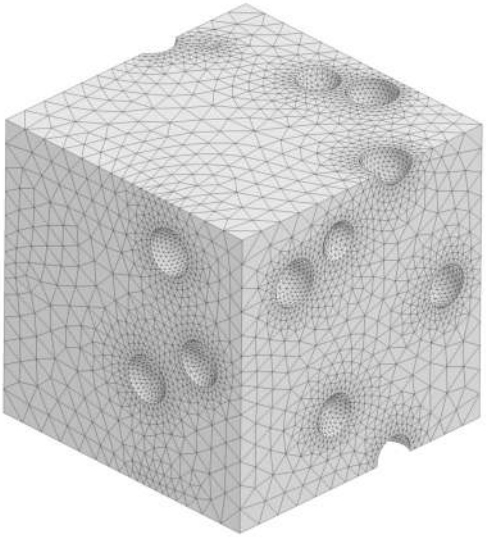

(a) Example of a random microstructure, with 27 voids

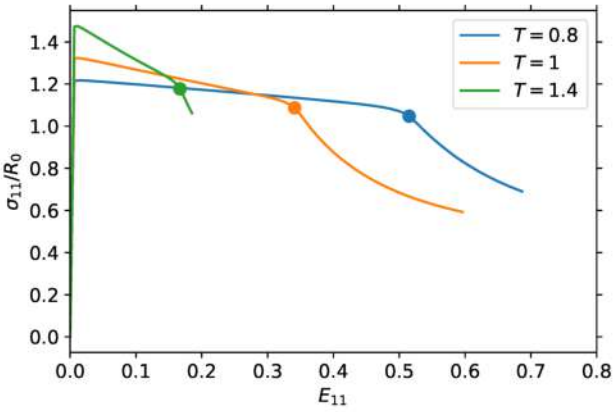

(b) Stress strain curves for several stress triaxiality levels on a random 27-void cell (perfect plasticity, $L = -1$)

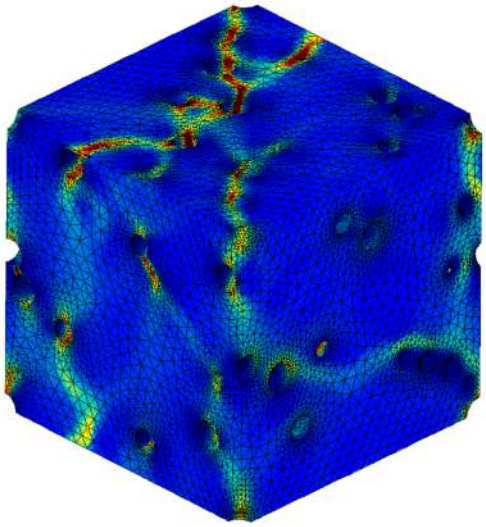

(c) Cumulative plastic strain field after failure, in a 125-void random microstructure (Loading conditions: $T = 1$, $L = -1$)

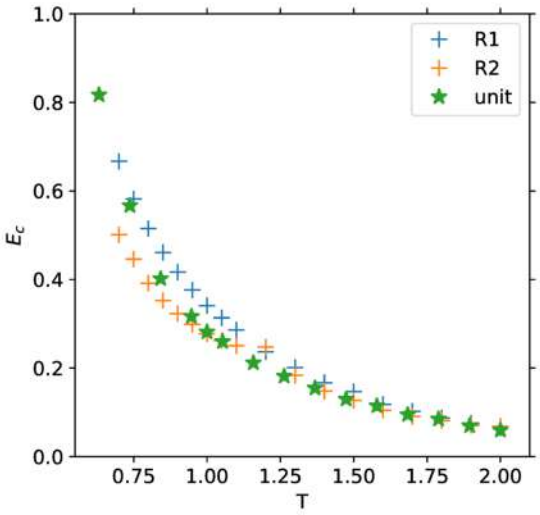

(d) Strain at failure depending on triaxiality, for two 27-void random microstructures $R1$ and $R2$, and a unit cell

Figure 1: Some typical results of simulations on random microstructures, with a perfectly plastic behavior

References

[1] Gurson, A. L. Continuum Theory of Ductile Rupture by Void Nucleation and Growth: Part IYield Criteria and Flow Rules for Porous Ductile Media. *Journal of Engineering Materials and Technology*, **99(1)**, 215, 1977.

[2] Fritzen, F., Forest, S., Bhlke, T., Kondo, D., Kanit, T. Computational homogenization of elasto-plastic porous metals. International Journal of Plasticity, **29**, 102119, 2012.

[3] Hure, J. Yield criterion and finite strain behavior of random porous isotropic materials. *European Journal of Mechanics - A/Solids*, **85**, 104143, 2021.

[4] Tvergaard, V., Needleman, A. Analysis of the cup-cone fracture in a round tensile bar. *Acta Metallurgica*, **32(1)**, 157169, 1984.

[5] Z-set, web site **www.zset-software.com**.

LOCALIZATION IN PSUEDOELASTIC NITI TUBES UNDER BIAXIAL STRESSES

Karlos Kazinakis[1] and Stelios Kyriakides [*1]
[1]Research Center for Mechanics of Solids, Structures & Materials, University of Texas at Austin, Austin, Texas, USA

Summary NiTi can undergo solid-state phase transformation at room temperature, which is responsible for the unique ability of the material to fully recover from strains of about 8%. Transformation under uniaxial tension leads to inhomogeneous deformation with transformed and untransformed material coexisting, and forming distinctive deformation patterns in the structure. NiTi tubes tested under combined tension and internal pressure have been shown to develop localized helical bands with helix angles that depend on the stress biaxiality. However, stress states close to equibiaxial tension do not induce localization. This complex interaction between the transformation induced material instability and the structure is reproduced by implementing a new constitutive model in a finite element analysis of tubes loaded proportionately under different biaxialities of internal pressure and tension.

INTRODUCTION

Under tension pseudoelastic NiTi traces a closed hysteresis with stress plateaus associated with the solid-state reversible transformation between the austenitic and martensitic phases. In the case of thin-walled tubes, the transformations take the form of multi-helical localization patterns of higher/lower strain that propagate while the two stress plateaus develop [1]. When the tubes are loaded under radial stress paths in the axial-hoop stress space [2], transformation again leads to localized helical deformation bands but with helix angles that change with the stress ratio. In addition, the transformation stresses trace a biaxial stress surface that is elongated along the equibiaxial direction, and stress plateau extents exhibit significant anisotropy between axial and hoop dominant stress paths. Furthermore, stress paths close to equibiaxial exhibit material hardening and homogeneous deformations. The present work uses finite element analysis coupled with the constitutive model of pseudoelastic behavior in [3], suitably extended to account for the strain anisotropy, to simulate this phenomena-rich biaxial behavior of NiTi tubes.

SIMULATION OF INHOMOGENEOUS BEHAVIOR OF NiTi TUBES UNDER BIAXIAL STRESS STATES

The tubes are discretized with solid incompatible elements and loaded under combined axial load and internal pressure. The radial stress paths are simulated in the manner followed in the experiments: prescribing for example the change in the volume of the incompressible fluid, monitoring the pressure and relating it to the prescribed axial force. The constitutive model of pseudoelastic behavior of NiTi in [3] capable of capturing the inhomogeneous evolution of phase transformation in tension, the nearly homogeneous behavior exhibited in compression, and reproducing the strong tension/compression asymmetry, is adopted. Figure 1 shows the measured and adopted stress-strain responses in compression and tension. Key feature of the latter is the softening branches that span the measured upper and lower stress plateaus. The model is extended in order to also address the recorded strain anisotropy. Here we outline the results of the simulations of three radial stress paths.

Figure 2 shows the measured and calculated nominal stress-"mean" strain responses in the hoop and axial directions for the stress ratio σ_x/σ_θ = 0.375 (strains are volumetric averages over the 8-diameter length of the tube). The specimen is deformed to a hoop strain of just under 6% and is unloaded. The closed hystereses involve upper stress plateaus during which the austenitic phase yields to the martensitic one, and lower plateaus when reverse transformation takes place. The calculated responses reproduce these plateaus as well as their extents. In the model, transformation is initiated from a small thickness depression close to the right end of the tube resulting in the stress peak and valley at the beginning of each stress plateau. In the experiment these were masked by the stress concentrations at the ends caused by the clamping of the tubes. The evolution of resultant localized deformation is illustrated by the accompanying nine tube deformed images with color contours of hoop strain superimposed. With the first load drop two bands of higher strain oriented at $\pm$ 34° to the axis of the tube nucleate from the depression. They first broaden uniformly as shown in image 1, but by image 2 the propagating front develops a second pair of symmetric bands, and subsequently additional ones as illustrated in images 3 and 4. With the completion of "transformation," deformation becomes uniform, and remains uniform during elastic unloading (image 5). The stress valley indicates the onset of reverse transformation that results in the nucleation of a single right-handed band (image 6). The band broadens as illustrated in images 7 and 8, but as the left end is approached it switches to a multi-pronged front as observed in 9.

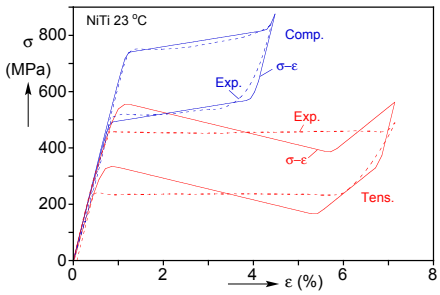

Figure 1. Measured and adopted tensile and compressive stress-strain responses.

Figure 3 shows results from an axial stress dominant case of σ_x/σ_θ = 2, where the axial strain exceeds 7%. The stress-mean strain responses of the experiments are reproduced quite well except that the lower stress plateaus are somewhat under-predicted. Two angled bands initiate again from the local imperfection (image 1) but now the angles are $\pm$ 57°.

*Corresponding author. E-mail: skk@mail.utexas.edu

The bands evolve into a symmetrical multi-pronged front (images 2 and 3), which closer to the left end yields to a left-handed spiral seen in image 4. Reverse transformation now initiates as a left handed single band, which first broadens and then switches to a left handed multipronged front seen in images 8 and 9.

Figure 4 shows the stress-mean strain responses for the equibiaxial stress path of $\sigma_x = \sigma_\theta$. The model captures the exhibited hardening as well as the strain asymmetry. Most importantly, the model tube deforms homogeneously as indeed was the case in the experiment. In summary, similar agreement between experiment and analysis will be reported for several other radial paths. The band angles in all cases agree with those of the experiments. The evolution of the localized deformation exhibit similar features as the experiments but one-to-one comparison is not appropriate as the model uses idealized boundary conditions.

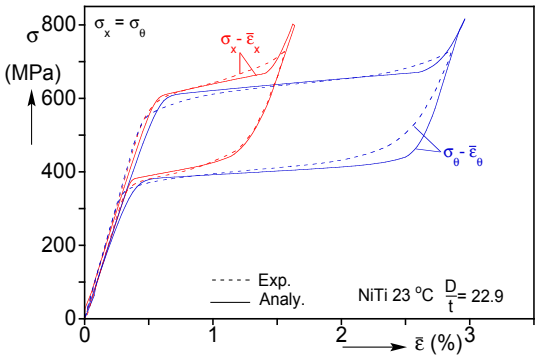

Figure 4. Measured hoop and axial stress-average strain responses for biaxial stress ration $\sigma_x = \sigma_\theta$.

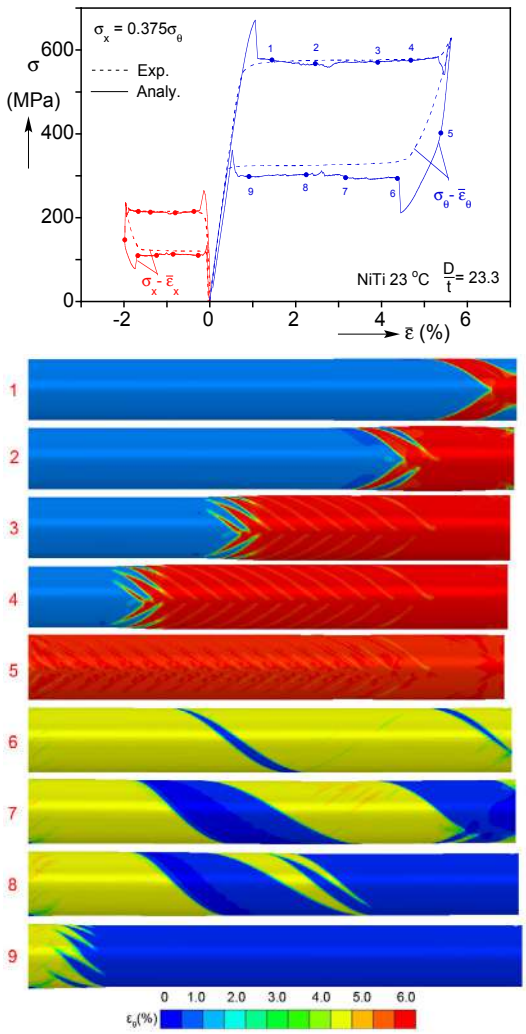

Figure 2. (a) Measured and calculated hoop–θ and axial–x stresses vs. average strains for biaxial stress ratio σ_x=0.375σ_θ. (b) Corresponding hoop strain contours.

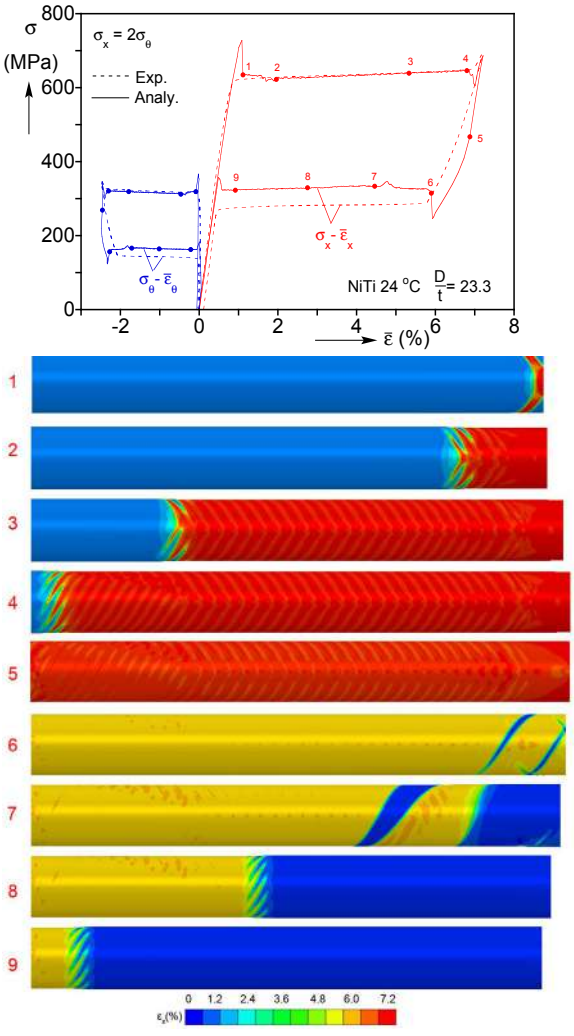

Figure 3. (a) Measured and calculated hoop and axial stresses vs. average strains for biaxial stress ratio $\sigma_x = 2\sigma_\theta$. (b) Corresponding axial strain contours.

References

[1] Jiang, D., Landis, C.M., Kyriakides, S. Propagation of Phase Transformation Fronts in Pseudoelastic NiTi Tubes under Uniaxial Tension. *Extr. Mech. Lett.* **15**, 113-121, 2017.

[2] Bechle, N., Kyriakides, S. Evolution of Localization in Psuedoelastic NiTi Tubes Under Biaxial Stress Stets. *Int'l J. Plast.* **82**, 1-13, 2016.

[3] Jiang, D., Landis, C.M., Kyriakides, S. Effects of Tension/Compression Asymmetry on the Buckling and Recovery of NiTi Tubes Under Axial Compression. *Int'l J. Solids Struct.* **100-101**, 41-53, 2016.

TUNABLE BUCKLING STRENGTH OF MAGNETICALLY ACTIVE ELASTIC SHELLS

Dong Yan*[1], Matteo Pezzulla [1], Lilian Cruveiller [2], and Pedro M. Reis [1]
[1]Flexible Structures Laboratory,Institute of Mechanical Engineering,Ecole Polytechnique Fédérale de Lausanne (EPFL), Switzerland
[2]Ecole Polytechnique,Palaiseau,France

Summary It is well-known that shell buckling is highly sensitive to material or geometric imperfections, causing critical loads to be significantly lower than classic predictions. The associated knockdown factor (ratio between the experimentally measured critical load and the classic theoretical prediction) is typically regarded as an intrinsic structural property; the imperfections are encoded into the shell during fabrication. Here, we demonstrate the ability to tune the knockdown factor of pressurized spherical shells actively using magnetic actuation. We fabricate our shells with a magneto-rheological elastomer by coating. The shells are first magnetized and then loaded by pressure under a uniform magnetic field. We find that, by adjusting the flux density and polarity of the field, the knockdown factor of our shells can be increased or decreased, on-demand, by up to 30%.

FABRICATION OF MAGNETICALLY ACTIVE SHELLS

Thin spherical shell specimens containing a precisely engineered imperfection were fabricated using a coating technique [1, 2] (see schematic in Fig. 1). These shells are made out of a magneto-rheological elastomer (MRE) mixture of vinylpolysiloxane (VPS 22) and NdPrFeB magnetic particles. This mixture was poured into a negative spherical mold (radius $R = 25.4\,\mathrm{mm}$), 100 s after the preparation. The elastic mold contains a circular soft spot with reduced thickness at the north pole, which, upon external pressurization during fabrication, deformed to produce a dimple-like geometric defect in the shell. After curing, we magnetized the specimens (along the z-direction) permanently using a strong applied magnetic field $B \approx 4.4\,\mathrm{T}$ to saturate the particles in the MRE. The effective residual flux density of our MRE is $B_\mathrm{r} = 63\,\mathrm{mT}$, which is set by the residual flux density of the saturated individual particles and the volume concentration (7%) of the mixture. We characterized the defect geometry using an optical profilometer, finding that its 2D profile can be described by $w = -\delta(1-\beta^2/\beta_0^2)^2$ (Fig. 2b) set by the deflection of the soft spot in the mold during fabrication under uniform pressure (zenith angle $\beta \le \beta_0$, assuming it is flat and clamped at the boundary). The defect amplitude, δ, and angular width, β_0, were determined through fitting. This fabrication technique allows us to engineer a precise geometric defect in the shell with an amplitude that can be systematically set during manufacturing.

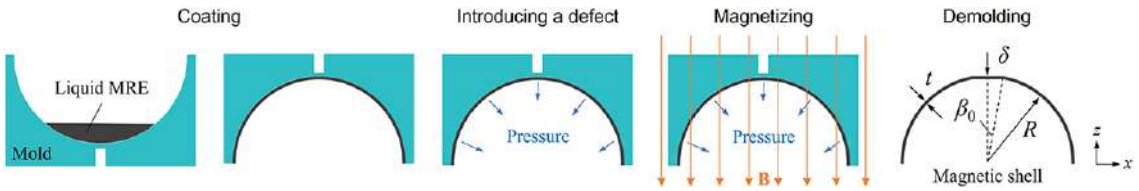

Figure 1: Schematic diagram of the experimental protocol used to fabricate a magnetic spherical shell containing a geometric defect.

TUNABLE CRITICAL BUCKLING PRESSURE

We investigate the onset of buckling of our magnetic shells under pressure loading. In the experiments, the shell was positioned in between Helmholtz coils, which generate a steady and uniform magnetic field (flux density B_e); see inset of Fig. 2a. Under this external magnetic field, the shell was then pressurized with an imposed volume change. We first focus on a shell containing a defect of amplitude $\delta/t = 0.38$ and width $\lambda_\beta = [12(1-\nu^2)]^{1/4}(R/t)^{1/2}\beta_0 = 3.16$. In Fig. 2a, we present curves of pressure versus volume change for this one shell at different levels of magnetic loading. In this plot, the pressure has been normalized by the classic critical pressure as $\overline{p} = p/p_\mathrm{c} = p/[2E(t/R)^2/\sqrt{3(1-\nu^2)}]$ [3] and the imposed volume change, $\Delta\overline{V}_\mathrm{i} = \Delta V_\mathrm{i}/\Delta V_\mathrm{c} = \Delta V_\mathrm{i}/[2\pi(1-\nu)R^2t/\sqrt{3(1-\nu^2)}]$, has been normalized by the corresponding critical volume change [4]. Without a magnetic field ($B_\mathrm{e} = 0\,\mathrm{mT}$), $\overline{p}$ increases linearly with $\Delta\overline{V}_\mathrm{i}$ during prebuckling. Buckling occurs accompanied by an abrupt pressure drop, and the normalized peak pressure is the knockdown factor, $\kappa_\mathrm{d} = 0.44$ for this particular curve. When a magnetic field is applied, the shell is active as long as the deformation breaks the alignment of its magnetization with the external field. As a result, distributed torques are applied to the shell, thereby affecting the buckling conditions. As shown in Fig. 2a, under a positive field (the field lines are parallel to the shell magnetization in the initial configuration), the knockdown factor is increased from 0.44 to 0.56 at $B_\mathrm{e} = 33\,\mathrm{mT}$, and to 0.68 at $B_\mathrm{e} = 66\,\mathrm{mT}$. The buckling also becomes less catastrophic with a smaller pressure drop. In contrast, the knockdown factor is decreased to 0.33 and 0.23 at $B_\mathrm{e} = -33\,\mathrm{mT}$ and $B_\mathrm{e} = -66\,\mathrm{mT}$, respectively, when the polarity of the magnetic field is flipped.

*Corresponding author. E-mail: dong.yan@epfl.ch.

Following the protocol detailed above, we fabricated different shells with a variety of defect amplitudes (Fig. 2b) and measured their knockdown factors as a function of the external flux density (see Fig. 2c). We find that, for the same shell, its buckling strength can be tuned actively by varying the applied external magnetic field. Within the range of flux density accessible in our experiments, κ_{d} can be increased or decreased up to a maximum change of $\approx 30\%$. In parallel to the experiments, we have developed an axisymmetric shell (1D) model within the framework of small strains and large displacements/rotations by minimizing the Helmholtz free energy [5] of the system (including both elastic and magnetic effects). Excellent agreement is found between this theory and the experiments (Fig. 2c).

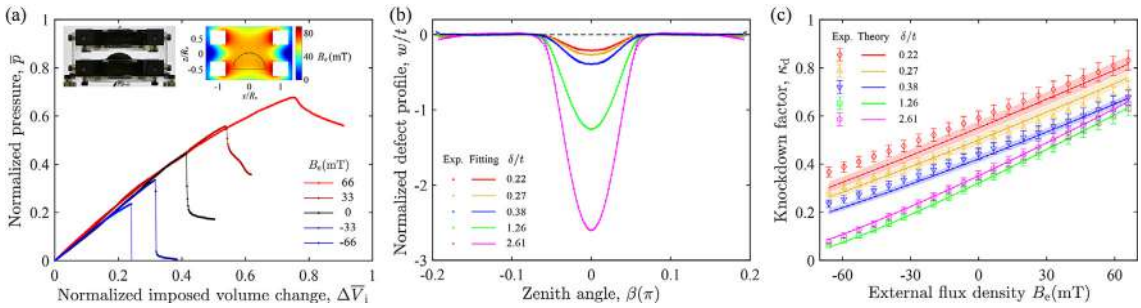

Figure 2: Tunable knockdown factor of magnetic shells. (a) Loading curves, $\overline{p}(\Delta\overline{V}_{\mathrm{i}})$, at different levels of external flux density, B_{e}, for the shell containing a defect of amplitude $\delta/t = 0.38$ and width $\lambda_\beta = 3.16$. Inset: Photograph of the shell positioned in between Helmholtz coils and the generated magnetic field calculated by COMSOL. (b) Defect profiles with different amplitude. (c) Knockdown factor, κ_{d}, versus the external flux density, B_{e}, for shells containing the defects shown in (b).

IMPERFECTION SENSITIVITY

We proceed to investigate the imperfection sensitivity of our magnetic shells by quantifying the relationship between the knockdown factor, κ_{d}, and the defect geometry. In the experiments, we varied the defect amplitude systematically and obtained the corresponding κ_{d} at different levels of external flux density. The latter is considered in the parameter $\lambda_{\mathrm{m}}R/t$, where $\lambda_{\mathrm{m}} = B_{\mathrm{e}}B_{\mathrm{r}}/\mu_0 E$ with μ_0 as the permeability of air and E as the Young's modulus of the MRE. In Fig. 3a, the same trend is observed for different cases of $\lambda_{\mathrm{m}}R/t$: κ_{d} is sensitive to small defects, but reaches a plateau for large δ/t. The onset of this plateau is shifted towards smaller or larger δ/t for a positive or negative field, respectively. In Fig. 3b, we plot the change of knockdown factor, $\Delta\kappa_{\mathrm{d}}$, as a function of defect amplitude at different levels of external flux density. We find that $\Delta\kappa_{\mathrm{d}}$ is significantly less sensitive to small defects and approximately constant when δ/t increases above a threshold. Although the buckling of magnetic shells is still sensitive to imperfections, the tuning of the knockdown factor is robust. We also find that the experimental data and theoretical curves for the knockdown factors of shells made with VPS 22 or VPS 32 collapse when they have the same value of $\lambda_{\mathrm{m}}R/t$. Therefore, $\lambda_{\mathrm{m}}R/t$ is a governing parameter of this problem, and the presented results are independent of the properties of MRE, shell radius to thickness ratio, and external flux density.

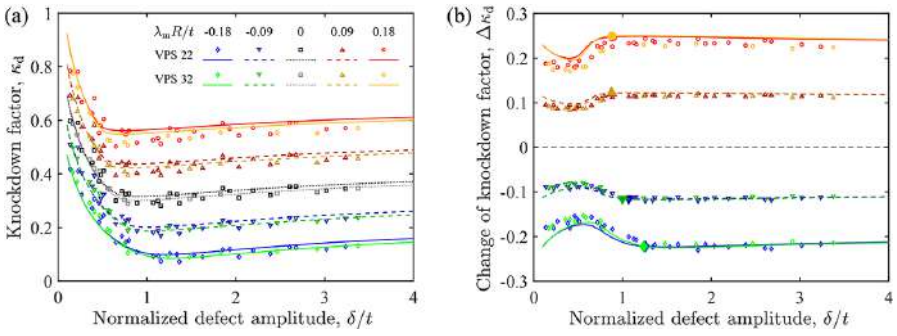

Figure 3: Imperfection sensitivity of magnetic shells. (a) Knockdown factor, κ_{d}, and (b) the change of knockdown factor, $\Delta\kappa_{\mathrm{d}}$, as a function of defect amplitude, δ/t. The parameter $\lambda_{\mathrm{m}}R/t$ is varied in the range {-0.18, -0.09, 0, 0.09, 0.18}. Defect width $\lambda_\beta = 3.16$ for shells made with VPS 22 and $\lambda_\beta = 3.35$ for shells made with VPS 32.

References

[1] Lee A., Brun P. -T., Marthelot J., Balestra G., Gallaire F., Reis P. M. Fabrication of slender elastic shells by the coating of curved surfaces. *Nat. Commun.* **7**: 11155, 2016.
[2] Lee A., López Jiménez F., Marthelot J., Hutchinson J. W., Reis P. M. The geometric role of precisely engineered imperfections on the critical buckling load of spherical elastic shells. *ASME J. Appl. Mech.* **83**: 111005, 2016.
[3] Zoelly R. Ueber ein knickungsproblem an der kugelschale. *PhD Thesis*, ETH Zürich, Zürich, Switzerland, 1915.
[4] Hutchinson J. W. Buckling of spherical shells revisited. *Proc. R. Soc. A* **472**: 20160577, 2016.
[5] Zhao R., Kim Y., Chester S. A., Sharma P., Zhao X. Mechanics of hard-magnetic soft materials. *J. Mech. Phys. Solids* **124**: 244-263, 2019.

CURVATURE TUNES WRINKLES IN TENSILE HYPERELASTIC SHELLS

Fan Xu*, Yifan Yang, and Ting Wang
Institute of Mechanics and Computational Engineering, Department of Aeronautics and Astronautics, Fudan University, Shanghai, China

Summary Transverse wrinkles usually occur in a uniaxially tensile elastic membrane and will be smoothed upon excess stretching. This instability-restabilization response (isola-center bifurcation) can originate from the nonlinear competition between stretching energy and bending energy. Here, we find a crucial factor, the curvature, which can control effectively and precisely the wrinkling and smoothing regimes. When the sheet is bent with curvature, the regime of wrinkling amplitude versus membrane elongation is narrowed, with local wrinkling instability coupled with global bending. There exists a critical curvature, where no wrinkles appear when the value is beyond this threshold. The curvature effects on wrinkling-smoothing behavior have been quantitatively explored by our theories, computations and experiments. The models developed in this work can describe large in-plane strains of soft shells to effectively capture this transition behavior, which build on general differential geometry and thus can be extended to arbitrary smooth surfaces with varying curvature such as torus. Our findings may shed light on designs of wrinkle-tunable membrane surfaces and structures.

INTRODUCTION

Recent studies revealed that curvature in conforming materials to rigid substrates has proven a versatile tool to guide the self-assembly of defects such as pleats [1] and crack paths [2]. Spontaneous curvature can induce rotational symmetry-breaking buckling and snapping instability in bilayered thin shells [3]. Understanding the mechanism of curvature effects on morphological evolution and pattern formation is, in fact, crucial for the effective use of wrinkling as a tool for realizing multifunctional surfaces. Do tensional wrinkles in thin films depend on geometric curvature? How does curvature affect pattern formation and pattern evolution? Whether curvature triggers or delays stretch-induced wrinkling behavior? These questions remain uncovered in prior works and will be addressed here.

This study quantitatively explores curvature effects on wrinkling-smoothing behavior of highly stretched soft shells by theories, computations and experiments. We design an experiment of stretching soft cylindrical shells, incorporated with 3D surface imaging technology to acquire spatial data from 2D images of structured-light projection, in order to examine the curvature effect on the wrinkling and smoothing regimes. Differential-geometry based shell models for mostly used hyperelastic materials are derived, which can be extended to arbitrarily curved surfaces. Numerical implementation [5] through coupling Chebyshev spectral collocation method for spatial discretization and *Asymptotic Numerical Method* (ANM) for nonlinear resolution is adopted to trace the nonlinear morphological evolution of wrinkles. Curvature effect on wrinkling-smoothing behavior of highly stretched cylindrical shells is carefully explored and a 3D phase diagram on stability boundaries is provided.

ARBITRARILY CURVED FINITE STRAIN SHELL MODELS

How to quantitatively predict the curvature effect on wrinkle-smooth evolution remains a theoretical challenge. Classical thin shell theories, *e.g.,* Donnell-Mushtari-Vlassov (DMV) model and Sanders-Koiter model, normally treat cases when the parametrization of the surface is prescribed and describe moderate rotation and deflection, yet small membrane strains with linear Hooke's law. Soft shells under overstretching, however, generally experience large deformations, and the existing small strain shell models become inadequate and fail in predicting isola-center bifurcation behavior considered here. For this purpose we derive more generalized shell models for commonly used hyperelastic materials, which build on general differential geometry and thus can be extended to arbitrarily curved surfaces. After some manipulations, the membrane strain tensor for cylindrical surface with finite curvatures reads

$$E_{\alpha\beta} = \frac{1}{2}(u_{\alpha,\beta} + u_{\beta,\alpha} + 2wb_{\alpha\beta}) + \frac{1}{2}(u_{\gamma,\alpha}u_{\gamma,\beta} + u_{\gamma,\beta}wb_{\gamma\alpha} + u_{\gamma,\alpha}wb_{\gamma\beta} + wb_{\gamma\alpha}wb_{\gamma\beta}) + \frac{1}{2}w_{,\alpha}w_{,\beta}, \tag{1}$$

where $b_{\alpha\beta}$ is the curvature tensor, Greek indices α, β,... take values in $\{1, 2\}$, u_α denotes the in-plane displacements, while w is the out-of-plane deflection. The linearized bending strain tensor for cylindrical surface with finite curvatures reads

$$K_{\alpha\beta} = -w_{,\alpha\beta} + \frac{1}{2}\left(u_{\gamma,\alpha}b^\gamma_\beta + u_{\gamma,\beta}b^\gamma_\alpha\right) + wb_{\gamma\alpha}b^\gamma_\beta. \tag{2}$$

Based on the well-known Euler-Lagrange equation, equilibrium governing equations can be obtained straightforwardly and the model is capable of accounting for various hyperelastic constitutive laws such as Saint-Venant Kirchhoff, neo-Hookean and Mooney-Rivlin, and even material anisotropy [4]. Furthermore, our finite strain shell model can be flexibly extended to soft shells with varying curvatures, *e.g.,* S-shape and C-shape surfaces.

*Corresponding author. E-mail: fanxu@fudan.edu.cn.

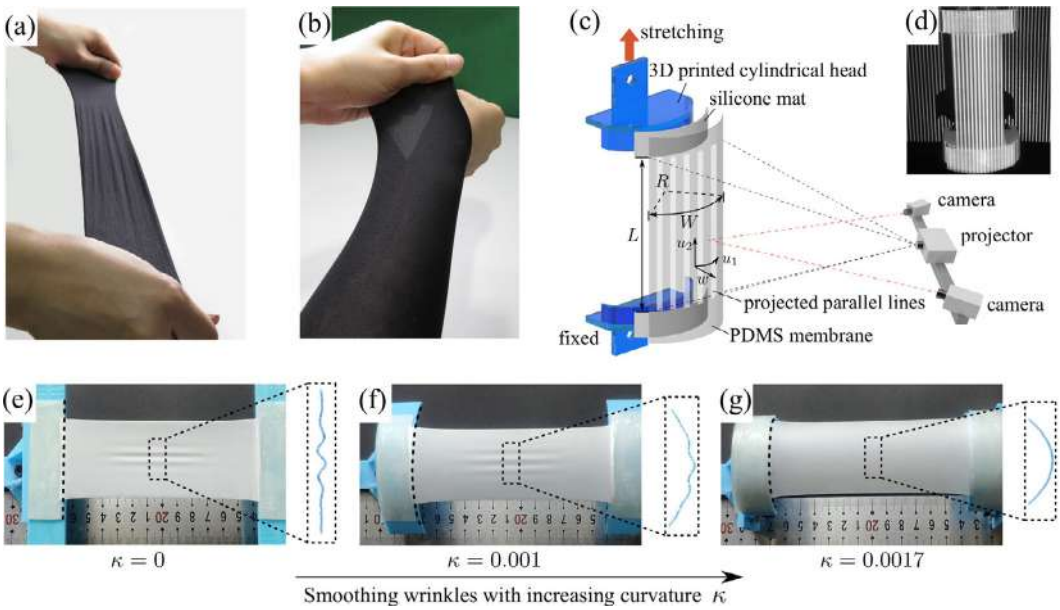

Figure 1: Transverse wrinkles appear in a stretched flat sleeve (a), while no wrinkles occur in a stretched cylindrical sleeve (b). (c) Sketch of the experimental setup and geometry of an open cylindrical shell. (d) Zebra lines (parallel and straight lines) are projected on the surface of tested sample. Wrinkles are smoothed with increasing curvatures $\kappa = h/R$ at the same stretching strain $\varepsilon = 0.1$: (e) $\kappa = 0$, wrinkling, (f) $\kappa = 0.001$, a coupling behavior of wrinkling and bending, (g) $\kappa = 0.0017$, global bending with smooth surface. In three cases, $L = 10$ cm, $W = 5$ cm and $h = 50$ μm.

RESULTS

We experimentally find that the curvature can smooth wrinkles and determine the wrinkling and smoothing responses (see Fig. 1(e)-(g)). Notably, with an increasing curvature, the wrinkling amplitude declines accordingly, showing a coupling behavior of global bending and local wrinkling instability (see Fig. 1(f)). However, there exists a curvature threshold κ_{cr} (depending on aspect ratios L/W and W/h), above which the wrinkling is avoided, with monotonic global bending deformation instead (see Fig. 1(g)). In theoretical computations, for a planar sheet, wrinkles occur first, then decrease, and finally disappear with continuous stretching, with demonstrating the entire path of morphological evolution namely isola-center bifurcation [5, 6]. However, for a curved surface, we find a novel nonlinear behavior coupling global bending and local wrinkling upon stretching, confirmed by experimental observations in Fig. 1(f). The regime of wrinkling amplitude *vs.* membrane elongation is narrowed with increasing curvature, and vanishes at a critical curvature. At the critical curvature and beyond, bending deformation dominates, with maintaining smooth surface. By varying the curvature, we can effectively tune and control the wrinkling and smoothing regimes, which would provide insights into fabricating topology-related functional membranes.

CONCLUSIONS

We have uncovered the curvature-tunable smooth-wrinkle-smooth transitions and postbuckling evolutions of a soft shell upon highly stretching, which can be quantitatively predicted by our general shell models that are developed for hyperelastic curved surfaces under large deformations, agreeing with carefully designed experiments. A remarkable finding lies in the motion and change of the curvature-determined wrinkling regime, the area of which can dramatically shrink with increasing curvature. Notably, no wrinkling happens above a critical curvature, yet demonstrating monotonic global bending deformation with smooth surfaces. Moreover, a 3D phase diagram of stability boundaries, based on our theoretical calculations and experimental data, was first provided. Understanding morphological evolution and in particular the dependence of wrinkling behavior on curvature (*e.g.*, 3D phase diagram of stability boundaries) is, in fact, crucial for the effective use of wrinkling as a tool for realizing multifunctional surfaces.

References

[1] Irvine, W.T.M., Vitelli, V., Chaikin, P.M. Pleats in crystals on curved surfaces. *Nature* **468**: 947–951, 2010.
[2] Mitchell, N.P., Koning, V., Vitelli, V., Irvine, W.T.M. Fracture in sheets draped on curved surfaces. *Nat. Mater.* **16**: 89–93, 2017.
[3] Pezzulla, M., Stoop, N., Steranka, M.P., Bade, A.J., Holmes, D.P. Curvature-induced instabilities of shells. *Phys. Rev. Lett.* **120**: 048002-1–048002-5, 2018.
[4] Liu, F., Xu, F., Fu, C. Orientable wrinkles in stretched orthotropic films. *Extreme Mech. Lett.* **33**: 100579-1–100579-9, 2019.
[5] Fu, C., Wang, T., Xu, F., Huo, Y., Potier-Ferry, M. A modeling and resolution framework for wrinkling in hyperelastic sheets at finite membrane strain. *J. Mech. Phys. Solids* **124**: 446–470, 2019.
[6] Wang, T., Fu, C., Xu, F., Huo, Y., Potier-Ferry, M. On the wrinkling and restabilization of highly stretched sheets. *Int. J. Eng. Sci.* **136**: 1–16, 2019.

FROM WRINKLES TO CREASES - ON STABLE LOCALIZED DEFORMATION SOLUTIONS IN HIGH SYMMETRY STRUCTURES USING GROUP THEORY

Shrinidhi S. Pandurangi[1], Ryan S. Elliott[2], Timothy J. Healey[1,3], and Nicolas Triantafyllidis*[4,5]
[1]Field of Theoretical and Applied Mechanics, Cornell University, Ithaca, NY, USA
[2]Aerospace Department and Mechanics, University of Minnesota, Minneapolis, MN, USA
[3]Department of Mathematics, Cornell University, Ithaca. NY, USA
[4]LMS,Ecole Polytechnique,CNRS UMR 7649,Institut Polytechnique de Paris,91128 Palaiseau,FRANCE
[5]Aerospace Eng. Dept. & Mechanical Eng. Dept. (emeritus) , University of Michigan, Ann Arbor, MI, USA

Summary We are motivated by the celebrated Biot problem ([1]) of surface instability in a hyperelastic half-space under axial compression and in particular the evolution, from an initially unstable bifurcated short wavelength, periodic deformation path to a stable solution involving a localized deformation. This feature is shared by other classical problems in mechanics, such as the problem of a beam on an elastic foundation which is used in modeling important technological problems including sun-kinking of railroads and failure in pipelines. A common feature in all these problems is their high initial symmetry (translational invariance) leading to a complex bifurcation pattern. Understanding the evolution of bifurcated solutions from a periodic pattern (wrinkling) to a highly localized one (crease) is the goal of this work. With an eye on relative simplicity, due to the complex structure of these nonlinear problems, we study here the behavior of an inextensible infinite Euler-Bernoulli beam that is subjected to a compressive axial force and connected to a nonlinear (polynomial) elastic foundation. We use group-theory methods to follow all bifurcated equilibrium paths in a systematic way and explore the emergence of stable localized solutions.

INTRODUCTION AND MOTIVATION

Surface instabilities in soft elastic materials under compression, leading to highly localized deformation regions known as creases, have been reported in the recent experiments by [2], thus providing renewed interest within the Mechanics community for the Biot problem (see [3]). Biot's original work applies the conventional method of bifurcation theory to the problem of an anisotropic, hyperelastic half space subjected to uniaxial far-field compressive stresses. Biot's results show that (a) the onset of instability occurs at an axial stretch of $\lambda = 0.544$ (for a Neo-Hookean solid) where a bifurcation occurs; (b) the associated bifurcation modes correspond to sinusoidal surface waves (wrinkles) whose amplitude decays with distance below the surface of the half space; and (c) wrinkles of all wavelengths become unstable at the critical stretch. Since creases, consisting of spatially localized finite-strain deformations typically involving self-contact, are often observed well before the Biot critical value, a portion of the Mechanics community has come to the conclusion that creases are a distinct *"nonconventional"* bifurcation phenomena, to be contrasted with *"conventional"* bifurcation phenomena. Numerical computations have been proposed to search for the creased solutions by introducing an *a priori* imperfection which biases the system to a desired configuration. This *ad-hoc* numerical search method does not fully explain the emergence of stable localized deformation solutions from the initially periodic ones, thus motivating the present investigation.

To avoid complicated numerical calculations in the reference continuum mechanics problem and gain insight, we revisit here the classic stability problem of the buckling of an inextensible, axially compressed beam on a nonlinear elastic foundation. This analytically tractable problem allows us to understand how localized deformation solutions emerge in Biot's problem and also in many other similar applications in mechanics problems with high initial symmetry. Instead of a numerical search for localized solutions using arbitrary imperfections – impossible due to the high initial symmetry of the problem and the multitude of closely spaced bifurcation points – we propose a systematic search using path-following bifurcation techniques and group-theoretic methods to find all the bifurcated solution orbits (primary, secondary etc.) of the system and examine their stability to establish their observability.

THEORY AND METHODOLOGY

The model adopted here is that of an inextensible, linear elastic beam resting on a nonlinear elastic foundation (with a cubic-quintic nonlinearity). A dimensionless version is hereby used. In order to make the problem manageable – and deal with compact symmetry groups – we will consider the L-periodic solutions of an infinite beam and then choose $L \gg 1$. The beam has bending stiffness $EI = 1$ and its undeformed centerline coincides with x-axis. The beam is subjected to an axially compressive load λ and has the lateral deformation $w(x)$. The total potential energy of the system is given by

$$\mathcal{E}(w(x);\lambda) = \frac{1}{L}\int_{-L/2}^{L/2}\left[\frac{1}{2}\left(\frac{d^2w}{dx^2}\right)^2 - \frac{1}{2}\lambda\left(\frac{dw}{dx}\right)^2 + \frac{1}{2}w^2 + \frac{\alpha}{4}w^4 + \frac{\gamma}{6}w^6\right]dx\ . \tag{1}$$

*Corresponding author. E-mail: nicolas.triantafyllidis@polytechnique.edu

The foundation force per unit length opposing a displacement w is $f = -(w + \alpha w^3 + \gamma w^5)$. Two different nonlinear foundation types will be considered: a "*softening foundation*" with $\alpha = -1$ and a "*hardening foundation*" with $\alpha = +1$. From the first category ($\alpha = -1$) we distinguish three different variations: the "*no re-hardening*" foundation where $\gamma = 0$, the "*mild re-hardening*" foundation where $\gamma = 0.25$ and the "*strong re-hardening*" foundation where $\gamma = 0.50$, resulting in a monotonically increasing foundation force-displacement response. We propose a systematic search using path-following bifurcation techniques and group-theoretic methods to find all the bifurcated solution orbits (primary, secondary etc.) of the system and examine their stability and hence their observability. Unlike previously proposed methods for the problem at hand that use multi-scale perturbative techniques near the critical load (see [4]), we show that to obtain a localized deformation equilibrium path for the perfect structure, one has to follow the secondary bifurcation with the longest wavelength far away from the critical load. The use of group-theory methods for this problem illustrates the general methodology for a systematic search in nonlinear problems in mechanics with a high degree of symmetry where localized deformation solutions do appear.

RESULTS AND CONCLUSION

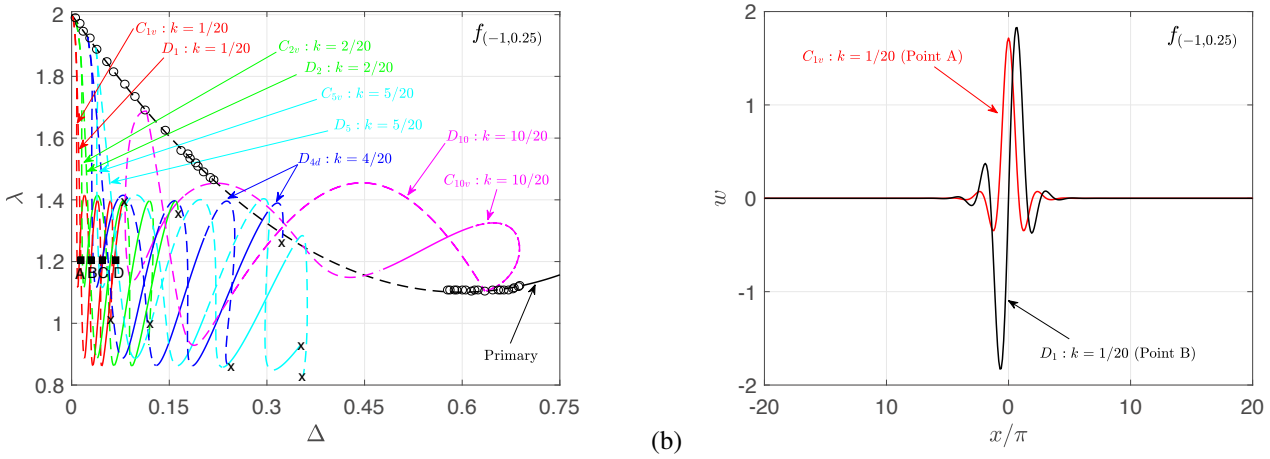

Figure 1: In (a) the load λ vs the work-conjugate dispacement Δ of a periodic beam of length $L = 40\pi$ (period of primary bifurcation is 2π) on a softening foundation with mild re-hardening ($\alpha = -1, \gamma = 0.25$) showing the primary and some of the secondary bifurcation orbits (labelled by their symmetry group), illustrating the problem's complex structure and multitude of equilibrium paths. In (b) stable localized solutions at points A and B of the secondary bifurcated orbits with the longest wavelength, i.e. the ones (marked in red) emerging from the primary orbit nearest the critical load $\lambda_c = 2$. NOTE: Stable segments of orbits are marked by a continuous line, while unstable ones by a dashed line.

The nonlinear beam model problem analyzed here, although it looks deceptively simple, has a very rich and complex set of solutions due to the high degree of its initial symmetry. We show that to obtain a stable localized deformation for the perfect structure, one has to follow the secondary bifurcating equlibrium path with the longest wavelength far away from the critical load. Although it is also necessary to have an initially softening foundation, a monotonically softening foundation precludes stable and hence observable localized deformation solutions, which require re-hardening of the nonlinear foundation. For monotonically stiffening foundations, no localized deformation modes can be found on the bifurcating solution branches. In addition to explaining how to find stable, localized deformation solutions in the problem at hand, the use of group-theory methods for this problem illustrates the general methodology for tackling nonlinear problems in mechanics with a high degree of symmetry for which the standard imperfection method is not a reliable option.

References

[1] Biot, M. A., Surface instability in finite anisotropic elasticity under initial stress. *Proc. R. Soc. A* **273**: 329–339, 1963.
[2] Gent A. N. and Cho I. S. Surface instabilities in compressed or bent rubber blocks. *Rubber Chemistry and Technology* **72**:253–262, 1999
[3] Cao, Y. and Hutchinson, J. W. From wrinkles to creases in elastomers: the instability and imperfection-sensitivity of wrinkling. *Proc. R. Soc. A* **468**: 94–115, 2012.
[4] Audoly, B. Localized buckling of a floating elastica. *Phys. Rev. E* **84**: 0116051–0116057, 2011.

AN ANALYTICAL METHOD FOR REPAIRED STEEL PLATE AFTER BUCKLING

Takuro Tomioka[1], Yasuhito Beppu [1]and Takumi Ito[1],
[1]Department of Architecture, Faculty of Engineering, Tokyo University of Science, Tokyo, Japan

Summary Recently, a digital fabrication method combined with 3D modelling, image analysis, and robotics is attracting, and which can realize the automation and sophistication under construction site. It is expected to support the quick restoration of damaged building after severe disasters. In this study, to investigate the feasibility of DF-method, the fundamental study is conducted on steel elementally member with local buckling. The simple and optimized shape of repair member is suggested which is assumed to be made of 3D-printting. Furthermore, the analysis method is suggested, and it can estimate the test result well.

INTRODUCTION

In recent years, there have been many reports of damaged buildings due to large earthquakes. In the stricken area, it is worried to keep the safety of investigators who conduct surveys and diagnoses, and to take a lot of time for recovery work of damaged buildings due to the shortage of materials and personnel. There is a need to resolve these issues and establish technical systems for the rapid restoration and reconstruction of seismic damaged cities.

Recently, to realize the automation and sophistication of construction procedure (new construction and renovation, etc.), ICT technology has been introduced. In addition, to speed up the construction and reduce the workers under the disaster-stricken buildings, an innovated system such as digital fabrication method has been discussed which combine the manufacturing technology using 3D printing and robots, and image analysis method for estimation of damage status of buildings.[1)]

Therefore, in this study, the optimal shape of repair member by 3D printing (Fig. 1) for the plastic deformation and buckling of the damaged steel member is examined. In addition, to estimate the recovered strength of repaired member, the analytical method is suggested. Also, the applicability is investigated here.

OUTLINE OF THE EXPERIMENT

In the case of damaged H-section steel members of earthquake-resisting steel frame, a repair method of linear lamination is assumed for local buckling of flanges. Therefore, an elemental test of a steel plate simulating a flange repair is performed using steel bar and steel plate, imitating the shapes of lines and plates that can be formed by 3D printing (Fig. 2).

Fig. 3 shows the dimensions of the test piece and Fig. 4 shows the setup diagram.

First, compression loading is performed on the base material (75×6×600mm, SM490B) (initial loading). Out-of-plane deformation was considered as parameters of the degree of damage. Three types of out-of-plane deformation, large (27mm), medium (17mm), and small (5mm) were assumed, which is based on the past test results of buckling waveform during the horizontal loading test of H-shaped steel members[2)].

Next, the damaged specimen is restored by welding a steel bar (SDG3K / SWRM8) or steel plate (SS400) as shown in Fig.5. Three types of repair positions were considered: on the load axis, outside and inside.

After that, compression loading is performed (secondary loading), and the repair effect is examined.

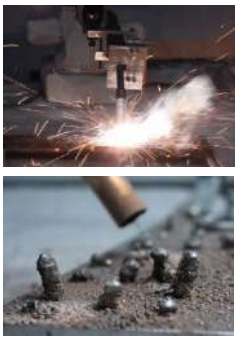

Figure 1. Robot welding and linear lamination

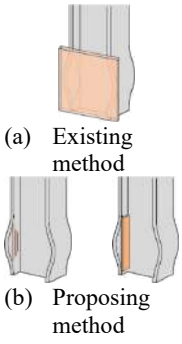

Figure 2. Repair method

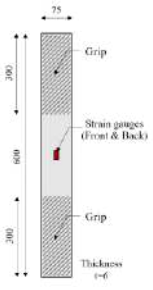

Figure 3. Specimen

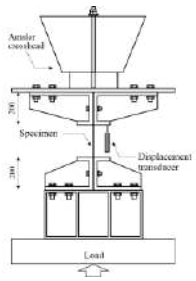

Figure 4. Setup diagram

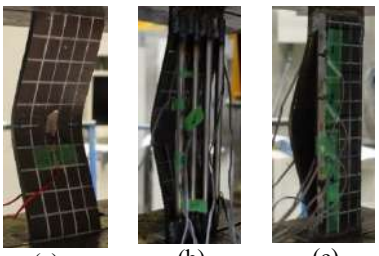

(a) Before repair (b) Steel rod repair (c) Steel plate repair

Figure 5. Specimen after repair

RESULT OF THE EXPERIMENT

Fig.6 shows the state of the specimen during the secondary loading. Four types of collapse modes were observed. Table 1 shows the ratio of the maximum proof stress, the rate of increase in strength, the ratio of the rigidity and the collapse mode of each specimen. It can be seen that when plate repair was performed on a specimen with a small degree

*Corresponding author. E-mail: **t.tkr28424@gmail.com**

of damage, both the maximum proof stress and rigidity were restored to the same level as the original state. In the case of bar repair, when Φ9mm was used rather than Φ6mm, both proof stress and rigidity were increased, and the repair effect was obtained. In the comparison of collapse modes, in modes A and B, high strength and rigidity were obtained after repair.

Table 1. Result of the experiment

No.	①	②	③	④	⑤	⑥	⑦	⑧	⑨	⑩	⑪	⑫	⑬	⑭	⑮	⑯	⑰	⑱
Damage degree	Small		Medium				Large											
Repair element	B	P	Bar		Plate		Bar					Plate						
Thickness / Diameter [mm]	6	6	6		6		6			9		4.5		6		9		12
Repair position	O	O	O	A	O	A	O	A	I	O	A	O	A	A	I	O	A	O
O : Outside, A : On axis, I : Inside																		
Maximum proof stress Ratio	0.64	0.97	0.34	0.34	0.66	0.70	0.28	0.26	0.22	0.56	0.52	0.41	0.54	0.68	0.33	0.66	0.49	0.72
Strength increase rate	1.37	1.55	1.35	1.35	2.64	2.81	1.49	1.36	1.16	2.99	2.79	2.21	2.87	3.60	1.78	3.51	2.62	3.86
Rigidity ratio	0.82	0.91	-	-	0.55	0.67	-	-	-	0.31	0.42	0.56	0.54	0.54	-	0.42	0.33	0.40
Collapse mode	C	B	B	C	B	D	B	C	C	B	D	B	C	C	D	A	D	A

ANALYTICAL STUDY FOR RECOVED STRENGTH OF REPAIRED STEEL MEMBER

A mechanical model is assumed based on the experimental results, and the proof stress is evaluated.

From Fig.6, it was observed that in Mode B, plastic hinges were generated near the upper and lower welded portions and in the center of the repair plate and they proceeded together with the hinges generated during the initial loading. Therefore, a dynamic model shown in Fig.7 is assumed. The full plastic moment of the base material is M_1, the hinge rotation angle is θ_1, the full plastic moment of the repair material is M_2, the hinge rotation angle is θ_2, and the hinge rotation angle of the initial load is θ_i.

$$P\delta=4M_1\theta_1+4M_2\theta_2 \quad \text{--- (1)}$$

Here,

$$(l/2)\cos\theta_i\,(1-\cos\theta_2)=\delta/2 \quad \text{--- (2)}$$

$$(l/2)\cos(\theta_1+\theta_i)=(l/2)\cos\theta_i\cos\theta_2 \quad \text{--- (3)}$$

From this equation, the relationship between P and δ is shown in Fig.8. This figure shows that the maximum proof stress of the analysis values is close to the experimental values. It seemed that the behaviour after buckling is almost the same.

Mode A Mode B Mode C Mode D

Figure 6. Specimen during second loading

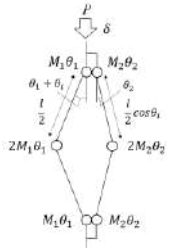

Figure 7. Dynamic model

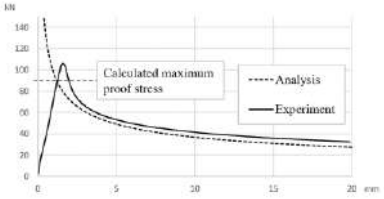

Figure 8. Relationship between P and δ

CONCLUSIONS

We proposed a plate-shaped and bar-shaped repair method for buckled steel plates, and the experimental results confirmed the repair effect of strength and rigidity. In particular, a high effect was obtained by repairing outside the buckling waveform. In the specimen with small damage, both the maximum proof stress and rigidity recovered to the same level as the original state. From the results of Mode B, the possibility of controlling the formation position of the plastic hinge after repair was shown. Based on the experimental results, a strength evaluation method using dynamic model was proposed and the possibility of evaluating the strength of the repaired part of H-shaped steel members was shown.

References

[1] Takumi Ito, Yasuhito Beppu, Kenjiro Mori, Ayumu Ushigome : Damage Detection Method by 3D-model Analysis of Damaged Steel Frames, Part 1 General Description of Diagnosis System and Experimental Study, Summaries of technical papers of annual meeting, Architectural Institute of Japan, pp183-184, 2019.9 (Japanese)

[2] Kenjiro Mori, Ayumu Ushigome, Yasuhito Beppu, Takumi Ito : Repairability and Recovery of Structural Performance of Damaged Steel Members with Buckling and Fractures, Part15 Proposal of a repair method by using intermittent steel plates and experimental study of repair effect, Summaries of technical papers of annual meeting, Architectural Institute of Japan, pp337-338, 2019.9 (Japanese)

TENSILE BUCKLING OF REPETITIVE RIGID RODS SYSTEMS WITH OVERLAPPING

Pedro Dias Simão[1,2] and Vítor Dias da Silva[1,2]
[1]INESC-Coimbra, Coimbra, Portugal
[2]Department of Civil Engineering, University of Coimbra, Coimbra, Portugal

Summary Overlapping is used to create innovative repetitive structural systems that buckle under tension, in the present case a one-dimensional frame made up by the sequential repetition of a module composed by a set of lined up rigid rods connected by rotational joints. Each module is composed by two main bars and two smaller bars overlapping the main ones. When tensioned, the global frame buckles, and it is observed that the tensile critical load shows little change when new modules are added to the system, in clear contrast with the compressive case. In addition, a global variation is imposed to a module's mechanical properties at each repetition step. Although smooth and kept within small values, this variation provokes significant changes in the tensile buckling behaviour of the global frame, here illustrated by a sequential buckling case. The findings pave the way to the future development of 2D or 3D innovative repetitive frames, deployable structures, cellular materials, polymer chains and origamis showing original buckling properties under tension, owing to overlapping.

THE STRUCTURAL SYSTEM WITH OVERLAPPING AND ITS MATHEMATICAL MODEL

In structural mechanics, buckling is usually associated with compressive stress and/or shortening deformation states, so that, for a frame under tension, buckling is not a concern. On the other hand, it is often considered that overlapping is a mere waste of material. In the present paper we prove this is not so. In fact, some original mechanical properties can be observed in frames showing secondary parts overlapping the main ones, such as tensile buckling. Pure tensile buckling was originally observed in members with transverse sliders [1], and in [2] we linked this phenomenon to alternative frames showing overlapping and rotational joints only. Besides, repetitive frames are widely used in nature and in engineering, owing to their strength and ease of erection. Within this context, we analyse a repetitive frame made up by the sequential repetition in series of the module presented in Fig. 1, for which the secondary bars [AB] and [CD] overlap the main ones [BC] and [DE], implying that $\overline{\mathrm{AB}}+\overline{\mathrm{CD}}$ must be always smaller than $\overline{\mathrm{BC}}$ or $\overline{\mathrm{DE}}$. By numbering sequentially all nodes of the frame, starting by denoting node A of the first module as node 0, and by relating each bar to the number index of its end node, the kinematic description of a frame made up by the repetition of n_M modules for node k is:

$$\begin{cases} u_k = 0+\sum_{i=1}^{k}(-1)^i L_i\left(\cos\theta_i-1\right) \\ w_k = 0+\sum_{i=1}^{k}(-1)^i L_i \sin\theta_i \end{cases} \tag{1}$$

to which corresponds the total potential energy of the system ($n_N = 4n_M$ is the index of the last node of the sequence, for bar i L_i is its length and θ_i its rotation, K_i is the stiffness coefficient of joint i, λ is a Lagrange multiplier associated with a restriction that forces the last node of the system to remain along the xx axis and P is the axial load, positive for tension):

$$V = \underbrace{\frac{K_0}{2}\theta_1^2+\sum_{i=2}^{n_N}\frac{K_{i-1}}{2}\left(\theta_i-\theta_{i-1}\right)^2+\frac{K_{n_N}}{2}\theta_{n_N}^2}_{V} \underbrace{-P\cdot\sum_{i=1}^{n_N}(-1)^i L_i\left(\cos\theta_i-1\right)}_{\Pi}+\underbrace{\lambda\sum_{i=1}^{n_N}(-1)^i L_i\sin\theta_i}_{G(\theta_i)} \tag{2}$$

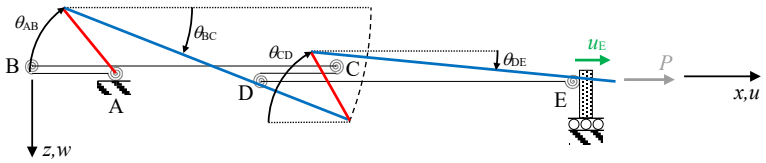

Figure 1. The rods module with overlapping bars.

BUCKLING BEHAVIOUR UNDER A TENSILE AXIAL LOAD

Application of the stability procedures [3] to expression (2) yields the stability behaviour of the structural system. Henceforth, all examples are kept dimensionless in order to allow any consistent set of units at macro or micro scales, and overlapping is mathematically modelled by factor $(-1)^i$ in expressions (1) and (2). Focusing now on the buckling behaviour of the system, Fig. 2 compares the tensile and compressive critical loads against the adopted number of modules associated in series considering, for all modules, all K_i equal to $1\times\kappa_{ref}$, lengths $\overline{\mathrm{AB}}$ and $\overline{\mathrm{CD}}$ equal to $1\times\Lambda_{ref}$ and lengths $\overline{\mathrm{BC}}$ or $\overline{\mathrm{DE}}$ equal to $3\times\Lambda_{ref}$. A relevant property is noticed immediately: the compressive buckling, arising from the lowest negative eigenvalue of the stability problem [3], is always smaller than the lowest tensile critical load, and it is much more sensitive to the number of adopted modules than the tensile critical load, which depends mainly on the ratio overlapping length/main length, constant as the number of modules increase.

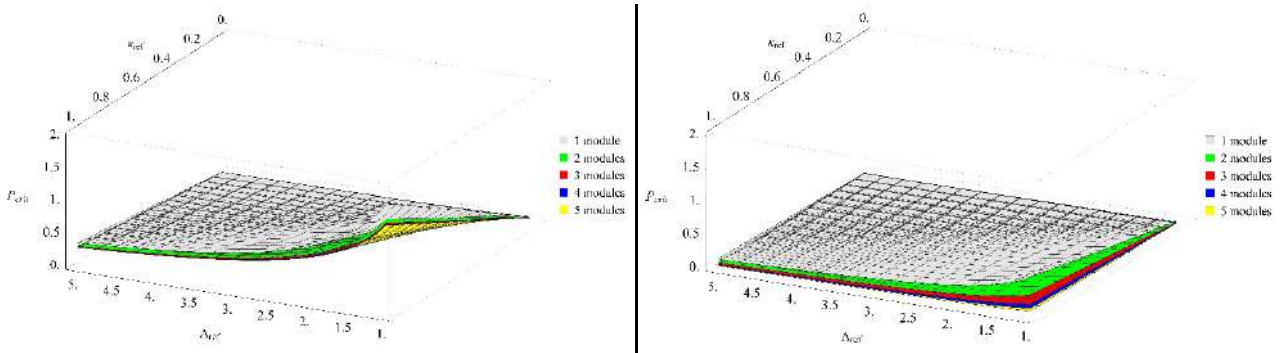

a) critical tensile loads b) critical compressive loads

Figure 2. Influence of the number of modules on the tensile and compressive buckling loads.

TENSILE POST-BUCKLING BEHAVIOUR AND THE INFLUENCE OF SMOOTH CHANGES OF THE MECHANICAL PROPERTIES ALONG THE FRAME

The repetitive frame just analysed considers a perfect repetition of the modes, in the sense that any new module added to the sequence is precisely equal to the previous one. It doesn't have to be always like that and, in nature or in engineering applications, we find often repetitive structures or cellular materials that, at each repetition step, show small changes in some module's mechanical properties, in order to better the performance of the whole system. By doing this, repetitive frames with original mechanical behaviours can be created [2] and so, in order to exemplify the effect of such variations on the tensile buckling behaviour of the frame made up by the sequential repetition of the module depicted in Fig. 1, we consider a structural systems composed by two modules, whose lengths are initially equal those of the previously analysed problem for $\Lambda_{ref}=1$. Then, the i^{th} rod's length is multiplied by $1+0.25\sin\left(\dfrac{i-1}{n_N-1}\pi\right)$, $i=1,\ldots,n_N$ (for the case with 2 modules $n_N=8$). The springs stiffness coefficients remain unchanged throughout the repetition process and, for each module, we consider $K_{\text{A}}=K_{\text{E}}=0$ and $K_{\text{B}}=K_{\text{C}}=K_{\text{D}}=1$. Fig 3 depicts the post-buckling behaviour, which constitutes a case of sequential tensile buckling. In fact, after the occurrence of a first critical load with value $P_{crit,1}=0.529$ along the trivial path, a second critical state occurs along the secondary path, for both branches, at $P_{crit,2}=0.684$. Fig. 3-a) depicts the deformed shape of the frame for $P=1.1\,P_{crit,1}$ and $P=2\,P_{crit,1}$ for the secondary and terciary paths respectively.

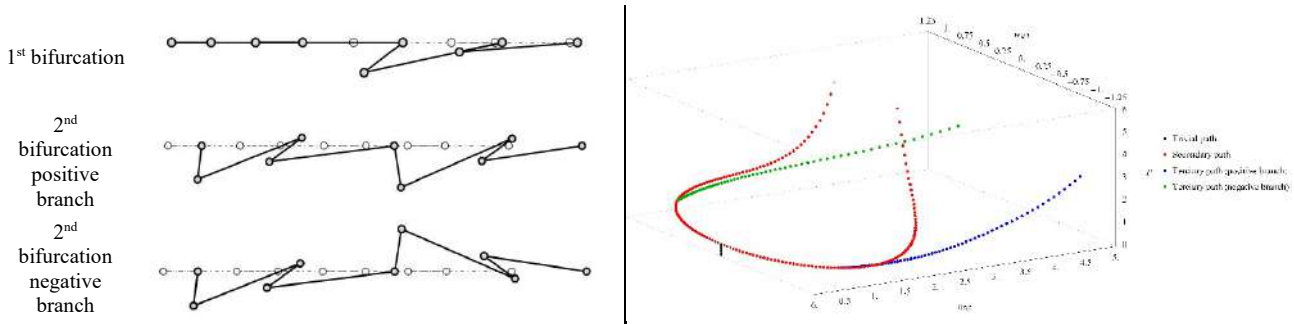

a) Post-buckling deformed shape (positive bifurcation only) b) Displacement (u,w) against P of point B of the second module

Figure 3. Post-buckling behaviour for a two modules structural system.

CONCLUSIONS

The tensile buckling behaviour for a repetitive frame with overlapping was analysed, showing some original properties. Bearing in mind that, nowadays, buckling is no longer seen as a mere route to collapse but also as a new way of creating structures and materials with original constitutive behaviours [4], we showed that this strategy can also be extended to frames under tension by means of overlapping. The findings pave the way to the development of innovative 2D and 3D repetitive frames, deployable structures, origamis or polymer chains showing original behaviours under tension.

References

[1] Zaccaria D., Bigoni D., Noselli G., Misseroni, D. Structures buckling under tensile dead load. *Proc. Royal Society of London*, **A–467**: 1686-1700, 2011

[2] Simão, P. D., Silva, V. D. Tensile buckling of repetitive rods systems with overlapping, *submitted to Elsevier*, 2020.

[3] Thompson J. M. T., Hunt, G. W. A general theory of elastic stability. John Wiley and Sons, London 1973.

[4] Reis P. M. A perspective on the revival of structural (in)stability with novel opportunities for function: from buckliphobia to buckliphilia. *ASME Journal of Applied Mechanics*, **82 (November)**, paper n. 111001, 2015.

PHASE TRANSITION AND LOCALIZATION IN INFLATED ARCHITECTURED ELASTIC PLATES (BAROMOPHS)

Emmanuel Siéfert[1],José Bico[1],Etienne Reyssat[1],and Benoît Roman*[1]
[1]PMMH, CNRS, ESPCI Paris, Universit PSL, Sorbonne Universit, Universit de Paris, F-75005, Paris, France

Summary In some systems, two very different equilibrium states exist for the same loading condition, and it is then often observed that an extended homogeneous system spontaneously divides spatially into coexisting regions in different states (or phase). These "propagating instabilities" [1]) (also denoted "localization") are in fact the equivalent in mechanics of phases transitions. Here we will show a new example of this type of instability in an architected elastomer plate including an internal network of airways ("baromorph" [2]) : although these systems are in this case designed to undergo homogeneous in-plane expansion, we find that they sometimes present very unusual three-dimensional shapes, that we interpret as buckling induced by phase-separation.

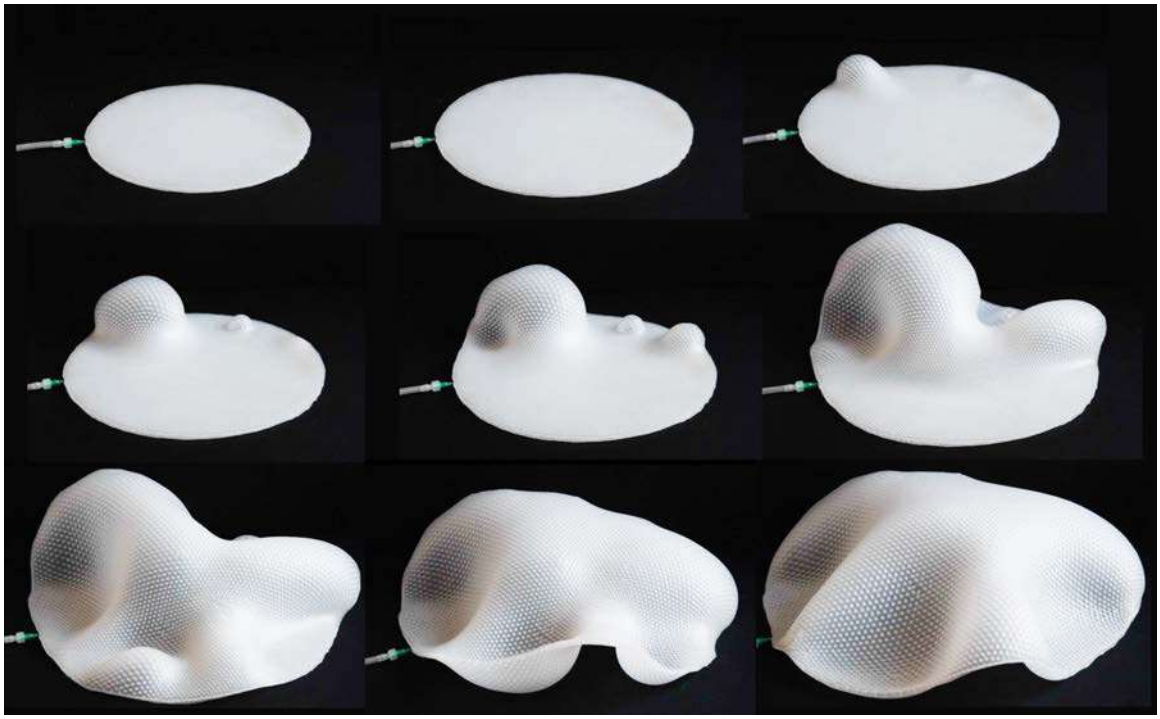

Figure 1: Series of pictures of a large plate embedding a regular hexagonal lattice of pillars upon inflation. Bulges appear in the plate and then propagate through the whole structure, at a nearly constant pressure.

We consider an architected elastomeric plate, with the following internal structure: a triangular network of cylindrical pillars connecting a top and bottom layer (thickness e), as in Fig. 2. When a pressure p is imposed in this internal chamber,

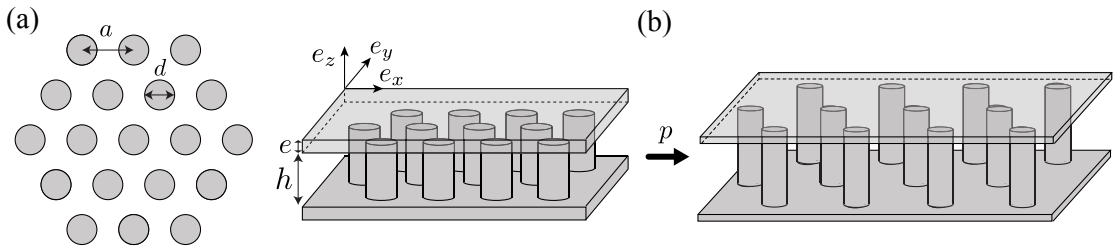

Figure 2: (a) (left) Schematic top view of the regular pillar lattice of pitch a, the diameter of the pillars being d. (right) Schematic 3D representation of a portion of the structure, e being the thickness of the top and bottom membranes, and h the height of the pillars. (b) Upon inflation, the structure deforms with a large in-plane expansion.

which has a internal structure everywhere identical, we would expect a uniform response of the material, so that the plate should simply expand everywhere by the same factor. But very surprising shape changes are observed at one critical pressure (pressure is approximately constant in all pictures except the first one on Fig. 1), where the structure locally

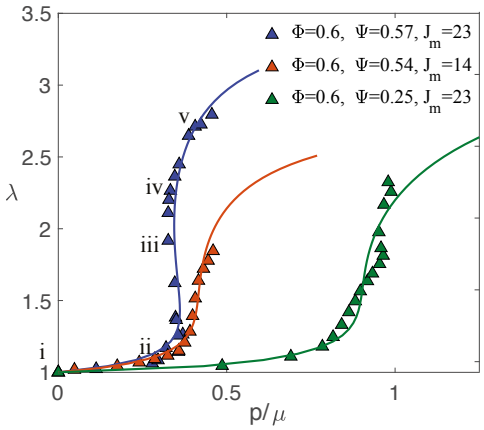

Figure 3: Deformation response of the plate as a function of the dimensionless applied pressure p/μ for various geometries of the inner architecture $\Psi = h/(h+2e)$ the relative height of the pillars compared to the total thickness of the plate, Φ the in-plane density of pillars, and J_m the maximum material stretching invariant in Gent's model [3] . Triangles correspond to experimental measurements, solid lines to the theoretical response

buckles out of plane in several areas, whereas the rest remains flat. As the air volume inside the plate is increased, the shape evolves, with the bumps progressively merge though a complex series of shapes in a very homogeneous structure.

In this presentation we wish to elucidate this instability. When computing the mechanical deformation of the inflated plate (assumed to be homogeneous), and we find that depending on the geometry and the material properties (see figure 3) several states may be attained for the same imposed internal pressure (a family of equilibrium states have a negative stiffness). A localization instability is therefore expected [4,5], with the coexistence of the two phases (in strongly different stretch state, which are thus geometrically incompatible). We interpret the complex shapes observed in Figure 1 as the result of out-of-plane buckling induced by such incompatible in-plane strains.

References

[1] Kyriakides,S. *Advances in applied mechanics* , 30,41993., 1993
[2] Siéfert, E and Reyssat, E and Bico, J and Roman, B *Nature materials* ,18, 1, 2019.
[3] Gent, A *Rubber chemistry and technology* 69, 1996.
[4] Ericksen J. of Elasticity 5,(191-201), 1975
[5] Santisi d'Avila,MP and Triantafyllidis, N. and Wen, G. *Journal of the Mechanics and Physics of Solids*, 97, (275-298), 2016

*Corresponding author. E-mail: benoit.roman@espci.fr

MAGNETICALLY CONTROLLED SURFACE PATTERNS OFBIAXIALLY PRE-STRAINED MULTI-LAYERED MAGNETO-ELASTICSTRUCTURES

Matthias Rambausek*[1] and Konstantinos Danas[2]
[1]Institute for Analysis and Scientific Computing, TU Wien, Wiedner Hauptstr. 8-10, 1040 Wien, Austria
[2]LMS,CNRS,École Polytechnique,Institut Polytechnique de Paris,Palaiseau,91128,France

Summary The research presented is concerned with instabilities in composites featuring layers of magnetorheological elastomers (MREs). It is already known that a thin magnetic film on an soft non-magnetic substrate exhibits complex surface patters in the post-bifurcation regime not only due to mechanical but also due to magneto-mechanical and purely magnetic loading. However, present literature mainly covers 1d surface patterns enforced by uniaxial mechanical pre-strain. In our current work we aim for full 2d surface patters as they appear in 3d structures under general conditions. Moreover, we generalize the basic thin-film-on-substrate-type structure to layers of MREs and non-magnetic elastomers and study their instabilities and post-bifurcation behavior. For this purpose we employ Fourier schemes for structures of infinite lateral extent combined with finite elements.

INTRODUCTION

Buckling and more complex instabilities such as folds and creases of slender or thin structures are a prominent field of study (not only) in mechanics and an important source of innovation. With the advent of finite-strain magneto-mechanics and the study of corresponding soft magneto-elastic composites it was only natural to explore instability phenomena also in the area of coupled magneto-mechanics [4]. One class of structures investigated for instabilities are thin films attached to soft substrates. In the purely mechanical case, such a structure exhibits instabilities resulting in one-dimensional or two-dimensional surface patterns, depending on the lateral loads [6, 5]. In case of magnetic films it has been shown that similar patterns can be initiated with applied magnetic fields in out-of-plane direction. Moreover, the critical magnitude of the magnetic field can be controlled via sub-critical mechanical pre-loads, ie. pre-stress or pre-strain. Uniaxial pre-strains have been shown to yield one-dimensional patterns such as wrinkling and more complex modes such as crinkling have been observed when going deeper in the post-bifurcation regime [1, 2]. As summarized in Figure 1, our current work is concerned with the effect of *biaxial* mechanical pre-loads on *magneto-mechanical* surface patterning which has not been investigated up to know. The idea behind is that biaxial pre-strains may be used to control the surface pattern obtained by increasing the magnetic load beyond the critical value. As a second generalization of prior work we study multi-layered magneto-elastic structures, ie. structures featuring more than one magnetic and non-magnetic layer.

For the exploration of critical loads we consider planar structures of infinite lateral extent. These results then serve as an important guide for real-world scenarios with structures of finite lateral extents treated with finite elements.

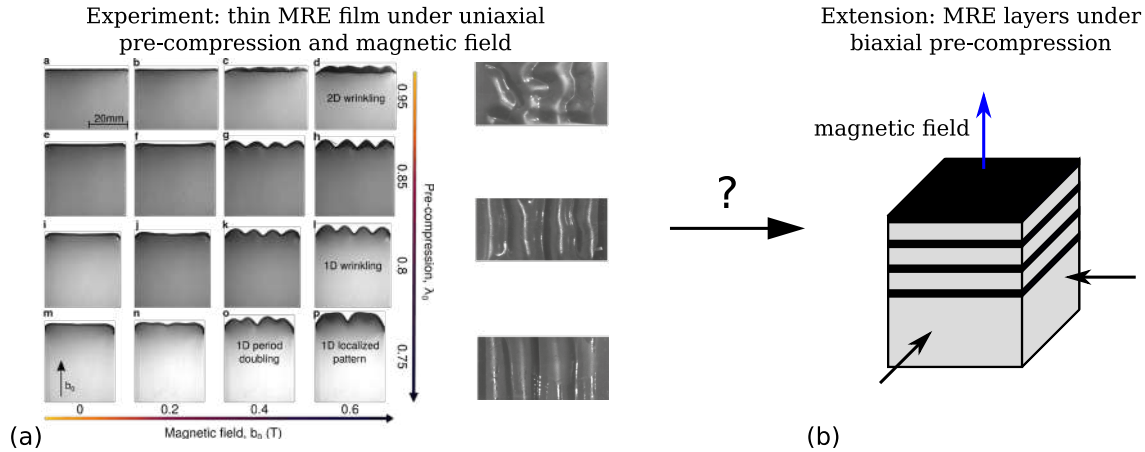

Figure 1: Prior experimental observations of a thin MRE film on a compliant substrate [1] (a) and scope of our current work (b): multiple layers of MREs under biaxial pre-compression and magnetic field.

THEORY

The study is within the scope of magneto-elasticity at finite strains and quasi-static conditions. We employ mechanical displacements $\boldsymbol{u}$ and the (referential) magnetic vector-potential $\boldsymbol{A}$ as primary fields. The corresponding governing variational principle can be found in, e.g., [3]. The body of interest is of infinite extent in the X_1-X_2-plane, where we may prescribe strains in either direction. As magnetic loading we prescribe $\boldsymbol{b}^\infty = (0, 0, b^\infty)$ in X_3 direction. Under such conditions, the principal solution of the problem yields states $\boldsymbol{F}$ (deformation gradient) and $\boldsymbol{B}$ (referential magnetic

*Corresponding author. E-mail: matthias.rambausek@tuwien.ac.at

field) that are uniform in the X_1-X_2-plane and piecewise constant in X_3. For our stability investigations we employ a Fourier-based discretization in X_1 and X_2 and finite elements (second-order Lagrange elements) in X_3. Accordingly, one *possible* Ansatz for an Eigen-mode is given as

$$\boldsymbol{u}(X_1, X_2, X_3) = \hat{\boldsymbol{u}}^c(X_3)\cos(\Omega_1 X_1 + \Omega_2 X_2) + \hat{\boldsymbol{u}}^s(X_3)\sin(\Omega_1 X_1 + \Omega_2 X_2) \tag{1}$$

$$\boldsymbol{A}(X_1, X_2, X_3) = \hat{\boldsymbol{A}}^c(X_3)\cos(\Omega_1 X_1 + \Omega_2 X_2) + \hat{\boldsymbol{A}}^s(X_3)\sin(\Omega_1 X_1 + \Omega_2 X_2), \tag{2}$$

where the amplitudes $\hat{\boldsymbol{u}}^c(X_3)$, $\hat{\boldsymbol{u}}^s(X_3)$, $\hat{\boldsymbol{A}}^c(X_3)$ and $\hat{\boldsymbol{A}}^s(X_3)$ have a standard finite element representation.

For given loading parameters $(b^\infty, \lambda_1, \lambda_2)$ we find the pair (ω_1, ω_2) which yields the smallest Eigenvalue of the system matrix. Then, the magnetic load is adjusted such that the smallest Eigenvalue is (numerically) zero, which marks the loss of stability.

A REPRESENTATIVE RESULT

We perform the procedure described above for a range of material parameters and combinations of material layers. In Figure 2 we show the critical magnetic load $b^{\infty,c}$ and the critical $(\omega_1^c = \Omega^c/\lambda_1, \omega_2^c = \Omega_2/\lambda_2)$ for a variety of pre-strains (λ_1, λ_2).

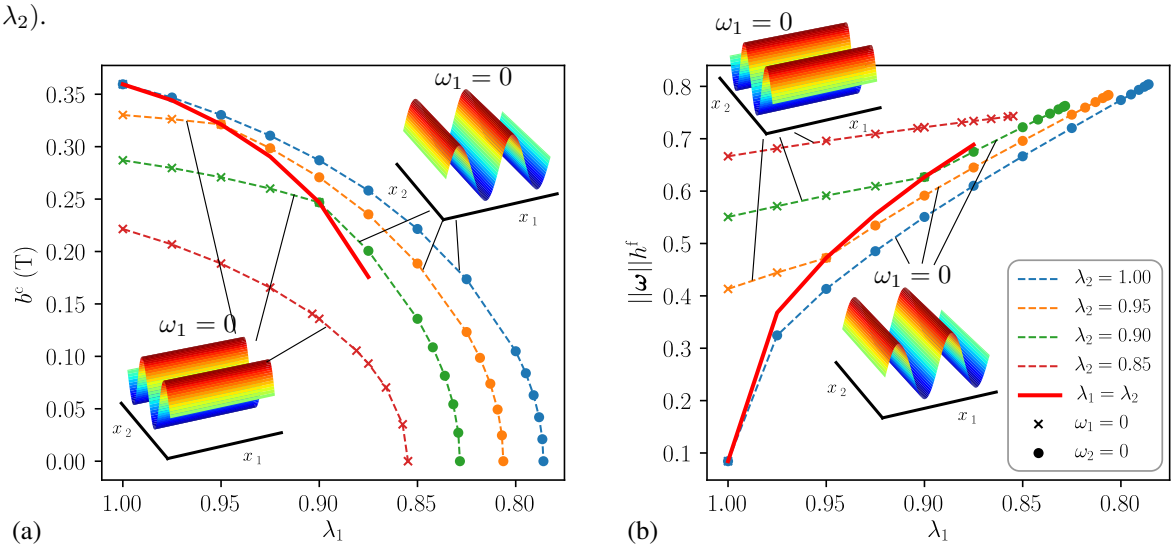

Figure 2: Critical applied magnetic field $b^{\infty,c}$ (a) and norm of critical Eulerian wave vector $||(\omega_1^c, \omega_2^c)||$ (b) for a set of pre-stretches in x_1 and x_2 direction, λ_1 and λ_2, respectively. The latter is plotted because the critical wave-numbers are not unique for the equi-biaxial case [5]. For non-equi-biaxial pre-stretches, the wave number in the direction of the larger pre-stretch is observed to be zero. Results for magnetic substrates and various topologies can be found in [7].

CONCLUSIONS

In our contribution we investigate the stability of multi-layered magneto-elastic structures of infinite lateral extent. Thereby, our research interest is two-fold: the first question is the magnetic loading required for loss of stability for a variety of pre-strains and combinations of layers. Second, we aim for a characterization of the stability of surface patters in the post-buckling regime. The results shown are intended to serve as a guideline for future studies in the nonlinear post-buckling regime and practical applications.

References

[1] Psarra, E., Bodelot, L. and Danas, K. Two-field surface pattern control via marginally stable magnetorheological elastomers. *Soft Matter* **13**:6576–6584, 2017.

[2] Psarra, E., Bodelot, L. and Danas, K. Wrinkling to crinkling transitions and curvature localization in a magnetoelastic film bonded to a non-magnetic substrate. *J. Mech. Phys. Solids* **133**:103734, 2019.

[3] Bustamante, R., Dorfmann, A. and Ogden, R. W. On Variational Formulations in Nonlinear Magnetoelastostatics. *Math. Mech. Solids* **13**:725–745, 2008.

[4] Danas, K. and Triantafyllidis, N. Instability of a magnetoelastic layer resting on a non-magnetic substrate. *J. Mech. Phys. Solids* **69**:67–83, 2014.

[5] Cai, S., Breid, D., Crosby, A. J., Suo, Z. and Hutchinson, J. W. Periodic patterns and energy states of buckled films on compliant substrates. *J. Mech. Phys. Solids* **59**:1094–1114, 2011.

[6] Audoly, B. and Boudaoud, A. Buckling of a stiff film bound to a compliant substrate–Part I. *J. Mech. Phys. Solids* **56**:2401–2421, 2008.

[7] Rambausek, M. and Danas, K. Bifurcation of magnetorheological film–substrate elastomers subjected to biaxial pre-compression and transverse magnetic fields. *Int. J. Nonlin. Mech.* **128**:103608, 2021.

INVESTIGATION OF INSTABILITY-INDUCED PATTERN TRANSFORMATIONS IN PERIODIC HYDROGELS BASED ON AN INCREMENTAL MINIMIZATION PRINCIPLE

Elten Polukhov[1] and Marc-André Keip*[1]
[1]Institute of Applied Mechanics, University of Stuttgart, Stuttgart, Germany

Summary The present contribution deals with swelling-induced pattern transformations of periodic hydrogels due to diffusion of solvent molecules. The deformation-diffusion processes are modeled by a rate-type variational formulation in terms of the deformation map and the solvent-volume flux as independent fields. This setting yields a minimization principle that is readily suitable for stability analysis. A conforming discretization requires edge-based finite elements for the flux degrees of freedom, which will be realized by Raviart–Thomas-type finite elements. Within the discussed framework, we investigate pattern transformations in periodic hydrogels using Bloch–Floquet wave analysis.

INTRODUCTION

Hydrogels are soft polymeric materials that have promising application areas in engineering, medicine and agriculture. Their advantageous properties, such as high porosity and biocompatilibity, and their characteristic swelling due to diffusion of solvents make them also attractive for developments in soft electronics as well as next-generation actuators and sensors. As could be shown in experiments, periodic porous hydrogel structures undergo swelling-induced instabilities that result in complex deformations in the form of pattern transformations [1, 2]. In hydrogel thin films such transformations do not only occur in the plane of periodicity, but also develop out of plane. As a result, related materials show complex three-dimensional patterns [3]. So far, associated studies of three-dimensional swelling-induced instabilities often rely on simplifying assumptions. Thus, the aim of the present contribution is twofold: We will (i) develop a versatile framework for the structural stability analysis of hydrogels within a variational minimization principle and (ii) exploit the variational framework for the investigation of pattern transformations of soft periodic hydrogels in two and three spatial dimensions.

VARIATIONAL FORMULATION OF DEFORMATION-DIFFUSION PROCESSES

We model the deformation-diffusion processes using a two-field variational minimization principle. This principle relies on the deformation map $\boldsymbol{\varphi} : \mathcal{B}_0 \times \mathcal{T} \to \mathcal{B}_t \subset \mathcal{R}^3$ and the solvent-volume flux $\mathbb{H} : \mathcal{B}_0 \times \mathcal{T} \to \mathcal{R}^3$ as independent fields. $\mathcal{B}_0$ and $\mathcal{B}_t$ denote the reference and current configuration of a hydrogel body, respectively [4]. To describe swelling phenomena, we introduce the concentration of the solvent volume $s : \mathcal{B}_0 \times \mathcal{T} \to \mathcal{R}$ which is related to the solvent flux via the conservation of the solvent-volume concentration via $\dot{s} = -\mathrm{Div}\mathbb{H}$. Due to the dissipative nature of deformation-diffusion processes, we model them using two constitutive functions given by the energy-storage function $\hat{\psi}(\boldsymbol{F}, s)$ and the dissipation-potential function $\hat{\phi}(\mathbb{H}; \boldsymbol{F}, s)$. The energy-storage function is assumed to depend on the deformation gradient $\boldsymbol{F}$ and the solvent-volume concentration s and, furthermore, is considered to have an additive form as $\hat{\psi}(\boldsymbol{F}, s) = \hat{\psi}_{mech}(\boldsymbol{F}) + \hat{\psi}_{chem}(s) + \hat{\psi}_{coup}(J, s)$. Here, $\hat{\psi}_{mech}$, $\hat{\psi}_{chem}$ and $\hat{\psi}_{coup}$ are the mechanical, chemical and coupling terms, respectively. Having introduced constitutive state variables and functions, we can determine the evolution of the deformation map and the solvent-volume flux from the rate-type variational formulation

$$\{\dot{\boldsymbol{\varphi}}, \mathbb{H}\} = \mathrm{Arg}\Big\{ \inf_{\boldsymbol{\varphi} \in H^1(\mathcal{B}_0)} \inf_{\mathbb{H} \in H(\mathrm{Div}, \mathcal{B}_0)} \int_{\mathcal{B}_0} \frac{\mathrm{d}}{\mathrm{d}t}\hat{\psi}(\boldsymbol{F}, s) + \hat{\phi}(\mathbb{H})\, \mathrm{d}V - \int_{\partial\mathcal{B}_0^t} \bar{\boldsymbol{t}} \cdot \dot{\boldsymbol{\varphi}}\, \mathrm{d}A - \int_{\partial\mathcal{B}_0^\mu} \bar{\mu}\mathbb{H} \cdot \boldsymbol{N}\, \mathrm{d}A \Big\}. \tag{1}$$

Above, $\bar{\boldsymbol{t}}$ and $\bar{\mu}$ denote the prescribed traction and chemical potential on $\partial\mathcal{B}_0^t$ and on $\partial\mathcal{B}_0^\mu$, respectively. In order to solve the above problem, we consider a space-time discretization of the variational principle using implicit Euler time integration and a Raviart–Thomas-type finite element formulation for the spatial discretization [4].

SWELLING-INDUCED STRUCTURAL STABILITY ANALYSIS OF PERIODIC HYDROGELS

We investigate the structural stability of periodic hydrogels by using Bloch–Floquet wave analysis [5, 6]. This allows us to determine possible pattern transformations that go beyond the periodicity of a typical periodic unit cell of the microstructure. In the finite-element setting, the structural stability of the hydrogel can be described by the condition

$$\Lambda = \min_{k_i \in [0,\pi]} \min_{\mathbf{d}} \left\{ \delta\mathbf{d}^T \left[\Pi^\tau(\mathbf{d})_{,\mathbf{dd}} \right] \delta\mathbf{d} / \|\delta\mathbf{d}\|^2 \right\} \begin{cases} > 0 & \text{for a stable solution state } \mathbf{d}^\star \\ \leq 0 & \text{for an unstable solution state } \mathbf{d}^\star \end{cases} \tag{2}$$

where $\mathbf{d}$ denotes the degrees of the freedom of the unit cell and k_i, $i = 1, 3$ are the components of the Bloch vector, see [6, 7] for implementations. The periodic degrees of freedom are subjected to the Bloch–Floquet-type boundary conditions $\delta\mathbf{d}(\boldsymbol{X}^+) = \delta\mathbf{d}(\boldsymbol{X}^-) \exp[\mathrm{i}\boldsymbol{k} \cdot (\boldsymbol{X}^+ - \boldsymbol{X}^-)]$ on the boundary of the unit cell.

*Corresponding author. E-mail: keip@mechbau.uni-stuttgart.de

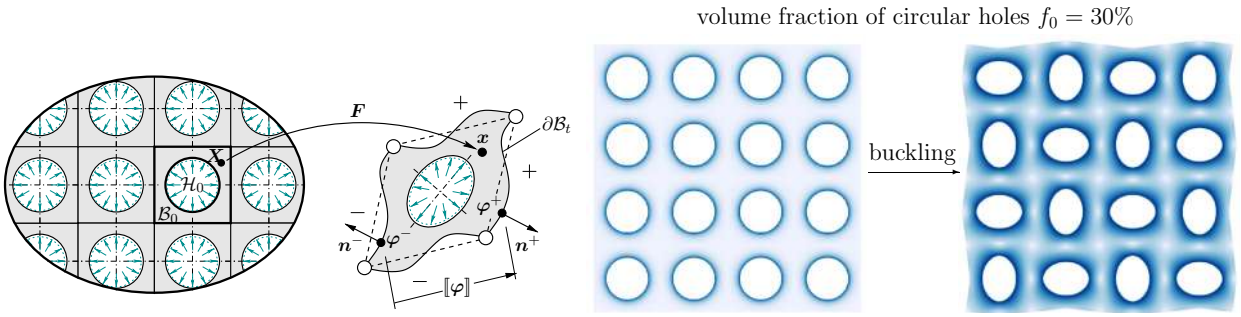

(a) (b)

Figure 1: Periodic hydrogel with voids. **a)** Experimentally motivated boundary conditions on a unit cell of a hydrogel microstructure. **b)** Swelling-induced pattern transformation.

NUMERICAL EXAMPLE

We present a numerical example to demonstrate a typical pattern transformation in a porous planar hydrogel. We assume that the considered hydrogel has a periodic microstructure as described in Fig. 1a. Periodic boundary conditions $[\![\boldsymbol{\varphi}]\!] = \overline{\boldsymbol{F}}[\![\boldsymbol{X}]\!]$, $[\![\mathbb{H}]\!] = \boldsymbol{0}$ on the external boundary of the unit cell $\partial\mathcal{B}_0$ are considered. Motivated by experiments [2] the hydrogel is exposed to solvent molecules through the internal boundary, i.e., $\mathbb{H} \cdot \boldsymbol{N} = H_D$ on $\partial\mathcal{H}_0$. The energy function is assumed to be of Flory–Rehner-type

$$\hat{\psi}(\boldsymbol{F}, s) = \tfrac{\gamma}{2}\big[\boldsymbol{F} : \boldsymbol{F} - 3 - 2\ln(\det \boldsymbol{F})\big] + \alpha\left[s\ln\big(\frac{s}{1+s}\big) + \frac{\chi s}{1+s}\right] + \frac{\epsilon}{2}\big(\det \boldsymbol{F} - 1 - s\big)^2 \tag{3}$$

and the dissipation-potential function is given in time-discrete form as $\hat{\phi}(\mathbb{H}; \boldsymbol{C}_n, s_n) = 1/(2Ms_n)\boldsymbol{C}_n : (\mathbb{H} \otimes \mathbb{H})$ [4].

In Fig. 1b, we present a detected buckling mode of the hydrogel. We observe that at a certain critical fluid content the circular voids deform to elliptic shapes with alternating orientations of their major axes. This particular pattern is referred to as diamond-plate pattern and has been experimentally shown in [1, 2].

OUTLOOK

Future work will be directed towards the three-dimensional extension of the stability analysis. This will allow us to detect complex three-dimensional instability patterns that usually occur in composite hydrogels composed of phases with different swelling properties. We refer to [3] for experimental studies on high-swelling hydrogels with embedded non-swelling discs. There, it could be shown that two-dimensional hydrogel thin films buckle out of plane to form convex-concave patterns, therewith minimizing the overall energy of the system.

References

[1] Zhang Y., Matsumoto E.A., Peter A., Lin P.-C., Kamien R. D., Yang S. One-step nanoscale assembly of complex structures via harnessing of an elastic instability. *Nano Lett.* **7**(4), 2008.

[2] Zhu X., Wu G., Dong R., Chen C.-M., Yang S. Capillarity induced instability in responsive hydrogels membranes with periodic hole array. *Soft Matter* **8**:8088–8093, 2012.

[3] Wang Z.J., Zhu C.N., Hong W., Wu Z.L., Zheng Q. Cooperative deformations of periodically patterned hydrogels. *Sci. Adv.* **3**:e1700348, 2017.

[4] Böger L., Nateghi A., Miehe C. A minimization principle for deformation-diffusion processes in polymeric hydrogels: constitutive modeling and FE implementation *Int. J. Solids Struct.* **121**:257–274, 2017.

[5] Geymonat G., Müller S., Triantafyllidis N. Homogenization of nonlinearly elastic materials, microscopic bifurcation and macroscopic loss of rank-one convexity. *Arch. Ration. Mech. Anal.***122**:231–290, 1993.

[6] Triantafyllidis N., Nestorović M.D., Schraad M.W. Failure surface for finitely strained two-phase periodic solids under general in-plane loading. *J. Appl. Mech.* **73**:505–515, 2006.

[7] Polukhov E., Vallicotti D., Keip M.-A. Computational stability analysis of periodic electroactive polymer composites across scales. *Comput. Methods Appl. Mech. Eng.* **337**:165–197, 2018.

INCREMENTAL CONSTITUTIVE TENSORS AND STRAIN LOCALIZATION FOR PRESTRESSED ELASTIC LATTICES

Giovanni Bordiga[1], Luigi Cabras[2], Andrea Piccolroaz*[1], and Davide Bigoni[1]
[1]Department of Civil, Environmental and Mechanical Engineering, University of Trento, Trento, Italy
[2]Department of Civil, Environmental, Architectural Engineering, University of Brescia, Brescia, Italy

Summary A lattice of elastic rods organized in a parallelepiped geometry can be axially loaded up to an arbitrary amount without distortion and then be subject to incremental displacements. Using both quasi-static and dynamic homogenization theories, this lattice can be made equivalent to a prestressed elastic solid subject to incremental deformation, in such a way to obtain extremely localized mechanical responses. Features such as for instance shear bands inclination, or emergence of a single shear band, or competition between micro (occurring in the lattice but not in the equivalent solid) and macro (present in both the lattice and the equivalent continuum) instabilities are analysed. The analysis of localizations is performed using a Green's function perturbative approach to highlight the correspondence between micromechanics of the composite and homogenized response of the equivalent solid.

INCREMENTAL RESPONSE OF LATTICES OF AXIALLY PRELOADED ELASTIC RODS

A two-dimensional periodic lattice of elastic rods, deformable in the plane both axially and flexurally, is considered, in which all structural members are axially prestressed from an unloaded reference configuration $\mathcal{B}_0$. The axial prestress $\boldsymbol{p} = \{p_1, p_2\}$ is assumed to be produced by dead loading acting at infinity, while body forces in the lattice are excluded for simplicity. It is assumed that the preload not only satisfies equilibrium, but also preserves periodicity and leaves the structure free of flexure.

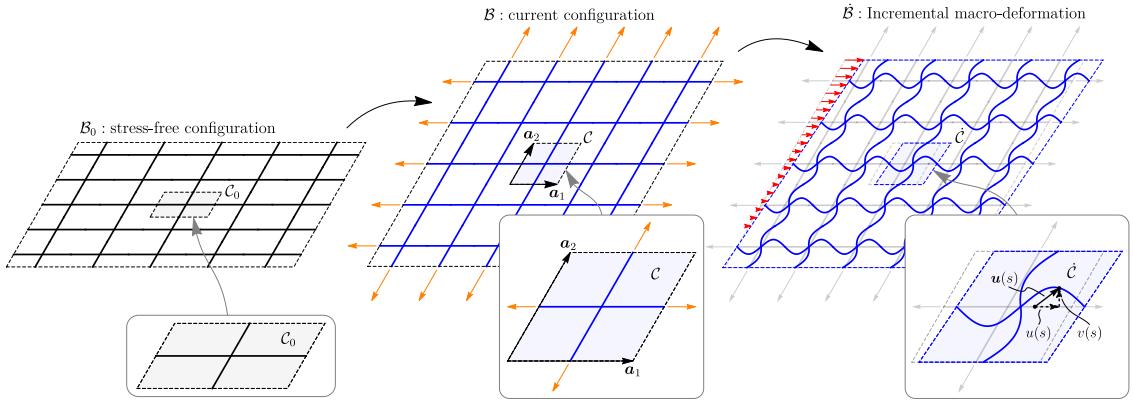

Figure 1: A periodic two-dimensional lattice of (axially and flexurally deformable) elastic rods is considered prestressed from the stress-free configuration $\mathcal{B}_0$ (left) by means of a purely axial loading state. The prestressed configuration $\mathcal{B}$ (center) can be represented as the tessellation of a single unit cell along the vectors of the direct basis $\{\boldsymbol{a}_1, \boldsymbol{a}_2\}$. Upon the current prestressed configuration, the incremental response (right) is defined by the incremental displacement field of each rod $\boldsymbol{u}(s)$, here decomposed in an axial and transverse component, $u(s)$ and $v(s)$.

QUASI-STATIC RESPONSE

A comparison is presented between the response of the lattice loaded with a concentrated force dipole and a dipole Green's function of the effective solid, in terms of maps of incremental displacements. The results are presented as contour plots in Fig. 2, where the color scale has been conveniently normalized according to the norm of the computed displacement field. In the upper part of the figure, results pertaining to the discrete lattice structure are presented, while, in the lower part, results are relative to the equivalent continuum, obtained via homogenization. The figures from left to right correspond to the application of increasing preloads, which approach the strong ellipticity boundary in the equivalent solid in situations where failure of ellipticity corresponds also to the occurrence of a macro bifurcation of infinite wavelength. The part (d) of the figure ($\boldsymbol{p} = 0.99\boldsymbol{p}_{\mathrm{E}}$) also illustrates a magnification of the lattice response in the neighborhood of the loading zone, thus disclosing the microscopic deformation pattern associated to the extreme mechanical response of the material when close to elliptic boundary.

*Corresponding author. E-mail: roaz@ing.unitn.it

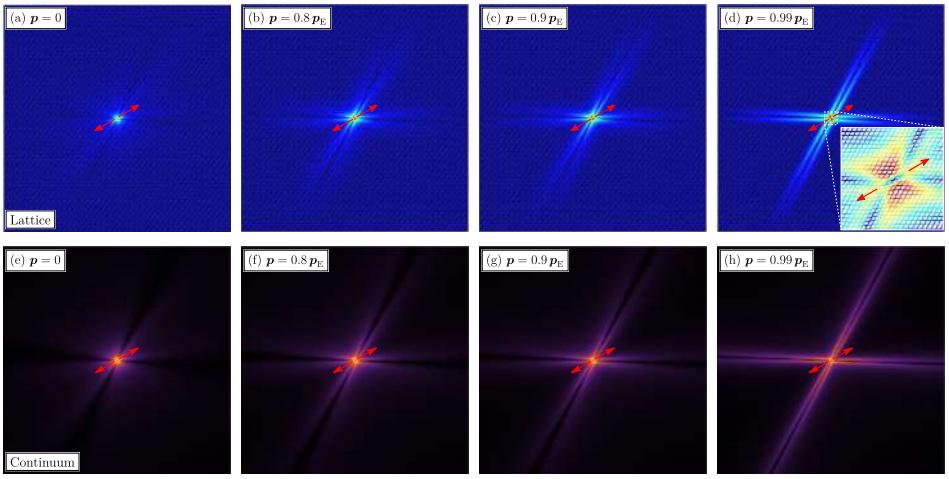

Figure 2: Progressive emergence at increasing load of two orthogonal shear bands visible in the displacement field generated by a diagonal force dipole applied to an orthotropic rhombic lattice (upper part, a–d, simulated via f.e.m.) compared to the response of the homogenized continuum (lower part e–h). From left to right the load increases towards failure of strong ellipticity $\boldsymbol{p}_E$. Shear bands are aligned parallel to the directions predicted at failure of ellipticity ($\theta_{cr} = 88.2°, 151.8°$).

INCREMENTAL DYNAMICS

By considering for instance a rhombic anisotropic grid, the deviation between the responses of the lattice (reported in blue in Fig. 3) and its equivalent continuum (reported in red in Fig. 3) can be visualized in terms of slowness contours computed at the frequency $\Omega = 0.01$. By comparing the contours for the four preload states, it can be appreciated that these are superimposed up $0.9\,\boldsymbol{p}_E$, so that the nonlinear dispersion of the lattice becomes non-negligible only when the material is very close to the elliptic boundary, namely, at a preload $0.99\,\boldsymbol{p}_E$, and only for waves close to the direction of ellipticity loss.

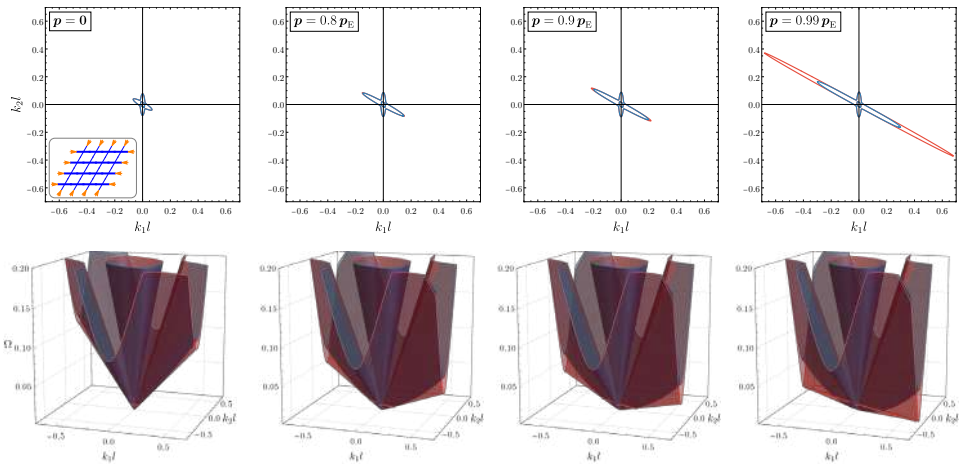

Figure 3: Slowness contours and dispersion surfaces for a rhombic anisotropic lattice (in blue) and for the effective Cauchy continuum (in red) at frequency $\Omega = 0.01$. The evolution of the contours and dispersion surfaces induced by a compressive preload of equal components $p_1 = p_2$ along two inclined directions demonstrates that the nonlinear dispersion of the lattice is negligible, except when the material is very close to the elliptic boundary, namely, for a prestress above $0.9\,\boldsymbol{p}_E$. The comparison between the behaviours of the lattice and its equivalent continuum shows a great agreement.

CONCLUSIONS

Homogenization of the incremental response of a lattice of elastic rods, axially pre-loaded to an arbitrary amount, has been shown to provide a superb tool for the design of cellular elastic materials of tunable properties and capable of extreme localized deformations.

References

[1] Bordiga G., Cabras L., Piccolroaz A., Bigoni, D. Incremental constitutive tensors and strain localization for prestressed elastic lattices: Part I - quasi-static response. *submitted*, 2020.

[2] Bordiga G., Cabras L., Piccolroaz A., Bigoni, D. Incremental constitutive tensors and strain localization for prestressed elastic lattices: Part II - incremental dynamics. *submitted*, 2020.

EFFECT OF FINITE THICKNESS ON WRINKLING OF ELASTIC BILAYERS

Takuya Morimoto*[1]
[1]Department of Mechanical, Electrical and Electronic Engineering, Shimane University, Shimane, Japan

Summary Surface instabilities in bilayer systems composed of a thin film bonded to a thick substrate have been studied extensively. Most of the previous papers have focused on the elastic bilayer with an infinite substrate to simplify the analysis by removing the lower boundary effect. Here this paper explores the effect of finite thickness on the wrinkling of elastic bilayers under film-only growth and elucidates the role of the boundary condition at the bottom through the incremental analysis. The standard incremental analysis reveals that the critical growth ratio and wavenumber have a large discrepancy between the displacement-free and traction-free boundaries as the ratio of the substrate thickness to the film thickness becomes small. The results show the possibility to control the wavenumber by tuning the thickness ratio in a combination of the boundary condition at the bottom surface.

INTRODUCTION

The incremental analysis of elastic bilayer applies to the problems of surface instability and can determine the stretches and wavenumbers at the critical thresholds. Most of the previous papers have analyzed on the bilayer with an infinite substrate to simplify the analysis by removing the lower boundary effect, except for Ref. [6] where the bilayer undergoes a whole compression. In this case, the boundary condition at the bottom surface does not affect the wrinkling pattern. However, if the film thickness is comparative to the substrate thickness, the difference of the boundary condition may affect and modifies it. Specifically, the case for the bilayer under film-only growth may enhance the finite thickness effect since the film growth makes its thickness thicker.

This paper explores the effect of finite thickness on the wrinkling of elastic bilayers under film-only growth and elucidates the role of the boundary condition at the bottom surface by the incremental analysis [1, 2]. The analysis reveals that the critical growth and wavenumber have a large discrepancy between the displacement-free and traction-free boundaries as the ratio of the substrate thickness to the film thickness becomes small as expected. The results show the possibility to control the wavenumber by tuning the thickness ratio in a combination of the B.C. at the bottom surface.

WRINKLING ANALYSIS

The incremental analysis is performed for wrinkling superimposed on a homogeneous film-only growth as shown in Fig. 1. Each layer is assumed to be incompressible neo-Hookean material with the strain energy density function $W_\alpha = \frac{\mu_\alpha}{2}(\lambda_1^2 + \lambda_2^2 + \lambda_3^2 - 3)$ where μ_α is shear modulus of layer $\alpha = (\mathrm{f}, \mathrm{s})$ where $\lambda_1 = 1/g_1 = 1/\gamma$, $\lambda_2 = g_1 g_3 = \gamma$ and $\lambda_3 = 1/g_3 = 1$ for growth in the $\mathbf{e}_1$-direction, and p is a Lagrange multiplier for imposing the incompressible constraint. The incremental equations composed of the equilibrium and constraint equations are given as $\mathrm{div}\,\boldsymbol{\Sigma} = \mathbf{0}$ and $\mathrm{tr}\,\boldsymbol{\Gamma} = \mathrm{div}\,\boldsymbol{u} = 0$ where $\boldsymbol{\Sigma} = \mathcal{A}_0\boldsymbol{\Gamma} + p\boldsymbol{\Gamma} - \dot{p}\mathbf{I}$, $\dot{p}$ is incremental Lagrange multiplier, the incremental displacement gradient $\boldsymbol{\Gamma} = \dot{\boldsymbol{F}}\boldsymbol{F}^{-1}$, and the incremental displacement $\boldsymbol{u}$. The elastic moduli $\mathcal{A}_0$ of the neo-Hooke material in Cartesian coordinates are given by $\mathcal{A}_{0ijkl} = \mu_\alpha \delta_{il} F_{jA} F_{kA}$ [1] with the Kronecker delta δ_{ij}. The boundary conditions are stress-free at the free surface and continuity at the interface between the film and the substrate. Here two types of boundary condition at the bottom surface are considered: (a) traction-free [6] or (b) displacement-free along the surface [3]. When the substrate is sufficiently thicker than the film, the boundary condition at the bottom surface should not affect the wrinkling pattern. On the other hand, if the film thickness is comparative to the substrate thickness, the difference of

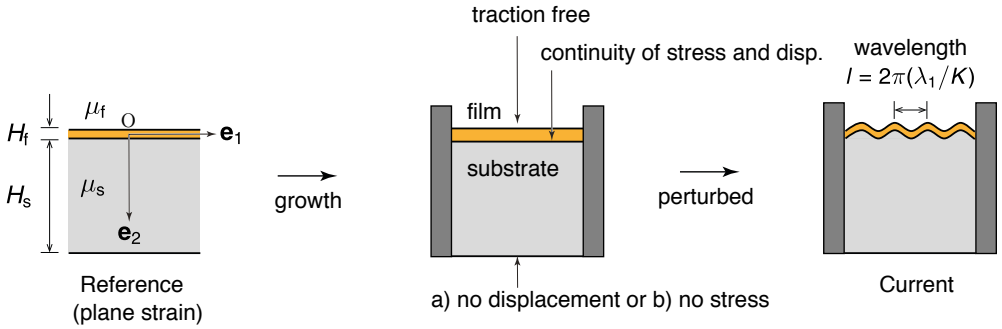

Figure 1: Elastic bilayer under film-only growth.

*Corresponding author. E-mail: morimoto@riko.shimane-u.ac.jp

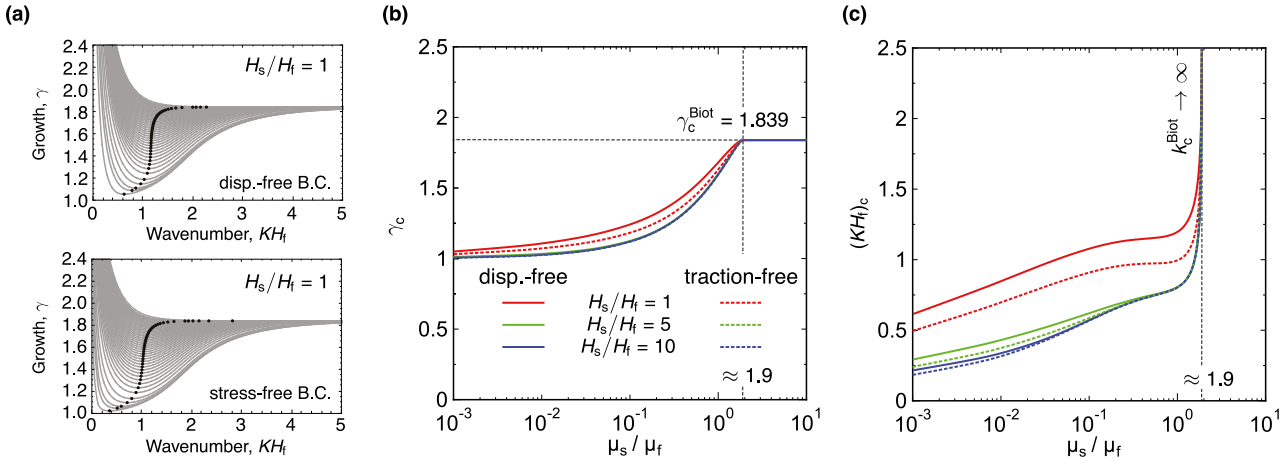

Figure 2: Critical conditions at the threshold of wrinkling for film-only growth. (a) Dispersion curves for a range of μ_s/μ_f values with $H_s/H_f = 1$. There is a slight difference between displacement-free B.C. (top) and stress-free B.C. (bottom) to the accuracy of visual inspection. The critical growth γ_c (b) and critical wavenumber (c) have a large discrepancy between displacement-free B.C and traction-free B.C. as H_s/H_f becomes small.

the boundary condition may affect and modifies it. This effect of finite thickness on the wrinkling of elastic bilayers is explored systematically.

The wrinkle mode may be expresses as the separation of variables $u_1 = f_1(x_2)\sin kx_1$, $u_2 = f_2(x_2)\cos kx_1$, $\dot{p} = f_3 x_2 \cos kx_1$ where $f_a(x_2)$ $(a = 1, 2, 3)$ is unknown functions and k is the wavenumber of wrinkle in a current configuration and relates to wavenumber in a reference configuration via $k = K/\lambda_1$. Substituting these $u_1, u_2, \dot{p}$ into the incremental equations, and then applying it to the boundary conditions [(i) or (ii)], we obtain eight equations for the constants $\mathbf{K}$ that can be written in a compact form as $\mathbf{MK} = \mathbf{0}$ where the matrix $\mathbf{M}$ is omitted for the brevity. The bifurcation condition $\mathbf{f}(\mu_s/\mu_f, H_s/H_f, KH_f, g_1) \equiv \det \mathbf{M} = 0$ determines the critical growth γ_c.

RESULTS AND DISCUSSION

Figure 2 shows the critical solutions value of growth and wavenumber as a function of μ_s/μ_f. The dispersion curves for a range of μ_s/μ_f values with $H_s/H_f = 1$. The growth rate γ increases from 1 and emerges the wrinkling solution at the minimum value of each dispersion curve which is marked point in the figure. There is a slight difference between displacement-free B.C. (top) and stress-free B.C. (bottom) to the accuracy of visual inspection, so that the minimum values are plotted as a function of μ_s/μ_f in Figs. 2(b) and (c). The critical growth ratio γ_c and wavenumber $(KH_f)_c$ decreases with increasing the substrate thickness. This tendency agrees with the theory [6] and experimental data [7] for a whole-domain compression. It is also confirmed that the solutions for $H_s/H_f \to \infty$ reduce to the same values in [4, 5]. As μ_s/μ_f increases, γ_c approaches $\gamma_c^{\mathrm{Biot}} = 1.839$ and the wavenumber first diverges at $(KH_f)_c \approx 1.9$ [4, 5], which are not dependence of the thickness ratio H_s/H_f. The critical growth γ_c [Fig. 2(b)] and critical wavenumber [Fig. 2(c)] have a large discrepancy between displacement-free B.C and traction-free B.C. as H_s/H_f becomes small as expected. The wrinkling pattern can be controlled by tuning the thickness ratio H_s/H_f in a combination of the B.C. at the bottom surface.

ACKNOWLEDGEMENTS

T.M. is indebted to Alain Goriely and to the Mathematical Institute at the University of Oxford for their hospitality during this work. This work is supported by JSPS KAKENHI Grant Numbers JP17KK0134, JP18K03838.

References

[1] Ogden R.W. Non-linear elastic deformations. Dover, New York 1997.
[2] Goriely A. The mathematics and mechanics of biological growth. Springer, New York 2017.
[3] Holland M.A., Li B., Feng X. Q., Kuhl E. Instabilities of soft films on compliant substrates. *J. Mech. Phys. Solids* **98**: 1–18, 2016.
[4] Tallinen T, Biggins JS. Mechanics of invagination and folding: hybridized instabilities when one soft tissue grows on another. *Phys. Rev. E* **92** 2015: 022720–8.
[5] Alawiye H., Kuhl E., Goriely A. Revisiting the wrinkling of elastic bilayers I: linear analysis. *Phil. Trans. R. Soc. A* **377** 2019: 20180076.
[6] Jin L., Auguste A., Hayward R. C., Suo Z. Bifurcation diagrams for the formation of wrinkles or creases in soft bilayers. *J. Appl. Mech.* **82**: 061008–11, 2015.
[7] Auguste A., Yang J., Jin L., Chen D., Suo Z., Hayward R.C. Formation of high aspect ratio wrinkles and ridges on elastic bilayers with small thickness contrast. *Soft Matt.* **14** 2018: 8545–51.

OPTIMISATION OF CONTINUOUS TOW-SHEARED CYLINDERS UNDER UNCERTAINTY

Reece Lincoln*[1], Paul Weaver[1,2], Alberto Pirrera[1], and Rainer Groh[1]
[1]Bristol Composites Institute (ACCIS), Department of Aerospace Engineering, University of Bristol, Bristol, BS8 1TR, UK
[2]Bernal Institute, School of Engineering, University of Limerick, Castletroy, V94 T9PX, Ireland

Summary The sensitivity to geometric imperfections limits the performance of thin-walled cylinders in compression buckling. The present work focuses on reducing the imperfection sensitivity of cylinders by using a novel manufacturing technique for composite materials known as Continuous Tow Shearing (CTS). CTS allows curvilinear steering of carbon fibre tows by shearing the carbon fibre tape, a 50 mm-wide strip of carbon fibre, that is placed via a robot arm. Steering of the carbon fibre tapes by shearing induces a smooth increase in the thickness of the tape and these localised thickness build-ups are used as a symmetry-breaking device to limit the impact of imperfections. The localised thickness build-ups are used to create embedded-stringers and -hoops that tailor the load path within the CTS cylinder. To maximise the effectiveness of the CTS cylinders, an optimisation framework that accounts for uncertainty is used. The results of the optimisation are corroborated with a Monte-Carlo analysis. The first optimisation goal is to maximise the thickness-normalised, mass-normalised buckling load of a CTS cylinder. The second optimisation goal is to minimise mass of a CTS cylinder under a specific load.

INTRODUCTION

The fuel and oxidizer cylindrical tanks of heavy launch vehicles are a large percentage of their total dry mass (60–70%). Using composite materials instead of current generation Li-Al fuel tanks is estimated to save up to 30% in mass and 25% in recurring manufacturing costs [1]. Several research programs have aimed to use composite materials to capitalise on these savings [2, 3] but have used blade-stiffened shells or foam/honeycomb sandwich structures. Few programmes have considered novel monocoque shell architectures due in part to their well-documented geometric imperfection sensitivity when loaded in compression—the design load case of heavy launch vehicles. Typically, the imperfection sensitivity is captured in the design phase using knockdown factors (KDFs), that are applied to the theoretical critical buckling load derived from a linear eigenvalue analysis. The classical KDFs of the NASA SP-8007 [4] guideline are still industry-standard but have been acknowledged to be too conservative for modern materials and manufacturing tolerances. Contemporary knockdown factors have been created that are less conservative [2, 5], but still show the imperfection sensitivity of cylindrical shells.

This paper looks at designing monocoque cylinders that are imperfection *insensitive* by tailoring load paths by using a novel variable-angle composite manufacturing technique, Continuous Tow Shearing (CTS) [6]. Preliminary work has found that CTS cylinders are less imperfection sensitive than straight-fibre cylinders [7, 8, 9]. It has also been shown that the imperfection sensitivity of composite cylinders can be decreased with Automated Fibre Placement (AFP) [10]. However, CTS has several benefits over AFP as a result of shearing the tows instead of bending the tows, *e.g.,* no in-plane bending; no fibre buckling or wrinkling; perfect tessellation of tows; smaller steering radii. In addition to these benefits, the shearing process couples the fibre angle change to the local thickness of the tow, enabling the formation of embedded stringers and hoops perpendicular to the fibre steering direction. Fibre paths are described using the notation $\phi\langle T_0|T_1\rangle^n$, where ϕ is the clockwise angle from the global x-axis that defines the refence axis for shearing; T_0 is the initial angle of shearing relative to ϕ; T_1 is shearing angle in the middle of the 'period' relative to ϕ; and n is the periodicity—the frequency of a $T_0 \rightarrow T_1 \rightarrow T_0$ cycle. For the sake of illustration, Figure 1 shows how a $0\langle 20|70\rangle^3$ layer and a $90\langle 0|30\rangle^2$ layer is defined.

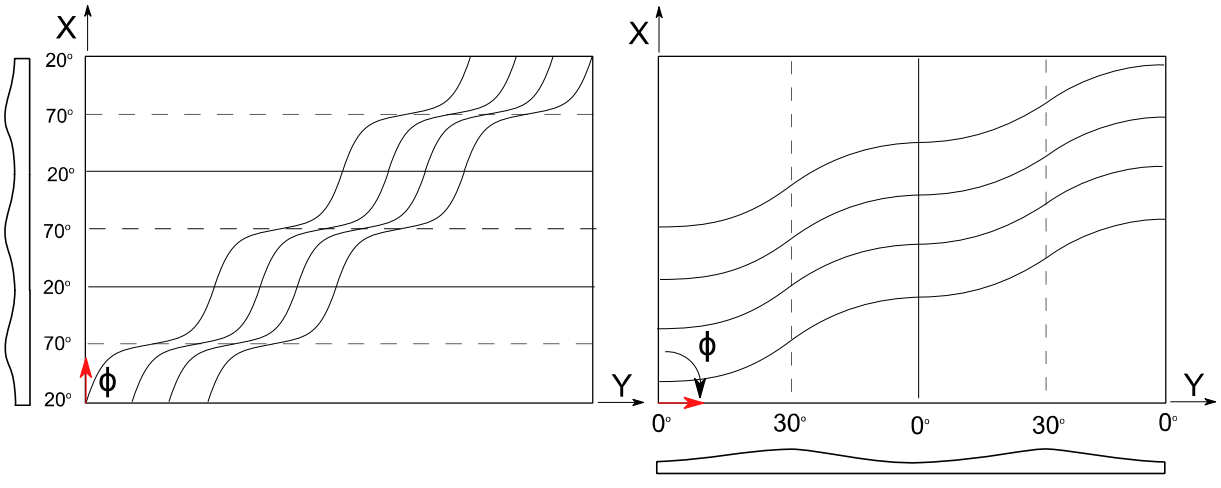

Figure 1 CTS lamina sheared where left is $0\langle 20|70\rangle^3$ and right figure is a $90\langle 0|30\rangle^2$ lamina.

*Corresponding author. E-mail: reece.lincoln@bristol.ac.uk.

FUTURE WORK

Two optimisations and a Monte-Carlo analysis will be carried out. The first optimisation will be to maximise the thickness-normalised and mass-normalised buckling load of a CTS cylinder. A by-product of the CTS process (where the local thickness of the tow is increased due to the shearing process) is that the average thickness of a CTS cylinder with shearing is greater than a straight-fibre cylinder. As the buckling load of a cylinder is proportional to t^2 and the mass of a cylinder proportional to t, the mass-normalised specific buckling load of a cylinder is proportional to t. Therefore, to ensure a fair comparison between CTS cylinders and straight-fibre cylinders, a thickness-normalised, mass-normalised buckling load is appropriate if the maximum load carrying capability of a structure is essential. The optimisation will use a reliability-based definition of buckling load. A forward-difference First-Order Second-Moment (FOSM) analysis will be used to calculate a conservative estimate of the buckling load. A realistic data bank of imperfections [11] will be spectrally decomposed into a five principal components that describe the data set. From the principal components, six FEA analyses of the CTS cylinder with different imperfections can approximate a distribution of buckling loads. A buckling load approximately equal to the mean buckling load minus three standard deviations will constitute P_{FOSM}, the buckling load calculated from the FOSM methodology. A Genetic Algorithm (GA) will be the framework in which the FOSM methodology is used to optimise towards maximising the thickness-normalised, mass-normalised P_{FOSM}. To test the robustness of the final result and the assumed distribution, a Monte-Carlo analysis of the converged value will be performed to ensure the assumptions are valid and the result is statistically significant.

As a secondary optimisation, the mass of a CTS cylinder will be optimised. The target function will be to minimise the mass of a CTS cylinder given certain loading criteria. A GA will be used as the optimisation framework. The buckling load will be calculated from the FOSM methodology previously described.

References

[1] D. A. McCarville, J. C. Guzman, A. K. Dillon, J. R. Jackson, and J. O. Birkland, “Design, manufacture and test of cryotank components,” *Compr. Compos. Mater. II*, vol. 3, pp. 153–179, 2018.
[2] M. W. Hilburger, “On the development of shell buckling knockdown factors for stiffened metallic launch vehicle cylinders,” in *AIAA/ASCE/AHS/ASC Structures, Structural Dynamics, and Materials Conference*, 2018, pp. 1–17.
[3] National Aeronautics and Space Administration, “Composite Cryotank Technologies and Demonstration,” 2013.
[4] National Aeronautics and Space Administration, “Space Vehicle Design: Buckling Thin-Walled Circular (SP-8007),” 1968.
[5] R. M. Groh, A. Pirrera, “On the role of localizations in buckling of axially compressed cylinders”, *Proc. Math. Phys. Eng. Sci.* 475 (2224).
[6] B. C. Kim, K. Potter, and P. M. Weaver, “Continuous tow shearing for manufacturing variable angle tow composites,” *Compos. Part A Appl. Sci. Manuf.*, vol. 43, no. 8, pp. 1347–1356, 2012.
[7] R. L. Lincoln, P. M. Weaver, A. Pirrera, and R. M. J. Groh, “Imperfection-Insensitive Continuous Tow-Sheared Cylinders,” *Compos. Struct.*, vol. 260, no. March, p. 113445, 2021.
[8] R. Lincoln, P. Weaver, A. Pirrera, and R. M. Groh, “Optimisation of Imperfection-Insensitive Continuous Tow Sheared Rocket Launch Structures,” *AIAA SciTech 2021 Forum*, no. January, pp. 1–19, 2021.
[9] S. C. White and P. M. Weaver, “Towards imperfection insensitive buckling response of shell structures-shells with plate-like post-buckled responses,” *Aeronaut. J.*, vol. 120, no. 1224, pp. 233–253, Feb. 2016.
[10] K. C. Wu, B. Farrokh, B. Stanford, and P. Weaver, “Imperfection Insensitivity Analyses of Advanced Composite Tow-Steered Shells,” in *57th AIAA/ASCE/AHS/ASC Structures, Structural Dynamics, and Materials Conference*, 2016, no. January, pp. 1–16.
[11] H. N. R. Wagner, C. Hühne, and I. Elishakoff, “Probabilistic and deterministic lower-bound design benchmarks for cylindrical shells under axial compression,” *Thin-Walled Struct.*, vol. 146, no. January, p. 106451, Jan. 2020.

BUCKLING INSTABILITY AND MATERIAL DAMAGE: TOWARDS A UNIFYING GENERAL THEORY

Anton Köllner*[1] and M. Ahmer Wadee[1]
[1]Department of Civil and Environmental Engineering, Imperial College London, London SW7 2AZ, United Kingdom

Summary An extension of the general elastic stability theory to systems undergoing inelastic deformation is discussed. The underlying idea is to derive an extended total potential energy, which is the governing functional during inelastic deformation but only depends on the configuration of the system. Thus, relationships are derived which describe the state of damage within the system by explicit functions of the configuration and applied loading. Such relationships are determined by investigating the change of elastic and inelastic energies with respect to a change in the damage state. With the aid of the proposed extension of the elastic stability theory, the effect of material damage and its propagation on the stability behaviour of structures can be analysed. This is demonstrated with the aid of the problem of delamination buckling in composite panels.

INTRODUCTION

The loss of structural stability in a mechanical system often constitutes a catastrophic failure scenario, where the system more or less abruptly loses its load carrying capability. This type of failure is strongly related with slender structures, which can be found in a vast variety of applications mainly in the transportation and construction industries. Over the last few decades, these slender structures have been made increasingly from composite materials, e.g. multi-layered carbon fibre reinforced polymer laminates that are also prone to various damage mechanisms, e.g. matrix damage growth and delamination growth, which may influence the global structural stability. This is visualized in Figure 1 (left), illustrating the compressive response of delaminated composite panels (with all boundaries being supported); an application example with special relevance for the aircraft/aerospace industry. As can be seen in Figure 1 (left), the onset of delamination growth and the initial propagation may be barely visible causing unexpected catastrophic failure whenever unstable delamination propagation occurs.

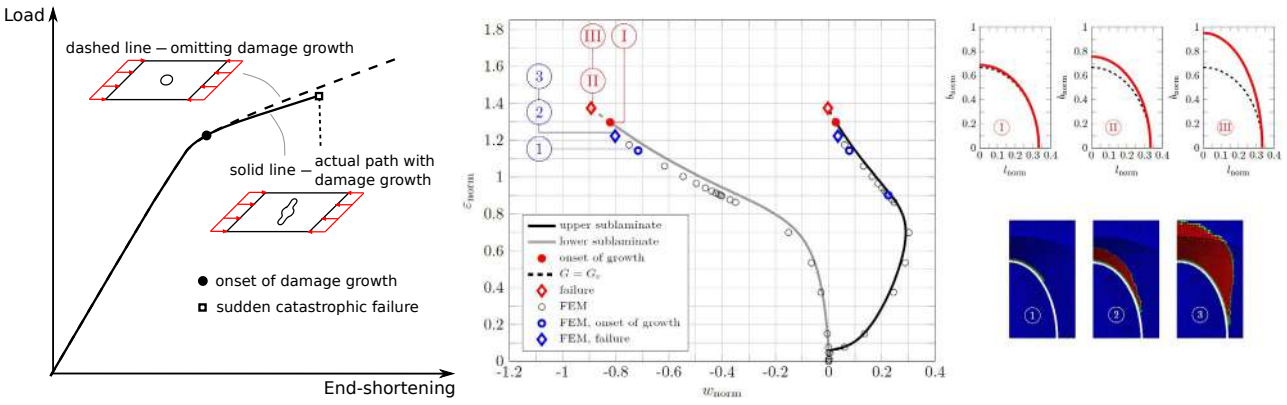

Figure 1: (left) Illustration of a characteristic compressive response of a delaminated composite panel; (middle) result in the form of applied compressive strain against midpoint deflection for an entire loading path up to failure with comparison against finite element (FE) simulations; (right) comparisons between model and FE simulation of delamination growth shapes associated with the deformation states shown in the middle graph.

Since the consideration of such damage mechanisms has had only limited relevance when using more traditional construction materials (e.g. structural steel), general theories of structural stability have hitherto tended only to consider elastic systems [1]. The current work aims at bridging the aforementioned gap in structural stability analysis techniques.

CONCEPT

A discrete coordinate approach is considered. Thus, all mechanical systems of interest are assumed to be fully defined by a set of generalized coordinates q_i, loading parameters λ_m and damage parameters ξ_k (i.e. internal state parameters) describing the configuration, applied loading and damage state respectively. During elastic deformation, i.e. whenever all damage parameters remain constant, the system is characterized by the total potential energy,

$$\Pi = \Pi(q_i, \lambda_m, \xi_k) \quad \text{with} \quad \xi_k = \text{const.} \tag{1}$$

and the well-known total potential energy principle $\delta\Pi(q_i) = 0$ yields the deformation path $q_i(\lambda_m)$. The damage parameters remain stationary so long as the thermodynamic forces f_k associated with the respective damage parameters ξ_k

*Corresponding author. E-mail: a.koellner@imperial.ac.uk

do not reach the thresholds required to cause damage growth which are denoted by g_k. The thermodynamic forces are determined by evaluating the change of the total potential energy with respect to the damage parameters, thus

$$f_k = -\frac{\partial \Pi}{\partial \xi_k}, \quad \text{whereas the thresholds are given by} \quad g_k = \frac{\partial W_\mathrm{d}}{\partial \xi_k}. \tag{2}$$

The later describes the change of the dissipative energy (W_d) with respect to the kth damage parameter. Whenever the thermodynamic forces f_k reach the respective thresholds required, i.e. $f_k \geq g_k$ damage growth is caused. As has been shown in [2, 3], equality between f_k and g_k holds during stable damage growth, such that the equality for these processes can be rewritten in terms of

$$f_k - g_k = D_k(q_i, \lambda_m, \xi_k) = 0. \tag{3}$$

From Eq. (3), the damage parameters are implicitly given as functions of the generalized coordinates and the loading parameters assuming that a unique solution exists, thus

$$D_k\Big[q_i, A_m, \xi_k(q_i, \lambda_m)\Big] \equiv 0. \tag{4}$$

The damage parameters are obtained in explicit form, $\xi_k = \xi_k(q_i, \lambda_m)$, by employing a TAYLOR series approximation around the deformation state causing damage growth (cf. [2]). With the damage parameters expressed in terms of the configuration and the applied loading, an extended total potential energy Π^* may be derived, i.e.

$$\Pi^* = \Pi^*\Big[q_i, \lambda_m, \xi_k(q_i, \lambda_m)\Big]. \tag{5}$$

The variational principle $\delta\Pi^*(q_i) = 0$ yields the deformation path $q_i(\lambda_m)$ considering damage growth starting from the deformation state at which growth is initiated. The behaviour of the damage parameters can then be determined by substituting the deformation path obtained into $\xi_k(q_i, \lambda_m)$.

DELAMINATION BUCKLING

The formalism is applied to study the compressive behaviour of delaminated composite panels, as illustrated in Figure 1 (left) [4]. A RAYLEIGH-RITZ formulation is employed approximating the displacement field. Loading in the form of in-plane compressive strain is applied and the delamination area is considered as an active damage parameter. Results presented in Figure 1 (middle and right) show that deformation paths for an entire loading process (until failure due to unstable delamination propagation, cf. red diamond symbols in Figure 1(middle)) can be determined with the aid of the extended total potential energy. The results obtained are verified by finite element (FE) simulations performed in Abaqus (cf. circle symbols in Figure 1(middle)). The delamination growth behaviour associated with the deformation path shown in Figure 1 (middle) is visualized in Figure 1 (right). Both deformation path and delamination growth characteristics are in good agreement with corresponding FE simulations.

CONCLUSIONS

A concept for extending the general elastic stability theory has been presented that enables the stability behaviour of structures undergoing inelastic deformation to be studied. The formalism has been successfully applied to model delamination buckling in multilayered composites. However, the interaction between multiple active damage parameters has not yet been addressed. Therefore, the respective variational inequalities are planned to be considered by introducing the well-known KUHN-TUCKER conditions. Upon a successful implementation, a generalized exposition for the stability analysis of structures undergoing inelastic deformation can be formulated.

References

[1] Thompson J. M. T., Hunt G. W. A general theory of elastic stability. John Wiley & Sons, 1973.

[2] Köllner A., Völlmecke C. An analytical framework to extend the general structural stability analysis by considering certain inelastic effects-theory and application to delaminated composites. *Compos. Struct.*, **170**: 261-270, 2017.

[3] Schapery R. A. A theory of mechanical behavior of elastic media with growing damage other changes in structure. *J. Mech. Phys. Solids*, **38**(2): 215-253, 1990.

[4] Köllner A., Völlmecke C. Post-buckling behaviour and delamination growth characteristics of delaminated composite plates. *Compos. Struct.*, **203**: 777-788, 2018.

EQUILIBRIUM AND STABILITY OF THE NONLINEARLY ELASTIC NONHOMOGENEOUS CYLINDER WITH INTERNAL STRESSES

Mikhail Karyakin*[1,2], Leonid Obrezkov [3]
[1]Southern Mathematical Institute – the Affiliate of VSC RAS, Vladikavkaz, Russia
[2]I.I.Vorovich Institute of Mathematics, Mechanics and Computer Science, Southern Federal University, Rostov-on-Don, Russia
[3]School of Engineering Science, Lappeenranta Technological University, Lappeenranta, Finland

Summary The problem of equilibrium of a nonhomogeneous cylinder subjected to simultaneous uniaxial tension/compression and inflation is considered within the framework of the three-dimensional nonlinear theory of elasticity. The effect of internal stresses caused by a linear defect such as a wedge disclination on the process of the buckling of the cylinder is investigated. For the analysis, the well-known models for describing compressible materials, Murnaghan model and Blatz & Ko model, were used. Two types of material inhomogeneity are considered. The stability analysis was carried out on the basis of a combination of the semi-inverse method of the nonlinear elasticity and bifurcation approach. The stability regions are presented as areas on the plane of loading parameters. The possibility of the bifurcation curves condensing was demonstrated.

Internal stresses caused by defects of crystal lattice draw an attention by the reason of a big impact to actual mechanical behaviour such as plasticity, creep, destruction and so on [1]. In the context of elasticity theory of finite strains much motivation for the research comes from soft tissue biomechanics, and for a recent discussion of internal stresses in artery walls [2]. In the present work some issues of effects of internal stresses on the equilibrium and stability of elastic cylinders were studied within the framework of nonlinear elasticity.

We present results on the one specific type of isolated defect, namely the wedge disclination (Fig.1). To describe the mechanical properties of a cylinder two constitutive models for compressible elastic solid were used: Murnaghan material and Blatz & Ko material [3]. The specific energy function W for these models has the following form (1) and (2) respectively:

$$W=\frac{1}{4}\left[W_1 I_1+W_2 I_1^2+W_3 I_2-mI_1 I_2+W_4 I_1^3+\frac{n}{2}(I_3-1)\right], \tag{1}$$

$$W=\frac{1}{2}\mu(1-\beta)\left[I_2 I_3^{-1}+\frac{1}{\alpha}\left(I_3^{\alpha}-1\right)-3\right]+\frac{1}{2}\mu\beta\left[I_1+\frac{1}{\alpha}\left(I_3^{-\alpha}-1\right)-3\right], \tag{2}$$

where

$$W_1=-3\lambda-2\mu+\frac{9}{2}l+\frac{n}{2},\ W_2=\frac{1}{2}(\lambda+2\mu-3l-2m),\ W_3=-2\mu+3m-\frac{n}{2},\ W_4=\frac{1}{6}(l+2m);$$

$\alpha,\beta,\lambda,\mu,l,m,n$ – material parameters, $I_k(k=1,2,3)$ – principal invariants of the right Cauchy–Green deformation tensor. The first model is usually used to account for geometrical nonlinearities while the second one describes physical nonlinearities also.

To model tension/compression as well as inflation of the hollow cylinder with wedge disclination at its axis we use following representation of the deformation:

$$r=f(R),\ \varphi=\kappa\Phi,\ z=\gamma Z \tag{3}$$

where R,Φ,Z and r,φ,z – cylindrical coordinates in the reference and actual configuration respectively, κ – parameter of the defect (proportional to the magnitude of the Frank vector of the disclination), γ – positive coefficient of the cylinder stretching or shortening. The function $f(R)$ in (3) describes radial (non-uniform, in general) displacement of the cylinder points.

The analysis of length changing of an unloaded cylinder due to the defect formation was performed. This changing is completely described by the dependence of γ on the disclination parameter κ at the absence of axial force. It was shown numerically that it is nonlinear effect and the elongation $(\gamma>1)$ or shortening $(\gamma<1)$ depends on material parameters of the mechanical models (1), (2). To verify the numerical results the asymptotic formula was obtained within the limits of the second-order effects theory [3]. To construct the solution of equilibrium equations in this case we replace $f(R)$ in (3) by a series in terms of powers of the parameter $\delta=\kappa-1$. Considering the sequence of tasks corresponding to different powers of δ we obtain the analytical relationship between length changing of the cylinder and material parameters. In particular, for the simplified version of Blatz & Ko model $(\alpha=0.5)$ the elongation–disclination relation has the form

$$\gamma-1=-\delta^2(0.121\beta-0.0605).$$

*Corresponding author. E-mail: karyakin@sfedu.ru

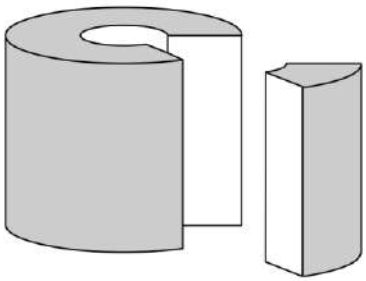

Figure 1. Scheme of the disclination formation in the hollow cylinder

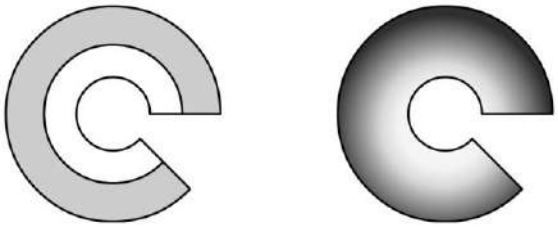

Figure 2. Two types of heterogeneity: composite cylinder and continuous inhomogeneity

To analyze the stability of a cylinder with isolated defect under tension and inflation the bifurcation approach was used based on linearization of the equilibrium equations in the neighborhood of the solutions obtained by means of the semi-inverse representation (3). Search of the bifurcation points is based on the analysis of the homogeneous linear boundary value problem of a six order, whose coefficients depend on radial displacement function $f(R)$ found in the first stage. The bifurcation point is treated as such value of the "loading" parameter – it can be the parameter of the defect, κ, or value of inflating pressure or axial force – for which the linearized problem has a nontrivial solution.

The semi-inverse approach based upon transformation (3) turns out to be applicable in some cases of an inhomogeneous cylinder. The most typical are two cases: a composite cylinder and a functional gradient material, in which the material parameters are continuous functions (Fig. 2).

In the first case, to determine the stress-strain state of the cylinder, that is, to find the function $f(R)$, it is required to solve a set of two second order ODE supplemented by the conditions of continuity of displacements and strains on the material dividing line. In the second case, coefficients of the equilibrium equation became variable and contain derivatives, $d\lambda/dR$, $d\mu/dR$ etc.

Numerical investigations of the problems under consideration showed, in particular, that the choice of the model had not a qualitative effect on the stress-strain state. If the parameters of the models were chosen so that in the linear approximation they corresponded to the same material, the difference in the distribution of normal stresses was no more than 10 percent. The effect of the choice of the model on the stability is much stronger. Special example of a variant of the Murnaghan material with a set of constants corresponding to plexiglass demonstrated the significance of the additional conditions of the Spector theorem in the analysis of the applicability of mathematical models of the behavior of elastic bodies in the region of large strains.

An important difference between thick and thin cylinders is the fact that the stability region is described by curves with different mode numbers. In addition, the condensing of bifurcation curves at one of the boundaries of the stability region was found for the case of the thick cylinder. Increasing the mode number n, starting from a certain value (about fifty), practically does not change the critical pressure. This fact agrees with the results obtained earlier in [1] for the harmonic material model. This, in particular, means that for such body it is impossible to predict the form of the stability loss based on the analysis of linearized equations. For a thinner cylinder, the $n=2$ mode is always preferred; the corresponding critical pressure is minimal. Another feature of thick cylinders is the existence of a zone where the loss of stability can occur only due to the presence of disclination without the application of external pressure. Such an area may be absent in the thinner cylinders.

Different types of the inhomogeneity of the cylinder material can also have noticeable influence upon the stability. In particular they can significantly change the region of stability of the unloaded cylinder having wedge disclination of the given strength. Although the shape of the stability region on the plane of loading parameters is generally preserved, it noticeably shifts depending on the parameters of the inhomogeneity. The direction of this bias, i.e., a positive or negative effect on stability, depends on both the type of heterogeneity and the disclination parameter.

Conclusions

The study of the equilibrium and stability of a hollow circular cylinder of compressible nonlinearly elastic material were carried out. Internal stresses in the cylinder are caused by the presence of a wedge disclination. A comparative analysis of the models used at various values of the parameters showed, in particular, that thick-walled cylinders are characterized by condensing of bifurcation curves, which can also occur in cases where there is no disclination, but its presence makes the condensation areas much more extensive. The presence of disclination can be both a stabilizing factor and vice versa – significantly reduce the value of the critical pressure. The type of inhomogeneity and its characteristics can also serve as a stability controlling factor.

References

[1] Zubov L.M. Nonlinear Theory of Dislocations and Disclinations in Elastic Bodies. Springer–Verlag, Berlin–Heidelberg–New York 1997.
[2] Taber L.A. Nonlinear theory of elasticity: applications in biomechanics. World Scientific, Singapore 2004.
[3] Lurie A.I. Nonlinear Theory of Elasticity. North-Holland, Amsterdam 1990.
[4] Kalashnikov V.V., Karyakin M.I. Second-order effects and Saint Venant's principle in the torsion problem of a nonlinear elastic rod. *Journal of Applied Mechanics and Technical Physics*, **47**(6), 879–885, 2006.

TEMPERATURE-DEPENDENT DOMAIN PATTERN EVOLUTION IN FERROELECTRIC CERAMICS: A PHASE-FIELD INVESTIGATION

Roman Indergand[1] and Dennis M. Kochmann *[1]
[1]Department of Mechanical and Process Engineering, ETH Zürich, Zürich, Switzerland

Summary We present a ferroelectric phase-field model, which has been successfully extended to finite-temperature applications and validated by various measurements of different types of lead zirconate titanate (PZT). The introduced temperature-dependent Ginzburg-Landau potential (GLP) is of importance for a realistic prediction of the temperature-dependent behavior of ferroelectric ceramics, including the spontaneous polarization (predicted accurately over a wide temperature range), and the strain hysteresis during bipolar electric cycling. Furthermore, we use statistical mechanics to account for thermal fluctuations in the ferroelectric constitutive model and show that these lattice vibrations, accounted for by a stochastic Allen-Cahn evolution equation, lead to realistic ferroelectric microstructures with nucleation of needle-shaped domains at locations with high stress concentrations.

STATE OF THE ART

Ferroelectrics are a frequently-used class of active materials whose mechanical and electrical properties are coupled: applying an electric field results in deformation, whereas an applied deformation produces an electric voltage in turn. This is a strongly nonlinear thermo-electro-mechanically coupled phenomenon caused by atomic-level interactions of the electric dipole moments and the lattice distortion. While the linear piezoelectric response under small applied fields is well described by phenomenological models, the complex nonlinear, time-dependent behavior, and the long-term stability threatened by material fatigue and failure are far from being understood nor reliably predictable. The current lack of understanding stems primarily from the large range of length and time scales involved (from atomic-scale interactions to macroscopic samples, from fast switching events to the experimentally-observed hysteresis). This makes the underlying phenomena difficult to model computationally and hard to access experimentally. Much prior work has focused on thin films, where both experimental TEM imaging of ferroelastic switching and atomistic simulations have helped understand the relation between domain wall motion and the collective switching behavior under electrical and mechanical loads. Less is known about bulk ferroelectrics. Predictive insight has been gained from first-principles [1] but is applicable only at zero temperature and has been used to derive energetic equilibrium properties but not the kinetics of ferroelectric switching.

TEMPERATURE-DEPENDENT PHASE FIELD MODEL

In this work, we emphasize the impact of temperature on the ferroelectric material response of bulk polycrystalline lead zirconate titanate (PZT). To this end, an existing zero-temperature phase-field description of ferroelectric ceramics [2] (solved via spectral homogenization) is extended to account for the influence of temperature. This is realized in two steps. First, the underlying DFT-informed Ginzburg-Landau potential is modified to depend on temperature by interpolating linearly between the known non-convex potential at zero Kelvin and the convex potential at the Curie temperature. Second, the ferroelectric constitutive model is extended by a new statistical mechanics-based approach to account for thermally induced lattice vibrations at the atomic level. This results in a stochastically perturbed Allen-Cahn equation with a space-time Gaussian noise contribution as the evolution law for the polarization, now accounting for thermal fluctuations.

RESULTS

We demonstrate that the finite-temperature Ginzburg-Landau potential predicts the temperature-dependent spontaneous polarization reasonably well in comparison with measurements of various types of lead-based perovskite ferroelectrics over a broad range of temperature. Furthermore, a more accurate prediction of the strain hysteresis is accomplished, as verified through a comparison of the bipolar cycling hysteresis with measurement from [3]. The stochastic Allen-Cahn equation with the random noise term results in a more realistic evolution of the ferroelectric domain pattern formation based on the nucleation of sharp need-like domains at local stress concentrations (such as grain boundaries and grain triple junctions), as illustrated in Fig. 1.

*Corresponding author. E-mail: dmk@ethz.ch

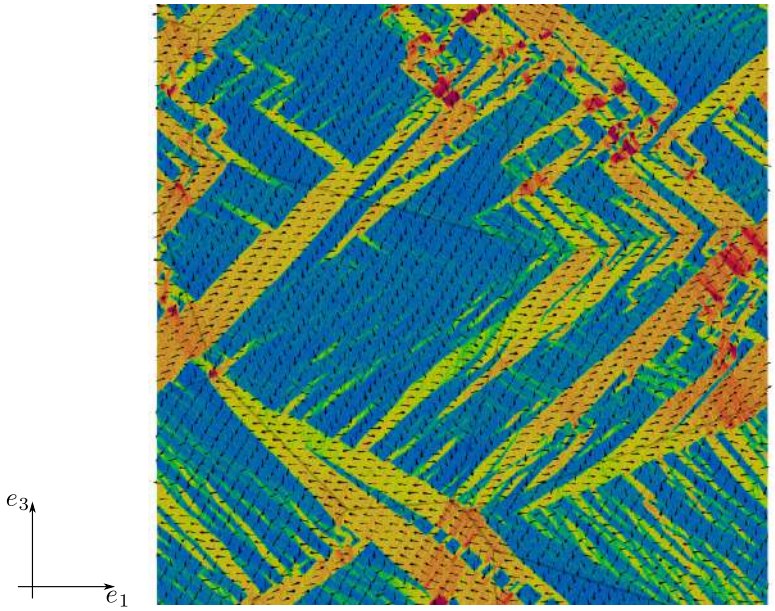

Figure 1: Snapshot of the computed domain pattern formation in a polycrystal after applying a constant electric field $E_3 = 8 \cdot 10^7$ V/m with the (normalized) polarization vector $\boldsymbol{p}(\boldsymbol{x}, t)/p_0$ visualized by small arrows. The color map indicates the (normalized) polarization in the vertical direction p_3, such that different ferroelectric domains can be recognized as: c^--domains (blue), c^+-domains (red), and $a^{-/+}$-domains (yellow).

References

[1] Völker, B., Marton, P., Elsässer, C. and Kamlah, M. Multiscale modeling for ferroelectric materials: A transition from the atomic level to phase-field modeling. *Conti. Mech. Thermodyn.* **23**: 435–451, 2011.

[2] Vidyasagar, A., Tan, W., Kochmann, D.M. Predicting the effective response of bulk polycrystalline ferroelectric ceramics via improved spectral phase field methods. *J. Mech. Phys. Solids.* **106**: 133–151, 2017.

[3] Tan, W., Faber, K., Kochmann, D.M. In-situ observation of evolving microstructural damage and associated effective electro-mechanical properties of PZT during bipolar electrical fatigue. *Acta Mater.* **164**: 704–713, 2019.

POST BULGE BUCKLING OF A FINITE HYPERELASTIC TUBE: THEORY AND EXPERIMENTS

Masoud Hejazi*[1] and A. Srikantha Phani[1]
[1]Department of Mechanical Engineering, University of British Columbia, Vancouver, BC, Canada

Summary A pre-stressed finite hyperelastic tube subjected to an internal pressure can bulge at a critical pressure. For a fixed axial stretch the bulge can either propagate or buckle before it ruptures, depending on the boundary conditions. We report experiments on the inflation of a finite rubber tube under tension and use bifurcation theory to construct a failure map in the stretch parameter space to delineate post bulge deformation regimes. We compare the experiments and theoretical predictions in the stretch parameter space. We find that buckling occurs when the pre-tension is insufficient to sustain a propagating bulge.

PROBLEM FORMULATION AND METHODOLOGY

It is well known that a pre-tensioned hyperelastic tube exhibits a spatially localized bulge instability under gradual inflation [1, 2, 3]. Earlier studies have addressed the conditions under which a bulge initiates and propagates. However the bulge propagation may no longer be sustained if the tension is insufficient for a fixed axial stretch: buckling of the initially straight bulged tube occurs under displacement control. The setup for the inflation test is shown in Fig 1. The tube is fixed at one end and the other end is attached to a tensile tester jaw (Instron 5969) in order to apply a fixed pre-tension and then hold the displacement during the inflation test. A compressed air supply inflates the tube quasi-statically leading to the initiation of a bulge at a local imperfection: in the post bulge regime it can propagate or buckle. A digital camera records the deformation of the tube during inflation and the pressure transducer records the internal pressure. An edge detection algorithm is used for calculating the internal volume and to extract the bulge profile and buckling amplitudes for different thicknesses and lengths of the tube, and for different initial pre-tension. Here, bulging is accompanied by a sudden reduction in the measured internal pressure, and buckling is observed through a sudden reduction in the axial load as measured by the tensile tester.

Earlier bifurcation analyses have identified the effect of aspect ratio, the validity of membrane assumption, and the effect of the stretch gradient in a diffuse interface model [4]. In this study, we employ a diffuse interface model to analyze the axisymmetric bifurcation condition (bulge formation). Nonlinear Euler buckling analysis is performed by extending an earlier study in [5] to include pre-tension and the existence of a propagating bulge.

Bifurcation analysis

We use two cylindrical polar co-ordinate systems: $R-\Theta-Z$ in the undeformed configuration and $r-\theta-z$ in the deformed configuration. The later is shown in Fig. 1c.

Axisymmetric bifurcation: To analyze the bifurcation condition for bulge formation, we use a diffuse interface model [4] for an axisymmetric membrane. The membrane energy per unit reference (undeformed) volume is

$$g_0(p,\lambda_z,\lambda_\theta) = w - p\frac{e}{2}\lambda_z{\lambda_\theta}^2, \tag{1}$$

where w is the strain energy density function, p is the internal pressure, λ_z is the longitudinal stretch, λ_θ is the circumferential stretch, and $e = R_i/H$ is the internal radius to thickness ratio. The axial equilibrium is set by $\partial g_0/\partial\lambda_z = 0$, which yields the longitudinal stretch as a function of internal pressure and circumferential stretch $\lambda = \lambda_0(p,\lambda_\theta)$. Introducing the circumferential stretch gradient, $\lambda_\theta^{'} = d\lambda_\theta/dZ$ in the Green-Lagrange strain the circumferential equilibrium condition follows as

$$h_l(p,\lambda_\theta(Z)) - \frac{1}{2}\frac{\partial G_l}{\partial\lambda_\theta}(p,\lambda_\theta(Z)){\lambda_\theta^{'}}^2(Z) + \frac{d}{dZ}(G_l(p,\lambda_\theta(Z))\lambda_\theta^{'}(Z)) = 0, \tag{2}$$

where $G_l = R_i^2/\lambda_0\,[\partial w/\partial\lambda_0(\lambda_0,\lambda_\theta Z)]$, and $h_l = \partial g_0/\partial\lambda_\theta(p,\lambda_0,\lambda_\theta)$. Under displacement (fixed boundary) control, the linear bifurcation analysis gives the bifurcation condition for the global axisymmetric deformation is

$$\frac{\partial h_l}{\partial\lambda_\theta}(p,\bar{\lambda}_\theta) = G_l(p,\bar{\lambda}_\theta)\frac{\pi^2}{L^2}. \tag{3}$$

which expresses the balance between the energy needed for radial expansion of the tube (left hand side in the above) and the energy required for bulge initiation.

Lateral bifurcation: The Buckling analysis begins with defining the incremental equilibrium based on Ogden's formulation $div\dot{\tilde{\mathbf{S}}}_0 = 0$. Where incremental nominal stress $\tilde{\boldsymbol{S}}_0$ is defined based on the gradient of the displacement field $\tilde{\boldsymbol{\eta}} = grad(\boldsymbol{U})$, strain energy function w, and Lagrange multiplier P to enforce incompressibility.

$$\dot{\tilde{\boldsymbol{S}}}_0 = \tilde{\boldsymbol{B}}\tilde{\boldsymbol{\eta}} + P\tilde{\boldsymbol{\eta}} - \dot{P}\boldsymbol{I}, \tag{4}$$

*Corresponding author. E-mail: masoud.hejazi@mech.ubc.ca

where $\dot{P}$ is the increment in Lagrange multiplier and $\tilde{\boldsymbol{B}}$ is the fourth-order tensor of instantaneous elastic moduli defined by strain energy function. We can construct an eigenvalue problem by defining the displacement vector components $\boldsymbol{U} = [u_r(\rho)\cos(m\theta)\cos(n\pi\zeta),\ u_\theta(\rho)\sin(m\theta)\cos(n\pi\zeta),\ u_z(\rho)\cos(m\theta)\sin(n\pi\zeta)]^T$, where m is the circumferential mode number, and n is the longitudinal mode number. $\rho = r/R_i$ and $\zeta = z/L$ are respectively the dimensionless radial and longitudinal coordinates. Solving with respect to boundary conditions (at inner $\boldsymbol{U}(0)$ and outer $\boldsymbol{U}(R_o)$ surfaces) by employing the state space approach and layer-wise method for laminated in-homogeneous tubes we obtain

$$\tilde{\boldsymbol{C}}\,[u_r(0), u_\theta(0), u_z(0), u_r(R_o), u_\theta(R_o), u_z(R_o)]^T = \boldsymbol{0}. \tag{5}$$

For non-trivial solution, the bifurcation condition is obtained by having $|\tilde{\boldsymbol{C}}| = 0$, where the elements of $\tilde{\boldsymbol{C}}$ are the functions of the longitudinal mode number, derivatives of strain energy function with respect to principal stretches ($\lambda_{r,\,\theta,\,z}$), and internal pressure.

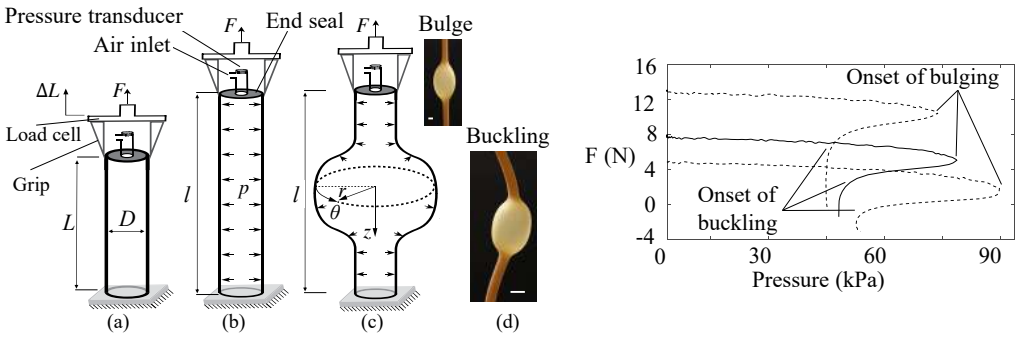

Figure 1: Left) Experiment overview. (a) Applying pre-tension by increasing the length from L to $l = L + \Delta L$; (b) Inflation due to internal pressure(p) while keeping the length constant; (c) Bulge formation and coordinate system. (d) Buckling; Scale bar indicates 1 cm. The axial force F is measured by Instron's load cell during inflation. Right) Longitudinal force vs. internal pressure for three different pre-stretches.

RESULTS AND CONCLUSION

Fig. 2a portrays different bifurcation regimes (axisymmetric and lateral) calculated using equations 3 and 5. The blue region (see color figure) right to the dashed line is the regime of bulge formation and the yellow region under the solid line is the buckling zone. The tube follows the path indicated by the dotted-dashed line during inflation, and the corresponding experimental data points are shown for three independent experiments. Experiments confirm the validity of our analysis. It is to be noted that the longitudinal and circumferential stretches have been measured during the inflation for section A-A (see Fig. 2a). Fig. 2b shows the stress distribution suggesting that the rupture is more likely to occur in the transition region (peak of the hoop stress calculated using strain energy function) between the uniform and the bulged portions of the tube. Our study shows the possible bifurcation behaviour of finite hyperelastic tubes. The critical and post-critical analysis for bulging has been addressed here. Post-bifurcation failure analyses are in progress and will be addressed in the future.

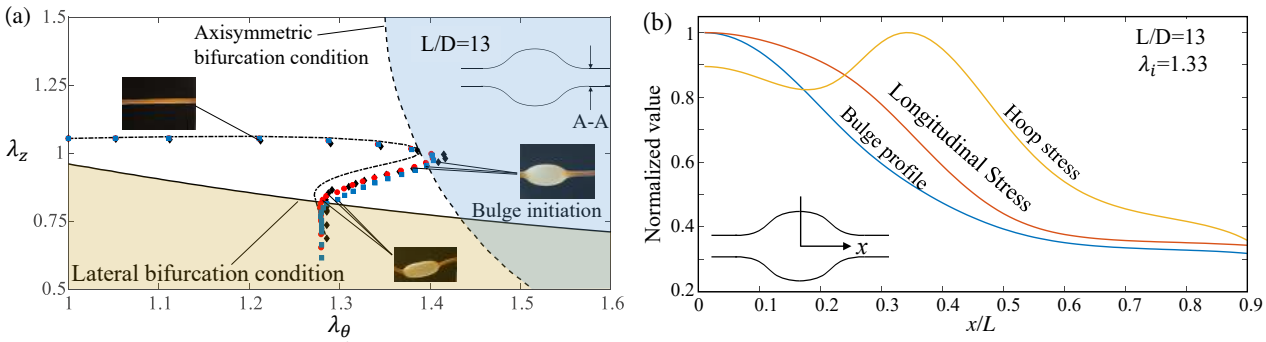

Figure 2: (a) Bifurcation phase diagram. (b) Stress distribution.

References

[1] Palmer A. C., Martin J. H. Buckle propagation in submarine pipelines. *Nature* **254**: 46, 1975.
[2] Chater E., Hutchinson J. W. On the Propagation of Bulges and Buckles. *J. Appl. Mech.* **51**: 269, 1984.
[3] Kyriakides S., Yu-Chung C. The initiation and propagation of a localized instability in an inflated elastic tube. *Int. J. Solids Struct.* **27**: 1085-1111, 1991.
[4] Lestringant C., Audoly B. A diffuse interface model for the analysis of propagating bulges in cylindrical balloons. *P. R. Soc-Math Phys. Sc.* **474**: 20180333, 2018.
[5] Goriely A., Vandiver R., Destrade M. Nonlinear euler buckling. *P. R. Soc-Math Phys. Sc.* **464**: 3003–3019, 2008.

JACOBI CONJUGATE POINTS, STABILITY AND COMPUTING END-TO-END PROBABILITIES FOR ELASTIC RODS

Giulio Corazza*, Raushan Singh, and John H. Maddocks
Laboratory for Computation and Visualization in Mathematics and Mechanics (LCVMM) Institute of Mathematics, Swiss Federal Institute of Technology (EPFL), CH-1015 Lausanne, Switzerland

Summary It is widely known how to efficiently compute equilibria of (hyper-)elastic rods subject to prescribed two-point boundary conditions, for example using the Hamiltonian form of the Euler-Lagrange equations for the associated energy [4, 6]. The classification of which equilibria are also stable in the sense of realising local minima of the energy can then be carried out using conjugate point theory, specifically, counting the number of zeros of a determinant evaluated on Jacobi fields associated with the second variation of the energy. What is less well-known is that the energy of equilibria combined with the actual value of the same Jacobi field determinant can be used to estimate probability densities for the distribution of end-to-end displacements when the rod is interacting with a heat bath (as is the case for example in elastic rod models of DNA). We demonstrate how to derive such an approximate conditional probability density function governing the relative location and orientation of the two ends, when the rod is subject to a prescribed external end-loading, in addition to external stochastic forcing from the heat bath (as happens in many single molecule experiments).

INTRODUCTION

Recent interest in the theory of special Cosserat rods has surged in part due to its applicability in molecular biophysics and modeling polymers. Starting from an assumed Boltzmann distribution on rod configurations, it is widely understood that a conditional probability can be expressed as the ratio of a Boltzmann weighted integral over all rod configurations or paths satisfying the desired end conditions, to the analogous weighted path integral over all admissible configurations. In turn these path integrals can be explicitly evaluated [3] if they can be transformed to be quadratic in appropriate variables, or if they can be approximated by a quadratic expansion about a minimum energy configuration satisfying prescribed end conditions. In particular, the contribution of local quadratic fluctuations around that minimum is captured by an appropriate modification of a conjugate point stability analysis. Our motivation for the present work is to exploit continuum mechanics models in order to evaluate conditional probability densities related to a wide range of applications, providing an extension of [1, 2] for dealing with systems driven by more general energies, e.g. including prescribed external end loadings, as arise for example in molecular tweezer experiments.

THE METHOD

Following the Cosserat theory of elastic rods, the configuration of the system is given by $\boldsymbol{q}(s) := (\boldsymbol{R}(s), \boldsymbol{r}(s)) \in SE(3)$, $s \in [0, L]$, where $\boldsymbol{r}(s)$ is the centerline vector in $\mathbb{R}^3$ and $\boldsymbol{R}(s) \in SO(3)$ is defined as the proper rotation relating a fixed, right-handed, orthonormal frame to the directors frame in $\mathbb{R}^3$, modeling the cross-section orientation of the rod. Under the assumption of linear hyper-elasticity, we consider a Lagrangian formulation of the problem, driven by the energy functional $E(\boldsymbol{q}(s)) = \int_0^L W(\boldsymbol{q}'(s), \boldsymbol{q}(s), s)\, ds$. The energy density W takes into account both the strain energy and the contribution coming from an external end loading $\boldsymbol{\lambda}$ at $\boldsymbol{q}_L := \boldsymbol{q}(L)$. When the system is at thermodynamical equilibrium, the conditional probability density in the variable $\boldsymbol{q}_L$ is given in terms of path integrals as

$$\rho(\boldsymbol{q}_0, \boldsymbol{q}_L; 0, L) := \frac{\int e^{-\beta E(\boldsymbol{q}(s))}\, \mathsf{D}[\boldsymbol{q}(s)]_{\boldsymbol{q}(0)=\mathbf{0}}^{\boldsymbol{q}(L)=\boldsymbol{q}_L}}{\int e^{-\beta E(\boldsymbol{q}(s))}\, \mathsf{D}[\boldsymbol{q}(s)]_{\boldsymbol{q}(0)=\mathbf{0}}}, \tag{1}$$

where $\beta = \frac{1}{k_B T}$, k_B is the Boltzmann constant, T is the temperature of the system and D is defined by discretization as a measure on the space of rod configurations. Notice that we can assume $\boldsymbol{q}_0 := \boldsymbol{q}(0) = (\mathbb{1}, \mathbf{0})$ for invariance under rigid body motions. The approximation method relies on a Laplace asymptotic technique for both numerator and denominator of (1) and it requires the existence of the following minima of the energy, respectively local (l) and global (g).

1. $\boldsymbol{q}^l(s)$ satisfying the boundary conditions $\boldsymbol{q}^l(0) = \boldsymbol{q}_0 = (\mathbb{1}, \mathbf{0})$, $\boldsymbol{q}^l(L) = \boldsymbol{q}_L = (\boldsymbol{R}_L, \boldsymbol{r}_L)$,
2. $\boldsymbol{q}^g(s)$ satisfying the boundary condition $\boldsymbol{q}^g(0) = (\mathbb{1}, \mathbf{0})$ and the natural boundary condition at $s = L$.

In particular, it is possible to show that $\rho(\boldsymbol{q}_0, \boldsymbol{q}_L; 0, L)$ is given by a component depending on the "distance" between the solutions of the Euler-Lagrange equations for the minima and another component depending on the "distance" between the solutions of the Jacobi equations on the minima. Specifically, we have that the approximation of $\rho(\boldsymbol{q}_0, \boldsymbol{q}_L; 0, L)$ is given by

$$\left(\frac{\beta}{\pi}\right)^3 \exp\left\{-\beta\left[E(\boldsymbol{q}^l) - E(\boldsymbol{q}^g)\right] - \frac{1}{2}\left[\ln Det[\boldsymbol{J}^l(0)] - \ln Det\,[\boldsymbol{J}^g(0)]\right]\right\},$$

where the Hamiltonian version of the Jacobi equation for $s \in [0, L]$ is driven by the symplectic skew-symmetric matrix

*Corresponding author. E-mail: giulio.corazza@epfl.ch

$\mathbb{E}$ and the symmetric matrix $\boldsymbol{S}$ coming from the second variation of the energy for the two minima. The boundary conditions determine a complete set of linearly independent solutions, which fully characterise the system by mean of linear differential equations as follow:

$$\begin{cases} \begin{pmatrix} \boldsymbol{J}^l \\ \boldsymbol{M}^l \end{pmatrix}' = \mathbb{E}\boldsymbol{S}^l \begin{pmatrix} \boldsymbol{J}^l \\ \boldsymbol{M}^l \end{pmatrix}, \\ \begin{pmatrix} \boldsymbol{J}^l \\ \boldsymbol{M}^l \end{pmatrix}(L) = \mathbb{E} \begin{pmatrix} \mathbb{1} \\ \mathbf{0} \end{pmatrix}, \end{cases} \qquad \begin{cases} \begin{pmatrix} \boldsymbol{J}^g \\ \boldsymbol{M}^g \end{pmatrix}' = \mathbb{E}\boldsymbol{S}^g \begin{pmatrix} \boldsymbol{J}^g \\ \boldsymbol{M}^g \end{pmatrix}, \\ \begin{pmatrix} \boldsymbol{J}^g \\ \boldsymbol{M}^g \end{pmatrix}(L) = \mathbb{E} \begin{pmatrix} \mathbf{0} \\ \mathbb{1} \end{pmatrix}. \end{cases}$$

A NUMERICAL EXAMPLE

We consider a family of cycling loadings applied to the L-tip of a rod deforming in the 3-dimensional space. As a roulette, there will be a configuration maximizing/minimizing the density. The end-loadings are given by

$$\boldsymbol{\lambda}_i = \frac{1}{20}\left(\sin(\theta_i), \cos(\theta_i), 0\right), \quad \theta_i = \frac{\pi}{4} i \ \text{ for } \ i = 1, ..., 8.$$

Thus we have 8 different global minima indexed by the related force, which are located around the minimizer of the elastic energy part, i.e the intrinsic configuration of the rod. Finally, for each load we are computing the conditional probability density for the end of the rod to be in a fixed prescribed configuration. Notice that the latter boundary condition determines the shape of the local minimum through the Euler-Lagrange equations. The experimental set up is shown in Fig. 1(a). Moreover, a Monte Carlo (MC) implementation [5] of the problem is provided in order to assess the accuracy level of the proposed approximation (Laplace). The comparison is displayed in Fig. 1(b).

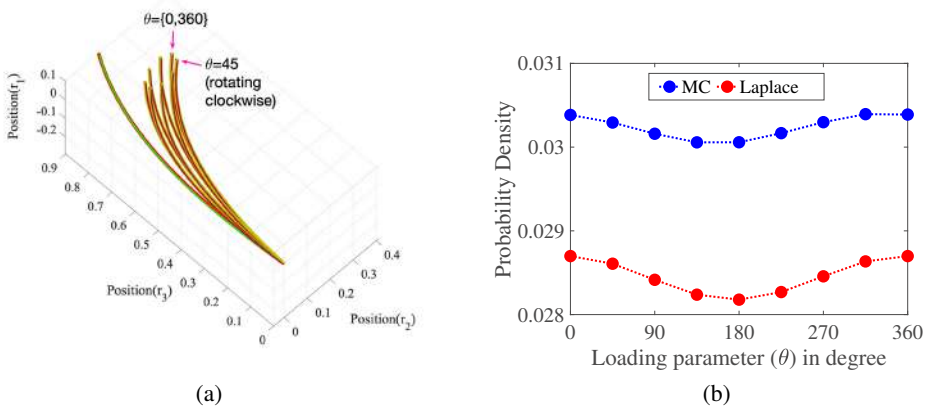

(a) (b)

Figure 1: (a) Profiles of global minima (red-yellow) for each load parametrized in degree. The local minimum is determined by the chosen boundary condition (red-green) (b) Conditional probability densities: comparison between Laplace theoretical values and Monte Carlo simulations.

CONCLUSIONS

We have described a new theory to estimate end-to-end probability distributions for an elastic rod that is subject to both a stochastic interaction with a heat bath and a deterministic end-loading. We have illustrated our analysis with a 3-dimensional example and computed an approximate probability density which gives a good agreement with direct Monte Carlo numerical simulations. The new method is of quite general applicability as no assumption is made on either uniformity, nor on the intrinsic shape, of the elastic rod model. Consequently our results can be exploited in a variety of interesting applications, such as the computation of looping probabilities for a DNA fragment of given sequence subject to end-loading, or other conditional probability densities for more general polymer systems.

References

[1] L. Cotta-Ramusino, J.H. Maddocks: *Looping Probabilities of Elastic Chains: A Path Integral Approach*, Physical Review E 82, 2010.
[2] L. Cotta-Ramusino: *A Path Integral Formalism of DNA Looping Probability*, Thesis n. 4017, EPFL, 2008.
[3] G. J. Papadopoulos: *Gaussian Path Integrals*, Physical Review D, Volume 11, Number 10, 1975.
[4] S. Kehrbaum and J.H. Maddocks: *Elastic rods, rigid bodies, quaternions and the last quadrature*, Philosophical Transactions Royal Society of London 355, 2117-2136, 1997.
[5] J.S. Mitchell, J. Glowacki, A.E. Grandchamp, R.S. Manning, J.H. Maddocks: *Sequence-Dependent Persistence Lengths of DNA*, Journal of Chemical Theory and Computation 13, 1539-1555, 2017.
[6] D. J. Dichmann, Y. Li, J.H. Maddocks: *Hamiltonian Formulations and Symmetries in Rod Mechanics*, Mathematical Approaches to Biomolecular Structure and Dynamics, IMA Volumes in Mathematics and its Applications 82, 71 - 113, 1996.

LOSS OF ELLIPTICITY IN SOFT COMPOSITES WITH FIBERPLASTICITY

Fernanda F. Fontenele[1], Michalis Agoras[2], and Nikolaos Bouklas*[1]
[1]Sibley School of Mechanical and Aerospace Engineering, Cornell University, Ithaca, NY, USA
[2]Department of Mechanical Engineering, University ot Thessaly, Volos, Greece

Summary This paper presents a modeling effort to capture global instability events, such as kink-band formation, during non-monotonic loading conditions of soft composites driven by fiber plasticity. This study brings new insight to damage initiation of biological fibrous tissues and engineered soft composites. To this end, a finite-strain phenomenological model that captures the effects of fiber plasticity by means of a back stress is proposed first and then the model is used to track the emergence of discontinuity fronts in the context of loss of ellipticity. It is confirmed that upon initial tensile loading in the direction of the fibers, and plastic deformation of the fibers, the composite can exhibit macroscopic localization during unloading. Contrary to past studies, loss of ellipticity in this case can occur as the composite is still under tensile loading; it is noteworthy that while the fiber stretch is tensile at loss of ellipticity, the elastic fiber stretch is contractile.

INTRODUCTION

Biological fiber-reinforced composites such as tendon, undergo cyclic loading and exhibit a complex damage response—from damage initiation in the form of kink band formation, fiber/matrix debonding, fiber rupture and to ultimate failure—and collagen fibril plasticity is known to play a crucial role in that damage cascade. In engineered fiber-reinforced soft composites, it is important to investigate the effects of fiber plasticity to optimize the strength and toughness of these materials. Localized deformation patterns of the kink-band type have been observed in biological composite materials such as mamalian tendon tissue, with uni-directional collagen-fibril reinforcement when subjected to tensile fatigue loading [3]. In the relevant literature, the formation of these kinks is not well understood, and they are only treated as a precursor to material failure. In parallel, apart from the finite elastic strains that are apparent in these materials, there is evidence of plastic deformation mechanisms present in collagen fibrils when loaded in uniaxial tension [4]. From a modeling perspective, loss of ellipticity of the governing equations of equilibrium, allows the prediction of emergence of macroscopic localization fronts. Loss of ellipticity of both phenomenological and micro-mechanical models has been extensively analyzed to investigate localized deformation patters in several classes of materials, including fiber-reinforced composites with hyperelastic or elastoplastic constituents ([5], [6], [2]). Most of these studies, however, focus on monotonic loading conditions involving compressive or tensile stresses along the fiber direction. In this paper, we focus in the emergence of localization in fiber-reinforced soft composites with elastoplastic fibers and elastic matrix under non-monotonic loading conditions.

CONSTITUTIVE MODELING

The soft materials of interest in this work are treated as fiber-reinforced composites, consisting of an elastic matrix reinforced by elastoplastic fibers at the microscopic scale, and assumed to be homogeneous, transversely isotropic, and incompressible solids at the macroscopic scale.

Consider a macroscopically homogeneous, but otherwise arbitrary, deformation of the composite from a given reference configuration described by a constant deformation gradient tensor $\mathbf{F}$, let $\mathbf{C} = \mathbf{F}^T\mathbf{F}$, and define the following set of independent transversely isotropic invariants of $\mathbf{C}$

$$I_1 = \mathrm{tr}\mathbf{C}, \quad I_2 = \frac{1}{2}\left[(\mathrm{tr}\mathbf{C})^2 - \mathbf{C}^2\right], \quad I_3 = \det\mathbf{C}, \quad I_4 = \mathbf{A}\cdot(\mathbf{C}\mathbf{A}) = \mathbf{C}:\mathbf{A}\otimes\mathbf{A}, \quad I_5 = \mathbf{A}\cdot(\mathbf{C}^2\mathbf{A}) \tag{1}$$

where $\mathbf{A}$ denotes the unit vector along the fiber direction in the reference configuration. For any given deformation path, we assume that the elastic part of the macroscopic constitutive relation of the composite is completely determined by means of the following strain energy density function

$$W(I_1, I_3, I_4, p; \lambda_f^p) = \frac{\mu}{2}(I_1 - 3) + p(I_3^{1/2} - 1) + \gamma(I_4 - (\lambda_f^p)^2)^2, \tag{2}$$

where μ and γ are the elastic moduli of the composite in the linearly-elastic regime, p is the Lagrange multiplier enforcing the incompressibility constraint, and λ_f^p is some effective measure of the accumulated plastic stretch in the fibers along $\mathbf{A}$ from the reference to the current configuration along the deformation path. Note that, in the context of (2), λ_f^p plays the role of an internal variable, which induces a back stress on the macroscopic response of the composite, and which may have a dramatic effect on the overall stability of the composite, as illustrated in the following section.

*Corresponding author. E-mail: nbouklas@cornell.edu

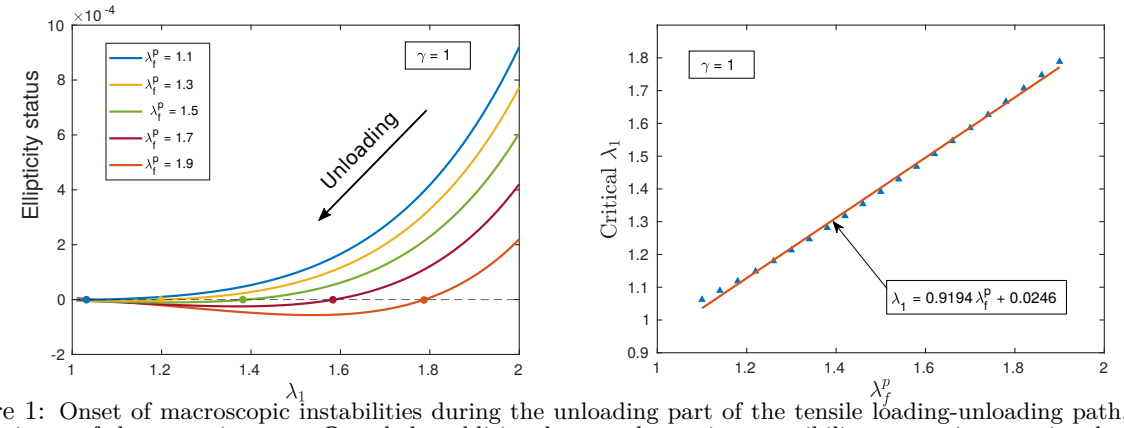

Figure 1: Onset of macroscopic instabilities during the unloading part of the tensile loading-unloading path. (a) The determinant of the acoustic tensor $\mathbf{Q}$ and the additional terms due to incopressibility constraint associated with (2) is shown as a function of the applied stretch λ for different values of the accumulated plastic stretch in the fibers λ_f^p. (b) The critical stretch λ_1^{cr} as a function of the plastic fiber stretch λ_f^p.

RESULTS AND DISCUSSION

For the purpose of this work, and given the space limitations, in the sequel we focus on the investigation of the overall stability of fiber-reinforced composites defined (partially) by (2) under a loading-unloading path of uniaxial tension along the fiber direction $\mathbf{A}$. In addition, we assume that the response of the composite is elastoplastic, stable, and known during loading and purely elastic, possibly unstable, and unknown during unloading. Hence, following the formulation by [7], [8], [2], we investigate the strong ellipticity condition for the strain energy function (2) during unloading, by treating the plastic stretch of the fibers λ_f^p as a known parameter. We remark that, the associated macroscopic stretch λ along the fiber direction may be decomposed as $\lambda = \lambda_f^e \lambda_f^p$, where λ_f^e is the elastic stretch of the fibers along $\mathbf{A}$.

Specific results for the loss of strong ellipticity of (2) during tensile unloading are shown in Fig. $1(a)$. These results illustrate that macroscopic strain localization is possible in the composite and occurs closer to the reference state for lower values of the plastic stretch λ_f^p. Fig.$1(b)$ shows results for the critical macroscopic stretch λ^{cr} at the onset of localization as a function of the plastic fiber stretchλ_f^p, also showing a linear fit between the two variables $\lambda^{cr} = 0.9194\lambda_f^p + 0.0246$. This allows the approximation of the critical elastic stretch $\lambda_f^{e,cr}$ of the fibers at loss of ellipticity as $\lambda e, cr_f = 0.9194 + 0.0246/\lambda_f^p$ which allways leads to $\lambda e, cr_f < 1$, as also verified by the exact results. We observe that the elastic stretch $\lambda_f^{e,cr}$ of the fibers at the onset of localization is contractile, even though the corresponding macroscopic stretch λ^{cr} is extensive. This is a critical detail, highlighting the effect of having an elastic mismatch between the plastically deforming fibers and the elastic matrix, which leads to the emergence of the localization fronts in the composite.

CONCLUSIONS

In this work, we have proposed a phenomenological, transversely isotropic model for the finite-strain, macroscopic response of soft fiber-reinforced composites, incorporating the effects of elastic deformations in the matrix and elastoplastic deformations in the fibers. In the context of this model, we found that plastic deformation induced to the fibers during tensile loading leads to loss of strong ellipticity during unloading while, macroscopically, the material is still in tension. However, when ellipticity is lost, it is observed that the elastic part of the fiber deformation is already contractile. The outcome of this analysis provides a first investigation and insight to an exciting new class of problems with significant biomechanical relevance.

References

[1] Agoras, M., Lopez-Pamies, O. and Ponte Castañeda, P. A general hyperelastic model for incompressible fiber-reinforced elastomers. *Journal of the Mechanics and Physics of Solids* **57**: 268-286, 2009.

[2] Agoras, M., Lopez-Pamies, O. and Ponte Castañeda, P. Onset of macroscopic instabilities in fiber-reinforced elastomers at finite strain. *Journal of the Mechanics and Physics of Solids* **57**: 1828-1850, 2009.

[3] Fung D. T., Wang V. M., Laudier D. M., Shine J. H., Basta-Pljakic J., Jepsen K. J., Schaffler M. B., Flatow E. L. Subrupture tendon fatigue damage. *J. Orth. Res.* **27, 2**: 264-273, 2009.

[4] Tang Y., Ballarini R., Buehler M. J., Eppell S. J. Deformation micromechanisms of collagen fibrils under uniaxial tension. *J. Ro. Soc. Int.* **7, 46**: 839-856, 2009.

[5] Triantafyllidis N., Abeyaratne R. Instabilities of a finitely deformed fiber-reinforced elastic material. *J. App. Mech.* **50, 1**: 149-156, 1983.

[6] Merodio J., Odgen R. W. Material instabilities in fiber-reinforced nonlinearly elastic solids under plane deformation. *Arch. Mech.* **54, 5-6**: 525-552, 2002.

[7] Knowles J. K., Sternberg E. On the ellipticity of the equations of nonlinear elastostatics for a special material. *J. El.* **5, 3-4**: 341-361, 1975.

[8] Triantafyllidis N., Abeyaratne R. Loss of ellipticity in plane deformation of a simple directionally reinforced incompressible nonlinearly elastic solid. *J. El.* **49, 1**: 1-30, 1997.

ELASTIC INSTABILITIES IN SOFT FIBER COMPOSITES

Nitesh Arora*[1], Jian Li[2], Viacheslav Slesarenko[3], and Stephan Rudykh[1]
[1]Department of Mechanical Engineering, University of Wisconsin–Madison, Madison, WI 53706, USA
[2]Department of Civil and Environmental Engineering, MIT, Cambridge, MA 02139, USA
[3]Freiburg Institute for Advanced Studies, University of Freiburg, Freiburg 79104, Germany

Summary In this work, we study the microscopic and long-wave instabilities in a class of non-Gaussian hyperelastic fiber composites with Gent phases. In particular, we investigate the influence of stiffening of phases on the onset of instabilities and the associated wavelengths. We derive an analytical expression to predict the onset of long-wave instabilities. By employing Bloch-Floquet analysis, we determine the critical parameters corresponding to the microscopic instabilities. The stiffening behavior of phases strongly defines the wavelength of the buckling patterns, together with the onset of instabilities. As a consequence, the interplay between long-wave and microscopic instabilities is highly dictated by the extent of phase stiffening. Hence, phases with pre-designed properties enable us to tailor the instability-induced patterns in soft fiber composites.

INTRODUCTION

Elastic instability phenomenon in soft microstructured materials has gained significant attention, since it can be used to trigger sudden microstructure transformations [1]. These transformations often accompany several unusual material properties, such as – instability-induced elastic wave band gaps [2], auxetic behavior [3], and the emergence of negative group velocity in marginally stable soft composites [4].

The onset of instabilities and the associated buckling patterns in soft composites are strongly defined by their microstructure [5,6] and contrast in the initial stiffness of the phases [7]. Additionally, the rich and complex behavior of soft phases, such as, viscoelasticity and stiffening effect, can further increase the admissible range of tunable microstructures. In this work, we study the influence of stiffening effects – stemming from the non-Gaussian statistics of polymer chains – on the stability of 3D fiber composites. Specifically, we examine the fiber composites with the phases characterized by the Gent model. We also study the interplay between the microscopic and macroscopic instabilities. To this end, we derive the analytical expression corresponding to the onset of long-wave instabilities using loss of ellipticity analysis, and employ Bloch-Floquet analysis superimposed on finite deformations to detect microscopic instabilities and associated buckling modes.

ANALYSIS

Consider the fiber composites being subjected to uniaxial deformation along the direction of fibers ($\mathbf{e_3}$) with macroscopic deformation $\bar{\mathbf{F}}$ gradient given as

$$\bar{\mathbf{F}} = \lambda^{-1/2}\left(\mathbf{e_1}\otimes\mathbf{e_1} + \mathbf{e_2}\otimes\mathbf{e_2}\right) + \lambda\mathbf{e_3}\otimes\mathbf{e_3}. \tag{1}$$

Next, we discuss the method used for detecting the onset of macroscopic and microscopic instabilities in fiber composites with Gent phases having strain energy density function: $\psi_G^{(f,m)} = -\frac{1}{2}\mu^{(f,m)}J_m^{(f,m)}\ln\left(1-\frac{I_1^{(f,m)}-3}{J_m^{(f,m)}}\right)$, where μ is the initial shear modulus, (f,m) corresponds to fiber or matrix phase and J_m is the dimensionless locking parameter, which accounts for the limiting polymeric chain extensibility. The lock-up phenomenon appears in the limit $(I_1-3)\to J_m$.

Long-wave instability

To predict the onset of long-wave instability, we use loss of ellipticity analysis. First, we calculate the effective elastic moduli tensor $A_{\alpha i\beta j}$ for transversely isotropic incompressible hyperelastic fiber composite with Gent phases for the uniaxial deformation (1). In the current configuration the effective elastic moduli is obtained as $A^0_{piqj} = J^{-1}\bar{F}_{p\alpha}\bar{F}_{q\beta}A_{\alpha i\beta j}$. Application of strong ellipticity condition on A^0_{piqj} results in a explicit polynomial in the critical stretch (λ_{cr}), namely $\sum_{i=0}^{12} a_i\lambda_{cr}^i = 0$, where coefficients a_i are the functions of material and geometry parameters [8].

Microscopic Instability

To predict the onset of microscopic instabilities, we have used a two-step analysis. First, we apply the macroscopic deformation gradient (1) by imposing the periodic boundary condition. Then, we superimpose the Bloch-Floquet periodicity conditions on the deformed state with incremental displacement as $\mathbf{u}(\mathbf{X}+\mathbf{R}) = \mathbf{u}(\mathbf{X})e^{i\mathbf{K}\cdot\mathbf{R}}$, where $\mathbf{K}$ is the Bloch-wave vector and $\mathbf{R}$ being the spatial periodicity vector. The corresponding eigenvalue problem is solved at each deformation level for a range of $\mathbf{K}$ until a non-trivial eigenvalue is detected. The strain level for which $\omega(\mathbf{K})=0$ appears, corresponds to the onset of instabilities. For detailed description, please see reference [7]. Note that the same scheme can be used for long-wave instability analysis [9].

*Corresponding author. E-mail: narora7@wisc.edu.

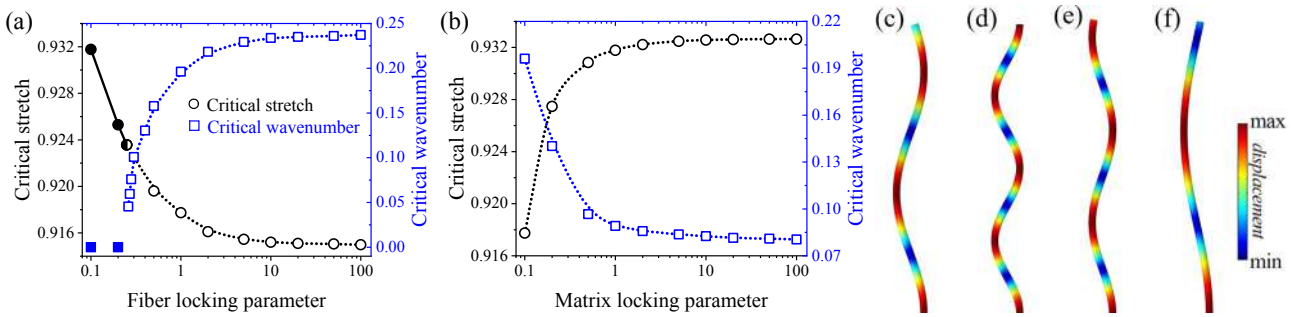

Figure 1: Dependence of critical stretch and normalized critical wavenumber on the fiber (a) and matrix (b) locking parameters; (c), (d), (e) and (f) represent the buckling modes of fibers for composites with various phase locking parameters. The color shows the magnitude of in-plane displacement.

RESULTS

Fig. 1 illustrates the dependence of critical stretch and the associated wavelengths (inverse of critical wavenumber) on the fiber locking parameter ($J_m^{(f)}$) (a) and matrix locking parameter ($J_m^{(m)}$) (b). The results are shown for the fiber composites with fiber volume fraction = 0.048, shear modulus contrast = 100, and $J_m^{(m)} = 0.1$ for subfigure (a) and $J_m^{(f)} = 1$ for subfigure (b). The filled and hollow symbols correspond to macroscopic and microscopic instabilities, respectively. The half-filled symbol marks the point corresponding to the transition of instability mode. We observe that the stability of the composites increases (critical stretch decreases) with an increase in the fiber locking parameter and/or decrease in the matrix locking parameter. Moreover, the critical wavelength corresponding to the microscopic instabilities increases with a decrease in the fiber locking parameter and/or with an increase in the matrix locking parameter. As a consequence, the composites with stiffening fibers tend to develop long-wave instabilities, whereas the composites with stiffening matrix phase are more prone to microscopic instabilities.

The subfigures (c), (d), (e) and (f) represent the buckling mode of fibers, which develop as a result of microscopic instabilities in the composites with various phase locking parameters. In particular, the locking parameters are: $J_m^{(f)} = 0.4$ and $J_m^{(m)} = 0.1$ (c); $J_m^{(f)} = 2$ and $J_m^{(m)} = 0.1$ (d); $J_m^{(f)} = 1$ and $J_m^{(m)} = 0.1$ (e); and $J_m^{(f)} = 1$ and $J_m^{(m)} = 1$ (f). The height of all the buckling modes is identical. It is evident from these buckling modes, that even a small variation in the locking parameters of phases results in significant changes in the shape of these patterns.

CONCLUSIONS

We have investigated the microscopic and long-wave instabilities in 3D fiber composites with Gent phases. Our results indicate that the critical strains and the associated wavelengths are significantly affected by the locking parameters of the phases. In summary, we show that the stiffening effect (stemming from the accurate non-Gaussian based models) together with instability phenomenon lead to the widening of admissible pool of tunable microstructures. Finally we note that practically, the extent of stiffening behavior can be regulated by varying the level of cross-linking.

References

[1] Li J., Dora T., Goshkoderia A.,Slesarenko V. and Rudykh S. Domain formations and pattern transitions via instabilities in soft heterogeneous materials. *Advanced Materials* **31**: 1807309, 2019.

[2] Rudykh S. and Boyce M. C. Transforming wave propagation in layered media via instability-induced Wrinkling interfacial Layer. *Physical Review Letters* **112**: 034301, 2014.

[3] Li J., Slesarenko V. and Rudykh S. Auxetic multiphase soft composite material design through instabilities with application for acoustic metamaterials. *Soft Matter* **14**: 6171-6180, 2018.

[4] Slesarenko V., Galich P., Li J., Fang N.X. and Rudykh S. Foreshadowing elastic instabilities by negative group velocity in soft composites. *Applied Physics Letters* **113**: 031901, 2018.

[5] Triantafyllidis N. and Maker B.N. On the comparison between microscopic and macroscopic instability mechanisms in a class of fiber-reinforced composites. *Journal of Applied Mechanics* **52**: 794-800, 1985.

[6] Galich P. I., Slesarenko V., Li J. and Rudykh S. Elastic instabilities and shear waves in hyperelastic composites with various periodic fiber arrangements. *International Journal of Engineering Science* **130**: 51-61, 2018.

[7] Slesarenko V. and Rudykh S. Microscopic and macroscopic instabilities in hyperelastic fiber composites. *Journal of the Mechanics and Physics of Solids* **99**: 471-482, 2017.

[8] Arora N., Li J., Slesarenko V., and Rudykh S. Microscopic and long-wave instabilities in 3D fiber composites with non-Gaussian hyperelastic phases. *Under review*

[9] Geymonat G., Muller S., Triantafyllidis N. Homogenization of nonlinearly elastic materials, microscopic bifurcation and macroscopic loss of rank-one convexity. *Archives for Rational Mechanics and Analysis* **122**: 231-290, 1993.

STABILITY OF NONLINEARLY ELASTIC SPHERE WITH DISTRIBUTED DISLOCATIONS

Evgeniya Goloveshkina *and Leonid Zubov
Institute of Mathematics, Mechanics, and Computer Science, Southern Federal University, Rostov on Don, Russia

Summary The formulation and solution of the stability problem for a three-dimensional elastic body is given, taking into account the microstructure. The buckling of a hollow nonlinear elastic sphere from a semi-linear (harmonic) material with edge dislocations is investigated. The study was carried out in the framework of the continuum theory of continuously distributed dislocations using the linearization method (the static Euler method). By solving a homogeneous linear boundary value problem, the minimum pressure value at which the sphere loses stability for the first time is found. The effect of dislocations on the buckling of thin and thick shells is analyzed.

Acknowledgments: The reported study was funded by the Russian Foundation of Basic Research, project number 19-31-90045.

INTRODUCTION

Dislocations, which are defects in a solid microstructure, have a significant effect on the deformation and strength properties of materials. Using dislocation models, one can describe other defects of crystalline materials, as well as such mechanical phenomena as inelasticity, crystal growth, fatigue, and some others [1, 2, 5]. In this paper, within the framework of the continuum theory of continuously distributed dislocations, we consider the stability problem for a nonlinearly elastic sphere with dislocations. Most studies concern the stability of thin rods, plates, and shells [6, 7, 8, 9]. However, the phenomenon of stability loss is advisable to study for three-dimensional elastic bodies too [3, 10].

STABILITY PROBLEM

In the framework of the three-dimensional nonlinear elasticity theory, the influence of distributed dislocation on the equilibrium stability of a thick-walled closed spherical shell loaded with external hydrostatic pressure is studied. The system of equations of the nonlinear dislocation theory consists of equilibrium equations

$$\mathrm{div}\mathbf{D} = 0,$$

constitutive equations of the material

$$\mathbf{D} = \mathrm{d}W(\mathbf{C})/\mathrm{d}\mathbf{C},$$

and incompatibility equations

$$\mathrm{rot}\mathbf{C} = \boldsymbol{\alpha}, \tag{1}$$

where $\mathbf{C}$ is the distortion tensor, $\mathbf{D}$ is the Piola stress tensor, W is the specific strain energy, and $\boldsymbol{\alpha}$ is the dislocation density tensor satisfying the solenoidality condition

$$\mathrm{div}\boldsymbol{\alpha} = 0\,.$$

In this paper, the gradient, rotor, and divergence operators are written in the reference configuration.

We consider a spherically symmetric distribution of edge dislocations defined by the dislocation density tensor

$$\boldsymbol{\alpha} = \beta(r)\left(\mathbf{e}_\varphi \otimes \mathbf{e}_\theta - \mathbf{e}_\theta \otimes \mathbf{e}_\varphi\right)\,. \tag{2}$$

Here $\beta(r)$ is a given function, r, φ, θ are the spherical coordinates, $\mathbf{e}_r$, $\mathbf{e}_\varphi$, $\mathbf{e}_\theta$ are the unit vectors tangent to coordinate lines.

For an isotropic material, by virtue of (2), the incompatibility equation (1) has a solution [4]

$$\mathbf{C}_0 = C_1(r)\mathbf{e}_r \otimes \mathbf{e}_r + C_2(r)\left(\mathbf{e}_\varphi \otimes \mathbf{e}_\varphi + \mathbf{e}_\theta \otimes \mathbf{e}_\theta\right), \tag{3}$$

and the Piola stress tensor according to (3) takes the form

$$\mathbf{D}_0 = D_1(r)\mathbf{e}_r \otimes \mathbf{e}_r + D_2(r)\left(\mathbf{e}_\varphi \otimes \mathbf{e}_\varphi + \mathbf{e}_\theta \otimes \mathbf{e}_\theta\right)\,.$$

Boundary conditions

$$D_1(r_0) = -p_0 C_2^2(r_0), \quad D_1(r_1) = 0 \tag{4}$$

*Corresponding author. E-mail: evgeniya.goloveshkina@yandex.ru.

mean the loading of the outer sphere's surface $r = r_0$ with the hydrostatic pressure p_0.

The equilibrium stability is studied by the static Euler method based on the linearization of a nonlinear boundary value problem in a neighborhood of a subcritical (unperturbed) state. The unperturbed state of the sphere is a spherically symmetric deformation and, in the case of a semi-linear (harmonic) material with constitutive equations [3]

$$\mathbf{D} = \frac{2\mu}{1-2\nu}\left(\nu \operatorname{tr}\mathbf{U} - 1 - \nu\right)\mathbf{A} + 2\mu\mathbf{C},$$

is described by the exact solution found earlier [5]. Here, $\mathbf{U}$ is the symmetric positive defined stretch tensor, $\mathbf{A}$ is the properly orthogonal rotation tensor, μ and ν are the constants. The linearized equilibrium and incompatibility equations are reduced to a system of three partial differential equations with respect to the components of the quasi-displacement vector field

$$\mathbf{w} = u(r,\theta)\mathbf{e}_r + v(r,\theta)\mathbf{e}_\theta\,.$$

For a semi-linear material, the linearized constitutive equations we obtain in the form

$$\dot{\mathbf{D}} = \frac{2\mu}{1-2\nu}\left(\nu \operatorname{tr}\mathbf{C}_0 - 1 - \nu\right)\frac{\dot{C}_{\theta r} - \dot{C}_{r\theta}}{C_{\theta\theta} + C_{rr}}\left(\mathbf{e}_\theta \otimes \mathbf{e}_r - \mathbf{e}_r \otimes \mathbf{e}_\theta\right) + \frac{2\mu}{1-2\nu}\left(\nu \operatorname{tr}\dot{\mathbf{C}}\right)\mathbf{E} + 2\mu\dot{\mathbf{C}},$$

where the distortion tensor in the unperturbed state $\mathbf{C}_0$ is determined according (3), $\mathbf{E}$ is the unit tensor, and

$$\dot{\mathbf{C}} = \frac{\partial u(r,\theta)}{\partial r}\mathbf{e}_r \otimes \mathbf{e}_r + \frac{\partial v(r,\theta)}{\partial r}\mathbf{e}_r \otimes \mathbf{e}_\theta + \frac{u(r,\theta) - v(r,\theta)\tan\theta}{r}\mathbf{e}_\varphi \otimes \mathbf{e}_\varphi$$
$$+ \left(\frac{\partial v(r,\theta)}{r\partial\theta} + \frac{u(r,\theta)}{r}\right)\mathbf{e}_\theta \otimes \mathbf{e}_\theta + \left(\frac{\partial u(r,\theta)}{r\partial\theta} - \frac{v(r,\theta)}{r}\right)\mathbf{e}_\theta \otimes \mathbf{e}_r\,.$$

Using Legendre polynomials for axisymmetric forms of the sphere's buckling, the variables r and θ are separated and the stability problem is reduced to finding nontrivial solutions of the linear homogeneous boundary value problem for the system of ordinary differential equations and determining the critical external pressure. The latter is solved numerically.

The effect of dislocations on critical pressure corresponding to the stability loss of both thin and thick-walled shells is analyzed. In particular, it is found that with increasing the dislocation density in a thick shell, the absolute values of the quasi-displacements in the meridian plane decrease. Inside the sphere there are spherical surfaces on which these displacements do not depend on the dislocation density. For a thin shell in different parts of it in the radial direction, an increase in density either increases displacements or decreases. A negative dislocation density decreases the critical pressure, while a positive one increases it. Cases when the shell loses stability in the absence of an external load due to eigenstresses caused by dislocations have been revealed.

CONCLUSIONS

The stability problem for a hollow sphere with edge dislocations is solved. The minimum value of the external hydrostatically distributed pressure at which the sphere loses stability for the first time is found. For thick and thin shells, the forms of stability loss corresponding to the found critical pressure values are determined. The effect of dislocations on the buckling of a spherical shell is analyzed. It has been established that edge dislocations have a nonlinear effect on displacements. Also, the shell buckling in the absence of an external load due to eigenstresses caused by dislocations is studied.

References

[1] Clayton J. D. Nonlinear Mechanics of Crystals. Springer, Dordrecht 2011.
[2] Maugin G. A. Defects, dislocations and the general theory of material inhomogeneity. *Generalized Continua and Dislocation Theory. CISM courses and lectures*. **537**: 1-83. Springer, Vienna 2012.
[3] Lurie A. I. Nonlinear Theory of Elasticity. North-Holland, Amsterdam 1990.
[4] Zubov L. M. Spherically symmetric solutions in the nonlinear theory of dislocations. *Dokl. Phys.* **59(9)**: 419-422, 2014.
[5] Zhbanova E. V., Zubov L. M. The influence of distributed dislocations on large deformations of an elastic sphere. *Advanced Methods of Continuum Mechanics for Materials and Structures, Advanced Structured Materials*. **60**: 61-76. Springer, Singapore 2016.
[6] Singer J., Arbocz J., Weller T. Buckling experiments: Experimental methods in buckling of thin-walled structures: Shells, built-up structures, composites and additional topics. **2**. John Wiley & Sons, Inc, New York 2002.
[7] Eggwertz S., Samuelson L. A. Shell stability handbook. Elsevier Applied Science, London 1992.
[8] Volmir A. S. Stability of Deformable Systems. Nauka, Moscow 1967.
[9] Tvergaard V. Buckling behaviour of plate and shell structures. *Proc. 14th IUTAM Congress*. **72**: 233-247. North-Holland, 1976.
[10] Guz A. Fundamentals of the Three-Dimensional Theory of Stability of Deformable Bodies. Springer-Verlag, Berlin 1999.

CONTACT STABILITY OF ACTIVE MECHANICAL LINKAGES

Neelima Sharma*[1] and Madhusudhan Venkadesan†[1]
[1]Department of Mechanical Engineering and Materials Science, Yale University, New Haven, USA, 06511

Summary For animals and robots, compliant limb joints are needed to safely interact with the environment. However, excessive compliance compromises stability and the limb may buckle under contact forces. Here we address the problem of designing compliant and stable limbs during static operation by analyzing actively driven kinematic chains with external contacts. We show that the minimum joint stiffness for stability is an affine function of the torques driving the joints. Thus driving the joints using muscle-like actuators, with stiffness linearly proportional to force, lends stability without feedback control. Furthermore, we show that designing open-loop stable controllers is a convex problem, thus enabling efficient solution methods. We demonstrate the method on a model of the human index finger and discuss the implications for robots, prosthetics, and the neural control of limbs.

INTRODUCTION

Actively-driven mechanical linkages with compliant joints are ubiquitous in physical and biological systems. Like hinged columns that buckle when compressed, a self-driven mechanical linkage could also buckle because of external forces. Unlike passive columns, the external forces on these active linkages typically arise as a result of internal actuation. In passive and active systems, having joints with high stiffness could prevent buckling and stabilize a desired static configuration. However, excessive joint stiffness impedes free motion and adaptability of active limbs. We present here a mathematical analysis of general actively-driven linkages and show how to manage the trade-off between stability and adaptability using variable stiffness actuators. We first find a lower bound for the stiffness needed to remain stable and derive a formulation to incorporate the stiffness-based stability condition as a convex constraint within a optimization framework. By applying our formulation to tendon-driven linkages, we find that the use of muscle-like variable stiffness actuators yields open-loop control strategies that are stable. We demonstrate these results using an anatomically detailed model of a human index finger that is pushing on a surface with the fingertip.

MODELING AND RESULTS

The governing equations for linkages with Pfaffian constraints and springy, actuated joints are,

$$\mathrm{M}(\vec{q})\ddot{\vec{q}} + \vec{c}(\vec{q},\dot{\vec{q}}) + \vec{\gamma}(\vec{q}) + \mathrm{A}^T(\vec{q})\vec{\lambda}(\vec{q},\dot{\vec{q}}) = \vec{\tau} - K(\vec{q}-\vec{q}_0), \quad \mathrm{A}(\vec{q})\dot{\vec{q}} = 0. \tag{1}$$

Pfaffian constraints admit all holonomic constraints, but restrict generalized nonholonomic constraints like $\vec{g}(\vec{q},\dot{\vec{q}}) = 0$ to the case $\partial\vec{g}/\partial\vec{q} = A(\vec{q})$. Many known physical nonholonomic systems such as the rolling penny or the Chaplygin sleigh are Pfaffian [1]. The other terms are the generalized actuation forces $\vec{\tau}$, stiffness K, neutral configuration $\vec{q}_0$, generalized constraint forces $\vec{\lambda}(\vec{q},\dot{\vec{q}})$, inertia matrix $\mathrm{M}(\vec{q})$, Coriolis and centripetal terms $\vec{c}(\vec{q},\dot{\vec{q}})$, and external forces $\vec{\gamma}(\vec{q})$ (e.g. gravity).

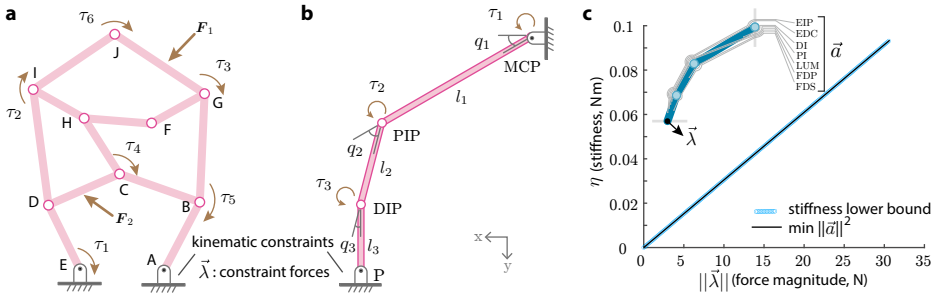

Figure 1: **a.** We consider open-loop stability of a prescribed configuration for general mechanical linkage networks with joint actuators (τ_{1-6}), external forces ($\vec{F}_{1-2}$) and kinematic constraints (A and E). In such active networks, actuation can induce constraint forces that destabilize the configuration, but the static pose can be stabilized if the joint stiffness matrix K is greater than a minimum stabilizing stiffness K_m. We show that this constraint can be incorporated within an optimal control framework as a set of linear convex constraints, formulated as a linear matrix inequality [2]. **b.** We apply this formulation to an index finger pushing on a surface by modeling the finger as a planar four-bar linkage driven by seven muscles. Muscle activation induces joint torques $\vec{\tau}$ and a joint stiffness matrix K. **c.** In a numerical demonstration of the index finger model, the stiffness matrix of a planar four-bar linkage that has only a single degree of freedom is parameterized by a scalar stiffness η. Solving an optimization problem to find a minimal effort solution, $\min\|\vec{a}\|^2$, results in activation patterns that satisfy $\eta > \eta_m$, as needed for open-loop stability (blue markers versus solid black line).

*E-mail: neelima.sharma@yale.edu
†E-mail: m.venkadesan@yale.edu

THEMATIC SESSION SM

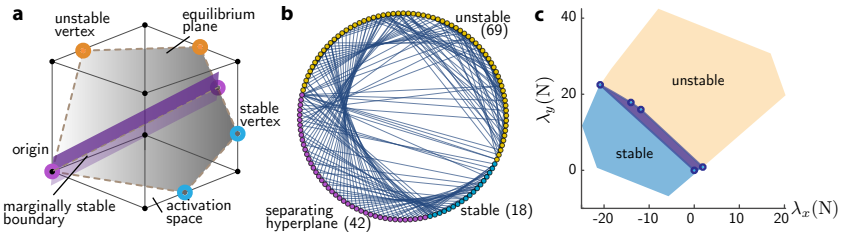

Figure 2: **a.** A cartoon to illustrate the geometric underpinnings of the control problem. The unit cube of normalized activations contains a lower-dimensional plane representing the torque-force equilibrium. A second lower dimensional plane shows marginal stability of the system and divides the equilibrium plane into stable and unstable regions with stable (blue), unstable (orange), and marginally stable (pink) vertices at the intersection with the unit cube. **b.** Circular embedding of the vertices of the equilibrium plane in 7D, showing the feasible muscle activations for an index finger and 18 stable, 69 unstable, and 42 marginally-stable vertices. **c.** The projection of the stable and the unstable regions from the 7D activation space onto the 2D fingertip force space. For every direction of force production, the boundaries of the marginally stable region show the largest force that can be stably produced.

The actuator torques $\vec{\tau}_0$ and stiffness K_m needed for stability depend on the desired static posture $\vec{q}_0$ and the desired contact forces $\vec{\lambda}_0$. With the definition $\mathrm{A}_0 = \mathrm{A}(\vec{q}_0)$, we find that $\vec{\tau}_0$ and K_m are affine functions of $\vec{\lambda}_0$ as given by,

$$\vec{\tau}_0 = \mathrm{A}_0^{\mathrm{T}} \vec{\lambda}_0 + \vec{\gamma}(\vec{q}_0), \quad \mathrm{K}_m = -\left(\frac{\partial \vec{\gamma}}{\partial \vec{q}} + \frac{\partial \mathrm{A}^T(\vec{q})\vec{\lambda}}{\partial \vec{q}} \right). \tag{2}$$

Inspired by biological limbs, we now focus on tendon-driven linkage networks with muscle-like actuators. The normalized vector $0 \leq \vec{a} \leq 1$ parametrizes muscle activations, which in turn induce joint torques $\vec{\tau} = \mathrm{RT}\vec{a}$ and joint stiffness $\mathrm{K} = \mathrm{R}\,\mathrm{K}_t\,\mathrm{diag}(\vec{a})\,\mathrm{R}^{\mathrm{T}}$. Normalized muscle activations are scaled to muscle forces by T, the matrix R that consists of the moment arms of the tendons about each joint maps muscle forces to torques, and the diagonal matrix K_t maps normalized muscle activations to muscle stiffness.

The problem is to find activations $\vec{a}$ that satisfy mechanical equilibrium between the torques and contact forces, and also stabilize the posture using muscle-induced stiffness. Typically, there are additional goals such as minimizing effort that are sought by the controller while subject to the mechanical constraints of equilibrium and stability. For a desired static limb posture $\vec{q}_0$ and desired contact forces $\vec{\lambda}_0$, the constrained optimization problem is given by,

$$\min \text{(objective function)}, \text{ subject to: } \mathrm{R}\,\mathrm{K}_t\,\mathrm{diag}(\vec{a})\,\mathrm{R}^{\mathrm{T}} - \mathrm{K}_m \succeq 0, \text{ and } \vec{\tau}_0 = \mathrm{RT}\vec{a} = \mathrm{A}_0^{\mathrm{T}}\vec{\lambda}_0 + \vec{\gamma}(\vec{q}_0). \tag{3}$$

Remarkably, the constraint of stability appears as a linear matrix inequality, which is convex in nature and thus can be solved by using established efficient numerical methods [2].

To demonstrate this formulation, we use a published model of an index finger that is applying a force with its tip such as during precision grips in humans [3]. The model is a planar three-link chain driven by 7 muscles and hinge constraints at both ends, making it a four-bar linkage with 1 net degree of freedom. Thus the joint stiffness K has only one non-zero eigenvalue η, which we use to quantify stiffness of the finger. We consider a convex (quadratic) objective function $\|\vec{a}\|^2$ and ignore gravitational forces. In this numerical example, we verify that the minimum stiffness for stability η_m is indeed a linear function of the tip force magnitude $\|\vec{\lambda}\|$, as is the muscle-induced stiffness η for the activation patterns found from the optimization (Fig. 1c). Furthermore, we use the constraint equations to map out the entire space of feasible activation patterns that satisfy equilibrium and stability constraints within the 7D space of activations (Fig. 2). This computation in 7D took 3 seconds on a 1.7 GHz 2-core Intel i7 running MATLAB version 9.8.0.1323502.

The projection of the stable and unstable equilibrium sets from 7D onto the 2D space of contact forces shows that larger forces are generally destabilizing (Fig. 2c). Such a comprehensive evaluation of the entire space of control strategies is made possible by formulating the open-loop control design problem as a linear convex problem. Future work could extend our formulation to dynamic conditions and to problems with nonholonomic constraints.

CONCLUSIONS

We derived the conditions for an active mechanical linkage that is stable and yet the softest possible. In the context of tendon-driven systems, such as prevalent in animals and some robots, the set of stable solutions form a convex polytope. Therefore, convex objective functions subject to the stability constraint may be easily solved, as we demonstrate for a 7D control space for an anatomically detailed model of the index finger.

References

[1] Ruina, A. (1998). Nonholonomic stability aspects of piecewise holonomic systems. *Reports on mathematical physics*, 42(1-2), 91–100.
[2] Boyd, S., El Ghaoui, L., Feron, E., & Balakrishnan, V. (1994). Linear matrix inequalities in system and control theory. *Society for industrial and applied mathematics*.
[3] Valero-Cuevas, F. J. (2000). Predictive modulation of muscle coordination pattern magnitude scales fingertip force magnitude over the voluntary range. *Journal of Neurophysiology*, 83(3), 1469–1479.

TRANSITIONS IN WRINKLING PATTERNS OF THIN ELASTIC FILMS ON COMPLIANT VISCOELASTIC SUBSTRATES

Jan Zavodnik*[1] and Miha Brojan[1]
[1]Laboratory for Nonlinear Mechanics, University of Ljubljana, Ljubljana, Slovenia

Summary Many viscoelastic structures are modelled in elastic (usually in short or long time) limits due to the considerable computational complexity. This way, a wide range of interesting phenomena from transient states is omitted. In this contribution we keep the time dependence of the viscoelastic material and study the transient states in large deformation regime during active deformation process, such as drying, swelling or growth of elastic films on viscoelastic substrates. We investigate the influence of viscous components on the deformation state of this structure and describe the transient deformation phenomena. We show that if the active deformation process is much faster than the viscous relaxation, the system can be driven out of equilibrium and in certain cases the transient shape modes can be "frozen" and remain in an "out of equilibrium" state for a considerable amount of time.

WRINKLING OF ELASTIC FILMS ON COMPLIANT VISOELASTIC SUBSTRATES

Wrinkling of thin elastic films on compliant viscoelastic substrates under compressive loads is an great toy model for studying interaction between the effects of the kinematic nonlinearity and viscoelastic material properties, because it is simple enough for analytical treatment and at the same time still maintains the effects of the viscoelasticity-nonlinear kinematics interaction. This kind of interaction occurs when the structure transitions from the initial, short time-limit to the final, long time-limit. The transition is essentially governed by the viscoelastic properties of the material. In the regime of the infinitesimal deformations the transition is trivial and therefore unsubstantial, but in the presence of nonlinear kinematic effects the transition becomes highly complex and more strongly dependent on initial conditions, perturbations and boundary conditions.

While the purely elastic theory offers discrete wrinkling deformation patterns as the solutions, the viscoelastic theory provides a framework to describe also the transition from the deformation patterns, e.g. from a pattern with a large number of wrinkles to the pattern with a small number of wrinkles. The complexity of this transition is a direct consequence of kinematic nonlinearities, because any rearrangement of wrinkles during the transition causes an energy dissipation while it does not affect the final elastic limit state. However, it can have an influence when the system arrives to the long time-limit state. If the initial energy dissipation during rearrangement of wrinkles is too large the system can become “frozen” in a non-equilibrium deformation state, which can be distinctly different from the purely elastic one. The system can remain there permanently if the system loses more energy than needed to overcome an energy barrier. Alternatively, the system can also transition so slowly that the environmental parameters change during the process and it can therefore remain in the out-of-equilibrium state permanently. Note that in general, these deformation states are unreachable for the elasticity alone [1]. In fact, this deformation patterns are very common in nature, e.g. in microbiology [2-4] and morphogenesis [5].

We analyse the elastic film and the viscoelastic compliant substrate decomposed, as displayed in Fig. 1. The elastic film is modelled with the use of Főppl-von Karman (weakly) nonlinear plate kinematic assumptions. On the other hand, the viscoelastic substrate is modelled as a continuum with infinitesimal deformation theory. Both elements are connected through the continuity of deformations and stresses in the structure.

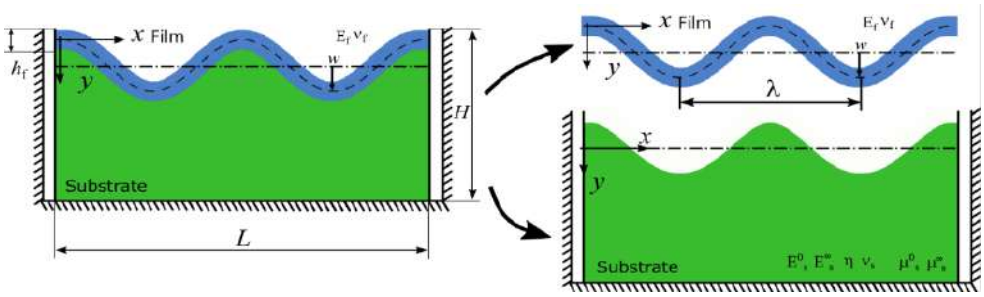

Figure 1: Elastic film and the viscoelastic substrate as separate structural elements.

To solve the obtained system of differential equations we approximate the wrinkles as a harmonic function of the form $w(x,t) = A(t)\cos k\,x$.

*Corresponding author. E-mail: jan.zavodnik@fs.uni-lj.si.

The system load in the form of confined growth, external forces etc. can be applied differently in the given time frame. We first analyse a step load. We show that an analytical implicit relation between the wrinkle amplitude A and time t and the wave number k can be obtained on an infinitely long structure with the use of total strain energy minimization,

$$t = \frac{C_1(\log A - \log A_0) - 12E^*_{s,ee}(1-\nu_f^2)\left(\log C_2(A) - \log C_2(A_0)\right)}{r\left(E_f h_f k\left(-h_f^2 k^2 + 12\varepsilon_g^0\right) - 24E^*_{s,e}(1-\nu_f^2)\right)}, \qquad k = 2\sqrt{\frac{\varepsilon_g^0}{3A^2 + h_f^2}}.$$

Here the C_1 and C_2 are some auxiliary functions made of material and geometric parameters, A_0 is the initial perturbation amplitude, E is Young's modulus, h is film thickness, ν is Poisson's ratio and r is a viscous relaxation rate. The indices "f" and "s" label the film and substrate properties, respectively. The time at which the wrinkles start to appear depends on the film growth amplitude ε_g^0. We show that if the growth amplitude is subcritical with respect to the long time-limit the wrinkles never appear and alternatively, if it is supercritical with respect to the long time-limit and supercritical with respect to the short time-limit then the wrinkles grow shortly after the growth is applied. Furthermore, if the growth amplitude is supercritical with respect to the short time-limit then wrinkles appear instantly and then continue to grow and transition towards the long time-limit deformation state. If the short time elastic equilibrium deformation pattern is qualitatively different from the long-time time deformation pattern, then the nontrivial transition will occur and the structure may become "frozen" in an out-of-equilibrium state.

In the case where the film growth is a ramp function the ratio between the compliant substrate relaxation rate and the active film growth rate is vitally important. In this case we performed numerical simulation where the growth magnitudes and elastic parameters of the structure were the same, only the ratio between the growth rate and viscoelastic relaxation rate were different. The long-time deformation patterns of two such structures are shown in Fig. 2. We observed that the two simulated structures converged to qualitatively different final deformation pattern.

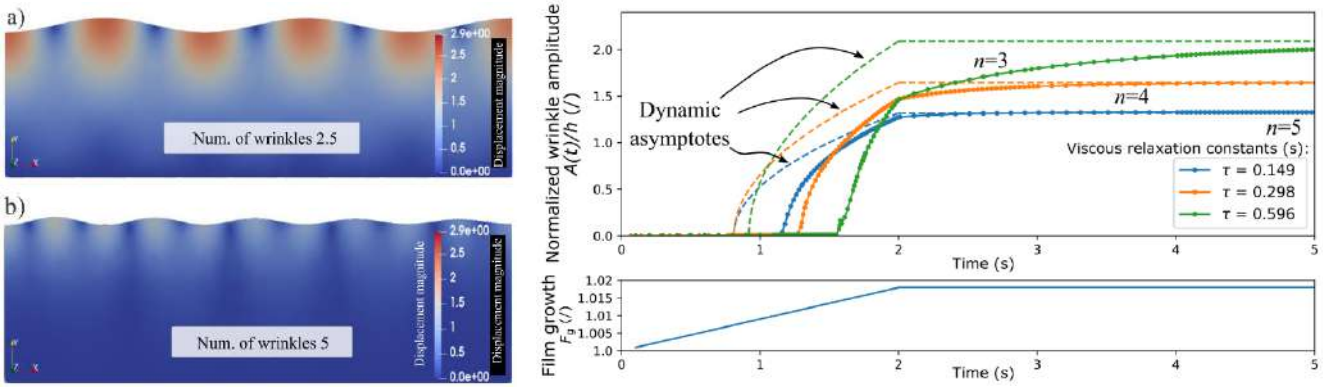

Figure 2: Left: Final deformation states of structures with the same elastic and different viscoelastic properties. Right: Wrinkle amplitude as a function of time for structures with the same elastic and different viscoelastic properties.

CONCLUSIONS

In this contribution, we show that viscoelastic properties of the material are crucially important for the final development of the pattern even though they seemingly affect only the transition period between the elastic short and long-time equilibrium states of the structure. The interaction between the viscoelastic material properties with the nonlinear kinematics produces interesting deformation patters otherwise unattainable for purely elastic systems. The theory and the principles described are also extremely useful in engineering applications because they allow much simpler fabrication of smart surfaces and coatings that at some point in fabrication behave viscoelasticity.

References

[1] D. A. Matoz-Fernandez, et al.: Wrinkle patterns in active viscoelastic thin sheets. Phys. Rev. Research 2(2020) p. 013165
[2] T. Ruiz-Herrero, et al.: Dynamics of Growth and Form in Prebiotic Vesicles Phys. Rev. Lett. 123(2019) p. 038102
[3] M. Nelson, et al.: Growth-induced buckling of an epithelial layer. Biomech. Model. Mechan. 10(2010) p. 883–900.
[4] D. Espeso, et al.: Differential growth of wrinkled biofilms. Phys. Rev. E, Stat. nonlin. soft matt. Phys. 91(2015) p. 022710
[5] R. de Rooij and E. Kuhl: Constitutive Modeling of Brain Tissue: Current Per-spectives. Appl. Mech. Rev. 68(2016) p. 010801

COMPETITION BETWEEN MULLINS AND CURVATURE EFFECTS IN THE WRINKLING OF STRETCHED SOFT SHELLS

Ting Wang, Yifan Yang, Chenbo Fu, and Fan Xu*
Institute of Mechanics and Computational Engineering, Department of Aeronautics and Astronautics, Fudan University, Shanghai, China

Summary A highly stretched hyperelastic shell experiences a coupled nonlinear behavior of local wrinkling and global bending within the stability boundary. Recently, we observed an interesting phenomenon that there are no wrinkles but global bending in the first loading for the stretched curved shell with certain curvature, while local wrinkling will appear in the first unloading process experimentally. Here, we investigate the effect of stress softening and residual strain, namely Mullins effect, in the cyclic loading process on this nonlinear response. To quantitatively explore the Mullins effect in the curved shell, we develop a pseudo-elastic shell model and our numerical results are consistent with the experimental phenomenon. Our findings reveal the competition between Mullins and curvature effects in the wrinkling behavior of a stretched shell.

INTRODUCTION

Recent research observed the inelastic behavior that there exists a permanent change in length of stretched sheets upon first loading experimentally, especially, a interesting Mullins effect was revealed in the cyclic loading process of stretched membrane [1]. Among many works established models to study the Mullins effect, Ogden and Roxburgh, Dorfmann and Ogden [2, 3] proposed a phenomenological model based on the theory of incompressible isotropic elasticity revised by incorporation of a damage parameter, which is a single continuous parameters, to account for the Mullins effect appearing in filled rubber elastomers. Based on the work of [2, 3], Feher *et al.* [1] developed a pseudo-elastic model to explain the longitudinal stress softening and residual strain occurring in the experiments of tensile membrane in the cyclic loading process. While their work is constraint to planar membrane. The mechanism and phenomenon of Mullins effect on the curved shell is under to be clarified.

This work experimentally and numerically investigates the Mullins effect in the cylindrical shell. We design an experiment of stretching cylindrical shells under cyclic loading. A pseudo-elastic shell model is established and numerical implementation through coupling *Asymptotic Numerical Method* (ANM) for nonlinear resolution and Chebyshev spectral collocation method for spatial discretization is adopted. The competition between Mullins and curvature effects in the instability behavior of a stretched shell is carefully examined.

PSEUDO-ELASTIC SHELL MODEL

Based on general differential geometry, the membrane strain tensor for cylindrical shell reads

$$E_{\alpha\beta} = \frac{1}{2}(u_{\alpha,\beta} + u_{\beta,\alpha} + 2wb_{\alpha\beta}) + \frac{1}{2}(u_{\gamma,\alpha}u_{\gamma,\beta} + u_{\gamma,\beta}wb_{\gamma\alpha} + u_{\gamma,\alpha}wb_{\gamma\beta} + wb_{\gamma\alpha}wb_{\gamma\beta}) + \frac{1}{2}w_{,\alpha}w_{,\beta}, \tag{1}$$

where Greek indices $\alpha, \beta, \ldots$ take values in $\{1, 2\}$, u_α denote the in-plane displacements, while w is the out-of-plane deflection. We employ Einstein's convention for implicit summation on repeated indices. The linearized bending strain tensor for cylindrical shell with finite curvatures reads

$$K_{\alpha\beta} = -w_{,\alpha\beta} + \frac{1}{2}\left(u_{\gamma,\alpha}b^{\gamma}_{\beta} + u_{\gamma,\beta}b^{\gamma}_{\alpha}\right) + wb_{\gamma\alpha}b^{\gamma}_{\beta}. \tag{2}$$

We consider pseudo-elastic model accounting for the stress-softening/residual strain [2, 3], the corresponding strain energy density function can be written as

$$\Psi = h\Psi_m(\mathbf{C}_s, \eta) + \Psi_b + h\Phi(\eta), \tag{3}$$

in which Ψ_m and Φ_b represent respectively the in-plane membrane strain energy density and volumetric bending energy density, η is a state variable with $\eta \leq 1$ and Φ is dissipation function, and $\mathbf{C}$ represents the right Cauchy-Green deformation tensor. The corresponding strain energy density function can be written as [1]

$$\Psi_m(\mathbf{C}_s, \eta) = p_1\left[\left((1+p_3)\,\eta - p_3\right)(C_{11} - 1) + \eta\,(C_{22} - 1) + \frac{1}{\det\mathbf{C}_s} - 1\right] + p_2\eta\left[\frac{\mathrm{tr}\mathbf{C}_s}{\det\mathbf{C}_s} + \det\mathbf{C}_s - 3\right], \tag{4}$$

where p_1 and p_2 are material constants, and $p_3 > 0$ is a fixed scalar parameter tuning the anisotropic damage ratio ($p_3 = 0$ corresponds to isotropic damage). When $\eta = 1$, the strain energy density function reduces to the Mooney-Rivlin (MR) model.

*Corresponding author. E-mail: fanxu@fudan.edu.cn.

RESULTS

For the hyperelastic stretched cylindrical shells, Wang *et al.*[4] has provided the 3D phase diagram (aspect ratio and curvature) of stability boundary. First, we consider the case with aspect ratio lower but close to the stability boundary and curvature is smaller than the critical value. Obviously, in the first loading process, there is no wrinkles but global bending when increasing stretching strain. After we stretch the shell to the maximum strain 0.66, the shell experiences the cyclic loading. Besides global bending is observed, the wrinkles will occur when the strain is unloaded to about 0.2 and the residual strain will appear. The evolutions of first loading and cyclic loading are displayed in Fig. 1, and the numerical phenomenon is consistent with the experimental results.

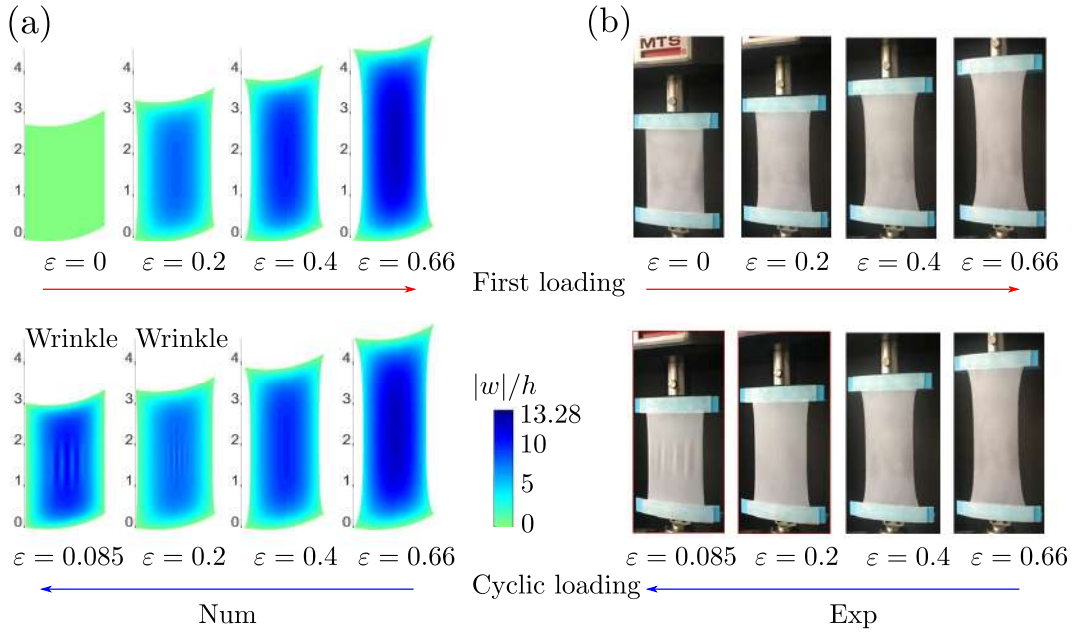

Figure 1: Evolutions in the first loading and cyclic loading process: (a) numerical results, (b) experimental results. The wrinkles will appear in the cyclic loading process. Geometric parameters: $W/h = 1600$, $L/W = 1.4$, $\kappa = 0.0002$.

CONCLUSIONS

we have experimentally and numerically revealed the Mullins effect in the cylindrical shell. For a curved shell with certain aspect ratio lower than the threshold or curvature larger than critical value, there is no wrinkles but global bending when increasing stretching strain, while in the unloading process, local wrinkling instability coupled with global bending is observed and residual strain occurs. We have established a pseudo-elastic shell model to quantitatively explore the Mullins effect in the curved shell. Our results clarified not only the inelastic behavior of the shells with cyclic loading but also the curvature effect on the response.

References

[1] Fehér, E., Healey, T.J., Sipos, A.A. The Mullins effect in the wrinkling behavior of highly stretched thin films. *J. Mech. Phys. Solids* **119**: 417–427, 2018.

[2] Ogden, R., Roxburgh, D. A pseudo-elastic model for the mullins effect in filled rubber. *Proc. R. Soc. A* **455**: 2861–2877, 1999.

[3] Dorfmann, A., Ogden, R. A constitutive model for the mullins effect with permanent set in particle-reinforced rubber. *Int. J. Solids Struct.* **41**: 1855–1878, 2004.

[4] Wang, T., Yang, Y., Fu, C., Liu, F., Wang, K., Xu, F. Wrinkling and smoothing of a soft shell. *J. Mech. Phys. Solids* **134**: 103738-1–103738-20, 2020.

STRUCTURAL STABILITY AND MECHANICAL PROPERTIES OF PRESSURE DEPENDENT PALLADIUM DIHYDRIDE

Zeliang Liu[1,2], Rajeev Ahuja[2,3], Wei Luo[2], and Huijian Li [*1]
[1]Key Laboratory of Mechanical Reliability for Heavy Equipments and Large Structures of Hebei Province, Yanshan University, Qinhuangdao, China
[2]Materials Theory Division, Department of Physics and Astronomy, Uppsala University, Uppsala, Sweden
[3]Applied Materials Physics, Department of Materials and Engineering, Royal Institute of Technology (KTH), Stockholm, Sweden

Summary The structural stability and mechanical properties of the potential structures of PdH_2 under pressure were studied based on the ab initio calculation. The Fm-3m phase is the most stable in thermodynamics at ambient pressure, and it is dynamically stable and mechanical stability. When the pressure up to 25.5 GPa, the structure transfer to mechanical instability. The P63mc phase is dynamic stability at pressures greater than 10 GPa. In the pressure range of 5.5-23.8 GPa, the P63mc phase is mechanical stability. When the pressure is greater than 75 GPa, the P63mc phase is the most thermodynamic stable. When PdH_2 is formed, it will decomposition into Pd and H_2. Therefore, the PdH_2 is a metastable structure under pressure. In addition, the single-crystal bulk modulus, shear modulus, Young's modulus, Poisson's ratio, and anisotropic properties of PdH_2 are obtained.

Results and discussions

Palladium hydrogen (Pd-H) system has been concerned since 1866, mainly due to large amount of hydrogen storage, reversible hydrogen absorption and desorption, and high superconducting transition temperature[1,2]. Previous studies focused on PdH_x ($x \leq 1$) with low hydrogen concentration. Theoretical and experimental studies on Pd-H structure with high hydrogen content show that the perfect stoichiometric palladium dihydride (PdH_2) structure cannot exist stably [3,4]. The calculation shows that PdH_2 will decompose rapidly into PdH and H_2 [5]. Although several PdH_2 structures, have been studied. However, the stability of PdH_2 is still an open question.

A crystalline structure is stable, in the absence of external load and in the harmonic approximation, if and only if (i) all its phonon modes have positive frequencies (dynamical stability), and (ii) the elastic energy, is always positive (Born stability criterion). The enthalpy differences and formation enthalpy are used to explain the favourable structure and reaction direction under pressure.

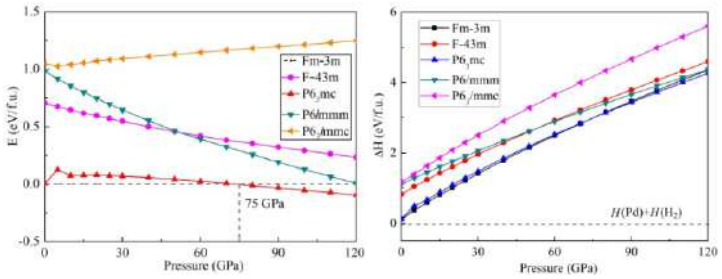

Figure 1. Thermodynamic stability: enthalpy difference and formation enthalpy.

The enthalpy differences for F-43m, P6/mmm, $P6_3/mmc$ structure is positive, indicating that these structures are unstable relative to the Fm-3m structure. It is noteworthy that the enthalpy difference between $P6_3mc$ and Fm-3m is negative when the pressure is greater than 75 GPa, indicating that $P6_3mc$ phase is more stable when the pressure is greater than 75 GPa. The formation enthalpy shows that all of the PdH_2 structures directly dissociate into Pd and H_2, and the higher the pressure, the easier the decomposition.

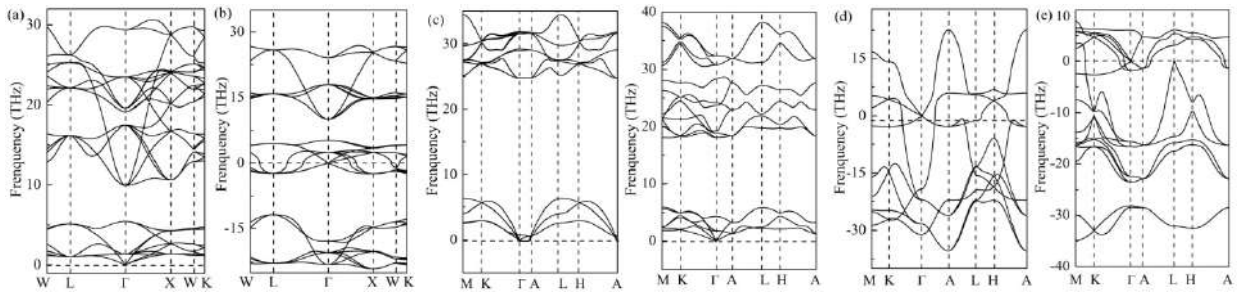

Figure 2 Dynamic stability: phonon dispersion (a) Fm-3m, (b) F-43m, (c) $P6_3mc$, (d) P6/mmm and (e) $P6_3/mmc$

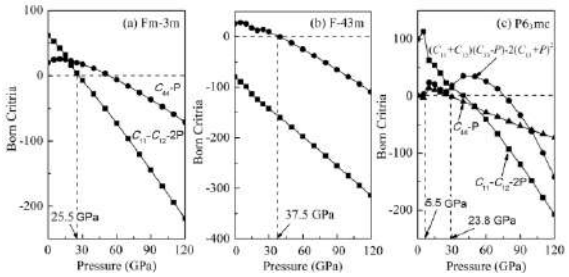

Figure 3. Mechanical stability: elastic constants

The inexistence of imaginary frequencies in phonon dispersion indicates the dynamic stability. The results show that Fm-3m phase is dynamic stable under environmental pressure. When the pressure increases to above 10 GPa, $P6_3mc$ phase is dynamic stable. The F-43m, $P6_3mc$, P6/mmm and P63/mmc phase are dynamic unstable under the environmental pressure. According to born stability criterion, when the pressure is less than 25.5 GPa, the Fm-3m phase is mechanically stable. In the pressure range of 5.5-23.8 GPa, the $P6_3mc$ phase is mechanically stable.

The elastic properties of Fm-3m and $P6_3mc$ phase PdH_2 are listed in table 1. The bulk modulus and Young's modulus increases with the increase of pressure. With the increase of pressure, the shear modulus increases little, and the Poisson's ratio remains about 0.42. Pugh ratio B/G is greater than 1.75, the material is generally ductile, otherwise it is brittle. The results show that the Fm-3m PdH_2 exhibits good ductility. The $P6_3mc$ PdH_2 shows ductility when the pressure up to 5 GPa, and with the increase of pressure, the ductility increases.

Table 1 The elastic properties of Fm-3m and $P6_3mc$ phase PdH_2

	Fm-3m					$P6_3mc$				
P (GPa)	*B* (GPa)	*G* (GPa)	*B*/*G*	*E* (GPa)	*v*	*B* (GPa)	*G* (GPa)	*B*/*G*	*E* (GPa)	*v*
0	150.9	24.2	6.2	68.9	0.42	30.5	19.2	1.6	47.6	0.24
5	169.6	30.3	5.6	85.8	0.42	63.8	18.6	3.4	50.9	0.37
10	186.3	33.9	5.5	95.9	0.41	155.5	32.1	4.8	90.0	0.40
15	202.6	36.2	5.6	102.4	0.42	172.6	33.4	5.2	94.1	0.41
20	215.9	35.9	6.0	102.1	0.42	187.3	32.6	5.8	92.3	0.42
25	230.6	36.8	6.3	104.7	0.42	202.1	32.0	6.3	91.3	0.42
30	245.5	37.7	6.5	107.6	0.43	221.4	35.0	6.3	99.8	0.42

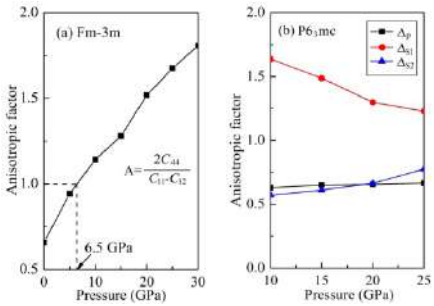

Figure 4. The anisotropic factor of Fm-3m phase and F-43m P63mc phase PdH_2 as a function of pressure

The anisotropy factor equal to 1, that is, the material is isotropic. For Fm-3m phase, PdH_2 is isotropic at 6.5 GPa. The farther the pressure is away from 6.5 GPa, the stronger the anisotropy is. For $P6_3mc$ phase, the anisotropy factors deviate from 1, indicating that PdH_2 is anisotropic. It should be noted that the pressure leads to a decrease in anisotropy.

CONCLUSIONS

Based on the density functional theory, the potential stable structure of PdH_2 is studied by the first principle theory. The thermodynamic stability, dynamic stability and mechanical stability under different structural pressures were calculated. The results indicate that PdH_2 is metastable under pressure. The elastic properties of Fm-3m and $P6_3mc$ PdH_2 under pressure are also reported, including bulk modulus, shear modulus, Young's modulus, Poisson's ratio and anisotropic properties.

References

[1] Graham T. On the relation of hydrogen to palladium[J]. *Proceedings of the Royal Society of London*, **17**: 212-220, 1869.
[2] Kawae T., Inagaki Y., Wen S. Superconductivity in Palladium Hydride Systems. *J. Phys. Soc. Jpn.* **89**, 051004, 2020.
[3] Wei S. H., Zunger A. Stability of atomic and diatomic hydrogen in fcc palladium. *Solid State Commun*. **73**: 327-330, 1990.
[4] Kuzovnikov M. A., Tkacz M. Dihydride formation in the palladium-rhodium alloys under high hydrogen pressure. *Int. J. Hydrogen Energ.* **42**: 340-346, 2017.
[5] Yang X, Li H, Ahuja R, et al. Formation and electronic properties of palladium hydrides and palladium-rhodium dihydride alloys under pressure. *Sci. Rep.* **7**: 3520, 2017.

A NOVEL BIFURCATING FORCE-LIMITING ELASTIC STRUCTURE

P. Koutsogiannakis*[1], F. Dal Corso[1], and D. Bigoni[1]
[1]Department of Civil, Environmental and Mechanical Engineering, University of Trento, Trento, Italy

Summary Force limiters have a wide range of uses, from car industry to medical fields. In the present work, a novel force-limiting mechanism is introduced, based on the instability related to a buckling elastic element. When the load applied to one end of the structure surpasses a critical value, the elastic element buckles and the mechanism is unlocked. By constraining the tip of the elastic element to move on a predefined curve, the response of the system can be controlled. The shape of the constraint curve can be optimized for specified behaviours by an optimization loop. The design can define a zone of greatly increased reaction forces at large deflections, providing a smooth transition towards the maximum allowable displacement.

Force limiting mechanisms find application in industrial problems. They are used where precise force control is critical, such as in medical tools, or where limiting loads is crucial to protect structures or humans from harm, like in the case of belt retractors, car seat belts, and seismic isolation devices. Various operational principles are deployed for different designs. These include the constricted displacement of air and the yielding of energy absorption elements.

In the present work, it is shown how a force limiting mechanism can be realized by exploiting buckling elastic elements. The proposed system consists of an elastic element connected to a moving clamp on one end and constrained to slide along a curve on the other end; see Fig. 1. The shape of the constraint curve can be selected so that the desired behavior of the device is achieved [1, 2]. Here this concept is used for producing force-limiting effects. More specifically, the elastic element remains straight until the external applied force surpasses a critical buckling value. This critical load depends on the curvature of the constraint curve at the position corresponding to the initial configuration. The resulting design is simpler than current commercial systems. In order to retain simplicity, a helicoidal spring is used as the elastic element, meaning that there will be a slight displacement before buckling happens. This effect is desirable as it can introduce tolerance for slight movements that should not activate the device. To the authors' knowledge no published studies on this concept can be found.

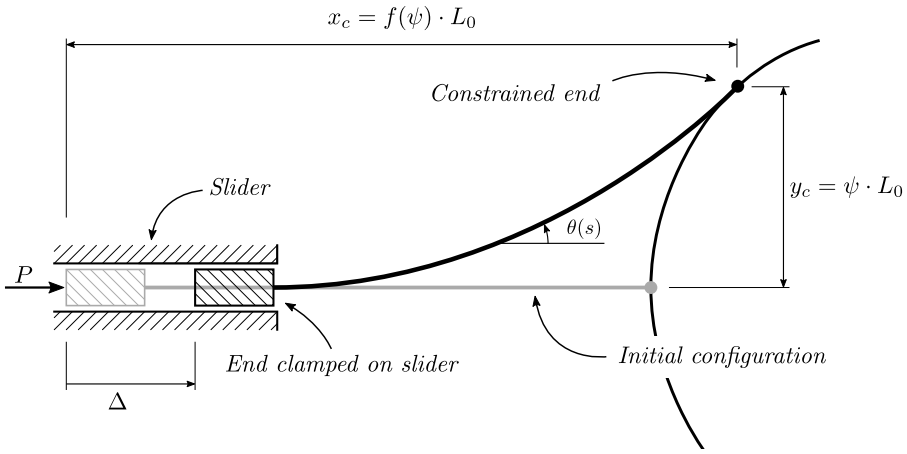

Figure 1: Drawing of the proposed design. The elastic element is connected to a movable clamp on one end, while at the other end is constrained to move along a predefined curve. In the undeformed configuration the slider remains locked until the load P exceeds a critical value.

For the fast and effective calculation of the response of the system, the spring is approximated by an elastic rod with bending stiffness B and axial stiffness K. These stiffnesses can be related to the parameters of the spring as follows

$$B = \frac{4L_0 EIG}{n\pi D(2G+E)}\,, \qquad K = \frac{Gd^4 L_0}{8D^3 n} \tag{1}$$

where L_0 is the free length of the spring, d the wire diameter, D the mean coil diameter, n the number of coils, G the shear modulus, E Young's modulus and EI the flexural rigidity of the wire cross section. The deformation of the spring is defined by the rotation $\theta(s)$ and the displacement $\delta(s)$, being $s \in [0, L_0]$ the curvilinear coordinate along the undeformed spring.

The shape of the constraint curve (in non-dimensional form) is considered to be represented by the even polynomial

$$f(\psi) = 1 + \frac{1}{2}\psi^2\, f''(0) \;+\; \sum_{i=0}^{n} c_i\, \frac{1}{(2i+1)(2i+2)}\, \psi^{2i+2} \tag{2}$$

*Corresponding author. E-mail: p.koutsogiannakis@unitn.it

where $\psi = \int_0^{L_0} \sin(\theta(s))ds$ is the vertical deflection of the elastic rod at the constrained tip. Considering function f given by eq. (2) ensures a null slope at the origin, $f(\psi = 0) = 0$, and a symmetric constraint curve, $f(-\psi) = f(\psi)$.

Assuming quasi-static conditions, the total potential energy of the system is

$$\mathcal{V} = \frac{1}{2}\int_0^{L_0} B\,(\theta'(s))^2\ ds\ +\ \frac{1}{2}\int_0^{L_0} K\,\delta^2(s)\ ds\ +\ P\,\Delta\,, \tag{3}$$

where Δ is the displacement of the movable clamped end, depending on the rotation $\theta(s)$ and the displacement $\delta(s)$ fields and the constraint curve shape $f(\psi)$. In this way, an extra equation can be derived that enforces the constraint on the elastic rod. The deformed shape of the spring will then be given by the configuration that minimizes the energy $\mathcal{V}$ of the system.

For the purposes of this work, the elastic element is modeled numerically by discrete springs, following the Discrete Element Method. An additional constraint is added to the resulting nonlinear system of equations to impose a specified displacement Δ. Then by varying the parameter Δ we can calculate the load P as a reaction force. Additionally, an outer optimization loop is used in order to adapt the response of the system to a reference Force-Displacement curve; see Fig. 2 (Left).

Finally, a smooth transition to a maximum allowable displacement can be achieved by introducing an additional term to the previous constraint shape,

$$f(\psi) = 1 + \frac{1}{2}\psi^2\ f''(0)\ +\ \sum_{i=0}^{n} c_i\ \frac{1}{(2i+1)(2i+2)}\ \psi^{2i+2} + f_a(\psi), \tag{4}$$

which has an effect only at deflection ψ greater in modulus than a specified value α as follows

$$f_a(\psi) = \begin{cases} 0, & \psi < |\alpha|, \\ c_a \cdot \left[\frac{1}{6}|\psi|^3 - \frac{\alpha}{2}\psi^2 + \frac{\alpha^2}{2}|\psi| - \frac{\alpha^3}{6}\right], & \psi \geq |\alpha|, \end{cases} \tag{5}$$

and preserves continuity of the second derivative of the constraint curve. By controlling this additional term $f_a(\psi)$, a zone can be designed, where the reaction force P gradually increases to values that are multiple times larger than the bifurcation load; see Fig. 2 (Right). Provided that the load P remains within a range of values close to the critical load, a maximum displacement exists. This property provides a 'cushioning effect' in the case that a maximum allowable displacement has to be imposed by external design constraints.

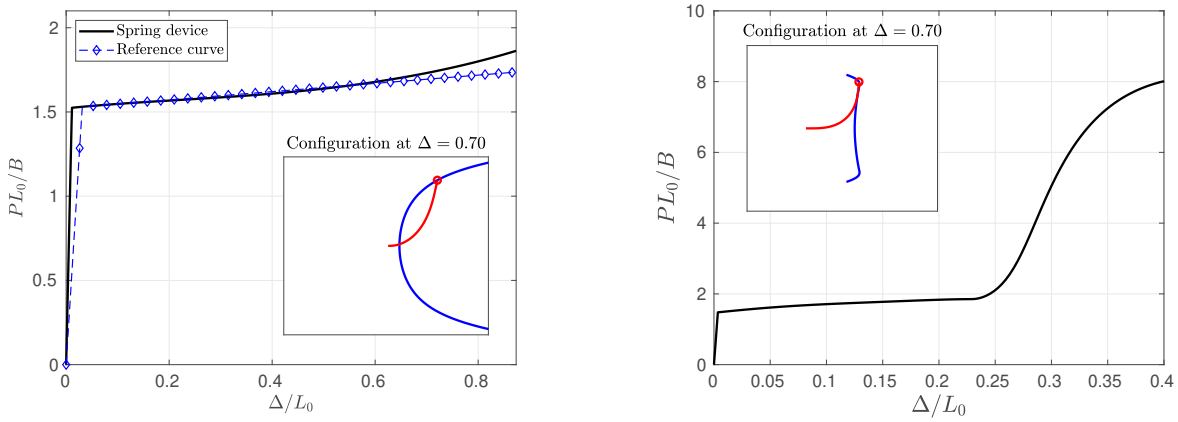

Figure 2: (Left) Force-Displacement curve of the proposed system adapted to a reference one by optimizing the constraint curve shape. The reference curve specifies a critical load and a small slope in order to keep the overall stiffness of the device positive at all displacements. (Right) Force-Displacement curve of the proposed system showcasing a secondary "locking" zone.

Acknowledgments. PK, FDC and DB gratefully acknowledge financial support from the European Union's Horizon2020 research and innovation programme under the Marie Sklodowska-Curie grant agreement 'INSPIRE - Innovative ground interface concepts for structure protection' PITN-GA-2019-813424-INSPIRE.

References

[1] Bigoni D., Misseroni D., Noselli G., Zaccaria D. Effects of the constraint's curvature on structural instability: tensile buckling and multiple bifurcations. *Proceedings of the Royal Society A: Mathematical, Physical and Engineering Sciences*, **468**, 2191-2209, 2012.

[2] Misseroni D., Noselli G., Zaccaria D., Bigoni D. The deformation of an elastic rod with a clamp sliding along a smooth and curved profile. *International Journal of Solids and Structures*, **69**, 491-497, 2015.

[3] Wahl A. M. Mechanical Springs. McGraw Hill, NY 1944.

TENSILE BUCKLING AND POSTBUCKLING BEHAVIOUR OF TRIANGULAR STRUCTURAL ELEMENTS UNDER DEAD LOADS

Nikolin Hima*[1], Francesco Dal Corso [1], and Davide Bigoni [1]
[1]Department of Civil, Environmental and Mechanical Engineering, University of Trento, Trento, Italy

Summary An elementary triangular frame structure comprised of rigid bars, a rotational spring, and a slider, is investigated under vertical and horizontal loading conditions. The slider in one of the bars of this structure enables for tensile bifurcation of the corresponding substructure element to occur. The overall mechanical response of the structure shows that it remains undeformed until a certain critical horizontal load is attained and the post-critical behaviour can be tuned to develop horizontal displacement without significant increase in load, until eventually locking occurs. The behaviour of this structure is driven by its base angles and the vertical load applied on it. The present work paves the way towards the design of a new generation of seismic isolators which provide protection for frequent seismic events without compromising the overall stability of the structure.

By implementing a slider in the middle of a bar (a slider is a device that imposes the same rotations angles and axial displacements to the connected parts, vanishing the shear force, and allowing only a relative sliding), Bigoni et. al. [1,2] have shown that bifurcation under tensile dead loading can occur. The present work makes use of this elementary device by incorporating it in a simple structure which is comprised of rigid bars connected to each other with hinges in a triangular shape. In the lower right node of this triangular truss-like structure a rotational spring is incorporated, and the bar in front of it is divided into two equal parts with a slider, as reported in Figure 1-a.

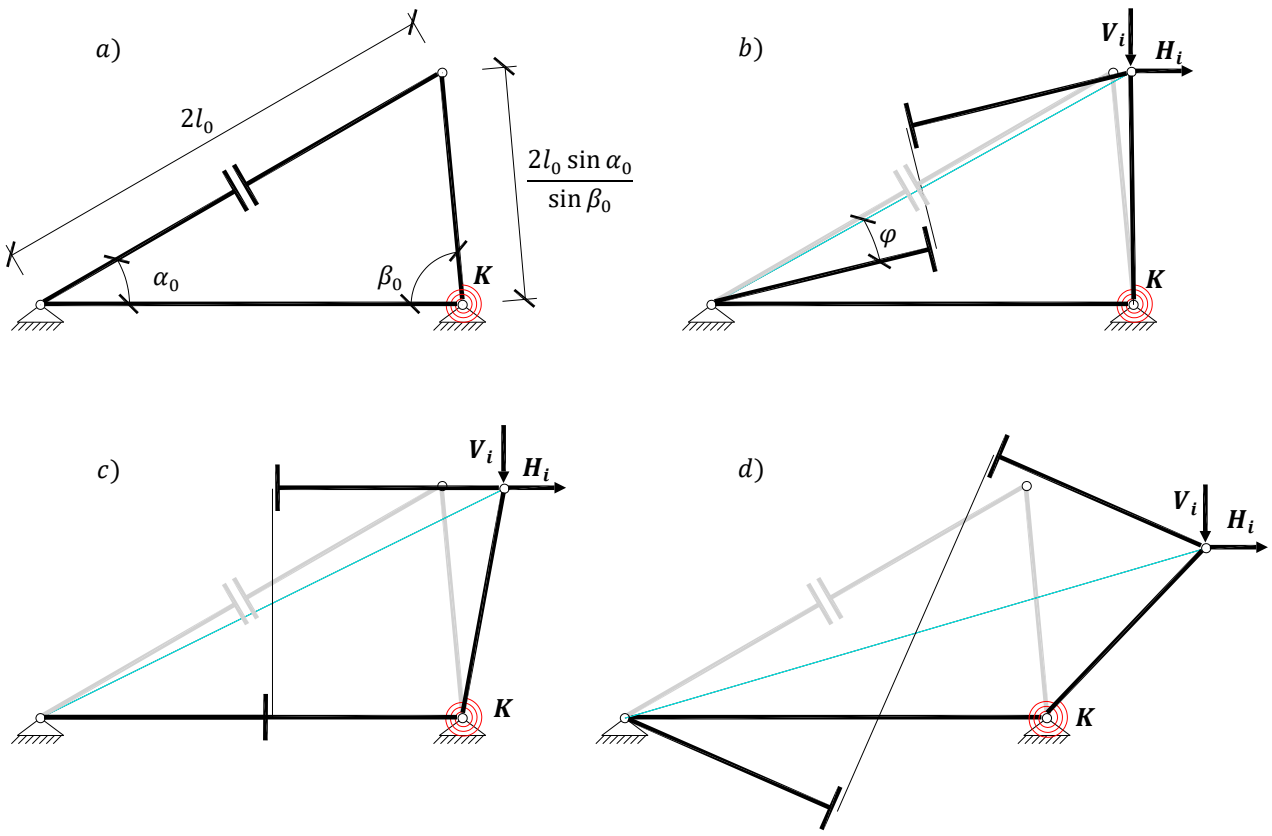

Figure 1: a) Undeformed triangular structure comprised of rigid bars connected with hinges, a rotational spring in the lower right node and a slider incorporated in the middles of the bar in front of the rotational spring. b) c) and d) Deformed configurations of the structure under vertical and horizontal loadings at the bifurcation angle $\varphi = \{15, 26, 40\}°$.

Theoretical formulation predicts that for a given vertical load (V) acting on the top node of the structure and a certain rotational stiffness (K) at the right lower node, the horizontal load applied at the top node, when large enough, can move the system towards the right, as reported in Figure 1-b. The movement occurs because the bar containing the slider, changes from a compressive (H=0) to a tensile state (for H=H_{crc}), so that the structure bifurcates, allowing the two parts of the bar to rotate with respect to one another (bifurcation angle φ). The structure develops the kinematics as reported in Figure 1-b,c,d.

*Corresponding author. E-mail: **nikolin.hima@unitn.it**

The mechanical response of the analysed structure depends on the initial angles between the bars at the base and on the vertical load. More specifically, the critical horizontal load necessary to bifurcation, is a function of the vertical load and the right base angle of the structure, $H_{i,crc} = V_i \cot \beta_0$. Moreover, the post buckling behaviour of the structure is also highly influenced by these parameters. Depending on the vertical load and the base angles the structure can return a force displacement curve that can range from softening to a flat and/or hardening curve, until eventually locking occurs. Through the rotational spring stiffness K and the reference bar half-length l_0, dimensionless horizontal and vertical forces can be introduced as:

$$H_i = \frac{H l_0}{K} \qquad V_i = \frac{V l_0}{K}$$

and the theoretical prediction for the dimensionless horizontal force – horizontal displacement curve is depicted in Figure 2 for initial base angles $\alpha_0 = 30°$ and $\beta_0 = 85°$ and vertical load $V_i = 1$ (so that $V_i/H_{i,crc} = \tan \beta_0 = 11.34$).

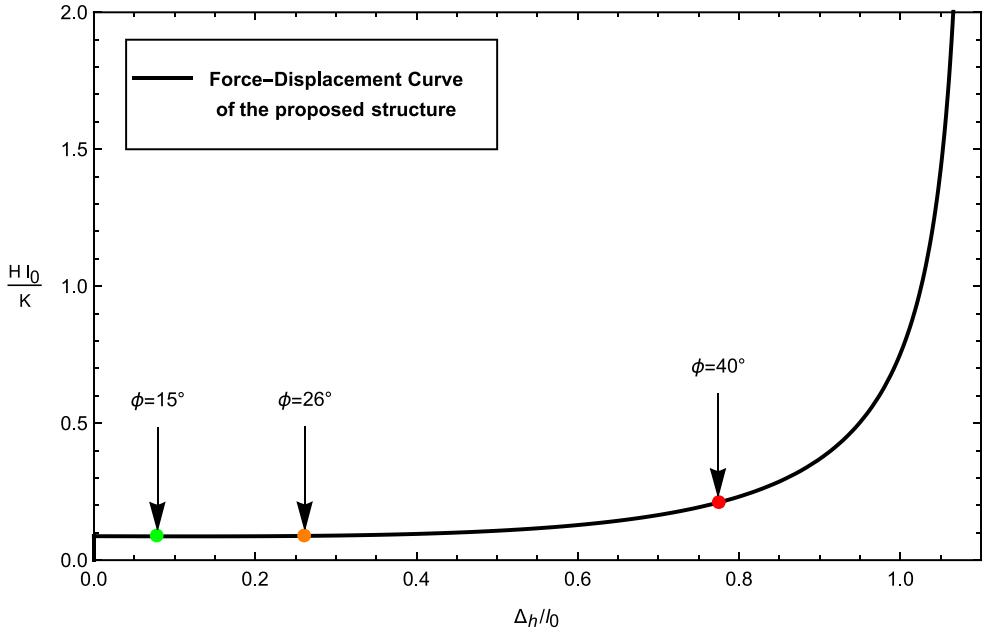

Figure 2: Dimensionless horizontal force-horizontal displacement curve for initial base angles $\alpha_0 = 30° \,\&\, \beta_0 = 85°$ and dimensionless vertical load $V_i = 1$. Force-displacement pairs corresponding to bifurcation angles $\varphi = \{15°, 26°, 40°\}$ displayed in Fig. 1 are highlighted.

The present work paves the way towards a new generation of seismic isolators which can self-activate and provide protection for frequent seismic events, without compromising the overall stability of the structure, and remaining rigid when exposed to other accidental loads such as wind or small impacts.

Acknowledgments. The authors gratefully acknowledge financial support from the European Union's Horizon2020 research and innovation programme under the Marie Sklodowska-Curie grant agreement 'INSPIRE – Innovative ground interface concepts for structure protection' PITN-GA-2019-813424-INSPIRE.

References

[1] Bigoni D., Bosi F., Misseroni D., Dal Corso F., Noselli G. (2015) New phenomena in nonlinear elastic structures: from tensile buckling to configurational forces. In: Bigoni D. (eds) Extremely Deformable Structures. CISM International Centre for Mechanical Sciences, vol 562. Springer, Vienna. https://doi.org/10.1007/978-3-7091-1877-1_2

[2] D. Zaccaria, D. Bigoni, G. Noselli, and D. Misseroni, "Structures buckling under tensile dead load," Proc. R. Soc. A Math. Phys. Eng. Sci., vol. 467, no. 2130, pp. 1686–1700, 2011, doi: 10.1098/rspa.2010.0505.

STRAIN GRADIENT PLASTICITY SIMULATION OF STRAIN LOCALIZATION AT LARGE STRAINS

Jean–Michel Scherer[1,2], Samuel Forest*[1], Jacques Besson[1], Jeremy Hure[2], and Benoit Tanguy[2]
[1]MINES Paris Tech,PSL University,Centre des matériaux,CNRSUMR7633,BP8791003 Evry,France
[2]DEN-Service d'Etudes des Matériaux Irradiés,CEA,Université Paris-Saclay,F-91191, Gif-sur-Yvette,France

Summary A micromorphic crystal plasticity model is used to simulate slip band localization in single crystals under simple shear at finite deformations. Closed form analytical solutions are derived for single slip in the case of positive, zero and negative strain hardening. Linear negative strain hardening, i.e. linear softening, leads to a constant localization slip bandwidth, while non linear softening and saturating behaviour results in an increasing bandwidth. An enhanced model is therefore proposed in order to maintain a bounded localization slip band-width when considering an exponential softening behaviour. Analytical solutions are used to validate finite element computation of the same boundary value problems. The enhanced micromorphic crystal plasticity model is then applied to predict the interaction between localized slip bands and voids encountered in porous irradiated materials. For that purpose, periodic porous unit cells are loaded in simple shear with a strain gradient crystal plasticity matrix material. The finite element simulation results show that, for a given void volume fraction, the larger the voids, the wider the localization band. However, for a given void size, the larger the void volume fraction, the narrower the localization band. In addition a satisfactory qualitative agreement of the rotation and elongation of the voids with the experimental observations made in irradiated materials is observed, where small voids are shown to remain ellipsoidal for larger shear strains. Large voids deform into peanut-like shapes.

REDUCED MICROMORPHIC MODEL

This work investigates the responses given in single slip for a strip in simple shear by a recently developed micromorphic crystal plasticity model [1, 2, 6]. It is used to simulate slip band localization in single crystals under simple shear at finite deformations. It is formulated at finite deformations as an extension of Mandel's classical theory based on a multiplicative decomposition of the deformation gradient. It involves a single microslip degree of freedom in addition to the usual displacement components. Two main variants of the constitutive equations were proposed. The first one relies on a Lagrangian microslip gradient and leads to a Laplace term in the isotropic hardening law. In contrast, the second formulation, based on a generalized strain measure defined with respect to the intermediate configuration, is shown to induce both isotropic and kinematic enhanced hardening. The first formulation is implemented in a 3D finite element code. The model is applied first to strain localization phenomena in a single crystal in tension undergoing single slip. The regularization power of the model is illustrated by mesh-independent simulations of the competition between kink and slip bands [4].

CONTROLLING SHEAR BAND WIDTH AT LARGE STRAINS

Closed form analytic solutions are derived for single slip in the case of positive, zero and negative strain hardening. Linear negative strain hardening, i.e. linear softening, leads to a constant localization slip band width, while non linear softening and saturating behavior results in an increasing band width. An enhanced model is therefore proposed in order to maintain a bounded localization slip band width when considering an exponential softening behavior. Analytic solutions are used to validate finite element computation of the same boundary value problems.

APPLICATION TO SHEAR BAND–VOID INTERACTION

The enhanced micromorphic crystal plasticity model is then applied to predict the interaction between localized slip bands and voids encountered in porous irradiated materials [3]. For that purpose, periodic porous unit cells are loaded in simple shear with a strain gradient crystal plasticity matrix material. Then the mechanism of dislocation channel deformation observed in irradiated steels and its interaction with voids is studied on a numerical perspective. The enhanced model is used to simulate the interaction of voids and localization bands in a softening material. Periodic perforated plate and cubic unit-cells are loaded in simple shear for different void content and characteristic length scales versus void radius ratios. The finite element simulation results show that, for a given void volume fraction, the larger the voids, the wider the localization band. However, for a given void size, the larger the void volume fraction, the narrower the localization band. In addition a satisfactory qualitative agreement of the rotation and elongation of the voids with the experimental observations made in irradiated materials is observed, where small voids are shown to remain ellipsoidal for larger shear strains. Large voids deform into peanut-like shapes [5].

*Corresponding author. E-mail: samuel.forest@mines-paristech.fr.

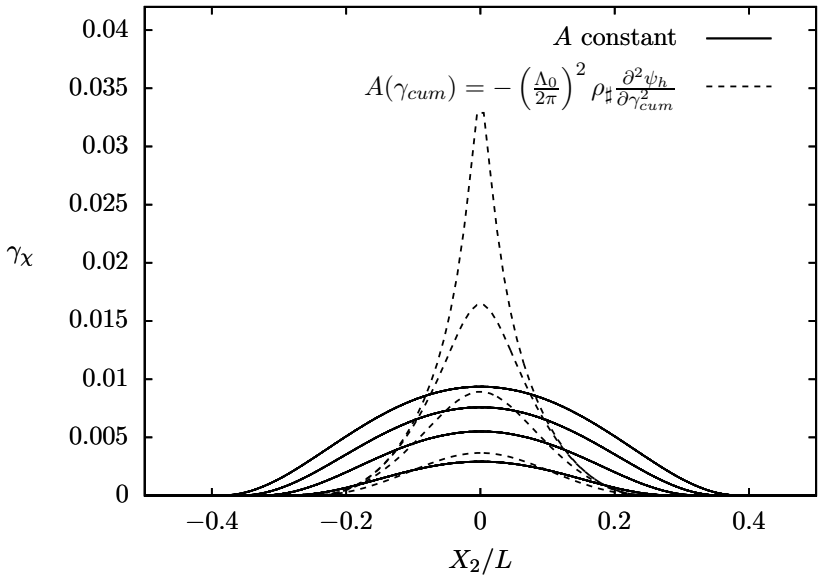

Figure 1: Finite element solutions of differential equation governing γ_χ for constant A displaying localization bandwidth widening (solid line) and for $A(\gamma_{cum}$ inducing a bounded localization bandwidth (dashed line), after [5].

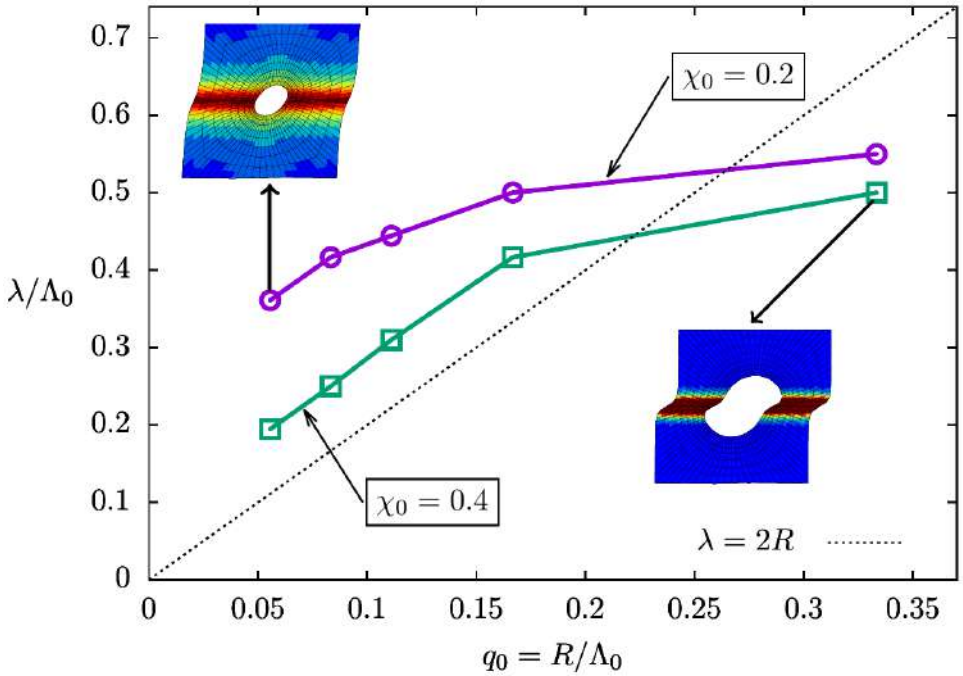

Figure 2: . Normalized localization slip bandwidth λ as a function of q_0 for two different void volume fractions at the overall shear value $\bar{F}_{12} = 0.025$. Insets correspond to snapshots at $\bar{F}_{12} = 0.15$, after [5].

References

[1] Forest S., Nonlinear regularization operators as derived from the micromorphic approach to gradient elasticity, viscoplasticity and damage. *Proc. R. Soc. A* 472:20150755, 2016.

[2] Ling, C., Forest, S., Besson, J., Tanguy, B. and Latourte, F. A reduced micromorphic single crystal plasticity model at finite deformations. Application to strain localization and void growth in ductile metals. *International Journal of Solids and Structures*, 134:43–69, 2018.

[3] Ling C., Besson J., Forest S., Tanguy B., Latourte F., Bosso E., An elastoviscoplastic model for porous single crystals at finite strains and its assessment based on unit cell simulations, *International Journal of Plasticity* 84:58-87, 2016.

[4] Marano, A., Gélébart, L. Forest, S. Intragranular localization induced by softening crystal plasticity: Analysis of slip and kink bands localization modes from high resolution FFT-simulations results. *Acta Materialia*, 15:262–275, 2019.

[5] Scherer, J. M., Besson, J., Forest, S., Hure, J., and Tanguy, B. Strain gradient crystal plasticity with evolving length scale: Application to voided irradiated materials. *European Journal of Mechanics - A/Solids*, 77:103768, 2019.

[6] Scherer J. M., Phalke V., Besson J., Forest S., Hure J. and Tanguy B.. Lagrange multiplier based vs micromorphic gradient-enhanced rate-(in)dependent crystal plasticity modelling and simulation. *Computer Methods in Applied Mechanics and Engineering*, page 113426, 2020.

K108980 - SM15 - Computational Solid Mechanics - Keynote

A MICROMORPHIC COMPUTATIONAL HOMOGENIZATION FRAMEWORK FOR PREDICTING MICRO AND MACRO BUCKLING OF MECHANICAL METAMATERIALS

Ondřej Rokoš[1,2], Sylviavan Bree[1], Martin Doškář[2], Ron Peerlings*[1], and Marc Geers[1]
[1]Department of Mechanical Engineering, Eindhoven University of Technology, Eindhoven, Netherlands
[2]Faculty of Civil Engineering, Czech Technical University in Prague, Prague, Czech Republic

Summary Mechanical metamaterials generally exhibit their unusual mechanical response by virtue of a coordinated local buckling of their microstructure. Capturing this behaviour in a mean sense presents a challenging problem for (computational) homogenization methods – particularly if the structural dimensions are such that the structure may also buckle globally. In this paper we develop a methodology which meets this challenge. It employs dedicated fluctuation functions which represent the potential local buckling patterns. The amplitudes of these patterns appear as micromorphic fields which need to be solved for at the macroscale – together with the conventional mean deformation. When solved by a full Newton solver, the resulting governing equations can capture local buckling, global buckling, as well as their interaction.

INTRODUCTION

Mechanical metamaterials feature engineered microstructures designed to exhibit exotic, and often counter-intuitive, effective behaviour such as negative Poisson's ratio or negative compressibility. Such a specific response is often achieved through instability-induced transformations of the underlying periodic microstructure into one or multiple patterning modes [1]. Due to a strong kinematic coupling of individual repeating microstructural cells, non-local behaviour and size effects emerge, which cannot easily be captured by classical homogenization schemes. In addition, the individual patterning modes can mutually interact in space as well as in time, while at the engineering scale the entire structure can buckle globally. For efficient numerical predictions of macroscale engineering applications, a micromorphic computational homogenization scheme has recently been developed by Rokoš et al. [2]. In follow-up work, a full Newton solver has been developed for the methodology, including derivations of the tangent operators at the microscale, macroscale and linking the two scales. The Newton solver renders simulations more efficient by ensuring quadratic convergence. But perhaps more importantly, the availability of the tangents allows one to perform a proper bifurcation analysis – at the macroscale as well as at the microscale – and in fact at both levels simultaneously when this is relevant.

In this contribution we demonstrate the performance of the developed methodology by a number of examples in which a competition between local and global buckling exists or where multiple patterning modes (local buckling modes) emerge.

METHODOLOGY

The micromorphic homogenization framework which we employ is founded on the following Ansatz for the full-scale displacement field $\vec{u}$:

$$\vec{u} = \vec{v}_0 + \sum_{i=1}^{n} v_i \vec{\varphi}_i + \vec{w} \tag{1}$$

where $\vec{v}_0$ and v_i, $i = 1, 2, \ldots, n$ vary slowly in space, i.e. at the scale of the macroscopic structure, whereas $\vec{\varphi}$ and $\vec{w}$ are rapidly fluctuating, at the scale of the metamaterial's microstructure. $\vec{v}_0$ represents the mean displacement, which one usually aims to capture by homogenisation. The fluctuation functions $\vec{\varphi}$ represent characteristic modes of deformation, or patterns, which the microstructure exhibits – typically the periodic local buckling modes which underly the metamaterial's particular response. They are defined either as analytical estimates or computed numerically in an off-line buckling analysis on a periodic cell. In either case, for the homogenisation they are known functions. It is the presence of these modes, and the terms in which they appear in (1), which renders the framework nonlocal and allows it to capture the interaction between adjacent microstructural cells. The fluctuation functions $\vec{\varphi}_i$ are modulated by the smooth amplitude functions v_i, which hence indicate how 'active' the individual modes are in the neighbourhood of a particular point of the (macro-)structure. $\vec{w}$, finally, is a remainder term which captures local features of the solution at the microscale. It is computed, as in conventional computational homogenization, on a periodic cell which is subjected to the average response as dictate by the other terms of expression (1).

The governing equations are established by formulating the total potential energy as a functional of $\vec{u}$, substituting the Ansatz (1) and minimizing with respect to $\vec{v}_0$, v_i and $\vec{w}$ (remember that $\vec{\varphi}$ are known functions). Minimizing with respect to $\vec{v}_0$ results in the conventional homogenized equilibrium equation, in which the stress however depends not only on the gradient of $\vec{v}_0$, but also on the amplitude functions v_i and their gradients, as well as $\vec{w}$. The minimization with respect to v_i, where $i = 1, 2, \ldots, n$, results in n additional, micromorphic equilibrium equations in terms of non-standard stresses. The minimization with respect to $\vec{w}$, finally, gives rise to microscale problems on a periodic cell attached to each macroscopic point. For details on these equations and their numerical implementation, we refer to Reference [2] and a forthcoming publication on the formulation of the Newton solver.

*Corresponding author. E-mail: r.h.j.peerlings@tue.nl.

EXAMPLE

An example of the results obtained with the framework, using the novel Newton solver, is shown in Figure 1. A rectangular domain of dimensions $W \times H$ is considered, where W and H are both multiples of the unit cell size l. It is loaded by a vertical compressive strain. The microstructure considered consists of an elastomer with a periodic array of circular holes in a square stacking. Under compressive loading, this arrangement is known to result in a periodic local buckling pattern in which the 'islands' between the holes alternatingly rotate clockwise and anti-clockwise. As a result, the incremental stiffness of the material is reduced drastically compared with its initial, unbuckled stiffness, cf. Reference [1].

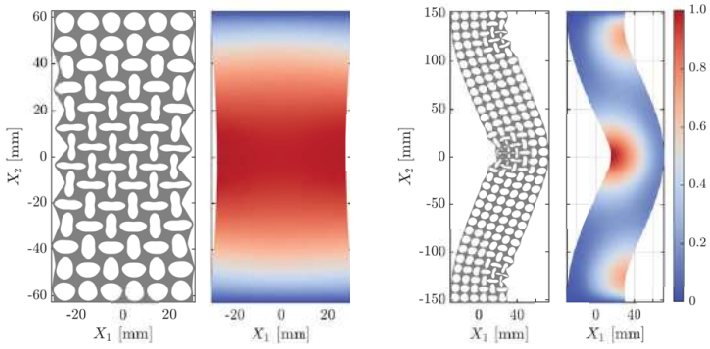

(a) DNS, $6\ell \times 14\ell$ (b) MM, $6\ell \times 14\ell$ (c) DNS, $6\ell \times 34\ell$ (d) MM, $6\ell \times 34\ell$

Figure 1: Comparison of the deformed shapes obtained from Direct Numerical Simulations (DNS) and from the micromorphic (MM) computational homogenization scheme. (a) DNS and (b) MM results for a $6l \times 14l$ specimen. (c) DNS and (d) MM results for a $6l \times 34l$ specimen. Local buckling emerges in (a) and (b), whereas global buckling occurs in (c) and (d). The colour in the MM plots indicates the magnitude of the v_1 field normalized by its extreme value. The results are shown for the overall applied strain $u/H = 0.1$.

Figures 1(a) and (c) show full-scale Direct Numerical Simulations (DNS) of the problem for two different aspect ratios H/W. For the smaller ratio, in Figure 1(a), we indeed observe the anticipated periodic local buckling pattern – except for boundary layers along the top and bottom boundaries of the domain, which are restricted in adopting the local buckling pattern by the kinematic boundary conditions along them. Notice also the auxetic effect, which is visible as a horizontal contraction of the sample at mid-height under vertical compression. Figure 1(c) shows that for a larger aspect ratio, i.e. a more slender sample, a global buckling deformation may be obtained which is similar to classical Euler beam buckling. In regions which are under compression, however, also some local buckling (patterning) is observed.

The predictions of the micromorphic computational homogenization framework for the two cases considered are shown in Figures 1(b) and (d), in which the mean deformation $\vec{v}_0$ is visualized by means of the deformed shape of the sample, and the amplitude of the local buckling mode v_1 by the color code. For both aspect ratios the homogenized solutions pick up the main features of the DNS. For the low aspect ratio, Figure 1(b) shows activation of the pattern (given by v_1) in most of the sample, except for two boundary layers at the top and bottom. The auxetic effect is also visible in the mean deformation. And for the slender beam, in Figure 1(d), global buckling is predicted into a mode which is not unlike that of the DNS, while local buckling is also predicted in the correct regions of the beam.

CONCLUDING REMARKS

A more extensive numerical study of the above example, not shown here, indicates that the micromorphic homogenization predicts the local to global buckling transition 4% of relative error in terms of the applied strain. Simulations of a microstructure with hexagonally stacked holes, for which three distinct patterns may be activated, show that the expected pattern combinations are triggered. The revised methodology employing the full Newton solver thus presents a powerful tool for the analysis and design of structures made of mechanical metamaterials.

References

[1] Bertoldi K., Boyce M. C., Deschanel S., Prange S. M., Mullin T. Mechanics of deformation-triggered pattern transformations and superelastic behavior in periodic elastomeric structures. *Journal of the Mechanics and Physics of Solids* **56**:2642–2668, 2008.

[2] Rokoš O., Ameen M. M., Peerlings R. H. J., Geers M. G. D. Micromorphic computational homogenization for mechanical metamaterials with patterning fluctuation fields. *Journal of the Mechanics and Physics of Solids* **123**:119–137, 2019.

A GRAPH THEORETIC FRAMEWORK FOR REPRESENTATION, EXPLORATION AND ANALYSIS ON COMPUTED SATES OF PHYSICAL SYSTEMS

Matthew Duschenes[1], Elizabeth Livingston[2], Gregory H. Teichert[2], Arjun Sundararajan[2], Xiaoxuan Zhang[2], and Krishna Garikipati *[3]
[1]Applied Physics, University of Michigan, Ann Arbor, USA
[2]Department of Mechanical Engineering, University of Michigan, Ann Arbor, USA
[3]Departments of Mechanical Engineering, and Mathematics; Michigan Institute for Computational Discovery & Engineering, University of Michigan, Ann Arbor, USA

Summary A graph theoretic view is taken for continuum physics, described by partial differential equations and solved by high-fidelity computations. We consider graph theoretic representations that are made possible by low-dimensional states, typically functionals of the high-dimensional solutions, that therefore retain important aspects of the high-fidelity information. Each state defines a vertex on a graph and edges are induced either by numerical solution strategies, or by the physics. Correspondences are drawn between the sampling of stationary states, or the time evolution of dynamic phenomena, and the analytic machinery of graph theory. A collection of computations is examined in this framework and new insights to them are presented through the graph theoretic representation. Additionally, we present a rigorous framework for reduced order modelling based on these graphs.

BACKGROUND

In this communication, we explore the casting of large-scale computations of continuum physics in the framework of graph theory. The motivation is to work with low-dimensional representations that encode the fidelity of very high-dimensional, computed solutions, and to develop effective methods to explore and extract further information that could have relevance to decision-making on natural or engineered systems. In this first presentation of ideas, the treatment is deterministic. No probabilistic considerations are invoked.

Of specific interest here are initial and boundary value problems (IBVPs) that span the range from stationary or steady-state systems through first- and second-order dynamics. Each computation of the IBVPs is at high spatial and/or temporal resolution, making for a high-dimensional and/or long time series numerical solution. While dimensionality reduction techniques such as proper orthogonal decomposition or tensor decomposition methods and their variants have been widely applied to high-dimensional problems, and compelling progress continues to be made on them, our approach is different. With an ultimate view to decision-making on these systems, we consider functionals defined on the high-dimensional numerical solutions, and that are induced by physics on the system-wide scale. Examples of these functionals include the lift, drag and thrust in computational fluid dynamics, the average strain, load at yield, failure strain or dissipated energy in computational solid mechanics, and phase volumes, total and interfacial free energies in computational materials physics. We consider as the state of the physical system, a low-dimensional Euclidean vector (typically of dimension $\sim \mathcal{O}(10^1)$) whose components are such functionals. The crux of our approach is to treat the states as vertices on a graph, which can then be completed by identifying edges between vertex pairs. We seek additionally to introduce edges that are induced by either (a) the numerical solution technique, or (b) a transition guided by some physical property. In the first case the existence of an edge is determined by convergence of a solution step between states. More alternatives present themselves for edge definition via the physics. We present examples that help make these notions more precise. The edges enable graph traversal by time as well as by enumeration of states guided by the numerics or physics in the low-dimensional space.

Graph theory has a well-appreciated relevance to physical systems, due in some measure to the fact that it underlies network analysis. Applications including traffic flow, electric power grids and neural circuits are well-known. However, its direct use in representing and analyzing physical phenomena that are described by partial differential equations appears relatively under-explored except for the following work: Graph vertices and edges have been used to represent vortices and their interactions, respectively, for the analysis of turbulent flows in computational fluid dynamics. Recently, graphs have been used to represent problem components such as governing equations, constitutive relations and initial/boundary conditions in the numerical framework of IBVPs. Graph vertices and edges also have been used to represent variables and relations between them, respectively, in a game theoretic approach to discovering constitutive response functions for material failure.

GRAPH THEORY FOR COMPUTATIONAL PHYSICS

We make the case that graph theory offers a framework for representation, exploration and analysis of large scale computed solutions. The fundamental insight required is that high-dimensional field solutions typically admit functional representations of low-dimensional states, which are the vertices of a graph. Transitions between states, which could

*Corresponding author. E-mail: krishna@umich.edu

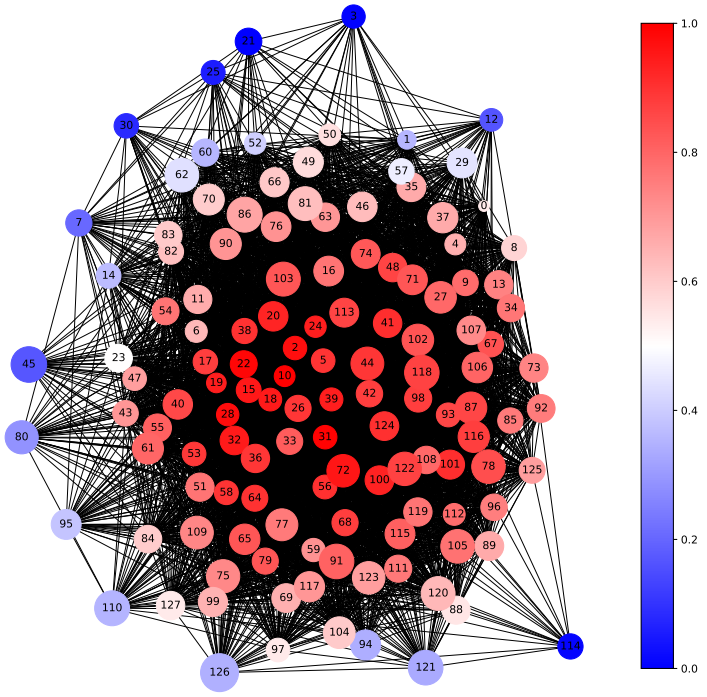

Figure 1: A graph of strain states in Kamada-Kawai layout. The vertices are shaded by their eigenvector centrality, while the area of each vertex symbol is proportional to the Frobenius norm of the strain.

either be a (nonlinear) solution step, or be defined by the change in a physical property, are the edges of the graph. With this foundation, isomorphisms can be identified between the computational and physical framework of states and transitions on one hand, and graph vertices and edges on the other. In this isomorphism, many properties of the numerical solution procedure and of the dynamical physical system are in correspondence with properties of graphs. This includes standard notions of weights, directedness of edges, connectedness of graphs, components, cliques and cycles. Other correspondences arise when considering specific dynamical systems as graphs.

In recent work [1] we have considered computations of IBVPs for stationary and steady-state systems, non-dissipative dynamics and dissipative dynamics, and connected them to specific types of graphs (see Figure 1). The standard machinery of graph theoretic definitions and results was invoked for this purpose. Specific examples were then drawn from computed solutions, and extensive Inferences and insights, not directly available from the high-dimensional numerical solutions, were drawn from analysis of the graphs using well-established concepts from graph theory, as well as algorithms that are motivated by the numerical solution or physics specific to each system.

CONCLUSIONS

Graph theory has, until recently, not had much impact on computational physics, and *vice versa*. Here we have proposed and demonstrated that there is a rich correspondence between these fields that presents many opportunities for representation, exploration and analysis.

References

[1] Banerjee, R., Sagiyama, K., Teichert, G.H. and Garikipati K. *A graph theoretic framework for representation, exploration and analysis on computed states of physical systems*. Computer Methods in Applied Mechanics and Engineering, Vol. **351**, 501-530, 2019, doi.org/10.1016/j.cma.2019.03.053.

MECHANICS OF INFLATABLE AND BISTABLE STRUCTURES

Katia Bertoldi*[1], David Melancon[1], Benjamin Gorissen[1], Ahmad Zareei[1], and Bolei Deng[1]
[1]1School of Engineering and Applied Sciences, Harvard University, Cambridge, United States

Summary Although the study of the effect of shape and geometry on the mechanical response of solid objects has a long history, the surge of modern techniques to fabricate structures of complex form paired with our ability to simulate and better understand their non-linear response has created new opportunities for the design of system with novel functionalities. In this talk I will focus on multistable structures (i.e. structures with multiple stable configurations) and show that they provide an ideal platform for the design of systems with new modes of functionality.

In recent years we have witnessed the emergence of soft structures for which the non-linear response has a prominent role and results in enhanced functionality. Here, I will focus on multistable structures (i.e. structures with multiple stable configurations) and show how numerical simulations can be used to identify new modes of functionality.

Harnessing snapping to make a soft actuator jump

Soft robots comprising several inflatable actuators made of compliant materials have drawn significant attention over the past few years because of their ability to produce complex and adaptive motions through nonlinear deformation. The simplicity of their design, ease of fabrication, and low cost sparked the emergence of soft robots capable of walking, crawling, camouflaging and assisting humans in grasping. However, the actuation speed of soft inflatable actuators is typically limited by the influx of fluid, resulting in slow moving soft robots. To overcome this limitation, we have developed a bistable elastic actuator with an isochoric snap-through (see Figure 1). As no external fluid input is needed to pass through this instability, the resulting actuator deformation happens quasi-instantaneous and is characterized by energy release. Besides optimizing the actuator's design for energy release, we also demonstrate its ability to be reset to the initial, undeformed state, enabling cyclic energy release.

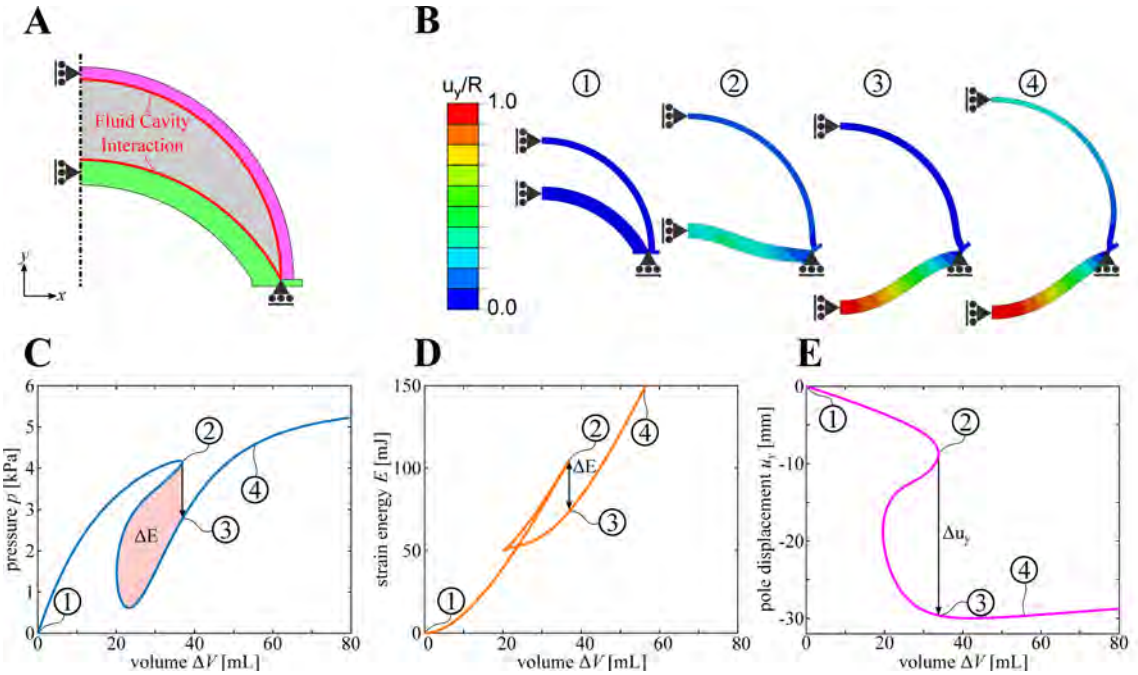

Figure 1: xisymmetric simulations of our actuators. **A.** Schematic of the axisymmetric model. **B.** Numerical snapshots of Design C at (1) rest, (2) before snapping, (3) after snapping, and (4) upon further inflation. **C.** Pressure vs. volume relation as predicted by our axisymmetric simulations for Design C. **D.** Strain energy vs. volume relation as predicted by our axisymmetric simulations for Design C. **E.** Pole displacement vs. volume relation as predicted by our axisymmetric simulations for Design C.

Harnessing transition waves to realize deployable structures

From foldable chairs, and umbrella to tents and solar panels, many structures are capable of quickly changing their shape and, therefore, function. The design of these deployable structures pose two main challenges. First, the transformation needs to be reliable and autonomous and, second, the systems have to be stable and locked in place in the deployed state. Using a combination of experiments and analyses, we demonstrate that bistable linkages and transition waves provide a powerful platform for realizing deployable structures. We first carefully design the bistable joints, so that the transition wave propagates through the entire linkage, transforming the initial straight structure into a curved one. Then, we use these elements as building blocks to create deployable 3D structures of arbitrary shape (Figure 2).

*Corresponding author. E-mail: bertoldi@seas.harvard.edu

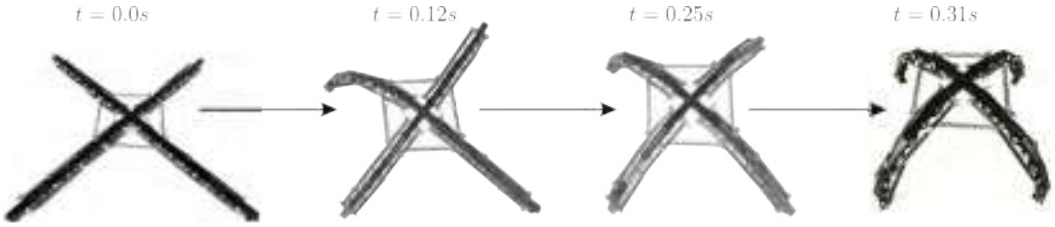

Figure 2: A four linkage structure transforms into a 3D dome-like shape. The four linkages are attached to a central rigid element and interconnected with linear springs.

ESTIMATION OF BIAXIAL STRESS-STRAIN CURVES FOR ALUMINUM ALLOY SHEETS USING DEEP NEURAL NETWORK

Akinori Yamanaka*[1], Kohta Koenuma[1], Ryunosuke Kamijyo[1], Ikumu Watanabe[2], and Toshihiko Kuwabara[1]
[1]Department of Mechanical Systems Engineering, Tokyo University of Agriculture and Technology, Tokyo, Japan
[2]Research Center for Structural Materials, National Institute of Materials Science, Ibaraki, Japan

Summary In order to understand elastoplastic deformation behaviour of aluminum alloy sheets under the biaxial stress condition, the biaxial stress-strain (SS) curves of the sheets have been measured by experimental biaxial tensile test using a cruciform specimen and predicted by numerical biaxial tensile test (NBT) based on the crystal plasticity finite element method. This study propose a new computational methodology for efficiently estimating the biaxial SS curves of the sheets using the deep neural network (DNN) with the convolution neural network. The results obtained in this study demonstrates that the DNN trained with the over 50000 training datasets generated by the NBTs quantitatively estimate the biaxial SS curves from an image of (111) pole figure of the crystallographic texture in the sheet.

INTRODUCTION

Aluminium alloy sheets have been widely used for lightweight automotive body. However, low formability of aluminium alloy sheets causes cracking and wrinkle of the sheets during plastic forming. To prevent the failures, we need to predict elastoplastic deformation behaviour of the sheets under biaxial stress condition. Kuwabara *et al.* [1] developed biaxial tensile testing method using a cruciform specimen as shown in Fig. 1(a) and (b). Although the experimental biaxial tensile test provides accurate stress-strain (SS) curve of sheet metals, the test have to be performed for various biaxial stress conditions. On the other hand, Hashimoto *et al.* [2] proposed virtual biaxial tensile testing method using crystal plasticity finite element method (CPFEM), called numerical biaxial tensile test (NBT). NBT enables us to predict SS curves under the biaxial tensile deformation only from crystallographic texture data (*e. g.* orientation distribution functions and pole figures) and uniaxial SS curve. However, NBT needs source code for CPFEM and is computationally expensive.

The purpose of this study is to propose a new computational methodology for efficiently estimating the biaxial SS curves of aluminium alloy sheets using the machine learning technique based on deep neural network (DNN). We develop a DNN with the convolution neural network (CNN) to estimate the biaxial tensile SS curves from an image of (111) pole figure which shows the crystallographic texture in the aluminium alloy sheet.

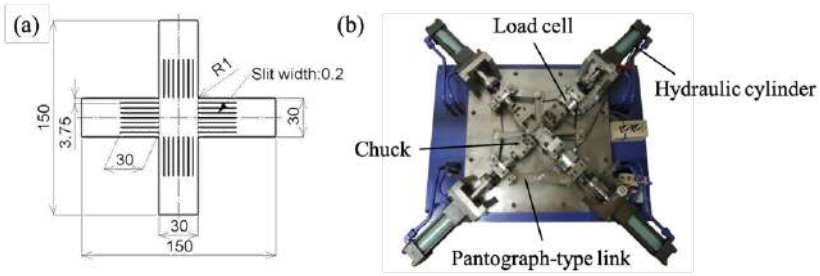

Figure 1. (a) Cruciform specimen and (b) experimental apparatus used for experimental biaxial tensile test [1].

DEEP NEURAL NETWORK

The DNN developed in this study is illustrated in Fig. 2. Input data of the DNN is the image of (111) pole figure of the texture in aluminum alloy sheet and a stress ratio between the true stresses along rolling direction (RD) and transverse direction (TD) of the sheet. The output data of the DNN is SS curves for RD and TD of the sheet. The DNN consists of two CNNs to capture the feature of (111) pole figure image.

A large amount of training datasets is needed for training the DNN. We generate synthetic datasets of crystallographic textures containing Cube, S, Copper, Brass, Goss and random components [3]. Total 5944 synthetic textures are generated by changing volume fraction, V_i, and standard deviation (SD), ξ_i, of the texture component i (i = Cube, S, Copper, Brass, Goss and random). The image files of (111) pole figure for the synthetic textures are generated in Portable Network Graphics (PNG) format with 128^2 pixels.

In order to obtain the biaxial SS curves which include the training datasets, we perform NBTs using the synthetic textures as the initial crystal orientation. The crystal plasticity constitutive equations [4,5] and those parameters used for the NBT are calibrated by SS curve obtained by experimental uniaxial tensile test of A5182-O aluminum alloy sheet. Using the calibrated parameters, NBTs for all the synthetic textures are performed to obtained SS curves for 9 linear stress paths: σ_{RD} : σ_{TD} = 1:0, 4:1, 2:1, 4:3, 1:1, 3:4, 1:2 and 0:1 where σ_{RD} and σ_{TD} denotes the true stress along RD and TD, respectively. Therefore, the NBTs are performed for 53496 times in total.

*Corresponding author. E-mail: a-yamana@cc.tuat.ac.jp.

In the training of the DNN, the mean squared error is used for the loss function. Adam [6] is used for optimization algorithm. Further information for the training of the DNN will be presented in the conference.

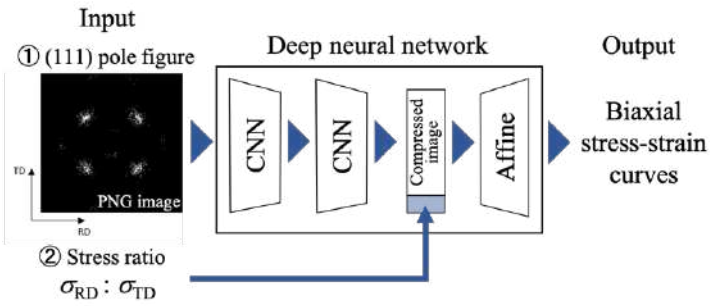

Figure 2. Schematic illustration of the deep neural network (DNN) developed in this study.

RESULTS

The trained DNN are validated by comparing the SS curves calculated by the NBT with those estimated by the trained DNN. Figure 3(a) shows the (111) pole figure of the synthetic texture used for the validation. The synthetic texture are generated based on real texture of the aluminium alloy sheet reported in the literature [6]: V_{Cube} = 18 %, V_S = 8 %, V_{Goss} = 10 %, V_{Brass} = 2 %, V_{Copper} = 4 % and V_{Random} = 58 %, ξ_{Cube} = 3.6°, ξ_S = 2.8°, ξ_{Goss} = 3.4°, ξ_{Brass} = 3.6° and ξ_{Copper} = 2.2°.

Figure 3 (b), (c) and (d) show the true stress-logarithmic plastic strain curves estimated by the DNN for the true stress ratio σ_{RD} : σ_{TD} = 1:0, 1:1, and 0:1, respectively. The result reveals that the trained DNN can quantitatively estimate the SS curves obtained by the NBT based on the CPFEM. Using the trained DNN, the biaxial SS curves can be estimated within a few seconds. In the conference, we will present the SS curves estimated for other synthetic textures and stress ratios.

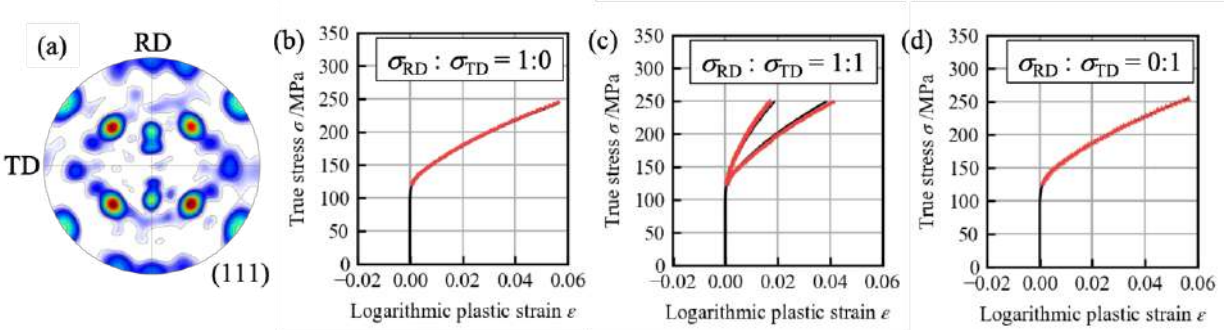

Figure 3. (a) (111) pole figure of the synthetic texture used for the validation of the DNN. Biaxial stress-strain curves obtained by the NBT (black line) and estimated by the trained DNN (red symbols) for the true stress ratios, σ_{RD} : σ_{TD} = (a) 1:0, (b) 1:1 and (c) 0:1.

CONCLUSIONS

In this study, we have proposed the efficient methodology for estimating the biaxial SS curves of aluminium alloy sheets from an image of (111) pole figure based on the machine learning using the DNN. To generate the training data for the DNN, over 5000 synthetic texture datasets were generated and over 50000 NBTs were performed based on the CPFEM. By training the DNN with the massive training data, the trained DNN shows a potential for quantitatively estimating the biaxial SS curves of aluminium alloy sheets.

References

[1] Kuwabara T., Ikeda, S., Kuroda K., Measurement and analysis of differential work hardening in cold-rolled steel sheet under biaxial tension. *J. Mater. Technol.* **80-81**: 517-523, 1998.

[2] Hashimoto K., Yamanaka A., Kawaguchi J., Sakurai T., Kuwabara T., Biaxial tensile deformation simulation of 5000 series aluminium alloy sheet using crystal plasticity finite element method based on homogenization method and its experimental validation, *J. Jpn. Inst. Light Met.*, **65**: 196-203, 2015.

[3] Koenuma K., Yamanaka A., Watanabe I., Kuwabara T., Estimation of texture-dependent stress-strain curve and *r*-value of aluminium alloy sheet using deep learning. *J. Jpn. Soc. Technol.* in print, 2020.

[4] Pan J., Rice J. R., *Int. J. Solids Struct.* **19**: 973-987, 1983.

[5] Hutchinson J. W., *Proc. R. Soc. Lond.* **A319**: 247-272, 1970.

[6] Kingma D. P., Ba J. L., Adam: A method for stochastic optimization, *arXiv:142.6980v9*, 2014

[7] Zeng X. H., Ahmad M., Engler O., Texture gradient, average texture, and plastic anisotropy in various Al-Li sheet alloys, *Mater. Sci. Technol.* **10**: 581-591, 1994.

CHEMO-MECHANICS MODELLING OF LITHIUM-ION BATTERY ELECTRODES

Bai-Xiang Xu*, Yang Bai, and Peter Stein
Division Mechanics of Functional Materials, Technische Universitaet Darmstadt, Darmstadt, Germany

Summary Research on the capacity loss of Lithium-ion batteries have highlighted a rich field of diffusion-induced mechanical phenomena. We summarize firstly our chemo-mechanical phase-field model and finite element simulations for the bulk. The study on the chemo-mechanical interplay at grain boundaries and at interface between the solid electrolyte and electrode is insufficient. We report then our recent progress on developing a chemo-mechanical interface model, which includes both the damage-dependent across-grain transport and the mechanical cohesive zone law. We show that the enhanced intergranular chemical inhomogeneity challenges the grain boundary mechanical strength, while the grain boundary damage influences or even blocks the across grain transport. Results explain well the experimentally observed features like chemical hot spots and surface layer delamination.

Chemo-Mechanics and its Modelling

Rechargeable Lithium-Ion Batteries (LIBs) are widely used in portable electronic devices and electric vehicles, and are also prominent solutions for the storage of intermittent renewable energies. Mechanics can have a critical influence on the performance and the lifetime of LIBs. Materials in LIBs experience breathing-like deformation during cyclic charging and discharging and suffer from considerable chemo-mechanical degradation. Understanding and controlling the effects of stress and strain on ion transport, phase transformations, and catalytic pathways in energy materials can be a key for improving the performance and the durability of battery devices. Figure 1 highlights the (a) mechanistic and (b) mechanical degradation in a typical battery cell.

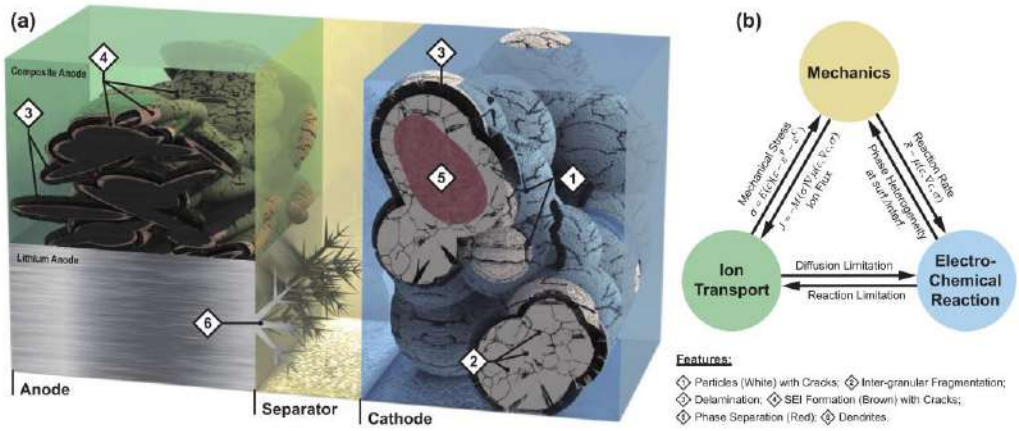

Figure 1. Schematics of (a) mechanistic and (b) mechanical degradation mechanisms of a lithium-ion battery cell with a composite anode and a lithium metal anode, respectively. [1]

To study the deformation of the active electrode materials in the framework of finite deformation elasticity, one can decompose the deformation gradient into the elastic distortion part (indicated by the superscript e) and the (de-)intercalation-induced swelling part (indicated by the superscript c). For the derivation of the coupled constitutive relation and the mass transport equation, we propose the following free energy density in the reference configuration (denoted by the subscript R), considering the Neo-Hookean elasticity, the dilute solution chemical bulk free energy and possible phase interface energy. From the thermodynamics and the phase-field theory, we obtain the second Piola–Kirchhoff stress tensor and the chemical potential contributions.

$$\psi_R(c_R, \nabla_R c_R, \mathbf{C}) = \psi_R^c(c_R) + \psi_R^i(\nabla_R c_R) + \psi_R^e(c_R, \mathbf{C})$$

$$\psi_R^c = c_R \ln c_R + (1 - c_R)\ln(1 - c_R) + \chi c_R (1 - c_R)$$

$$\psi_R^i(\nabla_R c_R) = \frac{1}{2}\kappa |\nabla_R c_R|^2$$

$$\psi_R^e(c_R, \mathbf{C}) = J^c[\frac{K}{2}(\frac{J}{J^c} - 1)^2 + \frac{G}{2}(\bar{I}_1 - 3)]$$

$$\mathbf{S} = \frac{\delta \psi_R}{\delta \mathbf{E}} = \frac{2\partial \psi_R^e}{\partial \mathbf{C}} = J^c[KJ^c(J^c - 1)\mathbf{C}^{-1} + GJ^{-\frac{2}{3}}(\mathbf{1} - \frac{1}{3}I_1\mathbf{C}^{-1})]$$

$$\mu^c = \frac{\partial \psi_R^c}{\partial c_R} = \ln c_R - \ln(1 - c_R) + \chi(1 - 2c_R)$$

$$\mu^i = \frac{\delta \psi_R^i}{\delta c_R} = -\kappa \nabla_R^2 c_R$$

$$\mu^e = \frac{\partial \psi_R^e}{\partial c_R} = \frac{\Omega K}{2}[1 - (J^e)^2] + \frac{\Omega G}{2}(\bar{I}_1 - 3)$$

The stress equilibrium and the mass conservations lead to the following governing equations, along with the boundary conditions:

$$\nabla \cdot \boldsymbol{\sigma} = \mathbf{0} \quad \text{in} \quad B \times (0, \mathcal{T})$$

$$\frac{\partial c}{\partial t} = \nabla \cdot (\mathrm{M} \nabla \mu) \quad \text{in} \quad B \times (0, \mathcal{T})$$

$$\mu = \mu^c + \mu^i + \mu^e \quad \text{in} \quad B \times (0, \mathcal{T})$$

$$-\mathrm{M} \nabla \mu \cdot \boldsymbol{n} = J_s \quad \text{on} \quad \partial B_c \times (0, \mathcal{T}),$$

$$\nabla c \cdot \boldsymbol{n} = 0 \quad \text{on} \quad \partial B \times (0, \mathcal{T}),$$

$$c(\mathbf{x}, 0) = c^0(\mathbf{x}) \quad \text{in} \quad B \times (0, \mathcal{T}),$$

$$\boldsymbol{u} = \hat{\boldsymbol{u}} \quad \text{on} \quad \partial B_u \times (0, \mathcal{T}).$$

More details can be found in our previous publication [2]. Thereby the ion flux *Js* is the (de-)intercalation of Lithium, which can be described by a phenomenological Butler-Volmer model in dependence on the (electro)chemical potentials of the particle and the electrolyte, as described in [1,2]. If the fracture inside the particles is addressed, one can make use additionally the phase-field fracture theory, by adding the damage-like order parameter and the related bulk and interface energies[3]. Through regularization, we considered even the (de-)intercalation of Lithium ion on the freshly created fracture surface denoted by the high gradient of the damage order parameter [4].

Chemo-Mechanical Grain Boundary Model

More recently, we studied also the grain boundary (GB) effect, since most electrode materials have a polycrystal or multi-grains structure. The unique mechanical or chemical properties of the grain boundary has been long recognized, but the chemical process and the mechanical degradation of the grain boundary are fully coupled and go hand-in-hand: the enhanced intergranular chemical inhomogeneity challenges the GB mechanical strength, while the GB damage influences in return the across grain ion transport as it is sensitive to or can be even blocked by GB delamination. For this purpose, we present here a chemically coupled cohesive zone GB model, which includes both the damage-dependent across-grain transport and the mechanical traction-separation cohesive law:

$$J^+ = -J^- = J^d, \quad J^d = (1-d)\left[M^+\nabla\mu^+ - M^-\nabla\mu^-\right]\vec{\mathbf{n}}$$

$$T_n^+ = T_n^- = T_n(\Delta_n, \Delta_t), \quad T_t^+ = T_t^- = T_t(\Delta_n, \Delta_t)$$

whereby d is the damage parameter of the grain boundary. For the grain interior, we employ a chemo-mechanical model described in the last subsection. The outlined chemo-mechanical models for the grain interior and grain boundaries were implemented in the finite element framework MOOSE. In particular, the Discontinuous Galerkin (DG) method is applied for the discontinuity of displacement and concentration at GBs. Numerical simulations were carried out for polycrystalline $Li(Ni_xMn_yCo_z)O_2$ cathode materials, comprising 89, 174 and 413 grains, with radius R = 5 µm, respectively. The 1C-rate discharge process is applied. Simulation examples on demonstrate the capability of our models. In particular, we reproduce the experimentally observed features including chemical hot spots and surface layer delamination (Fig.2), which otherwise cannot be understood using the conventional cohesive zone modelling.

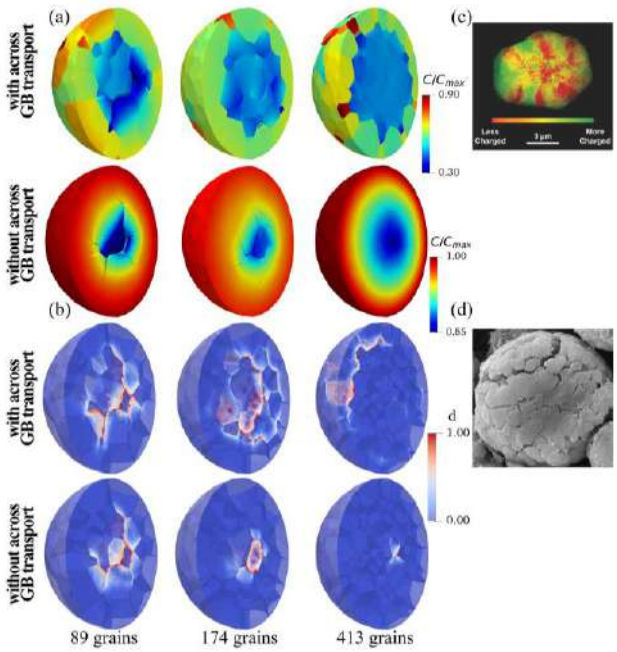

Figure 2. Comparison of the concentration distribution and the crack patterns between the cases with (a) and without (b) across GB transport. The simulated concentration hot spots and surface layer delamination demonstrate similarity to the experimental results (c,d) by Gent et al. Advanced Materials, 28, 2016; Sun et al. Extreme Mechanics Letters 9, 2016).

References

[1] Zhao Y., Stein P., Bai Y., Al-Siraj M., Yang Y., Xu B.-X. A Review on Modeling of Electro-Chemo-Mechanics in Lithium-Ion Batteries. *J. Power Sources* **413**: 259-283, 2019
[2] Zhao Y., Stein P., Xu B.-X. Isogeometric Analysis of Mechanically Coupled Cahn-Hilliard Phase Segregation in Hyperelastic Electrodes of Li-ion Batteries. *Computer Methods in Applied Mechanics and Engineering* **297**: 325-347, 2015
[3] Xu B.-X., Zhao Y., Stein P., Phase Field Modeling of Electrochemically Induced Fracture in Li-Ion Battery with Large Deformation and Phase Segregation. *GAMM-Mitteilungen* **39** (1):92-109, 2016
[4] Zhao Y., Xu B.-X., Gross D. Phase-Field Study of Electrochemical Reactions at Exterior and Interior Interfaces in Li-ion Battery Electrode Particles. *Computer Methods in Applied Mechanics and Engineering* **312**:428-446, 2016

MODEL-FREE DATA BASE-DRIVEN RVE WITHIN FE²: ANALYSIS OF CRACKED MEDIA

Georgios A. Drossopoulos [1], and Georgios E. Stavroulakis*[21]
[1]Department of Civil Engineering, University of KwaZulu-Natal, Durban, South Africa
[2]School of Production Engineering and Management, Technical University of Crete, Chania, Greece

Summary Fusion of data mining and computational mechanics is a modern approach for the exploitation of available data within rigorous modeling. Previous attempts have been focused on the usage of neural networks and other soft computing tools as metamodeling tools. This framework seems suitable for numerical homogenization techniques realized within the so-called FE² environment, where the lower level FEM of a detailed RVE is replaced by a data base. Extraction of homogenized material properties from the data base is based on classical interpolation or artificial neural networks. We investigate this approach here for the analysis of structures with distributed cracks including unilateral contact behaviour.

INTRODUCTION

Neural networks provide an effective approximator which can be used within nonlinear computational mechanics and replace classical material constitutive models. Replacement of lower level FEM analysis of a representative volume element, as used in multi-scale numerical homogenization, is proposed and tested here. Difficulties of implementing this approach will be discussed and comparison with previously published results, which used classical interpolation, will be shown.

DATA-DRIVEN HOMOGENIZATION ALGORITHM

Numerical homogenization and FE²

Within the classical multilevel approach based on FE² a detailed RVE model is used to calculate the mechanical response of every wished loading. The result is integrated into the nonlinear finite element analysis of macroscopic level, which does not contain all details (cracks, composite structure, microstructure) and is based on the homogenized properties. The authors proposed this scheme for the treatment of unilaterally affected structures in [1]. Due to the high computational cost of classical FE², the lower level has been replaced by an approximation based on a FEM-generated data base in [2]. A more efficient neural network approximator is used here, see Figure 1.

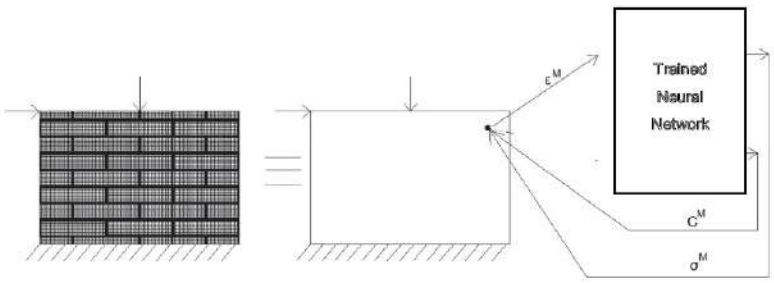

Figure 1. The proposed multilevel approach using a neural network approximation of RVE results.

Homogenized properties using data-base with RVE data

The mechanical response of the RVE is an unknown mapping between the deformation and stress tensors. Various realizations of this mapping have been calculated by a finite element RVE model and stored within a backpropagation artificial neural network of the type 3-10-10-3. The performance of the trained network on unknown deformation inputs is shown in Figure 2. On a randomly selected sample of 1000 inputs the neural network requires an average of 0.009926s for each calculation, in comparison to the 4.251175s required by the interpolation function of MATLAB, which has been used in [2].

1 Corresponding author, email: gestavr@dpem.tuc.gr

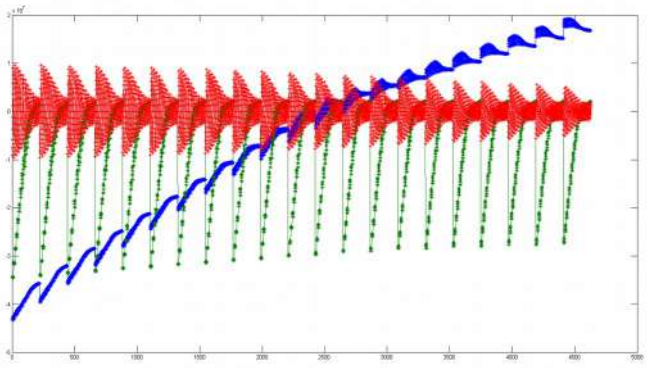

Figure 2. Approximation of RVE results for various load levels using neural networks. NN prediction of stresses for various strain levels.

ANALYSIS OF A CRACKED STRUCTURE

A masonry wall with cracks has been calculated by using the proposed algorithm. Results, like the ones shown in Figure 3, have been compared with previously published in [2].

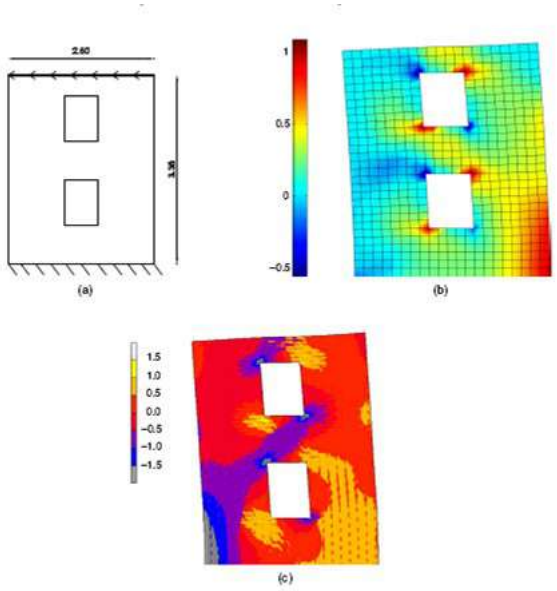

Figure 3. Solution of a cracked wall using the proposed multilevel approach (see [2] for details).

CONCLUSIONS

Data-driven, model-free computational mechanics is a modern approach which promises to give flexibility in using experimental data in the form of data bases [3]. It can be incorporated to make classical FE^2 more efficient by using numerically generated data and classical [2] or neural interpolation.

References

[1] Drosopoulos G.A. Wriggers P. Stavroulakis G.E. A muti-scale computational method including contact for the analysis of damage in composite materials. *Computational Materials Science* ***95***: 522-535, 2014.
[2] Drosopoulos G.A. Giannis K., Stavroulaki M.E., Stavroulakis G.E. Metamodeling-assisted numerical homogenization for masonry and cacked structures. *ASCE Journal of Engineering Mechanics* ***144(8)***: 04018072, 2018.
[3] Kirchdoerfer T. Ortiz M. Data-driven computational mechanics. *Computer Methods in Applied Mechanics and Engineering*, **304**: 81-101 2016.

EFFECT OF MAGNETIC FIELD ORIENTATION ON MAGNETOELECTRIC RESPONSE IN LAYERED COMPOSITES

S. Sudersan *[1] and A.Arockiarajan[1]
[1]Department of Applied Mechanics, Indian Institute of Technology Madras, Chennai, India

Summary Composites of magnetostrictive and piezoelectric systems find applications as gyrators, sensors, etc. These magnetoelectric (ME) composites develop voltage across the piezoelectric phase under applied magnetic field. A number of 1D models quantify the voltage, wherein effect of magnetic field orientation on ME response is often overlooked. Hence, a 2D nonlinear magnetostrictive constitutive relation coupled with First Order Shear Theory (FOST) is used to model the behavior of an ME composite under inplane magnetic fields. A finite element procedure is used to determine the static and resonant response of the structure. The influence of bias as well as AC field orientation on the net output voltage and a correlation between the two is determined in order to ensure maximum coupling. The resonant ME coupling under bending, twisting and axial vibrations has also been quantified.

INTRODUCTION

Magnetoelectric composites have been widely pursued for device applications due to their unique coupling behavior. These materials exhibit a nonlinear response under high magnitudes of applied magnetic fields and hence research has been focused on understanding their constitutive behavior [1]. While symmetric laminates offer the advantage of high ME coupling, they often have resonant frequencies of several kHz, making them difficult to use in practice. Unsymmetric laminates, though offering lower static ME coefficient, can be operated in bending resonant mode at much lower frequencies, thus compensating for weaker static coupling and hence resulting in a comparable response. Hence research works have focused on quantifying the resonant behavior of these laminates at bending and axial resonance [2]. Much of these works approximate the structure as a beam, restricting the magnetic field to the longitudinal direction. The objective of this work is thus to explore the effect of in-plane magnetic field orientation on the static and dynamic ME response of an ME bilayer. Finite element analysis in conjunction with First Order Shear Theory (FOST) is used to determine the nonlinear ME voltage as a function of the applied magnetic field.

CONSTITUTIVE RELATIONSHIP

The magnetostrictive layer is governed by nonlinear constitutive relations, relating the magnetic field vector and the magnetization vector as well as the strain tensor and the magnetic field vector. The piezoelectric layer is assumed to be governed by linear constitutive equations since the electric fields developed are too small to cause nonlinearity. These constitutive relations are linearized about the DC (bias) magnetic field, in order to determine the AC component of the magnetostrictive strain.

$$M_i = M_s f(k||\underline{H}||)\frac{H_i}{H} \quad ; \quad \lambda_{ij} = \frac{3}{2}\frac{\lambda_s}{M_s^2}M_i M_j \tag{1}$$

$$\delta\lambda_{ij} = \left.\frac{\partial\lambda_{ij}}{\partial H_k}\right|_{\underline{H}_b}\delta H_k = \frac{3f}{H^4}(kHf' - f)H_k\delta H_k H_i H_j + \frac{3}{2}\frac{f^2}{H^2}(H_i\delta H_j + H_j\delta H_i) - ff'k\delta_{ij}\frac{H_k\delta H_k}{H} \tag{2}$$

$$\delta\sigma^m_{ij} = C^m_{ijkl}\delta\epsilon_{kl} - q^m_{ijk}\delta H_k \quad ; \quad \delta\sigma^p_{ij} = C^p_{ijkl}\delta\epsilon_{kl} - e^p_{ijk}\delta E_k \tag{3}$$

$$\delta D_i = e^p_{ijk}\delta\epsilon^p_{jk} + \varepsilon^p_{ij}\delta E_j \tag{4}$$

$$\underline{H} = [\cos(\theta)\ \sin(\theta)\ 0]^T \quad ; \quad \underline{\delta H} = [\cos(\beta)\ \sin(\beta)\ 0]^T \tag{5}$$

An applied DC (bias) magnetic field causes a static deformation of the composite, which is then perturbed by an AC field. A dynamic analysis is thus conducted and the AC components of the resulting strains are determined. The open-circuit AC voltage in the piezoelectric layer is then determined by setting δD=0. The effect of the magnetic field is modeled as pseudo mechanical forces and moments on the beam given by

$$\delta N_{ij} = \int_{t^m} Q_{ij}\delta\lambda_i dz \quad ; \quad \delta M_{ij} = \int_{t^m} Q_{ij}\delta\lambda_i z dz \tag{6}$$

The equilibrium equations are given by

$$\delta N_{ij,j} = I_0\ddot{\delta u}_i + I_1\ddot{\delta\theta}_i \ ; \ \delta Q_{i,i} = I_0\ddot{\delta w} \ ; \ \delta M_{ij,j} - Q_i = I_1\ddot{\delta u}_i + I_2\ddot{\delta\theta}_i \tag{7}$$

The aforementioned equilibrium equations and the boundary conditions are used to set up the finite element equations of the form

$$(K_{ij} - \omega^2 M_{ij})d_i = F_i \tag{8}$$

which is subsequently solved to obtain the nodal degrees of freedom and hence the electric field.

*Corresponding author. E-mail: sudersansridhar@yahoo.co.in .

RESULTS AND DISCUSSION

The variation of the ME coefficient with the bias is shown in Fig. Bias(a) for different AC field orientations,β, at specified bias field orientations, θ. It is seen that that the ME coefficient drops rapidly with increasing β and when θ=0°, the ME coefficient vanishes at β=90°. Hence mutually perpendicular fields result in a vanishing ME coupling. It is also seen that the optimum bias at which the ME coefficient is maximum varies as a function of the AC field angle for nonzero θ values.

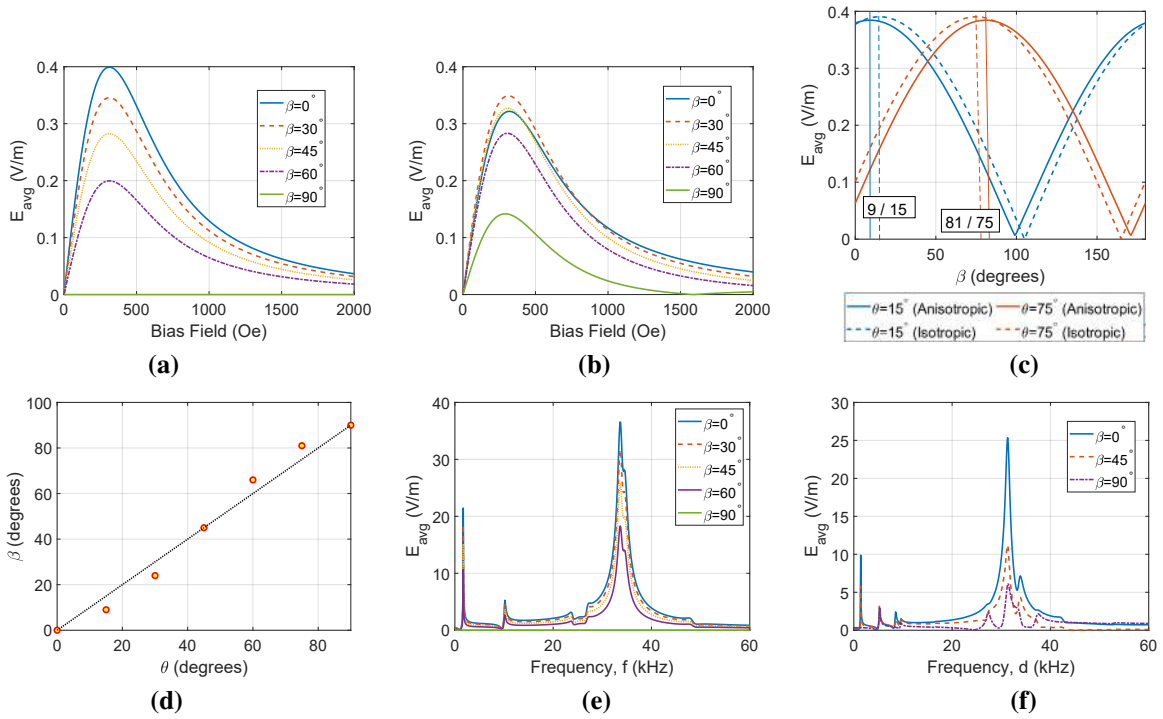

Figure 1: Output electric field at (a) θ=0° and (b) θ=30° (c) Effect of anisotropy of magnetostrictive phase at θ=15° and θ=75°, (d) Corresponding points between θ and β for the peak ME coupling, (e) Resonant electric field at θ=0° and (f) Resonant electric field at θ=45°.

Another point of interest is the effect of the anisotropy of the magnetostrictive phase. This is illustrated at θ=30° in Fig. 1(c) and (d). If the magnetostrictive layer is isotropic, the ME coupling is maximum at β=θ. However, this is not the case when the magnetostrictive layer is transversely isotropic. As can be seen from Fig. 1(c), a difference of about 6° exists between $\theta$and β at θ=15°. It is further noteworthy that at a complementary angle (θ=75°), the difference between θ and β corresponding to the peak values is numerically the same. It is observed that the variation of the ME coupling gets flipped with respect to β. This can be explained on the basis of the decreasing elastic modulus along the longitudinal direction and increasing contribution to the transverse directions. Fig. 1(d) shows the values of β at any given θ corresponding to maximum output electric field. The dotted line indicates the case under isotropic behavior.

The resonant ME electric field is determined at θ=0° and at θ=45°. The combined bending, twisting and axial vibration of the composite results in multiple peaks of the output field with respect to the frequency of the AC field. The results are shown in Fig. 1 (e) and (f) respectively. It is seen that at θ=45°, the bending resonant mode almost disappears as β increases. The additional peaks in comparison to Fig. 1(e) correspond to twisting modes of vibration due to an inclined bias field.

SUMMARY

Thus a nonlinear magnetostrictive constitutive relation has been used in combination with FOST and a finite element framework in order to determine the ME response of laminated magnetoelectric composites. The model predicts the ME coupling at quasi-static as well as resonant conditions. The effect of the bias and AC field orientations and the influence of the anisotropy of the magnetostrictive phase on the observed ME response have been elucidated. A detailed analysis of the system and confirmation of the observations with experiments is planned as future work.

References

[1] Nan, C.W., Bichurin, M.I., Dong, S., Viehland, D. and Srinivasan, G. Multiferroic magnetoelectric composites: Historical perspective, status, and future directions. *Journal of applied physics*, **103(3)**, p.1, 2008

[2] Sudersan, S., Maniprakash, S. and Arockiarajan, A. Nonlinear magnetoelectric effect in unsymmetric laminated composites. *Smart Materials and Structures*, **27(12)**, p.125005, 2018

CREEP-FATIGUE LIFE CALCULATIONS FOR TRANSPIRATION COOLED AEROFOILS

Christos Skamniotis*[1], Alan Cocks[1]
[1]Department of Engineering Science, University of Oxford, Parks Road, Oxford, OX1 3PJ,UK

Summary For further increase in gas turbine efficiency, engine temperatures need to exceed the physical capabilities of metals, necessitating advanced cooling technology, such as transpiration cooling systems. Despite their enormous benefits on cooling, these systems come at the cost of thermal stresses which continue to raise thermomechanical performance concerns. To accelerate the industrial implementation-design of such systems, we present new creep-fatigue life calculations of typical double-wall porous aerofoils under thermal cycling conditions. Our analytical, pseudo-analytical and Finite Element (FE) elastic-plastic-creep solutions provide the desirable parameters associated with geometry and thermal cycle characteristics, for which creep-fatigue life is maximized.

THERMOMECHANICAL PROBLEM

We consider the transpiration cooled aerofoil presented by Murray et al [1] (see Fig 1a), which consists of regularly spaced pedestals connecting an outer wall (skin 1) with effusion holes and an inner wall (skin 2) with impingement holes. The latter allow for injecting coolant fluid against the interior of the outer wall, while the effusion holes allow the coolant to escape at an angle (pitch) such that a protective film is formed against the hot mainstream gas flow. Due to convection, a thermal gradient, $\Delta T = T_{max} - T_{min}$, arises in the outer skin 1 (see Fig 1b), while the inner skin is assumed to remain at uniform temperature, T_{min} [2]. To firstly understand how stresses are induced by the gradient, ΔT, and how they can be minimized by first order geometric changes, holes are excluded from the analysis such that the system in Fig 1a can be represented by the repeating unit cell shown in Fig 1b. The latter is cut at its $r-z$ and $r-\theta$ bisectional planes to

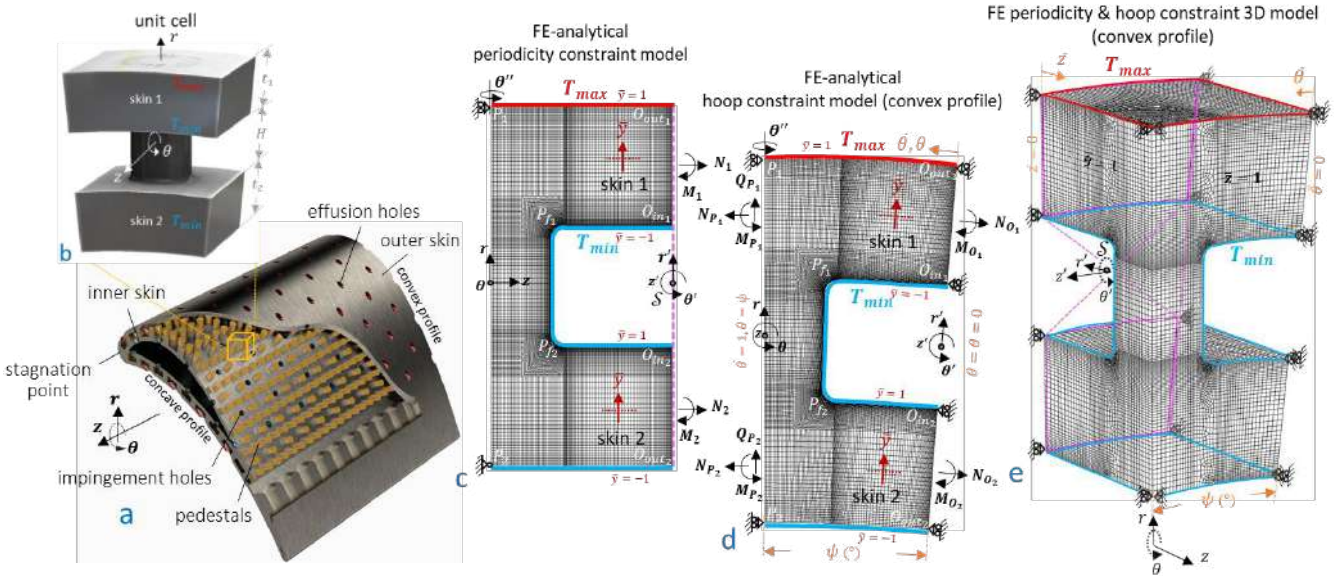

Figure 1. Thermomechanical analysis: (a) double-wall transpiration cooled aerofoil, (b) repeating unit cell, (c) FE-analytical 2D model – periodicity constraint, (d) FE-analytical 2D model – hoop constraint, (e) 3D FE model – combined periodicity and hoop constraints.

produce the 2D models in Fig 1c and Fig 1d, respectively, based on which analytical-FE solutions for stress in the corresponding z and θ directions are derived; the periodicity constraint model (Fig 1c) postulates common θ' −rotation between skins 1-2 at the plane $r'-z'$ [2], whereas the hoop constraint model (Fig 1d) requires zero θ' −displacement and z −rotation the plane $r'-\theta'$. The above conditions co-exist in the 3D unit cell FE model (Fig 1e) i.e. common θ' −rotation between skin 1-2 faces at $\bar{z}=0$ plane (outlined in purple) and symmetry conditions in all other bounding planes. After investigating the relevance of 2D analytical-FE stress field (Figs 1c-d) to the corresponding 3D FE stress field (Fig 1e), holes are added in the 3D model at the location $\bar{z}=\bar{\theta}=0$ (see Fig 2a); the effusion hole pitch is not considered here. The analytical 2D solutions (Figs 1c-d) are obtained based on beam-virtual work theory.

RESULTS: ELASTIC ANALYSIS – EFFECT OF GEOMETRY ON PEAK STRESSES

Based on the analytical-FE 2D analysis alone (Fig 1c-d), we find that minimizing skin spacing, H/t_1, and using low inner wall thickness, t_2, have both beneficial effects, whereas reducing the density of connecting pedestals may reduce compressive stress magnitudes, thus improve creep-fatigue life at the effusion holes at the outer blade surface (at $O_{out_{f_1}}$ location in Fig 2a), yet, it tends to increase tensile stresses at the pedestal-wall filleted corners (at P_{f_1}, P_{f_2} in Fig 2a). These conclusions are found to agree with 3D simulations (Fig 1e) which highlights the advantage of our simplified

*Corresponding author. Email: christos.skamniotis@eng.ox.ac.uk

approach in that it provides analytical relationships for the effect of a range of geometric parameters on nominal stresses. The latter is important because peak stresses at the critical locations of the system i.e. at effusion/impingement holes ($O_{out_{f_1}}$, $O_{in_{f_1}}$, $O_{in_{f_2}}$, in Fig 2a) and at pedestal-skin filleted corners (at P_{f_1}, P_{f_2} in Fig 2a), are found to be a multiple of these nominal stresses and of a stress concentration factor specific to the hole/fillet.

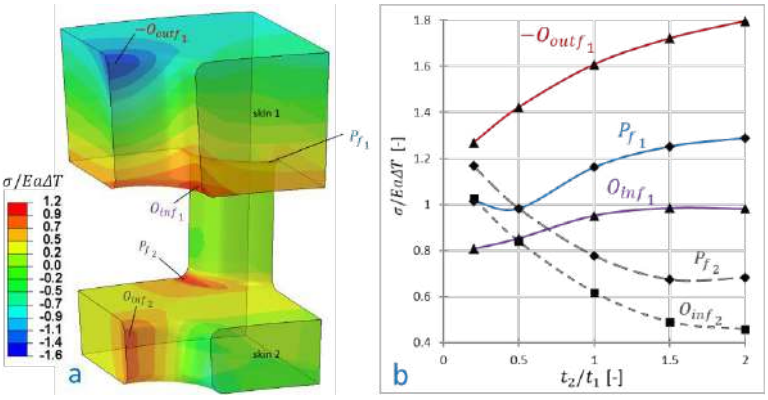

Figure 2. Summary of FE results from 3D model of Fig 1e with added impingement/effusion holes: (a) normalised absolute maximum principal FE stress contours, (b) FE peak stresses at critical points versus skin thickness ratio, t_2/t_1.

RESULTS: INELASTIC ANALYSIS – THE ROLE OF THERMAL CYCLE CHARACTERISTICS

For evaluating creep-fatigue life, we consider that inevitable creep deformation particularly at regions near the external surface of skin 1 (see Fig 1b), will in fact modify the stress field over time. To understand-predict the nature of the long-term stress state at critical points for a given thermal cycling history, we firstly obtain analytical, pseudo-analytical and FE 2D solutions (Fig 1c-d). These account for stress relaxation during the hot part of the thermal cycle i.e. when $\Delta T = T_{max} - T_{min}$ (see Fig 3a) based on a creep power law calibrated for the Nickle based superalloy CMSX-4, and also account for the resulting residual stress profile at the cold part of the cycle i.e. when $\Delta T = 0$ (see Fig 3a); plastic yielding also occurs when a constant Von Mises yield stress, σ_y, is exceeded. Three regimes of behaviour can prevail under these conditions: elastic-creep, reverse plasticity and shakedown; the latter here implies that a cycle state will occur where the total creep strain, ε_c, accumulated during the hot part of each cycle is equal and opposite to the total plastic strain, ε_p, growth at the cold part of each cycle. This gives rise to a cyclic inelastic strain range, $\Delta\varepsilon_i = 2|\varepsilon_p|$, which is related to the number of cycles, N_f, for fatigue failure based on the Coffin-Manson relationship: $\Delta\varepsilon_i = AN_f{}^a$ (A, a material constants). By calculating $\Delta\varepsilon_i$ analytically based on the 'rapid cycle' assumption, in Fig 3b we illustrate how N_f reduces with ΔT and cyclic time at high temperature, Δt_h (see Fig 1a) for a fixed T_{max}, as well as in Fig 3c how N_f decreases with T_{max} and ΔT for fixed Δt_h; less conservative N_f values are found by calculating $\Delta\varepsilon_i$ through other more accurate pseudo-analytical and FE schemes. Our inelastic calculations are extended to account for the 3D case (Fig 1e) including stress concentration at holes as well as for the combined thermal-inertial loading conditions that typically occur in aerofoil components. Our approach aims to reduce the total number of simulations required over the entire design process in double-wall transpiration cooled systems.

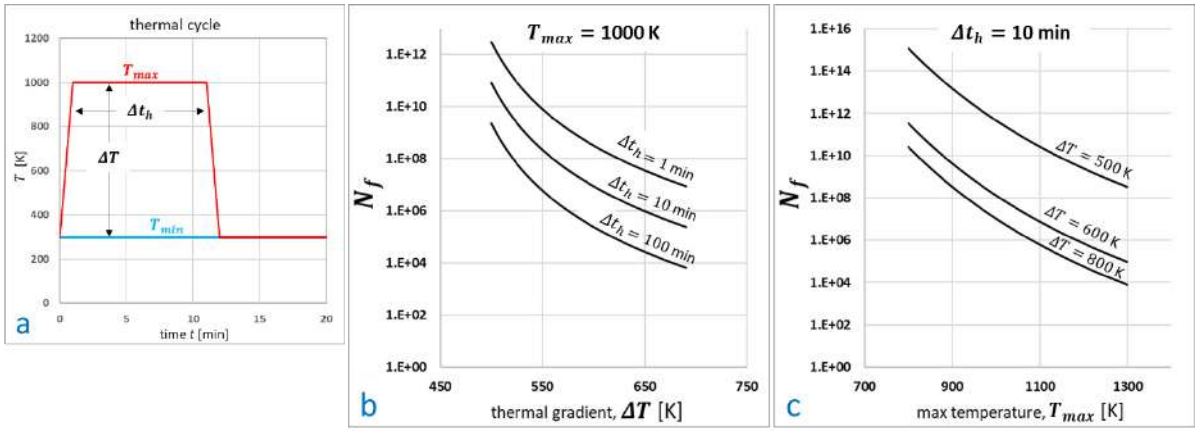

Figure 3. Thermal fatigue calculations: (a) typical thermal cycle, (b) number of cycles to failure, N_f, versus ΔT for varying Δt_h and fixed T_{max}, (c) N_f versus T_{max} for varying ΔT and fixed Δt_h.

References

[1] Murray, A.V., P.T. Ireland, and E.J.J.o.T. Romero, *Development of a Steady-State Experimental Facility for the Analysis of Double-Wall Effusion Cooling Geometries*. 2019. **141**(4): p. 041008.Icer D.F., Adams J.A. Mathematical Elements for Computer Simulation. McGraw Hill, NY 1977.

[2] Elmukashfi, E., Murray, A.V., Ireland, P.T. and Cocks, A.C.F., "Analysis of the Thermomechanical Stresses in Double-Wall Effusion Cooled Systems", ASME Journal of Turbomachinery, 2019 (in press).

TOWARDS THE SIMULATION OF THE FRICTION STIR WELDING PROCESS WITH THE SMOOTHED PARTICLE HYDRODYNAMICS METHOD

Elizaveta Shishova*[1], Florian Panzer[2], Siegfried Schmauder[2], and Peter Eberhard[1]
[1]Institute of Engineering and Computational Mechanics, University of Stuttgart, Stuttgart, Germany
[2]Institute for Materials Testing, Materials Science and Strength of Materials, University of Stuttgart, Stuttgart, Germany

Summary In contrast to common welding processes, Friction Stir Welding does not involve melting of the material. The occurring large deformations and topology changes are problematic to treat by conventional mesh-based discretization methods. Smoothed Particle Hydrodynamics provides an alternative, which is capable of dealing with these issues. This contribution handles various challenges associated with the joining process, combining numerous physical phenomena, such as an appropriate viscoplastic material model, solid-state bonding, thermoplasticity and contact, into one single SPH framework. Different simulation scenarios are performed with the help of the SPH code to ensure the appropriate consideration of each physical effect.

Friction Stir Welding (FSW) is a solid-state joining process [1], where the weld is produced not by melting of the base material like in common fusion processes, but by stirring it at elevated temperatures [2]. The thermal and deformation energies are generated by the tool rotating along the weldline. As a result the material is softened and mixed, producing a non-porous high-quality seam. In experiments, the observation of the material behavior and effects inside the workpiece is not possible, as the tool motion results in a complex, hidden, three-dimensional material flow [3]. Due to that, a vast effort is spent in FSW modeling with the help of different simulation techniques. As there are large deformations present in this joining process, conventional grid-based methods, such as the Finite Element Method, do not provide a reliable simulation model, result in mesh entanglement, and require remeshing. In contrast to that, Smoothed Particle Hydrodynamics (SPH) is a computational method that represents the continuum by discretization points, i.e., particles. This allows the material to follow topology changes and makes it possible to include voids and discontinuities. Besides large deformations, FSW is described by various linked physical phenomena. This contribution provides insight into an accurate implementation of thermo-mechanical simulation, which considers all the effects, which are essential for the FSW process. These include plasticity with high strains and strain rates, inelastic heat generation, friction, and solid-state bonding. In the work presented, the necessary constitutive laws were implemented in the SPH framework, combining thermal, mechanical, and contact effects. The simulation of FSW was performed alongside additional validation examples followed by comparison with analytical solutions, experiments, and conventional simulation techniques.

In literature, there are few examples of FSW simulated using the SPH method [4, 5]. However, a complete and accurate model that considers all of the crucial effects is absent. As an initial test, the existing SPH framework for solids [6] was used to simulate FSW, which can be seen in Fig. 1. However, remaining issues are a lack of a proper material model, the missing transition from contact to continuum during solid-state bonding, as well as the need for an enhanced stabilization technique. These problems have to be addressed separately in order to provide an accurate approximation of the process.

In this study, a new microstructure-based material model was developed in order to reproduce the viscoplastic material behavior in a more complete way, than, for example, the common empiric Johnson-Cook material model [7]. The FSW process is characterized by large strains, large strain rates, and elevated temperatures [8], which requires an improved constitutive law formulation. To do so, a new representation of the yield criteria was composed, which describes yield stress as a function of strain, strain rate, and temperature. In contrast to the Johnson-Cook material model, the influence

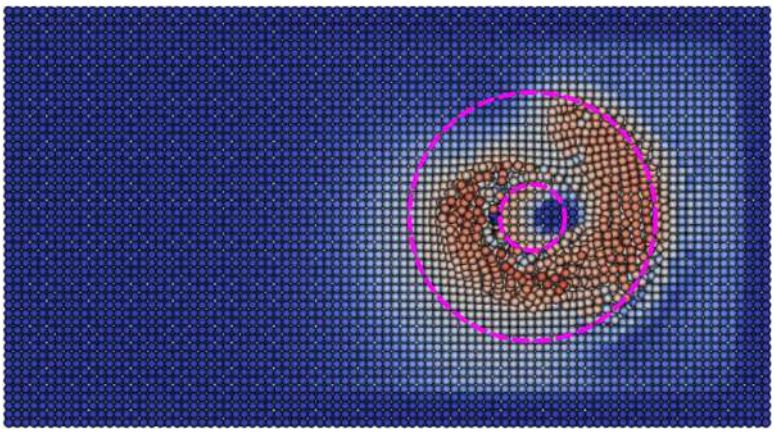

Figure 1: von Mises stress distribution during FSW. Blue: low stresses, red: high stresses.

*Corresponding author. E-mail: elizaveta.shishova@itm.uni-stuttgart.de

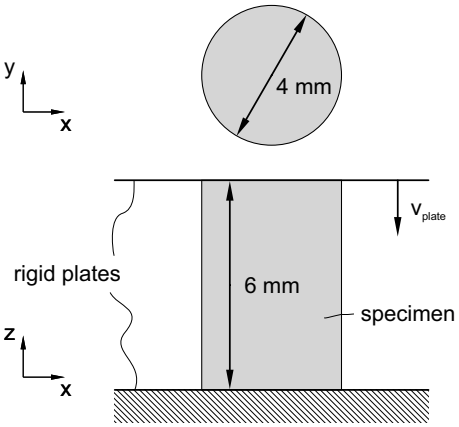

Figure 2: Setup of compression test model

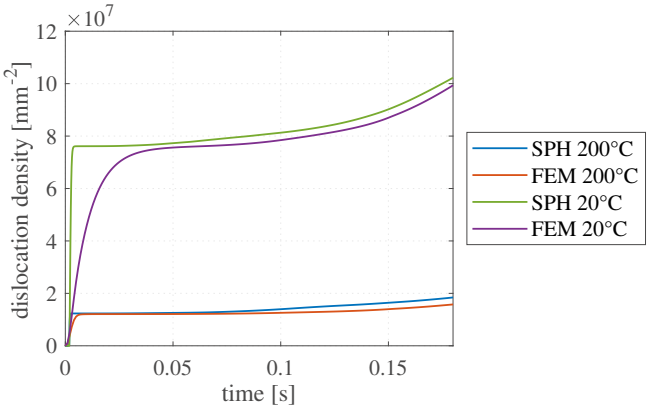

Figure 3: Dislocation density evolution for two different scenarios with isometric temperature $T = 20°\mathrm{C}$ and $T = 200°\mathrm{C}$ for $\dot{\epsilon} = 7\,\mathrm{s}^{-1}$.

of the material condition is not taken into consideration directly, but through a physical description defining the origin of plasticity on a microstructural level. The relationship describes the influence of grain size, dislocation densities, and solid solution on strengthening and softening of the material. In order to produce such a model, the compression tests were performed with different strain rates and temperatures at the Material Testing Institute (MPA). The resulting model was implemented in Abaqus and in the SPH-code Pasimodo [9]. A simple compression test was set up in both simulation frameworks and compared with each other, as well as with experimental results, in order to validate the implementation. The test setup is presented in Fig. 2, where the cylinder is compressed between two rigid planes. Figure 3 shows the evolution of the dislocation density for different temperature scenarios. As it would be expected, the plastic deformation at lower temperatures results in higher amount of dislocations.

There is no FSW model available today, that is able to represent the solid-state bonding, currently the welding interface is already connected before the actual joining happens. That results in an inability of the simulation to predict some specific defects, such as the kissing-bond phenomena. The implemented microstructural material model provides a base for a solid-state bonding criteria. That means that the interaction between SPH particles should be able to change from the normal and friction force interaction into SPH interaction representing a continuum under large deformations and elevated temperatures.

Another crucial aspect of the FSW process are thermal effects. Heat is generated through friction contact of the tool with the workpiece, as well as through large plastic deformations. Heat conduction is responsible for the heat transportation along the workpiece and heat dissipation results in loss of heat to the atmosphere. Additionally, the thermal and mechanical behavior of the model is strongly connected. Therefore, it is essential to simulate the thermal effects correctly. To that end, simulation models with separated effects were created. A nonisothermal compression test was used to validate the contribution of plastic work to thermal energy, as the strain rates can be controlled in this test.

As a final step, the improved SPH framework was used to assemble and simulate an enhanced FSW model, providing deeper insight into the quality and possible improvements of the joining method.

References

[1] Thomas W., Nicholas E., Needham J., Murch M., Temple-Smith P., Dawes C. Friction-Stir Butt Welding. *Great Britain Patent Application No. GB9125978.8*, 1991.

[2] Mahoney M.W., Rhodes C.G., Flintoff J.G., Bingel W.H., Spurling R.A. Properties of friction-stir-welded 7075 T651 aluminum. *Metallurgical and Materials Transactions A*, **29**: 1955-1964, 1998.

[3] Lorrain O., Favier V., Zahrouni H., Lawrjaniec D. Understanding the material flow path of friction stir welding process using unthreaded tools. *Journal of Materials Processing Technology.* **210**: 603-609, 2010.

[4] Pan W., Li D., Tartakovsky A., Ahzi S., Khraisheh M., Khaleel M. A new smoothed particle hydrodynamics non-Newtonian model for friction stir welding: Process modeling and simulation of microstructure evolution in a magnesium alloy. *International Journal of Plasticity*, **48**: 189-204, 2013.

[5] Fraser K. Robust and efficient meshfree solid thermo-mechanics simulation of friction stir welding. *PhD Thesis*, UQAC, Quebec, 2017.

[6] Shishova E., Spreng F., Hamann D., Eberhard P. Tracking of material orientation in updated Lagrangian SPH, *Computational Particle Mechanics*, **6**: 449-460, 2019.

[7] Johnson G.R., Cook W.H. A constitutive model and data for metals subjected to large strains, high strain rates and high temperatures.*Proceedings of the 7th International Symposium on Ballistics*, **21**, 1983.

[8] Kuykendall K., Nelson T., and Sorensen C. On the selection of constitutive laws used in modeling friction stir welding. *International Journal of Machine Tools and Manufacture*, **74**: 74-85, 2013.

[9] Pasimodo, web site **https://www.itm.uni-stuttgart.de/en/software/pasimodo**.

PARAMETRIC REDUCED ORDER MODELLING AND DEEP LEARNING TO ACCOMPLISH PATTERN RECOGNITION AND REGRESSION TASKS

Luca Rosafalco*[1], Andrea Manzoni[2], Stefano Mariani[1], and Alberto Corigliano[1]
[1]Dipartimento di Ingegneria Civile ed Ambientale, Politecnico di Milano, Milano, Italy ù
[2]MOX, Dipartimento di Matematica, Politecnico di Milano, Milano, Italy

Summary The use of high-fidelity physical/numerical models is still challenging when dealing with inverse problems aiming at parameter estimation. To enhance the solution of these problems in computational mechanics, we propose to train statistics-based regressors via input-output data ad-hoc generated from the physics-based model. The goal is to obtain an easy to use data analysis tool capable of performing pattern recognition and regression tasks, in compliance with the governing equations of the model. In particular, we combine: (i) parametric model order reduction techniques, to reduce the computational burden connected to the input-output pairs generation; (ii) deep learning architectures, for the sake of pattern recognition and regression tasks.

PROBLEM DEFINITION

Physics-based high-fidelity models enable the study of complex phenomena and deepen our understanding of reality. In recent times, the development of numerical methods, such as finite elements, have enlarged the domain of applications of such models to attain unprecedented success in building digital twins of real systems. Dealing with model uncertainties also becomes crucial in inverse problems; in several engineering applications, factors like the presence of noise or the redundancy of measurables make inverse problems hard to tackle with customary model updating tools, requiring the use of pattern recognition techniques. To overcome this bottleneck and also attain results in real time, physical models can be empowered by a coupling with statistical tools.

Our proposal consists in training statistics-based regressors via input-output data, ad hoc generated running mechanical models. A regressor is trained using: as input the J_0 displacements and/or acceleration recordings $\mathbf{X}^0 = \left[\mathbf{x}_1^0, \dots, \mathbf{x}_{J_0}^0\right]$ at a discrete locations over the structure in the time interval $[0, I]$; and as output the elastic properties (parametrized by the vector $\boldsymbol{\eta}$). The input $\mathbf{X}^0$ of the regressor is thus the output of the model, while the output $\boldsymbol{\eta}$ of the regressor is the input of the model; for this reason, the regressor is said to operate an output-input mapping.

Dealing with a semi-discretized version of the equations governing structural dynamics, the physical description of a mechanical system is provided by

$$\mathbf{M}\ddot{\mathbf{u}}\left(\boldsymbol{\eta}, t\right) + \mathbf{C}\dot{\mathbf{u}}\left(\boldsymbol{\eta}, t\right) + \mathbf{K}\left(\boldsymbol{\eta}\right)\mathbf{u}\left(\boldsymbol{\eta}, t\right) = \mathbf{f}\left(t\right) \quad t \in (0, T)$$

where: t is the time; $\mathbf{u}\left(\boldsymbol{\eta}, t\right)$ are the degrees of freedom of the mechanical system; $\mathbf{M}$, $\mathbf{C}$, $\mathbf{K}\left(\boldsymbol{\eta}\right)$ are the mass, damping and stiffness matrices, respectively; $\mathbf{f}\left(t\right)$ is the vector of external loads. The displacement/acceleration time recording $\mathbf{x}_j^0$, with $j = 1, \dots, J_0$, is obtained running the model in $[0, I]$ and sampling the structural response in time at the corresponding control points (e.g $x_{1j}^0 = \ddot{u}_n\left(t_1\right), \dots, x_{Ij} = \ddot{u}_n\left(t_I\right)$, where the acceleration of the j-th control point coincides with the n-th degree of freedom of the model).

Given that the generated input-output pairs satisfy the governing equations of the problem, also the regressor enjoys this property. Thanks to the optimization procedure on which the regressor training relies, the regressor acquires the ability of performing pattern recognition. Surrogate or reduced order models can be exploited in place of high-fidelity models, given that the training relies on the generated input-output pairs, and not on the mathematical structure of the model. Parametric model order reduction techniques are then employed due to their capacity of handling the input variability in a straightforward manner, due to the availability of a priori and a posteriori error analyses tools linked to the construction of the reduced order space [3]. Depending on the problem, several deep learning-based architectures may be used for the regressor; in our work [4], neural network architectures have been proven to be extremely powerful and versatile and have therefore been adopted even if, due to the complexity of the non-linear transformation involved, it is generally difficult to describe these algorithms in a close mathematical form.

The described approach has been adopted in numerical benchmarks where the elastic properties $\boldsymbol{\eta}$ of a specimen under partially unknown loading conditions must be determined on the basis of available displacement and/or acceleration recordings, as typically done in vibrational analysis. Given that such measurements are shaped as multivariate time series, fully convolutional networks featuring three convolutional layers have been exploited [1]. The l-th convolutional layer operates a non linear transformation of the incoming signal according to $\mathbf{X}^l = \sigma\left(\mathbf{W}^l * \mathbf{X}^{l-1}\right)$, where $\mathbf{X}^{l-1} = \left[\mathbf{x}_1^{l-1}, \dots, \mathbf{x}_{J_{l-1}}^{l-1}\right]$ is the input matrix; $\mathbf{X}^l = \left[\mathbf{x}_1^l, \dots, \mathbf{x}_{J_l}^l\right]$ is the output matrix; σ is an element-wise activation function, and $\mathbf{W}^l = \left[\mathbf{w}_1^l, \dots, \mathbf{w}_{J_l}^l\right]$ is a kernel matrix, being $\mathbf{w}_j^l$ a kernel with Q_l tunable parameters. The convolutional dot product $*$ reads $\mathbf{x}_j^l = \sigma\left(\mathbf{w}_j^l * \mathbf{X}^{l-1}\right)$ where, at a sliding step centered at i:

$$\left(\mathbf{w}_j^l * \mathbf{X}^{l-1}\right)_i = \sum_{q=0}^{Q_l} \sum_{k=0}^{J_{l-1}} w_{qj} x_{i+q,k}^{l-1} \, .$$

*Corresponding author. E-mail: luca.rosafalco@polimi.it.

APPLICATION

A numerical benchmark dealing with a classification task is adopted to assess the performance of the proposed approach. A cantilever beam, whose geometry is depicted in Fig.1, is loaded with a uniform load $\mathbf{f}$ that has a sinusoidal dependency on time, and whose magnitude and frequency are described by two uniform probability distributions $\mathcal{U}_1\,(0.075, 1.025)$ kN/m and $\mathcal{U}_2\,(25, 325)$ Hz, respectively. The beam domain Ω is divided into four parts Ω_r, $r = 1, \ldots, 4$, of equal length. The beam deflection is recorded in four points located on the upper surface of the beam at $x = 1, 2, 3, 4$ m. Considering a reference Youngs modulus $E = 210$ GPa, the goal is to understand which of five possible states has generated the pseudo-experimental measurements: in each damage state, E is reduced by 25% in one single domain, while the virgin state (baseline) is considered as state 0.

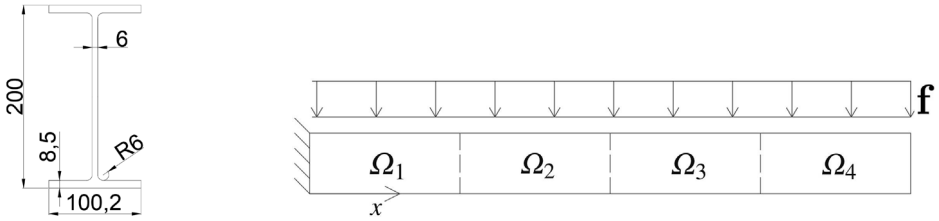

Figure 1: (left) IPE 200 cross section (dimensions in mm); (right) schematic representation of the problem.

Reduced basis techniques [2] have been used for the parametric order reduction of the model to treat the sources of variability of the mechanical system output, depending both on $\boldsymbol{\eta}$ and on the (partially unknown) loading conditions. Whenever non affine dependences on the input has been encountered, hyper-reduction techniques, such as the discrete empirical interpolation method, have been exploited.

The obtained results testify the potentialities of the approach: in Fig.2 the evolution of loss C and accuracy A on the training set $\mathbf{D}_{train}$ (used to train the fully convolutional network) and on the validation set $\mathbf{D}_{val}$ (used to interrupt the training when necessary) are depicted. The evolution of C and A are shown against the number of iterations performed by the training algorithm. In Fig.3 the confusion matrix obtained on the test set $\mathbf{D}_{test}$ (unseen by the network during training) is reported, highlighting an overall accuracy of around 98.7%. $\mathbf{D}_{train}$ and $\mathbf{D}_{val}$ have been constructed using the reduced order model, while $\mathbf{D}_{test}$ has been constructed using the high fidelity model, meant as a replica of reality.

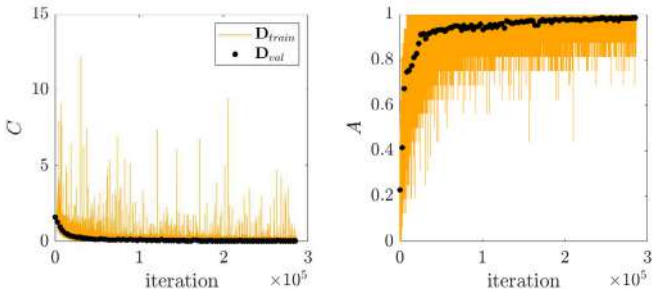

Figure 2: Left: evolutions of C (left) and A (right) on $\mathbf{D}_{train}$ and $\mathbf{D}_{val}$ during the training of the fully convolutional network.

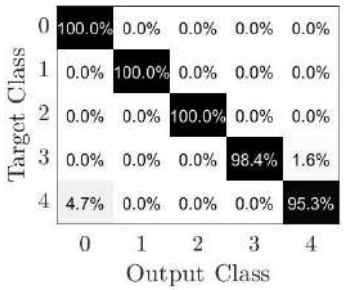

Figure 3: Confusion matrix related to the classification performance of the regressor on $\mathbf{D}_{test}$.

References

[1] Karim F., Majumdar S., Darabi H., Harford S. Multivariate LSTM-FCNs for time series classification. *Neural Networks* **116**: 237-245, 2019.

[2] Quarteroni A., Manzoni A., Negri F. Reduced basis methods for partial differential equations: an introduction. Unitext vol.92, Springer, Cham, Switzerland 2015.

[3] Rosafalco, L., Manzoni, A., Mariani, S. et al. Fully convolutional networks for structural health monitoring through multivariate time series classification. *Adv. Model. and Simul. in Eng. Sci.* 7, 38 (2020). https://doi.org/10.1186/s40323-020-00174-1

[4] Rosafalco, L.; Torzoni, M. Manzoni, A.; Mariani, S.; Corigliano, A. Towards Real time Structural Health Monitoring by Model Order Reduction and Deep Learning Algorithms. Submitted.

[5] Rosafalco, L.; Manzoni, A.; Mariani, S.; Corigliano, A. A Time Series Autoencoder for Load Identication empowered by Automatic Selection of the Latent Variables Number. Submitted.

A QUASI-EXTREMAL ENERGY PRINCIPLE IN RATE-INDEPENDENT PLASTICITY OF SINGLE CRYSTALS

Henryk Petryk[1]
[1]Institute of Fundamental Technological Research (IPPT), Polish Academy of Sciences, Warsaw, Poland

Summary A quasi-extremal energy principle has recently been proposed for non-potential problems in rate-independent plasticity for which the known extremal principles do not apply. The principle is extended here to small but finite increments, with the end-point values of displacements and plastic multipliers as unknowns in a computational approach. The aim is to overcome the difficulty related to non-uniqueness of incremental solutions for ductile single crystals characterized by a slip-system interaction matrix that is indefinite and non-symmetric. The extended principle is applied to numerical simulations of large plastic deformation of a single crystal with automatic selection of the currently active slip systems at each time step.

INTRODUCTION

There is a long-standing difficulty in solving incremental problems of rate-independent plasticity, which is related to non-uniqueness of solutions. Commonly known branching phenomena like buckling, necking, shear banding or subgrain formation require a criterion of choice of the post-critical deformation branch in numerical simulations. In crystal plasticity at finite strain [1, 2, 3], the difficulty appears already at the level of selection of active slip systems at a material point. If there exists an incremental potential then a computational approach based on the incremental energy minimization is available [4, 5, 6]. However, a generic rate-problem in crystal plasticity is of non-potential type, therefore the question arises how to select a physically meaningful solution among multiple possibilities when the known extremal principles do not apply.

Recently, a new energy-based variational formulation has been developed for a broad class of non-potential problems in rate-independent plasticity [7]. It has been shown that direct incremental energy minimization does not provide a proper solution to the rate-problem posed when the global stiffness matrix for active plastic deformation mechanisms is not symmetric. The correct rate-solution is then generated by a quasi-extremal energy principle in which the minimized function depends on an unknown solution as a parameter.

The aim of the present work is twofold. First, to extend the quasi-extremal energy principle, formulated originally for rate-solutions, to small but finite increments with the end-point values as unknowns in a computational approach. Second, to apply it in numerical simulations of large plastic deformation of a single crystal for automatic selection of the currently active slip systems at each time step, without assuming symmetry of the slip-system interaction matrix.

A QUASI-EXTREMAL ENERGY PRINCIPLE FOR A DISCRETIZED PROBLEM

A *quasi-extremal principle* (QEP) for a discretized plasticity problem takes the form

$$x = \arg\min_{z\in\mathbb{Z}} \mathcal{E}(z,x)\,, \qquad z=(\tilde{q},\tilde{\mu}), \qquad \mathbb{Z}=\mathbb{R}^m\times\mathbb{R}^n_+\,, \tag{1}$$

where the variable $z=(\tilde{q},\tilde{\mu})$ encompasses virtual increments $\tilde{q}=q^{k+1}-q^k\in\mathbb{R}^m$ of generalized displacements and non-negative plastic multipliers $\tilde{\mu}\in\mathbb{R}^n_+$. A characteristic feature of a quasi-extremal principle is that the minimized real-valued function $\mathcal{E}$ depends not only on variable z but also on an unknown solution x as a parameter. Function $\mathcal{E}$ has a particular energy-based form derived in [7]. It is essential that function $\mathcal{E}$ is generally non-convex when evaluated with accuracy to second-order terms. When extended to small but finite increments, it takes a fully analogous form,

$$\mathcal{E}(z,x)=\tilde{E}(z)+z\cdot Cx\,, \qquad C=-C^{\mathrm{T}}\,, \tag{2}$$

where the leading term is the incremental energy function defined for isothermal irreversible processes by

$$\tilde{E}=\tilde{\Phi}+\tilde{\Omega}+\tilde{\mathcal{D}}\,. \tag{3}$$

Here, a tilde over a symbol means an increment, Φ is the Helmholtz free energy, Ω the potential energy of external loads, and $\tilde{\mathcal{D}}$ is the incremental rate-independent dissipation in the case when all components of $\tilde{z}$ vary proportionally in time during a time step $[t^k,t^{k+1}]$. The term $z\cdot Cx$ in Eq. (2) is new and accounts for the loss of potentiality of the incremental problem. It is expressed through the anti-symmetric part $C=\frac{1}{2}(A-A^{\mathrm{T}})$ of a governing matrix A in constitutive equations $(\tilde{Q},\tilde{f})=Ax+o(t^{k+1}-t^k)$ that relate an incremental solution x to increments $\tilde{Q}$ of generalized forces and $\tilde{f}$ of yield functions. It has been shown that a solution x to QEP (1) solves the incremental quasi-static problem so that $\tilde{Q}$ satisfies the equilibrium conditions and $\tilde{f}$ the discrete consistency conditions at the end of a time step.

Moreover, QEP (1) includes also the energy criterion of stability of a solution path in the sense that small perturbing forces make a non-negative scalar product with a deviation δx they induce in the solution. QEP (1) with non-convex $\mathcal{E}$ provides thus a criterion of choice among multiple solutions that is not based on arbitrarily assumed imperfections or random selection but has a physical meaning. For potential problems we have $C=0$, and then QEP (1) reduces to direct minimization of $\tilde{E}(z)$ known as the energy criterion of path stability or as the incremental energy minimization approach.

SELECTION OF ACTIVE SLIP SYSTEMS IN A SINGLE CRYSTAL

Similarly to the incremental energy minimization limited to potential problems, QEP (1) can be used to overcome the difficulty related to non-uniqueness of incremental solutions to non-potential problems for ductile single crystals. In particular, it has been employed to select a non-uniquely defined set of active slip systems in a single crystal for which the energy function $\mathcal{E}$ is non-convex due to latent hardening higher than self-hardening. To solve the problem numerically, the constrained non-convex minimization problem in QEP (1) has been converted to a smooth unconstrained one by using the augmented Lagrangian method [8] in a manner fully analogous to that in [6].

The algorithm developed in [6] has been applied after modifying the incremental work expression by adding an extra term corresponding to the last term in Eq. $(2)_1$. Effectiveness of the algorithm for large plastic deformation is demonstrated by an example of simple shear λ relative to a fixed laboratory frame $\bar{X}_i$ initially aligned with crystallographic lattice direction [100] and plane (001) of an fcc single crystal with the full set of crystallographic slip systems. The results reported here have been obtained for the step size in λ equal to 0.01. The predicted material response and the changes of active slip systems caused by rotation of the crystallographic lattice are illustrated in Fig. 1.

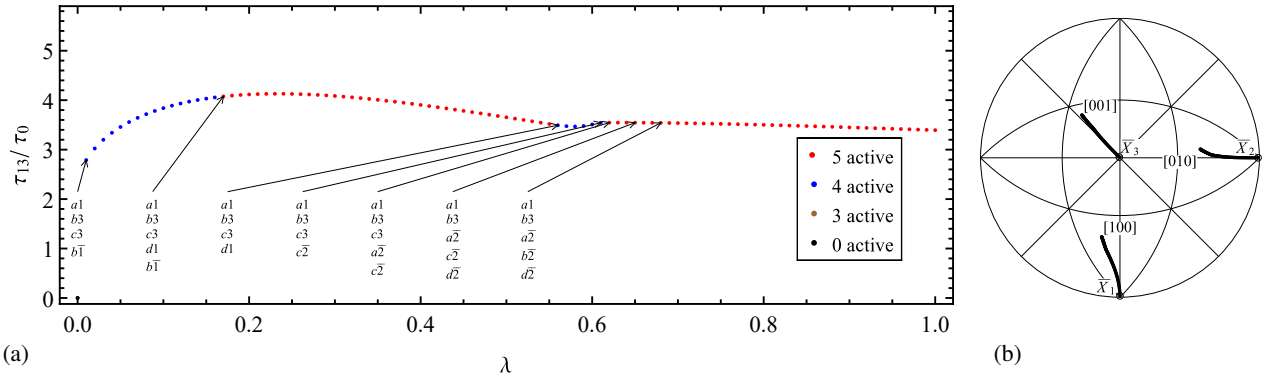

Figure 1: (a) Normalized shear stress vs shear strain for simple shear of a Cu single crystal, and (b) accompanying changes in the orientation of crystallographic axes.

The results are qualitatively similar to those obtained earlier in [6]. However, there are also quantitative differences due to the selective symmetrization of the slip-system interaction matrix used in [6] and absent here. The points marked by arrows in Fig. 1a correspond to unloading of some slip system and/or loading of some other system that reaches the current threshold value of the resolved shear stress. It is remarkable that the number of simultaneously active slip systems does not exceed five, which is in accord with experimental observations of polycrystals and results here from the energy criterion of path stability that is embedded in QEP (1).

Further work on non-unique deformation patterns computed with the help of the quasi-extremal energy principle is currently in progress.

CONCLUSION

- The recently proposed [7] quasi-extremal energy principle (QEP) for non-potential problems in rate-independent plasticity has been extended to small but finite increments with the end-point values as unknowns in a computational approach.
- Applicability of the QEP has been illustrated by the example of selection of active slip systems in a Cu single crystal under large plastic shear, without assuming symmetry of the slip-system interaction matrix.

References

[1] Hill R., Rice J. R. Constitutive analysis of elastic-plastic crystals at arbitrary strain. *J. Mech. Phys. Solids* **20**: 401–413, 1972.
[2] Peirce, D., Asaro, R. J., Needleman, A. An analysis of nonuniform and localized deformation in ductile single crystals.*Acta Metall.* **30**: 1087–1119, 1982.
[3] Franciosi P., Zaoui A. Crystal hardening and the issue of uniqueness. *Int. J. Plasticity* **7**: 295–311, 1991.
[4] Petryk H., Thermann K. On discretized plasticity problems with bifurcations. *Int. J. Solids Struct.* **29**: 745–765, 1992.
[5] Ortiz, M., Repetto, E. A., Stainier, L. A theory of subgrain dislocation structures. *J. Mech. Phys. Solids* **48**: 2077–2114, 2000.
[6] Petryk H., Kursa, M. Incremental work minimization algorithm for rate-independent plasticity of single crystals. *Int. J. Num. Meth. Engng.* **104**: 157–184, 2015.
[7] Petryk H. A quasi-extremal energy principle for non-potential problems in rate-independent plasticity. *J. Mech. Phys. Solids*, 2020, https://doi.org/10.1016/j.jmps.2019.103691.
[8] Bertsekas D.P. Constrained Optimization and Lagrange Multiplier Methods. Second ed., Athena Scientific, Belmont, MA 1996.

THEORETICAL AND COMPUTATIONAL RESULTS ON MATERIAL CONSTRAINTS IN ANISOTROPIC ELASTICITY

Michele Marino*[1] and Peter Wriggers[2]
[1]Department of Civil Engineering and Computer Science, University of Rome Tor Vergata, Rome, Italy
[2]Institute of Continuum Mechanics, Leibniz University, Hannover, Germany

Summary Incompressibility conditions and/or strong anisotropies introduce internal constraints in material deformation. Numerical simulations comprising "constrained" materials show an overstiff structural response, referred to as element locking. Implementations based on mixed variational methods can heal locking but several solutions adopted in the state-of-the-art are still non-optimal for anisotropic materials. This paper addresses this issue by proposing a novel decomposition of anisotropic deformation modes on the basis of kinematic and energy requirements. Theoretical results exploit the Walpole's formalism. A low-order mixed finite element formulation for dealing with quasi-inextensibility and/or quasi-incompressibility constraints is thus derived and analysed.

INTRODUCTION

Many engineering applications comprise materials with an anisotropic response [1]. For instance, in civil, aerospace and automative industries, fibrous or fiber-reinforced materials are widely employed since they gather lightweight properties with excellent strength behaviors and complex target responses. In the design of fiber-reinforced composite materials, structural requirements or production restrictions might lead to the use of highly-stiff fiber materials or matrix properties with small/negligible volumetric deformations. This occurs, for instance, in applications like soft actuators, textiles, rubberized concretes or laminates, but also in the domain of biological tissues [2]. Stiff responses along particular directions and/or in the volumetric behavior can be regarded as internal constraints in material response.

Numerical simulations are widely employed in technical applications to analyze material and/or structural behavior for design and verification purposes. Nevertheless, the robustness and accuracy of numerical simulations are highly affected by the presence of internal constraints in material response. Traditional finite element formulations exhibit poor convergence rates in the basic variables and the element response is overstiff. These phenomena are generally referred to as locking and they have been widely explored in the literature, for instance, for the case of incompressibility [3], fiber inextensibility or intra-ply fiber shear [4, 5, 6]. Clearly, when material constraints couple each other, like when inextensble fiber are embedded in an incompressible material, locking effects severly amplify. This work explores Hu-Washizu-like mixed formulations introduced for overcoming element locking in the case of anisotropic materials [7]. The analysis is restricted to linear elasticity with transversely isotropic material symmetries.

MIXED FORMULATIONS IN ANISOTROPIC ELASTICITY

Within a variational principle for mixed formulations, the internal energy density is enriched by means of Lagrange (stress-like) multipliers and deformation-like (energy-conjugate) variables. In order to deal with material constraints, the strain tensor is generally split in two contributions: a penalized contribution, associated with the material constraint, and the complementary part. Apart from mechanical equilibrium (i.e., the balance of linear momentum), stationary of the enriched potential energy leads to two additional (set of) equations. One is associated with kinematic compatibility, where the penalized strain (i.e., the displacement field) is controlled in terms of the introduced deformation-like variables. The other one is associated with the constitutive relationship, where the deformation-like variables are related to the Lagrange multipliers through the material constitutive response associated with the overstiff behavior (e.g., the bulk modulus for incompressibility or fiber stiffness for inextensibility). This rationale is here referred to as penalized-kinematics. If the introduced decomposition of the strain tensor respects energetically-orthogonality, the balance of linear momentum will not explicitly depend on the deformation mode associated with the material constraint, being fully replaced in its stress response by the introduced Lagrange multipliers. As a consequence, the material constants associated with the overstiff behaviour will also not explicitly appear. In this case, the associated mixed variational formulation is referred to as energetically-decoupled, since the penalized "constrained" deformation mode is decoupled in energy from the complementary "unconstrained" one.

In isotropic elasticity, the classical volumetric-deviatoric split leads to energetically-decoupled mixed variational formulations where the bulk modulus does not explicitly appear in the static equilibrium [3]. Anisotropy introduces relevant issues in the kinematic decomposition of material response for dealing with internal constraints. For instance, the classical volumetric-deviatoric split for treating incompressibility in the presence of anisotropic elasticity looses its significance (since it assumes an isotropic response). Moreover, in the presence of fiber inextensibility, existing mixed formulations for anisotropic materials are generally built exclusively upon a kinematic rationale (like the removal of the unidirectional elongation of fibers), hence violating energy-orthogonality requirements [4, 5]. A general constraint manifold theory which

*Corresponding author. E-mail: m.marino@ing.uniroma2.it

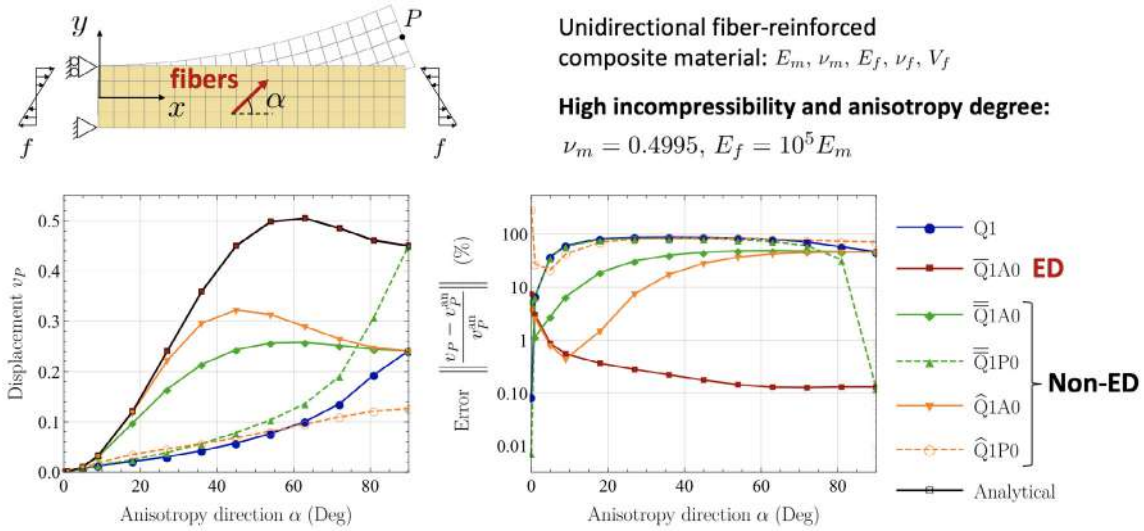

Figure 1: Vertical displacement v_P (left) and relative error (right) obtained in a pure bending test: comparison between the proposed energetically-decoupled (ED) Hu-Washizu formulation using the Walpole's formalism for strong transverse isotropy and high incompressibility with different non-energetically-decoupled (Non-ED) mixed potentials. Results are shown for different anisotropy direction (i.e., fiber angle α) on a structured mesh with element density $n_{el} = 10$.

introduces energetically-consistent Hu-Washizu formulations for incompressibility, inextensibility and inshearability has been recently discussed by Zdunek in Ref. [6].

The present work presents novel theoretical and computational results on transversely isotropic elasticity for different degrees of incompressibility and/or anisotropy. Results are built exploiting the convenient basis offered by the Walpole's formalism [8, 9]. A projector operator is built on the basis of kinematic and energy requirements and its effectiveness in terms of numerical results analysed.

NUMERICAL RESULTS

A low-order mixed finite element formulation based on the proposed kinematic split is introduced and tested on a number of benchmark tests and engineering case studies. Firstly, in order to investigate on the engineering relevance of the obtained theoretical results, the ineffectiveness of the classical volumetric-deviatoric split in anisotropic elasticity is investigated from the numerical point of view, showing that accuracy is lost even in the presence of mild anisotropy degrees. Moreover, the drawbacks of employing a non-energetically-decoupled formulation based only on a penalized-kinematics rationale are clearly shown in terms of accuracy, convergence properties and robustness with respect to material properties (see Fig. 1).

CONCLUSIONS

In this work, the theoretical derivation of energetically-orthogonal deformation modes in transversely isotropic linear elasticity was developed by exploiting the convenient representation offered by the Walpole's basis. A projector operator on the deformation field has been designed in order to satisfy kinematic and energy requirements. It has been proven that the projected strain contains the full volumetric deformation at hand. Accordingly, the proposed formulation allows to effectively deal with the presence of material constraints associated with quasi-inextensibility and/or quasi-incompressibility. Energetically-decoupled mixed variational formulations were introduced and implemented in low-order finite element models, investigating their numerical effectiveness.

References

[1] Kollar L.P., Springer G.S. Mechanics of Composite Structures, Cambridge University Press, Cambridge, UK, 2003.
[2] Aboudi J., Arnold S.M., Bednarcyk B.A. Micromechanics of Composite Materials, Butterworth-Heinemann, Elsevier, Oxford, UK, 2013.
[3] Zienkiewicz O.C., Taylor R.L., Zhu J.Z., 2013. The Finite Element Method: Its basis and fundamentals, 7th edn. Butterworth-Heinemann, Oxford.
[4] Wriggers P., Schröder J., Auricchio F., 2016. *Adv. Model. and Simul. in Eng. Sci.* **3**:25(18).
[5] Rasolofoson F., Grieshaber B.J., Reddy B.D., *Int. J. Numer. Methods Eng.* **117**:693–712, 2019.
[6] Zdunek A. *J. Elast*, doi:10.1007/s10659-019-09747-7, 2019.
[7] Washizu K. Variational Methods in Elasticity and Plasticity. Pergamon Press, Oxford, UK, 1975.
[8] Walpole L.J. *Adv. Appl. Mech.* **21**:169–242, 1981.
[9] Federico S., Grillo A., Imatani S. *Math. Mech. Solids* 20:643–662, 2015.

REDUCED ORDER MODELS FOR COMPOSITES WITH PLASTIC BEHAVIOR

Alfredo Castrogiovanni[1], Sonia Marfia[2], Elio Sacco[3] and Ferdinando Auricchio[1]
[1]Dipartimento di Ingegneria Civile e Architettura, Università di Pavia, Pavia, Italy
[2]Dipartimento di Ingegneria, Università di RomaTre, Roma, Italy
[3]Dipartimento Strutture per l'Ingegneria e l'Architettura, Università di Napoli "Federico II", Napoli, Italy

Summary The aim of the work is to study the overall mechanical response of periodic composite characterized by constituents with a nonlinear response. In particular, a plasticity material model with isotropic hardening is considered at the microscale. A representative volume element of the heterogeneous material is studied. The micromechanical problem is solved considering two different reduced order models, one based on Hashin-Shtrikmann homogenization scheme and the other one on the Transformation Field Analyses. Some numerical applications are carried out comparing the two presented techniques.

INTRODUCTION

Composite materials are used in several fields of structural engineering. Their heterogeneous and complex microstructure have to be considered in order to predict the macroscopic response of the composite material, taking into account the possible nonlinear response of the components. In this case, the study becomes more complex as the nonlinear effect occurring in the material has also be modeled. A large class of composite media are made of constituents that exhibit plastic behavior that requires the use of nonlinear elastoplastic material models.
One possibility to evaluate the overall mechanical response of these composite materials, which have complex microstructures and plastic effects in its constituents, is to adopt micromechanical procedures, that study a representative volume element (RVE), determining the behavior of the homogenized equivalent material. To this end, nonlinear finite element analyses can be developed to solve the micromechanical problem, requiring expensive computations, due to the large number of history variables and micromechanical unknowns, in view of multiscale analyses.
Thus, efficient tools able to determine the overall response of the material, taking into account its microstructure and the nonlinear phenomena occurring, are needed. For this reason, model order reduction techniques have been proposed in the literature.
The aim of this work is to study and compare two reduced order models (ROM) in order to underline advantages and disadvantages of these techniques. In particular, the study investigates the performances of the Hashin-Shtrikmann (HS) homogenization scheme, proposed in [1] and based on the Hashin and Shtrikman approach [2], and of the Piecewise Uniform Transformation Field Analysis homogenization technique, presented in [3] and based on Transformation Field Analysis proposed by Dvorak [4]. In particular, the HS technique is herein extended to plasticity with isotropic hardening adopting the Von Mises yield criterion.

REDUCED ORDER MODELS

Periodic composites are considered and a unit (UC), repetitive cell is studied. Indeed, composites with constituents characterized by a plastic behaviour are studied and, in particular, a plastic model based on the introduction of Mises yield function and isotropic hardening is considered.
The micromechanical problem of the UC is solved adopting two different reduced order models. In both the approaches the UC is divided in elastic and plastic clusters where constant plastic strains are considered.
The Piecewise Uniform Hashin-Shtrikman (PWUHS) is derived from the Hashin-Shtrikman variational formulation, which is based on the introduction of a linear-elastic reference medium characterized by an elastic tensor $\mathbf{C}_0$. A common choice is to consider the isotropic stiffness matrix according to the homogenization theory by Voigt, which assumes homogeneous strain throughout the composite material components. An alternative is provided by the overall elasticity matrix $\bar{\mathbf{C}}$ evaluated on the real composite. A constant eigenstress is introduced in each cluster to take into account the actual elastic properties of the cluster with respect to the linear-elastic reference medium and the plastic phenomena. The micromechanical problem is formulated considering the average strains in each cluster as primary unknowns and the uniform inelastic strain as internal variables. To improve the results of the procedure the elastic properties of the reference medium can be updated during the loading history according to the *secant modulus approach,* in order to take into account the plastic phenomena occurring in the heterogeneous material. The second approach is based on the Transformation Field Analysis in which the inelastic strain, assumed as internal variable, is considered uniform in each cluster (PWUTFA) and its evolution is governed by the average stress in the cluster. In both the approaches the numerical procedure is developed to solve the micromechanical problem in two dimensional framework. The unit cell is studied applying loading histories in terms of overall average strains. The two presented homogenization techniques are able to determine the overall stress in the UC taking into account the nonlinear phenomena.

NUMERICAL APPLICATIONS

Different numerical applications are carried out in order to study the convergence of the two approaches and the efficiency in evaluating the mechanical response of composites characterized by plastic matrix and elastic inclusions. The results

obtained by the homogenization techniques are compared with the one recovered solving the micromechanical problem by nonlinear finite element analysis.

A convergence study for the PWUHS is herein reported. In Figure 1(a) a UC characterized by a plastic matrix and an elastic inclusion with a volume fraction equal to 0.54, is represented (UC-1). Both the matrix and the inclusion are characterized by the same elastic properties (Young modulus equal to 210 GPa and Poisson coefficient equal to 0.3). The yield stress of the matrix is 300 MPa and the isotropic hardening modulus is 100 MPa. The reference elastic matrix is considered constant during the analysis or updating its properties. An increasing monotonic loading history is considered for the horizontal average strain. Several analyses are carried out for two possible scenarios considering only one cluster for the inclusion and an increasing number of clusters for the matrix or a completely refined inclusion (60 clusters) and an increasing number of clusters for the matrix. The method converges to the FE solution as reported in Figure 1(b) and (c) where the value of the overall stress at the end of the analysis is plotted versus the number of clusters in the matrix.

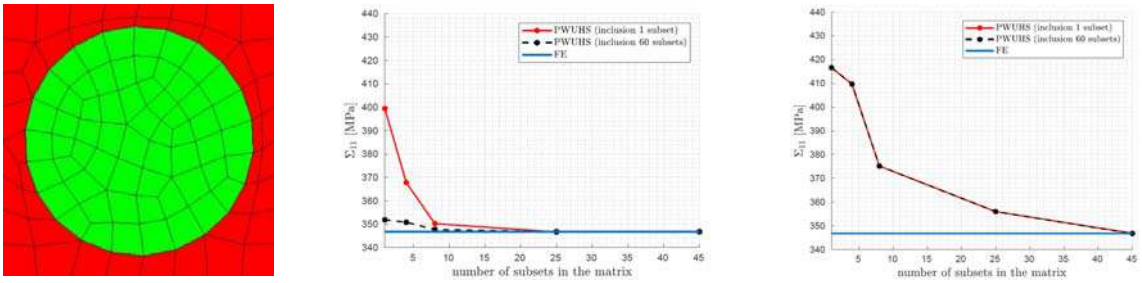

(a) (b) (c)

Figure 1. Geometry of the UC-1 (a). Analysis of convergence for an increasing horizontal average strain using the secant modulus approach (b) or using the initial $\mathbf{C}_0$ (c).

The results of the PWUHS are compared with a nonlinear finite element analyses (FE). It can be pointed out that the results of the PWUHS approach converge to the FE results increasing the number of clusters. The convergence is significantly faster in Figure 1(b) when the elastic properties of the reference medium are updated during the analyses according to the secant modulus.

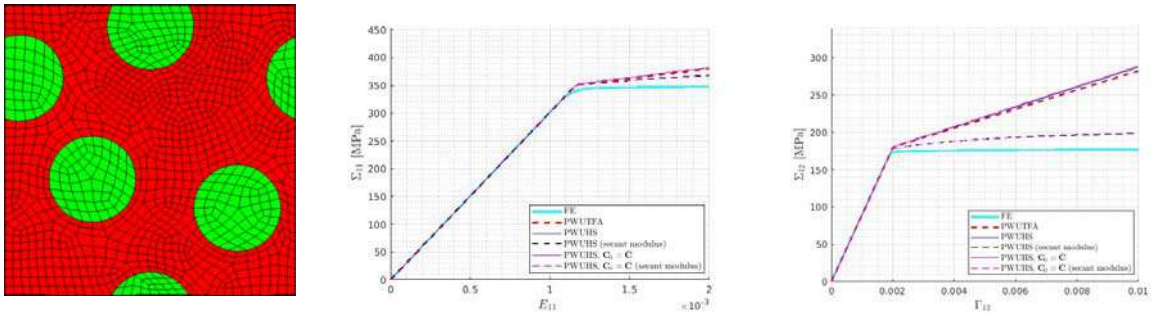

(a) (b) (c)

Figure 1. Geometry of the UC-2 (a). Analysis of convergence for an increasing horizontal average strain using the secant modulus approach (b) or using the initial $\mathbf{C}_0$ (c).

A comparison between the PWUHS and PWUTFA approaches is presented for the UC in Figure 2(a), when two clusters, one for the matrix and one for the inclusions, are considered having volume fractions respectively equal to 0.72 and 0.28. The material properties of the matrix remain unchanged if compared to UC-1 while the inclusions Young modulus and Poisson coefficient are, respectively, 300 GPa and 0.25. Results in terms of the macroscopic stresses are reported in Figure 2(b) for a horizontal increasing average strain and in Figure 2(c) for a monotonically increasing average shear strain. It can be noted that the two techniques give results in very good accordance, furthermore the correction of the elastic reference matrix sensibly increases the accuracy of the PWUHS.

CONCLUSIONS

Advantages and disadvantages of the two approaches, PWUHS and PWUTFA, are examined with the aim of developing an efficient novel Reduced Order Method. Further investigations on different microstructures are needed in order to build up a robust two-scale reduced order technique.

References

[1] Wulfinghoff, S., Cavaliere, F., Reese, S., Model order reduction of nonlinear homogenization problems using a Hashin-Shtrikman type finite element method, *Comput. Methods Appl. Mech. Engrg*, **330**: 149-179, 2017.

[2] Hashin, Z., Shtrikman, S., A variational approach to the theory of the elastic behaviour of multiphase materials, *Journal of the Mechanics and Physics of Solids*, **11**:127-140, 1963.

[3] Marfia S., Sacco E., Multiscale technique for nonlinear analysis of elastoplastic and viscoplastic composites, *Composites Part B*, **136**: 241-253, 2018.

[4] Dvorak, G. J., Transformation field analysis of inelastic composite materials. *Proceedings of the Royal Society of London*, **437**: 311-327, 1992.

DENUDED ZONES IN ZIRCONIUM PRESSURE VESSELS: OXYGEN'S ROLE EXAMINED VIA MULTI-SCALE DIFFUSION MODEL

Manura Liyanage*[1], Ronald Miller[2], and R. K. N. D. Rajapakse[3]
[1]Department of Civil and Environmental Engineering, Carleton University, Ottawa, ON, Canada
[2]Department of Mechanical and Aerospace Engineering, Carleton University, Ottawa, ON, Canada
[3]School of Engineering Science, Simon Fraser University, Burnaby, BC, Canada

Summary Zircaloy are used to make containers for nuclear fuel in nuclear reactors. Hydride formation can make them susceptible to failure, giving the need for continuous monitoring of the hydride content. Denuded zones sometimes found in surfaces of these tubes affect this monitoring process. We carried out a study which determines the effect of oxygen on hydrogen diffusivity in Zr, to check the validity of a hypothesis, suggesting that O slows the diffusion of H causing the hydrides formed to be smaller in size, and forms denuded zones. We estimated H diffusivity for different O concentrations, which shows that H diffusivity in Zr reduces with O concentration. Comparing these diffusivities against O profiles found in pressure tubes, we found that the reduction in diffusivity rates are insufficient to change the size of the precipitates to form denuded zones, in contradiction of the hypothesis.

INTRODUCTION

Zirconium alloys are used to make pressure tubes, which contains the nuclear fuel in the reactors, due to many advantageous properties [1, 2]. In the harsh service conditions of nuclear reactors, these alloys react with water to form zirconium oxide, while releasing hydrogen. Some of this hydrogen enters the metal which adversely changes its properties like the fracture toughness. Delayed hydride cracking can also occur if sharp flaws, cuts, and nicks suffered during operation coincide with regions under tensile stresses [3, 4, 5]. Hence, the hydride content in these pressure tubes are continuously monitored through scrape samples taken from their surfaces. Optical micrographs suggest that the size of hydrides close to the metal-oxide interface can be smaller than in the bulk which hinders the monitoring process [6, 7]. While the reasons for these hydride "denuded" zones are not exactly known, it is hypothesized that oxygen slows down the diffusion of H, forming smaller intragranular hydrides instead of the usual intergranular hydrides [6]. After an extensive literature review we didn't find any studies which has investigated this hypothesis through experimental or computational means.

We conducted a study to ascertain the diffusivities of H in hexagonal close packed (hcp or α phase) Zr at zero to moderate O concentrations. We also looked at the reasons for the variation in H diffusivity due to the presence of O by looking at the diffusion mechanics and diffusion paths taken by H atoms. Finally we determined the effect the changes in diffusivities calculated against the O concentrations expected in Zr pressure vessels to determine the effect it has on the sizes of the precipitates formed. Using these results we evaluated the validity of the above mentioned hypothesis and found that this hypothesis is unlikely to be the main reason for the formation of denuded zones in Zr pressure vessels.

METHODS

H atoms, which have a very small size, will diffuse via an interstitial mechanism in Zr, hopping between the available occupancy locations/interstitial sites. We used a multi-scale method to determine the diffusivity of H in α-Zr for three different O concentrations. This method was validated in our previous paper which looks at H diffusivity in pure Zr [8]. First-principles calculations were carried out to identify the occupancy locations and determine the rate constants for the transitions between these sites. The identified rate constants were used to estimate the diffusivity of H for each concentration with the use of Kinetic Monet Carlo (KMC) Simulations. Using oxygen concentration profiles found in Zr pressure vessels, we checked the effect on the hydride sizes found along the the pressure tube,using the determined diffusivity values, to look at the validity of the hypothesis being tested.

RESULTS AND DISCUSSION

From the first principles studies we identified the H occupancy sites for each O concentration and the possible transition mechanism between these sites. Rates for these transitions are then calculated with the semi classical Harmonic Transition State Theory (SC-HTST). These were used in KMC simulations to determine the diffusivities for the considered cases. The change of the diffusivity (logarithm of diffisivity) against the temperature (inverse of temperature) is as shown in figure 1. We can see the the change in diffusivity is relatively small for the low O concentrations (0.775% atm and 1.82% atm), where it is considerable for the 5.88% atm O concentration case.

If the size if the precipitates (hydrides) depend on the catchment volume, the size of the precipitates will be proportional to $D^{1.5}$. If we look at how this value changes with the O concentration we can understand the size variation to be

*Corresponding author. E-mail: manuraliyanage@cmail.carleton.ca

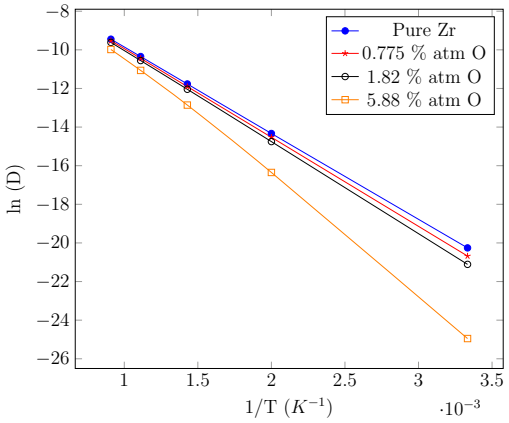

Figure 1: change in $ln(D)$ against $1/T$ for H diffusion in pure Zr, and for Zr with interstitial O

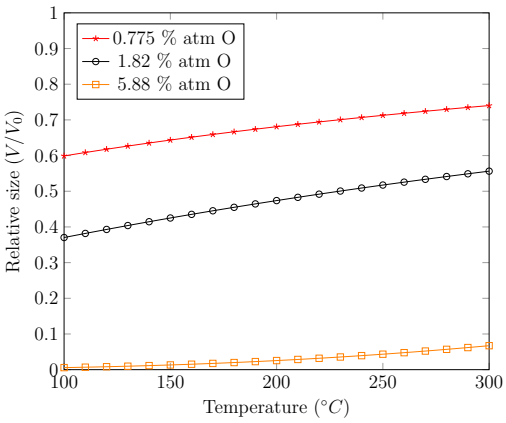

Figure 2: Relative size of the precipitates to the size of precipitates expected in pure Zr

expected in the precipitate sizes. Figure 2 looks at the relative size of precipitates expected for each different O concentration against the size of precipitates expected in pure Zr, where V is the size of the precipitates with O and V_0 is the size of precipitates in pure Zr at the same temperature. To have a noticeable decrease in the size of the precipitates they have to be smaller by a magnitude in the order of 10^{-2} (0.01 times). We can only see this in the case with 5.88% atm O concentration.

Looking at the O concentration profile found in Zr pressure vessels we find that it has is very high at the surface (approximately 27% atm) and decays exponentially to reach a value of 0.6% atm at a depth of about 32 μm. Comparing these distances with the denuded zone thickness (which can reach about $100 - 200$ μm) the depth is considerably lower. With this we can see that the amount of oxygen present in the denuded zones is not sufficient to slow the diffusion rates of H to cause significant reduction in the sizes of hydrides formed.

CONCLUSIONS

We looked at diffusivity of H in Zr with and without the influence of O using a combination of first principles methods and KMC simulation. The first principles calculations have been successfully used to determine the hopping rates for individual diffusion steps, validated from previous work carried out for H diffusion in pure Zr. This study show that H diffusion in Zr can be decreased by the presence of interstitial O and further decreased as the O concentration increases. We looked at the paths taken by H atoms and found that in addition to the decrease in hopping rates, H traps are formed by the amalgamation of occupancy sites, decreasing the diffusivity.

While this study proves that diffusivity of H in Zr is decreased by O, the amount of reduction in the diffusivity is not seen to be sufficient to decrease the size of the precipitates to be noticeable in the denuded zones. The O concentration profile suggests that the amount of O present in the denuded zone is not sufficient to decrease the diffusivity to a sufficient level to decrease the size of precipitates noticeably. Hence, we can disprove the hypothesis which sets forward the idea that denuded zones are formed by decrease of hydrogen diffusivity caused by the presence of interstitial oxygen.

This gives rise to the need to look at other mechanisms which could explain the formation of denuded zones in Zr pressure vessels.

ACKNOWLEDGEMENT

The authors gratefully acknowledge funding from NSERC's Discovery Grants program.

References

[1] Banerjee S. Nuclear Applications: Zirconium Alloys In *Encyclopedia of Materials: Science and Technology (2nd ed.)* (pp. 6287–6299). Elsevier, 2001.
[2] Féron D. Overview of nuclear materials and nuclear corrosion science and engineering In *Woodhead Publishing Series in Energy, Nuclear Corrosion Science and Engineering* (pp. 31–56). Woodhead Publishing, 2012.
[3] McRae G., Coleman C., Leitch B. *J. Nucl. Mater.* **396**: 130-143, 2010.
[4] De Las Heras M., Parodi S., Ponzoni L., Mieza J., Müller S., Alcantar S., Domizzi G. *J. Nucl. Mater.* **509**: 600-612, 2018.
[5] Murty T. N., Singh R., Såhle P. *J. Nucl. Mater.* **513**: 129-142, 2019.
[6] Hardie D. *J. Nucl. Mater.* **17**: 88-90, 1965.
[7] Cha H. J., Jang K. N., An J. H., Kim K. T. *Phys. Rev.* B **54**: 11169-11186, 1996.
[8] Liyanage M., Miller R., Rajapakse R. K. N. D. *Modelling Simul. Mater. Sci. Eng.* **26**: 085002, 2018.

COMPUTATIONAL HOMOGENIZATION FOR THE MULTISCALE ANALYSIS OF METAMATERIAL PLATES WITH LOCAL RESONANCES

Varvara Kouznetsova*[1], Lei Liu[1], Tom Lenders[1], and Marc Geers[1]
[1]Department of Mechanical Engineering, Eindhoven University of Technology, Eindhoven, The Netherlands

Summary This work presents a dynamic computational homogenization framework for transient and steady-state multi-scale analysis of locally resonant metamaterial panels. The approach relies on the relaxed separation of scales and combines the transient computational homogenization scale transition relations with the static-dynamic decomposition and mode synthesis, resulting in a computationally efficient closed-form formulation for a macroscopic shell continuum enriched with emergent degrees of freedom capturing the local resonance micro-inertia effects.

INTRODUCTION

Attenuation of low-frequency flexural waves in lightweight thin structures, such as beams or plates, presents an important engineering challenge. New promising solutions addressing this problem may be found in the emergent field of dynamic metamaterials. Dynamic metamaterials are materials designed for manipulation of elastic waves through specific interactions between propagating mechanical waves and fine scale micro-inertia mechanisms, based on either localized resonance or Bragg scattering, or their combination. This leads to exotic emerging phenomena, such as band gaps, negative refraction index etc., and opens possibilities for tunable waveguides, adaptive passive vibration control, superdamping, acoustic diodes, cloaking and focussing, noise insulation and (vibro-acoustic) energy harvesting. In particular, locally resonant metamaterials may be promising candidates for the low-frequency flexural wave attenuation in beam and plate structures, since they present exceptional wave manipulation properties in a subwavelength regime compared to the size of the unit cell.

The development and design of such metamaterials in general, and the locally resonant materials in particular, and devices/structures made thereof, requires advanced computational techniques. Such techniques should, on one hand, be capable to deal with complex geometries, boundary conditions and excitations, and on the other hand be computationally more efficient than direct numerical simulations. The latter become quickly computationally infeasible for locally resonant metamaterials due to the need to accurately resolve the fine scale resonator features, which are much smaller than the size of the large scale structure.

DYNAMIC HOMOGENIZATION FRAMEWORK

In this work, a computational framework for multi-scale dynamic analysis of locally resonant beams/plates is presented. As a point of departure, two previously developed computational homogenization methodologies have been used, i.e. a computational homogenization for plates/shells under static conditions [1] and dynamic computational homogenization for a general 3D continuum [2]. The homogenization framework proposed here employs a thin continuum shell description at the macroscale, while the (locally resonant metamaterial) microstructure is modelled as a full 3D solid continuum representing the full shell thickness. The application of the homogenization methodology is justified by the relaxed separation of scales regime, typically satisfied for locally resonant metamaterials, i.e. in the relevant frequency regime of interest, the matrix host medium is in the long wavelength regime, while the wavelength in the locally resonant inclusions can be comparable to the inclusion size, leading to non-negligible micro-inertia effects. Moreover, for the applicability of the thin shell theory, an additional condition is needed, restricting the analysis to flexural wavelengths much smaller than the shell thickness, which is obviously satisfied in the subwavelength regime.

The macroscopic and microscopic scales are coupled by consistent scale transition relations, involving the application of a localization operator to provide the macro-to-micro kinematic relations, and the Hill-Mandel condition, which establishes the micro-to-macro homogenization relations through energy consistency between the scales. For the dynamic homogenization of shells, the macroscopic kinematic quantities to be imposed on the microscopic unit cell consist of the macroscopic in-plane deformation gradient tensor, curvature tensor, the translational displacement of the reference lamina and the rotation of the director. The macroscopic resultant stress quantities extracted from the microscale include the thickness integrated stress and moment, as well as the translational and rotational momenta. The above described framework is formulated in the time domain. It is general and can be applied to a broad variety of transient problems, also those involving material and geometrical non-linearities. The computational costs are, however, rather high due to the need of the nested, coupled two-scale analysis at each time increment and at each macroscopic (integration) point.

In the linear elastic, small strain regime the computational costs can be significantly reduced through the use of the static-dynamic decomposition and mode synthesis at the micro-scale allowing the derivation of closed-form homogenized equations representing an enriched micromorphic continuum, in which additional field variables emerge to account for the micro-inertia effects [3]. In this case, the microscale problem has to be solved in the 'off-line' stage only, to obtain the static properties and identify the relevant local resonant modes and their frequencies. The microscale problem

*Corresponding author. E-mail: v.g.kouznetsova@tue.nl

is subsequently eliminated resulting in a compact closed-form description of the micro-dynamics that captures the local resonance phenomena. Upon substitution of the reduced microscale model into the scale transition relations, the resulting macroscale equations represent an enriched shell continuum with additional field variables accounting for the local resonance effects, which are absent in a classical shell continuum. Such an approach retains the accuracy and robustness offered by a two-scale coupled computational homogenization implementation, while significantly reducing the problem size and the computational time to the 'on-line' solution at the macro-scale only. Moreover, the obtained closed-form enriched formulation can be written in the time, as well as the frequency domains, thus enabling an efficient solution of transient or steady-state problems.

RESULTS

The developed framework has been validated against direct numerical simulations (DNS) and standard Bloch analysis by comparing the dispersion and transmission spectra of the homogenized model and the fully resolved model for a variety of microstructural unit cell designs and macroscopic beam/plate structures. An example is shown in Figure 1. The locally resonant unit cell and the macroscopic structure with its boundary conditions and applied harmonic excitation at the corner are shown in Figure 1a. For the numerical implementation of the macroscopic shell continuum, an isogeometric formulation has been used, while the microscale unit cell and DNS were solved using regular finite elements. The dimensions are such that the DNS problem involves 25x25 unit cells resulting in over 3 million degrees of freedom. The simulation results are shown in Figures 1b,c. In Figure 1b, an almost perfect match between the homogenized model and the reference DNS can be observed in the low frequency regime and the two locally resonant band gaps (shaded green). The slight discrepancy outside the band gap regions at higher frequencies is most probably due to the coarse macroscopic discretization. The computational gain achieved by the homogenized model compared to the DNS is almost a factor 50.

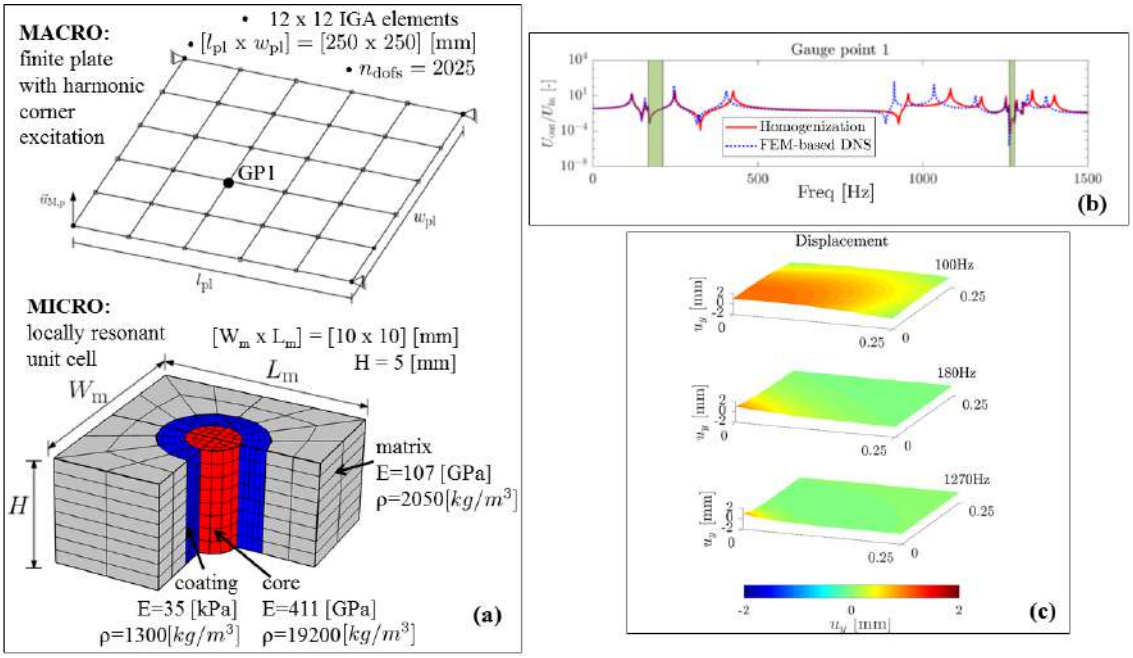

Figure 1: Application of the developed homogenization framework to a problem of a macroscopic plate with locally resonant substructure. (a) The macroscopic and microscopic problems. (b) Transmission at gauge point 1, compared to DNS. (c) Displacement of the plate at several excitation frequencies.

CONCLUSIONS

A new efficient dynamic computational homogenization framework for the multi-scale analysis of locally resonant metamaterial panels has been developed and validated. This approach can be used in the future for the design of metamaterial panels and beams for low-frequency flexural wave attenuation.

References

[1] Coenen E.W.C., Kouznetsova V.G., Geers M.G.D. Computational homogenization for heterogeneous thin sheets, *Int. J. Num. Meth. Engrg.*, **83**: 1180-1205, 2010

[2] Pham K., Kouznetsova V.G., Geers M.G.D. Transient computational homogenization for heterogeneous materials under dynamic excitation. *J. Mech. Phys. Solids*, **61**: 2125-2146, 2013

[3] Sridhar A., Kouznetsova, V.G., Geers M.G.D. Homogenization of locally resonant acoustic metamaterials towards an emergent enriched continuum. *Comp. Mech.*, **57**: 423-435, 2016

AN ENHANCED MAXIMUM-ENTROPY-BASED MESHLESS TECHNIQUE FOR STABLE SIMULATIONS OF SEVERE DEFORMATION

Siddhant Kumar[1], Yannick Hollenweger[1], Kostas Danas[2], and Dennis M. Kochmann*[1]
[1]Mechanics & Materials,Dept.of Mechanical & Process Engineering ETH Zürich,Zürich,Switzerland
[2]Laboratoire de Mécanique des Solides,C.N.R.S.,Ecole Polytechnique,Palaiseau,France

Summary We discuss a computational framework based on an enhanced local maximum-entropy approximation scheme for particle method-type simulations of severe elastic and inelastic deformation. Exploiting both total-Lagrangian and updated-Lagrangian settings, we demonstrate that this meshless approach not only enables the accurate prediction of large-deformation and large-rotation scenarios but it also comes with computational efficiency comparable to finite element-based schemes. We illustrate the performance of the technique through a suite of examples from metal forming and metal processing as well as extreme deformation of rubbery materials.

INTRODUCTION: MESHLESS TECHNIQUES

Meshless methods are popular computational mechanics tools for simulating scenarios in which classical mesh-based techniques – such as the finite element method (FEM) – reach their limits. This particularly applies to boundary value problems involving large deformation such as during metal forming (involving severe plastic deformation), the deformation of rubber (displaying even severe (visco-)elastic behavior), or fluid-structure interactions (in which the two worlds of classically Eulerian and Lagrangian settings collide). The large number of available meshfree techniques include, e.g., smoothed-particle hydrodynamics, the element-free Galerkin method, reproducing kernel particle methods, and material point methods – all of which circumvent mesh-related problems by treating nodes as interacting particles. However, such meshfree methods encounter alternative challenges that involve, among others, the treatment of discontinuities and boundary conditions as well as numerical instabilities. Specifically, all kernel-based meshfree methods experience a rank-deficiency instability that causes spurious modes[1]; when the discretization is formulated in an updated-Lagrangian setting, a purely numerical instability called *tensile instability* further arises from the changing nodal spacing and the associated localization of the shape function support [1]. Meshfree schemes also face challenges in accurately capturing material interfaces due to the smearing of discontinuous gradients induced by the nonlocal support.

ENHANCED LOCAL MAXIMUM-ENTROPY APPROXIMANTS

More recently, maximum-entropy approximation schemes have gained interest, which formulate meshless interpolants based on the maximization of information entropy [2]. Their extension to a Pareto compromise between shape function locality and maximization of information entropy resulted in the local maximum-entropy (*local max-ent*) shape functions [3], which we extend and exploit here. The local max-ent scheme is particularly attractive because it provides a seamless transition between a nonlocal approximation and a simplicial interpolation on a Delaunay triangulation (such as in classical FEM). The local max-ent interpolants further possess the weak Kronecker property, thus allowing for the direct application of essential boundary conditions and making the scheme attractive for fluid-structure interactions [4].

We recently introduced an improved meshfree approximation scheme [5] which adopts the original local maximum-entropy strategy as a compromise between shape function locality and entropy in an information-theoretical sense. This improved version is specifically designed for severe, finite deformation and offers significantly enhanced stability as opposed to the original formulation. This is achieved by (i) formulating the quasistatic mechanical boundary value problem in a suitable *updated-Lagrangian* setting, (ii) introducing *anisotropy in the shape function* support to accommodate directional variations in nodal spacing with increasing deformation and *eliminate tensile instability*, (iii) spatially bounding and *evolving the shape function support* to restrict the domain of influence and increase efficiency, (iv) *defining shape functions only locally* at material points, and (v) *truncating shape functions at interfaces* in order to stably represent multi-component systems like composites or polycrystals.

In a nutshell, the max-ent interpolation of all fields of interest is based on a set of *nodes*. The constitutive behavior is evaluated at a second, independent set of *material points* (the integration points), as in the classical optimal transportation meshfree (OTM) scheme [4]. Unlike previous implementations, the max-ent shape functions are defined only *locally* at the material points, and their *shape and support changes* with the current local state of deformation. The result is a versatile particle-type computational mechanics technique for the solution of static and dynamic boundary value problems, which we formulate in an *update-Lagrangian setting* (see Figure 1 for a schematic illustration). Beneficially, our formulation overcomes the phenomenon of tensile instability found in most competing meshless interpolation schemes.

*Corresponding author. E-mail: dmk@ethz.ch.

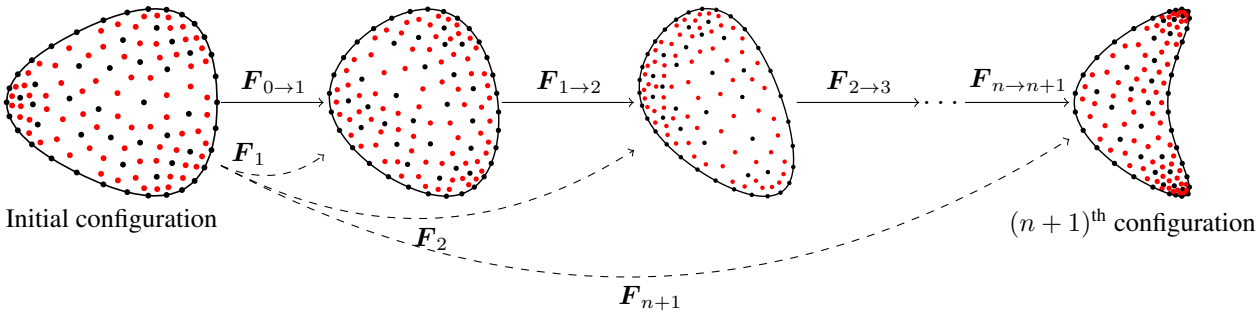

Figure 1: Illustration of the total-Lagrangian (dahsed lines) and updated-Lagrangian (solid lines) descriptions of the meshfree scheme based on improved local maximum-entropy interpolants [5]. Red and black points denote material points and nodes, respectively.

BENCHMARK EXAMPLES

We demonstrate the performance of our numerical scheme through a series of benchmark problems involving severe elastic and inelastic deformation. The accuracy of simulated results is evaluated by comparing, where applicable, to exact solutions or FEM simulations. In particular, we present simulations of rubber (hyper)elasticity [5] involving the extension of a rubbery block by several hundred percent strain, and the torsion of a rubbery block by more than 200° twist angle. In both cases, the meshless scheme outperforms state-of-the-art FEM techniques in a stable manner. We further showcase the capability of representing elastic-plastic behavior by simulating the classical Taylor-Anvil test of a metal sample impacting a rigid wall at high speed (which admits a quantitative accuracy assessment by comparison to prior simulations and to experiments). Finally, we apply the scheme to simulate equal-channel angular extrusion (ECAE) applied to polycrystalline pure copper billets [6, 7]. In addition to capturing boundary and end effects well, this latter scenario also serves as a demonstration of the ability to incorporate complex constitutive laws – we adopt a multiscale setting in which the local constitutive behavior at each material point is derived from an extended crystal plasticity model at the polycrystalline mesoscale including dynamic recrystallization [7] (of importance during ECAE at elevated temperature). We compare simulated results to experiments to highlight the applicability and accuracy of our approach.

CONCLUSIONS

We have extended the classical local maximum-entropy interpolation scheme into a versatile meshless framework which enables stable updated-Lagrangian (and total-Lagrangian) simulations of severe elastic and inelastic deformation [5], as demonstrated through examples from hyperelasticity, elasto-plasticity, and multiscale models for metal processing. Besides its superb accuracy and avoidance of the classical tensile instability, the efficiency of our particle-type scheme is comparable to competing finite element implementations.

References

[1] Belytschko T., Guo Y., Liu W. K. , Ping Xiao S. A unified stability analysis of meshless particle methods. *Ìnt. J. Numer. Meth. Engng.* **48**: 1359-1400 (2000).

[2] Sukumar N. Construction of polygonal interpolants: a maximum entropy approach. *Int. J. Numer. Meth. Engng.* **61**: 2159-2181 (2004).

[3] Arroyo M., Ortiz M. Local maximum-entropy approximation schemes: a seamless bridge between finite elements and meshfree methods, *Int. J. Numer. Meth. Engng.* **65**: 2167-2202 (2006).

[4] Li B., Habbal F., Ortiz M. Optimal transportation meshfree approximation schemes for fluid and plastic flows. *Int. J. Numer. Meth. Engng.* **83**: 1541-1579 (2010).

[5] Kumar S., Danas, K., Kochmann, D. M. Enhanced local maximum-entropy approximation for stable meshfree simulations. *Comput. Meth. Appl. Mech. Engng.* **344**: 858-886 (2019).

[6] Tutcuoglu A. D., Hollenweger Y., Stoy A., Kochmann D. M. High- vs. low-fidelity models for dynamic recrystallization in copper, *Materialia* **7**: 100411 (2019).

[7] Kumar S., Tutcuoglu A. D., Hollenweger Y., Kochmann D. M. A meshless multiscale approach to modeling severe plastic deformation of metals: application to ECAE of pure copper, *Comp. Mater. Sci.* (2019), in press (doi: 10.1016/j.commatsci.2019.109329).

THERMODYNAMICAL MODEL FOR STRAIN-INDUCED CRYSTALLIZATION IN POLYMERS

Serhat Aygün and Sandra Klinge*
Institute of Mechanics, TU Dortmund University, Dortmund, Germany

Summary The present work deals with the continuum mechanical model for the strain-induced crystallization covering mechanical and thermal properties of this phenomenon. The approach proposed relies on the minimum principle of the dissipation potential, which requires the Helmholtz free energy and the dissipation potential to be defined. These relationships are expressed in terms of external variables along with two internal variables, the network regularity and the thermal expansion. Advantageously, the model is able to simulate the reduction of crystalline regions followed by the heat release during the unloading phase, which is achieved by introducing shift terms in corresponding thermodynamic driving forces. The numerical results provide insights into the phenomena by illustrating the microstructural evolution within selected RVEs with a randomly generated initial microstructure.

THERMODYNAMICAL MODELING OF THE STRAIN-INDUCED CRYSTALLIZATION

High stretching of certain polymers, such as natural rubber, causes a partial transformation of the amorphous polymer chain structure, also known as strain-induced crystallization (SIC). Under a constant load, the crystalline regions remain stable, however, they gradually degrade and finally disappear during the unloading stage. The whole process is dissipative as shown by the experimental results on the stress strain behavior [1]. The proposed thermodynamically consistent model capturing mentioned properties of the process relies on the minimum principle of the dissipation potential. According to this approach, the Lagrangian $\mathcal{L}$ including the rate of Helmholtz energy $\dot{\psi}$ and the dissipation potential Δ is minimized with respect to the rates of internal variables $\dot{\boldsymbol{x}}$. The procedure yields the expressions for thermodynamic forces $\boldsymbol{q_x} \in \arg\min\{\mathcal{L} = \dot{\psi} + \Delta \mid \dot{\boldsymbol{x}}\}$ and, consequently, evolution equations for internal variables.

In the current work, the set of internal variables $\boldsymbol{x}$ includes the regularity of the polymer chain network (χ) and thermal expansion (α) due to the heat change by the SIC. Regularity χ takes the values in the range $[0, 1]$, such that zero value corresponds to the completely amorphous structure, and that the unity-value corresponds to a regular crystal structure. Moreover, the model uses the concept of large deformations and assumes a triple decomposition of the deformation gradient $\boldsymbol{F} = \boldsymbol{F}^{\mathrm{e}} \cdot \boldsymbol{F}^{\mathrm{c}} \cdot \boldsymbol{F}^{\mathrm{th}}$. Here, $\boldsymbol{F}^{\mathrm{e}}$ is the elastic deformation gradient, $\boldsymbol{F}^{\mathrm{c}}$ is the deformation gradient due to the crystallization and $\boldsymbol{F}^{\mathrm{th}}$ is the thermal deformation gradient. Quantities $\boldsymbol{F}^{\mathrm{c}}$ and $\boldsymbol{F}^{\mathrm{th}}$ are not listed in the set of internal variables, since they are defined in terms of χ and α as shown in the continuation.

Free energy and derivation of driving forces

For the previously defined framework, the Helmholtz free energy is assumed in the following form

$$\psi(J^{\mathrm{e}}, \boldsymbol{C}^{\mathrm{e}}, \chi, \alpha, \Theta) = \psi^{\mathrm{e}}_{\mathrm{AB}}(J^{\mathrm{e}}, \boldsymbol{C}^{\mathrm{e}}) + \psi^{\mathrm{th}}(\Theta) + c_1\,\chi + c_2\,\Theta\,\alpha + c_3\,\alpha\,. \tag{1}$$

Here, the Arruda-Boyce elastic energy $\psi^{\mathrm{e}}_{\mathrm{AB}}$ depends on the elastic Jacobian J^{e} and the elastic right Cauchy-Green tensor $\boldsymbol{C}^{\mathrm{e}}$, whereas the thermally stored energy ψ^{th} is used to define the heat capacity $c_p = -\Theta\frac{\partial^2\psi}{\partial\Theta^2}$, commonly assumed as a constant. The linear terms in (1) are responsible for shifts in driving forces, c_1 is the deformation dependent material parameter and c_2 and c_3 are material constants.

The model furthermore includes coupling conditions for velocity gradients and rates of corresponding internal variables: The crystalline velocity gradient $\boldsymbol{L}^{\mathrm{c}}$ is coupled to the rate of the regularity and the thermal velocity gradient $\boldsymbol{L}^{\mathrm{th}}$ to the rate of the thermal expansion

$$\boldsymbol{L}^{\mathrm{c}} := \dot{\boldsymbol{F}}^{\mathrm{c}} \cdot (\boldsymbol{F}^{\mathrm{c}})^{-1} = k_1\,\dot{\chi}\,\frac{\boldsymbol{M}^{\mathrm{c,dev}}}{\|\boldsymbol{M}^{\mathrm{c,dev}}\|}\,, \quad \boldsymbol{M}^{\mathrm{c,dev}} = \boldsymbol{M}^{\mathrm{c}} - \frac{\mathrm{tr}(\boldsymbol{M}^{\mathrm{c}})}{3}\boldsymbol{I}\,, \quad \boldsymbol{L}^{\mathrm{th}} := \dot{\boldsymbol{F}}^{\mathrm{th}} \cdot (\boldsymbol{F}^{\mathrm{th}})^{-1} = k_2\,\dot{\alpha}\,\boldsymbol{I}\,. \tag{2}$$

These conditions are expressed in terms of the Mandel stress tensor $\boldsymbol{M}^{\mathrm{c}}$ representing the thermodynamical couple of the $\boldsymbol{L}^{\mathrm{c}}$. Furthermore, $\boldsymbol{M}^{\mathrm{c,dev}}$ denotes the deviatoric part of $\boldsymbol{M}^{\mathrm{c}}$ and k_1 and k_2 are proportionality constants. Finally, the expressions for the reduced dissipation $\mathcal{D}^{\mathrm{red}}$ and thermodynamic forces q_χ and q_α are derived by using standard principles of thermodynamics and assumptions (1) and (2) [2, 3]:

$$\mathcal{D}^{\mathrm{red}} = \boldsymbol{M}^{\mathrm{c}} : \left(k_1\,\dot{\chi}\,\frac{\boldsymbol{M}^{\mathrm{c,dev}}}{\|\boldsymbol{M}^{\mathrm{c,dev}}\|}\right) + \boldsymbol{M}^{\mathrm{th}} : (k_2\,\dot{\alpha}\,\boldsymbol{I}) - \frac{\partial\psi}{\partial\chi}\dot{\chi} - \frac{\partial\psi}{\partial\alpha}\dot{\alpha} = q_\chi\,\dot{\chi} + q_\alpha\,\dot{\alpha} \geq 0\,, \tag{3}$$

$$q_\chi = k_1\|\boldsymbol{M}^{\mathrm{c,dev}}\| - c_1\,, \quad q_\alpha = k_2\,\mathrm{tr}(\boldsymbol{M}^{\mathrm{th}}) - c_2\,\Theta - c_3\,. \tag{4}$$

Here, $\boldsymbol{M}^{\mathrm{th}}$ is the thermodynamic couple of $\boldsymbol{L}^{\mathrm{th}}$ and c_1 and c_3 are shift terms chosen such that the unloading phase is characterized by negative driving forces.

*Corresponding author. E-mail: sandra.klinge@tu-dortmund.de.

Dissipation potential and derivation of evolution equations

The following dissipation potential including the absolute value of the regularity rate and a quadratic term of the expansion rate is proposed according to the behavior of crystalline regions under the different loading regimes:

$$\Delta(\dot{\chi},\dot{\alpha}) = (A+B)\,|\dot{\chi}| + \frac{D}{2}\dot{\alpha}^2\,, \quad \dot{B} = \frac{b}{f(\chi)}\,|\dot{\chi}|\,, \quad f(\chi) = a-(\chi-c)^d\,, \quad b = \begin{cases} b_1 & \text{if} \quad \dot{q}_\chi \geq 0\,, \\ b_2 > b_1 & \text{else}\,. \end{cases} \tag{5}$$

The definitions take the following notation: A is the crystallization limit, whereas B defines its evolution. Parameter b and function $f(\chi)$ regulates the change of B depending on the load type and the current value of regularity. Finally, D is a viscous type constant and a, c and d are material parameters. The minimization of the C^0 continuous Lagrange function is obtained by calculating the subdifferential, finally leading to the evolution equations

$$\dot{\alpha} = \frac{1}{D} q_\alpha\,, \qquad \dot{\chi} = \begin{cases} 0\,, & \text{if} \quad |q_\chi| \leq A+B\,, \\ \lambda\, q_\chi\,, \quad \lambda = \dfrac{f(\chi)\, q_\chi\, \dot{q}_\chi}{b\,(A+B)^2} \geq 0\,, & \text{else}\,. \end{cases} \tag{6}$$

The crystallization parameter λ in the expression for $\dot{\chi}$ is the result of the consistency condition $q_\chi\,\dot{q}_\chi = (A+B)\,\dot{B}$. Both evolution equations depend on thermodynamical driving forces defined in (4). Due to the influence of thermal effects, the full formulation of the problem also requires the consideration of the energy balance [3].

NUMERICAL RESULTS

The selected numerical example deals with the finite element simulation of a cyclic tensile test for a square sample with the dimensions 100×100 nm. The lower and the upper boundaries are constrained and the vertically applied stretch λ linearly increases and subsequently decreases in the interval $[1.0,\ 6.0]$. The total time amounts to 10 s and the time increment is 2×10^{-3} s. The initial values of the regularity are randomly generated over the sample. During the loading phase the regularity increases and its growth is favored in regions with the higher initial values (Fig. 1a). Figure 1b shows the state of the network regularity in the final (maximal) loading step, where fully crystalline regions are present. The crystalline regions decrease at a lower rate during the unloading phase (Fig. 1c).

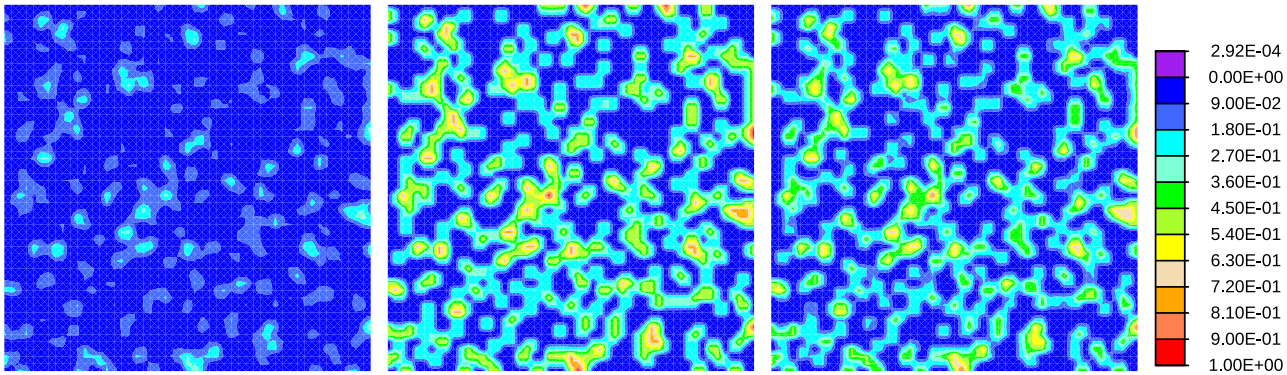

a) $\lambda = 4$ b) $\lambda = 6$ c) $\lambda = 4$

Figure 1: Cyclic tension test for a sample with the random initial microstructure. Snapshots: a) $\lambda = 4$ - loading stage, b) $\lambda = 6$ - end of the loading, c) $\lambda = 4$ - unloading stage. Applied material parameters: $A = 2 \times 10^5$ Pa, $b_1 = 5 \times 10^4$ Pa, $b_2 = 6 \times 10^4$ Pa, $k_1 = 6 \times 10^{-2}$, $k_2 = 0.1$, $D = 2 \times 10^6$ Pa, $c_2 = 4 \times 10^5$ Pa/K, $c_3 = -1.2 \times 10^8$ Pa and $c_p = 2 \times 10^7$ J/(kg K).

The present work shows a thermodynamical model for the SIC based on the assumptions for the Helmholtz energy and the dissipation potential. The model enables the simulation of the evolution of the microstructure during a complete cyclic tension test including the degradation of crystals and temperature reduction during the unloading phase. As a next step, the model will be implemented within the multiscale concept in order to study the influence of crystallization on the effective material behavior of polymers.

Acknowledgements

The authors gratefully acknowledge the financial support of the German Research Foundation (DFG), research grant number KL 2678/7-1.

References

[1] Candau, N., Laghmach, R., Chazeau, L., Chenal, J.-M., Gauthier, C., Biben, T., Munch, E. Influence of Strain Rate and Temperature on the Onset of Strain Induced Crystallization in Natural Rubber. *Eur. Polym. J.* **64**:244-252, 2015.
[2] Aygün, S., Klinge, S. Continuum Mechanical Modeling of Strain-Induced Crystallization in Polymers. *Int. J. Solids Struct.* 2019. Submitted.
[3] Aygün S., Klinge, S. Coupled Thermomechanical Model for Strain-Induced Crystallization in Polymers. *PAMM* **19**:e201900342, 2019.

COMPUTATIONAL THERMODYNAMICS OF STRAIN-INDUCED CRYSTALLIZATION

Vu Ngoc Khiêm*[1], Mikhail Itskov[1], and Jean-Benoît Le Cam[2]
[1]Department of Continuum Mechanics, RWTH Aachen University, Kackertstr. 9, 52072 Aachen, Germany
[2]Institut de Physique UMR 6251 CNRS/Université de Rennes 1, Rennes, France

Summary As a type of phase transition in natural rubbers, strain-induced crystallization is a phenomenon where amorphous polymer molecules transform to perfect order structures (crystallites) under the course of extension. Strain-induced crystallites are very important for the elastomer reinforcement and crack growth resistance in natural rubbers. This contribution presents a computational thermodynamic framework for filled natural rubbers. The proposed model is based on the analytical network-averaging theory [1,2,3]. In contrast to previous works on thermomechanics of natural rubbers, this model explicitly derives internal energy and entropy of polymer molecules in terms of state variables. Such methodology would allow for microscopic boundary conditions of the representative volume element, and shed new light on the multiaxiality of strain-induced crystallization.

INTRODUCTION

The thermomechanics of strain- induced crystallization in natural rubbers has not been properly described so far in spite of much effort applied to develop the kinetic theory [4, 5]. Most of the proposed theories fail to elucidate the Gough-Joule effect due to their isothermal nature. Besides, elastoplasticity-based models contradict calorimetric measurement [6] since they predict positive mechanical dissipation.

THERMOMECHANICAL FRAMEWORK

Free energy

The Helmholtz free energy of natural rubber in a material point of the continuum can be given by [2]

$$\Psi = U\left(\mathbf{F}, \Xi, T\right) - T\eta\left(\mathbf{F}, \Xi, T\right), \tag{1}$$

where U is the internal energy per unit referential volume and η is the network entropy. $\mathbf{F}$ is the deformation gradient, Ξ denotes an internal variable and T is the absolute temperature. The quantities $\mathbf{F}$, Ξ and T are state variables.

Energy balance

The energy transfer during the strain-induced crystallization can be analyzed by means of the first law of thermodynamics [2] as

$$\dot{U} = \mathbf{P} : \dot{\mathbf{F}} - \mathrm{Div}\,\boldsymbol{Q} + \hat{R}, \tag{2}$$

where $\boldsymbol{Q}$ is the heat influx per unit referential area, $\hat{R}$ denotes the heat supply per unit referential volume of the body, $\mathbf{P}$ is the first Piola-Kirchhoff stress tensor and the superposed dot indicates the material time derivative.

CRYSTALLIZATION KINETICS

This work assumes a two-step crystallization kinetics [2]. First, solid clusters of polymer segments (primary crystallites) are formed in the amorphous network at the onset of strain-induced crystallization. Afterwards, secondary crystallites grow from the nuclei. These steps are referred to as crystallization nucleation and growth, respectively.

Crystallization nucleation

The primary crystallite is assumed here to be bundle-like with a cylindrical geometry. Each crystallite is formed by K neighbouring polymer chains aligned in the stretching direction. Therefore, the primary crystallinity is proportional to the fraction of aligned chains.

By means of the nucleation theory [2], the primary crystallinity in each spatial direction i can be calculated as

$$\zeta_{Bi} = \zeta_{\mathrm{B}} \exp\left(-\frac{8\pi\gamma_t\gamma_s^2}{k_{\mathrm{B}}T\Delta\Psi_{\mathrm{i}}^2}\right), \tag{3}$$

where ζ_{B} denotes a material constant, γ_t is the surface tension at the top surfaces of the crystallite. γ_s is the surface tension on the side of the crystallite. $\Delta\Psi_{\mathrm{i}}$ is the difference in bulk free energies between the semicrystalline and the amorphous subnetworks.

*Corresponding author. E-mail: vu@km.rwth-aachen.de.

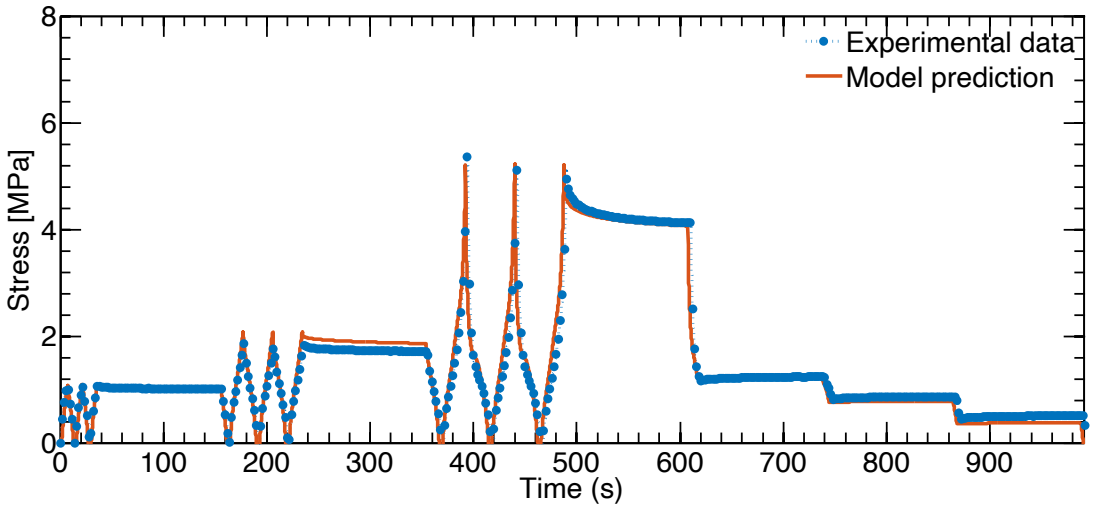

Figure 1: Comparison between model prediction and experimental data of a filled natural rubber under a multiple relaxation test.

Thus, the fraction of chains aligned in each spatial direction is proportional to ζ_{Bi} as

$$w_i = w_B \exp\left(-\frac{8\pi\gamma_t\gamma_s^2}{k_B T \Delta\Psi_i^2}\right), \tag{4}$$

where w_B is the limit of the chain alignment. According to the analytical network averaging theory [1, 2, 3], the microscopic boundary condition $\bar{\mathbf{\Lambda}}$ of the representative volume element (i.e. representative polymer molecule) is given by

$$\bar{\mathbf{\Lambda}} = \bar{\mathbf{\Lambda}}\left(\mathbf{F}, w_i\right). \tag{5}$$

Crystallization growth

The secondary crystallites grow from the primary nuclei. Thus, the secondary crystallinity ζ_{Ci} in each spatial direction i is a multiplication of the number of nuclei and the number of grown crystallites from each nucleus in this direction [2] as

$$\zeta_{Ci}\left(\mathbf{F}, \Xi\right) = \zeta_{Bi}\left(\mathbf{F}\right) \cdot \zeta_{Gi}\left(\mathbf{F}, \Xi\right). \tag{6}$$

The total crystallinity in each spatial direction is the sum of the primary and secondary crystallinity as

$$\zeta_i = \zeta_{Bi} + \zeta_{Ci}. \tag{7}$$

RESULTS

Finally, the proposed model is validated by comparing its prediction with a multiple relaxation test of a filled natural rubber (see Figure 1). Good agreement to the experimental data can be observed.

References

[1] Khiêm, V. N. & Itskov, M. Analytical network-averaging of the tube model: Rubber elasticity *J. Mech. Phys. Solids*, **95**: 254-269, 2016.

[2] Khiêm, V. N. & Itskov, M. Analytical network-averaging of the tube model: Strain-induced crystallization in natural rubber *J. Mech. Phys. Solids*, **116**: 350-369, 2018.

[3] Khiêm, V. N., Mai, T. T., Urayama, K., Gong, J. P. & Itskov, M. A Multiaxial Theory of Double Network Hydrogels *Macromolecules*, **52**, 15: 5937-5947, 2019.

[4] Plagge, J. & Klüppel, M. A Theory Relating Crystal Size, Mechanical Response, and Degree of Crystallization in Strained Natural Rubber *Macromolecules*, **51**, 10: 3711–3721, 2018.

[5] Gros, A., Huneau, B., Verron, E. & Tosaka, M. A physically-based model for strain-induce d crystallization in natural rubber . Part I : Life cycle of a crystallite *J. Mech. Phys. Solids*, **125**: 164-177, 2019.

[6] Samaca Martinez, J. R., Le Cam, J.-B., Balandraud, X., Toussaint, E. & Caillard, J. Mechanisms of deformation in crystallizable natural rubber. Part 2: Quantitative calorimetric analysis *Polymer*, **54**, 11: 2727-2736, 2013.

HYPERLEASTICITY IN TOPOLOGY OPTIMIZATION: A VARIATIONAL APPROACH

Philipp Junker*, Daniel Balzani
Institute of Continuum Mechanics, Ruhr University Bochum, Bochum, Germany

Summary A novel approach to the topology optimization of hyperalstic structures is presented. Applying variational techniques, an evolution equation for the density parameter is obtained that is solved simultaneously to the balance of linear momentum. Whereas for the latter a finite element strategy is employed, we make use of a newly introduced method using the strong form of the evolution equation for the density parameter. This neighbored element method allows for a fast numerical treatment.

TOPOLOGY OPTIMIZATION

Topology optimization is a key component in the design of structures. Here, the optimal shape is to be computed for a given design space and boundary conditions. Several approaches to solve this problem are available, such as SIMP (Solid Isotropic Material with Penalization), phase field methods, or level set strategies to mention just a few [1]. A huge challenge is to accurately treat the problem in a numerical sense since usually non-convex functions are used in order to find discrete black/white solutions with a minimum of gray transition regions between full and void material. The non-convex energies, however, render the problem ill-posed such that filter techniques or, more generally speaking, regularization strategies are inevitable. A prominent example is the checkerboard phenomenon that is present when no regularization is employed.

VARIATIONAL APPROACH

In the current talk, we present a variational approach to topology optimization which is based on methods known from material modeling [2-5]. We regularize the problem by introducing a convex gradient term to the optimization functional rendering the problem well-posed. Furthermore, we discuss how a parameterization of the density function allows for fulfilling the constraint of boundedness of the density function in]0,1]. This novel method for topology optimization is applied to hyperelastic structures, i.e. we are using a Neo-Hooke material for optimization. Along with the model derivation, several numerical examples and comparisons with results for Hookean materials proof the validity of our approach.

Figure 1. *Optimization result for a hyperelastic structure employing the novel variational approach.*

References

[1] Rozvany, G. I. (2009). A critical review of established methods of structural topology optimization. *Structural and multidisciplinary optimization*, ***37***(3), 217-237.
[2] Jantos, D. R., Junker, P., & Hackl, K. (2016). An evolutionary topology optimization approach with variationally controlled growth. *Computer Methods in Applied Mechanics and Engineering*, ***310***, 780-801.
[3] Jantos, D. R., Hackl, K., & Junker, P. (2019). An accurate and fast regularization approach to thermodynamic topology optimization. *International Journal for Numerical Methods in Engineering*, *117*(9), 991-1017.
[4] Jantos, D. R., Junker, P., & Hackl, K. (2018). Optimized growth and reorientation of anisotropic material based on evolution equations. *Computational Mechanics*, ***62***(1), 47-66.
[5] Gaganelis, G., Jantos, D. R., Mark, P., & Junker, P. (2019). Tension/compression anisotropy enhanced topology design. *Structural and Multidisciplinary Optimization*, ***59***(6), 2227-2255.

A DISCRETE BOUNDARY ELEMENT METHOD FOR 3D ATOMISTIC/CONTINUUM COUPLING

Ankit Gupta *[1], Max Hodapp[2], and W. A. Curtin[1]
[1]Laboratory for Multiscale Mechanics Modeling, EPFL, Lausanne, Switzerland
[2]Center for Energy Science and Technology, Skolkovo Institute of Science and Technology, Moscow, Russia

Summary The Coupled Atomistic/Discrete Dislocation (CADD) method has been successfully used to study multiscale phenomena such as plasticity in metals, but practical computational applications are currently limited to plane strain or infinite-space problems [2]. Here, we discuss a new Discrete Boundary Element Method (DBEM) that is combined with the flexible boundary condition method to enable efficient large-scale concurrent coupling of atomistic and DD domains, greatly reducing the computational cost of 3d plasticity problems.

THE DBEM AND ITS INTEGRATION WITH THE FLEXIBLE BOUNDARY CONDITIONS METHOD

The CADD method [5] concurrently couples atomistic and discrete dislocation domains which enables the study of non-linear, intrinsically atomistic, phenomena, such as dislocation emission near crack tips, using an atomistic material description while treating remote regions with the less-expensive DD method. Previously, the FEM which requires discretisation of entire domain, has been used to solve 3d DD problems in small systems, with large systems being computationally intractable. The problem of dealing with such large systems can be overcome by using the boundary element method based DBEM [4] in the continuum DD region and Sinclair's [7] flexible boundary condition method at the atomistic-continuum interface.

The governing equations for a general bounded DBEM problem shown in Fig. 1(a) containing finite lattice sites, represented by set Λ^c (inside dotted line), are as follows. The lattice sites comprise atoms interacting harmonically leading to a linear force displacement relationship represented by the force constant matrix $[\underset{\sim}{\boldsymbol{L}}_{\xi|\eta}]$ between atoms at sites ξ and η. We assert that the corresponding lattice green function matrix is $[\underset{\sim}{\boldsymbol{G}}_{\xi|\eta}] = [\underset{\sim}{\boldsymbol{L}}_{\xi|\eta}]^{-1}$. The $\partial\Lambda^- \subset \Lambda^c$(blue) and $\partial\Lambda^+$(green) outside the bounded region are sets of lattice sites that have non-zero forces when any atom in the other set are displaced. The displacement $\mathbf{u}_\xi$ of any atom at $\xi \in \Lambda^c$, subjected to external forces $[\mathbf{f}_\eta]$ and displacements $[\mathbf{u}_\eta]$ for atoms in $\eta \in \partial\Lambda^-$ and any internal forces $[\mathbf{f}^{in}_\eta]$ for atoms at $\eta \in \Lambda^{in}$, is given by

$$\mathbf{u}_\xi = -\sum_{\eta\in\partial\Lambda^-} \underset{\sim}{\boldsymbol{G}}_{\xi|\eta}\,\mathbf{f}_\eta + \sum_{\eta\in\partial\Lambda^-} \underset{\sim}{\boldsymbol{F}}_{\xi|\eta}\,\mathbf{u}_\eta + \sum_{\eta\in\Lambda^{in}} \underset{\sim}{\boldsymbol{G}}_{\xi|\eta}\,\mathbf{f}^{in}_\eta, \qquad \forall\xi\in\Lambda^c. \tag{1}$$

where $\underset{\sim}{\boldsymbol{F}}_{\xi|\eta} = \sum_{\zeta\in\partial\Lambda^+} \underset{\sim}{\boldsymbol{G}}_{\xi|\zeta}\underset{\sim}{\boldsymbol{L}}_{\zeta|\eta}$. This method requires no explicit discretisation $inside$ the domain, only the boundary conditions (displacements and/or forces) on the outer surface (set $\partial\Lambda^-$) are treated explicitly.

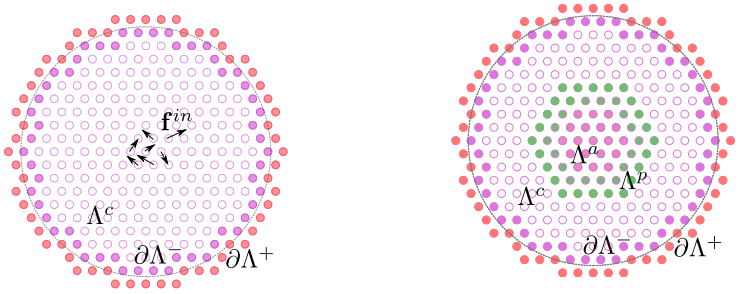

(a) bounded general DBEM problem

(b) coupled atomistic-continuum problem

Figure 1

We then consider the coupling of the continuum to an internal atomistic domain, represented by atoms Λ^a interacting according to specified interatomic potentials (Fig. 1(b)). The atoms in Λ^p around the interface are "pad" atoms that are in the continuum, and slaved to the continuum degrees of freedom, but serve to transmit forces and displacements to the atoms in Λ^a . This interface coupling is achieved using flexible boundary condtions, originally described by Sinclair [7].

The entire coupling methodology has been implemented with the molecular dynamics code LAMMPS [1]. As a demonstration case, we model a two-dimensional hexagonal lattice of atoms interacting via a Morse potential [6]. We subject the coupled problem to a rigid shift, i.e. a displacement boundary condition in which all the atoms on $\partial\Lambda^-$ are displaced by the same amount in the same direction. Fig. 2 shows various steps during the simulation: (a) initial undeformed system, (b) after displacement of the boundary atoms, (c) during iteration toward the solution, and (d) the final solution. The final solution has all atoms rigidly displaced by the displacment imposed on the boundary.

*Corresponding author. E-mail: ankit.gupta@epfl.ch

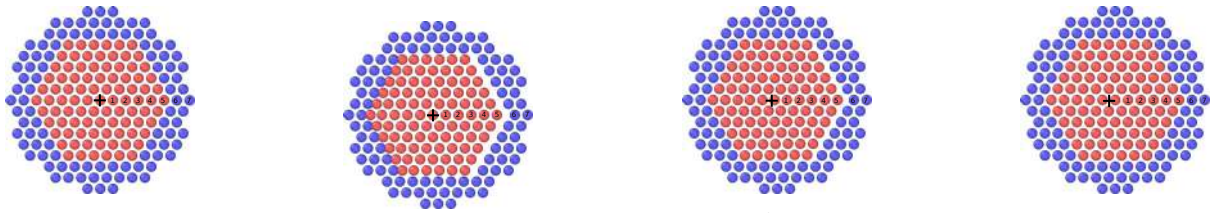

(a) reference positions of atoms at Λ^a(red) and Λ^p(blue)

(b) pad atoms moved according to Eq. (1)

(c) atoms at Λ^c kept fixed in new position and atoms in Λ^a are relaxed

(d) final positions of $\Lambda^a \cup \Lambda^p$ atoms after the simulation

Figure 2

EFFICIENT TREATMENT OF THE OUTER BOUNDARY

The governing equation for the DBEM requires atomic scale discretization of the entire outer surface (set $\partial\Lambda^-$). For 3d applications of CADD which are of practical interest, there can be millions of degree of freedom, and this is not computationally tractable. In most boundary value problems, the boundary conditions on the outer surface are varying very slowly over the atomic scale-it is only in the atomistic region and near dislocations where deformations are varying rapidly. Therefore, the atomistically-resolved boundary can be coarse grained. Specifically, the imposed forces and displacements can be approximated using local shape functions. Fig. 3 shows a schematic representation of $\partial\Lambda^-$ surface atoms represented by crosses with a reduced set of atoms chosen to form $\partial\Lambda_h \subset \partial\Lambda^-$(represented by squares) and local shape functions $\mathbf{\Phi}^\alpha$ defined for each lattice site α. $\partial\Lambda_\alpha$ denotes the atoms contained in support of $\mathbf{\Phi}^\alpha$. The displacement and forces for every atom on $\eta \in \partial\Lambda^-$ can be represented as $\mathbf{u}_\eta = \sum_{\alpha\in\partial\Lambda_h} \mathbf{u}_\alpha \mathbf{\Phi}^\alpha(\mathbf{x}_\eta)$ and $\mathbf{f}_\eta = \sum_{\alpha\in\partial\Lambda_h} \mathbf{f}_\alpha \mathbf{\Phi}^\alpha(\mathbf{x}_\eta)$. The local shape functions satisfy following property, $\mathbf{\Phi}^\alpha(\mathbf{x}_\eta) = \delta_{\alpha|\eta} \forall \eta, \alpha \in \partial\Lambda_h$. Using these shape function the governing equations are reduced to

$$\mathbf{u}_\xi = -\sum_{\eta\in\partial\Lambda_h} \tilde{\underset{\sim}{G}}_{\xi|\eta}\, \mathbf{f}_\eta + \sum_{\eta\in\partial\Lambda_h} \tilde{\underset{\sim}{F}}_{\xi|\eta}\, \mathbf{u}_\eta + \sum_{\eta\in\Lambda^{in}} \underset{\sim}{G}_{\xi|\eta}\, \mathbf{f}^{in}_\eta, \qquad \forall \xi \in \Lambda^c. \tag{2}$$

Here, $\tilde{\underset{\sim}{G}}_{\xi|\eta} = \sum_{\alpha\in\partial\Lambda_\eta} \underset{\sim}{G}_{\xi|\alpha} \mathbf{\Phi}^\eta(\mathbf{x}_\alpha)$ and $\tilde{\underset{\sim}{F}}_{\xi|\eta} = \sum_{\alpha\in\partial\Lambda_\eta} \underset{\sim}{F}_{\xi|\alpha} \mathbf{\Phi}^\eta(\mathbf{x}_\alpha)$. This matrix can be efficiently constructed using Hierarchical matrices [3], which involve low-rank approximations to $[\underset{\sim}{G}_{\xi|\eta}]$ and $[\underset{\sim}{F}_{\xi|\eta}]$. This reduces the number of degrees of freedom to $\mathcal{O}(N_h^2 \log(N))$ compared to $\mathcal{O}(N^2)$ required for exact solution of Eq. (1), where N and N_h are number of atoms in $\partial\Lambda^-$ and $\partial\Lambda^h$, respectively.

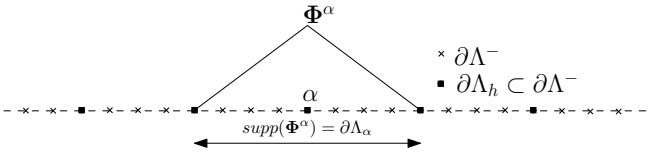

Figure 3

This new method for treatment of the outer boundary will be demonstrated on various sample problems to show the reductions in computational and memory costs and the relative error of the approximate solution with respect to an exact reference solutions.

CONCLUSIONS

We have successfully combined a DBEM method and Sinclair's scheme for large-scale 3d coupled Atomistic/Continuum boundary value problems. The implementation has been made within the open-source code LAMMPS, which will eventually enable wide dissemination of the methodology. The overall method has been demonstrated using various test problems, which serve as validation of the method and its computational efficiency.

References

[1] https://lammps.sandia.gov.
[2] G. Anciaux, T. Junge, M. Hodapp, J. Cho, J.-F. Molinari, and W. Curtin. The coupled Atomistic/Discrete-dislocation method in 3d part i: Concept and algorithms. *J. Mech. Phys. Solids*, 118:152–171, Sept. 2018.
[3] W. Hackbusch. Definition and properties of hierarchical matrices. In *Hierarchical Matrices: Algorithms and Analysis*, pages 119–154. Springer Berlin Heidelberg, 2015.
[4] M. Hodapp, G. Anciaux, and W. Curtin. Lattice green function methods for atomistic/continuum coupling: Theory and data-sparse implementation. *Comput. Methods Appl. Mech. Eng.*, 348:1039–1075, May 2019.
[5] R. E. Miller, L. Shilkrot, and W. A. Curtin. A coupled atomistics and discrete dislocation plasticity simulation of nanoindentation into single crystal thin films. *Acta Mater.*, 52(2):271–284, Jan. 2004.
[6] P. M. Morse. Diatomic molecules according to the wave mechanics. II. vibrational levels. *Phys. Rev.*, 34(1):57–64, July 1929.
[7] J. Sinclair, P. Gehlen, R. Hoagland, and J. Hirth. Flexible boundary conditions and nonlinear geometric effects in atomic dislocation modeling. *J. Appl. Phys.*, 49(7):3890–3897, July 1978.

COMPUTATIONAL MODELING OF CHEMO-THERMO-MECHANICAL CRACKING IN EARLY-AGE CONCRETE

Mehran Ghasabeh[1] and Serdar Göktepe*[1]
[1]Department of Civil Engineering, Middle East Technical University, 06800, Ankara, Turkey

Summary In this contribution, a chemo-thermo-mechanical modeling approach coupled with a cohesive phase field model is developed to address thermal cracking observed in massive concrete structures. The computational risk analysis of thermal cracking is of cardinal importance for massive concrete structures whose lifetime may be drastically reduced by early-age cracksif necessary precautions are not taken. The existing phase field-based approaches applied to multi-physics problems are predominantly restricted to brittle fracture. In this work, however, we extend the recently proposed cohesive phase field approach coupled with chemo-thermo-mechanical effects to predict thermal cracking in a roller-compacted concrete (RCC) structures where the stress concentrations arise from high temperature gradients generated by the highly exothermic hydration process.

INTRODUCTION

In cementitious composite materials, the durability problems generally arise from uneven volume changes that may result from heat generation and transfer due to hydration, moisture transfer, or chemical reactions at different ages of concrete. In the presence of restrictive boundary conditions, in particular on deformation, these non-uniform volumetric strains may result in stress concentrations. As the principal tensile stress values exceed the tensile strength of concrete, gained during the course of hydration, cracks start to onset [1]. This study is concerned with the computational prediction of thermal cracks that are initiated by high temperature gradients due to the heat generated through hydration and it convection and conduction in massive concrete structures. Therefore, the coupled problem of interest is governed by three equations where besides the displacement and temperature fields, the crack phase field is included to account for thermal cracking. To this end, a coupled chemo-thermo-mechanical approach [2] is developed to investigate the cross-effect of the evolution of both temperature and the degree of hydration on the durability and mechanical properties of concrete structures. Over a couple of decades, the phase-field approach has become popular in modeling failure mechanisms in solid bodies [3]. This approach has pronounced advantages over the other methods of the computational fracture mechanics in predicting complex crack topologies, curvilinear crack paths, crack kinking, and branching without requiring special extensions of discretization methods. In the literature, most of the studies tackling with coupled multi-physics problems employ the brittle phase field approach. The novel aspect of the proposed approach is that it extends the recently proposed quasi-brittle phase field approach [4] to account for thermal cracking in massive concrete structures within the framework of coupled chemo-thermo-mechanics. The capabilities of the developed model is demonstrated through a crack risk analysis of a roller-compacted-concrete dam [5].

GOVERNING EQUATIONS AND CONSTITUTIVE MODEL

A coupled problem of chemo-thermo-mechanics accompanied by the phase-field approach to the fracture is formulated in terms of four field variables, namely the total strain tensor $\boldsymbol{\varepsilon}(\boldsymbol{x},t) := \mathrm{sym}(\nabla_{\boldsymbol{x}}\boldsymbol{u})$, the absolute temperature field $\theta(\boldsymbol{x},t)$, the crack phase field $d(\boldsymbol{x},t)$, and the degree of hydration $\xi(\boldsymbol{x},t)$. While the evolution of the first three field variables is governed by the balance of linear momentum $\mathrm{div}(\boldsymbol{\sigma}) + \boldsymbol{b} = \boldsymbol{0}$, the transient heat conduction equation $\mathrm{div}(\boldsymbol{q}_\theta) + f_\theta = 0$, the non-local damage evolution equation $\mathrm{div}(\boldsymbol{q}_d) - \mathcal{H}_d + f_d = 0$, respectively, the evolution of the degree of hydration is described by an additional ordinary differential equation. To be able to solve these differential equations by discretizing them using the finite element method, the constitutive equations for the total stress $\boldsymbol{\sigma}$, the heat flux $\hat{\boldsymbol{q}}_\theta$, the crack phase-field diffusion $\hat{\boldsymbol{q}}_d$, the viscous heat resistance $\hat{f}_\theta$, and the crack phase-field resistance $\hat{f}_d$ must be specified. For this purpose, the positive and negative parts of the total stress tensor along with the elastic strain tensor are defined as follows

$$\begin{aligned} \boldsymbol{\sigma} = \hat{\boldsymbol{\sigma}}(\boldsymbol{\varepsilon},d,\theta,\xi) := \hat{\omega}(d)\,\boldsymbol{\sigma}_0^+ - \boldsymbol{\sigma}_0^- \quad \text{with} \quad \boldsymbol{\sigma}_0^\pm = \hat{\lambda}(\xi)\langle \mathrm{tr}\boldsymbol{\varepsilon}^{\mathrm{e}}\rangle_\pm + 2\hat{\mu}(\xi)\langle \boldsymbol{\varepsilon}^{\mathrm{e}}\rangle_\pm \\ \boldsymbol{\varepsilon}^e := \boldsymbol{\varepsilon} - \alpha\Delta\theta\boldsymbol{1} - \boldsymbol{\varepsilon}^{\mathrm{sh}} - \boldsymbol{\varepsilon}^{\mathrm{ttc}} \quad \text{with} \quad \boldsymbol{\varepsilon}^{\mathrm{sh}} := \langle \frac{\xi-\xi_0}{1-\xi_0}\rangle_+ \boldsymbol{1} \quad \text{and} \quad \dot{\boldsymbol{\varepsilon}}^{\mathrm{ttc}} := \lambda^{\mathrm{ttc}} \mid \dot{\theta} \mid \boldsymbol{\sigma}_0 \end{aligned} \tag{1}$$

where $\boldsymbol{\varepsilon}^{\mathrm{ttc}}$ and $\boldsymbol{\varepsilon}^{\mathrm{sh}}$ denote the transient thermal creep strain and the autogenous shrinkage strain, respectively. In the transient heat conduction, the heat flux vector $\boldsymbol{q}_\theta$ is defined according to the Fourier's law $\boldsymbol{q}_\theta = \hat{\boldsymbol{q}}_\theta(\theta) := -k_\theta \nabla_{\boldsymbol{x}}\theta$ in terms of the non-negative coefficient of thermal conductivity k_θ and the temperature gradient $\nabla_{\boldsymbol{x}}\theta$. Furthermore, the thermal energy storage is defined in terms of the the volume-specific heat capacity ρc, the latent heat of hydration Q_ξ, and the degree of hydration ξ

$$f_\theta = \hat{f}_\theta(\theta;\dot{\theta}) = \rho c\,\dot{\theta} - Q_\xi \dot{\xi} \tag{2}$$

*Corresponding author. E-mail: sgoktepe@metu.edu.tr

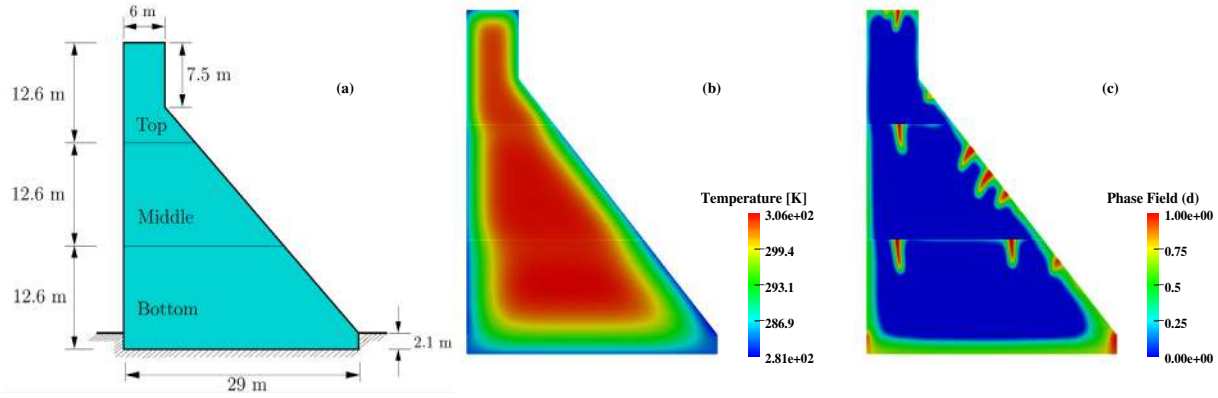

Figure 1: Roller-compacted-concrete dam: **(a)**: geometric dimensions, **(b)**: temperature distribution, **(c)** cracks propagation under coupled chemo-thermo-mechanical effect on 77th day.

where the last term represents the effect of hydration process on the evolution of temperature. Moreover, the crack phase-field flux $\boldsymbol{q}_d$ in the non-local damage evolution equation is defined as

$$\boldsymbol{q}_d = \hat{\boldsymbol{q}}_d(d, \xi) := -\frac{1}{c_0}\hat{G}_c(\xi)\,\ell\,\nabla_{\boldsymbol{x}} d \tag{3}$$

where $\hat{G}_c(\xi)$ is the age-dependent critical fracture energy, ℓ indicates an internal length scale regularizing the sharp crack, $c_0 > 0$ is a scaling parameter, and $\nabla_{\boldsymbol{x}} d$ stands for the spatial gradient of crack phase-field. The crack resistance is expressed as

$$f_d = \hat{f}_d(d; \dot{d}) = \frac{\hat{G}_c(\xi)\,\hat{\alpha}_d(d)}{\ell c_0} \tag{4}$$

where $\hat{\alpha}_d(d)$ represents the geometric crack function characterizing homogeneous evolution of the crack phase-field.

REPRESENTATIVE NUMERICAL EXAMPLES

To illustrate the capabilities of the proposed model, the thermal crack risk analysis of the roller-compacted-concrete (RCC) dam [5] is carried out. The geometric dimensions, the temperature distribution, and thermally induced cracks pattern in RCC dam are represented in Fig. 1. As shown, the RCC dam is mechanically fixed at the boundaries interacting with the soil. It is constructed in three parts. These parts from bottom to top were constructed in 42, 21, and 14 days, respectively. At the RCC-air boundaries of the model, the heat loss is simulated to investigate the effect of the ambient temperature on the behavior of the dam during its construction. In this problem the ambient temperature is dropped to 5°C as the interior part of the dam undergoes the temperature increase up to 33°C. The high temperature gradients between the interior and exterior of the dam causes cracks to initiate at the boundaries of the dam and to propagate towards interior part of the dam.

CONCLUSION

Through the numerical example represented above, it is demonstrated that the proposed coupled chemo-thermo-mechanical model along with the cohesive zone phase-field approach is capable of predicting the potential crack paths in the RCC dam under the coupled chemo-thermo-mechanical effects primarily governed by the ambient temperature at early ages.

References

[1] M. Cervera, J. Oliver, and T. Prato, "Simulation of construction of RCC dams. I: temperature and aging," *Journal of Structural Engineering*, vol. 126, no. 9, pp. 1053–1061, 2000.

[2] F. Ulm and O. Coussy, "Modeling of thermochemomechanical couplings of concrete at early ages," *Journal of Engineering Mechanics*, vol. 121, no. 7, pp. 785–794, 1995.

[3] C. Miehe, F. Welschinger, and M. Hofacker, "Thermodynamically consistent phase-field models of fracture: Variational principles and multi-field FE implementations," *International Journal for Numerical Methods in Engineering*, vol. 83, no. 10, pp. 1273–1311, 2010.

[4] J.-Y. Wu, "A unified phase-field theory for the mechanics of damage and quasi-brittle failure," *Journal of the Mechanics and Physics of Solids*, vol. 103, pp. 72–99, 2017.

[5] R. Lackner and H. A. Mang, "Chemoplastic material model for the simulation of early-age cracking: From the constitutive law to numerical analyses of massive concrete structures," *Cement and Concrete Composites*, vol. 26, no. 5, pp. 551–562, 2004.

BIPENALTY EXPLICIT FINITE ELEMENT ALGORITHM FOR THE SOLUTION OF CONTACT-IMPACT PROBLEMS

Dušan Gabriel*[1], Ján Kopačka[1], Radek Kolman[1], and Jiří Plešek[1]
[1]Institute of Thermomechanics of the Czech Academy of Sciences, Prague, Czech Republic

Summary In dynamic transient analysis, recent comprehensive studies have shown that using mass penalty together with standard stiffness penalty, the so-called bipenalty technique, preserves the critical time step in conditionally stable time integration schemes. In this paper, the bipenalty approach is applied in the explicit contact-impact algorithm based on the pre-discretization penalty formulation for the solution of 2D/3D problems. Several numerical examples are presented including the longitudinal impact of two thick plates, for which analytical solution is available and the Taylor high-velocity impact test with elastic-plastic flow model. In all the cases the superiority of the bipenalty method over the standard stiffness penalty method is demonstrated.

INTRODUCTION

In contact problems the contact constraints can be enforced either by the Lagrange multiplier method or by the stiffness penalty method. In practise the latter approach has gained in substantial popularity, because its implementation is easy, straightforward and has a clear physical meaning. On the other hand, the choice of the penalty parameter influences the accuracy of the approximate solution. In addition, in contact-impact applications the stiffness penalty method tends to decrease the critical time step in conditionally stable time integration schemes. This is due to the fact that the stiffness-type penalty can greatly enlarge the maximum eigenfrequency of a system.

In dynamic transient analysis, the penalty method can also be applied to the mass matrix. This technique is known as the mass penalty or the inertia penalty method. In contrast to the stiffness penalty approach, it significantly reduces one or more eigenfrequencies. In Reference [1] the bipenalty technique was introduced, where the both penalty formulations were used simultaneously. The goal of this method is to find the optimum of the so-called critical penalty ratio (CPR) defined as the ratio of stiffness and mass penalty parameters so that the maximum eigenfrequency and the critical time step are preserved. The calculation of CPR requires an analysis of the full bipenalised problem. Owing to mathematical difficulty, it limits the classes of elements that can be taken into account. In order to overcome this problem, a simple relationship between the CPR of an element and its maximum unpenalised eigenfrequency was derived in [2]. Thus, the multiple constraints and more complex element formulations can be directly accounted for [3]. In Reference [4] the stability of the bipenalty method has been studied for one-dimensional contact-impact problems. The main attention has been paid on an upper bound estimation of the stable Courant number for the bipenalty method with respect to stiffness penalty and mass penalty parameters.

BIPENALTY METHOD

Next, a brief description of the bipenalty method follows. Let us assume that the contact boundary Γ_c is known. The standard stiffness penalty method adds an extra term to the strain energy to enforce the zero gap g_N on the contact boundary

$$\mathcal{U}_p(\mathbf{u}) = \int_\Omega \frac{1}{2}\boldsymbol{\sigma} : \boldsymbol{\varepsilon}\, dV + \int_{\Gamma_c} \frac{1}{2}\epsilon_s g_N^2\, dS \tag{1}$$

Further, the inertia penalty term can also be added to the kinetic energy to enforce the zero gap rate $\dot{g}_N$ on the contact interface

$$\mathcal{T}_p(\dot{\mathbf{u}}) = \int_\Omega \frac{1}{2}\rho\dot{\mathbf{u}}\cdot\dot{\mathbf{u}}\, dV + \int_{\Gamma_c} \frac{1}{2}\epsilon_m \dot{g}_N^2\, dS \tag{2}$$

The penalised Lagrangian functional can be defined as

$$\mathcal{L}_p(\mathbf{u},\dot{\mathbf{u}}) = \mathcal{T}_p(\dot{\mathbf{u}}) - (\mathcal{U}_p(\mathbf{u}) - \mathcal{W}(\mathbf{u})) \tag{3}$$

where $\mathcal{W}(\mathbf{u})$ is the work done by external body forces $\mathbf{b}$ and traction forces $\mathbf{t}$. The unknown displacement field can be found as one which renders the penalised action functional stationary

$$\delta \int_0^T \mathcal{L}_p(\mathbf{u},\dot{\mathbf{u}})\, dt = 0 \tag{4}$$

where δ denotes the first variation or the directional derivative in the direction of virtual displacement $\delta\mathbf{u}$. Using the standard procedures one arrives to the principle of virtual displacement

$$\int_\Omega \rho\delta\mathbf{u}\cdot\ddot{\mathbf{u}}\, dV + \int_\Omega \delta\boldsymbol{\varepsilon} : \boldsymbol{\sigma}\, dV + \int_{\Gamma_c} \delta g_N(\epsilon_m\ddot{g}_N + \epsilon_s g_N)\, dS = \int_\Omega \delta\mathbf{u}\cdot\mathbf{b}\, dV + \int_{\Gamma_\sigma} \delta\mathbf{u}\cdot\mathbf{t}\, dS \tag{5}$$

*Corresponding author. Email: gabriel@it.cas.cz

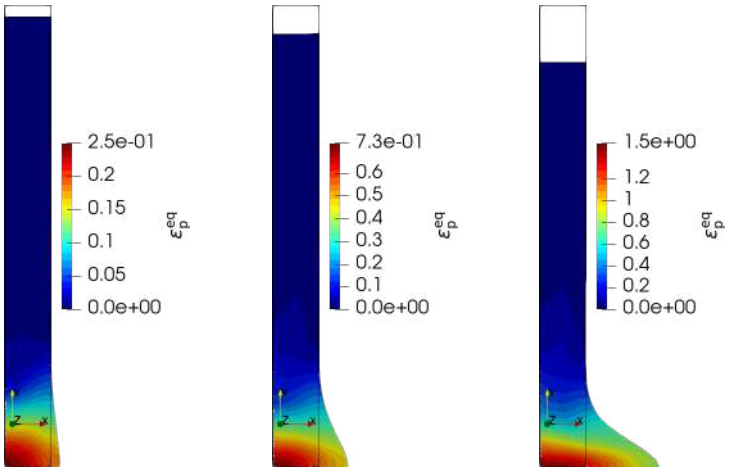

(a) $-100\,\mathrm{m/s}$ (b) $-250\,\mathrm{m/s}$ (c) $-500\,\mathrm{m/s}$

Figure 1: Taylor high-velocity impact test with elastic-plastic flow model.

which serves the base for the finite element discretization. The integrals (5) represent the virtual work of the inertia forces, internal forces, contact forces, body forces, and traction forces, respectively. Note that the integral of the virtual contact work is expressed with the aid of the inertia ϵ_{m} and the stiffness penalty ϵ_{s} simultaneously. The details concerning finite element implementation, explicit time integration including analysis of numerical stability can be found in Reference [4].

In this work, use of the bipenalty technique is extended for the solution of 2D/3D contact-impact problems. To this end, symmetry preserving explicit contact algorithm [5] has been modified to consider bipenalty treatment of contact constraints. Several numerical examples are presented including the longitudinal impact of two thick plates, for which analytical solution is available and the Taylor high-velocity impact test with elastic-plastic flow model shown in Figure 1.

CONCLUSIONS

In this paper, explicit symmetry-preserving contact-impact algorithm based on the bipenalty treatment of contact constraints was presented. It was shown that proposed algorithm preserved the stable critical time step during time integration by the central difference method regardless the values of stiffness penalty parameter. The effectiveness of proposed algorithm was tested by means of several numerical examples including the longitudinal impact of two thick plates, for which analytical solution is available and the Taylor high-velocity impact test. In all the cases the superiority of the bipenalty method over the standard stiffness penalty method is demonstrated.

ACKNOWLEDGEMENTS

The work was supported by the projects ERDF CZ.02.1.01/0.0/0.0/15_003/0000493 and CSF 19-04956S within institutional support RVO:61388998.

References

[1] Askes, H. Caramés-Saddler, M. ,Rodriguez-Ferran, A. Bipenalty method for time domain computational dynamics. *Proceedings of the Royal Society A: Mathematical, Physical and Engineering Sciences*, **466**, 1389–1408, 2010.

[2] Hetherington, J., Rodriguez-Ferran, A., Askes, H. A new bipenalty formulation for ensuring time step stability in time domain computational dynamics. *International Journal for Numerical Methods in Engineering*, **90**, 269–286, 2012.

[3] Hetherington, J., Rodriguez-Ferran, A., Askes, H. The bipenalty method for arbitrary multipoint constraints. *International Journal for Numerical Methods in Engineering*, **93**, 465–482, 2013.

[4] Kopačka, J., Tkachuk, A., Gabriel, D., Kolman, R., Bischoff, M., Plešek, J. On stability and reflection-transmission analysis of the bipenalty method in contact-impact problems: a one-dimensional, homogeneous case study. *International Journal for Numerical Methods in Engineering*, **113**, 1607–1629, 2018.

[5] Gabriel, D., Plešek, J., Ulbin, M. Symmetry preserving algorithm for large displacement frictionless contact by the pre-discretization penalty method. *International Journal for Numerical Methods in Engineering*, **61**, 2615–2638, 2004.

A PRIORI ENRICHMENTS FOR MACROSCOPIC PROBLEMS WITH EXPLICITLY RESOLVED MICROSTRUCTURAL DETAILS GENERATED BY THE CONCEPT OF WANG TILES

Martin Doškář*[1], Jan Novák[2], and Jan Zeman[1]
[1]Department of Mechanics, Faculty of Civil Engineering, Czech Technical University in Prague, Prague, Czech Republic
[2]Experimental centre, Faculty of Civil Engineering, Czech Technical University in Prague, Prague, Czech Republic

Summary We present a numerical scheme that accelerates simulations of macroscopic problems with a resolved microstructural geometry generated by means of Wang tiles—an extension of the classical Periodic Unit Cell approach to microstructural characterization. Our approach builds on precomputed microstructure-informed enrichments that are extracted as a collective response of the compressed representation to a prescribed macroscopic loading represented by constant and linear macroscopic gradients. These enrichment fields are then combined with a macroscopic discretization using the ansatz of Generalized Finite Element method to produce reduced modes for a given macroscopic problem. Albeit universal in the sense they are extracted without any knowledge of the shape of a macroscopic domain or its loading, the introduced enrichments allow for a significant reduction in the number of unknowns.

MICROSTRUCTURAL REPRESENTATION

The macroscopic response of materials is predominantly dictated by their microstructural composition. Consequently, numerical models tend to incorporate more knowledge of the underlying material microstructure in order to increase their predictive capability. While the microstructural representation based on a Periodic Unit Cell (PUC) proved to be sufficient for nested multi-scale simulations, it induces an artificial periodicity and determinism when utilized for generating virtual samples of materials with a random heterogeneous microstructure.

In our previous works, e.g. [1, 2], we have generalized the standard PUC-based microstructural representation by replacing a single cell with the concept of Wang tiles, in which the microstructural information is stored in a set of small domains with pre-defined compatibility constraints. Using a stochastic algorithm, the domains—Wang tiles—can be almost instantly assembled into microstructural realizations (along with the corresponding finite element discretization) of an arbitrary size with suppressed periodicity artefacts. This approach thus represents a compromise between generating microstructural samples by the periodic extension of a PUC and methods that create a microstructural sample each time anew such as optimization algorithms. Consequently, it appeals to applications where a multitude of microstructural realizations are needed, such as identification of Representative Volume Element size [3, 4] or Monte-Carlo like analyses of the influence of microstructural randomness on the macroscopic response.

NUMERICAL SCHEME

In this contribution, we present a numerical scheme that exploits the repeating occurrence of individual tile types in the generated microstructural samples and accelerates solutions to problems with a fully resolved underlying microstructural geometry that was generated with the Wang tile concept. The proposed scheme consists of two parts.

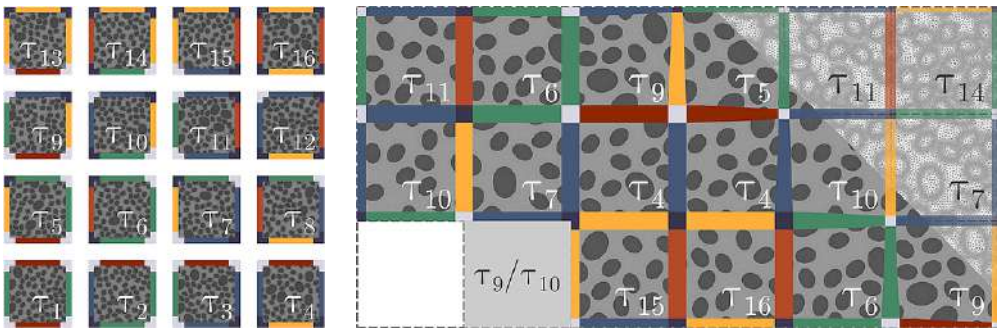

(a) (b)

Figure 1: Illustration of (a) a compressed microstructural representation by means of Wang tiles and (b) a partially assembled microstructural sample (along with a finite element discretization depicted in the upper right part) with highlighted tile edges whose colours encode the continuity constraints. Tile indices at the grey-shaded position indicate potential tiles to be placed.

*Corresponding author. E-mail: martin.doskar@fsv.cvut.cz

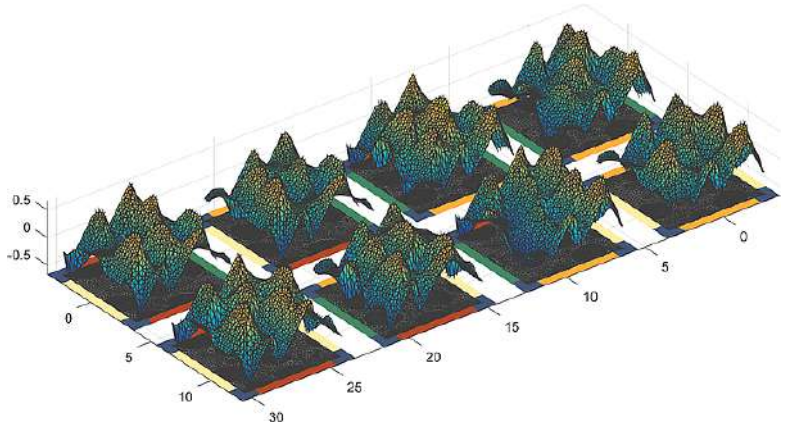

Figure 2: Illustration of a pre-computed characteristic fluctuation field, defined tile-wise and obtained for a unit macroscopic first-order gradient.

First, inspired in computational homogenization, we precompute the characteristic responses of a compressed microstructural representation to a prescribed loading parametrized with the first- and second-order macroscopic gradients. By construction, we constrain the responses to be continuous across the compatible tile edges, i.e., edges with the same attributed code. For the linear problems, as discussed in this contribution, it is sufficient to consider only the unit macroscopic excitations that form a basis in the parametrization space of the macroscopic gradients; however, the same procedure applies also to non-linear material behaviour of individual constituents except for the need for sampling the parametrization space and post-processing the sampled results with, e.g., Proper Orthogonal Decomposition. Since only the fluctuation part of the responses is stored, the tile-wise defined fields obtained for the same macroscopic loading can be subsequently assembled in the macroscopic domain in the same way the microstructural geometry was generated, forming a continuous approximation to the fluctuation part of the solution if the assembled domain was uniformly loaded.

However, the shape and loading of the macroscopic problem rarely yield a uniform distribution of macroscopic gradients, hence it is necessary to interpolate between the approximation fields. To facilitate such an interpolation, we adopt the ansatz of Generalized Finite Element Method (GFEM) as the second part of our scheme. In addition to a fine finite element discretization of a macroscopic domain, which comes from the assembled tiles and for which the characteristic fields are precomputed, we also define a coarse macroscopic discretization that does not resolve any microstructural details and serves mainly to capture the overall solution of the macroscopic problem and to interpolate between the precomputed fluctuation fields. The fields thus take the role of microstructure-informed enrichments, similar to the handbook solutions of Strouboulis et al. [5] or the global-local enrichments of Plews and Duarte [6]. Yet, we use the GFEM ansatz only to construct the problem-specific basis and the final problems is posed in the spirit of reduced order modelling, hence bypassing the need for a specific quadrature and the issues related to imposing Dirichlet boundary conditions by a simple Galerkin projection.

RESULTS AND CONCLUSIONS

We illustrate the proposed scheme with a scalar, elliptic, two-dimensional problem represented by a steady-state heat equation. We show that, albeit the considered microstructure-informed enrichment fields are universal in the sense they are extracted from the compressed system, i.e. without any knowledge on the shape of a macroscopic domain or its loading, the introduced enrichments allow for significant reduction in unknowns while achieving less than 3% relative error in the L_2-norm and energy difference, when compared to the results of the direct numerical simulation. Further improvements can be achieved by a progressive refinement of the coarse macroscopic discretization or by resorting to the fully resolved model in selected subdomains.

ACKNOWLEDGEMENT

This work has been supported by the Czech Science Foundation, grant No. 19-26143X.

References

[1] Novák, J., Kučerová, A., Zeman, J. *Phys. Rev. E* **86**: 040104. 2012.
[2] Doškář, M., Novák, J., Zeman, J. *Phys. Rev. E* **90**: 062118. 2014.
[3] Doškář, M., Novák, J. *Comput. Struct.* **166**: 33–41. 2016.
[4] Doškář, M., Zeman, J., Jarušková, D., Novák, J. *Eur. J. Mech. A-Solids* **70**: 280–295. 2018.
[5] Strouboulis, T., Zhang, L., Babuška, I. *Comput. Meth. Appl. Mech. Eng.* **192**: 3109–3161. 2003.
[6] Plews, J. A., Duarte, C. A. *Int. J. Numer. Methods Eng.* **102**: 180–201. 2015.

RECOVERY-BASED ERROR ESTIMATION AND MESH ADAPTIVITY FOR THE VIRTUAL ELEMENT METHOD

Antonio Maria D'Altri*[1], Stefano de Miranda[1], Luca Patruno[1], Edoardo Artioli[2], and Carlo Lovadina[3]
[1]Department of Civil, Chemical, Environmental, and Materials Engineering (DICAM), University of Bologna, Bologna, Italy
[2]Department of Civil Engineering and Computer Science, University of Rome Tor Vergata, Rome, Italy
[3]Dipartimento di Matematica, Università di Milano, Via Saldini 50, 20133 Milano, Italy

Summary In order to drive adaptive mesh refinement processes in 2D elasticity problems within the Virtual Element Method (VEM), a Recovery by Compatibility in Patches (RCP)-based *a posteriori* error estimator is herein proposed. RCP recovers stresses through the minimization of the complementary energy of patches of elements over a set of assumed equilibrated stress modes. RCP naturally appears suitable for the VEM, as the explicit knowledge of displacements is only requested along the patch boundaries. The error estimation is performed through the comparison of the stress field of a displacement-based VEM solution and the stress field obtained through RCP. The potential of this error estimator to drive mesh adaptivity is shown by means of several examples.

INTRODUCTION

The Virtual Element Method (VEM) is a recent and efficient discretization scheme, in which the shape functions are not known pointwise everywhere, while they are typically explicitly determined on the element boundary. The VEM is well known for its flexibility in handling general polygonal meshes, hanging nodes and non-conforming grids. Particularly, the VEM appears specifically suited for mesh adaptivity, as the use of hanging nodes and polygonal elements can facilitate the adaptive refinement, given that only local mesh modifications are generally required [1]. Accordingly, the development of reliable error estimators to drive adaptive mesh refinements in the VEM appears significant. However, only few *a posteriori* recovery-based error estimators have been developed for the VEM, see for example [1,2].

Recently, the Recovery by Compatibility in Patches (RCP) procedure [3], in which the stresses are recovered by enforcing compatibility over patches of elements, has been extended to the VEM [4]. Particularly, in RCP the stresses are recovered by minimizing the complementary energy functional associated to the patch considered as a separate system, leading to project the error between the displacement-based VEM strains and the strains coming from smoothed (equilibrated) stresses defined over the patch. Accordingly, the explicit knowledge of displacements is only needed along the patch boundaries, thus making the RCP naturally suitable for the VEM [4].

Here, an RCP-based *a posteriori* error estimator is proposed for the VEM, and it is utilized to drive adaptive mesh refinement processes in 2D linear elastic problems. The error estimation is *a posteriori* performed through the comparison of the stress field of a displacement-based VEM solution and the stress field obtained through RCP. The favourable features of the RCP procedure are exploited, e.g. its simplicity, the unnecessary *ad hoc* modification for small patches, and the unnecessary recourse to least-squares schemes. The potential of this error estimator to drive mesh adaptivity is shown by means of several examples.

ERROR ESTIMATION

The error in the displacement-based VEM solution can be suitably evaluated by adopting an integral measure of the distance between the stress field computed via the constitutive relationship and the exact stress field. The basic concept of the recovery-based error estimators consists of replacing the exact stress field by an improved (recovered) solution obtained by a suitable post-processing of the solution, in this case RCP.

The key idea of RCP is to consider each patch of elements (defined as the union of the elements surrounding a central element) as a separate system on which improved stresses are recovered by enhancing equilibrium and relaxing compatibility, i.e. by minimizing the complementary energy associated to the patch, among a set of equilibrated stress modes [3]. In order to minimize the patch complementary energy, the stress field to be recovered can be written as the sum of two contributions, which correspond to the divergence-free homogeneous part of the stress and a particular solution of the equilibrium equation. Various orders of approximation can be adopted for the homogeneous part, leading for example to linear (RCP1) and quadratic (RCP2) approximations.

An extensive numerical campaign is conducted to check the effectiveness of the RCP-based error estimator, see an example in Figure 1 (for a concave polygonal mesh) where the exact displacement field $\mathbf{u}(x,y) = \left[x(1-x)y(1-y)\tan^{-1}\left(\frac{20(x+y-1)}{\sqrt{2}} - 0.8\right), 0\right]^T$ is considered (θ is the effectivity index, defined as the ratio of the estimated to the exact error). A good performance of the RCP-based *a posteriori* error estimator is generally observed for both linear (RCP1) and quadratic (RCP2) approximations for the RCP recovery.

*Corresponding author. E-mail: am.daltri@unibo.it

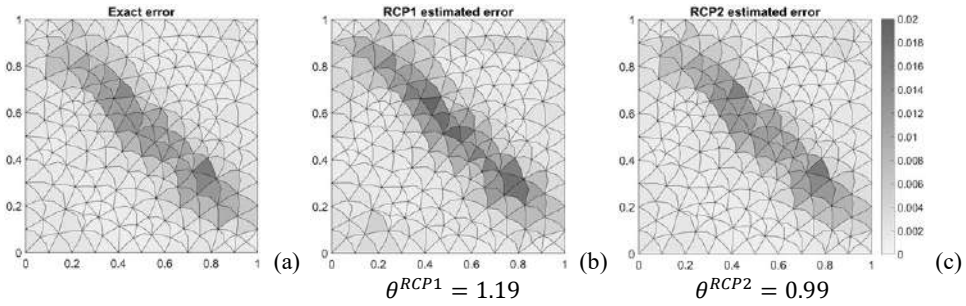

Figure 1. Error maps in energy norm: (a) exact error, (b) RCP1 estimated error, and (c) RCP2 estimated error.

MESH ADAPTIVITY

A "solve → estimate → mark → refine" mesh adaptivity strategy is herein implemented. Once the mesh is refined, it can be used as new input for the adaptive strategy, leading to an iterative adaptive procedure. A standard marking strategy is used to select the elements to be refined, i.e. the elements which show an error exceeding α times the maximum error recorded in the domain are marked for refinement, with $0 \leq \alpha < 1$ a user-defined threshold.

Several mesh refinement strategies can be followed within the VEM framework. In this study, the elements marked for refinement are split by connecting the middle point of each edge of the element to the element centroid. To save degrees of freedom and optimize the procedure, the hanging nodes belonging to elements marked for refinement are treated in a peculiar way, so that the aligned edges which have a hanging node in (at least) one extremity are considered as a unique edge, i.e. they are subdivided through just one middle point. In case the middle point corresponds with an existing hanging node, the existing node is used to describe the connectivity of the new elements.

A wide numerical campaign is conducted to test the efficacy of the RCP-based *a posteriori* error estimator to drive adaptive mesh refinements, see an example in Figure 2 where a cantilever deep beam benchmark is used to highlight the effectiveness of adaptive mesh refinement with respect to uniform mesh refinement (for a structured regular hexagon mesh). As can be noted in Figure 2, both RCP1 and RCP2 show good performances in driving mesh refinements within the VEM framework. Indeed, refinements are automatically performed around the two points with stress singularity (at the two corners of the clamped edge on the left), as expected. Furthermore, adaptive refinements appear to be able to restore the optimal convergence rate (i.e. 1), unlike the cases of uniform refinements.

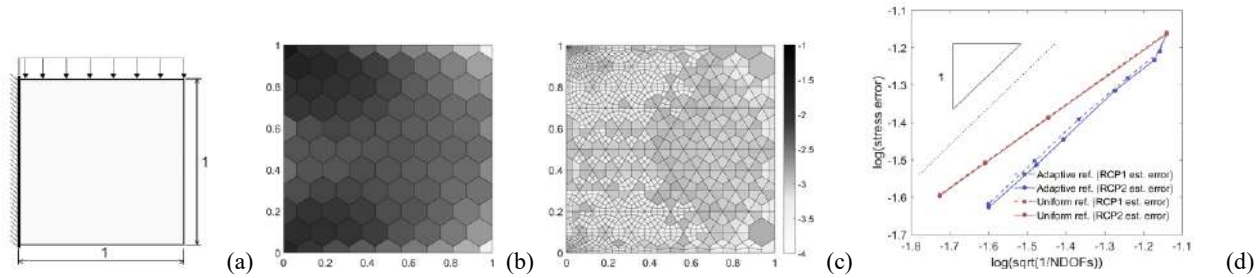

Figure 2. Cantilever deep beam: (a) boundary conditions, logarithmic error maps in energy norm (RCP1) for (b) the initial mesh, and (c) the final refinement, and (d) convergence of estimated error along with adaptive and uniform refinements.

CONCLUSIONS

In this research, a recovery-based *a posteriori* error estimator has been proposed to drive mesh adaptivity in the VEM. The recently developed RCP stress recovery procedure for VEM [4] has been used to recover stresses. The error estimation has been *a posteriori* performed through the comparison of the stress field of a displacement-based VEM solution and the stress field obtained through RCP. The potential of this RCP-based error estimator to drive adaptive mesh refinements has been demonstrated through a wide selection of meaningful numerical examples.

References

[1] Chi, H., Beirão da Veiga, L., & Paulino, G. H. (2019). A simple and effective gradient recovery scheme and a posteriori error estimator for the Virtual Element Method (VEM). Computer Methods in Applied Mechanics and Engineering, 347, 21–58.

[2] Nguyen-Thanh, V. M., Zhuang, X., Nguyen-Xuan, H., Rabczuk, T., & Wriggers, P. (2018). A Virtual Element Method for 2D linear elastic fracture analysis. Computer Methods in Applied Mechanics and Engineering, 340, 366–395.

[3] Ubertini, F. (2004). Patch recovery based on complementary energy. International Journal for Numerical Methods in Engineering, 59(11), 1501–1538.

[4] Artioli, E., de Miranda, S., Lovadina, C., & Patruno, L. (2018). An equilibrium-based stress recovery procedure for the VEM. International Journal for Numerical Methods in Engineering, 117(8), 885–900.

MODELLING RANDOM FIBRE NETWORKS BASED ON SEGMENT STRETCH DISTRIBUTIONS

Ben R. Britt*[1,2], Edoardo Mazza[1,2], and Alexander E. Ehret †[1,2]
[1]Empa, Swiss Federal Laboratories for Materials Science and Technology, 8600 Dübendorf, Switzerland
[2]ETH Zurich, Institute for Mechanical Systems, 8092 Zürich, Switzerland

Summary A new, generally non-affine modelling approach is proposed for random fibre networks. The approach is based on a mathematical description of the distribution of quantities that determine the energy of single fibre segments when the network deforms. For illustration, the new approach is exemplified in application to the affine microsphere model. If the strain-energy function depends on the segment stretch and is analytic, this special case provides a new physical perspective on existing full network models. Additionally, in this context a novel technique for the (spherical) integration of piecewise defined strain-energy functions, typically found in models with tension-compression asymmetry, is proposed.

INTRODUCTION

Network-like structures of randomly arranged and connected fibres are prevalent in a variety of natural as well as technical materials [1]. To understand, analyse and predict the behaviour of these materials, efficient and reliable models are of great interest for both fundamental research and applied engineering.

The random fibre network characteristics result from the network structure and the individual fibre material properties. Discrete network models to simulate these materials employ numerical multi-scale simulations with a finite amount of connected fibres and subsequent homogenization or averaging procedures [2]. Due to the statistical background of these simulations, the generalisability of the corresponding results is often difficult or limited, and additionally, the associated computational costs are high. Analytical approaches are based on physically motivated continuum mechanical models. Here, a constitutive assumption that relates the micro-kinematics of the single fibres with the macroscopic deformations of the network replaces simulations with discretised networks. While this approach is favourable with regard to computational costs, it is prone to oversimplifying the mechanisms responsible for the scale transition. Indeed, comparing the micro-kinematics revealed in multi-scale simulations and those stemming from common continuum mechanical models reveals large discrepancies [3, 4]. This highlights the need to reevaluate and reformulate the assumptions that govern the micro to macro transitions.

A NEW APPROACH TO NETWORK MODELLING

Here we propose a novel approach for constitutive modelling of random fibre networks that generally applies to non-affine fibre kinematics and includes affinity as a special case. Instead of defining the motion of a single fibre depending on its initial spatial orientation, the method developed here focuses on finding the probability distributions of energetically relevant quantities, such as the segment stretch, within the random fibre network. For example, given a central force network formed by homogeneous segments, the expected segment energy $E[\psi]$ is determined by the stretch distribution μ within the network, i.e.

$$E[\psi] = \int_0^\infty \psi(x) d\mu(x) \, .$$

APPLICATIONS AND RESULTS

Despite the generally non-affine deformation behavior of random fibre networks, we introduce the novel approach here by providing a new perspective on affine microsphere models [5]. The associated integration of constitutive equations $f(\lambda) = g(\Lambda)$ over the surface of the d-dimensional unit sphere $\mathcal{S}^{d-1}$ has been used as an averaging method in many branches of physics and engineering, including continuum mechanics. It is, e.g., the basic ingredient of the microsphere and full-network models for rubber-like materials [5] and the structural approach in biomechanics [6]. Only in few cases, the integral can be solved analytically so that, typically, quadrature is employed. If the integrand can be expressed as a finite power series, an invariant-based analytical integration can be performed, leading to an invariant-representation of the constitutive equations [7]. However, in many cases relevant to the mechanics of soft materials, the integrands are not analytic, e.g. due to piecewise definitions or asymptotic behaviour.

With the new approach the domain of integration changes from $\mathcal{S}^{d-1}$ to the one-dimensional open half-space formed by the stretch λ, respectively, its square $\Lambda = \lambda^2$ (Fig. 1). For the special case of the affine microsphere, the domain is bounded between the minimum and maximum (squared) principal stretch, and the value of the integral is the expectation of $f(\lambda) = g(\Lambda)$ given the affine distribution of the (squared) stretch. Interestingly, an investigation of the

*Corresponding author. E-mail: Ben-Rudolf.Britt@empa.ch
†Corresponding author. E-mail: Alexander.Ehret@empa.ch

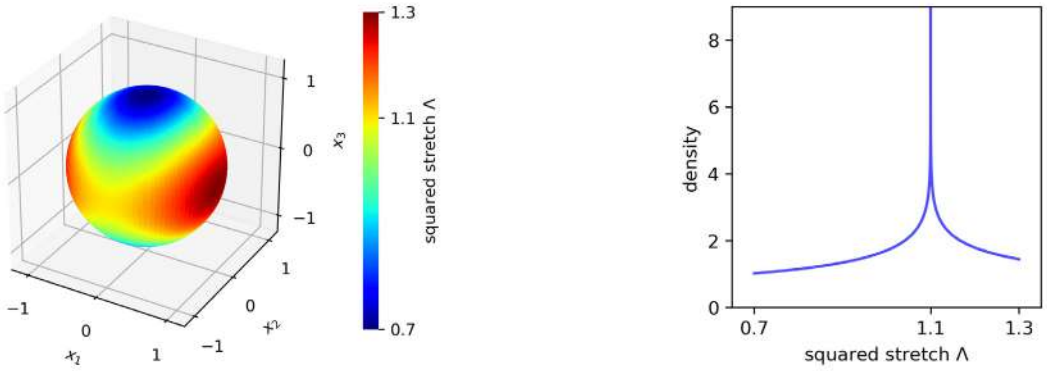

(a) (b)

Figure 1: Segment stretches for a global deformation characterised by the three squared principal stretches $\Lambda_3 = 0.7$, $\Lambda_2 = 1.1$ and $\Lambda_1 = 1.3$ under the affine assumption. (a) Directional squared stretch Λ for directions depicted on the surface of the three-dimensional unit sphere $\mathcal{S}^2$. (b) Density of the corresponding stretch distribution given an isotropic fiber distribution.

three-dimensional distribution of the stretch (square) reveals the very strong accumulation of stretches near the mid, i.e. non-extreme, principal stretch (Fig. 1b).

Based on this analysis, we recover the integration method proposed in [7] which is valid in case of an isotropic fibre distribution, and supplement it by a closed form expression, as well as a physical explanation. This enables the exact integration of polynomial functions of any order and allows an arbitrarily close approximation for analytic functions. Moreover, we show the benefits of the new approach for the integration of functions $g(\Lambda)$ or $f(\lambda)$ that are piecewise defined as polynomials, as they occur in case of a tension-compression asymmetry typical for e.g. collagenous networks, and the consequences for the tension-compression switch of fibres [8].

CONCLUSIONS

In the present contribution we delineate a new approach for constitutive modelling for random fibre networks, which provides a basis for the development of generally non-affine computationally efficient models. To validate and introduce the underlying concepts, the approach is employed here to revisit the affine microsphere model. This not only reveals interesting features of the affine stretch distribution but also provides an alternative justification of a previously proposed integration method. Finally, for piecewise defined integrands that are typically used in models to capture tension-compression asymmetry or that implement a tension-compression switch, we demonstrate the advantages concomitant with the new approach.

References

[1] Picu, R. C. Mechanics of random fiber networks – a review. *Soft Matter* **7(15)**: 6768-6785, 2011.
[2] Stylianopoulos, T., & Barocas, V. H. Volume-averaging theory for the study of the mechanics of collagen networks. *Computer Methods in Applied Mechanics and Engineering* **196(31-32)**: 2981-2990, 2007.
[3] Domaschke, S., Zündel, M., Mazza, E., & Ehret, A. E. A 3D computational model of electrospun networks and its application to inform a reduced modelling approach. *International Journal of Solids and Structures* **158**: 76-89, 2019.
[4] Zündel, M., Mazza, E., & Ehret, A. E. A 2.5D approach to the mechanics of electrospun fibre mats. *Soft Matter* **13**: 6407-6421, 2017.
[5] Miehe, C., Göktepe, S. & Lulei, F. A micro-macro approach to rubber-like materials – Part I: the non-affine micro-sphere model of rubber elasticity. *Journal of the Mechanics and Physics of Solids* **52(11)**: 2617-2660, 2004.
[6] Lanir Y. A structural theory for the homogeneous biaxial stress-strain relationships in flat collagenous tissues. *Journal of Biomechanics* **12**: 423–436, 1979
[7] Itskov, M., Ehret, A. E., & Dargazany, R. A Full-Network Rubber Elasticity Model based on Analytical Integration. *Mathematics and Mechanics of Solids* **15(6)**: 655–671, 2010.
[8] Holzapfel, G. A., Ogden, R. W. On the tension-compression switch in soft fibrous solids. *European Journal of Mechanics A/Solids* **49**: 561-569, 2015.

ROBUST FINITE ELEMENT MODELING OF CABLE SYSTEMS

Charlèlie Bertrand*[1],Claude Henr iLamarque[1],Vincent Acary[2],and Alireza Ture Savadkoohi[1]
[1]Univ Lyon, ENTPE, LTDS UMR CNRS 5513, Rue Maurice Audin 69518 Vaulx-en-Velin Cedex, France
[2]Univ. Grenoble Alpes, CNRS, Inria, Grenoble INP (Institute of Engineering Univ. Grenoble Alpes) , GIPSA-Lab, 38000 Grenoble, France

Summary Numerical simulation of cable systems remain delicate due to the effects of their curvature. Indeed finite element approaches (if not implemented carefully) fail to predict correct responses of cable structures. The major issue to be addressed is the ill-conditioning, starting configuration and wrong choice of descent direction during iterative methods. Some strategies to overcome spurious solutions for cable system will be presented accompanied with comparisons and potential experimental results.

CONTEXT

"Cable" stands for a slender structure which cannot resist compression and torque. Its equilibrium relies on the balance between its internal axial force and external forces and/or forcing [1]. Analytical studies account for the high diversity of its dynamics contents [2]. However, purely numerical methods for cable suffer from ill-conditioning, spurious solutions [3] and high frequency contents interference [4] regardless the type of finite element approach. Cable systems should be treated numerically in the framework of unilateral material (no tension materials [5, 6] or no-compression [7]). Main contribution of this work is the coupling between these conditions and the geometrical non linearity of the cable. Governing equation accompanied by unilateral dilatation condition reads:

$$\forall S \in \Omega, \forall t \quad \begin{cases} \rho\ddot{x} = EA\left((\|x'\| - 1)\dfrac{x'}{\|x'\|}\right)' + b \\ \varepsilon = \|x'\| - 1 \geq 0 \end{cases} \tag{1}$$

where space and time dependencies, resp. S and t, have been removed for conciseness. $\cdot'$ and $\dot{\cdot}$ respectevily stand for the derivation with respect to S and t. The latter may be understood as taking the following constitutive law for the cable:

$$T = \begin{cases} EA\varepsilon & ; \quad \varepsilon \geq 0 \\ 0 & ; \quad \varepsilon \geq 0 \end{cases} \tag{2}$$

FINITE ELEMENT IMPLEMENTATION OF NON-COMPRESSIBLE CABLE

The Finite Element Method [8] (FEM) formulation for an elastic non-compressible cable is derived accounting the fact that a cable can only undergo stretching (no compression). A cable element is formulated with regards to curvilinear mechanics [9], thus providing a Lagrangian viewpoint that may be used to compute large displacements. This unilateral formulation ($\varepsilon \geq 0$) results in a kind of active set FEM procedure [10]. Constrained optimization methods are used to impose connexion between cables and boundary conditions. The whole process yields to solve:

$$\begin{cases} 0 = \mathbf{M}\ddot{\mathbf{X}} + \mathbf{K}(\mathbf{X})\mathbf{X} - \mathbf{f} - \mathbf{A}^t\lambda \\ 0 = \mathbf{A}\mathbf{X} - \mathbf{c} \end{cases} \tag{3}$$

Where the $\mathbf{A}$ matrix embeds boundary condition and imposed connections between cables and $\mathbf{c}$ is a fixed column vector.
Modal analysis of such system can be performed provided suitable projection on the constraint operator null-space [11], i.e.:

$$\text{Find } (\omega, \mathbf{U}) \text{ such as: } \begin{cases} \omega^2 = \min\limits_{\mathbf{U}} \dfrac{\mathbf{U}^\top(\nabla\mathbf{K})\mathbf{U}}{\mathbf{U}^\top(\mathbf{M})\mathbf{U}} \\ 0 = \mathbf{A}\mathbf{U} \end{cases} \tag{4}$$

This methodology has been proven efficient to compute static cable equilibrium (Figure 1), modal analysis of cables or even cable networks (Figure 2) and also to perform some time integration (Figure 3) without violating the non compression condition.

CONCLUSIONS

Implementation of a numerical tool for a non-compressible cable equilibria have been discussed. Applications are possible for static analysis, modal analysis and time-integration.

ACKNOWLEDGMENTS

The authors kindly thank the french ministry "Ministère de la Transition Écologique et Solidaire" and the french institute "Service Technique des Remontées Mécanique et des Transports Guidés".

*Corresponding author. E-mail: charlelie.bertrand@entpe.fr

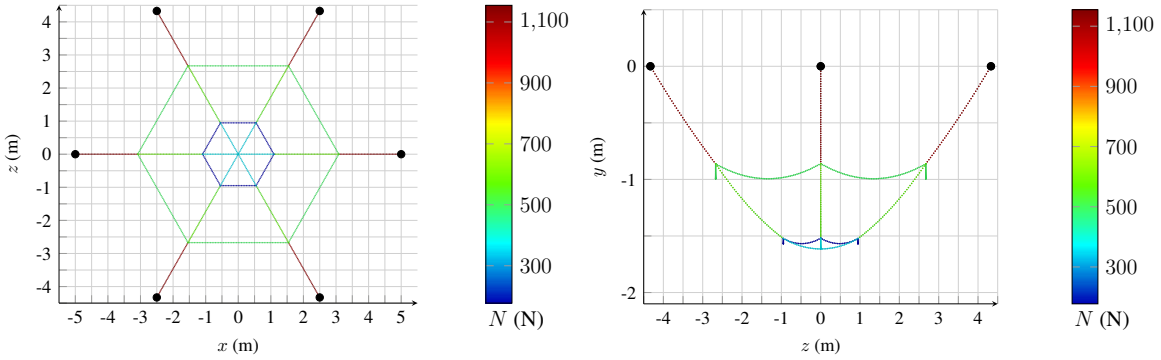

Figure 1: 3D Symmetric spider web superimposed with axial tension profile ; Views in the x-z and z-y planes

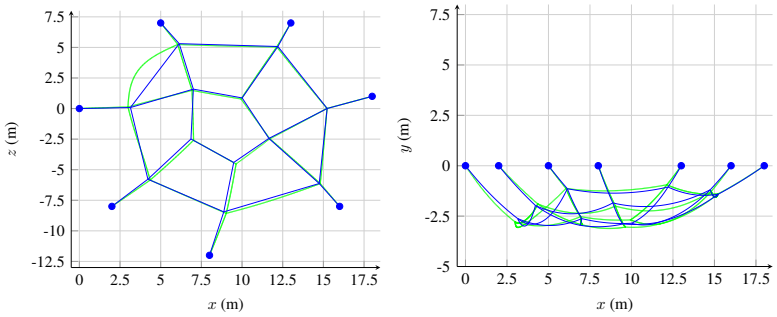

Figure 2: 3[rd] mode of a 3D non symmetric spider web ($\omega = 0.95$ rad/s) ; Views in the x-z and x-y planes

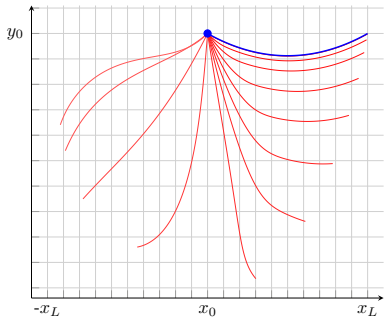

Figure 3: Stations of a falling cable in a similar fashion than [12]

References

[1] H. M. Irvine. *Cable structures*. Dover, New York, 1992. OCLC: 831328789.
[2] G. Rega. Nonlinear vibrations of suspended cables - Part I: Modeling and analysis. *Applied Mechanics Reviews*, 57(6):443, 2004.
[3] C. A. Felippa. Finite element analysis of dimensional cable structures. *Proc. 1st Int. Conf. Computational Mthods in Nonlinear Mechanics; Austin TX*, pages 311–324, 1974.
[4] M. Crusells-Girona, F. C. Filippou, and R. L. Taylor. A mixed formulation for nonlinear analysis of cable structures. *Computers & Structures*, 186:50–61, July 2017.
[5] P. D. Panagiotopoulos. Stress-unilateral analysis of discretized cable and membrane structure in the presence of large displacements. *Ingenieur-Archiv*, 44(5):291–300, 1975.
[6] M. Angelillo. A finite element approach to the study of no-tension structures. *Finite Elements in Analysis and Design*, 17(1):57–73, June 1994.
[7] Y. Kanno and M. Ohsaki. Minimum principle of complementary energy of cable networks by using second-order cone programming. *International Journal of Solids and Structures*, 40(17):4437–4460, August 2003.
[8] O. C. Zienkiewicz and R. L. Taylor. *The finite element method. Vol. 1: The basis*. Butterworth-Heinemann, Oxford, 5. ed., reprinted edition, 2002. OCLC: 249013082.
[9] J.-J. Marigo. *Mécanique des Milieux Continus I*. Paris, École polytechnique, August 2014. Lecture notes, HAL-ID: *cel-01023392*.
[10] S. Ueber, G. Stadler, and B. Wohlmuth. A primal-dual active set algorithm for three-dimensional contact problems with coulomb friction. *SIAM J. Scientific Computing*, 30.
[11] B. Fraejis de Veubeke, M. Gérardin, and A. Huck. *Structural dynamics*. LTAS, Liège, 1974.
[12] I. Fried. Large deformation static and dynamic finite element analysis of extensible cables. *Computers & Structures*, 15(3):315–319, January 1982.

CONSTITUTIVE ARTIFICIAL NEURAL NETWORKS (CANNS)

Kian P. Abdolazizi*[1], Kevin Linka[1], and Christian J. Cyron[1,2]
[1]Institute of Continuum and Materials Mechanics, Hamburg University of Technology, Hamburg, Germany
[2]Institute of Materials Research, Materials Mechanics, Helmholtz-Zentrum Geesthacht, Geesthacht, Germany

Summary This contribution aims to balance theory- and data-driven approaches to describe a material's mechanical response. We introduce so-called Constitutive Artificial Neural Networks (CANNs), a novel machine learning architecture. CANNs incorporate substantial prior knowledge from materials theory to reduce the need for experimental data while simultaneously taking account of material symmetries and internal constraints. Functional relations between stress and strain are not postulated a priori but rather learned from experiments. CANNs have the ability to incorporate stress-strain but also non-mechanical data, e.g., parameters from manufacturing processes or imaging data. Therefore, CANNs may serve not only as descriptive but also as predictive tool and open perspectives for the virtual design of new materials.

INTRODUCTION AND THEORETICAL BACKGROUND

The classical, theory-driven approach to describe the deformation of a material body relies on the formulation of constitutive equations connecting kinematic and kinetic quantities. Both phenomenological and micromechanically motivated constitutive equations typically exhibit a set of material parameters that have to be calibrated from experiments [1]. A drawback of this classical, theory-driven approach is the efforts that are typically required to develop appropriate functional relations that can describe the behavior of complex new materials. Furthermore, in this classical approach it is often difficult to incorporate information which is well-known to be strongly correlated with the behavior of the material but whose exact relation to the mechanical properties of a material cannot be strictly quantified. This is, for example, often the case for manufacturing parameters.

By contrast, current model-free data-driven methods [2, 3, 4] permit the numerical simulation based on experimental stress-strain measurements only, without postulating any constitutive model at all. These data-driven methods rely on material data bases that have to be sufficiently large in order to reflect the characteristics of a material appropriately. So far proposed methods of data-driven constitutive modeling often require a relatively large amount of (sufficiently accurate) material data, which may in practice often not be available.

In this contribution, we propose a novel hybrid approach that can help overcome the shortcomings and combine the strengths of both classical theory-driven and modern data-driven constitutive modeling by introducing so-called Constitutive Artificial Neural Networks (CANNs), a novel machine learning architecture. CANNs can learn constitutive models from given data while incorporating already significant prior theoretical knowledge, which reduces the amount of data required substantially.

Constitutive modeling

Anisotropic hyperelastic materials may be described by strain energy functions of the type

$$\Psi = \Psi\big(\tilde{I}_r, \tilde{J}_r, \mathrm{III}_{\mathbf{C}}\big) \tag{1}$$

with so-called (generalized) invariants [5]

$$\tilde{I}_r = \mathrm{tr}[\mathbf{C}\tilde{\mathbf{L}}_r], \qquad \tilde{J}_r = \mathrm{tr}[(\mathrm{cof}\,\mathbf{C})\tilde{\mathbf{L}}_r], \qquad \mathrm{III}_{\mathbf{C}} = \det\mathbf{C}, \qquad r = 1, 2, \ldots \tag{2}$$

Therein, $\mathbf{C}$ and $\tilde{\mathbf{L}}_r$ denote the right Cauchy-Green tensor and generalized structural tensors, respectively. The latter are defined as convex combinations of structural tensors $\mathbf{L}_i$ and corresponding weighting factors $w_i^{(r)} \geq 0$:

$$\tilde{\mathbf{L}}_r = \sum_{i=0}^{n} w_i^{(r)} \mathbf{L}_i, \qquad \sum_{i=0}^{n} w_i^{(r)} = 1, \qquad r = 1, 2, \ldots \qquad \mathbf{L}_0 = \frac{1}{3}\mathbf{I}, \tag{3}$$

where $\mathbf{L}_j = \boldsymbol{l}_j \otimes \boldsymbol{l}_j,\ j = 1, 2, \ldots, l$, is referred to as structural tensor and is represented by unit vectors $\boldsymbol{l}_j$ reflecting preferred material directions. Accordingly, the second Piola-Kirchhoff stress tensor $\mathbf{S}$ and the fourth-order material tangent tensor $\mathbb{C}$ are given by

$$\mathbf{S} = 2\frac{\partial\Psi}{\partial\mathbf{C}} - p\mathbf{C}^{-1}, \qquad \mathbb{C} = 2\frac{\partial\mathbf{S}}{\partial\mathbf{C}}, \tag{4}$$

with the Lagrange multiplier p enforcing incompressibility.

*Corresponding author. E-mail: kian.abdolazizi@tuhh.de.

Machine learning architecture

In this contribution, we are proposing a novel machine learning architecture based on feed-forwards artificial neural networks (ANNs), referred to as CANNs. By their very design CANNs incorporate theoretical domain knowledge as reflected by the above equations (1) – (4). Thereby, the amount of required training data is reduced, while the output of the CANNs is restricted to physically meaningful values, e.g. symmetric $\mathbf{S}$. Preferred material directions $\tilde{\boldsymbol{l}}_i$ and associated weights $w_i^{(r)}$ required for generalized invariants are learned automatically from given data by sub-ANNs. CANNs can receive as input not only stress-strain data but in fact also any additional information regarding the material of interest. During the training process the main network as well as the sub-ANNs are trained simultaneously by minimizing the mean squared error of the CANN in terms of stress response.

In-silico study

We tested the ability of CANNs using several examples. One was computational homogenization of representative volume elements (RVEs) for computing the macroscopic mechanical behavior of incompressible matrix inclusion composites. We considered the simple test case of a periodic composite material with spheroid inclusions centered in cubic RVEs. The length of the semi-axes of the inclusions was allowed to vary in a large range. We generated 500 different samples of this type of material with varying inclusion geometry. The inclusion geometry, the phase contrast of matrix and inclusion stiffness as well as the simulated mechanical behavior under a series of loading states (obtained from computational homogenization) of these 400 samples were provided as training data to a CANN. From these data, the CANNs were able to learn the constitutive behavior not only of matrix-inclusion composites with the phase contrasts and inclusion geometries as reflected by the training data but also to predict the constitutive behavior of matrix-inclusion composites (of the above type) with microstructures and phase contrasts not covered by the training data. In particular, CANNs proved able to identify from the training data automatically material symmetries. The predictive abilities of the CANN are illustrated in Figure 1a for three materials unknown to the CANN.

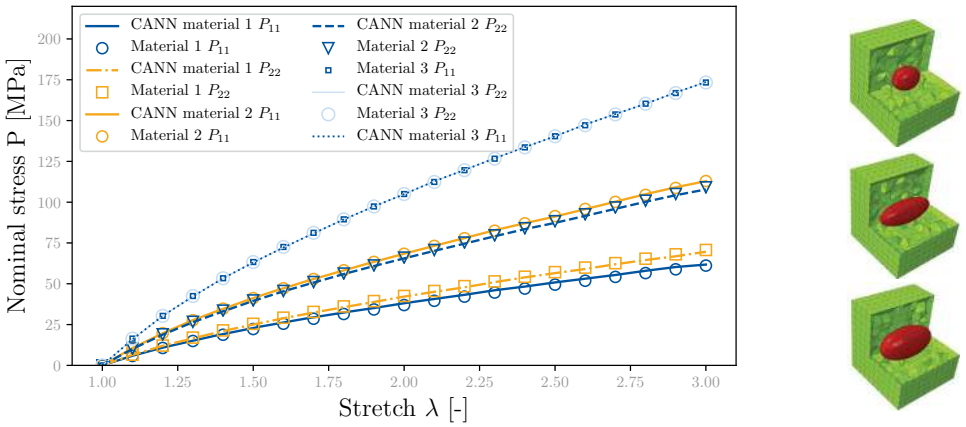

(a) (b)

Figure 1: Simulated stress-stretch responses (symbols) and CANN predictions (lines) for the three RVEs on the right, which did not form part of the CANN training data

CONCLUSIONS

CANNs are a novel machine learning architecturs capable to infer constitutive laws from stress-strain data (using thereby also additional non-mechanical data if provided). In contrast to other machine learning approaches in the field of constitutive modeling, which often aim for a mapping of strain tensor components to stress tensor components, the dimensionality of the feature space, from whom training data has to be sampled, is considerably reduced by incorporating knowledge from continuum mechanics. CANNs can easily and efficiently be implemented into widely-used finite element packages via user subroutines. Moreover, CANNs cannot only be used to describe the constitutive behavior of a given material but also to predict the one of new materials, opening up application scenarios in the area of virtual materials design.

References

[1] Ogden R.W. et al.: Fitting hyperelastic models to experimental data. *Computational Mechanics* 34, 484–502, 2004.
[2] Kirchdoerfer T., Ortiz M.: Data-driven computational mechanics. *Computer Methods in Applied Mechanics and Engineering* 304, 81–101, 2016.
[3] Leygue A. et al.: Data-based derivation of material response. *Computer Methods in Applied Mechanics and Engineering* 331, 184–196, 2018.
[4] Stainer L. et al.: Model-free data-driven methods in mechanics: material data identification and solvers. *Computational Mechanics* 64, 381–393, 2019.
[5] Ehret A.E., Itskov M.: A polyconvex hyperelastic model for fiber-reinforced materials in application to soft tissues. *Journal of Material Science* 42, 8853–8863, 2006.

SYSTEMATIC EXTENSION OF THERMOELASTIC-VISCOPLASTIC CONSTITUTIVE LAWS AT FINITE DEFORMATION: FORMULATION AND IMPLEMENTATION IN A COMMERCIAL FE CODE

Mohamed Abatour[1], Samuel Forest*[1], Kais Ammar[1], Cristian Ovalle[1], Nikolay Osipov[2], and Stéphane Quilici[2]
[1]MINES Paris Tech, PSL University, Centre des matériaux, CNRS UMR 7633, BP 87 91003 Evry, France
[2]Transvalor S.A., Centre d'affaires la Boursidière, 92357 Le Plessis-Robinson, France

Summary Most commercial finite element codes are based on hypoelastic formulations of thermoelasto-viscoplastic constitutive laws for metals or polymers. Their spurious effects, like unexpected ratcheting under cyclic loading, are well-known but generally overlooked for the sake of computational ease. An alternative systematic framework for the extension of nonlinear thermoelastic-(visco)plastic constitutive equations to finite deformations is proposed, based on a multiplicative decomposition of the deformation gradient into a thermoelastic part and an inelastic part. The questions of the choice of suitable hyperelastic potential, of hardening variables and of anisotropy evolution are discussed. The method is applied to a commercial FE code as an illustration.

SHORTCOMINGS OF EXISTING EXTENSIONS IN FE CODES

There is today no unified framework for the implementation of nonlinear constitutive equations at finite deformations in commercial finite element codes. A wealth of elastoviscoplastic constitutive equations are available for simulations at small strain involving kinematic and isotropic hardening variables, static and dynamic recovery and strain rate sensitivity. They are suitable for the thermo-mechanical behaviour of metallic alloys and polymers. They involve internal variables dedicated to dissipative processes including plasticity and damage.

Many codes rely on the so-called corotational extension of the laws developed at small strains, i.e. the pull-back of Eulerian variables in rotating objective frames [1]. The drawbacks of such a formulation are well–known: absence of elastic potential (hypoelasticity) and associated spurious ratcheting effects under cyclic non-proportional [2, 3]. The strain rate tensor D is pulled back in a cororational frame and split additively into thermal, elastic and (visco)plastic strains rates:

$$\dot{\boldsymbol{e}} = \boldsymbol{Q}\boldsymbol{D}\boldsymbol{Q}^T = \dot{\boldsymbol{e}}^e + \dot{\boldsymbol{e}}^{th} + \dot{\boldsymbol{e}}^p$$

As a consequence, the non-holonomic plastic strain $\boldsymbol{e}^p$ has no clear mechanical interpretation. This framework provides only limited description of anisotropy due to the absence of plastic spin in the standard framework. The use of extended anisotropic yield functions then assumes that the anisotropy axes rotate at the corotational rate. These limitations have been recently highlighted in [5]. The main advantage is that any set of nonlinear constitutive equations formulated at small strains (for example the whole sets of material descriptions proposed by Lemaitre and Chaboche [4]) can be translated into the corotational frame and deliver material frame-indifferent models for large deformations. This explains the wide use of these laws in commercial finite element codes [12].

There is a real need for thermodynamically consistent and systematic extensions of small strain constitutive laws for large deformations, that remain transparent for the user, namely engineers who often do not have a sufficient background for choosing intentionally specific finite deformation formulations.

MULTIPLICATIVE DECOMPOSITION AND CHOICE OF THE HYPERELASTIC LAW

Hyperelastic-viscoplastic constitutive laws are classically based either on additive decomposition of Lagrangian strain measures [6] or on Mandel's multiplicative decomposition of the deformation gradient:

$$\boldsymbol{F} = \boldsymbol{F}^{eth}\boldsymbol{F}^p$$

where $\boldsymbol{F}^{eth}$ is the thermoelastic part of deformation whereas $\boldsymbol{F}^p$ denotes all inelastic contributions due to viscoplasticity and damage. The attention is focused on the latter because it is more relevant for metallic alloys possessing isomorphic elastic ranges [7]. This avoids arbitrary multiple decompositions of the form $\boldsymbol{F} = \boldsymbol{F}^e\boldsymbol{F}^{th}\boldsymbol{F}^p\boldsymbol{F}^d$ or associated permutations that are often found in literature [8, 9]. Instead the inelastic deformation rate $\dot{\boldsymbol{F}}^p\boldsymbol{F}^{p-1}$ can be taken as the sum of the various viscoplastic and damage contributions, including corresponding spins accounting for anisotropy.

Inelastic strain is dominant in most metals and polymers (except elastomers) so that the choice of the hyperelastic law can be limited to a two–parameter elastic potential extending the small strain elastic moduli. Hence, the use of Saint-Venant Kirchhoff elastic law, or, preferably a polyconvex potential as proposed by [10], is recommended. The Helmholtz free energy potential is a function $\psi(\boldsymbol{E}^{eth} = \boldsymbol{F}^{ethT}\boldsymbol{F}^{eth}, T, \boldsymbol{\alpha})$ of thermoelastic strain, temperature and internal variables $\boldsymbol{\alpha}$. A quadratic elastic potential is retained in the theory:

$$\psi^{eth}(\boldsymbol{E}^{eth}, T) = \frac{1}{2}\boldsymbol{E}^{eth}\cdot\boldsymbol{C}\cdot\boldsymbol{E}^{eth} + (T - T_0)\boldsymbol{P}\cdot\boldsymbol{E}^{eth}$$

The inelastic flow rule follows from an assumption of normality for (possibly porous) metallic alloys. The question of plastic spin for anisotropic materials will be discussed at the light of the archetypal example of single crystal behaviour.

*Corresponding author. E-mail: samuel.forest@mines-paristech.fr.

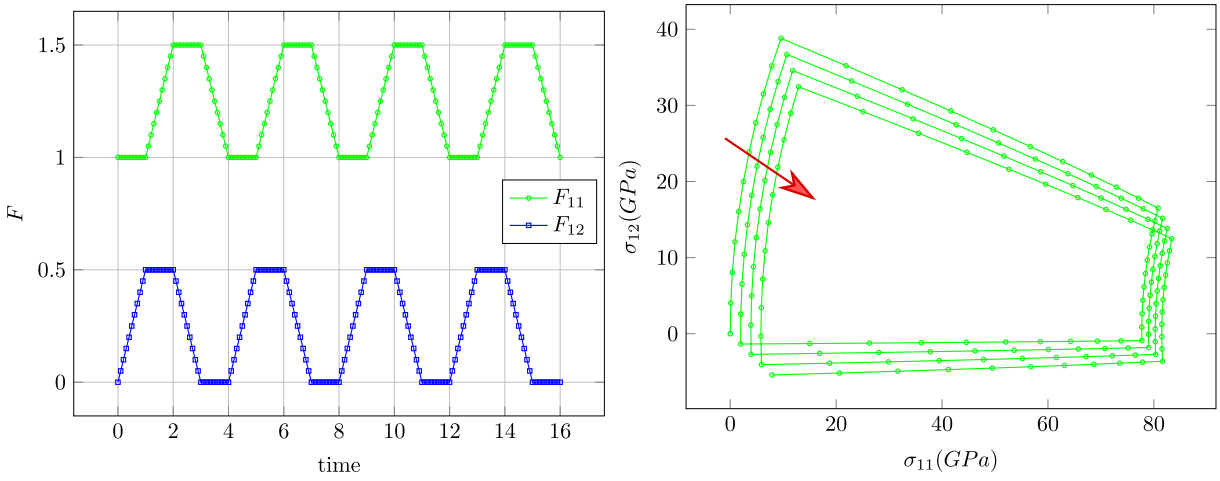

Figure 1: Spurious ratcheting under non-proportional cyclic loading for a hypoelastic formulation (Green-Naghdi rate). $E = 210GPa$, $\nu = 0.3$. The applied loading is shown left: all the other components are null except $F_{22} = F_{33} = 1$.

EXTENSION OF HARDENING LAWS DEVELOPED AT SMALL STRAINS

Extension of isotropic hardening rules based on scalar internal variables is rather straightforward. In contrast, kinematic hardening is associated with tensor internal variables and several large deformation extensions are possible as discussed in [11]. It can be shown that hypoelastic-plasticity with (non)linear kinematic hardening can lead to (pseudo)periodic stress response under simple shear [1].

A construction method of consistent tangent matrices for implicit integration of evolution equations and of the tangent operator for implicit global resolution is proposed, based solely on the associated small strain operator and appropriate pull back and push forward transports.

The proposed methodology is implemented in the commercial FE object-oriented code Zset [12]. It is shown in particular how the rich library of small strain nonlinear constitutive laws can be readily extended to finite deformations.

References

[1] Besson J., Cailletaud G., Chaboche J.L, Forest S., Blétry M. Non-linear mechanics of materials. Springer, 2010.

[2] Kojić M., Bathe K.-J. Studies of finite element procedures–Stress solution of a closed elastic strain path with stretching and shearing using the updated Lagrangian Jaumann formulation. *Computers & Structures* **26**: 175–179, 1987.

[3] Lin R. C., Schomburg U., Kletschkowski T. Analytical stress solutions of a closed deformation path with stretching and shearing using the hypoelastic formulations. *European Journal of Mechanics - A/Solids* **22**: 443–461, 2003.

[4] Lemaitre J., Chaboche J.-L. Mechanics of Solid Materials. Cambridge University Press, 1994

[5] Brepols T., Vladimirov I. N., Reese S. Numerical comparison of isotropic hypo- and hyperelastic-based plasticity models with application to industrial forming processes. *International Journal of Plasticity* **63**:18–48, 2014.

[6] Miehe C., Apel N., Lambrecht M. Anisotropic additive plasticity in the logarithmic strain space: modular kinematic formulation and implementation based on incremental minimization principles for standard materials. *Computer Methods in Applied Mechanics and Engineering* **191**: 5383–5425, 2002.

[7] Bertram A. An alternative approach to finite plasticity based on material isomorphisms. *International Journal of Plasticity* **15**: 353–374, 1999.

[8] Mićunović, M. A geometrical treatment of thermoelasticity of simple inhomogeneous bodies: I and II. *Bulletin de l'Académie Polonaise des Sciences, Série des Sciences Techniques* **22**: 579–588, and 633–641, 1974.

[9] Mcauliffe C., Waisman H. A unified model for metal failure capturing shear banding and fracture. *International Journal of Plasticity* **65**: 131–151, 2015.

[10] Wallin, M., Ristinmaa M. Deformation gradient based kinematic hardening model. *International Journal of Plasticity* **10**: 2025-2050, 2005.

[11] Vladimirov I. N., Pietryga M. P. and Reese S. Anisotropic finite elastoplasticity with nonlinear kinematic and isotropic hardening and application to sheet metal forming. *International Journal of Plasticity* **26**: 659–687, 2010.

[12] Zset finite element code, **http://www.zset-software.com**.

AN ENERGY-BASED DETWINNING MODEL FOR GRANDIENT NANOTWINNED METALS

Panpan Zhu[1], and Haofei Zhou*[1]
[1]Center for X-mechanics, Department of Engineering Mechanics Zhejiang University, Hangzhou, Zhejiang, PR China

Summary: Detwinning has been widely observed in both bulk and low-dimensional nanotwinend metals. The physical origin of detwinning is generally known to be the consecutive nucleation and movement of Shockley partial dislocations on the twin plane under a finite resolved shear stress. Here, we propose a detwinning model based on the concept of strain energy release rate in gradient nanotwinned metals, which is subjected to uniaxial loading nearly parallel to the twin boundaries. Although no apparent resolved shear stress is present on the twin plane, the difference in the elastic energy stored in neighboring grains is able to drive the migration of twin planes, leading to substantial detwinning in the gradient nanotwinned structure. We demonstrate the model with results from large-scale molecular dynamics simulations. Our findings not only point out the critical role of detwinning in the plasticity of gradient nanotwinned metals, but also shed light on previous experimental observation of detwinning in nanotwinned metals.

INTRODUCTION

Gradient nanostructured (GS) metals, including both gradient nanograined (GNG) and gradient nanotwinned (GNT) metals, have recently emerged as a new class of materials with tunable distribution of microstructures and have been shown to possess substantially enhanced mechanical properties compared to their gradient-free counterparts [Fang et al., 2011; Wei et al., 2014; Wu et al., 2014]. Due to their unique gradient microstructures, GS metals could be designed to exhibit an unusual combination of ultrahigh strength, good tensile ductility, enhanced strain hardening, superior fatigue and wear resistance. Our recent work [Cheng et al., 2018] shows that GNT metals exhibit extra strengthening and work hardening behaviors compared with uniform nanotwinned metals. The extra strengthening and work hardening of GNT metals was revealed to be controlled by high density of geometrically necessary dislocations in the form of concentrated dislocation bundles distributed in the grain interiors. Here, using large-scale molecular dynamics (MD) simulations, we report a strain energy release controlled detwinning mechanism that is dominant in the plasticity of GNT metals at large strains.

MD SIMULATION RESULTS

We performed MD simulations on fully three-dimensional GNT Cu samples with various structural gradients. We first created two homogeneous columnar-grained nanotwinned components, and then combined them together to form a GNT structure (Figure 1a). By varying the twin thickness of the individual components, GNT samples with various structural gradients can be generated. The same relaxation, tension, and visualization methods were adopted for the simulated samples [Cheng et al., 2018]. We performed uniaxial tensile loading on the structure with a large gradient in yield strength to demonstrate the detwinning-induced plasticty in GNT structures. The grain size and twin size of the two components NT-A and NT-B were selected such that the large gradient in yield strength ensures extensive detwinning process of GNT structures at large strains (Figure 1b). Twinning partial dislocations were emitted either from the GBs or the intersections of TBs and stacking faults.

AN ENERGY-BASED DETWINNIING MODEL

The extensive twin boundary migration and detwinning-governed deformation is unexpected because resolved shear stress along the twin planes is negligible with the loading axis parallel to the twin planes. Recently, an anomalous tensile detwinning mechanism governed by the migration of a unique TB-GB-TB structure was reported in a bitwinned metallic nanowire, which is apparently not the case in our simulations [Cheng et al., 2017]. Here, we develop a theoretical model

based on the concept of strain energy release rate to explain the substantial detwinning observed in the simulated GNT structures. Suppose the GNT structure has two components A and B with twin thickness $\lambda_A < \lambda_B$ and yield strength $\sigma_A > \sigma_B$. The stored strain energy density of the two components is different. The driving force for detwinning in GNT structure due to the gradient in yield strength can be derived as $\tau_d = \frac{\sigma_A^2 - \sigma_B^2}{2E}$, where E is the Young's modulus of the material. The detwinning rate can be related to the driving force as $n = A(\frac{\tau_d}{\tau_0})^\alpha$, where A, α, and τ_0 are material parameters. We created three different GNT samples with different structural gradients. NT-B is fixed. The twin thickness in NT-A varies from 0.63nm-1.25nm. Figure 1c shows the variation of the number of h.c.p. atoms in NT-A in these three GNT samples. The predicted detwinning rates at large strains match well with the simulations results, demonstrating that the proposed strain energy release driven detwinning mechanism is indeed dominant in the plasticity of GNT metals.

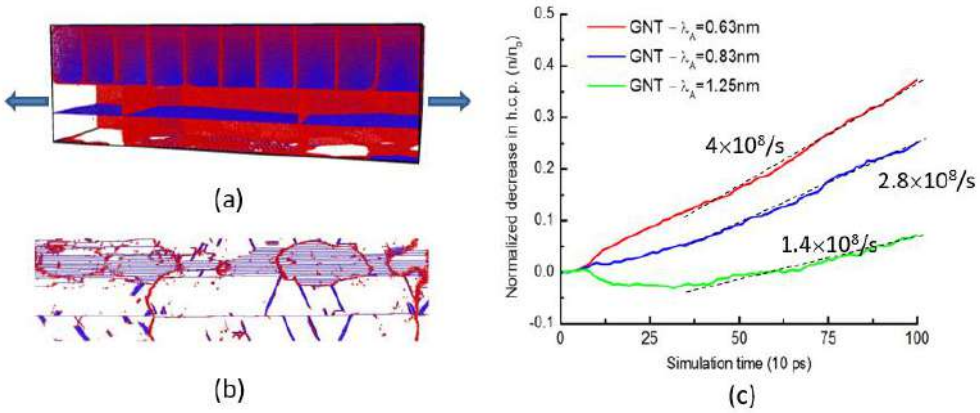

Fig. 1 (a) Three-dimensional GNT Cu samples. (b) Cross sectional snapshots of the detwinning process of GNT structures at 50% strains. (c) The number of h.c.p. atoms in NT-A change with simulation time of three GNT samples.

CONCLUSION

In this work, using MD simulations and theoretical modeling, we have demonstrated that a sufficiently large gradient in the stored strain energy in neighboring grains is able to induce substantial detwinning in a GNT Cu sample. In nanotwinned metals synthesized by electrodeposition or magnetic sputtering, the distribution of nanotwins is not ideally uniform but with local gradients in twin thickness and stored strain energy density. Our energy-based detwinning model may help understand the observation of detwinining in nanotwinned metals.

References

[1] Fang TH, Li WL, Tao NR, et al. Revealing Extraordinary Intrinsic Tensile Plasticity in Gradient Nano-Grained Copper[J]. *Science*, 2011, 331(6024):1587-1590.

[2] Wei Y, Li Y, Zhu L, et al. Evading the strength-ductility trade-off dilemma in steel through gradient hierarchical nanotwins. *Nature Communications*. 2014;5:3580.

[3] Wu X, Jiang P, Chen L, et al. Extraordinary strain hardening by gradient structure[J]. *Proceedings of the National Academy of Sciences*, 2014, 111(20):7197-7201.

[4] Cheng Z, Zhou HF, et al. Extra strengthening and work hardening in gradient nanotwinned metals.[J]. *Science (New York, N.Y.)*, 2018.

[5] Cheng G, Yin S, Chang TH, et al. Anomalous Tensile Detwinning in Twinned Nanowires[J]. *Physical Review Letters*, 2017, 119(25):256101.

AUTOMATIC DIFFERENTIATION FOR SOLID MECHANICS

Andrea Vigliotti*[1] and Ferdinando Auricchio[2]
[1] Innovative Materials Laboratory, Italian Aerospace Research Center, Capua, Italy
[2] Department of Civil Engineering and Architecture, University of Pavia, Pavia, Italy

Summary Automatic differentiation (AD) is an ensemble of techniques that allow to evaluate accurate numerical derivatives of a mathematical function expressed in a computer programming language. In this study we use AD for stating and solving solid mechanics problems. Given a Finite Element (FE) discretization of the domain, we evaluate the free energy of the solid as the integral of its strain energy density and we make use of AD for directly obtaining the residual force vector and the tangent stiffness matrix of the problem as the gradient and the Hessian of the free energy respectively. The result is a remarkable simplification in the statement and the solution of complex problems involving non trivial constraints systems and both geometrical and material non linearities.

Forward automatic differentiation through dual numbers

As opposite to finite differences, AD does not approximate the continuous derivatives with discrete differences, thus it does not suffer from truncation error, and it is capable of delivering machine precision exact derivatives. AD techniques exist in different fashions [1], nonetheless, in the current study we use dual numbers for the implementation of a forward mode AD scheme, which allows seamless integration with existing software programs. Dual numbers are an extension of the complex field with multiple higher dimensional parts [2]. In this work, dual numbers are the structure chosen to store, and operate, both on the value of a given parameter and on its derivatives. We define dual numbers of the second order and dimension N the quantities of the kind

$$\boldsymbol{x} \equiv x_0 + x_i \boldsymbol{\imath}_i + x_{ij} \boldsymbol{\imath}_{ij} \qquad \text{where } \boldsymbol{\imath}_i \text{ is the canonical base of } \mathrm{R}^N \text{ and } \boldsymbol{\imath}_{ij} \equiv \boldsymbol{\imath}_i \otimes \boldsymbol{\imath}_j + \boldsymbol{\imath}_j \otimes \boldsymbol{\imath}_i \,, \tag{1}$$

where the summands in the above expression are independent parts of $\boldsymbol{x}$, x_0 is the value part of $\boldsymbol{x}$, $x_i \boldsymbol{\imath}_i$ is the gradient part of $\boldsymbol{x}$, and $x_{ij} \boldsymbol{\imath}_{ij}$ the Hessian of part, sum on repeated index applies. Numbers of the type of (1) can be structured as to induce an algebra that allows to simultaneously evaluate the value, the first and the second derivatives, where they exist, with respect to the identified independent variables, of any function expressed in a computer programming language, in an automated way [3].

Equilibrium as a free energy minimum

Thermodynamics ensures that free energy is stationary for equilibrium configurations. Therefore, given a functional expression for the free energy of a body, subjected to given boundary conditions and to some external actions from the environment, stable equilibrium configurations can be found by minimizing this functional. Using a FE discretization we can approximate the free energy of a solid as a function of the nodal Degrees of Freedom (DoFs) of the FE model, $\boldsymbol{u}$, as follows

$$\Psi = \int_{V_0} (\phi - b_0) \, \mathrm{d}V_0 \quad \underset{\text{discretization}}{\overset{\text{Finte Elements}}{\Longrightarrow}} \quad \Psi(\boldsymbol{u}) = \sum_{k=1}^{N_E} \sum_{i=1}^{N_W^k} w_l^k \left[\phi - b_0\right]_{r_l^k} \,, \tag{2}$$

where surface forces have been neglected for brevity, V_0 is the volume occupied by the body in its reference configuration, ϕ is the strain energy density, and b_0 is the potential of the external body forces, per unit reference volume. The equation on the right side of the arrow in (2) expresses the Gauss-Legendre quadrature rule for Ψ, where N_E is the number of elements, N_W^k the number of Gauss points of the k-th element, w_l^k are the integration weights, and r_l^k are the positions where the bracket is evaluated. With reference to the FE discretization of Ψ, the minimum free energy principle can then be stated as follows

$$\delta\Psi = \frac{\partial \Psi}{\partial \boldsymbol{u}} \cdot \delta\boldsymbol{u} = 0 \quad \forall\, \delta\boldsymbol{u} \qquad \Longleftrightarrow \qquad \boldsymbol{r} = \frac{\partial \Psi}{\partial \boldsymbol{u}} = 0 \quad \text{with} \quad \boldsymbol{K}_t = \frac{\partial \boldsymbol{r}}{\partial \boldsymbol{u}} = \frac{\partial^2 \Psi}{\partial \boldsymbol{u} \partial \boldsymbol{u}} \tag{3}$$

where $\boldsymbol{r}$ is the residual force vector and $\boldsymbol{K}_t$ is the tangent stiffness matrix, that coincide with the gradient and the Hessian of the free energy, respectively, and can be *automatically calculated* from the last expression in equation (2), once the DoFs of the model, collected in $\boldsymbol{u}$, are treated as dual quantities of the type of (1).

Thus, with the approach described here, it is not necessary to explicitly write code for the evaluation of the components of the residual force vector and of the tangent stiffness matrix for a given configuration of the solid, but it suffices to write the functions that calculate the free energy of the configuration - which is a scalar quantity - and evaluate it over the dual number field, while its gradient and Hessian are automatically obtained as the higher order parts of the result [3]. We also remark that the methodology presented here allows to state and solve a FE problem without introducing the notion of a stress tensor, which is the usual starting point of FE formulations. This is an interesting effect of always remaining within the weak form of the problem.

Examples

In this section we illustrate a selection of solid mechanics problems that have been solved by means of the method outlined above. All problems include both geometric and material non-linearities, along with non trivial boundary conditions. All the script for the solution of the examples have been written in the Julia programming language [4], and are available, along with the input files, from [5] under a collaborative licence.

*Corresponding author. E-mail: a.vigliotti@cira.it.

The non linear truss

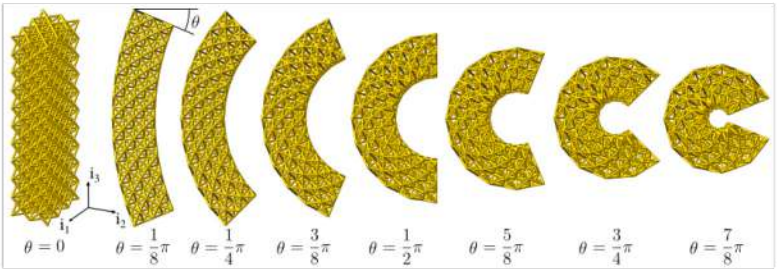

Figure 1: Deformation of a truss with large geometrical non linearities

Figure 1 shows the deformed configuration of a regular lattice structure. The truss is made of rod elements in a linear elastic material that can store deformation energy only because of length variations. The structure is obtained by replicating a regular octet cell along the coordinate directions. The boundary conditions have been applied to the nodes of the top and the bottom end, constraining them to remain on planes forming the same angle θ with direction i_3, with opposite sign.

Cylindrical symmetry problem with internal volume constraint

Figure 2 illustrates the modelling of a solid with cylindrical symmetry around the i_2 axis, featuring an internal cavity with circular cross section, in a Neo-Hookean material. Thanks to the symmetry of the problem, we only model a generic cross section of the solid with a plane including the symmetry axis, and the cylindrical formulation for the deformation tensor. The presence of an incompressible fluid within the cavity can be modelled by constraining the cavity volume to remain constant. Results are presented with and without the internal volume constraint.

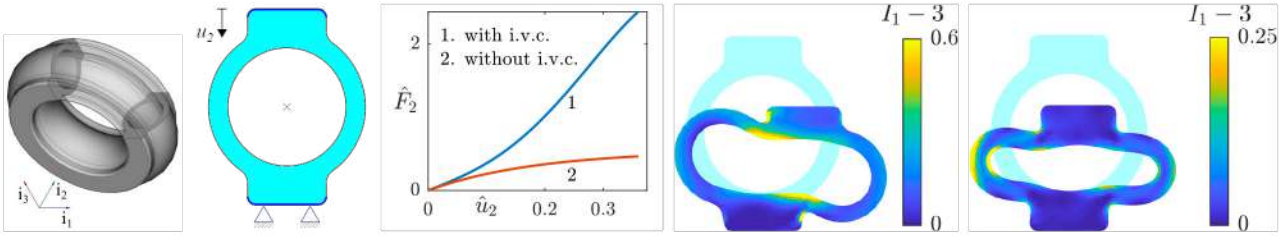

Figure 2: Axi-symmetric problem, simulation results. (a) Undeformed domain, (b) cross section and boundary conditions, (c) normalized force displacement plot, (d) deformed cross section with internal volume constraint (i.v.c.), and (e) without i.v.c. at maximum deformation, I_1 is the first invariant of the deformation tensor.

Three-dimensional solid with large geometrical non-linearities

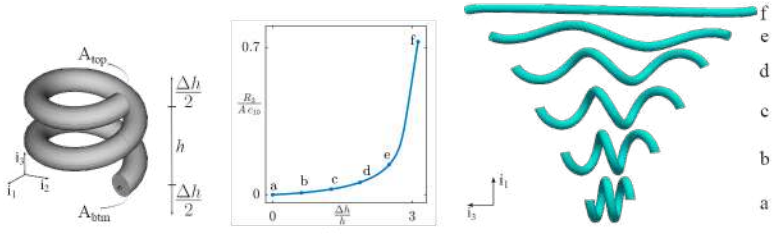

Figure 3: Three-dimensional solid. (a) Undeformed domain, (b) normalized force displacement plot, (c) deformed configurations at the stages of the simulation marked in (b).

Figure 3 shows the results of the simulation of a model made of continuous hexahedral elements in a Neo-Hookean material. The boundary conditions have been applied by constraining the centre of gravity of the top bottom section to produce the displacements shown in Figure 3a. As it can be observed the model captures the complex non linear geometry of the unfolding of the spring, followed by the material stiffening.

Conclusions

In this study we used AD for the implementation of the FE method for the solution of solid mechanics problems. The advantage in such approach is that it only requires to explicitly evaluate the free energy of a body in a given configuration, which is a simple scalar quantity, while the corresponding residual force vector and the tangent stiffness matrix are obtained automatically. In this way it is possible to state and solve complex problems, including geometrical and material non linearities and non trivial boundary conditions in a fast and simple way. This approach also exposes an interesting insight on the nature of the general problem of FE for solid mechanics, which is that the stress tensor can be seen as an intermediate variable, playing a lesser fundamental role in a formulation totally based on the energy balance.

References

[1] A. Griewank and A. Walther, *Evaluating Derivatives: Principles and Techniques of Algorithmic Differentiation*. SIAM, second ed., 2008.
[2] I. L. Kantor and A. S. Solodovnikov, *Hypercomplex numbers: an elementary introduction to algebras*. Springer, 1989.
[3] A. Vigliotti and F. Aurcchio, "Automatic differentiation for solid mechanics," *Arch. of Comp. Meth. in Eng.*, accepted, 2020.
[4] J. Perkel, "Julia: come for the syntax, stay for the speed," *Nature*, vol. 572, no. 7767, pp. 141–142, 2019.
[5] A. Vigliotti, "Automatic differentiation for solid mechanics, examples scripts." http://dx.doi.org/10.17632/ybbsszpbss.1, Mendeley, 2020.

ON THE UNIQUENESS PROBLEM ABOUT CENTRAL CONFIGURATIONS IN THE PLANAR CONVEX FOUR-BODY PROBLEM

Agnieszka Siluszyk*[1]
[1]Institute of Mathematics, Faculty of Exact and Natural Sciences, Siedlce University, Siedlce, Poland

Summary The classification of the planar central configurations consisting of two pairs of bodies located on parallel lines has been presented by M. Corbera, J.M. Cors, J. Llibre and E. Perez-Chavela. They have proved the existence of acute and obtuse trapezoid central configurations in the case of four positive masses and of non-symmetric trapezoid central configuration with two pairs of equal masses. Here, we deal with a quadrilateral configuration in the shape of a isosceles trapezoid. We consider the planar motion of four interacting material points when the masses m_1 and m_2 lie on the X-axis at $(R,0)$ and $(-R,0)$-vertices whilst the masses m_3 and m_4 lie at the $(\pm R\cdot cos\theta, R\cdot sin\theta)$ respectively, with $\theta\in(0,\pi)$. In this way, we consider the model which is constructed in the circle with the radius R. We show that there exist at most one convex central configuration for each cyclic order.

1.

Investigations of the N-body problem for $N=2,3$ which were initiated by I. Newton and continued by L. Euler, J.L. Lagrange, H. Poincare, A.M. Lyapunov, A. Wintner, and by others gave us the most complete analysis of these problems. The investigations of N bodies motion with masses m_i, $i=1,...,N$ in R^d, moving under the influence of the Newton's gravitational law, when $N\geq 3$ and $d=1,2,3$, are still open. A continuation of the famous Smale's list of problems concerned with relative equilibrium, under the potential, different from the Newtonian one, and may be with a weaker symmetry, the uniqueness problem, singularities, bifurcations, stability of relative equilibria have been proposed by A. Albouy, H.E. Cabral, A.A. Santos *Some problems on the classical n-body problem*, Celestial Mechanics and Dynamical Astronomy, 113(4), (2012), pp. 369-375.
To the list of classical central configurations given in XVIII- XX c. (see, e.g., [17], [13]), B. Elmabsout and E.A. Grebenikov have added some new ones with poorer symmetry, these configurations consisting of $2n$ equal point-masses, where n particles, with mass m_1 each, are located at the vertices of a n-gon, and others n particles with common mass m_2 lie at the vertices of another n-gon. Both n-gons are regular and concentric. Finally, a mass m_0 lies at the center of masses of such configuration. They have proved that such a configuration exists if and only if these two polygons are homothetic or differ by an angle of $\frac{\pi}{n}$ (see, [7, 10, 14]). Nowadays, such central configurations in the N-body problem are called *spiderweb central configurations* (see, [11]). A development of the numerical computer methods makes it possible to obtain the *N-body choreographies*, i.e., a periodic solution of the equal mass N-body problem in which all bodies follow the same path (see, [3, 16]).
In the list of new open problems, as the 10^{th} question, A. Albouy, H.E. Cabral, A.A. Santos formulate the following one: *For given four masses m_1,m_2,m_3,m_4 and with $a=-\frac{3}{2}$ does it exist only one convex central configuration for each cyclic order*? (Here, a is the value occurring in the potential of the Newtonian N-body problem, in the general case the potential have the form $U=-\frac{1}{2a}\sum_{i<j}m_im_jr_{ij}^{2(a+1)}$). One counts central configurations up to rotation and rescaling. Earlier, this uniqueness problem was considered by O. Dziobek [6] and W.D. Macmilian, W. Bartky [12]. Recently, the uniqueness and ordering questions of the bodies in the convex central configurations of the four-body problem has been studied by A. Albouy, Y. Fu, S. Sun [1], M. Corbera, J.M. Cors, J. Llibre and E. Perez-Chavela [4] and others [5, 8].

2.

The central configurations are very important in the analysis of simultaneous collisions, because it turns out that the configuration of gravitating points at the instant of a simultaneous collision is central (in the asymptotic sense). The points which in the beginning formed a central configuration and were at rest have their configuration which clearly does not change up to the instant of a simultaneous collision. [2]. Recall that by a planar central configuration in the N-body problem under the Newtonian potential $U=\sum_{1\leq i<j\leq N}\frac{m_i\,m_j}{|q_i-q_j|}$, $q_i\neq q_j$, $i\neq j$ we mean *an arrangement of N bodies $q_i\in R^2$, $i=(1,\ldots,N)$ with masses m_1, m_2,...,m_N satisfying the equation*

$$\nabla U(q)=\lambda\cdot m\cdot(q-c), \tag{1}$$

for some $\lambda\in R$, where $q=(q_1,q_2,\ldots,q_N)\in R^{2N}$, $m=diag(m_1,m_2,\ldots,m_N)$, and $c=(c_x,c_y)$ is the center of masses. The problem of counting the convex configurations and of their cyclic order of masses could be posed once the existence problem would be solved. In [15], we have stated necessary and sufficient conditions on the parameters for such a configuration to exist, in the case of four interacting material points with the masses m_1 and m_2 lying on the X-axis at $(R,0)$ and $(-R,0)$-vertices whilst the masses m_3 and m_4 lay at the $(-R\cdot cos\theta, R\cdot sin\theta)$ and $(R\cdot cos\theta, R\cdot sin\theta)$, respectively, with $\theta\in(-\frac{\pi}{2},\frac{\pi}{2})$. If the two ends of a diagonal have equal masses then the uniqueness problem of convex central configuration is known, but it is not known if, the masses being numbered 1,2,3,4 in cyclic order, satisfy or not the equalities $m_1=m_2$ and $m_3=m_4$ [1].

*Corresponding author. E-mail: agnieszka.siluszyk@uph.edu.pl

3.

For an isosceles trapezoid central configuration $q_i = (x_i, y_i)$, $(i = 1, 2, 3, 4)$ to exist, its parameters must satisfy the following system of equations [9]

$$\begin{cases} \omega^2(x_i - c_x) &= -\sum\limits_{j=1, i\neq j}^{N} m_j \frac{x_i - x_j}{q_{ij}^3}, \\ \omega^2(y_i - c_y) &= -\sum\limits_{j=1, i\neq j}^{N} m_j \frac{y_i - y_j}{q_{ij}^3}. \end{cases} \tag{2}$$

where $\omega^2 = -\frac{U(q)}{2I(q)}$ and $I(q) = \sum_{i=1}^{n} m_i \cdot \mid q_i \mid^2$ means the moment of inertia. By using CAS *Mathematica* we present below for $N = 4$ in Oxy a homographic interpretations of the system (2) for geometrical and physical values of the parameters.We have shown that if $\theta \in (-\frac{\pi}{2}, \frac{\pi}{2})$ then there don't exist a convex isosceles trapezoid central configuration with all positive masses.

In these figures we can see the functions ω and m_4 which are fulfilled eq.(2). These two parameters describe our

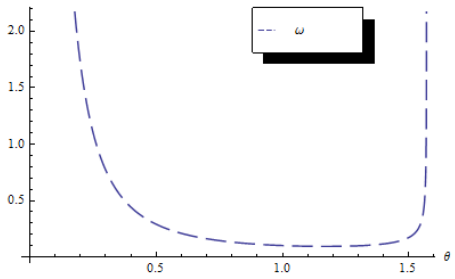

Figure 1: Function ω for $m_1 = m_2 = 0.1$, $R = 1$ and $\theta \in (0, \frac{\pi}{2})$

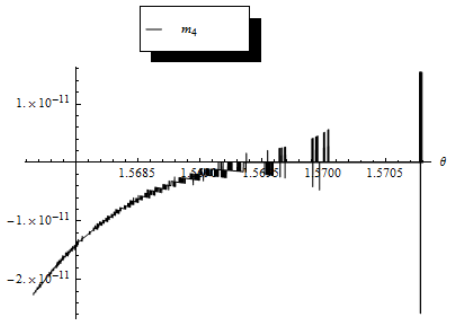

Figure 2: Function m_4 for $m_1 = m_2 = 0.1$, $R = 1$ and $\theta \in (\frac{499\pi}{1000}, \frac{\pi}{2})$

configuration.

References

[1] Albouy A., Fu Y., Sun S. Symmetry of planar four-body convex central configurations. *Proc. R. Soc. Lond. Ser.A, Math. Phys. Eng. Sci.* **464**: 1355-1365, 2008

[2] Arnold V.I., Kozlov V.V., Neishtadt A.I. Mathematical Aspects of Classical and Celestial Mechanics. Springer-Verlag, Berlin 2006

[3] Chenciner A., Gerver J., Montgomery R., Simó C. Simple choreographic motions of N bodies: a preliminary study. Geometry, mechanics, and dynamics, 287308, Springer, New York, 2002

[4] Corbera M., Cors J.M., Llibre J., Perez-Chavela E. Trapezoid central configurations. *Applied Mathematics and Computation* **346**: 127-142, 2019

[5] Corbera M., Llibre J. Central configurations of the 4-body problem with masses $m_1 = m_2 > m_3 = m_4 = m > 0$ and m small. *Applied Mathematics and Computation* **246**: 121-147, 2014

[6] Dziobek O. Die Mathematischen Theorien der Planeten-Bewegungen. J.A. Barth, Leipzig 1888.

[7] Elmabsout B. Nouvelles configurations d'equilibre relatif dans le probleme des N corps. *C. R. Acad. Sci.* **329 (Serie II)**: 467-472, 1991

[8] Fernandes A.C., Llibre J., Mello L.F. Convex central configurations of the 4-body problem with two pairs of equal masses. *Archive for Rational Mechanics and Analysis* **226**: 303-320, 2017

[9] Grebenicov E.A., Kozak-Skoworodkin D., Jakubiak M. Methods of Computer Algebra in Many-Body Problem. Ed. of UFP, Moscow 2002 (in Russian)

[10] Grebenicov E.A. Two New Dynamical Models in Celestial Mechanics. *Rom. Astron. J.* **10 (No.1)**: 13-19, 1998

[11] Hénot O., Rousseau Ch. Spiderweb central configurations. *Qual. Theory Dyn. Syst.* **18 (No.3)**: 1135-1160, 2019

[12] Macmilian W.D., Bartky W. Permanent configurations in the Problem of Four Bodies. *Trans. Amer. Math. Soc.* **34**: 838-875, 1932

[13] Moulton F.R. The straight line solutions of the problem of n bodies. *Ann. Math.* **12**: 1-17, 1910

[14] Siluszyk A. A new central configuration in the planar N-body problem. *Carpathian J. Math.* **30 (No.3)**: 401-408, 2014

[15] Siluszyk A. On unique convex isosceles trapezoid configuration, In: Computer Algebra Systems in Teaching and Research, A.N.Prokopenya, A.Gil-Swiderska (Eds.), UPH, Siedlce, **vol.VIII**: 232-242, 2019

[16] Simó C. New families of solutions in N-body problems. European Congress of Mathematics (Barcelona, 2000), Progr. Math., 201, Birkhuser, Basel, **vol.I**: 101-115, 2001

[17] Wintner A. The Analytical Foundations of Celestial Mechanics. Princeton University Press, New York 1941

NONDIMENSIONAL ANALYSIS OF TWO-DIMENSIONAL ELASTIC POROUS MATERIALS WITH REGULARLY DISTRIBUTED CIRCULAR HOLES

Mertol Tüfekci [1,2], Inci Pir*[1] and Ekrem Tüfekci[1]
[1]Faculty of Mechanical Engineering, Istanbul Technical Engineering, Istanbul, Turkey
[2]Department of Mechanical Engineering, Imperial College, London, United Kingdom

Summary In this study the static behaviour of two-dimensional (2D) elastic porous materials are investigated by using finite element models. The porous material is modelled using a 2D representative element (RE) which includes two quarter circular holes at diagonal corners and analysed under plane stress assumptions. The REs are prepared with different porosities from 5% to 70%. Effects of volume fraction of the pores on the maximum stresses occurring on the material are investigated. The results are nondimensionalized to generalise the behaviour of porous materials.

INTRODUCTION

Foams are becoming more popular over the last decades and widely used in more industrial applications. One of the most important reasons behind this is the need for construction of lighter structures. Another important reason for using foams is the need for wastewater treatment. There, porous membranes are used. properties of those porous materials are not the same or even similar to the bulk forms of the materials. There are numerous studies that investigate the mechanical behaviour of such materials with voids. Majority of the research using numerical methods to model those materials employ representative elements (RE) applying periodic boundary conditions (PBC) on them [1]. The REs can be categorised in two groups based on the distribution of the pores/voids, namely, REs with randomly distributed voids and REs with regularly distributed voids [2]. The distribution of particles are usually random in real materials and the distribution of the voids also affect the mechanical properties of the material [3,4]. However, generating modelling REs with randomly distributed voids is a lengthy process since they require multiple repetitions to find accurate averaged results. Considering that the mechanical properties of the REs with randomly distributed voids lie around an average value. Therefore, in some cases, random REs can be represented with regular REs to estimate the averaged effective properties [2,5]. This, of course, reduces the time to calculate the effective properties whereas it also reduces the accuracy of the estimations.

In this study, elastic foam materials are studied employing the finite element method. REs of these materials were modelled under PBC and a prescribed strain. The material is defined as isotropic and linear elastic. As the goal of this paper is to generalise the results for any linear elastic and isotropic material that are used to manufacture such 2D foams, the resultant stresses are plotted in nondimensional form.

ANALYSIS

The effect of porosity on the mechanical behaviour of REs of 2D materials is studied with finite element method. The REs that are analysed have the volume fractions from 5% to 70% with 5% incrementation. The radius and RE parameter are calculated to meet those volume fraction requirements and the REs are drawn. REs are modelled with 2D plane stress quadratic quadrilateral elements. It is also to be noted that, the necessary convergence studies for each RE are performed to check the meshing is done properly. The only parameter that is changed for this analysis procedure, is the volume fraction of the pores. A typical mesh of the 2D RE is represented in Figure 1.

Figure 1. A typical meshed RE.

The elastic properties are only defined for the execution of the numerical analysis. However, Young's modulus has no effect on the results presented in this paper as the results will be presented without dimensions. The only important elastic material parameter is the Poisson's ratio and it is kept constant as 0.44. The nondimensionalisation is done by

*Corresponding author. E-mail: pirin@itu.edu.tr.

dividing the resultant stresses and the effective elastic moduli by the elastic modulus of the material in bulk form which is the initial elastic modulus defined in the stiffness matrix.

The four sides are subjected to PBC where the sides that belong to the pores are set free. On one of the four sides, a tensional displacement which is the equivalent a strain 0.1% is applied.

RESULTS AND DISCUSSION

The maximum nondimensional Von Mises Stress values and nondimensional principal stress values are calculated for each RE under the conditions that are defined earlier. From those results, the approximate stress concentrations in the material structure can be estimated. As expected and as it is present in the literature, with increasing porosity, all types of stress values decrease. This is, of course, due to reduced stiffness and the imposed constant displacement which is the same for each RE. It is also to be noted that, since the stiffness is reduced, the capabilities of the structure/material to carry loads and the strength of the material will be also in question with increasing porosities. Therefore, it is an important issue to be taken care of during the design of components made of such foams. The plotted results are presented in Figure 2.

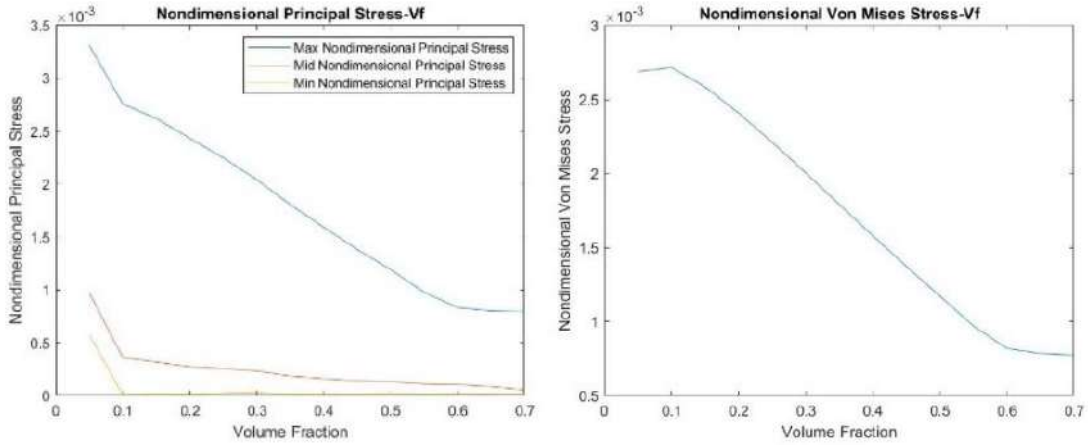

Figure 2. Nondimensional principal and Von Mises stresses.

CONCLUSIONS

The nondimensional results obtained in this paper can be used for any type of foams which are manufactured using linearly elastic and isotropic materials. The stress intensities that expected to occur near the voids are to be assessed with some resemblance. Under constant strain, the increasing amount of gaps in the material structure reduce the stiffness and therefore the stresses. Reduced stiffness also limits capacity to carry loads. Hence, if this analysis were run under the same loading conditions instead of prescribed displacement, the results would look different. For future works, this procedure can be applied with three-dimensional REs and also the dependence of the mechanical properties and stresses on Poisson's ratio can be investigated.

References

[1] Babaee S., Jahromi B. H., Ajdari A., Nayeb-Hashemi H., Vaziri A. Mechanical Properties of Open-Cell Rhombic Dodecahedron Cellular Structures. *Acta Mater.* ***60*****(6–7)**, 2873–2885, 2012

[2] Marur P. R. Numerical Estimation of Effective Elastic Moduli Of Syntactic Foams. *Finite Elem. Anal. Des.* **46(11)**, 1001–1007, 2010

[3] Nian G., Shan Y., Xu Q., Qu S. Effects of Hollow Particle Shape And Distribution on the Elastic Properties of Syntactic Foams: 3D Computational Modeling. *Comp. Mat. Sci.* **95**, 106–112, 2014

[4] Heitkam S., Drenckhan W., Titscher T., Weaire D., Kreuter D. C., Hajnal D., Piechon F., Fröhlich J. Elastic Properties of Solid Material with Various Arrangements of Spherical Voids. *Eur. J. Mech. A Solids*. **59**, 252–264, 2016

[5] Antunes F. V., Ferreira J. A. M., Capela C. Numerical Modelling of the Young's Modulus of Syntactic Foams. *Finite Elem. Anal. Des*, **47(2)**, 78–84, 2011

LATERAL COMPRESSION OF TUBES - NUMERICAL PREDICTIONS: REID AND REDDY REVISITED

Rokesh laishram [*1]
[1]Robert Bosch Centre for Cyber-Physical Systems, Indian Institute of Science, Bangalore-India

Summary Numerical validation is carried out to ensure the agreement between the predicted results and the actual observations in the experiment. This paper predicts some of the observations of T.Y. Reddy [1] on the experiments conducted on lateral compression of circular single tubes and crossed layers of tubes crushed between flat parallel platens. Quasi-static experimental results are predicted using the finite element LS_DYNA simulation software package. Other prediction includes the deformed shape of single tube and single crossed layer tubes. The predictions are carried out for aluminium specimens. The predicted load-displacement data matches well with the experimental results. It also captures small details like the change in load-deflection curve when the bottom tube touches the top platen and top tube touching the bottom rigid plate in cross tube experiment.

INTRODUCTION

The predicted load displacement curves of a single tube and of two overlapping crossed tubes being compressed laterally at a constant rate are predicted and presented in this paper. The main motivation of this article is the use of advanced computational tools to predict the coarse experimental data as well as other finer details observed experimentally, but that could not be predicted due to lack of technology at the time of experiment. Well designed and carefully conducted experiment, see Refs [1, 2] showed commendable observations, especially of contact, during the experiment. Above that, the emerging use of single circular tube as legs for Quaterpad robot Refs [8] or arms in Drone Refs [9] in major robotics industries and institutes (especially in Robert Bosch Centre for Cyber Physical Systems, IISc see Refs [10]) has triggered to work on this particular research area.

NUMERICAL PREDICTIONS

The shapes of a single tube at various stages of compression and deforming when compressed laterally between two flat parallel plates are shown in Fig. 1. The corresponding load curve with respect to deflection is shown in Fig. 4a. Fig. 4b shows correlation of the experiment and simulation (of two crossed tubes under compression) with details of contact between tubes with the platens, while Fig. 2 shows the physical deformations of the two tubes. In a crossed tube scenario, the analysis predicts that, of the two tubes, one tube deforms initially at the contact portion while the other starts when the first one deforms considerably. The physical dimensions of the tube and material properties used for numerical prediction are Density = 2700 kg/m^{3,} Young's modulus= 70 GPa, Yield strength = 350 MPa, Tangent modulus = 750 MPa, Tube length = 150mm, Tube outer diameter = 25mm and Thickness = 0.9mm.

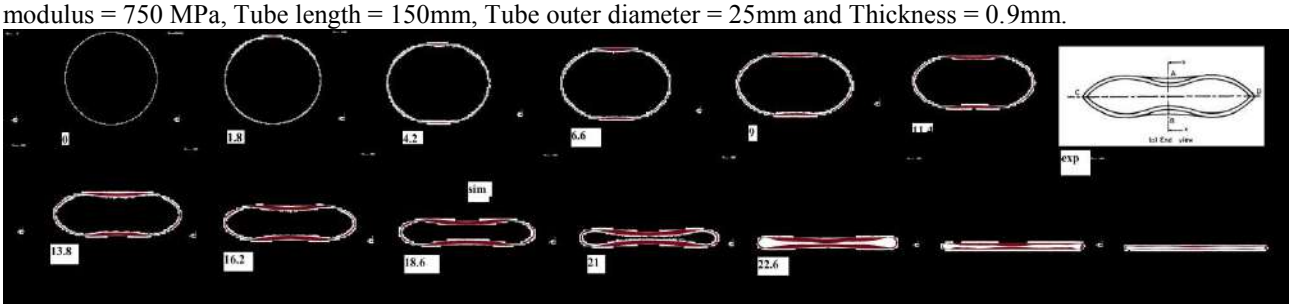

Figure 1: Simulated deforming shapes of a single tube upon compression by platen in mm (sim) and experiment (exp) Refs[2].

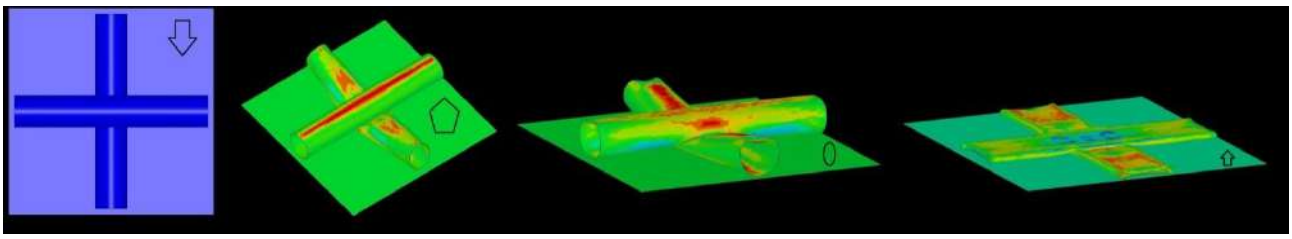

Figure 2: Deformed single crossed layer tubes upon compression.

The modelling details are as follows. The top platen is considered as non-deformable rigid body with material card MAT_20 MAT_RIGID and for aluminium MAT_24 MAT_ELASTIC-PLASTIC material card is used. 4 noded co-rotational shell elements are used for simulation with element form 16 (Fully integrated shell element) with HOURGLASS type 8. Contact is CONTACT_AUTOMATIC_GENERAL. Number of elements in a tube is 11849 with mesh size 1. Load collector used is BOUNDARY_PRESCRIBED_MOTION_RIGID where a constant load is being applied.

*Corresponding author. E-mail: **laishrams@iisc.ac.in / thoilai3@gmail.com**

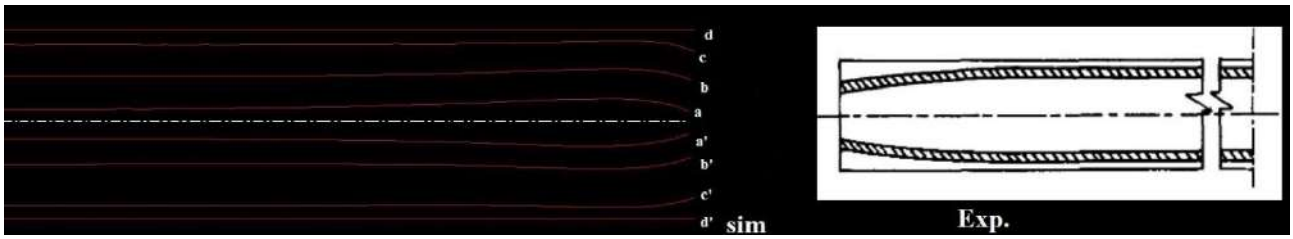

Figure 3: Sim – Sectional deformation view at the middle of tube from side at different stages a, b, c and d, Exp. – sectional view in Refs. [2]

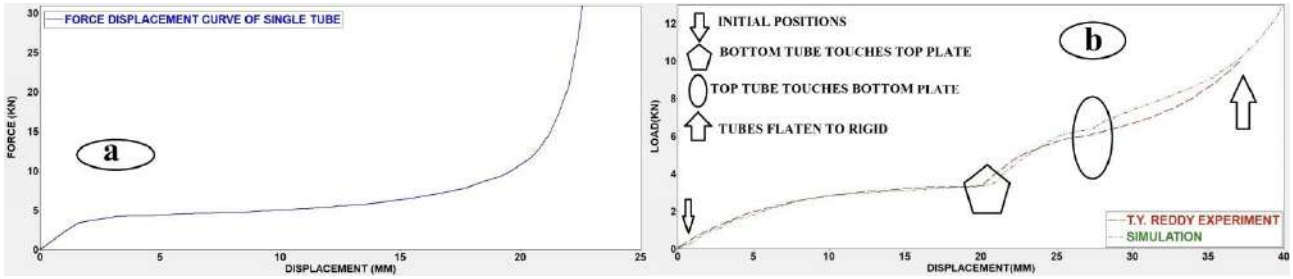

Figure 4: a) Load displacement curve of single tube, b) Experimental and predicted load displacement curve of crossed single tubes.

The anticlastic curvature effect could be seen clearly in the side sectional view of the tube upon compressing gradually both in simulation and experiment Refs [2]. Fig 3 sim shows the changes in curvature of the tube upon being compressed gradually at different stages Fig 3(d/d') initially the platen has whole length contact with the tube later at fig 3 (c/c') (b/b') the end of the tube starts bending and continued the bending in the middle of the tube as well at fig 3(a/a').

CONCLUSIONS

The work reported here is the prediction of some experimental data published in Refs. [1]. A lot of works related to lateral compression have been reported in Refs. [1-5] and the prediction of the experiments would be analysed numerically in future papers. The study would include loading laterally on nests of tubes (multiple layers of several tubes in each layer), compression of tubes with side constraint and dynamic behaviour with strain rate effects. Other observations like crack development on the side of the tubes and development of contact zone between two crossed tubes upon increasing compression load would also be studied. The study could be useful in designing drone arms and robot legs Refs. [6] where the arms/legs are circular and held tightly between two plates (also side constraints) which are similar to the experiments and numerical prediction done in this article. The main advantages for using circular tubes in robotic legs would be because of its ability to take lateral load uniformly from all directions i.e. when the robot is moving forward and sidewise and of its high axial load bearing capacity. The simulation result correlates well with the experimental data though slight disagreements are visible after the tube started touching the top platen and thus this model is validated and the properties could be used for further investigation of lateral compression of tubes with holes (.i.e. coupling point) and foam filled for robotic applications.

ACKNOWLEDGEMENT

I would like to thank Dr. Tirumagondanahalli Yella Reddy for allowing me to use his experimental results as well as for giving clarification on the experiments conducted and Dr. Debiprosad Roy Mahapatra (iMEMS lab, Aerospace Dept., IISc-Bangalore) for providing the computational facility for this article. I express my sincere thanks to Dr. S. Bharadwaj Amrutur (Chairman, RBCCPS, IISc.-Bangalore) for encouraging this research work.

References

[1] T. Y. Reddy, Impact Energy Absorption using Laterally Compressed Metal Tubes, Ph. D. Thesis, University of Cambridge, 1979.
[2] W. Johnson, S.R. Reid and T. Yella Reddy, The Compression of Crossed Layers of Thin Tubes, IJMS,19:423-437,1977.
[3] T.Yella Reddy and S.R. Reid, Phenomena Associated with the Crushing of Metal Tubes Between Rigid Plates, Int. J. Solids Structures,16:545-562,1979.
[4] S.R. Reid and T.Yella Reddy, Effect of Strain Rate on Dynamic lateral Compression of Tubes, Inst. Phys. Conf. Ser. No. 47:Chapter3, 1979.
[5] T. Yella Reddy and S.R. Reid, Lateral Compression of Tubes and Tube-Systems with side Constraints, IJMS, 21:187-199, 1979.
[6] Dhaivat Dholakiya, Shounak Bhattacharya, Ajay Gunalan, Abhik Singla, Salabh Bhatnagar, Bharadwaj Amrutur, Ashitava Ghosal and Shishir Kolathaya, Design,Development and Experimental Realisation of a Quadrupedal Research Platform: Stoch, arXiv:1901.00697v2,2019
[7] A. Otubushin, Detailed Validation of A Non-Linear Finite Element Code Using Dynamic Axial Crushing of a Square Tube, IJIE, 21:349-368, 1998.
[8] "Laikago robot", **http://www.unitree.cc/**.
[9] "DJI Matrice Drone", **https://www.dji.com/**.
[10] "RBCCPS" , https://cps.iisc.ac.in/

THERMOMECHANICAL ANALYSIS OF TWISTED BLADE

Aalok Kumar Jha *and Chandra Shekhar Upadhyay
Department of Aerospace Engineering, Indian Institute of Technology Kanpur, India

Summary It is always challenging to analyze twisted blade like structures and predict their life accurately due to their complex shapes, especially in high temperature and hostile environment. In the present study, the authors present a methodology by which finite element(FE) based geometric approximation as well as analysis approach has been efficiently and effectively implemented for the blade under thermomechanical load. The developed tool is an effort towards creating a reliable FE based analysis tool, which can be used to aid the design process.

INTRODUCTION

Thermomechanical analysis of a complex geometrical structure is still a challenging issue and the finite element (FE) method is one of the most popular and powerful methods for analysing such a problem. Accuracy in capturing curved boundaries and their discretization is a source of error in FE method, therefore approximation of geometry along with the approximation of solution field should be done carefully. A novel three dimensional FE tool has been developed for the thermomechanical analysis of generally twisted blade like structures, which creates a consistent representation of geometry, allowing for effective control of error emanating from inexact representation of the boundaries. The method further uses directional enrichment in order to capture localized three-dimensional effect due to change in material, boundary conditions or defect. Any extruded section which is tapered, bent and twisted can be efficiently analyzed by this technique. The computed stress and strain gives interesting and expected result which may be used for design and life prediction of such blade, specially in thermal environment, such as in gas turbine compressor and low pressure turbine blade.

GEOMETRICAL MODELLING

Inspired by the current focus on isogeometric formulation which has exciting possibilities of unifying both geometry description and the analysis, authors constructed a formulation which uses conventional FE representation up to higher order for both geometry as well as the analysis. Following the desire for unified modelling and analysis approach the authors have created a FE regime for representation of the geometry. The geometry will be represented in terms of FE basis functions, so that again analysis and geometry representation is done in same function space. This allows for easy manipulation of geometry data with desired accuracy in both representation of geometry and solution. It ensures that curved boundaries can be easily modelled for a given level of refinement of the mesh ensuring guaranteed bounds on the errors that arise due to both the geometrical approximation as well as the analysis.

Capturing the geometry of cross section

The cross-section of most of the gas-turbine(GT) engine blades are complicated aerofoil shapes, whose boundary surface data can be in the form of an explicit curve or in terms of point cloud. The developed tool is capable of fitting a curve which represents the actual boundary accurately. It is assumed that the given point cloud has sufficient data points to start with, i.e. it is not starved of data points. Fig. 1(a) shows fitted cubic curve from the tool. Utilizing the nodal points obtained from the boundary curve discretization the point set for the cross section has been generated. Fig. 1(b) shows point set for meshing of elliptical cross section by developed method. Once mapping of cross sectional area has been generated, for getting 3D representation an extrusion of 2D cross-sectional fit has been done. The extrusion can handle pre-bend,twist and taper. This gives the special element which is used for 3D thermo-mechanical analysis. Extruded twisted-tapered-bent beam obtained by this method can be seen in Fig.2, which shows the obtained thermomechanical field in the beam.

THERMO-MECHANICAL MODEL

In classical thermoelasticity the displacement field and thermal field are strongly coupled in transient condition and these fields can be expressed as

$$d = d(x, y, z, T, t)$$
$$T = T(x, y, z, t)$$

Where d is displacement, T is temperature, $X(x, y, z)$ is spatial co-ordinate and t is time. The classical coupled thermoelastic equation is derived in [3-5] and given by following coupled equations.

$$\sigma_{ij,j} + f_i - \rho\ddot{u}_i = 0 \quad (1)$$
$$q_{i,j} + \rho C\dot{\theta} + \beta_{ij}T_0\dot{\epsilon}_{ij} - Q^* = 0 \quad (2)$$

*Corresponding author. E-mail: aalokjha@iitk.ac.in

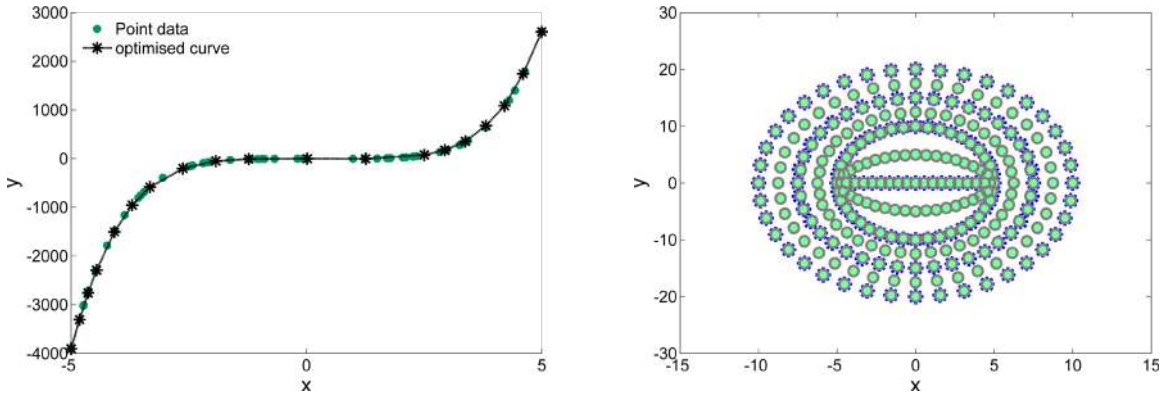

(a) (b)

Figure 1: Optimised geometrical fit obtained from proposed methodology (a) 2D curve fitting from given point-data (b) Fitting of elliptical boundary of cross section and generation of interior points for 2D mesh

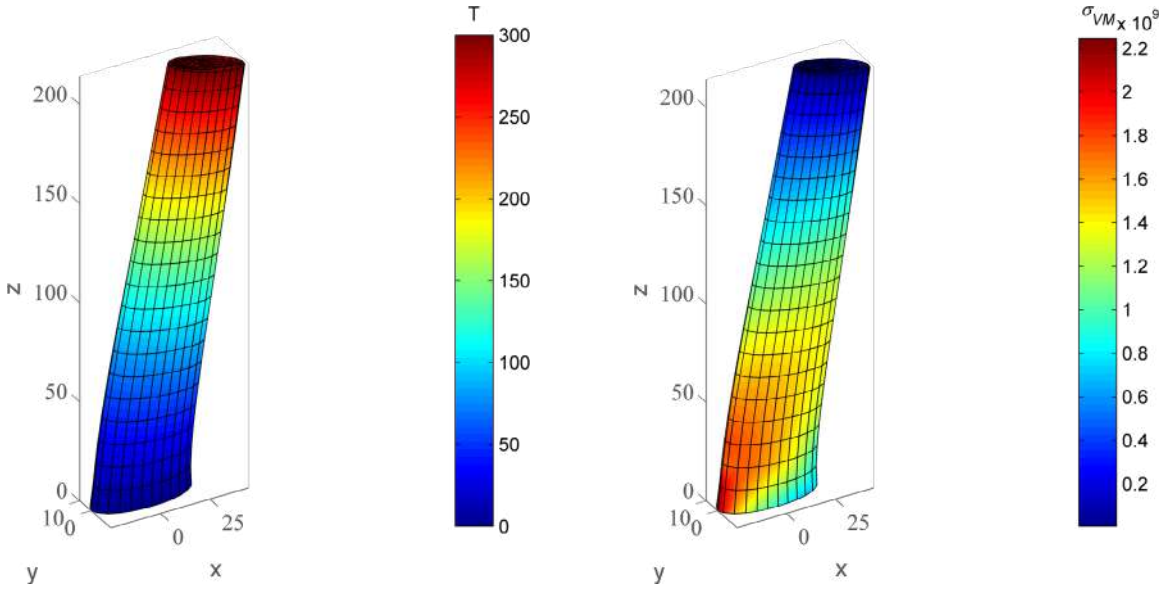

(a) (b)

Figure 2: Themomechanical results for twisted-tapered beam subjected to given end temperature ($T_{root} = 0°C$ and $T_{tip} = 300°C$) and transverse load ($P = 10kN$). Material properties are taken for mild steel ($\rho = 7850kg/m3, E = 200GPa, \mu = 1/3, \alpha = 12 \times 10^{-6}, k = 46.1W.(mK)^{-1}$). (a) Themperature distribution, (b)Von Mises stress distribution.

Where $[\sigma]$ is stress tensor, $\boldsymbol{f}$ is body force, $\boldsymbol{u}$ is displacement, $\boldsymbol{q}$ is heat flux, Q* is internal heat generation, θ is change in temperature, T_0 is initial temperature, ρ, C and β_{ij} are material constants.

CONCLUSIONS

The methodology developed for creating an optimised mesh with special element gives the exact representation of complex geometry and it's general nature allows for thermo-mechanical analysis of any arbitrary, curved 3D-beam of blade like structures. Meshing is automatically generated in this method. Hence, rigours meshing technique can be avoided, which saves time and resources. Further interaction with CAD model is not needed for analysis purpose. These features make the whole process very fast in comparison with the existing methods. This novel FE method predicts good results for elastic and thermoelastic problems. A typical result obtained from this method is shown in Fig.2.

References

[1] Zlamal M. Curved elements in the finite element method-I *SIAM J.Numer.Anal.*, Vol. 10, No. 1, 1973, pp.229–240.
[2] Hughes T.J.R.,Cottrell J.A.,Bazilevs Y. Isogeometric analysis: CAD, finite elements, NURBS, exact geometry and mesh refinement,*Comput. Methods Appl. Mech. Engrg.*, Vol. 194, 2005, pp.4135–4195.
[3] Stojanovic Rastko. Nonlinear Thermoelasticity, Springer-Verlag, 1972.
[4] Hsu Tai-Ran. The Finite Element Method In Thermomechanics, Allen and Unwin, 1986.
[5] Hetnarski, Richard B., and Eslami M. R., Thermal Stresses - Advanced Theory And Applications, Springer, 2009.

A STUDY ON COMPOSITEMATERIAL NON-LINEAR MECHANICAL RESPONSE BASED ON MICROMECHANICS FINITE ELEMENTMETHOD

Heyuan HUANG*[1], Meiying ZHAO [1],and Wenzhi WANG [1]
[1]Northwestern Polytechnical University,Xi'an,China

Summary The non-linear mechanical performance of a composite material, i.e. ZT7H/5429, was investigated in present paper in the micro-scale. Combining numerical simulation results with experimental data demonstrated that micro-crack accumulation and plasticity of matrix were the two dominant factors which can lead to nonlinear mechanical performance of ZT7H/5429.

1 Numerical analysis method

The paper provided an examination on the fiber random distribution modeling method. Particularly, an algorithm was developed for generating the equivalent RVE. With experimental statistical inputs, this algorithm generated RVE was statistically equivalent to real structures by probability equations, and solved the problem of smaller distance distribution, the generated finite RVE element model was shown in Figure 1(a). The corresponding model based on this RVE generation method was subsequently developed and used to accurately predict the mechanical properties of ZT7H/5429. Furthermore, a damage constitution was implemented into the RVE of this model to simulate the mechanical responses in transvers and in-plane directions as well as the damage evolution procedure, three dimensional periodic boundary conditions were shown in Figure 1(b).

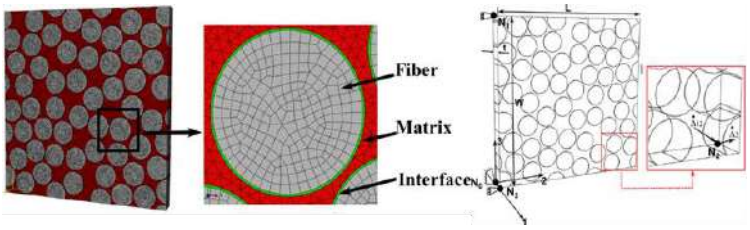

Fig.1 The RVE model schematic diagram: (a) finite element model; (b) periodic boundary conditions

2 Numerical simulation results and analysis

2.1 Damage propagation analysis

Compared with the experimental results, the RVE models could accurately simulate the damage propagation law of laminates under different loads. At the same time, it could be seen that the initiation of internal cracks in the element was gradually expanded from the beginning of the interface. Fig. 3~Fig. 5 were damage propagation schematic diagrams of RVE models under different load conditions.

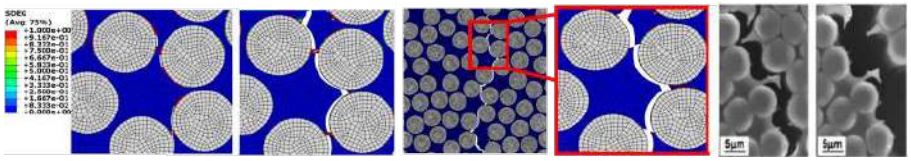

Fig. 3 Damage propagation process of RVE model under transverse tensile loading

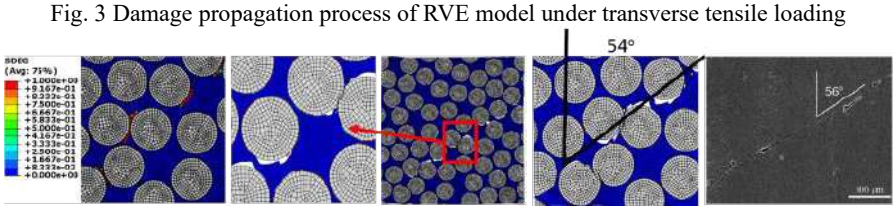

Fig. 4 Damage propagation process of RVE model under transverse compresssion loading

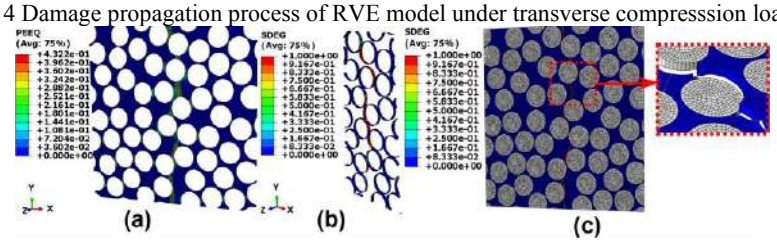

Fig. 5 Damage propagation process of RVE model under shear loading: (a) matrix damage; (b) interface damage; (c) failure mode

2.2 Analysis of nonlinear influence factors

By controlling the interface stiffness, a perfect interface was established to prevent crack initiation and the influence of the linear-elastic constitutive relation of the matrix was considered. The relationship between the micro-crack accumulation in the

*Heyuan HUANG. E-mail: huangheyuan@nwpu.edu.cn.

element and the plasticity of the matrix material and the macroscopic stress-strain curve nonlinearity are comprehensive researched.

Fig.6 compared the stress-strain curves of ZT7H/5429 composites of different interface stiffness. With the changes of interface stiffness, the strength limit of composite material was almost unchanged, but the curve slopes were obviously different, which proved that the micro crack initiation and accumulation have important influence on the non-linearity of the composite macro mechanical response. Fig.2-49 shown the stress-strain curves under different loads. As can be seen from the figures, stress-strain curves have weakly non-linear characteristics in elastic constitutive, but there was obvious error with the plastic constitutive, which indicated that the plasticity of matrix material is also an important reason for the non-linear stress-strain of materials.

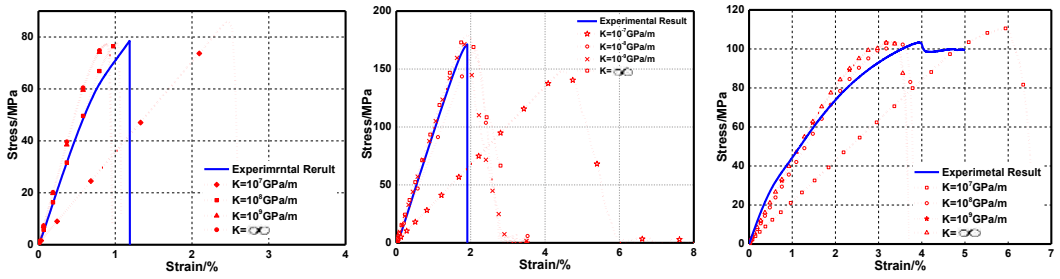

(a) (b) (c)

Fig.6 Stress-strain curves for different interface strengths：(a) Longitudinal Tension; (b) Transvers Compression;(c) In-plane Shear

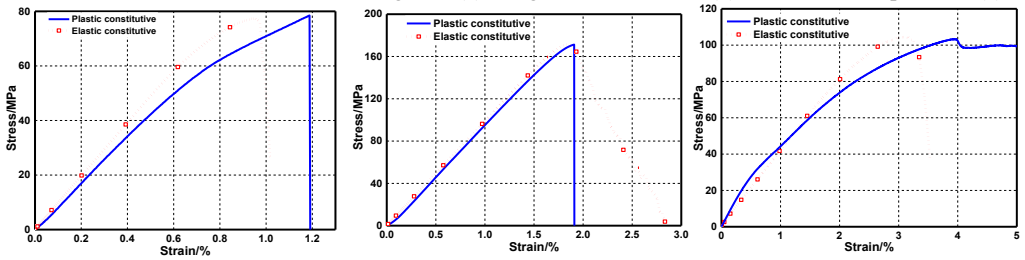

(a) (b) (c)

Fig.7 Stress-strain curves for different constitutive equations：(a) Longitudinal Tension;(b) Transvers Compression;(c) In-plane Shear

3 Conclusion

In this paper, the damage propagation mechanism of ZT7H / 5429 composites is analyzed comprehensively. The nonlinear characterization of macroscopic stress-strain curves of composite laminates was verified that the micro-crack accumulation and matrix plasticity were the two main factors caused of laminates macroscopic nonlinear mechanical characterization.

References

[1] Sun C T, Vaidya R S. Prediction of composite properties from a representative volume element[J]. Composites Science and Technology, 1996, 56(2): 171-179.

[2] Xia Z, Zhou C, Yong Q, et al. On selection of repeated unit cell model and application of unified periodic boundary conditions in micro-mechanical analysis of composites[J]. International Journal of Solids and Structures, 2006, 43(2): 266-278.

[3] Melro A R, Camanho P P, Pinho S T. Influence of geometrical parameters on the elastic response of unidirectional composite materials[J]. Composite Structures, 2012, 94(11): 3223-3231.

[4] Trias D, Costa J, Mayugo J A, et al. Random models versus periodic models for fibre reinforced composites[J]. Computational Materials Science, 2006, 38(2): 316-324.

[5] Hojo M, Mizuno M, Hobbiebrunken T, et al. Effect of fiber array irregularities on microscopic interfacial normal stress states of transversely loaded UD-CFRP from viewpoint of failure initiation[J]. Composites Science and Technology, 2009, 69(11): 1726-1734.

[6] Pyrz R. Quantitative description of the microstructure of composites. Part I: Morphology of unidirectional composite systems[J]. Composites Science and Technology, 1994, 50(2): 197-208.

[7] Totry E, González C, LLorca J, et al. Mechanisms of shear deformation in fiber-reinforced polymers: experiments and simulations[J]. International journal of fracture, 2009, 158(2): 197-209.

[8] Vaughan T J, McCarthy C T. Micromechanical modelling of the transverse damage behaviour in fibre reinforced composites[J]. Composites Science and Technology, 2011, 71(3): 388-396.

[9] Romanowicz M. Determination of the first ply failure load for a cross ply laminate subjected to uniaxial tension through computational micromechanics[J]. International Journal of Solids and Structures, 2014, 51(13): 2549-2556.

[10] Melro A R, Camanho P P, Andrade Pires F M, et al. Micromechanical analysis of polymer composites reinforced by unidirectional fibres: Part II–Micromechanical analyses[J]. International Journal of Solids and Structures, 2013, 50(11): 1906-1915.

[11] Yang L, Yan Y, Liu Y, et al. Microscopic failure mechanisms of fiber-reinforced polymer composites under transverse tension and compression[J]. Composites Science and Technology, 2012, 72(15): 1818-1825.

MODELING OF TRANSVERSALLY LOADED AXIALLY MOVING BEAM WITH CREEP

Helmut J. Holl*[1] and Gottfried Simon[2]
[1]Institute of Technical Mechanics, Johannes Kepler University, Linz, Austria
[2]Plasser & Theurer, Export von Bahnbaumaschinen GmbH, Linz, Austria

Summary For an axially moving beam which is supported by periodic discrete elastic springs and a given transversal load two mechanical models are derived, analysed and discussed. The first beam model applies global Ritz approximations for the spans between the spring supports whereas the second beam model uses a conventional FE description. Gauss integration points are used in longitudinal and transversal direction. The temperature distribution and pressure loads cause stresses, which lead to strain rates due to creep of the material so that a time dependent deformation between the discrete elastic supports results. The deflection of the axially moving beam model is computed considering various spans separated by elastic spring supports. The computed results of the two mechanical models are compared for a beam with two and ten spans.

INTRODUCTION

Transversally loaded beams under axial motion are studied in two different models. In [1] the axially moving viscoelastic web is simulated with varying normal force a high axial speed so that inertia terms are important in the equation of motion. For the process simulated here the axial motion is considered to be so slow that inertia effects can be neglected in the computation. The axial transport of the inelastic creep-strains has been considered in the computation in accordance with the axial speed. The temperature field is assumed to be constant in the beam and it is considered that the beam has a constant thickness.

MECHANICAL MODEL OF A MOVING BEAM WITH CREEP

The equations for an axially moving beam with transversal load considering creep deformations are given in [2], where also a method for the computation of ε^{cr} is proposed. The mechanical stress in the beam cross-section is computed by

$$\sigma_{XX} = E\left[-Zw''(X) - \varepsilon^{cr}(X,Z) - \varepsilon^{th}(X,Z)\right], \tag{1}$$

where E is the Young's Modulus, $w(X)$ is the deformation of the beam in transverse direction, ε^{cr} is the creep strain and $\varepsilon^{th}(X,Z)$ is the thermal strain. With the virtual displacement $\delta\varepsilon = -Z\delta w''$ the formulation of virtual work results to

$$\delta A = -\int_V \sigma_{XX}\delta\varepsilon dV + \int p_z \delta w dX - \sum_{k=1}^{N_k} F_k \delta w(X_k) \tag{2}$$

with the external transveral load p_z and the concentrated spring element forces F_k at the position X_k. The temperature is assumed to be constant in the computed examples so that $\varepsilon^{th}(X,Z) = 0$. The bending moment is computed from the stress distribution in the beam eq. (1) and $dV = dXdA$, where the part for the bending moment caused by the creep strain is $M^{cr} = \int EZ\varepsilon^{cr}dA$. Two different approximations are implemented and compared. In a first approach global shape-functions are derived, see [3], and inserted into the eq. (2). In a second approach local Ritz approximations analogous to the FE method are used. These two kinds of shape functions are arranged in the vector $\mathbf{W}(\mathbf{X}) = W\left(P_1, P_2, \ldots PN\right)^T$ for the global and $\mathbf{W}(X) = W\left(N_1, N_2, N_3, N_4\right)^T$ for local Ritz' approximation where the deflection is $w = \sum_0^n W_i q_i = \mathbf{W}(X)\mathbf{q}(t)$. Inserting $w(X)$ in eq. (2) gives a force term caused by the creep strain $\mathbf{f^{cr}} = \int M^{cr}\mathbf{W}''dX$. With these shape-functions the consistent force of the external load $\mathbf{f^0} = \int p_z \mathbf{W}(X)dX$ and the force caused by the spring elements $\mathbf{Q}_{Sk} = k\ \mathbf{W}(X_k)$ is computed. Finally the stiffness matrix results to $\mathbf{K} = \int EI \cdot \mathbf{W}''\left(\mathbf{W}''\right)^T dX$. The number of coordinates neccesary for a converged solution defines the size of the system of equations to be solved, $\mathbf{q}$ is the vector of the generalized coordinates or nodal degrees of freedom respectively, so we derive the system of equations

$$\mathbf{K}\,\mathbf{q} + \mathbf{Q}_S = \mathbf{f}^{cr} + \mathbf{f}^0. \tag{3}$$

DESCRIPTION OF THE AXIAL MOTION

In eq. (1) the stress depends on the longitudinal coordinate of the beam and is computed at the Gauss-points in the X,Z-plane of the beam. The integrals over the cross-section and the length are evaluated by Gauss-integration. The creep strain is computed from the constitutive equation of the material $\dot{\varepsilon}^{cr} = \gamma(\sigma, \varepsilon, t)$, see [5]. This ordinary differential equation is integrated in time with an implicite Runge-Kutta-Method to get the local creep increment $\Delta\varepsilon^{cr}_{t+\Delta t}$. Because of

*Corresponding author. E-mail: helmut.holl@jku.at.

the axial velocity v_0 the creep strain is transported with the material along the beam axis. The one-dimensional transport equation with homogeneous initial and boundary conditions

$$\frac{\partial \varepsilon^{cr}}{\partial t} + v_0 \frac{\partial \varepsilon^{cr}}{\partial x} = 0, \qquad \varepsilon^{cr}(x=0) = 0 \tag{4}$$

is used to compute the actual values of ε^{cr}. The Finite-Difference-Method (FDM) is applied to get a system of ODE's. Again the Gauss-points are used for the discretisation. This system of ODE's again has to be integrated in time to get the convective part of the inelastic strain. The total creep strain is

$$\varepsilon^{cr}_{t+\Delta t} = \varepsilon^{cr}_{con} + \Delta\varepsilon^{cr}_{t+\Delta t}. \tag{5}$$

COMPUTED RESULTS

A parametric study is carried out and two examples are presented. A two-span beam with a height of $h = 30$ mm is considered which is supported by one spring element with the stiffness $k = 4 \cdot 10^{12} \frac{\mathrm{N}}{\mathrm{m}}$. The lenght of the beam span is $a = 0.3$ m. Clamped boundary conditions on both ends. The applied constitutive relation taken for secondary creep is $\dot{\varepsilon}^{cr} = Ce^{-\frac{Q}{T}}|\sigma|^{n-1}\sigma$. and the parameters are taken form [5]. A constant transversal load of $p_z = 115.5 \frac{\mathrm{kN}}{\mathrm{m}}$, constant axial velocity of $v_0 = 1.6 \frac{\mathrm{m}}{\mathrm{min}}$ and a constant temperature of 1300 °C is applied. Due to the axial motion there is a steady state transversal deflection which means that the deformation does not change with time and $w(x,t) = w(x)$. The axial motion in combination with creep leads to an asymmetric result, see Fig. 1, whereas the load and the mechanical boundary conditions are symmetric. 14 global Ritz approximations are applied and for the FEM Method 50 beam elements are used to get a suitable convergence. The difference in the computed results between the Ritz- and the FE-Method in Fig. 1 is caused by a different discretisation with Gauss-points. For the second example of a ten-span beam the height is again $h = 30$ mm, the temperature is 1350 °C, the transversal load is $p_z = 700 \frac{\mathrm{kN}}{\mathrm{m}}$, the axial velocity is $v_0 = 0.85 \frac{\mathrm{m}}{\mathrm{min}}$. In the results in Fig. 2 the elastic and the total deflection of the beam is shown. Due to the axial velocity and creep again the transversal deformation is not symmetric with respect to the position of the supports.

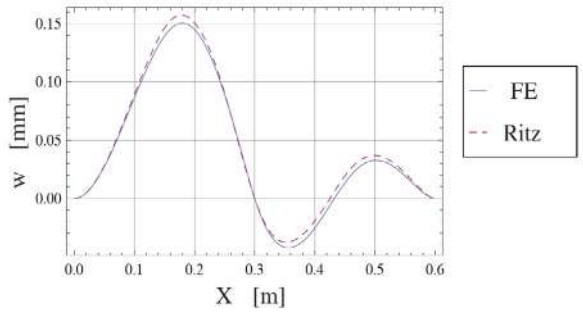

Figure 1: Deformation of the two-span beam

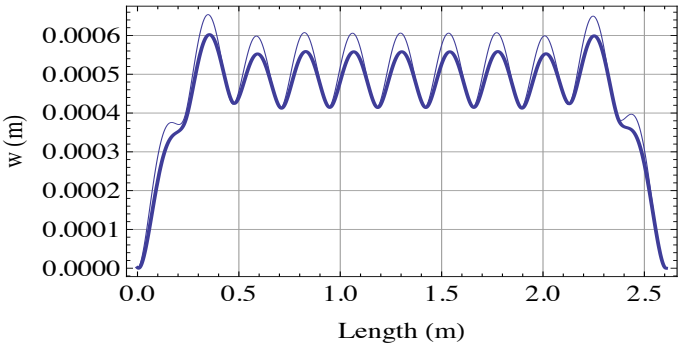

Figure 2: Deformation of the ten-span beam

CONCLUSIONS

The computation of the transversal deformation of an axially moving beam is performed for two different mechanical models applying local and global Ritz approximations. The computation results of the parametric study show that for the model with up to three spans the global Ritz approximations are computationally more efficient whereas for more spans the local Ritz approximations are preferable. A material with constitutive relations of secondary creep is used in the computation. The creep deflection depends on the axial velocity and shows a non-symmetric deflection within each span.

Acknowledgement

The support of this work by the Linz Center of Mechatronics (LCM) in the framework of the Austrian Comet K2 program is gratefully acknowledged.

References

[1] K. Marynowski, Non-linear vibrations of an axially moving viscoelastic web with time-dependent tension. Chaos, Solitons and Fractals **21**, 481-490 (2004)
[2] H.Altenbach, G. Kolarow, and K. Naumenko, Solution of Creep-Damage Problems for Beams and Rectangular Plates Using the Ritz and Finite Elemente Method. Tech. Mech. **19**, 249-258 (1999)
[3] M. Bestehorn, Hydrodynamik und Strukturbildung. (Springer-Verlag, Berlin, 2006).
[4] F. Ziegler, Technische Mechanik der festen und flüssigen Körper. (Springer-Verlag, Wien, 1998).
[5] P. Kozlowski, B. Thomas, J. Azzi, and H. Wang, Simple Constitutive Equation for Steel at High Temperature. Metal. Trans. **23**, 903-918 (1992)

DYNAMICS OF PARTICLE-STRUCTURE INTERACTIONS WITH LARGE-DEFLECTION CANTILEVER BEAMS: A DEM PERSPECTIVE

Prasenjit Ghosh*[1], Gondi K. Ananthasuresh[1]
[1]Department of Mechanical Engineering, Indian Institute of Science, Bengaluru, India

Summary The discrete element method (DEM) is a general discrete modelling technique widely used to model granular material and discontinuum phenomena such as fracture and fragmentation. This study investigates the efficacy of DEM to model deformable elastic continua like cantilever beams and capture geometric nonlinearity in their large-deflection response. It presents a numerical example to demonstrate the utility of this approach in particle-structure problems involving large structure displacements. The example simulates the capture of particles by slender protrusions called cilia present in living organisms. A DEM model consisting of cantilever beams that oscillate elastically in a particulate environment is constructed. The dynamics of the ensuing particle-structure interactions are simulated and factors governing the efficiency of particle capture are examined.

INTRODUCTION

The mechanical behaviour of deformable solid bodies in a particulate environment has been an area of increasing interest in recent years. Examples where discrete entities or particles interact with these bodies are ubiquitous in biology and more particularly, cell biology [1]. Mechanical microstructures like microcantilevers operate on biological elements and experience interactions with particles of myriad sizes and shapes. Examples also abound in the macroscopic world: debris flow mitigation by flexible barriers, dam-break tests, sea-ice loads on marine structures, etc.

Problems involving deformable solid continua present in conjunction with particles often necessitate a coupled continuum-discrete approach to describe the mechanics entailed. This study presents the discrete element method (DEM) as an alternative approach, especially in cases where (a) the mechanical responses of the solids and particles are coupled, and (b) the resulting interactions are dynamic in nature. DEM provides a natural route to modelling the dynamics of discrete entities [2]. For solids, it undertakes a mesoscopic discretization that is computationally tractable and characteristic of the macroscopic response [3]. This offers the advantage to recast all possible interactions as particle-particle interactions, which are naturally handled using the DEM technique. Furthermore, the interaction relations prescribed at the particle level are relatively simple and unencumbered by a large number of unknown parameters. Nonlinearity and complexity evolve dynamically in such a system. It may thus be worthwhile to explore the modelling of deformable solids, their capability to undergo large deformation, and their nature of interactions in a particulate environment, all using DEM.

GEOMETRICALLY NONLINEAR LARGE-DEFLECTION RESPONSE

In many problems of particle interactions, solids undergo small elastic deformation and large rotations and displacements. This commonly gives rise to an important class of nonlinear effects in the system: geometric nonlinearity. The first half of our work models an Euler-Bernoulli cantilever beam using DEM and examines the possibility of capturing geometric nonlinearity in its large-displacement behaviour. Deformation under static, dynamic and impact loading scenarios, each applied at the free end, is simulated. For static loading, we consider transverse force (P), axial force (nP), bending moment (M), and torsional moment (T), acting individually or in combination. For dynamic loading, we consider a sinusoidally varying transverse force. For impact loading, we consider a sphere transversely impacting the beam from a distance. Results for a beam with length L, area moment of inertia I, Young's modulus E, shear modulus G, and torsion constant K are shown in Figure 1.

Our numerical investigations with DEM-modelled cantilever beams capture geometric nonlinearity in large deformation under multiple loading scenarios. It is worthwhile to note that the nonlinearity emerges from the simple contact relations specified in the particle level. DEM is shown to reproduce this nonlinear behaviour in good agreement with solutions obtained from analytical and numerical methods within the framework of continuum mechanics. This provides us the necessary groundwork to subject flexible cantilever beams to a particulate environment and analyse the associated mechanics within the DEM framework.

PARTICLE-STRUCTURE INTERACTION: AN ILLUSTRATIVE EXAMPLE

The second half of our work presents a numerical example to demonstrate the utility of this approach in particle-structure problems involving large structure displacements. The genesis of this example lies in the capture of particles by beating cilia – slender and elastic hair-like structures that protrude from the surfaces of various cells in living organisms. An assemblage of beating cilia possesses two fundamental characteristics: (a) each cilium deforms asymmetrically in a periodic manner to generate a net effect of directed motion, and (b) neighbouring cilia oscillate with a difference in phase to generate a metachronal wave motion. To a first approximation, we model the cilia as an array of 10 cantilever beams, each of which undergoes large deflection sequentially and periodically due to a sinusoidal force F_n at the free end. To model metachronal motion, a constant phase difference is specified in the loads of consecutive beams such that for the n-th beam,

$$F_n = F_o \sin(\omega t + n\pi/10) \quad \text{where } n=1,2,3\ldots,10$$

*Corresponding author. E-mail: prasenjitg@iisc.ac.in

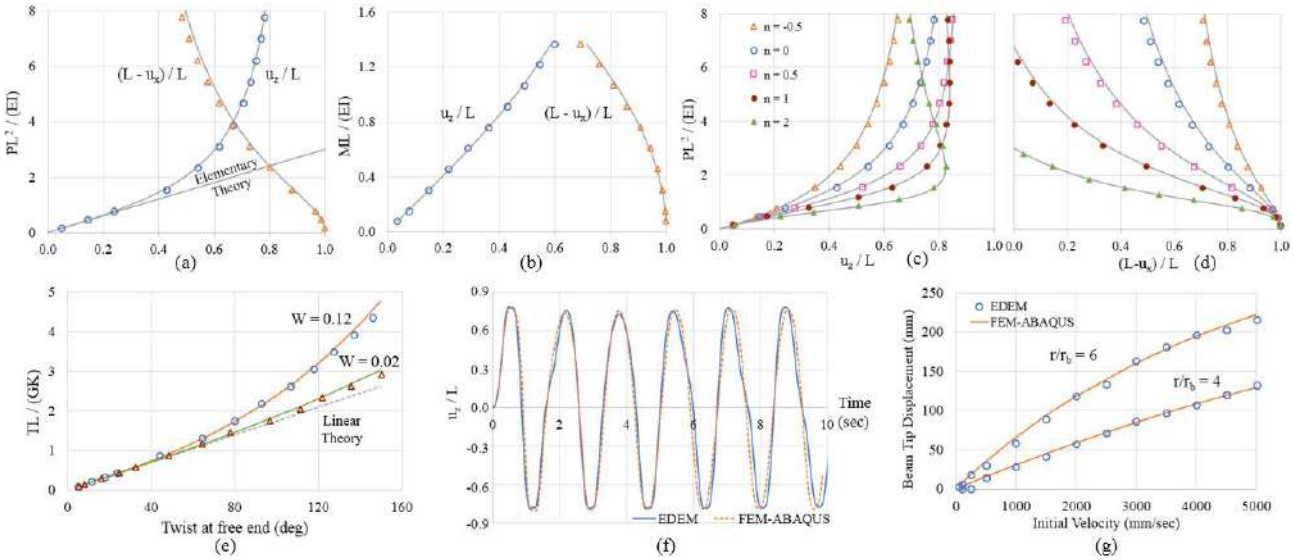

Figure 1: Generalized large-displacement solutions for an Euler-Bernoulli cantilever beam subjected to loading at free end. (a) and (b) correspond to transverse force and bending moment loads respectively. (c) and (d) correspond to combined transverse and axial forces. (e), (f) and (g) correspond to torsional moment, dynamic transverse force and transverse impact of a sphere respectively. The solid lines, unless otherwise indicated, represent continuum solutions.

The beam array oscillating in a rhythmic manner impacts a stream of incoming particles with the objective to drive them inside a particle collector placed underneath (Figure 2(a)-(b)). The impact dynamics determine whether particles are captured in the collector or thrown off. We are interested in analysing the capture characteristics of the array. We compute the capture fraction, the number of particles captured relative to a total of 100 incoming particles. We examine its dependence on three parameters: the frequency of oscillation, the flow velocity of incoming particles, and the incline angle denoting the asymmetry of oscillation. It is challenging to estimate a priori how a combination of these factors will affect the capture of particles. DEM enables the nonlinear dynamics of these factors of capture to be determined from the solution (Figure 2(c)-(d)).

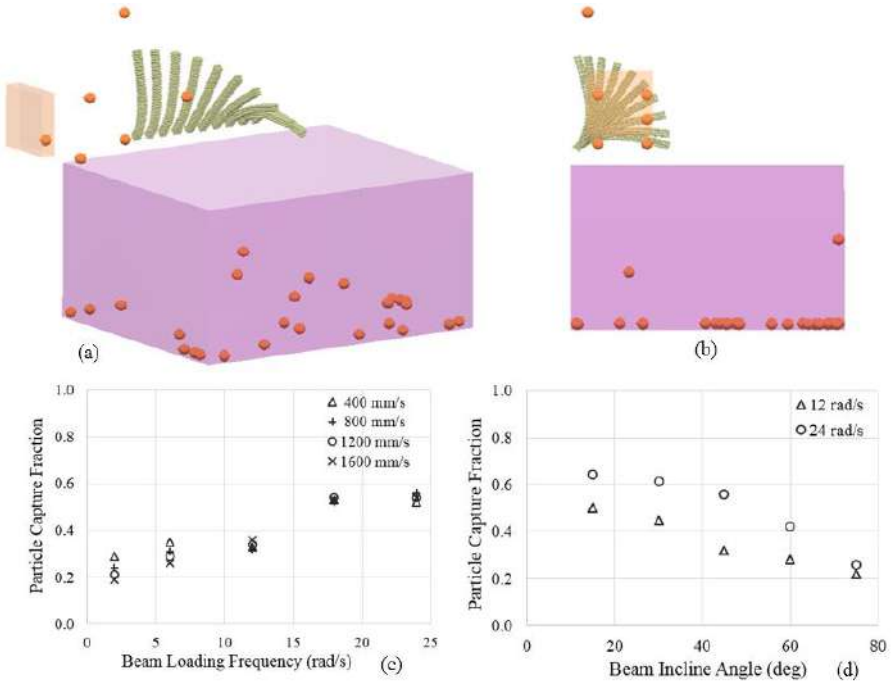

Figure 2: Particle interactions of an array of oscillating cantilever beams. (a) and (b) show a snapshot of the dynamic simulation from two views. (c) plots the variation of capture fraction with the frequency of oscillation and the flow velocity of incoming particles. (d) plots the variation of capture fraction due to change in the incline angle of each beam.

CONCLUSION

A DEM model is developed for the deformable solid continuum of a cantilever beam. This is shown to depict geometric nonlinearity in its large-deflection response for various cases of static, dynamic and impact loading applied at the free end. The DEM-modelled cantilever is further introduced in a particulate environment to simulate the capture of particles by biological cilia. Our results highlight the rich dynamics present in a simple model of a ciliated system capturing particles. This is where numerical experimentation using DEM can gain utility as an effective tool to capture the coupled dynamics of particle-structure systems.

REFERENCES

[1] Zhou, E. H., Martinez, F. D. & Fredberg, J. J. (2013). Cell rheology: mush rather than machine. *Nature materials*, 12(3), 184.
[2] Cundall, P. A. & Strack, O. D. (1979). A discrete numerical model for granular assemblies. *Geotechnique*, 29(1), 47-65.
[3] Potyondy, D. O. & Cundall, P. A. (2004). A bonded-particle model for rock. *Int. journal of rock mechanics and mining science*, 41(8), 1329-1364.

THE DISCONTINUITY LAYOUT OPTIMIZATION (DLO) FOR THE EVALUATION OF LIMIT LOAD OF NON-PERIODIC TEXTURES MASONRIES

Mattia Schiantella[1], Federico Cluni *[1], and Vittorio Gusella[1]
[1]Department of Civil and Environmental Engineering, University of Perugia, Perugia,Italy

Summary The Discontinuity Layout Optimization (DLO) is used to estimate the failure load of masonry walls having three different textures: periodic, quasi-periodic and chaotic. In particular, DLO belongs to the upper bound methods of limit analysis. The discontinuities associated with the failure mechanism can appear both in the mortar joints and inside the bricks. A Mohr-Coulomb failure criterion is used. The results are compared with those obtained with small samples made of one-fourth scaled down bricks.

INTRODUCTION

When dealing with cultural heritage constructions, very often the engineer has to face masonries realized with a non-periodic texture. In particular, when dealing with multi-leaf masonries, the exterior curtain is usually made with stones having equal size arranged in periodic pattern, while the inner leaf very often consist of quasi-periodic masonry, which is realized with blocks having different size arranged in such a way that blocks having approximately the same height are aligned to form horizontal rows; anyway, the length of the blocks inside a row and the height of each row vary in each sample. Moreover, is some cases the texture is chaotic, with absence of continuity in bed mortar joints due to the presence of stones having very different dimensions.

Since these masonry textures are not periodic, the usual methods available in literature (see, for example, [1] for a recent discussion) to estimate the failure surface cannot be used. Recently, in [2], the Authors proposed an approach where the effective texture of the masonry is taken into account, and the upper bound of the failure surface is estimated by means of Discontinuity Layout Optimization (DLO).

In DLO approach, which belongs to the field of limit analysis and was proposed in [3, 4], all possible discontinuities (according to an hypothesized failure mechanism) that can appear in the considered portion of the wall are considered, and by minimizing a suitable function the effective pattern of discontinuities at failure is estimated. One of the main advantage is that, if the function is a linear one, it can be minimized through linear programming techniques.

APPLICATION OF DLO TO MASONRY WALLS

In the present paper, the results of the application of DLO to masonries with different textures are reported. In particular the following textures have been analyzed, as shown in Fig. 1:

- periodic texture;
- quasi-periodic texture;
- chaotic texture.

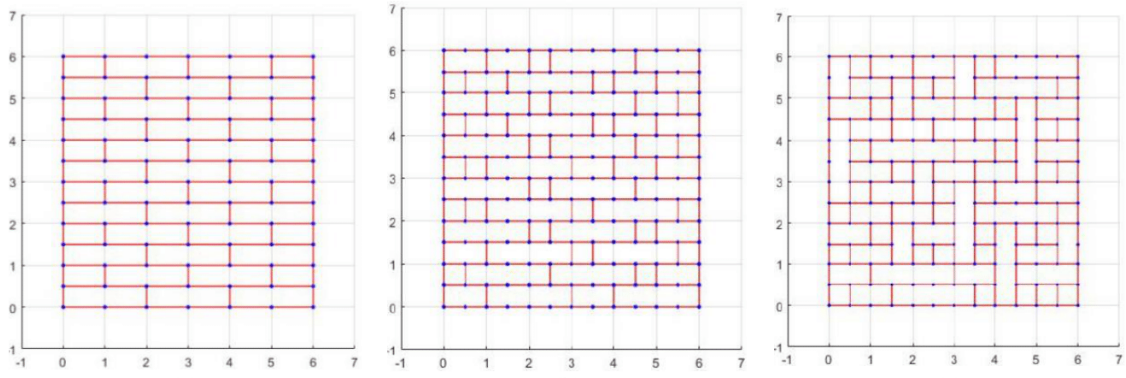

Figure 1: Masonry with periodic (a), quasi-periodic (b) and chaotic (c) textures.

The effect of the width-to-height ratio of the entire walls is evaluated. Moreover, the influence of the width-to-height ratio of the single brick is also taken into account. As an enhancement of the results shown in [2], it is assumed that the

*Corresponding author. E-mail: federico.cluni@unipg.it.

discontinuities could also appear inside the brick. The assumed failure criterion is the Mohr-Coulomb one, which allows to obtain a linear problem which could be solved by means of linear programming.

In order to validate the results, the obtained estimates of failure load are compared with the results of experimental tests, where specimens of small dimensions, realized with the bricks scaled down to about one-fourth of the real dimension to match exactly the texture used in the numerical simulations, are loaded until failure occurs.

CONCLUSIONS

The Discontinuity Layout Optimization approach is used to investigate the failure load of masonry having several different textures. The possible failure of both bricks and mortar joints is taken into account, adopting a Mohr-Coulomb criterion. The effects of geometric variability is taken into account. The results are compared with those obtained by means of experimental tests.

References

[1] Sacco E. New trends in mechanics of masonry. *Meccanica* **53**: 15651569, 2018.
[2] Cluni F., Gusella V., Schiantella M. Upper bound limit analysis of quasi-periodic masonry by means of discontinuity layout optimization (DLO). *Proc. AIMETA 2019*, 2019.
[3] Smith C., Gilbert M. Application of discontinuity layout optimization to plane plasticity problems. *Proc. Roy. Soc. A-Math Phy.* **463**: 2461-2484, 2007.
[4] Gilbert M., Smith C. Soil structure revolution. *Struct. Eng.* **88**: 18-22, 2010.

A METHOD OF PROCESSING RIGID BOUNDARY CONDITIONS IN THE MATERIAL POINT METHOD

Mengdi Zhou[1], Linfang Qian[1],Guangsong Chen [*1],Shijie Zhou[1]
[1]School of Mechanical Engineering, Nanjing University of Science and Technology, Nanjing, China

Summary A method for handling rigid boundaries in the cubic B-spline material point method (MPM) is proposed in the paper. The corrected shape function overcomes the inherent drawback that it is difficult for the original cubic B-spline function to deal with the rigid boundary conditions. Numerical tests are made to prove the feasibility and accuracy of this method. Results show that, when employed in MPM, the proposed method is superior to the original cubic B-spline function in preventing particles from crossing rigid boundaries.

CUBIC B-SPLINE CORRECTION SHAPE FUNCTION

MPM takes advantage of both Eulerian methods and Lagrangian methods [1]. The original version of MPM employs piecewise shape functions and suffers from noise when particles move through grid nodes. To eliminate noise and improve accuracy, the cubic B-spline is introduced as the shape function. However, it's difficult to deal with particles near rigid boundaries as the cubic B-spline spans four grid cells in each dimension.

A cubic B-spline function and its derivative have the following form [2]

$$N_{Ip}=\begin{cases}\frac{h^3}{6}+h^2+2h+\frac{4}{3}, h\in[-2,-1)\\ -\frac{h^3}{2}-h^2+\frac{2}{3}, h\in[-1,0)\\ \frac{h^3}{2}-h^2+\frac{2}{3}, h\in[0,1)\\ -\frac{h^3}{6}+h^2-2h+\frac{4}{3}, h\in[1,2)\\ 0, others\end{cases},\quad \nabla N_{Ip}=\begin{cases}\frac{h^2}{2}+2h+2, h\in[-2,-1)\\ -\frac{3h^2}{2}-2h, h\in[-1,0)\\ \frac{3h^2}{2}-2h, h\in[0,1)\\ -\frac{h^2}{2}+2h-2, h\in[1,2)\\ 0, others\end{cases} \tag{1}$$

where

$$h=\frac{x_p-x_I}{L} \tag{2}$$

where x_p denotes the spatial coordinates of a particle p , x_I denotes the spatial coordinates of the grid nodes which in the influence domain of p ,and L is a grid spacing.

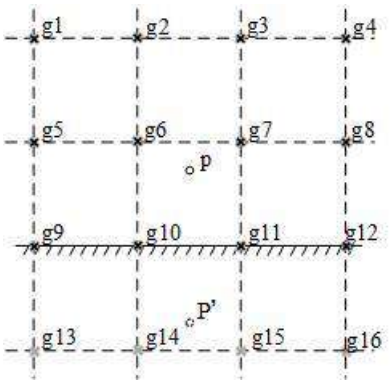

Figure 1. Particles and nodes

In 2D space, each particle should be related to sixteen nodes. When a particle is close to the boundary, its influence domain is beyond the computational domain. To handle rigid boundary conditions, Eulerian methods employ ghost cells while Lagrangian methods use mirror particles. As MPM is a mixed Eulerian-Lagrangian method, both ghost cells and mirror particles should be considered. This poses a challenge to computational efficiency.

For a long time, there has been a lack of one simple and efficient method to handle rigid boundary conditions in cubic B-spline MPM. Therefore, under this circumstance, the corrected shape function is proposed. When a particle is more than one cell away way from the boundary, the shape function and its derivative are expressed as Equation (1) ~ (2). When a particle moves into the cell adjoining the boundary, the shape function is corrected to replace the effect of ghost cells and mirror particles.

As shown in Figure 1, taking a particle near the bottom as an example. p' is the mirror particle of p, while $g13$ $g16$ are ghost nodes of $g5$ $g8$. There exist $x_{2,g14}=x_{2,g6}-2L$, $x_{2,p'}=2x_{2,g6}-2L-x_{2,p}$, and N_{Ip} is calculated as follows:

$$\left.\begin{aligned}h_{14p}&=h_{6p}+(0,2)^T\\ h_{6p'}&=-h_{6p}-(0,2)^T\end{aligned}\right\}\Rightarrow\begin{aligned}&N\left(h_{14p}\right)=N\left(\varphi\left(h_{6p}\right)\right)\\ &N\left(h_{6p'}\right)=N\left(-\varphi\left(h_{6p}\right)\right)=N\left(\varphi\left(h_{6p}\right)\right)\end{aligned} \tag{3}$$

where $\varphi(\xi)=\xi+2n$. n denotes the normal vector of boundary. ∇N_{ip} is calculated as follows:

$$\begin{aligned}\nabla N\left(h_{14p}\right)&=\nabla N\left(\varphi\left(h_{6p}\right)\right)\\ \nabla N\left(h_{6p'}\right)&=\nabla N\left(-\varphi\left(h_{6p}\right)\right)=-\nabla N\left(\varphi\left(h_{6p}\right)\right)\end{aligned} \tag{4}$$

*Corresponding author. E-mail: cgsnjust@njust.edu.cn

Obviously, $\nabla N\left(h_{6p'}\right)$ is the opposite of $\nabla N\left(h_{14p}\right)$. Meanwhile considering that the direction of variables such as normal velocity and normal force of ghost nodes is opposite to that of real grid nodes, the coefficient matrix C_{ij} is

$$C_{ij}=\begin{cases}1, j=\{1,2,\quad 12\}\\ |\tau_i|-|n_i|, j=\{13,14,15,16\}\end{cases} \tag{5}$$

where τ is the tangent vector of boundary and i denotes the dimension. The shape function of p is given by

$$N_{Ip}=C\left[N_{1p}\left(h_{1p}\right),N_{2p}\left(h_{2p}\right),\quad ,N_{13p}\left(\varphi\left(h_{5p}\right)\right),\quad ,N_{16p}\left(\varphi\left(h_{8p}\right)\right)\right] \tag{6}$$

Since the mass of mirror particles equals that of real particles, when calculating the grid nodal mass by mapping particles mass to grid nodes, Equation (6) becomes

$$N_{Ip}=\left[N_{1p}\left(h_{1p}\right),N_{2p}\left(h_{2p}\right),\quad ,N_{13p}\left(\varphi\left(h_{5p}\right)\right),\quad ,N_{16p}\left(\varphi\left(h_{8p}\right)\right)\right] \tag{7}$$

Numerical Examples

To test the performance of this correction shape function, we consider the compressible ring test, which involves a hollow elastic ring and a rigid boundary. The ring is made of a compressible Neo-Hookean with bulk modulus $K=121.7$Mpa , shear modulus μ=26.1Mpa and density ρ=1010kg/m^3 . The ring crashes to the rigid boundary at 30 miles per second. The comparative test is carried out by adopting the original cubic B-spline shape function and the corrected shape function.

Figure 2 shows the position of particles in the contrast test. Obviously, the proposed shape function succeeds in preventing particles from penetrating the boundary, thus improving the computational accuracy. To check the energy conservation, the internal and kinetic energy are computed for each time step. The evolution of these energies are given in Figure 3. The minimum time step used in our correction shape function increased as well.

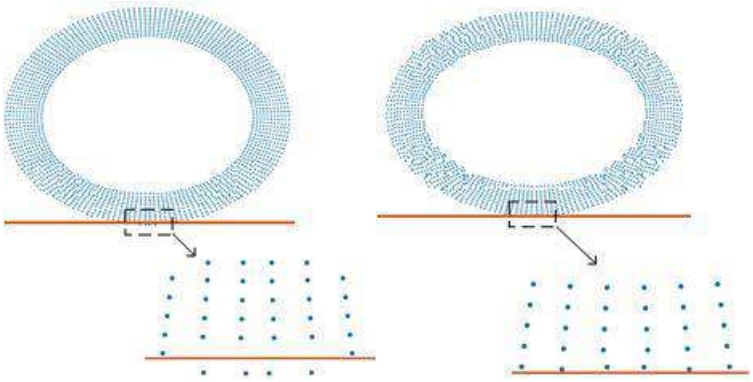

Figure 2. Comparison between original shape function (left) and correction shape function (right)

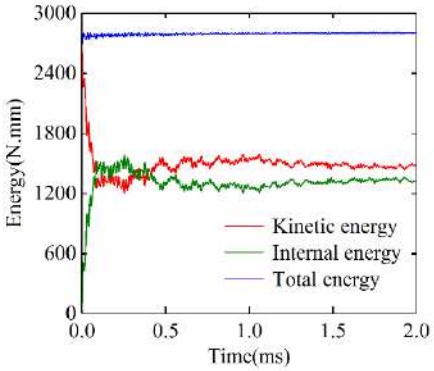

Figure 3. Energy evolution of ring

CONCLUSIONS

In this paper, a corrected cubic B-spline shape function is proposed to handle rigid boundary conditions in MPM. We replace the effect of mirror particles and ghost cells with corrected shape functions of particles near boundaries. The numerical results show that particles do not cross boundaries when our corrected shape function is employed, and the calculation efficiency is improved as well. The research could provide references for further development of MPM and other numerical simulation methods.

References

[1] Lian Y.P., Zhang X., Liu Y., Coupling of finite element method with material point method by local multi-mesh contact method. Comput. Methods Appl. Mech . Engrg. **200**: 3482-3494, 2011.

[2] Michael S., Robert M.K., Martin B., Analysis and reduction of quadrature errors in the material point method (MPM). *Int. J. Numer. Meth. Engng.* **76**:922-948, 2008.

A MULTI-BRANCHED CRACK TIPS TRACKING METHOD FOR DYNAMIC PHASE-FILED FRACTURE MODEL

Jun Zeng [1,2], Mengnan Zhang [1,2], Erjie Yang [1,2], Fucheng Tian[1,2]
[1]National Synchrotron Radiation Lab, University of Science and Technology of China, Hefei 230029, China
[2]Anhui Provincial Engineering Laboratory of Advanced Functional Polymer Film, University of Science and Technology of China, Hefei 230029, China

Summary The position of the diffuse crack tip is difficult to be accurately located, the currently widely used scheme is to consider the iso-contour endpoint (ICE) of a certain phase-field value as the crack tip [1, 2]. Despite the above method determines the crack tip quickly and easily, searching in the entire domain limits it to only track the tip at the forefront, which means it is unsuitable for branched cracks. A novel multi-branched crack tips tracking method termed multi-CTTM is proposed in this work, it allows locating the corresponding crack tip in each crack tip region (CTR) via ICE to track all tips of multi-branched crack. An instance of multi-branched crack propagation is simulated by dynamic phase-filed fracture model (PFM), and all tips of the multi-branched crack are tracked accurately utilizing the multi-CTTM.

Tracking process of multi-CTTM

For tracking the multi-branched crack tips, the discrimination of crack bifurcation is essential that is implemented by introducing a concept called the crack tip reference point in this work. As shown in Fig. 1, the one-dimensional phase-field curve along a straight line passing through the crack paths can be drawn within the CTR, which takes the y-coordinate of the nodes in the line as the horizontal axis and the phase-field value as the vertical axis. Thus, crack bifurcation is identified by judging the number of peaks in the one-dimensional profile curve which is consistent with the number of crack tips. The two-dimensional coordinates corresponding to peak sites of the phase-field-y curve are regarded as the mentioned crack tip reference point $\mathbf{P}_{CT}$.

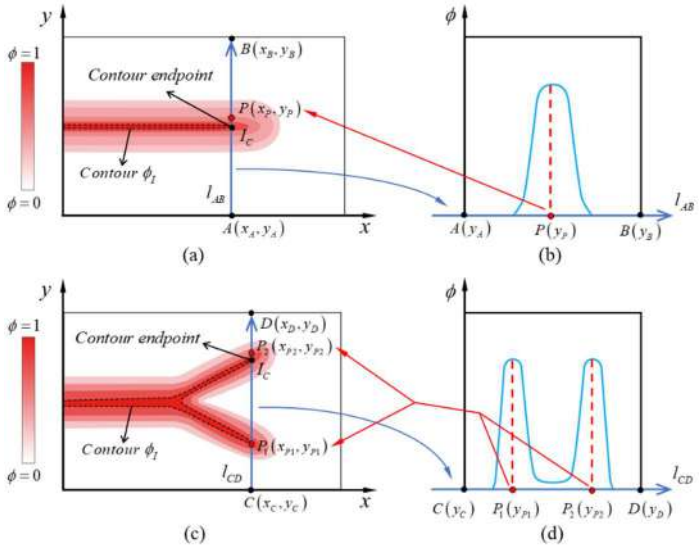

Figure 1. Schematic of the process of drawing the one-dimensional phase-field-y curves based on the two-dimensional diffuse cracks. (a), (b) and (c), (d) correspond to the single crack and the simple bifurcation crack, respectively.

The update of CTR relies on the tracking result of the previous step, implying that an initial CTR should be preset. For clarity, a schematic in Fig. 2 that demonstrates the update of the CTR with crack propagation and bifurcation is presented. Two reference points need to be introduced during the tracking process of CTR, one is the $\mathbf{P}_{CT}$ mentioned above and the other is called the crack tip region reference point donated as $\mathbf{P}_{CTR}$, where $\mathbf{P}_{CTR}$ are reference points used to calculate the coordinates of CTR corners, and they coincide with the side midpoint or corner of CTR. Once the crack starts, $\mathbf{P}_{CT}$ immediately moves forward while $\mathbf{P}_{CTR}$ and CTR remain unchanged until the distance d_{13} between $\mathbf{P}_{CT}$ and $\mathbf{P}_{CTR}$ exceeds a threshold d_0. For a single crack, the new CTR can be positioned with the new $\mathbf{P}_{CTR}$, and the CTR tracking process can be completed by looping the process described in Figs. 2(b) to (c). An increase in the number of $\mathbf{P}_{CT}$ from 1 to 2 indicates this crack is branched, the new $\mathbf{P}_{CTR}$ is no longer the midpoint of CTR-side but coincides with CTR-corner points of the upper and lower crack branch, respectively. Then, the number of CTR increases with the appearance of crack bifurcation and the tracking process of bifurcation can be completed according to Fig. 2(d) to (h). The CTR in Fig. 2(c) and (i) are in the same state, so the subsequent tracking process only needs to repeat the Fig. 2(c) to (i). The distinctive local positioning style of the multi-CTTM, which is based on the idea of tracking CTR and locating the crack tip within each CTR, endows its ability in tracking all crack tips of multi-branched crack.

*Correspondence author: tfc1992@ustc.edu.cn, Tel & Fax: +86-551-63602081

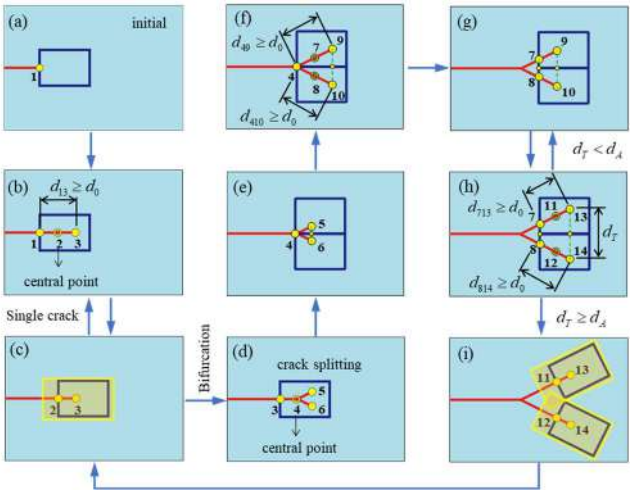

Figure 2. Illustration of automatically tracking the CTR with crack propagation. (a) is the initial CTR set in advance. (b)-(c) is the propagation process of single crack. (d)-(h) indicates crack bifurcation with a small opening, and (i) is the bifurcation of further opening. The CTR on each crack branch in (i) is essentially the same as that in (c), thus the process of (c)-(i) will proceed until the end of crack propagation.

Tracking result for the simulation of dynamic PFM

We employ the AT2 model to simulate the propagation of multi-branch cracks, and the distributions of CTR and crack tips at different time steps tracked by multi-CTTM are presented in Fig. 3.

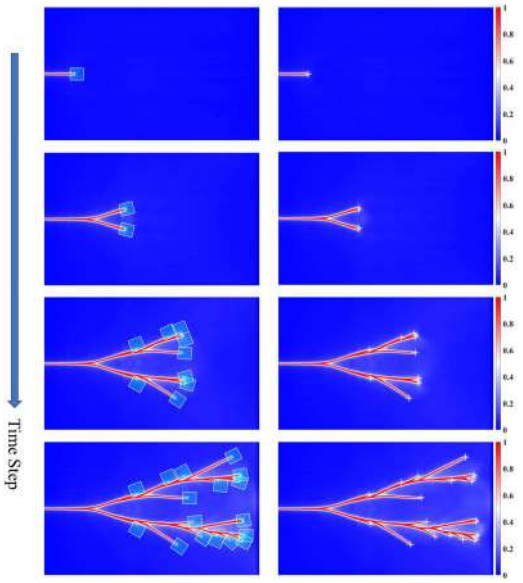

Figure 3. The distributions of CTR (light blue rectangle) and crack tips (white symbol '+') tracked by multi-CTTM at different time steps.

References

[1] J. Bleyer, C. Roux-Langlois, J.-F. Molinari, Dynamic crack propagation with a variational phase-field model: limiting speed, crack branching and velocity-toughening mechanisms, International Journal of Fracture, Vol.204 (2017) 79-100.
[2] J.-Y. Wu, V.P. Nguyen, C. Thanh Nguyen, D. Sutula, S. Bordas, S. Sinaie, Phase field modelling of fracture, Advances in Applied Mechanics, 53 (2019).

STRESS ANALYSIS NEAR THE CRACK TIP OF NACRE-LIKE BIOMATERIALS USING INCREMENTAL FEM

Xiaoyan Ye[1], Yusuke Doi[1], and Akihiro Nakatani *[1]
[1]Division of Mechanical Engineering, Graduate School of Engineering, Osaka University, Osaka, Japan

Summary This study is focused on the toughening mechanism of nacre-like biomaterials associated with crack expansion, which has attracted increasing attention in these years. This research simulated crack expansion using a two-dimensional model and studied the toughening mechanism of nacre-like biomaterials associated with crack expansion. And we found a huge process zone affected by the mechanical properties of debond cohesive zones (DCZ), which may be one reason why the toughness of nacre-like biomaterials is so excellent.

INTRODUCTION

As a variety of biomaterials that attracts increasing attention from many researchers, the nacre-like biomaterials show two distinctive characteristics. One is the hierarchical structure, comprised of hard and brittle tablet-like aragonite crystals and a small amount of soft proteins. The tensile force might cause these tablets to slide on each other, and then macroscopic deformation occurs. The other is excellent toughness[1], which is significantly higher than aragonite crystals. Many researchers have noticed the relationship between the toughness of nacre-like biomaterials and crack patterns like branches in recent studies. However, the toughening mechanism is still unclear. Therefore, it is necessary to conduct further study on the connection between the nacre-like biomaterials' crack patterns and toughness.

MODEL AND METHOD

In order to simulate the crack expansion, we simplify the actual nacre-like biomaterials into a two-dimensional model, as shown in Fig.1. The microstructure of the model consists of unit structures shown in Fig.1(b). Several kinds of cohesive zone (CZ) elements are introduced in the positions where cracks may occur to simulate the crack's expansion. This model consists of 20 layers of aragonite tablets, each layer contains 10 debond cohesive zones (DCZ) to simulate tensile fracture between tablets. Protein layers exist between the aragonite layers, and shear cohesive zones (SCZ) are introduced between protein and aragonite layers to mimic shear fracture. There is a pre-crack with a length of 5 layers at top center of the model (see Fig.1(e)). Furthermore, two kinds of boundary conditions are applied. Under constant displacement condition (see Fig.1(c)), the upper and lower boundaries are set as free boundaries, the left boundary is fixed horizontally, and the right boundary is given a forced displacement in the horizontal direction. Under the K-displacement field condition (see Fig.1(d)), the elastic asymptotic Model I in-plane displacement field is prescribed on the outer boundary. The CZ model used is the exponential model offered by Xu and Needleman[2]. The cohesive law is determined by the maximum traction

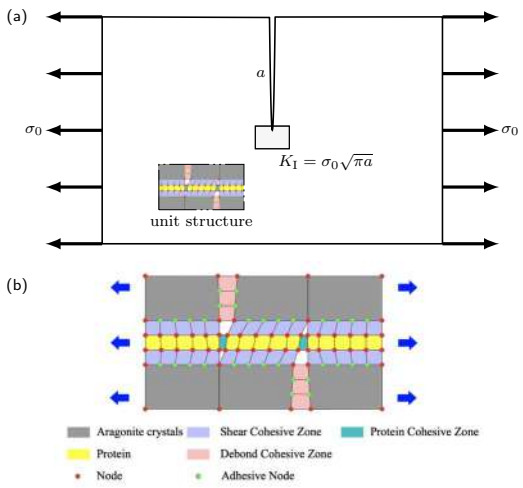

Figure 1: Diagram of analysis model. (a) Finite element mesh of the model. (b) Unit structure under tensile force. (c) Small specimen with prescribed displacement. (d) Small specimen with K_I-displacement field. (e) Discretization for FEA.

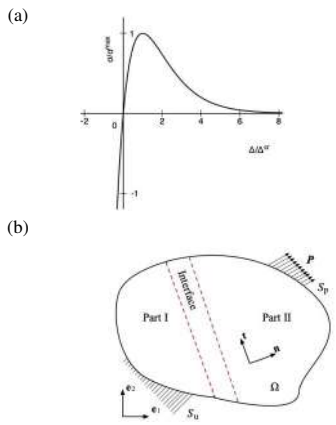

Figure 2: Cohesive zone model: (a) Cohesive law of normal direction. (b) Deformed condition of a continuum with a cohesive interface.

*Corresponding author. E-mail: nakatani@mech.eng.osaka-u.ac.jp

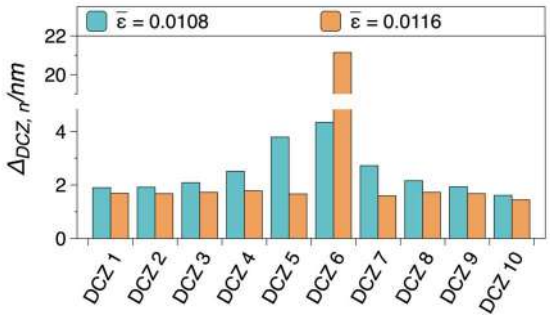

Figure 3: Separation of DCZs on the sixth layer before and after DCZ6 is weakened.

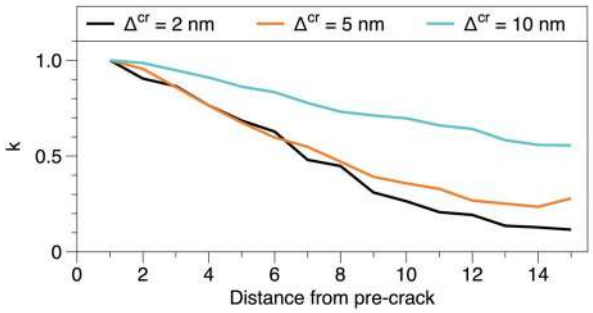

Figure 4: The strain concentration state of each layer before the pre-crack tip when the crack expands.

$\sigma^{\max}$ and critical weaken separation Δ^{cr} (see Fig.2(a)). Tensile deformation in the case of plane strain of the model is studied using the incremental finite element method.

A boundary value problem is solved in which the continuum Ω is fixed by the S_u boundary and deformed under the external load P existing on the S_p boundary (see Fig.2(b)). CZ elements exist at the interface where cracks may occur. $\mathbf{t}_0$ and $\mathbf{n}_0$ are the tangent unit vector and the normal unit vector of this interface, respectively. Under small deformation assumption,

$$\int_{\Omega} \dot{\sigma}_{ij}\delta\varepsilon_{ij}\mathrm{d}V = \int_{S_{\mathrm{coh}}} \left(\dot{\overline{T}}_{\mathrm{n}}\delta\Delta_{\mathrm{n}} + \dot{\overline{T}}_{\mathrm{t}}\delta\Delta_{\mathrm{t}}\right)\mathrm{d}S + \int_{S_p} \dot{P}_i\delta u_i \mathrm{d}S. \tag{1}$$

is obtained using the principle of virtual power at time t, where $\dot{(\cdot)}$ means material time derivative. Here, S_p is the outer surface, S_{coh} is the interface where CZ is introduced. σ_{ij} is the stress component, u_i is the displacement component, and P_i is the external force component. For CZ elements, P_i is always equal to 0. Therefore the nodal displacement under load conditions can be obtained by the incremental finite element method using Eq.1.

RESULT OF STRESS ANALYSIS

In this study, we have investigated the spatial distribution and temporal development of stress and strain near the crack tip in the early stages of crack extension when the model is under constant displacement boundary condition. Fig.3 shows the strain distribution in DCZs of the sixth layer before the crack extension. We found that the crack expansion process consists of two stages. The first is the "stable stage" (see Fig.3, $\bar{\varepsilon} = 0.0108$). Despite the stress concentration, there is a larger process zone near the crack tip than brittle ceramics. As the deformation increases, it enters the "unstable stage"(see Fig.3, $\bar{\varepsilon} = 0.0116$), the strain suddenly concentrates, and eventually, crack expansion occurs. In the "stable stage", the unique hierarchical structure avoids strain concentration, and it facilitates the lateral expansion of the crack. It means that more energy is released, making the material's toughness increase[3].

Also, we studied the influence of the critical weaken separation Δ^{cr} of DCZ on the size of the process zone near the crack tip. We keep the maximum traction $\sigma^{\max}$ constant and make the critical displacement equal to 2 nm, 5 nm, and 10 nm, respectively. When the crack expands to the sixth layer, each layer's strain concentration is shown in Fig.4. The horizontal axis means the distance to the crack tip. $k = \Delta^{\max}_{\mathrm{DCZ},n}/\Delta^{\max}_{\mathrm{DCZ},6}$, where $\Delta^{\max}_{\mathrm{DCZ},n}$ is the maximum separation of the DCZs of the n-th layer, while $\Delta^{\max}_{\mathrm{DCZ},6}$ is the maximum separation of the sixth layer. As the relative displacement of the critical softening of DCZ increases, the number of layers affected by cracks rises, and the size of the process zone also increases significantly.

CONCLUSIONS

In this study, we have investigated the spatial distribution and temporal development of stress and strain near the crack tip in the early stages of crack extension. We found a huge process zone, which is affected by the mechanical properties of CZ. It may be one reason of nacre-like biomaterials' excellent toughness, which will inspire subsequent studies on the toughness mechanism of nacre-like biomaterials and make it possible to design nacre-like artificial materials.

Acknowledgement: This work was partially supported by China Scholarship Council (Grant Number: 202008050310), and Japan Society for the Promotion of Science (JSPS) KAKENHI(Grant Number JP19K21921, JP20H02030).

References

[1] Barthelat F., Li C., Comi C., Espinosa H. D. Mechanical properties of nacre constituents and their impact on mechanical performance. *J. Mater. Res.* **21-8**, 1977, 2006.
[2] Xu, X.P., Needleman, A. Numerical simulations of fast crack growth in brittle solids. *J. Mech. Phys. Solids*. **42(9)**, 1397-1434, 1994.
[3] Rabiei, R., Bekah, S., Barthelat, F. Failure mode transition in nacre and bone-like materials. *Acta Biomater.*, **6(10)**, 4081-4089, 2010.

A GRADIENT SMOOTHED GFEM FOR 2D SOLID MECHANICS PROBLEMS

Jinsong Tang[1], Linfang Qian[1], Guangsong Chen*[1] and Shijie Zhou[1]
[1]School of Mechanical Engineering, Nanjing University of Science and Technology, Nanjing, China

Summary A gradient smoothed GFEM (GS-GFEM) without extra DOFs based on Taylor expansion is proposed in this work. The displacement field function of GS-GFEM consists of the finite element shape function and the node displacement function. The Taylor expansion is adopted for the nodal displacement function. The derivative term in Taylor expansion is obtained by using gradient smoothed technique. The finite element interpolation is employed for gradient smoothed operation. Through several typical numerical experiments and comparison with other methods (FEM-T3, FEM-Q4 and NS-FEM), the advantages of the proposed GS-GFEM including high accuracy, rapid error convergence, temporal stability etc. are demonstrated.

Displacement Function Discrete Strategy

The displacement field function can be expressed as the combination of the finite element shape function and the node displacement function:

$$u(\mathbf{x}) = \sum_{i=1}^{m} N_i(\mathbf{x}) u^i(\mathbf{x}) \tag{1}$$

The nodal displacement function is obtained by the second-order Taylor expansion:

$$\begin{aligned} u^i(\mathbf{x}) = u(\mathbf{x}_i) + (x-x_i)\tilde{u}_{,x}(\mathbf{x}_i) + (y-y_i)\tilde{u}_{,y}(\mathbf{x}_i) + \frac{1}{2}(x-x_i)^2 \tilde{u}_{,xx}(\mathbf{x}_i) + \frac{1}{2}(y-y_i)^2 \tilde{u}_{,yy}(\mathbf{x}_i) \\ + (x-x_i)(y-y_i)u_{,xy}(\mathbf{x}_i) \end{aligned} \tag{2}$$

According the gradient smoothed operation [1], the first order smoothed derivative term in the Taylor expansion can be expressed as:

$$\begin{aligned} u_{,l}(\mathbf{x}_i) &= \frac{1}{A}\int_{\Omega_i} u^i_{,l}(\mathbf{x})\mathrm{d}\Omega = \frac{1}{A}\int_{\Gamma_i} u^i(\mathbf{x}) n_l \mathrm{d}\Gamma \\ &= \frac{1}{A}\int_{\Gamma_i} \sum_{j=1}^{n_i} N_j(\mathbf{x}) u_j n_l \mathrm{d}\Gamma = \sum_{j=1}^{n_i} \frac{1}{A}\int_{\Gamma_i} N_j(\mathbf{x}) n_l \mathrm{d}\Gamma u_j \\ &= \sum_{j=1}^{n_i} N^l_j u_j \end{aligned} \tag{3}$$

where Ω_i is the smoothed domain, and its boundary is Γ_i, as shown in Figure 1. n_i is the number of nodes in the supported domain of node *i*. $N_j(\mathbf{x})$ is the linear finite element shape function and triangular element is adopted. $N^l_j(\mathbf{x})$ the smoothed derivation of $N_{j,l}(\mathbf{x})$ and $l = \{x, y\}$. The second-order smoothed derivative term can be obtained in the similar way.

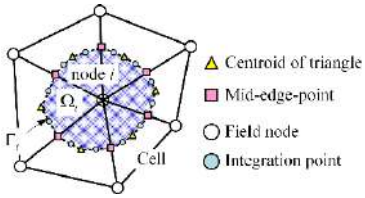

Figure 1. Nodal supported domain

Numerical Examples

Static analysis of cantilever beam

The geometric model of a cantilever beam is as shown in Figure 2. The right free end is subjected to a shear force. Some geometric and material parameters are listed in Table 1. Define the displacement error norm e_d and the strain energy norm e_e:

$$e_d = \sqrt{\frac{\sum_{i=1}^{N_d}\left(u_i^{\mathrm{ref}} - u_i^{\mathrm{num}}\right)^2}{\sum_{i=1}^{N_d}\left(u_i^{\mathrm{ref}}\right)^2}}, \quad e_e = \sqrt{\frac{\left|E_{\mathrm{num}} - E_{\mathrm{exact}}\right|}{E_{\mathrm{exact}}}}$$

in which, 'ref' represents the analytical solutions [1].

Figure 3 shows the convergence curves of displacement and strain energy error norms with four methods under different number of meshes. *R* represents the slope of each curve, namely the error convergence rate, which is obtained by linear fitting. Compared with the other three methods, the advantages of the proposed GS-GFEM in terms of accuracy and error convergence are intuitively reflected in results.

*Corresponding author. E-mail: cgsnjust@njust.edu.cn

Table 1. Parameters of cantilever beam

Parameters	Length (L)	Width (D)	Young's modulus (E)	Poisson's ratio (υ)	Shear force (P)
Value	48	12	3.0×10^7	0.3	1000

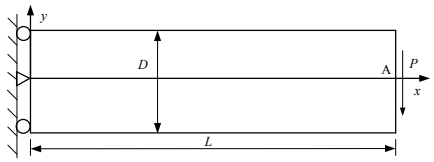

Figure 2. Cantilever beam geometric model

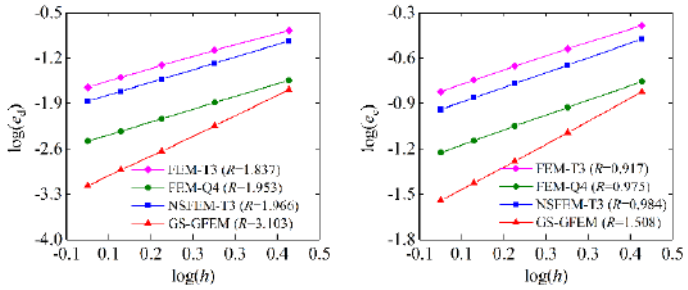

Figure 3. Convergence rate of displacement(left) and strain energy(right) error norms

Dynamical analysis of cantilever beam

As shown in Figure 4, a shear wall with four openings is studied. The boundary condition is set to the bottom edge fully clamped. The geometrical and material parameters are $E=10000\,\mathrm{N/m^2}$, $v=0.2$ and $\rho=1.0\ \mathrm{kg/m^3}$.

Firstly, the free vibration analysis of shear wall is carried out. The first eight mode frequencies are calculated as shown in Table 2. There is a severe temporal instability problem in the dynamical analysis of the NS-FEM method, and the free vibration analysis of the method have spurious non-zero energy modes, which is highlighted in bold in Table 2. The modes corresponding to spurious non-zero energy modes are shown in Figure 5. In contrast, the GS-GFEM method avoids this problem and the calculation results are in good agreement with the reference results.

Furthermore, the dynamic response of shear wall under a harmonic concentrated load is analyzed. The displacement response at point A is shown in Figure 6. Obviously, compared with NS-FEM, the proposed GS-GFEM offers superior performance on dynamic analysis.

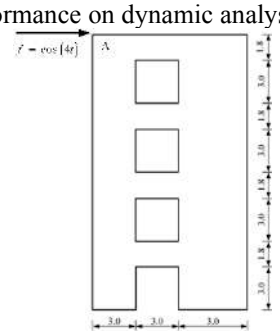

Figure 4. Shear Wall geometric model.

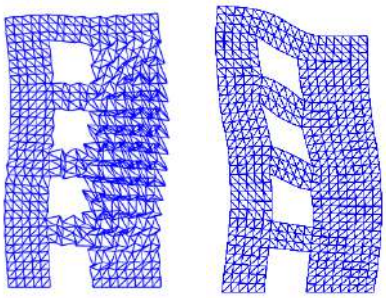

Figure 5. The 5th model shape with NS-FEM(left) and GS-GFEM(right).

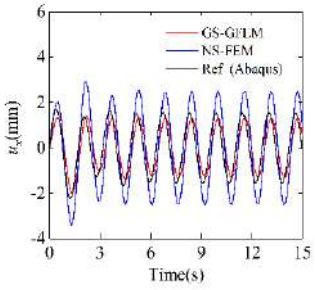

Figure 6. The displacement response at point A in the x direction.

Table 2. First eight mode frequencies with different methods

Model order	1	2	3	4	5	6	7	8
NS-FEM	0.2907	1.0365	1.1973	1.6163	**2.1838**	**2.3398**	**2.6970**	**2.7149**
GS-GFEM	0.3342	1.1376	1.2153	1.9414	2.4661	2.9277	3.1706	3.5508
Reference [1]	0.3309	1.1429	1.2166	1.8833	2.5381	2.9673	3.2258	3.6232

CONCLUSIONS

In this work, a GS-GFEM is proposed for 2D solid mechanics problems. Both static and dynamic analyses are conducted using the proposed GS-GFEM and compared with other methods. Some important conclusions can be summarized as follows:

(1) The GS-GFEM method proposed in this paper has the advantages of high accuracy and rapid error convergence, which are reflected from the static analysis results of the cantilever beam and the comparison with other numerical methods.

(2) GS-GFEM overcomes the temporal instability problem in NS-FEM. There are no spurious non-zero energy modes in free vibration analysis of GS-GFEM, showing brighter prospects in dynamic analysis.

(3) No extra DOFs are introduced in the derivation of GS-GFEM, and the formulation is very straightforward and the procedure is easy to implement.

References

[1] Chen G.S., Qian L.F., Ma J.. A Gradient Stable Node-Based Smoothed Finite Element Method for Solid Mechanics Problems. Shock and Vibration, 2019, 2019: 1-24.

AN EFFICIENT PARTICLE SUBDOMAIN QUADRATURE SCHEME FOR THE MATERIAL POINT METHOD

Zheng Sun* and Xiaomin Zhou
School of Civil and Surveying & Mapping Engineering, Jiangxi University of Science and Technology, Ganzhou, Jiangxi 341000, China

Summary MPM has been proved to be an effective numerical method for large deformation problems. However, MPM suffers from cell crossing error as that material particles are used to represent deformed material and perform particle quadrature. An efficient subdomain quadrature MPM is proposed to eliminate cell crossing error. Particle domain is approximated to be line segment, rectangle, and cuboid for 1-, 2-, and 3- D problems, respectively, which are divided into several different subdomains based on topological relationship between particle domain and background grid. A single Gauss quadrature point is placed at center of each subdomain and used for information mapping. Material quantities of each Gauss quadrature point are determined by corresponding material particle and subdomain volume without reconstruction algorithm. Numerical examples demonstrate effectiveness of the proposed method.

1 SUBDOMAIN QUADRATURE MATERIAL POINT METHOD (SQMPM)

The particle domain is assumed to be the line segment, rectangle, and cuboid for the 1D, 2D, and 3D problems, respectively, and the particle is positioned at the domain center, as illustrated in Fig. 1.

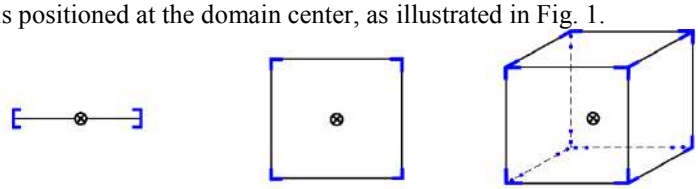

(a) Line segment for 1D **(b)** Rectangle for 2D **(c)** Cuboid for 3D

Fig. 1 Schematic illustration for (a) 1-dimensional, (b) 2-dimensional, and (c) 3-dimensional particle domain.

The changing of particle domain is tracked by:

$$\boldsymbol{r}_p^k = \boldsymbol{F}_p^k \boldsymbol{r}_p^0 \tag{1}$$

where $\boldsymbol{r}_p^k$ and $\boldsymbol{r}_p^0$ denote volume domain vectors of the particle p at the k-th time step and the initial state, respectively. $\boldsymbol{F}_p^k$ is the deformation gradient tensor of the particle p at the k-th time step. It should be noted that, for rectangular and cuboid particle domains, only diagonal terms of $\boldsymbol{F}$ are non-zero that means the rotation of the particle domain is neglected in this paper.

The code structure of particle domain partitioning strategies for the 1D case is presented as follows, and the bivariate and trivariate for the 2D and 3D cases could be obtained by tensor product structure.

Algorithm structure of the particle domain partitioning strategies for 1D case

Input: the background node position vector: $\{x_J\}$; the current position of particle p: x_p; the initial line segment domain of particle p: r_p^0; the current deformation gradient tensor of particle p: $\boldsymbol{F}_p$.

(1). Calculate the current line segment domain of particle p: $r_p = \boldsymbol{F}_p r_p^0$.

(2). Calculate the coordinate of the left boundary x_{pl} and the right boundary x_{pr} of the particle p: $x_{pl} = x_p - \frac{r_p}{2}$ and $x_{pr} = x_p + \frac{r_p}{2}$.

(3). Identify the J-th and K-th background elements that contain the x_{pl} and x_{pr}, respectively.

(4). Determinate the number of background nodes that are contained in the particle domain: $M=K-J$

(5). Divide the line segment domain of particle p into M+1 subdomain as:

$$\begin{cases} V_p = [x_{pl}, x_{pr}], & M = 0 \\ V_1 = [x_{pl}, x_{J+1}],\ V_2 = [x_{J+1}, x_{J+2}], \cdots, V_{M+1} = [x_K, x_{pr}], & M \geq 1 \end{cases}$$

Output: the number of particle subdomains: M; the size for each subdomain: $V_1, \ldots, V_i, \ldots, V_{M+1}$

*Corresponding author. E-mail: sunzheng@jxust.edu.cn

2 NUMERICAL EXAMPLES

2.1 Two-dimensional bending beam

The dynamic bending of a two-dimensional elastic beam is studied, which is induced by the initial velocity in the transverse direction. The simulating parameters of the beam are as follows: Length L = 0.06 m, Height H =0.01 m, Young's modulus E = 318 GPa, Poisson's ratio μ=0.054, density ρ= 1845 kg/m3, Y_{max}= 0.005 m, the background mesh size dx×dy=0.625 mm×0.625 mm, the particles per cell ppc=4×4, and the simulated time step $0.001\mu s$.

The distributions of the particle stress at t=8 μs calculated by the MPM and sqMPM method are presented in Fig. 2, where a close-up of particle domain at the top of the curved boundary segment for sqMPM is given in Fig. 2(c). The results show that severe stress oscillations are observed in the standard MPM, especially in the large deformation area. As expected, the oscillations of the particle stress found in the standard MPM is noticeably reduced by the sqMPM.

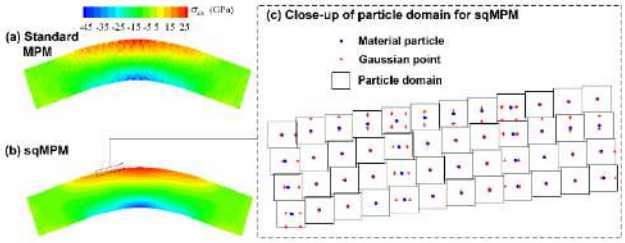

Fig. 2 Distributions of stress σ_{xx} at t = 8 μs obtained by (a) standard MPM and (b) sqMPM, and (c) a close-up of particle domain for the sqMPM method where the solid blue dot, red asterisk, and black rectangle denote the material particles and its corresponding Gaussian point and particle domain, respectively.

2.2 Three-dimensional cantilever beam

This example is the bending of a three-dimensional cantilever beam under the quasi-static concentrated force, which is linearly increased from zero to 1.5 kN in 30 seconds and is split across the material particles within the cells closest to the right boundary of the beam. The beam has an initial dimension l×b×h of 10 m×1 m×1 m. The material properties for the beam are Young's modulus E = 10 MPa, Poisson's ratio μ=0.2, and density ρ= 1000 kg/m^3, respectively. The background grid size dx=dy=dz=0.05 m, the particles per cell ppc=2×2×2, and the simulated time step 0.1 ms are chosen in both the standard MPM and sqMPM. The neutral axis of the beam is fixed at its left-hand edge, and roller boundary conditions are imposed on the other background grid nodes at the root of the beam. The static solution of the FEM method for this problem is also presented with a mesh of 0.05 m×0.05 m×0.05 m.

Fig.3 compares the distribution of the normal stressobtained by the standard MPM, sqMPM at t =30s, and the FEM method, respectively. As we can see, the sqMPM exhibits good agreements with the FEM, while the results obtained by the standard MPM are quite noisy, especially in the large deformation region.

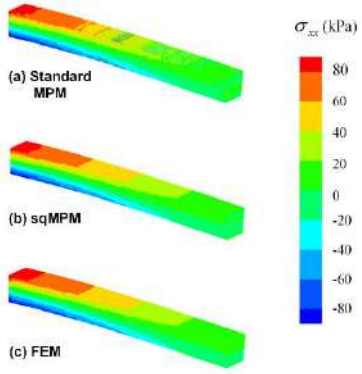

Fig. 3 Distributions of normal stress obtained by (a) standard MPM and (b) sqMPM at t =30s, and (c) the FEM method, respectively.

3. Conclusion

An efficient subdomain quadrature Material Point Method (sqMPM) has been developed to eliminate the cell crossing error of the standard MPM in this study. In the proposed method, the particle domain is assumed to be the line segment, rectangle, and cuboid for the 1D, 2D, and 3D problems, respectively. The particle domain is divided into several different subdomains based on the topological relationship of the particle domain and background grid. A single Gauss quadrature point is placed at the center of each particle subdomain and employed for the information mapping. The material quantities of each Gauss quadrature point are determined by the corresponding material particle and the subdomain volume without the cumbersome reconstruction algorithm as that in MLS. Numerical examples involving large deformation problems have been used to verify and demonstrate the proposed method. It is shown that the sqMPM eliminates the cell crossing error and exhibits better convergence than the MPM.

INFORMATION FUSION FOR COMPUTATIONAL RELIABILITY ANALYSIS

Carsten Proppe*[1]
[1]Chair of Engineering Mechanics, Karlsruhe Insitute of Technology, Karlsruhe, Germany

Summary Multifidelity estimation combines the output of simulation models of different approximation quality and from different sources in order to obtain efficient estimators for a quantity of interest. It relies on a model hierarchy that is established either by means of an approximation parameter or the Pearson correlation of the model outputs. Information fusion combines the results from the model hierarchy based on differences of the quantity of interest or on conditional probabilities. In this presentation, information fusion is combined with importance sampling and importance splitting (notably the moving particles method) in order to yield efficient estimators for reliability analysis. Importance sampling and importance splitting based multifidelity reliability estimation methods are developed and critically assessed based on numerical examples.

INFORMATION FUSION

Reliability estimation deals with the evaluation of the failure probability $P_F = \int_F p(\boldsymbol{\theta})\mathrm{d}\boldsymbol{\theta}$, where $F = \{\boldsymbol{\theta} \in \mathbb{R}^n | g(\boldsymbol{\theta}) < 0\}$ denotes the failure region and $p(\boldsymbol{\theta})$ the joint probability density function of the random vector $\boldsymbol{\Theta}$. In general, the performance function $g(\boldsymbol{\theta})$ is not known exactly, but is computed by numerical approximation. In the following, an ordered family of approximated performance functions $g_l(\boldsymbol{\theta})$, $l = 0, ..., L$ is considered, where the index l refers to the performance function of the lth model of the model hierarchy. The index $l = 0$ denotes the model with lowest fidelity and $l = L$ the high-fidelity model.

Additive Information Fusion

For additive information fusion, denote by Q_l a quantity of interest related to the lth model. In the context of reliability estimation, the quantity of interest could be the indicator function $I_{g_l<0}(\boldsymbol{\theta})$, i.e. $I_{g_l<0}(\boldsymbol{\theta}) = 1$, if $g_l(\boldsymbol{\theta}) < 0$ and $I_{g_l<0}(\boldsymbol{\theta}) = 0$ elsewhere. An estimator for such a quantity of interest that combines the information from the model hierarchy in an additive manner is obtained from the telescoping sum $E[Q_L] = E[Q_0] + \sum_{l=1}^{L} E[Q_l - Q_{l-1}]$. The aim is to compute each of the estimates on the right-hand side of this equation individually by Monte Carlo simulation. A reduction of the overall computational effort can be expected from the fact that the variance of the differences decreases to zero with increasing index l and thus, for a given coefficient of variation, estimates of the contributions from highly accurate performance function will require less samples.

Multiplicative Information Fusion

For multiplicative information fusion, one has with

$$p(\boldsymbol{\theta}_L) = \int ... \int p(\boldsymbol{\theta}_L, ..., \boldsymbol{\theta}_l, ..., \boldsymbol{\theta}_0)\mathrm{d}\boldsymbol{\theta}_L ... \mathrm{d}\boldsymbol{\theta}_l ... \mathrm{d}\boldsymbol{\theta}_0 = \int p(\boldsymbol{\theta}_L|\boldsymbol{\theta}_{L-1}) ... \int p(\boldsymbol{\theta}_1|\boldsymbol{\theta}_0)p(\boldsymbol{\theta}_0)\mathrm{d}\boldsymbol{\theta}_{L-1} ... \mathrm{d}\boldsymbol{\theta}_0 \qquad (1)$$

an expression for the high-fidelity probability density function that is computed from the low-fidelity contributions and can then be utilized to estimate the quantity of interest of the high-fidelity model.

INFORMATION FUSION AND IMPORTANCE SAMPLING

The aim of importance sampling is to reduce the variance of Monte Carlo simulation by sampling from an alternative density, the importance sampling density. To this end, the importance sampling density $p_{IS}(\theta)$ is introduced: $P_F = \int_F \frac{p(\boldsymbol{\theta})}{p_{IS}(\boldsymbol{\theta})} p_{IS}(\boldsymbol{\theta})\mathrm{d}\boldsymbol{\theta}$ and samples are drawn from $p_{IS}(\boldsymbol{\theta})$.

Additive information fusion

For additive combination of the model outputs, the importance sampling density for each expectation has to focus on the differences of the performance functions of neighboring models. Alternatively, the importance sampling estimators might be computed separately for each level and then the differences of the estimators are weighted. In the first case, the regions where the performance functions differ are small and widespread and it is difficult to cover these regions well. This may lead to an increase of the coefficient of variation of the estimator and also of the relative approximation error. In the latter case, a weighted sum of importance sampling estimates is computed. This approach requires unbiased importance sampling estimates. Thus, the importance sampling densities are calibrated by means of the different approximations of the performance function $g_i(\boldsymbol{\theta})$, $i = 1, ..., n$; however, the samples generated with the different importance sampling densities are evaluated with respect to the performance function $g_n(\boldsymbol{\theta})$ of highest fidelity. This is different from the other methods, where the generated samples are either evaluated by the performance function of the same or the next higher level. In order to be efficient, a reduction of the coefficient of variation for the weighted multifidelity estimator compared to the single level approach is therefore mandatory, such that in total, less samples are evaluated by the high-fidelity performance function.

*Corresponding author. E-mail: proppe@kit.edu.

Multiplicative information fusion

For multiplicative information fusion, the importance sampling density is based on the model with lower fidelity and pairs of output quantities for neighboring models are obtained for samples generated by means of the importance sampling density. These pairs of samples are then utilized to find a functional expression by regression that relates the high fidelity model output to the low fidelity model output. The relative error is comparable to that of the high fidelity model. Thus, the method considerably improves the approximations of the failure probability. However, the coefficient of variation of the multifidelity estimator is higher than that of the single level estimator. It scales with the coefficient of determination and thus might be attributed to the regression error.

INFORMATION FUSION AND IMPORTANCE SPLITTING

The idea of importance splitting in reliability estimation is to discard samples that are far away from the failure region and to split at least some of the remaining ones. This procedure is repeated gradually by introducing thresholds and retaining only those samples that pass the threshold. Importance splitting can also be interpreted as a special adaptive importance sampling procedure, where the final samples are drawn from the importance sampling density. The moving particles algorithm applies importance splitting to obtain an estimate of P_F. It starts with an initial Monte Carlo simulation (MCS) with N_m samples. These initial samples are then moved to the failure region by the following procedure: The values $g(\boldsymbol{\theta}_j)$, $j = 1, ..., N$, of the N samples are ranked. The sample with the maximum value of the performance function is moved: a Markov chain Monte Carlo simulation (MCMC) is carried out starting from one of the remaining samples and the final state of the Markov chain is accepted, if the value of the performance function could be reduced. Otherwise, the sample is simply replaced by the initial value of the Markov chain. The Markov chain can be generated either by application of the classical Metropolis-Hastings algorithm or by direct sampling from a normal transition kernel. For each initial sample, the number M of moves until the sample reaches the failure region is count. The number of moves to get an initial sample into the failure region follows a Poisson distribution with parameter $\lambda = -\log P_F$. The estimator for the parameter of the Poisson distribution can thus be obtained from $\lambda = E[M]$.

Additive information fusion

For the moving particles algorithm, the quantity of interest is the number of moves to reach the failure region. Denote by M_l the number of moves when the numerically computed performance function $g_l(\boldsymbol{\theta})$ is applied. Applying additive information fusion, the estimator for the Poisson distribution parameter at level L and thus for $-\log P_{F_L}$, where P_{F_L} denotes the failure probability computed with the approximated performance function $g_L(\boldsymbol{\theta})$ at approximation order L is obtained from the telescoping sum, where the quantity of interest is the number of moves ($Q_l = M_l$).

Multiplicative information fusion

For information fusion with multiplicative combination of the model outputs, consider again without loss of generality the bilevel situation with a high-fidelity and a low-fidelity model. M_h and M_l denote the random variables for the moves of the particles related to the high-fidelity and the low-fidelity model, respectively. As the low-fidelity model is assumed to be computationally more efficient, suppose that samples M_{l_i}, $i = 1, ..., N$, are generated for particles with the low-fidelity models and pairs of samples (M_{l_i}, M_{h_i}), $i = 1, ..., M$ that were obtained with both the low- and the high-fidelity model , where $M \ll N$. The objective is to estimate the parameters λ_l and λ_h of the two dependent Poisson distributed random variables M_h and M_l. To this end, three independent Poisson distributed random variables are introduced and the parameters of the three Poisson distributions are estimated by maximum likelihood estimation via the expectation maximization algorithm.

CONCLUSIONS AND OUTLOOK

This paper combines additive and multiplicative information fusion with importance sampling and importance splitting in order to efficiently obtain reliability estimates. Obtaining a good importance sampling density is still a challenging task, especially in high dimensions. This is also the case, if the importance sampling density should focus on level differences. It therefore appears to be more advantageous to combine different importance sampling estimators by a weighted sum, even if this approach requires unbiased estimators and thus the evaluation of all samples by the high-fidelity performance function. Multiplicative information fusion might have advantages compared to additive information fusion as it reduces the relative error and requires less samples to be evaluated by the high-fidelity performance function. However, multiplicative information fusion relies on establishing a relationship between the values of the performance function obtained with the model of lower and of higher fidelity. Importance splitting is a rather robust method to yield accurate reliability estimates. Taking advantage of Poisson process theory, both additive and multiplicative information fusion can be combined with the moving particles method in order to further increase the efficiency of the moving particles method.

In a Bayesian setting, the approaches can be extended by taking the data and model error into account. It is also noted that the methods presented in the paper can be applied to sensitivity analysis and Bayesian inference.

PHASE-FIELD STUDY OF HIGH TEMPERATURE OXIDATION AND AQUEOUS CORROSION OF METALS CONSIDERING MECHANICO-CHEMICAL COUPLING

Chen Lin*[1], Haihui Ruan [2], Sanqiang Shi [2]
[1]Sino-French Institute of Nuclear Engineering and Technology, Sun Yat-Sen University, Zhuhai, China
[2]Department of Mechanical Engineering, The Hong Kong Polytechnic University, Hong Kong, China

Summary Phase-field models were proposed to study high temperature oxidation and aqueous corrosion of metals. The reaction rate was expressed as a function of the electrochemical potentials of reactants and products and conforms to the generalized Butler-Volmer relationship. The Gibbs free energy was expressed as a sum of chemical potential, interfacial energy, electric potential energy, and mechanical energy of system. The governing equation of phase order parameter was derived from the equivalence of reaction rate and phase transformation rate, which captured the effects of reaction kinetics, elemental concentration, electric potential, and mechanical deformation. The mechanisms of chemo-mechanical coupling have been revealed for two typical scenarios: (i) the stress-oxidation interaction in growth of oxide and (ii) the localized corrosion in wet environment.

INTRODUCTION

Numerous experimental investigations indicate that corrosion (or oxidation) can be influenced by stress. However, the harsh service-environments and complex structures of materials lead to that all factors, involving: chemical, mechanical, and phase-field-kinetic, are generally interrelated and interactive during the corrosion (or oxidation). The major challenge stands out in revealing the mechanism of chemo-mechanical corrosion is to establish a multi-field coupling theory and develop its numerical method. In present talk, we propose the phase-field models to explore the chemo-mechanical coupling in high temperature oxidation and aqueous corrosion. We presented a set of examples to show the capability of our model to capture the effects of varies mechanical loading on complicated corrosion scenarios.

RESULTS AND CONCLUSIONSN

In a reactive system, the forward and backward reactions take place simultaneously, leading to the net reaction rate:

$$r = r - r = k_0\left(e^{-(\mu_{TS}-\mu_R)/RT} - e^{-(\mu_{TS}-\mu_P)/RT}\right), \quad (1)$$

where r and r represent the forward and backward reaction rate, respectively. They are further expressed in an Arrhenius form in Eq. (1), where k_0 is the rate coefficient; μ_R, μ_P are the chemical potentials of reactants and products, respectively; μ_{TS} is the chemical potential at the transition state. For a reaction involving multiple reactants and products, μ_R and μ_P, are $\mu_R = \sum_i n_i \mu_{R_i^{X_i}}$ and $\mu_P = \sum_j n_j \mu_{P_j^{Z_j}}$, respectively, where the chemical potential, μ_*, is the variational derivative of the total free energy, Ψ, with respect to the concentration, c_*. The reaction rate can be recast as generalized Allen-Cahn equation to govern the phase transformation. This reaction rate can also be expressed in the form of generalized BV equation, in which the overpotential is correlated with not only the species diffusion, electric field, but also the interfacial energy, mechanical deformation [1].

The proposed PF model was applied to two typical case:

In first case, we use the PF model to study a zirconia-zirconium bilayer with the initial thickness of zirconia. Through this numerical study, many experimentally observed but insufficiently understood phenomena can be well explained. Specifically, the numerical simulations (Fig. 1) reveal quantitatively the causes of interface roughening or smoothening during the inward oxide growth, the roughness-dependent oxide growth rate, and the nucleation sites of premature cracking. These numerical findings indicate that the durability of oxide scale can be significantly improved by the variation in the initial surface roughness and creep properties of zirconium alloy which can prolong the service life of zirconium-based alloy cladding used in the nuclear power plant.

*Corresponding author. E-mail: linch67@mail.sysu.edu.cn

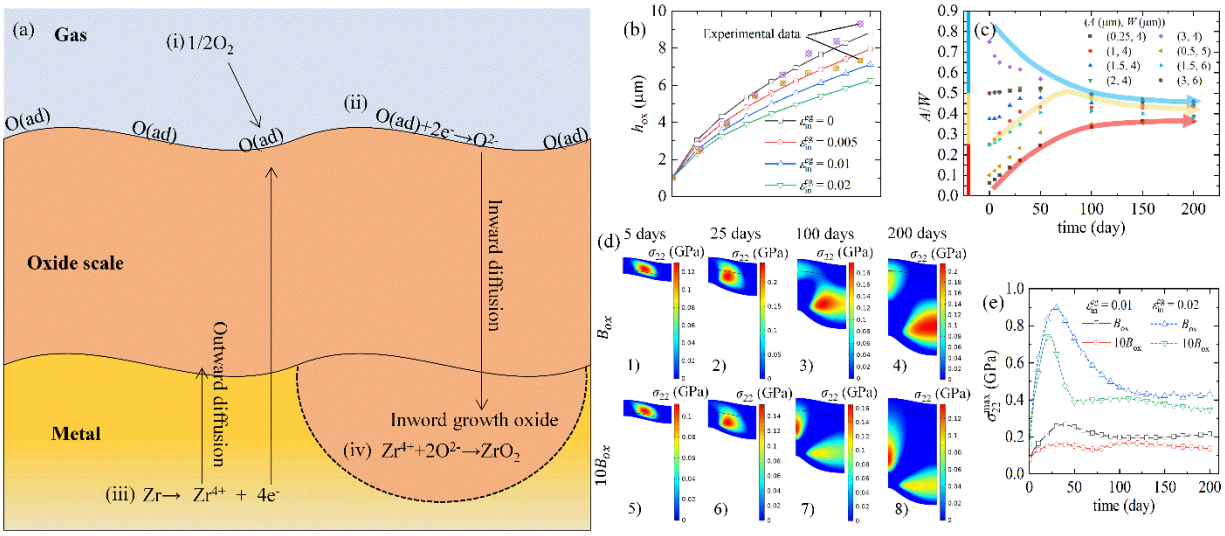

Fig. 1 (a) Schematics of zirconium oxidation; (b) Variations of oxide scale thickness different eigenstrains; (c) Variations of oxide interfacial roughness considering different initial interface morphologies; (d) Contour plots of the normal stress σ_{22} after different periods of oxidation for two creep rate coefficients; (e) Variations in the maximum tensile stress over time for different eigenstrains and creep rates.

In the case of aqueous corrosion [2]. We study a complex occluded cell corrosion process (Fig. 2) that involves mechano-electrochemical coupling, anodic dissolution, insoluble depositions formation, and resulted Galvanic-pitting corrosion. Based on a quantitative investigation into the effects of Cl^- concentration, pH value, mechanical loading, and electric field, we reveal the autocatalytic process of pitting assisted by increasingly aggressive chemical environment and concentrated stress and study how the external electric field can arrest assisted corrosion and prolong service lifetime. The computational model would be helpful for the lifetime management of metallic components serving in the ocean or other more aggressive environment.

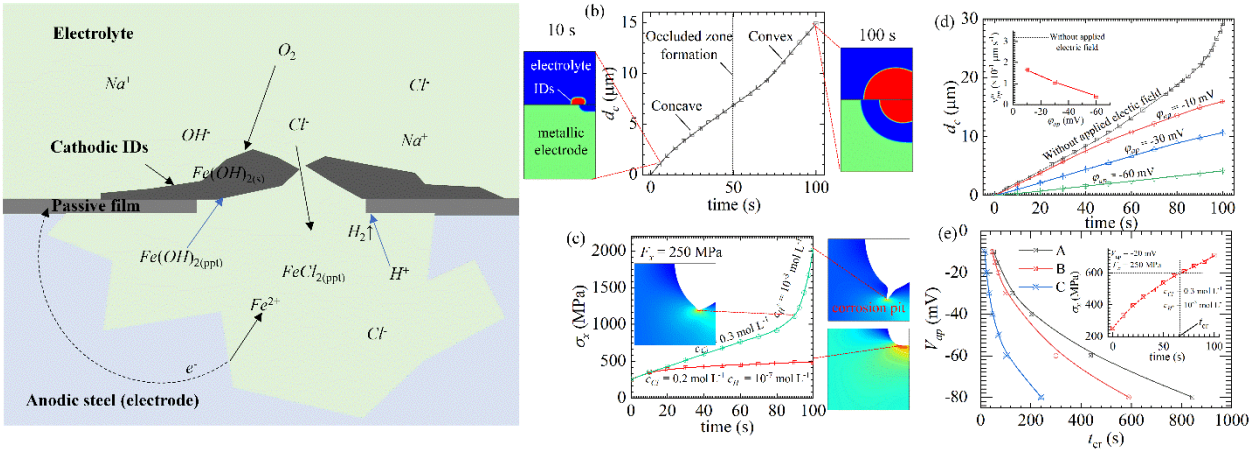

Fig. 2 (a) Schematics of occluded cell corrosion (b) formation of occluded corrosion cell; (c) corrosion assisted by mechano-electrochemical coupling; (d) and (e) corrosion arrested by cathodic protection.

References

[1] C. Lin, H.H. Ruan, S.Q. Shi, Mechanical–chemical coupling phase-field modeling for inhomogeneous oxidation of zirconium induced by stress–oxidation interaction. *npj Materials Degradation* **4 (1)**: 1-12, 2020.

[2] C. Lin, H.H. Ruan, Multi-phase-field modeling of localized corrosion involving galvanic pitting and mechano-electrochemical coupling. *Corrosion Science* **177**, 108900, 2020.

HIGHLY SENSITIVE AFM USING COUPLED RESONATORS UNDER NONLINEAR FEEDBACK

Hiroshi Yabuno*[1], Yubo Lin[1], Yasuyuki Yamamoto[2], and Sohei Matsumoto[3]
[1]Grad Sch Systems and Informat Eng, Univ. of Tsukuba, Tsukuba Science City, Ibaraki, Japan
[2]Nmij, Res Inst Engn Measurement, Fluid Property Stand Grp, Natl Inst Adv Ind Sci and Technol, Tsukuba Science City, Ibaraki, Japan
[3]Res Ctr Ubiquitous MEMS Micro Engn, Natl Inst Adv Ind Sci and Technol, Tsukuba Science City, Ibaraki, Japan

Summary The mass sensing based on the eigenmode shift in weakly coupled resonators has been attractive which is much higher sensitive than that based on the frequency shift of a single resonator. In a previous study, we have proposed the method based on the eignemode shift in coupled resonators to achieve a highly sensitive atomic force microscope (AFM). For the detection of the eigenmode shift, the self-excited oscillation has been utilized because the amplitude ratio between the coupled resonators under the self-excitation corresponds to the eigenmode in the state with small response amplitude. The self-excited oscillation produced by positive velocity feedback grows with time until the limitation of power in the actuator driver. In the present study, by adding the nonlinear feedback to the linear one, we restrict the amplitude growth using stable limit cycle and reduce the steady state amplitude. Experimental results by using coupled macrocantilevers demonstrate the reduction of the response amplitude.

INTRODUCTION

In the measurement methods as mass sensor, atomic force microscope (AFM), and so on, a single resonator has been utilized for the high sensitive measurement [1]. In AFM, the sensitivity, that is the natural frequency shift of the resonator due to the stiffness perturbation of the resonator due to the variation of the probe-sample distance, is $\frac{d\omega}{dk} = \frac{1}{2\sqrt{mk}}$, where ω, m, and k is the equivalent natural frequency, mass, and stiffness of the resonator. To increase the sensitivity much more, the miniaturization is essential, but restricted due to the limitation of fabrication techniques. There is the same situation in the mass sensing, in which the weakly coupled resonators have been introduced to improve the sensitivity not relying on the miniaturization. In most cases, two identical cantilevers as a coupled resonators are utilized. When a measured mass is attached to one of them, the eigenmode is changed from 1:1. The sensitivity of the eignmode shift with respect to the attached mass is increased by decreasing the coupling stiffness between the cantilevers [2]. We have introduced a weakly coupled cantilevers to realize the highly sensitive AFM [3]. For the detection of the eigenmode without being influenced by viscosity in measurement environments, the self-excitation is applied by using a positive linear velocity feedback. Then, the amplitude ratio of the self-excited coupled cantilevers corresponds to the eigenmode in the state where the response amplitude is small. Also for the noncontact sensing between the probe and sample, it is very important to produce the self-excited oscillation with small steady state amplitude. For the self-excited single resonator, the gain of the positive velocity feedback can be automatically changed in real time; this is called automatic gain control [1]. In this research, we add the nonlinear velocity feedback to the linear velocity feedback and produce the stable limit cycle. As a result, the steady state amplitude under the self-excitation can be decreased. The efficiency of the proposed amplitude control method is experimentally confirmed by using weakly coupled macrocantilevers.

ANALYTICAL MODEL AND EQUATIONS OF MOTION FOR COUPLED RESONATORS

Figure 1 show the analytical model of coupled resonators, where m, k, Δk, k_c and c are the mass of the resonator, the stiffness, the perturbation of the stiffness due to the atomic force, the coupling stiffness between the cantilevers, and the equivalent damping, respectively. x_1 and x_2 are the displacements of the resonators. The equations of motion for the cantilevers are expressed as

$$m\frac{\mathrm{d}^2(x_1+\Delta x)}{\mathrm{d}t^2} + c\frac{\mathrm{d}x_1}{\mathrm{d}t} + (k+k_c)x_1 - k_c x_2 = 0, \tag{1}$$

$$m\frac{\mathrm{d}^2(x_2+\Delta x)}{\mathrm{d}t^2} + c\frac{\mathrm{d}x_2}{\mathrm{d}t} - k_c x_1 + (k+k_c+\Delta k)x_2 = 0. \tag{2}$$

By applying the displacement excitation Δx as

$$\Delta x = \alpha \int x_1 dt, \tag{3}$$

*Corresponding author. E-mail: yabuno@esys.tsukuba.ac.jp.

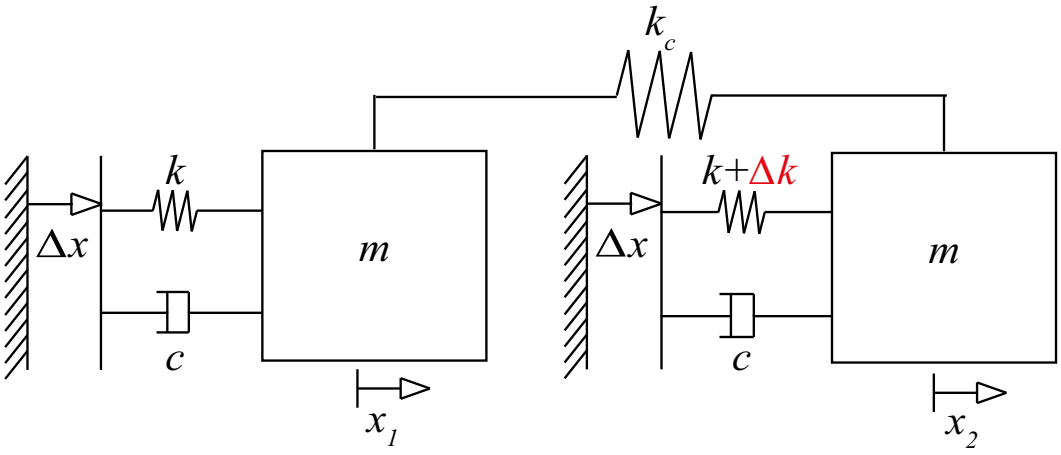

Figure 1: Analytical model of weakly coupled cantilevers.

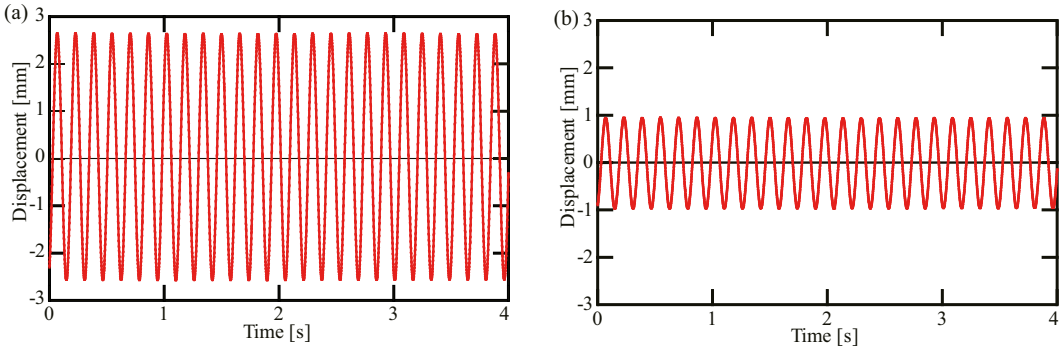

Figure 2: Experimental results. (a) without nonlinear feedback. (b) with nonlinear feedback.

we can apply the positive velocity feedback [3]. In this study, by adding the cubic nonlinear velocity feedback to Eq. (3) as

$$\Delta x = \alpha \int x_1 dt + \alpha_n \int x_1^3, \tag{4}$$

the resonators receive the force proportional to $x_1^2 \dfrac{\mathrm{d}x_1}{\mathrm{d}t}$, which is the same as the nonlinear damping in van der Pol oscillator and can make a stable limit cycle.

EXPERIMENTAL RESULTS

We use weakly coupled phosphor bronze macrocantilevers to compare the response amplitudes under self-excitation for the cases with and without nonlinear feedback. The length, width, and thickness of each cantilever are 215, 15, and 0.5mm, respectively [3]. Figures 2(a) and (b) show the time histories in the steady state for the cases without and with nonlinear feedback control, respectively. In the case without nonlinear feedback, the amplitude growth is restricted by the limited power supply to the actuator for the resonators. On the other hand, Fig. 2(b) shows the reduction of the steady state amplitude by the nonlinear feedback. The reduction eliminates the effect of the nonlinear stiffness of the cantilevers and realizes the accurate detection of the eigenmode.

ACKNOWLEDGEMENTS

The present study was supported in part by a Grant-in-Aid for Scientific Research B (Grant No. 19H0209B) from the Japan Society for the Promotion of Science (JSPS).

References

[1] T. Albrecht, P. Grütter, D. Horne, D. Rugar. *Appl. Phys. Lett.* **69**: 668, 1991.
[2] M. Spletzer, A. Raman, X. Wu, R. Reifenberger. *Appl. Phys. Lett.* **88**: 254102, 2006.
[3] Y. Lin, H. Yabuno, Liu X., Y. Yamamoto, S. Matsumoto. *Appl. Phys. Lett.* **115**: 133105, 2019.

WEAKLY NONLINEAR VIBRATIONS OF THERMOMECHANICALLY COUPLED PLATES: ASYMPTOTIC FORMULATION AND NUMERICAL CHARACTERIZATION

Valeria Settimi[1] and Giuseppe Rega*[1]
[1]Department of Structural and Geotechnical Engineering, Sapienza University of Rome, Rome, Italy

Summary Weakly nonlinear vibrations of composite plates with thermomechanical coupling are dealt with analytically and numerically, describing the main dynamical phenomena which characterize the involved pre- and post-buckling response scenarios. Static buckling and two resonance conditions around the unbuckled and buckled equilibria are investigated by the asymptotic method of multiple time scales and verified towards numerical bifurcation diagrams. Local and global aspects of the mechanical response are characterized in terms of attractors and cross-sections of the 4D basins of attractions, respectively.

INTRODUCTION

The nonlinear dynamical behavior of reduced order models of composite plates under different excitation conditions in a thermomechanical environment has been the subject of recent papers aimed at highlighting the role of multiphysics coupling and the main local and global features of the nonlinear response [1, 2]. The numerical analyses, carried out in strongly nonlinear regime and under different mechanical and thermal conditions, highlighted a rich and involved scenario characterized by multistability and possible chaos. Yet, the analytical treatment of the dynamical response can also represent a useful tool to predict, describe and possibly modify the behavior of the coupled system. Within this general framework, three main response phenomena in the weakly nonlinear regime are detected herein via the asymptotic method of multiple time scales [3], and the relevant mechanical and thermal vibrations are numerically characterized in both local and global dynamics terms.

ASYMPTOTIC AND NUMERICAL INVESTIGATION

With reference to a reduced model of rectangular laminated plate with von Kármán nonlinearities, third-order shear deformability and consistent cubic variation of the temperature along the thickness [4], the assumption of isothermal edges and free heat exchange on the upper and lower surfaces leads to the following nondimensional equations of motion describing the plate dynamics around primary resonance:

$$\begin{aligned} &\ddot{W}(t) + a_{12}\dot{W}(t) + (\Omega^2 - p)W(t) + a_{14}W(t)^3 + a_{15}T_{R1}(t) + a_{16}T_{R0}(t)W(t) - f\cos\Omega t = 0 \\ &\dot{T}_{R0}(t) + a_{22}T_{R0}(t) + a_{23}\alpha_1 T_\infty + a_{24}W(t)\dot{W}(t) = 0 \\ &\dot{T}_{R1}(t) + a_{32}T_{R0}(t) + a_{33}\dot{W}(t) = 0 \end{aligned} \tag{1}$$

in terms of the nondimensional reduced variables $W(t)$ (deflection of the center of the plate), $T_{R0}(t)$ (membrane temperature) and $T_{R1}(t)$ (bending temperature). The mechanical excitations consist of a uniform compressive force p on the plate edges and a distributed harmonic transverse excitation of amplitude f and frequency Ω. The thermal excitation is represented by the constant thermal difference between plate and environment T_∞, while a_{ij} are coefficients which incorporate the geometrical and physical properties of the model.

Local and global nonlinear dynamics have been investigated by considering the single or combined presence of thermal and mechanical excitations. In particular, the transition to mechanically- or thermally-induced buckled responses has been analyzed, with a variety of multistable scenarios being detected. With the aim to unveil the bifurcation phenomena

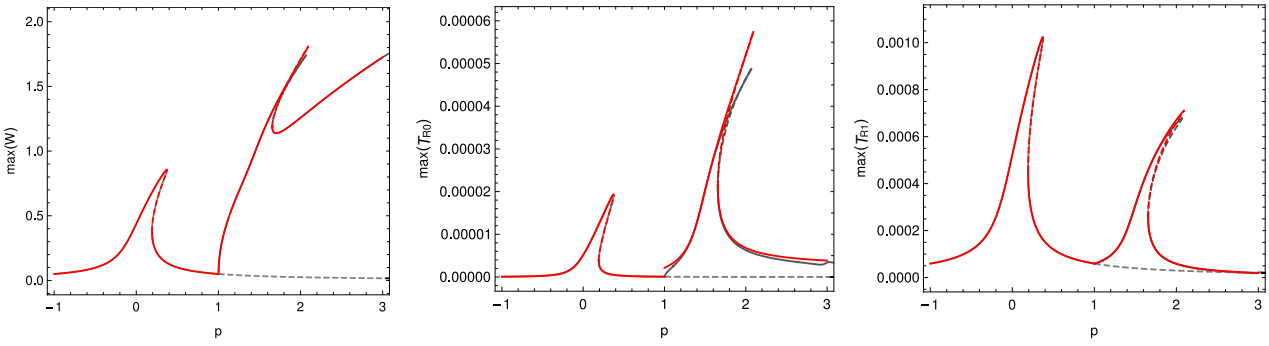

Figure 1: Numerical (gray) and analytical (red) bifurcation diagrams of mechanical and thermal variables. $\Omega = 1$, $f = 0.05$.

*Corresponding author. E-mail: giuseppe.rega@uniroma1.it.

triggering the development of such a rich scenario, identified in a strongly nonlinear regime, a lower forcing amplitude is considered herein, and three main dynamical phenomena are detected,i.e., a static pitchfork bifurcation inducing the mechanical buckling, and two resonance peaks occurring in the pre- and post-buckling branches. The first phenomenon occurs when the mechanical pretension p nullifies the linear mechanical stiffness, while the two peaks correspond to primary resonances of the external harmonic excitation with the pre- and post-buckling system frequencies, respectively.

The static buckling analysis is performed by obtaining the three equilibria $\boldsymbol{e} = \{\boldsymbol{W}_{\mathbf{e}}, \boldsymbol{T}_{\mathbf{R0e}}, \boldsymbol{T}_{\mathbf{R1e}}\}$ of the coupled system (1), which correspond to the pre-buckling configuration representing the mechanical rest position, and to the two stable buckled non-trivial (positive and negative) solutions arising after the pitchfork bifurcation. The two resonance conditions are analytically investigated by means of the asymptotic multiple scales method, in order to study the system nonlinear dynamics around the pre-buckling and post-buckling equilibria. The perturbation equations around the pre-buckling equilibrium have the same structure of Eqs. (1), while the analysis around the buckled position implies the presence of additional terms in the varied mechanical and membrane thermal equations. Consequently, the two asymptotic procedures require different assumptions in the scaling of variables and parameters, and consequently different expansions to higher orders in order to account for some main dynamic effects (due, e.g., to the occurrence of both quadratic and cubic nonlinearities). In both cases, they have been guided by the previous numerical investigations of strongly nonlinear scenarios, which have pointed out the contemporary presence of slow (thermal) and fast (mechanical) dynamics, and have allowed to discuss the role of the coupling terms inside the three equations [5]. They result to be crucial into the thermal equations in order to determine the temperature response, while they have a marginal effect on the mechanical equation, whose dynamics evolves much quicker than the coupled thermal one. The two procedures are developed separately, and the amplitude modulation equations are obtained together with the reconstructed steady state mechanical and thermal responses. Figure 1 shows a good agreement between analytical (red) and numerical (gray) bifurcation diagrams, also in the post-buckling scenario where the mechanical response is moderately severe.

The multistability regions are numerically characterized in global and local terms by the planar sections in the mechanical plane of the 4D basins of attraction, with trivial thermal initial conditions, and the mechanical phase portraits of the detected periodic solutions, shown in Fig. 2. In the pre-buckling region, the resonance condition induces a bistable behavior with (resonant, gray) high-amplitude and (nonresonant, pink) low-amplitude symmetric solutions (Fig. 2(a,b)). After buckling, the resonance peaks on the positive and negative branches cause the arise of a multistable regime characterized by two pairs of mirrored 1-period responses oscillating around the varied equilibria (Fig. 2(c,d)). The basin organization highlights an involved scenario on both sides of the two-well mechanical oscillator, with a substantially symmetric organization of the basins and a dominance of the low-amplitude buckled solutions in the post-buckling response.

CONCLUSIONS

Some main phenomena of the rich multistable scenario occurring in the weakly nonlinear dynamics of thermomechanically coupled plates are analyzed with the multiple scale method and verified through numerical bifurcation diagrams. The main periodic unbuckled and buckled responses are characterized in local and global terms via phase portraits and proper cross-sections of the 4D basins of attraction.

References

[1] Settimi V., Rega G., Saetta E. (2018) Avoiding/inducing dynamic buckling in a thermomechanically coupled plate: a local and global analysis of slow/fast response. *Proc. R. Soc. Lond., A*, **474(2213)**:20180206.
[2] Settimi V., Saetta E., Rega G. (2019) Nonlinear dynamics of a third-order reduced model of thermomechanically coupled plate under different thermal excitations. *Meccanica*, to appear.
[3] Nayfeh A.H., Mook D.T. (1979) Nonlinear oscillations. Wiley, NY.
[4] Saetta E., Rega G. (2017) Third-order thermomechanically coupled laminated plates: 2D nonlinear modeling, minimal reduction and transient/post- buckled dynamics under different thermal excitations. *Compos. Struct.*, **174**:420-441.
[5] Settimi V., Rega G. (2019) Thermomechanical coupling and transient to steady global dynamics of orthotropic plates. *in* Problems of Nonlinear Mechanics and Physics of Materials, Springer, pp:483-499.

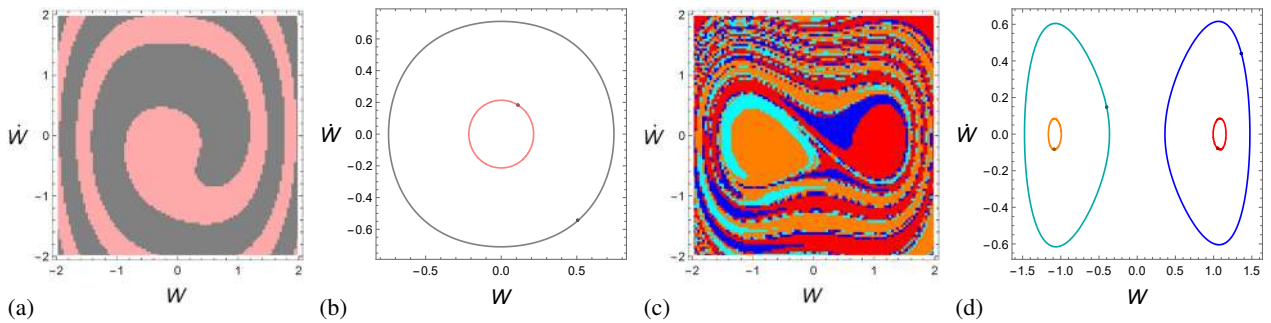

Figure 2: Basins of attraction in the mechanical plane and phase portraits of the relevant periodic solutions at $p = 0.25$ (a,b) and $p = 1.8$ (c,d).

EXPERIMENTAL STUDIES OF MASS EXCITED IMPACT OSCILLATOR

Dimitri Costa[1,2], Ekaterina Pavlovskaia*[1], Vahid Vaziri[1], Marcin Kapitaniak[1], and MarianWiercigroch[1]
[1]Centre for Applied Dynamics Research, University of Aberdeen, Aberdeen, Scotland, United Kingdom
[2]Center for Nonlinear Mechanics, COPPE, Universidade Federal do Rio de Janeiro, Rio de Janeiro, Brazil

Summary This work presents the dynamics of a new mass excited impact oscillator proposed in [1] which can be used for fundamental studies of impact phenomena including grazing. In this rig, the excitation force is generated electromagnetically and it acts directly on the mass in contrast to the most of the experimental set-ups where the excitation passes through the structure. A comparison with the previous base excited impact oscillator studies confirms that the rig is much more accurate as well as it has capability to generate a wide range of excitation patterns. The results obtained using a simple impact oscillator model are in a good agreement with the experimental findings, which indicates that the rig can also serves as a tool to study nonlinear control including bifurcation control and control of co-existing orbits.

INTRODUCTION

The study of impact systems represents an interesting field of research that has a wide range of applications including machining, drilling, and rotor dynamics among others. The understanding of impact phenomena and grazing occurrence is essential for getting a deeper insight into the intricacies of dynamical systems with impacts. In some cases, impacts are an essential part of system's operation, but in other instances, they can be a side effect due to ageing of the mechanical parts, thermal deformation or design tolerances. This work is motivated by the need to further enhance the understanding of impact phenomena and it focuses on the investigations of the dynamics of a newly constructed mass excited impact oscillator, its parameters characterisation and comparison with the results obtained using previous base excited impact oscillator rig [2, 3].

EXPERIMENTAL RIG

In this work dynamics of the impact oscillator rig shown in Fig. 1 is studied. It includes a stabilizing rigid structure mounted on the base plate to suppress any spurious external vibrations that may affect the main mass (highlighted in grey in Fig. 1). The main mass is attached to the leaf springs (coloured in red), which themselves are clamped between two beams and a grooved base, ensuring their proper alignment. A strong permanent cylindrical neodymium magnet, with a 15 kg pull is attached to one side of the main mass by a stainless steel rod and fixed by two stainless steel nuts. The magnet itself is placed approximately in the middle of an in-house built coil (coloured in orange), capable of generating a variable magnetic field that provides direct excitation to the system.

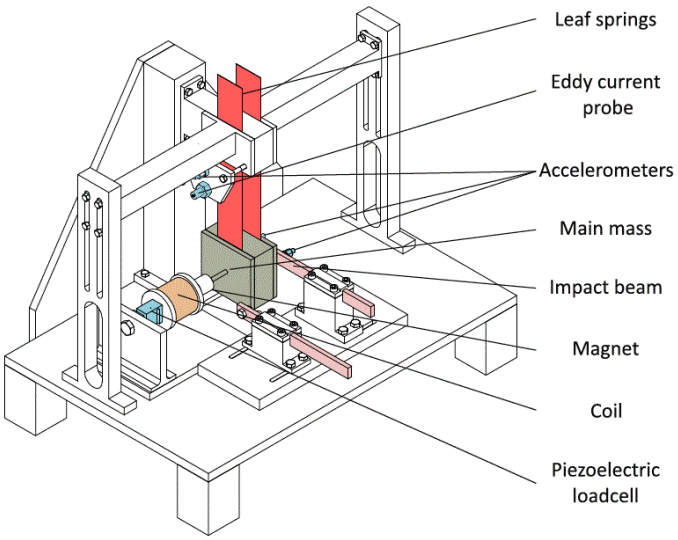

Figure 1: Schematic diagram of the experimental rig. The main components of the system are highlighted as: sensors (eddy current probe, piezoelectric load cell and accelerometers mounted on the mass, frame and impact beam) in blue, coil in orange, main mass in grey, impact beams in pink, leaf springs in red and permanent magnet in white.

The current I running through the coil is provided by a signal generator composed of a current amplifier, two power supplies and an NI® PCI-6251 board which can produce the desired signal. There are secondary supports on either side of the main mass (coloured in pink) made of the beams which can be inserted to produce impact.

*Corresponding author. E-mail: e.pavlovskaia@abdn.ac.uk.

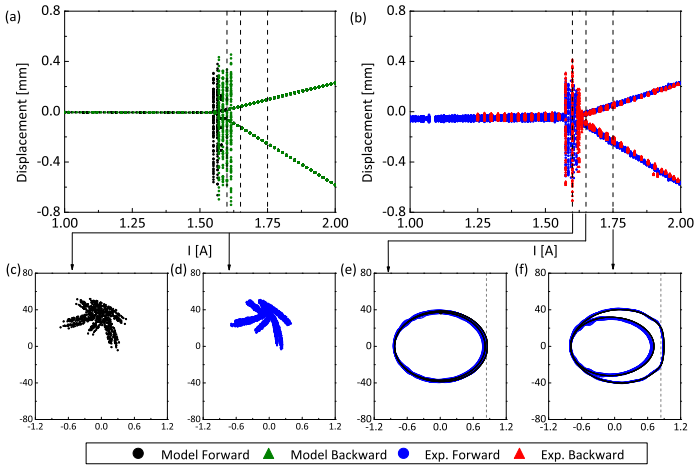

Figure 2: Bifurcation diagram obtained with input current amplitude as branching parameter with a gap of $g = 0.84$ mm and forcing frequency $f = 7.3$ Hz. Forward and backward (a) numerical and (b) experimental bifurcation diagrams. Here the black dashed vertical lines indicate the amplitude values where the trajectories on the phase planes are shown. (c) Numerical and (d) experimental Poincaré sections of chaotic response at the current amplitude of 1.605 A. (e) Period-2 orbits near internal grazing at 1.635 A. (f) Period-2 solutions recorded at 1.755 A. The dashed grey line on phase planes represents the impact boundary. Colours of the trajectories and Poincaré sections are the same as for the system responses shown in the bifurcation diagrams.

An acquisition system composed of an NI® PCI-6251 board and a LabVIEW® program is used to collect the experimental data. The coil input current is measured by a multi-meter, while the displacement of the main mass is measured by an eddy current probe attached to the structure close to the base of the leaf springs. Accelerometers are placed on the structure, the main mass and the impact beam, as shown in Fig. 1. Finally, a piezoelectric load-cell is also placed between the coil and the rigid structure to measure the reaction force due to the mass excitation.

EXPERIMENTAL AND NUMERICAL RESULTS

A piecewise linear impact oscillator model is used to describe the experimental rig. Here the displacement of the main mass m is X, the excitation force, F_{coil}, is applied directly onto the main mass, while the leaf springs are characterised by a linear stiffness k_1. The impact beam can be described by another linear spring of stiffness k_2, separated from the main mass by gap g. A linear viscous damping coefficient c is used to represent an equivalent damping in the system, leading to the equation of motion:

$$m\ddot{X} + c\dot{X} + k_1 X + k_2(X - g)H(X - g) = F_{coil}(t), \tag{1}$$

where H is a Heaviside step function and dot represents derivative with respect to time t.

The diagrams shown in Fig. 2a-b demonstrate an example of a comparison between the experimental and numerical results and are obtained for a forcing frequency of 7.3 Hz around the first grazing incidence. At lower amplitudes, the linear non-impacting response is observed up to the first grazing incidence where a narrow band region of chaotic behaviour [4] appears. As the current amplitude increases, it is followed by a period-2 response with one impact per period which is observed until the end of the diagrams. As can be seen from this figure, the experimental bifurcation diagrams and phase portraits have a good agreement with the numerical results obtained using the calibrated model.

CONCLUSIONS

In this work, the dynamics of a newly constructed mass excited impact oscillator was investigated both experimentally and numerically. It was shown that in this case a precise control of the excitation through the coil current becomes possible resulting in improvements in obtained resolution of the excitation amplitude and frequency for the construction of bifurcation diagrams. The comparison with previous base excited impact oscillator confirms that the rig has an ability to provide much more flexible excitation. Also, the rig is able to capture co-existent attractors and multi-stability experimentally by reproducing various predicted numerical responses, which was not possible before.

References

[1] Wiercigroch, M., Kovacs, S., Zong, S., Costa, D., Vaziri, V., Kapitaniak, M. and Pavlovskaia, E. *Nonlinear Dynamics*, doi:10.1007/s11071-019-05368-w, 2019.

[2] Ing, J., Pavlovskaia, E., Wiercigroch, M. and Banerjee, S. *Philosophical Transactions of the Royal Society A: Mathematical, Physical and Engineering Sciences* **366**(1866): 679-705, 2008.

[3] Ing, J., Pavlovskaia, E., Wiercigroch, M. and Banerjee, S. *Physica D: Nonlinear Phenomena* **239**(6): 312-321, 2010.

[4] Banerjee, S., Ing, J., Pavlovskaia, E., Wiercigroch, M. and Reddy, R. K. *Physical Review Letters E* **79**: 037201, 2009.

IS IT REALLY CHAOS?
THE COMPLEXITY OF TRANSIENT DYNAMICS OF DOUBLE PENDULA

Dawid Dudkowski*[1], Jerzy Wojewoda[1], Krzysztof Czołczyński[1], and Tomasz Kapitaniak[1]
Division of Dynamics, Lodz University of Technology, Stefanowskiego 1/15, 90-924 Lodz, Poland

Summary We study the dynamics of mechanical double pendula with parametric excitation (induced by the external shaker). The motion of the single oscillator has been investigated, showing that the system can behave chaotically, as well as periodically. Different types of patterns have been confirmed both numerically and experimentally. The bifurcation analysis of the double pendulum allowed to observe, that the character of dynamical response strictly depends on the excitation parameters, leading to the regions where the transitions from one type of pattern into another take place (periodic windows). In our research we have also examined a small network of two coupled double pendula, connected through a linear components (both upper and lower bobs of each unit), investigating the transient synchronization phenomenon. Our results exhibit, that the problem of transient dynamics may become very complex even for the simplest nonlinear systems, like the ones considered.

We investigate the numerical and experimental transient dynamics in parametrically excited double pendulum, which has been shown in Fig. 1.

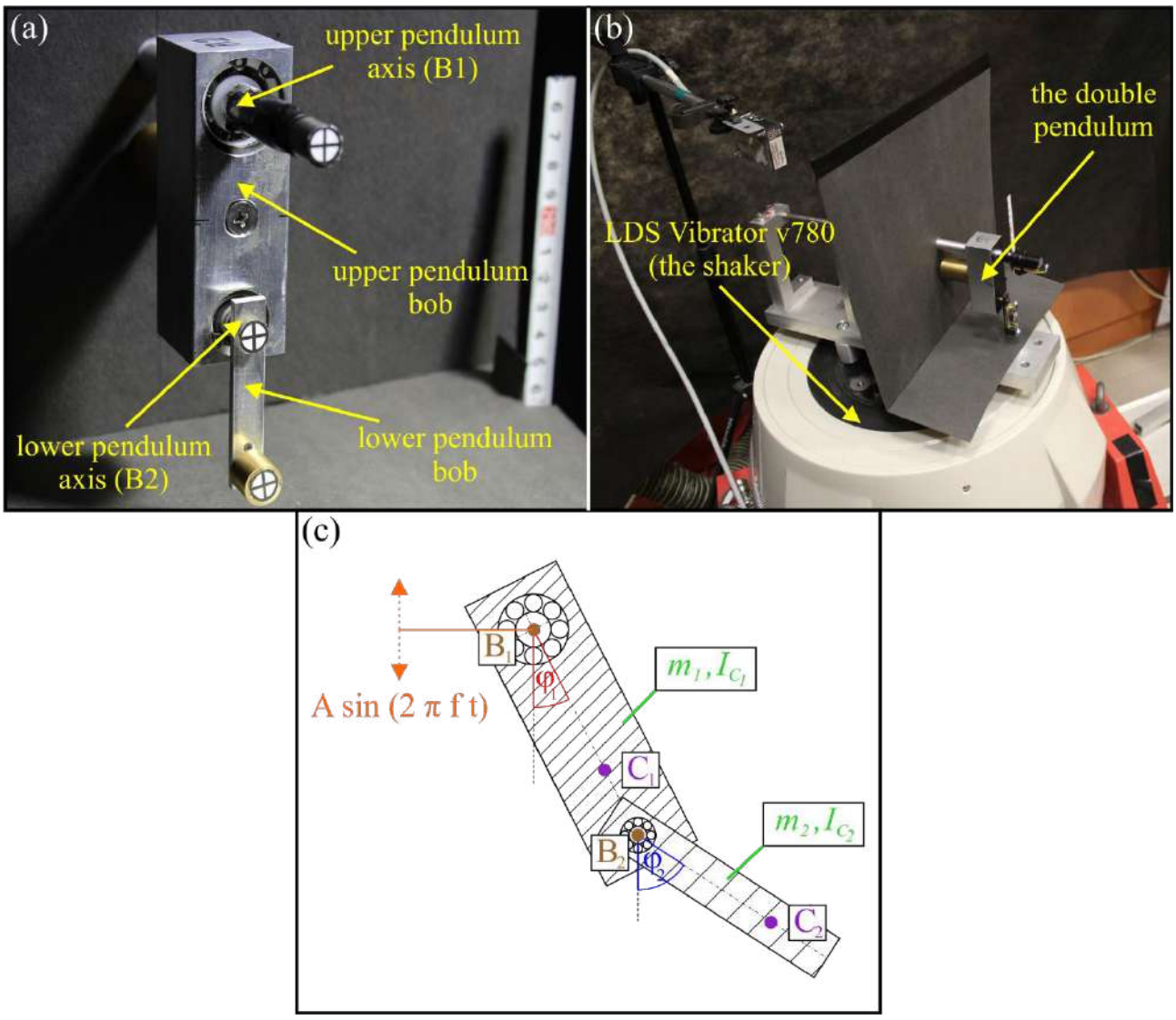

Fig. 1. A single experimental double pendulum (a) and the experimental rig of an oscillating platform with suspended unit (b). In (c) the scheme of considered model used to perform numerical research is presented.

*Corresponding author. E-mail: dawid.dudkowski@p.lodz.pl.

The double pendulum shown in Fig. 1 consists of two elements, i.e., the larger pendulum (upper bob) which holds the smaller one (lower bob). The upper bob can rotate or oscillate around the axis B1 (the upper bearing) connected to the periodically oscillating platform and the lower bob can rotate or oscillate around the axis B2 (the lower bearing). Both axis B1, B2 are perpendicular to the figure's plane. The larger and smaller bobs have respectively masses m_1, m_2 [kg] and moments of inertia I_{C1}, I_{C2} [kgm^2] (around the perpendicular axes which crosses bob's mass centers C_1, C_2). The oscillations of the platform are described by the harmonic function $A\sin(2\pi ft)$, where A [m] and f [Hz] are respectively amplitude and frequency.

In our research we present typical types of behaviors of the single double pendulum, including chaos, rotations and periodic oscillations. The bifurcation analysis is performed, exhibiting complex transitions from one type of motion into another. The character of observed dynamics is analyzed using Lyapunov exponents, which confirms the hyperchaotic nature of the system. We study the transient behaviors, showing that the length of the irregular motion can be extremely sensitive on both parameters and initial conditions. Apart from the single oscillator, in our numerical research we consider also the case of two coupled double pendula, connected by a typical linear scheme. Our results show, that depending on the network's parameters, one can observe the phenomenon of a transient chaotic synchronization, during which the units spontaneously synchronize and desynchronize. The loss of coherence is strictly related with the motion of the pendula around the unstable equilibrium of the system, which has been confirmed in the scenario of pure chaotic oscillations. We determine the regions of the occurrence of transient synchronization in the coupling parameters' plane, as well as study the statistical properties of observed patterns. Our analysis exhibits, that due to the unpredictable character of the phenomenon, the problem of determining the final dynamical attractor of the model can become not straightforward. Research presented in our study indicates the complexity of transient behaviors in nonlinear dynamical systems, which should be expected also in more complex models, including single and coupled oscillators.

NONLINEAR DYNAMICS OF A BEAM-LIKE TUBE WITH NON-RIGID CROSS-SECTION

Arnaldo Casalotti[1], Daniele Zulli*[1], and Angelo Luongo[1]
[1]Department of Civil, Construction-Architectural and Environmental Engineering, University of L'Aquila, Italy

Summary Nonlinear dynamics of a tubular beam are analyzed here via perturbation methods. The tube is modeled as a beam-like structure, with possibility of change in shape of the cross-section. In particular it becomes oval and performs warping under bending. Use of a nonlinear and coupled response function for the hyperelastic material is made, as it comes from a homogenization procedure from a three-dimensional, corresponding, body. Large amplitude vibrations are analyzed, with possible occurrence of loss of stability close to the Brazier limit point.

INTRODUCTION

Tubular beams are very common structures in civil and industrial applications, and their mechanical performance under external solicitations is a key point to be addressed for structural designers. The thin-walled nature of such structures requires, for engineers, to consider some specific aspects during analysis, being local effects and change in shape of the cross-section generally not negligible. Conveniently, beam-like models might be helpful in considering those aspects, possibly keeping the dynamic equations moderately handy. For instance, it is well known that ovalization of the cross-section, taking places when thin-walled circular tubes are bent over, may lead to instability phenomena, with consequent loss of carrying capacity of the whole structure. This behavior, known as Brazier effect [1], is due to the occurrence of a limit point in the bending moment-curvature relationship, as a consequence of the softening nature of such a law. In [2], this behavior is described in case of anisotropic materials. In [3, 4], multi-layered beams and cross-sectional models are addressed in the same framework. In [5], a homogeneous beam-like coarse model is adopted to describe the mechanics of thin-walled beams with possibility of cross-section distortion. In [6], static and free dynamic analysis of a homogeneous beam-like model is performed, after an identification procedure from a companion three-dimensional continuum. The same model is then extended in [7], where further parameters are introduced in order to take into account shear deformations in the multi-layered case.

Starting from the one-dimensional, non-standard, beam-like model presented in [7], where only static analysis is performed, inertial effects are here considered as well. The nonlinear equations of motion are taken on, and perturbation methods are used to evaluate approximated solutions, to be compared with outcomes of numerical integration. Dynamics close to the Brazier limit point are addressed, where possible intriguing dynamic response may occur.

EQUATIONS OF MOTION

A beam-like model is considered for describing the nonlinear dynamics of a thin annular tube. The beam model is shown in Fig. 1a, where the axis-line, spanned by the abscissa s running from 0 to l, is sketched together with the generic cross-section. In order to coarsely consider non-rigid behavior of the cross-sections, two s- and time-functions are introduced, a_p and a_w, besides the kinematic descriptors of planar Timoshenko beams, namely the longitudinal and transversal displacements of the axis line (u, v) and the cross-section bending rotation (ϑ). The kinematic equations are posed and the dynamic equilibrium equations of the beam evaluated from the consequential use of the virtual power theorem. The constitutive relations come from a homogenization procedure from a corresponding 3D model, shown in Fig. 1b, where the annular tube is assumed as realized by longitudinal rods and transversal ribs. For the homogenization purposes, the change in shape of the cross-section is described as in the GBT theory [8], namely the kinematic variables a_p and a_w multiply assumed functions, describing ovalization and warping, respectively, as shown in Fig. 2. The equations of motion are written below, where the linear part is made explicit:

$$\begin{aligned}
&c_1 u'' - m\ddot{u} + \mathcal{F}_1(u, v, \vartheta, a_p, a_w) + p_u = 0\\
&c_4(v'' - \vartheta') + c_5 a_g' + m\ddot{v} + \mathcal{F}_2(u, v, \vartheta, a_p, a_w) + p_v = 0\\
&c_7\vartheta'' + c_4(v' - \vartheta) + c_{11}a_g'' + c_5 a_g - I\ddot{\vartheta} + \mathcal{F}_3(u, v, \vartheta, a_p, a_w) + c = 0\\
&c_{19}a_p'' - c_{17}a_p + c_{20}a_w' - \mu\ddot{a}_p + \mathcal{F}_4(u, v, \vartheta, a_p, a_w) + q_p = 0\\
&c_{30}a_w'' - c_{26}a_w - c_{20}a_p' - \mu\ddot{a} + \mathcal{F}_5(u, v, \vartheta, a_p, a_w)_w + q_w = 0
\end{aligned} \tag{1}$$

while the nonlinear terms, expanded up to the third order, are collected in the functions $\mathcal{F}_n$, $n = 1, \ldots, 5$. Relevant boundary conditions are combined to Eqs. (1). The Multiple Scale Method is applied to Eqs. (1), when a shear force is exerted on the free tip, being the other terminal cross-section clamped. In particular, the shear force is assumed to be constituted by a static component, which modifies the equilibrium configuration of the beam and let the response close to the limit point, plus a time-harmonic, fluctuating component, which triggers intriguing dynamic evolution.

*Corresponding author. E-mail: daniele.zulli@univaq.it.

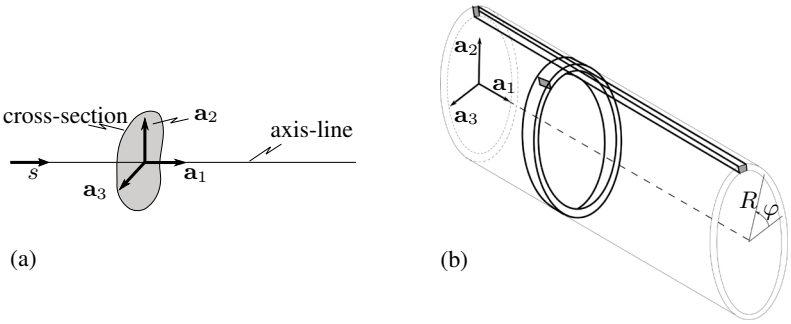

Figure 1: (a) The one-dimensional beam-like model; (b) the three-dimensional model with fibers and ribs.

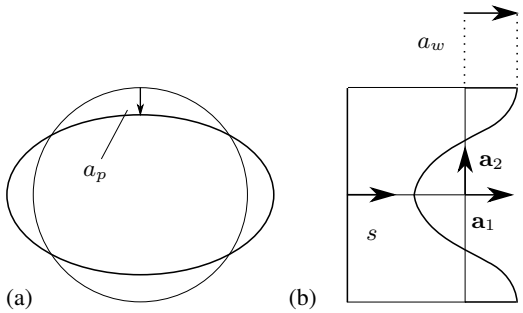

Figure 2: The change in shape of the cross-section: (a) ovalization; (b) warping.

CONCLUSIONS

Nonlinear dynamics of an annular thin tube is analyzed here. A beam-like model is introduced, where specific kinematic functions coarsely describe the change in shape of the cross-section, namely ovalization and warping. The nonlinear material response function comes from a homogenization procedure. Perturbation methods are applied to the equations of motion, in order to describe dynamic evolution close to the Brazier limit point .

References

[1] L. Brazier, On the flexure of thin cylindrical shells and other 'thin' sections, *Proc. Royal Society of London A*, **116** 104–114, 1927.

[2] D. Harursampath, D. Hodges, Asymptotic analysis of the non-linear behavior of long anisotropic tubes, *International Journal of Non-linear Mechanics*, **34** 1003–1018, 1999.

[3] L. Librescu, O. Song, Thin-walled Composite Beams. Theory and applications, Springer-Verlag, 2006.

[4] D. Hodges, Nonlinear Composite Beam Theory, American Institute of Aeronautics and Astronautics, 2006.

[5] S. Gabriele, N. Rizzi, V. Varano, A 1D nonlinear TWB model accounting for in plane cross-section deformation, *International Journal of Solids and Structures*, **94-95** 170–178, 2016.

[6] A. Luongo, D. Zulli, A non-linear one-dimensional model of cross-deformable tubular beam, *International Journal of Non-Linear Mechanics*, **66** 33–42, 2014.

[7] D. Zulli, A one-dimensional beam-like model for double-layered pipes, *International Journal of Non-Linear Mechanics*, **109** 50–62, 2019.

[8] R. Gonçalves, M. Ritto-Corrêa, D. Camotim, A large displacement and finite rotation thin-walled beam formulation including cross-section deformation, *Computer Methods in Applied Mechanics and Engineering*, **199** (23-24) 1627–1643, 2010.

NONLINEAR VIBRATIONS AND CONTROL OF ROTATING FLEXIBLE BEAMS

Jerzy Warminski *[1], Lukasz Kloda[1], Andrzej Mitura[1], and Jaroslaw Latalski[1]
[1]Department of Applied Mechanics, Faculty of Mechanical Engineering, Lublin University of Technology, Lublin, Poland

Summary Nonlinear dynamics of a rotor composed of a rigid hub and three flexible blades is presented in the paper. The model of blades which are made of isotropic and homogenous material, is based on Bernoulli-Euler beam theory. However, the model is extended and the beams are treated as extensional, and due to possible large oscillations, nonlinear curvatures are taken into account as well. The model considers also a lumped mass at the beams tip which allows studying more general case with dynamical boundary conditions. In order to control beams' vibrations active elements are embedded in each single beam. Free and forced oscillations and nonlinear normal modes are studied first analytically by the multiple time scale method and next the results are validated by a finite element model. Based on the developed model a strategy for active vibrations control is proposed.

INTRODUCTION AND PROBLEM FORMULATION

Rotating structural elements play a very important role in many aerospace, mechanical or civil engineering systems, for example arms of robotic manipulators, wind turbines, helicopter rotors, drones. Also micro or nano systems, or bio-inspired structures, include rotating flexible elements. Therefore, more and more sophisticated models are developed to get a proper description of a real object. The rotation of the structure may cause in some cases unexpected and not intuitive results. A numerical model with 'weak' formulation of a homogenous rotating beam, with coupling of bending-stretching, bending-twist and twist-stretching deformations taken into account, was presented in [1]. The importance of Coriolis effect and centrifugal stiffening were confirmed by that model. The effect of increased angular speed on the rotating nonlinear inextensible beam was presented in [2] and the hardening and also not intuitive softening phenomenon was presented in that paper.

The development of new materials and active elements enable to design a system with required properties. Furthermore, new active composite elements, which are very light and flexible, can be easily embedded into a rotating blade and, then used as sensors or/and actuators. The mathematical model of a rotating thin-walled blade made of composite material and embedded active piezoceramic layers was recently presented in paper [3]. Authors developed the two way coupled elecro-mechanical model considering linear constitutive equations for mechanical domain and nonlinear constitutive equations for electric field. The nonlinear electric characteristics of piezolayers affected the resonance curves leading to the softening phenomenon. In [4] active elements embedded into the beam were used to reduce forced vibrations by a simple PD control algorithm.

Rotation of the structure may lead to complex oscillations of the beams and therefore other control methods taking into account nonlinear and rotation effects should be tested. To reach this goal an enhanced model of a flexible rotor with active blades is developed in this paper. The model is composed of a rigid hub and a flexible blades oscillating in the plane defined by a preset angle θ as presented in Fig.1.

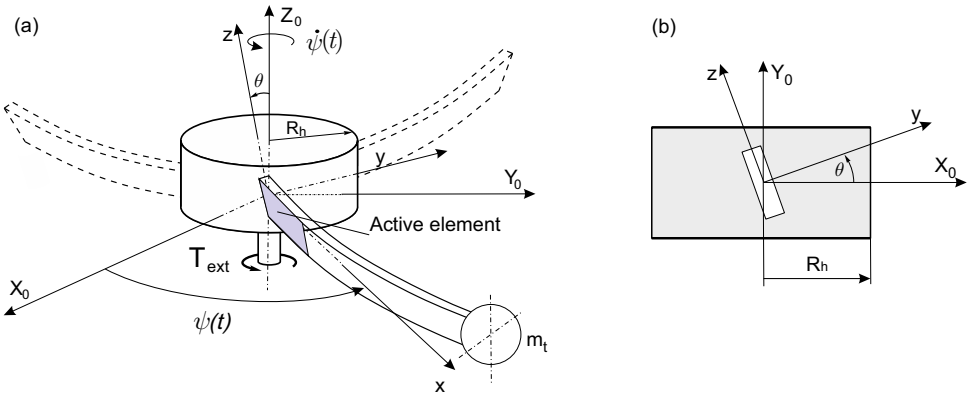

Figure 1: Rotor with blades and active elements, (a) general and (b) side view with coordinates and preset angle θ.

A lumped mass is added to the beam tip which allows to study more general case with dynamic boundary conditions. Furthermore, the mass can be used to tune the structure to the specific resonance conditions. The beam with a rectangular cross-section is made of isotropic material with linear material properties and is assumed to be slender thus, its mathematical model is based on Bernoulli–Euler beam theory. Nevertheless, due to possible large oscillations, the formulation is extended and takes into account geometric nonlinear terms and also both flexural and longitudinal deformations. It means

*Corresponding author. E-mail: j.warminski@pollub.pl.

that the beam is treated as *extensional* which can be crucial in some specific cases [5]. The rotation and oscillations of the system arise from the external torque imposed to the hub or periodic force applied directly to the beam. A pair of piezoelectric actuaturs/sensors are embedded into every single beam. The proposed mathematical model is rich and can be considered in many variants, in terms of nonlinear modes of the multi–bladed rotor, internal and external resonances with coupled transversal and longitudinal modes, vibrations control by using the active elements.

Dynamics of the rotor is governed by a set of nonlinear partial differential equations (PDEs) and associated dynamical boundary equations (BCs) not present in this abstract due to their long and complex forms. The PDEs together with BCs are solved analytically by the multiple time scales method up to the third order perturbation. Tip mass m_t, preset angle θ and angular velocity Ω are kept as bifurcation parameters and are varied in numerical analysis.

NUMERICAL EXAMPLE

As an numerical example we present dynamics of a single rotating nonlinear blade with tip mass and constant angular velocity $\dot{\psi} = \Omega$. The fixed parameters of the rotor take values: length of the beam - $L = 0.35$ m, mass per length - $\rho_1 = 0.04131$ kg/m, stiffness coefficients - $EI = 0.127883$ N/m^2, $EA = 1.89457 \times 10^6$ N. In this example we study the first and the second bending mode with light tip mass m_t equal to of 5% of beam's mass. The radius of the hub is fixed as 0.1 of the beam length L. Natural frequencies of the first bending modes take values: $\omega_{01} = 46.12$ rad/s, $\omega_{02} = 282.48$ rad/s.

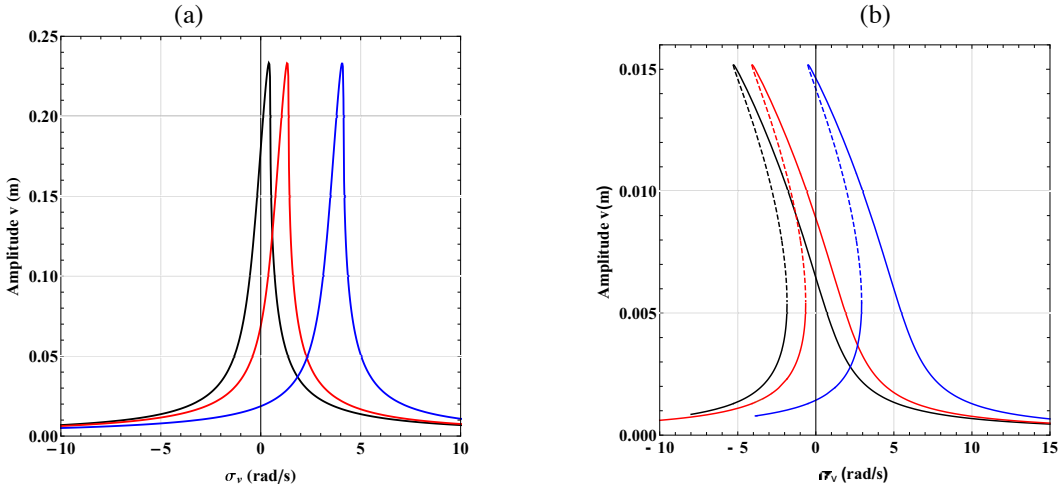

Figure 2: Resonance curves for selected angular velocity and tip mass $m_t = 0.05$, (a) first and (b) second flexural mode: $\theta = 45°$. $\Omega = 0$ - black, $\Omega = 10$ - red, $\Omega = 20$ - blue.

The resonance curves against detuning parameter σ_v defined as difference between excitation frequency ω and natural frequency ω_0, computed for fixed amplitude of transversal excitation ξ_v, and modal damping c_v, are presented in Fig. 2.

CONCLUDING REMARKS

The proposed mathematical model of the rotor takes into account large flexural displacements and *extensionality* of the beams. The influence of angular velocity, tip mass and preset angle on bifurcation scenario is analysed for selected resonance zones. The studied case of a single rotating beam with small tip mass and constant velocity demonstrates either stiffening effect, for the first flexural mode, or softening one, for the second flexural mode. The increased angular speed does not change the nature of the resonance curves but shifts them into higher frequencies direction. In the case of free vibrations of the multi–bladed rotor the hub inertia plays important role in nonlinear normal modes formulation. For forced vibrations mode localisation and synchronisation phenomena are observed. The embedded active elements enable blades vibration reduction or control.

Acknowledgements

The work is financially supported by grant 2016/23/B/ST8/01865 from the National Science Centre, Poland.

References

[1] Tian J., Su J., Kai Z., Hua H. A modified variational method for nonlinear vibration analysis of rotating beams including Coriolis effects. *J. Sound and Vib* **426**: 258—277, 2018.
[2] Thomas O., Sénéchal A., Deü J.F. Hardening/softening behavior and reduced order modeling of nonlinear vibrations of rotating cantilever beams. *Nonlin. Dyn.* **86**: 1293—1318, 2016.
[3] Latalski J., Warminski J. Nonlinear vibrations of a rotating thin-walled composite piezo-beam with circumferentially uniform stiffness (CUS). *Nonlin. Dyn.* **98**: 2509–2529, 2019.
[4] Lin S.M. PD control of a rotating smart beam with an elastic root. *J. Sound and Vib.* **312**: 109–124, 2008.
[5] Lenci S., Clementi F., Rega G. A Comprehensive analysis of hardening/softening behaviour of shearable planar beams with whatever axial boundary constraint. *Meccanica* **51**: 2589—2606, 2016.

COLOR SYMMETRY IN NONLINEAR NORMAL MODE VIBRATIONS OF A HYPERELASTIC MATERIAL

Ryuichi Tarumi*[1]
[1]Graduate School of Engineering Science, Osaka University, Osaka, Japan

Summary This study conducts numerical analysis for nonlinear normal mode vibrations of St.Venant−Kirchhoff hyperelastic material. The material has a two-dimensional rectangular shape which belongs to the point group $\mathbb{C}_{2v}$. A resonant state is obtained from a stationary condition to the action integral. A boundary condition requires that the stationary solution must satisfy the time reversal and time periodic symmetries. We solved the variational problem numerically using the Ritz method, where the basis functions include the higher-order harmonics. This analysis revealed that the vibration symmetry is classified on the basis of single color magnetic point group, $\mathbb{C}_{2v}(\mathbb{C}_{2v})$, and three types of bicolor magnetic point groups, $\mathbb{C}_{2v}(\mathbb{C}_2)$, $\mathbb{C}_{2v}(\mathbb{C}_{1h})$ and $\mathbb{C}_{2v}(\mathbb{C}'_{1h})$, rather than the conventional irreducible representations of $\mathbb{C}_{2v}$.

INTRODUCTION

Normal modes plays a central role to understand acoustic vibration of solids and structures. It is well known that the vibration symmetries are explained by group theory, *i.e.*, irreducible representations (IRs) of the point group. In other words, a dynamical matrix can be divided into a direct sum of sub-matrices which are spanned by invariant sub-spaces. This is the algebraic understanding for normal mode vibration of a linearized system. Normal modes in a nonlinear system is, however, still unclear and further investigation is required. In our recent studies, we revealed that the vibration symmetry of a nonlinear hyperelastic material is explained by the *magnetic point group*, rather than the conventional IRs of a point group [1, 2]. In the present study, we briefly summarizes our formulation as well as the results of numerical analysis.

MATHEMATICAL PRELIMINARIES

We consider normal mode vibration, or free-vibration acoustic resonance, of a two-dimensional St.Venant−Kirchhoff hyperelastic material. The material has a rectangular shape which is expressed as $\Omega = \{(x_1, x_2) | -L_i < x_i < L_i,\ i = 1, 2\}$. It belongs to the point group $\mathbb{C}_{2v}$, Let $u_i = u_i(x_i, t)$ be the displacement and let $\dot{u}_i$ and $u_{i,j}$ be the derivatives defined by $\dot{u}_i = \partial u_i/\partial t$ and $u_{i,j} = \partial u_i/\partial x_j$. Then, the action integral is define in the following form

$$I[u_i] = \int_0^{2\pi/\omega} \int_\Omega \left[\frac{1}{2}\rho \dot{u}_i^2 - \frac{1}{2}\lambda (E_{ii})^2 - \mu E_{ij} E_{ij} \right] dV dt. \tag{1}$$

Here, λ and μ are Lamé constants and E_{ij} is Green−Lagrange strain tensor defined by $E_{ij} = (u_{i,j} + u_{j,i} + u_{k,i}u_{k,j})/2$. The time domain $t \in (0, 2\pi/\omega)$ includes the angular frequency ω which is unknown in advance. Hence, Eq. (1) is defined on a variable time domain. A resonant state of the hyperelastic material is obtained from a stationary condition and which is solved numerically using the Ritz method. Note that, according to the boundary condition, the stationary solution must satisfy the time reversal symmetry with respect to $t = 0$ and time periodicity condition; $u_i(x_1, x_2, -t) = u_i(x_1, x_2, t)$. Hence, we assume that the solution $u_i = u_i(x_1, x_2, t)$ is expressed in the form of separation of variables such that

$$u_i(x_1, x_2, t) = \sum_{n=0}^{N} \sum_{m=1}^{M} F_i^{m,n}(x_1, x_2) \cos(n\omega t) \tag{2}$$

where $\sum_{m=1}^{M} F_i^{m,n}$ is Fourier series and $n \in \mathbb{N}$ is the order of harmonics up to $N = 3$. In order to avoid the trivial solution $u_i = 0$ $(\forall x \in \Omega)$, we impose a subsidiary condition at $t = 0$ such that $\|u_i\|_{L^2} = \text{const}$. Obviously, this condition defines the magnitude of vibration amplitude.

RESULTS AND DISCUSSION

Figure 1 shows the result of numerical analysis. Here, (a) shows a nonlinear vibration pattern of bending mode for half a period. (b) to (e) correspond to $n = 0, 1, 2, 3$ components in Eq. (2). In other words, the summation of (b) to (e) yields (a). As seen in the figure, the principal harmonic component (c) $n = 1$ shows bending mode vibration and which is expressed by B_1 in terms of IRs of the point group $\mathbb{C}_{2v}$. The same holds for the third-order harmonics of (e) $n = 3$. To our surprise, however, the (b) $n = 0$ and (d) $n = 2$ components show totally symmetric A_1 mode vibrations. Hence, the nonlinear normal mode vibration (a) includes two types of vibration symmetries, B_1 and A_1 symmetries, depending on the parity of the harmonics n.

*Corresponding author. E-mail: tarumi@me.es.osaka-u.ac.jp

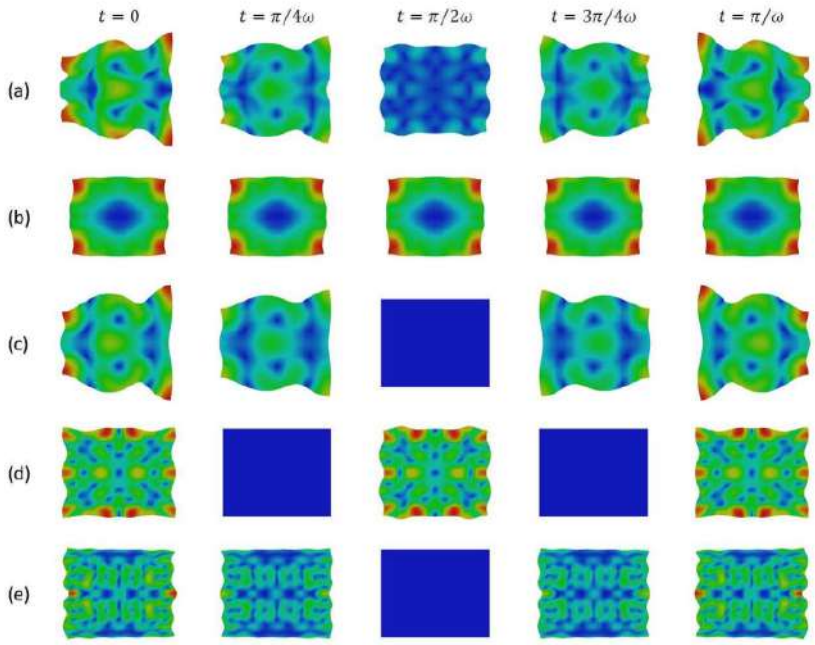

Figure 1: (a) Nonlinear vibration pattern obtained at the vibration amplitude $\|u_i\|_{L^2} = 0.05$ for half a period $t \in (0, \pi/\omega)$. (b)-(e) Displacement components for $n = 0, 1, 2, 3$; their superposition yields (a). The vibration symmetry for $n =$ odd components, namely (c) $n = 1$ and (e) $n = 3$, have B_1 symmetry. However, that for $n =$ even components, namely (b) $n = 0$ and (d) $n = 2$ have A_1. It indicates that two types of vibration symmetries are included in the nonlinear normal mode vibration (a).

As mentioned above, IRs span the invariant subspace of a linearized system. Hence, the mixing of vibration symmetries does not happen. It indicates that mode classification by conventional IRs no longer holds in the present nonlinear system. In this study, we introduce the magnetic point group (MPG) for the complete mode classification. The point groups $\mathbb{C}_{2v}$ consists of four symmetry operations including identity E, π-rotation C_2, mirror with respect to the x-plane σ_x and y-plane σ_y; $\mathbb{C}_{2v} = \{E, C_2, \sigma_x, \sigma_y\}$. Let us introduce the time reversal operator T which acts on the displacement such that $Tu_i(\cdot, t) = u_i(\cdot, -t)$ with respect to $t = \pi/2\omega$. According to the group theory, we can construct a magnetic point group (MPG) from the point group $\mathbb{C}_{2v}$ such that $\mathbb{C}_{2v}(\mathbb{C}_{1h}) = \{E, \sigma_y, TC_2, T\sigma_x\}$. Projection operator of the MPG is given by $P_{B_1} = \frac{1}{4}(E + \sigma_y + TC_2 + T\sigma_x)$. A direct calculation reveals that the operator P_{B_1} project-out the parity-dependent vibrations, *i.e.*, B_1 for $n =$ odd and A_1 for $n =$ even, from the overall displacements given in Eq. (2). Hence, the MGP $\mathbb{C}_{2v}(\mathbb{C}_{1h})$ completely explains the vibration symmetry shown in Fig. 1. Note that the point group $\mathbb{C}_{2v}$ has other three MPGs, $\mathbb{C}_{2v}(\mathbb{C}_{2v})$, $\mathbb{C}_{2v}(\mathbb{C}_2)$ and $\mathbb{C}_{2v}(\mathbb{C}'_{1h})$, in addition to $\mathbb{C}_{2v}(\mathbb{C}_{1h})$. Our numerical analysis revealed that vibration symmetry of the hyperelastic material can be classified by one of the four MPGs without any exception. It is worthwhile to note that the MPG also explains the symmetry of nonlinear normal mode vibration of molecules [3]. This result validates the results of present analysis.

CONCLUSIONS

In this study, we investigated the nonlinear normal mode vibration of a two-dimensional hyperelastic material. Present numerical analysis revealed that the vibration symmetry can be classified on the basis of magnetic point group, rather than the conventional IRs for linearized system. It demonstrates that there exists a new class of vibration symmetry, *i.e., the color symmetry*, in nonlinear normal mode vibrations of hyperelastic materials.

References

[1] Tarumi R. Emergence of Colour Symmetry in Free-Vibration Acoustic Resonance of a Nonlinear Hyperelastic Material. *Prof. R. Soc. A* **469** 20130275, 2013.

[2] Tarumi R., Yamaguchi Y., Shibutani Y. Theoretical Foundations of Resonant Ultrasound Spectroscopy at High Pressure. *Prof. R. Soc. A* **470** 20140448, 2014.

[3] Harris D. C., Bertolucci M. D. Symmetry and Spectroscopy; An Introduction to Vibrational and Electronic Spectroscopy, Dover, New York, 1978.

NONLINEAR DYNAMICS OF A CANTILEVERED BEAM WITH A TIP MASS: THEORY AND EXPERIMENTS

M. Reza Talebi Bidhendi*[1] and A. Srikantha Phani[1]
[1]Department of Mechanical Engineering, University of British Columbia, Vancouver, Canada

Summary Nonlinear dynamics of a cantilevered beam with an end mass excited through an electromagnetic shaker at its tip is investigated in this paper. Shaker-structure interaction imposes a near 2:1 frequency ratio between the first vertical and lateral modes of the structure. Experiments show the the lateral mode activation after a vertical force threshold with excitation frequency close to the first vertical natural frequency. Shaker-structure interaction in the multi-body dynamic model is through the external supports. Further, a minimal model which includes a mass restrained by linear spring-damper pairs is developed. The resultant restoring-damping force components produced by each pair introduce kinematic nonlinear terms in the governing equations. We find that the multi-body dynamic and minimal model are able to qualitatively explain the experimentally observed nonlinear responses.

PROBLEM STATEMENT

Cantilevered beam with tip mass is a canonical structure extensively studied under the tip excitation and under the base excitation [1]. Nonetheless, the present problem of a tip excited cantilevered beam with a tip mass connected to an electromagnetic shaker has not received much attention, and we are led to it through a friction control application in railways [2]. Similar systems can arise in the vibration energy harvesting, vibration mitigation, and sensing or actuating mechanisms [3]. Restoring force due to the elastic support leads to nonlinear forces of kinematic origin in the governing differential equations (DEs) of motion [4, 5]. A similar situation arises in our problem due to shaker-structure interaction, sketched in Fig.1(a). A long steel beam with a diameter of 4 mm and length of 254 mm is connected to an aluminum tip mass ($70\times50\times20$ mm^3) and a rigid rod of density of 7800 kg/m^3 and diameter of 4 mm and length of 40 mm. Shaker-structure interaction is through the external supports at the tip in the multi-body dynamic modelling, see Fig.1(b). The associated values of the support elements (c_x, c_y, k_x, k_y) are then found by making the frequency response functions of the multi-body dynamic model close to the experimental ones, Fig.1 (e) and Fig.1 (f). The experimental linear modal parameters of the structure (damping ratio(ζ), stiffness(k), natural frequency (f_n)) are $k_1 = 5328\ N/m, \zeta_1 = 0.1346, f_1 = 24.80\ Hz, k_2 = 2202\ N/m, \zeta_2 = 0.1234, f_2 = 12.37\ Hz$. Indices one and two refer to the vertical and the lateral directions, respectively. Using the linear modal properties of the structure, a minimal two-degree-of-freedom (DOF) model as shown in Fig.1(c) can be developed, with the governing equations:

$$m_2\ddot{x} + k_2(L_2 - x)\left(\frac{L_2}{\sqrt{(L_2-x)^2+y^2}} - 1\right) - k_1 x\left(\frac{L_1}{\sqrt{(L_1-y)^2+x^2}} - 1\right) + \left(\frac{c_2(x-L_2)}{(L_2-x)^2+y^2}\right)((x-L_2)\dot{x} + y\dot{y}) + \left(\frac{c_1 x}{(L_1-y)^2+x^2}\right)((y-L_1)\dot{y} + x\dot{x}) = 0 \tag{1}$$

$$m_1\ddot{y} + k_1(L_1 - y)\left(\frac{L_1}{\sqrt{(L_1-y)^2+x^2}} - 1\right) - k_2 y\left(\frac{L_2}{\sqrt{(L_2-x)^2+y^2}} - 1\right) + \left(\frac{c_1(y-L_1)}{(L_1-y)^2+x^2}\right)((y-L_1)\dot{y} + x\dot{x}) + \left(\frac{c_2 y}{(L_2-x)^2+y^2}\right)((x-L_2)\dot{x} + y\dot{y}) = -F\cos(2\pi f t) \tag{2}$$

where $m_i,\ L_i,\ c_i,\ i = 1, 2$ are the masses, initial lengths of the support elements, and damping coefficients respectively; F is the excitation amplitude, and f is the excitation frequency. The above equations are solved numerically for non-zero initial conditions, and compared with the full-scale multi-body dynamics model (no modal truncation) in ADAMS software and experiments.

RESULTS AND CONCLUSIONS

Force-response curves are calculated by fixing the excitation frequency (f) and increasing the excitation amplitude (F) [6]. When the excitation frequency is close to the first vertical natural frequency, ($f \approx f_1$), the first lateral mode is excited through a 2:1 internal resonance after a force threshold as shown in Fig.2(a). Furthermore, multi-body dynamic simulation and the minimal model show the activation of the lateral mode after a certain threshold. These validate the experimentally observed responses qualitatively, Fig.2(b) and Fig.2(c) . However, discrepancies in the vertical nonlinear response exist between the simulations (ADAMS model and the minimal model) and the experiments. This issue is to be addressed in the future studies through experimental quantification of nonlinearity [7] and considering the electro-mechanical coupling effects imposed by the external exciter [8]. Structure response due to the 2:1 internal resonance between two flexural modes with displacements in mutually orthogonal planes is almost similar to Froude oscillations of a ship. However, the reduced model does not show the saturation in the vertical response. This difference has to do with the retaining of all nonlinear terms in our minimal model.

*Corresponding author. E-mail: m.talebibidhendi@alumni.ubc.ca

References

[1] Meesala, V.C., Hajj, M.R. Parameter sensitivity of cantilever beam with tip mass to parametric excitation. *Nonlinear Dyn* **95(4)**:3375-3384, 2018.
[2] Talebi Bidhendi, M.R. An experimental study of nonlinear oscillations in railroad friction control systems (T). University of British Columbia. Retrieved from https://open.library.ubc.ca/collections/ubctheses/24/items/1.0371958, 2018.
[3] Harne, R.L., Wang, K.W. Harnessing bistable structural dynamics for vibration control, energy harvesting and sensing. *Wiley*, 2017.
[4] Mojahed, A., Moore, K., Bergman, L.A. and Vakakis, A.F. Strong geometric softening–hardening nonlinearities in an oscillator composed of linear stiffness and damping elements. *Int.J.Non-Linear Mech*, **107**:94-111, 2018.
[5] Yang, T.L., Rosenberg, R.M. On forced vibrations of a particle in the plane. *Int.J.Non-Linear Mech* **3(1)**:47-63, 1968.
[6] Nayfeh, A.H., Balachandran, B. Modal interactions in dynamical and structural systems. *Appl.Mech.Rev* **42(11S)**:175-201, 1989.
[7] Kerschen, G., Worden, K., Vakakis, A.F., Golinval, J.C. Past, present and future of nonlinear system identification in structural dynamics. *Mech. Syst. Signal Process*, **20(3)**:505-592, 2006.
[8] McConnell, K.G., Varoto, P.S. Vibration testing: theory and practice. *Wiley*, 1995.

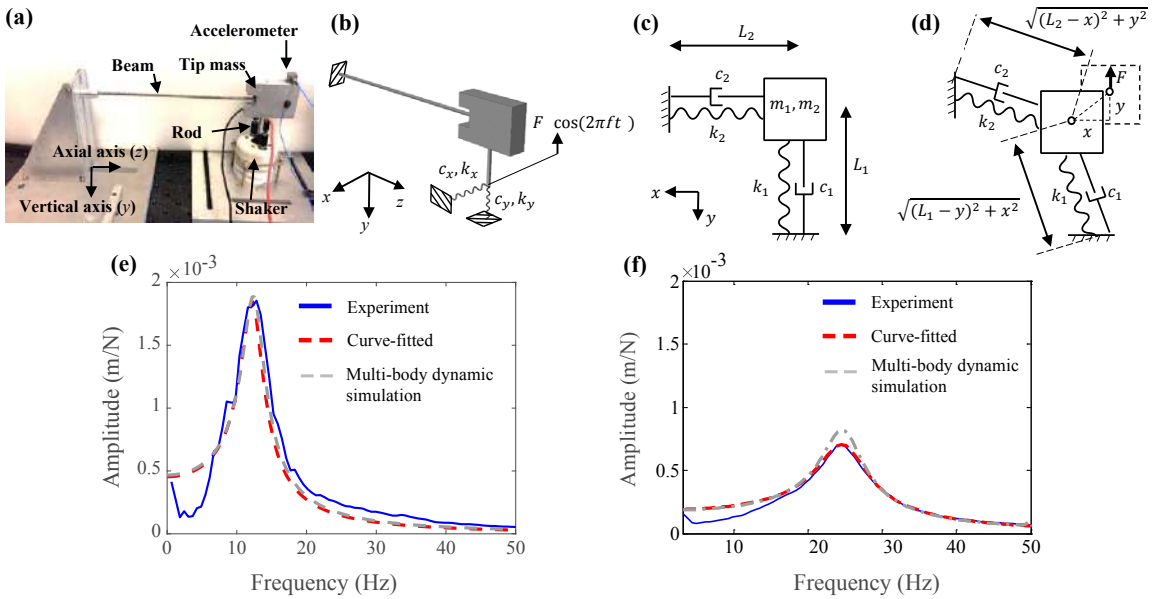

Figure 1: (a) Experimental setup of the cantilevered beam with tip mass connected to the shaker. (b) Multi-body dynamic model of the structure considering the shaker-structure interaction as pairs of spring and damper. (c) Minimal two-DOF model of the structure. (d) Deformed structure under the vertical excitation force. (e) Direct lateral FRF comparisons. (f) Direct vertical FRF comparisons. Note that the external support introduces kinematic nonlinearities and imposes two-to-one internal resonance in the structure. $c_x = 0.05\ N.s/m, c_y = 0.42\ N.s/m, k_x = 1800\ N/m, k_y = 5100\ N/m.\ L_1 = L_2 = 2.5\ mm.$

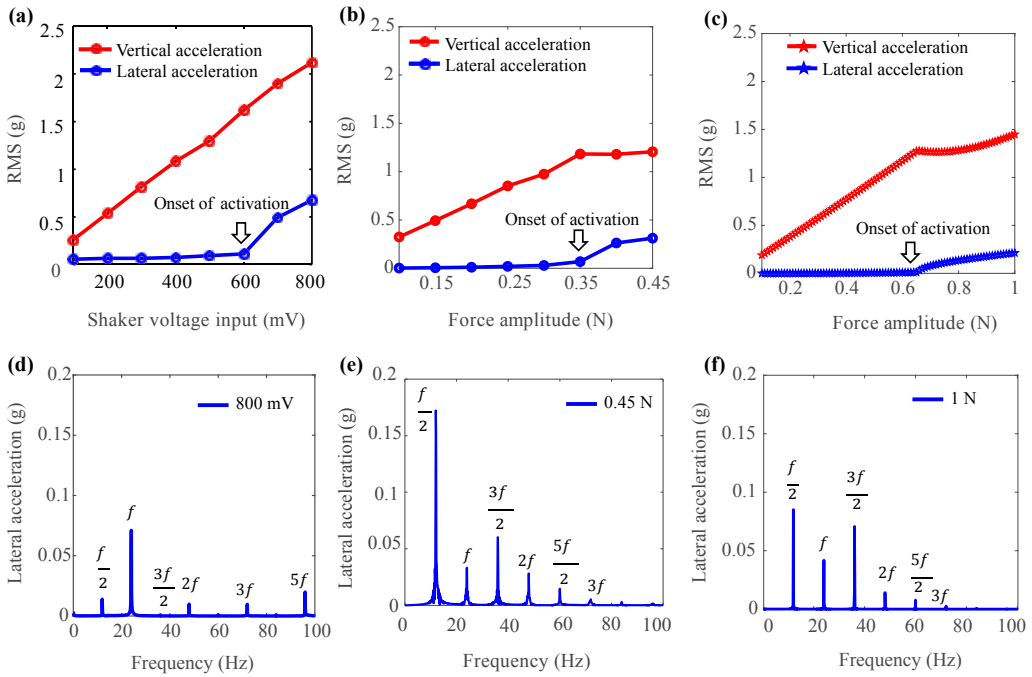

Figure 2: Activation of the lateral mode after certain excitation threshold, $f = 24\ Hz$. (a) Experiment. (b) Multi-body dynamic simulation. (c) Numerical calculation of the minimal model. Frequency response of the lateral mode after activation for (d) experiment, (e) Adams model, (f) minimal model.

BLOCH WAVE PROPAGATION IN MICROSTRUCTURED WAVEGUIDES WITH NONLINEAR INERTIA AMPLIFICATION

Valeria Settimi*[1], Andrea Bacigalupo[2], and Marco Lepidi[2]
[1]Department of Structural and Geotechnical Engineering, Sapienza University of Rome, Rome, Italy
[2]Department of Civil, Chemical and Environmental Engineering, University of Genoa, Genoa, Italy

Summary The free propagation of Bloch waves in acoustic metamaterials with nonlinear inertia amplification is investigated. A Lagrangian model is formulated to describe the nonlinear dynamics of a periodic chain of elastically coupled point masses (atoms), realizing a minimal acoustic waveguide with local inertia-amplifying oscillators. First, the nonlinear equations of motion governing the free undamped vibrations of the tetra-atomic periodic cell are formulated, and the linear frequency spectrum governing the small-amplitude range of wave propagation is determined in the complex wavenumber space via the linear map approach. Second, the harmonically-periodic solutions characterizing the high-amplitude range of wave oscillations are investigated, via the nonlinear map approach.

INTRODUCTION

The dispersion spectrum of periodic microstructured materials has long been attracting the scientific research in the fields of linear and nonlinear dynamics. Recently, a renewed interest has been paid to the parametric and computational design of architectured cellular materials, targeted at fine-tuning the periodic cell architecture to achieve unconventional, superior of functional dispersion properties. In particular, the growing technological request for low-density artificial materials serving as mechanical low-frequency filters or isolators has boosted the rapid diffusion and success of elastic microstructures locally coupled with undamped oscillators (*acoustic metamaterials*). Indeed, the mechanism of local resonance provided by the tuned oscillators (*resonators*) allows the opening, shifting and widening of frequency stop bands in the dispersion spectrum [1, 2]. From the physical viewpoint, low-frequency resonators suited for high-pass filtering applications tend to combine high flexibility with large inertial masses, conflicting with the requirement of low-density materials. In order to by-pass this stalemate, an effective dynamic solution leverages the panthographic mechanisms to artfully amplify the inertial properties of the material microstructure [3]. In this framework of high-performing functionalities, the combination of high microstructural flexibility, pantographically-amplified vibrations and minimal dissipative capabilities can also be the natural scenario for the development of nonlinear dynamic phenomena.

LAGRANGIAN MODEL OF THE ACOUSTIC METAMATERIAL

A Lagrangian model is formulated to describe the nonlinear dynamics of a periodic chain of undamped oscillators (Figure 1), in which only linear forces of attraction/repulsion are exchanged between any pair of adjacent point masses (*primary atoms*). The atomic chain represents a minimal physical realization of acoustic waveguide with inertia-amplifying auxiliary oscillators (*secondary atoms*), rigidly connected to the primary atoms by a panthographic mechanism.

Free wave propagation

Collecting the nondimensional displacement variables $u = U_1/L$, $w = (U_3 - U_1)/L$, $u_\ell = U_\ell/L$ and $u_r = U_r/L$ in the vector $\mathbf{u} = (u, w, u_\ell, u_r)$, the exact nonlinear equation governing the motion of the generic cell can be formulated. Expanding in Taylor series around the rest position $\mathbf{u} = \mathbf{0}$ and retaining terms up to the third order, the equation reads

$$\mathbf{M}\ddot{\mathbf{u}} + \mathbf{K}\mathbf{u} + \mathbf{m}_2(\dot{\mathbf{u}}, \dot{\mathbf{u}}) + \mathbf{n}_2(\ddot{\mathbf{u}}, \mathbf{u}) + \mathbf{m}_3(\mathbf{u}, \dot{\mathbf{u}}, \dot{\mathbf{u}}) + \mathbf{n}_3(\ddot{\mathbf{u}}, \mathbf{u}, \mathbf{u}) = \mathbf{0} \tag{1}$$

The quasi-static equilibrium at the cell boundary nodes is instead governed by the linear equation $\mathbf{K}_p\mathbf{u} = \mathbf{f}_p$, where the external forces $\mathbf{f}_p = (f_\ell, f_r)$ can easily be related to the internal stresses $\boldsymbol{\sigma} = (\sigma_\ell, \sigma_r)$. Partitioning the displacement vector $\mathbf{u}$, the inner and outer displacement subvectors read $\mathbf{u}_a = (u, w)$ and $\mathbf{u}_p = (u_\ell, u_r)$, respectively. Collecting all the outer variables in the vector $\mathbf{v} = (u_\ell, u_r, \sigma_\ell, \sigma_r)$, the quasi-static equilibrium equations can be inverted to obtain the static condensation rule $\mathbf{u}_a = \mathbf{S}\mathbf{v}$. After condensation, the nonlinear equations of motion reads

$$\mathbf{M}\ddot{\mathbf{v}} + \mathbf{K}\mathbf{v} + \mathbf{p}_2(\dot{\mathbf{v}}, \dot{\mathbf{v}}) + \mathbf{q}_2(\ddot{\mathbf{v}}, \mathbf{v}) + \mathbf{p}_3(\mathbf{v}, \dot{\mathbf{v}}, \dot{\mathbf{v}}) + \mathbf{q}_3(\ddot{\mathbf{v}}, \mathbf{v}, \mathbf{v}) = \mathbf{0} \tag{2}$$

Focusing the analysis on the only periodic solutions in the nondimensional τ-time domain, the real-valued unknown $\mathbf{v}(\tau)$ can conveniently be expressed in Fourier series (truncated to account for the first harmonic terms)

$$\mathbf{v}(\tau) = \sum_{-\infty}^{\infty} \mathbf{a}_k \, \mathrm{e}^{\imath k\omega\tau} \simeq \mathbf{a}\,\mathrm{e}^{\imath\omega\tau} + \bar{\mathbf{a}}\,\mathrm{e}^{-\imath\omega\tau}, \qquad \text{with} \quad k \in \mathbb{Z} \tag{3}$$

where the Fourier coefficient $\mathbf{a} = (A_\ell, A_r, B_\ell, B_r)$ serves as (unknown) amplitude of the first harmonic term and bar indicates complex conjugate. The nondimensional parameter ω plays the role of circular frequency for the mono-harmonic motion.

*Corresponding author. E-mail: valeria.settimi@uniroma1.it

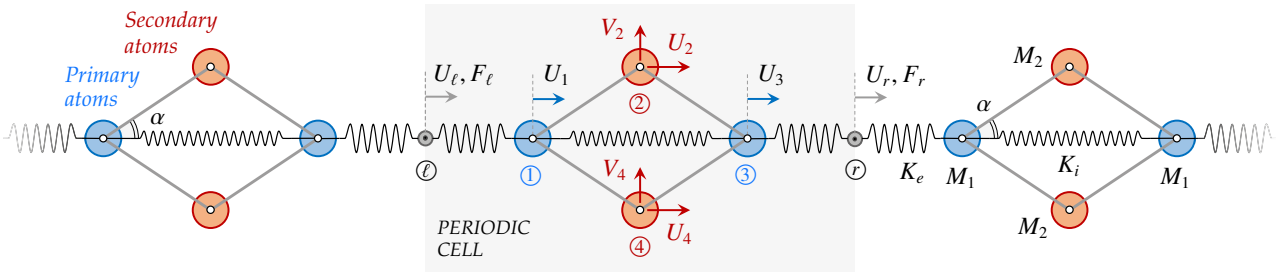

Figure 1: Acoustic metamaterial: (a) tetra-atomic crystal structure, (b) periodic cell of the Lagrangian model, (c) mechanical properties.

LINEAR AND NONLINEAR MAP APPROACH

The nonlinear equations of motion (2) can be linearized in the small-amplitude oscillation range. Therefore, the linear dispersion functions $\omega(\beta)$ relating the frequency ω to the nondimensional wavenumber β can be determined by applying either the Floquet-Bloch theory [4] or the linear map approach [5]. The latter technique employs the formal analogy between the wave periodicity (in the β-space) and the Lyapunov stability (in the τ-space) for discrete systems (Figure 2).

.5 The map approach can also be applied to the nonlinear systems governed by explicit equations $\dot{\mathbf{y}} = \mathbf{f}(\mathbf{y})$ to analyze the periodic solutions in the high-amplitude range of wave oscillations [6]. However, the nonlinear equations (2) can be manipulated to achieve only the implicit form $\mathbf{g}(\dot{\mathbf{y}}, \mathbf{y}) = \mathbf{0}$, which may require a different mathematical treatment [7]. Specifically, according to the most general definition of discrete implicit map, $\mathbf{y}_0$ is a p-periodic point of the implicit dynamic system $\boldsymbol{g}(\dot{\mathbf{y}}, \mathbf{y}, \boldsymbol{\alpha}) = \mathbf{0}$ if

$$\begin{cases} \boldsymbol{g}(\mathbf{y}_0, \mathbf{y}_1, \boldsymbol{\alpha}) = \mathbf{0} \\ \boldsymbol{g}(\mathbf{y}_1, \mathbf{y}_2, \boldsymbol{\alpha}) = \mathbf{0} \\ \dots \\ \boldsymbol{g}(\mathbf{y}_{p-2}, \mathbf{y}_{p-1}, \boldsymbol{\alpha}) = \mathbf{0} \\ \boldsymbol{g}(\mathbf{y}_{p-1}, \mathbf{y}_0, \boldsymbol{\alpha}) = \mathbf{0} \end{cases} \tag{4}$$

Therefore, the $\mathbf{y}_0$ stability can be analysed by introducing bifurcation conditions in order to assess the critical values of the parameter set $\boldsymbol{\alpha}$. The periodic points can be searched for the nonlinear system under investigation by setting $\dot{\mathbf{y}} = (A_r, B_r, \bar{A}_r, \bar{B}_r)$ and $\mathbf{y} = (A_\ell, B_\ell, \bar{A}_\ell, \bar{B}_\ell)$ and assuming ω as control parameter in the $\boldsymbol{\alpha}$-set.

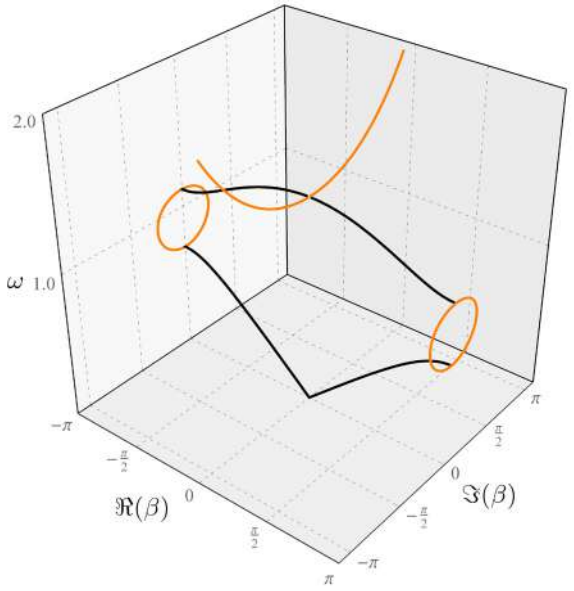

Figure 2: Linear spectrum in the ω-$\Re(\beta)$-$\Im(\beta)$ space.

Equations (4) can be stated and solved for particular p-cases ($p = 1, 2$), giving solutions $\omega(\mathbf{y}_0, \mathbf{y}_1)$ corresponding to $\beta = 2\pi/p$. Using polar representations $A_\ell = a_\ell \, \mathrm{e}^{\imath\phi}$ and $B_\ell = b_\ell \, \mathrm{e}^{\imath\varphi}$, the amplitude-dependent frequency solutions $\omega(a_\ell)$ or $\omega(b_\ell)$ are obtained by setting $\mathbf{y}_1 = \mathbf{y}_0 \, \mathrm{e}^{\imath \, 2\pi/p}$. The amplitude-dependent frequency curves have dominant softening behaviour for small amplitudes, as expected for inertial nonlinearities, and originate from the linear spectrum for null amplitudes. The softening behaviour may enlarge the amplitude-dependent stop bandwidth.

CONCLUSIONS

Nonlinear periodic solutions for the free Bloch wave propagation have been determined for an acoustic metamaterial waveguide with inertia amplification. The map approach has been employed to achieve the linear dispersion spectrum and nonlinear amplitude-dependent frequency functions for particular oscillation periodicities.

References

[1] Krushynska A.O., Kouznetsova V.G., Geers M.G. Towards optimal design of locally resonant acoustic metamaterials. *J Mech Phys Solids* **71**:179-196, 2014.
[2] Kamotski I.V., Smyshlyaev V.P. Bandgaps in two-dimensional high-contrast periodic elastic beam lattice materials. *J Mech Phys Solids* **123**:292-304, 2019.
[3] Yilmaz C. Kikuchi N. Analysis and design of passive low-pass filter-type vibration isolators considering stiffness and mass limitations. *J Sound Vib* **293**(1-2):171-195, 2006.
[4] Bacigalupo A., Lepidi M. Acoustic wave polarization and energy flow in periodic beam lattice materials. *Int J Solids Struct* **147**:183-203, 2018.
[5] Romeo F., Luongo A. Invariant representation of propagation properties for bi-coupled periodic structures. *J Sound Vib* **257**(5):869-886, 2002.
[6] Romeo F., Rega G. Wave propagation properties in oscillatory chains with cubic nonlinearities via nonlinear map approach. *Chaos Solitons Fractals* **27**(3): 606-617, 2006.
[7] Oliveira H.M. Bifurcation equations for periodic orbits of implicit discrete dynamical systems. *Nonlinear Dynamics* **91**(1):387-402.

SECOND-ORDER PERTURBATION BASED RECURSIVE UPDATE OF EIGEN-DECOMPOSITION FOR VIBRATION ANALYSIS

Paul Mucchielli[1], , Basuraj Bhowmik[1], Vikram Pakrashi[2], Budhaditya Hazra[3]
[1]Dynamic Systems Risk Laboratory, University College Dublin, Dublin, Ireland
[2]Department of Mechanical and Materials Engineering, University College Dublin, Dublin, Ireland
[3]Department of Civil Engineering, Indian Institute of Technology Guwahati, Guwahati, India

Summary This manuscript describes the work that was undertaken by the authors towards recursive eigen-decomposition update of a vibration signal. A Structural Health Monitoring (SHM) approach was adopted to extract the eigen-decomposition of a multivariate signal. This real-time implementation, requiring the intervention of a composite algorithm, can provide timely information as to the state of the structural system under study. This algorithm gathers both eigen-perturbation principles and the well-known Jacobi algorithm. Through the analysis of simulated signals of a 5 degrees of freedom system under white noise excitation, we explore the performance of such an algorithm in the extraction of accurate eigen-decomposition.

INTRODUCTION

The analysis of a system through its dynamical response to surrounding excitation has previously shown that external events could be correlated with changes in the dynamical behaviour of the system. In this context, we proposed to observe the dynamical response of a 5 degrees of freedom system through the analysis of a multivariate acceleration signal. The covariance matrix of this signal encloses information about the interaction between these degrees of freedom. In SHM, the modification of the dynamical response can often be assessed through the analysis of the covariance matrix through its principal components [1]. Indeed, a system under excitation, represented in time through a multivariate signal contained in the matrix $X^{n\times k}$ of n output acceleration traces has covariance matrix $C = {}^{1}/_{k}\, XX^{T}$ [1]. The update of eigenvalues and eigenvectors of the covariance matrix under a small perturbation is enabled using perturbation theory. The covariance matrix of a zero mean and unit variance multivariate signal can be updated over time according to,

$$C_{i+1} = \frac{i-1}{i} C_i + \frac{1}{i}\delta C, \tag{1}$$

The quantity $\delta C = {}^{1}/_{i}\, X_i X_i^{T}$ where X_i is the ith sample vector will experience a decrease proportional to the inverse of the time stamp. Therefore, the amplitude of the perturbation δC applied to C_i will reduce over time. We can update the eigenvectors (i.e. principal components) of the matrix C perturbed by δC at each time step. This process, known as eigen-perturbation, has been explored in previous works in the form of First Order Eigen-Perturbation (FOEP) for the approximation of eigenvalues and eigenvectors of a perturbed covariance matrix [1]. The works described here established the performance of Second Order Eigen-Perturbation (SOEP).

THEORY

The core of this method resides in computing extra perturbation terms to the FOEP formulation.

$$\underbrace{C}_{\substack{Original\\ covariance\ matrix}} \times \underbrace{V}_{\substack{Original\\ eigenvectors}} = \underbrace{\Lambda}_{\substack{Original\\ eigenvalues}} \times \underbrace{V}_{\substack{Original\\ eigenvectors}} \tag{2}$$

$$(C+\delta C)\left(\mathrm{V} + \underbrace{\delta \mathrm{V}}_{\substack{1^{st}\ order\\ perturbation}} + \underbrace{\delta^2 \mathrm{V}}_{\substack{2^{nd}\ order\\ perturbation}}\right) = \left(\Lambda + \underbrace{\delta\Lambda}_{\substack{1^{st}\ order\\ perturbation}} + \underbrace{\delta^2\Lambda}_{\substack{2^{nd}\ order\\ perturbation}}\right)\left(\mathrm{V} + \underbrace{\delta \mathrm{V}}_{\substack{1^{st}\ order\\ perturbation}} + \underbrace{\delta^2 \mathrm{V}}_{\substack{2^{nd}\ order\\ perturbation}}\right) \tag{3}$$

While FOEP would only see the terms marked as first order terms appear in the computations, the terms marked as second order would offer extra precision to the approximation of the new eigen-decompositions [2]. Expanding and simplifying this equation allows to develop simple rules for the calculation of $\delta\Lambda$, δV, $\delta^2\Lambda$, $\delta^2 V$ recursively by using the update in Equation (1).

As mentioned in perturbation literature, the one major disadvantage of perturbation bounds derived for the eigenvalue problem is their reliance on the spacing between two consecutive eigenvalues [3]. Indeed, the theory that governs the perturbation of an eigen-decomposition gravitates around the assumption of linear independence of the eigenvectors [4]. Once two or more eigenvalues are repeated or close, the rules obtained from Equation (3) cannot be used. That is why the Jacobi algorithm is used to handle those cases where eigen-perturbation is not appropriate. Consequently, in this specific situation, we rearrange the problem to display strong diagonal dominance and use the well-adapted Jacobi algorithm to compute the results [5], [6]. Since the Jacobi algorithm operates to eliminate the off-diagonal terms of the matrix, it is better suited to this problem than techniques requiring tridiagonalization. The detection of close eigenvalues was

performed using perturbation bounds that limited the maximum 2-norm relative eigenvector error to 1 % [7]. We refer to the algorithms that include Jacobi intercession as FOEPS and SOEPS.

RESULTS

We processed a 100 s-long simulation of a 5-DOF building system under white noise excitation and sampled at 100 Hz. The results for FOEP, FOEPS and SOEPS were compared against the sample wise eigen-decomposition of C performed by the QR algorithm [6]. Figure 1 shows the results in terms of Mean Absolute Percentage Error (MAPE) and Modal Assurance Criterion (MAC) [8].

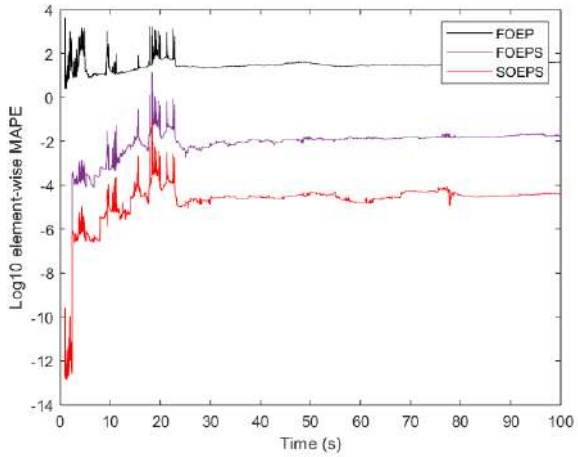

Figure 1. Plot of the log-10 MAPE against time for FOEP, FOEPS and SOEPS

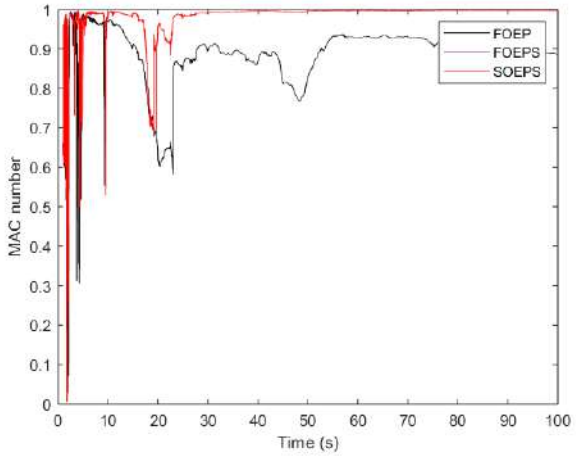

Figure 2. Plot of the MAC number with respect to the system modes against time for FOEP, FOEPS and SOEPS

DISCUSSION

Figure 1 shows that the first and second order frameworks that included Jacobi intercession performed quite significantly better. Indeed, while the first order technique output a median error of 29.3 %, including the intervention of the Jacobi algorithm reduced it to 1.29×10^{-2} % while the second order run reached 3.02×10^{-5} %. Considering the MAC, while FOEP is reaching a final 88.63 score, the FOEPS and SOEPS techniques both scored 99.76. This shows the potential of the FOEPS and SOEPS algorithm to provide more accurate and consistent (with the system modes) updates at each time step in a time series.

CONCLUSIONS

The superiority of SOEPS and its linking to a real-time recursive framework may be able to allow a more precise damage detection in all types of systems. Indeed, one can use recursive damage sensitive in conjunction with time-varying autoregressive coefficients all of which can be implemented with an eigen-perturbation framework [1].

Acknowledgments

This work was performed as part of the WindPearl project funded by the Sustainable Energy Authority of Ireland (Project number RDD/00263). The authors also acknowledge the support of Science Foundation Ireland Centre Marine and Renewable Energy Ireland (MaREI) and The Energy Institute, University College Dublin, Ireland. Dr. Vikram Pakrashi also acknowledges the support of the SIRMA project.

References

[1] B. Bhowmik, T. Tripura, B. Hazra, and V. Pakrashi, “First order eigen perturbation techniques for real time damage detection of vibrating systems: Theory and applications,” *Appl. Mech. Rev.*, no. c, 2019.
[2] T. Kato, *Perturbation theory for linear operators*. 1966.
[3] G. H. Golub and H. A. Van Der Vorst, “Eigenvalue computation in the 20th century,” *J. Comput. Appl. Math.*, 2000.
[4] P. D. Cha and A. Shin, “Perturbation Methods for the Eigencharacteristics of Symmetric and Asymmetric Systems,” *Shock Vib.*, vol. 2018, pp. 1–25, Oct. 2018.
[5] S. -H Chen, Z. -S Liu, C. -S Shao, and Y. -Q Zhao, “Perturbation analysis of vibration modes with close frequencies,” *Commun. Numer. Methods Eng.*, vol. 9, no. 5, pp. 427–438, May 1993.
[6] G. H. Golub and C. F. Van Loan, *Matrix Computations*. 1989.
[7] A. S. Deif, “Rigorous perturbation bounds for eigenvalues and eigenvectors of a matrix,” *J. Comput. Appl. Math.*, vol. 57, no. 3, pp. 403–412, Feb. 1995.
[8] R. J. Allemang, “The Modal Assurance Criterion,” *J. Sound Vib.*, vol. 1, no. August, pp. 14–21, 2003.

DYNAMIC ANALYSIS OF GRANULAR CHAIN USING COSSERAT DISCRETE MODELING

Sina Massoumi[*1], Noël Challamel[2], and Jean Lerbet [1]
[1]Department of Mechanical Engineering, Univ. Evry, University of Paris-Saclay, Evry, France
[2]Department of Civil Engineering, University of Bretagne Sud, Lorient, France

Summary This paper deals with the free vibration of a beam which is discretized by finite rigid granular elements and compared its exact solution to continuum local elasticity. This problem, which can be considered as a simple model to rigorously study the effect of the microstructure on the dynamic behavior of a equivalent continuum structural model, can be referred to Cosserat discrete chain or a lattice elastic model with shear interaction. This micro structured system consists of uniform grains elastically connected by shear and rotation springs. First the critical frequencies of the system which change the nature of the results, are obtained. Next, the natural frequencies of such as granular model are analytically calculated whatever the considered modes for the granular beam resting on two supports, starting from the resolution of the linear difference eigenvalue problem. It is shown that the discrete equations of this granular system, for an infinite number of grains, converge to the differential equations of the Bresse-Timoshenko beam resting on Winkler foundation (such a Bresse-Timoshenko beam can be also classified as a continuous Cosserat beam model). A gradient Bresse-Timoshenko model is constructed from continualization of the difference equations of the granular system. This continuous gradient elasticity Cosserat model is obtained from a polynomial or a rational expansion of the pseudodifferential operators, stemming from the continuualization process. The natural frequencies of the continuous gradient Cosserat models are compared with those of the discrete Cosserat model associated with the granular chain. Scale effects of the granular chain are clearly captured by the continuous gradient elasticity model. The results clarify the dependency of the beam dynamic responses to the beam length ratio.

***Keywords*:** Cosserat continuum, Discrete Cosserat formulation, Gradient elasticity, Timoshenko beam.

Introduction

In order to adapt a theory of continuous media to granular materials, it is necessary to introduce independent degrees of freedom of rotation, in addition to those conventional translation. Indeed, the relative movements between the microstructure and the average macroscopic deformations can be apprehended by additional degrees of freedom. Such enriched kinematics leads to non-classical continuous media or Cosserat-type theories [1], [2] which introduce intrinsic length scales via higher order gradients or additional degrees of freedom. Conversely, the classical mechanics of continuous media does not incorporate a rotational interaction between the particles, and does not allow to understand the size effects in these media.

The Bresse-Timoshenko beam model admits kinematics with two independent fields of transverse displacement and rotation [3], [4]. The exact calculation of natural frequencies for a Bresse-Timoshenko beam with any boundary conditions and in elastic interaction with a rigid medium was obtained by Wang and Stephens [5], [6]. Timoshenko beam is an example of Cosserat one-dimensional continuum considering the independent double rotation-displacement kinematics. The present study focuses on the vibration of the granular beam model resting on a linear Winkler foundation. Note that the difference equations of this granular chain coincide with the difference equations of the granular model of Pasternak and Mühlhaus [7] in the absence of elastic foundation, while differ from the ones of Duan et al [8] or Bacigalupo and Gambarotta [9].

Granular Model

A granular beam of length L resting on two simple supports is modeled by a finite number of grains interacting together. Such a model could be presented by considering the microstructured granular chain comprising $n+1$ rigid grain with diameter a ($a=L/n$) that are connected by n shear and rotational springs, as shown in figure 1.

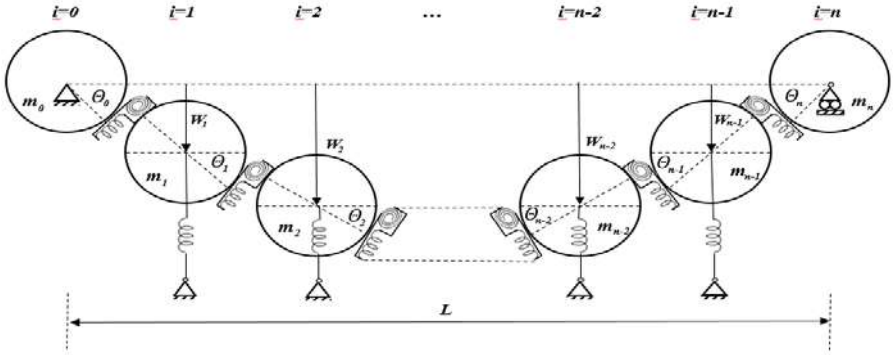

Figure 1. A discrete shear granular chain composed of n+1 grain

The Lagrangian relation of the granular system may be defined as

$$L = \left[\frac{1}{2}\sum_{i=0}^{n} m_i \dot{W}_i^{\,2} + \frac{1}{2}\sum_{i=0}^{n} I_{m_i}\dot{\Theta}_i^2\right] - \left[\frac{1}{2}\sum_{i=0}^{n-1} S\left(W_{i+1} - W_i - a\frac{\Theta_{i+1}+\Theta_i}{2}\right)^2 + \frac{1}{2}\sum_{i=0}^{n-1} C(\Theta_{i+1}-\Theta_i)^2 + \frac{1}{2}\sum_{i=0}^{n} KW_i^{\,2}\right] \quad (1)$$

where S is the shear stiffness and defined by $S = \frac{K_s GA}{a} = \frac{nK_s GA}{L}$. G is the shear modulus; A is the cross-sectional area of the beam and K_s is an equivalent shear correction coefficient. C is the rotational stiffness and can be expressed as $C = \frac{EI}{a} = \frac{nEI}{L}$, where E is Young's modulus and I is the second moment of area. $K=ka$ is the discrete stiffness of the elastic support.

From the Euler-Lagrange of the granular system by assuming a harmonic motion $W_i = w_i e^{j\omega t}$ and $\Theta_i = \theta_i e^{j\omega t}$ with $j^2=-1$, the following deflection equation could be obtained

$$[EI\delta_2{}^2 + \left(\rho I\omega^2 - \frac{kEI}{K_s GA} + \frac{EI\rho\omega^2}{K_s G}\right)\delta_2 + (k - \rho A\omega^2)\delta_0 - \frac{k\rho I\omega^2}{K_s GA} + \frac{\rho^2 I\omega^4}{K_s G}]w_i = 0 \quad (2)$$

The pseudo-difference parameters are defined as:

$$\delta_0 W_i = \frac{W_{i+1}+2W_i+W_{i-1}}{4}, \quad \delta_1 W_i = \frac{W_{i+1}-W_{i-1}}{2a}, \quad \delta_2 W_i = \frac{W_{i+1}-2W_i+W_{i-1}}{a^2} \quad (3)$$

The fourth-order difference equation (2) is equivalent to the one of Challamel et al. [10] in the static range ($\omega = 0$). Considering infinite number of grains ($n \to \infty$) for the continuum beam, the fourth-order differential equation valid for a Bresse-Timoshenko beam on Winkler elastic foundation is given by (4) which also could be compared well by [5], [6].

$$\frac{d^4w}{dx^4} + \left(\frac{\rho\omega^2}{E}\left(1 + \frac{E}{k_s G}\right) - \frac{k}{k_s GA}\right)\frac{d^2w}{dx^2} - \left(\frac{\rho\omega^2}{E}\left(\frac{A}{I} + \frac{k}{k_s GA} - \frac{\rho\omega^2}{k_s G}\right) - \frac{k}{EI}\right)w = 0 \quad (4)$$

Exact solution

For simply supported boundary conditions by assuming $w_0 = 0$; $\delta_1\Theta_0 = 0$ and $w_n = 0$; $\delta_1\Theta_n = 0$ the frequencies of the discrete system could be obtained by (5). The results are shown in figure 2.

$$\omega = \frac{1}{L^2}\sqrt{\frac{EI}{\rho A}}\sqrt{-\frac{n^2}{\mu_s r^{*2}}\left(1+\mu_s-\frac{1}{4r^{*2}n^2}\right)cos\left(\frac{p\pi}{n}\right)+\frac{k^*}{2}+\frac{1}{4\mu_s r^{*4}}+\frac{n^2}{\mu_s r^{*2}}(1+\mu_s) \pm \sqrt{\left(\frac{n^2}{\mu_s r^{*2}}\left(1+\mu_s-\frac{1}{4r^{*2}n^2}\right)cos\left(\frac{p\pi}{n}\right)-\frac{k^*}{2}-\frac{1}{4\mu_s r^{*4}}-\frac{n^2}{\mu_s r^{*2}}(1+\mu_s)\right)^2-\frac{n^4}{\mu_s r^{*4}}\left(\left(-\frac{r^{*2}k^*\mu_s}{n^2}+\frac{k^*}{4n^4}-4\right)2cos\left(\frac{p\pi}{n}\right)+\frac{k^*}{2n^4}+\frac{2r^{*2}k^*\mu_s}{n^2}+4+4\left(cos\left(\frac{p\pi}{n}\right)\right)^2\right)} \quad (5)$$

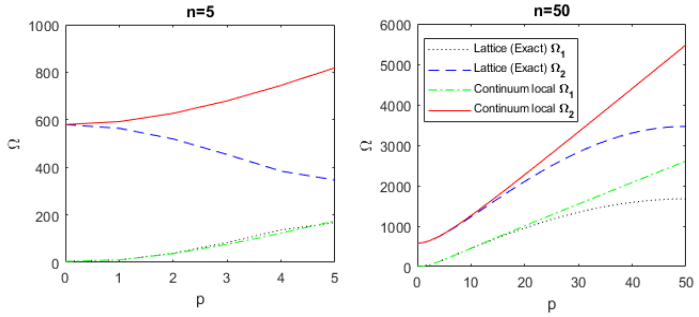

Figure 2. Comparison of the natural frequencies for the discrete exact and continuum solutions with respect to the mode number (p) and grain number $(n \in \{5,\ 50\})$ for $\mu_s = 4.28$, $r^* = 0.029$ and $k^* = 15$

CONCLUSIONS

This paper investigates the macroscopic free vibration behavior of a discrete granular system resting on a Winkler elastic foundation. It is shown that the discrete deflection equation of this granular system (Cosserat chain) is mathematically equivalent to the finite difference formulation of a shear deformable Bresse-Timoshenko beam resting on Winkler foundation. Next, the natural frequencies of such a granular model with simply supported ends are first analytically investigated, whatever considered modes through the resolution of a linear difference equation. The scale effects of the granular chain are clearly captured by the continuous gradient elasticity model. This scale effect is related to the grain size with respect to the total length of the Cosserat chain.

References

[1] E. Cosserat and F. Cosserat, Théorie des corps déformables, *A. Herrmann et Fils*, 226, 1909.
[2] W. Nowacki, The linear theory of micropolar elasticity, W. Nowacki and W. Olszak (eds.), Micropolar Elasticity. Wien, New York, Springer-Verlag, 1–43, 1974.
[3] J. A. C. Bresse, Cours de mécanique appliquée – Résistance des matériaux et stabilité des constructions 1859.
[4] S. P. Timoshenko, On the correction for shear of the differential equation for transverse vibrations of prismatic bars, *Philosophical Magazine*, 41, 744-746, 1921.
[5] T. M. Wang T. M. and J. E. Stephens, Natural frequencies of Timoshenko beams on Pasternak foundation, *J. Sound and Vibration*, 51, 2, 149-155, 1977.
[6] A. I. Manevich, Dynamics of Timoshenko beam on linear and nonlinear foundation: phase relations, significance of the second spectrum, stability, *J. Sound and Vibration*, 344, 209-220, 2015.
[7] E. Pasternak and H. B. Mühlhaus, Generalized homogenization procedures for granular materials, *J. Engineering Mathematics*, 51, 1, 2005.
[8] W. Duan, N. Challamel, C. M. Wang and Z. Ding, Development of analytical vibration solutions for microstructured beam model to calibrate length scale coefficient in nonlocal Timoshenko beams, *J. Applied Physics*, 114, 104312, 1-11, 2013.
[9] A. Bacigalupo and C. Gambarotta, Generalized micropolar continualization of 1D beam lattices, J. Mechanic Science, 155, 554-570, 2019.
[10] Challamel N.,Lerbet J.,Darve F. and Nicot F., Buckling of granular systems with discrete and gradient elasticity Cosserat continua, in preparation, 2019.

EXPERIMENTAL IDENTIFICATION OF CONTACT DAMPING IN ASSEMBLED STRUCTURES

Bálint Magyar[1], Balázs Pere[2], Gábor Csernák*[3], Roland Zana[1], Richárd Wohlfart[1], and Gábor Stépán[1]
[1]Department of Applied Mechanics, Budapest University of Technology and Economics, Budapest, Hungary
[2]Department of Applied Mechanics, Széchenyi István University, Győr, Hungary
[3]MTA-BME Research Group on Dynamics of Machines and Vehicles, Budapest, Hungary

Summary The energy dissipation in assembled metal structures is mainly related to various physical phenomena on the contact surfaces. To evaluate the role of contact in damping and to find a connection between the contact-related increase of modal damping and the mode shapes, the modal damping ratios of a monolithic body and a shrink-fitted assembly are compared in this paper. Based on the experiments, a finite element model was developed that is able to reproduce the measured modal damping values of the assembled structure at all the natural frequencies in the frequency range of the measurement. Moreover, a dimensionless quantity is introduced that seems to correlate with the contact-related component of damping.

INTRODUCTION

The modal analysis of monolithic structures by finite element method belongs to the routine tasks. However, in case of assemblies, there is no off-the-shelf solution: on the one hand, there is the uncertainty of the contact stiffness, on the other hand, the modelling of contact-related damping is extremely challenging. The present paper focuses on the latter problem, by comparing the measured damping characteristics of a monolithic structure and a shrink-fitted assembly. Two disc-shaped test specimens with identical material properties and macroscopic geometry (see Figure 1) had been carefully designed and manufactured for the experiments.

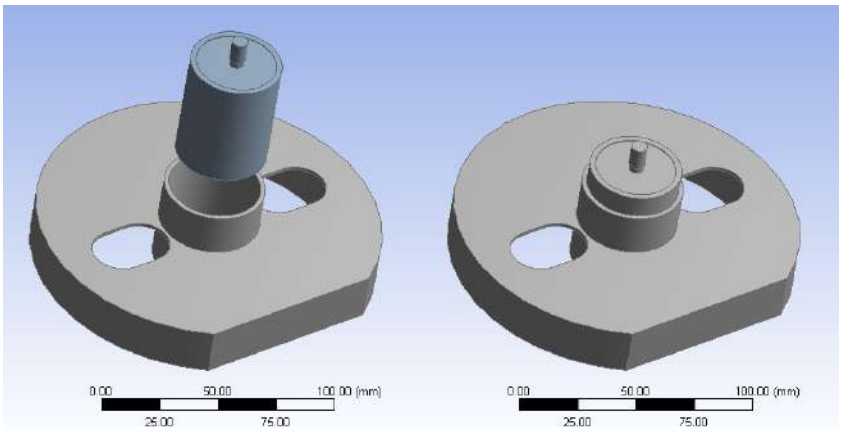

Figure 1: Test specimens. Left: shrink-fitted disc, right: monolithic disc.

An automated pneumatic ball shooter [1] was used for the excitation to ensure the initial conditions to be as identical as possible, while the vibrations were measured by lightweight accelerometers. Short-time Fourier transform was applied on the acquired acceleration signals, and the characteristic amplitude peaks – that had been identified by the finite element modal analysis of the monolithic disc – were traced during the decays.

EXPERIMENTAL RESULTS

The frequency range of the measurement made the analysis of the first five natural frequencies of both specimens possible. In Figure 2, the measured decays of the acceleration magnitudes are shown on a logarithmic scale for the first and the fifth natural frequencies. Different colours belong to different measurement locations, and solid lines represent the average decays. The fitted modal damping factors are listed in the legends of these charts.

As it can be seen, the damping was found to be linear in the whole range of the decay experiments. However, the corresponding damping factor values for the shrink-fitted disc are significantly higher compared to the monolithic specimen. The results also showed that the individual vibration modes are differently influenced by the contact damping.

Assuming that the dissipation at the contact surface depends on the local variation of stresses and strains, we found that an energy-like quantity may characterize the contact-related increase of damping. Thus, we defined a dimensionless strain energy $\tilde{u}_c$ as the ratio of a local strain energy in the neighbourhood of the contact surface and the total strain energy. $\tilde{u}_c$ could be calculated easily by the finite element analysis of the monolithic body for each vibration mode. The experimentally obtained relative increases of the damping ratio are plotted in Figure 3 versus the calculated values of $\tilde{u}_c$.

*Corresponding author. E-mail: csernak@mm.bme.hu.

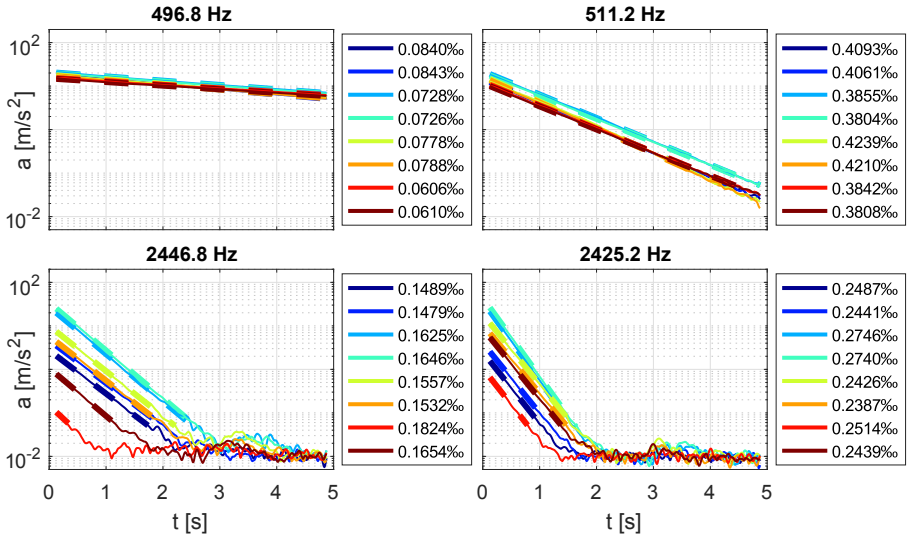

Figure 2: Free vibration decays of the acceleration magnitude peaks at eight points of the specimens. Left: monolithic disc, right: shrink-fitted assembly.

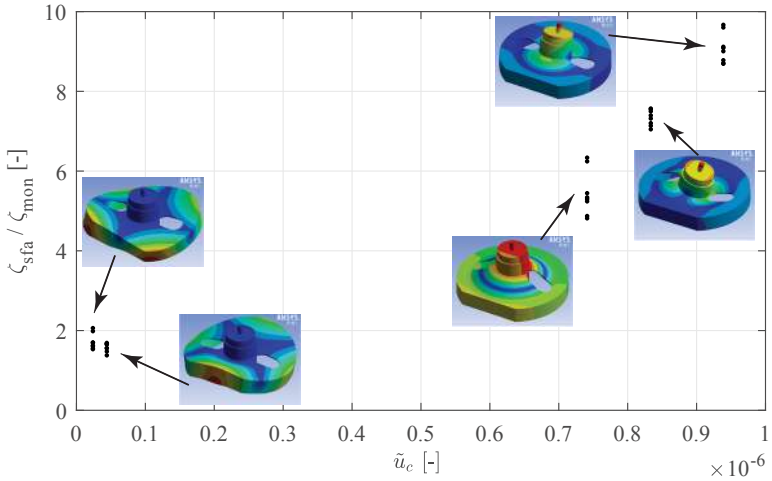

Figure 3: The measured increase in damping ratios due to contact versus the calculated dimensionless strain energy values for the first five modes. ζ_{sfa} and ζ_{mon} denote the damping ratios regarding to the shrink fitted assembly and the monolithic body, respectively.

CONCLUSIONS

The lowest vibration amplitudes that could be reliably measured were cca. 0.05 m/s^2 at 2450 Hz, hence the corresponding displacements were only cca. 200 pm = $2 \cdot 10^{-10}$ m. This value is in the order of magnitude of the atomic distances in the crystal structure. Even in the case of the first natural frequency, the smallest measured displacements were approximately 5 nm. Thus, a linear contact damping must be present besides the material damping even without macroscopic slips. We refer to this phenomenon as *quasi-slip*. To characterize the effect of contact on modal damping ratios, a dimensionless strain energy $\tilde{u}_{\mathrm{c}}$ was introduced. The correlation between the damping increase and $\tilde{u}_{\mathrm{c}}$ appears to be convincing, especially for relatively large values of $\tilde{u}_{\mathrm{c}}$. We claim that this result opens the possibility to predict how the individual modes are influenced by the contact damping.

Acknowledgements

The research reported in this paper has been supported by the National Research, Development and Innovation Fund (TUDFO/51757/2019-ITM, Thematic Excellence Program) and the Hungarian National Science Foundation under Grant No. NKFI-128422.

References

[1] Takács D., Wohlfart R., Miklós Á., Krajnyák G., Tóth A., Stépán G. Ball shooting tests for identification of modal parameter variation in rotating main spindles. *Procedia CIRP* **77**: 481484, 2018.

[2] Magyar B., Pere B., Csernák G., Zana R., Wohlfart R., Stépán G. Experimental analysis and numerical modelling of contact damping. Submitted to *Journal of Sound and Vibration.*

STABILITY OF TURNING PROCESS ON WORKPIECE SUBJECTED TO TIME-PERIODIC COMPRESSION

Bence Beri*, Gergely Meszaros, and Gabor Stepan
Department of Applied Mechanics, Budapest University of Technology and Economics, Budapest, Hungary

Summary The paper investigates the stability of turning processes where the workpiece is subjected to time-periodic axial force. Based on the Euler-Bernoulli beam theory, the workpiece is modelled as a beam with clamped end at the chuck and pinned end at the tailstock. To increase the stable parameter domain of the cutting operation in turning processes, the beam is excited by periodic compression. This results in the periodic change of the lateral stiffness of the workpiece, which varies the natural frequency of the system, too. It is shown that it has a positive effect on chatter avoidance at low cutting speeds.

MOTIVATION

Surface regeneration is almost always present is machining, which often results in self-excited vibrations called chatter. Chatter generally degrades the surface of the workpiece and might also decrease the lifespan of the cutting tool. It may arise due to the compliance of the tool and/or the workpiece due to the occurring relative vibrations between the workpiece and the tool. The regeneration effect was first modelled by Tobias [1] via time-delay equations. The tool cuts the surface that was machined in the previous revolution, thus, the chip thickness is given by the difference of the present and the previous position of the workpiece. The delay is the time period of workpiece rotation.

In machining, to increase productivity without undesired vibrations, the so-called stability lobe diagram is considered. It helps the machinist to avoid chatter by modifying the corresponding technological parameters: the spindle speed Ω and the depth of cut w at a given feed rate. An effective manner is the periodic modulation of the spindle speed Ω around a certain mean value with a given frequency and amplitude. Spindle speed variation is also dependent on the type of the modulation waveform such as triangular [2] or sinusoidal [3]. Segalman *et.al.* [4] applied the method of impedance modulation where the mechanical impedance of the underlying system is varied continuously. It results in the change of the natural frequency of the system, which may lead to an extended stable parameter region.

The purpose of the study is to propose an alternative way to increase the chatter-free domain by the application of time-periodic compression to the rotating workpiece. The effect of compression is taken into account through the lateral stiffness variation of the workpiece. For constant compression, the lateral stiffness, and thus the natural frequency of the system decreases, which leads to the reduction of the stable parameter region [5]. However, when the compressive force is modulated periodically with an appropriate time period, the destabilising nature of compression can be overcome, and it can even improve the stability properties of the system for the lower spindle speeds relevant in turning.

The approach may become beneficial in case of cutting slender shafts or tubes having low bending stiffness. For higher spindle speeds, the effect of the periodic axial excitation converges to the case when only constant compression is applied. Consequently, the stability analysis of the material removal process in question has to be carried out to reveal the viable spindle speed ranges where cutting efficiency can be increased.

MODELLING AND ANALYSIS

A one degree-of-freedom mechanical model is constructed for turning slender workpieces. The workpiece is modelled by a stepped beam that is compliant in the y direction shown in Fig. 1(a). This represents the most common configuration of turning where the workpiece is clamped at the chuck and pinned at the tailstock [6]. The tool position is given with the parameter a measured from the chuck. The normal cutting force F_y acting on the workpiece has empirical formulas in practice: while it is linearly proportional to the depth of cut w, it has a nonlinear dependence on the chip thickness h. An approved cubic approximation is $F_y(t) = w(\rho_1 h(t) + \rho_2 h^2(t) + \rho_3 h^3(t))$ where ρ_i, $i = 1,2,3$ are the cutting force parameters [1]. The regeneration effect develops in the chip thickness h that is given by the present and the previous position of the flexible workpiece. Thus, $h(t) = h_0 + y(t-\tau) - y(t)$ where h_0 is the desired chip thickness and $\tau = 2\pi/\Omega$.

The periodic axial force F_a causes the stiffness variation of the workpiece. The workpiece is assumed to be an inextensible, linearly elastic and isotropic beam. Based on the Euler-Bernoulli beam theory, the point-by-point lateral stiffness k_y of the workpiece can be calculated analytically. The compression F_a affects the lateral stiffness of the system linearly: $k_y = k_0 + k_1(F_a - F_0)$ where k_0 and k_1 are constant coefficients and F_0 is a precompression, while $F_a = F_0 + F_1\cos(2\pi t/T)$ (see Fig. 1(a)) where F_1 is the amplitude of excitation and T is the time-period of excitation. All this leads to a time-periodic delay differential equation. The motion of the workpiece can be decomposed into $y(t) = y_p(t) + \eta(t)$ where y_p is a periodic solution, and η is the small perturbation. Accordingly, the variational system yields

$$\dot{\mathbf{q}}(t) = \begin{bmatrix} 0 & 1 \\ -\left(\frac{k_0 + w(\rho_1 + 2h_0\rho_2 + 3h_0^2\rho_3)}{m} + F_1\frac{k_1\cos\left(\frac{2\pi}{T}t\right)}{m}\right) & -\frac{c_y}{m} \end{bmatrix}\mathbf{q}(t) + \begin{bmatrix} 0 & 0 \\ \frac{w(\rho_1 + 2h_0\rho_2 + 3h_0^2\rho_3)}{m} & 0 \end{bmatrix}\mathbf{q}(t-\tau) \qquad (1)$$

*Corresponding author. E-mail: beri@mm.bme.hu.

THEMATIC SESSION SM

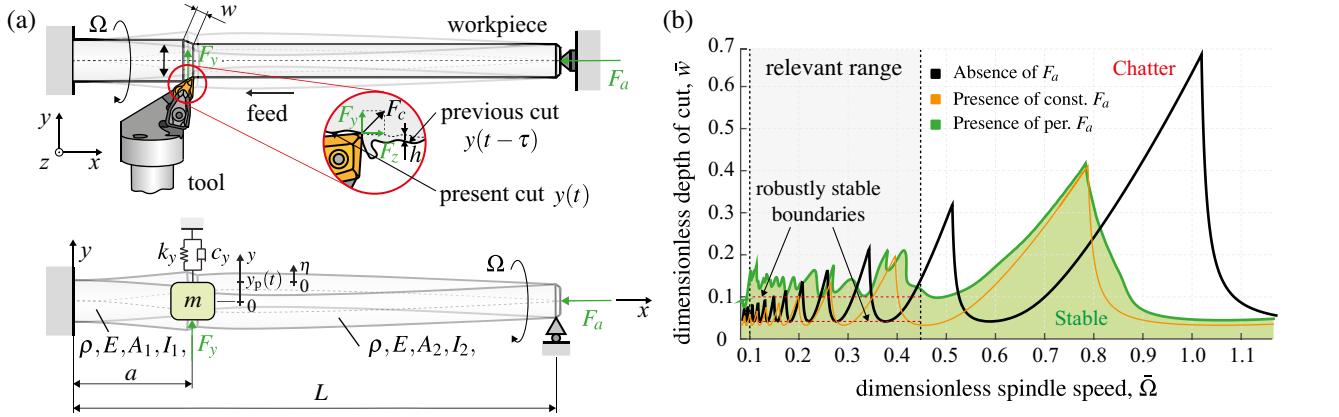

Figure 1: (a) 1 DoF dynamical model of turning process with flexible workpiece. (b) Stable parameter region of the material removal process for a certain tool position a and reliable precompression F_0.

where $\mathbf{q} = \mathrm{col}[\eta\ \dot{\eta}]$ is the state vector. It has to be noted that if τ and T are rationally dependent, the Floquet-theory can be applied [2, 7].

To identify the modal mass m of the workpiece at different tool positions a, the bending vibrations of a corresponding continuum beam model are investigated in the presence of a constant compression F_0. Since a one degree-of-freedom approximation is assumed in Fig 1(a), the first natural frequency of the system has to be fitted. It depends not only on the axial force but also on the cutting tool position because the length of the uncut segment of the workpiece changes.

The stability analysis of Eq. (1) is achieved by means of the semi-discretization method [7]. The dimensionless linearly stable parameter region of the operation can be seen in Fig. 1(b) where the lobe diagram indicated in black shows the stable domain in the absence of the axial force. When constant compression is applied, the natural frequency of the system decreases. It destabilizes the process in a way that the lobe diagram is shifted to the left and somewhat downward [5] (indicated in orange in Fig 1(b)). In contrast, when the compressive force is periodic about a precompression F_0 with a certain frequency, the stability boundary of the operation becomes more intricate (green region in Fig. 1(b)). While it does not mean too much for higher spindle speeds, a dedicated range can be found for operational turning where the compressive excitation predicts a reasonable increase in the size of the stable domain.

The lower envelope of the stability lobes represents robustly stable boundaries with respect to the spindle speed as shown in Fig. 1(b). For realistic parameters, the robust region is 2.5 times larger for periodic compression than for the non-compressed case.

CONCLUSIONS

The research presented was motivated by a novel option to achieve an increase in the stable parameter region for turning flexible workpieces. The workpiece is subjected to time-periodic compression. Even though compression has a destabilizing effect, periodic forcing improves the stability properties of the system. The results show that a dedicated parameter region can be proposed where high material removal rates can be attained for operational turning.

ACKNOWLEDGEMENT

This research was supported by the UNKP-19-3 New National Excellence Program of the Ministry for Innovation and Technology and the National Research, Development and Innovation Fund (TUDFO/51757/2019-ITM, Thematic Excellence Program.

References

[1] Tobias S.A. Machine tool vibration. London, Blackie, UK 1965.
[2] Seguy S., Insperger T., Arnaud L., Dessein G., Peign G. On the stability of high-speed milling with spindle speed variation. *International Journal of Advanced Manufacturing Technology* **48**: 883-895, 2010.
[3] Zatarain M., Bediaga I., Munoa J., Lizarralde R. Stability of milling processes with continuous spindle speed variation: Analysis in the frequency and time domains, and experimental correlation. *CIRP Annals* **57**: 379-384, 2008.
[4] Segalman D.J., Butcher E.A. Suppression of Regenerative Chatter via Impedance Modulation. *Journal of Vibration and Control* **6**: 243-256, 2000.
[5] Beri B., Stepan G. Stability of turning process with tool subjected to compression. *Procedia CIRP* **77**: 179-182, 2018.
[6] Stepan G., Kiss AK., Ghalamchi B., Sopanen J., Bachrathy D. Chatter avoidance in cutting highly flexible workpieces. *CIRP Annals* **66**: 377-380, 2017.
[7] Insperger T., Stepan G. Semi-Discretization for Time-Delay Systems. New York, Springer, NY 2011.

VIBRATION CHARACTERISTICS STUDY OF AIRCRAFT ELECTRIC BRAKE SQUEAL SYSTEM CONSIDERING MODALCOUPLING

Qiaozhi Yin*[1], Hong Nie[2], Xiaohui Wei[3] and Shuai Chen[4]
[1234]State Key Laboratory of Mechanics and Control of Mechanical Structures, Key Laboratory of Fundamental Science for National Defense-Advanced Design Technology of Flight Vehicle, Nanjing University of Aeronautics and Astronautics, Nanjing, P.R. China

Summary Based on the modal coupling theory, the rotor and stator contact stiffness and relative velocity are considered to build an electric aircraft brake dynamic system model in this study. The complex modal analysis is used to study the aircraft brake squeal performance and vibratory mechanism. Results show that the feed in energy is larger than the output energy in the brake rotor/stator module so that brake squeal takes place. Finally the transient dynamic analysis is adopted to verify the modeling approach and the complex modal analysis results.

INTRODUCTION

Aircraft brake squeal may cause the attrition and looseness of landing gear and brake components, influencing braking system security and passenger comfort[1]. Research on brake squeal performance and vibration system stability prediction can provide with theoretical foundation for the design of landing gear, braking system and system vibration reduction.

The complex modal analysis (CMA) and transient dynamic analysis (TDA) are usually used to study brake squeal[2]. Liu[3] built a set of perturbation equations of a hydraulic brake squeal system to study the vibration stability. Mercier[4] took the deviation of the relative velocities of each point at the interface into consideration and used springs to connect the rotors and the stators. The CMA is widely used in brake squeal study. But due to the difficulties in building a precise friction model between a rotor and a stator, the modal frequencies are not perfectly accurate. In this study, the contact stiffness and interface characteristics are considered to improve the accuracy of the brake squeal model.

The brake squeal model in TDA method is more precise but time consuming. A large amount of incrementation are used to calculate the motion states of every node in time domain. Nagy[5] proposed the TDA method to study brake squeal. The nonlinearity of brake pads interface is included. Sinou[6] adopted both stability and nonlinear TDA methods and pointed out that new fundamental frequencies can emerge due to the nonlinear contact of a frictional interface. Oberst[7] built a numerical model of a disc brake system to study the in-plane pad vibrations and the out-of-plane disc mode.

In this study, the aircraft electric brake squeal is analyzed. The rotor and stator contact stiffness and relative velocity are considered based on the modal coupling theory. Both the CMA and the TDA are applied to study the aircraft electric brake squeal mechanism.

AIRCRAFT ELECTRIC BRAKE SQUEAL MODEL

Aircraft electric brake mechanism consists of an electric actuator and a rotor/stator module, shown in Fig.1. The brake pressure P_b produced by the motor acts on the rotor/stator module to generate brake torque M_b. Brake squeal occurs during this braking process, resulting from the friction and relative motion at the interface of the rotors and stators. The modal coupling is considered so that a set of springs K_b connecting a rotor and a stator is built to simulate the interaction force in the brake squeal model. After discretizing the brake pads, the friction force matrix $\boldsymbol{F_f}$ can be expressed as:

$$\boldsymbol{F}_f = \mu_b \boldsymbol{P}_b + \mu_b K_b (\boldsymbol{U}_{sn} - \boldsymbol{U}_{rn}) \tag{1}$$

where, μ_b is the frictional coefficient. $\mu_b \boldsymbol{P_b}$ is the external excitation. $\boldsymbol{U_{sn}}$-$\boldsymbol{U_{rn}}$ is the relative displacement of the rotor and stator along the wheel axial direction. Therefore, the brake squeal dynamic model of a local mass block is:

$$\boldsymbol{MU} + \boldsymbol{CU} + (\boldsymbol{K} - \boldsymbol{K}_F)\ \boldsymbol{U} = 0 \tag{2}$$

where, $\boldsymbol{M}$, $\boldsymbol{C}$ and $\boldsymbol{K}$ are mass, damping and stiffness matrixes respectively. $\boldsymbol{U}$ is the nodal displacement vector. $\boldsymbol{K_F}$ is the coupling stiffness matrix, indicating the relationship between $\boldsymbol{F_f}$ and $\boldsymbol{U}$. $\boldsymbol{K_F}$ couples the nodal axial displacement and tangential friction force, thus $\boldsymbol{K}$-$\boldsymbol{K_F}$ is asymmetric. The aircraft brake rotor/stator FE model is illustrated in Fig. 2. Figure 3 shows the brake pressure distributes unevenly when braking and the separation takes place at the edge of the pads.

COMPLEX MODAL ANALYSIS

The system natural frequencies and the complex eigenvalues are obtained by complex modal analysis. The results are demonstrated in Fig. 4. If the real part of a complex eigenvalue is positive, the damping ratio is negative, indicating that the vibration system is unstable and brake squeal will occur. The modes with damping ratio ξ<-0.01 are regarded as the unstable modes. Figure 4 shows 21 unstable modes that may lead to brake squeal, among which most unstable modes are located at the frequencies of 4500Hz, 7300Hz, 8000Hz, 9700Hz and 11200Hz. Since the modal coupling exists in the brake squeal system, the intervals between these frequencies are different. In addition, the second-order modal frequency is much higher than that of the first-order.

*Corresponding author. E-mail: yinqiaozhi@nuaa.edu.cn.

The modal analysis is conducted and some typical unstable vibration modes are shown in Fig. 5. The out-of-plane vibration plays an important role in these modes. Only when the modal frequency is about 7574Hz, the pads vibrate with node-circles. At other frequencies lower than 10kHz, all the brake pads vibrate with 4-6 node-diameters. As the frequency increases, the vibration modes become more complex. The node-diameters increase and the modes among each pad are various. Therefore, the wheel axial direction modal coupling mainly results in aircraft brake squeal. From the perspective of modal coupling, the feed in energy is larger than the output energy in the system, so brake squeal finally takes place.

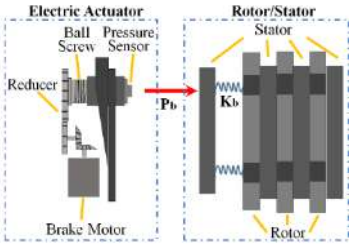

Figure 1. Aircraft brake mechanism model.

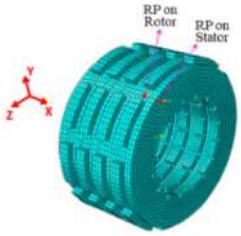

Figure 2. Brake rotor/stator FE model.

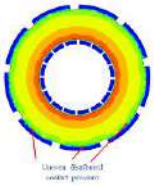
Figure 3. Contact pressure distribution when braking.

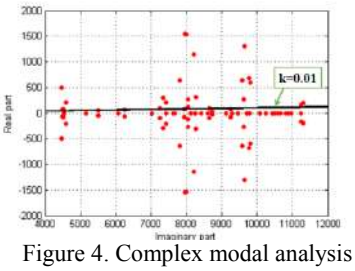

Figure 4. Complex modal analysis results.

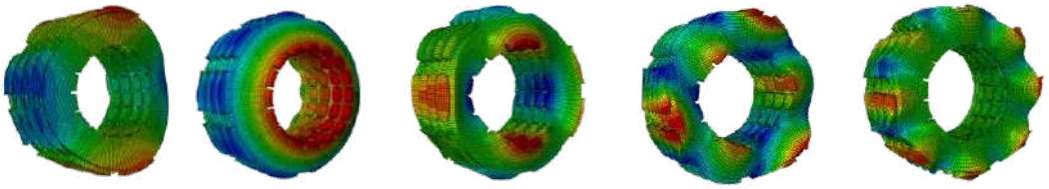
I=4572Hz, R=215 I=7574Hz, R=204 I=8101Hz, R=1150 I=9600Hz, R=1301 I=11205Hz, R=261

Figure 5. Some typical unstable vibration modes.

TRANSIENT DYNAMIC ANALYSIS

The TDA method is used to verify the correctness of the CMA results. The FE model is built considering the nonlinearities. The diagonal concentrated mass matrix and the central difference method are adopted to solve the vibration system responses. The reference points (RPs) on the rotor/stator and the reference frame are shown in Fig. 2. The vibrations along the y- and z-directions are slight, while the brake squeal appears along the x-direction. Figure 6 illustrates the x-directional displacement of RP on the stator. The results indicate that the squeal takes place mainly out of the plane, which is consistent with the CMA results. The amplitude-frequency curve in Fig. 6(b) shows that except a 13000Hz modal frequency appearing in TDA, the other modal frequencies all match the results in Fig. 4. This indicates that the aircraft brake dynamic system model considering the modal coupling can predict the brake squeal relatively accurately.

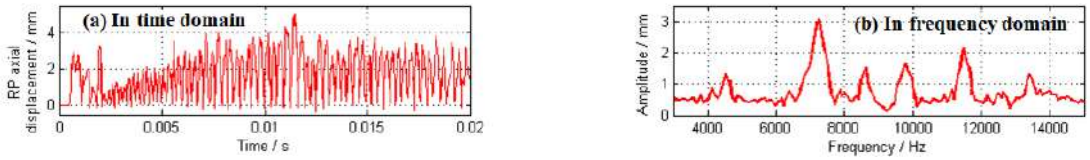

Figure 6. Transient dynamics analysis results.

CONCLUSIONS

The aircraft electric brake squeal system is studied based on the modal coupling theory. Both the CMA and the TDA are carried out to study the vibration performance. Results show that the brake dynamic model considering the modal coupling can predict the brake squeal relatively accurately. The vibration suppression methods will form part of our future work.

ACKNOWLEDGEMENT

This study was funded by the National Natural Science Foundation of China (Grant No. 51905264), the China Postdoctoral Science Foundation Funded Project (Grant No.2019M650115, and No.2020T130298), the National Defense Outstanding Youth Science Foundation (Grant No.2018-JCJQ-ZQ-053), the Fundamental Research Funds for the Central Universities (Grant No.NF2018001) and the Priority Academic Program Development of Jiangsu Higher Education Institutions.

References

[1] Gatt A, Besset S, Jézéquel L, et al. Reduction Methods Applied to Aircraft Brake Squeal Prediction and Simulation. *J. Aircr.* **54**: 1340-1349, 2017.
[2] Ouyang H, Nack W, Yuan Y, et al. Numerical Analysis of Automotive Disc Brake Squeal: A Review. *Int. J. Veh. Noise Vibr.* **1**: 207-231, 2005.
[3] Liu SY, Gordon JT and Ozbek MA. Nonlinear Model for Aircraft Brake Squeal Analysis: Model Description and Solution Methodology. *J. Aircr.* **35**: 623-630, 1998.
[4] Mercier A, Jezequel L, Besset S, et al. Nonlinear Analysis of the Friction-induced Vibrations of a Rotor-stator System. *J. Sound Vibr.* **443**: 483-501, 2019.
[5] Nagy LI, James C and Yu-Kan H. A New Method Development to Predict Brake Squeal Occurrence. *SAE Trans.* **103**: 416-423, 1994.
[6] Sinou JJ. Transient Non-linear Dynamic Analysis of Automotive Disc Brake Squeal – On the Need to Consider both Stability and Non-linear Analysis. Mech. Res. Commun. **37**: 96-105, 2010.
[7] Oberst S and Lai JCS. Nonlinear Transient and Chaotic Interactions in Disc Brake Squeal. *J. Sound Vibr.* **342**: 272-289, 2015.

NON-AXISYMMETRIC FREE VIBRATIONS OF A SPHERICAL SHELL UNDER PRESSURE

Suresh Shrivastava
Department of Civil Engineering, McGill University, Montreal, Quebec, Canada

Summary In a recent conference paper, Shrivastava [1], has derived the non-axisymmetric mode shapes and frequencies of a complete composite spherical shell under external or internal uniform pressure. The exact analysis took into account the transverse shear deformations and the rotary inertias. The analysis here is again exact, but is simpler by restricting it to homogeneous shell and neglecting the last two effects. Multiple non-axisymmetric modes exist for single frequencies.

1 INTRODUCTION

Many papers have appeared on the subject of frequencies of axisymmetric vibrations of thin elastic spherical shells beginning with the work of Lamb in 1893. Here, general frequencies and mode shapes are derived for a homogeneous elastic spherical shell under an all-around pressure. Transverse shear deformations and rotary inertia effects are neglected.

2 GOVERNING EQUATIONS, THEIR SOLUTION, DISCUSSION AND CONCLUSIONS

Let ϕ,θ,z be the meridional (+ zenith to nadir), azimuthal (+ counter clockwise), and radial (+ outward normal) coordinates of a shell point. The ratio of thickness h to the middle surface radius R is small. Let the coordinate displacements from equilibrium, after the uniform pressure is applied, be:

$$u(\phi,\theta)-z\alpha(\phi,\theta),v(\phi,\theta)-z\beta(\phi,\theta),w(\phi,\theta)$$

where u,v,w and α,β are the amplitudes of the middle surface displacements and rotations. The actual quantities are the amplitudes multiplied with $e^{i\omega t}$ where ω is a natural frequency. The displacement gradient and strain matrices are:

$$[L]=\begin{pmatrix} \frac{\partial u}{Rd\varphi}-z\frac{\partial\alpha}{Rd\varphi}+\frac{w}{R} & \frac{\partial u}{R\sin\phi d\theta}-z\frac{\partial\alpha}{R\sin\phi d\theta}-\frac{\cot\phi}{R}(v-z\beta) & -\alpha \\ \frac{\partial v}{R\partial\phi}-\frac{z\partial\beta}{R\partial\phi} & \frac{\partial v}{R\sin\phi\partial\theta}-z\frac{\partial\beta}{R\sin\phi\partial\theta}+\frac{\cot\phi}{R}(u-z\alpha)+\frac{w}{R} & -\beta \\ \frac{\partial w}{R\partial\phi}-\frac{u}{R} & \frac{\partial w}{R\sin\phi\partial\theta}-\frac{v}{R} & 0 \end{pmatrix}$$ and

$$[\varepsilon]=\begin{pmatrix} \frac{\partial u}{Rd\varphi}-z\frac{\partial\alpha}{Rd\varphi}+\frac{w}{R} & \frac{\partial u}{R\sin\phi d\theta}-z\frac{\partial\alpha}{R\sin\phi d\theta}-\frac{\cot\phi}{R}(v-z\beta) & 0 \\ \frac{\partial v}{R\partial\phi}-\frac{z\partial\beta}{R\partial\phi} & \frac{\partial v}{R\sin\phi\partial\theta}-z\frac{\partial\beta}{R\sin\phi\partial\theta}+\frac{\cot\phi}{R}(u-z\alpha)+\frac{w}{R} & 0 \\ \alpha=\frac{\partial w}{R\partial\phi}-\frac{u}{R} & \beta=\frac{\partial w}{R\sin\phi\partial\theta}-\frac{v}{R} & 0 \end{pmatrix}$$

where $[\varepsilon]=([L]^T+[L])/2$. The rotations $\alpha=(\partial w/R\partial\phi)-(u/R)$ and $\beta=(\partial w/R\sin\phi\partial\theta)-(v/R)$ have been chosen to render the transverse shear strains zero. The stresses due to pressure q are equi-biaxial compression (or tension) $P=h\sigma^o_{\phi\phi}=h\sigma^o_{\theta\theta}=qR/2$. For isotropic elastic shells, the additional stresses due to the above strains are $\sigma_{\phi\phi}=B\varepsilon_{\phi\varphi}+C\varepsilon_{\theta\theta},\sigma_{\theta\theta}=C\varepsilon_{\phi\varphi}+B\varepsilon_{\theta\theta},\sigma_{\phi\theta}=2F\varepsilon_{\phi\theta},\sigma_{zz}=\varepsilon_{\phi z}=\varepsilon_{\theta z}=\varepsilon_{zz}=0$ where $B=E/(1-\nu^2),C=\nu E/(1-\nu^2),$ $F=E/2(1+\nu),B-C=2F$, $\rho_a=\rho h$, where ρ is the mass density. $B_a=Bh,B_b=\frac{B_a}{12}$ etc. Washizu's formula gives the equilibrium equations $\int_V\{tr(([\sigma^o][L]^T[\delta L])+[\sigma][\delta L])\}dV=0$, δ denotes variation. D'Alembert's principle yields, the vibration equations, where ω is a natural frequency:

$$-\frac{\partial N_{\phi\phi}}{\partial\phi}-\cot\phi(N_{\phi\phi}-N_{\theta\theta})-\frac{\partial N_{\phi\theta}}{\sin\phi\partial\theta}-Q_\phi+P\{(\nabla^2-\cos ec^2\phi)\frac{u}{R}-2\frac{\cot\phi}{R\sin\phi}\frac{\partial v}{\partial\theta}+2\frac{\partial w}{R\partial\varphi}\}-R\rho_a\omega^2u=0,$$

$$-\frac{1}{\sin\phi}\frac{\partial N_{\theta\theta}}{\partial\theta}-\frac{\partial N_{\phi\theta}}{\partial\phi}-2\cot\phi N_{\phi\theta}-Q_\theta+P\{(\nabla^2-\cos ec^2\phi)\frac{v}{R}+2\frac{\cot\phi}{R\sin\phi}\frac{\partial u}{\partial\theta}+\frac{2}{R\sin\phi}\frac{\partial w}{\partial\theta}\}-R\rho_a\omega^2v=0,$$

$$-\frac{1}{\sin\phi}\frac{\partial Q_\phi\sin\phi}{\partial\phi}-\frac{1}{\sin\phi}\frac{\partial Q_\theta}{\partial\theta}+N_{\phi\phi}+N_{\theta\theta}+P\{(\nabla^2-2)\frac{w}{R}-\frac{2}{R}\frac{\partial u}{\partial\phi}-2\cot\phi\frac{u}{R}-\frac{2}{R\sin\phi}\frac{\partial v}{\partial\theta}\}-R\rho_a\omega^2w=0$$

where the stress resultants are:

$$N_{\phi\phi}=C_a\cot\phi\frac{u}{R}+(B_a+C_a)\frac{w}{R}+C_a\frac{\partial v}{R\sin\phi\partial\theta}+B_a\frac{\partial u}{R\partial\phi},N_{\theta\theta}=B_a\cot\phi\frac{u}{R}+(B_a+C_a)\frac{w}{R}+B_a\frac{\partial v}{R\sin\phi\partial\theta}+C_a\frac{\partial u}{R\partial\phi},,$$

$$N_{\phi\theta}=F_a(\cot\phi\frac{v}{R}+\frac{w}{R}+\frac{\partial u}{R\sin\phi\partial\theta}+\frac{\partial v}{R\partial\phi}),M_{\phi\theta}=\frac{h^2}{R}F_b(\frac{\partial u}{R\sin\phi\partial\theta}+\frac{\partial v}{R\partial\phi}+\cot\phi\frac{v}{R}+\frac{2\cot\phi\partial w}{R\sin\phi\partial\theta}-\frac{2\partial^2w}{R\sin\phi\partial\theta\partial\phi}),$$

$$M_{\phi\phi}=\frac{h^2}{R}(C_b\cot\phi\frac{u}{R}+C_b\frac{\partial v}{R\sin\phi\partial\theta}-C_b\frac{\partial^2w}{R\sin^2\phi\partial\theta^2}+B_b\frac{\partial u}{R\partial\phi}-C_b\cot\phi\frac{\partial w}{R\partial\phi}-B_b\frac{\partial^2w}{R\partial\phi^2}),$$

$$M_{\theta\theta}=\frac{h^2}{R}(B_b\cot\phi\frac{u}{R}+B_b\frac{\partial v}{R\sin\phi\partial\theta}-B_b\frac{\partial^2w}{R\sin^2\phi\partial\theta^2}+C_b\frac{\partial u}{R\partial\phi}-B_b\cot\phi\frac{\partial w}{R\partial\phi}-C_b\frac{\partial^2w}{R\partial\phi^2}),$$

$Q_\phi=\frac{\partial M_{\phi\phi}}{R\partial\phi}+\frac{1}{R\sin\phi}\frac{\partial M_{\phi\theta}}{\partial\theta}+(M_{\phi\phi}-M_{\theta\theta})\frac{\cot\phi}{R},Q_\theta=\frac{1}{R\sin\phi}\frac{\partial M_{\theta\theta}}{\partial\theta}+\frac{\partial M_{\phi\theta}}{R\partial\phi}+\frac{2\cot\phi}{R}M_{\phi\theta}$ $\nabla^2=\frac{\partial^2}{\partial\phi^2}+\cot\phi\frac{\partial}{\partial\phi}+\frac{1}{\sin^2\phi}\frac{\partial^2}{\partial\theta^2}$ is the Legendre operator. Substitution in the vibration equations gives the three governing equations in the variables u,v,w:

$$(-2F_a-2\frac{h^2}{R^2}F_b+B_a\cos ec^2\phi+\frac{h^2}{R^2}B_b\cos ec^2\phi)u-(F_a+\frac{h^2}{R^2}F_b)\frac{\partial^2u}{\sin^2\phi\partial\theta^2}-\frac{h^2}{R^2}B_b\frac{1}{\sin\phi}\frac{\partial}{\partial\phi}\sin\phi\frac{\partial u}{\partial\phi}-B_a\frac{1}{\sin\phi}\frac{\partial}{\partial\phi}\sin\phi\frac{\partial u}{\partial\phi}-R^2\rho_a\omega^2u+$$

$$(\frac{h^2}{R^2}(B_b+F_b)+(B_a+F_a))\frac{\cot\phi}{\sin\phi}\frac{\partial v}{\partial\theta}+\frac{h^2}{R^2}(-B_b+F_b-B_a+F_a)\frac{1}{\sin\phi}\frac{\partial^2v}{\partial\phi\partial\theta}-\frac{h^2}{R^2}2B_b\frac{Cot\phi}{\sin^2\phi}\frac{\partial^2w}{\partial\theta^2}-(2B_b-2F_a-2F_b\frac{h^2}{R^2})\frac{\partial w}{\partial\phi}-\frac{h^2B_b}{R^2}\frac{1}{\sin^2\phi}\frac{\partial w}{\partial\phi}$$

$$+\frac{h^2B_b}{R^2}\frac{1}{\sin^2\phi}\frac{\partial^3w}{\partial\theta^2\partial\phi}+\frac{1}{\sin\phi}\frac{\partial}{\partial\phi}(B_b\frac{h^2}{R^2}\sin\phi\frac{\partial^2w}{\partial\phi^2})+P\{(\nabla^2-\csc^2\phi)u-2\frac{\cot\phi}{\sin\phi}\frac{\partial v}{\partial\theta}+2\frac{\partial w}{\partial\phi}\}=0$$

$$(-\frac{h^2B_b}{R^2}-\frac{h^2F_b}{R^2}-B_a-F_a)\frac{\cot\phi}{\sin\phi}\frac{\partial u}{\partial\theta}+(-\frac{h^2B_b}{R^2}+\frac{h^2F_b}{R^2}-B_a+F_a)\frac{1}{\sin\phi}\frac{\partial^2 u}{\partial\phi\partial\theta}-\rho\omega^2 v-2F_a v-\frac{2h^2F_b}{R^2}v-\frac{h^2B_b}{R^2}\frac{1}{\sin^2\phi}\frac{\partial^2 v}{\partial\theta^2}-B_a\frac{1}{\sin^2\phi}\frac{\partial^2 v}{\partial\theta^2}-F_a\frac{\partial^2 v}{\partial\phi^2}-F_a\cot\phi\frac{\partial v}{\partial\phi}+\frac{F_a}{\sin^2\phi}v-$$
$$\frac{h^2F_b}{R^2}\frac{\partial^2 v}{\partial\phi^2}-\frac{h^2F_b}{R^2}\cot\phi\frac{\partial v}{\partial\phi}+\frac{h^2F_b}{R^2}\cos ec^2\phi v++\frac{2h^2B_b}{R^2}\frac{\cot\phi}{\sin\phi}\frac{\partial^2 w}{\partial\phi\partial\theta}+\frac{2h^2F_b}{R^2}\frac{\cot\phi}{\sin\phi}\frac{\partial^2 w}{\partial\phi\partial\theta}+2(\frac{h^2F_b}{R^2}-B_a+F_a)\frac{1}{\sin\phi}\frac{\partial w}{\partial\theta}+(\frac{h^2B_b}{R^2}\frac{1}{\sin^3\phi}\frac{\partial^3 w}{\partial\theta^3})(-2F_a-2\frac{h^2}{R^2}F_b+B_a\cos ec^2\phi+$$
$$\frac{h^2}{R^2}B_b\cos ec^2\phi)u-(F_a+\frac{h^2}{R^2}F_b)\frac{\partial^2 u}{\sin^2\phi\partial\theta^2}-\frac{h^2}{R^2}B_b\frac{1}{\sin\phi}\frac{\partial}{\partial\phi}\sin\phi\frac{\partial u}{\partial\phi}-B_a\frac{1}{\sin\phi}\frac{\partial}{\partial\phi}\sin\phi\frac{\partial u}{\partial\phi}-R^2\rho_a\omega^2 u+P\{(\nabla^2-\csc^2\phi)v+2\frac{\cot\phi}{\sin\phi}\frac{\partial u}{\partial\theta}+2\frac{\partial w}{\sin\phi\partial\theta}\}=0$$

$$-\frac{h^2}{R^2}B_b\frac{\partial^3 u}{\partial\phi^3}-\frac{2h^2B_b}{R^2}\cot\phi\frac{\partial^2 u}{\partial\phi^2}+(-\frac{2h^2F_b}{R^2}+2B_a-2F_a+\frac{h^2B_b}{R^2}+\frac{h^2B_b}{R^2}\cos ec^2\phi)\frac{\partial u}{\partial\phi}+(-\frac{2h^2F_b}{R^2}+2B_a-2F_a-\frac{h^2B_b}{R^2}\cos ec^2\phi)\cot\phi u-\frac{h^2B_b}{R^2}\cos ec^2\phi\frac{\partial^3 u}{\partial\phi\partial\theta^2}+(-\frac{2h^2F_b}{R^2}+2B_a-2F_a$$
$$-\frac{h^2B_b}{R^2}\cos ec^2\phi)\cot\phi u-\frac{h^2B_b}{R^2{}_b}\cos ec^2\phi\frac{\partial^3 u}{\partial\phi\partial\theta^2}-\frac{h^2B_b}{R^2{}_b\sin^2\phi}\frac{\cot\phi}{\partial\theta^2}\frac{\partial^2 u}{\partial\theta^2}-\frac{h^2B_b}{R^2{}_b}\frac{1}{\sin\phi}\frac{\partial^3 v}{\partial\theta\partial\phi^2}-\frac{h^2B_b}{R^2}\frac{1}{\sin^3\phi}\frac{\partial^3 v}{\partial\phi^3}+\frac{h^2B_b}{R^2}\frac{\cot\phi}{\sin\phi}\frac{\partial^2 v}{\partial\phi\partial\theta}+\frac{2h^2F_b}{R^2}\frac{\cot\phi}{\sin\phi}\frac{\partial^2 v}{\partial\phi\partial\theta}+(-\frac{2h^2F_b}{R^2}+2B_a-2F_a-$$
$$\frac{h^2B_b}{R^2}\cos ec^2\phi)\cos ec\phi\frac{\partial v}{\partial\theta}+\frac{h^2B_b}{R^2}\frac{\partial^4 w}{\partial\phi^4}+\frac{2h^2B_b}{R^2}\cot\phi\frac{\partial^3 w}{\partial\phi^3}+(-\frac{2h^2B_b}{R^2}+-\frac{2h^2F_b}{R^2})\frac{\partial^2 w}{\partial\phi^2}+(+\frac{h^2B_b}{R^2}+\frac{2h^2F_b}{R^2}++\frac{2h^2F_b}{R^2}\sin^2\phi)\frac{\cot\phi}{\sin^2\phi}\frac{\partial w}{\partial\phi}+\frac{h^2B_b}{R^2\sin^4\phi}\frac{\partial^4 w}{\partial\theta^4}+\frac{2h^2B_b}{R^2\sin^2\phi}\frac{\partial^4 w}{\partial\phi^2\partial\theta^2}-$$
$$\frac{2h^2B_b}{R^2}\frac{\cot\phi}{\sin^2\phi}\frac{\partial^3 w}{\partial\phi\partial\theta^2}+(\frac{2h^2B_b}{R^2}\cot^2\phi+\frac{2h^2B_b}{R^2}\cos ec^2\phi+\frac{2h^2F_b}{R^2}\cos ec^2\phi)\frac{1}{\sin^2\phi}\frac{\partial^2 w}{\partial\theta^2}+(4B_a-4F_a)w-R^2\rho\omega^2 w+P\{(\nabla^2-2)w-2\frac{\partial u}{\partial\phi}-2u\cot\phi-2\frac{\partial v}{\sin\phi\partial\theta})=0$$

Separation of variables can be made: $u(\phi,\theta)=u'(\phi)\cos(m\theta), v(\phi,\theta)=v'(\phi)\sin(m\theta), w(\phi,\theta)=w'(\phi)\cos(m\theta)$ where m is an integer. This results in three ordinary differential equations in ϕ. Equations belonging to u', v' can be manipulated (1) by eliminating w' from them, and (2) by forming an equation with terms like $\nabla^2 w'$ in it. A function $\chi(\phi)$ such that $u'(\phi)=\frac{d\chi(\phi)}{d\phi}, v'(\phi)=-\frac{m\chi(\phi)}{\sin(\phi)}$ satisfies the newly formed first equation identically. The second new equation and the old third equation are now the two homogeneous equations in variables χ and w', In matrix form:

$$\begin{pmatrix} -(\frac{h^2B_b}{R^2}+B_a-P)\nabla^4-(\frac{2h^2F_b}{R^2}+2F_a+R^2\rho_a\omega^2)\nabla^2 & \frac{h^2B_b}{R^2}\nabla^4+2(\frac{h^2F_b}{R^2}+F_a-B_a+P)\nabla^2 \\ -\frac{h^2B_b}{R^2}\nabla^4-2(\frac{h^2F_b}{R^2}+F_a-B_a+P)\nabla^2 & \frac{h^2}{R^2}B_b\nabla^4+(2\frac{h^2}{R^2}F_b+P)\nabla^2+4B_a-4F_a-2P-R^2\rho_a\omega^2 \end{pmatrix}\begin{pmatrix}\chi\\ w\end{pmatrix}=\begin{pmatrix}0\\0\end{pmatrix}$$

For a non-trivial solution, let $\chi=A_1P_m^n(\cos\phi), w=A_2P_m^n(\cos\phi)$ where A_1, A_2 are arbitrary constants, and $P_m^n(\cos\phi)$ are the Associated Legendre Functions. These have the property that $\nabla^2P_m^n(\cos\phi)=-\mu, \nabla^4P_m^n(\cos\phi)=\mu^2, \mu=n(n+1)$. Thus, the mode shapes clearly satisfy the above equations. The frequency equation (the determinant of the above matrix) contains only μ, i.e. only n but not m. The frequencies are independent of m as long as $0\le m\le n$. Frequencies obtained by presuming only the axisymmetric deformations ($m=0$) are therefore correct. For any $m>n$, the Associated Legendre Function is zero. Thus for every n^{th} frequency there are $n+1$ distinct modes, n non-axisymmetric and always one axisymmetric. For any one frequency, a linear combination of all permissible modes can appear simultaneously. The figure below shows the modes for $P=0$ and $n=12$, four distinct modes out of the possible 13 are shown.

For $n=\mu=m=P=0$, the vibration is purely radial with the frequency exactly that in Love. For $n=1$,regardless of the pressure, $\omega=0$, signifying two rigid body modes, one axisymmetric and the other non-axisymmetric. The present frequencies are compared with the axisymmetric theoretical results, and their experimental results given in Duffey et al. [2]. The experiments were done for a steel shell with $R=4.4688$ in, $h=0.0625$ in, psi, $\rho=0.000751$ lbf-sect/in^4, $E=28\times10^6$ psi, $\nu=0.28$ and $P=0$ were employed. As seen in Table 1, the present theoretical results match the reported ones, exactly with the refined analysis [1]. The theoretical results agree quite well with the experiments. Table 2 shows the frequencies under $\sigma_{\phi\phi}^o=\sigma_{\theta\theta}^o=15{,}000$ psi. Results are as expected; the frequencies increase with internal pressure and decrease with the external one. The conclusion is that the results of the present simpler theory are quite good.

Table 1. Theoretical and experimental verification, frequencies in Hz

Freq. No.	Mean Experiments	Analytical Duffey et al	Analytical Previous[1]	Analytical Present
n = 2	5088	5078	5078	5078
n = 3	6028	6005	6005	6006
n = 4	6379	6378	6378	6379
n = 5			6581	6583
n = 6	6680	6729	6729	6732

Table 2. Frequencies in Hz for Duffey shell with $\sigma^o=\pm15{,}000$ psi

Freq. No.	No pressure	σ^o comp	σ^o tensile
n = 0	6078	6078	6078
n = 1	0	0	0
n = 2	5078	5071	5086
n = 3	6005	5987	6024
n = 4	6378	6345	6412
n = 5	6581	6531	6634
n = 6	6729	6732	6804

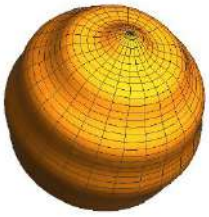

Mode Shape for n = 12 and m = 0, Axisymmetric

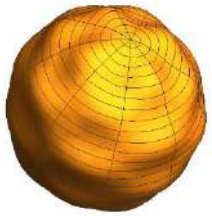

Mode Shape for n = 12 and m = 4, Non-axisymmetric

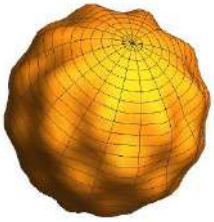

Mode Shape for n = 12 and m = 8, Non-axisymmetric

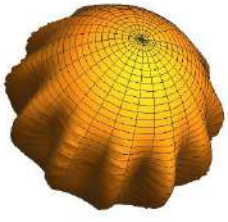

Mode Shape for n = 12 and m = 12, Non-axisymmetric

REFFERENCES: [1] Shrivastava, S. 2019, Frequencies of Vibrations of a Spherical Shell with All-Around Pressure, Proceedings of the SEMC Seventh International Conference, Cape Town, South Africa.[2] Duffey, T.A, Romero, C., Robertson, A.N. & Steinzig, M.L. 2005. Vibrations of Complete Spherical Shell with Imperfections, International Modal Analysis Conference (IMAC XXIII), Orlando, USA.

ON THE CAUSE OF DISAGREEMENT BETWEEN SIMULATED AND EXPERIMENTAL RESULTS FOR THE STABILITY PROBLEM OF INVERTED STABILIZED PENDULUMS (BASED ON NATURE PAPER BY D. ACHESON, T. MULLIN)

Vladimir A. Gribkov* and Yaroslav D. Gordin
Department of Aerospace Systems,
Bauman Moscow State Technical University (National Research University), Moscow, Russia

Abstract This paper determined the cause of strong disagreement between simulated and experimentally determined regions of stability of inverted stabilized pendulums presented in a well-known Nature paper by D. Acheson and T. Mullin. The reason is a large error of experimental determination of higher natural frequencies of the double and triple pendulums using parametric resonance. The regions of stability determined using D. Acheson's pendulum theorem based on the corrected simulated natural frequencies have better agreement with the experimentally determined regions of stability. Additional experimental verification was done using pendulums with parameters different from those used by D. Acheson and T. Mullin. The verification confirmed the correctness of the proposed cause of disagreement and validated the D. Acheson theorem.

One of the most known papers devoted to the experimental investigation of the stability of vibration stabilized inverted pendulums is the paper by D. Acheson, T. Mullin published in Nature [1].

Although this paper was published a long ago, it is still one of the most reputable experimental investigations of the systems of this class. The goal of that study was to do an experimental verification of the pendulum theorem [2] proposed by D. Acheson.

Single, double, and triple inverted pendulums, which are parametrically stabilized by harmonic oscillations of the pivot axes, were chosen as study subjects in [1]. Fig. 1a shows the stability diagram made based on the results of [1]. This diagram is plotted as dimensionless amplitude excitation parameter vs. dimensionless frequency parameter.

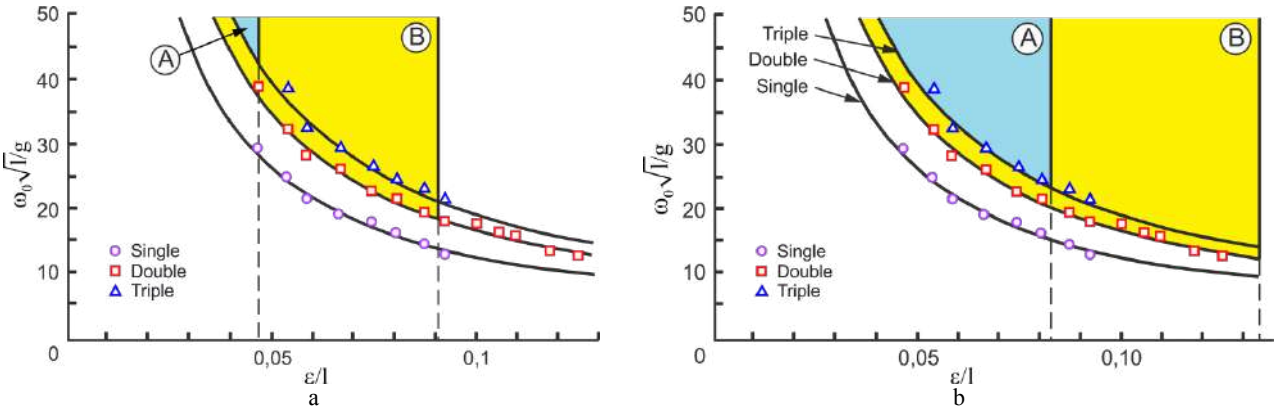

Figure 1. Calculated and experimental regions of stability of three pendulums from the paper by D. Acheson and T. Mullin; (a) – using data from [1], (b) – using refined parameters

The calculated stability boundaries were obtained using the pendulum theorem, and they are in good agreement with a set of experimental points (markers) on the quasi-static boundary of the stability region for a single, double, and triple pendulums. These are the left stability region boundary curves. Fig. 1a also shows two straight right boundary lines, which were also obtained using the pendulum theorem. When the right straight boundary lines are crossed, the double and triple pendulums lose dynamic stability (dynamic boundary line). The calculated results for plotting the second (dynamic) boundary line of the stability region were given in [1], but they were not shown at the stability diagram. In Fig. 1a, the stability regions of the triple and double pendulums are denoted as Region A (blue fill) and Region B (yellow fill), accordingly.

Based on results obtained by D. Acheson and T. Mullin, the pendulum theorem was not confirmed experimentally. Most of the experimental results for the double pendulum and all results for the triple pendulum lie beyond the boundaries of the calculated region of stability (Fig. 1a).

According to the pendulum theorem, the boundary lines of the region of stability are determined from natural frequencies of the pendulums in the gravity field in the natural (lower non-inverted) position with a stationary pivot axis. The quasi-static boundary lines are determined by the lowest pendulum natural frequency, and the dynamic boundary line is determined by the highest natural frequency. In [1], these frequencies were determined experimentally using parametric resonance.

The strong disagreement between the calculated and experimental regions of stability in [1] might have been caused by the error of measuring higher natural frequencies via parametric resonance. The assumption can be tested by calculating these natural frequencies of the pendulums. However, some of the pendulums' parameters required for the calculation were not given in [1]. The missing parameters (material properties of links and pivots, geometric and

*Corresponding author. E-mail: zenit-ab@mail.ru.

physico-mechanical parameters of the pendulums' elements) were obtained from the simulation in SolidWorks (SW) and MSC.Adams. Tables 1 and 2 present the refined parameters used for calculations. The parameters are denoted as follows: m_i – pendulum link mass; l_i – pendulum link length; l_{ci} – distance from link pivot to the link's center of mass; I_i – link's moment of inertia about its center of mass. Table 2 presents lower/higher natural frequencies determined using refined and restored pendulums' parameters.

Table 1. Pendulums' links' parameters

Link number	m_i, g	l_i, mm	l_{ci}, mm	I_i, g/mm^2
1	19.164	190	111.411	112848.476
2	19.164	190	111.411	112848.476
3	11.846	184	64.066	43034.804

Table 2. Natural frequencies

Number of links	Experiment, Hz	Modeling in SW, Hz
1	1.227	1.288
2	0.935/2.510	0.927/2.094
3	0.824/3.660	0.829/2.654

Fig. 1b shows the calculated boundary lines of the stability regions for the double and triple pendulums. The calculation results were obtained based on refined values of natural frequencies. It is evident that all experimental points for the double pendulum (Region A) and most of the points for the triple pendulum (Region B) are on the boundaries of the corresponding stability regions. The agreement between the calculated and experimental stability regions validates the pendulum theorem.

For additional verification of the pendulum theorem and harmonizing the boundaries of the calculated and experimental regions of stability, we used the results obtained in [3]. The results were obtained for the single, double, and triple (See Fig. 2a) pendulums with parameters given in [3]. The stability diagrams of dimensional frequency vs. amplitude of the pendulum's pivot axis are shown in Fig. 2(b-d). Here, the X-axes represent the excitation amplitude in mm, and the Y-axes represent the parametric excitation frequency in Hz. The calculated results are plotted with lines, and the experimental results are plotted with markers. The regions of stability are filled.

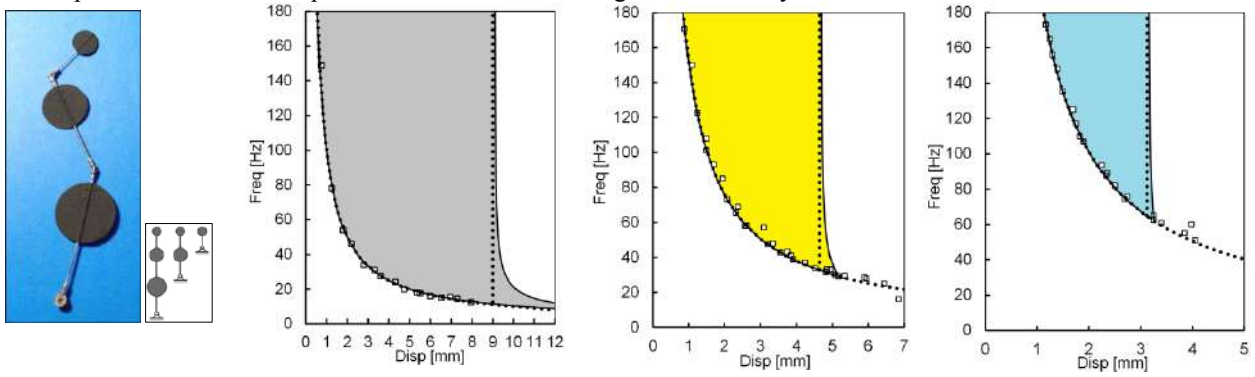

Figure 2. Stability regions of three pendulums: single (b), double (c) and triple (d)

The calculated results were obtained using the pendulum theorem (dotted line) and the method described in [4] (solid line). For the left (quasi-static) boundary line, the results coincide. For the right (dynamic) boundary, the results obtained with the pendulum theorem somewhat differ from the results obtained in [4]. The agreement between the calculated and experimental results is good. For the left boundary, they practically coincide, except for several experimental points for the double and triple pendulum, which have crossed the calculated stability region. This phenomenon is probably caused by neglecting dissipation in the system during simulations.

References

[1] Acheson D.J., Mullin T. Upside-down pendulums // Nature. 1993. 366. p. 215–216.

[2] Acheson D.J. A pendulum theorem // Proc. Roy. Soc. London. 1993. Ser. A. V. 443. p. 239-245.

[3] Gribkov V.A., Khokhlov A.O. Experimental Study of Inverted Regulable Pendulum Stability // Vestn. Mosk. Gos. Tekh. Univ. im. N.E. Baumana. Estestv. Nauki [Herald of the Bauman Moscow State Tech. Univ. Nat. Sci.], 2017, no.2. pp. 22-39. DOI: 10.18698/1812-3368-2017-2-22-39. (in Russian).

[4] Gribkov V.A., Khokhlov A.O. A method to simplify of stability problem for parametrically stabilized statically unstable pendulum systems // Izvestiya vysshikh uchebnykh zavedeniy. Mashinostroenie [Proceedings of Higher Educational Institutions. Mashine Building]. 2015, no. 6. pp. 29-38. DOI: 10.18698/0536-1044-2015-11-29-38. (in Russian).

MULTI BALLS ROTATING IN A CIRCULAR TRACK EFFICIENTLY MITIGATE FLOW-INDUCED VIBRATIONS

Michael M. Selwanis[1,2], Guilherme Rosa Franzini[3], Cédric Béguin[1], and Frédérick P. Gosselin*[1]
[1] Department of Mechanical Engineering, Polytechnique Montréal, Québec, Canada
[2] Aerospace Engineering Department, Military Technical College, Cairo, Egypt
[3] Offshore Mechanics Laboratory, Escola Politécnica, University of São Paulo, Brazil

Summary Galloping, as a critical type of flow-induced vibration (FIV), has a destructive effect on different structures subjected to wind. In this paper, we introduce a simple, low-cost device able to absorb the energy of vibrating structures and reduces its galloping amplitudes. This purely nonlinear energy sink (NES) consists of multi balls rotating freely in a circular track without direct coupling with the primary system. We assess the benefit of the proposed NES in mitigating galloping of a square prism through wind tunnel tests. NES balls rotate due to dynamic interaction with the vibrating structure providing a way of nonlinear energy absorption, enhanced by ball impacts in a multi-ball NES. We test different NES configurations varying the number of NES balls to demonstrate the effect of the balls' number. Whereas a single ball NES with a mass 8% that of the prism can increase the reduced velocity of large-amplitude galloping by 68%, a 2 or 3-ball NES of the same total mass increases this critical velocity by 87%.

INTRODUCTION

Transverse galloping generated during heavy winds can lead to natural disasters putting bridges and skyscrapers at risk. A linear tuned mass damper (TMD) is a simple solution for damping the vibration of high buildings. However, it works only in a narrow frequency band and changes the characteristics of the primary system adding new frequencies. A different type of vibration absorbers known as Nonlinear energy sinks (NES) can overcome the drawbacks of the TMD [1]. The non-linearizable stiffness of such a suppressor enables it to engage with the dynamics of the primary structure, mitigating its vibration amplitudes over a wide band of frequencies [3].

Developing a purely NES, composed of a metal ball rotating freely in a circular track without direct coupling with the primary structure, was a considerable simplification in the NES design [2]. That should extend the industrial applications of such types of NESs, taking into consideration their significant effect on mitigating FIV. As an extension of this research, we introduce a multi-ball NES that depends on the impact between balls to improve the energy absorption efficiency. In this paper, wind tunnel tests validate the effect of the multi-ball NES in mitigating the galloping of a square prism. Depending on the design of the presented NES, we change the NES track dimensions by swapping some parts to use a different number of balls without changing the NES total mass.

METHODOLOGY

We follow the same methodology presented in Ref.[2] performing the experiments in the closed-loop wind tunnel (Model 407-B, ELD, Lake City, MN, USA) of the mechanical engineering department of Polytechnique Montréal. Fig. 1(a) presents the experimental set up in detail; a lightweight model of a square prism of 5 cm side length and 58 cm height is mounted by two identical elastic supports, located at the upper and lower sides of the wind tunnel test section. The prism can oscillate only in the transverse direction to the flow, behaving as a single degree of freedom (DOF) system. We installed a pair of plates at the two ends of the square prism to prevent the escape of airflow from the wind tunnel test

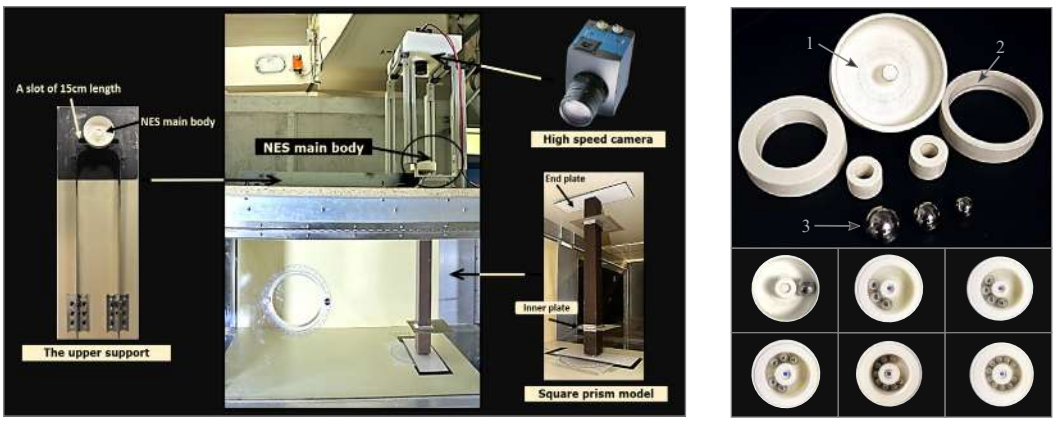

(a) (b)

Figure 1: (a) Experimental setup. (b) Exploded view for NES parts: 1- main body, 2- bushings, 3- steel balls, and different configurations of the multi-ball NES of equivalent mass.

*Corresponding author. E-mail: frederick.gosselin@polymtl.ca.

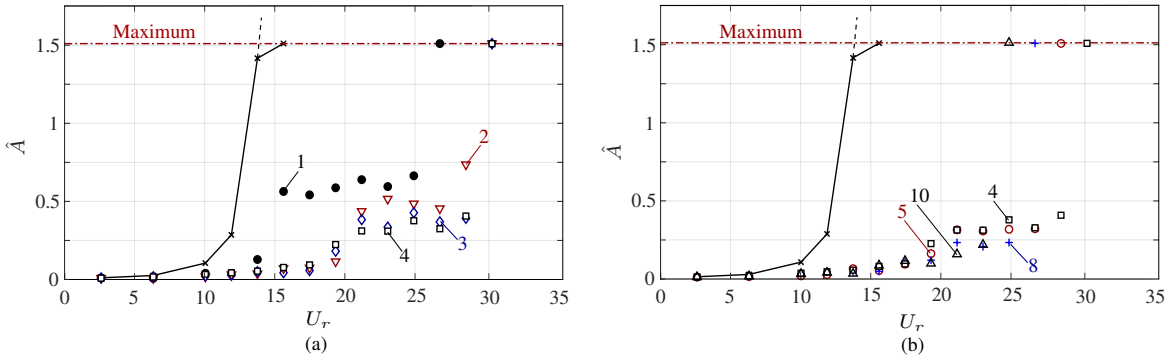

Figure 2: Amplitude response of: (a) the prism without NES ×, with 1-ball NES •, with 2-ball NES ▽, with 3-ball NES ◇, and with 4-ball NES □; (b) the prism without NES , with 4-ball NES □, with 5-ball NES ○, with 8-ball NES +, and with 10-ball NES △.

section. Two smaller plates were installed 8 cm away from each end to help approach two-dimensional flow conditions. Our experimental setup allows a maximum amplitude A of 7.5 cm (equal to 1.5 times the square prism side length). A high-speed Camera (Motion BLITZ Cube 4, MIKROTRON) recorded the motion of the vibrating prism with a resolution of 0.085 mm. A MATLAB code, developed for image analysis, traces the time histories of the prism vibration displacement y. We repeated the measurement at various flow speeds to illustrate the prism response by plotting the maximum amplitude A $versus$ flow speed U in the non-dimensional form for generalization.

The Multi-ball NES of Figure 1(b) consists of the main body (1), various size bushings (2), and steel balls (3). We printed the main body and the bushings using a 3D printer (Ultimaker3, Ultimaker) with white Poly-Lactic Acid (PLA) plastic. Swapping some parts allows easily changing the dimension of the NES track to accommodate different ball sizes. To figure out how the variation of ball quantity affects the NES behaviour, we tested various configurations of multi-ball NES, varying numbers and size of balls without changing the total mass of the NES.

RESULTS

We define the flow speed range where the NES can reduce the vibration amplitude of the prism as the NES working range. Figure 2(a) compares the responses of the prism with 1 ball, 2 balls, 3 balls and 4 balls at different flow speeds. Using two balls instead of one significantly reduces the prism vibration amplitudes and eliminates the amplitude jump which appears at a reduced velocity $U_r = 15.6$. The working range of the 2-ball NES increases to $U_r = 30$ as compared to 27 for the 1-ball NES. Increasing the number of balls to three then four, reduces the vibration amplitudes of the prism at $U_r \geq 20.5$ with no effect on the NES working range. However, the 2-ball NES shows better behavior at $U_r = 19$. Focusing on the flow speed range $16 < U_r < 20.5$, we can observe a gradual jump in the response of the prism with the 4-ball NES. This jump is more significant and delayed to $U_r = 22.5$ in the case of using the 2-ball NES. Figure 2(b) presents the responses of the prism with 4-balls, 5-balls, 8-balls and 10-balls at different flow speeds. At low flow speeds $U_r < 17$, no considerable change appears in the behavior of the prism with the different NESs. For higher flow speeds, increasing the number of balls above four reduces the vibration amplitudes of the prism. Additionally, it limits the NES working range to flow reduced velocities 24, 22.5 and 21 for the 5-ball, 8-ball, and 10-ball NESs, respectively.

CONCLUSIONS

The single ball NES presented in the literature is a simple, low-cost way for damping flow-induced vibration. In this paper, we propose a multi-ball NES as a more beneficial NES. The impact between balls is an efficient way of energy absorption that adds an advantage for the multi-ball NES. An increase in the number of NES balls reduces the vibration amplitudes of the prism. This trend remains throughout all the experiments using one to ten balls. Regarding the NES effective range, we observe two opposite trends. The use of two smaller balls instead of one large ball increases the NES working range then it remains the same for the 3-balls and 4-ball NESs. Any further increase in the number of NES balls reduces the NES working range. The overcrowdedness of the NES track results in fewer beneficial impact between balls at higher flow speeds. The 4-ball NES increases the reduced velocity of large-amplitude galloping by 10 % compared to the 1-ball NES of equivalent mass.

References

[1] Lu, Zheng, Zixin Wang, Ying Zhou, and Xilin Lu. "Nonlinear dissipative devices in structural vibration control: A review." Journal of Sound and Vibration 423 (2018): 18-49.

[2] Michael M. Selwanis, Guilherme Rosa Franzini, Cédric Béguin, and Frédérick P. Gosselin. "Wind tunnel demonstration of galloping mitigation with a purely nonlinear energy sink." Journal of Fluids and Structures 100 (2020): 103169.

[3] Ueno, Tatiana, and Guilherme Rosa Franzini. "Numerical studies on passive suppression of one and two degrees-of-freedom vortex-induced vibrations using a rotative non-linear vibration absorber." International Journal of Non-Linear Mechanics 116 (2019): 230-249.

ANALITICAL SOLUTIONS OF AN OSCILLATING ELASTIC CABLE LOADED WITH A CONCENTRATED MASS

Enrico Pagani*[1] and Markus Wenin[2]
[1]Department of Mathematics, University of Trento, Trento, Italy [2]CPE Computational Physics and Engineering, Lana (BZ), Italy

Summary We present a new analytical study of the oscillations of an elastic cable, loaded with a point mass in the center of the span. The solutions of the equations of motion represent a generalization of the linear theory of Irvine [**?**], [**?**] for the empty elastic cable, i.e. we find the transcendental equations to determine the eigenfrequencies for symmetric/antisymmetric modes of oscillations, as well as the eigenfunctions to determine the displacement of the cable. To test our analytical results we used a simple model of discrete mass points in the gravitational potential, connected by massless elastic rods.

INTRODUCTION

We generalize the theory of Irvine which treats oscillations of empty suspended elastic cables with small midspan catenary sag. Here we consider an elastic cable loaded with a point mass in the center of the span and investigate the in–plane oscillations of this system. Problems of this kind arise in many practical situations, for example when one studies the motion and in particular the vehicle–oscillations of ropeways. For the authors the content of this paper represents a tentative of an analytic approach to the problem of oscillations of cables in presence of a concentrated mass fixed in a given point of the cable using the theory and the approximations of Irvine.

ELEMENTS OF THE THEORY

We introduce a material point of mass m, fixed in the center of the cable. The coordinates of the suspension points are $(x = 0, y = 0)$, $(x = l, y = 0)$, and the point mass, at the equilibrium, has coordinates $(x = l/2, y = D$, see Fig. **??**). Denoting (improperly) with K the horizontal component of the cable tension, constant along the whole cable, the static configuration of the cable is described by the formula

$$y_0(x) = \frac{\rho g(l + \frac{m}{\rho})}{2K}\left[x - \frac{x^2}{(l + \frac{m}{\rho})}\right], \quad x \in [0, l/2] \tag{1}$$

(symmetric for $x \in (\frac{l}{2}, l]$), in which the relation between K and the sag D is given by

$$D = y_0\left(\frac{l}{2}\right) = \frac{\rho g l^2}{8K}\left(1 + \frac{2m}{\rho l}\right) . \tag{2}$$

Concerning dynamics, let's denote with $x = x_0(s)$, $y = y_0(s)$ and $T(s)$ the parametric representation of the cable and the tension in the equilibrium configuration, and with $u = u(t, s)$, $v = v(t, s)$ and $T(s) + \tau(t, s)$ the horizontal and vertical displacements of the points of the cable and the tension at the point of curvilinear parameter s at time t. The functions $u = u(t, s)$, $v = v(t, s)$ and $\tau(t, s)$ satisfy the linearized equations of motion:

$$\frac{\partial}{\partial s}\left(T(s)\frac{\partial u(t,s)}{\partial s} + \frac{dx_0(s)}{ds}\tau(t,s)\right) = \rho\frac{\partial^2 u(t,s)}{\partial t^2} \quad s \neq s^* , \tag{3}$$

$$\frac{\partial}{\partial s}\left(T(s)\frac{\partial v(t,s)}{\partial s} + \frac{dy_0(s)}{ds}\tau(t,s)\right) = \rho\frac{\partial^2 v(t,s)}{\partial t^2} \quad s \neq s^* , \tag{4}$$

$$\left[\frac{dx_0(s)}{ds}\tau(t,s) + T(s)\frac{\partial u(t,s)}{\partial s}\right]_{|(t,s^*)} = m\frac{\partial^2 u(t,s^*)}{\partial t^2} , \tag{5}$$

$$\left[\frac{dy_0(s)}{ds}\tau(t,s) + T(s)\frac{\partial v(t,s)}{\partial s}\right]_{|(t,s^*)} = m\frac{\partial^2 v(t,s^*)}{\partial t^2} , \tag{6}$$

$[F(t,s)]_{|(t,s^*)} := F(t,(s^*)^+) - F(t,(s^*)^-)$ denoting the jump of the function $F(t,s)$ at s^*, namely at the point in which the concentrated mass m is present.

*Corresponding author. E-mail: enrico.pagani@unitn.it

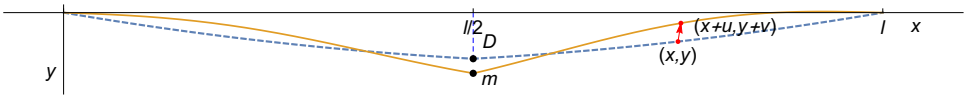

Figure 1: Sketch of the system under consideration. Dashed line: equilibrium configuration $y_0(x)$. Solid line: cable out of equilibrium, where a point undergoes the displacement $(x, y) \to (x + u(t, x), y + v(t, x))$.

RESULTS - SYMMMETRIC AND ANTISYMMETRIC MODES OF OISCILLATIONS

Adopting the definition of Irvine a mode of oscillation is called *symmetric (resp. antisymmetric)* if the vertical displacement $v(t, x)$ is symmetric (resp. antisymmetric) with respect to $x = \frac{l}{2}$. We have no space to present here in details the analytic approach and we give the results of a comparison of the analytic approach with a numerical example, using the following parameters: linear density $\rho = 1$ kg/m, span $l = 100$ m, $A_c E_c = 10^5$ N. The static midspan sag for the empty cable is $d =$ 5m and the horizontal component of the tension is $K = 2450$ N. We compare our analytical results with the ones obtained by evaluation of a model, consisting of a set of discrete mass points in a gravitational potential (each with a mass $m_p = 2.396$ kg) connected by massless rods with appropriate elastic constant and rest length. We consider the case of an empty cable, and with a concentrated load $m = 6m_p = 14.37$ kg. The resulting values are collected in the tables that appear below, together with the numerical values for the different loading cases and modes (symmetric (s) and antisymmetric (a)) of oscillation. Unfortunately, we have no space to exhibit the corresponding eigenfunctions.

A NUMERICAL EXAMPLE

The presented tables show a comparison of both approaches for the empty and the loaded cable respectively.

n	1 (s)	2 (a)	3 (s)	4 (a)	5 (s)	6 (a)
ω_n analytical	1.92	3.11	4.68	6.22	7.78	9.33
ω_n numerical	1.92	3.06	4.63	6.14	7.68	9.18

Table 1: First 6 eigenfrequencies (Hz) for the empty cable ($m = m_p$). The analytical results agree with the theory of Irvine. The letters (a), (s) denote antisymmetric/symmetric modes respectively.

n	1 (s)	2 (a)	3 (s)	4 (a)	5 (s)	6 (a)
ω_n analytical	1.81	3.19	4.34	6.40	7.28	9.60
ω_n numerical	1.81	3.14	4.31	6.34	7.21	8.97

Table 2: First 6 eigenfrequencies (Hz) for the loaded cable with $m = 6m_p$.

References

[1] Irvine H. M., and Caughey T. K., The linear theory of free vibrations of a suspended cable, *Proc. R. Soc. London A* **341**: 299-315, 1974.
[2] Irvine H. M., Studies in the statics and dynamics of simple cable systems DYNL-108, California Institute of Technology, 1974.

BAND-GAP CHARACTERISTICS OF A TRI-LIGAMENT CHIRAL STRUCTURE WITH FLEXURE HINGES

Tan Wangxi[1], Su Xunwen*[1], An Ning[1]
School of Technology, Beijing Forestry University, Beijing, China

Summary In order to study the characteristics of band gap of low frequency and wide bandwidth, we proposed a tri-ligament chiral structure with flexure hinges, which is convenient to adjust the band gap without changing the geometric parameters of the chiral structure. Finally, we performed a numerical simulation using the finite element method.

MODEL OF TRI-LIGAMENTS CHIRAL STRUCTURE WITH FLEXURE HINGES

Chiral structure, consisting of a node and ligaments tangent to the node, is a hotspot in engineering because of its light weight, good impact resistance and excellent vibration isolation performance. The difficult point is adjusting band gap of low frequency and broad bandwidth. The former researches suggest that the influence of the geometric parameters of the chiral structure on the band gap distribution is complex and coupled. So a new tri-ligament chiral structure with flexure hinges is proposed, as shown in figure 1. This structure makes it easier to adjust the band gap by adding an arc flexible hinge to the ligament.

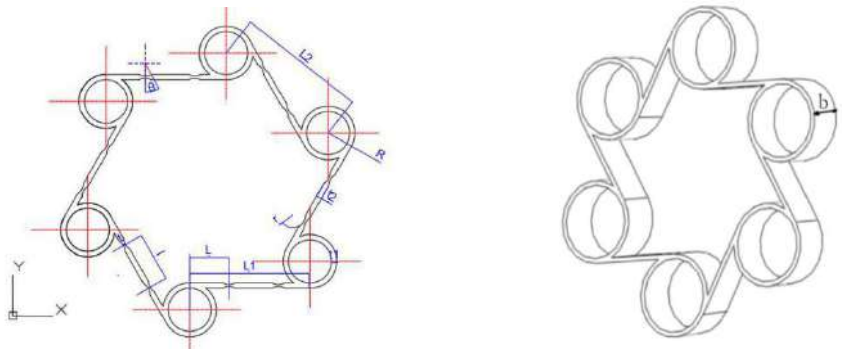

Fig. 1 Geometric parameters of the three-ligament chiral structure with flexure hinges

Calculation models are built by finite element method. According to the previous study of Su[1], a structure containing 23 cells is established in the part module of SolidWorks based on the two-dimensional shell element, and ANSYS is used to handle the model based on the harmonic response analysis, as shown in figure 2 . Four parameters are changed to observe the influence of the flexure hinge on the frequency response characteristics, including radius of the notch arc r, center angle of the notch arc θ, quantity of arc flexure hinges and length between centers of the notch arc of two flexure hinges l.

*Corresponding author: Su Xunwen, E-mail: suxw0703@gmail.com

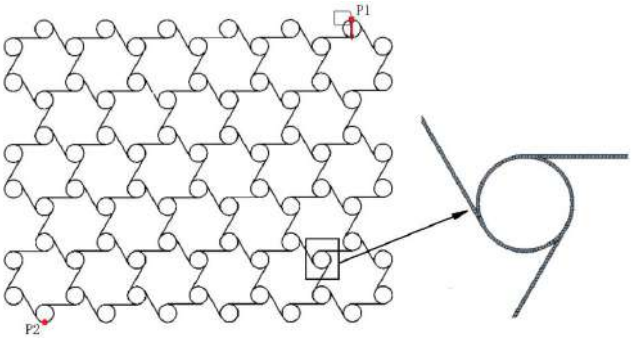

Fig. 2 Schematic diagram of the loading and mesh of the chiral structure with flexure hinges

CONCLUSIONS

The main results of the research are as follows. The research in this paper can provide basis and reference for the chiral structure design of variant aircraft in the aviation field in the future.

(1) When the radius of the notch arc r is 3mm, 4mm, 5mm, 6mm, 7mm and 8mm respectively, the starting frequency and bandwidth are shown in figure 3. The results show that as the radius increases, the starting frequency decreases and the bandwidth increases. When the radius increases to 6mm, the change is most dramatic.

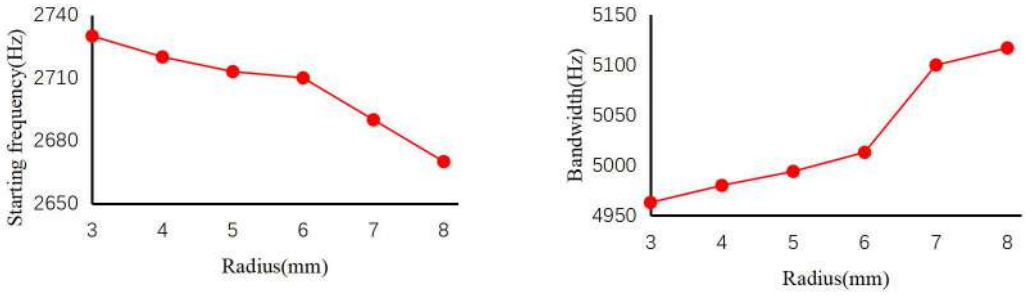

Fig. 3 Starting frequency and bandwidth under different radius of the notch arc

(2) Radius of the notch arc, center angle of the notch arc, quantity of the arc flexure hinges and length between the centers of the notch arc of two flexure hinges also have an impact on the starting frequency and bandwidth. As the parameters increase, the starting frequency decreases and the bandwidth increases. Results show that the most effective way to adjust the band gap probably is to change the number of flexible hinges., and adjusting center angle affects more than radius.

(3) The recommended structure is radius of the notch arc of 7mm, the center angle of the notch arc of 25°, 7 arc flexure hinges and the length between the centers of the notch arc of two flexure hinges 6.8mm.

References

(1) Su, X. Zhu, D. Zheng, C. and Tomovic Mileta M. Frequency response characteristics of finite periodic chiral structures with three ligaments[J]. *Proceedings of the Institution of Mechanical Engineers*, 233(12), 2019.

APPLICATION OF VIRTUAL SENSING TO VIBRATIONAL DATA FROM A HIGH-SPEED AXIAL COMPRESSOR

Mona Amer*[1], Clemens Groß[2], and Joerg Seume[1]
[1]Institut für Turbomaschinen und Fluid-Dynamik,Leibniz Universität Hannover,Germany
[2]Institut für Land-und Seeverkehr,Technische Universität Berlin,Germany

Summary In order to reduce sensor count of acceleration sensors used to monitor the vibrational behaviour of industrial machinery, virtual sensing approaches are studied and employed. Virtual sensors are used to predict the vibrational behaviour virtually without using a physical sensor. The application of this approach aims at solving the conflict of interests: On one hand, a low number of sensors is required, among others, for economic reasons. On the other hand, the vibrational behaviour of the mechanical system should be represented as realistically as possible and, therefore, requires a high number of sensors. In the present case, analytical models like the statistic energy analysis using structural mechanics correlations as well as novel data-driven approaches based on artificial intelligence are applied to acceleration sensors on a high-speed axial compressor.

INTRODUCTION

Virtual sensors are often employed for economic, environmental, or technical reasons when the use of physical sensors is restricted. Liu et al. [4] reviewed different virtual sensing (VS) technologies focusing on active noise cancellation. The automotive industry also makes use of VS, e.g. torsional load data from power trains have been gained by using a nonlinear Kalman filter approach [1] and Hirsenkorn et al. [2] applied VS to driver assistance systems. VS is applied in civil engineering applications for structural health monitoring (SHM) as well. Kullaa et al. [3] presented a hybrid approach for SHM on the basis of VS. Large machines are also controlled by vibration sensor technology to ensure a safe operation because an increased vibration level over a long period of time can lead to mechanical failure. The objective of the operator will always be the minimisation of the sensor count, as accessability and economic reasons lead to increased cost. VS could offer suitable alternatives as studied below.

METHODOLOGY

The VS methodology is applied to an axial compressor test rig which is shown in Fig. 1. The objective is to eliminate

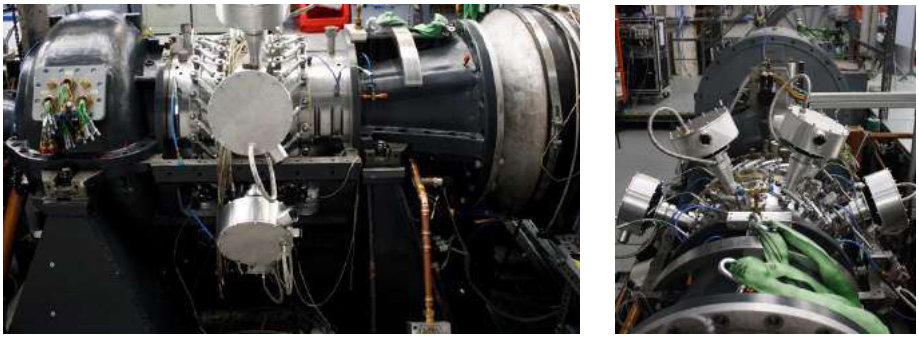

Figure 1: Axial compressor test rig at the Institute of Turbomachinery and Fluid Dynamics (TFD)

one or more physical sensors using a virtual model. The data set is derived from the monitoring system of the axial compressor. The highly resolved acceleration data is integrated and provides time-averaged root mean square (RMS) values $x_{\mathrm{RMS}} = \sqrt{\frac{1}{T}\int_0^T x^2(t)dt}$ sampled with 5 Hz. This data set is more suitable for VS than acceleration data with a high sampling frequency as the RMS values show less rapid fluctuations. Overall, 10 sensors are used, measuring the axial and horizontal vibration of the free and fixed bearing support, the gearbox, and the motor. The design of VS is split into two parts; firstly the dependence on other parameters has to be established and secondly a linking function between the predicted variable and the influencing variables has to be defined. Approaches to VS can be divided into model-driven, data-driven, and hybrid methods. Model-based and hybrid approaches assume a physical model, which is guided by data and physical laws at the same time. The statistical energy analysis (SEA) is a model-driven method, which considers the transmission behaviour of vibrations. It is based on the principle of energy conservation. The system is divided into subsystems described by an equation set for the input, storage, transmission and dissipation of energy within the subsystems. The coupling coefficients required are determined iteratively by comparing the reconstructed signal with the measured data. The acceleration can finally be derived from the energy Π^{in} into a subsystem $\Pi^{\mathrm{in}} = \frac{1}{2}\Re\{m\ddot{X}\dot{X}\}$ with $x(t) = X(\omega)e^{i\omega t}$. Data-driven approaches include, among others, statistical methods such as correlation models

*Corresponding author. E-mail: amer@tfd.uni-hannover.de.

(CM) and regression analysis (RA). For the use of CM, impulse response coefficients have to be determined by establishing a relationship between input and output. RA include, among others, polynomial and nonlinear methods. Another field of applied statistics provides artificial intelligence (AI) approaches such as neural networks (NN). Again, different approaches exist like feed-forward NN (FFNN), recurrent NN (RNN), the output of a layer can be fed back as an input, and long short-term memory (LSTM) NN, which is basically a further development of recurrent NN. Another version of NN, belonging to the hybrid approaches, is the physics-informed NN (PINN). These approaches are applied to a data set, consisting of approximately 1 million samples.

RESULTS

The vibration data from the fixed bearing can be replaced best by VS, therefore, it is the basis of the following comparison. To compare the different approaches, an error function is introduced

$$\epsilon = \frac{1 - n_{0.5}}{n} \cdot 100\% \tag{1}$$

with n being the length of a chosen interval and $n_{0.5}$ being the number of samples in this interval which are not outside the ± 5 % measurement uncertainty bound of the sensors. The value corresponds to an average of the horizontal and vertical sensor signal at the fixed bearing support. Table 1 summarises the quality of all approaches considered. For the

Method	Approach		ϵ
Model driven	SEA		23.4%
Hybrid	PINN		84.6%
Data driven	CM		62.4%
	RA	polynomial	76.3%
		nonlinear	76.6%
	NN	R	74.3%
		FF	87.5%
		LSTM	89.4%

Table 1: Comparison of the quality of the approaches applied

SEA, the mass of the different components needs to be determined in order to calculate the resulting energy $E = \frac{1}{2} m \dot{x}^2$. Hence, the weight of the entire motor is approximated to be 12 times the mass assumed for the fixed and free bearing support. It is assumed that the transmitted energy into the axial compressor and into the bearing support is dissipated into the foundation. Nevertheless, the SEA shows poor results, as the complexity of the test stand is too high for this approach. It can be noticed that it still gives a good estimation of the current RMS value. For the PINN, the result of the SEA is fed into a FFNN and shows good accordance with the real sensor data but also requires a high implementation effort. The phenomenon of overfitting excludes polynomial RAs of high order. Hence, order 3 is presented in Tab. 1. For the nonlinear RA wavelet functions are examined. The LSTM approach shows the best result overall, which confirms the development of NN in the literature. Besides, the quantitative evaluation other criteria can be taken into account like complexity and computational effort, NN approaches show good results here too. It is noticeable, that leaving out the standstill data leads to a more accurate replication of the physical sensor signal. The incorporation of additional data from the monitoring system like pressure and temperature values did not improve the VS approach, which were used to model operating conditions. The replication of a second sensor still shows acceptable agreement with the original data.

CONCLUSIONS

Different VS approaches – model-driven hybrid and data-driven approaches – were successfully applied to vibration data from an axial compressor test rig. The time-averaged RMS values were most suitable for this use case. The results indicate that the vibrational behaviour is not or weakly dependent on the operating point. Data-driven approaches have proven to be more efficient and provide a more accurate prediction of the physical sensor outputs. The complexity of the test stand led to poor results derived from the model purely based on theoretical mechanics principles. As a next step an evaluation of significance of the changes in predictive quality associated with AI methods will be pursued. This study represents a first step towards the application of VS to industrial machines with fewer installed sensors.

Acknowledgements The author kindly thanks Mikail Aydin for a first study regarding this topic within his bachelor thesis.

References

[1] Forrier, B., et al. Broadband Load Torque Estimation in Mechatronic Powertrains Using Nonlinear Kalman Filtering, IEEE Transactions on Industrial Electronics 65, 2018.
[2] Hirsenkorn, N., et al. Virtual sensor models for real-time applications, Advances in Radio Science 14, 2016.
[3] Kullaa, J., et al. Combined empirical and analytical virtual sensing for full-field dynamic response estimation, Helsinki, 2016.
[4] Liu L., et al. Virtual sensing techniques and their applications. International Conference on Networking, Sensing and Control, 2009.

DYNAMIC RESPONSE OF FRACTIONALLY DAMPED MULTIPLATE SYSTEMS

Marina Shitikova*[1,2], Olga Zhavoronkova[1]
[1]Department of Structural and Theoretical Mechanics, Moscow University of Civil Engineering, Moscow, Russia
[2]Research Center on Dynamics of Solids and Structures, Voronezh State Technical University, Voronezh, Russia

Summary In the present paper, a vertically inhomogeneous viscoelastic plate is modelled as a multiplate system, i.e. a set of thin plates interconnected with each other in terms of fractional derivative Kelvin-Voigt elements. The procedure allowing one to reduce the analysis of the dynamic response of such rather complex system to the solution of the characteristic equations of fractional oscillators with two retardation times and two fractional parameters has been proposed, that is to simplify significantly the solution of the problem under consideration.

INTRODUCTION

During the last three decades, fractional calculus entered the main stream of engineering analysis and has been widely applied to structural dynamic problems both in discrete and continuous equations, considering stationary and transient dynamic response of oscillators, beams, plates, cylindrical shells. The overview of recent publications could be found in [1,2]. The results obtained in the field have been critically estimated in the light of the present view of the place and role of the fractional calculus in engineering problems and practice.

In the present paper, the dynamic behaviour of a viscoelastic plate with nonhomogeneity varying with its width is considered utilizing the multilayered model involving different combinations of fractionally damped layers.

PROBLEM FORMULATION METHOD OF SOLUTION

One of the approaches for simulating multilayered structures is to consider a sandwich structure as a multibeam or multiplate system, in which deformable elastic or viscoelastic bodies (beams or plates) are interconnected by distributed light viscoelastic constrain elements which have the ability to resist axial deformation under static and dynamic conditions [3].

Let us consider a discrete-continuum inhomogeneous vertical chain system (Figure 1) involving a set of N thin viscoelastic plates with different material constants but with the same boundary contours and boundary conditions, which are interconnected with by N-1 viscoelastic constraint layers with equal material constants. The number of degrees of freedom of such a multilayered structure is equal to N-infinity, where N is a number of deformable plates in the chain, in so doing each Kirchhoff-Love plate admits the dynamic deflection $w_i(x,y,t)$. The plates may be subjected to transverse distributed external loads $q_i(x,y,t)$.

The dynamic response of such a viscoelastic plate with nonhomogeneity varying with its height, or a viscoelastic layer connected multiple plate system, could be described by the following system of the N governing coupled partial differential equations:

$$\tilde{D}_i \nabla^2 w_i + \rho_i h_i \ddot{w}_i = q_i + F_{i+1} - F_i \qquad (i = 1,2,...,N) \tag{1}$$

$$F_1 = \tilde{\lambda}_1 w_1, \qquad F_i = \tilde{\lambda}_i (w_i - w_{i-1}) \qquad (i = 2,3,...,N-1), \qquad F_N = \tilde{\lambda}_N w_N \tag{2}$$

formulated in terms of N unknown transverse displacements $w_i(x,y,t)$, where F_i is the reaction of the ith viscoelastic layer, $\tilde{D}_i$ is the cylindrical rigidity of the ith plate, Young's modulus $\tilde{E}_i$ of the ith plate and the coefficient of rigidity of the connecting viscoelastic layer $\tilde{\lambda}_i$ are the following Kelvin-Voigt-type operators of the fractional order

$$\tilde{D}_i = \frac{h_i^3 \tilde{E}_i}{12(1-\nu_i^2)}, \qquad \tilde{E}_i = E_{0(i)}(1+\tau_1^{\gamma_1} D^{\gamma_1}), \qquad \tilde{\lambda}_j = \lambda_{0(j)}(1+\tau_2^{\gamma_2} D^{\gamma_2}), \tag{3}$$

where $E_{0(i)}$ and $\lambda_{0(j)}$ are prolonged magnitudes of coefficients of rigidity for the ith plate and jth layer, respectively, τ_1, γ_1 and τ_2, γ_2 are the retardation time and fractional parameter for plates ans layers, respectively, D^γ is the Riemann-Liouville fractional derivative [1], and $0 < \gamma < 1$ is the order of the fractional derivative (fractional parameter).

Note that adding the Nth layer to this system allows one to consider the dynamic response of a multilayered plate on a viscoelastic foundation.

Supposing the solution of Eqs (1)-(3) in the modal form

$$w_i(x,y,t) = \sum_{m=1}^{\infty}\sum_{n=1}^{\infty} W_{(1)mn}(x,y) x_{(i)mn}(t), \qquad i = 1,2,...,N \tag{4}$$

*Corresponding author. E-mail: mvs@vgasu.vrn.ru

dividing Eq. (1) by $\rho_i h_i$, substituting (2)-(4) in Eq. (1), multiplying each equation by $W_{(1)mn}(x,y)$, after integrating along the plates' length and width, and considering the orthogonality conditions and corresponding equal boundary conditions of the plates yield to the *mn*-family of systems containing coupled only *N*-ordinary fractional-order differential equations for the determination of unknown generalized displacement functions $x_{(i)mn}(t)$ $(i=1,2,....N, \quad m,n=1,2,...,\infty)$:

$$\ddot{x}_{(i)mn}+\Omega^2_{(i)mn}(1+\tau_1^{\gamma_1}D^{\gamma_1})x_{(i)mn}+\frac{\lambda_{0(i)}+\lambda_{0(i+1)}}{\rho_i h_i}(1+\tau_2^{\gamma_2}D^{\gamma_2})x_{(i)mn}-\frac{\lambda_{0(i+1)}}{\rho_i h_i}(1+\tau_2^{\gamma_2}D^{\gamma_2})x_{(i+1)mn}$$
$$-\frac{\lambda_{0(i)}}{\rho_i h_i}(1+\tau_2^{\gamma_2}D^{\gamma_2})x_{(i-1)mn}=P_{(i)mn}(t), \tag{5}$$

where

$$P_{(i)mn}(t)=\frac{\int_0^a\int_0^b q_i(x,y,t)W_{(1)mn}(x,y)dxdy}{\rho_i h_i\int_0^a\int_0^b[W_{(1)mn}(x,y)]^2dxdy}, \qquad \Omega^2_{(i)mn}=\frac{h_i^2\tilde{E}_i}{12\rho_i(1-\nu_i^2)}\nabla^2 W_{(1)mn}(x,y).$$

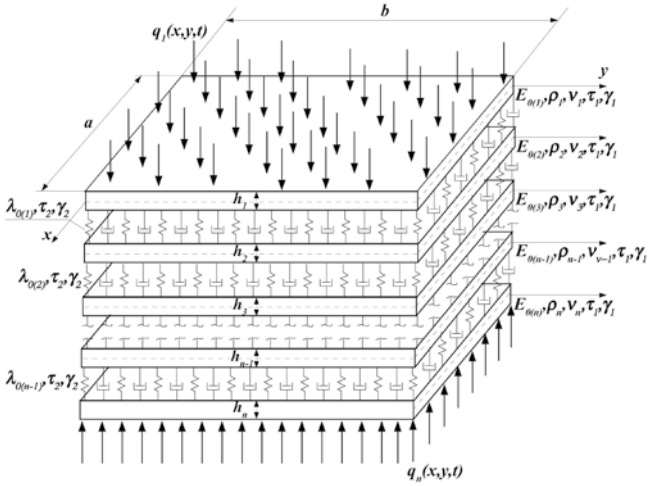

Figure 1. Scheme of a multiplate system.

Applying the Laplace transform to Eqs. (5), int to the sets of roducing the change of variables $\bar{x}^*_{(i)mn}=\bar{x}_{(i)mn}\sqrt{\rho_i h_i/\rho_1 h_1}$, and expanding the vectors $\bar{x}^*_{(i)mn}$ in terms of the eigenvectors, the governing equations in the Laplace domain could be reduced to the *n* sets of decoupled equations, each of which describes forced vibrations of an uncoupled Kelvin-Voigt fractional derivative oscillator with two retardation times and two fractional parameters. The solution of such characteristic equations was proposed in [4].

CONCLUSIONS

Thus, it has been shown how rather complex system modelling the dynamic response of the multilayered plate can be reduced to the sets of uncoupled fractionally damped oscillators characterized by two retardation times and two fractional parameters, what allows one to simplify significantly the solution of the problem under consideration.

The approach described above enables one to consider any number of elastic/viscoelastic plates interconnected by viscoelastic (or elastic) layers in the case when welded or sliding contact between the layers is ignored. For example, it could be applied with great success for finding an approximate solution of the dynamic problem of a simply supported elastic Kirchhoff-Love-type plane damped by a viscoelastic layer.

Acknowledgement. This research has been supported by the Russian Foundation for Basic Research, Project No. 20-01-00443.

References

[1] Rossikhin Yu. A., Shitikova M. V. Application of fractional calculus for dynamic problems of solid mechanics: Novel trends and recent results. *Appl. Mech. Rev.* **63**: PaperID 010801, 2010.

[2] Rossikhin Yu. A., Shitikova M. V. Fractional calculus in structural mechanics. In: *Handbook of Fractional Calculus with Applications*. Vol. 7: Applications in Engineering, Life and Social Sciences, Part A (D. Baleanu, A.M. Lopes, Eds.) De Gruyter, 159-192, 2019.

[3] Hedrih K.F. Linear and nonlinear dynamics of hybrid systems. *Proc. IMechE Part C: J. Mech. Eng. Sci.* DOI: 10.1177/0954406220957699, 1-34, 2020.

[4] Rossikhin Yu. A., Shitikova M. V. Analysis of the viscoelastic rod dynamics via models involving fractional derivatives or operators of two different orders. *Shock Vib. Dig.* **36**: 3-26, 2004.

MULTI-SCALE INTERACTION WITH FLOWS OF KIRIGAMI STRUCTURES

Tom Marzin [1], Kerian Le Hay [1], Emmanuel de Langre [1], and Sophie Ramananarivo*[1]
[1]LadHyX, Department of Mechanics, Ecole polytechnique, Institut polytechnique de Paris, France

Summary We study the deformation of a kirigami- that is a sheet slit with a network of cuts- in a water flow. When stretched, the kirigami significantly opens up and thus acts as a poro-elastic surface that lets fluid through. We characterize experimentally and theoretically the relation between the cuts geometry and the resulting shape transformation. We show that macroscopic morphing is dictated by interactions with fluid at the scale of individual pores, whose geometry changes in turn with the sheet elongation. Understanding those multi-scale couplings provides a novel way to control and program shape-shifting in flows through the reverse-engineering of cut motifs.

INTRODUCTION

Lightweight compliant surfaces are commonly used as roofs (awnings), filtration systems or propulsive appendages, that operate in a fluid environment. Their flexibility allows for shape to change in fluid flows, to better endure harsh or fluctuating conditions. Alternatively, those passive deformations can be exploited for enhanced locomotion [1] or energy extraction from flows. The way the structure deforms is however key to fulfill its function, prompting the need for control levers.

Thin surfaces undergo primarily length-preserving deformations, which places severe restriction on accessible shapes. A way around such limitations is to add a network of cuts to the flat surface, a technique that is specific to kirigamis. The slits enable the material that remains to either rotate in plane or buckle out of plane (see Fig.1a), transforming the flat sheet into arbitrarily complex three-dimensional shapes. This technique has recently drawn the attention of scientists and engineers, as it also allows the design of tunable and predictable mechanical properties, such as extreme stretchability [2]. This enlarged design space offers exciting opportunities to control and program shape transformations under fluid loading.

An interesting feature of kirigamis from the perspective of fluid mechanics, is that stretching occurs through significant opening up of the material. It thus acts as an adaptive poro-elastic structure, where a flow deforms the kirigami and opens pores, which in turn alter the fluid loading. Local forces exerted by the fluid flowing through individual pores are then likely to condition the global behavior of the structure. The aim of this study is to understand those multi-scale fluid/structure interactions. We approach this problem on a first type of kirigami characterized by a pattern of parallel rows of slits (illustrated in Fig.1a).

EXPERIMENTAL SET-UP

The kirigami is made by laser cutting a 100 µm-thick mylar sheet. It is clamped at its two ends and placed in a cross flow generated by a water tunnel, where it occupies the whole test section of 15x15cm (see Fig.1b). A camera placed on top of the channel records the quasi-2D deformation induced by the fluid. Fig 1.c shows typical shapes extracted through image analysis, when regularly increasing the flow speed from 4 to 22 cm.s^{-1}. The amplitude of the deformation eventually tends to saturate for strong flows, and we note a surprising breaking of left-right symmetry that will be discussed later.

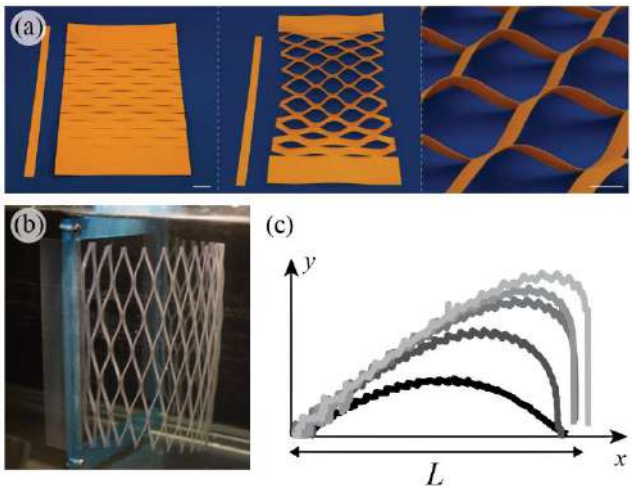

Figure 1. (a) Kirigami with a parallel arrangement of slits allowing for the struts in between to buckle out of plane [2]. (b) Deformation in a steady water cross-flow. (c) Typical shapes extracted from top-view pictures of the kirigami of length L, when increasing the flow speed (denoted by the grayscale).

Kirigamis with different elastic properties are tested, changing the length of the slits L_s, the distance between cuts within a row d_x, and the distance between rows d_y. Structural properties are characterized with an Instron, which records the force required to stretch the structure. We show that within the range of deformation explored in the experiments, the force-displacement curves are linear. An effective stiffness K is extracted from the slope, which scale as $K \sim \frac{Et^3 d_x}{(L_s - d_y)^3} \frac{N_y}{2N_x}$, with E the Young modulus, t the sheet thickness, and N_x and N_y the numbers of vertical and horizontal cut units. In the spirit of [3], this result is consistent with viewing the kirigami as a collection of plates that are bending, and act as spring assembled in parallel and in series. The three parameters L_s, d_x, and d_y effectively set the width and length of those plates, determining their 'stiffness'.

*Corresponding author. E-mail: sophie.ramananarivo@ladhyx.polytechnique.fr

GLOBAL DEFORMATION OF THE PORO-ELASTIC SURFACE

We first characterize the fluid-induced shape changes by measuring the amplitude of the deformation y_{max} in the flow direction. This y_{max}, is nondimensionalized by the kirigami length L and shown in the inset of Fig.2a as a function of the flow speed U. The blue-to-yellow color gradient differentiates kirigamis with increasing slit length. Deformation increases with U, and is all the more pronounced for large L_s that correspond to smaller effective stiffness. A natural step is then to replot those data as a function of a Cauchy number $C_y = \rho H U^2 / K$. (with H the height of the kirigami and ρ the water density), that compares the fluid loading to elastic restoring forces. Fig.2a then shows a collapse of the data onto a single curve for the three series of kirigamis tested with varying L_s, d_x and d_y, respectively denoted by circle, triangle and square symbols. The competition between elastic and fluid opposing effects thus captures the amount of deformation of the kirigami. A finer study of coupling with flows is however required to interpret features such as the saturation of deformation observed for strong flows. This effect could in particular be attributed to the opening of porosity when stretching the surface, which tends to reduce the fluid loading. We thus set to investigate the detail of local interactions with flows at the individual pore level. Such information will also provide clues to understand the symmetry breaking in the shape transformation.

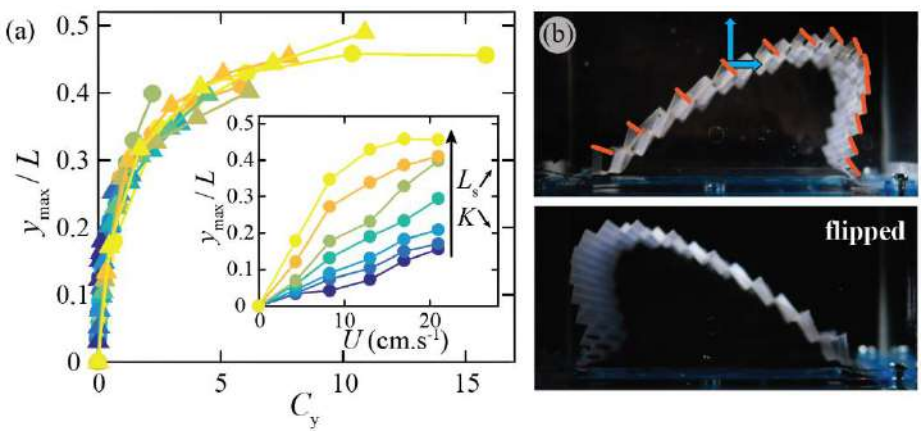

Figure 2. (a) [Inset] Dimensionless maximum deformation y_{max}/L as a function of flow speed U, for kirigamis with increasing slit length L_s and thus decreasing stiffness K (differentiated by a blue-to-yellow gradient). Results replotted as a function of a Cauchy number C_y (see main text) for different cut patterns. (b) The post-buckling tilting of the struts (outlined by orange lines) induces lateral forces, breaking the deformation symmetry. Flipping the kirigami upside down reverses the direction of the asymmetry.

LOCAL INTERACTIONS WITH FLOWS

The opening up of the kirigami with stretching can be characterized by measuring the evolution of the porosity Φ, that is the fraction of void area on the total area. Expectedly, porosity increases with the elongation ε, but the relation $\Phi(\varepsilon)$ also has the particularity of being independent of the slit length and inter-slit distances. This observation is directly explained by geometry arguments considering the out-of-plane tilting of strips within stretched kirigamis [3].

This out-of-plane buckling is also an important feature from a fluid dynamics viewpoint. Transverse lift forces are generated, and induce local tension leading to the observed assymetrical deformation (see top panel of Fig.2b). This asymmetry is prescribed by the strips orientation –which turns out to be highly biased by the fabrication process here-, but the direction spontaneously reverses upon flipping the kirigami upside down (bottom panel of Fig.2b).

To control and program shape shifting, local fluid forces need to be determined. Since those are difficult to measure in-situ, we devise a model system that reproduces the strip geometry and can be mounted on a force sensor. It consists of an assembly of 8 to 12 parallel blades, where the inter-blades spacing can be modified, as well as their orientation with respect to an incoming water flow. A six-axis force sensor measures forces both in the direction parallel and transverse to flow, to extract effective drag and lift coefficients. Those informations are used as input to model the two-dimensional deformation of the kirigami. The latter is modelled as an extensible thread –neglecting bending moments- and subjected to normal and transverse fluid forces that depend on local elongation. Model predictions show reasonable agreement with experimental results, providing clues to understand the feedback loop between local deformation and fluid forces.

Note that while the strips all buckle in the same direction in Fig.1a, it is not necessarily the case, and orientation could be varied throughout the sheet to access different deformations. It was shown in particular that buckling orientation can be controlled and programmed using notches in the material to guide the tilting [4]. Targeted macroscopic shape transformations could then be achieved through reverse-engineering of cut motif. This approach offers promising applications for intelligent structures for robotic and engineering, which passively adapt to changes in their fluid environment, such as filtration system with tunable filter mesh, or shape-shifting screens.

References

[1] Ramananarivo, S., Godoy-Diana, R., and Thiria, B. Rather than resonance, flapping wing flyers may play on aerodynamics to improve performance. *PNAS*, *108*(15), 5964-5969, 2011.
[2] Callens, S. J., and Zadpoor, A. A. From flat sheets to curved geometries: Origami and kirigami approaches. *Mater. Today*, *21*(3), 241-264, 2018.
[3] Isobe, M., and Okumura, K. Initial rigid response and softening transition of highly stretchable kirigami sheet materials. *Sci. Rep.*, *6*, 24758, 2016.
[4] Tang, Y., Lin, G., Yang, S., et al. Programmable Kiri-Kirigami Metamaterials. *Adv. Mater.*, *29*(10), 1604262, 2017.

MEASURING LOCAL RATE-DEPENDENT PROPERTIES OF SOFT MATERIALS USING VOLUME CONTROLLED CAVITY EXPANSION

Christine Roth[1,2] and Tal Cohen[*1,3]
[1]Department of Civil and Environmental Engineering, Massachusetts Institute of Technology, Cambridge, MA, USA
[2]Institute of Mechanical Engineering, École Polytechnique Fédérale de Lausanne (EPFL), 1015 Lausanne, Switzerland
[3]Department of Mechanical Engineering, Massachusetts Institute of Technology, Cambridge, MA, USA

Summary. By manipulating the volume of an incompressible fluid droplet formed at the tip of a needle that is injected into a soft material, and measuring the resisting pressure, it is shown that a clear signature of the nonlinear rate-dependent properties of the subjected material can be captured. Comparison of theoretical predictions and experiments then allows for identification of an appropriate constitutive model and quantification of the material parameters.

INTRODUCTION/MOTIVATION

The ability to locally probe rate-dependent properties of soft and biological materials presents opportunities in various fields, from food science, biomechanics, and pharmaceuticals, to soft robotics, and medical diagnosis. However, while standard rheological methods are well suited to measure the response of homogeneous materials, they require the preparation of samples with particular shapes and sizes to be tested outside of their natural environment. Hence, if the material properties are heterogeneous, or when removal of the material from its natural environment can affect its mechanical response, these methods are limited. To address this challenge, recent advancements [1-3] that build on the methodology of Needle Induced Cavitation Rheology (NICR) [4,5], have been shown to capture the local nonlinear response of soft materials. There, by controlling the volume of a cavity formed at the tip of a needle, and measuring the resisting pressure, the pressure-volume response can be obtained (even beyond the fracture limit [3]). By comparison with theoretical predictions, the nonlinear constitutive model and fracture resistance is determined. This technique, which we refer to as Volume Controlled Cavity Expansion (VCCE), has been shown to produce repeatable measurements in both synthetic and biological materials, however it is limited to rate-independent properties. In this talk, I will present recent advancements in extending this technique to capture rate-dependent properties. I will discuss experimental challenges and will outline the theoretical model and constitutive relations that are used to characterize the large deformation rate dependent response of polymers with tuned properties.

References

[1] Raayai-Ardakani, S., Chen, Z., Earl, D.R. and Cohen, T. Volume-controlled cavity expansion for probing of local elastic properties in soft materials. Soft matter, 15(3), (2019) pp.381-392.
[2] Raayai-Ardakani, S., Earl, D.R. and Cohen, T. The Intimate Relationship between Cavitation and Fracture. Soft Matter, 15, (2019) 4999-5005.
[3] Raayai-Ardakani, S. and Cohen, T. Capturing Strain Stiffening Using Volume Controlled CavityExpansion. Extreme Mechanics Letters, 31 (2019) 100536.
[4] Zimberlin, J.A., Sanabria-DeLong, N., Tew, G.N. and Crosby, A.J. Cavitation rheology for soft materials. Soft Matter, 3(6), (2007) pp.763-767.
[5] Crosby, A.J. and McManus, J. Blowing bubbles to study living material. Physics Today, 64(2), (2010) pp.62-63.

*Corresponding author. E-mail: talco@mit.edu.

DIMENSION REDUCTION FOR SOFT SLENDER STRUCTURES

Basile Audoly[1] and Claire Lestringant[1]
[1]Laboratoire de mécaniquedes solides,CNRS,Institut Polytechnique de Paris,Palaiseau,France
[2]Mechanics & Materials,Department of Mechanical and Process Engineering,ETH Zürich,8092 Zürich, Switzerland
[2]Structures Research Group, Department of Mechanical and Process Engineering, University of Cambridge, United Kingdom

Summary We propose a method for obtaining one-dimensional models for slender elastic structures. The method accounts for large changes in the shape of the cross-sections, as happens typically in structures undergoing finite strain. It yields an equivalent one-dimensional energy functional in terms of (apparent) macroscopic strain. The energy functional captures both the non-linear dependence on the local apparent strain, as well as the dependence on the strain gradient, and is suitable for the analysis of phenomena such as localization.

When applied to a slender elastic body in three dimensions, dimension reduction classically yields the celebrated Euler-Bernoulli rod model. The equivalent elastic moduli of the one-dimensional model can be expressed in terms of elastic and geometric properties of the cross-section. This classical approach to dimension reduction is limited to situations where all the cross-sections deform almost rigidly. In this case, the dimension reduction involves solving a problem of linear elasticity in every cross-section.

A number of slender structures deform in a way such that cross-sections do not deform rigidly at all. Consider the inflation of thin cylindrical balloon (*i.e.*, a cylindrical party balloon), for instance: the formation of localized bulges during inflation has been successfully described using membrane theory[2] but this inflation entails variations in the cross-sectional radius that are well beyond 100%, and the finite-strain version of the membrane theory is required[1]. Another example is the bending and twisting of thin elastic ribbons: when these ribbons are deformed with macroscopic bending and twisting strain comparable to the inverse of the width, the cross-sections deform into arcs of circle so as to preserve the inextensibility of the mid-surface. By treating the cross-sections as essentially rigid, the equivalent Navier-Bernoulli rod model misses important features of these slender structures, and provides a poor approximation to the essentially non-linear way in which these structures deform.

In this talk, we present an approach to dimension reduction for slender elastic structures that is applicable to slender structures possessing highly deformable cross-sections. The approach proceeds as follows. The deformed structure is parameterized in terms of a geometric center-line, and of local degrees of freedom. The strain energy is then worked out in terms of the geometric properties of the center-line and of the local degrees of freedom. A relaxation problem is considered, whereby the local degrees of freedom are relaxed while the geometry of the center-line is kept constant. A one-dimensional strain energy functional is defined as the strain energy of this relaxed configuration, seen as a function of the properties of the center-line. Next, we work out this one-dimensional strain energy functional in powers of the successive gradients of the apparent stretching, bending and twisting strain of the center-line[4]. At dominant order, we find a non-linear, possibly non-convex, energy functional depending on the local apparent strain of the center-line. To derive this energy, one has to analyze the homogeneous solutions in a non-linear setting, and this is how large changes in the cross-sections are resolved accurately. At the next order, we find a correction to the energy arising from the gradient of the apparent strain, in the form of a diffuse-interface model.

This general strategy is applied to derive accurate, explicit one-dimensional models for slender non-linear structures such as an inflated axisymmetric balloon[4], a hyper-elastic cylinder undergoing necking[3], a thin elastic ribbon, or a tape spring. The strain-gradient corrections, which are obtained systematically from the general procedure and are asymptotically exact, allow us to analyze various types of localization phenomena easily and accurately.

References

[1] E. Chater and J. W. Hutchinson. On the propagation of bulges and buckles. *Journal of Applied Mechanics*, 51(2):269–277, 1984.
[2] S. Kyriakides and Y.-C. Chang. On the inflation of a long elastic tube in the presence of axial load. *International Journal of Solids and Structures*, 26(9–10):975–991, 1990.
[3] B. Audoly and J. W. Hutchinson. Analysis of necking based on a one-dimensional model. *Journal of the Mechanics and Physics of Solids*, 97:68–91, 2016.
[4] C. Lestringant and B. Audoly. A diffuse interface model for the analysis of propagating bulges in cylindrical balloons. *Proceedings of the Royal Society A: Mathematical, Physical and Engineering Sciences*, 474:20180333, 2018.
[5] C. Lestringant and B. Audoly. Asymptotically exact strain-gradient models for nonlinear slender elastic structures: a systematic derivation method. *Journal of the Mechanics and Physics of Solids*, 2019.

FINITE STRING RADIUS STRONGLY MODIFIES THE CLASSIC CAPSTAN PROBLEM

Harmeet Singh*[1] and John H. Maddocks[1]
[1]Institute of Mathematics, École Polytechnique Fédérale de Lausanne, Switzerland

Summary In the classic capstan problem the maximum possible tension in a flexible string wrapped around a rigid tube with frictional contact grows exponentially with the wrapping angle. This result relies only on force balance taken with two tacit assumptions: 1) The thickness of the string is negligible, and 2) there is a single contact line. Motivated by recent experimental work in modelling knots, we generalise the classic analysis to allow A) finite string thickness, and B) double contact lines, which can arise when the rigid tube is itself curved. Finite thickness requires that moment balance must be considered in addition to force balance. As a consequence the maximum tension growth is decreased. In contrast, double contact lines lead to an increase in the effective friction coefficient, and an associated increased maximal growth in tension.

THE PROBLEM

The classic capstan problem in mechanics entails determining the maximum possible increase in tension in a completely flexible string that is wrapped around a (planar, perpendicular, but possibly non-circular) cross-section of a rigid capstan with a frictional interaction governed by Coulomb's Static Inequality Law. This problem is treated in many places, e.g. [1]. Motivated by contemporaneous analytical and experimental work in modelling knots where neither of the two assumptions 1) and 2) above is a good approximation, we have generalised the classic capstan analysis to allow for A) finite string thickness, and B) double contact lines, which can arise when the capstan is itself a rigid, but curved, tubular surface.

RESULTS FOR FINITE THICKNESS WITH A SINGLE CONTACT LINE

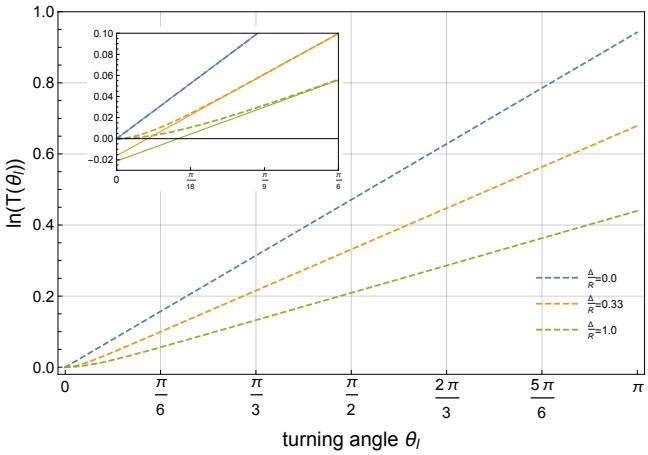

Figure 1: Natural log of maximal tension growth vs. wrapping/turning angle θ_l (scaled with unit tension at the initial zero turning angle, and in the case of a circular capstan cross-section). In all three cases shown, the asymptotic maximal growth rate is linear with slope $(1-\frac{\Delta}{R+\Delta})\mu$ where Δ and R are respectively the string and capstan radii, and $\mu = 0.3$ is the assumed Coulomb coefficient of static friction. For our generalisation to the case of non-zero string radius, there is also an initial layer with sub-exponential growth in the tension (cf. inset, where the straight line asymptotes are also shown).

We argue that finite string thickness implies that moment balance of the flexible string must be considered in addition to force balance, and as a consequence (whenever there is still a single, planar, contact line) the maximal asymptotic growth remains locally exponential, but with a significantly reduced growth constant involving a geometrical (possibly variable) pre-factor times the coefficient of friction (Figure 1). We also predict the existence of a non-exponential initial layer for the maximal tension at small wrapping/turning angles which further reduces (albeit only slightly) the maximal possible tension (Figure 1 inset).

The data of Figure 1 is obtained by considering the following ODE IVP which expresses balance of forces and moments on a planar configuration for a string that supports no internal bending moment

$$T' = (1-\kappa)f\,, \quad (\kappa f)' = T - \Lambda\,, \tag{1}$$

$$T(0) = 1\,, \quad f(0) = 0\,, \tag{2}$$

$$\text{subject to} \quad |f| \le \mu\Lambda\,. \tag{3}$$

Here T is the tension scaled by its initial value, and expressed as a function of turning angle θ_l, κ is the curvature of the string centreline scaled by the tube radius Δ ($\kappa = \frac{\Delta}{R+\Delta}$ a constant in the case when the capstan cross-section is an arc of a circle of radius R), f is the frictional contact force per unit turning angle, which is related to the normal contact pressure per unit turning angle $\Lambda \ge 0$ via the Coulomb inequality (for densities) with coefficient of friction μ. The initial condition $f(0) = 0$ arises as part of moment balance.

Consideration of the above system reveals that maximal tension growth arises for $f \ge 0$ and the largest possible value of $-\Lambda$ i.e. in the Coulomb friction inequality, the equality bound $\Lambda = \frac{f}{\mu}$ always holds. Then for maximal tension growth we eliminate Λ to arrive at the system

$$T' = (1-\kappa)f\,, \quad (\kappa f)' = T - \frac{f}{\mu}\,, \quad T(0) = 1\,, \quad f(0) = 0\,. \tag{4}$$

The classic capstan system arises in the singular limit $\kappa \equiv 0$, so that $T' = \mu T$, $T(0) = 1$, whose exponential solution is one curve in Figure 1. The two other curves are numerical solutions of the system (4) for two constant values of $\kappa = \frac{\Delta}{R+\Delta}$.

*Corresponding author. E-mail: harmeet.singh@epfl.ch

RESULTS FOR DOUBLE CONTACT LINES

Our motivation for this investigation is to obtain a mechanical analysis of knots. A typical situation in that context is two tubes, both flexible, with circular cross-sections of comparable radii, interacting with each other through mutual volume exclusion and with friction at the contact interface. Through a small generalisation of remarkable results of Starostin [2] for (the four-fold symmetric case of) the orthogonal clasp, we obtained one-parameter families of pairs of U-shaped planar tube configurations (red and blue in Figure 2b panel b)) that are in equilibrium for two flexible strings interacting without friction. We have shown four snapshots from a continuous family in which the opening angle of the red tubes is constant while the opening angle of the blue tube is varied. The main point of interest for us is that there are double contact lines (shown in green) between the pairs of tubes in each member of this family.

These tubular configurations with double contact lines are equally valid as configurations when we assume that the red tubes are entirely rigid, so that they can be taken as forming a capstan. Then we can solve the analogous versions of the balance laws above, but now in the case of double contact lines, in order to compute the maximal possible tension growth in the blue tubes in the presence of friction. The results are plotted in panel a). The four coloured dots are the maximal possible end tensions for each of the four cases, with the associated coloured dot-dashed lines being the internal distribution of tension on the maximal tension growth equilibria (where in the case of the shortest blue tube the internal tension distribution is not visible at this scale). The black solid line indicates the maximal end tension along the entire one-parameter family of double contact line equilibria as a function of the end opening angle for the blue tubes. It is this line that is comparable to the single contact line results presented in Figure 1 for various values of $\frac{\Delta}{R}$ and varying turning angle. In particular for the same value of friction coefficient μ, and for each overall opening angle, the possible maximal tension in the finite-radius $\frac{\Delta}{R} = 1$ double-contact case with a highly curved capstan tube, is less than for the classic idealised zero radius case $\frac{\Delta}{R} = 0$, but greater than for the comparable finite radius $\frac{\Delta}{R} = 1$ single contact line case, that arises for a right cylindrical capstan.

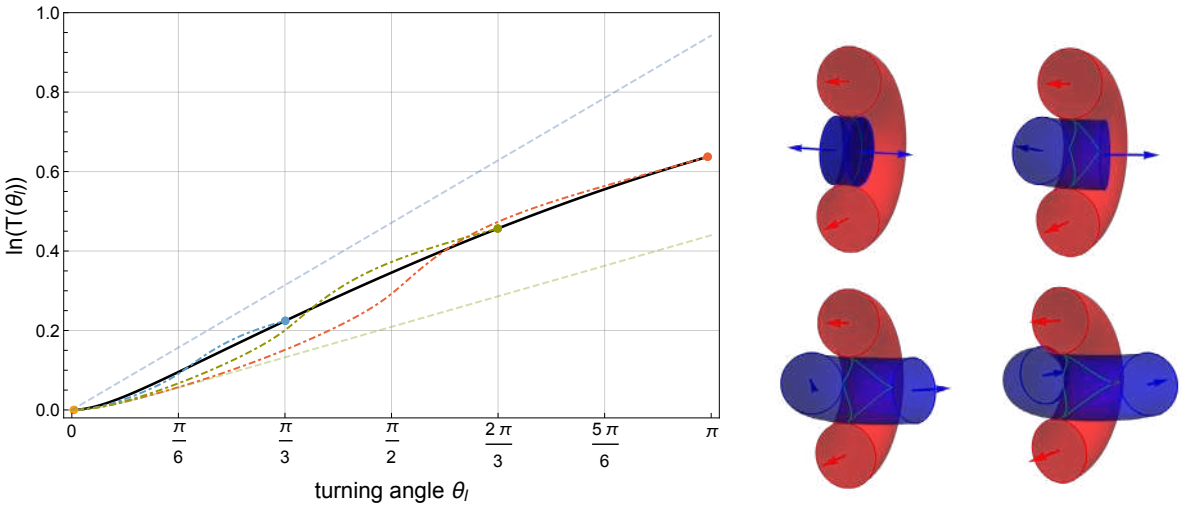

(a) (b)

Figure 2: (a) Natural log of the maximum tensions in the flexible string (blue) plotted against its turning angle θ_l around the red tube (assumed to be rigid). The end opening angle of the red tube/capstan is held fixed at π radians in the four cases. The dot-dashed curves represent tension profiles for the four cases $\theta_l = \{0, \frac{\pi}{3}, \frac{2\pi}{3}, \pi\}$ of end opening angles for the blue tube. The two dashed curves correspond to the single contact case for $\frac{\Delta}{R} = \{0, 1\}$ from Figure 1 shown here for comparison. (b) Equilibrium configurations showing the double contact lines (in green) between the two tubes corresponding to the four cases in (a).

CONCLUSIONS

We have shown that considering a finite tube radius as a generalisation of the classic capstan problem has two opposing effects. If the capstan has a geometry that still gives rise to single contact lines, then finite tube thickness decreases the maximal possible tensions, due to the necessity to balance moments. However if the rigid capstan is itself a sufficiently deformed tube, then finite radius geometry can also give rise to double contact lines, which in turn allow an increase in maximum tension distributions. In the classic case of $\frac{\Delta}{R} = 0$ the shape of the capstan outside its planar cross-section can play no role. For the examples shown here, the increases in maximal tension distributions due to double contact, do not approach the classic bounds that pertain in the singular limit of vanishing tube radius. We believe that to fully understand the mechanics of three-dimensional knots these competing consequences of finite tube radii need to be better understood.

References

[1] Maddocks, J.H., Keller, J.B., Ropes in Equilibrium. *SIAM Journal on Applied Mathematics* **47** (6): 1185-1200, 1987.
[2] Starostin E. L. , A Constructive Approach to Modelling the Tight Shapes of Some Linked Structures. *Forma* **18**: 263-293, 2003.

EXPERIMENTS AND MODELING OF THE VISCOELASTIC BEHAVIOR OF POLYMERIC GELS

Nikola Bosnjak[1] and Shawn A. Chester *[1]
[1]Mechanical Engineering, New Jersey Institute of Technology, Newark, NJ USA

Summary A polymeric gel is a cross-linked polymer network swollen with a solvent. Also, as is well known many polymeric materials exhibit viscoelastic behavior in their mechanical response. In this work, we report on our recent experimental observations and theoretical modeling involving the change in the viscoelastic response of the polymeric material VHB caused by equilibrium swelling in multiple solvents. To characterize this change, we have developed an experimental procedure that includes mechanical testing when virgin, free swelling, mechanical testing when swollen, and mechanical testing after drying. A model is used to help interpret the experimental results. The key finding of this work is that our results indicate that the viscoelastic behavior of initially dry VHB, reversibly, becomes essentially hyperelastic when swollen to equilibrium in multiple solvents.

INTRODUCTION

When exposed to a suitable solvent, many polymeric materials will imbibe the solvent. During this process, the polymer network expands, and the fluid molecules migrate into the polymer microstructure, forming a solid-fluid continuum known as polymeric gel. And many polymeric gels are classified as active materials due to their ability to respond to various stimuli.

The goal of this project is to characterize the viscoelastic response of both dry and fully swollen polymeric gels through experimental observations and continuum level modeling. Towards our goal, we have developed an experimental procedure intended to capture the major aspects of the non-linear mechanical behavior of polymeric gels, including the viscoelastic response. To complement the experimental observations, we calibrate a constitutive model for viscoelastic polymeric gels. In what follows, we restrict our attention to the specific cases where the material is either completely dry, or fully swollen.

For our experiments we have chosen the commercially available material VHB 4910, since it is well known exhibit viscoelastic behavior in the absence of fluid. Also, we have observed that VHB 4910 swells when in contact with suitable solvents. Therefore all of our experiments make use of n-Pentane, o-Xylene, and Toluene, as solvents in conjunction with VHB 4910 to create our polymeric gels. The continuum-level constitutive model is mechanically incompressible, includes viscoelasticity, and does not explicitly take diffusion into account. That is to say we consider time dependence in the mechanical response, however not in the diffusive response of the solvent, which is taken to be at a known and fixed degree of swelling.

Readers are referred to [1] for full details related to this project.

EXPERIMENTAL RESULTS

We use dog-bone shaped specimens, and virgin samples are cut out from a roll of VHB 4910 tape using an ASTM D638-V cutting die. The nominal length, width, and thickness of the virgin gauge section are 9.49 mm, 3.18 mm, and 1 mm respectively. The results of some of our uniaxial tests on virgin specimens are shown in Figure 1. The dry virgin material exhibits pronounced rate-dependent behavior, which is observed in Figures 1b and 1a, and Figure 1b shows the measured stress relaxation behavior at an applied stretch of $\lambda = 2$. And in Figure 1c the large deformation quasi-static tension test results at a rate of 10^{-4}s^{-1} are plotted along with the long term creep and relaxation data at equilibrium. Since the large deformation quasi-static tensile response has some hysteresis, we interpolated the creep and relaxation data (utilizing the `smooth` function in MATLAB) to obtain the time-independent response of the material. Figure 2a shows a subset of our data with multiple stretch-stress curves all superimposed atop each other, and immediately the change in behavior is visible. The behavior of virgin samples shows clear viscoelastic effects. However, the fully swollen results show no signs of rate dependency, nor hysteresis, with load-unload stretch-stress curves obtained at different rates being almost completely on top of each other. Measurements of the hysteresis, stiffness, and stress-stretch behavior all lead toward the hypothesis that *the fully swollen material has lost nearly all viscoelasticity, and the fully swollen material behaves like a non-linear elastic material.* To assess if swelling causes irreversible changes to the mechanical behavior, we solvent cycle — freely swell, then freely dry — and then use those samples for uniaxial tests. For samples that have been solvent cycled five times, Figure 2b shows the reappearance of the viscoelastic response for uniaxial load-unload experiments. These results show that *prior solvent cycling has no significant residual effects on the overall response of the polymer, which we take as an indication of the reversibility of the process.*

*Corresponding author. E-mail: shawn.a.chester@njit.edu.

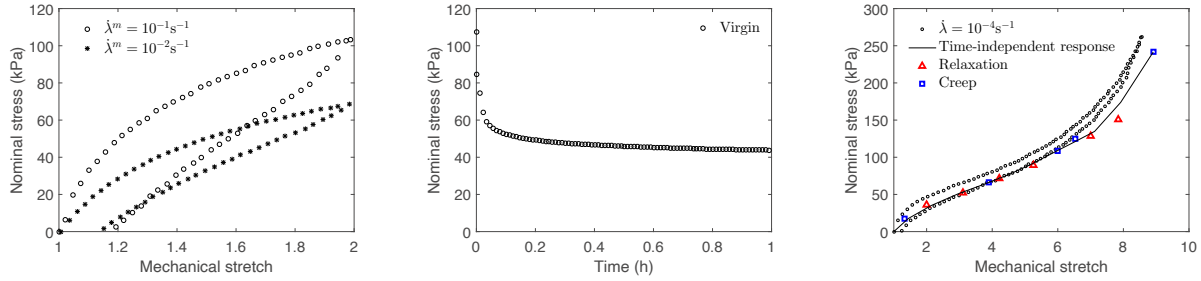

a) b) c)

Figure 1: Uniaxial experimental results for dry virgin specimens. a) moderate rate load-unload uniaxial tensile tests, with nominal stress as a function of mechanical stretch. b) Stress relaxation for an applied mechanical stretch of 2. And c) comparison between the quasi-static large deformation tensile test and the time-independent behavior obtained through combination of stress relaxation and creep testing.

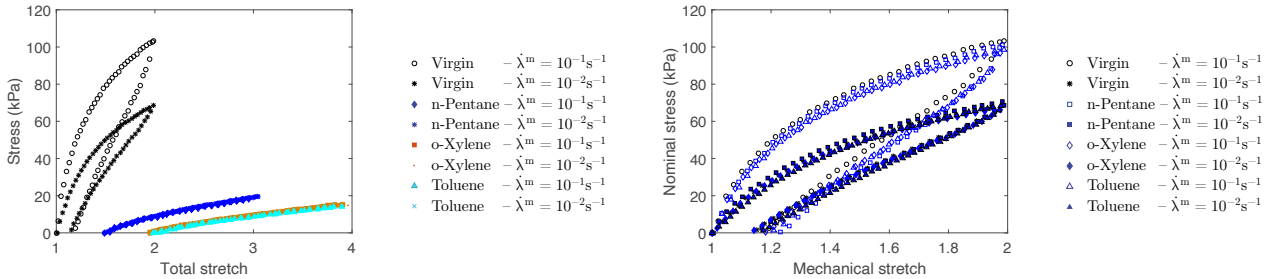

a) b)

Figure 2: a) A subset of the experimental results showing the load-unload response for moderate rates displaying the clear affect of equilibrium swelling on the behavior. b) Uniaxial load-unload tensile test results after solvent cycling 5 times with n-Pentane, o-Xylene and Toluene. For ease of comparison, we also show the virgin results.

CONTINUUM LEVEL MODEL

Our continuum-level constitutive model for polymeric gels is provided in detail in [1], it is only overviewed here. The large deformation time-independent response of the polymer is modeled employing a non-Gaussian statistical mechanics model, which takes into account the limited extensibility of polymer chains, as well as a scaling exponent on the swelling ratio to account for the change in effective stiffness. Viscous effects are modeled following a micromechanically motivated approach. Lastly, the mixing between the polymer network and solvent is accounted for by the Flory-Huggins model.

CONCLUSIONS

Using VHB 4910 along with three different solvents, n-Pentane, o-Xylene and Toluene, we have measured the mechanical response in (i) quasi-static uniaxial large deformation tension, (ii) uniaxial load-unload at multiple rates, and (iii) stress relaxation; when virgin, fully swollen, and solvent cycled. The most notable result of these experiments being the apparent loss of viscoelasticity in the response due to the uptake of solvent. Additionally, through solvent cycling, our measurements show the reappearance of viscoelasticity, suggesting the process is reversible. In addition, we have developed a continuum-level constitutive model for viscoelastic polymeric gels. Our model is successfully calibrated against the obtained experimental data, thus proving capable to replicate the major features of viscoelastic gel behavior observed in our experiments. The calibration of our constitutive model showed (i) low utilization of the time-dependent stress contribution for the samples fully swollen in n-Pentane; (ii) almost complete absence of the time-dependent stress contribution for samples fully swollen with o-Xylene and Toluene. Although not the aim of this study, we have found the failure of the material fully swollen with o-Xylene and Toluene to be occurring at the stretch at which the dry material (both virgin and solvent cycled) is still intact. That is a very interesting result that indicates there is more to learn, however we leave it for future work. Lastly, while we characterized the behavior of a viscoelastic gel when fully swollen, the mechanical response at intermediate degrees of swelling is yet to be determined and is the focus of our future work.

References

[1] Bosnjak, N., Nadimpalli, S., Okumura, D. and Chester, S.A. Experiments and modeling of the viscoelastic behavior of polymeric gels. *Journal of the Mechanics and Physics of Solids* **137**: 103829, 2020.

SHAPE-CHANGING ELASTOMER VIA LIQUID-GAS PHASE TRANSITION

Saint-Jean Maïka*[1], Etienne Reyssat[1], José Bico[1], Benoît Roman[1]
[1]PMMH, CNRS, ESPCI Paris, Université PSL, Sorbonne Université, Université de Paris, Paris, France

Summary: We use the liquid-gas transition of droplets dispersed in an elastomer matrix to design reversible shape changing materials. More specifically, we use droplets of alcohol trapped in silicone rubber. Upon heating, the liquid boils inside the cavities, leading to a rise of the inner pressure and to the global expansion of the material. Our goal is to design planar sheets that can evolve to controlled 3D structures. The strategy adopted here is to use an embedded structure to geometrically constrain the deformations of the material.

INRODUCTION

Shape changing materials is currently an active field of research, motivated by potential applications in minimally invasive surgery [1], tissue engineering [2], soft robotics [3] and, more generally, in smart materials [4]. One possible strategy consists in embedding a network of airways in plates made of an elastomeric matrix [5]. Upon inflation, the airways deform anisotropically, leading to local metric change through the plate. As a consequence, the plate buckles and adopts a 3D shape prescribed by the architecture of the airways. Following this work, we propose a different strategy where an embedded skeleton limits the extension of the material in certain directions, leading to programmed 3D shapes.

METHODS AND RESULTS

The growing matrix used in this study is inspired by the recent work of Miriyev *et al.* [6]. This technique is based on thermal actuation of an elastomer material in which ethanol droplets are dispersed. When heated, ethanol vaporizes, which increases the pressure inside the cavities and induces a large expansion of the material. This action is, in principle, reversible as the pressure is released when the ethanol goes back to its liquid state (although in practice we observe-some aging of the material due to the diffusion of ethanol through the matrix).

Our goal is to use this expanding material to design objects than can change shape upon heating. The strategy selected here is to control in-plane metric deformation by locally constraining the expansion along given directions. To this aim, custom meshes made out of thin ~~cut~~ Mylar sheets are embedded in the matrix.

Technically, two identical meshes are disposed symmetrically on both sides of a plate of elastomer to prevent spontaneous bending by bilayer effect. Each mesh is finally covered with a thin layer of raw elastomer to prevent alcohol leaks (Figure 1a).

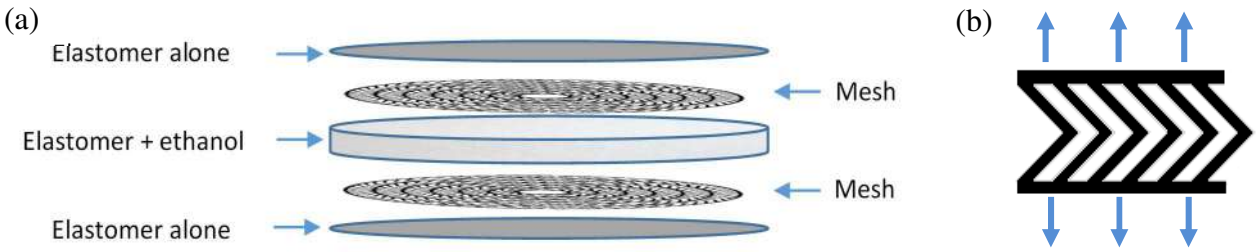

Figure 1: (a) Composition of the sample. Two identical thin meshes are placed on each side of a plate of active matrix (elastomer with alcohol droplets) and then covered with a layer of pure elastomer. (b) Typical chevron pattern of the mesh that permits an expansion in the vertical direction but blocks the horizontal direction.

The meshes used are designed differently according to the desired 3D shape. Different types of designs are developed: like chevrons (Figure 1.b). Depending on the pattern, both positive and negative Gaussian curvatures can be obtained from planar shapes. Having both negative and positive Gaussian curvatures allows us to potentially design any shape. The orientation and angle of the patterns of the mesh determine the final shape of the object (Figure 2). The kinematics of the embedded mesh can be rationalized with simplified designs that lead to uniaxial extension.
Under high extension the mesh reaches a maximum deformation dictated by geometry. Such finite extensibility stiffens the composite material. As a consequence, in addition to dictating the shape, the embedded meshes also tend to rigidify the final structure.

*Corresponding author. E-mail: maika.saint-jean@espci.fr

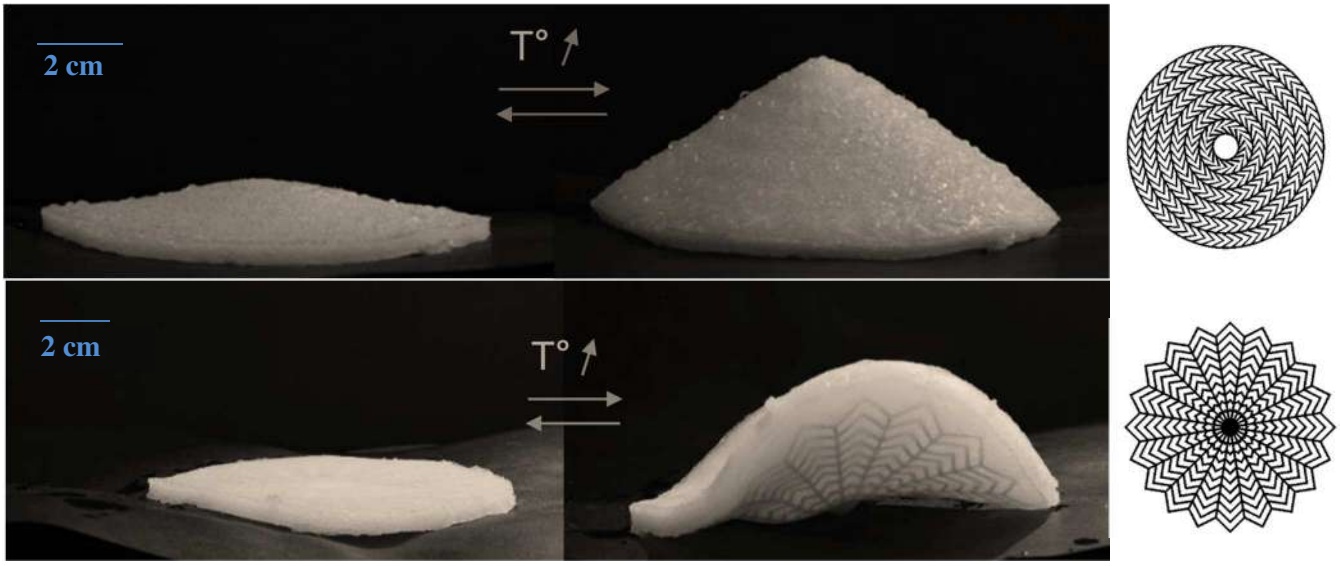

Figure 2: Deformation of samples upon heating. Chevrons are oriented azimuthally and induce a positive Gaussian curvature (top) or they are oriented radially and lead to a negative Gaussian curvature (bottom).

ACKNOWLEDGMENTS

We thank the "Agence Innovation de Défense" and the "Direction Générale de l'Armement" for their financial support.

References

[1] Cianchetti, M. et al. (2014). Soft robotics technologies to address shortcomings in today's minimally invasive surgery: The stiff-flop approach. *Soft Robotics* **1**, 122-131.
[2] Gao, B. et al. (2016). 4D bioprinting for biomedical applications. *Trends Biotechnol.* **34**, 746-756.
[3] Shepherd, R. F. et al. (2011). *Multigait soft robot. Proceedings of the national academy of sciences* **108**, 20400-20403.
[4] McEvoy, M. A. & Correll, N. (2015). Materials that couple sensing, actuation, computation, and communication. *Science* **347**, 1261689.
[5] Siéfert, E., Reyssat, E., Bico, J., & Roman, B. (2019). Bio-inspired pneumatic shape-morphing elastomers. *Nature materials,* **18** (1), 24.
[6] Miriyev, A., Stack, K., & Lipson, H. (2017). Soft material for soft actuators. *Nature communications*, **8** (1), 596.

ON THE MECHANICS OF *E*-CONES

Souhayl Sadik*[1] and Marcelo Azevedo Dias †[1]
[1]Department of Engineering, Aarhus University, 8000 Aarhus C, Denmark

Summary In this work, we study the most basic and fundamental geometric building block of Kirigami: a thin sheet with a single cut. We consider the deformation of a circular thin plate with a radial slit following the opening of the slit by a given excess angle. In the isometric limit—as the thickness of the disk approaches zero—the elastic energy has no stretching contribution and the shape of the disk is governed by the bending energy as it approaches that of an *e*-cone: a conical solution where all the generators remain straight and intersect at a singularity at its apex. We solve the geometrically nonlinear boundary value problem for a Saint Venant-Kirchhoff constitutive plate model to find the geometry of the e-cone as well as the surface stresses and couple-stresses (moments). We further investigate the local singular behaviour of the slit near the crack tip by relaxing the inextensibility condition and discarding the conical ansatz in an attempt to access the stretching region around the apex.

KINEMATICS

Kirigami, the Japanese art of paper cutting, offers unexplored ways to tailor the morphology of thin elastic sheets. Indeed, by exploiting the fundamental principles of this art and carefully tuning the geometry and the topology of the cuts, it unlocks a great potential to control the structural and mechanical properties of thin sheets across multiple scales [1]. In order to generate predictable and adaptable patterns or motion control as well as regulate the multi-stable nature of these structures, one would need to understand the fundamental behaviour of such structures [2]. In this work, we explore the emergent local non-linear effects in Kirigami by focusing our attention on the study of the deformation of a single cut and the inherent interplay of geometry and mechanics.

We consider a reduced two-dimensional shell model $\mathcal{H}$ for a circular thin disk with a radial slit extending from its centre to its boundary. We assume an excess angle of ψ and look for a developable conical solution: the disk deforms in $\mathbb{R}^3$ such that all its radial generators remain straight and unstretched. In terms of the deformation embedding, it amounts to assuming the conical ansatz for the deformation mapping $\varphi(R,\Phi) = (R, \theta(\Phi), \phi(\Phi))$, where $\{R, \Phi\}$, $0 \leq \Phi \leq 2\pi$ is a polar coordinates system on $\mathcal{H}$ such that its origin sits at the center of $\mathcal{H}$ and $\Phi = 0$ and $\Phi = 2\pi$ arbitrarily correspond to the two lips of the slit, and $\{r, \theta, \phi\}$, $0 \leq \theta \leq \pi$, $0 \leq \phi < 2\pi$ is a spherical coordinate system in $\mathbb{R}^3$. We further assume the following boundary conditions to enforce the opening of the slit by an angle ψ and control the angles of rotation of its lips by η_1 and η_2 : $\theta(0) = \theta(2\pi) = \frac{\pi}{2}$, $\phi(0) = \frac{\psi}{2}$, $\phi(2\pi) = 2\pi - \frac{\psi}{2}$, $\theta'(0) = \eta_1$, and $\theta'(2\pi) = \eta_2$.

In the deformed configuration $\varphi(\mathcal{H}) \subset \mathbb{R}^3$, we denote the normal of the surface by $\boldsymbol{n}$ and its first and second fundamental forms by $\boldsymbol{g} = \bar{\boldsymbol{g}}_{|\varphi(\mathcal{H})}$ and $\boldsymbol{\beta} = -(\nabla^{\bar{\boldsymbol{g}}}\boldsymbol{n})^{\flat}$,[1] respectively. To quantify the strain, we define an intrinsic strain measure $\boldsymbol{C} = \varphi^*\boldsymbol{g}$ [2]—the right Cauchy-Green deformation tensor;[3] and an extrinsic strain measure $\boldsymbol{\Theta} = \varphi^*\boldsymbol{\beta}$. We denote by J the Jacobian of the deformation $J = \sqrt{\frac{\det \boldsymbol{C}}{\det \boldsymbol{G}}}$. We define the convected manifold $(\mathcal{H}, \boldsymbol{C}, \boldsymbol{\Theta})$ as the Riemannian manifold resulting from pulling-back the geometry of the deformed surface onto $\mathcal{H}$, i.e., taking $\boldsymbol{C}$ and $\boldsymbol{\Theta}$ to be the first and second fundamental forms of $\mathcal{H}$, respectively.

The inextensibility yields that $\phi(\Phi) = \frac{\psi}{2} + \int_0^{\Phi} \frac{\sqrt{1-\theta'^2(\eta)}}{\sin[\theta(\eta)]}\, d\eta$, and it follows that the deformed fundamental forms read

$$\boldsymbol{C} = \begin{pmatrix} 0 & 0 \\ 0 & R^2 \end{pmatrix}, \quad \boldsymbol{\Theta} = \begin{pmatrix} 0 & 0 \\ 0 & R\kappa(\Phi) \end{pmatrix},$$

where we introduce the normal curvature $\kappa(\Phi) := \frac{\cot[\theta(\Phi)]\left(1-\theta'^2(\Phi)\right) - \theta''(\Phi)}{\sqrt{1-\theta'^2(\Phi)}}$.

BALANCE LAWS

We assume that the disk is made of a material with a Saint Venant-Kirchhoff constitutive model. In the convected manifold $(\mathcal{H}, \boldsymbol{C}, \boldsymbol{\Theta})$, the strain energy density $\mathcal{W}$ of the material reads[4]

$$\mathcal{W} = \frac{h}{4}\left\{\mu \mathrm{tr}\left[(\boldsymbol{C}-\boldsymbol{G})^2\right] + \frac{\mu\lambda}{2\mu+\lambda}\left[\mathrm{tr}\,(\boldsymbol{C}-\boldsymbol{G})\right]^2\right\} - \boldsymbol{p}:(\boldsymbol{C}-\boldsymbol{G}) + \frac{h^3}{12}\left\{\mu \mathrm{tr}\left[(\boldsymbol{\Theta}-\boldsymbol{B})^2\right] + \frac{\mu\lambda}{2\mu+\lambda}\left[\mathrm{tr}\,(\boldsymbol{\Theta}-\boldsymbol{B})\right]^2\right\},$$

*E-mail: souhayl.sadik@eng.au.dk.
†E-mail: madias@eng.au.dk.

[1]The flat symbol in $(.)^{\flat}$ denotes the operator for lowering tensor indices.

[2]φ^* denotes the pullback by the diffeomorphism φ. As examples, the pullback of a $\binom{0}{2}$-rank tensor $\boldsymbol{w}$ reads in local coordinates $(\varphi^*\boldsymbol{w})_{AB} = \frac{\partial\varphi^a}{\partial X^A}\frac{\partial\varphi^b}{\partial X^B} w_{ab}$; and the pullback of a $\binom{2}{0}$-rank tensor $\boldsymbol{\omega}$ reads in local coordinates $(\varphi^*\boldsymbol{\omega})_{AB} = \frac{\partial\varphi^{-A}}{\partial x^a}\frac{\partial\varphi^{-B}}{\partial x^b}\omega^{ab}$.

[3]Note that the right Cauchy-Green deformation tensor is typically defined as $\boldsymbol{F}^{\mathsf{T}}\boldsymbol{F}$ where $^{\mathsf{T}}$ denotes the transpose operator. In our notation, we have $\boldsymbol{C} = \left(\boldsymbol{F}^{\mathsf{T}}\boldsymbol{F}\right)^{\flat}$.

[4]Note that in the convected manifold, one has $C^{AK}C_{KB} = \delta^A{}_B$ so that raising $((.)^{\sharp})$ and lowering $((.)^{\flat})$ tensor indices is performed using the convected metric $\boldsymbol{C}$, e.g., $T^A{}_B = C^{AK}T_{KB}$. Also, the trace of a tensor is computed by using the convected metric $\boldsymbol{C}$, e.g., $\mathrm{tr}\,(\boldsymbol{T}) = C^{AB}T_{AB}$ and $\mathrm{tr}\,(\boldsymbol{C}) = 3$.

where h is the thickness of the disk, μ and λ the Lamé coefficients, and $\boldsymbol{p}$ the $\binom{2}{0}$-rank tensor Lagrange multiplier enforcing the inextensiblity condition $\boldsymbol{C} = \boldsymbol{G}$. Without any loss of generality, we assume the following form for the Lagrange multiplier $\boldsymbol{p}$

$$\boldsymbol{p}(R,\Phi) = \begin{pmatrix} p_1(R,\Phi) & \frac{\tau(R,\Phi)}{R} \\ \frac{\tau(R,\Phi)}{R} & \frac{p_2(R,\Phi)}{R^2} \end{pmatrix}$$

In the convected manifold $(\mathcal{H}, \boldsymbol{C}, \boldsymbol{\Theta})$, the balance laws for the disk read

$$\mathrm{Div}_{\boldsymbol{C}} \left(\boldsymbol{\Sigma} + \boldsymbol{C}^\sharp \cdot \boldsymbol{\Theta} \cdot \boldsymbol{\Lambda} \right) + \boldsymbol{C}^\sharp \cdot \boldsymbol{\Theta} \cdot \mathrm{Div}_{\boldsymbol{C}} (\boldsymbol{\Lambda}) = \boldsymbol{0}\,, \tag{1a}$$

$$\left(\boldsymbol{\Sigma} + \boldsymbol{C}^\sharp \cdot \boldsymbol{\Theta} \cdot \boldsymbol{\Lambda} \right) : \boldsymbol{\Theta} - \Delta_{\boldsymbol{C}} (\boldsymbol{\Lambda}) = 0\,, \tag{1b}$$

where $\mathrm{Div}_{\boldsymbol{C}}$ and $\Delta_{\boldsymbol{C}}$ respectively denote the divergence and the Laplace operators in the convected manifold; they read as follow $\mathrm{Div}_{\boldsymbol{C}}\, \boldsymbol{\Sigma} = \Sigma^{AB}{}_{||B}$ and $\Delta_{\boldsymbol{C}} \boldsymbol{\Lambda} = \Lambda^{AB}{}_{||AB}$, where a subscript double stroke $||$ denote covariant differentiation with respect to $\boldsymbol{C}$ taken as a metric on $\mathcal{H}$. Reducing $\boldsymbol{p}$, the balance laws (1) reduce to a single equation governing the normal curvature κ and it reads

$$\kappa''(\Phi) + \frac{\kappa^3(\Phi)}{2} + \left(1 + \alpha - \frac{3(\lambda+2\mu)}{h^3 \mu(\lambda+\mu)} \int_0^\Phi b(\eta)\, d\eta \right) \kappa(\Phi) = 0\,. \tag{2}$$

Note that for $b = 0$, Cerda and Mahadevan [3], Guven and Müller [5], and Efrati et al [**?**] have all obtained the same elastica equation governing the normal curvature κ from a reduced conical model. Using the solution $\boldsymbol{p}$ of (1), we may write the radial and circumferential effective surface traction $\boldsymbol{f}$ and effective surface shear s as follow

$$\begin{aligned}
\bar{\boldsymbol{f}}_R &= \left[\frac{h^3\mu(\lambda+\mu)}{3(\lambda+2\mu)} \frac{\frac{1}{2}\kappa^2(\Phi)+\alpha}{R^2} - \frac{a'(\Phi) + (\ln(R)+1)b'(\Phi) + \int_0^\Phi b(\eta)d\eta}{R^2} - \frac{c(\Phi)}{R} \right] \boldsymbol{u} - \left[\frac{a(\Phi)+\ln(R)b(\Phi)}{R^2} \right] \boldsymbol{t}\,; \\
\bar{s}_R &= \frac{h^3\mu(\lambda+\mu)}{3(\lambda+2\mu)} \frac{\kappa(\Phi)}{R^2}\,; \quad \bar{\boldsymbol{m}}_R = \frac{h^3\mu\lambda}{6(\lambda+2\mu)} \frac{\kappa(\Phi)}{R}\, \boldsymbol{u}\,; \\
\bar{\boldsymbol{f}}_\Phi &= -\left[\frac{a(\Phi)+\ln(R)b(\Phi)}{R^2} \right] \boldsymbol{u} + \left[-\frac{h^3\mu(\lambda+\mu)}{3(\lambda+2\mu)} \frac{\frac{1}{2}\kappa^2(\Phi)+\alpha}{R^2} + \frac{\int_0^\Phi b(\eta)d\eta}{R^2} \right] \boldsymbol{t}\,; \\
\bar{s}_\Phi &= \frac{h^3\mu(\lambda+\mu)}{3(\lambda+2\mu)} \frac{\kappa'(\Phi)}{R^2}\,; \quad \bar{\boldsymbol{m}}_\Phi = \frac{h^3\mu(\lambda+\mu)}{3(\lambda+2\mu)} \frac{\kappa(\Phi)}{R}\, \boldsymbol{t}\,;
\end{aligned} \tag{3}$$

for some constant α and some functions a, b, and c of the angle Φ; where $\boldsymbol{t} = \varphi_* \partial_\Phi$ and $\boldsymbol{u} = \varphi_* \partial_R$. Note that $\boldsymbol{t}$ and $\boldsymbol{u}$ are respectively the tangent and the in-surface normal of any curve in the deformed configuration that resulted from the deformation of a circle centered at the origin in the reference configuration of the disk—the curve that is parametrized by the assumed conical ansatz for a fixed R. We have hereby obtained more general results on the state of stress in the *e*-cone which are nonetheless consistent with the results found by Cerda and Mahadevan [3] and Guven and Müller [5].

CONCLUSIONS

We have achieved a full description of the geometry and the mechanics of the *e*-cone. However, it is easy to see that the apex represent a singularity for the curvature, the stress, and the energy—it is indeed a singularity for all quantities. Indeed, for a small region near the apex, the deformation of the e-cone is regularised by an added contribution of the stretching energy on top of the bending energy. This resolves the singularity by eliminating the inexentensibility condition and the conical ansatz. As such, the local solution near the apex is no longer invariant under a radial dilation with respect to its centre. We are currently investigating this region and have so far obtained by rescaling the problem scaling laws in the apex area and consequently proven that the stretching and bending contributions are of the same order.

References

[1] Dias, M. A., et al. Kirigami actuators. *Soft matter*, 13(48):9087-9092, 2017.
[2] Yang, Y., Dias, M. A., & Holmes, D. P. Multistable kirigami for tunable architected materials. *Physical Review Materials*, 2(11):110601, 2018.
[3] Cerda, E. and Mahadevan, L. Confined developable elastic surfaces: cylinders, cones and the *elastica*. *Proceedings of the Royal Society A: Mathematical, Physical and Engineering Sciences*, 461(2055):671-700, 2005.
[4] Guven, J. and Müller, M. M. How paper folds: bending with local constraints. *Journal of Physics A: Mathematical and Theoretical*, 41(5):055203, 2008.
[5] Efrati, E. et al Confined disclinations: exterior versus material constraints in developable thin elastic sheets. *Physical Review E*, 91(2):022404, 2015.

FROM BIFURCATION TO SNAP-THROUGH BUCKLING OF ELASTIC THIN SHELLS WITH LARGE AXISYMMETRIC IMPERFECTION

Chuan Qiao, Lu Liu, and Damiano Pasini*
Department of Mechanical Engineering, McGill University, Montreal, Canada

Summary Elastic thin shells are well-known for their highly unstable post-buckling response that exhausts their pressure bearing capacity and leads to catastrophic collapse. This paper examines elastic thin shells with a large axisymmetric imperfection that can escape the classical bifurcation of perfect spherical shells. The results show that the imperfect shell undergoes snap-through buckling followed by a stable post-buckling that offers increasing resistance to pressure over a large shell deformation. In addition, a sensitivity analysis on the role of defect geometry reveals the emergence of four buckling modes. The findings show that harnessing defect geometry can be effective in programming the post-buckling characteristics and transition between buckling modes, thus offering potential routes for the design of soft metamaterials.

INTRODUCTION

The post-buckling response of elastic thin shells subject to prescribed uniform external pressure is highly unstable [1]. This phenomenon deprives shell functionality and has two main features. First, prior to bifurcation, the shell deformation, in particular the displacement of the pole, is tiny compared to the shell radius thereby yielding almost no change in volume. Second, under a given pressure the shell is unstable for the entire post-buckling regime, showing the inability to resist any increase in pressure and spontaneous marching towards full eversion.

To escape the classical bifurcation of perfect spherical shells, this paper examines elastic thin shells with a large axisymmetric imperfection [2] and compares its buckling response with that of perfect shells subject to a uniform external pressure. We present a theoretical model that uses exact expressions of stretching and bending strains for axisymmetric deformations without any restrictions on the magnitude of displacements and rotations, along with a campaign of experiments on fabricated shell samples and a comprehensive computational study. The results can capture the defect sensitivity of imperfect shells to selected parameters of shell and defect geometry.

GEOMETRY OF THE IMPERFECT SHELL

We examine an imperfect shell (Figs. 1 a and b) with a large imperfection in the form of an axisymmetric circular-arc indentation that can vary in amplitude, angular width, and meridional angle. The arc can collapse to a line segment for a small amplitude or a semicircle for a large amplitude. The imperfection is also assumed to lie between the equator and the upper pole of the semi circumference. The slenderness of the shell is defined by the radius to thickness ratio.

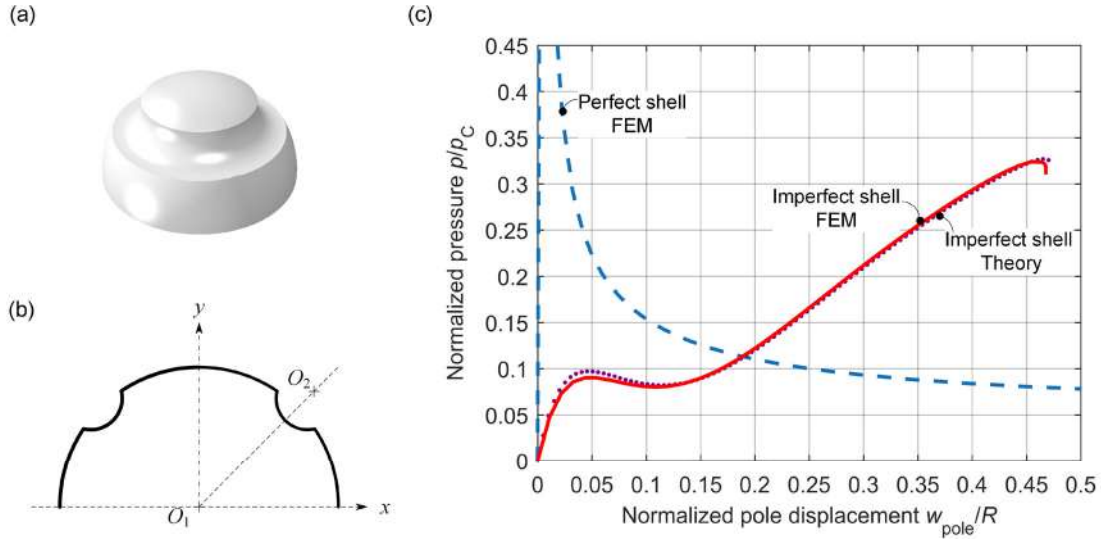

Figure 1. (a) Three-dimensional view and (b) cross-section view of an imperfect hemispherical shell with a large axisymmetric imperfection. (c) Responses of perfect and imperfect hemispherical shells under uniform pressure for axisymmetric deformations.

COMPARISON BETWEEN THE BUCKLING OF THE PERFECT AND IMPERFECT SHELLS

Figure 1c shows three curves, one of which is obtained from a theoretical model that uses exact expressions of stretching and bending strains for axisymmetric deformations. The blue dashed line is for the perfect baseline hemispherical shell and represents the classical buckling response extensively investigated in literature [1]. Normalized

*Corresponding author. E-mail: damiano.pasini@mcgill.ca.

with the Zoelly's buckling pressure p_C [3], the pressure rapidly increases with tiny pole displacement up to unity. Post bifurcation, a monotonic plunge of pressure appears, followed by a gradually descending plateau (just below 0.1) that spans the entire range.

The purple and red curves in Figure 1c refer to the imperfect shell with uniform thickness. The former (purple dots) is the pressure provided by our theoretical model, which employs exact expressions of stretching and bending strains for axisymmetric deformations, and the latter (red solid line) that obtained by our numerical model (ABAQUS). The difference between the maximum pressure predicted by the theoretical and FEM models is below 1%. At the normalized pole displacement of $w_{pole} / R = 0.04$, the pressure of the imperfect shell enters a region of snap-through buckling, after which the pressure monotonically increases to reach a maximum value of $p / p_C = 0.33$ at $w_{pole} / R = 0.46$.

A number of differences emerge between the perfect and imperfect shell shown in Figure 1c. The main one is their buckling mode. The imperfect shell first undergoes snap-through buckling at a pressure lower than the maximum pressure, and then it regains stability as the pressure increases to the maximum, a phenomenon not observed in the perfect spherical counterpart. In contrast, the perfect shell undergoes bifurcation buckling for a tiny value (below 1%) of the normalized pole displacement, where the pressure reaches its maximum without undergoing snap-through instability. After the bifurcation point, the post-buckling pressure decreases monotonically until the shell is everted, thereby denying the chance for the shell to regain stability [1].

SENSITIVITY TO IMPERFECTION GEOMETRY

Figure 2 shows four possible modes for the imperfect shell to respond to pressure. Mode 1 resembles the classical instability of a perfect spherical, i.e. an inward dimple-like shape (Figure 2a) and it is governed by small values of the imperfection. Mode 2 identifies a post-buckling response with deformation localized within the imperfection region (Figure 2b). This mode indicates a transition from bifurcation to snap through buckling. It is governed by a larger imperfection size. Figure 2c illustrates mode 3, a snap-through buckling controlled by a localized deformation accrued below the imperfection. This response is caused by increasing values of the imperfection size. For all of the aforementioned buckling modes (1, 2, and 3), the shell collapses once the prescribed pressure exceeds the buckling pressure. Mode 4 (Figure 2d) describes a scenario where snap-through buckling with mode 2 arises before the attainment of the maximum pressure with mode 3. This behaviour is triggered by a large width and moderate amplitude of the imperfection.

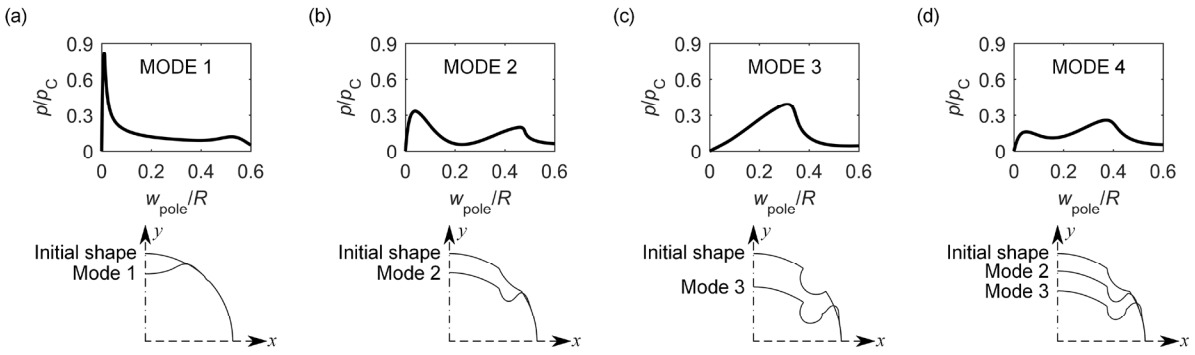

Figure 2. Possible deformation modes leading to shell collapse. (a) Bifurcation buckling. (b), (c), and (d) Snap-through buckling.

CONCLUSIONS

This paper has investigated the impact of a large axisymmetric imperfection on the buckling response of a thin elastic shell subject to uniform external pressure. A large axisymmetric imperfection can cause the shell response to depart from bifurcation buckling, i.e. the classical dimple-like shape of perfect shells typically triggered by a tiny pole displacement. Our shell theory formulation with exact stretching and bending strain measures shows quantitative agreement with FEM simulations for large shell displacements and rotations. Four modes have been identified: bifurcation instability caused by small sized imperfections, and three snap-through responses generated by large sized imperfections. These results highlight that a sizeable snap-through tunability could be exploited for the design of soft robots and morphing metamaterials.

Acknowledgements. This work was supported by the Natural Sciences and Engineering Research Council of Canada.

References

[1] Hutchinson J.W. Buckling of spherical shells revisited. *Proc. R. Soc. A-Math. Phys. Eng. Sci.* **472**: 20160577, 2016.
[2] Qiao C., Liu L., Pasini D. Elastic thin shells with large axisymmetric imperfection: from bifurcation to snap-through buckling. Manuscript submitted for publication, 2019.
[3] Zoelly, R. Ueber ein knickungsproblem an der kugelschale. *Ph.D. thesis*, ETH Zurich, Zurich, Switzerland, 1915.

SOFT ELASTICITY BY DOMAIN FORMATION IN MAGNETOACTIVE COMPOSITES

Pedro Ponte Castañeda*[1,2] and Joshua Furer[2]
[1]Department of Mechanical Engineering & Applied Mechanics, University of Pennsylvania, Philadelphia, USA
[2]Graduate Program in Applied Mathematics & Computational Sciences, University of Pennsylvania, Philadelphia, USA

Summary Reinforced elastomeric composites with periodic microstructures can undergo both microscopic and macroscopic instabilities. This paper is concerned with the post-bifurcation response of magneto-active elastomeric composites after the possible development of a macroscopic instability. By means of the relaxation or quasiconvexification of the principal solution for the homogenized energy function, it is shown that the response after the onset of a macroscopic instability corresponds to domain formation and is associated with soft modes of deformation that can be controlled by an externally applied magnetic field.

EXTENDED SUMMARY

This paper deals with the stability and post-bifurcation response of magneto-active elastomeric composites. In the purely mechanical context, it has been known for a long time [1, 2] that elastomeric composites with periodic microstructures can undergo both microscopic (short wavelength) and macroscopic (long wavelength) instabilities, which can be estimated from their incremental or *local* energy. In addition, it is also known that macroscopic instabilities can be detected by loss of strong ellipticity of the incremental homogenized response in both periodic and random systems [2, 3], but the behavior of the composites after the onset of such macroscopic instabilities is less well understood. Consistent with experimental observations in nanostructured thermoplastic elastomers [4], recent theoretical work [5, 6] indicates that, under appropriate loading conditions, it is possible for the "principal" solution, i.e. the solution before the onset of any instability, to bifurcate into a lower-energy solution by the formation of domains (see Fig. 1). These domains form on a scale much larger than that of the heterogeneity, but still small when compared to the original macroscopic scale, and are associated with "soft modes" of deformation. Mathematically, the post-bifurcation behavior after the onset of a macroscopic instability can be related to the relaxation or quasiconvexification of the principal solution for the homogenized energy function, which in turn can be estimated by means of the rank-1 convexification. As it turns out, this *global* approach provides estimates for the onset of macroscopic instabilities that can be different from those that can be generated by checking loss of ellipticity of the incremental or *local* response, but that are more consistent with the definition of the homogenized energy function [2, 3].

In the context of dielectric elastomer laminates with periodic microstructures, the onset of microscopic and macroscopic instabilities has also been investigated based on the incremental or local response [7]—and they have been found to depend on the magnitude and orientation of the applied electric field. Analogous results have been obtained for macroscopic instabilities in magneto-active elastomer with random distributions of aligned short fiber [8]. In this paper, we consider a different approach based on the global homogenized energy of magneto-elastic composites [5, 6] and investigate the post-bifurcation response after the development of macroscopic instabilities. For analytical ease, we consider a simple laminate consisting of two isotropic neo-Hookean phases with linear magnetic responses. Making use of generalized notions of quasiconvexification and rank-1 convexification in the magneto-elastic context, we obtain estimates for the relaxation of the magneto-active composites and find long wavelength instabilities and soft modes of deformation under appropriate loading conditions. In particular, we consider the application of a magnetic field parallel and perpendicular to the layers.

The first important conclusion drawn in this work is that, as in the purely mechanical context, in the generalized magneto-elastic setting, strict global rank-one convexity of the principal solution is generally lost prior to strong ellipticity, as measured by the generalized strong ellipticity condition making use of the incremental magneto-elastic moduli of the principal solution. In fact, only under pure shear loading with a magnetic field parallel and perpendicular to the layers (in the undeformed configuration) are strong ellipticity and strict rank-one convexity lost simultaneously. For more general loading, rank-one convexity can be lost significantly earlier than strong ellipticity.

While the relaxation can only be computed exactly for certain loading conditions, upper and lower bounds based on the rank-1 convexification and polyconvexity, respectively, remain rather tight so long as the alignment of the magnetic field with the layers is not too close. Even still, the difference between the bounds decreases as the magnetic field comes into alignment with the layers, whereby the upper bound can give an accurate prediction of the relaxation for all loading conditions.

In addition, and consistent with the incremental approach [8], a magnetic field perpendicular to the layers tends to destabilize the composite. It is therefore interesting that our knowledge of the relaxation is best in these destabilized states. In investigating the behavior of the laminate, we found that the mechanism of instability, namely sufficient compression along the layers, can either be promoted or inhibited, depending on the orientation of the applied magnetic field. In

*Corresponding author. E-mail: ponte@upenn.edu.

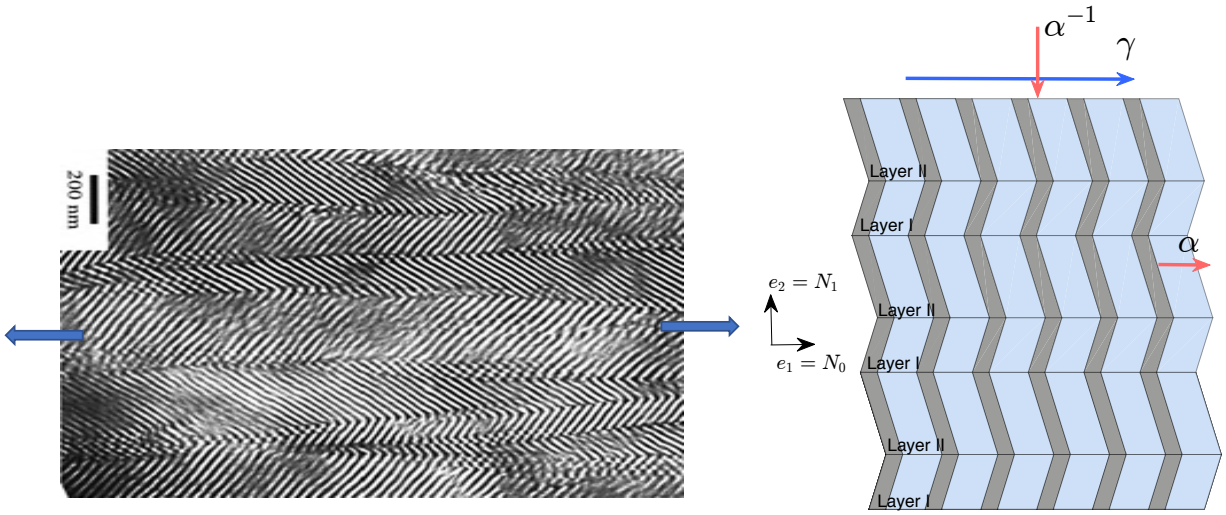

(a) (b)

Figure 1: (a) Domain formation in Oriented Lamellar Block Copolymer Films: TEM image of a "chevron" structure formed by perpendicular deformation to 300% strain [4]. (b) Rank-1 convexification construction for relaxation of neo-Hookean laminates.

particular, the application of a magnetic field perpendicular to the layers has the effect of reducing the value of the axial stretch (relative to the value in the purely mechanical case) necessary for an instability to develop. In fact, we found that a macroscopic instability can be triggered just by prescribing such a magnetic field, in the undeformed configuration. Such instabilities result in the formation of lamellar domains, and the construction is found to be similar to that in the purely mechanical case. In all cases, stability can be regained through the application of sufficient shear, and the relaxation not only induces mechanical softening, but can also lead to an increase or decrease in the macroscopic magnetic response, depending on the orientation of the magnetic field.

References

[1] Triantafyllidis, N., Maker, B. N. On the comparison between microscopic and macroscopic instability mechanisms in a class of fiber-reinforced composites. *Journal of Applied Mechanics* **52**, 794-800, 1985.

[2] Geymonat, G., Müller, S., Triantafyllidis, N. Homogenization of nonlinearly elastic materials, microscopic bifurcation and macroscopic loss of rank-one convexity. *Archive for Rational Mechanics and Mathematics* **122**, 231-290, 1993.

[3] Lopez-Pamies, O., Ponte Castañeda, P. On the overall behavior, microstructure evolution, and macroscopic stability in reinforced rubbers at large deformations. *Journal of the Mechanics and Physics of Solids* **54**, 807-863, 2006.

[4] Cohen, Y. Albalak, R.J., Dair, B.J., Capel, M.S., Thomas, E. L.. Deformation of Oriented Lamellar Block Copolymer Films. *Macromolecules*, **33**, 6502-6516, 2000

[5] Avazmohammadi, R., Ponte Castañeda, P. Macroscopic constitutive relations for elastomers reinforced with short aligned fibers: Instabilities and post-bifurcation response. *Journal of the Mechanics and Physics of Solids* **97**, 37-67, 2016.

[6] Furer, J., Ponte Castañeda, P. Macroscopic instabilities and domain formation in neo-Hookean laminates. *Journal of the Mechanics and Physics of Solids* **118**, 98-114, 2018.

[7] Bertoldi, K, and Gei, M. Instabilities in multilayered soft dielectrics. *Journal of the Mechanics and Physics of Solids* **59**, 18-42, 2011.

[8] Galipeau, E., Ponte Castañeda, P. A finite-strain constitutive model for magnetorheological elastomers: Magnetic torques and fiber rotations. *Journal of the Mechanics and Physics of Solids* **61**, 1065-1090, 2013.

DISTRIBUTED PREDICTION OF MECHANICALLY UNSAFE CONFIGURATIONS BY A SYSTEM OF ROBOTIC BLOCKS

Benoît Piranda[1], Paweł Chodkiewicz[2], Paweł Hołobut[3], Stéphane Bordas[4], Julien Bourgeois[1], and Jakub Lengiewicz *[3,4]
[1]Université BourgogneFranche-Comté, FEMTO-ST Institute, CNRS, France
[2]Faculty of Automotive and Construction Machinery Engineering, Warsaw University of Technology, Poland
[3]Institute of Fundamental Technological Research, Polish Academy of Sciences, Warsaw, Poland
[4]Faculty of Science, Technology and Medicine, University of Luxembourg, Luxembourg

Summary We present a computational scheme for predicting whether addition of new modules to an existing modular robotic structure will mechanically overload the system, causing it to break or lose stability. The algorithm is executed by the modular robot itself in a distributed way, and relies on the iterative solution of mechanical equilibrium equations derived from a simple Finite Element model of the robot. In the model, inter-modular connections are represented as beams and the contact between modules and external supports is accounted for by a predictor-corrector scheme. The algorithm is verified through simulations in the Programmable Matter simulator *VisibleSim* and real-life experiments on the modular robotic system *Blinky Blocks*.

MOTIVATION

This work stems from investigations into self-reconfigurable modular robots with a view towards Programmable Matter [1]. Such systems are built of simple robotic units—modules—which can compute, exchange information, join, disjoin, and move over one another. If the modules were sufficiently small, numerous and well-powered, they could potentially form a highly-versatile active metamaterial, with shape- and microstructure-changing capabilities.

Much work on self-reconfigurable robots focuses on kinematics and is devoted to reconfiguration planning—designing such module movements which allow the entire ensemble to transition from one configuration into another [2]. The present work, by contrast, focuses on mechanics of modular structures [3] and is purely static. We consider the rarely-discussed problem of mechanical safety of a modular structure, which is crucial for the structure's functionality as a physical system and reconfiguration in particular [4].

PROBLEM STATEMENT

The modular structure rests on the ground, or is otherwise in contact with external supports, loaded by its own weight. If additional modules are attached to the system, two failure scenarios may occur. Either some inter-modular connection may become overloaded and break (Fig. 1) or the center of gravity of the system may shift insecurely causing the structure to topple (Fig. 2). The task is to predict if the structure will fail or not, knowing the strength of connectors and the places where new modules will be added to the system. The prognosis should be obtained by the modular system itself using its distributed MIMD computational structure with a mesh connection topology, as it was outlined in [4].

METHODS

We focus on cubic modules attached side to side, and thus on structures arranged over a cubic Cartesian grid (Figs. 1 and 2). Despite this narrow scope, the proposed methods are general and can be used with other setups as well.

In the algorithm, the modular structure is represented as a Finite Element (FE) model whose nodal values are stored by the modules in a distributed fashion. We use a simple FE model in which each module corresponds to a single node with 6 degrees of freedom (3 displacements and 3 rotations), while connections between modules are represented as elastic beams with respective nodes as endpoints [5]. Each module only stores its own 6 nodal values. The contact with external supports is also modeled using beams, but ones having variable elastic parameters—during the iterative solution, a predictor-corrector scheme is employed to emulate unilateral connections. Further, selected modules simulate the presence of the new modules which will be added to the system.

The solution is obtained using the weighted Jacobi iterative scheme [6]. The main advantage of this procedure is that computations can be done locally—each module computes its own nodal values at step $i+1$ using only the values at step i from its immediate neighborhood. After the iterations have converged to a desired tolerance, each module checks if any of its connections is overloaded by comparing the junction forces predicted by the beam model with the strength of connectors. This addresses the bond breakage problem. Modules also aggregate information about the active points of contact with external supports, and are able to predict if the structure will tip over or not. This addresses the stability problem.

*Corresponding author. E-mail: jleng@ippt.pan.pl.

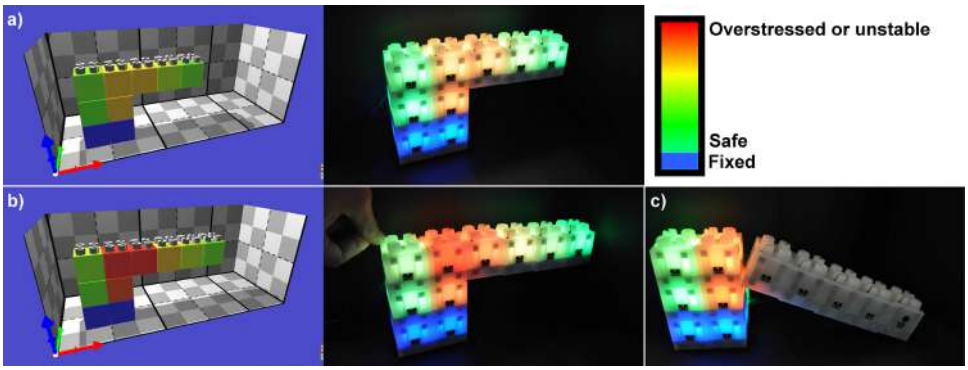

Figure 1: An example of bond breakage. Adding successive modules overloads magnetic connectors and causes the cantilever to break. The blue modules are assumed to be fixed. Left—simulations in *VisibleSim*; center and right—experiments on *Blinky Blocks*.

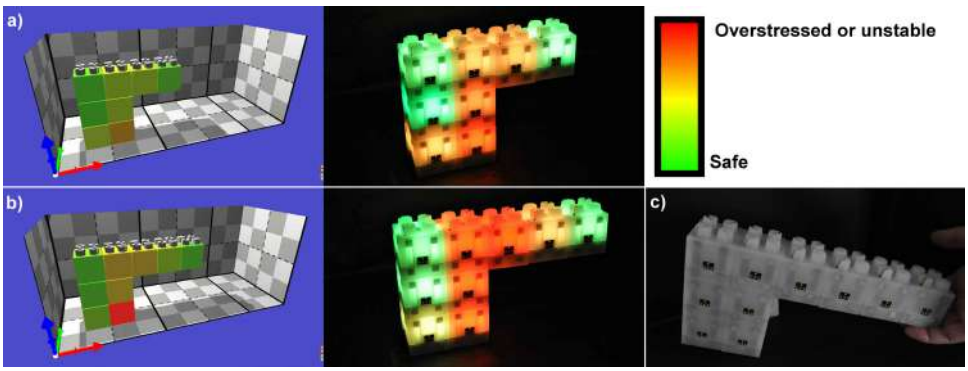

Figure 2: An example of stability loss. Adding successive modules moves the center of gravity of the cantilever beyond the supports and the structure tips over. Left—simulations in *VisibleSim*; center and right—experiments on *Blinky Blocks*.

RESULTS

Tests were performed in the dedicated simulator *VisibleSim* [7] and on the static robotic modules *Blinky Blocks* [8]. The attachment forces of Blinky Blocks were determined experimentally, while their elastic parameters assessed. Hardware experiments, like those presented in Figs. 1 and 2, revealed that the algorithm correctly predicts the mechanical behavior of small ensembles of modules, despite its crude FE representation of connected modules and the simple contact model. The weighted Jacobi solution scheme converges slowly, as expected, which will have to be addressed in the future by applying more complex alternatives like Krylov subspace methods or multigrid methods [6].

ACKNOWLEDGEMENTS

This work was partially supported by the EU Horizon 2020 Marie Sklodowska Curie Individual Fellowship *MOrPhEM* (H2020-MSCA-IF-2017, project no. 800150), by the Project "Micromechanics of Programmable Matter" (Contr. No. 2011/03/D/ST8/04089 with the National Science Centre in Poland), by the ANR (ANR-16-CE33-0022-02), the French Investissements d'Avenir program, ISITE-BFC project (ANR-15-IDEX-03), Labex ACTION program (ANR-11-LABX-01-01) and Mobilitech project.

References

[1] Goldstein S. C., Campbell J. D., Mowry T. C. Programmable Matter. *IEEE Computer* **38(6)**: 99-101, 2005.
[2] Thalamy P., Piranda B., Bourgeois J. A Survey of Autonomous Self-Reconfiguration Methods for Robot-Based Programmable Matter. *Robotics and Autonomous Systems* **120**: 103242, 2019.
[3] Lengiewicz J., Kursa M., Hołobut P. Modular-Robotic Structures for Scalable Collective Actuation. *Robotica* **35**: 787-808, 2017.
[4] Hołobut P., Lengiewicz J. Distributed Computation of Forces in Modular-Robotic Ensembles as Part of Reconfiguration Planning. in *Proceedings of the IEEE International Conference on Robotics and Automation*: 2103-2109, 2017.
[5] White P. J., Revzen S., Thorne C. E., Yim M. A General Stiffness Model for Programmable Matter and Modular Robotic Structures. *Robotica* **29**: 103-121, 2011.
[6] Saad Y. Iterative Methods for Sparse Linear Systems. Society for Industrial and Applied Mathematics, 2nd ed., 2003.
[7] Piranda B. VisibleSim: Your Simulator for Programmable Matter. in *Algorithmic Foundations of Programmable Matter (Dagstuhl Seminar 16271)*: 12, 2016.
[8] Kirby B. T., Ashley-Rollman M., Goldstein S. C. Blinky Blocks: A Physical Ensemble Programming Platform. in *CHI'11 Extended Abstracts on Human Factors in Computing Systems*: 1111-1116, ACM, 2011.

WRINKLING ANALYSIS OF THE FILM IN A SANDWICH SYSTEM UNDER BI-DIRECTIONAL PRESSURES

Guohua Nie*[1], and Guohang Shao [1]
[1]Institute of Applied Mechanics, School of Aerospace Engineering and Applied Mechanics, Tongji University, Shanghai 200092, China

Summary The 2D wrinkling of the film in a layer-film-layer sandwich system under the action of bi-directional uniform pressures is presented. The analytical relation between the pressure and wave number is derived based on classical thin-plate theory for the film and 3D elasticity theory for the two compliant layers, which is readily used to predict appearance of wrinkling and do a parametric analysis. Numerical examples are given to illustrate critical wave length and strain for various ratios of moduli of the system for the cases that both the layers are all fixed at their exterior surfaces or one layer is free while the other is fixed. The present results are compared with finite element simulation on equivalent thermal buckling by relating critical thermal strain to critical pressure. A comparison indicates that the present solution is valid and accurate enough in computation.

INTRODUCTION

A stiff thin film bonded to the surface of a compliant substrate can buckle to form periodic wrinkling patterns under compressive stresses [1]. The wrinkling patterns have a huge potential for various applications, e.g., wrinkles may be used as stretchable and foldable electronics, etc. In the fabrication of such electronic devices, a layer-film-layer sandwich system is of particular importance. To avoid delamination of the circuit (film-layer system) and/or fracture of metal interconnects (film) under high bending, an additional encapsulating layer is introduced on top of the circuit to improve adhesion and alleviate the strain level because such sandwich system shifts the neutral mechanical plane to the film plane [2]. For 1D sinusoidal interfacial wrinkling in a film-layer or sandwich system under unidirectional pressure, some theoretical solutions for critical pressure and wave number for the onset of interfacial wrinkles have been proposed by combination of thin-plate theory for the film with the solution for boundary value problem under plane strain condition for one layer or bi-layer materials [3,4]. However, the plane strain condition will no longer exist for the layers for two dimensional wrinkling of film (e.g., square checkerboard mode, etc.) induced by action of bi-directional pressures. This paper aims to present a theoretical solution for 2D wrinkling of the film in the sandwich system.

ANALYSIS AND RESULTS

As shown in Figure 1, a thin plate (film) of height h is assumed to be bonded to two corresponding surfaces of upper and lower compliant layers (substrates) with heights of H_u and H_l, respectively. When there exists 2D wrinkling in the sandwich system under combined uniform bi-directional pressures N, the governing equation for buckling of the film is $D_f\nabla^4 w=\Delta p-N\nabla^2 w$, where w and Δp are the deflection of the film and pressure difference from two substrates respectively and $D_f=E_f h^3/12\left(1-\mu_f^2\right)$ in which E_f,μ_f are elastic modulus and Poisson's ratio, respectively. It is assumed that the deflection takes the bi-directional (periodic) sinusoidal form of $w=A\cos(kx)\cos(ky)$ where A and k are amplitude and wave number, respectively. Due to a linear perturbation procedure [4], the relation between the pressure and wave number can be derived as $N=2D_f k^2-\left(\bar{g}_u\bar{E}_u-\bar{g}_l\bar{E}_l\right)/2k$, where $\bar{E}_{u,l}=E_{u,l}/(1-\mu_{u,l}^2)$ and $E_{u,l},\mu_{u,l}$ are elastic moduli and Poisson's ratios of the upper and lower substrates, respectively. The two unknown quantities, $\bar{g}_u,\bar{g}_l$, relate to wave number k and are determined by using a three dimensional elastic solution described below for the two compliant layers together with boundary conditions for the layers and continuous conditions between the film and layers. The critical wave number k_c can be obtained by condition of extremum, i.e., $\partial N/\partial k=0$, and the critical pressure N_c causing the 2D wrinkling of the film is thus evaluated as $N_c=N\big|_{k=k_c}$.

To deduce the 3D solution for the two compliant layers, the equilibrium equations can be expressed in terms of the displacement components u_i^s as $(1-2\mu_s)u_{i,jj}^s+u_{j,ji}^s=0\ (i,j=1,2,3)$, where $s=u,l$ stands for the upper and lower layers (substrates) respectively and u_1^s,u_2^s and u_3^s are three components in the x-, y-, and z-directions, respectively. The displacement fields can be taken the form of $u_1^s=u_x(z)\sin(kx)\cos(ky)$, $u_2^s=u_y(z)\cos(kx)\sin(ky)$, $u_3^s=u_z(z)\cos(kx)\cos(ky)$ where $u_x(z),u_y(z)$ and $u_z(z)$ are resulted from the above equilibrium equations as $u_x=\sum_{p=1}^{6}C_p^s f_p(z)$, $u_y=\sum_{p=1}^{6}C_p^s g_p(z)$ and $u_z=\sum_{p=1}^{6}C_p^s h_p(z)$ in which coefficients $C_p^s\ (p=1,2,...,6)$ are determined by specific boundary conditions for the lower and upper layers and continuous conditions between the film and layers while $f_p(z),g_p(z),h_p(z)$ are the resulting explicit functions of z and k. Here two cases for boundary conditions are considered: (a) Clamped Condition (CC), where a compliant layer is fixed at its exterior surface; and (b) Free Condition (FC), where the layer is free at its exterior surface. Based on the resulting displacement fields for the compliant layers,

*Corresponding author. E-mail: ghnie@tongji.edu.cn

the corresponding stress components can be determined. The above unknown quantities $\bar{g}_u, \bar{g}_l$ have the results of $\bar{g}_u = \sum_{p=1}^{6} C_p m_p(z)\big|_{z=h/2} / \bar{E}_u kA, \bar{g}_l = \sum_{p=1}^{6} C_p m_p(z)\big|_{z=-h/2} / \bar{E}_l kA,$ which results in an analytical expression for the pressure N.

To verify the present theoretical model a finite element simulation is performed by using ANSYS code. The 3D element (Solid70) is chosen for the sandwich system. The thermal buckling analysis is performed to simulate the corresponding wrinkling of the system under uniform pressures. Based on the Lanczos method is used to determine the critical strain ε_c by $\varepsilon_c = \alpha \times \Delta T_c$ where α and ΔT_c are thermal expansion coefficient and critical temperature, respectively. The critical temperature is determined by using Eigen Buckling in the code. Test of convergence of the finite element model is done by changing the numbers of elements of the film and substrates. The total number is around 300,000 for a valid finite element simulation. The critical wave length λ_c is thus obtained. The critical pressure N_c and wave number k_c for the finite element simulation can be determined by $\varepsilon_c = (1-\mu_f) N_c / h E_f$ and $\lambda_c = 2\pi / k_c$.

In computation for finite element model it is assumed that the thicknesses of substrates and film are $H_u = H_l = 10h$ and $h = 2.0\,\text{nm}$, respectively. The Poisson's ratios are $\mu_u = \mu_l = \mu_f = 0.3$, and the elastic moduli of upper and lower substrates are $E_u = E_l = E_s = 1.0\,\text{GPa}$ where E_s denotes the same value of the two moduli. The change in non-dimensional critical wave length $\lambda^* = \lambda_c / h$ and strain ε_c with non-dimensional modulus of the film E_f / E_s is shown in Figure 2 for two cases of CC-CC and CC-FC where the first shorthand notation (CC) represents boundary condition for the lower substrate layer while the second notation (CC or FC) stands for condition for the upper substrate layer. When the critical wave length increases substantially with the ratio of modulus when $E_f / E_s < 50.0$ and increases slowly with a larger ratio of modulus. In contrast, the critical strain presents an opposite trend, which indicates that a stiffer film causes easily wrinkling of the film. The comparison shows that the present theoretical results agree well with the data from finite element simulation.

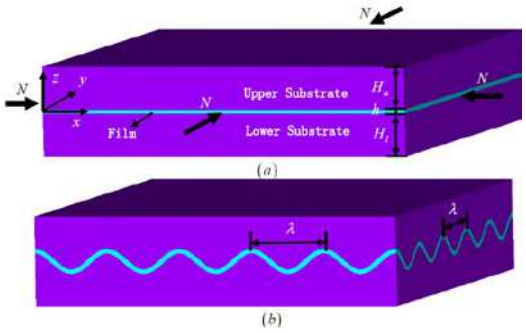

Figure 1. A sandwich system of layer-film-layer. (a) geometry of the system; and (b) wrinkling mode

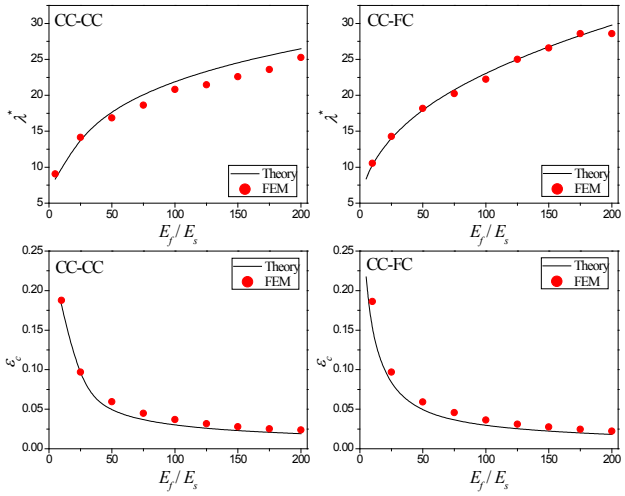

Figure 2. Comparison of critical wave length and strain for various ratios of moduli

CONCLUSIONS

A theoretical solution is proposed to predict two dimensional (periodic) sinusoidal wrinkling of the film in a layer-film-layer sandwich system under the action of bi-directional uniform pressures. The analytical relation between the pressure and wave number is derived based on classical thin-plate theory for the film and 3D elasticity theory for the two compliant layers (substrates) in connection with boundary conditions for the lower and upper layers and continuous conditions between the film and layers. Numerical examples are given to verify the present model. The resulting relation between the pressure and wave number can be readily used to predict and evaluate the appearance of wrinkling in the sandwich system.

References

[1] Li B., Cao Y. P., Feng X. Q., Gao H. Mechanics of Morphological Instabilities and Surface Wrinkling in Soft Materials: A Review. *Soft Matter* **8**: 5728-5745, 2012.

[2] Kim D. H., Ahn J. H., Choi W. M., Kim H. S., Kim T. H., Song J., Huang Y., Liu Z., Lu C., Rogers J. A. Stretchable and Foldable Silicon Integrated Circuits. *Science*, **320**: 507-511, 2008.

[3] Huang Z. Y., Hong W., Suo Z. Nonlinear Analyses of Wrinkles in a Film Bonded to a Compliant Substrate. *Journal of the Mechanics and Physics of Solids*, **53**: 2101-2118, 2005.

[4] Yang J. W., Nie G. H. Analysis of Sinusoidal Interfacial Wrinkling of an Anisotropic Film Sandwiched Between Two Compliant Layers, *ASME J. Appl. Mech.* **81**: 091013, 2014.

ELASTO-ACTIVE INSTABILITIES OF SOLVENT-FILLED SPHERICAL MICROCAPSULES

Michele Curatolo[1] and Paola Nardinocchi*[1]
[1]Department of Structural and Geotechnical Engineering, Sapienza Università di Roma, Roma, Italy

Summary We investigated the occurrence of instability modes in water-filled microcapsules under drying through a multi-physics model. We show as a necessary condition to start instability is the occurrence of water-under-tension inside the cavity and as it is determined by some key geometrical and mechanical parameters of the structure.

INTRODUCTION

Instabilities of spherical shells have been largely studied starting from the major contribution by Koiter in the 1960s with specific reference to pressurized shells, as discussed in [1]. Typically, these shells were acted by an external pressure field and their instability modes have been studied in terms of pressure versus change in volume curves and pressure versus normal deflection curves, through exact formulations and differently approximated formulations.
Instabilities may also occur in solvent-filled spherical microcapsules due to solvent release processes, initiated by different causes, which determine critical loads on microcapsules walls. Nature delivers a few examples of soft capsules confining microscopic cavities undergoing a dehydration process; for example, in Fern Sporangium, it drives the conditions to realize spores dispersion [2, 3]. The working principles of these mechanisms in Nature have been classified and studied in terms of the specific functional demands that they fulfill [4]. On the contrary, analysing the possibility to reproduce them in soft polymers, which requires an accurate modeling and the identification of the determinants of the key mechanism, is still lacking.
Inspired by these observations, we investigated the occurrence of instability modes in water-filled microcapsules under drying through a multi-physics model which has been elaborated and successively tested in different situations by the Authors (see [5, 6] and references therein). A necessary condition to start instability is the occurrence of water-under-tension inside the cavity. It determines a negative pressure field on the inner walls of the microcapsules, also breaks the smooth drying process induced by water evaporation and drives a sharp change in pressure under constant volume within the confined cavity. The onset of the process has been shown to depend on geometrical and mechanical parameters and is realised through bending of the cavity's walls [6]. However, when spherical confined cavities are involved, bending is not realized due to the high geometric stiffness of the structure and it is the presence of small inhomogeneities of the microcapsule walls which breaks the symmetry and determine different instability modes.

ELASTO-ACTIVE SPHERICAL MICROCAPSULES

Spherical microcapsules are thin closed spherical shells which have a fixed geometrical size at the dry state $\mathcal{B}_d$ defined by the thickness h and the radius R of the middle surface. We describe their chemo-mechanical state by the displacement field $\mathbf{u}_d$ and the water concentration c_d, per unit dry volume, and discuss the hydration and de-hydration processes induced by different environmental conditions, as represented by the cartoons in figure 1. The hydration process corresponds to

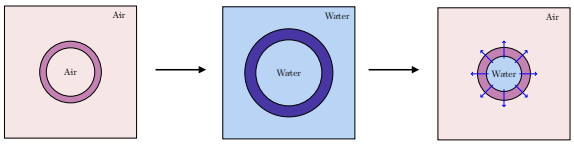

Figure 1: Cycle of hydration and de–hydration of a spherical capsule, from left to right.

embed the dry capsule (left cartoon in figure 1) into a bath until the walls are fully swollen and the cavity filled with water (middle cartoon in figure 1). The swelling-induced deformation which produces the fully swollen and stress-free state is a homothety whose value λ_o is determined from the following equation

$$\mathcal{R}\,T\Big(\log\frac{\lambda_o^3-1}{\lambda_o^3}+\frac{1}{\lambda_o^3}+\frac{\chi}{\lambda_o^6}\Big)+\frac{G_d}{\lambda_o}\Omega=\mu_e\,, \tag{.1}$$

with R, T, χ, G_d, Ω and μ_e the gas constant, the temperature, the Flory parameter, the shear modulus of the dry polymer, the water molar volume and the chemical potential of the bath. The successive de-hydration process, that is especially interesting with respect to the possible instability modes of the capsules, starts from the fully swollen state and proceeds by de-hydrating the body from the outside. It corresponds to pull out the swollen spherical shell, with its cavity filled with water, from the bath and to expose it to air. The dynamics of the process is based, as usual, on the standard equations of

*Corresponding author. E-mail: paola.nardinocchi@uniroma1.it

balance of forces and solvent mass; the dry-reference stress $\mathbf{S}_d$ and solvent flux $\mathbf{h}_d$ are constitutively prescribed within the context of Flory thermodynamics and the two state variables of the problem are coupled by the volumetric constraint $\det \mathbf{F}_d = 1 + \Omega c_d$, being $\mathbf{F}_d = \mathbf{I} + \nabla \mathbf{u}_d$, which forces the volume change $\det \mathbf{F}_d$ due to the displacement to be equal to the one due to solvent absorption or release.
Those standard equations are here joined with a new global volumetric constraint and distinguished boundary conditions, in the following explained. We assume that

$$\mathbf{S}_d\,\mathbf{m} = -p_e\,\mathbf{F}_d^{\star}\,\mathbf{m} \quad \text{and} \quad \mathbf{S}_d\,\mathbf{m} = -p_i\,\mathbf{F}_d^{\star}\,\mathbf{m} \tag{.2}$$

on the outer and inner boundary of the capsule, respectively. The internal pressure $p_i = p_i(t)$ is a key element in the analysis of the drying-driven suction effect, as already discussed [6]. It arises as reaction to the volumetric coupling $v_c(t) = v_w(t)$ between the water volume $v_w = v_w(t)$ and the cavity volume $v_c = v_c(t)$, and represents the pressure corresponding to the so-called suction effect. Finally, to break the spherical symmetry, we added two stiffer regions around the poles characterised by a *deepness* parameter $\bar{\theta}$ and a *stiffness amplifier* parameter α.
A first analysis of the problem has shown that the mechanical phenomenon resembles the buckling of pressurised spherical shells, largely studied in the Literature (see [1] and references therein) also in presence of softer regions around the poles. However, there are important differences between the two situations: (**i**) water fills cavity and constraints cavity volume; (**ii**) the pressure is not a control parameter of the process, which is a dynamical process driven by the de-hydration of the shell; (**iii**) the de-hydration process realises a differential swelling across the thickness of the shell so equipping the shell with a natural curvature which can play a role in the mechanical instability we observed. We found that, with these conditions, the de-hydration process can induced an instability mechanism whose characteristics are controlled by $\bar{\theta}$ and α. A first analysis of the problem in terms of dimensionless inner pressure p_i/G_d and change in volume v_c/v_{co} of the cavity with respect to the initial volume v_{co} shows a sharp change in pressure as identifier of the instability mechanism. Our conjecture is that different values of the α and $\bar{\theta}$ parameters produce different instability modes.

CONCLUSIONS

We presented the first results of a study focused on elasto-active instabilities in spherical microcapsules. Due to the complexities of the computational analysis, our next steps will be supported with semi-analytical methods which will start from the analysis presented in [7].

References

[1] Hutchinson J. W. Buckling of spherical shells revisited. *Proceedings of the Royal Society A* **472**: 20160577, 2016.
[2] Noblin X., Rojas N. O., Westbrook J., Llorens C., Argentina M. and Dumais J. The Fern Sporangium: A Unique Catapult. *Science* **335**: 1322, 2012, 335, 1322.
[3] Llorens C., Argentina M., Rojas N. O., Westbrook J., Dumais J. and Noblin X. The fern cavitation catapult: mechanism and design principles. *Proceedings of the Royal Society A* **114**: 20150930, 2016.
[4] Sakes A., van der Wiel M., Henselmans P.W.J., van Leeuwen J.L., Dodou D. , Breedveld P. Shooting Mechanisms in Nature: A Systematic Review. *PLoS ONE* **11(7)**: e0158277, 2016.
[5] Lucantonio A., Nardinocchi P. and Teresi L. Transient analysis of swelling-induced large deformations in polymer gels. *Journal of the Mechanics and Physics of Solids* **61**: 205–218, 2013.
[6] Curatolo M., Nardinocchi P. and Teresi L. Driving water cavitation in a hydrogel cavity. *Soft Matter* **14**: 2310, 2018.
[7] Holmes D.P., Lee J., Park H.S., Pezzulla M. The nonlinear buckling behavior of a complete spherical shell under uniform external pressure and homogenous natural curvature. *arXiv:1810.04078*.

MODELING AND INSTABILITIES IN MAGNETICALLY HARD, VISCOELASTIC MAGNETORHEOLOGICAL ELASTOMERS

Dipayan Mukherjee*[1] and Kostas Danas[1]
[1]LMS, C.N.R.S, École Polytechnique, Institute Polytechnique de Paris, Palaiseau, 91128, France

Summary We present a family of unstable microstructural responses of hard magnetic particle-filled, viscoelastic magnetorheological elastomers. Energy dissipates in such two phase magneto-active composites primarily due to two distinct mechanisms, namely, (a) magnetic hysteresis in the hard-magnetic inclusions and (b) viscous dissipation in the mechanically soft elastomeric matrix. Full-field numerical computations are performed by employing an augmented incremental variational principle, which enables the computation of the effective magnetization and magnetostriction, without considering the effect of the background Maxwell stress. While the MREs with circular inclusions only exhibit particle rearrangements, the elliptical inclusions, in contrast, lead to instability via rotating rapidly to align themselves along the direction of applied magnetic fields.

INTRODUCTION

NdFeB particle-filled, mechanically soft magnetorheological elastomers (MREs) find application in a wide range of engineering devices ranging from smart sensors to soft robotic manipulators. In contrast to the traditional carbonyl iron particle (CIP)-filled MREs, the NdFeB particles in the composites exhibit magnetic hysteresis, leading to an overall hard-magnetic response of the composite. Thus, NdFeB particle-filled MREs are also referred to be hard MREs (or h-MREs in short).

Despite several analytical, numerical and experimental investigations for the modeling and instabilities in the CIP-filled MREs have been performed [1, 2, 3, 5], very few numerical and experimental investigations have been reported for this novel class of h-MREs. The present work employs an augmented, incremental variational principle to investigate the material and the microstructure dependence of the effective response of h-MREs. The following section lays down the choice of internal variables and the local constitutive models of the particle and matrix phases.

LOCAL CONSTITUTIVE BEHAVIOR

The hard magnetic NdFeB particles are also mechanically stiff. Thus, the energy dissipation in the particle phase is considered solely due to the magnetic hysteresis. The hysteretic constitutive response is modeled via first considering an additive decomposition of the magnetic h-field, such that $\mathbf{H} = \mathbf{H}_e + \mathbf{H}_r$, where $\mathbf{H}$ is the total h-field, while $\mathbf{H}_e$ and $\mathbf{H}_r$ are the energetic and remanent components of $\mathbf{H}$, respectively. Then we employ the evolving switching surface (ESS) model [4] that is developed in terms of the generalized standard materials (GSM) framework, which leads to thermodynamically consistent dissipation models, provided the associated dissipation potential remains strictly convex. The thermodynamic internal variable in the ESS model is considered to be $\mathbf{H}_r$. The resulting hysteretic magnetization response is shown in Fig. 1a.

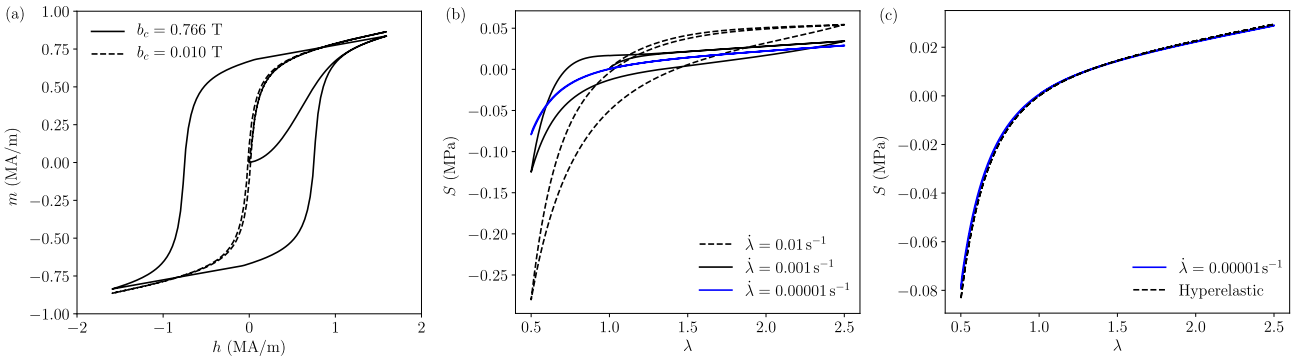

Figure 1: (a) Magnetic hysteresis loop obtained from the ESS model. (b) Rate-dependent, viscoelastic stretch-stress response of the matrix. (c) Hyperelastic stress-stretch response in the limit of quasi-static loading.

The elastomer matrix, on the other hand, is magnetically inert but mechanically viscous in nature. The viscoelastic response of the matrix is modeled via first considering a multiplicative decomposition of the total deformation gradient $\mathbf{F}$, such that $\mathbf{F} = \mathbf{F}_e\mathbf{F}_v$, where the subscripts e and v represents energetic and viscous part of $\mathbf{F}$, respectively. The GSM framework is also applied in this case, in order to obtain a thermodynamically consistent and objective viscoelastic model. Here the internal variable is considered to be $\mathbf{F}_v$. The local stretch-stress response of such viscous elastomers are shown in Fig. 1b. Notably, the dissipative viscoelastic model leads to the energetic hyperelastic model in the limit of quasi-static loading (see Fig. 1c).

*Corresponding author. E-mail: dipayan.mukherjee@polytechnique.edu.

EFFECT OF MAGNETIC HYSTERESIS AND VISCOELASTICITY ON PARTICLE ROTATIONS

Numerical computations are carried out via employing an augmented, incremental variational principle [2] that enables us to eliminate the effect of the background Maxwell stress while computing the effective magnetostriction and also facilitates the application of an Eulerian h-field across the periodic representative volume elements (RVEs). Two sets of 2-dimensional RVEs are considered for our investigations having (a) randomly distributed circular particles and (b) single elliptic inclusions with various volume fractions, aspect ratios and initial orientations.

A representative computed response for an elliptical inclusion in mechanically hard and soft matrices is shown in Fig. 2. Here we observe that a soft matrix — facilitating easy rotations — leads to microstructural instabilities. Thus, it is

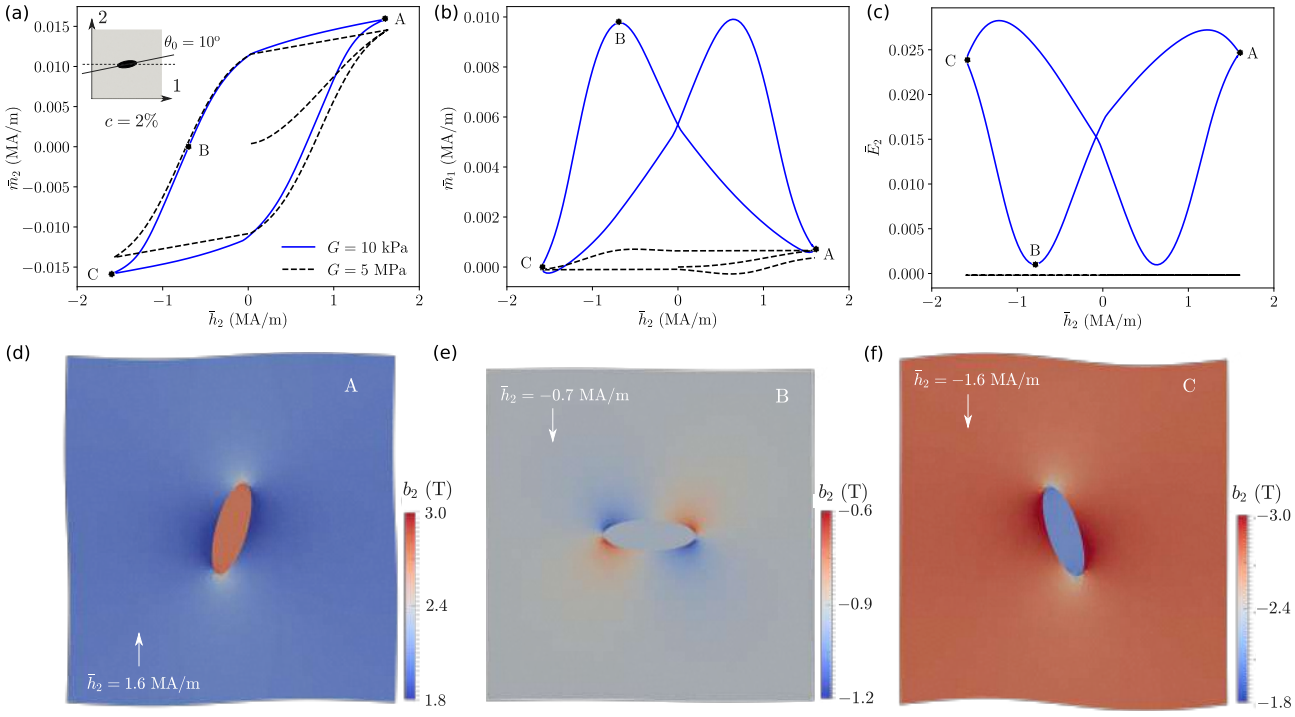

Figure 2: Effective (a) parallel and (b) transverse magnetization and (c) transverse magnetostriction of the MREs with a single elliptical inclusion in mechanically soft (solid lines) and hard (dashed lines) matrices. (a) (inset) Initial configuration of the elliptical inclusion. (d-f) Contours of the local parallel magnetic field in the RVE under different applied h-fields indicated by A,B and C on a-c.

noted that the magnetization in the particle never vanish, rather, the permanently magnetized particle becomes unstable via rotating rapidly to align itself along the reversed loading direction. By contrast, a standard magnetization-demagnetization response along with a negligibly small magnetostriction is observed in the MREs with a mechanically hard matrix, which, in turn, hinders the rotation of the elliptical inclusion.

CONCLUSIONS

The unstable magneto-mechanical response of magnetically hard but mechanically soft MREs are observed to be strongly dependent on the elastic modulus of the matrix for the elliptical inclusions. The circular inclusions, on the other hand, undergoes only particle rearrangements and thus, do not exhibit microstructural instabilities. However, the effective magnetostriction in the latter, in turn, depends strongly on the matrix elastic modulus and the rate of magnetic loading/unloading. Thus, the microstructural instabilities in the h-MREs are found to be strongly dependent on the morphology of the inclusions as well as on the elastic and viscous properties of the matrix.

References

[1] Kankanala S. V., Triantafyllidis N. On finitely strained magnetorheological elastomers. *J. Mech. Phys. Solids* **52**: 2869-2908, 2004.
[2] Danas K. Effective response of classical, auxetic and chiral magnetoelastic materials by use of a new variational principle. *J. Mech. Phys. Solids* **105**: 25-53, 2017.
[3] Lefevre V., Danas K., Lopez-Pamies O. A general result for the magnetoelastic response of isotropic suspensions of iron and ferrofluid particles in rubber, with applications to spherical and cylindrical specimens. *J. Mech. Phys. Solids* **107**: 343-364, 2017.
[4] Mukherjee D., Danas K. An evolving switching surface model for ferromagnetic hysteresis. *J. Appl. Phys.* **123**: 033902, 2019.
[5] Mukherjee D., Bodelot L., Danas K. Microstructurally-guided explicit continuum models for isotropic magnetorheological elastomers with iron particles. *Int. J. Nonlin. Mech.* in press, 2020.

ULTRA-SOFT ELASTIC CYLINDERS DEFORMED BY THEIR OWN WEIGHT

Serge Mora*[1], Edward Ando`[2], Jean-Marc Fromental[3], Ty Phou[3], and Yves Pomeau[4]
[1]Laboratoire de Mécanique et de Génie Civil, Université de Montpellier and CNRS, Montpellier, France.
[2]Laboratoire 3SR, Université Grenoble Alpes and CNRS, Grenoble, France.
[3]Laboratoire Charles Coulomb, Université de Montpellier and CNRS, Montpellier, France.
[4]University of Arizona, Department of Mathematics, Tucson, USA.

Summary Deformations of hanging elastic cylinders subjected to the Earth's gravity field are investigated. The specimens, made of polyacrylamide hydrogels, are attached from their top circular cross section to a rigid plate. An equilibrium configuration results from the interplay between gravity that tends to deform the cylinders downwards under their own weight, and elasticity that resists these distortions. The corresponding steady state exhibits fascinating shapes which are measured with lab-based micro-tomography. For any given initial radius to height ratio, the deformed cylinders are no longer axially symmetric beyond a critical value of a control parameter that depends on the volume force, the height and the elastic modulus: self-similar wrinkling hierarchies develop, and dimples appear at the bottom surface of the shallowest samples. We show that these patterns are the consequences of elastic instabilities.

INTRODUCTION

Many materials such as biological tissues can withstand huge elastic deformations over more than several hundred percent. Fascinating and puzzling shapes can result from these large deformations which have to be better understood in view of emerging applications as computer-assisted precision surgery involving human organs among which some are elastic and can undergo large deformations. A physical rationalization of these phenomena requires first to model materials subjected to basic external loads in simple geometries.

We present here an experimental study of the deformations of elastic cylinders attached to a rigid plate at the upper cross section, and submitted to a downwards constant volume force in the vertical direction. This minimal system is enough to exhibit intriguing shapes such as those encountered in more complex systems with practical applications.

MATERIALS AND METHODS

We use aqueous polyacrylamide gels, that can be considered as incompressible with a mass density ρ almost equal to that of water. They behave as elastic material for strains up to several hundreds percent, whose shear modulus μ can be tuned by varying the concentrations in monomers and cross-linkers.

In these experiments, the reagents generating the gels are first dissolved into ultra-pure water and poured into cylindrical dishes up to the brim. After the gel is cured into the dish, its top surface is attached by capillary action onto a rigid horizontal surface coated with a sheet of paper, and the dish is gently removed from below. This results in a hanging cylinder of gel attached from the top and deformed by the gravitational acceleration g. The radius of the dishes, R, and the height, h, are between $36\,\mathrm{mm}$ and $150\,\mathrm{mm}$ and between $8\,\mathrm{mm}$ and $40\,\mathrm{mm}$ respectively. The shear modulus of the gel lies between 10 and $160\,\mathrm{Pa}$, a value compared to modulus of tissues (as liver or brain).

The dimensionless gravity acceleration α is defined as the ratio of the characteristic gravitational stress, $\rho g h$, to the shear modulus: $\alpha = \rho g h/\mu$. α lies between 1 and 16 in the experiments reported here. Surface tension is not always negligible with soft solids [2], and the dimensionless parameter α has to be complemented with another one, namely $\beta = \gamma/(\mu h)$, with γ the surface energy per unit area. For polyacrylamide gels in air, $\gamma \simeq 70\,\mathrm{mN\,m^{-1}}$. Taking for instance $\mu \sim 35\,\mathrm{Pa}$ and $h \sim 20\,\mathrm{mm}$ as characteristic shear modulus and height, one gets $\beta \sim 0.1$.

CASCADE OF WRINKLES

The equilibrium shapes of the hanging cylinders are acquired using x-ray tomography. The observed deformed shapes are axially symmetric for the samples with $\alpha < 4.7$. For samples with $\alpha = 4.7$, wrinkles appear, and upon increasing α, a second generation in the wrinkles hierarchy of size appears for samples with $\alpha > 6.02$, leading to hierarchical structures (Fig. 1-(a-c)). The amplitude of the wrinkles as well as the degree of branching is the highest at the top of the shape decreasing downwards until vanishing at the bottom of the hanging cylinder.

These hierarchical wrinkles result from a Biot-like elastic instability [3] : once the surface deformation of the elastic gel reach a threshold, wrinkles develop, releasing a part of the accumulated stress. If the remaining surface strain is again larger than the threshold, a new generation of wrinkles develops [1].

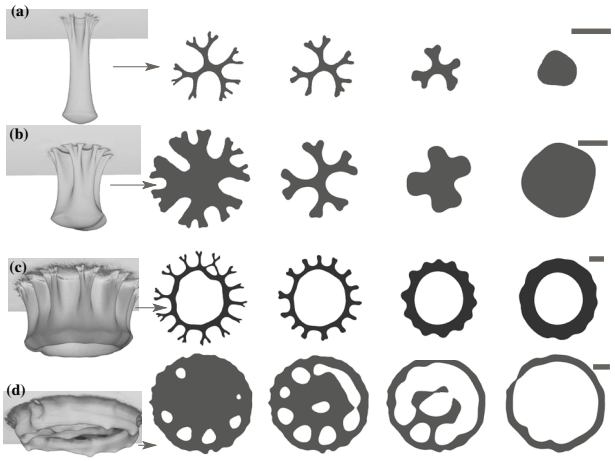

Figure 1: Three-dimensional views and horizontal slices at various heights (from the top to the bottom of the samples) of 4 hanging cylinders with initial dimensions ($R \times h$) and shear modulus: $22\,\mathrm{mm} \times 25\,\mathrm{mm}$, $\mu = 27.4 \pm 1.5\,\mathrm{Pa}$ (a); $37\,\mathrm{mm} \times 24\,\mathrm{mm}$, $\mu = 29.2\,\mathrm{Pa}$ (b); $69\,\mathrm{mm} \times 17\,\mathrm{mm}$, $\mu = 18.6\,\mathrm{Pa}$ (c); $72\,\mathrm{mm} \times 9\,\mathrm{mm}$, $\mu = 12.9\,\mathrm{Pa}$ (d). In the slices, the gel is in black; the white areas continuously surrounded by black areas correspond to the central depression (c,d) or to dimples (d). The dimensionless accelerations (α) and surface tensions (β) for these samples are respectively $(8.94,\ 0.1)$ for (a);$(8.05, 0.1)$ for (b); $(8.96\ , 0.2)$ for (c); and $(6.84\ , 0.6)$ for (d). Gray bar length is $2\,\mathrm{cm}$. From [1].

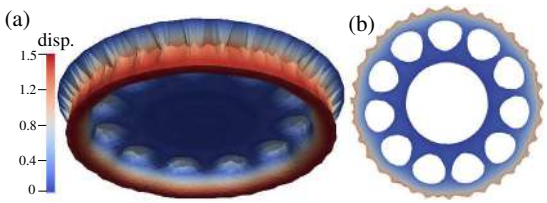

Figure 2: **(a)** Deformed shape computed with $R/h = 8$, $\alpha = 5.58$ and $\beta = 0$. Colors indicate the ratio of the total displacement to the initial height. **(b)** Horizontal slice of the previous deformed shape (a) at the distance h below the rigid plate. From [1].

DEPRESSIONS AS A RESULT OF A RAYLEIGH-TAYLOR MECHANISM

In addition to wrinkles, quasi-regular dimples appear at the lower surface of samples with large aspect ratios (see Fig. 1(d)). Finite element (FE) simulations consisting of minimizing the sum of gravity and neo-Hookean elastic energies of a hanging cylinder have been carried out, with a quantitative agreement with the experiments, indicating that the formation of the dimples are the consequence of the Elastic Rayleigh-Taylor instability [4, 5, 1]

CONCLUSIONS

X-ray micro-tomography has proved to be a powerful technique capable of capturing complex equilibrium shapes of hydrogels subjected to large deformations, whereas conventional optical methods are more difficult to handle with these transparent and folded samples.
Although the system consisting of a hanging elastic cylinder is probably one of the simplest in order to study the mechanical response of highly stretchable elastic material, the resulting deformations are manifold, whose underlying mechanisms have been unveiled in this paper.

References

[1] S. Mora, E. Ando, JM Fromental, T. Phou, and Y. Pomeau. The shape of hanging cylinders. *Soft Matter*, 15:5464–5473, 2019.
[2] S. Mora, C. Maurini, T. Phou, J. M. Fromental, B. Audoly, and Y. Pomeau. Solid drops: Large capillary deformations of immersed elastic rods. *Phys. Rev. Lett.*, 111:114301, 2013.
[3] MA Biot. Surface instability of rubber in compression. *Appl. Sci. Res.*, A12:168–182, 1963.
[4] S. Mora, T. Phou, J. M. Fromental, and Y. Pomeau. Gravity driven instability in solid elastic layers. *Phys. Rev. Lett.*, 113:178301, 2014.
[5] A. Chakrabarti, S. Mora, F. Richard, T. Phou, J.-M. Fromental, Y. Pomeau, and B. Audoly. Selection of hexagonal buckling patterns by the elastic Rayleigh-Taylor instability. *Journal of the Mechanics and Physics of Solids*, 121:234–257, 2018.

*Corresponding author. E-mail: serge.mora@umontpellier.fr

NETWORK THEORY FOR MORPHOLOGICAL CONTROL OF SOFT ROBOTS

Edoardo Milana*[1], Joost Jennen[1,2], Giorgio Oliveri [2], Benjamin Gorissen[1,3], Johannes Overvelde[2]and Dominiek Reynaerts[1]
[1]Department of Mechanical Engineering, KU Leuven, Leuven, Belgium
[2]AMOLF, Amsterdam, The Netherlands
[3]John A. Paulson School of Engineering and Applied Sciences, Harvard University, Cambridge, Massachusetts

Summary Simplified design of soft robots, featuring continuum actuators, conflicts with the opportunity of independently controlling different degrees of freedom associated with dedicated actuation. The use of nonlinearities can help bridging the gap. Indeed, nonlinearity can be an opportunity for morphological control, where groups of actuators are actuated using a single input signal and functionality emerges from the interplay of nonlinearities and environmental triggers. In this work we will detail on a framework to analyze and design this actuation behavior in a morphological setting, using electrical network theory. To demonstrate the strength of this approach, we demonstrate actuation sequencing using fluidic actuation technology where the order of sequence can be altered by varying the amplitude of the single input signal.

INTRODUCTION

Advances in polymer synthesis and their digital manufacturing processes paved the way for the rapid advancement of the field of soft robotics where materials are used with stiffness comparable to biological tissue [1]. Inherent safety, large deformations and adaptability to unstructured environments are few of the reasons why soft robots are outperforming conventional rigid robots in applications that necessitate interactions with unpredictable surroundings such as navigating uneven terrains or handling amorphous objects [2]. Instead of sensing the environment and adapting the actuator behavior in a feedback loop, soft robots can display the same functionality since the environment is able to directly influence the robot hardware. This concept is referred to as embodied intelligence which is in stark contrast to the central intelligence paradigm in conventional robotics. Instead of concentrating all computational power in the software, it was shown by Pfeifer and Bongard [3] that in nature intelligent behaviors are not simply encoded in the brain of a living agent, but they rather emerge due to body-environment interactions. Muscles and tendons, similarly to soft actuators, harness their elasticity to adapt their response to different tasks without being continuously controlled by the brain. This phenomenon in particular is referred to as morphological computation and underline the fact that complex and adaptable responses can be achieved with simple low-level software control in addition to morphological intelligence.

The field of soft robotics is highly compatible with the concept of embodied intelligence, which has been recently displayed in literature. In previous work, we were able to [4] harness the elastic snap-through instability of soft balloon-like actuators for event triggering in a network of such actuators. We used the same type of nonlinear inflatable actuators to drive ambulatory locomotion in a soft articulated robot [5] where 8 actuators were sequenced using only one pressure input. However, a general analysis tool that takes into account additional fluidic effects is missing, making it difficult to design the morphological response of a network of inflatable actuators. In this work we apply a modeling framework that uses an electrical circuit analogy to analyze the global behavior of such fluidic network [6], in particular we apply it to snap-through actuators. This tool will be applied to a fluidic network where the actuation sequence of a nonlinear 2-actuator system will be analyzed. We show that this sequence can be altered by changing the amplitude of the input signal, which directly follows from a parameter sensitivity analysis using the same tool.

NONLINEAR FLUIDIC NETWORKS

Inflatable soft robotic systems can be thought of as a network of inflatable actuators that are linked to each other using tubing as fluidic interconnections. Inflatable actuators are characterized by a pressure-volume relationship, and tubing by a pressure-flow relationship. As volume-pressure-flow are analogous to the electrical quantities of charge-voltage-current, it is possible to convert a network of inflatable actuators and tubing, to an equivalent electrical circuit if nonlinear impedances are used to mimic the nonlinear fluidic characteristics. A schematic of the fluidic-electric analogy can be seen in Fig. 1a. Distribution of charge over time is analogue to the fluid volume distribution in the system, which for inflatable actuators is directly linked to their deformation.

MORPHOLOGICAL CONTROL

In order to obtain a sequential response of the actuators in the system, nonlinearities need to be incorporated in the fluidic network. In this work we use inflatable actuators that exhibit an isochoric snap-through, where a rubber cavity is enclosed by a conically shaped membrane, similar to the actuators used in [7]. This membrane will go through an elastic structural instability and snaps out of the cavity with a sudden and significant deformation (fig. 1b). The nonlinear pressure-volume characteristic shows two local extrema (a peak and a valley, fig. 1c) corresponding to the snapping pressures. Extrema can be tuned by varying some geometrical parameters of the actuator such as membrane thickness and

*Corresponding author. E-mail: edoardo.milana@kuleuven.be

membrane angle. The highly nonlinear pressure-volume relationship of this actuator can be translated to an electrical analogue, by a stepwise linear interpolation of capacitors, as shown on figure 1c.

As case study of morphological control, we analyze the response of a network composed of two such nonlinear actuators having different pressure peaks and interconnected through flow restrictors (fig. 1d-e). The main goal is to obtain a sequential actuation with a single pressure input and to change the sequence by only acting on the input. Indeed, if the pressure input amplitude is low, pressure drops caused by flow restrictors can be neglected. In this case the actuators will move in the sequence prescribed by the pressure peaks locations of their characteristic (fig. 1f, dashed lines). In contrast, for high amplitude inputs, pressure drops play a significant role and according to the position of the flow restrictors in the network, the actuation sequence can change. If the actuator with the lowest pressure peak has the highest flow restrictor in series, it snaps after the motion of the other actuator (fig. 1f, continuous lines). Thanks to the electric circuit analogy, the system can be analyzed numerically through Simulink and compared against experiments.

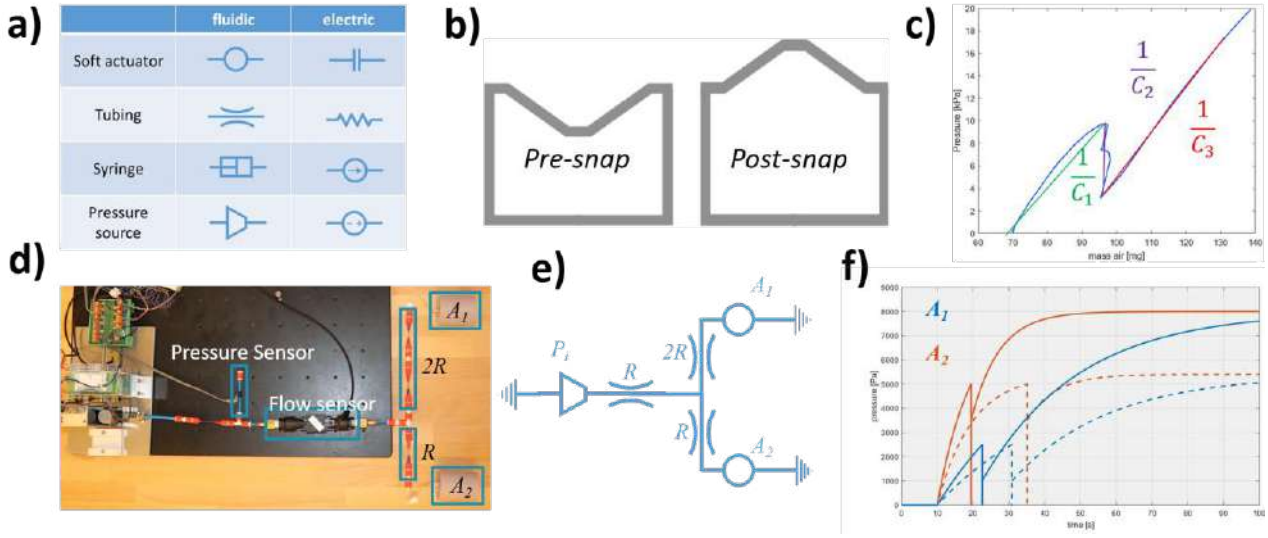

Figure 1. a) Impedance analogy for soft fluidic networks. b) Deformation sketch of the nonlinear snapping actuator. c) Nonlinear characteristics of the soft actuator and its stepwise linear approximation. d) Experimental setup comprising two nonlinear actuators and flow restrictors. e) Circuit scheme of the setup. f) Time response of the two actuators for an high pressure amplitude step (continuous line) and low amplitude (dashed line). Snapping times are different leading to a change of the actuation sequence.

CONCLUSIONS

A network of nonlinear inflatable actuators that are connected using fluidic tubes can be analyzed using electrical network theory as volume-pressure-flow is analogous to charge-voltage-current. With this technique, the response of an arbitrary network of nonlinear building blocks can be simulated in Simulink, which can be loaded by either a pressure or volume input. This has been done to analyze morphological control of 2-actuators nonlinear system, where we showed that the actuation sequence can be changed by varying the input amplitude thanks to their highly nonlinear response. This design strategy can further be used to develop highly complex soft robotic behaviors, emerging from the interaction of simple nonlinear building blocks, in an effort to simplify control schemes.

References

[1] Whitesides GM Soft Robotics, *Angewandte Chemie - International Edition*, **57**. Wiley-Blackwell, 4258–4273, 09-Apr-2018.
[2] Rus D and Tolley MT 2015 Design, fabrication and control of soft robots *Nature* **521** 467–475.
[3] Pfeifer R and Bongard J How the Body Shapes the Way We Think, in *How the Body Shapes the Way We Think*, The MIT Press, 2006.
[4] Overvelde JTB Kloek T D'haen JJ a and Bertoldi K 2015 Amplifying the response of soft actuators by harnessing snap-through instabilities. *Proc. Natl. Acad. Sci. U. S. A.* **112** 10863–8.
[5] Gorissen B *et al.* 2019 Hardware Sequencing of Inflatable Nonlinear Actuators for Autonomous Soft Robots *Adv. Mater.* **31** 1–7.
[6] Vasios N Gross AJ Soifer S Overvelde JTB and Bertoldi K 2019 Harnessing Viscous Flow to Simplify the Actuation of Fluidic Soft Robots *Soft Robot.* **00** soro.2018.0149.
[7] Rothemund P *et al.* 2018 A soft, bistable valve for autonomous control of soft actuators *Sci. Robot.* **3** eaar7986.

SNAP-SHAPING GROOVY SHEETS

Anne Meeussen*[1,2] and Martin L. van Hecke [1,2]
[1]Designer Matter Department, AMOLF, Amsterdam, The Netherlands
[2]Leiden Institute of Physics, Leiden University, Leiden, The Netherlands

Summary Thin sheets show unusual behaviour, from curve-stiffening [1] to crumpling [2]. These phenomena arise from a geometry-mediated competition between stretching and bending energies, which produces rich emergent effects. Here, we harness a thin sheet with a simple geometry—a *groovy sheet* with parallel undulations—to create a multistable structure with minimal preprogramming. We show that our groovy sheets exhibit rapid, easy-to-actuate, and reversible shape-switching between a large array of out-of-plane states via snap-through instabilities. Our work opens up new vistas for the design of shape-shifting materials, leveraging thin sheets' potential for large elastic deflections.

COMPLIANT ORIGAMI

Origami, the archetypical shape-shifting material, is often modelled as having stiff facets and perfectly soft hinges. However, real origami structures' facets and hinges may bend and stretch. Adding compliance to rigid origami models enriches their behaviour, leading especially to the creation of mechanically multistable structures [3]. Compliance thus opens up a new design space for shape-shifting structures, with the potential to formulate design rules for controlling a structure's stable configurations.

SNAPPING GROOVY SHEETS

We explore this new shape-design space using a compliant *groovy sheet*, consisting of thin, soft plates connected by parallel curved hinges (Fig. 1a, left). When point loads are applied to the sheet's edges (Fig. 1a, middle), the structure undergoes a rapid, elastic snap-through instability into a new stable configuration with a distinct curled shape (Fig. 1a, right).

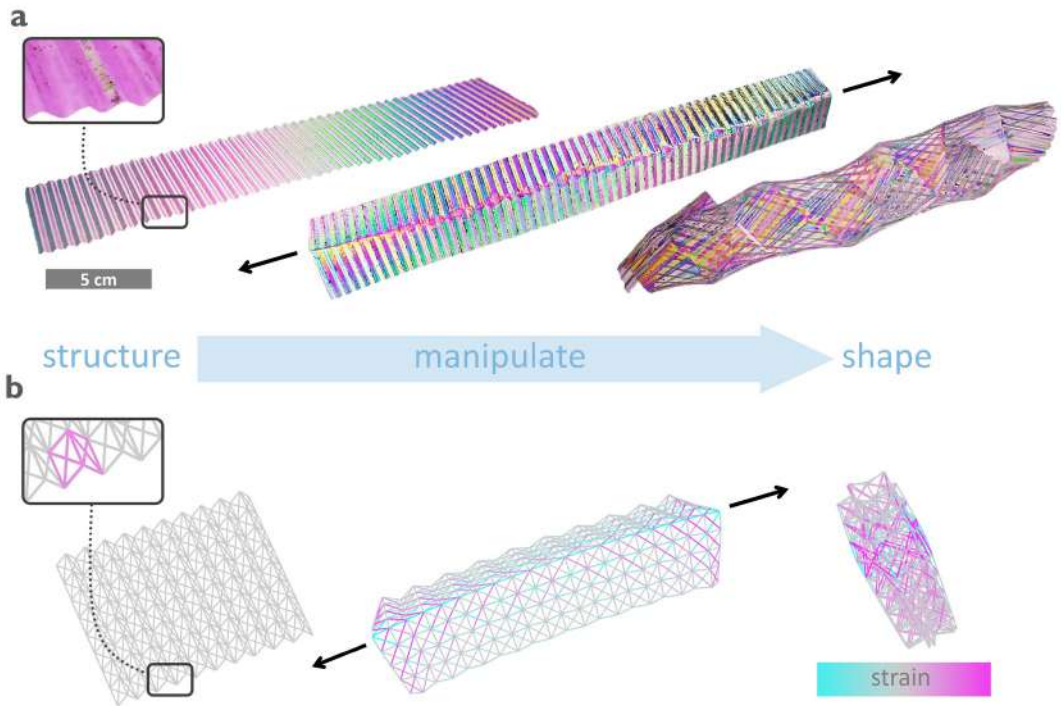

Figure 1: **A groovy sheet snaps through into a new, stable shape. a)** A sheet made of 15 μm thick PET film, consisting of soft plates and parallel hinges that form a series of grooves (inset) is shown. The colouring is obtained by photographing the strip between crossed polarisers. Under external point forces (dark arrows), the sheet snaps through into a new, stable, spiralling shape. **b)** The behaviour of the groovy sheet is simulated using a simplified network model, consisting of stiff linear springs connected by soft torsional springs (inset). Under external loading, the simulated network finds a new stable configuration that reproduces the rolling shape of the real sheet.

*Corresponding author. E-mail: a.meeussen@gmail.com

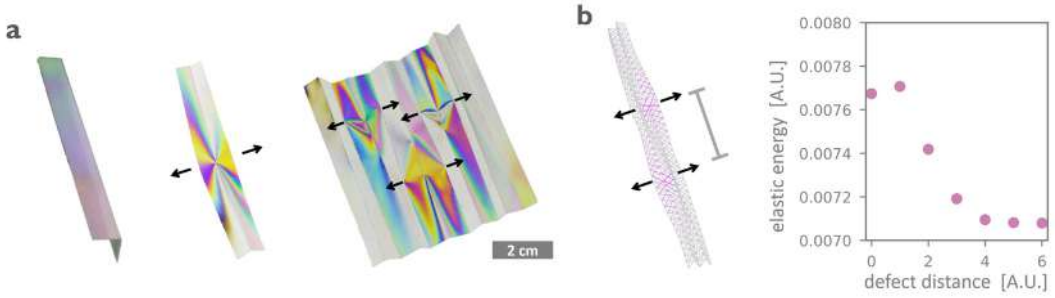

Figure 2: **Individual snap-through defects in each groove are responsible for the reshaping behaviour of the sheet. a)** A single PET film groove (23 μm thick) undergoes a snap-through instability into a new, stable state under external forcing. A stretched defect is created at the snap-through location. In a large groovy sheet, this local stretching leads to geometric interactions between defects. **b)** Defect interactions can be investigated using the discrete model shown in Fig. 1b, by calculating the network's elastic energy as a function of the distance between defects (indicated left). The results (shown right) indicate that defects created close together will stay that way to minimize their energy; conversely, defects created at a distance will repel.

Bistability from groove geometry

This reshaping is purely a result of the presence of compliance in the sheet's grooves, which produces a geometry-mediated energetic competition between stretching and bending in the underlying material of the sheet. We confirm that geometric coupling between stretching and bending in the groovy sheet leads to bistable behaviour via a simple computational model, illustrated in Fig. 1b.

Local defects shape the sheet

We further show that the reshaping capacity of the groovy sheet is contained in the snapping behaviour of its individual groove [4]: each groove may snap through into a configuration with a locally stretched defect (Fig. 2a, left). In a large sheet, adjacent local defects result in a geometrically incompatible structure- it is energetically costly to accommodate defect clusters. As a result, defects will interact and move to minimize geometric frustration (Fig. 2a, right). The interaction between defects depends on their mutual distance; our network model indicates that nearby defects will attract, while distant defects repel (Fig. 2b). A line of neighbouring defects in a groovy sheet will therefore be stable, minimizing the overall energy. The resulting geometry produces a characteristic spiralling shape.

CONCLUSIONS

In conclusion, we show that compliance of thin sheets—that is, their geometry-mediated competition between bending and stretching—leads to a rich design space of multistable structures. We show here that the range of available multistable shapes of a thin, groovy sheet can be explored and understood with straightforward experimental tools and minimal numerical models.

References

[1] Pini, V., Ruz, J.J., Kosaka, P.M., Malvar, O., Calleja, M., and Tamayo, J. How two-dimensional bending can extraordinarily stiffen thin sheets. *Sci. Rep.* **6**:29627, 2015.
[2] Witten, T. Stress focusing in elastic sheets. *Rev. Mod. Phys.* **79**:643-675, 2007.
[3] Silverberg, J., Na, J.H., Evans, A.A., Liu, B., Hull, T.C., Santangelo, C.D., Lang, R.J., Hayward, R.C., and Cohen, I. Origami structures with a critical transition to bistability arising from hidden degrees of freedom. *Nat. Mater.* **14**:389-393, 2015.
[4] Lechenault, F., and Adda-Bedia, M. Generic bistability in creased conical surfaces. *Phys. Rev. Lett.* **115**:1-5, 2015.

MECHANICS-INFORMED PROGRAMMING OF PASSIVELY CONTROLLED, UNTETHERED SOFT ROBOTS

Connor McMahan[†1], Arda Kotikian[†2], Emily C. Davidson[2], Jalilah M. Muhammad[2], Robert D. Weeks[2], Chiara Daraio[*1], Jennifer A. Lewis[*2]
[1]Division of Engineering and Applied Science, California Institute of Technology, Pasadena, CA, USA
[2]John A. Paulson School of Engineering and Applied Sciences, Wyss Institute of Biologically Inspired Engineering, Harvard University, Cambridge, MA, USA

Summary Most soft robots require a tether to rigid power and control systems to locomote. An alternative to this approach is to use soft active materials that exert work in response to various environmental stimuli. However, the creation of untethered, active matter-based robots presents challenges. Predicting the kinematics of these systems is not straightforward because they often operate in nonlinear elastic regimes, and programming the sequential actuation of different robotic components requires understanding the effect of chemistry and geometry on responses to stimuli. Here, we showcase the programming of a "rollbot" that morphs into a prism and self-propels when heated. To do so, we control the chemistry and geometry of liquid crystal elastomer bilayer hinges during 3D printing, informed by thermo-mechanical characterizations of the materials.

BACKGROUND

Untethered self-propulsion is a requirement for robotic systems that navigate large distances. Given that untethered operation often requires carrying power and control systems that add mass to the robot, active matter that self-actuates in response to external stimuli (e.g., temperature, light, chemical gradients, and electric fields) has been explored as an alternative to soft robotic systems that rely on pneumatics or onboard electronics [1].

Precisely controlling the kinematics of soft robots that rely on pneumatic systems or active matter can be challenging because of their operation in nonlinear elastic regimes [2]. Origami-based strategies address this challenge by localizing large, predictable shape changes of the overall structural frame to discrete creases [3]. Origami-inspired approaches become especially compelling when implemented with active materials that can be programmed to actuate creases in a desired sequence in response to an external stimulus, as this broadens the space of achievable geometries and enables multi-gait locomotion. However, many active materials lack energy density or the capability to deform reversibly [4]. These features are necessary for applications that involve bearing large loads or self-propelling over many actuation cycles.

Liquid crystal elastomers (LCEs) have recently emerged as a promising class of soft active matter because they generate large, powerful, and repeatable deformations upon heating above their nematic-to-isotropic transition temperature (T_{NI}), thus meeting the demands of soft robotic applications specified above. The direction of contractile strain (director) can be programmed by aligning rigid mesogens during fabrication [5].

SUMMARY OF RESULTS

Toward the objective of creating soft robots that can shape-morph and self-propel repeatedly in response to external stimuli, we 3D printed LCE in the form of active hinges that interconnect passive polymeric tiles. When heated above their actuation temperatures, the printed LCE hinges exhibit a large, reversible bending response. To achieve controlled bending, we fabricated each LCE hinge in a bilayer design in which the two halves have orthogonal directors. A spontaneous strain mismatch caused each hinge to bend when heated above their actuation temperature. Using this method, the folding orientation, hinge angles, torque output, and actuator geometry are fully programmable by adjusting the print path. By printing LCE inks with different T_{NI}, we created soft robotic matter with predetermined folding sequences upon heating. These materials generate torques capable of lifting objects that were more than two orders of magnitude heavier than the hinges themselves, and torque remained constant over multiple heating and cooling cycles, which is essential for repeatable propulsion in untethered robots.

We use a multi-material 3D printing approach to demonstrate simple embodiments of origami-inspired soft robots that are manufactured in a single step. Upon deployment, shape-morphing and self-propulsion were passively controlled via the constitutive response of the printed matter. Among the soft robotic structures created using this manufacturing approach, we highlight an initially flat structure that reconfigured to a pentagonal prism and propelled itself by rolling on a hot surface, which we refer to as a "rollbot." The thermo-mechanical characterization of bilayers of varied chemistry and printed geometry informed the programming of the hinge actuators so that they met the kinematic and torque requirements of the "rollbot," shown in the figure below.

[†]These authors contributed equally to this work.
[*]Corresponding authors. E-mails: daraio@caltech.edu (C.D.); jlewis@seas.harvard.edu (J.A.L.)

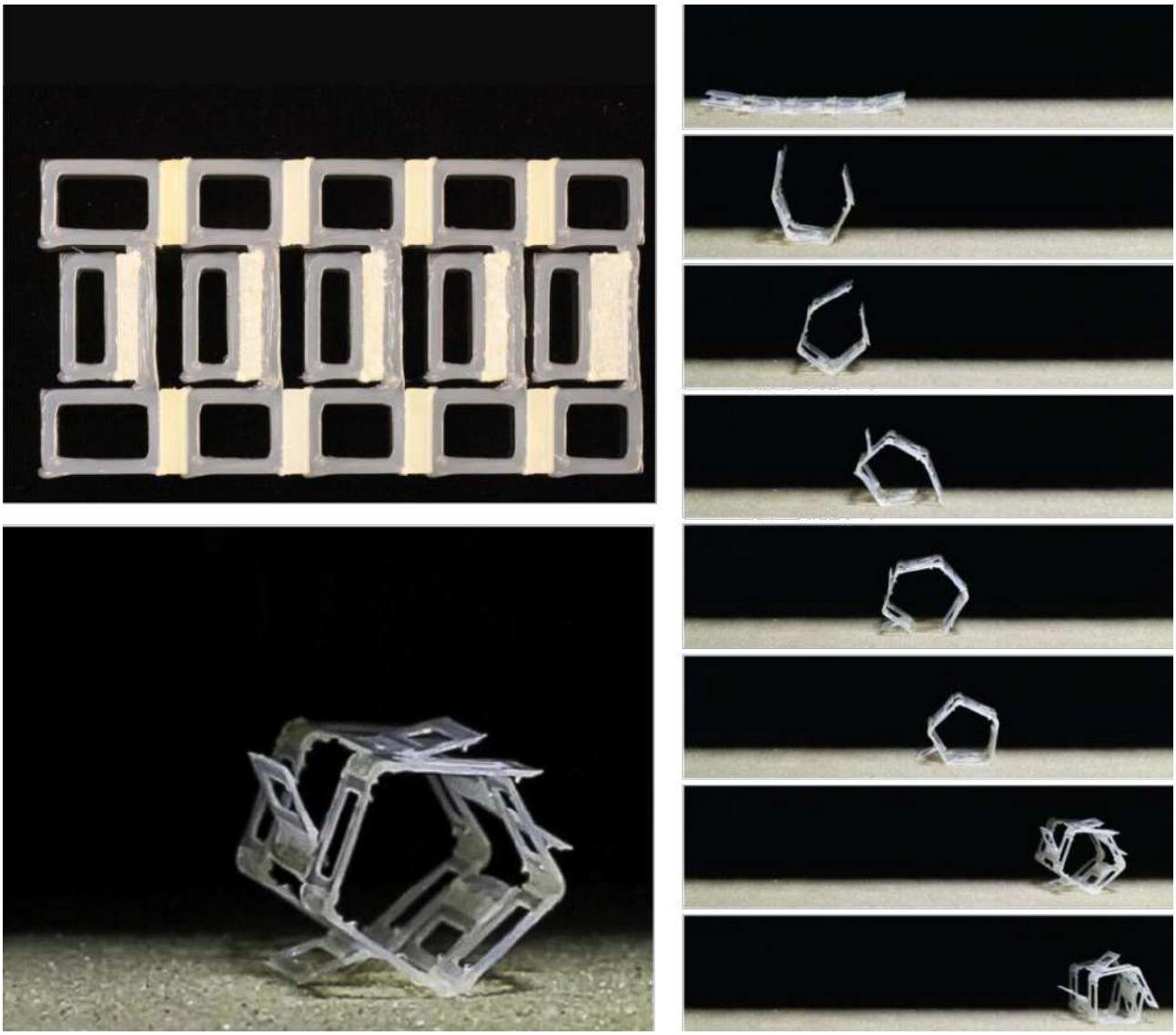

Figure 1. Passive control of self-assembly and propulsion in a rolling architecture (i.e., rollbot). The entire structure was printed flat (top left). The structural frame was composed of two outer rails that use low-T_{NI} LCE hinges to morph from a flat state to a pentagonal prism. These rails were connected by bridges that hold propelling high-T_{NI} LCE hinges. A hot plate and a convective environment were used to passively induce the desired assembly (bottom left) and rolling motion (right). In the assembled 3D configuration, the high-T_{NI} LCE hinges actuated when in contact with the hot plate, rolling the structure over the adjacent vertex and onto the next hinge, which carried out the same action. Both low-T_{NI} and high-T_{NI} LCE hinge dimensions were chosen based on thermo-mechanical characterizations of the materials. Because these hinges unfolded away from the hot surface, their repeated actuation was possible.

CONCLUSIONS

Using an additive manufacturing approach that enables us to program the response of active materials to external stimuli and integrate them with several materials, we have created passively controlled shape-morphing and self-propelling structures. This method enables programming the actuation temperature, folding angle and orientation, and torque output of LCE hinges. Importantly, these materials actuate reversibly and their torque outputs are large enough for self-propulsion and for lifting objects that are much heavier than the hinges themselves. Given the modular nature of the additive manufacturing approach, we envision incorporating LCEs that respond to other stimuli (e.g., light, pH, and humidity) within these printed architectures in the future.

References

[1] Palagi S., et al. Structured Light Enables Biomimetic Swimming and Versatile Locomotion of Photoresponsive Soft Microrobots. *Nat. Mat.* **15**: 647-653; 2016.
[2] Shepherd R. F., et al. Multigait Soft Robot. *PNAS.* **108**: 20400-20403; 2011.
[3] Rus D., Tolley M. T. Design, Fabrication and Control of Origami Robots. *Nat. Rev. Mater.* **3**: 101-112; 2018.
[4] Chen T., et al. Harnessing Bistability for Directional Propulsion of Soft, Untethered Robots. *PNAS.* **115**: 5698-5702; 2018.
[5] Kotikian A., et al. 3D Printing of Liquid Crystal Elastomeric Actuators with Spatially Programed Nematic Order. *Adv. Mater.* **30:** 1706164; 2018.

A NUMERICAL MODEL FOR SOFT TWO-DIMENSIONAL MATERIALS

Daniele Liprandi[1], Federico Bosia[2], and Nicola Maria Pugno [*1,3]
[1]Department of Civil, Environmental and Mechanical Engineering, Università di Trento, Trento, Italy
[2]Department of Applied Science and Technology, Politecnico di Torino, Torino, Italy
[3]School of Engineering and Materials Science, Materials Research Institute, Queen Mary University of London, London, UK

Summary Many soft materials are implemented in devices that mechanically interact with other bodies. When a soft two-dimensional membrane touches another body or a substrate it becomes impossible to analytically predict its exact behaviour. Adhesion, friction, stress and fracture propagations are important rulers of the mechanical responses. In this work, we propose numerical models which are able to quickly calculate complex mechanical responses of soft membranes interacting with a substrate. The Lattice Spring Model is used to discretize the continuous membrane and allows the definition of heterogeneous materials. We show how this can be applied to soft biological membranes and how different parameters affect their mechanical responses.

INTRODUCTION

The term "soft materials" covers polymeric materials, such as rubbers, gels and self-adhesive materials, but also many biological and bio-inspired materials such as living tissues. Soft materials have now attracted high interest from the robotic and biomedical fields as they can be the elementary bricks for the development of new devices.
A common problem in the development of new devices is the need of thin materials able to interact and adhere to a surface, sustain large deformations before failing and having predetermined mechanical responses [1,2]. The interaction between surfaces is one of the major rulers of the behaviour of these adhesive membranes and has been intensively studied in the past years both theoretically and experimentally. Even so, the adhesive and frictional properties of two generic surfaces for three-dimensional problems are far to be understood. If we don't consider particular symmetries or homogeneous conditions, it is almost impossible to predict how stresses and strains will distribute during the adhesive interaction between the two materials. This is caused by the high number of interplaying parameters, which comprehend the geometrical and mechanical properties of the materials, the substrate properties and the adhesive potentials connecting them. The number of parameters further increases when composite, heterogeneous or hierarchical materials are considered. Nonhomogeneous materials are of particular interest for their tunability, often proved by the multiple instances which can be found in nature. To tackle these problems, we developed a theoretical-numerical approach to simulate the behaviour of a heterogeneous membrane-like soft structure interacting with a rigid substrate.

METHOD

We use two discretization techniques for both the soft membrane and the interface. We apply the framework method to discretize continuous surfaces using structured lattices. The lattice definition is based on the framework method and the Lattice Spring Model. The Lattice Spring Model allows us to simulate heterogeneous soft membranes as shown in Figure 1. The interaction between the structure and the rigid substrate is simulated by a fibrillar three-dimensional cohesive law. We have developed a hand-written C++ code, which allows our model to have both great portability and versatility.

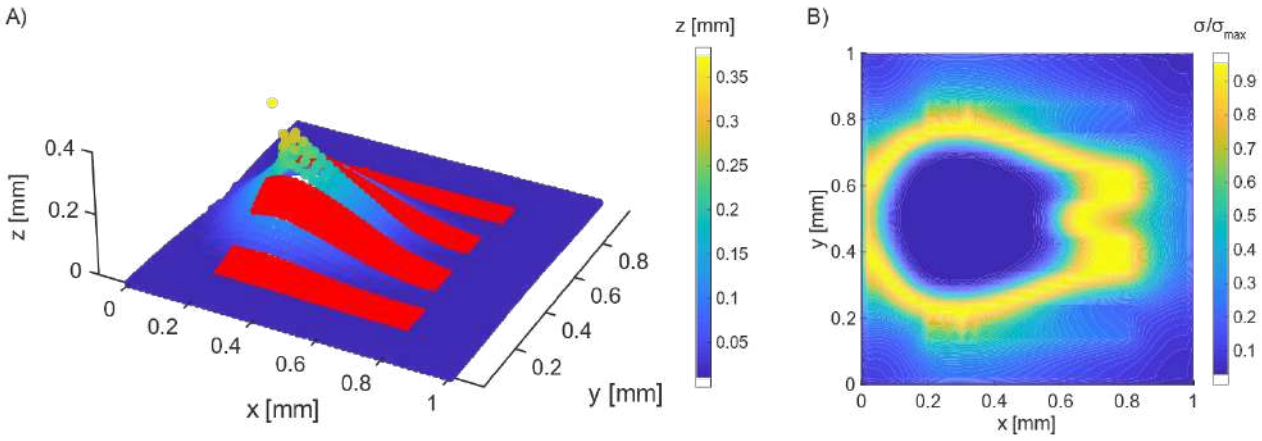

Figure 1. A) 3D Membrane displacement map of a composite membrane being pulled from a substrate in a single point at an angle $\theta = 60°$. The red parts of the membrane have a higher Young modulus. The colormap indicates the vertical displacement. B) Normalized interface stress map.

* Corresponding author. E-mail: Nicola.pugno@unitn.it

RESULTS

The results presented show how the stress and strain distributions are influenced by the system parameters. We apply the model to a spider disc attachment-like structure, explaining the evolutionary path of the geometrical parameters. We show how the geometrical properties of the membrane rule the maximal pull-off force and extensibility of the system, and how tearing phenomena and heterogeneous mechanical properties change the behaviour of the peeling process.

References

[1] Costantino Creton and Matteo Ciccotti *Rep. Prog. Phys.* **79**, 046601, 2016
[2] Shull, K.R. *Mater. Sci. Eng. R Reports* 36, 1–45, 2002.

RIGOROUS NUMERICAL 1D MODEL FOR HYPERELASTIC SLENDER SOLIDS

Helen Liedtke*[1], Claire Lestringant[1,2], and Dennis Kochmann[1]
[1]Mechanics & Materials, Department of Mechanical and Process Engineering, ETH Zurich, Zurich, Switzerland
[2]Structures Research Group, Department of Engineering, University of Cambridge, Cambridge, United Kingdom

Summary We introduce a computational mechanics approach for the dimensional reduction of slender structures at finite strains with generic cross-sections and hyperelastic constitutive behaviour following a formal asymptotic approach. We validate our model with a suite of test cases.

Slender structures undergoing extreme deformations are of interest in many disciplines and applications such as biology [1], soft robotics [2] and 4D printing [3]. Finding efficient and accurate models for these structures at finite strains is an important challenge arising in all these different fields. In particular, when slender elements are combined with nonlinear and/or heterogeneous material behaviour and have complex cross-sectional shapes, classical 1D models often lose applicability. Recent efforts, see [4], propose a formal asymptotic dimension reduction approach that starts from a general, nonlinear 2D or 3D model. Following this approach, we propose to implement a systematic numerical method to define and solve accurate 1D models for hyperelastic slender solids at finite strains for a variety of cross-sectional geometries as well as constitutive behaviours.

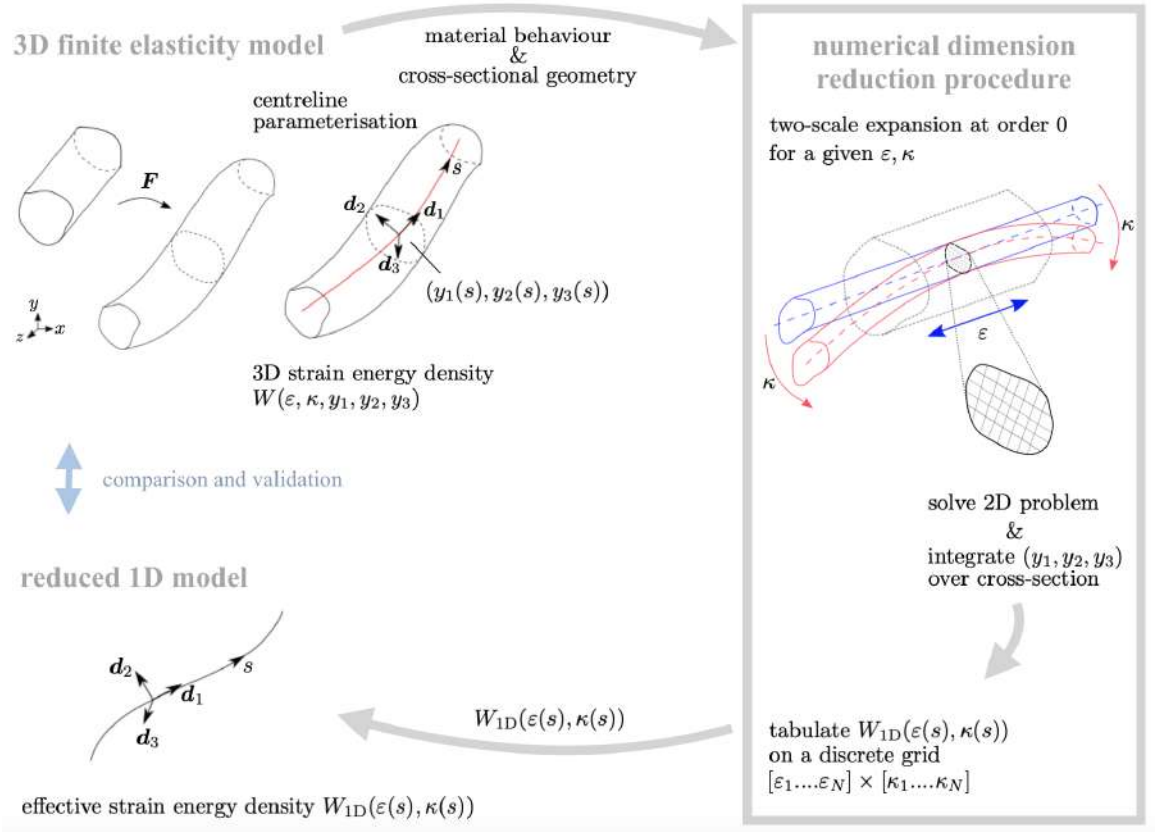

Figure 1: A flowchart showcasing the dimension reduction procedure.

Starting from a generic 3D slender structure, as shown in Figure 1, we parameterise the centreline as shown in red with the Lagrangian curvilinear coordinate s. At every s, an orthonormal set of material frame directors $(\boldsymbol{d}_1, \boldsymbol{d}_2, \boldsymbol{d}_3)$ defines the average orientation of the cross-section, while the coordinates (y_1, y_2, y_3), which depend on the position s, capture the geometry of the deformed cross-section. The information on the material behaviour and the cross-sectional geometry is passed to the numerical dimension reduction algorithm for a given load case, i.e. the axial strain ε and/or the curvature κ. Using a two-scale expansion, we rescale the longitudinal coordinate s by a small parameter η (typically of dimension of the cross-section over the length). Consequently, all axial gradients disappear at order 0 and the solution is homogeneous

*Corresponding author. E-mail: helen.liedtke@mavt.ethz.ch.

along the length. We are left with a 2D finite elasticity problem on a generic cross-section of the solid, that can be solved with standard FE. We then integrate the coordinates (y_1, y_2, y_3) over the cross-section, which yields the reduced 1D strain energy density, which is ultimately tabulated for a catalogue of different strains. The resulting reduced 1D energy allows us to define a 1D model that depends on the centerline's deformations ε and κ only (for 2D deformations). The latter is solved with an in-house nonlinear discrete beam framework [5].

We present the theoretical foundation, implementation and evaluate the accuracy of the reduced model by solving a set of test cases for which we solve both the original 3D problem and the reduced nonlinear 1D model. Our comparison includes hyperelastic models as well as cross-sectional shapes both in linear and nonlinear regimes, as well as a comparison of the efficiency of the two approaches.

References

[1] Moulton D.E., Lessinnes T., Goriely A. Morphoelastic rods. Part I: A single growing elastic rod. *Journal of the Mechanics and Physics of Solids*, **61**: 398-427, 2013.

[2] Kotikian A., McMahan C. Davidson, E.C., Muhammad J.M., Weeks R.D., Daraio C., Lewis J.A. Untethered soft robotic matter with passive control of shape morphing and propulsion, *Science Robotics*, Vol4 Issue 33, 2019.

[3] Ding Z., Weeger O., Qi H.J., Dunn M.L. 4D rods: 3D structures via programmable 1D composite rods. *Materials and Design*, **137**:256:265, 2018.

[4] Lestringant C., Audoly B. Asymptotically exact strain-gradient models for nonlinear slender elastic structures: a systematic derivation method. *Journal of the Mechanics and Physics of Solids* pp.103730 in press, hal-02347666, 2019.

[5] Lestringant C., Audoly B., Kochmann D.M. A discrete, geometrically exact method for simulating nonlinear, elastic and inelastic beams. *Computer Methods in Applied Mechanics and Engineering* 112741 in press, 2019.

PLAYING WITH A ROPE ON THE GROUND: A TOY-MODEL FOR DYNAMICAL ELASTIC CONTACTS.

Benoît Seron and Gregory Kozyreff*
Optique Non linéaire Théorique,Département de Physique,Université libre de Bruxelles(U.L.B.)CP231,Campus de la Plaine, Bruxelles, Belgium

Summary We study theoretically, numerically, and experimentally the dynamics of a rope laid on the ground when one end is lifted and harmonically vibrated vertically with a small amplitude around a given value. Intuitively, at small frequencies, only the part of the rope that is lifted should be set into motion, the rest of it remaining inert. Meanwhile, the location of the first contact with the ground, $x_c(t)$, should advance and recede, following the up and down motion at the lifted end of the rope. Next, a critical frequency is expected, above which waves are radiated along the rope away from the vibrated end. Our study confirms this intuition and yields the critical frequency of this transition. However, further investigation reveals that the dynamics is much richer than anticipated. Firstly, the location $x_c(t)$ tends to display a strongly anharmonic behaviour even well below the critical frequency. Secondly, we find that an infinity of secondary critical frequencies exist and that the stability diagram is actually covered by Arnold's tongues.

INTRODUCTION

Problems of contact between deformable bodies are among the most difficult ones in elasticity, and only a few are exactly solvable [1, 2, 3]. Aside from the fundamental interest of the subject, structures containing parts that enter in contact and transfer loads between each other abound in engineering. Hence, the study of elastic contact is of significant practical importance.

Here, we explore the physics of a slender body in dynamical contact with an obstacle: namely a rope laid on the ground with one of its ends vibrated vertically around a given altitude. Our motivation is primarily fundamental; we note, however, that some connection can be made with the dynamics of strands of hair making contact with the human body, the mechanics of rugs [4, 5] or the mechanical instabilities affecting rods injected in cylinders [6, 7], borehole drilling [8, 9] and ocean cable laying [10].

The system we consider is depicted in Fig. 1 and the simplest possible mathematical model for the elevation $w(x,t)$ of the rope is that of a nearly horizontal elastic beam [3]:

$$\rho\frac{\partial^2 w}{\partial t^2} = T\frac{\partial^2 w}{\partial x^2} - B\frac{\partial^4 w}{\partial x^4} - \rho g, \qquad w \geq 0, \tag{1}$$

$$w - Z(t) = \frac{\partial^2 w}{\partial x^2} = 0, \qquad x = 0, \tag{2}$$

$$w = \frac{\partial w}{\partial x} = \frac{\partial^2 w}{\partial x^2} = 0, \qquad x = x_c(t). \tag{3}$$

with ρ, T, B and g respectively the linear density, tension, bending stiffness and the acceleration of gravity. At $x = 0$, the rope is lifted to a height $Z(t)$ and the point of contact between the rope and the ground is located at $x_c(t)$, to be found as a functional of $Z(t)$. Although Eq. (1) is formally linear, the above differential problem is in fact strongly nonlinear, since $w(x,t)$ is nonlinearly coupled to the location $x_c(t)$ where Eq. (3) is imposed, and $x_c(t)$ is to be found as part of the solution.

Above, the tension T is difficult to predict and control, experimentally, as it is affected by the friction between the ground and the rope. Nevertheless, it greatly simplifies the analysis if we assume that it is constant and that it dominates bending: $B\partial^4 w/\partial x^4 \ll T\partial^2 w/\partial x^2$. In that limit, bending stiffness only manifests itself in boundary layers and can be neglected in first approximation. Finally, the excitation of the rope is given by

$$Z(t) = Z_0 + \epsilon z(t), \qquad z(t) = \cos(\omega t), \tag{4}$$

and we wish to establish a map of the possible dynamical behaviours in the (ω, ϵ) plane.

RESULTS

In the absence of harmonic excitation ($\epsilon = 0$) and in the limit of small bending stiffness, it is easy to find that

$$x_c = x_{c,0} = \left(\frac{2TZ_0}{\rho g}\right)^{1/2}\left[1 + O\left(\beta^{1/2}\right)\right], \qquad \beta = \frac{\rho g B}{2T^2 Z_0} \ll 1. \tag{5}$$

Next, in the limit $0 < \epsilon \ll 1$, we find that

$$x_c \sim x_{c,0}\left[1 + \frac{\epsilon}{2}\frac{\pi\omega/\omega_c}{\sin(\pi\omega/\omega_c)}\cos(\omega t) + O\left(\epsilon^2\right)\right], \qquad \omega_c = \left(\frac{\pi^2 g}{2Z_0}\right)^{1/2}. \tag{6}$$

*Corresponding author. E-mail: gkozyref@ulb.ac.be

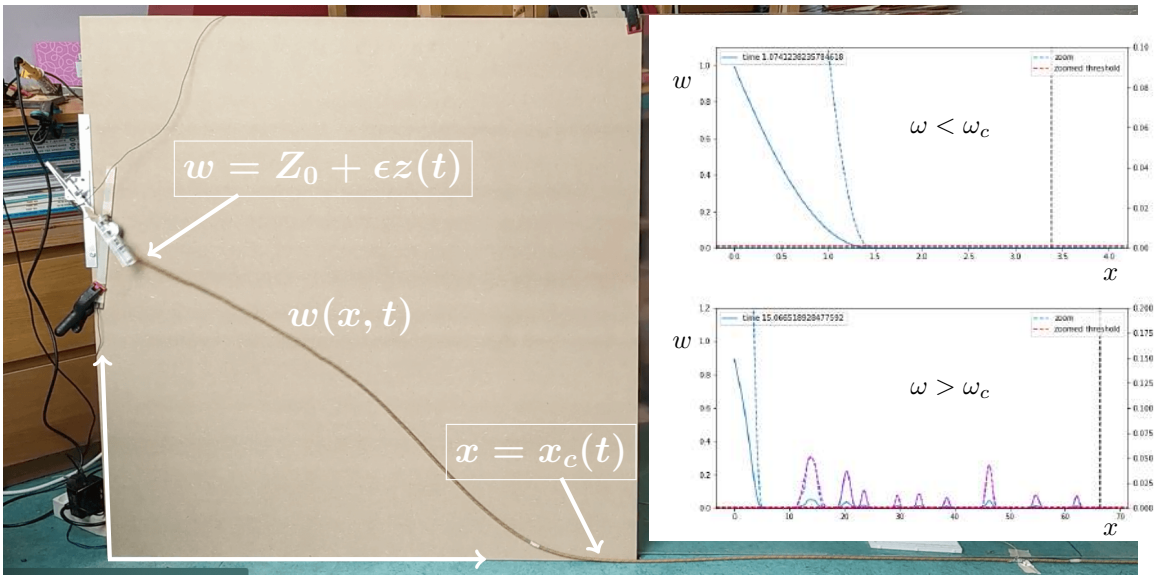

Figure 1: Experimental set-up. Top inset: snapshot of numerical simulation below instability threshold. Bottom inset: unstable regime. Full lines: $w(x,t)$, dotted lines: $10 \times w(x,t)$. Parameters: $Z_0 = 1$m, $\epsilon = 0.2$, $\beta = 0.1$.

The above result indicates that the response diverges as $\omega \to \omega_c$ and the expression for ω_c makes the rope appear as a pendulum of effective length $2Z_0/\pi^2$. Interestingly, the tension T does not appear in the expression for the resonant pulsation ω_c. This is because $x_{c,0}$ is naturally adjusted so that the propagation time of a disturbance between the vibrated end and the first contact point is independent of T.

As one approaches the resonant pulsation ω_c, the amplitude of vibration of the rope increases to such an extent that the rope can enter in contact with the ground at an intermediate location x^* between $x = 0$ and $x = x_c$. The region of the rope that is lifted in the range $x^* < x < x_c$ subsequently splits into one or more bumps that moves away from the origin. Thus, a dynamical transition is observed between a state of localised oscillations and a state of wave radiation along the rope. This dynamical scenario is confirmed both experimentally and by numerical simulations, performed with a code adapted from the work of Liakou *et al.* [8]. In Fig. 1, a close-up on the pulses in the radiation regime show that they are accurately given by fundamental travelling wave solutions of the beam equation [3].

A closer inspection of numerical simulations well below ω_c reveals that $x_c(t)$ can display quite an erratic behaviour, far from the simple harmonic form suggested by Eq. (6). This arises from the fact that the spectral response function actually contains a discrete infinity of resonances, at $\omega_n = n\omega_c$ ($n \geq 1$). These can easily be excited if special care is not taken to switch on the oscillations $z(t)$ sufficiently gradually. This infinite set of resonances indicates that the rope is a more complicated dynamical object than a simple pendulum: They are the signature of delayed interactions mediated by waves travelling up and down the rope.

A second surprise comes from carrying the perturbative analysis to higher orders in ϵ. At each new order, new harmonics are born due to the nonlinearity. For instance, at $O(\epsilon^2)$, the rope vibrates at a pulsation 2ω. As 2ω becomes close to ω_c the corresponding $O(\epsilon^2)$ amplitude diverges and a new region of instability is produced in the (ω, ϵ) plane. More generally, at $O(\epsilon^p)$ terms of frequency $p\omega$ are found and these are liable to diverge if they come close to $q\omega_c$. Therefore and infinity of nonlinear resonances actually exist, given by $(p/q)\omega$ with arbitrary integers p and q. Numerically, we have been able to observe regions of instability in the vicinity of $\omega_c/2$ and $2\omega_c/3$ in the form of Arnold's tongue.

References

[1] Heinrich Hertz. Über die Berührung fester elastischer Körper. *J. Reine Angew. Math.*, 92:156–171, 1881.
[2] K.L. Johnson, K. Kendall, and A.D. Roberts. Surface energy and the contact of elastic solids. *Proc. Roy. Soc. A*, 324:301–313, 1971.
[3] Peter Howell, Gregory Kozyreff, and John Ockendon. *Applied solid mechanics*. Cambridge University Press, 2009.
[4] Dominic Vella, Arezki Boudaoud, and Mokhtar Adda-Bedia. Statics and inertial dynamics of a ruck in a rug. *Phys. Rev. Lett.*, 103:174301, 2009.
[5] John M. Kolinski, Pascale Aussillous, and L. Mahadevan. Shape and motion of a ruck in a rug. *Phys. Rev. Lett.*, 103(17), oct 2009.
[6] I McCourt, T Truslove, and J Kubie. On the penetration of tubular drill pipes in horizontal oil wells. *Proc. Instn of Mech. Engrs C: J. Mech.*, 218(9):1063–1081, sep 2004.
[7] J.T. Miller, T. Su, E.B. Dussan V., J. Pabon, N. Wicks, K. Bertoldi, and P.M. Reis. Buckling-induced lock-up of a slender rod injected into a horizontal cylinder. *Int. J. Solids Struct.*, 72:153–164, oct 2015.
[8] Anna Liakou, Vincent Denoël, and Emmanuel Detournay. Fast in-plane dynamics of a beam with unilateral constraints. *J. Eng. Mech.*, 143(2):04016116, feb 2017.
[9] M.F. Shakib, E. Detournay, and N. van de Wouw. Nonlinear dynamic modeling and analysis of borehole propagation for directional drilling. *Int. J. Non-Linear Mech.*, 113:178–201, jul 2019.
[10] E. E. Zajac. Dynamics and kinematics of the laying and recovery of submarine cables. *Bell Sys. Tech. J.*, 36:1129, 1957.

DYNAMICS OF PHASE SEPARATION WITH NONLINEAR ELASTIC EFFECTS

Mrityunjay Kothari[1] and Tal Cohen [*1,2]
[1]Department of Civil and Environmental Engineering, Massachusetts Institute of Technology, Cambridge, MA, USA
[2]Department of Mechanical Engineering, Massachusetts Institute of Technology, Cambridge, MA, USA

Summary. Phase separation in binary liquid mixtures is arrested in the presence of elastic networks and leads to a nearly uniformly-sized distribution of the dilute-phase droplets. The droplets show a directional preference to migrate in presence of elastic property gradients. We model the dynamics of the resulting front propagation and discuss how elasticity controls the entire process.

INTRODUCTION

Phase separation is observed across the scales and in a variety of physical processes that range from the fields of biology to metallurgy. Liquid-liquid phase separation and subsequent species migration is understood to be a crucial mechanism for regulating the normal bodily functions of a cell. For instance, P-granule assembly is believed to employ phase separation as a mechanism to polarize the cell along its anterior-posterior axis as a precursor to cell differentiation [1]. The dynamics of this process is dependent on the cytoplasm and its properties. Similarly, phase separation phenomena are commonly observed in metals [2,3]. In the case of metals, elastic fields in the matrix are well known to affect the phase transitions; they can either inhibit or promote the growth of precipitates [4]. While important work has been carried out, both experimentally and theoretically, in understanding the elastic effects on phase separation and species migration in soft-material systems, understanding the dynamics of these processes still presents many challenges. In practical applications, the matrix properties are often heterogeneous, and the phase separation process is sensitive to these non-uniformities. In this talk, we will focus on 1D heterogeneity in elastic properties of the matrix and will examine the long-time dynamics of phase separation. In particular we explain through our model the observation of a propagating droplet dissolution front in a composite elastic sample made of stiff and soft materials [5]. We will discuss quantitatively how elasticity controls the speed of the front. We will also extend the model to analyse a graded elastic material and its effects on phase separation.

References

[1] Brangwynne, Clifford P., et al. "Germline P granules are liquid droplets that localize by controlled dissolution/condensation." *Science* 324.5935 (2009): 1729-1732.
[2] Rao, C. N. R., P. V. Vanitha, and Anthony K. Cheetham. "Phase separation in metal oxides." *Advances In Chemistry: A Selection of CNR Rao's Publications (1994–2003)*. 2003. 37-44.
[3] Edwards, Peter P., and M. J. Sienko. "Phase separation in metal solutions and expanded fluid metals." *Journal of the American Chemical Society* 103.11 (1981): 2967-2971.
[4] Johnson, W. C. "On the elastic stabilization of precipitates against coarsening under applied load." *Acta Metallurgica* 32.3 (1984): 465-475.
[5] Rosowski, Kathryn A., et al. “Elastic ripening and inhibition of liquid-liquid phase separation.” https://arxiv.org/abs/1907.08465

*Corresponding author. E-mail: talco@mit.edu.

MECHANICAL RESPONSE OF WRINKLED STRUCTURES

Sijie Tong[1] and Andrej Košmrlj*[1]
[1]Department of Mechanical and Aerospace Engineering, Princeton University, Princeton, NJ, USA

Summary The wrinkling instability of compressed stiff thin films bound to soft substrates has been recently exploited to create structures with tunable drag, wetting and adhesion. While these studies successfully demonstrated the proofs of concepts, the quantitative understanding is still lacking, because we don't know how wrinkled surfaces deform in response to interactions with environment. To address this issue, we systematically study how wrinkled structures respond to infinitesimal surface forces both in the vertical and horizontal directions. We find that the linear response diverges near the onset of wrinkling instability and then decays away from this critical threshold. Our theory can be further used to study the response of wrinkled structures to more complicated distributions of external forces and can thus provide insights for the above-mentioned applications.

Wrinkling instability of compressed stiff thin films bound to soft substrates has been studied for many years and the formation and evolution of wrinkles is well understood [1, 2, 3]. In recent years, the wrinkling instability has been exploited to create structures with tunable drag [4], wetting [5], adhesion [6], and to create a template for DNA wire formation [7]. While these studies successfully demonstrated the proofs of concepts, the quantitative understanding is still lacking, because we don't know how wrinkled surfaces deform in response to interactions with environment. In this talk, I will discuss how we try to address this issue by systematically studying theoretically and numerically how wrinkled structures respond to infinitesimal surface forces both in the vertical and horizontal directions. We find that the linear response diverges near the onset of the wrinkling instability and then decays away from this critical compression threshold (see Fig. 1). The mechanical response near the critical compression threshold can be understood exclusively in terms of the dominant characteristic Fourier mode of wrinkles, which is decoupled from other modes. In analogy with the critical phenomena in ferromagnets, we can introduce the critical exponents for the response of the characteristic modes of wrinkles, which are consistent with the Landau theory [8] (see Fig. 1). However, away from the critical compression threshold, the coupling between different Fourier modes becomes significant and it affects the mechanical response. Our theory can be further used to study the response of wrinkled structures to more complicated distributions of external forces and can thus provide insights for the above-mentioned applications.

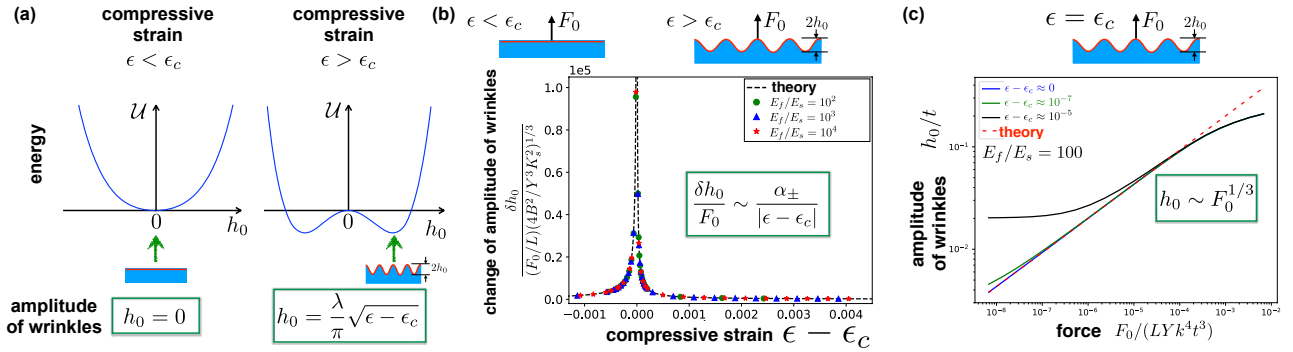

Figure 1: Relation between mechanical response of wrinkled structures and the Landau's theory of phase transition in ferromagnets, where the compressive strain ϵ, amplitude of wrinkles h_0 and external force F_0 are analogous to temperature, magnetization and magnetic field, respectively. (a) Energy landscape of wrinkled structures in the absence of external force as a function of compressive strain ϵ. Above the critical compressive strain ϵ_c the amplitude of wrinkles increases as $h_0 \propto \sqrt{\epsilon - \epsilon_c}$, which is analogous to spontaneous magnetization in ferromagnets below the critical temperature. (b) Linear response to vertical force diverges near the critical compressive strain as $\delta h_0/F_0 \sim |\epsilon - \epsilon_c|^{-1}$, which is analogous to the diverging susceptibility in ferromagnets near the critical temperature. (c) Exactly at the critical compressive strain ($\epsilon = \epsilon_c$) the amplitude of wrinkles grows nonlinearly with the applied force as $h_0 \sim F_0^{1/3}$, which is analogous to the nonlinear relation between magnetization and applied magnetic field in ferromagnets at the critical temperature.

References

[1] Allen H. G. Analysis and design of structural sandwich panels: the commonwealth and international library: structures and solid body mechanics division. Elsevier, 1969.
[2] Audoly B., Boudaoud A. Buckling of a stiff film bound to a compliant substrate–Part I:: Formulation, linear stability of cylindrical patterns, secondary bifurcations. *J. Mech. Phys. Solids.* **56(7)**: 2401-2421, 2008.
[3] Brau F., Damman P., Diamant H., Witten T. A. Wrinkle to fold transition: influence of the substrate response. *Soft Matter* **9(34)**: 8177-8186, 2013.
[4] Terwagne D., Brojan M., Reis P. M. Smart morphable surfaces for aerodynamic drag control. *Adv. Mater.* **26(38)**: 6608-6611, 2014.
[5] Chung J. Y., Youngblood J. P., Stafford C. M. Anisotropic wetting on tunable micro-wrinkled surfaces. *Soft Matter* **3(9)**: 1163-1169, 2007.
[6] Lin P. C., Vajpayee S., Jagota A., Hui C. Y., Yang S. Mechanically tunable dry adhesive from wrinkled elastomers. *Soft Matter* **4(9)**: 1830-1835, 2008.
[7] Nagashima S., Ha H. D., Košmrlj A., Stone H. A., Moon M.-W. Spontaneous formation of aligned DNA nanowires by capillarity-induced skin folding. *Proc. Natl. Acad. Sci. U.S.A.* **14(24)**: 6233-6237, 2017.
[8] Landau L. D., Lifshitz E. M., Statistical Physics. Butterworth-Heinemann, 1980.

*Corresponding author. E-mail: andrej@princeton.edu

ON THE DEFORMATION DEPENDENCE OF SURFACE STRESSES IN SOFT SOLIDS

Stefanie Heyden*[1], Robert W. Style[1], and Eric R. Dufresne[1]
[1]Department of Materials, ETH Zürich, 8093 Zürich, Switzerland

Summary Surface tension effects dominate the material behavior at scales below the elastocapillary length, which extends to the range of micrometers for increasingly soft materials such as hydrogels. Recent experiments using static wetting techniques suggest stretch-dependent surface stresses of soft solids [1, 2]. In this work, we present analytical solutions to the static wetting problem on stretched substrates. Following a Green's function approach, we extend the generalized Flamant-Cerruti problem, regularized by the addition of surface stresses, to furthermore account for uniaxial pre-stretches of the substrate. Symmetry breakage thereby allows us to gain insight into the intermediate-deformation regime between the two extreme cases of Youngs law for wetting on rigid substrates and Neumann's triangle for wetting on liquid substrates. Surface profiles and opening angles of wetting ridges are calculated and discussed in both frameworks of linearized and finite kinematics and compared to available experimental data [2].

OUTLINE OF THE PROBLEM

The analytical problem which originates from the static wetting framework is depicted in Figure 1. A liquid droplet is deposited on a soft substrate subjected to a finite pre-stretch λ. At the solid-vapor interface, forces originating from the liquid surface tension γ_l and the solid surface stresses γ_{sl} and γ_{sv} are balanced. Here, we focuse on the limiting case of large droplets, for which droplet curvature may be neglected and liquid surface tension acts along a straight contact line. The substrate is furthermore assumed to be neutrally-wetted. Due to pre-stretches applied to the solid substrate, the emergent surface stresses are rendered anisotropic. The fully three-dimensional surface profile upon static wetting is recovered by allowing solutions to account for varying in-plane angles between the applied pre-stretch and the in-plane direction perpendicular to the contact line.

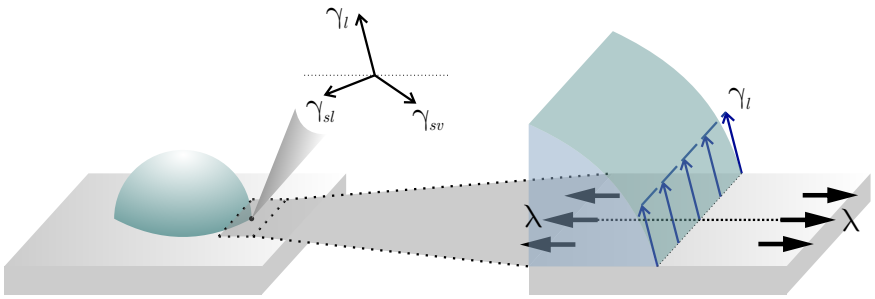

Figure 1: Sketch of the static wetting scenario: A liquid droplet is deposited on a soft substrate subjected to a finite pre-stretch λ. At the solid-vapor interface, forces originating from the liquid surface tension γ_l and the solid surface stresses γ_{sl} and γ_{sv} are balanced.

BULK ELASTICITY

To solve for the resulting substrate deformations due to the presence of the droplet within the framework of linearized kinematics, we follow a classical Green's function approach. The Navier–Lamé equations are simplified based on the assumption of plane strain conditions within the in-plane direction parallel to the contact line as prevalent in the large-droplet limit. Further, application of Fourier transforms results in a system of ordinary differential equations. Here, we aim to solve for substrate displacements at the surface only, for which tractions and displacements may be related via a generic spring constant $\hat{Q}_{ij}$.

SURFACE STRESSES

In order to take into account surface stresses counteracting the tractions applied at the substrate's surface, we start from a force balance at the surface. Surface stresses counteracting both normal- and in-plane tractions are derived, and the generic spring constant $\hat{Q}_{ij}$ is generalized to furthermore account for the additional action of surface stresses. To model anisotropic surface stresses based on an applied substrate pre-stretch, resultant surface stresses are calculated within the frameworks of both linearized kinematics and finite kinematics. In the latter case, we linearize about the configuration of an applied finite pre-stretch preceding droplet deposition.

*Corresponding author. E-mail: stefanie.heyden@mat.ethz.ch.

CONCLUSIONS

In this work, we present analytical solutions to the static wetting problem on an anisotropically stretched substrate. The generalized Flamant-Cerruti problem (regularized by the addition of surface stresses) is hence extended to furthermore account for anisotropic pre-stretches of the substrate. Moreover, solutions allow us to recover the full three-dimensional surface profile. By comparison to available experimental data, we show that a theoretical model of deformatio- dependent surface stresses predicts opening angles of the wetting ridge within experimental error measures.

References

[1] Xu, Q., Jensen, K.E., Boltyanskiy, R., Safarti, R., Style, R.W., Dufresne, E.R. Cooler A. S. Direct measurement of strain-dependent solid surface stress. *Nature Communications* **555(8)**, 2041-1723, 2017.

[2] Xu, Q., Style, R.W., Dufresne, E.R. Surface elastic constants of a soft solid. *Soft Matter* **14(916)**, 916-920, 2018.

THE ELASTIC CLASP: MECHANICS OF TWO DEFORMABLE FILAMENTS IN FRICTIONAL CONTACT

Paul Grandgeorge*[1], Changyeob Baek[1,2], Paul Johanns[1], Tomohiko Sano[1], and Pedro M. Reis[1]
[1]Flexible Structures Laboratory, Institute of Mechanical Engineering, Ecole Polytechnique Fédérale de Lausanne (EPFL), Lausanne, Switzerland
[2]Department of Mechanical Engineering, Massachusetts Institute of Technology, Boston, USA

Summary Knots, knits, weaves, and braids are but a few examples of intricate filaments in mechanical contact. Despite our broad empirical experience with such systems, there is a striking lack of fundamental understanding to predictively model their mechanical behavior. Indeed, the intricacy of entangled filaments coupled to the strong geometrical and material non-linearities involved make it challenging to develop high-fidelity quantitative models. Here, we adopt state-of-the-art 3D-imaging tools (X-ray tomography) combined with mechanical testing to investigate a canonical configuration of this class of problems; we focus on the frictional behavior of two elastic rods brought orthogonally into mechanical contact and made to slide against each other. We demonstrate how the frictional behavior between these two rods is closely related to the shape and size of their contact region.

MECHANICAL RESPONSE OF TWO ELASTIC RODS LOADED INTO FRICTIONAL CONTACT

Knotted filaments are ubiquitous across a wide range of length scales to moor ships to docks, secure adventurous climbers, or ensure the robustness of medical sutures. Yet, our understanding of the mechanical behavior of these intricate structures remains primarily empirical, gained through millennia of hands-on experience. This striking lack of fundamental understanding stems from the non-trivial coupling between topology, geometry, and mechanics in these systems. Past studies have either focused on ideal knots where no elasticity is taken into account [1] or on loose elastic knots [2, 3]. The latter are not representative of practical knots, which are usually tight. To gain a more in-depth mechanical insight into the primary mechanical ingredients underlying knotted structures, we investigate the mechanics of a minimal, yet representative, configuration of this class of problems: two elastic rods loaded into frictional contact.

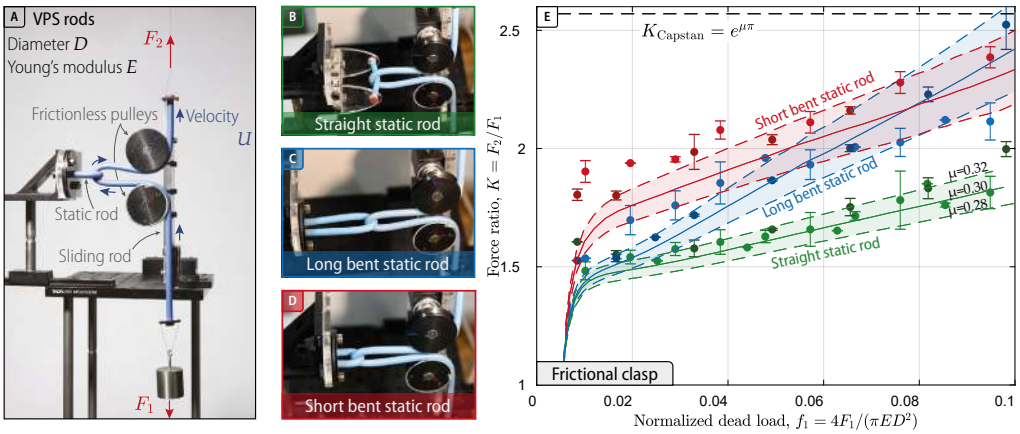

Figure 1: **Frictional clasp. A** – Experimental setup to quantify the force jump that an elastic rod is subjected to when sliding against another (static) elastic rod. A dead load F_1 is applied at one end of the sliding rod, and the stationary force F_2 required to achieve a constant upward velocity U of the upper end of the sliding rod is measured. The static rod configurations are shown in panels **B**, **C** and **D** and the experimental and numerical results of the force ratio $K = F_2/F_1$ as a function of the dimensionless dead load $f_1 = 4F_1/(\pi E D^2)$ a presented in panel **E**.

In Figure 1-**A**, we present our experimental apparatus comprising a long sliding *rod I* that is guided by two frictionless pulleys to thread through a second static *rod II* attached to a rigid frame. Rod II can be initially set to be either straight or pre-bent. We refer to this configuration of two elastic rods in crossing contact as the *elastic clasp*. The two rods composing this clasp are fabricated in-house out of Vinylpoly-Siloxane (VPS). Their Young's Modulus is varied using two different grades of VPS ($E = 0.52$ and 1.2 MPa). The sliding rod is weighted by a dead load F_1 attached to its lower extremity so as to study how this loading influences the mechanical response of the system. We focus on three different static rod configurations. In the first case (Figure 1-**B**), the static rod is set straight. In the two other configurations (Figure 1-**C** and **D**) the static is initially pre-bent by clamping its ends close to each other.

A typical experimental test involves using an Instron machine to impose the displacement of the upper end of the sliding rod that is loaded at the other end by the dead weight, F_1, and measuring the reaction force using a load cell.

*Corresponding author. E-mail: paul.grandgeorge@epfl.ch

This force first increases quickly before reaching a stationary plateau at F_2. In Figure 1-**E**, we plot the force ratio $K = F_2/F_1$ as a function of the normalized dead load $f_1 = 4F_1/(\pi ED^2)$ for the three static rods configurations. The experimental results (data points) are in good agreement with finite element (FEM) simulations (solid lines) using a friction coefficient of $\mu = 0.30 \pm 0.02$. The shaded region associated with the FEM results corresponds to the propagation of the uncertainty in μ. The friction coefficient was independently measured, and a value of μ =0.30 ±0.03 was obtained. Surprisingly, the force ratio K increases with f_1 for the three static rod configurations. By contrast, a classic *Capstan analysis* for an inextensible belt with no bending stiffness wrapped around a rigid cylinder, would predict a constant force ratio $K_C = e^{\mu\alpha} = 2.57$ for $\mu = 0.30$ and an imposed contact angle $\alpha = \pi$. The discrepancy between experimental (and FEM) results and the Capstan model is due to the elasticity of the rods (bending, torsion, and stretching). Elastic deformation plays a major role in setting the local geometry of the contact region by affecting both the global shape of the rods, as well as the local deformation of the cross-section near the region of contact between the two rods.

X-RAY TOMOGRAPHY TO CHARACTERIZE THE CONTACT REGION

To investigate the mechanics of the frictional elastic clasp in more detail, we first experimentally characterize its geometry in the frictionless case. In this set of experiments, two rods are clamped at both of their ends and brought into mechanical contact by increasing the distance between the two supporting walls. Using state-of-the-art X-ray micro computed tomography (μCT) and mechanical tensile testing, we experimentally assess the geometry of this system at different levels of loading. A 3D-image processing algorithm developed in-house then allows us to quantify relevant geometric properties of the clasp, including the Cosserat frame of the rod and the local opening angle $\theta_{\mathrm{I,II}}$. The latter is defined as the angle described by the tangents of the centerline at the first and last contact point along the arc-length of either rod (rod I or II, see Figure 2-**A**). In Figure 2-**B**, we plot the results for the measured opening angle of the orthogonal clasp as a function of the dimensionless force applied at its ends, $f_y = 4F_y/\pi ED^2$, for different configurations (similar to the ones analyzed in the frictional case). As the vertical force applied by the two walls ($2F_y$) to the rod ends increases, the opening angle decreases for the pre-bent rods. Moreover, the strongly heterogeneous contact pressure map, computed using FEM (Figure 2-**C**), encodes information on how this contact region will lead to non-trivial frictional behavior.

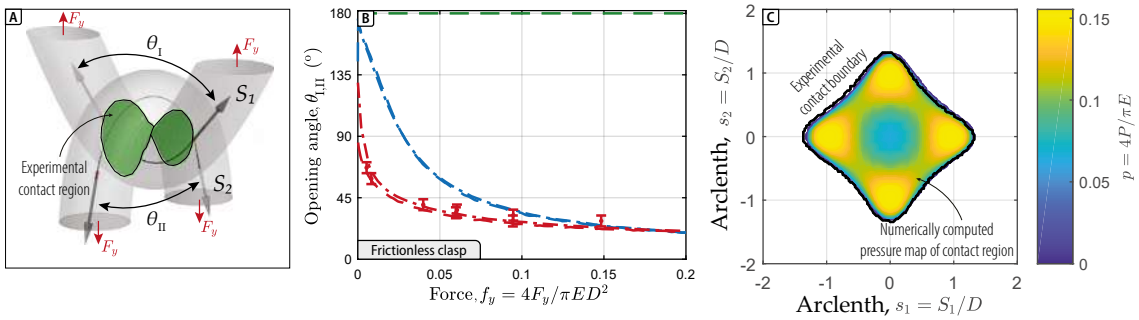

Figure 2: **Geometry of the contact region in an elastic clasp.** **A** – X-ray tomographic reconstruction of an experimental scan showing the centerline of the two rods (solid lines) and the contact surface (in green). **B** – Opening angle measured for different clasp configurations, the red (blue) curves correspond to rods of length $L = 60$ mm ($L = 160$ mm) clamped at their ends at a distance $W = 16$ mm, in contact with a rod either in this same configuration or with a rod whose ends are clamped further apart, at a distance $W = 0.7L$. The opening angle of one rod is almost unaffected by the configuration of the rod it is in contact with. Note that the green dashed line represents the opening angle of fiber kept straight (180°). **C** – FEM computed heterogeneous pressure map of a symmetric elastic clasp.

Modeling efforts are currently ongoing to study the influence of geometric reconfigurations of the contact region between two rods on the tension drop observed in this frictional clasp by adapting the modified capstan theory for elastic rods, as proposed by Jung *et al.* [4]. We believe such a fundamental understanding and characterization of the interplay between geometry, elasticity, and friction will help unravelling the behavior of more complex intricate filaments systems such as knots, knits, braids, and weaves.

References

[1] Maddocks J. H. and B. Keller J. B. Ropes in Equilibrium *SIAM Journal on Applied Mathematics* **47**: 1185–1200, 1987.

[2] Clauvelin N., Audoly B. and Neukirch S. Matched asymptotic expansions for twisted elastic knots: A self-contact problem with non-trivial contact topology. *Journal of the Mechanics and Physics of Solids* **57**: 524–534, 2009.

[3] Jawed M. K., Dieleman P., Audoly B. and Reis P. M. Untangling the Mechanics and Topology in the Frictional Response of Long Overhand Elastic Knots. *Physical Review Letters* **115** (11) 118302, 2015.

[4] Jung J. H., Ning Pan N. and Kang T. J. Generalized capstan problem: Bending rigidity, nonlinear friction, and extensibility effect. *Tribology International* **41**: 524–534, 2008.

ON THE ROLE OF THE INCOMPRESSIBILITY CONSTRAINT IN SOFT DIELECTRIC COMPOSITES

Valentina Volpini[1], Lorenzo Bardella*[2], and Massimiliano Gei†[3,4]
[1]Department of Engineering Enzo Ferrari, University of Modena and Reggio Emilia, Modena, Italy
[2]Department of Civil, Environmental, Architectural Engineering and Mathematics, University of Brescia, Brescia, Italy
[3]Department of Civil, Environmental and Mechanical Engineering, University of Trento, Trento, Italy
[4]School of Engineering, Cardiff University, Cardiff, UK

Summary In this work we demonstrate that the incompressibility constraint customarily adopted in literature to model soft dielectric composites may lead to incorrect predictions. In fact, although in these composites each phase may individually be assumed to be incompressible, for high-phase contrast in terms of elastic moduli the volumetric deformation of the softest phase can provide a non-negligible contribution to the effective behaviour. To reach our goal, we determine the effective electric response of a two-phase Dielectric Laminated Composite (DLC) actuator, whose softest phase is described by a constitutive law admitting volumetric deformation. Our results, discussed in the light of the limit case in which the softest phase consists of void, are expected to aid the design of high-performance hierarchical DLCs.

PROBLEM STATEMENT

We investigate the two-phase DLC actuator illustrated in Figure 1, which is built by repeating a unit cell constituted by an incompressible phase a and a considerably softer phase b, the latter being compressible. We describe the DLC effective behaviour in terms of the macroscopic deformation gradient $\mathbf{F}$ and the nominal electric field $\mathbf{E}$, along with their work-conjugate first Piola-Kirchhoff stress $\mathbf{S}$ and nominal electric displacement $\mathbf{D}$. All the microscopic fields and the material constants (such as the shear modulus μ and the electric permittivity ϵ) are indicated with the subscripts a and b, depending on the phase.

We assume the following free-energy density for the phase a, based on neo-Hookean hyperelasticity [1, 2]:

$$W_a = \frac{\mu_a}{2}\left[\mathrm{tr}(\mathbf{F}_a^{\mathrm{T}}\mathbf{F}_a) - 3\right] - \frac{\epsilon_a}{2}|\mathbf{F}_a^{-\mathrm{T}}\mathbf{E}_a|^2 \tag{1}$$

where tr and $^{\mathrm{T}}$ are the trace and transpose operators and $|\mathbf{v}|$ is the modulus of $\mathbf{v}$. For the phase b, we adopt the following *decoupled* free-energy density:

$$W_b = \frac{\mu_b}{2}\left(\frac{\mathrm{tr}(\mathbf{F}_b^{\mathrm{T}}\mathbf{F}_b)}{J_b^{2/3}} - 3\right) + \frac{K_b}{2}\left(\frac{J_b^2 - 1}{2} - \ln J_b\right) - \frac{\epsilon_b J_b}{2}|\mathbf{F}_b^{-\mathrm{T}}\mathbf{E}_b|^2 \tag{2}$$

in which $J_b = \det \mathbf{F}_b$ and K_b is the bulk modulus.

We consider a voltage-driven actuator subject to the following macroscopic boundary conditions. We apply increasing transverse nominal electric field $E_2 = \Delta\phi/h_0$ (see Figure 1), whereas we disregard edge effects, such that $E_1 = 0$. For what concerns the mechanics, we assume plane-strain and hamper macroscopic shear deformations, such that the sole non-vanishing components of $\mathbf{F}$ are the longitudinal stretch $F_{11} \equiv \lambda_1$, the transverse stretch F_{22}, and $F_{33} = 1$. Correspondingly, the effective direct stress components vanish, that is $S_{11} = 0$ and $S_{22} = 0$, while, in general, $S_{12} \neq 0$, $D_1 \neq 0$, $D_2 \neq 0$. We solve the problem by the homogenisation approach for hierarchical DLCs based on the continuity relationships holding at the interfaces [3, 1, 2, 4], assuming that the microscopic fields are spatially uniform in each phase.

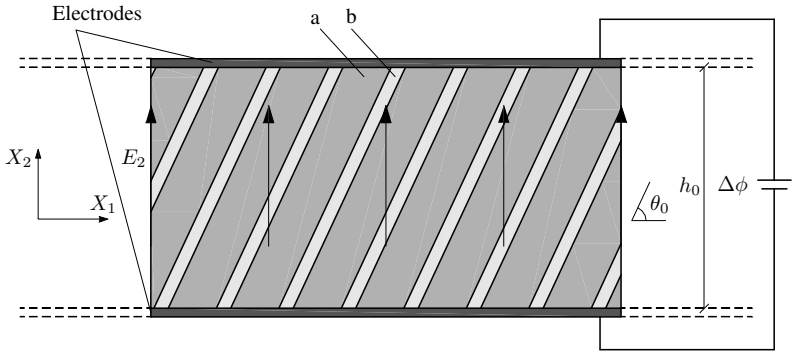

Figure 1: Geometric parameters of the DLC actuator consisting of incompressible phase a and compressible phase b. $\Delta\phi$ is the applied voltage drop across the electrodes, h_0 is the actuator thickness in the undeformed configuration, and θ_0 is the lamination angle.

*Corresponding author. E-mail: lorenzo.bardella@ing.unibs.it.
†Corresponding author. E-mail: geim@cardiff.ac.uk.

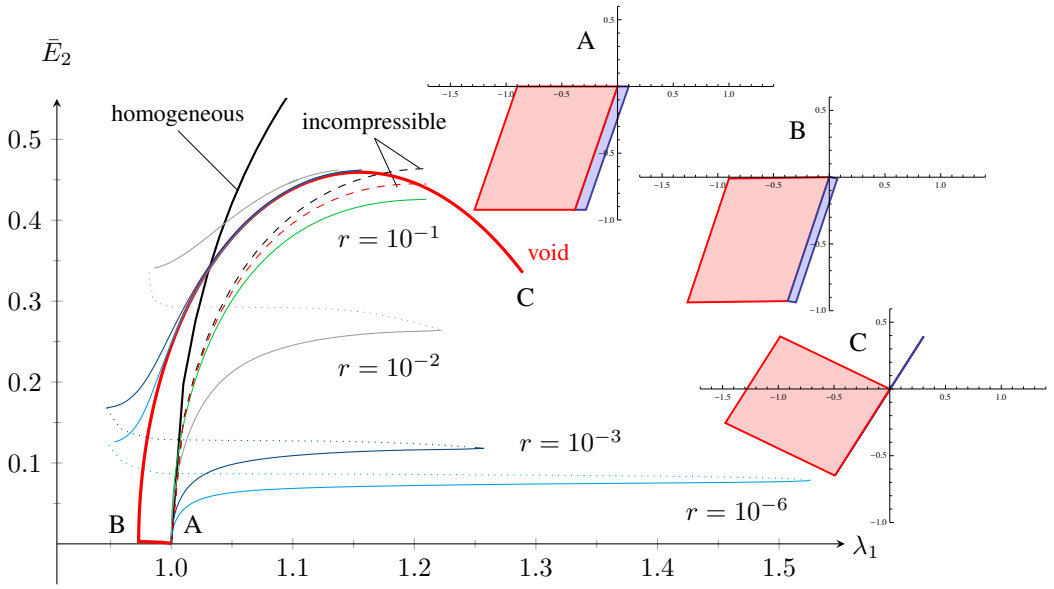

Figure 2: Performance of the compressible DLC actuator for varying $r = K_b/\mu_a$. Other parameters are $\theta_0 = 3\pi/8$, initial volume fraction of the compressible phase equal to 0.1, $\mu_a/\mu_b = 3 \times 10^3$, and $\epsilon_a/\epsilon_b = 10$. For the case in which phase b is void (red curves) we refer to $\mu_a = 10$ MPa and provide the configurations assumed by the two-phase unit cell at stages A (rest), B, and C.

RESULTS, DISCUSSION, AND PERSPECTIVES

Figure 2 illustrates the actuator response in terms of λ_1 as a function of the nondimensional electric field $\bar{E}_2 = E_2\sqrt{\epsilon_a/\mu_a}$, by varying the bulk modulus K_b through the ratio $r = K_b/\mu_a$. To discuss the results, we consider the case, referred to as the "limit case", in which the compressible phase b is void, for which the potential (2) has the electrostatic contribution only. In this case, we observe a behaviour characterised by three branches. The first branch (from A to B) is an initial *transient*, in which phase b suddenly shrinks whereas the continuity condition of stress at the interfaces cannot be properly satisfied. After this transient, a state of microscopically uniform *Cauchy* shear stress is reached all over the DLC. In this situation, holding up to the final stage C, all the electromechanical conditions are satisfied, as we can analytically prove. Our analysis also sets $\theta_0 = 3\pi/8$ as the lamination angle maximising J_b after the initial transient. After stage B, a second branch with increasing $\bar{E}_2$ follows, in which the DLC elongates as the result of local shear deformations and rotations. This branch ends with a maximum that we ascribe to the onset of a pull-in electromechanical instability. In the final branch $\bar{E}_2$ must decrease and the analysis ends when the phase b completely vanishes.

For a solid compressible phase b, the curves in Figure 2 share important features with the limit case, after an interesting high-performance branch. Then, in a transient response (dotted part of the curves), analogous to the first branch in the limit case, phase b largely shrinks while violating interface stress continuity. After this transient, the response approaches the limit case (from the left in Figure 2) for suitably small r. About the actuation response, for relative small r we observe an enhancement with respect to both the homogeneous DLC consisting of the sole phase a (black curve) and the incompressible DLC (black dashed curve), whose response is predicted through the effective potential obtained in [2]. Interestingly, the latter behaviour is very close to that of the incompressible DLC whose phase b is void (red dashed curve), which, in turn, is significantly different from the limit case, or any case with small r. This gives a clear indication that the incompressibility constraint in dielectric composites with large phase contrast should be cautiously adopted.

The foregoing results summarise those under publication in [5]. In this contribution we aim at further explaining the behaviour above by resorting to two strategies, towards relaxing the problem at hand and modelling actual hierarchical DLCs. First, we will consider imperfect interfaces. Second, we will allow the DLC to experience a non-vanishing macroscopic shear deformation F_{12}, to be constitutively related to the shear stress S_{12} through a linear law. Such a relation may, in fact, be particularised to both the case above and the case where one sets $S_{12} = 0$ to leave F_{12} free, for which, for any solid phase b, the obtained actuation responses continuously satisfy all the electromechanical conditions, being free from transients such as those reported above [5].

References

[1] Gei M., Springhetti R., Bortot E. Performance of soft dielectric laminated composites. *Smart Mater. Struct.* **22**: 104014, 2013.
[2] Spinelli S. A., Lopez-Pamies O. Some simple explicit results for the elastic dielectric properties and stability of layered composites. *Int. J. Eng. Sci.* **88**: 15-28, 2015.
[3] deBotton G. Transversely isotropic sequentially laminated composites in finite elasticity. *J.Mech. Phys. Solids* **53**: 1334-1361, 2005.
[4] Volpini V., Bardella L., Gei M. A note on the solution of the electro-elastic boundary-value problem for rank-two laminates at finite strains. *Meccanica* **54(13)**: 1971-1982, 2019.
[5] Volpini V. Analysis of sensing and actuation in electroactive soft composites. *PhD Thesis*, University of Brescia, Brescia, 2020.

SHAPE MORPHING VIA INFLATABLE ZIGZAGS

Tian Gao*[1],Emmanuel Siéfert[1],José Bico[1],Etienne Reyssat[1],Benoît Roman[1],and Antonio De Simone[2,3]
[1]Physique et Mécanique des Milieux Hétérogènes (PMMH),ESPCI Paris,PSL University,CNRS,Sorbonne Universités,Université de Paris,75005Paris,France
[2]MathLab, SISSA-International School for Advanced Studies, 34136 Trieste, Italy
[3]The Biorobotics Institute, Scuola Superiore Sant'Anna, 56127 Pisa, Italy

Summary Zigzags structures are found in a wide variety of fields. For instance, the future leaves of hornbeam are folded in the buds into zigzagging features that deploy as the leaves grow. This natural example has been the source of inspiration to develop origami designs. Here, we present a novel strategy where inextensible thin patches are sealed along zigzag paths to generate complex shape transformation under applied pressure. We investigate the change in metrics induced by the inflation of these paths and the consequent transformation of the initially flat patches into 3D structures. We also study the case of asymmetric zigzags, which leads to a rotation of the average deformation tensor and widens the routes for reverse-engineering. We finally propose a theoretical model based on zigzagging paths to program the deployment of flat sheets into 3D shapes.

INTRODUCTION

The concept of shape morphing has received great attention in a range of fields from dynamic optics, tissue engineering, aeronautics to soft robotics. Although inspired by biological morphogenesis, programming shapes from 2-dimensional (2D) to 3-dimensional (3D) is essentially a geometrical challenge. More specifically, one needs to control the metric tensor at every point to define the target Gaussian curvatures. From a physical standpoint, shape transformation requires materials to modify intrinsically their geometry in reponse to external stimuli, such as chemical swelling, dielectric elastomers, liquid crystal elastomers or magnetic responsive materials. In our previous research, we introduce **baromorph** [1] as a pneumatic shape-morphing structure made of stretchable material which encodes the target 3D shape by embedding a specific network of airways. Here, we provide a new platform by writing zigzags on quasi-inextensible thin sheets, along with an inverse problem model.

EXPERIMENT AND MECHANISM

This inflatable structure is primarily made of two superimposed thermoplastic sheets that are sealed together along a zigzag path. A soldering iron mounted on an XY-plotter or a CNC-machine directly "writes" heat-sealed zigzag seams on the two superimposed sheets (Fig.1(a)) [2]. Zigzags are characterized by their angle θ_0 at rest (Fig. 1(c)). Inflating these flat "zigzags" involves contraction of the material both along and perpendicular to the average zigzag direction (Fig. 1(b)(c)). Indeed, in the case $\theta_0 = 0$ (no zigzags),the contraction is purely perpendicular, whereas for large angles $\theta_0 \simeq \pi/2$, contraction occurs mostly along the zigzag direction. Fig.1(d) shows the quantitative agreement between the experimental measurements and the theoretical prediction for the typical contraction rate $\bar{\lambda} = 0.77$. It is interesting to notice that changing the angle of the zigzags does not impact the overall area contraction upon inflation, which remains equal to $\bar{\lambda}$.

INVERSE PROBLEM AND RESULTS

We are interested in inducing controlled changes of the shape of the material surface by generating changes of lengths and angles of its material fibers through actuation, described by changes of the metric tensor from its reference value g_0 to a new value g. The possibility of changing the curvature (morphing) of a surface by acting on its metric relies on a remarkable theorem by Gauss, the celebrated *theorema egregium*, stating that the Gaussian curvature K of a surface (the product of its principal curvatures) can be computed by differentiating the components of its metric tensor. The interpretation of Gauss' theorem as a morphing scheme has been suggested in the pioneering work of Klein et al. (2007) [3]. This approach has been exploited in Arroyo et al. (2012) [4]; Arroyo and DeSimone (2014) [5]; to model shape-shifting envelopes of unicellular organisms, and we follow the approach of these papers closely.

Let us consider a stretch with principal directions along the coordinate lines

$$g = \begin{bmatrix} \lambda^2 & 0 \\ 0 & \mu^2 \end{bmatrix} \tag{1}$$

where $\lambda = \lambda(u,v) \in (0,+\infty)$ and $\mu = \mu(u,v) \in (0,+\infty)$ are the stretches along the $u-$ and $v-$ coordinate lines, respectively. By setting $\lambda\mu = \bar{\lambda}$ (fixed area ratio), we obtain after some calculations

$$K = -\frac{1}{\bar{\lambda}^2}((\lambda\lambda_{,v})_{,v} + (\mu\mu_{,u})_{,u}) \quad (\lambda\mu = \bar{\lambda}) \tag{2}$$

Experimental realisations of structures of constant positive and constant negative GC may be found in Fig. 2.

*Corresponding author. E-mail: tian.gao@espci.fr

THEMATIC SESSION SM

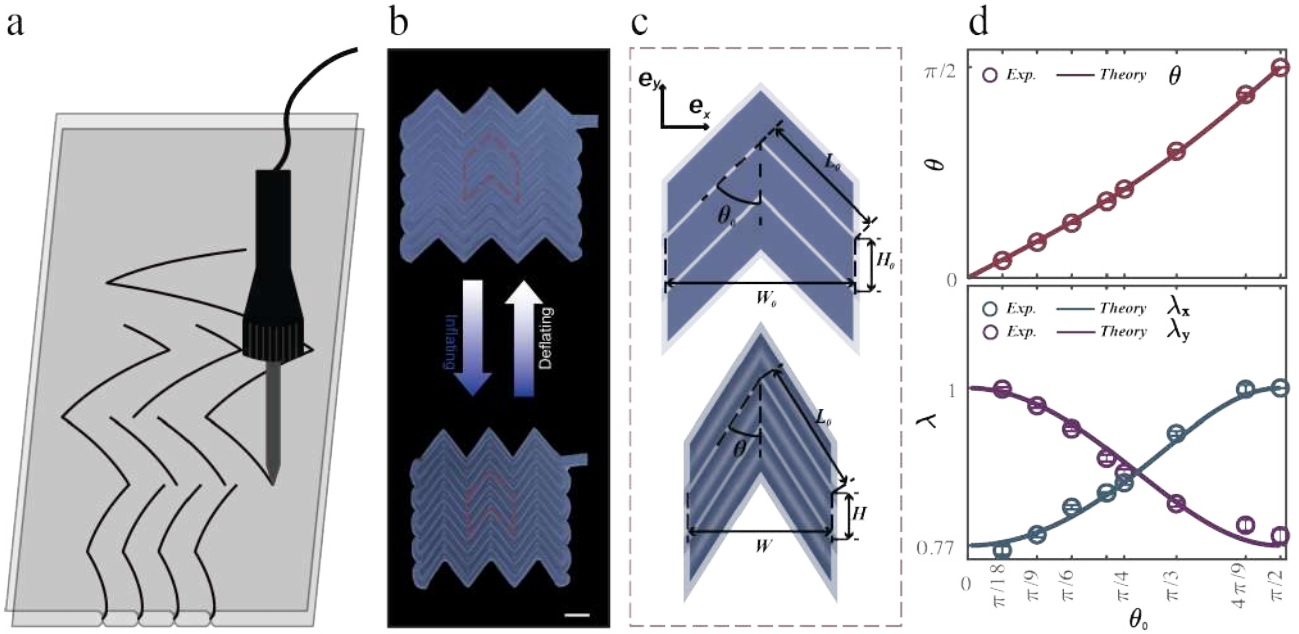

Figure 1: Fabrication and deformation of inflated zigzag patterns. (a) A soldering iron is mounted on an XY-plotter and writes "zigzags" on two superimposed flat heat-sealable sheets. (b) Photo of a sheet with zigzags of original angle $\theta_0 = \pi/4$ at rest. Upon inflation, the contraction perpendicular to the seam lines induces the sharpening of the angle.(Scale bar, 20 mm.) (c) Schematic of the mechanism: change in angle and distances along and perpendicular to the zigzags. (d) Angle θ in the inflated state and principal stretches parallel (λ_x) and perpendicular (λ_y) to the zigzag direction measured experimentally as a function of the original angle θ_0. The solid line corresponds to the theoretical model.

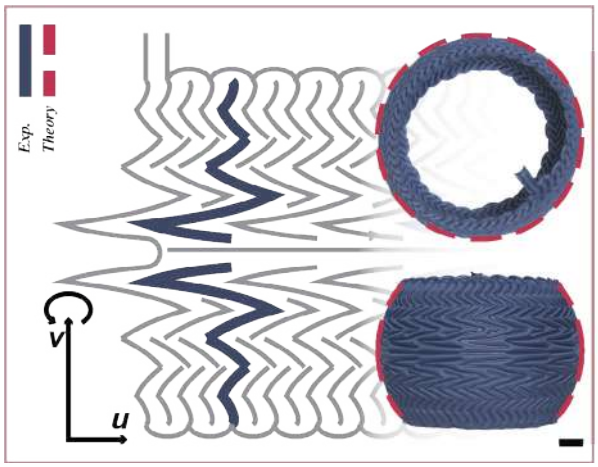

Figure 2: Programmable *Gaussian Curvatures* from writing "zigzags". A part of sphere: the Gaussian Curvature here is positive and constant. The pattern in the background is the "zigzag" path used on heat-sealable sheets to program the deployed shape. Solid and dashed lines respectively correspond to experimental realisation and theoretical model (Scale bar, 20 mm.)

References

[1] E. Siéfert, E. Reyssat, J. Bico, B. Roman. Bio-inspired pneumatic shape-morphing elastomers. *Nat. Mater.* **18**: 24–28, 2019.

[2] E. Siéfert, E. Reyssat, J. Bico, B. Roman. Programming curvilinear paths of flat inflatables. *Proc. Nat. Acad. Sciences USA* **116**: 16692-16696, 2019.

[3] Klein, Y., Efrati, E., Sharon, E. Shaping of elastic sheets by prescription of non-Euclidean metrics. *Science* **315**: 1116-1120, 2007.

[4] Arroyo, M., Milan, D., Heltai, L., DeSimone, A. Reverse engineering the euglenoid movement. *Proc. Nat. Acad. Sciences USA* **109**: 17874-17879, 2012.

[5] Arroyo, M., DeSimone, A. Shape control of active surfaces inspired by the movement of euglenids.*J. Mech. Physics Solids* **62**: 99-112, 2014.

PIERCING SOFT SOLIDS: A MECHANICAL THEORY FOR SURFACE RUPTURE

Stefano Fregonese[1], Mattia Bacca[1]
[1]Department of Mechanical Engineering, University of British Columbia, Vancouver, Canada

Summary The determination of the critical force to be applied to a needle in order to pierce a soft material is key in order to improve surgical technology (e.g. robotic surgery), manufacturing (food processing) and in-situ material characterization. Previous investigations unravelled the force required in order to deeply penetrate a soft rubber once the needle is already inserted but did not determine the critical force for needle insertion (the piercing force creating surface rupture). Recent investigations proposed a phenomenological analysis for the determination of such force based on experimental observations but without providing a quantitative mechanical theory to support their conclusions. We propose a mechanistic theory based on energetic analysis to finally obtain a quantitative prediction of the critical piercing force based on needle geometry and material behaviour.

INTRODUCTION

The deep penetration of a soft solid by a punch is of widespread technological importance, with application for robotic surgery, piercing the skin by needling and injection of liquid, penetration of rubber packaging and food processing. Despite the luck of standardization, there are many industries in which the mechanism of surface rupture plays an important role and affects not only the cutting process but often has a direct influence on human life. Applications such as measuring mechanical properties of biological tissue are of technological importance for remote robotic surgery, where the needs of having in situ measurements are fundamental. Robotic control of deformable objects is a topic of increasing importance in the textile, medical and food processing domains. However, the interaction with deformable materials remains unsolved issue principally due to the variability in mechanical behaviour. Previous attempts to solve this issue have generated some partially complete solutions [1-2] and empirical data [3]. We propose here a simple mechanical theory to finally calculate the critical force and depth to rupture a soft material via needle insertion.

MECHANICAL THEORY

We propose here an energetic approach to quantify the critical rupture force and penetration depth of a soft material by needle insertion. The method is based on an energetic comparison between two distinct configurations in the system: (i) Deep indentation and (ii) deep penetration. The former considers the needle to be pushed against the free surface of the material without any penetration, while the latter considers the needle is already inserted in the material. Take d to be the depth at which the needle is being pushed toward the free surface of the material from an initial state of zero force applied and the tip of the needle touching the free surface. Both configurations are characterized by a force applied to the back of the needle $F_i(d)$, and $F_{ii}(d)$ ($F(0) = 0$ in both cases), and the mechanical work required to reach the depth d in both configurations is $w_i(d) = \int_0^d F_i(d)\delta d$ and $w_{ii}(d) = \int_0^d F_{ii}(d)\delta d$.

Surface rupture occurs when d reaches the critical depth d_c. At $d < d_c$, we have $w_i(d) < w_{ii}(d)$, *i.e.* deep indentation requires less mechanical work, hence configuration (i) is favoured. Conversely, for $d \geq d_c$, we have $w_i(d) \geq w_{ii}(d)$, giving configuration (ii) to be energetically favoured, hence promptings surface rupture.

Our model system considers a needle of cylindrical shape with a spherical tip (Figure 1).

Deep indentation

We calculate the indentation energy via finite element analysis (FEA). The mechanical behaviour of the material is described with a single term Ogden strain energy density

$$u(\lambda_1, \lambda_2, \lambda_3) = \frac{\mu}{\alpha}(\lambda_1^\alpha + \lambda_2^\alpha + \lambda_3^\alpha - 3) \quad (1)$$

with λ_1, λ_2 and λ_3 the principal stretches, $2\mu = \alpha\mu$ the shear modulus of the material and α a dimensionless material parameter. $F_i(d)$ is expressed in dimensionless form as a Taylor expansion around the resting condition $F_i(0) = 0$, as

$$\frac{F_i(d)}{\mu R^2} = \sum_{k=1}^{n} a_k \left(\frac{d}{R}\right)^k \quad (2)$$

with R the radius of the needle (see Figure 1*a*), a_k the Taylor series coefficients, and n the number of terms of the series needed to fit the results obtained with FEA. From Eq. (2) the mechanical work due to deep penetration, in dimensionless form, is then

$$\frac{w_i(d)}{\mu R^3} = \sum_{k=1}^{n} \frac{a_k}{k+1} \left(\frac{d}{R}\right)^{k+1} \quad (3)$$

*Stefano Fregonese. E-mail: fregonese.stefano88@gmail.com.

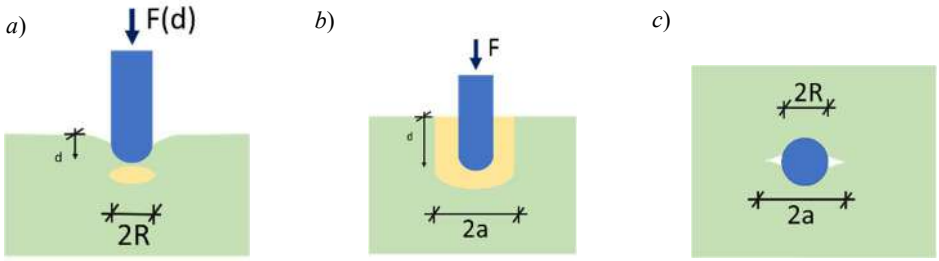

Figure 1: *a*) Deep indentation (i), side view; *b*) Deep penetration (ii), side view; *c*) Deep penetration (ii), top view

Deep penetration

The mechanical work due to deep penetration is calculated from two energetic contributions: (1) the work of fracture; (2) the work of spacing [1-2]. The former is the work done to the material to create a fracture-slit capable of allocating needle penetration and is done via rupture of molecular bonds in the material (see Figure 1*b*). The latter is the work done to the material to space it in order to accommodate the presence of the needle (see Figure 1c). We have then $w_{ii}(d) = w_{(1)}(d) + w_{(2)}(d)$, with

$$\frac{w_{(1)}(d)}{\mu R^3} = 2\left(\frac{G_c}{\mu R}\right)\left(\frac{a}{R}\right)\left(\frac{d}{R}\right) \qquad (4a)$$

$$\frac{w_{(2)}(d)}{\mu R^3} = h(a/R)\frac{d}{R} \qquad (4b)$$

where G_c is the toughness of the material, a is the size of the fracture-slit (Figure 1*b-c*) and $h(a/R)$ is a dimensionless spacing-function [1]. Both $h(a/R)$ and a are calculated from FEA as a function of the dimensionless term $G_c/\mu R$. The surface rupture condition $w_i(d_c) = w_{ii}(d_c)$ to obtain d_c and then the critical force $F_c = F_i(d_c)$ for surface rupture is finally calculated numerically from Eq. (2-4).

RESULTS

We adapted our theory to calculate the critical force F_c and depth d_c needed to puncture a gel ($\mu = 7{,}2kPa, G_{IC} = 25N/m$), and compared our predictions with experiments [3], as shown in Figure 2.

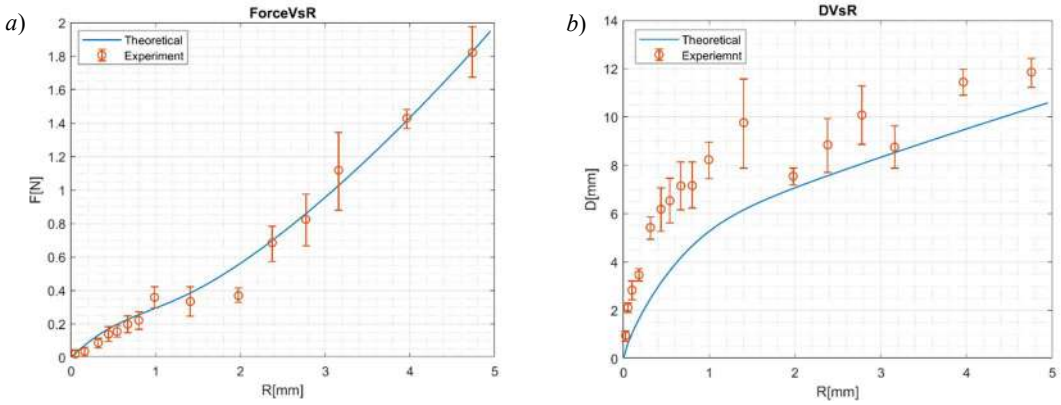

Figure 2: Surface rupture conditions, theory (blue lines) versus experiments (orange circles) [3]: *a*) Critical force for surface rupture F_c; *b*) Critical depth d_c

DISCUSSION AND CONCLUSIONS

From Figure 2, we can conclude that our theory provides quantitative agreement with the experiments in predicting the critical force, F_c, and qualitative agreement in predicting the critical depth, d_c. In Figure 2*b*, it can be seen that our model underestimates the experiments for smaller R, where d_c/R is larger. The material behavior is described with the simple Eq. (1), thus a loss of accuracy is expected for larger d_c/R. We expect an improvement in accuracy in Figure 2*b* from the use of more sophisticated models in replacement of Eq. (1).

References

[1] O. A. Shergold, N. A. Fleck, Experimental Investigation into the Deep Penetration of Soft Solids by Sharp and Blunt Punches, With Application to the Piercing of Skin. ASME, 838 / Vol. 127, 2005.

[2] O. A. Shergold, N. A. Fleck, Mechanisms of deep penetration of soft solids, with application to the injection and wounding of skin. *The royal society.* **460, 3037–3058**, 2004.

[3] S. Fakhuri, S. B. Shelby, A. J. Crosby, Puncture mechanics of soft solids. *Soft Matter, 2015, 11, 4723--4730*, 2015.

SIMULATING COMPLIANT CREASES, CONTACT, AND THICKNESS IN ORIGAMI

Yi Zhu[1], and Evgueni Filipov[1]
[1]Department of Civil and Environmental Engineering, University of Michigan, Ann Arbor, MI

Summary This work presents a set of recent advancements in mechanical modelling of deformable origami structures. We use a bar and hinge model where bars represent in-plane stiffness of the thin sheet while rotational hinges represent bending stiffness of the sheet and the prescribed fold lines. First, we introduce a modification that allows the model to simulate compliant creases with a non-negligible width. This modification is important for capturing the true geometry of the origami system, and for better approximating the crease flexibility for extensional and torsional deformation modes. Next, we introduce a model that can detect contact within the origami, initiate and disengage contact interactions, prevent penetration of the thin sheet panels, and provide force continuity for the mechanical simulation. When combined with the compliant crease modification, this contact model can also mimic the effects of thickness in origami structures. These bar and hinge derived models use a sparse nodal representation of the origami which makes them computationally efficient and versatile for simulating a vast assortment of origami geometries. These advancements in mechanical modelling are important for simulating the geometry, self-assembly, bistability, contacts, and resulting mechanical behaviours in origami structures.

INTRODUCTION

The principles of folding thin sheets into origami have inspired a variety of practical engineering applications ranging from metamaterials and medical robotics, to deployable space structures and adaptable architectures. Advantages of these systems include self-assembly from flat sheets, compact stowing and deployment, geometric reconfiguration, tuneable mechanical properties, and more. Over the past decade, a bar and hinge based modelling approach emerged as a convenient, efficient, and versatile method for simulating the geometric, kinematic, and mechanical characteristics of origami structures [1-3]. In contrast to discretized finite element methods, each flat panel of the origami is approximated only with several bars and rotational hinges. This sparsity makes the model efficient and generally appropriate for estimating the global mechanics of the origami which are highly dependent on the system geometry. This work enhances the capability of bar and hinge models by enabling the simulation of compliant creases, contact and thickness.

COMPLIANT CREASE MODIFICATION

Many origami-inspired structures do not have a discrete hinge element (concentrated along a line), but instead have a flexible and compliant crease region where distributed folding occurs (Figure 1). These compliant regions, are especially common in micro fabricated structures, where the compliant crease also often acts as an active actuator that is used to accomplish the folding of the origami. This compliant crease region is important for the final folded geometry of the origami [4] and can be responsible for bistable behaviours in the system [5]. We discretize the compliant crease region by adding new bar and hinge elements as shown in Figure 1(a). The axial stiffness of the bar elements was derived based on plate theory, while the bending stiffness of the hinge elements was derived based on a pseudo-rigid-body model. These formulations were verified using a finite element simulation that captures the full mechanical behaviour of the origami [6-7]. The bar and hinge approximation performs well for tension, shear, bending (both small and large deformations), and torsion of the compliant crease. The proposed model produces the best estimate of structural stiffness when the crease aspect ratio is $\alpha \approx 0.1$ and the panel thickness ratio is $\beta \approx 3.0$. These ratios are representative of real origami systems with compliant creases. When the compliant creases are modeled appropriatley, the bar and hinge model can better approximate the final folding geometries and mechanical behaviors of the origami [6-7].

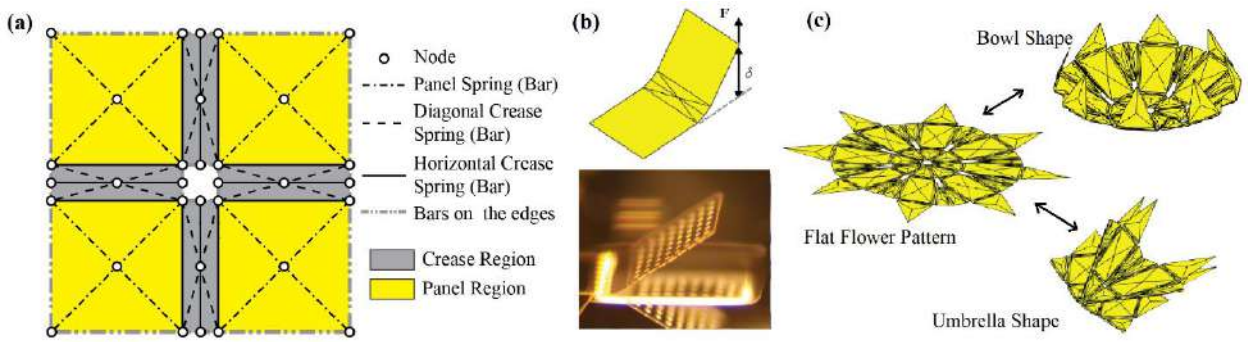

Figure 1. (a) An origami vertex discretized with compliant crease regions. Additional bars and rotational hinges can better capture the geometry and deformations of the crease. (b) A compliant crease model with a similar shape to electro-thermally activated micro-origami fabricated in our laboratory. (c) Possible folding of complex shapes with compliant hinges. All images are from [6].

CONTACT MODEL

The presence of self-contact within origami patterns has been difficult to simulate, yet it has significant implications on the foldability, kinematics and resulting mechanical properties of the final origami system. We present a contact model

that is based on the principle of stationary potential energy and assumes that the contact forces are conserved. The contact potential is formulated to approach infinity as the distance d between the contacting panel and node approaches zero:

$$\Pi(d(\boldsymbol{x})) = \begin{cases} k_e \left\{ \ln\left[\sec\left(\frac{\pi}{2} - \frac{\pi d}{2d_0}\right)\right] - \frac{1}{2}\left(\frac{\pi}{2} - \frac{\pi d}{2d_0}\right)^2 \right\}, & (d \le d_0) \\ 0 & (d > d_0) \end{cases},$$

where d_0 is the contact threshold distance, and k_e is a constant used to scale the magnitude of the potential. The corresponding internal force vector is calculated by taking the gradient of the potential, and the stiffness matrix is calculated from the Hessian of the potential. In our recent paper [8], we verified that this contact model (1) produces a continuous force field; (2) prevents penetration by giving infinite forces and stiffness as d approaches zero; and (3) has a piecewise formulation that allows initiation and disengagement of contact. To implement contact detection into the bar and hinge model we do a double loop over all flat panels and nodes, to determine the distances and initiate contact as necessary. Self-assembly or mechanical loading of the system is done incrementally [3], and the potential energy can successfully capture contact when it occurs (Figure 2). Contact within origami systems often leads to locking and stiffening of the structure, which is also approximated with the simplified bar and hinge model. When the contact model is implemented with compliant creases, we can set d_0 to be the thickness of the panels and k_e to be a relatively large value; as such the model effectively mimics the thickness of the origami panels as shown in Figure 3.

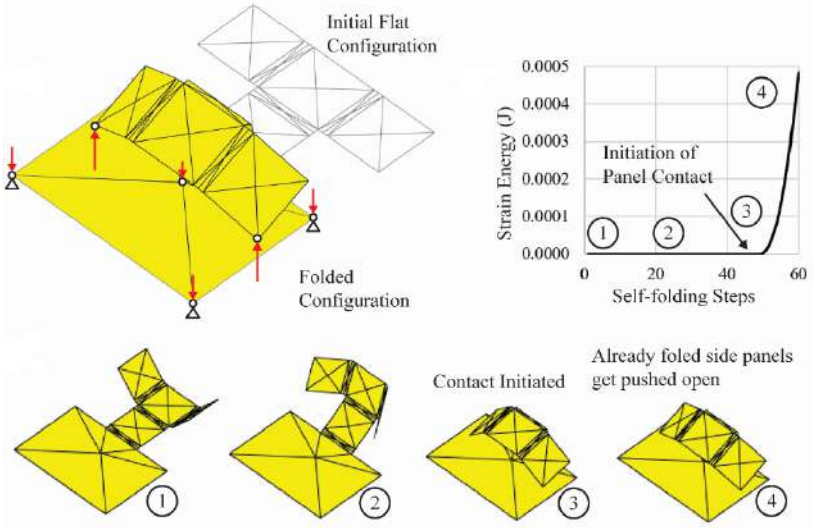

Figure 2. Self-assembly of an origami that experience self-contact during the folding sequence. This contact creates strain energy in the system. Images are from [8].

CONCLUDING REMARKS

This work presents a new method for simulating compliant creases, contact, and thickness in origami-inspired structures. Capturing these effects is important for better approximating the folded geometry, and predicting the mechanical characteristics of thin deformable sheets. The existence of compliant hinges can allow for bistable behaviours in the origami, and can allow for more complex geometries to be folded. The new contact model can evaluate if the folding of an origami pattern will be influenced by contact, and can capture relevant mechanical behaviours in the structure after contact occurs. These simulation approaches can enable the advanced study and design of new origami inspired structures and metamaterials with advanced mechanical properties and functionality.

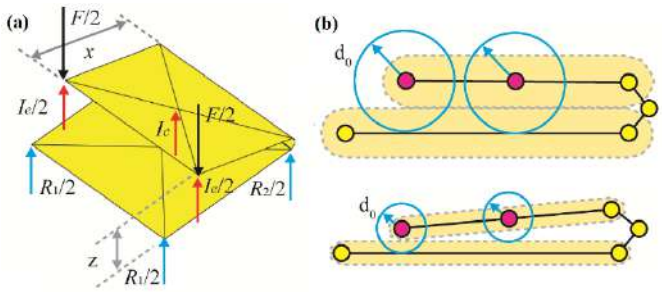

Figure 3. When the contact model is used with the compliant creases, it is possible to mimic thickness in the origami. A single crease shown in (a) isometric, and (b) side views with different d_0. Images are from [8].

References

[1] Schenk M., and Guest S.D. (2010) "Origami Folding: A Structural Engineering Approach," *In Origami5,Proceedings of 5OSME* pp. 293–305 Singapore.

[2] Filipov E.T., Liu K., Tachi T., Schenk M., Paulino G.H. (2017) "Bar and Hinge models for Scalable Analysis of Origami," *International Journal of Solids and Structures*. Vol. 124 No. 1 pp. 26-45. (DOI: https://doi.org/10.1016/j.ijsolstr.2017.05.028)

[3] Liu K., and Paulino G.H., (2017) "Nonlinear mechanics of non-rigid origami: an efficient computational approach." *Proceedings of Royal Society - A* Vol. 473, No. 2206. (DOI: https://doi.org/10.1098/rspa.2017.0348)

[4] Hernandez E.P., Hartl D.J., Akleman E., and Lagoudas D.C., (2016) "Modeling and analysis of origami structures with smooth folds," *Computer-Aided Design* Vol. 78, pp. 93–106. (DOI: https://doi.org/10.1016/j.cad.2016.05.010)

[5] Faber J., Arrieta, A.F., and Studart, A.R., (2018), "Bioinspired Spring Origami", *Science*, Vol. 359, No.6382, pp.1386,1391. (DOI: https://doi.org/0.1126/science.aap7753)

[6] Zhu Y., Filipov E.T. (2019) "Simulating Compliant Crease Origami with a Bar and Hinge Model," *ASME 2019 IDETC Conference*. Aug 18-21, Anaheim, CA, USA. (DOI: https://doi.org/10.1115/DETC2019-97119)

[7] Zhu Y., Filipov E.T. 2020. "A Bar and Hinge Model for Simulating Bistability in Origami Structures with Compliant Creases," *Journal of Mechanisms and Robotics*. (In Press) (DOI: https://doi.org/10.1115/1.4045955)

[8] Zhu Y., Filipov E.T. (2019). "An Efficient Numerical Approach for Simulating Contact in Origami Assemblages," *Proceedings of the Royal Society - A*. Vol. 475 No. 2230. (DOI:https://doi.org/10.1098/rspa.2019.0366)

A HIGHLY STRETCHABLE MAGNETIC DOUBLE-NETWORK COMPOSITE

Xiangchao Feng[1], Zhuo Ma[2], and Wei Hong[3]
[1]Qian Xuesen Laboratory of Space Technology, Beijing, China
[2]Department of Aerospace Engineering, Iowa State University, Ames,USA
[3]Department of Aerospace Engineering, Southern University of Science and Technology, Shenzhen,China

Summary This paper presents the manufacturing and testing results of a magnetic double network composite, consisting of permanent magnet chains and polymer matrix. The initially connected permanent magnet chains were used as sacrificial and reconnecting components in the composite. The strength of the composite was limited by the magnetic attractions while the maximum stretch was limit by the stretchability of the matrix. The composite was significantly tougher than either of the constituents. A one-dimensional model is developed to examine the mechanical and the damage distribution and energy dissipation process of DN magnetic composite. To further study the property and fracture toughness of the DN magnetic composite, a quasi-static, two-dimensional phase-field model of fracture are developed. Simulations have shown that an effective fracture energy one order of magnitude higher than the base polymer material.

INTRODUCTION

Double-network (DN) gels and elastomers have been of great interest to researchers in the last decades for their superior mechanical characteristics including both high strength and high toughness [1]. The desirable features endow DN gels and elastomers with applications in various areas[1-4]. Inspired by the salient self-healing capabilities of the ionic crosslinks in the tough gels, we designed and tested a magnetic DN composite capable of large and recoverable deformation in this work. In analogy to the reversible ionic crosslinks in self-healing hydrogels [5-6], permanent magnets were used as the sacrificial and reconnecting components in the composite. The strength of the composite was limited by the magnetic attractions while the maximum stretch was limit by the stretchability of the matrix. The composite was significantly tougher than either of the constituents. Upon unloading, the magnetic attraction between neighboring magnetics held them back again and the composite's stiffness and strength were fully recovered. To better understand the mechanical properties of the magnetic DN composite, a quasi-static continuum model is developed to study the damage distribution and energy dissipation process. The model predicts the stress-strain relation of the magnetic DN composite with various magnetic lattice compositions in the uniaxial tension test; the results agree well with experimental results.

EXPERIMENTATION

The magnetic DN composite samples were prepared by first pouring the well-mixed Polydimethylsiloxane (PDMS, WACKER SILICONES) precursor solution around the chains of cylindrical permanent magnets of two different sizes (φ4mm×10mm, φ2mm×1mm) inside rectangular molds. Once fully cured, the PDMS-magnet samples were removed from the molds for testing. The mechanical tests were carried out with an Instron 5960 dual column testing system. Each sample was held vertically by metallic grips with the magnetic chains aligned in the loading axis.

RESULTS AND DISCUSSION

A typical force–extension curve of a PDMS-magnetic DN composite subjected to uniaxial tension is shown in Fig.1(a), together with the reference curves measured from the base materials. Corresponding to the stress plateau in stage II was the coexistence of two phases: a partially damaged phase with separated magnet links and an intact phase with connected magnet links, as shown by the insets of Fig.1(a). Over the stress plateau, further stretch was manifested by the growth of the partially damaged zones at the expense of the intact magnetic links. Stage II continued until all the magnets were separated. In stage III, deformation was accompanied by further stretching of the matrix and sliding between the magnets and the matrix. The force needed to separate two magnets is much higher than the force two highly-separated magnets require to snap together. Such an asymmetry between loading and unloading results in a hysteresis over the stress-strain curve Fig.1(b). When reloaded, the nominal stress plateaued at the same level as in previous cycles， indicating that both the stiffness and the strength of the composite were recovered. The total free energy stored in the magnetic DN composite may be divided into two parts: the energy stored in the permanent magnets W_m and the energy stored in the polymer matrix W_e . The energy stored in the permanent magnets attenuates quickly as the inter-particle distance increases. The second network is stretchable and will hold the integrity of structure. We write the free energy density function to include three contributing terms:

$$W = W_{\mathrm{m}} + \mathrm{g}(\phi)W_e + W_d[1 - g(\phi)] + \frac{\kappa}{2}(\nabla\phi)^2 \qquad (1)$$

The third term on the right-hand side of Eq. (1) represents the energy associated with material damage. When the strain energy at a material particle exceeds the threshold W_d, the damaged state with $\phi = 0$ becomes energetically favorable. The gradient energy term is added to regulate the transition between the coexisting states.

In the fracture tests of pre-cracked sample, as shown by Fig.2., a large process zone formed near the crack tip by fragmenting the connected magnet chains to resist crack propagation. The local deformation and damage fields of representative results in 2D energy snapshots are shown in Fig.2. In the process zone, the initial damage pattern propagates in the shear band direction before reflected by boundary, the fracture process zone encompasses the entire

sample prior to the crack propagation. In the second stage, the crack tip in polymer matrix propagates, and the cracks advances.

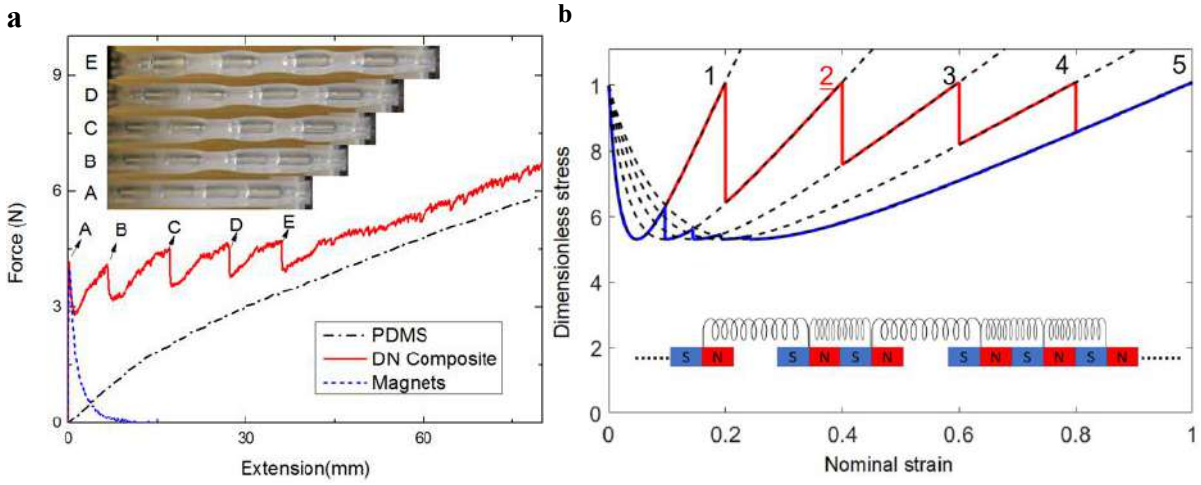

Figure 1. (a)Force-Extension curves of PDMS-Magnets composite, and DN composite with single chain of magnets. The insets A–E are the snapshots of the sample corresponding to the specific points along the loading curves. Over the stress plateau (A-E), partially damaged regions coexisted with the undamaged regions, and the extension was accompanied by the growth of the "damaged" regions. (b). Theoretical dimensionless stress-strain curves of one DN composite for case when 1,2,3,4 and 5 pairs of magnets are separated and reconnect. The sketch of magnets chain in bottom was indicate 2 unit cells are open.

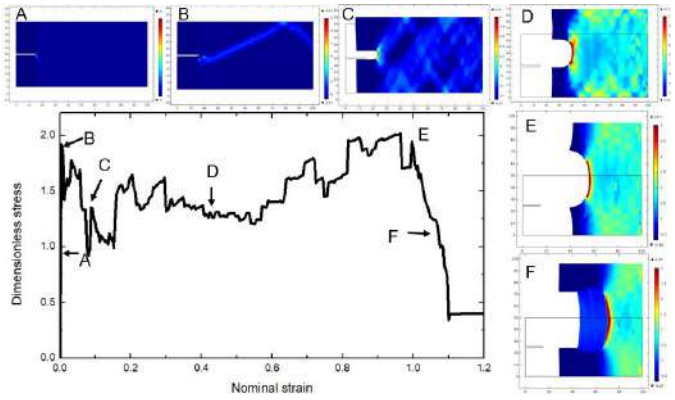

Figure 2. A typical dimensionless stress-strain curve of magnetic DN composites under fracture test. The insets A-F are the snapshots corresponding to the specific points along the loading curves. The color scale shows the nominal free energy density. Over the stress plateau (B-E), partially damaged regions coexisted with the undamaged regions, and the stretch was accompanied by the growth of the damaged regions. The snapshot E is taken at the moment before the crack starts to propagate. The snapshots F were captured during the crack propagation.

CONCLUSIONS

In analogy to the reversible ionic crosslinks in self-healing hydrogels, permanent magnets were used as the sacrificial and reconnecting components in the DN composite. We designed and tested a magnetic DN composite capable of large and recoverable deformation in this work. The theoretical model predicts the stress-strain relation of the magnetic DN composite with various magnetic lattice compositions in the uniaxial tension test; the results agree will with experimental results. Through visualizing the damage evolution, it may provide insights towards further understanding the toughening mechanism and optimizing of magnetic DN composites for enhanced properties.

References

[1] Gong, J.P., Katsuyama, Y., Kurokawa, T. and Osada, Y., 2003. Double-network hydrogels with extremely high mechanical strength. *Advanced Materials*, *15*(14), pp.1155-1158.

[2] Keplinger, C., Sun, J. Y., Foo, C. C., Rothemund, P., Whitesides, G. M., & Suo, Z. (2013). Stretchable, transparent, ionic conductors. Science, 341(6149), 984-987.

[3] Gong, Jian Ping. "Materials both tough and soft." Science 344.6180 (2014): 161-162.

[4] Sun, T. L., Luo, F., Kurokawa, T., Karobi, S. N., Nakajima, T., & Gong, J. P. (2015). Molecular structure of self-healing polyampholyte hydrogels analyzed from tensile behaviors. Soft matter, 11(48), 9355-9366.

[5] Sun, Jeong-Yun, et al. "Highly stretchable and tough hydrogels." Nature 489.7414 (2012): 133.

[6] Ducrot, Etienne, et al. "Toughening elastomers with sacrificial bonds and watching them break." Science 344.6180 (2014): 186-189.

THE INTRINSIC APPROACH IN LIQUID CRYSTALS: COMPATIBILITY, FRUSTRATED PHASES, AND INVERSE DESIGN PROBLEMS.

Efi Efrati[1]
[1]Department of Physics of Complex Systems, Weizmann Institute of Science, Rehovot, Israel

Summary :
Unlike Lego bricks that perfectly assemble next to one another, in many molecular assemblies and modern applications of responsive materials some misfit is almost always present. The constituents of such structures must distort in order to fit next to one another resulting in geometrically frustrated structures that possess no stress-free rest state. The elastic behavior of such structures is thus best described through local intrinsic geometric quantities such as their metric. In this talk, I will discuss the notion of compatibility, geometric frustration and the intrinsic approach as it arises in two-dimensional liquid crystals. I will show that the intrinsic approach does not only accurately describe frustrated states but also allows us to solve inverse design problems that were previously inaccessible analytically.

Geometrically Frustrated Assemblies

Geometrically frustrated assemblies are structures comprised of ill-fitting building blocks, typically possessing two or more mutually contradicting geometric tendencies.[1] Such structures lack a stress free rest state precluding the use of standard elastic treatments, which are based on the displacement vectors. The conformations such structures adopt are thus compromises between their mutually contradicting intrinsic geometric tendencies. This can give rise to elaborate conformations that arise from very simple input. Geometrically frustrated structures display super extensive elastic energy, a tendency for filamentation, and exotic response properties.[2]

Frustrated assemblies arise in a wide variety of systems in soft matter including chiral colloids[3], twisted molecular crystals[4], macromolecules, and commonly arises in plastic deformations, in viscoelastic solids and in hygro-morphing plants. The lack of a stress free configuration in these systems motivates a description that utilizes intrinsic geometric quantities such as the reference metric of the material manifold. Such descriptions were recently applied to molecular crystals revealing the gradual untwisting of twisted molecular crystal as the crystal's cross-section grows.[4] For uniform frustration in 2D the metric description predicts an elastic energy that scales like the area cubed for isotropic domains, while narrow ribbons show extensive elastic energy growing linearly with the area.[2] For thin elastic sheets the metric approach accurately predicts both the morphology and the non-trivial elastic response properties. Most recently, the metric approach was used to predict the future stability of viscoelastic structures.[5]

The key elements of a successful intrinsic description of a frustrated structure is the identification of the relevant intrinsic variables that fully characterise the system, and the common relations these quantities must obey to describe a viable structure. In what follows we do so for two-dimensional liquid crystals. We identify two scalar quantities that fully describe the phase, and one differential relation these quantities must satisfy. We conclude by demonstrating the power of this approach in solving the inverse problem of the nematic elastomers.

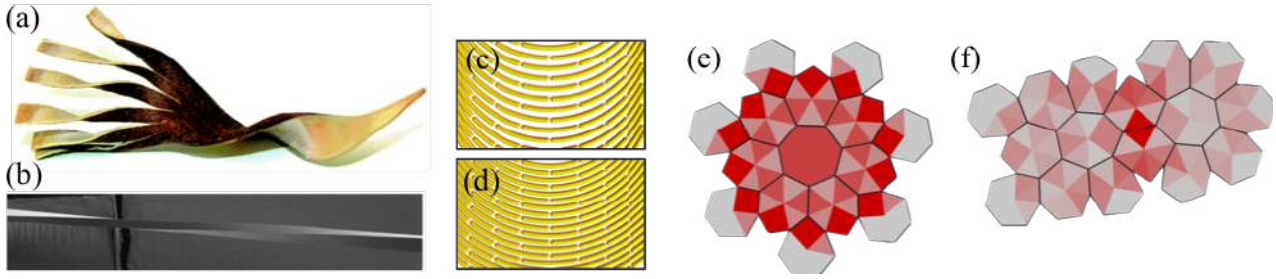

Figure 1. Frustrated assemblies. (a) Cutting a frustrated structure will cause it to deform to partially alleviate frustration. (b) SEM image of a twisted molecular crystal of Hippuric acid. (c) and (d) show a constant bend and zero splay planar arrangements of bent rods. However, the two cannot be simultaneously achieved. (e) and (f) show an isotropic and narrow assembly of 15 elastic heptagons in the plane colored by elastic energy. The filamentous structure shows much less elastic frustration. Panels (a), (b), (c) and (d) adapted from references 2,4 and 7.

The intrinsic approach for two dimensional liquid crystals

The simplest liquid crystalline phase is the simple nematic, in which molecules elongated along one axis orient on average to point in the same direction uniformly. Deviations of the orientations field, termed the director, from this uniform phase create gradients in the director both along the director, called bend deformations, and transversely giving rise to splay deformations. The bend and splay are given by $b = |(n \cdot \nabla)n|$ and $s = |(n_\perp \cdot \nabla)n|$ respectively, where n denotes the director unit field, and $n_\perp$denotes the director perpendicular direction. If two director fields share the same bend and splay functions they differ only by a rigid motion. The splay and bend uniquely characterize director fields, yet not every two scalar functions could constitute the splay and bend of a director field. It is well known that there is no director with zero splay and constant non-zero bend in the plane. Moreover, bend core liquid crystals, under the appropriate conditions, locally favour this inaccessible phase.

We next obtain the compatibility conditions for two-dimensional directors in arbitrarily curved surfaces. We begin with identifying the bend with the geodesic curvature of the director integral curves, and the splay with the geodesic curvature of the perpendicular integral curves. A careful implementation of the Gauss-Bonnet theorem yields

$$b^2 + s^2 + n \cdot \nabla s - n_\perp \cdot \nabla b = -K,$$

where K is the local Gaussian curvature of the surface in which the director is embedded. The above equation must hold at every point on the surface for b and s to be the bend and splay functions of a director on the surface. If the above equation holds one can find a director field n such that its splay and bend function read s and b respectively, unique up to rigid motions. Considering the case of uniform fields is particularly elucidating; the equation $b^2 + s^2 = -K$ implies that for the flat case where K=0 yields that only the trivial nematic with vanishing splay and bend is compatible. In positively curved spaces (like the surface of the sphere) where 0<K there are no compatible phases of uniform bend and splay. Last, for hyperbolic surface there are many such phases.

The compatibility condition above not only allows us to identify if an attempted phase is frustrated, but identifies the phases that are admissible. This replaces the elastic question of mechanical equilibrium with one of an optimal embedding, the cost function determined by materials constitutive relations. For the case of an attempted phase of vanishing splay and a constant bend in a domain of width W and length L the theory predicts an elastic energetic cost that scales as $E_{el} \propto W^3 L$.[6] For an Isotropic domain this implies a super-extensive elastic energy that scales with the area squared. For ribbons of constant width the energy becomes extensive. Thus, much like frustrated solids the ordered domains will tend to filament.

The nematic elastomer inverse design problem

The intrinsic approach to liquid crystals is not only useful for understanding frustrated states, but also allows solving analytically the inverse design problem of nematic elastomers. Nematic elastomers are elastomeric solids that possess an internal uniaxial orientational order. The locally preferred direction (director field) in the material can be externally prescribed during fabrication. Upon heating the orientational order is lost and the metrial shrinks by a factor λ along the director, and expands by a factor $\lambda^{-\nu}$ in the perpendicular direction. This in turn distorts the initially planar manifold to form a curved metric of Gaussian curvature

$$K = (\lambda^{2\nu} - \lambda^{-2}) \times \left(\cos(2\theta)[\left(\partial_y\theta\right)^2 - (\partial_x\theta)^2 + \partial_x\partial_y\theta] + \frac{1}{2}\sin(2\theta)\left[(\partial_x\theta)^2 - \left(\partial_y\theta\right)^2 - 4\partial_x\theta\,\partial_y\theta\right)\right).$$

The above equation is straightforward to implement if θ is known and we seek to learn what surface would be obtained upon actuation. However, recent advances in material science including programmable nematic elastomers, 4D printing applications and pneumatic soft actuators motivate the inverse problem: Given a desired surface with a prescribed K can we design a director that would realize it upon actuation. This amounts to finding a solution $\theta(x,y)$ in the plane to the above equation. There are two main impediments to reaching a solution. The first is that the Gaussian curvature is given on the distorted surface with respect to some intrinsic coordinates $K(u,v)$, whereas the unknown field and differential relation are in the (x,y) plane. The second impediment is the inaccessibility of the information that the initial state is flat. Setting $\lambda = 1$ above (which corresponds to the flat configuration before actuation) yields zero on both side of the equation and adds no information.

If we rewrite the equation above using the intrinsic approach we obtain $-K = \lambda^2(s^2 + n \cdot \nabla s) + \lambda^{2\nu}(b^2 - n_\perp \cdot \nabla b)$. Setting $\lambda = 1$ and $K = 0$ yields an independent equation. We may now solve for the splay and bend on the distorted surface, or equivalently on the plane solving simultaneously for $u(x,y), v(x,y), s(x,y)$ and $b(x,y)$. We perform this to produce the director field that would distort into the surface resembling a face, see figure 2. The initial data to the hyperbolic partial differential equations are given as two mutually perpendicular curves on the distorted surface which we interpret as integral curves of n and $n_\perp$.

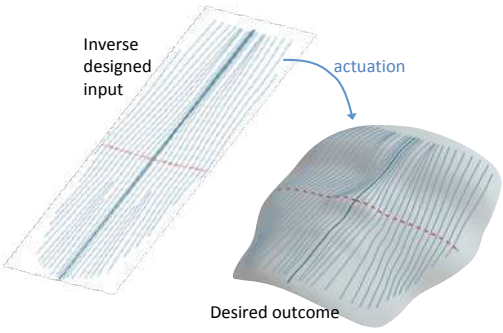

Figure 2. Solving the nematic elastomer inverse design. Adapted from 6.

CONCLUSIONS

We show that the splay and bend scalar fully describe a 2D director field, and provide the relation these fields must satisfy to describe a realizable field on arbitrary surfaces[7]. This intrinsic description allows us to solve the inverse design problem which is relevant to a variety of shaping mechanisms from nematic elastomers[6], to 4D printing and baromorphing[8].

References

[1] G.M. Grason, Perspective: Geometrically-Frustrated Assemblies, Journal of chemical Physics 145(11):110901, 2016.
[2] E. Efrati, E. Sharon, and R. Kupferman. The metric description of elasticity in residually stressed soft materials. Soft Matter, 9(34):8187, 2013.
[3] T. Gibaud, et al. Reconfigurable self-assembly through chiral control of interfacial tension. Nature 481, 348–351, (2012).
[4] Haddad, A., et-al. Twist renormalization in molecular crystals driven by geometric frustration. Soft Matter 15, 116–126, (2018).
[5] E.Y. Urbach and E. Efrati, Delayed instabilities in viscoelastic solids through a metric description. arXiv:1711.09491, (2017).
[6] I. Griniasty, H. Aharoni, and E. Efrati, Curved Geometries from Planar Director Fields. Phys. Rev. Lett. 123, 127801, (2019).
[7] I. Niv and E. Efrati, Geometric frustration and compatibility conditions for two-dimensional director fields. Soft Matter 14, 424–431, (2018).
[8] E. Efrati, Inflating to Shape. Nature Materials 18,2–3 (2019).

MULTIFUNCTIONAL VISCOELASTIC COMBINATORIAL METAMATERIALS

David M.J. Dykstra*[1], Aleksi Bossart[1,2], Jop van der Laan[1], and Corentin Coulais[1]
[1]Institute of Physics, University of Amsterdam, Amsterdam, the Netherlands
[2]School of Engineering, Ecole polytechnique fédérale de Lausanne, Lausanne, Switzerland

Summary Mechanical metamaterials are structured forms of matter that can exhibit advanced functionalities such as non-reciprocity [1], shape-shifting [2, 3, 4], strain-rate dependency [5] and negative responses [6]. To date, most metamaterials only have a single functionality, underpinned by a single soft deformation mode or an uncontrollable extensive number of modes. Here, we introduce a novel class of combinatorial metamaterials that are multifunctional. We find a rich design space, which can host multiple yet a sub-extensive number of soft deformation modes. We demonstrate the multifunctional nature of such metamaterials using viscoelasticity. In particular, we realize a metamaterial that has a negative (positive) Poisson's ratio for low (high) compression rate. This makes our metamaterial an early example of multi-functional matter, thus paving the way for robust and adaptable devices.

BACKGROUND

Relating architectural details to emerging properties is a daunting challenge for the design of metamaterials. In particular, metamaterials so far exhibit either only a single deformation mode—which limit their functionality to a single shape-change or a single property— or exhibit a number of deformations modes or deformation branches that grow linearly or exponentially with the system size [2, 4], which are very difficult to actuate — in practice only one deformation mode or deformation branch can be actuated. To attack this challenge, we restrict our attention to combinatorial metamaterials [3], where the structural complexity is reduced to a discrete design space, typically by controlling the orientation of the constitutive unit cells. Such discreteness makes the design space much easier to explore and has been leveraged to create non-periodic metamaterials with shape-changing [3] and topological properties [7], yet, only for single mode metamamaterials so far.

COMBINATORIAL MODEL

Here, we introduce a novel unit cell with two soft deformation modes (Fig. 1a). In order to understand the structure and number of zero modes, we introduce a combinatorial model that maps out angle deformations onto a directed graph. To obtain it, we begin by linearizing the geometric constraints for a single cell at rest, which allows us to express three angles in terms of the other two. Conveniently, this relationship between small angle deformations has integer coefficients, allowing for a neat graphical representation of single-cell deformations (Fig. 1a) as arrows on a vertex with 5 edges (Fig. 1b). We can then construct a variety of tessellations of this unit cell. By construction, each edge corresponds to a hinge in real space, for which the sum of angles on either side remains constant (Fig. 1c). This makes it possible to draw only one group of arrows per edge; geometric constraints are easily propagated from one vertex to its neighbours. Hence, each configuration of arrows on this graph corresponds to a zero mode and provides an intuitive representation of the mechanical deformations it entails. This is reminescent of the integrable vertex models found in 2D statistical physics [8, 9], since it also amounts to counting arrow configurations that respect a set of local constraints, including the ice rule. Even though its algebraic structure remains a largely uncharted territory, this model provides a powerful graphical design tool that provides direct insight in the behaviour of combinatorial metamaterials.

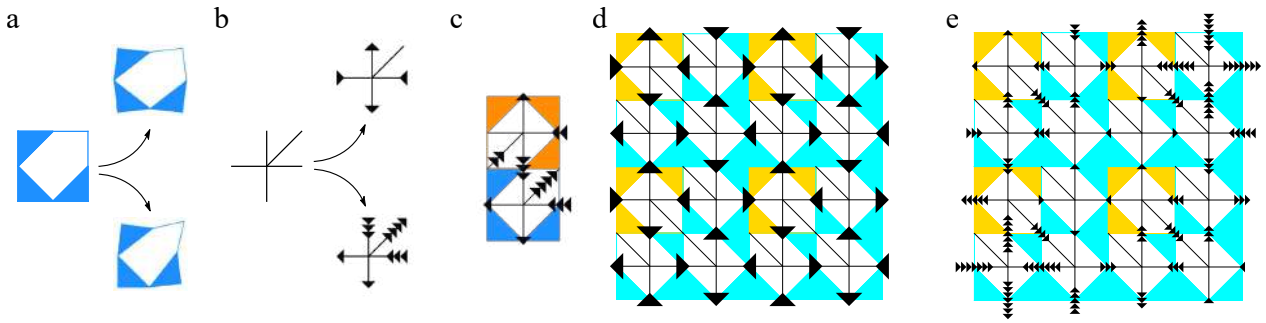

Figure 1: **Modes structure and vertex representation.** (a) Unit cell with two possible deformation modes (b) Vertex model representation. (c) Combinatorial index matching. (d) Counter-rotating squares in bimodal design. (e) Second bulk bi-domain mode.

Our new tool allows us to explore a variety of tessellations. An example of a periodic tessellation is shown in Fig. 1d, with a counter-rotating zero mode visualised using the vertex representation, which can be found for any rectangular

*Corresponding author. E-mail: d.m.j.dykstra@uva.nl

tessellation of our unit cell and has been studied extensively in the past [6]. What makes this specific tiling interesting is that it also features, regardless of system size, exactly one alternative bulk mode (Fig. 1e), which can be classified as a bi-domain mode, symmetric about the diagonal from north-west to south-east, increasing its deformation linearly when moving away from the symmetry axis. Other tesselations can offer a variety of zero mode counts, such as an extensive number of modes growing with system size, a finite number of modes larger than one or only the single mode of Fig. 1d.

MULTIFUNCTIONAL VISCOELASTICITY

In the following, we demonstrate that we can use these modes to generate multifunctional materials, harnessing strain-rate dependent viscoelasticity. To do so, we use a combination of additive manufacturing and casting to produce the architecture of Fig. 1d-e, resulting in the metamaterials of Fig. 2a. The sample of Fig. 2a features a hinge geometry that favours bending, with elastic hinges (green) and viscoelastic hinges (grey). For short time scales ($<$ 1sec) the viscoelastic material is stiffest and for long time scales ($>$ 1sec), it undergoes stress-relaxation and become softer than the elastic material. We compress the metamaterials at slow ($\dot{\varepsilon} = 9.3 \cdot 10^{-6} s^{-1}$) and fast ($\dot{\varepsilon} = 0.11 s^{-1}$) loading rates. We observe that the metamaterial responds in the counter-rotating mode when actuated slowly (Fig. 2c) and in the bi-domain mode when actuated rapidly (Fig. 2b). This can be explained as follows: for fast compression at short time scales, the elastic hinges are relatively softer and hence deform and lead to the bi-domain mode, while for slow compression at long time scales, the elastic hinges are relatively stiffer and hence not deform, thus leading to the the counter-rotating mode.

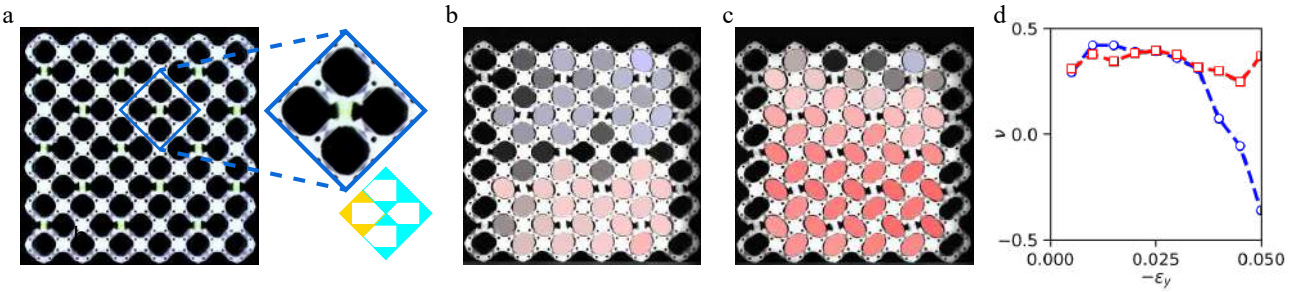

Figure 2: **Multifunctionality mediated by viscoelasticity** (a) Bimode metamaterial at rest and close up on a unit cell with schematic representation. (b-c) Snapshot of the metamaterial and reconstructed ellipses after a compression $\varepsilon = 0.056$ at a strain rate $\dot{\varepsilon} = 0.11 s^{-1}$ (b) and $\dot{\varepsilon} = 9.3 \cdot 10^{-6} s^{-1}$ (c). (d) Incremental Poisson's ratio vs. compressive strain ε for compression at a strain rate $\dot{\varepsilon} = 0.11 s^{-1}$ (blue circles) and $\dot{\varepsilon} = 9.3 \cdot 10^{-6} s^{-1}$ (red squares).

Interestingly, these two modes induce different Poisson's ratios (Fig. 2d). Namely, the counter-rotating deformation mode leads to a response with a negative Poisson's ratio while the bi-domain mode induces a positive Poisson's ratio. Therefore, our metamaterial is multifuntional, non-auxetic under fast compression rate and auxetic at slow compression rate.

CONCLUSIONS

To conclude, we have created a novel class of multifunctional metamaterials, that harness a combinatorial architecture to exhibit multiple modes, which we use to generate loading-rate dependent multifunctionality. Our work significantly advances the field of metamaterials and could be used to generate new kinds of multifunction materials.

References

[1] C. Coulais, D. Sounas, and A. Alù. Static non-reciprocity in mechanical metamaterials. *Nature*, 542:461–464, 2017.
[2] Yigil Cho, Joong-Ho Shin, Avelino Costa, Tae Ann Kim, Valentin Kunin, Ju Li, Su Yeon Lee, Shu Yang, Heung Nam Han, In-Suk Choi, and David J. Srolovitz. Engineering the shape and structure of materials by fractal cut. *Proc. Natl. Acad. Sci. USA*, 111(49):17390–17395, 2014.
[3] C. Coulais, E. Teomy, K. de Reus, Y. Shokef, and M. van Hecke. Combinatorial design of textured mechanical metamaterials. *Nature*, 535:529–532, 2016.
[4] C. Coulais, A. Sabbadini, F. Vink, and M. van Hecke. Multi-step self-guided pathways for shape-changing metamaterials. *Nature*, 561:512–515, 2018.
[5] D.M.J. Dykstra, J. Busink, B. Ennis, and C. Coulais. Viscoelastic snapping metamaterials. *J. Appl. Mech.*, 86(111012), 2019.
[6] T. Mullin, S. Deschanel, K. Bertoldi, and M.C. Boyce. Pattern transformation triggered by deformation. *Phys. Rev. Lett.*, 99(084301), 2007.
[7] A.S. Meeussen, E.C. Oguz, Y. Shokef, and M. van Hecke. Topological defects produce exotic mechanics in complex metamaterials. *arXiv:1903.07919*, 2019.
[8] E.H. Lieb. Residuaal entropy of square ice. *Phys. Rev.*, 162(162), 1967.
[9] E.K. Sklyenin, L.A.Takhtadzhyan, and L.D. Faddeev. The quantum method of the inverse problem and the heisenberg xyz model. *(Russ. Math. Surveys*, 5:11–68, 1979.

PRESSURE-INDUCED COMPOSITION CHANGES IN A GEL FORCED TO MOVE BETWEEN TWO PLATES: THE ROLE OF ELASTIC AND OSMOTIC PROPERTIES

Fernando P. Duda*[1], Angela C. Souza[2], and Eliot Fried[3]
[1]Programa de Engenharia Mecanica - COPPE, Universidade Federal do Rio de Janeiro, Rio de Janeiro, Brasil
[2]Programa de Engenharia Mecanica - TEM, Universidade Federal Fluminense, Niteroi, Brasil
[3]Mathematics, Mechanics, and Materials Unit, Okinawa Institute of Science and Technology Graduate University, Okinawa, Japan

Summary We present a theory for the coupling between large deformation and fluid permeation in polymer gels that allows for the presence of sharp interfaces separating regions of high and low polymer volume fraction. The theory is specialized to study the problem of pressure driven fluid flow through a gel-filled channel, with the aim of investigating how the elastic and osmotic properties of the gel and the applied pressure gradient affect the composition, and hence the fluid flow, through the initially uniform gel under steady-state conditions. For a gel defined by Gent and Flory-Huggins models for elastic and mixing free energies, we demonstrate that the applied pressure gradient leads to a non-uniform polymer distribution across the channel which under appropriate circumstances is associated with the formation of regions of high and low polymer volume fraction separated by sharp interfaces.

PRELIMINARIES

Following Duda, Souza & Fried (2010), we present a theory for the coupling between large deformation and fluid permeation in polymer gels that allows for the presence of sharp interfaces separating regions of high and low polymer volume fraction. The main novelty here is the introduction of an extra force balance to account for the power expenditure associated with interface motion. Thus, by combining the basic balances of the theory, namely network content conservation, fluid content balance, mechanical force balance, and configurational force balance, with a constitutive theory compatible with thermodynamics, we derive the governing equations of the theory. Using the standard notation of continuum mechanics, we write the spatial version of these equations as follows:

- Bulk equations

$$\begin{aligned} &\phi \det \mathbf{F} = \phi_0, \\ &\operatorname{div}\,(\mathbf{T}_{\mathrm{n}} - p\mathbf{I}) = \mathbf{0}, \\ &\operatorname{div}\,(\upsilon \boldsymbol{\jmath} + \mathbf{v}) = 0, \end{aligned} \tag{1}$$

with the constitutive equations for network stress $\mathbf{T}_{\mathrm{n}}$ and fluid flux $\boldsymbol{\jmath}$ given by

$$\begin{aligned} &\mathbf{T}_{\mathrm{n}} = \frac{2}{\sqrt{I_3}}\left(\frac{\partial \tilde{\psi}_e(I_1,I_2)}{\partial I_1}\mathbf{B} + \frac{\partial \tilde{\psi}_e(I_1,I_2)}{\partial I_2}(I_1\mathbf{I}-\mathbf{B})\mathbf{B}\right) - \hat{\pi}(\phi)\mathbf{I}, \\ &\boldsymbol{\jmath} = -\upsilon\, \hat{m}(\phi)\operatorname{grad} p. \end{aligned} \tag{2}$$

Here and henceforth, $\mathbf{F}$ is the deformation gradient, ϕ and ϕ_0 the polymer volume fractions in the reference and actual configurations, p the interstitial fluid pressure, υ the volume occupied by an individual fluid molecule, $\mathbf{v}$ the network velocity, (I_1, I_2, I_3) the list of the principal invariants of the left Cauchy-Green tensor $\mathbf{B} = \mathbf{F}\mathbf{F}^{\top}$, $\hat{\psi}_e$ the elastic free energy response, $\hat{\pi}$ the osmotic pressure response, which is related to mixing free energy response $\hat{\psi}_m$ by the relation $\hat{\pi} = (\phi^2/\phi_0)\partial\hat{\psi}_m/\partial\phi$, and $\hat{m}$ the fluid mobility response. External body forces, inertial effects, and solvent supply are neglected here;

- Interface equations

$$\begin{aligned} &[\phi]u - [\phi\mathbf{v}]\cdot\mathbb{m} = 0, \\ &[\mathbf{T}_{\mathrm{n}}]\mathbb{m} = \mathbf{0}, \\ &[c]u - [c\mathbf{v}]\cdot\mathbb{m} = [\boldsymbol{\jmath}]\cdot\mathbb{m}, \\ &[\hat{\psi}_e(\mathbf{F}) + \hat{\psi}_m(\phi)] - |\mathbf{F}^*\mathbb{n}|^2\,\mathbf{T}_{\mathrm{n}}\mathbb{m}\cdot[\mathbf{F}]\,(\mathbf{F}^*)^{-1}\,\mathbb{m} = 0, \end{aligned} \tag{3}$$

where u is the interface speed, $\mathbb{m}$ ($\mathbb{n}$) the normal to the (referential) interface, c the fluid number density, and $\mathbf{F}^*$ the cofactor of $\mathbf{F}$. We have assumed a coherent interface across which the fluid pressure was continuous.

Next, we apply the foregoing theory to study the steady-state behavior of a gel of uniform composition placed between two flat plates and forced by a pressure gradient.

*Corresponding author. Email: duda@mecanica.coppe.ufrj.br

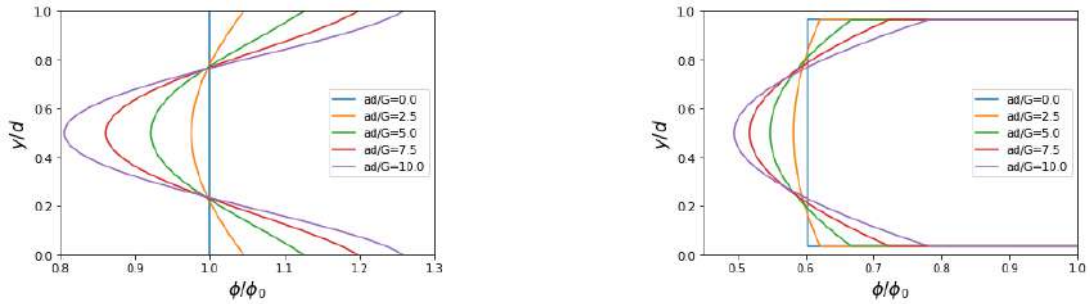

(a) (b)

Figure 1: Polymer volume fraction profile across the channel for $\phi_0 = 0.1$, $J_m = 10.$, $(k_BT)/(\upsilon G) = 100.$, and different values of ad/G. (a) $\chi = 0.2$ and (b) $\chi = 1.0$.

PRESSURE-DRIVEN FLOW THROUGH A GEL-FILLED CHANNEL

Consider the space between two infinitely long parallel plates separated by a gap d and completely filled by a gel which is fixed to and impermeable at the plates. We introduce a Cartesian coordinate system with the x-axis chosen parallel to the flow, the y-axis orthogonal to the plates, and z-axis orthogonal to the (x, y)-plane. We take the plates to be located at $y = 0$ and $y = d$. Initially, the gel is in a stress-free state with polymer volume fraction constant and equal to ϕ_0. Then, a pressure gradient a is applied causing the fluid to flow through the gel, which in turn deforms locally according to the deformation gradient

$$[\mathbf{F}] = \begin{bmatrix} 1 & \gamma & 0 \\ 0 & \eta & 0 \\ 0 & 0 & 1 \end{bmatrix}. \tag{4}$$

This implies that that $\mathbf{F}$ is a superimposition of an uniaxial extension with stretch η on a simple shear with amount γ. These unknown quantities, which are functions y, are obtained by considering two distinct situations according to which interfaces are absent not.

In absence of interfaces, η and γ are smooth functions and must obey the set equations

$$\begin{aligned} &\hat{\tau}(\gamma(y), \eta(y)) = -a(y - d/2), \\ &\hat{\sigma}(\gamma(y), \eta(y)) = k, \\ &\int_0^d (1/\eta(y))\, dy = d, \end{aligned} \tag{5}$$

with k an unknown constant to be determined. The first two equations above follows from the combination of $(1)_2$, $(2)_1$, and (4), where $\hat{\tau}$ and $\hat{\sigma}$ are the constitutive for the shear and normal stresses acting in a plane normal to the y-direction.

We now consider the presence of two interfaces located symmetrically with respect to the central line between the two plates. In this case, η and γ are smooth away from and display jump discontinuity across the interfaces located at $y = w$ and $y = d - w$, with $w < d/2$. Thus, our problem reduces to the determination of γ and η for each y away from the interface, the corresponding limit values at the interfaces, and the location of the interfaces. Thus, we have to supplement $(5)_{1,2}$, which now hold only for points away from the interfaces, and $(5)_3$ with the following interface conditions obtained from (3):

$$\begin{aligned} &\hat{\tau}(\gamma_+, \eta_+) = -a(w - d/2), \qquad \hat{\sigma}(\gamma_+, \eta_+) = k, \\ &\hat{\tau}(\gamma_-, \eta_-) = -a(w - d/2), \qquad \hat{\sigma}(\gamma_-, \eta_-) = k, \\ &[\hat{\psi}_e(I_1, I_2) + \hat{\psi}_m(\eta)] + a(w - d/2)(\gamma_+ - \gamma_-) - k[\eta] = 0. \end{aligned} \tag{6}$$

These relations hold at $y = w$ and involves the limit values $\gamma_\pm$ and $\eta_\pm$ pf γ and η. The relations holding at $y = d - w$ are, by symmetry, redundant and for this reason are not displayed here.

We now consider a gel defined by Gent and Flory-Huggins models for $\hat{\psi}_e$ and $\hat{\psi}_m$, respectively. These models involves the following parameters: shear modulus G, finite extensibility parameter J_m, Boltzmann constant k_B , absolute temperature T, and the Flory-Huggins interaction parameter. Figure 1 plots the profile for $\phi/\phi_0 (= 1/\eta)$ for $\phi_0 = 0.1$, $J_m = 10.$, $k_BT/(\upsilon G) = 100.$, and two values of χ: (a) $\chi = 0.2$ (good solvent) and (b) $\chi = 1.$ (bad solvent). The same values of ad/G were adopted in both cases.

References

[1] Duda F.P., Souza A.C., Fried E.: A theory for species migration in a finitely strained solid with application to polymer network swelling. J. Mech Phy Sol 58:515-529, 2010.

OSCILLATING CONFIGURATIONAL CONSTRAINTS AND NONLINEAR DYNAMICS OF EXTREMELY DEFORMABLE STRUCTURES

F. Dal Corso*[1], P. Koutsogiannakis[1], D. Misseroni[1], T. Papathanasiou[2], and Davide Bigoni[1]
[1]Department of Civil, Environmental and Mechanical Engineering, University of Trento, Trento, Italy
[2]Department of Civil & Environmental Engineering, Brunel University London, Uxbridge, UK

Summary The motion of an elastic rod, constrained with a frictionless sliding sleeve periodically oscillating in time, is analyzed. Based on an analytical formulation and a numerical resolution, the resulting nonlinear dynamic response is shown to be heavily influenced by the configurational tangential reaction generated at the sliding sleeve constraint. More specifically, the system response features three characteristic motion patterns: (i.) the final complete injection, (ii.) the final complete transverse ejection, or (iii.) an initial ejection along the longitudinal direction (despite gravity) followed by an injection resulting to a steady small amplitude oscillation around a non-null external length value. Dynamic simulation of all characteristic motion patterns is achieved by means of an in-house Finite Element solver. The present results pave the way to longitudinal actuation by means of transverse non-periodic oscillations and control theory could be a powerful tool for optimal actuators.

Nonlinear structural dynamics breaks the limits of traditional linear elastic design, to create elements working beyond the realm of linearized kinematics, fully inside the nonlinear range, therefore meeting the strong requirements imposed by soft robotics, flexible locomotion devices, metastructures, architected structures for vibration mitigation, and morphable structures. Within this context, the influence of configurational (or 'Eshelby-like') forces on the nonlinear dynamics of structures is investigated in the presence of periodically oscillating sliding sleeves.

Configurational forces were introduced by Eshelby [10] to describe the motion of defects within solids and have been shown recently to act on elastic rods constrained by sliding sleeves [5]. In particular, the sliding of an elastic rod through a frictionless sleeve generates at the constraint exit an 'Eshelby-like' force with direction parallel to that of sliding. Recent studies have utilized the action of configurational forces to explain unexpected quasi-static response [4, 7, 8] of structures, analyze propulsion characteristics [6, 9], through a material force balance [11, 14], and investigate constrained buckling problems [12, 13]. Moreover, recent research on configurational forces in structural mechanics has eventually inspired a new interpretation of their action in solids [2].

The analysis of configurational forces acting on structures was recently extended to the dynamic framework [1] and developed in the special case of a moving mass m attached to an elastic rod of bending stiffness B and external length $\ell(t)$ varying in time t. Similar to the quasi-static case, the configurational force under dynamic conditions was found to be proportional to the square of the bending moment at the sliding sleeve entrance. Complex and often counterintuitive motion of the mass was also revealed, leading to complete rod injection and ejection from the sleeve constraint. In this study, the influence of the sliding sleeve constraint periodic transverse oscillation $\bar{u}_g \sin \omega t$ is considered (Fig. 1 (left)).

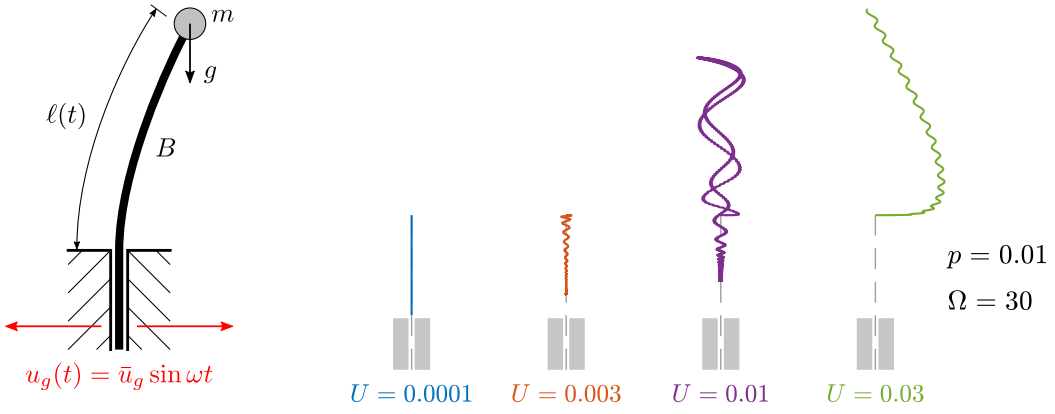

Figure 1: (Left) A lumped mass attached to an elastic rod slipping into a frictionless sliding sleeve parallel to the gravity direction and subject to an oscillatory transverse motion. The part of rod outside the configurational constraint has external length $\ell(t)$ varying in time. (Right) Theoretical predictions of the lumped mass trajectory for $p = 0.01$, $\Omega = 30$, and varying $U = \{0.0001,\ 0.003,\ 0.01,\ 0.03\}$, showing a final complete injection ($U = 0.0001$), an initial longitudinal ejection followed by an injection ending with a stationary motion at almost constant external length ($U = 0.003$ and 0.01), and a final complete transverse ejection ($U = 0.03$).

To numerically simulate this system, an in-house Finite Element (FE) code has been developed. The formulation extends a recently developed methodology [3] by including the effects of sliding sleeve constraints. The time response is computed assuming negligible elastic rod inertia by solving a nonlinear Differential-Algebraic Equation (DAE) system. In

*Corresponding author. E-mail: francesco.dalcorso@unitn.it

addition to possible dissipation sources, the time evolution is found to depend only on the following three dimensionless parameters

$$p = \frac{m\,g\,\ell_0^2}{B}, \qquad \Omega = \omega\sqrt{\frac{m\ell_0^3}{B}}, \qquad U = \frac{\overline{u}_g}{\ell_0},$$

where g is the gravity acceleration (acting parallel to the sliding direction) and ℓ_0 is the value of the external length $\ell(t)$ at the initial state ($t = 0$).

The structure response is observed to dramatically change with varying values of p, Ω, and U. More specifically, the system shows two limit states corresponding to complete injection or complete transverse ejection of the rod. Furthermore, a third, qualitatively different and intriguing motion, has been found. In this third case, the rod is initially ejected along the longitudinal direction (despite gravity) and then injected settling to a steady small oscillation around a non-null external length value. Theoretical predictions for the mass trajectory are reported in Fig. 1 (right), while the $\ell(t)$ values are depicted in Fig. 2 for a system with $p = 0.01$, and $\Omega = 30$, and $U = \{0.0001,\ 0.003,\ 0.01,\ 0.03\}$.

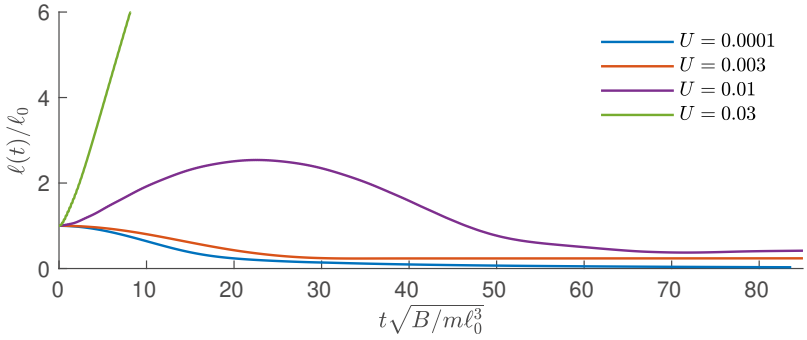

Figure 2: Evolution in time t of the external length ℓ for a system with $p = 0.01$ and $\Omega = 30$, with varying $U = \{0.0001,\ 0.003,\ 0.01,\ 0.03\}$.

The present results pave the way to longitudinal actuation by means of non-periodic transverse oscillations, where control theory could be employed for optimization purposes.

Acknowledgments. FDC, PK, DB gratefully acknowledge financial support from the European Union's Horizon2020 research and innovation programme under the Marie Sklodowska-Curie grant agreement 'INSPIRE - Innovative ground interface concepts for structure protection' PITN-GA-2019-813424-INSPIRE, TP gratefully acknowledges support by the Brunel Research Initiative & Enterprise Fund BRIEF 2018/2019-award number 1069 and DM gratefully acknowledges funding by the 'LIGHTEN - Ultralight membrane structures towards a sustainable environment' H2020-MSCA-ITN - 2020-LIGHTEN-956547. Funding from the Italian Ministry of Education, University and Research (MIUR) in the frame of the "Departments of Excellence" grant L. 232/2016 is also acknowledged.

References

[1] Armanini C., Dal Corso F., Misseroni D., Bigoni D. Configurational forces and nonlinear structural dynamics. *J. Mech. Phys. Sol.*, **130**, 82-100, 2019.
[2] Ballarini R., Royer-Carfagni G. A Newtonian interpretation of configurational forces on dislocations and cracks. *J. Mech. Phys. Sol.*, **95**, 602-620, 2016.
[3] Bartels S. A simple scheme for the approximation of elastic vibrations of inextensible curves. *IMA Journal of Numerical Analysis*, **36**, 1051-1071, 2016.
[4] Bigoni D., Bosi F., Dal Corso F., Misseroni D. Instability of a penetrating blade. *J. Mech. Phys. Solids*, **64**, 411–425, 2014.
[5] Bigoni D., Dal Corso F., Bosi F., Misseroni D. Eshelby-like forces acting on elastic structures: theoretical and experimental proof. *Mech. Mater.*, **80**, 368–374, 2015.
[6] Bigoni D., Dal Corso F., Misseroni D., Bosi F. Torsional locomotion. *Proc. R. Soc. A*, **470.2171**, 20140599, 2014.
[7] Bosi F., Misseroni D., Dal Corso F., Bigoni D. An elastica arm scale. *Proc. R. Soc. A*, **470**, 20160870, 2014.
[8] Bosi F., Misseroni D., Dal Corso F., Bigoni D. Self-encapsulation, or the 'dripping' of an elastic rod. *Proc. R. Soc. A*, **471**, 20150195, 2015.
[9] Dal Corso F., Misseroni D., Pugno N.M., Movchan A. B., Movchan N. V., Bigoni D. Serpentine locomotion through elastic energy release. *J. R. Soc. Interface*, **14**, 20170055, 2017.
[10] Eshelby J. D. The continuum theory of lattice defects. *Solid State Phys.*, **3.C**, 79–144, 1956.
[11] Hanna J. A., Singh H., Virga E. G. Partial Constraint Singularities in Elastic Rods. *J. Elas.*, **133**, 105-118, 2018.
[12] Liakou A. Constrained buckling of spatial elastica: Application of optimal control method. *J. App. Mech. ASME*, **85**, 081005, 2018.
[13] Liakou A. Application of optimal control method in buckling analysis of constrainedelastica problems. *Int. J. Sol. Struct.*, **141-142**, 158-172, 2018.
[14] O'Reilly O. M. Some perspectives on Eshelby-like forces in the elastica arm scale. *Proc. R. Soc. A*, **471**, 20140785, 2015.

EXACT MINIMAL PARKING GARAGES: HELICAL MOTIFS IN OPTIMALLYPACKED LAMELLAR STRUCTURES ARE PITCH BALANCED

Luiz C. B. da Silva*[1] and Efi Efrati [1]
[1]Department of Physics of Complex Systems, Weizmann Institute of Science, Rehovot, Israel

Summary It has been recently found that the lamellar structure of plant thylakoids and the endoplasmic reticulum are abundant with helical motifs connecting adjacent layers. In addition, both right- and left-handed motifs were observed in distributions suggesting total pitch balance. So far, the analytical treatment of such motifs embedded in minimal surfaces has been limited to the small-slope approximation, which breaks in the relevant biological regimes. Here, we provide a method for building exact and analytically tractable minimal surfaces containing any desired distribution of helical motifs. We then consider the fundamental structure and interaction between two motifs of either opposite or similar handedness. Finally, we use our new method to construct minimal surfaces with an arbitrary array of N helical motifs and show that local area minimization leads to global pitch balance.

INTRODUCTION

Minimal surfaces arise as the ground state of a variety of manmade and naturally occurring membranes and lamellar structures. They minimize area among all surfaces with a given boundary and should naturally appear when surface tension is the dominant effect. Minimal surfaces can also be relevant in systems dominated by membrane bending energy as they form a special class of critical points of the Helfrich free energy [4]. Recently, helical motifs were found in the lamellar structures of plant thylakoids [5] and the endoplasmic reticulum [6], where both right and left handed motifs were observed in stoichiometry suggesting total pitch balance [2, 6]. To better understand these structures we require the ability to build minimal surfaces in which the appropriate helical motifs are present.

In the modeling of endoplasmic reticulum, the inter-layer connections are arranged in a checkerboard array of oppositely handed helical motifs [6]. Despite that the modeled structures are not minimal surfaces, it was argued that they possess a low bending energy which in fact places an upper bound on the amount of bending the true smoothed texture is expected to display. In contrast, the helical motifs in thylakoids have distinct pitch and core radius distributions yet still display total pitch balance on average [2]. In trying to model these system analytically, Guven et al [3] considered the small slope approximation whose main advantage is that minimal surfaces are represented by the graph of harmonic functions and, consequently, it allows for the simple addition of helical motifs of arbitrary geometry and topology due to the additivity of harmonic functions. However, the resulting surfaces are not exactly minimal, what is exceptionally apparent in the immediate vicinity of the helical structures, i.e., within a distance of a few pitch lengths from the core of each motif. Unfortunately, this imposes limitations for this type of approach as in the biologically and physically relevant regimes the helical motifs are commonly separated by a distance comparable to the pitch, rendering the small slope approximation irrelevant for these structures [2, 6].

To address this issue, in this work we provide a recipe for constructing exact minimal surfaces with an arbitrary distribution of helical motifs. This is based on a representation of minimal surfaces known as *Enneper immersion* [1], from which follows that any harmonic graph can be deformed into an exact minimal surface through an explicit, yet non-local operation. In other words, we correct an approximate minimal surface given as a harmonic graph over the plane such that it becomes an exact minimal surface by only exploiting lateral displacements and not varying the height data.

CONCATENATING TWO HELICAL MOTIFS

Consider a surface given by a harmonic function h over a domain $\Omega \subset \mathbb{C}$: $\mathbf{r}(z = x + iy) = (z, h(z))$, $\partial_{\bar{z}}\partial_z h = 0$, where $\bar{z} = x - iy$, $\partial_z \equiv \frac{\partial}{\partial z}$ and $\partial_{\bar{z}} \equiv \frac{\partial}{\partial \bar{z}}$. The mean curvature satisfies $H \propto \mathcal{O}(\|\nabla h\|^2)$ and the surface is considered minimal within the small slope approximation, i.e., when terms of order $\mathcal{O}(\|\nabla h\|^2)$ are omitted. One can then "add" helical motifs due to the additivity of harmonic functions. Indeed, the surface $\mathbf{r}(z) = (z, p_0 \arg(z - z_0))$ yields a helicoid of pitch p_0 centered around z_0 which is exactly minimal. One can explicitly construct a surface which includes N helical motifs located at the points z_i and of corresponding pitches p_i through $\mathbf{r}(z) = (z, \sum_{i=1}^{N} p_i \arg(z - z_i))$. Its mean curvature, however, does not vanish identically. To fix this, we apply to an approximately minimal surface in the form of a harmonic graph lateral displacements leading to a new surface, the Enneper immersion of h, which is an exact minimal surface [1]: $\mathbf{r} = (z - \overline{P(z)}, h(z))$, where $P(z) = \int (\partial_z h)^2 \, dz$. This operation provides a conformal parameterization whose area element dA and Gaussian curvature K read $dA = (1 + \frac{1}{4}\|\nabla h\|^2)^2 dx\, dy$ and $K = -4\frac{|\partial_{zz} h|^2}{(1+|\partial_z h|^2)^4} = \frac{h_{xx}h_{yy} - h_{xy}^2}{[1+\frac{1}{4}(h_x^2+h_y^2)]^4}$.

We now come to analyze the fundamental problem of adding two helical motifs of similar and opposite handedness. Given two helical motifs of pitches p_1 and p_2 located at $z_1 = \frac{R}{2}$ and $z_2 = -\frac{R}{2}$, $R > 0$, the corresponding harmonic function is $h(z) = p_1 \arg(z - z_1) + p_2 \arg(z - z_2)$ whose graph is only minimal up to $\mathcal{O}(\|\nabla h\|^2)$. Integrating $(\partial_z h)^2$, we have

$$P(z) = \frac{p_1^2}{4(z - \frac{R}{2})} + \frac{p_2^2}{4(z + \frac{R}{2})} + \frac{p_1 p_2}{2R}\left[\ln(z + \frac{R}{2}) - \ln(z - \frac{R}{2})\right]. \quad (1)$$

*Corresponding author. E-mail: luiz.da-silva@weizmann.ac.il

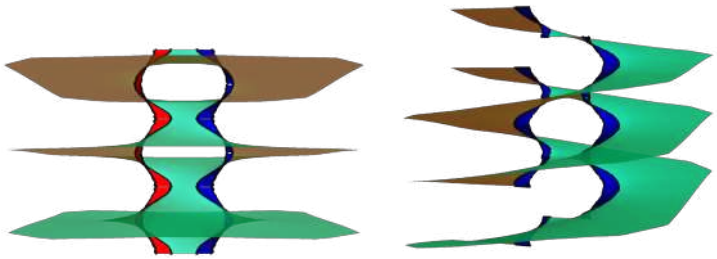

Figure 1: Layers of minimal dipole (left) and non-dipole (right) obtained by concatenating two helical motifs. (In the figures, $|p_1| = |p_2| = 0.15$ and $R = 1$.) The inner rims colored in red and blue emphasize the distinct handedness of the motifs.

The first two terms are the sum of $P_{\{z_1,p_1\}}(z)$ and $P_{\{z_2,p_2\}}(z)$ associated with two helicoids around $\pm\frac{R}{2}$, while the last term creates an interaction between them required to make the parameterization a conformal minimal immersion. In addition, since P decays as $1/|z|$, the harmonic graph of h is a good approximation for the corresponding Enneper immersion at large distances from the core. However, the approximated and exact minimal surfaces differ in the immediate vicinity of the helical core. The same reasoning equally applies for the addition of an arbitrary number of helical motifs since $P = \sum_i \frac{p_i^2}{4(z-z_i)} - \sum_{i<j} \frac{p_i p_j}{z_j - z_i}[\ln(z-z_j) - \ln(z-z_i)]$.

We start by considering the symmetric problem of gluing two identical motifs such that $p_1 = p_2 = p$. We next come to analyze a single leaf bearing in mind that the full structure is comprised of two such leaves repeated periodically. To describe the geometry of the helical core, we may compute the gradient and Hessian of $h(z) = p\arg(z+\frac{R}{2}) + p\arg(z-\frac{R}{2})$. The area of an annulus with radii $r_2 > r_1 \gg R$ is then $\int_{r_1}^{r_2} dA \approx \pi(r_2^2 - r_1^2) + 4\pi p^2 \ln(r_2/r_1) + \mathcal{O}((r/R)^{-2})$, $r = |z|$, while the Gaussian curvature is $K \approx -\frac{4}{R^2}\left(\frac{p}{R}\right)^2\left(\frac{r}{R}\right)^{-4}$, $r \gg R$. As expected, up to a small correction, the area of a minimal pair of identical motifs behaves for large distances as the area of two interlaced helicoids of pitch $p_0 = 2p$. The same is valid for the Gaussian curvature: $K \approx -4p^2/r^4$, which is precisely the asymptotic behavior for a helicoid of pitch $p_0 = 2p$.

For the case of a pair of oppositely handed motifs, $p = p_1 = -p_2$, the associated harmonic function is $h(z) = p\arg(z+\frac{R}{2}) - p\arg(z-\frac{R}{2})$. Here, we have $\int_{r_1}^{r_2} dA \approx \pi(r_2^2 - r_1^2) + \mathcal{O}((r/R)^{-2})$, $r_2 > r_1 \gg R$, whose non-trivial contribution is the area of a planar annulus. This confirms that for large distances, a minimal pair of opposite helical motifs is approximated by parallel stacked planes. The Gaussian curvature behaves as $K \approx -\frac{4}{R^2}\left(\frac{p}{R}\right)^2\left(\frac{r}{R}\right)^{-6}$, $r \gg R$. Notice that K decays faster than the Gaussian curvature of a minimal pair with $p_1 + p_2 \neq 0$.

CONCLUSIONS

We provided a recipe for constructing exact minimal surfaces with an arbitrary distribution of helical motifs, which in particular corrected the small slope approximation in the immediate vicinity of the helical structures. The process is described by the addition of helicoidal motifs but also taking into account an effective interaction between them necessary to guarantee minimality of the surface. Moreover, at large distances from the helical core, the corresponding exact minimal surface is well approximated by a helicoid whose pitch equals the total pitch of the helical structure. This implies that the boundary conditions at the far field regime is not altered by our deformation process. Our method can also be used for determining the attraction/repulsion between any two motifs, as well as to prove that strict area minimization favors global pitch balance.

References

[1] Andrade P. Enneper immersions. *J. Anal. Math.* **75**: 121–134, 1998.
[2] Bussi Y., Shimoni E., Weiner A., Kapon R., Charuvi D., Nevo R., Efrati E., and Reich Z. Fundamental helical geometry consolidates the plant photosynthetic membrane. *Proc. Natl. Acad. Sci.* **116**: 22366–22375, 2019.
[3] Guven J., Huber G., and Valencia D. M. Terasaki spiral ramps in the rough endoplasmic reticulum. *Phys. Rev. Lett.* **113**: 188101, 2014.
[4] Helfrich W. Elastic properties of lipid bilayers: theory and possible experiments. *Z. Naturforsch. C* **28**: 693–703, 1973.
[5] Mustárdy L., Buttle K., Steinbach G., and Garab G. The three-dimensional network of the thylakoid membranes in plants: quasihelical model of the granum-stroma assembly. *Plant Cell* **20**: 2552–2557, 2008.
[6] Terasaki M., Shemesh T., Kasthuri N., Klemm R. W., Schalek R., Hayworth K. J., Hand A. R., Yankova M., Huber G., Lichtman J. W., Rapoport T. A., and Kozlov M. M. Stacked endoplasmic reticulum sheets are connected by helicoidal membrane motifs. *Cell* **154**: 285–296, 2013.

CHARACTERIZINGHIGH-RATE, FINITE MATERIAL DEFORMATIONS OF SOFT MATERIALS IN INERTIAL MICROCAVITATION

Selda Buyukozturk[1,2], and Christian Franck [2]
[1]School of Engineering, Brown University, Providence, Rhode Island, USA
[2]Department of Mechanical Engineering, University of Wisconsin - Madison, Madison, Wisconsin, USA

Summary We recently developed a new method to characterize the constitutive behavior of soft materials undergoing high-strain rate deformations using laser-induced cavitation, called Inertial Microcavitation Rheometry. However, the current theoretical framework was developed with limited experimental modulation of bubble amplitude limiting the regime of accessible material deformations. The model also neglects to address inelastic material behavior at large material stretches. This study focuses on experimentally identifying critical material stretches during the transition from viscoelastic to inelastic behavior by systematically controlling bubble amplitude and material deformations over a large stretch range. This critical experimental data will lay the foundation for incorporating damage and failure mechanisms of inelastic behavior of soft materials undergoing high-strain rate deformations.

MOTIVATION

The motivation of this study is to develop a deeper understanding of inertial cavitation and its resulting bubble dynamics in soft materials, which has significant applications in the study of biological tissues, polymeric coatings, biofouling, composites and other synthetic materials. Laser-induced cavitation (LIC) is a thermally driven inertial process with the ability to characterize material behavior at high-strain rate ($10^3 - 10^8\ s^{-1}$) deformations. Through the integration of appropriate theoretical framework, material stresses and strains during cavitation can be estimated for homogeneous, isotropic materials through Inertial Microcavitation Rheometry (IMR), a tool we recently developed to characterize the non-linear viscoelastic properties of soft materials at high strain rates [1].

The previous development of IMR has considered only a limited material stretch ratio regime, neglecting to incorporate inelastic material behavior. This study aims to: (1) identify the critical material stretches exhibited at the transition from viscoelastic to inelastic material behavior and (2) develop new experimentation for the modulation of LIC bubble amplitudes. Experimental methods to achieve these aims include varying cavitation laser energy and using micron-sized heat sink particles to drive bubble nucleation. This characterization will pave the way to future work in the development and incorporation of damage and failure mechanisms into the theoretical framework.

BACKGROUND

LIC is a reliable and robust experimental method for generating spatially-controlled microns sized cavitation bubbles in soft materials. Complex nucleation physics generally results in the ionization and formation of a bubble consisting of an approximate two-phase vapor and gas mixture. The resulting oscillating bubble interacts with the surrounding material and is modelled to determine constitutive behavior to predict material stresses and strains at high-strain rates.

Inertial Microcavitation Rheometry (IMR)

IMR uses the experimentally obtained high-speed time-lapse data of bubble oscillations within the given material of interest, and for spherically symmetric bubbles computes the temporal evolution of the bubble radius, R(t) [1]. The normalized value $R(t) / R_{eq}$ is also defined to be the material stretch, $\lambda(t)$. Assuming spherical bubble symmetry and near-field material incompressibility, the 1D momentum balance and conservation of mass equations, with the incorporation of traction and kinematic boundary conditions of the bubble, present the Keller-Miksis equation,

$$(1-\frac{\dot{R}}{c})R\ddot{R}+\frac{3}{2}(1-\frac{\dot{R}}{3c})\dot{R}^2=\frac{1}{\rho}(1+\frac{\dot{R}}{c})(p_b-\frac{2\gamma}{R}+S-p_\infty)+\frac{1}{\rho}\frac{R}{c}\overline{(p_b-\frac{2\gamma}{R}+S)}^{\cdot} \quad (1)$$

R is bubble radius, c is material wave speed, ρ is mass density, p_b is bubble pressure, γ is surface tension, and p_∞ is far-field pressure. S describes the constitutive material behavior as a function of hoop and radial stress. IMR employs the least squares method to best fit material parameters across several constitutive models to determine the best material fit.

EXPERIMENTAL APPROACH

A Q-switched 532nm Nd:YAG laser (Amplitude) with 6ns pulse is aligned into the back port of a Ti2 Nikon Microscope. As shown in Figure 1a, a dichroic notch filter is used to path the laser into the back aperture of a microscope objective to focus the beam within the volume of a hydrogel to initiate cavitation. Bubble kinematics are imaged through the objective using a high-speed camera. Laser energy attenuation is controlled with Neutral Density (ND) filters placed in beam path and laser energy is measured with an EnergyMax Sensor (Coherent). Isotropic homogeneous polyacrylamide hydrogels are used for cavitation: “soft” and “stiff” gels with quasi-static shear moduli, $G_{\infty,soft}$=0.461 kPa and $G_{\infty,stiff}$=2.97 kPa. Separate polyacrylamide samples were made with 20μm polystyrene particles with conductive paramagnetic coating. These particles, hereto referred to as heat sink particles, are used to lower the bubble nucleation threshold in the gels.

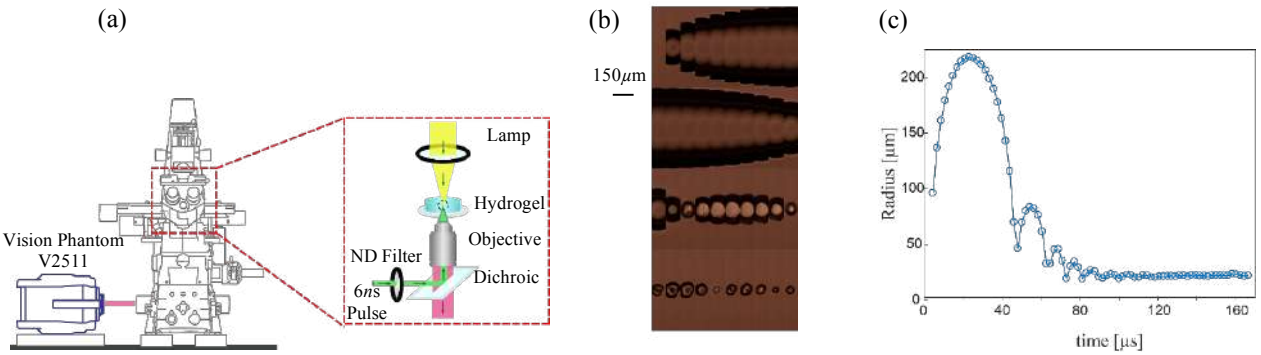

Figure 1. (a) LIC experimental setup on Ti2 Nikon Microscope (b) LIC bubble time-lapse (2-3μs per frame) in polyacrylamide (c) Radius vs. time of LIC bubble in polyacrylamide (sampled at 480k fps)

PRELIMINARY RESULTS & CONCLUSIONS

Polyacrylamide hydrogels undergoing large finite deformations at high strain-rates have been measured and fitted to a non-linear Kelvin-Voigt model, which extends the traditional quasi-static Neo-Hookean description of polyacrylamide to include dynamic shear viscosities [1]. However, at high laser energies, the model may fail to capture the complete bubble dynamics due to unaccounted inelastic material behavior. Experimentally, this is reflected in loss of bubble amplitude, as well as bubble asphericity. As schematically depicted in Figure 2a, experimental bubble radius vs. time is compared to its simulated IMR curve. The first peak consistently fits well, but there is a discrepancy for subsequent peaks unaccounted for by the current IMR nonlinear viscoelastic model.

In Figure 2b, bubbles in polyacrylamide were nucleated at relatively high laser energies. An increase in laser energy increased the maximum bubble radius, in line with other energetics studies performed in literature [2]. At the same laser energies, "soft" polyacrylamide exhibited a higher bubble amplitude than "stiff".

R_{max} and R_{eq} scale with laser energy and within this regime, the maximum material stretch ratio is relatively constant. For "soft" polyacrylamide for example, the maximum stretch ratio is approximately 9 across all energy levels. When laser energy is drastically decreased, the energy threshold may be too low to overcome the dielectric breakdown barrier required for bubble nucleation. In this presentation, we will show that when a lower energy laser is focused at a micron-sized heat sink particle, a bubble will not only successfully nucleate, but the material stretch ratio will drastically decrease. Preliminary results indicate the ability to change the material stretch experimentally to explore the complete finite deformation range of polyacrylamide.

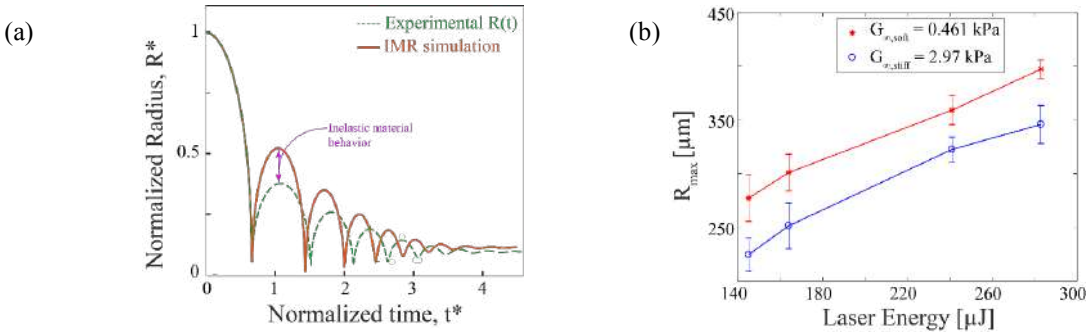

Figure 2. (a) Schematic showing IMR simulation at large material stretches and experimental discrepancy (b) R_{max} vs. laser energy

This study will test the limitations of current IMR model to identify critical stretches at the transition from viscoelastic to inelastic material behavior, as well as provide new experimental methods for controlled bubble amplitude modulation. The experimental acquisition of a full finite deformation regime will lay the foundation for the incorporation of inelastic material behavior into the theoretical framework. Studies such as energy loss through the material, asphericity, rupture, wrinkling, and more may be included ultimately improving our fundamental understanding of the high-rate deformation behavior of soft materials and improve our ability to predict constitutive material properties and material performance.

References

[1] Estrada, Jonathan B., et al. "High strain-rate soft material characterization via inertial cavitation." *Journal of the Mechanics and Physics of Solids* 112 (2018): 291-317.

[2] Quinto-Su, Pedro A., Madoka Suzuki, and Claus-Dieter Ohl. "Fast temperature measurement following single laser-induced cavitation inside a microfluidic gap." *Scientific reports* 4 (2014): 5445.

THE ONSET OF PLASTICITY THROUGH INFLATION OF THIN FILMS

Federico Bosi*[1] and Khurram Suleman[1]
[1] Department of Mechanical Engineering, University College London, London, UK

Summary We present a novel approach that enables a reliable characterisation of the yield strength through the sharp change in strain distribution that develops at the onset of plasticity when soft membranes are inflated. The method is based on a finite strain solution for the mechanical response of pressurised elastoplastic thin films, analytically obtained and numerically validated. Non-contact optical experiments are performed on different materials and prove the accuracy of the proposed technique, thus opening new perspectives for the prediction of the yield stress of structural membranes in a wide range of thermo-mechanical loading conditions.

INTRODUCTION

The use of thin films in lightweight structures is rapidly increasing, with applications ranging from soft robotics to advanced aerospace systems. Therefore, a comprehensive understanding of membranes governing deformation mechanisms is required to predict their complex time and temperature-dependent responses [1]. In particular, it is recognised that a reliable experimental method to assess the onset of plasticity in thin films is missing [2], and it limits the knowledge of the yield condition, thus preventing an optimal design of membrane structures. Currently, the experimental determination of the yield strength in structural thin sheets strongly depends on the methodology employed for its detection, leading to unacceptable variability in the results. In order to overcome the difficulty of a precise measurement of the (visco)elastoplastic threshold, an alternative material-independent imaging technique is here developed.

FINITE STRAIN ELASTOPLASTIC INFLATION OF SOFT MEMBRANES

The mechanics of pressurised membranes has been treated by several authors, who investigated the elastic, hyperelastic and perfectly plastic inflation of circular isotropic thin sheets [3, 4]. However, the mechanical response of an elastoplastic thin film has never been studied before, and it is presented here as the foundation of the proposed experimental technique to assess the onset of plasticity. A flat circular membrane of initial radius r_0 and thickness h_0 is subjected to a pressure p. Under the plane stress assumption, the finite strain formulation can be obtained by rearranging the equilibrium equations and compatibility conditions into a system of differential equations

$$\begin{cases} r\dfrac{d\epsilon_\theta}{dr} = e^{\epsilon_r-\epsilon_\theta}\sqrt{1-e^{-2\epsilon_r}\left(\dfrac{dw}{dr}\right)^2}-1 \\ \dfrac{2}{\sqrt{3}}re^{\epsilon_\theta}\left(\dfrac{d\bar{\sigma}}{dr}\cos\phi-\bar{\sigma}\sin\phi\dfrac{d\phi}{dr}+\bar{\sigma}\cos\phi\dfrac{d\epsilon_h}{dr}\right)+\bar{\sigma}\left(\dfrac{1}{\sqrt{3}}\cos\phi-\sin\phi\right)\sqrt{e^{2\epsilon_r}-\left(\dfrac{dw}{dr}\right)^2}=0 \\ \dfrac{dw}{dr} = -\dfrac{\sqrt{3}rp}{4h_0\bar{\sigma}\cos\phi}e^{\epsilon_r+\epsilon_\theta-\epsilon_h} \end{cases} \tag{1}$$

where w is the vertical displacement, $\bar{\sigma}$ and ϕ are introduced to parametrise the stress components σ_r and σ_θ and r, θ, h represent the radial, circumferential and thickness directions, respectively. The strain components $\epsilon_r, \epsilon_\theta, \epsilon_h$ are defined by an isotropic strain hardening bilinear constitutive model, characterised by the yield stress σ_y, Fig. 1a. Therefore, the unknowns $\bar{\sigma}, \phi, w$ can be obtained by numerically solving eq. (1) through the Euler method, iterating over the radial domain for different values of the pressure p until the boundary condition $w(r_0) = 0$ is satisfied.

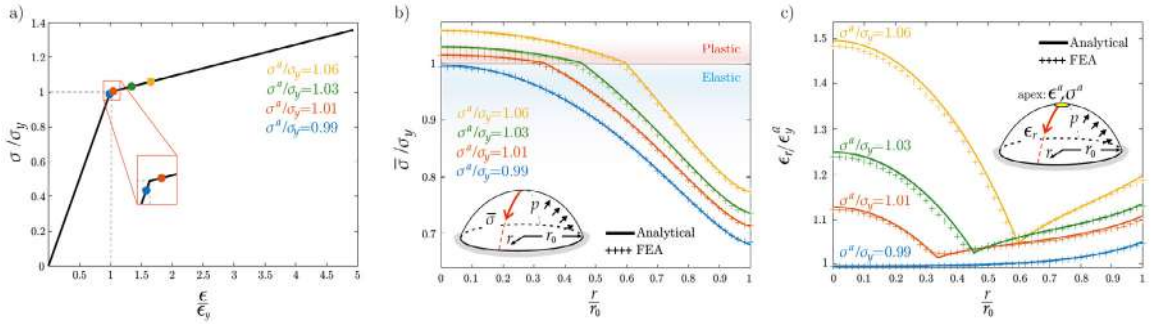

Figure 1: Inflation of circular elastoplastic membranes: (a) strain hardening bilinear constitutive relation; comparison between analytical and FEA solutions for the radial distribution of normalised equivalent stress $\bar{\sigma}/\sigma_y$ (b) and normalised radial strain ϵ_r/ϵ_y^a (c).

*Corresponding author. E-mail: f.bosi@ucl.ac.uk

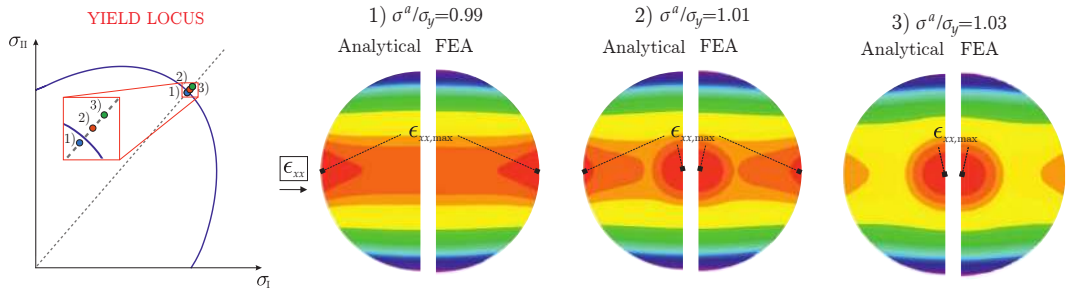

Figure 2: Yield domain and comparison between analytical and FEA contour plots of the horizontal strain ϵ_{xx} across the membrane, showing the sudden and distinct change in maximum strain distribution ($\epsilon_{xx,\text{max}}$) that characterises the onset of plasticity.

The obtained results are presented in Fig. 1b,c together with the finite element solution (Abaqus, Dassault Systèmes), which validates the theoretical approach. The dimensionless equivalent stress $\bar{\sigma}/\sigma_y$ and normalised radial strain ϵ_r/ϵ_y^a (ϵ_y^a is the yield strain at the apex) are reported for four different values of the dimensionless equibiaxial apex stress $\sigma^a/\sigma_y = [0.99, 1.01, 1.03, 1.06]$ in the proximity of the onset of plasticity. Fig. 1c shows the drastic change in strain distribution when plastic deformations develop from the centre of the thin film. In particular, when the membrane is in the elastic regime (blue curve, $\sigma^a/\sigma_y = 0.99$), the maximum radial strain lies at the edge of the membrane, while immediately after the onset of irreversible deformations (red curve, $\sigma^a/\sigma_y = 1.01$), the highest radial strain moves to the centre, which corresponds to the apex of the inflated membrane.

The rapidly developing strain localisation associated with the onset of plasticity is highlighted in Fig. 2, which reports the yield surface for J2 plasticity and the contour plots of the horizontal strain ϵ_{xx} for three subsequent normalised stress values at the membrane apex, corresponding to different inflation pressures. This phenomenon, demonstrated here for an elastoplastic bilinear model, can be proven for distinct constitutive relations and materials. Therefore, the observed localisation can be employed for the development of a novel imaging technique to assess the yield strength in thin films.

EXPERIMENTAL DETERMINATION OF THE ONSET OF PLASTICITY

The abrupt change in strain distribution that emerges at the onset of plasticity has been experimentally validated on a custom made setup, where the in-plane strains of LLDPE membranes were measured through digital image correlation (VIC3D, Correlated Solution). Fig. 3 reports the horizontal strain across the thin sheets, highlighting the localisation that suddenly develops when the yield domain is reached. Since the maximum horizontal (and radial) strain quickly change location when plasticity develops, moving from the edges to the centre, we can assume that yielding develops when $\epsilon_{xx,\text{edge}} = \epsilon_{xx,\text{centre}}$. Therefore, we were able to measure in real-time the yield strength of the viscoelastic material for a wide range of temperatures and strain rates, with a maximum relative error of 7% when compared with the time-consuming strain recovery procedure, considered the most reliable one [5]. The proposed experimental method has been further proven by applying it to aluminium foils and PEEK films, showing excellent results in the yield stress prediction.

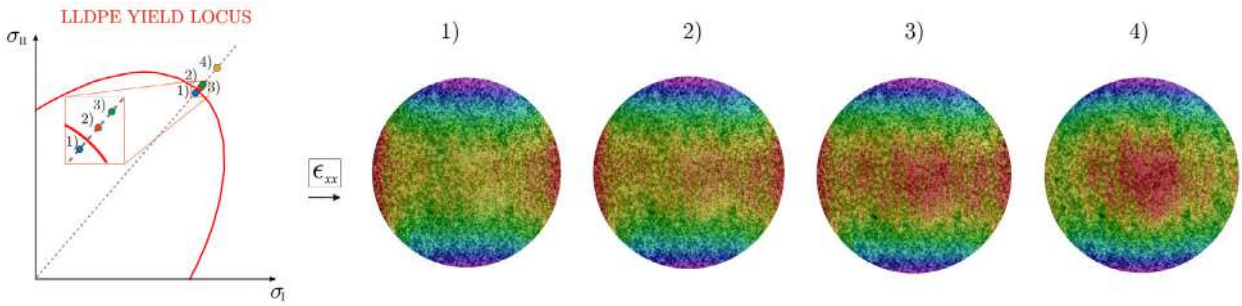

Figure 3: Experimental observation of strain localisation in LLDPE inflated membranes: yield surface and ϵ_{xx} strain contour plots. The abrupt change in strain distribution that develops at the onset of plasticity is employed for a reliable assessment of the yield stress.

References

[1] Bosi F., Pellegrino S. Nonlinear thermomechanical response and constitutive modeling of viscoelastic polyethylene membranes.*Mech. Mater.* **117**, 9-21, 2018.
[2] Gurmessa B., Croll A. Onset of plasticity in thin polystyrene films. *Phys. Rev. Lett.* **110**, 074301, 2013
[3] Adkins J. E., Rivlin R. S. Large elastic deformations of isotropic materials IX. The deformation of thin shells. *P. Roy. Soc. A*, **244**, 505-531, 1952.
[4] Wang N. M., Shammamy M. R. On the plastic bulging of a circular diaphragm by hydrostatic pressure. *J. Mech. Phys. Solids*, **61**, 17-43, 1969.
[5] Bosi F., Pellegrino S. Molecular based temperature and strain rate dependent yield criterion for anisotropic elastomeric thin films.*Polymer* **125**, 144-153, 2017.

FLUTTER OF ELASTIC RODS SUBJECT TO ZIEGLER AND REUT LOADS

Davide Bigoni[1]
[1]Department of Civil, Environmental and Mechanical Engineering, Università di Trento, Trento, Italy

Summary Flutter and divergence instabilities are theoretically and experimentally analysed in elastic structures subject to follower loads of the Ziegler type and to loads acting on a line of the Reut type. It is shown how these loads can be obtained through an exploitation of Coulomb friction. Computer simulations and experiments on scale models reveal how flutter and divergence develop and how they are influenced by dissipation.

INTRODUCTION

Non-conservative loads are advocated as sources of dynamic instabilities such as flutter and divergence. One of these loads is the tangential follower force considered by Ziegler [10] and another is a force constrained to act along a fixed straight line, as introduced by Reut [8], see also Bolotin [4].

The problem with these loads is their realization, which has been considered impossible during the last fifty years [5, 6].

REALIZATION OF THE NON-CONSERVATIVE FORCES

Following Bigoni and Noselli [3], Bigoni et al. [1] and Bigoni and Misseroni [2] it is shown, both theoretically and experimentally, how to obtain the Ziegler's (Fig. 1) and Reut's (Fig. 2) forces by exploiting contact with Coulomb friction.

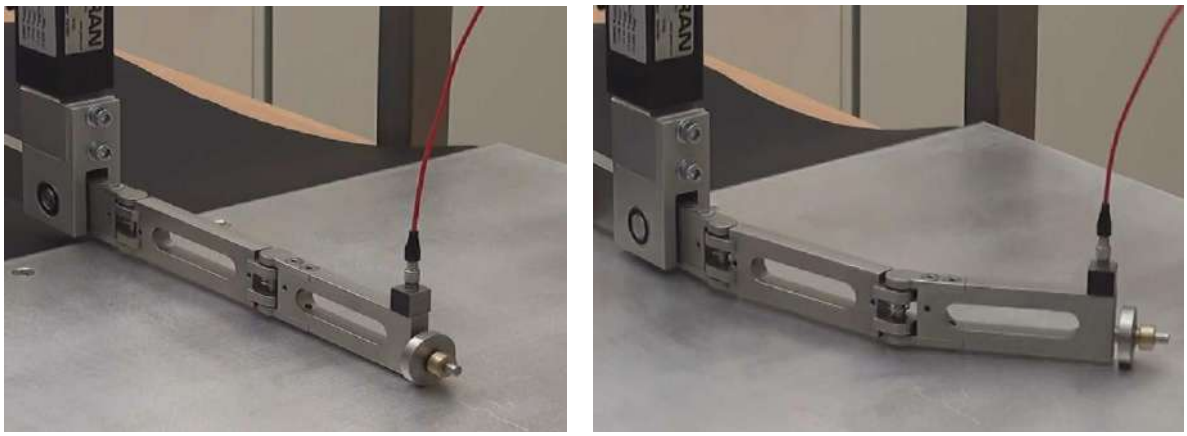

Figure 1. The realization via Coulomb friction of the follower load postulated by Ziegler.

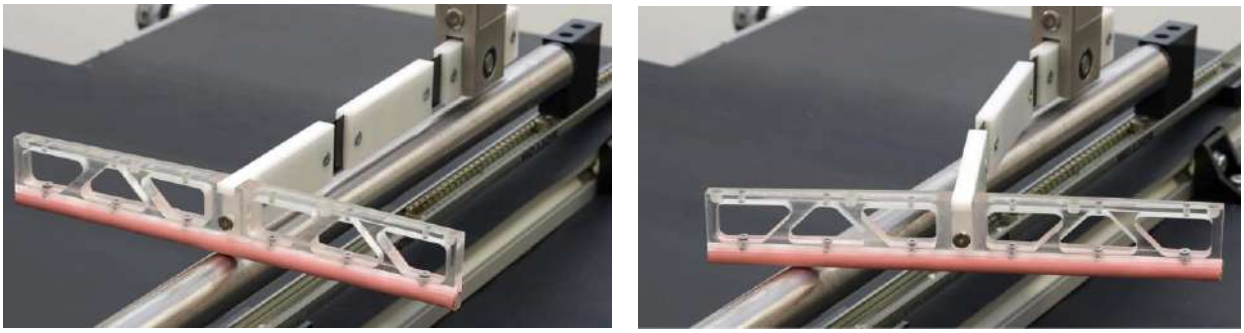

Figure 2. The realization via Coulomb friction of the follower load postulated by Reut.

FLUTTER & DISSIPATION-INDUCED INSTABILITIES

Viscosity was theoretically proven to have a detrimental effect on the stability with respect to flutter and Hopf bifurcations [7, 9]. In the limit of vanishing viscosity, the so-called Ziegler paradox was found, which corresponds to a discontinuity in the critical load occurring in the limit. Effects related to the viscosity remained so far not validated experimentally, so that an experimental campaign was performed to highlight these. Experiments are shown to provide positive evidence to the theoretical results.

CONCLUSIONS

Flutter and divergence instabilities, as well as the detrimental effect of viscosity on critical loads, are documented indisputably, thus bringing an end to a long debate and opening a new research area, with perspective applications to mechanical actuators, high-precision cutting tools, or energy harvesting devices.

References

[1] Bigoni, D., Kirillov, O., Misseroni, D., Noselli, G.Tommasini, M. Flutter and divergence instability in the Pflüger column: Experimental evidence of the Ziegler destabilization paradox. *J. Mech. Phys. Solids* **116**: 99-116, 2018.

[2] Bigoni D. and Misseroni D. Structures loaded with a force acting along a fixed straight line, or the "Reut's column problem" *J. Mech. Phys. Solids* **134**: 103741, 2020.

[3] Bigoni, D., Noselli, G. Experimental evidence of flutter and divergence instabilities induced by dry friction. *J. Mech. Phys. Solids* **59**: 2208-2226, 2011.

[4] Bolotin, V.V. Nonconservative problem of the theory of elastic stability. Pergamon Press, New York, 1963.

[5] Elishakoff, I. Controversy associated with the so-called "follower force": critical overview. *Appl. Mech. Rev.* **58**: 117-142, 2005.

[6] Koiter, W.T. Unrealistic follower forces. *J. Sound Vibration* **194**: 636-638, 1996.

[7] Krechetnikov, R., Marsden, J.E. Dissipation-induced instabilities in finite dimensions. *Rev. Modern Phys.* **79**: 519-553, 2007.

[8] Reut, V.I. About the Theory of Elastic Stability. *Proceedings of the Odessa Institute of Civil and Communal Engineering* **1**, 1939.

[9] Tommasini, M., Kirillov, O., Misseroni, D., Bigoni, D. The destabilizing effect of external damping: Singular flutter boundary for the Pfluger column with vanishing external dissipation *J. Mech. Phys. Solids* **91**, 204-215, 2016.

[10] Ziegler, H. Die Stabilitätskriterien der Elastomechanik *Ing. Archiv* **XX**, 49-56, 1952.

INFLATABLES MAZES: FROM FLAT SHEETS TO 3D STRUCTURES.

Emmanuel Siéfert[1], Julian Panetta[2], Tian Gao[1], Étienne Reyssat[1], José Bico*[1], Mark Pauly[2], and Benoît Roman[1]
[1]Physique et Mécanique des Milieux hétérogènes, CNRS, ESPCI Paris, PSL Research University, Sorbonne Université and Université de Paris, France
[2]Computer Graphics and Geometry Laboratory, EPFL, Lausane, Switzerland

Summary We present a simple technique to encode 3D shapes on flat fabrics through metric changes. Our technique is inspired by curved folded and Miura-ori origami and is based on the inflation of a channel network obtained by heat-sealing two opposite pieces of fabric. Similarly to folds in origami, inflated channels induce a strongly anisotropic in-plane contraction which dictates the Gaussian curvature of the deployed structure. We present different strategies to control such differential contraction and discuss a numerical inverse model. In addition to shapes, we describe the mechanical properties of the inflated structure that involve both material properties and pressure.

INTRODUCTION: CHANGING METRICS TO CHANGE SHAPES

Cartographers have long been faced with the problem of deforming the continents in order to project the Earth on a flat map. Similarly, wrapping a ball with a sheet of paper induces wrinkles where the excess of paper is stored. Indeed, changing the Gaussian curvature of a surface (the product of both main curvatures) requires a change in metrics, i.e. the distances between material points along the surface. Many living structures, e.g. plant leaves, rely on differential growth to adopt complex 3D shapes [1]. Differential growth has been a source of inspiration for recent developments such as swelling hydrogels [2, 3, 4], liquid crystal elastomers [5, 6], dielectric elastomers [7, 8] or *baromorph* materials [9]. However, these systems are based on soft elastomers and large size structures tend to sag under their own weight.
Traditional origami is also an elegant way to transform an unstretchable flat sheet into a complex 3D structure. In this case, folds may accommodate the excess of surface resulting from a change in the apparent metric of the structure [10, 11]. As the sheet is locally simply bent, stiff materials may be used, e.g. polymers, metals or event graphene sheets [12]. However, folding flat origami outlines into shape can be complex.

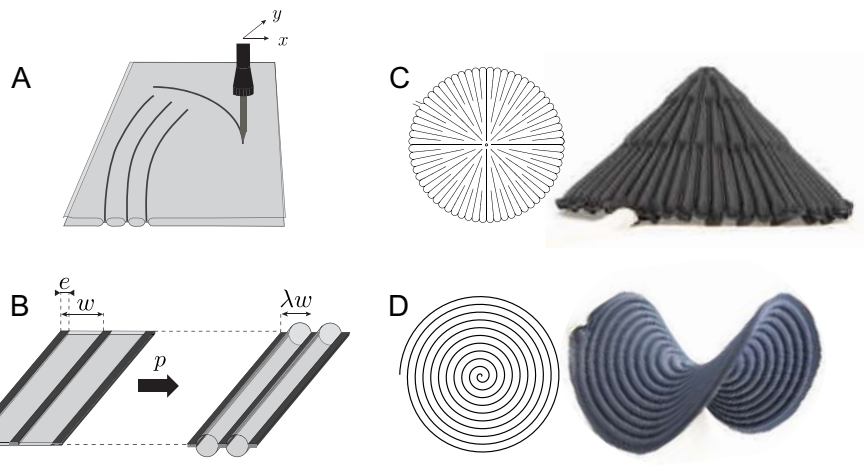

Figure 1: **A** Heal-sealing process: a network of channels is printed on two superimposed pieces of fabric coated with a thermoplastic layer. **B** Upon inflation, the section of the channels contracts while the length remains unchanged which induces differential metric change of the fabric. **C** Conical shape obtained with radial channels. **D** Saddle shape resulting from orthoradial channels.

INFLATING MAZES

We present here an alternative concept to transform initially flat sheets into stiff and lightweight inflatable shells (Fig.1A). Two flat superimposed sheets (typically made of thermoplastic coated fabric) are sealed together along a specific pattern of seam lines, defining a "maze" of channels. A soldering iron mounted on an XY-plotter directly prints the pattern [13]. Inflation induces in-plane contraction perpendicular to the channels through the local bending of the sheets. This contraction mechanism plays the same role as a fold in origami: the seam lines are equivalent to the positions of valley folds, with mountain folds in between (Fig. 1B). As a simple example, a structure with radial seams adopts a conical shape

*Corresponding author. E-mail: jose.bico@espci.fr

(Fig. 1C), as radial folds in a disk of paper would lead to a cone. Conversely, a disk with circular channels buckles into a saddle shape (Fig. 1D) equivalent to origami structures involving circular folds [14]. In contrast with standard origami, the deployment of the 3D structure is here spontaneous and does not require mechanical actuation of individual folds. Moreover, while rigidly-foldable origami tessellations may involve soft deployment modes, the effective folding angle of inflatable mazes is fixed by volume maximization. The shape is dictated by the design of the maze and does not rely on a complex assembly of flat patches, as in common inflatable structures [15]. We present and rationalize three different strategies (curved channels, seams of varying width, zig-zag seams) to distort the metrics and propose analytic ways to program simple geometric shapes ranging from domes to helices (Fig. 2). Such strategies are the source of an inverse model solved with numerical tools developed in the computer graphics community. We finally discuss the mechanical properties of the inflated structures. Internal pressure p provides stiffness to the resulting structure that is similar to other large scale inflatables, such as fabric air beams, stratospheric balloons or architectural buildings [16]. We show how the bending and stretching rigidity of these inflates mazes both depend on the applied pressure and on material stiffness.

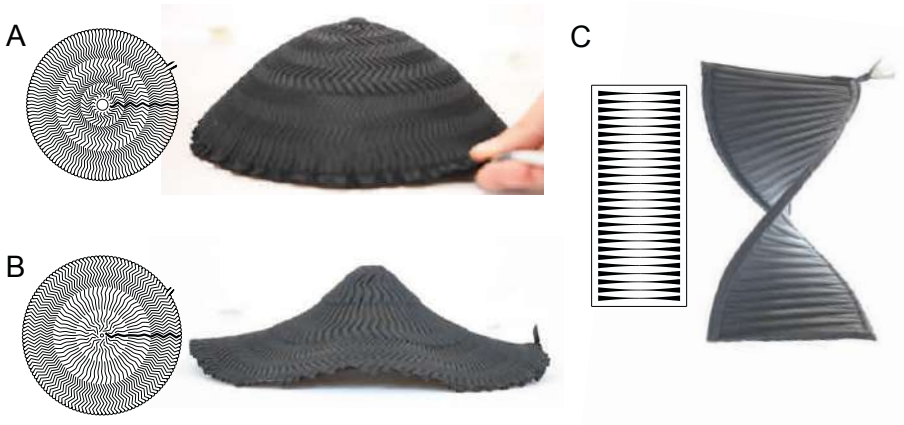

Figure 2: **A** and **B** Dome and hat obtained with a zig-zag pattern reminiscent of Miura-ori tesselation. **C** Helix obtained by tuning the width of the seam lines.

References

[1] U. Nath, B. Crawford, R. Carpenter, and E. Coen. Genetic control of surface curvature. *Science*, 299:1404, 2003.

[2] Yael Klein, Efi Efrati, and Eran Sharon. Shaping of elastic sheets by prescription of non-euclidean metrics. *Science*, 315, 2007.

[3] Jungwook Kim, James A. Hanna, Myunghwan Byun, Christian D. Santangelo, and Ryan C. Hayward. Designing responsive buckled surfaces by halftone gel lithography. *Science*, 335(6073):1201–1205, 2012.

[4] A. Sydney Gladman, Elisabetta A. Matsumoto, Ralph G. Nuzzo, L. Mahadevan, and Jennifer A. Lewis. Biomimetic 4d printing. *Nature Materials*, 15(413), 2016.

[5] Cyrus Mostajeran, Mark Warner, Taylor H Ware, and Timothy J White. Encoding gaussian curvature in glassy and elastomeric liquid crystal solids. *Proceedings of the Royal Society A: Mathematical, Physical and Engineering Sciences*, 472(2189):20160112, 2016.

[6] H. Aharoni, Y. Xia, X Zhang, R.D. Kamien, and S. Yang. Universal inverse design of surfaces with thin nematic elastomer sheets. *Proc. Natl. Acad. Sci.*, 2018.

[7] Hadrien Bense, Miguel Trejo, Etienne Reyssat, José Bico, and Benoît Roman. Buckling of elastomer sheets under non-uniform electro-actuation. *Soft matter*, 13(15):2876–2885, 2017.

[8] Ehsan Hajiesmaili and David R Clarke. Reconfigurable shape-morphing dielectric elastomers using spatially varying electric fields. *Nature communications*, 10(1):183, 2019.

[9] E Siéfert, E Reyssat, J Bico, and B Roman. Bio-inspired pneumatic shape-morphing elastomers. *Nature materials*, 18(1):24, 2019.

[10] Levi H Dudte, Etienne Vouga, Tomohiro Tachi, and L Mahadevan. Programming curvature using origami tessellations. *Nature materials*, 15(5):583, 2016.

[11] Yan Zhao, Yuki Endo, Yoshihiro Kanamori, and Jun Mitani. Approximating 3d surfaces using generalized waterbomb tessellations. *Journal of Computational Design and Engineering*, 5(4):442–448, 2018.

[12] Marc Z Miskin, Kyle J Dorsey, Baris Bircan, Yimo Han, David A Muller, Paul L McEuen, and Itai Cohen. Graphene-based bimorphs for micron-sized, autonomous origami machines. *Proceedings of the National Academy of Sciences*, 115(3):466–470, 2018.

[13] J. Ou, M. Skouras, N. Vlavianos, F. Heibeck, C.-Y. Cheng, J. Peters, and H. Ishii. aeromorph-heat-sealing inflatable shape-change materials for interaction design. In *Proceedings of the 29th Annual Symposium on User Interface Software and Technology*, pages 121–132. ACM, 2016.

[14] M.A. Dias, L.H. Dudte, L. Mahadevan, and C.D. Santangelo. Geometric mechanics of curved crease origami. *Physical review letters*, 109(11):114301, 2012.

[15] M. Skouras, B. Thomaszewski, P. Kaufmann, A. Garg, B. Bickel, E. Grinspun, and M. Gross. Designing inflatable structures. *ACM Trans. Graph.*, 33(4):63:1–63:10, July 2014.

[16] T. Herzog. *Pneumatic Structures: a hanbook of inflatable architecture*. Oxford University Press, 1976.

EXTREME DEFORMATION OF AUXETIC RUBBER SHEETS: AN EXPERIMENTAL AND NUMERICAL ANALYSIS

Filippo Agnelli[1], Pierre Margerit[1], Andrei Constantinescu *[1], Paolo Celli[2], and Chiara Daraio[3]
[1]LMS,CNRS,École polytechnique,Institut polytechnique de Paris,Palaiseau,France.
[2]Department of Civil Engineering, Stony Brook University, Stony Brook, USA
[3]Department of Mechanical and Civil Engineering, California Institute of Technology, Pasadena, CA, USA

Summary Imparting elastic sheets with a controlled pattern enables the creation of materials with unusual characteristics. Herein, we analyse the tensile and shear response of laser cut rubber sheets featuring an auxetic pattern designed via topology optimization. A set of dedicated experimental and numerical tools are adapted for this purpose. Quasi-static mechanical tests up to 50% effective strain, associated with image processing techniques and a robust digital image correlation permit to detect the geometry contour and measure displacements and strains fields. The results are compared with a FE-analysis, undertaken using a hyper-elastic Mooney-Rivlin constitutive law. The numerical results remarkably grasp the experiments, and appear as a good indicator to assess the impact of the manufacturing process, geometry non-linearity and base material non-linearity on the final properties.

Keywords auxetic, rubber, digital image correlation, identification

Soft elastomers readily change their shapes in response to external stimuli, such as mechanical load or heat. Their high thoughness and capability to withstand large deformations have been harnessed in a wide range of emerging fields including stretchable electronics, soft robotics and biomimetics [9, 8, 10, 6]. Poisson's ratio is another key parameter to consider, as it determines the deformation shape of the material and has a major contribution to modulate shear modulus and bulk modulus from the solid mechanics background. Remarkably, the Poisson's ratio of elastomers is contained in a narrow range with a value close to 0.5, and nearly invariant in all directions [7]. Alternatively, the Poisson's ratio of a material can deviate from its inherent value by introducing cellular structures [4]. Additionally, in thin sheets, architectured cut patterns are easily fabricated via subtractive technologies. Auxetics are materials that expand transversely under an applied uniaxial stretch load and vice versa by means of a tailored structural mechanism. Classical embodiments enable the control over a small range of strains ($\sim 10\%$).

In this work, we investigate the evolving pattern transformation under uniaxial loading at finite strain of laser cut rubber sheets with a periodic pattern derived from a topology optimization procedure, through experiments and simulations. After introducing the experimental facility, testing method, material models and modelling strategy, we discuss the observed effective properties and compare them to the finite element simulations.

EXPERIMENTAL AND COMPUTATIONAL METHODOLOGY

More precisely, we analyze the deformation of rubber sheets patterned with an auxetic design proposed in [2]. The design of the elementary unit cell, illustrated in Figure 1(a-b), results from a topology optimization procedure combining the level set method and the asymptotic homogenization theory [3] with the objective of prescribing effective elasticity tensor and more specifically Poisson's ratio. The designed geometry resembles a typical re-entrant honeycomb structure, with trusses of varying width. The macroscopic behaviour of the periodic unit cell carries an orthotropic symmetry. To identify experimentally the complete two-dimensional constitutive behaviour, 3 sorts of specimen were devised (2 specimens for vertical and horizontal uniaxial tensile tests respectively, 1 specimen for a shear test) consisting of a periodical assembling from the optimal unit cell. The repetition of unit cell was adapted, such that the local constraints of the clamps cause minor deviations when evaluating the elastic properties at the center of the specimen. The specimen were laser cut from a 1.5mm-thick natural rubber sheet, then mechanically tested on a universal Instron 10kN tensile machine (mounted 50N load cell) up to 50% effective strain. For the shear test, a specific set-up consisting of 2 plexiglass plates was required to constrain the deformation in the focal plane, as shown in Figure 1(c). During the mechanical tests, a digital camera recorded images of the specimen surface to allow for displacement field measurements via digital image correlation. A black and white speckle pattern was applied on the specimen surface using sprayed paint to increase the image contrast. The mechanical properties of natural rubber were equally explored through uniaxial tensile tests on standard dog-bone specimens. A Mooney-Rivlin incompressible hyper-elastic model, acceptable for intermediate elongations (50-100%), was selected to fit the experimental stress–strain response and calibrate material parameters. Using the experimental data, local and global approaches to digital image correlation were employed to measure displacement and strain field. Elastic properties of the macroscopic continuum could be identified, and their evolution at finite strain could be tracked. Full-field measurements by means of digital image correlation (DIC) were carried out using an in house programming operating on MATLAB software. The experimental mesh was obtained using classical image processing on the reference image of the specimen surface. In complement to experiments, finite element computation were undertaken under the assumption of large transformations, plane stress using the finite element solver Cast3M 2018 [1]. The mesh was obtained using image processing from the binarized images of the optimal level set function, from Figure 1(a) and completed to the sample geometry. The material parameters of the hyper-elastic model were identified from the tensile curve of the base material.

*Corresponding author. E-mail: andrei.constantinescu@polytechnique.edu.

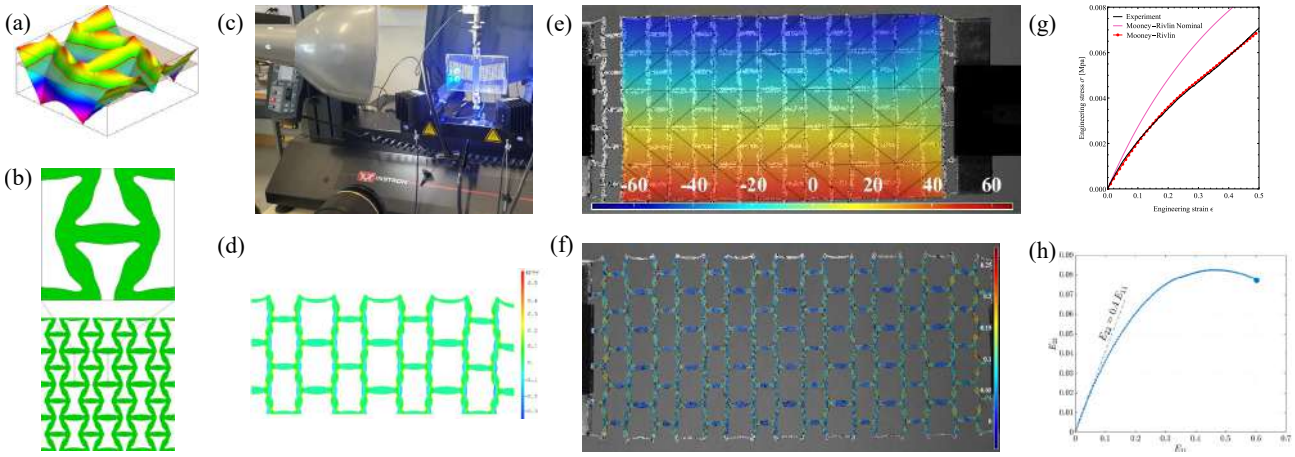

Figure 1: An overview of the experimental and numerical protocol. (a) Level set function to characterize the geometry of the unit cell. (b) Unit cell and of a 4×4 assembly. (c) Experimental setup for the shear test, the sample, constrained between 2 plexiglas plates, is pulled in its center and held at each borders. (d). Strain field resulting from FE-analysis. (e) Vertical displacement field in pixels using local-DIC, i.e. tracking locally the displacement of the hinges (f) Strain field, global-DIC. (g) Stress-strain curve for horizontal tension, comparison with the numerical model (h) Evolution of the apparent Poisson's ratio with respect to the longitudinal strain.

RESULTS AND DISCUSSION

During both horizontal and vertical tensile extensions, a lateral expansion indicating a negative Poisson's ratio was clearly visible. A first local-DIC measurements was performed to comfort this visual observations. We measured the macroscopic displacement at each nodes of the honeycomb, and derived a strain field, as illustrated in Figure 1 (e). The ratio of the averaged strain components yields an effective Poisson's ratio. The displacements fields obtained using global-DIC measurements permit a further comparison with predictions and give an insight of the deformation mechanism of the samples, i.e. how the structure moves and deforms. The specimens exhibited a structural deformation at small strain, where different parts of the "lattice" behave as rigid struts and deformable hinges, in spite of the soft natural rubber. Regarding the Poisson's ratio, the results show that the initial measure was close to the predictions in the optimization process and was not degraded by the manufacturing process. Conversely, the stiffness of the honeycomb turned out to be extremely sensitive to the manufacturing uncertainties. A comparison between experimental results (in black) and the numerical simulation (in pink), depicted in Figure 1(g) reveals a significant gap in stiffness by looking at the effective stress strain curve. An observation under an optical microscope revealed that the trusses of the fabricated specimen were $\sim 100\,\mu m$ thinner than the model. The calculation gave a better prediction when using the experimental DIC mesh (curve in red). The good agreement between simulation and experiments further permits to estimate the stress distribution during shear, the experimental measures being biased by the frictions in the channel. At finite strains, the mechanical behaviour shifts rapidly, indicating in particular a decrease of the "auxeticity" of the specimen. Beyond 10% effective strain, the Poisson's ratio is no longer in agreement with the desired value. The evolution of the Poisson's ratio with applied strain has already been observed and discussed in [5] on polymeric filament structure. In complement, they arrived to correct the phenomenon up to 20% strain using a non-linear material behaviour in the optimization process. In the case of the design procedure used here, the extension to non-linear material behaviour is currently under investigation and will appear in subsequent work of the authors.

References

[1] Cast3M, http://www-cast3m.cea.fr (2018)
[2] F. Agnelli, A. Constantinescu, G. Nika. *Contin. Mech. Thermodyn.* (2019). doi: 10.1007/s00161-019-00851-6
[3] G. Allaire, C. Dapogny, G. Delgado, G. Michailidis. *ESAIM Control Optim. Calc. Var.* (2014). doi: 10.1051/cocv/2013076
[4] P. Celli, C. McMahan, B. Ramirez, A. Bauhofer, C. Naify, D. Hofmann, B. Audoly, C. Daraio. *Soft Matter* (2018). doi: 10.1039/c8sm02082e
[5] A. Clausen, F. Wang, J.S. Jensen, O. Sigmund, J.A. Lewis. *Adv. Mater.* (2015). doi: 10.1002/adma.201502485
[6] A.S. Gladman, E.A. Matsumoto, R.G. Nuzzo, L. Mahadevan, J.A. Lewis. *Nat. Mater.* (2016). doi: 10.1038/nmat4544
[7] G.N. Greaves, A.L. Greer, R.S. Lakes, T. Rouxel. *Nat. Mater.* (2011). doi: 10.1038/nmat3134
[8] Y.J. Lee, S.M. Lim, S.M. Yi, J.H. Lee, S. Kang, G.M. Choi, H.N. Han, J.Y. Sun, I.S. Choi, Y.C. Joo. *Extreme Mech. Lett.* (2019). doi: 10.1016/j.eml.2019.100516
[9] J.T. Muth, D.M. Vogt, R.L. Truby, Y. Mengüç, D.B. Kolesky, R.J. Wood, J.A. Lewis. *Adv. Mater.* (2014). doi: 10.1002/adma.201400334
[10] M. Wehner, R.L. Truby, D.J. Fitzgerald, B. Mosadegh, G.M. Whitesides, J.A. Lewis, R.J. Wood. *Nature* (2016). doi: 10.1038/nature19100

ISOGEOMETRIC OPTIMAL DESIGN OF NONLINEAR LATTICE STRUCTURES WITH FRICTIONLESS BEAM-TO-BEAM CONTACT

Myung-Jin Choi*[1], Thang X. Duong[2], Sven Klinkel[1], and Roger A. Sauer[3,4,5]
[1]Chair of Structural Analysis and Dynamics, RWTH Aachen University, Aachen, Germany
[2]Department of Continuum Mechanics, RWTH Aachen University, Aachen, Germany
[3]Aachen Institute for Advanced Study in Computational Engineering Science (AICES), RWTH Aachen University, Aachen, Germany
[4]Faculty of Civil and Environmental Engineering,Gdan´sk University of Technology,ul.Gdan´sk,Poland
[5]Department of Mechanical Engineering, Indian Institute of Technology Kanpur, UP, India

Summary We derive analytical design sensitivity analysis formulation using an adjoint variable method, based on an isogeometric finite element formulation of geometrically and materially nonlinear Timoshenko beams, which incorporates in-plane deformation of the cross-section described by two extensible directors [1], and frictionless beam-to-beam contact. Further, we present an optimal design in three-dimensional beam lattice structures undergoing large deformations with contact interactions of constituent ligaments. The developed gradient-based design optimization method is combined with a stochastic approach in order to avoid multiple local minima. Our application is to design an auxetic structure having an extremal and constant negative Poisson's ratio during large compressive deformations.

ABSTRACT

Periodic slender structures or lattice structures have been widely studied due to their low weight, outstanding structural performances, and possibility of tailoring effective mechanical properties. For design problems in material microstructures, mathematical optimization methods are often exploited to achieve a target mechanical property. However, an incorporation of contact interactions of constituent ligaments to the lattice structural design optimization framework is significantly challenging, and to the best of our knowledge, it still remains unexplored. In this research, we develop a gradient-based optimal design method for three-dimensional beam lattice structures considering contact constraints. A target application of the developed method is a lattice structure with enhanced impact energy-absorption properties like auxetic structures. We particularly deal with large deformations, where the effective Poisson's ratio strongly depends on the magnitude of applied loads. Choi et al. [2] obtained two- and three-dimensional beam lattice structures having a negative Poisson's ratio -2 along specific directions in both tension and compression loadings (see Fig. 1); however, due to the absence of contact condition in the simulations, the maximum load magnitude was limited to avoid unphysical overlap between ligaments. Fig. 2 shows an experimental verification of the two-dimensional auxetic structure.

Beam contact formulations have been successfully exploited in deformation analyses of slender bodies with contact interactions. For example, in Sauer and Mergel [3], a geometrically exact shear-deformable planar beam model with varying cross-section along the beam length was employed to describe adhesion and debonding of thin film. Also, a contact interaction in a biopolymer network was simulated in Meier et al. [4] using a Kirchhoff beam model with a unified contact formulation, which combines a point-to-point and a line-to-line contact formulations using a variationally consistent transition between those two formulations. However, in those previous works, no cross-section deformation was assumed, although local contact may lead to a significant influence on the deformation of cross-sections. In the present research, we employ the formulation of geometrically and materially nonlinear Timoshenko beams, which considers in-plane deformation of the cross-section described by two extensible directors [1]. This formulation allows direct application of nonlinear three-dimensional constitutive laws without zero stress conditions.

ACKNOWLEDGEMENTS

M.-J. Choi gratefully acknowledges the financial support by a Humboldt post-doctoral research fellowship from the Alexander von Humboldt foundation.

References

[1] Myung-Jin Choi, Roger A. Sauer, and Sven Klinkel. An isogeometric finite element formulation for geometrically exact timoshenko beams with extensible directors. *arXiv: 2010.14454*, 2020.
[2] Myung-Jin Choi, Se-Hyeon Kang, Myung-Hoon Oh, and Seonho Cho. Controllable optimal design of auxetic structures for extremal Poisson's ratio of -2. *Composite Structures*, 226:111215, 2019.
[3] Roger A. Sauer and Janine C. Mergel. A geometrically exact finite beam element formulation for thin film adhesion and debonding. *Finite Elements in Analysis and Design*, 86:120–135, 2014.
[4] Christoph Meier, Wolfgang A. Wall, and Alexander Popp. A unified approach for beam-to-beam contact. *Computer Methods in Applied Mechanics and Engineering*, 315:972–1010, 2017.

*Corresponding author. E-mail: choi@lbb.rwth-aachen.de

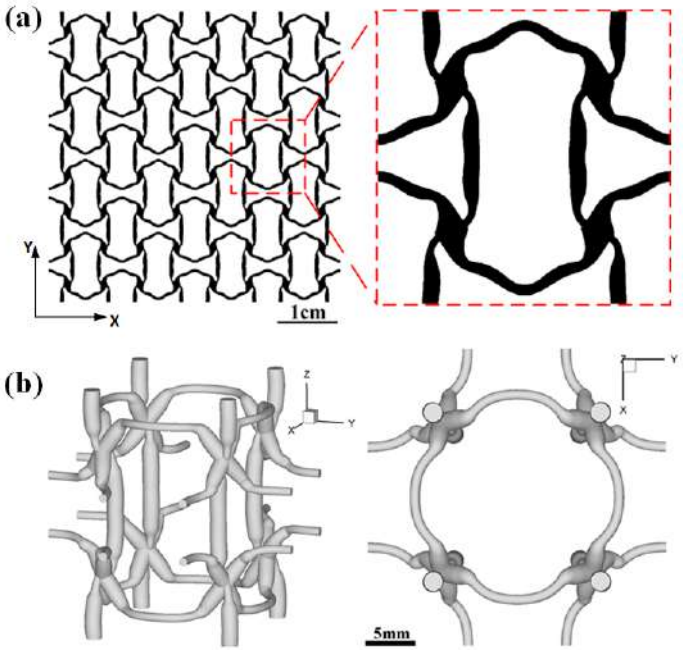

Figure 1: Undeformed shapes of optimal designs [2]. (a) Two-dimensional structure with an effective Poisson's ratio $\nu_{21} = -2$, (b) Three-dimensional structure with effective Poisson's ratios $\nu_{31} = \nu_{32} = -2$. $\nu_{21} \equiv -\varepsilon_X/\varepsilon_Y$, $\nu_{31} \equiv -\varepsilon_X/\varepsilon_Z$, and $\nu_{32} \equiv -\varepsilon_Y/\varepsilon_Z$, where ε_X, ε_Y, and ε_Z are nominal strains in X-, Y-, and Z-directions, respectively.

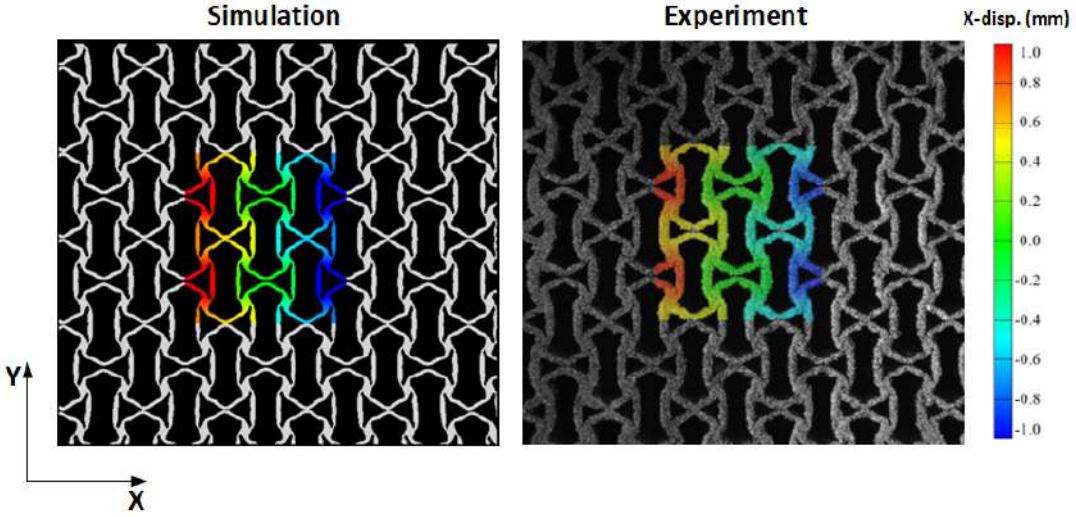

Figure 2: Comparison of deformed shapes and X-displacement contours from the simulation and experiment of the two-dimensional auxetic structure [2]. 3.75% nominal compressive strain applied.

AN "ELASTICA ROBOT": TIP CONTROL IN TENDON-DRIVEN ELASTIC ARMS

Ramsharan Rangarajan*[1] and Poornakanta Handral[1]
[1]Department of Mechanical Engineering, Indian Institute of Science Bangalore, India

Summary Various applications ranging from pipeline inspection to robot-assisted surgery require highly maneuverable devices with precisely controllable tips. In this contribution, we propose and experimentally validate a mechanics-based approach to quasistatically manipulate the tip location of a flexible arm by controlling the tensions in a pair of cables attached to its centerline. We show that by adopting a geometrically nonlinear elastica model for the arm, by carefully accounting for configuration-dependent tendon loadings, and by interpreting the problem of manipulating the arm as one of load optimization, it is possible to realize a high degree of accuracy. The resulting device functions as an energy-efficient robot that is well suited for miniaturization.

INTRODUCTION

An emerging class of robots is composed of flexible structures and function by exploiting the compliances of their constitutive elements. Such robots are aimed at applications that demand high maneuverability for navigation in closed or cluttered environments, that require interaction with compliant substrates, and at applications where energy-efficiency is critical. Their operating principle stands in stark contrast to traditional robots typically composed of networks of links with actuated joints whose compliances are generally considered to be a hindrance for controlled operation. Our work here is motivated by the observation that developments in strategies for controlling flexible elements in robots lags behind technologies for designing and fabricating them.

The arrangement in Fig. 1a shows of a slender flexible arm clamped at one end and loaded by a pair of cables. We demonstrate that by modeling the highly deformable arm as an elastica and by posing control as a problem of optimizing tensions in the cables, the tip of the arm can be accurately positioned within a feasible workspace. Our choice of tendon actuation is based on its simplicity, ease of experimental realization and its suitability for space applications.

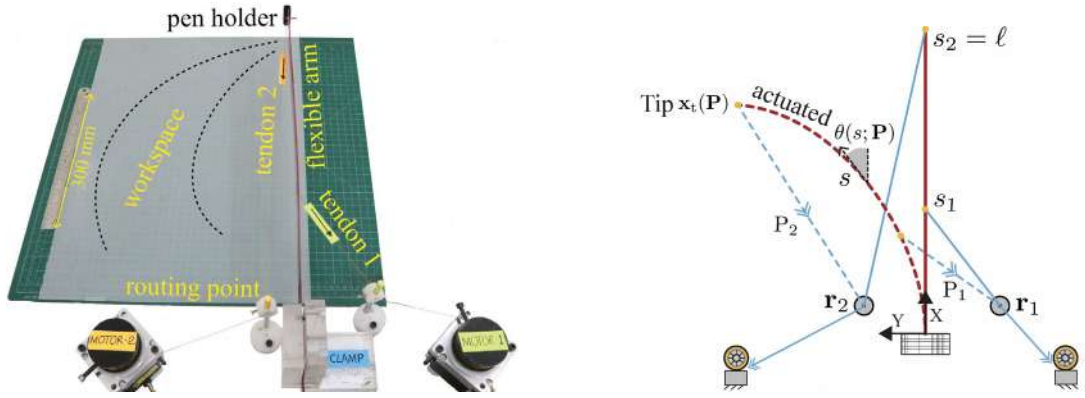

(a) (b)

Figure 1: Illustration of the experimental setup in (a) and its idealization in (b). The arm is made of Polycarbonate and is about 600 mm long. The first tendon is attached at $s_1 = 200\,\mathrm{mm}$ and the second at $s_2 = 600\,\mathrm{mm}$. The total cost of the setup is about $255.

AN INVERSE PROBLEM FOR ELASTICA CONTROL

The schematic in Fig. 1b represents an idealization of the setup in Fig. 1a. A straight elastic arm of length ℓ is loaded by a pair of tendons attached at distances $s = s_1$ and $s = s_2$ along its centerline, where $s \in [0, \ell]$ denotes the arc-length parameter of the centerline measured from the clamped end and $0 < s_1 < s_2 = \ell$. For simplicity, we set $s_2 = \ell$ and assume actuation using two tendons. We presume the arm to be inextensible and its cross sections to be rigid and unshearable. The deformation of the arm that results from imposing tensions $\mathbf{P} = (\mathrm{P}_1, \mathrm{P}_2)$ in the two tendons can hence be parameterized by the inclination angle $s \mapsto \theta(s;\mathbf{P})$ of the tangent to the centerline. Referring to the Cartesian system indicated in the figure, coordinates of the deformed centerline follows as $s \mapsto \mathbf{x}(s;\mathbf{P}) = \int_{\xi=0}^{s} (\cos\theta(\xi;\mathbf{P}), \sin\theta(\xi;\mathbf{P}))\, d\xi$. In particular, $\mathbf{x}_1(\mathbf{P}) \triangleq \mathbf{x}(s_1;\mathbf{P})$ and $\mathbf{x}_2(\mathbf{P}) = \mathbf{x}(s_2;\mathbf{P})$ identify the points of attachment of the tendons in the deformed configuration. The second argument $\mathbf{P}$ of θ and $\mathbf{x}$ explicitly denote their dependence on the loading.

Presuming a linear relationship between the curvature $\theta' = d\theta/ds$ of the centerline and the moment, force balance in the arm is succinctly stated as

$$\mathrm{B}\theta''(s;\mathbf{P}) + \mathbf{x}'(s;\mathbf{P}) \times (\mathrm{H}(s_1 - s)\mathbf{F}_1(\mathbf{P}) + \mathbf{F}_2(\mathbf{P})) = 0, \tag{1}$$

*Corresponding author. E-mail: rram@iisc.ac.in

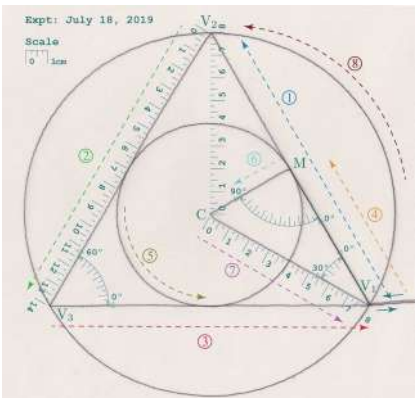

(a) Tracing geometric shapes (experiment in black).

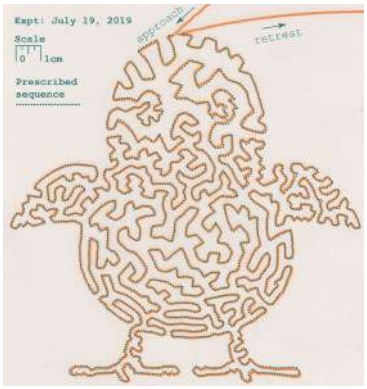

(b) Sketching a convoluted curve. Prescribed points appear in green and the expt. in orange.

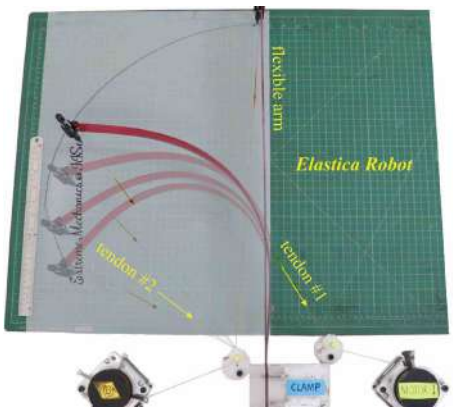

(c) Cursive writing.

Figure 2: Demonstrating versatility and accuracy of experimentally realized tip control using the setup shown in Fig. 1. Deviations in distances and angles consistently remain smaller than $2\,\mathrm{mm}$ and 1°, respectively.

where B is the bending stiffness, H is the Heaviside function, $\mathbf{F}_i(\mathbf{P}) = \mathrm{P}_i(\mathbf{r}_i - \mathbf{x}_i(\mathbf{P}))/\|\mathbf{r}_i - \mathbf{x}_i(\mathbf{P})\|$ for $i = 1, 2$ are the tendon loadings resulting from the imposed tensions P_1 and P_2, and $\mathbf{r}_1, \mathbf{r}_2$ are the fixed routing points of the two cables. Equation (1) is supplemented with boundary conditions $\theta(0, \mathbf{P}) = \theta'(\ell, \mathbf{P}) = 0$ representing the clamped and moment-free ends. Nonlinearity in the model represented by eq. (1) is purely geometrical and stems from three sources—computing curvatures of the centerline exactly, measuring moment arms of loads without approximation, and accounting for the dependence of tendon inclinations on the deformation.

We formulate the control problem of placing the tip $\mathbf{x}_\mathrm{t}(\mathbf{P})$ of the flexible arm at a desired location $\mathbf{x}_\mathrm{d}$ as one of computing optimal cable tensions. Introducing the cost function $\mathrm{E}(\mathbf{P}) = \|\mathbf{x}_\mathrm{d} - \mathbf{x}_\mathrm{t}(\mathbf{P})\|^2/2$ to measure the deviation of the tip from the desired position, we pose tip-control as a parameter optimization problem for P_1 and P_2:

$$\text{Find } \mathbf{P} \in \arg \min_{\mathbf{P} \in [\mathbb{R}_{\geq 0}]^2} \{\mathrm{E}(\mathbf{P}) \,:\, \theta(s; \mathbf{P}) \text{ solves eq. (1)}\}. \tag{2}$$

In the talk, we will discuss key aspects of resolving the minimization problem in eq. (2) by explicitly computing the sensitivities of the state $\theta(s; \mathbf{P})$ to the tensions P_1 and P_2. These sensitivities reveal an innate coupling between the independent actuations arising from the configuration dependence of loading directions.

EXPERIMENTAL REALIZATION

Fig. 1a shows the experimental setup used. Small holes located along the centerline of the arm serve as attachment points for two stiff metal-reinforced cables. The length of the arm is short enough so that its centerline does not visibly sag due to gravity, and its width is large enough to reduce axial twisting caused by small deviations from idealized loading conditions. Each cable is routed through a fixed point to a motorized spool, which reels in/out the cable, thereby controlling its length and in turn the tension it bears. A light attachment holds a pen to trace the location of the tip as the arm deforms to monitor the accuracy of tip-control realized. Although it is possible to impose the computed optimal tensions $(\mathrm{P}_1, \mathrm{P}_2)$ by coupling each cable with a tension gauge, for the sake of simplicity and to avoid errors caused by friction between cables and their routing posts, we instead impose the computed cable lengths instead. Hence, actuating the arm simply requires prescribing the number of revolutions for each motor. Fig. 2 shows representative examples demonstrating the accuracy of tip control realized in the experiments.

More remarks in the talk. In the talk, we will discuss key aspects determining the workspace of the proposed robotic device. We will also discuss how the proposed framework can be easily adapted for shape control of the elastica. Such problems arise when manipulating surgical instruments or inspection devices in constrained environments. We will highlight interesting aspects of the tendon-controlled elastica problem, including the possibilities of and distinctions between instabilities in load and length-controlled settings.

References

[1] Nayak A., Handral, P., Rangarajan, R. Shape control for the Elastica through load optimization. *J. Appl. Mech.* **86(1)**: 011011, 2019.
[2] Handral P., Rangarajan, R. An elastica robot: Tip-control in tendon-actuated elastic arms. *Extreme Mechanics Letters*, **in press**. 2019.

AN EXPERIMENTAL INVESTIGATION OF MODELS FOR ELASTIC RIBBONS

Arun Kumar[1] and Ramsharan Rangarajan *[1]
[1]Department of Mechanical Engineering, Indian Institute of Science Bangalore, India

Summary Understanding the feature-rich buckling dominated behavior of thin elastic ribbons is ripe with opportunities for fundamental studies in exploring the nexus between geometry and mechanics. Predictive mechanical models play an instrumental role to this end. Here, we critically examine common modeling approaches for elastic ribbons using carefully designed experiments and detailed shape measurements. Specifically, we demonstrate simple and practically realizable ribbon deformations that easily contradict assumptions underlying nonlinear rod and von Karman plate models, resulting in large discrepancies between model predictions and experimental measurements. We identify and validate, seemingly for the first time, the applicability of the 1-director Cosserat plate model for elastic ribbons subject to a useful range of loading conditions. In the process, we discover interesting aspects of the behavior of annular ribbons. We also establish them to be prototypical systems with a tunable degree of geometric nonlinearity, making them well suited for (in)validation of dedicated ribbon models proposed in the literature.

INTRODUCTION

Ribbons are slender structures characterized by three disparate geometric dimensions— length ℓ, width w and thickness h, which are ordered such that $\ell \gg w \gg h$. The pair of slenderness ratios ℓ/w and w/h dictate its rich buckling-dominated mechanical behavior independently of the material constitution. In many ways, the growing body of literature on the mechanics of ribbons is exemplary of an evolving paradigm that considers buckling and related geometric nonlinearities as features to be exploited in applications ranging from flexible robotics to miniaturized electronic devices, rather than as modes of failure

Our goal in this contribution is to critically examine commonly used modeling approaches for ribbons by comparing their predictions with detailed measurements from quasi-static experiments. Specifically, we consider modeling elastic ribbons as nonlinear rods with highly anisotropic cross-sections, as Kirchhoff-Love plates, as von Karman plates, as 1-director Cosserat plates, and as developable surfaces. The theories examined span the gamut of linear, weakly nonlinear and fully nonlinear one/two dimensional models. Through carefully designed table-top experiments, we highlight the significance of geometric nonlinearities stemming from assumed strain-displacement relationships in these models.

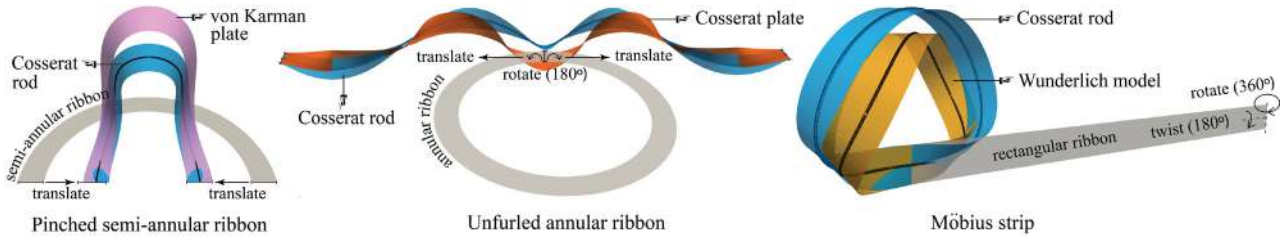

Figure 1: Simple experiments exposing unambiguous differences in the predictions of four models for elastic ribbons. Our primary goal in this contribution is to critically examine the accuracies of these predictions using simple experiments and detailed measurements.

NOT ALL RIBBON MODELS ARE CREATED EQUAL

Figure 1 succinctly summarizes the motivation behind our investigation. The figure illustrates three simple virtual experiments that involve rotating and translating clamped ends of semi-annular, annular and rectangular ribbons. Therein, we show predictions of the Cosserat rod model alongside those of von Karman plate, Cosserat plate, and Wunderlich models. Each prediction represents a converged numerical simulation for the respective model. In each case, we find that a pair of models make drastically different predictions for the shape of the ribbon. The figure then evokes the obvious question— *which model is right?* Or, adopting a very skeptical point of view, could it be that all the predictions shown in the figure are inaccurate?

Experiments to settle the debate. We resort to simple physical realizations of the experiments depicted in fig. 1 along with detailed measurements to settle the debate. The setup used in our experiments is shown in Fig 2, and consists of a pair of translatable clamps to hold an annulus and semi-annulus shaped ribbon. The clamps are additionally rotatable about an axis perpendicular to the direction of translation. We use ribbon specimens cut from flat radiography sheets. The difference between the inner and outer radii defines the width w, while the circumference along the mean radius furnishes the length scale ℓ. The mean radius also endows the ribbon with a non zero geodesic curvature. Roughly speaking, when

*Corresponding author. E-mail: rram@iisc.ac.in

its ends are translated and rotated relative to each other, the ribbon responds to compression along its peripheries by assuming buckled three-dimensional configurations. The resulting deformations are reminiscent of undulations observed in fabrics, edges of leaves/petals, or in ripped plastic sheets as a result of growth, thermal expansion, plastic deformation or residual stresses. Our experiments exploit the difference in dimensions between the inner and outer circumferences of the ribbon to produce a similar effect.

For measuring shapes of deformed ribbons, we sample the exposed surfaces using a line laser scanner mounted on a portable coordinate measuring machine to determine a dense point cloud representation. We directly compare shapes digitized in this way, with configurations predicted by various models and compute quantitative measures of deviations. Using novel algorithmic techniques, we compute detailed differential geometric quantities including mean and Gaussian curvatures from the measured data, which facilitate detailed full field comparisons with strain invariants predicted by the different models.

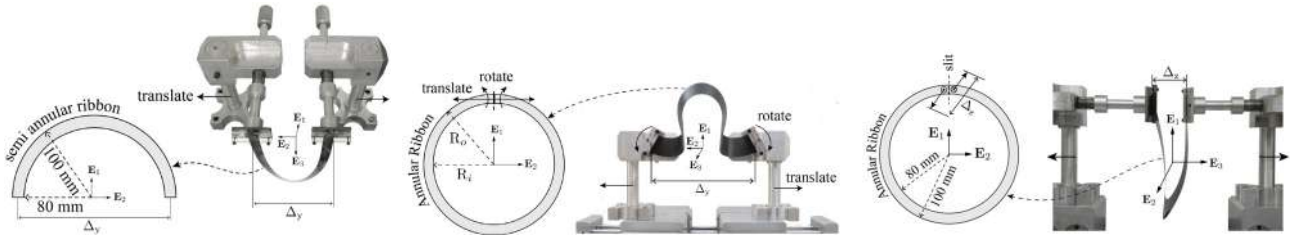

(a) Pinched semi annular ribbon (b) Unfurled annular ribbon (c) Transversely displaced annular ribbon

Figure 2: Experimental setup showing a slit annular ribbon whose edges held in clamps. The three tests shown consist in rotating the edges about the $\mathbf{E}_3$ axis and linearly translating them along an orthogonal direction, causing the ribbon to deforms into complex three-dimensional shapes.

KEY FINDINGS

- Our experiments reveal annular ribbons to be prototypical systems which exhibit varying degrees of geometric nonlinearity in response to simple displacement and rotation boundary conditions. We demonstrate the existence of multiple stable equilibria, bifurcation phenomena that appear to be correlated with the number of zero crossings in the mean curvature of the ribbon, emergence of creases and localization of energy.

- By scrutinizing an obstacle course of test cases, we identify a set of simple experiments, including the ones shown in Figs. 1 and 2, that highlight the consequences of kinematic relations assumed in the Kirchhoff-Love plate, von Karman plate, Cosserat plate and nonlinear Cosserat rod theories. Measurements from these experiments enable us to decisively (in)validate the applicability of the various ribbon models considered. They highlight assumptions underlying that Kirchhoff rod and von Karman plate models that render them inadequate for modeling a seemingly practical range of deformations of elastic ribbons. These observations are not criticisms of the latter two models, but a reminder that their underlying kinematic assumptions are easily violated when considering deformations of ribbons.

- We find the 1-director Cosserat plate model to be in very good agreement with a broad range of experimental measurements. In particular, for the problem of predicting shapes of Möbius strips, both the Cosserat plate and Wunderlich model predict solutions that agree well with experimental measurements.

- Our study establishes a clear way to test dedicated one-dimensional ribbon models proposed in the literature. Specifically, simulations using 1-director Cosserat plates can serve as benchmark solutions against which to compare predictions of various ribbon models. The narrow width model of Sadowsky, the finite width model of Wunderlich, and the rod-based model of [2] are appealing candidates for such validations. Ribbon models derived by dimensional reduction from von Karman plate theories will benefit from such validations, especially in light of our observations concerning the von Karman plate model.

References

[1] Audoly, B. and Pomeau, Y. Hair Curls to the Non-linear Response of Shells. Wrinkles, and Loops in Twisted Ribbons. *OUP Oxford.* 2010

[2] Dias,M. and Audoly,B. Wunderlich, meet Kirchhoff: A general and unified description of elastic ribbons and thin rods. *Journal of Elasticity.* **119**: 2015

[3] Starostin E. and Van Der Heijden G. The shape of a Möbius strip. *Nature Materials.* **6(8)**: 563-567, 2007.

ANALYSIS OF SOFT SHELLS OF REVOLUTION AT LARGE DEFORMATIONS

Ekaterina Korovaytseva
Institute of Mechanics, Lomonosov Moscow State University, Moscow, Russia

Summary An algorithm of soft shells of revolution axisymmetric dynamic deformation problems solution is represented in the work. The algorithm imposes no restrictions on the form of meridian of the shell, values of deformation investigated or physical relations describing behavior of shell material. Features of software implementation of the algorithm are pointed out. Characteristics of calculation process which influence calculation stability, iteration process convergence and solution accuracy are specified. The result of test calculation of hemispherical shell made of Treloar material inflation is represented.

In a general case statements of geometrically and physically nonlinear problems concerning investigation of soft shells at large deformations behavior are quite complicated. Owing to this complexity reported studies on the dynamic problems of soft shells are quite scarce. In the works studied only solutions of concrete applied problems or specific problems of soft shells with the simplest meridian form deformation are represented.

In the work given an algorithm of axisymmetric dynamic deformation of unbranched soft shells of revolution with arbitrary meridian form calculation is suggested. The algorithm imposes no restrictions on values of deformation investigated or physical relations describing behavior of shell material. For the purpose of generalization of problem statement we use vector-matrix formalization of resolving equation system and subsequent transformations of vector functions of vector variables.

We suppose soft shell to be loaded by internal pressure. Let it stress state be biaxial in the general case. We construct the resolving equation system on the basis of general theory of soft shells [1]. This system includes two differential equations of motion, two differential geometrical equations, eight additional algebraic equations and two physical relations. In order to simplify mathematical manipulation we shall represent the resolving system of equations in vector-matrix form:

$$\frac{\partial \vec{y}_i}{\partial x_i} = f_i(x_i, y_i, z_i, \mu_i, q_i) + M_i \cdot \frac{\partial^2 \vec{y}_i}{\partial t^2}, \; i \in [1, N] \tag{1}$$

$$\varphi_i(x_i, y_i, z_i, \mu_i, q_i) = 0. \tag{2}$$

Boundary conditions have the form

$$\psi_1(x_{1,b}, y_{1,b}, z_{1,b}, \mu_{1,b}, q_{1,b}) = 0; \quad 1 \quad 2, \; x_{1,b} \quad x_{N,e}, \tag{3}$$

and conjunction conditions for the segments of the shell can be written as

$$y_j(x_{j,e}) = y_{j+1}(x_{j+1,b}), \; j \in [1, \; N-1]. \tag{4}$$

Here y_i is resolving variables vector, z_i is additional variables vector, q_i is vector of given surface loads; μ_i is vector of characteristic geometrical parameters; M_i is mass matrix of the *i*-th segment of the shell; ψ_1, ψ_2 are vector functions of given boundary conditions with the number of components p and s respectively, where $p + s = n$; $f_i(x_i, y_i, z_i, \mu_i, q_i)$ is vector function of n components of right-hand side of the resolving equation system; $\varphi_i(x_i, y_i, z_i, \mu_i, q_i)$ is vector function of nonlinear additional algebraic equations; N is a number of segments of the boundary problem, indices b and e denote beginning and end of a segment.

For the solution of nonlinear boundary problem (1)-(4) we use method of lines, replacing time derivatives by finite differences. Thus the system (1) turns into the system of ordinary nonlinear differential equations, for solution of which we use parameter differentiation method. According to the concept of parameter differentiation method, instead of given loads we introduce variable loads with the same meridian distribution, but depending on nonlinear boundary problem solution step process parameter α : $q_i^*(x_i) = \alpha \cdot q_i(x_i)$. As a result the problem (1)-(4) can be written at each time step $t = t_k$:

$$\frac{dy_{i,k}}{dx_i} = f_{i,k}^*(x_i, y_{i,k}, q_{i,k}^*, \mu_{i,k}); \quad i \in [1, N] \tag{5}$$

$$\varphi_{i,k}(x_i, y_{i,k}, z_{i,k}, \mu_{i,k}, q_{i,k}^*) = 0. \tag{6}$$

$$\psi_{1,k}(x_{1,b}, y_{1,b}, z_{1,b}, \mu_{1,b}, q_{1,b}) = 0; \quad 1 \quad 2, \; x_{1,b} \quad x_{N,e}, \tag{7}$$

$$y_{j,k}(x_{j,e}) = y_{j+1,k}(x_{j+1,b}), \; j \in [1, \; N-1]. \tag{8}$$

Solution of the problem (5)-(8) at $\alpha = 1$ corresponds to the solution of the problem (1-4).

According to the procedure of parameter differentiation method [2], we differentiate the relations (5)-(8) of the problem with respect to some chosen parameter T. Then, expressing the speed of additional variables vector $z_i = dz_i / dT$ from the differentiated algebraic relations (6), we obtain the following quasilinear boundary problem in speeds of vector variables:

$$\frac{dy_{i,k}}{dx_i} = A_{i,k}^{*}(x_i, \vec{y}_{i,k}, \vec{z}_{i,k}, \vec{\mu}_{i,k}, \vec{q}_{i,k}, \alpha)\vec{y}_{i,k} + \vec{a}_{i,k}^{*}(x_i, \vec{y}_{i,k}, \vec{z}_{i,k}, \vec{\mu}_{i,k}, \vec{q}_{i,k}, \alpha)\alpha; \quad i \in [1, N] \tag{9}$$

with boundary conditions

$$\frac{\partial \psi_{1,k}}{\partial \acute{o}_{1,k,b}} \acute{o}_{1,k,b} + \frac{\partial \psi_{1,k}}{\partial z_{1,k,b}} z_{1,k,b} + \frac{\partial \psi_{1,k}}{\partial q_{1,k,b}} q_{1,k,b}\alpha = 0; \quad 1 \quad 2; \quad 1,b \quad N,e \tag{10}$$

and conjunction conditions

$$y_{j,k}(x_{j,e}) = y_{j+1,k}(x_{j+1,b}), \ j \in [1, N-1]. \tag{11}$$

Here dots above the variables y_i, z_i, α denote derivative with respect to parameter T, and

$$A_{i,k}^{*}(x_i, y_{i,k}, z_{i,k}, \mu_{i,k}, q_{i,k}, \alpha) = \frac{\partial f_{i,k}^{*}}{\partial y_{i,k}} - \frac{\partial f_{i,k}^{*}}{\partial z_{i,k}} \left(\frac{\partial \varphi_{i,k}}{\partial z_{i,k}} \right)^{-1} \cdot \frac{\partial \varphi_{i,k}}{\partial y_{i,k}};$$

$$a_{i,k}^{*}(x_i, y_{i,k}, z_{i,k}, \mu_{i,k}, q_{i,k}, \alpha) = \frac{\partial f_{i,k}^{*}}{\partial q_{i,k}} q_{i,k} - \frac{\partial f_{i,k}^{*}}{\partial z_{i,k}} \left(\frac{\partial \varphi_{i,k}}{\partial z_{i,k}} \right)^{-1} \cdot \frac{\partial \varphi_{i,k}}{\partial q_{i,k}} q_{i,k}.$$

Solution of the problem (9)-(11) can be obtained using method of initial parameters. Initial problems of subsequent calculation of the variables themselves have the form

$$\begin{aligned} \frac{dy_{i,j}}{dT} &= y_{i,j}(y_{i\,j}\ z_{i\,j,}\ x_{i\,j}, T, \quad), \\ \frac{dz_{i,j}}{dT} &= z_{i,j}(y_{i\,j}\ z_{i\,j,}\ x_{i\,j}, T, \quad) \ j \in [\ N\ ]\ j \in [\ N_j\ ] \\ \frac{d\alpha}{dT} &= \alpha(y_{i,j}\ T\ ) \end{aligned} \tag{12}$$

Cauchy problem (12) is nonlinear, and the right-hand side of it is known only in discrete form. Besides, the value of parameter increment depends on iteration process convergence rate and cannot be predicted. That is why for the solution of the problem (12) we use specially developed methods of solution of Cauchy problems with right-hand side known at discrete values of variable step.

It should be mentioned that in the absence of prestress the matrix of partial derivatives $\frac{\partial \varphi_{i,k}}{\partial z_{i,k}}$ is singular, which makes the represented algorithm using difficult at the first step of the solution. So regularization of system (5)-(8) solution is required when starting calculation process. Regularization means constructing resolving equation system of soft shells theory with a solution close to the solution of the initial problem. But this new equation system must be well-conditioned.

The algorithm described was tested for the solution of problem of hemispherical shell dynamic inflation. We considered different boundary conditions for the shell. Nonlinear Treloar physical relations were taken to describe properties of soft shell material.

It was established that stability and convergence of calculation process realizing the algorithm represented depend on a number of factors: shell material type, prestress existence, value of pre-pressure, boundary conditions, value of initial increment of parameter T, number of steps for which solution regularization is carried out, number of integration points along the meridian of the shell, time step, way of acceleration finite-difference approximation. Recommendations concerning establishing values of calculation process parameters allowing obtaining correct solution were drawn up.

The reported study was funded by RFBR and Moscow city Government, according to the research project No. 19-38-70005 mol_a_mos.

References

[1] Usyukin V.I. On equations of soft shells large deformations theory. *Izv AN USSR. Mechanics of Solids.* **1**: 70-75, 1976.
[2] Davidenko D.F. One a new method of numerical solution of nonlinear equation system. *Dokl. AN USSR.* **88** (4): 601-602, 1953.

MACROSCOPIC FRACTURE CRITERION OF LITHIUM-ION BATTERY ELECTRODE

Yoshinao Kishimoto*[1], Yukiyoshi Kobayashi[1], Toshihisa Ohtsuka[1], Kyohei Nakamura[1], Yuki Tsukagoshi[1], Shota Ono[1] and HiroshiYamazaki[1]
[1]Department of Mechanical Engineering, Tokyo City University, Tokyo, Japan

Summary Lithium-ion batteries are widely used as power sources for mechanical structures such as electric vehicles. Damages of electrodes cause performance deterioration and abnormal heating of lithium-ion batteries. This study has proposed a macroscopic fracture criterion of electrodes based on a mechanical model. The microscopic fracture of electrodes occurs when binder resins connecting active materials break. The mechanical model approximates alignment of particles as the body-centred cubic (bcc) and the face-centred cubic (fcc) which are the well-known crystal lattices. The tensile test results agreed with the tensile strength of electrodes calculated by the mechanical model. In the bending tests and the buckling tests, crack initiation of electrodes could be predicted by the macroscopic fracture criterion.

INTRODUCTION

Lithium-ion batteries (LIBs) which has high energy density is expected to be main power sources of electric vehicles. For application to automobiles, the reliability of LIBs should be guaranteed against various external loads. Damages of electrodes cause performance deterioration and abnormal heating of lithium-ion batteries [1], [2]. Most of the studies agree in that microscopic structure of electrodes is bridged structure in which particles of active material (AM) are bonded by binder, and fracture of electrodes is due to fracture of binder. Numerical simulations by the discrete element method seems to be the most exact approach to evaluate basic mechanical properties of electrodes [3]. However, actual alignment of particles of AM is random, and the high-cost simulations must be iterated for enormous numbers of alignment cases. This study has proposed a simple and macroscopic fracture criterion of electrodes based on a mechanical model.

MACROSCOPIC FRACTURE CRITERION

Figure 1 shows schematics of the microscopic model of electrode material. Although actual alignment of particles of AM is random, this study approximates the alignment as the body-centred cubic (bcc) and the face-centred cubic (fcc) which are the well-known crystal lattices. Then, the macroscopic stress σ on the bulk and the microscopic stress σ_t on each binder are related by the following equation.

$$\sigma = \frac{8\alpha_b}{\zeta N} \times \sigma_t \tag{1}$$

where α_b is volume ratio of binder. ζ is constant value (= 0.589 (bcc model), 0.438 (fcc model)) and N is coordination number (= 8 (bcc model), 12 (fcc model)). Therefore, $8 / \zeta N$ is set to 1.61 on average. Equation (1) gives a macroscopic fracture criterion of electrodes if tensile strength of binder is substituted into the stress σ_t.

SPECIMEN AND EXPERIMENT PROCEDURE

Specimens are prepared by pasting graphite powder and thermoplastic fluropolymer binder (polyvinylidene fluoride, PVDF) on copper foil by reference to negative electrodes for LIBs. The mean diameter of the graphite powder is d = 5 μm. The compounding weight ratio Graphite:PDVF is from 94:6 to 50:50. In the tensile tests, uniaxial tensile load is applied on the electrode material removed from the copper foil, and the tensile strength of the electrode material is measured. In the bending tests and the buckling tests, bending moment and uniaxial compressive load is respectively applied on the specimens by attaching both ends of the copper foil on the testing machines.

RESULTS AND DISCUSSION

Figure 2 shows results of the tensile tests. The macroscopic fracture of the electrode material is brittle fracture. Many marks of fractured binder are observed by SEM images. The tensile strength is proportional to the volume ratio of the binder, and the experimental values agree with the theoretical line. In this respect, the binder clearly supports the structure.

Figure 3 shows results of the bending tests and the buckling tests. A crack initiated in some of the specimens. The tensile stress on the surface of the specimen is estimated by the following equation.

$$\sigma = \frac{8\alpha_b}{\zeta N} \times \frac{E_b}{\zeta}\left(\varepsilon + \frac{t}{\rho}\right) \tag{2}$$

where E_b is Young's modulus of the electrode material (= 1 GPa). ζ is set to 0.5 on average. ε, t, ρ are measured strain of the surface of the copper foil, thickness of the electrode material and curvature radius of the specimens, respectively. As shown in Fig. 3, the estimated stress of most of the cracked specimens is equal to or more than the tensile strength of the electrode material. Therefore, the macroscopic fracture criterion can predict the crack initiation of the electrodes.

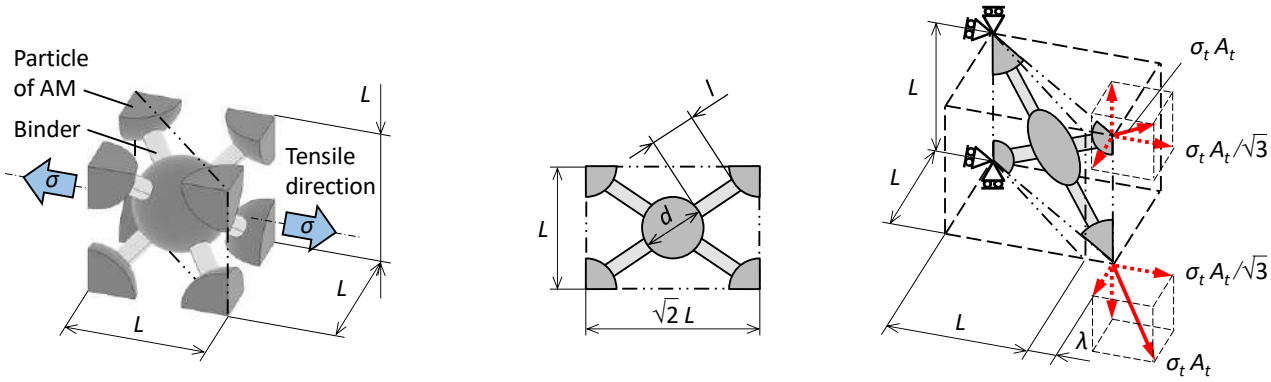

Figure 1. Microscopic model of electrode material (bcc model)

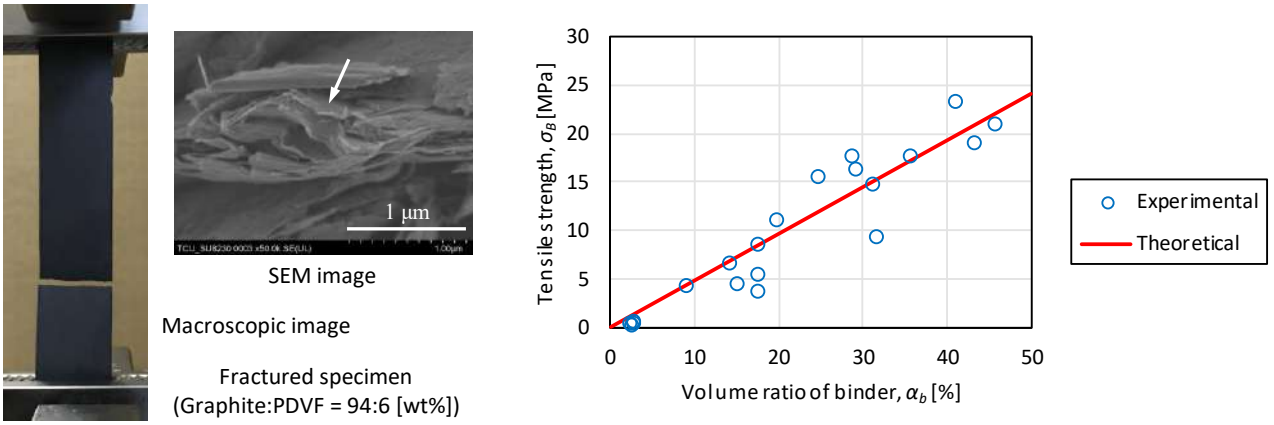

Figure 2. Results of tensile tests of electrode material

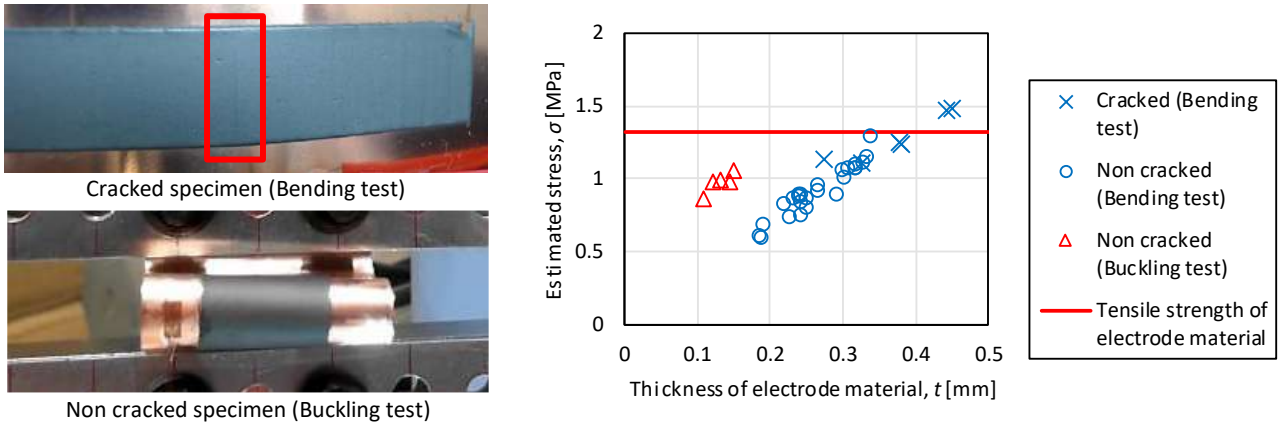

Figure 3. Results of bending tests and buckling tests (Compound weight ratio of specimen, Graphite:PVDF = 94:6 [wt%])

CONCLUSIONS

This study has proposed a simple and macroscopic fracture criterion of electrodes based on the bcc model and the fcc model. The tensile test results agreed with the tensile strength of electrodes calculated by the mechanical model. In the bending tests and the buckling tests, the macroscopic criterion could predict the crack initiation of the electrodes. This work was supported by JSPS KAKENHI Grant Numbers JP16K05989 and JP19K04078.

References

[1] Cai, W., Wang, H., Maleki, H., Howard, J. and Lara-Curzio, E., Experimental simulation of internal short circuit in Li-ion and Li-ion-polymer cells, *Journal of Power Sources*, **196**: 7779–7783, 2011.

[2] Ren, F., Cox, T. and Wang, H., Thermal runaway risk evaluation of Li-ion cells using a pinch–torsion test, *Journal of Power Sources*, **249**: 156–162, 2014.

[3] Giménez, C. S., Finke, B., Nowak, C., Schilde, C. and Kwade, A., Structural and mechanical characterization of lithium-ion battery electrodes via DEM simulations, *Advanced Powder Technology*, **29**: 2312–2321, 2018.

ANALYTICAL METHOD OF HORIZONTAL RESISTANT MECHANISM OF STRUCTURAL PLYWOOD ON HYBRID STEEL-WOOD STRUCTURE

Haruka Kataoka*[1], Takumi Ito[1*], Tsubasa Saito [1*]
[1]Department of Architecture, Faculty of Engineering, Tokyo University of Science, Tokyo, Japan

Summary Authors has suggested a structural sandwich panel which a steel column is sandwiched by thick plywood connected by bolt joints. In this paper, the horizontal loading test of structural plywood is performed as parameter with bolt joint method, whether the steel hardware is installed or not. Also, based on the test study, the analytical method of horizontal resistant mechanism is proposed. From the comparison with test result, the proposed method can estimate the strength of the sandwich panel structure.

INTRODUCTION

Recently, in Japan, to promote the use of domestic wood in architectural engineering field such as Olympic Stadium 2020 Tokyo, a various kind of hybrid structural system using wood and steel has been proposed. Authors have proposed the composite structural panel system and joint method, which steel column is sandwiched by thick plywood connected by bolt joints and the steel hardware [1] (see Fig.1). Furthermore, from the past experimental study, the proposed sandwich panel presents the high strength and rigidity due to composite effect.

This study aims the application of this system for prefab low-rise steel frame which has narrow space, a composite of 12mm-thick structural plywood is applied. And the feasibility study and analytical study are performed.

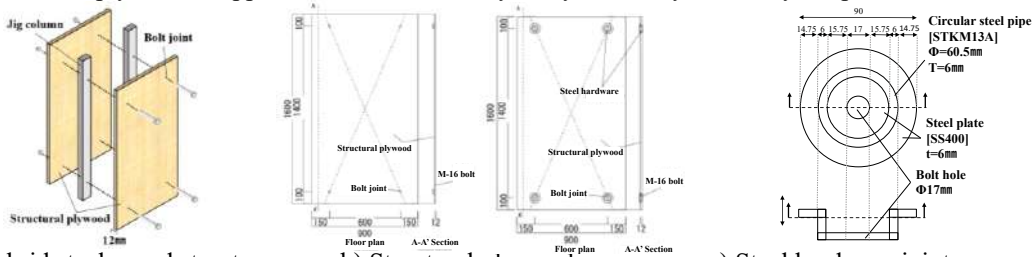

a) Hybrid steel-wood structure b) Structural plywood c) Steel hardware joint

Fig.1 Conceptual diagram of hybrid steel-wood structure and steel hardware joint

OUTLINE OF EXPERIMENT STUDY

To investigate the resistant mechanism of structural plywood on hybrid steel-wood structure, the fundamental loading test is conducted only on structural plywood. Here, a steel member is assumed as rigid with pin-supported, and the two sheets of plywood are fastened with M-16 bolt on the steel pillar.

The test setup is presented on Fig.2, and the cyclic loading with incremental amplitude is done. The loading jack is set on the top of steel jig column, and the out-of-plane deformation is supported by linear-guide. The horizontal load is measured by load cell, and horizontal displacement is measured by displacement meter. The strain gauges are put on the surface of plywood.

The size of structural plywood of specimen is 910×1600×12mm. The horizontal loading test is performed as parameter with bolt joint method, whether the steel hardware is installed or not. The steel hardware is made by steel plate (SS400) and steel pipe (STKM13A) are welded. The clearance of joint hole is 2.5mm in case of the specimen not using steel hardware and 1mm in case of the specimen using steel hardware. The list of test specimens is summarized on Table.1.

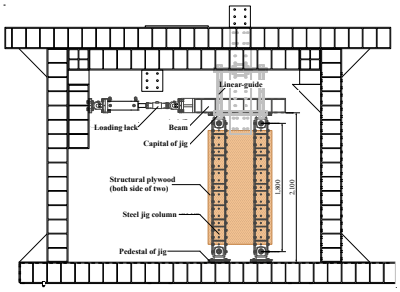

Fig.2 Test setup (unit: mm)

Table.1 List of test specimen

Specimen name	Steel hardware	Load method
N-C	Not	Cycle
S-C	Being	

N: not using the steel hardware, S: using the steel hardware
※Not→Not using, Being→Using, Load method→Load pattern, Cyclic→Cyclic by incremental amplitude

From the test study, the results of strength and rigidity are summarized on Table 2. And the ultimate state of test specimen is shown in Fig.3. From Table.2, the specimen with steel hardware presents high strength. From Fig.3, the end opening fracture and out-of-plane deformation are observed during cyclic loading. Also, from the test result of strain and inter deformation angle of bolt joint, it is predicted that the resistant mechanism as brace mechanism subjected to horizontal load is appeared as shown in Fig.4. Furthermore, the horizontal load on steel column is translated throw the bolt, and the bearing resistant mechanism is occurred between the bolt and plywood.

Table.2 Result of experiment

Specimen name	proportional limit [kN]	maximum bearing force [kN]	rigidity [kN/mm]
N-C	4.1	5.8	0.25
S-C	10.6	14.3	1.3

a)N-C b)S-C

Fig.3 Ultimate state of test specimen

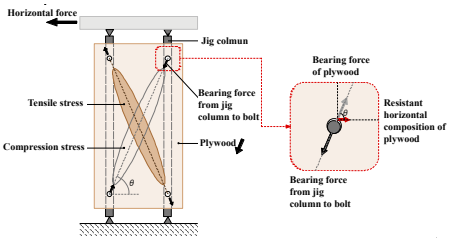

Fig.4 Conceptual diagram of brace resistant mechanism

ANALYTICAL METHOD AND CONSIDERATION

From the test results as previous mentioned, the resistant mechanism with diagonal brace on plywood is occurred, and the bearing force translates the horizontal load on steel member. Here, the analytical model of whole resistant mechanism of plywood (see Fig.5) and the bearing model on bolt joint (see Fig.6) are assumed to estimate the strength.

First, the horizontal force P as shown Fig.5 is evaluated as follows:

$$P = \frac{\mathrm{H}\times\mathrm{T}\times\cos\theta}{\mathrm{L}} \qquad \text{(Formula.1)}$$

Where, H: height of plywood, T: bearing force of bolt joint, L: distance between steel column.

The bearing force of bolt joint T_u (see Fig.6) are presented as follows:

$$Tu = \frac{2\times d\times\delta\times Fe}{\cos\theta} \qquad \text{(Formula.2)}$$

Where, d: thickness of plywood, δ: effective diameter on bearing, Fe: bearing strength of plywood (=19.4N/mm^2 (base bearing strength of 0° fiber direction)) [4]

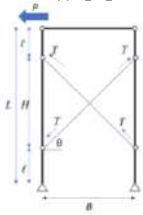

Fig.5 Analytical model of whole resistant mechanism of plywood

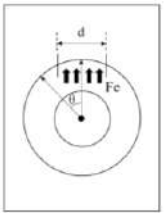

Fig.6 Bearing model on bolt joint

The size and material properties of plywood are summarized on Table.3, and the test result and analysis compare on Table.4. A direction of bearing force is assumed as 0°, and the bearing strength of bolt joint is calculated here.

From the comparison of Table 4, in case of N-C, the horizontal strength of experimental result shows 2 times comparing with analysis results. This error is derived from the strength of bearing of bolt joint, that is, the other resistant mechanism is predicted such as hardening, stress concentration. However, the whole resistant mechanism as shown in Fig.4 can chase the test result. Next, in case of S-C, the analysis result show good agreement of test result. It means that the bearing strength under wide area can be estimated by Formula 1.

Table.3 Size and material properties

Specimen name	maximum bearing force mechanism model				bearing force mechanism model			
	H [mm]	L [mm]	B [mm]	cosθ	d [mm]	δ [mm]	Fe [N/mm^2]	cosθ
N-C	1400	1800	910	0.55	12	16	19.4	1.1
S-C						61.2		

Table.4 Comparison of test results and analysis

Specimen name	bearing force [kN]		T/Tu	maximum bearing force [kN]		P/Pu
	experiment T	analysis Tu		experiment P	analysis Pu	
N-C	13.7	8.1	1.691358	5.8	3.4	1.7058824
S-C	33.7	31	1.0870968	14.3	13.1	1.0916031

CONCLUSIONS

From the test study, the specimen with steel hardware presents high strength, and the end opening fracture and out-of-plane deformation are observed during cyclic loading. Also, from the test result of strain and inter deformation angle of bolt joint, it is predicted that the resistant mechanism as brace mechanism. The analytical model of whole resistant mechanism of plywood and the bearing model on bolt joint are assumed to estimate the strength. The analysis result show that the bearing strength under wide area can be estimated.

Acknowledgment

This study was supported by Naito House Corp.

References

[1] SHINKENCHIKU 2017 January pp.90-93

[2] A. Otsuka, K. Takahashi, W. Kanbe, T. Ito : In - plane share test of thick plywood connected by bolts, Proceeding of the architectural research meetings, Kanto Chapter, Architectural Institute of Japan I pp.317-320

[3] Fundamental Theory of Timber Engineering pp.92-93, 190-194

[4] Design Manual for Engineering Timber Joints pp.277

THROW EFFICIENCY OF ELASTIC BEAMS IN SIMPLE EJECTION EXPERIMENTS

Guillaume Giombini*[1], Joachim Mathiesen[2], Médéric Argentina[1], Franck Celestini[1], and Christophe Raufaste[1]
[1]Université Côte d'Azur, CNRS, Institut de Physiqu ede Nice, 06100 Nice, France
[2]Niels Bohr Institute, University of Copenhagen, Copenhagen, Denmark

Summary We are interested in the energy transfer between a throwing engine and slender elastic projectiles. We have recently shown that the deformation dynamics of a projectile plays a major role in tuning its throw efficiency [1]. Here we investigate the case of slender elastic objects that are subject to bending deformations, such as arrows and spears. Different kind of projectiles are designed to investigate this question. A bow-like throwing engine is built to accelerate projectiles up to 100 times the standard gravity. The deformation dynamics is of paramount importance for the energy transfer and a gain of 150% can be reached for an optimal projectile. A simple model determines the relevant dimensionless parameters and is in good agreement with the experimental data.

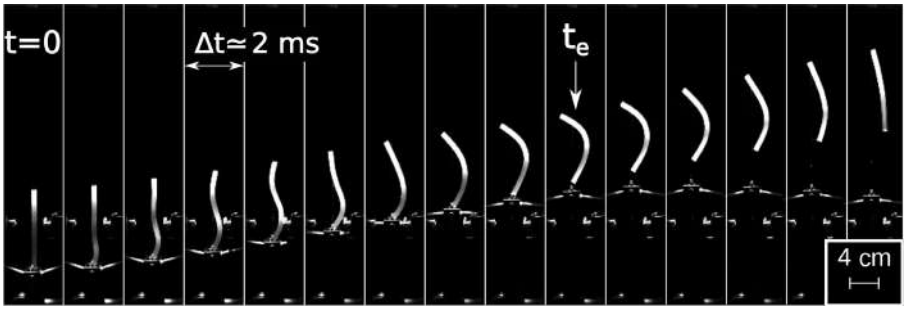

Figure 1: Image sequence displaying the deformation of a projectile while accelerated by the throwing engine. The projectile is made of a synthetic elastomer.

INTRODUCTION

Throwing objects is relevant for many natural processes [2] and is central to many technological innovations in human history. This is the case of bow-assisted shots in primitive societies or ejections by means of medieval catapults [3]. A recent study [1] has shown that elastic objects thrown by a catapult-like engine can obtain a 250% gain of kinetic energy as compared to a rigid projectile thrown in the same conditions. This phenomenon, called "superpropulsion", appears when the time scales of the object deformation and of the throwing engine acceleration are of the same order. While this phenomenon was characterized with longitudinal deformations, we investigate here the case of slender elastic projectiles that bend and exhibit transverse deformations.

EXPERIMENTAL SETUP

We perform experiments by throwing elastic beams. Several materials are tested, from soft elastomers to metallic rods (Fig. 1). The projectiles are vertically accelerated up to 100 times the standard gravity by a bow-inspired throwing engine. We vary numerous parameters systematically: mass (0.1 - 1 g), length L (1-10 cm), diameter (0.2-5 mm) and Young modulus of the projectile E (50 MPa-140 GPa), as well as the amplitude A (1-8 cm) and frequency f of the throwing engine (around 20 Hz). This engine has a harmonic motion described by $z(t) = A\,[1 - \cos(2\pi f t)]$ with a maximal velocity $V_p = 2\pi A f$. In order to have good time and space resolutions of our data, the experiments are imaged by a high-speed camera with a frame rate of 10^4 frames per second. We use an algorithm to track automatically the positions of the different parts of the system (masses and throwing engine). From these positions, we are able to measure the velocity of each object over time and particularly the ejection velocity of the projectile V_e at the time t_e as well as V_p, the velocity at which a rigid projectile would take off.

RESULTS

The efficiency is characterized by the energy transfer factor $\alpha = \left(\frac{V_e}{V_p}\right)^2$. We present results from four projectiles with same diameter, elastic modulus and mass but different lengths. The values obtained for α depend strongly on the

*Corresponding author. E-mail: guillaume.giombini@unice.fr

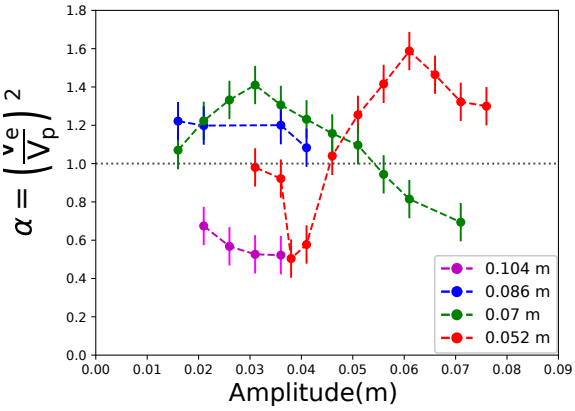

Figure 2: α as a function of the loading amplitude for four projectiles with the same diameter, mass and elastic modulus but different lengths. We see here a common behaviour: α increases, exhibits a maximum value and then decreases. The amplitude of the optimum depends on the length.

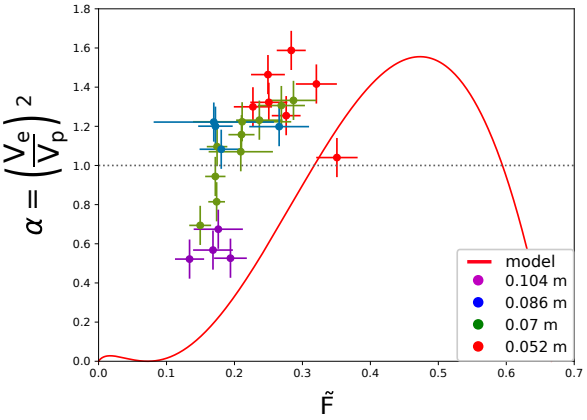

Figure 3: α as a function of the force ratio $\tilde{F}$ for the same lengths studied in Fig. 2. We see that the data align on a trend similar to the one predicted by the model (red solid line) with no free parameter, but slightly shifted towards the left.

amplitude (Fig. 2). At small ones, the projectile acts as a rigid object without any kinetic energy gain. For intermediate amplitudes, we observe transverse deformations that can lead to a kinetic energy gain of 150%. At large amplitudes, α decreases and the projectile exhibits very large deformations that can be irreversible and lead to failure of the beam. The effect of the amplitude emphasizes a nonlinear dynamics and the amplitude at optimal ejection is found to depend on the projectile length.

MODEL

We built a model to find the relevant dimensionless parameters. The projectiles are modeled by massless elastic beams with two point masses at the edges. In that case, the elastic beam pushes on the point masses with a constant force, equal to Euler's load, as soon as it bends. Within the frame of the model, the deformation dynamics can be calculated and the set of equations emphasizes two relevant parameters: the ratio of the amplitude to length and the ratio of the elastic force to the inertia force, which is a function of the amplitude and frequency of the throwing engine as well as the mass of the projectile. We find that the previous results are no longer disperse but follow a single trend when expressed as a function of the force ratio instead of the amplitude, in relative good agreement with the model (Fig. 3).

CONCLUSION

We have shown that the efficiency of a deformable beam can reach 150% the one of a rigid projectile thrown in the same conditions and that this effect is nonlinear since it depends on the amplitude of the throwing engine. A simple model gives the relevant dimensionless parameters, in good agreement with experiments. This study could be relevant for archery and the way arrows are shot from a bow: we expect a matching between bows and arrows to maximize the transfer of energy.

References

[1] Raufaste C., Ramos Chagas G., Darmanin T., Claudet C., Guittard F., and Celestini F. Superpropulsion of droplets and Soft Elastic Solids, *Physical Review Letters*, 119, 108001, 2017.

[2] Forterre Y. Slow, fast and furious: understanding the physics of plant movements. *Journal of Experimental Botany* 64(15):4745–4760, 2013.

[3] Denny M. Siege engine dynamics. *European Journal of Physics* 26(4):561, 2005.

WRINKLING INSTABILITY OF MICROCAPSULES IN EXTENSIONAL FLOW

Revaz Chachanidze,Kaili Xie,Clément de Loubens*,and Marc Leonetti†
Univ. Grenoble Alpes, CNRS, Grenoble INP, LRP, 38000 Grenoble,France

Summary Soft microcapsules are core-shell particles, i.e viscous droplets bounded by a soft elastic membrane and embedded in another viscous fluid. If buckling of capsules under pressure or local indentation has been investigated in literature, this is certainly not the case in simple flows. Well-defined wrinkles and folds are experimentally first observed on the membrane of stretched capsules by extensional flow when the hydrodynamic stress is above a threshold. It depends on the membrane elastic properties and the capsule's size. A master curve for wrinkling bifurcation is demonstrated. The scaling of the wrinkle's wavelength with microcapsule's characteristics is determined in the limit of small wavelength compared to the capsule's size. The phase diagram is established.

INTRODUCTION

Microcapsules are droplets bounded by a solid membrane characterized by a Young modulus which can vary on several order of magnitudes, depending on the applications. They are used to protect internalized molecules of interest, to convey and to deliver their contents in food, cosmetics and medecine... Soft microcapsules in flow model also the behavior of biological cells in living fluids such as blood. Indeed, soft deformable particles such as vesicles, polymersomes and capsules exhibit analog spatiotemporal dynamics than Red Blood Cells in shear flow. These shape instabilities are more or less oscillations of the global shape, i.e without wrinkles for example.

However, in the 70s, [1] observed a shape modulation when RBCs are stiffened, a phenomenon explained by buckling. [2] studied large capsules of several millimeters moving inside channels. If the study is only focused on the curvature inversion at the rear as RBCs, wrinkles can be visualized (but not mentioned) on figures. Finally, [3] visualize also wrinkles at the membrane of one kind of small capsules in shear flow. However, if compressive domains due to fluid-structure coupling are expected at membrane [4, 5], neither scaling, nor phase diagram were established.

Here, we study experimentally the emergence of the wrinkling instability of capsules with well controlled mechanical properties in a planar extensional flow.

MATERIALS AND METHODS

Microcapsule fabrication

The microcapsule membrane is formed via electostatic complexation of chitosan (CAS 9012-76-4, Sigma-Aldrich) with phosphatidic acid [6]. Chitosan is dissolved in demineralized water at concentration 0.05 - 3.0 g/L (pH of water is adjusted to 3.0 by adding hydrochloric acid). Phosphatidic acid (AMP 4455, Palsgaard) is dissolved in rapeseed oil. Microfluidic generation of chitosan droplets in the oil phase allows to create uniform in size capsules (30 - 400 μm). The complexation time for membrane formation takes 2-30 minutes. After that in order to stop the reaction the capsules are washed in cyclohexane (CAS 110-82-7, purity 99.5%, Sigma Aldrich) an resuspended in silicon oil AP1000 (IMCD, viscosity 1.18 Pa·s - 22°C). The membrane thickness (20 nm - 1 μm) is estimated with atomic force microscopy (for the details see Xie *et al.*, [7]). Typically, the Young modulus E is 4 MPa.

Microfluidic chamber

The microfluidic chamber with a 1 x 1 mm^2 cross section is composed of two intersecting channels and is used to create a planar extensional flow [8, 9]. The capsule suspension is pushed through the chamber and visualised with a bright field microscope (Olympus IX-71) equiped with a 20x objective and a fast camera (Photron Fastcam SA3). The surface shear elastic modulus G_s is determined in the limit of small deformations by applying hydrodynamic stress to a capsule, where deformation is defined as the Taylor parameter $D = (L - S)/(L + S)$. Here, S and L are the small and big axes of the capsule respectively Figure 1.

RESULTS AND DISCUSSION

The microcapsules, initially spherical, deform into ellipsoids under hydrodynamic stress. Their membrane experiences the wrinkling instability when the stress surpasses a threshold which depends on membrane properties: figure 1-a,b. The wavelength changes strongly between both cases as the thickness. This trend is similar to the case of flat soft films under static extension [10]. Thicker membrane, larger critical hydrodynamic stress: figure 1-c.

*Corresponding author. E-mail: clement.de-loubens@univ-grenoble-alpes.fr.
†Corresponding author. E-mail: leonettm@univ-grenoble-alpes.fr.

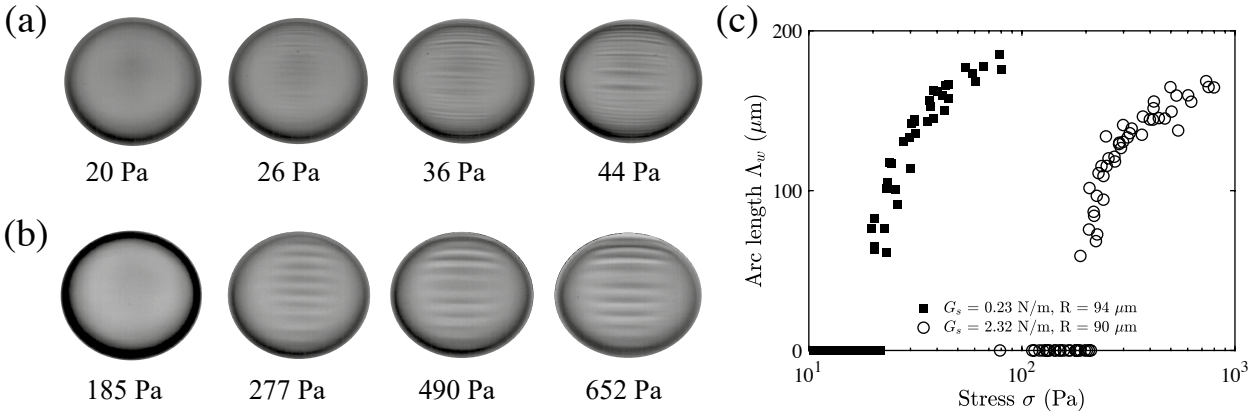

Figure 1: **(a, b)** : Development of the wrinkles on the capsules with 60 $\pm$ 8 nm **(a)** and 650 $\pm$ 80 nm **(b)** thick membrane. In the case a, focalized structures can be observed at 44 Pa. **(c)**: Wrinkling lenght Λ_w as a function of hydrodynamic stress σ,

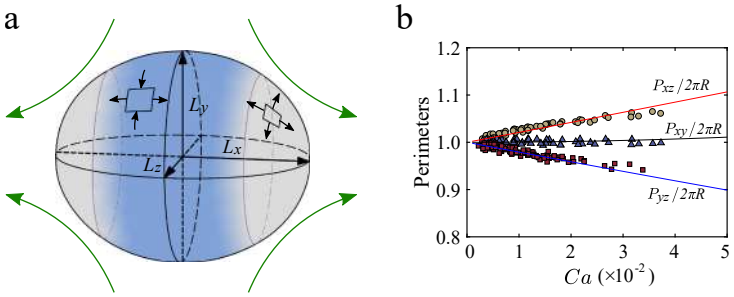

Figure 2: **(a)**: Schematic depiction of a capsule in an elongational flow. The blue zone corresponds to the domain under azimuthal compression. **(b)**: Evolution of a capsule perimeter in three principal planes of deformation

In this flow configuration, capsules are stretched in the direction flow (positive membre tension) while at the center, membranes become under compression even at small stress (negative membrane tension). See the compressive zone schematically depicted in blue color on the figure 2-a and is quantified with the decrease of the perimeter in the orthogonal plane (x-z) on the figure. 2-b.

We study the nature of this instability by quantifying the length of the wrinkles presented on the figure 1-c. We observe that the wrinkling threshold depends on the surface shear elastic modulus G_s of a capsule as well as on its radius R leading to recasting all the results on a master curve using the dimensionless elastic capillary number. Thus the critical capillary number is unique and does not depend on thickness contrary to the theory [11]. By an original optical set-up, the section is also visualized to determine accurately the scaling of the wavelength. A phase diagram is established.

CONCLUSION

In flow microcapsules can experience wrinkling instability which can be fully characterised experimentally.

References

[1] Fischer, T. M., Haest, C. W. M., Stàhr, M., Kamp, D., & Deuticke, B. (1978). Biochimica et Biophysica Acta (BBA)-Biomembranes, 510(2), 270-282.
[2] Seshadri, V., Hochmuth, R. M., Croce, P. A., & Sutera, S. P. (1970). Microvascular research, 2(4), 434-442.
[3] Walter, A., Rehage, H., & Leonhard, H. (2001). Colloids and Surfaces A: Physicochemical and Engineering Aspects, 183, 123-132.
[4] Secomb, T. W., Skalak, R., àzkaya, N., & Gross, J. F. (1986). Journal of Fluid Mechanics, 163, 405-423.
[5] Lac, E., Barthes-Biesel, D., Pelekasis, N. A., & Tsamopoulos, J. (2004). Journal of Fluid Mechanics, 516, 303-334.
[6] Gunes, D. Z., Pouzot, M., Rouvet, M., Ulrich, S., & Mezzenga, R. (2011). Soft Matter, 7(19), 9206-9215.
[7] Xie, K., De Loubens, C., Dubreuil, F., Gunes, D. Z., Jaeger, M., & Léonetti, M. (2017). Soft matter, 13(36), 6208-6217.
[8] de Loubens, C., Deschamps, J., Georgelin, M., Charrier, A., Edwards-Levy, F., & Leonetti, M. (2014). Soft matter, 10(25), 4561-4568.
[9] de Loubens, C., Deschamps, J., Boedec G., & Leonetti, M. (2015). Journal of Fluid Mechanics, 767, R3.
[10] Cerda, E., & Mahadevan, L. (2003). Physical review letters, 90(7), 074302.
[11] Finken, R., & Seifert, U. (2006). Journal of Physics: Condensed Matter, 18(15), L185.

PUMPING FLUID WITH A THIN-WALLED PNEUMATIC SOFT ACTUATOR

Maziar arfaee[1], Johannes T.B. Overvelde*[2], and Jolanda Kluin [1]
[1]Department of Cardiothoracic surgery, Academic medical centre, Amsterdam, Netherlands
[2]AMOLF, Amsterdam, Netherlands

Abstract: Soft actuators are becoming increasingly popular for application where adaptability is important, due to their embodied intelligence. They are typically light-weight, easy to process, safe in human-body interaction and also low cost in fabrication. In the following, we will introduce a thin-walled soft actuator made by heat sealing two thin layers of materials. Our system is actuated pneumatically and can have various motions based on the sealing pattern. We demonstrate our approach by fabricating a prototype of a soft pump that can be used as an artificial heart, and demonstrate promising results for this system in terms of efficiency.

BACKGROUND

Soft robotics is a recent field of robotics, in which intelligence is embodied in the robot by way of compliance of materials. Soft actuators are being developed to make motions in soft robots and can work as a part of industrial systems or medical devices, that can be safer than solid actuators in combination with a soft end effector. This is because both the actuator and end effector have the capability of adapting their shape to their environment. Moreover, soft actuators are getting popular to study due to their low manufacturing cost, safe human-machine interaction [1], light-weight and also ease of process. However, this comes at a cost of high precision [2]. Importantly, many motions can be embedded in soft actuators by manufacturing them in different shapes, such that simple outputs could potentially lead to various and complex outputs [3].

Soft actuators can be actuated pneumatically, hydraulically, by heat, chemical reactions, or electric fields [4][5]. Among these ways of actuating, soft pneumatic actuators have become popular as they are powerful and also relative easy to control. Several studies have been done on design and optimization of such soft pneumatic actuators during the last decade, with a main focus on: (i) Development of different geometrical designs to have various motions; (ii) increase power output; (iii) Try to find analytically model the actuators in order to predict and optimize the behavior before fabricating. Studies have shown geometrical design can affect the output motion significantly [1][6]. Also the behavior of the actuator can be changed by using different materials which have different properties. Finally, as it is possible to fabricate soft actuators with biocompatible materials, they can be utilized in devices aimed to interact with human body like rehabilitation devices, surgical devices for minimal invasive surgery and prosthesis [2].

THIN-WALLED SOFT ACTUATOR

In this study, we propose a thin-walled soft pneumatic actuator which can be made by any thin thermoplastic sheets, for example in this study we used thermoplastic polyurethane sheets with a thickness of 0.3 millimeters. The actuator is made of two layers which are sealed together using a custom heat sealer, in which particularly channels and chambers are embedded to program the actuator with certain behavior upon inflation. The pattern of sealing determines the channel arrangements and so the behavior. By inflating the actuator, the channels are inflated, which effectively reduces the distance between the sealing lines, such that the whole actuator shrinks perpendicular to the channel walls (i.e. sealing direction). Therefore, the shrinkage pattern can be modified by analyzing and designing different patterns of channels. The simplest motion of the thin-walled soft actuator is contraction in one direction which is similar to the motion needed for artificial muscles [7].

Here we demonstrate the actuators by building a prototype for a soft pump, in which we enclose a volume by our inflatable actuators. By inflating the walls we are able to reduce the enclosed volume, and pump a certain volume. In particular, we are interested in pumping a large amount of fluid, while only inflating the walls by a small amount. In other words, we would like to achieve transmission ratio higher than one. Moreover, we aim to achieve high transmission ratios with high efficiency of this pumping. Therefore, we have developed a measurement platform which allows us to determine both quantities accurately. Initial tests showed that the outflow can rise up to twice as the inflow regarding the inside pressure, with efficiencies up to 80 percent.

CONCLUSIONS

We have just started to explore the potential of these thin-walled pneumatic actuators, and initial results shown great potential. Our goal in the future will be to optimize the design of the actuators, to improve transmission ratios, while keeping high efficiencies, with the ultimate goal to develop a soft total artificial heart.

* Corresponding author. E-mail: overvelde@amolf.nl

References

[1] Herianto, et al., Design and fabrication in the loop of soft pneumatic actuators using fused deposition modelling. Sensors and Actuators A: Physical, 2019. 298.
[2] Azami, O., et al., Development of the extension type pneumatic soft actuator with built-in displacement sensor. Sensors and Actuators A: Physical, 2019. 300.
[3] Connolly, F., C.J. Walsh, and K. Bertoldi, Automatic design of fiber-reinforced soft actuators for trajectory matching. Proc Natl Acad Sci U S A, 2017. 114(1): p. 51-56.
[4] Wang, T., L. Ge, and G. Gu, Programmable design of soft pneu-net actuators with oblique chambers can generate coupled bending and twisting motions. Sensors and Actuators A: Physical, 2018. 271: p. 131-138.
[5] Ding, L., et al., Design of soft multi-material pneumatic actuators based on principal strain field. Materials & Design, 2019. 182.
[6] Siefert, E., et al., Bio-inspired pneumatic shape-morphing elastomers. Nat Mater, 2019. 18(1): p. 24-28.
[7] Oguntosin, V. and A. Akindele, Design and characterization of artificial muscles from wedge-like pneumatic soft modules. Sensors and Actuators A: Physical, 2019. 297.

SOFT CELLULAR METAMATERIALS WITH PROGRAMMABLE DEFORMATION-CONTROLLED SHAPE

Zhaohang Zhang[1], Anastasiia O. Krushynska*[1]
[1]Engineering and Technology Institute Groningen, Faculty of Science and Engineering, University of Groningen, Groningen, The Netherlands

Summary Rich microstructure makes cellular metamaterials promising candidates for delivering programmable behaviour. In this paper, we develop a comprehensive method based on theoretical, numerical and experimental analysis aimed to program the shape of soft cylindrical structures subject to tensile deformation. The programmable response originates from a combination of auxetic and conventional honeycomb unit cells with different geometric parameters allowing to control the structural shape. First, we theoretically study the dependence of the mechanical properties on the geometric parameters of honeycomb unit cells. Then, we introduce a theory-driven design approach to program the structural shape. Further, we explore the possibilities of an experiment-driven optimization to find more complex programmable designs. For that, the cylindrical honeycomb structures are fabricated by means of additive manufacturing techniques and will be tested experimentally. The prescribed deformation of a complex shape has great application potential in the fields of medical equipment and intelligent structures, while further development of programmable and even automated design methods can facilitate their eventual use.

INTRODUCTION

Rapid advances in additive manufacturing, computational design and conceptual breakthroughs have allowed considering the material design not only as a means to solve practical problems, but also as a catalyst for unveiling novel material functionalities [1]. Rationally designed architectures give rise to unprecedented mechanical properties that can be exploited to create advanced materials with novel functionalities [2]. The recent paradigms of shape-morphing, topological and nonlinear metamaterials have opened roadmaps for the development of truly smart materials, e.g. those with a complex response to a single stimulus [3]. When realized in a two- or three-dimensional setting, these metamaterials can be used to switch, activate or regulate the mechanical structural response and associated functionalities. Specifically, they have a promising potential in flexible electronics and wearable devices, like prosthetics and orthotics [4].

Mechanical cellular metamaterials form an ideal platform for the development of novel smart and multi-functional materials thanks to their high-dimensional design space determined by a variety of geometric parameters and bulk material properties [5]. On the one hand, their architectural elements, including cell arrangement, corner angle, cell length, strut width, etc., provide sufficient degrees of freedom (DOFs) to design new functionalities [6]. On the other hand, an enormous amount of available DOFs makes it very challenging to find the most feasible solution. To address this challenge, it is promising to exploit computational design and optimization tools helping to avoid tedious trial-and-error procedures and excessive experimentation.

In this work, we focus on the design of soft cylindrical structures formed by a combination of auxetic and conventional honeycomb unit cells (e.g. star-shaped and octagon unit cells) and propose two techniques to achieve their programmable mechanical response driven by external deformation.

METHODS & RESULTS

To study the described structures and to implement their programmable behaviour, we use a combination of theoretical methods, numerical simulations, and experiments supplementing each other as described below.

Honeycomb unit cells analysis

Among different kinds of honeycomb unit cells, we consider star-shaped and octagon honeycomb configurations (SOH) with a biaxial symmetry (Fig. 1a) to facilitate their integration in a single structure when geometric parameters are varied. It is well-known that the mechanical properties of cellular materials are governed by their geometric parameters. For our SOH unit cells, these are the wall thickness and the inner angle between adjacent struts. As the angle changes from 10° to 180°, the unit-cell geometry is transformed from auxetic ($10° < \theta < 53°$) to conventional ($53° < \theta < 180°$) characterized by a positive and negative Poisson's ratio, respectively. The effective Young's modulus and Poisson's ratio of each unit cell were evaluated theoretically by means of the beam theory that accounts for tensile and bending deformations. The obtained results are approximate, though they can be used as a rough reference for programmable designs.

Programming of the honeycomb structures

One of the key parameters governing the deformation of the whole structure is the effective Poisson's ratio of a unit cell. Since its value was shown to be regulated by the inner angle and/or the wall thickness, the deformation and thus the final shape of the structure can be programmed by e.g. varying the inner angle. To achieve this, one can use different techniques, e.g. the theory-driven derivation or the experimental-driven optimization method.

The theory-driven derivation implies the use of 1D periodic unit cells in the 2D arrangement (Fig. 1b), where the inner angle of the unit cells is different along the y-direction and remains unchanged along the x-direction. In this case, the

*Corresponding author. E-mail: **a.o.krushynska@rug.nl**

linear-elastic strain in the y-direction, induced by forces on the left- and right-hand sides of the structure, will be inversely proportional to the effective Young's modulus of each column. The linear-elastic strain in the x-direction will be then proportional to the ratio of the effective Poisson's ratio and effective Young's modulus. The combination of these strains will influence the structural shape. We have verified this in numerous numerical simulations. Two of the pre-programmed structural shapes are shown in Figs.1c, d. However, soft materials are usually deformed in a nonlinear regime. Thus, to properly estimate the structural response, we are planning to consider large deformations as well.

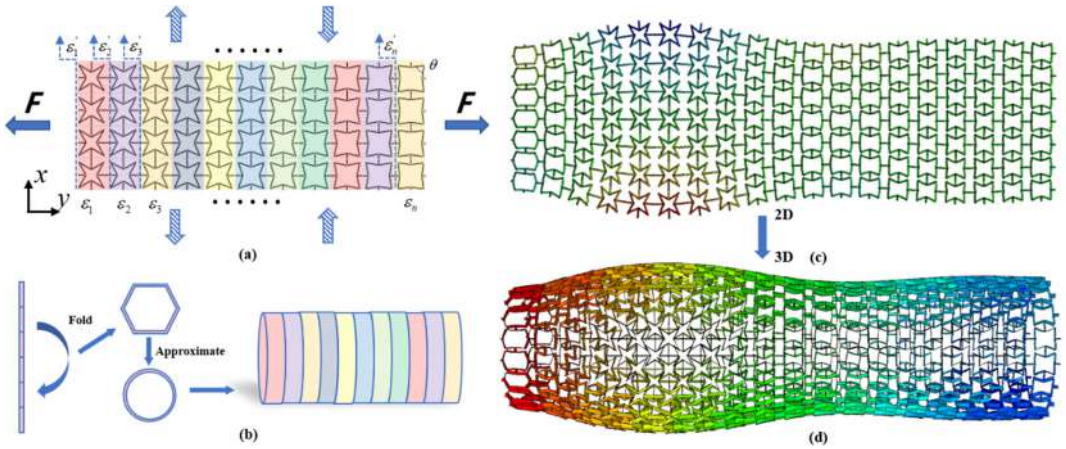

Figure 1. Schematic demonstration of (a) the deformation of 1D-periodic cellular metamaterial under tensile load and (b) the conversion of a flat honeycomb structure to a cylindrical one. Examples of (c) a flat honeycomb cellular meta-structure of pre-programmed shape and (d) a cylindrical cellular meta-structure of a pre-programmed shape.

The second, experiment-driven optimization technique allows considering a fully 2D arrangement of the unit cells. The main idea of this approach is that meta-structures can be fabricated, e.g. by additive manufacturing techniques, and tested experimentally to study the effect of the design parameters on the structural response. The experimental data supplemented by relevant numerical results form a benchmark for further optimization that can deliver more complex designs tailored to demand. To implement this approach, we have fabricated several samples by means of 3D-printers Form2 and Objet260 Connex3 from tough and soft resin, respectively. The experimental tests including tensile and compression analysis are underway.

CONCLUSIONS

We preliminary demonstrated that simple cellular honeycomb structures are excellent candidates for delivering a programmable mechanical response. The theory-driven derivation was shown to be an effective tool to program the shape of cylindrical honeycombs with a 1D-periodic arrangement of auxetic and conventional unit cells. The alternative experimental-based optimization will be used to design more complex arrangements, and, ultimately, to automate the design process to a certain degree. Therefore, we believe that the proposed techniques will be of use for the design of truly programmable metamaterials and will eventually facilitate their application in the fields of medical equipment and smart industry.

References

[1] Bertoldi K., Vitelli V., Christensen J., van Hecke M. Flexible mechanical metamaterials. *Nat. Rev. Mater.* **2(11)**:1–11, 2017.
[2] Kadic M., Milton G. W., van Hecke M., Wegener M. 3D metamaterials. *Nat. Rev. Phys.* **1(3)**:198–210, 2019.
[3] Zadpoor A. A. Mechanical meta-materials. *Mater. Horiz.* **3(5)**:371–81, 2016.
[4] Mirzaali M. J., Janbaz S., Strano M., Vergani L., Zadpoor A.A. Shape-matching soft mechanical metamaterials. *Sci. Rep.* **8(1)**:965, 2018.
[5] Guttag M., Yan D., Reis P. M. Programmable Aerodynamic Drag on Active Dimpled Cylinders. *Adv. Eng. Mater.* **21(7)**:1801315, 2019.
[6] Yang W., Liu Q., Gao Z., Yue Z., Xu B. Theoretical search for heterogeneously architected 2D structures. *PNAS.* **115(31)**: E7245-E7254, 2018.

A FINITE STRAIN PLATE MODEL FOR WRINKLING IN ANISOTROPIC HYPERELASTIC FILMS

Yifan Yang and Fan Xu*
Institute of Mechanics and Computational Engineering, Department of Aeronautics and Astronautics, Fudan University, Shanghai, China

Summary Transverse wrinkles commonly occur in a uniaxially tensile elastic membrane and can vanish upon excess stretching. The wrinkling direction is usually perpendicular to the stretching direction under isotropic elasticity. Here, we show that wrinkles are orientable by material anisotropy, such as in fiber-reinforced or fibrous films, and the wrinkling orientation can be tuned by varying the stiffness and direction of fibers. To quantitatively describe large anisotropic deformations and predict morphological evolution, we develop a finite strain model by introducing anisotropic, hyperelastic constitutive law into the geometrically extended Föppl-von Kármán nonlinear plate theory. We find that the shear modulus ratio between fibers and matrix significantly affects the critical buckling threshold, restabilization point and wrinkling amplitude. The shear modulus ratio above a critical value prevents the appearance of wrinkles. Effects of the angle between fibers and stretching direction on the oblique wrinkling orientation are carefully examined. The findings could provide an effective way to design wrinkle-tunable surfaces for fiber-reinforced or biomimetic membranes.

INTRODUCTION

Surface wrinkling instability is widely used to realize multifunctional smart structures and devices, such as the measurement of material properties, controllable optical transmittance, topology optimization, synthetic camouflaging skins, reprogrammable Braille designing and bioinspired surface structured sensors. Most previous efforts were made on isotropic materials and little is known about wrinkling response of anisotropic films. Here, we fill this gap by developing a mathematical model through introducing anisotropic, hyperelastic constitution into the geometrically extended Föppl-von Kármán (FvK) nonlinear plate theory, to quantitatively explore fiber-related wrinkles and their morphological evolution. We derive a simple yet effective anisotropic finite strain plate model inspired by the classical Gent constitutive law [1], while it is not difficult to implement other types of anisotropic hyperelastic materials with multiple families of fibers. Based on our model, we find that shear modulus ratio between fibers and isotropic matrix significantly affects the critical buckling threshold, restabilization point and wrinkling amplitude. Moreover, the shear modulus ratio above a critical value can even resist wrinkles. We reveal that the orientation of oblique wrinkles strongly depends on the fibers stiffness and the angle between fibers and stretching direction.

EXTENDED FÖPPL-VON KÁRMÁN PLATE MODEL WITH ANISOTROPIC HYPERELASTICITY

Let us consider a simple case that a single family of fibers reinforces the isotropic matrix. Motivated by Gent model, Horgan [1] presented a three-parameter strain energy for neo-Hookean materials reinforced by a family of fibers. Taking the incompressibility condition $J = 1$ into account, the strain energy function can be expressed as

$$\Psi = \frac{\mu}{2}\left(I_1 - 3\right) + \frac{\mu_1}{2}\left(I_4 - 1\right)^2 - p\left(J - 1\right), \tag{1}$$

where p denotes a Lagrange multiplier that can be identified as hydrostatic pressure.

For thin films, the direction of fibers is usually restricted in plane and thus the unit vector of fibers can be expressed as $\boldsymbol{a}_{0s} = (\cos\varphi_0, \sin\varphi_0)^T$, in which $\varphi_0 \in [0, 90°]$ represents the angle between fibers and stretching direction in the initial reference configuration. Combining the Kirchhoff-Love hypothesis and plane stress condition, the in-plane second P-K stress tensor is written as

$$\mathbf{S}_s = \mu\mathbf{I}_s + 2\mu_1\left(I_4 - 1\right)\boldsymbol{a}_{0s} \otimes \boldsymbol{a}_{0s} - p\mathbf{C}_s^{-1}. \tag{2}$$

Based on the extended FvK nonlinear plate theory [2], the 2D membrane energy is given by

$$W_m\left(\mathbf{C}_s^{\circ}\right) = h\Psi\left(\mathbf{C}_s^{\circ}\right), \tag{3}$$

and the bending energy density $W_b\left(\mathbf{K}_s\right)$ can be written as the contributions of the matrix [2] and fibers [3]:

$$W_b\left(\mathbf{K}_s\right) = \frac{Eh^3}{24\left(1-\nu^2\right)}\left(\nu\mathrm{tr}(\mathbf{K}_s)^2 + (1-\nu)\mathbf{K}_s \cdot \mathbf{K}_s\right) + \frac{\mu_1 h^3}{6}\left(\boldsymbol{a}_{0s} \cdot \mathbf{K}_s \cdot \boldsymbol{a}_{0s}\right)^2, \tag{4}$$

in which E and ν represent the initial Young's modulus and Poisson's ratio in the linear elastic regime, respectively. The potential energy $\mathcal{P}$ of the membrane reads

$$\mathcal{P} = \int_{\Omega_{2D}} \left[W_m\left(\mathbf{C}_s\right) + W_b\left(\mathbf{K}_s\right)\right] \mathrm{d}\Omega. \tag{5}$$

*Corresponding author. E-mail: fanxu@fudan.edu.cn

The first variation of the potential energy (5) with respect to the components of displacement field yields the Euler-Lagrange equilibrium equations:

$$\nabla_s \cdot [(\mathbf{I}_s + \nabla_s \mathbf{u}) \cdot \mathbf{S}_s] = \mathbf{0}, \tag{6}$$

$$\nabla_s \cdot (\nabla_s \cdot \mathbf{M}_s) + h \nabla_s \cdot (\mathbf{S}_s \cdot \nabla_s w) = 0, \tag{7}$$

in which $\nabla_s \cdot (\nabla_s \cdot)$ denotes the surface divergence and $\mathbf{M}_s := \partial W_b(\mathbf{K}_s)/\partial \mathbf{K}_s$ represents bending moment.

RESULTS

We set the fiber direction along the stretching direction ($\varphi_0 = 0°$). An isola-center bifurcation phenomenon is observed in Fig. 1, where the instability boundary shrinks with increasing k, and the membrane remains flat when $k \geqslant 0.2$. This fact implies a promising way for wrinkle-free or wrinkle-resistant surface design.

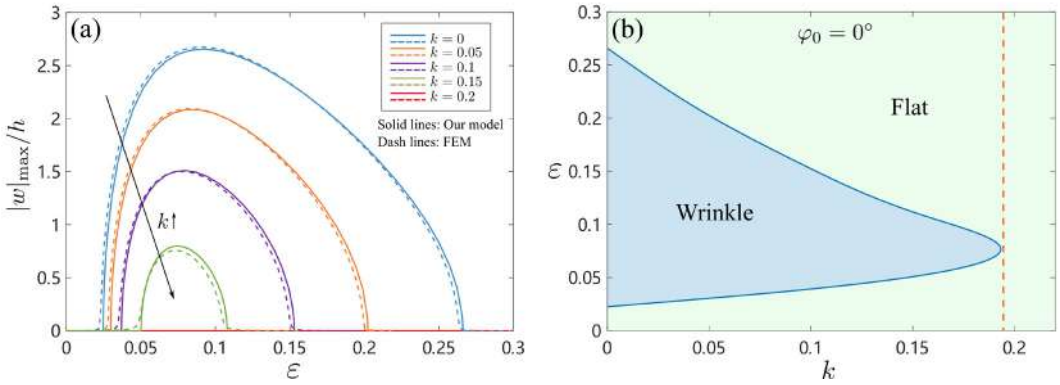

Figure 1: (a) Isola-center bifurcation diagram of uniaxially stretched membranes with varying shear modulus ratio ($k = \mu_1/\mu$). The solid lines represent predictions by our model, while the dash lines stand for those computed by FEM. With the increase of k, the isola-center bifurcation cycle dramatically shrinks. (b) Calculated phase diagrams on stability boundaries determined by the shear modulus ratio k and tensile strain ε. The anisotropic membranes wrinkle when their parameters are located in the blue region, while remain flat in the green region. Fiber angle $\varphi_0 = 0°$.

We find that the fiber direction determines the oblique angle of wrinkles, as shown in Fig. 2. The contours of compressive stresses in the pre-buckling stage of anisotropic membranes are drawn in the third line of Fig. 2. It can be seen that the compressive stress has the similar distribution as the wrinkling orientation (maximum compression parallel to wrinkling direction). Altering the material anisotropy, *i.e.*, the angle between fibers and stretching direction, is shown to be a feasible way for the formation of orientation-tunable wrinkling patterns.

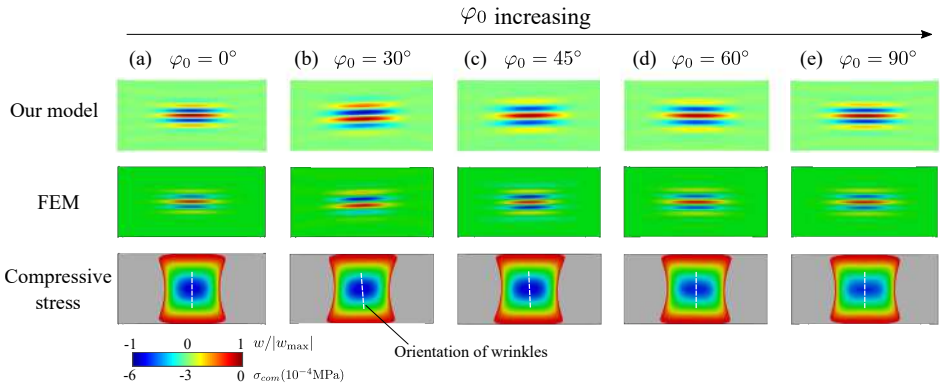

Figure 2: Oriented oblique wrinkles and contours of compressive stresses for various angles between material anisotropy and stretching direction. Shear modulus: $k = 0.15$.

References

[1] Horgan, C.O. The remarkable Gent constitutive model for hyperelastic materials. *Int. J. Nonlinear Mech.* **68**, 9-16, 2015.

[2] Fu, C., Wang, T., Xu, F., Huo, Y., Potier-Ferry, M. A modeling and resolution framework for wrinkling in hyperelastic sheets at finite membrane strain. *J. Mech. Phys. Solids* **124**, 446-470, 2019.

[3] Yang, Y., Fu, C., Xu, F. A finite strain model predicts oblique wrinkles in stretched anisotropic films. *Int.l J. Eng. Sci.* **155**, 103354-1–103354-14, 2020.

A BI-SHELL VALVE UTILIZING SHELL SNAPPING INTERACTION FOR FAST ACTUATION OF PNEUMATIC SOFT ROBOTS

Chuan Qiao, Lu Liu, and Damiano Pasini*
Department of Mechanical Engineering, McGill University, Montreal, Canada

Summary Fast actuation of pneumatic soft robots is typically achieved through either pressure-controlled strategies involving a bulky system of pressure supply, or actuators engaging structural instabilities or chemical explosions. All these routes are not straightforward to realize and have their own challenges. In this paper, we introduce a bi-shell valve that can operate through the slow deflation of a syringe to produce a fast volume output for rapid actuation. The valve leverages the snapping and interaction of its constituent shells, whose geometry can be effectively tuned to maximize its volume change output. Our valve works through deflation, yet its architecture can be adapted to work as a rapid inflation valve or pneumatic volume fuse, hence offering additional routes for soft robot control and actuation.

INTRODUCTION

Rapid actuation is challenging to achieve for most pneumatic and hydraulic soft robots. The most widely used approach is to quickly inflate a soft actuator through a pressure controlled system. This requires a cumbersome setup f pressure supply, sensors, hard valves and a control algorithm. Alternative strategies exists, and propose fairly sophisticated modifications to the actuator which needs to be embedded in the soft robot. These mainly rely on the integration of structural instabilities in the actuator architecture [1] or on the use of explosive chemical reactions [2].

In this paper, we provide a volume-controlled solution, a bi-shell valve, that bypasses the requirements above [3]. Its operation needs only a slowly dispensed volume input to deliver fast volume output. The function this valve can deliver is unattainable by existing soft valves, which can either fully (on-off control) or partially (flux control) block a fluid flow. Its hallmarks are also distinct over current valve concepts: the architecture encompasses two shells (one spherical cap and one imperfect shell), and its physics is underpinned by the cooperative deformation and snap-through interaction of its constituent shells.

DESIGN OF THE BI-SHELL VALVE

The design of the bi-shell valve (Figure 1a) consists of two elastic shells, a shallow spherical cap and an imperfect hemispherical shell with a large indentation in the form of an axisymmetric elliptical arc. Both shells are mounted on a input chamber, which is used to deflate them by a slow volume-controlled input from the inlet. The spherical cap is also enclosed by an output chamber that capitalizes on its snapping to deliver a fast volume output.

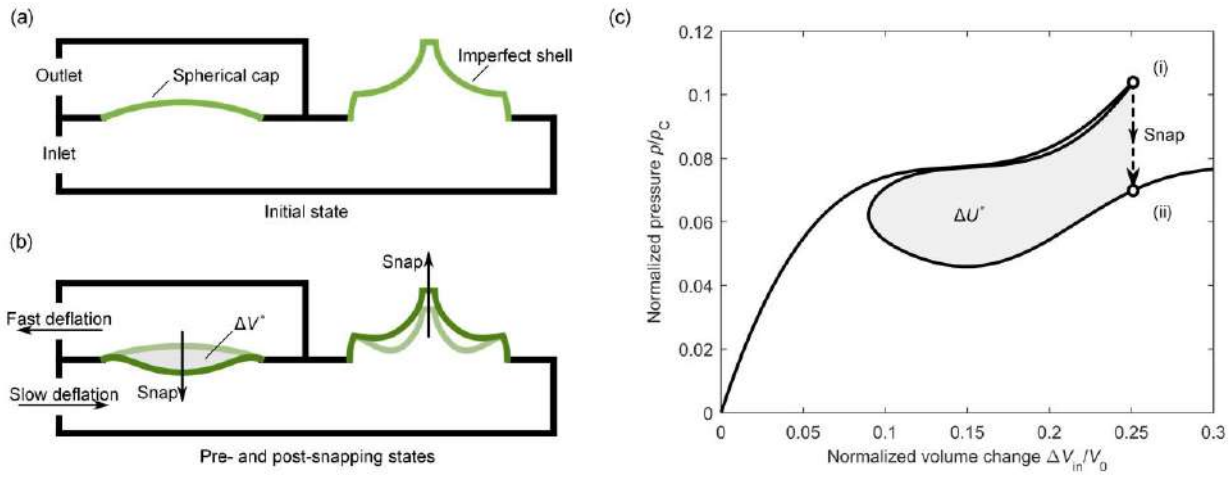

Figure 1. (a) Schematic of the bi-shell valve. (b) The configuration of the bi-shell valve in pre- and post-snapping states. (c) Pressure-volume response of the bi-shell valve.

Figure 1b shows the configuration of the bi-shell valve in its pre- and post-snapping states. When the input chamber of the bi-shell valve is slowly deflated from the inlet, the imperfect shell first deflates during the pre-snapping state (light green), while storing volume change and energy. During this phase, the spherical cap stays almost in its initial shape. After snapping (dark green), the imperfect shell springs up towards its undeformed state, releasing the volume change and energy stored during pre-snapping. The spherical cap, on the other hand, snaps downward to a fully everted state. The sudden collapse of the spherical cap generates a fast volume change ΔV^*, which is depicted by the grey area (Fig. 1c) bounded by the pre- and post-snapping states of the spherical cap. This volume change is captured by the output chamber and is made readily available to rapidly deflate any soft robots that is connected to the valve outlet.

*Corresponding author. E-mail: damiano.pasini@mcgill.ca.

Figure 1c shows the pressure volume response of the bi-shell valve obtained from our analysis. The pressure is normalized with the theoretical buckling pressure p_C of an elastic spherical shell with a radius identical to the radius of the imperfect shell, whereas the volume change is normalized with the volume of a hemisphere V_0. Upon deflation, the pressure gradually increases to the snapping pressure at the pre-snapping state (i), followed by an abrupt drop in pressure when the bi-shell valve snaps to the post-snapping state (ii). During snapping, the bi-shell valve releases the elastic energy ΔU^* (the grey area in Figure 1c), which can be used for rapid actuation of soft robots.

INDIVIDUAL RESPONSE AND INTERACTION OF THE CONSTITUENT SHELLS

Figure 2 shows the individual response (pressure-volume change) of the spherical cap (left - a) and the imperfect shell (right - b). The former exhibits a highly unstable response that is characteristic of elastic spherical thin shells. This is expressed by the quick escalation of pressure to a high critical value (state i) in response to a small volume change, followed by a drop to a lower plateau that spans a wide range of volume change before raising again. On the other hand, the latter shows a stable pressure response over a large volume change, with a buckling mode enabled by the type and geometry of the imperfection. In this case, the pressure-volume response displays three portions: an initial regime where the pressure increases quickly, followed first by a plateau with a mild increase in pressure, and finally by a rapid increase of pressure.

When the shells are connected through the input chamber of the valve, their concerted deformation is governed by the equilibrium of pressure and volume. This condition requires that their pressure must be equal, and that their total volume change should equal the input volume change. At the pre-snapping state (i), both shells share the identical value of pressure. With further deflation, the buckling of the spherical cap triggers a sudden decrease in the pressure resistance of the cap, which forces the bi-shell system to snap and regain the balance of pressure in a new stable state, i.e. the post-snapping state (ii). During snapping, the spherical cap is deflated by ΔV^*, while the imperfect shell is inflated by the same amount of volume change. The total energy released during snapping ΔU^* (Fig. 1c) is the difference between the energy released by the imperfect shell ΔU_2^* (Fig 2b) and the energy stored by the spherical cap ΔU_1^* (Fig 2a).

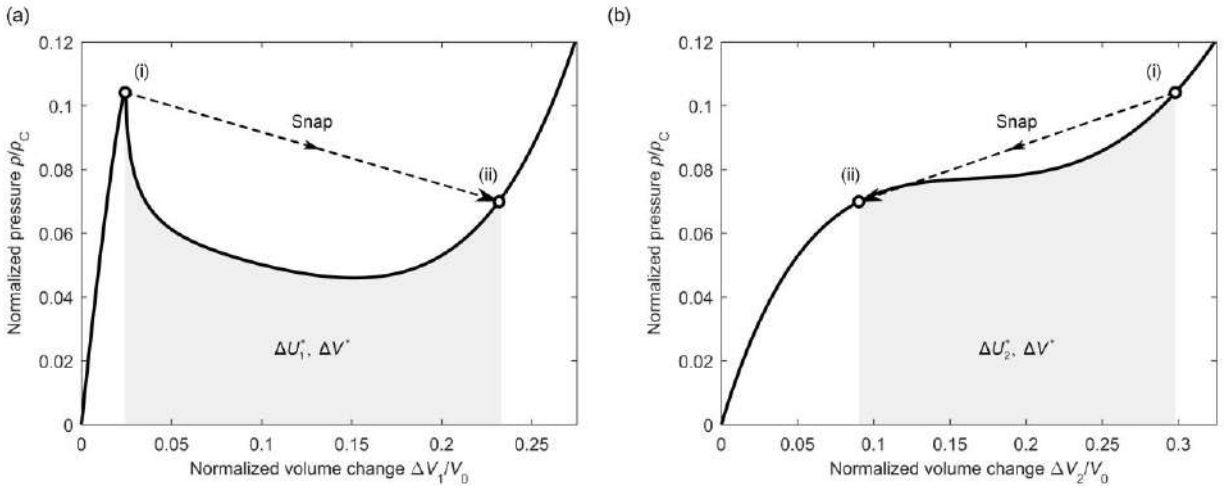

Figure 2. Pressure-volume change responses of the constituent shells. (a) The spherical cap. (b) The imperfect shell.

CONCLUSIONS

This work has introduced a bi-shell valve that harnesses the snapping and interaction of its constituent shells to convert a slow volume input into a fast volume output for fast actuation of soft robots. The valve can be directly connected to a soft robot without modifications to its design, and its performance can be controlled passively by simply tuning the shape of its constituent shells. The bi-shell valve concept introduced in this work along with its variational designs can offer new routes to provide actuation and control of soft pneumatic actuators.

Acknowledgements. This work was supported by the Natural Sciences and Engineering Research Council of Canada.

References

[1] Gorissen B., Melancon D., Vasios N., Torbati M., Bertoldi K., Inflatable soft jumper inspired by shell snapping. *Sci. Robot.* **5**: 1967, 2020.

[2] Shepherd R. F., Stokes A. A., Freake J., Barber J., Snyder P. W., Mazzeo A. D., Cademartiri L., Morin S. A., Whitesides G. M., Using explosions to power a soft robot. *Angew. Chem.-Int. Edit.* **52**: 2892-2896, 2013.

[3] Qiao C., Liu L., Pasini D. Elastic thin shells with large axisymmetric imperfection: from bifurcation to snap-through buckling. *J. Mech. Phys. Solids* **141**: 103959, 2020.

NON-ORIENTABLE MECHANICS IN METAMATERIALS

Xiaofei Guo*[1,3], Marcelo Guzman[2], Denis Bartolo[2], David Carpentier[2], and Corentin Coulais[1]
[1]Institute of Physics, University of Amsterdam, Amsterdam, Netherlands
[2]Ecole Normale Supérieure de Lyon,Lyon,France
[3]Harbin Technology of Institute, Harbin, China

Summary Non-orientability is a topological property, which has potential to achieve novel and unusual mechanical behaviours. However, the complex geometry of non-orientable structures limits their applications in the real world. Here we show that it is possible to achieve non-orientable mechanics in an orientable metamaterial. This is achieved by geometrical frustration, which generates a single movable domain wall in periodic structures during loading. The moving path of the domain wall can be controlled by the loading sequence, which leads to different mechanical responses. In other words, the proposed metamaterial can break abelian rules and has a sequential memory. Based on the sequential memory, we build a mechanical sequential logic gate, which can achieve the same value table as a Set-Reset latch, one of the most basic sequential logic gates in electronic fields. The concept of non-orientable mechanics opens up a new avenue for new designs of metamaterials and mechanical logic gates.

BACKGROUND

Unlike avoiding imperfections in traditional metamaterials, flexible metamaterials harness instability, defect and frustration to achieve novel functionalities, such as pattern and shape transformations[1, 2], reprogrammable property[3] and multistability[4]. However, few studies have focused on the mechanics in non-orientable structures, which has potential to achieve new functionalities. But the non-orientability generally leads to complex geometries, which limits applications. Here we achieve non-orientable mechanics in an orientable structure using instability and frustration. The concept of non-orientable mechanics provides new ideas for metamaterials designs.

NON-ORIENTABLE MECHANICS

Orientability is a topological property of surfaces, which describes whether it is possible to make a consistent choice of surface normal vector at every point. A Mobius strip is the simplest non-orientable surface. Due to the non-orientability, Out-of-plane deformations or shear deformations must pass through zero in one round of a Mobius strip[5], which is robust and topologically protected. The topologically protected zero point is the characteristic of non-orientable mechanics.

Here we show that it is possible to achieve non-orientable mechanics in an orientable metamaterial: the rotating-square mechanism. The unit cell of rotating-square mechanisms includes up and down two squares and arranges along the horizontal direction (Fig.1(a)). In an open rotating-square chain, adjacent unit cells always trend to rotate in opposite directions like a mechanical antiferromagnet[6]. Once a rotating-square chain is closed by joining its ends together, the mechanism of a rotating-square ring depends on the parity of total number of unit cells. If the number of unit cells is even, it still can follow the compatible antiferromagnetic mechanism. If the number of unit cells is odd, the rotating-square ring forms a frustrated mechanism (Fig.1(a)). The frustration leads a conflict between two opposite rotating mechanisms. The junction between two rotating mechanisms is defined as a domain wall, at where the rotation is zero. Therefore, an odd number rotating-square system always has a zero deformation point, like the non-orientable mechanics in a Mobius strip.

NON-ABELIAN MECHANICS

Due to the single domain wall, rotating-square ring can achieve non-abelian mechanics under three compressive forces. Three forces applied on the rotating-square ring are marked as A, B and C. The response of the loading sequence as A→B→C is different from the response of the loading sequence as A→C→B (Fig.1(b)). Therefore, the proposed mechanism has a sequential memory. It also can be represented as non-abelian mechanics, i.e. $A+B+C \neq A+C+B$. The reason of realizing non-abelian mechanics includes the characteristic property of buckling and the move of the domain wall. Different loading sequences push the domain wall along different paths(Fig.1(b)), which leads to different responses of deformations and achieves non-abelian mechanics in statics.

SEQUENTIAL LOGIC GATES

The non-abelian property of non-orientable mechanics gives a system sequential memories, which enables it to achieve a mechanical sequential logic gate. Unlike combinatorial logic, the output of sequential logic not only depends on the current input, also its previous states. To achieve a mechanical logic gate by the rotating-square ring, input and output codes are defined as follows. Similar to the previous discussion, three forces A, B and C are applied. The force A is defined as a pre-load, which is not included in the input. Therefore, there are two inputs, force B and C, which are applied

*Corresponding author. E-mail: x.guo2@uva.nl

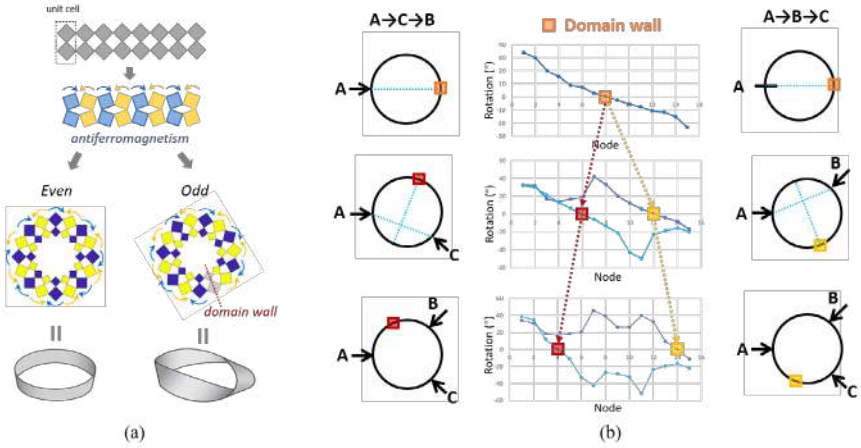

Figure 1: **Non-orientable mechanical metamterials.** (a) The antiferromagnetic rotating mechanism. If the number is odd(even), the rotating-square ring has the similar non-orientable(orientable) mechanics as a Mobius(cylinder) strip. (b) The moving path of the domain wall of the rotating-square ring depends on the loading sequences, which leads to different mechanical responses and achieves non-abelian mechanics, $A + B + C \neq A + C + B$.

by actuators (Fig.2(a)). Their actuated states are respectively represented as R and S. If the actuator is on(off), S or R is coded as 1(0). The outputs are the deformations of two unit cells between two actuators. If the unit cell rotates anticlockwise(clockwise), it is coded as 1(0). Since the adjacent unit cells rotate in different direction, the two outputs are marked as Q and $\bar{Q}$. All responses of this mechanical logic gate exactly conform to the value table of a Set-Reset flip-flop (Fig.2(b)(c)), one of the most basic sequential logic gates.

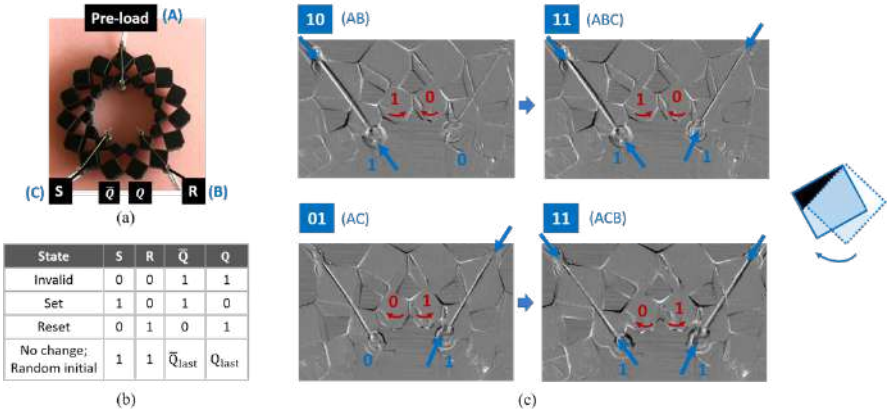

State	S	R	$\bar{Q}$	Q
Invalid	0	0	1	1
Set	1	0	1	0
Reset	0	1	0	1
No change; Random initial	1	1	$\bar{Q}_{last}$	Q_{last}

(b)

Figure 2: **Mechanical sequential logic gates.** (a) The setup used to achieve a mechanical Set-Reset flip-flop, one of the most typical sequential logic gates. (b) The value table of a Set-Reset flip-flop. (c) The responses under different actuation states in experiments. The rotation direction of unit cells is marked by black and white triangles.

CONCLUSIONS

In summary, we proved that it is possible to achieve non-orientable mechanics in a flat orientable metamaterial. It is achieved by the antiferromagnetic rotating mechanism. When the number of unit cells is odd, the antiferromagnetic mechanism forms a frustration. The frustration automatically generates a domain wall, which is similar to the topologically protected zero point in a Mobius strip. The moving path of the domain wall depends on the loading sequences and achieves non-abelian property. A mechanical sequential logic gate was built using the sequential memory of the rotating-square ring. The concept of non-orientable mechanics opens up a new avenue for metamaterials designs.

References

[1] B. Haghpanah et al. Multistable shape-reconfigurable architected materials. *Adv. Mater.*, 28, 7915–7920, 2016.
[2] C. Coulais et al. Multi-step self-guided pathways for shape-changing metamaterials. *Nature*, 561, 512-515, 2018.
[3] J. L. Silverberg et al. Using origami design principles to fold reprogrammable mechanical metamaterials. *Science*, 345, 647–650, 2014.
[4] S. Shan et al. Multistable architected materials for trapping elastic strain energy. *Adv. Mater.*, 27, 4296, 2015.
[5] D. Bartolo and D. Carpentier. Topological Elasticity of Nonorientable Ribbons. *Phys. Rev. X.*, 9(4), 041058, 2019.
[6] S. Kang et al. Complex Ordered Patterns in Mechanical Instability Induced Geometrically Frustrated Triangular Cellular Structures. *Phys. Rev. Lett.*, 112(9), 098701, 2014.

A SIMPLE MACROSCALE MODEL OF THERMOMECHANICAL RESPONSE OF TCPF ACTUATORS

Miha Brojan*[1] and Jan Zavodnik[1]
[1]Laboratory for Nonlinear Mechanics, University of Ljubljana, Ljubljana, Slovenia

Summary The recent discovery of a negative effective thermal expansion in twisted and coiled polymer fibres (TCPFs), has opened new routes for development of systems that can mimic natural skeletal muscles. It was shown that TCPF actuators are a viable alternative to pneumatic, hydraulic and electric actuators due to their ability to develop a significant force per unit mass, low cost of manufacture and ease of operation. To optimize the development and functionality of TCPFs, a comprehensive modelling of thermal untwist and the TCPF shortening is of great importance. For this purpose, we present a concise and simple mathematical model capable of describing thermally induced deformation and additionally, elastic deformations caused by mechanical loads and residual torsion from the fabrication process. We show a remarkable match between the theory and experiments.

TCPF CONTRACTION MECHANISM

Twisted and coiled polymer fibres (TCPFs, shown in Fig. 1) have been proposed by Haines et al. [1]. Since then this system has attracted a lot of attention as it has found use in many applications, e.g. as pneumatic and hydraulic actuator alternatives, for residual energy harvesting, as limb actuators, robotic arms, self-regulating relayes, etc. The main advantages of the TCPF actuators are their low production cost, simplicity and the ability to perform large strokes.

The TCPFs are essentially twisted and then coiled crystalline polymeric fibres of nylon, polypropylene or some other polymers, which exhibit a thermal expansion anisotropy in the longitudinal/transverse fibre direction. The thermal expansion anisotropy is a direct consequence of the polymer chain orientation following the extrusion process. It is precisely this anisotropy that causes the twisted fibres to untwist during heating, resulting in a change of the helix angle and an effective shortening of the twisted and coiled polymer fibre. This large effective shortening of the TCPF is harvested in actuator applications, as large strokes are often required in various applications.

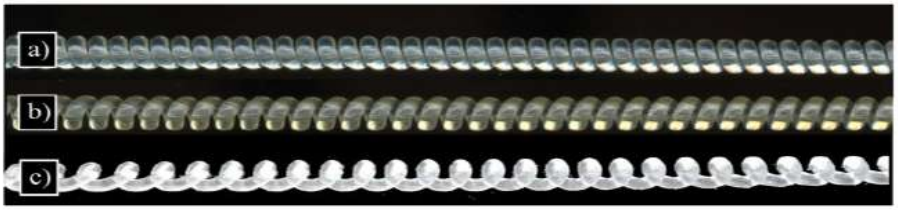

Figure 1. a) Coiled virgin TCPU b) Thermally treated TCPU c) Plastically deformed TCPF.

Several models that describe the TCPF behaviour have been proposed. The commonality between the models is that they are often either too simple to accurately describe the phenomenon or are way too convoluted to enable a deep understanding and rapid parametric analysis of the TCPF response. In our study we focused on understanding the TCPF mechanics via concise theoretical modelling and precise experiments. We therefore present a simple, concise, yet accurate mathematical model to predict and describe the mechanisms that govern the TCPF contraction and force production.

The first part of our model describes the temperature expansion fiber untwist with the use of a simple transverse anisotropic thermal expansion material model. The twisted fibre thermal expansion anisotropy is modelled in the local coordinate system that follows the rotation of polymer chains rather than in a global coordinate system that is fixed to the fibre. Therefore, we can more easily follow the untwist of the fibre. We find that a model reduction in terms of assuming axial symmetry of the polymer fibre, assuming that untwist is constant along the fibre and employing an averaging in the radial direction can significantly simplify the solution procedure while maintaining a remarkable accuracy of the problem within the performance limits of the TCPFs. This way we find that the temperature and axial loading cause an effective fibre untwist which can be written as

$$\Delta\phi^{\mathrm{eff}}(T,F)=\frac{4\varepsilon(\phi_0+\Delta\phi_F)}{\gamma_{l\phi,0}^4}\left(\gamma_{l\phi,0}^2-(1-2\varepsilon(T))\ln\left(1+\frac{\gamma_{l\phi,0}^2}{1-2\varepsilon(T)}\right)\right)+\Delta\phi_F(T,F).$$

Here ϕ_0 is the initial fibre twist, $\gamma_{l\phi,0}=\phi_0 r_0/l_0$ is the dimensionless initial fibre twist with r_0 as initial outer fibre radius, l_0 is the initial fibre length, ε labels the difference between the longitudinal and the circumferential/radial polymer thermal expansion, expression $\Delta\phi_F(T,F)$ is the axial force caused untwist that depends on the force F and the temperature dependent material parameters. This axial force caused untwist can be calculated e.g. from the principle of virtual work.

*Corresponding author. E-mail: miha.brojan@fs.uni-lj.si

The second part of our model describes the kinematic connection between the thermally caused untwist $\Delta\phi^{eff}$ and the TCPF effective shortening. Our kinematic relation between the fibre untwist and helix angle stems directly from the differential geometry where the change of twist is described as

$$\tau = |\frac{\partial^2 r}{\partial s^2}|^{-2}\left[\frac{\partial \boldsymbol{r}}{\partial s}, \frac{\partial^2 \boldsymbol{r}}{\partial s^2}, \frac{\partial^3 \boldsymbol{r}}{\partial s^3}\right].$$

Here $\boldsymbol{r}$ is the position vector describing the spatial curve and s is the arc-length parameter. The total twist can therefore be calculated as $\phi = \tau l + \Gamma$, where Γ is the residual twist emanating from fabrication. From here the kinematic relation for a helix is written as

$$\Delta\phi = 2\pi n(\cos\tilde{\theta} - \cos\theta),$$

where n is the number of coils, $\tilde{\theta}$ is the deformed helix angle and θ is the initial helix angle. This relation offers a direct insight into the behaviour of the TCPFs.

Furthermore, a simple, low-cost, but effective experimental setup (not shown here) that allows the study of TCPF fabrication mechanics and the validation of the theory was also developed. The fabrication process itself is not complex but requires at least a qualitative knowledge of the physical phenomena at play in order to successfully fabricate a high quality TCPF. With the use of our experimental setup, we explore and describe the good practice and underlying mechanism of the coiling process in order to successfully fabricate a high performance TCPF. An excellent agreement between our theoretical results and the results from the literature [2,3,4] is shown in Fig. 2.

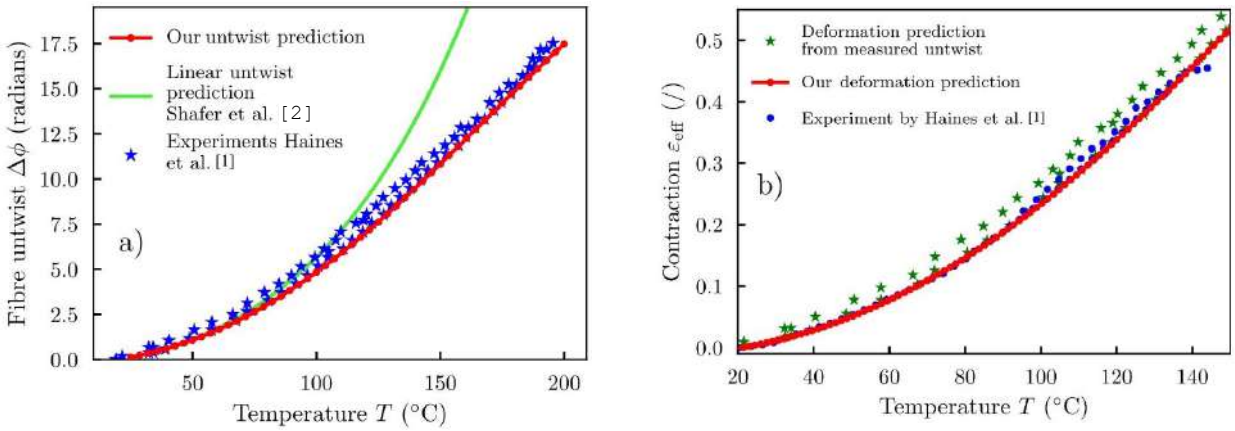

Figure 2: Comparison between our theoretical predictions, experiments by Haines et al. [1] and model by Shafer et al. [2]. a) Fibre untwist as a function of temperature. b) TCPF contraction as a function of temperature.

CONCLUSIONS

In our study we focused on understanding of the TCPF mechanics via concise theoretical modelling and precise experiments. We have developed a simple and accurate theoretical model to describe the behaviour of TCPFs in which we consider thermally induced deformation, elastic deformations caused by mechanical loads and residual torsion from the fabrication process. The proposed model describes the anisotropy without unnecessary complexity and is accurate within the performance limits of the TCPFs. With the use of our model and experimental setup we described the underlying mechanism of the coiling process to successfully fabricate a high performance TCPF. We show a very good match between the theory and experiments.

References

[1] C. S. Haines et al., Artificial Muscles from Fishing Line and Sewing Thread. Science 343:6173 (2014) p. 868-872.
[2] M. Shafer et al., First steps in modeling thermal actuation of twisted polymer actuators using virgin material properties. In: Modeling, Simulation and Control; Bio-Inspired Smart Materials and Systems; Energy Harvesting, Vol. 2. American Society of Mechanical Engineers, (2016).
[3] C. Haines et al., New twist on artificial muscles. Proceedings of the National Academy of Sciences of the United States of America Vol. 113, (2016).
[4] Q. Yang and G. Li, A top-down multi-scale modeling for actuation response of polymeric artificial muscles. Journal of the Mechanics and Physics of Solids 92, (2016) p. 237-259.

PIECEWISE VARIABLE STRAIN APPROACH FOR THE MODELING OF SOFT ROBOTS: THEORY AND APPLICATION

Costanza Armanini*[1], Frederic Boyer[2], and Federico Renda[1,3]
[1]Department of Mechanical Engineering, Khalifa University of Science and Technology, Abu Dhabi, UAE
[2]LS2N lab, Institut Mines Telecom Atlantique, 44307 Nantes, France.
[3]Khalifa University Center for Autonomous Robotic Systems (KUCARS), Khalifa University of Science and Technology, Abu Dhabi, UAE

Summary One of the main challenges in the soft robotics field is the development of mathematical models capable of describing the complex deformed configurations with both accuracy and simplicity. In an effort to develop models based on continuum mechanics and parametrized by a small set of relative, serial-link DOFs, the Piecewise-Constant-Strain (PCS) approach has been proposed [1] to efficiently model soft, rigid and hybrid multi-body systems within the same framework. Here, the PCS approach is generalized to the case of non-constant strains and applied to the static equilibrium of soft manipulators internally actuated by tendon and/or fluidic chambers with general routing [2]. Moreover, we present an example of application of the modeling approach for the design and development of a novel generation of macro-scale underwater propellers that draw their inspiration from flagellated organisms.

DISCRETE VARIABLE-STRAIN MODEL

Continuum kinematics and statics

A Cosserat rod is a continuous stack of rigid cross-sections parametrized by a material curvilinear abscissa $X \in [0, L]$ where L is the total length of the rod. Identifying each rigid cross-section with the moving frame rigidly attached to it, the configuration space of the rod is completely defined by a curve $\boldsymbol{g}(\cdot) : X \mapsto \boldsymbol{g}(X) \in SE(3)$ represented by the homogeneous matrix:

$$\boldsymbol{g} = \begin{pmatrix} \mathbf{R} & \mathbf{r} \\ \mathbf{0}^T & 1 \end{pmatrix}, \tag{1}$$

where $\mathbf{r}(X) \in \mathbb{R}^3$ is the position vector of the origin of the moving frame and $\mathbf{R}(X) \in SO(3)$ is the rotation matrix representing its orientation with respect to the spatial frame. Considering the Lie algebra $\mathfrak{se}(3)$ of $SE(3)$, the derivative of $\boldsymbol{g}$ with respect to X defines the strain state of the rod $\widehat{\boldsymbol{\xi}}(\cdot) : X \mapsto \widehat{\boldsymbol{\xi}}(X) \in \mathfrak{se}(3)$, while the equality of mixed partial derivatives of $\boldsymbol{g}$ with respect to space X and time t yields the velocity of the moving frame $\widehat{\boldsymbol{\eta}}(\cdot) : X \mapsto \widehat{\boldsymbol{\eta}}(X) \in \mathfrak{se}(3)$:

$$\boldsymbol{g}' = \boldsymbol{g}\widehat{\boldsymbol{\xi}}\,, \qquad\qquad \boldsymbol{\eta}' = \dot{\boldsymbol{\xi}} - \mathrm{ad}_{\boldsymbol{\xi}}\boldsymbol{\eta}\,, \tag{2}$$

where ad is the adjoint map. We consider now the static equilibrium of a Cosserat rod internally actuated by a distributed tendons and/or fluidic chambers. Taking the equilibrium of a section of an elastic rod and limiting the length of the section to zero, the static ordinary differential equation and its final value are obtained:

$$\begin{aligned} &(\boldsymbol{\mathcal{F}}_i - \boldsymbol{\mathcal{F}}_a)' + \mathrm{ad}^*_{\boldsymbol{\xi}}(\boldsymbol{\mathcal{F}}_i - \boldsymbol{\mathcal{F}}_a) = \mathbf{0}\,, \\ &\boldsymbol{\mathcal{F}}_i(L) = \boldsymbol{\mathcal{F}}_a(L)\,, \end{aligned} \tag{3}$$

Above, $\boldsymbol{\mathcal{F}}_i(X)$ and $\boldsymbol{\mathcal{F}}_a(X)$ represent the internal elastic and the actuation load respectively, given by:

$$\boldsymbol{\mathcal{F}}_i(X) = \boldsymbol{\Sigma}(X)\left(\boldsymbol{\xi}(X) - \boldsymbol{\xi}^*\right) \qquad \boldsymbol{\mathcal{F}}_a(X) = \begin{bmatrix} \tilde{\boldsymbol{d}}(X)\boldsymbol{t}(X) \\ \boldsymbol{t}(X) \end{bmatrix} \tau\,, \tag{4}$$

where $\boldsymbol{\Sigma}(X)$ is the elasticity tensor matrix, $\boldsymbol{d}(X)$ represents the distance from the mid-line to the internal actuator, $\boldsymbol{t}(X)$ is the unit vector tangent to the actuator path, and τ is the magnitude of the actuation force given by the tension of the tendon or by fluid pressure for a fluidic actuation.

Discrete model

The infinite dimensional strain field $\boldsymbol{\xi}$ can be discretized by selecting a set of vector functions to form a finite basis for the field. This can be represented as:

$$\boldsymbol{\xi}(X) = \boldsymbol{B}_q(X)\boldsymbol{q} + \boldsymbol{\xi}^*\,, \tag{5}$$

where $\boldsymbol{B}_q(X) \in \mathbb{R}^{6\times n}$ is a matrix function whose columns form the basis for the strain field $\boldsymbol{\xi}$ and $\boldsymbol{q} \in \mathbb{R}^n$ is the vector of coordinates in that basis, n being the number of degrees of freedom. Inserting the strain discretization, the velocity-strain equation can be analytically integrated:

$$\boldsymbol{\eta}(X) = \left[\mathrm{Ad}^{-1}_{\boldsymbol{g}} \int_0^X \mathrm{Ad}_{\boldsymbol{g}}\boldsymbol{B}_q ds\right]\dot{\boldsymbol{q}} = \boldsymbol{J}(\boldsymbol{q}, X)\dot{\boldsymbol{q}}\,, \tag{6}$$

*Corresponding author. E-mail: costanza.armanini@ku.ac.ae.

which defines the geometric Jacobian $\boldsymbol{J}(\boldsymbol{q}, X) \in \mathbb{R}^{6\times n}$ for a variable-strain soft manipulator. Finally, it is now possible to obtain the generalized static equation of the system by virtue of the D'Alembert's principle:

$$\int_0^L \boldsymbol{B}_q^T \boldsymbol{\mathcal{F}}_i dX = \int_0^L \boldsymbol{B}_q^T \boldsymbol{\mathcal{F}}_a dX \,, \qquad \boldsymbol{\mathcal{F}}_a(X) = \boldsymbol{B}_\tau(\boldsymbol{q}, X)\boldsymbol{\tau} \,, \tag{7}$$

where $\boldsymbol{B}_\tau(\boldsymbol{q}, X) \in \mathbb{R}^{6\times n_a}$ is a matrix function whose columns are given by vector functions and $\boldsymbol{\tau} \in \mathbb{R}^{n_a}$ is the vector of magnitude actuation forces. In Figure 1, we present the modeling of a conical arm, with linear and helical path actuators in the reference configuration, i.e.: the distance $\boldsymbol{d}(X)$ to the center-line has respectively linear and sinusoidal coordinates in the local frame.

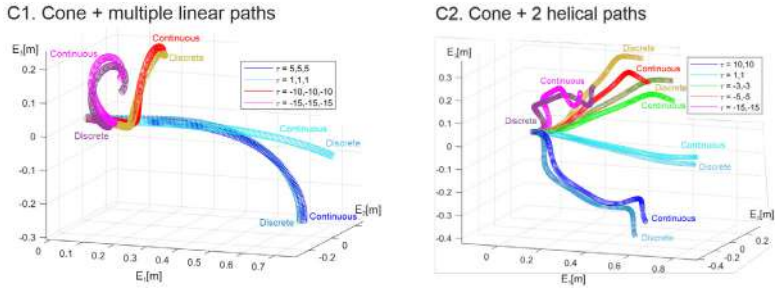

Figure 1: Example of a conycal manipulator with (left) linear and (right) helical path actuators.

A FLAGELLUM PROPELLER: MODELLING AND TESTING

The proposed model is employed to design a macro-scale aquatic soft robot propeller inspired by flagellated prokaryotic bacteria. Interacting with the surrounding fluid, the propeller exploits the compliance of its own body to passively attain a range of stable helical waves which are responsible for the generation of positive net thrust. We investigate the relationship between actuation frequency and material elasticity in determining the steady-state configuration of the system and its thrust output. Different experiments are performed and finally a complete robot is fabricated.

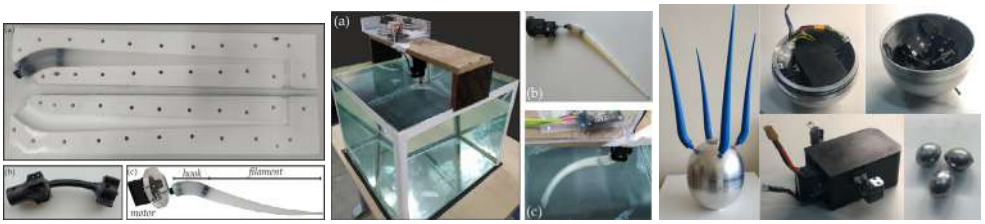

Figure 2: Photos of the proposed propeller: (left) the flagellum propeller with the mold used to fabricate it; (center) photos taken during one of the experiment; (right) the underwater robot prototype combining the action of 4 propellers.

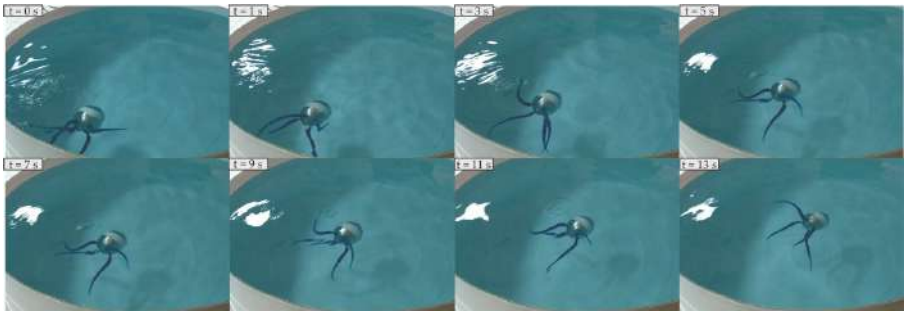

Figure 3: Screenshots taken during an experiment with the 4-flagelleted underwater robot

References

[1] Renda F., Boyer F., Dias J. and Seneviratne L. Discrete Cosserat approach for multisection soft manipulator dynamics. *IEEE Transactions on Robotics*, 34(6):15181533, 2018.

[2] Renda F., Armanini C., Lebastard V., Candelier F. and Boyer F. A Geometric Variable-Strain Approach for Static Modeling of Soft Manipulators With Tendon and Fluidic Actuation *IEEE Robotics and Automation Letters*, 5, 4006-4013, 2020.

ACKNOWLEDGEMENT

This research is based upon work supported by the Khalifa University of Science and Technology under Award No. FSU-2018-08, Research Excellence (AARE) 2018-05 and CIRA-2020-074.

A THEORETICAL STUDY ON THE TRANSIENT MORPHING OF LINEAR POROELASTIC PLATES

Dario Andrini[1], Alessandro Lucantonio[2], and Giovanni Noselli[1]
[1]Department of Mathematics, SISSA–International School for Advanced Studies, Trieste, Italy
[2]Department of Excellence in Robotics & AI, The BioRobotics Institute, Scuola Superiore Sant'Anna, Pisa, Italy

Summary Based on their shape-shifting capabilities, soft active materials have enabled new possibilities for the engineering of sensing and actuation devices. While the relation between strains and equilibrium shapes has been fully characterized, the transient morphing of thin structures is rather unexplored. Here we focus on polymer gel plates and derive a reduced linear model to study their time-dependent response. We show that independent control of stretching and bending deformations in stress-free conditions allows to realize spherical shapes with prescribed geometry of the mid-plane. Further, we demonstrate that tensile (compressive) membrane stresses delay (accelerate) swelling-induced shape transitions, as compared to the stress-free evolution. We believe that these effects should be considered for the accurate design of smart systems and may contribute to explain the complexity of natural shapes.

A LINEAR MODEL FOR THIN POROELASTIC PLATES

Understanding the way natural systems control and exploit shape changes to achieve biological functions is currently the subject of intense research inspiring the realization of synthetic replicas of natural shape morphing mechanisms using smart materials. Particular attention has been devoted to thin structures, such as plates and shells and to the exploration of their final equilibrium configurations. However, very little is known about the transient processes of morphing, apart from mainly experimental reports [1].

In this work, we focus on the transient shape morphing of poroelastic plates made of swelling gels. Despite geometric non-linearities play a crucial role in determining the configurations of active plates, we employ a linearized theory that is amenable to explicit analytical treatments.

The system of evolution equations for Kirchhoff linear poroelastic plates was first derived by Taber [2] starting from the three-dimensional setting, and later justified in [3]. Here we proposed an alternative derivation, following a formal asymptotic expansion approach inspired by Miara [4].

Let $\mathcal{B} = \omega \times (-h/2, h/2) \subset \mathbb{R}^3$ be the undeformed equilibrium configuration of the plate (ω is the mid-surface whereas h denotes the thickness). We write $(\mathbf{x}, x_3) \in \omega \times (-h/2, h/2) \subset \mathbb{R}^3$ for a point of the plate. The state of the plate is determined by the in-plane and transverse displacement fields $\mathbf{u}$ and u_3 respectively and the chemical potential μ. We finally introduce the in-plane strain $\mathbf{E} = \operatorname{sym} \nabla \mathbf{u}$ and curvature $\mathbf{K} = -\nabla\nabla u_3$ tensors.

We will consider cases where a free standing poroelastic plate is immersed into a solvent bath: null tractions are imposed on $\partial\omega$ and Dirichlet conditions $\mu = \mu_\star^\pm$ on $\omega \times \{\pm h/2\} := \omega^\pm$.

The symmetries of the governing equations allow to establish the dependence of the solution on the boundary conditions. We have that $\mathbf{E} = \mathscr{P}[\mu_m]$ and $\mathbf{K} = \mathscr{Q}[\mu_d]$ where $\mathscr{P}$ and $\mathscr{Q}$ are two linear operators and $\mu_m = (\mu_\star^+ + \mu_\star^-)/2$, $\mu_d = (\mu_\star^+ - \mu_\star^-)/2$. As a consequence of this $\mu_\star^+$ and $\mu_\star^-$ can be chosen so as to select any of the admissible evolutions of in-plane strain and curvature corresponding to given values of μ_m and μ_d, respectively. Consequently, there is no mutual influence between strain and curvature dynamics, a feature of interest in the context of the shape control of thin structures. We remark that this decoupled response is not expected to occur in the context of non-linear theories.

ANALYSIS OF THE STRESS-FREE PROBLEM

We now focus on a special class of solutions whose (thickness averaged) in-plane stress ($\mathbf{N}$) and bending moment ($\mathbf{M}$) are null everywhere in ω. We will refer to this problem as the stress-free problem.

First we derive necessary and sufficient conditions for the boundary conditions on μ to produce stress-free solutions. They need to satisfy $\Delta\mu_m = 0$ and $\nabla\mu_d = 0$ such that $\mu_\star^+$ and $\mu_\star^-$ are harmonic functions whose difference must be constant. As a consequence of that we conclude that stress-free configurations correspond to spherical shapes with any prescribed geometry of the mid-plane.

Next we obtain an analytical solution using the method proposed by Taber [2], in particular the procedure requires to take the Laplace transform of the governing equations in time. However the inverse transform cannot be analytically computed and so we present approximate solutions which are shown to be of significant accuracy. Interestingly these reveal an exponential decay through which the process reaches the stationary state. More specifically $\mathbf{u}$ and u_3 decay like $e^{-\pi^2 B_\eta t}$ and $e^{-4\pi^2 D_\eta t}$ respectively. The coefficients B_η and D_η have an explicit expression depending on the parameter $\eta = G/\lambda$ where G and λ are the shear and the bulk moduli respectively. Their dependence on η is depicted in Figure 1a. Notice that larger values of η correspond to slower shape changes.

We remark that, in general, the equation regulating solvent diffusion inside the gel is coupled to the displacement field through $\operatorname{tr}\mathbf{E}$ and $\operatorname{tr}\mathbf{K}$. This is not the case in the limit of $\eta \to 0$ where the governing equation for solvent diffusion

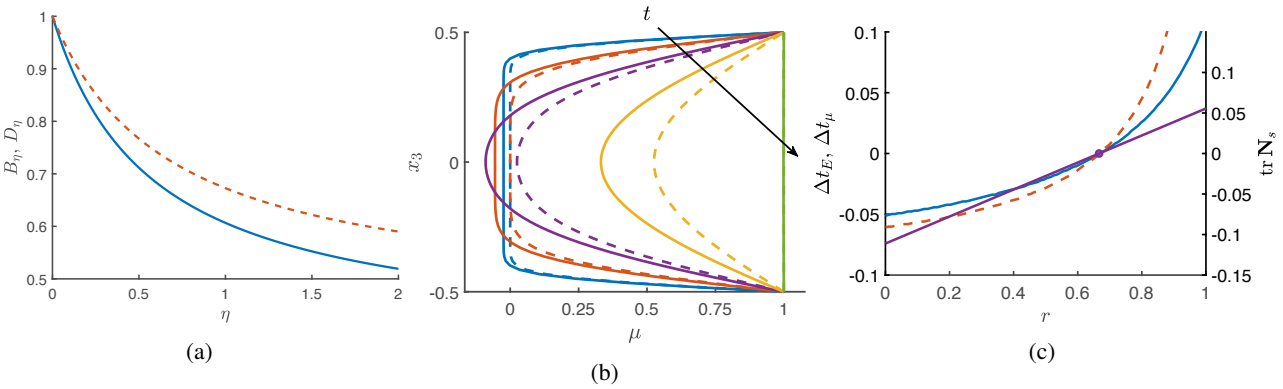

(a) (b) (c)

Figure 1: (a) Plots of B_η (solid blue line) and D_η (dashed red line) as functions of η. (b) Evolution in time for the chemical potential for $\mu_m = 1$, $\mu_d = 0$. Continuous line correspond to $\eta = 0.5$ while dashed lines to $\eta = 0$. (c) Time differences Δt_E (solid blue line) and Δt_μ (dashed red line) as functions of the radial coordinate. The purple line represents the trace of $\mathbf{N}$ at equilibrium. The crossover point of $\Delta t_E = \Delta t_\mu$ corresponds to the location where $\mathrm{tr}\,\mathbf{N}_s$ vanishes.

becomes a standard heat equation for μ. Hence Figure 1a shows that the weaker the coupling between diffusion and mechanics, the faster is the process. Finally we compared in Figure 1b the evolution of the profile for the chemical potential in the cases when $\eta = 0.5$ and $\eta = 0$.

EFFECT OF STRESSES ON THE SWELLING DYNAMICS: AN EXAMPLE

Differently from the stress-free case, where the time evolution of fields leading to stationarity is influenced only by mechanical parameters and is independent on the in-plane coordinate, the general fully coupled problem is sensitive to the internal stress distribution. To explore such sensitivity we computed a *semi-analytical* (numerical tools are used to invert the Laplace transform) solution of a specific problem where ω is the unit disk and $\mu_\star^\pm$ are taken with circular symmetry. In particular we chose $\mu_m(r) = 1 - r$ and $\mu_d(r) = 0$ where r is the radial coordinate. Observe that such a distribution of μ_m is not harmonic thus not allowing for a stress-free solution. Our analysis reveals how internal stresses affect pointwisely the process of shape change by swelling. As an average measure of swelling rate, we define the time $t_E(r)$ needed for $\mathrm{tr}\,\mathbf{E}$ to reach its steady state value within a tolerance of 0.1%. We notice that such a measure is conveniently a constant, t_{SF}, which only depends on η for any stress-free problem as already anticipated. Analogously, we introduce $t_\mu(r)$ for $N_\mu := \int_{-h/2}^{h/2} \mu \, \mathrm{d}x_3$. In Figure 1c we report results for $\Delta t_E = t_E/t_{SF} - 1$ and $\Delta t_\mu = t_\mu/t_{SF} - 1$, along with the steady state value of $\mathrm{tr}\,\mathbf{N}$. We notice that *compressive (tensile) stresses promote faster (slower) swelling with respect to the stress-free case*.

CONCLUSIONS

In this work, we have derived trough an asymptotic procedure a linear poroelastic plate model. First, we have studied a stress-free problem that has allowed us to obtain explicit, approximate solutions for the state fields. Then, we have presented a problem where elasticity and solvent transport are fully-coupled, namely, the planar swelling of a circular plate, which we have solved using a semi-analytical approach. We have found that tensile (compressive) membrane stresses delay (accelerate) swelling. Even though such an example concerns a specific choice of geometry and boundary conditions, our results highlight the impact of stresses on the dynamics of swelling of poroelastic plates. Given the theoretical nature of the present paper, we also plan to carry out experiments to validate our conclusions. Future works will be devoted to generalizing our findings, as well as extending the model to the non-linear regime.

References

[1] Amirali Nojoomi, Hakan Arslan, Kwan Lee, and Kyungsuk Yum. Bioinspired 3d structures with programmable morphologies and motions. *Nature Communications*, 9(3705), 2018.

[2] Larry A Taber. A theory for transverse deflection of poroelastic plates. *Journal of Applied Mechanics*, 59(3):628–634, 1992.

[3] Anna Marciniak-Czochra and Andro Mikelić. A rigorous derivation of the equations for the clamped biot-kirchhoff-love poroelastic plate. *Archive for Rational Mechanics and Analysis*, 215(3):1035–1062, 2015.

[4] B Miara. Justification of the asymptotic analysis of elastic plates, I. the linear case. *Asymptotic analysis*, 9(1):47–60, 1994.

[5] Dario Andrini, Alessandro Lucantonio, and Giovanni Noselli. A theoretical study on the transient morphing of linear poroelastic plates. *Journal of Applied Mechanics*, pages 1–10, 10 2020.

THE NON-HERMITIAN PHYSICS OF NON-RECIPROCAL ROBOTIC METAMATERIALS

Corentin Coulais*[1]
[1]Institute of Physics, University of Amsterdam, the Netherlands

Summary We create 1D and 2D robotic mechanical metamaterials wherein we use local control loops to break reciprocity at the level of the interactions between the unit cells to probe a wide range of non-Hermitian phenomena, ranging from the non-Hermitian skin effect, to non-Hermitian topological bulk-edge correspondence and odd-elasticity.

INTRODUCTION

Non-reciprocal transmission of motion is potentially highly beneficial to a wide range of applications, ranging from wave guiding to shock and vibration damping and energy harvesting. To date, large levels of non-reciprocity have been realized using broken spatial or temporal symmetries, yet mostly in the vicinity of resonances, bandgaps or using non-linearities, thereby non-reciprocal transmission remains limited to narrow ranges of frequencies or input magnitudes and sensitive to attenuation. Here, we create 1D and 2D robotic mechanical metamaterials wherein we use local control loops to break reciprocity at the level of the interactions between the unit cells to probe a wide range of non-Hermitian phenomena.

In such systems, we first show theoretically and experimentally that first-of-their-kind spatially asymmetric standing waves at all frequencies and unidirectionally amplified propagating waves emerge. These findings realize the mechanical analogue of the non-Hermitian skin effect. Second, we use this platform to discover a novel form of topological bulk-edge correspondence in a purely non-Hermitian setting. Third, we extend our explorations to the non-linear regime and observe the emergence of non-reciprocal solitons. Finally, we generalise our robotic metamaterials in 2D to create non-reciprocal shape-changing structures that realize odd elasticity.

UNIDIRECTIONALLY AMPLIFIED WAVES

Inspired by recent developments in robotics and active metamaterials, we create a robotic mechanical metamaterial (Fig. 1a) that uses distributed active control to break reciprocity at the level of the interactions between the building blocks themselves (Fig. 1b) [1]. This work builds on the field of active metamaterials, yet with a key new twist: while active metamaterials only have actuating elements, robotic metamaterials include a combination of local sensing, computation, communication, and actuation. As a result, they feature unique wave phenomena, namely asymmetric modes at all frequencies and unidirectional amplification (Fig. 1cb), and in turn realize large, broadband, linear, and self-amplified nonreciprocal transmission of mechanical waves. These findings realize the classical counterpart of the so-called non-Hermitian skin effect, recently theoretically introduced in quantum mechanics. These findings can be further generalized in the nonlinear regime and can lead to the emergence of non-reciprocal dissipative solitons.

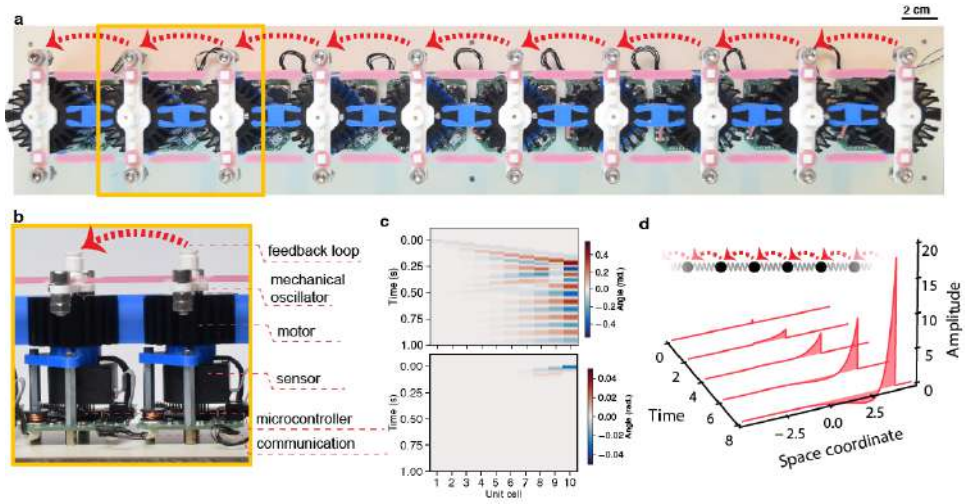

Figure 1: :(a) Mechanical 1D robotic mechanical lattice with 10 unit cells comprising internal feedback loops. (b) close-up on two robotic unit cells. (c) Experimental space-time diagram of the response to a pulse on the left (top) and right (bottom) and (d) theoretical prediction (Greens function) of the response to a pulse of a non-reciprocal mass-and-spring 1D lattice (continuum approximation), both showing the amplification (attenuation) for left-to-right (right-to-left) propagation..

*Corresponding author. E-mail: coulais@uva.nl

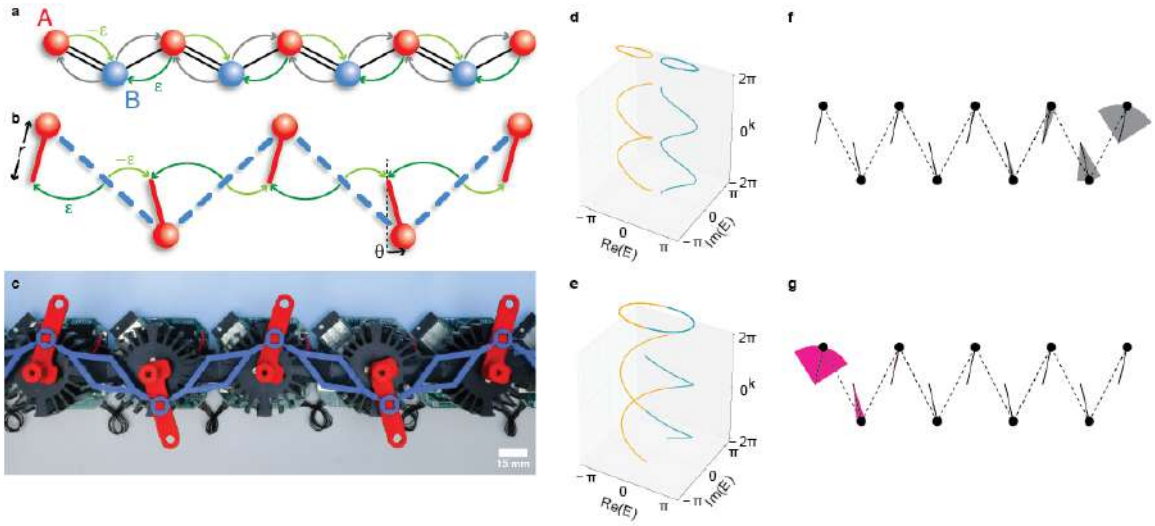

Figure 2: : Quantum-to-classical mapping of a chain with non- Hermitian topology and non-Hermitian bulk-edge correspondence. (a): An SSH chain with two sublattices, A (in red) and B (in blue), augmented with non-reciprocal variations in the hopping amplitudes (indicated by $\pm\varepsilon$). (b): The non-reciprocal classical analogue of the augmented SSH chain, in which the classical masses (in red) correspond to the A sites in the quantum model, while the non-reciprocal springs (in blue) are analogous to the B sites. (c) Picture of the mechanical metamaterial realizing the non-reciprocal classical analogue of the augmented SSH model. (d-e) The real and imaginary parts of the energies of the two bands $E_-(k)$ (orange) and $E_+(k)$ (blue) as a function of wave number k, along with their projections onto the $k = 0$ plane. The energies form either disconnected bands (d) or wind around other (e) forming trivial (d) or winding non-Hermitian (e) topology. (f-g) Corresponding edge mode localized on the right (f) or left (g) for trivial and winding topology, respectively.

NON-HERMITIAN TOPOLOGY AND BULK-EDGE CORRESPONDENCE

In a second time, we endow our 1D robotic metamaterials with non-Hermitian topological properties [2]. In particular, by generalizing the quantum-to-classical analogy to a non-Hermitian setting (Fig. 2), we establish a bulk-edge correspondence for this new type of truly non-Hermitian topology. We find that a change in the non-Hermitian topological invariant is accompanied by a localization change in the zero-energy edge modes (Fig. 2ef). We establish this non-Hermitian bulk-edge correspondence experimentally by measuring both bulk-invariants and edge modes and observe that a change in the non-Hermitian topological invariant coincides with the localization change of the topological edge mode, thus proving the robustness of the theoretical prediction.

ODD-ELASTICITY

Finally, we extend our robotic metamaterial platform to 2D and implement a recent proposal to realize non-symmetric elastic tensors, termed odd-elasticity [3]. Combining experiments, numerics and theory, we demonstrate that 2D non-reciprocal robotic metamaterials can realize non-reciprocal shear-extension coupling, wherein extension induces shear but shear does not induce extension as well as wave propagation even in overdamped conditions. We further evidence peculiar nonlinear behavior, in the form of self-oscillations and multistable response.

CONCLUSIONS

We have shown that non-reciprocal robotic metamaterials can realize a number of intriguing non-Hermitian phenomena and as such are a prime platform to explore non-Hermitian physics. Exciting further works include miniaturization, other non-Hermitian approaches and generalization beyond mechanics.

References

[1] Brandenbourger M., Locsin X., Lerner E. and Coulais C. Non-reciprocal robotic metamaterials *Nat. Comm.* **10**: 4608-4608, 2019.
[2] Ghatak A., Brandenbourger M., van Wezel J., Coulais C. Observation of non-Hermitian topology and its bulk-edge correspondence arXiv preprint arXiv:1907.11619, 2019
[3] Scheibner C., Souslov A., Banerjee D., Surowka P., Irvine W.T.M., Vitelli V. Odd elasticity arXiv preprint arXiv:1902.07760, 2019

PHYSICAL BASIS OF THE WILLI-FORM EQUATIONS AND SOME RELATED APPLICATIONS

Zhihai Xiang*[1], Hexuan Gao[1], Yixiao Sun[1], and Zhuyou Hu[1]
[1]Department of Engineering Mechanics, Tsinghua University, Beijing, China

Summary The form-invariant property of wave equations is essential to the success of using transformation methods to design metamaterials. It is well known that the classical elastodynamic equations are not form-invariant, but the Willis equations have this property. We have proved that the Willis-form equations with displacement coupling terms can be naturally obtained by using the transformation method in time domain. Here we show that these equations can also be obtained through energy approach and have clear physical meanings. Based on these understandings, at least three applications are possible. The first is developing a general method to design elastic metamaterials by minimizing the coupling terms. The second is proposing an efficient geometrically nonlinear finite element method with the help of the coupling terms. The third is identifying the distribution of residual stresses based on the coupling terms.

INTRODUCTION

Transformation methods have achieved great success in designing optic and acoustic metamaterials [1]. However, the development of elastic metamaterials is rather slow, because Milton et al. have proved that classical elastodynamic equations in frequency domain transform to the following new elastodynamic equations, which are form-invariant [2]:

$$\boldsymbol{\Sigma} = \boldsymbol{C} : \nabla \boldsymbol{U} + \boldsymbol{S} \cdot \boldsymbol{U} \tag{1a}$$

$$\nabla \cdot \boldsymbol{\Sigma} = \boldsymbol{S}^{\mathrm{T}} : \nabla \boldsymbol{U} - \omega^2 \overline{\boldsymbol{\rho}} \cdot \boldsymbol{U} \tag{1b}$$

where $\boldsymbol{\Sigma}$ and $\boldsymbol{U}$ are amplitudes of stresses and displacements, respectively; $\boldsymbol{C}$ is the elasticity tensor; $\boldsymbol{S}$ is a third-order tensor; $\overline{\boldsymbol{\rho}}$ is the effective mass density that is the function of angular frequency ω.

The unclear physical meaning of $\boldsymbol{S}$ impedes using Eq. (1) to design elastic metamaterials. However, it is interesting that Eq. (1) can be regarded as a special case of the Willis equations in time domain established several decades ago [3]:

$$\langle \boldsymbol{\sigma} \rangle = \boldsymbol{C}_{eff} \otimes \langle \boldsymbol{e} \rangle + \boldsymbol{S}_{eff} \circ \langle \dot{\boldsymbol{u}} \rangle \tag{2a}$$

$$\nabla \cdot \langle \boldsymbol{\sigma} \rangle + \boldsymbol{f} = \boldsymbol{S}_{eff}^{\dagger} \circ \langle \dot{\boldsymbol{e}} \rangle + \boldsymbol{\rho}_{eff} \odot \langle \ddot{\boldsymbol{u}} \rangle \tag{2b}$$

where $\boldsymbol{\sigma}$ is the stress; $\boldsymbol{u}$ is the displacement; $\boldsymbol{e}$ is the linear strain; $\boldsymbol{f}$ is the body force; $\langle\ \rangle$ denotes the ensemble average; the superposed dot denotes the differentiation with respect to time t; $\boldsymbol{C}_{eff}$, $\boldsymbol{S}_{eff}$ and $\boldsymbol{\rho}_{eff}$ are operators related with a dynamic Green's function; $\otimes$, $\circ$ and $\odot$ are non-local operators involving time and space convolutions [4].

However, if we apply transformation method in time domain, we can naturally obtain [5]:

$$\boldsymbol{\sigma} = \boldsymbol{C} : \boldsymbol{e} + \boldsymbol{S} \cdot \boldsymbol{u} \tag{3a}$$

$$\nabla \cdot \boldsymbol{\sigma} + \Delta \boldsymbol{f}_e = \boldsymbol{S}^{\mathrm{T}} : \boldsymbol{e} + \boldsymbol{K} \cdot \boldsymbol{u} + \boldsymbol{\rho} \cdot \ddot{\boldsymbol{u}} \tag{3b}$$

where $\Delta \boldsymbol{f}_e$ is the incremental external body force. When deformation gradient is adopted to connect the displacement before and after transformation, Eq. (3) in frequency domain are the same as Eq. (1). Later on, we proved that Eq. (3) has clear relations with the gradient of pre-stress $\boldsymbol{\sigma}^0$ through differential approach [6], i.e., $\boldsymbol{S} = \boldsymbol{\sigma}^0 \nabla$ and $\boldsymbol{K} = (\nabla \cdot \boldsymbol{\sigma}^0) \nabla$. They can be verified by an experiment of rotational spring [7], and can ensure time synchronization when only spatial transformation is applied [8]. By noticing the differential property of time convolution, Eq. (2) and Eq. (3) are mathematically equivalent [7]. In addition, since pre-stress gradients are explicitly involved, Eq. (3) is also non-local and could be regarded as a special case of Eq. (2), similar to its frequency counterparts of Eq. (1). In this sense, Eq. (3) is reasonably named *the Willis-form equations*.

In the following text, we will derive the Willis-form equations through energy approach, and show that they have solid physical basis. Then, some examples are briefly introduced to demonstrate some potential applications.

THE WILLIS-FORM EQUATIONS FROM ENERGY POINT OF VIEW

In an inhomogeneous media with initial configuration B^0, a material point locates at position $\boldsymbol{x}^0$ in the global Cartesian coordinate system with pre-stress $\boldsymbol{\sigma}^0$. This material point moves to position $\boldsymbol{x}^1$ in the deformed configuration B^1 after a small perturbation, corresponding to a small displacement $\boldsymbol{u} = \boldsymbol{x}^1 - \boldsymbol{x}^0$ and a linear strain $\boldsymbol{e}$. Since the media is inhomogeneous, the strain energy density of this material point is an explicit function of the spatial position [9, 10], which can be presented as:

$$W(\boldsymbol{x}^1, \boldsymbol{e}) \approx W(\boldsymbol{x}^0, \boldsymbol{0}) + \frac{\partial W(\boldsymbol{x}^0, \boldsymbol{0})}{\partial \boldsymbol{e}} : \boldsymbol{e} + \frac{\partial W(\boldsymbol{x}^0, \boldsymbol{0})}{\partial \boldsymbol{x}} \cdot \boldsymbol{u} + \frac{1}{2} \left(\boldsymbol{e} : \frac{\partial^2 W(\boldsymbol{x}^0, \boldsymbol{0})}{\partial \boldsymbol{e} \partial \boldsymbol{e}} : \boldsymbol{e} + \boldsymbol{u} \cdot \frac{\partial^2 W(\boldsymbol{x}^0, \boldsymbol{0})}{\partial \boldsymbol{x} \partial \boldsymbol{x}} \cdot \boldsymbol{u} + 2\boldsymbol{e} : \frac{\partial^2 W(\boldsymbol{x}^0, \boldsymbol{0})}{\partial \boldsymbol{e} \partial \boldsymbol{x}} \cdot \boldsymbol{u} \right) \tag{4}$$

According to the theory of thermodynamics, the stress of this material point in B^1 is $\partial W(\boldsymbol{x}^1, \boldsymbol{e}) / \partial \boldsymbol{e}$, which can be presented in configuration B^0 according to Eq. (4), i.e., the second Piola-Kirchhoff stress of this material point is:

*Corresponding author. E-mail: xiangzhihai@tsinghua.edu.cn.

$$\boldsymbol{\sigma}^1\left(\boldsymbol{x}^0\right) \approx \frac{\partial W\left(\boldsymbol{x}^0,\mathbf{0}\right)}{\partial \boldsymbol{e}} + \frac{\partial^2 W\left(\boldsymbol{x}^0,\mathbf{0}\right)}{\partial \boldsymbol{e}\partial \boldsymbol{e}} : \boldsymbol{e} + \frac{\partial^2 W\left(\boldsymbol{x}^0,\mathbf{0}\right)}{\partial \boldsymbol{e}\partial \boldsymbol{x}} \cdot \boldsymbol{u} = \boldsymbol{\sigma}^0\left(\boldsymbol{x}^0\right) + \boldsymbol{C}\left(\boldsymbol{x}^0\right) : \boldsymbol{e} + \left[\boldsymbol{\sigma}^0\left(\boldsymbol{x}^0\right)\nabla\right]\cdot\boldsymbol{u} \tag{5}$$

Thus, the incremental second Piola-Kirchhoff stress is $\boldsymbol{\sigma} = \boldsymbol{\sigma}^0 - \boldsymbol{\sigma}^0 = \boldsymbol{C}:\boldsymbol{e} + (\boldsymbol{\sigma}^0\nabla)\cdot\boldsymbol{u}$, which is the same as Eq. (3a).

To derive the equation of motion, we firstly establish the incremental Lagrangian function $\Delta L = \Delta W + \Delta V - \Delta T$, where $\Delta W = W(\boldsymbol{x}^1,\boldsymbol{e}) - W(\boldsymbol{x}^0,\boldsymbol{e})$ is the incremental strain energy density; $\Delta V = -\boldsymbol{f}_e^0\cdot\boldsymbol{u} - \boldsymbol{u}\cdot\left(\boldsymbol{f}_e^0\nabla\right)\cdot\boldsymbol{u}/2 - \Delta\boldsymbol{f}_e\cdot\boldsymbol{u}$ is the incremental potential density of external body force (denoted by subscript e); and $\Delta T = \dot{\boldsymbol{u}}\cdot\boldsymbol{\rho}\cdot\dot{\boldsymbol{u}}/2$ is the incremental kinetic energy density. Then, we can obtain the effective body force in configuration B^1 as $\boldsymbol{f}^1 = -\partial\left(\Delta W + \Delta V\right)/\partial\boldsymbol{u} = \boldsymbol{f}_e^0 + \Delta\boldsymbol{f}_e + \left(\boldsymbol{f}_e^0\nabla\right)\cdot\boldsymbol{u} - \left(\boldsymbol{\sigma}^0\nabla\right):\boldsymbol{e} - W^0\nabla - \left(W^0\nabla\nabla\right)\cdot\boldsymbol{u}$, where $W^0 = W(\boldsymbol{x}^0,\boldsymbol{e})$. Therefore, it is obvious that $\boldsymbol{f}^0 = \boldsymbol{f}_e^0 - W^0\nabla$. Here, we can see the extra body force $-W^0\nabla$ due to the inhomogeneous strain energy density and the extra body force $\left(\boldsymbol{f}_e^0\nabla\right)\cdot\boldsymbol{u} - \left(\boldsymbol{\sigma}^0\nabla\right):\boldsymbol{e} - \left(W^0\nabla\nabla\right)\cdot\boldsymbol{u}$ activated by deformation.

Noticing $\nabla\cdot\boldsymbol{\sigma}^0 + \boldsymbol{f}^0 = \mathbf{0}$ in B^0, the incremental equation of motion from B^0 to B^1 can be obtained by [10]:

$$\frac{\partial\left(\Delta L\right)}{\partial\boldsymbol{u}} - \frac{\mathrm{d}}{\mathrm{d}\boldsymbol{x}}\frac{\partial\left(\Delta L\right)}{\partial\boldsymbol{e}} - \frac{\mathrm{d}}{\mathrm{d}t}\frac{\partial\left(\Delta L\right)}{\partial\dot{\boldsymbol{u}}} = 0 \quad\Rightarrow\quad \nabla\cdot\boldsymbol{\sigma} + \Delta\boldsymbol{f}_e = \left(\boldsymbol{\sigma}^0\nabla\right)^{\mathrm{T}} : \boldsymbol{e} + \left[\left(\nabla\cdot\boldsymbol{\sigma}^0\right)\nabla\right]\cdot\boldsymbol{u} + \boldsymbol{\rho}\cdot\ddot{\boldsymbol{u}} \tag{6}$$

which is the same as Eq. (3b).

APPLICATIONS

Since the Willis-form equations have very clear physical meanings, it is possible to explore related applications.

The first application is based on the finding that the elastic potential energy is nearly form-invariant after conformal mappings, when the longitudinal wave velocity is much larger than the transverse wave velocity [11]. This means that it is possible to use the transformation method to design elastic metamaterials by minimizing the extra coupling term. Experimental results of a vibration isolator [11] and an elastic wave concentrator [12] designed in this way demonstrate that these metamaterials have good low frequency performances through wide frequency bandwidths.

Another application aims at utilizing pre-stress gradients to construct a natural secant stiffness matrix. In this way, we can accelerate the geometrically nonlinear finite element analyses, and introduce natural perturbations near the critical point [13]. Without assuming the form of imperfections, the obtained buckling loads are about 10% lower than those of perfect shells by using classical numerical methods and are very close to experimental results for nearly perfect shells.

Since the Willis-form equations contain the pre-stress gradients, they can be used to identify the distribution of residual stresses, especially around notches [14]. Experimental re • sults demonstrate that this identification method can achieve high accuracy if the residual stresses gradient is significant compared with material tangent stiffness.

CONCLUSIONS

Here we clarify the physical basis of the Willis-form equations. Since pre-stress gradients are explicitly included, these equations are intrinsically non-local and can be regarded as special cases of the original Willis equations. We can envisage that the potential applications of these equations are not limited to the examples given here.

Acknowledgment: This work was supported by the National Science Foundation of China with grant number 11672144.

References

[1] Ball P. Bending the laws of optics with metamaterials: an interview with John Pendry. *Natl. Sci. Rev.* **5**: 200-202, 2018.
[2] Milton G.W., Briane M., Willis J.R. On cloaking for elasticity and physical equations with a transformation invariant form. *New J. Phys.* **8**: 248, 2006.
[3] Willis J.R. Variational principles for dynamics problems in inhomogeneous elastic media. *Wave Motion* **3**: 1-11, 1981.
[4] Willis J.R. From statics of composites to acoustic metamaterials. *Philos Trans R Soc Lond A* **377**: 20190099, 2019.
[5] Xiang Z.H. The form-invariance of wave equations without requiring a priori relations between field variables. *SCI CHINA PHYS MECH* **57**: 2285–2296, 2014.
[6] Xiang Z.H., Yao R.W. Realizing the Willis equations with pre-stresses. *J Mech Phys Solids* **87**: 1-6, 2016.
[7] Yao R.W., Gao H.X., Sun Y.X., Yuan X.D., Xiang Z.H. An experimental verification of the one-dimensional static Willis-form equations. *Int J Solids Struct* **134**: 283-292, 2018.
[8] Yao R.W., Xiang Z.H. One dimensional Willis-form equations can retain time synchronization under spatial transformations. *Int J Solids Struct* **141-142**: 73-77, 2018.
[9] Nemat-Nasser S., Hori M. Micromechanics: Overall Properties of Heterogeneous Materials, Chapter II. North Holland, Amsterdam 1993.
[10] Kienzler R., Herrmann G. Mechanics in Material Space. Springer-Verlag., Berlin, 2000.
[11] Gao H.X., Xiang Z.H. Manipulating elastic waves with conventional isotropic materials. *Phys. Rev. Appl.* **11**: 064040, 2019.
[12] Gao H.X., Liu W., Sun Y.X., Xu L., Xiang Z.H. Omnidirectional broadband low-frequency elastic wave concentrator. *Phys. Rev. Appl.* **12**: 064020, 2019.
[13] Sun Y.X., Xiang Z.H. Buckling analyses of spherical shells by the finite element method based on the Willis-form equations. *Int J Appl Mech* **11**: 1950091, 2019.
[14] Hu Z.Y, Xie J.N., Zhao J.L., Sun Y.X., Xiang Z.H., Identify the distribution of 2D residual stresses around notches based on the Willis-form equations. *Inverse Probl. Sci. Eng.*, 2020: DOI:10.1080/17415977.2020.1813126

NONLINEAR DYNAMICS OF MECHANICAL METAMATERIALS MADE OF SNAPPING SHALLOW ARCHES

Eleonora Tubaldi[*1], Gabriele Librandi[2], and Katia Bertoldi[*2]
[1]Department of Mechanical Engineering, University of Maryland, College Park, USA [2]School of Engineering and Applied Sciences, Harvard University, Cambridge, USA

Summary Classic snap-through buckling behavior of shallow arches represents a source of inspiration for engineering new nonlinear mechanical metamaterials. In this study, we realize snapping bistable nonlinear structures using arches as building block. The goal is to allow signal transmission by exploiting the sudden reconfiguration of a system of arches excited in one single element. To this end, two designs are proposed: (i) sequence of elastic shallow arches (i.e. buckled beams) with progressively decreasing rises, and (ii) sequence of elastically and plastically deformed shallow arches with the same rise. These nonlinear mechanical metamaterials are designed to manipulate the propagation of elastic pulses in unprecedented ways.

ANALYSES AND EXPERIMENTS

Dynamics of a single shallow arch has been studied for decades and snap-through instability has been investigated under several loading conditions [1-3]. Recent studies have focused even further on the snap-through instability of this structural element discovering new interesting features (critical slowing down [4]) and applications for jumping poppers [5]. Snap-through instability can also be exploited for mechanical signal transmission [6, 7].
A straight steel beam (Figure 1(a)) can be manufactured into a shallow arch by either plastically deform it (Figure 1(b)) or by elastically buckle it (Figure 1(c)). The elastic shallow arch (Figure 1(c)) is a symmetric element that can snap between two equilibrium conditions associated to the same potential energy wells. Thus, the snapping of a series of arches connected by rotating hinges is limited by the damping of the system that will eventually stop the snapping motion. We propose two strategies to overcome this issue and realize a chain of "energetic favorable" snap-through instabilities: (i) progressively decreasing the rise of a chain of arches reducing the energy barrier to overcome between the two stable equilibrium configurations (Figure 1(d,f)), (ii) introducing a plastically deformed shallow arch (Figure 1(b)) in its inverted configuration (Figure 1(e,g)).

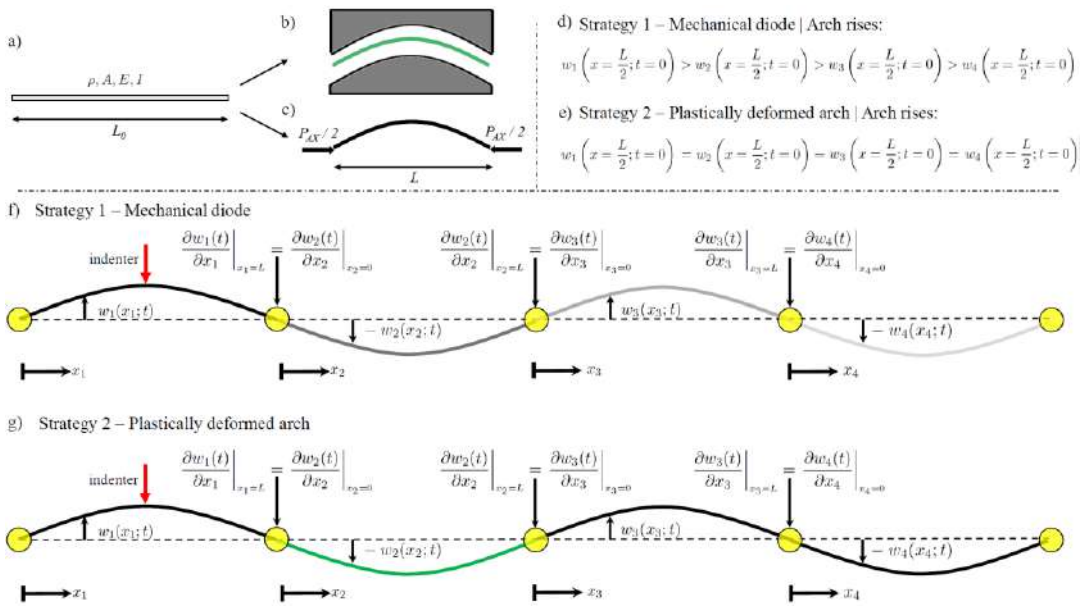

Figure 1. (a) A straight steel beam is manufactured into a shallow arch by (b) either plastically deform it or by (c) elastically buckle it. Both the plastically deformed arch and the buckled beam have an end-to-end distance equals to $L < L_0$. Arch rise sequence of (d) Strategy 1 and (e) Strategy 2. (f-g) Schematic of Strategy 1 and 2, respectively. All the arches are simply supported and the hinges are represented by the yellow circles. Hinges impose the rotation of two consecutive arches to be the same.

Thanks to the first strategy we can design a reversible and tunable mechanical diode that allows the propagation of incoming signals from one direction but blocks the ones propagating in the other one. The mechanical diode is also reversible because in the transmitting direction multiple signals can propagate. To propagate a signal in a sequence of arches with the same rise, the second strategy requires the introduction of an element that acts as a "battery" and it releases energy once activates. This element is represented by the plastically deformed shallow arch (green arch in Figure 1) which snaps between two asymmetric equilibrium conditions undergoing a large, nonlinear displacement. In its initial

*Corresponding authors. E-mail: etubaldi@umd.edu, bertoldi@seas.harvard.edu.

configuration, the plastic shallow arch is placed in its high energy well which is given by its inverted equilibrium condition. Then, the transition from its high energy well to the lower energy well is triggered by the snapping of the preceding elastic arch. This tailorable transition from high to low strain potential energy results in a release of energy that is exploited to propagate a stable signal in the "metastructure" of these bistable elements at an arbitrary distance.
We use a combination of experiments and analytical modelling to investigate both systems. Experiments have been performed on sequences of four shallows arches for both strategies. In Figure 2, experimental results for the Strategy 1 are showed. The rises of the four arches are slightly decreasing in such a way that the arch with the blue circle has a biggest rise and the last arch with the green circle has the smallest rise. The indenter pushes the first arch downwards and the arch is in contact with the indenter up to t = 0.85s. It is worth noticing that at t = 0.85s, while the hinge between the first and second arch has started to rotate inducing a motion to the second arch, the third and fourth arches still do not perceive the motion of the other arches. For t > 0.85s the first arch reaches an unstable configuration and quickly snap downwards to its stable and inverted state. At this point the entire chain is forced to snap generating a mechanical signal from left to right. At t = 1.10s the chain is found to be in a new and still stable configuration. A similar behaviour has been experienced with Strategy 2, but reversibility is lost.
A theoretical model is developed to accurately predict the snapping behaviour of both plastic and elastic shallow arches. The deformation of the arches has been tracked and reconstructed by placing markers on the structure and it has been compared with the theoretically predicted one showing an impressive agreement.

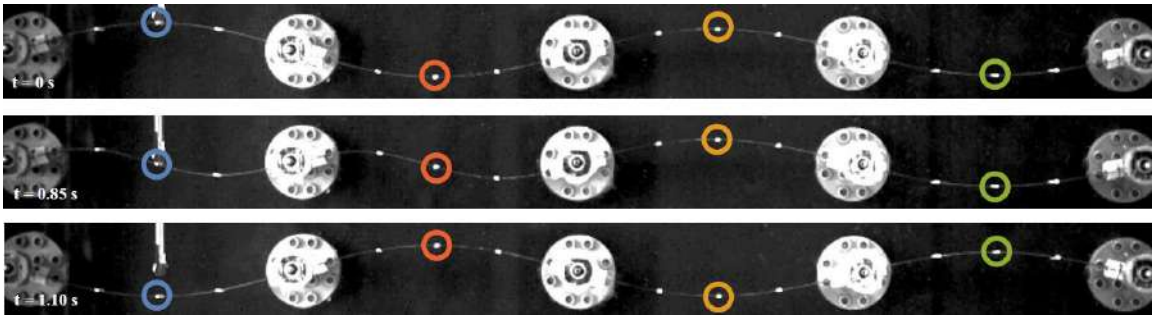

Figure 2. Snapshots of experimental representation of Strategy 1 with four arches.

CONCLUSIONS

We are able to harness the snapping of a series of shallow arches to achieve mechanical signal transmission. We propose two strategies to guarantee the robustness of the proposed design. In the first strategy, a reversible mechanical diode is obtained by carefully modulating the sequence of the rise of the arches. The second strategy counts on the introduction of "batteries" which snap between two stable configurations with different energy wells granting a surplus of energy which allows the chain reaction. This opens avenues to new applications of nonlinear mechanical metamaterials for signal transmission purposes.

References

[1] Lock M.H., Snapping of a Shallow Sinusoidal Arch under a Step Pressure Load. AIAA Journal VOL. 4, NO. 7, JULY 1966
[2] Simitses G.J., Dynamic Stability of Suddenly Loaded Structures, Springer-Verlag 1990
[3] Plaut R.H., Snap-Through of Shallow Elastic Arches Under End Moments. Journal of Applied Mechanics, VOL. 76, 2009
[4] Gomez M., Moulton D. E., Vella D., Critical slowing down in purely elastic 'snap-through' instabilities. Nature Physics, VOL. 13, 2017
[5] Pandey A., Moulton D.E., Vella D., Holmes D.P., Dynamics of snapping beams and jumping poppers. Europhysics Letters Physics. February 2014, VOL. 105
[6] Nadkarni N., Arrieta A.F., Chong C., Kochmann D.M., Daraio C., Unidirectional transition waves in bistable lattices. Physical Review Letters.,116(24):24450, 2016
[7] Raney J. R., Nadkarni N., Daraio C., Kochmann D. M., Lewis J. A., Bertoldi, K. Stable propagation of mechanical signals in soft media using stored elastic energy. Proceedings of the National Academy of Sciences, 113(35), 9722-9727, 2016

INVESTIGATIONS OF AN EFFECTIVE META-INTERFACE MODEL THROUGH TIME-DOMAIN WAVE PROPAGATION SIMULATIONS

Marie Touboul[1],Kim Pham[2],Agnés Maurel[3],Jean-Jacques Marigo[4],Bruno Lombard*[1],and Cédric Bellis[1]
[1]Aix Marseille Univ, CNRS, Centrale Marseille, LMA UMR 7031, Marseille, France
[2]IMSIA, CNRS, ENSTA Paris, Palaiseau, France
[3]Institut Langevin, CNRS, ESPCI Paris, Paris, France
[4]Laboratoire de Mécanique des Solides,CNRS,Ecole Polytechnique,Palaiseau,France

Summary With an adequate scaling on the physical parameters, resonances are possible in the inclusions of a thin micro-structured medium. The homogenization of such media yields jump conditions that are non-local in time. Auxiliary variables are used to take into account the resonant behaviour and perform time domain simulations. These simulations are compared with simulations in the microstructured original medium to discuss the accuracy of the homogenized model obtained.

EFFECTIVE MODEL

The physical problem concerns the propagation of scalar waves within the framework of the linear anti-plane elasticity in 2D across a periodic row of inclusions $\cup_i \Omega_i$ embedded within a homogeneous matrix Ω_m, with both media being assumed to be isotropic. The thickness and the periodicity of the row are denoted by e and h respectively and we assume that $e = \mathcal{O}(h)$. The spatial coordinates are denoted by $\boldsymbol{X} = (X_1, X_2)$ respectively, with X_2 being the direction of periodicity of the inclusions as shown in Figure 1. The mass density ρ and the shear modulus μ are piecewise constant as:

$$(\rho, \mu)(\boldsymbol{x}) = \begin{cases} (\rho_m, \mu_m) & \text{in the matrix} \\ (\rho_i, \mu_i) & \text{in the inclusions.} \end{cases}$$

The wavelength λ within the matrix is assumed to be much larger than the spacing h between inclusions. Defining the wavenumber within the matrix as $k_m = 2\pi/\lambda$, we introduce the ratio $\eta = k_m h$ that satisfies $\eta \ll 1$ for the configurations of interest. This geometrical assumption allows to homogenize the microstructure in the long-wavelength regime [1]. However, these results do not apply to microstructures with high material contrast as the latter can be the seat of local resonances. In particular, they can occur for a low contrast in mass density $\rho_i/\rho_m = \mathcal{O}(1)$ and a high contrast in shear modulus $\mu_i/\mu_m = \mathcal{O}(\eta^2)$, a configuration which we consider in the present study.

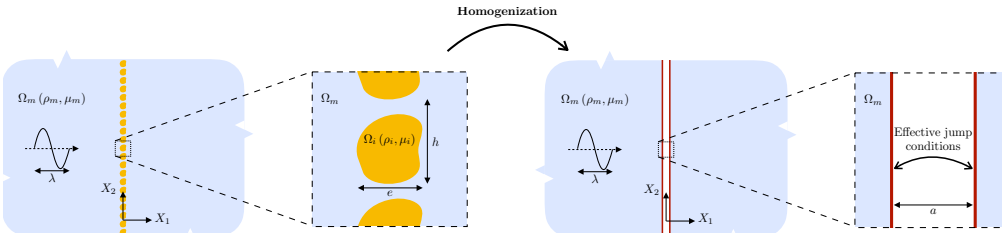

Figure 1: Homogenization process for a single periodic row of inclusions.

Under these asumptions, the microstructured problem can be replaced by an equivalent homogenized problem. It consists in solving the evolution equations around an enlarged interface of thickness a, and jump conditions on the velocity V and the normal stress vector Σ_1 across this enlarged interface. These jump conditions take into account the microstructure characteristics and read in the time-domain :

$$\begin{cases} [\![V]\!]_a &= B_1 \langle \partial_{X_1} V \rangle_a + B_2 \langle \partial_{X_2} V \rangle_a, \\ [\![\Sigma_1]\!]_a &= C_{11} \langle \partial_{X_1} \Sigma_1 \rangle_a + C_{12} \langle \partial_{X_2} \Sigma_1 \rangle_a + C_{22} \langle \partial_{X_2} \Sigma_2 \rangle_a + hD * \langle \boldsymbol{\nabla} \cdot \boldsymbol{\Sigma} \rangle_a, \end{cases} \tag{1}$$

where we have defined

$$[\![f]\!]_a (X_2) = f\left(\frac{a}{2}, X_2\right) - f\left(-\frac{a}{2}, X_2\right), \tag{2}$$

$$\langle f \rangle_a (X_2) = \frac{1}{2}\left(f\left(\frac{a}{2}, X_2\right) + f\left(-\frac{a}{2}, X_2\right)\right) \tag{3}$$

being the jump of f across the homogenized enlarged interface and the mean value of f, respectively. D encapsulates the resonant behaviour of the inclusions and its Fourier transform can be written as [2]:

$$\hat{D}(\omega) = \alpha_0 - \sum_{n \geq 1} \alpha_n^2 \frac{\omega^2}{\omega^2 - \omega_n^2}, \tag{4}$$

where the set of $\{\omega_n\}$ denote resonant frequencies, with $\{\omega_n^2\}$ linked to eigenvalues of the Laplacian in an inclusion. Stability of such system is linked to energy considerations and is guaranteed for a specific interface thickness $a \geq e$.

*Corresponding author. E-mail: lombard@lma.cnrs-mrs.fr

NUMERICAL MODELING

Formulating the system in the time domain with a convolution product is very costly numerically and would reduce the computational gains obtained from homogenization. To avoid this, auxiliary fields [3] are formally introduced in the frequency-domain formulation of the homogenized problem [2] due to the expression of $\hat{D}$ (4). We introduce the original variable set $\boldsymbol{u} = (V, \boldsymbol{\Sigma})^\top$ and the set $\boldsymbol{w}$ of auxiliary variables. The system in the time-domain now consists of first-order equations in time that are complemented by jump conditions that are local in time. Considering the complete set of variables $\tilde{\boldsymbol{u}} = (\boldsymbol{u}, \boldsymbol{w})^\top$ it can be written in a compact form for all $t > 0$ as:

$$\begin{cases} \partial_t \boldsymbol{u} + \mathbb{A}_j \partial_j \boldsymbol{u} = \boldsymbol{0} & (|X_1| \geq a/2, X_2 \in \mathbb{R}), \\ \partial_t \boldsymbol{w} + \mathbb{B} \langle \partial_j^2 \partial_\ell \boldsymbol{u} \rangle_a + \mathbb{C} \boldsymbol{w} = \boldsymbol{0} & (X_2 \in \mathbb{R}), \\ [\![\boldsymbol{u}]\!]_a = \mathbb{D}_j \langle \partial_j \boldsymbol{u} \rangle_a + \mathbb{E} \boldsymbol{w} & (X_2 \in \mathbb{R}), \end{cases} \tag{5}$$

using the Einstein summation convention for repeated indices and where the matrices $\mathbb{A}_j$, $\mathbb{B}$, $\mathbb{C}$, $\mathbb{D}_j$ and $\mathbb{E}$ concatenate the parameters characterizing the resonant meta-interface model considered. This formulation is at price of handling $2N_R$ auxiliary variables, with N_R the number of resonances chosen to truncate the sum in (4), introduced only along the enlarged interface.

An explicit finite-difference scheme is used to solve numerically the homogenized problem (5). The scheme has to be adapted because the solution is not defined in the enlarged interface. This modification will take into account the jump conditions. A point M is called an irregular point if the stencil at M requires nodes that are in the enlarged interface where the solution is not defined. For these points, some phantom values values will be used in the enlarged interface, and direct numerical values will be used otherwhise. These phantom values are constructed as a smooth extension of the solution on the interfaces using the jump conditions. Their construction is detailed in [4] for the non-resonant case and is adapted here in the resonant case.

NUMERICAL EXPERIMENTS

For a plane wave and a plane or circulat resonant meta-interface, a semi-analytical solution of the homogenized problem can be computed. Comparisons of both semi-analytical and numerical solutions allow to validate the numerical method. After this validation, we can compare numerical solutions of time-domain simulations in the microstructured configuration and effective configuration. The numerical error measured will provide an estimation of the global modeling error and will be used to assess the validity of the homogenized model. Fields and profiles are presented in Figure 2 for $\eta = 0.4$. As expected, the solutions agree for a low value of η and deviate from one another as it goes to 1.

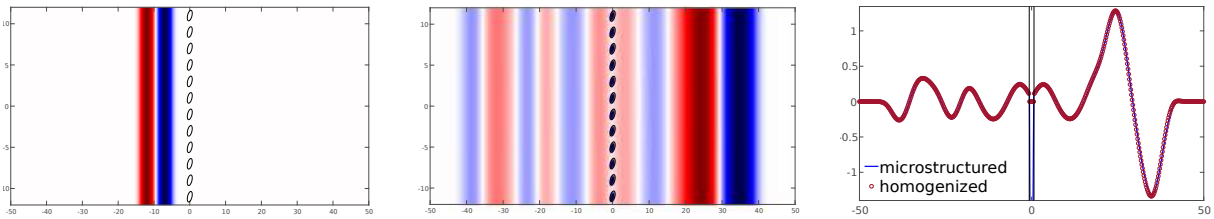

(a) Velocity field at the initial time

(b) Velocity field at the final time in the microstructured configuration

(c) Comparison of the profiles in the homogenized and microstructured configurations at the final time

Figure 2: Velocity fields in the microstructured configuration and corresponding profiles for both configurations.

CONCLUSIONS

Performing the homogenization process directly in the time-domain for this hightly contrasted inclusions leads to jump conditions that are stable for an enough enlarged interface but non-local in time. Introducing auxiliary variables allows to build a numerical approach to perform time-domain simulations in the effective medium and compare its solutions with simulations involving the original microstructure. It is discussed how it deteriorates as the frequency increases.

References

[1] J.-J. Marigo, A. Maurel, K. Pham, and A. Sbitti, Effective Dynamic Properites of a Row of Elastic Inclusions: The Case of Scalar Shear Waves, *Journal of Elasticity*, **128** (2017), pp. 265–289

[2] K. Pham, A. Maurel, and J.-J. Marigo, Two scale homogenization of a row of locally resonant inclusions - the case of shear waves, *Journal of the Mechanics and Physics of Solids*, **106** (2017), pp. 80–941

[3] C. Bellis and B. Lombard, Simulating transient wave phenomena in acoustic metamaterials using auxiliary fields, *Wave motion*, **86** (2019) , pp. 175–194

[4] B. Lombard, A. Maurel, and J.-J. Marigo, Numerical modeling of the acoustic wave propagation across an homogenized rigid microstructure in the time domain, *Journal of Computational Physics*, **335** (2017), pp. 558–577

DYNAMICS OF TWO-DIMENSIONAL NON-HERMITIAN ELASTIC LATTICES WITH NON-LOCAL FEEEDBACK CONTROL INTERACTIONS

Massimo Ruzzene[1] and Matheus I. N. Rosa [1]
[1]Department of Mechanical Engineering, University of Colorado Boulder, Boulder, USA

Summary We investigate a family of elastic lattices where non-local feedback control interactions lead to a series of unconventional phenomena stemming from their non-Hermiticity. In two-dimensional lattices, the feedback interactions produce directional and non-reciprocal wave amplification, occurring in multiple frequency/wavenumber bands depending on the non-local nature of the control interactions. Moreover, the non-Hermitian skin effect manifests as modes localized at the boundaries of finite lattice strips, whose combined effect in two directions leads to the existence of bulk modes localized at corner of finite two-dimensional lattices. Our results describe fundamental properties of non-Hermitian elastic lattices, opening new possibilities for the design of active metamaterials with novel functionalities related to selective wave filtering, amplification and localization.

INTRODUCTION

Non-Hermitian systems are non-conservative systems where loss and/or gain are inherently present from interactions with the environment, and have been the focus of many research efforts by the physics and engineering communities. By carefully engineering the balance between gain and loss, unconventional phenomena such as unidirectional invisibility [1] and enhanced sensitivity to perturbations [2] have been demonstrated. Unique topological features have also been explored, such as the non-Hermitian skin effect [3], whereby all eigenstates of one-dimensional (1D) systems are localized at a boundary, in sharp contrast with the extended Bloch modes of Hermitian counterparts.

In this context, feedback control was recently introduced as a strategy to design mechanical metamaterials with non-reciprocal couplings [4,5], opening a new avenue for the exploration of the unique properties of non-Hermitian systems. Following such notable contributions, we study the dynamics of a family of one and two-dimensional elastic lattices with local and non-local feedback interactions [6], revealing a series of unconventional phenomena associated with their non-Hermiticity. Among the key results, we demonstrate non-reciprocity associated with attenuation and amplification for waves propagating along different directions in 1D and 2D lattices, illustrating that multiple non-reciprocal bands can be established by engineering the non-local nature of the control interactions. We also study the topological properties associated with the complex dispersion bands, resulting in localization of bulk modes at edges and corners according to the non-Hermitian skin effect. The talk will focus mostly on the properties of two-dimensional lattices, such as directional and non-reciprocal wave amplification, tunability, the effects of the non-local nature of the feedback interactions, and bulk modes localized at corners of finite two-dimensional lattices.

TWO-DIMENSIONAL ELASTIC LATTICES WITH FEEDBACK INTERACTIONS

We consider a 2D lattice of equal masses m connected by springs k, separated by a unit distance in both x and y directions (Fig. 1a). Each mass moves along the perpendicular z direction, so that the springs react with a force proportional to the relative vertical motion of neighboring masses. Feedback interactions are defined by an additional force applied to mass n,m proportional to the elongation of a spring a units behind in the x and y directions, which is expressed as $f_{n,m} = k_{c_x}\left(u_{n-a,m} - u_{n-(a+1),m}\right) + k_{c_y}\left(u_{n,m-a} - u_{n,m-(a+1)}\right)$, where k_{c_x} and k_{c_y} are the proportionality constants for elongations of springs aligned with the x and y directions, respectively. By imposing Bloch wave solutions of the form $u_{n.m} = Ue^{i(\omega t - \mu_x n - \mu_y m)}$, where ω denotes angular frequency while μ_x and μ_y are the wave vector components along x and y, the following dispersion relation can be obtained:

$$\Omega^2 = 2\left(2 - \cos\mu_x - \cos\mu_y\right) - \gamma_x e^{i\mu_x a}\left(1 - e^{i\mu_x}\right) - \gamma_y e^{i\mu_y a}\left(1 - e^{i\mu_y}\right),$$

where $\Omega = \omega/\omega_0$, with $\omega_0 = \sqrt{k/m}$, while $\gamma_x = k_{c_x}/k$ and $\gamma_y = k_{c_y}/k$. The feedback interaction makes the right-hand side of the dispersion relation generally complex, which results in complex frequencies $\Omega = \Omega_r + i\Omega_i$. The solutions are associated with a wave $u_{n,m} = Ue^{i(\Omega_r\tau - \mu_x n - \mu_y m)}e^{-\Omega_i\tau}$ that travels along the direction defined by the wave-vector components ($\theta = \tan^{-1}(\mu_y/\mu_x)$), and that is exponentially attenuated (amplified) in time when Ω_i is positive (negative).

Figures 1(b,c) display the real and imaginary iso-frequency contours of the dispersion surfaces for a representative case with $\gamma_x = \gamma_y = 0.1$ and local control interactions ($a = 0$). While the real part (Fig. 1b) closely resembles that of a passive 2D lattice, the imaginary part of the frequency contours (Fig. 1c) exhibits directional dependent attenuation and amplification zones. In particular, a region for which $\Omega_i < 0$ is identified in the third quadrant of the μ_x, μ_y plane, revealing a range of directions for wave amplification. This is further illustrated by considering a frequency of $\Omega = 0.7$, whose corresponding contour in the Ω_r map, highlighted by the thick black line in Fig. 1b, is approximately circular, possibly suggesting isotropic propagation. However, the wave vector components at this frequency (also highlighted by the thick black line in Fig. 1c), cross regions of positive and negative imaginary frequency. The angular dependence of

Ω_i is displayed in Fig. 1d, where it is plotted in polar form versus the propagation angle θ. In the figure, the thick blue lobe denotes amplification corresponding to $\Omega_i < 0$, while the thin red line defines the angular range associated with attenuation. The plot shows that maximum amplification is found for $\theta \approx 225^o$, which corresponds to waves traveling towards the left bottom corner of a square lattice. We illustrate this by considering a transient time domain simulation on a lattice with 100 x 100 masses, with a force consisting of a 5-cycle sinusoidal burst of frequency $\Omega = 0.7$ applied to the center mass of the lattice. Snapshots of the lattice motion at two subsequent time instants displayed in Figs. 1(e,f) confirm that waves are preferentially amplified as they travel towards the bottom left corner of the lattice.

The talk will describe further properties of the non-Hermitian lattices such as tunability based on anisotropic control parameters ($\gamma_x \neq \gamma_y$), multiple non-reciprocal frequency bands for lattices with non-local control ($a > 0$), topological properties of the complex dispersion bands in terms of winding numbers and their relation to skin modes localized at the edges of finite lattice strips, and bulk modes localized at corners of finite two-dimensional lattices. Multiple avenues for future work are suggested such as possibilities for experimental implementation, exploration of different geometries, modulations of control parameters, modification of control laws (*e.g.* derivative and integral controls), as well as the introduction of non-linearities.

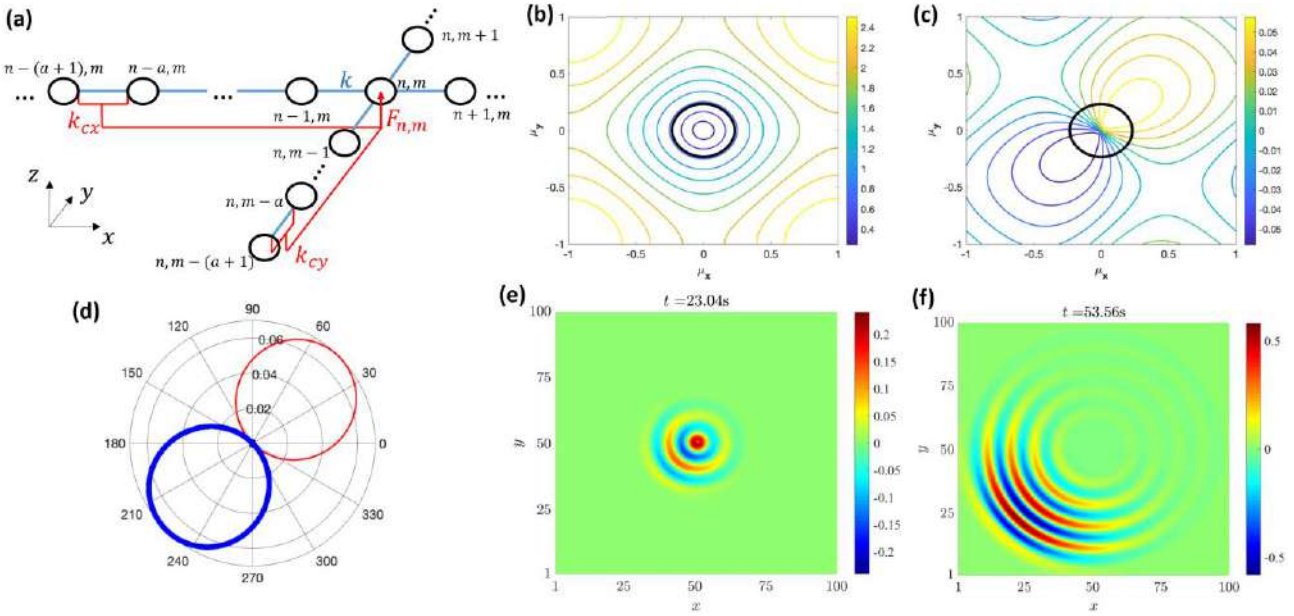

Figure 1. Non-reciprocal wave amplification in two-dimensional lattice with feedback interactions. (a) Schematic of 2D lattice where a feedback force is applied to each mass along the lattice, reacting proportionally to the strain of springs a units behind in the x and y directions. (b,c) Iso-frequency contours corresponding to the real part Ω_r (b), and imaginary part Ω_i (c) of the dispersion $\Omega(\mu_x, \mu_y)$. The thick black line outlines the contour for $\Omega_r = 0.7$, and defines the wave vector components governing propagation at the considered frequency. (d) Angular variation of Ω_i highlighting the angular range of amplification (thick blue line) and attenuation (thin red line). (e,f) Snapshots of transient response to a tone-burst excitation at $\Omega = 0.7$ applied to the center mass of the lattice, illustrating that waves traveling towards the bottom left corner are preferentially amplified.

ACKNOWLEDGEMENTS

This work is supported by the National Science Foundation (NSF) through the EFRI 1741685 grant and by the Army Research Office (ARO) through grant W911NF-18-1-0036.

References

[1] R. Fleury, D. Sounas, A. Alu. An invisible acoustic sensor based on parity-time symmetry. *Nature communications*, 6:5905, 2015.
[2] H. Hodaei *et. al*. Enhanced sensitivity at higher-order exceptional points. *Nature*, 548(7666):187, 2017.
[3] S. Yao and Z. Wang. Edge states and topological invariants of non-hermitian systems. *Physical review letters*, 121(8):086803, 2018.
[4] A. Ghatak, M. Brandenbourger, J. V. Wezel and C. Coulais. Observation of non-hermitian topology and its bulk-edge correspondence. *arXiv preprint* 1907.11619, 2019.
[5] M. Brandenbourger, X. Locsin, E. Lerner and C. Coulais. Non-reciprocal robotic metamaterials. *arXiv preprint* 1903.03807, 2019.
[6] M. I. N. Rosa and M. Ruzzene. Dynamics and topology of non-Hermitian elastic lattices with non-local feedback control interactions. *arXiv preprint* 2001.01817, 2020

BAND GAPS AND SIZE-EFFECTS IN A HETEROGENEOUS CAUCHY MATERIAL IN THE DYNAMIC FRAMEWORK

Gianluca Rizzi*[1], Patrizio Neff[2], and Angela Madeo[1]
[1]Laboratoire GEOMAS, INSA Lyon, Lyon, French
[2]Fakultät für Mathematik,Universität Duisburg-Essen,Essen,Germany

Summary The mechanical response of a heterogeneous Cauchy material (see Fig. 1) subjected to dynamic solicitations cannot always be adequately represented via a classic homogeneous model. To overcome this problem, it is possible to use an enriched continuum such as a *relaxed micromorphic model* to catch phenomenons like *band gaps* and *size-effect*.

INTRODUCTION

It is clear nowadays that both in statics and dynamics, the presence of heterogeneities or microstructures within a solid can cause micromechanical effects which can only be described through non local and higher-order models [1]-[2]. In particular, these effects are magnified for a finite-size domain when its dimensions are comparable to the size of its unit cell.

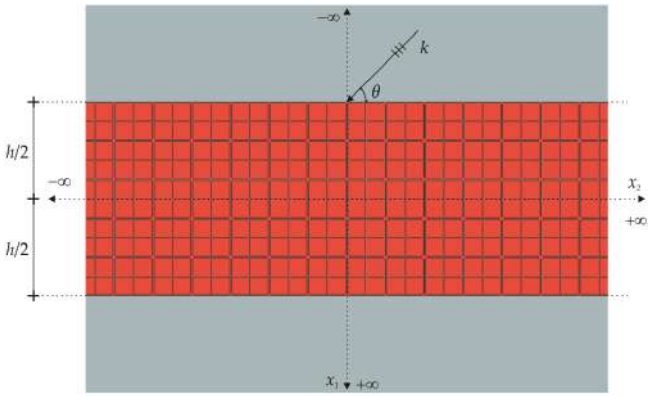

Figure 1: Inclusion of a microstructured Cauchy material embedded between two homogeneous media.

Two examples of micromechanical effects are the so called *size-effects* and *band gaps*. The *size-effect* consists in how the mechanical response of a solid changes when changing the ratio between the characteristic size of the macroscopic specimen and that of the unit cell (in dynamics it is also important the ratio between the wavelength of the incident wave and both the size of the unit cell and the size of the solid considered). On the other hand, *band gaps* are frequency ranges for which waves do not propagate due to scattering or local resonance phenomena at the level of the microstructure. In order to be able to replicate both these micromechanical effects in a continuum mechanics framework, a relaxed micromorphic model is here proposed [3]-[4].

The jump conditions at the interfaces consist in the continuity of the displacement and of the generalized traction for both the relaxed micromorphic and Cauchy continuum and, additionally, null double force for the relaxed micromorphic continuum (see [4] for more details).

We use this model to explore the scattering response of a finite-size metamaterial slab embedded between two homogenous media (see Fig. 2 and Fig. 3). The obtained response is than compared with that retrieved via a FEM simulation of the microstructured material.

RELAXED MICROMORPHIC MODEL

The expression of the kinetic energy density for a relaxed micromorphic continuum is:

$$\begin{aligned} J\left(u_{,t}, \nabla u_{,t}, P_{,t}\right) = \quad & \tfrac{1}{2}\rho\langle u_{,t}, u_{,t}\rangle + \tfrac{1}{2}\mathbb{J}_{micro}\langle \mathrm{sym}P_{,t}, \mathrm{sym}P_{,t}\rangle + \tfrac{1}{2}\mathbb{J}_{c}\langle \mathrm{skew}P_{,t}, \mathrm{skew}P_{,t}\rangle \\ & + \tfrac{1}{2}\mathbb{T}_{e}\langle \mathrm{sym}\nabla u_{,t}, \mathrm{sym}\nabla u_{,t}\rangle + \tfrac{1}{2}\mathbb{T}_{c}\langle \mathrm{skew}\nabla u_{,t}, \mathrm{skew}\nabla u_{,t}\rangle, \end{aligned} \tag{1}$$

where u is the macroscopic displacement field, $P \in \mathbb{R}^{3x3}$ is the non-symmetric micro-distortion tensor, ρ is the macroscopic apparent density, and $\mathbb{J}_{micro}$, $\mathbb{J}_c$, $\mathbb{T}_e$, $\mathbb{T}_c$ are 4th order micro-inertia tensors [4] whose coefficients are dynamic characteristic lengths (L_i, $\overline{L}_i$ with $i = 1, 2, 3, 4$).

*Corresponding author. E-mail: gianluca.rizzi@insa-lyon.fr

The expression of the strain energy density for a relaxed micromorphic continuum is:

$$W\left(\nabla u, P, \mathrm{Curl}P\right) = \begin{aligned} &\tfrac{1}{2}\mathbb{C}_e\langle \mathrm{sym}\left(\nabla u - P\right), \mathrm{sym}\left(\nabla u - P\right)\rangle + \tfrac{1}{2}\mathbb{C}_{micro}\langle \mathrm{sym}P, \mathrm{sym}P\rangle \\ &+\tfrac{1}{2}\mathbb{C}_c\langle \mathrm{skew}\left(\nabla u - P\right), \mathrm{skew}\left(\nabla u - P\right)\rangle + \tfrac{\mu_{micro}L_c^2}{2}\langle \mathrm{Curl}P, \mathrm{Curl}P\rangle, \end{aligned} \tag{2}$$

where $\mathbb{C}_e$, $\mathbb{C}_{micro}$, and $\mathbb{C}_c$ are 4th order tensors and μ_{micro} and $\mathbf{L_c}$ are scalar quantities [4]. The micro-inertia and the elastic parameter numerical values can be found in [4] and a the solution considered is time-harmonic.

RESULTS

The comparison in terms of reflection coefficient between the microstructured material (MM), the Cauchy material (CM) (Fig. 2), and the realxed micromorphic material (RMM) (Fig. 3) is here presented for the case of study of a slab (Fig. 1) of thickness 20 and 30 cells. For the sake of compactness, we only present the case of an in-plane pressure incident wave, but analogous conclusions can be drawn for the case of shear incident ones.

As it can be seen, the band gaps are captured very well by the relaxed micromorphic material while not at all by the correspondent Cauchy counterpart.

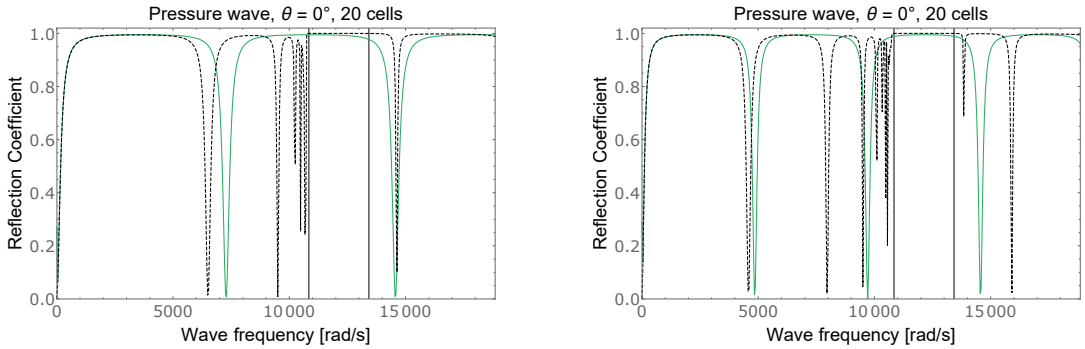

Figure 2: Comparison between the microstructured material (dashed black) and the effective Cauchy continuum (green) in terms of reflection coefficient for two slabs of 20 and 30 cells thick.

It is also important to underline that the position of the band gaps (Fig. 3) are due to the coefficient L_i and $\overline{L}_i$.

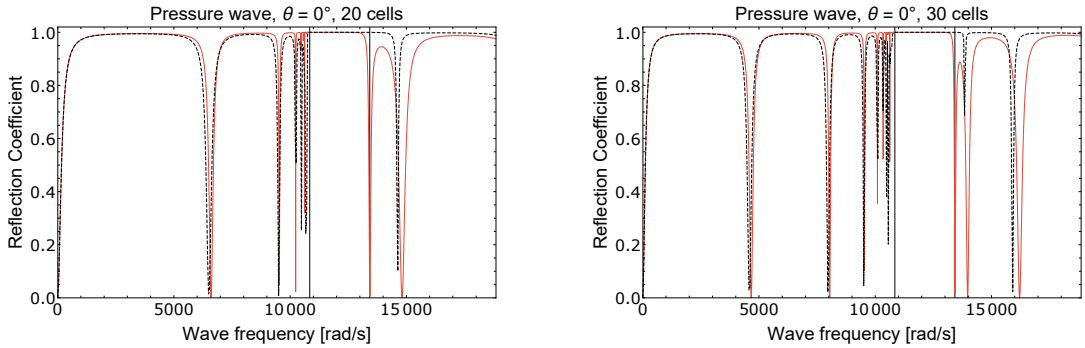

Figure 3: Comparison between the microstructured material (dashed black) and the effective relaxed micromorphic continuum (red) in terms of reflection coefficient for two slabs of 20 and 30 cells thick.

References

[1] Beveridge A.J., Wheel M.A., Nash D.H., The micropolar elastic behaviour of model macroscopically heterogeneous materials,International Journal of Solids and Structures, v50, pp 246-255, 2013.

[2] Buechner P. M., Lakes R. S., Size effects in the elasticity and viscoelasticity of bone, Biomechanics and Modeling in Mechanobiology, v1, pp 295–301, 2003.

[3] d'Agostino M.V., Barbagallo G., Ghiba I.D., Eidel B., Neff P., Madeo A., Effective description of anisotropic wave dispersion in mechanical band-gap metamaterials via the relaxed micromorphic model. *Journal of Elasticity*, pp 1-31, 2019.

[4] Rizzi G., Collet M., Demore F., Eidel B., Neff P., Madeo A., Exploring metamaterials' structures through the relaxed micromorphic model: switching an acoustic screen into an acoustic absorber. *submitted*.

Acknowledgements: Angela Madeo acknowledge funding from the French Research Agency ANR, "METASMART" (ANR-17CE08-0006). Angela Madeo and Gianluca Rizzi acknowledges support from IDEXLYON in the framework of the "Programme Investissement d'Avenir" ANR-16-IDEX-0005.

INVESTIGATING THE DYNAMICS OF SURFACE WAVES IN RESONANT HALF-SPACES

Antonio Palermo[1], Farhad Zeighami[1], and Alessandro Marzani *[1]
[1]Department of Civil, Chemical, Environmental and Materials Engineering, University of Bologna, Bologna,Italy

Summary We study the dynamics of vertically polarized surface waves propagating in elastic half-spaces patterned with locally resonant inclusions. By employing an effective medium description able to capture the low-frequency dynamics of the inclusions, we derive a closed-form dispersion relation of Rayleigh-like waves and discuss their dispersive features, including the formation of surface waves band gaps.

BACKGROUND

Elastic metamaterials are artificial composites with local resonant particles or structures of subwavelength dimensions hosted in an elastic medium [1]. When elastic waves propagate through a resonant medium, they hybridize with the local resonant modes of the inclusions, leading to frequency band gaps generated from the avoided crossing behavior between repelling modes. These band gaps arise in the narrow frequency range between the resonance and antiresonance mode of the inclusions. Homogenization techniques have been employed to model the dispersive properties of one-dimensional, two-dimensional, and bulk resonant media. Additionally, resonant boundary conditions have been used to describe the dynamics of resonant structures placed on the surface of elastic half-spaces, for Rayleigh and Love waves control [2]. Nonetheless, the dynamics of surface waves in a half-space equipped with resonant inclusions through its whole depth remains still unexplored. Hence, in what follows, we describe the dynamics of Rayleigh-like waves in a resonant half-space, summarizing and complementing with further numerical results, some of the analytical developments and numerical models presented in our earlier work [3].

ANALYTICAL MODEL AND RESULTS

We investigate the propagation of vertically polarized surface waves in a homogeneous elastic resonant half-space (see Fig. 1a). The resonant medium is formed by a periodic arrangement of hard cylindrical inclusions (i), covered by soft coating layers (c) and embedded in an elastic hosting matrix (h).

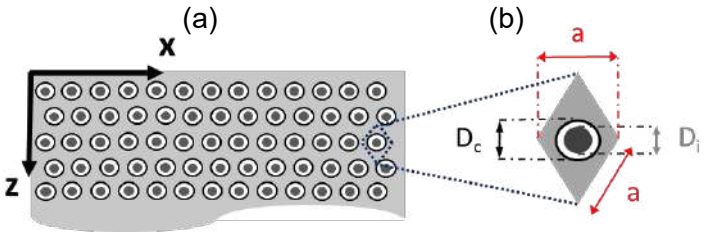

Figure 1: (a) Schematic of a two-dimensional (2D) resonant half-space. (b) Basic unit cell.

For the example of choice, the inclusions are arranged in a triangular lattice of spacing $a = 3\ cm$. We adopt an effective medium description to provide closed-form expression of the effective mass density ρ_{eff} and elastic moduli λ_{eff}, μ_{eff}, able to correctly capture the low-frequency dynamics of the composite medium. In detail, for the effective density, we adopt the closed-form expression provided by Liu [4]:

$$\rho_{eff}(\omega) = \phi_h \rho_h + (\phi_c + \phi_i)\rho_c \left[g_1(\omega) - g_2(\omega) \frac{g(\omega)}{R(\omega) - \frac{\rho_i}{\rho_c}} \right] \tag{1}$$

where ρ_h, ρ_c and ρ_i, are the mass densities, ϕ_h, ϕ_c, and ϕ_i are the filling fractions of the host, coating, and inclusion, respectively, and $g_1(\omega)$, $g_2(\omega)$, $g(\omega)$ and $R(\omega)$ are frequency-dependent functions given in Ref. [4].
Conversely, for the effective elastic moduli, we employ a two-step homogenization procedure, adapting the static approximation employed by Mei et al. [5] for a bi-phase composite. Hence, we first calculate the effective elastic parameters of the resonant inclusion, combining the hard cylindrical particle with its soft interface. The effective elastic moduli of such bi-composite, $\mu_{i,c}$ and $\lambda_{i,c}$, are obtained from the equations [5]:

$$\begin{aligned} \frac{\mu_{i,c} - \mu_c}{\mu_{i,c} + \mu_c} &= \phi_{i,c} \frac{\mu_i - \mu_c}{\mu_i + \mu_c}, \\ \frac{(\lambda_{i,c} + \mu_{i,c}) - (\lambda_c + \mu_c)}{\lambda_{i,c} + \mu_{i,c} + \mu_c} &= \phi_{i,c} \frac{(\lambda_i + \mu_i) - (\lambda_c + \mu_c)}{\lambda_i + \mu_i + \mu_c}, \end{aligned} \tag{2}$$

*Corresponding author. E-mail: alessandro.marzani@unibo.it

where $\phi_{i,c} = (D_i/D_c)^2$ is the filling ratio of the cylinder within the resonant inclusion.
The homogenization procedure is repeated by combining the homogenized resonant inclusion ($\mu_{i,c}$, and $\lambda_{i,c}$) and the host material to obtain the effective parameters μ_{eff} and λ_{eff}. Equipped with effective density and elastic moduli of the composite medium, we obtain the dispersive longitudinal $c_{L,eff}(\omega)$ and shear $c_{T,eff}(\omega)$ effective bulk velocities as:

$$c_{T,eff}(\omega) = \sqrt{\frac{\mu_{eff}}{\rho_{eff}(\omega)}},\ c_{L,eff}(\omega) = \sqrt{\frac{\lambda_{eff} + 2\mu_{eff}}{\rho_{eff}(\omega)}} \tag{3}$$

At this stage, the dispersive properties of Rayleigh waves in a resonant half-space are calculated by adopting the expressions in Eqs. (2) and (3) in the standard Rayleigh wave dispersion law [6].

$$\left(2 - \left(\frac{\omega}{kc_{T,eff}}\right)^2\right)^2 - 4\sqrt{1 - \left(\frac{\omega}{kc_{T,eff}}\right)^2}\sqrt{1 - \left(\frac{\omega}{kc_{L,eff}}\right)^2} = 0 \tag{4}$$

Fig. 2 shows (in continuous black lines) the complex wavenumber ($k = k_r + ik_i$) of Eq. (4) calculated for a composite medium consisting of aluminum inclusions ($\rho = 2.7 \times 10^3 kg/m^3$, $\mu = 2.59 \times 10^{10} N/m^2$ and $\lambda = 6.05 \times 10^{10} N/m^2$), coated with rubber ($\rho = 1.3 \times 10^3 kg/m^3$, $\mu = 5 \times 10^5 N/m^2$ and $\lambda = 5 \times 10^6 N/m^2$), and embedded in epoxy matrix ($\rho = 1.18 \times 10^3 kg/m^3$, $\mu = 1.59 \times 10^9 N/m^2$ and $\lambda = 4.43 \times 10^9 N/m^2$). Analytical solutions, provided in terms of non-dimensional complex wavenumber $k' = ka/\pi$ vs. non-dimensional angular frequency $\omega' = \omega/\omega_r$, where ω_r is the angular resonance frequency of the resonant system, agree well with numerical solutions obtained via finite element modelling of the composite material. The dispersion curve highlights the existence of a band gap where the propagation of Rayleigh waves is forbidden. The gap occurs in the same frequency region where bulk waves are hindered.

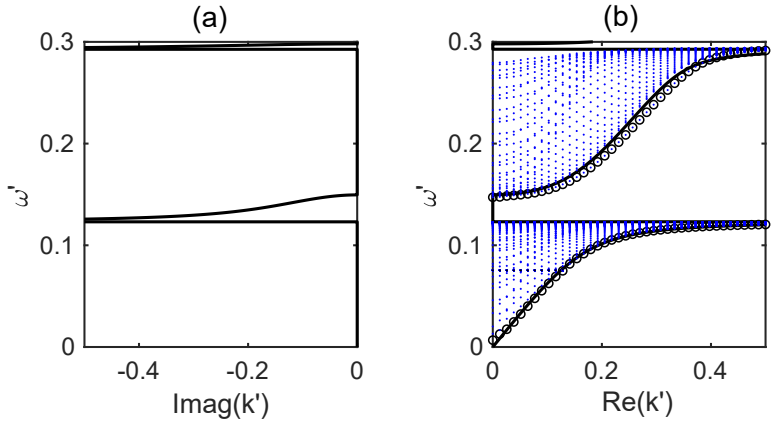

Figure 2: (a) Imaginary and (b) real wavenumbers of vertically polarized surface waves in the resonant half-space. Blue dots and black circles mark bulk and surface modes predicted by FE simulations, respectively.

CONCLUSIONS

In this work, we investigate the propagation of vertically polarized surface waves in resonant half-spaces. We derive effective parameters of the resonant medium via homogenization approaches and develop an analytical dispersion law for the interaction of Rayleigh waves existing in the resonant half-space. According to our model, band gaps exist around the resonance frequencies of the inclusions. An in-depth analysis on the band gap frequency width as well as on its dependence on the depth of the resonant inclusions will be presented at the conference.

References

[1] Hussein M. I., Leamy M. J., Ruzzene M., *Appl. Mech. Rev.* **66**, 40802, 2014.
[2] Palermo A., Krödel S., Marzani A., Daraio C., *Sci. Rep.* **6**, 39356, 2016.
[3] Palermo A., Zeighami F., Marzani A., Submitted to *J. Mech. Phys. Solids*, 2020.
[4] Liu Z., Chan C.T., Sheng P., *Phys. Rev. B* **71**, 014103, 2005.
[5] Mei J., Liu Z., Wen W., and Sheng P., *Phys. Rev. B* **76**, 134205, 2007.
[6] Graff K.F., Wave motion in elastic solids. Dover, New York, NY 1991.

CANONICAL QUASICRYSTALLINE MULTILAYERED METAMATERIALS

Lorenzo Morini*[1], Zhijiang Chen[1], and Massimiliano Gei[1,2]
[1]School of Engineering, Cardiff University, Cardiff, UK
[2]Department of Civil, Environmental and Mechanical Engineering, University of Trento, Trento, Italy

Summary A new class of two-phase periodic laminates with a *quasicrystalline* structure (generated by the Fibonacci substitution rule) is introduced. Recently, we found that the Floquet-Bloch spectrum of antiplane waves propagating in this particular type of layered composite has a self-similar layout which can be characterized through an invariant function of the frequency, the so-called Kohmoto invariant. Moreover, for particular ratios between the geometrical and constitutive parameters of the two constituent phases (*canonical* ratios), the spectra are periodic. We illustrate how these two unique properties can be used to design quasicrystalline lamitates providing negative refraction of an antiplane wave obliquely incident at the interface with an elastic substrate. It is shown that, beyond a certain frequency threshold, high order Fibonacci laminates allow negative refraction of a single transmitted mode at lower frequencies with respect to a periodic classical bilayer. The attained results represent an important advancement towards the realisation of multilayered quasicrystalline metamaterials with the aim to control negatively refracted elastic waves.

QUASICRYSTALLINE-GENERATED LAMINATES

We define a class of two-dimensional, two-phase quasicrystalline laminates with layering direction parallel to the axis y (see Fig. 1/(A)). Each of its elements is composed of a repeated elementary cell $\mathcal{F}_i$ where the two basic components, A and B, are arranged in series according to the standard Fibonacci sequence, which is based on the following substitution rule $A \to AB,\ B \to A$. The repetition of the fundamental cells assures global periodicity along axis x and the possibility of applying the Floquet-Bloch technique in order to study harmonic wave propagation in these systems.

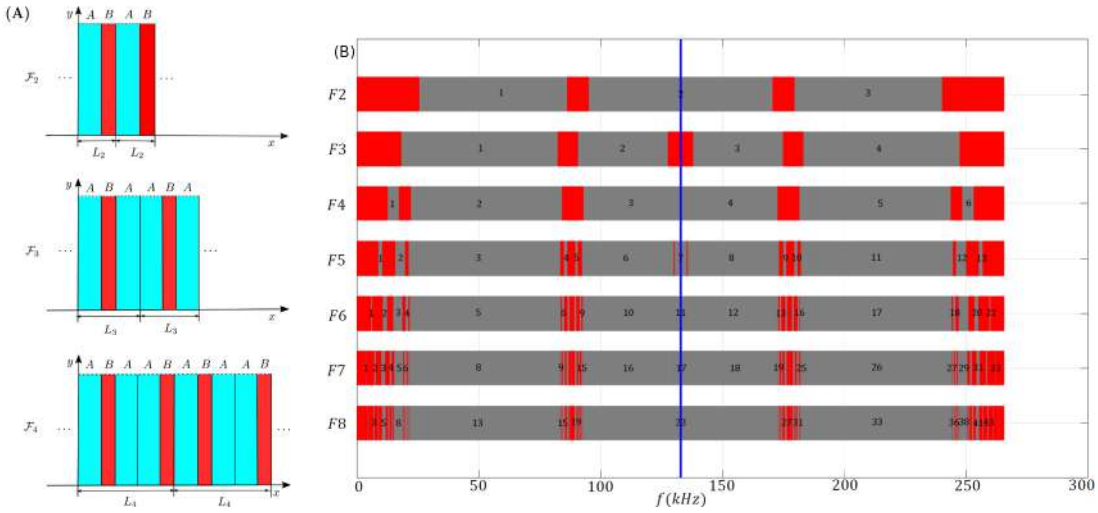

Figure 1: (A): two-dimensional laminates assembled according to $\mathcal{F}_2$, $\mathcal{F}_3$ and $\mathcal{F}_4$ Fibonacci cells. (B): Diagram reporting, in the grey zones, the number N_i^f of real solutions K_y of the dispersion relation for cells $\mathcal{F}_2$ to $\mathcal{F}_8$ as a function of the frequency. Transition zones are highlighted in red.

The dispersion relation for Floquet-Bloch harmonic antiplane waves propagating in Fibonacci laminates as those illustrated in Fig. 1/(A) assumes the form

$$\cos\left(K_x L_i\right) = \frac{1}{2}\mathrm{tr}\mathbf{M}_i(f, K_y), \tag{1}$$

where $\mathbf{M}_i$ is the trasmission matrix of the ith-order cell $\mathcal{F}_i$, L_i is the total length of the cell, $f = \omega/2\pi$ is the wave frequency, K_x and K_y are the components of the wave vector directed along $x-$ and $y-$ axis, respectively. $\mathbf{M}_i$ is unimodular, i.e. $\det\mathbf{M}_i = 1$, and follows the recursion rule $\mathbf{M}_{i+1} = \mathbf{M}_{i-1}\mathbf{M}_i$, with $\mathbf{M}_0 = \mathbf{M}_B$ and $\mathbf{M}_1 = \mathbf{M}_A$ [1]. Assuming a given wave frequency f, for any real value of K_x we found a finite number N_i^f of real and an infinite number of imaginary solutions K_y of the dispersion relation (1) [2]. This means that for any real K_x we have N_i^f propogating waves and infinite evanescent modes along the $y-$direction. The numerical solution of (1), obtained for a determinate set of frequencies by varying K_x along the intervals $0 \le K_x \le m\pi/L_i$, $m \in \mathbb{N}$ (*Brillouin zones*), shows that: i) assuming given values of f and K_x, N_i^f increases for high order Fibonacci cells $\mathcal{F}_i$ [3]; ii) if f belongs to some particular frequency ranges, N_i^f depends on the value of K_x and we have $N_i^f = t-1$ for $0 \le K_x \le \overline{K}_x$ and $N_i^f = t$ for $\overline{K}_x \le K_x \le m\pi/L_i$. We denote these frequency ranges as *transition zones*. The t-th transition zone is that where N_i^f switches from $t-1$ to t.

*Corresponding author. E-mail: morinil@cardiff.ac.uk.

SELF-SIMILAR TRANSITION ZONE LAYOUT AND CANONICAL RATIO

An example of transition zone layout for laminates designed according to cells $\mathcal{F}_2$ to $\mathcal{F}_8$ is reported in Fig. 1/(B) as a function of the frequency. We note that they are disposed according to a self-similar pattern. The analysis of the dispersion curves obtained assuming $K_y = 0$ (transverse wave propagation in the laminate) reveals that for any cell $\mathcal{F}_i$ the position of pass bands coincide with that of transition zones. In this specific case, the transfer matrix $\mathbf{M}_i$ and the dispersion relation (1) become identical to those defined in [1] and [5]. Consequently, the self similarity is governed by a local scaling whose factor is analogous to that used in those papers for studying the spectrum of quasicrystalline-generated structural waveguides:

$$\kappa_0^+(f) = \frac{1}{4}\left(\sqrt{4+(4+I_0(f))^2}+(4+I_0(f))\right)^2, \tag{2}$$

where $I_0(f)$ is the so-called Kohmoto's invariant [4]. A transition zone $f_i^B - f_i^A$ of the cell $\mathcal{F}_i$ centred at a frequency f^* is related to the transition zone $f_{i+6}^B - f_{i+6}^A$ of $\mathcal{F}_{i+6}$ centred almost about the same value f^* by the scaling law $f_{i+6}^B - f_{i+6}^A \approx (f_i^B - f_i^A)/\kappa$, where $\kappa = \kappa_0^+(f^*)$. Similarly, $f_{i+3}^B - f_{i+3}^A \approx (f_i^B - f_i^A)/\lambda$, with $\lambda = \sqrt{\kappa}$.
By observing Fig. 1/(B), we also note that for any cell $\mathcal{F}_i$, the arrangement of the transition zones is periodic. This is achieved for rational values of the ratio $\beta = c_A h_B / c_B h_A$, where h_A and h_B are the thicknesses of phases A and B, c_A and c_B the shear wave speed in materials A and B, respectively. We denote β as *canonical ratio*, and the laminates characterized by $\beta \in \mathbb{Q}$ as *canonical laminates* (for the case shown in Fig.1/(B), $\beta = 2$).

NEGATIVE REFRACTION USING QUASICRYSTALLINE LAMINATES

We now use the quasicrystalline laminates to obtain negative refraction of an antiplane wave across an interface with an elastic substrate (schematic of the problem reported in Fig.2/(A)). For each value of K_x corresponding to a given frequency and an arbitrary angle of incidence in the interval $0 \leq \theta \leq \pi/2$, we have N_i^f real solutions of the dispersion relation (1). These real solutions correspond to propagating modes transmitted at the interface. In order to have only one single negatively refracted mode (*pure negative refraction*), the incident wave frequency should belong to the interval $f_i^{min} \leq f \leq \tilde{f}_i$ [3], where $f_i^{min} = \sqrt{\mu_0}/(2L_i\rho_0)$ (with μ_0 and ρ_0 shear modulus and mass density of the substrate, respectively), and $\tilde{f}_i$ is the highest frequency of the second transition zone. Remembering the spectrum analysis reported in the first section, we can calculate $\tilde{f}_i$ for any Fibonacci cell $\mathcal{F}_i$. Moreover, using the scaling factor (2) together with the associated scaling relationships and the condition of periodicity $\beta \in \mathbb{Q}$, we can design canonical laminates providing pure negative refraction in several ranges of frequencies considering different elastic substrates. The results illustrated in Fig.2/(B) for a PMMA-steel laminate bonded to a polyethylene substrate show that, by considering the same angle of incidence ($\theta = 20°$) high-order Fibonacci cells yield single negatively refracted modes at lower frequencies with respect to standard two-phase periodic laminates (represented by cell $\mathcal{F}_2$).

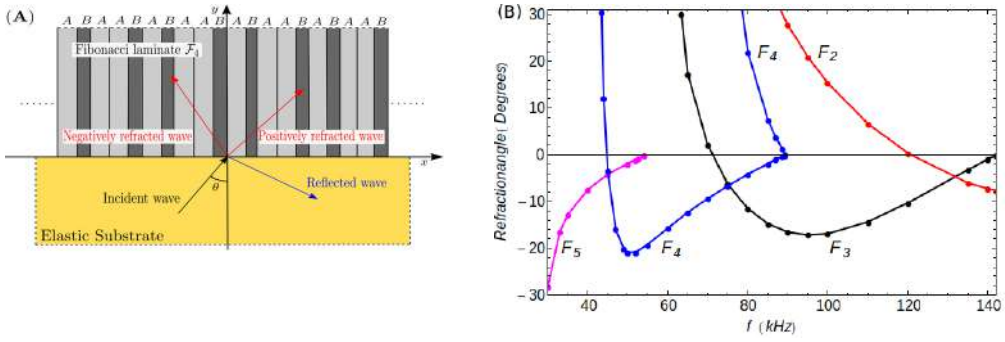

Figure 2: (A): Schematic of the problem of an antiplane wave approaching the interface between an elastic substrate and a Fibonacci laminate $\mathcal{F}_4$. (B): Angles of refraction corresponding to an incident angle $\theta = 20°$ plotted versus the frequency for cells $\mathcal{F}_2$ to $\mathcal{F}_5$.

CONCLUSIONS

The propagation of antiplane shear waves in two-phase periodic quasicrystalline-generated laminates following the Fibonacci substitution rules has been studied. The Floquet-Bloch analysis reveals that particular ranges of frequencies, called transition zones, are disposed in the dispersion diagrams according to a self-similar pattern. Numerical results show that these self-similarity properties together with the condition for the periodicity of the spectrum can be used to design high order Fibonacci laminates allowing negative wave refraction of a single transmitted mode at lower frequencies with respect to a classical periodic bilayer.

References

[1] Gei M. Wave propagation in quasiperiodic structures, stop/pass band distribution and prestress effects. *Int. J. Solids Struct.* **47**: 3067-3075, 2010.
[2] Willis J. Negative refraction in a laminate. *J. Mech. Phys. Solids* **97**: 10-18, 2016.
[3] Morini L., Eyzat Y., Gei M. Negative refraction in quasicrystalline multilayered metamaterials. *J. Mech. Phys. Solids* **124**: 282-298, 2019.
[4] Kohmoto M., Oono Y. Cantor spectrum for an almost periodic Schoedinger equation and a dynamical map. *Phys. Lett.* **102A**: 145-148, 1984.
[5] Morini L., Gei M. Waves in one-dimensional quasicrystalline structures: dynamical trace mapping, scaling and self-similarity of the spectrum *J. Mech. Phys. Solids* **119**: 82-103, 2018.

CLOAKING OF MULTIPLE INTERACTING VOIDS

Diego Misseroni*[1]
[1]Department of Civil, Environmental and Mechanical Engineering, Università di Trento, Trento, Italy

Summary A new approach, based on the concept of the redistribution of the mass and the stiffening of the boundary, is proposed for the cloaking of multiple interacting voids embedded into an elastic plate. This new method is validated via both numerical simulations and experiments. This technique, very simple in principle, produces invisibility of the randomly located voids to flexural waves over a wide range of frequencies. The proposed design can find applications in mechanical problems ranging from the micro-scale to the macro-scale.

THE CLOAKING DESIGN

In elasticity, the invisibility of a defect (such as a void or an inclusion) embedded into a vibrating plate is achieved when the vibration propagating within the medium is not perturbed by its presence. In the last decades, several methods have been proposed in the attempt to make an object invisible to flexural vibrations. Usually, they are based on the so-called *cloaking transformation*, a concept originally developed in electromagnetism and optics [1, 2, 3, 4]. The 'perfect cloak' of an object implies omnidirectional and total scattering elimination over a wide frequency range, a goal that should be achieved with a sufficiently thin coating, of simple design and realization.

A radically new design concept is introduced to make voids invisible within an extremely broad range of frequencies, never challenged so far. Without recurring to the concept of cloaking transformation, a simple procedure to strongly reduce scattering is proposed, based on mass and moment of inertia conservation and elastic stiffening averaging along the boundary of the void, as shown schematically in Fig. 1. Such a cloaking design is introduced regarding an elastic plate perforated with several voids, randomly located and inclined.

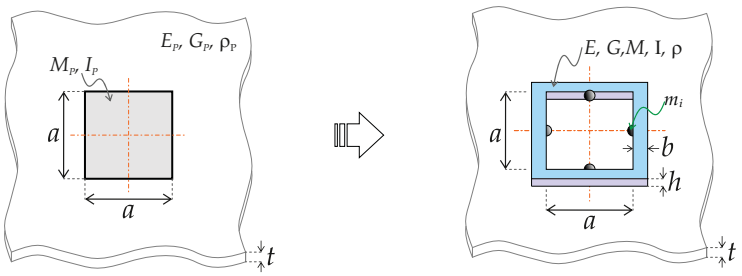

Figure 1: Sketch of the cloaking design. (left) A void of dimension $a \times a$ has to be cloaked in an elastic plate. (right) A stiffer and heavy frame is placed along the boundary of the void to maintain the same mass, the same moment of inertia around the axes of the void and the same bending stiffness eliminated by the void.

NUMERICAL VALIDATION

Numerical simulations were performed in Abaqus to demonstrate omnidirectionality of the cloak and multiple invisibility for several voids randomly located and inclined. An out-of-plane vibration is applied at one end of three different plates: i) an intact plate, ii) a plate with reinforced voids and iii) a plate with unreinforced voids. The frequency of the excitation is continuously varied until resonance, to show that the eigenmodes of the intact plate and the plate with cloaked voids are the same, while the resonance modes of the perforated plate with uncloaked voids are different. In Fig. 2 the modes associated with three frequencies for which the cloak works exceptionally well so that multiple and omnidirectional invisibility is almost perfect) are reported. The plate with cloaked voids is shown to behave almost identically with the intact plate, while it strongly differs from the perforated plate, which remains almost undeformed (because it vibrates far from resonance).

EXPERIMENTAL PROOF

In addition to the numerical simulations, resonance experiments were carried out to validate the efficiency of the proposed method exploiting the experimental setup shown in Fig 3. The resonance is detected using a stroboscopic light and the experiments exactly confirm the expectation (a set of photos is shown in Fig. 4) and show coincidence up to the fourth mode of vibration for the intact plate and the perforated plate with cloaked voids, while the plate with the unreinforced voids vibrates far from its resonance frequency and thus appears only slightly deformed.

*Corresponding author. E-mail: diego.misseroni@unitn.it

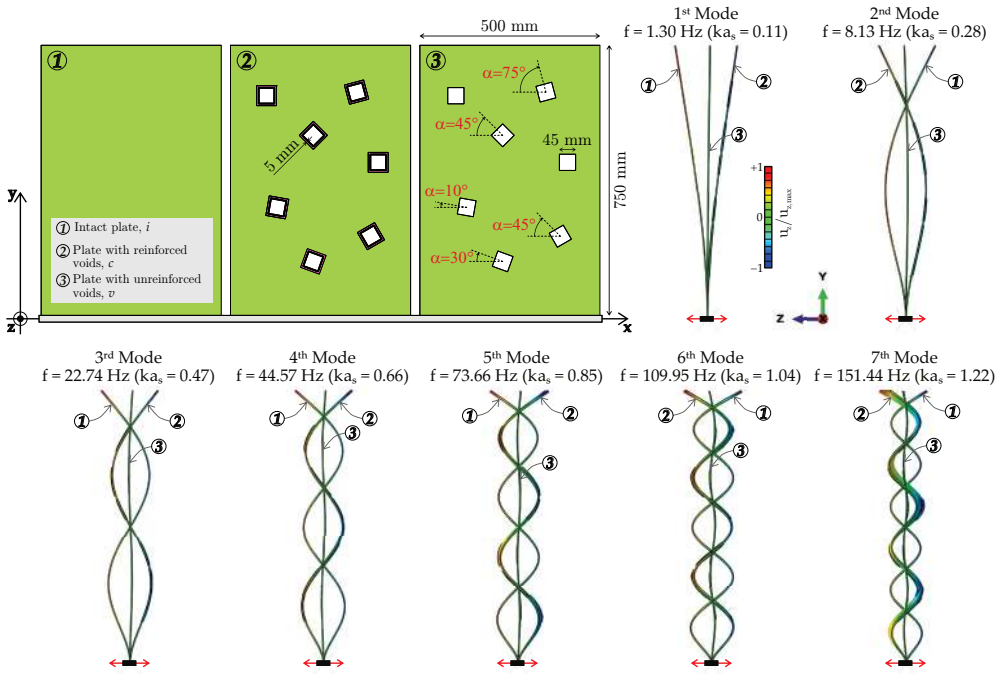

Figure 2: Omnidirectional cloak and multiple invisibility of 7 randomly located and inclined voids. The eigenmodes of the intact plate and the plate with cloaked voids coincide up to (and beyond) the 7^{th} mode and are different from those of the plate with unreinforced voids.

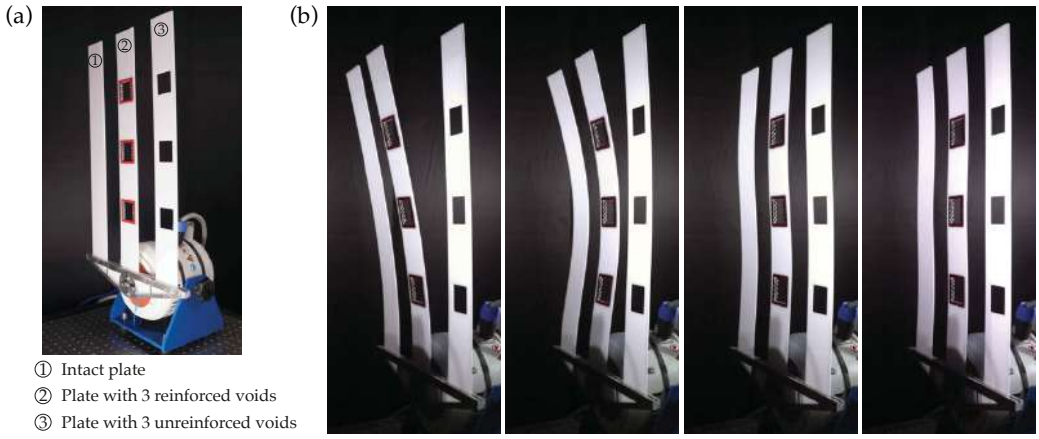

Figure 3: (a) Experimental setup employed to impose the flexural vibration at one end of the elastic plates. (b) Stroboscopic snapshots taken during the resonance experiments. The intact plate behaves the same as the plate with the reinforced voids. The plate with unreinforced voids remains almost undeformed because it vibrates at a frequency far from its resonance.

CONCLUSIONS

A new method, based on the mass redistribution and the stiffening of the boundary, is proposed to obtain the invisibility of square voids embedded in elastic plates. The efficiency of the method was tested through both numerical simulations and real experiments performed on a proof-of-concept cloaking model. The obtained outcomes fully confirm the goodness of the method and pave the wave to the achievement of an 'ideal' cloak.

Acknowledgement: The author gratefully acknowledges financial support from the 'UNITN Starting Grant Young Researchers 2019'

References

[1] Schurig D., Mock J. J., Justice B. J., Cummer S. A., Pendry J. B., Starr A. F., Smith D. R. 2006 Metamaterial electromagnetic cloak at microwave frequencies. *Science*, **314**, 977980.

[2] Fleury R., Alù A.. 2014 Cloaking and invisibility: A review. In *Progress In Electromagnetics Research*, **147**, 171-202, 2014.

[3] Colquitt D. J., Brun M., Gei M., Movchan A. B., Movchan N. V., Jones I. S. 2014 Transformation elastodynamics and cloaking for flexural waves. *J. Mech. Phys. Solids*, **72**, 131-143.

[4] Misseroni D., Colquitt D. J., Movchan A. B., Movchan N. V., Jones I. S. 2016 Cymatics for the cloaking of flexural vibrations in a structured plate. *Sci. Rep.*, **6**, 23929.

BIO-INSPIRATION IN PHONONIC CRYSTALS: THE EFFECT OF HIERARCHY ON THE WAVE ATTENUATION

M. Miniaci*[,1], A. Krushynska[2], A. S. Gliozzi[3], N. Kherraz[2], F. Bosia[3]and Nicola Maria Pugno[4,5]
[1]Univ. Lille, CNRS, Centrale Lille, ISEN, Univ. Valenciennes, UMR 8520—IEMN, F-59000 Lille, France
[2]Department of Physics, University of Torino, Via P. Giuria 1, 10125 Torino, Italy
[3]Department of Applied Science and Technology, Politecnico di Torino, Corso Duca degli Abruzzi 24, 10124 Torino, Italy 6Laboratoryof
[4]Bio-Inspired and Graphene Nanomechanics, Department of Civil, Environmental and Mechanical Engineering, University of Trento, Via Mesiano77, 38123 Trento, Italy
[5]School of Engineering & Materials Science, QueenMary University of London, Mile End Road, London E1 4NS, UK

Summary Nature has engineered complex designs to achieve advanced properties and functionalities over hundreds of thousands of years. For instance, a hierarchical organization over multiple length scales allows enhanced quasistatic mechanical properties (such as high specific strength, stiffness, and toughness). While largely investigated in the quasistatic domain, the role of hierarchy in the dynamic behaviour of metamaterials remains largely unexplored. Here we numerically and experimentally investigate the influence of bio-inspired hierarchical organization on the wave dispersion diagram in metamaterials with self-similar structures at various spatial scales. The study reveals that the hierarchical architecture provides advantages for the dynamic performance with respect to conventional metamaterials.

INTRODUCTION

Hierarchical structures with constituents over multiple length scales are found in various natural materials like bones, shells, spider silk and others, all of which display enhanced quasi-static mechanical properties, such as high specific strength, stiffness and toughness, attributed to hierarchy [1-3]. However, the role of hierarchy in the dynamic behaviour of metamaterials remains largely unexplored. This work assesses the effect of bio-inspired hierarchical organization on the band structure of continuous mechanical metamaterials [4].

Although optimized conventional metamaterial configurations have recently been proposed [5, 6], elementary unit cells comprising single inclusions or cavities often provide limited frequency band gaps (BGs), so that lightweight, practically oriented meta-structures with multi-scale wave attenuation remain to be achieved.

MODELS AND METHODS

One way to potentially overcome the mentioned limitations is to exploit bio-inspired structural hierarchy. Structural hierarchy is here understood in the sense that a representative metamaterial unit cell comprises multiple arrangements of inhomogeneities at various size scales. If the same arrangement occurs at every scale, the pattern is called self-similar. We consider single-phase metamaterials formed by self-similar unit cells with different hierarchical levels, as schematically shown in Figure 1A.

We consider small-amplitude waves. In the case of a linear elastic medium, in the absence of external forces, the wave field is described by standard wave equations for two-dimensional displacements. The analysis is restricted to harmonic waves and forms a necessary basis for studying other types of wave motions. Due to the structural periodicity of the metamaterials, the displacements are also periodic in space and thus can be represented using the Floquet-Bloch expansion theorem. This allows to restrict the analysis of an infinite periodic medium to that of a representative unit cell only (Figure 1A) with Bloch periodic conditions at the unit cell boundaries [7].

RESULTS

The dispersion diagrams for the hierarchical cross-like metamaterial with regular and external hierarchical organization is shown in Figures 1B-D. It clearly appears that the wide band gap ranging from approximately 42 kHz to 96 kHz is almost preserved. Pass bands located inside the latter band gap are represented by mostly flat lines corresponding to localized modes. These modes do not couple with external field in realistic structures, which always have a certain level of energy dissipation.

Also, the introduction of hierarchy allows to shift the band gap corresponding to the ordinary unit cell to an approximately 3 times lower frequency. Several other band gaps appear at the band gap frequencies of the regular structure [4].

* Corresponding author: marco.miniaci@gmail.com

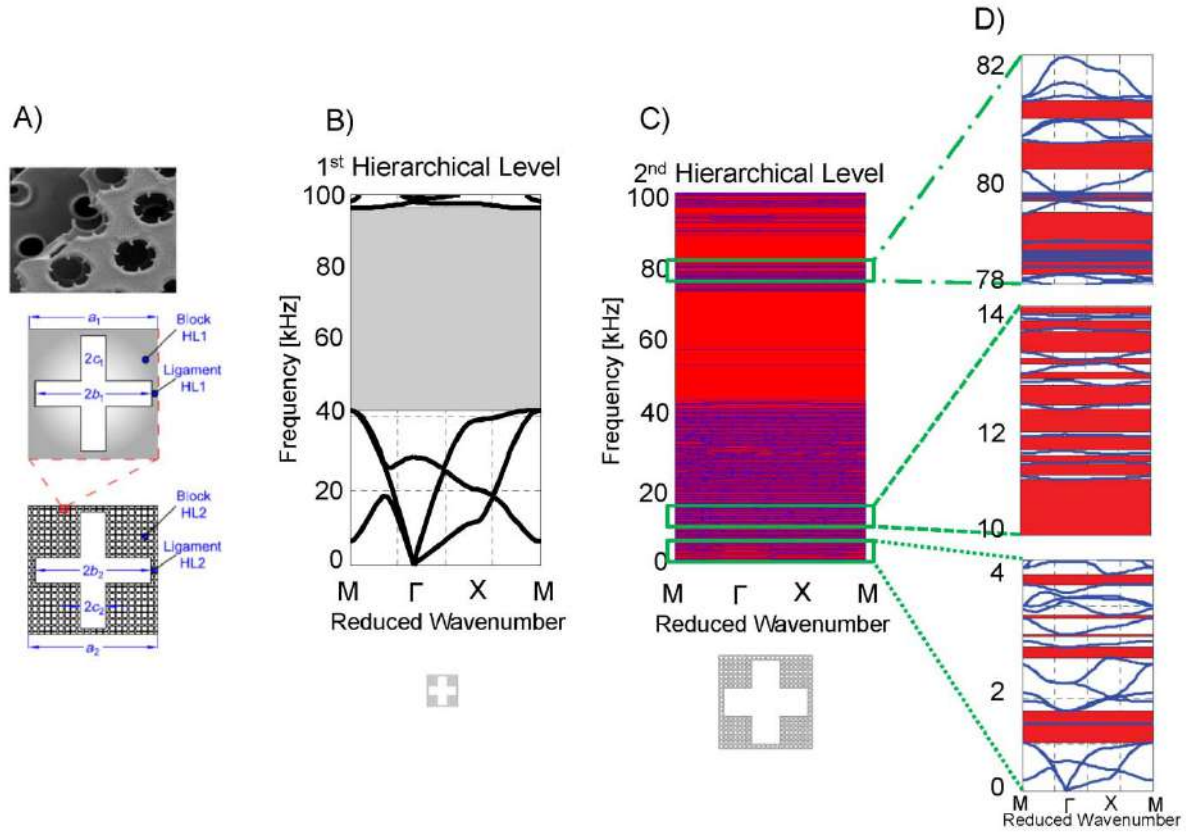

Figure 1. (A) Hierarchical structures found in natural materials, diatom cell walls (top) presenting holes at different spatial scales and the corresponding bio-inspired hierarchical metamaterial unit cells (bottom). The structure is made of cross-like cavities repeated over multiple scales. Dispersion diagrams for the regular cross-like metamaterial with (B) regular and (C) hierarchical organization. (D) Zoomed regions of the dispersion diagram. The hierarchical organization at different spatial scales allows preserving the BG originating from a smaller constitutive geometry and opening frequency band gaps at lower frequencies.

CONCLUSIONS

We have numerically and experimentally investigated the influence of bio-inspired hierarchical organization on wave dispersion in metamaterials with self-similar constituents at various spatial scales. Various advantages are found and here summarized:
(1) partial conservation of the band gaps induced by the constitutive regular geometries;
(2) nucleation of additional hierarchically induced band gaps;
(3) similar wave dynamics at low frequencies for hierarchical and corresponding regular structures;
(4) shift of band gaps to lower frequencies due to the effective mass and stiffness reduction.

References

[1] M. Meyers, P. Chen, A. Lin and Y. Seki, " Biological materials: Structure and mechanical properties," Prog. Mater. Sci., vol. 53, pp. 1-206, 2008.
[2] S. Cranford, A. Tarakanova, N. Pugno and M. Buehler, "Nonlinear material behaviour of spider silk yields robust webs," Nature, vol. 482, pp. 72-91, 2012.
[3] M. Miniaci, A. Krushynska, A. B. Movchan, F. Bosia, and N. M. Pugno, Appl. Phys. Lett. 109, 071905, 2016.
[4] M. Miniaci, A. Krushynska, A. S. Gliozzi, N. Kherraz, F. Bosia, and N. M. Pugno, "Design and Fabrication of Bioinspired Hierarchical Dissipative Elastic Metamaterials", Phys. Rev. Applied 10, 024012, 2018.
[5] M. I. Hussein, M. J. Leamy and M. Ruzzene, Appl. Mech. Rev., 66(4), 040802, 2014.
[6] M. I. Hussein, K. Hamza, G. M. Hulbert, R. A. Scott and K. Saitou, Struct. Multidisc. Optim., 31, 60-75, 2006.
[7] A. S. Gliozzi, M. Miniaci, F. Bosia, N. M. Pugno and M. Scalerandi, Appl. Phys. Lett. 107, 161902, 2015.
[8] D. Mousanezhad, S. Babaee, H. Ebrahimi, R. Ghosh, A. S. Hamouda, K. Bertoldi and A. Vaziri, Sci. Rep., 5, 18306, 2015.

DAMPING IN PHONONIC AND ACOUSTIC METAMATERIALS: FROM UNDERSTANDING TO TAILORABLE BEHAVIOR

Anastasiia O. Krushynska[1]
[1]Engineering and Technology Institute Groningen (ENTEG), Faculty of Science and Engineering, University of Groningen, Groningen, the Netherlands

Summary This work is focused on establishing fundamental relations between architecture-driven dynamics of phononic & acoustic metamaterials and material properties of their constituents. First, by considering acoustic waves in thermoset and thermoplastic polymers, we summarize two key structure-driven mechanisms for wave manipulation and investigate the effects of material viscosity on them. Then we introduce a particle wave damping for 3D-printed metamaterials and prove that it has a strong potential for achieving controllable wave dissipation. All the reported results are verified experimentally on full-scale polymeric and metallic samples.

INTRODUCTION

Phononic and acoustic metamaterials are known for their superior abilities to control acoustic and ultrasonic waves at various frequency ranges. During the last three decades, a plethora of fascinating experimental works demonstrated intriguing dynamic phenomena, including wave attenuation at extremely low frequencies, subwavelength focusing and imaging, cloaking, scattering-free and one-way wave propagation, etc. [1]. These and other functionalities arise due to a tailored metamaterial architecture, rather than constituent materials. However, for acoustic waves in solids, material properties can significantly influence wave propagation in metamaterials and even cancel wave manipulation mechanisms induced by architecture. Prominent examples are frequency band gaps in polymeric phononic meta-structures, where material viscosity can shift the band gaps or even completely wash them out [2, 3]. In other cases, wave energy dissipation in a constituent material can be of advantage, as e.g. in metallic phononic structures with Bragg's scattering mechanism, when dissipation losses could be used to decrease a large number of the metamaterial unit cells necessary to reach a certain attenuation level [4].

Proper understanding of the influence of viscoelastic and other nonlinear material properties on the wave dynamics in metamaterials requires a rigorous theoretical treatment, thorough experimental testing and accurate data for all relevant material parameters. In the first part of this talk, we show how this problem can be tackled for phononic structures made of thermoset and thermoplastic polymers.

On the other hand, it is highly desirable to be able to control the level of material damping with the aim to enable even more advanced manipulation of elastic waves in metamaterials. As the material viscosity governed by complex molecular interactions might be very challenging to manipulate (if possible at all), we propose to harness a particle-driven damping widely used in vibration and noise reduction technologies. This mechanism can be easily employed due to recent advances in additive manufacturing techniques allowing to manufacture structures of arbitrary complex shapes. The working principle and potential of the particle-driven damping will be discussed in the second part of this talk.

WAVE DYNAMICS OF VISCOELASTIC POLYMERIC PHONONIC MATERIALS

As the dynamics of elastic waves in phononic and acoustic metamaterials is mainly governed by their tailored architecture, rather than constituents, it is common, in the first approximation, to model the material response as linear elastic neglecting any possible nonlinearities [1]. This approach, however, often fails in case of polymeric materials characterized by frequency-dependent viscoelastic losses [2,3]. Simplified viscoelastic models with a few viscous parameters cannot always capture related viscoelastic effects due to a broad frequency content of the material relaxation moduli commonly expanded over several orders of frequency magnitude, while the use of multi-mode models is restricted either by a lack of experimentally measured relaxation data or limitations of commercial finite-element software packages to deal with complex-valued dynamic characteristics [5]. In overall, it is unclear which material models should be used to correctly describe wave propagation in viscoelastic phononic and acoustic metamaterials.

Here, we present a thorough study of viscoelastic effects in thermoset and thermoplastic polymers on wave attenuation in phononic materials with the Bragg and local resonance wave manipulation mechanisms. The theoretical analysis is based on the in-house numerical framework developed previously to investigate wave dispersion in dissipative phononic meta-structures, which is capable of dealing with arbitrary complex linear viscoelastic models [6], and finite-element transmission simulations performed by means of the COMSOL Multiphysics. The material response is represented by the relaxation moduli accurately measured over the frequency range from 10^{-2} to 10^{7} Hz that distinguishes this study from other works using approximate or limited (in frequencies) data. Based on the obtained results, we derive clear guidelines on the validity of the commonly used simplified viscoelastic models depending on the working frequency ranges of a phononic material and suggest how the structural response can be analysed in the cases when the simplified models are inapplicable. The obtained results are verified in experimental tests on PMMA phononic plates exhibiting band gaps at various frequency scales (see Fig. 1). More details on the experimental measurements are given below.

PARTICLE-DRIVEN WAVE DISSIPATION IN 3D-PRINTED METAMATERIALS

Particle damping is a technique allowing to achieve energy dissipation in a vibrating cavity filled with particles. The damping mechanism, governed by collisions and friction between particles and the cavity walls, is widely used for reduction of vibrations in compressors, gears, and even rocket engines. With the advances in additive manufacturing techniques, the particle-driven damping can easily be implemented in phononic and acoustic metamaterials.

This work introduces the concept of phononic materials with architectural units partially or completely filled with particles. We first design simple solid 3D phononic configurations with the Bragg scattering and local resonance mechanisms and then analyse how the particle-driven damping implemented in various parts of these structures influences their wave attenuation abilities at band-gap frequencies. Careful analysis of the metamaterial microstructure filled with particles allows us to derive useful effective characteristics in order to correctly describe the particle damping at the macroscopic scale. The obtained results, confirmed by experimental measurements on metallic samples, reveal that the designed meta-structures are characterized by enhanced wave dissipation and can also exhibit tailorable energy dissipation by simply varying the volume of cavities filled by particles. Hence, the particle-driven damping opens promising avenues for further improving the control over wave dynamics in phononic metamaterials and their exploitation in multiple engineering applications.

EXPERIMENTAL TESTING

The theoretically derived results on wave dissipation in metamaterials are verified by performing transmission pitch-catch tests on polymeric phononic plates and 3D-printed metallic metamaterial samples (Fig. 2). The specimens are made with a milling machine from pristine PMMA thermoplastic plates and by means of SLM 3D-printing technique from 316L stainless steel, respectively. The wave propagation is excited using either a frequency sweep in a target frequency range by means of an amplified vibration exciter (TIRA, Shaker 51110) glued to the specimen surface, or broadband piezo-transducers at higher frequencies. The measured data are in an excellent agreement with the numerical predictions.

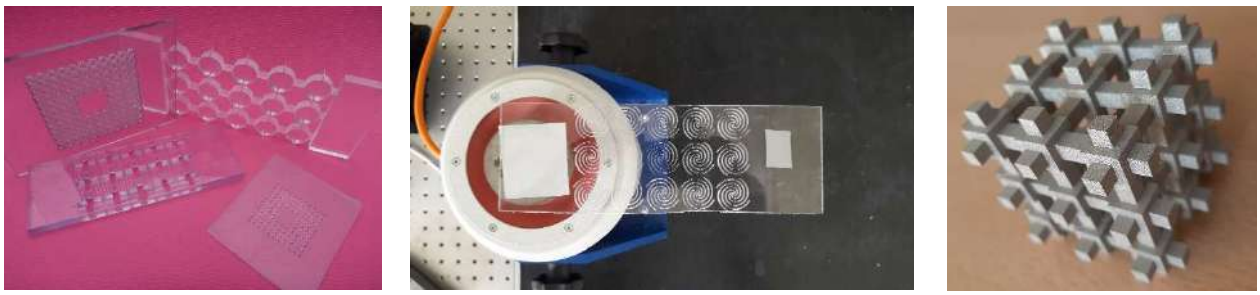

Figure 1. (*from left to right*) Polymeric (PMMA) phononic plates for experimental validation of viscoelastic effects on the dynamics of elastic waves controlled by the Bragg scattering and local resonance mechanisms; a part of the experimental setup for the transmission pitch-catch experiments in a low-frequency sonic frequency range; a metallic (stainless steel 316L) phononic crystal with particle-driven wave attenuation mechanism.

ACKNOWLEDGEMENT

The author would like to thank Profs. F. Bosia, A.S. Gliozzi and M. Scalerandi (Polytechnic University of Turin, Italy) and Dr. S. Ghio and Prof. N.M. Pugno (University of Trento, Italy) for their indispensable contribution in manufacturing of the polymeric samples, experimental testing and their continuous support of this project. Special appreciation goes to Dr. M. Acuautla Meneses, M. Stokroos (Discrete Technology and Production Automation Group, University of Groningen, the Netherlands), and Dr. T. Pijper (Phillips, Innovation cluster Drachten, the Netherlands) for the experimental measurements and manufacturing of the 3D-printed metallic samples.

References

[1] Craster R.V., Guenneau S. Acoustic Metamaterials: Negative Refraction, Imaging, Lensing and Cloaking. Springer Science & Business Media, 2012.

[2] D'Alessandro L., Ardito R., Braghin F., Corigliano A. Low Frequency 3D Ultra-Wide Vibration Attenuation via Elastic Metamaterial. *Sci. Rep.* **9**: 8039, 2019.

[3] Matlack K.H., Bauhofer A., Krödel S., Palermo A., Daraio C. Composite 3D-Printed Metastructures for Low-Frequency and Broadband Vibration Absorption. *Proc. Nat. Acad. Sci.* **113**: 8386-8390, 2016.

[4] Gliozzi A.S., Miniaci M., Krushynska A.O., Morvan B., Scalerandi M., Pugno N.M. Bosia F. Proof of concept of a frequency-preserving and time-invariant metamaterial-based nonlinear acoustic diode. *Sci. Rep.* **9**: 1-9, 2019.

[5] Krushynska A.O., Bosia F., Gliozzi A.S., Krushinsky D., Ghio S., Pigno N.M. Dynamics of dissipative polymeric phononic materials: experimental and numerical study. *Appl. Mech. Rev.*(in preparation).

[6] Krushynska A.O. Kouznetsova V.G., Geers M.G.D. Visco-elastic effects on wave dispersion in three-phase acoustic metamaterials. *J. Mech. Phys. Solids* **96**: 29-47, 2016.

[7] Krushynska A.O., Acuautla Meneses M. Particle-driven attenuation in 3D-printed phononic materials. *J. Acoust. Soc. Am.* (in preparation).

SURFACE WAVES FROM FLEXURAL AND COMPRESSIONAL RESONANCES OF BEAMS

Kim Pham*[1], Jean-Jacques Marigo[2], Agnès Maurel[3], and Sébastien Guenneau[4]
[1] IMSIA, CNRS, ENSTA Paris Tech, 828Bd des Maréchaux, 91732 Palaiseau, France
[2] LMS, Ecole Polytechnique, Route de Saclay, 91120 Palaiseau, France
[3] Institut Langevin, CNRS, ESPCI ParisTech, 1 rue Jussieu, 75005 Paris, France
[4] UMI 2004 Abraham de Moivre-CNRS, Imperial College, London SW7 2AZ, UK

Summary We present a three-dimensional model describing the propagation of elastic waves in a soil substrate supporting an array of cylindrical beams with flexural and compressional resonances. The resulting surface waves are of two types : hybridized Rayleigh waves in the sagittal plane with bandgaps resulting from an interplay between flexural and compressional resonances, and a surface wave with displacements perpendicular to the sagittal plane; this latter wave is the elastic analog of electromagnetic spoof plasmons and it is sensitive to flexural resonances only. Similar, yet quantitatively different, physics is reported in a two-dimensional setting involving resonances of plates.

We consider an array of beams atop a semi-infinite soil substrate $z \in (-\infty, 0)$. The beams are slender bodies, which means that their radius r_b is much smaller than their height h_b and we denote $(\rho_\mathrm{b}, E_\mathrm{b}, \nu_\mathrm{b})$ their mass density, Young's modulus and Poisson ratio. For the soil, $(\rho_\mathrm{s}, \lambda_\mathrm{s}, \mu_\mathrm{s})$ are the mass density and the two Lamé's coefficients. We have shown in [1] that the presence of an array of beams or plates can be encapsulated in effective boundary conditions on the soil surface which read

$$\sigma_{x\alpha}(\boldsymbol{x}, 0) = \mu_\mathrm{s} k_\mathrm{T} \varepsilon \, f_\mathrm{F}(\Omega) \, u_\alpha(\boldsymbol{x}, 0), \quad \alpha = x, y \quad \text{and} \quad \sigma_{zz}(\boldsymbol{x}, 0) = \mu_\mathrm{s} k_\mathrm{T} \varepsilon \, f_\mathrm{C}(\Omega) \, u_z(\boldsymbol{x}, 0), \tag{1}$$

where ω is the frequency, $k_\mathrm{T} = \omega\sqrt{\rho_\mathrm{s}/\mu_\mathrm{s}}$, $\Omega = \omega/\omega_0$ a dimensionless frequency with $\omega_0 = \frac{1}{\mathcal{S} h_\mathrm{b}}\sqrt{\frac{E_\mathrm{b}}{\rho_\mathrm{b}}}$, $\varepsilon = \frac{\theta}{\mathcal{S}}\sqrt{\frac{\rho_\mathrm{b} E_\mathrm{b}}{\rho_\mathrm{s}\mu_\mathrm{s}}}$ a coupling parameter with : for beams (3D) $\mathcal{S} = 2h_\mathrm{b}/r_\mathrm{b}$, $\theta = \pi r_\mathrm{b}^2/a^2$ and for plates (2D) $\mathcal{S} = \sqrt{3(1-\nu_\mathrm{b}^2)}h_\mathrm{b}/r_\mathrm{b}$, $\theta = 2r_\mathrm{b}/a$. The displacements associated to surface waves are written in terms of the elastic potentials $(\varphi, \boldsymbol{\psi})$, with

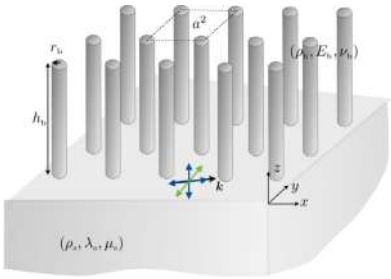

Figure 1: Soil substrate supporting an array of beams with flexural and compressional resonances. Hybridized Rayleigh waves with motions in the sagittal plane (blue arrows) and out-of-plane elastic SPPs (green arrows).

$\boldsymbol{u} = \Re\left[\boldsymbol{\nabla}\varphi + \boldsymbol{\nabla} \times \boldsymbol{\psi}\right]$ and $\boldsymbol{\nabla} \cdot \boldsymbol{\psi} = 0$. Making use of the isotropy of the medium, we define

$$\varphi(\boldsymbol{x}, z) = -\frac{iA}{k} \, e^{k\alpha_\mathrm{L} z + i\boldsymbol{k}\cdot\boldsymbol{x}}, \quad \boldsymbol{\psi}(\boldsymbol{x}, z) = \frac{1}{k}\left(B_n \boldsymbol{n} + B_t \boldsymbol{t} + iB_z \boldsymbol{e}_z\right) e^{k\alpha_\mathrm{T} z + i\boldsymbol{k}\cdot\boldsymbol{x}}, \tag{2}$$

with $B_n + \alpha_\mathrm{T} B_z = 0$, and where $\boldsymbol{k} = k\boldsymbol{n}$ and $\boldsymbol{t} \cdot \boldsymbol{n} = 0$. With β the ratio of the celerities of the Rayleigh wave c and of the bulk shear wave c_T, we have $\beta = \frac{k_\mathrm{T}}{k}$, $\quad 1 - \alpha_\mathrm{T}^2 = \beta^2$, $\quad 1 - \alpha_\mathrm{L}^2 = \xi\beta^2$, where $\xi = \mu_\mathrm{s}/(\lambda_\mathrm{s} + 2\mu_\mathrm{s})$. Doing so provides two families of surface waves. In the sagittal plane, hybridized Rayleigh waves have a dispersion of the form

$$\left(1 + \alpha_\mathrm{T}^2\right)^2 - 4\alpha_\mathrm{T}\alpha_\mathrm{L} + C_\varepsilon(\beta, \Omega) = 0, \quad \text{with} \quad C_\varepsilon(\beta, \Omega) = \varepsilon\beta^3 \left[f_\mathrm{C}\alpha_\mathrm{L} + f_\mathrm{F}\alpha_\mathrm{T}\right] + \varepsilon^2\beta^2 f_\mathrm{C} f_\mathrm{F}\left(\alpha_\mathrm{L}\alpha_\mathrm{T} - 1\right). \tag{3}$$

(where f stands for $f(\Omega)$). Next, displacement perpendicular to the sagittal plane is associated with a surface wave whose dispersion $\beta = \frac{1}{\sqrt{1+\varepsilon^2 f_\mathrm{F}^2(\Omega)}}$, $f_\mathrm{F}(\Omega) \geq 0$, is the elastic analog of electromagnetic spoof plasmons. As one would expect for $\varepsilon = 0$, the classical Rayleigh waves is recovered, and the elastic SPP disappears (with $k = k_\mathrm{T}$). Typical exemples of the dispersion of hybridized Rayleigh waves are reported in Fig. 2 for beams and plates (numerical validations are provided in this case). For plates, the overall agreement between direct numerics and our model is good. In particular, the coexistence of two branches in frequency ranges below the flexural resonances is confirmed. Next, as expected, the dispersion observed for an array of beams significantly differs from that observed for an array of plates.

*Corresponding author. E-mail: kim.pham@ensta-paris.fr

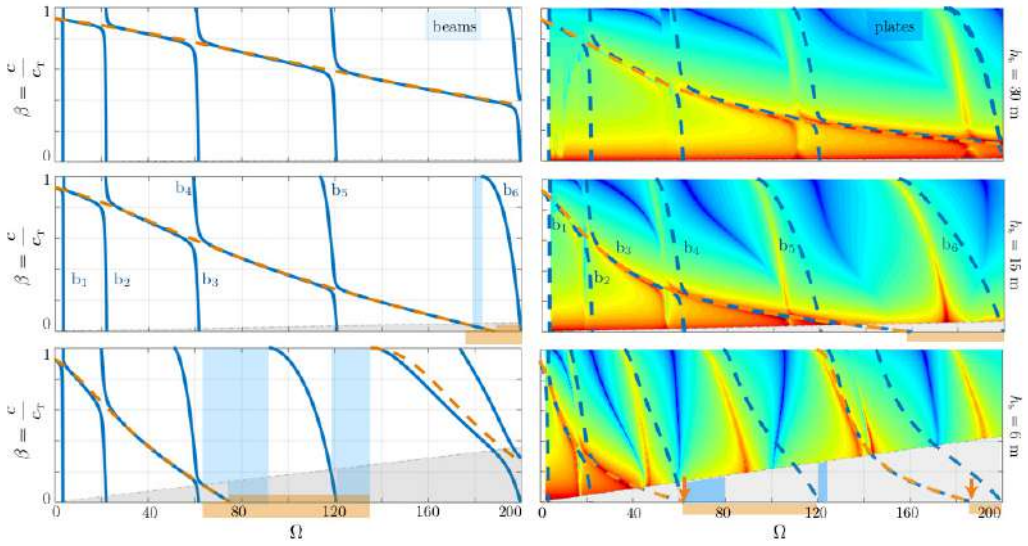

Figure 2: Dispersion of the hybridized Rayleigh wave for 3D beams and 2D plates – dimensionless velocity c/c_T versus $\Omega = \omega/\omega_0$ (blue lines). Dashed red lines show the dispersion produced by the compressional resonances on their own ($f_F = 0$). Bandgaps can be opened by periodicity (light blue region in the Brillouin zone) or they can be intrinsic (light blue region outside of the Brillouin zone, independent of a) and enlarged by periodicity.

The ellipticity χ of surface waves of the Rayleigh type (horizontal to vertical displacement ratio) characterizes the displacements at the soil surface. In the absence of out-of-plane displacements, from (3), it reads

$$\chi = \frac{\alpha_T\beta^2 + \varepsilon\beta f_C(\alpha_L\alpha_T - 1)}{2\alpha_L\alpha_T - (1+\alpha_T^2)} = \frac{2\alpha_L\alpha_T - (1+\alpha_T^2)}{\beta^2\alpha_L + \varepsilon\beta f_F(\alpha_L\alpha_T - 1)}, \tag{4}$$

whose variations versus Ω are reported in Fig. 3 for $h_b = 15$ m (middle panels in Fig. 2). In the reported cases, the branches b_n, $n = 1$ to 5, are below the first compressional resonance. From (4) and (3), these branches have 3 typical points: (i) the starting point ($\beta = 1$) for which $\chi = \varepsilon f_C$ which increases when $n = 1, \cdots, 5$ increases as f_C does; (ii) the frequency at which the wave motion transitions from prograde to retrograde with $\chi = 0$ when $f_F \to \infty$ and this is consistent with (1) which predicts $u_n = 0$ at the flexural resonances, (iii) the ending point for $\beta \to 0$ resulting in $\chi = -1/\xi$ for any branch. Next the branch b_6 appears just before the longitudinal resonance where $f_C \to \infty$ imposes $u_z = 0$. It results high values of χ in the neighbourhood of the singularity and it is worth noting that this affects a branch which is dictated by the interplay of flexural and compressional resonances.

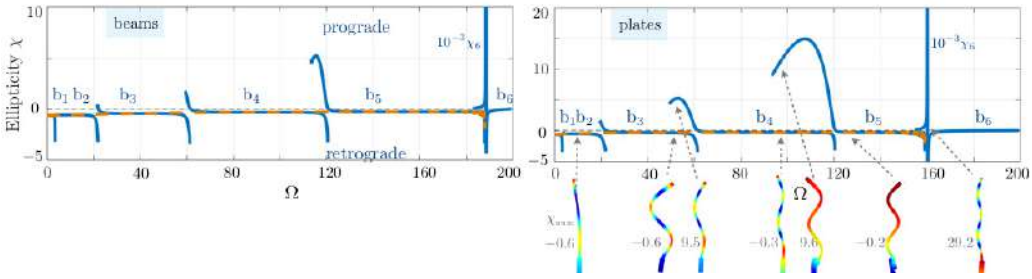

Figure 3: Ellipticity χ of the hybridized Rayleigh waves versus Ω – Blue lines show χ from (4), dashed red lines neglecting the flexion. Insets show the deformations in the plates atop the soil in a single cell.

We shall discuss the following points (i) The hybridized Rayleigh waves have an important part of their spectrum associated with celerities larger than that of the classical Rayleigh waves; (ii) These waves are associated with prograde or retrograde motion at the soil interface with large variations of the ellipticity; (iii) The existence of an out-of-plane surface wave, with infinite ellipticity on its own. This should be useful for the analysis of the displacement components in particular on records of the ambient noise for which the horizontal displacement is the sum of the two contributions [2, 3].

References

[1] J.J Marigo, K. Pham, A. Maurel, and S. Guenneau, arXiv:submit/3006447
[2] E.F. Manea, C. Michel, M. Hobiger, D. Fäh, C.O. Cioflan, and M. Radulian, Geophys. J. Int. **210**(3), 1609-1622 (2017).
[3] M. Lott, P. Roux, S. Garambois, P. Guéguen, and A. Colombi, Geophys. J. Int. **220**(2), 1330-1339 (2019).

PROGRAMMING TEMPORAL MORPHING OF SELF-ACTUATED SHELLS

Ruslan Guseinov[1],Connor McMahan[2],Jesús Pérez[1,3],Chiara Daraio*[2],and Bernd Bickel†[1]
[1]Institute of Science and Technology Austria, Klosterneuburg, Austria
[2]California Institute of Technology, Pasadena, USA
[3]Universidad Rey Juan Carlos, Madrid, Spain

Summary Advances in shape-morphing materials, such as hydrogels, shape memory polymers and light-responsive polymers have enabled prescribing self-directed deformations of initially flat geometries. However, most proposed solutions evolve towards a target geometry without considering time-dependent actuation paths. To achieve more complex geometries and avoid self-collisions, it is critical to encode a spatial and temporal shape evolution within the initially flat shell. Recent realizations of time-dependent morphing are limited to the actuation of few, discrete hinges and cannot form doubly curved surfaces. Here, we demonstrate a method for encoding temporal shape evolution in architected shells that assume complex shapes and doubly curved geometries. The shells are non-periodic tessellations of pre-stressed contractile unit cells that soften in water at rates prescribed locally by mesostructure geometry. The ensuing midplane contraction is coupled to the formation of encoded curvatures. We propose an inverse design tool based on a data-driven model for unit cells' temporal responses.

INTRODUCTION

Morphing flat sheets into complex, three-dimensional geometries is a challenge that has been pursued for centuries by artists, and more recently by mathematicians and scientists. In engineering, the search for materials suitable for such transformations has been motivated by the ease of two-dimensional fabrication, which relies on subtractive processes, such as punching, machining, water jetting or laser cutting. Flat objects can be stacked in volumetrically efficient arrangements, which simplifies transportation and storage. While flat sheets are easy to fabricate and store, many structural and functional applications across scales rely on changing surface curvatures (e.g., tunable mirrors [1, 2] and parabolic antennae [3]). Morphing between flat geometries and desired curved surfaces requires methods for prescribing local deformations.

Here, we show that spatio-temporal information can be embedded in the geometry of architected shells that morph from flat to smooth three-dimensional shapes. This programmed temporal evolution enables reaching target geometries that would be impeded by collisions if shells actuated with uniform or unplanned deformation rates. Furthermore, our shells use polymers that actuate when the temperature in their environment is set to a critical value. At room temperature, they remain flat, storing the energy necessary to drive the deformation.

SPATIO-TEMPORAL PROGRAMMING OF SELF-ACTUATED SHELL MECHANISMS

We propose an inverse design algorithm for shell architectures and the temporal evolution of their shapes (Fig. 1). The algorithm collects user inputs at two stages: the first input is the desired 3D target surface, and the second is the specification of local deformation rates. We term this temporal map input an *actuation time landscape*. The algorithm outputs the mesostructure for initially flat shells that we fabricate and test. These shells have three layers, with a ~ 4.6 mm total thickness. The two outer layers are 3D-printed tessellations of non-uniform unit cells, made of Vero PureWhite (Stratasys). The middle layer is a 0.5 mm thick pre-stretched elastic membrane, which stores the energy required to drive the morphing process. Actuation from the flat to the curved profile is triggered by immersing the shells into $56°$ C water, which causes the outer layers to soften over the course of approximately 30 to 80 s.

The unit cells have a grid spacing of $\sim$ 10 mm, and are composed of cylindrical bases connected at the external shell surfaces by pairs of V-shaped brackets (Fig. 2). The bases serve as attachment points to the elastic membrane and as mounting points for the brackets. The brackets serve as nonlinear springs: they hold the structure flat prior to being placed in water, and then they guide the temporal morphing process, softening at rates determined by their geometric parameters when heated (thicker brackets soften at slower rates). There are also bumpers attached to the bases in the space between the brackets, which collide when the local contraction reaches the target magnitude and control the contact angle between adjacent unit cells. The membrane provides energy for actuation, compressing the brackets as they soften. All of these components play an important role for reaching targeted geometries through spatio-temporal programming. For example, the petalled structure shown in Fig. 3 has been programmed so that the petals reach their target shape sequentially, actuating from smallest to largest. If all petals deformed at the same rate, they would collide and would not reach the target geometry.

We incorporated a discretized mechanical model of our shells in an inverse design algorithm for obtaining desired temporal morphing. Given a target geometry and a smooth time landscape, the algorithm automatically generates the flat shell mesostructure that will produce the corresponding morphing process. The selection of bracket thicknesses is governed by the designer's specification of the actuation time landscape. Thicker brackets soften at a slower rate than

*Corresponding author. E-mail: daraio@caltech.edu.
†Corresponding author. E-mail: bernd.bickel@ist.ac.at.

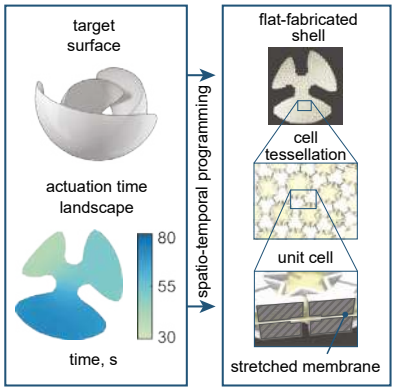

Fig. 1. A user-specified target surface and actuation time landscape are inputs to an inverse design procedure that defines the mesostructure of flat-fabricated shells that morph into the target geometries

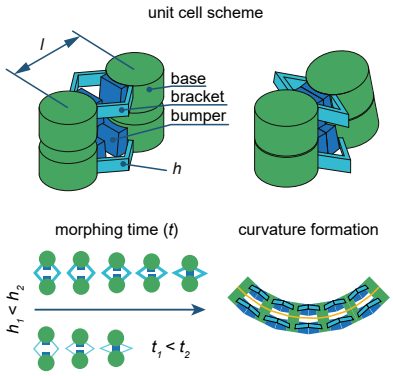

Fig. 2. Each unit cell has an initial central length *l*. Brackets control actuation time through their softening rate, which is controlled by their thickness, *h*, and a set of bumpers prescribe final local curvatures upon collision.

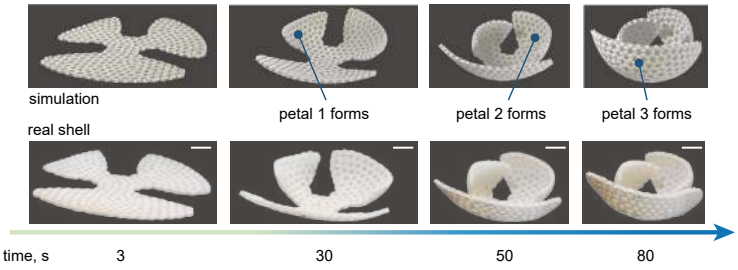

Fig. 3. Morphing of a petalled structure with an actuation time landscape ensuring that larger petals cover their smaller neighbors avoiding collisions on the way. Simulation and experiments are compared at 3, 30, 50, and 80 seconds in water. The structure replicates the encoded actuation time landscape shown in Fig. 1. Scale bars, 3 cm.

Fig. 4. A self-interweaving shell. Scale bar, 3 cm.

narrower ones, enabling distinct target deformation times to be realized in each region of the shell for collision avoidance, visual impression or other desired functionalities. Given that there can be a broad range of morphing sequences that yield certain target geometries, the morphing process can be designed according to the designer's goals by iterating through actuation time landscapes and observing their effect.

We showcase the complexity of achievable shapes through a set of examples, the most challenging of which is the self-interweaving structure shown in Fig. 4.

CONCLUSION

The significance of this method is that it enables collision-avoidance during deformations from flat shapes to curved geometries. We built a design system based on a data-driven mechanical model of mesostructures to predict shape evolution in time, enabling temporal morphing design. Applications of self-actuating shells to biomedical and construction industries are close to becoming reality with the fast advances in this field of study. Further generalizations of our approach to other materials such as liquid-crystal elastomers, bio-compatible polymers, and conventional engineering materials whose properties evolve in time due to other stimuli such as temperature, humidity, light, pH, etc., could enable rapid manufacturing of load-bearing structures that can only assume desired geometries through temporally planned deformations upon deployment as well as robotic materials temporally programmed for a broader range of functionalities.

This work was supported by the European Research Council (ERC) under grant agreement No 715767 - MATERIALIZABLE: Intelligent fabrication-oriented Computational Design and Modeling, by the European Union's Horizon 2020 Marie Sklodowscka-Curie COFUND Action ISTPlus under Grant Agreement No. 754411, by the US Army Research Office Grant W911NF-17-1-0147, and by a NASA Space Technology Research Fellowship.

References

[1] Mark Clampin. Status of the james webb space telescope (jwst). In *Space Telescopes and Instrumentation*, volume 7010, 2008.
[2] Wei Liu and Joseph J Talghader. Current-controlled curvature of coated micromirrors. *Optics letters*, 28(11):932–934, 2003.
[3] E. Peral, S. Tanelli, Z. Haddad, O. Sy, G. Stephens, and E. Im. Raincube: A proposed constellation of precipitation profiling radars in cubesat. In *2015 IEEE International Geoscience and Remote Sensing Symposium (IGARSS)*, pages 1261–1264, July 2015.

DYNAMIC FLOPPY EDGE MODES AND ASYMMETRIC TRANSMISSION IN TOPOLOGICAL LATTICES

Jihong Ma[1], Di Zhou[2], Kai Sun[3], Xiaoming Mao[3], and Stefano Gonella*[4]
[1]Center for Nanophase Materials Sciences, Oak Ridge National Laboratory, Oak Ridge, TN, USA
[2]Department of Physics, Georgia Institute of Technology, Atlanta, GA, USA
[3]Department of Physics, University of Michigan, Ann Arbor, MI, USA
[4]Department of Civil, Environmental and Geo- Engineering, University of Minnesota, Minneapolis, MN, USA

Summary Topological Maxwell lattices are known to support floppy edge modes on selected boundaries according to their polarization vector. For ideal lattices consisting of links connected by perfect hinges, the edge modes occur at zero frequency. For realistic lattices, whose hinges are ligaments with finite bending stiffness, the floppy modes morph into low-frequency edge phonons that coexist with the acoustic bulk modes. In this work, we experimentally document the existence of these modes, we investigate their dependence upon the hinge parameters and we exploit them to realize configurations with low-frequency asymmetric wave transport capabilities.

BACKGROUND INFORMATION

In recent years, substantial efforts have been devoted to applying the conceptual framework of topological states of matter, initially introduced for electronic and quantum systems, to classical mechanical systems. It has been shown that mechanical systems can acquire unconventional mechanical behaviors, such as one-way wave transport characteristics, that are rooted in the topological states of their phonon band structures. An especially interesting family of systems is represented by the so-called *Maxwell lattices* [1], i.e., lattices that contain an equal number of degrees of freedom and constraints in the bulk and, for this reason, are *on the verge of mechanical instability*. For an ideal system consisting of point masses connected by harmonic springs and forming a periodic lattice in d-dimensional space, the condition for a Maxwell lattice is $\langle z \rangle = 2d$, where $\langle z \rangle$ is the mean coordination number. This condition comes from balancing the degrees of freedom per site, d, with the average number of constraints per site, $\langle z \rangle / 2$.

These systems are known to feature topologically protected *floppy modes* (i.e., states of deformation that do not cause stresses in the ligaments and do not cost any energy) [2] and *states of self stress* (i.e., states of stress that are self equilibrated without external forces). These modes can be established either at the lattice *edges* (or boundaries) or at internal *domain walls* (or interfaces) between lattice sub-domains.

A topological invariant $\boldsymbol{R}_{\mathrm{T}}$, called *topological polarization vector*, was introduced by Kane and Lubensky in [3] to characterize the localization of floppy modes and states of self stress. Interestingly, $\boldsymbol{R}_{\mathrm{T}}$ can be constructed using information of the lattice unit cell and can therefore be seen as a *property of the bulk*. Nevertheless, it controls phenomena (e.g., the manifestation of floppy edge modes) *that manifest at the edges*. This fact can be seen as a clear example of the so-called *bulk-edge correspondence*, which is a fundamental principle underpinning many phenomena in topological mechanics, according to which certain classes of phenomena, despite being intimately controlled by the bulk, ultimately manifest at the edges. *Reconfigurable kagome lattices* have also been studied in which, by rotating the triangular elements about the hinges, it is possible to change not only the lattice geometry, but also the polarization vector, turning on/off floppy edge modes as well as dynamically deciding on which edge these modes will be observed.

The static behavior of ideal topological lattices has been extensively studied using ball-and-spring models. In contrast, experimental validations addressing the dynamic behavior of realistic lattices with finite hinges have been much sparser. In this work, we report on computational and experimental work that attempts to fill this gap in the literature.

RESULTS OF NUMERICAL AND EXPERIMENTAL ANALYSIS

We consider a strip of twisted and deformed kagome lattice, as shown in Fig. 1(a). The triangles in the unit cell are connected through thin, yet finite, ligaments, as shown in the inset. For the corresponding ideal lattice, the polarization vector points to the top edge, deeming it as the floppy edge and leaving the bottom edge as the non-floppy, or stiff, boundary. To verify whether the polarization is preserved even in the presence of ligaments at the hinges, we perform a supercell analysis. To this end, we consider a strip of cells spanning from top to bottom edge and we impose Bloch conditions in the direction of the arrow. The super cell band diagram reveals the existence of two low-frequency branches in the frequency range of the non-dispersive region of the canonical bulk acoustic modes. Since these modes do not appear in the band diagram of the unit cell, they cannot be bulk modes. Inspection of the mode shapes for these new branches confirms that they correspond to deformation mechanisms that localize at the edges, deeming them as *edge modes*. Two mode shapes associated with short-wavelength excitations ($\xi \to \pi$, where ξ is the non-dimensional wavenumber) of the lowest edge mode are reported in Fig. 1(b). *In essence, the observed edge modes are the dynamical counterparts of the zero-frequency floppy edge modes of ideal polarized Maxwell lattices, which have "migrated" towards finite frequencies.*

*Corresponding author. E-mail: sgonella0@umn.edu.

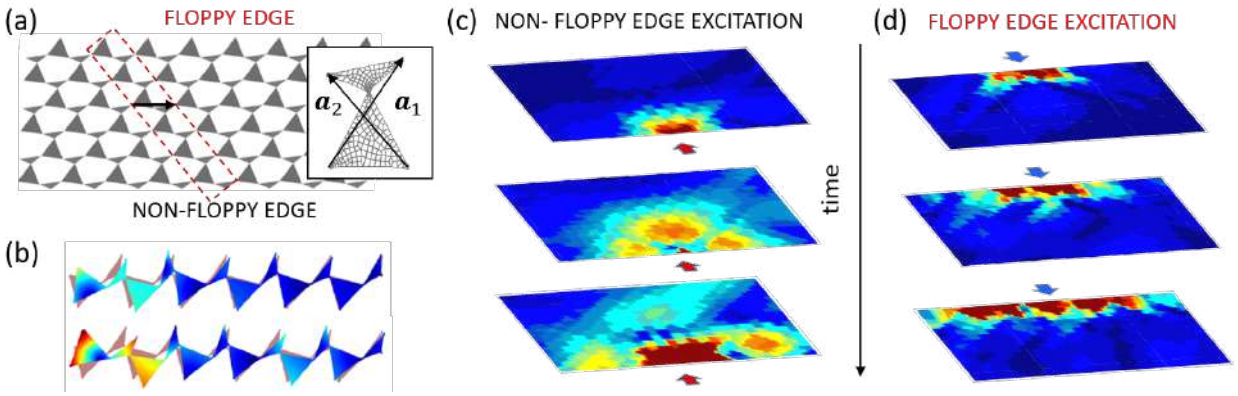

Figure 1: Dynamical behavior of topologically polarized Maxwell lattice. (a) Lattice geometry with unit cell featuring finite-thickness ligament hinge highlighted in the inset, super-cell encapsulated by dashed box, and floppy and non-floppy edges marked. (b) Two short-wavelength mode shapes for the first edge mode, revealing localization of deformation at the floppy edge. (c) Snapshots of wavefield for excitation at the non-floppy edge showing long-wavelength wave propagation in the bulk. (d) Snapshots of wavefield for excitation at the floppy edge, featuring localization at the excited edge.

To confirm the polarized behavior, we conduct dynamical experiments on a lattice specimen obtained from a sheet of acrylonitrile butadiene styrene (ABS) using water-jet cutting [4]. In this physical realization, the ligaments connecting the triangular elements of the kagome cell are slender elements endowed with finite thickness which can deform both axially and flexurally in the plane of the lattice. We excite the specimen with burst excitations in the frequency band of the edge mode. We conduct two separate tests in which we excite the structure from the non-floppy and from the floppy edge, respectively. The in-plane response of the lattice is captured using a 3D Scanning Laser Doppler Vibrometer. When we excite from the non-floppy edge, we mostly activate long-wavelength bulk waves that rapidly transport signal across the specimen, as shown in Fig. 1(c). In contrast, when we prescribe excitation a the floppy edge, we observe an edge wave in which the energy remains localized within a thin strip of lattice at the excited edge, as shown in Fig. 1(d). This behavior can be explained by recalling that, while in both cases the excitation frequency lives in the band of the edge mode, only an excitation prescribed at the floppy edge can directly activate the mechanisms associated with the edge modes.

To show that the asymmetric wave transport is frequency-dependent and confined to low frequencies, we perform a sweep of the carrier frequency in which, for each value of ω, we measure the displacement transmissibility between the excitation edge and the opposite edge. Again, we compare excitations prescribed at the floppy edge against excitations imposed at the non-floppy one. The results suggest that a significant difference in transmissibility between the two scenarios is observed over the entire frequency interval of the edge mode. Above the cut-off of the edge mode branch, the trasmissibility behavior is instead insensitive to the excitation edge selection. To further understand the effect of the bending stiffness of the hinges, we conduct FEM simulations for lattices with identical lattice vectors and connectivity but featuring ligaments with different thickness. The simulations reveal that, with thicker hinges, the polarization is further diluted and considerable leakage is observed in the bulk, where a mixture of bulk and edge phonons is observed.

By means of simulations, we also study the behavior of topologically polarized Maxwell lattices on elastic foundations operating in the nonlinear regime. We show that the simultaneous availability of nonlinearity (from large deformations) and asymmetry in the response (here guaranteed by the asymmetric behavior of the edges) can be leveraged to realize non-reciprocal phonon transmission. The non-reciprocal wave transmission can be switched on/off via topological phase transitions, paving the way to the design of metamaterials that can serve as tunable topologically protected phonon diodes.

CONCLUSIONS

In conclusion, we experimentally demonstrate that the topological characteristics of Maxwell lattices are overall preserved at finite frequencies when the non-ideality of their hinges is relaxed. However, with thicker ligaments, the behavior starts to deviate from that of an ideal topological lattice, as the polarization predicted for ideal lattices becomes progressively less adequate to capture the actual conditions established with continuum elasticity.

The authors acknowledge support of the National Science Foundation (NSF Grant EFRI-1741618).

References

[1] Maxwell J. C. On the Calculation of the Equilibrium and Stiffness of Frames. *Philos. Mag.* **27 (182)**: 294-299, 1864.
[2] Sun K., Souslov A., Mao X., Lubensky T.C. Surface phonons, elastic response, and conformal invariance in twisted kagome lattices. *Proc. Natl. Acad. Sci. U.S.A.* **109 (31)**: 12369-12374, 2012.
[3] Kane C.L., Lubensky T.C. Topological boundary modes in isostatic lattices. *Nat. Phys.* **10**: 39-45, 2014.
[4] Ma J., Zhou D., Sun K., Mao X., Gonella S. Edge Modes and Asymmetric Wave Transport in Topological Lattices: Experimental Characterization at Finite Frequencies. *Phys. Rev. Lett.* **121**: 094301, 2018.

NON-LOCAL DYNAMIC CONTINUALIZATION OF DISCRETE PERIODIC MATERIALS VIA INTEGRAL TRANSFORM

Andrea Bacigalupo[1], Luigi Gambarotta[*1], Marco Lepidi[1] and Francesca Vadalà[1]
[1]Department of Civil, Chemical and Environmental Engineering, University of Genoa, Genoa, Italy

Summary A continualization of lattice-like materials based on a non-local integral down-scaling law is proposed. The difference equation of motion of the Lagrangian system is transformed into an integro-differential equation or a partial differential equation of infinite order. The resulting integral non-local continuum presents a Floquet-Bloch spectrum coinciding with the actual Lagrangian one. By a multi-variate expansion of the kernels of the integro-differential equation and retaining a prescribed number of higher-order terms, the governing equations of the higher order continuum are obtained, which are characterized by non-local constitutive and inertial tensors. Moreover, it is shown that the equivalent continuum governed by this field equations exhibit frequency band structures which are convergent to the actual Lagrangian one in the first Brillouin zone.

INTRODUCTION

The characterization of non-local continua to approximate the dynamic behavior of lattice-like materials presents some critical points regarding the energetic consistency of the equivalent continuum (see for reference [1-4]). To overcome these drawbacks, an energetically consistent continualization scheme has been proposed for beam-lattice materials for the optimal design of hyper-performance wave guides [5]. This approach resulted in a good approximation in simulating both the boundary layer effects and the frequency band structure of 1D beam lattices with lumped mass. In the present work a generalization of the previous formulation [5] is proposed and extended to 2D lattice-like materials.

DISCRETE AND CONTINUUM MODELS

Let us consider the pre-stressed cable net shown in Figure 1.a. The net is made of N pre-stressed massless strings of equal length ℓ connected at the nodes. Each node having mass m undergoes transverse motion and may be subjected to transverse forces. The resulting lattice-like material is characterized by the coordination number n representing the number of strings departing from the reference node $(i_1,...,i_{n/2})$ whose non-dimensional displacement $\psi_{i_1,...,i_{n/2}} = v_{i_1,...,i_{n/2}}/\ell$ is involved in the its dynamic balance equation

$$\begin{aligned}&\alpha_{i_1-1,...,i_{n/2}}\psi_{i_1-1,...,i_{n/2}} + \alpha_{i_1+1,...,i_{n/2}}\psi_{i_1+1,...,i_{n/2}} + \alpha_{i_1,...,i_{n/2}}\psi_{i_1,...,i_{n/2}} + ... + \\ &+\alpha_{i_1,...,i_{n/2}-1}\psi_{i_1,...,i_{n/2}-1} + \alpha_{i_1,...,i_{n/2}+1}\psi_{i_1,...,i_{n/2}+1} + f_{i_1,...,i_{n/2}} = I_\psi \ddot{\psi}_{i_1,...,i_{n/2}}\end{aligned} \quad (1)$$

being $f_{i_1,...,i_{n/2}} = \mathrm{f}_{i_1,...,i_{n/2}}/N$, $I_\psi = m\ell/N$ and $\alpha_{i_1,...,i_{n/2}}$ coefficients depending on the topology of the cable net.

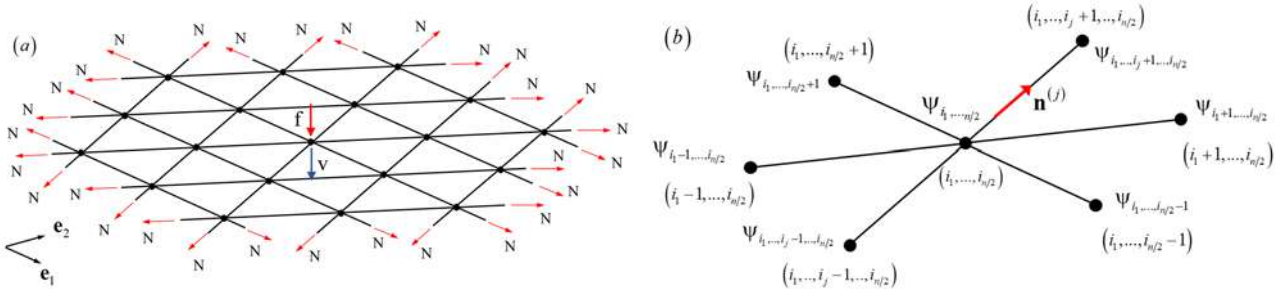

Figure 1. (a) Triangular prestressed cable net; (b) the reference node and the adjacent nodes with the connecting strings.

By introducing the multi-dimensional Z-transform $\hat{\psi}(z_1,..,z_{n/2},t) = Z\left[\psi_{i_1,...,i_{n/2}}\right] = \sum_{-\infty}^{+\infty}\cdots\sum_{-\infty}^{+\infty}\psi_{i_1,...,i_{n/2}}(t)\,z_1^{-i_1}\cdots z_{n/2}^{-i_{n/2}}$, with $z_j \in \mathbb{C}$, equation (1) may be reformulated as follows

$$\begin{pmatrix}\alpha_{i_1-1,...,i_{n/2}}z_1^{-1} + \alpha_{i_1+1,...,i_{n/2}}z_1 + \alpha_{i_1,...,i_{n/2}} + ...\\ ..... + \alpha_{i_1,...,i_{n/2}-1}z_{n/2}^{-1} + \alpha_{i_1,...,i_{n/2}+1}z_{n/2}\end{pmatrix}\hat{\psi}(z_1,..,z_{n/2},t) + \hat{f}(z_1,..,z_{n/2},t) = I\ddot{\hat{\psi}}(z_1,..,z_{n/2},t). \quad (2)$$

Let us consider the mapping $z_j = \exp\left(I\, n_r^{(j)} k_r \ell\right)$ on the unit circle (with $j = 1,..,n/2$ and $r = 1,2$) together with a continuum field $\Psi(x_1,x_2,t)$ in the physical space related through its Fourier transform $\mathcal{F}\left[\Psi(x_1,x_2,t)\right]$ to the Z-transformed nodal displacements defined as

*Corresponding author. E-mail: luigi.gambarotta@unige.it

$$\hat{\psi}\left(k_1,k_2,t\right) = Z\left[\psi_{i_1,\ldots,i_{n/2}}\right]\Big|_{z_j=\exp\left(In_r^{(j)}k_r\ell\right)} \doteq \mathcal{F}\left[\Psi\left(x_1,x_2,t\right)\right] = \hat{\Psi}\left(k_1,k_2,t\right) \quad . \tag{3}$$

As a consequence, equation (2) takes the form of governing equation of an integral non-local continuum as follows

$$\begin{aligned}&\mathcal{F}^{-1}\left[\begin{pmatrix}\alpha_{i_1-1,\ldots,i_{n/2}}\exp\left(-I\,n_r^{(1)}k_r\ell\right)+\alpha_{i_1+1,\ldots,i_{n/2}}\exp\left(I\,n_r^{(1)}k_r\ell\right)+\alpha_{i_1,\ldots,i_{n/2}}+\ldots\ldots+\\ +\alpha_{i_1,\ldots,i_{n/2}-1}\exp\left(-I\,n_r^{(n/2)}k_r\ell\right)+\alpha_{i_1,\ldots,i_{n/2}+1}\exp\left(I\,n_r^{(n/2)}k_r\ell\right)\end{pmatrix}\hat{\Psi}\left(k_1,k_2,t\right)\right]+\\ &+\mathcal{F}^{-1}\left[\hat{F}\left(k_1,k_2,t\right)\right]=I_\psi\mathcal{F}^{-1}\left[\ddot{\hat{\Psi}}\left(k_1,k_2,t\right)\right] \quad .\end{aligned} \tag{4}$$

The dispersion function associated to equation (4) is coincident by definition with the corresponding one of the Lagrangian model. By expanding the kernel in Taylor series and after truncation at the *H* order, a differential equation in terms of the continuum displacement field $\Psi\left(x_1,x_2,t\right)$ is obtained to which corresponds to a Lagrangian function having constitutive potential energy density not positive defined (*standard continualization*). Moreover, such equation presents only local/standard inertial terms. These problems may be circumvented by introducing a proper defined mapping of the transformed displacements $\hat{\Psi}\left(k_1,k_2,t\right)$ in the Fourier space into a new auxiliary regularizing continuum field $\hat{\Psi}^R\left(k_1,k_2,t\right)$ in the same space as follows

$$\hat{\Psi}^R\left(k_1,k_2,t\right) \doteq \prod_{j=1}^{n/2}\frac{\exp\left(In_r^{(j)}k_r\ell\right)-\exp\left(-In_r^{(j)}k_r\ell\right)}{2I\,n_r^{(j)}k_r\ell}\;\hat{\Psi}\left(k_1,k_2,t\right) \quad . \tag{5}$$

In this case a new integro-differential equation is obtained, which involves two kernels: the constitutive and the inertial ones. By expanding the kernels in Taylor series and after truncation at the *H* order, a differential equation in terms of the continuum displacement field $\hat{\Psi}^R\left(k_1,k_2,t\right)$ is obtained to which a Lagrangian function corresponds having both the constitutive potential energy and the kinetic energy density positive defined. In this case also inertial non-locality is consistently obtained (*enhanced continualization*). The frequency dispersive functions in the first Brillouin zone are represented in Figure 2 for the discrete Lagrangian model and the continuum models obtained via *standard* and *enhanced continualization*.

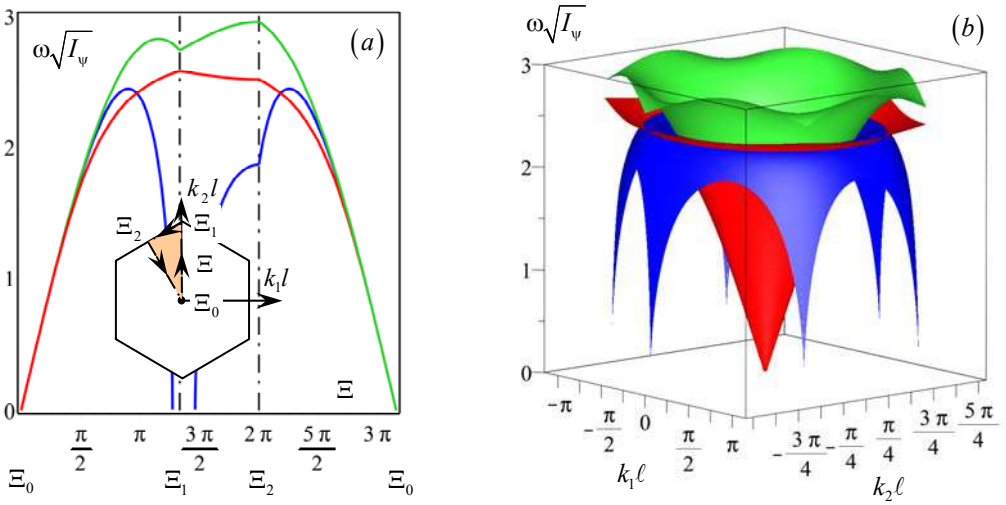

Figure 2. Frequency dispersive functions of the triangular pre-stressed cable net: Lagrangian model (green); 4th order standard continualization (blue); 4th order enhanced continualization (red).

Acknowledgements

The authors acknowledge financial support of MIUR in the framework of the research MIUR Prin15 project 2015LYYXA8, Multi-scale mechanical models for the design and optimization of micro-structured smart materials and metamaterials, coordinated by prof. A. Corigliano.

References

[1] Rosenau P., Dynamics of dense lattices, Phys. Rev. B, **36**: 5868-5876, 1987.

[2] Bacigalupo A., Gambarotta L., Wave propagation in non-centrosymmetric beam-lattices with lumped masses: discrete and micropolar modelling, *Int. J. Sol. and Struct.*: **118-119**: 128-145, 2017.

[3] Bacigalupo A., Gambarotta L., Dispersive wave propagation in two-dimensional rigid periodic blocky materials with elastic interfaces, *J. Mech. Phys. Sol.*, **102**: 165-186, 2017b.

[4] De Domenico D., Askes H., Nano-scale wave dispersion beyond the First Brillouin zone simulated with inertia gradient continua, *J. App. Phys.*, **124**: 205107, 2018.

[5] Bacigalupo A., Gambarotta L., Generalized micropolar continualization of 1D beam lattice, *Int. J. Mech. Sci.*, **155:** 554-570, 2019.

MICROSCALE BISTABLE TENSEGRITY STRUCTURES

Zacharias Vangelatos[1], Andrea Micheletti[2], Costas Grigoropoulos[1], and Fernando Fraternali[3]
[1]Department of Mechanical Engineering, University of California, Berkeley, Berkeley, CA, USA
[2]Department of Civil and Computer Science Engineering, University of Rome Tor Vergata, Rome, Italy
[3]Department of Civil Engineering, University of Salerno, Fisciano (Salerno), Italy

Summary We design and fabricate through multiphoton lithography microscale tensegrity lattices that exhibit bistable mechanical response. The examined structures tesselate tensegrity prisms in the three-dimensional space. Such units undergo a snapping twisting transformation between two stable configurations under compression loading. In situ indentation tests show the activation of the snapping event at the end of a primary softening response branch in the examined lattices, and the repetition of such a transition under loading-unloading cycles. The presented numerical and experimental results lead us to conclude that multiphoton lithography offers an accurate procedure to fabricate multi-cell tensegrity lattices with multi-stable response, which may feature unconventional static and dynamic responses, energy absorption capacity and solitary wave dynamics.

FABRICATION OF MICROSCALE TENSEGRITIES

The structures examined in the present study were fabricated by multiphoton lithography [1] using the experimental setup shown in Fig. 1. The employed material is a hybrid organic-inorganic material Zr-DMAEMA consisting of 70 wt% zirconium propoxide, 10 wt% (2-dimethylaminoethyl) methacrylate (DMAEMA) (Sigma-Aldrich), and 20 wt% ASTM type II deionized, distilled water. Briefly, 1.4 ml of 3-(trimethoxysilyl)propyl methacrylate (MAPTMS) (Sigma-Aldrich) were first mixed with 0.14 gr of hydrochloric acid in a vial. Then, in another vial, 137.7 μl of DMAEMA were mixed with 0.66 ml of zirconium (IV) propoxide solution containing 70 wt% 1-propanol. After intermixing the two mixtures, they were placed in a vial diluted with 0.2 ml of distilled water and 0.016 gr of photoinitiator consisting of 4,4′-bis(diethylamino)benzophenone (Sigma-Aldrich). Before the fabrication, the experimental material was placed on glass substrates and heated at 40 ºC for 2 hr in vacuum. Details about the material synthesis and experimental setup have also been reported elsewhere [1]. It should be noted that multiphoton lithography is the only fabrication technique with the resolution needed to construct the structures examined in this study. The only challenge with this technique is the perception of the 3D space when designing these geometries. All of the metamaterial structures were fabricated several times to ensure repeatability. The unit cells height was 10 μm and the beam diameter was 0.5 μm. The structures were fabricated with constant cross sections, since variance of the thickness at the hinges resulted in inept photopolymerization of the structure. Figure 2 illustrates the fabricated structures.

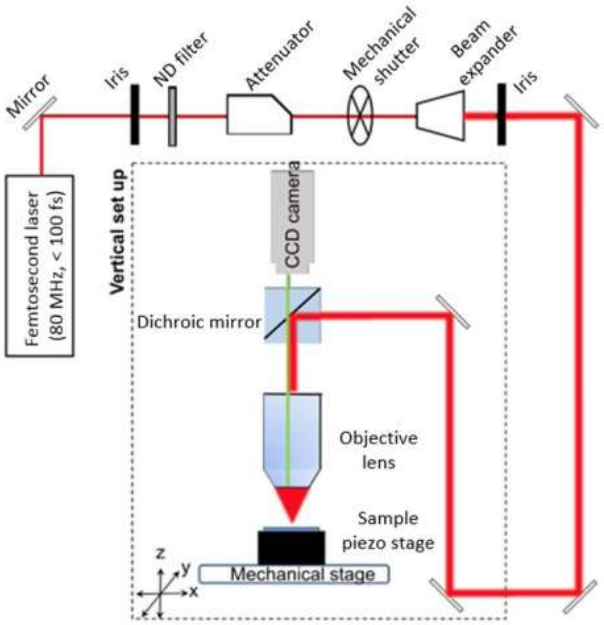

Figure 1. Schematic of the multiphoton lithography experimental setup.

MECHANICAL TESTING

In situ indentation tests were performed with a nanoindentation apparatus (PI 85 SEM PicoIndenter, Hysitron) placed inside a scanning electron microscope (FEI Quanta 3D FEG), thus enabling high-precision nanomechanical testing and real-time recording of the deformation. The molybdenum tip (Model # 72SC-D3/035 (407A-M)) was cut to a diameter of

75 μm by a femtosecond laser and was finished with a Focused Ion Beam (FIB) to be flat. The maximum tip displacement was set at 10 μm. A triangular force function with loading and unloading rates both set at 0.2 μm/s was used in all the tests. To ensure the repeatability of the measurements, each experiment was repeated at least three times. The force-displacement plots of 3D assemblies of bistable tensegrity prisms reveal a softening behavior during loading form the first stable configuration, up to a snapping event that drives the structure into a second stable configuration (Fig. 3). The twisting mechanism that characterizes such a transition is preserved after unloading and during repeated loading-unloading cycles.

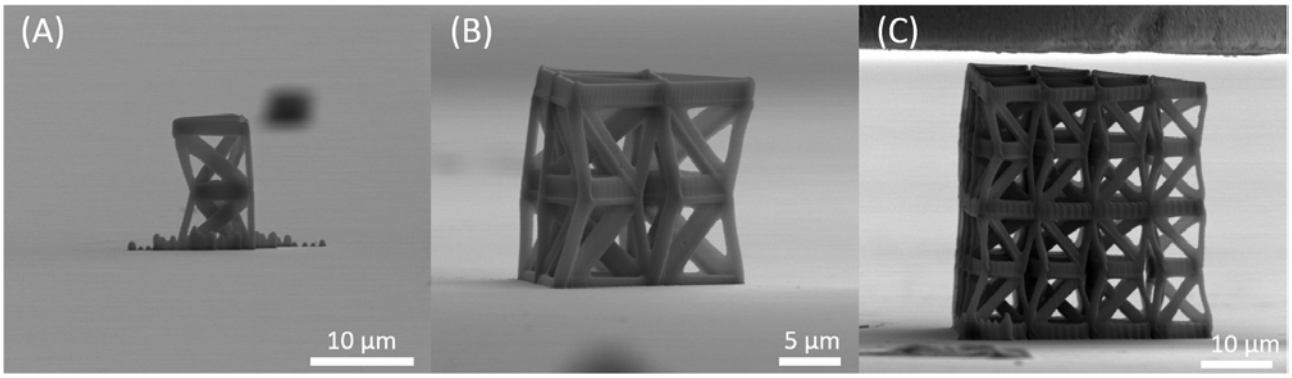

Figure 1. Fabricated Geometries of Structures. (A) Individual unit cells. (B) Arrays of 3 unit cells in one layer. (C) Arrays of two layers with ten unit cells at each layer.

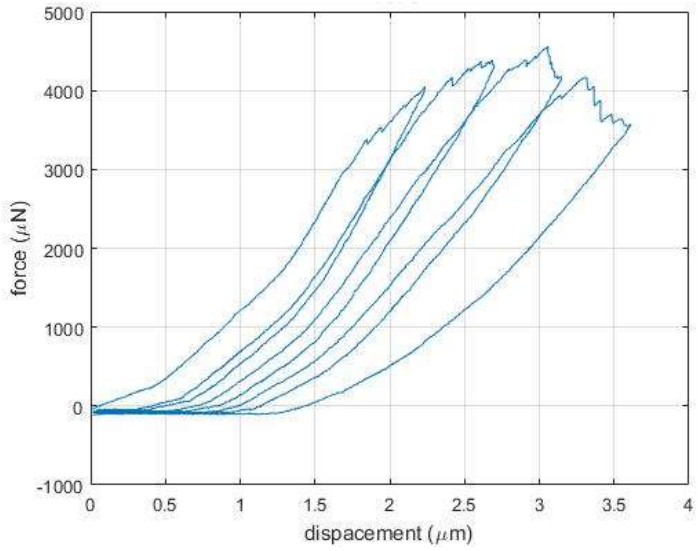

Figure 3. Force-displacement plot of an in-situ indentation test.

CONCLUSIONS

The results of the present study demonstrate that fabrication of multistable tensegrity lattices is highly feasible via multiphoton lithography, and pave the way to the fabrication of multi-cell tensegrity metamaterials with unprecedented static and dynamic responses [3-5] at the microscale.

.

References

[1] Ovsianikov, A, et al... Ultra-low shrinkage hybrid photosensitive material for two-photon polymerization microfabrication. *ACS Nano* **2**: 2257–2262, 2008.

[2] Vangelatos Z, Komvopoulos K, Grigoropoulos C. Vacancies for controlling the behavior of microstructured three-dimensional mechanical metamaterials. *Math. Mech. Solids* **24**: 511-524, 2018.

[3] Fraternali, F., Carpentieri, G., Amendola, A., Skelton, R.E., Nesterenko, V.F. Multiscale tunability of solitary wave dynamics in tensegrity metamaterials. *Appl. Phys. Lett.* **105**: 201903, 2014.

[4] Fraternali, F., Carpentieri, G., Amendola, A. On the mechanical modeling of the extreme softening/stiffening response of axially loaded tensegrity prisms. *J. Mech. Phys. Solids* **74**: 136-157, 2015.

[5] Micheletti, A., Ruscica, G., Fraternali F. On the compact wave dynamics of tensegrity beams in multiple dimensions. *Nonlin. Dynam.* **98**: 2737–2753, 2019

SELF-LOCKING ORIGAMI MECHANICAL METAMATERIALS: PROGRAMMABLE STIFFNESS AND PARAMETER IDENTIFICATION

Hongbin Fang*[1], Zuolin Liu[2], and Jian Xu[2]
[1]Institute of AI and Robotics, Fudan University, Shanghai, China
[2]School of Aerospace Engineering and Applied Mechanics, Tongji University, Shanghai, China

Summary Origami has been recognized as an important resource for designing mechanical metamaterials. Based on the single-collinear degree-4 vertex origami tessellation, it is found that each unit cell can self-lock at a non-flat configuration. Experiments and numerical analyses show that by switching the deformation modes of the constituent cell from pre-locking folding to post-locking pressing, its stiffness experiences a sudden jump. Such a stiffness jump is generalized to a multi-segment piecewise stiffness profile in a multilayer mechanical metamaterial. Note that for a given self-locking origami metamaterial, the constitutive relation (including the model and the parameters) is always completely opaque and unmeasurable. Hence, based on the piecewise linear assumption, a *physically-interpretable* neural-fuzzy network is built to construct the model and identify the unknown parameters.

INTRODUCTION

Single-collinear degree-4 vertex origami unit would self-lock at a non-flat configuration owing to the collision of facets. This property can be utilized to develop self-locking origami mechanical metamaterials. We show that kinematically, self-locking origami mechanical metamaterials possess wide design space to adjust its foldability and relative density [1,2]. Experiments and finite element analyses are combined to demonstrate that by switching the deformation modes of the constituent cell from pre-locking folding to post-locking pressing, which essentially, is a phase change, its stiffness would experience a sudden jump. By tessellating multiple layers into an n-layer metamaterial, an n-segment piecewise stiffness profile can be achieved. Furthermore, by strategically switching the constituent cells' deformation modes through active methods, the n-layer metamaterial's stiffness is controllable among $2n$ target stiffness values [2].

Note that practically, for a finished self-locking origami mechanical metamaterial, the number of locking points, the positions of locking points, and the stiffness value in each deformation stage are always difficult to be accurately obtained a priori through simple measurements, which makes the constitutive relation (i.e., the force-deformation profile) completely or partly opaque. This arouses interests in adopting inverse approaches, i.e., dynamic identification methods, to precisely estimate the parameters and build the model. Aiming at this specific problem, the piecewise linear constitutive relation is determined using a physically-interpretable neural-fuzzy network [3].

LOCKING-INDUCED PROGRAMMABLE PIECEWISE STIFFNESS

A single self-locking origami cell would experience two deformation modes that are qualitatively different when being compressed: the pre-locking folding mode and the post-locking pressing mode (Fig. 1(a)). In the folding mode, the cell exhibits relatively low stiffness that originates from the rotational stiffness of the creases; while in the pressing mode, the cell receives a significant increase in stiffness that comes from the bending or twisting of the origami facets. By connecting n origami cells in series by assuming force balance at the connections, a self-locking origami structure can be obtained (Fig. 1(b)).

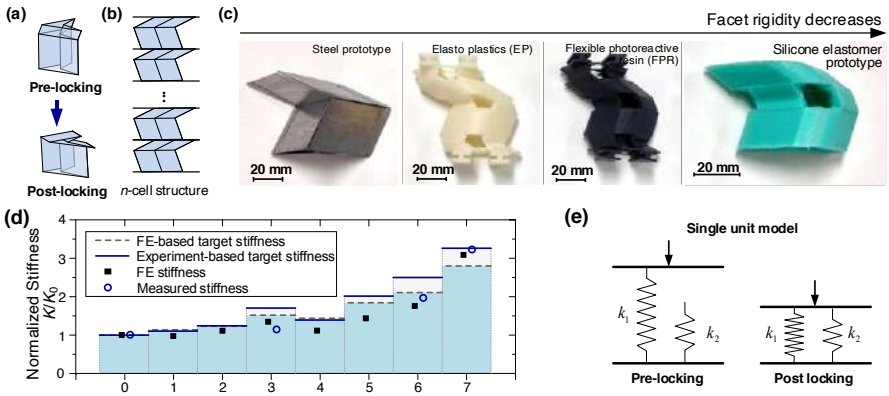

Figure 1. Self-locking origami mechanical metamaterials. (a) A single unit at the pre-locking and the post-locking modes; (b) a n-cell self-locking origami structure; (c) experimental prototypes made of different materials; (d) FE and experimental results; (e) equivalent lumped mass model of a single unit.

Theoretically, if without any internal actuation or control to individually deform the constituent cells, the overall structure can exhibit n+1 stiffness values in a passive compression/tension process. Each time when a constituent cell reaches or leaves its self-locking configuration, the overall stiffness of the structure will undergo a jump. On the other

* Corresponding author. E-mail: fanghongbin@fudan.edu.cn.

hand, if internal actuations are applied, each constituent cell's folding and locking can be actively controlled. In such a scenario, the overall structure is capable of reaching 2^n stiffness values by strategically switching the constituent cells' deformation modes between pre-locking folding and post-locking compressing.

Based on different materials and via different methods, proof-of-concept unit prototypes are fabricated (Fig. 1(c)). Particularly, quasi-static tests and finite element analyses are performed on a 3-layer prototype made of flexible photoreactive resin (FPR) via 3D printing. The predicted 4 (n+1=4) stiffness segments in a passive compression process and the predicted 8(2^n=8) stiffness segments in an active folding process are verified (Fig. 1(d)). Moreover, to quantify such piecewise stiffness profile, an equivalent spring model is also developed (Fig. 1(e)).

IDENTIFICATION OF THE PIECEWISE LINEAR CONSTITUTIVE RELATION USING A PHYSICALLY-INTERPRETABLE NEURAL-FUZZY NETWORK

The self-locking origami metamaterial can be utilized as nonlinear damper, where the load mass may be subjected to force excitation. In such a scenario, the number and positions of the non-smooth points and the linear parameters of each segment of the piecewise-linear constitutive relation is completely unknown; they need to be determined via dynamic identifications.

In this research, after processing the data based on B-Spline Galerkin finite element and integration by parts, a local linear neural-fuzzy network (LLNFN) is built (Figure2). The LLNFN consists of three layers: the input layer, the hidden layer that symbolizes the fuzzy rules, and the output layer. Numerical experiments show that the built network could effectively determine the form and the parameters of the piecewise-liner constitutive relation. Moreover, unlike conventional neural network that the components are not physically interpretable, here, the constructed neural network possesses specific physical meaning of its components: the number of neurons relates to the number of piecewise segments (i.e., the number of self-locking origami cells), the coefficients of the local linear models relate to the parameters of the constitutive relation in each segment (i.e., the pre-locking and post-locking stiffness of each self-locking origami cell), and the validity functions relate to the positions of non-smooth points (i.e., locking position of the origami cell).

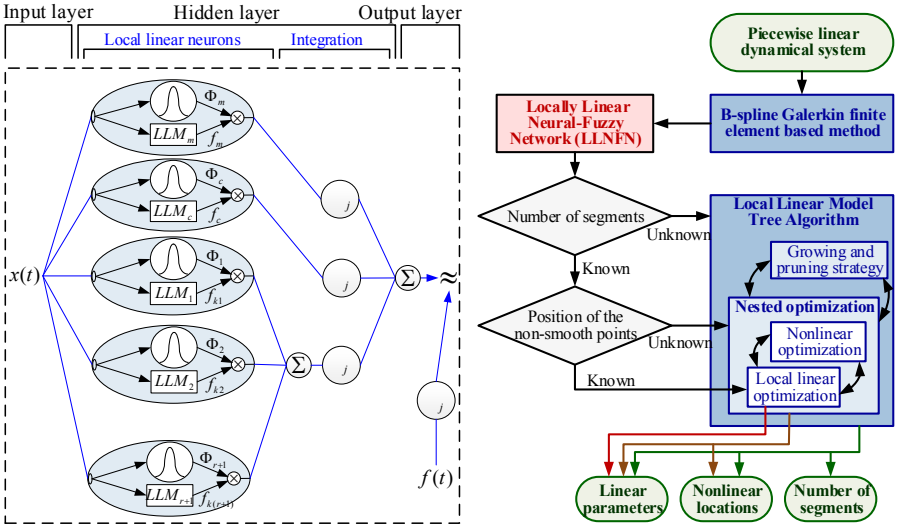

Figure 2. The constructed neural-fuzzy network used for identifying the unknown piecewise linear constitutive relation of the self-locking origami structure.

CONCLUSIONS

Through experimental and numerical efforts, we demonstrate that the self-locking degree-4 vertex origamis provide a new platform for the design of metamaterials with programmable kinematic and mechanical properties, including programmable deformability, programmable density, and programmable stiffness. The programmability originates from the locking and the locking-induced stiffness jump of the non-flat-foldable origami. On the other hand, acquiring the constitutive force-deformation relations of the self-locking origami structures is of practical importance for applying them into engineering systems, especially for dynamic applications. This is achieved in this research through a physically-interpretable neural-fuzzy network. This research would therefore establish a solid foundation for exploring the mechanical and dynamical properties of the self-locking origami metamaterials, and meanwhile, significantly advance their engineering applications [4].

ACKNOWLEDGMENTS

This research was supported by the National Natural Science Foundation of China under award No. 11902078 and No. 11932015, and the Major Research Plan of the National Natural Science Foundation of China under grant no. 91748203.

References

[1] Fang H., Li S., and Wang K.W. *Proc. R. Soc. A Math. Phys. Eng. Sci.*, **472**, 20160682, 2016.
[2] Fang H., Chu S. A., Xia Y., and Wang K.W. *Adv. Mater.*, **30**, 1706311, 2018.
[3] Liu Z., Fang H., and Xu J. *Neural Networks*, **116**, 74-87, 2019.
[4] Li S., Fang H., Sadeghi S., Bhovad P., and Wang K.W., *Adv. Mater.*, **31**,1805282, 2019.

ELASTIC METASURFACES FOR WAVE MANIPULATION AND ENERGY HARVESTING

Jacopo M. De Ponti*[1,2], Andrea Colombi [3], Raffaele Ardito [1], Francesco Braghin [2], Alberto Corigliano [1] and Richard V. Craster [4,5]
[1]Department of Civil and Environmental Engineering, Politecnico di Milano, Milano, Italy
[2]Department of Mechanical Engineering, Politecnico di Milano, Milano, Italy
[3]Department of Civil, Environmental and Geomatic Engineering, ETH Zürich, Zürich, Switzerland
[4]Department of Mechanical Engineering, Imperial College London, London, United Kingdom
[5]Department of Mathematics, Imperial College London, London, United Kingdom

Summary Precise control of elastic waves along surfaces is a challenge for many applications in the field of mechanical vibrations, ultrasonic inspection and energy harvesting. Graded arrays of rods on elastic substrates recently revealed superior performances for broadband wave trapping and mode conversion. In this study, we present elastic metasurfaces able to govern waves at different scales and to increase energy harvesting using the Rainbow effect. The efficiency of the proposed metasurfaces is supported by analytical, numerical and experimental results, demonstrating the energy harvesting advantages of such designs.

INTRODUCTION

Metamaterials concepts are receiving increasing popularity for wave control across much of physics and engineering in electromagnetism, optics, acoustics and elasticity. While the momentum initially focused on the subwavelength bandgaps generated by the resonance, the research has delivered new forms of control, encompassing tailored graded designs to obtain spatially varying refractive index, wide bandgaps and mode conversion [1-3]. To capitalize on recent elastic metamaterial designs, energy harvesting is an attractive application [4] useful to self-power small electronic components, avoiding periodic battery replacement and chemical waste.

RESULTS

Starting from the seminal work on the resonant metawedge that supports both conversion and broadband reflection [2], we have restricted the problem to the case of a plate with graded rod-like resonators. Because each rod has a different resonance frequency, trapping varies spatially according to the frequency content of the incident wave, giving rise to the Rainbow effect [5]. By grading the array from short to tall resonators the group velocity tends to zero at the turning point

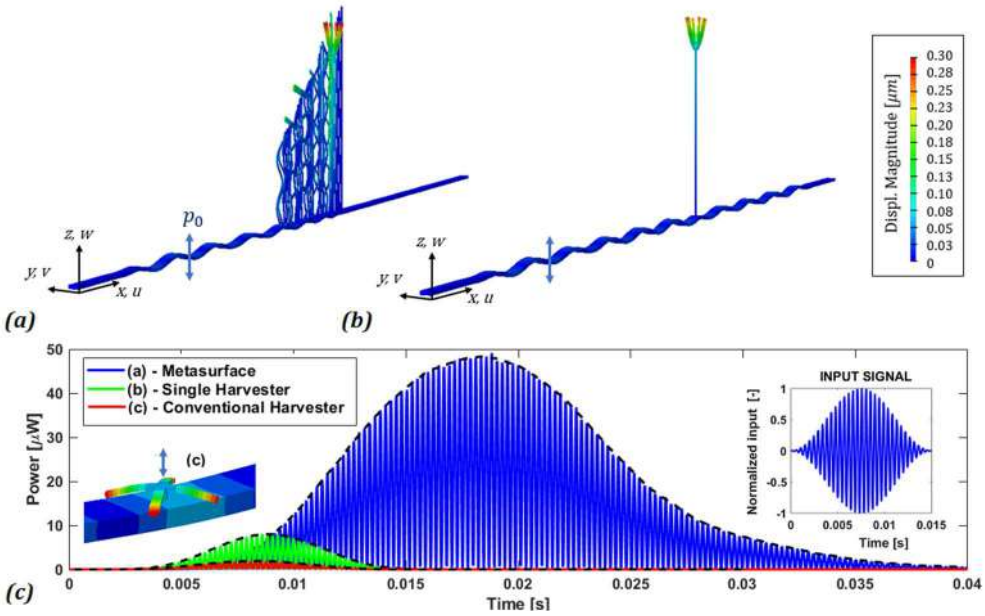

Figure 1. Harvester on a plate strip with (a), and without (b), the metasurface at time t = 10 ms. Electrical power for a maximum input acceleration of 1g at 2.15 kHz with, and without, the metasurface and compared to conventional cantilever beam scheme (c).

and the wave slows down and therefore spends time in the vicinity of the resonator feeding energy into it. Introducing in the array a properly designed piezo-augmented resonator is it possible to increase harvesting efficiency with respect to

*Corresponding author. E-mail: jacopomaria.deponti@polimi.it

conventional solutions (Figure 1) [6].
A similar effect can be obtained with horizontal beams directly attached on the plate strip, obtaining a device easy to manufacture also at microscale (Figure 2).

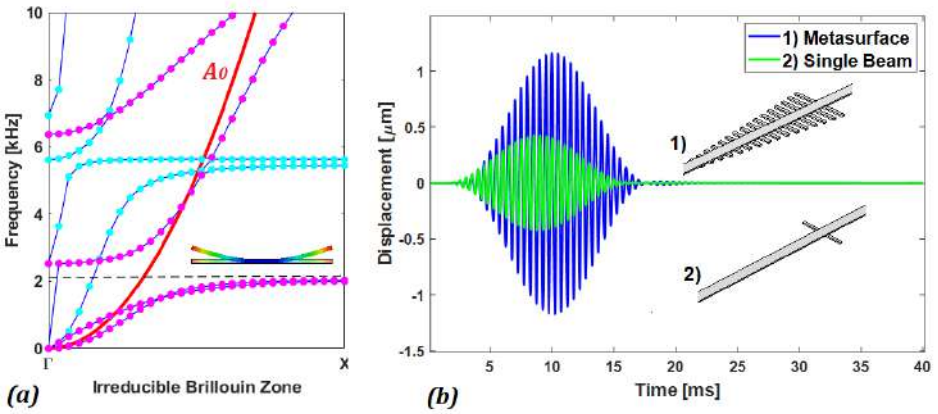

Figure 2. Rainbow trapping with horizontal beams directly attached on a plate strip. Dispersion curves (colors represent wave polarization: purple vertical, light blue horizontal) for a unit cell with a beam at right and left side (a). Tip displacement of the same beam inside 1) and outside 2) the metasurface (b) at 2.15 kHz.

After an introduction of the control capacity of graded elastic metasurface, the talk will present the numerical optimization of the trapping capacity and the results from an experiment in the kHz range. The experimental setup will be discussed in detail, showing the importance of a correct realization of Absorbing boundaries using the Acoustic Black Hole effect (Figure 3) [7].

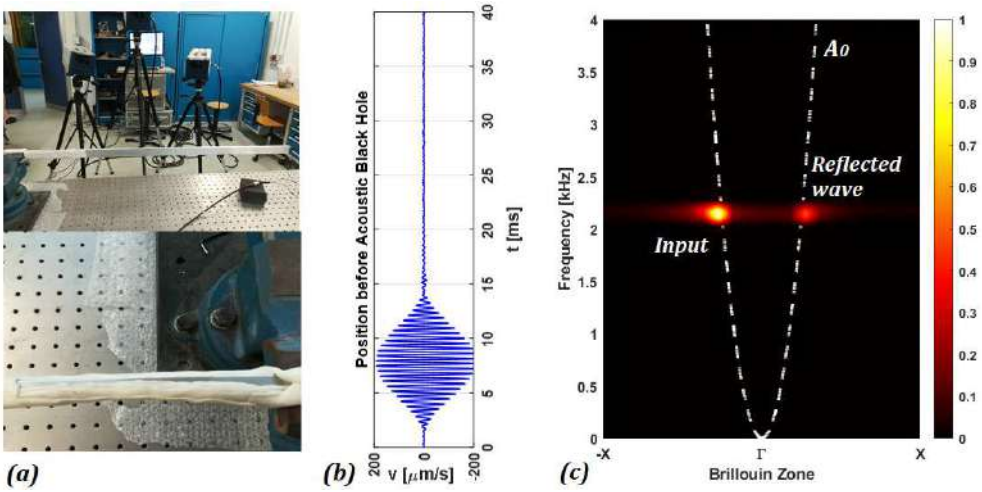

Figure 3. Experimental results on the Acoustic Black Hole. Experimental setup and Acoustic Black hole at the edge of the plate strip (a), velocity field before the Black Hole (b) and experimental dispersion showing the reflected wave reduction (c)

CONCLUSIONS

Efficient wave manipulation for enhanced energy harvesting is demonstrated using graded metasurfaces with different configurations. Energy is trapped in the position of the harvester, providing strong amplification. Broadband behavior can be achieved placing more than one harvester or exploiting nonlinear effects.

References

[1] A. Colombi, "Resonant metalenses for flexural waves", *J. Acoust. Soc. Am.* 140, EL423, 2016.
[2] A. Colombi, D. Colquitt, P. Roux, S. Guenneau, and R.V.Craster. "A seismic metamaterial: The resonant metawedge", *Sci. Rep.*, 6:27717, 2016.
[3] E. A. Skelton, R V Craster, A Colombi, and D J Colquitt, "The multi-physics metawedge: graded arrays on fluid-loaded elastic plates and the mechanical analogues of rainbow trapping and mode conversion", *New Journal of Physics*, 20(5):053017, 2018.
[4] M Carrara, MR Cacan, J Toussaint, MJ Leamy, M Ruzzene, A Erturk,, "Metamaterial-inspired structures and concepts for elastoacoustic wave energy harvesting", *Smart Materials and Structures* 22 (6), 065004 , 2013.
[5] K. L. Tsakmakidis, A. D. Boardman, and O. Hess, "Trapped rainbow storage of light in metamaterials", *Nature*, 450:397–401, 2007.
[6] J. M. D. Ponti, A. Colombi, R. Ardito, F. Braghin, A. Corigliano, R. V. Craster, "Graded elastic metasurface for enhanced energy harvesting", *New Journal of Physics* (2019), URL http://iopscience.iop.org/10.1088/1367-2630/ab6062
[7] D.J. O'Boy, V.V. Krylov, V. Kralovic, "Damping of flexural vibrations in rectangular plates using the acoustic black hole effect", Journal of Sound and Vibration 329 (2010) 4672–4688 (1)

ELASTIC METASURFACES

Richard Craster[1,2]
[1]Department of Mathematics, Imperial College London, London, UK
[2]Department of Mechanical Engineering, Imperial College London, London, UK

Summary This talk will provide an overview of elastic metasurfaces in the context of phononic crystals, gradient index lenses, transformation optics and resonant graded surface arrays and will draws upon analogies in the field of optics, photonic crystals and electromagnetism.

INTRODUCTION

Elastic metasurfaces can be constructed in several different ways, some of which bear more relation to phononic crystals than to metamaterials based upon resonances. I will cover both and discuss their relative merits, as shown in Fig. 1, and discussed in [1], it is possible to use surface resonance to tune and manipulate Rayleigh waves.

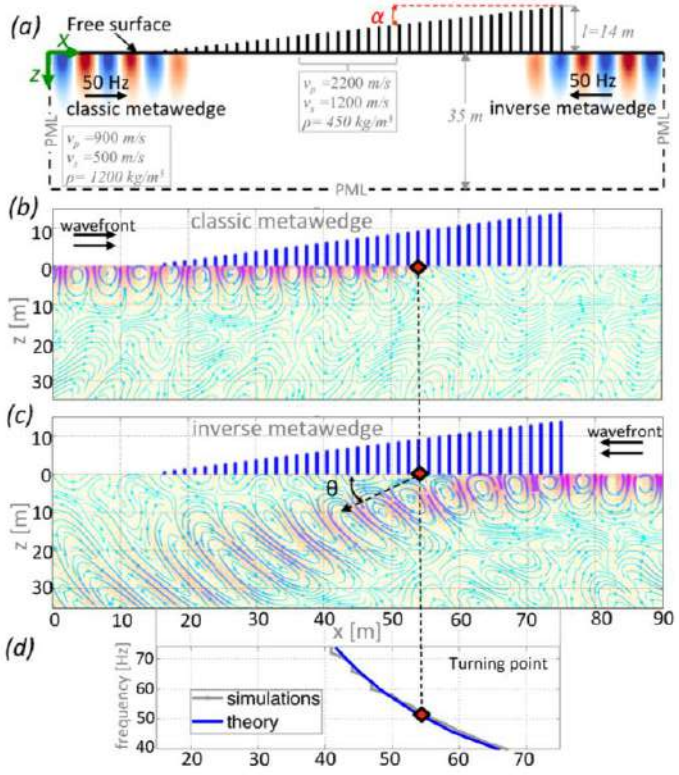

Figure 1. The metawedge from [1] is shown in (a)-(d) showing the effect of grading a surface array of rods that have resonances. In particular (b) shows frequency spatial selection and the ability to separate out frequency, panel (c) shows conversion from surface Rayleigh wave into bulk shear waves.

It is also possible to manipulate surface Rayleigh waves using ideas from transformation optics, this is an approach that has several merits. An initial attempt to steer surface waves using Luneburg lenses is in [2] and one aim of this talk is to discuss this approach in more detail.

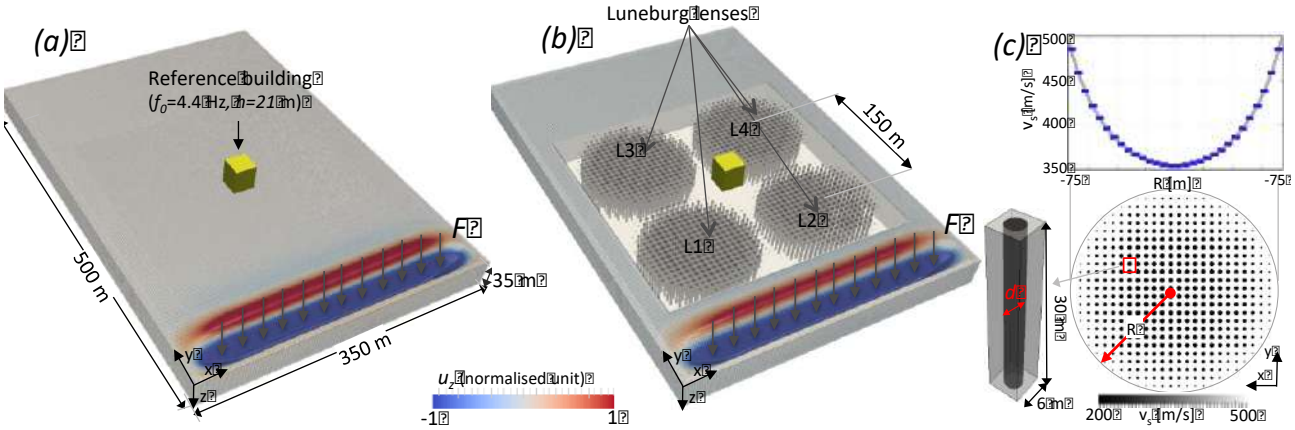

Figure 2. Using an arrangement of Luneburg lenses to steer surface elastic Rayleigh waves.

References

[1] A. Colombi, D. Colquitt, P. Roux, S. Guenneau, R. V. Craster, Scientific Reports, 6, 27717, 2016
[2] A. Colombi, D. Colquitt, S. Guenneau, P. Roux, and R. V. Craster, Scientific Reports, 6, 25320 2016

A TRULY RE-PROGRAMMABLE MECHANICAL METAMATERIAL USING MAGNETIC ACTUATION

Tian Chen*[1,2], Mark Pauly[2], and Pedro Reis[1]
[1]Flexible Structures Laboratory,Ecole Polytechnique Fédérale de Lausanne,Switzerland
[2]Computer Graphics and Geometry Laboratory,École Polytechnique Fédérale de Lausanne,Switzerland

Summary Mechanical metamaterials are engineered systems that exhibit physical properties that may not exist in conventional bulk materials. The periodicity or the internal unit structure of a mechanical metamaterial is often optimized for specific mechanical behavior. During fabrication, such architected materials are effectively "programmed" once and for all, and their functionality cannot be altered *a posteriori*. Here, we show a truly programmable metamaterial with fixed periodicity and internal structure, but each unit cell can be independently and reversely programmed on-demand. Programming of individual cells is achieved by switching between the equilibrium states of a bistable elastic shell using magnetic actuation. A tiled sheet of such unit cells exhibits tunable mechanical properties, including its stiffness, and yield strength and ultimate strength.

MAGNETIC PROGRAMMING OF UNIT CELLS

We propose a novel concept for a mechanical metamaterial that combines the versatility of a standard metamaterial (*i.e.*, periodicity and identical internal structure) with the targeted functionality of an architected structure [1], and with the novelty of repurposing after fabrication. In our system, each unit cell be switched to undergo a state change independently of the nearby cells, which we refer to as *programming*. Similar to a computer function, once programmed, the metamaterial maps the input (*e.g.*, quasi-static compression) to a set of desired outputs (*e.g.*, effective properties such as stiffness, yield strength, and ultimate strength). For a different set of desired outputs, the our metamaterial can be reprogrammed, reversibly, and on demand.

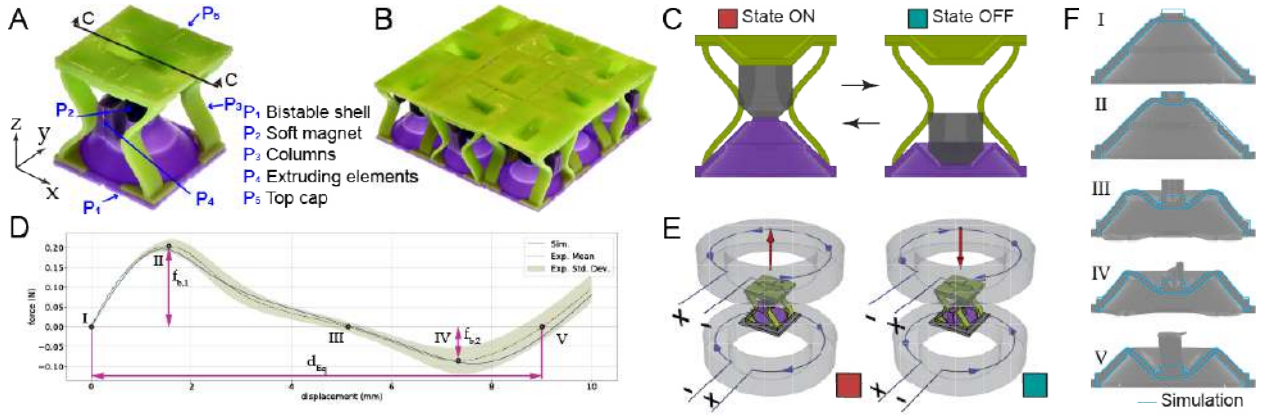

Figure 1: Design of one unit cell and its programming procedure. A: Fabricated and assembled unit cell using VPS. B: An tiled array of the unit cell. C: Geometry of the two equilibrium states. D: Force displacement behavior of the elastic bistable shell. E: Programming method using electromagnetic coils. F: CT imagery and simulation of the bistable shell under increasing displacement.

The unit cell of our elastic system (Fig. 1A) comprises a bistable elastic shell P_1, a soft magnet P_2, two set of naturally-curved columns P_3, two extruding elements P_4 and the top cap P_5. All parts are cast using Vinyl Polysiloxane (VPS) with the molds printed using Stereolithography. Each unit cell is cubic in shape and has an edge length of $30\,\mathrm{mm}$. Multiple cells can be tiled in a square lattice configuration (Fig. 1B). Each unit cell has two stable equilibrium states (Fig. 1C). The ON state is the state at which the unit cell is fabricated. In this state, the soft magnet is in contact with the top cap, and the columns are in contact with the extruding side elements. In the OFF state, the bistable shell snaps to a second equilibrium configuration, and both contacts are lost. Magnetic interactions are leveraged to switch between the ON and the OFF states, thereby enabling programming[2].

Programming is performed by moving the entire array on the x-y plane so that the intended unit cell is positioned at the center of the two electromagnetic coils of radius R and a separation distance of $\sqrt{3}R$. This is referred to as the Maxwell configuration. With equal current in the two coils, a constant gradient field ∇B is created. Consequently, a constant force f_m is experienced by the soft magnet. Hence, the behavior is analogous to a force boundary condition, *i.e.*, when the force at the apex of the shell reaches $f_{\mathrm{b},1}$, it will snap beyond the second equilibrium position. When the field is turned off, the shell will return to the second equilibrium (Fig. 1D). By reversing the polarity, the opposite effect is achieved. Since the

*Corresponding author. E-mail: tian.chen@epfl.ch

absolute value of $f_{b,1}$ is higher than that of $f_{b,2}$ and ∇B is constant within the predicted movement of the soft magnet, the magnetic field only needs to deliver a force greater than $f_{b,1}$ to enable programming and reprogramming. The dimensions of the elastic shell are optimized to maximize $f_{b,1}$ so long as it is lower than f_m. The optimized design allows for the ratio $f_{b,2}/f_{b,1}$ to be increased so that the stability of the second equilibrium state is maximized and to maximize d_{Eq} to widen the difference in mechanical behavior. X-ray micro computed tomography (μCT) is used to obtain a volumetric scan of the sample and help validate Finite Element Modeling (FEM) predictions (Fig. 1F).

MECHANICAL BEHAVIOR OF THE METAMATERIAL

Both a single unit cell and the assembled square array of 3×3 unit cells are tested under quasi-static cyclic compression from 0 to a strain of 0.26 at a rate of $1\,\mathrm{mm\,s^{-1}}$. Our results show a significant difference between the mechanical behavior of the two states in the quantities of interest, namely, stiffness, yield, and ultimate strength (Fig. 2A). Two topological changes contribute to this difference. Firstly, the switchable contact of the center (soft magnet and the bistable shell) to the top cap allows for the load to be carried axially, instead of only through bending of the columns (Fig. 2B, LP_1). Secondly, the confinement of the extruding elements exerted by the two columns again creates an axial load path (Fig. 2B, LP_2). Note that boundaries of the unit cell do not experience significant strain, and remain compatible with neighboring cells.

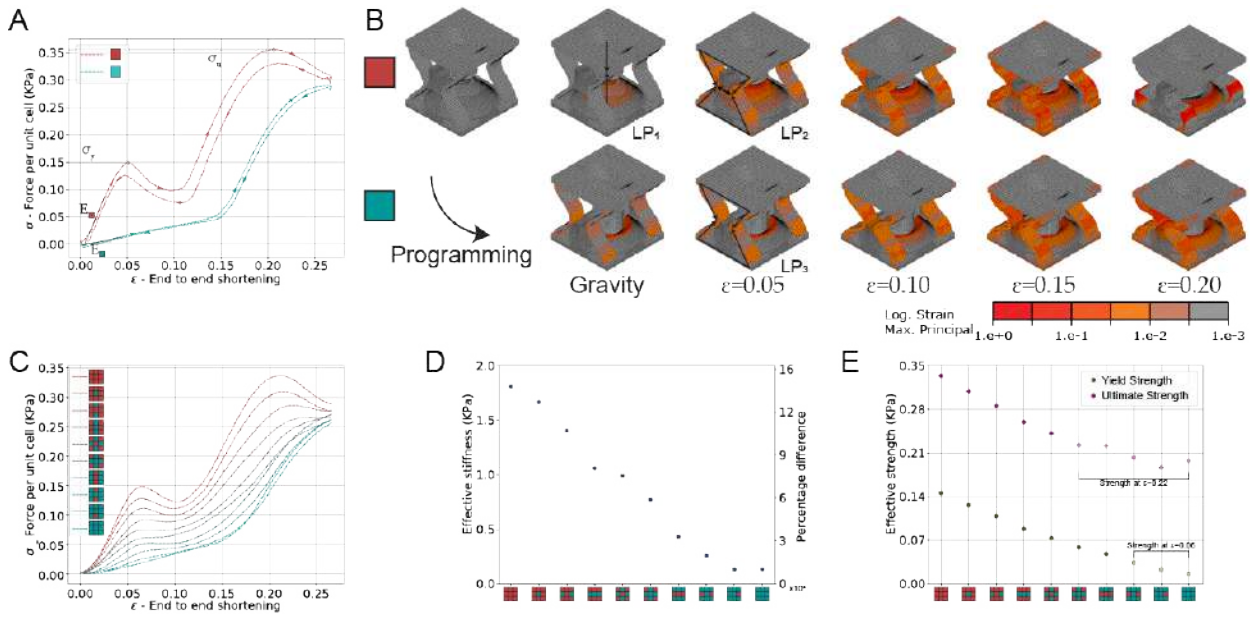

Figure 2: Mechanical response of the metamaterial under a compressive displacement. A. Behavior of one unit cell in both ON and OFF states. B. Corresponding simulation of a single unit cell, showing principal strains at different compression. C. Behavior of a 3×3 array in all possible combinations. D. Effective stiffness of each combination. E. Effective yield and ultimate strength of each combination.

As in a computer program, the execution of a function should not change the function itself, *i.e.* the programming should not be undone under compression. In our system, the programming procedure also involves a compressive load on the bistable shell. Nonetheless, due to the interaction between the buckled columns and the extruding element upon compression of the entire unit cell, these two processes are decoupled. Load and unloading of a unit cell in either state show a reversible stress-strain behavior with small loss due to viscoelasticity (Fig. 2A).

The loading part of the behavior of a 3 by 3 array (Fig. 2C) show interpolations between the two states of ON and OFF, thereby enabling a finer tunability of properties. All 9 combinations of the states are tested, with programming done with coils installed on the Instron testing machine. The stiffness is calculated by finding the maximum gradient prior to the yield. A near linear increase is observed as more unit cells are switched from the OFF to the ON state (Fig. 2D). The maximum increase is approximately $1500\,\%$. Similar tunability is exhibited with yield and ultimate strength. Note that these quantities cannot be unambiguously defined if most unit cells are in the OFF state. Therefore end-to-end shortening strain of 0.06 and 0.22 are used to provide a measure of the yield and ultimate strength respectively.

References

[1] Coulais, C., Teomy, E., de Reus, K., Shokef, Y., and van Hecke, M., Combinatorial design of textured mechanical metamaterials. *Nature.* **535**:7613, 2016.

[2] Bilal, O.R., Foehr, A., and Daraio, C., Reprogrammable Phononic Metasurfaces. *Adv Mater.* **29**:39, 2017.

[3] Clausen, A., Wang, F., Jensen, J.S., Sigmund, O., and Lewis, J.A., Topology Optimized Architectures with Programmable Poisson's Ratio over Large Deformations. *Adv Mater.* **27**:37, 2015.

ONE-WAY FLEXURAL WAVES IN PLATES WITH CHIRAL RESONATORS

Giorgio Carta*[1], Daniel J. Colquitt[2], Alexander B. Movchan[2], Natasha V. Movchan[2], and Ian S. Jones[3]
[1]Department of Mechanical, Chemical and Materials Engineering, University of Cagliari, Cagliari, Italy
[2]Department of Mathematical Sciences, University of Liverpool, Liverpool, UK
[3]Mechanical Engineering and Materials Research Centre, Liverpool John Moores University, Liverpool, UK

Summary In this contribution, we show how flexural waves can be forced to propagate in a single preferential direction within a thin elastic plate. This phenomenon is attained by introducing a periodic system of chiral resonators, consisting of elastic beams connected to gyroscopic spinners. The junction conditions between the beams and the plate are derived analytically by means of asymptotic techniques and employing the new concept of "logarithmic rotational spring". One-way wave propagation is generated by a time-harmonic force at the interface between two sub-domains of the structure, where the gyroscopic spinners rotate in opposite directions. The proposed system is versatile, as the direction of propagation and the frequency at which the phenomenon is observed can be varied by changing the rotations of the gyroscopic spinners.

INTRODUCTION

Phononic crystals and elastic metamaterials have received increasing attention from the scientific community in recent years [1]. In this context, chirality (the property of an object that cannot be superimposed onto its mirror image) has been used to design auxetic media [2] and alter the dispersive features of discrete systems [3]. Generally, these structures are geometrically chiral. In this paper, we consider an active chiral system, where chirality is induced by the mechanical action of gyroscopic spinners.

The aim of the present paper is to show the possibility of generating flexural waves in an elastic plate that propagate in one direction only. One-way edge modes immune to backscattering were firstly observed in photonic crystals and associated with the quantum Hall effect [4]. In elasticity, topologically protected edge and interfacial modes have been realised, for example, in plates [5, 6, 7, 8, 9] and lattices [10, 11, 12, 13]. Here, we exploit the preferential directionality conferred by gyroscopic spinners to create one-way interfacial waves in an elastic plate.

MODEL DESCRIPTION: PERIODIC ARRAY OF CHIRAL RESONATORS CONNECTED TO A PLATE

The system under consideration is illustrated in Fig. 1a. It consists of an elastic plate, connected to a doubly-periodic array of chiral resonators, represented by elastic beams whose tips are attached to gyroscopic spinners. The latter are solids of revolution characterised by mass m, moments of inertia I_1 and I_0 (about the axis of revolution and about the two perpendicular axes passing through the spinner's base, respectively) and gyricity Ω, representing the sum of the spinner's initial precession and spin rates. In [14] it is proved that the gyricity remains constant during the spinner's motion. The junction conditions between the beam and the plate are derived analytically in [15].

The elementary cell of the periodic system is assumed to be square. The band diagram of the system is determined for the case when the gyricity is uniform throughout the structure. Fig. 1b shows the band diagram when $\Omega = 100$ rad/s along the path Γ X M Y Γ, drawn in the inset. In the computations, the side length of the elementary cell is taken as $L = 2$ m. The plate has thickness $h = 0.01$ m, Young's modulus $E_\mathrm{p} = 70$ GPa, Poisson's ratio $\nu_\mathrm{p} = 0.3$ and density $\rho_\mathrm{p} = 2700$ kg/m^3. The beams have length $l = 1$ m, circular cross-section of radius $a = 0.02$ m, and the same elastic constants and density as the plate. The gyroscopic spinners are characterised by $m = 1$ kg, $I_0 = 4$ kg m^2 and $I_1 = 2$ kg m^2.

From Fig. 1b, it can be noticed that a narrow stop-band appears at low frequencies. The eigenmodes of the periodic cell for a given wave vector and frequency exhibit rotation of the beam around the z-axis. In addition, we note that the directions of rotation of the beam for two eigenmodes above and below the stop-band are opposite. This behaviour is exploited to create unidirectional waves, as discussed in the following.

ONE-WAY LOCALISED WAVES PRODUCED BY A TIME-HARMONIC FORCE

We consider a plate divided into two sub-domains, where the gyroscopic spinners rotate in opposite directions (see Fig. 1a). The system is excited by a time-harmonic force, applied at the upper end of a beam close to the interface between the two sub-domains. If the frequency of the force is taken inside the stop-band, for instance $\omega = \omega^* = 19.8$ rad/s (refer to Fig. 1b), waves are likely to propagate along the interface, in one specific direction.

In the numerical simulations, performed in the finite element software *Comsol Multiphysics*, the plate is made of 50×50 elementary cells. In order to avoid reflections of waves at the boundaries, PML (*Perfectly Matched Layers*) are inserted near the edges of the computational model. Fig. 1c presents the colour map of the plate's transverse displacement amplitude W_p due to a force of amplitude 1 N. It is apparent that waves propagate only to the left of the force and are localised at the interface.

*Corresponding author. E-mail: giorgio_carta@unica.it.

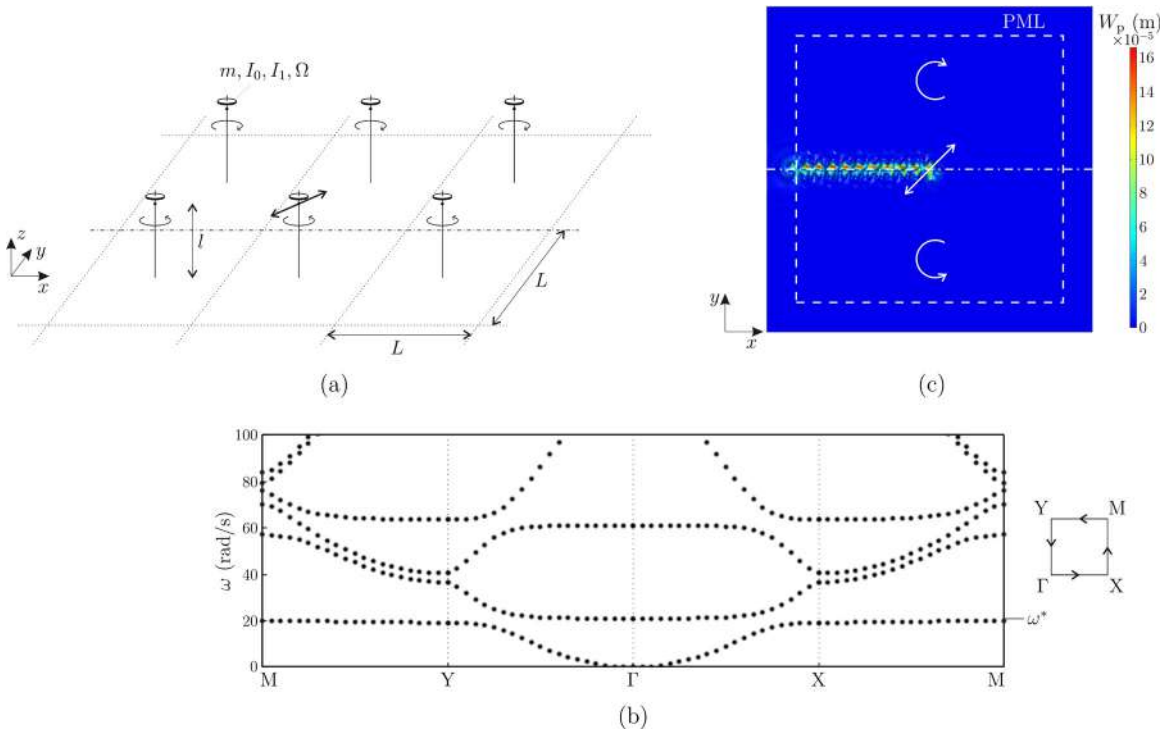

Figure 1: (a) Plate connected to a doubly-periodic array of beams with gyroscopic spinners; (b) band diagram of the periodic system along the path Γ X M Y Γ; (c) displacement amplitude field produced by a time-harmonic force with frequency ω^*, indicated in (b).

CONCLUSIONS

The results of Fig. 1 demonstrate that the proposed system, consisting of a plate attached to a doubly-periodic array of chiral resonators, is capable of supporting one-way interfacial waves. The model is flexible in that the same phenomenon can be replicated at different frequencies and with opposite direction of propagation by changing the value or the sign of the gyricity Ω. More sophisticated models can be designed and constructed, such as the system described in [16], incorporating double resonators made of two beams and two gyroscopic spinners.

We envisage that the chiral structure described here can have important applications in mechanical and civil engineering, for the control of vibrations in structural systems and mechanical elements.

References

[1] Laude V. Phononic Crystals: Artificial Crystals for Sonic, Acoustic, and Elastic Waves. De Gruyter Studies in Mathematical Physics 26, Walter de Gruyter GmbH, Berlin/Boston 2015.
[2] Prall D., Lakes R. S. Properties of a chiral honeycomb with a Poisson's ratio of −1. *Int. J. Mech. Sci.* **39**: 305-314, 1997.
[3] Spadoni A., Ruzzene M., Gonella S., Scarpa F. Phononic properties of hexagonal chiral lattices. *Wave Motion* **46**: 435-450, 2009.
[4] Raghu S., Haldane F. D. M. Analogs of quantum-Hall-effect edge states in photonic crystals. *Phys. Rev. A* **78**: 033834, 2008.
[5] Pal R. K. , Ruzzene M. Edge waves in plates with resonators: an elastic analogue of the quantum valley Hall effect. *New J. Phys.* **19**: 025001, 2017.
[6] Jin Y., Torrent D., Djafari-Rouhani B. Robustness of conventional and topologically protected edge states in phononic crystal plates. *Phys. Rev. B* **98**: 054307, 2018.
[7] Makwana M. P., Craster R. V. Geometrically navigating topological platonic modes around gentle and sharp bends. *Phys. Rev. B* **98**: 184105, 2018.
[8] Makwana M. P., Craster R. V. Designing multi-directional energy-splitters and topological valley supernetworks. *Phys. Rev. B* **98**: 235125, 2018.
[9] Chaplain G. J., Makwana M. P., Craster R. V. Rayleigh-Bloch, topological edge and interface waves for structured elastic plates. *Wave Motion* **86**: 162-174, 2019.
[10] Wang P., Lu L., Bertoldi K. Topological phononic crystals with one-way elastic edge waves. *Phys. Rev. Lett.* **115**: 104302, 2015.
[11] Nash L. M., Kleckner D., Read A., Vitelli V., Turner A. M., Irvine W. T. M. Topological mechanics of gyroscopic metamaterials. *Proc. Natl. Acad. Sci.* **112**: 14495-14500, 2015.
[12] Garau M., Carta G., Nieves M. J., Jones I. S., Movchan N. V., Movchan A. B. Interfacial waveforms in chiral lattices with gyroscopic spinners. *Proc. Roy. Soc. A.* **474**: 20180132, 2018.
[13] Garau M., Nieves M. J., Carta G., Brun M. Transient response of a gyro-elastic structured medium: Unidirectional waveforms and cloaking. *Int. J. Eng. Sci.* **143**: 115-141, 2019.
[14] Nieves M. J., Carta G., Jones I. S., Movchan A. B., Movchan N. V. Vibrations and elastic waves in chiral multi-structures. *J. Mech. Phys. Solids* **121**: 387-408, 2018.
[15] Carta G., Colquitt D. J., Movchan A. B., Movchan N. V., Jones I. S. Chiral flexural waves in structured plates: Directional localisation and control. Accepted in *J. Mech. Phys. Solids*, 2020.
[16] Carta G., Colquitt D. J., Movchan A. B., Movchan N. V., Jones I. S. One-way interfacial waves in a flexural plate with chiral double resonators. *Phil. Trans. R. Soc. A* **378**: 20190350, 2019.

PERIODIC GEOMETRIC TRANSFOMATION FOR OUT-OF-PLANE SHEAR WAVES

Bibinur Meirbekova[1,2] and Michele Brun*[1]
[1]Department of Mechanical, Chemical and Material Engineering, University of Cagliari, Cagliari 09123, Italy
[2]Department of Mechanics and Mathematics, Al-Farabi Kazakh National University, Almaty 050040, Kazakhstan

Summary A two-dimensional periodic geometric transformation is considered for the problem of out-of-plane shear wave propagation in an elastic media. The transformation leads to the design of a doubly periodic particulate medium with a system of anisotropic and inhomogeneous interfaces surrounding the void or rigid inclusions. The dynamic properties of the system are determined comparing the dispersion properties before and after the geometric transformation.

The analysis of dispersive properties reveals the invariance of the dynamic behavior for a "regular" transformation, but also the possibility to obtain new effects for "overlapping" and "unfolding" transformations.

Due to periodicity, it is possible to cloak an arbitrarily large region with multiple large holes, or to obtain a highly reflective interface in presence of holes of negligible size.

DOUBLY PERIODIC GEOMETRIC TRANSFORMATIONS

Geometric transformation techniques have been extensively applied to design cloaking system capable to hide defects. The basic idea is that a simply connected region, most often a circle, is mapped into a multiply connected one (an annulus). Greenleaf, Lassas and Uhlmann [1] showed that singular transformations lead to cloaking for conductivity, while [2, 3] applied this technique to achieve cloaking for electromagnetic waves. In vector elasticity, the wave equations are not invariant under a general mapping [4, 5, 6], while the biharmonic equation for flexural wave propagation in Kirchhoff plates is transformed into an equation of an inhomogeneous and anisotropic plate in presence of in-plane stress [7, 8]. Extended reviews on transformation optics in metamaterials in different fields, with a focus on experimental results, can be found in [9, 10].

Here, a doubly periodic geometric transformation is considered, as shown in Figure 1. In each cell, the non singular local radial transformation from the original local coordinate R to the transformed one r is

$$r = g(R) = R_0 + \frac{R_0 - R_2}{R_0 - R_1}(R - R_0), \tag{1}$$

where the homogeneous isotropic interface in $R \in [R_1, R_0]$ is mapped into the inhomogeneous anisotropic interface in $r \in [R_2, R_0]$.

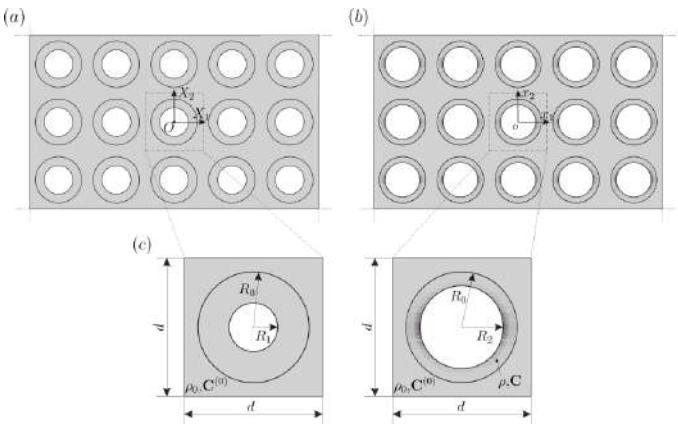

Figure 1: Double periodic geometric transformation of the perforated medium. Each homogeneous interface (a,c) of internal and external radii R_1 and R_0, respectively, is transformed into an interface (b,c) of internal and external radii R_2 and R_0, respectively.

*Corresponding author. E-mail: mbrun@unica.it

Filtering properties

Thanks to the periodicity of the transformation, it is possible to cloak multiple inclusions in an arbitrary large region, also in the case of relatively large defects. Additionally, by taking advantage of periodicity, it is possible to design a grating interface, with voids of negligible size, that shows extremely high reflection in a broad frequency and angle of incidence interval.

In Figure 2, the particular case of an interface in a waveguide is reported. An interface made of five void inclusions is present. In the upper part of the figure, in presence of relatively large voids ($2R_2/d = 0.8$), the incident wave

$$u_I = e^{ik_1 x_1 \cos\left(\frac{\pi x_2}{d}\right)} \tag{2}$$

is practically totally transmitted.

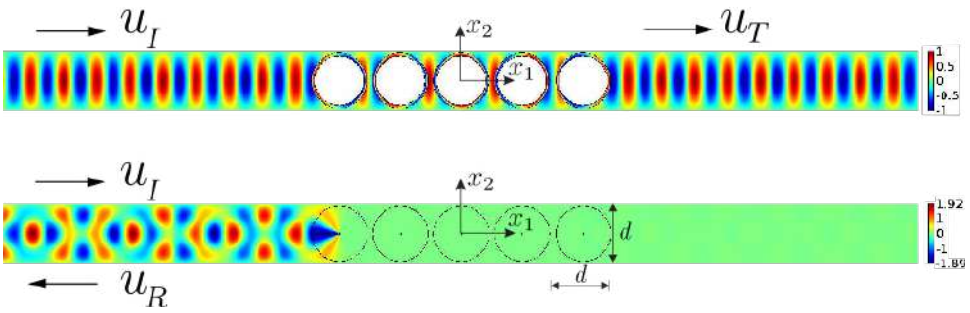

Figure 2: Wave transmission in a waveguide throughout an interface made of five void inclusions. Extremely high transmission and reflection in presence of, respectively, large and small holes are shown.

In the second case, while the size of the voids is relatively small ($2R_2/d = 0.01$), the incident wave is practically totally reflected. Such response is present in the all frequency interval that has been analysed with except of some peaks of transmission associated to the classical Fabry-Perot resonance.

CONCLUSIONS

The proposed elastic phononic crystal combines the properties of single inclusion cloaks with those of periodic systems in order to cloak multiple inclusion in a wide region or to reflect the incident energy. The filtering system is passive and does not need any active control.

References

[1] Greenleaf A., Lassas M., Uhlmann G. On nonuniqueness for Calderón's inverse problem. *Mathematical Research Letters*, **5**: 685-693, 2003.
[2] Pendry J. B., Schurig D., Smith D. R. Controlling electromagnetic fields. *Science*, **5781**: 1780-1782, 2006.
[3] Leonhardt U. Optical conformal mapping. *Science*, **5801**: 1777-1780, 2006.
[4] Milton G. W., Briane M., Willis J. R. On cloaking for elasticity and physical equations with a transformation invariant form. *New Journal of Physics*, **8**: 248, 2006.
[5] Brun M., Guenneau S., Movchan A.B. Achieving control of in-plane elastic waves. *Applied Physics Lettters*, **94**: 061903, 2009.
[6] Norris A. N., Shuvalov, A. L. Elastic cloaking theory *Wave Motion*, **48**: 525-538, 2011.
[7] Colquitt D., Brun M., Gei M., Movchan A. B., Movchan N.V., Jones I.S. Transformation elastodynamics and cloaking for flexural waves. *Journal of the Mechanics and Physics of Solids*, **72**: 131-143, 2014.
[8] Brun M., Colquitt D. J., Jones I.S., Movchan A.B., Movchan N.V. Transformation cloaking and radial approximations for flexural waves in elastic plates. *New Journal of Physics*, **16**: 093020, 2014.
[9] Kadic M., Bückmann T., Schittny R., Wegener M. Metamaterials beyond electromagnetism. *Reports on Progress in Physics*, **76**: 12, 126501 ,2013.
[10] Fleury R., Alù A., Cloaking and Invisibility: a Review. *Progress In Electromagnetics Research*. **147**: 171-202, 2014.

BAYESIAN MACHINE LEARNING IN METAMATERIAL DESIGN: FRAGILE BECOMES SUPER-COMPRESSIBLE

Miguel A. Bessa*[1], P. Glowacki [1], and M. Houlder[1]
[1]Materials Science and Engineering, Delft University of Technology, Delft, The Netherlands

Summary We present the data-driven discovery of a metamaterial exhibiting recoverable super-compressibility. Unlike the usual materials design process that is guided by trial-and-error experimentation, we follow a unique computational data-driven approach where Bayesian machine learning guides the design process while experimentation is used for validation, not discovery. This enabled the design and additive manufacturing of a lightweight, recoverable and super-compressible metamaterial achieving more than 90% compressive strain without damage, despite using brittle base materials (fracture strain $\varepsilon_f < 4\%$). More importantly, within minutes, the machine learning model can be optimized to adapt the designs to different base materials, length-scales and manufacturing processes. The complete article has been published recently [1], and the computer code is released as open-source to promote future data-driven discoveries in multiple fields: https://github.com/mabessa/F3DAS

INTRODUCTION

Our data-driven exploration follows a framework that is opening new avenues in the design of materials and structures [2, 3, 4]. This modular framework integrates (1) design of experiments to sample the input variables, (2) efficient predictive analyses to generate the output database, (3) machine learning to establish input-output relationships from the database, and (4) optimization to determine optimum designs from the machine learning model. Different methods can be chosen for each module depending on the problem's dimensionality, size of database needed for the learning process, and whether the phenomena of interest is probabilistic or deterministic. Here, we focus on designing a new metamaterial based on a concept design introduced in the aerospace literature: the deployable mast [5]. Since our mechanical metamaterial undergoes probabilistic responses due to buckling/postbuckling mechanisms, and involves a moderate number of design parameters, we used a recent Bayesian machine learning method called sparse Gaussian processes [6] to fulfill these requirements while being sufficiently scalable.

DATA-DRIVEN DISCOVERY OF METAMATERIAL

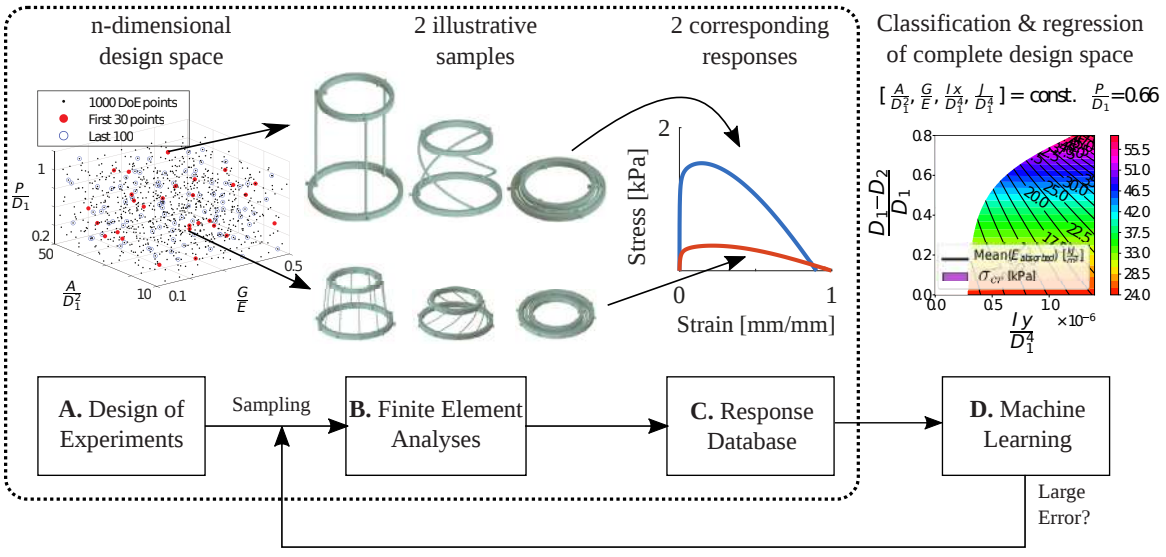

Figure 1: Data-driven design of super-compressible metamaterial building block using 7 design variables. [1]

Figure 1 summarizes the data-driven design of the metamaterial concept. First, the metamaterial is parameterized according to the design variables that define the geometry (top and bottom base diameters, D_1 and D_2, height P, and four parameters that define the cross-section of the vertical elements (longerons): the cross-sectional area A, moments of inertia I_x and I_y, and torsional constant J_τ). In addition, since the metamaterial is targeted to be reversibly deformable, any chosen base material is defined by its elastic constants: the Young's modulus E and the shear modulus G. Given that this is a nonlinear elastic mechanics problem we know *a priori* that the geometric variables can be scaled by one of the dimensions, chosen here as D_1, and that we can consider the ratio of elastic constants G/E. These seven input variables are then sampled according to a Sobol sequence (Figure 1A), finite element simulations for each sampling point (Figure

*Corresponding author. E-mail: M.A.Bessa@tudelft.nl

1B) create a database (Figure 1C), that is then evaluated by Bayesian machine learning to classify and regress the design space (Figure 1D).

The obtained machine learning model provides the relationship between the input design variables and the output quantities of interest: buckling strength and toughness of the metamaterial. This machine learning model can then be used as a surrogate model on which sensitivity analysis, dimensionality reduction or gradient based optimization techniques can be used. This has enabled us to predict viable designs of the super-compressible metamaterial and 3D print them at different length-scales. Figure 2 shows the microscopic design after being tested with a nanomechanical testing device. As shown in the figure, the metamaterial recovers from multiple cyclic loads and achieves unprecedented compressibility and strength. The macroscopic example (not shown for conciseness) achieves over 95% compressibility.

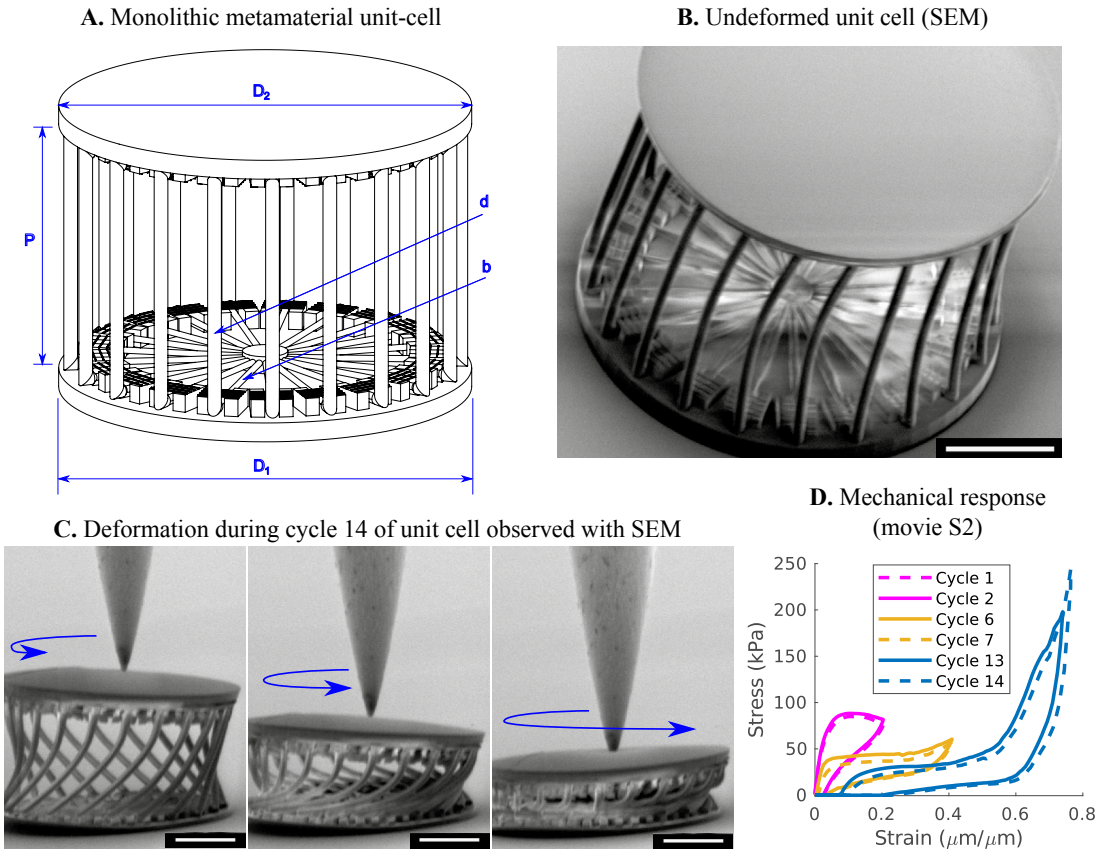

Figure 2: Monolithic metamaterial obtained with two-photon nanolithography. [1]

CONCLUSIONS

We demonstrate that inverting the design process from experimentally-guided to data-driven is possible and advantageous even when computational models are missing some information. This approach is widely applicable to design and analyze different materials and structures. The essential requisites are that "enough" data about the problem of interest is available, and that the data is sufficiently accurate. This data does not need to be exclusively computational, as it could also be analytical or experimental. Therefore, we believe that machine learning will play an ever-increasing role in the quest for the best materials, but it is in tuning them for unforeseen scenarios where it may be most attractive to use it.

References

[1] Bessa M. A., Glowacki, P., Houlder, M. Bayesian machine learning in metamaterial design: fragile becomes super-compressible. *Advanced Materials* (2019).

[2] Bessa M. A., Bostanabad R., Liu Z., Hu A., Apley D., Brinson C., Chen W., and Liu W. A framework for data-driven analysis of materials under uncertainty: Countering the curse of dimensionality. *Computer Methods in Applied Mechanics and Engineering* 320 (2017): 633-667.

[3] Bessa M. A., and Pellegrino S. Design of ultra-thin shell structures in the stochastic post-buckling range using Bayesian machine learning and optimization. *International Journal of Solids and Structures* 139 (2018): 174-188.

[4] Mozaffar M., Bostanabad R., Chen W., Ehmann K., Cao J., and Bessa M. A. Deep learning predicts path-dependent plasticity. *Proceedings of the National Academy of Sciences* 116, no. 52 (2019): 26414-26420.

[5] Pellegrino S., ed. Deployable structures. Vol. 412. *Springer*, 2014.

[6] Ghahramani Z. Probabilistic machine learning and artificial intelligence. *Nature* 521, no. 7553 (2015): 452.

BROADBAND CONTROL OF WATER WAVE ENERGY AMPLIFICATION IN CHIRPED ARRAYS

Aidan Archer[1], Hugh Wolgamot[1], Jana Orszaghova[1], Luke Bennetts*[2], Malte Peter[3], and Richard Craster[4]
[1]Wave Energy Research Centre, University of Western Australia, Australia
[2]School of Mathematical Sciences, University of Adelaide, Australia
[3]Institute of Mathematics, University of Augsburg, Germany
[4]Department of Mathematics, Imperial College London, UK

Summary Water waves in natural environments are typically broadband, nonlinear and dynamic phenomena. Taking concepts developed for slow light in optics, we address the challenge of designing arrays to control the spatial distribution of wave energy, and amplify target frequencies at specified locations. Experiments on incident waves interacting with a chirped array of eight vertical cylinders demonstrate significant amplifications, as predicted numerically, providing motivation for application to energy harvesting.

The ability of chirped (or graded) arrays to create slow light or sound waves, confine them, and filter them spatially according to frequency is attractive for wave control. There is a comprehensive body of work, primarily in optics, plasmonics and electromagnetism, which forms a paradigm for the control of waves more broadly, and has been extended to the field of elasticity [1], where it is used to generate mode conversion devices that hybridise surface waves to body waves. A feature less often exploited is that energy can accumulate in regions where the group velocity tends to zero [2]. Assuming the local behaviour in the array is dominated by neighbouring elements enables the implied local periodicity to predict band-gaps (or forbidden frequencies), and the band-gap edges determine a relation between local array properties and frequencies at which group velocities are zero.

In a seemingly disparate branch of ocean engineering, there has been intense activity on methods to harvest the vast quantity of renewable energy carried by ocean waves. Many wave energy converter (WEC) designs have been proposed [3], and a very large class of WECs are tuned to resonate with the dominant frequencies in a sea-state, but suffer from having small bandwidth compared to the bandwidth of the (random) incident waves [4]. In any practical application, multiple interacting WECs will be present, and much research has focussed on regular arrangements of these [5].

We address the pressing question of whether it is possible to take advantage of generic chirped-array concepts from optics in a (potentially nonlinear and dissipative) water wave system, to yield amplification of chosen frequencies at different locations, where (in an absorbing array) the energy could conceivably be captured by suitably tuned WECs. We do so through careful experimentation on waves of length order metres, interacting with an array of eight identical fixed bottom-mounted cylinders arranged along the centreline of a wave flume, and with chirped spacing (Fig. 1 left).

Guided by band-gap theory of doubly-periodic infinite arrays, we probe the resonant modes using regular incident waves of angular frequency $\omega = 6.50\,\mathrm{rad\,s^{-1}}$ and amplitude $a_{\mathrm{inc}} = 0.01\,\mathrm{m}$. Eulerian point measurements of the free surface elevation, η, are recorded at the centre of each of the first six spacings. Linear time-series responses show large amplifications in spacing 3, and minimal transmission farther along the array (Fig. 1 middle), consistent with theoretical predictions. Further, similar mode shapes to those predicted by linear theory were observed, as indicated by the wetted surface of the cylinders (Fig. 1 right).

Focussed incident wave packets are used to investigate the overall spectral structure of the response. The transfer function

$$\mathcal{A}(\omega) = \frac{\mathcal{F}(\eta)}{\mathcal{F}(\eta_{\mathrm{inc}})} \quad \text{where} \quad \mathcal{F} \text{ denotes the Fourier transform,}$$

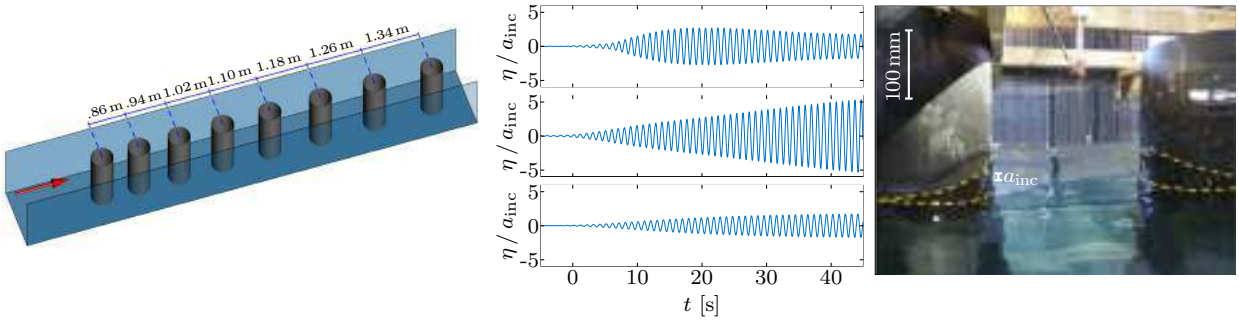

Figure 1: Left: Experimental set-up. Middle: Measured surface elevations for $\omega = 6.50\,\mathrm{rad\,s^{-1}}$ in spacing 1 (top), 3 (middle) and 5 (bottom), showing resonance at spacing 3, as predicted by band-gap theory. Right: Photo of spacing 3 with wetted cylinder surface indicating resonant mode shape.

*Corresponding author. E-mail: luke.bennetts@adelaide.edu.au

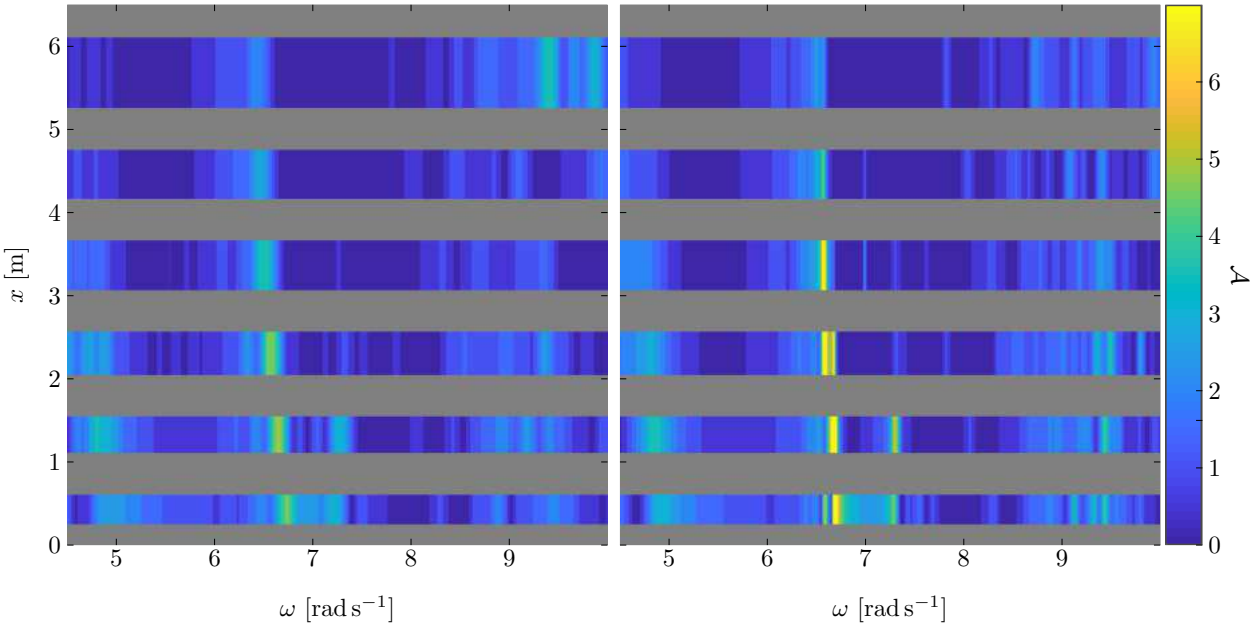

Figure 2: (a) Experimental and (b) numerical amplitude transfer functions, at wave probe locations along the array (shown as constant in each spacing). Grey strips represent spatial locations of cylinders 1–7.

is used to quantify amplitude amplifications over the frequency spectrum. Fig. 2 shows the amplitude transfer function calculated from a linear numerical model (right) and from focussed wave group experiments (left). The experimental and numerical transfer functions are in excellent agreement, notwithstanding the expected larger and sharper amplifications in the numerical model. Amplifications on the first and second bands are evident, along with the spectral downshift along the array.

We have presented results from wave-flume experiments that demonstrate localisation and amplification of water waves along a chirped array of bottom-mounted cylinders, despite the challenges of working with highly resonant systems in a finite-length flume. Linear theory was shown to predict the amplification spectrum accurately in frequency–distance space, including peak resonance locations and spectral downshifts along the array. Moreover, even for the rather small array of eight cylinders used, the amplification locations, at which the group velocity slows to zero, were shown to be consistent with the band structure of infinite periodic arrays using local cylinder spacings. The outcomes suggest future strategies for ocean wave energy harvesting should consider taking advantage of the broadband response and precise control demonstrated here. We have not attempted a parametric study to optimise such an array; this will be a future undertaking.

References

[1] Colombi, A., Colquitt, D., Roux, P., Guenneau, S., Craster, R. V. A seismic metamaterial: The resonant metawedge. *Sci. Rep.* **6**, 27717, 2016.
[2] Romero–Garcia, V., Pico, R., Cebrecos, A., Sanchez-Morcillo, V. J., Staliunas, K. Enhancement of sound in chirped sonic crystals. *Appl. Phys. Lett.* **102**, 091906, 2013.
[3] Babarit, A. Ocean wave energy conversion: resource, technologies and performance, Elsevier, 2017.
[4] Falnes, J. A review of wave-energy extraction. *Mar. Struct.* **20**,185–201, 2007.
[5] Tokic, G., Yue, D. K. P. Hydrodynamics of periodic wave energy converter arrays. *J. Fluid Mech.* **862**, 34–74, 2019.

TUNING EFFECTIVE DYNAMICAL PROPERTIES OF PERIODIC MEDIA BY FFT-ACCELERATED TOPOLOGICAL OPTIMIZATION

Rémi Cornaggia [1] and Cédric Bellis*[1]
[1]Aix-Marseille Univ, CNRS, Centrale Marseille, LMA UMR 7031, Marseille, France

Summary In the context of waves in periodic media, we propose an iterative algorithm that determines an optimal material distribution to reach target effective dispersive properties. It relies on an homogenized model of this medium, an update procedure based on the topological derivative concept, and on an efficient FFT-accelerated method to solve cell problems.

INTRODUCTION

We are interested in standing waves in unbounded two-dimensional domains filled with a periodic medium, *e.g.* antiplane elastic shear waves. The material is made of cells $Y_\ell = \ell Y$, where Y is the reference unit cell and ℓ the characteristic periodicity length (Fig. 1). At circular frequency ω, the wave amplitude u_ℓ obeys the equation:

$$\boldsymbol{\nabla} \cdot \left(\mu_\ell \boldsymbol{\nabla} u_\ell\right) + \rho_\ell \omega^2 u_\ell = 0, \tag{1}$$

where μ_ℓ and ρ_ℓ are the Y_ℓ-periodic shear modulus and density of the medium.

In the long wavelength regime ($\lambda > \ell$), the motion can be described approximatively by the superposition of a slowly varying mean field U and higher-order (in $\varepsilon = \ell/\lambda$) oscillating correctors. Given an effective (homogenized) model satisfied by U, the effective dispersion of the medium is characterized by the variations of the phase velocity $c(k, \boldsymbol{d}) = \omega(k, \boldsymbol{d})/k$ of a plane wave $U(\boldsymbol{x}) = \exp(\mathrm{i}k\boldsymbol{d} \cdot \boldsymbol{x})$ when the wavenumber k and direction $\boldsymbol{d}$ vary. Here we adopt the following direction-dependant dispersion indicator:

$$\gamma(\boldsymbol{d}) := \left.\frac{\partial^2 c^2(k, \boldsymbol{d})}{\partial k^2}\right|_{k=0}. \tag{2}$$

In this work, the goal is to optimize the material distribution within the unit cell Y to reach some target effective dispersive properties, in particular to maximize their anisotropy. The proposed method relies on four main components: a second-order homogenized effective model, the topological derivatives of the model's coefficients, an iterative topological optimization algorithm for the unit cell, and an efficient fixed-point FFT method to evaluate these topological derivatives at each iteration. These components are now described in more details.

SECOND-ORDER HOMOGENIZED MODEL

The two-scale asymptotic homogenization method [1, 3] is a popular way to derive an effective model from the equation (1). One obtains a fourth-order wave equation for the mean field U:

$$\boldsymbol{\mu}^0 : \boldsymbol{\nabla}^2 U + \omega^2 \varrho^0 U + \ell^2 \left[\boldsymbol{\mu}^2 :: \boldsymbol{\nabla}^4 U + \omega^2 \boldsymbol{\varrho}^2 : \boldsymbol{\nabla}^2 U\right] = 0, \tag{3}$$

where $(\boldsymbol{\mu}^0, \varrho^0, \boldsymbol{\mu}^2, \boldsymbol{\varrho}^2)$ are constant tensors computed by solving cell problems over Y [3], ":" and "::" indicate inner products between second- and fourth-order tensors, and $\boldsymbol{\nabla}^j = \boldsymbol{\nabla}(\boldsymbol{\nabla}^{j-1})$. Moreover, this model coincides with the one obtained by the Bloch-Floquet wave method (see [1, Sect. 3] for the case $\rho_\ell = 1$). The dispersion indicator γ defined by (2) is then simply given by:

$$\gamma(\boldsymbol{d}) = 2\ell^2 \left[\frac{\boldsymbol{\varrho}^2 \otimes \boldsymbol{\mu}^0 - \varrho^0 \boldsymbol{\mu}^2}{(\varrho^0)^2}\right] :: (\boldsymbol{d} \otimes \boldsymbol{d} \otimes \boldsymbol{d} \otimes \boldsymbol{d}). \tag{4}$$

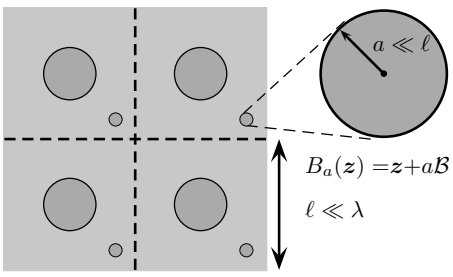

Figure 1: Periodic material and small phase change

*Corresponding author. E-mail: bellis@lma.cnrs-mrs.fr.

TOPOLOGICAL OPTIMIZATION OF THE UNIT CELL

To reach a target dispersive behavior, one first defines a cost functional to be minimized, *e.g.*

$$J(Y;\boldsymbol{d}_1,\boldsymbol{d}_2,\ldots,\boldsymbol{d}_{N_d}) = \frac{1}{2}\left(\sum_{j=1}^{N_d} w_j \left[\gamma(\boldsymbol{d}_j)\right]^{\alpha_j}\right), \tag{5}$$

where each exponent α_j is fixed to 2 (resp -2) to minimize (resp. maximize) the dispersion in direction $\boldsymbol{d}_j$ and the positive constants w_j are user-defined weights that balance the contribution of each term in the cost functional. This cost functional depends on the cell Y implicitely through the homogenized coefficients that intervene in the expression (4) of γ.

An iterative topological optimization algorithm, already used in microstructural optimization of static properties [2], is then adapted to the present situation. We restrain ourselves to two-phase cells, which are described thanks to a level-set function ψ. At each iteration, the update of this function is based on the concept of topological sensitivity (TS) of the cost functional to an infinitesimal phase change at point $\boldsymbol{z}$, supported by a small disc B_a of size $a \ll \ell$, as depicted in Figure 1. This TS, denoted $\mathcal{D}J$, is the leading-order coefficient of the following expansion of the perturbed cost functional J_a:

$$J_a = J + (a/\ell)^2 \mathcal{D}J(\boldsymbol{z}) + o\left((a/\ell)^2\right).$$

The negative minima of the map $\boldsymbol{z} \mapsto \mathcal{D}J(\boldsymbol{z})$ thus indicates the locations in Y where a small phase change would decrease J the most. Following [2], the level-set update $\psi_n \to \psi_{n+1}$ is done by partial projections of ψ_n onto the TS $\mathcal{D}J$. The algorithm stops when the optimality condition $\mathcal{D}J > 0$ is reached, indicating a local minimum of J.

COMPUTATIONAL CONSIDERATIONS

At each iteration, the TS $\mathcal{D}J$ is computed by simple algebraic combinations of the TSs of the four coefficients $(\boldsymbol{\mu}^0, \varrho^0, \boldsymbol{\mu}^2, \boldsymbol{\varrho}^2)$ whose evaluation requires the resolution of 12 direct and adjoint scalar potential problems on the current material configuration of the cell Y, as specified in [3].

To solve these problems, we adopted the FFT-accelerated algorithm proposed by Moulinec and Suquet in the 90's (see *e.g.* the introduction of [4]), that permits (i) a meshless representation of the unit cell as an image, (ii) a very simple implementation of the whole procedure and (iii) good computational performances.

An example of microstructure obtained with the proposed procedure is presented in Fig. 2. We also note that a similar study is conducted in [1], using the shape derivative of the homogenized coefficients rather than their topological derivative to update the level-set.

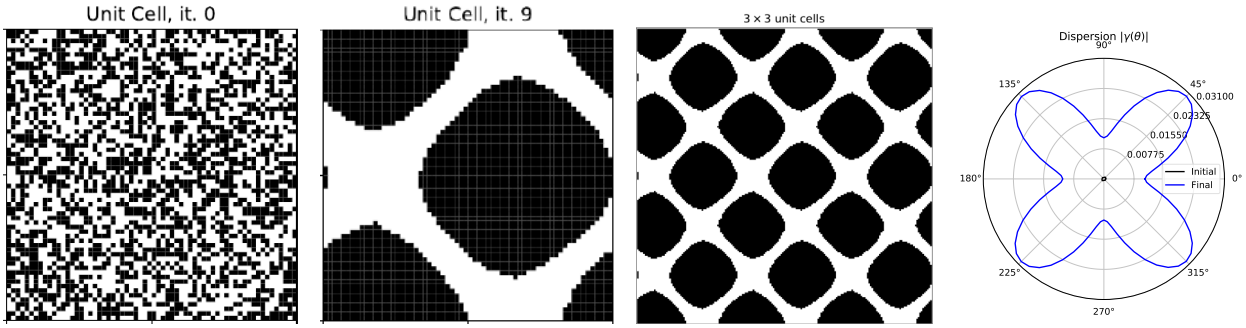

(a) Initial unit cell (b) Final unit cell (c) Resulting microstructure (3×3 unit cells) (d) Final dispersion indicator γ

Figure 2: Microstructure optimization to maximize the dispersion in the directions $\theta = \pm\pi/4$ and minimize it in the directions $\theta = 0,\ \pi/2$ ($N_d = 4$ in the definition (5) of J). The unit cell is discretized into 128×128 pixels and initialized with a random distribution of materials 1 (white pixels) and 2 (black pixels). The material ratios are $\mu_2/\mu_1 = 6$ and $\rho_2/\rho_1 = 1.5$. The optimality condition was reached after 9 iterations.

References

[1] G. Allaire and T. Yamada. Optimization of dispersive coefficients in the homogenization of the wave equation in periodic structures. *Numerische Mathematik*, 2018

[2] S. Amstutz, S. M. Giusti, A. A. Novotny, and E. A. de Souza Neto. Topological derivative for multi-scale linear elasticity models applied to the synthesis of microstructures. *Int. J. Numer. Methods Eng.*, 2010.

[3] M. Bonnet, R. Cornaggia, and B. Guzina. Microstructural topological sensitivities of the second-order macroscopic model for waves in periodic media. *SIAP*, 2018.

[4] H. Moulinec, P. Suquet, and G. W. Milton. Convergence of iterative methods based on Neumann series for composite materials: Theory and practice. *Int. J. Numer. Methods Eng.*, 2018.

A PHONONIC CRYSTAL FOR RADIAL TORSIONAL WAVES

Ignacio Arretche[1], and Kathryn H. Matlack [1]
[1]Department of Mechanical Science and Engineering, University of Illinois Urbana-Champaign, Illinois, USA

Summary: We present a phononic crystal that exhibits periodic behavior in terms of radial torsional waves, even though its unit cells are geometrically different. The phononic crystal is motivated by a lumped parameter model and consists of a series of alternating steel and rubber rings of different thicknesses that provides unit cells with constant effective properties even though they have different dimensions. The system exhibits the typical stop band of a monoatomic lattice, paving the way for vibration suppression of radially propagating torsional waves.

INTODUCTION

Torsional vibrations in rotating and reciprocating machinery are one of the main reasons for their failure and rapid wear [1]. Current solutions to reduce torsional vibration usually involve addition of mass or complex mechanisms. On the other hand, architected metamaterials and phononic crystals have shown promise in terms of reducing vibrations [2]. Proposed metamaterials for torsional vibration suppression have been limited to one-dimensional chains of ring resonators attached to a central shaft [3]. These systems deal with the propagation of plane torsional waves in the axial direction and require long chains of rings that may be impractical where space is limited. An alternative approach is to attenuate vibrations as they propagate radially outward from the center of a ring, such as in a gearbox. However, this presents additional challenges, mainly due to difficulties in achieving periodic coefficients when the wave equation is expressed in cylindrical coordinates, which inhibits the application of Floquet theory for analysis. In fact, most work in metamaterials and phononic crystals deals with Cartesian plane waves and only a few studies have considered cylindrical wave fronts [4,5]. For example, radial propagation of torsional vibrations through finite metamaterials made of equal alternating radial rings have been studied using a localization factor method [4]. However, vibration transmission of these metamaterials is strongly dependent on where the infinite system is truncated to make the finite metamaterial. Other solutions involve anisotropic mass density to achieve invariance to radial translation in the equations of motion [5], but these material properties may be hard to achieve. Here, we instead impose periodicity by starting with an infinite lumped parameter model that exhibits invariance to radial translation. We then construct a numerical model of the system using alternating non-periodic layers of rubber and steel of different thicknesses. The outcome is a phononic crystal that behaves as a periodic media although is not geometrically periodic.

PHONONIC CRYSTAL MODEL AND RESULTS

We first analyze a lumped parameter model consisting of an infinite chain of rigid rings of equal mass moment of inertia and torsional springs of equal torsional stiffness (Fig. 1a). We define the unit cell as one rigid ring and one torsional spring. Note that this definition is based on equal effective properties (i.e. inertia of the rigid rings and torsional stiffness of torsional springs) and not geometry. The infinite lumped parameter model is a radial tessellation of unit cells and the equation of motion of the n^{th} unit cell can be expressed as:

$$I\ddot{\theta}_n = \beta_T\theta_{n-1} + \beta_T\theta_{n+1} - 2\beta_T\theta_n \tag{1}$$

where θ_n is the angular displacement of the rigid ring of the n^{th} unit cell, I is the mass moment of inertia of the rigid rings and β_T is the torsional stiffness of the torsional springs. The equation of motion is invariant to radial translations of the form $r = r + n\Delta r$. Thus, we seek Bloch plane wave solutions:

$$\theta_n = Ae^{i(kn\Delta r - \omega t)} \tag{2}$$

where k is the wavenumber and Δr is the lattice constant (Fig. 1a). Introducing equation (2) into equation (1), we obtain the dispersion relation, which is equivalent to that of a monoatomic one dimensional phononic crystal (Fig. 1c):

$$\omega(k) = 2\sqrt{\frac{\beta_T}{I}}\left|\sin\left(\frac{k\Delta r}{2}\right)\right| \tag{3}$$

Like the monoatomic phononic crystal, this model shows a cut-off frequency above which no propagating solution exists, i.e. there is attenuation of radially propagating torsional waves above such frequency.

The main challenge with this simple lumped parameter system is translating it to a phononic crystal geometry, as the dimensions must be carefully chosen to obtain equal rotational inertia and torsional stiffness in each unit cell (equations (4) and (5) below). We propose a unit cell made of one steel and one rubber ring (Fig. 1b). The rubber rings, which have low density and low stiffness, approximate the torsional springs, and the steel rings, which have high density and high stiffness, represent the rigid rings. The torsional stiffness of each rubber ring (β_T) [6] and rotational inertia of each steel ring (I) can be calculated as:

*Corresponding author. E-mail: ia6@illinois.edu

$$\beta_T = \frac{4\pi r_{r2n}^2 r_{r1n}^2 h_r}{r_{r2n}^2 - r_{r1n}^2}\mu_r \tag{4}$$

$$I = \frac{\rho_s \pi h_{sn}}{2}(r_{s2n}^4 - r_{s1n}^4) \tag{5}$$

where r_2 is the external radius of each ring, r_1 is the internal radius of each ring, h is the height of the ring, ρ is the material density, μ is the material shear modulus, and subscripts s, r, and n represent steel, rubber, and unit cell number, respectively. Equations (4) and (5) show that in order to keep the effective torsional stiffness and inertia the same for all unit cells, the thicknesses of both steel and rubber rings must be different for each unit cell. In addition, for equation (3) to be valid the lattice constant (Δr) must also be kept constant, thus the sum of the steel and rubber ring thicknesses of each unit must be equal for all unit cells. To satisfy this, we use different steel ring heights in each unit cell.

To analyze the validity of this approach we model a 4-unit cell phononic crystal (Fig. 1b). We choose dimensions of each unit cell such that they all have the same moment of inertia of the steel ring, the same torsional stiffness of the rubber ring, and the same lattice constant. We use finite element methods to simulate a frequency sweep analysis by applying an angular harmonic displacement on the internal boundary of the inner ring and fixing the external boundary of the external ring. We calculate transmission as the ratio of reaction moment on the external ring to reaction moment on the internal ring. Comparison between transmission curves (Fig. 1d) and the stop band predicted by the lumped parameter model (Fig. 1c) indicates that the finite phononic crystal behaves as the infinite lumped parameter model. Furthermore, analysis of 3 phononic crystals with different internal radius (r_0), different lattice constant, and equal predicted cut-off frequency shows the response of the finite phononic crystal is independent of where we truncate the infinite chain. This is further proof that the finite phononic crystal behaves as an infinitely periodic system. Most importantly, the proposed system behaves as a periodic system to radially propagating torsional vibrations solely due to the periodicity of its effective material properties. The novelty of this analysis and design lies in introducing a phononic crystal that exhibits behavior of typical periodic media even though all of its unit cells are geometrically different.

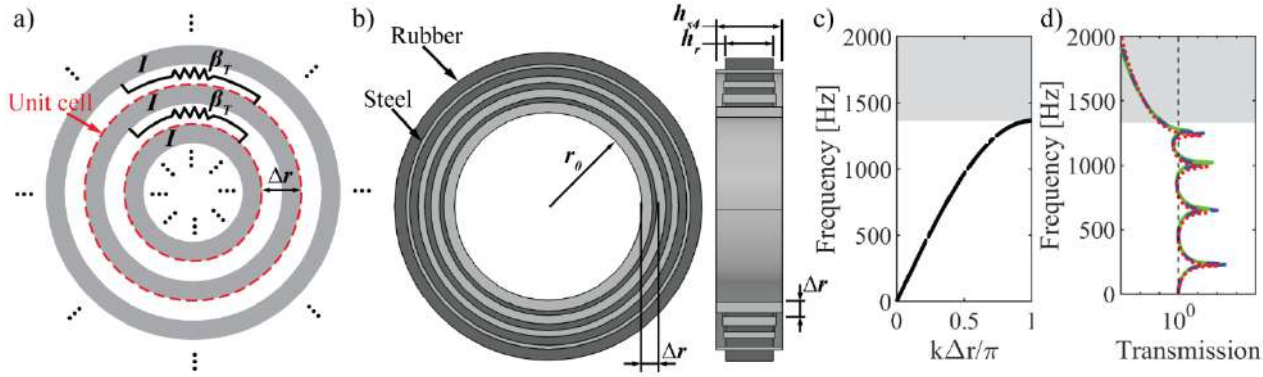

Figure 1. a) Infinitely periodic lumped parameter model (red-dashed lines show the unit cell). b) Phononic crystal for radial torsional waves. Rubber and steel rings are shown in dark and light grey, respectively. c) Dispersion relation obtained from periodic lumped parameter model. Shaded region shows stop band. d) Finite element transmission curves of phononic crystal for $r_0 = 10mm, \Delta r/r_0 = 0.36$ (green-solid), $r_0 = 25mm, \Delta r/r_0 = 0.16$ (blue-dashed), and $r_0 = 100mm, \Delta r/r_0 = 0.04$ (red-dotted).

CONCLUSION

We presented a phononic crystal for radially propagating torsional waves. The design is developed from a simple lumped parameter system that shows radial translational invariance of its equations of motion. We model the phononic crystal by using series of concentric rings of steel and rubber of different thicknesses. We show that even though the phononic crystal is not geometrically periodic (i.e. each unit cell is geometrically different), it behaves as a periodic system to radially propagating torsional waves. The capability of torsional wave attenuation above a cut-off frequency makes the design applicable for torsional vibration suppression.

References

[1] Feese, T., and Hill, C., 2009, "Prevention of Torsional Vibration Problems in Reciprocating Machinery," *Proceedings of the 38th Turbomachinery Symposium*, pp. 213–238.
[2] Matlack, K. H., Bauhofer, A., Krödel, S., Palermo, A., and Daraio, C., 2016, "Composite 3D-Printed Metastructures for Low-Frequency and Broadband Vibration Absorption," Proc. Natl. Acad. Sci., **113**(30), pp. 8386–8390 DOI: 10.1073/pnas.1600171113.
[3] Yu, D., Liu, Y., Wang, G., Cai, L., and Qiu, J., 2006, "Low Frequency Torsional Vibration Gaps in the Shaft with Locally Resonant Structures," Phys. Lett. A, **348**(3–6), pp. 410–415 DOI: 10.1016/j.physleta.2005.08.067
[4] Haisheng, S., Liqiang, D., Shidan, L., Wei, L., Shaogang, L., Weiyuan, W., Dongyan, S., and Dan, Z., 2014, "Propagation of Torsional Waves in a Thin Circular Plate of Generalized Phononic Crystals," J. Phys. D. Appl. Phys., **47**(29) DOI: 10.1088/0022-3727/47/29/295501.
[5] Torrent, D., and Sánchez-Dehesa, J., 2009, "Radial Wave Crystals: Radially Periodic Structures from Anisotropic Metamaterials for Engineering Acoustic or Electromagnetic Waves," Phys. Rev. Lett., **103**(6) DOI: 10.1103/PhysRevLett.103.064301
[6] García Tárrago, M. J., Kari, L., Viñolas, J., and Gil-Negrete, N., 2007, "Torsion Stiffness of a Rubber Bushing: A Simple Engineering Design Formula Including the Amplitude Dependence," J. Strain Anal. Eng. Des., **42**(1), pp. 13–21 DOI: 10.1243/03093247JSA246

ELASTIC WAVE TRANSMISSION IN LOCALLY RESONANT MATERIALS WITH VARIABLE RESONATORS

Jacopo Maria De Ponti[1], Stefano Iannaccio[1], and Raffaele Ardito[*1]
[1]Department of Civil and Environmental Engineering, Politecnico di Milano, Milano, Italy

Summary A special case of locally resonant material (LRM) is considered, with unit cells constituted of a frame-like 3D structure and resonating cantilevers attached to each node. The resonators can be suitably tuned in order to have low-frequency, complete and wide band gaps. The present study deals mainly with the wave transmission through non-periodic assemblies, given by the juxtaposition of cells endowed with different resonators. The transmission plots are obtained by means of finite element analyses and shows the presence of band gaps also for the non-periodic media, even though the performances are not comparable to the periodic cases. Remarkably, the transmission is highly affected by the sense of wave propagation.

INTRODUCTION

Locally resonant materials (LRMs) are engineered materials, typically represented by a periodic repetition of a unit cell, with special effective properties that, in some specific situations, may lead to the presence of frequency ranges in which wave propagation is prohibited (band gaps). Such a property can be used in many different ambits, with the purpose of controlling and manipulating elastic wave propagation. As an example, LRMs can be adopted for the elimination of machine vibrations, see e.g. [1, 2]. The vibration suppression is achieved if the leading frequency of the input vibration that, for the case of rotating machinery, is relatively low (about 50 Hz), lies within the band gap. LRMs are based on the local vibrations of its components, thus it is possible to obtain band gaps with a central frequency which is well below the frequency of the wave associated to the cell dimension of the metamaterial [3,4].

The present paper deals with a frame-like 3D structure with resonant cantilevers attached to the nodes, as originally proposed in [5]. Such a design is endowed with some specific advantages: an extremely lightweight structure is obtained, with global stiffness regulated by the dimensions of the frame and low-frequency bandgap governed by the features of the resonators. The LRM is made of a single material, so that the manufacturing process is highly simplified. The main purpose of the present paper is the numeric analysis of the LRM, both in terms of wave dispersion diagram for an infinite periodic medium and for the wave transmission behaviour of finite assemblies. More specifically, transmission analyses are referred to the presence of different unit cells, with the same frame structure but different resonators. The effects of such a non-periodic arrangement are studied from a computational point of view.

METHODS

The considered metamaterial is given by the three-dimensional assembly of unit cells, endowed with cubic symmetry (see Fig. 1). The cell is constituted of a regular frame, with three mutually perpendicular beams (square cross-section, side w) whose span is equal to the unit cell size a. A set of cantilever resonators is attached in correspondence of the nodal points of the frame. Each resonator is given by a cylindrical beam (diameter w_{res}) and a spherical tip mass (radius R_{res}). The theoretical analysis of LRM shows that the band gap width is increased if the mass of the resonator m_R is large with respect to the non-resonating mass m (namely, the mass of the frame plus the part of the resonator that is not excited). Therefore, the design of the unit cell is studied to maximize the tip mass and the number of resonators.

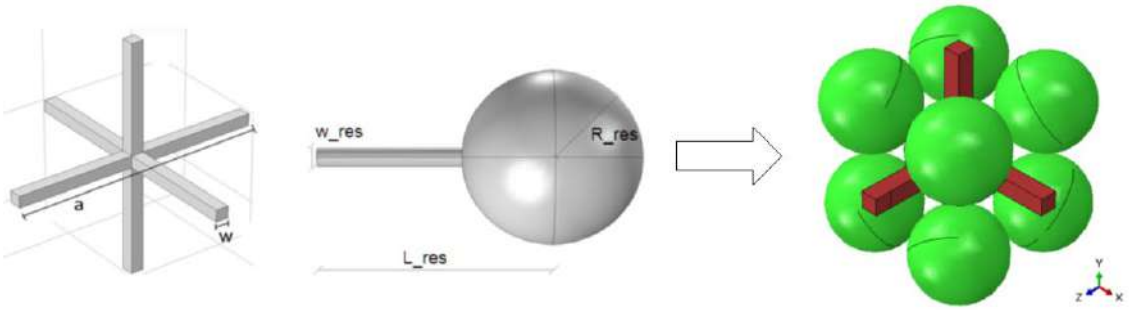

Figure 1 – Design of the unit cell of the considered LRM

To investigate the performance of the LRM as a filter for elastic waves, two types of analyses are executed: wave dispersion analysis on the unit cell, provided that suitable Bloch-Foquet boundary conditions are introduced for periodicity; wave transmission, in the frequency domain, on a finite 3D assembly of a certain number of unit cells. The analyses are carried out via the Finite Element Method, using the software ABAQUS with ad hoc user subroutines to implement Bloch-Floquet conditions. The transmission through finite realizations is computed via a frequency response

*Corresponding author. E-mail: raffaele.ardito@polimi.it

analysis, with input acceleration on one side of the structure. The convergence is achieved for a quite refined mesh, so that the analyses are burdensome.

RESULTS

The results are referred to a specific material, i.e. Nylon PA12, since a set of prototype is realized via additive manufacturing (Selective Laser Sintering [6]) for future experimental tests. The geometric features are selected with the purpose of having band gaps around the frequency of interest for machine vibration. The size of the unit cell is $a = 50$ mm, and the width of the frame element is $w = 4$ mm. Three different unit cells are considered, with resonators tuned at $f_1 = 38$ Hz, $f_2 = 45$ Hz, $f_3 = 50$ Hz. The finite structure is constituted of three layers, 2x2 cells each, with the sequence of the above mentioned resonators. The dispersion plot is represented in Figure 2 and it is compared to the three cases of homogeneous cells (periodic structures). It is possible to notice that the non-periodic structure is still endowed with band gaps, but their width is smaller than the periodic case. Indeed, the largest band gap for the non-periodic material starts in correspondence of f_3, but the closing point is characterised by a frequency much lower than the case of periodic LRM. Similar results are obtained for other cases, with a large number of cells with resonating frequency varying according to a predefined law. An interesting result is represented by non-reciprocity of the band gap: the transmission plot in one sense is by far different if the opposite propagation verse is considered. More specifically, the band gap regions are modified, so that for some frequencies an elastic wave is strongly attenuated in one sense and amplified in the opposite one. Such a property, not shown for paucity of space, is reproduced for different non-periodic arrangements.

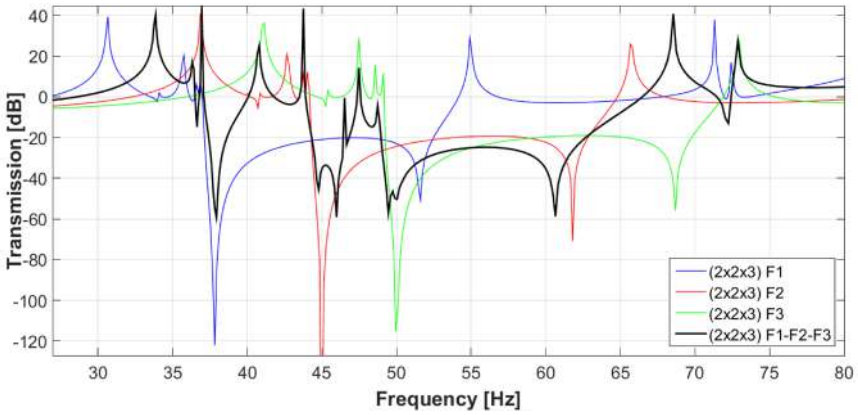

Figure 2 – Transmission plot for the periodic LRMs (blue, red, green lines, with resonators tuned at $f_1 = 38$ Hz, $f_2 = 45$ Hz, $f_3 = 50$ Hz) and the non-periodic arrangement of the three layers (black line).

CONCLUSIONS

The present study is referred to the performance assessment of an innovative LRM, via computational analysis. Focus is on the wave transmission through non-periodic LRMs, with a progressive variation of the resonating frequency in the different layers. The results show that non-periodic LRMs are still endowed with low-frequency band gap, even though it is not possible to merge the overlapped gaps for different resonators. It is worth noting that wave transmission is very different if the verse if propagation is changed. Such a feature could be of interest for the development of innovative metamaterials in the elastic field and deserves future research, also by means of the execution of experimental tests on prototypes realized via additive manufacturing.

References

[1] S. Krödel, N. Thom, C. Daraio, Wide band-gap seismic metastructures, Extreme Mechanics Letters 4 (2015) 111–117.
[2] A. Colombi, P. Roux, S. Guenneau, P. Gueguen, R. V. Craster, Forests as a natural seismic metamaterial: Rayleigh wave band gaps induced by local resonances, Scientific Reports 6 (2016) 19238.
[3] V. Laude, Phononic Crystals: Artificial Crystals for Sonic, Acoustic, and Elastic Waves, De Gruyter, 2015.
[4] Z. Liu, X. Zhang, Y. Mao, Y. Y. Zhu, C. T. C. Zhiyu Yang, P. Sheng, Locally resonant sonic materials, Science 289 (2000) 1734–1736.
[5] L. D'Alessandro, E. Belloni, G. D'Alò, L. Daniel, R. Ardito, A. Corigliano, F. Braghin, Modelling and experimental verification of a single phase three-dimensional lightweight locally resonant elastic metamaterial with complete low frequency bandgap, in: Metamaterials 2017, 2017, 70–72.
[6] L. D'Alessandro, E. Belloni, R. Ardito, A. Corigliano, F. Braghin, Modeling and experimental verification of an ultra-wide bandgap in 3D phononic crystal, Appl. Phys. Lett. 109 (22) (2016) 221907.

ON THE SMOOTHNESS OF BOUNDARIES FOR THE COMPUTATIONAL DESIGN OF PHONONIC CRYSTALS

Sanne J. van den Boom[1], Fredvan Keulen[1], and Alejandro M. Aragón*[1]
[1]Precision and Microsystems Engineering, Delft University of Technology, Delft, the Netherlands

Summary Acoustic/elastic metamaterials and phononic crystals (PnCs) have received increased attention in recent years due to the presence of bandgaps. Their computational design has relied to a great extent on topology optimization (TO), a technique that combines finite element analysis (FEA) with a gradient-based optimizer. However, standard density-based and Ersatz material level-set-based TO schemes use a diffuse representation of the geometry that does not accurately capture material boundaries. In this presentation we show the effect of boundary representation on the design of PnCs. We also introduce an enriched TO technique that greatly reduces the computational cost of design by improving the accuracy of the field at boundaries. The technique shows great potential for the design of PnCs and other metamaterials that interact with waves, whose optimal geometry is expected to be smooth.

INTRODUCTION

Metamaterials (MMs) obtain peculiar functionality by means of an engineered structure. MMs are usually created from a building block—a periodic unit cell (PUC)—that is replicated in space to amplify the desired behavior. Although initially developed in electro-magnetism, mechanical MMs have showed incredible potential in other realms of physics. Acoustic/elastic MMs and phononic crystals (PnCs), which are engineered to interact with waves, are of particular interest because of the presence of bandgaps, *i.e.*, ranges of mechanical wave frequencies that do not propagate through the metamaterial. These MMs are currently being considered for energy harvesting, communication, thermal barriers, elastic/acoustic filters, vibrationless environments for high-precision equipment, improved transducers, waveguides, acoustic lasers (phasers), sound protection devices, and earthquake shields.

Given a target functionality, it is not straightforward to obtain an optimal PnC design because of the complexity of the periodic structural configuration; therefore, the ineffective empirical trial-and-error approach to design has to be replaced by adequate numerical tools to obtain the most out of the metamaterial. The design of PnCs is extremely challenging not only because it has to be tailored to a particular application, but also because current design tools demand for vast computational resources. Standard TO or Ersatz level-set-based TO have limited applicability in PnC design due to a poor topological representation caused by the use of structured meshes, which can reproduce at best *pixelized* or *staircase* boundaries with density properties that do not correspond to void nor material. In this talk we show that this geometry representation and modeling is detrimental for the design of materials whose geometry is expected to be smooth, as is the case with MMs that interact with waves. We compare the results with diffuse interfaces commonly used in density-based TO with those obtained by enriched FEA that captures the geometry smoothly. We also introduce an enriched TO framework and discuss its performance for maximizing PnCs' bandgaps.

METHODS

The band structure of a PnC is commonly obtained by analyzing its periodic unit cell (PUC). We first consider a PUC with a simple geometry: a square domain containing a circular inclusion with contrasting material properties. In both material phases the behavior is governed by the elastodynamic wave equation, whose variational form is discretized straightforwardly by following standard finite element procedures. With $\boldsymbol{u}^h$ denoting the finite element approximation, which is a function of both coordinate $\boldsymbol{x}$ and time t, we prescribe Bloch-Floquet periodic boundary conditions $\boldsymbol{u}^h(\boldsymbol{x}+\boldsymbol{a},t) = e^{i(\boldsymbol{k}\cdot\boldsymbol{a})}\boldsymbol{u}^h(\boldsymbol{x},t)$, where $\boldsymbol{a}$ is the lattice vector between two periodic edges and $\boldsymbol{k} \in \mathcal{K}$ is a wave vector of a finite set $\mathcal{K}$ along the edge of the irreducible Brillouin zone. The band structure is then obtained by solving an eigenvalue analysis for each wave vector $\boldsymbol{k} \in \mathcal{K}$ along the edge of the irreducible Brillouin zone:

$$\left[\tilde{\boldsymbol{K}} - \omega_j^2 \tilde{\boldsymbol{M}}\right] \tilde{\boldsymbol{V}}_j = \boldsymbol{0}, \qquad j = 1, \ldots, N, \qquad \forall \boldsymbol{k} \in \mathcal{K}, \tag{1}$$

where ω_j is jth numerical frequency out of N bands considered, $\tilde{\boldsymbol{V}}_j$ the corresponding eigenvector, $\tilde{\boldsymbol{K}} = \boldsymbol{T}^{\mathsf{H}}\boldsymbol{K}\boldsymbol{T}$ and $\tilde{\boldsymbol{M}} = \boldsymbol{T}^{\mathsf{H}}\boldsymbol{M}\boldsymbol{T}$, $\boldsymbol{T}$ is complex valued and depends on $\boldsymbol{k}$, and $\boldsymbol{K}$, $\boldsymbol{M}$ are the global stiffness and mass matrices, respectively.

Both standard and enriched finite element spaces are considered. For the latter, the approximation is given by [1, 2]

$$\boldsymbol{u}^h(\boldsymbol{x}) = \underbrace{\sum_{i \in \iota_h} N_i(\boldsymbol{x})\, \boldsymbol{U}_i}_{\text{standard FEM}} + \underbrace{\sum_{i \in \iota_w} \psi_i(\boldsymbol{x})\, \boldsymbol{\alpha}_i}_{\text{enrichment}}, \tag{2}$$

where the standard FE term—comprised of Lagrange shape functions N_i and corresponding degrees of freedom (DOFs) $\boldsymbol{U}_i$—is augmented by an enrichment term that captures, by means of enrichment functions ψ_i and corresponding enrichment DOFs $\boldsymbol{\alpha}_i$, a smoother (piecewise linear) description of the circular inclusion. As a result, the enriched finite element solution captures more accurately the field along material interfaces and boundaries.

*Corresponding author. E-mail: a.m.aragon@tudelft.nl

EFFECT OF GEOMETRY DESCRIPTION FOR BANDGAP ANALYSIS

We conduct band structure analysis focusing on the first five bands ($N = 5$), and compare the results obtained by standard and enriched FEA. While enriched FEA captures smooth boundaries by means of enrichment functions, standard FEA uses the pixelized representation commonly used in standard TO. We quantify the error in the band structure by:

$$\epsilon = \sqrt{\frac{1}{|\mathcal{K}|\,N}\frac{\sum_{\boldsymbol{k}\in\mathcal{K}}\sum_{j=1}^{N}(\omega_j-\omega_j^\star)^2}{\sum_{\boldsymbol{k}\in\mathcal{K}}\sum_{j=1}^{N}\omega_j^{\star 2}}}, \tag{3}$$

where $|\cdot|$ denotes set cardinality, $\omega_j^\star$ is the *reference* jth frequency for wave vector $\boldsymbol{k}$, obtained by an *overkill* FE analysis.

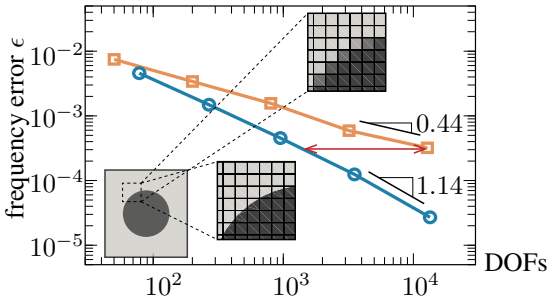

Figure 1: Error given by (3), showing the adverse effect of the pixelized boundary.

Figure 1 shows the mesh convergence analysis, where (3) is plotted against the total number of DOFs—which is proportional to the cost of solving the problem and increases with finer FE meshes. The results reveal that using a pixelized representation is detrimental to band structure analysis, as it has a considerable error in predicting the bandgap. The enriched FEA has not only higher accuracy but also a higher convergence rate (1.44 vs. 0.44).

COMPUTATIONAL DESIGN VIA ENRICHED TOPOLOGY OPTIMIZATION

Topology optimization (TO) was introduced in the late 80s as a means to find optimal structural designs. In a nutshell, in TO an optimal structure is obtained through an iterative procedure that performs FEA and uses sensitivity information to improve topology for the next iteration. Building on the aforementioned advantages of enriched FEA, we propose an enriched TO approach to design a PnC. The objective of the optimization is to maximize the width of the bandgap, which is expressed mathematically as

$$\begin{aligned}\boldsymbol{\phi}^\star &= \arg\max_{\boldsymbol{\phi}\in\mathcal{D}} \mathcal{F} = \min\left(\omega_4^2\right) - \max\left(\omega_3^2\right)\\ &\text{such that } \left[\tilde{\boldsymbol{K}}\left(\boldsymbol{\phi}\right) - \omega_j^2\tilde{\boldsymbol{M}}\left(\boldsymbol{\phi}\right)\right]\tilde{\boldsymbol{V}}_j = \boldsymbol{0} \quad \forall \boldsymbol{k}\in\mathcal{K}, \quad V_{\Omega_i}\le V_c, \quad \phi_{\min}\le\phi_i\le\phi_{\max},\end{aligned} \tag{4}$$

where ω_3 and ω_4 denote the frequencies corresponding to the bands that define the first bandgap, $\boldsymbol{\phi}$ is a vector of design variables, restricted to minimum and maximum values, and we place a constraint on the target volume of inclusion V_{Ω_i}.

Figure 2 shows the results of the enriched TO applied to a PUC composed by two materials. Figure 2a shows the dispersion diagram for an initial PUC design seeded with 25 inclusions—for which there is no bandgap—and Figure 2b shows the band structure obtained after just 50 iterations.

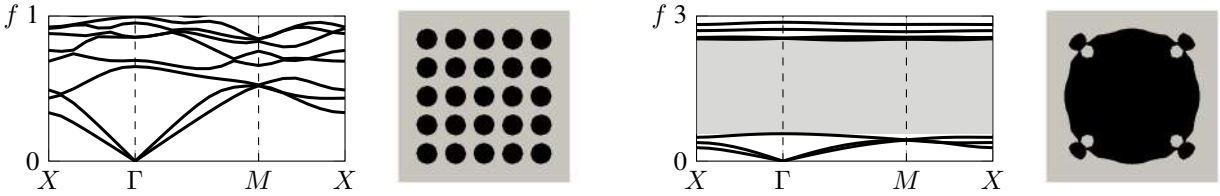

(a) (b)

Figure 2: (a) Band structure obtained for the initial bimaterial design shown; and (b) wide bandgap obtained at the 50th iteration of topology optimization that uses enriched FEA.

CONCLUSIONS

The bandgap mesh convergence results of Figure 1 illustrate that enriched FEA has a clear edge over standard FEA for band structure analysis. About an order of magnitude less DOFs is required for the same level of accuracy, and because DOFs are directly proportional to the cost of solving the problem, for a given accuracy enriched FEA can save considerably on computational costs. Because optimization is essentially a loop over FEA, the cost advantages discussed for bandgap analysis carry over to TO. As a proof of concept, the enriched TO technique was used to design of a phononic crystal composed of two materials for maximizing bandgap. The proposed technique shows tremendous potential for the design of this and other metamaterials that interact with waves.

References

[1] Soghrati *et al.* An interface-enriched generalized FEM for problems with discontinuous gradient fields. *Int. J. Numer. Meth. Eng.* **89**: 991-1008, 2012.

[2] van den Boom *et al.* A stable interface-enriched formulation for immersed domains with strong enforcement of essential boundary conditions. *Int. J. Numer. Meth. Eng.* **120**: 1163–1183, 2019.

AMPLITUDE DEPENDENT EDGE STATES AND DISCRETE BREATHERS IN NON- LINEAR SPATIALLY MODULATED ELASTIC LATTICES

Matheus I. N. Rosa[1], Michael J. Leamy[2] and Massimo Ruzzene [1]
[1]Department of Mechanical Engineering, University of Colorado Boulder, Boulder, USA
[2]School of Mechanical Engineering, Georgia Institute of Technology, Atlanta, USA

Summary We investigate the amplitude dependent behaviour of the spectral properties of elastic lattices with spatial stiffness modulation and cubic non-linearities via a harmonic balance approach. We demonstrate that edge states localized at the boundaries of finite lattices, whose existence are attributed to non-trivial topological properties defined in the linear regime, are robust with non-linearities within a certain amplitude range, although some reduction in the degree of localization may occur. We also demonstrate that bulk modes may experience transitions to discrete breathers localized in the interior of the domain as a function of amplitude. The predicted spectral behaviour is confirmed by forced response computations and direct time domain simulations, and possibilities for future work such as amplitude-driven mode transitions are discussed.

INTRODUCTION

In this work we investigate the role of weak non-linearities on the dynamics of spatially modulated one-dimensional (1D) elastic lattices. In the linear regime, the spatial stiffness modulation was shown to produce non-trivial topological properties characterized by integer-valued Chern numbers [1]. As a result, edge states localized at the boundaries of finite lattices are found to span the spectral gaps as a function of the phase of the stiffness modulation. A transition of the edge states can be exploited for topological pumping by smoothly modulating the stiffness phase along a second dimension, resulting in a robust edge-to-edge transport of energy. This phenomenon may be useful in technological applications and devices that rely on manipulating information through elastic waves.

When it comes to the effects of non-linearities in topological states, previous work has demonstrated amplitude dependent behaviour of topological interface states and 2D edge modes in discrete lattices with cubic non-linearities, suggesting potential for tunable devices based on amplitude-dependent localization and wave transport [2]. A more recent study has demonstrated, numerically and experimentally, an edge-to-bulk transition of 1D interface states using fidget spinners with magnetic interactions [3]. These results suggest that non-linear interactions may lead to amplitude-dependent tunable devices, but also that possible limitations related to the loss of topological protection may need to be considered.

Motivated by these works, we here consider the effects of non-linearities on the edge states of spatially modulated elastic lattices [1]. Seeking to understand the limitations of topological protection, our results indicate that the edge states maintain robustness within a certain amplitude range, but the degree of localization may decrease when their branch tangentially approximates the bulk. We also explore mode transitions experienced by the bulk modes as they become localized in the interior of the lattice for increasing amplitudes, in a manner reminiscent of discrete breathers [4]. Our results are obtained through a harmonic balance approach and confirmed by forced response computations and direct time domain simulations.

NON-LINEAR SPATIALLY MODULATED ELASTIC LATTICES

We consider one-dimensional (1D) lattices of equal masses m connected by springs whose constant k_n is defined by the sampling of a sinusoidal function (Fig. 1a), *i.e.* $k_n = k_0[1 + \alpha\cos(\frac{2\pi np}{q} + \phi)]$. By fixing $\frac{p}{q} = 1/3$, we define a periodic lattice with 3 masses per unit cell (since $k_{n+3} = k_n$), whose topological properties are interpreted based on variations of the phase ϕ [1]. Non-linearities of the cubic type are introduced by considering restoring forces of the from $F = k_n(\Delta x + \epsilon\Delta x^3)$, where ϵ is a small parameter. The governing equation of motion for a mass with index n is expressed as

$$m\ddot{u}_n + k_n(u_n - u_{n+1}) + k_{n-1}(u_n - u_{n-1}) + \epsilon k_n(u_n - u_{n+1})^3 + \epsilon k_{n-1}(u_n - u_{n-1})^3 = 0.$$

We investigate the behaviour of a free-free finite lattice comprising $N = 42$ masses with parameters $m = k_0 = 1, \alpha = 0.6, \phi = 0.35\pi,$ and $\epsilon = 0.01$ via a Harmonic Balance (HB) approach, resulting in the amplitude dependent spectrum of Fig. 1b. In the figure, blue dots correspond to frequencies ω that numerically solve a set of non-linear algebraic equations (resulting from the HB approach) when a certain amplitude level is imposed, here corresponding to the L_2 norm of the displacements of all masses along the lattice. Shaded grey areas correspond to the limits of the dispersion bands, also estimated as a function of amplitude via a Multiple Time Scales analysis [5]. For very low amplitudes ($A \approx 0$), the linear analysis predicts the existence of a left-localized edge state (branch a) and a right-localized edge state (branch c) inside the gaps [1], while bulk modes within shaded grey regions are non-localized, globally spanning modes. As amplitude increases, the frequencies of the finite lattice modes tend to shift to the right, representing the typical hardening behaviour associated with positive cubic non-linearities. The evolution of the mode shapes of the edge states with amplitude (first harmonic) are displayed in Figs. 1(c,d), while the behaviour of two bulk modes (branches

d and e) are also tracked as a function of amplitude and are reported in Figs. 1(e,f). We note that the branch of the first edge state (branch a) remains within the gap for the considered amplitude range, and as a result it maintains its left-localized nature (Fig. 1c). However, the branch of the second edge state (branch c) slowly approaches a region populated by bulk modes, and as a result its degree of localization decreases (Fig. 1d). The branch of this edge state remains tangential with the bulk, and does not cross or enter the bulk region, which suggests that topological protection is maintained even though resulting in a lower degree of localization. Finally, we observe that a few bulk modes (such as branches d and e) detach from the bulk regions as a function of amplitude, resulting in a transition of their mode shapes to localized at one or more regions in the interior of the lattice, which is reminiscent of discrete breathers. This behaviour is aligned with observations in the literature of discrete breathers where modes of this kind are formed through bifurcations of band edge plane waves in monoatomic lattices [4].

In the talk we also show results for forced response computations to confirm the amplitude dependent behaviour of the finite lattice spectrum, in addition to direct time domain simulations. We discuss further possibilities associated with amplitude-driven mode transitions, such as edge-to-edge transitions (topological pumping) or even edge-to-interior localization transitions by exploiting the discrete breathers.

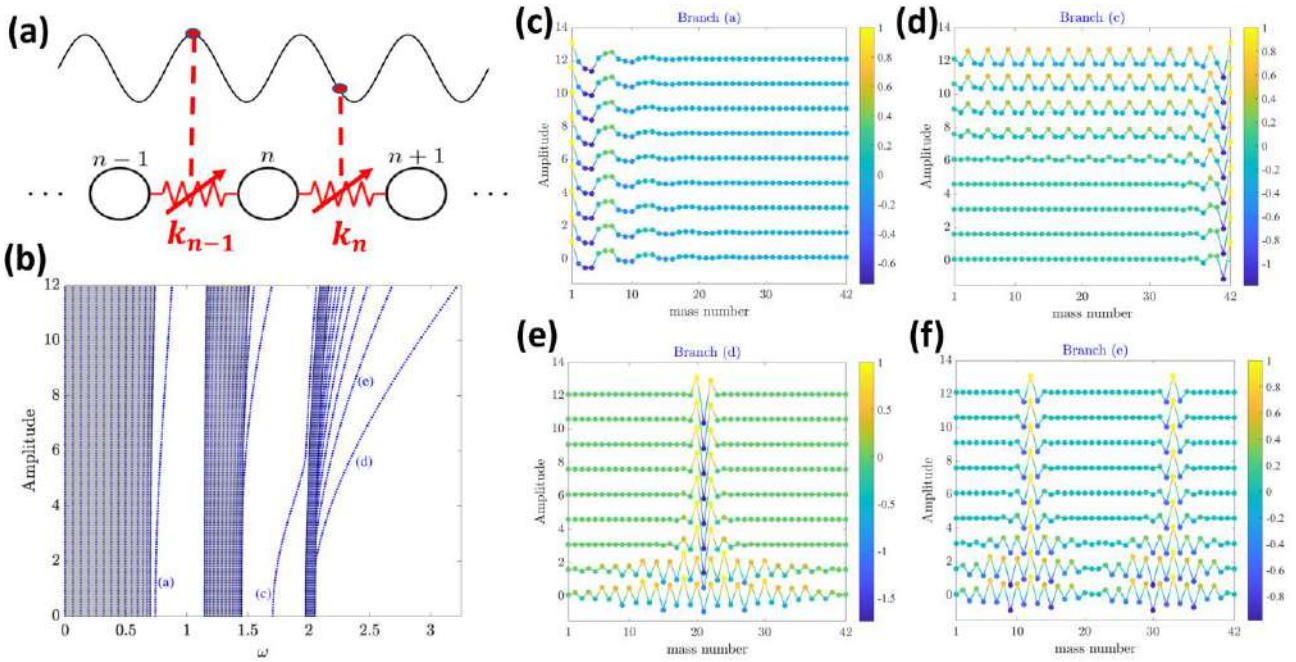

Figure 1. Amplitude dependent behaviour of non-linear spatially modulated elastic lattices. (a) Schematic of 1D lattice of masses connected by non-linear springs that provide a restoring force $F = k_n(\Delta x + \epsilon \Delta x^3)$, whose constant k_n is defined by the sampling of a sinusoidal function, *i.e.* $k_n = k_0[1 + \alpha \cos(2\pi np/q + \phi)]$. (b) Amplitude dependent spectrum of finite lattice with N=42 masses with free-free boundary conditions and parameters $m = k_0 = 1, \alpha = 0.6, \phi = 0.35\pi,$ and $\epsilon = 0.01$. Blue dots correspond to modes of the finite lattice as a function of amplitude, while shaded grey areas denote the limits of the dispersion bands as a function of amplitude. The variation of the mode shape of the edge states (branches a,c) with amplitude are displayed in (c,d), while transitions from globally spanning to discrete breather experienced by bulk modes (branches d and e) are illustrated in (e,f).

ACKNOWLEDGEMENTS

This work is supported by the National Science Foundation (NSF) through the EFRI 1741685 grant and by the Army Research Office (ARO) through grant W911NF-18-1-0036.

References

[1] M. I. N. Rosa, R. K. Pal, J. R. F. Arruda and M. Ruzzene. Edge States and Topological Pumping in Spatially Modulated Elastic Lattices. *Physical review letters*, 123 (3): 034301, 2019.

[2] R. K. Pal, J. Vila, M. Leamy and M. Ruzzene. Amplitude-dependent topological edge states in nonlinear phononic lattices. *Physical review E*, 97 (3): 032209, 2018.

[3] J. Vila, G. H. Paulino, M. Ruzzene. Role of nonlinearities in topological protection: Testing magnetically coupled fidget spinners. *Physical Review B*, 99 (12): 125116, 2019.

[4] F. Sergej and C. R. Willis. Discrete Breathers. *Physics reports* 295.5 181-364, 1998.

[5] M. D. Fronk and M. J. Leamy. Direction-dependent invariant waveforms and stability in two-dimensional, weakly nonlinear lattices. *Journal of Sound and Vibration*, 447 137-154, 2019.

NEGATIVE REFLECTION AND POLARIZATION CONTROL OF ELASTIC WAVE VIA BROADBAND METAMATERIAL

Rui Zhu*[1], Zhou Hu [1], Mingye Zheng [1]and Gengkai Hu [1]
[1]School of Aerospace Engineering, Beijing Institute of Technology, Beijing, China

Summary In this work, a non-resonant metamaterial supporting single polarized elastic wave is designed, which provides an excellent solution for broadband wave mode control and can lead to novel elastic wave phenomena. Particularly, total polarization separation, conversion and negative reflection are demonstrated in this presentation by using the so-called singly polarized solid (SPS). Furthermore, by delicate design, the Littrow configuration of elastic wave is demonstrated for the first time. Noting that the extraordinary wave phenomena only depend on the engineered elasticity tensor of the solid metamaterial and therefore, are intrinsically broadband, which can be beneficial for various elastic wave applications.

Introduction

Elastic waves possess various polarization characteristics that are absent in its acoustic and electromagnetic counterparts. Due to the complex polarization nature, achieving broadband control of elastic waves has been proved to be more difficult [1]. Resonance-based elastic metamaterials have been harnessed for peculiar elastic wave manipulations [2,3], but unfortunately, only in a narrow band near the resonant frequency of the metamaterial's microstructure. Recently, phase shifting via metasurfaces demonstrates the capability to separate different polarized waves, which, however, still suffers the narrow-band problem [4]. On the other hand, pentamode metamaterials supporting only one stress state offer a non-resonant way to manipulate elastic wave in a much wider frequency range [5]. In this presentation, a non-resonant metamaterial supporting only one elastic wave mode, called singly polarized solid (SPS), is proposed. Three interesting and potentially useful elastic wave phenomena including polarization separation, mode conversion and negative reflection are demonstrated.

Results

Different from the ordinary solids that support two polarized waves, for example isotropic solids support both longitudinal and transverse waves, the proposed SPS can only support singly polarized wave due to its engineered elastic tensor as

$$C=\begin{bmatrix} C_{11} & \gamma\sqrt{C_{11}C_{22}} & 0 \\ \gamma\sqrt{C_{11}C_{22}} & C_{22} & 0 \\ 0 & 0 & 0 \end{bmatrix}, \tag{1}$$

where $\gamma=\pm1$. For $\gamma=1$, the SPS can only support quasi-longitudinal wave. Especially, under the condition of $C_{11}=C_{12}$, it supports longitudinal wave omnidirectionally as a fluid-like solid. For $\gamma=-1$, the SPS can support longitudinal wave along its principal axis and transvers wave along a particular direction of $\varphi=\tan^{-1}\sqrt[4]{C_{11}/C_{22}}$. Here, we focus on the SPS with $\gamma=-1$ which has richer controllability on wave polarizations.

First, the elastic wave transmission in an ultrathin SPS layer sandwiched between semi-infinite isotropic solids is explored with the parameters running over the full material anisotropy and principal orientation. Selective wave mode filtering is observed in a broad frequency range by only changing the principal orientation of the ultrathin metamaterial layer, as shown in Figure 1 (a) and (b), respectively. Furthermore, by conducting transient elastic wave simulations in the non-resonant metamaterial layer, longitudinal and shear waves can be controlled independently to enable total wave transmission as well as total wave isolation, as shown in Figure 1 (c) and (d), respectively.

Then, mode converting and negative reflection in anisotropic SPS are demonstrated. The equi-frequency curve (EFC) of the SPS is shown in Fig. 2(a), which indicates the unique singly polarized wave supportability. The negative reflection region is marked with yellow colour, which means that the energy flux of reflected wave and incident wave locate in the same side of the surface normal of the traction free boundary. Fig. 2(b) shows that negative reflection occurs after a longitudinal incident wave interacting with the traction free boundary of the anisotropic SPS. Finally, by carefully designing the negative reflection angle and the microstructure of the SPS, a Littrow configuration of elastic wave is achieved for the first time, as shown in Fig. 2(c).

*Corresponding author. E-mail: rzhu83ac@gmail.com

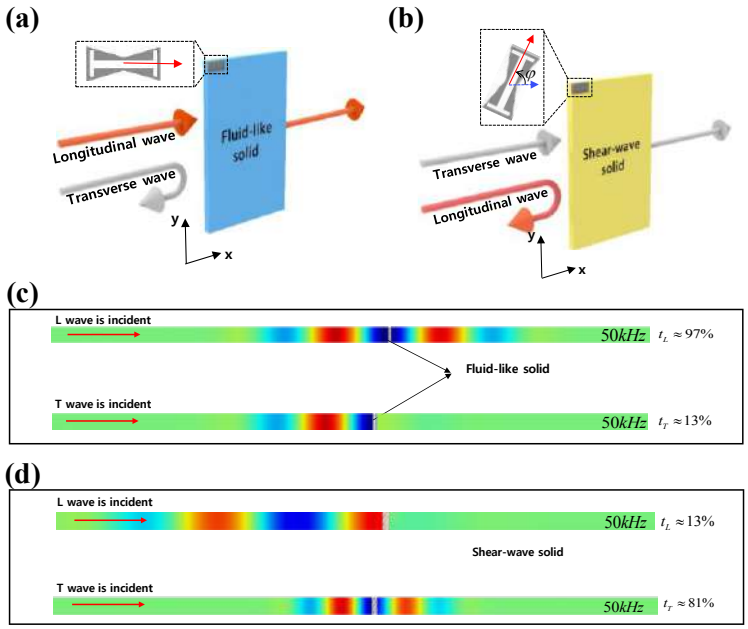

Figure 1. Mode separation in the negative SPS layer (a) without or (b) with rotation of the principal axis of the microstructure, respectively.

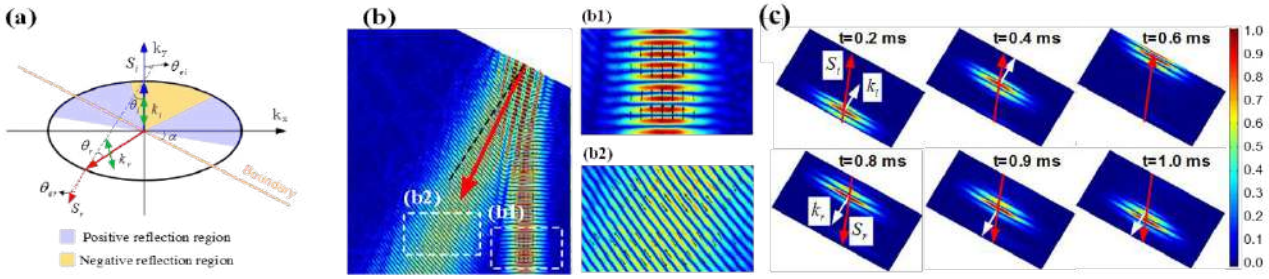

Figure 2. Total mode conversion and negative reflection of elastic wave in an anisotropic SPS.

CONCLUSIONS

In this presentation, the non-resonant metamaterial called SPS is investigated and peculiar elastic wave manipulations are demonstrated. By harnessing the engineered wave properties in SPSs, three interesting and potentially useful elastic wave phenomena including total wave mode separation and conversion, complete negative reflection are theoretically predicted as well as numerically demonstrated. More importantly, unlike other metamaterial-based wave control, those extraordinary wave phenomena do not rely on any resonance and therefore, are intrinsically broadband.

References

[1] Graff K. F. Wave Motion in Elastic Solids. Dover, NY 1975.
[2] Zhu R., Liu X. N., Hu G. K., Sun C. T., Huang G. L. Negative Refraction of Elastic Waves at the Deep-Subwavelength Scale in a Single-Phase Metamaterial. *Nat. Comm.* **5**:5510, 2014.
[3] Kim M. S., Lee W. R., Kim Y. Y., Oh J. H. Transmodal Elastic Metasurface for Broad Angle Total Mode Conversion. *Appl. Phys. Lett.* **112**: 241905, 2018.
[4] Su X. S., Lu Z. C., Norris A. N. Elastic Metasurfaces for Splitting SV- and P-waves in Elastic Solids. *J. Appl. Phys.* **123**:091701, 2018.
[5] Milton G. W., Cherkaev A. V. Which Elasticity Tensors Are Realizable? *J. Eng. Mat. Tech.* **117**:483-493, 1995.
[6] Zheng M. Y., Liu X. N., Chen Y., Miao H. C., Zhu R., Hu G. K. Theory and Realization of Nonresonant Anisotropic Singly Polarized Solids Carrying Only Shear Waves. *Phys. Rev. Appl.* **12**:014027, 2019.

PROGRAMMING MECHANICAL METAMATERIALS BY PERMANENT MAGNETS

Viacheslav Slesarenko*[1,2]
[1]Freiburg Institute for Advanced Studies, Freiburg, Germany
[2]Cluster of Excellence livMatS @ FIT, University of Freiburg, Freiburg, Germany

Summary The enrichment of the design space of mechanical metamaterials by harnessing non-mechanical interactions is in the scope of this research. In particular, it is revealed that the energy landscape of the mechanical metamaterials can be tuned through the embedment of the permanent magnets into the architecture of the metamaterial. The control over the mechanical behavior of the metamaterials consisting of rotating squares through embedment of the modified elementary cells with attractive and repulsive configurations of the magnets is demonstrated experimentally and numerically. Moreover, this approach is shown to be effective in introducing multistability into the materials with initially single equilibrium state. The capacity to manipulate the energy landscape on the global and local scales provides powerful means for the design of advanced mechanical metamaterials.

Nowadays, mechanical metamaterials are mostly treated as functional materials rather than structural, so there is an ongoing quest to add new functionalities and make metamaterials responsive, adaptive, or programmable. One of the ways to achieve these goals is to go beyond mechanical interaction between elements of the metamaterial and harness other physical phenomena. Among a wide variety of the designs, stimuli-responsive metamaterials capable of reacting to the external magnetic field were demonstrated [1]. Unfortunately, a high magnetic field is required for the successful activation, making such metamaterials unfeasible for the practical applications. At the same time, there is another potential approach to harness magnetic interaction by employing permanent magnets embedded into the architecture of the metamaterial. Recently, it was shown in practice that the permanent magnets could provide powerful means to adjust the behavior of the mechanical metamaterials [2], origami structures [3], and energy harvesters [4]. In this study, a new way to program the performance of the metamaterials by modifying their energy landscape through embedment of the permanent magnets in the different configurations is proposed and studied both experimentally and numerically [5].

A classical design of the metamaterial consisting of the rotating squares connected by the soft hinges was adopted for this study (Figure 1e). Under biaxial compression, this particular metamaterial undergoes a buckling-driven transformation from the initial open state to the closed state, as shown in Figures 1a,b for the elementary cell consisting of four rotating squares. In order to program the behavior of the metamaterial, some elementary cells were modified through the embedment of the cubic permanent magnets inside of each rotating square. For the permanent magnets with magnetic moments perpendicular to the metamaterial, each of the modified elementary cells can exist in three configurations: neutral (no embedded magnets) (a), repulsive (c), and attractive (d) (see Figure 1). To study the contribution of the magnetic interaction, the numerical simulations of the infinite structure using FEA software COMSOL 5.4 were performed. The unit cell of the studied metamaterial with the embedded magnets is shown by a dashed square in Figure 1e. The unit cell was subjected to biaxial compression with lateral displacement D_b, while the maximal rotation of the squares was limited by 45° to prevent the contact between squares. The magnetic interaction between two out-of-plane magnets was treated as dipole-dipole interaction with the total force exerted on the second magnet

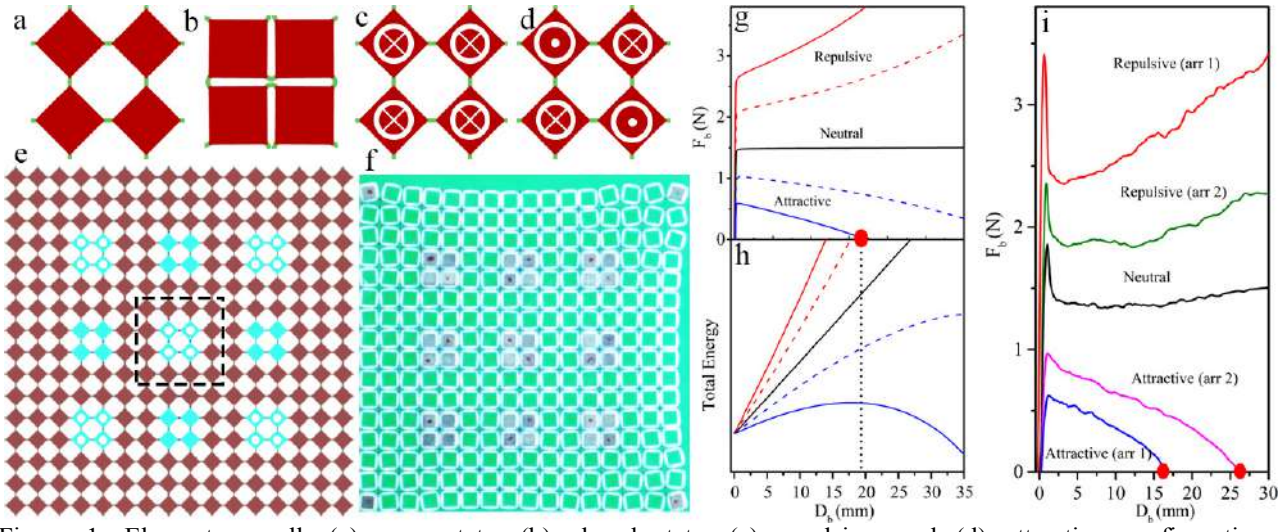

Figure 1. Elementary cell. (a) open state, (b) closed state, (c) repulsive, and (d) attractive configurations. (e) 16x16 metamaterial. Blue squares and white circles – locations of the magnets in arrangements 1 and 2, respectively, dashed square – elementary cell for FEM simulations (f) 3D printed sample (arrangement 1) after snap-through. (g) Numerically obtained force-displacement curves. D_b and F_b are the horizontal displacement and force scaled to 16x16 metamaterial. (h) Dependencies of total energy on the displacement D_b. The curves are independently shifted vertically to have origin in (0, 0). (i) Experimentally obtained and smoothed force-displacement curves for 16x16 metamaterial.

*Corresponding author. E-mail: viacheslav.slesarenko@livmats.uni-freiburg.de, sl.slesarenko@gmail.com

calculated as $\boldsymbol{F} = s\frac{3\mu_0 m^2}{4\pi|\boldsymbol{r}|^5}\boldsymbol{r}$, where $\mu_0 = 4\pi \times 10^{-7}$ H/m is the permeability of the vacuum, $\boldsymbol{r}$ is the vector connecting centers of the first and second magnets, m is the value of a magnetic moment, and $s = +1$ for co-directed (repulsive) configuration or $s = -1$ otherwise. Therefore, the magnetic energy of the elementary cell is equal to $U = \frac{\mu_0}{4\pi}\sum_{ij}\frac{s_{ij}m^2}{|\boldsymbol{r}_{ij}|^3}$, where the sum is taken for all pairwise combinations of magnets. The magnetic interaction between different elementary cells was neglected. The magnetic moment $m = 0.105$ Am^2 was used in simulations due to the good approximation of the magnetic behavior of cubic $5 \times 5 \times 5$ mm Nd-magnets of N42 grade used in the experimental study. The rotating squares were treated as rigid bodies, while the soft hinges were considered as neo-Hookean solids with shear modulus $\mu = 1.1$ MPa and Poisson's ratio of $\nu = 0.46$. For comparison reasons, the biaxial displacement D_b and corresponding force F_b were recalculated for the metamaterial with 16x16 rotating elements.

Figure 1g shows the force-displacement curves obtained for the mechanical metamaterial with a periodic distribution of the modified elementary cells in a neutral (black), repulsive (red), and attractive (blue) configurations. Dashed lines are obtained for metamaterial with weaker magnets ($m = 0.075$ Am^2). Being subjected to equibiaxial compression, the metamaterial with a neutral configuration of the modified elementary cells undergoes buckling which leads to the drastic drop in the effective elastic modulus due to the replacement of initially compressive state of the hinges by the bending in the post-buckling regime. The metamaterials with non-neutral configurations of the modified cells also undergo similar buckling; however, the embedment of the repulsive configuration leads to the increase in the critical buckling force. Moreover, the increase in the magnetic moment for this configuration leads to an increase in the slope of the force-displacement curve in the post-buckling regime, making metamaterial less compliant. In contrast, for the metamaterial with attractive configuration, the slope of the curve becomes negative. Moreover, when the decreasing force reaches zero during loading (red circle on the blue curve), the snap-through to the closed state of the metamaterial rapidly occurs. This instability-driven transition can be explained by examining the total energy of the metamaterial calculated as a sum of magnetic and elastic components (Figure 1h). The energy of the metamaterial with repulsive configuration is a convex function with only one minimum corresponding to the open state. At the same time, the reduction of the distance between attractive magnets leads to a significant decrease in magnetic energy during compression. As a result, the energy function becomes concave, and for large enough m, it has a maximum that corresponds to zero force and leads to subsequent realization of snap-through instability during compression. Therefore, modified metamaterial has two stable equilibrium states, proving that the embedment of attractive magnets can be employed for modification of the energy landscape.

To verify the predicted behavior of the metamaterial with modified elementary cells, 3D-printed mechanical metamaterials with the same design were tested experimentally (Figure 1f). The voids in the interior of the rotating squares enable the quick reconfiguration of the metamaterial to reprogram its behavior through the embedment of the permanent magnets in various configurations. The samples with two various arrangements of the modified elementary cells (blue squares and white circles in Figure 1e) were subjected to the equibiaxial compression in the special transparent fixtures preventing out-of-plane deformation. The force-displacement curves for the displacement D_b and force F_b are shown in Figure 1i. As in the numerical study, for both studied arrangements of the magnets, the repulsive configuration leads to the increase in the buckling strain, and the positive slope of the curve is observed in the post-buckling regime. While the numerical results show that the value of the magnetic moment affects the observed behavior, by experimentally comparing the mechanical performances for two arrangements, a similar role can be assigned to the density of the modified elementary cells in the mechanical metamaterial. The increase in the number of the modified elementary cells amplifies the contribution of the magnetic energy. The snap-through behavior is also captured experimentally for the metamaterials with attractive configurations, as marked by red circles in Figure 1i. Upon reaching the critical strain, the metamaterial rapidly switches to the closed configuration by rotating all square elements until their contact and remains in the closed state even after removal of the external load.

Therefore, it is shown both experimentally and numerically that the rational embedment of the interacting permanent magnets inside the structure of the mechanical metamaterials enables the enhanced control over their performance and can be exploited to introduce multistability to the systems with initially single equilibrium state. In general, this approach can be applied to manipulate the energy landscape of mechanical metamaterials on the global and local scales by harnessing the intricate interplay between elastic and magnetic energies. It can provide a powerful means to design advanced mechanical metamaterials with programmable behavior.

The research leading to these results has received funding from the European Union's Horizon 2020 research and innovation programme under the Marie-Sklodowska-Curie grant agreement №754340. The research received support by the Deutsche Forschungsgemeinschaft (DFG) under Germany's Excellence Strategy – EXC-2193/1-390951807.

References

[1] K. Yu, et al. Magnetoactive Acoustic Metamaterials. *Adv. Mater.* **30**: 1706348, 2018.
[2] K. K. Dudek, R. Gatt, J. N. Grima. 3D composite metamaterial with magnetic inclusions exhibiting negative stiffness and auxetic behaviour. *Mater. Des.* **187**: 108403, 2020
[3] H. Fang, T.-S. Chang, K. W. Wang. Magneto-origami structures: engineering multi-stability and dynamics via magnetic-elastic coupling. *Smart Mater. Struct.* **29**:015026, 2019.
[4] X. Tan, et al. Design, fabrication, and characterization of multistable mechanical metamaterials for trapping energy. *Extreme Mech. Lett.* **28**: 8–21, 2019.
[5] V. Slesarenko. Planar mechanical metamaterials with embedded permanent magnets. *Materials* **13**(6): 1313, 2020.

WAVES IN ENGINEERED METAMATERIAL LATTICES: FROM ELASTIC TOPOLOGICAL STATE TO PIEZOELECTRIC ENERGY HARVESTING

Tian-Xue Ma*[1], Quan-Shui Fan[2], Chuanzeng Zhang[1], and Yue-Sheng Wang[3,2]
[1]Department of Civil Engineering, University of Siegen, Siegen, D-57076, Germany
[2]Institute of Engineering Mechanics, Beijing Jiaotong University, Beijing 100044, China
[3]School of Mechanical Engineering, Tianjin University, Tianjin 300350, China

Summary Recently, the topological interface/surface states are of great interest as they are robust against the local defects and immune from the back-scattering. In this paper, the topological properties of the engineered metamaterial SSH lattices are studied. The metamaterial lattices are formed by locating the metamaterial cavities in desired positions. By varying the coupling strengths between these cavities the topological interface and edge states obtained, which are robust to the local disorder. Based on the topological states, we propose the piezoelectric energy harvester.

INTRODUCTION

In recent years, the field of topological matters is growing rapidly in condensed matter physics. The topological interface/surface states are robust against the local defects and immune from the back-scattering. Recently, the concept of topological matters was extended to classical waves in artificial periodic structures, for example, electromagnetic waves in electromagnetic metamaterials and acoustic/elastic waves in acoustic/elastic metamaterials [1, 2]. Piezoelectric energy harvesting by converting ambient vibrations into low-power electricity is of interest as the rapid development of the electronic industry [3]. As the topological states are usually highly confined at interfaces or edges, these topological states show potential applications in energy harvesting.

RESULTS AND DISCUSSION

It is known that cavities (or the so-called point defects) can be introduced into a perfect elastic metamaterial by breaking the lattice periodicity at desired positions. Since the displacement fields are usually confined in the cavities, the interactions between these cavities can be described by the tight binging model, which is widely used for predicting the band structures of electronic materials. Thus, the cavities can be arranged into any specific lattice, such as the Su-Schrieffer-Heeger (SSH) model, and then the topological characteristics of the elastic waves in such an elastic metamaterial lattice can be mapped to the classic electronic system with the same lattice.

The unit-cell of a two-dimensional (2D) elastic metamaterial slab is illustrated in the inset of Fig. 1(a). The elastic pillars are periodically deposited on a homogeneous slab. The band structure of the unit-cell is shown in Fig. 1(a), where the results are calculated by the finite element method (FEM). It is seen that an absolute phononic band gap (the yellow shadow in Fig. 1(a)) can be obtained in such an elastic metamaterial, which is fundamental for the cavities (the cavity modes). The cavity is formed by removing a pillar from the perfect elastic metamaterial. A metamaterial cavity can support several cavity modes with frequencies inside the phononic band gap. The displacement distribution of the 1st cavity mode is shown in Fig. 1(b). It is clearly observed that the elastic energy is highly confined inside the cavity region. Then various forms of metamaterial lattices can be constructed by using the cavity modes.

We construct the one-dimensional (1D) SSH lattice by the metamaterial cavities. The classic SSH model is given in Fig. 2, where the unit-cell (in the dashed rectangle) is composed of two atoms A and B with the nearest-neighbor coupling. The intra- and inter-coupling strengths are denoted by γ_{a} and γ_{b}, respectively. The super-cell (in the dashed rectangle) of the metamaterial lattice which contains two cavities is shown in Fig. 3(a). The coupling strength between the neighboring cavities can be tuned by altering the distances between the cavities. The wave characteristics of the metamaterial SSH lattices are analyzed by both the FEM and tight binding model. The effective Hamiltonian is derived from the analytic model, and the topological phase of the phononic band gaps can be characterized by the winding number. The results show that when the intra-coupling strength is larger (smaller) than the inter-coupling strength, the phononic band gap is topologically trivial (non-trivial).

The topological interface state can be achieved by connecting the metamaterial lattices with different topological phases, as shown in Fig. 3(b). From the modal distribution one can observe that the elastic waves are highly localized in near the interface. Notably, such topological interface state is robust to the local disorder. Moreover, the topological edge states can be found at the edge of metamaterial lattice with the topological non-trivial phase. In addition, the topological interface and edge states are verified in the fabricated samples. Finally, the mechanical energy of the topological states is collected by utilizing the piezoelectric patches. Compared with the reference slab, the output electric power of the topological metamaterial lattice is significantly increased.

*Corresponding author. E-mail: tianxue.ma@uni-siegen.de

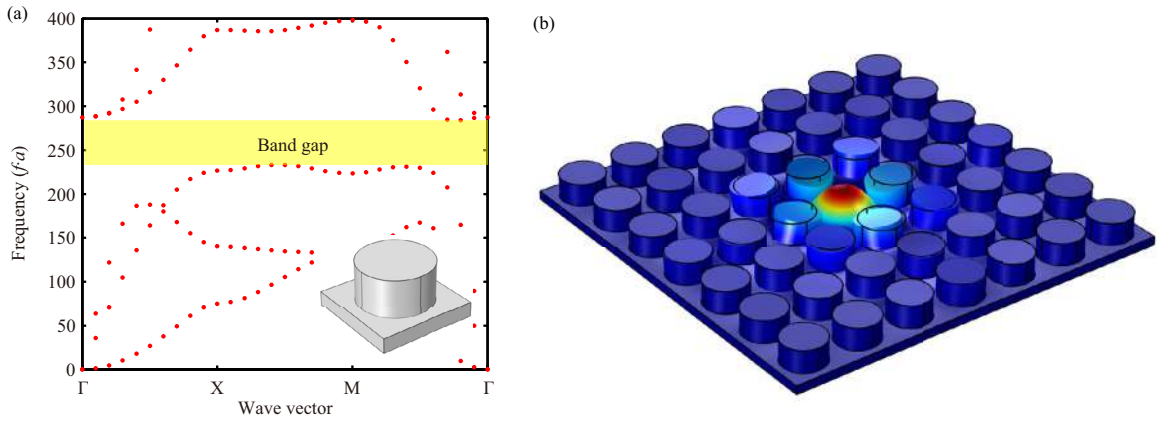

Figure 1: (a) Band structure of the elastic metamaterial slab, where the absolute phononic band gap is indicated by the yellow shadow. The schematic diagram of the unit-cell is plotted in the inset. (b) Displacement field distribution and deformation pattern of the cavity mode.

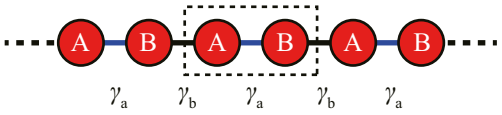

Figure 2: Schematic diagram of the classic SSH model.

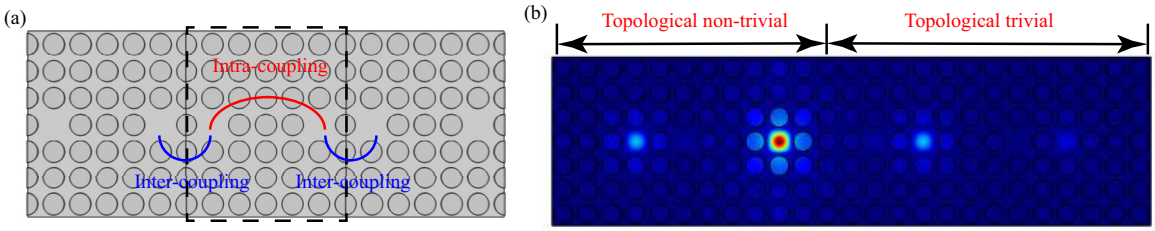

Figure 3: (a) Schematic diagram of the super-cell of the metamaterial SSH lattice. (b) Displacement field distribution of the topological interface state, where the interface is formed by connecting the metamaterial lattices with topological non-trivial and trivial phases.

CONCLUSIONS

The topological properties of the engineered metamaterial SSH lattices are studied. The topological interface and edge states obtained, which are robust to the local disorder. Additionally, the piezoelectric energy harvester is proposed by utilizing the topological states. Note that various phenomena in electronic or quantum systems may be realized in the elastic or acoustic systems using the engineered material lattices.

References

[1] Huber S. D. Topological mechanics. *Nat. Phys.* **12**: 621, 2016.
[2] Ma G, Xiao M., Chan C. T. Topological phases in acoustic and mechanical systems. *Nat. Rev. Phys.* **1**: 1, 2019.
[3] Erturk A., Inman D. J. Piezoelectric energy harvesting. Wiley, 2011.

A KIND OF SINGLE-PHASE FULL BANDGAPS PHONONIC CRYSTALS AND EXPERIMENTAL EVIDENCE

Tianyan Liu*[1], Pengzhou Li [1], and Kun Zhang[1]
[1]Reactor Engineering Sub-institute, Nuclear Power Institute of China, Chengdu, China

Summary Based on understanding of the dynamical explanation of locally resonant phononic crystals, a one-dimensional simple mechanical model is established based on the mass-spring chain model, which can accurately and easily predict the lower and upper frequencies of the first bandgap in locally resonant phononic crystals. In addition, the dynamic model can explain the modal and vibration response of locally resonant phononic crystals. On the basis of the model, a kind of single-phase PCs structure with full-bandgaps is designed, which can omnidirectionally obtain locally resonant bandgaps in a very low frequency range by using the cantilever beam, which have great potential in the field of large-scale mechanical vibration isolation. As a verification, we also made steel samples of this kind of PCs, and the existence of full-bandgaps is confirmed in the experiment.

INTRODUCTION

The phononic crystals make the propagation of vibrations forbidden (infinite structure) or greatly suppressed (finite structure) within the band gap. This characteristic of phononic crystals enables them to be applied in the field of vibration isolation of large mechanical devices[1–3]. However, in some special environments, such as the nuclear island environment, the traditional phonon crystal structure cannot work efficiently. Thus, it is necessary to design a phononic crystals vibration isolation structure composed mainly of steel materials. In this paper, a dynamic model for predicting the upper and lower bandgap edge of locally resonant phononic crystals is proposed. On this basis, a kind of single-phase locally resonant phononic crystals with full bandgap is designed, and its energy band structure and transmission are analyzed. In additional, a steel PCs sample was made, and the existence of full-bandgaps is confirmed in the experiment.

MECHANICAL MODEL

In the reference[4], the modal at the bandgap boundary is divided into two vibrational forms, the one is the natural mode of the resonator structure, and the other is one that the free vibration between the resonator and the matrix. Thus, a mass-spring chain model, shown in the fig.1, is proposed.

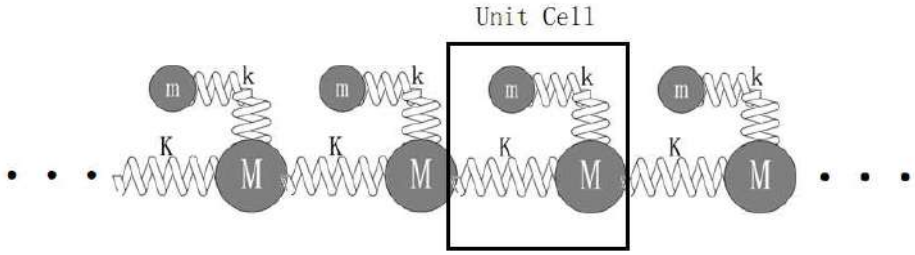

Figure 1. Mass-spring chain schematic diagram. As an one-dimensional infinite model of locally resonant PCs, there are four units' cells (one of them is enclosed by a solid box), which repeat indefinitely on both sides, shown in the figure.

The one-dimensional PCs has periodicity in the direction between left and right, based on Bloch Theorem, both U_L and U_R are demanded to satisfy the constrain determined by the following equation,

$$U_R = U_L e^{ik(-r_R+r_L)} = U_L e^{-ik_p a}. \quad (1)$$

According to the relationship of U_L and U_R determined in Eq. (1), we define k_p as the wave vector in the propagation direction, and introduce a new variable stiffness K',

$$K' = (e^{ik_p\frac{a}{2}} - e^{-ik_p\frac{a}{2}})^2 K. \quad (2)$$

By employing variable K', the unit cell model can be changed to the two-degree-of-freedom model. This 2-DOF model has two eigenvalue branches, which describe two coupled vibration modes of the locally resonant PCs in physics. Fig. 2(a) depicts the vibration mode of upper edge and Fig. 2(b) depicts the vibration mode of lower edge. These two diametrically opposite modes of vibration cut off the vibration transmission. There will be no vibration modes between these vibration modes frequency, which is the first forbidden band of the locally resonant PCs.

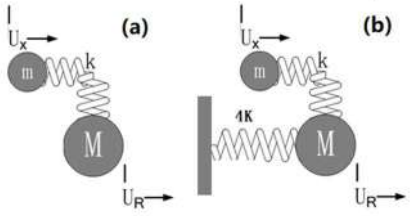

Figure 2. Vibration mode of unit cell.

GEOMETRIC DESIGN AND EXPERIMENTAL EVIDENCE

*Corresponding author. E-mail: rexroi@hotmail.com.

In order to apply it in the vibration isolation structure of the common device, the unit cell size is limited to 10 cm, the thickness of phononic crystal plate is 3 cm, and the lower edge frequency of first band gap generated by the phononic crystal plate should be less than 600 Hz, which covered most pump electromagnetic vibration frequency. According to the requirements, as shown in Fig. 3, it is designed the phononic crystal unit cell structure in this work.

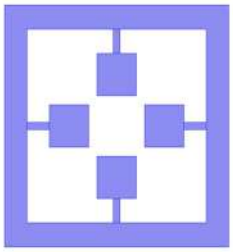

Figure 3. Schematic view of unit cell

The band structure of this PCs is fully discussed in Fig. 4, including isotropic and anisotropic situation. Furthermore, as a validation, the numerical simulation results are compared with the experimental results. Similar transmission is obtained in FIG. 5, which prove the existence of low-frequency bandgaps of single-phase locally resonant PCs.

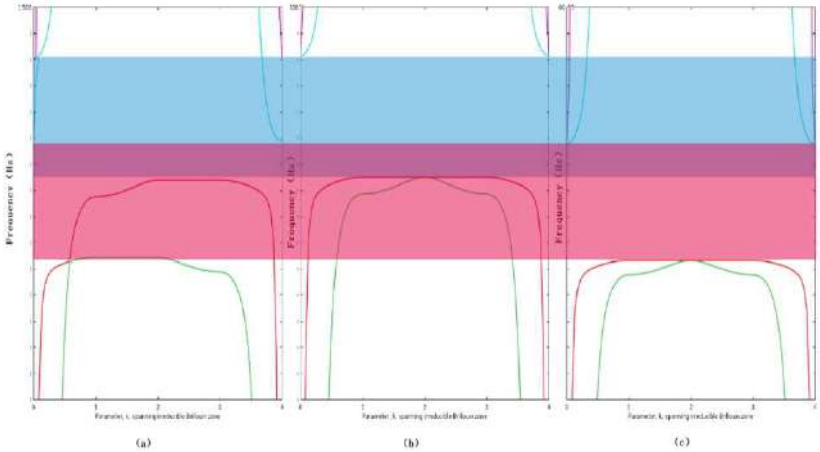

Figure 4. The band structure of designed PCs.

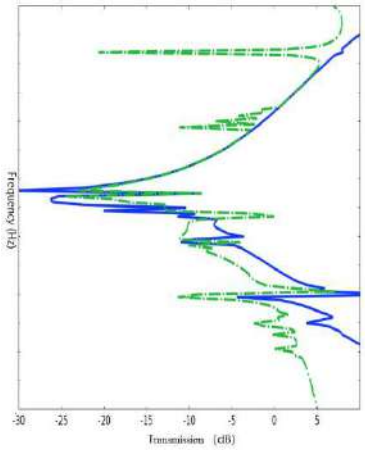

Figure 5. Transmission spectra.

CONCLUSIONS

Through lucubration of the proposed dynamic model, a kind of single-phase locally resonant phononic crystals with very low frequency bandgaps was designed and experimentally verified.These PCs have guiding significance to the design of vibration isolation structures of nuclear devices.

References

[1] Lisenkov I V, Nikitov S A, Popov R S and Koo C 2007 Propagation of Elastic Waves in Phononic Crystals *RADIO Phenom. SOLIDS PLASMA* **52** 1037–48
[2] Hirsekorn M, Delsanto P P, Batra N K and Matic P 2004 Modelling and simulation of acoustic wave propagation in locally resonant sonic materials *Ultrasonics* **42** 231–5
[3] Z. Liu, X. Zhang Y M 2000 Locally resonant sonic materials *Science (80-.).* **289** 1734–6
[4] Gang W, Li-Hui S, Yao-Zong L and Ji-Hong W 2006 Accurate evaluation of lowest band gaps in ternary locally resonant phononic crystals *Chinese Phys.* **15** 1843–8

A NOVEL HIERARCHAL METAMATERIAL WITH TUNABLE BANDGAPS

Hamid Jafari, Soroush Sepehri, Mahmoud Mosavi Mashhadi, Mohammad Reza Hairi Yazdi, and Mir Masoud Seyyed Fakhrabadi *
School of Mechanical Engineering, College of Engineering, University of Tehran, Tehran, Iran

Summary Designing an acoustic/elastic metamaterial with wide and tunable band gaps has been one of the significant fields of study for structural engineers and scholars, and applying hierarchy is one of the latest developed methods to tune the attenuation zones of an elastic metamaterial. In this manuscript, a novel hierarchal concept structure able to exhibit tunable bandgaps is presented. Aside from the geometrical changes occurred in the structure due to the hierarchy, the effect of the change in the elastic modulus and density of the inner structure of the proposed geometry on the dispersion curves of the hierarchal structure is studied numerically using the finite element method and applying Bloch's theorem. The results of the present study can pave the way for designing elastic metamaterials with the ability to present wider and more tunable band gaps in the future.

BACKGROUND

Due to their exceptional mechanical, vibrational, and thermal characteristics, periodic lattice materials have been the subject of numerous studies in the past 20 years. One of the most notable features of such structures is their ability to attenuate specific ranges of frequency in the dispersion curve. In such ranges, which are called bandgaps by many researchers, the wave motion stops, and thus it cannot propagate any further. This phenomenon serves as the main principle in designing the vibration, acoustic and elastic filters. Recently, Jafari et al. [1] studied the wave propagation behavior of architected microtubule-based nano-bio-filters of various topologies and concluded that the geometry and relative density of an architected structure plays a vital role in the wave propagation characteristics of periodic architected structures.

The performance of a filter is evaluated by the location and width of the occurring bandgaps and how it can serve a specific need. In order to be able to engineer and design tunable elastic/acoustic metamaterial, one has to understand the underlying mechanisms of forming bandgaps fully. Typically, two different mechanisms are noted as the main reasons for forming the bandgaps, namely the Bragg scattering [2] and local resonance [3]. While the bandgaps induced by the Bragg scattering phenomenon are typically formed in the wavelengths in the order of the lattice constant, energy localization of the propagating waves is the reason behind the locally resonant bandgaps, which are formed in lower frequencies. Hence, aside from the geometry, mechanical parameters such as the elastic modulus and density may affect the band diagram of the system and lead to the formation of new bandgaps in different regions.

In the present study, a concept hierarchal lattice structure is presented with the ability to exhibit tunable bandgaps. Aside from the topological changes made in the structure by introducing hierarchy, different materials are used in different levels of hierarchy to measure the material effects of the bandgap formation and behavior. Further, the concept of functionally graded thickness is introduced in the structure for various levels of hierarchy, and its effects on the performance of the periodic lattice metamaterials are studied. The structures are modeled using the finite element method, and the wave propagation analysis is carried out by implementing the Bloch's theorem on the provided 2-D hierarchal structures.

FORMULATION

By applying Bloch's theorem, the wave propagation behavior of a periodic structure can be studied by analyzing a single unit cell, thus saving us a lot of time and processing power. According to this theorem, the following equation can be written to describe the deformation of specific point with position vector $q(\vec{R})$ to its corresponding position vector in the reference unit cell $q(\vec{R}_i)$ [4]:

$$q(\vec{R}) = q(\vec{R}_i)e^{\vec{\kappa}.(\vec{R}-\vec{R}_i)} = q(\vec{R}_i)e^{\vec{\kappa}.(m_1\vec{a}_1+m_2\vec{a}_2)} = q(\vec{R}_i)e^{(k_1m_1+k_2m_2)} \quad (1)$$

In the previous equations, $\vec{\kappa}$ is the wave vector with components κ_1 and κ_2 in the direction of $\vec{a}_1$ and $\vec{a}_2$, respectively. Further, the components κ_1 and κ_2 are in a complex form with real part (δ) and an imaginary part (ϵ), serving as the attenuation and phase constants, respectively. Since in the present study, the waves are propagating without attenuation, the real parts are assumed to be zero; hence, the description of the wave vectors components can be reduced to $\kappa_1 = i\epsilon_1$ and $\kappa_2 = i\epsilon_2$.

The schematics of a hierarchal lattice structure of proposed topology are depicted in Figure 1 along with its reciprocal lattice and Brillouin zones. Implementing the finite element method to model the structure, the following eigenvalue problem can be solved to find the dispersion curves of the present structures in the reduced coordinates:

$$\left(\tilde{K}(k_1,k_2) - \omega^2\tilde{K}(k_1,k_2)\right)\begin{bmatrix}q_1\\q_2\\q_i\end{bmatrix} = 0 \quad (2)$$

THEMATIC SESSION SM

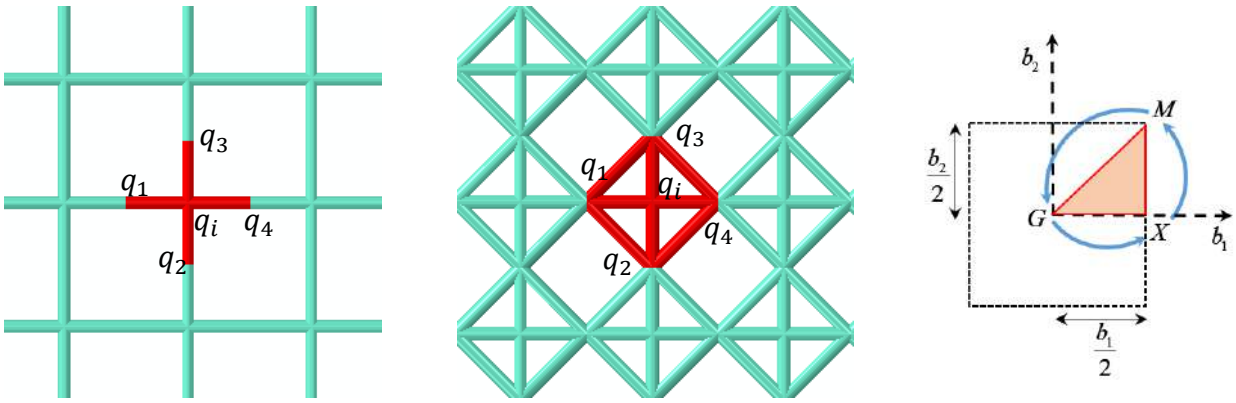

a) b) c)

Figure 1. Periodic tunable architected structure a) Base model b) First order of hierarchy (unit cell as red one) c) FBZ and IBZ

RESULTS AND DISCUSSIONS

The dispersion curves of the rectangular periodic architecture are depicted in Figure 2 along with the band diagram of a hierarchal unit cell. It is observed that increasing the connectivity number of nodes via adding including hierarchy leads to opening new locally resonant bandgaps. The local resonance nature of this bandgap is designated by the flat lower band. Further, since the plotted frequencies are normalized against the first natural frequency of the lateral vibration of a clamped-clamped beam with the same length as that of the rectangular structure, the occurrence of local resonance at points close to the normal frequency $\omega = 2$ proves that the added hierarchy is responsible for the energy localization in the structure. Performing a careful parameter study on the length and mechanical properties of the added hierarchal levels, one can tune this local resonance (and possible other resonances), leading to designing a periodic lattice structure with the ability to exhibit bandgaps in desired frequency ranges.

Another effect of changing the topology of the structure by introducing hierarchy is the widening of the directional band gaps as a result of adding stiffer elements to the structure. This phenomenon can also be tuned by changing the material composition of the whole structure by using different materials for different levels of hierarchy.

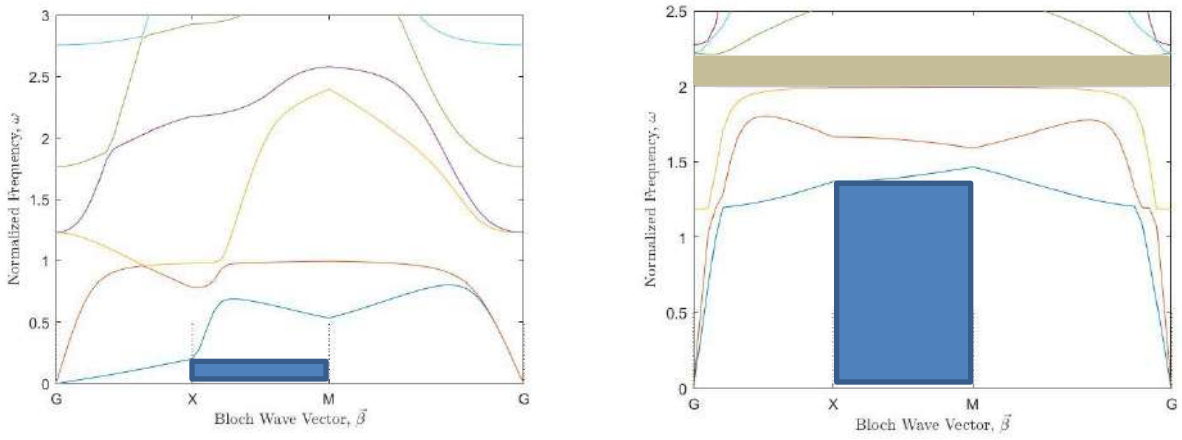

a) b)

Figure 2. dispersion curves of a) rectangular lattice b) hierarchal rectangular lattice

CONCLUSION

In the present manuscript, a novel hierarchal architected structure, capable of exhibiting tunable bandgaps, is presented and its wave propagation behavior is studied using the finite element method and Bloch's theorem. In addition to the geometrical changes made to the structure by adding hierarchy, the effect of the elastic modulus ratio on the dispersion curves is illustrated and further, the implementation of functionally graded thickness in different levels of hierarchy is further scrutinized. The results of the current study prove that by adding different levels of hierarchy to the structure, it can exhibit bandgaps induced by local resonance. This phenomenon opens ways to tune the bandgap position by changing geometrical and material properties of the hierarchal periodic lattice structure.

References

[1] H. Jafari, M. R. H. Yazdi, and M. M. S. Fakhrabadi, "Wave propagation in microtubule-based bio-nano-architected networks: A lesson from nature," *Int. J. Mech. Sci.*, vol. 164, 2019.

[2] M. S. Kushwaha, P. Halevi, G. Martínez, L. Dobrzynski, and B. Djafari-Rouhani, "Theory of acoustic band structure of periodic elastic composites," *Phys. Rev. B*, vol. 49, no. 4, pp. 2313–2322, 1994.

[3] P. Sheng, X. X. Zhang, Z. Liu, and C. T. Chan, "Locally resonant sonic materials," *Phys. B Condens. Matter*, vol. 338, no. 1–4, pp. 201–205, 2003.

[4] A. S. Phani, J. Woodhouse, and N. A. Fleck, "Wave propagation in two-dimensional periodic lattices," *J. Acoust. Soc. Am.*, vol. 119, no. 4, pp. 1995–2005, 2006.

INTEGRATED DESIGN OF MECHANICAL REINFORCEMENT AND MICROWAVE ABSORPTION FOR LIGHTWEIGHT METASTRUCTURE

Yixing Huang[1], Mingji Chen[2]and Daining Fang*[1,2]
[1]State Key Laboratory for Turbulence & Complex Systems, College of Engineering, Peking University, Beijing 100871, P. R. China
[2]Institute of Advanced Structure Technology, Beijing Institute of Technology, Beijing 100081, P. R. China

Summary Poor mechanical properties of microwave absorbing materials which are widely used to protect aircrafts and vessels from radar detection limit seriously their further applications. A metastructure with integrated design of mechanical reinforcement and broadband microwave absorption is optimized and fabricated with nano lossy composites. Theoretical stress solution is given to improve structural parameters with better stress distribution. Lightweight design is achieved by internal cavity carving in the metastructure. The improved flexural strength and absorption performance exhibit effective coordination of multi-scale mechanical strengthening and electromagnetic resonance with small thickness.

INTRODUCTION

Covering microwave absorbing (MA) materials on metallic surfaces is the major way to reduce radar cross section and protect targets from radar detection, which is seriously significant for unit survival in battle fields. However, poor mechanical properties of MA coatings, which is used dominantly in current situation, limit their further application to a great extent[1, 2]. MA Coating peeling, crush and smash are inevitable in the short-term usage period because of mechanical impact and loading in working conditions. Thus, mechanical reinforcement is essential to improve working efficiency and reduce cost of MA materials in engineering sense. In recent years, proposal of metastructure concept makes it possible to integrate spatial mechanical lattice and microwave absorbers into one practical structure, which is promising to enhance the structural mechanical strength of the metastructure for broadband microwave absorption. Typical microwave metastructure is designed with lattice to generate spatial electromagnetic resonance so that more microwave energy in broader frequency bands can be dissipated. The lattice for microwave absorption is often fabricated with polymer embedded with metallic resonant circuit, which is of poor load bearing, while mechanical lattice is usually fabricated with aluminium or steel which is complete microwave reflectors. Thus, combining the function of microwave absorption and mechanical resistance is challenging. In this paper, the metastructure fabricated by nano lossy lattice and carbon/glass fibres with microwave dissipation and mechanical reinforcement is presented, which is promising to solve the conflict between mechanical and electromagnetic designs.

THEORETICAL STRESS DISTRIBUTION

The proposed metastructure is composed of glass fibre reinforced composite (GFRC), carbon fibre reinforced composite (CFRC) and nano lossy lattice made of epoxy resin (ER), multiwall carbon nanotube (MWCNT) and spherical carbonyl iron particles (CI) as shown in Figure 1 (a). In order to enhance the mechanical strength of the metastructure and achieve lightweight properties, the stress should be reduced by optimizing the lattice structural parameters under the same load. The three-point bending model of the metastructure is shown in Figure 1 (a). Five dangerous points that are supposed to be subject to the maximum stress are marked as a_1, a_2, a_3, a_4 and a_5 respectively. Under the circumstances of three-point bending working condition, point a_1 is subject to the maximum compressive stress on the top of the GFRC, point a_2 is subject to shear stress on the interface between the lattice core and the GFRC, point a_3 is subject to shear stress that may tear the rib and the substrate apart in the lattice, point a_4 is subject to shear stress on the interface between the lattice and the CFRC, and point a_5 is subject to the maximum tensile stress at the bottom of the CFRC. According to Euler–Bernoulli beam theory and assumption of plane cross section, the normal stress of GFRC and CFRC in the metastructure under three-point bending can be written as

$$\sigma_{GF}=\frac{MyE_{GF}}{E_{GF}I_{GFz}+E_LI_{Lz}+E_{CF}I_{CFz}}\ (1)\quad \sigma_{CF}=\frac{MyE_{CF}}{E_{GF}I_{GFz}+E_LI_{Lz}+E_{CF}I_{CFz}}\ (2),$$

where E_{GF} (16.43GPa), E_L (4.15GPa) and E_{CF} (21.73GPa) are the measured elastic modulus of the GFRC, lattice core and CFRC respectively, I_{GFz}, I_{Lz} and I_{CFz} are the inertia moment of the GFRC, lattice core and CFRC with respect to the cross section, and M is the moment applied to the metastructure, y is the vertical coordinate. The shear stress of the metastructure can be written as

$$\tau_{xy}=\begin{cases}-\dfrac{F_S\left[E_{CF}S^*_{CF1z}+E_LS^*_{L1z}\right]}{2(P-L)\left(E_{GF}I_{GFz}+E_LI_{Lz}+E_{CF}I_{CFz}\right)}, & (0<y\le A_1+A_3-y_{C1})\\ \dfrac{F_S\left[E_{GF}S^*_{GF1z}+E_LS^*_{L2z}\right]}{2(P-L)\left(E_{GF}I_{GFz}+E_LI_{Lz}+E_{CF}I_{CFz}\right)}, & (A_3-y_{C1}\le y\le 0)\end{cases}\quad (3),$$

where

$$I_{GFz}=\frac{PA_3^3}{6}+2PA_3\cdot\left(y_{C1}-\frac{A_3}{2}\right)^2\ (4)\quad I_{CFz}=\frac{PA_4^3}{6}+2PA_4\cdot\left(H-\frac{A_4}{2}-y_{C1}\right)^2\ (5)\quad I_{Lz}=\frac{(P-L)A_1^3}{6}+2\left(y_{C1}-A_3-\frac{A_1}{2}\right)^2(P-L)A_1+\frac{PA_2^3}{6}+2\left(A_1+A_3+\frac{A_2}{2}-y_{C1}\right)^2PA_2\ (6)$$

$$S^*_{CF1z}=(2H-A_4-2y_{C1})PA_4\ (7)\quad S^*_{L1z}=PA_2\left(2A_1+2A_3+A_2-2y_{C1}\right)+\left(A_1+A_3-y_{C1}+y\right)\left(A_1+A_3-y_{C1}-y\right)(P-L)\ (8)$$

* Corresponding author. E-mail: fangdn@pku.edu.cn

$$S^*_{GF1z}=(A_3-2y_{C1})PA_3 \text{ (9)} \quad S^*_{L2z}=-(y_{C1}-A_3+y)(y_{C1}-A_3-y)(P-L) \text{ (10)} \quad y_{C1}=\frac{PA_3^2+(2H-A_4)PA_4+(2A_3+A_1)(P-L)A_1+(2A_1+2A_3+A_2)PA_2}{2P(A_2+A_3+A_4)+2(P-L)A_1} \text{ (11).}$$

S^*_{CF1z} and S^*_{GF1z} are the inertia moment of the CFRC and the GFRC with respect to the neutral surface, S^*_{L1z} and S^*_{L2z} are the inertia moment of the lattice part which is below or above the calculated point's y coordinate with respect to the neutral surface, and $H=A_1+A_2+A_3+A_4$. Since the shear stress condition above and below the neutral surface is different, the shear stress distribution is in a different pattern when coordinate y is larger or smaller than zero. The designed load is 1100N.

When increasing the height of the lattice rib A_1 from 0.1mm to 5mm, the normal stress in point a_1 and a_5 decreases dramatically from 1200MPa to 200MPa, while the normal stress in point a_2 and a_4 changes slightly (Figure 1 (b)). Thus the design dimension A_1 is essential for dangerous point a_1 and a_5. Shear stress in point a_2 and a_3 also decreases from -70MPa to -20MPa with A_1 increased (Figure 1 (c)). However, when increasing the cavity side length L from 3mm to 20mm, the shear stress in point a_2 and a_3 increases drastically from -20MPa to -150MPa. Considering the stress level, the final parameters are optimized as P=20mm, L=17.5mm, A_1=2mm, A_2=1mm, A_3=0.5mm.

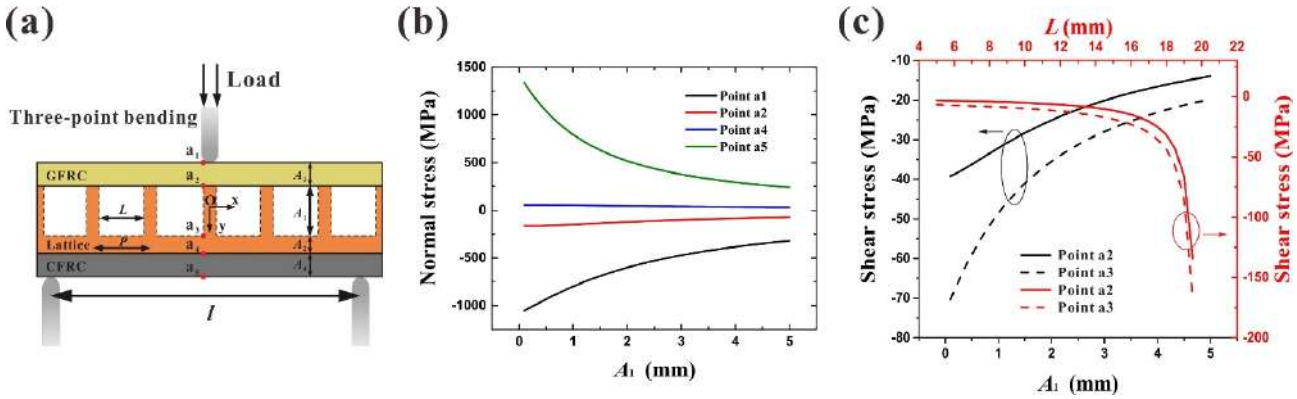

Figure 1: (a) The three-point bending model of the metastructure and dangerous points. (b) The normal stress in the dangerous points in the metastructure when varying A_1. (c) The shear stress in the dangerous points in the metastructure when varying A_1 and L.

MECHANICAL-MICROWAVE ABSORPTION PERFORMANCE

The nano lossy lattice reinforced by MWCNT and CI (ER:MWCNT:CI=48vol%:2vol%:50vol%) in micro-scale and meso-scale and by CFRC and GFRC in macro-scale is the essential way to replace steel-made lattice for broadband microwave absorption (Figure 2 (a)). The measured load-deflection curve in three-point bending test and experimental reflectivity measured by NRL arch method exhibit effective load bearing with maximum load of 1111N and broadband microwave absorption with -9dB bandwidth from 2.54GHz to 22.81GHz crossing the S, C, X, Ku and K bands (Figure 2 (b)). The metastructure is able to resist loading from the deflection of 3mm to 12mm even after the fracture of GFRC (the maximum load), indicating the reliable mechanical reinforcement. Compared with structures reported in previous typical studies[1, 2], the proposed metastructure improves both the flexural strength and the -10dB effective bandwidth-thickness ratio up to 126.2MPa and 2.99GHz/mm, which suggests that the structural design is reasonable to maintain microwave absorption and mechanical resistance in one structure (Figure 2 (c)). With cavity design, the areal density of the metastructure is only 4.11kg/m^2, one-third of the plate form with the same thickness. The combined design methodology of mechanics-electromagnetics is promising for multifunctional structure development.

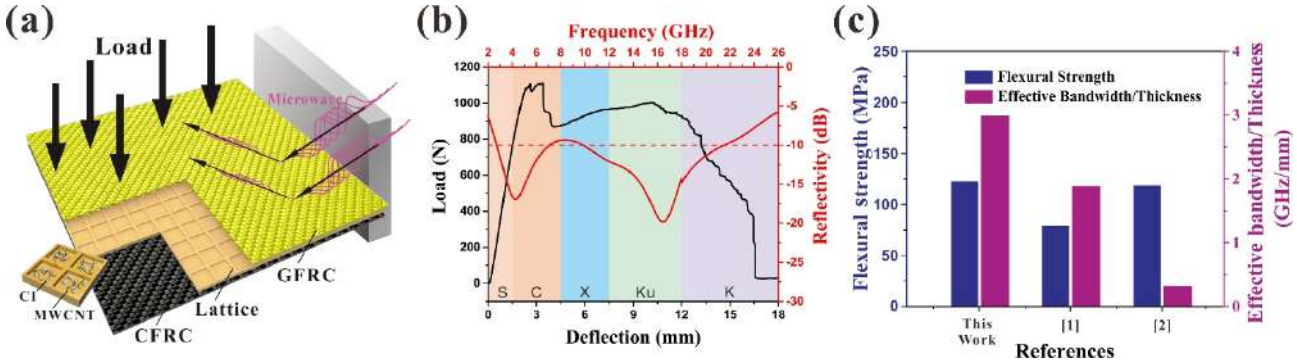

Figure 2: (a) The illustrative diagram of the metastructure with integrated design of mechanical reinforcement and microwave absorption. (b) The load-deflection relationship under three-point bending and reflectivity of the metastructure. (c) Flexural strength and microwave absorption efficiency comparison with counterparts.

References

[1] Khurram A. A., Raza M. A., Zhou P., Subhani T., A Study of The Nanocomposite Sandwich Structures for Broadband Microwave Absorption and Flexural Strength. *J. Sandw. Struct. Mater.* **18 (6)**: 739-753, 2016.

[2] Yang L., Fan H., Liu J., Ma Y., Zheng Q. Hybrid Lattice-core Sandwich Composites Designed for Microwave Absorption, *Mater. Des.* **50**: 863-871, 2013.

NON-RECIPROCAL SOLITONS IN ROBOTIC METAMATERIALS

Martin Brandenbourger*[1], Hans Dekker[1], and Corentin Coulais[1]
[1]Institute of Physics, University of Amsterdam, Amsterdam, the Netherlands

Summary The recent development of robotic metamaterials, which are assemblies of building blocks integrating sensors and actuators, enables the implementation of non-conservative interactions within mechanical systems. This opens the way to the emergence of unique large scale mechanical properties. Here, we use this new platform to generate soliton waves that indefinitely propagate in only one direction. We show that these waves emerge from a balance between mechanical non-linearities and linear non-reciprocal interactions, namely, which preferably transmit motion in one direction. We rationalize the conditions of existence of these solitons and demonstrate that they exist even in the presence of friction. These results establish new ways to reliably transport mechanical energy.

INTRODUCTION

Over the last few years, there has been an explosion of activity on non-reciprocal metamaterials [1, 2, 3], namely, which transmit motion in one direction, but block it in the other. However, to date, non-reciprocal transmission has only been achieved for a limited range of frequencies and input magnitudes. The recent development of robotic metamaterials, which are assemblies of building blocks integrating sensors and actuators, enables the implementation of non-conservative interactions within mechanical systems. Using this approach, recent research [1] have created robotic mechanical metamaterials that break reciprocity at the linear level and have shown that first-of-their-kind unidirectionally amplified waves emerge. This first observation opens the way to new wave manipulations in active metamaterials. Here, we show that the same platform can generate soliton waves that indefinitely propagate in only one direction. We rationalize the conditions of existence of these solitons and demonstrate that they exist even in the presence of friction, which qualifies them as dissipative solitons [4, 5, 6, 7]. These results establish new ways to reliably transport mechanical energy and to store mechanical waves.

OBSERVATION OF A SOLITON

Our metamaterial consists of 20 robotic building block with rotational degrees of freedom (Fig. 1A). Each robotic unit cell consists of a mechanical rotor with a rotational moment of inertia J, of a local control system, and is mechanically coupled to its neighbors via pre-stretched elastic beams with a torsional stiffness C (Fig. 1B). The rotors are made out of a 3D printed pieces mounted on a rotor shaft, and are housed in units that are placed equidistantly in a circle. The local control system takes as input the signals from the angular sensors of neighboring building blocks, and computes an output torque which the motor applies to the rotor. The output torque on a building block i, τ_i, is computed using the non-reciprocal feedback rule $\tau_i = \epsilon(-\phi_{i-1} + \phi_{i+1})$. The parameter ϵ is a feedback parameter indicating the strength of the non reciprocal interaction and ϕ_{i-1} (ϕ_{i+1}) is the angular displacement of the rotor $i-1$ ($i+1$). Once the robotic metamaterial excited with a pulse, a solitary wave packet propagates through the system in only one direction (Fig. 1C). By analyzing this wave, we verify that it is characterized by a constant shape and velocity over time, which qualifies it as a soliton.

REGIME OF EXISTENCE

In Hamiltonian systems, classical soliton theory applies and the soliton stability is only governed by the balance between dispersion and non-linearity. For a given system, a range of solitons shapes and velocities exist, depending on the initial conditions. However, energy is constantly injected in our system via the robotic parts and the viscous friction of each rotor dissipates energy. Therefore, the unidirectional wave observed in our system has to be described by dissipative soliton theory [4, 5, 6, 7], where the balance between dispersion and non-linearity is complemented with a balance between dissipation and driving. These solitary waves are characteristic of active systems and are found in semiconductors, nonlinear optical systems and chemical systems. In this growing field of research, the complexity of the experiments often makes difficult the control of each parameter, in particular the balance between dissipation and driving. This robotic mechanical metamaterial, with its unique control over the driving via the parameter ϵ, enables a fine tuning of this balance. Therefore, we generated a diagram of soliton stability, where the feedback parameter ϵ and the initial velocity of the pulse ω_0 have been varied. The stability of the solitary wave is described by a characteristic exponential time decay α. The experimental phase diagram (Fig. 1D) shows a soliton region (black crosses) that starts at high initial pulses and expands toward lower initial pulses for higher feedback parameters ϵ. As expected, solitons are not observed for low feedback parameters, in which case the wave slowly decreases in amplitude over time, and for high feedback parameters, in which case the wave amplitude self-amplifies and explodes as it propagates. According

*Corresponding author. E-mail: martinbdbg@gmail.com

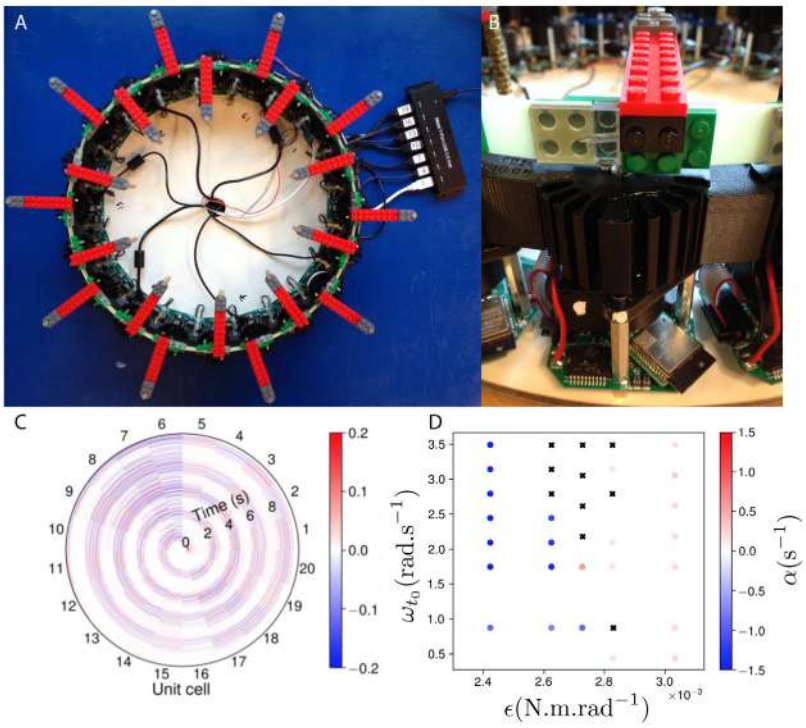

Figure 1: (A) Top view of the mechanical metamaterial constituted of 20 building blocks connected to each other via green elastic rubber bands. (B) Side view of one building block, where the bottom part corresponds to the local control system enabling linear non-reciprocity. (C) Measurement of a solitary wave propagating along the robotic metamaterial. The unit cells are numbered from 1 to 20. The color scale corresponds to the amplitude of oscillation of an oscillator in radians. (D) Phase diagram describing the region of existence of dissipative solitons (black crosses) as a function of the initial speed of the pulse ω_{t_0} and the feedback parameter ϵ. The parameter α describes the characteristic decay time of the propagating waves.

to dissipative soliton theory, for every value of driving, there should be a distinct soliton in terms of its velocity and wave form, irrespectively of the initial conditions. This is confirmed experimentally as we observe that the soliton speed increases linearly a function of the balance between driving and dissipation. Furthermore, for specific initial conditions, we observe breathing solitons, where the wave form of the soliton oscillates between two shapes. This phenomenon has been observed in other discrete systems, such as photonics crystals [5], Josephson junctions [6] and Bose-Einstein condensates [7] and has been referenced as localized breathers. The simplicity of the present mechanical systems brings unique opportunities to study in details the breathing behavior of solitons.

CONCLUSION

By adding nonlinear interactions in a linearly non-reciprocal metamaterial, we observed for the first time a unidirectional dissipative soliton. Its existence is governed by the balance between both dispersion versus non-linearity and driving versus friction. The robotic nature of this metamaterial enables easy exploration of the influence of driving on the active system via a feedback parameter. We show that the dissipative soliton exists for a fixed range of feedback parameters and input velocities. For specific initial conditions, we observe breathing solitons, where the wave form of the soliton oscillates between two shapes. The constant nature of the soliton wave and the fine control that we have over its properties opens new ways of creating materials that act as tunable, non-reciprocal waveguides.

References

[1] Brandenbourger, M., Locsin, X., Lerner, E., and Coulais, C., Non-reciprocal robotic metamaterials. *Nat. commun.*, **10**: 4608-4608, 2019.
[2] Fleury, R., Sounas, D. L., Sieck, C. F., Haberman, M. R. and Alu, A. Sound isolation and giant linear nonreciprocity in a compact acoustic circulator. *Science* **343**: 516519 2014.
[3] Estep, N. A., Sounas, D. L., Soric, J. and Alu, A. Magnetic-free non-reciprocity and isolation based on parametrically modulated coupled-resonator loops. *Nat. Phys.* **10**: 923927 2014.
[4] Gurevich, S. V., Amiranashvili, S., and Purwins, H. G Breathing dissipative solitons in three-component reaction-diffusion system. *Physical Rev.E* **7**: 066201 2006.
[5] Mingaleev, S. F., and Kivshar, Y. S., Self-Trapping and Stable Localized Modes in Nonlinear Photonic Crystals *Phys. Rev. Lett.* **86**: 5474 2001.
[6] Trias, E., Mazo, J. J., and Orlando, T. P., Discrete Breathers in Nonlinear Lattices: Experimental Detection in a Josephson Array *Phys. Rev. Lett.* **84**: 741 2000.
[7] Trombettoni, A., and Smerzi, A., Discrete Solitons and Breathers with Dilute Bose-Einstein Condensates *Phys. Rev. Lett.* **86**: 2353 2001.

MACHINE LEARNING OF MECHANISMS IN COMBINATORIAL METAMATERIALS

Ryan van Mastrigt*[1,2], Corentin Coulais[1], Martin van Hecke[2,3], and Marjolein Dijkstra[4]
[1]Institute of Physics, University of Amsterdam, Amsterdam, the Netherlands
[2]AMOLF, Amsterdam, the Netherlands
[3]Leiden Institute of Physics, Leiden University, Leiden, the Netherlands
[4]Debye Institute, Utrecht University, Utrecht, the Netherlands

Summary Combinatorial metamaterials are metamaterials designed by combining unit cells picked from a discrete set. This discretised design space allows us to explore the limitless structural complexity of metamaterials in a controlled manner. However, analytical and conventional numerical approaches have difficulty in efficiently navigating large design spaces, which grow exponentially with system size. Here we employ machine learning techniques to explore combinatorial metamaterial design. We show that trained convolutional neural networks are able to classify never before seen configurations near perfectly. To study the scalability of this long-correlation classification problem, we investigate the relation between network complexity and configuration size. Our work provides insight into application and scaling of neural networks to complex discrete structure-property maps.

BACKGROUND

Most mechanical metamaterials are designed by tiling a unit cell on a particular grid. The zero-energy deformations, or floppy modes, of such a material depend strongly on how the adjacent unit cells interact with each other, i.e. if they allow for compatible zero-energy deformations. By varying the grid or the design of them, it is possible to design materials with a wide range of exotic properties[1].
More complex metamaterial designs can be explored in a controlled manner by expanding the design space to designs composed by selecting unit cells from a finite set, which allows for exotic material behaviour such as specific deformation response[2], strain rate selectable modes[3], or control of defects[4]. However, for large configuration sizes the design space increases exponentially, which hinders analytic and numeric exploration of the full design space.

RULES FOR LINE MODES

Here, we focus on the design of 2D metamaterials composed by periodic tiling of $n \times n$ super cells on a square grid, where the latter are in turn composed by tiling of $k \times k$ unit cells selected from a finite set. This set consists of a singular bimodal fundamental unit cell and its three 90°rotations, the unit cell and its two deformation modes are shown in figure 1**a**. The complete metamaterial thus consists of a $nk \times nk$ grid of unit cells as is shown in figure 1**b**.
Depending on the precise configuration of the super cell, the metamaterial is able to host a number of floppy modes M_n^k. As n increases, for some super cell configurations M_n^k increases linearly with n. This is due to the configuration supporting line modes - deformations that span the whole material along one spatial direction. It turns out that all super cell configurations can be classified as either having a line mode (class B) or not (class A).
For a super cell to allow for a line mode to exist in the horizontal (vertical) direction, a set of adjacent rows (columns) of unit cells must allow for compatible periodic deformations in the horizontal (vertical) direction while inducing no or the counter-rotating squares mode in the unit cells outside of the set. Thus recognising line modes in super cell configurations means recognising compatible local deformations throughout the whole material, i.e. a set of abstract rules to be followed throughout the material.

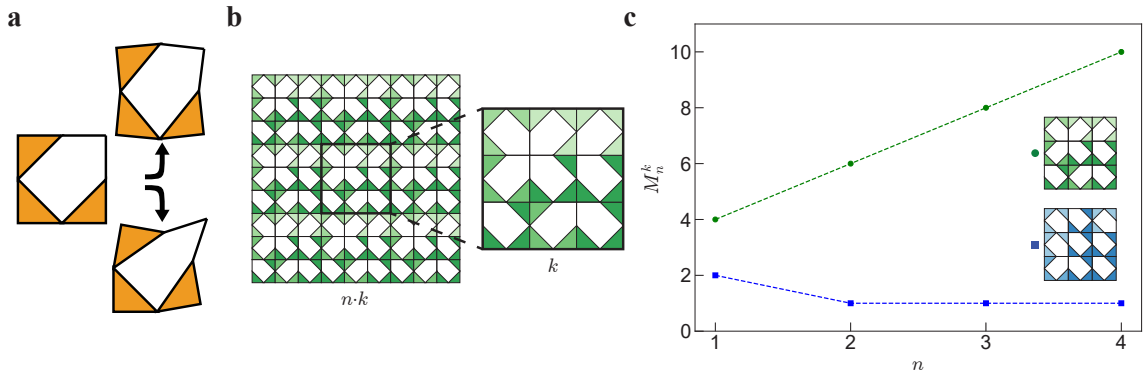

Figure 1: **Material hierarchy and mode scaling. a.** Unit cell with two possible deformation modes. **b.** Super cell (right) tiled periodically in the metamaterial (left). **c.** Number of floppy modes with obc M_n^k as a function of n for two $k = 3$ super cells shown in the legend.

*Corresponding author. E-mail: r.vanmastrigt@uva.nl.

MACHINE LEARNING LINE MODES

However, in general it may be difficult to define such rules, especially for complex unit cells. In the following, we study the application of machine learning to reduce the combinatorial search space for line modes.
A large number of very simple, minimal convolutional neural networks (CNNs) are trained and assessed over training and test sets respectively for a range of super cell sizes. Each CNN consists of a single convolutional layer of n_f filters, a single hidden layer of n_h neurons, and an output layer of two neurons.
In order to fairly assess the performance of the trained nets over the different configuration sizes, recall is used as the performance measure. The recall is defined as the ratio of correctly classified class B configurations over all class B configurations, which is invariant to the class balance of the test set.
The recall as a function of the hyperparameters n_f and n_h is shown in figure 2. Clearly, for sufficiently large neural networks the recall is very high and the performance of the networks are excellent. However, when the network has a relatively small number of parameters, the performance worsens. The difference between the configuration sizes is striking, indicating that non-trivial scaling between line mode complexity and neural network performance is present.

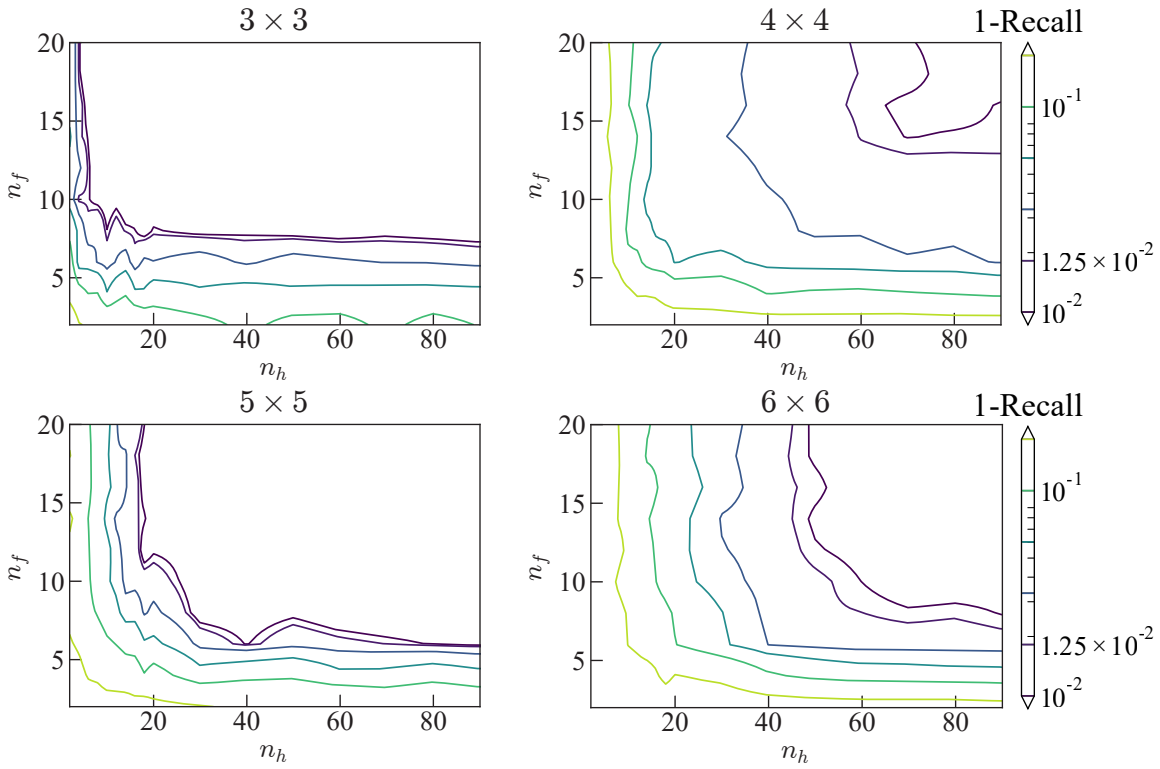

Figure 2: **Trained CNN performance.** The recall as a function of the number of filters n_f and hidden neurons n_h for neural networks trained on different configuration sizes $k \times k$.

CONCLUSIONS

To conclude, we have created a metamaterial that is capable of deforming periodically along a spatial direction, given that the super cell configuration supports such a mode. We have shown that with convolutional neural networks, we are able to classify - with high accuracy - super cells that are able to do this, over a range of super cell sizes. Further analysis of underparameterised neural networks trained on this problem, has shown the presence of a non-trivial scaling relation between super cell size and neural network performance. We intent to explore this scaling further, through rescaling of the recall and in depth analysis of size effects on line modes. Understanding how size effects in metamaterial design propagate through neural network learning is key in further application of neural networks to material design problems.

References

[1] Bertoldi, K., Vitelli, V., Christensen, J., Van Hecke, M. Flexible mechanical metamaterials. *Nature Reviews Materials* **11**: 1-11, 2017.
[2] Coulais, C., Teomy, E., De Reus, K., Shokef, Y., Van Hecke, M. Combinatorial design of textured mechanical metamaterials. *Nature* **535, no. 7613**: 529-532, 2016.
[3] Bossart, A., Dykstra, D.M., van der Laan, J., Coulais, C., Oligomodal mechanical metamaterials. *arXiv preprint arXiv*: **2006.05149**, 2020.
[4] Meeussen, A.S., Oğuz, E.C., Shokef, Y., Van Hecke, M., Topological defects produce exotic mechanics in complex metamaterials. *Nature Physics*: pp.1-5, 2020.

CONSTRUCTION OF DISPERSION CURVE BY PARTS THROUGH ASYMPTOTIC MULTI-SCALE METHOD

Antoine Rallu*[1], Claude Boutin[1], and Stéphane Hans[1]
[1] LTDS CNRS UMR 5513 ENTPE, Vaulx-en-Velin, France

Summary Dynamics at low frequencies of periodic heterogeneous media is conventionally described by the method of homogenization of periodic media, when it exists a scale separation between displacements and the characteristic size of a cell irreducible from the media. At higher frequency, this separation of scales is lost and the homogenization method becomes obsolete. To cross this barrier, a multi-scale method is propose to consider periodic modes over a period composed of several irreducible cells. Around the eigenfrequencies of these multicells periods with periodic boundary conditions, large evolution situations emerge. A new separation of scales is therefore defined between the amplitude of the mode and the characteristic size of the period. The equations governing the modulation are thus obtained, and their nature differs if the mode considered is single or multiple. From the macroscopic modulation equations we can extract an approximation of the fundamental dispersion curve, in the vicinity of the periodic eigenmodes of the multi-cells period. Consequently, a construction by parts of the fundamental dispersion curve is provided.

INTRODUCTION

The goal of this paper is to describe the methodology of construction of parts of the dispersion curve of periodic elastic networks. This process is full and clearly described on a periodic network of elastic resonators : First, a multi-cells approach is presented in order to identify the situation of large scale evolutions, which correspond to the frequency ranges around the eigenfrequencies of the multi-cells period Ω_p, that is a period constituted by p irreducible cells Ω, with periodic boundary conditions. Then, in these situations, the framekork of asymptotic analysis of high-frequency modulation [Rallu *et al.*, 2018] in periodic systems is a applied and yields the equations governing the large scale modulations. This method is illustrated on the case of periodic framed beams, that is periodic structures made of the 1D-repetition of a frame, see Figure 1.

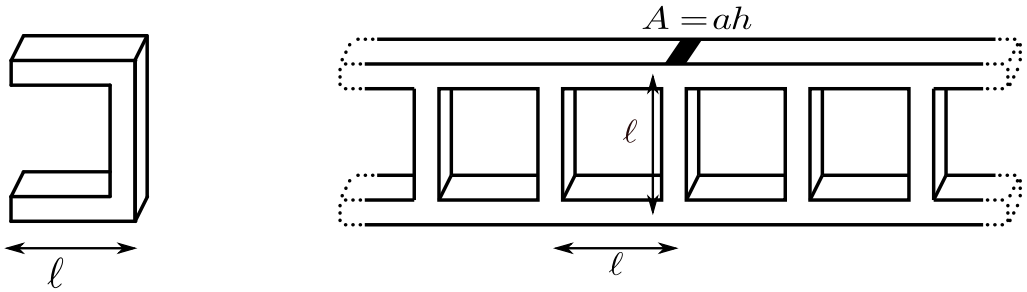

Figure 1: Left : Cell Ω of the reticulated beam. Right : periodic framed beam.

METHODOLOGY

This asymptotic approach is closely related to the HPDM method [Caillerie *et al.*, 1989] and to the modulation analysis of elastic composites [Craster *et al.*, 2010], [Boutin *et al.*, 2012]. At first, one focuses on p-cells period Ω_p, whose angular eigenfrequencies for periodic boundary conditions are denoted ω_J. For frequencies close to ω_J, the modal amplitude envelop varies at a large scale L compared to the length $\ell_p = p\,\ell$ of Ω_p. This assumption of scale separation allows us to define the small parameter $\varepsilon_p = \ell_p/L = p\,\ell/L \ll 1$.

Then the procedure is splitted into the following key steps. 1. Reduce the studied structure to an equivalent discrete model. This is obtained by condensing the balance equations of the beam elements within the period at the nodes of the period. 2. Establish an exact recurrence equation by expressing the balance of the edges nodes of the considered (multi-)cells period. 3. Identify the periodic eigenmodes and eigenfrequencies of the (multi-)cell. 4. Consider frequencies close to a given eigenfrequency and assume a large scale modulation. Then rewrite the recurrence equation in terms of Taylor expansions of the continuous variables that describe the amplitude of the eigenmode. 5. Introduce the asymptotic expansions of the variables and rescale the physical parameters of the element constituting the period. Here, all the local frames are identical, and we consider a slenderness contrast of the local frame as $\ell/a = O(\varepsilon_p^{-1})$. 6. Deduce the various envelope models that apply close to the eigenfrequencies of the considered (multi-)cells.

This approach applied on the transversal kinematics allows to extract the approximation of dispersion curve around the periodic eigenmodes of periods made of one, two and three irreducible cells. All the equations are detailed in [Rallu *et al.*, 2018]. These approximations are given in dashed lines on Figure 2.

*Corresponding author. E-mail: antoine.rallu@entpe.fr

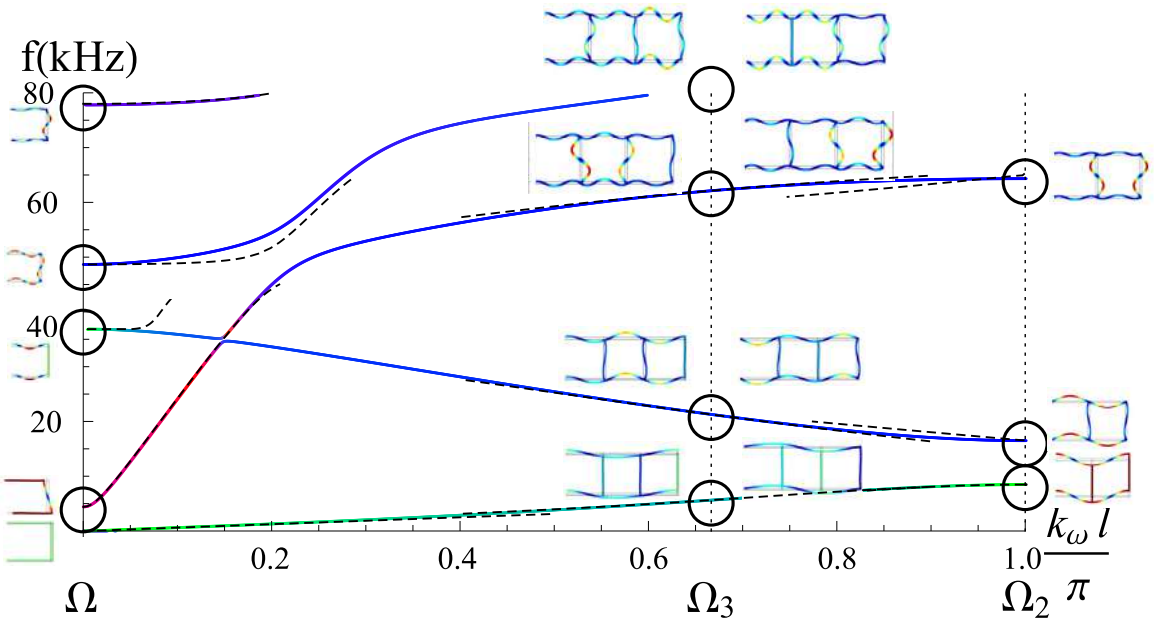

Figure 2: Dispersion curve in the half on the first Brillouin zone for the transversal kinematics. Black circles correspond to the Bloch modes for periods made of one cell (Ω), two cells (Ω_2) and three cells (Ω_3). In dashed lines the asymptotic description of the dispersion curves derived by modulation analysis.

NUMERICAL RESOLUTION

From the finite difference relation established on the first step of the previous methodology, the dispersion tensor of the system can be reached, whose the null determinant yields the dispersion relations. Their numerical resolutions are performed point by point by sampling half of the first Brillouin zone for a sufficiently large number of points. Furthermore, for each solution, the kernel of the dispersion tensor is calculated to identify the associated kinematics. As an illustration the dispersion of the transversal waves of a framed beam whose wall and floor elements are identical is studied. In addition, the kernel kinematics is also depicted, in attributing a given color for each component namely the color of the dot being the linear combination of the three colors weighted by the proportion of each component.

CONCLUSIONS

At low frequencies, the modulation approach matches the classical homogenization method. But at higher frequencies, the nature of the descriptions departs from the usual macroscopic formulation : (i) the macroscopic operator is applied on the amplitude of the periodic eigenmodes, (ii) instead of an unique equivalent model, a family of descriptions is derived for modulation phenomena; this family is associated to the modes of the irreducible or the multiple cells, (iii) the nature of the modulation equations is different whether the mode is simple or multiple. Thanks to these macroscopic descriptions, a piecewise built of the dispersion curve is possible in the vicinity of the periodic eigenfrequencies of Ω_p. Finally, compared to Floquet-Bloch theory, the specificity of the modulation approach is to extract the frequency bands where the large scale modulations are allowed and to determine their governing equations. As an illustration, we applied this methodology to reticulated beams, whose the enriched kinematics and the continuous distribution of mass and stiffness involve wave dispersion curves with several branches. The main outcomes are (i) a given dispersion branch may involves different kinematics, (ii) the modulation analysis performed on multi-cell around rational Bloch number allows to build by parts the dispersion curves and to relate them to an effective analytical description, (iii) these approximations are reliable in a range such that the kinematics do not significantly changed. These results established on a particular beam lattices may be extended to more complexe periodic structures and clarify the physics behind the dispersion curves.

References

[Boutin *et al.*, 2012] BOUTIN, C., RALLU, A. et HANS, S. (2012). Large scale modulation of high frequency acoustic waves in periodic porous media. *The Journal of the Acoustical Society of America*, 132(6):3622–3636.

[Caillerie *et al.*, 1989] CAILLERIE, D., TROMPETTE, P. et VERNA, P. (1989). Homogenisation of periodic trusses. *In IASS Symp. 10 Years Prog. Shell Spat. Struct.*, Madrid.

[Craster *et al.*, 2010] CRASTER, R. V., KAPLUNOV, J. et PICHUGIN, A. (2010). High-frequency homogenization for periodic media. *In Proceedings of the Royal Society of London A: Mathematical, Physical and Engineering Sciences*, page rspa20090612. The Royal Society.

[Rallu *et al.*, 2018] RALLU, A., HANS, S. et BOUTIN, C. (2018). Asymptotic analysis of high-frequency modulation in periodic systems. analytical study of discrete and continuous structures. *Journal of the Mechanics and Physics of Solids*, 117:123 – 156.

Thematic Session FS

K108858 - FS01 - Acoustics - Keynote

ACOUSTICS OF WHISTLING KETTLES, MATING MICE AND DRIPPING TAPS

Anurag Agarwal* [1]
[1]Department of Engineering, University of Cambridge, Cambridge, United Kingdom

Summary In this talk, we will explore the sound generation mechanisms from three everyday phenomena.

WHISTLING KETTLES

The whistle in a steam kettle provides a good example of a hole tone system, in which two orifice plates are held a short distance apart in a cylindrical duct. This setup leads to distinct audible tones for a large range of flow rates. In this talk we will see that the whistle's behaviour is divided into two regions of operation Reynolds numbers (based on orifice diameter and jet velocity). Below a critical Reynolds number the whistle exhibits a near-constant frequency behaviour. A mathematical model based on a Helmholtz resonator explains this behaviour well. Above the critical Reynolds number, the whistle exhibits a constant Strouhal number behaviour. We will see that in this regime the resonant modes of the upstream duct are coupled with the vortex shedding at the jet exit.

MATING MICE

Mice produce ultrasonic mating calls in the form of a whistle. Our experimental results show that the whistle is not caused by a hole tone mechanism or superficial vocal fold vibrations as previously thought. We will see that mice use a wall/edge-jet based resonance mechanism to produce robust ultrasonic whistles.

DRIPPING TAPS

A leaky dripping tap produces a distinctive and irritating plink. The plink is caused by a small drop falling into a larger body of liquid and has been the subject of scientific curiosity for more than a century. Previous investigators have determined that the source of the sound is a pulsating air bubble trapped under the surface of the water during the drop impact. However, it was not clear just how the underwater bubble produces the plink heard above water by the human ear. Through a series of synchronised high-speed video and audio measurements we will see that the airborne sound field is not simply the underwater field propagating through the water-air interface, as had previously been assumed. We propose an alternative hypothesis that the oscillating bubble induces oscillations of the water surface itself, giving a more efficient mechanism by which the underwater bubble drives the airborne sound field. A model for this new hypothesis produces good agreement with experimental data.

ACKNOWLEDGEMENT

The work presented in this talk was made possible through collaborations with Ross Henrywood, Elena Mahrt, Coen Elemans, Sam Phillips, and Peter Jordan.

References

[1] R. H. Henrywood and A. Agarwal. The aeroacoustics of a steam kettle. *Physics of Fluids*, 25(10):1–23, 2013.
[2] E. Mahrt, A. Agarwal, D. Perkel, C. Portfors, and C. Elemans. Mice produce ultrasonic vocalizations by intra-laryngeal planar impinging jets. *Current Biology*, 26(R1–R3), 2016.
[3] S. Phillips, A. Agarwal, and P. Jordan. The sound produced by a dripping tap is driven by resonant oscillations of an entrapped air bubble. *Scientific Reports*, 8(1):1–12, 2018.

*Corresponding author. E-mail: aa406@cam.ac.uk.

EDUCING NOZZLE REFLECTION-COEFFICIENTS FROM TURBULENT JET DATA

Robin Prinja* [1], Eduardo Martini[2], Peter Jordan[1], Aaron Towne[3], and André V. G. Cavalieri[2]
[1]Département Fluides, Thermique et Combustion, Institut Pprime, Université de Poitiers, Poitiers, France
[2]Instituto Tecnológico de Aeronáutica, São José dos Campos/SP, Brazil
[3]Department of Mechanical Engineering, University of Michigan, Ann Arbor, MI 48109, USA

Summary This work studies resonance mechanisms that underpin tones that occur in high Mach-number subsonic jets due to resonance between upstream and downstream traveling waves that are coupled by reflection in the nozzle plane and at downstream turning points. Local stability analysis is used based on mean velocity profiles near the nozzle exit plane. Projection of Large Eddy Simulation (LES) data on the eigenbasis shows that Kelvin-Helmholtz (KH) and a small selection of upstream and downstream traveling guided modes have substantial amplitudes, and they accurately reconstruct the LES data illustrating the low-rank nature of the resonance. Following the eduction of mode amplitudes, a procedure is implemented in order to compute reflection-coefficients in the nozzle plane, which are necessary for developing predictive resonance models.

INTRODUCTION

Acoustic tones observed in Mach 0.9 jet have been shown to be associated with a family of linear waves that resonate in the jet between the nozzle exit plane and downstream turning points ([1] and [2]). The same waves have been shown to be responsible for jet-flap interaction tones [3]. At the end locations, the resonance models ([3]) require knowledge of reflection-coefficients. The goal of this work is to educe these coefficients using LES data.

METHODOLOGY

It has been shown that waves in turbulent jets can be modelled using linear stability theory ([1] and [2]), where stability analysis is done on the time-averaged mean flow. We perform a local analysis at $0.3D$ downstream from the nozzle exit. Mean flow from LES is fitted with $tanh$ analytical profile. We consider azimuthal mode, $m = 0$ and Strouhal number, $St = fD/U_{jet} = 0.39$, which corresponds to the resonance mode. The normal mode ansatz is,

$$q = q(r)e^{i\alpha x}e^{-i2\pi ft} \tag{1}$$

where, α is the axial wavenumber and $q(r)$ is the radial structure of the fluctuation. Formulating the system as an eigenvalue problem ($Aq = i\alpha Bq$), we get the eigenspectrum as shown in Fig. 1(a). The modes of interest are marked with crosses (for details about other modes, see [4]). The only unstable mode is KH ($\times$, k^+_{KH} mode). The resonating modes are indicated by green, blue and red crosses: ($\times$, k_2^+), ($\times$, k_1^-) & ($\times$, k_3^-), where the superscripts - and + refer to the generalised group velocity.

Biorthogonal projections

Instability wave amplitudes, undetermined in linear analysis, are obtained by biorthogonal projections. Prior to projection, the eigenfunctions are normalised such that they have (i) $\int_0^\infty [\mid u'_x \mid^2 + \mid u'_r \mid^2] r\, dr = 1$ (ii) $\angle u'_x = 0^o$ at $r = 0$, where u'_x and u'_r are axial and radial fluctuations respectively, and r is the radial coordinate. The LES data is then projected on to 4 modes of interest as follows:

$$\mathbf{a}_i(n) = (q_i^{ad})^H\ B\ q_n^{LES} \tag{2}$$

where, q_i^{ad} is the adjoint eigenfunction of the i^{th} mode, H is the hermitian transpose and q_n^{LES} is the LES fluctuation data from n^{th} LES realization (we have 153 realizations) and $\mathbf{a}_i$ is the vector of projection coefficients for the i^{th} mode. A rank-4 reconstruction of the LES data, using these modes, is shown by plotting u'_x PSD in Fig.1(b).

Reflection-coefficient evaluation

In the nozzle exit plane, we compute reflection-coefficients for 2 pairs of modes (k_2^+/k_1^- and k_2^+/k_3^-). Each pair involves a k^- wave that reflects at the nozzle exit plane. As we have projection coefficients at $x/D = 0.3$, we shift them to $x/D = 0$ using the ansatz (equation 1). From here onwards, we refer to the projections coefficient vector at $x/D = 0$ as $\mathbf{a}$.

The amplitude of a k_2^+ wave is related to the amplitudes of k^- waves through the reflection-coefficients as,

$$\mathbf{a}_2^+ = R_2^1\ \mathbf{a}_1^- + R_2^3\ \mathbf{a}_3^- + R_2^o\ \mathbf{a}_o \tag{3}$$

*Corresponding author. E-mail: robin.prinja@univ-poitiers.fr.

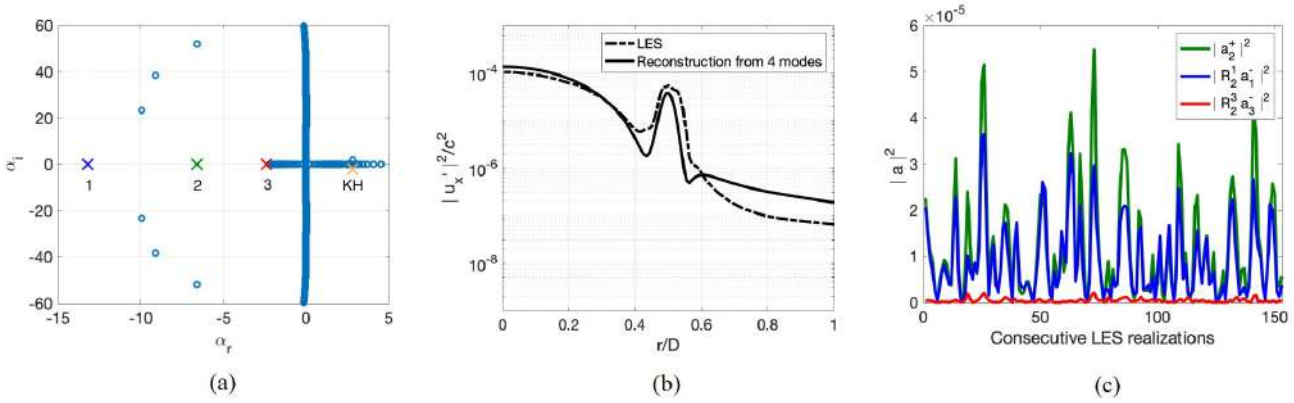

Figure 1: $St = 0.39$, $m = 0$. **(a)** Eigenspectrum. **(b)** Rank-4 reconstruction of u_x' PSD (here, c is the sound speed). **(c)** $\mid \mathbf{a}_2^+ \mid^2$, $\mid R_2^1\, \mathbf{a}_1^- \mid^2$ and $\mid R_2^3\, \mathbf{a}_3^- \mid^2$ (see equation 3 for reference) are plotted against consecutive LES realizations.

The last term on the R.H.S. accounts for reflections from other upstream traveling waves and transmissions from nozzle boundary layer fluctuations. Taking the dot product of equation 3 with $\mathbf{a}_1^{-H}$ leads to,

$$\mathbf{a}_2^+ \cdot \mathbf{a}_1^{-H} = R_2^1\, \mathbf{a}_1^- \cdot \mathbf{a}_1^{-H} + R_2^3\, \mathbf{a}_3^- \cdot \mathbf{a}_1^{-H} \tag{4}$$

where we have assumed that all other waves are uncorrelated with the k_1^- wave (i.e. $\mathbf{a}_o \cdot \mathbf{a}_1^{-H} = 0$). This assumption is supported by the negligible projection coefficients obtained for all other modes and by the accurate reconstruction of the LES by the rank-4 model. Similarly, taking the dot product of equation 3 with $\mathbf{a}_3^{-H}$ and using $\mathbf{a}_o \cdot \mathbf{a}_3^{-H} = 0$, we get,

$$\mathbf{a}_2^+ \cdot \mathbf{a}_3^{-H} = R_2^1\, \mathbf{a}_1^- \cdot \mathbf{a}_3^{-H} + R_2^3\, \mathbf{a}_3^- \cdot \mathbf{a}_3^{-H} \tag{5}$$

We can solve the equations 4 and 5 together to obtain the reflection-coefficients.

RESULTS

A coherence analysis is performed using the educed wave amplitudes to establish which modes are resonating at a given frequency. The mode pairs identified by this analysis are consistent with the scenarios proposed by [1]. Reflection-coefficients (RC) are then computed using the approach described above, giving the following results for the RC magnitudes,

$$\mid R_2^1 \mid = 0.62\ (k_2^+/k_1^-\ \text{pair})\ \&\ \mid R_2^3 \mid = 0.89\ (k_2^+/k_3^-\ \text{pair}).$$

The respective contribution of k_1^- and k_3^- modes to the k_2^+ considered can be appreciated in Fig. 1(c), where the square magnitude of projection coefficients for k_2^+, and the contributions of k_1^- and k_3^- modes are plotted w.r.t FFT realisations. Fig. 1(c) shows that k_2^+ sharply follows the k_1^- demonstrating that k_2^+ is primarily driven by the reflection of k_1^- in the nozzle plane, consistent with the scenario proposed in [1].

A similar approach was implemented for other frequencies and will be shown at the conference.

CONCLUSIONS

Reflection-coefficients in the nozzle plane of a turbulent jet of Mach 0.9 were educed from LES data. The approach involved: (i) the eduction of wave amplitudes from the turbulent data by its projection on the eigenbasis of a local stability analysis in the vicinity of the nozzle plane, and (ii) the calculation of RC via consideration of a low-rank model of the resonance dynamics.

References

[1] Towne, A., Cavalieri, A. V., Jordan, P., Colonius, T., Schmidt, O., Jaunet, V., Brès, G. A. Acoustic resonance in the potential core of subsonic jets. *J. Fluid Mech.* **825**: 1113-1152, 2017.

[2] Schmidt, O., Towne, A., Colonius, T., Cavalieri, A., Jordan, P., Brès, G. Wavepackets and trapped acoustic modes in a turbulent jet: Coherent structure eduction and global stability. *J. Fluid Mech.* **825**: 1153-1181, 2017.

[3] Jordan, P., Jaunet, V., Towne, A., Cavalieri, A. V., Colonius, T., Schmidt, O., Agarwal, A. Jet–flap interaction tones. *J. Fluid Mech.* **853**: 333-358, 2018.

[4] Rodríguez, D., Cavalieri, A. V., Colonius, T., Jordan, P. A study of linear wavepacket models for subsonic turbulent jets using local eigenmode decomposition of PIV data. *European J. Mech.-B/Fluids* **49**: 308-321, 2015.

A LINEAR STABILITY APPROACH FOR EVALUATION OF THE REFLECTION COEFFICIENT OF A KELVIN-HELMHOLTZ WAVE INCIDENT ON A NORMAL SHOCK

M. Mancinelli* [1], E. Martini[2], V. Jaunet[1], P. Jordan[1], A. V. G. Cavalieri[2], A. Towne[3], and Y. Gervais[1]
[1]Département Fluides Thermique et Combustion, Institut Pprime - CNRS-Université de Poitiers-ENSMA, 11 Boulevard Marie et Pierre Curie, 86962 Chasseneuil-du-Poitou, Poitiers, France
[2]Divisão de Engenharia Aeronáutica, Instituto TecnolÓgico de Aeronáutica, São José dos Campos, São Paulo, Brazil
[3]Department of Mechanical Engineering, University of Michigan, 2350 Hayward Street, Ann Arbor, MI 48109, USA

Summary We present a linear stability-based, mode-matching approach for the evaluation of reflection and transmission coefficients associated with waves generated by interaction between a Kelvin-Helmholtz instability wave and a normal shock. We use vortex-sheet and finite-thickness linear-stability models to compute the initial amplitudes of the upstream-travelling guided jet modes generated by the said interaction, which are now known to close the feedback loop that underpins screech in imperfectly expanded supersonic jets.

INTRODUCTION

The problem we consider is motivated by the sound generated by under-expanded, supersonic jets, and, in particular, the phenomenon known as screech, a mechanistic explanation for which was first provided by Powell [4]. The mechanism involves turbulence structures that convect through the shock-cell pattern; this Shock-Turbulence Interaction (STI) results in the generation of upstream-travelling waves. When the phases of the upstream-travelling waves and downstream-travelling turbulence structures are suitably matched, at the jet exit plane and at the STI locations, resonance may occur. The turbulence structures considered important for screech are what are often referred to as coherent structures. Downstream-travelling coherent structures can be modelled using linear theory and are largely underpinned by Kelvin-Helmholtz (K-H) instability of the mean flow [1]. The upstream-travelling waves important for screech were considered by Powell [4] to be free-stream sound waves. This approach has been questioned by Shen & Tam [5], who suggested that the upstream-travelling disturbance might comprise a family of guided jet modes that can be described using linear stability theory. A simplified screech-tone prediction model based on this idea has been developed and validated by Mancinelli *et al.* [2]. In this model, the spatial growth of the K-H instability is ignored, and a phase-matching criterion is sufficient to provide a reasonable prediction of screech-tone frequencies. In a more complete model [3], where the spatial growth rates of the upstream- and downstream-travelling waves are included, knowledge of the reflection coefficient in the jet exit plane and at the location of STI is required.

It is this that motivates the study we report. We use linear theory to consider the interaction between a downstream-travelling K-H wave and a normal shock. We consider the transmitted and reflected waves, and employ a mode-matching procedure to determine the reflection coefficient at the STI location that determines the initial amplitude of the upstream-travelling guided jet waves active in the screech loop. We consider vortex-sheet and finite-thickness flow models.

MODELLING FRAMEWORK

We consider an axisymmetric shock-containing supersonic jet. The shock is assumed to be normal. We assume an incident K-H wave on the shock with unitary amplitude, $I = 1$. The interaction of the incoming wave with the shock generates a collection of reflected (R) and transmitted (T) modes. A mode is identified as (i) reflected, if upstream of the shock (subscript 1) and upstream-travelling, (ii) transmitted, if downstream of the shock (subscript 2) and downstream-travelling. The propagation direction of waves is determined using the Briggs-Bers criterion.

The shock discontinuity is divided along the radial distance r into infinitesimal control volumes $\mathrm{d}V$ and conservation equations are applied on these. Performing Reynolds decomposition and assuming a normal-mode ansatz, the linearised jump equations for normal shock can be written in a compact form as follows,

$$\mathbf{A}_1 \left(I\hat{\mathbf{q}}_{1I} + \sum_{n=1}^{\infty} R_n \hat{\mathbf{q}}_{1R,n} \right) = \mathbf{A}_2 \sum_{n=1}^{\infty} T_n \hat{\mathbf{q}}_{2T,n}, \tag{1}$$

where $\mathbf{A}_1$ and $\mathbf{A}_2$ are operators depending on the mean flow upstream and downstream of the shock, respectively. The vectors of eigenfunctions $\hat{\mathbf{q}}_n = \left\{ \hat{\rho}, \hat{u}_x, \hat{u}_r, \hat{u}_\theta, \hat{T}, \hat{p} \right\}$ are computed using either a vortex-sheet (V-S) model or a finite-thickness linear-stability model based on the Rayleigh Equation (RE). For the latter, we use for the mean flow the following hyperbolic-tangent velocity profile: $\overline{u}_x(r) = \frac{1}{2} M_a \left(1 + \tanh\left(\frac{R}{4\theta_R} \left(\frac{R}{r} - \frac{r}{R} \right) \right) \right)$, with $R/\theta_R = 30$, where R is the radius, θ_R the shear-layer momentum thickness and M_a the acoustic Mach number.

*Corresponding author. E-mail: matteo.mancinelli@univ-poitiers.fr

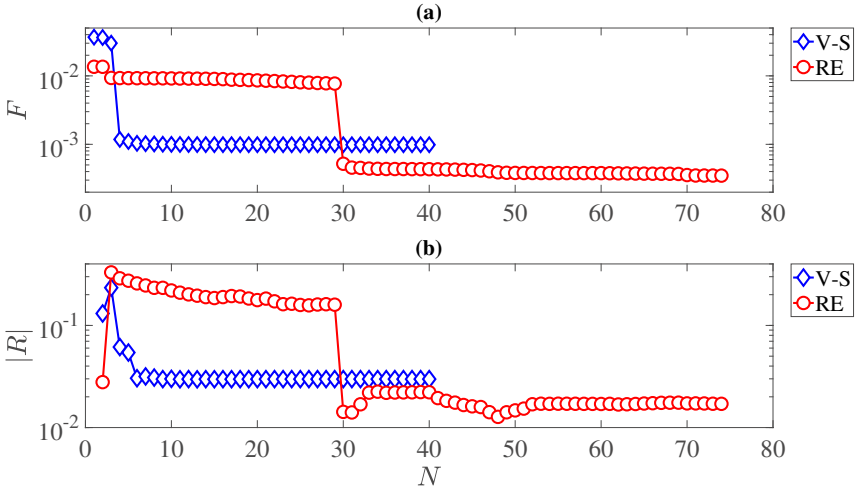

Figure 1: Evolution of the solution as a function of the number of modes considered: (a) objective function to minimise, (b) reflection-coefficient amplitude. ◇ refer to results obtained using a vortex-sheet model, ○ to Rayleigh equation.

Reflection-coefficient calculation

Equation (1) is exact if all jet modes are considered. If we truncate the sum to a finite number of modes N, an error $\epsilon\,(r)$ is introduced for each conservation equation. Equation (1) can thus be written as follows,

$$\mathbf{A}_1\left(I\hat{\mathbf{q}}_{1I}+\sum_{n=1}^{N}R_n\hat{\mathbf{q}}_{1R,n}\right)-\mathbf{A}_2\sum_{n=1}^{N}T_n\hat{\mathbf{q}}_{2T,n}=\boldsymbol{\epsilon}, \tag{2}$$

where $\boldsymbol{\epsilon}\,(r)$ is the vector of errors associated with each conservation equation. It is clear that $\boldsymbol{\epsilon}\to 0$ if the number of modes $N\to\infty$. The reflection and transmission coefficients associated with each mode R_n and T_n, respectively, can be computed by a least-mean-square minimization of the errors:

$$[R_{opt,n},T_{opt,n}]=\min_{R_n,T_n\in\mathcal{C}}\underbrace{\int_0^{\infty}|\boldsymbol{\epsilon}^2\,(r)\,|\,\mathrm{d}r}_{F} \tag{3}$$

where F is the objective function to minimise. The minimization problem is solved using the Nelder-Mead algorithm, which is a heuristic direct-search algorithm based on the simplex method. A convergence analysis is carried out by increasing the number of modes N.

RESULTS

Figure 1 shows the evolution of the objective function and the reflection-coefficient amplitude associated with the upstream-travelling guided jet mode as a function of the number of modes considered. Results obtained using both V-S model and Rayleigh equation to describe the jet wave dynamics are reported. We note that the solution appears to have converged for both flow models. The effect of the shear-layer thickness results in a reduction of $|R|$ of about 40% when free-stream acoustic modes of the continuous branches and critical-layer modes are included in the computation.

CONCLUSIONS

We present a linear stability-based, mode-matching approach to calculate the reflection coefficient associated with an upstream-travelling guided jet mode generated by the interaction between a K-H instability wave and a normal shock. The jet wave dynamics are modelled using a cylindrical vortex-sheet model as well as the compressible Rayleigh equation, in order to highlight the role played by the shear-layer thickness.

References

[1] Cavalieri, A. V. G., Jordan, P., Lesshafft, L. Wave-packet models for jet dynamics and sound radiation. *App. Mech. Rev.* **71**: 020802, 2019.
[2] Mancinelli, M., Jaunet, V., Jordan, P., Towne, A. Screech-tone prediction using upstream-travelling jet modes. *Exp. Fluids* **60**: 22, 2019.
[3] Mancinelli, M., Jaunet, V., Jordan, P., Towne, A., S. Girard. Reflection coefficients and screech-tone prediction in supersonic jets. 25^{th} AIAA/CEAS Aeroacoustics conference: 2522, 2019 .
[4] Powell A. On the mechanism of choked jet noise. *Proc. Phys. Soc. London, Sec. B* **66**: 1039, 1953.
[5] Shen, H. and Tam, C. K. W. Three-dimensional numerical simulation of the jet screech phenomenon. *AIAA J.* **40**: 33-41, 2002.

ACOUSTICS OF CEREBRAL ANEURYSMS

Amélie Lamarquette * [1] and Anurag Agarwal[1]
[1]Department of Engineering, University of Cambridge, Cambridge, United Kingdom

Summary Cerebral aneurysms are common lesions that can be life threatening. They are known to generate a narrowband sound, the mechanism of which remains poorly understood. Previous studies suggest that the lesions act as resonators in a self-excited system. However, this hypothesis has never been validated, partly because of a lack of experimental evidence. This paper presents an experimental study in which aneurysms are modelled by flexible bulbs. The results reveal the presence of two different sources of vibrations: periodic flow structures and structural vibrations. When the frequencies associated with these two sources coincide, resonance can occur that can help explain the observed sound from aneurysms.

INTRODUCTION

Brain aneurysms are localised expansions of a blood vessel that carry a significant risk of bursting. These lesions occur in about 3.2% of the population [11]. While most of them are asymptomatic and will remain harmless [10], ruptured cerebral aneurysms are the primary cause of spontaneous subarachnoid haemorrhage, a devastating type of stroke. Unfortunately, the mechanics of the rupture of an aneurysm is still not fully understood. For instance, even though bigger aneurysms are thought of as having a higher chance of bursting, small ruptured aneurysms are encountered more often than large ruptured aneurysms (van Gijn et al. [8]). Hence, a better understanding on the rupture of aneurysms is needed to distinguish between benign and life-threatening lesions.

In 1970, during exposed surgeries, Ferguson [4] recorded musical sound, or *bruits*, from 10 out of 17 aneurysms. The mechanism behind bruit generation remains unexplained. However, the main hypotheses include the presence of flow turbulence in the lesion [4], as well as self-excited vibrations in which aneurysms act as resonators [5]. Arterial wall vibrations and turbulence are known to affect the wall integrity [2, 3]. Therefore, understanding the generation of aneurysmal sound may reveal important phenomena behind ruptured aneurysms.

Recent studies to explain the sound have been based on CFD and have focused on the high-frequencies present in the flow using CFD [6, 9]. They have ignored the possibility of the resonance of aneurysms. This loss of interest is likely caused by earlier research that suggested that aneurysms are stable [7, 1]. However, these studies did not include the possibility of high-frequency flow structures able to excite aneurysm vibration, and thus the possibility of self-excited oscillations cannot be disregarded. This paper presents an experimental study that investigates the vibrations of a model aneurysm arising from the interaction of fluid flow and structural vibrations.

EXPERIMENTAL SET-UP AND RESULTS

In the experiments carried out, the blood vessels are modelled by a rigid structure and aneurysms by flexible bulbs immersed in water. Blood was replaced with a mixture of water and glycerol, which was pumped through the rig at a constant velocity. Figure 1 presents the design used and highlights the important geometrical parameters. Additional parameters include flow speed U, fluid viscosity ν, Young modulus E, fluid density ρ_f and bulb material density ρ_s. For a typical Reynolds number ($Re = UD/\nu$) at the systole phase of the cardiac cycle, other non-dimensional numbers were identified to scale the system to a convenient size. Their values are outlined in table 1. The sound from the system was recorded with a hydrophone.

Non-dimensional numbers	Physiological	Model 1	Model 2
Re	1220	1077	1088
$E/\rho_f U^2$	811	954	58
ρ_f/ρ_s	1.06	1.15	0.92
d/D	0.70	0.67	0.71
a/D	1.1	1.1	0.52-1.1
a_0/D	1.9	2.7	2.9
h/D	0.12	0.20-0.40	0.15-0.22
α	100°	100°	100°

Table 1: Typical physiological and experimental values of the parameters.

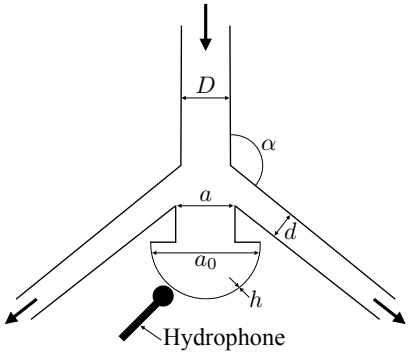

Figure 1: Design of the aneurysm model

*Corresponding author. E-mail: al858@cam.ac.uk.

Figure 2 displays spectra obtained from the hydrophone recordings for different Reynolds numbers. For each Reynolds number, it is possible to identify two frequencies of interest in the spectrum. One corresponds to the natural vibrations of the bulb (dashed line in figure 2), which is fixed with the flow rate, the other is a peak that increases in frequency with increasing Reynolds numbers (arrows in figure 2). At a Reynolds number of about 484 (red curve), the two frequencies coincide resulting in a larger amplitude indicative of resonance. Past that value (blue curve), the peak related to the flow moves to the right of the resonance frequency. Similar results have been found for different bulb thicknesses and artery geometry. The resonance frequency seems to be independent of the artery geometry but increases with bulb thickness and decreases with bulb size. The frequency of the flow is however related to the diameter of the incoming tube. To compare the results from all of the geometries investigated here, the Strouhal number $St = fD/U$ was analysed as a function of the Reynolds number (figure 3). The experimental data collapse well around a fitted curve using a power law.

The results are representative of a self-excited system, in which the bulbs are excited by periodic flow features. However, to the authors' knowledge, there is no theoretical model available in the literature that can accurately predict the resonance frequency of the system.

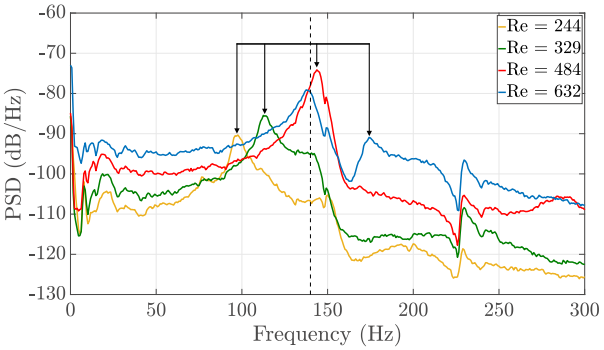

Figure 2: Power spectra for various Reynolds numbers

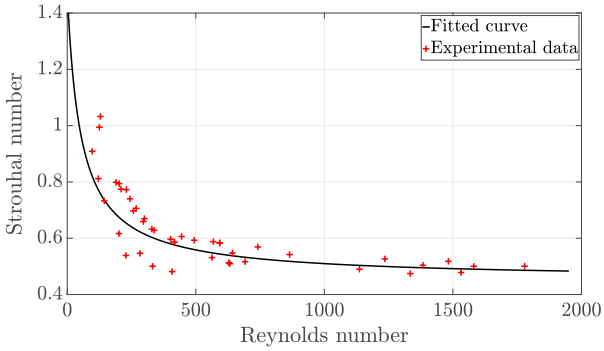

Figure 3: Strouhal number as a function of the Reynolds number

CONCLUSIONS

Our experiments show the presence of two separate frequencies, one related to the flow and the other to the bulb (the aneurysm). As the flow frequency increases with the Reynolds number and the bulb frequency remains constant, there is a critical flow speed at which the two frequencies coincide, leading to the resonance of the system. The results are indicative of a self-excited oscillation mechanism, and suggest that previous studies that concluded that the lesions are not subject to resonance may have overlooked the importance of flow-structure interactions.

We are currently developing a theoretical model to predict the resonance frequency of such systems. In parallel, a flow visualisation study is being carried out to understand the onset of the periodic flow structures, which will help us understand the conditions necessary for the onset of self-excited oscillations.

This work is supported by the Cambridge Commonwealth, European & International Trust (Cambridge European & Churchill Pochobradsky scholarship).

References

[1] D. Aranda-Iglesias, C. Ramón-Lozano, and J. A. Rodríguez-Martínez. Nonlinear resonances of an idealized saccular aneurysm. *International Journal of Engineering Science*, 121(Supplement C):154–166, 2017.

[2] D. R. Boughner and M. R. Roach. Effect of Low Frequency Vibration on the Arterial Wall. *Circulation Research*, 29(2):136–144, 1971.

[3] P. F. Davies, A. Remuzzi, E. J. Gordon, C. F. Dewey, and M. A. Gimbrone. Turbulent fluid shear stress induces vascular endothelial cell turnover in vitro. *Proceedings of the National Academy of Sciences*, 83(7):2114–2117, 1986.

[4] G. G. Ferguson. Turbulence in human intracranial saccular aneurysms. *Journal of neurosurgery*, 33(5):485–497, 1970.

[5] T. D. Mast and A. D. Pierce. A theory of aneurysm sounds. *Journal of Biomechanics*, 28(9):1045–1053, 1995.

[6] T. Natarajan, D. E. MacDonald, M. Najafi, P. W. Coppin, and D. A. Steinman. Spectral decomposition and illustration-inspired visualisation of highly disturbed cerebrovascular blood flow dynamics. *Computer Methods in Biomechanics and Biomedical Engineering: Imaging & Visualization*, DOI:10.1080/21681163.2019.1647461, 2019.

[7] A. D. Shah and J. D. Humphrey. Finite strain elastodynamics of intracranial saccular aneurysms. *Journal of Biomechanics*, 32(6):593–599, 1999.

[8] J. van Gijn, R. S. Kerr, and G. J. Rinkel. Subarachnoid haemorrhage. *The Lancet*, 369(9558):306–318, 2007.

[9] N. Varble, J. Xiang, N. Lin, E. Levy, and H. Meng. Flow instability detected by high-resolution computational fluid dynamics in fifty-six middle cerebral artery aneurysms. *Journal of Biomechanical Engineering*, 138(6):061009, 2016.

[10] C. Vega, J. V. Kwoon, and S. D. Lavine. Intracranial aneurysms: current evidence and clinical practice. *American Family Physician*, 66(4):601, 2002.

[11] M. H. Vlak, A. Algra, R. Brandenburg, and G. J. Rinkel. Prevalence of unruptured intracranial aneurysms, with emphasis on sex, age, comorbidity, country, and time period: a systematic review and meta-analysis. *The Lancet Neurology*, 10(7):626–636, 2011.

EXPERIMENTAL INVESTIGATION OF UAV ROTOR NOISE

Romain Gojon* [1], Hélène Parisot-Dupuis[1], Thierry Jardin[1], and Jean-Marc Moschetta[1]
[1]ISAE-SUPAERO, Université de Toulouse, Toulouse, France

Summary The present work outlines efforts at ISAE-SUPAERO to reduce the aeroacoustic footprint of rotors operating at low Reynolds and low Mach numbers typical of small and medium scale Unmanned Air Vehicles (UAVs). An experimental campaign is presented that serves as a basis for the validation of several numerical approaches, from high fidelity LES to low order models like BEMT and NVLM coupled with a FW-H formulation. Two off-the-shelf rotors and four rotors of canonical shape are considered. Aerodynamic and acoustic results from the two first rotors allow to validate the experimental setup. The four canonical rotors are printed at the laboratory using stereolithography, and corresponding results help unravel the physics behind UAV rotor noise.

EXPERIMENTAL SETUP

An experimental campaign that aims at investigating rotor noise is conducted in an anechoic chamber whose wedge-tip to wedge-tip dimensions are $5.02 \times 5.24 \times 5.34$ m^3 and anechoicity is validated between 80 Hz and 16,000 Hz. The rotor is located at the acoustic center of the chamber, at the top of a 2.8 m height pylon visible in figure 1. Just under the rotor, a Faulhaber 327-024 BP4 electric motor is mounted. This motor is expected to radiate less noise than conventional off-the-shelf small scale motors [1].

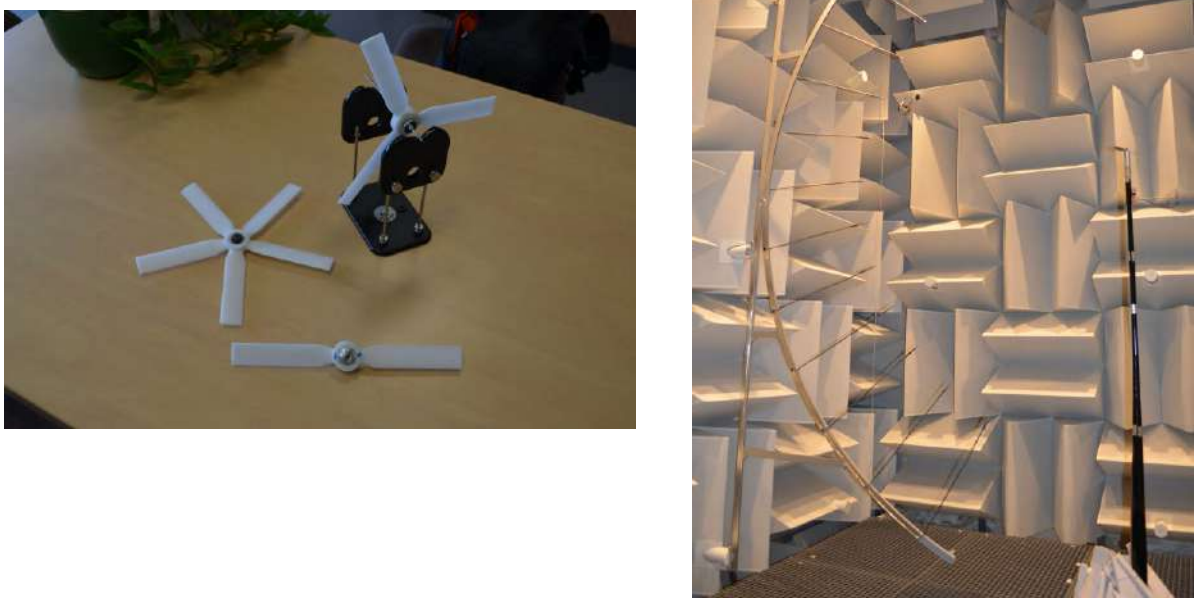

Figure 1: Canonical rotors printed by stereolithography (left) and experimental setup (right).

A six-axis ATI load-cell is positioned directly underneath the motor to measure aerodynamic loads. Moreover, a three-axis accelerometer from DJB Instruments is mounted on the pylon, 25 cm below the rotor plane, to monitor possible vibrations transmitted to the pylon. Acoustic measurements are performed using 1/4" GRAS 40PH microphones of sensitivity 50 mv.Pa^{-1}. In order to study the far-field noise, a directivity antenna is used with 13 microphones, located at a constant distance of 162.0 cm from the rotor center each 10 degrees from 30 to 150 degrees (90 degrees being the rotor plane). A near-field microphone is also placed 25 cm below the rotor plane and 25 cm away in the radial direction. The numerical setup is visible in figure 1.

Two rotors from the literature (APC 9x6 SF and 11x4.7 SF) and four rotors of canonical shape are considered. Aerodynamic and acoustic results from the two first rotors allow to validate the experimental setup against other experimental results from the litterature [2, 1]. The four canonical rotors are printed at the laboratory using stereolithography, some of which are visible in figure 1. They have a NACA0012 profile with a uniform chord length and a constant pitch angle of 10 degrees. The diameter and the chord are 12.5 cm and 2.5 cm respectively. Cases with two blades, three blades, four blades and five blades are considered. They are presented in table 1. Note that the simulation of those rotors using a NVLM approach coupled to a FW-H formulation has been performed recently [3].

*Corresponding author. E-mail: romain.gojon@isae-supaero.fr

Table 1: Canonical rotors geometries and operating conditions

	Value
Number of blades (N_B)	$2, 3, 4, 5$
Radius (R)	12.5 [cm]
Chord length (c)	2.5 [cm]
Advance ratio (J)	0
Free-stream velocity (v_∞)	0 [m/s]
Rotating speed (Ω)	$1,000 \rightarrow 10,000$ [RPM]
Reynolds number (chord-based, at the tip)	$\rightarrow 220,000$
Mach number (at the tip)	$\rightarrow 0.38$

RESULTS

Acoustic spectra are calculated from pressure signals whose sampling rate and total duration are $25,600$ Hz and 16 s. The Fourier transform is applied on 100 blocks with a 50% overlap and the frequency resolution is 3.125 Hz. Far-filed spectra in the rotor plane obtained for the APC 9X6 SF rotor are depicted in figure 2.

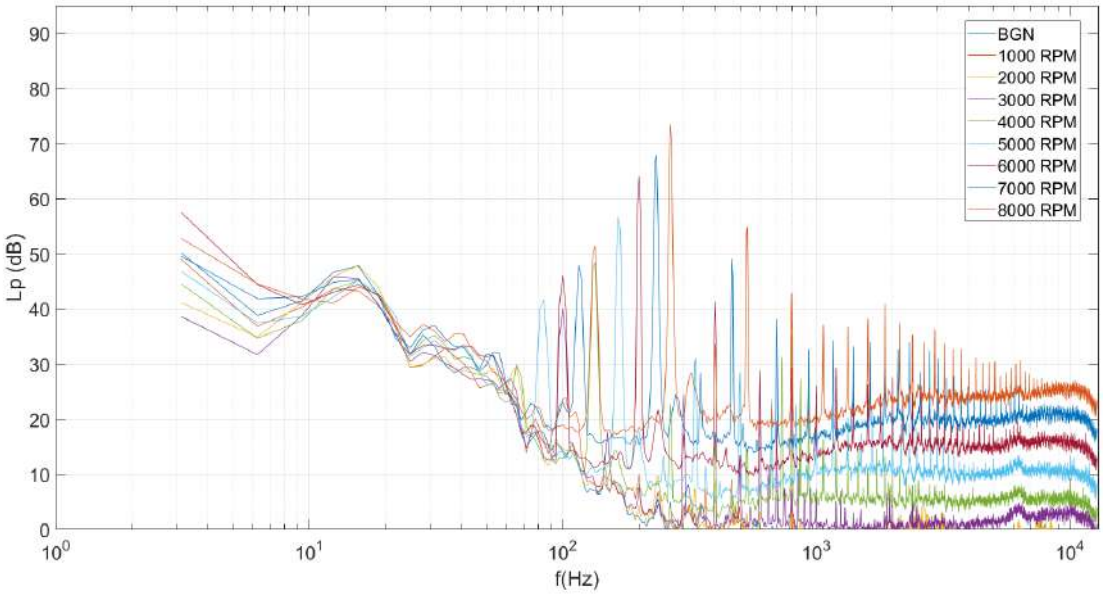

Figure 2: Acoustic spectra in the far-field in the rotor plane for the rotor APC 9X6 SF.

A background noise is presented to compare with. Data obtained for various rotation speeds are plotted, from $1,000$ to $8,000$ RPM. The dominant tone corresponds to the blade passing frequency in all cases, as expected. Its amplitude is increasing with the rotation speed. A high frequency broadband noise is also observed with an amplitude increasing with the rotation speed and with a dipole-like directivity pattern (not shown here).

CONCLUSIONS

An experimental campaign is conducted to study UAV rotor noise. The numerical setup is validated using data from the literature. Then canonical rotors are tested in order to unravel the noise source mechanisms.

References

[1] Zawodny, N. S. and Boyd Jr, D. D. and Burley, C. L. (2016). coustic characterization and prediction of representative, small-scale rotary-wing unmanned aircraft system components. Nasa Report.

[2] Brandt, J.B. and Deters, R.W. and Ananda, G.K. and Selig M.S., UIUC Propeller Database, University of Illinois at Urbana-Champaign, retrieved from http://m-selig.ae.illinois.edu/props/propDB.html.

[3] Jo, Y. and Jardin, T. and Gojon, R. and Jacob, M. C. and Moschetta, J.M. (2019). Prediction of Noise from Low Reynolds Number Rotors with Different Number of Blades using a Non-Linear Vortex Lattice Method. In 25th AIAA/CEAS Aeroacoustics Conference (p. 2615).

ACTIVE CONTROL OF INSTABILITY WAVES IN JET SHEAR LAYER IN VIEW OF JETWING INTERACTION NOISE REDUCTION

Victor Kopiev[1], Georgy Faranosov*[1], Oleg Bychkov[1], Vladimir Kopiev[1], Ivan Moralev[2] and Pavel Kazansky[2]
[1]Central Aerohydrodynamic Institute (TsAGI), Moscow, Russia
[2]Joint Institute of High Temperature RAS, Moscow, Russia

Summary This work demonstrates the possibility of active control of low-frequency jet-wing interaction noise when the wing is close to the jet shear layer. The main idea of the proposed approach is connected with the reduction of the amplitude of instability waves developing in the jet shear layer in the form of wave packets. Jet-wing interaction noise is related to the scattering of jet near-field pressure pulsations, which are footprints of instability waves, by the wing trailing edge. Therefore, mitigation of instability waves should directly lead to noise reduction. Active control system is developed and tested in experiments. Control action is provided by a dielectric barrier discharge plasma actuator mounted inside the nozzle. It is shown for a subsonic jet that the system is capable to reduce jet-wing interaction noise at the target frequency by about 3 dB.

INTRODUCTION

Application of turbofan engines with high and very high bypass ratio implies that nozzle diameter increases. Corresponding reduction of jet velocity leads to a significant reduction of jet noise. However, larger engines have to be more integrated into airframe. In case of such a tight engine-airframe integration, the jet issuing from the engine's nozzle may pass rather close to the wing so that intensive jet-wing interaction noise arises. This effect was studied in a number of publications [1-5]. It was demonstrated that additional low-frequency hump in noise spectrum is related to the scattering of the jet near-field hydrodynamic pulsations by the wing trailing edge [3-5]. These near-field pulsations can be considered as footprints of coherent structures evolving in the jet shear layer in the form of instability wave-packets of different azimuthal numbers [3, 5]. Thus, jet-wing interaction noise reduction strategy can be formulated in terms of instability wave control [6] as it is sketched in Figure 1.

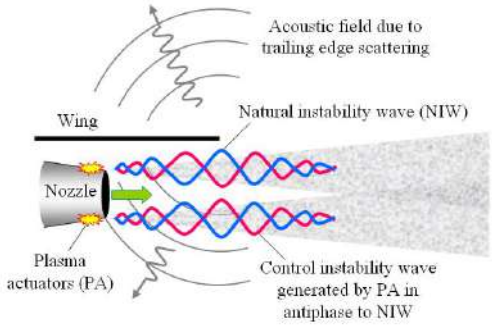

Figure 1. Control strategy for jet-wing interaction noise reduction.

Plasma actuators are widely used for realization of control action in flow control applications [7], including attempts of flow/noise control of standalone jets [8-10]. Current work continues our previous studies [10] where it was demonstrated the possibility of control of artificially excited instability waves in the jet shear layer by means of high-frequency dielectric barrier discharge (HF DBD) plasma actuators. The main idea of control in [10] was based on the generation by the plasma actuator of an instability wave which is of the same amplitude but in antiphase to the instability wave artificially excited in the jet shear layer. In this study, we extend the concept tested for tone excited jets [10] for the case of natural unexcited jets in accordance with the control strategy described in [6]. It is shown that the proposed approach makes it possible to reduce instability wave intensity in unexcited jet (and hence jet-wing interaction noise) in the narrow band around the target frequency.

EXPERIMENTAL SETUP AND MAIN RESULTS

Small-scale model that simulates jet-wing configuration was studied experimentally in the anechoic chamber AC-2 at TsAGI. The diameter of the nozzle was $D = 50$ mm and the wing was simulated by a flat plate of dimensions 1.2m x 0.35m x 0.003m (Figure 2). The trailing edge of the plate was shifted downstream from the nozzle exit plane by $1.7D$, the distance between the jet axis and the plate was $0.9D$. Several jet Mach numbers in the range 0.4-0.9 were considered.

As shown in [4, 5], only the first two near-field azimuthal modes significantly contribute to the low-frequency jet-wing interaction noise. Therefore, in the current work the control system were designed with the aim to reduce axisymmetric part of the near-field pressure pulsations. It was realized by HF DBD plasma actuator with a ring-like electrode mounted inside the nozzle near the nozzle edge (3-5 mm from the nozzle exit) as shown in Figure 2. Generally, the configuration of the actuator is similar to that used for the case of artificially excited instability wave control [10] with the difference that metal nozzle covered by a dielectric (using the technique of detonation deposition of a dielectric barrier), rather than the fully dielectric nozzle [10], is used in the current study. The control strategy, proposed in [6], is implemented as follows. It consists in the narrowband sliding filtration of the original signal measured by the reference microphone flush-mounted on the plate near its trailing edge and the formation of a narrowband control action. Signal filtration is realized by the AD/DA converter integrating a digital signal processor (DSP). The signal is processed in real time by the DSP. The code of the module driver is modified to include digital

*Corresponding author. E-mail: georgefalt@rambler.ru

filtering of the signal from the reference microphone and correct phase and amplitude distortions. The processed signal is then used for modulating the voltage at the discharge on the actuator in order to generate instability wave of proper amplitude in antiphase to that measured by the reference microphone. The control system and experimental setup are shown in Figure 2. To reduce jet installation noise, the signal amplification and phase delay were manually adjusted step-by-step by the DSP reprogramming and analyzing of the spectrum on the reference microphone. To monitor the response of the system to the control action, several microphones were distributed in the near and far field of the jet: five microphones in the far field (Bruel & Kjaer, ½'', type 4189, at an arc of 30*D* radius) and six microphones in the near field (Bruel & Kjaer, ¼'', type 4935) as shown in Figure 2 (right).

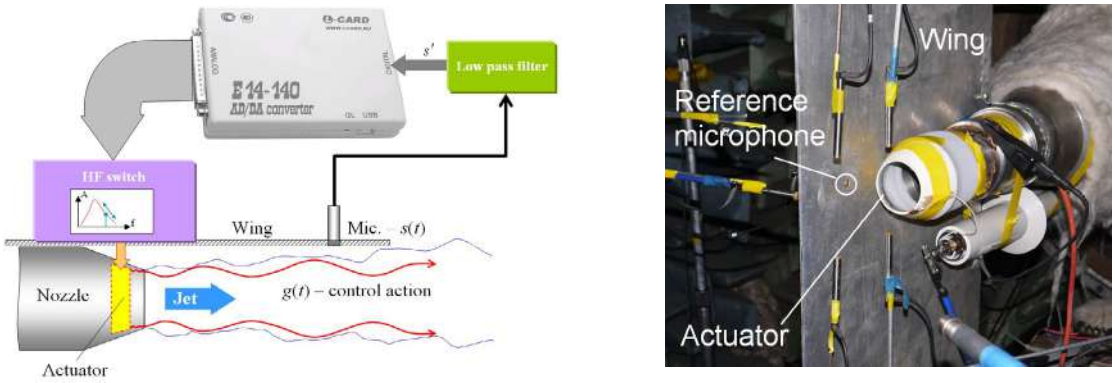

Figure 2. Sketch of the control system.

As soon as the proper parameters of the transfer function were defined, the effect of noise reduction in the far-field could be observed in a narrow band around the target frequency with minor penalties at both sides of the filter band. Corresponding results for Mach 0.4 jet are shown in Figure 3. It can be seen that the value of noise reduction reaches 3 dB. The effect of noise reduction becomes less pronounced for the microphones located downstream due to the cardioid-like directivity of the jet-wing interaction noise. At these observation angles the signal is dominated by the jet noise and less sensitive to the control.

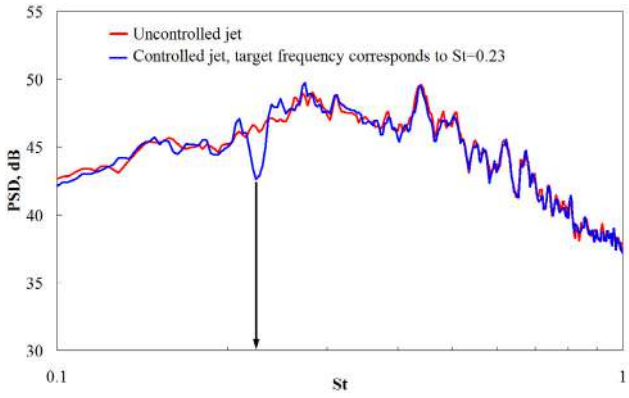

Figure 3. Acoustic spectra on the "under-the-wing" microphone in the far field. Jet Mach number 0.4. Target control frequency corresponds to Strouhal number St ≈ 0.23.

ACKNOWLEDGMENTS

The work is partly supported by the Russian Foundation for Basic Research and Moscow city Government, project 19-31-70005.

References

[1] Kopiev V.F., Faranosov G.A., Zaytsev M.Yu., Vlasov E.V., Karavosov R.K., Belyaev I.V., Ostrikov N.N. Intensification and Suppression of Jet Noise Sources in the Vicinity of Lifting Surfaces. *Proc. of the 19th AIAA/CEAS Aeroacoustics Conference*, AIAA paper 2013-2284, 2013.
[2] Lawrence J. Aeroacoustic Interactions of Installed Subsonic Round Jets. *PhD thesis*, Univ. of Southampton, 2014.
[3] Cavalieri A.V.G., Jordan P., Wolf W.R., Gervais Y. Scattering of Wavepackets by a Flat Plate in the Vicinity of a Turbulent Jet. *J. Sound Vibr.***333**:6516-6531, 2014.
[4] Lyu B., Dowling A.P., Naqavi I. Prediction of Installed Jet Noise. *J. Fluid Mech.***811**:234–268, 2017.
[5] Bychkov O.P., Faranosov G.A. An Experimental Study and Theoretical Simulation of Jet-Wing Interaction Noise. Acoustical Physics **64(4)**:437–452, 2018.
[6] Belyaev I.V., Bychkov O.P., Zaitsev M.Y., Kopiev V.A., Kopiev V.F., Ostrikov N.N., Faranosov G.A., Chernyshev S.A. Development of the Strategy of Active Control of Instability Waves in Unexcited Turbulent Jet. *Fluid Dynamics* **53(3)**:347–360, 2018.
[7] Samimy M., Webb N., Esfahani A. Reinventing the Wheel: Excitation of Flow Instabilities for Active Flow Control Using Plasma Actuators. *Journal of Physics D: Applied Physics* **52**: 1-16, 2019.
[8] Samimy M., Kearney-Fischer M., Kim J.-H., Sinha A. High-speed and high-Reynolds-number jet control using localized arc filament plasma actuators *J. Propul. Power* **28**: 269-280, 2012.
[9] Kopiev V.F., Bityurin V.A., Belyaev I.V., Godin S.M., Zaytsev M.Yu., Klimov A.I., Kopiev V.A., Moralev I.A., Ostrikov N.N. Jet noise control using the dielectric barrier discharge plasma actuators. *Acoustical Physics* **58(4)**:436-443, 2012.
[10] Kopiev V.F., Akishev Y.S., Belyaev I.V., Berezhetskaya N.K., Bityurin V.A., Faranosov G.A., Grushin M.E., Klimov A.I., Kopiev V.A., Kossyi I.A., Moralev I.A., Ostrikov N.N., Taktakishvili M.I., Trushkin N.I., Zaytsev M.Yu. Instability wave control in turbulent jet by plasma actuators. *Journal of Physics D: Applied Physics* **47**:1-18, 2014.

JET NOISE SOURCE ESTIMATION USING RESOLVENT ANALYSIS

Filipe R. Amaral* [1] and André V. G. Cavalieri[1]
[1]Divisão de Engenharia Aeroespacial, Instituto Tecnológico de Aeronáutica, 12228-900 São José dos Campos, Brazil

Summary A resolvent-based method is applied to estimate the flow state and the noise source statistics from a small number of measurements of both a synthetic line wavepacket source model and a large eddy simulation database of a Mach 0.4 fully turbulent jet. Good agreement is observed for both cases with near exact match for the synthetic case. The results highlight the pertinence of resolvent-based estimation in aeroacoustics, as the method avoids the compact-source assumption used in beamforming frameworks and is thus suitable for the estimation of source statistics using microphone arrays, which can also be placed in the near pressure field of the source. Future work will include a more complete formulation of the Lighthill's tensor to improve the accuracy of source estimation.

INTRODUCTION AND METHODS

The estimation of aeroacoustic noise sources is an important step for the understanding of physical mechanisms behind the sound generation and for further development of noise control strategies. Acoustic beamforming [1] is a well-established technique aimed at noise source estimation employing a limited number of probes. Such a technique assumes a distribution of uncorrelated monopole point sources as a premise, which is not an adequate hypothesis for jet noise source estimation, since the presence of organized large-scale structures, modeled as wavepackets, are not taken into account.

In this work, the recently developed resolvent-based methodology estimation [5] is thus applied to estimate the source forcing cross-spectral density (CSD) and consequently the flow state. Such a method employes the Lighthill's acoustic analogy written in operator notation, casting the problem in the input (source distribution, $P_{ff} = \mathcal{E}(\mathbf{f}\mathbf{f}^*)$, where $\mathbf{f}$ is the source term, * indicates the Hermitian transpose and $\mathcal{E}$ is the expected-value operator) / output (radiated pressure, $P_{qq} = \mathcal{E}(\mathbf{q}\mathbf{q}^*)$) framework [4]. For the Lighthill's acoustic analogy, the resolvent operator $\mathbf{R}$ can be obtained using the analytical free-field Green's function with integration weights. Hence, the pressure field (flow response) is related to the source distribution (forcing) by $P_{qq} = \mathbf{R}\, P_{ff}\, \mathbf{R}^*$. In most situations, one has limited information on the flow state at an array of sensors $\mathbf{y}$ distributed along a few positions. In this case, the resolvent operator may be used to estimate source statistics from sensor data and, subsequently, obtain the radiated sound in other locations [5].

In order to verify if the resolvent-based methodology is suitable to estimate the source statistics from a limited set of know data, two test cases were employed. The first case consists of a line source modeled as a wavepacket of amplitude-envelope length scale L, coherence decay characteristic length L_c and hydrodynamic wavenumber k_h [3]. The values of $L_c = L$ and $k_h L = 5$ where chosen in order to obtain a source that is both partially desynchronized regarding to the spatially evolving wavepacket fluctuations and an extended wavepacket, mimicking the main features of sound radiation by a Mach 0.6 jet. The second case comprises a large eddy simulation (LES) database of an isothermal Mach 0.4 turbulent jet [2], from which the axisymmetric pressure fluctuations were taken.

PRELIMINARY RESULTS

The analytical pressure CSD [4] was sampled, or measured, with a 38-probe array distributed along a line. Such a line of equally-spaced probes is centered on the source origin $x/L = 0$, distant of $h/L = 1$ regarding the source vertical position h and extends between $-4 \leq x/L \leq 4$ (closed circles near the source origin in Fig. 1a). The probes thus mimic a near-field array of microphones. Figure 1b shows the source CSD (P_{ff}) estimated from the near-field array, clearly recovering the signature of a jittering wavepacket [4]. The Power Spectral Density (PSD) of the estimated state $\mathbf{q}$ is shown in Fig. 1c, given by the P_{qq} line. A remarkable agreement with the probe PSD, $P_{yy,nf}$, is observed, which confirms that the identified source matches nearly exactly the fluctuations at the probe array. The identified source of Fig. 1b is then propagated to a far-field array (closed triangles in Fig. 1a). The PSDs of both far-field data ($P_{yy,ff}$ line) and propagated pressure field from the identified source ($RP_{ff}R^\dagger$ line) are shown in Fig. 1c. An excellent agreement is obtained up to a polar angle of $120°$ measured from the downstream axis.

Figure 2a exhibits a 100-probe array employed to acquire pressure data from the LES. The array was positioned along a $7°$-inclined line, extending between $0 \leq x/D \leq 30$. Such probes, displayed in the figure as closed circles, were equally-spaced and the first array probe is positioned at the jet lip line. The LES jet noise estimated line-source CSD (P_{ff}) is shown in Fig. 2b for Strouhal number $St = 0.2$, whereas the PSD of the estimated state is displayed in Fig. 2c. The measured and the estimated noise spectra, given by $P_{yy,nf}$ and P_{qq} lines in Fig. 2c show good agreement, although the estimated state P_{qq} underestimate the measured PSD $P_{yy,nf}$ by approximately 5 dB for $x/D \geq 15$. Figure 2c also displays the jet noise P_{ff} propagated to a 30-probes array positioned in the acoustic field (shown as closed triangles in Fig. 2a). The overall levels are predicted by the source, but with discrepancies likely due to the line-source simplification and the consideration of only longitudinal quadrupoles in Lighthill's analogy.

*Corresponding author. E-mail: filipefra@ita.br.

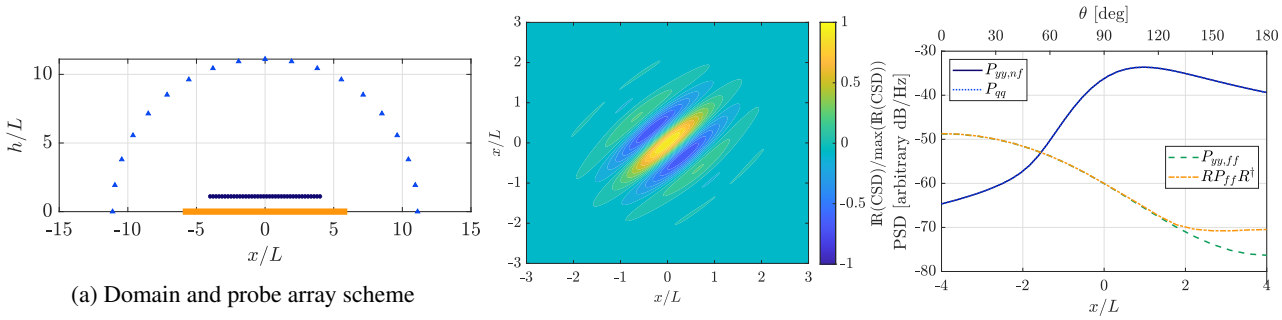

(a) Domain and probe array scheme

(b) Forcing CSD (P_{ff})

(c) PSD (P_{qq}) at the probe positions

Figure 1: Analytical wavepacket line source estimation results.

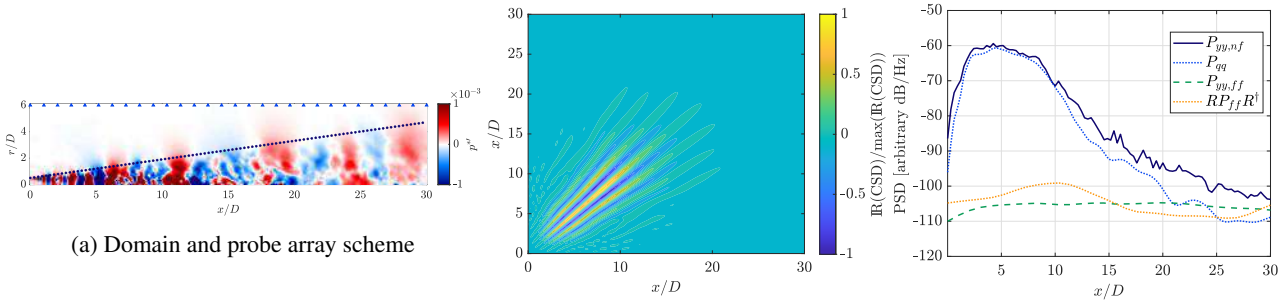

(a) Domain and probe array scheme

(b) Forcing CSD (P_{ff})

(c) PSD (P_{qq}) at the probe positions

Figure 2: LES jet noise source estimation results, $St = 0.2$.

CONCLUSIONS

In this extended abstract we have shown results of a resolvent-based estimation applied to jet noise obtained with limited number of probes. An analytical wavepacket line source model, mimicking jet noise source features, and an LES jet database were employed as test cases. The method successfully estimated the forcing source P_{ff} and the state P_{qq}, particularly for the analytical source, which was tailored for the simplifications used here (line distribution of longitudinal quadrupoles). Nonetheless, the method is a viable alternative to acoustic beamforming, particularly for non-compact sources typical in aeroacoustics, whose wavepacket features are accurately identified in both cases. We are currently developing a formulation of the Lighthill's stress tensor in order to achieve better accuracy for the LES database and further improve our estimations.

ACKNOWLEDGMENTS

F.R.A. received funding from the Sao Paulo Research Foundation (FAPESP/Brazil), grant #2019/02203-2. A.V.G.C. received support from National Council for Scientific and Technological Development (CNPq/Brazil), grant #310523/2017-6.

References

[1] Amaral, F. R. and Pagani Jr, C. C. and Medeiros, M. A. F. Improvements in closed-section wind-tunnel beamforming experiments of acoustic sources distributed along a line. *Appl. Acoust.* **156**: 336-350, 2019.

[2] Brès G. A., Lele, S. K. Modelling of jet noise: a perspective from large-eddy simulations. *Philos. Trans. R. Soc. A* **377**: 20190081, 2019.

[3] Cavalieri A. V. G., Agarwal, Anurag. Coherence decay and its impact on sound radiation by wavepackets. *J. Fluid Mech.* **748**: 399-415, 2014.

[4] Cavalieri A. V. G., Jordan P., Lesshafft L. Wave-packet models for jet dynamics and sound radiation. *Appl. Mech. Rev.* **71(2)**: 020802, 2019.

[5] Martini E., Jordan P., Cavalieri A. V. G., Towne A., Lesshafft L. Optimal estimation of responses and forces from low rank measurements. *J. Fluid Mech. (submitted)*, 2020.

STRATEGIES FOR THE EVALUATION OF THE FLUID-DYNAMIC ACOUSTIC POWER PRODUCED BY AN ORIFICE

Luca Fenini[1], Luca Nicola Quaroni* [2], Gabriele Mazzaro[3], and Stefano Malavasi[4]
[1,2,4]Department of Civil and Environmental Engineering, Politecnico di Milano, Milano, Italy
[3]Engineering department, Pibiviesse S.r.l., Nerviano (MI), Italy

Summary A novel approach to numerically estimating the acoustic power produced by gas flow through control devices is presented. The procedure is based on the simulation of stationary fluid flow by means of the Reynolds Averaged Navier-Stokes (RANS) equations employing Computational Fluid Dynamics (CFD) techniques. An appropriate expression for the acoustic power density as defined by existing literature allows to obtain the acoustic power by integrating over an aptly-defined source region. A discussion of the results obtained for a single-hole orifice plate through the proposed and the reference international standards' procedure follows.

INTRODUCTION

Several fluid-dynamic processes in industrial settings are managed by means of flow-control devices, either fixed (e.g. orifice plates) or mobile (e.g. valves). The working principle of such devices is the conversion of part of the mechanical energy of the flow into turbulent kinetic energy. While most of such energy is dissipated into heat, a small portion escapes the flow as acoustic pressure fluctuations which are then transmitted to the medium surrounding the pipe though the vibration of its walls [1]. This phenomenon is particularly important for gas flows, where it may result in sound pressure levels dangerously high for the health and wellbeing of the work personnel. The international standard regulating the acoustic emissions of gas flow-control devices and reference for this short paper is the IEC 60534-8-3 [2]. Such standard provides a procedure for estimating the sound pressure level of a control device based on the definition of an acoustical efficiency for the conversion of mechanical power into acoustic power. A major drawback for the provided approach is however that such acoustical efficiency only indirectly takes into consideration the specific flow characteristics of a given type of device, as it's dependent on a factor which is constant for any given flow-control device category (e.g. orifice plates, gate valves...). In the present work, an approach developed by Fenini [3] based on the computation of the acoustic power density as defined by Proudman [4] is applied to a single-orifice plate. The acoustical power is estimated directly from the flow field, leading to a more case-dependent computation of the acoustic emissions of the device. The choice of the single-hole orifice plate is justified by the relative simplicity of its flow field and by the possibility of using the results as a starting point for the more complex geometries relevant to the industrial world.

MODEL FORMULATION

Computational model of the plate

The single-hole orifice plate subject of the present manuscript is characterized by an orifice-to-line diameter ratio $\beta = d/D$ of 0.4 and sharp edges. The diameter of the test line D and the thickness of the plate t are respectively set equal to 24.3 mm and 10 mm. A computational domain of $10D$ upstream and $15D$ downstream of the device is chosen so as to guarantee that the upstream and downstream boundaries' velocity profiles don't influence the results. The symmetric domain allows for a reduction of the required computational resources by simulating only a quarter of the pipe's section.

The flow simulations were performed using the finite-volume-based code *ANSYS Fluent 19.1*. An hexahedral mesh was built and through a sensitivity analysis a ratio of $2 \cdot 10^{-2}$ between the cell's size in the proximity of the orifice and the line's diameter was found to provide results independent of the grid. The chosen working fluid is dry air, whose equation of state is set as the ideal gas law; its viscosity is instead kept constant and independent of temperature. The effects of turbulence on the mean flow are accounted for through the choice of the RNG $k-\varepsilon$ model. Due to the moderate compressibility of the flow, the implicit *coupled* pressure-based algorithm is chosen as solver. As for the boundary conditions, an inlet absolute pressure of 6 bar and progressively decreasing static pressures at the outlet are imposed. Temperature is set equal to 293 K at both inlet and outlet.

Acoustic power estimation

The following approach for computing the acoustic power W_a of the flow was developed by Fenini [3]. The *acoustic power density* P is calculated at every cell's centroid employing the definition given by Proudman [4]:

$$P(\mathbf{x}) = \alpha_P \rho \varepsilon \left(\frac{\sqrt{2k/3}}{c} \right)^5 \tag{1}$$

where ρ is the fluid density, ε is the turbulent dissipation rate, k is the turbulent kinetic energy, c is the local speed of sound and α_P is a numerical constant set equal to 3.804 in this study [5]. The acoustic power can be computed by integrating P over an aptly-defined source region S:

$$W_a = \int_S P(\mathbf{x}) d\mathbf{x} \tag{2}$$

*Corresponding author. E-mail: lucanicola.quaroni@mail.polimi.it

where S is defined in this study as the fluid volume for which the turbulent kinetic energy k is greater than 20% of the maximum value reached in the domain. For comparison, the expression for W_a as provided by the international standard has the shape:

$$W_a = 10^{A_\eta} \cdot f\,(regime) \tag{3}$$

where A_η is the *valve correction factor for acoustical efficiency* and f is an expression dependent on the flow regime, which is itself defined based on the value of the relative pressure drop $x = (p_1 - p_2)/p_1$ (p_1 and p_2 respectively the static pressure measured at $2D$ upstream and $6D$ downstream of the device, see [2]). None of the quantities in eq. (3) directly takes into account the characteristics of the flow field developed at the control device. In particular the value for A_η is provided as constant for each specific device typology (e.g. -4.8 for orifice plates, -4 for a generic dipole source) thus neglecting the substantial differences in geometry which may be present within the same category (e.g. round- v.s. sharp-edged orifices).

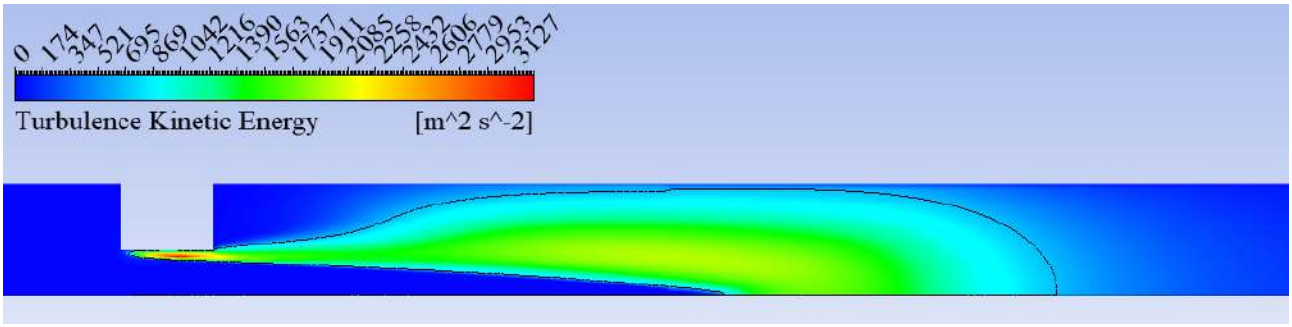

Figure 1: Turbulent kinetic energy and acoustic source region S (enclosed by the black contour line) for $x = 0.2$. Threshold value for $k = 0.2 \cdot k_{max} \approx 627\, m^2/s^2$. Flow is from left to right.

RESULTS

The acoustic power for varying x computed through the proposed approach and the international standard's procedure (for A_η equal to -4.8 and - 4) is reported in fig. (2). The A_η factor for varying x obtained by inverting eq. (3) once the acoustic power was known from eq. (2) is also reported.

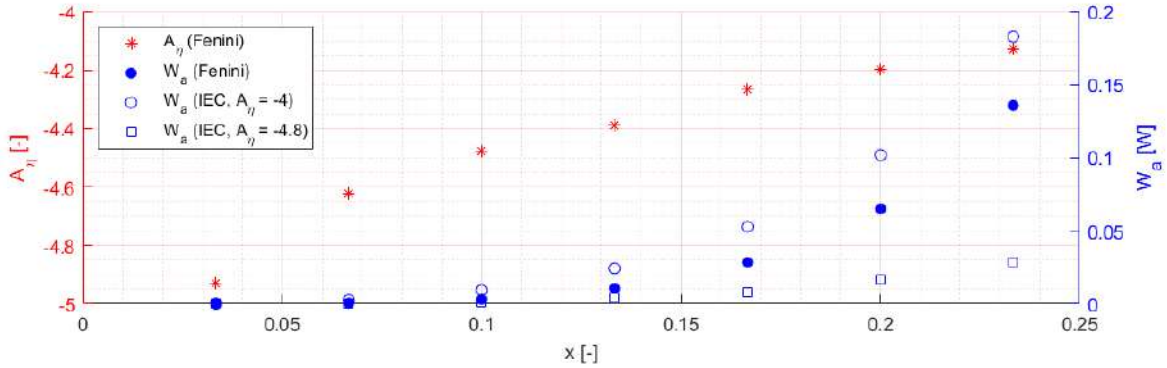

Figure 2: Acoustic power W_a and valve correction factor for acoustical efficiency A_η for varying x as computed through Fenini's procedure. The acoustic power calculated using the international standards' procedure is also displayed for comparison.

The acoustic power W_a shows a qualitatively similar behaviour between the two approaches. More quantitatively however, as x increases, the acoustic power computed through eq. (2) tends to the values obtained using the standard's procedure with $A_\eta = -4$. Such a behaviour can be better appreciated by looking at the A_η obtained through the proposed approach, which tends to the value the international standard suggests for general dipole sources. This indicates that the procedure outlined in [2] may underestimate the acoustic power emissions, and therefore the resulting sound pressure level produced by flow-control devices. An experimental plant is under construction at the "G. Fantoli" Hydraulics' Laboratory of Politecnico di Milano. Once completed, the above findings will be validated experimentally and further tests will be carried out on more complex geometries.

References

[1] Lighthill, J. On sound generated aerodynamically - I. General theory. *Proc. R. Soc. Lond. A* **211(1107)**: 564-587, 1952.
[2] IEC 60534-8-3:2010 Industrial-process control valves - Part 8-3: Noise considerations – Control valve aerodynamic noise prediction method.
[3] Fenini, L. Numerical modelling of flow-induced noise emitted by control devices. *Ph.D. thesis*, Politecnico di Milano, DICA, Milan, 2019.
[4] Proudman, I. The generation of noise by isotropic turbulence. *Proc. R. Soc. Lond. A* **214(1116)**: 119-132, 1952.
[5] Sarkar, S. & Hussaini, M.Y. Computation of the sound generated by isotropic turbulence. *Technical report*, Institute for Computer Applications in Science and Engineering-, Hampton, Virginia, 1993.

STREAMING IN A KUNDT'S TUBE OF AN ARBITRARY DIAMETER

Alen Pavlic[1] and Jürg Dual [1]
[1]Institute for Mechanical Systems, ETH Zurich, Zurich, Switzerland

We solve an axisymmetric streaming problem in a Kundt's tube that follows from the perturbation expansion of the governing equations for a compressible Newtonian fluid. No restriction is imposed on the diameter of the rigid tube with respect to the viscous boundary layer thickness and acoustic wavelength. We show that the streaming torus bounded by the wall expands towards the center of the tube with the increase of the relative thickness of the viscous boundary layer. An additional (Rayleigh) streaming torus is bounded by the aforementioned streaming and is gradually reduced as the viscous boundary layer expands. Furthermore, we analyse cases exceeding the critical viscous boundary layer thickness relative to the tube radius, at which the Rayleigh streaming disappears.

INTRODUCTION

Kundt's tube is a well-known experiment for measuring the speed of sound in fluids [1]. In 1876, Dvorak [2] observed a steady fluid flow in a Kundt's tube, i.e. the acoustic streaming, and ever since, the challenge of analytically modelling such flows exists. In 1884, Rayleigh derived the first analytical solution [3], which assumes a 2D channel geometry, and a small viscous boundary layer. Rayleigh's solution predicts that the fluid flows from a velocity antinode to the node along the middle of the channel, and in the opposite direction near the wall. The direction of the flow was later validated experimentally by Andrade [4].

Here, we present an analytical solution for the streaming in a Kundt's tube without restrictions on the tube diameter with regards to the viscous boundary layer thickness and acoustic wavelength. The solution is used to numerically investigate the streaming patterns in some cases that are beyond the scope of Rayleigh's theory.

We show that when the viscous boundary layer thickness becomes comparable to the tube diameter, Rayleigh streaming disappears, and only the oppositely directed Schlichting streaming remains. This transition is invariant of the material properties when the acoustic wavelength is large compared to the tube radius. When the acoustic wavelength is comparable to the tube radius, a large-scale Eckart-like streaming supersedes the Rayleigh streaming.

PROBLEM STATEMENT

The viscous fluid is, initially at rest, placed in an infinite rigid tube with an inner diameter of $2a$. Two counterpropagating harmonic weakly decaying travelling waves are assumed in the fluid, oriented along the axis of the tube (pseudo-standing wave). Thermal effects are neglected, and the fluid motion is therefore governed by the Navier-Stokes equations, the continuity equation, and the equation of state, namely,

$$\rho \frac{\partial \boldsymbol{v}}{\partial t} + \rho(\boldsymbol{v}\cdot\boldsymbol{\nabla})\boldsymbol{v} = -\boldsymbol{\nabla}p + \eta\nabla^2\boldsymbol{v} + \left(\eta_\mathrm{B} + \frac{\eta}{3}\right)\boldsymbol{\nabla}(\boldsymbol{\nabla}\cdot\boldsymbol{v})\,,$$

$$\frac{\partial \rho}{\partial t} + \boldsymbol{\nabla}\cdot(\rho\boldsymbol{v}) = 0\,,$$

$$p = p(\rho) \quad (p_1 = c_\mathrm{f}^2\rho_1 \rightarrow \text{at the first order}).$$

The three variables in the governing equations are the velocity $\boldsymbol{v}$, pressure p, and density ρ. Material constants defining the viscous fluid are the equilibrium density ρ_0, the speed of sound c_f, and the dynamic and bulk viscosity, η and η_B, respectively. The problem is constrained by the no-slip boundary condition at the wall.

By applying a regular perturbation technique, the problem can be solved in successive steps of increasing order in terms of small Mach number. The perturbed variables can then be written in a series form, namely, $(\,) = (\,)_0 + (\,)_1 + (\,)_2 + \cdots$, where the subscript denotes the order in the perturbation expansion, and where $(\,)_1 \gg (\,)_2$.

RESULTS

The defined problem has been divided onto the first- and second-order problems, and solved in two consecutive steps. The procedure of solving the problem analytically is described in detail by Pavlic and Dual [5]. The solution has no restriction on the thickness of the viscous boundary layer δ. Here, we use the derived expression for the Eulerian streaming velocity $\langle\boldsymbol{v}_2\rangle$ and for the average mass transport velocity, defined as $\langle\boldsymbol{v}_2\rangle^\mathrm{M} = \langle\boldsymbol{v}_2\rangle + \langle\rho_1\boldsymbol{v}_1\rangle/\rho_0$, for numerical analysis of the evolution of streaming patterns inside the tube.

The analysis revealed, as indicated in Figure 1, three distinct regimes of streaming possible within a Kundt's tube. When the ratio $\Xi = a/\delta$ is larger than the critical ratio Ξ_S, we observe coexistence of the Rayleigh and the oppositely directed Schlichting streaming. Rayleigh streaming being the flow from the velocity node towards the antinode along the center of the tube, and in the opposite direction near the wall. If the radius is decreased below Ξ_S, only the Schlichting streaming remains.

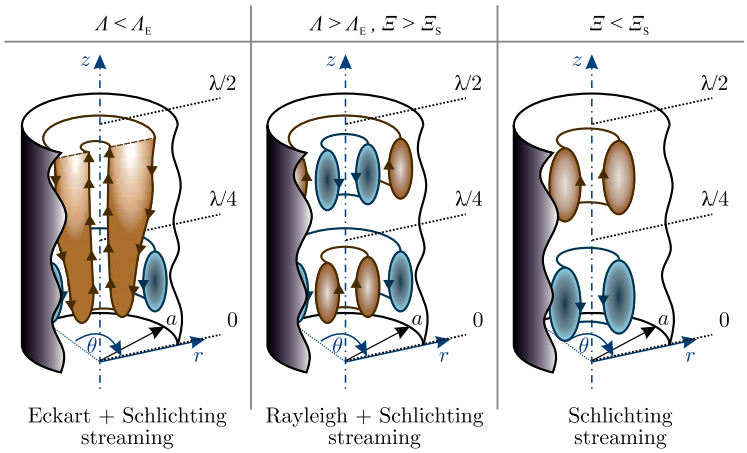

Figure 1. Different streaming regimes that depend on the ratios $\Xi = a/\delta$ and $\Lambda = \lambda/a$ relative to the critical ratios Ξ_S and Λ_E.

Critical ratio Ξ_S, at which the transition between streaming regimes appears, was found to be invariant of material properties when the acoustic wavelength $\lambda = c_f/f$ is large compared to the tube radius. The distinct values appear to be $\Xi_S = 5.6$ and $\Xi_S^M = 6.2$, for the Eulerian streaming velocity and for the average mass transport velocity, respectively. When the acoustic wavelength is smaller than $\sim 10a$, the streaming becomes qualitatively affected by the ratio $\Lambda = \lambda/a$. For glycerol, at $\Xi = 22.5$, the transition between Rayleigh and Eckart-like streaming appears at critical ratio $\Lambda_E = 3.1$ for $\langle \boldsymbol{v}_2 \rangle$ and at $\Lambda_E^M = 3.5$ for $\langle \boldsymbol{v}_2 \rangle^M$. Some exemplary streaming patterns for an oil are depicted in Figure 2. The frequency of the standing wave with a pressure amplitude (at $z = 0$) of 100 kPa is 100 kHz. The oil used for the analysis has the dynamic viscosity of $\delta = 41.5$ mPa s, the bulk viscosity of $\delta = 89.3$ mPa s, the density of $\rho_0 = 922.6$ kg m^{-3}, and the speed of sound of $c_f = 1445$ m s^{-1}.

The average mass transport velocity patterns shown in Figure 2 indicate the reversal of the direction of the streaming as the relative radius Ξ is decreased from 22.5 to 3.33 ($< \Xi_S$). Furthermore, a non-periodicity of the streaming pattern along the axis of the tube (z) appears due to the decoupling of the exponential amplitude dependency of the first-order solution to the sum of exponential and sinusoidal parts at the second order. The magnitude of the streaming velocity at the center of the tube was found to approach the simplified solution by Schuster and Matz [7], provided that $\Xi \geq 20$.

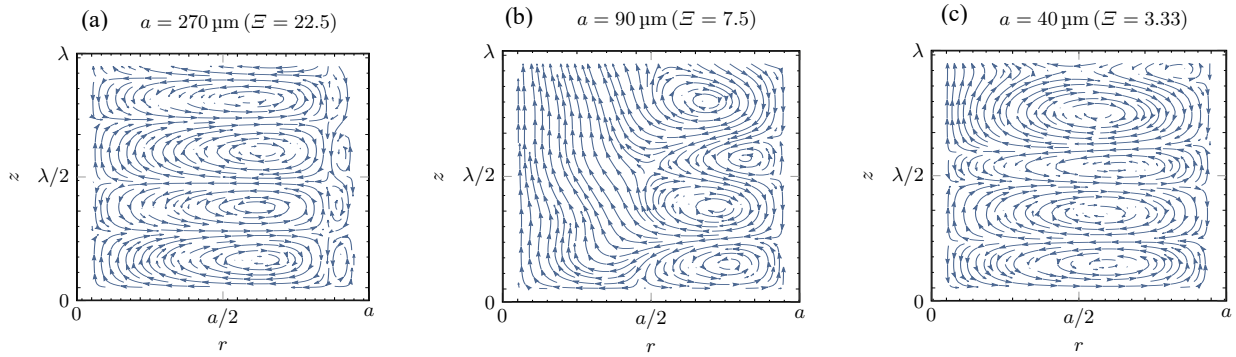

Figure 2. Average mass transport velocity patterns inside oil, at 100 kHz and with a pressure amplitude of 100 kPa. The arrows indicate the direction of the flow, and reveal the reversal of the streaming direction as Ξ is decreased (a) 22.5 to (c) 3.33.

CONCLUSIONS

The patterns that result from the analytical solution for the streaming in a Kundt's tube reveal an interesting and complex steady behaviour in such systems. This could be relevant for the design of acoustofluidic devices for manipulation of microparticles and cells.

References

[1] Kundt A. Ueber eine neue Art akustischer Staubfiguren und über die Anwendung derselben zur Bestimmung der Schallgeschwindigkeit in festen Körpern und Gasen. *Annalen der Physik* **203**: 497-523, 1866.

[2] Dvorak V. Ueber die akustische Anziehung und Abstofsung. *Annalen der Physik* **157**: 42-73, 1876.

[3] Rayleigh L. On the circulation of air observed in Kundt's tubes, and on some allied acoustical problems. *Philosophical Transactions of the Royal Society of London* **175**: 1-21, 1884.

[4] Andrade E. N. D. C. On the circulations caused by the vibration of air in a tube. *Proceedings of the Royal Society of London. Series A, Containing Papers of a Mathematical and Physical Character* **134**: 445-470, 1931.

[5] Pavlic A., Dual J. On the streaming in a microfluidic Kundt's tube. To be submitted.

[6] Schuster K., Matz W. Über stationäre Strömungen im Kundtschen Rohr. *Akustische Zeitschrift* **5**: 349-352, 1940.

MULTI PHYSICAL MODELLING OF COMPOSITE CELLULAR PIEZOCRYSTALLINE WAVEGUIDES

Ara S. Avetisyan* [1] and Vazgen M. Khachatryan[1]
[1]Department of Deformable Systems Dynamic and Coupled Fields, Institute of Mechanics of National Academy of Sciences of Armenia, Yerevan, Armenia

Summary Some possible variants of elastic multipartial waves formation and propagation in three-layer reticular waveguide with canonical rectangular cells of different piezo-crystals are considered. The cells are in acoustic contact. In neighboring cells of different piezo-materials, four-partial electroelastic wave of anti-plane strain and six-partial electroelastic wave of plane stress-strain state are formed simultaneously. The composite waveguide is modelled as a periodic structure of longitudinally inhomogeneous columns. The formation of electroelastic wave over the thickness of the composite waveguide is studied, and dispersion equations for electroelastic wave signal frequency filtration along the waveguide are obtained. It is shown that, by a proper choice of material pairs and relative thicknesses of layers, it is possible to achieve diverse schemes of wave formation and frequency filtration in the composite waveguide.

STRUCTURE OF THE WAVEGUIDE AND MATHEMATICAL BOUNDARY-VALUE PROBLEM

Consider a piezoelectric waveguide with reticular inner structure (see Figure 1(a)), which allows propagation of multiportional high-frequency electroelastic wave signal. The rectangular cells are in non-acoustic contact. The piezoelectric materials and the sagittal sections of the cells are chosen in such a way that, in neighbouring cells "B" and "R", two-partial electroelastic wave of anti-plane strain state of SH type and three-partial electroelastic wave of plane stress-strain state of P& SV type, respectively, occur simultaneously [1]. The three-layer waveguide is represented as a one-layer periodically-inhomogeneous waveguide with elastic composite columns (see Figure 1(b)).

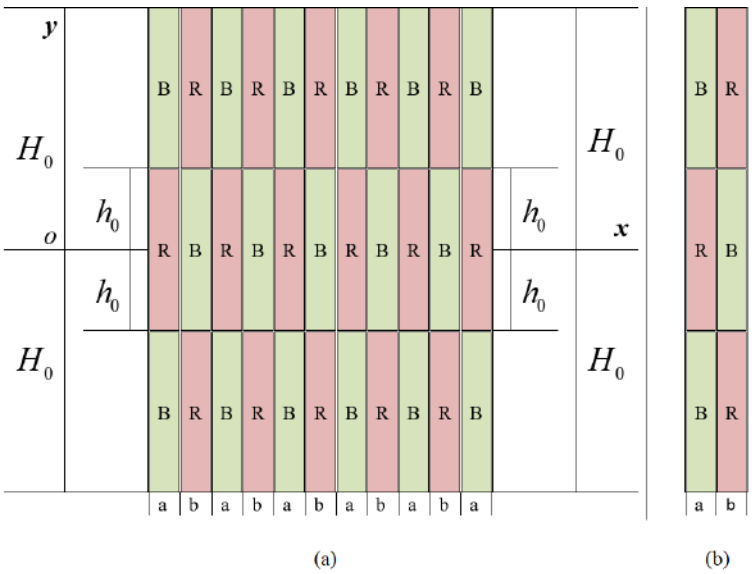

Figure 1: Structure of the waveguide. (a) Schematic representation of longitudinal section, (b) Periodically repeated unit.

The mathematical boundary-value problem consists of a system of equations for the two-partial and three-partial electroelastic waves of anti-plane strain state and plane stress-strain state in respective piezoelectric cells of the composite waveguide, of boundary conditions on surfaces of non-acoustic contact of "B" and "R" cells, as well as of boundary conditions on external shielded surfaces of the waveguide.

PROPAGATION OF NORMAL WAVE SIGNAL IN RETICULAR WAVEGUIDE

Electroelastic wave signal $\{f^{(j)} \cdot \exp(-i\omega t)\}$ forms two-partial and three-partial vibrations in respective cells of the reticular waveguide. The longitudinally periodic structure of the waveguide (see Figure 1(b)), allows propagation of periodic Floquet-type wave modes [2, 3].

*Corresponding author. E-mail: ara.serg.avetisyan@gmail.com.

In the case when electroacoustic signal occurs, in cells of "B" type, four-partial electroelastic shear wave occurs. Anti-plane elastic shear displacements $W_{mn}(x,y,t)$ and vibrations of electric field $\Phi_{mn}(x,y,t)$ in each cell of "B" type of the waveguide read as

$$f_m^{(B)}(x,y) = \sum_{n=1}^{4} Y_{mn}^{(B)}[y, k_m(\omega)\cdot p_{mn}^{(B)}(k_m(\omega))]\cdot X_{mn}^{(B)}[x, k_m(\omega)].$$

In cells of "R" type, six-partial electroelastic wave of plane stress state occurs. Elastic displacements $U_{mn}(x,y,t)$ and $V_{mn}(x,y,t)$, as well as the corresponding vibrations of electric field $\Phi_{mn}(x,y,t)$ in each cell of "B" type of the waveguide read as

$$f_m^{(R)}(x,y) = \sum_{n=1}^{6} Y_{mn}^{(R)}[y, k_m(\omega)\cdot p_{mn}^{(R)}(k_m(\omega))]\cdot X_{mn}^{(R)}[x, k_m(\omega)]$$

The coefficient of the solution periodicity in the waveguide, $\mu = \exp[(a+b)\cdot k_m^*(\omega)]$, the step of wave-forms in sub-layers, $\lambda_m(\omega) = 2\pi/k_m(\omega)$, and the coefficients of wave-forms formation in each cell, $p_{mn}^{(B)}(k_m(\omega))$ and $p_{mn}^{(R)}(k_m(\omega))$, are defined in terms of geometry material characteristics of the cells and frequency of the incoming wave signal.

When high-frequency electroacoustic signal is propagating, hybrid electroacoustic waves occur in the waveguide. Then, in cells of "B" type, localization of wave energy of Blustein-Gulyaev type occur near the surface. In cells of "R" type, localization of wave energy of Rayleigh type occur near the surface. Localization of energy of electro-active elastic vibrations occur also near the mechanically free, shielded surfaces $y = \pm H_0$, and near internal surfaces $y = \pm h_0$ of non-acoustic contact of the cells.

Near-surface localizations of wave energy near two different surfaces of each cell are qualitatively similar, but differ quantitatively. The distributions of electromechanical characteristics in neighboring composite sub-layers of "B-R-B" and "R-B-R" (see Figure 1(b)) types also differ.

The waveguide is represented as a three-channel waveguide with corresponding domains of admissible (forbidden) wave lengths

$$\lambda_m^*(\omega) = \frac{2\pi(a+b)}{\arccos\left[C_{Bt}, C_{Rt}, C_{Rl}, k_m(\omega), k_{m+1}(\omega), p_{m\alpha}^{(B)}(k_m(\omega)), p_{m\pm1\alpha}^{(R)}(k_m(\omega))\right]}, \quad \alpha = 1,2,3, \quad m = 1,2.$$

Obviously, the domains of admissible wave lengths of the external layers coincide, i.e., $\{\lambda_1^*(\omega)\} = \{\lambda_2^*(\omega)\}$. When $\{\lambda_0^*(\omega)\}\cap\{\lambda_2^*(\omega)\} \neq \varnothing$, i.e., the corresponding domains of admissible wave lengths have common points, the waveguide will be three-channel with two similar channels (for the given frequency). When $\{\lambda_0^*(\omega)\}\cap\{\lambda_2^*(\omega)\} = \varnothing$, the hybrid wave will propagate through one of the waveguide layers.

CONCLUSIONS

It is possible to generate electroactive hybrid elastic wave with cycle of transformation of anti-plane strain state to plane stress-strain state in reticular piezoelectric waveguide.

In the case of high-frequency electroacoustic signal, near the mechanically free shielded surfaces of a three-layer waveguide and near the inner surfaces of non-acoustic contact between the waveguide cells, localization of wave energy of hybrid electroacoustic waves of Blustein-Gulyaev and Rayleigh types occurs.

The reticular waveguide may functionate as in single-channel, as well as in multi-channel of wave modes transfer. By a proper choice of material characteristics and geometry of cells, the composite waveguide may serve as filter and resonator of electroelastic waves.

References

[1] Avetisyan A. S., Two-Dimensional Problem of Electroacoustics in Homogeneous Piezoelectric Crystals. *Proc. of NAS Armenia, Mechanics.* **72**(3): 56-79, 2019 **http://doi.org/10.33018/72.3.4**

[2] Avetisyan A. S., Khachatryan V. M., The Formation and Propagation of Elastic (SH) Shear Waves in a Cellular Composite Waveguide. *Proc. of NAS Armenia, Mechanics.* **71**(3): 55-73, 2018 **http://doi.org/10.33018/71.3.7**

[3] Piliposian G.T., Avetisyan A.S., Ghazaryan K.B., Shear wave propagation in periodic phononic/photonic piezoelectric medium. *I. J. Wave Motion.* **49**(1): 125–134, 2012 **https://doi.org/10.1016/j.wavemoti.2011.08.001**

COUPLING FLEXIBLE STRUCTURE AND VISCOUS, COMPRESSIBLE FLUID: A CASE FOR MODEL ORDER REDUCTION

Florian Toth* [1], Hamideh Hassanpour[1], and Manfred Kaltenbacher[1,2]
[1]Institute of Mechanics and Mechatronics, TU Wien, Vienna, Austria
[2]Institute of Fundamentals and Theory in Electrical Engineering (IGTE), Graz University of Technology, Graz, Austria

Summary We present a finite element formulation for the coupled modeling of a flexible structure and a viscous, compressible fluid. The coupling is realized using a non-conforming grid technique based on Nitsche's method. Employing the reduced basis method the typically very large system of equations resulting from the finite element discretisation is reduced dramatically using only a few natural modes as generalized degrees of freedom in a reduced-order model. Finally, the accuracy and computational performance of the reduced and full model are compared.

INTRODUCTION

In classical acoustics where the acoustic wave equation is employed, the fluid is often assumed as inviscid. This assumption is justified in cases where the relevant problem dimensions are large compared to the viscous boundary layer thickness, which depends on the viscosity of the medium and the frequency of interest. Especially on small scales, e.g. in MEMS applications, viscous effects should be considered. A similar reasoning applies to thermal effects (i.e. thermal conductivity in the fluid). Both can be modeled very efficiently by employing the finite element method (FEM) for the acoustic wave equation and modeling the acoustic and thermal boundary layer effects by impedance type boundary conditions [1]. Another common approach is to use a linearisation of the compressible flow equations, and use FEM to solve for pressure, velocity, and temperature field [2]. Coupling between fluid and flexible structure can be done using non-conforming grids [3, 4, 5], enforcing the interface conditions in the weak sense, and removing the need for a conforming mesh on the fluid-structure interface. Since the computational effort for the described method is rather high, we employ model order reduction based on the eigenmodes of the coupled system.

PHYSICAL MODEL

For the sake of simplicity, we disregard thermal effects, allowing us to treat the fluid problem using balance of mass and momentum only. To obtain the governing equations in linearised form, one first employs a perturbation ansatz for the fluid pressure, i.e. $\bar{p}(\boldsymbol{x},t) = p_\mathrm{f}(\boldsymbol{x}) + p(\boldsymbol{x},t)$, density $\bar{\rho}_\mathrm{f}(\boldsymbol{x},t) = \rho_\mathrm{f}(\boldsymbol{x}) + \rho(\boldsymbol{x},t)$ and velocity $\bar{\boldsymbol{v}}_\mathrm{f}(\boldsymbol{x},t) = \boldsymbol{v}(\boldsymbol{x},t)$, where the background fluid is assumed at rest and fulfilling the equilibrium condition. Furthermore, we assume a linearised equation of state relating pressure and density variation by $p\rho_\mathrm{f} = K_\mathrm{f}\rho$ where K denotes the bulk modulus. Using above assumptions one obtains the linearised version of the compressible flow equations describing the fluid by

$$\frac{\rho_\mathrm{f}}{K_\mathrm{f}}\frac{\partial p}{\partial t} + \nabla\cdot(\rho_\mathrm{f}\boldsymbol{v}) = 0, \quad \text{and} \quad \rho_\mathrm{f}\frac{\partial \boldsymbol{v}}{\partial t} - \nabla\cdot\boldsymbol{\sigma}_\mathrm{f} = \boldsymbol{0}, \quad \text{in } \Omega_\mathrm{f}. \tag{1}$$

The fluid is assumed as isotropic and Newtonian, i.e. the fluid stress tensor is written as

$$\boldsymbol{\sigma}_\mathrm{f} = -p\boldsymbol{I} + \big(\nabla\boldsymbol{v} + (\nabla\boldsymbol{v})^T\big) - \big(\frac{2}{3}\mu - \eta\big)\boldsymbol{I}\nabla\cdot\boldsymbol{v}, \tag{2}$$

where the parameters μ and η denote the shear and bulk viscosity, respectively, and $\boldsymbol{I}$ is the unit tensor.

The behavior of the elastic structure is described by the balance of momentum written in terms of the displacement $\boldsymbol{u}$ as

$$\rho_\mathrm{s}\frac{\partial^2\boldsymbol{u}}{\partial t^2} - \nabla\cdot\boldsymbol{\sigma} = \boldsymbol{0} \quad \text{in } \Omega_\mathrm{s}. \tag{3}$$

Assuming a linear elastic material and small stains the stress tensor is described as

$$\boldsymbol{\sigma} = \boldsymbol{C} : \boldsymbol{\mathcal{B}}(\boldsymbol{u}), \quad \text{with} \quad \boldsymbol{\mathcal{B}}(\boldsymbol{u}) = \frac{1}{2}\big(\nabla\boldsymbol{u} + (\nabla\boldsymbol{u})^T\big), \tag{4}$$

where $\boldsymbol{C}$ denotes the stiffness tensor, and $\boldsymbol{\mathcal{B}}$ the strain tensor.

Finally fluid and solid domains are coupled by enforcing the kinematic and dynamic interface conditions

$$\frac{\partial \boldsymbol{u}}{\partial t} = \boldsymbol{v}, \quad \text{and} \quad \boldsymbol{\sigma}_\mathrm{f}\cdot\boldsymbol{n} = \boldsymbol{\sigma}_\mathrm{s}\cdot\boldsymbol{n}, \quad \text{on } \Gamma_\mathrm{i}. \tag{5}$$

*Corresponding author. E-mail: florian.toth@tuwien.ac.at.

FINITE ELEMENT FORMULATION

The corresponding weak form is derived in the standard procedure by introducing suitable test functions, denoted by $()'$, assuming homogeneous Neumann boundary conditions in the integration by parts for the sake of simplicity. Coupling of solid and fluid domain based on Nitsche's method is done by summing the respective momentum balance equations, using the dynamic interface condition and introducing a penalty term to enforce the kinematic interface condition, yielding

$$\int_{\Omega_\mathrm{f}} p' \nabla \cdot \boldsymbol{v} \,\mathrm{d}\Omega + \int_{\Omega_\mathrm{f}} p' \frac{\rho_\mathrm{f}}{K_\mathrm{f}} \frac{\partial p}{\partial t} \,\mathrm{d}\Omega = 0, \tag{6}$$

$$\int_{\Omega_\mathrm{f}} \rho_\mathrm{f} \boldsymbol{v}' \cdot \frac{\partial \boldsymbol{v}}{\partial t} \,\mathrm{d}\Omega + \int_{\Omega_\mathrm{f}} \nabla \boldsymbol{v}' : \boldsymbol{\sigma}_\mathrm{f} \,\mathrm{d}\Omega + \int_{\Omega_\mathrm{s}} \boldsymbol{u}' \cdot \rho_\mathrm{s} \frac{\partial^2 \boldsymbol{u}}{\partial t^2} \,\mathrm{d}\Omega + \int_{\Omega_\mathrm{s}} \nabla \boldsymbol{u}' : \boldsymbol{\sigma}_\mathrm{f} \,\mathrm{d}\Omega$$
$$- \int_{\Gamma_\mathrm{i}} (\boldsymbol{u}' - \boldsymbol{v}') \cdot \boldsymbol{\sigma}_\mathrm{s} \cdot \boldsymbol{n} \,\mathrm{d}\Gamma + \beta \int_{\Gamma_\mathrm{i}} (\boldsymbol{u}' - \boldsymbol{v}') \cdot (\frac{\partial \boldsymbol{u}}{\partial t} - \boldsymbol{v}) \,\mathrm{d}\Gamma = \boldsymbol{0}, \tag{7}$$

where the penalty factor β was introduced. Above mixed formulation contains pressure, velocity and displacement degrees and can be discretised using nodal finite elements. Ensuring the order of the ansatz functions for the pressure degrees of freedom is one lower than for the velocity results in a stable formulation.

MODEL ORDER REDUCTION

Introducing the ansatz $\boldsymbol{w}(t) = \hat{\boldsymbol{w}} e^{\lambda t}$ for the vector of unknowns, the discretised system can be written in the form

$$\boldsymbol{M}\lambda^2 \hat{\boldsymbol{w}} + \boldsymbol{D}\lambda \hat{\boldsymbol{w}} + \boldsymbol{K}\hat{\boldsymbol{w}} = \boldsymbol{0}, \tag{8}$$

representing a quadratic eigenvalue problem. Computing a set of eigenvalues and corresponding modes enables us to obtain a reduced order system by projecting onto the modal basis. Since the mass matrix $\boldsymbol{M}$ has no full rank and the damping and stiffness matrices $\boldsymbol{C}$ and $\boldsymbol{K}$ are not symmetric, the projection to the modal system needs left and right eigenvectors.

CONCLUSION

The finite element formulation was implemented in the open source code openCFS [6]. The reduced basis method offers an attractive option to speed up the solution of systems where a small number of modes are of interest. This is usually the case in fluid-solid coupled systems where the structural modes usually dominate the behaviors of the system, and the fluid is responsible for the damping effect, which can be accurately modeled by the presented strategy.

References

[1] Berggren M, Bernland A, Noreland D. Acoustic boundary layers as boundary conditions. *Journal of Computational Physics* oct 2018; **371**:633–650.

[2] Kampinga WR, Wijnant YH, de Boer A. Performance of several viscothermal acoustic finite elements. *Acta Acustica united with Acustica* jan 2010; **96**(1):115–124.

[3] Flemisch B, Kaltenbacher M, Wohlmuth BI. Elasto-acoustic and acoustic-acoustic coupling on nonmatching grids. *Int. J. Numer. Meth. Engng* 2006; **67**(13):1791–1810.

[4] Alauzet F, Fabrèges B, Fernández MA, Landajuela M. Nitsche-xfem for the coupling of an incompressible fluid with immersed thin-walled structures. *Computer Methods in Applied Mechanics and Engineering* 2016; **301**:300–335.

[5] Burman E, Fernández MA. An unfitted nitsche method for incompressible fluid–structure interaction using overlapping meshes. *Computer Methods in Applied Mechanics and Engineering* 2014; **279**:497–514.

[6] openCFS: open source Coupled Field Simulation based on the Finite Element Method. https://opencfs.org.

EFFICIENT "MATRIX-FREE" PARTIAL-ASSEMBLY ALGORITHMS FOR HIGH-ORDER ALE HYDRODYNAMICS ON GPUS

Robert N. Rieben[1], Arturo Vargas *[1]
[1]Weapons and Complex Integration, Lawrence Livermore National Laboratory, Livermore, USA

Summary In this talk, we present our two-fold approach in tailoring Blast, an arbitrary Lagrangian-Eulerian (ALE) multi-material hydrodynamics code developed at LLNL, for advanced architectures. A distinguishing feature of Blast is the choice of high order finite element methods leading to higher arithmetic intensity per data access; a trait favored by modern computing processors. Our first approach leverages partial assembly techniques and exploits the tensor product structure of quad/hex elements. Through this approach, the action of global operators only requires values at quadrature points enabling reduced storage and on the fly calculations. Second, to remain portable across computing platforms, our implementation builds on the RAJA programming model and Umpire resource manager. Together RAJA and Umpire enable maintaining a single source code suitable for heterogenous computing systems.

With the introduction of advanced architectures such as GPUs, a major effort has been set forth to develop algorithms and implementations for hydrodynamics codes which can realize performance on next gen computer systems. MARBL is a next generation Multiphysics code for modelling ICF/pulsed power experiments and is being developed at LLNL as part of the Exascale Computing Project. A core component of MARBL is the high-order, multi-material, arbitrary Lagrangian-Eulerian (ALE) module based on high-order finite elements, called BLAST [1]. A distinguishing feature of BLAST is the choice of high order finite element methods leading to higher arithmetic intensity per data access; a trait favored by modern computing processors. In this talk, we discuss our two-fold strategy for achieving high-performance on advanced architectures like GPUs which includes adoption of efficient "matrix-free" methods and use of the RAJA performance portability abstraction layer [2] for on-node parallelism.

The core of BLAST is the Lagrange phase where we solve the time dependent Euler equations of compressible gas dynamics on a moving mesh with explicit high order time-stepping. This algorithm requires the solution of a global linear system for solving the momentum conservation equation, involving both a "mass" and a rectangular "force" matrix. In our standard solution approach, we fully assemble global, sparse, parallel distributed matrices for the momentum solve. This approach has poor scaling characteristics as a function of the polynomial degree of the finite elements used for discretization. In addition, solution of the global linear system for momentum requires parallel matrix-vector multiplies which is a bandwidth limited computational kernel.

The first component of our approach for achieving high-performance on advanced architectures refactors the Lagrange phase of BLAST to bypass the assembly of global operators and only assemble data at quadrature points. This partial assembly strategy enables us to decompose the action of global matrices into a set of element wise operator evaluations (i.e. computing the action of the operator per element). At high finite element orders, this results in a compute bound algorithm that is well suited for GPU acceleration. In addition, it enables us to exploit the tensor product structure of finite element basis functions on quadrilateral/hexahedral elements leading to a reduction in required operations. To explore the properties of this approach, we have developed a miniapp, called LAGHOS [3], which captures the key properties of the Lagrange phase of BLAST. LAGHOS supports both full and partial assembly methods.

The second component of our high-performance strategy is the use of the RAJA abstraction layer to support on node threading along with the Umpire resource manager developed at LLNL. Together, RAJA and Umpire enable maintaining a single source code suitable for heterogenous computing systems. We report on performance characteristics of both LAGHOS and BLAST using the partial assembly approach combined with RAJA and discuss the code changes that were required to enable this.

This work performed under the auspices of the U.S. Department of Energy by Lawrence Livermore National Laboratory under Contract DE-AC52-07NA27344, LLNL-ABS- 800797.

References

[1] V. Dobrev, T. Kolev, R. Rieben, "High order curvilinear finite element methods for Lagrangian hydrodynamics," SIAM J. Sci. Comp, 34(5), P606-641, 2012.
[2] RAJA Performance Portability Layer. **https://github.com/LLNL/RAJA**.
[3] LAGHOS Miniapp: **https://github.com/CEED/Laghos**.

*Corresponding author. E-mail: vargas45@llnl.gov.

LARGE-SCALE SIMULATIONS IN TURBULENT CONVECTION

J. Schumacher* [1,2], K. P. Iyer[2], D. Krasnov[1], J. D. Scheel[3], A. Pandey[4], and K. R. Sreenivasan[2,4]
[1]Department of Mechanical Engineering, Technische Universität Ilmenau, Ilmenau, Germany
[2]Tandon School of Engineering, New York University, New York, USA
[3]Department of Physics, Occidental College, Los Angeles, USA
[4]Center for Space Science, New York University Abu Dhabi, Abu Dhabi, UAE

Summary High-resolution direct numerical simulations of Rayleigh-Bénard convection have contributed significantly to our better understanding of structure formation and transport processes in turbulent convection flows which are driven by buoyancy forces. In this presentation two particular applications of supercomputing to turbulent Rayleigh-Bénard convection are discussed in more detail: (1) convection in slender cells for very high Rayleigh numbers up to $\mathrm{Ra} = 10^{15}$ at a Prandtl number $\mathrm{Pr} = 1$, and (2) convection in horizontally extended domains at a very low Prandtl number $\mathrm{Pr} = 10^{-3}$ for Rayleigh numbers up to $\mathrm{Ra} = 10^{6}$. It is explained why both cases are important in view to applications of convection and why they require massively parallel simulations.

INTRODUCTION

Turbulent Rayleigh-Bénard convection (RBC), triggered in a fluid layer which is uniformly heated from below and cooled from above, is considered the paradigm for many examples of buoyancy-driven turbulence reaching from stellar convection via atmospheric and oceanic turbulence to cooling blankets in nuclear engineering or the storage of renewable energy in liquid metal batteries (see e.g. [1, 2] for more details). Central questions in RBC are related (1) to the fundamental law governing the global turbulent transport of heat and momentum across the convection layer and (2) the characteristic scales and times of large-scale convection patterns in extended layers as a function of dimensionless parameters characterizing the flow . These parameters are the Rayleigh number $\mathrm{Ra} = g\alpha\Delta T H^3/(\nu\kappa)$, which quantifies the relative magnitude of the thermal driving to the viscous and diffusive forces of the fluid motion and is directly proportional to the temperature difference $\Delta T = T_{\mathrm{bottom}} - T_{\mathrm{top}}$ maintained between the top and bottom plates, and the Prandtl number $\mathrm{Pr} = \nu/\kappa$, which is the ratio of momentum and thermal diffusivities denoted by ν and κ, respectively. Here, g, α, and H are the acceleration due to gravity, the isobaric thermal expansion coefficient, and the fluid layer height H, respectively. A third parameter is the aspect ratio Γ that relates a horizontal scale of the setup, such as a diameter d of the closed (cylindrical) cell or the horizontal length L to the height H.

Direct numerical simulations (DNS) which resolve all scales face significant challenges to advance towards parameter regimes of realistic convection flows in nature. Figure 1 illustrates this circumstance for the example of solar convection. Turbulent convection inside the Sun operates at Prandtl numbers $\mathrm{Pr} \sim 10^{-6}$ and (local) Rayleigh numbers $\mathrm{Ra} \sim 10^{22}$ and should be considered in domains $\Gamma \gg 1$. Despite the fact that a RBC model neglects additional important physical processes which interact in solar convection, the values of Ra and Pr will not be accessible in foreseeable future. Some progress can be made however along two lines, either for small aspect ratio cells in order to advance to the highest accessible Rayleigh numbers or for moderate Rayleigh number in order to advance to the lowest accessible Prandtl numbers in horizontally extended domains. Both routes are followed in supercomputer simulations of RBC which apply the spectral element code nek5000 [3] or a finite difference method [4] and will be discussed here. See again figure 1 for the accessible range of both simulation series which we denote as DNS 1 and DNS 2 in the following.

CONVECTION IN SLENDER CELL AT VERY HIGH RAYLEIGH NUMBER

The global transport of heat and momentum in turbulent convection is constrained by thin thermal and viscous boundary layers at the heated and cooled boundaries of the system. This bottleneck is thought to be lifted once the boundary layers themselves become fully turbulent at very high values of the Rayleigh number Ra. Laboratory experiments in cylindrical cells for $\mathrm{Ra} \geq 10^{12}$ have reported different outcomes on the existence of the transition to such an "ultimate" state of turbulent convection. We showed by series DNS 1 of three-dimensional RBC in a slender cylindrical cell with $\Gamma = 1/10$ that the ultimate state does not occur even at $\mathrm{Ra} = 10^{15}$, and relate the result to the flow structure, in particular inside the boundary layers [5]. Figure 1 displays a temperature snapshot close to the heated bottom plate. We find that the Nusselt number — the dimensionless measure of heat transport — follows the power law of $\mathrm{Nu} = (0.055 \pm 0.010) \times \mathrm{Ra}^{0.33\pm0.01}$, which is almost identical to the classical prediction based on marginally stable boundary layers. Intermittent fluctuations in the wall stress, a blueprint of turbulence in the vicinity of the boundaries, manifest at all Ra considered here, increase with increasing Ra, and demonstrate that no abrupt transition of the boundary layer to turbulence is likely. The largest direct numerical simulations at $\mathrm{Ra} = 10^{15}$ were conducted with more than 17 million spectral elements and used 524,288 Message Passing Interface (MPI) processes on the Blue Gene/Q supercomputer Mira at the Argonne National Laboratory that alone required more than 100 million core-hours.

*Corresponding author. E-mail: joerg.schumacher@tu-ilmenau.de

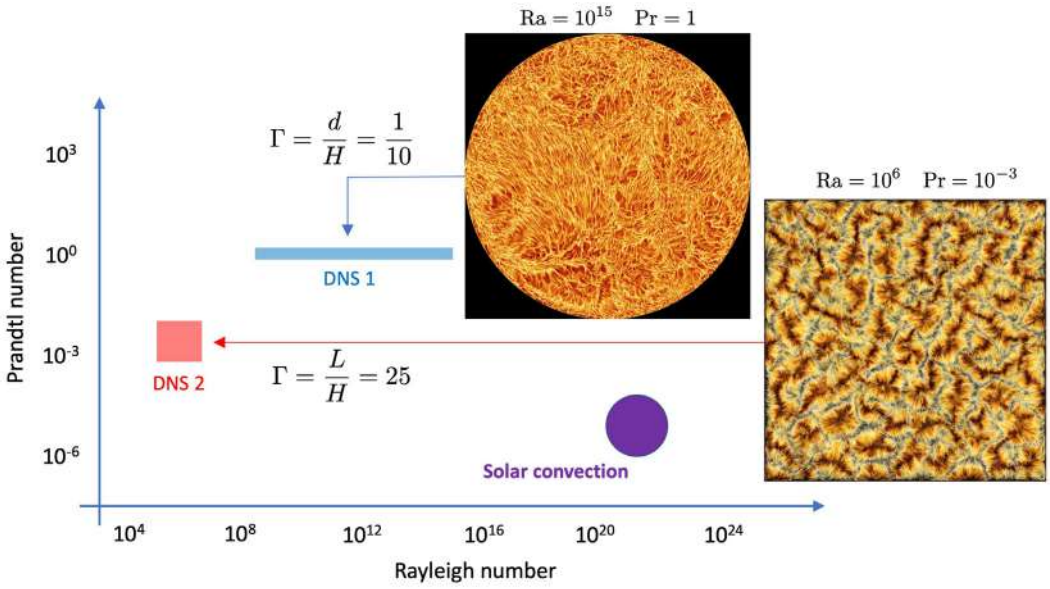

Figure 1: The parameter plane, which is spanned by the Rayleigh number Ra and the Prandtl number Pr, is shown together with the two series of DNS of turbulent Rayleigh-Bénard convection. For both series, a snapshot picture is added. DNS 1: contours of the temperature field close to the heated bottom plate of the slender cylindrical cell. DNS 2: Top view on the convection domain with streamlines of the velocity field colored by velocity magnitude. Also indicated is the typical range of Rayleigh and Prandtl number in solar convection.

CONVECTION IN EXTENDED LAYER AT VERY LOW PRANDTL NUMBER

RBC flows in horizontally extended domains show an organisation into regular large-scale patterns which are termed *turbulent superstructures* of convection [6]. They are reminiscent to the patterns in the weakly nonlinear regime of thermal convection for Rayleigh numbers right above the linear instability threshold. We have studied these patterns as a function of Rayleigh and Prandtl numbers in rectangular simulation domains with a large aspect ratio of $\Gamma = 25$ and obtained characteristic spatial and time scales as a function of $(\mathrm{Ra}, \mathrm{Pr})$. The analysis of these large-scale computations require a strong data reduction, e.g., to reveal the role of turbulent superstructures for the global heat transfer across the layer. Therefore, we applied deep convolutional neural networks to reduce the raw 3d simulation data to a planar dynamic ridge network and to quantify the turbulent heat transfer that is connected with this structure [7]. A particular challenge are RBC simulations at very low Prandtl number in this setting (see DNS 2 in figure 1 again). The reason is that the fluid turbulence becomes highly inertial at low Prandtl numbers. This requires very fine computational grids, both, in the boundary layers and in the bulk. The largest DNS, which was conducted at $\mathrm{Ra} = 10^6$ and $\mathrm{Pr} = 10^{-3}$ on the SuperMUC NG computer at the Leibniz Rechenzentrum Garching, used a non-uniform finite-difference Cartesian grid with a resolution of $N_x : N_y : N_z = 12800 : 12800 : 800$ points that sum up to more than 131 billion grid points.

Acknowledgements. The present DNS 1 were enabled by an award of computer time provided by the Innovative and Novel Computational Impact on Theory and Experiment (INCITE) program, and used resources of the Argonne Leadership Computing Facility, which is a DOE Office of Science User Facility supported under Contract DE-AC02-06CH11357. DNS 2 were enabled by Grant No. HIL12 of the John von Neumann Institute for Computing in Jülich (Germany) and Grant No. pr62se of the Gauss Centre for Supercomputing (Germany). JDS and JS are supported by the Priority Programme DFG-SPP 1881 "Turbulent Superstructures" of the Deutsche Forschungsgemeinschaft (DFG). DK is supported by DFG Grant No. KR 4445/2-1.

References

[1] Chillà F., Schumacher J. New perspectives in turbulent Rayleigh-Bénard convection. *Eur. Phys. J. E* **35**: article no. 58, 2012.
[2] Schumacher J., Sreenivasan, K.R. Unusual dynamics of convection in the Sun. *Rev. Mod. Phys.*, submitted, 2019.
[3] Nek 5000, web site **https://nek5000.mcs.anl.gov**.
[4] Krasnov, D., Zikanov, O., Boeck, T. Comparative study of finite difference approaches in simulation of magnetohydrodynamic turbulence at low magnetic Reynolds number. *Comput. Fluids* **50**: 46–59, 2011.
[5] Iyer, K.P., Scheel, J.D., Schumacher, J., Sreenivasan, K.R. No ultimate turbulent convection in slender cell up to $\mathrm{Ra} = 10^{15}$. *Proc. Natl. Acad. Sci. USA*, submitted, 2019.
[6] Pandey, A., Scheel, J.D., Schumacher, J. Turbulent superstructures in Rayleigh-Bénard convection. *Nat. Commun.* **9**: article no. 2118, 2018.
[7] Fonda, E., Pandey, A., Schumacher, J., Sreenivasan, K.R. Deep learning in turbulent convection networks. *Proc. Natl. Acad. Sci. USA*, **116**, 8667–8672, 2019.

UNCERTAINTY QUANTIFICATION TECHNIQUES FOR SCALE-RESOLVING SIMULATIONS OF WALL-BOUNDED TURBULENCE

Saleh Rezaeiravesh[1,2], Narges Tabatabaei[1,2], Ricardo Vinuesa[1,2], and Philipp Schlatter * [1,2]
[1]Linné FLOW Centre, KTH Mechanics, Royal Institute of Technology, Stockholm, Sweden
[2]Swedish e-Science Research Centre (SeRC), Stockholm, Sweden

Summary Scale-resolving simulations of wall-bounded turbulent flows can be very expensive and, on the other hand, their performance depends on various numerical and modeling parameters. Dealing with these challenges can be facilitated by making use of novel techniques from the field of uncertainty quantification (UQ). In this regard, two connected paths of research are pursued here. First, using a combination of stochastic collocation and polynomial chaos expansion (PCE) methods with global sensitivity analysis, a framework is developed to efficiently assess accuracy, sensitivity, and robustness of scale-resolving simulations when different numerical parameters are allowed to vary. In the second path, multifidelity models are developed which are beneficial for constructing predictive models over the input space of high-fidelity flow simulations. Such models provide the possibility of conducting robust optimization and uncertainty quantification studies involving wall-resolving simulations. The frameworks in this study are software-independent, however, the main focus is on Nek5000 [1] that is an open-source high-order highly-scalable spectral-element flow solver. The presented UQ techniques are particularly relevant in the view of large-scale (exascale) computing.

INTERFACES BETWEEN UQ AND TURBULENCE SIMULATIONS

Assessment of Numerical Uncertainties

Numerical solutions of the Navier–Stokes equations for turbulent flows can be contaminated by some level of uncertainties and errors originating from different sources, including the followings: the projection, discretization of spatial and temporal derivatives, velocity-pressure coupling, imposing initial and boundary conditions, meshing, bugs in the code, limited sampling time, etc. A part of this study aims at investigating how the accuracy and certainty of the quantities of interest (QoIs) of canonical wall-bounded turbulent flows are sensitive to various numerical parameters and time averaging. Assume $\varphi_h(\mathbf{x},t)$ represents a discrete flow quantity obtained by direct numercal simulation (DNS) or large-eddy simulation (LES), where $\mathbf{x}$ is the position vector and t is time. The averaged value of $\varphi_h(\mathbf{x},t)$ over statistically homogeneous directions and finite time T is considered to be a QoI and represented by $\langle\varphi_h(\mathbf{x},t)\rangle_T$. Given a reference true data, $\langle\varphi_h^\circ(\mathbf{x},t)\rangle$, we can write,

$$\|\langle\varphi_h(\mathbf{x},t)\rangle_T - \langle\varphi_h^\circ(\mathbf{x},t)\rangle\| \leq \|\langle\varphi_h(\mathbf{x},t)\rangle - \langle\varphi_h(\mathbf{x},t)\rangle_T\| + \|\langle\varphi_h(\mathbf{x},t)\rangle - \langle\varphi_h^\circ(\mathbf{x},t)\rangle\| \,.$$

On the right-hand side, the first and second terms represent the uncertainties due to finite time-averaging (sampling error), $\mathcal{E}_T$, and the combination of all other numerical and modeling errors (excluding the projection error), $\mathcal{E}_n$, respectively. To estimate the uncertainty in the QoIs due to time averaging, $\mathcal{E}_T$, the use of different techniques such as classical, batch-based and autoregressive methods is discussed, see e.g. [2] and the references therein. Due to the dominant non-linearity of the Navier–Stokes equations and the fact that various numerical and modeling errors are intertwined, deriving accurate a-posteriori estimates for $\mathcal{E}_n$ in turbulent flows is not feasible. Here, the strategy is to study the sensitivity and behavior of the $\mathcal{E}_n$ of different QoIs with respect to several sources of uncertainty through systematic flow simulations, see *e.g.*[3, 4]. Therefore, a UQ forward problem is formulated in which the numerical parameters, such as grid resolution and filtering parameters, are considered to be uncertain. The associated uncertainties in these parameters (hereafter shown by $\mathbf{q}$) are propagated into the responses or quantities of interest $\mathcal{R}$. The parameters $\mathbf{q}$ are allowed to vary over the presumed admissible space Q. Using polynomial chaos expansion (PCE) [5] with stochastic collocation samples in a non-intrusive way, surrogates are constructed for $\mathcal{R} = \tilde{f}(\mathbf{q})$. Employing the surrogates, the portraits of the errors in the QoIs are obtained over the whole space Q and stochastic moments of QoIs are estimated. Moreover, the Sobol indices [6] provide a quantitative basis to compare the global sensitivity of different errors with respect to variation of $\mathbf{q}$.

Figure 1 shows a set of described analysis for wall-resolved simulations of channel flow at $\mathrm{Re}_\tau = 300$, where Re_τ is based on friction velocity and channel half-height. The uncertain parameters $\mathbf{q}$ are Δx^+ and Δz^+, the inner-scaled average distance between collocation points in the streamwise and spanwise directions, respectively. Variation of the error in mean streamwise velocity, $\langle u\rangle$, in the admissible space of parameters $\mathbf{q}$, sensitivity indices of the errors in different QoIs with respect to these parameters, and robustness of the QoIs when $\mathbf{q}$ vary over Q are illustrated in Figure 1. The study also investigates the impact of filtering approach and associated parameters in addition to grid resolution controllers.

Multifidelity Models

Uncertainty quantification, prediction and robust optimization for problems involving wall-bounded turbulent flows can be very expensive, since exploration of the input space demands several realizations. Therefore accurate yet cost-effective models are required for such purposes. The present study reports our recent progress on further developing and exploiting multifidelity models which rely on Gaussian processes [7]. Following Goh et al. [8], at each hierarchical level

*Corresponding author. E-mail: pschlatt@mech.kth.se.

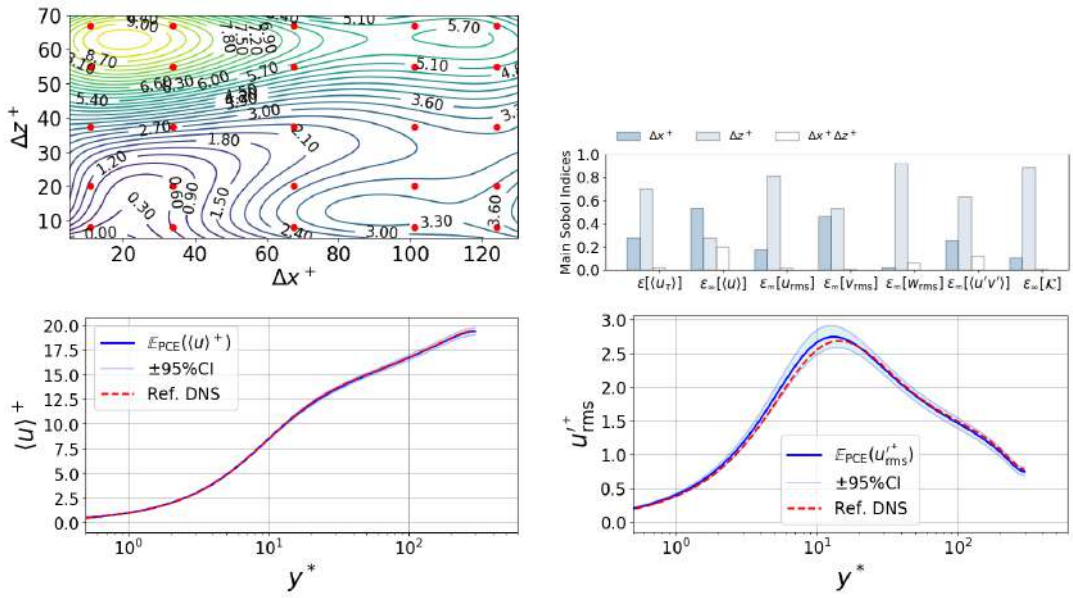

Figure 1: UQ study of turbulent channel flow at $\mathrm{Re}_\tau = 300$ when inner-scaled grid resolutions in wall-parallel plane are allowed to vary: variation of error in $\langle u \rangle$ in Δx^+-Δz^+ plane (top-left), Sobol sensitivity indices for different QoIs with respect to Δx^+ and Δz^+ which are varying over $[5, 50]$ and $[5, 30]$, respectively (top-right) with resulting propagation of uncertainty in the inner-scaled mean and rms streamwise velocities (bottom).

in our multifidelity model, the Kennedy-O'Hagan model [9] is used which allows for considering both model inadequacy and aleatoric uncertainties in the process of data fusion. Using a limited number of realizations (mostly by running low-fidelity simulations), the calibration parameters and hyperparameters appearing in the multifidelity model are estimated within a Bayesian framework. The constructed model can then be employed for uncertainty propagation and prediction over the whole input space. In particular, the turbulent flow around a standard NACA airfoil is considered with time-averaged aerodynamic characteristics as QoIs. The input variables (uncertain and controlled parameters) include the angle of attack, Reynolds number, and specific locations on the airfoil. To construct the multifidelity model, data from wall-resolved LES, Reynolds-averaged Navier-Stokes (RANS) simulations, and panel method are employed. Upon availability, new experimental measurements are also considered. The accuracy and credibility of the model predictions and their sensitivity with respect to various influential factors will be discussed.

CONCLUSIONS

It is shown how UQ techniques can be extremely helpful in studies involving simulations of wall turbulence. Such techniques make it possible to rank the parameters which influence the accuracy, sensitivity and robustness of the numerical simulations. Moreover, they can be used for development of a framework for quantitative comparison between different flow solvers. Multifidelity models can be utilized as an efficient surrogate for actual wall-resolving simulations in problems where exploration of a parameter/input space is required. The insights gained from this study will pave the way for the further development of the multifidelity models for wall-bounded turbulent flows, and will also allow us to design future high-fidelity simulation campaigns for airfoils and wings. This project is in the context of the Excellerat EU Centre of Excellence.

References

[1] Nek5000, web site **https://nek5000.mcs.anl.gov/**.
[2] Russo S., Luchini P. A fast algorithm for the estimation of statistical error in DNS (or experimental) time averages. *Journal of Computational Physics*. **347**, 328-340, 2017.
[3] Rezaeiravesh S., Liefvendahl M. Effect of grid resolution on large eddy simulation of wall-bounded turbulence *Phys. Fluids*, **30**, 055106, 2018.
[4] Mariotti A., Siconolfi L., Salvetti M. Stochastic sensitivity analysis of large-eddy simulation predictions of the flow around a 5:1 rectangular cylinder. *Eur. J. Mech. B/Fluids* , **62**, 149:165 2017.
[5] Ghanem R. G., Spanos P. D. Stochastic Finite Elements: A Spectral Approach. Springer-Verlag. NY, 1991.
[6] Sobol I. M. Global sensitivity indices for nonlinear mathematical models and their Monte Carlo estimates, *Mathematics and Computers in Simulation*, **55**, 271:280, 2001.
[7] Rasmussen C. E., Williams C. K. I., Gaussian Processes for Machine Learning, MIT Press, 2005.
[8] Goh J. et al. Prediction and computer model calibration using outputs from multifidelity simulators, *Technometrics*, **55**, 501:512, 2013.
[9] Kennedy M. C., O'Hagan A. Bayesian calibration of computer models, *J. R. Statist. Soc. B*, **63**, 425:464, 2001.

LARGE EDDY SIMULATION OF FLOWS OVER POROUS STRUCTURES WITH A MASSIVELY PARALLEL ADAPTIVE LATTICE BOLTZMANN METHOD

Ralf Deiterding and Mikaël P. Grondeau
Aerodynamics and Flight Mechanics Research Group, University of Southampton
Boldrewood Innovation Campus, Southampton, SO16 7QF, United Kingdom

Summary We discuss the construction and parallel performance of our self-developed parallel and dynamically adaptive lattice Boltzmann software AMROC-LBM. We apply the code to large eddy simulations of turbulent boundary layer flows over rough and permeable surfaces. Beside the fluid mechanical results, the computational performance of AMROC-LBM in dynamically adaptive as well as in unigrid mode on large-scale and massively parallel supercomputer systems is discussed.

INTRODUCTION

Predicting turbulent boundary layer flows over complex porous surfaces accurately requires a low-dissipation computational approach with high temporal and spatial fidelity. While compressible large eddy simulation (LES) in the transonic or supersonic regime is best accomplished with high-order finite volume schemes, the lattice Boltzmann method (LBM) has emerged as a particularly powerful alternative for LES or direct numerical simulation of subsonic flows.

Being a type of immersed boundary method, the LBM is well suited for modelling porous structures. A unique capability of our LBM implementation is the seamless integration into a fully parallelized block-structured adaptive mesh refinement algorithm implemented in our generic massively parallel framework AMROC [1], thereby allowing local resolution increases on-the-fly and depending on the local flow field. Here, we sketch the inner workings of AMROC-LBM [2,3] and report on first LES results of boundary layer development over a prototypical rough wall scenario consisting of regularly arranged spheres of identical size [4]. Parallel performance of our implementation on dynamically evolving as well as on static uniform grids is discussed.

METHODS

The LBM is based on solving a simplified Boltzmann equation with a time-explicit streaming and collision algorithm on a Cartesian lattice. The streaming step is exact, and the scheme exhibits very low numerical dissipation. Here, we employ the single-relaxation-time (SRT) collision operator, for which it is mandatory to apply a turbulence model in high Reynolds number situations. We adopt an LES approach with eddy viscosity model [3], which can easily be considered in the LBM by adding a turbulent eddy viscosity, evaluated locally in each cell, to the kinematic viscosity of the gas. Here, we have used the constant coefficient Smagorinsky model.

Our LBM is implemented on finite volume type meshes and considers geometrically complex boundaries with a level-set-based ghost-fluid-type approach. Dynamic mesh adaptation can be applied in addition in order to increase the local resolution based on the level set function and features detected in the flow field, as provided by out MPI-parallelized structured adaptive mesh refinement (SAMR) software system AMROC. In the SAMR approach, cells are clustered with a special algorithm into non-overlapping rectangular grids. Refinement levels are integrated recursively. See [1] for details. Distributions streaming across refinement boundaries are fully considered in AMROC-LBM by a specially designed correction algorithm [2,3]. For mesh partitioning, AMROC uses a space filling curve algorithm.

RESULTS

An adaptive LBM-based LES of the boundary layer flow over a prototype porous surface using AMROC is shown in Fig. 1. Two levels of dynamic mesh resolution have been used in this preliminary computation. Inspired by a case studied by Stoesser et al. [4], flow of air imposed by a flume at velocity of U=8m/s, modelled as a surface sliding in the x-direction at the top domain boundary, passes over two layers of 18x10 regularly positioned spheres of D=12mm diameter on top of a flat fixed wall bottom (x-y-plane). The distance of the flume is H=41mm above the sphere surfaces, giving a Reynolds number of the bulk channel flow of $\mathrm{Re}=UH/\nu=20372$. Figure 1 is depicting the instantaneous velocity in the x-direction after approximately 12 flow periods through the domain, when the boundary layer is reasonable well formed. Figure 2 shows the averaged x-velocity above the spheres in locations of minimal and maximal porosity compared to the reference data by Stoesser et al. While the resolution of the LBM computation is still coarser, convergence can be clearly by inferred.

Strong scalability benchmarks on the Archer system of AMROC-LBM have been also been carried out for the prototype setup. Starting from a 360x240x108 base grid and adding dynamically up to 2 additional levels refined in all spatial directions by factors 2 and 4, respectively, the benchmark computation corresponds to a uniform mesh of 2880x1920x864 = 4.78e9 cells. The benchmark computed 80 timesteps on the finest grid level and included 4 complete parallel mesh redistributions. 24,844,504 cells where used at the end of this test on the first refinement level and 10,838,016 on the second. The left plot of Fig. 2 displays the speedup of the parallel computation with increasing core count compared to the ideal linear line. Since the LBM is computationally rather inexpensive, parallel scalability on very large processor

number is difficult to achieve when mesh adaptation is employed. At least until 1536 cores the performance gains from using more processors are quite acceptable for our implementation. For comparison, the right plot of Fig. 2 shows the speedup for the initial 80 timesteps for this case when using a uniform and static mesh of 1440x1920x432 = 1.19e9 cells.

CONCLUSIONS

LES of turbulent boundary layer flow over a generic prototype rough and permeable surface have been carried out with our self-developed parallel and dynamically adaptive lattice Boltzmann code AMROC-LBM. Good agreement with available reference data is achieved and verifies the correctness of the adaptive LBM and LES implementation.

While scalability of the explicit AMROC-LBM code when running in static uniform grid mode is up to O(10,000) cores, first benchmark computations have confirmed good scalability of AMROC-LBM on hierarchical, self-adapting meshes on O(1000) cores for a prototype surface. At the conference significantly higher resolved simulations of LES over technically relevant surface geometries will be presented. The preliminary studies discussed here have confirmed the suitability of our overall approach.

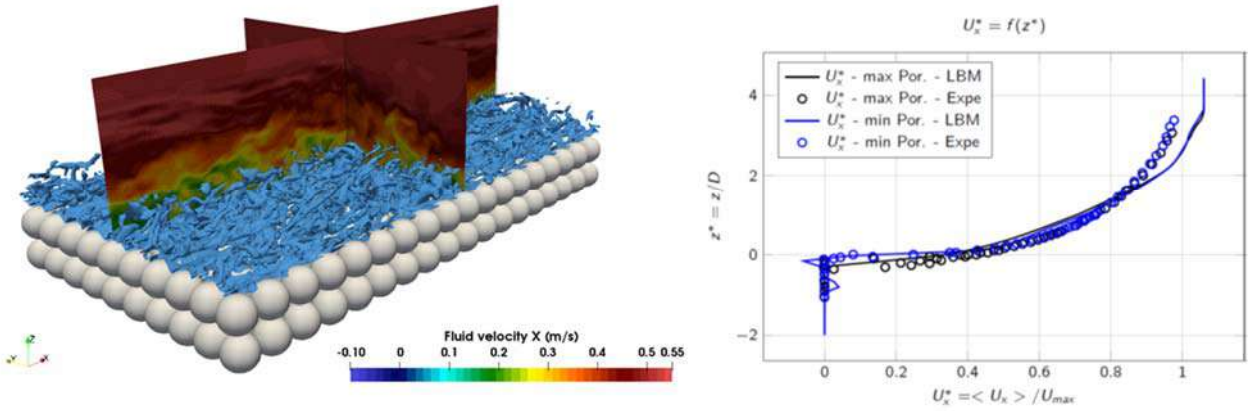

Figure 1. Left: LES of turbulent boundary layer flow over surface consisting of two regular layers of spheres with the adaptive LBM. Colour plot of tangential velocity field with overlaid mesh resolution and blue isoline to display the vortices near the surface. Right: Averaged velocity in tangential direction in the present computation (LBM) vs. reference result (Expe).

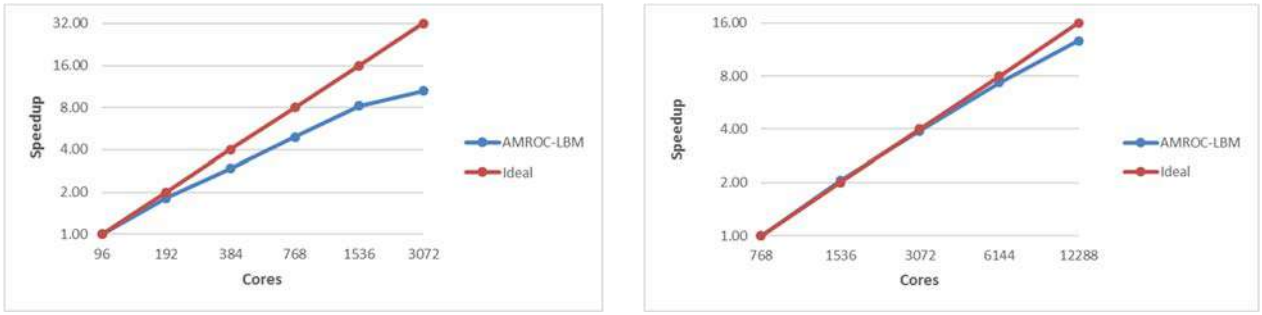

Figure 2. Strong scalability of AMROC-LBM. Left: dynamically changing SAMR mesh. Right: static uniform mesh.

The authors would like to acknowledge support from EPSRC (Engineering and Physical Sciences Research Council) under the Grant No. EP/S013296/1.

References

[1] Deiterding, R. Block-structured adaptive mesh refinement - theory, implementation and application, European Series in Applied and Industrial Mathematics: Proceedings **34**: 97-150, 2011.

[2] Feldhusen, K., Deiterding, R., Wagner, C. A dynamically adaptive lattice Boltzmann method for thermal convection problems. *Int. J. Applied Mathematics and Computer Science* **26(4)**: 735-747, 2016.

[3] Deiterding, R., Wood, S. L. Predictive wind turbine simulation with an adaptive lattice Boltzmann method for moving boundaries. *Journal of Physics: Conference Series* **753**(82005) 2016.

[4] Stoesser, T., Fröhlich, J., Rodi, W. Large eddy simulation of open-channel flow over and through two layers of spheres, 7th Int. Conf. on Hydroscience and Engineering (ICHE-2006) 2006.

ULTRA HIGH RESOLUTION TOPOLOGY OPTIMIZATION FOR SHELL STRUCTURES

Erik A. Träff[1], Niels Aage[1], and Ole Sigmund[1]
[1]Department of Mechanical Engineering, Technical University of Denmark, Lyngby, Denmark

Summary Topology optimization for shell structures has numerous applications, such as optimizing shell thickness, shell reinforcement, and fiber orientation. Performing high resolution topology optimization on shell structures remains challenging due to high condition numbers of the resulting stiffness matrices, which stems both from the shell geometry and from the material heterogeneity. The proposed design methodology consists of a novel combination of methods to perform topology optimization in extreme resolutions for shell structures. The approach is showcased on an aircraft fuselage which is resolved with 4.2 million shell elements, which is a factor of 50 times larger than the current state-of-the-art for shell topology optimization.

INTRODUCTION

A range of structural optimization problems can be solved by applying topology optimization to shell structures, including thickness optimization, reinforcement placement, and fiber orientation. All such problem formulations have potential uses in larger structures such as wind turbine blades, ship hulls, and aircrafts. To be successful, this requires efficient methods to perform topology optimization with shell formulations. The use of shells in high resolution models is complicated by the high condition numbers which usually accompany thin walled structures [1], decreasing the rate of convergence in iterative solvers.

SHELL ELEMENT

The shell element used here is a linearised version of the solid shell formulation presented in [2]. The shell is modelled as a hexahedral element, with three displacement degrees of freedom at each node. In order to increase accuracy, the element is modelled using several alternate strain interpolations to alleviate locking phenomena. The formulation also supports integrating multiple material layers throughout the thickness, which is used to implement passive regions in the optimization. In order to reduce the increased condition number associated with thin shells the Scaled Thickness Conditioning (STC) [3] is applied to the formulation. The accuracy of the resulting linear element is validated against a set of test cases and found to be sufficiently accurate.

MULTIGRID FOR SHELLS

In order to solve the resulting system of equations a geometric multigrid precondtioner is employed. The used multigrid interpolation corresponds to the method presented in [4] applied to a solid shell element. A standard V-cycle multigrid scheme is used with Galerkin projections. The prolongation is constructed by projecting a query point onto the quadrilateral mid-plane of the coarse element, where the interpolation is obtained using quadrilateral shape-functions. An algebraic multigrid preconditioned conjugate gradient method is finally used to approximate the coarse space correction in the multigrid scheme, as also done in [5].

ULTRA FINE RESOLUTION EXAMPLE

To show the efficiency of the presented method, an example using the aircraft fuselage from the NASA common research model is presented [6]. The model consists of 4.2 million shell elements, or 19 million degrees of freedom. The shell is modelled with a passive outer shell of thickness 0.025mm, and an interior support layer of 2.4975cm which is optimized using SIMP and a PDE based filter with filter radius of 5cm [7, 8]. At this point the mesh is refined to an extent where the average element side-length of 1cm is smaller than the modelled shell thickness of 2.5cm. As the number of shells only quadruples every time the average element size is halved, very fine resolutions can be obtained using only

Figure 1: Side view of aircraft fuselage after 200 iterations of optimization. The mesh consists of 4.3 million shell elements, resulting in an average element side length of 1 cm. Red colour indicates the existence of supporting 2.4975cm of material, while blue indicates the absence of support resulting in only the passive shell of thickness 0.025mm.

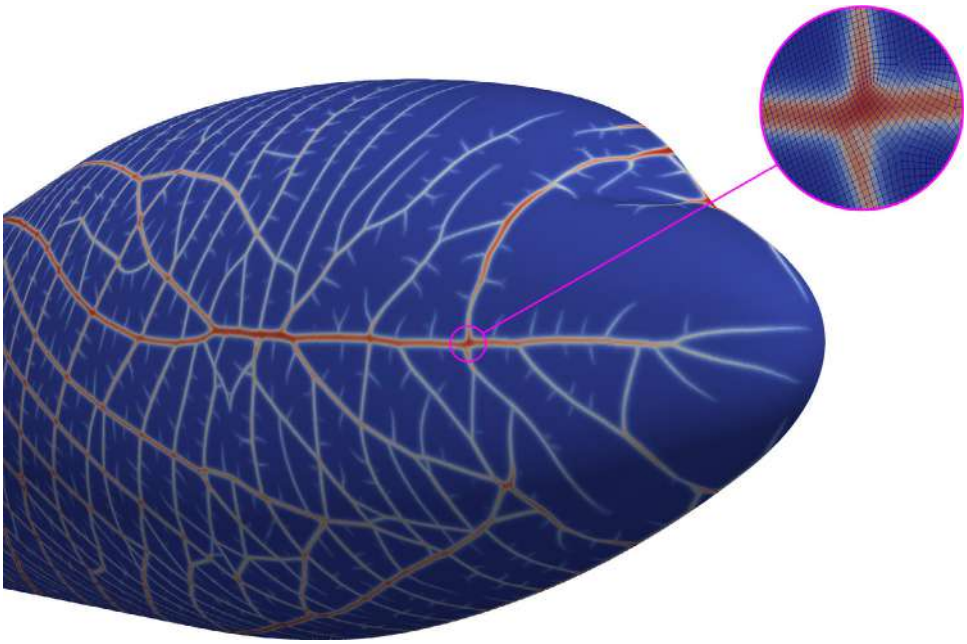

Figure 2: Close up on aircraft fuselage mesh, in order to visualize the element size. Red colour indicates the existence of supporting 2.4975cm of material, while blue indicates the absence of support resulting in only the passive shell of thickness 0.025mm.

millions of elements. The fuselage is modelled without an interior structure and with simplified boundary conditions and loading. Therefore the resulting structure should not be considered in itself, but rather as a showcase of the efficiency of the presented approach. The presented solution was computed on 15 nodes, each with two Intel Xeon E5-2680v2 CPUs, totalling in 300 cores. Finally, it should be noted that the computational obstacle in achieving higher resolution is no longer solving the state equation, but rather constructing the unstructured mesh, as this is a sequential process.

CONCLUSION

The presented approach using linear shell elements is demonstrated to be able to solve extremely finely resolved systems, where the shell thickness becomes larger than the element sizes. This is considered sufficient for most practical applications, although the mesh only consists of millions of elements, in comparison with the billion elements required in similar three-dimensional solid cases [5].

References

[1] M. Papadrakakis, A. Samartin, E. O. (eds, W. A. Wall, M. Gee, E. Ramm, W. A. Wall, M. Gee, and E. Ramm, "The challenge of a three-dimensional shell formulation, the conditioning problem," 2000.

[2] S. Klinkel, F. Gruttmann, and W. Wagner, "A continuum based three-dimensional shell element for laminated structures," *Computers & Structures*, vol. 71, no. 1, pp. 43 – 62, 1999.

[3] T. Klöppel, M. W. Gee, and W. A. Wall, "A scaled thickness conditioning for solid- and solid-shell discretizations of thin-walled structures," *Computer Methods in Applied Mechanics and Engineering*, vol. 200, no. 9, pp. 1301 – 1310, 2011.

[4] J. Fish, L. Pan, V. Belsky, and S. Gomaa, "Unstructured multigrid method for shells," *International Journal for Numerical Methods in Engineering*, vol. 39, no. 7, pp. 1181–1197, 1996.

[5] N. Aage, E. Andreassen, B. S. Lazarov, and O. Sigmund, "Giga-voxel computational morphogenesis for structural design," *Nature*, vol. 550, no. 7674, p. 84, 2017.

[6] "Nasa common research model." https://commonresearchmodel.larc.nasa.gov/, 2019.

[7] M. Bendsøe and O. Sigmund, *Topology optimization. Theory, methods, and applications. 2nd ed., corrected printing*. 01 2004.

[8] B. S. Lazarov and O. Sigmund, "Filters in topology optimization based on helmholtz-type differential equations," *International Journal for Numerical Methods in Engineering*, vol. 86, no. 6, pp. 765–781, 2011.

LARGE-SCALE SPECTRAL-ELEMENT SIMULATIONS OF COMPLEX TURBULENT FLOWS THROUGH ADAPTIVE MESH REFINEMENT

Daniele Massaro* [1], Nicolas Offermans[1], Adam Peplinski[1], and Philipp Schlatter[1]
[1]Linné FLOW Centre, KTH Mechanics, Royal Institute of Technology, Stockholm, Sweden

Summary The present investigation focuses on the adaptive mesh refinement technique applied in fully turbulent flows. In particular for large-scale problem, where the solution behaviour is in general not a-priori known, such adaptive techniques are necessary to assess the committed error. In that regard, the strive towards exascale calculations needs to go along with appropriate control of errors in the full domain. In the present study, a number of direct numerical simulations of three-dimensional incompressible flow in relatively complex geometries, *e.g.* the flow in a constricted periodic channel or around a stepped cylinder, have been performed. Results are aimed to assess the efficacy of different error indicators and eventually contribute to the understanding of the complex physics involved in such flows.

MOTIVATION

The study of fluid dynamics appears to be fundamental in most human activities, such as predicting weather patterns or transportation by car, bicycle, plane and so on. In most situations the flow is transitional or turbulent, in which special attention needs to be paid to the proper resolution of the small scales, in particular in DNS and (high-resolution) LES. In complex geometries understanding in advance where a refine mesh is required and where a coarse is enough is far from trivial. The experience and intuition may give us good guesses, but a-priori knowledge of the flow physics is generally not available. This is even more important of large-scale simulations on forthcoming computer systems, where more and more of the complex physics is incorporated into the simulation. In these situations, it is absoutely necessary to control the arising errors, and adapt the meshes adequately. This work is in the context of the Excellerat Centre of Excellence, where the simulation fidelity has been identified as one of the relevant points towards exascale.

The adaptive-mesh-refinement (AMR) technique allows to automatically refine or coarsen the mesh based on the characteristics of the flow, avoiding a long-standing issue in Computational Fluid Dynamics (CFD) [1, 2]. The objective of AMR is to increase the accuracy of the solution at a lower computational cost than what was achievable with a fixed mesh. The two main ingredients of AMR are computational tools to adapt the mesh, and to efficient and accurately estimate the local error. Obviously the choice of these two affects the entire simulation.

When it comes to high-order methods such as the spectral element method, a previous study was carried out on a steady and unsteady flow around two-dimensional cylinder in a sub and super-critical Reynolds regime [4, 3]. We have also considered more complex geometries, *e.g.* the turbulent boundary layer on a wing [6], and the fully turbulent three-dimensional flow in a constricted periodic channel (periodic hill, [3]). In this contribution we would like to focus on a case with intermediate complexity, but yet the clear need for AMR: The turbulent flow around a stepped cylinder, which consists of two attached cylinders with different diameters.

METHOD AND PRELIMINARY RESULTS

A number of direct numerical simulations (DNS) have been performed in three-dimensional turbulent incompressible flows, *i.e.* the periodic hill and the stepped cylinder. The implementation is carried out in Nek5000, an open-source, highly scalable and portable code based on the spectral-element method (SEM). Initially, we define a coarse mesh with the aim to refine only those regions pointed out by the chosen error indicator. The three possible strategies consist in moving the existing grid points (r-refinement), locally increasing the number of grid points (h-refinement) or locally increasing the polynomial order (p-refinement). The h-refinement has been used in our study for its flexibility and relative ease of implementation. For the future, in particular p-refinement in the proximity of wall appears as another promising approach.

The committed error has been defined and measured in an appropriate and numerically efficient way. Indeed errors resulting from the discretization and resolution of partial differential equations with SEM arise from different sources. In practice, we assumed the mathematical model to be consistent and the adequate finite accuracy of computers sufficient. We are left with the truncation error, which arises because the solution is approximated by a finite spectral expansion, and the quadrature error, related to the discrete integration. In order to estimate these errors we employ two methods used in our study: The spectral error indicator, developed by [7], relies on the local properties of the solution. For simplicity we introduce here the formulation for a 1D solution $u(x)$ and its spectral transformation $u(x) = \sum_{k=0}^{\infty} \hat{u}_k L_k(x)$, where L_k is the Legendre polynomial at order k, which is the polynomial basis implemented in Nek5000, and $\hat{u}_k$ is the k-th spectral coefficient. Looking at the N–order of the polynomial expansion, we obtain the spectral element solution $[\mathbf{u}_N, p_N]$ and the error indicator, which is $\epsilon_{ind} \approx \|u - u_N\|_{L^2}$, reads:

$$\epsilon_{ind} = \left(\int_N^{\infty} \frac{\hat{u}(k)^2}{\frac{2k+1}{2}} dk + \frac{\hat{u}_N^2}{\frac{2N+1}{2}} \right)^{\frac{1}{2}} \tag{1}$$

*Corresponding author. E-mail: dmassaro@kth.se

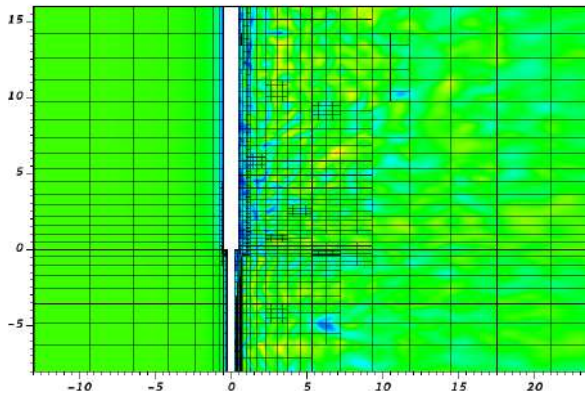

Figure 1: Velocity field of the external 3D flow around a stepped cylinder where the mesh has been refined few times. The simulation is carried out at $Re = 1000$. Individual shed vortices can be tracked, leading to refinement and de-refinment as the simulation proceeds. Alternatively, a static (non-conformal) mesh can be defined based on the sensitivity of turbulence statistics.

where the decay of the spectral element coefficients is assumed to be $\hat{u}_k \sim \hat{u} = cexp(-\sigma k)$. Previous works ([3]) pointed out that this estimator is the best to track the error in flow with high gradients and aims to uniformly reducing the error on the solution.

On the other hand we have implemented the adjoint error estimator. This kind of error estimators are goal-oriented and generate an estimation of the committed error based on a functional of interest. In this case we used the method of the adjoint-weighted residuals by [8], which combines local info in the form of strong residuals and the global sensitivity given by the computation of the dual problem. Firstly we need to define the functional of interest J. In an unsteady turbulent flow, the functional of physical interest is commonly a time-averaged quantity, *e.g.* stresses, mean fluxes, drag or lift coefficients. The averaging time T is chosen long enough for the statistics to convergence. An estimation of the error on the functional is computed as:

$$\begin{aligned}
\delta J &= |J(\mathbf{u}, p) - J(\mathbf{u}_N, p_N)| = \\
&< \sum_{e=1}^{E} \frac{1}{T} \int_O^T \Big[|R_1(\mathbf{u}_N, p_N)|_{L^2(\Omega_e)} \cdot |\mathbf{u}^+ - \mathbf{u}_N^+|_{L^2(\Omega_e)} + \\
&+ |R_2(\mathbf{u}_N, p_N)|_{\Gamma_e} \cdot |\mathbf{u}^+ - \mathbf{u}_N^+|_{\Gamma_e} + \\
&+ \|R_3(\mathbf{u}_N, p_N)\|_{L^2(\Omega_e)} \cdot \|p^+ - p_N^+\|_{L^2(\Omega_e)} \Big] \mathrm{d}t
\end{aligned} \tag{2}$$

where R_1 and R_3 are the strong residuals of the momentum and continuity equations, R_2 correspond to the jump in the stresses at the interface between elements (usually neglected). The terms $|\mathbf{u}^+ - \mathbf{u}_N^+|$ and $\|p^+ - p_N^+\|$ represent the interpolation error on the adjoint field and are estimated with the spectral error indicator [5]. The adjoint error estimators are analytically elegant, but suffer from the problem of the stability of the adjoint equation in the context of turbulent (chaotic) flows.

Figure 1 shows a snapshot of the velocity field around a stepped cylinder, which represents a fully three-dimensional case with curved elements. In the final contribution, we compare the various error estimators on this case, and provide a physical description of the flow physics based on refined meshes. Some perspectives, related to the savings in grid points and gains in accuracy, are given, motivated also by flow cases relevant to aeronautics [6].

References

[1] R. D. Henderson. Adaptive spectral element methods for turbulence and transition. *High-Order Methods for Computational Physics* pp.: 225–324.Berlin, Springer Berlin Heidelberg, 1999.

[2] J. Hoffman, J. Jansson, N. Jansson, & R. Abreu. Towards a parameter-free method for high Reynolds number turbulent flow simulation based on adaptive finite element approximation. *Computer Methods in Applied Mechanics and Engineering* **288**: 60-74, 2015.

[3] N. Offermans, Aspects of adaptive mesh refinment in the spectral element method. *PhD Thesis*, KTH, Stockholm, Sweden, 2019.

[4] N. Offermans, O. Marin, A. Peplinski, P. F. Fischer & P. Schlatter. Towards adaptive mesh refinement for the spectral element solver Nek5000. DLES 11: Direct and Large Eddy Simulation. Pisa, Italy, 2017.

[5] N. Offermans, O. Marin, A. Peplinski & P. Schlatter. Adjoint error estimators in Nek5000. Nek5000 Users meeting. Tampa, Florida, USA, 2018.

[6] A. Tanarro., F. Mallor, N. Offermans, A. Peplinski, R. Vinuesa & P. Schlatter Using adaptive mesh refinement to simulate turbulent wings at high Reynolds numbers. TSFP11, 2019.

[7] C. Mavriplis. A posteriori error estimators for adaptive spectral element techniques. In Notes on Numerical Fluid Mechanics (ed. P. Wesseling), pp. 333–342, 1990.

[8] W. Bangerth & R. Rannacher. Adaptive Finite Element Methods for Differential Equations. Birkhäuser, Basel, 2002.

IMPROVING STRONG SCALABILITY LIMITS OF ENGINEERING SIMULATIONS

Niclas Jansson * [1] and Rahul Bale[2]
[1]PDC Center for High Performance Computing, KTH Royal Institute of Technology, Stockholm, Sweden
[2]RIKEN Center for Computational Science, Kobe, Japan

Summary Engineering simulations based on finite volume codes scale reasonably well as long as each core has sufficient amount of local work that can balance communication costs. However, achieving efficient performance at exascale will require unreasonable large problem sizes, in particular for low-order methods, where the small amount of work per grid point already is a limiting factor on current post petascale machines. For multi-block Cartesian based methods, one of the key bottlenecks is the halo-exchange, where communication latency starts to limit performance as the number of cores increases. We present our work on improving strong scalability of the multiphysics code CUBE using multithreaded halo-exchange algorithms based on lightweight one-sided communication. A description of these new communication kernels is given, and we present a detailed performance analysis.

INTRODUCTION

To strongly scale finite volume codes on future exascale systems will require either unreasonable large problem sizes to balance communication costs, or algorithmic developments need to be achieved which retain strong scalability even for very few grid points per core. This is in particular the case for low-order methods, where the small amount of work per grid points already is a limiting factor on current post petascale machines. One of the key bottlenecks is halo-exchange, where communication costs starts to limit performance as the number of cores increases.

The message passing paradigm has been the dominating programming model for writing highly scalable scientific applications for decades. Among several implementations, the Message Passing Interface (MPI) has over the years come out as the de facto standard. Based upon a two-sided communication schematics, it is a challenge to handle large amount of fine-grained parallelism. A common optimization is to use non blocking communication, which allows overlapping computation and communication. However, with very few grid points per core, even overlapping techniques will fail, and both latency and synchronization costs of communication will severely limits the strong scalability of an application.

Today at the dawn of exascale computing, some concerns have been raised whether current parallel programming models are capable of delivering the needed performance on future systems. Therefore a large investment has been made in various exascale computing projects worldwide to provide novel programming models, suitable for expressing the massive parallelism that exascale computing will offer. Another key aspect of these new models is their lower latency and synchronization costs, allowing for good performance even for very small problem sizes per core.

ENSURING STRONG SCALABILITY VIA NOVEL PROGRAMMING MODELS

We present our work on improving strong scalability for for Complex Unified Building cubE (CUBE) [1], a multiphysics framework for solving complex engineering problems with moving geometries. The framework is based on a block-structured Cartesian meshing technique called Building Cube method (BCM) [2], with a constraint based immersed boundary method, based upon Lagrangian particles, to represent the complex geometries encountered in industrial applications. The halo-exchange kernel in CUBE is based on a multithreaded two-sided message passage implementation, which overlaps the communication and computation on both a intra- and inter-node level.

To improve the performance of our communication kernels, we replace the two-sided MPI with lightweight, low latency one-sided communication offered by the Partitioned Global Address Space (PGAS) extensions of Fortran 2008 (co-arrays). Using co-arrays we observe an improved strong scalability limit due to the low-latency of PGAS. This allows good performance even with very few grid points and improves exascale readiness of CUBE.

ACKNOWLEDGMENTS

The first author would like to acknowledge the financial support from the Swedish Research Council under grant number: 2019-04723. The computations were performed on resources provided by the Swedish National Infrastructure for Computing (SNIC) at PDC Center for High Performance Computing.

References

[1] N. Jansson, R. Bale, K. Onishi, and M. Tsubokura. *CUBE: A scalable framework for large-scale industrial simulations*, The International Journal of High Performance Computing Applications, 33(4), pp. 678–698, 2019

[2] K. Nakahashi, *Building–Cube Method for Flow Problems with Broadband Characteristic Length*, Computational Fluid Dynamics 2002, Springer Berlin Heidelberg, pp. 77–81, 2003

*Corresponding author. E-mail: njansson@kth.se.

FAST IN-SITU TOMOGRAPHY OF MECHANICAL TESTS

Clément Jailin* [1] and Stéphane Rouxy[1]
[1]Université Paris-Saclay, ENS Paris-Saclay, CNRS, Laboratoire de Mécanique et Technologie, Cachan, France

Summary In situ mechanical tests in a tomograph may provide a remarkable wealth of information resolving both microstructure and 4D (space and time) displacement fields from Digital Volume Correlation (DVC). The limiting point of this technique is the duration of tomographic acquisitions. Projection-based DVC (P-DVC) breaks this barrier and opens up the possibility to complete a mechanical test, which can be quantitatively exploited for identification of mechanical quantities of interest, *in about one minute*. Two examples of application will be discussed, namely, the identification of an elastoplastic constitutive law and a fracture test.

INTRODUCTION

Successive tomographic scans of a mechanically loaded specimen at different levels of load brings an extraordinarily rich amount of information. Not only from the microstructure, and its changes (e.g., pores in ductile fracture, microcracks for damaging materials) but also from complete 3D displacement fields within the specimen as can be retrieved from the use of Digital Volume Correlation (DVC) [1].

However, lab-scale tomographs usually require a rather lengthy acquisition time (typically from several tens of minutes to a few hours) during which the specimen has to remain perfectly motionless. As a consequence, in situ mechanical testing in a tomograph appears as intrinsically limited to quasistatic loadings, unless one resorts to synchrotron facilities where high-rate tomography can be achieved [2, 3]. Moreover, each 3D image usually displays the very same microstructure up to its warping due to mechanical deformations. Hence, the long duration of the acquisition is needed to resolve small details of the microstructure that do not convey a very rich information for the kinematics. But, when a subvoxel displacement resolution is sought, it is necessary to have a highly resolved image and therefore one cannot be satisfied with a coarse resolution in spite of its faster acquisition. This limitation may seem impossible to overcome.

One way out is not to perform a reconstruction of the microstructure, but rather to only address the kinematics from radiographs (or equivalently projections) acquired on-the-fly as the mechanical test is performed, together with the same sample rotation as classically used in tomography. The only requirement then becomes that the specimen should not move significantly during the exposure time of *one radiograph*, which is typically 1,000 times less demanding than for a full scan. However, a single projection cannot allow for the inversion of the full 3D displacement field at each instant of time, as motions along the X-ray beam do not influence the projection, thereby making the problem severely ill-posed. One key ingredient to make the problem well-posed is to introduce a parameterization in time that couples different projection angles. Dealing with a nonlocal in time measurement of the kinematics only requires a smooth temporal evolution, a requirement that is expected to hold true most of the time in the course of mechanical tests. The resulting technique is called Projection-based DVC or P-DVC [4].

PROJECTION-BASED DIGITAL VOLUME CORRELATION

It is assumed that prior to the mechanical test, a full tomography of the specimen has been acquired, following a standard acquisition and reconstruction. The resulting 3D image is denoted as $f(\boldsymbol{x}, t_0)$, giving the coefficient of absorption f at voxel position $\boldsymbol{x}$. Time t_0 is used to refer to the initial state. This 3D image is reconstructed from the projection data, $p(\boldsymbol{r}, \theta)$, which is computed from the radiograph $I(\boldsymbol{r}, \theta)$ acquired when the specimen has been rotated by an angle θ, and the flat field $I_0(\boldsymbol{r})$ radiograph acquired without specimen, $p(r, \theta) = -\log(I(\boldsymbol{r}, \theta)/I_0(\boldsymbol{r}))$. The linear projection operator is denoted Π_θ so that the reconstruction is obtained from the inversion of the set of equations

$$\Pi_\theta[f(\boldsymbol{x}, t_0)] = p(\boldsymbol{r}, \theta) \tag{1}$$

where Π sums up all absorption coefficients $f(\boldsymbol{x}, t_0)$ encountered along the X-ray hitting the detector at position $\boldsymbol{r}$.

In the proposed approach, $f(\boldsymbol{x}, t_0)$ being known, projections $p(\boldsymbol{r}, t, \theta(t))$ are acquired at different instants of time t with varying load and rotation angle $\theta(t)$. P-DVC then consists in solving

$$\Pi_\theta[f(\boldsymbol{x} - \boldsymbol{u}(\boldsymbol{x}, t), t_0)] = p(\boldsymbol{r}, t, \theta(t)) \tag{2}$$

for the *Eulerian* displacement field, $\boldsymbol{u}(\boldsymbol{x}, t)$, which is parameterized as

$$\boldsymbol{u}(\boldsymbol{x}, t) = \sum_i a_i \boldsymbol{\chi}_i(\boldsymbol{x}, t) \tag{3}$$

*Present address: GE Healthcare – General Electric Medical Systems, Buc, France
†Corresponding author. E-mail: stephane.roux@ens-paris-saclay.fr

To make the problem better conditioned, a reduced kinematic basis may be considered. As earlier mentioned, having an extended support is needed to make the problem well-posed. For kinematic basis reduction, different routes may be followed:

- One possibility consists in exploiting prior knowledge on the studied material or its constitutive law. Here a finite-element (FE) modeling may be used where the degrees of freedom become the unknowns of the model, which are the boundary conditions and possibly one or several constitutive parameters. The basis functions $\boldsymbol{\chi}_i(\boldsymbol{x},t)$ are thus computed from the FE modeling, which itself involves a mesh that is tailored to the studied domain.
- An alternative comes from a more agnostic reduced-basis representation of the kinematics. For instance, a separated representation $\boldsymbol{\chi}_i(\boldsymbol{x},t) = \phi_{i_1}(t)\boldsymbol{\psi}_{i_2}(\boldsymbol{x})$ is known to be quite efficient at extracting a reduced basis. Here, the scalar functions $\phi_j(t)$ or vector fields $\boldsymbol{\psi}_k(\boldsymbol{x})$ can be computed to be the most suited to hierarchically account for most of the signal. Depending on the norm used to evaluate these "modes," this approach can be termed differently, namely, Proper Orthogonal Decomposition (POD) for an Euclidian metric or Proper Generalized Decomposition (PGD) if a more physically motivated variational principle is used to weight the modes. For P-DVC, the PGD norm may originate from the minimization of the quadratic differences between left and right members of Equation (2), or it may come from the mechanical model itself.

Let us emphasize that the second strategy leaves more freedom to account from deviations from an a priori postulated model. Likewise, it also receives less guidance from such a modeling and hence may generate poorer conditioning. Thus, there is nothing like a unique optimal way to proceed, the best choice has to rely on the degree of confidence that one has on the proposed model. It is also important to stress that, in the end, a given choice of strategy will lead to a solution, with which a residual (i.e., difference between acquired and modeled projections) should be computed. The compatibility of the residual with the statistical characteristics of noise will finally validate or not the choice, and possibly invite one to revisit the modeling.

EXAMPLES

Elastoplastic calibration

In the first example, detailed in Refs. [5, 6], a slender dog-done specimen was used in a uniaxial tensile test. The studied material was chosen to be nodular graphite cast iron loaded until fracture. The test was performed in less than 5 minutes, and was interrupted by a sudden localization leading to the initiation of a crack that broke the specimen into two pieces. For this test, a first parameterization was used in the same spirit as beam theory where each section along the specimen axis z was considered to be essentially rigid-body motions, parameterized by z [5]. A second version involving an elastoplastic law was further used to calibrate the constitutive parameters [6].

Fracture test

In the second example, a refractory material was used and the goal of the test was to determine its toughness [7]. The duration of the test was less than 30 seconds. In spite of the fact that the sample geometry was adjusted in order to stabilize crack propagation, the crack fractured the sample into two blocks as soon as it initiated. However, the last load level that the specimen could withstand and the first one where it could not resist provides a bounding interval for toughness.

CONCLUSION

The possibility of performing fast mechanical tests in a tomograph offers a novel playground for studying viscoelastic materials (e.g., elastomers, gels, polymer matrix composites). If combined with the ultra-fast tomographic devices available at synchrotron facilities, even higher time resolutions are envisioned. Yet, the rotation rate of the specimen is likely to be the ultimate limiting factor!

As a side result, let us also note that the underlying mathematical problem of dealing with highly lacunar data for PGD or POD is addressed in the above approaches through an original algorithm [8] that outperforms classical "Gappy-POD" procedures in terms of convergence speed and noise robustness.

References

[1] Buljac, A. *et al.*, Digital volume correlation: review of progress and challenges, *Exp. Mech.*, **58**: 661–708, 2018.
[2] Maire, E. and Withers, P.J., Quantitative X-ray tomography, *Int. Mat. Rev.*, **59**: 1–43, 2014.
[3] Maire, E. *et al.*, 20 Hz X-ray tomography during an in situ tensile test, *Int. J. Fracture*, **200**: 3–12, 2016.
[4] Leclerc, H. *et al.*, Projection savings in CT-based digital volume correlation, *Exp. Mech.*, **55**: 275–287, 2015.
[5] Jailin, C. *et al.*, Fast four-dimensional tensile test monitored via X-ray computed tomography: Single projection-based digital volume correlation dedicated to slender samples, *J. Strain Anal. Eng. Design*, **53**: 473–484, 2018.
[6] Jailin, C. *et al.*, Fast four-dimensional tensile test monitored via X-ray computed tomography: Elastoplastic identification from radiographs, *J. Strain Anal. Eng. Design*, **54**: 44–53, 2019.
[7] Jailin, C. *et al.*, Sub-minute in situ fracture test in a laboratory CT scanner. *Int. Mat. Manuf. Innov.*, **8**: 413–422, 2019.
[8] Jailin, C. and Roux, S., Modal decomposition from partial measurements, *Compt. Rend. Méca.*, **347**: 863–872, 2019.

ON A VOLUMETRIC TEMPERATURE AND VELOCITY MEASUREMENT TECHNIQUE FOR SUB-MILLIMETER SCALES

Christian Cierpka
Institute of Thermodynamics and Fluid Mechanics, Technische Universität Ilmenau, Ilmenau, Germany

Summary The development and the validation of a volumetric measurement technique for the simultaneous determination of temperature and velocity in small geometries will be presented. The technique is based on the so-called astigmatism particle tracking velocimetry which uses the defocus effect including an additional cylindrical lens in the system. Particle images appear elliptically distorted on the camera sensor depending on their three-dimensional position within the measurement volume. Using classical image processing or neural networks the volumetric particle position can be determined reliably. In order to measure the temperature two fluorescent dyes (EuTTA and Perylen) are incorporated in the particles. The luminescence lifetime and intensity of the Europium-complex is temperature sensitive. Thus either evaluating the lifetime using a high speed camera, or evaluating the intensity of the particle images by a monochrome or color camera will enable the estimation of the particle temperature. Within the presentation an overview of the various approaches will be given, advantages and drawbacks as well as examples of applications will be discussed.

Introduction of the measurement technique

Heat and mass transfer is important in many engineering applications. Especially in microfluidic devices where the surface to volume ratio is largely increased and the velocity field is always three-dimensional, measurements are often the only tool to evaluate the flow as boundary conditions may be unknown. A measurement technique that allows for three-dimensional velocity field measurements with only one optical access is the astigmatism particle tracking velocimetry (APTV) [1]. The images of small tracer particles in the flow are used to determine their displacement between two successive time instants. In order to measure the out-of-plane position an additional cylindrical lens is introduced in the system and the particle images appear as ellipses on the camera sensor. The size of the major axes depend on their depth position in the volume. Using particle tracking the volumetric trajectories of the particles can be determined. Using fast cameras that allow for time resolved measurements Lagrangian velocities and acceleration can be estimated precisely with a higher spatial accuracy than typically achieved in correlation based techniques like µPIV. If the flow is steady the spatial resolution can also be much higher than for µPIV. One of the main advantages of APTV is the ability of volumetric measurements using standard equipment with only one optical access and the addition of one low cost cylindrical lens.
However, very often also scalar fields like temperature, concentration or pH are of interest. Therefore the particles were incorporated with two temperature sensitive fluorescent dyes, an Europium-complex (EuTTA) and perylen [2]. EuTTA shows a significant change in the luminescence intensity and lifetime with temperature, whereas perylen is insensitive to temperature variations when illuminated with ultraviolet light. The use of the two dyes allows to correct for variations in light source intensity. A big advantage of this combination is, that the emission spectra of perylene (~420–550 nm) and EuTTA (~575–635 nm) are far apart from each other and do not overlap. This makes it easy to filter the respective signals with corresponding wavelength filters using two cameras. A drawback of such a procedure is that the images of both cameras have to be overlapped for data evaluation. However, also a single color camera using a Bayer mosaic can be used as the cross talk for the different color pixels is quite low. To test both approaches a heated flow in a microchannel was used. The setups are shown in Fig. 1. Both approaches are generally well suited. The one camera approach is much simpler to use but smaller uncertainties could be reached by the two camera setup if a high signal to noise ratio (>10) can be achieved [3].

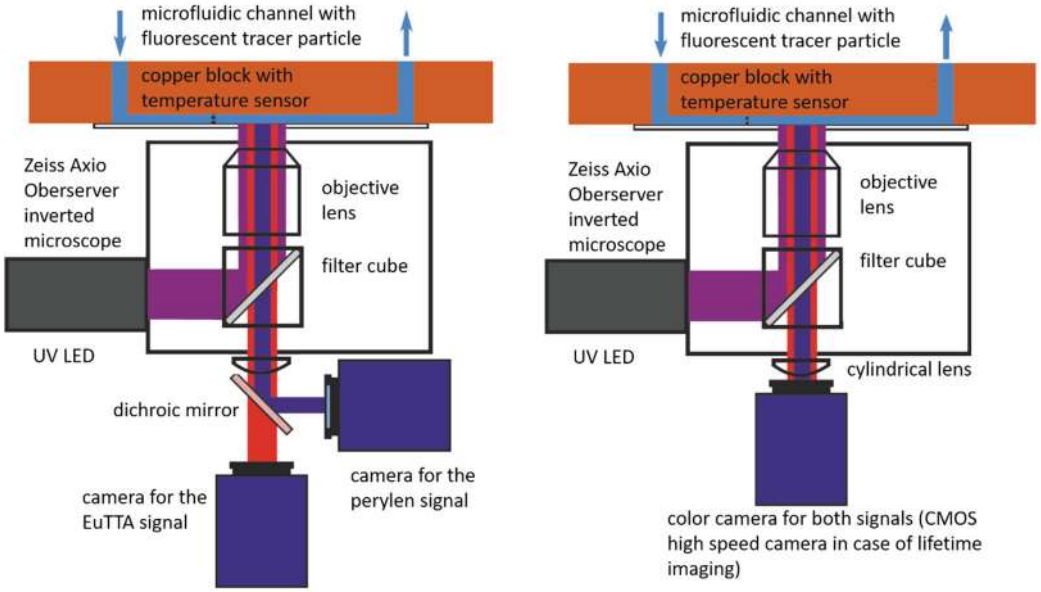

Figure 1. Setup for the different temperature measurement approaches (two color intensity – left, color camera intensity of lifetime imaging - right) adopted from [3].

If a high speed camera is available also the luminescent lifetime can be evaluated with a similar setup as for the color camera (see Fig. 1, right). Although the timing scheme is much more complex to decouple the velocity estimation from the temperature measurement, the uncertainty was shown to be lower especially in the case of varying illumination intensity as for example in multi-phase flows or complex geometries [4].

Results

The developed technique was applied to measure the Marangoni flow and the temperature field around an electrochemically produced hydrogen bubble on a microelectrode. The results helped to clarify the origin of the gradients in surface tension [5]. In Fig. 2 (top - left) the velocity field in the close vicinity of the bubble foot is shown. A vertical structure can clearly be seen. The origin of this flow is the surface tension that varies with temperature. Since Joule heating causes a higher temperature the electrode (as can be seen on Fig. 2 top-right) the surface tension at the electrode is lower which causes the Marangoni flow to evolve. Furthermore, the application of the technique to investigate a heating system for a fast start-up of a direct methanol fuel cell (see Fig. 2 bottom) will be discussed in the talk [6].

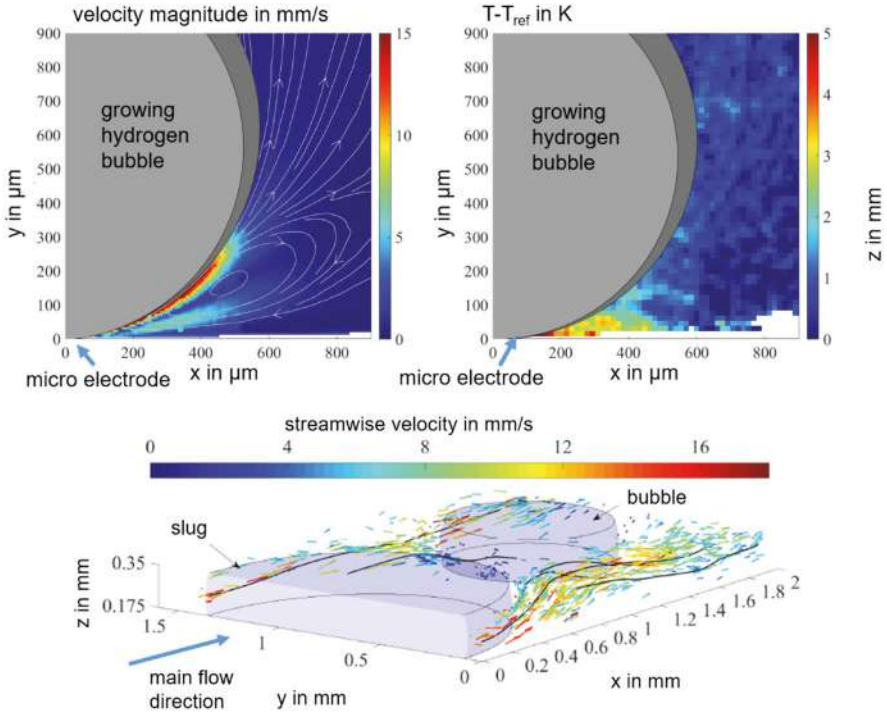

Figure 2. Velocity in the close vicinity of a hydrogen bubble generated by electrolysis at a micro electrode (top-left) and corresponding temperature field measured by lifetime imaging (top-right) adopted from [5]. Flow field around a gas bubble in a direct methanol flue cell (bottom) adopted from [6].

Conclusion and Outlook

It was shown that the measurement technique allows for reliable measurements in complex geometries including multi-phase flows. Either intensity of lifetime of the luminescence of the particles can be used for the additional temperature determination. Using the lifetime evaluation for the temperature shows lower uncertainties for the sake of higher equipment costs and higher timing complexity to have the temperature and velocity measurement independent of each other. This allows for a high flexibility of the system. Further improvements of the technique will be the application of deep neural networks to determine the particle position, temperature and eventually also classify particles. This would be advantageous for systems with multi-disperse particle mixtures, as typically in process engineering and biological applications. Since neural networks are also more robust using different shaped for the particles mono-disperse high cost particles are not anymore necessary.

References

[1] C. Cierpka, C. J. Kähler (2012), Journal of Visualization 15, 1-31, DOI: 10.1007/s12650-011-0107-9, open access
[2] J. Massing, D. Kaden, C.J. Kähler, C. Cierpka (2016), Measurement Science and Technology 27, 1153014, DOI: 1088/0957-0233/27/11/115301
[3] J. Massing, C.J. Kähler, C. Cierpka (2018), Technisches Messen 85, 97-103, DOI: 10.1515/teme-2017-0094
[4] J. Massing, C.J. Kähler, C. Cierpka (2018), Experiments in Fluids 59, 163, DOI: 10.1007/s00348-018-2616-y
[5] J. Massing, G. Mutschke, D. Baczyzmalski, X. Yang, K. Eckert, C. Cierpka (2019) Electrochimica Acta 297, 929-940, DOI: 10.1016/j.electacta.2018.11.187
[6] J. Massing, N. van der Schoot, C. J. Kähler, C. Cierpka (2019) International Journal of Hydrogen Energy 44, 26517-26529, DOI: 10.1016/j.ijhydene.2019.08.107

EXPLORATION OF DYNAMICAL PROPERTIES OF TURBULENT NEAR WAKES FOR DRAG REDUCTION

Y. Haffner[1], J. Boreé[1], A. Spohn[1], T. Castelain[2]
[1]Institut Pprime, UPR-3346 CNRS, ENSMA, Université de Poitiers, France
[2]CNRS-LMFA UMR 5509, UDL, Univ. Claude Bernard Lyon I, Ecole Centrale de Lyon, INSA Lyon, France

Summary A fascinating aspect of turbulent aerodynamics of bluff bodies at large Reynolds number is the wide range of length and time scales that one has to explore in order to understand the flow dynamics. Based on a long-standing experience obtained in our large scale subsonic wind-tunnel, our goal is here to illustrate on two typical examples the temporal and spatial resolution requirements for coupled pressure and velocity measurements. A short physical analysis and details on experimental techniques are provided below for this invited contribution in the thematic session on Experimental Methods in Mechanics. Research supported by the French Agence Nationale pour la Recherche (ANR) through the project Activ_ROAD (ID ANR-15-CE22-0002) and the CPER Feder program Transport.

Drag reduction of ground vehicles has become a major challenge for the transport industry due to increasing need for reducing fuel consumption and carbon pollution. Flows around such bluff bodies contain massively separated flow regions which lead to wake flows. Our aim is to understand the origins of wake flow changes and associated drag variations by developing wake control strategies. A fascinating aspect of these turbulent aerodynamics at large Reynolds number ($\approx 10^6$) is the interaction between a wide range of length and time scales. At the length scale of the body, an absolute instability leading to periodic vortex shedding is responsible for self-sustained oscillations. Reflectional symmetry breaking, leading to random switching with a long time dynamic, is also observed. Specific flow structures, namely turbulent shear layers surrounding the near wake and, in case of slanted geometries, 3D conical vortices of trailing type, interact producing significant drag contributions.
Modifications of these wakes can be obtained using so called "wake pressure control" devices which change the orientation of mean streamlines at separation using fixed geometrical tapering, moving flaps [1] or steady blowing [2]. Another way, named here "turbulence control", is to modify the dynamical state of the separating shear layers by altering mass and momentum exchanges as well as interactions between shear layers in order to change the mean near wake and to reduce the drag [3]. High frequency pulsed jets interacting with control surfaces [4, 5] combine both strategies. Capturing the dynamics of the unsteady jets, their interactions with small control surfaces and with the turbulent shear layers is thereby of utmost importance.
Experimental and numerical approaches are very complementary. Large Eddy Simulation [6] provide a wealth of information. However, it remains out of reach to compute the long-time dynamics for such a large range of space and time scales in particular when resolving actuations at small scale. Experiments are therefore needed and must be performed on models having a noticeable size (of order 1 meter) in order to reach Reynolds numbers of order 10^6. Recent experimental research has focused on resolving tri-dimensional (3D) characteristics using a scan of particle image velocimetry (PIV) [7], stereo-PIV fields [8] or tomo-PIV [9]. Our goal is here to discuss temporal and spatial resolution requirements for coupled pressure and velocity measurements obtained with typical flow geometries.

Analysis of transient near wake reversals and their consequences on drag [10].
The main objective is here to illustrate the reduction in base drag observed during wake reversals. Indeed, we will show that the flow structure for transient symmetric states explored during the reversals differ from those of static symmetry-breaking states. During the wake reversals, the disorganization of the recirculating flow leads to a transient symmetric state with a reduced interaction between opposed shear layers. A transient drag reduction of 8 % is measured when compared to asymmetric states.
In such a situation, one has to capture spatial and temporal dynamics not only at the scale of separating shear layers but also at the scale of the body because one needs to analyse the interaction of the shear layers. The experiments are performed inside the working section of a subsonic wind-tunnel of 2,4m width and 2,6m height. The turbulence intensity of the upstream flow is of the order of 0.3 % with flow homogeneity better than 0.5 %. The model with height H = 0,3 m, width W = 0,36m and length L = 1m (aspect ratio H/W = 0,83) is fixed on a raised false floor with a ground clearance G = 0,05m which corresponds to about five times the thickness of the turbulent boundary layer upstream of the model. Experiments discussed are performed at $U_0 = 25m/s$ or $Re_H = HU_0/\nu = 5310^5$ where ν is the kinematic viscosity of the air at operating temperature. The boundary layer at separation along the rear edges of the model is fully turbulent with a characteristic momentum thickness of $\theta_0 = 2.2310^{-3}m$ measured using hot-wire anemometry. "Time Resolved" particle image velocimetry (TR-PIV) is performed in the near-wake of the model to gain insight in the flow structure. The setup is associated to a large field of view (FOV) spanning the whole recirculating wake (approx. 1,8H X 1,3H) in the horizontal plane of symmetry of the model. A Phantom VEO4K 990 camera (sensor of 4096 X 2300 px) coupled to a Sigma DG Macro 105 mm objective captures this FOV in a double-frame mode at a frequency of 500 Hz. In order to ensure sufficient illumination of the PIV plane, two lasers Continuum Terra PIV 2 x 30 mJ and Quantronix Darwin Duo 18 mJ are synchronously fired from each side of the test section. The flow is seeded with 1µm-diameter particles. Multi-pass cross-correlation is performed using Davis 10.1 with a final interrogation window of 12 x 12 pixels and overlap of 50 %. For this setup, care is taken to resolve both temporally and spatially all relevant scales in the wake. The frame rate is sufficient to resolve the smallest time-scales associated to the initial shear layer instability after separation of the

turbulent boundary layer. This frequency-scale is estimated to be $f_\theta = St_{\theta_0} U_0/\theta_0 \approx 230Hz$ where $St_{\theta_0} = 0{,}022$ is the initial most amplified time-scale in a turbulent shear layer according to [11]. Similarly the spatial resolution of the velocity measurements is around 1mm which is less than half of θ_0.

Analysis of Unsteady Coanda effect for drag reduction.

The second example is a situation where a noticeable drag decrease is obtained by fluidic boat tailing in combination with the unsteady Coanda effect [4, 5]. Our results point to the need of a careful matching between the jet forcing frequency and the size of the curved surfaces to gain the maximum potential out of the unsteady Coanda effect for drag reduction. Indeed for high frequencies of order $O(U_0/r)$ where r is the size of the flap, strong vortical coherent structures produced by the interaction of the pulsed jets and the separating shear layer not only delay the separation of the boundary layer but also induce a favourable curvature of the shear layer immediately downstream separation. This leads to drag reductions up to 12%. Therefore, in such a problem, one has not only to resolve statistical properties of the wake at a large scale but also scales imposed by actuation. To this end, two planar two-component setups are used. A large field of view (FOV) covering the whole recirculation region in the wake in the vertical plane of symmetry of the model and a smaller FOV localized in the same plane covering the beginning of the top shear layer. Both FOV are captured by a LaVision Imager LX 16Mpx equipped with respectively a a Zeiss Makro-Planar ZF 50 mm lens and a Nikon AF Micro-Nikkor 400 mm lens. A laser light sheet of 1 mm thickness is provided by a Quantel EverGreen 2 x 200 mJ laser. For the small FOV, although the pulsed jets are not directly seeded, the aspiration phase of the forcing still allows for a weak presence of particles in the laminar flow coming from the jets, which leads to satisfactory seeding of the flow. For each configuration studied, the acquisition of 1000 image pairs with an acquisition rate of 4 Hz led to satisfactory convergence of the second order statistics. Image pairs are processed by Davis 8.4 software with a final interrogation window of 16x16 pixels and overlap of 50% leading to a velocity vector each 1.2mm and 0.15mm respectively for both types of field of view. Additional phase-locked measurements using as reference the command signal of the forcing system are performed for the small FOV. In this case, between 500 and 1000 images are acquired for each phase, and each pulsing period is split into 7 to 13 phases. For the small FOV, specific surface treatment is applied on the curved surfaces in order to limit the laser light reflexions. Two additional steps are used in the processing of image pairs: a sliding minimum subtraction in order to eliminate residual laser light reflexions near the curved surface, and an image translation to correct for the small displacements of the model due to relative flexibility of the aerodynamic balance which can result in 1-2 pixels displacement for this PIV setup with high magnification factor.

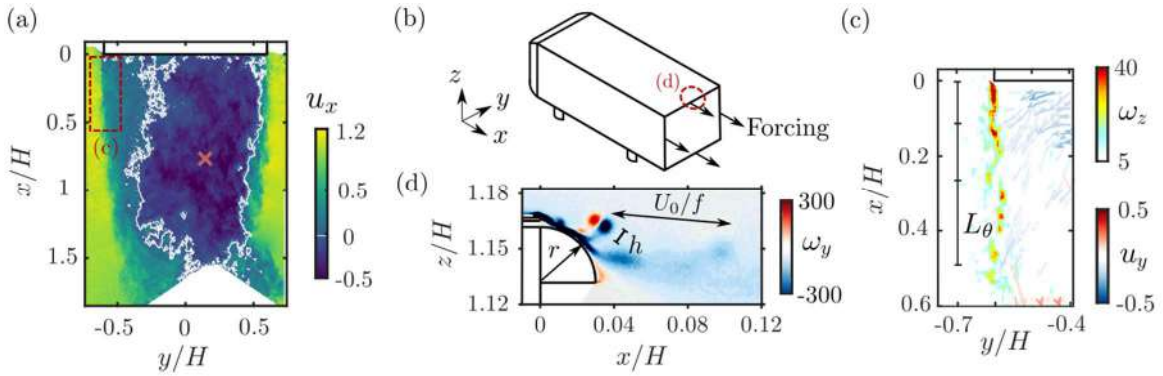

Figure 1. Various length scales of the turbulent near wake. (a) Wake flow in the horizontal symmetry plane of the model with reflectional symmetry-breaking at a scale H. (b) Bluff body. (c) Zoom on shear layer surrounding the recirculation region (red rectangle in (a)). The vorticity sheet rolls-up at length scales of order $L_\theta = T_\theta\, U_0/2 \approx 0.1H$. (d) Flow around an edge of the base (red circle in (b)) forced periodically at frequency f. The forcing produces coherent vortical structures at a scale$3h \approx 0.01H$ periodically repeated at a scale$3U_0/f$. All quantities are made non-dimensional with U_0 and H.

References

1. Brackston, R.D., A. Wynn, and J.F. Morrison, *Modelling and feedback control of vortex shedding for drag reduction of a turbulent bluff body wake.* Int. J. of Heat and Fluid Flow, 2018. **71**: p. 127-136.
2. Pfeiffer, J. and R. King, *Robust control of drag and lateral dynamic response for road vehicles exposed to cross-wind gusts.* Experiments in Fluids, 2018. **https://doi.org/10.1007/s00348-017-2479-7**: p. 59:45.
3. Li, R., et al., *Drag reduction mechanisms of a car model at moderate yaw by bi-frequency forcing.* Phys. Rev. Fluids 4, 034604, 2019.
4. Barros, D., et al., *Bluff body drag manipulation using pulsed jets and Coanda effect.* J. Fluid Mech. , 2016. **805**: p. 422–459.
5. Haffner, Y., et al., *Unsteady Coanda effect and drag reduction of a turbulent wake.* Jour. of Fluid Mech., 2020. **vol. 899, A36**
6. Dalla Longa, L., O. Evstafyeva, and A.S. Morgans, *Simulations of the bi-modal wake past three-dimensional blunt bluff bodies.* J. Fluid Mech., 2019. **866**
7. Venning, J., et al., *The effect of aspect ratio on the wake of the ahmed body.* Exp. in Fluids, 2015. **56(6)**: p. 1-11.
8. Rossitto, G., et al., *Influence of afterbody rounding on the pressure distribution over a fastback vehicle.* Exp. in Fluids, 2016. **57, 3**.
9. Pavia, G., et al., *Three dimensional structure of the unsteady wake of an axisymmetric body.* Phys. of Fluids, 2019. **31(2)**
10. Haffner, Y., et al., *Mechanics of bluff body drag reduction during transient near wake reversals.* Jour. of Fluid Mech., 2020. **Vol. 894**
11. Zaman, K.B. and F. Hussain, *Turbulence suppression in free shear flows by controlled excitation.* Jour. Fluid Mech., 1981. **103**: p. 389-414.

FROM UNSTEADY INFLOW TO DEFORMATION - AN EXPERIMENTAL STUDY ON THE AERODYNAMICS AND STRUCTURAL BEHAVIOR OF A ROTOR BLADE

Tom T. B. Wester* [1], Lars Kröger[1], Apostolos Langidis[1], Martina Göring[2], Simon Nietiedt[2], Thomas Luhmann[2], Joachim Peinke[1], and Gerd Gülker[1]
[1]University of Oldenburg, ForWind and Institute of Physics, Küpkersweg 70, 26129 Oldenburg, Germany
[2]Jade University of Applied Sciences, Institute of Applied Photogrammetry and Geoinformatics (IAPG), Ofener Str. 16/19, 26121 Oldenburg, Germany

Summary The aim of the present study is the investigation of the flow field around a wind turbine rotor blade under periodic changes of the angle of inflow. Additionally, also the resulting deformation of the blade is tracked to examine the impact of such inflow on the structure itself. For this purpose wind tunnel experiments are carried out on a clamped rotor blade of the Oldenburg wind turbine model called MoWiTO 1.8. During the experiment the global forces as well as the local flow around the blade are measured. In addition to this also a photogrammetry system for measuring the blade deformation is used. A 2D active grid is used to create customized flow conditions based on real flow situations at a rotating turbine. For the measurement of the respective span, the wind speed of the wind tunnel was also adapted to the rotating case.

INTRODUCTION

In free field operation wind turbines face a broad range of inflow conditions. In most cases the inflow is of turbulent nature resulting in changes of the incoming wind velocities and direction. Such changes result in angle of attack (AoA) variations for the rotating turbine blade and as a result fast fluctuations of lift and drag force take place. These recurring fluctuations can then lead to wear and tear of the system, which means that the planned service life cannot be achieved. To build more durable turbines it is therefore essential to understand the influence of turbulent flow on the aerodynamics of the rotor blade. Furthermore, the resulting material and torsional behavior due to turbulent inflow need to be understood to adapt the blades to the given flow situation.
This study will present a novel setup with a combination of two state of the art measurement systems. For resolving the flow field around the blade at different spans a high-speed PIV system is used. This techniques allow the investigation of the direct influence of the imposed flow on the rotor blade aerodynamics. In addition, a synchronized photogrammetry multi-camera system is used, which can measure the global deflections of the blade. By simultaneous measurement it is possible to draw direct conclusions about the interaction between inflow, aerodynamics and structural deformations.
The long term objective of the experiment are measurements on a rotating wind energy system. Therefore, it shall also be tested whether the effects on a rotating and pitching system can be simulated with the setup presented here.

EXPERIMENT

The experiment is performed in a wind tunnel of the University of Oldenburg. A schematic sketch of the used setup is shown in figure 1 including all used measurement equipment. The wind tunnel itself has an outlet of 0.8×1.0 m^2 and a test section length of 1.8 m. During the experiments the wind tunnel is operated in open test section configuration. A 2D active grid [1] is attached to the outlet of the nozzle to generate sinusoidal angle of inflow (AoI) changes with a frequency of 8 Hz corresponding to the rotational frequency of the model wind turbine. The experiment focuses on a single wind turbine blade of the Oldenburg model wind turbine called MoWiTO 1.8 [2]. The blade is attached to force and torque sensors 1.1 m behind the 2D active grid. The force and torque sensors are used to measure the global acting forces with a sampling frequency of 1 kHz. To investigate the local flow field a high-speed stereoscopic PIV system is used, which is represented in the figure 1 by grey cameras. For illumination a double pulsed laser with a repetition rate of 1 kHz is used, which is coupled into the wind tunnel from downstream. Since it is only possible to investigate the flow field in discrete planes, the flow fields at 25%, 30%, 35% and 70% of the blade span are investigated during the experiment. To adapt the flow fields to the rotating system, the wind speed of the tunnel is adjusted to the respective span. The generated flow field is based on the rotating and pitching system presented at the wind energy science conference 2019 and shall be compared with the presented results.
In addition to the investigation of the flow field, this study also investigates the deformation and deflection of the rotor blade itself. A photogrammetry system consisting of four high-speed cameras and high power pulsed LEDs [3]. These are represented in the figure 1 by the blue cameras. In contrast to the PIV measurement system, the photogrammetry system is able to record the deformation of the entire rotor blade in all three dimensions. The measured data of both systems are transformed into a common 3D coordinate system. This combination of force, flow and deformation measurements can then be used to analyze the fluid structure interaction (FSI), which was previously only possible in computational fluid dynamics (CFD) in such high temporal resolution and combination.

*Corresponding author. E-mail: tom.wester@uol.de.

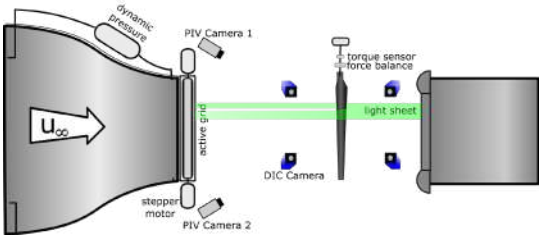

Figure 1: Sketch of the used experimental setup. Shown is the PIV Setup consisting of the two grey cameras and the green light sheet as well as the photogrammetry setup represented by the blue cameras.

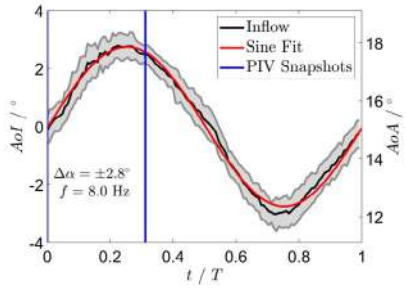

Figure 2: Generated angle of inflow (AoI) and resulting angle of attack (AoA) variations during the measurement at 25% span. Added to the phase averaged measurement in black is a sinusoidal fit in red and the vertical lines in blue represent the times of the PIV Snapshots in figure 3.

AERODYNAMIC RESULTS

As an example, the abstract here will only deal with the case of the 25% span, focusing on aerodynamics. Further comparisons as well as the integration of the deflection will be postponed to the presentation.
Figure 2 shows the generated sinusoidal inflow with an angle of inflow (AoI) amplitude of $\pm 2.8°$ and a frequency of 8 Hz resulting in an angle of attack (AoA) change for the blade from $12.3°$ up to $17.9°$. The wind tunnel velocity during the experiment is set to $u_\infty = 15.9\frac{m}{s}$. With the corresponding chord length c this results in a reduced frequency of $k = \frac{\pi c f}{u} = 0.13$, which is highly unsteady [4].
Figure 3 shows on the left side the vorticity field at an AoI of $0°$. In the figure it is easy to see that the shear layer between wing and free flow is very small here. In comparison, the right side of the figure shows the vorticity field near the maximum of the AoI. Here, a much more pronounced shear layer is visible, which indicates that the flow here is no longer fully attached. This is in agreement with the findings from the measurements from the rotating system and the pitching airfoil.
Besides the flow measurements, other cases of the measurement campaign with focus on the blade deflection have already been presented in [3]. The results were very promising and showed a deformation well correlated with the given flow field.

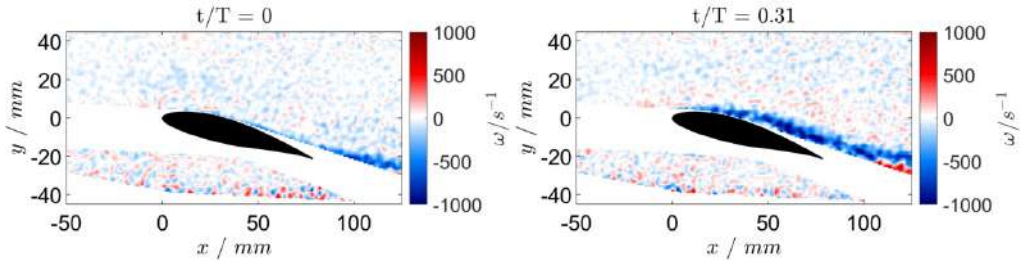

Figure 3: Phase averaged vorticity field for an AoI of $0°$ on the left side and near the maximum AoI on the right side.

CONCLUSION

In the presented study an innovative setup was tested, in which two powerful and non-intrusive optical measurement systems were combined to get new insights into the complex fluid structure interaction. The results that can be achieved by this setup will enable future investigations of FSI in the rotating system under turbulent inflow. Furthermore, the results from the non-rotating system are in good agreement with those from the rotating system, indicating that the flow modulation with the 2D active grid can reflect the real conditions of a rotating system very well. This could significantly reduce the complexity of some investigations in the future.

References

[1] T. T. B. Wester et al.: High speed PIV measurements of an adaptive camber airfoil under highly gusty inflow conditions, *IOP Conf. Series: Journal of Physics: Conf. Series* **1037**: 072007, 2018
[2] Frederik Berger et al.: Scaled wind turbine setup in a turbulent wind tunnel, *IOP Conf. Series: Journal of Physics: Conf. Series* **1044**: 01202, 2018
[3] S. Nietiedt et al.: Measurement of Fluid-Structure Interaction of Wind Turbines in Wind Tunnel Experiments - Concept and First Results, *ISPRS, XLII-2/W18* **143-149**, 2019
[4] G. J. Leishman: Principles of helicopter aerodynamics with CD extra, *Cambridge university press*

MEASUREMENTS WITH A NEW STEREO-DUAL-PIV SYSTEM IN A FORWARD-FACING STEP FLOW

Christopher J. Schauerte[1], Deepak Prem Ramaswamy * [1], and Anne-Marie Schreyer[1]
[1]Institute of Aerodynamics and Chair of Fluid Dynamics, RWTH Aachen University, Aachen, Germany

Summary A new stereo-dual-PIV system to analyze turbulent flows with unsteady effects has been developed. Our particular interest is the investigation of complex high-speed flows; the associated conditions thus define the design parameters of the system. After system validation, first measurements were performed in a low-speed forward-facing step flow, featuring multiple instances of flow separation and reattachment, enclosing recirculation zones. The design of the measurement system will be presented, along with results and a detailed discussion of the turbulence and unsteady flow patterns in the fully turbulent flow over a forward-facing step geometry at 10 m/s. Based on measurements of all three components of the mean and turbulent velocity vector throughout the flow field along with the temporal auto-correlation coefficient for several small time delays, we will analyze the flow topology.

MOTIVATION AND APPROACH

To be able to analyze the turbulence and spatio-temporal links in complex high-speed flows, we developed a stereo-dual-particle image velocimetry (Stereo-Dual-PIV) system. In particular, the system was designed to analyze shock wave/turbulent boundary layer interactions (SWTBLI) with separation, a type of flow with major impact and relevance for numerous aerospace-transportation and -propulsion applications [1]. These three-dimensional and highly unsteady flows impose demanding requirements on a measurement system: a very large range of characteristic frequencies, ranging from O(100 Hz) for the low-frequency unsteadiness of the separation bubble/shock system, over O(10 kHz) for large-scale coherent turbulent structures to O(100 kHz) for small-scale boundary-layer turbulence [2], needs to be resolved. High spatial and temporal resolutions are required for accurate measurements of the turbulent quantities in wall-bound flows. To be able to analyze space-time links across the interaction, which is required to better understand the underlying mechanisms in the flow, we need a relatively large field of view that covers the entire interaction flow field and thus allows simultaneous measurements across the field. Due to the three-dimensionality of the flow field, we desired measurements of all three velocity components. Furthermore, a high laser-pulse energy is needed to provide sufficient illumination for the small tracer particles required in high-speed flows. Existing PIV systems cannot provide the temporal and spatial resolutions required in high-speed flows at the same time. Classic PIV measurement systems typically feature high-resolution CCD sensors, allowing for a sufficiently high spatial resolution, but no temporal resolution. On the other hand, high-speed PIV systems using CMOS sensors can provide reasonable temporal resolutions up to O(50 kHz) [5] but cannot provide the required spatial resolution.

Therefore, a carefully synchronized multi-frame approach was chosen for our system: two Stereo-PIV systems, each of them delivering all three components of the velocity vector in the measurement plane, are arranged such that they observe the exact same field of view. Two sets of PIV-image pairs at a preselected, arbitrarily small temporal delays can thus be recorded. With measurements at a number of time delays, temporal and thus also spectral information becomes available.

The validation of the PIV system was performed based on the subsonic flow across a forward-facing step measured in a continuously running subsonic wind tunnel. The large installation space and continuous run times at the low-speed facility have proven advantageous to validate different systems against each other. Care was taken to choose appropriate validation parameters that are transferable to the high-speed flows of interest. This flow topology is well suited to show the capabilities of the new measurement system and is also of inherent scientific interest for multiple reasons: the flow configuration forming at a two-dimensional forward-facing step is of highly dynamic behavior and complexity, featuring several closed separation zones and an unsteadiness of the separation bubble [4], which is typically similar to the unsteadiness occurring in shock-induced separation [2]. The prevailing flow features, namely two distinct separation regions [3], recirculation zones, and reattachment events are of immense importance and interest, also taking into consideration the actually targeted supersonic flow pattern. The results presented on this flow field will therefore help understand high-speed flows with separation, especially the influential phenomenon of the low-frequency unsteadiness, and also demonstrate the capabilities of the Stereo-Dual-PIV system.

EXPERIMENTAL SETUP

Experimental facility and model

The experiments for this study were performed in the closed-circuit low-speed wind tunnel at the Institute of Aerodynamics, RWTH Aachen University. The open test-section has a total length of 1.8 m and a cross section of 1.2 m x 1.2 m. The turbulence intensity based on the freestream velocity fluctuation of the wind tunnel is below 0.3%.

*Corresponding author. E-mail: a.schreyer@aia.rwth-aachen.de.

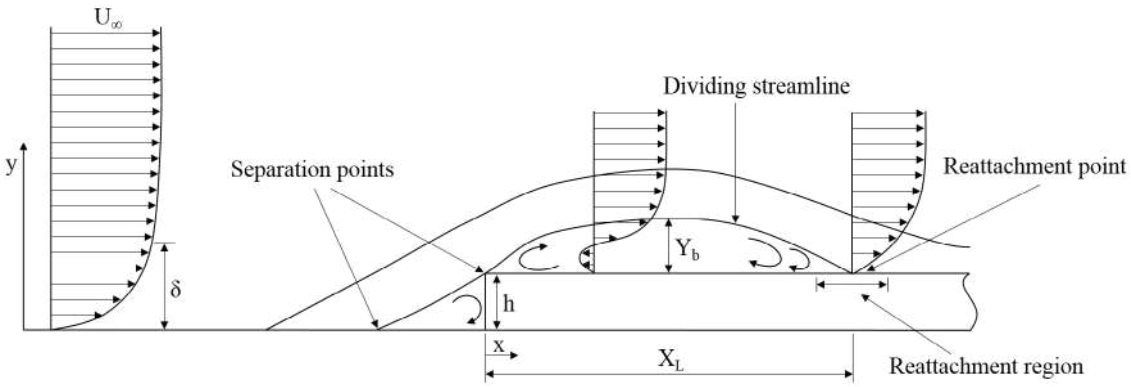

Figure 1: Schematic of the flow topology in the flow across a forward-facing step. Figure from Sherry et al. [6]

The experimental model consisted of a flat plate of 1350×2030 mm (width x length) mounted horizontally in the test section. A rectangular forward-facing step was installed onto the flat plate. The leading edge of the flat plane was a half ellipse, and a tripping wire with a diameter of 0.5 mm installed downstream of the leading edge was used to ensure a fully developed turbulent boundary layer at the measurement region. The step induces large-scale separation, a schematic of the establishing flow topology is shown in Figure 1.

The Stereo-Dual-PIV system

The PIV system is a further development of the Dual-PIV system described by Schreyer et al. [5]. The setup is composed of two separate, but synchronized Stereo-PIV systems, each of them including a double-pulse PIV laser and two 11 megapixel CCD cameras, corresponding to a sensor resolution of 4008 x 2672 pixels. Consequently, each subsystem provides access to all three spatial components of the velocity vector in the measurement plane. Both systems are carefully aligned, such that image sequences of the identical section of the flow field are captured. The temporal delay between the systems is precisely adjustable and can be chosen arbitrarily small. Measurements at a preselected set of time delays thus make the desired temporal and thus spectral information accessible. Frequency-based image separation, which is based on the application of two lasers emitting at slightly distinct wavelengths, combined with high-quality color filters installed in front of the cameras, allows to separate the recorded images of the subsystems. This allows the choice of lasers with similar characteristics and an equally large laser pulse energy of 200 mJ/pulse, enabling a high signal-to-noise ratio that is equally large for both subsystems.

CONCLUSIONS

The high accuracy in the system alignment and the high-quality image separation that can be obtained with the presented setup allow measurement data of very high quality, suitable for turbulence measurements in wall-bound flows. Furthermore, the setup provides a very low measurement noise level. Based on measurements of all three components of the mean and turbulent velocity vector throughout the flow field along with the temporal auto-correlation coefficient for several small time delays, the flow topology and dynamics in complex unsteady three-dimensional flows in both high- and low-speed flows can be assessed and analyzed.

ACKNOWLEDGMENTS

The financial support of the German Research Foundation (DFG) in the framework of the Emmy Noether-Programme (grant SCHR 1566/1-1) is gratefully acknowledged.

References

[1] Délery J. M., Marvin J. G. Shock-wave boundary layer interactions, *AGARDograph No.280*. NATO Advisory Group for Aerospace Research and Development, 1986.

[2] Dupont P., Haddad C., Debiève J. F. Space and time organization in a shock-induced separated boundary layer. *J. Fluid Mech.* **559**: 255–277, 2006.

[3] Graziani, A., Kerhervé, F., Martinuzzi, R.J. et al. *Exp Fluids* **59: 154**, 2018. https://doi.org/10.1007/s00348-018-2608-y

[4] Pearson D. S., Goulart P. J., Ganapathisubramani B. Turbulent separation upstream of a forward-facing step. *J. Fluid Mech.* **724**: 284–304, 2013.

[5] Schreyer A.-M., Lasserre J.-J., Dupont P. Development of a Dual-PIV system for high-speed flow applications. *Experiments in Fluids* **56 (10)**, 2015.

[6] Sherry M., Lo Jacono D., Sheridan J. An experimental investigation of the recirculation zone formed downstream of a forward facing step. *Journal of Wind Engineering and Industrial Aerodynamics* **98 (12)**: 888–894, 2010.

DEEP RECURRENT NETWORKS FOR PARTICLE IMAGE VELOCIMETRY

Christian Lagemann* [1], Kai Lagemann [2], Michael Klaas[1], and Wolfgang Schröder[1]
[1]RWTH Aachen University, Chair of Fluid Mechanics and Institute of Aerodynamics, Aachen, Germany
[2]German Center for Neurodegenerative Diseases, Bonn, Germany

Summary For many years, convolutional neural networks have successfully been used in a variety of tasks, e.g., image classification, object detection, and pattern recognition, and have been recently adapted to improve post-processing steps in Particle-Image Velocimetry (PIV), one of the most important measurement techniques in experimental fluid dynamics. These supervised and unsupervised learning based approaches show promising results but often fail to generalize well to real-world applications. Changing light and diverse particle conditions are still major challenges for achieving high robustness in end-to-end learning based PIV processing. To tackle these challenges in general PIV applications, we apply a novel deep neural network architecture for optical flow estimation called Recurrent All-Pairs Field Transforms (RAFT) [1]. Using RAFT as an optical flow estimation backbone achieves a new state-of-the-art accuracy on public PIV datasets, generalizes well to unknown real-world experimental data, and allows for a significantly higher spatial resolution compared to state-of-the-art PIV algorithms based on cross-correlation methods.

INTRODUCTION

In recent years, common tasks of computer vision, e.g., object detection and recognition, have improved dramatically due to significant advances in the field of machine learning. Low-cost high performance processing units in combination with a higher amount of reasonable training data led to outstanding breakthroughs in deep learning and convolutional neural networks (CNNs). Deep learning methods have shown to side-step the problem of explicitly formulating an optimization pipeline and directly adjust the parameters of an end-to-end network in a general fashion to estimate optical flow. Motivated by the successes of end-to-end deep learning, CNNs have been suggested for addressing current challenges in PIV processing and started to match or even outperform state-of-the-art algorithms in terms of efficiency, accuracy, or spatial resolution. Cai et al. [3] formulated a first dense optical flow estimator for PIV problems achieving decent accuracy while significantly improving the spatial resolution compared to cross-correlation based methods. Adapting a lighter network architecture like LiteFlowNet [2] further increased accuracy and reduced the number of trainable parameters. The major task of current research is to identify network architectures that perform better, train more easily, and achieve good robustness to changing light and particle conditions in novel scenes.

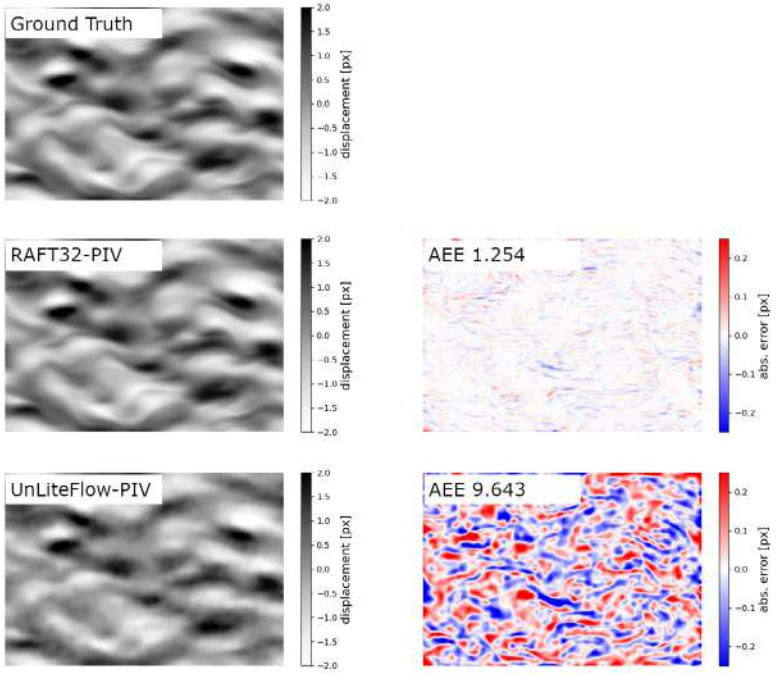

Figure 1: Optical flow prediction of different network architectures (left) and absolute error between ground truth flow and network predictions in vertical flow direction (right: lighter is better).

To tackle these challenges, we apply a novel deep neural architecture for optical flow estimation called Recurrent All-Pairs Field Transforms (RAFT) [1] to general PIV applications. RAFT extracts per-pixel features, computes a 4 level multi-scale correlation volume for all pairs of pixels, and iteratively updates a flow field using a convolutional gated recurrent unit. Compared to other optical flow networks, it is unique in the sense that it operates at a single resolution using a large number of lightweight, recurrent update operators. Using RAFT as optical flow backbone achieves state-of-the-art

*Corresponding author. E-mail: c.lagemann@aia.rwth-aachen.de

accuracy on synthetic PIV datasets, generalizes well to unknown real-world experimental data, and opens the door for further self-supervised or unsupervised learning approaches. We trained our RAFT model on a publicly available synthetic PIV image dataset and further designed more challenging datasets increasing the maximum particle shift to a maximum of $\pm 20px$ while significantly decreasing the number of particles within an image domain at the same time. Finally, we applied our trained model to experimental data performing on pair with state-of-the-art PIV algorithms.

RESULTS

Fig. 1 depicts the predefined reference displacement data of a direct numerical simulation of isotropic turbulence together with the computed estimates of our RAFT based method and a state-of-the-art unsupervised PIV network. Analyzing the absolute error distribution clearly reveals that our RAFT based method outperforms state-of-the-art PIV networks. In addition, RAFT provides a second major benefit over traditional cross-correlation PIV algorithms, the high spatial resolution, since it computes per-pixel flow estimates. In our test cases, the RAFT based flow predictions have a 64 times higher resolution compared to our cross-correlation based PIV approach. Especially in turbulent flows characterized by strong fluctuations and gradients, a higher spatial resolution allows to resolve finer flow structures. We evaluate this benefit for a transitional turbulent boundary layer of an incompressible flow over a flat plate with an elliptical leading edge. These results are provided in the final manuscript.
Finally, we applied our models to real-world experimental PIV data. The test case is taken from a measurement dealing with a turbulent wavy channel flow as described in [4]. The PIV images are analyzed using our in-house code PascalPIV. Fig. 2 clearly depicts that our RAFT approach performs on pair with available cross-correlation PIV methods while significantly increasing the spatial resolution. Furthermore, RAFT outperforms state-of-the-art PIV networks and shows less noisy results due to its iterative nature. These results as well as the findings of various synthetic and experimental data will thoroughly be discussed in the final manuscript.

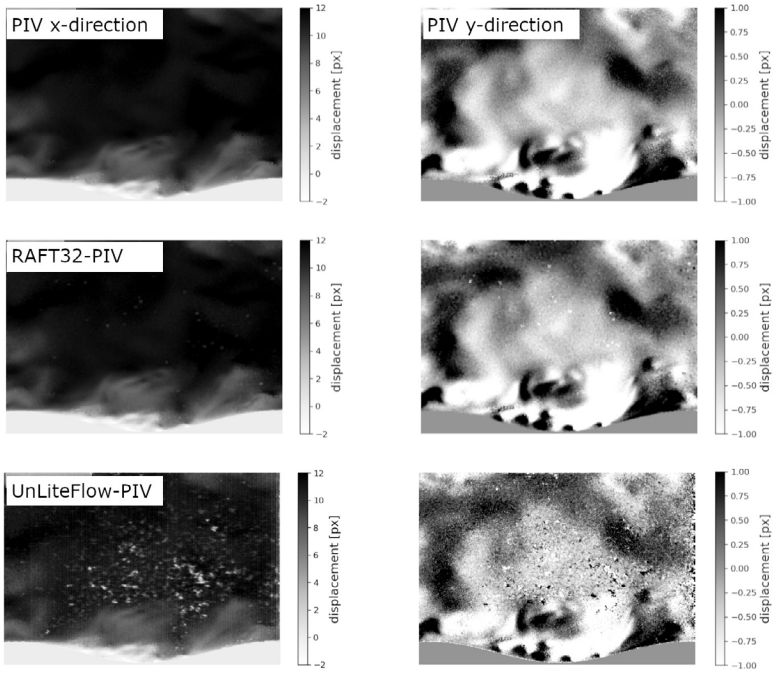

Figure 2: Visual comparison of our RAFT models and state-of-the-art PIV algorithms as well as PIV networks.

CONCLUSIONS

Several deep neural network architectures used for PIV processing were evaluated. Our RAFT based models achieve a new state-of-the-art accuracy on a public PIV image dataset and outperform available supervised and unsupervised learning based approaches. We demonstrate that our RAFT models also perform well in significantly more challenging flow field and image conditions, e.g., low particle density and changing light conditions, again outperforming available PIV networks. Furthermore, we apply our RAFT models to real-world experimental PIV data performing on pair with sophisticated state-of-the-art PIV algorithms while significantly improving the spatial resolution.

References

[1] Teed Z. and Deng J. RAFT: Recurrent All-Pairs Field Transforms for Optical Flow. *arXiv preprint* **arXiv:2003.12039** , 2020.
[2] Hui T., Tang X., and Change Loy C. Liteflownet: A lightweight convolutional neural network for optical flow estimation. *Measurement Science and Technology* **28**, 2017.
[3] Cai S., Liang J., Gao Q., Xu C., and Wei, R. Particle image velocimetry based on a deep learning motion estimator. *IEEE Transactions on Instrumentation and Measurement*, 2019.
[4] Rubbert A., Albers M., and Schröder W. Streamline segment statistics propagation in inhomogeneous turbulence. *Physical Review Fluids* **4**, 2019.

3D STRAIN FIELD EVOLUTION DURING TENSILE LOADING OF PAPERBOARD

Sara Johansson[1]*, Stephen Hall[1], Jonas Engqvist[1], and Johan Tryding[1]
[1]Division of Solid Mechanics, Lund University, Lund, Sweden

Summary Paperboard is subject to a range of mechanical deformations during package processing and there is a need for an increased understanding of deformation mechanisms to optimize these processes. In this study, the 3D strain field evolution of single-ply paperboard samples were investigated during in-plane uniaxial tension tests using X-ray tomography and digital volume correlation. The loading was applied in two directions; along and across the main fibre direction. Full 3D strain tensor fields were analysed in an incremental manner across four consecutive load steps before material failure. The strain field patterns differed between samples loaded along and across the main fibre direction. However, for both types of samples, strain localization occurred early and the established patterns intensified with further loading.

INTRODUCTION: DAMAGE MECHANISMS IN PAPERBOARD

Paperboard is an essential component to many food and beverage products. During the package processing the paperboard is subject to a range of mechanical deformations that are necessary for the forming of the package, but could also compromise the overall product performance. Numerical modelling has become an important tool towards optimising the package forming processes[1], but more detailed models require more detailed experimental support in terms of the material structure and deformation mechanisms. In this work we investigate the 3D evolution of paperboard microstructures based on 4D x-ray tomography imaging and Digital Volume Correlation (DVC) to quantify the development of the 3D tensor strain fields leading to damage. Furthermore, as paperboard is a highly anisotropic material, we investigate how the direction of loading with respect to the material microstructure affects the development of strain fields and damage in the lead up to material failure.

MATERIAL AND METHODS: X-RAY TOMOGRAPHY AND DIGITAL VOLUME CORRELATION

The material studied here is a single-ply paperboard consisting of bleached fibres and coated with two layers of clay/latex on one side. Notched samples from this paperboard (see sketch in Figure 1, left) were subjected to in-plane uniaxial tension tests in two different material directions; the Machine Direction (MD) and the Cross machine Direction (CD). The tensile loading was performed using a small custom-built tensile test device designed to be used within an x-ray tomograph. Loading was carried out in load steps with x-ray tomography acquisitions after each step to image the internal microstructures in the material. The MD and CD samples were loaded in load steps of 15N and 8N, respectively, resulting in four load steps before the peak force was reached and failure occurred in the samples.

X-ray tomography imaging was performed using a Zeiss Xradia XRM520, at the 4D Imaging Lab at Lund University. The x-ray source parameters were set to 110kV and 10W. 1601 projections were collected during 360º rotation, which resulted in scanning times of around 1 hour and 10 minutes. The final 3D images had cubic voxels of side length 4 µm.

To obtain the full tensor strain fields in 3D, the x-ray tomography images were analysed by DVC. DVC was performed in an incremental manner (comparing strain evolution across each consecutive load step) using the tomography volumes corresponding to these loading steps. The open source Python code Spam 0.4.3[2] was used for the DVC analysis. After an initial registration of rigid body motions, a node spacing 20 voxels and a correlation window size of 21 voxels was chosen for the DVC, as it resulted in relatively high resolution of the strain fields and reasonable computation times.

RESULTS AND DISCUSSION: STRAIN FIELD EVOLUTION

The macroscopic stress-displacement curves for the MD and CD samples are shown in Figure 1 (middle), where the loading steps are marked with red circles. Stress relaxation occurring during the x-ray tomography data collection can be observed for all load steps. The sample loaded in the MD experienced a relatively steep increase in stress up to around 60 MPa, followed by a rapid drop to 10 MPa when the sample failed. The stress/strain curve measured on the CD sample has a wider shape and becomes significantly nonlinear as the maximum stress around 40 MPa is approached. After the failure, the stress drops to around 10 MPa and continues to decrease gradually with further material separation.

Also shown in Figure 1 (right) are 2D visualizations of the samples after failure (load step 06, central plane). In the MD sample, the fracture (as indicated by the zone with low fibre density) extends from the upper parts of both notches and approximately diagonally towards the centre of the sample. The central part contains slightly higher amounts of fibres compared to the edges. The fracture in the CD sample runs roughly diagonally from the upper part of the left notch towards the lower part of the right notch. On average, the sample looks more damaged close to the right notch compared to the left.

Although the full strain tensor is obtained from the DVC analysis, we focus on the volumetric strain field here. Figure 2 shows, for both samples, 3 orthogonal sections through the volumetric strain field volumes and for three loading increments before material failure. In both cases, patterns of elevated strain developed already at early load increments and increased in magnitude with further loading, but the patterns remained similar throughout the loading. The areas of

*Corresponding author. E-mail: sara.johansson@solid.lth.se.

elevated strain also extend further to neighbouring parts of the sample at later load increments. The patterns differ between the MD and CD samples in both plane view and the thickness directions. In MD, the strain localisation starts at the notches and extend towards the centre in apparently diagonal directions (at least partly). The strain is, on average, high close to the notches compared to the centre; a pattern that can be recognized from the fracture at load step 06 in Figure 1. In the thickness directions, the strain is localized in the central parts of the sample which indicates that the sample started to delaminate and increase in thickness. The CD strain field developed mainly from the right notch (where the major fracture zone appeared after failure, Figure 1) and extended in a roughly horizontal direction towards the left notch. The diagonal or vertical patterns observed in the MD strain fields cannot be distinguished in the CD strain fields. In the last loading increment, high strains developed throughout the sample width.

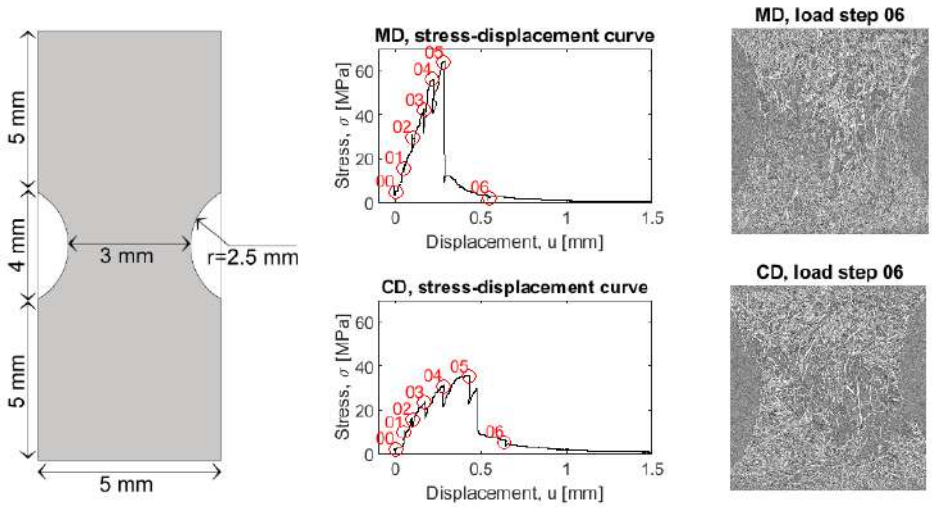

Figure 1. Left: Sketch and dimensions of the samples. Middle: Macroscopic stress-displacement curves. Right: Visualisation of the fractured samples at loading step 06 (centre of the image stacks).

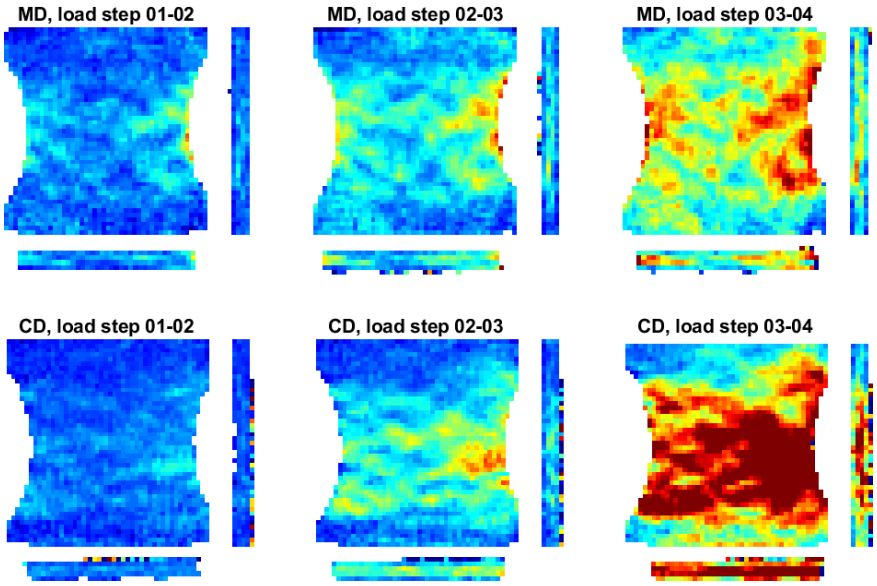

Figure 2. Volumetric strain fields (colour scale -1-8%). The 2D visualisations represent the centre of the volume in each direction.

The difference between MD and CD in terms of strain field evolution and fracture patterns is interpreted as a consequence of the main fibre direction, i.e. vertical in MD and horizontal in CD. A possible explanation is that the CD sample failure results from separation of fibres, while in the MD sample, vertically aligned fibres might break or elongate. More analysis at the resolution of single fibre behaviour is needed to verify these hypotheses and to fully understand the processes underlying the strain field evolution and fracture processes.

References

[1] Borgqvist, E., Wallin, M., Ristinmaa, M., Tryding, J. An anisotropic in-plane and out-of-plane elasto-plastic continuum model for paperboard. *Compos. Struct.* **126**: 184-195, 2015.

[2] Andò, E., Cailletaud, R., Roubin, E., Stamati, O. and the spam contributors. {spam}: The Software for the Practical Analysis of Materials, web site **https://ttk.gricad-pages.univ-grenoble-alpes.fr/spam/**, 2017.

A TRANSIENT THERMAL ANALYSIS OF A FAST RESPONSE HEAT FLUX SENSOR

Konstantin Huber* [1] and Tim Rödiger † [1]
[1]Department of Mechanical Engineering, University of Applied Sciences Landshut, Landshut, Germany

Summary The measurement principle of heat flux sensors based on the transversal Seebeck effect (TSE) require homogeneous temperature differences across their active layers. A transient thermal analysis using 3D FEA is applied to investigate the TSE-based Atomic Layer Thermopile (ALTP) sensor in combustion environments. Studying the location depending temperature difference of the top and bottom side of the active layer while applying highly transient thermal engine loads shows a homogeneous distribution over the active surface. The results indicate that the presented sensor design leads only to small thermal disturbance effects within the active layer and make it applicable to engine diagnostics.

SENSOR DESIGN

The active layers of TSE-based ALTP sensors have a thin tilted layer structure made out of Yittrium-Barium-Copperoxid (YBCO) and Copperdioxide ($Cu0_2$) with approx. $500 - 700\,\mathrm{nm}$ thickness and an active surface of $1 - 6\,\mathrm{mm}^2$ fabricated on top of a strontium titanate substrate ($SrTiO_3$). The induced output voltage U_{ALTP} is calculated by

$$U_{ALTP} = 0.5\, l\, \sin 2\gamma\, \Delta S\, \Delta T\, d^{-1} \tag{1}$$

and directly proportional to the incident heat flux density, when a constant temperature difference over the sensor's active layer (top vs. bottom side) is present (γ is the tilt angle, d is the thickness and l the length of the active film, ΔS is the difference of the Seebeck coefficients of the two materials) [1]. Previous studies concerning measurements in supersonic wind tunnels demonstrated the accuracy and time constant in the microsecond range in short-duration measurements based on a semi-infinite wall assumption for the substrate [2].

However, long duration measurements like combustion applications violate the semi-infinite wall assumption and lead to significant changes in the boundary conditions of the active layer. This study investigates therefore changes in the temperature distribution leading to resulting voltage and calibration assumptions. The electrical signal connection to the active layer is made via a thin gold layer, an electric conductive adhesive and copper cables (Figure 1a).

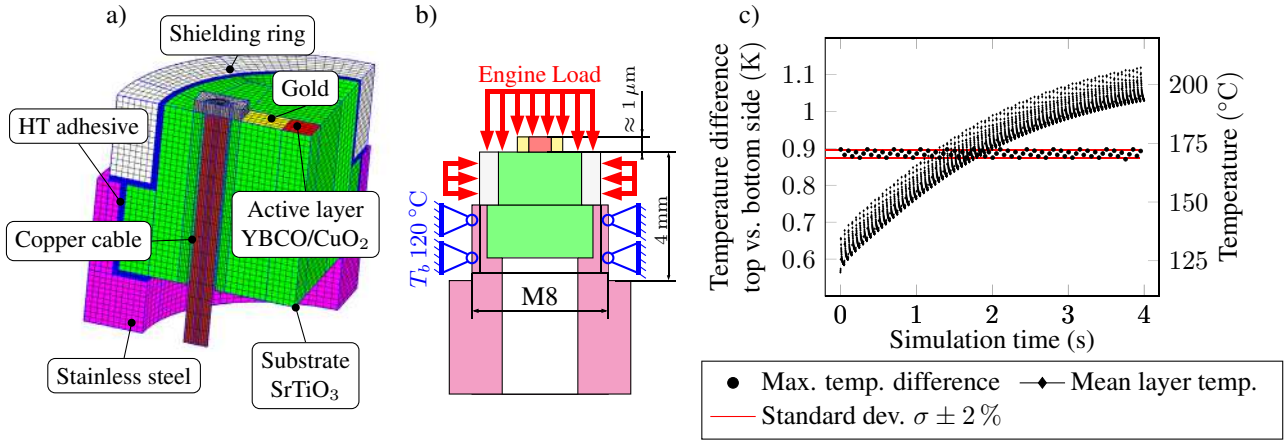

Figure 1: a) Schematic view of the discretized ALTP module, b) sectional view of the module and its thermal boundary conditions, c) time progression diagram of the temperature difference and the mean temperature of the active layer.

SIMULATION SETUP AND RESULTS

The sensor module is discretized using micrometer scaled hexahedron second order elements (C3D20). Making use of symmetry characteristics in two directions lead to a quarter model (Figure 1a). The active layer and the gold contact are modeled with 10 layers and an overall thickness of $1\,\mu\mathrm{m}$ with increasing discretization fineness towards their contact region. The anisotropic active film (nm-layered) was modeled like the rest of the sensor module as homogeneous isotropic structure with thermal parameters proposed by Zeuner [3]. Due to fast changing thermal loads on the front surface, the time step is chosen to $0.7\,\mathrm{ms}$.

*Corresponding author. E-mail: konstantin.huber@haw-landshut.de
†E-mail: tim.roediger@haw-landshut.de

It should be noted that this study constitutes an ideal situation with regard to disturbing effects like location depending thermal loads, contact resistances (neglected) or differences in the manufacturing process of the active layer. As thermal boundary conditions a constant thread temperature of $T_b = 120\,°\mathrm{C}$ is assumed (Figure 1b). The thermal load on the front side is discretized in $10\,°\mathrm{CA} - 0.7\,\mathrm{ms}$ steps, measured for a single cylinder 4-stroke engine with a cylinder volume of $485\,\mathrm{cc}$ and manifold injection operating at $2400\,\mathrm{rpm}$ and $4.4\,\mathrm{bar}$ mean effective pressure [4].

In order to investigate possible temporal variation in the temperature difference of the active layer, the mean nodal temperature values of the top- and bottom side are subtracted from one another and displayed in Figure 1c. Despite slightly varying maximum values ($\sigma \pm 2\,\%$) for each load peak the temperature difference stays constant over time although the mean layer temperature illustrated in diamonds rises by approx. $80\,\mathrm{K}$ and highly transient loads are present.

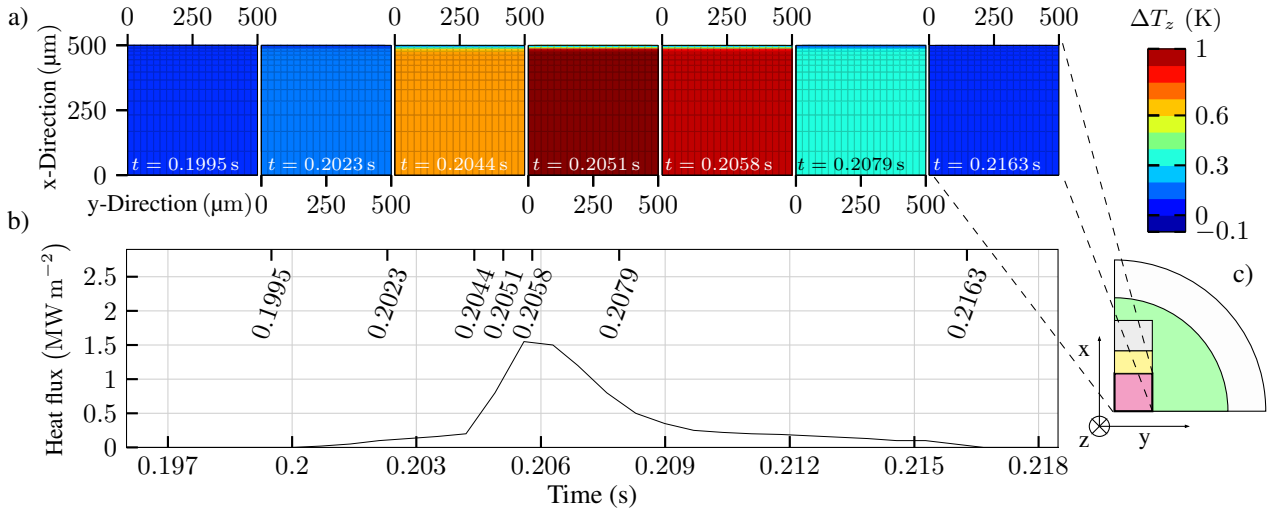

Figure 2: The time and location depending 2D-temperature difference distribution (Fig. 2a) of the active layer for one load cycle (Fig. 2b) is shown. Fig. 2c displays a top view schematic of the considered active film area for better orientation.

Figure 2a shows the temperature difference distributions of the active layer for selected time steps along the load cycle. The temperature difference rises and reaches a maximum of approx. $1\,\mathrm{K}$ for $t = 0.2051\,\mathrm{s}$ shortly before the maximum heat load in the cycle. Afterwards the temperature difference decays again and reaches around $0\,\mathrm{K}$ as at the beginning of the cycle.

The temperature distribution is homogeneous over the active surface along the entire cycle, only for $x > 490\,\mu\mathrm{m}$ a trend towards reduced local temperature differences can be observed when thermal loads are present. This reduction can be explained by the adjacent gold layer for $x > 500\,\mu\mathrm{m}$ (not displayed in Fig. 2a) with a much higher thermal product as the active layer that acts as heat sink. In the immediate vicinity of the gold layer the temperature difference is reduced to approx. one hundredth of the difference in the unaffected area. This reduction could lead to measurement errors of the heat flux sensor and different boundary discretizations varying in their fineness are used to estimate the affected active sensor area. The discretization study shows that the affected area for which $\Delta T < 0.9 \cdot \Delta T_{\mathrm{unaffected}}$ is rather small and makes up only $2\,\%$ of the overall active surface area.

CONCLUSION

FEA analysis can be used for the design and layout of heat flux sensors based on TSE. It is possible to estimate local and time-dependent temperature difference disturbances of the active layer that can lead to systematic errors of their working principle. The FEA investigation of a specific ALTP-sensor in a combustion induced load cycle shows a fairly constant temperature difference distribution over the top and bottom side of the active layer and a homogeneous temperature distribution over the surface. The studied design seems promising for the use in long duration and highly transient scenarios like combustion engine measurements.

References

[1] Renk, K. F., Betz J., Zeuner S., Lengfellner H., Prettl W. Thermopile effect due to laser radiation heating in thin films of high-Tc materials. *Physica C: Superconductivity* **235-240**: 37-40, 1994.

[2] Roediger T., Knauss H., Smorodsky B. V., Estorf M., Schneider S. P. Hypersonic instability waves measured using fast-response heat-flux gauges. *AIAA: Journal of Spacecraft and Rockets* **46**(2): 266-273, 2009.

[3] Zeuner S. Atomlagenthermosäulen in Hochtemperatur-Supraleitern als schnelle Strahlungsdetektoren. *PhD Thesis*, Physics Dept., Regensburg, 1994.

[4] Wimmer A. Oberflächentemperaturaufnehmer zur experimentellen Bestimmung des instationären Wärmeübergangs in Verbrennungsmotoren. *Mitteilung des Institutes für Verbrennungskraftmaschinen und Thermodynamik* **62**: 191-218, 1991.

MULTISCALE DIC APPLIED TO METAMATERIALS

François Hild* [1], Anil Misra[2], and Francesco dell'Isola[3]
[1]Laboratoire de Mécanique et Technologie (LMT), ENS Paris-Saclay, Cachan, France
[2]Civil, Environmental and Architectural Engineering Department, University of Kansas, Lawrence (KS), USA
[3]International Research Centre on Mathematics and Mechanics of Complex Systems (M&MoCS) and
Dipartimento di Ingegneria Civile-Edil, e Architettura e Ambientale, Università degli Studi dell'Aquila, L'Aquila, Italy

Summary The deformation of a metamaterial (i.e., millimetric pantograph) in a bias extension test is measured via digital image correlation (DIC) performed at different scales. Thanks to the gray level residuals, the microscale results are found to be in better agreement with the experiment than mesoscale and macroscale analyses. Fine analyses around the hinges show that relative displacements occur between the two beam layers of the pantograph.

INTRODUCTION

Pantographic structures are characterized by two families of equally spaced beams interconnected at their intersection points via cylindrical pivots. These structures, realized by using standard devices in additive manufacturing (3D printing), can be described as metamaterials since they have been designed upon the basis of 2nd gradient theories of continuum mechanics [1, 2]. Such material systems are peculiar due to their ability to undergo large deformation (> 50 % stretch) while remaining elastic. The present effort is motivated by the requirement to characterize the detailed deformation of pantographic unit cells formed of two orthogonal sets of 3 beams. They are subjected to tensile experiment and digital image correlation (DIC) will be applied to extract the details of their deformation.

DIC consists in registering images acquired during mechanical tests [3]. From such analyses, displacement, strain and residual fields are obtained. For the experiment reported herein, FE-based DIC will be applied at three different scales. Hencky-type regularization (i.e., incremental elastic regularization) is implemented [4]. Thanks to such type of regularization, large strains can be achieved without penalizing too much the registration scheme. Further, focused analyses about the hinges will also be carried out via global DIC at the microscale.

DIC ANALYSES OF BIAS EXTENSION TEST

The specimen considered in this analysis was designed to represent the unit cell behavior of pantographic structures. The sample was fabricated using a 3D printer using the SLS (selective laser sintering) technology with polyamide powder (PA2200) with average grain size of 56 μm. The pantographic unit cell specimen was subjected to tensile loading in step-by-step quasi-static conditions in displacement control mode. The grips connecting the specimen to the loading machine are designed to apply an axial tensile action and resist the overall specimen rotation about the loading axis. For measurements of displacement fields, the specimen grips were sprayed on their surface to make a black speckle pattern prior to the testing. However, the surface of the beams was just marked by a set of crosses whose distance is about 30 pixels. Such situation required the regularization to be adapted and a size of $\ell_{reg} = 150$ pixels enabled all DIC calculations reported herein to converge.

Multiscale Meshes

Each of the following meshes is made of 3-noded triangles (T3). First, a macroscopic mesh encompassing the pantographic structure is considered (Figure 1(a)). The sought kinematics then corresponds to the macroscopic response of such materials. The average element size ℓ, which is defined as the square root of the mean element surface, is equal to 12 pixels.

Second, T3-based DIC registrations are also performed at the mesoscale. The external geometry of the pantographic structure is explicitly accounted for, but the kinematics is that of an underlying FE mesh in which the hinges are not explicitly described (Figure 1(b)). The mesh is tailored to the pantograph surface via simple morphological operations [2]. The average element size ℓ is equal to 10 pixels.

To account for the 11 hinges, a third (i.e., microscopic) mesh is constructed. Each beam of the pantograph is individually meshed (Figure 1(c)) with a mean element size $\ell = 11$ pixels. Consequently, the two meshes overlap in the intersection areas about each hinge. An additional operation was needed, namely backtracking the mesh constructed on the nominal geometry of the pantograph [4]. The hinges can then be recreated by using Lagrange multipliers prescribing the corresponding kinematic constraints (in terms of nodal displacements) in the registration systems to solve, or the kinematics of two beam systems can be left free. The beams were therefore allowed at least to rotate about each hinge, which was not possible in the mesoscopic analyses. The two supports of the pantograph were also meshed with two triangular elements and connected to the corresponding hinges of the pantograph.

*Corresponding author. E-mail: francois.hild@ens-paris-saclay.fr

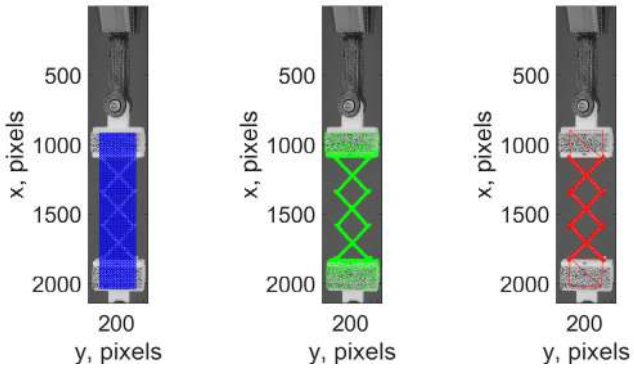

(a) Macro (b) meso (c) µicro

Figure 1: Different meshes used in DIC analyses at (a) macroscopic, (b) mesoscopic, and (c) microscopic scales

Comparison of Different Kinematic Hypotheses

In the following analyses, only the state corresponding to the maximum stretch will be reported. From the measured displacement field, the strain field is computed by exact differentiation of the shape functions of T3 elements. In the present case, the Green-Lagrange strain measure will be reported. The maximum level of the color bar corresponds to 1.5 times the overall Green-Lagrange strain (i.e., computed from the length variation between the two supports). Figure 2 shows the maximum principal strain fields for global DIC analyses at different scales. For the macroscopic mesh (Figure 2(a)), the strains are very high in most of the sample. For the mesoscopic mesh (Figure 2(b)), the strains concentrate in the vicinity of the hinges, but the beams also experience significant elongations, except those that are connected to the two supports. For the microscopic mesh, the strains remain lower everywhere and do not concentrate around hinges (Figure 2(c)). However, the strains in the beams do not vanish, which indicates that some strain energy was stored in the pantograph.

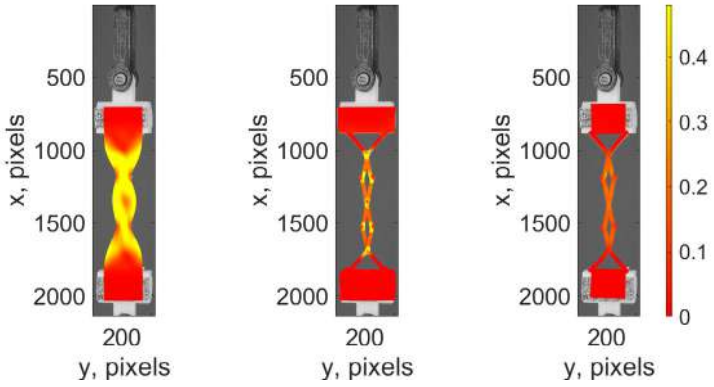

(a) Macro (b) meso (c) µicro

Figure 2: Maximum principal strain for DIC analyses at various scales

Table 1: RMS residuals (expressed in gray levels) corresponding to the analyses shown in Figure 2

Scale	RMS(ρ)
Macro	30 GL
meso	15 GL
µicro	8 GL

The choice of any discretization is probed by computing the correlation residual field ρ and its RMS level. The lower the latter, the more trustworthy the measured displacement field. Table 1 shows that the macroscopic kinematics leads to an RMS level that is twice as high as that at the mesoscale, itself twice as high as that at the microscale when no kinematic constraint is applied to the hinges. Such results are very useful for devising models that can be written at various scales.

References

[1] Turco E. et al. Enhanced piola–hencky discrete models for pantographic sheets with pivots without deformation energy: Numerics and experiments. *Int. J. Solids Struct.*, **147**: 94-109, 2018.

[2] Dell'Isola F. et al. Pantographic metamaterials: an example of mathematically driven design and of its technological challenges. *Cont. Mech. Thermod.*, **31**(4): 851-884, 2019.

[3] Sutton M.A. et al. Image correlation for shape, motion and deformation measurements: Basic Concepts, Theory and Applications. Springer, New York, NY (USA), 2009.

[4] Dell'Isola F. et al. Advances in Pantographic Structures: Design, Manufacturing, Models, Experiments and Image Analyses. *Cont. Mech. Thermod.*, **31**(4): 1231-1282, 2019.

SPATIALLY DISTRIBUTED TRANSVERSE ISOTROPY AROUND A HOLE: FROM PARAMETER IDENTIFICATION TO VALIDATION

Stefan Hartmann* [1], Rose Rogin Gilbert[1], and Ali Kheiri Marghzar[1]
[1]Institute of Applied Mechanics, Clausthal University of Technology, Clausthal-Zellerfeld, Germany

Summary Usually fiber-reinforced composite sheets are drilled to join them together with rivets. In this case, the fibers are cut and the load cannot be transferred directly via the fibers. Alternatively, the fibers can be bypassed around the holes leading to a different stress-strain state. To investigate the structural behavior, we have to model the spatially distributed anisotropy, where we draw on a model of transverse isotropy, and to determine the material parameters. Thus, a detailed discussion of both the spatially distributed fiber orientation as well as material parameter identification has to be held, especially if the parameters should be addressed uniquely. Experiments for the purposes of both parameter identification as well as validation are proposed.

INTRODUCTION

We follow a question in composite technology to avoid the drilling of fibers to obtain holes inside a composite plate, see sketch 1. In this case, the fibers are placed around the hole leading to a different stress and strain state. Here, we restrict

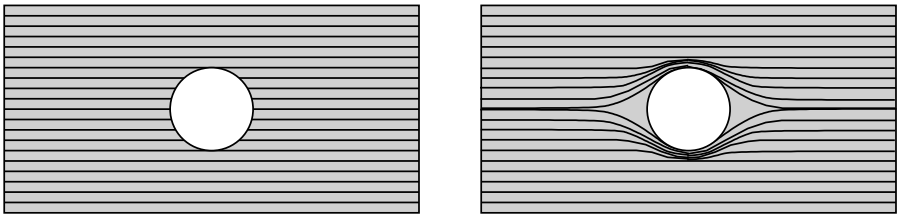

Figure 1: Comparison of two fiber orientation samples (left: uniform, unidirectional fiber orientation – classical technology, where the fibers are drilled; right: fibers bypassing a hole)

ourselves to unidirectional fiber orientations. The classical approach, we call it *uniform, unidirectional fiber orientation*, the material properties are assumed to be constant over the specimen. The case where the fibers are placed around the hole is called the *bypassing case*. From the perspective of modeling, we need the material parameters for transverse isotropy, where we assume small strains and linear elasticity. Even this seemingly simple approach reveals some challenges: first, the modeling of the fiber orientation, and, second, the unique determination of the material parameters.

B-SPLINE APPROACH FOR FIBER ORIENTATION

A common approach in finite element simulations is to assign an estimated but constant fiber orientation to a small region. This yields discontinuities in the stress-strain behavior. In [1] a first continuous approach using streamlines around a circular region is proposed. Although this leads to reasonable results, it does not reflect the real fiber orientation. Therefore, digital images were taken during the manufacturing process of the composite plates, where the fiber orientation could be seen. Afterwards, the images are evaluated and B-splines are chosen to interpolate the coordinates assigned to the fibers. One of the two coordinate lines of the B-splines "surfaces" represent the fiber line, and the orientation can be determined by the tangent vectors, see [2]. Consequently, a continuously spatial representation of the fiber orientation is available so that individual fiber orientations at each Gauss-point within a finite element can be assigned.

PARAMETER IDENTIFICATION OF TRANSVERSE ISOTROPY

The second question to be addressed is the issue of unique parameter identification to determine the five material parameters of linear elastic, transverse isotropy. A current approach is the application of digital image correlation systems (DIC-system) and to evaluate three different orientations of the fibers in an uniaxial tensile test (e.g. fiber angles relative to loading direction $\gamma = 0°, 45°, 90°$) and compare it to finite element solution. However, it turns out that this does not address all parameters. A concept to obtain a hint whether the parameters are identifiable is given by [3]. In this case, the Hessian of a quadratic Taylor-series in the solution of the optimizer is drawn on and its determinant is investigated. If it is singular, the parameters cannot be identified uniquely. This, however, has to be done with the same experimental process, but with a re-identification step using purely numerical results, see [4]. Alternatively, a detailed study using analytical results is provided in [5] showing that various experiments are required, tension for $\gamma = 0°, 90°$, shear, and a particular compression test. This compression test requires either a new (and very sensitive) experimental device or

*Corresponding author. E-mail: stefan.hartmann@tu-clausthal.de.

using a numerical representative volume element, where at the pure matrix material the elastic parameters have to be determined as well. We combine the DIC/FEM-approach with the necessary experiments as well as the evaluation of identifiability leading to reliable parameters. Accordingly, we require four tests for the composite plus one test at the pure matrix material times five repetitions for reproducibility aspects. The whole concept and the experiments are shown in detail.

VALIDATION

After the determination of the parameters, the comparison of plates with a hole where the fibers are cut, and where the fibers bypass the holes is performed both experimentally and numerically. For this purpose, experiments for the different samples are performed and the surface strains are determined using a DIC-system. To circumvent the critical approach of comparing only optically resulting images, the surface strains of the DIC-system and those of the finite element simulations are evaluated numerically. Consequently, we obtain real errors between the finite element simulation and the DIC results, see Fig. 2. In this context, it must be mentioned that the evaluation of displacements implies the

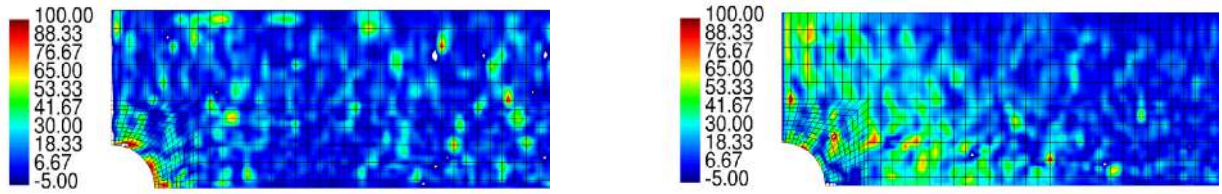

(a) Unidirectional fiber orientation (b) Bypass approach

Figure 2: Relative strain error of maximum principal strain. Comparison of unidirectional fiber orientation and bypassing approach. Here, only one-eighth of the sample and the DIC-region is shown (modeled with 20-noded hexahedral elements).

consideration of the rigid body motion of the experimental device, which is very difficult to avoid. Thus, the strain determination concept in [6] is drawn on, where the strain data of one program (e.g. DIC) can be projected to the other system (e.g. FEM).

CONCLUSIONS

A detailed study to obtain both the continuous fiber distribution as well as unique material parameters for linear elastic, transverse isotropic material is provided using a DIC/FEM approach. Particularly, identifiability is a specific challenge. Moreover, the continuous representation of the spatially inhomogeneous fiber orientation is a further issue, where one possibility is the application of B-splines. Various experimental tests are performed to identify the parameters and to validate plates with a hole, where, on the one hand, uniform fiber directions are chosen and the holes are drilled, and, where, on the other hand, the fibers bypass the holes. The validation examples provided show direct numerical errors, and not a statement of a visual comparison whether the simulation is good or bad.

References

[1] Hartmann, S., Kheiri Marghzar, A. Modeling of fiber circumplacement around a hole using a streamline approach. *Universal Journal of Mathematics and Applications* **1**: 17–28, 2018.

[2] Hartmann, S., Kheiri Marghzar, A., Gilbert, R. R., Pangboonyanon, W., Meiners, D. Experiment, modeling and simulation of bypassing holes in composites. accepted for publication in *Composite Structures*: 2019.

[3] Beck, J. V., Arnold, K. J. *Parameter estimation in engineering and science*. John Wiley & Sons, New York, 1977.

[4] Hartmann, S., Gilbert, R. R. Identifiability of material parameters in solid mechanics. *Archive of Applied Mechanics* **88**(1): 3–26, 2018.

[5] Christensen, R. M. *Mechanics of composite materials*. Dover Publication, Mineola, N.Y., 2005.

[6] Hartmann, S., Rodriguez, S. Verification examples for strain and strain-rate determination of digital image correlation systems. in: *Advances in Mechanics of Materials and Structural Analysis. Advanced Structured Materials*, Altenbach, H., Jablonski, F., Müller, W., Naumenko, K., Schneider, P. (Eds.), Springer International Publishing, Cham, 135–174, 2018.

DELAMINATION TESTS ON CFRP-REINFORCED MASONRY PILLARS: EXPERIMENTS, OPTICAL MONITORING AND FINITE ELEMENT MODELLING

Roberto Fedele[1], Gianpaolo Rosati[1], Marco Scaioni[2], Gabriele Milani[2]
[1]Department of Civil and Environmental Engineering (DICA), Politecnico di Milano, Milano, Italy
[2]Department of Architecture, Built Environment and Construction Engineering (ABC), Politecnico di Milano, Milano, Italy

Summary Masonry pillars constituted of historical bricks and mortar joints, externally reinforced by CFRP strips, were subjected to 1-tonn delamination tests to investigate their mechanical response up to failure. The experiments were monitored by conventional point gauges and by no contact, full field 2D Digital Image Correlation technique. Recourse was made to a three dimensional, heterogeneous finite element model with isotropic damage, under the simplifying assumption of perfect adhesion of the reinforcement sheet, to simulate the macroscopic behaviour of the reinforced pillar as a function of complex dissipative mechanisms which develop inside the quasi-brittle bulk.

RETROFITTING AND REPAIRING INTERVENTIONS

For the historical heritage and monumental buildings, possibly affected by chemical–physical ageing processes and deteriorated by past accidental events (such as earthquakes), there is a special need for sustainable retrofitting and repairing interventions, to increase the in-plane shear resistance, to provide out-of-plane bearing capacity, or also to reduce seismic vulnerability, see e.g. [1-2]. Fiber-Reinforced-Polymers (FRP), and especially those made of carbon fibers (CFRP), are available as stiff sheets ready to be glued to the support, or alternatively as multi-directional tissue to be embedded into grout and adhesive layers. Since one decade at least, such reinforcements have been widely used in rehabilitation works for several reasons: (i) they do not increase the structural mass, due to their excellent "specific" stiffness and strength; (ii) they are extremely simple to apply and can adhere to differently shaped surfaces such as arches and vaults [3], even irregular or very rough; (iii) they turn out to be non-intrusive and non-destructive since exhibit low impact on the pre-existing scenario. Due also to the technical progress in high strength adhesives, the CFRP/masonry interface has to be considered no longer as the weakest element of the system, and complex damage mechanisms are expected to develop within the bulk of quasi-brittle masonry when loaded up to failure.

SINGLE-LAP SHEAR TESTS

The effectiveness of the glued reinforcement on the overall behaviour of the structural element was assessed by single-lap shear tests, see [1]. An ad hoc steel frame, with additional stiffening rods, was realized to prevent rigid body motion of the pillar during the 1-tonn experiments, whilst prescribing a tangential slip between the reinforcement and the support, see Figure 1. The experiments were performed under closed loop control, with feedback signal provided by a clip gauge located at the anchor of the strip. This provision allowed a stable control of the tests also along the post peak branch, which would result in a snap back behavior if referred not only to the stroke but even to the LVDTs located closely to the notch. The clip gauge measured the tangential slip of the reinforcement with respect to the substrate, disregarding the overall deformation of the pillar and a large part of the initial, elastic deformation of the FRP strip itself. A single camera was utilized to monitor in real time the reinforced surface (average pixel footprint on the object was about 84 μm), exploiting the natural texture of the masonry, and picture sequence was processed by 2D Digital Image Correlation (DIC), see [4-8]. Sources of inaccuracies for the kinematic measurements by a single camera were carefully assessed by comparative benchmark tests, and corrective provisions were implemented including camera calibration by Brown's model and homography registration [1]. Full field measurements allowed us to detect local slips of the reinforcement with respect to the underlying masonry substrate. In the present scenario, data from DIC were especially useful to estimate the "actual" history of relative displacements at the notch of the reinforcement, to be prescribed to the finite element model as boundary conditions. Moreover, kinematic measurements were utilized to calibrate the effective elastic properties of the reinforcement, resulting from the superposition of several layers (primer, grout and epoxy adhesive). In fact, Young's modulus of the CFRP strip turned out to be markedly different from the nominal value corresponding to the carbon fibers, and in agreement with a basic mixture rule. As expected, the nonlinear response up to failure of the reinforced pillar was dominated by the strength of the substrate, namely by damage mechanisms occurring within the masonry bulk: this circumstance was confirmed by post-mortem inspection of the debonded material, including thick layers of the substrate.

FINITE ELEMENT MODELLING

A three dimensional, heterogeneous model of the pillar was developed in Abaqus® environment [9], enriched by a VUmat Fortran routine [10] for user defined constitutive relationships. Brick and mortar were described as elastic damageable phases by an isotropic damage model, see [1-2,11]: their different parameters were estimated on the basis of compressive tests, when necessary integrated by literature suggestions. The FRP reinforcement was assumed to behave elastically and to perfectly adhere to the substrate, without the need of intermediate layers closely to the interface. A strategy for fracture energy regularization based on a characteristic length was implemented at the level of element routine,

leading to a satisfactory objectivity of the overall response, resulting almost independent of the adopted discretization. In the presence of severe damage, recourse was made to an explicit integration scheme for the simulation of the quasi-static tests. Small time steps (corresponding to about 10^{-6} of the final prescribed displacement) were required for the conditional stability of the analyses, confirmed by an amount of kinematic energy not increasing along time and negligible with respect to cumulated internal energy. To decrease the computational effort (up to 120,000 elements were included within the finest discretization), 8-node brick elements with reduced integration were utilized. Moreover, when local value of damage variable exceeded a suitable threshold (close to unity), elements were deleted from the analysis ("erosion" strategy). Model predictions indicated, along the initial branch, damage propagating within a thick region close to the reinforcement: at approaching the overall peak, a wide, spoon shaped damaged region developed starting from the strip anchor, see [11]. This scenario was in satisfactory agreement with post mortem analyses of debonded material.

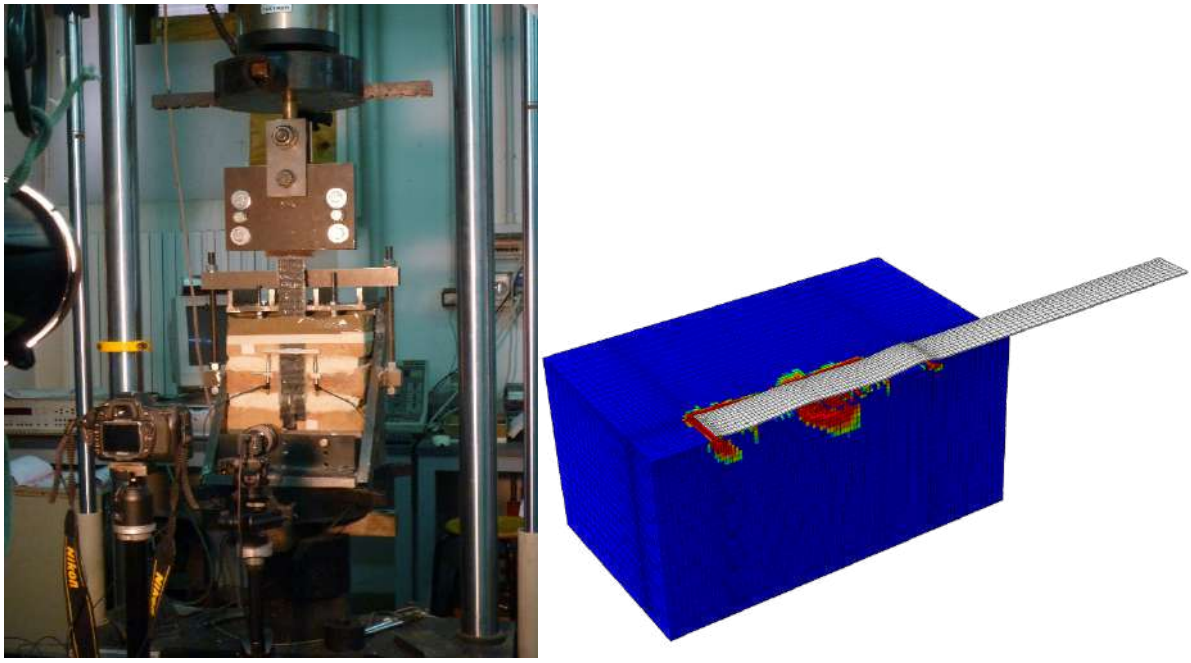

Figure 1. Delamination experiments on reinforced masonry pillars (left), monitored by digital cameras, and their finite element simulation (right), with highlighted damaged regions and amplified deformed shape.

References

[1] Fedele R., Scaioni M., Barazzetti L., Rosati G., Biolzi L. Delamination tests on CFRP-reinforced masonry pillars: optical monitoring and mechanical modelling. *Cement Concrete Comp.* **45**: 243-254, 2014.

[2] Basilio I., Fedele R., Laurenço P.B.. Milani G. Assessment of curved FRP-reinforced masonry prisms: experiments and modelling. *Constr. Build. Mater.* **51**:492–505, 2014

[3] Bertolesi E., Milani G., Fedele R. Fast and reliable non-linear heterogeneous FE approach for the analysis of FRP-reinforced masonry arches. *Comp. Part B* **88**:189 – 200, 2016.

[4] Fedele R., Raka B., Hild F., Roux S. Identification of adhesive properties in GLARE laminates by Digital Image Correlation. *J. Mech. Physics Solids* **57(7)**:1003-1016, 2009

[5] Fedele R., Galantucci L., Ciani A. Global 2D Digital Image Correlation for motion estimation in a finite element framework: a variational formulation and a regularized, pyramidal, multi-grid implementation. *Int. J. Num. Meth. Engn.* **96(12)**:739-762, 2013.

[6] Fedele R., Galantucci L., Ciani A., Casalegno V., Ventrella A., Ferraris M. Characterization of innovative CFC/Cu joints by full-field measurements and finite elements. *Mat. Science & Engn. A* **595**:306-317, 2014.

[7] Fedele R. Simultaneous Assessment of mechanical properties and boundary conditions based on Digital Image Correlation. *Exp. Mech.* **55**:139-153, 2015.

[8] Barazzetti L., Scaioni M. Crack measurement: development, testing and applications of an automatic image-based algorithm. *ISPRS J. Photogramm. Remote Sens.* **64**(3):285–96, 2009.

[9] ABAQUS/Standard and Explicit User's Manual, Version 6.10. Dassault Systèmes Simulia Corp, Providence, RI (USA), 2014.

[10] Comi C., Fedele R., Perego U. A chemo-thermo-damage model for concrete affected by alkali-aggregate reaction. *Mech. Mater.* **41**:210–230, 2009.

[11] Fedele R., Milani G. Three dimensional effects induced by FRP-from masonry delamination. *Comp. Struct.* **93**(7):1819–1831, 2011.

IN-SITU KINEMATIC TRACKING VIA RUGGED MULTI-SENSOR MEMS UNITS

Andrin Caviezel * [1], Adrian Ringenbach[1], Miguel Sanchez[1], Marc Christen[1], Philipp Mayer[2], Michele Magno[2], Luca Benini[2], and Perry Bartelt[1]
[1]WSL Institute for Snow and Avalanche Research SLF, Davos, Switzerland
[2]ETH Zurich, Integrated Systems Lab IIS, Zurich, Switzerland

Summary The development in miniaturised microelectronic mechanical systems (MEMS) sensors during the last decade driven by growing needs for autonomous driving and unmanned aerial vehicle navigation lead to a giant performance increase. Here, we present data acquired via rugged low-power multi-sensor nodes, that have been designed to acquire and log accurate inertial sensor measurements during induced in-field experiments with falling rocks and moving avalanches. Field experiments have been carried out with several differently shaped rocks on typical terrain in the Swiss alpine region. The sensor streams are integral part of an excessive experimental campaign, studying influence of rock shape and mass. Using equally shaped rocks with masses up to 2670 kg offers for the first time systematic insights on rock kinematics and its dependence on the rock mass.

INTRODUCTION

Rockfall hazard engineers face the erratic problem of predicting runout distances, jump heights and lateral dispersion of falling rocks. The better the accuracy of this information the more reliable are the design of danger maps and the higher the cost-efficiency of protection methods such as rockfall dams and nets. With the advent of affordable and available computer power such risk assessments rely on three-dimensional rockfall modelling as standard technology. The calibration and refinement of any used model pose a challenging task and to date relies heavily on case study back calculations. Experimental trajectory analysis paired with in-situ MEMS data can help to calibrate constitutive models and/or numerical model input parameters [1]. Here, we present for the first time in-situ acceleration and gyroscope data streams covering the a mass range from 45 kg up to 2670 kg used at the experimental campaign *Chant Sura* [2] gathered over the last three summer seasons.

INERTIAL MEASUREMENT UNIT DEDICATED TO HIGH IMPACT KINEMATICS

The hardware platform used in the presented work has been under development since 2016 and has been steadily upgraded and improved. Selection of suitable MEMS is of upmost importance for a reliable and functional design of a sensor node dedicated to high impact and high speed motions. In the fast evolving electronic world, consumer grade chips in the range up to ± 16 g and ± 2000 °/s are succumbed to even shorter support times and decommissioning cycles. The used, specialised InvenSense ITG-3701 full scale range 3-axis gyroscope for high impact wearable, high speed motion applications with maximum measurment range of ± 4000 °/s as well as the STM accelerometer H3LIS331DL with its maximal range of ± 400 g have been active and supported for new designs over the last years. Both sensors allow for a sampling rate of 1 kHz, resolving the short duration impact kinematics in rock-ground or rock-net interactions. The so-called *StoneNode v4.0* is the upgraded version of an earlier design presented in Ref. [3]. The most recent layout is shown in Fig. 1a with its three- jaw fixation chuck used to place at the centre of mass of any given test block in induced rockfall experiments shown in Fig. 1b. Upgrades for extended pressure measurement options are the Bosch Sensortec BMP3870 and the STM LSPS22HH targeting consumer drone applications and therefore rather high sampling rates of 200 Hz included in redundant design in the *SnowNode* option (see Fig. 1c).

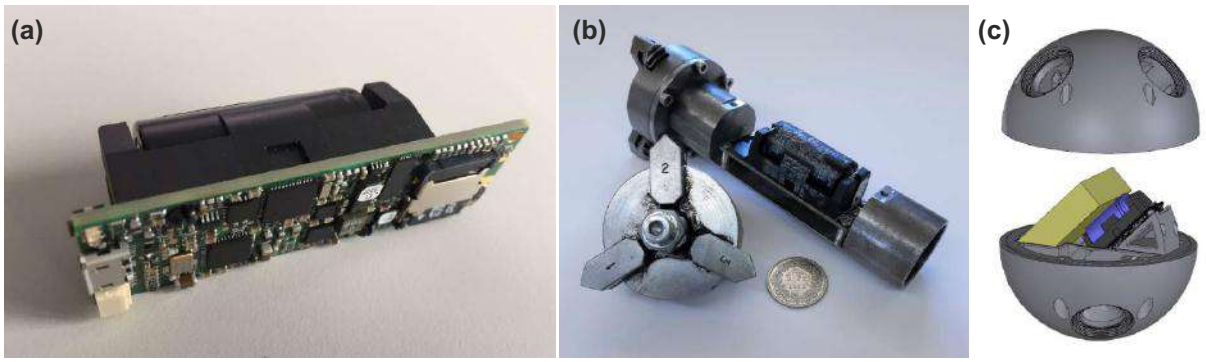

Figure 1: Dedicated inertial measurement unit for high angular velocity, high acceleration kinematics. **(a)** Assembled PCB with a 1200 mAh battery pack. **(b)** Three jaw fixation chuck with mounted IMU. **(c)** Prototype of a *SnowNode* design with barometric pressure sensor add-ons to regular IMU design for deployment in blasted avalanches. The yellow box indicates spare space for an avalanche beacon for easier retrieval.

*Corresponding author. E-mail: caviezel@slf.ch.

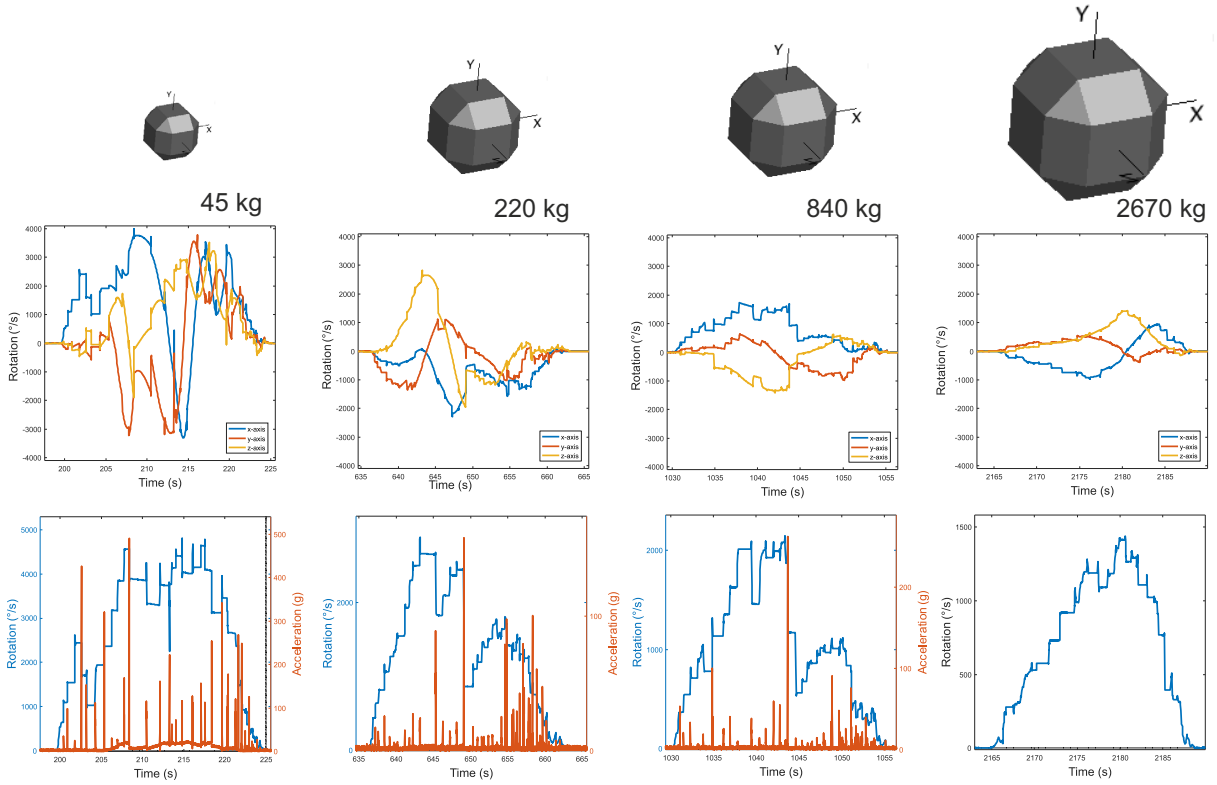

Figure 2: Dedicated inertial measurement unit for high angular velocity, high acceleration kinematics. **(a)** Assembled PCB with a 1200 mAh battery pack. **(b)** Three jaw fixation chuck with mounted IMU. **(c)** Prototype of a *SnowNode* design with barometric pressure sensor add-ons to regular IMU design for deployment in blasted avalanches. The yellow box indicates spare space for an avalanche beacon for easier retrieval.

RESULTS

Figure 2 shows the gyroscope and accelerometer sensor stream for selected runs for cubic EOTA rocks (norm rock of the European Organisation for Technical Assessment used in standardised rock fence testing procedures in official European Technical Approval Guidelines) with masses between 46 and 2670 kg collected at the *Chant Sura* test site [2]. Sensor failure prevents the acceleration data of the 2670 kg block to be present. The gyroscope plots feature a maximum ordinate range of 4000°/s, the maximum measurement range. The decrease in rotational speed owing to an ever growing moment of inertia is nicely visible. While the rotational velocity pattern of the EOTA_{45kg} and EOTA_{2670kg} feature a rather continuous increase and decrease - the pattern of a rock speeding up in a homogeneous slope and continuously rolling out due to flatter terrain - the EOTA_{220kg} and EOTA_{840kg} resultant angular velocity features sharp drops signifying heavily energy dissipating impacts. The individual nature of such an impact needs detailed analysis as such pattern can arise due to a heavily scarring impact into soft, compactable soil or due to opposing faces of rigid objects alike.

CONCLUSIONS

We present novel data from *StoneNode* IMUs a rugged low-power sensor device dedicated to the acquisition of rockfall dynamics in induced experiments. Such real scale tests are vital ingredients for the development and refinement of constitutive laws for accurate simulation models. The selected approach to deploy equally shaped rocks in different masses strives towards coming up with generic rock-terrain contact models that are independent of rock size and shape. The presented in-situ data allows do gain direct insights into the different impact behaviour caused by varying boundary conditions and configurations. The acting forces act over very short time periods and are impossible to average or linearize. Further analysis will allow to come up with empirically based laws for the rock-terrain contact and reconstruct and forecast acting forces for varying impact conditions. Future application might feature trajectory reconstruction via sensor fusion approaches complementing existing techniques based on external surveying techniques.

References

[1] Giani, G. P., Giacomini, A., Migliazza, M., and Segalini, A.: Rock Mechanics and Rock Engineering, **37**: 369–389, 2004
[2] Caviezel, A., Demmel, S. E., Ringenbach, A., Bühler, Y., Lu, G., Christen, M., Dinneen, C. E., Eberhard, L. A.,, von Rickenbach, D., Bartelt, P. Earth Surface Dynamics, **7(1)**: 199-210, 2019.
[3] Caviezel A., Schaffner M., Cavigelli L., Niklaus P., Bühler Y., Bartelt P., Magno M. and Benini L. *IEEE Trans. Instrum. Meas.* **67**: 767-779, 2018.

SIMULTANEOUS STRAIN AND TEMPERATURE FIELD MEASUREMENT TECHNIQUE BASED ON DIGITAL IMAGE CORRELATION AND THERMOGRAPHIC PHOSPHOR THERMOMETRY

Tao Cai[1], Taekyung Lee[1], Yoon Seong Park[1], Kyung Chun Kim*,[1]
[1] School of Mechanical Engineering, Pusan National University, Busan 46241, Korea

Summary: A two-dimensional (2D) phosphorescence-based strain and temperature simultaneous measurement technology is presented in this study. Here, 6 μm size MFG phosphor particles was sprayed to the surface of test target as sensor. A measurement system was established which included a high-speed camera, a 385nm LED, and a signal generator. The signal generator controls the LED to output a 100 Hz pulse light to excite the phosphor. The phosphorescence was then detected by the high-speed camera with a frequency of 10 kHz. The temperature information was obtained by the phosphorescent decay rate using lifetime method. The digital image correlation (DIC) method was then used with the random markings formed by spraying. A 100 Hz temperature and strain measurement technology is implemented based on the current experimental conditions. The measurement procedure was used for measurements of temperature and deformation of aluminum plate with pulsed current. The results from experiments showed the possibility of 2D measuring surface temperature and strain in a harsh environment with a non-invasive method.

INTRODUCTION

Temperature and strain/stress are usually highly coupled in many areas such as electronics package[1], electricity transportation[2], aerospace engine[3], new type battery[4], and so on. The acquisition of accurate temperature and stress-strain fields will help optimize the product and improve the engineering quality. Besides, an important capability is to measure both temperatue and strain/stress at the same time, which could continue to further the understanding of mechanics, suhc as thermal stress/strain. However, in many cases, the measurement environment is very harsh (high temperature, high voltage, high magnetic field), which limited access to these parameters. Therefore, a non-contact or semi-contact optical technology for multi-physics measurement of temperature and strain/stress is need to meet the needs.

DIC is an importantand widely used non-contact technique for measuring material strain[5]. It can obtain the strain information by calculating the displacement of the feature points of the two images. At present, it has been developed into two-dimensional or even three-dimensional measurement technology. Although it has been highly developed, the only access to strain information limits its application. Thermographic phosphor thermometry (TPT) is a temperature measurement technique based on the thermal dependence of phosphor luminescence[6]. Due to its non-intrusiveness, high accuracy, and high spatial resolution, TPT has clear advantages over traditional techniques, such as thermocouples, pyrometry, and infrared thermography. During the application of TP, the phosphor particles usually be sprayed onto the surface of the object to be measured. Uneven spraying will create random speckles on the surface.

Based on the speckles created by the spray, it is possible to achieve a simultaneous measurement of temperature and strain combined with DIC technique. In the present work, the lifetime method has been used to measure a two-dimensional temperature distribution. Simultaneously, the DIC will be used to caculated the strain during the temperature changes.

METHOLODLOGY

In current measurement technique, a signal generator was used to control the excitation and high-speed camera. The timing chart of excitation light (here is a UV LED) and camrea is shown in figure 1. The LED will output a f_{Ex}=100 Hz pulse light to excite the phosphor. At the same time, the high-speed camera will record the excitation and decay of the phosphorescent signal at a frequency of f_{Ca}=10 kHz. Figure 2 shows the excitation and decay of phosphorescence over two cycles using the high-speed camera. As shown in Figure 2, the temperature information could be obtained by the decay of phosphorescence. Simultaneously, using the random speckles (shown in Figure 3, right) as feature points, strain

*Corresponding author: Kyung Chun KIM. E-mail: kckim@pusan.ac.kr

information could be obtained by DIC technique. Both of the frequency of temperature and strain acquisition is 100 Hz.

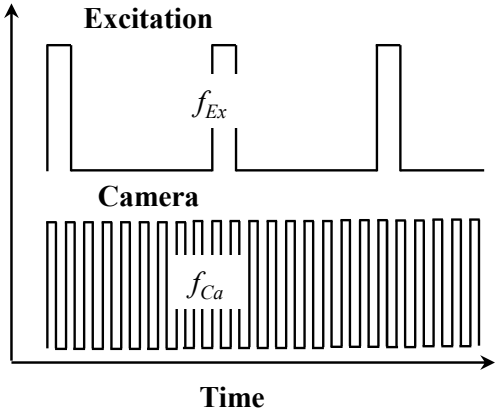

Figure 1 Timing chart

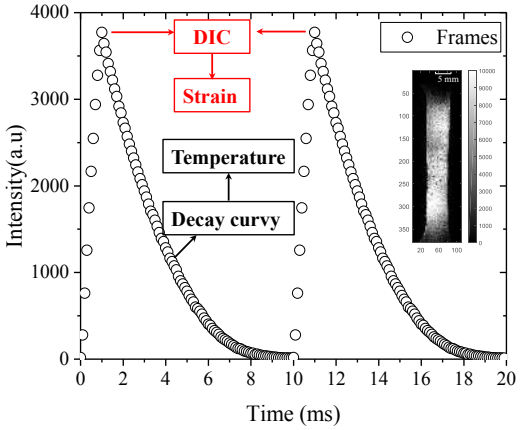

Figure 2 Schematic diagram of obtaining temperature and strain

The technique was applied in the measurement of heating and thermal strain of a aluminum strip during a high voltage current passing through it. The experimental setup was shown in figure 3. A pulse current of up to 1000 A will pass through the aluminum strip. Due to the self-existing resistance, the aluminum strip will instantly be heated up and deformed. Figure 4 shows the measured temperature and strain fields.

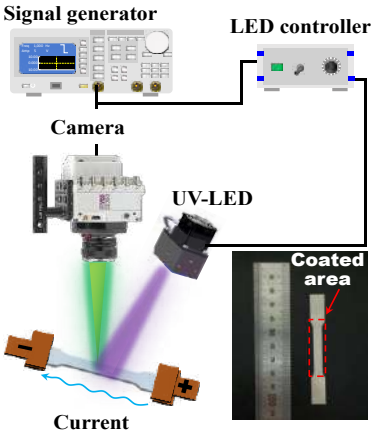

Figure 3 Experimental setup

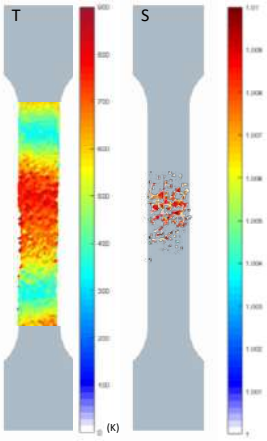

Figure 4 Measured temperature and strain

REFERENCES:

[1] Z. Zhong, S. Nah, Thermal strain analysis of an electronics package using the SEM Moiré technique, Soldering & surface mount technology, 15(2003) 33-5.

[2] C.A. Randall, A. Kelnberger, G. Yang, R. Eitel, T.R. Shrout, High strain piezoelectric multilayer actuators—a material science and engineering challenge, Journal of electroceramics, 14(2005) 177-91.

[3] R. Quentmeyer, Rocket combustion chamber life-enhancing design concepts, 26th Joint Propulsion Conference1990, p. 2116.

[4] C.-K. Lin, T.-T. Chen, Y.-P. Chyou, L.-K. Chiang, Thermal stress analysis of a planar SOFC stack, Journal of Power Sources, 164(2007) 238-51.

[5] W. Peters, W. Ranson, Digital imaging techniques in experimental stress analysis, Optical engineering, 21(1982) 213427.

[6] S. Allison, G. Gillies, Remote thermometry with thermographic phosphors: Instrumentation and applications, Review of Scientific Instruments, 68(1997) 2615-50.

P113158 - FS03 - Experimental Methods in Mechanics - Poster

A TRIBOLOGICAL SCALE DOWN FROM RIG TEST TO LAB TEST: ANALYSIS ON SRV EXPERIMENTAL RESULTS AS A SCREENING FOR FZG RIG TEST

Davide Massocchi[1]*, Marco Lattuada[2], Paolo Pennacchi[1], Steven Chatterton[1]
[1]Department of Mechanical Engineering, Politecnico di Milano, Milano, Italy [2] Eni SpA, Downstream product R&D, Milano, Italy

Summary Governments and institutions have sustainable development goals: the improvement of energy efficiency and the reduction of CO_2 emissions, in a "green economy" approach, currently become the fundamental drivers that push research and development activity towards the optimization of rotating machines components, in the industrial sector, with special focus on lubrication systems too. In order to face the numerous challenges of the future, Eni and PoliMI (Politecnico di Milano) have decided to support a doctoral research activity on the specific topic of Tribological Methodologies [1] to support the development of innovative lubricating oils. Basically, the activity is directed towards the optimization of tribological testing methods and equipment for better discriminate the performance of lubricants in operating conditions as much predictive as possible of real applications. In this context, the present paper describes the results of an experimental campaign based on the use of a well selected SRV* tribometer procedure as a screening of a rig test, the FZG** test, leading to concrete benefits as saving time and operative costs. Four cases for the determination of failure load stage of SRV have been defined and, in many cases, a good correlation with FZG rig test has been found. A very good repeatability of this method has been proven too. The aim of the authors is to continue the experimentation, thus providing a more robust evaluation also considering the impact of lubricant formulation.

Keywords: Tribological test, energy efficiency, rig test, screening

1. Method setup

A widely used test method to evaluate load carrying capacity in industrial oils is the FZG test A/8.3/90. A-type gears, wheel and pinion, are loaded stepwise in 12 load step stages from a Hertzian stress of 146 to 1841 N/mm^2. The step time duration is 15 minutes and the starting oil temperature is 90 ± 3 °C, under conditions of dip lubrication without cooling. Gear flanks are inspected after each load stage for scuffing marks. Failure load stage is indicated when the wear area detected on all pinion teeth exceeds the area of a single tooth. The Optimol method[3] aims to screen and reproduce the scuffing rig test using the SRV tribometer. The concept is to reproduce the Hertzian contact pressure used in the FGZ test rig using the cylinder on disk contact for the SRV test: the load steps for the SRV EP procedure are presented in Table 1.

FZG load step	1	2	4	6	8	10	12	14	16	18
Hertzian surface pressure [N/mm²]	146	295	621	929	1223	1539	1841	2170	2465	2777
SRV® normal force [N]	7	28	126	282	489	774	1107	1538	1985	2520

Table 1 Loads of SRV procedure according to Hertzian contact pressure in FZG loads steps[2]

The duration of each step is 217 seconds, which is a result of prior investigations [5]. The conditions for the step test are the following: the temperature is 98°C, stroke is 2 mm and frequency is 50 Hz. We have defined threshold values of some parameters for test execution, the so-called cut-off values. In particular, for this experimental campaign we set the following cut-off values of COF and stroke: 0.3 as maximum COF and a stroke deviation of maximum 55%. We fixed these values for two main reasons: on one hand for safety operation, as to quickly block test run while high seizure occurs; on the other, the above limits selected allow us to detect also microseizures and seizure (of limited intensity) helping in the qualitative analysis of COF profile. The SRV (Fig. 1) is a very versatile device for measuring the coefficient of friction and the wear and EP characteristics of lubricating oils and greases under various operating conditions. In addition to the standard tests this equipment is very well suitable for in-house tests in order to simulate, on a laboratory scale, operating conditions that often occur in operation of machinery/components/circuits. For the evaluation criteria of oil performances and failure load stage assignment, in our experimental campaign we defined four cases described in the third section.

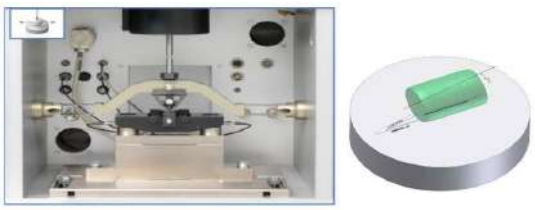

Fig. 1 SRV tribometer & Cylinder on disk[3]

2. Experimental campaign

The coupling selected, for the experimental campaign, is cylinder on disk. The lower specimen is a disk Ø 24 x 7.9 mm, made of hardened rolling bearing steel AISI 52100 / 100Cr6. The upper surface is polished and aligned at 10° to the direction of movement along its longitudinal axis (cf. Fig. 1). The lubricants tested are commercial gear oils, turbine oils and circulating oils. Specimens' surfaces were ultrasonically cleaned in ethanol for 5 min; after mounted and locked with a torque wrench with a load of 30N. We use the SRV EP procedure with the only difference of temperature (T = 90°C instead of 98°C). A very small amount of oil sample is needed and the operator should dry both the upper and lower specimens during the setting phase. The procedure is done for each oil for a minimum of three repetitions and is defined as good repeatability a difference of ± 1 stage.

*SRV stands for Schwingung (Oscillating), Reibung (Friction), Verschleiž (Wear)
* *FZG stands for "Forschungsstelle fur Zahnrader und Getriebebau", the Technical Institute for the Study of Gears and Drive Mechanisms

3. Experimental results discussion and conclusion

In this section we present in detail some experimental results and we discuss the relationship between rig test and laboratory test. Fig. 2 shows the simplest case: during the test we detect the presence of a net COF peak; in correspondence of this the tested oil reaches the failure load stage. In Fig. 3, in the last steps, we see an increase in the COF profile without huge peak or multiple small peaks and any thickening of the curve; for this reason, we can conclude that the oil has passed all steps of the procedure. In our campaign we assign to this oil an SRV failure load stage >12, even if the stages of SRV procedure are 17. In fact, in order to be comparable to FZG, it is enough for us that it exceeds the 12th SRV stage (so that, if the SRV failure load stage is greater than 15th or reaches the end, it would not be so relevant). In Fig. 4 we see a lot peaks attributable to microseizures phenomena in the final steps; after the first microseizure, the COF curve presents other peaks of higher intensity. In our analysis we assign the failure load stage at the stage where a series of microseizures occurs and continues for at least few seconds. In Fig.5 we see a special and unique case in our experimentation. At the middle of the test, COF profile changes, becoming flat and reaching high values as in the first steps. This behavior has occurred quite exactly in all the test repetitions. We categorize this report as Case 4.

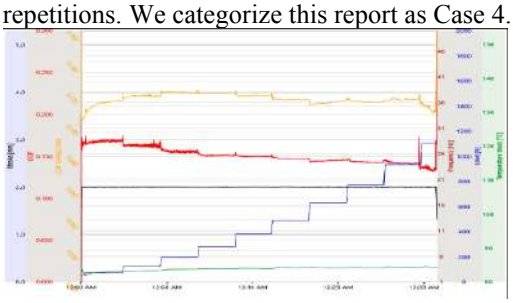

Fig.2 Case 1: example

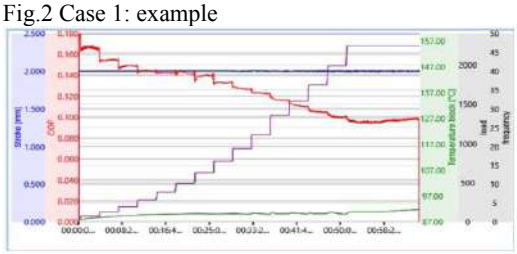

Fig.3 Case 2: example

Oil type	Viscosity grade	SRV failure load stage	FZG failure load stage
gas turbine oil	ISO VG 15	11	12
gas turbine oil	ISO VG 32	11	12
gas turbine oil	ISO VG 46	12	12
turbine oil	ISO VG 46	8	9
gear oil	ISO VG 320	>12	>12
gear oil	ISO VG 460	>12	>12
circulating oil	ISO VG 68	>12	>12
circulating oil	ISO VG 68	n.d.	12
circulating oil	ISO VG 68	>12	n.a.
circulating oil	ISO VG 68	>12	12

Table 2 Experimental results: tribo and rig tests

In Table 2 we report the results of SRV test, as an average value between the repetitions we carried out for each oil and in the last column FZG data to easily compare both machines tests. For only one product we do not have FZG data and for one oil we do not assign the SRV failure load stage (it belongs to case 4). For the others we notice a difference of only ± 1 stage and based on this, a good correlation between SRV and FZG tests has been found, appropriately distinguished in the cases previously identified (the oils tested mainly belong to case 1 and 2).

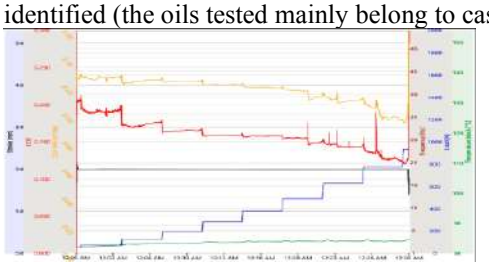

Fig.4 Case 3: example

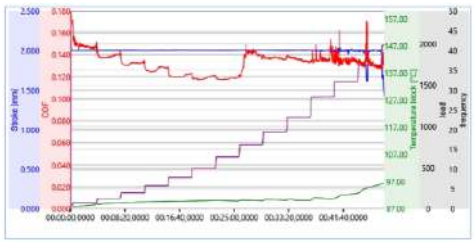

Fig.5 Case 4: example

The aim of the authors is to continue the experimentation by using other procedures and investigate the impact of lubricant formulation: to predict, estimate or determine synergistic/antagonistic effect of oil components. The results obtained and those that we are going to collect in the next experimental activity provide useful preliminary indications on the behavior of the lubricant thus helping a formulator in a lubricating oil development. Finally, from the work carried out, the importance of optimizing tribological test methods really emerges: advantages from the point of view of product development and final machine performance, being an extremely useful tool for the constant improvement of the energy efficiency of modern industrial systems.

References

[1] Massocchi, D.; Lattuada, M.; Assanelli, G.; Pennacchi, P. E. L. M.; & Chatterton, S. Nuove metodologie di testing a supporto dello sviluppo di oli lubrificanti “energy-saving” per applicazioni industriali. In 7° Workshop AIT “Tribologia e Industria”, 2020.

[2] Chatterton, S.; Pennacchi, P.; Vania; A.; De Luca, A.; & Dang, P. V. Tribo-design of lubricants for power loss reduction in the oil-film bearings of a process industry machine: Modelling and experimental tests. Tribology International, 130, 133-145, 2019.

[3] Baumann, C.; Patzer, G. Screening Engine Oils Using Piston Parts on a Translatory Oscillation Tribometer (SRV®). 한국윤활학회 학술대회, 75-76, 2018.

[4] Lattuada, M.; Manni, M. A new methodology for the experimental evaluation of organic antifriction additives, ISFL, International symposium on fuel and lubricants, New Delhi, 2016.Hoehn, B.-R.; Michaelis, K.; Oster, P. New Test Methods for the Evaluation of Wear, Scuffing and Pitting Capacity of Gear Lubricants. AGMA, 1998.

[5] Patzer, G.; Ebrecht, J.; Vorstellung eines Pruefkonzepts als Screeningmethode für Getriebeoele auf dem translatorischen Oszillationstribometer (SRV®); Tribologie + Schmierungstechnik, expert Verlag, Renningen, Germany; 63, 2/2016.

FABRICATION OF 2D DENSE SUSPENSIONS OF SOFT PARTICLES IN MICROFLUIDIC CHANNELS

Lars Kool[1], K. Lawrence Galloway[2], Paulo Arratia[2], and Anke Lindner*[1]
[1]Laboratoire de Physique et Méchanique des Milieux Hétérogènes, ESPCI, Paris, France
[2]Department of Mechanical Engineering and Applied Mechanics, University of Pennsylvania, Philadelphia, PA, USA

Summary To properly understand the macroscopic response of soft particle glasses to stress/strain, an understanding of the material microstructure and its dynamics upon exposure to stresses is required. Here, we present a versatile experimental system to study the microstructure and dynamics of 2D hydrogel ensembles as function of the applied stress. This system is based on the in-situ fabrication of PEGDA hydrogel particles by UV-crosslinking. When a stress is applied, by flowing uncured solution over and under the particles, the packing compresses. We were able to extract several microstructural quantities, such as inter-particle forces and excess entropy, as well as several dynamical quantities, such as D^2_{min} and visco-elastic timescales. This experimental model system could give key insights in the connection between the microstructure and dynamics of soft particle glasses.

INTRODUCTION

Soft particle glasses (SPG's) are ubiquitous, from emulsions and foams, to pastes and dry food products, and are therefore of great industrial relevance. Over the last decades, our knowledge on SPG's has increased significantly, thanks to both numerical and experimental studies. However, experimental studies focus mainly on the macroscopic response of the SPG's to stress/strain, whereas microscopic studies have received much less attention, as they have proven to be difficult or require expensive equipment, like X-ray or NMR machines. But, for a proper interpretation of the macroscopic measurements, an understanding of the material microstructure and its response to forces and stresses is required. Another problem that arises while studying the effects of particle softness, is that it is complicated to isolate the effects of just the particle softness. As changing the Young's modulus often requires to change the material, which inevitably lead to changes in properties like friction coefficient, surface roughness, and/or interparticle interactions. Here, we present an experimental system with an unprecedented degree of control. By fabricating hydrogel particles inside a microfluidic channel, we can control shape and size of the system, as well as the size, shape, and Young's modulus of the particles with little to no additional effort. This method will allow us to isolate the effects of particle softness on the response of SPG's to compressive stress.

METHOD

Experimental sytem

In our experiments, the particles are contained inside a microfluidic device, made by casting poly-dimethylsiloxane (PDMS) over a positive master mould. The casted PDMS is then bonded to a PDMS coated glass slide to form the final microfluidic device (Figure 1A). As PDMS is porous to gases, our microfluidic devices allow for the diffusion of oxygen into the PEGDA solution. This locally inhibits the UV-polymerization reaction, causing the particles to not stick to the channel walls. By placing a wall with small perforations near the outlet of the microfluidic channel, we created a uni-axial compression system (Figure 1B). However, this wall can also easily be fitted with an orifice to form a silo, or angled to form a hopper (Figure 1C)

Figure 1: A) Schematic representation of the hydrogel particle fabrication (Adapted from Bechert et al. 2019 [2]). B) Example of a channel that can be used for compressional experiments. C) Example of a 2D hopper in a microfluidic channel. D) Typical packing of bidisperse particles.

*Corresponding author. E-mail: anke.lindner@espci.fr

Soft particles

The soft hydrogel particles were fabricated in-situ by UV-crosslinking polyethylene glycol diacrylate (PEGDA) (Figure 1A). The UV-light first passes through a shutter, to control the exposure of the solution to UV-light. Then, the light passes through the field-stop position. By placing a mask in the field stop position of the microscope, we are able to give the particle the desired size (ranging from as small as $\sim 10\ \mu m$ to several mm), as well as shape (Figure 2C) [1]. Finally, the light passes through the objective of the microscope, which focusses the UV-light on the desired spot in the channel. The Young's modulus of the particles can be controlled over 3 orders of magnitude (between $\sim$ 10 kPa and $\sim$ 10 MPa), by either changing UV-exposure time and/or by diluting the PEGDA solution with polyethylene glycol (PEG) [3]. By moving the focal spot through the channel using an automated stage, we fabricated large ensembles ($\sim$ 2000 particles) of these particles, with initial configuration obtained from DEM or MD simulations (Figure 1D).

RESULTS & OUTLOOK

We are able to impose a hydrodynamic compressive force on the packing, by imposing a flow of uncured PEGDA solution over and under the particles using a pressure controller, allowing for step stress and oscillatory compression experiments. An add advantage of our system is that one can interrogate the material microstructure, as a function of the applied forc. This allows us to obtain microstructural quantities such as the force network (calculated using Hertzian contact theory, Figure 2A-C) and excess entropy (calculated from the pair correlation function), and link them to dynamical quantities such as local rearrangements (quantified by the local non-affine deformation D^2_{min}, Figure 2D) and relaxation timescales (obtained from step-stress/relaxation experiments, Figure 2E). For example, we observed an anisotropy in the average interparticle force (a microstructural quantity, Figure 2C), which is not expected in the quasi-static regime. We hope to be able to link this dynamical quantities, such as the difference in visco-elastic time-scales or a possible anisotropy in the number of local rearrangements during compression and decompression.

We envision that this technique could play a key role in determining the development of an (empirical) microstructural model to describe the behavior of granular materials and the influence of particle softness and particle shape, on the behavior of granular materials, by linking material microstructure to its dynamics.

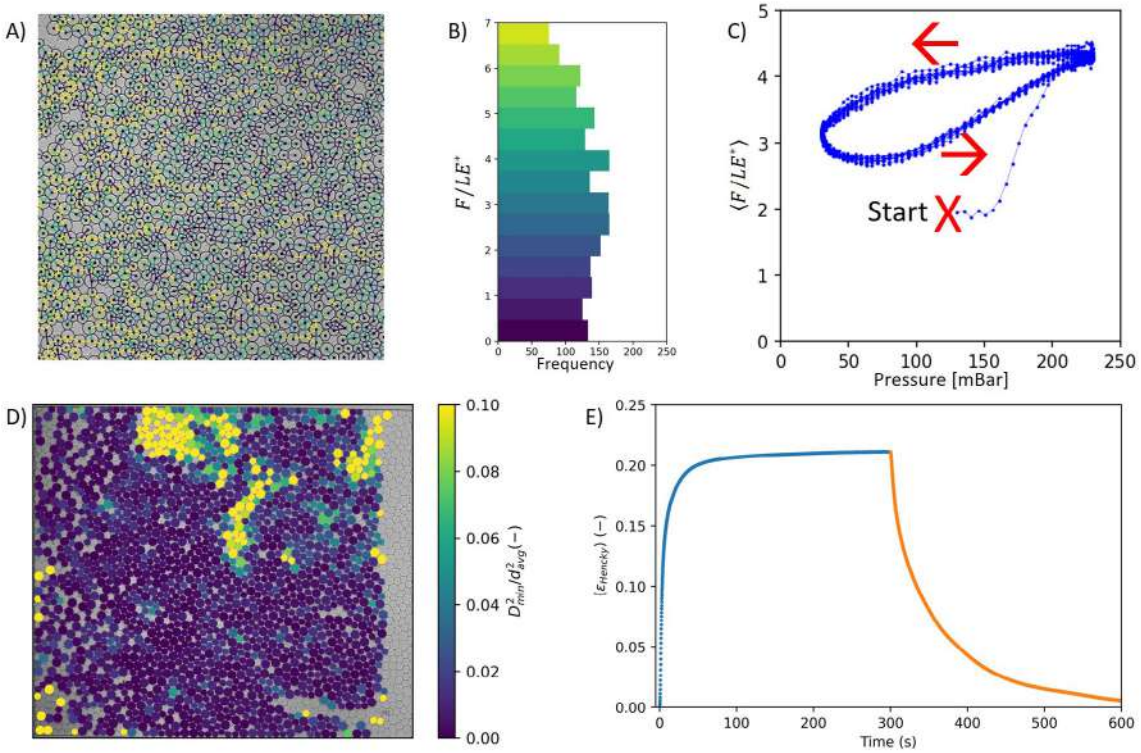

Figure 2: A) Visualization of the local rearrangements (quantified by D^2_{min}) during oscillatory compression experiments. B) Strain response over time after a step stress (blue), and step relaxation (orange). C) Visualization of the force network, as calculated from the interparticle distances (colorbar identical to Fig. 2D. D) Histogram of the observed interparticle forces in Fig. 2C. E) Average interparticle force, as function the applied pressure.

References

[1] Dendukuri et al., Continuous-flow lithography for high-throughput microparticle synthesis, *Nature materials*, **5(5)**, 365-369, 2006
[2] Bechert et al., Controlling transport dynamics of confined asymmetric fibers, *EPL*, **126**(4): 44001, 2019
[3] Cappello et al., Microfluidic In-Situ Measurement of Poisson's Ratio of Hydrogels, *Micromachines*, **11**(3): 318, 2020

DETERMINING COMPLEX SPATIAL PATTERNS DURING CRYSTALLISATION OF SOFT MATTER

Priya Subramanian * [1] and Alastair Rucklidge[2]
[1]Mathematical Institute, University of Oxford, Oxford UK
[2]School of Mathematics, University of Leeds, Leeds UK

Summary Soft matter systems display a wide range of spatial patterns as asymptotic states during crystallisation and can be modelled as a pattern forming system governed by a conserved dynamics. Traditional first tools for analysis of such pattern forming systems include linear stability analysis and a weakly nonlinear analysis. In addition, numerical continuation and direct simulations can be employed to determine invariant solutions. In this work, we show that combining equivariant bifurcation theory and numerical continuation with numerical algebraic geometry allows us to determine all solutions with a chosen symmetry subgroup. We explore the advantages of this method in identifying co-existing metastable states, unearthing invariant solutions with reduced symmetry and in identifying parameter regimes with multiple solutions.

Soft matter such as polymers crystallise when cooled from a melt and can self-assemble into a variety of spatially complex patterns [1]. Phase field crystal (PFC) models that include information about small length scales and operate over diffusive time scales have been employed to model the crystallisation of soft matter [2]. This PFC model is also known as the conserved Swift-Hohenberg equation. When analysing this model beyond linear stability thresholds using a weakly nonlinear analysis, the resulting normal form equations are usually in the form of coupled ordinary differential equations (ODEs) for the amplitudes of the active modes, i.e., modes that are growing or neutrally stable.

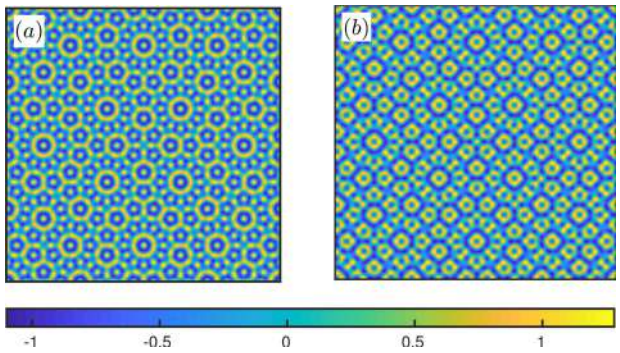

Figure 1: Figure 1: Variation of scalar density in a 2D soft matter system modelled using in a PFC model showing co-existing dynamically stable dodecagonal quasicrystal states.

We use homotopy methods from numerical algebraic geometry to solve for all solutions of the chosen amplitude equations in a non-iterative method [3]. Solutions obtained this way are used as initial guesses for numerical continuation to determine invariant solutions to the full model. Starting with dodecagonal symmetry in 2D, we discover multiple co-existing metastable states at the same parameters with the same symmetry as shown in Figure 1 (a) and (b).

Effects of broken symmetry can also be investigated robustly by solving amplitude equations corresponding to reduced symmetry subgroups. In Figure 2, we show results obtained from starting with full 3D icosahedral symmetry and relaxing constraints to investigate states with different reduced symmetries. We obtain four different metastable states: two different periodic stackings of 2D decagonal QCs, an aperiodic stacking of 2D decagonal QC and the globally stable fully symmetric 3D icosahedral QC at the same parameter combination.

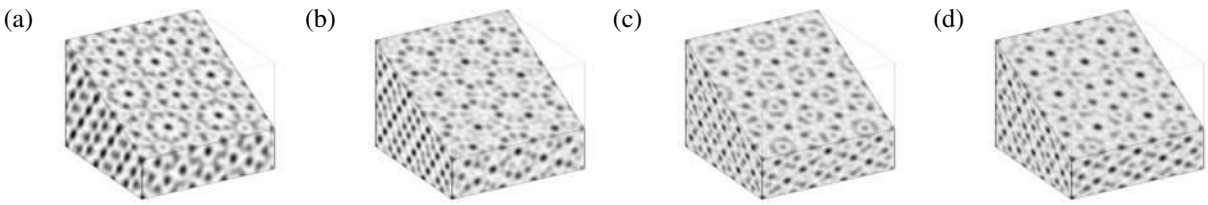

Figure 2: Variation of scalar density in a 3D soft matter system modelled using in a PFC model, sliced along the plane (1.618, 0, 1) for extended dynamically stable states of (a) a periodic stacking of 2D decagonal QC with large stacking wavelength, (b) a periodic stacking of 2D decagonal QC with small stacking wavelength and (c) an aperiodic stacking of 2D decagonal QC and (d) a fully symmetric icosahedral QC.

Combining equivariant bifurcation theory along with numerical algebraic geometry allows us to obtain multiple co-existing metastable states with same symmetry properties, obtain solutions for reduced symmetry subgroups and makes it feasible to probe multi-parameter ranges in pattern forming system to identify interesting parameter regimes with multiple invariant solutions.

References

[1] Zeng X, Ungar G, Liu Y, Percec V, Dulcey A. E., Hobbs J. K. Supramolecular dendritic liquid quasicrystals. *Nature* **428**: 157-160, 2004.
[2] Subramanian P, Archer A. J., Knobloch E., Rucklidge A. M. Three-dimensional icosahedral phase field quasicrystal. *PRL* **117**: 075501, 2016.
[3] Bates D. J., Hauenstein J. D., Sommese A. J., Wampler C. W. Bertini:Software for Numerical Algebraic Geometry. SIAM, Philadelphia 2013.

*Corresponding author. E-mail: priya.subramanian@maths.ox.ac.uk

INVARIANT SOLUTIONS UNDERLYING LOCALIZED BURSTING SPOTS IN INCLINED CONVECTION

Florian Reetz[1] and Tobias M. Schneider * [1]
[1]Emergent Complexity in Physical Systems Laboratory (ECPS), École Polytechnique Fédérale de Lausanne, Lausanne, Switzerland

Summary Convection in a fluid layer inclined against gravity exhibits a large variety of flow patterns including intermittent bursting spots. Here localized regions of strong convection spontaneously emerge in a regularly patterned background and subsequently decay. We identify exact invariant solutions of the nonlinear flow equations underlying the transiently emerging bursting spots and thereby rationalize both temporal and spatial properties of the observed convection pattern. This work highlights the power of nonlinear dynamical systems approaches for explaining patterns in driven dissipative systems well above the onset of linear instability.

INTRODUCTION

Thermal convection in a fluid layer inclined against gravity shows a large variety of self-organized flow patterns. As a function of the externally controlled temperature difference or Rayleigh number Ra, the inclination angle γ and the material dependent Prandtl number Pr patterns of various complexity ranging from unpatterned laminar flow and spatially periodic stationary convection rolls to spatio-temporal chaos and turbulence are observed in experiments and simulations [1].

For $\mathrm{Pr} = 1.07$ (compressed CO_2) and an inclination of $\gamma = 78°$, the laminar base flow loses stability to two types of stationary convection rolls, longitudinal rolls (LR) aligned with the incline and transverse roles (TR) oriented in perpendicular direction, at almost identical critical values of $\mathrm{Ra}_c = 8078$. Above the critical threshold, for $0 < \epsilon < 0.1$ with $\epsilon = \mathrm{Ra}/\mathrm{Ra}_c - 1$, a spatio-temporally intermittent convection pattern is observed, previously termed 'transverse bursts' [2]. The bursting phenomenon is characterised by spatially localized spots of intense convection that transiently emerge and decay within a background of weak longitudinal rolls. The aim of the present study is to explain these *bursting spots* including their two key features: (i) Intermittent time evolution of spontaneously arising and decaying bursts of convection and (ii) spatial localization of a chevron-like convection pattern within a background of longitudinal rolls.

INTERMITTENT TIME EVOLUTION

Following the recent identification of exact invariant solutions of the three-dimensional Oberbeck-Boussinesq equations underlying less complex spatially periodic patterns at other values of the control parameters [3, 4], we here describe two unstable equilibrium solutions whose dynamical connection supports the temporal dynamics of bursting spots. A chevron equilibrium (CH) is identified that captures the internal structure of the spots and coexists with the longitudinal roll equilibrium (LR) in the state space of the system. In a doubly periodic domain of extent $[L_x, L_y, H] = [4.5, 4, 1]$,

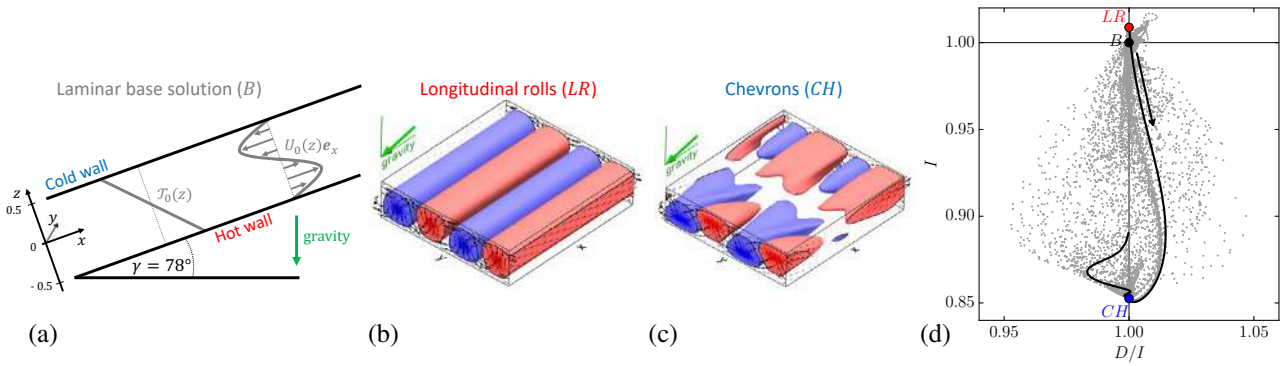

Figure 1: The intermittent temporal dynamics of bursting spots in ILC at $\epsilon = 0.05$ transiently visits three unstable equilibrium solutions: (a) the schematically shown laminar base solution, B, (b) longitudinal rolls, LR, (c) a previously unknown chevron equilibrium solution, CH, resembling the core pattern of bursting spots. The 3D contours illustrate temperature fluctuations around B. In panel (d), a two-dimensional state space projection (I: energy input, D: dissipation) of a simulated state vector trajectory reveals intermittent dynamics shadowing a dominant dynamical connection $LR \to CH$ (black curve). Since CH is a saddle point, the dynamics departs from CH following a decaying chaotic trajectory (only the initial part of the trajectory is shown). The background point cloud, extracted from a long simulation over 10 000 free fall time units, illustrates the chaotic attractor. Equilibrium solutions and time evolution are computed using the open-source spectral code *Channelflow-ILC* [5] at control parameters $[\gamma, \mathrm{Pr}, \epsilon] = [78°, 1.07, 0.05]$ in a doubly periodic domain of extent $[L_x, L_y, H] = [4.5, 4, 1]$.

*Corresponding author. E-mail: tobias.schneider@epfl.ch.

both equilibria are dynamically unstable. State space projections of the simulated time evolution indicate that the chaotic trajectory shadows a dominant rapidly traced dynamical connection $LR \rightarrow CH$. The trajectory than slowly departs from the unstable chevron equilibrium along a complex trajectory and decays towards LR from where the next burst $LR \rightarrow CH$ is triggered (Figure 1). Thus, both unstable equilibrium solutions together with their dynamical connection support the observed intermittent temporal dynamics of the bursting spots.

LOCALIZATION IN SPACE

To explain the dynamics of *spatially localized* bursting spots, invariant solutions must capture the spatial coexistence of the chevron pattern and the longitudinal rolls. We construct localized variants of the chevron equilibrium by extending the lateral size of the numerical domain, first in the spanwise direction and then in both, spanwise and streamwise direction. The constructed collection of spanwise and doubly localized invariant solutions includes equilibrium solutions, traveling waves and periodic orbits that all capture the localized pattern of bursting spots. Numerical continuation of these unstable invariant solutions in ϵ traces their solution branches and reveals their subcritical bifurcations from the spatially periodic CH solution. Moreover, the solutions branches continue to control parameters where laminar ILC is linearly stable, $\epsilon < 0$. There, the branches undergo homoclinic snaking which changes the number of localized chevron structures and leads to spot patterns of arbitrary size (Figure 2). Consequently, pattern forming bifurcations create localized invariant solutions capturing the spatial coexistence of two types of convection patterns as observed within bursting spots.

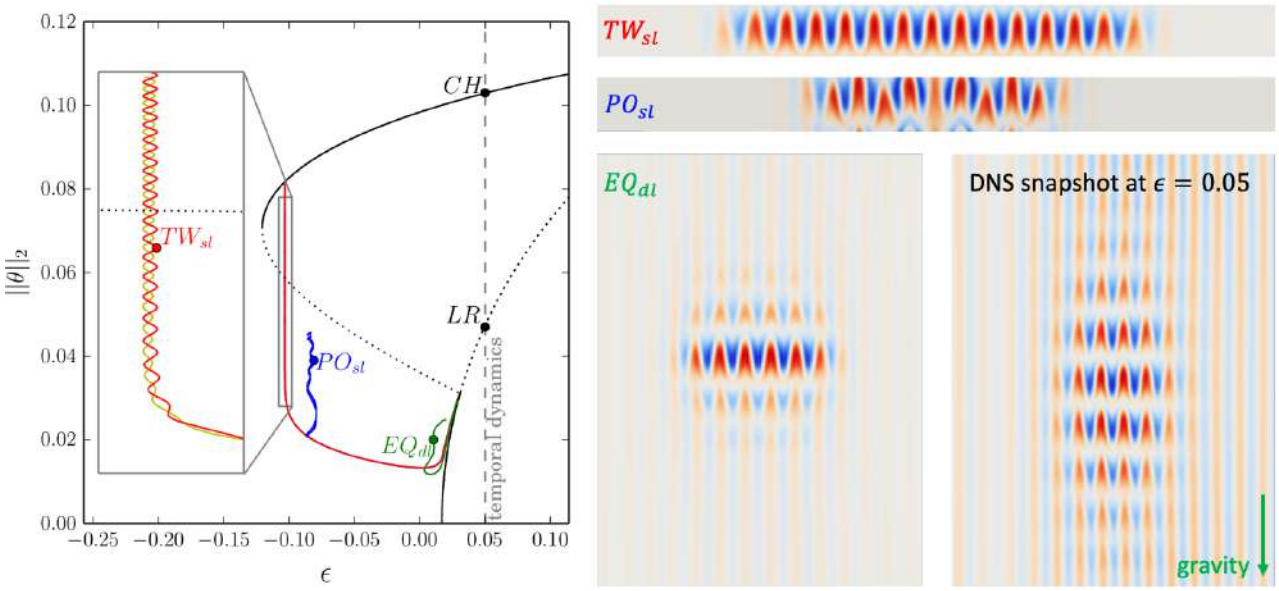

Figure 2: Subcritical bifurcations give rise to spatially periodic, spanwise localized (sl), and doubly localized (dl) variants of the chevron equilibrium, CH. Localized invariant solutions include equilibria (EQ), traveling waves (TW) and periodic orbits (PO). Selected invariant solutions along the branches are visualized in terms of midplane temperature contours and compared to a snapshot from a direct numerical simulation (DNS) in a large domain. While TW_{sl} undergoes regular snaking bifurcations, the spanwise localized periodic orbit, PO_{sl}, and the doubly localized equilibrium EQ_{dl} undergo irregular snaking bifurcations. $||\theta||_2$ is the norm of the temperature fluctuations around B.

CONCLUSIONS

The discussed exact invariant solutions of the nonlinear flow equations capture both temporal and spatial properties of bursting spots in inclined layer convection. This work highlights the power of fully nonlinear dynamical systems approaches for explaining patterns in driven dissipative systems well above the onset of linear instability.

References

[1] Subramanian P., Brausch O., Daniels K. E., Bodenschatz E., Schneider T. M., Pesch W. Spatio-temporal patterns in inclined layer convection. *J. Fluid Mech.* **794**: 719-745, 2016.

[2] Daniels K. E., Wiener R. J., Bodenschatz E. Localized transverse bursts in inclined layer convection. *Phys. Rev. Lett.* **91**: 114501, 2003.

[3] Reetz F., Schneider T. M. Invariant states in inclined layer convection. Part 1. Temporal transitions along dynamical connections between invariant states. **arXiv:1911.02836**.

[4] Reetz F., Subramanian P., Schneider T. M. Invariant states in inclined layer convection. Part 2. Bifurcations and connections between branches of invariant states. **arXiv:1911.02873**.

[5] Channelflow 2.0, web site **http://www.channelflow.ch**.

FARADAY PILOT WAVES IN A CAVITY: A HYDRODYNAMIC CORRAL

Paul A. Milewski * [1] and Matthew Durey[2]
[1]Department of Mathematical Sciences, University of Bath, Bath, UK
[2]Department of Mathematics, MIT, Cambridge, USA

Summary Millimetric droplets may bounce periodically on the surface of a vertically vibrating bath of the same fluid, each impact exciting a wave-field subcritical Faraday waves. The cumulative generated wavefield can then guide the droplet's horizontal motion, providing the system with memory of both the past path and the geometry of the fluid domain. In particular, the droplet may be confined by a submarine "corral" which modulates the Faraday waves. Experiments show that this configuration can lead to dynamics bearing striking resemblance to quantum mechanical corrals. We describe a framework for understanding the fluid dynamical problem that is derived from first principles, and is simple enough for mathematical and efficient numerical treatment.

EXTENDED ABSTRACT

A millimetric droplet may bounce periodically on the surface of a vertically vibrating bath of the same fluid; the thin air layer separating the droplet from the bath during impact prevents coalescence. Each impact excites a wave-field consisting primarily of subcritical temporally decaying (due to viscous effects) Faraday waves, whose longevity depends inversely on the closeness of the shaking strength to the Faraday instability threshold (Couder et. al. 2005). As the shaking strength increases, and due to the generated wavefield, the bouncing destabilizes to horizontal "walking" across the bath, whereby the droplet is propelled at each impact by the slope of its associated Faraday wave field generated at previous impacts. In the walking regime the droplet may then be confined by either an external field or by submarine "corral" topography that modulate the Faraday wavefield and hence modify the path of the drop (Harris et. al. 2013). In this context, the decay time of the Faraday waves result in a "path-memory" of previous impacts, which encode the topographical information of the domain (Fort et. al. 2010).

The resulting non-Markovian dynamics are similar in many respects to the pilot-wave dynamics envisaged by de Broglie as a physical framework for understanding quantum mechanics (Bush 2015).

We have developed a hydrodynamic pilot-wave model, formulated from first principles, that exhibits the behaviour observed in the laboratory experiments. In describing the wave field, our approach is a linear quasi-potential flow description inspired by the inviscid theory of Benjamin & Ursell (1954), with viscous damping being incorporated in the manner outlined by Lamb (1932). The droplet-bath interaction, in its simplest form, is modelled with a periodic, instantaneous and localised impact on the surface. These allow for an elegant reduction of the full hydrodynamic coupled system to period map to account for the fluid evolution followed by jump conditions at each impact that generate the new waves and guide the horizontal trajectory of the particle (see Durey & Milewski 2017). The model is sufficiently simple for a mathematical study of the bifurcations and stability of the system.

This model can be simulated very efficiently and is therefore appropriate for elucidating certain statistical long-time behaviour inaccessible to more detailed computations of impact wave generation such as those of Milewski et. al. (2015) or Galeano-Rios et. al (2017, 2019). For example, we can show that in confined states and near the Faraday threshold, a mean hydrodynamic pilot wave field arises from the stationary distribution of droplet positions. We prove a relation between the droplet position distributions and this mean wave-field, rationalising aspects of the dynamics at high memory (Durey et. al. 2018). All prior realistic fluid dynamical simulations of this system were based on a fluid domain without underlying geometry where the droplet was trapped by an external potential instead.

Herein we present the first model capable of the capturing the dynamics in a corral that confines the droplet. The corral consists of a cavity with a deep cylindrical region surrounded by shallow region which prevents the particle and waves to propagate into it (see Figure 1). We use a domain decomposition method to compute the Dirichlet to Neumann map for the velocity potential at the surface, which allows us to compute the cavity wave modes of the system. We can then apply the above-described discrete methods to generate waves at each impact and evolve the pilot wave system achieving efficient simulation speeds. We find all the states described experimentally and some new ones: centre and off-centre

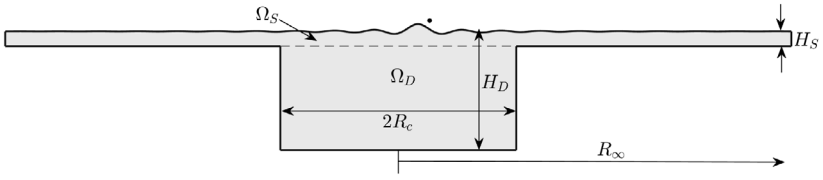

Figure 1: Geometry of cylindrical hydrodynamic corral.

*Corresponding author. E-mail: p.a.milewski@bath.ac.uk

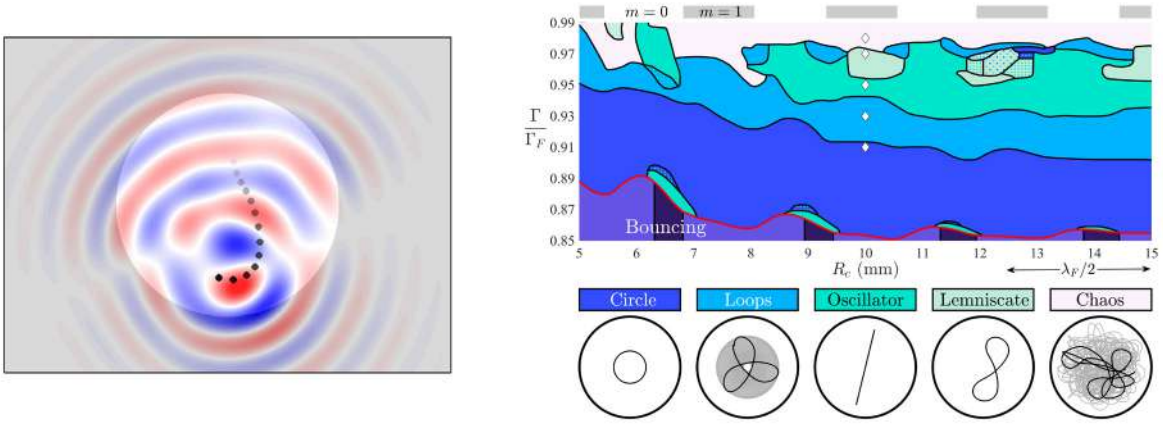

Figure 2: Left: Typical trajectory at intermediate memory showing droplet path and Faraday pilot waves. Right: Diagram indicating various observed dynamics as a function of corral radius and forcing strength.

bouncers, circular orbits, oscillators, lemniscates, n-foils and chaotic motion. A typical trajectory and wave-structure, together with a summary of the behaviour of the system for varying corral radii and forcing is shown in Figure 2. We deduce the stability of the trajectories, compare these trajectories to experimental works, and rationalise the observations, in particular we highlight the importance of whether the most unstable mode is axisymmetric. We compare some features of the dynamics to the case without topography, but instead with an external potential. Finally, in the chaotic regime, we obtain droplet distributions that have some spatial structure but do not reproduce the "cavity mode" feature seen in experiments. We postulate that the differences between our model and experimental results arise from the assumption of periodic impacts and discuss how to remove this assumption in the model.

References

[1] Benjamin, T. B. & Ursell, F. 1954 The Stability of the Plane Free Surface of a Liquid in Vertical Periodic Motion. Proc. R. Soc. Lond. A 225, 505–515.

[2] Bush, J. W. M. 2015 Pilot-Wave Hydrodynamics. Annu. Rev. Fluid Mech. 47, 269–292.

[3] Couder, Y., Fort, E., Gautier, C.-H. & Boudaoud, A. 2005a From Bouncing to Floating: Noncoalescence of Drops on a Fluid Bath. Phys. Rev. Lett. 94, 177801.

[4] Durey, M. & Milewski, P. A. 2017 Faraday wave-droplet dynamics: discrete-time analysis. J. Fluid Mech. 821, 296–329.

[5] Durey, M., Milewski, P. A. & Bush, J. W. M. 2018 Dynamics, emergent statistics, and the mean-pilot-wave potential of walking droplets. Chaos: An Interdisciplinary Journal of Nonlinear Science 28 (9), 096108.

[6] Fort, E., Eddi, A., Boudaoud, A., Moukhtar, J. & Couder, Y. 2010 Path-memory induced quantization of classical orbits. PNAS 107 (41), 17515–17520.

[7] Galeano-Rios, C. A., Milewski, P. A. & Vanden-Broeck, J.-M. 2017 Non-wetting impact of a sphere onto a bath and its application to bouncing droplets. J. Fluid Mech. 826, 97–127.

[8] Galeano-Rios, C. A., Milewski, P. A. & Vanden-Broeck, J.-M. 2019 Quasi-normal free-surface impacts, capillary rebounds and application to Faraday walkers. J. Fluid Mech. 873, 856–888.

[9] Harris, D. M., Moukhtar, J., Fort, E., Couder, Y. & Bush, J. W. M. 2013 Wavelike statistics from pilot-wave dynamics in a circular corral. Phys. Rev. E 88, 011001.

[10] Milewski, P.A., Galeano-Rios, C.A., Nachbin, A. & Bush, J.W.M. 2015 Faraday Pilot- Wave Dynamics: Modelling and Computation. J. Fluid. Mech 778, 361–388.

SURFACTANTS DRIVEN OUT OF EQUILIBRIUM BY A FLOW

Shreyas Mandre* [1]
[1]Mathematics Institute, University of Warwick, Coventry UK

Summary The description of the flow driven only by a point source of surfactant is complicated by the multitude of the surfactant's physico-chemical parameters. The value of these parameters in practice depends on the local surfactant concentrations, which in turn depends on the flow. For flow driven by a point source of surfactant, the radial velocity decays as r^n, where two values of n, $-3/5$ and -1, are experimentally observed. Previous work (J. Fluid Mech., 832, 777-792, 2017; Phys. Rev. Lett, 119, 26501, 2017) has explained the exponents through two different surfactant models, without the knowledge or estimation of any of the surfactant physico-chemical parameter. Here we present a unified model for the surfactant, where the two exponents are realized as two asymptotic limits.

INTRODUCTION TO SURFACTANTS

Surfactants are chemical compounds, which by virtue of its molecular structure adsorbs onto a fluid-fluid interface and reduces its surface tension. In equilibrium, the dissolved and adsorbed concentrations of the surfactant are uniform, and the Gibbs adsorption isotherm relates them to each other and to the surface tension of the interface. For dilute solutions of the surfactant, the adsorbed concentration increases linearly with the dissolved concentration, and so does the reduction in surface tension. As the solution gets more concentrated, the adsorbed concentration saturates owing to overcrowding of molecules on the interface and the surface tension also levels out.

The picture is richer when the system is out of equilibrium, in which case the surfactant distribution need not be uniform. A gradient of surface tension due to a non-uniform distribution of surfactants, known as the Marangoni stress, drives a flow, which in turn transports the surfactant. Mathematical models of surfactant-driven flows couple the Navier-Stokes equations with the surfactant dynamics. The surfactant dynamics themselves consist of the chemical kinetics between and the transport of the adsorbed and the dissolved phases. However, the plethora of surfactant physico-chemical parameters poses a challenge for use of such models for prediction in experimental systems. It is so especially because the values of these parameters changes with surfactant concentration. These concentrations themselves are also difficult to measure *in situ*.

Here we consider the case of a point source of surfactant on a liquid interface, which drives an axisymmetric flow away from the source (see Figure 1). Such a flow is inspired by two experiments on the air-water interface: (i) the flow due to a static disc of camphoric acid [1], and (ii) the flow due to the injection of surfactant from a narrow tube [2]. Experiments revealed that the velocity away from the source decayed with distance either as r^{-1} or as $r^{-3/5}$, depending on the nature of the source. A theoretical explanation of the resulting flow has been sought before [3], but the flow could only be explained recently [4] in terms of the dynamics being dominated by either the dissolved or adsorbed surfactant phases. Remarkably, this conclusion could be reached without the explicit knowledge or estimation of the surfactant's physico-chemical parameters.

Here starting from the general surfactant dynamics model, we derive two asymptotic limits under which the two power-laws for the decay of velocity are observed.

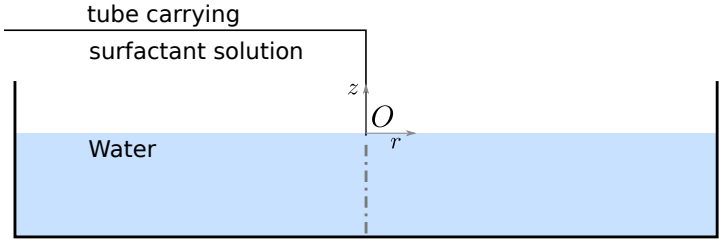

Figure 1: Schematic of a flow driven by a point source of surfactant. The experimental setup consists of a pool of water several centimeters in depth. The surfactant is released at point O on the air-water interface. The resulting gradients in surface tension drive a flow, which inturn also transport the surfactant.

*Corresponding author. E-mail: shreyas.mandre@warwick.ac.uk.

ASYMPTOTICS OF SURFACTANT DYNAMICS

The general surfactant dynamics model invokes the concentration of the dissolved phase c and that of the adsorbed phase Γ. The dissolved concentration follows the transport equation

$$c_t + \boldsymbol{u} \cdot \boldsymbol{\nabla} c = D\nabla^2 c \quad \text{in the fluid,} \tag{1}$$

and the adsorbed concentration follows

$$\Gamma_t + \boldsymbol{\nabla} \cdot (\boldsymbol{u}_s \Gamma) = D_s \nabla_s^2 \Gamma + j \quad \text{on the interface.} \tag{2}$$

The exchange flux, j, between the two depends on the degree of departure from equilibrium and for dilute concentrations may be written as

$$j = -\boldsymbol{\nabla} c \cdot \hat{\boldsymbol{n}} = k_a c - k_d \Gamma, \tag{3}$$

where k_a and k_d are reaction rate constants for the adsorption and desorption process. The surface tension σ decreases linearly with Γ, i.e. $\sigma - \sigma_0 = -K\Gamma$, where σ_0 is the surface tension of pure water. Note that the diffusion term in (2) can be neglected because the advection term dominates over it, but the one in (1), while also small, must be retained because the formation of a boundary layer of thickness $\delta = \sqrt{DL/T}$ perpendicular to the interface.

Two timescales of relevance to the dynamics are the hydrodynamic timescale L/U, where L is the characteristic radial length scale for the flow and U the characteristic speed in the radial direction, and the kinetic timescale $1/k_d$. When the hydrodynamic timescale is much faster than the kinetic (i.e. when the reaction is much slower than the time the flow takes the transport the chemicals), the exchange flux j can be neglected and the equation (2) governing Γ decouples from (1). In other words, the terms Γ_t balances $\boldsymbol{u}_s \cdot \boldsymbol{\nabla}\Gamma$, whilst j is an order $k_d L/U$ smaller. The surface tension depends only on Γ and, therefore, only on (2). The dissolved concentration evolves independently according to (1), but with a no-flux condition on the interface. This limit is dominated by adsorbed surfactant, in which case previous work [4, 1] showed that the radial velocity decays as $r^{-3/5}$.

The other asymptotic limit is the one where the adsorption-desorption kinetics are much faster than the hydrodynamics, so that the exchange flux saturates the interface to equilibrium, i.e., $k_a c = k_d \Gamma$. In this case, $\Gamma = (k_a/k_d)c$ and c is governed by (1), while (2) becomes $j \approx 0$. The adsorbed surfactant dynamics are thus eliminated. This is the limit dominated by dissolved surfactant, in which case previous work [4, 1] showed that the radial velocity decays as r^{-1}.

CONCLUSION

I showed in a previous article [4] that in the case dominated by adsorbed surfactant, the radial velocity decays as $r^{-3/5}$, and in the case dominated by dissolved surfactant the velocity decays as r^{-1}. The agreement of the power-law decay of velocity is not a coincidence but a direct consequence of the two limits of surfactant dynamics is demonstrated by comparing the three-dimensional profile of radial velocity [1]. Here we have shown that the two possibilities arise from a unified model of surfactant dynamics.

References

[1] Bandi, M. M., Akella, V. S., Singh, D. S., Singh, R. S., and Mandre, S, *Phys.Rev. Lett.* **119**, 264501, 2017.
[2] Roche, M., Li, Z., Griffiths, I. M., Le Roux, S., Cantat, I., Saint-Jalmes, A., and Stone, H. A., *Phys.Rev. Lett.* **112**, 208302, 2014.
[3] Le Roux, A., Roché, M., Cantat, I., and Saint-Jalmes, A., *Phys. Rev. E* **93**, 013107 (2016).
[4] Mandre, S., *J. Fluid Mech.* **832**, 777–792, 2017.

MODEL SELECTION OF PDES FOR PATTERN FORMATION

Natsuhiko Yoshinaga * [1,2] and Satoru Tokuda[2,3]
[1]WPI - Advanced Institute for Materials Research, Tohoku University, Sendai 980-8577, Japan
[2]MathAM-OIL, AIST,Sendai 980-8577, Japan

Summary We propose an inverse problem of partial differential equations (PDEs) for pattern formation[1]. From one snapshot of a target pattern, we successfully estimate the best model and its parameters using Bayesian model selection. The success of our method is achieved by (i) making a family of the models from which we select the best, (ii) defining an order parameter which characterises features of a ordered pattern, and (iii) efficient sampling of posterior distribution in the parameter space by using the replica exchange Monte Carlo method. We demonstrate our method for a two-dimensional dodecagonal quasi crystal.

INTRODUCTION

Partial differential equations (PDE) have been widely used to reproduce patterns in nature. To understand the mechanism of pattern formation, nonlinear PDEs have been employed for fluid convection[2], microphase separation of block copolymers[3], and crystals[4]. Despite a number of PDE models have been proposed, they rely on pre-request knowledge of physical laws and symmetries, and it requires significant efforts to develop a model reproducing a desired pattern. The challenge is quantitative and physically interpretable modelling of a complex phenomenon, which demands both developing a model and parameter estimation. The identification of a model equation is a recent key topic of machine leaning and data science. Several methods have been proposed to derive PDEs from time series data[5].

In this study, we propose the method to select a PDE model and its parameters to reproduce a given snapshot of a pattern, and from that, to get a physical insight of the target pattern[1]. We apply our method to two-dimensional nontrivial patterns, namely quasi-crystal with twelve-fold symmetry reproduced by using a family of phase-field crystal models. Our method not only estimates the parameters to reproduce these patterns but also gives an insight on the appropriate number of characteristic length scales hidden in the patterns.

MODEL SELECTION OF PDE

We consider a pattern that is expressed by the scalar density field $\psi(\mathbf{x})$. An example of a dodecagonal quasicrystal is shown in Fig. 1(a). We explorer a model to reproduce a target pattern $\hat{\psi}(\mathbf{x})$ at the steady state of an unknown model described by nonlinear PDEs, $\partial_t \psi(\mathbf{x}) = f_\mu[\psi(\mathbf{x})]$ with parameters μ. Our target pattern is ordered and has many invariants under translation, rotation, and also the action of symmetry group that the pattern has. In order to extract these features of the pattern $\psi(\mathbf{x})$, we define the order parameter $\Psi[\psi(\mathbf{x})]$. The model is specified by the functional form of $f[\psi(\mathbf{x})]$. We consider a family of the models based on a phase-field crystal (PFC) model in which each model has m length scales. For a given target pattern, we estimate the appropriate number of length scales by estimating the best model, and also estimate the parameters in the model. The estimation is performed by the Bayesian model selection in which we compute posterior distribution of parameters and marginal likelihood using the replica exchange Monte Carlo (REMC) sampling[6].

Order Parameter

To quantify the similarity between a target pattern $\hat{\psi}(\mathbf{x})$ and a pattern $\psi(\mathbf{x})$ that we get from the candidate model, we consider the cost function, which is zero when the two patterns are identical while it is larger when the obtained pattern is far from the target pattern. We define the order parameter, $\mathbf{\Psi}[\psi(\mathbf{x})] = (\Psi_1, \Psi_2, \ldots, \Psi_l)$, and the cost function, $E = \frac{1}{2}\sum_{l=1}^{l_0} \left|\Psi_l[\psi] - \hat{\Psi}_l\right|^2$ where l denotes a mode of the order parameter and l_0 is the maximum mode number. Here, $\hat{\Psi}_l = \Psi_l[\hat{\psi}]$ is the order parameter for the target pattern. The order parameter is rotational invariant form of the quantity A_l. This is given in two dimensions, by $A_l[\psi] = \int |\psi(\mathbf{k})| e^{il\theta_k} d\mathbf{k}^2$ where θ_k is a polar angle in the Fourier space. We consider appropriate norm that is invariant under rotation, $\Psi_l = |A_l|$.

Family of models

We consider a pattern described by a scalar density field $\psi(\mathbf{x})$ in a box with a periodic boundary condition. The density field $\psi(\mathbf{x})$ is obtained by a candidate model of a PDE. We focus on a family of the PFC models given by $\partial_t \psi = \mathcal{L}\psi + \Delta\psi^3$ with the linear operator is denoted by $\mathcal{L}$. The family is constructed by modifying the linear operator $\mathcal{L}$ so that the system has one or more characteristic length scales. The simplest PFC model is nothing but a conserved version of the Swift-Hohenberg (SH) equation. The SH equation reproduces a stripe and hexagonal patterns in two dimensions.

The conventional PFC equation has a single characteristic length at which a real part of the eigenvalue is positive.In order to consider the arbitrary number of length scales, we use m characteristic wave numbers, $q_0, q_1, \cdots, q_{m-1}$, and the values of the spectral, $a_0, a_1, \cdots, a_{m-1}$, at the wave number $k = q_i$. A family of our models is described in the Fourier transformation of the density field $\psi(\mathbf{k}) = \mathcal{F}[\psi(\mathbf{x})]$ with $\mathcal{L}_k = a_0 S_0(k) + \cdots + a_m S_m(k) + k^2\left(1-k^2\right)^2 \cdots \left(q_m^2 - k^2\right)^2$.

*Corresponding author. E-mail: yoshinaga@tohoku.ac.jp

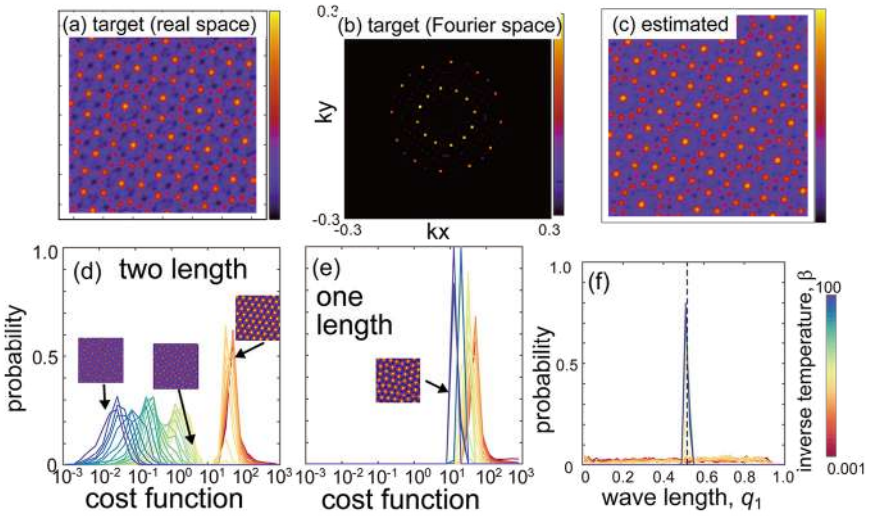

Figure 1: (a,b) The target pattern of dodecagonal quasicrystal in real space (a) and Fourier space (b). (c) The estimated pattern. (d,e) Histograms of the cost function, E, for $m = 2$ (d) and $m = 1$ (e). (f) The estimated parameter in $m = 2$. The vertical lines show the true parameter value to reproduce the target pattern.

RESULTS

In REMC, we perform parallel MC sampling for various inverse temperature, β, chracterising the likelihood ($P[\mu|\psi] \propto e^{-\beta E}$)[6]. Efficient search in the parameter space μ is capable by this method. At the low temperature (large β), we obtain the pattern very similar to the target pattern as demonstrated in Fig. 1(c,d). The estimated parameters are also well agree to the parameters that we used to generate the target pattern (Fig.1(f)). The estimate length scale is $q_1 = 0.52$ with the second length scale $q_0 = 1$. The ratio between them is agree to $q_0/q_1 = 2\cos(\pi/12) \approx 1.9319$, which is necessary value to generate this pattern[7]. Our method automatically estimates this ratio. The estimation works also for other parameters.

The model with two length scales ($m = 2$) can reproduce the quasicrystal pattern whereas the model $m = 1$ cannot. This is demonstrated by the histogram of the cost function (Fig. 1(d,e)). The latter model $m = 1$ has hexagonal patterns and higher E. From the marginal likelihood, we may conclude that the model with two length scales is indeed likely.

Our method is not restricted to estimation of parameters that numerically generates the target pattern. A target pattern is produced by properly superposing plane waves. The simplest case is a stripe pattern, which is expressed by one wave in one direction in two-dimensional space. This target pattern is not necessarily a steady solution of one of the candidate models. Nevertheless, we may estimate approximated parameters and the best model that can reproduce the pattern.

We demonstrate this idea using a two-dimensional dodecagonal quasi-crystal, which is generated by $\psi = \sum_{i=1}^{12} \cos(\mathbf{k}_i \cdot \mathbf{x})$ in which the wave vectors $\mathbf{k}_i$ are appropriately chosen[7]. The pattern is similar to numerically generated quasi-crystal, but in the current case there is no true parameters $\hat{\mu}$ and model. Using the pattern generated by analytic function, our method estimates quasi-crystal patterns, and both in two-length-scale and three-length-scale models reproduce quasi-crystal patterns. The estimated parameters reproduce the inherent ratio of the length scales $q_0/q_1 = 1.948 \approx 2\cos(\pi/12)$.

CONCLUSIONS

We demonstrated that the method can not only estimate the parameters that reproduces a target pattern, but also estimate the most likely model. The success of our approach relies on the order parameters, Bayesian model selection, and a family of models. The order parameters can extract symmetries of the pattern, and distinguish two visually similar patterns produced with different number of characteristic length scales. In order to perform model selection, we use REMC, which efficiently compute posterior probability distribution. This enables us to evaluate marginal likelihood of each model. Our approach can be applied to other family of models as well as three dimensional patterns[1].

References

[1] Yoshinaga N., Tokuda S. Bayesian Modelling of Pattern Formation from One Snapshot of Pattern. *arXiv:2006.06125*, 2020.
[2] Swift J., Hohenberg P. C. Hydrodynamic Fluctuations at the Convective Instability. *Phys. Rev. A*, **15**: 319–328, 1977.
[3] Ohta T., Kawasaki K. Equilibrium Morphology of Block Copolymer Melts. *Macromolecules*, **19**: 2621–2632, 1986.
[4] Elder K. R., Katakowski M., Haataja M., Grant M.. Modeling Elasticity in Crystal Growth. *Phys. Rev. Lett.*, **88**: 245701, 2002.
[5] Rudy S. H., Brunton S. L., Proctor J. L., Kutz J. N.. Data-Driven Discovery of Partial Differential Equations. *Sci. Adv.*, **3**: e1602614, 2017.
[6] Hukushima K., Nemoto K.. Exchange Monte Carlo Method and Application to Spin Glass Simulations. *J. Phys. Soc. Japan*, **65**: 1604–1608, 1996.
[7] Lifshitz R., Petrich D. M. Theoretical Model for Faraday Waves with Multiple-Frequency Forcing. *Phys. Rev. Lett.*, **79**: 1261–1264, 1997.

NUMERICAL SIMULATION OF WAVY MODULATION OF FARADAY WAVES

Laurette S. Tuckerman * [1] and Rahul Agrawal[2]
[1]Physique et Mécanique des Milieux Hétérogènes (PMMH), ESPCI Paris, CNRS, PSL Research University, Sorbonne Université, Université de Paris, F-75005 Paris, France
[2]Department of Mechanical Engineering, Indian Institute of Technology Bombay, Maharashtra, India 400076

Summary Numerical simulations are carried out of an experimentally observed modulational instability of Faraday waves [1] in which the regular pattern of square waves acquires a large-scale low-frequency spatio-temporal waviness.

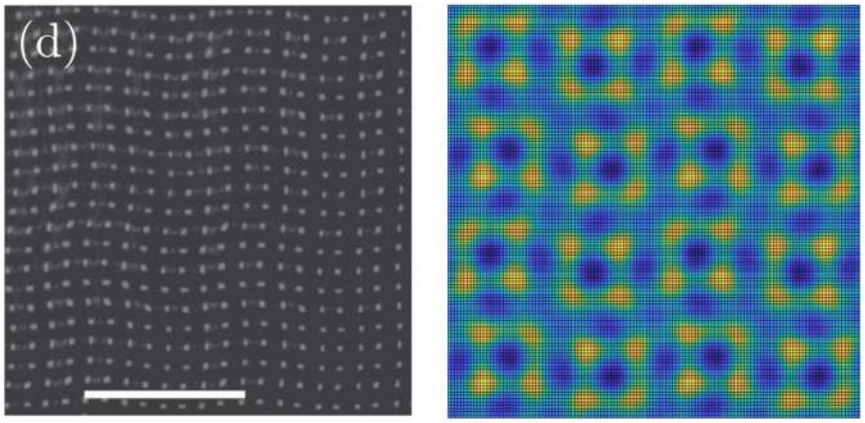

Figure 1: Faraday pattern with wavy large-wavelength modulation. Left: experiments [1]. Right: Initial condition for our simulations.

When a fluid layer is subjected to vertical vibrations of sufficient amplitude, standing waves appear at the surface via the classic Faraday instability. The pattern often forms a square grid, and at a higher oscillation amplitude, these regular squares may rearrange themselves into larger structures. In our group, Périnet et al. [2] produced the first numerical simulations of Faraday waves. For vibration amplitudes in a small range approximately twice the Faraday threshold, Domino et al [1] observed experimentally a wavy large-wavelength modulation of a square pattern of Faraday waves, shown in figure 1 (right). The spatial wavelength of the wavy modulation is four times that of the basic square pattern, while the temporal period is about 20 times as long.

We have investigated this pattern numerically using the massively parallel code `BLUE` written by Shin et al. [4]. This multiphase code BLUE is based on recently developed hybrid front-tracking/level-set interface methods. Both the fluid layer and the air above it are represented by a single field, with a density and viscosity which take on different values in the two phases. A 3D Cartesian mesh is used to represent the field, while the free surface is represented by triangles on a Lagrangian interface mesh. Kahouadji et al. [3] have previously used this code to study supersquares, a different variant of a regular square pattern, in which the grid of standing waves spontaneously partitions itself into two-by-two blocks, with the diagonal blocks in phase with one another.

To simulate the pattern in [1], we use an initial condition which is constructed to resemble the large-scale pattern; see the right portion of figure 2. The pattern appears persists for several long oscillation periods but eventually reverts to a basic square pattern, in contrast to the permanent waviness in the experiments; see figure 2. Domino et al [1] proposed an interpretation of the wavy instability in terms of the theory of elasticity. Numerical simulations produce accurate global quantities such as the kinetic energy and the total surface area as a function of time, as well as the complete velocity field and position of the surface. We analyze this detailed information to learn more about the secondary pattern and the mechanism responsible for its instability.

References

[1] L. Domino, M. Tarpin, S. Patinet, A. Eddi. Faraday wave lattice as an elastic metamaterial. *Phys. Rev. E* **93**: 050202(R), 2016.
[2] N. Périnet, D. Juric & L.S. Tuckerman. Numerical simulation of Faraday waves. *J. Fluid Mech.* **635**: 1–26, 2009.
[3] L. Kahouadji, N. Périnet, L.S. Tuckerman, S. Shin, J. Chergui, D. Juric. Numerical simulation of supersquare patterns in Faraday waves. *J. Fluid Mech.* **772**: R2, 2015.
[4] S. Shin, J. Chergui, D. Juric. A solver for massively parallel direct numerical simulation of three-dimensional multiphase flows. *J. Mech. Sci. Tech.* **31**: 1739-1751, 2017.

*Corresponding author. E-mail: laurette@pmmh.espci.fr.

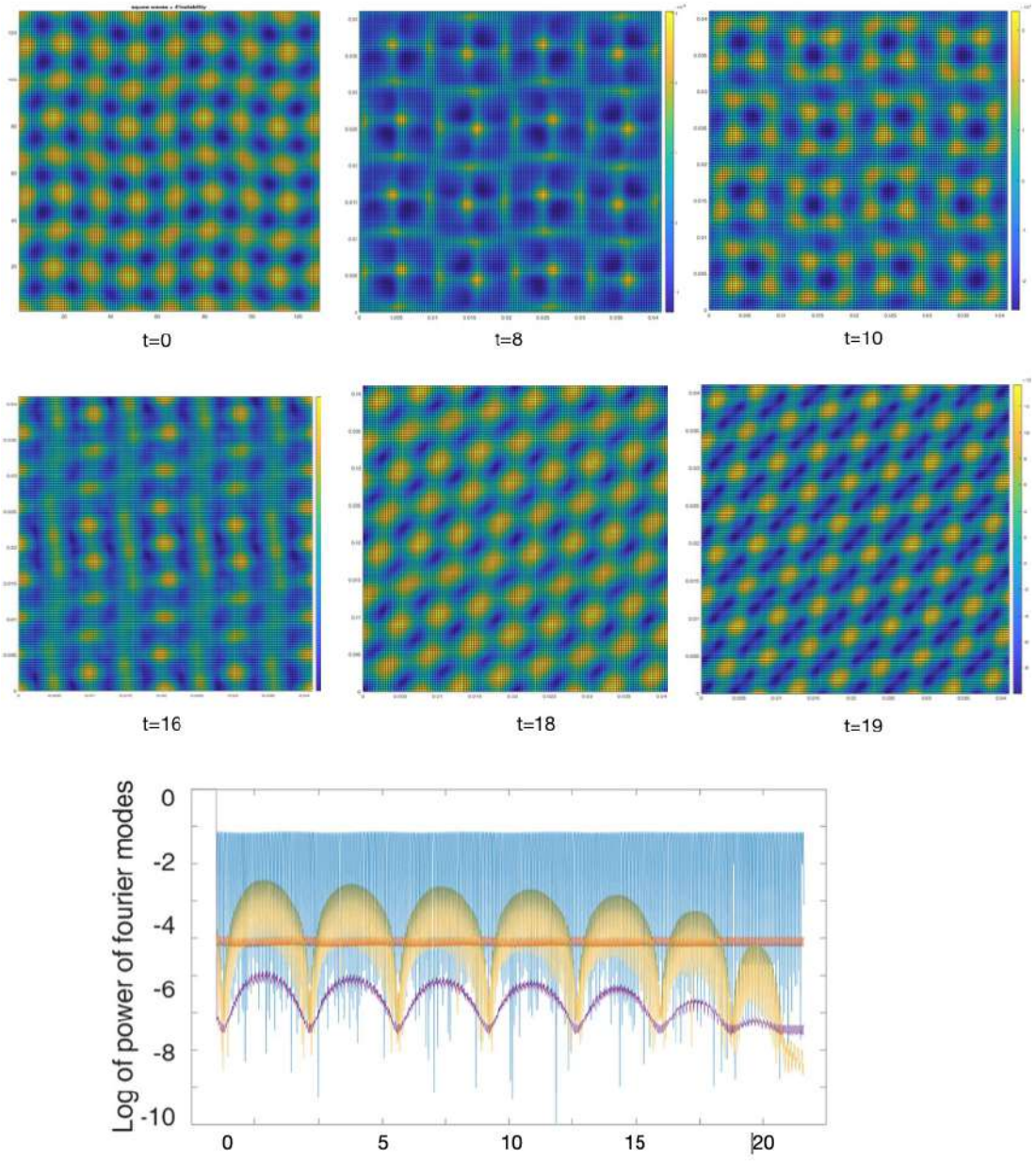

Figure 2: Numerical simulation of Faraday waves starting from a synthetic initial condition consisting of a wavy modulation of a square pattern. Above: visualisations. The pattern resembles that observed experimentally [1] until $t = 10$, then evolves towards a regular square or hexagonal pattern. Below: amplitude of the spatial Fourier modes corresponding to the basic square pattern (blue, red) and those corresponding to the wavy pattern (yellow, purple), with a longer spatial wavelength and temporal period.

SHORT-TERM PREDICTION OF A BUOYANCY-DRIVEN TURBULENT FIRE UNDER LOW-GRAVITY ENVIRONMENT

Takumi Tokami[1], Yushi Ozaki*[1], Takayoshi Hachijo[1], Takaya Miyano[2] and Hiroshi Gotoda[1]
[1]Department of Mechanical Engineering, Tokyo University of Science, Tokyo, Japan
[2]Department of Mechanical Engineering, Ritsumeikan University, Shiga, Japan

Summary We numerically study the spatiotemporal dynamics and short-term predictability of a buoyancy-driven turbulent fire under low-gravity environment. We observe a significant transition from order to disorder structures in the degree in the spatial horizontal visibility graph. The entropy transport from temperature to streamwise flow velocity fluctuations is predominant near the interface between hot combustion products and cold surrounding air. The transfer entropy is an important measure for determining the predictability of the flow velocity fluctuations in the near-field.

The complex coupling of hydrodynamic flow, heat/mass diffusion, and a rapid chemical reaction gives rise to a rich variety of flame front instabilities. Buoyancy-driven flame puffing is an important class of flame front instabilities in diffusion flames. Our recent study [1] using a large-eddy simulation has shown the existence of two important dynamical states in a mid-scale buoyancy-driven turbulent fire: low-dimensional deterministic chaos in the near-field and high-dimensional deterministic chaos in the far-field. These dynamical states have been reasonably identified by the advanced analyses based on symbolic dynamics and statistical complexity [2]. In this study, we clarify the mutual interaction between flow velocity and temperature fluctuations in a buoyancy-driven turbulent fire under low-gravity environment using the symbolic recurrence plots (SRPs) [3] and the transfer entropy [4]. In addition, we examine the predictability of streamwise flow velocity fluctuations using the echo state networks as one of promising machine learning technologies.

We obtain the numerical data of a spatiotemporal structure in a buoyancy-driven turbulent fire under low-gravity environment from large-eddy simulation [1,2]. The governing equations, the discretization method of the governing equations, and the boundary conditions are all the same as those in the previous studies [1,2]. In this study, the computational domains in the x, y, and z directions are set to 2.0 m, 2.0 m, and 5.0 m. Methane gas is supplied from a square central area with dimensions of 1 m × 1 m. The gravity level G (= g_a/g, where g is the gravitational acceleration under normal-gravity and g_a is the gravitational acceleration under low-gravity) is set to 0.8. Similarly to in the previous studies [1, 2], we analyse the streamwise flow velocity and temperature fluctuations for a sufficient interval of 28 s during a turbulent fire.

Recurrence plots [3] enable us to capture the dynamical changes to chaos via bifurcations. They are constructed by computing the distances between all sets of points in a phase space. Symbolic recurrence plots (SRPs), which are an extended version of the recurrence plots, incorporate the rank order patterns in time series [5], and are effective for capturing the similarity of two dynamical states [6]. In this study, we use SRPs to evaluate the similarity of streamwise flow velocity and temperature fluctuations. The adjacency matrix of SRPs is obtained as Eq. (1).

$$R_{ij} = \begin{cases} 1 & \pi^D_{w'}(t_i) = \pi^D_{T'}(t_j) \\ 0 & \text{otherwise} \end{cases} \tag{1}$$

Here, $\pi^D_{w'}(t_i)$ and $\pi^D_{T'}(t_j)$ are the rank order patterns of the streamwise flow velocity fluctuations w' and the temperature fluctuations T', and D is the embedding dimension. In this study, we estimate the recurrence rate S_{RR} to quantify the similarity of w' and T'.

$$S_{RR} = \frac{1}{N-(D-1)-|\tau|} \sum_{i=1}^{N-(D-1)-|\tau|} R_{ij} \tag{2}$$

S_{RR} represents the density on the diagonal in SRPs, and approaches to unity as w' and T' reach a similar dynamical state. Note j is set to $i+\tau$.

Transfer entropy is one of the useful measures to estimate the causality between two time series [4]. In this study, we estimate the transfer entropy defined as Eq. (3) to clarify the mutual interaction of the streamwise flow velocity and temperature fluctuations.

$$S_{E,T'\to w'} = \sum_{i=1}^{N-\tau} p(w'(t_{i+\tau}), \mathbf{w}_i^k, \mathbf{T}_i^l) \log \frac{p(w'(t_{i+\tau}) \mid \mathbf{w}_i^k, \mathbf{T}_i^l)}{p(w'(t_{i+\tau}) \mid \mathbf{w}_i^k)} \tag{3}$$

A machine learning called reservoir computing is an effective model-free predictor [7]. Reservoir computing has been applied to chaotic time series (e.g., Lorentz equation and Kuramoto-Sivashinsky equation) [7,8]. In this study, we consider the echo state networks and use T' as the input data to obtain the future state of w' as the output data.

Figure 1(A) shows the variation in S_{RR} as a function of τ_a for different z at G = 0.8. Note that τ_a is set to the actual delay time (=$\tau\Delta t$, where Δt is the time resolution). S_{RR} takes high values at $z \sim 1.0$ m, indicating that T' and w' are synchronized each other. S_{RR} periodically changes in terms of τ_a, indicating the strong periodicity of both fluctuations. S_{RR} reaches to approximately 0.3 and the periodic dynamical structure disappears in the far-field. In the previous studies

*Corresponding author. E-mail: 4520516@ed.tus.ac.jp

[1,2], we have reported that high randomness of the streamwise flow velocity and temperature fluctuations in the far-field is attributed to the formation of high-dimensional chaos. This leads to the formation of non-synchronized state in the far-field. Figure 1(B) shows the spatial distribution of ΔS_E ($= S_{E,T'\to w'} - S_{E,w'\to T'}$). ΔS_E takes high positive values near the shear layer region between hot combustion products and cold surrounding air. This means that the temperature fluctuations strongly affect the streamwise flow velocity fluctuations at this region. These suggest that the transfer entropy is useful for extracting the driving region of a buoyancy-driven turbulent fire. Figure 2 shows the variation in the ΔS_E and correlation coefficient C between the predicted values and the corresponding reference values of w' as a function of x for different z at $G = 0.8$. The spatial distribution of ΔS_E reasonably corresponds to that of C in the near-field. This means that ΔS_E has a significant impact on the predictability of the streamwise flow velocity fluctuations in the near-field. These results show that the transfer entropy is an important measure for determining the predictability of the streamwise flow velocity fluctuations in the near-field under low gravity environment.

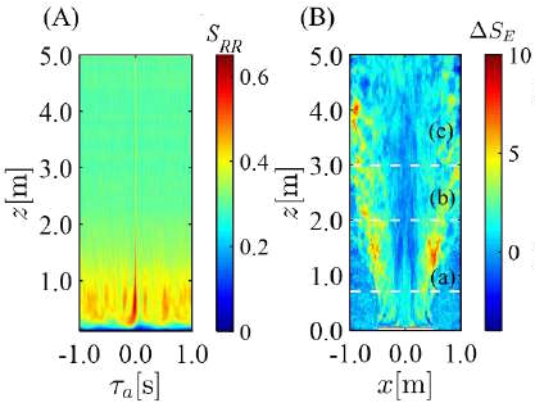

Figure 1. (A) Variation in S_{RR} as a function of τ_a for different z and (B) spatial distribution of ΔS_E at G =0.8.

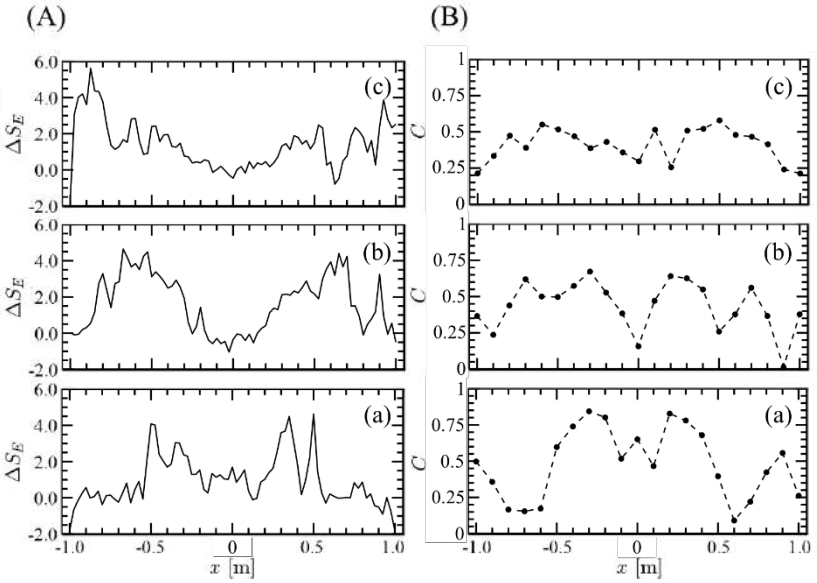

Figure 2 Variations in (A) ΔS_E and (B) C as a function of x for different z at G =0.8. (a) z = 0.7 m, (b) z = 2.0 m, (c) z = 3.0 m.

References

[1] K. Takagi, H. Gotoda, I. T. Tokuda, and T. Miyano, Phys. Rev. E 96, 052223 (2017).
[2] K. Takagi, H. Gotoda, I. T. Tokuda, and T. Miyano, Phys. Lett. A 382, pp. 3181-3186 (2018).
[3] N. Marwan, M. C. Romano, M. Thiel, and J. Kurths, Phys. Reports 438, 237 (2007).
[4] T. Schreiber, Phys. Rev. Lett. 85, 461 (2000).
[5] C. Bandt and B. Pompe, Phys. Rev. Lett. 88, 174102 (2002).
[6] A. Groth, Phys. Rev. E 72, 046220 (2005).
[7] J. Pathak, B. Hunt, M. Girvan, A. X. Lu, and E. Ott, Phys. Rev. Lett. 120, 024102 (2018).
[8] J. Pathak, Z. Lu, B. R.Hunt, M. Girvan, and E. Ott, Chaos 27, 121102 (2017).

FARADAY INSTABILITY IN 1D CAVITIES : TIME CRYSTALS AND MODE SELECTION

Guillaume d'Hardemare [1], Antonin Eddi *[2] and Emmanuel Fort [1]
[1] Institut Langevin, ESPCI Paris, CNRS, PSL University, 1 rue Jussieu, F-75005 Paris, France
[2] PMMH, CNRS, ESPCI Paris, Universit PSL, Sorbonne Université, Universit de Paris, F-75005, Paris,France

Summary Faraday instability is equivalent to a time crystal, where the parametric amplification leads to the apparition of k-gaps, formally analogous to the energy band gap is solid-state physics. As energy is not conserved, this results in an unstable domain in k-space where modes grow. Here, we investigate experimentally Faraday instability in 1D cavities, where we can tune the excited mode by changing the cavity length. This allows us to probe the amplification band of the instability. Abruptly changing the phase of the excitation further allows us to observe the overdamped modes of the instability, measuring for the first time their decay rate predicted theoretically but never observed so far.

FARADAY INSTABILITY AS A TIME CRYSTAL

Faraday instability is observed when a liquid bath is vertically shaken above a certain threshold [1]. It has been extensively studied experimentally and theoretically as an instability in the stationary regime, with focus on the forcing threshold, pattern formation and the various dissipation processes or the hydrodynamic associated phenomena. This parametric instability can be revisited within the framework of Floquet time crystals. For an inviscid fluid in a bath submitted to vertical acceleration $a_0\cos(2\omega_f t)$, the modes are given by a Mathieu equation [2]. The free surface elevation $\xi(\mathbf{r},t)$ at position $\mathbf{r}$ and time t can be decomposed in Fourier modes $\hat{\xi}(\mathbf{k},t)$ of wavevector $\mathbf{k}$ following:
$\frac{\partial^2\hat{\xi}(\mathbf{k},t)}{\partial t^2} + \omega_0^2(\boldsymbol{k})\hat{\xi}(\mathbf{k},t) = -a_0 \mathrm{k}\cos(2\omega_f t)\,\hat{\xi}(\mathbf{k},t)$ with $\omega_0(\mathrm{k})$, the angular frequency given by the dispersion relation for gravity-capillary waves and k, the wavenumber. This equation describes the modes in a medium with a gravity modulation. The variation of the effective gravity induces a speed modulation of the gravito-capillary waves which can be seen as a modulation of the refractive index [4,5]. The solutions of the Mathieu equation are given by the Bloch-Floquet theorem while in the case of liquid with a small viscosity ν, a damping term $-2\gamma\partial\hat{\xi}/\partial t$ should be added to the Mathieu equation, γ being the damping rate related to the fluid viscosity by $\gamma = 2\nu\mathrm{k}^2$ [3]. Figure 1 shows a typical complex dispersion curve obtained with a small viscosity, with vertical k-gaps (in momentum). These k-gaps are the analog of the horizontal energy gaps observed in spatial crystals in which the waves cannot propagate. Within the k-gaps, the vertical excitation of the bath leads to two possible solutions: one being overdamped compared to a bath at rest, the other being underdamped. For sufficient forcing, the Faraday instability is observed and a standing wave at half the excitation frequency appears on the surface.

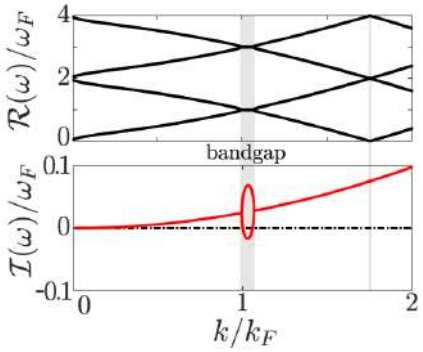

Figure 1: Dispersion relation showing the band structure of the Faraday instability as a water wave time crystal. Top: real part $\Re(\omega)$ of the angular frequency ω versus the normalized wavenumber k/k_F with k_F being the Faraday wavenumber Bottom: Imaginary part $\Im(\omega)$ of the angular frequency as a function of k/k_F. The small parabolic variation corresponds to the viscous damping

EXPERIMENTS

We now focus on a versatile implementation of a 1D time crystal based on Faraday instability. It consists in a 1D wave cavity whose length L can be tuned that is submitted to vertical harmonic vibrations. Faraday waves are excited at half the forcing frequency Ω_F. The associated wavelength λ_F is given by the capillary-gravity dispersion relation for water-waves and is chosen so that it equals twice the width of the tank to excite the first transverse mode of the cavity. We measure the exponential growth rate of the waves which corresponds to the imaginary part of the Floquet exponent $\Im(\omega)$ as well as the wavelength λ inside the cavity. The growth rates (Fig. 2a) exhibit peaks separated by half a Faraday wavelength λ_F. These peaks correspond to matching between a mode associated to the Faraday instability and a resonant mode of the cavity which wavelength satisfies $\lambda = 2L_{\mathrm{eff}}/n$, n being the mode number and L_{eff}, the effective cavity length taking into account the boundary conditions. Varying the cavity length results in scanning the k-gap associated to the Faraday instability (Fig. 2b). The curve of the growth rate thus corresponds to a periodic scanning of the k-gap with maxima obtained for cavity lengths satisfying $L_{\mathrm{eff}} = n\lambda_F/2$.
Last, we introduce a topological defect in the time crystal by suddenly π-shifting the excitation period which results in concatenating two time crystals with opposite phase. At the interface, the existing mode is turned into the overdamped one. By extracting the damping rate, we are thus able to measure the entire complex dispersion inside the k-gap of the Faraday time crystal.

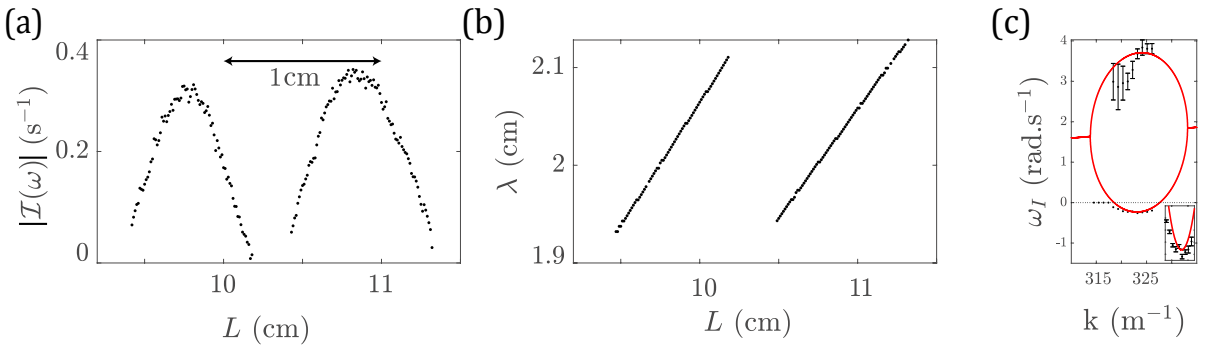

Figure 2: (a) Growth rate of the amplitude $|\Im(\omega)|$ and (b) wavelength λ of the mode in the cavity as a function of the cavity size L. The peaks are associated to the matching between the Faraday instability k-gap modes and the ones of the cavity. (c) Measurement of growth and decay rates inside the k-gap. The solid red curves give the result of the computation based on a damped Mathieu equation using experimental values of the viscosity. The inset provides a zoom on the lower part of the curve.

References

[1] Faraday, M. On a Peculiar Class of Acoustical Figures; and on Certain Forms Assumed by Groups of Particles upon Vibrating Elastic Surfaces. *Philos. Trans. R. Soc. Lond.* **121**, 299–340 (1831).

[2] Benjamin, T. B. & Ursell, F. J. The stability of the plane free surface of a liquid in vertical periodic motion. *Proc R Soc Lond A* **225**, 505–515 (1954).

[3] Kumar, K. & Tuckerman, L. S. Parametric instability of the interface between two fluids. *J. Fluid Mech.* **279**, 49 (1994).

[4] Bacot, V., Labousse, M., Eddi, A., Fink, M. & Fort, E. Time reversal and holography with spacetime transformations. *Nat. Phys.* 1–6 (2016).

[5] Bacot, V., Durey, G., Eddi, A., Fink, M. & Fort, E. Phase-conjugate mirror for water waves driven by the Faraday instability. *Proc. Natl. Acad. Sci.* **116**, 8809–8814 (2019).

GROWTH AND DECAY OF ISOLATED TURBULENT BAND IN PLANE-COUETTE FLOW

Jianzhou Lu, Jianjun Tao *, and Weitao Zhou
SKLTCS, Department of Mechanics and Engineering Science, College of Engineering, Peking University, Beijing, P.R. China

Summary The transition of plane Couette flow is numerically investigated in a large computational domain. It is found that the averaged period of the transient growth reduces slowly with the decrease of the Reynolds number (Re) except when Re is close to a threshold value of 286. During the decay process, the band contracts from its both ends with a statistical constant velocity, but keeps its center, width, and tilt angle statistically unchanged. For self-sustained turbulent band, three growth styles are observed. At moderate Re, the isolated band extends obliquely as what happens in plane Poiseuille flow. With the increase of Re, transverse split occurs and the band breaks into several attached segments, forming a shape of 'F'. Further increasing Re leads to a longitudinal split, i.e. the isolated band becomes wider at first and then splits into two parallel bands.

INTRODUCTION

It is known that plane Couette flow (PCF) is always linearly stable, but may turn to be turbulent at moderate Reynolds numbers by the subcritical transition. Leutheusser and Chu [1] studied the flow between a moving water surface and an upper flat stationary plate, and determined the transitional Reynolds number as 280. It should be noted that the spanwise aspect ratio of the experimental channel was small and the water flow was turbulent, suggesting that the water surface was rough. From then on, substantial progresses have been made and the localized turbulent band or stripe is found to be a key structure for the transition in channel flows [2]. The band growth and decay processes have been simulated in large domains with under-resolution simulations [3, 4], and it was mentioned that the low resolution lowered the threshold for sustained turbulence from 325 to 210 [3] and impeded reliable predictions for fully resolved cases. Therefore, the spatio-temporal evolution of the isolated turbulent bands still requires fully-resolved numerical investigations.

METHODS AND RESULTS

We conduct numerical simulations on the PCF in a large domain of the size $800h \times 2h \times 712h$, and a spectral code [5] is used to solve the incompressible Navier-Stokes equations, where the velocity field is expanded in a basis of Fourier modes (in the streamwise x- and spanwise z-directions) and Chebyshev polynomials (in the wall-normal direction y). The numerical resolution is 2048 spectral modes in x, 33 in y, and 2048 in z. The boundary conditions are periodic in the x- and z-directions and there is no-slip at the walls ($y = \pm h$). The half of the velocity difference between the boundaries U and the half channel gap h are chosen as the characteristic velocity and the length scale, respectively. In the following simulations, an isolated turbulent band, i.e., a unique straight band whose length is several times smaller than the domain size, is used as the initial perturbation.

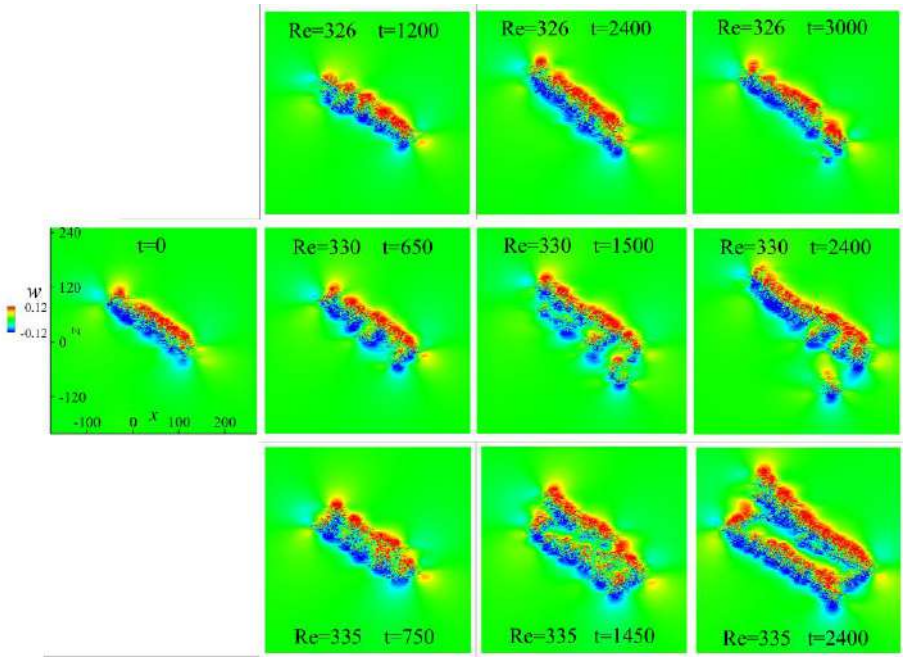

Figure 1: Iso-contours of the spanwise velocity in the mid-plane. The initial fields are the same for all three cases.

*Corresponding author. E-mail: jjtao@pku.edu.cn

As shown in Fig. 1, there are three different growth styles for localized turbulence. For moderate Re, e.g. Re=326, the isolated band extends obliquely with time as what occurs in plane Poiseuille flow but with a much lower extension velocity. When Re increases to 330, transverse split occurs and the band breaks into attached segments, forming a shape of 'F'. It seems that the transverse split may lead to the lateral branching observed in the previous under-resolution simulations [4]. A longitudinal split happens when Re is further increased, e.g. Re=335 as shown in Fig. 1, the isolated band becomes wider at first and then splits into two parallel bands. In fact, the later growth style includes the former one(s), and hence the turbulence spreads more and more efficiently with the increase of Re.

Since the disturbance kinetic energy of the main body of the isolated band is statistically uniform and the band is straight with a finite width, its shape may be simplified as a tilted rectangle. The center, width, length, and tilt angle of the rectangle can be determined based on the disturbance kinetic energy of the band in the midplane with the method proposed for plane Poiseuille flow [6]. According to the simulations for Re=314, 317, and 318, the position of the band center varies stochastically but does not move much during a period more than 3000 time units, reflecting that the convective velocity of such a localized structure is nearly zero. After an initial period of adjustment, the band contracts longitudinally, i.e. its length decreases generally while its width and tilt angle remain statistically constants. The temporal variation of the band length may be fitted linearly, suggesting a constant contraction velocity. A similar contraction phenomenon was observed before in an under-resolved simulation, where the position of the band center and the shape parameters (e.g., the tilt angle) were not analyzed quantitatively [3]. For the present decaying isolated band, the tilt angle is $(27 \pm 3)^\circ$ when Re is between 314 and 318.

In order to study the statistical properties of the decay process (Fig. 2a), ten samples are calculated for each Reynolds number, and the initial flow fields are composed by the same band and different random disturbances in the whole fields. We define a parameter, the transient-growth time T_{grow}, which is the ensemble average of the mean periods obtained from different samples when the growth rate of E_{k} is positive, and draw it in Fig. 2(b). It is shown that T_{grow} decreases monotonically by lowering Re, and there is a drastic decline of T_{grow} as Re reduces to 286, indicating a threshold for the transient growth of the turbulent band. When Re<286, the probability of the transient growth is very small, implying that the turbulent band can hardly be formed from the transient growth of any initial disturbances.

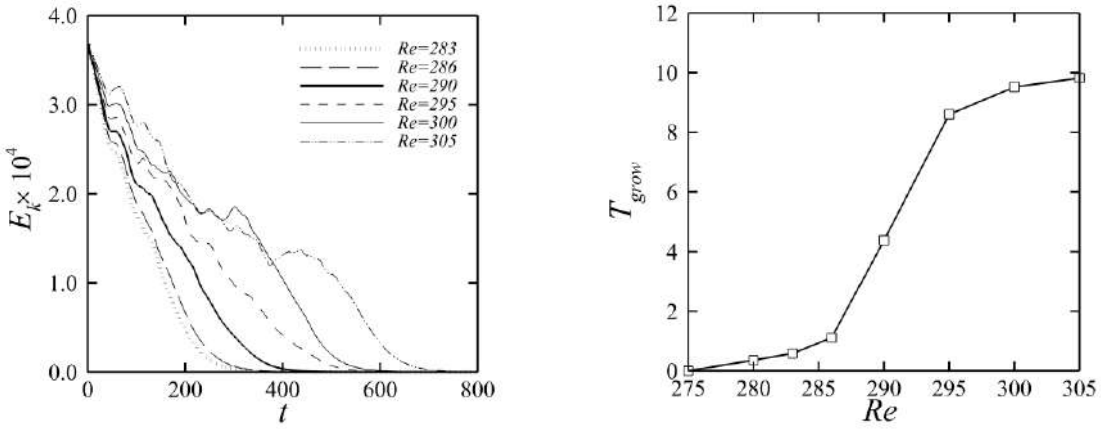

Figure 2: Time series of the volume-averaged disturbance kinetic energy E_{k} at different Reynolds numbers obtained with the same initial turbulent band; (b) transient-growth time T_{grow} as a function of Re

CONCLUSIONS

Direct numerical simulations are carried out to study the subcritical transition of plane Couette flow in a large computational domain. It is found that the isolated turbulent band decays in a style of longitudinal contraction at low Reynolds numbers, and the lower bound Reynolds number of the transient-growth regime is defined as 286. In addition, three different growth styles of the isolated turbulent band are illustrated, i.e. the oblique extension, transverse split, and the longitudinal split. It is believed that their joint action leads to the formation of labyrinthine patterns observed in simulations and experiments.

References

[1] Leutheusser H. J. Chu V. H. Experiments on plane Couette flow. *Journal of the Hydraulics Division, ASCE*, **97**: 1269–1284, 1971.
[2] Tuckerman L. S., Chantry M., Barkey D. Patterns in wall-bounded shear flows. *Annu. Rev. Fluid Mech*. **52**:343–67, 2020.
[3] Manneville P. On the decay of turbulence in plane Couette flow. *Fluid Dyn. Res.* **43**, 065501, 2011
[4] Manneville P. On the growth of laminar-turbulent patterns in plane Couette flow. *Fluid Dyn. Res.* **44**, 031412, 2012.
[5] Chevalier M., Schlatter P., Lundbladh A., and Henningson D.S.: SIMSON a pseudo-spectral solver for incompressible boundary layer flows, Technical Report TRITA-MEK 2007:07, 2007.
[6] Tao J. J., Eckhardt B., Xiong X. M. Extended localized structures and the onset of turbulence in channel flow. *Phys. Rev. Fluids*, **3**, 011902(R) 2018.

BISPECTRAL MODE DECOMPOSITION FOR DISCOVERY OF TRIADIC INTERACTIONS FROM FLOW DATA

Oliver T. Schmidt * [1]
[1]Department of Mechanical and Aerospace Engineering, University of California San Diego, La Jolla, CA, USA

Summary Bispectral mode decomposition is introduced as a mean of detecting triadic nonlinear interactions in flow data. The method leverages the fact that triadic interactions are characterized by quadratic phase coupling. The proposed decomposition computes modes that optimally represents the data in terms of an integral measure of the bispectral density, which in turn detects quadratic phase coupling in deterministic signals. The two main outputs of the method are the mode bispectrum and the corresponding bispectral modes. The mode bispectrum indicates triadically interacting frequency triplets and the corresponding modes reveal the coherent flow structures generated by the interaction. We demonstrate the method on direct numerical simulation data of planar cylinder flow at $Re = 500$ and particle image velocimetry data of massively separated turbulent flow behind a flat plate at high angle of attack.

INTRODUCTION

Triadic interactions are the fundamental mechanism of energy transfer in fluid flows. They result from the quadratic nonlinearity of the Navier-Stokes equations and manifest as triads,

$$\mathbf{k}_j \pm \mathbf{k}_k \pm \mathbf{k}_l = \mathbf{0}, \quad f_j \pm f_k \pm f_l = 0,$$

in Fourier space, i.e., triplets of three wavenumber vectors, $(\mathbf{k}_j, \mathbf{k}_k, \mathbf{k}_l)$, or frequencies, (f_j, f_k, f_l), that sum to zero. The latter condition implies that triads of wavenumber vectors and frequencies form triangles in their respective spaces. The turbulent cascade of energy, from large to small scales, is a well-known result of triadic interactions (see, e.g., Kraichnan, 1967).

As the Fourier transform of the third statistical moment, the bispectrum is a direct measure of non-Gaussianity of a stochastic signal. Most important in the context of three-wave interactions is the observation that the bispectrum correlates two frequency components with the frequency component corresponding to the sum of these two frequencies. This can be seen from its definition in terms of the expectation operator,

$$S_{qqq}(f_1, f_2) = \lim_{T\to\infty} \frac{1}{T} E[\hat{q}(f_1)^* \hat{q}(f_2)^* \hat{q}(f_1 + f_2)]. \tag{1}$$

The goal of this work is to devise a modal decomposition that reveals the presence of triadic nonlinear interactions from multidimensional data. Since quadratic phase coupling is characteristic of these interactions, the bispectrum defined in equation (1) can be used to detect them. To compute modes that exhibit quadratic phase coupling over extended portions of the flow field, we require the decomposition to optimally represent the data in terms of an integral measure of the bispectral density. These requirements translate into the problem of finding the vector that maximizes the Rayleigh quotient of a non-Hermitian matrix. We solve this problem using a slightly modified version of the algorithm by He and Watson (1997) for the computation of the numerical radius of a general complex matrix.

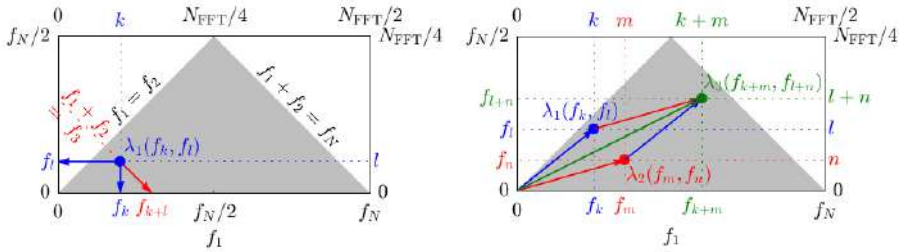

Figure 1: Frequency triads in the principal region of the mode bispectrum. Left: a local maximum $\lambda_1(f_k, f_l)$ indicates phase-coupling between the components of the triad (f_k, f_l, f_{k+l}) due to quadratic nonlinearity. Harmonics and the mean flow distortion (not shown) are generated by self-interactions like (f_k, f_k, f_{2k}) and $(f_k, f_{-k}, 0)$, respectively. Right: two triads (f_k, f_l, f_{k+l}) and (f_m, f_n, f_{m+n}) can interact to generate a new wave component (f_{k+m}, f_{l+n}).

The resulting decomposition may be understood as the extension of the analysis of time signals using higher-order spectra to multidimensional datasets, or *vice versa*, as an extension of spectral proper orthogonal decomposition to higher-order spectra. The two main results of this bispectral mode decomposition are the mode bispectrum and bispectral modes. As an estimator for the mode bispectrum we adapt Welch's method (Welch, 1967), which is an asymptotically consistent spectral estimator for the power spectral density that may equally be used to converge third-order statistics.

*Corresponding author. E-mail: oschmidt@ucsd.edu.

Figure 1 shows a schematic of the principal region of the mode bispectrum. All other regions contain redundant information or lie outside of the Nyquist limit. It hence suffices to plot this region. For brevity, we will use integer frequency index doublets (k, l) instead of physical frequency doublets (f_k, f_l) or triplets (f_k, f_l, f_{k+l}) to represent triads. Also discussed in figure 1 is the generation of new wave components through triad interactions.

Database						Spectral estimation		
Case	Variables	N_x	N_y, N_r	N_t	Δt	N_{FFT}	N_{ovlp}	N_{blk}
Cylinder DNS	u, v	250	125	4096	0.06	1024	512	7
Plate PIV	u, v	120	69	$2.5 \cdot 10^4$	$0.002s$	5000	0	50

Table 1: Parameters of the example databases and spectral estimation parameters. The DNS data are non-dimensionalized by the cylinder diameter and freestream velocity and the PIV data are given in SI units.

To demonstrate the method, we investigate the two flows summarized in table 1. The direct numerical simulation data of planar cylinder flow at $Re = 500$ is a canonical example of a laminar flow with strong nonlinear dynamics. The second example is that of particle image velocimetry (PIV) data of a flat plate at a high angle of attack. It is characterized not only by nonlinear dynamics at a wide range of scales down to turbulence, but also high levels of measurement noise. Figure 2 shows a flow visualization and of the PIV data, as well as the mode bispectrum and two examples of modes obtained from bispectral mode decomposition. In this example, the triad corresponding to the self-interaction of the fundamental bluff body vortex shedding is analyzed. The bispectral mode (11,0) shown in figure 2d corresponds to this fundamental instability evolving on the mean flow. By comparing the fundamental mode with its self-interaction, i.e., mode (11,11) shown in 2e, it becomes evident that the fundamental self-interaction occurs for a phase angle of 90° and generates a structure of twice the fundamental streamwise wavenumber (and frequency). As anticipated, the mode bispectrum shown in figure 2c confirms that the fundamental self-interaction is the dominant nonlinear triad in this flow, i.e. it attains its maximum at (11,11). This can be seen more clearly in the insert, in which the fundamental and its self-interaction triad are marked by circles. The cylinder flow example will be presented in the talk. Furthermore, we will introduce the summed mode bispectrum and the bispectral interaction map. The summed mode bispectrum is a compact representation of the mode bispectrum that permits comparison with classical spectra. The bispectral interaction map indicates where in physical space triadic interactions are active.

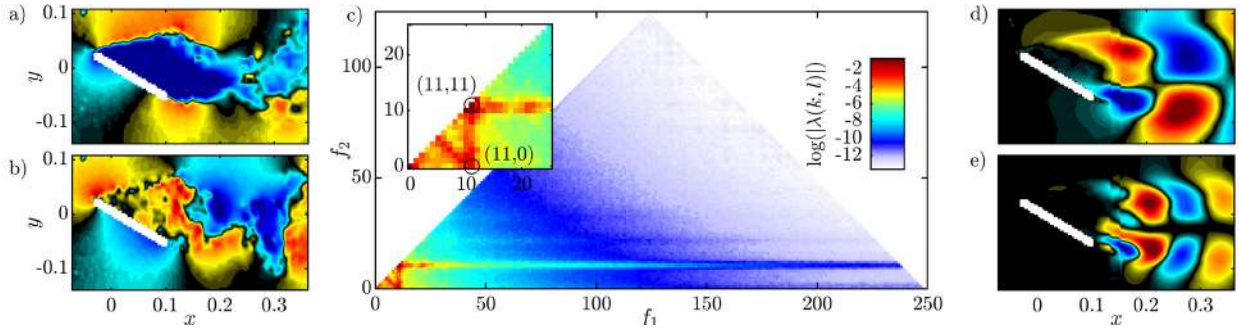

Figure 2: Bispectral mode analysis of PIV data of a flat plate at high angle of attack: (a,b) instantaneous streamwise and transverse velocity field; (c) mode bispectrum; (d) bispectral mode (11,0) corresponding to the fundamental bluff body vortex shedding frequency; (e) bispectral mode (11,11) resulting from the self-interaction of the fundamental mode. The streamwise velocity component is shown in (d,e). PIV data courtesy of Karen Mulleners, EPFL.

References

He C, Watson GA (1997) An algorithm for computing the numerical radius. IMA Journal of Numerical Analysis 17(3):329–342

Kraichnan RH (1967) Inertial ranges in two-dimensional turbulence. Physics of Fluids 10(7):1417–1423

Welch P (1967) The use of fast Fourier transform for the estimation of power spectra: a method based on time averaging over short, modified periodograms. IEEE Transactions on audio and electroacoustics 15(2):70–73

AN ADJOINT PRECURSOR OF EXTREME EVENTS IN CHAOTIC SYSTEMS

Alberto Racca * [1] and Luca Magri[1,2]
[1]Department of Engineering, University of Cambridge, Cambridge, United Kingdom
2Institute of Advanced Studies, Technische Universität München, Munich, Germany (visiting)

Summary We propose an *adjoint precursor* for real-time prediction of extreme events in chaotic systems. The precursor is calculated in the adjoint tangent space, which is decomposed by Covariant Lyapunov Vectors (CLVs) analysis. To quantify the performance of the adjoint precursor, we introduce a figure of merit in the time domain, which is compared with the traditional statistical figures of merits. We test the formulation on a variety of chaotic fluid systems: Rayleigh-Bénard convection, turbulent shear flow, and electrodissolution. In this abstract, we report the results for the electrodissolution system.

INTRODUCTION

Extreme events, which are sudden and violent changes of a state or an observable, arise in a large spectrum of fluid mechanics systems such as oceanic rogue waves, weather patterns, electrodissolution, combustion instabilities and turbulence. Because extreme events are typically undesirable in engineering systems, robust statistical methods for their prediction have been proposed recently [1, 2]. In this work, we use covariant Lyapunov vector (CLV) analysis combined with an adjoint method to propose a new precursor in a chaotic system. Covariant Lyapunov Vectors provide a basis of the tangent space of a chaotic attractor, which is split into unstable, stable and neutral subspaces. The CLVs determine the directions along which an infinitesimal perturbation to the system evolves exponentially with rates given by the Lyapunov Exponents [3]. In stability analysis, [4] mathematically and numerically showed that CLV analysis is a generalization of eigenvalue and Floquet theory to chaotic systems. Only recently a stable numerical algorithm for computing CLVs has been proposed [5]. This algorithm was employed to investigate chaotic fluid systems such intermittency in turbulence [6] and acoustics [4]. We employ CLV analysis to find a basis of the adjoint space, which is necessary to design the proposed precursors.

METHODS

We consider a fluid system that can be described as a nonlinear dynamical system $\dot{\mathbf{q}} = \mathbf{F}(\mathbf{q})$. The tangent equation $\dot{\mathbf{y}} = \mathbf{J}\mathbf{y}$, where $\mathbf{J} \equiv d\mathbf{F}/d\mathbf{q}$ is the Jacobian, governs the dynamics of an infinitesimal perturbation $\mathbf{y}$ to the solution $\mathbf{q}$. We consider the adjoint equation, $\dot{\mathbf{y}}^+ = -\mathbf{J}^T\mathbf{y}^+$, in which the adjoint variables are denoted by the superscript +. We express the adjoint solutions with the mapping $\mathbf{M}^+(t_0, t^*)$, which is defined as $\mathbf{y}^+(t^*) = \mathbf{M}^+(t_0, t^*)\mathbf{y}^+(t_0)$. We define the adjoint precursor

$$\lambda^{+(i)}_{\Delta T}(t) = \frac{1}{\Delta T}\ln\left(\frac{||\mathbf{M}^+(t-\Delta T, t)\mathbf{y}^+_{\mathbf{v}^+_i}(t-\Delta T)||}{||\mathbf{y}^+_{\mathbf{v}^+_i}(t-\Delta T)||}\right), \tag{1}$$

where $\mathbf{v}^+_i$ is the i-th adjoint CLV associated with the i-th adjoint Lyapunov exponent. We introduce the quantity $x_{max}(t) = \max_{t' \in (t+\tau)}(x(t'))$ [1] to assess the causality relation between a precursor ν and an observable x, where $\tau = [t_i, t_f]$ is the time interval in which the precursor spikes to foretell the occurrence of an extreme event. We compare the entire time series of the candidate precursor with x_{max} to evaluate the correlation between the earlier spike of ν with a future burst in x. The threshold that defines an extreme event is $x > x_{ee}$, whereas the threshold that defines a precursor for an extreme event is $\nu > \nu^*$. While the former is set a priori, the latter is chosen a posteriori depending on which predictive capability we want to maximize. To assess the performance of any pair (ν^*, x_{ee}), we compute statistical metrics for the classification of imbalanced data sets such as precision, recall and the F_1 score [7], which are based on the probability density functions (PDFs) $\mathcal{P}(\nu, x_{max})$, $\mathcal{P}(\nu)$ and $\mathcal{P}(x_{max})$. Statistical metrics are informative, but they cannot quantify the precursor's capability of correctly predicting an extreme event in the time domain. This is because statistical metrics are computed from the continuous overlapping of the two time series, but we are interested in correlating the spike of the precursor with the burst of the observable (rather than comparing the entire set of values in the interval τ). Therefore, we also assess the performance by evaluating the discrete matching between the two peaks in the time domain. We consider that an extreme event is correctly predicted if, during τ prior to the event, the precursor takes a value $\nu > \nu^*$ during a maximum. Subsequently, we define the Percentage of Predicted Peaks (POPP) as the number of correctly predicted extreme events over the total number of extreme events in the time series. With the POPP and the percentage of true positives over the total number of predictions (TPP), in a similar fashion to the F_1 score, we define a quantity F_{ee} to quantify the performance of the precursor in the time domain

$$F_{ee} = \frac{2}{\text{POPP}^{-1} + \text{TPP}^{-1}}. \tag{2}$$

*Corresponding author. E-mail: ar994@cam.ac.uk

RESULTS AND DISCUSSION

We test the formulation on a variety of chaotic fluid systems: Rayleigh-Bénard convection [8], turbulent shear flow [9], and electrodissolution [2]. Here, we report the results for an electrodissolution system, which displays homoclinic chaos. We time integrate the three nonlinear ordinary differential equations for 4×10^4 time units. The left panel of Fig. 1 shows the extreme events of the observable x, which phisycally is a current, preceded by spikes in the adjoint precursor associated with the unstable CLV direction, $\nu(t) = 1/\tau_{avg} \int_{t-\tau_{avg}}^{t} \lambda_{0.01}^{+(1)}(t')dt'$, $\tau_{avg} = 1.5$. The average over τ_{avg} is performed to filter out high amplitude and frequency oscillations that are related to the fast dynamics of the bursts. We set $x_{ee} = 15.0$, which is a threshold such that EE% $= 2.2\%$ of the total time is covered by extreme events (755 spikes). In the right panel of Fig. 1, we plot the figures of merit as a function of ν^* for a selected range of the threshold and prediction interval $\tau = [3.3, 4.0]$ along with the statistical False Positive Rate (FPR). The value $\nu_1^* = 1.336$ that maximizes the conventional statistical score, $F_1 = 0.603$, is not suitable for assessing extreme event prediction in the time domain because of the large number of false positives (POPP = 1, TPP = 0.616, FPR/EE% = 0.276 and $F_{ee} = 0.763$). On the other hand, the choice $\nu_2^* = 1.619$, which maximizes the proposed time-domain metric, $F_{ee} = 0.964$, is able to predict 97.5% extreme events with a low rate of false positives of 3.6% (POPP = 0.975, TPP = 0.964, FPR/EE% $= 0.023$). (Note that the intermediate value $\nu_3^* = 1.563$ ensures POPP $= 1$, but it provides more false positives: TPP $= 0.883$, FPR/EE% $= 0.044$ and $F_{ee} = 0.939$ (right panel of Fig. 1).)

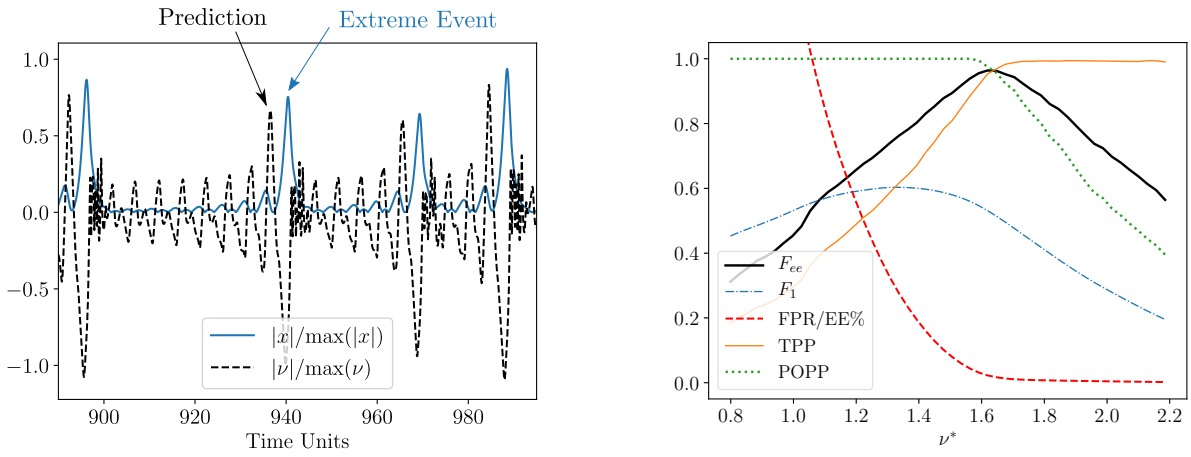

Figure 1: Left: Observable with extreme events and adjoint precursor. Right: different figures of merit as a function of the precursor threshold ν^*.

In conclusion, we propose an adjoint precursor for predicting the onset of extreme events in chaotic systems. We test the precursor in chaotic fluids systems, showing the results for an electrodissolution problem. We quantify the performance of the adjoint precursor with both statistical and time-domain figures of merit. The adjoint precursor performs well against both figures of merits. This work opens up new possibilities for the prediction of extreme events in deterministic systems. Current work is devoted to scaling this method up to high-dimensional turbulent flows.

References

[1] Farazmand, M.& Sapsis T. P. Extreme Events: Mechanisms and Prediction. *Appl. Mech. Rev.*, **71(5)**, 2019.
[2] Beims, M. W. & Gallas, J. A. Predictability of the onset of spiking and bursting in complex chemical reactions. *Phys. Chem. Chem. Phys.*, **20(27)**, 2018.
[3] Oseledets, V. I. A multiplicative ergodic theorem: Lyapunov characteristic numbers for dynamical systems. *Trans. Moscow Math. Soc*, **19**, 1968.
[4] Huhn, F. & Magri, L. Stability, sensitivity and optimisation of chaotic acoustic oscillations. *J. Fluid Mech*, **882**, 2020.
[5] Ginelli, F., Poggi, P., Turchi, A., Chaté, H., Livi, R. & Politi, A. Characterizing dynamics with covariant Lyapunov vectors. *Phys. Rev. Lett.*, **99(13)**, 2007.
[6] Kobayashi, M. U. & Yamada, M. Temporal intermittency in a shell model turbulence in terms of covariant Lyapunov vectors. *J. Phys. A*, **46(25)**, 2013.
[7] He, H., & Garcia, E. A. Learning from imbalanced data. *IEEE Trans. Knowl. Data Eng.*, **21(9)**. 2009.
[8] Pomeau, Y., & Manneville, P. Intermittent transition to turbulence in dissipative dynamical systems. *Commun. Math. Phys.* **74(2)**, 1980.
[9] Moehlis, J., Faisst, H. & Eckhardt, B. A low-dimensional model for turbulent shear flows. *New J. Phys*, **6(1)**, 2004.

ODE TO AN ICICLE: ON THE GROWTH MECHANISM OF RIPPLED ICICLES

John Ladan * [1] and Stephen W. Morris[1]
[1]Department of Physics, University of Toronto, 60 St George St.,Toronto, Ontario, Canada, M5S 1A7.

Summary Icicles are familiar ice formations with a distinctive morphology. Icicles form when water drips from a point of support into sub-freezing air. Liquid water flows over the icicle's evolving shape, onto which some of the water freezes, while the remaining water drips from the tip. Icicles often have a rippled shape, which has been traced to an instability triggered by the presence of small amounts of impurities in the water. We grew rippled icicles under controlled laboratory conditions using a dye as the impurity. The dye allowed the exterior flow of the water over the icicle surface to be visualized. In addition, we examined cross sectioned icicles and used the pattern of inclusions observed to study the concentration dependence of the ripple wavelength. Both these studies shed new light on the unexplained mechanism of the rippling instability.

Introduction

Icicles are deceptively simple-looking natural ice formations. They are an example of "wet" ice growth [1], in which a gravity-driven thin-film flow of the liquid phase control the ice growth mechanism. While ordinary icicles are obviously mostly harmless, similar wet ice build-up processes can be a significant hazard if they occur on power lines [2] or aircraft wings [3]. Accounting for the shape of such ice formations is a difficult free-boundary growth problem with a natural time scale separation between the slowly evolving shape that forms the substrate for the relatively fast flow of the liquid water. This flow in turn determines the availability of water for ice formation as well as controlling the flux of latent heat away from the freezing surface and into the surrounding cold air. The emergent shape of an icicle is thus the result of a highly non-equilibrium growth process [4].

Rippled icicles

It is commonly observed that some natural icicles exhibit a rippled shape, while others are smooth. The wavelength of the ripple pattern is remarkably constant, close to 1 cm, independent of the growing conditions. This suggests that icicle growth is subject to a strongly wavelength-selective morphological instability. In the first detailed laboratory study of icicle formation and morphology, Chen *et. al* [5] showed that the presence of impurities in the water is responsible for this instability. The growth rate of the ripple pattern was roughly logarithmic in the impurity concentration. No threshold concentration was observed for the onset of the instability, which is apparent even at very low concentrations (around 20 ppm of NaCl), however icicles grown from distilled water are smooth. For concentrations below 300ppm, ripples travel slowly and consistently upward during growth. Previous theories of the rippling instability [6, 7, 8] assumed pure water and thus completely fail to account for the dependence of the instability on impurities.

In the present study, we extend and improve upon the experimental results of Chen *et. al* [5], using an updated version of the same apparatus. In addition to using NaCl, we employed a strong dye (sodium fluorescein) as an impurity, and take sections of the icicle to observe the interior. The dye allowed tracking of the impurities visually — appearing orange when trapped inside the ice, but fluorescing green when in liquid on the surface. We propose that the mixed-phase nature of the ice and the rivulet pattern on the surface are intrinsic to the mechanism of ripple formation.

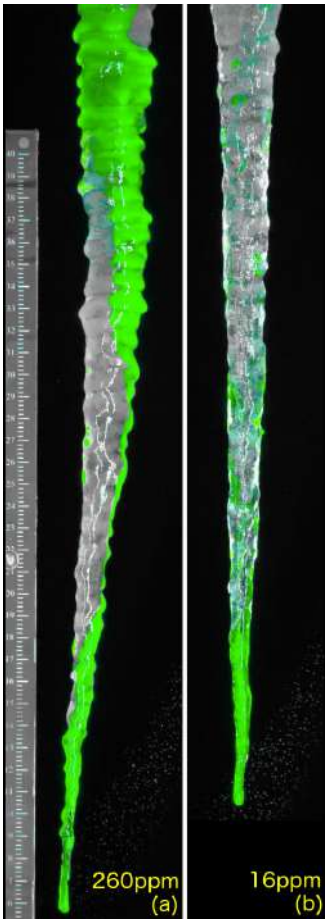

Figure 1: False-colour images of two icicles. The liquid on the surface is highlighted green. The 260ppm icicle (a) has significant ripples and much more liquid covering the surface than the 16ppm icicle (b).

Surface coverage of liquid

Sodium fluorescein only emits green light when in liquid, providing a visualization of the rather complex pattern of water flow over the surface of the growing icicle (Figure 1). The fluorescence shows that the surface flow is entirely different than the full-coverage thin shear flow assumed by existing models of the rippling instability [6, 7, 8]. This flow turns out not to wet the entire surface of the icicle, but rather is confined to rivulets. The complex and shifting pattern of rivulets interacts with the topography of the ripples.

Isolating the liquid covered parts of the icicle, we observe that the amount of surface covered increases with concentration, and the liquid tends to sit atop the ripples. The location of the water appears to coincide with regions of higher growth, consistent with the upward travel direction of the ripples.

*Corresponding author. E-mail: jladan@physics.utoronto.ca.

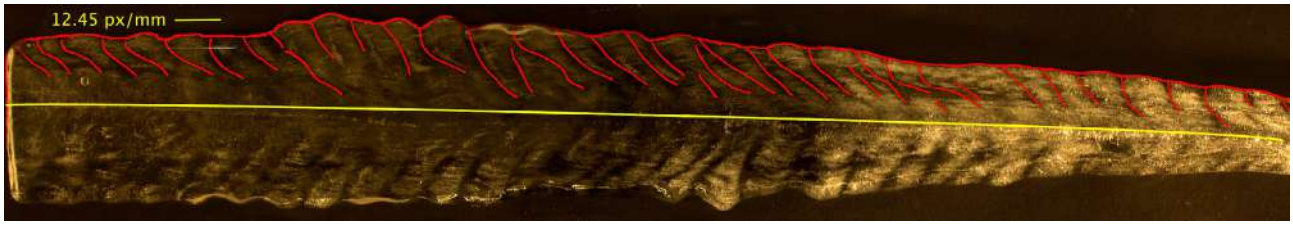

Figure 2: A longitudinal section of an icicle grown with 80ppm NaCl with clear sections of ice highlighted above the centreline. Down is to the right. The upward angle of the inclusions matches the upward growth direction of the ripples, and the median distance between lines matches the wavelength of the ripples. Near the middle of the icicle, there is evidence of wavelength selection where a band of inclusions is edged out by its neighbours.

Trapped impurities

When rippled icicles are cross-sectioned, a chevron pattern of inclusions within the ice is observed [4], which is correlated with the exterior rippled shape. We made the first systematic study of the pattern of inclusions, which contain much more information about the rippling instability than is available from the exterior topography alone. When viewed closely, inclusions appear to be small bubbles inside of the ice. However, when a dye (sodium fluorescein) is used, we can observe that the inclusions are actually filled with the instability-driving impurities.

Longitudinal sections give a view of the growth of the icicle over time. The inclusions have a chevron-shape (Figure 2), with a median centre-to-centre distance between bands matching the wavelength of the ripples (typically 7-10 mm). The upward slope of the inclusions matches what we expect from the ascending ripples observed in past experiments [5]. The concentration dependence of the spacing between bands of inclusions is weak, as shown in Figure 3.

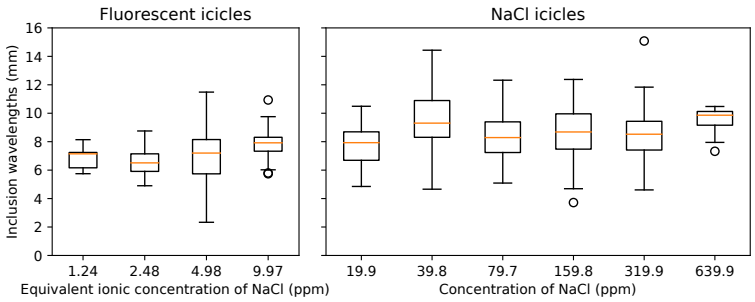

Figure 3: Measured centre-to-centre distances of inclusion bands in icicles. The values match previous measurements of the ripple wavelength [5]. The slight increasing trend with concentration is not statistically significant with this number of measurements.

Unsurprisingly, the amount of the inclusions increases with salt concentration. At the lowest concentrations (less than 20ppm NaCl), the ice is nearly pure. When ripples are visible on the icicle (between 20ppm and 200ppm NaCl) the chevron pattern is clear in the interior. At higher concentrations in this range, there are also signs of wavelength selection, as some bands of inclusions are squeezed out by their neighbours. Above roughly 300ppm NaCl (one tenth the concentration of sea water), there is no longer a chevron pattern and the entire interior appears to be mixed-phase even though ripples are still present. This is also the concentration above which the phase-speed of the ripples (up or down the icicle) is unpredictable, which suggests the bands of pure ice may control the travel of the ripples.

Conclusions

There exists no complete theory of icicle growth which includes impurity effects and the rippling instability. Our observations suggest that the instability is not simply due to freezing point depression or the complete rejection of impurities from the ice. A complete theory needs to account for the pattern of trapped inclusions, as well as for the incomplete surface coverage due to the varying surface properties of the ice.

References

[1] L. Makkonen, Phil. Trans. R. Soc. A, **358**, 2913, (2000).
[2] M. Farzaneh (ed.), *Atmospheric Icing of Power Networks* (Springer, Netherlands, 2008).
[3] R. W. Gent, N. P. Dart, and J. T. Cansdale, Phil. Trans. R. Soc. A **358**, 1776 (2000).
[4] L. Makkonen, J. Glaciol. **34**, 116 (1988).
[5] A. S-H. Chen and S. W. Morris, New Journal of Physics, **15**, 103012 (2013).
[6] K. Ueno, Phys. Rev. E **68**, 021603 (2003); Phys. Rev. E **69**, 051604 (2004); Phys. Fluids **19**, 093602 (2007).
[7] K. Ueno and M. Farzaneh, Phys. Fluids **22**, 017102 (2010).
[8] K. Ueno, M. Farzaneh, S. Yamaguchi, and H. Tsuji, Fluid Dyn. Res. **42**, 025508 (2010).

LIFE AND FATE OF A BUBBLE IN A CONSTRICTED HELESHAW CHANNEL

Antoine Gaillard[1], Jack S. Keeler[2], Alice B. Thompson[2], Andrew L. Hazel[2], and Anne Juel *[1]
[1]MCND and Department of Physics & Astronomy, University of Manchester, UK
[2]Department of Mathematics and MCND, University of Manchester, UK

Summary We study experimentally a geometrically-perturbed Hele-Shaw channel which supports several stable invariant modes of bubble propagation. We investigate the evolution of a centred bubble of fixed volume as a function of flow rate and initial shape. We find that the bubble frequently changes topology through the exploration of multiple-tipped modes and that in the long term, either a single bubble may be recovered or multiple bubbles remain, whose relative distance increases with time. We find numerically that these dynamics are orchestrated by weakly-unstable, two-bubble edge states of the system. We also study how the bubble becomes increasingly sensitive to initial conditions and exhibits long and disordered transients as the flow rate increases.

INTRODUCTION

Two-phase displacement flow in a confined geometry is a fundamental problem in fluid mechanics with applications in biomechanics, geophysics and industry. A canonical example is the viscous fingering instability which occurs when air displaces a viscous fluid in a Hele-Shaw channel of width much greater than its depth. A single finger of air, symmetric about the centreline of the channel, is formed following the destabilisation of an initially flat interface [1]. Beyond a threshold value of the driving parameter that depends on the roughness of the channel, this finger becomes unstable to tip-splitting leading to the emergence of complex patterns [2]. As the steady solution is found to be linearly stable for all computed flow rates [3], any further instabilities observed must arise subcritically; that is, they result from finite amplitude perturbations which drive the system away from equilibrium. In addition, the depth-averaged model of this two-phase flow contains alternative families of multiple-tipped symmetric solutions and asymmetric solutions, which are weakly unstable [4].

Recent experiments and numerical simulations [4] have shown that with the introduction of a depth-perturbation to the bottom of the channel henceforth referred to as a rail (Fig. 1a,b), the system retains similar modes of finger or bubble propagation as in the Hele-Shaw channel of rectangular cross-section, but their stability is altered so that several stable invariant solutions occur for the same imposed flow rates, as indicated by the solid lines in the numerical bifurcation diagram of Fig. 1c.

Hence, several long-term invariant outcomes are possible for a bubble propagating from a centred initial position but the bubble may also undergo changes in topology by breaking up into multiple bubbles [5]. In this talk, we characterise the transient evolution of propagating bubbles from controlled initial conditions. We compare our results with numerical simulations which indicate that when the flow-rate is large enough the bubble evolution is guided by transient exploration of the stable manifolds of weakly unstable two-bubble edge states of the system [5].

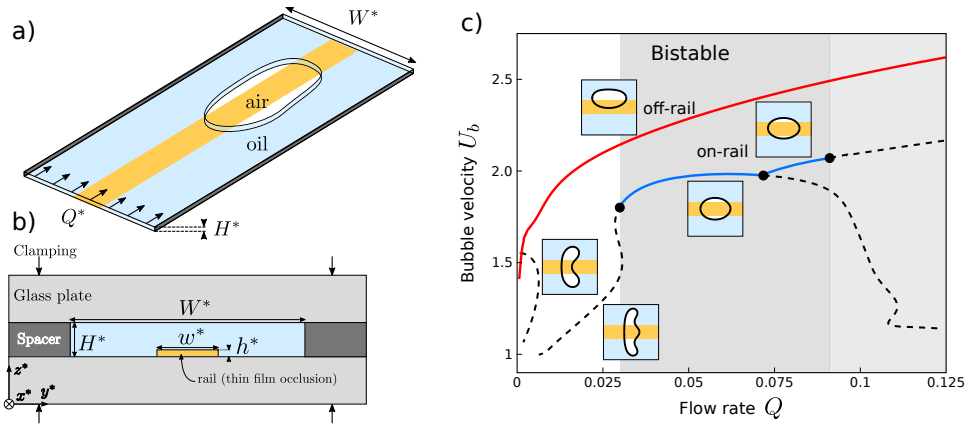

Figure 1: (a) Top-view of the experimental channel with an axially uniform, centred rail. (b) Cross-section of the channel. (c) Numerical bifurcation diagram depicting the steady modes of bubble propagation in terms of the bubble velocity as a function of the flow rate [5]. Stable and unstable modes are indicated by solid and dashed lines, respectively. The red line corresponds to stable off-rail solutions, which are asymmetric about the centreline of the channel and the blue lines to stable on-rail symmetric and asymmetric solutions.

*Corresponding author. E-mail: anne.juel@manchester.ac.uk

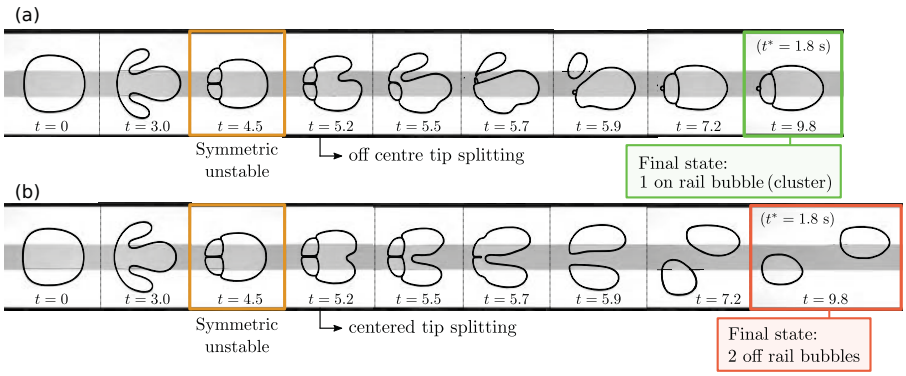

Figure 2: Sensitivity to initial conditions. (a) and (b) show different bubble evolutions starting from bubbles of similar shapes with initial bubble width $b = 0.58$ at relatively large flow rate $Q = 0.10$.

EXPERIMENT

The experimental channel is shown schematically in Fig.1a,b. The channel aspect ratio is fixed at 40, and the rail occupies 25% of the channel width and 2.4% of its height. An air bubble of controlled volume is injected at one end of the channel and propagated by infusing silicone oil at a constant flow rate with a non-dimensional flow rate $Q = \mu Q^* / (W^* H^* \sigma)$, where μ is the dynamic viscosity of the oil, σ the surface tension, $W^* H^*$ the cross-section of the unoccluded channel and Q^* the dimensional flow rate. We impose controlled initial conditions by deforming a centred bubble to a width $b = b^* / W^*$, and propagating it from rest. We track its evolution in top-view with a camera that moves with the bubble.

RESULTS

We find that depending on the initial bubble shape and the value of the flow rate, an initially centred bubble may evolve towards the on-rail or off-rail invariant modes (see Fig. 1c) or undergo a change in topology by breaking up into two bubbles, whose relative distance increases as they propagate. There is a rich variety of transient evolution scenarios leading to these long-term outcomes, which each occurs in well-defined regions of the parameter plane spanning flow rate and initial bubble width.

Above a threshold flow rate, initially slender bubbles tend to evolve towards on-rail invariant modes, often through a complex transient evolution involving break-up and recombination events. By contrast, initially wide bubbles break up into two separating bubbles. Examples of these long-term outcomes are shown in the images of the final states in Fig. 2.

For initially wide bubbles, the early-time evolution leads to a double-tipped bubble reminiscent of the weakly unstable state shown in Fig. 1c. As the bubble propagates, the two tips elongate until break-up into two bubbles on either side of the rail. These two newly formed bubbles may either remain on separate sides of the rail or one may migrate over the rail to recombine with the other. Numerical simulations of this process indicate that the evolution of this newly formed two-bubble system is orchestrated by weakly unstable two-bubble steady solutions whose existence depends on the flow rate and the relative bubble sizes.

For more slender bubbles, the early-time evolution is to a triple-tipped bubble similar to the unstable steady solution in Fig. 1c. The triple-tipped bubble breaks up into three bubbles which recombine into a compound bubble, as illustrated by the first three snapshots in Fig. 2(a-b). This symmetric bubble then breaks up into two bubbles which either recombine into an on-rail asymmetric compound bubble (a) or separate indefinitely (b). Fig. 2 also illustrates the sensitivity of the system at high flow rate since both figures correspond to the same initial condition within experimental resolution. In fact, as the flow rate is increased, the evolution becomes increasingly disordered and the bubble can break up into multiple parts, some of which are sufficiently small to rapidly separate from the larger bubbles as they propagate, resulting in a loss of volume of the remaining parts.

References

[1] Saffman, P.G. & Taylor, G.I. The penetration of a fluid into a porous medium or Hele-Shaw cell containing a more viscous liquid. Proc. R. Soc. A 245, 312–329, 1958.
[2] Tabeling, P., Zocchi, G. & Libchaber, A. An experimental study of the Saffman–Taylor instability. J. Fluid Mech. 177, 67–82, 1987 .
[3] Bensimon, D. Stability of viscous fingering. Phys. Rev. A 33, 1302–1308, 1986.
[4] Franco-Gómez, A., Thompson, A. B., Hazel, A. L. & Juel, A. Sensitivity of Saffman–Taylor fingers to channel-depth perturbations. J. Fluid Mech. 794, 343–368, 2016.
[5] Keeler, J.S., Thompson, A.B., Lemoult, G., Juel, A. & Hazel, A.L. The influence of invariant solutions on the transient behaviour of an air bubble in a Hele-Shaw channel. Proc. R. Soc. A 475, 20190434, 2019.

LOCALISED RADIAL PATTERNS ON THE FREE SURFACE OF A FERROFLUID

D. J. Hill *[1], D. J. B. Lloyd[1], and M. R. Turner[1]
[1]Department of Mathematics, University of Surrey, Guildford, Surrey GU2 7XH, UK

Summary This paper investigates the existence of localised axisymmetric (radial) patterns on the surface of a ferrofluid; smooth, bounded solutions which decay exponentially away from the pattern's centre (core). Results are shown for an unbounded cylinder of ferrofluid equipped with a linear magnetisation law, where a uniform magnetic field is applied vertically through the fluid. For a critical applied field strength, three classes of stationary radial solutions are found: spots A & B which have a larger magnitude at the core, and rings which have algebraic decay towards the core. These correspond exactly to the classes of radial solutions found for the Swift-Hohenberg equation [1, 2]. The values of the linear magnetisation μ and depth D of the ferrofluid are investigated and parameter regions in which localised radial solutions emerge are identified.

INTRODUCTION

Localised patterns appear in many physical and biological settings; vegetation in arid-climates [3] and crime hotspot modelling [4] to name but a few. Studying the Rosensweig instability, a normal-field instability where peaks spontaneously emerge from the free surface of a ferrofluid when a supercritical vertical magnetic field is applied, allows analytical investigations to be motivated by experimental results. Localised radial peaks (spots) have been observed by Richter (2005) [5] for local perturbations of the applied magnetic field, which persist when the perturbation is removed.

By setting up the problem as a free-surface variational problem, the ferrohydrostatic equations greatly resemble the equations for the emergence of gravity-capillary waves, which have been studied in great detail. There are also ample examples of using invariant manifold theory to find radial localised solutions for ODEs. However, three significant problems arise for the radial ferrohydrostatic case:

1. The ferrohydrostatic equations include non-autonomous terms, meaning that standard water waves techniques might not apply.
2. The localised radial patterns observed in [5] are dominated by the dynamics near the core, so techniques to find homoclinic solutions, such as in the one-dimensional ferrohydrostatic problem [6], are no longer sufficient.
3. The ferrohydrostatic equations form a quasilinear PDE system, where invariant manifold theory is not currently established, except for periodic solutions [7].

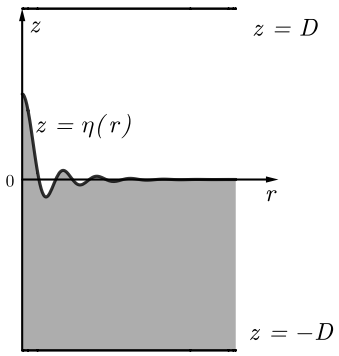

Figure 1: The domain of the problem; a ferrofluid (shaded) below air (white).

This work establishes a formal-analytic approach to finding the existence of radial solutions for the ferrohydrostatic problem, providing a framework for a rigorous proof at a later time. It also contributes techniques for future investigations of localised solutions to a PDE system.

THEORY & RESULTS

The domain is defined as two immiscible fluids from $-D < z < \eta(r)$ and $\eta(r) < z < D$, respectively, separated by a free surface at $z = \eta(r)$, see Fig. 1. The ferrohydrostatic system consists of solving Maxwell's equations in both fluids with a linear magnetisation law $\mathbf{B} = \mu_0\mu\mathbf{H}$ for respective induction and magnetizing fields $\mathbf{B}$ and $\mathbf{H}$ in the ferrofluid, as well as solving the Bernoulli equation at the interface. Applying standard transformations, as seen in [6], the full problem can be reduced to a six-dimensional PDE system of the form

$$\frac{\mathrm{d}}{\mathrm{d}r}\mathbf{u}(r,z) = \mathbf{L}(r)\mathbf{u} + \mathcal{F}(\mathbf{u},\varepsilon,r), \tag{1}$$

where ε is the bifurcation parameter such that $\varepsilon = 0$ is the bifurcation point, $\mathbf{L}(r)$ is a linear non-autonomous differential operator containing ∂_{zz} terms, and $\mathcal{F}$ is the collection of all nonlinear terms. In order to reduce this PDE system to an ODE system, an r-independent basis is required. The operator $\mathbf{L}_0 := \lim_{r\to\infty}\mathbf{L}(r)$ has eigenvalues $\pm ik$ with double multiplicity and $\pm\lambda_j \in \mathbb{R}$ for $j \in \mathbb{N}$, with respective eigenvectors $\{\mathbf{e}, \mathbf{f}, \overline{\mathbf{e}}, \overline{\mathbf{f}}\}$ and $\{\mathbf{e}_j, \mathbf{e}_{-j}\}$ for $j \in \mathbb{N}$. This is a complete basis, and so we can write

$$\mathbf{u}(r,z) = a(r)\,\mathbf{e} + b(r)\,\mathbf{f} + \overline{a}(r)\,\overline{\mathbf{e}} + \overline{b}(r)\,\overline{\mathbf{f}} + \sum_{n=1}^{\infty}\left\{a_n(r)\,\mathbf{e}_n + a_{-n}(r)\,\mathbf{e}_{-n}\right\}. \tag{2}$$

Projecting onto each respective eigenvector, the system reduces to an infinite number of nonlinear, non-autonomous amplitude equations for $a(r), b(r), a_j(r)$.

*Corresponding author. E-mail: d.j.hill@surrey.ac.uk

For $|\varepsilon| \ll 1$, we calculate solutions to the linear amplitude system and construct a fixed-point equation, parametrising the core manifold $\mathcal{W}^{cu}_{-}$, containing all small amplitude solutions that are bounded as $r \to 0$, for all $r \in [0, r_0]$. Next, the far-field manifold $\mathcal{W}^{s}_{+}$, containing all small amplitude solutions that exponentially decay to zero as $r \to \infty$, is parametrised. Stable foliations are constructed such that $\mathcal{W}^{s}_{+}$ can be written as a small perturbation from the stable part of a centre manifold $\mathcal{W}^{c}_{+}$, as seen in Fig. 2. In order to parametrise coordinates on $\mathcal{W}^{c}_{+}$ that decay to zero as $r \to \infty$, it is prudent to introduce geometric blow-up coordinates.

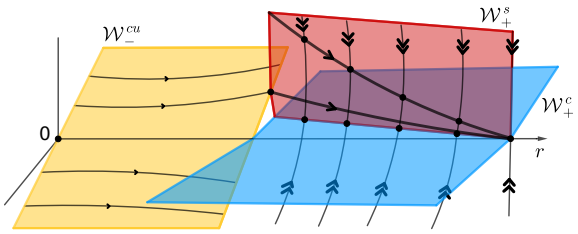

Figure 2: Schematic of the parametrisation of $\mathcal{W}^{s}_{+}$ and matching core & far-field manifolds.

By rescaling the variable $r \to s := \sqrt{\varepsilon} r$, the far-field equations restricted to $\mathcal{W}^{c}_{+}$ reduce to the nonautonomous real Ginzburg-Landau equation

$$\frac{\mathrm{d}^2}{\mathrm{d}s^2}\widetilde{a} = -\frac{1}{s}\frac{\mathrm{d}}{\mathrm{d}s}\widetilde{a} + \frac{1}{4s^2}\widetilde{a} + c_0\widetilde{a} + c_3\widetilde{a}^3, \qquad \widetilde{a} \in \mathbb{R},\ s \in \mathbb{R}^+, \tag{3}$$

where $\widetilde{a} := a/\sqrt{\varepsilon}$, c_0 and c_3 are both constants, $c_0 > 0$ and $c_3 < 0$ for particular values of parameters D, μ and the spatial wavenumber k. This has unique nontrivial decaying solutions that are defined for $\delta_0 < s < \infty$, where $\delta_0 > 0$ is a constant. However, as $\varepsilon \to 0$, control of the point $r = s/\sqrt{\varepsilon} = \delta_0/\sqrt{\varepsilon}$ is lost. Thus, a second change of coordinates must be introduced to control the transition from $r = \delta_0/\sqrt{\varepsilon}$ to the matching point $r = r_0$, see [2]. Having parametrised $\mathcal{W}^{s}_{+}$ at the matching point $r = r_0$, three distinct classes of solutions are found; spot A, spot B, and ring solutions. The spot A solution exists for all $0 < k \neq k_c$, for some critical wave number $k_c > 0$. These solutions remain close to the trivial state and have a free surface profile of the form

$$\eta_A(r) = C_A \varepsilon^{\frac{1}{2}} J_0(kr) + \mathrm{O}(\varepsilon), \qquad 0 \leq r \leq r_0, \tag{4}$$

where $C_A \neq 0$ is a constant, $\mathrm{sgn}(C_A) = \mathrm{sgn}(k - k_c)$, and J_ν is the ν-th order standard Bessel function of the first kind.

The spot B & ring solutions both require the coefficient c_3 in (3) to be negative in order to emerge, see Fig. 4. These solutions remain close to the trivial state and have profiles of the form

$$\eta^{\pm}_B(r) = \pm C_B \varepsilon^{\frac{3}{8}} J_0(kr) + \mathrm{O}(\varepsilon^{\frac{1}{2}}) \qquad 0 \leq r \leq r_0,$$
$$\eta^{\pm}_R(r) = \pm C_R \varepsilon^{\frac{3}{4}} \left[r J_1(kr) + b J_0(kr) \right] + \mathrm{O}(\varepsilon),$$

respectively, where $C_B, C_R, b > 0$ are all constants.

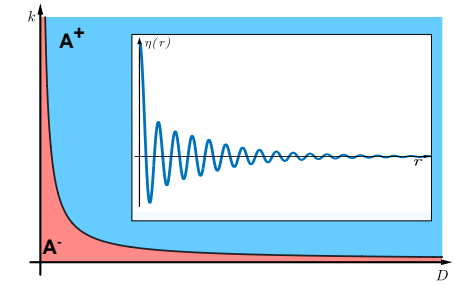

Figure 3: Plot of k in terms of D; spot A solutions have an elevation the blue region (A^+) and a depression in the red region (A^-).

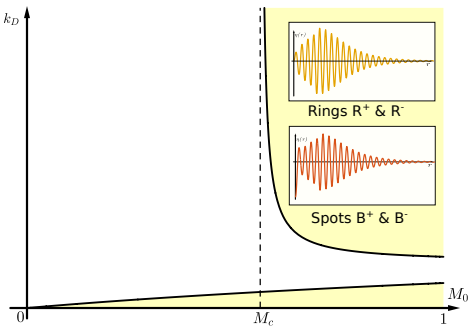

Figure 4: Plot of $k_D := kD$ in terms of $M_0 := \frac{\mu-1}{\mu+1}$; ring & spot B solutions emerge in the yellow regions.

CONCLUSIONS

For the radial ferrohydrostatic problem, one can formally show the existence of three classes of solutions; spot A, spot B, and rings. These solutions scale with the bifurcation parameter ε by $\varepsilon^{1/2}$, $\varepsilon^{3/8}$, and $\varepsilon^{3/4}$, respectively. Given a fixed depth D, localised patterns emerge for a sufficiently large magnetisation M_0. There is a critical spatial wave number k_c such that, for all $k > k_c$, spot A solutions exhibit an elevation at their core. Spot B and ring solutions require a magnetisation M_0 larger than a critical M_c in order to emerge. Existence regions of these localised radial patterns in (M_0, D) parameter space can be seen in Fig. 5.

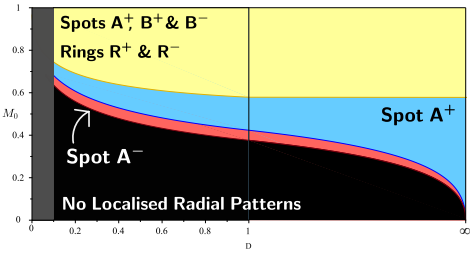

Figure 5: Existence regions of localised radial patterns for varying depth D and magnetisation M_0.

References

[1] Lloyd, D.J.B. & Sandstede B. Localized radial solutions of the Swift-Hohenberg equation. *Nonlinearity.* **22**: 485-524, 2009.
[2] McCalla, S.G. & Sandstede, B. Spots in the Swift-Hohenberg equation. *SIAM J. Appl. Dyn. Syst.* **12**: 831-877, 2013.
[3] Sheffer, E. et al. Why do plants in resource-deprived environments form rings? *Ecol. Complex.* **4**: 192-200, 2007.
[4] Short, M.B., Bertozzi, A.L. & Brantingham, P.J. Nonlinear patterns in urban crime: hotspots, bifurcations, and suppression. *SIAM J. Appl. Dyn. Syst.* **9**: 462-483, 2010.
[5] Richter, R. & Barashenkov, I.V. Two-dimensional solitons on the surface of magnetic fluids. *Phys. Rev. Lett.* **94**: 184503, 2005.
[6] Groves, M.D., Lloyd, D.J.B. & Stylianou, A. Pattern formation on the free surface of a ferrofluid: Spatial dynamics and homoclinic bifurcation. *Phys. D.* **350**: 1-12, 2017.
[7] Scheel, A. Radially symmetric patterns of reaction-diffusion systems. *Mem. Amer. Math. Soc.* **165**: viii+86, 2003.

DYNAMICS OF MULTIPLE BUBBLES IN A CONSTRICTED HELE-SHAW CHANNEL

Jack S. Keeler[1], Antoine Gaillard[2], Alice B. Thompson[1], Anne Juel[2], and Andrew Hazel * [1]
[1]MCND and Department of Mathematics, University of Manchester, UK
[2]Department of Physics & Astronomy and MCND, University of Manchester, UK

Summary We study the dynamics of multiple air bubbles driven by the motion of a suspending viscous fluid within a constricted Hele-Shaw channel via numerical simulation of a depth-averaged model. Despite its apparent complexity the bubbles' transient behaviour is organised by a number of weakly unstable invariant solutions, so-called edge states. An unusual feature of the system is that changes in topology due to bubble break up or coalescence lead to changes in the invariant-solution structure during temporal evolution. Families of two-bubble and single-bubble invariant solutions can be related in the sense that their propagation speeds are identical, but there are two-bubble solutions that do not have single-bubble equivalents.

INTRODUCTION

The motion of one or more bubbles through confined rigid geometries otherwise filled by a viscous fluid is a fundamental problem in fluid mechanics. Recent work has shown that propagation of a single bubble through a Hele-Shaw channel containing a centred, depth-perturbation exhibits a rich and complex dynamics with regions of bistability, symmetry-breaking and evidence of stable and unstable time-periodic solutions [1, 2]. Despite its non-trivial dynamics, the system remains sufficiently simple to be effectively modelled using a depth-averaged theory [2]. Another important feature is that for a sufficiently viscous suspending fluid, the only nonlinearity arises due to the presence of the interface between the two fluids and hence different solutions can be distinguished using only the interfacial morphology. Based on the morphologic similarities between transient interface shapes and known unstable solutions of bubbles in Hele-Shaw cells, Franco-Gómez *et al.*[1] conjectured that the dynamics is organised by weakly unstable invariant solutions of the system. Here, we investigate this conjecture by directly relating the transient dynamics to invariant solutions of the depth-averaged model system. A complicating factor is that the bubble often breaks up into two or more bubbles during its evolution. In some cases, the resulting bubbles will coalesce to recover a single bubble state; in others the bubbles remain separate. Given the prevalence of bubble break up into two smaller bubbles, here we concentrate on two-bubble dynamics.

MODEL

We consider the propagation of two bubbles, each assumed to be a fixed volume of inviscid fluid at constant pressure, through a rectangular (Hele-Shaw) channel of geometry chosen to match that of our experimental studies [1]. The cross-sectional aspect ratio, width (W^*) / height (H^*), is fixed at 40 and the base of the channel contains a centred depth-perturbation, see Fig. 1, occupying 25% of the channel width and 2.4% of the channel height. The bubbles are surrounded by a viscous oil that is extracted at a constant flow rate Q^* from one end of the channel.

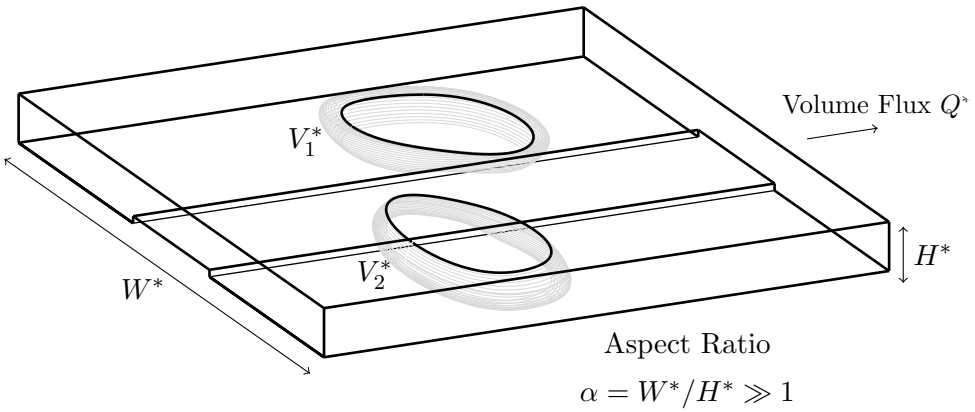

Figure 1: Two bubbles of volumes V_1^* and V_2^* propagate through an axially-uniform channel that contains a small centred geometric perturbation on its base. The suspending viscous fluid is extracted at a constant flow rate of Q^*.

The depth-averaged model system has been previously described [2] and the weak form of the governing equations is solved numerically using a finite element method implemented in the software library `oomph-lib` [4]. The library allows us to compute invariant solutions, determine their stability and perform time simulations all within the same framework. The key governing parameters are the dimensionless flow rate $Q = \mu Q^*/(W^* H^* \sigma)$ and dimensionless volumes of the two bubbles. Here, μ is the dynamic viscosity of the suspending fluid and σ is the constant surface tension at the bubble interface.

*Corresponding author. E-mail: Andrew.Hazel@manchester.ac.uk

RESULTS

In order to identify invariant solutions we use edge tracking techniques [3] combined with time simulations. For the case of two unequal bubbles with a volume ratio of 2:1 illustrative results are shown in Fig. 2 by plotting the trajectories of the centre of mass (x_1, y_1) of the larger bubble.

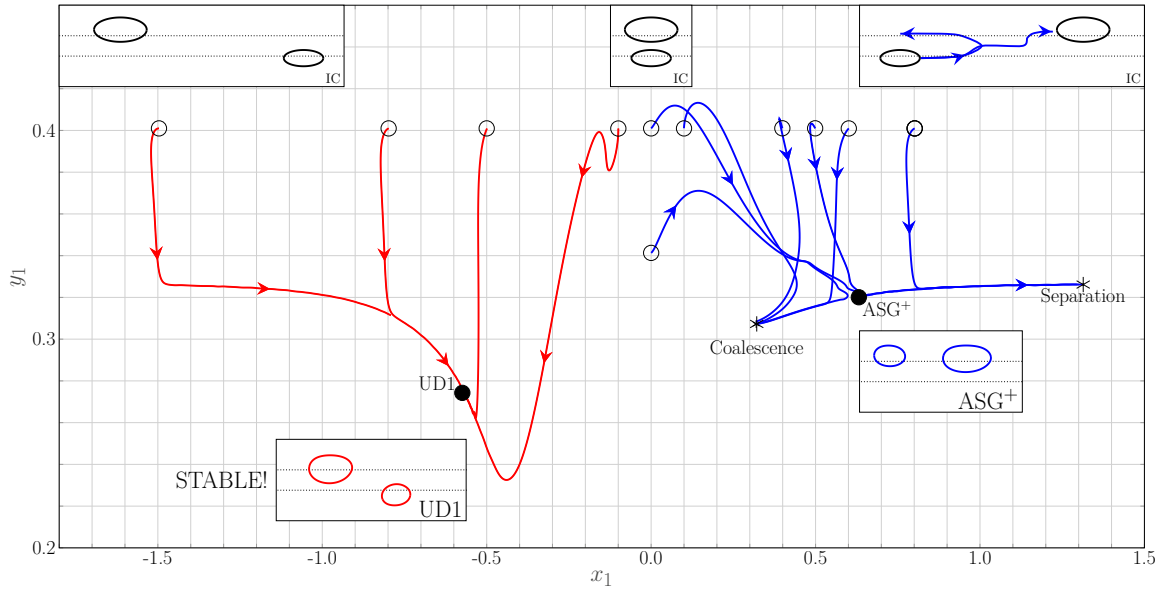

Figure 2: The temporal evolution of a system of two unequal bubbles at $Q = 0.04$ is represented by the trajectories of the centre of mass of the larger bubble: x_1 is the axial distance from the overall centre of mass of the two bubbles and y_1 is the cross-channel distance from the centreline. Initial conditions are shown as open circles and top-view snapshots of three initial conditions are shown as insets labelled IC. The evolution of the system is governed by steadily propagating invariant solutions indicated by filled circles with corresponding snapshots shown as insets labelled UD1 and ASG$^+$.

At the chosen flow rate, $Q = 0.04$, the larger bubble in isolation moves at a greater speed than the smaller bubble. Hence, the larger bubble will move towards the smaller if it is initially upstream ($x_1 < 0$) and the system evolves towards a stable two-bubble state, marked as UD1 in Fig. 2 (red trajectories). If the larger bubble is initially downstream ($x_1 > 0$) the system is instead influenced by a weakly unstable two-bubble state, ASG$^+$ (blue trajectories). If the bubbles are sufficiently close to each other they will eventually coalesce, but otherwise they separate. Thus ASG$^+$ acts as an edge state whose stable manifold divides the initial conditions leading to coalescence from those leading to separation. We use continuation methods to track the location of two-bubble invariant solutions under variations in the flow rate and bubble volumes. The weakly unstable state ASG$^+$ is equivalent to a single-bubble asymmetric solution in the sense that a single bubble of the same volume as the larger of the two bubbles propagates at the same speed for a given flow rate. The stable state UD1 does not have a single bubble equivalent. We find a variety of additional two-bubble invariant solutions not all of which have single-bubble equivalents and conjecture that the number of invariant solution branches increases with the number of bubbles.

CONCLUSIONS

We find considerable evidence that the transient dynamics of two bubbles moving in a constricted Hele-Shaw channel is organised by the many invariant solutions of the system. The propensity of the bubbles to split and coalesce leads to dynamic changes in the invariant solution structure and the number of invariant solutions increases with the number of bubbles, leading to increased complexity. There appears to be a direct correspondence between certain multiple-bubble solutions and single-bubble states, which may explain why the system is able to transition so readily between different bubble topologies.

References

[1] Franco-Gómez, A. *et al.* Bubble propagation in Hele-Shaw channels with centred constrictions. *Fluid Dynamics Research.* **50**:021403, 2018.
[2] Keeler, J. S. *et al.* The influence of invariant solutions on the transient behaviour of an air bubble in a Hele-Shaw channel. *Proc. R. Soc. Lond. A.* **879**:1–27, 2019.
[3] Kerswell, R. R. Recent progress in understanding the transition to turbulence in a pipe. *Nonlinearity.* **18**:R17–R44, 2005.
[4] `oomph-lib` web site **http://www.oomph-lib.org**.

THE ROLE OF A CAPILLARY MENISCUS ON THE FARADAY INSTABILITY

Alessandro Bongarzone[1], Francesco Viola[2], Simone Camarri[3], and François Gallaire*[1]
[1]Laboratory of Fluid Mechanics and Instabilities, École Polytechnique Fédérale de Lausanne, Lausanne, CH-1015, Switzerland
[2]GSSI, Viale F. Crispi, 7, 67100 L'Aquila, Italy
[3]Dept. of Industrial and Civil Engineering, Università di Pisa, Pisa, Italy

Summary The Faraday instability has been classically studied under the assumption of a free surface intersecting orthogonally the rigid container sidewalls. Here, the full system of equations, in both the inviscid and viscous cases, is solved asymptotically via a weakly nonlinear analysis using the multiple scale method; the resulting amplitude equation enables us to introduce the meniscus effects and to investigate how its presence disturbs the stability of the interface associated with the fundamental sub-harmonic parametric resonance. Two extreme cases of free slip and a pinned contact line are considered. Under certain combinations of external control parameters, the static meniscus may strongly modify the transition curves, commonly known as Faraday tongues; furthermore, when viscous dissipation is introduced, the meniscus also influences the instability thresholds.

INTRODUCTION

When a vessel containing liquid undergoes periodic vertical oscillations, the free liquid surface may be parametrically excited, emitting standing waves, depending on the combination of oscillation amplitude and frequency. This instability was first studied by [7], who observed experimentally that the frequency of the fluid oscillations was typically equal to half of the external frequency. Faraday waves have been often studied in analogy with the parametric excitation of systems having one degree of freedom, i.e. a pendulum whose length varies in time, that is governed by Mathieu's equation [5] with the fundamental, sub-harmonic, parametric resonance. Nevertheless, while the natural frequency of the simple parametric pendulum is unique, the fluid system has a countable infinity of eigenfrequencies (and associated eigenmodes) in a finite-size container.

Using the linear dispersion of gravito-capillary waves, [1] determined that the linear stability of the flat free surface of an ideal fluid is governed by a system of Mathieu's equations, whose solutions confirm Faraday's observation that the fundamental free surface response is sub-harmonic. With the exception of [2], the effect of viscous dissipation has been usually introduced a posteriori in the inviscid solution as a linear damping term. These linear analyses have been complemented by weakly nonlinear analysis in a sequence of papers over the last forty years [5, 3, 4].

All these studies, however, are based on the fundamental assumption that the free liquid surface is initially flat, which is necessary for an analytical solution of the problem. This assumption is reasonable in a large container (with respect to the capillary length) but is unrealistic for smaller containers where capillary effects at the meniscus are expected. Under vertical oscillations of arbitrary frequency and amplitude, any non horizontal meniscus emits surface waves that are synchronized with the excitation frequency. Indeed, in a non-inertial reference framework, the vertical periodic oscillations reduce to a modulation of the gravitational acceleration resulting in an oscillating capillary length. As explained by [3], these harmonic waves are not originated by the parametric resonance, but they are always present, even below the instability threshold. Hence, when the conditions for the Faraday instability are met, the Faraday waves evolve on the top of meniscus waves that behave as an unsteady base state, possibly perturbing the classical parametric instability analysis.

INVISCID CASE

We consider a planar (2D) container of height H, width $2L$ and aspect ratio L/H. The importance of the capillary effects is characterized by a Bond number $Bo = \frac{\rho g L^2}{\gamma}$ where ρ is the density, g the gravitational acceleration and γ the surface tension. In addition the wetting angle is denoted by θ_s.

In essence, the multiple scale approach proceeds by considering an order parameter ϵ and expanding the flow oscillation into an $\mathcal{O}(\epsilon)$ response at an eigenfrequency ω_n of amplitude A, and three contributions at order $\mathcal{O}(\epsilon^2)$: (i) the linear meniscus wave response to the vertical forcing $\epsilon^2 F \exp(i\Omega t)$ of small amplitude $\epsilon^2 F$ and frequency $\Omega = (2\omega_n + \epsilon^2 \Lambda)$ slightly detuned (by an order ϵ^2 difference in frequency) from the second harmonic of the considered sloshing wave, and (ii)-(iii) terms stemming from the inviscid flow nonlinearities, oscillating respectively at $2\omega_n$ and 0 frequency.

A very classical weakly nonlinear amplitude equation is obtained at order $\mathcal{O}(\epsilon^3)$ as a solvability condition. However its coefficients intrinsically account for the linear flow response at the forcing frequency, i.e. for the

*Corresponding author. E-mail: francois.gallaire@epfl.ch

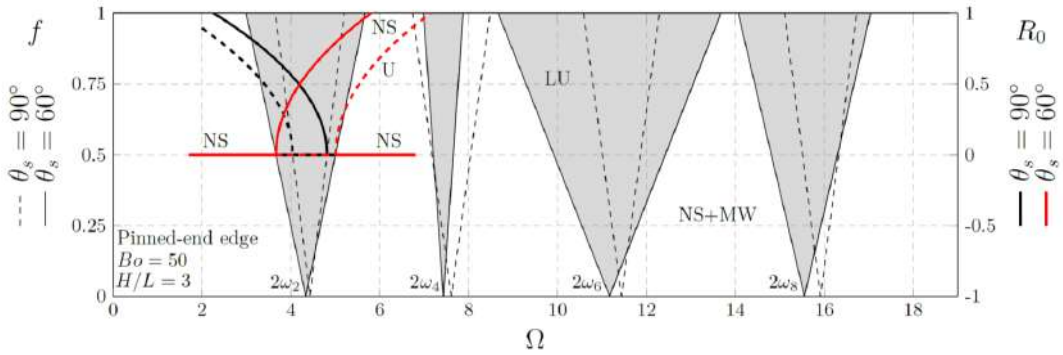

Figure 1: Thin lines: sub-harmonic Faraday tongues for the first four symmetric sloshing modes and pinned-end edge contact line. The unstable regions associated with the antisymmetric modes are not represented; dashed and solid lines are referred to $\theta_s = 90°$ and $\theta_s = 60°$ respectively; thick lines: nonlinear wave amplitude saturation associated with the first symmetric inviscid sloshing mode; black and red lines refers to $\theta_s = 90°$ and $\theta_s = 60°$; here the dashed lines mean the unstable branches, $Bo = 50$.

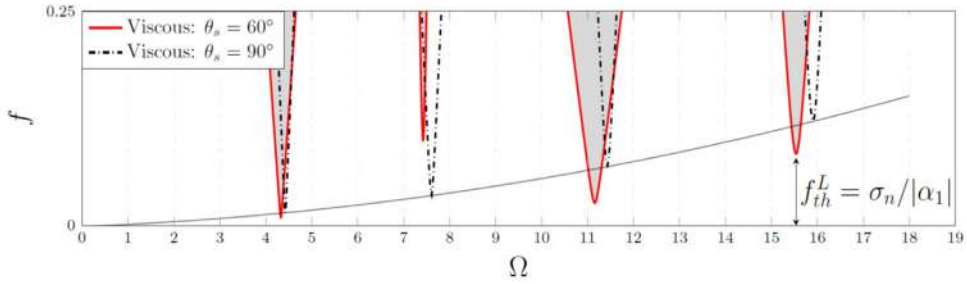

Figure 2: Viscous Faraday tongues for $\theta_s = 60°$ compared with their flat surface analogous case: the effect of the static meniscus on the instability threshold is markedly visible. $Re = 7363$, $Bo = 50$, $L/H = 3$.

meniscus waves. As seen in figure 1, for the a pinned contact line, an aspect ratio of the vessel of $L/H = 3$ (already in the deep water limit) and a Bond number $Bo = 50$, the presence of meniscus waves considerably alters the opening of the different Faraday tongues pertaining to the first four sloshing eigenfrequencies. In addition, they can even reverse the direction of hysteresis in the nonlinear response [3].

VISCOUS CASE

A very similar strategy can be followed including a finite viscosity μ, as long as the Reynolds number is large enough $Re = \frac{\rho g^{1/2} L^{3/2}}{\mu} \sim \epsilon^{-2}$, however to the price of increasingly complex algebraic calculations. Results are reported in figure 2, for $H/L = 3$, $Re = 7363$ and $Bo = 50$. It is seen that the meniscus waves also significantly affect the instability thresholds pertaining to the different tongues.

CONCLUSIONS

We have demonstrated that including the linear response of the flow in presence of a capillary meniscus has significant effects on the sub-harmonic instability tongues of invisicid and viscous Faraday instabilities. The generalization of this approach to higher order resonances hinges on the algebraic complexity of the asymptotic calculations.

References

[1] Benjamin, T. B. and Ursell, F. J., The stability of the plane free surface of a liquid in vertical periodic motion Proceedings of the Royal Society of London. Series A, 225, 1954.
[2] Kumar, K. and Tuckerman, L. S., Parametric instability of the interface between two fluids J. Fluid Mech., 279, 1994.
[3] Douady, S., Experimental study of the Faraday instability J. Fluid Mech., 221, 1990.
[4] Rajchenbach, J. and Clamond, D., Faraday waves: Their dispersion relation, nature of bifurcation and wavenumber selection revisited J. Fluid Mech. 777, 2015.
[5] Fauve, S., Pattern forming instabilities, Hydrodynamics and nonlinear instabilities, C. Godreche and P. Manneville ed., Cambridge University Press, 1998.
[6] Miles, J. W. and Henderson, D., Parametrically forced surface waves, Annual Review of Fluid Mechanics, 22(1) 1990.
[7] Faraday M., Phil. Trans., 1831.

STRONGLY NONLINEAR PATTERNS IN SLOW–FAST QUASI-LINEAR SYSTEMS

Gregory P. Chini * [1], Guillaume Michel[2], Alessia Ferraro[3], and Colm-cille Caulfield[4]
[1]Program in Integrated Applied Mathematics, University of New Hampshire, Durham, NH USA
[2]Institut d'Alembert, Sorbonne Université, Paris, France
[3]Department of Mechanical Engineering, EPFL, Lausanne, Switzerland
[4]DAMTP and BP Institute, University of Cambridge, Cambridge, UK

Summary The quasilinear (QL) reduction provides an effective starting point for the construction of pattern formation theories of certain strongly nonlinear and even ostensibly turbulent phenomena. The QL approximation can be asymptotically justified in the limit that suitably-defined fluctuations evolve rapidly relative to the mean fields about which their dynamics is linearized. Here, a new multiscale pattern formation formalism is developed for slow–fast QL systems susceptible to fast instabilities. A slaving relation for the fluctuation amplitude is derived that obviates the need to temporally resolve the fast dynamics by exploiting the tendency of these systems to self-organize on a *marginal-stability manifold*.

THE QUASI-LINEAR REDUCTION

The quasilinear (QL) or mean-field reduction [1] has proved surprisingly useful in the investigation of a wide variety of forced–dissipative pattern-forming fluid systems. The QL approximation involves parsing flow variables into suitable mean and fluctuation fields and then retaining fluctuation-fluctuation nonlinearities only where they feed back onto the mean fields through Reynolds stress divergences. Here, *quasilinear* should not be conflated with 'weakly nonlinear': indeed, the QL fluctuation fields are sufficiently strong to induce $O(1)$ changes in the mean fields, to which they are two-way coupled. Although increasingly invoked as a useful but *ad hoc* approximation, the QL reduction is asymptotically exact when the mean and fluctuation dynamics are scale separated in time. In particular, the approximation can be justified even for certain constrained or anisotropically-forced systems exhibiting fast *instabilities*, making it a potentially useful framework for the reduced description of strongly nonlinear patterns – the aim of the present work. Noteworthy examples include QL models of strongly-stratified free shear flows [2] (see below) and of various exact coherent states (ECS), e.g. equilibria, traveling waves, and periodic orbits, arising in constant-density wall-bounded flows [3].

A NEW MULTISCALE FORMALISM FOR SLOW–FAST QUASI-LINEAR SYSTEMS

A vexing attribute of slow–fast QL systems is that when the slow mean fields are locally frozen in time, exponential growth of the fluctuations is possible, invalidating the asymptotic reduction. To overcome this difficulty, a new multiscale formalism recently has been introduced [4], which is illustrated here by analyzing the following system of 1D PDEs:

$$\partial_t U = P(z,t) - U - \eta^2, \tag{1}$$
$$\epsilon\partial_t \eta = U\eta + \partial_z^2\eta - \epsilon\eta^3. \tag{2}$$

$P(z,t)$ is a specified inhomogeneous forcing, z is a spatial coordinate, and t is the time variable. As the parameter $\epsilon \to 0$, $U(z,t;\epsilon)$ and $\eta(z,t;\epsilon)$ are slow and fast fields, respectively. Indeed, formally introducing two time scales, $\tau \equiv t/\epsilon$ and $T \equiv t$, so that $U(z,t;\epsilon) \to U(z,\tau,T;\epsilon)$ and $\eta(z,t) \to \eta(z,\tau,T;\epsilon)$, and expanding U and η in an asymptotic power series in ϵ, the following leading-order system is obtained:

$$\partial_T \overline{U}_0 = P - \nu\overline{U}_0 - \overline{\eta_0^2}, \tag{3}$$
$$\partial_\tau \eta_0 = \overline{U}_0\eta_0 + \partial_z^2\eta_0. \tag{4}$$

Here, $\overline{(\cdot)}$ denotes a fast-time average. Unlike (1)–(2), the system (3)–(4) is quasilinear. Exploiting the separation in time scales between the mean and fluctuation dynamics enables the fluctuation equation to be treated as an eigenvalue (rather than initial-value) problem upon substituting the ansatz $\eta_0 = A(T)\hat{\eta}_0(z,T)e^{\sigma(T)\tau}$ into (4). For bounded solutions on the slow time scale, the only acceptable possibilities are that (real) leading eigenvalue $\sigma < 0$, in which case the amplitude $A(T)$ is set to zero, or $\sigma = 0$, in which case the resulting 'Reynolds stress' feedback $\overline{\eta_0^2} = |A|^2|\hat{\eta}_0|^2$ in (3).

For a given mean field, the eigenvalue problem for $\hat{\eta}_0$ is linear. The standard approach for deriving a slow-time (and potentially a slow-space) evolution equation for A – namely, by ensuring that the equations for higher-order fluctuations are solvable – fails to close. Instead, for slow–fast QL systems, $A(T)$ is constrained by the requirement that, once $\sigma = 0$, the fluctuation amplitude must self-consistently adjust to ensure the continued *emergent* marginal stability of the slowly-evolving mean field. Accordingly, a slow-time evolution equation for the growth rate rather than the amplitude is sought by taking the T derivative of the leading-order eigenvalue problem. The associated solvability condition requires

$$\frac{d\sigma}{dT} = \alpha - \beta|A|^2, \tag{5}$$

*Corresponding author. E-mail: greg.chini@unh.edu

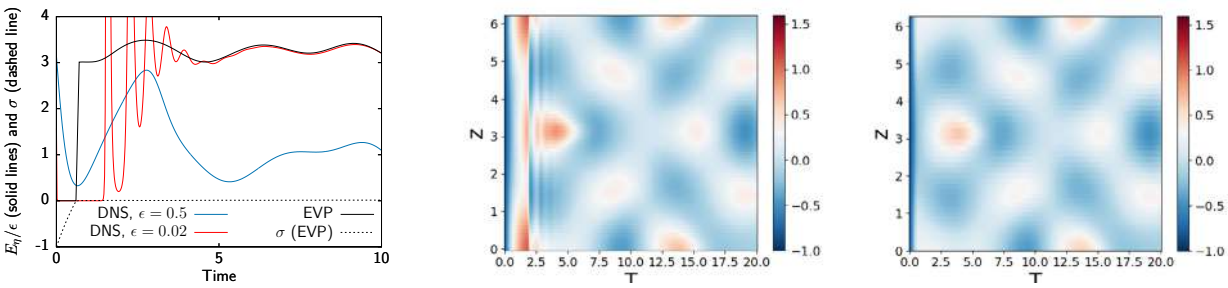

Figure 1: Comparison of the reduced model, in which (4) is treated as an eigenvalue problem (EVP) and solved at each slow-time step of (3) and A is prescribed according to (6), with DNS of (1)–(2). E_η is the fluctuation energy averaged over the fast-time scale. The right-hand plots show the space-time evolution of the slow field U from DNS (middle) and the multiscale algorithm (far right).

where $\alpha = \int_0^L \left(P - \nu \overline{U}_0^2\right) |\hat{\eta}_0|^2 \, dx$ and $\beta = \int_0^L |\hat{\eta}_0|^4 \, dx$ [4]. Recognizing that if $\sigma = 0$ at some slow time instant then $\mathrm{d}\sigma/\mathrm{d}T = 0$ must be enforced to preclude exponential fluctuation growth on the fast time scale (at least for $\alpha > 0$), the slow evolution of the amplitude is determined according to the following algorithm:

$$A(T) = \begin{cases} 0 & \text{if } \sigma < 0 \\ \sqrt{\alpha/\beta} & \text{if } \sigma = 0 \text{ and } (\alpha, \beta) \geq 0. \end{cases} \tag{6}$$

In figure 1 (left), the slow evolution of the fluctuation energy E_η (proportional to $|A|^2$) obtained from the mutiscale QL algorithm (EVP) is compared to that computed via direct numerical simulation (DNS) of the original system (1)–(2) for $\epsilon = 0.02$. The evolution of the leading eigenvalue also is shown, confirming that the algorithm succeeds in locking onto a marginal stability manifold. The right-hand plots provide a comparison of the space-time evolution of the mean field [5].

CONCLUSIONS AND FUTURE WORK

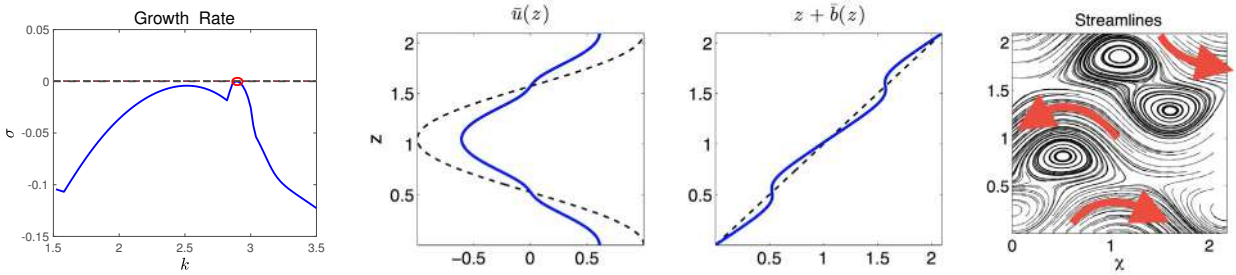

Figure 2: Computation of exact coherent states (ECS) in density-stratified Kolmogorov flow. In the absence of instabilities, the laminar state consists of a sinusoidal shear flow $\bar{u}(z)$ and linear buoyancy profile $z + \bar{b}(z)$, as shown by the dashed curves in the middle plots. In the dual asymptotic limits of large Reynolds number and strong stratification, a slow–fast QL reduction of the governing (2D) Boussinesq equations is possible. Application of the new multiscale formalism has enabled ECS to be obtained in this extreme parameter regime (as depicted by the solid profiles in middle plots and streamline pattern on the far right). For this 2D system, the algorithm ensures that the maximum growth rate $\sigma \leq 0$ over all 'fast' horizontal (χ) wavenumbers k (left-hand plot).

A new, multiscale formalism for slow-fast QL systems has been derived. The approach exploits the tendency of these systems to tune toward a marginal stability manifold, a manifestation of self-organized criticality. The slow evolution of the amplitude is determined via a slaving relationship to the mean field. Interestingly, this slaving is not associated with the usual strong dissipative contraction to a slow manifold but rather is effected by the Reynolds stress feedback from the fluctuations onto the mean field. In ongoing work, the new multiscale formalism is being used to compute ECS in strongly stratified shear flows (figure 2). Since the fluctuation fields are 2D, a further challenge arises [5]: predicting the slow temporal evolution of the 'fast' horizontal wavenumber k of the marginal mode(s) (figure 2, left). Future efforts will aim to incorporate a slow horizontal spatial coordinate (X) in addition to the fast horizontal coordinate (χ), yielding a systematically-reduced description of strongly nonlinear pattern formation in extended domains.

References

[1] Herring J. R. Investigation of problems in thermal convection. *J. Atmos. Sci.* **20**:325–338, 1963.
[2] Rocha C. Coupled Reduced Equations for Strongly Stratified Flows. *Proc. Woods Hole Summer GFD Program*. Woods Hole, MA 2015.
[3] Beaume C., Chini G., Julien K., Knobloch E. Reduced description of exact coherent states in parallel shear flows. *Phys. Rev. E* **91**:043010, 2015.
[4] Michel G., Chini G. Multiple scales analysis of slow–fast quasi-linear systems. *Proc. Roy. Soc. A* **475**:20180630, 2019.
[5] Ferraro A. Exploiting Marginal Stability in Slow–Fast Quasilinear Dynamical Systems. *Proc. Woods Hole Summer GFD Program*. Woods Hole, MA 2019.

THE EDGE OF CHAOS AS A LAGRANGIAN COHERENT STRUCTURE

Miguel Beneitez * [1], Yohann Duguet[2], Philipp Schlatter[1], and Dan S. Henningson[1]
[1]Linné FLOW Centre and SeRC, KTH Engineering Mechanics, Royal Institute of Technology, Stockholm, Sweden
[2]LIMSI, University Paris-Saclay, Orsay, France

Summary Subcritical transition to turbulence in shear flows rests on a dividing manifold called the edge, delimiting trajectories approaching the laminar state from those approaching the turbulent state, in an appropriate state space. We apply here concepts and tools from Lagrangian analysis of material barriers, applied to investigate the edge manifold directly in the state space of autonomous arbitrary high-dimensional dissipative system, in which it is re-interpreted as a Lagrangian Coherent Structure (LCS). Two different diagnostics, Finite-time Lyapunov exponents and Lagrangian Descriptors, are used and compared with respect to their ability to identify the edge and their properties. They are illustrated on several low-order models of hard transition of increasing dimension and complexity, as well on well-resolved simulations of the Navier-Stokes equations in the case of plane Couette flow.

INTRODUCTION

A stimulating breakthrough occurred in the research on transition to turbulence, when researchers started adopting tools from deterministic chaos theory and dynamical systems, supported by the on-going progress of computer simulations. Among these recent developments, a central idea is that of "edge states": nonlinear flow structures living at the dynamical border between laminar and turbulent flow [1]. Being saddles of the system, they guide the evolution of the flow going towards turbulence [2]. Their stable manifold, called the edge of chaos, is of codimension one. Although the numerical bisection method used to identify such states is now classical, its limitations were pointed out in the case of spatially boundary layer flows [3]. In a radically different framework, there was recent progress in Lagrangian studies of tracers. The concept of Lagrangian Coherent Structure (LCS), i.e. sets of specific trajectories structuring the volume-preserving state space of the tracers, has gained maturity [4]. In particular the edge manifold mentioned above can be described efficiently as a hyperbolic repelling LCS of infinite dimension [5].

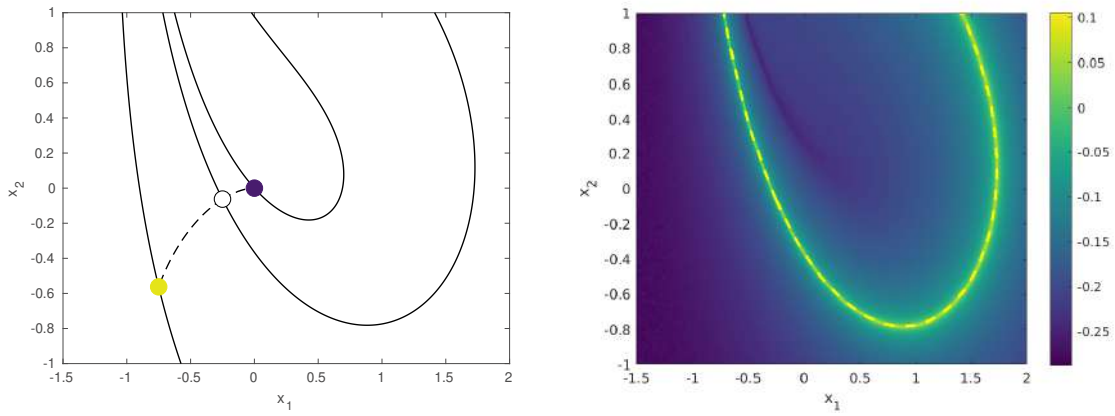

Figure 1: Left: state space for the two-dimensional Dauchot-Manneville system [7], solid points are stable fixed points and the empty point is a saddle node edge state. Solid lines are the stable or superstable manifolds of the fixed points and the dashed line is the unstable manifold of the edge state. Right: Stable manifold of the edge state visualised using isocontours of Finite-time Lyapunov exponents (FTLEs) for T=60. The ridge in the FTLEs captures efficiently the stable manifold of the edge state displayed in the left figure.

NEW INDICATORS TO LOCATE THE EDGE MANIFOLD

The main idea of this contribution is to use tools used in the study of LCSs, usually restrained to fields such as oceanography, to investigate the high-dimensional state space associated with transitioning flows. The main scalar indicator used in LCS studies is the finite-time Lyapunov exponent (FTLE), defined from the the leading eigenvalue of the right Cauchy-Green tensor. FTLEs measure a rate of divergence around a given finite-time trajectory defined between two times t and $t+T$. The challenge is to transfer a concept stemming from low-dimensional volume-preserving systems to arbitrary-dimensional dissipative systems. In autonomous systems, repelling hyperbolic LCSs can be well identified by ridges of FTLEs [4]. Being barriers to transport in state space, they nicely correspond to the notion of a dividing manifold except that they can be defined from finite-time data.

*Corresponding author. E-mail: beneitez@kth.se

An alternative to FTLEs consists of the Lagrangian Descriptors (LDs) described in Ref. [6]. Forward LDs measure a norm akin to the arclength along a finite-time trajectory between two times t and $t+T$. Their advantage is their ease of computation, their scalabilty and their ability to identify stable manifolds in the dissipative context.

Both indicators (FTLEs/LDs) have been tested to highlight the edge manifold in a series of low-dimensional models of increasing dimension. This is illustrated here in Fig. 1 for the case of the two-dimensional Dauchot-Manneville model [7], in which the edge is simply the stable manifold of the edge state, in this case the only saddle point of the system. This example is visually striking since the whole state space can be understood in one look.

EDGE TRACKING REVISITED

Incorporating ideas from the LCS community and extending them to arbitrary dimension makes it possible to revisit the edge tracking algorithm and make it more efficient computationally speaking. Since LCS can be identified by ridges of the FTLEs, the numerical optimisation of the FTLEs can be used to land exactly on the edge manifold. The same strategy has been used for LDs to detect edge trajectories and the related edge states in an almost infinite-dimensional case: a well-resolved direct numerical simulation plane Couette flow in a periodic cell. The associated state space has a dimension of $O(10^5)$. For both descriptors the algorithm finds the edge state fast and with arbitrary accuracy. While both methods outperform the classical bisection in terms of numerical efficiency, the revised bisection method based on LDs (which does not rely on an estimations of the Chauchy-Green tensor) has proved to be one order of magnitude faster for the studied cases, and relies on smaller values for the time horizon T.

CONCLUSIONS

In this conference contribution, we generalise here the popular notion of LCS to high-dimensional dissipative systems. The concept of edge manifold nicely corresponds to a subset of the repelling LCSs that can be identified using such descriptors as FTLEs or LDs. The advantage is not only a revised and more rigorous definition of the edge, but also faster algorithms for the numerical identification of edge states.

References

[1] Skufca, J. D., Yorke, J. A. and Eckhardt, B. Edge of chaos in a parallel shear flow. *Phys. Rev. Lett.*, **96**, 174101, (2006).

[2] Khapko, T., Kreilos, T., Schlatter, P., Duguet, Y., Eckhardt, B. and Henningson, D.S. Edge states as mediators of bypass transition in boundary-layer flows. *J. Fluid Mech.* **801**, R6, (2016).

[3] Beneitez, M., Duguet, Y., Schlatter, P., and Henningson, D. S. Edge tracking in spatially developing boundary layer flows. *J. Fluid Mech.*, **881**, 164-181, (2019).

[4] Haller, G. Lagrangian coherent structures. Annual Review of Fluid Mechanics. *Annu. Rev. Fluid Mech.* **47**: 137-162, (2015).

[5] Beneitez, M., Duguet, Y., Schlatter, P., and Henningson, D. S. Edge manifold as a Lagrangian coherent structure in a high-dimensional state space. *Phys. Rev. Research*, **2**, 033258, (2020).

[6] Mancho, A. M., Wiggins, S., Curbelo, J., Mendoza, C. Lagrangian descriptors: A method for revealing phase space structures of general time dependent dynamical systems. *Commun. Nonlinear Sci.*, **18**, 3530-3557, (2013)

[7] Dauchot, O., and Manneville, P. Local versus global concepts in hydrodynamic stability theory. *J. de Phys.*, **7**, 371-389, (1997).

FLOW REVERSALS IN THE SPHERICAL RAYLEIGH-BÉNARD PROBLEM

Philippe Beltrame * [1]
[1]Avignon Université, INRAE, UMR EMMAH, Avignon, France

Summary The aim of the paper is to find and analyze flow reversals in the spherical Rayleigh-Bénard problem. The (3,4) mode interaction near the onset of convection is studied using amplitude equations by the center manifold reduction. We showed the existence of aperiodic flow reversals involving non-axisymmetric state-states, namely with octahedral symmetry. These dynamics are related to the existence of heteroclinic cycles of steady-states. The spherical symmetry plays a crucial role in their existence. The heteroclinic cycles may be not stable and intermittencies between flow reversals and chaotic dynamics are observed. Our results differ from the existing models of reversals in the geophysical context.

INTRODUCTION

Initially motivated by geophysical experiments (GEOFLOW project [1]), this study investigates numerically and theoretically the flow reversals of thermal convection in a spherical shell under a central force field. The problem is invariant by the $O(3)$ spherical symmetry and the case of a small rotation is studied as a perturbation. Since Friedrich and Haken [2] it is known that flow reversals between axisymmetric steady-states may occur when the spherical modes $\ell = 1$ and 2 are in competition. Chossat and Guyard [3] have shown the existence of heteroclinic cycles due to the spherical symmetry for the $(\ell, \ell + 1)$ mode interaction. These cycles induce reversals between axi-symmetric steady-states. Recently, we showed for the (3,4) mode interaction the existence of heteroclinic cycles involving steady-states with octahedral symmetry [4]. The dynamics is much more complex than for the reversals between axi-symmetry solutions. After a recall of the method and theoretical tools, we focus on the existence of flow reversals for the (3,4) mode interaction.

MODELING AND THEORETICAL TOOLS

The Rayleigh-Bénard convection is studied considering an incompressible Newtonian fluid under the Boussinesq approximation. The fluid is confined between two concentric spheres of radii R_{in} and R_{out} ($R_{in} < R_{out}$). A radial force field proportional to $g(r)$ acts on the fluid. When the inner sphere is heated uniformly at T_{in} and the outer sphere is cooled uniformly at $T_{out} < T_{in}$ a temperature gradient appears. The gravity field $g(r)$ encountered in the geophysical context for low-density fluid surrounding a high-density ball (like the Earth's inner core) is mainly proportional to $1/r^2$. In the laboratory, the dielectrophoretic central force field is $1/r^5$-dependent field as for the GEOFLOW experiment. In this work we focused on force fields due either to gravity or dielectrophoretic effect. The thermal convective flow depends on three non-dimensional parameters: the aspect ratio $\eta = \frac{R_{in}}{R_{out}}$, the Prandtl number Pr (ratio of kinematic viscosity to thermal diffusivity) and the Rayleigh number Ra measuring the buoyancy force. The resulting equations with no-slip boundary conditions can be found for instance in [5].
For a critical Rayleigh number and aspect ratio, the marginal modes of the linear problem span the space V of eigenmodes with the spherical modes $\ell = 3$ and 4. It is a well-established fact that the Rayleigh-Bénard problem satisfies the hypothesis of the center manifold reduction theorem, which allows to reducing the system of Partial Differential Equations (PDE) to an Ordinary Differential Equations (ODE) defined in the space V. The spherical symmetry is responsible for the high dimension of the center manifold, i.e. $\dim V = 16$ for the (3,4) mode interaction. The use of concepts and techniques of Equivariant Bifurcation Theory [6] is of crucial importance in the bifurcation analysis. For instance, the isotropy subgroups lattice identifies the possible bifurcated steady-states and their symmetry and helps to find possible heteroclinic cycles. According to [4], the onset of convection has to be a codimension 3 bifurcation in order to obtain complex time-dependent dynamics as intermittent-like behaviours. In the next section, we focus to flow reversals dynamics and their link with the structure of heteroclinic cycles of steady-states or rotating waves.

FLOW REVERSALS

Intermittent like behavior appears for specific parameter domains: long periods of quasi steady-states (axisymmetric or octahedral patterns) followed by sudden excursions to regimes far from equilibrium and relamination to another steady-state. Some of these dynamics result from a cycle of heteroclinic connections between steady-states. An example of this dynamics is displayed in Fig. 1(a). The plateaux displayed in the time evolution correspond to long duration near the steady-states with octahedral symmetry. The short transition between reversed steady-states appears with the sudden wake-up of the mode 3. The symmetry of steady-states is broken during the transitions between equilibria: the first transition corresponds to the di-hedral symmetry of order 6 and the back transition has the tetrahedral symmetry (see snapshots in Fig. 1).

*Corresponding author. E-mail: philippe.beltrame@univ-avignon.fr.

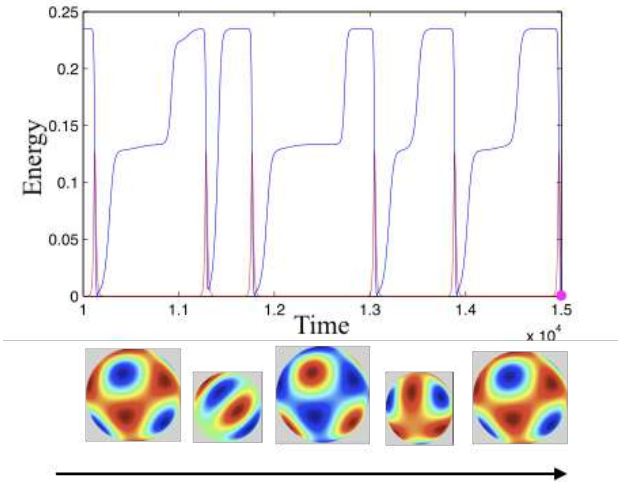

(a)

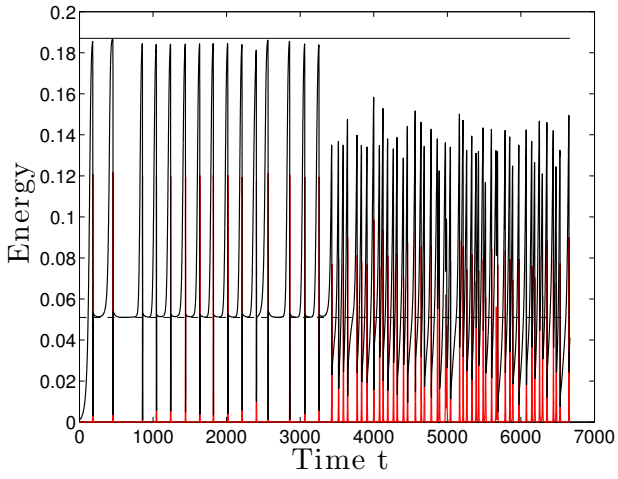

(b)

Figure 1: (a) [Top] Time evolution of the energy of the modes 3 and 4 (red and blue lines respectively) during the heteroclinic cycle. [Bottom] Evolution of the temperature field during the heteroclinic cycle. Large snapshots represent steady-states with octahedral symmetry and smaller snapshots represent a state during flow reversals. (b) Time evolution of the energy of the mode 3 [red] and mode 4 [black]. Firstly, the dynamics is close to a heteroclinic cycle similar to the one in Fig. 1 and suddenly ($t > 3500$) a chaotic dynamics takes place.

The heteroclinic cycles are not asymptotically stable in the usual sense [8]: the phase-space trajectories remain in the vicinity of heteroclinic connections but do not converge to the steady-states. As a consequence, the duration near the steady-states do not increase cycle by cycle. Indeed, the heteroclinic cycle may be unstable leading to intermittencies between the reversal and chaotic dynamics. In Fig. 1b the time evolution of the (3,4) modes lets appear a dozen of reversals disrupted by an irregular dynamics for which no steady-state is observed during for a long time. The heteroclinic cycle is in competition with a chaotic set which has repellent manifolds.
These reversals differ from the mechanism proposed in literature. The transitions between reversals are not identical as in [7]. Moreover, the noise is not required to escape from the steady-states in contrast to [7] and [8] .

These complex dynamics may remain in the rotating case. The equilibria become rotating waves (see for instance [9]) and the axis of these rotating waves coincides with the rotation axis. The consequence of this prevailed axis is that a part of the dynamics complexity vanishes but not the phenomenon of flow reversals.

CONCLUSION

We showed the existence complex aperiodic flow reversals between octahedral equilibria. The spherical symmetry plays a key role in their existence. The reversal mechanisms differ from the literature regarding the dynamo problem. The persistence of flow reversals in the rotating case spurs to study the case of higher rate rotation that is relevant in the geophysical context.

References

[1] I. Mutabazi, H. N. Yoshikawa, M. T. Fogaing, V. Travnikov, O. Crumeyrolle, B. Futterer, and C. Egbers, *Thermo-electro-hydrodynamic convection under microgravity: a review*, Fluid Dynamics Research, 48 (2016), p. 061413.

[2] R. Friedrich and H. Haken, *Static, wavelike, and chaotic thermal convection in spherical geometries*, The American Physical Society, 34 (1986), pp. 2100–2120.

[3] P. Chossat and F. Guyard, *Heteroclinic cycles in bifurcation problems with $o(3)$ symmetry and in the spherical bénard problem*, J. Nonlinear Sci., 6 (1996), pp. 201–238.

[4] P. Beltrame and P. Chossat, *Onset of intermittent octahedral patterns in spherical bénard convection*, European Journal of Mechanics - B/Fluids, 50 (2015), pp. 156 – 174.

[5] V. Travnikov, F. Zaussinger, P. Beltrame, and C. Egbers, *Influence of the temperature-dependent viscosity on convective flow in the radial force field*, Phys. Rev. E, 96 (2017), p. 023108.

[6] P. Chossat and R. Lauterbach, *Methods in Equivariant Bifurcations and Dynamical Systems*, World Scientific, Singapore, 2000.

[7] F. m. c. Pétrélis, S. Fauve, E. Dormy, and J.-P. Valet, *Simple mechanism for reversals of earth's magnetic field*, Phys. Rev. Lett., 102 (2009), p. 144503.

[8] P. Chossat and D. Armbruster, *Dynamics of polar reversals in spherical dynamos*, Proc. R. Soc. Lond. A, 459 (2003).

[9] F. Feudel, N. Seehafer, L. S. Tuckerman, and M. Gellert, *Multistability in rotating spherical shell convection*, Phys. Rev. E, 87 (2013), p. 023021.

A PROBABILISTIC PROTOCOL TO ASSESS THE CONTROL OF FINITE-AMPLITUDE INSTABILITIES: APPLICATION TO TRANSITIONAL FLOWS

Cédric Beaume * [1], Anton Pershin[1], and Steve Tobias[1]
[1]School of Mathematics, University of Leeds, Leeds LS2 9JT, United Kingdom

Summary Transition to turbulence is an instability in which a laminar flow becomes chaotic. In most canonical flow setups, this occurs due a finite-amplitude instability: a perturbation of sufficient energy is necessary to trigger transition. Assessing the robustness of the laminar flow and, thus, the likelihood of observing transition to turbulence, is not straightforward: perturbations of different amplitude, but also of different shapes, behave differently. To reliably quantify the laminar flow robustness, we determine the probability that random perturbations decay as a function of their amplitude. We apply the same protocol in the presence of a well-known control strategy aimed at suppressing transition to quantify its efficiency. The protocol introduced here is versatile and can be used to study any finite-amplitude instability.

INTRODUCTION

In a large number of applications involving fluid transport, it is critical to maintain the flow in its laminar state, where it is associated with a relatively low dissipation rate. If left uncontrolled, the flow might transition to turbulence and yield substantial energy losses and increased wall-friction. Such an instability does not necessitate any additional physics than that of a sheared flow and is thus determined entirely by one parameter, the Reynolds number (hereafter Re). As a result of its simplicity, it has been studied for more than a century [1] in simple wall-bounded flows driven only by a pressure gradient (e.g. pipe flow) or by wall motion (e.g. plane Couette flow).

We focus here on plane Couette flow, the viscous incompressible flow confined between two parallel walls moving in opposite directions. The last decade saw substantial progress in the description of this flow as a dynamical system. In particular, the complexity of the edge of chaos, the separatrix between the basins of attraction of the laminar and turbulent flows, has been characterised [2], the local attractor on the edge has been computed in small [3] and large domains [4], the smallest perturbation to transition, or minimal seed, has been found [5]. Further to these findings, the instability has been characterised statistically and related to directed percolation [6, 7].

The most natural way to determine the success or failure of a control strategy in suppressing transition to turbulence is to verify whether or not it increases the robustness of the laminar flow to perturbations. This is not easily achieved: the statistical threshold for transition [6] does not inform on how sensitive the flow is in the subcritical regime; and the minimal seed [5] and the edge states [3] only represent single points on the edge. In this Paper, we propose a probabilistic protocol to quantify the robustness of the laminar flow to perturbations and extend it to quantify the efficiency of control strategies.

RESULTS

In plane Couette flow, the laminar flow is linearly stable and turbulence can be thought of as a statistically persistent state for $Re > 325$ [6]. The edge of chaos then corresponds to the separatrix between the basin of attraction of the laminar flow and that of turbulence. To completely understand the robustness of the laminar flow, one would ideally require knowledge of the full structure of the edge of chaos. Unfortunately, the edge is an intricate manifold [2] and an exhaustive characterisation seems out of reach. Instead of fully determining the location of the edge, we proceed by approximating the probability of being on either side of it for a given value of the perturbation energy.

We consider plane Couette flow in a domain of (nondimensional) size 4π in the streamwise direction, 2 in the wall-normal direction and $32\pi/15$ in the spanwise direction and fix the Reynolds number to a value larger than required to observe turbulence: $Re = 500$. We generate a set of random perturbations at 40 equidistributed kinetic energy levels between $E = 0$ and $E = 0.04$. The perturbations are expressed in the following way: $\mathbf{u} = A\mathbf{u}_\perp + B\mathbf{U}_{\mathbf{lam}}$, where $\mathbf{U}_{\mathbf{lam}}$ is the laminar flow, $\mathbf{u}_\perp$ is the projection of the perturbation in the space orthogonal to the laminar flow and A and B are coefficients. To generate $\mathbf{u}$, we first choose B and $\mathbf{u}_\perp$ randomly, then compute A so that the perturbation has the prescribed kinetic energy E. We then time-integrate the initial conditions $\mathbf{u_0} = \mathbf{U_{lam}} + \mathbf{u}$ until transition or laminarisation is observed according to the following rules: transition is observed if the flow kinetic energy exceeds E_{turb}, the average turbulence kinetic energy, and does not laminarize within 400 time units; laminarisation is observed when the kinetic energy of the flow decays below $E_{turb}/100$.

We show in the left panel of figure 1 the results obtained for 200 perturbation per energy levels in plane Couette flow and expressed via the laminarisation probability P_{lam}. The laminarisation probability can be fitted by a lower incomplete gamma function (more details in [8]) to exhibit similar behavior to the data and particularly its monotonic decay from $P_{lam} = 1$ to a non-zero value. At sufficiently large perturbation energy, the laminarisation probability can be seen to

*Corresponding author. E-mail: c.m.l.beaume@leeds.ac.uk.

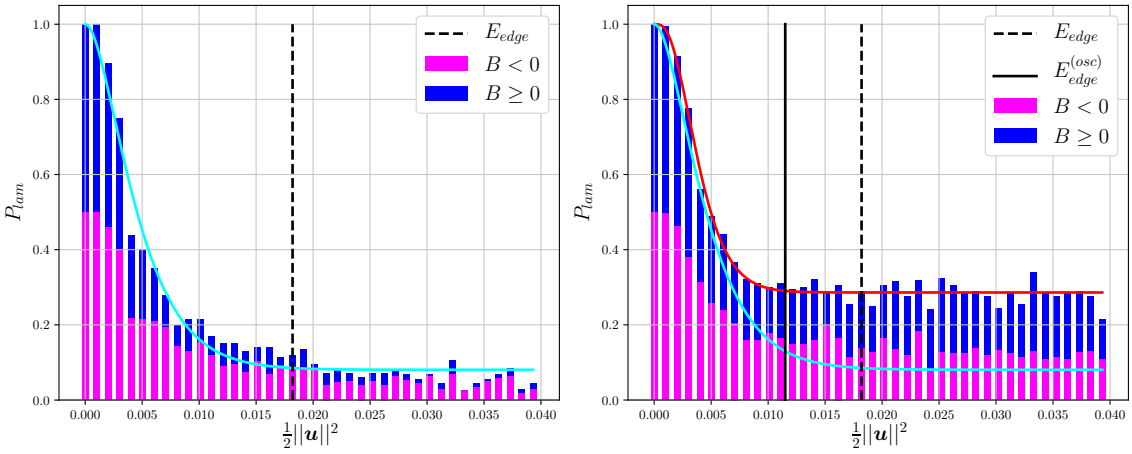

Figure 1: Laminarization probability P_{lam} for 40 perturbation energy $||\mathbf{u}||^2/2$ levels in plane Couette flow. The results are shown in the absence of control (left panel) and in the presence of control via wall oscillation (right panel, see text for details). In both cases, the contribution of shear enhancing perturbations is shown in blue while that of shear weakening ones is shown in pink. The solid blue (resp. red) curve corresponds to a fitting function in the absence (resp. presence) of control as explained in the text. The vertical dashed (resp. solid) line corresponds to the kinetic energy of the edge state in the absence (resp. presence) of control.

reach a plateau where virtually no shear enhancing perturbation ($B \geq 0$) laminarizes but where a non-negligible fraction of shear weakening perturbations ($B < 0$) laminarizes.

We reproduced the same study in the presence of control via wall oscillation: in addition to moving in the streamwise direction at constant (but opposite) speeds, the walls are oscillating in phase in the spanwise direction, a technique known to reduce turbulent drag [9] and increase the energy of the minimal seed [10]. We chose a control setup close to optimal according to [10]: the oscillation frequency is set to $1/16$ and the amplitude to 0.3. We chose the phase of oscillation randomly as part of the perturbation generation procedure. The results are shown on the right panel of figure 1. The control is successful: oscillating the walls increased the fraction of laminarizing perturbations at virtually all energy levels, and most noticeably for $E > 0.005$. The laminarization probability plateaux at values around 29% against 8% in the absence of control. Although wall oscillation stabilized approximately 10% of the shear weakening perturbations, its major effect is to stabilize a large number of shear enhancing perturbations, most of which would have triggered transition in the absence of control. Lastly, the energy of the edge state is lower in the presence of control than in its absence, a fact that might be misinterpreted as negative control without knowledge of the laminarization probability.

DISCUSSION

In this paper, we have introduced a protocol to characterise the robustness of the laminar flow to perturbations in plane Couette flow. The underpinning problem is that of transition to turbulence and the protocol used to quantify the efficiency of a control strategy based on wall oscillations. Given the nature of the protocol described here, it is clear that it has the potential to be a useful tool to assist the investigation of other finite-amplitude instabilities.

References

[1] Reynolds O. *Phil. Trans. R. Soc. London* **174**, 1884.
[2] Chantry M., Schneider T. *J. Fluid Mech.* **747**, 2014.
[3] Schneider T., Gibson J., Lagha M., De Lillo F., Eckhardt B. *Phys. Rev. E* **78**, 2008.
[4] Duguet Y., Schlatter P., Henningson D. *Phys. Fluids* **21**, 2009.
[5] Rabin S., Caulfield C., Kerswell R. *J. Fluid Mech.* **712**, 2012.
[6] Shi L., Avila M., Hof B. *Phys. Rev. Lett.* **110**, 2013.
[7] Chantry M., Tuckerman L., Barkley D. *J. Fluid Mech.* **824**, 2017.
[8] Pershin A., Beaume C., Tobias S. *arXiv:1908.03050* , 2019.
[9] Baron A., Quadrio M. *Appl. Sci. Res.* **55**, 1995.
[10] Rabin S., Caulfield C., Kerswell R. *J. Fluid Mech.* **738**, 2014.

EXTENDING BARKLEY'S PIPE FLOW MODEL TO PLANE COUETTE FLOW

Cristóbal Arratia *
Nordita, KTH Royal Institute of Technology and Stockholm University Roslagstullsbacken 23, SE-106 91 Stockholm, Sweden

Summary We present our attempt at developing an extension of Barkley's pipe-flow model to plane Couette flow. Drawing a connection between amplitude equations and large-scale flows around turbulent spots, we propose an effective local model which presents a bifurcation scenario that is consistent with the phenomenology observed in small domains. We also find that the obliqueness of the laminar-turbulent patterns cannot be described purely as a Turing instability. We will discuss some additional elements that can be included and describe how the resulting spatiotemporal dynamics compares with transitional plane Couette flow in large domains.

INTRODUCTION

The coexistence between laminar and turbulent regions is generic to the subcritical transition to turbulence of wall-bounded shear flows. Relevant examples are laminar-turbulent patterns in plane Couette and other two-dimensionally extended flows [1, 2], and turbulent puffs and slugs in pipe flow [3]. An effective description of such structures in terms of a single bistable variable $q(\boldsymbol{x}, t)$, a 'turbulent intensity' representing a competition between laminar and turbulent states as a phase transition [4], provides a helpful but incomplete conceptual picture [5]; such a simplified reaction-diffusion model does not capture much of the distinctive dynamics of the laminar-turbulent interfaces.

The ability to mimic the evolution of laminar-turbulent interfaces throughout the transitional regime is a central aspect of the success of Barkley's pipe-flow model [3, 5], which he accomplished by adding an extra variable field $u(x, t)$. Physically, the new variable $u(x, t)$ plays a double role in modelling the effects of (i) the mean shear relevant to inhibit/promote the presence of turbulence in a certain region, and (ii) the large-scale advection of the laminar/turbulent interfaces.

EXTENSION TO TWO DIMENSIONS

While the use of an effective variable describing (i) the local retroaction between the mean shear and the turbulence intensity $q(x, z, t)$ can be directly transferred to the 2D case, the impossibility of describing (ii) the large-scale advection with a scalar variable in 2D is an important obstacle. Accordingly, we use $s(x, z, t)$ instead of $u(\boldsymbol{x}, t)$ to represent the mean shear only. The large scale advection, however, has been the object of much attention and cannot be dismissed since the large scale flows around turbulent patches are important to their evolution [2]. We propose to effectively describe this large scale advection from spatial gradients of the model variables. In particular, the quadrupolar flow structure observed around turbulent spots could be described, at the laminar-turbulent interfaces, roughly as $(v_x, v_z) = (\partial_x q, -\partial_z q)$. As a consequence, terms that one may expect in the form $\beta \boldsymbol{v} \cdot \nabla q$ and $\gamma(\nabla \cdot \boldsymbol{v})q$, for some constants β and γ, become

$$\beta(\partial_x q)^2 - \beta(\partial_z q)^2 + \gamma q \partial_x^2 q - \gamma q \partial_z^2 q. \tag{1}$$

These terms, which represent nonlinear advection and nonlinear diffusion, appear in a non-variational extension of the Swift-Hohenberg equation known to display complex spatiotemporal behaviour and patterns. Remarkably, this non-variational amplitude equation has been shown to generically govern the order parameter around bifurcations of codimension-3 involving the appearance of bi-stability together with the onset of a long wave Turing instability [6]. Note that a Turing instability was proposed by Manneville as a possible mechanism to explain the appearance of the laminar-turbulent patterns in the framework of effective reaction-diffusion models [7].

These considerations provide some promising ingredients in view of developing an effective model for transitional shear flow with two extended dimensions. The terms (1) are consistently generated in multiscale expansions used for deriving amplitude equations around a specific type of bifurcation [6]. This gives a specific clue for constructing an extension of Barkley's model with a local dynamics that generate the nonlinear advection and diffusion terms in (1). The extension, however, is not straightforward, since the 'nascent bistability' [6] of the codimension-3 bifurcation cannot physically correspond to the bistability between laminar and turbulent states of shear-flow transition, which are from the onset at a finite distance in state-space. Still, we can construct a local model with a similar bifurcation, and whose dynamics is qualitatively consistent with transition to turbulence of plane Couette flow in small domains.

A model of local dynamics

Consider the temporal dynamics given by

$$\frac{\mathrm{d}q}{\mathrm{d}t} = f(q, s) f_\infty(q, s) = q\left(-\delta + r + s + \alpha q - r q^2\right) f_\infty(q, s), \tag{2a}$$

$$\frac{\mathrm{d}s}{\mathrm{d}t} = g(q, s) g_\infty(q, s) = \left[1 - s - \alpha\rho q^2 + \frac{\alpha}{3} q^3\right] g_\infty(q, s), \tag{2b}$$

*E-mail: cristobal.arratia@gmail.com.

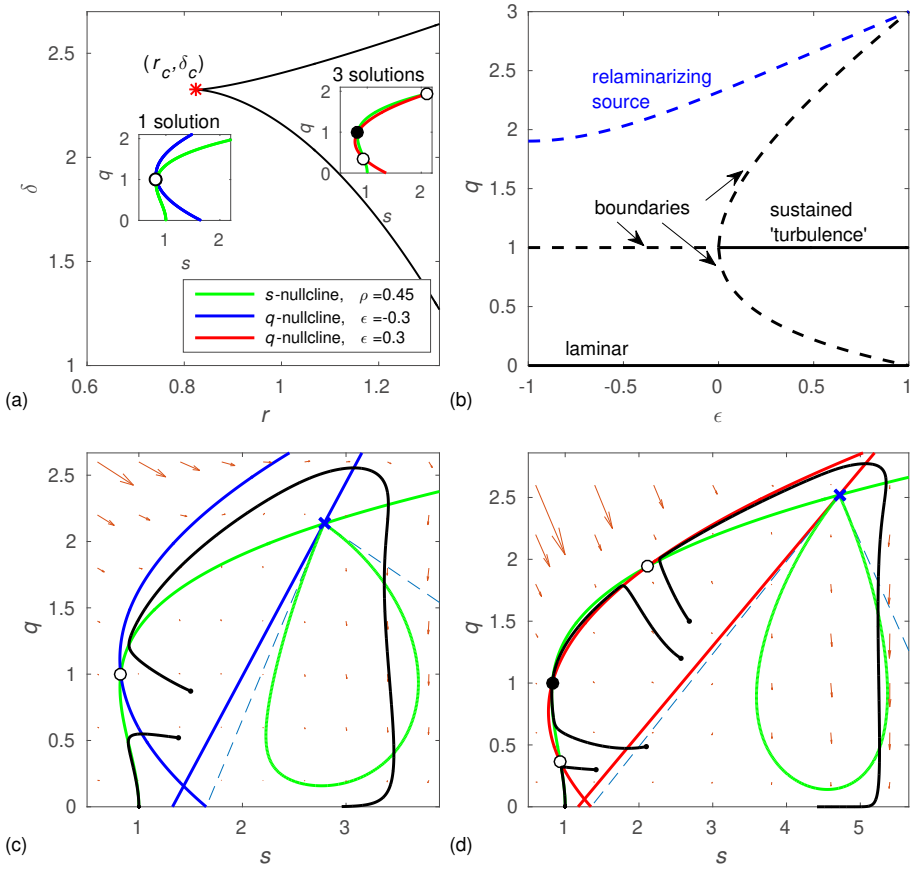

Figure 1: Qualitative properties of the local model for transitional turbulence in plane Couette flow. (a) Regions of the parameter space (r, δ) with different number of solutions. In addition to the laminar and the *ad-hoc* relaminarizing solutions, one or three other solutions exist to the left or right of the cusped line, respectively. The insets show the configuration of the nullclines. (b) Bifurcation diagram with control parameter $\epsilon = 3(r - r_c)/\alpha$ and fixed $\delta = \delta_c$. A state of (locally) sustained 'turbulence' appears at $\epsilon = 0$ through a subcritical pitchfork (local) bifurcation. (c,d) Temporal dynamics of the local model (2) in the (q, s)-plane. Black lines show sample trajectories, red arrows the state-space flow field, and coloured lines are nullclines as given in the legend of (a).

where q and s are the effective turbulent intensity and mean shear variables, and δ and r are control parameters with r the main bifurcation parameter (a 'Reynolds number'). $\alpha > 0$ and $0 \leq \rho \leq 2/3$ are free parameters at this stage. Stationary solutions given by $f(q, s) = g(q, s) = 0$ (defined implicitly by the second equalities in (2)) include a laminar state $(q, s) = (0, 1)$ and a 'turbulent' state where $q \equiv q_t$ is finite.

The main characteristics of the local model are described in Figure 1. There is a cusp in the (r, δ)-plane (point (r_c, δ_c) in Fig. 1(a)), for which three solutions $q_t = 1$ coincide. When increasing r with $\delta = \delta_c$ fixed, the saddle $q_t = 1$ is stabilized through a subcritical pitchfork bifurcation at $r_c = \alpha(1-\rho)$ (Fig. 1(b)). The functions $f_\infty(q, s)$ and $g_\infty(q, s)$ add a straight line and a 3-ellipse as q- and s-nullclines, respectively, whereby an *ad-hoc* solution is added that prevents the blow-up of the model by enforcing 'relaminarization'. Similar to plane Couette flow in small domains, there is a subcritical region with 'turbulent transients' (Fig. 1(c)) and a supercritical one where 'turbulence' is locally stable (Fig. 1(d)).

Spatial effects

Different diffusivities for $q(x, z, t)$ and $s(x, z, t)$ together with anisotropies along x and z is the first element considered when dealing with the spatiotemporal setting. A relevant observation is that, regardless of the anisotropy, the onset of the Turing instability develops always parallel to one of the axes. This implies that the obliqueness of the laminar turbulent bands cannot be described purely as a Turing instability of a reaction-diffusion model which satisfies the reflection symmetries around the x- and z-axes that are externally imposed. Further aspects of these developments will be discussed.

References

[1] A. Prigent, G. Grégoire, H. Chaté and O. Dauchot. Long-wavelength modulation of turbulent shear flows. *Physica D*, **174**(1-4):100 – 113, 2003.
[2] L. S. Tuckerman, M. Chantry and D. Barkley. Patterns in Wall-Bounded Shear Flows. *Annu. Rev. Fluid Mech.*, 52(1):343–367, 2020.
[3] D. Barkley, B. Song, V. Mukund, G. Lemoult, M. Avila, and B. Hof. The rise of fully turbulent flow. *Nature*, **526**, 2015.
[4] Y. Pomeau. Front motion, metastability and subcritical bifurcations in hydrodynamics. *Physica D: Nonlinear Phenomena*, 23(1):3 – 11, 1986.
[5] D. Barkley. Theoretical perspective on the route to turbulence in a pipe. *J. Fluid Mech.*, 803, Sep 2016.
[6] G. Kozyreff and M. Tlidi. Nonvariational real swift-hohenberg equation for biological, chemical, and optical systems. *Chaos*, 17(3):037103, 2007.
[7] P. Manneville. Turbulent patterns in wall-bounded flows: A turing instability? *Europhys. Lett.*, 98(6):64001, 2012.

EFFECTS OF AN IMPOSED AXIAL FLOW ON A FERROFLUIDIC TAYLOR-COUETTE FLOW

Sebastian Altmeyer* [1] and Younghae Do[2]
[1]Castelldefels School of Telecom and Aerospace Engineering, Universitat Politcnica de Catalunya, Barcelona, 08034, Spain
[2]Department of Mathematics, KNU-Center for Nonlinear Dynamics, Kyungpook National University, Daegu 41566, South Korea

Summary We investigate the effects of an externally imposed axial mass flux [1, 2] (axial pressure gradient, axial through flow) on ferrofluidic Taylor-Couette flow under the influence of either an axial or a transverse magnetic field [3]. Without imposed axial through flow, due to the symmetry-conserving axial field and the symmetry-breaking transverse field, it gives rise to various vortex flows in ferrofluidic Taylor-Couette flow such as wavy Taylor vortex flow (wTVF), wavy spiral vortex flow (wSPI) and wavy vortex flows (wTVFHx and wSPIHx), which are typically produced by a non-linear interaction of *rotational, shear* and *magnetic instabilities*. In addition, when an axial through flow is imposed to a ferrofluidic Taylor-Couette flow in the presence of such a magnetic field, new helical vortex structures are born. In particular, we uncover *'modulated Mixed-Cross-Spirals'* with a combination of at least *three different* dominant azimuthal wavenumbers.

FIXED TRANSVERSAL MAGNETIC FIELD.

To investigate the effects of an externally imposed axial through flow Re, for a fixed transversal magnetic field ($s_x = 0.6$), examine dynamics of flow states by varying Re, specially focusing on bifurcation phenomenon for two fixed inner Reynold numbers, $Re_i = 110$ and 270. Due to a transversal magnetic field, all flow states are *inherently* $3D$ and wavy-like modulated flow [4] containing specific higher modes $m \pm 2$.

BIFURCATION SCENARIO

For $Re_i = 110$ and $Re = 0$ the system shows *multistability* having three stable states, $L1 - wSPI_{H_x}$, $R1 - wSPI_{H_x}$ and $wTVF_{H_x}$. By increasing Re, both flow states $R1 - wSPI_{H_x}$ and $wTVF_{H_x}$ move to $L1 - wSPI_{H_x}$, and then follow the destiny of $L1 - wSPI_{H_x}$ (Fig. 1(a)).

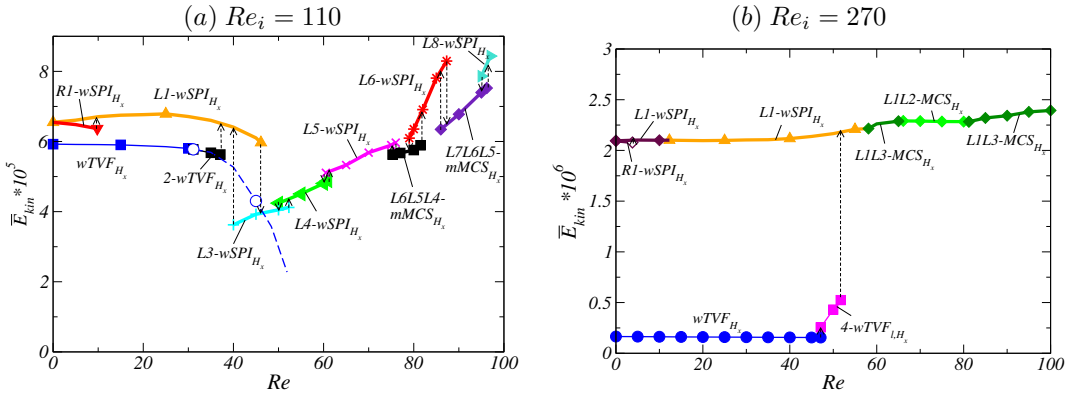

Figure 1: Bifurcation scenarios vs. imposed axial through flow Re. Bifurcation scenarios for (a) $Re_i = 110$ and (b) $Re_i = 270$, respectively. Shown is the total (time-averaged) modal kinetic energy E_{kin}. Different flow structures are labeled. Vertical arrows illustrate the transition direction to another stable state, when a flow state loses its stability. Thin [thick] lines correspond to toroidally closed [helical] flow states.

Increasing Re the state $wTVF_{H_x}$ becomes unstable at $Re \approx 35$, where a wavy flow state $2 - wTVF_{H_x}$ with dominant mode amplitudes $(2, \pm 1)$ bifurcates. At $Re \approx 38$, $2 - wTVF_{H_x}$ finally loses its stability, and moves towards a modulated helical spiral state $L1 - wSPI_{H_x}$. The helical downward propagating state $R1 - wSPI_{H_x}$ becomes unstable at $Re \approx 10$, and then moves toward a stable helical upward propagating state $L1 - wSPI_{H_x}$. Starting with $L1 - wSPI_{H_x}$, one obtains the following sequence of flow states (Fig. 1(a)):

$$\begin{aligned} L1 - wSPI_{H_x} \rightarrow L3 - wSPI_{H_x} \rightarrow L4 - wSPI_{H_x} \quad &\rightarrow \quad L5 - wSPI_{H_x} \rightarrow \\ L6L5L4 - mMCS_{H_x} \rightarrow L6 - wSPI_{H_x} \quad &\rightarrow \quad L7L6L5 - mMCS_{H_x} \rightarrow L8 - wSPI_{H_x}. \end{aligned}$$

While most steps in this scenario can be anticipated, i.e. increasing the helicity - larger azimuthal modes m with increasing Re one eventually finds a *new* type of *mixed mode states* as non-linear interaction. We will call this states *modulated Mixed-Cross-Spirals* ($mMCS_{H_x}$)[5] as they appear with *three* dominant azimuthal wavenumbers. For instance, $L6L5L4 - mMCS_{H_x}$ and $L7L6L5 - mMCS_{H_x}$.

*Corresponding author. E-mail: sebastian.andreas.altmeyer@upc.edu.

At larger $Re_i = 270$ (Fig. 1(b)) the sequence of flow state appearing out of $wTVF_{H_x}$ with increasing Re is quite different: $wTVF_{H_x} \rightarrow 4 - wTVF_{l,H_x} \rightarrow L1 - wSPI_{H_x}$.
At $Re \approx 47.6$, $wTVF_{H_x}$ bifurcates to $4 - wTVF_{l,H_x}$ with dominant azimuthal wavenumber $m = 4$. However flow states with lower azimuthal wavenumber m, as $2 - wTVF_{l,H_x}$ and $3 - wTVF_{l,H_x}$ were temporarily observed as *unstable* and only *transient* states. Further, at $Re \approx 52$, $4 - wTVF_{l,H_x}$ loses its stability, and then moves towards the helical $L1 - wSPI_{H_x}$. As before, within this transition process, $5 - wTVF_{l,H_x}$ and $6 - wTVF_{l,H_x}$ appear as *unstable transient* states. Interestingly we could not observe any other stable $wTVF_{l,H_x}$ with larger azimuthal wavenumber $m \geq 7$.

MODULATED MIXED-CROSS-SPIRALS

The spatial structure of a *stable* $L6L5L4 - mMCS_{H_x}$ (Fig. 2), which exists between $L5 - wSPI_{H_x}$ and $L6 - wSPI_{H_x}$ clearly illustrates the dominance of the largest mode $m = 6$ while at the same time the influence and modulation of *both* other dominant modes $m = 5$ and $m = 4$ are visible. The dominant azimuthal wavenumber m is decreasing from the inner towards the outer cylinder (Fig. 2(4)). Due to the symmetry-breaking effect of a transversal magnetic field,

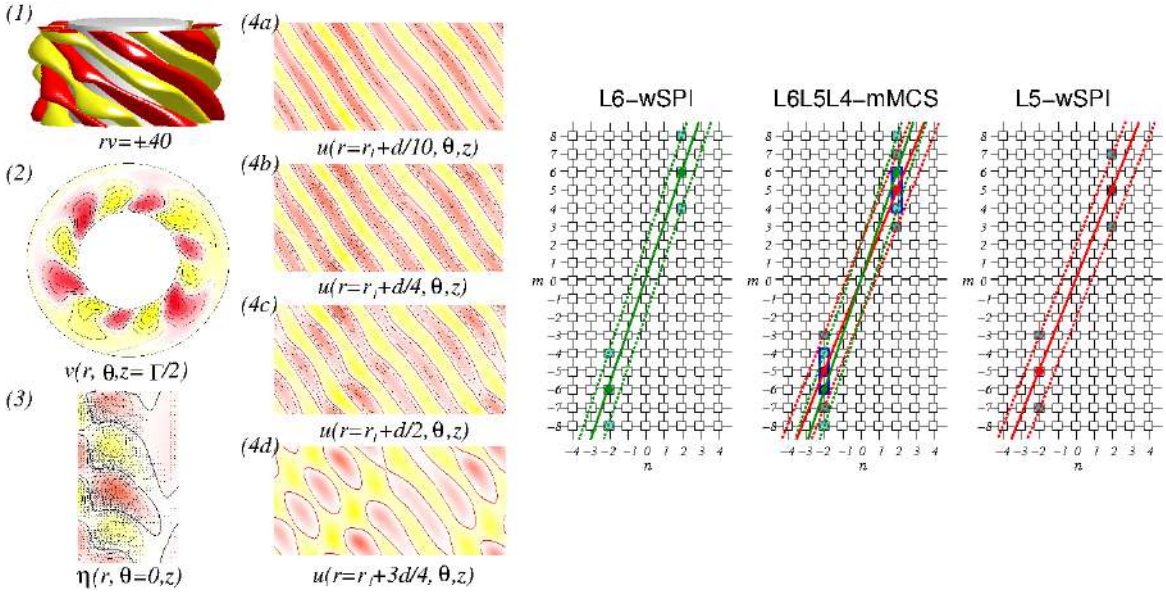

Figure 2: *Left:* Flow visualization of flow states L6L5L4-mMCS$_{H_x}$ at $s_x = 0.6$ & $s_z = 0.0$, $Re_i = 110$ and fixed axial through flow $Re = 82$. (1) Isosurface of rv; (2) The azimuthal velocity $v(r, \theta)$ at mid-plane; (3) Vector plot $[u(r, z), w(r, z)]$ of the radial and axial velocity components including color-coded azimuthal vorticity $\eta(r, \theta = 0, z)$). $(4a - d)$ The radial velocity $u(r, \theta, z)$ at different radial positions as indicated. *Right:* Dominant excited modes (colored squares) of the different solutions in the two-dimensional Fourier mode space (m, n). Filled circles denote linearly driven modes and linear Fourier mode subspaces are indicated by thick lines. They represent $L5 - wSPI_{H_x}(5n \pm 2, n)$, $L6 - wSPI_{H_x}(6n \pm 2, n)$, and a combination of both in $L6L5L4 - mMCS_{H_x}$.

the helical state $L5 - wSPI_{H_x}$ [$L6 - wSPI_{H_x}$] has its dominant mode $m = 5$ [$m = 6$] and an additionally stimulated modes $m \pm 2 = \{3, 7\}$ [$m \pm 2 = \{4, 8\}$] [4], respectively. When the states $L5 - wSPI_{H_x}$ and $L6 - wSPI_{H_x}$ come *close* in Re, they stimulate one of these additional modes (here $m = 4$) as a *nonlinear interaction* of dominant modes and thus a new state with *three* dominant modes is born. The correspondingmode space of $L6L5L4 - mMCS_{H_x}$ can be (linearly) constituted as a combination of two mode spaces of $L5 - wSPI_{H_x}$ and $L6 - wSPI_{H_x}$ [$(5n \pm 2, n)$ and $(6n \pm 2, n)$].

CONCLUSIONS

When an axial mass flux is applied to a ferrofludic system, the dynamics of a system can be described by results of competition of the *three* different instabilities; *centrifugal instability* due to rotation, *shear instability* due to axial mass flux and *magnetic instability* due to applied magnetic fields. Due to competition of these instabilities, previously unknown *new* flow states appear. These are *localized wavy Taylor vortices* ($wTVF_l$ and $wTVF_{l,H_x}$) and *modulated Mixed-Cross-Spirals* ($mMCS_{H_x}$). $mMCS_{H_x}$ appear as a byproduct of an interaction of an axial through flow and a transversal magnetic field. In fact the symmetry breaking nature of a transverse magnetic field is responsible for the appearance of $mMCS_{H_x}$ due to its additionally stimulated modes $m \pm 2$.

References

[1] Chossat P., and Iooss G., The Couette-Taylor Problem. (Springer, Berlin, 1994).
[2] Hoffmann C., Lücke M., and Pinter A., Spiral vortices and Taylor vortices in the annulus between rotating cylinders and the effect of an axial flow. *Phys. Rev. E* **69**, 056309, 2004.
[3] Altmeyer S., and Do Y., Effects of an imposed axial flow on a Ferrofluidic Taylor-Couette flow. *Scientific Reports* **9**, 15438, 2019.
[4] Altmeyer S., Hoffmann C., Leschhorn A., and Lücke M., Influence of homogeneous magnetic fields on the flow of a ferrofluid in the Taylor-Couette system. *Phys. Rev. E* **82**, 016321, 2010.
[5] Altmeyer S., and Hoffmann C., Secondary bifurcation of mixed-cross-spirals connecting travelling wave solutions. *New J. Phys.* **12**, 113035, 2010.

FARADAY INSTABILITY IN 1D CAVITIES : TIME CRYSTALS AND MODE SELECTION

Guillaume d'Hardemare [1], Antonin Eddi*[2] and Emmanuel Fort [1]
[1] Institut Langevin, ESPCI Paris, CNRS, PSL University, [1] rue Jussieu, F-75005 Paris, France
[2] PMMH, CNRS, ESPCI Paris, Université PSL, Sorbonne Université, Université de Paris, F-75005, Paris, France

Summary Faraday instability is equivalent to a time crystal, where the parametric amplification leads to the apparition of k-gaps, formally analogous to the energy band gap is solid-state physics. As energy is not conserved, this results in an unstable domain in k-space where modes grow. Here, we investigate experimentally Faraday instability in 1D cavities, where we can tune the excited mode by changing the cavity length. This allows us to probe the amplification band of the instability. Abruptly changing the phase of the excitation further allows us to observe the overdamped modes of the instability, measuring for the first time their decay rate predicted theoretically but never observed so far.

FARADAY INSTABILITY AS A TIME CRYSTAL

Faraday instability is observed when a liquid bath is vertically shaken above a certain threshold [1]. It has been extensively studied experimentally and theoretically as an instability in the stationary regime, with focus on the forcing threshold, pattern formation and the various dissipation processes or the hydrodynamic associated phenomena. This parametric instability can be revisited within the framework of Floquet time crystals. For an inviscid fluid in a bath submitted to vertical acceleration $a_0\cos(2\omega_f t)$, the modes are given by a Mathieu equation [2]. The free surface elevation $\xi(\mathbf{r},t)$ at position $\mathbf{r}$ and time t can be decomposed in Fourier modes $\hat{\xi}(\mathbf{k},t)$ of wavevector $\mathbf{k}$ following:
$\frac{\partial^2\hat{\xi}(\mathbf{k},t)}{\partial t^2} + \omega_0^2(\boldsymbol{k})\hat{\xi}(\mathbf{k},t) = -a_0 \mathrm{k}\cos\left(2\omega_f t\right)\hat{\xi}(\mathbf{k},t)$ with $\omega_0(\mathrm{k})$, the angular frequency given by the dispersion relation for gravity-capillary waves and k, the wavenumber. This equation describes the modes in a medium with a gravity modulation. The variation of the effective gravity induces a speed modulation of the gravito-capillary waves which can be seen as a modulation of the refractive index [4,5]. The solutions of the Mathieu equation are given by the Bloch-Floquet theorem while in the case of liquid with a small viscosity ν, a damping term $-2\gamma\partial\hat{\xi}/\partial t$ should be added to the Mathieu equation, γ being the damping rate related to the fluid viscosity by $\gamma = 2\nu\mathrm{k}^2$ [3]. Figure 1 shows a typical complex dispersion curve obtained with a small viscosity, with vertical k-gaps (in momentum). These k-gaps are the analog of the horizontal energy gaps observed in spatial crystals in which the waves cannot propagate. Within the k-gaps, the vertical excitation of the bath leads to two possible solutions: one being overdamped compared to a bath at rest, the other being underdamped. For sufficient forcing, the Faraday instability is observed and a standing wave at half the excitation frequency appears on the surface.

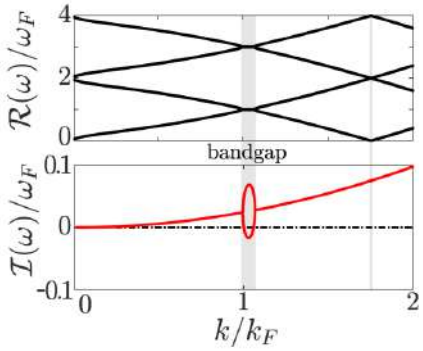

Figure 1: Dispersion relation showing the band structure of the Faraday instability as a water wave time crystal. Top: real part $\Re(\omega)$ of the angular frequency ω versus the normalized wavenumber k/k_F with k_F being the Faraday wavenumber Bottom: Imaginary part $\Im(\omega)$ of the angular frequency as a function of k/k_F. The small parabolic variation corresponds to the viscous damping

EXPERIMENTS

We now focus on a versatile implementation of a 1D time crystal based on Faraday instability. It consists in a 1D wave cavity whose length L can be tuned that is submitted to vertical harmonic vibrations. Faraday waves are excited at half the forcing frequency Ω_F. The associated wavelength λ_F is given by the capillary-gravity dispersion relation for water-waves and is chosen so that it equals twice the width of the tank to excite the first transverse mode of the cavity. We measure the exponential growth rate of the waves which corresponds to the imaginary part of the Floquet exponent $\Im(\omega)$ as well as the wavelength λ inside the cavity. The growth rates (Fig. 2a) exhibit peaks separated by half a Faraday wavelength λ_F. These peaks correspond to matching between a mode associated to the Faraday instability and a resonant mode of the cavity which wavelength satisfies $\lambda = 2L_{\mathrm{eff}}/n$, n being the mode number and L_{eff}, the effective cavity length taking into account the boundary conditions. Varying the cavity length results in scanning the k-gap associated to the Faraday instability (Fig. 2b). The curve of the growth rate thus corresponds to a periodic scanning of the k-gap with maxima obtained for cavity lengths satisfying $L_{\mathrm{eff}} = n\lambda_F/2$.
Last, we introduce a topological defect in the time crystal by suddenly π-shifting the excitation period which results in concatenating two time crystals with opposite phase. At the interface, the existing mode is turned into the overdamped one. By extracting the damping rate, we are thus able to measure the entire complex dispersion inside the k-gap of the Faraday time crystal.

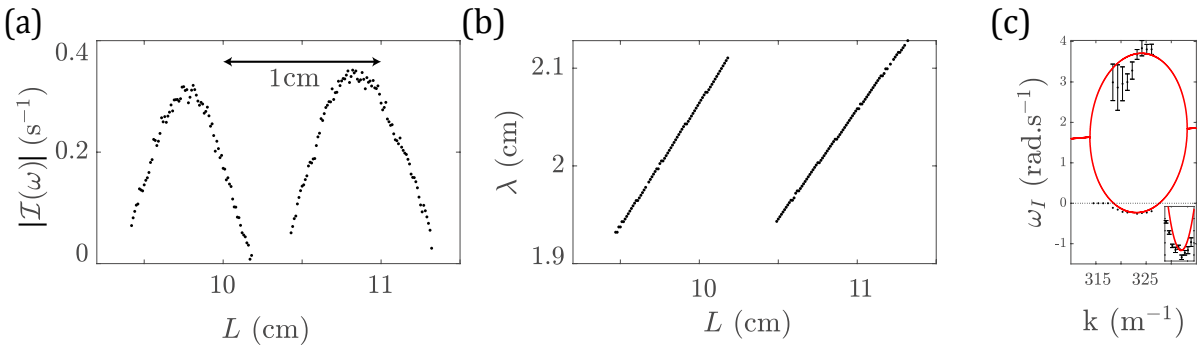

Figure 2: (a) Growth rate of the amplitude $|\Im(\omega)|$ and (b) wavelength λ of the mode in the cavity as a function of the cavity size L. The peaks are associated to the matching between the Faraday instability k-gap modes and the ones of the cavity. (c) Measurement of growth and decay rates inside the k-gap. The solid red curves give the result of the computation based on a damped Mathieu equation using experimental values of the viscosity. The inset provides a zoom on the lower part of the curve.

References

[1] Faraday, M. On a Peculiar Class of Acoustical Figures; and on Certain Forms Assumed by Groups of Particles upon Vibrating Elastic Surfaces. *Philos. Trans. R. Soc. Lond.* **121**, 299–340 (1831).

[2] Benjamin, T. B. & Ursell, F. J. The stability of the plane free surface of a liquid in vertical periodic motion. *Proc R Soc Lond A* **225**, 505–515 (1954).

[3] Kumar, K. & Tuckerman, L. S. Parametric instability of the interface between two fluids. *J. Fluid Mech.* **279**, 49 (1994).

[4] Bacot, V., Labousse, M., Eddi, A., Fink, M. & Fort, E. Time reversal and holography with spacetime transformations. *Nat. Phys.* 1–6 (2016).

[5] Bacot, V., Durey, G., Eddi, A., Fink, M. & Fort, E. Phase-conjugate mirror for water waves driven by the Faraday instability. *Proc. Natl. Acad. Sci.* **116**, 8809–8814 (2019).

NON-LINEAR PRE AND POST BUCKLING BEHAVIOUR OF A TIMOSHENKO BEAM

Marwan Hariz* [1], Loïc Le Marrec † [1], and Jean Lerbet ‡ [2]
[1]Univ Rennes, CNRS, IRMAR - UMR 6625, F-35000 Rennes, France.
[2]Université d'Evry, CNRS, LaMME - UMR 8071, F-91037, Evry, France.

Summary Plane bending of a Timoshenko beam is derived using Cosserat formulation by the mean of a material curve and a moving director frame. Equilibrium relations are derived in the case of linear stress-strain relations and for both large strains and large displacements. Beam bending is controlled by magnitude and direction of a force and a bending moment. By a series of transformations, equilibrium equations are rearranged where pre and post buckling solutions are given in terms of Jacobi elliptic functions. From our knowledge this is the first attempt where such solution are derived by taking account a control of the bending moment.

KINEMATICS AND INTERNAL FORCES UNDER COSSERAT FORMULATION

We consider a Timoshenko model for plane motion of an homogeneous straight beam of length L. In a Cartesian frame, the beam axis is oriented along $\boldsymbol{e_z}$ in the stress-free configuration, and the motion lies in the $(\boldsymbol{e_x}, \boldsymbol{e_z})$-plane. However, for such a Cosserat-like structure it is justified to use a moving director frame $(\boldsymbol{d_1}, \boldsymbol{d_2}, \boldsymbol{d_3})$ for which $\boldsymbol{d_2} = \boldsymbol{e_y}$ and $\boldsymbol{d_3}$ is normal to the cross-section, because this basis is orthonormal $\boldsymbol{d_1} = \boldsymbol{d_3} \wedge \boldsymbol{d_2}$. In the stress-free configuration this basis coincide with the Cartesian frame, however during motion, the orientation of the section is not uniform, $\{\boldsymbol{d_i}(S)\}$ depends on the curvilinear abscissa S of the beam. $\boldsymbol{d_3}$ is not tangent to the center line as in the Euler-Bernoulli model.
Kinematics of the beam are governed by the placement $\boldsymbol{\varphi}(S)$ of the center line and rotation $\theta(S)$ of the section around $\boldsymbol{d_2}$. Following [6], deformation are described thanks to the curvature $\boldsymbol{\kappa}(S)$ and generalized strains $\widetilde{\boldsymbol{\varepsilon}}(S)$ with

$$\boldsymbol{\kappa} := \frac{\partial \theta}{\partial S}\,\boldsymbol{d_2} = \kappa_2 \boldsymbol{d_2}\,, \qquad \widetilde{\boldsymbol{\varepsilon}} := \frac{\partial \boldsymbol{\varphi}}{\partial S} - \boldsymbol{d_3} = \varepsilon_1 \mathbf{d_1} + (\varepsilon_3 - 1)\boldsymbol{d_3}\,. \tag{1}$$

Hereafter the kinematical variables are the component $\kappa_2(S)$ of the curvature and components $\varepsilon_1(S)$ and $\varepsilon_3(S)$ of the deformation $\frac{\partial \boldsymbol{\varphi}}{\partial S}$ of the center-line. In particular ε_1 is the shear strain and $\varepsilon_3 - 1$ is the longitudinal strain. Internal force acting on a section is $\boldsymbol{N} = N_1 \boldsymbol{d_1} + N_3 \boldsymbol{d_3}$ where N_1 and N_3 are the shear and normal components respectively. Internal moment is $\boldsymbol{M} = M_2 \boldsymbol{d_2}$ where M_2 is the bending moment.
Linear constitutive law is assumed : $N_1 = GA\varepsilon_1$, $N_3 = EA(\varepsilon_3 - 1)$ and $M_2 = EI\kappa_2$ where A and I are the area and the quadratic moment of the section, E and G are the Young modulus and shear modulus (including eventually a shear correction factor) of the beam material.

EQUILIBRIUM RELATIONS

Equilibrium relations for this static problem states [1, 2] :

$$\frac{\partial \boldsymbol{N}}{\partial S} = 0\,, \qquad \frac{\partial \boldsymbol{M}}{\partial S} + \frac{\partial \boldsymbol{\varphi}}{\partial S} \wedge \boldsymbol{N} = 0\,. \tag{2}$$

Non-dimensional kinematical variables are given thanks to the gyration radius $\varrho = \sqrt{I/A}$:

$$s = \frac{S}{\varrho}, \quad \ell = \frac{L}{\varrho}\,, \quad \varepsilon_i(s) = \varepsilon_i(S)\,, \quad \kappa_2(s) = \varrho\,\kappa_2(S)\,, \qquad i = 1, 3\,. \tag{3}$$

Last, a material parameter $g = E/G$ is introduced. Note that $g \simeq 2(1+\nu)$ where ν is the Poisson's ratio, then $2 \lesssim g \lesssim 3$. Hence (2) become in a non-dimensional form (the prime stands for derivation over s) :

$$\varepsilon_1' + g(\varepsilon_3 - 1)\kappa_2 = 0 \tag{4}$$
$$g\,\varepsilon_3' - \varepsilon_1 \kappa_2 = 0 \tag{5}$$
$$g\,\kappa_2' + \varepsilon_1 \varepsilon_3 - g\,\varepsilon_1(\varepsilon_3 - 1) = 0 \tag{6}$$

In order to prevent rigid motion $\theta(0)$ and $\boldsymbol{\varphi}(0)$ are set to zero. In this work boundary conditions are fixed by imposing force and moment at $s = \ell$. Let us denote $\boldsymbol{N_\ell} := \boldsymbol{N}(\ell)$ and $\boldsymbol{M_\ell} := \boldsymbol{M}(\ell)$. In terms of force, either orientation ϕ_ℓ and magnitude N_ℓ or equivalently shear and longitudinal components $N_{1\ell}$ and $N_{3\ell}$ may be prescribed. Here ϕ_ℓ is measured from the opposite normal of the section, then $N_{1\ell} = -N_\ell \sin(\phi_\ell)$ and $N_{3\ell} = -N_\ell \cos(\phi_\ell)$.

*marwan.hariz@univ-rennes1.fr
†loic.lemarrec@univ-rennes1.fr
‡jlerbet@gmail.com

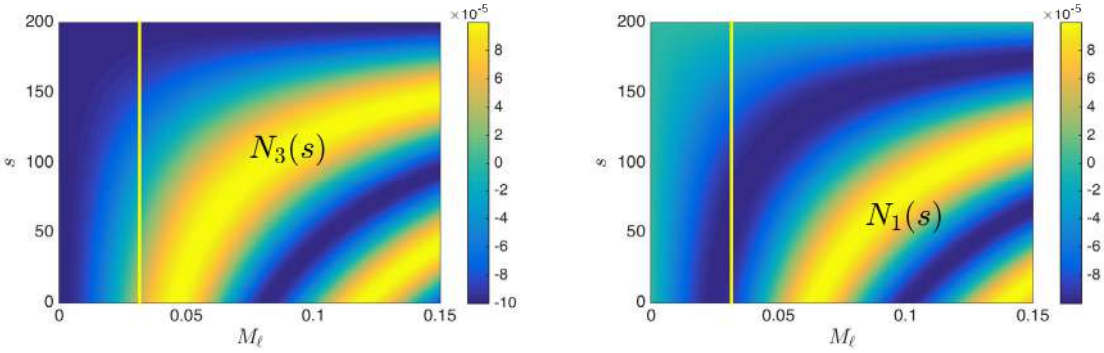

Figure 1: Internal longitudinal force $N_3(s)$ and shear force $N_1(s)$ for various bending moments at boundary $M_2(\ell) = M_\ell$. Here $\ell = 200$, $g = 2.5$ and the external load $N_\ell = 10^{-4}$ is fixed and purely longitudinal ($\phi_\ell = 0$ then $N_{1\ell} = 0$). Note that for such material the Euler critical buckling is $P_e = g\pi^2/\ell^2 \sim 6 \cdot 10^{-4}$ then a priori $|N_{3\ell}| < P_e$. The yellow line $M_\ell = 2\sqrt{gN_\ell} \sim 0.03$ splits the M_ℓ domain where $a < 0$ (left) and $a > 0$ (right).

PRE AND POST BUCKLING SOLUTIONS

From the first relation of (2), the force is uniform $\boldsymbol{N}(s) = \boldsymbol{N}_\ell$. This motivate us to introduce $\phi(s) \in]-\pi;\pi[$ such that $N_1(s) = -N_\ell \sin(\phi(s))$ and $N_3(s) = -N_\ell \cos(\phi(s))$ with $\phi(\ell) = \phi_\ell$. According to (4) or (5) it is straight forward to obtain $\phi' = -\kappa_2$. Injecting this relation into (6) we obtain after integration

$$-(g\phi')^2 + 2gN_\ell \cos\phi + (g-1)N_\ell^2 \cos^2\phi = \mu_\ell\,. \tag{7}$$

The constant of integration μ_ℓ is imposed by boundary conditions as $\mu_\ell = -M_{2\ell}^2 - 2gN_{3\ell} + (g-1)N_{3\ell}^2$. With the change of variable $t(s) = \tan(\phi(s)/2)$, (7) may be written as

$$(t')^2 = a(t^2-\alpha_-)(t^2-\alpha_+) \quad \text{with} \quad a = \frac{(g-1)N_\ell^2 - 2gN_\ell - \mu_\ell}{4g^2} \quad \alpha_\mp = \frac{(g-1)N_\ell^2 + \mu_\ell \mp 2N_\ell\sqrt{g^2+(g-1)\mu_\ell}}{(g-1)N_\ell^2 - 2gN_\ell - \mu_\ell}$$

that is completely determined by μ_ℓ and magnitude N_ℓ. Let us note $\omega_\mp = |\alpha_\mp|$. For practical application $\alpha_+ < 0$ but sign of α_- and a may vary according to the set $\{\mu_\ell, N_\ell\}$. This would strongly affect the solution of the differential equation:

If $a < 0$ and $\alpha_- < 0$ no real-valued solution

If $a < 0$ and $\alpha_- > 0$ $t(s) = \pm\sqrt{\omega_-}\,\mathrm{sn}\Big(\sqrt{|a|\omega_+}(s-s_0)\,\Big|\,-\dfrac{\omega_-}{\omega_+}\Big)$ or $t(s) = \pm\sqrt{\alpha_-}$

If $a > 0$ and $\alpha_- < 0$ $t(s) = \pm\sqrt{\omega_-}\,\mathrm{sc}\Big(\sqrt{|a|\omega_+}(s-s_0)\,\Big|\,1-\dfrac{\omega_-}{\omega_+}\Big)$

where s_0 is a constant choosen in order to satisfy boundary conditions. Jacobian functions $\mathrm{sn}(z\,|\,m)$ and $\mathrm{sc}(z\,|\,m)$ are defined according to [3].
An illustration is given for a practical application in Fig.1. It must be emphasized that for moderates bending momentum at the boundary, some homogeneous solutions may appears in addition to the non-homogenous ones depicted in the figures. Hence three equilibrium positions are possible for moderate bending boundary condition. The non-homogeneous solution observed for moderate bending moment corresponds to solution observed after such iterative process (i) impose a large external load in order to reach buckling (ii) reduce progressively the external load.
It is then interesting to investigate the stability of all these solutions in order to complete the analysis.

References

[1] L. Le Marrec, J. Lerbet, L. R. Rakotomanana, Vibration of a Timoshenko beam supporting arbitrary large pre-deformation. Acta Mechanica, 229.1 (2018), 109-132.
[2] Bažant, Z., Cedolin, L.: Stability of Structures: Elastic, Inelastic, Fracture and Damage Theories. Oxford University Press, New York (1991)
[3] Walker, P., 2003. The analyticity of Jacobian functions with respect to the parameter k. Proceedings of the Royal Society of London. Series A: Mathematical, Physical and Engineering Sciences, 459(2038), pp.2569-2574.
[4] Batista, M., 2016. A closed-form solution for Reissner planar finite-strain beam using Jacobi elliptic functions. International Journal of Solids and Structures, 87, pp.153-166.
[5] Humer, A., 2013. Exact solutions for the buckling and postbuckling of shear-deformable beams. Acta Mechanica, 224(7), pp.1493-1525.
[6] Simo, J.C., 1985. A finite strain beam formulation. Comput Methods Appl Mech Eng, 49,70.

NUMERICS AND EXPERIMENTS OF NONLINEAR MHD WAVES IN DIFFERENTIALLY ROTATING SPHERICAL GEOMETRY

Ferran Garcia * [1,2], Jude Ogbonna[1], Martin Seilmayer[1], André Giesecke[1], and Frank Stefani[1]
[1]Helmholtz-Zentrum Dresden-Rossendorf, Bautzner Landstraße 400, D-01328 Dresden, Germany.
[2]Anton Pannekoek Institute for Astronomy, University of Amsterdam, 1090 GE Amsterdam, The Netherlands.

Summary An overview of the nonlinear dynamics of the magnetised spherical Couette flow is presented. This problem is fundamental for understanding magnetohydrodynamic MHD instabilities occurring when a liquid metal flow, driven by the rotation of the inner boundary in a spherical shell, is subjected to an axial magnetic field. The analysis, at a moderate rotation rate and applied magnetic fields, is based on direct numerical simulations and numerical tools from dynamical systems and chaos theory, as well as laboratory experiments. Several type of MHD waves are classified and a reasonable agreement between simulations and experiments is obtained.

THE MAGNETISED SPHERICAL COUETTE MODEL

The magnetized spherical Couette (MSC) system models the HEDGEHOG experiment (Hydromagnetic Experiment with Differentially Gyrating sphEres HOlding GaInSn) at the Helmholtz-Zentrum Dresden-Rossendorf. The set-up consists of a liquid metal (GaInSn), filling the gap between two differentially rotating spheres, subjected to an axial magnetic field. This model gives rise to a rich variety of nonaxisymmetric induction-free instabilities related to the hydrodynamic jet instability, a return flow instability and the Kelvin-Helmholtz-like Shercliff layer instability, and thus its study is fundamental in MHD. Indeed, MSC is important from an astrophysical point of view: MHD flows measured in previous sodium experiments [10] were interpreted as magnetorotational instability (MRI) on a background of a fully turbulent flow. However, the observed fluctuations were attributed in [6, 5] to the turbulent analogues of the above mentioned MSC instabilities.

Previous nonlinear studies [6] and the references therein, are build on a basis of few direct numerical simulations (DNS). Very recently the authors of [7] compared DNS with experimental data obtaining reasonable agreement. The latter studies motivated recent work [4, 3] for a deep analysis of the nonlinear dynamics, by means of continuation and bifurcation methods, of each MHD instability, providing a classification of rotating and modulated waves (periodic and quasiperiodic flows) bifurcated from the basic flow.

The inductionless approximation of the Navier-Stokes and induction equations, which is valid for liquid metals as GaInSn, give rise to

$$\begin{aligned} \partial_t \mathbf{v} + \mathrm{Re}\,(\mathbf{v}\cdot\nabla)\,\mathbf{v} &= -\nabla p^* + \nabla^2\mathbf{v} + \mathrm{Ha}^2(\nabla\times\mathbf{b})\times\hat{\mathbf{e}}_z, \\ 0 &= \nabla\times(\mathbf{v}\times\hat{\mathbf{e}}_z) + \nabla^2\mathbf{b}, \end{aligned}$$

where p^* is the dimensionless pressure containing all the potential forces, $\mathbf{v}$ the velocity field and $\mathbf{b}$ the magnetic field perturbation. The system is governed by 3 non-dimensional numbers:

$$\mathrm{Re} = \frac{\Omega_i r_i L}{\nu}, \quad \mathrm{Ha} = B_0 L\sqrt{\frac{\sigma}{\rho\nu}}, \quad \eta = \frac{r_i}{r_o},$$

with $\sigma = 1$ the electrical conductivity of the fluid, ν the kinematic viscosity, $L = r_o - r_i$ the gap width, Ω_i the rotation rate of the inner sphere and B_0 the strength of the applied (axial) magnetic field. The simulation of the system is performed with a modified version of the pseudospectral code described in [2] that uses high order (up to 5) time integration IMEX-BDF methods.

The HEDGEHOG experiment can operate with two different aspect ratios $\eta = 0.35, 0.5$ and is designed to run in a quasi-laminar regime ($\mathrm{Re} \in [10^3, 10^4]$ and $\mathrm{Ha} < 10^3$) rather than the previous experiments of turbulent liquid sodium [10]. This regime is also suitable for studying helical [11] and azimuthal [9] MRIs.

NONLINEAR WAVES

The MSC system is $\mathbf{SO}(2)\times\mathbf{Z}_2$-equivariant, i. e., invariant by azimuthal rotations and reflections with respect to the equatorial plane. In this class of dynamical systems the type of solutions appearing at successive bifurcations from the base state is theoretically known [8, 1]. From a primary Hopf bifurcation of the basic Couette flow, several branches of periodic rotating waves (RW) appear [4], which in turn give rise to quasiperiodic modulated rotating waves (MRW) at a secondary Hopf bifurcations [3]. Continuation methods [4] allow to obtain the curves of rotating waves to study the dependence of the rotating frequency upon the Hartman number. Comprehensive explorations of the parameter space by means of DNS of flows bifurcated from these rotating waves allows to find regions of multistability of flows with quasiperiodic

*Corresponding author. E-mail: f.garcia-gonzalez@hzdr.de.

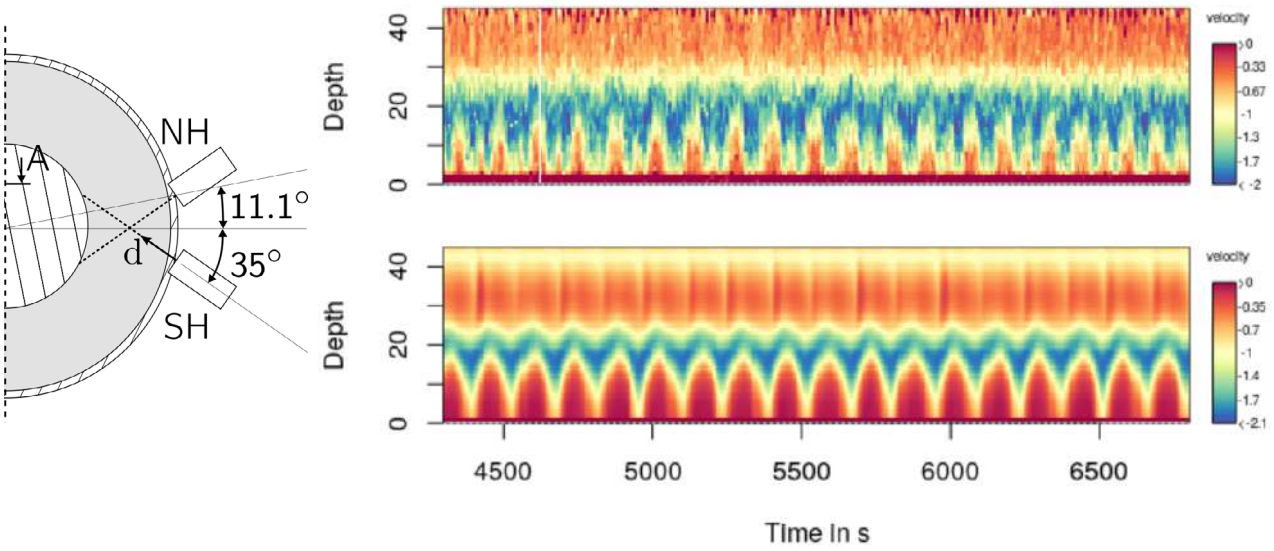

Figure 1: Left: Meridional section displaying the position of the ultrasonic Doppler velocimeter (UDV) DOP3010 probes. For each sensor the velocity along the dashed line is measured. Right: Experimental measurements (top) taken at one sensor on the north hemisphere (NH) and the corresponding numerical simulation (bottom). This radial jet instability corresponds to a modulated rotating wave at $\mathrm{Re} = 10^3$ and $\mathrm{Ha} = 2.5$.

and complex dependence [3]. The understanding and classification of the different types of azimuthal symmetries and temporal dependence of multistable flows is crucial for a successful comparison with experimental measurements.

Figure 1 illustrates the comparison of numerical and experimental velocities (mms^{-1}), along a line contained in a meridional plane (see figure caption), at $\mathrm{Re} = 10^3$ and $\mathrm{Ha} = 2.5$. According to the numerical simulations at these parameters several type of flows with azimuthal symmetry $m = 1$ are stable. The main difference between them is the azimuthal wave number, m_{max}, which mostly contributes to the flow kinetic energy. Concretely, two modulated rotating waves with $m_{\mathrm{max}} = 2$ and $m_{\mathrm{max}} = 3$ are found numerically and are stable at $\mathrm{Ha} = 2.5$. Because the experimental set-up consist of 6 UDV measuring sensors evenly displayed in the azimuthal direction, the $m = 2$ and $m = 3$ components of the flow can be estimated. In the case of Fig. 1 the main contribution to the kinetic energy of the experimental flow comes from the mode $m = 2$, and thus is compared with the simulated modulated wave with $m_{\mathrm{max}} = 2$. As displayed in Fig. 1 the amplitude and time dependence of the numerical solution and the experimental measurements are in good agreement.

CONCLUSIONS

A clear picture of complex nonlinear dynamics appearing in differentially rotating MHD flows in spherical geometry is revealed when analysing the system in terms of dynamical systems and bifurcations theory. In particular, the presence of different symmetry classes of rotating and modulated waves and their importance in the development of more complex flows can be understood. Indeed, regions of multistability can be determined with reasonable accuracy. This is of special relevance for understanding the origin of experimental flows and thus for the proper design of measurement techniques to capture flow symmetries.

References

[1] Crawford J. D., Knobloch E. Symmetry and symmetry-breaking bifurcations in fluid dynamics. *Ann. Rev. Fluid Mech.* **23(1)**:341-387, 1991.
[2] Garcia F., Net M., García-Archilla B., Sánchez J. A comparison of high-order time integrators for thermal convection in rotating spherical shells. *J. Comput. Phys.* **229**:7997-8010, 2010.
[3] Garcia F., Seilmayer M., Giesecke A., Stefani F. Modulated rotating waves in the magnetized spherical Couette system. *J. Nonlinear Sci.* **29(6)**:2735-2759, 2019.
[4] Garcia F., Stefani F. Continuation and stability of rotating waves in the magnetized spherical Couette system: Secondary transitions and multistability. *Proc. Roy. Soc. Lond. A* **474**:20180281, 2018.
[5] Gissinger C., Ji H., Goodman J. Instabilities in magnetized spherical Couette flow. *Phys. Rev. E* **84**:026308, 2011.
[6] Hollerbach, R. Non-axisymmetric instabilities in magnetic spherical Couette flow. *Proc. Roy. Soc. Lond. A* **465**:2003-2013, 2009.
[7] Kasprzyk C., Kaplan E., Seilmayer M., Stefani F. Transitions in a magnetized quasi-laminar spherical Couette flow. *Magnetohydrodynamics* **53(2)**:393-401, 2017.
[8] Rand D. Dynamics and symmetry. Predictions for modulated waves in rotating fluids. *Arch. Ration. Mech. An.* **79(1)**:1-37, 1982.
[9] Seilmayer M., Galindo V., Gerbeth G., Gundrum T., Stefani F., Gellert M., Rüdiger G., Schultz M., Hollerbach R. Experimental evidence for nonaxisymmetric magnetorotational instability in a rotating liquid metal exposed to an azimuthal magnetic field. *Phys. Rev. Lett.* **113**:024505, 2014.
[10] Sisan D. R., Mujica N., Tillotson W. A., Huang Y. M., Dorland W., Hassam A. B., Antonsen T. M., Lathrop D. P. Experimental observation and characterization of the magnetorotational instability. *Phys. Rev. Lett.* **93**:114502, 2004.
[11] Stefani F., Gerbeth G., Gundrum T., Hollerbach R, Priede J., Rüdiger G., Szklarski J. Helical magnetorotational instability in a Taylor-Couette flow with strongly reduced Ekman pumping. *Phys. Rev. E 80*:066303, 2009.

RESOLVING SIMULATED SEQUENCES OF EARTHQUAKES AND FAULT INTERACTIONS

Valère Lambert[1]*, and Nadia Lapusta [1,2]
[1]Seismological Laboratory, California Institute of Technology, Pasadena, USA
[2] Department of Mechanical and Civil Engineering, California Institute of Technology, Pasadena, USA

Summary We examine the sensitivity of fault interactions in numerical simulations of sequences of earthquakes and aseismic slip (SEAS) to choices in numerical discretization and physical approximations of inertial effects, using a rate-and-state crustal fault model with two co-planar segments separated by a strong creeping barrier. We find that some physical fault and earthquake rupture quantities can be reliably determined from adequately resolved numerical models, however other quantities, such as the probability of a rupture jumping from one fault segment to another, are highly sensitive to modeling choices. Our findings suggest that some hazard parameters, such as the probability of multi-fault ruptures, may be extremely sensitive to both numerical and physical perturbations, and thus may be impractical to estimate in a reliable manner for natural faults.

Physics-based numerical modeling of earthquake source processes aims to combine available real-world data and physical principles to improve our understanding of fault behavior. There is growing interest in using numerical earthquake models of fault networks to directly determine quantities of interest for seismic hazard, such as the probability of an earthquake rupture jumping from one fault segment to another. However, the outcomes of numerical simulations can be subject to choices in numerical procedures and physical approximations, and assessing the predictive power of numerical models remains a topic of active research.

We investigate the sensitivity of numerical simulations of long-term sequences of earthquakes and aseismic slip to choices in numerical discretization and approximations for inertial (wave-mediated) effects, using a simplified 2-D elastodynamic continuum model of a crustal fault with two co-planar segments separated by a relatively strong creeping barrier (Figure 1A). Our simulations demonstrate that the frequency of two-segment ruptures and the complexity of the resulting earthquake sequences significantly depend on the modeling assumptions. In part, simulations with different numerical discretization (including insufficient discretization) and treatments of inertial effects may produce similar complexity of earthquake sequences but have very different probabilities of multi-segment ruptures.

Even among simulations that are well-resolved by standard considerations, some properties of simulated events are similar and some are not, when the fault is long enough compared to the nucleation size. That parameter regime promotes a wider distribution of rupture sizes and results in long-term differences in the simulated sequences of events. Typically, the most constraining discretization condition has been the need to resolve the cohesive zone, i.e., the region at the rupture front where shear resistance breaks down and all variables rapidly evolve, by more than 3 cells (Figure 1B; Day et al., 2005; Lapusta and Liu, 2009). While earthquake sequence behavior is virtually indistinguishable for some initial period of adequately resolved simulated sequences, the sequences of slip events eventually begin to diverge due to the subtle accumulation of numerical differences interacting with the highly nonlinear nature of the problem (Figure 1C-D).

In our models, we find that some relationships among physical properties, such as average slip, average static stress drop, and the history of average shear stress on the fault, are generally stable among adequately resolved simulations, suggesting that they may be reliably estimated from well-formulated numerical models (Figure 2). However, others properties, such as the probability of an earthquake rupture jumping from one fault segment to another, are highly sensitive to physical assumptions and numerical discretization, and hence vary even among well-resolved simulations and cannot be reliably inferred from such numerical studies (Figure 1C-D).

Our results emphasize the general need to examine the potential procedural dependence of simulation outcomes, including to resolution, particularly when assessing their predictive value for seismic hazard assessment. In addition, the significant sensitivity of some hazard parameters, such as the rate of multi-segment ruptures, to small perturbations in numerical models implies that the hazard parameters may also be extremely sensitive to physical perturbations on natural faults, suggesting that such hazard parameters are highly unstable and may be impractical to estimate in a reliable manner. This motivates the exploration of more meaningful metrics for constraining long-term fault behavior and assessing seismic hazard.

*Corresponding author. E-mail: vlambert@caltech.edu.

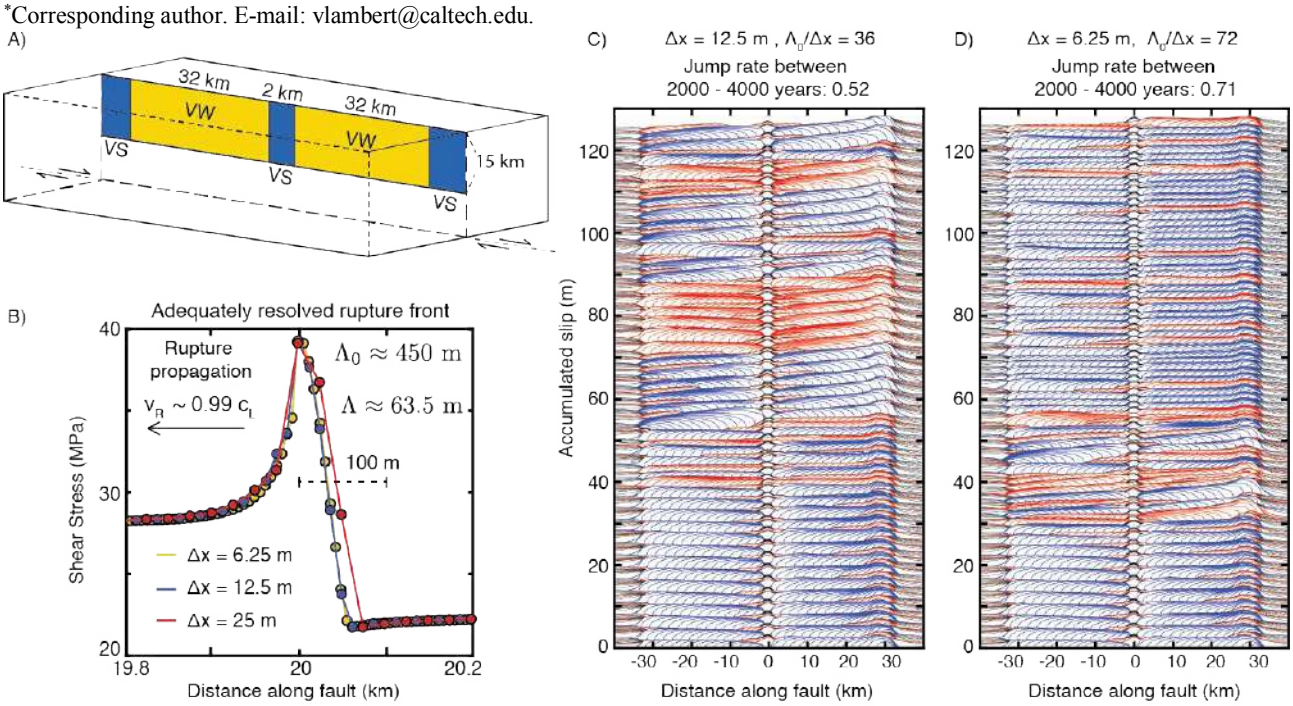

Figure 1. Sensitivity of simulated long-term interactions between two fault segments to numerical discretization even for well-resolved simulations. A) Schematic for a 2D plane-strain problem of a fault with two velocity-weakening segments separated by a velocity-strengthening barrier. B) Standard discretization considerations suggest the need to resolve the quasi-static cohesive zone size Λ_0 by at least 3 cells. During dynamic rupture the actual cohesive zone Λ shrinks as the rupture speed increases towards the limited wave speed (Day et al., 2005; Lapusta and Liu, 2009). (C-D) Slip history over 4000 years in two well-resolved simulations of earthquake sequences; e.g., the quasi-static cohesive zone size Λ_0 is resolved by 36 and 72 cells, respectively. The first 1000 years of simulated time are virtually indistinguishable. However, the long-term response, including the rate of two-segment ruptures, eventually begins to differ due to the compounded effects of small numerical differences and high nonlinearity of the problem, despite the simulations being well-resolved by any standard considerations. D)

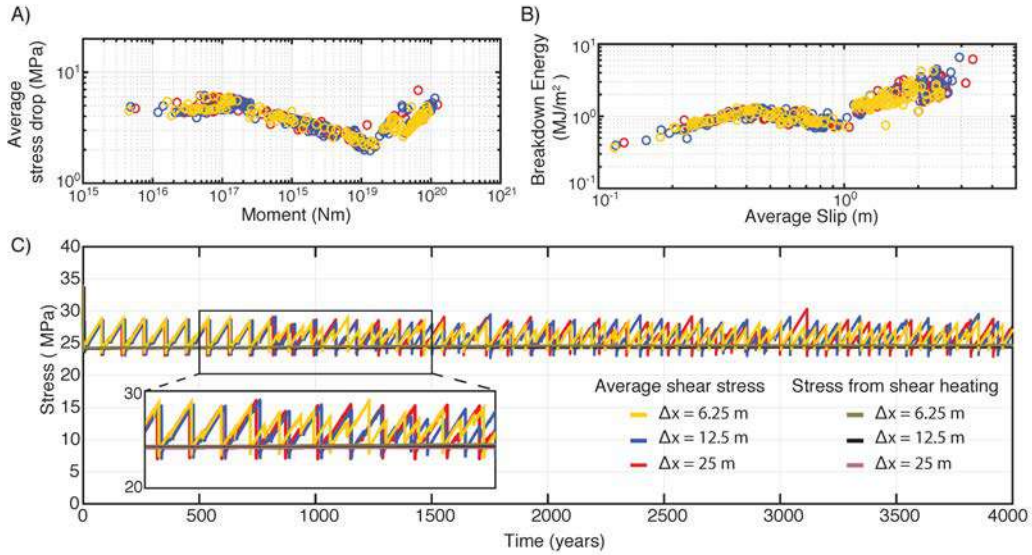

Figure 2. Consistent earthquake and fault properties among adequately resolved simulations. Despite differences in the simulated earthquake sequences, some simulated rupture and fault properties, such as the A) scaling of average static stress drop with seismic moment, B) scaling of average breakdown energy with slip, and C) evolution of average shear stress on the fault, are consistent among adequately-resolved simulations, suggesting that they may be reliably inferred from well-formulated numerical models.

References

[1] Day, S. M., L. A. Dalguer, N. Lapusta, and Y. Liu. Comparison of finite difference and boundary integral solutions to spontaneous rupture, *J. Geophys. Res.* 110, B12307, 2005.

[2] Lapusta, N, Liu, Y. Three-dimensional boundary integral modeling of spontaneous earthquake sequences and aseismic slip, *J. Geophys. Res.* 114, 2009.

MODERN PERSPECTIVES TO STATISTICAL CHARACTERIZATION OF HETEROGENEOUS POROUS MEDIA

Alberto Guadagnini
Department of Civil and Environmental Engineering, Politecnico di Milano, Milano, Italy

Summary Characterization of the spatial variability of attributes of natural porous media is critical in several environmental settings. Quantities such as, e.g., permeability, porosity, or geochemical parameters of natural systems typically exhibit spatial variations, their heterogeneous pattern being linked to the size of observation/measurement/support scale. As the latter becomes coarser, the system is seemingly associated with a decreased degree of heterogeneity. As such, sets of data linked to differing support scales provide diverse amounts of information. Here, we address the way stochastic representations of multiscale heterogeneity can be employed to assess documented manifestations of scaling of statistics of hydrological and soil science variables. We focus on perspectives associated with modern interpretive approaches to scaling of the main statistical descriptors of heterogeneity observed at diverse scales. We also include an appraisal of the potential of embedding elements of information theory in the analysis, as applied to the quantification of the information content related to data collected at differing measurement scales within a porous domain.

INTRODUCTION

Geostatistical approaches considered for the analysis of the major features associated with the spatial heterogeneity of quantities related to subsurface flow and transport processes assume that available observations of a target variable are sampled from a random field with a given distribution. The main statistics inferred from datasets of hydrogeological properties, including, e.g., hydraulic conductivity [1, 2, 3], electrical resistivity [2], log-permeability [4, 5, 6, 7], and neutron porosity [8] observations are characterized by distinct features. Spatial (or temporal) increments, $\Delta Y(\mathbf{s}) = Y(\mathbf{x}+\mathbf{s}) - Y(\mathbf{x})$, evaluated over the separation distance (or lag) $\mathbf{s}$, of a quantity $Y(\mathbf{x})$ ($\mathbf{x}$ denoting a position vector) display distributions characterized by peaks that become sharper and tails that tend to become heavier with decreasing lag. Distributions transitioning from heavy tailed at small lags to seemingly-Gaussian at increased lags are documented for a variety of spatial and/or temporal increments of environmental data, including sediment transport processes (e.g., [9]) and fully developed turbulence [10] as well as datasets of Earth, environmental and several other variables. Such a scale dependence is directly imprinted to the associated (statistical) moments of increment distributions, these and other aspects of statistical scaling being manifest in porous as well as fractured media characterized by either one or a hierarchy of spatial correlation scales.

In this broad context, several studies clarify that values of variables such as permeability and their associated statistics depend on a multiplicity of scales. These include the data support (or measurement scale), the size of the observation domain, and typical length scales describing spatial correlation (see e.g., [11, 12, 13, 14 and references therein]). As an example, we focus here on the length scale characterizing data sampling (i.e., the support or measurement scale). Laboratory- and field-scale evidences indicate that the mean value and the correlation length of a permeability field tend to increase with the size of the data support, the opposite behavior being displayed by the variance of data samples.

All of the above mentioned patterns suggest that the spatial distribution of permeability and other quantities tends to display an increased degree of homogeneity (as given by a decreased variance and an increased spatial correlation) with increasing support/measurement scale. These findings are also typically associated with the intuition that upscaling (here corresponding to data associated with increasing measurement/support scale) leads to a loss of information about the degree of spatial organization of the system property, corresponding to a loss of details.

THEORETICAL ELEMENTS AND SHOWCASES

The scale-dependent behavior of the probability density function (pdf) of incremental quantities can be captured through a Generalized Sub-Gaussian (GSG) model [8]. Such a theoretical framework describes the random field $Y(\mathbf{x}) = \langle Y \rangle + Y'(\mathbf{x})$, $\langle Y \rangle$ and $Y'(\mathbf{x})$ being the ensemble mean and a local zero-mean fluctuation, respectively, can be interpreted as $Y'(\mathbf{x}) = U(\mathbf{x})G(\mathbf{x})$, where $G(\mathbf{x})$ is a zero-mean, generally (but not necessarily) multi-scale Gaussian random field and $U(\mathbf{x})$ is a *subordinator*. The latter is independent of G and consists of statistically independent identically distributed non-negative random variables. The underlying Gaussian random field generally (but not necessarily) displays a multi-scale (statistical) nature. The latter can be captured, for example, through a geostatistical description based on a Truncated Power Variogram (TPV) model (e.g., [14] and references therein).

Here, we show how the original GSG model formulation can be generalized to include alternative distributional forms of the subordinator and present the ensuing analytical formulations. We then demonstrate the applicability of the theoretical framework by analyzing two datasets associated with differing processes and observation scales: (*i*) a dataset collecting measurements of surface topography of a (millimeter-scale) calcite sample resulting from induced mineral dissolution and (*ii*) a set of neutron porosity data sampled from a (kilometer-scale) deep vertical borehole in a reservoir.

We then rely on numerical simulations of conservative transport in a three-dimensional bounded porous medium and Quadratic Discriminant Analysis to document how different conservative transport observables might help in the non-univocal discrimination of model and parameters, thus translating into uncertain model outcomes. Our results document how the (ensemble averaged) longitudinal dispersion of a solute plume is scaled down in Sub-Gaussian fields with respect to their Gaussian counterparts after the solute has migrated across distances corresponding to a few integral scales of the conductivity field. This aspect is not clearly inferred from the analysis of individual realizations. We also find that the action of local dispersion tends to increase difficulties in the delineation of the influence of Sub-Gaussianity on transport. This reveals that one may not be able to discriminate between non-Gaussian and Gaussian conductivity fields relying solely on observations of the behavior of solutes migrating within the domain.

We then widen the scope of the analysis by relying on the unique datasets provided by Tidwell and Wilson [12, 13] and collecting the results of measurement campaigns targeted at the evaluation of air permeability data across the faces of a Berea Sandstone and a Topopah Spring Tuff blocks, considering different support/measurement scales. We leverage on such a truly multiscale datasets to address research questions such as "How much information is lost as the support scale increases?" and "How informative are data taken at a coarser support scale(s) with respect to those associated with a finer support scale?". The genuinely multi-scale nature of the data is analyzed through elements of Information Theory and enables us to quantify the way information is shared across measurement scales. On these bases, one can clearly identify information losses and/or redundancies that can be associated with the joint use of data sampled at differing scales.

We finally merge all of the above mentioned elements within a geostatistical interpretation of the system based on the GSG approach where a Truncated Power Variogram (TPV) model is employed to represent the underlying correlation structure. By doing so, we propose a way in which these models allow conditioning the spatial statistics of such fields on multiscale measurements via multiscale co-kriging.

CONCLUSIONS

This work is keyed to an appraisal of a variety of approaches aiming at the characterization of subsurface heterogeneity and focusing on the way statistical descriptors of the system transition across scales. We rely on interpretations based on geostatistical concepts, as integrated within a Generalized Sub-Gaussian model depicting the spatially correlated attributes of porous media at multiple scales. We then discuss the way elements of Information Theory can contribute to quantify the degree of information shared by data collected across differing scales and suggest an approach according to employ these to effectively yield a description of the main statistics of a given field at a desired scale.

The nature of the approaches makes these potentially amenable to be transferred to analyze settings involving other kinds of datasets associated with diverse hydrogeological quantities or considering joint assessment of data stemming from measurement/sampling devices of diverse designs. Future developments could also include exploring the possibility of embedding the approach within the workflow of optimal experimental design and/or data-worth analysis strategies.

References

[1] Painter S., Evidence for non-Gaussian scaling behavior of heterogeneous sedimentary formations, *Water Resour. Res.* **32**(5): 1183-1195, 1996.
[2] Painter S., Flexible scaling model for use in random field simulation of hydraulic conductivity. *Water Resour. Res.* **37**: 1155-1163, 2001.
[3] Meerschaert M.M., Kozubowski T.J., Molz F.J., Lu S., Fractional Laplace model for hydraulic conductivity. *Geophys Res Lett*. **31**, L08501, 2004.
[4] Siena M., Guadagnini A., Riva M., Neuman S.P., Extended power-law scaling of air permeabilities measured on a block of tuff, *Hydrol. Earth Syst. Sci*. **16**: 29-42, 2012.
[5] Siena M., Riva M., Giamberini M., Gouze P., Guadagnini A., Statistical modeling of gas-permeability spatial variability along a limestone core, *Spatial Statistics* **34**: 71-85, 2019.
[6] Riva M., Neuman S.P., Guadagnini A., Sub-Gaussian model of processes with heavy tailed distributions applied to permeabilities of fractured tuff, *Stoch. Environ. Res. Risk Assess.* **27**: 195-207, 2013.
[7] Riva, M., Neuman S.P., Guadagnini A., Siena M., Anisotropic scaling of Berea sandstone log air permeability statistics. *Vadose Zone Jour.* **12**(3): https://doi.org/10.2136/vzj2012.0153, 2013.
[8] Riva M., Neuman S.P, Guadagnini A., New scaling model for variables and increments with heavy-tailed distributions. *Water Resour. Res.* **51**(6): 4623-4634, 2015.
[9] Ganti V., Singh A., Passalacqua P., Foufoula-Georgiu E., Subordinated Brownian motion model for sediment transport. *Phys. Rev. E* **80**: 011111, 2009.
[10] Boffetta G., Mazzino A., Vulpiani A., Twenty-five years of multifractals in fully developed turbulence: a tribute to Giovanni Paladin. *J. Phys. A: Math. Theor.* **41**: 363001, 2008.
[11] Neuman S.P., Generalized scaling of permeabilities: Validation and effect of support scale, *Geophysical Research Letters* **21**(5): 349-352, 1994.
[12] Tidwell V.C., Wilson J.L., Permeability upscaling measured on a block of Berea Sandstone: Results and interpretation. *Math. Geol.* **31**(7): 749-769, 1999.
[13] Tidwell V.C., Wilson J.L., Upscaling experiments conducted on a block of volcanic tuff: Results for a bimodal permeability distribution. *Water Resour. Res*. **35**(11): 3375-3387, 1999.
[14] Neuman S.P., Di Federico V., Multifaceted nature of hydrogeologic scaling and its interpretation. *Reviews of Geophysics*. **41**: 1014, 2003.

WHAT WE CAN LEARN ABOUT INTERNAL TRANSFER MECHANISMS IN POROUS MEDIA (IMBIBITION, DRYING, COLLOID TRANSPORT, PHASE CHANGES) FROM MAGNETIC RESONANCE IMAGING AND OTHER NMR TECHNIQUES

Philippe Coussot
Université Paris-Est, Laboratoire Navier (ENPC-CNRS-IFSTTAR), Champs sur Marne, France

Summary Transport or transfers in porous media are often studied or described from global characteristics such as the amount of some quantity (liquid or particle mass) entering or exiting the sample, which precludes a deep understanding of local processes in time. Beyond the basic (non-quantitative) MRI technique, various techniques relying on NMR allow to provide a wide set of information on the quantitative evolution of the local liquid, porous structure, or solid-liquid interaction characteristics in time. We review several applications of these techniques and how they provided new information on the internal transfer mechanisms in porous media.

INTRODUCTION

Transport or transfers in porous media are often studied or described from global characteristics such as the amount of some quantity (liquid or particle mass) entering or exiting the sample, which precludes a deep understanding of local processes in time. Various more or less sophisticated techniques (confocal microscopy in transparent medium [1], neutron radiography or X-ray μ-CT [2], etc) allow to get some insight on the internal mechanisms. Here we focus on techniques relying on NMR (Nuclear Magnetic Resonance) which provide a wide set of information on the evolution of the local liquid or structure characteristics in time. NMR is based on the measure of the signal resulting from the resonance on the proton spins. For applications in porous media essentially the atoms in the liquid state are of interest. The basic MRI (Magnetic Resonance Imaging) technique relies on the distinction of the density of resonant spins at different places, but this approach is not quantitative and it resolution is generally not sufficient to get a precise information on the process characteristics at the pore scale. However, for processes homogeneous in the (cylindrical) sample cross-section, which may be checked from basic 2D MRI, it is possible to acquire the total signal in a thin cross-sectional layer and draw the distribution profile of liquid along the sample axis with an improved spatial resolution. Moreover, the NMR signal is not only sensitive to the spin density but also to its relaxation time which, roughly speaking, varies with the local solid-liquid interactions, and, under a field gradient, to its displacement. Coupling these characteristics with basic MRI widely opens the field of possibilities of measurements.

For sufficiently slow transient liquid transport processes such as imbibition, drying, phase changes, etc, following the liquid distribution in time provides a precise view of the internal processes. The sensitivity to displacement allows to measure the local velocity field or, alternatively but more precise as it does not suffer from resolution limitations, the probability density function of the velocity. The sensitivity to the solid-liquid interactions allows to measure the local concentration of suspended colloid particles, the local pore size, the water amount in the different possible states (e.g. free of bounded, in either large or small pores), etc. Such measurements make it possible to significantly progress in the knowledge of the transfer mechanisms in porous media. Here we review a series of examples of such approaches.

DRYING AND IMBIBITION

The evolution of the liquid distribution profile in a drying sample makes it possible to have a direct view of the liquid transport processes. This for example made it possible to show that, as long as gravity effects are negligible, from the very first times of drying the liquid fraction in a simple porous medium decreases homogeneously in time [3-4], a process which often lasts until a saturation of the order of 10%. Such an effect is due to capillary re-equilibration processes. However MRI also allowed to show that an almost homogeneous desaturation also occurs in porous materials with nanometric pores, whereas in such cases standard capillary effects cannot take place [4].

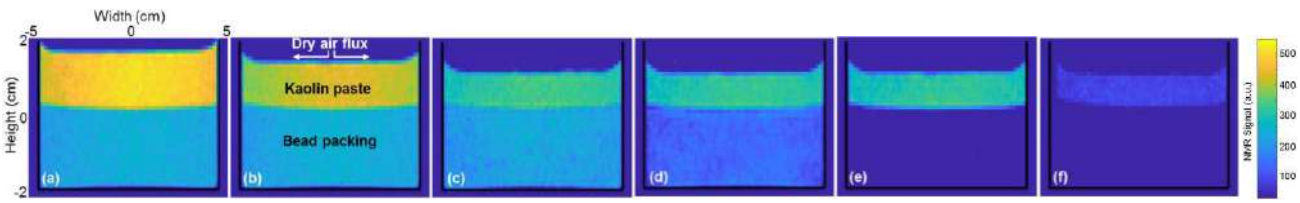

Figure 1: Qualitative (T2-weighted) 2D MRI Images of the kaolin paste (top) - bead packing (bottom) system at different times during drying: (a) 0, (b) 16 h, (c) 34 h, (d) 52 h, (e) 75 h, (f) 100 h. The NMR signal on the color scale is for each phase an increasing, but non-linear, function of the local water amount. Data from [5].

This technique appeared particularly useful for studying "composite" systems, made of layers of different types of porous materials, as it allows to quantify the liquid transfers between the layers. For example, it was shown that during the drying of a composite system made of a bead packing (substrate) covered by a clay paste, the substrate still undergoes a long homogeneous desaturation while the paste remains saturated (see Fig.1) [5]. The inverse situation of imbibition from a paste in a bead packing could also be studied [6] with this technique.

The power of NMR remarkably appears for the study of the imbibition or drying of complex porous systems containing several types of pores. For example, for hardwood, which contains free water inside long large vessels and small fibers, and bound water in the cell-walls, it was possible to distinguish the progression of the bound water and that of the free water, from which it appeared that the bound water surprisingly progresses faster (although by diffusion through the cell-walls) than the free water, an effect correlated to the strongly damped dynamics of imbibition as compared to the standard Washburn prediction [7]. At last the transfers between two phases can be followed by analysing the distribution of relaxation times when the relaxation times in the two phases are sufficiently different. This allows to follow the transfers between the different phases of a homogeneous system such as a hemp concrete or a cement paste containing aggregates.

TRANSPORT, DEPOSIT OR DISPERSION OF COLLOIDAL PARTICLES

In a saturated flow, the deposited fraction of colloid particles in a porous medium may be directly determined from the local liquid fraction with regards to liquid fraction before any deposit. This made it possible to observe the progressive deposition of non-colloidal particles by geometrical exclusion effects inside a 3D model porous medium, and to show that their concentration decreases exponentially with the distance from the entrance, which can described by a simple probabilistic model [8]. In general the NMR relaxation time of the liquid phase decreases with the ratio of the liquid volume to the area of the solid-liquid interface. This in particular implies that it will be smaller when the liquid is in smaller pores or the aspect ratio of the liquid volume is larger (e.g. films). This also implies that the relaxation time will be smaller for larger concentration of suspended solid particles. This made it possible to carry out relaxation-weighted measurements on pulses of suspensions of superparamagnetic colloidal particles injected in a granular packing and directly determine the dispersion coefficient from a straightforward analysis of the time evolution of the concentration profiles inside the sample (see Fig.2) [9]. The values obtained for this (directly observed) dispersion coefficient appeared to almost ten times lower than the commonly accepted values. This technique also made it possible to determine the local concentration in the flowing suspension in a different situation, if a fraction of particles is adsorbed onto the walls [10].

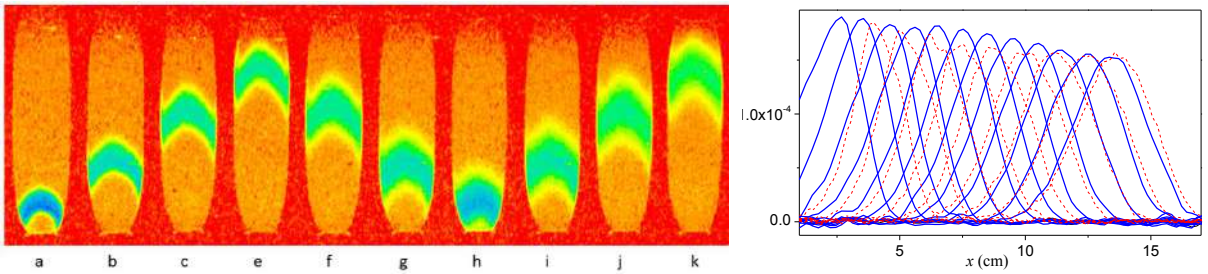

Figure 2: Left: Images of the particle distribution along longitudinal cross-sections at successive times during the flow through a bead packing (570 µm) with a pulse of colloid suspension : first upstream flow (a, b, c, d), downstream flow (e, f, g), second upstream flow (h, i, j). Color scale from maximum concentration to zero: blue-green-yellow-orange. Right: 1D quantitative profiles measured with another NMR technique. Data from [10].

NON-NEWTONIAN FLOWS IN POROUS MEDIA

Since yield stress fluids such as foams, emulsions, concentrated suspensions, exhibit a strongly non-linear constitutive equation, i.e. they behave as liquids above a critical stress and as solids otherwise, one expects that for such materials the Darcy's law will be strongly non-linear, which appeared to be effectively the case [11], but the question of the physical origin of such a law and of its coefficients remains open. It was suggested that such flows exhibit two original trends [12]: as the pressure drop increases a wider region of fluid starts to flow, an effect occurring at a local scale; at a macroscopic scale the flow starts only along a specific path throughout the porous medium and as the pressure drop is increased more flowing paths progressively form within the porous medium. However, with a simple porous medium (granular packing), from measurements using a NMR technique (pulsed-gradient spin echo (PGSE)), it was shown [13] that the probability density function of the velocity is similar to that for a Newtonian fluid, which suggests that this is the same for the local velocity field, while the stress needed to impose such a flow is non-linear.

References

[1] Gerber G, Bensouda M, Weitz DA, Coussot P, *Phys. Rev. Lett.*, **123**, 158005 (2019)
[2] Lal S, Poulikakos L, Partl M, Derome D, Carmeliet J, ICTAM Montreal, **vol.3**, p.3188 (2016)
[3] Pel L, Brocken H, Kopinga K, *Int. J. Heat Mass Transfer*, **39**, 1273 (1996)
[4]Thiery J, Rodts S, Weitz DA, Coussot P, *Phys. Rev. Fluids*, **2**, 074201 (2017)
[5] Ben Abdelouahab N, Gossard A, Rodts S, Coussot P, *Soft Matter*, **15**, 6732-6741 (2019)
[6] Ben Abdelouahab N, Gossard A, Rodts S, Coasne B, Coussot P, *Eur. Phys. J. E*, **5**, 66 (2019)
[7] Zhou M, Caré S, Courtier-Murias D, Faure P, Rodts S, Coussot P, *Wood Science and Technology*, **52**, 929-955 (2018)
[8] Gerber G, Rodts S, Aimedieu P, Faure P, Coussot P, *Physical Review Letters*, **120**, 148001 (2018)
[9] Lehoux A, Faure P, Michel E, Courtier-Murias D, Rodts S, Coussot P, *Transport in Porous Media*, **19**, 403-423 (2017)
[10] Lehoux A, Rodts S, Faure P, Michel E, Courtier-Murias D, Coussot P, *Phys. Rev. E* , **94**, 053107 (2016)
[11] T. Chevalier et al., *J. Non-Newt. Fluid Mech.*, **195**, 57-66 (2013)
[12] M.T. Balhoff, K.E. Thompson, *AIChE J.*50, 3034 (2004); M. Sahimi, *AIChE J.* **39**, 369 (1993).
[13] T. Chevalier et al., *Phys. Rev. E*, **89**, 023002 (2014)

A TALE OF X-RAY IMAGING AND MINIMAL SURFACES: REALIZING THE REVOLUTION IN ROCK CHARACTERIZATION

Martin J. Blunt, Branko Bijeljic, Qingyang Lin, Ali Raeini and Ying Gao
Department of Earth Science and Engineering, Imperial College, London, UK

Summary Recent developments in pore-scale modelling and imaging are reviewed, with an emphasis on three-dimensional X-ray visualizations of multiphase flow and reaction at reservoir conditions of temperature and pressure. Fundamental properties, such as contact angle, interfacial curvature, and pore-scale fluid distributions may be derived directly from these images, providing a powerful test for numerical models. We show how these pore-scale observations can be combined with measurements of pressure differential, which allow relative permeability and capillary pressure to be found simultaneously. We demonstrate how the morphology and curvature of the fluid interfaces impacts recovery. Modelling approaches are briefly reviewed, emphasizing that a hierarchy of methods are required to characterize flow.

OVERVIEW AND MOTIVATION

The understanding of multiphase flow in porous media is vital to address several important societal challenges, namely improved hydrocarbon production from underground reservoirs and the storage of the carbon dioxide produced from the burning of these fossil fuels [1]. Indeed, without widespread implementation of large-scale carbon capture and subsurface storage, underpinned by a fundamental understanding of subsurface flow processes, we are likely condemned to dangerous climate change combined with energy shortages.

We study the pore-scale fluid dynamics relevant for oil recovery and carbon dioxide storage, using high-resolution X-ray imaging and modelling calibrated to match the results of the experiments. Pore network modelling is introduced as a flexible upscaled formulation which uses experiments and direct numerical simulation to inform the pore-averaged properties used in the model.

MINIMAL SURFACES AND MODELLING

Figure 1 shows images highlighting the oil/water interfaces in a water-wet and a mixed-wet sandstone during waterflooding [2]. In a water-wet medium, the interfacial curvature is positive – oil bulges into water – which allows oil to be trapped. In the mixed-wet system, we see, remarkably, an approximately zero curvature, but where in one direction oil bulges into water and in the other water bulges into oil. The interfaces are approximately minimal surfaces, representing interfaces that minimize surface energy while being pinned at contact points. These minimal surfaces provide connectivity for oil and water and provide a topological explanation for the high oil recovery observed.

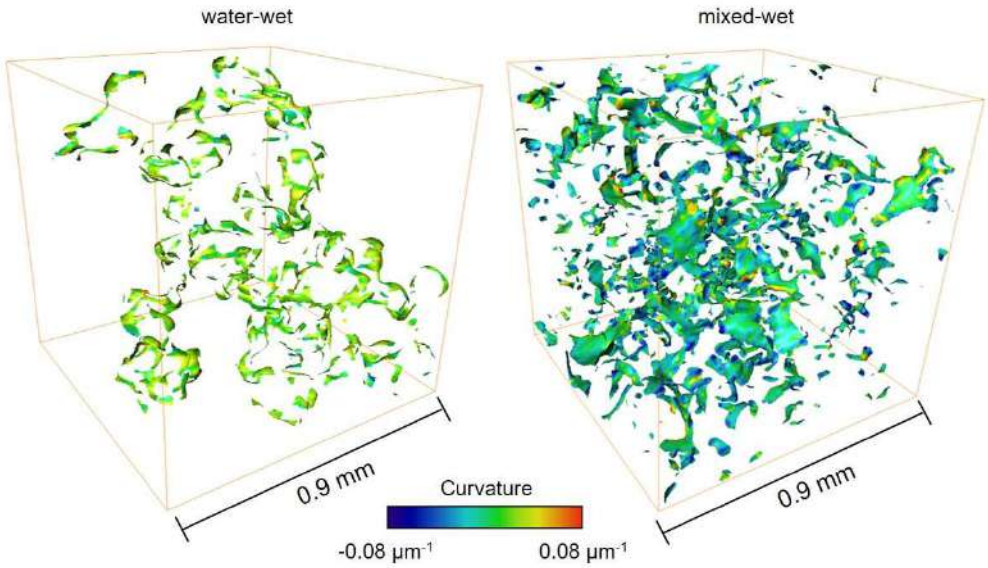

Figure 1. An illustration of the oil/water interface imaged in a water-wet (left) and mixed-wet (right) sandstone. The interfacial curvature is shown.

Figure 2 shows measured steady-state waterflood relative permeability on a mixed-wet reservoir carbonate from a producing reservoir in the Middle East where the pore-scale distribution of fluid has also been imaged [3]. The water connectivity is also shown – water preferentially fills water-wet pores and larger oil-wet pores throughout the sample, but this water is poorly connected, resulting in a low water relative permeability until a high saturation is reached and the

water clusters percolate in the macroscopic pore space. This leads to favourable local displacement efficiency, as the water is held back in the pore space.

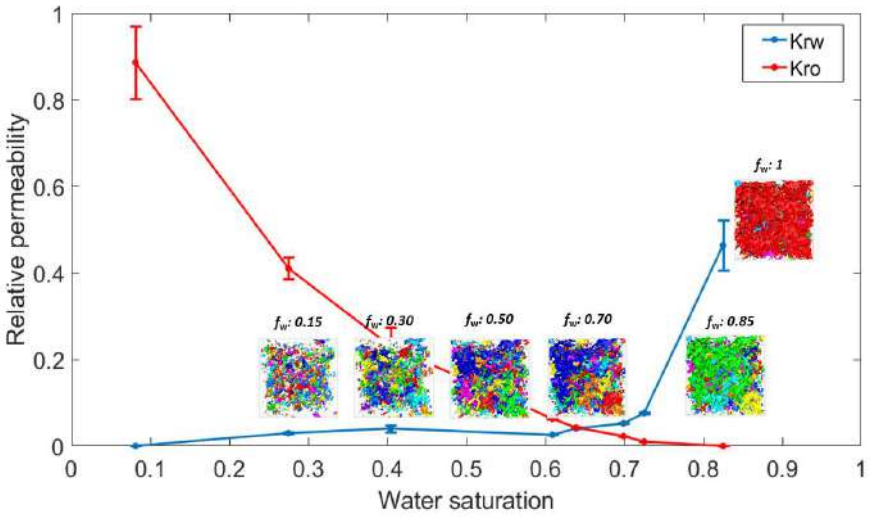

Figure 2. The waterflood relative permeability measured on a mixed-wet reservoir carbonate. Clusters of the water in macro-porosity are shown in different colours, indicating that water only percolates through the large pores at a high saturation, which explains the shape of the relative permeability function.

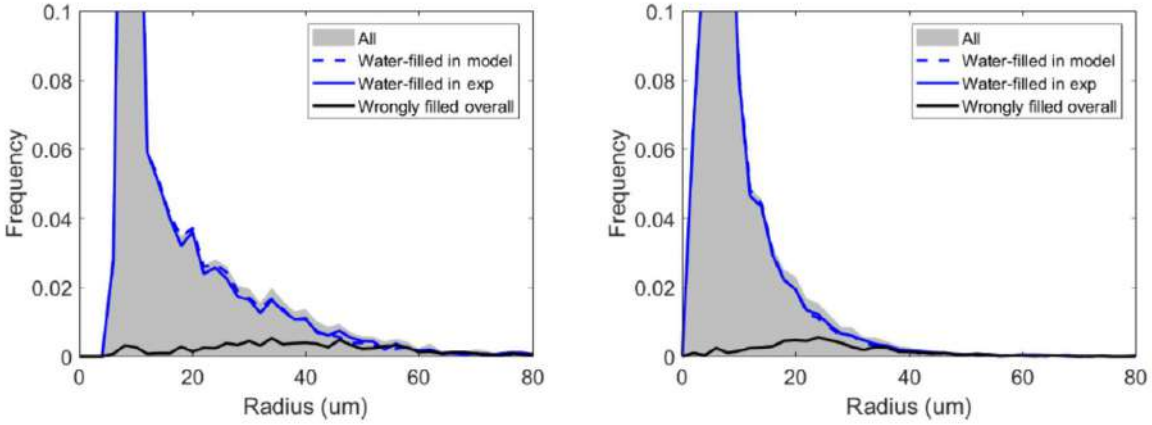

Figure 3. Pore-scale modelling results showing how the predictions of occupancy compares to direct imaging experiments. It is possible to almost exactly reproduce the correct sequence of filling with an appropriate assignment of wettability.

Figure 3 shows the results of pore-network modelling studies. If we assign wettability on a pore-by-pore basis we can reproduce almost exactly the sequence of displacement observed in the experiments. This provide a validated methodology to predict multiphase flow processes.

Further work will involve the combination of imaging, analysis and modelling to predict and interpret displacement processes for different porous materials and displacement processes.

Acknowledgments
We thank Shell under the Digital Rocks Programme and ADNOC for funding the research presented here.

References

[1] Blunt M. J. *Multiphase Flow in Permeable Media: A Pore-Scale Perspective*, Cambridge University Press, 2017.
[2] Lin Q., Bijeljic B., Berg, S., Pini, R., Blunt, M. J., and Krevor, S. "Minimal surfaces in porous media: Pore-scale imaging of multiphase flow in an altered-wettability Bentheimer sandstone," *Physical Review E*, **99,** 063105, 2019.
[3] Alhammadi, A. M., Gao, Y., Akai, T., Blunt, M. J., and Bijeljic, B. "Pore-scale X-ray imaging with measurement of relative permeability, capillary pressure and oil recovery in a mixed-wet micro-porous carbonate reservoir rock," *Fuel* (in press) 2020.

A FRAMEWORK FOR THE EXACT RECONSTRUCTION OF DEVELOPED MACRO-SCALE FLOW IN MICRO-CHANNELS WITH LARGE ARRAYS OF PERIODIC SOLID STRUCTURES

Arthur Vangeffelen * [1,2,3], Geert Buckinx[1,2,3], Maria Rosaria Vetrano[1,3], and Martine Baelmans[1,3]
[1]Department of Mechanical Engineering, KU Leuven, Celestijnenlaan 300A, 3001 Leuven, Belgium
[2]VITO, Boeretang 200, 2400 Mol, Belgium
[3]EnergyVille, Thor Park, 3600 Genk, Belgium

Summary A modelling framework is presented for the exact reconstruction of the developed macro-scale flow in micro-channels with arrays of periodic solid structures. Here, the macro-scale velocity and pressure are obtained from the Navier-Stokes equations by a double volume-averaging operator. That way, the constant macro-scale pressure gradient in the developed core region can be correlated to the macro-scale velocity by solving the periodically developed flow equations on a unit cell. For an exact reconstruction of the developed macro-scale velocity in the near-wall region, the equations are solved on an extended unit cell, containing part of the side walls. The channel's overall pressure drop and mass flow rate can then be related by a macro-scale velocity coefficient and coefficients for the macro-scale pressure drop over the in- and outlet region, as for channels without solid structures.

INTRODUCTION

For the characterisation of the incompressible laminar flow in micro-channels with large arrays of periodic solid structures, direct numerical simulation requires an enormous amount of computational resources. For this reason, generally, only a unit cell of the array is considered, and the bulk average flow variables of the entire channel are extracted under the assumption of periodically developed flow. By using this approach, friction factors for the pressure drop can be correlated to the bulk average velocity and thus to the fluid mass flow rate [1, 2]. For the exact calculation of the pressure drop over the entire channel, also the entrance and exit lengths as well as the pressure losses over the in- and outlet region of the channel need to be determined. In the literature, these lengths and loss coefficients are solely available for pipes or plate-channels without solid structures [3, 4].

For channels with solid structures, however, a macro-scale description based on bulk average quantities is not always appropriate. In our previous work [5, 6], it has been shown that an exact macro-scale description of the periodically developed flow and heat transfer regimes requires a double volume-averaging operation, as was first described by Quintard and Whitaker [7]. This filtering operation yields a spatially constant macro-scale pressure gradient and velocity, as well as a spatially constant heat transfer coefficient in the developed core region of the channel, whose relationship can be correlated through a flow simulation on a unit cell. At present, such closure correlations are only known for a few types of solid structures, and yet incompletely. Furthermore, it is not clear how the entrance and exit effects can be consistently incorporated in the context of a macro-scale description based on the double volume-averaging filter. Therefore, in this work, the macro-scale framework of [5, 6] is extended with more complete closure correlations for offset strip fins and square pin fins. In addition, the latter framework is used to formulate well-defined pressure-drop coefficients for the channel's in- and outlet regions, analogous to those for channels without solid structures. It is shown that in this framework, a macro-scale velocity coefficient can be derived, which incorporates the influence of the side walls of the channel.

EXACT RECONSTRUCTION OF THE MACRO-SCALE FLOW

Provided that the macro-scale velocity $\langle \mathbf{u} \rangle_m$ and pressure gradient $\nabla \langle p \rangle_m^f$ are computed through a double volume-averaging operator, these variables become constant in the periodically developed core region of the channel, as shown in figure 1a. In this region, the macro-scale velocity then equals the volume-averaged velocity over the unit cell $\langle \mathbf{u} \rangle$, and the macro-scale pressure gradient equals the pressure gradient over the unit cell $\nabla \mathrm{P}$:

$$\langle \mathbf{u} \rangle_m = \langle \mathbf{u} \rangle, \text{ and } \nabla \langle p \rangle_m^f = \nabla \mathrm{P}. \tag{1}$$

As a consequence, the relation between $\langle \mathbf{u} \rangle_m$ and $\nabla \langle p \rangle_m^f$ can be determined by solving the Navier-Stokes equations for periodically developed flow in a single unit cell. For an array of offset strip fins, the latter relationship can be represented in the form of the closure equation:

$$\nabla \mathrm{P} = -7.5 \cdot 10^5 \left(\frac{\mu}{l^2}\right) \frac{(1-e)^2}{e^3} \langle \mathbf{u} \rangle - 8.0 \left(\frac{\rho}{l}\right) \frac{(1-e)}{e^3} \|\langle \mathbf{u} \rangle\| \langle \mathbf{u} \rangle, \text{ with } e = \left(1 - \frac{t}{s}\right)^{0.18} \left(1 - \frac{t}{h+t}\right)^{0.18}, \tag{2}$$

where the geometry is characterised by the fin thickness t, height h, lateral spacing s, and length l [1, 2]. The closure equation (2) has been calculated numerically for $t/l = 0.02$ over the ranges $Re_l = \rho \|\langle \mathbf{u} \rangle\| l/\mu = 10 - 300$, $h/l = 0.12 - 1.00$, and $s/l = 0.12 - 0.48$, and has been fitted in analogy to the Ergun equation [8].

As schematically depicted in figure 1a, the macro-scale velocity and pressure gradient are not spatially constant over the in- and outlet region of a channel, but depend on the coordinate perpendicular to the main stream direction (dashed

*Corresponding author. E-mail: arthur.vangeffelen@kuleuven.be (A. Vangeffelen)

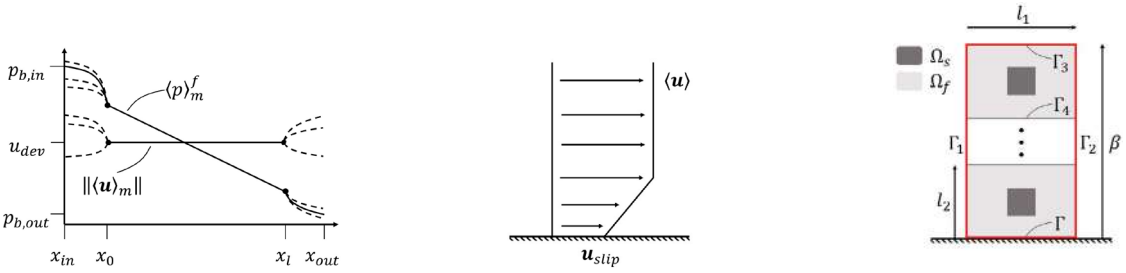

(a) Macro-scale velocity and pressure as a function of the streamwise channel position

(b) Macro-scale velocity profile contraction in the near-wall region

(c) Extended unit cell (within red outline) in near-wall region (Ω_s: solid domain, Ω_f: fluid domain)

Figure 1: Schematics for the reconstruction of the macro-scale flow

lines). On the other hand, the bulk averaged pressures $p_{b,in}$ and $p_{b,out}$, which are obtained by integration over the channel inlet and outlet respectively and which determine the pumping power for the flow, do not depend on the position in the channel. Therefore, in order to include inlet and outlet pressure drops into the macro-scale description of [5, 6] by means of spatially constant loss coefficients K_{in} and K_{out}, the following relations are defined:

$$K_{in} = \frac{p_{b,in} - \langle p \rangle_m^f|_{\mathbf{x}_0} - \nabla \mathrm{P} \cdot (\mathbf{x}_{in} - \mathbf{x}_0)}{\frac{1}{2}\rho \|\langle \mathbf{u} \rangle\|^2}, \text{ and } K_{out} = \frac{-p_{b,out} + \langle p \rangle_m^f|_{\mathbf{x}_l} + \nabla \mathrm{P} \cdot (\mathbf{x}_{out} - \mathbf{x}_l)}{\frac{1}{2}\rho \|\langle \mathbf{u} \rangle\|^2}, \tag{3}$$

where $\mathbf{x}_0$ and $\mathbf{x}_l$ correspond to the onset point and end point of the periodically developed flow region. In accordance with equation (3), the entrance and exit length are thus respectively defined as $l_0 = \|(\mathbf{x}_0 - \mathbf{x}_{in})\|$ and $l_l = \|(\mathbf{x}_{out} - \mathbf{x}_l)\|$, as $\mathbf{x}_{in}$ and $\mathbf{x}_{out}$ denote the coordinate of the inlet and outlet sections. In absence of solid structures, the definitions (3) become equivalent to the loss coefficients which are used for channels without solid structures. Table 1 shows by way of illustration the entrance and exit lengths for an array of square pin fins, with a porosity of 0.75, as a function of the Reynolds number Re_l. It is clear that the entrance length increases with Re_l, while the exit length remains nearly constant over the entire range of Reynolds numbers.

Table 1: Entrance and exit lengths for a square pin fin array with a porosity of 0.75

Re_l	25	50	75	100	125	150	200
l_0/l	6.1	10.1	12.6	14.5	16.3	17.2	18.4
l_l/l	3.00	3.14	3.00	3.00	3.00	3.00	3.60

The macro-scale velocity $\langle \mathbf{u} \rangle_m$ varies over space in the near-wall region of the channel and hence differs from the constant value $\langle \mathbf{u} \rangle$ in the core. Therefore, for the inclusion of these effects on the mass flow rate, a macro-scale velocity coefficient α can be defined, which is the ratio of the macro-scale velocity in the core region of the array $\|\langle \mathbf{u} \rangle\|$ and the bulk averaged velocity $\|\mathbf{u}_b\|$. The coefficient α depends on the nature of the macro-scale velocity profile in the near-wall region (figure 1b) and hence on the macro-scale slip velocity at the side wall $\mathbf{u}_{slip}$. This macro-scale velocity profile can be determined by solving the flow equations on an extended unit cell, which contains a part of the channel's side walls (figure 1c). In this extended unit cell, the flow velocity satisfies periodicity between the boundaries Γ_1 and Γ_2, and Γ_3 and Γ_4, as well as the no-slip condition on the channel side wall Γ. For the studied arrays of offset strip fins and square pin fins, the width of the extended unit cell β has been found to equal twice the lateral geometry period l_2.

CONCLUSION

This work has presented a framework for the exact reconstruction of the macro-scale flow, defined through a double volume-averaging operation, in a micro-channel with arrays of periodic solid structures. A correlation between the macro-scale velocity and pressure gradient in the developed core region of the channel has been derived for offset strip fin arrays. Consistent definitions of loss coefficients for the channel's in- and outlet, analogous to definitions for channels without solid structures, have been proposed. Additionally, the effect of the channel's side walls on the macro-scale velocity has been taken into account by means of a velocity coefficient.

References

[1] Kays, W. M., & London, A. L. "Compact heat exchangers." 1984.
[2] Manglik, R. M., & Bergles, A. E. "Heat transfer and pressure drop correlations for the rectangular offset strip fin compact heat exchanger." *Experimental Thermal and Fluid Science* **10.2**: 171-180, 1995.
[3] Menon, S. "Piping calculations manual." *McGraw Hill Professional* 2004.
[4] Shah, R. K., & London, A. L. "Laminar Flow Forced Convection in Ducts." *Academic Press*, 1978
[5] Buckinx, G., & Baelmans, M. "Multi-scale modelling of flow in periodic solid structures through spatial averaging." *Journal of Computational Physics* **291**: 34-51, 2015.
[6] Buckinx, G., & Baelmans, M. "Macro-scale heat transfer in periodically developed flow through isothermal solids." *Journal of Fluid Mechanics* **780**: 274–298, 2015.
[7] Quintard, M., & Whitaker, S. "Transport in ordered and disordered porous media II: Generalized volume averaging." *Transport in porous media* **14.2**: 179–206, 1994.
[8] Ergun, S. "Fluid flow through packed columns." *Chem. Eng. Prog.* **48**: 89-94, 1952.

A MODEL FOR THE DRYING SHRINKAGE OF POROUS MATERIALS THAT TAKES INTO ACCOUNT BOTH CAPILLARY AND SURFACE ADSORPTION EFFECTS

Ginger El Tabbal[1,2,3], Patrick Dangla*,[2], Matthieu Vandamme[2], Marina Bottoni[1,3], and Sylvie Granet[1,3]
[1]IMSIA, UMR9219, EDF-CNRS-CEA-ENSTA Paris Tech, Palaiseau, France
[2]Laboratoire Navier, UMR 8205 Ecole des Ponts Paris Tech, UGE, CNRS, Champs-sur-Marne, France
[3]EDF R&D, Palaiseau, France

Summary Upon their drying, porous media mostly shrink. Depending on its pore size distribution and on the relative humidity, the porous medium can be deformed by the water in its pores through different physical processes, in particular through capillary effects and through surface adsorption effects. In porous media with a wide pore size distribution, such as cement-based materials, clay-based rocks, or wood, those 2 effects occur concomitantly: both contribute to drying shrinkage. Here we derive and validate a model of drying shrinkage that takes into account both capillary and surface adsorption effects, thus providing a model relevant over a large range of relative humidity. The derivation is performed by relying extensively on thermodynamics. The validation is performed based on shrinkage and adsorption data obtained on different materials (i.e., cement, concrete, and Vycor glass).

INTRODUCTION

Porous media are ubiquitous: e.g., wood, bones, sponges, concrete, soils are all porous. When such porous media are dried, they mostly shrink, as can be observed with a sponge. Such shrinkage is called drying shrinkage. One reason why drying induces a shrinkage is capillary effects: upon drying, surface tension and the curvature of the air-water meniscus in the pores makes that the pore water is more and more in tension and pulls more and more on the pore walls. Several poromechanical models (e.g., the Biot-Bishop model, the Coussy et al. model… all compared in [1]) consider this capillary effect as the main driving force for drying. However, for cement-based materials, such models have been shown [1] to fail at low relative humidity (i.e., below ~40%). One reason for such failure is that those models neglect the fact that, when a pore has lost most of its water and is filled with air, a layer of adsorbed water remains at the surface of the pores. Such adsorption of water at the pore surface contributes to the deformation, which is called the Bangham effect.

Presently, no thermodynamically-derived model of drying shrinkage exists, that considers both capillary and surface adsorption effects concomitantly. There is only one model [2] that does consider those two effects, but it was proposed based on a phenomenological approach. However, such thermodynamically-sound model is needed. Indeed, many materials, such as cement-based materials, clay-based rocks, wood… exhibit a very large pore size distribution (from macropores down to nanometer-sized pores), so that, at a generic relative humidity, part of the porosity (the finer one) is filled with liquid water subjected to capillary effects, while the other part of the porosity (the larger one) is unsaturated (i.e., filled with gas (i.e., air)) but sees its pore walls covered with a layer of adsorbed water whose thickness depends on relative humidity (see Fig. 1).

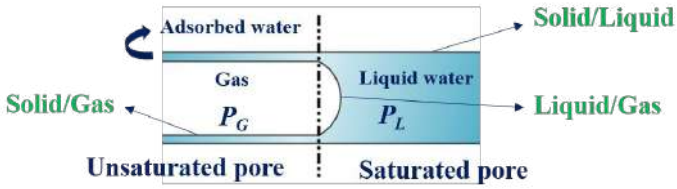

Figure 1. Schematics of a partially saturated pore system. The various interfaces at stake are indicated in green.

In this work we derive and validate a poromechanical model of drying shrinkage that takes into account both capillary and surface adsorption effects. First, we introduce the assumptions made in the derivation and discuss the resulting model. The model validation is then presented on 2 materials (namely a Vycor glass and a cement paste) and the insight that the model provides on the drying shrinkage process is briefly discussed.

DERIVATION AND DISCUSSION OF MODEL

The spirit of the model is to make it possible to predict drying shrinkage strains based on properties of the porous medium measured with classical techniques. We hence consider that the pore size distribution is measured with an adsorption isotherm analyzed with the BJH method, which assumes that pores are cylindrical. In accordance with the spirit with which we derive our model, we thus assume that pores are cylindrical. The model is derived for a linear elastic isotropic porous medium of bulk modulus K, Biot coefficient b, porosity ϕ_0, specific surface area A_0 per unit volume. The porous medium is partially filled with gas (i.e., air) at pressure P_G and liquid water (of density ρ_w and molar mass M_w) at pressure P_L. The relation $P_c(S_L)$, which relates the capillary pressure $P_c = P_G - P_L$ with the Lagrangian saturation S_L of the saturated pores in free water (and is therefore slightly different from the usual retention curve, which considers all water in the sample, not only the free one), is a characteristic of the pore size distribution. Likewise, we introduce a relation $\omega_G(S_L)$, which is the Lagrangian surface fraction of the walls of the unsaturated pores in the porous body and is also a characteristic of the pore size distribution. The capillary pressure P_c is related to the relative humidity

h_R through Kelvin's equation. The thickness $t(h_R)$ of adsorbed water on the walls of the unsaturated pores depends on the relative humidity h_R (or on its chemical potential μ): here we consider this dependence to be given by Badmann's equation. We finally assume that the amount of water adsorbed on the surface of the walls of the unsaturated pores does not depend on the surface strain of those walls.

After an extensive use of thermodynamics, we find that the variation $\Delta\varepsilon$ of volume strain of the porous solid during the drying process is given by $\Delta\varepsilon = b \cdot \Delta\pi/K$, where $\Delta\pi$ is the variation of a hydric stress π whose expression is:

$$\pi = P_L \cdot S_L + P_G \cdot (1 - S_L) + \frac{2}{3}\int_1^{S_L} P_c(S_L) \cdot dS_L + \frac{2}{3}(A_0/\phi_0) \cdot \left(\int_0^{\mu} \omega_G \cdot \frac{\rho^w}{M^w} \cdot t(h_R) d\mu - \left(\frac{\partial\gamma}{\partial\varepsilon}\right)\Big|_{\mu} \cdot \omega_G\right) \qquad (1)$$

where $\partial\gamma/\partial\varepsilon|_{\mu}$ is a parameter (assumed independent of relative humidity) that we call Shuttleworth parameter. In this expression, the first three terms capture the capillary effects. The fourth term captures the Bangham effect. The last term stems from the fact that, on solid surfaces, surface stress and surface tension are two different thermodynamic entities, as identified first by Shuttleworth. In the model derived phenomenologically in [2], this last term was missing.

VALIDATION OF MODEL

The model is validated on shrinkage data measured on Vycor glass, on cement paste, and on concrete. On those materials, on top of some basic properties (porosity ϕ_0, bulk modulus K…) and of the shrinkage upon drying, adsorption isotherms were also measured. By analyzing those isotherms with the BJH method, pore size distributions and hence the functions $P_c(S_L)$ and $\omega_G(S_L)$ are known, so that the only unknown parameters are the Biot coefficient b and the Shuttleworth parameter $\partial\gamma/\partial\varepsilon|_{\mu}$.

Figure 2 displays the predicted shrinkage strains for the Vycor glass and the cement paste upon their drying, for 2 reasonable Biot coefficients, by fitting the Shuttleworth parameter or setting it to zero. From this figure, it is clear that the model predicts the drying shrinkage strains satisfactorily on the full range of relative humidities. In particular, the model correctly captures the fact that, when relative humidity is decreased, the strain of the cement paste sample (Figure 2b) plateaus around h_R=0.35 and the strain of the Vycor glass (Figure 2a) even increases back (which is quite a counterintuitive phenomenon) around h_R=0.7.

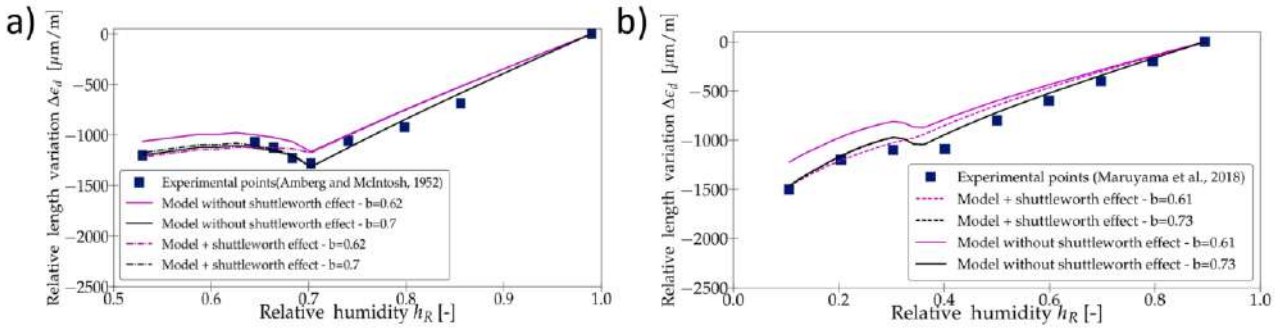

Figure 2. Predictions of drying shrinkage strains for (a) a Vycor glass and (b) a cement paste. Data are from [3] and [4], respectively.

An application of the model to those data also makes it possible to calculate the contribution of the various terms that intervene in Eq. (1). This application shows that the relative humidity at which the strain plateaus or even increases back (i.e., h_R=0.35 for the cement paste sample (Figure 2b) and h_R=0.7 for the Vycor glass (Figure 2a)) corresponds to a critical relative humidity above which capillary effects dominate and below which surface adsorption effects dominate.

CONCLUSIONS

In this work, we derived a model that predicts drying shrinkage by taking into account both capillary effects and surface adsorption effects. Most inputs to the model are rather simple properties of the porous medium (i.e., porosity, bulk modulus…) or can be obtained through the analysis of an adsorption isotherm. The model was validated on several materials over a large range of relative humidities. Using this model makes it possible to quantify, at a given relative humidity, the relative contribution of capillary effects and surface adsorption effects to the drying shrinkage strain.

References

[1] Wyrzykowski M., Bella C. D., Lura P. Prediction of Drying Shrinkage of Cement-Based Mortars with Poroelastic Approaches—A Critical Review, in: *Poromechanics VI. The Sixth Biot Conference on Poromechanics*, American Society of Civil Engineers, Paris, France, pp. 579–586, 2017.
[2] Rahoui H. Contribution to Understanding the Action of SRA in Cementitious Materials: Experiments and Modeling. *Ph.D. Thesis,* Univ. Paris-Est. 2018
[3] Amberg C., McIntosh R. A Study of Adsorption Hysteresis by Means of Length Changes of a Rod of Porous Glass. *Can. J. Chem.* 30, 1012–1032, 1952.
[4] Maruyama I. Origin of Drying Shrinkage of Hardened Cement Paste: Hydration Pressure. *J. Adv. Concr. Technol.* 8, 187–200, 2010.

STOKES FLOW COUPLED WITH NON HOMOGENEOUS POROELASTICITY

Matteo Taffetani * [1], Ricardo Ruiz Baier[2], and Sarah Waters[1]
[1]Mathematical Institute, University of Oxford, Oxford, United Kingdom
[2]School of Mathematics, Monash University, Clayton, Australia

Summary To engineer artificial tissue, a poroelastic biomaterial scaffold seeded with cells may be cultured within a perfusion bioreactor. Cells are mechanosensitive entities so the local mechanical environment may be tuned by controlling the spatial distribution of the porosity of the two phase poroelastic scaffold. To determine the impact of the heterogeneity on the kinematic variables and on the associated load distribution, we describe the porous domain using the equations of linear poroelasticity with the permeability and the shear modulus dependent upon the initial porosity field. We first show how the pressure and the strain fields are related to the permeability and the elastic properties solving the proper one dimensional problem and evaluating their asymptotic structure in the lubrication limit. Then we compute the full 2D fields by means of finite element simulations.

INTRODUCTION

The mechanical behaviour of the poroelastic domain in bioreactors for tissue growth is affected by a large variety of features including large deformations, growth of the cellular phase, remodelling of the solid phases, inhomogeneous and anisotropic description of the material properties. Often, as in the case of the perfusion system where the fluid is continuously force to flow through it, the porous domain is surrounded by a single phase fluid domain, and the interface mechanics is markedly different from the bulk mechanics.

To make quantitative advancements in the understanding of such fluid-poroelastic systems, we consider the problem of two domains, one fluid and one porous, that interface with each others through a single boundary, as in a perfusion bioreactor [1]. In addition to the presence of the interface, within the approach proposed here we retain the heterogeneous distribution of the material properties in the poroelastic domain, contrarily to [2] for example, and evaluate their effect on pressures, strains and velocities.

THEORETICAL FRAMEWORK

In the fluid domain we consider an incompressible Newtonian fluid whose flow is governed by the Stokes and the continuity equations.

Inertial effect are neglected also in the poroelastic domain and we consider a biphasic mixture of two intrinsically incompressible constituents. We let the permeability K and the solid shear modulus μ_s to be isotropic but inhomogeneous, depending on the spatial coordinate $\mathbf{x}$ through the porosity distribution $\theta(\mathbf{x})$: the function K is described through a Kozeny-Carman law [4] while the function μ_s through a linear dependence in $\theta(\mathbf{x})$. Under these assumptions, the non-linear description of the porous domain is given by a system of three equations in three unknowns (solid displacement, fluid pressure and variation of porosity). Linearising in the limit of small strain, the problem reduces to the classic pressure-displacement formulation [3], in which the equation for the variation of the fluid content decouples and with the initial porosity distribution $\theta_0(\mathbf{x})$ entering the expressions for K and μ_s.

To close the system we provide suitable initial data and boundary conditions related to the specific cases investigated. At the interface we follow [6] and we account for the continuity of normal fluxes, the continuity of the traction, the balance of the normal components of the stress in the fluid phase with the pressure in the porous domain, and the so-called Beavers-Joseph-Saffman condition.

NUMERICAL IMPLEMENTATION

We rewrite the poroelasticity equations using a three fields approach [7] (displacement, fluid pressure and total pressure), and note that since fluid pressure in the poroelastic domain has sufficient regularity, we do not require a Lagrange multiplier to enforce the coupling conditions. Another advantage of the present approach, inherited from [7] is that the formulation is robust with respect to the Lamé constants of the poroelastic structure, which is of particular importance when we test variations of the flow response to changes in the material properties of the skeleton and when the effective bulk modulus is large. All routines have been implemented using the open source finite element library FEniCS [8].

*Corresponding author. E-mail: matteo.taffetani@maths.ox.ac.uk.

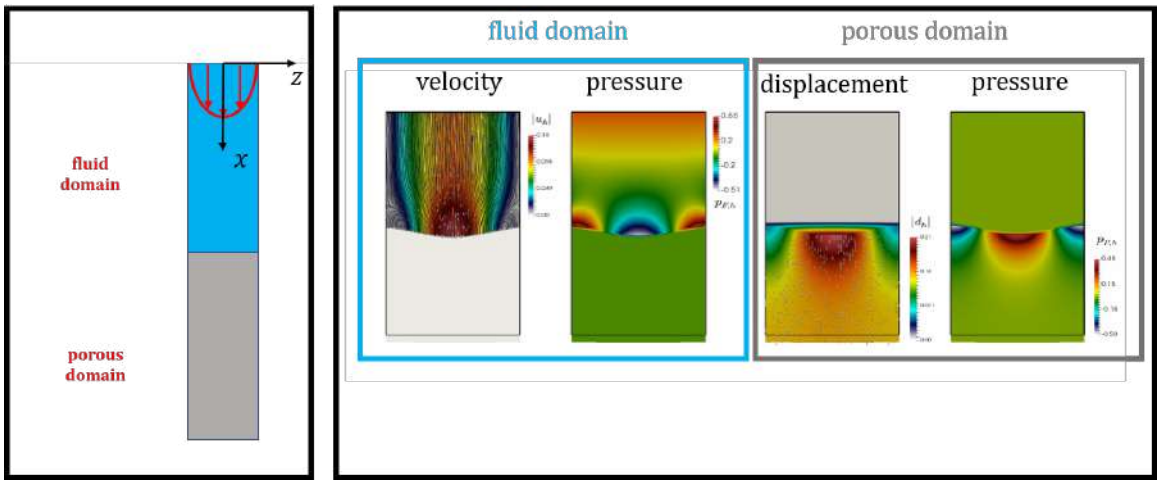

Figure 1: (left panel) Geometry under consideration. (right panel) Example of the velocity and pressure profiles in the fluid domain (blue panel) and the solid displacement and fluid pressure profiles in the porous domain (grey panel) as a response of an imposed Poiseuille profile for the velocity in the fluid domain on the top boundary.

RESULTS

We utilize this framework to consider the perfusion within a model bioreactor whose geometry is shown in figure 1 (left panel); fluid pressure and radial displacement are set to zero on the bottom edge of the porous domain while a prescribed flux is imposed at the inlet.

In the proper one dimensional reduction along the x direction and when a stationary flux is imposed, the fluid velocity throughout is constant while, in the porous domain, the pressure is described by $\int 1/K(\theta_0(x))$ and the longitudinal strain in term of $\int 1/\left(K(\theta_0(x))\left(2\mu_s(\theta_0(x))+\tilde{\lambda}\right)\right)$, where $\tilde{\lambda}$ is related to the effective compressibility of the porous domain. In the lubrication limit, where the aspect ratio of the channel is assumed to be small, we extend part of results in [2], being able to characterize the asymptotic behaviour of the deformation field in the deformable porous domain. An example of the full two dimensional fluid velocity, solid displacement and pressures maps obtained from finite element simulations is show in figure 1 (right panel).

CONCLUSION

Here we study the behaviour of a model perfusion bioreactor where the poroelastic domain is interfaced with the fluid domain. In the former, we employ the equations of linear poroelasticity when the material properties are kept inhomogeneous depending on a given prescribed initial porosity field. We first characterize the kinematic variables and compute the stress distributions when considering the proper one dimensional reduction and the lubrication limits: that allows to derive analytical relations useful to understand how these variables are related to the varying material properties. Then we compute the full two dimensional maps using finite element simulations.

This study opens toward the design of patterned porous scaffold for tissue growth, showing the possibility to compute *a priori* the local heterogeneous stress/strain distribution that a cell culture would sense.

References

[1] O'Dea R.D., Nelson M.R, El Haj A.J., Waters S.L., Byrne H.M. *Math. Med. Biol.* **32**: 345-366, 2015.
[2] Dalwadi M.P., Chapman S.J., Waters S. L., Oliver J.M. *J. Fluid Mech.* **798**: 88-139, 2016.
[3] Coussy O. Poromechanics, JohnWiley & Sons Ltd, Chichester, 2004.
[4] MacMinn C. W., Dufresne E.R., Wettlaufer J.S. *Phys. Rev. Appl.* **5**: 044020, 2016.
[5] Cowin S. C., Doty S. B. Tissue Mechanics, Springer-Verlag, New York, 2007.
[6] Badia S., Quaini A., Quarteroni A. *J. Comp. Phys/* **228**: 7986–8014, 2009.
[7] Oyarzua R., Ruiz-Baier R. *J. Num. Analysis* **54**: 2951–2973, 2016.
[8] Alnaes M. S., Blechta J., Hake J., Johansson A., Kehlet B., Logg A., Richardson C., Ring J., Rognes M. E., Wells G. N. *Archive of Numerical Software* **3**: 9–23, 2015.

INTERFACE CONDITIONS BETWEEN A FREE-FLUID REGION AND A POROUS MEDIUM

Sahrish B. Naqvi and Alessandro Bottaro *
Department of Civil, Chemical and Environmental Engineering, University of Genoa, Genoa, Italy

Summary Interfacial conditions at the dividing surface between a free-fluid and a porous region are of utmost importance when a two-domain approach is used to treat a coupled problem. Such conditions are here derived on the basis of adjoint homogenization [3] and the arising coefficients computed for the case of isotropic porous media. The conditions are then successfully tested for the case of a stagnation-point flow over a porous bed.

BACKGROUND

The problem of the interface coupling between a free-fluid region and a porous domain has been widely discussed analytically, numerically and experimentally (see e.g. [1]-[3]), most often with reference to simple uni-directional flows of the Poiseuille type. Recently, [2] approached the problem on the basis of homogenization theory, and derived conditions for both the slip velocity and the pressure jump across the dividing surface. Such conditions are derived here on the basis of adjoint homogenization [3], and a validation is provided against feature-resolving simulations for a flow with significant velocity components both tangent and normal to the interface.

THE MODEL

The microscopic domain (a *unit cell*) which crosses the dividing surface is illustrated in figure 1 (red lines). Small letters represent the variables for the microscopic problem while capital letters are used for the macroscopic one. The parameter used to expand the variables is $\epsilon = l/L$, ratio of small to large characteristic scales. The unit cell is periodic along the directions parallel to the dividing surface (x and z); along the interface-normal direction (y) the cell extends from the porous layer, assumed isotropic far from boundaries, to the free-fluid region. If l is the characteristic size of a unit cell

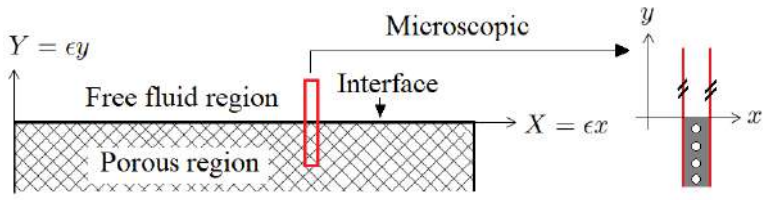

Figure 1: Sketch of the flat plate with overlaying porous bed (micro- and macro-scopic view).

deep within the porous layer, the interface-normal extent of the domain is typically four-times-l, both above and below the dividing surface (which we place in $y = 0$). It has been verified that such a y-length is adequate to produce results which are independent of the unit-cell size. Deep within the porous layer the fluid flow is induced by a macroscopic pressure gradient $\frac{\partial \bar{P}}{\partial X_i}$, whereas macroscopic shear ($\mu \frac{\partial U}{\partial Y}$) drives the flow in the free-fluid region. Assuming slow flow, the microscopic equations in the unit cell are:

$$\frac{\partial u_i}{\partial x_i} = 0, \quad -\frac{\partial p}{\partial x_i} + \mu \frac{\partial^2 u_i}{\partial x_j^2} = H(-y)\frac{\partial \bar{P}}{\partial X_i}, \tag{1}$$

with $H(y)$ the Heaviside function. At the lower end of the microscopic cell we assume periodicity to hold; on the upper boundary we enforce

$$\frac{\partial u}{\partial y} = \frac{\partial U}{\partial Y}, v = 0, \frac{\partial w}{\partial y} = \frac{\partial W}{\partial Y}. \tag{2}$$

The variables u_i and p are expanded in power series of ϵ; developing the problem at leading order it is found that the macroscale velocity components at the interface are

$$U|_{Y=0} = \epsilon \lambda \frac{\partial U}{\partial Y} - \epsilon^2 \mathcal{K}^{itf} \frac{\partial P}{\partial X}, \tag{3}$$

and likewise for W, whereas V (component of the velocity across the interface) is simply given by Darcy's law (and thus relies on a scalar permeability, denoted by $\mathcal{K}$), because of mass conservation.
There is also a pressure condition to be enforced; if we call P^+ and P^- the values of the pressure sufficiently above and sufficiently below the dividing surface in $Y = 0$, it is found that $P^+ - P^- = -a_j \frac{\partial P}{\partial X_j} + b_j \frac{\partial U_j}{\partial Y}$. The resolution of

*Corresponding author. E-mail: naqvi.sehrish@yahoo.com

the macroscopic problem proceeds iteratively, by first solving for the flow in the free-fluid region subject to no-slip and no-transpiration conditions at $Y = 0$; once the interface pressure is computed it is used as a boundary condition for the subsequent resolution of the flow in the porous domain. The solution of this problem is turn permits to correct the slip and transpiration velocities for the problem in the free-fluid region. The equations need to be iterated a few times between the two domains before convergence is reached. Of course, the accuracy of the whole procedure relies on the accuracy of the coefficients, $\mathcal{K}, \mathcal{K}^{itf}, \lambda, a_j$ and b_j, which are available from the numerical resolution of auxiliary problems in the unit cell.

MICRO- AND MACRO-SCOPIC RESULTS

The numerical simulation of the microscale problem (1)-(2) over a unit cell is done using circular or spherical grains; the results are displayed in figure 2 in terms of $\mathcal{K}, \mathcal{K}^{itf}$ and λ. These coefficients are then used in the slip condition (3) to simulate the macroscopic coupled flow between the free-fluid and the porous regions. The pressure coefficients a_j and b_j for isotropic porous inclusions vanish, i.e. there is no pressure jump at the dividing surface.

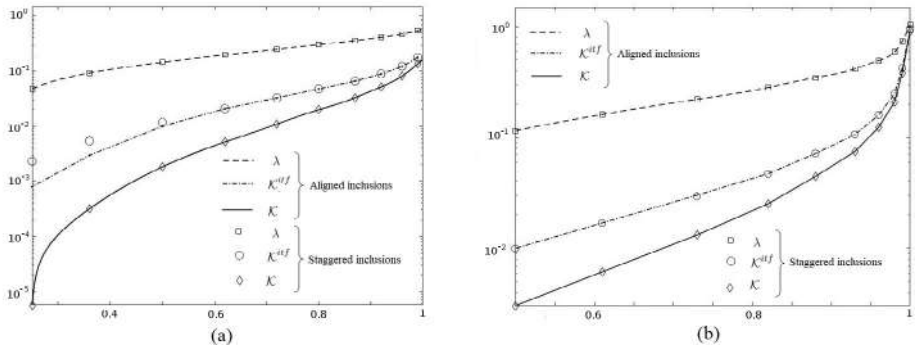

Figure 2: Macroscopic coefficients for (a) 2D (b) 3D isotropic grains, as function of porosity.

In the solution of the macroscale problem, a domain of size $15L$ and $Y = 5L$ in the X and Y direction, respectively, is considered. The situation considered is that of a stagnation point flow at $Re = 50$. Figure 3 shows the longitudinal velocity as function of Y, across the whole domain, both obtained from the model simulation (solid lines) and from a feature-resolved simulation (symbols) which captures the motion through the pores. The observed agreement is good.

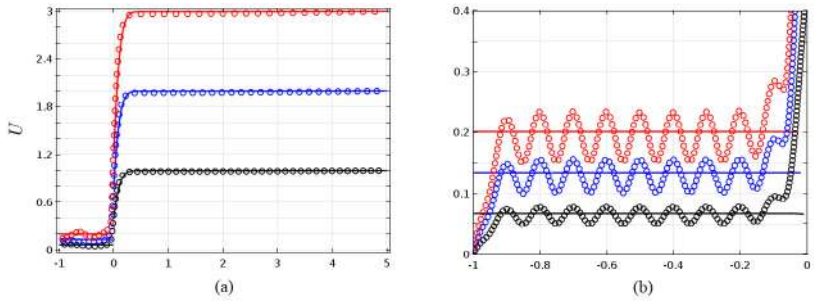

Figure 3: (a) Wall tangent velocity as a function of Y at three values of X (b) Close up of the flow field in the porous domain.

CONCLUSIONS

The interface conditions arising from homogenization theory at the dividing surface between a free-fluid and a porous region have been derived by homogenization, and the coefficients have been computed for some isotropic porous media as function of the porosity. The use of such conditions, which require no empirical coefficients, permits to reduce the computational resources needed in solving flow configurations where an interface of this kind appears. The stagnation point flow above a flat plate, covered by a porous bed, has been used as a test case. It is demonstrated that the derived conditions and coefficients yield very good results, againt fully-resolved simulations, at a fraction of the cost.

References

[1] G. S. Beavers and D. D. Joseph. Boundary condition at a naturally permeable wall. Journal of Fluid Mechanics, 30(1):197-207, 1967.
[2] U. Lãcis, Y. Sudhakar, S. Pasche, S. Bagheri. Transfer of mass and momentum at rough and porous surfaces. Journal of Fluid Mechanics, 884: A21, 2020.
[3] A.Bottaro. Flow over natural or engineered surfaces: an adjoint homogenization perspective. Journal of Fluid Mechanics, 877:1-91,2019.

VISCOELASTIC FLOW PAST A BIPERIODIC ARRAY OF CYLINDERS

Omar Mokhtari[1], Yohan Davit*[1], Jean Claude Latché[2], Romain de Loubens[3], and Michel Quintard[1]
[1]Institut de Mécanique des Fluides de Toulouse (IMFT), Université de Toulouse, CNRS, Toulouse, France
[2]Institut de Radioprotection et de SÛreté Nucléaire (IRSN), Cadarache, France
[3]Total E&P, CSTJF, Pau, France

Summary We investigate numerically two and three-dimensional creeping viscoelastic flow past a biperiodic array of cylinders. The viscoelastic fluid is modeled using both the Oldroyd-B and FENE-CR constitutive models of dilute polymer solutions. The space discretization is based on the so-called Rannacher-Turek (RT) scheme. The time discretization uses a fractional-step algorithm where the solution of the Navier-Stokes equations is first obtained by a projection method and then the transport-reaction equation for the conformation tensor is solved by a finite-volume scheme. We show that vortices are generated upstream of the cylinder and study their evolution with the Weissenberg number. We also analyze the evolution of the permeability with the different regimes.

INTRODUCTION

Dilute and semi-dilute polymer solutions used in engineering applications, such as bioremediation or enhanced oil recovery, typically exhibit viscoelastic behaviors [1]. Understanding the complex interplay between the nonlinear rheology of the fluid and the porous structure [2] is of great importance to enhance macroscale models and to understand the connection between pore-scale phenomena and macroscale behavior. Here, we explore this problem using computational fluid dynamics and solve the flow problem at pore-scale to understand fundamental aspects of the physics.

CONSTITUTIVE MODEL

Here, we consider viscoelastic models for polymeric incompressible liquids governed by the following system of equations:

$$\rho(\partial_t \mathbf{u} + \xi \mathbf{u}\cdot\boldsymbol{\nabla}\mathbf{u}) = -\boldsymbol{\nabla} p + \operatorname{div}\boldsymbol{\tau}_s(\mathbf{u}) + \operatorname{div}\boldsymbol{\tau}_p + \mathbf{F}, \quad \boldsymbol{\tau}_p = \frac{\eta_p}{\lambda}\mathbf{f}(\mathbf{c})(\mathbf{c}-\mathbf{I_d}), \tag{1a}$$

$$\operatorname{div}\mathbf{u} = 0, \tag{1b}$$

$$\partial_t \mathbf{c} + \mathbf{u}\cdot\boldsymbol{\nabla}\mathbf{c} - (\boldsymbol{\nabla}\mathbf{u})\,\mathbf{c} - \mathbf{c}\,(\boldsymbol{\nabla}\mathbf{u})^t + \frac{1}{\lambda}\mathbf{g}(\mathbf{c})(\mathbf{c}-\mathbf{I_d}) = 0, \tag{1c}$$

where the constant coefficients ρ, η_s, η_p and λ are the fluid density, the solvent viscosity, the polymer viscosity and the polymer retardation time. The vector-valued function $\mathbf{u}$ is the velocity of the fluid, p is the pressure and $\boldsymbol{\tau}_s = \eta_s(\boldsymbol{\nabla}\mathbf{u} + (\boldsymbol{\nabla}\mathbf{u})^t)$ is the Newtonian stress tensor for the solvent. The tensor $\boldsymbol{\tau}_p$ is the part of the stress accounting for the presence of polymers and $\mathbf{c}$ is the conformation tensor. The vector $\mathbf{F}$ corresponds to a given body force. The coefficient ξ is zero for unsteady Stokes equations and $\xi = 1$ for Navier-Stokes equations. The functions $\mathbf{f}(\mathbf{c})$ and $\mathbf{g}(\mathbf{c})$ depend on the model. For example (see [3] for a review), the Oldroyd-B model is given by $\mathbf{f}(\mathbf{c}) = \mathbf{g}(\mathbf{c}) = \mathbf{I_d}$, and the Fene-CR model corresponds to $\mathbf{f}(\mathbf{c}) = \mathbf{g}(\mathbf{c}) = \frac{b}{b-\operatorname{tr}(\mathbf{c})}\mathbf{I_d}$, with b a real number greater than the space dimension. This system must be complemented by initial conditions for the velocity and the conformation tensor, and by suitable boundary conditions.

NUMERICAL METHOD

We developed a numerical scheme for the solution of System (1) based on the following technology. The space discretization is based on the so-called Rannacher-Turek (RT) scheme (see [5]). The time discretization uses a fractional-step algorithm where the solution of the Navier-Stokes equations (1a)-(1b) is first obtained by a standard projection method and then the transport-reaction equation for the conformation tensor (1c) is solved by a finite-volume scheme. The development of this scheme faces two essential difficulties. Firstly, we use a weak formulation of (1a) for the discretization of the term $\operatorname{div}\boldsymbol{\tau}_p$, which yields an essential ingredient for the scheme stability and a built-in Lax-Wendroff weak consistency property. Secondly, the solution of Equation (1c) requires special care due to the stiffness of the term $(\boldsymbol{\nabla}\mathbf{u})\,\mathbf{c} + \mathbf{c}\,(\boldsymbol{\nabla}\mathbf{u})^t$. In the spirit of [6], solution of Equation (1c) is split in pure convection steps, with a change of variable from $\mathbf{c}$ to $\log(\mathbf{c})$, and a reaction step, which consists in solving one ODE per cell thanks to the piecewise constant discretization of $\mathbf{c}$. In contrast with [6], ODEs are solved directly for $\mathbf{c}$, and not $\log(\mathbf{c})$, so as to avoid any artificial introduction of nonlinearities. We further use a local time step for each cell, which ensures scheme stability and prevents from a blow-up of the CPU cost. Computations are run (in parallel) with a dedicated module of the IRSN open-source CALIF3S software [4] developped at IMFT.

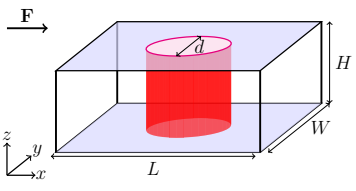

Figure 1: Flow geometry.

*Corresponding author. E-mail: yohan.davit@toulouse-inp.fr

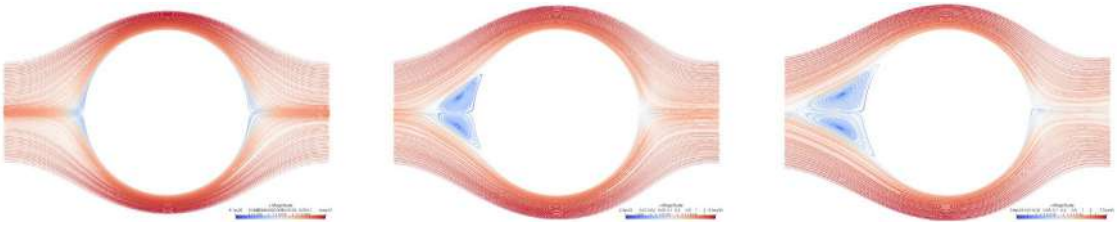

Figure 2: Streamlines with corresponding velocity magnitude in log scale. Two-dimensional case with $L = W = 2d$. From left to right: $W_i = 0.03$, 3.2 and 4.7. The flow is imposed from left to right.

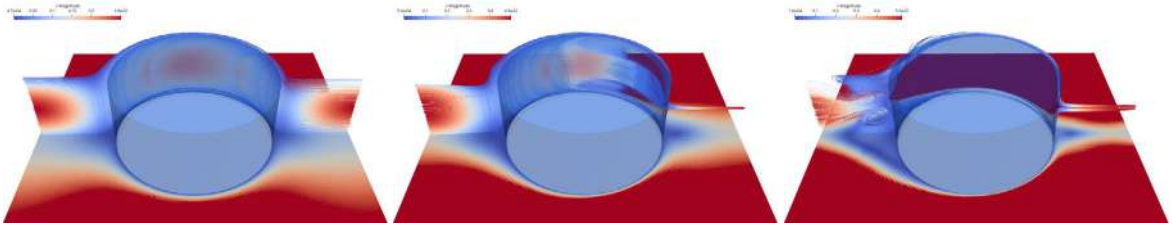

Figure 3: Streamlines and map of velocity magnitude. Three-dimensional case with $L = W = 2d$ and $H = d/2$. From left to right: $W_i = 0.5$, 1.5 and 2.5. The flow is imposed from left to right.

RESULTS

We consider the flow through a biperiodic array of cylinders. The flow length (x-direction) and width (y-direction) are L and W respectively. The cylindrical obstacle has diameter d. In the three-dimensional case, the height of the cylinder is H, see Figure 1. At the cylinder surface and the two horizontal planes (3D case), no-slip conditions are imposed and periodic boundary conditions are prescribed on vertical surfaces. The flow, is driven by a body force $\mathbf{F} \geq 0$ exerted on the fluid in the x-direction. We measure the resulting flowrate Q, defined as the constant integral of the normal velocity accross a plane normal to O_x. We then determine the corresponding Weissenberg number defined here as $W_i = \lambda U/d$, based on the cylinder diameter and the mean flow velocity U. The Reynolds number Re is set to zero ($\xi = 0$). We study the variation of the flow structure with the Weissenberg number. By increasing the Weissenberg number in the range 0.001 to 5, we first observe a Newtonian regime in the limit $W_i \to 0$ and then the appearance of stationary vortices upstream of the cylinder. For the 2D case (see Figure 2), the two vortices are counter-rotating on each side of the symmetry line. The same 2D structure of the upstream vortices have been observed experimentally [8]. In the 3D case, the vortices are 3D structures and at $W_i = 2.5$ we observe a complex structure with helically coiled streamlines (see Figure 3).

For porous media applications, we are also interested in characterizing the permeability, defined by

$$< \mathbf{u} >= \frac{K}{(\eta_s + \eta_p)}\mathbf{F} \tag{2}$$

as a function of the Weissenberg number. We observe first an increase of the permeability, followed by a sharp decrease with a minimum for Weissenberg numbers of about 0.4. This apparent thickening effect is known experimentally and has already been captured numerically (see [7]). Here, we observe that this permeability downturn corresponds to the appearance of the stationary vortices upstream of the cylinder and we study the phenomenon through energetic considerations.

References

[1] R. P. Chhabra, J. Comiti, and I. Macha. Flow of non-newtonian fluids in fixed and fluidised beds. Chemical Engineering Science 56:1–27 (2001).
[2] R. G. Larson, Eric S. G. Shaqfeh, and S. J. Muller. A purely elastic instability in taylor-couette flow. J. Fluid Mech. 218:573–600 (1990).
[3] R.B. Bird, J.M. Wiest: Constitutive Equations for Polymeric Liquids p. 25.
[4] CALIF^{3}S: A software components library for the computation of fluid flows. https://gforge.irsn.fr/gf/project/califs
[5] D. Grapsas, R. Herbin, W. Kheriji, J.C. Latché, : An unconditionally stable staggered pressure correction scheme for the compressible Navier-Stokes equations. SMAI Journal of Computational Mathematics **2**, 51–97 (2016).
[6] T.W. Pan, J. Hao, R. Glowinski: On the simulation of a time-dependent cavity flow of an Oldroyd-B fluid. International Journal for Numerical Methods in Fluids **60**, 791–808 (2009).
[7] E. J. Hemingway, A. Clarke, J. R. A. Pearson, and S. M. Fielding. Thickening of viscoelastic flow in a model porous medium. Journal of Non-Newtonian Fluid Mechanics 251:56–68 (2017).
[8] D. Kawale, E. Marques, P. L. J. Zitha, M. T. Kreutzer, W. R. Rossen, and P. E. Boukany. Elastic instabilities during the flow of hydrolyzed polyacrylamide solution in porous media: effect of pore-shape and salt. Journal of Non-Newtonian Fluid Mechanics 13(4):765–775 (2017).

CATCH AND RELEASE OF BUBBLES IN A SOFT GRANULAR MEDIUM

J. H. Guan[1,2], O. Dorostkar[1,3], S. Lee[4], and C. W. MacMinn*[,1]
[1]Department of Engineering Science, University of Oxford, Parks Road, Oxford, UK
[2]Department of Mathematics, University of North Carolina at Chapel Hill, Chapel Hill, North Carolina, USA
[3]Department of Mechanical and Process Engineering, ETH Z urich, Zürich, Switzerland
[4]Department of Mechanical Engineering, University of Minnesota, Minneapolis, Minnesota, USA

Summary A liquid-saturated packing of soft particles can behave like a complex fluid or like a porous solid, depending on the solid fraction. In the fluid-like state, invading gas bubbles will rise through the packing due to buoyancy with a rise velocity that decreases as the solid fraction increases. In the solid-like state, invading gas bubbles cannot rise unless their buoyancy overcomes the capillary entry pressure between the particles, in which case they will rise by migrating through the pore space of the packing. Here, we combine quasi-2D and 3D laboratory experiments with discrete-element simulations to show that the motion of gas bubbles through such a packing can be controlled by exploiting this dichotomy: Active manipulation of the solid fraction in a soft granular medium can be used for the on-demand catch and release of individual gas bubbles.

INTRODUCTION

The buoyancy-driven migration of gas bubbles through a liquid-saturated granular medium is important for a variety of natural and industrial processes, including the venting of biogenic gases from lakebed and seabed sediments [*e.g.*, Scandella et al., 2011], the venting of gases from industrial waste ponds [*e.g.*, Johnson et al., 2018], the venting of volatile gases from magma [*e.g.* Parmigiani et al., 2016], and the operation of many biological and chemical reactors.

There are several different mechanisms by which buoyant gas bubbles can migrate upward through and escape from a saturated granular medium, depending on bubble size, grain properties (*i.e.*, grain size, cohesion, and contact friction), and confining stress. In most applications, gas is unlikely to invade the pore space between the grains because of the large capillary entry pressure (*i.e.*, small grain size). Instead, for weak cohesion and low confining stress, sufficiently large gas bubbles will yield the medium and rise upward by fluidising the surrounding liquid-grain mixture. For stronger cohesion and/or higher confining stress, sufficiently large gas bubbles will instead "fracture" the medium by opening and then venting upward through a narrow pathway between the grains [*e.g.*, Lee et al.].

An important but ultimately unsurprising observation from field measurements of methane venting from lakes is that the venting rate varies inversely with fluctuations in confining stress [*e.g.*, Scandella et al., 2011]. A sudden decrease in confining stress tends to mobilise gas bubbles by weakening the sediment, making it easier for bubbles to displace the grains; a sudden increase in confining stress tends to arrest the motion of rising gas bubbles by strengthening the sediment, making it more difficult for gas bubbles to displace the grains. Here, inspired by this natural phenomenon, we study the impact of variations in confining stress on the motion of buoyant gas bubbles in a soft granular medium.

EXPERIMENTAL SYSTEM

We study this problem using quasi-2D and fully 3D experiments, as well as 3D discrete-element simulations. Our experimental system is a water-saturated packing of polyacrylamide hydrogel spheres with a mean diameter of $\sim 2\,\mathrm{mm}$. We pack these particles into a rigid container with a semi-permeable lid that constrains the particles but not the fluids, and which can be raised or lowered on-demand via a computer-controlled actuator. Lowering the lid increases the mean solid fraction in the container (*i.e.*, the mean density of the packing), which is analogous to increasing the confining stress; raising the lid does the opposite. We inject individual air bubbles into this system from below and record their motion with a digital camera.

RESULTS & DISCUSSION

We study this problem in three parts. We begin by studying the impact of different fixed initial solid fractions ϕ_s on the motion of bubbles through the packing, showing that the typical rise velocity decreases strongly as ϕ_s increases, and vanishes at a critical value $\phi_s^\star$ that depends weakly on bubble size. For $\phi_s > \phi_s^\star$, bubbles are unable to rise through the packing. We also measure the deformation of the packing as bubbles rise, finding that a rising bubble is surrounded by a fluidised zone in which particles flow around the bubble; particles outside of this zone are nearly stationary. The characteristic size of the rearrangement zone decreases as ϕ_s increases and vanishes at $\phi_s^\star$ (Figure 1).

We next study the transient response of the packing to sudden motions of the lid in the absense of bubbles. Specifically, we suddenly compress the packing by lowering the lid by an amount δ, and then subsequently allow the packing to relax by raising the lid by the same amount. We show that lowering the lid results in a poromechanical compaction front that propagates relatively quickly through the medium as the lid actively squeezes liquid out of the packing; in contrast,

*Corresponding author. E-mail: christopher.macminn@eng.ox.ac.uk

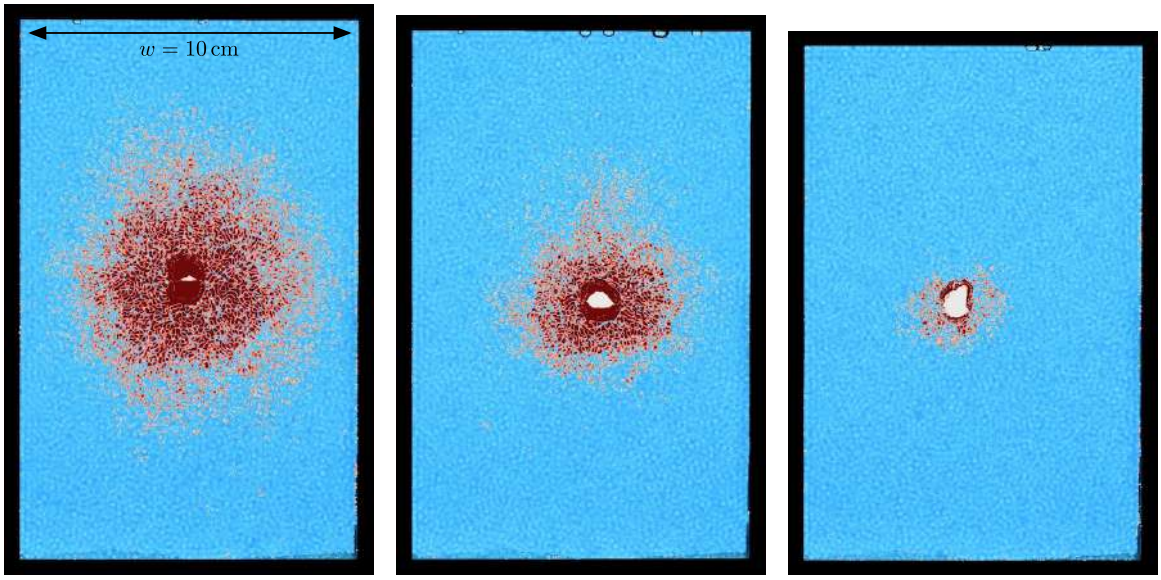

Figure 1: Snapshots of individual gas bubbles as they rise through a quasi-2D packing of soft particles for three different fixed mean solid fractions ϕ_s (increasing from left to right). We increase ϕ_s by lowering the lid, thus decreasing the height of the packing h. The red color indicates the fluidised zone around the bubble, as calculated from the motion of the particles. The size of this zone decreases strongly as ϕ_s increases (h decreases), as does the bubble velocity (not visible here). The bubble itself is partially obscured by the red color, but it is about the same size in all three cases.

raising the lid results in a poromechanical relaxation front that propagates relatively slowly through the medium as elastic expansion of the packing gradually sucks liquid back in. We also compare our experimental and simulation results with the predictions of a uniaxial model based on large-deformation poromechanics.

Finally, we study the consequences of raising or lowering the lid as a bubble actively rises through the packing. Specifically, we inject an air bubble into a packing for which $\phi_s < \phi_s^\star$ and then show that this rising bubble can be immobilised and re-mobilised on-demand by manipulating ϕ_s above and below $\phi_s^\star$ by lowering and raising the lid. We characterise this process by drawing on our earlier results for bubble migration at fixed ϕ_s and compaction and relaxation in the absense of a bubble.

CONCLUSIONS

We show here that active manipulation of the confining stress and/or the solid fraction in a soft granular medium can be used for the on-demand catch and release of individual gas bubbles. The physical insight developed in this study will contribute to our understanding of a variety of natural and industrial processes involving bubble migration in saturated granular media. In addition, we expect the active manipulation of confinement to be a useful tool for controlling bubble migration.

References

M. Johnson, J. Peakall, X. Jia, M. Fairweather, D. Harbottle, S. Biggs, and T. N. Hunter. Enhanced gas migration through permeable bubble networks within consolidated soft sediments. *AIChE Journal*, 64(11):4131–4147, 2018. doi: 10.1002/aic.16223.

S. Lee, J. Lee, R. Le Mestre, F. Xu, and C. W. MacMinn. Capturing gas in a soft granular material. Available at https://arxiv.org/abs/1808.02921.

A. Parmigiani, S. Faroughi, C. Huber, O. Bachmann, and Y. Su. Bubble accumulation and its role in the evolution of magma reservoirs in the upper crust. *Nature*, 532(7600):492—495, 2016. doi: 10.1038/nature17401.

B. P. Scandella, C. Varadharajan, H. F. Hemond, C. Ruppel, and R. Juanes. A conduit dilation model of methane venting from lake sediments. *Geophysical Research Letters*, 38:L06408, 2011. doi: 10.1029/2011GL046768.

MULTISCALE POROMECHANICAL MODEL FOR CO_2-ENHANCED COALBED METHANE RECOVERY INCLUDING GAS ADSORPTION EFFECTS

Tien Dung Le*[1], Quoc Dat Ha[1], Christian Moyne[1]
[1]Laboratoire Energies et Mécanique Théorique et Appliquée (Nancy, France)

Summary: In this work we develop a three-scale poromechanical model for CO_2-enhanced coalbed methane recovery. Coal seam is composed of two levels of porosity associated with nanopores and fracture network (cleats). Adsorption isotherms in the nanopores are computed by using the Density Functional Theory for calculating gas mixture density profiles and solvation force in complex geometries, showing a much more pronounced adsorption potential of CO_2 compared to CH_4. At the microscale, a modified form of the effective stress principle is derived incorporating the solvation force effects. The poromechanics of the matrix is then homogenized with the cleat network giving rise to a macroscopic model ruled by the effective stress and Lagrangian porosity. Numerical simulations illustrate the cleat closure phenomena experimentally observed.

INTRODUCTION

CO_2-Enhanced CoalBed Methane Recovery consists of unconventional gas resource which combines CH_4 production with CO_2 sequestration. Coal seam is composed of a coal matrix containing pores of several nanometers with adsorbed CH_4 and a natural fracture network (cleats) with high permeability filled by water. Production of gas consists simply in reducing the pressure in the coal seam which first produces water from the cleats and subsequently gas desorbed from the matrix. The enhanced coalbed methane recovery consists of a CO_2 injection process into the reservoir taking advantage of its huge adsorption potential. However, unsuitable injection pressure may cause cleat closure near the injection well and shut down the injection process. In this work we propose a three-scale poromechanical model to describe the matrix swelling and cleat closure phenomena during CO_2 injection. Particular attention is paid to describe the gas mixture adsorption problem in the nanopores and its influence on the mechanics at the macroscale. To accomplish this task, in the framework of the Density Functional Theory (DFT), a novel numerical method is proposed to compute the gas density profiles and the solvation force for complex pore geometries. Since the solvation force is much higher than the bulk pressure, this force modifies considerably the mechanical properties of the matrix. Macroscopic governing equations are then derived by the homogenization method [1] where we upscale the anomalous behavior of the binary gas mixture in the nanopores. Finally, a 2D reservoir simulation of methane production enhanced by CO_2 injection is presented to illustrate the potential of the multiscale model.

GAS MIXTURE ADSORPTION AND SOLVATION FORCE

The Density Functional Theory (DFT) is applied to describe precisely the gas mixture adsorption phenomena in nanopores [2,3,4]. The adsorbed gas density profiles and the pressure exerted on the solid wall by the fluid (or solvation force) are numerically computed for an oblate spheroidal pore with two semi-major axes $a=b=4{,}5d_{CH4}$ and semi-minor axis $c=3d_{CH4}$, d_{CH4} is the CH_4 diameter. Fig. 1(a) displays the gas density profiles of CH_4 (blue curve) and CO_2 (red curve) according to the small axis Oz. We can observe much higher adsorption peaks of CO_2 compared to CH_4 with the same bulk gas densities. Fig. 1(b) displays the solvation force profile according to the small axis Oz. We can observe that the solvation force is negative, not uniform in the case of an ellipsoid and much higher in absolute order of magnitude than the bulk pressure P_b=8 MPa. Fig. 1(c) shows the dependence of the solvation force on the partial bulk pressure for a spherical pore of diameter $D=6d_{CH4}$. For high CO_2 bulk pressure, the solvation force decreases with CO_2 bulk pressure which may cause the matrix swelling.

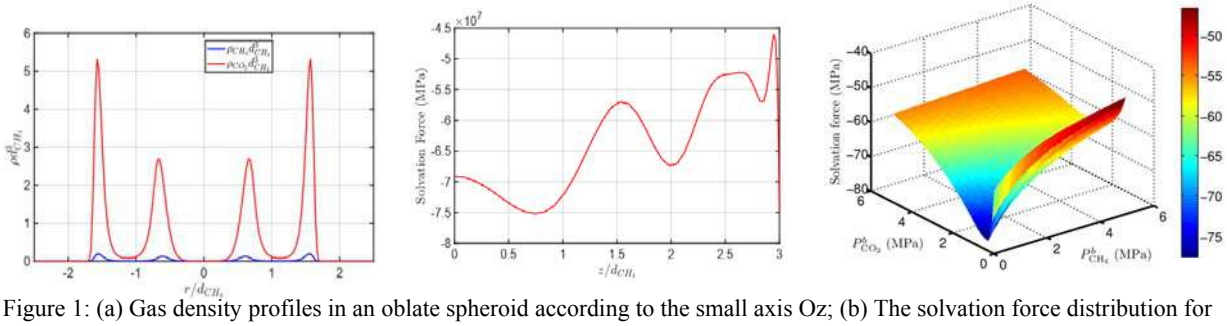

Figure 1: (a) Gas density profiles in an oblate spheroid according to the small axis Oz; (b) The solvation force distribution for an oblate spheroidal pore according to the small axis Oz (c) Dependence of the solvation force on the partial bulk pressures

*Corresponding author. E-mail: tien-dung.le@univ-lorraine.fr

MACROSCOPIC MODEL DERIVED FROM HOMOGENIZATION

At the microscale, a modified form of the effective stress principle is derived incorporating the solvation force effects. By linearizing the poromechanics around a reference state, the microscopic governing equations are rephrased with new coefficients strongly dependent on the solvation force. In Fig. 2(a), we can observe that the modified Biot-Willis coefficients of the matrix depending on the bulk pressure for each gas component can be larger than one in contrast to the classical poroelasticity due to the gas confinement effects, in particular for CO_2 (here i=1,2 correspond to CH_4 and CO_2 respectively). The poromechanics of the matrix is then homogenized with the cleat network giving rise to a three-scale model ruled by the effective stress, Lagrangian cleat porosity and permeability. The macroscopic laws of the effective stress tensor and Lagrangian cleat porosity are reconstructed in incremental forms where the effective coefficients are taken constant over each time interval and then updated to compute the next time interval. It should be noted that the proposed three-scale poromechanical model can be coupled with a multiscale transient model for flow and transport problems developed in other work in order to simulate the CO_2 injection process, the change of permeability and to predict the gas production curve.

Numerical simulations of the proposed poromechanical model coupled with the multiscale transient model are carried out in COMSOL Multiphysics software. Fig. 2(b) illustrates the ratio between the cleat permeability and its initial value. Near the injection well (lower left corner), the cleat permeability decreases significantly due to a matrix swelling induced by CO_2 adsorption. As observed at the nanoscale by the DFT approach, the adsorption potential of CO_2 is higher than CH_4. Therefore, CO_2 can replace CH_4 in the nanopores inducing a less attractive force which swells the matrix. Particular attention must be paid to the injection pressure to avoid total cleat closure near the injection well.

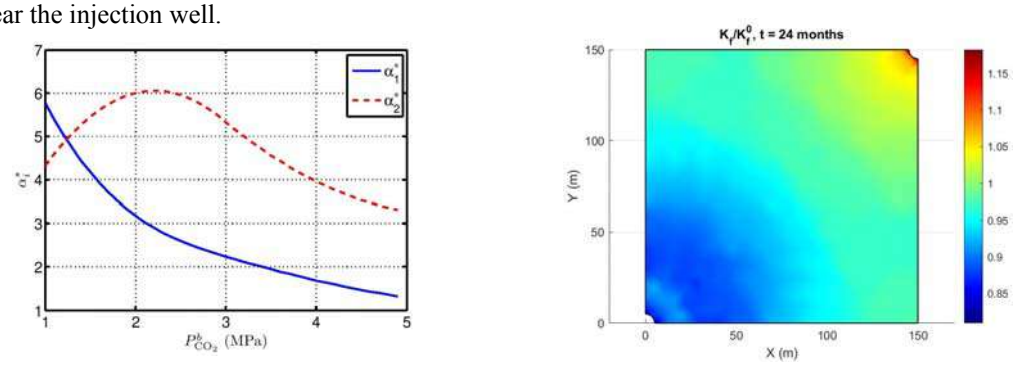

Figure 2: (a) Dependence of modified Biot-Willis coefficient on bulk pressure; (b) Ratio between the cleat permeability and its initial value after 24 months of gas production, P injection = 5 MPa

CONCLUSIONS

In this work we have constructed a three-scale model to describe the poromechanics of swelling porous media incorporating the deformation induced by solvation forces. A novel numerical method for solving the DFT equations allowed reconstructing numerically the fluid density profiles and the solvation force in complex pore geometry. After a first homogenization procedure to obtain the modified effective stress principle for the homogenized matrix including the contribution of solvation force, we highlight the magnitude of the Biot-Willis coefficient of the matrix which under adsorption effects can be greater than one. A second homogenization procedure was applied to construct the three-scale poromechanical model incorporating the cleat network. Such an approach was capable of incorporating the influence of solvation forces on the effective stress principle and the macroscopic nonlinear poroelastic coefficients. The proposed model can explain the experimentally observed cleat closure phenomena during CO_2 injection. Such a remarkable result illustrates the potential of the proposed approach in bridging highly complex adsorption phenomena at the nanoscale and the homogenized poromechanical behavior at the reservoir scale.

References

[1] Auriault J.-L., Boutin C., Geindreau C., Homogenization of Coupled Phenomena in Heterogeneous Media, ISTE Ltd and John Wiley and Sons, Inc, 2009.

[2] Le T. D., Murad M. A., Pereira P. A. and Boutin C., Bridging Between Macroscopic Behavior of Shale Gas Reservoirs and Confined Fluids in Nanopores, Computational Geosciences, pp 1-21, 2015.

[3] Le T. D., Moyne C., Murad M. A., Panfilov I., A three-scale poromechanical model for swelling porous media incorporating solvation forces: Application to enhanced coalbed methane recovery, Mechanics of Materials, pp 47-60, 2019.

[4] Le T. D., Ha Q. D., Panfilov I., Moyne C., Multiscale model for flow and transport in CO_2-enhanced coalbed methane recovery incorporating gas mixture adsorption effects, Advance in Water Resources, 103706, 2020.

UPSCALED MODEL FOR NON-STEADY INERTIAL FLOW IN HOMOGENEOUS POROUS MEDIA

Didier Lasseux* [1], Francisco J. Valdés-Parada[2], and Fabien Bellet[3]
[1]CNRS, UMR 5295, Univ. Bordeaux, Talence, France
[2]Universidad Autónoma Metropolitana-Iztapalapa, Mexico City, Mexico
[3]CNRS, CentraleSupélec, Univ. Paris-Saclay, France

Summary A macroscopic model for non-steady and inertial one-phase incompressible flow in rigid porous media is presented using an upscaling technique. The resulting model is non-local in time and involves two effective coefficients, namely, a dynamic apparent permeability tensor and a vector accounting for the time-decaying influence of the flow initial condition. Ancillary closure problems are provided, which allow computing the effective coefficients. Symmetry and positiveness analyses of the apparent permeability are carried out. The performance of the macroscopic model for different macroscopic forcing is examined along with validation with direct numerical simulations. It is shown that the purely heuristic classical model, consisting in a Darcy-like model complemented with an accumulation term on the filtration velocity, is not appropriate.

MICROSCALE EQUATIONS AND UPSCALING

The commonly employed model to described non-steady one phase incompressible and creeping flow in homogeneous porous media is a heuristic Darcy equation to which an accumulation term on the filtration velocity is added [1, 2]. This empirical macroscale momentum equation has never been established on a theoretical basis. The purpose of this work is hence to formally derive a macroscopic non-steady model for one-phase flow (including inertia) in rigid and periodic porous media. The procedure starts with the classical Navier-Stokes equations at the pore-scale considering a no-slip boundary condition at the solid-fluid interface together with the velocity initial condition. An upscaling procedure, based on a short-cut version of the volume averaging method [3], is then applied to the pore-scale equations. Due to the non-linear character of the Navier-Stokes equation, a pseudo-linearization is applied considering Reynolds numbers smaller than the critical value corresponding to the first Hopf bifurcation. Nevertheles, this pseudo-linearization does not introduce any approximation [4].

MACROSCOPIC MODEL

The macroscopic mass and momentum equations, valid in the homogeneous part of the porous medium and obtained from upscaling, are given by

$$\nabla \cdot \langle \mathbf{v} \rangle = 0, \quad t > 0 \tag{1a}$$

$$\langle \mathbf{v} \rangle = -\frac{1}{\mu} \int_{t_0=0}^{t_0=t} \left. \frac{\partial \mathbf{H}_t}{\partial t} \right|_{t-t_0} \cdot \left(\nabla \langle p \rangle^\beta - \rho \mathbf{b} \right)\Big|_{t_0} + \boldsymbol{\alpha}, \quad t > 0 \tag{1b}$$

Here, $\langle \psi \rangle$ and $\langle \psi \rangle^\beta$ denote the superficial and fluid-phase (β) intrinsic averages of ψ. In addition, $\mathbf{v}$, p and t are the velocity, pressure and time whereas μ and ρ are the dynamic viscosity and density, both being constant. In the macroscopic momentum equation, $\rho\mathbf{b}$ is the body force per unit volume, $\mathbf{b}$ being space-independent (but eventually time-varying). In equation (1b), which is non-local in time, $\mathbf{H}_t$ is the dynamic apparent permeability tensor (it is apparent due to the inertial effects) whereas $\boldsymbol{\alpha}$ is an effective coefficient which only contains a source due to the initial velocity field, $\mathbf{v}_0$, and is zero when $\mathbf{v}_0 = \mathbf{0}$. The tensor $\mathbf{H}_t$ depends on $\mathbf{v}_0$ and on the macroscopic forcing. These two effective coefficients are determined from the solution of two closure problems [4]. In the long time limit, $\mathbf{H}_t \to \mathbf{H}$, $\mathbf{H}$ being the steady apparent permeability tensor introduced earlier [5]. The final value theorem applied to equation (1b) conveniently yields the steady form of the macroscopic inertial momentum equation also reported in [5]. Moreover, using a formalism reported in [6], it can be shown that $\mathbf{H}_t$ is non-symmetric, the skew symmetric part being only due to inertial effects. In the frequency domain, the dynamic apparent permeability is shown to be a positive definite tensor. Clearly, the macroscopic momentum equation (1b) contrasts with the classical heuristic model given by $\frac{\rho}{\varepsilon}\rho\frac{\partial\langle\mathbf{v}\rangle}{\partial t} = -\left(\nabla\langle p\rangle^\beta - \rho\mathbf{b}\right) - \mu\mathbf{H}^{-1}\cdot\langle\mathbf{v}\rangle, \quad t > 0.$

RESULTS

To illustrate the relevance and accuracy of the macroscopic model reported above, its predictions are compared to the results of direct numerical simulations (DNS) of the initial pore-scale equations. To do so, a two-dimensional model pore-structure made of a square pattern of parallel cylinders of square cross section is considered. Periodicity is applied in the vertical (y-) direction allowing to consider a single row of n cylinders ($n = 21$) in the horizontal (x-) direction.

*Corresponding author. E-mail: didier.lasseux@u-bordeaux.fr

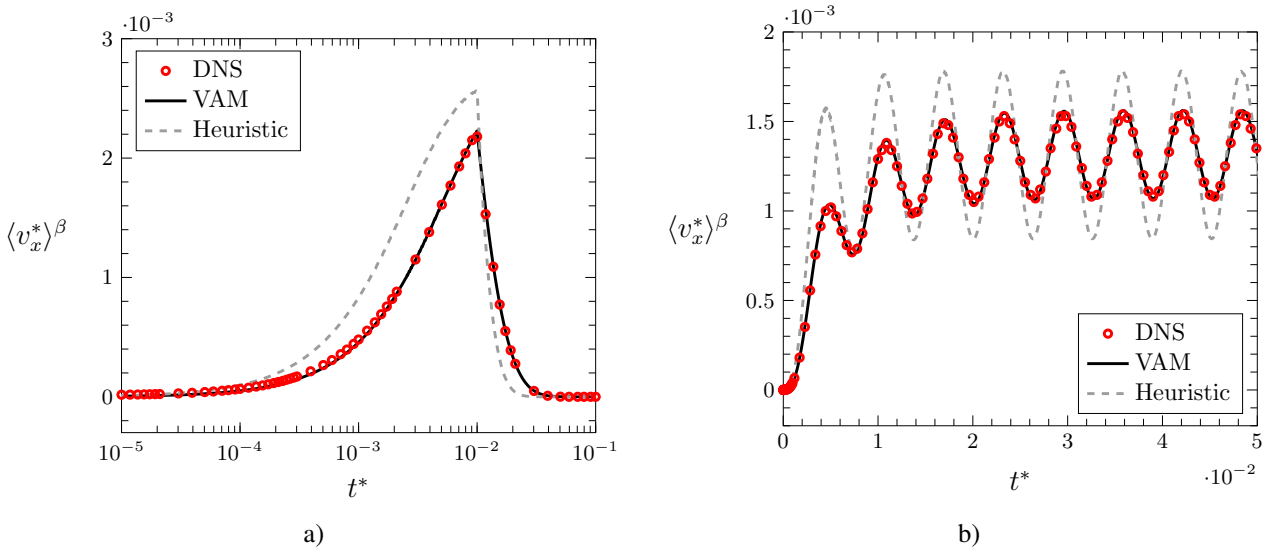

Figure 1: Dynamics of the x-component of the macroscale velocity as a response to a) a macroscopic pressure gradient pulse and b) an oscillatory macroscopic pressure gradient (see text for their expressions). Results from direct numerical simulations, from the solution of the macroscale model obtained by the volume averaging method (VAM) and from the heuristic model. In both cases, fluid is at rest at $t^\star = 0$. The porosity of the medium is 0.4 and the Reynolds number is $Re = 10^3$.

For the DNS, a pressure signal is imposed at the entrance of the medium ($x = 0$) while, at the exit, a zero pressure is maintained. For comparison with the macroscopic model, results are averaged over the central unit cell (*i.e.* far from the macroscopic boundaries where the medium is reasonnably homogeneous). For the macroscopic model, which reduces to 1D, a macroscopic pressure gradient, corresponding to that at the microscale, is applied in the x-direction.

Two different forms of the dynamic macroscopic pressure gradient were considered. The first one is a pulse given by $-\partial\langle p^\star\rangle^\beta/\partial x^\star = a$ with $a = 0,\ t^\star \leq 0;\ a = 1,\ 0 < t^\star < 10^{-2};\ a = 0,\ t^\star \geq 10^{-2}$. The second one corresponds to an oscillatory dimensionless pressure gradient given by $-\partial\langle p^\star\rangle^\beta/\partial x^\star = 0.5\,(1 - \cos(1000t^\star))$. In both cases, the initial velocity is $\mathbf{v}_0 = \mathbf{0}$.

Results on the dynamics of the dimensionless x-component of the intrinsic average velocity, $\langle v_x^\star\rangle^\beta$, are represented for the two cases in figure 1. The results from the macroscpoic model obtained with the volume averaging method (VAM) are compared to the DNS results and to the prediction of the heuristic model. This figure clearly shows that, in both cases, the dynamics of the velocity is perfectly predicted by the macroscopic model as it coincides with the DNS results. Moreover, the results obtained from the heuristic model poorly perform, proving the inadequacy of this model.

CONCLUSIONS

A macroscopic model for non-steady (inertial) one-phase Newtonian flow in a rigid homogeneous porous medium was formally derived in this work by upscaling the pore-scale mass conservation and Navier-Stokes equations. This macroscopic model is non local in time and involves a dynamic apparent permeability tensor together with an effective coefficient which accounts for the initial condition effects. Both effective parameters can be computed from the solution of two time-dependent closure problems. The macroscopic model contrasts with the heuristic model classically employed in the literature for which the macroscopic momentum equation is a Darcy-like equation to which an accumulation term on the filtration velocity is added. Numerical simulations on model test cases show that the macroscopic model derived here accurately predicts the velocity dynamics and is validated by comparison with direct numerical simulation of the pore-scale problem. The comparison also indicates that the prediction of the heuristic model poorly performs, making this model inadequate in the general case.

Apart from the fundamental interest in this formal macroscopic model, this represents an important step for further upscaling. Among many applications, it is also of major concern for the interpretation of non-steady experiments in which inertial effects and the influence of the initial condition are to be considered.

References

[1] Hill A. A. and Straughan B. Poiseuille Flow in a Fluid Overlying a Porous Medium. *J. Fluid Mech.* **603**, 137-149, 2008.
[2] Jin Y. and Kuznetsov A. V. Turbulence Modeling for Flows in Wall Bounded Porous Media: an Analysis Based on Direct Numerical Simulations. *Phys. Fluids* **29**(4), 045102, 2017.
[3] Whitaker S. The Method of Volume Averaging. Kluwer, Springer, Dordrecht, 1999.
[4] Lasseux D., Valdés-Parada F. and Bellet F. Macroscopic Model for Unsteady Flow in Porous Media. *J. Fluid Mech.* **862**: 283-311, 2019.
[5] Whitaker, S. The Forchheimer Equation: a Theoretical Development. *Trans. Porous Med.* **25**, 27-61, 1996.
[6] Lasseux D. and Valdés-Parada F. J. Symmetry Properties of Macroscopic Transport Coefficients in Porous Media. *Phys. Fluids* **29**, 043303, 2017.

STRUCTURE GENERATED TURBULENCE IN STOCHATIC POROUS MEDIA

Kyung Chun Kim[1]*, Chanhee Moon[1], and Youngwoo Kim [1]
[1]School of Mechanical Engineering, Pusan National University, Busan, Korea

Summary This study investigates turbulence characteristics of flow inside a stochastic metal foam. Using micro-tomography and stereo-lithography, a transparent stochastic foam was printed. Quantitative flow visualization was performed using refractive index matching technique and time-resolved particle image velocimetry. Mixing and turbulence characteristics were discussed with various length scales. The structure generated turbulence is compared to the grid generated turbulence.

INTRODUCTION

Metal foam is a metallic sponge which consists of many struts and nodes interconnect the struts. The struts are the product of plateau borders and they form irregular cellular configurations. This metal foam structures have been of interest because their geometrical characteristics are theoretically desirable to many applications such as heat exchanger, chemical reactor, filter, etc. Metal foam geometry provides high porosity ($\varepsilon > 0.9$), high specific surface area, and complex flow path. Although the annual publication rate on the metal foam is constantly increasing, most of them have only considered lump parameters like pressure drop and Nusselt number based on the inlet/outlet data. In order to observe the flow structure inside the metal foams, the numerical methods mostly have been used. To the authors' knowledge, only Onstad et al. [1] experimentally observed the flow characteristics inside a 4x scaled opaque metal foam replica through magnetic resonance velocimetry under a turbulent flow condition. The reason for the low number of papers on the flow inside the metal foam is because the fabrication of a transparent metal foam replica was practically impossible. Current 3-D printing technology supports the fabrication of a transparent metal foam replica.

Cellular structures like metal foams can make jet flows inside themselves and these jets cause flow instability. A comprehensive study of the effects of the structure on the flow behavior should be conducted based on instantaneous and time-averaged data. In this study, flow characteristics through a 10 PPI (pores per inch) transparent metal foam replica have been investigated under laminar flow condition.

EXPERIMENTAL METHOD

A 10 PPI aluminum foam was prepared for the metal foam sample. An X-ray computed tomography system was used to obtain a 3-D CAD (Computer-aided design) file. Under 200 kV, 200μA and 267ms condition, 743 x 740 x 459 voxels were generated with a spatial resolution of 0.032 mm. The voxels were converted to a 3-D CAD file. In CAD software, a part of the metal foam replica CAD file is cropped into a perfect hexagon that has a size of 10 mm x 10 mm x 25 mm. Because of the resolution of the 3-D printer, the size of the cropped model was doubled. Therefore, the final size of the metal foam replica file is 20 mm x 20 mm x 50 mm. The metal foam replica was printed by Polyjet type 3-D printer (Objet Eden260VS, Stratasys Ltd.). Vero Clear resin and water-soluble support material (SUP707) were selected as printing materials.

The refractive index of Vero Clear material is 1.515 for 532 nm. Refractive index matched (RIM) solution based on NaI was prepared. As shown in Fig. 1., an acrylic square duct, which has size of 20 mm x 20 mm x 500 mm, was manufactured. That duct has one inlet and one outlet, and they are positioned above the duct to observe the flow in the spanwise plane. 3-D printed metal foam replica is placed 15 D away from the inlet. A test loop has been configured to circulate the RIM solution through the test section. As shown in Fig. 1., it consists of a RIM solution container, a gear pump, a flowmeter, a bubble trap, a test section, and a traverse to move the test section. The RIM solution container is partially immersed in water bath. A constant temperature hot plate with 25°C was placed bottom of the water bath to maintain the temperature of RIM solution. The RIM solution is transported by the gear pump. Flowrate was measured by a turbine type flowmeter.

One CMOS high-speed camera (1k x 1k resolution) and one continuous wave laser (532 nm, 5 W) power were used to conduct time-resolved 2-D PIV experiment. Because equivalent diameter of struts is 0.8±0.06 mm, the thickness of laser sheets was set to 0.5 mm. Rhodamine B coated fluorescence polymer particle (1-20 μm) was used as tracer.

RESULTS AND DISCUSSION

Figure 2 shows the flow characteristics through the metal foam replica. The two graphs on the left side of Figure 2 show turbulent kinetic energy and Reynolds stress components on the streamwise center plane. Each value is normalized by the square of the mean bulk velocity, and the range of the y-axis is -0.1 to 0.5. When a flow with a turbulence intensity close to zero is introduced, it can be seen that the turbulent intensity increases while passing through the metal foam replica. The turbulence decays after passing through the replica, all the values recover to zero again. This characteristic can also be confirmed by the vorticity shown on the right side of Figure 2. Up to a and the metal foam inlet b show no vortical structures, but a large number of vortex structures are generated from c. These vortices decay downstream of the

*Corresponding author. E-mail: kckim@pusan.ac.kr

metal foam. In this study, the decay exponent for decay power law is -0.6 to -2.1, and the spatial mean value is -1.4, which is similar to grid-generated turbulence. This represents there is no turbulence production downstream. The integral length scale was investigated to determine the streamwise jet coherence length. The length is indicated as about 7 mm, similar to the size of one cell. This is different from the result reported by Onstad et al. [1], but this is because the shape of the metal foam and the investigated Reynolds number are different.

We call this turbulence generated by metal foam structure as structure generated turbulence. The irregularly arranged pore network of the metal foam interacts with the flow to generate transverse flow motion [2]. Flow separation from the metal foam struts can increase flow fluctuations, and this effect should be investigated. Further investigation will be performed at various Reynolds numbers.

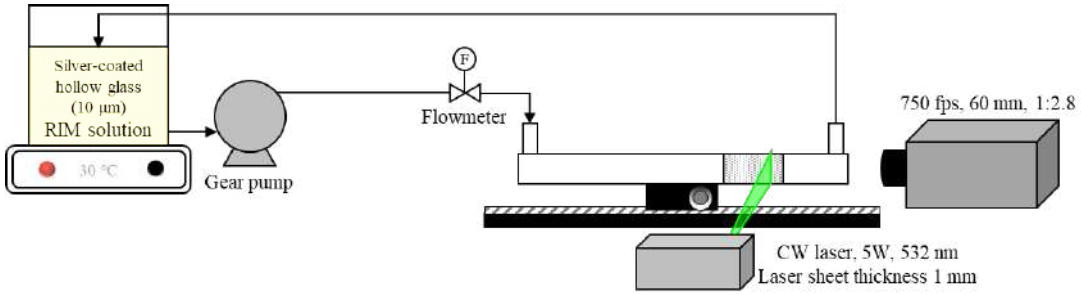

Figure 1. Experimental setup

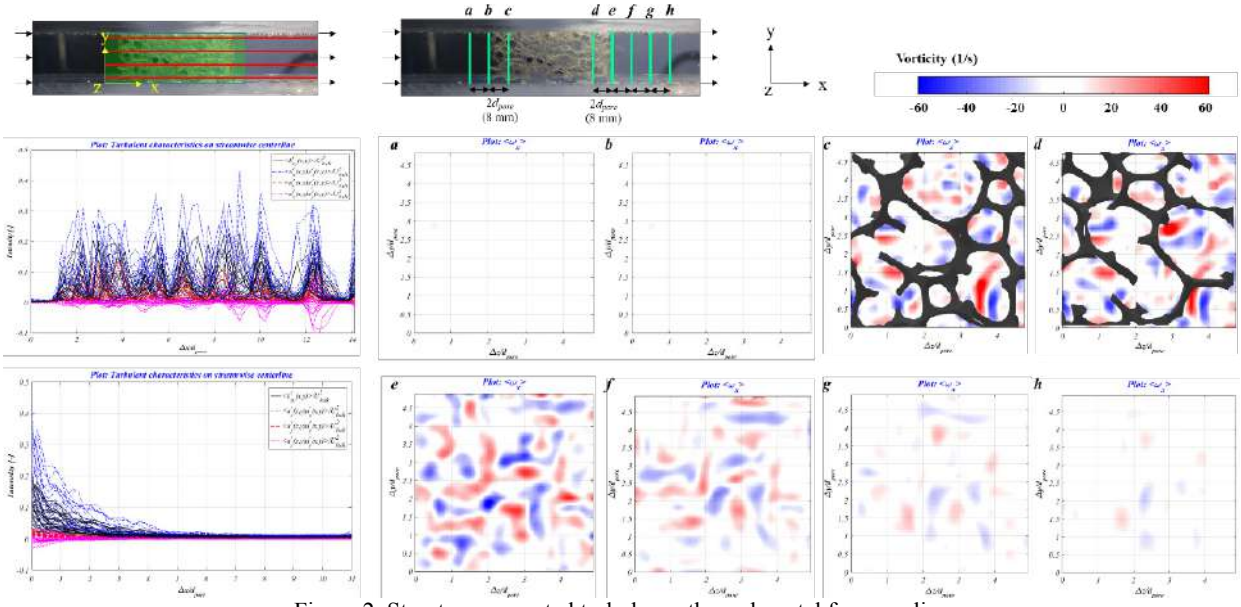

Figure 2. Structure generated turbulence through metal foam replica

CONCLUSIONS

Fluid flow entering the metal foam structure shows turbulent features. Jet-like flows are generated by the pore network, and the flow is furcated and interflowed successively. Shear layers generated by a jet are disturbed by interflowing jets. Strong transverse velocity was generated by 23% of U_b, and this was consistent with Onstad et al. [1]'s prediction that the strong transverse motion in a metal foam may occur even in laminar flow condition. Evolution of the spanwise vorticity in the metal foam structure was presented. Spanwise vorticity shows considerable fluctuation due to the complexity of flow motion in the metal foam structure. These turbulent characteristics were generated by the irregular metal foam structure: Structure generated turbulence. However, in this study, the investigation was conducted only for a single Reynolds number and single metal foam geometry. Present channel size is also not large enough to avoid wall effect. It is necessary to study the flow characteristics under the various Reynolds number and metal foam structures.

References

[1] Onstad A.J., Elkins C.J. et al.: Full-field measurements of flow through a scaled metal foam replica. *Exp. in Fluids.* ***50 :*** *1571-1585*, 2011.
[2] Pope S.B.: Turbulent Flows., Cambridge., 2013.

IMPACT OF WETTABILITY ON MULTIPHASE FLOW AND GRANULAR MECHANICS

Yue Meng[1], Bauyrzhan K. Primkulov[1], Zhibing Yang[2], Chung Yee Kwok[3], and Ruben Juanes*[1]
[1]Department of Civil and Environmental Engineering, Massachusetts Institute of Technology, Massachusetts, USA
[2]State Key Laboratory of Water Resources and Hydropower Engineering Science, Wuhan University, Wuhan 430072, China
[3]Department of Civil Engineering, The University of Hong Kong, Pokfulam Road, Hong Kong, China

Summary. We study fluid-induced deformation of granular media, and the fundamental role of capillarity and wettability on the emergence of fracture patterns. We develop a hydromechanical computational model, coupling a "moving capacitor" dynamic network model of two-phase flow at the pore scale with a discrete element model of grain mechanics. We simulate the slow injection of a less viscous fluid into a frictional granular pack initially saturated with a more viscous, immiscible fluid. We study the impact of wettability and initial packing density, and find four different regimes of the fluid invasion: cavity expansion and fracturing, frictional fingers, capillary invasion, and capillary compaction. We explain fracture initiation as emerging from a jamming transition, and synthesize the system's behavior in the form of a novel phase diagram of jamming for wet granular media.

INTRODUCTION AND METHODS

As one of the factors that influences multiphase flow in porous media, wettability (the relative affinity of the substrate to each of the fluids, and measured by the contact angle θ) has been studied for decades. While much is now known about the role of wettability on multiphase displacements in porous media, fundamental gaps remain in the context of grain-scale mechanisms and their macroscale consequences. Given the importance of capillarity on fracture of granular packs [1,2], here we focus on the impact of wetting properties on the emergence of such fracture patterns. We also adopt packing density as a control parameter, since it can lead to a transition from Saffman–Taylor instability to dendritic (or ramified) fingering patterns, or from frictional fingering to stick-slip bubbles [1].

In this work, we uncover four fluid-invasion morphological regimes under different initial packing densities and substrate wettabilities: cavity expansion and fracturing, frictional fingers, capillary invasion, and capillary compaction. To rationalize these simulation outputs, we propose to analyze the evolution of the system as one approaching a jamming transition, which provides new insights that allow us to map the wealth of behavior onto a novel phase diagram of jamming for wet granular media.

We adopt a recently developed "moving capacitor" dynamic network model to simulate fluid-fluid displacement at the pore level [3]. The model employs an analog of the pore network geometry, where resistors, batteries and capacitors are responsible for viscous, out-of-plane, and in-plane Laplace pressure drops, respectively. The fluid-fluid interface is represented as a moving capacitor—when the interface advances, the Laplace pressure increases until it encounters a burst (equivalent to a Haines jump), touch (touches the nearest particle), or overlap event (coalesces with a neighboring interface) [4,5]. These events determine how the interface advances, enlisting one or more new particles when a node on the interface reaches its filling capacity and becomes unstable. This model reproduces both the displacement pattern and the injection pressure signal under a wide range of capillary numbers and substrate wettabilities [4–6].

To capture particle motion, we couple the dynamic flow network model with a discrete element model (DEM), PFC2D® [7]. Hydromechanical two-way coupling is achieved from three perspectives: (1) the fluid pressures calculated from the moving-capacitor flow model exert forces on particles, and lead to particle rearrangement and deformation; (2) particle movements change the geometric configuration of the granular pack, which in turn changes the pore network topology and throat conductances and capillary entry pressures; and (3) expansion of the central cavity around the injection port "consumes" injected fluid, which decreases the flow of fluid permeating through the granular pack.

RESULTS AND DISCUSSION

We simulate immiscible fluid-fluid displacement through a granular pack confined in a circular flow cell, by setting a constant injection rate at the center, and constant pressure at the perimeter. The invading and defending fluid viscosities are set to $\eta_{\text{inv}} = 8.9 \times 10^{-4}$ Pa · s for water, and $\eta_{\text{def}} = 0.34$ Pa · s for oil, respectively, and the interfacial tension is set to $\gamma = 13 \times 10^{-3}$ N · m^{-1}. These parameters are chosen to mimic the experiments of [6]. The granular pack has an outer and inner radius of $R_{\text{out}} = 13.25$ mm, $R_{\text{in}} = 0.5$ mm, and a height $h = 330$ μm. We adopt a simplified Hertz–Mindlin contact model [7] for particles in the granular pack, with the following properties: shear modulus $G = 50$ MPa, Poisson ratio $\nu = 0.5$ (quasi-incompressible), coefficient of friction $\mu = 0.3$, fluid density $\rho = 1040$ kg · m^{-3}, and mean grain diameter $d = 300$ μm with 10% standard deviation. We choose an injection rate $Q_{\text{inj}} = 4.3 \times 10^{-11}$ m^3 · s^{-1}, corresponding to a modified capillary number $\text{Ca}^* = \eta_{\text{def}} Q_{\text{inj}} / (\gamma h d^2) = 0.5$ [2], for which viscous pressure gradients have time to relax between front movements, and capillary effects govern the displacement. We conduct simulations in which we fix these parameters, and we vary the contact angle θ from 140° (drainage) to 46° (imbibition),

*Corresponding author. E-mail: juanes@mit.edu

and the initial packing density ϕ_0 from 0.68 (loose pack) to 0.84 (dense pack). In Figure 1, we show the fluid invasion morphologies that result from injection in the form of a visual phase diagram for different values of θ and ϕ_0. The collection of patterns at breakthrough—when the invading fluid first reaches the outer boundary—exhibits four different regimes:

1. *Regime I: Cavity expansion and fracturing.* When the injection pressure from fluid injection is sufficient to push particles outwards, the cavity keeps expanding until the energy input becomes insufficient to compact the granular pack further; the point at which fractures emerge.
2. *Regime II: Frictional fingers.* At only weakly-wetting conditions, the injection pressure is positive but smaller than in drainage. In this case, the injected fluid pushes away particles in certain directions, preferably those with loosely packed particles, and develops frictional fingers.
3. *Regime III: Capillary invasion.* When particles have been densely packed initially, a small injection pressure (either positive or negative) is insufficient to overcome the established chains of contact forces, and thus particles do not move. In this case, we observe patterns of capillary fluid invasion in rigid media.
4. *Regime IV: Capillary compaction.* In strong imbibition the injection pressure is negative, and for sufficiently loose granular packs, particles are dragged into the invading fluid under the out-of-plane curvature effect, leading to capillary compaction.

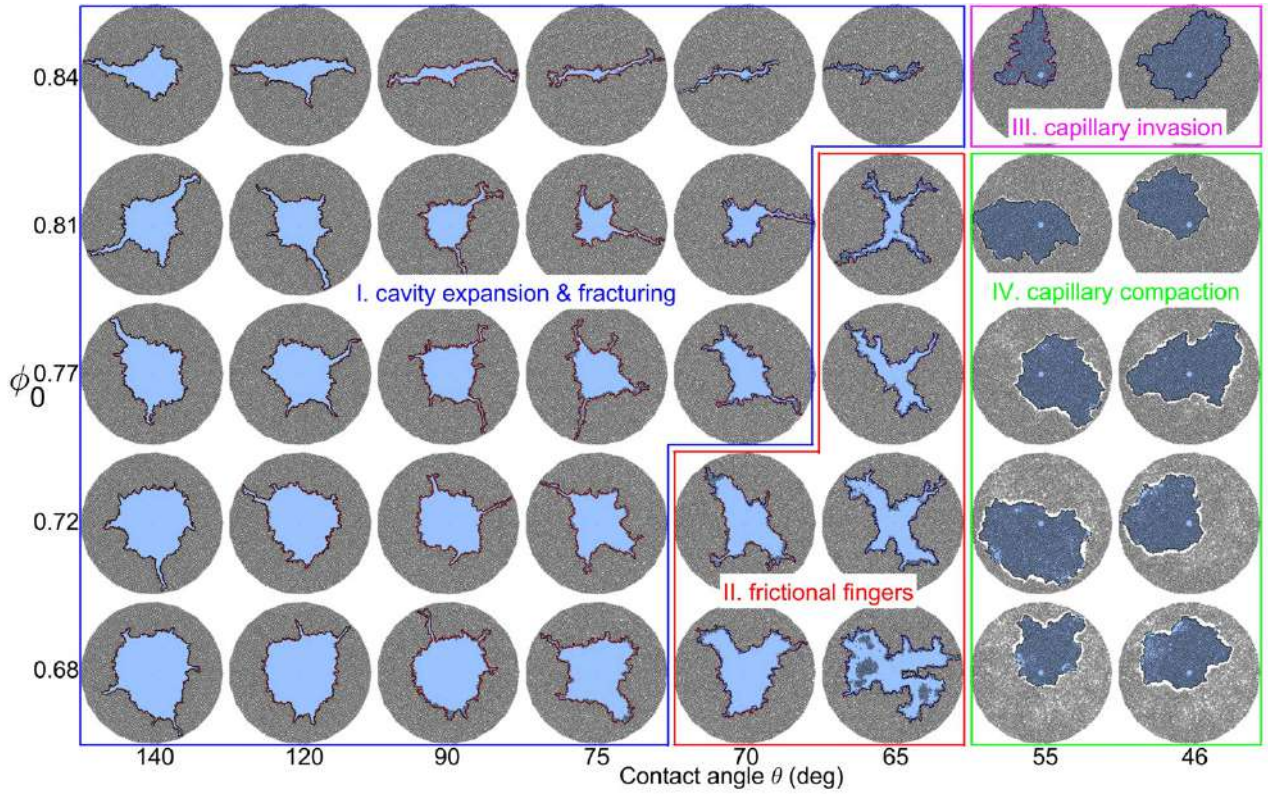

Figure 1. Visual phase diagram of the invading fluid morphology at breakthrough corresponding to different substrate wettabilities (contact angle θ) and initial packing densities ϕ_0.

CONCLUSIONS

In summary, we have studied morphological transitions in granular packs as a result of capillary-dominated fluid-fluid displacement via a novel, fully-coupled model of two-phase flow and grain mechanics. Simulations of fluid injection into a granular pack with different initial packing densities and substrate wettabilities have led to uncovering four invasion regimes: cavity expansion and fracturing, frictional fingers, capillary invasion, and capillary compaction. In particular, we have identified the emergence of fracture, and its surprising and unexplored dependence on the system's wettability.

References

[1] B. Sandnes, E. Flekkøy, H. Knudsen, K. Maløy, and H. See, *Nature Comm.* **2**, 288 (2011).
[2] R. Holtzman, M. L. Szulczewski, and R. Juanes, *Phys. Rev. Lett.* **108**, 264504 (2012).
[3] B. K. Primkulov, A. A. Pahlavan, X. Fu, B. Zhao, C. W. MacMinn, and R. Juanes, *J. Fluid Mech.* **875**, R4 (2019).
[4] M. Cieplak and M. O. Robbins, *Phys. Rev. B* **41**, 11508 (1990).
[5] B. K. Primkulov, S. Talman, K. Khaleghi, A. R. Shokri, R. Chalaturnyk, B. Zhao, C. W. MacMinn, and R. Juanes, *Phys. Rev. Fluids* **3**, 104001 (2018).
[6] B. Zhao, C. W. MacMinn, … and R. Juanes, *Proc. Natl. Acad. Sci. USA* **120**, 13799 (2019).
[7] ITASCA, PFC2D, v3.1 – Theory and Background, Itasca Consulting Group, Inc., Minneapolis, MN (2004).

DIFFERENTIAL DIFFUSIVITY EFFECTS ON REACTIVE CONVECTIVE DISSOLUTION IN A POROUS MEDIUM

Mamta Jotkar*[1], Laurence Rongy[1], and Anne De Wit [1]
[1]Nonlinear Physical Chemistry Unit, Université libre de Bruxelles, Brussels, Belgium

Summary Dissolution-driven convection is relevant in the context of CO_2 capture and sequestration and occurs in a host phase, initially separated from the dissolving species A, when a buoyantly unstable stratification develops upon dissolution. When all species diffuse equally, an A+B→C reaction is known to accelerate or decelerate the convective dynamics when C is denser or less dense than B, respectively. However, in practice, most species diffuse at different rates and alter the dynamics entirely. We observe that when B diffuses faster than C, the density profiles contain a local minimum below the reaction front and a double-diffusive instability occurs below the reaction front. When B diffuses slower than C, the density profiles contain a local minimum at the reaction front followed by a local maximum below, giving rise to diffusive-layer convection below the reaction front.

INTRODUCTION

Dissolution-driven convection, occurring in a host phase initially separated from the dissolving species A, when a buoyantly unstable stratification develops upon dissolution, has received significant attention due to its relevance in CO_2 capture and sequestration (CCS). In this technique, CO_2 is captured at production sites, transported through pipelines and injected into geological storage sites, such as saline aquifers for its long-term isolated storage. When CO_2 (phase A) is injected into an aquifer, it rises above the brine (host phase) up to an impermeable cap rock and a two-layer stratification develops. The two phases are partially miscible and initially separated by an interface. The subsequent dissolution of CO_2 in brine leads to a buoyantly unstable stratification due to the CO_2-rich brine being denser than the resident brine. This triggers a fingering instability and the resultant convective pattern is favourable to the sequestration technique since it accelerates the transfer of CO_2 towards the trapping host phase.

In the recent years, it has been demonstrated that chemical reactions have a strong impact on the convective dynamics. For example, when all species diffuse equally, an A+B→C reaction can accelerate or slow down the dissolution rate of species A, depending on the relative contribution to density of the reactant B and product C [1]. More precisely, when C is denser than B, the monotonically decreasing density profiles give rise to strong convective motion and accelerates the dissolution of A into the host phase. Conversely, when C is less dense than B, the density profiles are non-monotonic with a local minimum that acts as a barrier and prohibits the progression of the fingers. Consequently, the convective dynamics and dissolution rate is slowed down. So far, most of the studies in the literature have considered that all the species diffuse at equal rates. However, in practice, it is most likely that the species diffuse differently, as suggested by experiments and field investigations.

Following this motivation, we numerically study dissolution-driven convection in two partially miscible phases when the dissolving phase A, upon dissolution into the host phase reacts with a reactant B initially present in the host phase to produce C via an A+B→C type of reaction. Since all three species contribute to the density of the host phase and diffuse at different rates, it is possible to alter the buoyancy-driven instability by selecting the properties of B for a given A. In particular, we consider the impact of differential diffusivities δ_B and δ_C of B and C, respectively on the convective dynamics when C is denser or less dense than B. We quantify the dissolution flux, onset time for convection and asymptotic fluxes, which are essential in predicting the efficiency of a given sequestration technique.

PROBLEM FORMULATION

We consider a homogeneous, isotropic, isothermal porous medium, in which two partially miscible aqueous phases are initially separated in space by a horizontal interface. The gravitational field **g** points downwards along the vertical z-axis and is perpendicular to the horizontal x-axis. The phase A dissolves from above into the host phase containing a reactant B with an initial concentration B_0 to generate the product C via a second order reaction of the type A+B→C. All species contribute to the density stratification and diffuse at different rates. We assume a local chemical equilibrium such that the concentration of A at the interface (z = 0) remains constant in time, and is equal to its finite solubility A_0 in the host phase. The host phase extends from x = 0 to x = L in the horizontal direction and from z = 0 to z = H in the vertical direction.

The reaction-diffusion-convection equations govern the temporal evolution of the solutal concentration of the species A, B and C. These equations are complemented by Darcy's equation for an incompressible flow in a porous medium and a linear equation of state for the density. Periodic boundary conditions are imposed at x = 0 and x = L, no vertical flow and no flux conditions are used for A, B and C at z = H (bottom boundary) while at z = 0 (interface), no vertical flow and no flux conditions are used for B and C along with A = 1. Since we focus on the differential diffusivity effects, the relevant parameters are the Rayleigh numbers, determining the contribution to density of species B and C, R_B and R_C

*Corresponding author. E-mail: mmtjotkar@gmail.com, mjotkar@ulb.ac.be.

and the diffusivities of B and C, δ_B and δ_C, respectively. We maintain Rayleigh number of A as $R_A = 1$ and the ratio of initial concentration B_0 of B with respective to solubility A_0 as $\beta = B_0/A_0 = 1$. For numerical simulations, we have used YALES2 software with the DARCY_module.

RESULTS

We classify the reaction-diffusion density profiles in the δ_B/δ_C versus R_B/R_C parameter space, consistent with the literature [2]. When B diffuses sufficiently faster than C, we observe that the density profiles contain a local minimum below the reaction front. Conversely, when B diffuses sufficiently slower than C, the density profiles contain a local minimum at the reaction front followed by a local maximum below it. We observe that an addition convection zone develops below the reaction front when all the species diffuse differentially due to a local stratification consisting of less dense fluid lying on top of a denser one. When B diffuses sufficiently faster than C, the stratification consisting of denser fluid layer rich in A lying above the less dense one at the reaction front containing A and C, develops primary fingers due to Rayleigh-Taylor (RT) instability. Below the reaction front, the slow-diffusing less dense fluid layer rich in B and C overlies fast-diffusing denser fluid containing B, which leads to double-diffusive (DD) instability with secondary fingers at the tips of the primary ones (figure 1, left). Conversely, when B diffuses sufficiently slower than C, we observe two zones of convection: above the reaction front, the primary fingering is due to RT instability and below the reaction front, a secondary convective pattern marked by antenna-like structures arises due to the less dense fast-diffusing fluid layer rich in B and C overlying a denser slow-diffusing fluid one consisting of B (figure 1, right). This is diffusive-layer convection (DLC) instability [3]. We then study the impact of these mechanisms on the temporal evolution of the dissolution flux of species A into the host phase and the onset time for convection.

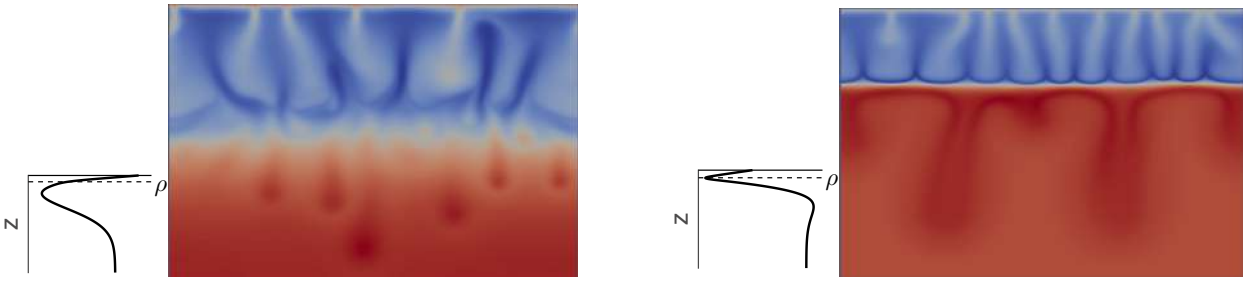

(a) DD-RT (b) DLC-RT

Figure 1. (a) Reaction-diffusion (RD) density profile (*left*) and density field (*right*) when reactant B diffuses faster than product C. Double diffusive (DD) convection influencing Rayleigh-Taylor (RT) instability has a destabilizing effect on the nonlinear dynamics. Density scale varies between 3 (red) and 1.4 (blue). (b) RD density profile (*left*) and density field (*right*) when reactant B diffuses slower than product C. Diffusive-layer convection (DLC) influencing RT instability has a stabilizing effect. Density scale varies between 3.26 (red) and 1.243 (blue).

CONCLUSIONS

We have shown that differential diffusivities of the species have a significant impact on the convective dynamics including the presence of an additional zone of convection below the reaction front and the occurrence of double-diffusive convection. In general, when B diffuses faster than C, the effect is destabilizing and the onset time is reduced and conversely, when B diffuses slower than C, it has a stabilizing effect and the onset time is larger; for both C denser and less dense than B. Our results are crucial in the context of CO_2 capture and sequestration (CCS) technique for predicting its efficiency, since it is most likely that all species diffuse differentially and alter the dynamics.

Acknowledgement

We gratefully acknowledge the financial support from the *Fondation ULB* and from the *FRS-FNRS PDR CONTROL* project.

References

[1] Jotkar M., De Wit A. and Rongy L. **Enhanced convective dissolution due to an A+B→C reaction: control of the non-linear dynamics via solutal density contributions**, *Phys. Chem. Chem. Phys.* **21**: 6432-6442, 2019.

[2] Loodts V., Trevelyan P. M. J., Rongy L. and De Wit A. **Density profiles around A+B→C reaction-diffusion fronts in partially miscible systems: A general classification**, *Phys. Rev. E* **94**: 043115, 2016.

[3] Carballido-Landeira J., Trevelyan P. M., Almarcha C. and De Wit A., **Mixed-mode instability of a miscible interface due to coupling between Rayleigh-Taylor and double-diffusive convection modes**, Phys. Fluids **25**: 024107, 2013.

THE IMPACT OF FLOW CONDITIONS ON THE CLOGGING OF A PORE BY COLLOIDAL PARTICLES

Delouche Nolwenn[1]*, Tabuteau Hervé [1]
[1]Institut de Physique de Rennes, Université de Rennes, France

Summary We use particle tracking to determine the hydrodynamical conditions of the abrupt flux decline during the clogging process of a pore by colloidal particles. We can detect every deposition event during the clogging with the measure of the average particle velocity and volume fraction of the particle accumulation behind the clog. Thanks to the Kozeny-Carman relation, we connect particles velocity and permeability of the clog. This approach helps us to determine the impact of the variation of the hydrodynamic conditions on the clogging process.

INTRODUCTION

The transport of dilute colloidal suspension through a porous medium like a filter or a soil, leads to the formation of clogs. This process is quite complex and results from a coupling between hydrodynamics and physicochemical parameters. Thanks to microfluidics, transparent porous media have been designed and allow monitoring the clogging process at the pore scale. Experimental studies have explored the geometry parameters promoting the fouling, like curvature at the pore entrance, shape and dimensions of the pore or confinement [1,3]. The investigation of the role of particle-wall or particle-particle interactions have also improved the understanding of the partial or total clogging conditions [2,4].
During such experiments there is an abrupt flux decline which corresponds to the clogging transition. Up to now, no quantitative link has been made between those two phenomena. Our experimental work helps to understand the dynamics of clog formation at the particle scale, relating each particle capture event to the corresponding decreases of the average variation of the particle velocity within the pore, using particle tracking. This approach also provides direct measurement of the volume fraction of both the flowing suspension and within the clog. Here we first determine the features of the clog transition and then we investigate the impact of the flow conditions on this transition as well on the subsequent growth of the clog.

MATERIALS AND METHODS

We flow a diluted suspension of polystyrene particles ($\phi = 5.10^{-3}$) under fixed pressure (fig.1a) through a constriction (fig.1b). A camera provides pictures at 100 frames/s that allows us using an algorithm sufficiently sensitive to track particles and get the spatial evolution of their velocity as they flow around the constriction.

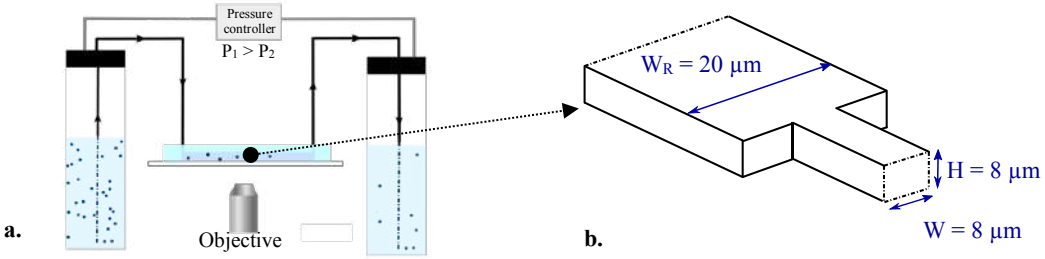

Figure 1: a. Schematic of the setup. b. Zoom in the central part of the channel in the constriction zone

RESULTS

We observe two significant steps during the clogging process. First, a partial clogging where the progressive particle deposition leads to a limited particle velocity decline (fig.2: a-f and plot). These deposits reduce the pore section until its complete clogging. At the very end of this process, an object is responsible of the final clogging which result in the most abrupt increase of the hydraulic resistance (image e to f). Later on, particles just pile up at the clog front leading to a slower increase of the channel resistance (fig.2 from image g up to l). The corresponding decrease of the velocity is also less abrupt since particle accumulation takes place into a wider part of the channel just upstream of the constriction zone, which thus has a lower hydraulic resistance.
We observe that the variation of the flow conditions has a direct consequence on particle deposition, while at high pressure the flow detaches some particles, in the lower range it limits their attachment. One may wonder if these erosion-deposition processes have also an impact of the structure of the clog and thus also on its hydraulic resistance. We investigate this by varying the pressure so that we get a large variation of the average particles velocity at the beginning of the experiment. The temporal evolution of the average particle velocity is reported in figure 3a. All the curves collapsed onto a master curve (insert figure 3b) indicating that the clogs formed for each applied pressure have the same permeability since the flow decline is identical.

*Corresponding author. E-mail: nolwenn.delouche@univ-rennes1.fr

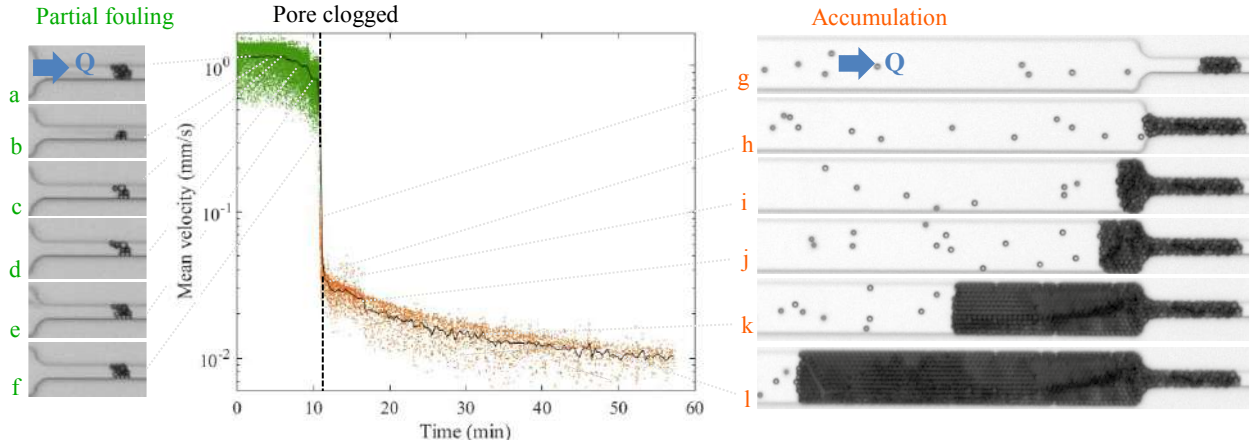

Figure 2: The two steps of the clog formation in a constriction: the partial clogging (a-f) followed by the particle accumulation (g-l). The plot is the temporal evolution of all the particle velocity that flow through the pore during the clogging process, with the continuous and the dotted lines corresponding respectively to the average velocity and the moment when the pore is clogged, i.e. when particle pile up at the clog front.

We use the Kozeny-Carman equation to determine the hydraulic resistance and the permeability of the packing of spherical particle from the constriction. From this equation we deduce that the fluid and also the particle velocity V vary as the inverse of the clog length L_c with a prefactor involving permeability. Based on independent measurement, made from image analysis we obtain a constant volume fraction $\phi_{exp} = 0.60 \pm 0.025$ for all pressures, which helps us to calculate the hydraulic resistance from the Kozeny-Carman equation. By plotting the average particle velocity against the clog length (fig.3b) we confirm that $V = A/L_c$, A being a constant irrespective of applied pressure. Therefore, we conclude that the hydraulic resistance of a colloidal clog does not depend on its dynamics of formation obtained with various flow conditions.

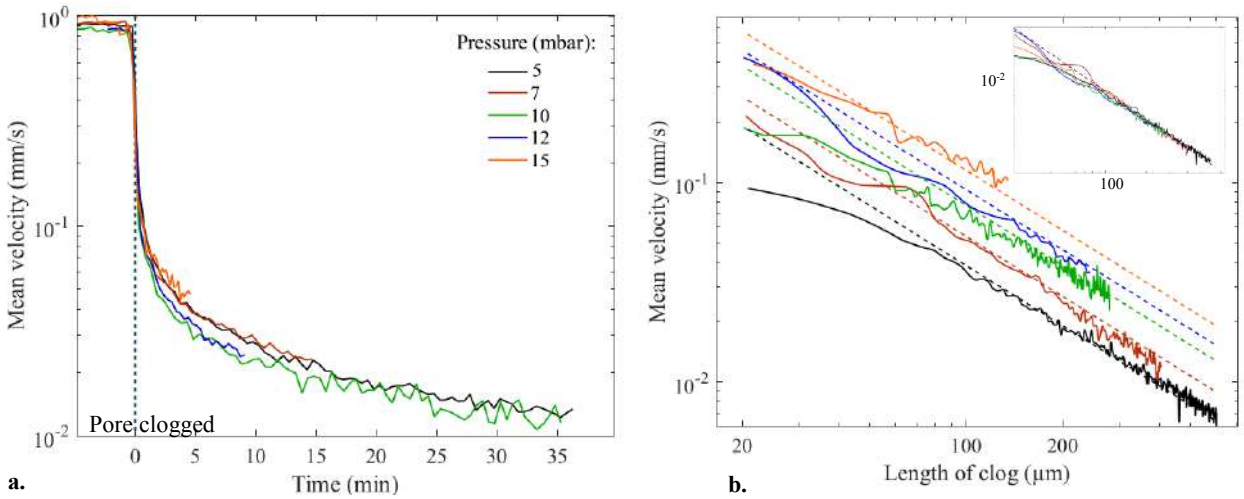

Figure 3: a. Temporal evolution of the average scaled velocity. The time is rescaled such that particle accumulation starts at zero for each applied pressure. b. Hydraulic resistance for a spherical packed bed, for different pressures. The continuous lines correspond to the experimental data while the dotted lines are fit by the Kozeny-Carman equation. Insert: master curve.

CONCLUSION

Coupling image analysis of the forming clog and tracking of flowing particles inside a pore help us to determine the dynamics of the clogging transition and also of the subsequent growth of the clog. We get a good estimate of the volume fraction of the clog which helps us to determine the hydraulic resistance of the clog. We show that this resistance does not change when we form clogs with different applied pressure. This new methodology can be easily implemented in order to study the evolution of hydraulic resistance of interconnected 2D porous media fouled by colloidal particles.

References

[1] Dersoir, B., de S. Vincent, M.R., Abkarian, M. Tabuteau H., *Microfluid Nanofluid* **19,** 953–961 (2015)
[2] Bacchin P**,** Marty A**,** Duru P**,** Meireles M**,** Aimar P**.,** *Adv Colloid Interface Sci*. 11;164(1-2):2-11 (2011)
[3] Wyss HM, Blair DL, Morris JF, Stone HA, Weitz DA, *Phys Rev E* 74(6):061402 (2006)
[4] Sendekie Z.B. Bacchin P., *Langmuir* 32, 6, 1478-14884, (2016)

EXPERIMENTAL INVESTIGATIONS OF CONVECTIVE DISSOLUTION OF CO2 IN 3-D POROUS MEDIA

Christophe Brouzet * [1], Yves Méheust[2], and Patrice Meunier[1]
[1]Aix Marseille Univ, CNRS, Centrale Marseille, IRPHE - Marseille, France
[2]Univ. Rennes, CNRS, Géosciences Rennes - UMR 6118, 35000 Rennes, France

Summary Geological storage of CO_2 in deep saline aquifers is a promising measure to mitigate global warming by removing this greenhouse gas from the atmosphere and trapping it into such subsurface formations. When CO_2 is injected in these porous media, it dissolves in the interstitial brine rendering it denser than the resident brine below, which creates a convective instability. This instability contributes to accelerating CO_2 sequestration but remains poorly understood. In this paper, we demonstrate a combination of experimental techniques which makes it possible to measure for the first time the characteristics of this instability in a 3-D porous medium, using both Refractive Index Matching and Planar Laser Induced Fluorescence. The measured characteristics of the instability will be compared to the theoretical and numerical models available in the literature.

INTRODUCTION

Nowadays, about 32 gigatonnes of carbon dioxide (CO_2) are released annually into the atmosphere due to human activities [1]. As CO_2 is a greenhouse gas, this leads to a global warming of our planet representing a potentially disastrous global problem. One solution to mitigate this issue is to capture and store CO_2 in deep saline aquifers and depleted oil reservoirs, which are typically porous structures filled with brine. Once the CO_2 is injected into such formations, its motion through the reservoir is controlled by fluid mechanics. Being supercritical, it first rises to the top of the reservoir, displacing the brine and positioning itself above it. By dissolving into the brine, CO_2 then densifies it locally which creates a convective instability, thus increasing storage efficiency [2].

This instability is characterised by the Rayleigh and Darcy numbers

$$\mathrm{Ra} = \frac{K\Delta\rho g H}{\mu\phi D} \text{ and } \mathrm{Da} = \frac{K}{H^2}, \tag{1}$$

where K, H and ϕ are the permeability, the height and the porosity of the porous medium, g the gravity acceleration, μ the viscosity of the fluid, and D the diffusion coefficient of CO_2 in water. $\Delta\rho$ is the density difference between the CO_2-laden brine and that devoid of CO_2. Several theoretical and numerical studies have already discussed the typical characteristics of the instability (wavelength, growth rate, and onset time) as a function of the Rayleigh number [3, 4], assuming that Darcy's law is valid in the porous media they consider. Recently, experiments performed in a Hele-Shaw cell mimicking a two-dimensional porous medium have validated the theoretical and numerical results at low Rayleigh numbers [5]. However, to our knowledge, no experimental studies of this instability in a real porous medium have been reported yet. It is the goal of this paper to demonstrate the experimental technique we develop to study convective dissolution in a 3-D porous medium. In particular, the question of whether the description based on Darcy's law is relevant, when the wavelengh of the instability is on the order of the grain size, remains open. By varying the Rayleigh number in our experiments, we can change the wavelength of the instability and see how far the theory based on Darcy's law holds.

EXPERIMENTAL SETUP

The experimental setup consists in a 30 cm large, 1.5 cm thick, 30 cm high, closed and transparent tank. The bottom half is filled with a porous medium and salt water while the top half contains air at atmospheric pressure and a CO_2 sensor. The z-direction points downward and its origin $z = 0$ is set at the interface between the porous medium and the air. At time $t = 0$, part of the air in the top half of the tank is removed and replaced by CO_2, leading to a sudden increase of the CO_2 partial pressure above the porous medium. In this configuration, the density difference $\Delta\rho$ is therefore proportional to that partial pressure. In order to visualise the instability inside the granular medium, we use the combination of two different techniques: Refractive Index Matching to see through the porous medium and Planar Laser Induced Fluorescence to detect the presence of CO_2 in the interstitial fluid.

Refractive Index Matching and porous medium

Refractive Index Matching is known to allow optical access to the bulk of dense suspensions and porous media [6], by matching the optical indices of the fluid and solid phases. Therefore, these two phases have to be carefully chosen. In our experiments, we use FEP (fluorinated ethylene propylene) transparent particules, with an optical index close to water that can be matched with salt water at a density $\rho \approx 1.060$ g/cm^3. These particles have a typical size of 2 to 3 mm, and resemble flatten spheres or oblate spheroids. Their shape is not classical but relatively regular over the different particles. They provide us with a porosity $\phi \approx 40\%$ and a permeability $K \approx 2 \times 10^{-9}$ m^2. The thickness of the tank, about 5 to 7 particles, is small compared to the two other dimensions ensuring that the instability remains two-dimensional but is large enough so that the flow is fully three-dimensional in the bulk of the porous medium.

*Corresponding author. E-mail: christophe.brouzet@univ-amu.fr.

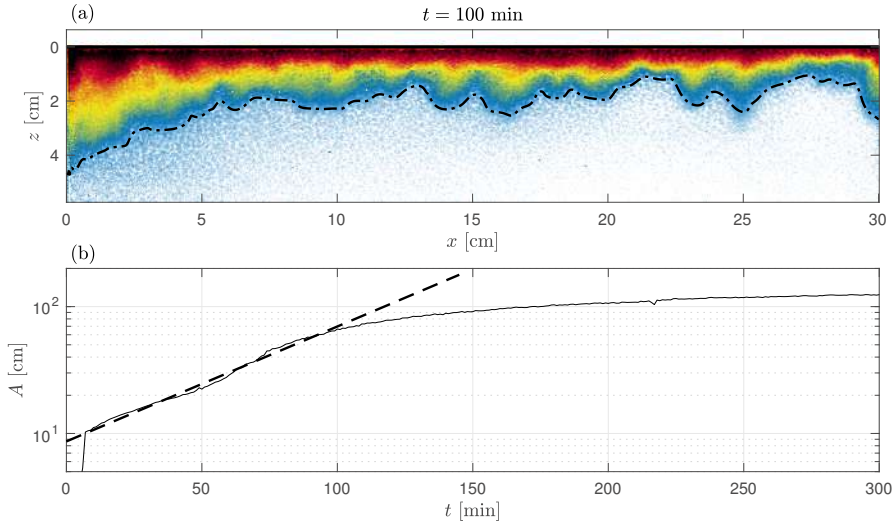

Figure 1: (a) Visualisation of the instability in a granular porous medium using Refractive Index Matching and Planar Laser Induced Fluorescence. The colors correspond qualitatively to different pH, correlated to CO_2 concentrations inside the porous medium. The detected front is shown with a dashed-dotted black line. (b) Lin-log plot of the front corrugation amplitude A as a function of time. The dashed thick line shows the slope from which the growth rate is measured.

Planar Laser Induced Fluorescence and instability characterization

The interstitial fluid, i.e. salt water, contains fluorescein at a given concentration of 10^{-6} mol/l. The tank is illuminated from the top, using a laser sheet obtained with a Powell lens to insure a homogeneous intensity along the sheet. The tank is filmed from its largest side using a camera equipped with a green light filter centred around the fluorescein emission wavelength. As the development of the instability is relatively slow, the frame rate is set to 1 image per minute. The presence of dissolved CO_2 acidifies the interstitial fluid and decreases the pH locally. As fluorescein light emission is pH-dependent [7], the emitted intensity at a position in the tank is correlated to the pH and therefore to the CO_2 concentration at that position. It is therefore possible to observe the instability by normalising the image at time t by the image at time $t = 0$, as shown in Figure 1(a). It allows us to detect the front of the instability $z_F(x, t)$, shown with a dashed-dotted black line in the figure. Using this quantity, one can measure the growth rate, the wavelength and non-linear time of the instability [5]. Indeed, the growth rate is measured by plotting the front corrugation amplitude $A(t)$, defined as the standard deviation of the front $z_F(x, t)$ along x, as a function of time. An example is shown in Figure 1(b), exhibiting a clear exponential growth of the amplitude at the beginning of the experiment. The time where the curve deviates from the exponential growth is defined as the non-linear time and the wavelength can be deduced from a Fourier transform of the front at that time.

ONGOING WORK TOWARDS FULL CHARACTERIZATION OF THE CONVECTIVE DISSOLUTION

We are currently performing experiments to measure the evolution of the characteristics of the instability (namely growth rate, non-linear time and wavelength) as a function of the Rayleigh number. This parameter is mainly changed by varying the CO_2 partial pressure above the porous medium. The experimental results will be compared to the theoretical and numerical results reported previously [3, 4] in order to evaluate over which range of Rayleigh numbers the predictions obtained with models based on Darcy's law remain valid. Moreover, by doing a careful calibration of fluorescein emitted light versus pH, it will be possible to obtain the CO_2 concentration from the images, and therefore the CO_2 flux in the experiments, which is crucial to estimate the characteristic time scale of CO2 storage, in particular towards industrial applications [1]. These investigations are ongoing and the results will be reported at the conference.

References

[1] Huppert H. E., Neufeld J. A. The Fluid Mechanics of Carbon Dioxide Sequestration. *Annu. Rev. Fluid Mech.* **46**: 255-272, 2014.
[2] MacMinn C. W., Szulczewski M. L., Juanes R. CO_2 migration in saline aquifers. Part 2. Capillary and solubility trapping. *J. Fluid Mech.* **688**:321-351, 2011.
[3] Riaz A., Hesse M., Tchelep H. A., Orr F. M. Onset of convection in a gravitationally unstable diffusive boundary layer in porous media. *J. Fluid Mech.* **548**: 87-111, 2006.
[4] Hassanzadeh H., Pooladi-Darvish M., Keith D. W. Scaling Behavior of Convective Mixing, with Application to Geological Storage of CO_2. *AIChE J.* **53**(5), 2007.
[5] Vreme A., Nadal F., Pouligny B., Jeandet P., Liger-Belair G., Meunier P. Gravitational instability due to the dissolution of carbon dioxide in a Hele-Shaw cell. *Phys. Rev. Fluids* **1**(064301), 2016.
[6] Dijksman J. A., Rietz F., Lórincz K. A., van Hecke M., Losert W. Refractive index matched scanning of dense granular materials. *Rev. Sci. Instrum.* **83**(011301), 2012.
[7] Diehl H., Markuszewski R. The fluorescence of fluorescein as a function of pH. *Talanta* **36**(3): 416-418, 1989.

HOMOGENIZATION-INFORMED CONVOLUTIONAL NEURAL NETWORKS FOR QUANTIFICATION OF EFFECTIVE PROPERTIES OF POROUS MEDIA IN ENERGY STORAGE DEVICES

Ross Weber[1], Svyatoslav Korneev * [2], and Ilenia Battiato[1]
[1]Department of Energy Resources Engineering, Stanford University, Stanford, USA
[2]Palo Alto Research Center (PARC), Palo Alto, USA

Summary Lithium-ion battery modeling remains a challenge due to multiple physical phenomena occurring at multiple length and time scales. A multiscale model is derived via homogenization, where effective properties are determined by solving a closure problem on a representative unit cell at the particle scale. The closure problem, however, still requires solving a partial differential equation (PDE) in a 3D space, which is computationally expensive. We develop a Convolutional Neural Network (CNN) to determine effective parameters of porous media from pore-scale images of the microstructure. The CNN is trained from PDE solutions of the closure problem on randomly generated images of porous electrodes that have varying topological properties. Results demonstrate that the CNN is significantly more accurate than the frequently-used porosity-conductivity relation, also known as Bruggeman equation.

INTRODUCTION

Lithium-ion batteries (LIBs) have become the dominant energy storage for consumer electronics due to their extraordinary energy and power density. Upscaling them for electric vehicles and grid storage, however, remains a challenge in part due to the complexity and computational cost of modeling with pore-scale resolution. A major challenge is that microscale information is needed to describe macroscopic responses. The goal of present work is to create a mechanism to incorporate particle-scale physics in a macroscopic model through effective transport parameters while keeping computational costs contained. The baseline macroscale electrochemical model for LIBs is known as the Doyle-Fuller-Newman (DFN) model and has been widely applied to model charge/discharge behavior. The DFN assumes each electrode is composed of equally-sized spherical particles and resolves radial diffusion within these particles, as well as ion diffusion and electromigration across the electrolyte. In this technique, effective parameters Ψ_{eff}, such as diffusion and conductivity, are often obtained from their intrinsic counterparts Ψ by the Bruggeman relation $\Psi_{\text{eff}} = \eta\tau^{-1}\Psi$ with $\tau = \gamma\eta^{-\alpha}$, where τ is tortuosity and η is the electrode porosity. The constants α and γ are fitting parameters that can be determined analytically for idealized geometries or empirically. The Bruggeman equation is useful as it defines crucial dynamic properties as a function of porosity alone, but it has multiple drawbacks. First, it assumes isotropy and thus cannot account for direction-dependent phenomena, which are very pronounced in certain LIB electrodes, especially graphite, the most common anode material. Additionally, electrodes of the same porosity can exhibit very different transport behavior, as the specific morphology and orientation of the particles plays a significant role. As a result, the Bruggeman relation can lead to significant errors in estimating effective parameters.

ELECTROCHEMICAL MODEL AND CLOSURE PROBLEM

The homogenized model describes the macroscopic response of a LIB to input current and temperatures, which informs crucial metrics such as state-of-charge (SOC) and state-of-health (SOH) [1]. The macroscale mass and charge transport equations are obtained by upscaling the pore-scale Possion-Nernst-Planck equations, as described by Arunachalam *et al.* [2]. The electrode of length L is assumed to be composed of periodic unit cells of length ℓ, and a scale separation parameter is defined as $\epsilon = \ell/L \ll 1$. Averaged electrode and electrolyte concentration and potential $(\bar{c}_s, \bar{c}_e, \bar{\phi}_s, \bar{\phi}_e)$ in each cell are resolved by the macroscopic model. Within the unit cell, a closure variable χ is computed to determine effective transport parameters. This process is schematically indicated in Figure 1(Left), where the closure problem and the effective parameters are defined in terms of χ.

CONVOLUTIONAL NEURAL NETWORK

The aim of this work is to train a CNN to estimate the solutions of the closure problem presented in Figure 1(Left), and thus reduce the computational cost of parameter estimation. The input for the network is chosen to be a $60x60$ pixel binary image. To obtain sufficient training data, images were computer-generated to mimic porous electrodes. The image generation algorithm consisted of placing a *random* number of *randomly* shaped circle-like particles in *random* positions throughout an originally empty canvas. Example images generated are shown in Figure 1. The input images are a binary grid with $1s$ (white pixels) representing the electrolyte and $0s$ (black pixels) to denote active particles. $100,000$ images were generated of which $90,000$ were randomly selected as the training set, $5,000$ were used as the development set to tune hyperparameters, and $5,000$ were set aside as the test set to evaluate the performance of the CNN on unseen data.

*Corresponding author. E-mail: ictam2020@aimgroup.eu.

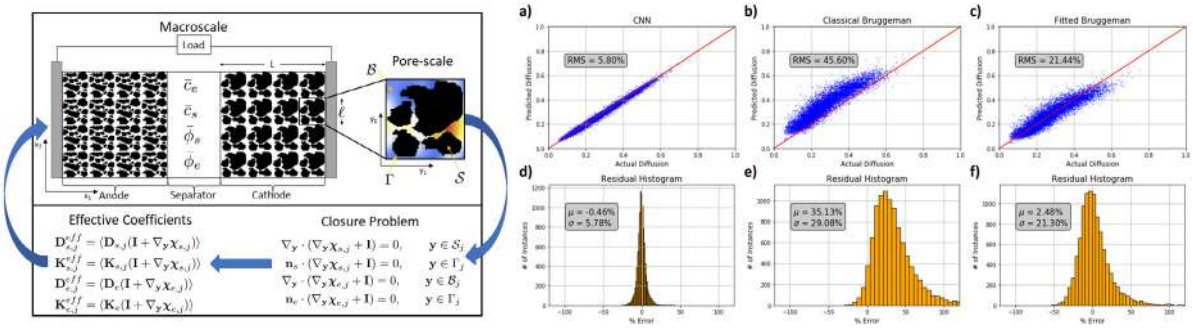

Figure 1: (**Left**) Schematic representation of the homogenization model and closure problem. The resolved χ variables are used to determine the effective dispersion and conductivity tensors from the solution of a closure problem on a pore-scale structure of arbitrary complexity. (**Right**) Top row: predicted dispersion coefficient vs actual for (a) CNN, (b) Classical Bruggeman, and (c) Fitted Bruggeman. Bottom row: histogram of the normalized error for each model. The solution to the closure problem is considered the actual dispersion coefficient because that is what the network was trained on.

Scatter plots showing the fit of the CNN, classical Bruggeman, and fitted Bruggeman model are shown in the top row of Figure 1(Right), where the "true" dispersion coefficients are taken as the closure problem solution because that is how the network was trained. The overall RMS error of the validation set was 6.26%. Using the classical and fitted Bruggeman resulted in RMS errors of 45.60% and 21.44% respectively, so the CNN made more than a $3x$ improvement.

RESULTS AND CONCLUSIONS

A preliminary investigation of the CNN on real images is performed in this section. The two real images considered were an SEM of a Lithium Cobalt Oxide ($LiCoO_2$) cathode from Hutzenlaub *et al.* [3], commonly used in LIBs for portable electronics, and of a Ni-yttria stabilized zirconia (Ni-YSZ) anode from Iwai *et al.* [4], a popular fuel cell anode. Each image is first processed to be consistent with the CNN input requirement by resizing to $60x60$ pixels and binarizing so that solid materials appear black and the electrolyte is white. Each transformed image is then put through the CNN from this work. The original and transformed images for each material are shown in the bottom-left corner of Figure 2a-b, which displays boxplots of the distribution of CNN predictions for each direction and their mean. The reference-provided effective coefficients are shown in green, and the fitted Bruggeman coefficients are shown in red. The classical Bruggeman predictions of 0.196 for $LiCoO_2$ and 0.327 for Ni-YSZ are not shown because they are well above the top of the plot. The results demonstrate that the mean CNN prediction is superior to the Bruggeman models. Furthermore, the shape of the boxplots suggests that the network consistently makes reliable predictions on real images.

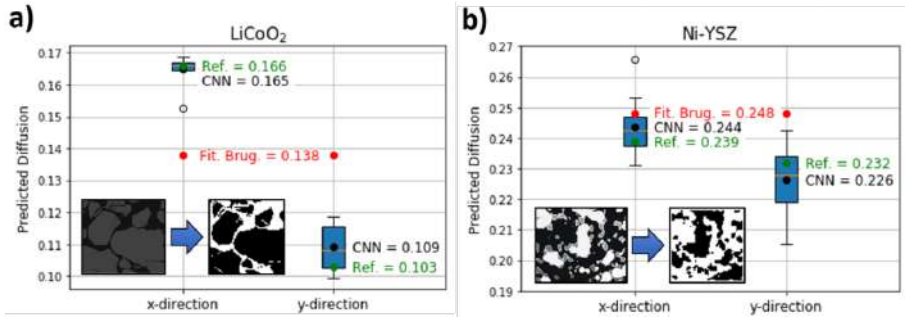

Figure 2: Box plots showing the x and y-components of the CNN-predicted transport tensors from real SEM images of (a) $LiCoO_2$ [3] and (b) Ni-YSZ [4]. The mean prediction is shown in black, the reference-provided coefficient is green, and the fitted Bruggeman output is in red. In the bottom-left of each subfigure, the original and transformed images are shown.

References

[1] H. Arunachalam, "A new multiscale modeling framework for lithium-ion battery dynamics: Theory, experiments, and comparative study with the doyle-fuller-newman model," *PhD Dissertations*, 2017.

[2] H. Arunachalam, S. Onori, and I. Battiato, *J. Electrochem. Soc*, vol. 162, no. 10, pp. A1940–A1951, 2015.

[3] T. Hutzenlaub, A. Asthana, J. Becker, D. Wheeler, R. Zengerle, and S. Thiele, *Electrochemistry Communications*, vol. 27, pp. 77 – 80, 2013.

[4] H. Iwai, N. Shikazono, T. Matsui, H. Teshima, M. Kishimoto, R. Kishida, D. Hayashi, K. Matsuzaki, D. Kanno, M. Saito, H. Muroyama, K. Eguchi, N. Kasagi, and H. Yoshida, *Journal of Power Sources*, vol. 195, no. 4, pp. 955 – 961, 2010.

MODELLING TRANSFER OF MASS MOMENTUM INTO A POROUS MEDIA FROM OVERLYING FLOWS

Ugis Lacis[1] and Shervin Bagheri * [1]
[1]Department of Engineering Mechanics, KTH, Stockholm, Sweden

Summary Today, effective models of single-phase fluid flow inside dense porous materials (such as Darcy's law) are well established. However, much less is known on how to couple such models to a domain where the fluid flows unobstructed. This is despite the importance in many applications of characterising how entrainment, mixing and dispersion inside a porous material depends on the external fluid environment. Here, we present effective coupling conditions between free flows and porous media that takes into account the microstructure of porous material both in the bulk and at the interface. Our model consists of slip velocity, transpiration velocity and pressure jump condition for coupling Navier-Stokes equations to Darcy's law. These conditions are derived from conservation of mass and momentum and linear theory and constitute a subset of high-order boundary conditions that can be derived from a formal asymptotic expansion. Using a number of rather complicated 2D and 3D flow configurations, we will show that our model constitutes a practical approach to model the transfer mass and momentum between free flows and porous media, with no free empirical parameters and direct link to the pore microstructure.

INTRODUCTION

Models of free flows over porous surfaces would be valuable in a range of problems, including predicting the mixing of fresh water with groundwater in hyperheic zone in rivers, estimating the supply of nutrients and bioactive agents to porous scaffolds to stimulate tissue growth and for enhancing removal of water in gas-diffusion layers in fuel cells by imposing external gas flow. In these applications, the microstructure of the porous skeleton plays a central role in determining the entrainment of heat, mass, nutrients, ions, proteins and other particles from the external environment into the porous medium. Therefore, effective models with predictive capabilities need to take into account the microstructure of porous material both in the bulk and at interfaces with their external environment.

The challenge in modelling the interface between an unobstructed unsteady shear flow and a complex anisotropic porous bed is twofold. First, the form of boundary conditions that couple Navier-Stokes equations for the external flow with effective models of porous materials (such as Darcy's or Brinkman equations) is still unclear. Different combinations of velocity and pressure conditions have been suggested, but there has yet emerged a complete set of conditions as a clear winner. Second, given a particular form of coupling conditions, it unclear on how to determine the constitutive parameters appearing in the conditions. Different approaches to determine constitutive parameters of varying complexity have been suggested, but a few of them are practical from an engineering viewpoint.

Similar to bulk porous media, where Darcy's law is unquestioned for creeping single-phase flows and the components of the permeability tensor can be determined either from experiments or from unit-cell computations, we aim to establish a complete set of coupling conditions and an accompanying practical procedure to determine the associated constitutive parameters.

BACKGROUND

Let us provide a familiar example of a set of coupling boundary conditions using a two-dimensional configuration. We denote the streamwise and wall-normal coordinates by x and z and impose the effective boundary conditions at an interface plane at coordinate $z = z_i$. For rigid porous surfaces with a pore size l, one may impose the following effective velocity boundary conditions,

$$u_x = -\frac{K}{\mu}\frac{\partial p^-}{\partial x} + L\frac{\partial u_x}{\partial z}, \qquad u_z = -\frac{K}{\mu}\frac{\partial p^-}{\partial z} \qquad \text{on} \qquad z = z_i. \tag{1}$$

In the above expression, u_x is the tangential velocity component at the interface, u_z is the wall-normal velocity component and p^- is the pore pressure. Moreover, μ is the fluid viscosity, and $K \sim l^2$ is the interior permeability of the porous substrate, $L \sim l$ is the slip length. The first condition in the expression above was suggested by Beaver and Joseph [3]. Here, the slip length is the distance that the relative velocity at the interface has to be linearly extrapolated to reach zero value. The second condition for the penetration velocity imposes a continuity with the interior Darcy flow in the normal direction. An additional boundary condition for pore pressure p^- at the interface is required to solve for the interior Darcy flow. Until relatively recently pressure continuity was imposed $p^- = p$, where p is the pressure of the overlying free fluid. However, current state-of-the-art [4] is a jump in pressure given by

$$p^- - p = -\mu C_\pi \frac{\partial u_x}{\partial z} - 2\mu\frac{\partial u_z}{\partial z}.$$

Here, C_π (which is non-zero only for anisotropic porous surfaces) is a stabilisation parameter derived from matching boundary layer solutions with exterior solutions.

*Corresponding author. E-mail: shervin@mech.kth.se

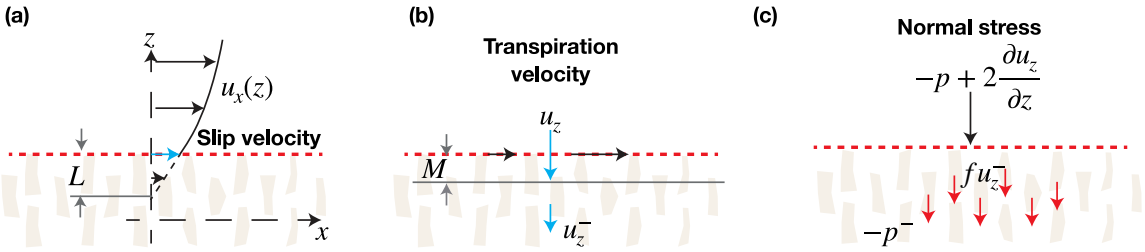

Figure 1: Schematics of the slip length L (a), the transpiration length M (b) and the resistance coefficient f (c).

RESULTS

In this talk, we aim to present a simple physical model for coupling Stokes equations to Darcy's law. The model, called Transpiration-Resistance Model (TRM), can be derived from assuming linearity and scale separation. The TR model captures the transport of interface tangential momentum as well as the transport of mass and interface normal momentum. It consists of the slip boundary condition given in equation (1) for the interface tangential velocity. The penetration velocity is extended with an additional term,

$$u_z = -\frac{K}{\mu}\frac{\partial p^-}{\partial y} - M\frac{\partial u_x}{\partial x} = u_z^- - M\frac{\partial u_x}{\partial x} \qquad \text{on} \qquad z = z_i \tag{2}$$

The new term quantifies how much a surface texture allows exchange of mass with the surrounding fluid due to a streamwise variation of the slip velocity. Geometrically (figure 1b), the transpiration length M is the distance below the interface for which a non-zero transpiration velocity u_z can exist due to fluctuating overlying shear flow. In the TRM, for a porous surface, the pressure condition reads,

$$-p + 2\mu\frac{\partial u_z}{\partial z} = -p^- + fu_z^-.$$

Here, the left-hand side is the normal stress of the outside free flow on the interface plane, and the right-hand side is the normal stress from the porous material. The resistance coefficient f quantifies the friction force that the Darcy seepage velocity generates while passing through the interface.

Figure 1 shows the interpretation of slip length L, transpiration coefficient M and resistance coefficient f. The TRM can be derived from linear theory by assuming; i) creeping flow assumption $Re < 1$; ii) scale separation assumption between system scale (H) and pore scale $\epsilon = l/H \ll 1$ and that iii) the surface is homogeneous i.e. it consists of repeating geometric entities or elements. Under these assumptions, the slip length, the transpiration length and the resistance coefficients are properties of the surface texture only, and can be computed by solving five fundamental Stokes problems. For a given texture, the knowledge of these effective coefficients provides important information on the diffusive/advective transport into the material as well as the ability of the solid skeleton to resist an externally imposed shear stress.

In this talk, we aim to present

- the validation of the suggested TRM by making use of pore-resolved two and three dimensional numerical simulations of shear flows over anisotropic porous media. Examples include a lid-driven cavity and separated backward-facing step with porous/textured surfaces. It will be shown that compared to other existing techniques, the transfer of mass and momentum is improved, allowing for better prediction of transport mechanisms across porous interfaces [1].
- an outline a mathematical derivation of high-order homogenized coupling conditions between Stokes equations and Darcy's law. These conditions, which are derived from asymptotic expansion, constitute a generalization of the TRM model [2].
- provide a simple and practical (numerically cheap) procedure to determine the constitutive parameters appearing in the coupling boundary conditions for TRM given a sample of periodic unit of the porous material.

References

[1] U. Lacis, Y. Sudhakar, S. Pasche, S. Bagheri, "Transfer of mass and momentum at rough and porous surfaces", in J. Fluid Mech. Vol. 884, 2020.
[2] Y. Sudhakar, U. Lacis, S. Pasche, S. Bagheri, "Higher order homogenized boundary conditions for flows over rough and porous surfaces", Submitted to Transp. Porous Media, 2019.
[3] Beavers, G. S., Joseph, D. D. "Boundary conditions at a naturally permeable wall" J. Fluid Mech. 30 (1), 197?207, 1976.
[4] Carraro, T., Goll, C., Marciniak-Czochra, A., Mikelic, A. "Pressure jump interface law for the Stokes?Darcy coupling: confirmation by direct numerical simulations" J. Fluid Mech. 732, 510?536, 2013

STEAM-WATER RELATIVE PERMEABILITY AND THERMAL CONDUCTIVITY IN FRACTAL TREE-LIKE NETWORKS

Pengliang Yu[1] and Rosalind Archer [1]
[1]Department of Engineering Science, University of Auckland, Auckland, New Zealand

Summary This paper derives new expressions for steam-water relative permeability and thermal conductivity in fractal tree-like networks. The work was motivated by the need to enhance these properties in enhanced geothermal systems, where fractures are created in the reservoir rock to enhance its permeability. The derivation combines Darcy's law and the Young-Lapace equation (to handle capillarity) to model two-phase laminar flow in a branching network of cylindrical flow paths. The overall behaviour of the network is considered by equating the flow/thermal performance to a equivalent single flow path. The results are likely to be useful for interpreting tests from enhanced geothermal wells, and for establishing parameters in numerical models of these systems.

INTRODUCTION

Two-phase flow (steam and water) in enhanced geothermal systems occurs in networks on fracture in the rock that this work models as a fractal tree like network. The network can be described as:

$$l_k = l_0\alpha^k = l_m\alpha^{k-m} \tag{1}$$

$$d_k = d_0\beta^k = d_m\beta^{k-m} \tag{2}$$

$$N = \alpha^{-D_l} = \beta^{-D_d} \tag{3}$$

Where l_0 and d_0 are the length and diameter of the 0^{th} branching level, respectively, D_l is the fractal dimension of channel length distribution, and D_d is the fractal dimension for diameter distribution.

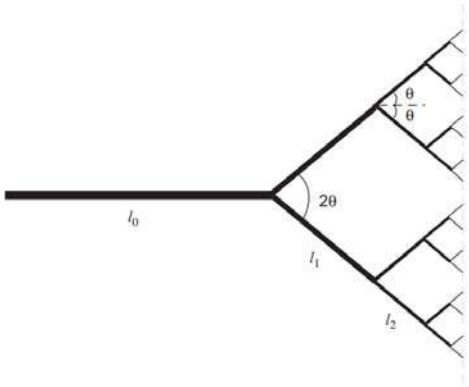

Figure 1. Fractal-like tree network model

The model assumes the flow through each channel is laminar and fully developed, thermally and hydrodynamically. In the case of an interface between steam and water phases (with saturations S_g and S_w) in a channel the Young-Laplace equation is used to model the relationship between the pressures in each phase. The channel is assumed to be water-wet with a connate water saturation (S_{wc}). Relative permeability for each phase compares the flow rate of that phase, to the flow rate which would exist in single phase flow. Flow rates are modelled using Darcy's law, so the length of the flow path is relevant. This work develops expressions for steam and water flow relative permeability in branched tree-like networks by equating the network to an equivalent single flow path (an approach taken by Xu et al. (2006) for hydraulic conductivity). Space constraints mean the full derivation is not presented, however one pivotal part of the derivation is equation (4) which defines the length of the total flow path in the network.

$$L_0 = l_0 + \sum_{k=1}^{m} l_k \cos\theta = l_0\left[1 + \frac{\alpha\left(1-\alpha^m\right)}{1-\alpha}\cos\theta\right] \tag{4}$$

The thermal conductivity of the network is considered using electrical engineering analogues (of resistance in series and parallel).

RESULTS

The effective (i.e. single phase) permeability (K) in the channel of 0th level (which has a diameter d_0) can be expressed by Equation 5.

$$K_{e\_0} = \frac{d_0^2}{32}\left(1 - S_{wc}\right)^2 \tag{5}$$

The relative permeability for water and steam in the network is derived (when taking into account capillary pressure effects, s and viscosity, m) to be:

$$k_{rw}^{+} = \frac{K_w}{K_{e\_0}} = \frac{S_w\left(S_w - S_{wc}\right)^2}{\left(1 - S_{wc}\right)^2}\left[\frac{1-\alpha}{1-\alpha^{m+1}}\frac{1-\alpha/N\beta^4}{1-\left(\alpha/N\beta^4\right)^{m+1}}\right]^{1/2}\left[1 + \frac{\alpha\left(1-\alpha^m\right)}{1-\alpha}\cos\theta\right] \tag{6}$$

$$k_{rg}^{+} = \frac{\sigma_1}{2\sigma_2 - \sigma_1}\left[\frac{\mu_w\left(1-S_w\right)^3 + 2\mu_g\left(1-S_w\right)^2\left(S_w - S_{wc}\right)}{\mu_w\left(1-S_{wc}\right)^2}\right]\left[\frac{1-\alpha}{1-\alpha^{m+1}}\frac{1-\alpha/N\beta^4}{1-\left(\alpha/N\beta^4\right)^{m+1}}\right]^{1/2}\left[1 + \frac{\alpha\left(1-\alpha^m\right)}{1-\alpha}\cos\theta\right] \tag{7}$$

The effective (e) thermal conductivity (k) of the network can be also be derived to be:

$$k_e = \left(k_w S_w + k_g S_g\right)\left(\frac{1 - N^{-(m+1)/D_l}}{1 - N^{-1/D_l}}\right)^2 \frac{1 - N^{1-\frac{2}{D_d}-\frac{1}{D_l}}}{1 - N^{(m+1)\left(1-\frac{2}{D_d}-\frac{1}{D_l}\right)}} \frac{1 - N^{\frac{2}{D_d}-\frac{1}{D_l}-1}}{1 - N^{(m+1)\left(\frac{2}{D_d}-\frac{1}{D_l}-1\right)}} \tag{8}$$

CONCLUSIONS

These results give fundamental insight into the flow and thermal behaviour of fractured porous media. The derivations were done with a view to using these results in an inverse modelling sense, i.e. in the interpretation of the response (pressure, temperature, flowrate) of wells in enhanced geothermal systems to infer the nature of the fracture networks in the reservoir. The results are also useful in establishing parameter values for numerical models of these systems which often use effective values to represent more complex porous medium properties.

References

[1] Xu, P., Yu, B., Feng, Y. and Liu, Y. Analysis of permeability for the fractal-like tree network by parallel and series models. *Physica A: Statistical Mechanics and its Applications*, ***369***, *2, 884 – 894, 2006.*

FINITE ANALYTIC METHOD FOR SINGLE AND MULTI-PHASE FLOWS IN HETEROGENEOUS POROUS MEDIA

Xiao-Hong Wang* and Zhi-Feng Liu
Department of Thermal Science and Energy Engineering, University of Science and Technology of China, Hefei, Anhui 230026, P.R. China

Summary It is a challenge and long-standing problem to numerically describe fluid flows in porous media with permeability variations. With the traditional numerical scheme, the refinement ratio for the grid cell needs to be increasing dramatically to get an accurate result. We find out that this difficulty is caused by the singularities the problems. The finite analytic numerical scheme is proposed to solve the single-phase and multi-phase fluid flows in heterogeneous porous media to avoid the difficulty of the singularities.

Natural reservoirs exhibit wide permeability variations. In this case, the nodal flow effects will lead the flow fingering to the high permeability region (see figure 1). It is a challenge problem to numerically describe the nodal fingering effects. With the traditional numerical scheme, refining the coarse grid enough is the only manner to describe the flow pattern accurately.

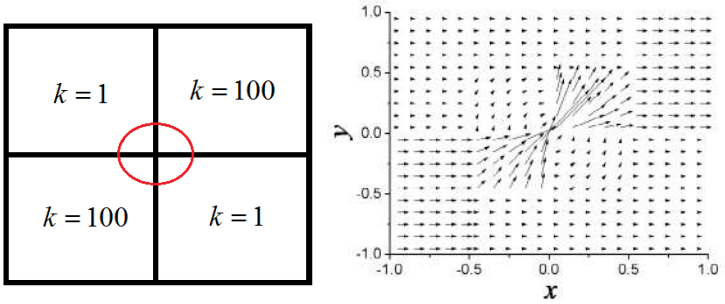

Figure 1. Velocity vector field on the 2×2 checkerboard for permeability ratio k_2/k_1=100.

For 2D problem with the heterogeneous scalar permeability distribution, enlightened from the numerical calculations on the flow pattern in the canonical 2×2 block with checkerboard geometry, which show that the pressure and its spatial gradient exhibit the power-law behaviors and especially the pressure gradient will tend to infinity when approaching the node joining different permeability domains, a local analytical nodal solution is derived. Based upon the analytical nodal solution, a finite analytic scheme is formulated for solving the fluid flows in 2D heterogeneous porous media. Numerical examples show that the detailed flow pattern can be reconstructed with the proposed numerical scheme under few grid refinements. Especially, only with 2×2 or 3×3 subdivisions, the proposed numerical scheme can provide rather accurate solutions. The convergent speed of the numerical scheme is independent of the permeability heterogeneity (see figure 2). In contrast, when using he traditional numerical schemes to simulate flow through a strong heterogeneous porous medium, the refinement ratio for the grid cell needs to be increasing dramatically to get an accurate result [1,2].

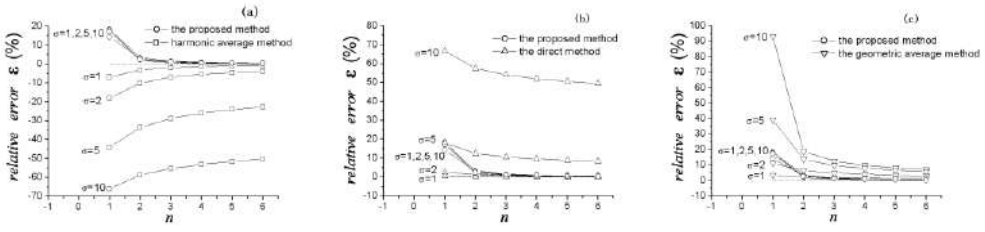

Figure 2. Plot of the relative errors of the equivalent permeabilities as a function of the grid refinement parameter n, calculated from different numerical schemes.

For 3D problem with the heterogeneous scalar permeability distribution, it is pointed out that the 3D flow will reduce to the 2D one in the neighborhood around each edge. Based upon the quasi-2D hypothesis, the 3D finite analytical numerical scheme can be constructed. Only with 2×2×2 or 3×3×3 subdivisions, the proposed numerical scheme can provide rather accurate solutions. The convergent speed of the numerical scheme is independent of the permeability heterogeneity (see figure.3). In contrast, when using the traditional numerical schemes to simulate flow through a strong heterogeneous porous medium, the refinement ratio for the grid cell needs to be increasing dramatically to get an accurate result [3].

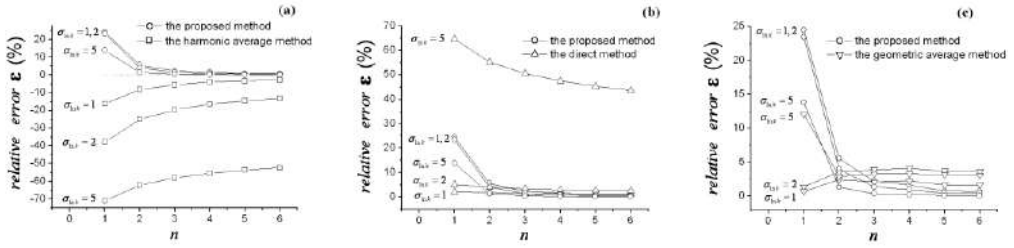

Figure 3. Plot of the relative errors of the equivalent permeabilities as a function of the grid refinement parameter n, calculated from different numerical schemes.

The finite analytic method is also developed to solve the 2D and 3D fluid flow in heterogeneous porous media with permeability in tensor form [4,5]. For the unstructured grids, a finite analytic scheme is constructed based upon the power-law analytic nodal solution in the angular domain with arbitrary shape. When approaching the grid node joining the subdomains, three different flow patterns may exist: power-law flow, linear flow or the stagnant flow. Numerical examples show that the proposed numerical scheme makes the convergences much quickly than the traditional methods [6].

For multi-phase flow in porous media, we construct a finite analytic numerical scheme [7]. Numerical examples show that the proposed scheme makes the convergences much faster as the refinement parameter increases, and the accuracy is independent of the heterogeneity. In contrast, when using the traditional numerical schemes to simulate flow through a strong heterogeneous porous medium, the refinement ratio for the grid cell needs to increase dramatically to get an accurate result (See figure. 4).

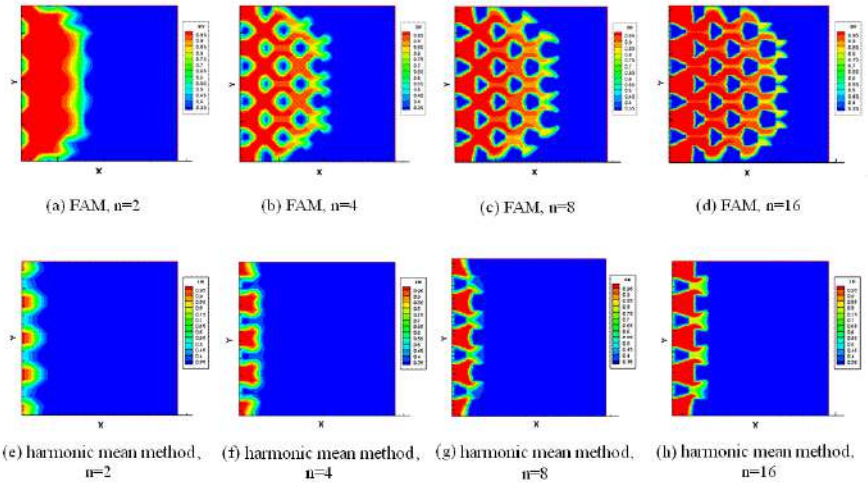

Figure 4. The saturation field calculated from the FAM and traditional IMPES under different grid refinement parameter n.

References

[1] Liu Z.-F. and Wang X. -H.: Finite Analytic Numerical Method for Two-dimensional Fluid Flow in Heterogeneous Porous Media. *Journal of Computational Physics* **235**: 286-301, 2013.

[2] Qu Z. -X., Liu Z. -F. and Wang X. -H.: Finite Analytic Numerical Method for Solving Two-Dimensional Quasi-Laplace Equation. *Numerical Methods for Partial Differential Equations* **30**: 1755-1769, 2015.

[3] Wang Y. -F., Liu Z. -F. and Wang X. -H.: Finite Analytic Numerical Method for Three-Dimensional Fluid Flow in Heterogeneous Porous Media. *Journal of Computational Physics* **278**; 169-181, 2014.

[4] Liu Z. -F. Liu Z. -F. and Wang X.-H.: Finite Analytic Method for 2D Fluid Flow in Porous Media with Permeability in Tensor Form. *Journal of Porous media* **19**: 539–555, 2016.

[5] Wang M, Wang Y. -F., Liu Z. –F, Wang X. –H, Wang Y. and Cao W. –D.: Finite Analytic Numerical Method for Three-Dimensional Quasi-Laplace Equation with Conductivity in Tensor Form. *Numerical Methods for Partial Differential Equations* **33**:1475-1492, 2017.

[6] Wang G. -W., Liu Z. -F. and Wang X.-H.: Finite Analytic Method for 2D Steady Fluid Flows in Heterogeneous Porous Media with Unstructured Grids, *International Journal for Numerical Methods in Engineering* **113**:742-766, 2018

[7] Zheng X. -H, Liu Z. -F, Wang X. -H and Shi A. –F: Calculating the Internodal Transmissibilities Using Finite Analytic Method and Its Application for Multi-Phase Flow in Heterogeneous Porous Media, *International Journal for Numerical and Analytical Methods in Geomechanics* **41**: 79–92, 2017.

MISCIBLE RADIAL VISCOUS FINGERING WITH FINITENESS

Vandita Sharma* [1], Yuichiro Nagatsu[2], and Manoranjan Mishra[1]
[1]Department of Mathematics, Indian Institute of Technology Ropar, Punjab, India
[2]Department of Chemical Engineering, Tokyo University of Agriculture and Technology, Tokyo, Japan

Summary Finiteness in the porous medium flows may result from the oil trapped in the porous reservoirs after oil recovery or in the contaminant transport in aquifers. We focus on numerically understanding the effect of finiteness on the miscible viscous fingering. We consider the more viscous fluid occupying a fixed area and surrounded by the less viscous fluid. Further injection of the less viscous fluid results in a finite layer of the more viscous fluid, whose affect on the VF dynamics is explored. Depending upon the initial area, different fingering dynamics are reported. It is observed that there exists a critical area occupied by more viscous fluid for the fingering to occur. The numerical results are in good agreement with the existing experiments.

INTRODUCTION

Viscous fingering (VF) is a hydrodynamic instability ubiquitous in various porous media flows like enhanced oil recovery, CO_2 sequestration, contaminant transport in aquifers, to name a few [1]. The mobility gradient during the displacement of a more viscous fluid by a less viscous one results in finger like patterns, termed as VF. The displacement is broadly classified as rectilinear and radial displacement depending upon whether one fluid displaces the other linearly or radially and we term the VF in the corresponding geometry as rectilinear VF or radial VF. The rectilinear displacement is characterised by a uniform flow velocity while a non-uniform, spatially varying velocity is observed in the radial displacement. Consequently the VF dynamics are known to be affected by the kind of displacement [2]. In this work, we focus on the radial VF when more viscous fluid exists in finiteness between the layers of the less viscous fluid as commonly observed during enhanced oil recovery. We mathematically model the flow problem using COMSOL Multiphysics® [3] to examine the effect of finiteness of the more viscous fluid on VF dynamics. The finite element based COMSOL Multiphysics® helps to model the radial source flow by considering a disconnected domain to include the hole used for injection of the fluids as utilised in the VF experiments using Hele-Shaw cell [4, 5].

MATHEMATICAL MODELLING

We use the *two phase Darcy law (tpdl)* module of COMSOL Multiphysics® to model the flow of miscible, non-reactive, incompressible, Newtonian fluids through a two dimensional porous medium. The governing equations in the *tpdl* module are

$$\frac{\partial \epsilon_p \rho}{\partial t} + \vec{\nabla} \cdot (\rho \vec{u}) = 0, \tag{1}$$

$$\vec{u} = -\frac{\kappa}{\mu} \vec{\nabla} p, \tag{2}$$

$$\rho = \rho_1 s_1 + \rho_2 s_2, \tag{3}$$

$$\frac{1}{\mu} = s_1 \frac{\kappa_{r_1}}{\mu_1} + s_2 \frac{\kappa_{r_2}}{\mu_2}, \tag{4}$$

$$s_1 + s_2 = 1, \tag{5}$$

$$\frac{\partial \epsilon_p c_1}{\partial t} + \vec{\nabla} \cdot c_1 \vec{u} = \vec{\nabla} \cdot (D_c \vec{\nabla} c_1), c_1 = s_1 \rho_1, \tag{6}$$

where ϵ_p, κ are the porosity and the permeability of the porous medium. s_i, ρ_i and $\mu_i, i = 1, 2$ are respectively the saturation, density and viscosity of the two fluids ($i = 1$ denotes more viscous fluid and $i = 2$ denotes less viscous fluid). Equation (1) is the equation for the conservation of mass which reduces to the continuity equation for incompressible fluids for a constant ϵ_p and ρ. The conservation of momentum for flow through porous medium is given by the Darcy's law (equation (2)), where $\vec{u}$ is the Darcy velocity and p is the fluid pressure. The viscosity is specified as $\mu_1 = \mu_2 = \mu_{ref} \exp(R s_1)$, where $R = \ln(\mu_1/\mu_2)$ is a non-dimensonal parameter dealing with the viscosity contrast between the fluids and $\mu_{ref} = 1$ mPas. Further, the equation (6) is associated with the following initial condition in order to incorporate the effect of finiteness

$$s_1(x, y, t = 0) = \begin{cases} 1, & 0 < x^2 + y^2 \leq r_1^2 \\ 0, & \text{Otherwise} \end{cases} \tag{7}$$

Here r_1 is the radius of the circle occupied by more viscous fluid. The less viscous fluid is injected from the source using the inlet condition with an injection velocity U_0. Thus there exist three layers of fluids; first of the continuously injected less viscous followed by the finite layer of more viscous fluid which is further surrounded by the less viscous fluid as shown in figure 1. The width of the middle layer is modified by varying r_1 and various values of r_1 result in the different area occupied by the more viscous fluid.
A customised free traingular mesh of fluid dynamics is used for all the simulations.

*Corresponding author. E-mail: vandita.sharma@iitrpr.ac.in

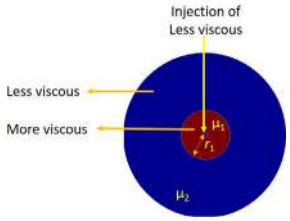

Figure 1: Schematic of the flow problem with an injection hole in the centre, showing the more viscous fluid surrounded by less viscous fluid. Injection of less viscous fluid results in finiteness of the more viscous fluid.

RESULTS AND DISCUSSION

The finiteness results in two interfaces, an *inward* interface where injected less viscous fluid displaces the more viscous fluid and an *outward* interface initially at a distance r_1 from the source, where more viscous fluid displaces the less viscous one. We show the density plots of saturation in figure 2 for different area occupied by more viscous fluid denoted by r_1. Depending upon the area occupied by the more viscous fluid, the two interfaces interact affecting VF dynamics. For a smaller area, the two interfaces are close enough for the diffusion to smear out concentration and hence viscosity gradient. Thus the unfavourable viscosity gradient at the *inward* interface may not be sufficient to trigger instability for smaller r_1. We perform a series of numerical simulations and observe that there exists a critical area occupied by more viscous fluid for the fingering to occur, which depends on R and U_0. The effect of finiteness is evident in figure 2 (a), b)) in which the *inward* interface is stable for $r_1 = 5$ mm while unstable for $r_1 = 30$ mm at $t = 180$ s for $R = 1, U_0 = 1.5$ mm/s. These results are consistent with the experimental results [5]. Further, if we increase R, intrinsic VF patterns are observed independent of the finiteness up to the time when the two interfaces are far apart (see figure 2c)). Once the two interfaces come in contact, the *outward* interface acts as a barrier preventing the fingers from growing further as evident in figure 2d).

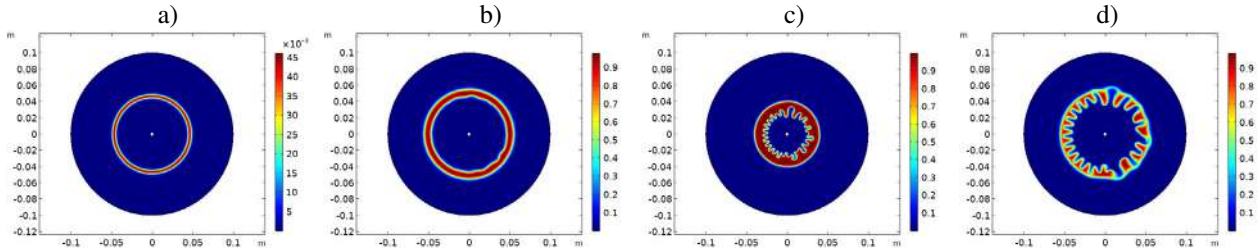

Figure 2: Density plots of saturation for a) $R = 1, U_0 = 1.5$ mm/s at $t = 180$ s for a) $r_1 = 5$ mm, b) $r_1 = 30$ mm, $R = 2, U_0 = 1.5$ mm/s, $r_1 = 30$ mm at c) $t = 60$ s, d) $t = 180$ s.

CONCLUSIONS

Finite element based COMSOL Multiphysics® is used to numerically capture the effect of finiteness under the similar experimental conditions utilised by Hamirul [5]. It is observed that the finiteness can result in a stable displacement despite an unfavourable viscosity gradient. In fact depending upon R, U_0, there exists a critical area for the fingering to occur, which is in agreement with the experiments. The effect of R is explored and it is found that the *outward* interface hinders growth of fingers resulting in the backward fingers.

Acknowledgement MM acknowledges the financial support from SERB, Government of India through project grant number MTR/2017/000283.

References

[1] Mishra, M., Martin, M., De Wit, A. Differences in miscible viscous fingering of finite width slices with positive or negative log-mobility ratio. *Phys. Rev. E* **78**: 066306, 2008.

[2] Sharma, V., Pramanik, S., Chen, C.-Y., Mishra, M. A numerical study on reaction-induced radial fingering instability. *J. Fluid Mech.*, **862**: 624-638, 2019.

[3] COMSOL Multiphysics® v. 5. 4. **www.comsol.com**. COMSOL AB, Stockholm, Sweden.

[4] Nagatsu, Y., Othman, H. B., Mishra, M., An experimental study of miscible viscous fingering of annular ring, *70th Annual Meeting of the APS Division of Fluid Dynamics*, **62**, 14, November 1921, 2017; Denver, Colorado, USA. *J. Fluid Mech.* **571**: 475-493, 2007.

[5] Hamirul Bin Othman, Radial viscous fingering of finite miscible ring: An experimental study, *Bachelor Thesis*, Tokyo University of Agriculture and Technology (2016).

OPTIMAL WETTABILITY DURING WATERFLOODING: DEPENDENCE ON STRUCTURAL FACTORS

Fanli Liu[1], Moran Wang *[1]
[1]Department of Engineering Mechanics, Tsinghua University, Beijing, China

Summary Oil recovery by waterflooding is known to heavily rely on the wetting condition of the reservoir. However, the common belief in low salinity waterflooding studies that a more water-wet condition is better seems to be in contradiction with many coreflooding experiments, where the maximum in oil recovery was found at near-neutral wettability.
This work offers an insight that the optimal wettability can be dependent on the structure of porous media. Theoretical derivations are done for simple geometries to show that modifying the structure can shift the optimal wettability. The rules are then applied in porous media and numerical simulations are carried out to validate the theoretical prediction. Finally, the dependence of the optimal wettability on several structural factors is studied and summarized and certain parameters are proposed to describe the relation.

INTRODUCTION

Waterflooding is a vastly applied oil recovery technique, during which water is injected from the injection well to displace oil inside porous rock towards the production well. The wetting condition of the reservoir is known to have a big impact on the displacing process and thus on the oil recovery by waterflooding. Moreover, wettability alteration has been recognized as the major mechanism of low salinity waterflooding or modified salinity waterflooding, a promising enhanced oil recovery technique where the ionic compositions are modified in the injected brine compared with traditional waterflooding. It is generally believed that, during low salinity waterflooding, altering the rock to a more water-wet condition leads to higher oil recovery.

However, there has been contradictory findings in terms of the optimal wettability for oil recovery. Jadhunandan and Morrow conducted more than 50 coreflooding experiments and found that the maximum in oil recovery occurred at close-to-neutral wettability, not strongly water-wet as many believed. They proposed that this was due to the snap-off mechanism which tended to happen in strongly water-wet condition and led to more trapped oil. A few follow-up experiments observed the same trend that weakly water-wet or neutrally wet was best for oil recovery. Simulation studies, on the other hand, has obtained various results where the optimal wettability could be strongly water-wet, neutrally wet or even oil-wet. So far there has been a lack of explanation for such contradictions.

This work offers a new insight in terms of what wetting condition is better for oil recovery by proposing that the optimal wettability can be dependent on the structure of the porous media. First, it is theoretically derived that for simple structures, how the change in structure can lead to the change in the optimal wettability and general rules are obtained. Then the rules are applied in porous media to predict the optimal wettability and two-dimensional simulations of waterflooding are conducted to validate the predictions. Finally, discussions are made on the impact of structural factors and how it can shed light on studies and applications of waterflooding.

THEORETICAL DERIVATION

In this section, it is theoretically derived that for some simple geometries weakly water-wet condition leads to the best oil recovery instead of strongly water-wet one. In addition, a minor change in the structure can reverse the trend and make strongly water-wet the best, indicating how the optimal wettability can be dependent on the structure. Some general rules are obtained in the derivation.

The derivation is done in the following manner. Consider a waterflooding process in the structure where the inlet boundary provides constant flux and the outlet boundary keeps constant pressure. The flow resistance in all possible flow paths from the inlet to the outlet is each calculated and the progress of flow is predicted as it should favour the path with the lowest resistance. Note that the resistance consists of the viscous term, the capillary term and the structural term due to the momentum loss where there is a sudden change of structure. As the flow advances, the configuration changes and the flow resistance is updated, which in term determines the flow path in the next step. By repeating such analysis, the overall flow path and thus oil recovery are obtained.

SIMULATION RESULTS

The rules obtained in the previous section on simple geometries can be extended to porous media. In this section, two-dimension numerical simulations of waterflooding are conducted to study the impact of structural factors on the optimal wettability and to validate the prediction by theory. The color-gradient two-phase lattice Boltzmann model is adopted. The porous media are first reconstructed from micro-CT images of sandstone, then modified in different manners in order to achieve different optimal wettability based on the theory.

Results show that the rules from simple geometries still apply for porous media to some extent. By modifying the porous structure, the optimal wettability can shift from strongly water-wet to weakly water-wet, as illustrated in Figure 1.

*Corresponding author. E-mail: mrwang@tsinghua.edu.cn.

DISCUSSION

In this section, the impact of structural factors on the optimal wettability is discussed based on the theoretical derivation and simulation results, with certain parameters proposed to describe such impact. It is also discussed how the findings can explain some contradictions in the previous studies.

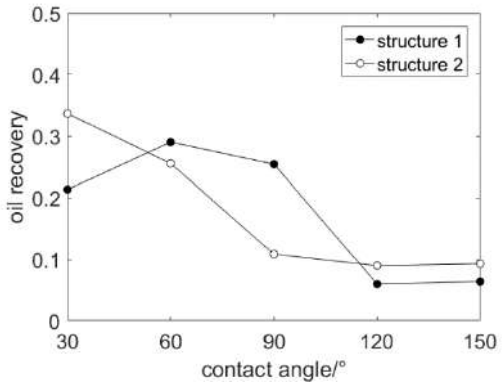

Figure 1. Oil recovery by waterflooding in different wetting conditions. Structure 1 and 2 are modified from the same micro-CT image of sandstone in different manners.

CONCLUSIONS

This work studies the dependence of the optimal wettability on structure factors by theoretical analyses and numerical simulation. It is found that weakly water-wet can be the optimal wettability instead of the commonly believed strongly water-wet, but changes in the structure can shift the optimal wettability towards more water-wet conditions. Certain parameters are proposed to describe the dependence and it is discussed how the findings can help further waterflooding studies.

References

[1] Jadhunandan, P. P., & Morrow, N. R. Effect of wettability on waterflood recovery for crude-oil/brine/rock systems. *SPE reservoir engineering*. **10**(01): 40-46, 1995.

[2] Sheng, J. J. Critical review of low-salinity waterflooding. *Journal of Petroleum Science and Engineering*. **120**: 216-224, 2014.

[3] Tian, H., & Wang, M. Electrokinetic mechanism of wettability alternation at oil-water-rock interface. *Surface Science Reports*. **72**(6), 369-391, 2017.

NUMERICAL SIMULATION OF THERMO-HYDRO-MECHANICAL EFFECTS OF STEAM INJECTION IN POROUS MEDIA

Anastasiia Kostina *, Maxim Zhelnin and Oleg Plekhov
Laboratory of Solid Thermomechanics, Institute of Continuous Media Mechanics of the Ural Branch of Russian Academy of Science, Perm, Russia

Summary The work is devoted to the development and computer implementation of a coupled three-dimensional mathematical model of steam-assisted gravity drainage. The model describes filtration of the three-phase fluid in porous media, convective heat transfer, evaporation of water and steam condensation, effect of pore pressure on stress-strain state of a reservoir and porosity evolution. The developed model takes into account specific data on location and number of wells, structural features of oil reservoirs as well as all stages of steam chamber initiation and evolution. The obtained results are in a good agreement with the experimental data of Yarega oil field.

INTRODUCTION

Steam-assisted gravity drainage (SAGD) is one of the most effective ways to enhance heavy oil recovery. The aim of this method is to decrease oil viscosity by injection of hot steam into reservoir. Temperature rise reduces oil viscosity and increases oil mobility. Application of this technique is accompanied by complex interaction between thermal, mechanical and hydrodynamic processes occurring in a fluid-saturated media. As a result, permeability and porosity of the reservoir undergo substantial changes which have significant effect on oil recovery.

The aim of this work is to develop three-dimensional mathematical model of SAGD and propose algorithm for its computer realization. The model describes following effects: change in thermophysical and hydrodynamic properties of multiphase flow; convective heat transfer; phase change due to condensation and evaporation of water; effect of pore pressure on stress-strain state of the reservoir; thermal expansion of solid grains; evolution of porosity due to the volumetric strains and pore pressure.

MATHEMATICAL MODEL

The developed mathematical model is based on the assumption that pore fluid consists of three immiscible components (water, steam and oil) [1]. The mathematical formulation includes mass balance equations for water, oil and steam saturations. Filtration of each component is described Darcy's law. The energy balance equation incorporates convective heat transfer term and additional source term [2] describing phase change process. The mechanical part of the model includes momentum balance equation, geometric relation and Hook's law for effective stresses. Evolution of the porosity due to the thermal and mechanical loading of the reservoir is determined according to the model proposed in [3].

RESULTS OF NUMERICAL SIMULATION

Numerical algorithm was based on the pressure-saturation formulation using total flow velocity [4]. Spurious oscillations caused by convection were stabilized by artificial diffusion. The obtained system of equations was solved in finite-element software Comsol Multiphysics® using Weak Form PDE Interface, Heat Transfer and Structural Mechanics modules.

Analysis of porosity models has shown that there are three qualitatively different pictures of porosity distribution near the wells (Fig.1). If the pore pressure is a prevailing mechanism of porosity evolution (Fig 1 (a)) then the high-porous area and low-porous area are formed. Influence of the thermal expansion leads to the increase in porosity (Fig. 1 (b)). If the prevailing mechanism is compression of the reservoir due to the steam injection (Fig.1 (c)) then the "ring-shaped" low-porous area corresponding to the thermal front is formed. The obtained results have shown that accurate description of steam chamber shape and sizes and, as a consequence, of oil production rate in arbitrary reservoir requires identification of the prevailing mechanism of porosity evolution.

The developed model was applied to simulation of oil recovery by SAGD in Yarega oil deposit (Russian crude oil deposit in Komi Republic). This type of reservoir is characterized by porosity rise of 1%-3%. Therefore, the porosity equation in the proposed model combines two mechanisms of porosity increase (pore pressure and thermal expansion). Figure 2 shows results of the steam chamber formation in Yarega oil deposit using the proposed model. Homogeneous initial porosity (Fig. 2 (a)) gives the shape of the steam chamber close to the inverted triangle which is similar to the assumptions made in analytical models [5]. Heterogeneous initial distributions (Fig. 2 (b)-(c)) lead to the qualitatively different steam chamber shapes. Initial porosity with the predominant spatial orientation (Fig. 2 (c)) shows the difference in merging time of the neighboring wells. These results are confirmed by experimental studies of the steam chamber evolution in the reservoir which has different permeability in horizontal direction [6].

*Corresponding author. E-mail: kostina@icmm.ru.

Verification of the proposed model is based on the thermal monitoring data obtained by the observation well which is located on the distance of 134 m from the utmost pair of wells. Comparison between the calculated and experimentally measured temperature in the depth interval from 194 to 204 m has shown that the proposed model can predict the temperature with an accuracy of 0.5^0C.

The work was supported by Russian Science Foundation [grant No. 19-77-30008].

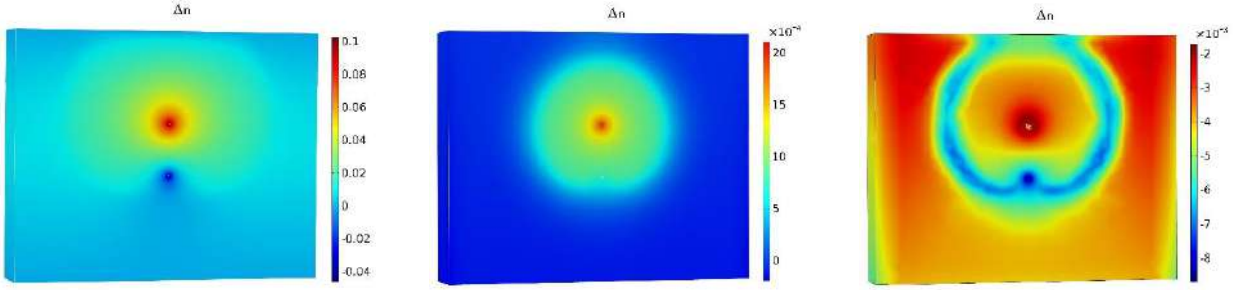

(a) (b) (c)

Figure 1. Effect of pore pressure (a), temperature expansion (b), reservoir compression (c) on porosity evolution.

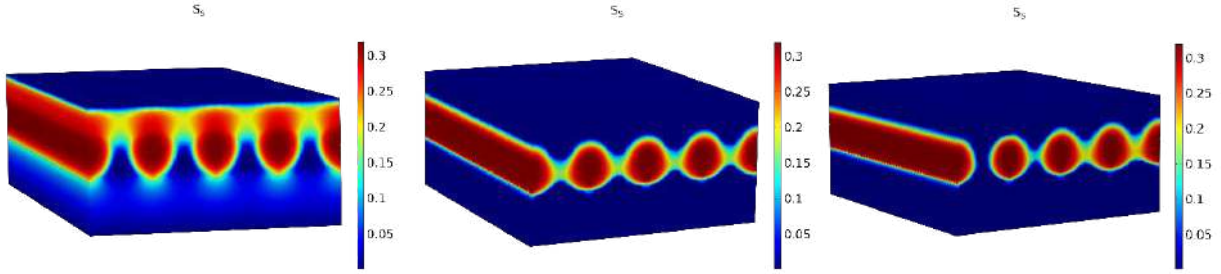

(a) (b) (c)

Figure 2. Steam chamber after 20 days of steam injection: homogeneous initial porosity (a), initial porosity with random distribution (b), initial porosity with the given predominant distribution (c).

CONCLUSIONS

The work is devoted to three-dimensional numerical simulation of fully coupled thermo-hydro-mechanical processes occurring in porous media during oil recovery by steam-assisted gravity drainage method. The developed model takes into account specific data on location and number of wells, structural features of oil reservoirs as well as all stages of steam chamber initiation and evolution. Verification of the model has shown good agreement with the field thermometry data of Yarega oil deposit.

References

[1] Lin B., Chen S., Jin Y. Evaluation of reservoir deformation induced by water injection in SAGD wells considering formation anisotropy, heterogeneity and thermal effect. *J. Petrol. Sci. Eng*. **157**: 767-779, 2017.

[2] Lee H., Kharangte C.R., Mascarenhas N. Experimental and computational investigation of vertical downflow condensation. *Int. J. Heat Mass Transfer*. **85**: 865-879, 2015.

[3] Wang Y., Lu B. A coupled reservoir-geomechanics model and applications to wellbore stability and sand prediction. *SPE International Thermal Operations and Heavy Oil Symposium,* Porlamar, 2001, SPE-69718-MS.

[4] Chen Z., Ewing R.E. Comparison of various formulations of three-phase flow in porous media. *J. Comput. Phys*. **132**: 362-373, 1997.

[5] Butler R.M., McNab G.S., Lo H.Y. Theoretical studies on the gravity drainage of heavy oil during in-situ steam heating. *Can. J. Chem. Eng*. **59**: 455-460, 1981.

[6] Liu H., Cheng L., Huang S., Jia P., Chen M. Evolution characteristics of SAGD steam chamber and its impacts on heavy oil production and heat consumption. *Int. J. Heat Mass Trans*. **121**: 579-596, 2018.

SLOSHING IN HIGHLY PERMEABLE POROUS MEDIA

Xiaoning Di*[1], Yohan Davit[1], Michel Quintard[1]
[1]Institut de Mécanique des Fluides de Toulouse (IMFT), Université de Toulouse, CNRS, Toulouse, France

Summary Sloshing in highly permeable porous media is an interesting research topic that has received little attention in the literature. Here, we use the numerical models based on the Volume of Fluid method to investigate sloshing dynamics in highly permeable porous structures. At first, sloshing is studied at pore-scale for a two-dimensional tank with several fixed particles, the size of which is typical of highly permeable porous media. Then, we develop a macro-scale model based on the VOF method, corresponding to a thin saturation front. The model effective properties are calculated for a Unit-Cell representative of the medium. A comparison between the pore-scale and the macro-scale results shows that the macro-scale model accurately predicts the transient location of the sloshing surface. Results also emphasize that inertia correction may play an important quantitative role.

PORE-SCALE MODELLING OF SLOSHING

Pore-scale numerical results based on VOF modelling were obtained using the OpenFOAM® implementation for a 2D tank cavity filled with a staggered array of discs. Results, presented Figure 1, show that the porous medium filling cavity yields more dissipation and modifies significantly the sloshing dynamics. Results for the column on the left correspond to a pure-fluid cavity and results on the right are for a porous cavity. As observed in [1], the amplitude of the surface movement is more important for pure-fluid sloshing than in the presence of a porous filled cavity because of the resistance produced by the particles. Results also indicate that the sloshing surface is not spread locally over more than one Unit-Cell for such a high permeability medium, and this is in favour of the development of a macro-scale VOF model.

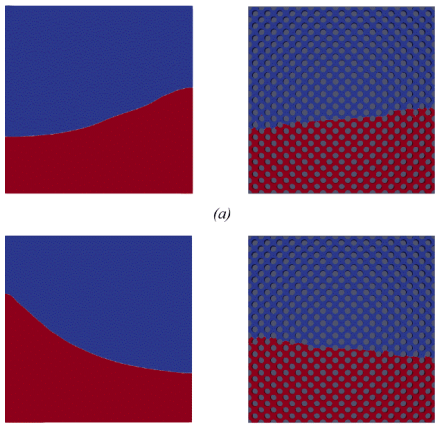

Figure 1. Comparison between pure fluid cavity and porous medium cavity sloshing (roll angle A=5°, sloshing period T=0.5 s, the length and height of cavity L=H=0.15 m, the diameter of particles d=0.5 cm, depth of cavity h=0.06 m). (a): t=0.5 s (b): t=0.75 s.

MACRO-SCALE MODELLING OF SLOSHING

A macro-scale model was established based on a VOF method and following the guidelines of a volume average method [2, 3]. The model takes into account the solid phase movement, a full anisotropic permeability tensor and a generalized term accounting for inertial effects. The macro-scale momentum equation reads

$$\rho\left(\frac{\partial \mathbf{U}}{\partial t}+\mathbf{U}\cdot\nabla\mathbf{U}\right)=-\nabla p+\rho\mathbf{g}+\nabla^2\mathbf{U}+k\sigma\nabla\alpha-\varepsilon\mu\mathbf{K_{app}}^{-1}\cdot\left(\mathbf{U}-\mathbf{U_{moving}}\right) \quad (1)$$

The last term on the right-hand side represents the resistance for flow in a moving porous medium. In this term, $\mathbf{U}$ is the intrinsic average velocity, α is the fluid volume fraction, $\mathbf{U_{moving}}$ is the local velocity of the moving porous medium and $\mathbf{K_{app}}$ is the apparent permeability taking into account all friction effects including inertia. In this study, we wrote $\mathbf{K_{app}}$ in the following form based on the work in [2, 3]

$$\mathbf{K_{app}}=\left(1+f(\mathrm{Re},\theta)\right)^{-1}\mathbf{P}\cdot\mathbf{K_0} \quad (2)$$

*Corresponding author. E-mail: xiaoning.di@toulouse-inp.fr.

where f is a non-linear inertia correction term, $\mathbf{K_0}$ the intrinsic permeability, $\mathbf{P}$ a rotation tensor that handles the additional anisotropic effects due to inertia. Therein, f and $\mathbf{P}$ depend on the Reynolds number Re and the orientation of the macro-scale pressure gradient, θ, with

$$\mathbf{P} = \begin{pmatrix} cos\left(\beta(\mathrm{Re},\theta)\right) & -sin\left(\beta(\mathrm{Re},\theta)\right) \\ sin\left(\beta(\mathrm{Re},\theta)\right) & cos\left(\beta(\mathrm{Re},\theta)\right) \end{pmatrix} \tag{3}$$

Further, β is also a function of θ and Re and it represents the angle between the orientations of macro-scale actual velocity and the macro-scale Darcy velocity that would be induced by the applied pressure gradient. Figure 2 shows an example of REV and the f - Re relationship in the situation $\theta = 0$ °.

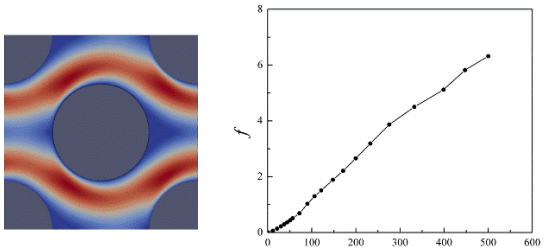

REV

(a) (b)

Figure 2. (*a*) Velocity field in the REV (Re = 56.73, $\theta = 0$ °); (*b*) The inertial correction f versus Re ($\theta = 0$ °).

All the equations presented above were implemented into a VOF solver in the computational fluid dynamics software OpenFOAM®.

Figure 3 shows the comparison between macro-scale and pore-scale sloshing at the same moments. It can be seen that the free surfaces are quite similar, indicating the ability of the macro-scale VOF model to reproduce the sloshing phenomena for highly permeable porous media. Further, through the comparison between the macro-scale results with and without inertia correction, it is obvious that the inertia correction plays an important role, particular for sloshing with short period which causes a high Re number. Without an inertia correction, the porous medium resistance is accordingly decreased inducing a movement of the free surface with larger amplitude.

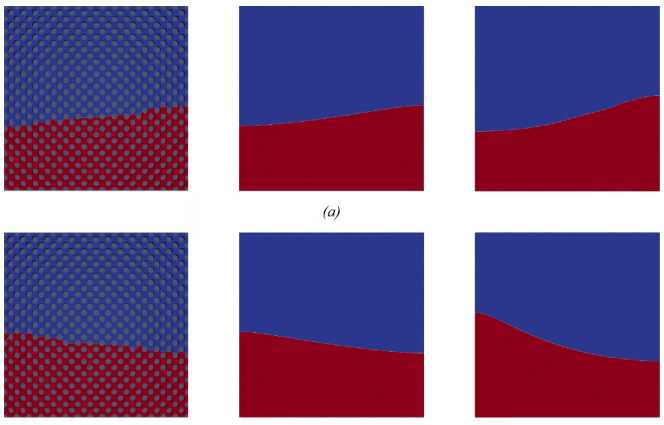

(a)

(b)

Figure 3. Comparison between porous medium cavity sloshing, macro-scale sloshing with and without inertia correction (roll angle A=5°, sloshing period T=0.5 s, the length and height of cavity L=H=0.15 m, the diameter of particles d=0.5 cm, depth of cavity h=0.06 m). (*a*): t=0.5 s (*b*): t=0.75 s.

CONCLUSIONS

In this study, we have established a macro-scale VOF model for describing sloshing situations in highly permeable porous media. A comparison with direct numerical simulation at the pore-scale showed the ability of the macro-scale model to reproduce the observed results. The investigation also emphasized the need for a correct estimate of effective properties, including inertia correction.

References

[1] Abbaspour.M, Ghodsi Hassanabad.M. SCI IRAN. 17: 93-101, 2010.
[2] Zami-Pierre. F, de Loubens. R, Quintard. M, Davit. Y. J Non-newtonian Fluid. 261: 99-110, 2018.
[3] Pauthenet. M, Davit. Y, Quintard. M, Bottaro. A. Transport Porous Med. 125: 211-238, 2018.

ON THE ACCURACY OF DEVELOPED CLOSURE CORRELATIONS FOR MODELLING THE LAMINAR MACRO-SCALE FLOW IN CHANNELS WITH LARGE ARRAYS OF SOLID STRUCTURES.

Geert Buckinx * [1,2,3]
[1]Department of Mechanical Engineering, KU Leuven, Celestijnenlaan 300A, 3001, Leuven, Belgium
[2]VITO, Boeretang 200, 2400 Mol, Belgium
[3]EnergyVille, Thor Park, 3600 Genk, Belgium

Summary In this work, laminar flow through channels with large arrays of solid structures is modelled from a macro-scale viewpoint, through spatially averaged Navier-Stokes equations which take account of the presence of porosity gradients and channel boundaries. The accuracy of employing a double-volume-averaging operator in combination with closure correlations that are exact for the periodically developed regime, is evaluated for parallel-plate channels with arrays of square pin fins. It is shown that a fairly good agreement with direct numerical simulation can be obtained, when the macro-scale velocity profile in the near-wall region is known a priori.

INTRODUCTION

For the modelling of laminar incompressible flow through channels with large arrays of periodic solid structures, direct numerical simulation (DNS) of the Navier-Stokes equations is usually infeasible, as it necessitates supercomputing infrastructure. Therefore, macro-scale models have been proposed in the literature, which offer an approximative description of the average flow in such channels, while requiring significantly less computational resources. In essence, these macro-scale models enable us to restrict our analysis of the detailed flow to just one unit cell of the array.

Although the majority of macro-scale models for laminar channel flows have been formulated on empirical grounds, e.g. [1], most of the theoretical framework is adapted from the volume-averaged flow equations that describe the macro-scale flow through porous media [2]. As a consequence, the available macro-scale flow models incorporate different assumptions and approximations which have been verified for some classes of porous media, yet not for channel flows.

First, the volume-averaged flow equations for porous media neglect the spatial moments of the array of solid structures [3, 4]. For that reason, they do not recover a constant macro-scale pressure gradient when the flow in the array is periodically developed, like it has been assumed in the literature. As a result, the developed flow regime in channels cannot be reconstructed in exact agreement with results from DNS, unless the volume-averaged flow equations are replaced by spatially filtered flow equations [4]. The latter filtered flow equations are derived from the Navier-Stokes equations by applying a double-volume-averaging operator, or filter, which was originally proposed by Quintard and Whitaker [3].

Secondly, the volume-averaged flow equations presented in the literature rarely if ever take porosity gradients or domain boundaries into account. As such, they lose their validity near the inlet and outlet of the channel, as well as near the channel walls.

In order to circumvent the previous modelling inaccuracies, this work explores a macro-scale description of laminar channel flow which is based on a double-volume-averaging operator and closure correlations that are (nearly) exact for the periodically developed regime. The presented macro-scale flow equations take porosity gradients and domain boundaries into account. Furthermore, the accuracy of this macro-scale modelling approach is compared with DNS for arrays of square pin fins.

MACRO-SCALE FLOW EQUATIONS WITH DEVELOPED CLOSURE CORRELATIONS

When gradients of the porosity ϵ_{fm} and the presence of domain boundaries are taken into account, the macro-scale velocity $\langle \boldsymbol{u} \rangle_m$ and macro-scale pressure $\langle p \rangle_m$ are the solution of the following filtered Navier-Stokes equations:

$$\nabla \cdot \langle \boldsymbol{u} \rangle_m = 0 \,, \tag{1}$$

$$\rho_f \nabla \cdot \left(\epsilon_{fm}^{-1} \langle \boldsymbol{u} \rangle_m \langle \boldsymbol{u} \rangle_m \right) = -\nabla \langle p \rangle_m + \mu_f \nabla^2 \langle \boldsymbol{u} \rangle_m + \boldsymbol{b} + \langle \boldsymbol{f} \rangle_m \,. \tag{2}$$

Here, $\langle\ \rangle_m$ denotes the double-volume-averaging operator, so $\langle \boldsymbol{f} \rangle_m$ corresponds to the spatially averaged body force.

The closure force $\boldsymbol{b}$ in the macro-scale momentum equation (2) contains in good approximation only contributions from the viscous forces and pressure at the fluid-solid interface and the channel walls, as we can show that macro-scale momentum dispersion is negligible for (quasi-developed) laminar channel flows.

In the core of the channel, where the flow through the array of solid structures is periodically developed, the closure force is a spatially constant vector, $\boldsymbol{b}_{\text{dev}}$, which can be correlated to the macro-scale velocity in an exact manner by solving the periodic flow equations on a unit cell of the array [4]. For an array of square pin fins of width w, whose inter-fin spacing ℓ is equal to the channel height, this correlation takes the form

$$\boldsymbol{b}_{\text{dev}}(\epsilon_{fm}, \langle \boldsymbol{u} \rangle_m) \simeq -75 \frac{\mu_f}{\ell^2} \frac{(1-\epsilon_{fm})^{1/3}}{\epsilon_{fm}^3} \langle \boldsymbol{u} \rangle_m - 0.006 \frac{\rho_f}{\ell} \frac{(1-\epsilon_{fm})^{0.5}}{\epsilon_{fm}^3} \| \langle \boldsymbol{u} \rangle_m \| \langle \boldsymbol{u} \rangle_m \,. \tag{3}$$

*Corresponding author. E-mail: geert.buckinx@kuleuven.be

The latter correlation has been fitted numerically over a wide range of Reynolds numbers $Re_{\text{unit}} \triangleq \rho_f \|\langle \boldsymbol{u} \rangle_m\| \ell / \mu_f \in [0, 200]$ and porosities $\epsilon_{fm} = 1 - (w/\ell)^2 \in [0.5, 1]$, and holds as long as the directions of $\boldsymbol{b}_{\text{dev}}$ and $\langle \boldsymbol{u} \rangle_m$ are more or less aligned.

In the regions of the channel where porosity gradients are present, the closure force can be approximated in agreement with the closure mapping from [2, 3], which leads to

$$\boldsymbol{b}(\epsilon_{fm}, \langle \boldsymbol{u} \rangle_m, \langle p \rangle_m) \simeq \epsilon_{fm}^{-1} \langle p \rangle_m \nabla \epsilon_{fm} + \mu_f \nabla \epsilon_{fm} \cdot \nabla \left(\epsilon_{fm} \langle \boldsymbol{u} \rangle_m \right) + \boldsymbol{b}_{\text{dev}}(\epsilon_{fm}, \boldsymbol{G} \cdot \langle \boldsymbol{u} \rangle_m) \,, \tag{4}$$

where $\boldsymbol{G}$ equals the identity tensor $\boldsymbol{I}$ inside the core of the channel.

In the near-wall region, the tensor $\boldsymbol{G}$ maps the local macro-scale velocity to the (nearly) spatially constant macro-scale velocity in the core. This tensor can be constructed from the macro-scale velocity profile in the wall region, which is approximately linear when the distance between the array and the channels walls is less than the characteristic size ℓ of the unit cell. Therefore, $\boldsymbol{G}$ can be constructed from the slip-length l_{slip} of the macro-scale velocity at the channel wall, by solving the periodically developed flow equations on a unit cell in the near-wall region.

VALIDATION THROUGH COMPARISON WITH DNS

In order to validate the accuracy of the filtered flow equations (1)-(2) and developed closure correlations (3)-(4), a series of DNS experiments has been carried out for parallel-plate channels containing arrays of square pin fins. In these numerical experiments, the Reynolds number based on the bulk velocity was varied over the range $Re \triangleq \rho_f u_b \ell / \mu_f \in [25, 250]$, while the width of the fins was chosen as $w/\ell \in \left\{ \frac{1}{2}, \frac{1}{3}, \frac{1}{4} \right\}$.

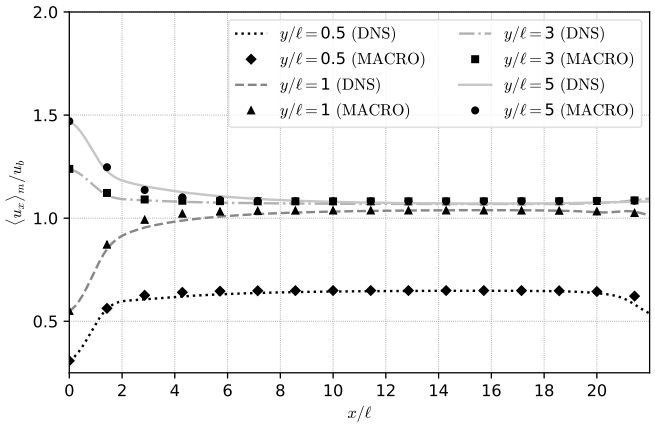

Figure 1: Macro-scale velocity $\langle u_x \rangle_m$ in the main flow direction x of a channel with an array of 20×10 pin fins, at different positions y along the width of the channel. ($w/\ell = 0.5$, $Re = 25$)

An example of the outcome of these DNS experiments is given in Figure 1, which shows the macro-scale velocity component $\langle u_x \rangle_m$ along the main flow direction x in a channel with an array of 20×10 pin fins with $w/\ell = 0.5$, for $Re = 25$. As it can be observed from Figure 1, the developed closure correlations (3)-(4) are capable of reproducing the macro-scale velocity in qualitatively good agreement with DNS at different positions y along the width of the channel, when the slip length is known a priori: $l_{\text{slip}}/\ell \simeq 0.25$ in this case. The relative point-wise difference between the results of the macro-scale model and DNS in terms of $\langle u_x \rangle_m$ is less than 5% in the core of the channel ($1 < y/\ell < 9$) and less than 15% in the near-wall region ($y/\ell \leq 1$ or $y/\ell \geq 9$) in this case. A comparable accuracy has been observed for the higher Reynolds numbers and higher porosities, as well as for larger arrays (for instance, of 60×10 pin fins).

CONCLUSIONS

By employing a double-volume-averaging operator and closure correlations that are exact for the periodically developed regime, the laminar macro-scale flow in simple parallel-plate channels can be reconstructed with point-wise differences of less than 15 to 20% with respect to direct numerical simulation, provided that the slip-length is known.

References

[1] Sbutega, K., Geb, D., Catton, I., "Chapter One - Modeling of Multiscale Heat Transfer Systems Using Volume Averaging Theory." *Adv. Heat Transfer* **47**: 1-165, 2015.

[2] Whitaker, S., "The Forchheimer equation: A theoretical development." *Transport Porous Med.* **25: 27**: 27–61, 1996.

[3] Quintard, M., Whitaker, S., "Transport in ordered and disordered porous media II: Generalized volume averaging." *Transport Porous Med.* **14.2**: 179–206, 1994.

[4] Buckinx, G., Baelmans, M., "Multi-scale modelling of flow in periodic solid structures through spatial averaging," *J. Comput. Phys.* **291**: 34-51, 2015.

MULTISCALE SIMULATION OF GAS TRANSPORT IN POROUS MEDIA

Wei Su*[1], Minh Tuan Ho[1], Yonghao Zhang[1], and Lei Wu[2]
[1]School of Engineering, The University of Edinburgh, Edinburgh, UK
[2]Department of Mechanics and Aerospace Engineering, Southern University of Science and Technology, Shenzhen, China

Summary The general synthetic iterative scheme is proposed to solve gas kinetic equations for multiscale gas dynamics with the Knudsen number spanning a wide range, where the traditional Navier-Stokes equations fail. Macroscopic equations of conservative laws are solved alongside the mesoscopic equations to guide the evolution of molecular velocity distribution functions. Constitutive relations to close the macro equations are strictly derived from the gas kinetic equations. The scheme can accurately obtain steady-state solutions within dozens of iterations at any Knudsen number and asymptotically preserve the Navier-Stokes limit on coarse meshes. The advantages make the scheme a promising tool to model gas transport in porous media. As an example, we quantify the apparent gas permeability of porous media and try to find a universal slop in the Klinkenberg's correlation.

INTRODUCTION

Gas flows through porous media is found in a variety of engineering applications, such as the next-generation technologies of carbon capture and utilization, productions of unconventional gas to offset the decline of conventional fossil fuels, membrane oxygenation for extracorporeal life support, and fast-responding pressure-sensitive paint for flow-field measurement. The development of the new technologies requires research advances in not only new materials and industrial processes but also improved knowledge about the underlying physics of gas transport. However, the latter has largely been neglected due to lack of experimental and computational capabilities.

The characteristic length of the gas flows in the above applications is usually multiscale, e.g. gas evolution and production in shale sediments contain flows in fine-grained formation at the nano/microscale, through fracturing networks at the mesoscale and from reservoirs to wellbores at the macroscale. As a consequence, the flow can span over a wide range of the Knudsen numbers (*Kn*, the ratio of the mean free path of gas molecules to the characteristic flow length), where the traditional Navier-Stokes equations fail to model the flows while the gas kinetic theory is required. So far, very few numerical methods are designed to efficiently solve multiscale gas dynamics. Particularly, the conventional iterative scheme (CIS) in solving the gas kinetic equations suffers difficulties as the Knudsen number approaches to the continuum limit: it requires the cell size of the spatial grid to be smaller than the molecular mean free path, in order to suppress numerical dissipations; it costs hundreds of thousands iterations to obtain steady-state solutions because information propagation becomes very inefficient when molecular collisions dominate. Therefore, the scheme is prohibitively expensive for realistic engineering problems.

In this work, we introduce a novel iterative scheme to solve gas kinetic equations, which is proven to be a promising tool for efficient and accurate simulation of multiscale gas dynamics. Then, as an application, we use this tool to find a universal slip factor in the Klinkenberg's correlation of apparent gas permeability in porous media.

GENERAL SYNTHETIC ITERATIVE SCHEME FOR MULTISCALE SIMULATION

To tackle the difficulties of CIS in simulating small-Kn flows, we have proposed the general synthetic iterative scheme (GSIS) [1,2]. The key of GSIS is that the macroscopic equations of conservative laws are simultaneously solved alongside the gas kinetic equations, from which the macroscopic flow properties are obtained to guide the evolution of molecular velocity distribution functions. The constitutive relations of the stress tensor and the heat flux for the closure of the macro equations are strictly derived from the kinetic equations, which explicitly contain the Newtonian and Fourier's laws as well as the high-order terms beyond the Navier-Stokes limit. Therefore, GSIS can obtain steady-state solutions within dozens of iterations at any Knudsen number while predicting accurate results when the rarefied effects intensify.

Rigorous analyses of Fourier stability and Chapman-Enskog expansion show that [3]: the residue of solutions between two successive iterative steps can be reduced by at least three orders of magnitude only after 10 iterations, allowing the scheme to achieve fast convergence over the whole flow regime; the macro synthetic equations are reduced to the Navier-Stokes equations when the Knudsen number approaches zero, guaranteeing the scheme to obtain accurate solution in the near-continuum region on a spatial grid with cell size much larger than the molecular mean free path. These advantages make the GSIS a particularly promising tool in simulating multiscale gas transport through porous media.

ON SLIP FACTOR IN THE KLINKENBERG'S CORRELATION

The apparent gas permeability (AGP) of a porous medium is an important parameter to predict the production of unconventional gas. Due to the gaseous slippage at solid surfaces, AGP can be much larger than the intrinsic permeability. One of the most popular empirical estimation to quantify AGP is the Klinkenberg's correlation, which states that the ratio of AGP to the intrinsic permeability of a porous medium is approximately a linear function of reciprocal mean gas

*Corresponding author. E-mail: wei.su@ed.ac.uk.

pressure. Significant efforts have been made to construct a universal expression for the slope in the correlation. However, the major challenges remain: it is difficult to define the effective flow length in the Knudsen number for complex porous geometries; thus the slop in the Klinkenberg's correlation may significantly vary for different geometries such that a universal expression seems nearly impossible.

Using the developed GSIS, we solve the linearized Boltzmann kinetic equation to evaluate AGPs in simplified porous media represented by the two-dimensional Sierpinski fractal model, see Figure 1(a) and a pore body/throat system. Figure 1(b, c) compares the number of iteration steps and the obtained AGP between the GSIS and CIS, where it is found the GSIS can obtain the same results as the CIS but with significantly smaller computational effort, especially when Kn becomes small. Finally, a new definition of the characteristic flow length in porous media is proposed, which is a function of the porosity, tortuosity and intrinsic permeability. A unique slop of about 7 in the Klinkenberg's correlation can be found for the geometries considered, when the Knudsen number characterized by the new flow length (Kn*) is within the slip flow regime, see Figure 1(d). Note that the GSIS is also used to find the intrinsic permeability in the continuum region with $Kn = 10^{-5}$, which just needs no more than 20 steps and a few minutes of CPU time on a single processor to obtain the converged solutions. Compared with the solutions from lattice Boltzmann calculations, the GSIS can predict accurate results on the coarse meshes even with the maximum cell size being 6000 times the mean free path length of gas molecules, due to its asymptotic preserving.

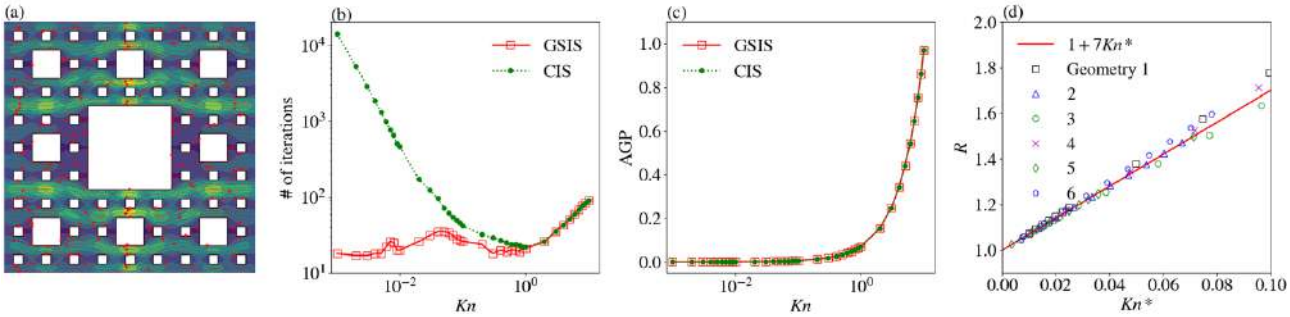

Figure 1: (a) Gas flow through Sierpinski fractal model; (b) Number of the iteration steps to obtain steady-state solutions; (c) Apparent gas permeability; (d) Ratio of AGP to intrinsic permeability (R) against Kn* using the new definition.

References

[1] Su W., Zhu L., Wang P., Zhang Y., Wu L. Can we find steady-state solutions to multiscale rarefied gas flows within dozens of iterations? *J. Comput. Phys.* **407**: 109245, 2020.

[2] Su W., Zhang Y., Wu L. Multiscale simulation of molecular gas flows by the general synthetic iterative scheme. Comput. Methods Appl. Mech. Engrg. **373**: 113548, 2021.

[3] Su W., Zhu L., Wu L. Fast convergence and asymptotic preserving of the general synthetic iterative scheme. SIAM J. Sci. Comput. 2020.

DEFORMATION-DRIVEN SOLUTE TRANSPORT IN SOFT POROUS MEDIA

Matilde Fiori*[1], Satyajit Pramanik [2], and Christopher W. MacMinn[1]
[1]Department of Engineering Science, University of Oxford, Oxford, UK
[2]Discipline of Mathematics, Indian Institute of Technology Gandhinagar, Gandhinagar, India

Summary Solute transport plays an important role in many soft porous materials, including the movement of contaminants in soils and the movement of nutrients and waste in living tissues and tissue-engineering scaffolds. These systems are also often exposed to large, periodic loading and deformation, which drives nontrivial fluid motion and changes in pore structure. Here, we study the strong coupling between fluid flow and mechanical stimulation during periodic deformations using a 1D continuum model based on large-deformation poroelasticity. We show that these reversible deformations lead to non-reversible spreading and mixing, even in a homogeneous medium. We analyse the three primary mechanisms of solute transport (advection, molecular diffusion, and mechanical dispersion) and study their separate impacts on the solute distribution. We also identify the key dimensionless parameters that govern deformation-driven transport, and we study their qualitative and quantitative impacts on solute spreading and mixing.

INTRODUCTION

Soft porous media are characterized by a highly deformable porous solid skeleton in which the pore space is occupied by a fluid phase. These materials can experience large volume changes, due to influx or efflux of the fluid. Internal fluid flow and external mechanical deformation are therefore highly coupled, through rearrangements of the pore structure [1].

The transport and mixing of solutes can be crucial in some soft porous media, from contaminants in soils to nutrients in biological tissues. In many cases, these materials are exposed to periodic deformations, which influence the resultant fluid flow and consequently impact on solute movements. In general, solute transport in soft porous media is driven by three main mechanisms – advection, molecular diffusion, and hydrodynamic dispersion. [2, 3]. Deformations affect these three phenomena by modifying the pore space – and, therefore, the fluid fraction in the domain at each time-step. Moreover, periodic deformations continuously alter the fluid and solid velocities, thus directly influencing advection and mechanical dispersion.

Here, by considering a simple one-dimensional model, we aim to describe the fundamental physics regulating the problem. We hence perform simulations to observe how a certain initial concentration profile is affected by changing some relevant parameters. Furthermore, we focus on the individual role of the three main transport mechanisms to fully characterise the effects of large periodic deformations on solute transport and mixing

PROBLEM FORMULATION AND THEORETICAL MODEL

Domain

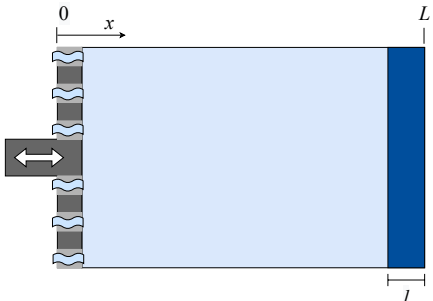

Figure 1: Scheme of the considered domain.

A schematic representation of the considered domain is shown in figure 1. We consider a soft porous medium of length L, subject to a periodic loading. The deformation is applied at the left boundary, which is, therefore, a moving boundary. Moreover, the left boundary is permeable, thus allowing fluid movement due to the applied stimulation. The right boundary is instead assumed to be fixed and impermeable. The solute is initially localised against the right boundary in a strip of width l. This formulation allows a one-dimensional analysis along the loading axis (x).

Theoretical Model

Our model comprehends a mechanical formulation – describing the coupling between deformation and fluid flow – and a transport formulation – providing the effects of fluid flow on the solute movements.

For the mechanical aspects, we formulate an evolution equation for the porosity field following the model developed by MacMinn *et al.* [1], through a rigorous nonlinear kinematic approach. We therefore apply the conservation of mass

*Corresponding author. E-mail: matilde.fiori@eng.ox.ac.uk

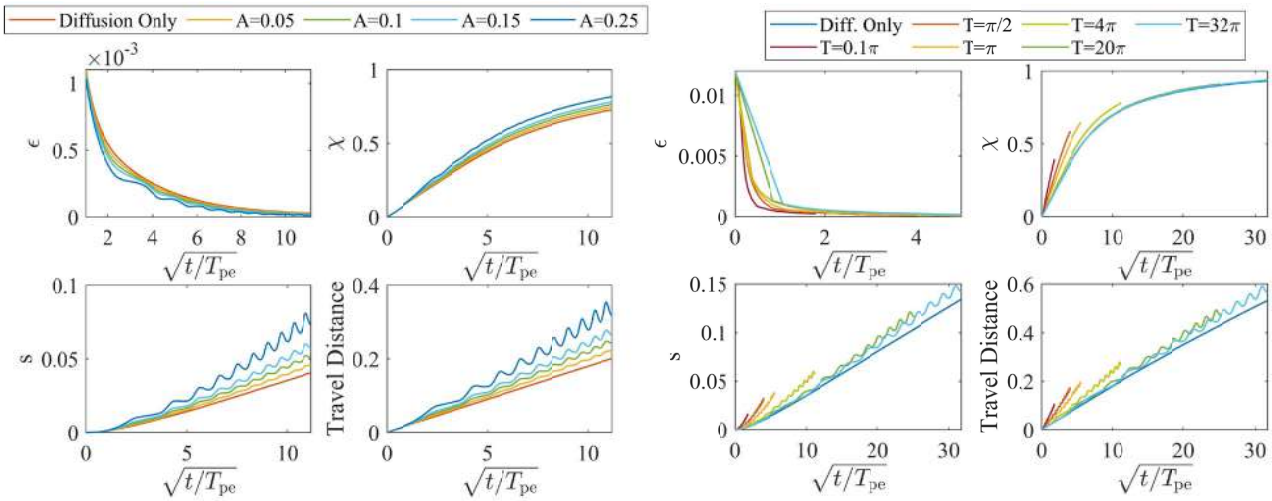

Figure 2: Results of varying the loading amplitude A (left) and the loading period T (right). In both cases, from left top to right bottom, the mixing rate ϵ, degree of mixing χ, spread s and travel distance are reported.

and Darcy's law, coupled with mechanical equilibrium through Terzaghi's effective stress. For the constitutive behaviour of the solid, we assume a deformation-dependent permeability and Hencky elasticity.

The evolution equation regulating solute transport is again formulated in terms of the evolving porosity field – weighted by the solute concentration – and includes contributions from advection, molecular diffusion and hydrodynamic dispersion, through the relevant coefficients.

RESULTS AND DISCUSSION

Isolation of transport mechanisms

In the first part of the study, we are able to isolate and examine the effects on the initial concentration profile of the transport phenomena by showing how each mechanism is individually responsible for a specific change in the shape and spread of the concentration profile. Moreover, we demonstrate that spread and contraction of the profiles are due the periodic changes in the pore space and fluid velocity. This analysis allows us to understand how the transport mechanisms are regulated by the evolving porosity and by the complex coupling between deformation and velocity fields.

Parameter Exploration

Next, we observe the effects on solute mixing and transport due to several parameters, like the loading amplitude, period and number of cycles, the values of the diffusion and dispersion coefficients, the amount of fluid and the amount of solute initially in the domain. In figure 2 we show two examples: in the first plot, we compare how mixing and transport of solutes are affected by different loading amplitude, while in the second plot we analyse different loading periods, keeping the amplitude fixed. From these examples, we can conclude that higher amplitudes lead to higher mixing and travelling of the solutes, as advection and hydrodynamic dispersion are enhanced. When considering different stimulation frequencies, instead, we show that longer periods behave more like pure molecular diffusion, while shorter periods highly enhance advection and hydrodynamic dispersion.

Overall, we observe that a periodic and reversible deformation for the material does not lead to reversible solute profiles. Furthermore, solute transport and mixing are highly dependent on several parameters describing the load applied and the material properties.

CONCLUSIONS

We provide a computational analysis to describe solute transport and mixing in soft porous media subject to large periodic deformation.

Overall, our results can have two main applications: first, they can be useful to predict solute transport and mixing given a certain set of fixed parameters; on the other hand, they can be used to control the final solute distribution by tuning the relative conditions. In the future, we will need to validate the model experimentally.

References

[1] C. W. Macminn, E. R. Dufresne, and J. S. Wettlaufer, Large Deformations of a Soft Porous Material, *Physical Review Applied*, **5**(4): 044020, 2016.
[2] D. R. Lester, G. Metcalfe, and M. G. Trefry, Is chaotic advection inherent to porous media flow? *Phys. Rev. Lett.* **111**(17): 174101, 2013.
[3] M. Dentz, M. Icardi, and J. J. Hidalgo, Mechanisms of dispersion in a porous medium *J. Fluid Mech.*, **841**: 851-882, 2018.

INTERMITTENT WATER TRANSFER: A WETTABILITY MODEL FOR POROUS MEDIA

Florian Cajot*[1] and Philippe Beltrame †[2]
[1]INRAE, UMR EMMAH, Avignon, France
[2]Avignon Université, INRAE, UMR EMMAH, Avignon, France

Summary We simulate water transfer in partial wetting porous media especially hydrophobic. A variant of Darcy-Richards model is considered by taking into account interactions between free surface of water and the porous matrix surface. These interactions lead to introduce new terms in the capillary pressure : effective repellent interaction and effective surface tension. The summation of the capillary pressure and the repellent pressure allows to represent partial wetting phenomena as the dis- and con-joining pressures for thin film on substrate. Using a 1D Finite Elemental code, we observe numerically a finite water spreading in the porous medium and we capture intermittent-like behavior at the interface of a stratified medium with two different grain sizes.

INTRODUCTION

Water transfer in unsaturated porous media displays phenomena still poorly understood as the fingering instability of the wetting front, water pinning and depinning in heterogeneous media. These phenomena are enhanced in the presence of hydrophobicity due, for instance, to organic matter. In the Darcy-Richards equation, the wetting property is defined via the capillary rise and the pressure head. In such a model, the water content diffuses towards the dryer region and thus cannot reproduce the water trapping. To take into account the front hysteresis, models based on the analogy of the contact angle of a water front on the surface are found in literature, for instance in [4].
In contrast, in the present study, we aim at describing the wettability via surface energy at interfaces. An effective term of short-range repulsion is introduced modeling the interaction between the porous matrix and thin water films. According to [1], this term is non negligible at low saturation. The sum of this repulsive term with the capillary pressure constitutes the analogous of con- and dis-joining pressures describing the interaction of partial wetting liquid [6]. An effective surface tension proposed in [3] is also taken into account. After detailing the model, we apply the model for stratified media with different porosity. The 1D simulation is performed using Finite Element Method.

MODEL

Our model is a generalization of Darcy-Richards equation of a porous medium with saturation s. Initially the Darcy-Richards equation only takes into account the hydraulic conductivity $K(s)$, the gravity $g_r\vec{x}$ and the capillary pressure $P_c(s)$ given by the Genutchen Mualem model [7]. Partial wetting or hydrophobicity are modeled by adding a repellent pressure $P_r(s)$ with opposite sign to the capillary pressure. Note that for hydrophilic media as sand, this term exists as reported by the experiments in [1] pointing out the hydrophobic behavior for low saturation in the sand. Therefore, we note the disjoining pressure of the porous medium $\Pi(s) = P_c - P_r$. The graph of the variation of Π and P_c w.r.t. the saturation s are displayed (Fig. 1a). The disjoining pressure differs from the capillary pressure only for low saturation.
Finally, we introduce a macroscopic surface tension T as described in [3] which takes into account the additional surface energy due to the water free surface. This term has also proved crucial in regularising instabilities generated by repulsive pressure. Thus, the generalized Darcy-Richards equation reads in dimensionless form:

$$\frac{\partial s}{\partial t} + \nabla \cdot \left[K(s)\nabla\left(\Pi(s) + g_r x + T\Delta s\right)\right] = 0. \tag{1}$$

where Δs is the Laplacian operator applied to s and according to [3] it represents the pressure contribution due to the effective surface tension.
Eq. (1) is a fourth order and nonlinear Partial Differential Equations (PDE). This equation is reminiscent of the lubrication equation with wettability in the thin film theory [6]. We expect then front instability and intermittent flow as shown in [2].

RESULTS

We mainly focus on 1D stratified media consisting of a silica sand layers alternating fine and coarse grains as presented in [5]. The experiment of this reference shows that when the wetting front arrives from fine-grain to a coarse-grain layer, the front progress stops. This stage is followed by the development of protrusions, which rapidly grow into fully fledged finger structures.
To model the stratified medium, we consider a variable conductivity $K(s, x)$ depending on the depth x and also a variable disjoining pressure $\Pi(s, x)$. Indeed, when the grain size increases surface area of the grains per unit volume decreases

*Corresponding author. E-mail: florian.cajot@inrae.fr
†Corresponding author. E-mail: philippe.beltrame@univ-avignon.fr

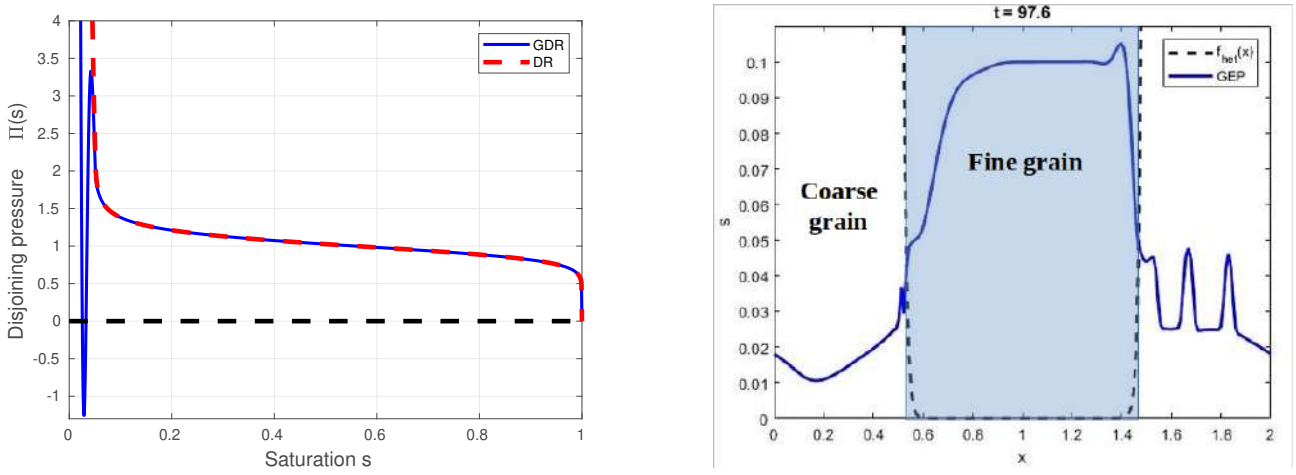

(a) (b)

Figure 1: (a) Disjoining pressure [red] in Darcy-Richards model and [blue] in the variant form. (b) Saturation time evolution in depth x, in a stratified porous medium. [black] boundary of the different layers : coarse and fine, [red] initial saturation s_0 and [blue] intermittent like behavior. The conductivity contrast $C_K = 0.048$ and the wettability contrast is $C_W = 5$.

leading to lower amplitude of the disjoining pressure. Then, we define the wettability contrast C_W by the ratio of the disjoining amplitude in the fine-grain layer over the amplitude in the coarse-grain layer. In a similar way, we define the conductivity contrast C_K.

The time integration of Eq. (1) shows that the profile $s(x,t)$ converges to a stationary state where the water saturation is larger in the fine grain than in the coarse grain layer. However, for specific parameters the flow can be intermittent (Fig.1b). We identify two main parameters providing intermittent flow. Firstly, the wettability contrast should be large enough, in the simulation (Fig. 1b), the wettability amplitude decreases by 80%. Secondly, the coarse-grain layer has to be dry, i.e. the saturation has to be about 5%. This value of saturation points out the key role of the repellent pressure $P_r(s)$.

Note that the effective surface tension is not the cause of the intermittent behavior but it plays a role on the quantitative properties of the intermittent dynamics.

CONCLUSION

Taking account to surface energies especially wettability by a disjoining pressure into a variant model of Darcy-Richards equation, we capture intermittent-like behavior in a stratified medium. This study showed that the relevance of a repellent contribution in the interaction at low saturation, even if the medium is hydrophilic.

The results suggests that the front can be unstable, in coming works, we will develop a 2D code to study fingering phenomenon.

Finally, This model could be applied to hydrophobic porous media such as soils in the presence of organic matter.

References

[1] Bachmann J., Liu H., Ju Z., Ren T. and Horton R., *Moisture-Dependent Wettability of Artificial Hydrophobic Soils and Its Relevance for Soil Water Desorption Curves*, Soil Sci. Soc. Am. J.,**76** : 342-349, 2012.

[2] Beltrame P. and Thiele U., *Time integration and steady-state continuation for 2d lubrication equations*, SIAM J. Appl. Dyn. Syst.,**9** : 484-518, 2010.

[3] Cueto-Fuelgueroso L. and Juanes R., *Stability analysis of a phase-field model of gravity-driven unsaturated flow through porous media*, Physical Review E, **79**, 2009.

[4] Rätz, A. and Schweizer, B. *Hysteresis models and gravity fingering in porous media* ZAMM - Journal of Applied Mathematics and Mechanics : 1–12, 2012.

[5] Sililo O. and Tellam J., *Fingering in Unsaturated Zone Flow: A Qualitative Review with Laboratory Experiments on Heterogeneous Systems*, Ground Water, **38** : 864-871, 2000.

[6] Thiele U., *Structure Formation in Thin Liquid Films*, Thin films of soft matter, Ed. Springer, **490** : 25-93, 2007.

[7] Van Genutchen M.T., *A closed-form equation for predicting the hydraulic conductivity of unsaturated soils*, Soil Sci. Soc. Am. J.,**44** : 892-898, 1980.

NON-STATIONARY LIMIT CYCLE OSCILLATIONS OF A RESTRAINED SLENDER POINTED BODY WITH A BLUNT ELLIPTICAL BASE AT HIGH INCIDENCE

Oded Gottlieb, Mark Ishay, and David Degani
Department of Mechanical Engineering, Technion – Israel Institute of Technology, Haifa, Israel

Summary: The response of a restrained slender pointed body with a blunt elliptical base is investigated numerically at high incidence in uniform flow. The flow is three-dimensional and laminar (with 30,000 Reynolds and 0.2 Mach numbers), whereas the body is restrained to rotate in the yaw direction only. The solutions are determined after removal of an initial disturbance and loss of periodicity is determined via Poincare' sampling of the upward zero-crossing side force. The resulting yaw response exhibits an intricate bifurcation structure that includes bi-stable periodic (finite amplitude) and non-stationary (small amplitude) limit cycles for moderate angles of attack, and non-stationary (finite amplitude) oscillations for high angles of attack. Investigation of the restraint torsion stiffness reveals an amazing resonant lock-in phenomena with quasiperiodic solutions for a 40° angle of attack.

INTRODUCTION

The flow around a pointed slender body of revolution at high incidence can generate significant side forces. The flow field can be so unstable that even upcoming turbulence or a small upstream disturbance can change the flow abruptly. It has been shown that these side forces can be altered by placing small irregularities near the body tip. Thus, when such a slender-body model is mounted on a balance in a wind tunnel, the nonlinear interaction between the flow and the structure can play a significant role on the configuration stability, and therefore, on the measurements. A numerical investigation of the fluid-structure interaction taking into account the elastic effects of the restraint has revealed existence of periodic and nonstationary oscillations for moderate and large angles of attack [1] culminating with an intricate bifurcation structure that included coexisting quasiperiodic tori and chaotic solutions foliated with periodic ultra-subharmonics [2]. Furthermore, a numerical investigation of a free-to-roll slender rigid-body of revolution placed in a wind tunnel at a high angle of attack (where the resistance to roll moment and bearing friction were represented by a linear viscoelastic torsion spring) revealed bi-stable periodic limit-cycle oscillations, which lost their periodicity with increasing stiffness of the restraining spring [3]. To date, the effect of the body's end on flow instabilities has not been systematically investigated and most research has focused on the effect of the pointed forebody as the body was very long and the base flow had little effect on the flow at the front of the body. Thus, in order to investigate the influence of a blunt elliptical base on the fluid-structure interaction of a slender pointed body, we consider a short inclined rigid tangent ogive-cylindrical body mounted on a viscoelastic torsion spring that is restrained to yaw (see Fig.1-left where spring is located at the coordinate system origin) and represents the resistance to a side-force induced moment and bearing friction. We focus on the self-excited limit cycle oscillations describing the restrained yaw response and the resulting wake pattern. The body is subjected to three-dimensional, compressible, laminar flow with a body diameter based Reynolds number of 30,000 and Mach number of 0.2. The second-order implicit Beam-Warming finite-difference scheme is employed to numerically solve the full Navier-Stokes equations, whereas the coupled structural equation is solved by an explicit 4th-order Runge-Kutta method. We employ a sub-iteration procedure for the flow-structure coupling and investigate the response after removal of an initial disturbance located near the ogive point.

RESULTS

We summarize the behaviour of the restrained yaw limit cycles for a fixed value of torsion stiffness in a bifurcation diagram (see Fig.1-right) which depicts four distinct regions of maximal limit cycle amplitude vs angle of attack (α): i) unique finite amplitude periodic oscillations [0°<α<20°], ii) coexisting bi-stable periodic finite amplitude and non-stationary small amplitude oscillations, [20°<α<35°], i) unique finite amplitude periodic oscillations [35°<α<45°], and iv) non-stationary finite amplitude oscillations, [α>45°].

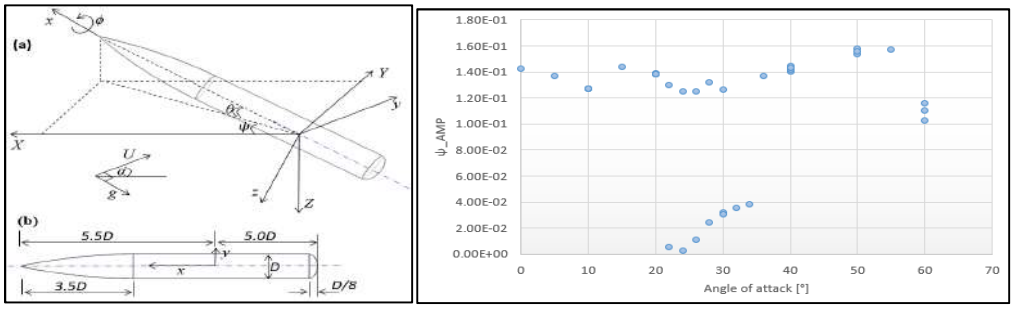

Figure 1. Body and coordinate system (left), and bifurcation diagram of yaw amplitude (right).

A comparison of the yaw phase planes with overlaid Poincare' maps and span-wise helicity contours between the moderate (α=30°) and high (α=50°) angles of attack (see Fig.2) clearly demonstrates the transition from a periodic structure with regular shedding of a fluctuating wake along the body (Fig.2-top) to a non-stationary structure with an irregular fluctuating wake (Fig.2-bottom). We note that limit cycle periodicity was determined by the yaw power spectra (not shown) the Poincare' map sampled every upward zero-crossing of the corresponding side force [2].

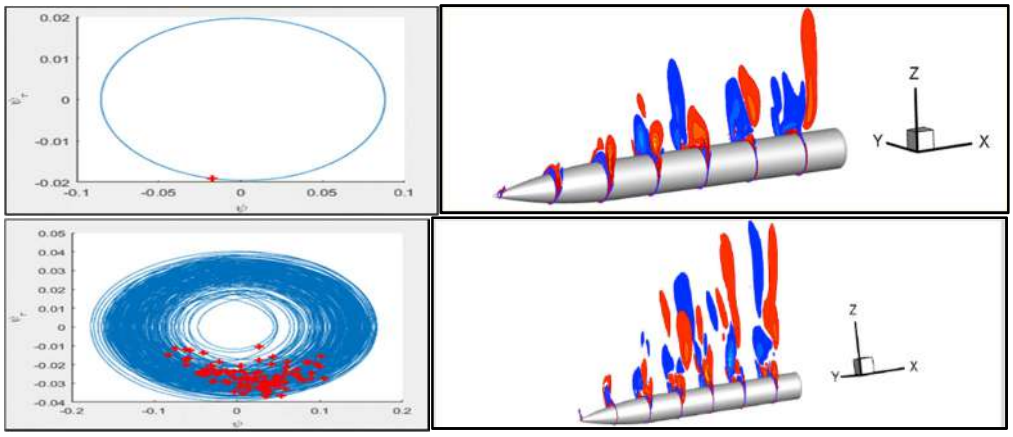

Figure 2. Yaw phase plane overlaid with Poincare' map (left) and span-wise helicity contours (right) for a finite amplitude periodic and nonstationary responses for moderate (top - α=30°) and high (bottom - α=50°) angles of attack respectively.

We also summarize the effect of the torsion spring stiffness on the yaw amplitude (see Fig.3-left) for a moderate angle of attack (α=40°) via the system reduced velocity (U*) defined here by the ratio of Mach number and the square root of the system torsional stiffness [$U^*=(U_\infty/Df_n)=(2\pi Ma/\sqrt{k_\psi})$]. The results reveal a distinct region of synchronization [4<U*<12] where the governing limit cycle frequency was very close to the system natural frequency and two desynchronized regions below and above the synchronized region. This phenomena represents resonant or lock-in behaviour found for both restrained circular cylinders [4] and tethered spheres [5] in uniform laminar flow but for significantly lower Reynolds numbers. A striking difference between the response here and results in literature for cylinders and spheres (where the synchronized response is periodic), is the appearance of synchronized quasiperiodic yaw in the resonant lock-in range (see Fig.3-midle) possibly due to the high Reynolds number of this work.

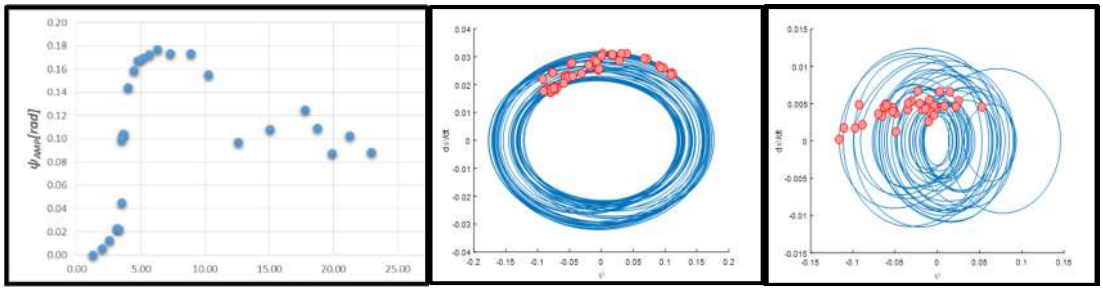

Figure 3. Maximal yaw angle amplitude (ψ_{AMP}) vs reduced velocity (U*) for α=40° (left) and phase planes overlaid with Poincare' maps for reduced velocities in the resonant lock-in range (middle- U*=6.3) and in the desynchronized range (right- U*=21.2).

CLOSING REMARKS

A numerical investigation of a pointed slender body of revolution restrained to yaw reveals an intricate bifurcation structure that includes: (i) periodic limit cycles for small angles of attack, (ii) bi-stable periodic (finite amplitude) and non-stationary (small amplitude) limit cycles for moderate angles of attack and (iii) non-stationary oscillations for large angles of attack. We note that the effect of the blunt elliptical base on the response of the short ogive-cylinder is to modify the classical supercritical bifurcation structure [2] where no restrained body motion was observed below a specific threshold whereas the response here (Fig.1-left) is reminiscent of a galloping like structure augmented by finite amplitude periodic limit cycles below the threshold for small amplitude oscillations.

References

[1] Gendel S., Gottlieb O. and Degani D. *AIAA J.* **53**: 1309-1318, 2015.
[2] Kleiman A., Gendel S., Degani D., and Gottlieb O. Nonlinear Dynamics, **86**: 2207-2230, 2016.
[3] Degani D., Ishay M. and Gottlieb O. Physics of Fluids, **29**: 037106, 1-13, 2017.
[4] Williamson C. and Govardahn R. *Annual Review of Fluid Mechanics*, **36**: 413-455, 2004.
[5] Rajamuni M., Thompson M. and Hourigan K. *J. Fluid Mechanics* **837**: 931-966, 2018.

FLEXIBLE FSI: FROM CARDIOVASCULAR MODELING TO AIR BLAST

Yuri Bazilevs*[1]
[1]School of Engineering, Brown University, Providence, RI, USA

Summary A general, flexible FSI framework is developed to accommodate a variety of applications of contemporary interest and importance in engineering and sciences. The framework is specialized to a set of concrete applications, and its veracity and potential are shown for cardiovascular mechanics, wind energy, and air blast applications.

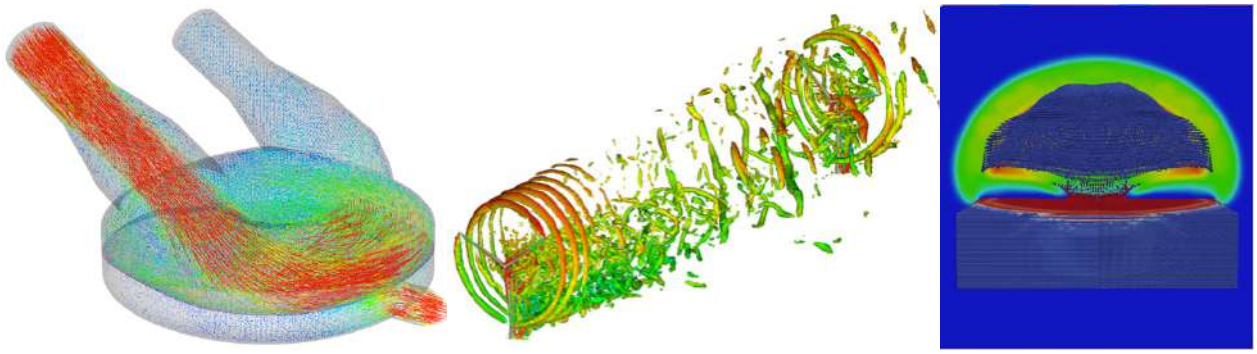

(a) (b) (c)

Figure 1. FSI simulation of (a) Pediatric Ventricular Assist Device (PVAD); (b) Two back-to-back 5MW wind turbines operating in thermally stratified atmospheric boundary layer flow; (c) Detonation of a cone-shaped explosive over a concrete block.

FLEXIBLE FSI FRAMEWORK

Fluid–structure interaction (FSI) simulations at full scale are essential for accurate modeling in engineering and sciences. The motion and deformation of the solid/structure depends on the flow of the surrounding fluid, and the fluid flow patterns depend on the motion and deformation of the solid/structure. In order to simulate the coupled problem, the equations governing the fluid and structural mechanics need to be solved simultaneously, with proper kinematic and dynamic conditions coupling the two physical systems. Without that the modeling cannot be realistic.

To obtain high-fidelity predictive simulation of science and engineering systems of interest, 3D modeling is essential. However, such simulations engender a number of challenges that need to be addressed. The flow is often fully turbulent or transitional, requiring accurate and robust approaches to modeling turbulence, as well as the use of increased grid resolution. The presence of fluid boundary layers, where turbulence is created, complicates the situation further. Structures are often geometrically complex and slender, while solids often exhibit nearly incompressible behavior and localization of deformation due to strain softening constitutive behavior, all of which requires numerical approaches that are geometrically flexible, and avoid locking and other instabilities. FSI of structural systems often involves moving and stationary components, which require special treatment. Finally, algorithms for FSI coupling must be accurate, efficient and robust to preclude divergence of the computations.

To address the aforementioned challenges, in [1], we developed a framework for (FSI) modeling and simulation with emphasis on non-matching fluid–structure interface discretizations. We take the augmented Lagrangian approach to FSI as a point of departure. Here the Lagrange multiplier field is defined on the fluid–structure interface and is responsible for coupling of the two subsystems. Thus the FSI formulation does not rely on the continuity of the underlying function spaces across the fluid–structure interface in order to produce the correct coupling conditions between the fluid and structural subdomains. However, in deriving the final FSI formulation the interface Lagrange multiplier is formally eliminated and the formulation is written purely in terms of primal variables. Avoiding the use of Lagrange multipliers adds efficiency to the proposed formulation. As an added benefit, the ability to employ non-matching grids for multi-physics simulations leads to significantly relaxed requirements that are placed on the geometry modeling and meshing tools.

APPLICATIONS

Cardiovascular FSI Modeling

In patient-specific cardiovascular FSI, the vascular wall motion, in many cases, is relatively modest. The motion occurs largely due to the global pressure variations in the blood vessel during the heart beat cycle, and it does not produce a significant effects on the global features of the blood flow. The influence of vascular wall elasticity is most pronounced when it comes to predicting wall quantities, such as the wall shear stress (WSS) and oscillating shear index (OSI), which

are well known key factors that influence the onset and progression of atherosclerosis. As a result, staggered or block-iterative solution strategies for FSI [2], which essentially involve a sequence of standalone fluid and structural mechanics solves, present an efficient way of dealing with this problem class. When it comes to the simulation of cardiovascular devices, such as pulsatile ventricular assist devices (PVADs, see Figure 1 and [3]) or prosthetic heart valves [4], the underlying structural motions are complex, often times exhibiting topology change (or near topology change). The structure added mass is often high, requiring the use of quasi-direct FSI solution strategies [2] in order to make the computation converge. We focus on FSI of PVADs [3] and simulate the Berlin Heart, a pediatric pump that is known to cause a large number of thrombolytic events. To address the blood clotting issue, we developed a technique that allows us to assess the pump efficiency on terms of average particle residence time in the blood chamber, which is known to correlate with blood clotting. A formal shape optimization framework is deployed in conjunction with FSI modeling and particle-residence-time computation to obtain a new pump design that minimizes average particle residence time in the blood chamber.

Wind-Turbine FSI Modeling

We make use of the flexible FSI framework developed to target more advanced FSI simulations of wind turbines. For this, we illustrate how the recent advances in Isogeometric Analysis (IGA) [5] of thin structures may be used for efficient structural mechanics modeling of full wind turbine structures, including tower, nacelle, and blades. We consider both horizontal axis and vertical axis wind turbine designs. We enhance the sliding–interface formulation of aerodynamics [6], to handle flows about mechanical components in relative motion such as rotor–tower interaction to allow nonstationary sliding interfaces. To accommodate the nonstationary sliding interfaces, we developed a new mesh moving technique and present its mathematical formulation. The numerical examples include structural mechanics verification for the new offshore wind turbine blade design, FSI simulation of a horizontal axis wind turbine undergoing yawing motion as it turns into the wind and FSI simulation of a vertical axis wind turbine. The FSI simulations are performed at full scale and using realistic wind conditions and rotor speeds. We conclude by presenting the FSI simulation of two 5MW wind turbines operating in a thermally-stratified atmospheric boundary-layer (ABL) flow (see Figure 1(b)).

Air-Blast FSI Modeling

The flexible FSI methodology is more recently extended to develop a computational framework for air-blast FSI applications that combines the attractive features of both Eulerian- and Lagrangian-frame based methods [7,8]. The underlying numerical formulation makes use of two meshes – background and foreground – to discretize, in the variational (e.g., Galerkin) framework, the governing equations of the coupled FSI problem. The foreground mesh is "immersed" in the background mesh, and thus the proposed methodology belongs to a class of immersed methods. The background mesh basis functions approximate the kinematic and field variables (i.e., velocity, temperature, etc.) of the coupled problem in the variational framework. The foreground mesh, which is moving with the material-particle velocity computed on a background mesh, is used to track the material interfaces, to carry out the numerical quadrature of the solid domain, to perform the stress update, and to solve auxiliary ordinary or partial differential equations (PDEs) employed in the modeling framework in order to represent additional phenomena. Figure 1(c) shows a 3D simulation of cone blast near a concrete block. Interaction of air, detonation gas products, and concrete is simulated. Mushroom cloud of the detonation gas products (blue) is immersed into the air domain. Concrete particles (red) separate from the block forming a crater on the top surface.

References

[1] Y. Bazilevs, M.-C. Hsu, and M.A. Scott, "Isogeometric Fluid--Structure Interaction Analysis with Emphasis on Non-Matching Discretizations, and with Application to Wind Turbines", *Computer Methods in Applied Mechanics and Engineering*, 249-252 (2012) 28-41.

[2] Y. Bazilevs, K. Takizawa, and T.E. Tezduyar, "Computational Fluid--Structure Interaction: Methods and Applications", Wiley 2013.

[3] C.C. Long, A.L. Marsden, and Y. Bazilevs, "Fluid--structure interaction simulation of pulsatile ventricular assist devices", *Computational Mechanics*, 52 (2013) 971-981.

[4] D. Kamensky, M.-C. Hsu, D. Schillinger, J.A. Evans, A. Aggarwal, Y. Bazilevs, M.S. Sacks, and T.J.R. Hughes, "An immersogeometric variational framework for fluid–structure interaction: application to bioprosthetic heart valves", *Computer Methods in Applied Mechanics and Engineering*, 284 (2015) 1005-1053.

[5] T.J.R. Hughes, J.A. Cottrell, and Y. Bazilevs, "Isogeometric analysis: CAD, finite elements, NURBS, exact geometry and mesh refinement", *Computer Methods in Applied Mechanics and Engineering*, 194 (2005) 4135-4195.

[6] Y. Bazilevs, A. Korobenko, X. Deng, and J. Yan, "Novel structural modeling and mesh moving techniques for advanced FSI simulation of wind turbines", *International Journal for Numerical Methods in Engineering*, 102 (2015) 766–783.

[7] Y. Bazilevs, K. Kamran, G. Moutsanidis, D.J. Benson, and E. Onate, "A new formulation for air-blast fluid–structure interaction using an immersed approach. Part I: Basic methodology and FEM-based simulations", *Computational Mechanics* 60 (2017) 83–100.

[8] Y. Bazilevs, G. Moutsanidis, J. Bueno, K. Kamran, D. Kamensky, M.C. Hillman, H. Gomez, J.S. Chen, "A new formulation for air-blast fluid–structure interaction using an immersed approach. Part II: Coupling of IGA and meshfree discretizations", *Computational Mechanics* 60 (2017) 101–116.

STABILITY BOUNDARIES AND FLUID DAMPING OF ELASTICALLY-MOUNTED PITCHING SWEPT WINGS

Yuanhang Zhu* , Yunxing Su, and Kenneth Breuer
School of Engineering, Brown University, Providence, RI 02912, USA

Summary We experimentally study the nonlinear stability characteristics and the role of fluid damping for elastically-mounted pitching swept wings using a cyber-physical system. We show that the onset of large-amplitude limit-cycle oscillations (LCOs) depends on the static characteristics of the wing. The non-monotonic variation of the stability boundary for different sweep angles is conjectured to be the competition between two mechanisms: (*a*) the stabilization of leading-edge vortices (LEVs) by wing sweep, which promotes LCOs and thus destabilizes the system, and (*b*) fluid damping, which damps out LCOs and thus stabilizes the system. We characterize the fluid damping by performing 'ring down' experiments in quiescent water and show that fluid damping increases with sweep angles.

INTRODUCTION AND EXPERIMENTAL SETUP

Fluid-structure interactions of elastically mounted pitching wings is central in many applications. Recent works explored the effect of different parameters on the dynamics and flow physics of such systems. Menon and Mittal [1] numerically investigated the effects of structural damping, initial angle of attach (AOA) and the location of pivot axis on the flow-induced oscillations of passively pitching two-dimensional wings. Zhu *et al.* [2] experimentally studied the effect of inertia and stiffness on the stability boundaries of a cyber-physical pitching two-dimensional wing and reported super- and sub-critical transitions to large-amplitude LCOs for low- and high-inertia wings respectively. However, the effect of wing sweep on the stability characteristics of elastically mounted pitching wings remains unclear. We address this problem in the present study.

A schematic of the experimental setup is shown in Figure 1(*a*). Five NACA 0012 wings with sweep angle $\Lambda = 0°, 10°, 15°, 20°, 25°$ are tested in the present study. All the wings have a chord length of $c = 0.1$ m and a span of $s = 0.3$ m. The pivot (elastic) axis is a vertical line passing through the mid-chord point on the mid-span plane. A side view of the five wings is shown in Figure 1(*b*). The wing is mounted vertically in a water tunnel with a zero initial AOA. An endplate is added to the top of the wing to eliminate tip vortices at wing root. The structural properties of the wing are controlled by a cyber-physical system. The non-dimensional parameters used in the present study are inertia, I^*, damping, b^*, stiffness, k^*, and the fluid force (moment coefficient), τ_f^*. The inverse of k^* is the Cauchy number Ca, which defines the ratio between the fluid inertia force and the elastic restoring force. The Reynolds number, Re, is kept at 50,000 for all the stability boundary tests and static force measurements (Figure 1(*b*)(*c*)). For all the experiments testing the fluid damping (Figure 2), the water is quiescent. Detailed description and validation of the cyber-physical system and the definition of non-dimensional parameters can be found in [2].

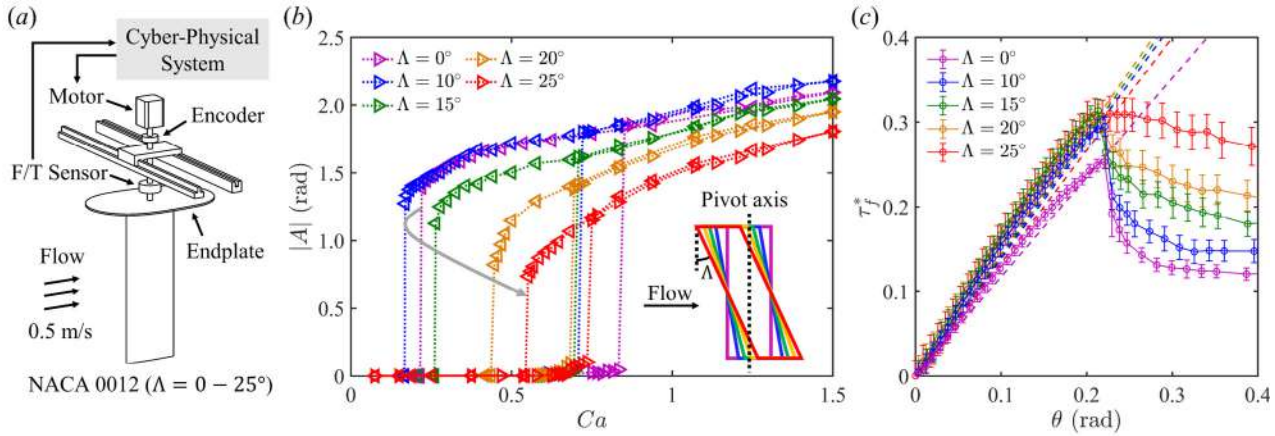

Figure 1: (*a*) A schematic of the experimental setup. (*b*) Bifurcation diagram at $I^* = 10.6$ and $b^* = 0.13$ for five wings ($\Lambda = 0°, 10°, 15°, 20°, 25°$). ▷: increasing Ca, ◁: decreasing Ca. (*c*) Static moment measurements.

RESULTS AND DISCUSSION

Stability boundaries of elastically mounted pitching swept wings

In the experiments, we fix $I^* = 10.6$ and $b^* = 0.13$, and incrementally vary Ca to define the stability boundaries of five wings with different sweep angles. Figure 1(*b*) shows the bifurcation diagram, in which the system response is represented by the pitching amplitude $|A|$. For all the wings, as Ca is increased, the system undergoes a subcritical bifurcation to large-amplitude LCOs, evidenced by an abrupt amplitude jump and a region of hysteretic bistability [2]. It is shown that both the onset and extinction of large-amplitude LCOs vary with the sweep angle. We attribute the difference in the onset point to the different static characteristics of the wings. Figure 1(*c*) shows that the static moment coefficient of the five wings can be divided into two groups, because the $\Lambda = 0°$ wing experiences lower static fluid force compared to the other four wings. This grouping is also evident in the results presented in Figure 1(*b*), where large-amplitude LCOs

*Corresponding author. E-mail: yuanhang_zhu@brown.edu

are seen to occur at a higher critical Ca for the $\Lambda = 0°$ wing. The critical elastic restoring force, $k_c^*\theta$, where k_c^* is the critical wing stiffness, is plotted using dashed lines in Figure 1(c) for all the five wings. It can be observed that all of the dashed lines coincide with the static stall point, which further suggests that the onset of large-amplitude LCOs is related the static characteristics of the wing.

As shown by the gray arrow in Figure 1(b), the extinction point (i.e. the saddle-node (SN) point) of the large-amplitude LCOs changes non-monotonically with the sweep angle. We conjecture that this non-monotonic behavior is due to the competition between two mechanisms, the destabilizing effect brought by the wing sweep and the stabilizing effect caused by the fluid damping. For $\Lambda = 0° - 10°$, the SN point extends to lower Ca, indicating that the system becomes more unstable. Previous studies [1, 2] have shown that large-amplitude LCOs are associated with the formation and shedding of strong LEVs. The persistence of LCOs at lower Ca for $\Lambda = 10°$ indicates that LEVs become more stable as compared to $\Lambda = 0°$. This agrees with previous findings [3, 4] that the wing sweep has a stabilization effect on LEVs by strengthening spanwise vorticity transport. For higher sweep angles ($\Lambda = 10° - 25°$), the large-amplitude LCOs die down at higher Ca, suggesting that a stabilizing mechanism comes into play. We think this stabilizing mechanism is fluid damping, because under the same pitching amplitude, wings with a higher sweep angle move more fluid due to larger tip motion. Due to high fluid damping, the pitching amplitude also decreases with Λ.

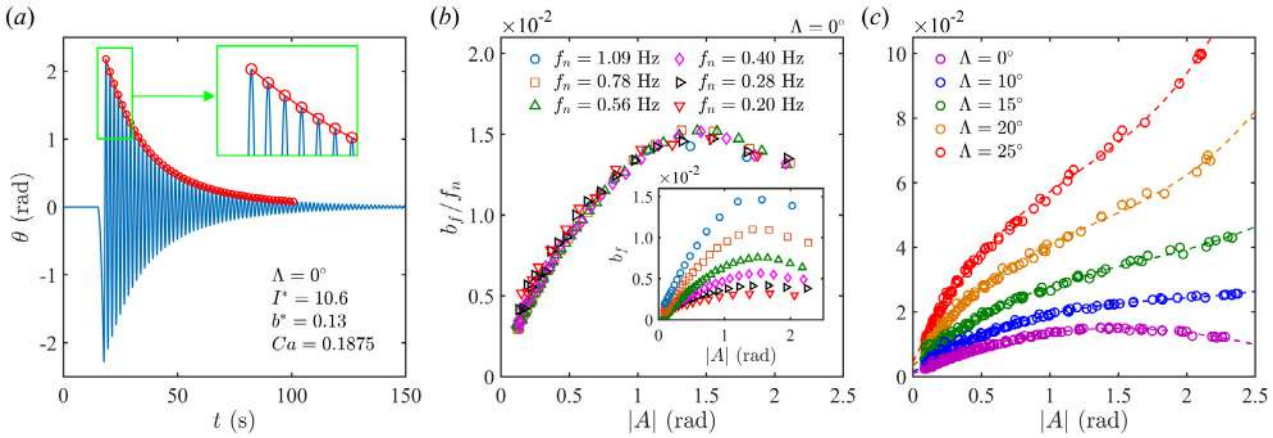

Figure 2: (a) An example of free damped oscillations. (b) Fluid damping scaling for the $\Lambda = 0°$ wing. Inset: Fluid damping versus pitching amplitude. (c) Fluid damping scaling for different wings. Note that (b) and (c) share the same y-axis label.

Fluid damping of swept wings in quiescent water

To characterize the fluid damping, we perform 'ring down' experiments in quiescent water, where we perturb the elastically mounted wing and analyze the amplitude evolution of the free oscillation. Figure 2(a) shows the result from a typical 'ring down' experiment. As shown in the zoom-in inset, for every two adjacent peaks (one cycle), we calculate the total cycle-averaged damping of the system by fitting an damped exponential to the two peaks. The structural damping is then subtracted from the total damping to get the cycle-averaged fluid damping, b_f. The corresponding pitching amplitude, $|A|$, is calculated to be the average amplitude of the two peaks. By changing the combination of I^* and k^*, we repeat the 'ring down' experiments for six different natural frequencies (f_n) and plot the result in the inset of Figure 2(b). It is seen that b_f increases non-monotonically with $|A|$ for a fixed f_n, and monotonically with f_n for a fixed $|A|$. When b_f is divided by f_n (Figure 2(b)), all the data points for different f_n collapse into one curve, indicating b_f/f_n is a good scaling parameter for the fluid damping. The 'ring down' experiments are repeated for the other four swept wings ($\Lambda = 10° - 25°$) and for each Λ, we are able to collapse the data points for different f_n using b_f/f_n, as shown in Figure 1(c). We observe that for a fixed $|A|$, b_f indeed increases with Λ. The b_f/f_n for each Λ can be accurately fit by a 3rd-order polynomial curve (dashed lines), and when Λ is high, b_f/f_n increases sharply, indicating the strengthening of nonlinear effects.

CONCLUSIONS AND FUTURE WORK

The onset of large-amplitude LCOs has been shown to depend on the static characteristics of the wing. The non-monotonic variation of the SN point has been attributed to the competition between a destabilizing mechanism brought by the stabilization of LEVs and a stabilizing mechanism caused by fluid damping. We have characterized the fluid damping for swept wings in quiescent water. A fluid damping scaling has been proposed and it has been shown that wings with higher sweep angles experience higher fluid damping. Our hypothesis that the system becomes more unstable because LEVs are stabilized by the wing sweep requires more experimental evidence and the next step is to characterize the effect of wing sweep on the LEV stability using 3D PIV experiments.

References

[1] Menon, K. and Mittal, R. Flow physics and dynamics of flow-induced pitch oscillations of an airfoil. *J. Fluid Mech.* **877**: 582–613, 2019.
[2] Zhu, Y., Su, Y. and Breuer, K. Non-Linear Stability Boundaries of an Elastically-Mounted Pitching Wing. *AIAA SciTech Forum*, AIAA 2020-1052, 2020.
[3] Onoue, K. and Breuer, K. A scaling for vortex formation on swept and unswept pitching wings. *J. Fluid Mech.* **832**: 697–720, 2017.
[4] Wong, J. G. and Rival, D. E. Determining the relative stability of leading-edge vortices on nominally two-dimensional flapping profiles. *J. Fluid Mech.* **766**: 611–625, 2015.

DEFORMATION OF FLEXIBLE MICRO HELICES UNDER FLOW-INDUCED VISCOUS FORCES

Lucas Prévost* [1], Marine Daïeff[1], Dylan M. Barber[2], Alfred J. Crosby[2], Anke Lindner[1], and Olivia du Roure[1]
[1]Laboratoire de Physique et Mécanique des Milieux Hétérog`enes (PMMH), UMR7636 CNRS, ESPCI Paris, PSL Research University, Sorbonne Université, Université de Paris, Paris, France
[2]Polymer Science and Engineering Department, University of Massachusetts, Amherst, MA, USA

Summary The study of fluid structure interactions between helix-shaped particles and viscous flows is of importance for both fundamental science and technological applications. The constitutive chirality of such particles indeed induces breaking of the time-reversal symmetry associated with viscous flows. This effect is exploited by microorganisms, such as E. coli bacteria, to propel themselves through viscous media by rotating helically shaped flagella. In this work, we fabricate flexible micro-helices with vanishing pitch and report use of material creep under stress to modify in a controlled way the helical pitch. We study experimentally the deformation of helical ribbons under flow-induced viscous forces and quantify the influence of the pitch. We report an effective stiffening of the helix as the helix pitch increases.

CONTEXT

In parallel to theoretical studies, biological flagella have been used to understand the viscous flow-helix interactions, highlighting effects such as drifting in simple shear flows [1] or flagella polymorphic transition under high-stress [2]. But the use of these biological systems is intrinsically limited, as their mechanical and geometrical properties (notably chirality) are biologically determined and thus scarcely tunable. As a consequence, numerous methods have been proposed to fabricate tunable artificial helical structure to serve as model systems. Such artificial systems have allowed quantification of the influence of bacterial head size [3] or helix pitch angle [4] on swimming efficiency. These systems open up numerous technological applications such as micro robots for targeted drug delivery [5] or flow sensors. But the influence of the helix elasticity has been so far mostly neglected, as it heavily complexifies both theoretical and experimental approaches. The fabrication of flexible chiral structure at the micro-scale is indeed a challenge.

HELIX FABRICATION AND PITCH CONTROL

In this work, we use ribbons fabricated through an evaporative assembly technique called flow coating [6]. Two different materials were used: poly(methyl methacrylate) (PMMA) and modified poly(2-dimethylaminoethyl methacrylate) (dPDMAEMA). As a result of the asymmetric cross section of the ribbons, ribbons spontaneously coil when immersed into liquids, forming helices. The preferred helix radius is given by a balance between surface tension and elasticity and can be controlled by the ribbon thickness [7]. The preferred helix pitch is zero but a small pitch is observed nonetheless due non-overlap of the ribbon.

We demonstrate that, by taking advantage of the creeping of the material under stress, it is possible to obtain a permanent non-vanishing pitch. This effect is reported for both materials (PMMA and dPDMAEMA). The stress is induced by immersing the helix in a uniform flow, which extends the helix. When the flow is stopped, we observe a persistent non-homogeneous increase of the helix pitch as seen in Figure 1. The pitch change can be controlled by tuning the duration or the intensity of the flow. The stress can also be induced by an end-point force, *i.e.* pulling on both sides of the helix. In this case, preliminary experiments show a uniform increase of the pitch. These observations are consistent with the fact that for viscous forces, the resulting stress is distributed along the helix whereas for end-point forces, the stress is uniform. We note that as a side effect of the applied forces, the helix radius is also modified. Similarly, the subsequent radius change is non-homogeneous for flow-induced stress and homogeneous for stress induced by end-point forces.

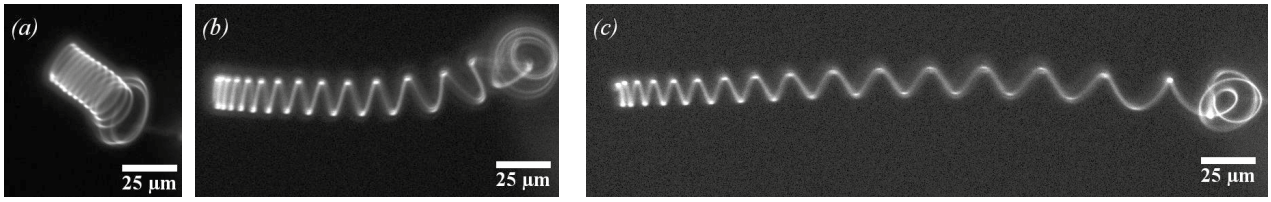

Figure 1: PMMA-made helical ribbon observed under fluorescent microscopy without any flow (a) in its initial state upon release and coiling of the ribbon ; (b) after immersion for 30 min in a water flow ; (c) after immersion for another 30 min in a water flow of identical flow rate. The helix is held on its right by a glass capillary.

*Corresponding author. E-mail: lucas.prevost@espci.fr

HELIX DEFORMATION IN FLOW

This fabrication technique allows us to obtain helical ribbons of controllable pitch. But more importantly, it allows us to vary the pitch of a given helix in a controlled way, all other parameters being unaffected (notably material modulus and ribbon cross-section). We use this effect to isolate and probe the influence of the helical pitch on the deformation of helices in flow. Experiments are conducted as follows: a given flow rate is applied in a microfluidic channel of known dimension, in which a helix is held by a glass capillary. The subsequent helix deformation is tracked by measuring the helix axial length H. The flow is parabolic in the channel but as typical helical radii are small compared to the channel size, we consider that the helix is immersed in a locally uniform flow. The velocity of this flow V is estimated from the computed velocity field and the position of the helix within the channel.

We define a *flow cycle* as a series of flow steps imposed upon a helix at increasing flow rate. A typical flow cycle is shown in Figure 2.(a) along with the measured helix axial extension. For each flow cycle, a velocity-extension curve $\Delta H(V)$ is obtained and the slope α of the linear regime is extracted, as shown in Figure 2.(b). The so-called flow stiffness α quantifies how much a helix is stretched for a given flow velocity. This work-flow is repeated on the same helix for different values of the pitch, which is modified using the procedure described in the previous section. As shown in Figure 2.(c), data suggest that an increase in the helix pitch angle is associated with a smooth decrease in the flow stiffness *i.e.* an effective stiffening of the helix. Possible aging effects were discarded by letting helices sit in water for $24\,\mathrm{h}$ prior to experiments.

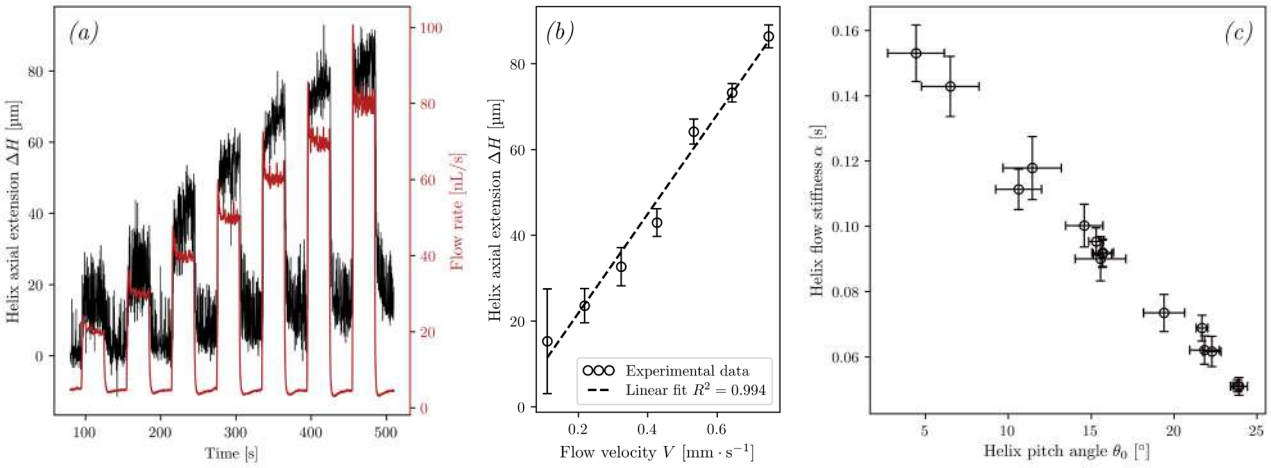

Figure 2: (a) Typical flow cycle applied upon a dPDMAEMA-made helix: the applied water flow rate (in red) and measured axial extension (in black) are plotted as a function of time. (b) Velocity-extension curve obtained from (a) and linear fitting to extract the helix flow stiffness. (c) Helix flow stiffness as a function of the helix pitch angle θ_0, defined as the angle subtended between a circumferential line and the pitch of the helix *i.e.* $\tan\theta_0 = p/2\pi R$.

CONCLUSION AND PERSPECTIVES

We have shown how to fabricate flexible micro helices of controllable radius and pitch. This fabrication method has allowed us to probe the influence of the helical pitch on the helix flow stiffness. We have acquired data suggesting an effective stiffening of the helix as the pitch increases. These experimental findings need to be confronted to recent theoretical modelings [8] to link the helix behavior to material and ribbon properties. A fine understanding of this link can allow characterization of the material, such as measurement of the Young's modulus [9]. Finally these micro-helices can be used to address more complicated problems, such as dynamics of freely transported helically shaped objects.

References

[1] Fu, Henry C., Thomas R. Powers, and Roman Stocker. "Separation of microscale chiral objects by shear flow." *PRL* **102.15** (2009): 158103.
[2] N. C. Darnton, et al. "Force-extension measurements on bacterial flagella: triggering polymorphic transformations." *Biophys. J.* **92.6** (2007): 2230-2236.
[3] Zhang, Li, et al. "Characterizing the swimming properties of artificial bacterial flagella." *Nano letters* **9.10** (2009): 3663-3667.
[4] Liu, Bin, et al. "Force-free swimming of a model helical flagellum in viscoelastic fluids." *PNAS* **108.49** (2011): 19516-19520.
[5] Zhang, Li, et al. "Artificial bacterial flagella: Fabrication and magnetic control." *Applied Physics Letters* **94.6** (2009): 064107.
[6] Lee, Dong Yun, et al. "Macroscopic nanoparticle ribbons and fabrics." *Advanced materials* **25.9** (2013): 1248-1253.
[7] J. T. Pham, et al. "Highly stretchable nanoparticle helices through geometric asymmetry and surface forces." *Adv. Mater.* **25.46** (2013): 6703-6708.
[8] Katsamba, Panayiota, and Eric Lauga. "Propulsion by stiff elastic filaments in viscous fluids." *PRE* **99.5** (2019): 053107.
[9] J. T. Pham, et al. "Deformation and shape of flexible, microscale helices in viscous flow." *PRE* **92.1** (2015): 011004.

UNDERACTUATED FLUIDIC CONTROL OF A CONTINUOUS MULTISTABLE MEMBRANE

Ofek Peretz[1], Anand Kumar Mishra[2] , Robert F. Shepherd[2] , and Amir D. Gat[1]
[1]Faculty of Mechanical Engineering, Technion - Israel Institute of Technology, Haifa 3200003, Israel
[2]Sibley School of Mechanical and Aerospace Engineering, Cornell University, Ithaca, NY, USA.

Summary This work addresses the challenge of underactuated pattern generation in continuous multistable structures. The examined configuration is a slender membrane which can concurrently sustain two different equilibria states, separated by transition regions, and is actuated by a viscous fluid. We first demonstrate the formation and motion of a single transition region and then sequencing of several such moving transition regions to achieve arbitrary patterns by controlling the inlet pressure of the actuating fluid. Finally, we show that non-uniform membrane properties, along with transient dynamics of the fluid, can be leveraged to directly snap-through any segment of the membrane.

INTRODUCTION

Pressurization of confined fluids is a leading method for the actuation of such bistable elements, yielding governing dynamics involving both viscous and elastic effects. While the interaction of fluids bounded by elastic structures was extensively studied in recent years (see [1-3] as well as discussion in [4]), only a few researchers examined viscous flow interacting with bi-stable elasticity (e.g., [5-7]). So far, all previous works examined the actuation dynamics of either a single bi-stable element [8,9] or multistable structures [10,11], which are an assembly of discrete bistable elements. In this work, we present, for the first time, analysis and demonstration of fluidic-control of a continuous multistable structure. In contrast with discrete multistable configurations, such continuous structures inherently have infinite possible stable patterns. Importantly, in many of these works, each element has its own control input for inducing transitions between its bi-stable states [13,14]. Therefore, generating complex deformation patterns of such a multistable structure, typically requires control of multiple inputs, which greatly complicates the systems operation. We thus focus on achieving underactuated fluidic control, enabling to arbitrarily pattern such continuous structures by a single pressure inlet.

THEORETICAL AND EXPERIMENTAL RESULTS

The configuration studied in this work is presented in Fig. 1a, showing the experimental setup, including the membrane and a transition region separating between the two different equilibria states. The x coordinate denotes the streamwise direction, where the inlet is located at x = 0. The location of the transition region is denoted by $x_s^-(t) < x < x_s^+$. Initially, the entire membrane is at the snapped-up state. A sudden decrease in inlet pressure initiates snap-down near the inlet (Fig. 1a, region 1). A transition region (Fig. 1a, region 2) then starts propagating, separating the snapped-down region from the membrane segment which remained at the initial snapped-up state (Fig. 1a, region 3). To achieve two stable equilibria states at rest (meaning fluidic gauge pressure $p = 0$), we require both $p_s^{down} < 0$ and $p_s^{down} > 0$. Using this setup, in Fig. 2a we demonstrate the propagation of a single transition region in the channel. The initial state of the membrane is at a snapped-up state, and then we apply a Heaviside inlet pressure function of $p_{in} = -10\,kPa$ at $t = 0\,sec$. The negative inlet pressure creates transition to snap-down near the inlet as well as a transition region separating the snapped-up state far from the inlet. As time progresses, the transition region propagates along the flow direction, and the membrane gradually changes its state from snapped-up to snapped-down. The shape of the membrane at different time intervals is presented in Fig. 2a, where the blue and black lines represent the theoretical and experimental location of the transition region x_s vs. time t. To obtain insight regarding these results, we derived a theoretical model for the propagation of a single transition region in a multi-stable channel (Fig. 2a, black line denotes experimental results, blue line denotes theoretical results and red line denotes inlet pressure profile).

Above, we analytically analyzed and experimentally demonstrated the emergence and motion of a single transition region, and showed that when the inlet pressure returns to its nominal value, the membrane's shape remains nearly unchanged. Thus, by sequencing several inlet pressures, any pattern of a snapped-down and snapped-up regions along the channel can be created. Figure 2b shows the evolution of the membrane shape and presents the location of the transition regions, vs. time, as well as snapshots of the membrane shape at different time intervals. Initially, the channel is entirely at the snapped-up state. Then we applied alternating positive and negative gauge inlet pressures (see red line in Fig. 2b, denoting inlet pressure) to generate moving snap-down and snap-up transition regions, thus patterning the equilibrium state of the continuously multistable membrane.

CONCLUSIONS

To conclude, in this work we addressed the challenge of underactuated control of continuous multistable structures, which could play a vital role in the fields of soft robotics, MEMS, and meta-materials. We focused our study on a simple illustrative configuration composed of an slender elastic membrane, which is actuated by a viscous fluid. The membrane is able to concurrently sustain two different modes of stable cross-section shapes at different segments of the membrane. These different segments are shown to be separated by transition regions, and the location of these regions sets the stable equilibrium shape of the membrane. We theoretically analyzed and experimentally demonstrated the formation and motion of a single, and multiple, transition regions due to manipulation of the fluidic inlet pressure. We showed that sequencing of multiple transition regions enables to achieve underactuated control of the membrane equilibria shape.

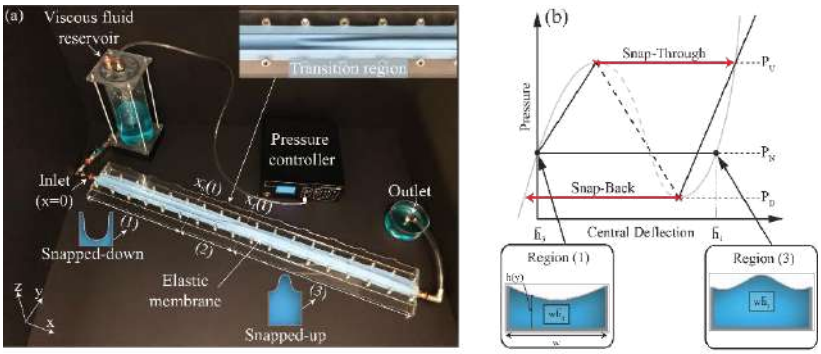

Figure 1: Panel (a) presents an illustration of a bi-stable behavior of a clamped-clamped curved elastic membrane. At the initial state (A), the configuration is at a stable deformation pattern. When pressure is applied on the bottom surface of the membrane, the component deforms gradually until a critical value of the pressure (denoted by p_s^{up}). At this point, the component snaps-through a region of unstable deformation shapes (B) until reaching a second stable deformation pattern (C). At state (C), decreasing the pressure below p_s^{up} will not bring the membrane back to state (A), due to hysteresis effect of the bi-stable dynamics. Snapping back to state (A) requires reaching a different lower critical value (denoted by p_s^{down}), associated with state (C). Panel (b) presents the experimental setup.

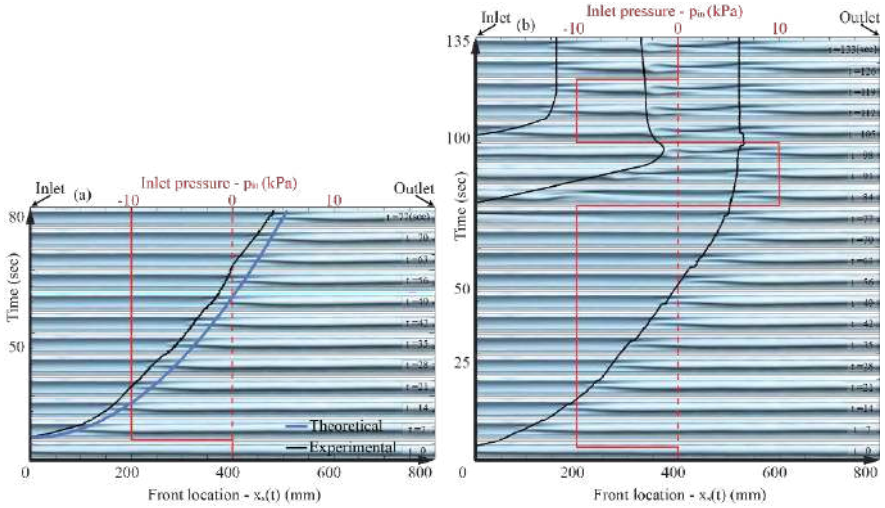

Figure 2: Panel (a) presents experimental and analytical results for a single transition region propagation and the location of the transition region at different time intervals (from 0-80 sec) and at varying inlet pressure ($p_{in} = 0\ to\ -10kPa$). Panel (b) presents experimental results of patterning using multiple transition regions propagation. Initially, the channel is at snapped-up state. Then we applied varying inlet pressures between negative and positive gauge values (red line, denoting inlet pressure) to generate moving snap-down and snap-up transition regions, which allow patterning of the continuously multistable membrane. After sequencing three transition regions (denoted in black line), separating four different stability states are obtained, we removed pressure actuation and the membrane pattern remained stable (see $t = 133\ sec$).

References

[1] JB Grotberg, OE Jensen, Biofluid mechanics in flexible tubes. Annu. review fluid mechanics 36 (2004).
[2] JR Lister, Buoyancy-driven fluid fracture: the effects of material toughness and of low viscosity precursors. J. Fluid Mech. 210, 263–280 (1990).
[3] B Mosadegh, et al., Pneumatic networks for soft robotics that actuate rapidly. Adv. Functional materials 24 (2014).
[4] C Duprat, HA Stone, Fluid-Structure Interactions in Low-Reynolds-Number Flows. (Royal Society of Chemistry), (2015).
[5] D Glozman, N Hassidov, M Senesh, M Shoham, A self-propelled inflatable earthworm-like endoscope actuated by single supply line. IEEE Transactions on Biomed. Eng. 57, 1264– 1272 (2010).
[6] M Heil, AL Hazel, Fluid-structure interaction in internal physiological flows. Annu. review fluid mechanics 43, 141–162 (2011).
[7] M Heil, Stokes flow in collapsible tubes: computation and experiment. J. Fluid Mech. 353, 285–312 (1997).
[8] Z Zhakypov, K Mori, K Hosoda, J Paik, Designing minimal and scalable insect-inspired multilocomotion millirobots. Nature 571, 381–386 (2019).
[9] J Vandermarlière, On the inflation of a rubber balloon. The Phys. Teach. 54, 566–567 (2016).
[10] G Puglisi, L Truskinovsky, Mechanics of a discrete chain with bi-stable elements. J. Mech. Phys. Solids 48, 1–27 (2000).
[11] W Dreyer, I Müller, P Strehlow, A study of equilibria of interconnected balloons. The Q. J. Mech. Appl. Math. 35, 419–440 (1982).
[12] T Cohen, S Givli, Dynamics of a discrete chain of bi-stable elements: a biomimetic shock absorbing mechanism. J. Mech. Phys. Solids 64, 426–439 (2014).
[13] L Hines, K Petersen, M Sitti, Inflated soft actuators with reversible stable deformations. Adv. Mater. 28, 3690–3696 (2016).
[14] Y Fei, W Pang, Analysis on nonlinear turning motion of multi-spherical soft robots. Nonlinear Dyn. 88, 883–892 (2017).

EFFECT OF CHORDWISE FLEXIBILITY ON PROPULSIVE PERFORMANCE OF HIGH INERTIA OSCILLATING FOILS

Peter Oshkai*[1], Dylan Iverson[1], Mostafa Rahimpour[1], Waltfred Lee[1], and Takahiro Kiwata [2]
[1]Department of Mechanical Engineering, University of Victoria, Victoria, Canada
[2]School of Mechanical Engineering, Kanazawa University, Kanazawa, Japan

Summary This work studies the effects of chordwise flexibility and inertia on propulsive performance of an oscillating foil. The foil was undergoing pitch and heave motions in a uniform flow at Re = 80000. Forces exerted on the foil were directly measured using a load cell and were used to calculate the thrust and efficiency values. The phase-averaged quantitative flow patterns in the wake of the foil were obtained using particle image velocimetry. The circulation in the wake was related to the loading on the foil by calculating the moments of vorticity with respect to the pitching axis of the foil. Inertial and pressure forces were responsible for foil deformation at the different phases of the oscillating cycle. The deformation of the foil resulted in an increased wake width, leading to increases in amplitudes of the instantaneous loading on the foil and in the generated thrust coefficient.

INTRODUCTION

The prevalence of oscillating wings found in nature warrants research into the associated biomimetic technologies that could be developed from these principles. When acting as a thrust generator, oscillating-foil designs propose an elegant alternative to conventional rotary propellers, which have limited ranges of operational speeds where efficiency is maximum [1]. Advances in numerical and experimental capabilities in recent years has renewed interest in the subject and facilitated many novel studies including those on flexible foils. It was highlighted that passive chordwise flexibility of the wing or foil can improve propulsive efficiency at the expense of small decreases in net thrust [2]. Research into the effect of inertial properties and its relation to performance of flexible foils has been mainly limited to numerical campaigns, in which this structural property may be varied readily [3], [4]. The present work analyzes flexible foils with high inertia values in a wide parametric space of pitch amplitude and oscillating frequency combinations.

EXPERIMENTAL SYSTEM AND TECHNIQUES

The experiments were performed in a recirculating water channel with a test section that had a length of 250 cm and a cross section of 45x45 cm. The ambient turbulence intensity of the flow was less than 1% for the range of velocities used in the current study. A schematic of the experimental apparatus is shown in Fig. 1a. The foil was centered in the cross section of the flow channel. Heave and pitch motions were controlled independently by separate servo motors. The heave motor was rigidly mounted onto the water channel frame and connected to a linear carriage that generated the heave motion. The pitch motor was mounted onto the heave carriage, to which a loadcell and the test foil were attached. Both heave and pitch motion profiles were sinusoidal, with a phase difference of 90° between them, as shown in Fig. 1b.

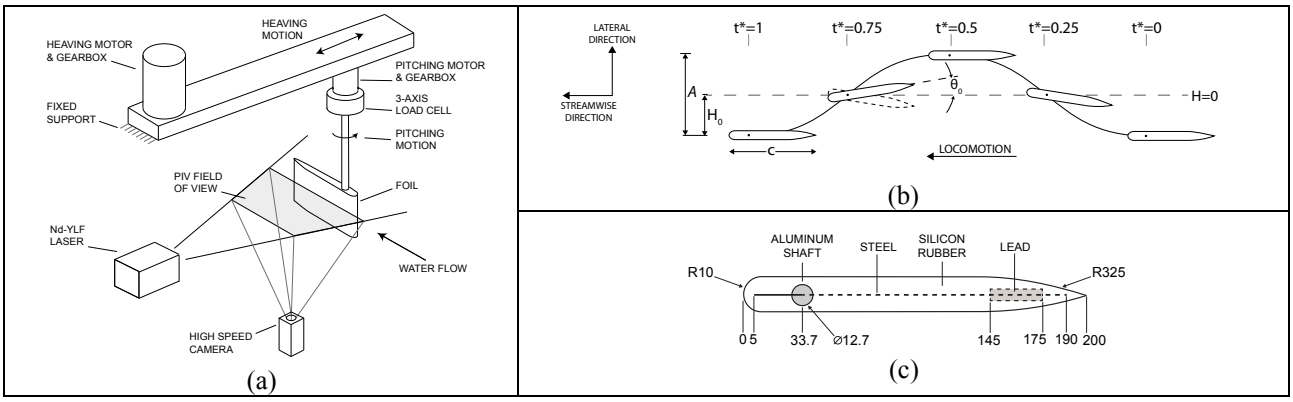

Figure 1. Schematics of the fully-passive turbine (a) and the PIV system (b).

Three foils of identical shape, but with different structural parameters, were used in experiments. All foils had a chord length of c = 200 mm and a span length of b = 140 mm. The cross-section of the foils is shown in Fig. 1c. This geometry was created to allow a weight to be embedded near the trailing edge of one of the foils, positioned at a distance 0.8c from the leading edge. The foil 'R', was constructed of plastic that is from a practical standpoint assumed to be fully rigid. The other two foils were constructed of a flexible silicon rubber. Flexible foil 'A' had a mass of 140 g embedded at the trailing edge location, and was reinforced in the chordwise direction by a stainless steel sheet. The second flexible foil, 'B', was constructed without the steel sheet or lead mass, and consequently was 34% less stiff than foil 'A'.

*Corresponding author. E-mail: poshkai@uvic.ca.

Fluid velocity was measured using high-speed particle image velocimetry (PIV) as shown schematically in Fig. 1a. The flow was seeded with tracer particles with a mean diameter of 10 μm that were illuminated by a pulsed laser. The images were processed with Davis LaVision 8.3 software using a multipass cross correlation technique. The smallest interrogation windows used were 12 pixels x 12 pixels, yielding a resolution of 0.26 vectors/mm.

RESULTS

All experiments were performed at $Re_c = 80000$ and with a heave amplitude $H_0 = 0.188c$. The recorded measurements for cycle-averaged thrust production $\overline{C_T}$ and efficiency η are presented in Fig. 2 for each of the three foils. The generated thrust values monotonically increased as a function of St for any given pitch angle, for all foils. Large positive pitch angles were necessary for high thrust production by the rigid foil, but they were not needed for high thrust production by both flexible foils. Moreover, the flexible foils showed significant increases in efficiency compared to their rigid counterpart.

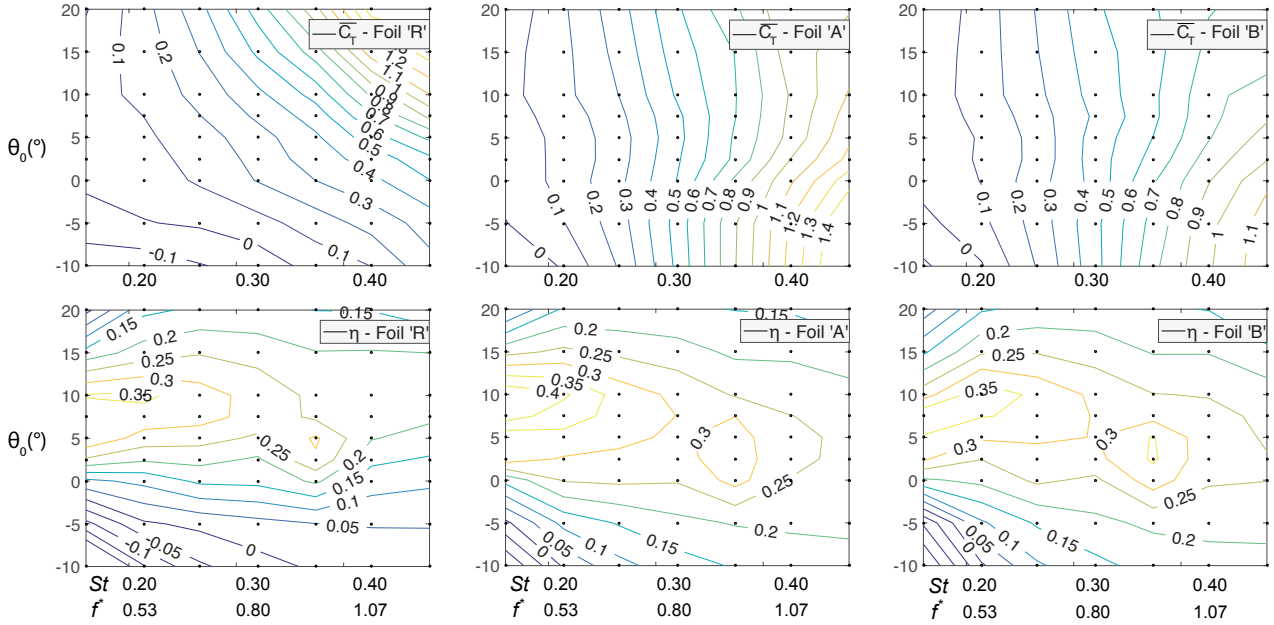

Figure 2. Thrust coefficient (top row) and efficiency (bottom row) as function of pitch angle and Strouhal number for foil 'R' (left column), foil 'A' (middle column) and foil 'B' (right column).

The PIV measurements (not shown herein) indicate that the transverse deflection of the trailing edge, which defined the effective instantaneous angle of attack, determined the timing of the trailing edge vortex shedding and, in turn, the generated thrust and efficiency.

CONCLUSIONS

The trends of propulsive performance observed for rigid and flexible foils differed in terms of response to pitch angles. Inertial forces were the dominant mechanism producing foil deformation at the beginning and at the end of a heave cycle. At the midstroke of the heaving motion, pressure forces were responsible for the majority of deformation. There appears to exist an optimal stiffness level that would result in maximum thrust and efficiency at all St in the considered range. In this scenario, the trailing edge would deform to ~15° when prescribed a pitch angle of ~5°.

References

1. Fish, F. and G. Lauder, *Passive and active flow control by swimming fishes and mammals.* Annu. Rev. Fluid Mech., 2006. **38**: p. 193-224.
2. Katz, J. and D. Weihs, *Hydrodynamic propulsion by large amplitude oscillation of an airfoil with chordwise flexibility*. Journal of Fluid Mechanics, 1978. **88**(3): p. 485-497.
3. Zhu, Q., *Numerical simulation of a flapping foil with chordwise or spanwise flexibility.* AIAA journal, 2007. **45**(10): p. 2448-2457.
4. Yin, B. and H. Luo, *Effect of wing inertia on hovering performance of flexible flapping wings.* Physics of Fluids, 2010. **22**(11): p. 111902.

LOCK-IN IN FLOW-INDUCED VIBRATION OF SPLITTER PLATES AND MEMBRANES

Mohd Furquan *[1], Tulsi Ram Sahu[1], and Sanjay Mittal[1]
[1]Department of Aerospace Engineering, Indian Institute of Technology Kanpur, Kanpur, India

Summary The phenomenon of lock-in is investigated for flow-induced vibration of flexible structures at low Reynolds numbers. The structures considered are flexible plate attached to cylinder(s), a sail modelled by a flexible membrane mounted normal to the incoming flow, and inflation of a balloon. For the splitter plate, various configurations of the cylinder(s) are considered: a stationary cylinder, a freely vibrating cylinder on elastic support and two stationary side-by-side cylinders. The effect of varying the flexibility of the splitter plates is studied. Lock-in is found to occur with the first two Euler-Bernoulli modes of the splitter plate. The cylinder on elastic support vibrates out-of-phase with the tip of the plate when the plate is very flexible, and in-phase when the plate is stiff. This reversal in phase is explored by examining the normal modes of the structure.

INTRODUCTION

Flow-induced vibration (FIV) of flexible structures exhibit a number of interesting dynamical phenomena. Some of them, such as lock-in and hysteresis, have been extensively studied in the context of FIV of rigid bodies mounted on elastic support. Lock-in is said to occur when the frequency of FIV attains a value close to the natural frequency of the structure. Large amplitude of vibration is observed during lock-in. Its onset is dependent on whether the state is approached by increasing or decreasing the control parameter, generally Reynolds number or inverse of (non-dimensionalized) natural frequency. This dependence of lock-in/no lock-in on initial condition is called hysteresis.

The vibration of flexible structures is, however, far more complex. In addition to the modification of the lock-in regimes, these systems exhibit phase reversal and appearance of chaos even at low Re. We investigate some of these phenomena for vibration of splitter plates behind bluff bodies, flutter of a sail like body and ovalling oscillation of an inflating balloon.

COMPUTATIONAL METHOD

All computations are done via an in-house fluid-structure-interaction (FSI) set-up based on a partitioned approach. Incompressible Navier-Stokes equations are solved using space-time SUPG/PSPG stabilized FEM [1]. Three different structure models are used: nonlinear elastic model [1], Timoshenko beam model [2] and nonlinear membrane model [3]. All three are solved using semi-discrete Galerkin FEM. Fluid mesh is deformed to conform the fluid-solid interface by modeling it as a linear elastic pseudo-solid [1].

RESULTS AND DISCUSSION

The effect of flexibility of a splitter plate behind a circular cylinder on FIV is studied for three different configurations. Flexibility of the plate is characterized using the reduced speed U_p^*, defined as the inverse of first natural frequency of the plate non-dimensionalized by freestream speed and cylinder diameter (D). The Reynolds number, mass-ratio and length of the splitter plate are fixed at 150, 10 and $3.5D$, respectively. First, flow past a fixed cylinder with flexible plate is considered. Figures 1(a) and (b) show the time history of tip displacement and instantaneous vorticity fields at $U_p^* = 5$ and 60, respectively. These values of U_p^* correspond to the peaks of the first two, amongst the several, lock-in regions observed. The first lock-in has a smaller peak amplitude with frequency close to the first natural frequency of the plate. Plate deformation during first lock-in is accounted completely by the first Euler-Bernoulli bending mode. The second lock-in corresponds to a mix of the first two bending modes and a much larger peak amplitude. The frequency of vibration stays close to the second natural frequency of the plate. The two lock-in regions are separated by a range of U_p^* in which very small amplitude vibration at a frequency close to that for a rigid plate is observed. This region is analogous to the desynchronization region for VIV of an isolated cylinder. The second configuration consists of a cylinder vibrating freely on a spring with compliance $U_s^* = 6$. U_s^* is defined as the inverse of natural frequency of the spring-mass system when the plate is taken to be rigid. In case both cylinder and plate are free to vibrate, the structure is characterized by the pair (U_s^*, U_p^*). Figures 1(c) and (d) correspond to $(U_s^*, U_p^*) = (6, 5.36)$ and $(6, 12)$, respectively. The cylinder and the plate vibrate in-phase in the first case and out-of-phase in the second. However, in either case the plate shape resembles the first Euler-Bernoulli mode. Normal mode analysis of the structure reveals that such behaviour is a representative of the first two eigenmodes of an elastically mounted cylinder with flexible plate. A parametric study of the FIV further shows that the transition between these two modes, as U_p^* increases, is sudden in nature. Transition from in-phase (figure 1(e)) to out-of-phase vibration (figure 1(f)), with U_p^*, is also observed between flexible plates behind two fixed cylinders. However, there are no underlying structure modes responsible for this transition. In fact, the switch in phase relation occurs purely due to hydrodynamic coupling between identical bending modes of the two plates.

*Corresponding author. E-mail: mfurquan@iitk.ac.in.

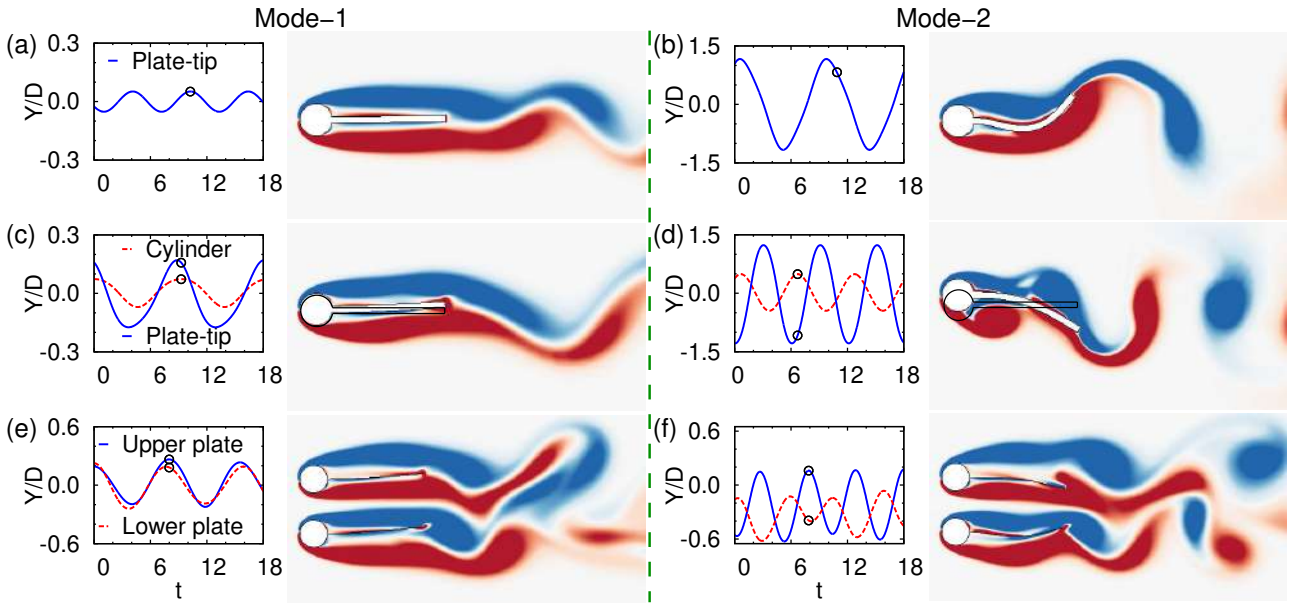

Figure 1: Flow past different configurations of circular cylinder(s) with flexible splitter plate(s) at $Re = 150$. Time history of tip displacement and instantaneous vorticity field for: fixed single cylinder at (a) $U_p^* = 5$ and (b) $U_p^* = 60$; elastically mounted cylinder at (c) $(U_s^*, U_p^*) = (6, 5.36)$ and (d) $(U_s^*, U_p^*) = (6, 12.8)$; two fixed cylinders at (e) $U_p^* = 4$ and (f) $U_p^* = 16$.

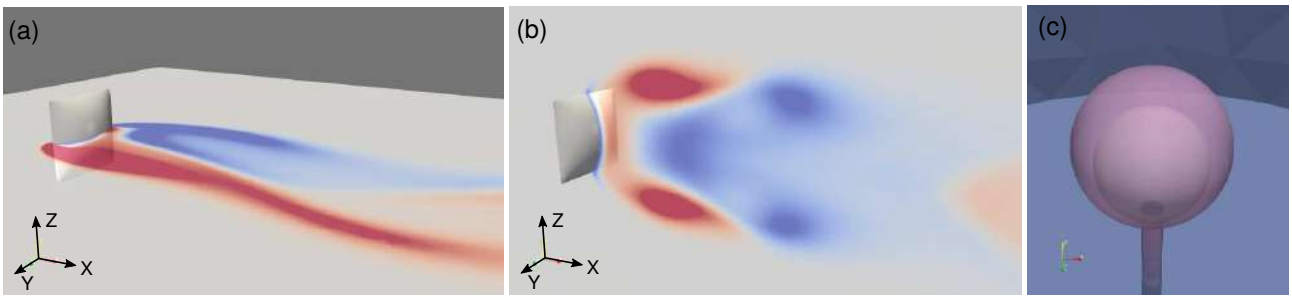

Figure 2: (a,b) Flow past a flexible square membrane sheet at $Re = 150$, $Ae = 5$ and $m^* = 10$: (a) Z-voriticty and (b) Y-vorticity fields along sectional planes through the center. (c) An inflated balloon undergoing ovalling oscillations for $Re = 500$, $Ae = 0.025$ and $m^* = 5$. Also shown for reference is the original un-inflated balloon.

FIV of membrane structures is studied. The membrane is characterized by stiffness $Ae = E/\rho_f U^2 L$ and mass-ratio $m^* = \rho_s/\rho_f L$, where E is Young's modulus, U is the characteristic speed, L is the characteristic length and ρ_f and ρ_s are the fluid and the membrane density. We first study the flow past a rectangular membrane held normal to an incoming uniform stream (along X axis). Figure 2(a) and (b) show the deformed membrane shape and Z and Y vorticity fields in two mid-sectional planes. The shape of the membrane resembles the first eigenmode of the structure. The vortex shedding is symmetric in the XZ plane and alternate in the XY plane. Figure 2(c) shows an initially spherical balloon undergoing ovalling oscillations as it inflates due to an applied pressure gradient in the inlet.

CONCLUSIONS

FIV of different structures is studied by varying flexibility. For a fixed cylinder with flexible plate, lock-in is observed with first, for $3 \lesssim U_p^* \lesssim 10$, and second, for $U_p^* \gtrsim 25$, Euler-Bernoulli modes. where the exact value of U_p^* for the onset of a lock-in is dependent on the initial condition used for computations. A stiff splitter plate, $U_p^* \lesssim 6$, vibrates in-phase with a freely oscillating cylinder due to lock-in with the first eigenmode of a vibrating cylinder with non-rigid plate. For $U_p^* \gtrsim 6$, the response is dominated by the second mode, leading to a reversal of the phase relation. Phase reversal, by increasing U_p^*, is also observed for two fixed cylinders with flexible plates.

References

[1] Furquan M. and Mittal S. Flow past two square cylinders with flexible splitter plates. *Comput. Mech.* **55**(6): 1155-1166, 2015.

[2] Simo, J.C. and Vu-Quoc, L. On the dynamics of flexible beams under large overall motions the plane case: Part II. *J. Appl. Mech.* **53**: 855-863, 1986.

[3] Taylor, R.L., Onate, E. and Ubach, P.A. Finite element analysis of membrane structures. In *Textile Composites and Inflatable Structures*, Onate, E. and Kroplin, B. (ed.). 2005.

FLOW-INDUCED DEFORMATION OF A BISTABLE ORIGAMI PATTERN

Tom Marzin[1], Emmanuel de Langre[1], and Sophie Ramananarivo* [1]
[1]LadHyX, Department of Mechanics, Ecole polytechnique, Institut polytechnique de Paris, France

Summary We experimentally investigate the elastic deformation of a 'waterbomb' folding unit in a controlled air flow. This fundamental origami base is selected for its large shape changes as well as its bistable properties. We measure the drag force experienced by the system as it reconfigures in the flow, and show an atypical drag-versus-flow speed curve, with abrupt changes in fluid loading. An analytical model is developed to corroborate our experimental results based on an energy balance between the elastic potential energy of the folds and the work of fluid forces. Understanding the behavior of such architected surfaces paves the way to control and program passive elastic response in flows.

INTRODUCTION

Flexibility allows for a structure to change shape in a flow and passively adapt to a varying fluid environment. Such reconfiguration offers a strategy for drag reduction through the combined effect of streamlining and reduction of frontal area [1]. The way the structure bends is determined by its elastic properties and its geometry: for example, a circular sheet cut along a radius rolls up into a cone when immersed in a flow [2]. Origamis, which recently emerged as a tool to engineer mechanical properties, represents an interesting opportunity to broaden the framework of flow-induced reconfigurations.

Origamis are sheets folded along crease patterns. Those patterns condition the morphing, allowing for extreme shape changes that can be exploited to deploy solar sails or foldable antenna. Targeted mechanical properties can also be implemented, such as auxetic behavior or multistability. Those features are interesting from the perspective of fluid/structure interaction as fluid loading is highly sensitive to large variations in area or shape.

Here, we study the behavior of origami in a controlled flow, starting with a single folding unit. We selected the so-called 'waterbomb' motif as one of the fundamental origami bases, that consists in an alternation of mountain or valley folds radiating from a single vertex (see Fig.1a). In the approximation of rigid faces, the kinematics is entirely prescribed by the motion of the folds [4]. The waterbomb motif then deforms along a single degree of freedom (DOF), but presents two stable equilibriums [3] (see Fig.1a). It would allow the structure to deploy in an incoming flow, before snapping past a critical speed.

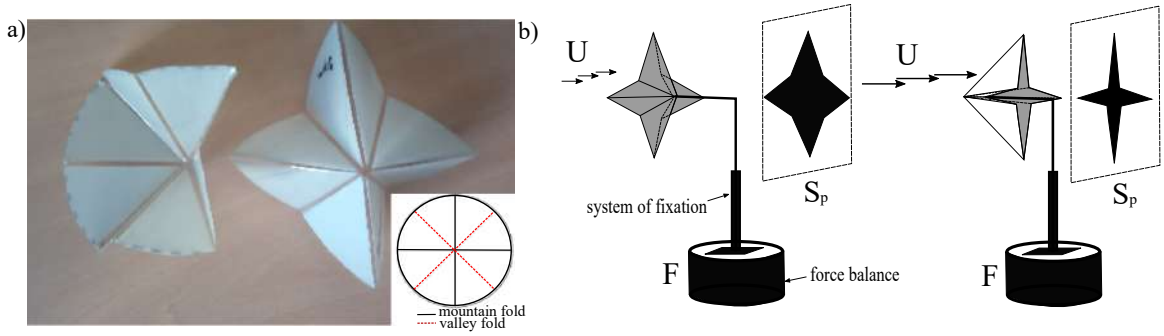

Figure 1: (a) 'Waterbomb' origami with rigid faces, assembled out of superposed mylar sheet. This base fold presents two stable states [Inset : crease pattern in the unfolded state]. (b) Experimental setup of a waterbomb base placed in an incoming flow of speed U. Past a critical speed, the structure snap-through. This reconfiguration leads to large changes of the projected surface S_p and the drag force F measured by a force balance.

EXPERIMENTAL SET UP AND RESULTS

The origami with rigid faces is implemented experimentally by superposing two mylar sheets of different thickness (Fig.1a), a thin one for the folds and a thicker one for the faces. The structure is placed in an open wind tunnel, that generates a controlled flow with velocity $U \sim 0 - 18\,m.s^{-1}$, with Reynolds numbers $Re \sim 10^3 - 10^4$. The drag force F experienced by the origami is measured by a precision balance, while we simultaneously record shape changes with a camera placed downstream of the air flow that extracts the projected surface S_p (Fig.1b). The origami is initially positioned with its concave side facing the flow, in order to study both its opening and closing. We vary the radius of the origami R, the stiffness of the folds κ as well as the opening angle in the unstrained state, and the number of folds N.

Fig.2a-b respectively show the projected surface S_p nondimensionalized by the unfolded surface S_0, and the drag force F, as a function of U wind velocity for the different parameters. The origami first deploys in the incoming flow and the increase in frontal area leads to a drag increase. Past a critical velocity, the deployed origami undergoes a snapping

*Corresponding author. E-mail: sophie.ramananarivo@ladhyx.polytechnique.fr

transition leading to an abrupt change in S_p and F. Past this point, the structure closes up in the flow and we observe the presence a force plateau, where drag no longer depends on the flow speed. As expected, larger the origamis (dark red curves, with $*$ symbols) tend to snap at lower critical wind velocity, with fluid forces acting on a greater area. Conversely, rigid origamis (dark red curves, with square symbols) require a higher U.

To capture the physical behavior of the system we define a Cauchy number $C_Y = \rho U^2 S_0/\kappa$ (with ρ the air density), that compares the fluid loading and the rigidity. The insets of Fig.2a-b show the results replotted in a non-dimensional form with $C_d = F/\rho U^2 S_0$ the drag coefficient as a a function of C_Y. The collapse of the curves shows that the behavior of the origami is set by the competition between the elastic restoring force of the folds and fluid forces. Note that C_Y however does not capture the effect of the number of folds or of changing the rest angle of the waterbomb, whose results are not shown in Fig.2.

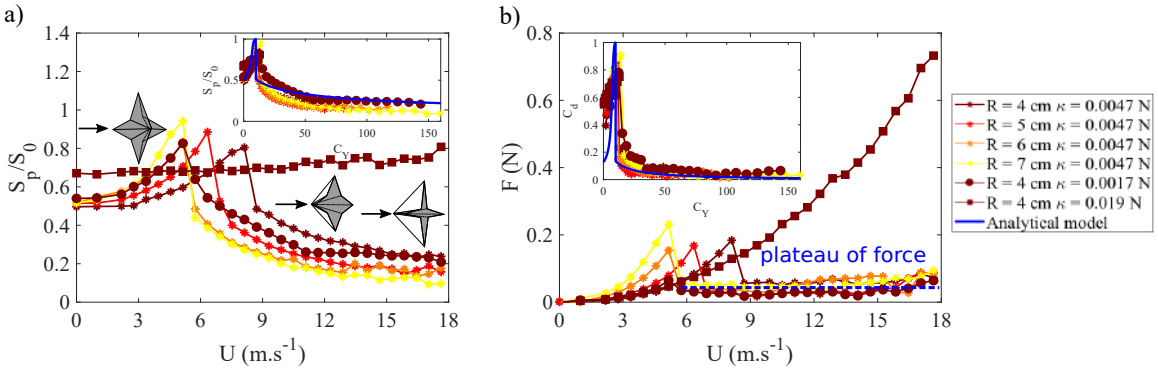

Figure 2: (a) Evolution of the relative projected surface S_p/S_o as a function of the flow speed U [Inset : data replotted as a function of the Cauchy number C_Y (see text), and compared to the model predictions]. (b) Drag force F as function of U, exhibiting a plateau at high speeds [Inset : Drag coefficient C_d vs. C_Y, with model predictions].

ANALYTICAL MODEL AND DISCUSSION

To rationalize our experimental results, we devise a simplified model to predict the static equilibrium of the waterbomb base structure under fluid loading. Our analytical model considers the energy of the origami that is the sum of two terms $E = E_{el} + W$, where E_{el} is the elastic potential energy obtained by modeling each fold as a torsional spring of linear rigidity κ and length R [3]. The second term W corresponds to the work done by fluid pressure forces acting on each face. Similarly to [1], we assume that the flow encountered by the origami is the far field one of speed $\underline{U}$, which exerts on each face a force $\underline{F_n}$ proportional to the momentum carried in the direction normal to the face $\underline{n}$: $\underline{F_n} = 1/2\rho S_0(\underline{U}.\underline{n})^2\underline{n}$. The energy of the structure that is to be minimized then writes :

$$E = \frac{N\kappa R}{4}[(\gamma_m - \gamma_m^0)^2 + (\gamma_v - \gamma_v^0)^2] - N\int \underline{F_n}.\underline{\delta r}, \tag{1}$$

Where $\underline{\delta r}$ is the trajectory of the face, and γ_m and γ_v are the mountain and valley folds angles respectively (the ^{0} denote the initial unstrained angles). It should be noted that E only depends on one variable as the origami deforms along a single DOF. This equation is solved numerically and the obtained predictions are compared to experimental data in the insets of Fig.2a-b. Despite strong hypothesis on the fluid, the opening and reconfiguration phases as well as the reversal threshold (critical Cauchy) are well predicted by our analytical model.

We showed that the extreme shape changes and bistable properties of the studied origami allow for an atypical non-monotonic drag-vs-speed curve. In strong flows, the fluid force experienced by the system also no longer depend on speed. This unusual behavior could be attributed to the localisation of deformation in the folds, an intrinsic feature of origamis. In the limit case of large deformation, the faces of the origami align with the flow, so that its radius R becomes irrelevant for the pressure drag. In the absence of any other lengthscale, dimensional analysis then suggests that fluid forces only scale with the rigidity of the folds. Finally, this system represents an interesting strategy for passive valves or hydraulic diode, that would expand in a water pipe and obstruct it, and eventually snap past a given threshold velocity to let fluid through. To control and program the pressure/flow rate curve of such system, it is then key to understand the fluid-elastic response of the origami, as well as effects of confinement.

References

[1] Gosselin F. de Langre E. and Machado-almeida A. Drag reduction of flexible plates by reconfiguration *J. Fluid Mech.* , 2009.
[2] Schouveiler L. Boudaoud A. The rolling up of sheets in a steady flow *J. Fluid Mech.* , vol. 563, pp. 71–80, 2006.
[3] Hanna B. et al. Waterbomb base: a symmetric single-vertex bistable origami mechanism *Smart Materials and Structures* **23**, 2014.
[4] Lechenault F. Thiria B. Mechanical Response of a Creased Sheet *PRL* **112**, 2014.

COUPLED DYNAMICS AND SELF-INDUCED VIBRATION OF FLEXIBLE MEMBRANE WINGS AT MODERATE REYNOLDS NUMBER

Guojun Li* [1], Boo Cheong Khoo[1], and Rajeev Kumar Jaiman[2]
[1]Department of Mechanical Engineering, National University of Singapore, Singapore, Singapore
[2]Department of Mechanical Engineering, University of British Columbia, Vancouver, Canada

Summary The aeroelastic interaction between a flexible membrane structure and the surrounding unsteady flow is ubiquitous in nature and engineering systems. The present study aims to investigate the synchronized coupling between the vortex shedding and the flexible membrane at moderate Reynolds number. In particular, we examine the self-induced vibration and the lock-in phenomena during nonlinear unsteady fluid-membrane interaction. With the aid of the Global Fourier Mode Decomposition (GFMD) method, the most energetic aeroelastic modes are identified from the coupled fluid-elastic fields and the mode migration between different states is explored as functions of aeroelastic parameters. Based on the coupled modal analysis, we propose a feedback loop between the vortex shedding, the induced pressure fluctuations and the multimodal membrane vibration.

INTRODUCTION

During the past decades, morphing wings with elastic membrane components have received substantial attention from the aerospace engineering community in the context of bio-inspired flying vehicles. As demonstrated in [1, 2], the elastic membrane wings may possess superior aerodynamic performance with improved lift-to-drag ratio, delayed stall and enhanced flight stability while maintaining light-weight structures, compared to conventional aircraft wings. In previous studies on the membrane dynamics [3, 4], it was found that the coupled dynamics of the flexible membrane wings are strongly influenced by the aeroelastic parameters namely, the angle of attack, Reynolds number, mass ratio and the aeroelastic number. Specifically, the migration of the membrane modes [3] and the transition from thrust to drag [5] were observed in the coupled aeroelastic system with different parameters. Furthermore, the aerodynamic performance and the flow dynamics of flexible membranes are related to vibration modes. It is necessary to fully understand the coupling mechanism between multiple excited modes and their corresponding flow patterns when designing efficient flying vehicles. The intertwined modes of the unsteady flow and the membrane deformation pose serious challenges from a physical analysis standpoint. In particular, the lock-in mechanism and the structural mode migration related to the vortex-membrane interaction require further investigation.

In the current study, we consider a three-dimensional rectangular membrane wing and analyze the nonlinear fluid-membrane interaction as functions of the aeroelastic parameters. We focus on the four key questions: (i) Which types of membrane vibrations and wake patterns are dominant in the fluid-membrane interaction and how do we identify these dominant aeroelastic modes? (ii) What is the intrinsic relationship between the flow features and the flow-induced structural modes? (iii) How do the aeroelastic parameters influence the fluid-membrane interaction? (iv) What is the trigger factor of the structural mode migration and the membrane lock-in at various flow conditions? A global mode decomposition method based on the Fourier transform is employed to identify the dominant aeroelastic modes from the overlapped fields by estimating the contribution of the dominant mode and its harmonics to the overall membrane dynamics quantitatively. A series of numerical simulation is performed to investigate the evolution of the coupled dynamics of the flexible membrane wing and the trigger factor of the structural mode migration and the membrane lock-in phenomena.

HIGH-FIDELITY AEROELASTICITY FRAMEWORK

A recently developed high-fidelity aeroelasticity framework [2] is employed for the current study. The incompressible Navier-Stokes equations and the flexible multibody structural equations are integrated in a partitioned manner and the aeroelastic governing equations are solved based on a typical predictor-corrector scheme. An efficient and energy-conserving method based on the radial basis function (RBF) is employed to transfer the aerodynamic forces and the structural displacements along the fluid-structure interface with non-matching meshes. The extended RBF method is used to update the fluid meshes in the fluid domain by following the deformation of the flexible membrane wings. A nonlinear iterative force correction (NIFC) scheme [6] is implemented to address the numerical stability caused by the strong inertia effects during fluid-membrane interaction.

RESULTS AND DISCUSSION

A two-dimensional flexible membrane wing with fixed leading and trailing edges and a three-dimensional rectangular membrane wing with all fixed edges conducted by Rojratsirikul et al. [1] are simulated by the high-fidelity aeroelastic framework to study the fluid-membrane coupling dynamics and mechanism with various aeroelastic parameters. The

*Corresponding author. E-mail: e0204974@u.nus.edu

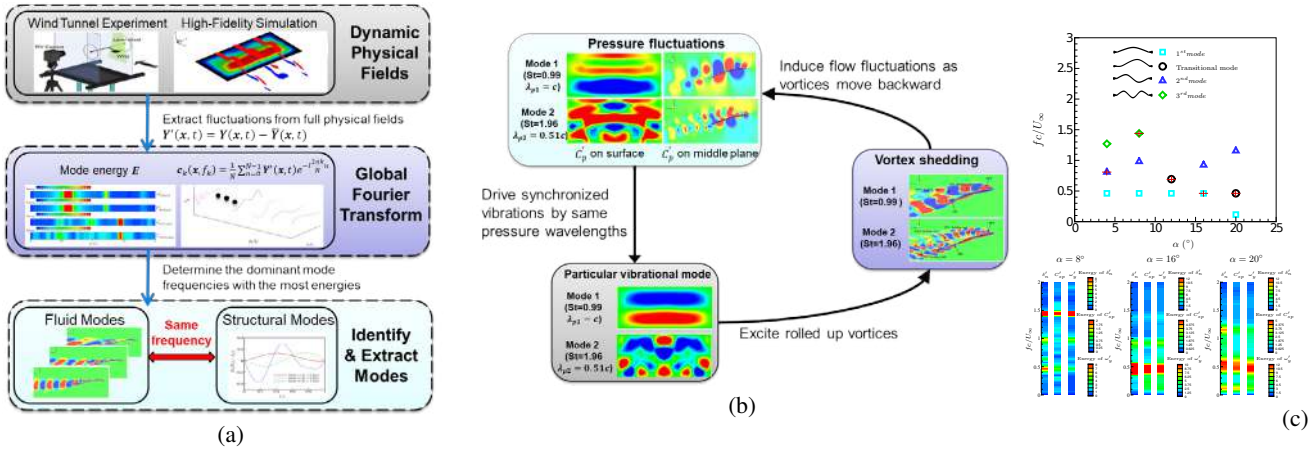

Figure 1: Flow-induced vibration of a flexible membrane wing: (a) a graphical illustration of Global Fourier Mode Decomposition (GFMD), including data pre-processing, mode decomposition and aeroelastic mode identification, (b) an illustration of fluid-membrane coupling mechanism at $Re = 24300$ and $\alpha = 15°$, and (c) mode migration map and global spatial mode energy spectra by decomposing the membrane deflection fluctuation, the surface pressure coefficient fluctuation and the spatial Y-vorticity fluctuation as a function of angle of attack α for a two-dimensional membrane wing at $Re = 2500$.

Global Fourier Mode Decomposition (GFMD) method is employed to decompose the full physical fields into particular aeroelastic mode ranked in frequency. A graphical illustration and the procedure of GFMD is presented in figure 1a.

With the aid of the GFMD method, we build a direct connection between the particular vibration modes and the induced flow patterns. We study how the flexible membrane interacts with the unsteady viscous flow to sustain the free vibration of a flexible membrane wing. Figure 1b illustrates a schematic of the fluid-membrane coupling mechanism for a three-dimensional flexible membrane wing. The flow-induced membrane vibration excites rolled up vortices near the leading edge. Subsequently, a chain of vortices moves backward resulting in the flow fluctuations in the flow domain as well as on the membrane surface. The induced pressure fluctuations drive the synchronized membrane vibrations by the same pressure wavelength. This feedback loop between the membrane vibration, the wake instability and the pressure fluctuations reveals how the structural mode is selected for the unsteady flow past the flexible membrane. The mode migration map and the global mode energy spectra are presented in figure 1c. As the angle of attack increases, the dominant mode migrates from 2^{nd} to 3^{rd} at $\alpha = 8°$, then it transits to the lower mode. Furthermore, it can be inferred from the energy spectra that the frequency of leading-edge vortex shedding synchronizes with the selected membrane mode. With regard to the relative inertial coupling, we consider a range of mass ratio $m^* \in [0.72, 14.4]$ at $\alpha = 15°$ and $Re = 24300$. Four distinctive membrane dynamic states are identified as a function of m^*, namely (i) deformed steady state, (ii) antisymmetry mode, (iii) transitional mode and (iv) symmetry mode. As the inertia effect becomes stronger, the 1^{st} mode turns to be the dominant mode when its mode energy exceeds that of the 2^{nd} mode.

CONCLUSIONS

We presented a series of aeroelastic simulations to investigate the coupled dynamics and self-induced vibration of the flexible membrane wings immersed in the incompressible unsteady viscous flow as functions of the angle of attack, Reynolds number and mass ratio. GFMD method was employed to isolate the dominant aeroelastic modes from the overlapped physical fields to connect the unsteady flow and the flow-excited vibration via the same mode frequency. A feedback loop between the membrane vibration, the wake instability and the induced pressure fluctuations was proposed for the coupled dynamics and self-induced vibration during fluid-membrane interaction. We found that the mode migration is triggered through the synchronized mode coupling between the multiple flow-excited modes.

References

[1] Rojratsirikul P., Genc M., Wang Z., Gursul I. Flow-induced vibrations of low aspect ratio rectangular membrane wings. *J. Fluids and Structures* **27**: 1296-1309, 2011.

[2] Li G., Law Y. Z., Jaiman R. K. A novel 3D variational aeroelastic framework for flexible multibody dynamics: Application to bat-like flapping dynamics. *Computers & Fluids* **180**: 96-116, 2019.

[3] Sun X., Wang S. Z., Zhang J. Z., Ye Z. H. Bifurcations of vortex-induced vibrations of a fixed membrane wing at Re <1000. *Nonlinear Dynamics* **91**: 2097-2112, 2018.

[4] Tiomkin S., Raveh D. E. On membrane-wing stability in laminar flow. *J. Fluids and Structures* **91**, 2019.

[5] Tzezana G. A., Breuer K. S. Thrust, drag and wake structure in flapping compliant membrane wings. *J. Fluid Mechanics* **862**: 871-888, 2019.

[6] Jaiman R. K., Pillalamarri N., Guan M. A stable second-order partitioned iterative scheme for freely vibrating low-mass bluff bodies in a uniform flow. *Comput. Methods Appl. Mech. Eng.* **301**: 187-215, 2016.

RELIABILITY STUDY OF A FULLY-PASSIVE OSCILLATING-FOIL TURBINE CONCEPT

Dylan Iverson[1], Waltfred Lee[1], Guy Dumas [2], and Peter Oshkai*[1]
[1]Department of Mechanical Engineering, University of Victoria, Victoria, Canada
[2]Department of Mechanical Engineering, Laval University, Quebec City, Canada

Summary A fully-passive flapping-foil hydrokinetic turbine prototype was subjected to flow at Re = 21000 in a water channel. The prototype was exposed to symmetric vortices shed from an oscillating foil placed upstream, boundary layer tripping by distributed roughness on its surface and freestream turbulence introduced via fractal grid turbulence generator. The potential of power extraction of the foil undergoing elastically constrained oscillations in heave and pitch under these nonideal, unsteady flow conditions was quantified by implementing an eddy current brake. When placed in the wake of an upstream oscillating foil, the turbine was sensitive to the frequency of the shed vortices in the incoming flow. An overall increase in power extraction was observed when the turbine was subjected to high freestream turbulence, while the surface roughness had insignificant effect on turbine performance.

INTRODUCTION

The use of oscillating foils for hydrokinetic energy harvesting has received much interest in recent years. These systems consist of a foil that translates and rotates in a cyclic and periodic manner. These lift-based devices have been shown to reach energy extraction efficiencies competitive with their conventional rotary counterparts [1].

In the present study, a self-sustained fully-passive flapping-foil hydrokinetic turbine prototype [2] that is able to achieve efficiency of power extraction up to 31% with a NACA 0015 foil is investigated experimentally. This fully-passive turbine concept inherently relies on a two-way coupled fluid-structure interaction to develop motion responses leading to useful energy extraction. This feature leads to the question of how sensitive this design may be to disturbances in the flow field, where certain flow perturbations may significantly alter the passive response of the foil. The current study aims at qualifying this potential sensitivity.

EXPERIMENTAL SYSTEM AND TECHNIQUES

The experiments were performed in a recirculating water channel with a test section that has a length of 250 cm and a cross section of 45x45 cm. The ambient turbulence intensity of the flow was less than 1% for the range of velocities used in the current study.

A schematic of the two-degree-of-freedom turbine system is shown in Fig. 1a. The NACA 0015 foil of chord length c was constrained to move only in a linear heave motion $h(t)$, and a rotational pitch motion $\theta(t)$ about its pitching axis, located a distance x_p from the leading edge. Both degrees-of-freedom were elastically mounted, and a linear damping was applied independently to the heave degree-of-freedom. The blade positions in heave and in pitch were recorded at a sampling frequency of 83.3 Hz and during 120 s, which roughly corresponds to 100 oscillations of the blade, with two rotary encoders generating10000 pulses per revolution.

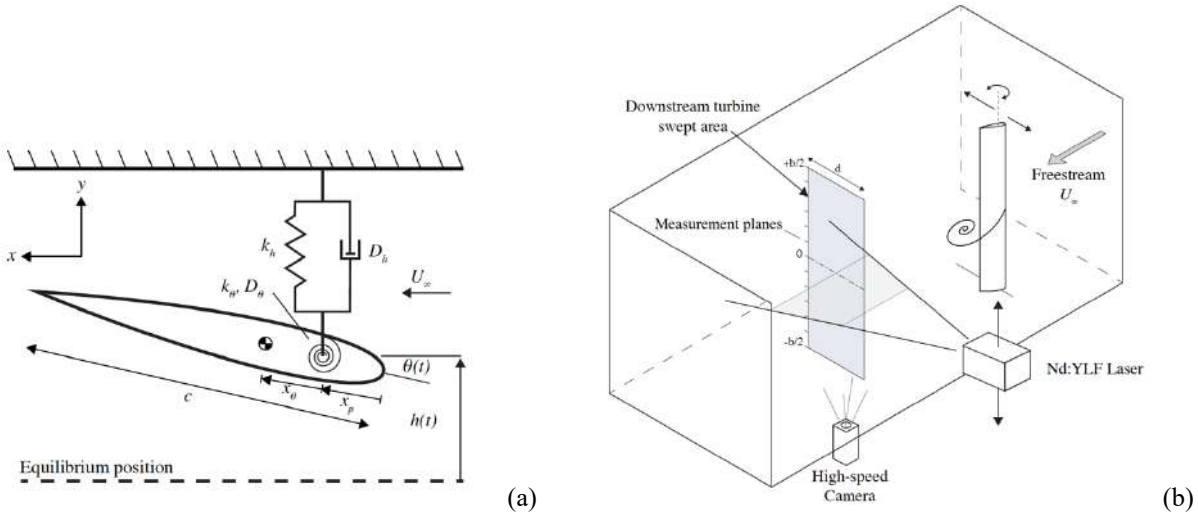

Figure 1. Schematics of the fully-passive turbine (a) and the PIV system (b).

Fluid velocity was measured using high-speed particle image velocimetry (PIV) as shown schematically in Fig. 1b. The flow was seeded with tracer particles with a mean diameter of 10 μm that were illuminated by a pulsed laser. The

*Corresponding author. E-mail: poshkai@uvic.ca.

images were processed with Davis LaVision 8.3 software using a multipass cross correlation technique. The smallest interrogation windows used were 12 pixels x 12 pixels, yielding a resolution of 0.26 vectors/mm.

RESULTS

As shown in Fig. 2a, when the turbine was placed in the wake (6.5*c* downstream) of a similar foil undergoing prescribed periodic motions, the power extraction was significantly lower than that of the baseline case without an upstream foil, which had a value of power coefficient $C_p = 0.62$. This result is not unexpected, considering the momentum deficit in which the turbine operated as shown by the streamwise velocity fields of Fig. 2b. The spanwise structure of the wake of the upstream foil is also shown through the different vertical planes of Fig. 2b. Moreover, stable oscillations of the fully-passive foil were observed in a relatively narrow range of reduced frequencies of the upstream foil corresponding to $f^{*\prime} < 0.125$, as illustrated in Fig. 3.

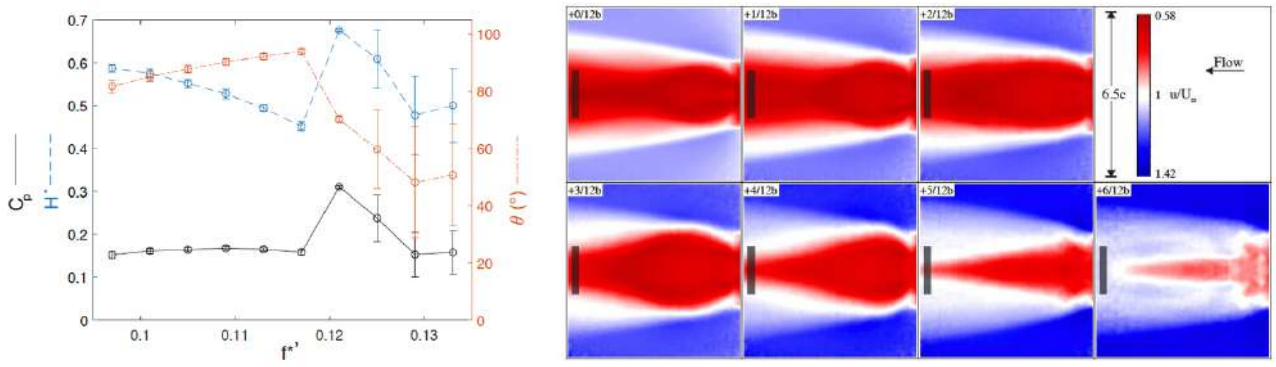

(a) (b)

Figure 2. (a) Averaged power coefficient, heave amplitude, and pitch amplitude of the fully-passive turbine. $f^{*\prime}$ is the reduced frequency of the upstream foil. (b) Time-averaged PIV images of normalized streamwise velocity in the wake of the upstream foil. Grey bars represent location of the downstream turbine.

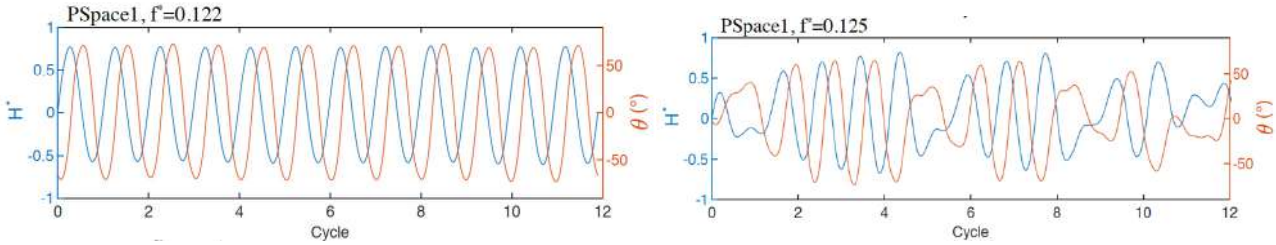

Figure 3. Heave and pitch amplitudes as functions of time over twelve cycles of turbine oscillation for two values of reduced frequency of the upstream foil.

When the boundary layer of the turbine was tripped by applying a strip of distributed roughness elements along the span of the blade, no significant improvement of turbine performance was observed presumably due to predominant stall condition that existed for a large portion of the oscillation cycle or ineffectiveness of the trip due to the relatively low Reynolds number.

On the other hand, when the turbulence level of the inflow was increased to 10% by installing a fractal grid upstream of the test section in the water channel, the power extraction increased by 5% - 13% relative to the baseline case of ambient turbulence. The heave amplitude also increased. It is hypothesized that the incoming turbulence delayed the stall by stimulating boundary layers transition or by increasing momentum transfer into the boundary layer or by reducing the coherence of the primary stall vortex.

CONCLUSIONS

When the fully-passive oscillating-foil turbine was placed in the wake of another foil undergoing a prescribed motion, the turbine performance was sensitive to the frequency of the generated vortices in the incoming flow. Regular oscillations were observed only in a narrow range of upstream kinematics. However, the prototype exhibited stable, and sometimes improved, performance when it was subjected to unstructured disturbances in the form of high freestream turbulence.

References

1. Young, J., J.C. Lai, and M.F. Platzer, A review of progress and challenges in flapping foil power generation. *Progress in Aerospace Sciences*, 2014. **67**: p. 2-28.
2. Boudreau, M., et al., Experimental investigation of the energy extraction by a fully-passive flapping-foil hydrokinetic turbine prototype. *Journal of Fluids and Structures*, 2018. **82**: p. 446-472.

AEROELASTICITY OF HOVERING AND FLYING BATS

Vaibhav Joshi* [1] and Rajeev Kumar Jaiman[1]
[1]Department of Mechanical Engineering, University of British Columbia, Vancouver, Canada

Summary Wings of natural flyers such as bats have evolved over millions of years to adapt and articulate the flexibility of the wings for better flight performance, maneuverability and agility. With aim to understand this flapping phenomenon of bats, we investigate the aeroelastic effects of articulated membrane flexibility on the flow structures and their relation with the aerodynamic performance. We find that the flexibility increases the unsteady lift generation as well as reduces the mean drag due to the large deformation of the flexible wing compared to the rigid counterpart, as a result of larger downwash.

INTRODUCTION

Biologically inspired flying vehicles based on flapping motion of wings have gained recent attention in the aerodynamics community due to their characteristics of high agility and hovering capabilities, flexible and soft material wings and lower frequency of wing motion. Compared to the flying vehicles or drones such as Quadcopters which employ the rotary motion of wings, such bio-inspired vehicles made from flexible materials could be much safer and energy-efficient alternative. Of particular interest is the bat-inspired wing design which allows for better control of the wing motion and a simpler design from manufacturing point of view than a bird-inspired wing. According to the quasi-steady state aerodynamics, a bat flying at slow speed or hovering should not be able to generate sufficient lift to balance its weight. Therefore, an unsteady lift generation mechanism was proposed in [1] by studying the vortex generated by a bat via digital particle image velocimetry. It was found that the unsteady lift is generated by the articulated flexibility of the wing membranes which led to attached leading-edge vortices and the phenomenon of delayed stall. A recent study of mimicing the kinematics of bat flight using a robot [2] demonstrated the capability of better flight control by dynamically changing the wing conformations by adjustment of the bone fingers and joint actuator in the robot (Fig. 1(a)). Therefore, the multibody nature of the bat wing design allows for (i) wing membrane articulated flexibility giving the advantage of delayed stall, (ii) evolving wing span based on the aerodynamic requirements and (iii) better control of the wing kinematics by adaptive adjustment of the bone fingers and joints.

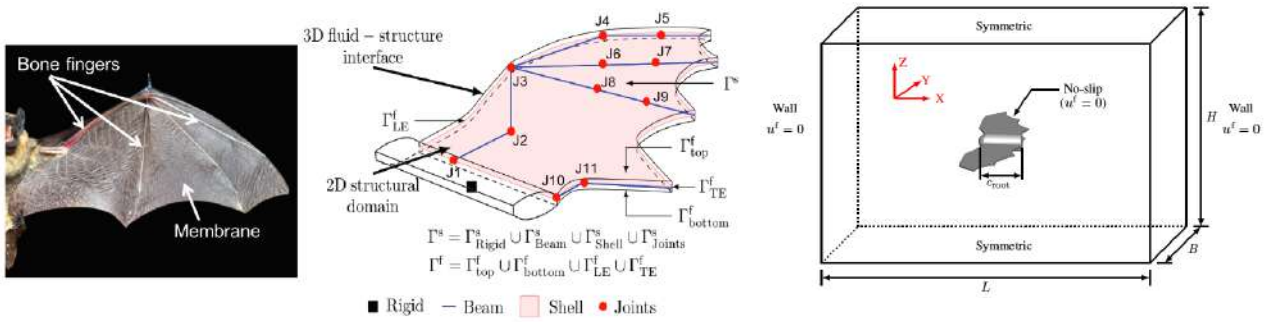

(a) (b)

Figure 1: (a) Flexible multibody nature of the bat wing and (b) problem setup for the numerical study.

The current numerical work aims to understand this relation between the articulated flexibility and the mechanism of unsteady lift generation. We employ a flexible multibody aeroelastic numerical framework to simulate the wing kinematics of a bat and understand the physical mechanisms of unsteady lift generation in various flight regimes. We intend to answer the following key questions in this work: (i) Does the flexibility in the membranes during passive flapping of the wing increase aerodynamic efficiency? (ii) How does the change in the wing deformation transform the flow structures around the bat wing? (iii) Can we optimize the articulated flexibility for maximizing the aerodynamic performance?

FLEXIBLE MULTIBODY AEROELASTIC FRAMEWORK

A generic flexible multibody wing of a bat is shown in Fig. 1(a) where the wing consists of bone fingers, membranes and joints which can be modeled as beam, thin shell element and revolute joints respectively. We employ a co-rotational transformation for the components of the multibody system where the rotation matrix is parametrized by conformal rotation vectors. The joints in the multibody system are solved as constraint to the structural equations. The structural domain is coupled with a three-dimensional incompressible Navier-Stokes variational framework by satisfying the kinematic and dynamic continuity along the fluid-structure interface. This is carried out with the help of an interpolation matrix which is formed by radial basis function approximation. A recent work on the formulation and the radial basis coupling can be found in [3].

*Corresponding author. E-mail: vjoshi02@mail.ubc.ca

RESULTS AND DISCUSSION

To understand the effect of membrane flexibility on the aerodynamic performance, we perform two-sets of high-fidelity aeroelastic simulations for passive flapping of wings in a bat flight. The first set of studies correspond to hovering flight by considering two wing flapping configurations (Fig. 1(b)) with anisotropic structural properties: (1) rigid flapping wing (RFW) and (2) flexible flapping wing (FFW). The Reynolds number is defined based on the maximum wing-tip velocity U_{tip} of the rigid wing ($Re = \rho^{\text{f}} U_{\text{tip}} c/\mu^{\text{f}} = 574$), ρ^{f} and μ^{f} being the density and dynamic viscosity of air and c is the mean chord of the bat wing. The Aeroelastic number is defined as the ratio of the structural stiffness to the inertia of the flow ($Ae = Eh/(1/2\rho^{\text{f}} U_{\text{tip}}^2 c)$), where E and h are the Young's modulus and thickness of the structure respectively. It is in the range of $10^4 - 10^9$ for the FFW and 10^{16} for the rigid wing. The mass ratio is given as $m^* = \rho^{\text{s}} h/(\rho^{\text{f}} c)$, ρ^{s} being the density of the structure. It ranges from $1 - 46$ for FFW and is at a constant value of 116 for RFW. The observed vortex structures agree with the proposed model in [1] where the trailing edge vortex is connected to the leading edge vortex via the tip vortices, forming one vortex loop per wing (Fig. 2(a)). These vortices evolve and form a rectangular vortex ring near the wing tip with vorticity being supplied in each stroke of the wing. The size of the vortex ring is found to be comparatively larger for FFW suggesting a relatively larger circulation. It was observed that the large wing tip deformation for the FFW (Fig. 2(a)) leads to high wing tip velocity which induces more effective downwash leading to larger circulation and unsteady lift (41% higher), compared to the RFW. The flapping efficiency is also quantified with the help of the lift force F_z^{s}, wing tip velocity $u_{z,\text{tip}}^{\text{s}}$ and the swept area of the wing A_s as $\eta = (F_z^{\text{s}} u_{z,\text{tip}}^{\text{s}})_{\max}/(1/2\rho^{\text{f}} U_{\text{tip}}^3 A_s)$, and is found to be 38% higher for the flexible wing.

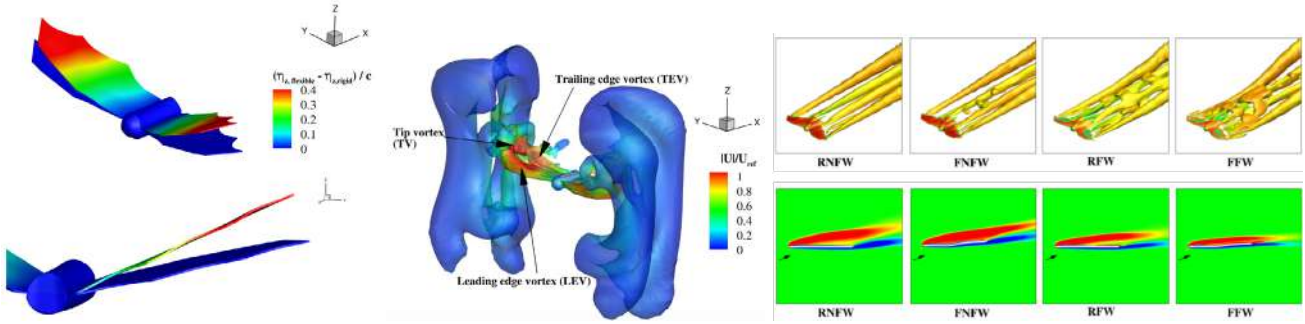

(a) (b)

Figure 2: (a) Comparison of the deformation of the FFW and the RFW for hovering flight. The large displacement of the FFW generates rectangular vortex rings with relatively larger circulation near the wing tip during hovering flight, and (b) vortex structures as well as streamwise vorticity during forward flight at 10° angle of attack at different wing configurations show the deformation of the flexible wing leading to delayed stall and reduced drag.

The second set of preliminary studies correspond to forward flight at 10° angle of attack with the following additional wing configurations than: rigid non-flapping wing (RNFW) and flexible non-flapping wing (FNFW). In this case, the Reynolds number, $Re = 12,000$ and is defined based on the incoming free-stream velocity; $Ae = 120 - 9 \times 10^6$ and $m^* = 4 - 30$ for the flexible wing and 9×10^6 and 30 for the rigid case respectively. The computations show that the mean drag is reduced by about 13% due to the adaptive alignment of the flexible wing with the flow. Furthermore, an 80% increase in the maximum unsteady lift is observed for the FFW compared to the RNFW. The vortex structures depict a delayed stall due to the attachment of the leading edge vortex as a consequence of the large deformation of the flexible wing (Fig. 2(b)).

CONCLUSIONS

Numerical studies are carried out to investigate the effects of membrane flexibility of the wing in bat flight on the aerodynamic performance with the help of a flexible multibody aeroelastic framework. It is observed that for both the flight regimes (hovering and forward flight), the unsteady lift is much higher for the flexible wings compared to the rigid counterpart. The efficiency for the flexible wing is found to be 38% higher than the rigid wing. The unsteady lift is generated due to the large wing tip displacement for the flexible wing leading to higher downwash velocity and circulation. In the forward flight regime, the flexible membrane deforms substantially leading to the attachment of the leading edge vortex as well as reduced drag, thus changing the vortex pattern so as to improve C_L/C_D by 10%.

References

[1] Mujires F. T., Johansson L. C., Barfield R., Wolf M., Spedding G. R., Hedenström A. Leading-edge vortex improves lift in slow-flying bats. *Science* **319**:5867, 1250-1253, 2008.

[2] Ramezani A., Chung S-J., Hutchinson S. A biomimetic robotic platform to study flight specilizations of bats. *Science Robotics* **2**: eaal2505, 2017.

[3] Li G., Law Y. Z., Jaiman R. K. A novel 3D variational aeroelastic framework for flexible multibody dynamics: Application to bat-like flapping dynamics. *Computers and Fluids* **180**: 96-116, 2019.

COLLECTING MIST WITH A FIBROUS NET

Adèle Moncuquet[1], Romain Labbé[1], Alexander Mitranescu[1], Ana Rewakowicz[1], Xavier Amandolese[1,2], Sophie Ramananarivo[1], and Camille Duprat*[1]
[1]LadHyX, Department of Mechanics, Ecole polytechnique, Institut polytechnique de Paris, France
[2]LMSSC, Conservatoire National des Arts et Métiers, Paris, France

Summary Capturing droplets from a stream with a fibrous material is a well-known and well-used process, from coalescence filters to fog harvesting. Here, we report experimental measurements of collection efficiency using a simple net arrangement consisting in an array of vertical fibres. Accounting for the growth of drops on fibres in a simple inertial impaction model allows predictive and quantitative comparisons with experiments, and we propose a simple structural change based on an elastocapillary effect in order to suppress drop growth and improve the collection efficiency. We then report drag force measurements on a fibrous net, and look for an optimal design of wind-resistant collecting nets.

INTRODUCTION

The filtration, or collection, of liquid droplets from mist is generally done by placing a fibrous structure in the path of the mist. In particular, coalescence filters are used to remove liquid from aerosols [1] and for a couple of decades, fog harvesting, i.e. the collection of fresh water from fog, has been developed for domestic use or for agriculture/livestock, as well as for reforestation projects [2]. The fog droplets are captured as they impact the wires of the fibrous nets; the water is then collected as drops fall along the mesh. Here, we focus on the collection of mist using a model system of parallel fibres. In particular, we identify the key role played by the drop distribution on the fibres on the collection efficiency of a single fibre, and propose a simple structural change to suppress drop growth thus overcoming this limitation. We then investigate the efficiency of a fibrous net, and report measurements of the drag on a fibrous panel, as a route toward the optimization of collecting nets.

CAPTURING DROPLETS WITH A FIBER

Using a custom made environmental wind tunnel, we produce an homogenous, laminar and well controlled flow of fog, composed of micron-sized droplets with a narrow size distribution and a mean droplet radius $r_d = 3.9\mu m$, carried at varying velocities $2 < U < 10$ m.s^{-1} with a constant water flow Q_w. We place a model net of surface S_f, composed of N_f fibers of diameter d_f, at the exit of the tunnel (of cross section S_{wt}) and measure the collected water volume as a function of time. We first focus on widely spaced fibers, i.e. with a spacing between fibres e_f sufficiently large to avoid interactions (typically $e_f = 10d_f$). As the mist passes through the mesh, fog droplets starts collecting on the fiber; drops appear on the fiber, grow, coalesce and fall periodically. The volume of collected water increases linearly with time, i.e. the collection rate Q_c is constant. We define the collection efficiency E as the ratio of the collected flow of water to the flow of water passing through the net $E = Q_c S_{wt}/(Q_w S_f)$. The main mechanism for the collection is the inertial impact of droplets on the fibres: a droplet carried in the flow can either follow the streamlines, and avoid the obstacle, or impact the fiber provided it has enough inertia [3]. The trajectory of the droplet, and thus the condition for impact and

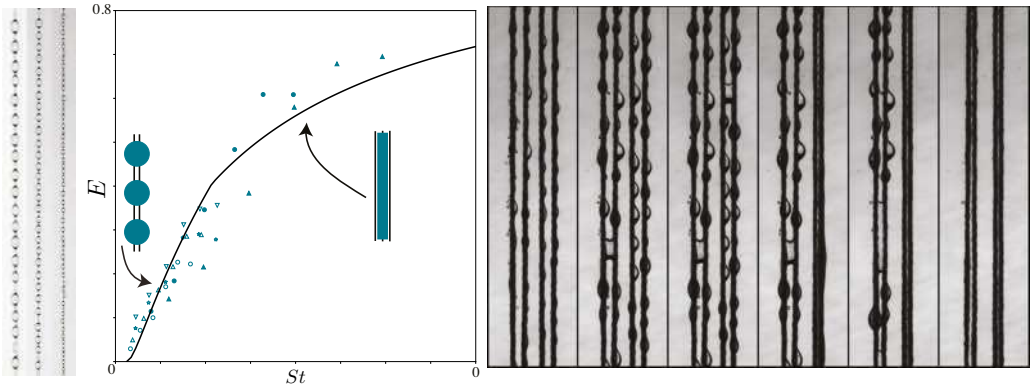

Figure 1: (a) Uniform drop distribution observed on fibres of different diameter during fog collection. (b) Evolution of the collection efficiency as a function of Stokes number, for individual fibres (open symbols corresponding to various diameter and wind velocities), and for liquid columns (filled symbols). Line corresponds to the inertial impaction model; here the definition of efficiency and Stokes is modified to take into account the presence of drops on fibers (open symbols) or to consider a perfectly hydrophilic fibre without drop growth (filled symbols). (c) Formation of liquid columns between two adjacent flexible fibres.

*Corresponding author. E-mail: camille.duprat@ladhyx.polytechnique.edu

the collection rate, depends on a single dimensionless parameter given by the ratio of inertial force to viscous drag, i.e. the Stokes number $St = \frac{4\rho_d r_d^2 U}{9\mu d_f}$ (where ρ_d is the density of the liquid drop and μ the viscosity of air). A first solution to this problem was given in [3] and is widely used in filtration models [1]. We report precise measurements of collection efficiency over a large range of parameters, and observe that the collection mostly occurs on the drops growing on the fibres, and thus strongly depends on the drop distribution. Due to a growth and coalescence process, this drop distribution evolves toward a regular pattern of uniformly distributed drops, and a balance between capillarity and gravity sets an average drop size (Fig. 1 (a)) [4]. Accounting for these effects in the simple inertial impaction model allows predictive and quantitative comparisons with experiments (Fig. 1 (b)). The collection is thus limited by the growth of drops on the fibres; a small change in the structure of the net allows to create super- hydrophilic fibers, i.e. suppress drop growth, by simply bringing adjacent fibers closer in order to form continuous liquid columns (Fig. 1 (c)). This may be easily induced by using flexible fibers that collapse under the capillary forces generated by the drops [5]. Incoming droplets immediately coalesce with these wet columns, and the overall efficiency is significantly increased (Fig. 1 (b)).

FIBROUS NETWORKS: TOWARDS AN OPTIMAL NET

In order to define the efficiency of a net, we evaluate the collection rate of an assembly of fibers, of overall width L, with varying inter-fiber distances e_f, i.e. different solidities $s = N_f d_f / L$ (solidity is inversely proportional to the inter-fibre distance e_f). We extend our model to take into account the interactions between fibers. In particular, as the flow passes through the net, its velocity is modified as the permeability decreases, and thus the collection rate is modified. We measure the drag force exerted on a porous net of surface S, composed of parallel fibers, using a close wind tunnel. We report the evolution of the pressure loss coefficient $C_o = \Delta p/(0.5\rho U^2)$, or equivalently the drag force $D = \Delta p S$, as a function of the solidity of the net for fibers either spanning the entire width of the wind tunnel, or smaller fibrous panels around which flow deviations may occur (Fig. 2(a)). In the latter case, the collection efficiency should decrease with increasing solidity, i.e. for smaller interfibre distances, due to a blockage effect and thus a decrease of the water flow passing through the net. However, decreasing the distance between adjacent fibers also increases the number of fibers per unit area, and thus increase the overall collection of the net, i.e. the collection per unit area. There is thus an optimal value for collection, independent of the velocity, corresponding to the maximal number of fibers that can be placed in the net without a decrease in single fiber collection rate (Fig. 2(b)). Using our previous result, the efficiency can be further increased by forming super-hydrophilic liquid columns between adjacent fibres (inset in Fig. 2(b)), which also avoids clogging of the net with drops and thus ensures a constant solidity. Using our drag measurements and collection model, we look for the optimal solidity, i.e. the optimal arrangement for collection. Measurements of the efficiency of several nets with different structures/arrangements, fibre diameters and flexibilities, along with aerodynamic and aeroelastic characterizations are on going in order to design an optimal net.

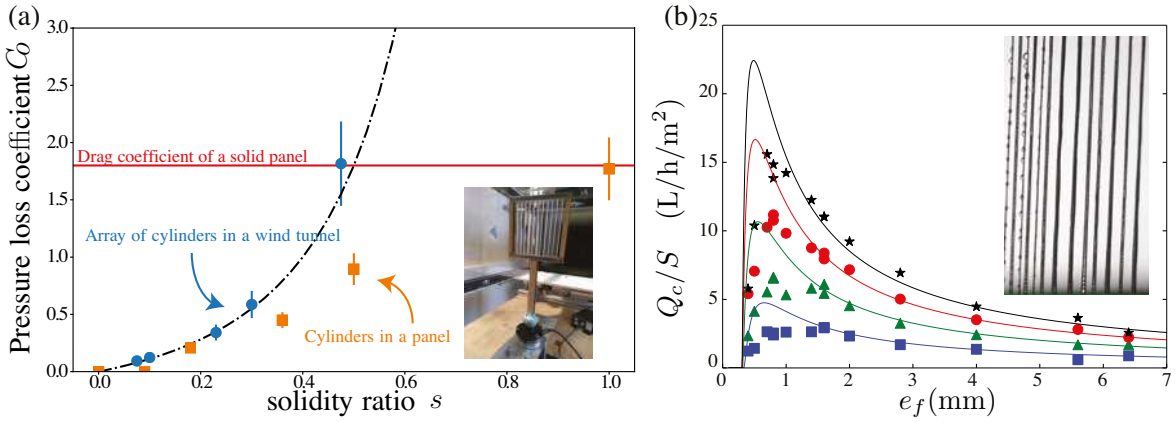

Figure 2: (a) Evolution of the pressure loss coefficient C_o as a function of the net solidity for an array of cylinders (blue circles) or a finite fibrous panel (orange squares). Dashed line corresponds to the theoretical model for a porous net. (b) Evolution of the net efficiency Q_c/S for a given surface S and fibre diameter d_f as a function of the spacing between fibres e_f for different incoming velocities U (from 1 to 4 m/s). Inset: a net composed of "super-hydrophilic" liquid columns between adjacent fibres.

References

[1] R. Mead-Hunter, A. J. King and B. J. Mullins, Aerosol-mist coalescing filters: a review, *Separation and Purification Technology* **133**, 2014,
[2] O. Klemm et al. Fog as a fresh-water resource: Overview and perspectives, *Ambio* **41**, 2012.
[3] I. Langmuir and K. Blodgett, Mathematical investigation of water droplet trajectories, 1945
[4] R. Labbé and C. Duprat, Capturing aerosol droplets with fibers, *Soft matter* **15**, 2019
[5] C. Duprat and S. Protière, Capillary stretching of fibers, *EPL* **111**, 2015

A LAGRANGIAN APPROACH FOR FLUID-STRUCTURE INTERACTION VIA PARTICLE FINITE ELEMENT (PFEM) MODELING

Massimiliano Cremonesi* [1], Simone Meduri[2], and Umberto Perego[1]
[1]Department of Civil and Environmental Engineering, Politecnico di Milano, Milano, Italy
[2] Phononic Vibes, Milano, Italy

Summary A Lagrangian fully explicit approach for the co-simulation of 3D Fluid-Structure Interaction (FSI) problems is here presented. The fluid domain is modelled as a weakly compressible material through an explicit version of the Particle Finite Element Method (PFEM) while the structure is modelled with standard FEM. The strong coupling of the partitioned approach is ensured by a domain decomposition algorithm allowing an incompatible space-time discretizations in the two subdomains. A novel and efficient mesh smoothing procedure is proposed to remove bad quality elements that may arise due to frequent remeshing in the PFEM. The fully Lagrangian description of the present method is particularly effective in problems characterized by strong variations in the fluid boundaries and in the fluid-structure interface. Moreover, the highly parallelizable and fully explicit nature of the equations of the global solver is appealing for real-scale engineering applications.

INTRODUCTION

In many fields of engineering and technology, the numerical simulation of large scale three-dimensional Fluid-Structure Interaction (FSI) problems is of growing interest. A possibility to efficiently deal with these problems is to use partitioned approaches because they allow for the use of existing software. The present work presents a partitioned approach coupling an explicit version of the Lagrangian Particle Finite Element Method (PFEM) [1, 2] for the fluid sub-problem and a standard commercial FEM (SIMULIA Abaqus/Explicit) for the structural one. A domain decomposition approach based on the Gravouil and Combescure (GC) algorithm [3] is here employed for fluid-structure coupling. The key features of this approach are the possibility of different time-steps in the two subdomains and the use of non-conforming meshes at their interface [4].

Moreover, the fully Lagrangian nature of this coupled approach is particularly suited for the description of free surface flows and FSI problems with large structural displacements. The position of the fluid mesh nodes defines automatically the boundaries with no need for interface tracking algorithms. Unfortunately, the Lagrangian motion of the fluid nodes can lead to overly distorted meshes. This issue can be overcome generating a new mesh when the current one gets too distorted. The PFEM makes use of a Delaunay Tassellation coupled with a distortion criterion to efficiently generate a new connectivity for the mesh nodes. Unlucky, in 3D the Delaunay Tassellation may generate bad tetrahedra which, following an explicit approach, can lead to a vanishing stable time step size. To overcome the problem, a novel efficient smoothing technique has been developed to produce a regular mesh, with a reasonably large stable time increment for the explicit solver. This smoothing algorithm is fully explicit and parallelizable, because it exploits the same architecture of the fluid solver thanks to an elastic analogy [5].

The proposed approach is validated through test cases proposed in the literature and used to solve real-scale engineering problems. The comparison with the available solutions confirms the accuracy of the partitioned solver and the effectiveness of the smoothing technique.

COUPLING SCHEME

In the present approach, a partitioned strategy is employed to solve the FSI problem: the explicit version of the PFEM [2] is used for the fluid subdomain, while the commercial software SIMULIA Abaqus/Explicit is used for the structural subdomain. The two solvers are coupled at the interface with the Gravouil and Combescure (GC) algorithm [3], which is a Domain Decomposition method initially proposed for structural dynamics problems and then extended to FSI problems, e.g. in [6]. The key idea behind the algorithm is to split the kinematic solution of each subdomains into two terms, denoted as *free* and *link* solutions, respectively. The former is related to the free motion of each subdomain as if they were not interacting with each other. The latter evaluates the correction to this solution. This is done applying boundary tractions at the fluid-structure interface that play the role of Lagrange multipliers for the imposition of the kinematic constraint. These tractions restore the compatibility at the interface and ensure the strong coupling of the partitioned approach.

The GC algorithm allows for the use of different time steps in the two subdomains, as well as non-conforming meshes at the interface. The resulting interface problem consists of a system of fully decoupled equations, in the case of conforming meshes, and of only weakly coupled equations otherwise, leading to an efficient global explicit solver. The explicit time integration can be an appealing choice for many engineering applications where the time step size is intrinsically small, namely in large scale real applications with fast dynamics, high degree of non-linearity and in extremely large scale problems, where implicit methods may become computationally ineffective. A more detailed description of the proposed approach can be found in [4].

*Corresponding author. E-mail: massimiliano.cremonesi@polimi.it.

ELASTIC ANALOGY FOR 3D MESH SMOOTHING

The problem of mesh distortion related to the adoption of a Lagrangian description for viscous fluid flows is solved in the PFEM through the introduction of a new mesh when the current one gets too distorted. This is done exploiting the Delaunay Tassellation, combined with a distortion criterion, the α-shape method, to recover the correct domain boundaries. However, while in 2D the Delaunay algorithm ensures excellent mesh quality, in 3D bad elements may be generated. This represents a strong limitation for the use of explicit solvers because it leads to vanishing stable time step size. For this reason, a novel efficient mesh smoothing approach based on an elastic analogy has been developed to improve the worst elements insphere radii, with a computational cost compatible with the frequent remeshing procedure required by the PFEM. The mesh regularization is the result of the deformation produced in a fictitious elastic problem under the action of a suitable distribution fictitious pressures in highly distorted tetrahedra.

The resulting final smoothing algorithm is explicit and highly parallelizable and exploits the same algorithmic structure of the fluid solver. Its efficiency allows to obtain remarkable improvements on the stable time steps of the explicit fluid solver in a reasonable computational time that is compatible with its frequent application due to the remeshing procedure of the PFEM approach. A detailed description of the smoothing algorithm can be found in [5].

EXAMPLE

The proposed approach has been tested and validated on different test cases. Here, to show the potential of the proposed technique, a dam break with deformable obstacle is presented. On the left side of a tank, a column of water is initially sustained by a rigid wall that is instantaneously removed at the beginning of the analysis, letting the water flow inside the tank and hit an elastic deformable body clamped in the middle of the tank. The impact bends the obstacle, while the resulting long wave hits the right rigid wall of the tank (see Figure 1).

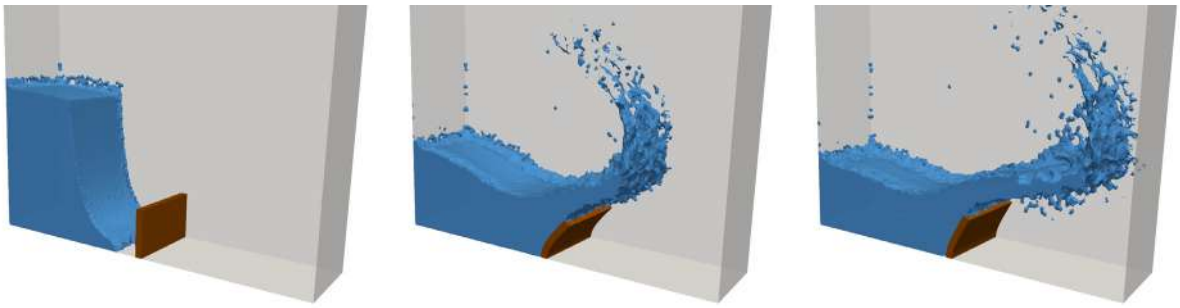

(a) $t = 0.10\ s$ (b) $t = 0.25\ s$ (c) $t = 0.30\ s$

Figure 1: Dam Break with elastic obstacle. Snapshot of the simulation at different time steps

CONCLUSIONS

This work presents a fully Lagrangian explicit partitioned approach for FSI problems, coupling the Particle Finite Element Method for the fluid subdomain and the commercial FEM software Abaqus/Explicit for the structural subdomain. The Lagrangian description of the Particle Finite Element Method for the fluid subdomain is particularly effective for free surface flows and large structural displacements. The coupling is achieved by means of the GC algorithm, which ensures strong coupling as well as the possibility to use incompatible space-time discretizations in the two subdomains. In the 3D framework, a novel efficient smoothing techique based on an elastic analogy has been presented. The considered numerical tests confirm the accuracy of the coupled approach, as well as the effectiveness of the smoothing procedure.

References

[1] Oñate, E., Idelsohn, S.R., del Pin, F. and Aubry, R. The Particle Finite Element Method. An Overview. *Int J Computational Method* **1**:267–307, 2004.

[2] Cremonesi, M., Meduri, S., Perego, U. and Frangi, A. An explicit Lagrangian finite element method for free-surface weakly compressible flows *Comp. Particle Mech.* **4**:357–369, 2017.

[3] Combescure, A. and Gravouil, A. A time-space multi-scale algorithm for transient structural nonlinear problems *Mecanique et Industries* **2**:43–55, 2001.

[4] Meduri, S., Cremonesi, M., Perego, U., Bettinotti O., Kurkchubasche, A. and Oancea, V. A partitioned fully explicit Lagrangian finite element method for highly nonlinear fluid-structure interaction problems *Int J Numer Meth Eng* **113**:43–64, 2018.

[5] Meduri, S., Cremonesi, M. and Perego, An efficient runtime mesh smoothing technique for 3D explicit Lagrangian free-surface fluid flow simulations *Int J Numer Meth Eng* **117(4)**:430-452, 2019.

[6] Li, Z., Leduc, J., Nunez-Ramirez, J., Combescure, A. and Marongiu, J. C. A non-intrusive partitioned approach to couple smoothed particle hydrodynamics and finite element methods for transient fluid-structure interaction problems with large interface motion *Comp Mech* **55**:697-718, 2015.

FLUID-STRUCTURE INTERACTION OF A CYLINDER IN A STRATIFIED FLUID

Sarah Christin*[1], Patrice Meunier [1], and Stéphane Le Dizès [1]
[1] Aix Marseille Univ, CNRS, Centrale Marseille, IRPHE

Summary This experimental study focuses on the flow induced vibrations of a circular cylinder horizontally translated at a constant speed in a stratified fluid. A mode analogous to vortex induced vibrations of the cylinder is observed as in a homogeneous fluid, but for a different frequency range, due to the additional restoring force of the stratification. Furthermore, a large amplitude galloping mode has been observed in contrast to a homogeneous circular cylinder wake where this type of oscillations cannot occur.

INTRODUCTION

Fluid-structure interactions have been widely studied in the past century, mainly under the angle of Vortex Induced Vibration (VIV) where the structure oscillates when the vortex shedding frequency induced by the flow is close to the structure natural frequency. This is a crucial problem in the design of civil engineering structures such as bridges or marine cables because this resonance phenomenon could lead to the breaking of the structure if the induced motion is too large. However, although most geophysical fluids are stratified, this kind of study has never been carried out in a non-homogeneous fluid. The goal is here to characterize the influence of a continuous stratification on flow induced vibrations.

A STRATIFIED VIV EXPERIMENT

The classical experiment of a spring-mounted cylinder is adapted to the case of a stratified fluid. The flowing water channel is replaced by a 4m-long towing tank, filled with stratified salted water (see figure 1). Cylinders of various diameters D (3, 4 and 6 cm) are towed horizontally at a velocity U using flat blade-shaped arms of length L (of 15, 30 or 50cm). The arms are free to rotate around their end thanks to ball bearings, thus allowing vertical oscillations of the cylinder. The drag creates a restoring force which mimics the action of a spring in classical VIV experiments. The mass ratio m* is finely adjusted to 1 such that the arms remain nearly horizontal.

The oscillations are studied as a function of non-dimensional parameters: the Reynolds number Re=UL/ν, the Froude number Fr=U/ND and the ratio L/D (N being the buoyancy frequency and ν the kinematic viscosity).

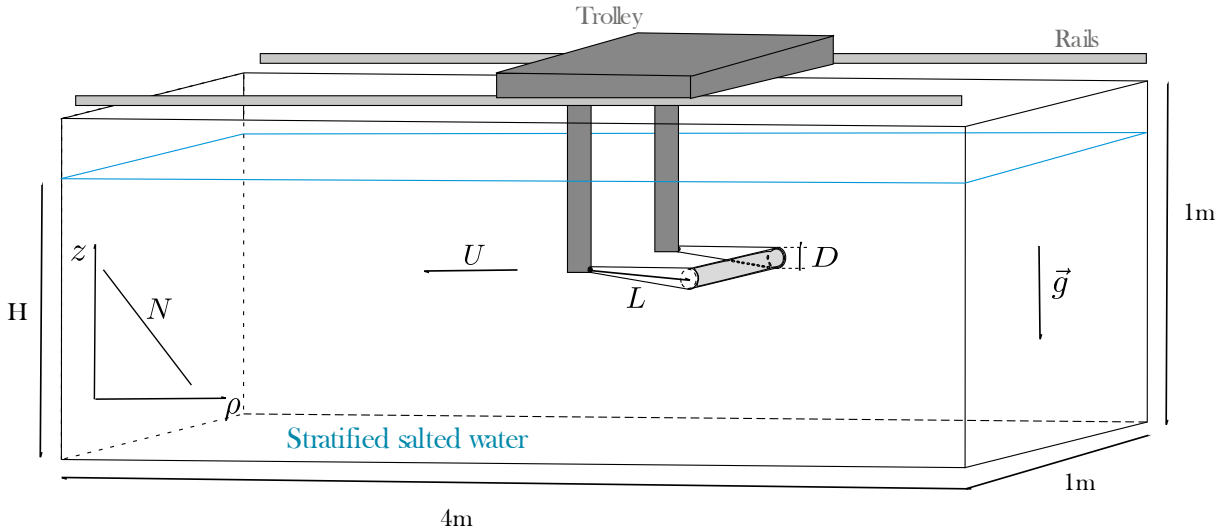

Figure 1. Sketch of the experimental setup

LARGE AMPLITUDE VIBRATIONS OF THE CYLINDER

Figure 2(a) shows the vertical position of the cylinder as a function of time in both the stratified and homogeneous cases for a specific Reynolds number as an example. Two things can be concluded: first, oscillations caused by a coupling between a structure and a flow also occur in a stratified fluid; second, the amplitude of these oscillations are far greater (more than a factor 10) in the stratified case than in the homogeneous case for the same parameters.

* E-mail: sarah.christin@univ-amu.fr.

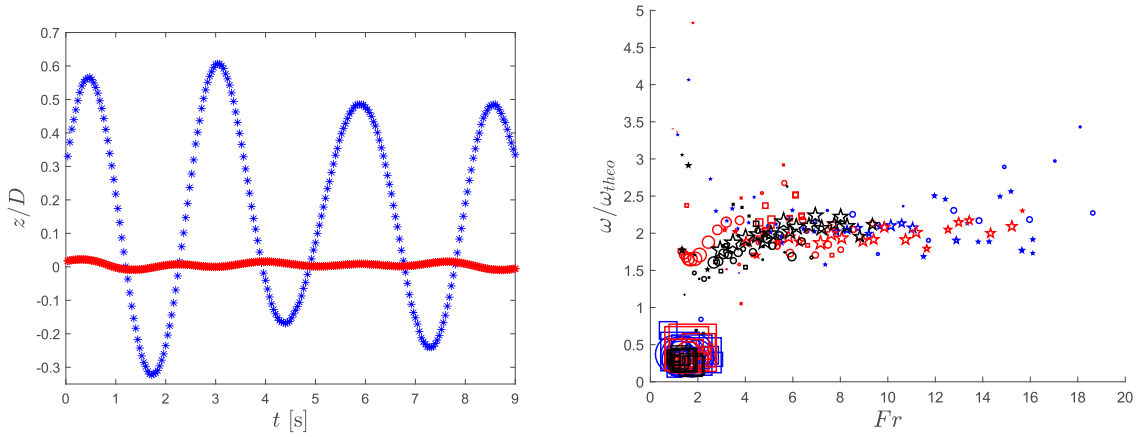

Figure 2. (a) Vertical position of the cylinder in a homogeneous fluid (red stars) and in a stratified fluid with Fr = 9.25 (blue stars). Here, L/D = 3.75 and Re = 6361. (b) Measured frequency ω as a function of the Froude number. The symbol's size is proportional to the oscillation's amplitude. Blue, red and black symbols stand for D=3, 4 and 6 cm, respectively, while squares, circles and stars stand for L= 50, 30 and 15 cm, respectively.

By varying the main parameters D, L and U, different Re, Fr and L/D are explored. A compilation of measures in all these cases is plotted in Figure 2(b), showing the existence of two modes of oscillations. The first one has low frequencies, is localized at small Fr and is favoured by a large L/D ratio. The second one has higher frequencies, can be observed for larger Fr and is favoured by low L/D ratio.

The VIV-like mode

The mode with higher frequencies is analogous to a classical VIV mode. Indeed, the natural frequency of the oscillator can be derived by summing the restoring forces on the cylinder due to the drag and to the stratification. It is equal to : $\omega_{theo} = \sqrt{\frac{N^2}{2} + \frac{C_D U^2}{\pi L D}}$, (where C_D, set to 1, is the drag coefficient of the cylinder). Figure 2(b) shows that the lock-in frequency is close to $2\omega_{theo}$, in good agreement with the VIV predictions for weak reduced mass m* (see Khalak and Williamson 1999 [1]). The stratification does not modify the physical origin of this oscillation. It simply increases the natural frequency, thus shifting the resonant band to larger ratios L/D. In a homogeneous fluid the oscillations would be locked for L/D smaller than 1. In our stratified experiment, they can be locked for L/D as large as 10.

The galloping mode

At lower Fr, and especially for large L/D ratio, a vibration mode comparable to a galloping mode is observed: oscillations with low frequencies and very high amplitudes (up to 2D) occur. In a homogeneous fluid, galloping is obtained when a symmetry is broken in the system (e.g. for a rectangular cylinder, see Bokaian and Geoola 1984 [2]) but is not observed with a circular cylinder. In the presence of stratification, the top/bottom symmetry is automatically broken. We show numerically that a weak tilt of the cylinder trajectory with respect to the horizontal creates a destabilizing lift. We argue that this effect is responsible of the galloping instability that is observed.

CONCLUSIONS

This study shows that stratification has a strong influence on the flow induced vibration phenomena affecting a moving cylinder. The stratification enhances a VIV-like mode: it leads to high amplitude oscillations even outside the classical band of resonance. It also induces new instabilities such as galloping.

References

[1] Khalak A., Williamson C.H.K., Motions, forces and mode transitions in vortex-induced vibrations at low mass-damping. *J. Fluid. Struct.* 13:813-51, 1999.

[2] Bokaian A.R., Geoola F., Hydroelastic instabilities of square cylinders, *J. Sound and Vibration*, **92**(1), 117-141, 1984

THE ROLE OF FREE-SURFACE ON VORTEX-INDUCED VIBRATION OF A SPHERE

Amir Chizfahm[1], Vaibhav Joshi [1], and Rajeev Jaiman* [1]
[1]Department of Mechanical Engineering, The University of British Columbia, Vancouver, Canada

Summary Fluid-structure interaction (FSI) of submerged or floating spherical bodies has various applications in marine and offshore engineering. In this study, we aim to understand the dynamics of vortex-shedding modes and the free-surface effects on the flow-induced vibration (FIV) response of a freely vibrating sphere with fully and partially submerged configurations. To analyze the vortex synchronization regimes and the wake patterns, We systematically examine the mode transitions and the motion trajectories for a range of Reynolds number $Re \in [2000 - 15000]$. we find that the mode transition is strongly sensitive to the Reynolds number. Finally, we look into the effect of free surface on the FIV response of the sphere piercing the free surface. The maximum amplitude response of $\sim 2D$ is observed for the sphere at lock-in state which is greater than all the submerged cases studied.

INTRODUCTION

Flow-induced vibrations (FIV) of floating spheres can be useful for power generation and wave energy harvesting while such vibrations could be undesirable for spherical marine/offshore structures such as low-aspect-ratio escort tug-boats. Unlike a vast amount of literature available on two-dimensional geometry of elastically-mounted circular cylinders, there are limited studies on a three-dimensional geometry of a sphere undergoing flow-induced vibration. Besides, most of the studies on the FIV of the sphere performed for the flow past a fully submerged structural body with no free surface, to identify the modes of vibrations and motion trajectories [1]. Furthermore, there are only limited experimental studies considered the hydrodynamic effects of free-surface on FIV of the three-dimensional geometry of a sphere. The recent experimental study by [2] investigated the effect of proximity to the free surface on VIV of a fully and semi-submerged configurations of the sphere. Various regimes based on the amplitude response and the immersion ratio for the fully submerged and piercing sphere configurations were discussed. They observed that the sphere amplitude response is increased while it is piercing the free-surface for a range of immersion ratios $h^* = h/D$, where h is the distance from the top of the sphere to the free-surface and D is the sphere diameter. However, no specific wake mode was identified for the cases of piercing spheres in the study performed in [2].

In the current study, for the first time, successful validation of the 1-DOF vibrating sphere by considering the effect of the free-surface is established through detailed quantitative and qualitative comparisons with the experiments. We systematically explore the effect of Reynolds number on the mode transitions at VIV regime for a freely vibrating sphere, and its substantial effect on the coupled dynamical behavior and motion trajectories. The insight gained is used for identifying the wake modes and coupled dynamical interactions that lead to vortex-induced motion (VIM) with a large amplitude response for the sphere configuration piercing the free-surface.

HIGH-FIDELITY FSI NUMERICAL FRAMEWORK

The present study employs a first-principle based fully-coupled continuum mechanics formulation for solving a multi-phase fluid-structure interaction at high Reynolds number. The underlying formulation combines the fluid flow, structure, turbulence, two-phases and the mesh movement in an efficient and robust manner. The incompressible multiphase Navier-Stokes equations are solved via a stabilized variational framework which is coupled with a nonlinear elastic structural solver to solve the fluid-structure interaction problem. The free-surface effects are taken into account by modeling the air-water interface with the help of phase-field based Allen-Cahn equation and the turbulence is modeled via dynamic large eddy simulation (LES). The flow equations are solved in an arbitrary Lagrangian-Eulerian (ALE) framework for the mesh movement. For the stability and robustness purpose, these multi-fields are solved in an implicit manner [3].

RESULTS AND DISCUSSION

A representative schematic and the associated boundary conditions of the problem domain are shown in Fig. 1a. The root-mean-squared values of the amplitude response are compared with the recent experimental data of [2]. Our VIV results show a good agreement with the experimental data. Fig. 1b shows the trajectory response at the lock-in regime for two different Reynolds numbers. The motion trajectories for the cases in the range of $Re \in [2000 - 6000]$ are showing circular-type motion at stationary state. However, at higher Reynolds numbers ($Re = 12000, 15000$) the behaviour of the motion trajectories is found to be changing substantially at the periodic state, experiencing a combination of linear and circular-type movement. At $Re \in [2000 - 6000]$, the sphere starts to move with a linear trajectory motion with hairpin-type vortex structures shed behind the sphere body Fig. 1(b-middle), however at the stationary state, the sphere motion changes to circular-type trajectory with the vortex shedding mode transforming to spiral mode, Fig. 1(b-bottom). The mode transition for the higher Reynolds number cases however is quite different where the vortex structure modes

*Corresponding author. E-mail: rjaiman@mech.ubc.ca

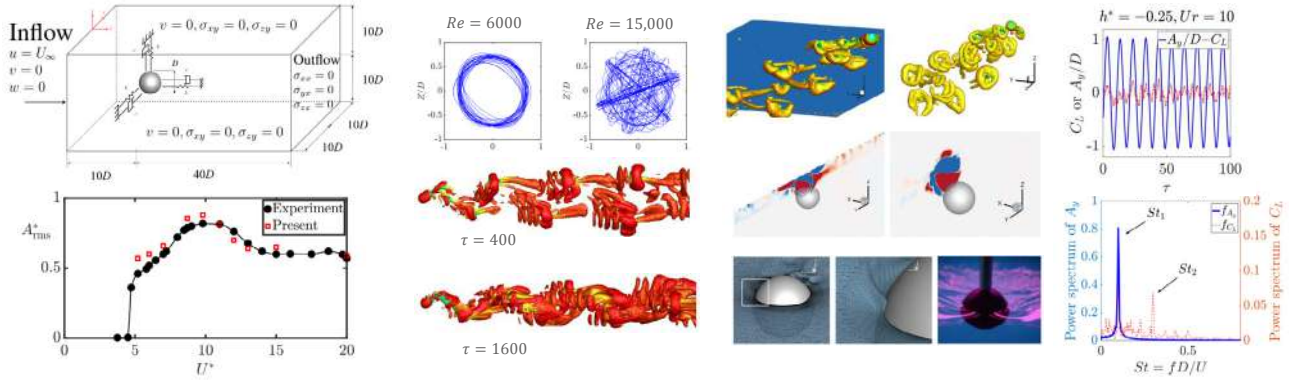

(a) (b) (c) (d)

Figure 1: (a) The schematic of the problem setup and the associated boundary conditions; The r.m.s amplitude response of the sphere at $h^* = 1$ with the experimental data of [2], (b) Trajectory response of the 3-DOF sphere motion in cross-flow plane at lock-in state; Iso-surface of wake structures formed behind the sphere at transient and stationary states at $Re \approx 2000$, where $\tau \equiv tU/D$. (c) Wake structures, stream-wise x-vorticity (ω_x) contour, and qualitative comparison of the free-surface deformation for the piercing sphere case with the experimental observation in [2], at $Re \approx 15,000$. (d) Time histories of the amplitude response and the lift coefficient and the corresponding power spectrum analysis versus the normalized frequency f^*.

transform with a mode shift frequency at the periodic state. The mode shift transforms the linear motion (due to the harpin mode), to circular-type motion (due to the spiral mode) and *vice versa* with the specific frequency. In addition, the sphere linear trajectory motion response is tilted at each mode shift.

The existence of hairpin wake modes even when the sphere is piercing the free-surface is found in our numerical analysis. We find that the vortex loop patterns that were observed for the submerged case (Fig. 1 (c-top-right)) are slightly stretched to elliptical loops for the piercing case (Fig. 1 (c-top-left)). In addition, Fig. 1(c-middle) qualitatively compares the wake dynamics of the fully-submerged sphere at ($h^* = 1$) and piercing sphere at ($h^* = -0.25$). As it can be seen the x-vorticity contour for the piercing case is quite similar with the submerged case except some added stretched vorticity formation at the top. Fig. 1d shows the time histories of the amplitude response at $h^* = -0.25$. For the case of the piercing sphere, the maximum peak-to-peak amplitude response of $\sim 2D$ is observed at the stationary state which is larger than all the submerged cases studied. Further analysis of the power spectrum is shown in Fig. 1d, where two dominant frequencies of the vortex shedding at $St_1 = 0.1$ and $St_2 = 0.29$ are found for the piercing sphere case. The existence of a higher-harmonic behaviour due to the non-symmetric geometry of the piercing sphere at the air-water interface is expected to be a major cause for the large amplitude response for the case of the piercing sphere.

CONCLUSIONS

In the present study, we have successfully employed our in-house coupled multifield solver to simulate two-phase fluid-structure interaction of a spherical body. We found that the effect of Reynolds number on the wake mode transitions and motion trajectories for a freely vibrating sphere at VIV regime is substantial. Despite the circular-type motion at stationary state at $Re \in [2000 - 6000]$ for the 3-DOF sphere, the trajectories for higher Reynolds numbers showed a combination of linear and circular motions with a tilt frequency at the periodic state. The insight gained is used to identify the wake modes and coupled dynamical interactions of the sphere piercing the free-surface. We observed that stretched hairpin-type wake loops are formed behind the sphere when it pierces the free-surface at VIV regime. The wake structures induce large amplitude oscillations ($A_{\max} \sim 2D$) that are greater than the fully submerged cases studied. The existence of higher-harmonic behaviour is observed due to non-symmetric geometry of the piercing case. It can be deduced that the geometry change at the discontinuous air-water interface has a significant impact on the synchronization of the vortex shedding and the vibration frequency, and could be the major cause of the large amplitude response.

References

[1] Rajamuni. MM et al. Vortex-induced vibration of elastically-mounted spheres: A comparison of the response of three degrees of freedom and one degree of freedom systems *J. Fluids and Structures*, 2019.

[2] Sareen. A et al. Vortex-induced vibrations of a sphere close to a free surface *J. Fluid Mech.* **846**: 1023–1058, 2018.

[3] Joshi. V, Jaiman. R A hybrid variational Allen-Cahn/ALE scheme for the coupled analysis of two-phase fluid-structure interaction *International J. for Numerical Methods in Engineering* **117**: 405-429, 2018.

EFFECTS OF LUBRICATION AND OSMOTIC PRESSURE ON SOLVENT PERMEATION THROUGH A MEMBRANE AT LOW PECLET NUMBER

Shuji Yamada * [1], Asahi Tazaki[1], Tomohiko Sakamoto[1], Shintaro Takeuchi[1], and Takeo Kajishima[1]
[1]Department of Mechanical Engineering, Osaka University, Osaka, Japan

Summary To understand the lubrication-dominated solvent permeation through a membrane in mass transfer, numerical simulation of permeation through a moving semi-permeable membrane of corrugated geometry is carried out with a fully validated numerical method. In mass transfer under the lubrication, the solvent permeation is induced by the discontinuities in hydrostatic pressure and osmotic pressure, which are respectively caused by the lubrication and concentration jump of solute at the membrane. An analytical model of asymptotic permeate flux of solvent (under an infinitesimal permeability condition) is presented by solving the Reynolds lubrication equation and the convection–diffusion equation of the solute. Through comparisons between the numerical and the asymptotic analytical results, the effect of permeation on lubrication in mass transfer is discussed and the significance of considering osmotic pressure in mass transfer under the lubrication is highlighted.

GOVERNING EQUATIONS, PROBLEM STATEMENT AND ASSUMPTIONS

The fluid is an incompressible Newtonian fluid with a constant density (ρ) and constant viscosity (μ). The governing equations of the fluid are the equation of continuity and Navier-Stokes equation, and the concentration obeys the convection-diffusion equation:

$$\nabla \cdot \boldsymbol{u} = 0, \qquad \frac{\partial \boldsymbol{u}}{\partial t} + \boldsymbol{u} \cdot \nabla \boldsymbol{u} = -\frac{\nabla p}{\rho} + \frac{\mu}{\rho}\nabla^2 \boldsymbol{u}, \qquad \frac{\partial c}{\partial t} + \boldsymbol{u} \cdot \nabla c = \nabla \cdot (D \nabla c),$$

where $\boldsymbol{u}$ is the velocity, t is the time, p is the pressure, μ is the viscosity, c is the concentration and D is the diffusivity.

The volumetric flux of the fluid across the membrane is modelled by the following equation: $\boldsymbol{J}_n = L_p([\![p]\!] - [\![\Pi]\!])\boldsymbol{n}$, where $\boldsymbol{n}$ is unit normal vector pointing from the rear side of the membrane Ω_1 to the front side Ω_2, L_p is the permeability for pure fluid, and $[\![p]\!]$ is the hydrostatic pressure jump (i.e., discontinuity) across the membrane calculated with the limiting pressure values at the interface, p_1 and p_2, on the respective sides of the membrane as $[\![p]\!] = p_1 - p_2$. Assuming that the solution is a dilute solution, the osmotic pressure Π is given by van't Hoff's law: $\Pi = cRT$, where R is the ideal gas constant and T is the temperature. Note that the concentration represents the molar concentration. Then, the volumetric flux is described by following equation:

$$\boldsymbol{J}_n = L_p([\![p]\!] - RT\,[\![c]\!])\boldsymbol{n}. \tag{1}$$

We study the permeation across a corrugated semi-permeable rigid membrane in a parallel channel moving at a constant velocity (U_0), as schematically shown in Fig.1. The membrane has an infinitesimal thickness. The geometry of the corrugation and its prescribed motion are given by the following function: $h(x,t) = h_0(1 + \delta\cos[k(x - U_0 t)]$, where $k(= 2\pi/l)$ is the wave-number and δ is a parameter between 0 and 1. The corrugation has an infinite extension in the x direction. We assume that the amplitude of corrugation δh_0 is sufficiently small with respect to the half-channel width h_0 (i.e., $\delta \ll 1$) and that h_0 is much smaller than the wavelength of the corrugation (i.e., $h_0 \ll 2\pi/k$) which is equivalent to aspect ratio $\varepsilon(= h_0/l)$ being sufficiently small, i.e.,$\varepsilon \ll 1$. We solve the concentration field under the prescribed Dirichlet conditions on the top and bottom walls: $c_{\mathrm{top}}(x) = c_0(1 + \sin(kx))$ and $c_{\mathrm{bot}}(x) = c_0(1 - \sin(kx))$.

In the present study, the permeation is solved by transforming the frame to that attached on the membrane for simplicity. When ε and the Reynolds number $\mathrm{Re} = \rho U_0 H/\mu$ satisfy $\varepsilon \ll 1$ and $\varepsilon\mathrm{Re} \ll 1$, the flow can be described by the Reynolds lubrication equation in both Ω_1 and Ω_2 regions. In addition, when ε and the Peclet number $\mathrm{Pe} = U_0 H/D$ satisfy $\varepsilon \ll 1$ and $\varepsilon\mathrm{Pe} \ll 1$, the concentration filed is determined by the diffusion in the y direction.

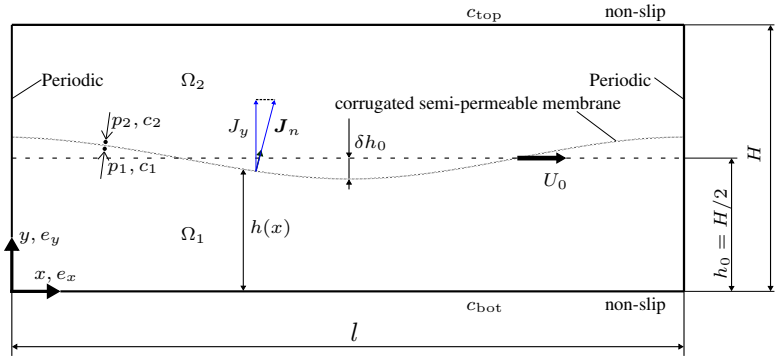

Figure 1: A corrugated semi-permeable membrane travelling at constant speed U_0 in $+x$ direction in a parallel channel

*Corresponding author. E-mail: yamada@fluid.mech.eng.osaka-u.ac.jp

ASYMPTOTIC PERMEATION FLUX AND OUTLINE OF NUMERICAL METHOD

With a membrane of infinitesimal permeability ($L_p \to 0$, and therefore $J_y \to 0$), the pressures in Ω_1 and Ω_2 regions, $p_1(x)$ and $p_2(x)$, follow separate Reynolds lubrication equations. By solving the Reynolds lubrication equation, the pressure in Ω_1 is given as follows:

$$p_1(x,t) = -6\mu U_0 \frac{h(x,t)+h_0}{(2\pi\varepsilon)^2(2+\delta^2)} \frac{\partial h^{-1}(x,t)}{\partial x}. \tag{2}$$

From the geometric symmetry of Ω_1 and Ω_2 (see Fig.1) and the one-dimensional nature of the lubrication pressures, the pressure in Ω_2 is given as $p_2(x,t) = p_1(x+\pi/k,t)$, and then $[\![p]\!]$ can be calculated. On the other hand, the concentrations in Ω_1 and Ω_2, $c_1(x,y)$ and $c_2(x,y)$, follow the respective diffusion equations. Under $\varepsilon \ll 1$ and $\varepsilon \mathrm{Pe} \ll 1$, c_1 and c_2 become independent of y, and the values are homogeneous in the y direction being fixed at the respective boundary values, $c_{\mathrm{bot}}(x)$ and $c_{\mathrm{top}}(x)$. Finally, under an infinitesimal L_p, the permeate flux is given by the sum of the permeations due to the discontinuities in the hydrostatic and osmotic pressures: $J_y(x,t) = L_p([\![p]\!] - RT\,[\![c]\!])$. By substituting Eq.(2) and $c_{\mathrm{top/bot}}$ into this J_y, the asymptotic permeate flux is obtained as

$$\frac{J_y(x,t)}{U_0} = -\frac{96L}{4\pi\varepsilon}\frac{\delta}{2+\delta^2}\frac{\sin\left[k(x-U_0t)\right]}{\left(1-\delta^2\cos^2\left[k(x-U_0t)\right]\right)^2} - \omega L\mathrm{Re}\sin(kx), \tag{3}$$

where L is the non-dimensional permeability defined as $L_p\mu/H$ and ω is the ratio of osmotic pressure to hydrostatic pressure defined as $2RTc_0/\mu U_0 H^{-1}$. Hereafter, we refer J_y under an infinitesimal L_p as asymptotic permeate flux.

For comparison, the fluid motion is numerically solved on a Cartesian fixed mesh system with a uniform mesh size (Δ). The membrane is represented by connected Lagrangian marker points. For coupling the fluid and object motions, an original discrete-forcing immersed boundary method [2] is employed, which is characterised by (i) the direct discretisation of the governing equations even at the grid points adjacent to the interface and (ii) the consistent coupling of the incompressible velocity and pressure fields. The same strategy is applied for discretising the concentration field near the interface. The above two features of the method enable capturing the sharp discontinuity of the pressure and concentration. For more details on the numerical method, refer to Ref. [2].

RESULTS AND DISCUSSION

In the present study, the domain length l is fixed at $5H$ $(= 10h_0)$; the aspect ratio of each flow region is sufficiently small, $\varepsilon = 0.1$. The amplitude parameter δ is fixed at 0.1. The Reynolds and Peclet numbers are set at $\rho U_0 h_0/\mu = 0.5$ and $U_0 h_0/D = 0.5$, and the reference concentration and the pressure ratio are fixed at $c_0 = 0.5$ and $\omega = 1$, respectively. Numerical simulation is carried out at the spatial resolution $h_0/\Delta = 20$ and the time increment $\Delta t/(H/U_0) = 5\times10^{-5}$. To see the asymptotic trend of J_y as $L \to 0$, the permeability is varied in the following range: $10^{-2}, 10^{-3}, 10^{-4}$ and 10^{-5}. Note that, depending on the phase difference between the corrugation and the boundary profiles of c, the above solvent fluxes $J_y(x,t)$ will encounter the weakening and strengthening instants. Figure 2 compares the longitudinal distributions of $J_y/(U_0L)$ at three different cases: (a) steady solvent flux induced only by $[\![p]\!]$ (i.e., $\omega = 0$), and the two cases of $\omega = 1$ in (b) the weakening configuration at $t/(H/U_0) = 7.5$ and (c) the strengthening configuration at $t/(H/U_0) = 10.0$. The figure highlights the effects of osmotic pressure on permeation under the lubrication. The asymptotic analytical prediction, Eq.(3), reasonably approximates the asymptotic permeate flux distributions, and, in the presentation, the difference from the numerical result will be discussed with the induced flux due to the effect not described by the Reynolds equation. [3].

References

[1] Takeuchi, S., Tazaki, A., Miyauchi, S. and Kajishima, T., *Journal of Membrane Science*, Vol.582 pp.91-102 (2019)
[2] Takeuchi, S., Fukuoka, H., Gu, J., Kajishima, T., *Journal of Computational Physics*, Vol.371, pp.1018-1042 (2018)
[3] Takeuchi, S., Gu, J., *Physical Review Fluids*, Vol.4(11), 114101 (2019)

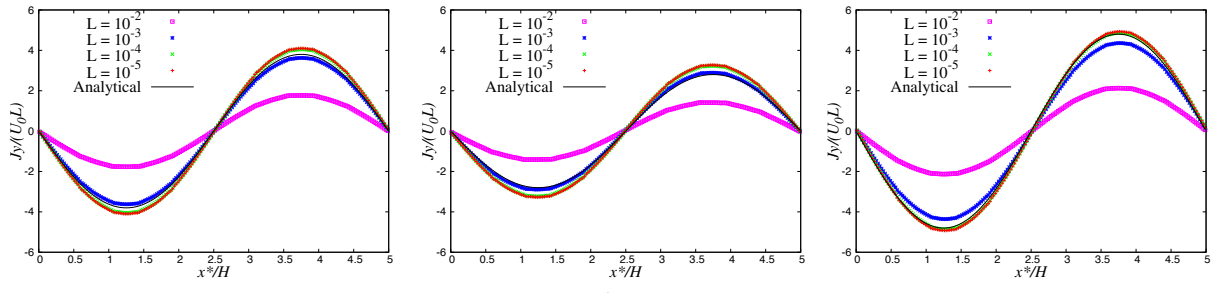

Figure 2: Asymptotic trends of solvent permeation flux $J_y(x)$ against the permeation coefficients $L = 10^{-2}, 10^{-3}, 10^{-4}$ and 10^{-5} at $\delta = 0.1$; the solvent flux (a) by $[\![p]\!]$ (without concentration condition, $\omega = 0$) under steady state, and by both $[\![p]\!]$ and $[\![c]\!]$ ($\omega = 1$) in (b) the weakening and (c) strengthening configurations. In the figure, "Analytical" means the prediction by Eq.(3) and $x^* = x - U_0 t$.

A NEW MECHANISM OF TRANSITION TO AEROELASTIC DIVERGENCE

Vasily Vedeneev *
Institute of Mechanics, Lomonosov Moscow State University, Moscow, Russia

Summary There are two types of aeroelastic instabilities: flutter, which is an oscillatory loss of stability, and divergence, which is a static instability. A general divergence mechanism described in textbooks consists of decrease of one of natural frequencies down to zero due to negative aerodynamic stiffness, coalescence with its paired frequency, and transformation to one damped and one growing frequency. Most examples of this mechanism use quasi-steady aerodynamics. In this study we show that when using unsteady aerodynamics, analytical structure of eigenfrequencies essentially changes; namely, no frequency coalescence occurs; instead, structural eigenfrequencies stay damped. The divergence mode is not a continuation of a structural mode, but separates from a continuous spectrum that exists in the aeroelastic system when unsteady aerodynamics is used, but is absent in quasi-steady case.

INTRODUCTION

In most of aeroelasticity textbooks [1–3], divergence and flutter are considered separately: divergence as static instability, where steady aerodynamics is employed, and flutter as dynamic instability, where the use of unsteady aerodynamics is crucial for flutter prediction. Even when divergence is considered within the framework of a dynamic system, still, at best, quasi-steady aerodynamics is used. In this study we re-analyse the classical problem of instability of two-degree-of-freedom (bending and torsional) system, focusing on divergence, but using fully unsteady Theodorsen aerodynamics.

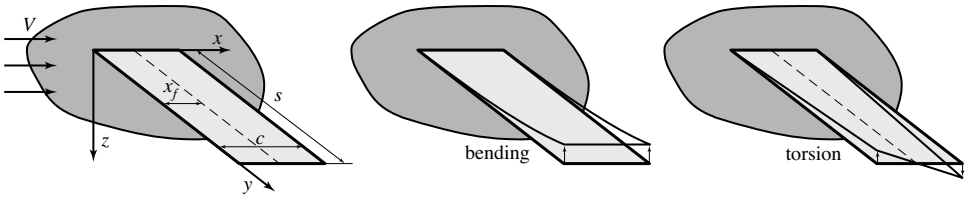

Figure 1: Rectangular wing and its bending and torsional degrees of freedom.

PROBLEM FORMULATION AND RESULTS

Wing model

We consider a classical two-degree-of-freedom aeroelastic model of a thin rectangular wing (Fig. 1) in incompressible fluid flow. To derive equations of motion, we follow a standard procedure, applying Largange equation as done in [3, §10.2.1]. To calculate unsteady aerodynamic lift and moment, we use a strip theory, assuming that aerodynamic forces produced by each cross-section can be taken from corresponding two-dimensional problem. We will restrict ourselves to harmonic motion of the wing, which is sufficient for both divergence and flutter analyses. Taking time dependence in the form $e^{i\omega t}$, the two-dimensional aerodynamic forces are readily given by Theodorsen theory [1, §5-6], [2, §6.9], [3, §9.3]. After standard algebra, we obtain aeroelastic equations of motion that yield the following eigenvalue problem:

$$\mathcal{F}(\omega) = \det(-\omega^2\mathbf{M} + i\omega\mathbf{D}_a(k) + (\mathbf{K}_a(k) + \mathbf{K})) = 0, \tag{1}$$

where $\mathbf{M}$ and $\mathbf{K}$ are structural mass and stiffness matrices, $\mathbf{D}_a(k)$ and $\mathbf{K}_a(k)$ are aerodynamic damping and stiffness matrices. While structural matrices are constant, aerodynamic matrices are expressed through the Theodorsen function $C(k) = K_1(ik)/(K_0(ik) + K_1(ik))$, where K_n are modified Bessel functions of the second kind, and $k = \omega c/(2V)$ is the reduced frequency.

Numerical results

The eigenvalue problem (1) is solved numerically by an iterative method. Calculations are started at sufficiently small flow speed V, where each solution is associated with a wing eigenmode in still air. Next, V is gradually increased so that continuous branch of eigenfrequencies is obtained. Parameters used in [3, §10.8] are considered here as an example.

Figure 2a shows the eigenfrequency loci when using quasi-steady aerodynamics. It is seen that when the flow speed is increasing, bending frequencies ω_2 and ω_4 move just slightly, while torsional frequencies ω_1 and ω_3 move toward each other, coalesce at the imaginary axis, and transform to damped and divergence modes. This behaviour represents classical divergence mechanism [1–3]. However, the use of full unsteady aerodynamics yields completely different eigenfrequency loci shown in Figure 2b. Torsional frequencies do not approach each other and do not interact, but become highly damped. The divergence mode also exists for $V \geq V_{div}$, being the fifth mode. But for $V < V_{div}$ no divergence root is found. Hence, at subcritical flow speed only structural modes are present. Note that the eigenvalue problem (1) is not algebraic, because eigenfrequency ω is not only explicitly present in the equation, but is also implicitly present in aerodynamic matrices, which are functions of the reduced frequency k. That is why constant number of roots cannot be guaranteed.

*E-mail: vasily@vedeneev.ru. This work is supported by the Russian Foundation for Basic Research (project 18-31-20057).

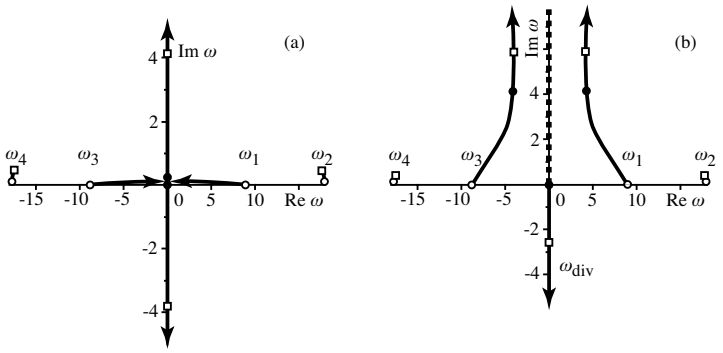

Figure 2: Eigenfrequency loci when changing the flow speed V from $V = 10$ m/s (○) to $V = V_{div} = 54.9$ m/s (●) and further to $V = V_{div} + 5 = 59.9$ m/s (□). Quasi-steady aerodynamics (a), full unsteady aerodynamics (b).

Proof of the non-existence of the divergence mode and subcritical flow speeds

To avoid numerical issues, a rigorous analysis of (1) in the vicinity of the divergence speed has been conducted. Let us have the solution $\omega = k = 0$ at $V = V_{div}$. We take a small velocity deviation $V = V_{div} + V'$ and find a solution of (1) that tends to zero as $V' \to 0$, i.e. find the divergence mode frequency in the vicinity of the divergence boundary. Neglecting ω^2 term as infinitesimal, and considering the asymptotic expansion of Theodorsen function at small k, we find simplified eigenfrequency equation (1) near the divergence boundary. Its rigourous analysis yields the following: the divergence root exists at $V \geq V_{div}$, but no root exists at $V < V_{div}$. In other words, the divergence mode is not a continuation of a natural mode of the wing but is an additional eigenmode that exists only for $V \geq V_{div}$.

Mathematically, this phenomenon is due to logarithmic singularity of Theodorsen function at $k = 0$, and it does not manifest itself if simplified quasi-steady aerodynamics is used.

Initial-value problem and the continuous spectrum

To understand the origin of the divergence mode, we solve the initial-value problem by using Laplace transformation technique. The general solution ($q_{b,t}$ are generalised coordinates corresponding to bending and torsion) has the form

$$q_{b,t}(t) = \frac{1}{2\pi}\int_0^{+i\infty} [\xi]_{b,t}(\omega) e^{i\omega t} d\omega + \sum_{n=1}^{p} i \frac{C_{b,t}(q^n_{b,t}, \omega_n)}{\partial \mathcal{F}(\omega_n)/\partial \omega} e^{i\omega_n t}, \tag{2}$$

where $[\xi]_{b,t}$ and $q^n_{b,t}$ are expressed through the initial conditions. It is seen that the solution is the linear combination of two terms: eigenmodes that form discrete spectrum of the problem (p is the number of eigenfrequencies), and the integral over pure imaginary damped frequencies that form continuous spectrum. Mathematically, the continuous spectrum is present due to the branch cut of the Theodorsen function. Its physical nature originates from the wake behind the oscillating wing: the wake is convected downstream but 'remembers' the wing motion in the past and affects the aerodynamic loading.

It is now clear that the divergence eigenmode that exists only at $V \geq V_{div}$ (Fig. 2b) does not come from "nowhere" but separates from the continuous spectrum at $V = V_{div}$. If quasi-steady aerodynamics is used, then aerodynamic matrices are constant, and no continuous spectrum is present. This reflects the fact that, physically, quasi-steady aerodynamics ignores the wake behind the wing and, consequently, the wake influence on the aerodynamic loads.

CONCLUSIONS

We have proved that when using fully unsteady aerodynamics for aeroelastic calculations, first, in addition to discrete spectrum of eigenfrequencies, there exists a continuous spectrum consisting of monotonically damped frequencies, which originates from the wake behind the oscillating wing. Second, the growing divergence eigenfrequency is not a smooth continuation of 'structural' natural frequency. Instead, all structural frequencies become damped at postcritical flow velocity, whereas the divergence mode is an additional mode which exists only at post-critical speeds and separates at the divergence speed out the continuous spectrum at $\omega = 0$.

Present results are compared with other studies that used unsteady aerodynamics for the divergence analysis [4–6] and with experimental divergence study [6], where divergence not originating from structural modes was observed. 'Practical' methods of aeroelastic analysis, such as k, p-k, g methods, are discussed.

References

[1] Bisplinghoff R.L., Ashley H., Halfman R.L, *Aeroelasticity*. Addison-Wesley, Cambridge, 1955.
[2] Fung Y.C., *An introduction to the Theory of Aeroelasticity*. Dover, New York, 1969.
[3] Wright J.R., Cooper J.E., *Introduction to Aircraft Aeroelasticity and Loads*. John Wiley & Sons, Chichester, 2015.
[4] Edwards J.W. Unsteady Aerodynamic Modeling for Arbitrary Motions. *AIAA J.* **17(4)**: 365–374, 1979.
[5] Edwards J. W., Wieseman C. D. Flutter and divergence analysis using the generalized aeroelastic analysis method. *J. Aircraft*. **45(3)**: 906-915. 2008.
[6] Heeg J. Dynamic Investigation of Static Divergence: Analysis and Testing. NASA/TP-2000-210310, 2000.

SUPERSONIC FLUTTER OF ELASTIC PANEL UNDER DIFFERENT DISTURBANCES

A.S. Shishaeva[1,2], V.V. Vedeneev[1], G.B.Sushko[2], A.A. Aksenov[2]
[1]Lomonosov Moscow State University, Moscow, Russia
[2]Tesis LTD, Moscow, Russia

Summary We investigate elastic panel behavior under different external disturbances in a constant, accelerated and decelerated supersonic flow. We obtain that the most dangerous disturbance is the third mode disturbance in gas flow with Mach number $1.45 < M < 1.6$.

INTRODUCTION

Aeroelastic instability of skin panels in supersonic gas flow, known as panel flutter, can be either single mode or coupled mode flutter. The coupled-mode panel flutter occurs at high supersonic gas speed [1], while at low supersonic speed the single-mode flutter is dominating [2]. A single-mode flutter regime is more energy-intensive and, thus, more dangerous. In our study [3] we considered instability of a skin panel in a constant subsonic and supersonic gas flow under a small external disturbance. Gas speed was varying from M=0.7 to M=1.7. We obtained that there are different types of single-mode flutter at small supersonic gas speeds: simple first mode flutter ($1 < M < 1.12$, $1.41 < M < 1.7$), 1:2 resonant flutter ($1.12 < M < 1.33$), high-frequency non-periodic flutter ($1.33 < M < 1.41$). Resonant flutter includes first and second natural modes and internal resonance between them. High-frequency non-periodic flutter includes two, three or more natural modes and an internal resonance between them. In our study [4] we considered instability of a skin panel in accelerating and decelerating gas flow under a small external disturbance. We obtained that there is a strong effect of the acceleration or deceleration on the panel. For example, high acceleration of deceleration eliminates high-frequency non-periodic flutter. Different limit cycles can realize at the same flow conditions in dependence of a form and power of external disturbance. Moreover, in that case one limit cycle can be transformed to another by applying a single disturbance to the plate. In this work we study an effect of a disturbance applied to the plate.

STATEMENT OF THE PROBLEM

We consider an interaction of an elastic plate with an external supersonic flow of air considered as inviscid perfect gas. The gas flows over one side of the plate with Mach number varied in the range $1<M<1.7$. At the other side of the plate, a pressure equal to the undisturbed flow pressure is specified, such that the undisturbed pressure difference along the plate is zero. The elastic plate of length $L_p = 0.3$ m and thickness $h_p = 0.001$ m is mounted into a rigid plane (see Figure 1). The plate is made of steel with Young's modulus $E = 2 \cdot 10^{11}$ Pa, Poison coefficient $\nu = 0.3$ and density $\rho_m = 7800$ kg/m^3. In dimensionless terms, the plate stiffness and length are: $D = D_p/(a^2 \rho_m h^3) = 21.4$, $L = L_p / h_p = 300$, where $D_p = Eh^3/(12(1-\nu^2))$ is the dimensional plate stiffness, and $a = 331$ m/s is the speed of sound in the air. The plate is described by the nonlinear Mindlin plate model, where elastic strains are calculated through Koiter–Sanders shell theory. During small initial period of time, disturbance is applied to the panel, and its evolution is analysed.

The subsequent plate-flow interaction is calculated using two coupled solvers: Abaqus for simulating the plate deformation and FlowVision for simulating the gas flow. The interaction between the programs is organized through the direct coupling mechanism along the surface of the deformed plate. Investigation of grid, time and domain convergence, testing of the model on coupled and single mode flutter at constant flow speed are described in [3].

Figure 1. Statement of the problem.

RESULTS

We consider two statements: panel behavior in a constant flow and in an accelerated or decelerated flow. In the first statement an effect of the first, second and third mode disturbance with significant load applied to the panel is considered. We compare these results with the behavior under disturbance with small load [3]. We analyze shape of the plate oscillations and dimensionless total energy. Dimensionless total energy is calculated as $W = (W_{kinetic}+W_{strain})/0.5\rho V^2 Ldz$. We obtain that there is a significant effect of initial disturbance for $M > 1.2$. If we apply second mode disturbance with significant amplitude to the panel in Mach number range $1.2 < M < 1.5$, than a second mode flutter is realized. Total energy of the second form flutter of the panel in Mach number range $1.4 < M < 1.48$ is two times larger than for small amplitude (see Figure 2, blue marker). If we apply third mode disturbance with significant initial amplitude to the panel in Mach number range $1.33 < M < 1.6$, a third mode flutter is realized. The total

energy of the panel under the third mode disturbance with large amplitude is two times larger than for a small amplitude in Mach number range $1.33 < M < 1.45$ (see Figure 2, green marker), and ten times larger in Mach number range $1.45 < M < 1.6$ than the largest energy of flutter realized under the small load in all investigated Mach numbers.

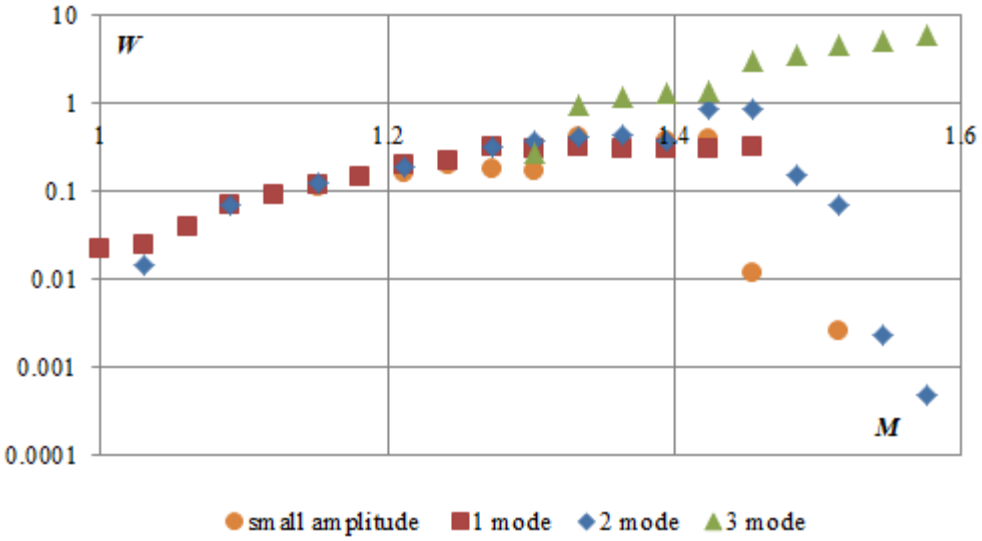

Figure 2. Dimensionless vibration energy of the panel (W) via Mach number (M).

In the second problem statement we investigate the evolution of the disturbance in the accelerated and decelerated supersonic flow. We obtain that the most significant effect takes place for the third mode disturbance with large amplitude at $1.4 < M < 1.7$.

CONCLUSIONS

The investigation shows that disturbances of higher modes (second and third) with large initial amplitude may induce single mode high-frequency vibrations with high energy. That vibrations are more energetic and dangerous than others so that it is important to avoid such kind of disturbances or flow conditions.

ACKNOWLEGEMENT

This work is supported by the grant of Russian Foundation for Basic Research (project 18-01-00404).

References

[1] Dowell E.H.: Aeroelasticity of Plates and Shells. Kluwer Academic Publishers, 1974.
[2] Vedeneev V.V.: Panel Flutter at Low Supersonic Speeds. *Journal of Fluids and Structures*. **29**:79–96, 2012
[3] Shishaeva, A.S., Vedeneev, V.V., Aksenov A.A. Nonlinear single-mode and multi-mode panel flutter oscillations at low supersonic speeds. *Journal of fluids and structures*. **56**: 205-223, 2015.
[4] Shishaeva A. S., Vedeneev V. V., Aksenov A. A., Sushko G. B.. Transonic panel flutter in accelerating or decelerating flow conditions. *AIAA Journal*. **56(3)**: 1-14, 2018.

INTERMITTENCY IN FLOW FIELD OF PLUNGING TEARDROP FOIL

Chhote Lal Shah* [1], Dipanjan Majumdar[1], and Sunetra Sarkar[1]
[1]Department of Aerospace Engineering, Indian Institute of Technology Madras, Chennai-600036, Tamilnadu, India.

Summary Flapping wings with suitable wing kinematics, wing shapes, and flexible structures can enhance lift as well as thrust by exploiting large-scale vortical flow structures under various conditions. However, it is also necessary to understand the dynamics of the flow field, which may influence the flyers. In the present study, an elliptic foil with an attached tail at the trailing edge is considered for studying the dynamics of the flow field. The present work focuses on analysing the dynamics with an increase in the flexibility of the tail structure. Although a perfectly rigid tail enhances the aerodynamic performance, it can also take the system to aperiodicity. However, a flexible tail has the ability to stabilize the system.

INTRODUCTION

Biologically inspired insect flight mechanisms have recently become a primary research subject, mainly to use in micro air vehicles (MAVs) for defense surveillance and environmental monitoring. The prime source of inspiration in this regard with the reliance on natural selection comes from the natural flyers due to the similar Reynolds number regime in which they fly. Natural flyers utilize the unsteady aerodynamics around their flapping wings to generate the lift and thrust. These aerodynamic loads are related to the formation and shedding of the vortices into the flow which are again dependent on different wing shapes, structural flexibility and wing kinematics. A rigid elliptic foil plunging in uniform stream results in a drag producing von-Karmann wake, thrust producing reverse Karmann wake and deflected reverse Karmann wake with the increase in plunge velocity kh (where $k = \frac{2\pi fc}{U_\infty}$ is reduced frequency, f is frequency, c is chord length of elliptic foil, U_∞ is free stream velocity, and h is nondimensional plunge amplitude) [1]. With further increase in kh the flow field transitions into the aperiodic regime and eventually to chaos [2]. However, a more realistic design of a bio-inspired wing would consist of a flexible trailing part attached to the stiff leading portion. Such models are typically called a teardrop model [3]. Heathcote and Gursul [3] reported that the enhancement in mean thrust is possible by using such a teardrop model. Likewise, Mia and Ho [4] noted that a flexible foil with a pre-defined deformation could increase the propulsive efficiency. Further, Heathcote et al. [5] showed that the thrust/input-power ratio was significantly high for flexible airfoils than rigid airfoils. Also, they observed that at high plunging frequencies, moderately flexible airfoil generates the largest thrust, while highly flexible systems show larger thrusts at low frequencies.

Most of the literature mentioned above focused on enhancing the aerodynamic performance. However, the dynamical transitions in the flow field of such a teardrop model have not been investigated earlier. The focus of this study is to explore the dynamics associated with the flow field for different levels of flexibility for the teardrop model. This study is of importance from the MAVs design point of view as one must avoid the system from entering into an aperiodic state in a broad sense.

COMPUTATIONAL METHODOLOGY

A teardrop airfoil with a rigid elliptic part (with major axis length as c) and a flexible tail of length $0.3c$ is considered here. A sinusoidal plunge motion is provided at the center of the elliptic foil. The trailing part of the teardrop is modeled as an inextensible flexible filament [6] and is allowed to oscillate passively. The flow around the oscillating body is governed by the incompressible Navier-Stokes equations. An in-house flow solver has been developed following the discrete forcing Immersed Boundary Method (IBM) proposed by Kim et al. [7]. In the present Fluid-Structure Interaction (FSI) framework, the structural solver and the IBM solver are coupled in a weak coupling approach where both flow and structural solvers exchange information explicitly at every time-step. The Reynolds number is kept constant at 300 throughout the study. The simulations are run after performing domain and grid convergence studies. A time step of 0.0004 has been considered after performing a time convergence test and has been used for the rest of the simulations.

RESULTS AND DISCUSSIONS

Simulations have been performed for a wide range of kh values. In order to study the effect of tail flexibility on the flow dynamics, different levels of rigidity with γ (nondimensional bending rigidity) = ∞ (rigid case), 1.0 and 0.1 have been considered. It is observed that the inclusion of a tail at the trailing edge of the elliptic foil enhanced the aerodynamic performance. At lower kh, the flow field, as well as aerodynamic loads, remain periodic for all the cases. However, the present study focuses on $kh = 1.5$, which is in the aperiodic regime. Time history of drag coefficient (C_D) and corresponding Morlet wavelet spectra [8] in terms of scalogram plots are presented in Figure 1. The scalograms are the visual representation of the wavelet transforms in which the x-axis represents time, and the y-axis represents the time-evolution of the frequency content of a signal.

*Corresponding author. E-mail: lal.chhote.shah@gmail.com

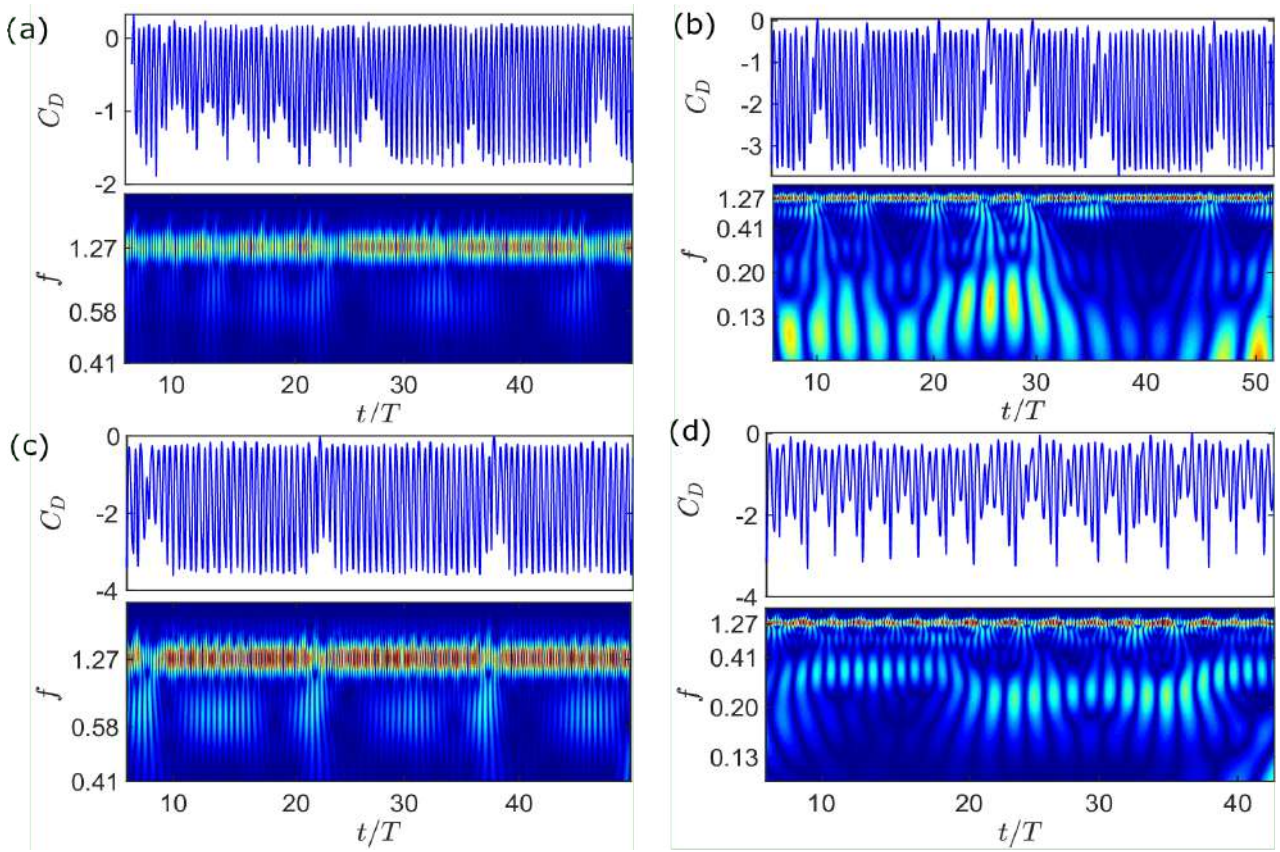

Figure 1: C_D time histories and corresponding scalogram of the wavelet coefficients for $kh = 1.5$; (a) elliptic foil without aft tail, (b) elliptic foil with rigid aft tail, (c) elliptic foil with flexible aft tail of $\gamma = 1.0$, and (d) elliptic foil with flexible aft tail of $\gamma = 0.1$.

The C_D time history for the rigid foil without tail exhibits an intermittent behavior that shows quasiperiodic time windows interspersed by chaotic windows (Figure 1 (a)). With the addition of a rigid tail, the mean thrust also increases notably. However, the system also enters into sustained aperiodicity (chaos) as is strongly suggested by the broad banded frequency spectrum in the scalograms in Figure 1 (b). As the rigidity of the tail is reduced, at $\gamma = 1.0$, the leading edge separation behavior again shows intermittency, which is clearly reflected in the C_D time history and corresponding wavelet spectra (Figure 1 (c)). With further decrease in the rigidity, for $\gamma = 0.1$, the flow field, and hence the C_D, becomes quasiperiodic. The quasiperiodic nature is confirmed from the modulation in the C_D time history caused by incommensurate frequency bands shown in the scalogram plot in Figure 1 (d).

CONCLUSIONS

In this study, the transition in flow dynamics of a sinusoidally plunging teardrop airfoil has been investigated. The existence of intermittency has been observed at $kh = 1.5$. Scalogram is used to characterise the dynamics associated with the time histories. The inclusion of a rigid tail at the trailing edge of the foil gives better aerodynamic performance, but the system also enters into a chaotic regime. However, with an increase in flexibility, the system no longer exhibits chaos, and the dynamics gets stabilized. Further time series analyses on the characterization of different dynamic states and the details of the flow field could not be shown here for the sake of brevity but will be shared during the presentation. The present study contributes towards the design of flexible flapping wings for the development of micro-air vehicles.

References

[1] Jones K.D., Dohring C.M., Platzer M.F., Experimental and Computational Investigating of the Knoller-Betz Effect. *AIAA J.* **36**: 1240-1246, 1998
[2] Badrinath S., Bose C., Sarkar S., Identifying the Route to Chaos in the Flow Past a Flapping Airfoil. *Eur. J. Mech.B Fluids* **66**: 38-59, 2017
[3] Heathcote S., Gursul I., Flexible Flapping Airfoil Propulsion at Low Reynolds Numbers. *AIAA J.* **45**: 1066-1079, 2007
[4] Miao J.M., Ho H.M., Effects of Aerodynamic Propulsive Efficiency of Flapping Flexible Airfoil. *J. Fluid and Struct.* **22**: 401-419, 2006
[5] Heathcote S., Martin D., and Gursul I., Flexible Flapping Airfoil Propulsion at Zero Freestream Velocity. *AIAA J.* **42**: 2196-2204, 2004
[6] Huang W., Shin S.J. Sung H.J, Simulation of Flexible Filaments in a Uniform Flow by the Immersed Boundary Method. *J. Comput. Phys.* **226**: 2206-2228, 2007
[7] J. Kim, D. Kim, H. Choi, An immersed-boundary finite-volume method for simulations of flow in complex geometries. *J. Comput. Phys.* **171**: 132-150, 2001
[8] Grossmann, A., Kronland-Martinet, R., and Morlet, J., Reading andUnderstanding Continuous Wavelet Transforms,"Wavelets. *Springer* 2–20, 1990.

ON DYNAMICS OF AN AEROELASTIC SYSTEM WITH TWO TRANSLATIONAL DEGREES OF FREEDOM

Yury D. Selyutskiy[1]
[1]Institute of Mechanics, Lomonosov Moscow State University, Moscow, Russia

Summary An aeroelastic system is considered which consists of two bodies that can move translationally in the direction transversal to the incoming flow. It is assumed that one of these bodies is bluff, and the aerodynamic load upon the other body is negligible. It is shown that if parameters of the system meet certain conditions then the trivial equilibrium can be destabilized by increasing of stiffness of one of the mounting springs. Dependence of amplitudes of limit cycles arising in the system on the mounting stiffness is studied.

INTRODUCTION

Aeroelastic systems consisting of a bluff body that can move translationally across the incoming flow (which means that the system has one translational degree of freedom) are intensively studied for many years. It is known that the so called galloping can arise in such systems, when the "natural" (or "trivial") equilibrium becomes unstable if the flow speed gets large enough, which results in the onset of self-sustained oscillations. This effect is of great interest from the point of view of engineering: on the one hand, it can lead to the fatigue and break of structures; on the other hand, such oscillations can be used for power generation purposes.

Different aspects of the influence of various parameters on the galloping behaviour of rectangular cylinders were investigated numerically and experimentally, in particular, in [1], [2].

Questions of using this phenomenon for energy harvesting were discussed, e.g., in [3], where the influence of electric load on the onset and characteristics of galloping oscillations were analysed.

In the present work, we consider an aeroelastic system with two translational degrees of freedom.

PROBLEM STATEMENT

Consider an aeroelastic system consisting of rigid bodies M_1 and M_2 connected with springs and able to move translationally along the axis OY (see Fig. 1). The body M_2 has a shape of rectangular cylinder.

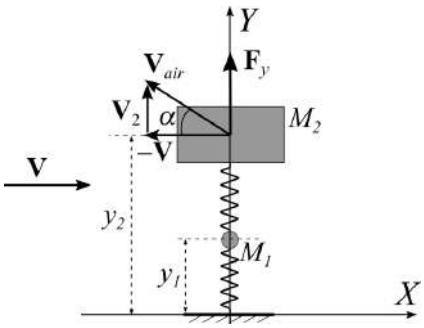

Figure 1. Aeroelastic system with two translational degrees of freedom.

This system is placed in the airflow; the air speed V is constant and perpendicular to the line of motion of bodies. We assume that the body M_2 interacts with the flow, while the aerodynamic load upon the body M_1 is negligible.

Here, we consider a modification of the conventional system, which comprises two bodies instead of one. Taking into account the above mentioned, the equations of motion can be written as follows:

$$m_1 y_1 + k_1 y_1 + h_1 y_1 + k_2(y_1 - y_2) + h_2(y_1 - y_2) = 0,$$
$$m_2 y_2 + k_2(y_2 - y_1) + h_2(y_2 - y_1) = F_y.$$

Here $y_{1,2}$ are coordinates of bodies; $k_{1,2}$ and $h_{1,2}$ are coefficients of stiffness and damping of springs; F_y is aerodynamic force acting upon the body M_2 and directed along the OY axis:

$$F_y = \frac{\rho S}{2} V_{air}^2 C_y(\alpha), \quad V_{air} = \sqrt{V^2 + V_2^2} = \sqrt{V^2 + y_2^2}, \quad \alpha = -\arctan\frac{y_2}{V},$$

where ρ is the air density, S is the cross-section area of the body M_2, V_{air} is the speed of this body with respect to the incoming flow, C_y is a non-dimensional coefficient.

From symmetry considerations, it is clear that $C_y(0) = 0$, and the system has the trivial equilibrium: $y_1 = y_2 = 0$.

RESULTS AND DISCUSSION

For simplicity sake, we normalize equations using characteristic length $L_c = b$ (the width of the body M_2), characteristic time $T_c = b/V$, and characteristic mass $m_c = \mu\rho Sb/2$ (where μ is a non-dimensional coefficient characterizing the ratio of average density of the body M_2 to the air density).

In order to illustrate the behaviour of the system for different values of parameter k_1 changes, numerical simulations were performed. Data for C_y are from [1]. The following values of parameters were used: $m_1 = m_2 = 1$, $k_2 = 1.5$, $u = 1$, $h_1 = -C_y^\alpha + 0.3$, $h_2 = -C_y^\alpha + 0.5$ (here $C_y^\alpha = \left(dC_y/d\alpha\right)\Big|_{\alpha=0}$).

From the point of view of flow energy harvesting, it is important that an attracting limit cycle exists in the system. We denote the amplitude of oscillations of the second body in limit cycle (when it exists) with X_2.

Evolution of X_2 with the change of k_1 is shown in Fig. 2. The solid line corresponds to attracting cycles, and the dashed line, to repelling ones. Plus signs show the intervals of k_1 where the trivial equilibrium is asymptotically stable.

It should be noted that the trivial equilibrium is asymptotically stable for sufficiently small and sufficiently large values of the stiffness of the first spring. For $k_1 \approx 0.86$ and $k_1 \approx 3.6$, subcritical Hopf bifurcations occur, when a repelling limit cycle merges with stable fixed point. For "moderate" values of k_1, the equilibrium is unstable.

It is interesting to note that making the system more "stiff" doesn't necessarily make it stable. Such effect is illustrated in Fig. 3, where the instability area is shown in plane (k_1, k_2). In some cases, simultaneous increase in stiffness coefficients of both springs results in destabilization. Moreover, in some situations it is sufficient to decrease stiffness coefficient of one spring to ensure the stabilization. Such effect of change in stiffness looks somewhat unconventional. Similar phenomenon was reported for an aeroelastic system with one translational and one rotational degrees of freedom in [4].

Thus, increase in stiffness can result in stability loss. In order to make the equilibrium stable again, it is necessary to increase k_1 considerably.

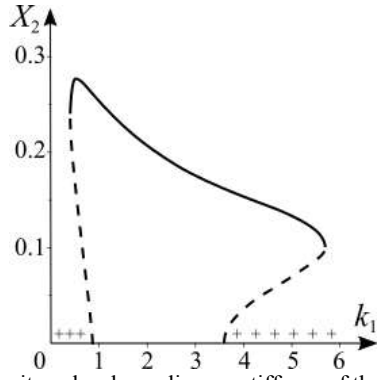

Figure 2. Limit cycles depending on stiffness of the first spring.

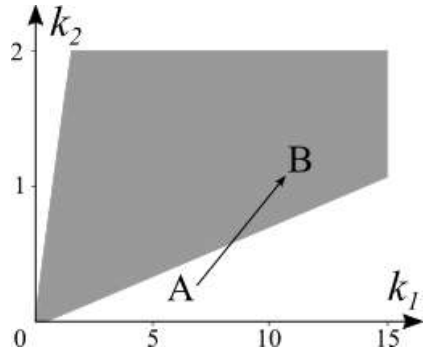

Figure 3. Domain of instability (grey colored): effect of stability loss induced by increase in stiffness

An attracting limit cycle exists in the system in wide enough range of parameters. Its amplitude decreases as k_1 increases. For sufficiently small and sufficiently large values of stiffness of the first spring, no limit cycle was found.

CONCLUSIONS

The discussed aeroelastic system with two translational degrees of freedom is subject to flow-induced vibrations. Proper choice of parameters (such as mounting stiffness) can ensure large enough amplitudes of oscillations. So, this system has the potential to be used as an element of oscillatory-type wind power harvesting devices.

References

[1] Massai T., Zhao J., Lo Jacono D., Bartoli G., Sheridan, J. The effect of angle of attack on flow-induced vibration of low-side-ratio rectangular cylinders. J. Fluids & Struct. **82**: 375-393, 2018

[2] Luo S.C., Chew Y.T., Ng Y.T. Hysteresis phenomenon in the galloping oscillation of a square cylinder. J. Fluids & Struct. **18(1)**: 103-118, 2003.

[3] Abdelkefi A., Hajj M.R., Nayfeh A. Power harvesting from transverse galloping of square cylinder. Nonlinear Dyn. **70(2)**: 1355–1363 (2012).

[4] Selyutskiy Y.D. On dynamics of an aeroelastic system with two degrees of freedom. Appl. Math. Mod., **67**: 449–455, 2019.

FLUID-STRUCTURE INTERACTION ANALYSIS OF CORRUGATED DACRON GRAFT USED FOR AORTIC REPLACEMENT

Raja Jayendiran[1], Bakr Nour[2] and Annie Ruimi*[1]
[1] Mechanical Engineering Program, Texas A&M University at Qatar, Doha, Qatar
[2]Weill Cornell Medicine-Qatar, Doha, Qatar

Summary Aortic dissection (AD) is a serious medical condition characterized by a tear in the intima, the inner layer of the aortic walls. In such occurrence, blood is diverted to the media layer and may result in patient death if not quickly attended. Treatment involves replacing the diseased portion of the aorta with a graft made of Dacron, a synthetic fabric. Dacron has corrugation folds, with a distinctive accordion-like structure. Here we use the GHO anistropic hyperelastic model combined to a fluid-structure interaction analysis to understand how the blood flow affects the graft-aorta mechanical behaviour. The results show that the model is able to predict the graft nonlinear behavior and its progressive increase in rigidity due to Dacron stretching in the radial direction. This study allows to predict the graft-aorta mechanical response when subjected to realistic conditions.

INTRODUCTION

The aorta is the largest artery in the human body. Its primary function is to distribute oxygenated cells to other parts of the body. Among complications, aortic dissection (AD) is a very serious although not common condition, in which blood is being diverted to other parts of the aorta as a result of a tear in the intima, the inner layer of the aortic walls. The tear can occur in any of the aortic segments and treatments vary depending on the location. Among surgical techniques, one involves resecting (removing) and replacing the damaged portion of the aorta with a polyester graft [1]. The Food & Drug Administration (FDA) qualifies the aortic graft as a cardiovascular prosthetic device (CPD). Graft materials used in aortic replacement procedures include Dacron, which possesses a distinctive accordion-like structure due to corrugations. It is popular for its superior biocompatibility and its low incidence of rejection. It is also strong, flexible and durable. However, differences in the mechanical response of the Dacron fabric and the aorta can result in non-optimal conditions and affect the heart functions [2]. Clinical observations also report a radial stretching of the Dacron caused by internal pressure after being placed in the aorta [3]. This affects the overall rigidity of the structure. Here, we employ a three-dimensional fluid-structure interaction (FSI) analysis to understand how the blood flow affects the mechanical response of the Dacron/aorta taking into account the graft evolving geometry.

METHODOLOGY

For this study, the FSI simulations are performed on the commercial software package Abaqus/Simulia (2013), running on a desktop (i7-4790 CPU). Solidworks is used to generate the graft and the aorta geometry. The graft is modeled as a cylindrical structure 62 mm long, 32 mm diameter and 0.328 mm thickness with 31 corrugation folds. Figure 1 shows the graft straight configuration and the 90 ^{0} (i.e. 2θ) configuration. Other curvatures have been studied. The aorta is idealized as a cylindrical shell 31 mm long and 16 mm radius. It is made of three concentric layers (of total thickness 2.61 mm) which account for the intima, media and adventitia layers. The graft is attached to the aorta at its ends. The graft is modeled as an anisotropic structure due to the corrugations, which will cause its response to depend on the directions. Similarly, it is well established that human tissues exhibit anisotropic properties due to the presence of fibers with various orientations. Both the Dacron graft and the aortic segment have been modeled with the Gasser-Ogden-Holzapfel (GHO) model [4], a sophisticated anisotropic hyperelastic formulation. To obtain parameters representing the anisotropy of the Dacron fabric, we used experimental stress-strain curves generated by Amabili et al. (2018) [5] on a corrugated Dacron woven graft specimen. We used a generic algorithm available on MathWorks (2015) to obtain the material property for the hyperelastic model. The algorithm involves minimizing the error of an R-squared function where σ_{exp} is the value of the stress obtained experimentally and σ is the value of the theoretical Cauchy stress.

$$R - Squared = \frac{\sum_{i=1}^{n}(\sigma_{exp}(i) - \sigma(i))^2}{\sum_{i=1}^{n}(\sigma_{exp}(i) - (\sigma_{exp}^{mean}))^2} - 1$$

Blood is modeled as a Newtonian medium, incompressible and turbulent. The no-slip condition is enforced on the walls of the fluid domain. At the interface of the fluid and the solid domains, the components of the displacement and velocity are equal and the tractions are equal.

RESULTS

The anisotropy parameters obtained from the minimisation function were given as input to the hyperelastic material model. Figure 2 indicates good agreement between the stress-strain curves obtained experimentally and with the hyperelastic GHO material model. Using these parameters, we were able to launch a FSI analysis on a Dacron/aorta structure subjected to blood flow. Stress, strain and wall-shear stress contours on straight as well as curved configurations were obtained (Figure 3). We found that the maximum circumferential strain on the Dacron-graft was 1.9%, comparable to the experimental measurement obtained by Bustos et al. [2] at 110 mmHg. The Dacron is sutured onto the adventitia

layer and stress exceeding its ultimate strength may cause rupture. Results indicate that for all the cases, the von Mises stress computed at the junction between the Dacron and aorta was 1.13 MPa (for curved geometry), below the ultimate strength of the adventitia layer (1.4 MPa [6]). In the literature [7], WSS under 0.4 Pa are reported to generate endothelial proliferation and dysfunction accompanied by apoptosis (cell death). As WSS decreases, the walls weaken further and may also rupture. The WSS values obtained here ranged between 2.2 Pa and 5.2 Pa. We also found that the graft curvature had a noticeable effect on the computed quantities.

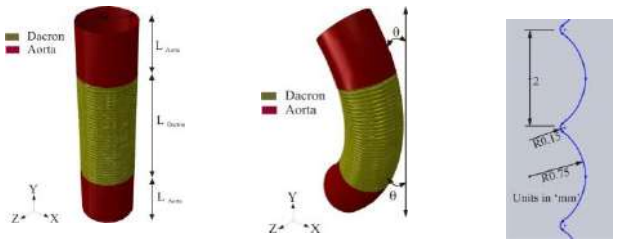

(a) (b) (c)

Figure 1. Schematic representation of Aorta-Dacron graft a) straight b) 90° (2θ) curved and c) dimension of the corrugation folds

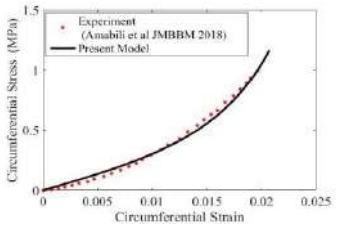

Figure 2. Anisotropic Dacron parameter fitting with hyperelastic material model and experimental data:

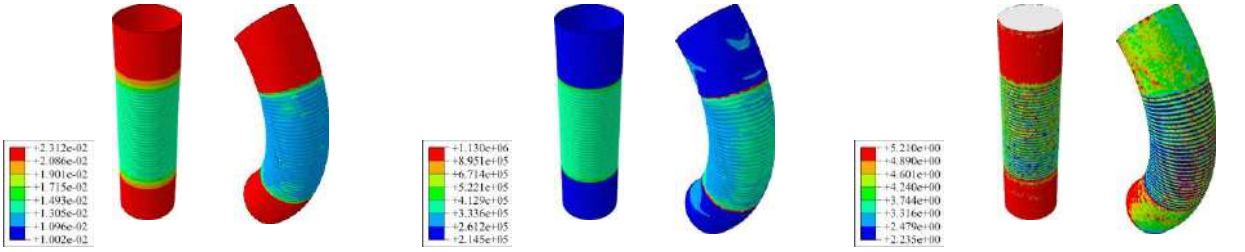

(a) (b) (c)

Figure 3. Contours showing (a) Strain, (b) Stress (in Pa) and (c) Wall Shear Stress (in Pa) on the aorta-Dacron graft at peak systole for straight and 90° curved geometries.

CONCLUSION

We conducted a FSI analysis to understand the mechanical response of a Dacron graft used for aortic replacement when subjected to a hemodynamic load. The accordion-like structure of the Dacron fabric was responsible for its anisotropic response. Straight as well as curved configurations of the aorta/graft assembly were studied. Strains and WSS decreased for the curved geometry while stress concentrations appeared at the junction Dacron/aorta. This study can help us predict the graft-aorta mechanical response when subjected to realistic blood flow conditions.

References

[1] Silver F. H., Biomaterials, Medical Devices and Tissue Engineering: An Integrated Approach. Springer-Science & Business Media, 1994.

[2] Bustos C. A., Herrera C. M. G., Celentano D. J., Modelling and simulation of the mechanical response of a Dacron graft in the pressurization test and an end-to-end anastomosis, J. Biomech. 61: 36 -44, 2016

[3] Etz C. D., Homann T., Silovitz D., Bodian C. A., Luehr M., Luozzo G. D., Plestis K. A., Griepp R. B., Vascular Graft Replacement of the Ascending and Descending Aorta: Do Dacron Grafts grow?, Ann. Thorac. Surg 2007; 84:1206-13, 2007

[4] Gasser, T. C., G. A. Holzapfel, and R. W. Ogden, "Hyperelastic Modelling of Arterial Layers with Distributed Collagen Fibre Orientations," Journal of the Royal Society Interface, vol. 3, pp. 15–35, 2006

[5] Amabili M., Balasubramanian P., Breslavsky I., Ferrari G., Tubaldi E., Viscoelastic characterization of woven Dacron for aortic grafts by using direction-dependent quasi-linear viscoelasticity, J. Mech. Behav. Biomed. Matl. 82:282-290, 2018

[6] Holzapfel, G.A., Sommer, G., Gasser, C.T., Regiting, P.,. Determination of layer specific mechanical properties of human coronary arteries with nonatherosclerotic intimal thickneing and related constitutive modeling. Am. J. Physiol. Heart Circ. Physiol. 289, H2048–H2058, 2005

[7] Boussel L. et. al., Aneurysm Growth Occurs at Region of Low Wall Shear Stress, Stroke 39:2997-3002, 2008

NONLINEAR DYNAMICS OF TUBE-DEBRIS INTERACTION AND TUBE WEAR

Njuki Mureithi*[1], Loay Alyaldin[1], Abdallah Hadji[1] , Huy Peter Pham[1], James Benson [2] and Sean Kil [2]
[1]Department of Mechanical Engineering, Polytechnique Montreal, Canada
[2]Electric Power Research Institute (EPRI), Palo Alto, CA, USA

Summary The flow induced dynamics of foreign objects (debris) in tube arrays of nuclear steam generators is addressed in the present work. Objects undergoing flow-induced motion while in constant contact with neighboring tubes can cause tube wear and compromise tube integrity. In cases where the debris cannot be removed, an analysis to estimate expected tube wear rate is imperative. This paper presents work done to develop and test a quasi-steady nonlinear theoretical model for debris dynamics and tube wear estimation.

INTRODUCTION

Much remains unknown regarding the flow-induced dynamics of small objects (debris) located within tube arrays subjected to transverse (cross-) flow. In particular, the characteristics of fluid forces acting on such objects located within tube arrays remain poorly understood.
Debris found in tube-and-shell heat exchangers, and in particular nuclear steam generators, poses a problem due to the risk of tube wear induced by loose debris moving in contact with the tubes due to flow turbulence-induced motion. Fig.1 shows an example of debris (a screw) found in a nuclear steam generator. Such debris stays permanently in the SG, unless manually removed during a plant shutdown. For operating plants, the practical engineering problem, when the debris cannot be removed (e.g. due to inaccessibility), is the estimation of the limiting debris residence time beyond which tube integrity is compromised.

Fig.1 Screw debris object in steam generator

DYNAMICAL MODEL

The work reported here investigates the dynamics of small rigid or flexibly lodged objects (debris) within a tube array subjected to high turbulence flow and undergoing nonlinear interaction with tubes. Fig.2 shows the typical configuration of a debris object in contact with two tubes. Debris-tube contact is maintained by the flow drag. The object is also subjected to turbulence lift and drag forces. The resulting problem is a nonlinear turbulence-induced 'vibration' problem.

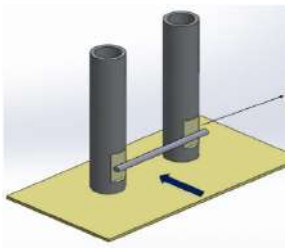
(a)

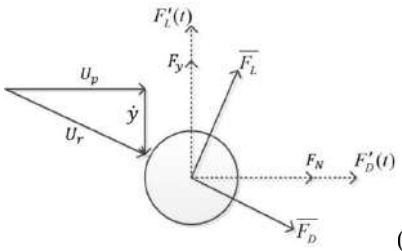

(b)

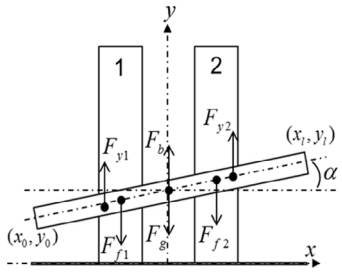

(c)

Fig.2(a) Object-tube configuration, (b) flow and fluid forces, (c) 2 *d.o.f.* dynamic model.

Due to the presence of the surrounding tubes, the array generated turbulence intensity may be up to 30% or higher. Fig.3 shows an example of the computed flow structure within a tube array relative to the size of a typical debris object. The primary source of nonlinearity is the friction contact between the object and the tubes. The second important nonlinearity is the lift force generated when the objects approaches the bottom wall (tube-sheet region of the steam generator). In the more general case, impacting should also be considered; impact occurs between the object and tubes as well as the object and the bottom wall.

*Corresponding author. E-mail: njuki.mureithi@polymtl.ca.

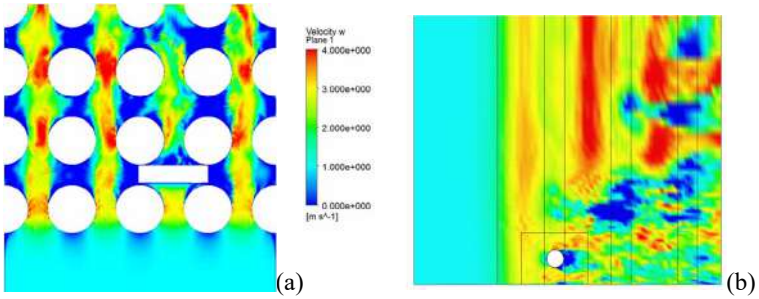

Fig.3 Top view and side view of flow around a debris object within a tube array of tube pitch-diameter ratio P/D=1.42; $\mathrm{Re} \approx 18000$, based on tube diameter.

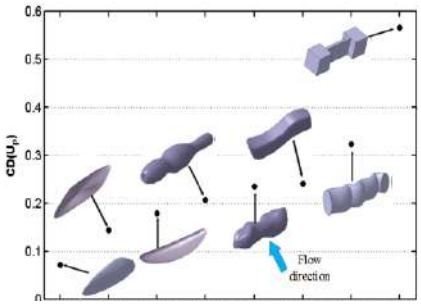

Fig.4 Drag coefficients for typical debris

Fig.2(b) shows the local flow velocity vectors and the fluid forces acting on the object. In the model developed here, a quasi-steady approach is taken in order to account for object-motion dependent forces. Motion independent fluid forces include the turbulence-induced lift ($F_L'(t)$) and turbulence-induced drag ($F_D'(t)$)forces as well as the steady drag ($\overline{F}_D$) and the fluid buoyancy force (F_b). Motion-dependent unsteady fluid forces are generated when the object moves. In a linear quasi-steady formulation, the resulting motion dependent forces are considered to be proportional to FO acceleration, velocity and displacement. The motion independent forces (in Fig.2) are obtained by CFD analysis (e.g. Fig.3) and directly from experimental measurements, Fig.4. To cover a wide class of general object geometries (e.g. Fig.4), pertinent geometry parameters must be obtained to allow the definition of drag force coefficients and dimensionless turbulence spectra. In the quasi-steady approximation, the change in the effective angle of attack of the flow relative to the moving object is also taken into consideration. This introduces a velocity dependent (damping) force component which slightly reduces the energy available for tube wear.

FLOW-INDUCED OBJECT DYNAMICS AND TUBE WEAR

The debris object flow-induced motion is obtained by solving the nonlinear governing equations for the model of Fig.2. In addition to the object motion, the debris-tube contact force histories are also obtained. To estimate the tube wear, the debris normal wear work-rate is computed as the product of the normal contact force and the object velocity, $\dot{W}(t) = F_N(t)|\dot{y}(t)|$. The curved plate debris shown in Fig.5 caused tube through-wall wear in approximately 3 months. The model predicted wear work-rate is presented in the same figure. This corresponds to the energy transfer rate to the tube wear process.

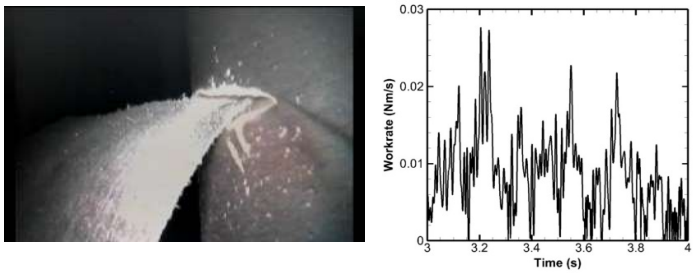

Fig.5 Plate debris in tube contact and model predicted wear work rate

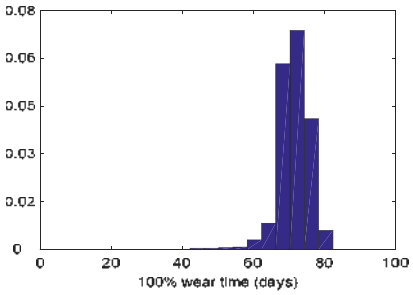

Fig.6 Monte Carlo analysis results

Using the work-rate, and the tube wear scar geometry, the wear time to a given tube wall depth can be estimated in a Monte Carlo analysis. Fig.6 shows the estimated probability distribution of wear times for 100% wall-wear time; analysis results yield 71 days, versus the maximum wear time of 115 days estimated by the plant operator. The Monte Carlo analysis accounts for the uncertainties in the various parameters governing the object dynamics. For practical plant operations, wear time estimates within days are considered quite acceptable and realistic. The analysis results obtained in this work raise some important fundamental questions on the effect of friction nonlinearities on the turbulence induced excitation of arbitrary geometry objects. The effect of turbulence on flutter instability also arises. While turbulence effect on bluff body flutter has been studied (e.g. for bridge decks), the governing mechanisms here are quite different. For bridge decks, for instance, turbulence affects flutter via reduced correlation of the fluidelastic forces along the bridge span. For debris in tube arrays, the flutter derivatives themselves (in particular the fluid force phases) are strongly affected by turbulence. As a result, the instability can potentially be altogether eliminated by high turbulence.

IN SITU MEASUREMENTS OF A HARP FOG COLLECTOR

Adèle Moncuquet[1], Sophie Ramananarivo[1], Xavier Amandolese[2], and Camille Duprat * [1]
[1]Laboratoire d'Hydrodynamique (LadHyX), Ecole polytechnique, Palaiseau, France
[2]LMSSC, Conservatoire National des Arts et Métiers, Paris, France

Summary Experimental measurements on a fog collector in real-life conditions are considered here. Full-scale tests are conducted for future comparison with wind tunnel measurements and literature. The collector is made of parallel nylon fibers, its porosity is around 60%. Three force sensors are fixed between the collector and the main structure in order to investigate the drag on this porous elevated panel. Furthermore, the collector is placed within a measurement site, the SIRTA-ReOBS, where fog episodes due to radiative cooling and stratus lowering are frequent. Fog water collection can then be relied to visibility and wind speed, during fog events.

INTRODUCTION

Fog collection using fibrous nets has been used since the 50's, mostly for chemical analysis and to collect drinkable water. They're used in arid location with frequent fog events, with a collection of up to ten litres of water per day per square meter [1]. Fog water collection is mainly due to the inertial impaction mechanism, i.e the deviation of the droplets from the stream lines toward the collector's fibers [2]. The Wind flow is modified when it passes around and through the porous panel, which modifies the collection efficiency. Moreover the net is deformable and get charged in water. The geometrical characteristics are changed and thus the wind loads. There are few experimental studies on the wind effects on collectors of this porosity. We present here a specifically designed fog collector made of parallel fibers (see figure.1). It is installed in the atmospheric observatory SIRTA-ReOBS located in the south of Paris. The collector instrumentation consists of a rain gauge, four anemometers and three force sensors to respectively measure collection efficiency, wind reduction across the collector and the panel drag. Force measurements are compared to previous studies on permeable cladding, with equivalent porosity (i.e its degree by which the net is penetrable by the air), reviewed in 2012 in - [3]. We also aim to relate collection efficiency to measured wind speeds and, thanks to IRTA-ReObs data base - [4], visibility, precipitation and drop sizes measurements.

ENVIRONMENT AND FOG COLLECTION

The collector is set on a plain located 20km southwest of Paris (France). On this site, fog appears because of radiative cooling, when the air get saturated in water vapor because of infrared cooling near the ground surface, and when lowering stratus i.e descent of a cloud [5].The collector is aligned with the North ($\equiv 0°$) and face the dominant wind coming from the West ($\equiv 270°$). In the following we keep the meteorological definition of the wind direction.

(a)  (b)  (c) 

Figure 1: Set-up for fog collection measurement with vertical fibers on the SIRTA. (a) Complete set-up : The fog collector, 2m long, 1m high, on a supporting structure ; One rain gauge of 0.1mm resolution ; Four wind sensors : two on the West side, two on the East side; Three force sensors: two on each upper corners of the frame, one on the bottom side, in the center. (b) Water flowing in the gutter to the rain gauge at the bottom of the collector. (c) Zoom on the pairs of nylon fibers stitched to PVC plates.

The net parameters are chosen to optimize the collection efficiency and to avoid blockage effect. Nylon fibers of diameter $d = 0.3mm$, are placed in pairs in order to form liquid columns [2]. They are separated by $e = 2.2d$ along a length $L = 2m$ leading to a porosity $p = 59\%$. Efforts have been made in order to manually ensure homogeneous tension and spacing throughout the net (see figure.1(c)).

Four cup-anemometers are installed by pairs to measure the wind profiles (figure 1(a)). The first pair is located 4 meters upstream (with respect to the dominant wind coming from the $West$). They measure the wind speed at the center of the mesh (1m90 from the ground), to reach higher wind speeds. and 1m above. The second set is located 3 meters downstream. Finally, custom made force sensors are clamped between the frame and the support structure.

*Corresponding author. E-mail: camille.duprat@ladhyx.polytechnique.fr

RESULTS

Fog is defined as a visibility reduction below $1km$. A SIRTA's measurement of visibility for December 16^{th} 2019 is reported on figure.2 (a)-(black curve), with our water collection (discrete line blue lines). Fog appears around 8:30 pm, the first water collection appears one hour later. Associated wind speed and direction are reported on figure.2 (b). The winds come from North-East ($\equiv 45°$), to South-Est ($\equiv 140°$), (black dashed line in 2 (b)), its speed is below $1m/s$ (blue pointed line and orange full line). The low collection rate can be explained by low wind speeds ($< 0.6m/s$), and deviation from the collector surface's normal, (90°- red line 2 (b)). Finally a wind reduction is visible when the wind direction is around $90°$. Gathering data for several fog events during the fog season, we aim at linking the collection trend to the visibility, wind speeds and drop sizes measurements. Results will also be compared to empirical model made in the Canary Islands, Spain -[6].

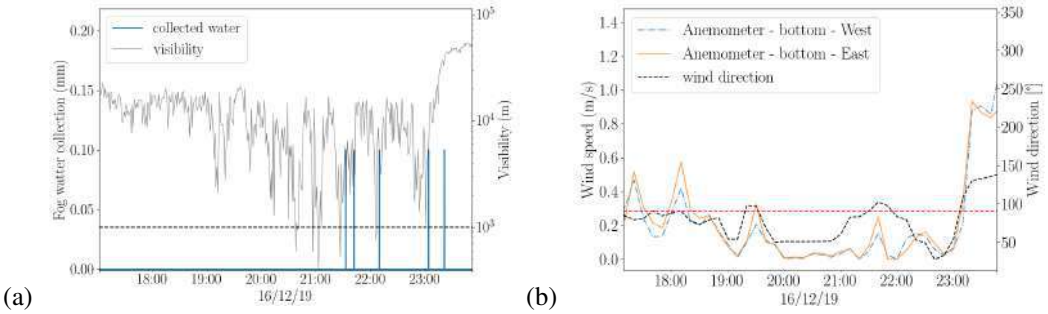

Figure 2: (a) Fog water collection (vertical lines) and visibility as a function of the hour. The horizontal line represent a visibility of $1km$, meaning the presence of fog. (b) Wind speed measurements downstream and upstream the collector at 1m94 high (clear lines), and wind direction measurements (black, dashed line) averaged over 5min. The Net is aligned with the North (see red, horizontal line)

The force acting on the panel, in the direction normal to the net's surface, as a function of the wind speed measured 3m upstream, at mid-height of the panel, is plotted in figure.3. The points correspond to all the measurements made from December 11^{th} to Decmber 25^{th} 2019. Following the work of Richards and Robinsons (1999), the wind velocity has been corrected by a wind direction factor, $cos(\frac{\pi}{2} - \beta)$ where β is the wind direction in radians. Measurements for wind coming from both sides of the net follow the expected trend given by the empirical formula $D = \frac{1}{2}\rho(U * cos(\frac{\pi}{2} - \beta))^2 S(1 - p)Cd_{pe}$, where ρ is the mass density of the air and $Cd_{pe} = 1.15$ is the drag coefficient of a solid (in opposition to porous), elevated panel, of this aspect ratio - [3]. However, some discrepancies can be observed, that can be due to the effect of water collection on drag and measurements uncertainties increased when $\beta \neq \pi[\pi]$. Works are ongoing to clarify that point with the help of additional wind tunnel tests.

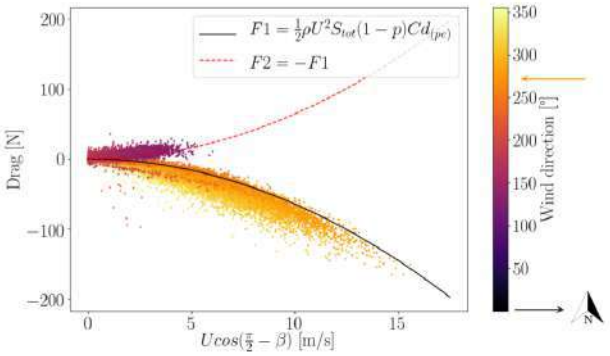

Figure 3: (a) Force measurements for different wind directions, as a function of the corrected wind speed. Positive force is a traction of the captor, negative force is a compression. Solid and dashed lines correspond to the empirical formula cited in [3]. Orange arrow corresponds to the direction normal to the collector, black one is the North.

References

[1] Schemenauer RS, Cereceda P. A proposed standard fog collector for use in high elevation regions. *Journal of Applied Meteorology* ;33:1313–1322, (1994).
[2] R. Labbé, C. Duprat Capturing aerosol droplets with fibers, *Soft Matter* 15, 6946-6951 (2019)
[3] A. Giannoulis, T. Stathopoulos, D. Briassoulis, A. Mistriotis, Wind loading on vertical panels with different permeabilities, *Journal of Wind Engineering and Industrial Aerodynamics*, Volumes 107–108, pp. 1-16, (2012).
[4] Chiriaco M., Dupont J.-C., Bastin S., Badosa J., López J., Haeffelin M., Chepfer H., Guzman R., 2018: ReOBS: a new approach to synthesize long-term multi-variable dataset and application to the SIRTA supersite. *Earth System Science Data*, Copernicus Publications, 10 (2), pp.919 - 940.
[5] Mazoyer, M. and Burnet, F. and Denjean, C. and Roberts, G. C. and Haeffelin, M. and Dupont, J.-C. and Elias, T., Experimental study of the aerosol impact on fog microphysics, *Atmospheric Chemistry and Physics*, 19,7,4323–4344, (2019).
[6] Carlos M. Regalado, Axel Ritter, On the estimation of potential fog water collection from meteorological variables, *Agricultural and Forest Meteorology*, Volumes 276–277, (2019).

RESPONSE OF A PLATE TO SUPERSONIC WIND TUNNEL START INCLUDING INTERACTION WITH CAVITY AND THE FREE STREAM FLOW

Maxim Freydin * [1] and Earl H. Dowell[1]
[1]Mechanical Engineering and Materials Science, Duke University, Durham, North Carolina, US

Summary A theoretical/computational model is proposed to analyze the linear stability and the nonlinear time response of a plate with supersonic (or hypersonic) flow on one side and a cavity with stationary fluid on the other. The plate's dynamic coupling with the fluid in the cavity, as well as aerodynamic heating and static deformation due to static pressure differential, are shown to affect the linear stability envelope and the limit cycle oscillation (LCO) amplitude and frequency (in post flutter condition). The coupled plate-cavity-flow model is linearized at a nonlinear deformation of the plate (due to static pressure and temperature differentials) and an eigenvalue problem is formulated to obtain the system's natural frequencies, mode shapes and determine its stability. Direct time integration is also performed and the results are correlated with wind tunnel tests.

THEORETICAL MODEL

The structural model derivation consists of formulating the elastic and kinetic energies of a flat plate with general in-plane stiffness distribution at the edges in terms of three displacement components (in contrast to previous literature where the Airy stress function and a single transverse displacement are employed). Then, the Rayleigh-Ritz approach is applied with Lagrange's Equations to obtain the equations of motion. The full derivation is provided by Freydin and Dowell in [1], including first order Piston Theory (PT) aerodynamics and a simplified cavity model which only includes the added stiffness effect and neglects added mass. The simplified cavity model is an approximation used when the first natural frequency of the cavity is much greater than that of the plate. In this work, the model is improved by replacing the simplified cavity model by the wave equation for the acoustic pressure perturbation and then coupling the equations as outlined in [2]. Figures 1 and 2 show schematic views of the problem. Equation 1a describes the system of structural

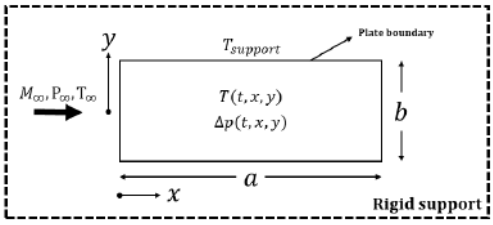

Figure 1: Plate top view with free stream flow

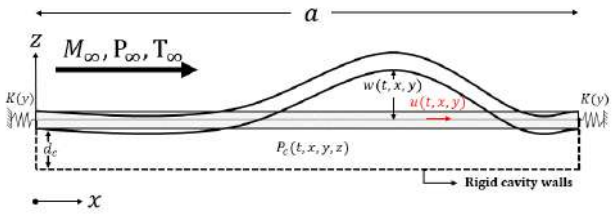

Figure 2: Plate, cavity and free stream flow side view, cross section at $-b/2 < y < b/2$

equations of motion in modal coordinates with important terms underlined. Equation 1b describes the system of cavity dynamical equations in modal coordinates. The coupled system in Equation 1 is solved as an eigenvalue problem for dynamic linearization about a nonlinear statically deformed plate and by direct time integration for the full dynamically nonlinear model. Each approach has advantages and provides different information about the fluid-structure system. Fast computation times make the eigenvalue approach suitable for design while direct time integration provides insight into nonlinear behavior of the system in post flutter conditions that lead to LCO.

$$M_{nk}\ddot{w}_k + \underbrace{A_{\dot{w}_{nk}}\dot{w}_k + A_{w_{nk}}w_k}_{\text{PT aerodynamics}} + G^{(2)}_{nk}w_k + \underbrace{D^{(2)}_{nkrs}w_k w_r w_s}_{\text{NL structural stiffness}} - \underbrace{L^c_{kn}P_k}_{\text{cavity coupling}} + \underbrace{Q^s_n}_{\text{static pressure differential}} = 0 \qquad (1a)$$

$$\underbrace{\rho_c L^c_{nk}\ddot{w}_k}_{\text{plate coupling}} + \underbrace{\frac{1}{a_c^2}M^c_{nk}\ddot{P}_k + K^c_{nk}P_k}_{\text{acoustic wave eqn.}} = 0 \qquad (1b)$$

RESULTS AND DISCUSSION

The proposed model is utilized to correlate and analyze results obtained in an experimental wind tunnel study by Spottswood at el. [3]. This work focuses on data measured during the supersonic wind tunnel start. Free stream static

*Corresponding author. E-mail: maxim.freydin@duke.edu.

pressure and plate temperature transient measurements are plotted on the p_∞ vs ΔT stability maps of static nonlinear/dynamical linear plates loaded with a uniform static pressure differential. Figures 3 and 4 show results without and with the effect of a cavity, respectively. Regions of instability are highlighted in red color and show that the location of these zones is sensitive to whether a cavity is present or not. An additional important difference is the flutter frequency in each zone changes drastically due to coupling with cavity natural modes (which are usually much greater in frequency than the plate's several first natural modes). Figure 5 shows how the natural frequencies of the full coupled system vary with ΔT on a single slice of Figure 4 at $p_\infty = 30kPa$. The three flutter regions are characterized by different frequencies and rates of exponential growth in time (quantified by the positive damping, not presented here). It can be shown (using either eigenvalue analysis or time integration) that the first and third flutter branches will reach a steady limit cycle much slower than the second branch.

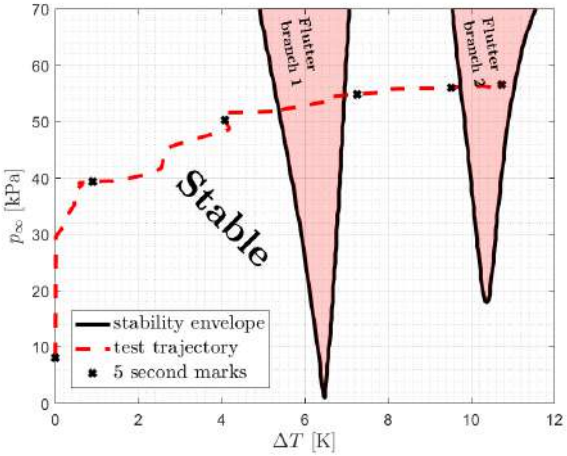

Figure 3: Nonlinear static/linear dynamic stability envelope for $\Delta p = 3kPa$ **without** cavity effect

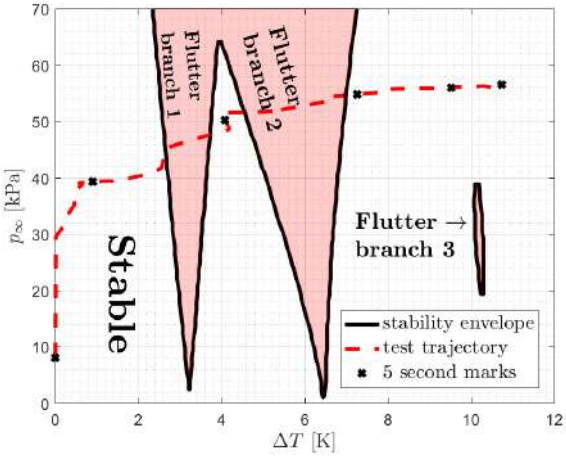

Figure 4: Nonlinear static/linear dynamic stability envelope for $\Delta p = 3kPa$ **with** cavity effect, $p_c = p_\infty - \Delta p$

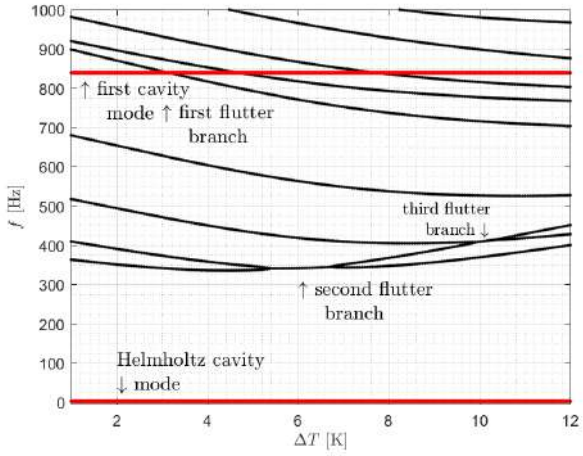

Figure 5: Plate-cavity-flow system's natural frequencies variation vs ΔT for $p_\infty = 30kPa$, $\Delta p = 3kPa$, $p_c = p_\infty - \Delta p$

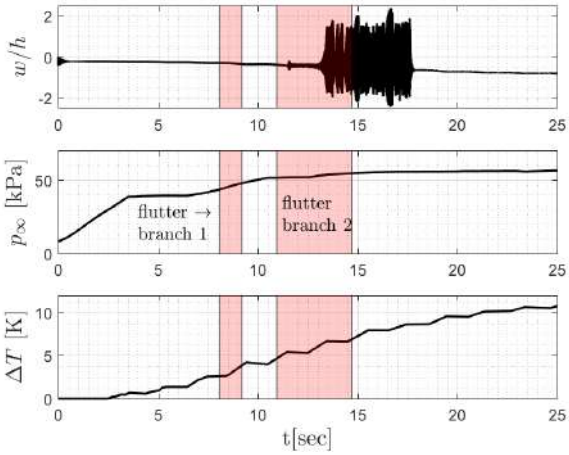

Figure 6: Direct time integration, $\Delta p = 3kPa$, $x/a = 1/4$

Figure 6 shows time series obtained using the direct time integration approach. The $p_\infty(t)$ and $\Delta T(t)$ functions were extracted from [3] and represent the "test trajectory" curve in previous figures. It is clear that while crossing the first and second flutter branches the plate does not have enough time to reach a steady LCO. On the 15th second, the plate has exited the 2nd flutter branch but has yet to stabilize. This suggests that a region of hysteresis exists and can be explored using this model. The presented analysis and results agree well with the qualitative behavior observed in [3].

References

[1] Freydin M., Dowell E. H. Nonlinear Theoretical and Computational Aeroelastic Model of a Plate: From Free to Fixed In-Plane Boundary Constraints. *J. Fluids and Structures*, under review, submitted on Sep. 2019.
[2] Dowell E. H. Aeroelasticity of Plates and Shells. Noordhoff International Publishing (now Springer), 1974.
[3] Spottswood S. M., Beberniss T. J., Eason T. G., Perez R. A., Donbar J. M., Ehrhardt D. A., Riley Z. B. Exploring the response of a thin, flexible panel to shock-turbulent boundary-layer interactions. *J. of Sound and Vibration* **449**: 74-89, 2019.

THE ADDED MASS EFFECT IN FLUID STRUCTURE INTERACTION PROBLEMS

Galina Dynnikova*[1], Sergey Guvernyuk[1]
[1]Lomonosov Moscow State University, Research Institute of Mechanics, Moscow, Russia

Summary The fundamental property of the added masses tensor in a viscous incompressible fluid is discussed and demonstrated by numerical simulation of bodies' movement in a viscous liquid based on Navies-Stokes equations. It is confirmed that the tensor of the added masses is independent of viscosity and is the same as in potential flows of an ideal fluid. The stable numerical scheme is proposed for solving the tasks of fluid structure interaction in the case of light bodies with great added masses.

Added or virtual mass is an unsteady fluid dynamic effect that has been discussed in the literature for over a century beginning with [1] up to the present time (see for example [2]). Most researchers are of the opinion that the added masses are independent of viscosity, based on experimental observations and some theoretical considerations. At the same time, in some recent works the values of the added masses are used as dependent on viscosity (see for example [3]).

In work [4], a theorem is strictly proved, which states that the hydrodynamic force acting on a body in a viscous incompressible fluid of constant density is the sum of two forces $\mathbf{F}_H = \mathbf{F}_{stat} + \mathbf{F}_{add}$, where the force $\mathbf{F}_{stat}$ corresponds to motion without acceleration for a given distribution of vorticity, and $\mathbf{F}_{add}$ is the force of the added mass which depends only on acceleration and geometry but not on viscosity, hence it is the same as in potential flows of an ideal fluid.
In this work the mentioned theorem is illustrated by numerical simulation of an unsteady body motion.

In Figure 1 the numerical results are presented for the following task.
Airfoil NACA0015 moves at an angle of attack of 5 degrees with a speed $\mathbf{U} = -U\mathbf{e}_x$, where time dependence of U is following (see Fig.1b)

$$U = \begin{cases} 2t, & 0 < t < 0.25 \\ 0.5, & 0.25 < t < 0.5 \\ 2t - 0.5, & 0.5 < t < 0.75 \\ 1, & 0.75 < t < 1 \end{cases}$$

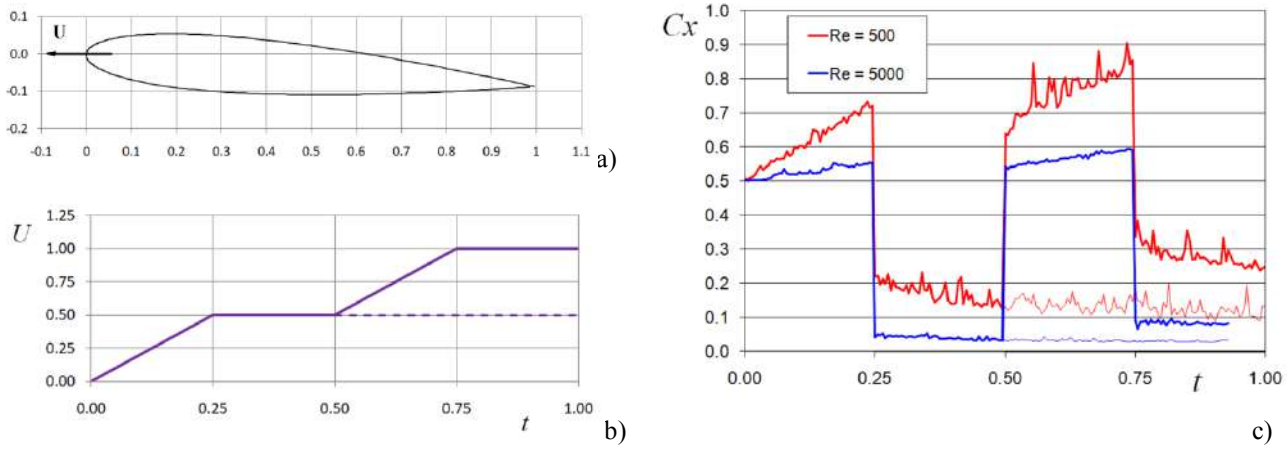

Figure 1. Movement of airfoil NACA0015 with the piecewise constant acceleration. a) airfoil NACA0015; b) time dependence of velocity U; c) time dependences of drag coefficient at Re = 500 and Re = 5000

Dimensionless acceleration is equal to 2 at time intervals $0 < t < 0.25$ and $0.5 < t < 0.75$, and the rest of the time, acceleration is equal to zero. In Fig. 1c, time dependences of drag coefficient are shown at Re = 500 and Re = 5000. The Reynolds numbers are based on the velocity at $t = 1$. The calculations were performed by a meshless Lagrangian method VVD [5]. One can see from Figure 1 that in the moments when acceleration is switched, the drag coefficients changes abruptly. The jump value is constant and does not depend on Re, $|\Delta C_x| = 0.5 \div 0.52$ that corresponds to the added mass $M_{add} = (0.125 \div 0.13)\rho C^2$ (here ρ is fluid density, C is chord length). The theoretical value of the added mass in potential flow for this case is equal to $0.127\rho C^2$. That confirms the theorem mentioned above. Similar calculations with the same results were performed for flat plate, cylinder, sphere, and disk.

Accurate knowledge of the attached masses is useful in solving the flow structure interaction problems, especially in the case of light bodies. It is known that numerical schemes with splitting are unstable in this case. Therefore the monolithic schemes have to be used. But they are more complicated. The use of attached masses allows

*Corresponding author. E-mail: dyn@imec.msu.ru

us to apply the schemes with splitting for light bodies up to bodies with zero mass. For this purpose, at each time step, a force $\mathbf{F}_{stat}$ corresponding to the movement without acceleration should be calculated. After that, the acceleration vector $\mathbf{a}$ is calculated from the equation $m\mathbf{a} = \mathbf{F}_{stat} - \mathbf{M}\mathbf{a} + \mathbf{F}_{ex}$, where m is body's mass, $\mathbf{M}$ is tensor of added mass, $\mathbf{F}_{ex}$ is external force if it exists.

Such method was applied for simulation of oscillation of the cylinder elastically fixed in the fluid with one degree of freedom. Movement of the cylinder is described by the equation $mY = F_H - kY$. Calculation has been performed in dimensionless variables, where the linear sizes are related to the cylinder diameter D, time is related to $t_0 = 2\pi\sqrt{\frac{m}{k}}$, density of the cylinder ρ is related to the fluid density, forces are related to $m_0 D/t_0^2$, where m_0 is displaced mass of fluid. In Fig. 2 the numerical results are presented for the case ρ = 2, Re = $D^2/(\nu t_0)$ = 50. Calculations were performed by the method VVD with modification developed especially for a flow around a cylinder [6]. The scheme with splitting was applied. In fig 2b, the components of the hydrodynamic force F_{stat} and F_{add} are shown. One can see that the force F_{stat} is mainly opposite to speed U that provides the damping. The force F_{add} is co-directed with the deflection of the cylinder, and therefore directed opposite to the force of the spring action. This leads to a change in the oscillation period. In this case, it is 1.29, which is approximately equals to value $\sqrt{(m+M)/m} = \sqrt{3/2} = 1.22$. This task has been solved also with use of the monolithic scheme, described in [7]. The results coincided with high precision.

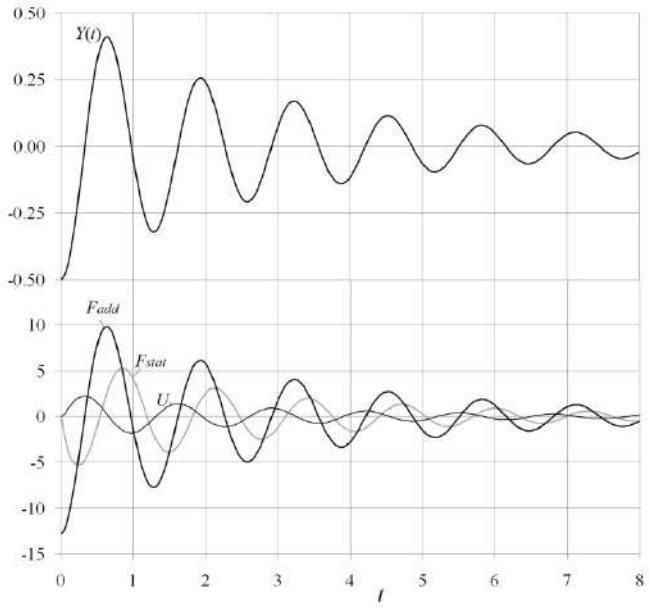

Figure 2. Oscillation of the cylinder in the fluid; a) time dependence of the cylinder centre coordinate; b) components of the hydrodynamic force F_{stat} F_{add} and cylinder velocity U.

Acknowledgements

This work is partially supported by the Russian Foundation for Basic Research (project 18-31-20057).

References

[1] Lamb H. Hydrodynamics. Cambridge University Press. 1895

[2] Corkery S.J., Babinsky H. And Graham W.R. Quantification of added-mass effects using particle image velocimetry data for a translating and rotating flat plate. Journal of Fluid Mechanics, 2019-07-10 DOI: 10.1017/jfm.2019.231

[3] Fischer P., Schmitt M., Tomboulides A. Recent Developments in Spectral Element Simulations of Moving-Domain Problems. In: Melnik R., Makarov R., Belair J. (eds) Recent Progress and Modern Challenges in Applied Mathematics, Modeling and Computational Science. Fields Institute Communications, vol 79. Springer, New York, NY. 2017. DOI https://doi.org/10.1007/978-1-4939-6969-2_7

[4] Dynnikova G.Y. Added mass in a model of a viscous incompressible fluid. Doklady Physics. 2019. Vol. 64, no. 10. P. 397–400. DOI: **https://doi.org/10.1134/S1028335819100045**

[5] Guvernyuk S. V., Dynnikova G. Y. Modeling the flow past an oscillating airfoil by the method of viscous vortex domains // Fluid Dynamics. 2007. Vol. 42, no. 1. P. 1–11.

[6] Dynnikova G.Y. Calculation of flow around a circular cylinder on the basis of two-dimensional Navier-Stokes equations at large Reynolds numbers with high resolution in a boundary layer // Doklady Physics. 2008. Vol. 53, no. 10. P. 544–547.

[7] Andronov P.R., Dynnikov Y.A., Dynnikova G.Ya., Guvernyuk S.V.. Flow-induced oscillations of circular cylinder in a narrow channel. Aerospace Science and Technology. 2019. Vol. 93. № 105348. DOI 10.1016/j.ast.2019.105348

MIXING AND THERMAL ENHANCEMENTS THROUGH FLOW-INDUCED OSCILLATIONS OF A THIN ELASTIC PLATE ATTACHED TO A BLUFF BODY

Mayank Verma[1] and Ashoke De*[1]
[1]Department of Aerospace Engineering, Indian Institute of Technology Kanpur, Kanpur, India

Summary: The flow-induced oscillations of the thin, flexible plate after a bluff body have several promising engineering applications. In the present study, we have compared the characteristics of the flow induced by the motion of the thin plate with two different bluff bodies, i.e. a circular and a square cylinder, respectively. A partitioned approach is employed to solve the fluid-structure coupled problem. The Reynolds number based on the hydraulic diameter is 200. The results suggest that the flexible plate sweeps almost the same pattern for both the cylinders. Although, the square cylinder produces higher amplitude of the plate oscillations with a lesser frequency as compared to the circular cylinder at the same Reynolds number, resulting in the enhanced mixing and strong vorticity field in the domain. Also, the settling time for the oscillations of the square cylinder is observed to be lesser than that of the circular cylinder. Further, the square cylinder with a flexible plate indicates more convection resulting in the reduced thermal boundary layer.

INTRODUCTION

Many researchers have extensively studied control of the flow over bluff bodies with a thin plate due to its prominent practical applications and interesting fluid-dynamic phenomena associated with it. The rigid thin plates are commonly used for controlling vortex shedding, while the flexible plates are utilized to enhance the vortex shedding behind the bluff bodies. Recently, researchers have studied the effect of the oscillations of the flexible plate, with [1] or without [2] a bluff body, on the mixing and thermal augmentation. However, the literature lacks the comparative study of the flow-induced motion of the plate attached to circular and square cylinders. In the present study, we have attempted to compare the effect of the bluff bodies on the flow-induced motion of the plate. Further, based on the analysis of the mixing and thermal enhancement due to the shed vortices, the authors recommend the square cylinder over the circular cylinder for mixing and thermal enhancements.

PROBLEM DESCRIPTION

The geometry of the fluid-structure domain is shown in Fig. 1a. The analysis is restricted to 2D only. Two different types of bluff bodies, viz. a circular cylinder and a square cylinder is placed before the thin plate. One end of the thin plate is fixed to the rear side of the bluff body and the length of the plate is kept the same for both the bodies. The bluff bodies are rigid and the plate is flexible with the properties: density of plate, $\rho_s = 1000\ kg/m^3$, Young's modulus of the plate, $E = 5.6 \times 10^6\ N/m^2$, and Poisson's ratio, $\mu_s = 0.4$. The uniform velocity of 2 m/s is prescribed at the inflow boundary of the domain. The flow properties considered for the simulation are: temperature of the fluid at the inlet, $T_{inlet} = 300\ K$, density of the fluid, $\rho_f = 1000\ kg/m^3$, kinematic viscosity, $\vartheta_f = 0.001\ m^2/s$, thermal diffusivity, $\alpha_f = 0.001\ m^2/s$. The channel walls are at a constant temperature of 360 K. The mesh used for discretization of the flow domain consists of 96,498 finite volume cells while the thin plate is discretized with 1232 finite element cells. The coupled simulation is steered with a time-step of 0.001 s.

NUMERICAL METHODOLOGY

Solvers:

Fluid Solver: An open-source incompressible flow solver *thermoPimpleFOAM* of OpenFOAM [3], a modified version of *pimpleFOAM*, is used to solve the temperature scalar equation along with the governing equations of the fluid.

$$\frac{\partial T}{\partial t} + \nabla \cdot T = \alpha_f \cdot \nabla^2 T \tag{1}$$

where T is the temperature and α_f is the thermal diffusivity constant.

Solid Solver: CalculiX [4], an open-source Finite Element based solver, is used to solve the governing equations of the solid.

Fluid-Solid System Coupling: In order to facilitate the exchange of data between the Fluid and Solid solvers at the interface, we have employed preCICE [5], an open-source coupling library for partitioned multi-physics simulation.

Numerical Validation:

In order to confirm the validity of the numerical setup, a benchmark problem proposed by Turek and Hron [6] is attempted. The x and y displacement of the flexible plate at $Re = 100$, are compared with the benchmarked results. The results are found to be in good agreement and are shown in Fig. 1 b.

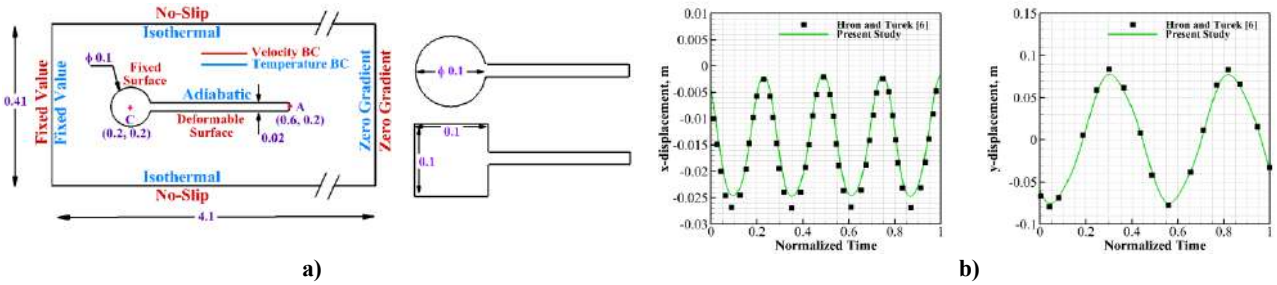

a) b)

Figure 1. **a)** Computational Domain with the corresponding boundary conditions (*#all dimensions are in m*); **b)** Study of the numerical validation of the computational methodology.

RESULTS AND DISCUSSION

Flow-Induced Motion of the Plate:

The vortex shedding is the most common phenomenon associated with bluff bodies. The vortices force the attached thin plate to oscillate. At the initial time, the amplitude of the oscillations is small but increases with the time as can be seen in Fig. 2 a), and c). Further, after a certain time, the plate oscillates with the fixed amplitude. The settling time of the oscillations for the square cylinder with a flexible plate is found to be less. The square cylinder generates higher amplitude and lesser frequency vortices. The plate sweeps almost the same pattern during its operation for both the cylinders as depicted in Fig. 2 b).

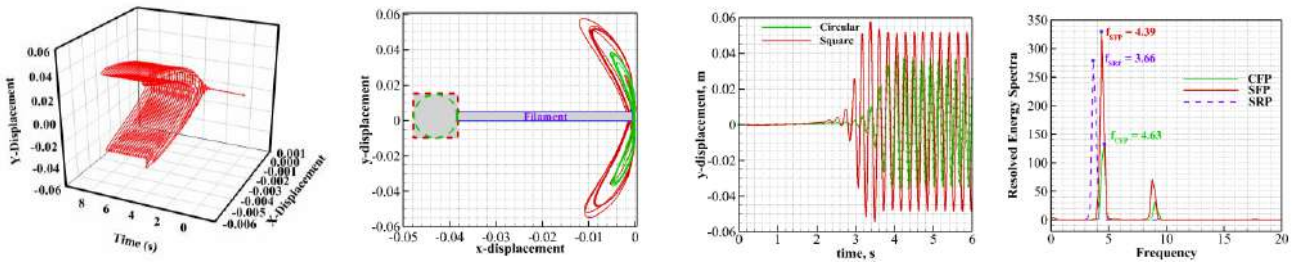

a) **b)** **c)** **d)**

Figure 2. **a)** 3-D development of flow-induced motion of the point A; **b)** 2-D pattern swept by the point-A at the plate for square and circular cylinder respectively; **c)** comparison of the y-displacement of the tip of the plate; **d)** FFT of the vortex shedding signal [***CFP:*** *Circular cylinder with flexible plate;* ***SFP:*** *Square cylinder with flexible plate;* ***SRP:*** *Square cylinder with rigid plate*]

Vorticity magnitude and enhancement of fluid mixing due to FSI:

Fig. 3 a) and b) shows the vorticity contours for the rigid plate and the flexible plate, respectively. From Fig. 3 a), we observed no vortex shedding for the case CHF and CRP, while for SRP, the vortex shedding frequency was found to be 3.66 Hz, as shown in Fig. 2 d). Introducing flexibility in the plate enables the circular cylinder to shed vortices at the frequency 4.63 Hz (case CFP), while for the square cylinder (case SFP), it increases the vortex shed frequency to 4.39 Hz. The vorticity magnitude of SFP is found to be more than that of CFP. Thus, the wake vortices of SFP sweeps higher vorticity regions which further aids in the enhanced mixing of the fluid. Further, Fig. 3 c) depicts the reduction in the thermal boundary layer thickness at the locations of the convected vortices due to the enhanced convection caused by the swept vortices.

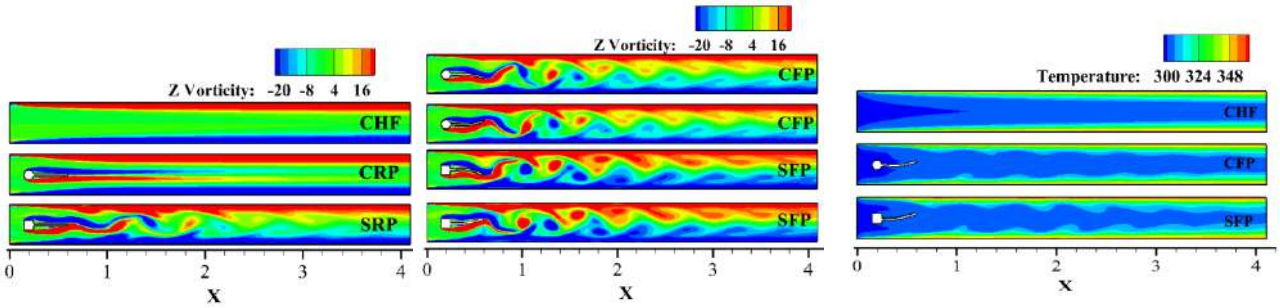

a) **b)** **c)**

Figure 3. Vorticity contours in a channel for **a)**rigid plate setup; **b)** flexible plate setup; **c)** Temperature contours [***CHF:*** *Channel flow;* ***CRP:*** *Circular cylinder with rigid plate*]

CONCLUSIONS

The comparative study has been performed on the flow-induced motion of the thin plate attached to two different bluff bodies, i.e., a circular and a square cylinder, respectively. The square cylinder with the flexible plate sweeps the higher amplitude and lesser frequency vortices. The settling time of the oscillations is found to be less for the square cylinder. Further, the square cylinder with the flexible plate imparts the higher vorticity magnitude in the domain resulting in the enhancement of the mixing of the fluid. The enhanced mixing promotes improved convection and indicates the reduction in the thermal boundary layer at the locations of the swept vortices. Thus, the authors recommend the use of a square cylinder with a flexible plate over the circular cylinder arrangement for the effective cooling of the electronics contained in enclosures through the flow-induced motion of the plate.

References

[1] Soti, Atul Kumar, Rajneesh Bhardwaj, and John Sheridan. "Flow-induced deformation of a flexible thin structure as manifestation of heat transfer enhancement." *International Journal of Heat and Mass Transfer* 84: 1070-1081, 2015.

[2] Ghalambaz, Mohammad, et al. "Fluid-structure interaction study of natural convection heat transfer over a flexible oscillating fin in a square cavity." *International Journal of Thermal Sciences* 111: 256-273, 2017.

[3] Greenshields, Christopher J. "Openfoam user guide." *OpenFOAM Foundation Ltd, version* 3.1: e2888, 2015.

[4] Dhondt G.,"Calculix: A free software three-dimensional structural finite element program.", http://www.calculix.de/

[5] Bungartz, Hans-Joachim, et al. "preCICE–a fully parallel library for multi-physics surface coupling." *Computers & Fluids* 141: 250-258, 2016.

[6] Turek, Stefan, and Jaroslav Hron. "Proposal for numerical benchmarking of fluid-structure interaction between an elastic object and laminar incompressible flow." *Fluid-structure interaction*. Springer, Berlin, Heidelberg: 371-385, 2006.

EVALUATION OF A QUADRATIC ELASTICITY FORMULATION FOR FLUID-STRUCTURE INTERACTION

Ridhwaan Suliman* [1]
[1]Advanced Mathematical Modelling, CSIR, Pretoria, South Africa

Summary The deformation of slender elastic structures due to the motion of fluid around it is a common multi-physics problem encountered in many applications. This work details the development and implementation of a numerical model capable of solving such strongly-coupled fluid-structure interaction problems. A thorough stability analysis of finite elastic plates in uniform flow is conducted, and validation of the results with those from analytical methods is done. An analysis of the dynamic interactions between multiple finite plates in various configurations is also conducted.

INTRODUCTION

In most fluid-structure interaction problems the deformation of the slender elastic bodies is significant and cannot be described by a purely linear analysis. We present a new formulation to model these larger displacements. Examples of such FSI systems include wing flutter on aircraft, aeroelasticity of turbomachinery blades, flows in elastic pipes and blood vessels, heart valve dynamics, swimming of fish and in the processing of paper. In this work, we make use of a blend of mathematical and computational approaches to study strongly-coupled fluid-structure interaction problems involving long thin structures.

STRONGLY-COUPLED FLUID STRUCTURE INTERACTION

Two computational fluid-structure interaction approaches are implemented in a partitioned manner: a finite volume method for discretisation of both the fluid and solid domains and the quadratic modal formulation for the structure coupled with a finite volume fluid solver. Strong-coupling is achieved by means of a fixed-point solver with dynamic relaxation. The fluid-structure interaction approaches are validated and compared on benchmark problems of increasing complexity and strength of coupling between the fluid and solid domains.

Governing Equations

The equations governing viscous incompressible isothermal fluid flow in an arbitrary-Lagrangian-Eulerian (ALE) reference frame [1] are given by the continuity and Navier-Stokes equations. To close the governing equations, a constitutive relation for stress is required. We assume a Newtonian fluid to relate the stress to strain. The partial differential equations that describe a homogeneous isotropic elastic solid undergoing large, non-linear deformation are given by Cauchy's first equation of motion [2]. Assuming an isotropic hyperelastic St. Venant–Kirchhoff material model, the stress-strain relationship is given in terms of the second Piola–Kirchhoff stress. The first Piola–Kirchhoff stress is related to the second Piola–Kirchhoff stress by the deformation gradient, which relates quantities in the undeformed configuration to their counterparts in the deformed configuration. The constitutive stress-strain relationship is given in terms of the Green–Lagrange strain, which is related to the displacement field through the gradients of displacement.

Modal FSI Analysis

Tangential to the full finite volume FSI approach, a reduced-order modal approach to solving the structural equations has been implemented and coupled with an incompressible finite volume fluid solver in OpenFOAM. For a modal structural analysis, Lagrange's equations of motion in the general case are used, which provides an expression for the eigenvalues or natural frequencies and eigenvectors or mode shapes. By extending the standard modal analysis technique for linear structural analysis, the governing equations and boundary conditions are updated to account for the leading-order non-linear terms and a new modal formulation with quadratic modes is derived. Strong-coupling of the fluid and solid domains is achieved by means of a fixed-point solver using a dynamic relaxation parameter based on Aitken's method.

Fluid-Solid Coupling

The coupling between the fluid and solid is done once at the beginning of every time-step when movement of the mesh occurs. The fluid flow provides a traction onto the structure. This results in a deformation of the structure which in turn affects the fluid flow. Coupling conditions for the traction, displacement and velocity are applied to ensure momentum conservation or force equilibrium at the interface, as well as to enforce the kinematic or geometric continuity and no-slip conditions respectively. The above conditions require an iterative procedure such that a strongly-coupled solution is obtained. A strongly-coupled fixed-point solver with dynamic relaxation, has been implemented in this work. It is the most basic of the above approaches yet is highly robust and efficient. The fixed point solver uses a relaxation parameter based on Aitken's method. The solver was modified to call the mesh movement algorithm after every iteration, thus allowing a re-calculation of interface forces, displacements and velocities with every iteration hence resulting in a fully-coupled scheme upon convergence.

*Corresponding author. E-mail: rsuliman@csir.co.za

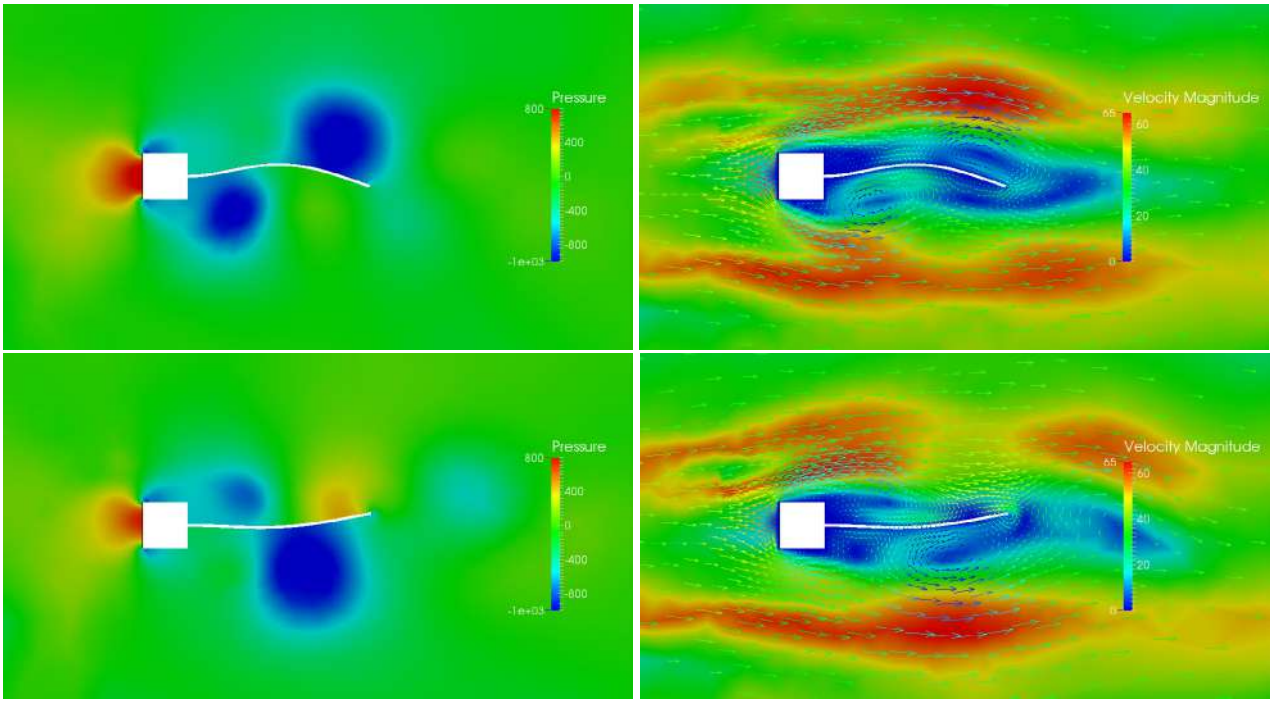

Figure 1: Pressure (left) and velocity contours (right) for the block-tail test-case with the beam oscillating in its second mode of vibration

Two-dimensional Flapping Beam

Both FSI approaches have been successfully validated and compared on benchmark cases and the results for a common FSI benchmark problem, proposed by Turek and Hron [3], of an elastic beam in the wake of a cylinder undergoing vortex-induced vibration are included here. The properties of the fluid and solid are as described by Turek and Hron [3]. A uniform constant fluid velocity, Reynolds number, Re = 100, was applied at the inlet while at the exit pressure was set to zero. Flow is assumed to be laminar. Snapshots of the beam deflection and velocity contours at various times are shown in Figure 1, showing large oscillations of the beam in its second mode of vibration as vortices are shed periodically from either side of it. The finite volume FSI results, however, required a very fine mesh for the solid domain and consequently a long run-time. Upon further investigation of just a cantilever beam under a tip load it was found that the finite volume method for structural mechanics suffered from a phenomenon of shear locking. When the aspect ratio of the elements (ratio of element width to height) is large, a numerical shear strain component is produced in addition to a bending strain. This absorbs strain energy and results in a decrease in displacement or stiffening. In addition, an evaluation of the accuracy of the finite volume scheme shows that the scheme is only first-order accurate, which also explains the slow convergence in the result.

CONCLUSIONS

Two computational fluid-structure interaction approaches have been successfully implemented and validated on benchmark problems. Whilst the partitioned finite volume FSI method displayed accurate results, fine meshes and hence long computational times were required. It was shown that the finite volume method for modelling solid mechanics has a number of deficiencies, especially with regards to long thin structures where locking occurs. The modal FSI solver was successfully validated on a wide range of test-cases. Strong-coupling and the handling of the mesh movement showed promising results. The linear and quadratic modal solutions converged to the same result when the structure undergoes small linear displacement, while the quadratic approach showed substantial improvement in predicting the transient response of FSI systems where the structure undergoes significant deflections. The prediction of the frequency and dynamic behaviour of strongly-coupled fluid-loaded structures compared well with those from full FSI solutions.

References

[1] Hirt, C., Amsden, A., and Cook, J., 1974. An arbitrary Lagrangian-Eulerian computing method for all flow speeds. *Journal of Computational Physics* **14**: pp. 227-253.

[2] Holzapfel, G., 2001. Nonlinear Solid Mechanics: A continuum Approach for Engineering. John Wiley & Sons Ltd., West Sussex, England.

[3] Turek, S., and Hron, J., 2006. Proposal for numerical benchmarking of fluid-structure interaction between an elastic object and laminar incompressible flow. *Lecture Notes in Computational Science and Engineering* **53**: 371.

STABILISING THE FLOW-FIELD OF A HEAVING FOIL USING A FLEXIBLE AFT TAIL ATTACHED AT THE TRAILING EDGE

Chhote Lal Shah* [1], Dipanjan Majumdar[1], and Sunetra Sarkar[1]
[1]Department of Aerospace Engineering, Indian Institute of Technology Madras, Chennai-600036, Tamilnadu, India.

Summary Flapping wings with suitable wing kinematics, wing shapes, and flexible structures can enhance lift as well as thrust by exploiting large-scale vortical flow structures under various conditions. However, it is also necessary to understand the dynamics of the flow-field, which may influence the flying performance. In the present study, an elliptic foil with an attached tail at the trailing edge is considered for studying the dynamics of the flow-field. The current work focuses on analysing the dynamics with an increase in the flexibility of the tail structure. Although a perfectly rigid tail enhances the aerodynamic performance, it can also take the system to aperiodicity. However, a flexible tail has the ability to change the dynamics and stabilise the system.

INTRODUCTION

Biologically inspired insect flight mechanisms have recently become a primary research subject, mainly to design efficient micro air vehicles (MAVs) used for defence surveillance and environmental monitoring. The prime source of inspiration in this regard with the reliance on natural selection comes from the natural flyers due to the similar Reynolds number regime in which they fly. Natural flyers utilise the unsteady aerodynamics around their flapping wings to generate the lift and thrust. These aerodynamic loads are related to the formation and shedding of the vortices into the flow which are again dependent on different wing shapes, structural flexibility and wing kinematics. A rigid elliptic foil plunging in uniform stream results in a drag producing von-Karmann wake, thrust producing reverse Karmann wake and deflected reverse Karmann wake with the increase in plunge velocity κh (where $\kappa = \frac{2\pi f c}{U_\infty}$ is reduced frequency, f is frequency, c is chord length of elliptic foil, U_∞ is free stream velocity, and h is nondimensional plunge amplitude) [1]. With further increase in κh, the flow-field transitions into the aperiodic regime and eventually to chaos [2]. However, a more realistic design of a bio-inspired wing would consist of a flexible trailing part attached to the stiff leading portion. Heathcote and Gursul [3] reported that the enhancement in mean thrust is possible by inclusions of an aft tail attached to the foil. Likewise, Mia and Ho [4] noted that a flexible foil with a pre-defined deformation could increase the propulsive efficiency. Further, Heathcote et al. [5] showed that the thrust/input-power ratio was significantly high for flexible airfoils than rigid airfoils. Also, they observed that at high plunging frequencies, moderately flexible airfoil generates the largest thrust, while highly flexible systems show larger thrusts at low frequencies. Most of the literature mentioned above focused on enhancing the aerodynamic performance. However, the dynamical transitions in the flow-field of a heaving foil with an attached tail at the trailing edge have not been investigated earlier. The focus of this study is to explore the dynamics associated with the flow-field for different levels of flexibility of the aft tail structure. This study is of importance from the MAVs design point of view as one must avoid the system from entering into an aperiodic state in a broad sense.

COMPUTATIONAL METHODOLOGY

A foil with a rigid elliptic part (with major axis length as c) and a flexible tail of length $0.3c$ is considered here. A sinusoidal plunge motion is provided at the center of the elliptic foil. The trailing part of the foil is modelled as an inextensible flexible filament [6] and is allowed to oscillate passively. The flow around the oscillating body is governed by the incompressible Navier-Stokes equations which are numerically solved using an in-house solver [2] developed based on the discrete forcing type imersed boundary method (IBM). In the present Fluid-Structure Interaction (FSI) framework, the structural solver and the IBM solver are coupled in a weak coupling approach where both flow and structural solvers exchange information explicitly at every time-step [7]. The Reynolds number is kept constant at 300 throughout the study. The simulations are run after performing domain and grid convergence studies. A time step of 0.0004 has been considered after performing a time convergence test and has been used for the rest of the simulations.

RESULTS AND DISCUSSIONS

Simulations have been performed for a wide range of κh values. In order to study the effect of tail flexibility on the flow dynamics, different levels of rigidity with γ (non-dimensional bending rigidity) $\approx \infty$ (rigid case), 1.0 and 0.1 have been considered. It is observed that the inclusion of a tail at the trailing edge of the elliptic foil enhanced the aerodynamic performance. At lower κh, the flow-field, as well as aerodynamic loads, remain periodic for all the cases. However, the present study focuses on $\kappa h = 1.5$, which is in the aperiodic regime. Time history of drag coefficient (C_D) and corresponding Morlet wavelet spectra [8] in terms of scalogram plots are presented in Figure 1. The scalograms are the visual representation of the wavelet transforms in which the x-axis represents time, and the y-axis represents the time-evolution of the frequency content of a signal. The C_D time history for the rigid foil without tail exhibits quasi-periodic

*Corresponding author. E-mail: lal.chhote.shah@gmail.com

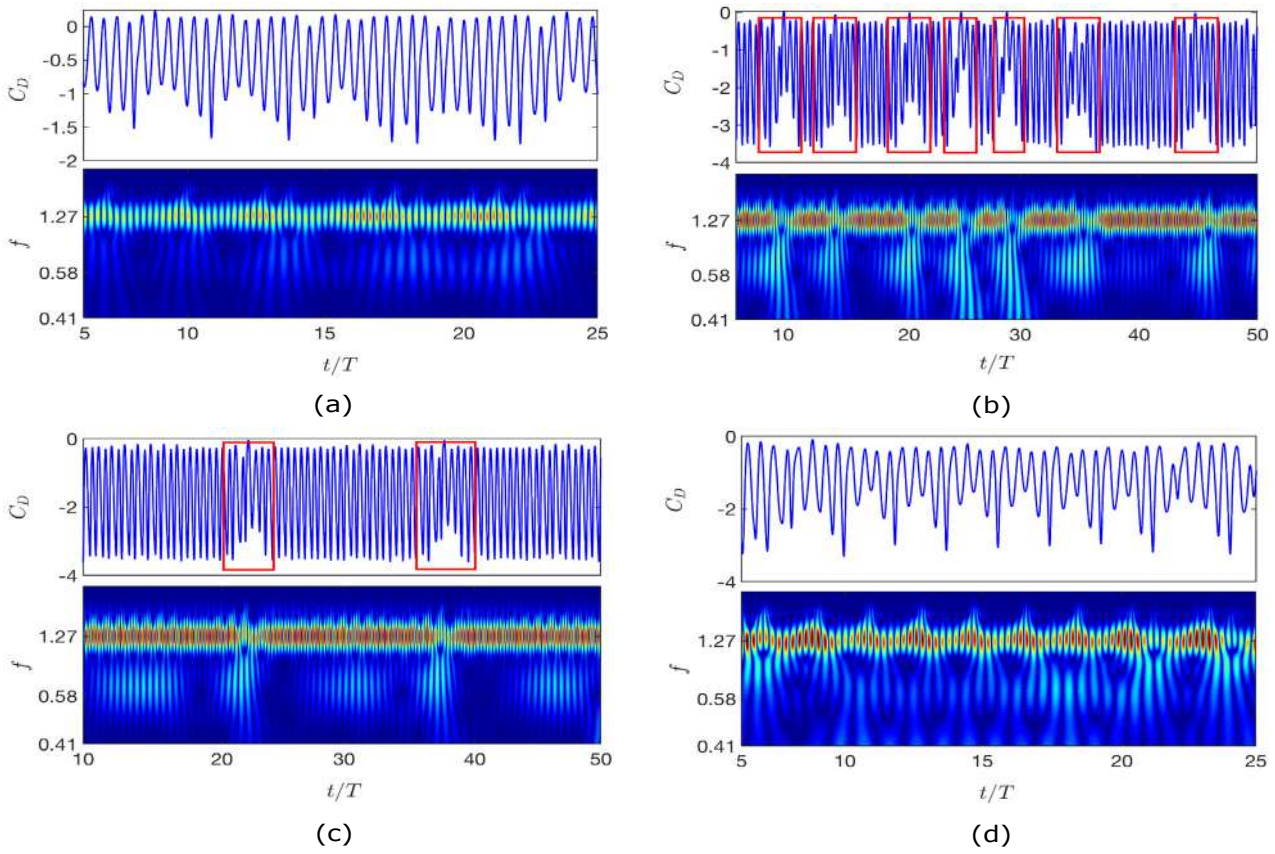

Figure 1: C_D time histories and corresponding scalogram of the wavelet coefficients for $\kappa h = 1.5$; (a) elliptic foil without aft tail, (b) elliptic foil with rigid aft tail, (c) elliptic foil with flexible aft tail of $\gamma = 1.0$, and (d) elliptic foil with flexible aft tail of $\gamma = 0.1$.

behavior which is evident by the presence of incommensurate frequency bands shown in the scalogram plot (Figure 1 (a)). With the addition of a rigid tail, the mean thrust increases notably. However, the system manifests intermittency as evident by the presence of quasi-periodic windows interspersed by the chaotic windows shown in Figure 1 (b). As the rigidity of the tail is reduced, at $\gamma = 1.0$, the leading edge separation behavior still remain intermittent. However, the system behaviour has now become regularised compared to the rigid tail case; see Figure 1 (c). In this case, the length of the quasi-periodic windows has increased and the aperiodic windows has reduced. With further decrease in the rigidity, for $\gamma = 0.1$, the flow-field, and hence the C_D, returns back to the quasi-periodic dynamics which is confirmed from the modulation in the C_D time history caused by incommensurate frequency bands (Figure 1 (d)).

CONCLUSIONS

In this study, the transition in flow dynamics of a sinusoidally heaving foil with flexible aft tail has been investigated. The existence of intermittency has been observed at $\kappa h = 1.5$. Scalogram is used to characterise the dynamics associated with the time histories. The inclusion of a rigid tail at the trailing edge of the foil gives better aerodynamic performance, but the system also shows intermittency. However, with an increase in flexibility, the system no longer exhibits intermittency, and the dynamics gets stabilised. Further time series analyses on the characterisation of different dynamic states and the details of the flow-field could not be shown here for the sake of brevity but will be shared during the presentation. The present study contributes towards the design of flexible flapping wings for the development of micro-air vehicles.

References

[1] Jones K.D., Dohring C.M., Platzer M.F., Experimental and Computational Investigating of the Knoller-Betz Effect. *AIAA J.* **36**: 1240-1246, 1998.
[2] Majumdar D., Bose C., Sarkar S., Capturing the dynamical transitions in the flow-field of a flapping foil using Immersed Boundary Method. *J. Fluids Struct.* **95**: 102999, 2020.
[3] Heathcote S., Gursul I., Flexible Flapping Airfoil Propulsion at Low Reynolds Numbers. *AIAA J.* **45**: 1066-1079, 2007.
[4] Miao J.M., Ho H.M., Effects of Aerodynamic Propulsive Efficiency of Flapping Flexible Airfoil. *J. Fluid and Struct.* **22**: 401-419, 2006.
[5] Heathcote S., Martin D., and Gursul I., Flexible Flapping Airfoil Propulsion at Zero Freestream Velocity. *AIAA J.* **42**: 2196-2204, 2004.
[6] Huang W., Shin S.J. Sung H.J., Simulation of Flexible Filaments in a Uniform Flow by the Immersed Boundary Method. *J. Comput. Phys.* **226**: 2206-2228, 2007.
[7] Shah C.L., Majumdar D., Sarkar S., Performance Enhancement of an Immersed Boundary Method Based FSI Solver Using OpenMP. 21^{st} Annual CFD Symposium, NAL Bangalore, India, August 8-9, 2019.
[8] Grossmann A., Kronland-Martinet R., and Morlet J., Reading andUnderstanding Continuous Wavelet Transforms,"Wavelets. *Springer* 2–20, 1990.

LAMINAR SEPARATION FLUTTER OF A NACA0012 AIRFOIL AS A GLOBAL INSTABILITY

D. Sabino[1,2], O. Marquet *[1], V. Mons[1], and D. Fabre[2]
[1]ONERA-DAAA, 8 rue des Vertugadins, 92190 Meudon, France
[2]Institut de Mécanique des Fluides de Toulouse (IMFT), Université de Toulouse, CNRS, Toulouse, France

Summary The onset of pitch-oscillations of a NACA0012 airfoil mounted on a torsion-spring is investigated by the means of a global stability analysis. Experimental studies from literature have shown this configuration undergoing on a flutter behaviour for a close range of Reynolds. This phenomenon is attributed to the laminar character of the boundary layer and to its detachment, transition and subsequent reattachment on the airfoil surface. In this regard, we carried out a linear stability analysis of the mean flow field, issued from a RANS simulation, using a Spalart–Allmaras model. A careful choice of the inlet conditions revealed to be necessary to capture a laminar separation and, as the incidence increases, a laminar separation bubble (LSB).

INTRODUCTION

The first investigation of the aeroelastic behaviour of a NACA0012 airfoil was conducted by Poirel *et al.* (2008), with an experimental set up on a Reynolds number range of $4.5 \times 10^4 < Re < 1.35 \times 10^5$. The airfoil was free to rotate in the pitch degree of freedom, presenting a self-sustained behaviour around a mean angle of attack of zero degrees and an amplitude around $5.5°$. The primary driver for this behaviour was associated to the laminar boundary layer separation on the second half of the airfoil surface, with a subsequent flow transition to a turbulent state an reattachment, forming a Laminar Separation Bubble (LSB).

Subsequent works have reproduced the same phenomenon, performing large-eddy simulations of forced pitch oscillations (Poirel & Yuan 2010) or numerical time-marching fluid-structure-interaction simulations using turbulence modelling for the Navier–Stokes equations (Poirel *et al.* 2011), to name a few. In continuation of these works, Poirel & Mendes (2014) performed experiments in the same transitional Reynolds range, but with both pitch and heave degrees of freedom, obtaining both small and large amplitude oscillations.

More recently, an aeroelastic linear stability using a mean flow from 3D DNS simulations was investigated by Negi (2019), showing a static eigenvalue that indicates a divergent behaviour of the airfoil from its equilibrium position at $\alpha = 0°$. Further, they associated the subsequent non-linear oscillation to a sub-critical mode, which is non-linearly excited.

The present study aims to understanding of the laminar separation flutter, by highlighting this divergent onset that leads the airfoil to a new equilibrium point where an unstable eigenvalue is then responsible for the non-linear onset dynamics.

MEAN FLOW ANALYSIS

We consider a flow described by the incompressible Reynolds-Averaged Navier–Stokes equations (RANS) with a closure obtained from the Spalart–Allmaras model. This model was intended to be used in a fully turbulent configuration where no laminar separation was able to appear. This turbulent behaviour is commanded by the inlet condition on the eddy viscosity which is recommended to be $\nu_t^\infty = 3\nu$.

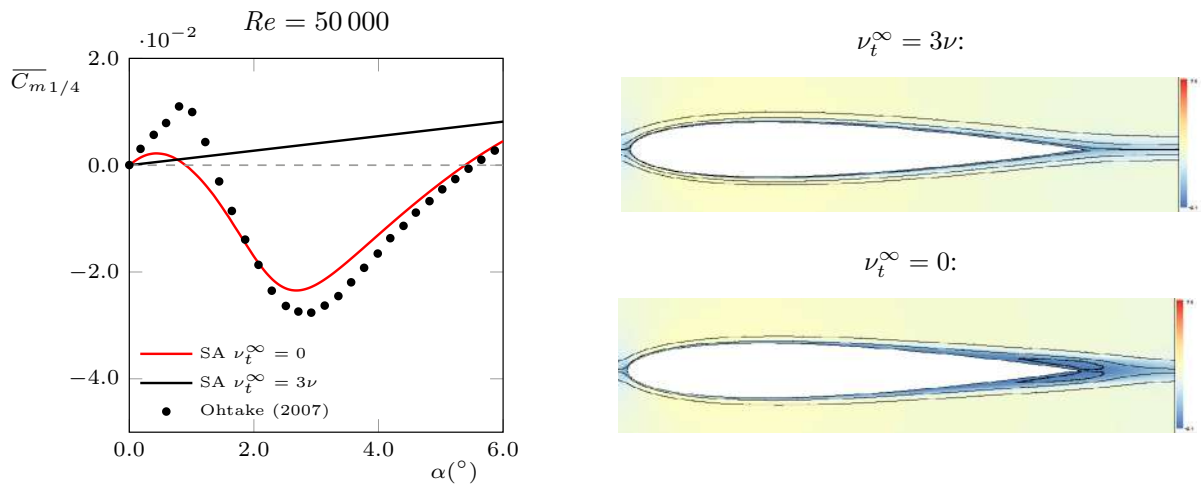

Figure 1: At right, the evolution of the mean flow moment coefficient with the incidence. At left, the streawise velocity for $Re = 50\,000$ for $\alpha = 0°$ and $\alpha = 4°$, showing a detached flow and a laminar separation bubble, respectively.

*Corresponding author. E-mail: diogo.ferreirasabino@toulouse-inp.fr.

THEMATIC SESSION FS

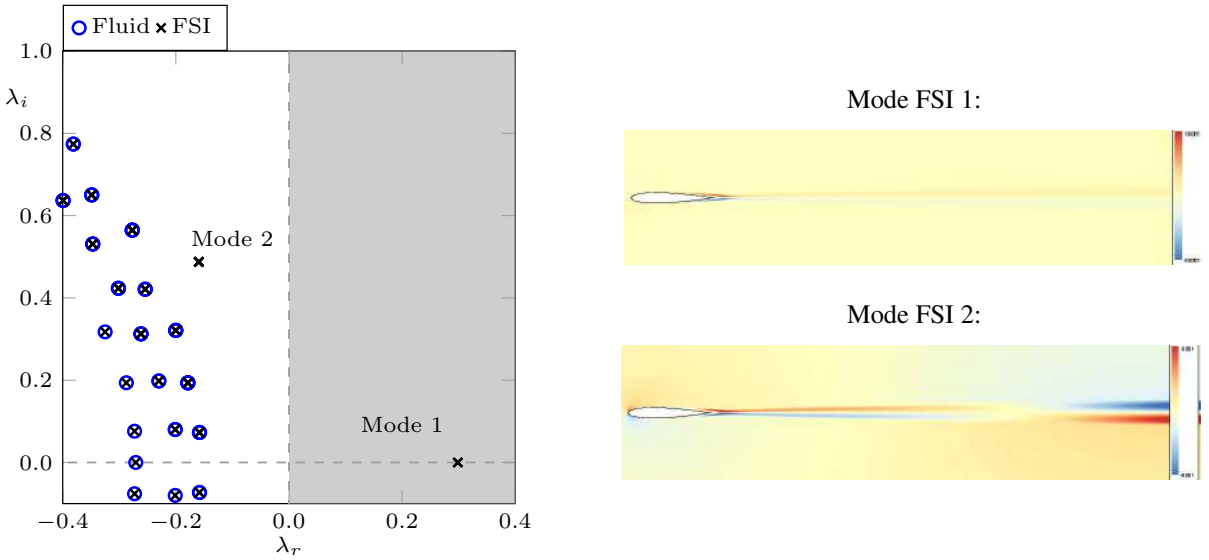

Figure 2: At left, a comparison between the fluid and a fluid structure spectra, the latter presenting a static unstable eigenvalue. At right, the streamwise velocity field for the two FSI modes.

However, recent studies have used this model to describe laminar separation flow, being able to capture the transition triggered by a separated flow (Crivillini & D'Alessandro 2014). The key ingredient of this procedure was the use of very small turbulent variable free-stream conditions, ideally at $\nu_t^\infty = 0$.

Following this idea, we carried out several RANS simulations for different airfoil incidences. The evolution of the mean flow moment coefficient is depicted in figure 1, for two different values of ν_t^∞.

It can be observed that the nonlinear behaviour of the flow field at low incidences cannot be captured by a fully turbulent simulation ($\nu_t^\infty = 3\nu$), whereas a laminar approach was able to capture it, when comparing with the experimental data from Ohtake (2007). The comparison between the flow fields is depicted at the left of figure 1, where a recirculation bubble can be observed for the laminar separated case.

FLUID STRUCTURE LINEAR STABILITY ANALYSIS

In a second time, a global stability analysis was carried out at $\alpha = 0°$ for the case where $\nu_t^\infty = 0$. The FSI stability analysis revealed two additional eigenvalues, associated to the pitching degree of freedom, that are not present when studying a pure hydrodynamic case. This comparison is detailed in figure 2, at left. The FSI stability analysis was carried out with a stiffness, damping and inertia coefficients of $K_s = 0$, $D_s = 0.0$ and $I_s = 0.00135$, respectively. The mode 1 is associated to the divergent linear departure from the equilibrium position. The correspondent spatial structure is depicted at right of figure 2. The second mode, although stable, and can be responsible for the onset of the pitching oscillation, by a non-linear excitation for large enough oscillation amplitudes.

CONCLUSIONS

A global linear stability analysis is performed for a torsion-spring airfoil configuration at the Reynolds number of 50 000. The mean flow field is obtained solving the RANS equations coupled to the Spalart–Allmaras turbulence model, with $\nu_t^\infty = 0$. The stability analysis around $\alpha = 0°$ shows a divergent eigenmode responsible for the departure of the airfoil from this equilibrium position. The subsequent the onset of the pitching oscillation could be explained by a non-linear excitation of a second structure mode.

References

[1] Poirel, D., Harris, Y & Benaissa, A. 2008 Self-sustained aeroelastic oscillations of a NACA0012 airfoil at low-to-modelate Reynolds numbers. *J. Fluid and Struct.* **24**: (5), 700 – 719.
[2] Poirel, D. & Yuan, W. 2010 Aeodynamics of laminar separation flutter at transitional Reynolds number. *J. Fluid and Struct.* **26**: (7), 1174 – 1194.
[3] Poirel, D., Métivier, V & Dumas, G. 2011 Computational aeroelastic simulations of self-sustained pitch oscillations of a NACA0012 at transitional Reynolds numbers. *J. Fluid and Struct.* **27**: (8), 1262 – 1277.
[4] Poirel, D. & Mendes, F. 2014 Experimental small-amplitude self-sustained pitch–heave oscillations at transitional Reynolds numbers. *AIAA J.* **52**: (8), 1581 – 1590.
[5] Negi, P. S. 2019 Stability and transition in pitching wings. *PhD thesis* Royal Institute of Technology in Stockholm
[6] Andrea Crivellini, Valerio D'Alessandro 2014 Spalart–Allmaras model apperent transition and RANS simulations of laminar separation bubbles on airfoils. *Inter. J. of Heat and Fluid Flow* **47**: 70 – 83.
[7] Tomohisa Ohtake, Yusuke Nakae, Tatsuo Motohashi 2007 Nonlinearity of the Aerodynamic Characteristics of NACA0012 Aerofoil at Low Reynolds Numbers. *J. of the Japan Society for Aeronautical and Space Sciences* **55**(644): 439 – 445.

EXTENDED KINETIC THEORY FOR A DENSE, COLLISIONAL, SHEARING FLOW ABOVE AN INCLINED PARTICLE BED

James T. Jenkins*[1] and Diego Berzi [2]
[1]School of Civil and Environmental Engineering, Cornell University, Ithaca, NY, USA
[2] Department of Civil and Environmental Engineering, Politecnico di Milano, Milano, Italy

Summary We outline the physics and provide the equations and boundary conditions that govern the behavior of steady, dense, collisional sharing flows above an inclined particle bed. These may be employed to formulate and solve the boundary problem that gives profiles of particle concentration, average velocity, and the strength of the velocity fluctuations through the depth of the flow.

INTRODUCTION

Balance laws and constitutive relations based on kinetic theory [1] form the basis for the description of many shearing flows of inelastic spheres. However, when flows are sufficiently dense, such kinetic theories fail. For example, in flows down inclines, they predict increases in average density with inclination, significant variation in density across the flow, and limited increases in depth with volume flow rates than are different from those observed in numerical simulations [2,3]. The problem is that they fail to incorporate velocity correlations that develop [4] at particle concentrations above 0.49, at which a transition to an ordered collisional gas is possible in an equilibrated system of elastic spheres [5].

An attempt to correct kinetic theory in order to incorporate the influence of the velocity correlations involves the introduction of an additional length scale in the rate of collisional dissipation of energy [6-8]. The length scale is determined by a phenomenological balance between the orienting influence of the mean shearing and the randomizing influence of collisions. Its presence permits realistic predictions of the behavior seen in dense inclined flows [9,10]; it also allows the resulting theory to be related to simpler phenomenological descriptions of dense flows [11-14] that have recently become popular.

Often, dense collisional shearing flows occur over a particle bed. In this case, particle collisions persist within the bed, but are accompanied by ephemeral chains of contacting particles that transmit force within the bed. The resulting elasticity associated with the existence of force chains and the collisional transfer of momentum associated with their breaking may be incorporated into the stress [10].

Here, we focus on the collisional flow above the bed and collect the elements of the extended kinetic theory that describe the flow. These include balance laws for particle momentum and fluctuation energy, constitutive relations for stress, energy flux, and the rate of energy dissipation, and the associated boundary conditions.

THEORY

We consider steady, two-dimensional shearing flows of a dense aggregate of identical spheres of diameter d, mass density ρ_s, and solid volume fraction, or concentration, ν over an inclined particle bed in the absence of side walls. The spheres have a coefficient of sliding friction μ, and a restitution coefficient e. The x-axis is taken to be in the direction of flow and at an angle of ϕ to the horizontal, the y-axis is perpendicular to it and directed upward. The gravitational acceleration is g, the average particle flow velocity is u, the granular temperature T is one-third the square of the magnitude of the particle velocity fluctuations, and a prime denotes a derivative with respect to y.

Momentum Balance

The particle shear stress s and particle pressure p satisfy familiar forms of the balance of momentum. In flow and normal directions, $s' = \rho_s \nu g \sin\phi$ and $p' = -\rho_s \nu g \cos\phi$. With a free surface at $y = h$, these integrate to $s/p = \tan\phi$; and, when ν does not vary much from a typical value $\overline{\nu}$, as is often the case, $p = \rho_s \overline{\nu} g (h - y)\cos\phi$.

We consider only flows in which $\nu \geq 0.49$ and, in the constitutive relations [1] retain only terms that result from collisions. In this case, $s = 8\hat{J} d \rho_s \nu (1+e) G T^{1/2} u' / (5\pi^{1/2})$, where [1] $\hat{J} = 1/2 + (\pi/4)(3e-1)(1+e)/[24-(1-e)(11-e)]$; and $p = 2\rho_s \nu (1+e) G T$, where [15] $G = 5.69\nu(\nu_c - 0.49)/(\nu_c - \nu)$, with ν_c the value of the solid fraction at which spheres first touch along the axis of compression and the formation of a bed becomes possible. The value of this concentration depends on μ [8,16]: $\nu_c = 0.58 + (0.64 - 0.58)\exp(-4.5\mu)$. The common dependence of the pressure and shear stress upon ν and G allows the shear stress to be expressed as a function of p, rather than ν: $s = 4\hat{J} d (p/T^{1/2}) u' / (5\pi^{1/2})$. This is an advantage, because the distribution of pressure is often known. Inverting the relation for the shear stress results in an equation to be integrated for the average velocity: $u' = 5\pi^{1/2}(T^{1/2}/d)\tan\phi/(4\hat{J})$, once T is determined.

*Corresponding author: e-mail: jtj2@cornell.edu

Energy balance

The temperature is determined by an energy balance associated with the particle velocity fluctuations. It involves the divergence of a flux of fluctuation energy Q, the working of the shear stress through the velocity gradients, and a rate of dissipation Γ of fluctuation energy in collisions: $-Q' + su' - \Gamma = 0$. Here, $Q = -4\hat{M}d\rho(1+e)GT^{1/2}T'/\pi^{1/2}$, where [1] $\hat{M} = 1/2 + (9\pi/8)(2e-1)(1+e)/[16-7(1-e)]$, or $Q = -2\hat{M}d(p/T^{1/2})T'/\pi^{1/2}$; and $\Gamma = (12/\pi^{1/2})\left(1-\varepsilon^2\right)\rho GT^{3/2}/L$, or $\Gamma = (6/\pi^{1/2})(1-\varepsilon)pT^{1/2}/L$, where ε is an effective coefficient of restitution, $\varepsilon = e - \left(3/2\right)\mu\exp(-3\mu)$, that incorporates both restitution and friction [17-19], and L is the correlation length, given in a balance between the mean shearing and the temperature as $L/d = fdu'/T^{1/2} = f5\pi^{1/2}\tan\phi/(4\hat{J})$, in which the dependence on ν and ε enter through f, determined in numerical simulations [8] to be $f^2 \equiv 2\hat{J}/[15\left(1-\varepsilon\right)]\left[1+(26/15)(1-\varepsilon)(\nu-0.49)/(0.64-\nu)\right]^3$. When the constitutive relations for Q, s, and Γ are employed in the energy balance and the result expressed in terms of $w \equiv T^{1/2}$, the fluctuation velocity, a linear equation for w results: $d^2w'' + d^2(p'/p)w' + \left[5\pi\tan^2\phi/(8\hat{J}) - 3\left(1-\varepsilon\right)/L\right]w/(2\hat{M}) = 0$. However, in this equation, the pressure and the correlation vary with concentration through the depth of the flow.

In any case, the normal component of the momentum balance, used with the constitutive relation for the pressure, provides a first-order differential equation equation that involves both ν and w. This may be used with the linear equation for the fluctuation velocity and appropriate boundary conditions to determine the variation of both fields through the flow. Then, given w, the inversion of the constitutive relation for the stress may be integrated for the average particle velocity, subject again to an appropriate boundary condition.

Boundary conditions

Here, we assume that at the surface of the bed the concentration is very near ν_c, the average particle velocity is small enough to be neglected, and that particle velocity fluctuations persist into the bed [20]. Then, in the bed, we assume there is a rough balance between the first and last terms in the equation for the fluctuation velocity: $d^2w'' - \lambda^2 w = 0$, where $\lambda^2 = 3d\left(1-\varepsilon\right)/(2\hat{M}L_0)$ and the subscript indicates that L is evaluated at the surface of the bed. Integrating this give a condition on the energy flux at the surface of the bed: $Q = -4\hat{M}p\lambda w/\pi^{1/2}$, or $w'\big|_0 = \lambda w_0/d$. At the free surface, we take $\nu = 0.49$, $s = p\tan\phi$, $w' = 0$. These conditions permit the determination of the profiles of ν, u, and w and the thickness, h, of the flow.

CONCLUSIONS

We have outlined the physics and provided the equations and boundary conditions that govern the behavior of a steady, dense, collisional, sharing flow above an inclined particle bed. The resulting relatively simple system of equations may be employed in, for example, the Matlab solver bvp4c to determine the profiles of particle concentration, average velocity, and fluctuation velocity through the depth of the flow.

References

[1] Garzo V., Dufty J.W. Dense fluid transport for inelastic hard spheres. *Phys. Rev. E* **59**:5895–5911, 1999.
[2] Silbert L.E., Ertas D., Grest G.S., Halsey T.C., Levine D., Plimpton S. J. Granular flow down an inclined plane: Bagnold scaling and rheology. *Phys. Rev. E* **64**:051302, 2001.
[3] Mitarai, N., Nakanishi, H. Bagnold scaling, density plateau, and kinetic theory analysis of dense granular flow. *Phys. Rev. Lett.* **94**:128001, 2005.
[4] Mitarai, N., Nakanishi, H. Velocity correlations in dense granular shear flows: effects on energy dissipation and normal stress. *Phys. Rev. E* **75**:031305, 2007.
[5] Adler B.J., Wainwright T.E. Phase transition for a hard sphere system. *J. Chem. Phys.* **27**:1208-1209, 1957.
[6] Jenkins J.T. Dense shearing flows of inelastic disks. *Phys. Fluids* **18**:103307, 2006.
[7] Jenkins J.T., Berzi, D. Dense inclined flows of inelastic spheres: tests of an extension of kinetic theory. *Granul. Matt.* **12**:151-158, 2010.
[8] Berzi, D., Vescovi, D. Different singularities in the functions of extended kinetic theory at the origin of the yield stress in granular flows. *Phys. Fluids* **27**:013302, 2015.
[9] Gollins D., Berzi D., Bowman, E.T. Extended kinetic theory applied to inclined granular flows: role of boundaries. *Granul. Matt.* **19**:56-73. 2017.
[10] Berzi D., Jenkins J.T., Richard P. Extended kinetic theory for granular flow over and within an inclined erodible bed. *J. Fluid Mech.* **885**:A27,1-24, 2020.
[11] GDR MiDi On dense granular flows. *Eur. Phys. J. E* **14**:341–365, 2004.
[12] Forterre Y., Pouliquen O. Flows of dense granular media. *Annu. Rev. Fluid Mech.* **40**:1-24, 2008.
[13] Kamrin K., Koval G. Nonlocal constitutive relation for steady granular flow. *Phys. Rev. Lett.* **108**:178301, 2012.
[14] Kamrin K., Henann D.L. Nonlocal modeling of granular flows down inclines. *Soft Matt.* **11**:1744–6848, 2015.
[15] Torquato S. Nearest-neighbor statistics for packings of hard spheres and disks. *Phys. Rev. E* **51**:3170–3182, 1995.
[16] Chialvo S., Sun, J., Sundaresan, S. Bridging the rheology of granular flows in three regimes. *Phys. Rev. E* **85**:021305 2012.
[17] Jenkins, J.T., Zhang C. Kinetic theory for identical, frictional, nearly elastic spheres. *Phys. Fluids* **14**:1228–1235, 2002.
[18] Chialvo S., Sundaresan, S. A modified kinetic theory for frictional granular flows in dense and dilute regimes. *Phys. Fluids* **25**:070603, 2013.
[19] Larcher M., Jenkins J.T. Segregation and mixture profiles in dense, inclined flows of two types of spheres. *Phys. Fluids* **25**:113301, 2013.
[20] Jenkins J.T., Askari E. Boundary conditions for rapid granular flows: phase interfaces. *J. Fluid Mech.* **223**:497–508, 1991.

FLOW AND PACKING BEHAVIOR OF COHESIVE AND ASPHERICAL PARTICLES IN HOPPERS

Jennifer Sinclair Curtis[1], Yu Guo[2], and Henna Tangri[3]
[1]Department of Chemical Engineering, UC Davis, Davis, CA, USA
[2]School of Aeronautics and Astronautics, Zhejiang University, Hangzhou, China
[3]Chemical Engineering Department, University of Florida, Gainesville, FL, USA

Summary This presentation outlines advances in DEM to simulate the motion of cohesive and/or aspherical particles. Aspherical grains are described either as perfect cylinders or disks of varying aspect ratio or described using a linked and overlapping sphere approach. Using this linked approach, the flow of flexible aspherical particles can also be treated via a bonded particle model which incorporates normal and shear forces as well as bending and torsional moments. The bonded particle model also allows for breakage of aspherical particles during impact. Cohesion between particles is described as originating from surface moisture, described by a liquid bridge force model in the case of pendular liquid bridges. DEM simulations of wet, aspherical particles are validated via experiments of hopper discharge and measurements of particle-phase stress in a ring shear cell.

RESULTS: Hopper Discharge of Dry, Aspherical Particles

DEM has been shown to be a powerful simulation tool to predict the flow behaviour of spherical particles in hoppers – both in wet and dry states ([1],[2],[3]). Here, the discharge of non-spherical particles, specifically cylindrical particles, from a rectangular hopper is investigated. The behavior of both steel and plastic cylindrical particles with varying aspect ratio (same diameter, different lengths) is simulated via DEM and validated via corresponding experimental measurements. In addition, the effects of fill height, particle-particle friction, and hopper cone angle (90 and 55 degrees) are explored and compared with previously published results for spherical particles. A representative computational set up is shown in Figure 1, along with the detailed information regarding particle velocities for various heights in the hopper. The cylindrical particles are simulated using the contact detection as outlined in [4].

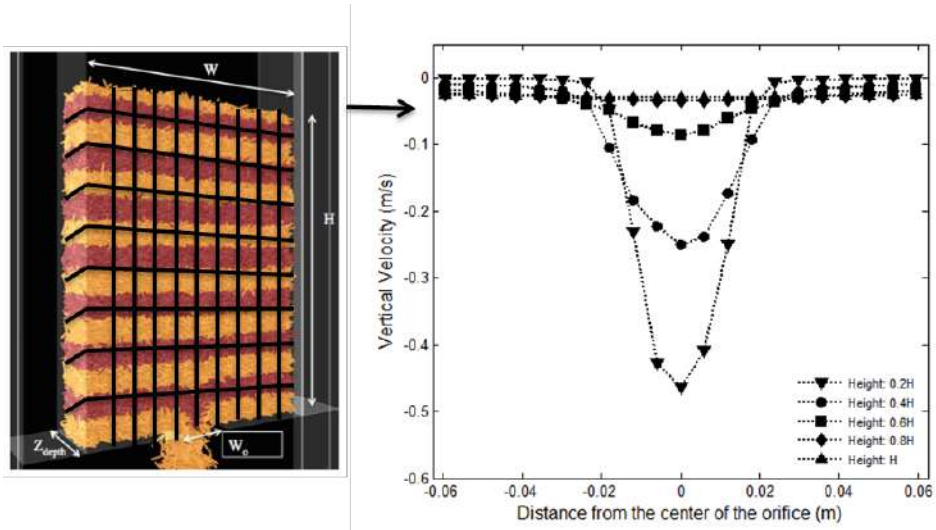

Figure 1. DEM simulation and representative grid (left) used to compute local particle velocities with the hopper (right)

The DEM simulations show that the discharge rate of aspherical particles are drastically different from their spherical counterpart, with the discharge rate decreasing with increasing aspect ratio or decreasing sphericity. This trend is valid even taking into account the increase in equivalent diameter of the aspherical particle. This is shown in Figure 2 by a comparison of the discharge rate of spherical particles, based on the Myers and Sellers hopper discharge rate correlation ([5]), with the discharge rate of aspherical particles with the same equivalent volume diameter. Also, Figure 2 shows that the DEM simulations are fully capable of predicting the discharge rate of the aspherical particles. The coefficient of friction also strongly affects the discharge rate – increasing friction significantly decreases the discharge rate. The critical value of friction coefficient in which the discharge becomes independent of friction is 0.1. The DEM simulations also show that discharge rate of cylindrical particles varies with the orifice width raised to the power 3/2, similar to the case with spherical particles. In addition, decreasing the hopper angle from 90 degree to 55 degrees decreases the discharge rate and further decreases in hopper angle increase the discharge rate. Based on a wide range of simulation and experimental data, a new hopper discharge rate correlation is proposed which incorporates the particle sphericity and longest particle dimension and is applicable to both spherical and aspherical particles.

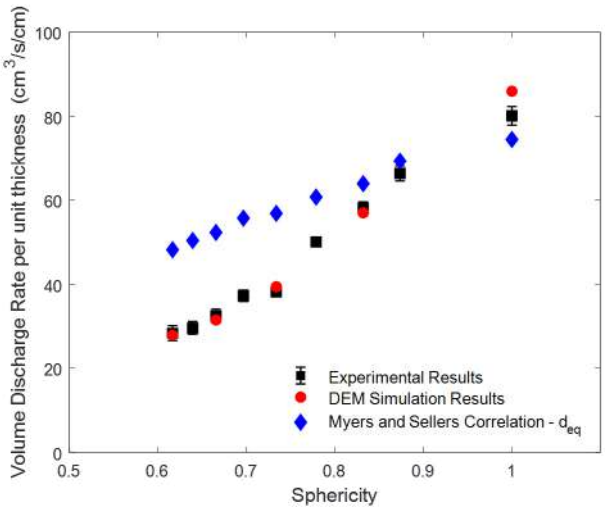

Figure 2. Hopper discharge for particles of varying sphericity from [6]

RESULTS: Hopper Discharge of Wet, Aspherical Particles

When aspherical particles are wet, the cohesive forces associate with the liquid bridges that form between particles affect the discharge rate. As the amount of liquid on the particle surface increases, the rupture distance of the pendular bonds that form between particles increases. A premeasured amount of liquid is added to the particles, and the particle-liquid mixture is thoroughly mixed for uniform distribution of liquid before charging the hopper. The discharge rate of wet steel spheres and wet cylindrical steel particles were measured at varying liquid quantities. Figure 3 shows the effect of silicon oil content on the discharge rate of steel particles. The discharge rate decreases upon the addition of a small amount of surface liquid but further increases in surface liquid do not affect the discharge rate.

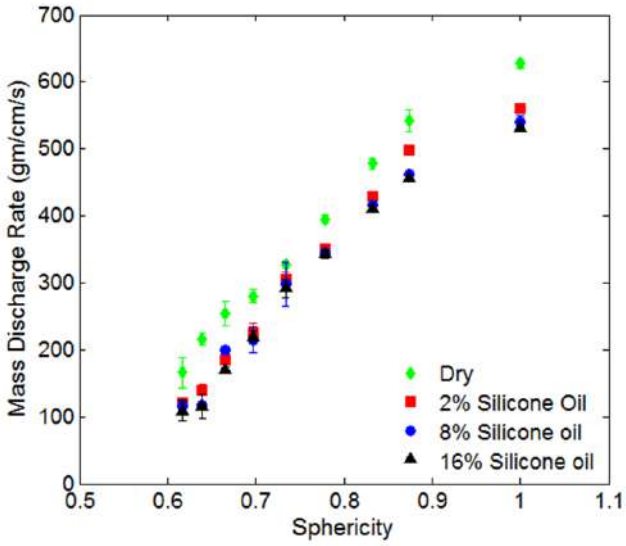

Figure 3. Hopper discharge for varying levels of surface liquid on aspherical particles

References

[1] Guo, Y. and J. Curtis, "Discrete Element Method Simulations for Complex Granular Flows" (Invited), *Annual Review of Fluid Mechanics*, **47**, 21-46 (2015)
[2] Anand A., Curtis, J.S., Wassgren, C.R., Hancock, B.C., Ketterhagen, W.R., Predicting discharge dynamics from a rectangular hopper using the discrete element method (DEM), *Chemical Engineering Science*, **63**, 5821-5830 (2008)
[3] Anand, A., J. Curtis, C. Wassgren, B. Hancock and W. Ketterhagen, "Experimental Study of Wet Cohesive Particles Discharging from a Rectangular Hopper", *I&EC Research*, **54**, 4545-4551 (2015)
[4] Kodam, M., R. Bharadwaj, J. Curtis, B. Hancock, and C. Wassgren, "Cylindrical Object Contact Detection for Use in Discrete Element Method Simulations, Part I – Contact Detection Algorithms", *Chemical Engineering Science*, **65**, 5852-5862 (2010)
[5] Myers, M.E., Sellers, M., Chemical Engineering, Tripos Part 2. Research Project Report, University of Cambridge (1971)
[6] Tangri, H., Y. Guo, and J. Curtis, "Hopper Discharge of Elongated Particles of Varying Aspect Ratio: Experiments and DEM Simulations" *Chemical Engineering Science: X*, 100040 (2019)

LATERAL BOUNDARY INFLUENCE ON TURBULENT BED-LOAD FLOWS FROM REFRACTIVE-INDEX-MATCHED EXPERIMENTS

Hervé Capart *[1] and Wei-Jay Ni [1]
[1]Department of Civil Engineering and Hydrotech Research Institute,National Taiwan University, Taipei, Taiwan

Summary We report experiments aimed at characterizing the influence of lateral boundaries on turbulent bed-load flows. Three types of lateral boundaries are examined: symmetric smooth walls, symmetric rough walls, and an asymmetric half-channel configuration featuring an erodible bank on one side and a smooth wall on the other. In all cases, an erodible loose bed is considered. To image the internal structure of the resulting flows, refractive-index-matching and laser scanning are used, making it possible to measure both the liquid and granular flux distributions over the flow cross-section.

INTRODUCTION

For simplicity, most detailed experiments on turbulent bed-load flows conducted so far have focused on the vertical flow structure. In particular, such experiments have documented the transition from a liquid-dominated upper flow layer to the loose static bed, across a bed-load layer featuring strong concentration and velocity gradients (Sumer et al. 1996; Capart and Fraccarollo, 2011; Revil-Baudard et al., 2015). To achieve quasi-two-dimensional flows, symmetric channels with smooth sidewalls are typically used, and measurements acquired either near the wall, or inside the flow using optical or acoustic methods.

In industrial and natural flows, however, lateral boundaries are typically more complex, and may produce strong gradients in both the lateral and vertical directions. For rigid walls, this will occur if the lateral boundaries are sufficiently rough. Many natural channels, moreover, feature erodible banks that will likewise produce lateral flow variations over the channel width. To investigate such effects, we conducted experiments with different lateral boundaries, examining how they influence the cross-sectional flow and transport distributions.

EXPERIMENTAL METHODS

As illustrated in Fig. 1, we conduct experiments in a sloping open channel, alimented with constant liquid and granular discharges. To gain optical access to the interior of the three-dimensional flows, we use transparent liquid and granular materials with closely matched refractive indexes. The mixture then becomes optically homogeneous, making it possible to observe the undistorted shapes, positions and motions of grains or tracer particles inside the medium. For the present experiments, we adopt the refractive index matched liquid-solid pair proposed by Haam et al. (2000), which we used successfully in previous work (Ni and Capart, 2015, 2018). The transparent liquid is the specialty organic liquid para-cymene, while the solid grains are spheres made from transparent PMMA (polymethyl metacrylate).

To measure the resulting flows, laser scanning is conducted using different orientations of the laser sheet, respectively parallel to the (x,y), (x,z), and (y,z) planes (see Fig. 1 for the axis directions), slowly translating the laser sheet in the normal direction. The (x,z) and (x,y) laser scans make it possible to capture the different components of the liquid and granular velocities, using particle tracking velocimetry. The (y,z) laser scans, on the other hand, capture grain crossing events from which both the granular concentration and granular flux can be estimated. Averaged over the channel cross-section, the resulting measurements produce maps of velocities, concentration and flux intensity at sub-grain diameter resolution (for details regarding the imaging algorithms and averaging methods, see Ni and Capart, 2015 and Ni, 2018).

EXPERIMENTAL RESULTS

Results will be compared for three types of lateral boundaries: symmetric smooth walls, symmetric rough walls, and an asymmetric half-channel configuration featuring an erodible bank on one side and a smooth wall on the other. In all cases, an erodible loose bed is considered. Results for symmetric smooth walls have been reported previously (Ni and Capart 2018), and correspond to quasi-two-dimensional flows with limited near-wall effects.

For symmetric rough walls, however (see Fig. 1), both the granular and liquid flux intensity become strongly non-uniform over the width. The bed-load transport layer acquires a lenticular shape, with a thickness that grows with distance from the wall. The liquid flux distribution, likewise, is strongly affected, with maximas occurring below the free surface near the rough walls. Near the walls, similar intensities are observed for the lateral and vertical gradients.

For the asymmetric half-channel configuration, experiments are more complex because erosional bank migration produces unsteady flows. The granular flux, moreover, appears to play a significant role in destabilizing the bank. At different stages during the resulting evolution, the liquid and granular fluxes again exhibit strong lateral variations. Although ideally the smooth sidewall would represent a symmetry plane of an equivalent full channel configuration, some wall effect are present, hence the effective symmetry plane is displaced into the channel some distance away from the wall.

*Corresponding author. E-mail: hcapart@yahoo.com.

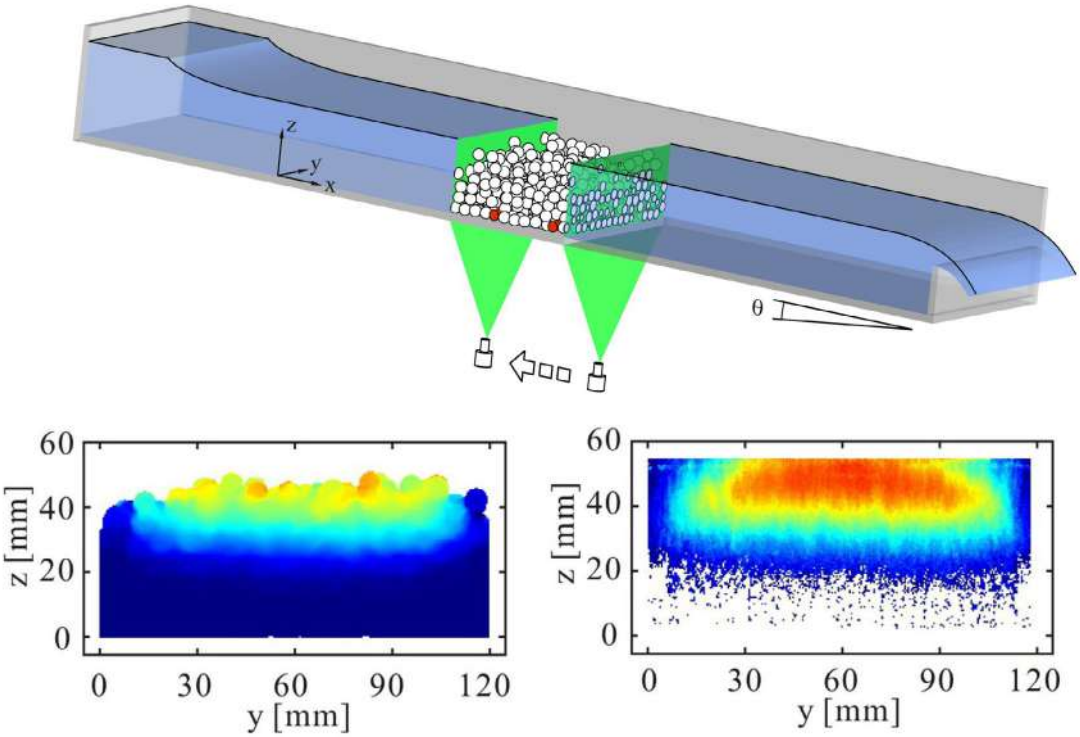

Figure 1: Principle and capabilities of the experimental approach. Top: laser scanning across a three-dimensional flow volume made transparent by using refractive-index-matched liquid and solid materials. Bottom: measurements of the granular (left) and liquid flux distribution (right) over the flow cross section (here for symmetric rough walls).

CONCLUSIONS

Using refractive-index-matching and laser scanning, we obtain detailed cross-sectional maps of liquid and granular fluxes in turbulent bed-load flows with different lateral boundaries. The results show that lateral boundaries exert a very significant influence on the flow and transport distributions. Unlike smooth rigid walls, rough rigid and erodible boundaries produce lateral and vertical gradients of similar strengths.

References

[1] Sumer B. M., Kozakiewicz J., Fredsøe J., Deigaard R. Velocity and concentration profiles in sheet flow layer of movable bed. *J. Hydr. Eng.* **122**: 549–558, 1996.

[2] Capart H., Fraccarollo L. Transport layer structure in intense bed-load. *Geophys. Res. Lett.* **38**: L20402, 2011.

[3] Revil-Baudard T., Chauchat J., Hurther D., Barraud P.-A. Investigation of sheet-flow processes based on novel acoustic high-resolution velocity and concentration measurements. *J. Fluid Mech.* **767**: 1–30, 2015.

[4] Haam S. J., Brodkey R. S., Fort I., Klaboch L., Placnik M., Vanecek V. Laser Doppler anemometry measurements in an index of refraction matched column in the presence of dispersed beads: Part I. *Int. J. Multiphase Flow* **26**: 1401–1418, 2000.

[5] Ni W.-J., Capart H. Cross-sectional imaging of refractive-index-matched liquid-granular flows. *Exp. Fluids* **56**(8): art. no. 163, 2015.

[6] Ni W.-J., Capart H. Stresses and drag in turbulent bed load from refractive index-matched experiments. *Geophys. Res. Lett.* **45**(14): 7000-7009, 2018.

[7] Ni W.-J. Turbulent bed-load made transparent: internal flow structure from refractive-index-matched experiments. *PhD thesis*, National Taiwan University Civil Eng. Dept, Taipei, 2018.

SPONTANEOUS CLUSTERING IN A SUBMONOLAYER OF GRAINS UNDER HORIZONTAL SHAKING

Song-Chuan Zhao* [1] and Thorsten Pöschel[2]
[1]State Key Laboratory for Strength and Vibration of Mechanical Structures, School of Aerospace Engineering, Xi'an Jiaotong University, Xi'an 710049, China
[2]Institute for Multiscale Simulation, Friedrich-Alexander-Universität, Caustra e [3], 91058 Erlangen,Germany

Summary Granular matters often display clustering instability, a signature of its non-equilibrium state. Nevertheless, the mechanism leading to clustering varies. We study here the spontaneous clustering of a submonolayer of beads under horizontal circular shaking. The clustering is triggered by increasing the oscillation amplitude. It turns out that the observed clustering is due to the formation of density wave, which travels along with the oscillation at the same frequency. The key ingredient of its formation is a type of multiplicative driving resulting from the interplay between the friction between grains and the the frictional driving of the substrate. A phenomenological model shows that the instability arises by increasing the oscillation amplitude and further captures the non-monotonic dependence of the transition amplitude of the clustering on the global density of the system.

BACKGROUND

Owing to the non-equilibrium nature granular materials exhibit self-organization across orders of magnitude, from gold panning to astrophysics. Those phenomena are largely represented by the clustering instability, non-uniform density distribution developing out of an initially homogeneous state. Clustering has been observed both in freely cooling granular gas and in driven systems. Such a collective behavior leads to pattern formation, segregation and phase separation. Though clustering of granular matter exhibits some generic features across various systems, there are peculiarities in any particular system that need to be taken into account, *e.g.,* the type of energy input. In this paper we studied a submonolayer of beads under horizontal oscillations. The constant frictional driving of the substrate distinguishes it from the vertical vibrated system. Strip-like pattern was reported in such a system subjected to one-dimensional oscillation [1]. Under two-dimensional oscillation liquid-solid transition was found, and the solid phase is reached by increasing the oscillation amplitude [2], an example of 'freezing by heating'. However, the mechanism of the spontaneous clustering in such a system is still unknown. Here, we untangle this issue by combining experiments, a phenomenological model and molecular-dynamic simulations.

EXPERIMENTS AND PHENOMENOLOGY

For the system studied here, there are at least three aspects of experimental parameters: the oscillation strength, the global packing density and the ratio of the grain size to that of the container. For simplicity, we first constraint the parameter as follows, and in the end we will expand the parameter space and discuss the consequences. The submonolayer consists of $N_{tot} = 6930$ polydisperse ceramic beads of which the range of diameter is between 0.6 mm to 0.8 mm. The mean diameter is used to denote the grain size $d_g = 0.7\mathrm{mm}$. The grains sitting on a bottom plate are confined by a circular side wall with diameter $D = 82\mathrm{mm}$. The global packing density is given by the area ratio $\phi_0 = N_{tot}(d_g/D)^2$. The inclination of the bottom plate is smaller than 0.02 mm/m. The container is subjected to anti-clockwise circular oscillation in the x-y plane. The oscillation frequency is fixed at 5 Hz. The oscillation amplitude A is varied in the range between 5 mm and 13 mm. Note that here the amplitude represents the diameter of the circular oscillation path (figure 1c). In this range of agitation grains rarely jump over each other, and thus the packing remains two-dimensional. The system is illuminated by a LED panel from bottom, and the dynamics are captured by a high speed camera at the top. The camera is fixed in the laboratory frame of reference. Without specifications the analysis in the following is done in this frame for reference.

In figure 1 snapshots of the packing at two oscillation amplitudes are shown. For $A = 5\mathrm{mm}$ the packing is homogeneous (figure 1a). By increasing A to 11 mm a cluster of grains can be seen at the center (figure 1c). The observed clustering is very sensitive to the oscillation amplitude. The dense area is destroyed within 10 cycles after decreasing A from 11mm to 10mm. This transition is thus second-order like. This highlights the uniqueness of the clustering in the current work with respect to that in a vertically vibrated monolayer [3]. There, the clustering is triggered by decreasing the oscillation strength after fluidization, and the cluster consists of low-velocity particles. Furthermore, in our experiments the dense area appears to move anti-clockwisely, the same direction as the oscillation, and seems to be in phase with the oscillation.

In figure 1b there are dense areas also along periphery of the packing. Those dense boundary layers may be sustained over cycles and moves in a counter-intuitive way, opposite to the oscillation (not shown here). Nevertheless, its formation is not surprising. The rotational degree of freedom of grains reduces the linear momentum transfer from the substrate. Therefore, grains move more slowly than the container, and those close to the side wall is condensed during certain oscillation phases. In contrast, the spontaneous clustering at the center of the packing can not be explained by the same reason, as there are no obvious condensers at the center.

*Corresponding author. E-mail: songchuan.zhao@xjtu.edu.cn

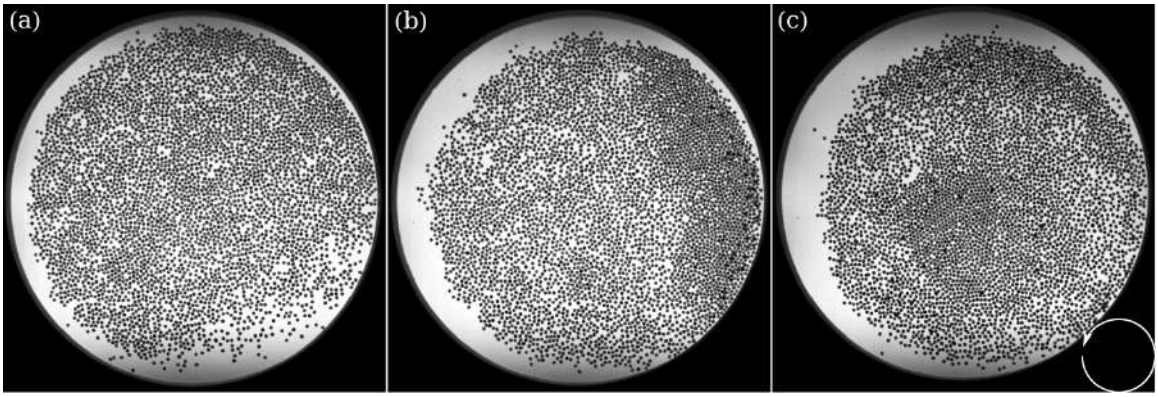

Figure 1: Snapshots of the packing for two oscillation amplitudes: (a) $A = 5\mathrm{mm}$, (b) $A = 8\mathrm{mm}$ and (c) $A = 11\mathrm{mm}$. A dense area can be seen at the center for (c). The white circle at the bottom right indicates the anti-clockwise oscillation path in scale.

THE UNDERLYING MECHANISM OF THE CLUSTERING

To unravel its formation mechanism we perform particle tracking and look into the dynamics for clues. We follow the motion of one grain in the central region. Its neighborhood experiences periodic compression and dilation. It is remarkable that the speed of the grain v_g follows the same periodic pattern and shows a positive correlation with ϕ_{loc}, *i.e.*, a grain in a denser neighborhood tends to move faster. This feature, the dependence of the speed of individual particles on the local density of the local neighborhood remains for $A < 11\mathrm{mm}$ as well, though clustering is not observed.

Considering the continuity equation, it is readily to show that as an increasing function of ϕ_{loc} the velocity $v(\phi_{loc})$, the advection term, promotes the formation of density shocks, similar to Burgers' equation. On the other hand, the finite transition amplitude of the clustering ($A \geq 11\mathrm{mm}$) suggests that the collisions between grains introduce an equivalent term of pressure and competes with the advection term. In addition to the continuity equation, we introduce a phenomenological equation of the velocity field incorporating these two aspects. The stability analysis of the model shows that the uniform flow state becomes unstable against density fluctuations when increasing A beyond the transition amplitude A_c, and the density wave develops into the clustering. This corresponds to the observed 'freezing by heating'. Furthermore, according to the model the transition amplitude is expected to be non-monotonic which is indeed observed in experiments.

The key ingredient promoting the clustering is the dependence of the speed of grains on the the local density. Why such a dependence exists? We believe that it is a consequence of the interplay between the friction between grains and that between grain and the substrate. μ_{gg} and μ_{gs} denote the friction coefficients of the former and the latter respectively, and F_{gg} and F_{gs} are the corresponding frictional forces. Upon agitation F_{gs} accelerates not only the linear momentum but also the angular momentum of individual grains. It has been shown that the faster a grain rolls, the slower its linear speed is [1]. On the other hand, during collisions F_{gg} counteracts the rolling of grains which in turn increases the moment of the inertia with respect to F_{gs} and effectively enhances the linear momentum transfer. F_{gg} is expected to increase with ϕ_{loc} and A. Therefore, grains tend to move faster in denser areas and/or under stronger agitations. This results into the observation where v_g increases with ϕ_{loc} and A. To examine this speculation molecular-dynamic simulations are performed. For a given μ_{gs} and A, the clustering is suppressed by decreasing μ_{gg}.

References

[1] Krengel D., Strobl S., Sack A. and Heckel M. and Pöschel T. Pattern Formation in a Horizontally Shaken Granular Submonolayer. *Granul Matter* **15**: 377-387, 2013

[2] Aumaître S., Schnautz T., Kruelle C. A. and Rehberg I. Granular Phase Transition as a Precondition for Segregation. *Phys. Rev. Lett.* **90**: 114302, 2003

[3] Olafsen J. S. and Urbach J. S. Clustering, Order, and Collapse in a Driven Granular Monolayer. *Phys. Rev. Lett.* **81**: 4369, 1998

DYNAMICS OF A HORIZONTALLY WIGGLING INTRUDER IN A DENSE GRANULAR MEDIUM

Bitang Kwrung Tripura[1], Sonu Kumar[1], and Katha Anki Reddy * [1]
[1]Department of Chemical Engineering, Indian Institute of Technology Guwahati, Guwahati 781039, India

Summary We have investigated the effect of an intruder object(IO) shape, and its orientation has on the rise or sink when oscillated horizontally within a granular medium. For the simulations, the discrete element method (DEM)[1] has been used. We have considered six different shapes in our study: a square, two rectangle with different aspect ratio , a disc, an equilateral triangle, and an inverted equilateral triangle. The intruders were oscillated at a varying range of oscillating amplitude(A) and frequency(f). With time the oscillating IO settles down at a specific position within the granular media depending upon the A and f. The rise is seen from its initial position for the intruders at higher oscillating frequencies and the opposite at lower frequency for most of the IO for a given A. It is observed that there is a minimum amplitude(A_{min}) below which the position of the IO remains unaltered even after varying the f. The maximum amount of positive rise is observed for square and inverted triangle shapes. The orientation of the IO plays a significant role in its rise or sink within the media. The two triangles having different orientations have shown to have completely opposite rise behavior to each other. With the equilateral triangle showing negative lift at higher amplitude($A > 1d$) for all the f, while the inverted equilateral triangle has shown to have a positive lift at higher amplitude($A > 1d$) in all the cases. The average drag force calculated is seen to remain the same for all the shapes at the same phase angle.

INTRODUCTION

Granular material is a collection of discrete solid particles that show the property of both solid and fluid depending upon its volume fraction[2]. They can be seen in various forms in nature, ranging from sand particles in the desert to a group of floating iceberg in the ocean. It is one of the most manipulated materials in the industry after water. In recent years studies were performed to understand the dynamics of granular material in various configurations [3, 4, 5]. Many of these studies were aimed at understanding the organizational dynamics of granular material when a disturbance is applied in the system. In our work, we have highlighted one such problem where the movement of a self-energized intruder object oscillating horizontally within the granular media is studied. Such dynamics can be helpful to understand problems such as the brazil nut effect[6] and the use of wave like motion by the sand lizard[7] for its movement when under the surface in desert.

SIMULATION METHODOLOGY

A two-dimensional simulation system is considered for the study with dimensions of 300d×200d along x and y-axis, as shown in Fig. 1, where d is the mean particle diameter. The intruder object(IO) is placed at a depth of h=105d from the top free surface and then oscillated at varying A and f. We have employed Discrete element method(DEM)[1] for the

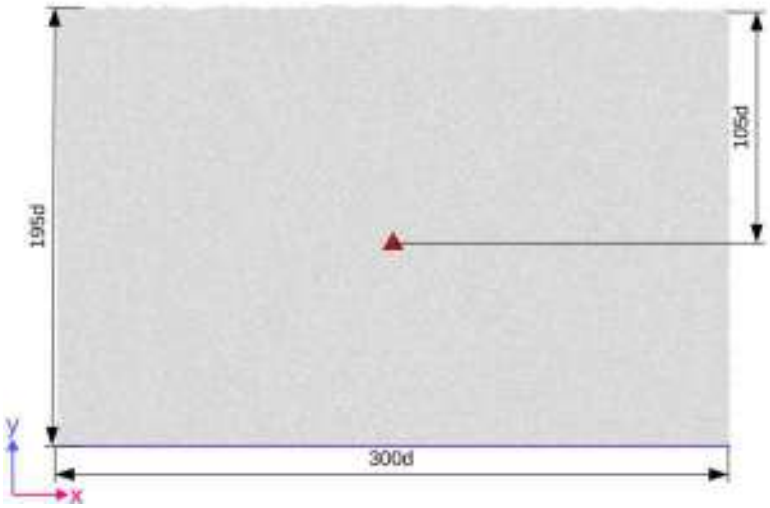

Figure 1: Initial configuration for one of the shapes (equilateral triangle) at a depth $h = 105d$. The x-direction is periodic while y-direction is confined by a wall at $y = 0$ made of particles of size $1d$(blue particles) while the top surface is free to move

simulation i.e used widely to simulate granular materials. While for particle interaction contact force model[8] is applied. The normal and tangential forces experienced by the interacting particles are given from the force model:

$$F_n = \sqrt{(R_{eff}\delta)}(K_n\delta - m_{eff}\gamma_n v_n) \quad (1)$$

*Corresponding author. E-mail: anki.katha@iitg.ac.in

$$F_t = -min(\mu F_n, \sqrt{(R_{eff}\delta)}(K_t\Delta)s_t + m_{eff}\gamma_t v_t) \quad (2)$$

RESULTS

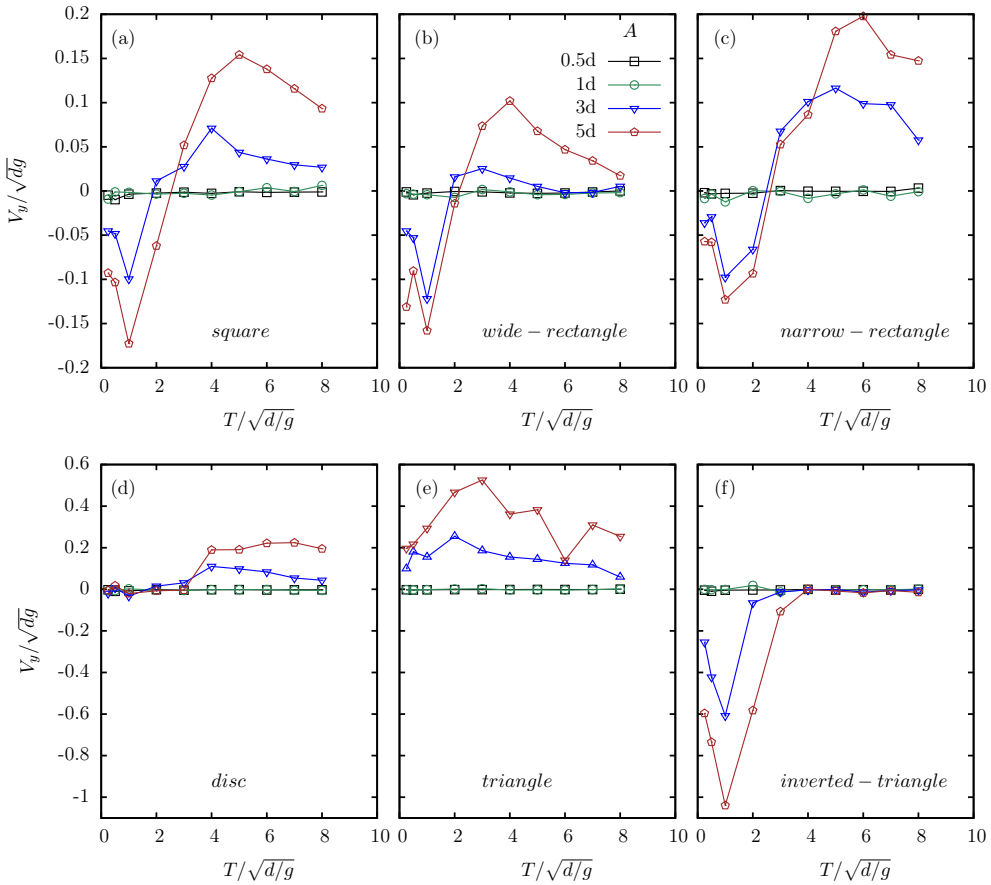

Figure 2: The rise rate(V_y) of the intruder object has been shown as a function of its oscillating time-period(T) for all the amplitude for (a) square (b) wide-rectangle and (c) narrow-rectangle(d) disc (e) triangle and (f) inverted triangle shaped intruder object.

CONCLUSIONS

Due to its continues oscillation, there was a rise or sink observed for the IO from its initial position within the granular medium for all the shapes. It was observed that for oscillation amplitude of 1d or less than it there was negligible change from its initial position of oscillation for all the IO. The maximum amount of rise from its initial position was observed for square and inverted triangular shapes. Some interesting outcome was also seen for the two triangular shapes used. With the equilateral triangle showing negative lift at higher amplitude($A > 1d$) for all the oscillated frequencies, while the inverted triangle has shown completely opposite result showing positive lift at higher amplitude($A > 1d$) in all the cases. The shape and orientation of the intruder object is seen to have an important role in the rising and sinking.

References

[1] Peter A Cundall and Otto DL Strack. A discrete numerical model for granular assemblies. *geotechnique*, 29(1):47–65, 1979.
[2] Heinrich M Jaeger, Sidney R Nagel, and Robert P Behringer. Granular solids, liquids, and gases. *Reviews of modern physics*, 68(4):1259, 1996.
[3] K Wieghardt. Forces in granular flow. *Mechanics Research Communications*, 1(1):3–7, 1974.
[4] Junfei Geng and Robert P Behringer. Slow drag in two-dimensional granular media. *Physical review E*, 71(1):011302, 2005.
[5] Yang Ding, Nick Gravish, and Daniel I Goldman. Drag induced lift in granular media. *Physical Review Letters*, 106(2):028001, 2011.
[6] Matthias E Möbius, Benjamin E Lauderdale, Sidney R Nagel, and Heinrich M Jaeger. Brazil-nut effect: Size separation of granular particles. *Nature*, 414(6861):270, 2001.
[7] Ryan D Maladen, Yang Ding, Paul B Umbanhowar, Adam Kamor, and Daniel I Goldman. Mechanical models of sandfish locomotion reveal principles of high performance subsurface sand-swimming. *Journal of The Royal Society Interface*, 8(62):1332–1345, 2011.
[8] Nikolai V Brilliantov, Frank Spahn, Jan-Martin Hertzsch, and Thorsten Pöschel. Model for collisions in granular gases. *Physical review E*, 53(5):5382, 1996.

QUASISTATIC BEHAVIOUR OF LOOSE COHESIVE GRANULAR MATERIALS: A NUMERICAL STUDY

Walid Lammali[1], Vinh-Du Than[1], Anh-Minh Tang[1], and Jean-Noël Roux * [1]
[1]Lab. Navier, Univ. Gustave Eiffel, Ecole Nationale des Ponts et Chaussées, CNRS, Champs-sur-Marne, France

Summary The quasistatic mechanical behaviour of model cohesive granular materials is studied by discrete, grain-level (DEM) simulations. Representative (periodic) samples of 4000-9000 spherical beads of diameter d, for which elastic-frictional contacts are endowed with capillary or van der Waals cohesion, are assembled in loose states (solid fraction Φ down to 0.3). The mechanical response is largely determined by the reduced pressure $P^* = Pd^2/F_0$ comparing applied stress P to tensile strength F_0 in adhesive contacts. In isotropic or oedometric compression, Φ irreversibly increases with P^* in range $0.01 \leq P^* \leq 10$, while the apparent internal friction in triaxial compression is strongly enhanced, compared to the cohesionless case. Relations of such macroscopic behaviours to initial state, mechanical parameters and microstructure are discussed.

INTRODUCTION

While discrete-element (DEM) simulations have repeatedly been applied to investigate the quasistatic mechanical properties of assemblies of cohesionless grains [1], the behaviour of cohesive granular materials, which may form very loose structures [2] remains virtually unexplored. We present a DEM study of such a model material, made of cohesive spherical beads, initially assembled at low density.

MODEL AND SAMPLE PREPARATION

We consider spherical beads of diameter d, interacting in their contacts by elastic-frictional forces. We use the elasticity of glass and friction coefficient $\mu = 0.3$ in the contacts. Attractive forces press contacting particles against one another, which we model with a force law approximating the capillary attraction in pairs joined by a bridge formed by a wetting liquid, taking maximum value $F_0 = \pi\Gamma d$ at contact (Γ being the liquid surface tension). A meniscus of volume V_m is assumed to form as soon as grains touch, and a decreasing force subsists in receding pairs as long as the separation distance does not exceed $V_m^{1/3}$. The V_m-independent F_0 value given above holds for small V_m. The limit of very small V_m, then devoid of hysteresis, might be regarded as a simplified model for van der Waals attraction (Γ now representing a solid surface tension). The contact laws are described in detail in Refs. [3, 2]. Despite the simplifications, quantitative agreement was obtained with some experiments on polystyrene beads in simple shear flow [4, 5]. All results are presented in dimensionless form and are therefore valid for arbitrary materials. An essential dimensionless control parameter in these cohesive systems is the reduced pressure $P^* = Pd^2/F_0$: cohesive forces dominate and stabilize loose structures at small P^* and become negligible for large P^*. Reproducible and consistent results are obtained for samples of N beads, with $N = 4000$ or $N = 8788$, with periodic boundary conditions. Loose solid aggregates form by ballistic aggregation at constant solid fraction Φ_0, their structure depending on initial velocities (Fig. 1): better coordinated structures form with larger velocities, but with larger density inhomogeneities.

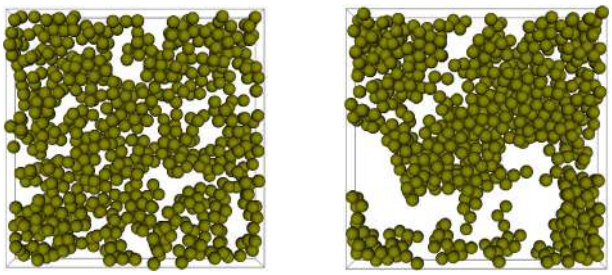

Figure 1: Aspect of aggregated structures formed at solid fraction $\Phi_0 = 0.3$ (front views of slabs of thickness $3d$), with small (left) and large (right) initial agitation velocity.

RESPONSE TO ISOTROPIC OR OEDOMETRIC COMPRESSION

Upon increasing P^* in quasistatic compression, such loose structures irreversibly collapse, and a quasilinear variation of void ratio $e = -1 + \frac{1}{\Phi}$ with $\log P^*$ is observed in some range. As shown in Fig. 2 this behaviour is influenced by the initial structure. We also investigated its dependence on Φ_0 and possible rolling resistance at contacts (also affecting the initial structure).

*Corresponding author. E-mail:jean-noel.roux@univ-eiffel.fr

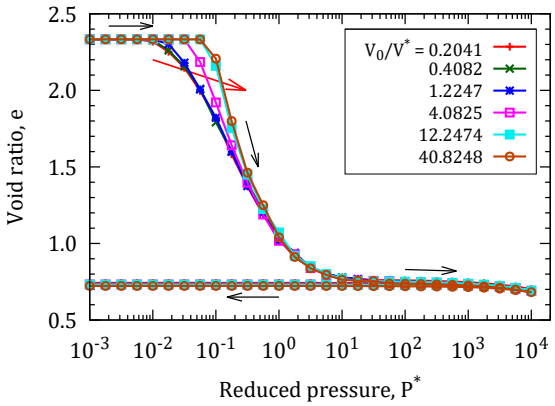

Figure 2: Compression curves showing void index versus $\log P^*$ in isotropic compression for different values of initial agitation velocity V_0. Note irreversibility (arrows) in pressure cycle.

TRIAXIAL COMPRESSION TESTS

Fig. 3 shows how the cohesion increases the deviator stress to lateral stress ratio (the cohesionless value being retrieved for the larger P^* values). The approach to the critical state plateau is delayed for small P^* while the density increases through a large contractance interval of strain.

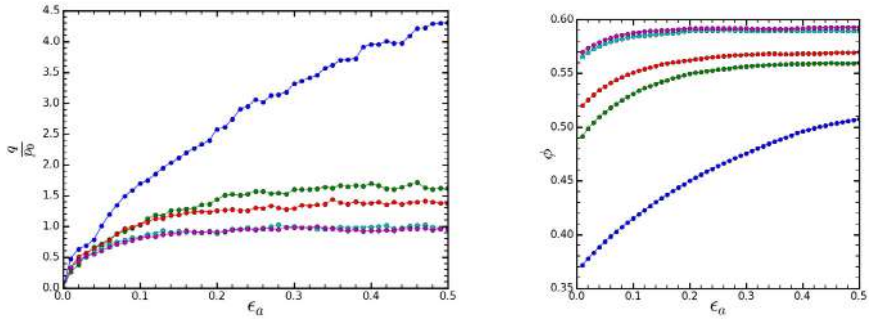

Figure 3: Results of triaxial compression tests: deviator normalized by constant lateral stress (left), and solid fraction (right) versus axial strain. Different initial P^* values: 0.1 (dark blue), 0.62 (green), 1 (red), 6.23 (light blue), 10 (pink).

PERSPECTIVES

We are currently systematically investigating the triaxial response of the model material. In parallel, the considerably greater wealth of microstructures available to cohesive systems is being characterized. Generic features should emerge at both scales, applying to a variety of materials, from clays to powders and colloidal gels.

References

[1] F. Radjaï and F. Dubois, editors. *Discrete-element modeling of granular materials*. Wiley, 2011.

[2] V.-D. Than, S. Khamseh, A.-M. Tang, J.-M. Pereira, F. Chevoir, and J.-N. Roux. Basic Mechanical Properties of Wet Granular Materials: A DEM Study. *ASCE Journal of Engineering Mechanics*, 143(SI1):C4016001, 2017.

[3] S. Khamseh, J.-N. Roux, and F. Chevoir. Flow of wet granular materials: a numerical study. *Phys. Rev. E*, 92:022201, 2015.

[4] M. Badetti, A. Fall, F. Chevoir, and J.-N. Roux. Shear strength of wet granular materials: Macroscopic cohesion and effective stress. *European Physical Journal E*, 41:68, 2018.

[5] M. Badetti, A. Fall, D. Hautemayou, S. Rodts, and J.-N. Roux. Rheology and microstructure of unsaturated wet granular materials: Experiments and simulations. *J. of Rheology*, 62:1175–1186, 2018.

EULERIAN MULTI-PHASE FLOW MODELING FOR GRAIN-SIZE SEGREGATION IN BEDLOAD TRANSPORT

Hugo Rousseau* [1], Remi Chassagne[1], Julien Chauchat[2], and Philippe Frey[1]
[1]University of Grenoble Alpes, INRAE, UR ETNA, 38000 Grenoble, France
[2]University of Grenoble Alpes, LEGI, G-INP, CNRS, Grenoble, France

Summary In this contribution we develop a Eulerian multi-phase flow model for bidisperse grain size-segregation in bedload transport. The closures used for the particle-particle drag and buoyancy forces are improved using recent advancement in the understanding of particle-particle interaction forces for a large particle in a bath of small. The two-phase flow model is then validated against recent DEM simulations of bidisperse grain-size segregation in bedload transport ([1]). The new model reproduces accurately the segregation dynamics in bedload transport and provides a better understanding of the segregation and remixing fluxes.

Rivers carry sediments that have a wide grain size distribution. This can lead to the grain size segregation phenomenon which has huge consequences on sediment fluxes. Among the various segregation processes, kinetic sieving is a key mechanism in bedload transport: the moving particles on top of the granular layer act as a random fluctuating sieve in which small particles are more likely to percolate down under the action of gravity than coarse particles. Accurate modeling of this phenomenon with continuous equations is a key step to upscale in sediment transport models.
Using the mixture theory, [4] and [2] developed continuous equations for bidisperse segregation. Based on the momentum balance of small particles, a simple advection-diffusion equation for the segregation of small particles was derived which makes it possible to explicit an advection and a diffusion coefficients. However they do not depend immediately on physical parameters of the granular flow.

Recently, Chassagne and co-workers [1] investigated grain-size segregation in bedload sediment transport using a coupled fluid-Discrete Element Method (DEM). The authors results showed that the small particles, initially at the bed surface, percolates through the bed made of large particles as the logarithm of time as a layer with a constant thickness. They developed an analytical solution for the space-time evolution of the concentration depth profile of small particles which shows that the advection and diffusion coefficients of the advection-diffusion model are power laws of the inertial number. However the link with the grain-scale physics and the actual formulation of the particle-particle forces is still lacking.

Using DEM simulations Guillard and co-workers [3] showed that the segregation force applied on a large intruder in a bath of small particles can be seen as a buoyancy force proportional to the pressure and the shear stress gradient. Also using DEM, [5] demonstrated that the drag force experienced by a denser particle in a sheared granular flow can be recasted as a Stokesian drag force proportional to the granular viscosity with a linear dependency to the relative velocity. However, the proportionality coefficient might not be 3 as in the classical Stokes drag law. Based one these new results a force balance for a single large particle in a dense granular flow made of small particles is infered in figure 1.

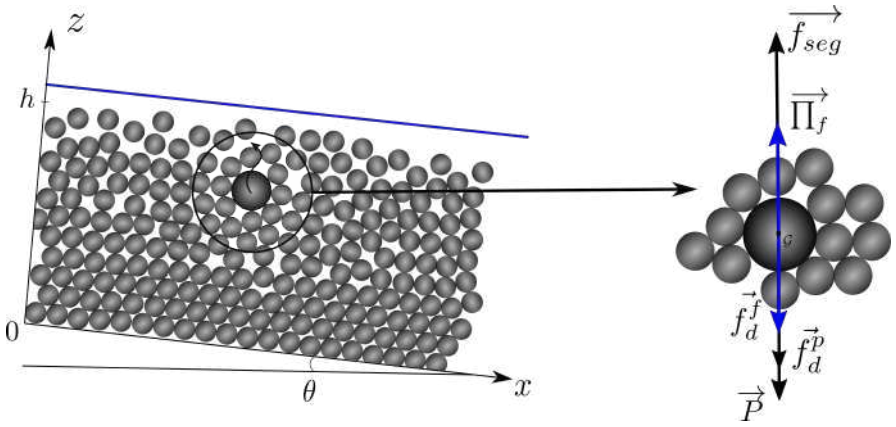

Figure 1: Forces acting on a large particle embedded in small ones. $\vec{\Pi_f}$ is the buoyancy due to the fluid and $\vec{f_{seg}}$ is the segregation force from [3]. The drag forces $\vec{f}_d^p$ and $\vec{f}_d^f$ are respectively due to the interaction with small particles [5] and the fluid.

Using the formulation of the forces presented above, a Eulerian multi-class model is developed to describe grain-size segregation in bed-load transport. The system of partial differential equation in the vertical direction is solved using a 1D Finite Volume Method for the concentration and the velocity of the fluid and of the large and small particles. The

*Corresponding author. E-mail: hugo.rousseau@inrae.fr

numerical results for the small particles are compared with the coupled-fluid DEM simulations from [1] in terms of space-time diagram for the concentration of small particles (see figure 2). It appears that the multi-class model based on the forces proposed by [3] and [5] reproduced accurately the logarithmic layer descent of small particles with time. However figure 2 shows that the thickness of the layer is different from DEM. Possible origins are the calibration of the segregation force because [3] developed it for disks or the calibration of the proportionality coefficient in the solid drag force of [5]. A complete sensitivity analysis on these parameters will be presented. Then, using the advection diffusion equation, an improved formulation inspired from DEM will be proposed.

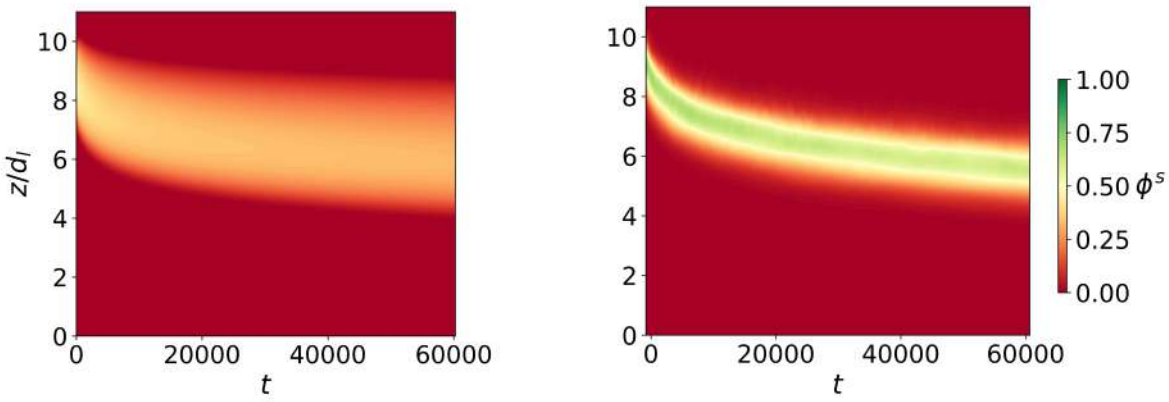

Figure 2: Concentration of small particles ϕ^s with the time in the bed. Left figure is the concentration obtained with the multi-phase model. Right figure shows the DEM results of [1].

References

[1] Chassagne R., Maurin R., Chauchat J., and Frey P. Discrete and continuum modeling of grain-size segregation during bedload transport. *J. Fluid Mech.*. 2020 (in revision).

[2] Gray J. M. N. T., and Chugunov V. A. Particle-size segregation and diffusive remixing in shallow granular avalanches. *J. Fluid Mech.*. 569: 365-398, 2006.

[3] Guillard F. Forterre Y., and Pouliquen O. Scaling laws for segregation forces in dense sheared granular flows. *J. Fluid Mech.*. 807, R1, 2016.

[4] Thornton A. R., Gray J. M. N. T., and Hogg A. J. A three-phase mixture theory for particle size segregation in shallow granular free-surface flows. *J. Fluid Mech.*. 550: 125, 2006

[5] Tripathi A., and Khakhar D. V. Numerical simulation of the sedimentation of a sphere in a sheared granular fluid: a granular stokes experiment. *Phys. Rev. Lett.*. 107, 108,001, 2011

GENERALIZATION OF SHIELDS CRITERION FOR WEAKLY CEMENTED GRAINS

Pierre Philippe*[1], Zeyd Benseghier[1], Florian Brunier-Coulin[2], Li-Hua Luu[1], Pablo Cuéllar[3], and Stéphane Bonelli [1]
[1]RECOVER, INRAE Aix Marseille Univ., Aix-en-Provence, France
[2]Irph , Aix Marseille Univ., Marseille, France
[3]BAM, Federal Institute for Materials research and Testing, Berlin, Germany

Summary Despite many usual geological or industrial processes include erosion of sediments by a superficial fluid flow, there is still a lack of fundamental knowledge about erosional processes, notably as regards the impact of internal cohesive or adhesive stresses. This contribution focuses on the surface erosion by a submerged impinging jet flow and investigates more specifically the influence of cohesion by solid bonding between grains, i.e. cemented granular soils. The methodology relies on both laboratory tests with artificially bonded granular materials and numerical simulation through DEM-LBM calculations. The critical erosion onset condition obtained from our experimental and numerical results is proved to be satisfactorily accounted for through a new generalized form of the usual Shields criterion based on a common definition of a cohesion number from yield tensile values.

MOTIVATION

The ubiquitous occurrence of sediment erosional processes in natural or industrial contexts calls for an accurate prediction of soils resistance to surface erosion by a fluid flow. Following the pioneering work of A. F. Shields [1], erosion of strictly non-cohesive materials (sand, small pebbles, etc…) is interpreted as an individual process whose onset can be deduced from a critical value of the dimensionless Shields number Sh_0, defined as the ratio between the fluid shear stress exerted by the fluid flow at the sediment bed and the buoyant weight of a particle. This critical value varies by less than one order of magnitude according to the particle shear Reynolds number Re_τ and lies approximately along the so-called Shields curve. The complexity grows substantially for cohesive materials, such as benthic sediments, clayey soils or cemented calcareous sands. Indeed, internal attractive forces between particles induce more collective processes during erosion that preclude the previous scheme and consequently discard the related Shields approach.

However, for rather weakly cohesive soils, several attempts to generalize the Shields number have been proposed in the literature and rely notably on a comparison between a characteristic cohesive force and the particle's buoyant weight, thus defining a dimensionless cohesion number often denoted granular Bond number Bo_g [2]. The present contribution continues this approach by extending the applicability of the Shields criterion for the case of weakly cemented granular materials based on both experimental and numerical results in the specific situation of soil's erosion by a submerged impinging jet flow.

METHODOLOGY

In this study, we specifically address surface erosion of soil samples caused by a submerged impinging jet which is a standard experimental test, called Jet Erosion Test (JET), and enables quantifying soil's resistance to erosion either in the lab or in situ. Here, a micro-scale investigation is implemented by means of both numerical simulation and experiments. On the one hand, our numerical modelling uses a bi-dimensional coupled fluid-particle flow scheme, based on the Lattice Boltzmann Method (LBM) for the fluid phase combined with the Discrete Element Method (DEM) for the mechanical description of the solid grains interacting by contacts [3]. On the other hand, our experiments are performed on artificially bonded granular materials in an optically adapted device that permits a direct visualisation of the scouring process at the jet apex by means of the refractive index matching technique [4]. More precisely, our artificial soils are constituted of spherical glass beads bonded by solid bridges made of polyurethane resin.

Both investigations aim at assessing and modelling the effect on the resistance to erosion of a granular sample when additional internal stresses exist between the soil's particles. In our artificial cemented soils, this inter-granular cohesion induced by solid bonds, to be further used through the granular Bond number, is either quantified by traction tests or given by a specific model of the solid bond rheology [3].

RESULTS FOR EROSION ONSET CONDITIONS

We implemented similar protocols in the numerical simulations and in the experiments: the mean jet velocity at injection is progressively increased until first detachment of grains at the upper surface of the artificial soil. The critical injection velocity at erosion onset is thus measured with reasonable accuracy. A recent study based on our 2D LBM-DEM modelling in laminar flow regime [5] can provide the maximal bed shear-stress value in 2D and is extended to 3D in the experiments. Then, the bed shear-stress at erosion onset τ_s^* for both our numerical simulations and our experiments can

*Corresponding author. E-mail: pierre.philippe@inrae.fr.

be deduced from the critical injection velocity based on these 2D and 3D expressions, respectively. Figure 1 shows the Shields diagrams obtained during the numerical, where the critical values of the usual Shields number $Sh_0{}^* = \frac{\tau_s{}^*}{\Delta\rho g d}$ (with d the mean grain diameter and $\Delta\rho = \rho_g - \rho_f$ the difference of density between the grains and the fluid) are plotted versus the particle shear Reynolds number $Re_\tau{}^* = \sqrt{\frac{\tau_s{}^*}{\rho_f}}\frac{d}{\nu_f}$ (with ν_f the fluid dynamic viscosity). A very similar graph is obtained with the experimental data.

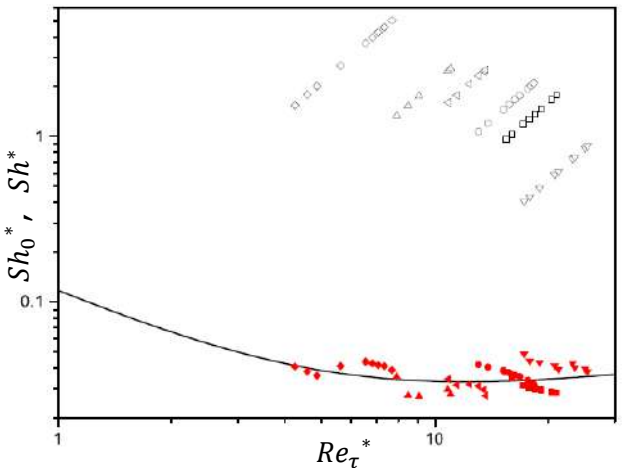

Figure 1. Critical values of the usual Shields number $Sh_0{}^*$ (black open symbols) and generalized Shields number Sh^* (red closed symbols) versus critical friction particular Reynolds number $Re_\tau{}^*$ obtained in the 2D numerical simulations.

As can be seen on these diagrams, the critical values of the usual Shields number $Sh_0{}^*$ increasingly deviate from the Shields curve as $Re_\tau{}^*$ increases, or equivalently as adhesion gets higher. Obviously, the usual Shields number Sh_0 is no more relevant to account for the erosion onset of our cemented granular soils and adhesive stresses must be included in addition to friction and gravitational contributions.

PROPOSAL OF A GENERALIZED SHIELDS CRITERION

We propose here to extend the definition of Sh_0 in a straightforward way by simply adding the adhesive stress, assumed to be directly proportional to the macroscopic yield tensile stress τ_Y, to the buoyant weight. By the end, the following expression is obtained for the generalized Shields number: $Sh = \frac{\tau_s}{\Delta\rho g d + \alpha\tau_Y} = \frac{Sh_0}{1+\alpha Bo_g}$, with introduction of the granular Bond number $Bo_g = \frac{\tau_Y}{\Delta\rho g d}$ and where the empirical coefficient α, expectedly of order 1, can be more precisely determined by linear regression. We found $\alpha_{2D} = 2.69 \pm 0.06$ and $\alpha_{3D} = 2.26 \pm 0.27$ from the numerical and experimental results, respectively. With these values of α, the critical values of the generalized Shields number Sh^* are found to lie approximately on the Shields curve and can consequently advantageously replace the usual $Sh_0{}^*$ in the Shields diagrams of Figure 1. It also manages to reconcile the data for cohesive and cohesion-less materials.

CONCLUSIONS

By means of both a 2D numerical modelling and real 3D experiments of erosion induced by submerged impinging jets on artificial weakly cemented materials, the present study has investigated the critical flow condition at erosion onset and proposed a generalization Sh of the Shields number through addition of cohesion by solid bonding between grains to buoyant weight with the dimensionless granular Bond number Bo_g. This approach is in rather satisfactory agreement with the usual Shields curve and offers a general framework for both cohesion-less (i.e. $Bo_g \sim 0$) and cohesive samples (i.e. $Bo_g > 1$), at least for weakly cemented soils as tested here ($Bo_g < 300$).

References

[1] Buffington J. M. The legend of A. F. Shields. *J. Hydraul. Eng.* **125(4)**: 376-387, 1999.
[2] Nase S.T., Vargas W.L., Abatan A.A., McCarthy J.J. Discrete characterization tools for cohesive granular material. *Powder Technol.* **116**: 214-223, 2001.
[3] Benseghier Z., Cuéllar P., Luu L.-H., Bonelli S., Philippe P. A parallel GPU-based computational framework for the micromechanical analysis of geotechnical and erosion problems. *Comput. Geotechn.***120**: 103404, 2020.
[4] Brunier-Coulin F., Cuéllar P., Philippe P. Erosion onset of a cohesionless granular medium by an immersed impinging round jet. *Phys. Rev. Fluids* **2(3)**: 034302, 2017.
[5] Benseghier Z., Cuéllar P., Luu L.-H., Delenne J.-Y., Bonelli S., Philippe P. Relevance of the free jet model for the soil erosion by impinging jets. *J. Hydraul. Eng.* **141(4)**: 04019047, 2019.

VISUALIZATION AND COMPUTATION ANALYSIS OF GRANULAR FLOW CAUSED BY EMBEDDED RIGID BODY MOTION

Hideto Nonoyama[1], and Yoshihisa Miyata [1]
[1]Department of Civil and Environmental Engineering, National Defense Academy, Yokosuka, Japan

Summary The visualization and computation analysis of granular flow caused by embedded rigid body motion are discussed. The outline of model test apparatus and observation system by using transparent granular for the granular flow are introduced. In a series of model tests, effects of the density of granular media and the position of the embedded rigid body were investigated. The observed granular flows were simulated by finite element analysis with four different constitutive models for granular materials.

INTRODUCTION

The granular flow induced by the embedded rigid body is an important research subject in civil engineering and chemical engineering. Since the actual internal behaviour of granular flow cannot be seen from the outside, only the relationship between the force-displacement relationships acting on the rigid body in the granular media has been discussed in previous researches. The authors have developed an observation system to visualize the granular flow. In the system, transparent granular is used. By applying the refractive index matching, the three-dimensional behaviour of the granular flow can be visualized time-successively. This paper introduces the outline of the observation system, results of the visualization and computation analysis for model tests are shown.

MODEL TEST AND VISUALIZATION TECHNIQUE

Granular materials are opaque to visible light, so the classical way to visualize internal granular flow is utilizing methods with X-rays, computerized tomography, or magnetic resonance imaging cameras. Those are very expensive and difficult to use. Visualization technique with transparent granular has been developed as a means of overcoming these difficulties. Transparent granular are two-phase media made by refractive index matching of granular materials and the fluids to saturate the void of granular. By using this technique and recent computational visualization techniques such as PIV and PTV, internal granular flow can be visualized [Inskander et al., 2015]. The authors applied this technique in this study.

Fig. 1 shows the outline of the model test apparatus in this study. Size of the testing box is 195mm in width, 600mm in height, and 195mm in depth. Two side of the testing box is made from acrylic plates and digital cameras were set at each observation windows. In a series of tests, a fan-shaped steel plate (radius B=50mm) was embedded in the granular media. The plate was pulled out at constant speed as 1mm/min. Quartz glass particles (particle density=2.214 g/cm^3, average diameter=1.0 mm, refractive index 1.4585) were used as transparent granular to made model media. The liquid paraffin was used to fill the void of the granular materials, whose refractive index is the same as quartz glass particles. As shown in Fig.2, tracer particles in granular media can be observed.

Model tests were performed in dense condition (relative density, Dr=80%) and loose condition (Dr=40%) of granular media. For each granular density condition, effect of steel plate depth was investigated. Investigated depth condition was D/B=2 and D/B=4, where D is depth of steel plate from the surface of granular media and B=radius of steel plate.

RESULTS OF MODEL TESTS, VISUALIZATION AND COMPUTATION ANALYSIS

Observed pull-out loads-D/B relationships are shown in Fig.3(a) (b) respectively. As is well known, the higher the density of the granular material and the deeper the embedded rigid body (steel plate), the greater the pull-out resistance of the plate. Observed granular flow in D/B=2 and Dr=40% is shown in Fig.4(a). In this figure, the slip line proposed by Clemnce and Veesaert (1977) is also shown. The granular flow occurs around the plate and does not reach the upper part of the granular media.

The authors analysed the observed granular flow by finite element method. Four kinds of constitutive models were used for a series of analysis such as 1) linear elastic model, 2) nonlinear elastic model, 3) classical elasto-plastic constitutive model based on Drucker-Prager yield function, and 4) subloading model proposed by Hashiguchi (2014), respectively. Model parameters were determined by triaxial compression tests for transparent granular sample in Dr=40, 80% under confining pressures: 50, 75, and 100kPa. Computed pull-out loads-D/B relationships are shown in Fig.3. Analysis using linear, non-linear and classical elasto-plastic model overestimates the observed load. Only analysis using subloading model can capture observed load behaviour. A comparison between observe granular flow and analysed results are shown in Fig.4. In D/B=2 and Dr=40%, analysed granular flow is similar to the observed one. In the case of simple and classical constitutive models, analysed granular flow is not local and top of the flow reaches to the surface of granular media. Non-linear plastic deformation should be considered for analysis of the granular flow.

CONCLUSION

Visualization technique using transparent granular is useful for investigating of granular flow. Especially, visualization using multi-camera is very powerful. Complicated granular flow can be simulated by finite element method considering non-linear plastic deformation. Combing the visualization technique with the computational analysis may contribute develop simple engineering solution.

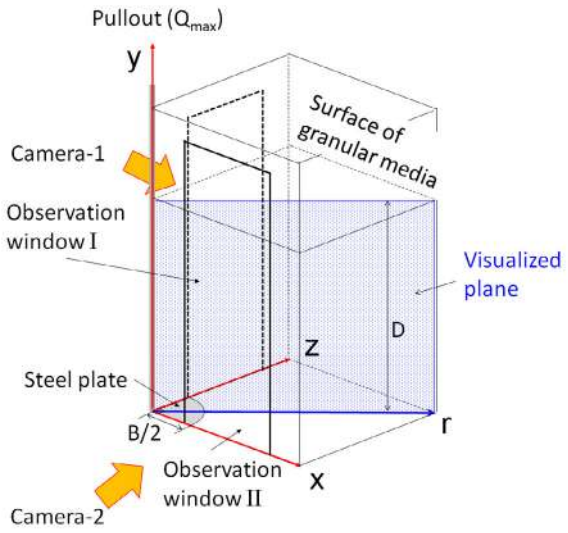

Figure 1. Model testing apparatus.

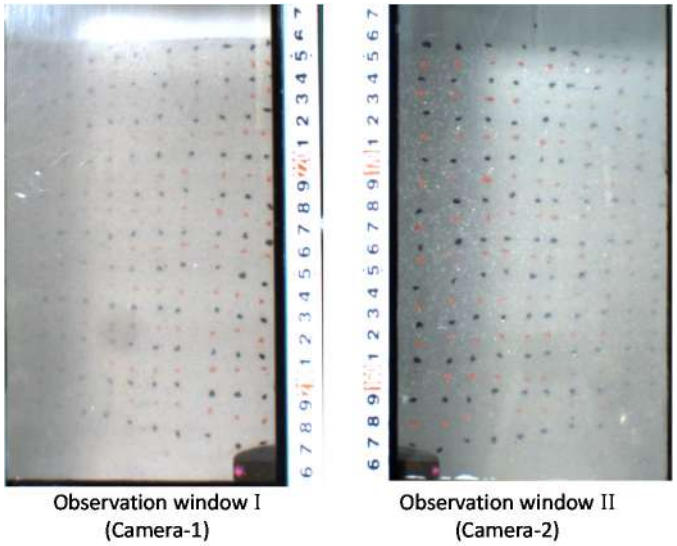

Figure 2. Particle tracers in granular media.

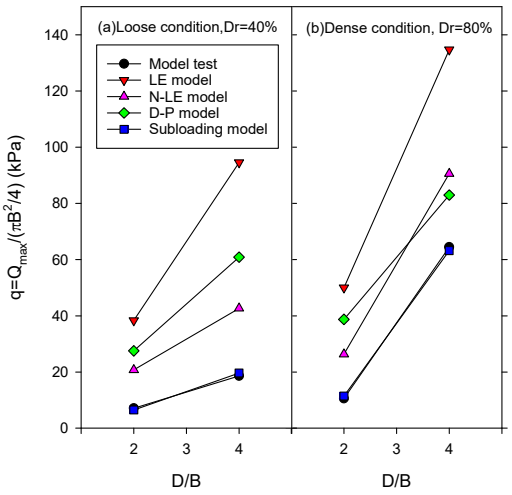

Figure 3. Normalized pull-out load and D/B relationship.

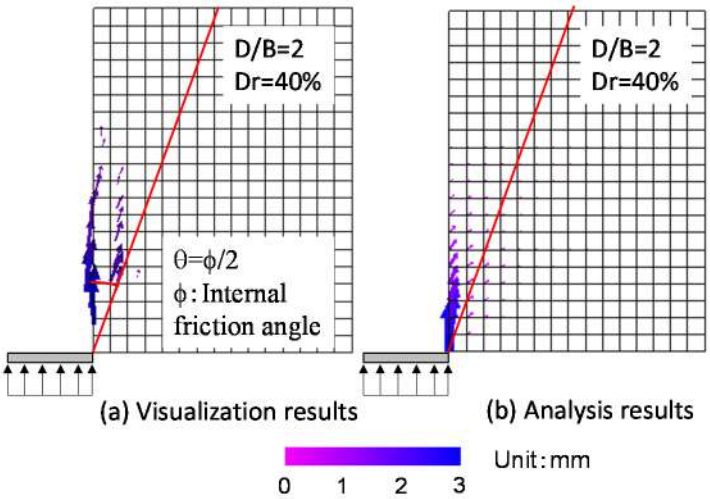

Figure 4. Results of visualization and computation analysis.

References

[1] Iskander, M., Bathurst, R.J. and Omidvar, M.: Past, Present, and Future of Transparent Soils, Geotechnical Testing Journal 38(5), DOI: 10.1520/GTJ20150079, 2015.

[2] Clemence, S.P. and Veesaert, C.J.: Dynamic Pullout Resistance of Anchors in Sand, Proc. of the Int. Conf. on Soil-Structure Interaction, Roorkee, India, 389-397, 1977.

[3] Hashiguchi, K.: Elastoplasticity Theory, second Edition, Lecture Notes in Applied and Computational Mechanics 69, Springer, 2014.

TEMPLATE FOR ICTAM2020 SHORT PAPER (MAXIMUM 2 PAGES)

Ben Nadler *[1]
[1]Department of Mechanical Engineering, University of Victoria, Victoria, BC, Canada

Summary Flow of ellipsoidal grains shows a complex macro-scale response that raises from the micro-scale alignment and relative slipping and collisions of the grains. This complex response is associate with the anisotropy induced by the micro-scale grains' orientation and alignment with respect to each other and the flow. In addition, the grains orientation is governed by the grains shape, the flow, the grain orientation in their surrounding and the interaction with the boundary. Observations from experiments and micro-scale simulations are used to construct a complete continuum model. The proposed model includes a constitutive law for the stresses, evolution law of the micro-scale grain rearrangement and the associate boundary conditions. The model shows good agreement with experimental and micro-scale numerical simulations.

ABSTRACT

Ellipsoidal grains show a complex macro-scale behavior associate with their ability to orient, align and slip with respect to each other. These additional micro-scale degrees of freedom are an evolving property that gives rise to a complex macro-scale anisotropic rheological response associate with micro-scale arrangement of the grains with respect to each other and the flow. Available continuum constitutive models of dense granular materials typically only consider grain size while ignoring grain shape, orientation and alignment and their effect on the rheological response.

Here a simple generalization of the inertia rheology [1] of spherical grains to ellipsoidal grains is proposed. The developed continuum model explicitly accounts for the grain shape and the micro-scale arrangement, while, the construction of the mathematical model is motivated by physical observations. The continuum model consists of a constitutive law that accounts for the grain shape, micro-scale arrangement and their role in the development of stresses when subjected to flow as well as an evolution law for the micro-scale arrangement.

Limited meaningful experimental and micro-scale simulation data on the rheology of ellipsoidal grain is available in the literature, which mainly consists of Discrete Element Method simulations of simple shear (Couette) flow [2, 3]. The response of the ellipsoidal grains subjected to simple shear flow shows nonmonotonic response with respect to the grains' aspect ratio, that is, ellipsoidal grains with small deviation from spheres, show higher resistant to shear flow than spherical grains. However ellipsoidal grains with high aspect ratio show much lower resistance to shear than spherical grains. It is proposed that this complex response is attributed to the arrangement of the grains in the micro-scale. Additionally, it was observed that grains subjected to simple shear tend to partially align with the stream lines which is enhanced with the aspect ratio. As a result, as grains becomes more aligned with respect to the flow the resistant to slip with respect to each other is reduced yielding a lower flow resistance.

The available experimental and micro-scale simulation data is used to determine the model parameters and to investigate its performance. Comparison of the model predictions with micro-scale simulations of simple shear flow shows that the model captures the complex mechanical response that is induced by the grain shape and the micro-scale arrangement as depicted in figure below.

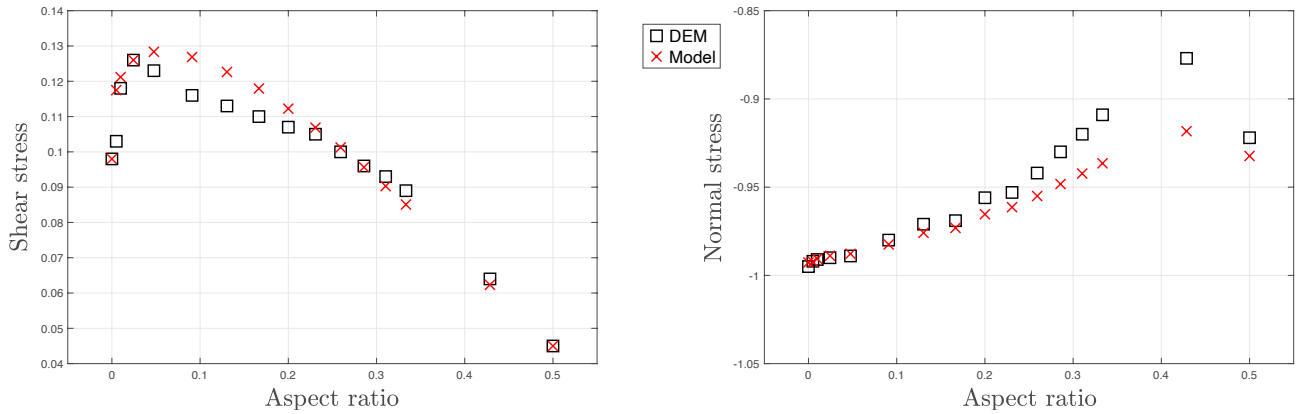

Figure 1. The macro-scale stress response as a function of the aspect ratio for frictionless grains subjected to simple shear

The main limitation of the available experiment and micro-scale simulations of simple shear data is that it is homogenous field and does not provide insight into the influence of inhomogeneity of the grain's alignment and flow. Experiments and Discrete Element Method simulations of flow of elongated grains down an incline plane [4] yields inhomogeneous flow and micro-scale grains arrangement, and hence provides some valuable insights. These observations suggest that the micro-scale

*Corresponding author. E-mail: bnadler@uvic.ca.

alignment diffuses spatially as the grains alignment at a point influence the orientation of its surrounding. This is induced by the characteristic of the collisions between grains that is sensitive to the gains' relative orientation. In addition, the interaction of the grains with the boundaries drives grains toward alignment with the boundary's topography. These observations motivative the introduction of a diffusion-like term in the evolution law of the micro-scale arrangement and treatment of the associate boundary conditions. Such a diffusion term and boundary conditions are proposed in the modified model. The modified continuum model is used to simulate flow down incline plan and it shows agreement with the experimental and micro-scale simulations observation.

CONCLUSIONS

The complex mechanical response of ellipsoidal grains is attributed to the micro-scale arrangement of the grains that is governed by the grain shape, flow and boundary conditions. An intuitive (and simple) continuum model is proposed to rational and predict, their mechanical response by an explicit consideration of the macro-scale arrangement. The model shows good agreement with experimental and micro-scale numerical simulations.

References

[1] P. Jop, Y. Forterre and O. Pouliquen, A constitutive law for dense granular flows, *Nature,* **441**: 727-730, 2006.
[2] B. Nadler, F. Guillard and I. Einav, Kinematic model of transient shape-induced anisotropy in dense granular flow. *Phys. Rev. Lett.,* **120**: 198003, 2018.
[3] D. Nagy, P. Claudin, T.B. Borzaonyi and E. Somfai, Rheology of dense granular flow of elongated particles. *Phys. Rev. E.*, **96**: 062903, 2017.
[4] R.C. Hidalgo, B. Szabo, K. Gillemot, T. Borzsonyi and T. Weinhart, Rheological response of nonspherical granular flows down an incline. *Phys. Rev. Fluids,* **3**: 074301, 2018.

EXPERIMENTAL STUDY OF CYLINDRICAL PARTICLES ORIENTATION IN RANDOM PACKED BEDS

Maciej Marek[1], Paweł Niegodajew[1], Przemysław Rajca[2] and Konrad Gruszka[3]
[1]Czestochowa University of Technology, Department of Thermal Machinery, Częstochowa, Poland
[2]Czestochowa University of Technology, Department of Production Management, Częstochowa, Poland
[3]Czestochowa University of Technology, Department of Physics, Częstochowa, Poland

Summary The present work employs a new experimental method to investigate cylindrical particles' orientation in cylindrical columns of different diameters. The idea of the method is to employ as particles cylindrical transparent capsules filled with water and paraffin. The capsules are dumped into the container after they are heated so that the paraffin is in liquid state, then can be freely removed when the paraffin cools down and turns back into solid. The original orientation of the particle can be assessed by the inclination of the liquid-solid interface within a capsule. Sample results on orientation distribution of particles of various aspect ratios are presented.

INTRODUCTION

Random packed beds of particles in a cylindrical container (column) are widely employed in many areas of process engineering as a medium enhancing the contact surface between reacting substances – e.g. in absorbers and strippers [1]. As the information about the bed structure is essential for proper design of the system, substantial effort has been put into experimental and numerical investigations of random packed beds. Detailed studies of a random packed bed structure typically require complex and expensive experimental methods e.g. computer tomography in various forms (X-ray or gamma-ray). To face that problem, a number of numerical methods allowing to reconstruct 3-dimensional geometries of packed beds have been developed. Most of works employing such models focuses on estimation of void fraction distributions which is an important parameter, however, as the beds typically consist of randomly oriented particles, more detailed information about the bed structure, in particular the orientation of particles in various regions of a bed, is of high interest. While the simulation may successfully reproduce void fraction distribution, it may fail in prediction of the particles orientation distribution [2]. As a lot of works deal with numerical generation of non-spherical packings like cylinders [3], spherocylinders [4], frustums and full cones [5], octahedrons [6], tetrahedrons [7], rodlike [8], elliptical particles [9] and rings [10], more experimental data concerning orientation of particles in random packed beds should facilitate the validation of these models. In the present work a new experimental method is used for studies of orientation of cylindrical particles randomly dumped in a cylindrical column.

EXPERIMENTAL PROCEDURE

The experimental stand consists of a cylindrical column of a diameter D_c, an industrial stove for heating of the particles and a large number of transparent particles-capsules. The particles should have only one axis of symmetry (e.g. cylinders or spherocylinders), so that their orientation can be defined by only one angle – between particle's axis and the container's axis. In the initial stage, the capsules must be filled with two substances, denoted here as "*L*" and "*S*", both of approximately the same volume equal to the half of the capsule volume. The substances should have the following properties: a) they should be immiscible (a distinct interface must be formed between *L* and *S*), b) *S* should solidify at temperature T_S above ambient temperature T_0, c) T_S should be lower than T_{max} – the maximum temperature permitted for the material of the capsules, d) shrinkage of *S* cannot be too large and the substance cannot adhere too much to the walls of a capsule – the interface should be essentially flat in both liquid and solid state in order to measure the inclination angle with sufficient accuracy, e) there should be only a slight difference between densities of *L* and *S* in the liquid state.

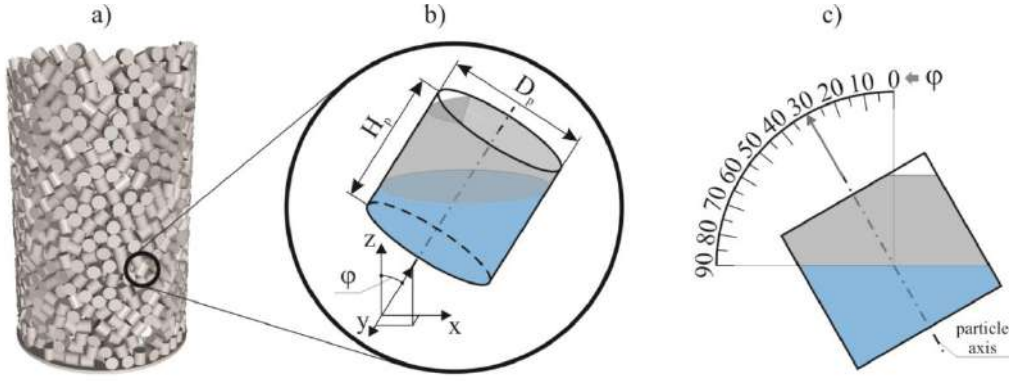

Figure 1. Experimental procedure: a) random packed bed, b) transparent particle-capsule with two immiscible fluids inside *L* and *S* at ambient temperature, c) measurement of the orientation angle

The experiment is performed in three main stages: (1) the capsules are heated in the stove to temperature *T* higher than T_S but lower than T_{max}. Both substances should turn into liquid state. (2) the capsules are randomly dumped into the

container and form a fixed structure. Then, the bed is left until ambient temperature T_0 is attained by all capsules. Additional cooling or ventilation can be considered for acceleration of this process. (3) at ambient conditions S solidifies and the interface between L and S remains at a fixed position related to the original particle-capsule orientation within the bed. Thus, the inclination of the interface can be easily measured (see Fig. 1c). If we are only interested in a global orientation distribution, the capsules may be removed freely but the method offers also possibility of local investigations (e.g. core of the bed, near wall or near bottom region). In such a case, the capsules should be removed with care in order not to alter their original position (not necessarily the orientation) of the remaining capsules within the bed.

SAMPLE RESULTS

In order to test the proposed method, two series of the experiment have been performed: one with 1100 polycarbonate cylindrical screw capsules of diameter D_p=25.6 mm and height H_p=28.5 mm (H_p/D_p=1.11) filled with water (L) and paraffin (S) and then dumped into a column of diameter D_c=387 mm (D_c/D_p=15.1); the second one with 900 capsules of diameter D_p=38 mm and height H_p=32 mm (H_p/D_p=0.84) in a column of diameter D_c=250 mm (D_c/D_p=6.6) . The capsules were sealed with silicone gel sealant and heated in a stove to 80°C. The probability distribution of the measured orientation angles are shown in Fig. 2. The capsules were removed from the container layer by layer, thus the results could be obtained not only for the bed as a whole (global distribution in Fig. 2) but also for the bed with the bottom region removed ("bottom excluded" in Fig. 2, representing the particles positioned higher than $3D_p$ over the bottom). A characteristic feature of the global distribution is the presence of two distinct peaks at 0 and 90° significantly reduced with the bottom section excluded, which means that the main contribution to these peaks comes from the bottom layers. The probability distributions for the case of the narrow column show a strong contribution of the so called "wall effect" – a pronounced peak in the central part of the graph (see also [10]).

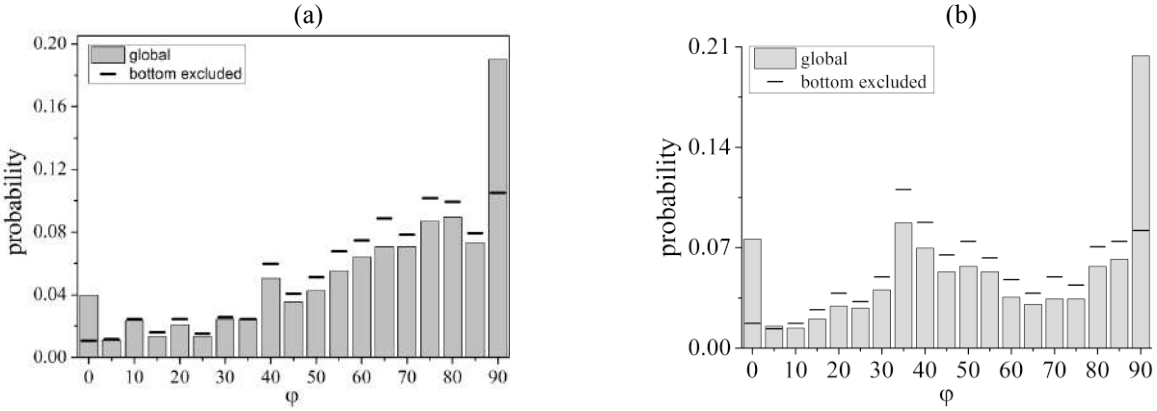

Figure 2. Probability distribution of the orientation angle of cylindrical particles with and H_p/D_p=0.84 (D_c/D_p=6.6) (a) and H_p/D_p=1.11 (D_c/D_p=15.1) (b).

CONCLUSIONS

This work demonstrates a new low-cost method alternative to tomographic techniques that can be used in examination of orientation distribution in random packed beds. This method can be used to analyse the orientation of particles of wide range axisymmetric shapes and sizes. A preliminary results showed that distribution of particles is strongly influenced by bottom region as the global probability distribution of the angle φ differs significantly from the one obtained for the upper part of the bed. The future work will cover the experiments with considerably larger number of particles-capsules, local analysis concerning orientation distribution in various bed zones and wider range of column sizes.

ACKNOWLEDGMENTS

The investigation was supported by National Science Centre, Poland under the Grant No. UMO-2018/31/D/ST8/00199.

References

[1] P. Niegodajew, D. Asendrych, Appl. Math. Model. 40 (2016) 10222–10237.
[2] R. Caulkin, X. Jia, C. Xu, M. Fairweather, R. a. Williams, H. Stitt, M. Nijemeisland, S. Aferka, M. Crine, A. Léonard, D. Toye, P. Marchot, Ind. Eng. Chem. Res. 48 (2009) 202–213.
[3] M. Kodam, R. Bharadwaj, J. Curtis, B. Hancock, C. Wassgren, Chem. Eng. Sci. 65 (2010) 5852–5862.
[4] L. Meng, Y. Jiao, S. Li, Powder Technol. (2016).
[5] J. Zhao, S. Li, P. Lu, L. Meng, T. Li, H. Zhu, Powder Technol. 214 (2011) 500–505.
[6] L. Liu, P. Lu, L. Meng, W. Jin, S. Li, Phys. A Stat. Mech. Its Appl. 444 (2016) 870–882.
[7] S. Zhao, X. Zhou, W. Liu, C. Lai, Particuology 23 (2015) 109–117.
[8] W. Nan, Y. Wang, Y. Liu, H. Tang, Adv. Powder Technol. 26 (2015) 527–536.
[9] W.X. Xu, H.S. Chen, Z. Lv, Phys. A Stat. Mech. Its Appl. 390 (2011) 2452–2467.
[10] P. Niegodajew, M. Marek, Powder Technol. 297 (2016) 193–201.

RATE EFFECTS AND SHEAR BANDING DURING ORTHOGONAL CUTTING OF SAND

Abhijit Hegde *[1], and Tejas Murthy [1]
[1]Department of Civil Engineering, Indian Institute of Science, Bengaluru, India, 560012

Summary We report an extensive experimental study on the orthogonal cutting of a cohesionless soil (a model granular material) under plane strain conditions. Experiments have been carried out over a range of cutting speeds. High resolution images of the region of cutting were captured and analyzed using Particle Image Velocimetry(PIV) that allowed quantification of the deformation fields. We make detailed observations on the regions of velocity discontinuities (shear bands) in our ensemble as the tool ploughs through the pile of glass ballotini. The shear band initiates from the tip of the tool and propagates towards the free surface, akin to metal cutting. Consequently, the effective depth of cut increases as the glass ballotini start to rise along the tool face and begin to repose under gravity. As we continue to cut, the system reaches a steady state of deformation.

INTRODUCTION

Ploughing/trenching of soil is an earthmoving process generally carried out with the help of blades or ploughs. Every year humans move trillions of kilograms of earth and soil for various purposes like mining, excavation for road works, dredging, and therefore the problem deserves a proper scientific treatment to get a better physical understanding of the process and hence design more efficient tools for ploughing. The ploughing process in general can be modelled as an orthogonal cutting problem, a framework well established in the field of metal cutting, wherein a preset depth of soil is removed by moving the tool/blade in a direction normal to the embedment of the tool. Hettiaratchi and Reece (1974), McKyes and Ali (1977) have come up with analytical models to theoretically predict the forces on the tool. Further efforts have been made to numerically model the ploughing process using FEM by Szymanski et al.(2011) and using DEM(Discrete Element Method) by Gravish et al. (2010) while Coetzee (2014) has performed a detailed numerical analysis of the soil cutting problem using a meshless Material Point Method(MPM). Palmer (1999) has performed extensive cutting experiments on submerged sand and have studied the effect of pore water pressure on the draft/cutting forces.

EXPERIMENTS

For studying the deformations encountered during the cutting process, we have performed orthogonal, plane strain cutting experiments with dry glass beads-as a model granular material. The cutting operation was carried out on a CNC machine and to capture the images for analysis we use a PCO 1200HS camera. A rectangular box of dimensions 55.5cm x 16cm x 1.5cm, made of high-speed steel was used to contain the glass beads. The dimension of the box was intentionally made small in one of the directions-perpendicular to front face of the cutting box- to ensure plane strain conditions during cutting. The cutting box is first mounted onto the translation stage of the CNC. The motion of the tool is restricted to the vertical direction while the box can only move in a horizontal plane. A glass plate is then carefully attached to the front face of the box. Glass beads are then poured into the box through the open top face with the help of a funnel till the desired depth of cut is reached. A camera is then setup in front of the cutting box to capture the images of the ploughing process. A light source was used to illuminate the region of interest around the tool. A PIV algorithm was used to analyze the images captured through the ploughing process. PIV is an indirect, non-intrusive, whole field velocity measurement technique used extensively in the study of fluid flows and also has been used to study deformation fields in soil.

RESULTS

A series of cutting experiments at different cutting speeds was carried out in this research programme. A preset depth of cut equal to $5d_p$, d_p being the size of glass beads(2.5mm), and a rake angle of 0^0 degrees was used in our experiments. In Figure1(a), we show a sample image of the cutting process captured after a tool displacement of $34d_p$. The material undergoes large deformations and with prolonged ploughing the system seems to reach a steady state. This can be verified by either measuring the angle of repose of the pile formed in front of the tool during ploughing or by looking at the evolution of the effective strain rate in a region surrounding the tool (Figure1(c)). In Figure1(b), we show the corresponding velocity field obtained from our PIV analysis. The direction of motion of the glass beads are apparent from the quiver plots overlaid on top of a contour map which shows the magnitude of the velocity. The bulk velocity of the material, till the tip of the tool, moves at a constant velocity prescribed by the cutting speed. At the tool tip, we observe a bifurcation in the velocity field, i.e. the velocity changes direction, leading to the formation of a shear band, which extends from the tool tip to the material surface. As the ploughing progresses, the material removed from the surface, after undergoing a change in the direction at the tool tip, rises along the surface of the tool, begins to repose and forms a pile in front of the tool. This effectively increases the depth of cut during the ploughing. With prolonged ploughing, the surface angle of the pile remains constant while the height of the pile keeps increasing. In figure1(d) we show the effective shear strain rate field corresponding to the velocity field map shown in Figure1(b). In this figure, we observe the formation of a distinct shear band, a region of very high strain rate, at the tool tip and extending through the thickness of the pile and

*Corresponding author. E-mail: abhijithegde@iisc.ac.in

reaching the free surface. This clearly indicates that the material undergoes strain localization across which a change in the velocity of glass beads is observed, when subjected to severe plastic deformation due to cutting. We also observe shear bands along the free surface of the pile and shearing occurring at the interface between the material and the rake face. We observe formation of a dead zone next to the tool face, the size of which increases as we continue to plough through the material and hence increases the effective rake angle of tool. The effective strain rate is maximum along the shear plane originating at the tool, with a magnitude of $0.0015s^{-1}$ and increased with the speed of cut. The shear strain map also allowed us to accurately measure the thickness and inclination angle of the shear bands. We find that at steady state, the thickness of the shear band was around $7d_p$ and the inclination angle was 42^0. Both the thickness and inclination angle of the shear bands was found to be insensitive to the speed of cut, over the range of speeds tested in our experiments.

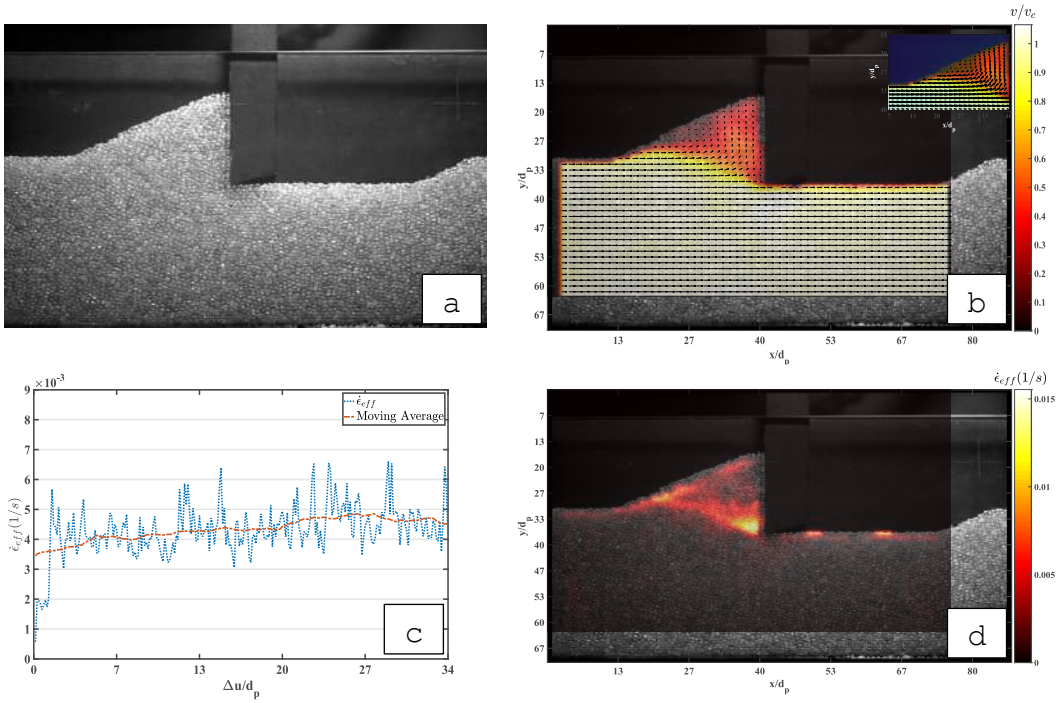

Figure 1(a)-Sample image corresponding to a tool displacement of $34d_p$. Figure1(b)- Velocity field contour map obtained from PIV. Figure1(c)-Evolution of shear strain averaged over the entire ensemble. Figure1(d)- Shear strain contour map.

CONCLUSIONS

Forces exerted on the tool/blade during cutting of soil has been well studied but the deformation undergone by the material itself has often been overlooked. Using PIV, we. have been able to obtain the deformation and velocity fields observed during the ploughing process. We observe formation of shear bands in the material as a result of large plastic deformations imparted on the material during ploughing. With prolonged ploughing, the system reaches a steady state of deformation, as indicated by the slope of the pile formed in front of the tool which also results in an increase in the depth of cut. The problem of orthogonal cutting allows an in-depth examination of the formation and propagation of shear bands in granular materials.

References

[1] Hettiaratchi, D. and Reece, A. (1974). "The calculation of passive soil resistance." *Geotechnique*, 24(3), 289–310Icer D.F., Adams J.A. Mathematical Elements for Computer Simulation. McGraw Hill, NY 1977.

[2] McKyes, E. and Ali, O. (1977). "The cutting of soil by narrow blades." *Journal of Terramechanics* Icer D.F., Adams J.A. Mathematical Elements for Computer Simulation. McGraw Hill, NY 1977.

[3] Shmulevich, I., Asaf, Z., & Rubinstein, D. (2007). Interaction between soil and a wide cutting blade using the discrete element method. *Soil and Tillage Research*, *97*(1), 37-50

[4] Gravish, N., Umbanhowar, P. B., and Goldman, D. I. (2010). "Force and flow transition in plowed granular media." *Physical review letters*, 105(12), 128301.

[5] Coetzee, C. (2014). "Discrete and continuum modelling of soil cutting." *Computational Particle Mechanics*, 1(4), 409–423

[6] Palmer, A. (1999). "Speed effects in cutting and ploughing." *Geotechnique*, 49(3),285–29

COMPACTION DYNAMICS OF GRANULAR COLUMNS FROM FLUIDIZATION BURSTS

Georges Gauthier* and Philippe Gondret
Université Paris-Saclay, CNRS, Laboratoire FAST, 91405, Orsay, France

Summary How to arrange a packing of spheres is a scientific question that aroused many fundamental works since a long time from Kepler's conjecture to Edward's theory [1], where the role traditionally played by the energy in statistical problems is replaced by the volume for athermal grains. In a recent study [2] we have shown that compaction of a liquid immersered granular pile can be achieved by small upward continuous or bursting flow at low Reynolds number. We now focus on the influence of different flow parameters such as the amount of fluid during each burst, the Reynolds and Stokes numbers, and on the detail mechanism of compaction at the grain scale.

INTRODUCTION

Though the solid fraction in the tetrahedral arrangement of four equal spheres in contact is 0.78, the highest solid fraction that can be achieved in a large packing is 0.74 and corresponds to the densest periodic arrangement of equal spheres. Any other ordered or disordered packing has lower solid fractions. Random packings of equal spheres have a solid fraction $\phi = 0.6 \pm 0.04$ with a Random Loose Packing limit (RLP) $\phi_{RLP} \simeq 0.56$ and a Random Close Packing (RCP) $\phi_{RCP} \simeq 0.64$. For granular systems that are athermal and dissipative, the exploration of the different possible arrangements cannot be driven by temperature but some external energy must be injected continuously. The most classical way of compaction is the mechanical shaking of the container by successive taps [3, 4]. The compaction time dynamics displays a first quick increase of the solid fraction followed by a much slower increase. For rather confined systems with non negligible wall effects, a logarithmic law is often used to describe the evolution of the solid fraction ϕ from the initial packing value ϕ_0 to the final one ϕ_∞ as a function of the number of taps $\mathcal{N}$ [3]:

$$\frac{\phi(\mathcal{N}) - \phi_0}{\phi_\infty - \phi_0} = 1 - \frac{1}{1 + B \ln\left(1 + \mathcal{N}/\mathcal{N}_c\right)}, \tag{1}$$

where $\mathcal{N}_c$ is a characteristic number of taps and the parameter B is related to the compaction efficiency. In the tapping experiments of monodisperse spheres, the solid packing fraction increases from typically $\phi_0 \simeq 0.58$ to $0.61 \lesssim \phi_\infty \lesssim 0.63$. As for dry packings, compaction of liquid immersed granular packings can be achieved by taps with a maximum solid volume fraction $\phi_\infty \simeq 0.64$. A more efficient process consists in shearing the granular packing (*e.g.* [6, 7]) which may lead to solid fraction up to $\phi_\infty \simeq 0.69$ after a few 10^4 cycles, with thus some local ordering. We here present experiments in which liquid immersed piles can be efficiently compacted using small burst upward flows.

EXPERIMENTAL SET-UP

The experimental set-up is sketched in figure 1a. The suspension consists in glass beads of radius $a = 1\,\mathrm{mm}$ and density $\rho_p = 2.3 \times 10^3\,\mathrm{kg/m^3}$ dispersed in a water-glycerol mixture of density $\rho = 1235\,\mathrm{kg/m^3}$ and viscosity $\eta = 0.156\,\mathrm{Pa \cdot s}$ at $T = 24\,^\circ\mathrm{C}$, characterized by a low particulate Reynolds number ($Re_p \simeq 10^{-1}$ when based on the settling velocity of an isolated particle) and low Stokes number ($St \simeq 10^{-1}$).

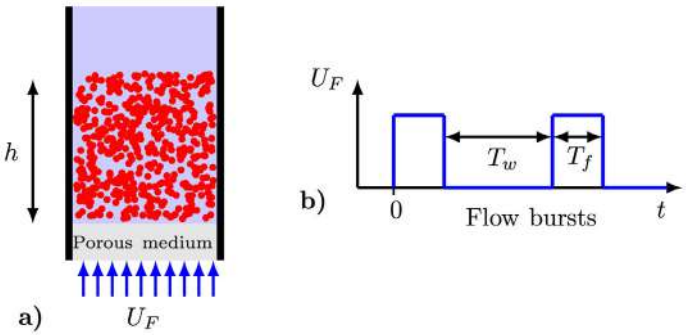

Figure 1: (a) Sketch of the experimental set-up with upward flow U_F across a bed of height h. (b) Burst flow with the time period $T = T_w + T_f$ made of successive flow bursts of time duration T_f with $U_F \neq 0$ sepatated by rest time T_w without flow ($U_F = 0$).

*Corresponding author. E-mail:gauthier@fast.u-psud.fr

The granular pile is contained in a vertical parallelepipedic cell of 50 cm high and of rectangular cross-section $S = 8 \times 2\,\mathrm{cm}^2$. The fluid is injected through a porous media located at the bottom of the cell, with a permeability which is two orders of magnitude lower than the permeability of the granular bed to minimize any possible effect from the evolution the granular bed on the flow injection. The upward flow rate is fixed using a gear pump, controlled with a wave generator, allowing bursting flow with short flow time period T_f at constant flow rate $U_F \neq 0$ followed by a long resting T_w time period without flow ($U_F = 0$) before the next flow time, as sketched in figure 1b. The waiting time has been chosen long enough for the grains to settle before the next flow burst. Images of the cell are taken by a video camera at the maximum rate of 15 images per second. From each image, the bed surface is tracked and averaged spatially to obtain the mean instantaneous height $h(t)$ of the bed. The mean solid volume fraction ϕ of the bed after each burst $\mathcal{N}$ is then deduced from $h(t)$ as $\phi(t) = M_p/\rho_p S h(t)$, where M_p is the total mass of particles.

RESULTS

Figure 2a presents the evolution of the height of the pile during the three first bursts, for two different flow rates. At a burst flow rate U_F above the fluidization threshold $U_{Fc} \simeq 0.32$ mm/s (—), one can see a small increase of the height of the pile followed by a larger decrease down to a lower value before same at the next burst. More surprisingly, below the fluidization threshold ($U_F < U_{Fc}$) (– –), the pile still compacts even though no expansion can be seen. In both

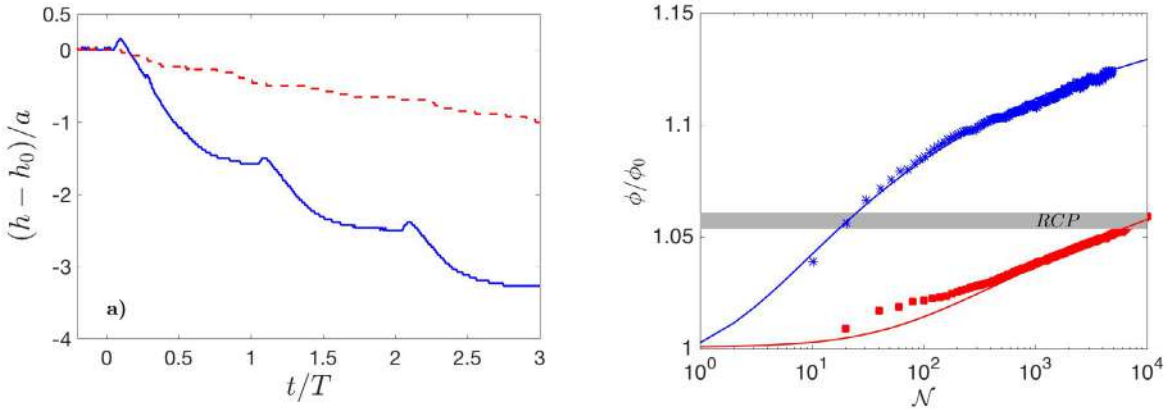

Figure 2: (a) Time evolution of the relative normalized pile height $(h(t) - h_0)/a$ for two burst flow rates U_F : (– –) $U_F = 0.6U_{Fc}$ ($T_f = 0.26T$) and (—) $U_F = 2.6U_{Fc}$ ($T_f = 0.08T$). (b) Evolution of the normalized solid fraction ϕ/ϕ_0 with the number $\mathcal{N}$ of bursts at two flow rates : (■) $U_F = 0.4U_{Fc}$ and (*) $U_F = 2.6U_{Fc}$, together with (—) best fits by eq. (1) with $\phi_\infty = 0.74$ and with (*) $B = 0.07$ and $\mathcal{N}_c = 63$, or (×) $B = 0.21$ and $\mathcal{N}_c = 3$.

cases the evolution of the solid volume fraction ϕ with the number of bursts reasonably follows a logarithmic law of eq. (1) as shown in figure 2b. For $U_F > U_{Fc}$, the final solid volume fraction is observed to exceed ϕ_{RCP} with thus some local ordering. When increasing the flow rate by keeping constant the injected fluid during each burst (fluid displacement $U_F T_f = cte$), we observe a sharp transition in the compaction efficiency across the fluidization threshold U_{Fc}: the parameter B increases from $B \simeq 0.1$ up to $B \simeq 0.2$ and the characteristic number of taps decreases from $\mathcal{N}_c \simeq 60$ down to $\mathcal{N}_c \simeq 3$ [2].

CONCLUSIONS

We have shown that efficient compaction of immersed granular pile can be achieved from bursting upward flow at low particulate Reynolds number. Additional experiments are ongoing to understand the effects of the injected fluid amount, together with the effect of the Reynolds and Stokes numbers. We are also investigating the particle motions that lead to the observed progressive compaction.

References

[1] Edwards S.F., Oakeshott R.B.S. Theory of powders. *Physica A: Stat. Mech. Appl.* **157**, 1080-1090, 1989.
[2] Gauthier G., Gondret P. Compaction of liquid immersed granular packings by small upward flows. *Phys. Rev. Fluid* **4**, 074308, 2019.
[3] Knight J.B., Fandrich C.G., Lau C.N., Jaeger H.M., Nagel S.R., Density relaxation in a vibrated granular material. *Phys. Rev. E* **51**, 3957 (1995).
[4] Dijksman J.A., Van Hecke M. The role of tap du- ration for the steady-state density of vibrated granular media. *Europhys. Lett.* **88**, 44001 (2009).
[5] Boutreux T., de Gennes P-G. Compaction of granular mixtures: a free volume model. *Physica A: Stat. Mech. Appl.* **244**, 59-67 (1997).
[6] Pouliquen O., Belzons M., Nicoals M. Fluctuating particle motion during shear induced granular compaction. *Phys. Rev. Lett.* **91**, 014301 (2003).
[7] Rietz F., Radim C., Swinney H.L., Schroter M. Nucleation in sheared granular matter. *Phys. Rev. Lett.* **120**, 055701 (2018).

EXPERIMENTAL STUDY OF THE COLLAPSE OF COHESION-CONTROLLED GRANULAR MATERIALS

Adrien Gans* [1], A.Abramian [3], Maxime Nicolas [1], Olivier Pouliquen[1], Alban Sauret[2], and P.-Y. Lagrée [3]
[1]Aix Marseille Univ, CNRS, IUSTI, Marseille, France
[2]University of California, Santa Barbara, USA
[3]Institut Jean le Rond d'Alembert, Sorbonne Université Paris, France

Summary We present an experimental investigation of the collapse of a cohesive granular column. The granular material is made of glass beads coated with a thin polymer layer, which controls the cohesion. As observed for cohesionless granular material by previous studies, the front velocity and the run-out length L_f are mainly controlled by the aspect ratio a. The effect of the cohesion on the dynamics and the final deposit of the collapse is also compared with numerical simulations.

INTRODUCTION

Cohesive granular media are encountered in many geophysical and industrial applications: cement, pharmaceutical powders, and flours among other examples. Whereas many progresses have been made in the description of dry granular flows, the behavior of cohesive powders remains elusive. In particular, one difficulty lies in the cohesion force between the particles. Using our recently developed method to create a cohesion-controlled granular material [1], we experimentally consider the collapse of a column made of cohesive spherical grains. This configuration has been extensively studied in the case of dry granular material: when the grains are released, the granular mass spreads and stops at a finite distance [2]. The morphology of the deposit is mainly controlled by the initial aspect ratio and is independent of the material properties. Yet, for cohesive powders, the inter-particle forces strongly affect the collapse. In this study, we characterize the effects of the cohesion on the collapse dynamics, the run-out length, and the final morphology of the deposit. These experiments illustrate that cohesive forces between particles introduce an additional complexity in this system through a new parameter. Our experiments are compared with numerical simulations performed by A. Abramian and P.-Y. Lagrée at d'Alembert Institute, Paris, in the framework of the COPRINT project (ANR-17-CE08-0017). These simulations are based on a Navier-Stokes solver with a cohesive $\mu(I)$ granular rheology.

EXPERIMENTS

The cohesive granular material is made of glass beads (diameter $d = 800$ μm), coated with polyborosyloxane (PBS) made from a -OH terminated Polydimethylsiloxane (PDMS) cross-linked with H_3BO_3 boric acid [4]. The thickness b of the PBS layer coating the glass beads is the control parameter of the inter-particle cohesion. From our previous study [1], inter-particle force is captured by the expression $F_c = 1.5\pi\gamma d\left(1 - \mathrm{e}^{-b/B}\right)$ where $B \approx 230$ nm and γ is the surface tension of the PDMS. We have also shown that the cohesive stress of the bulk material τ_c is linearly related to the microscopic inter-particle force F_c. Changing the PBS thickness b is a convenient way to control the bulk cohesion of the granular material. To describe the flow under gravity, we define the cohesion length $l_c = \tau_c/(\phi\rho g)$, which represents the characteristic length where gravity effects are balanced by cohesion effects.

The experimental set-up is made of a rectangular channel [Fig. 1(a)], with a removable door sliding upwards, allowing us to build a column of cohesive grains with an aspect ratio $a = H_i/L_i$ where H_i is the initial height and L_i the initial width of the granular column. We investigate the role of the cohesion on the collapse dynamics and the final morphology of the deposit. The experiments are performed using three batches of particles: dry granular beads and cohesive beads with coatings $b = 200$ nm and $b = 300$ nm, respectively.

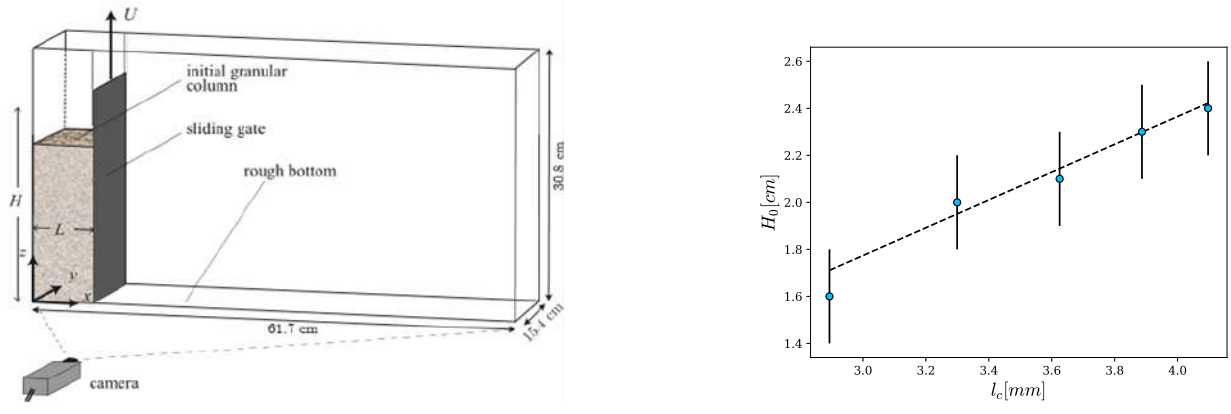

(a) (b)

Figure 1: (a) Experimental setup. (b) Maximum height of a stable cohesive granular column.

*Corresponding author. E-mail: adrien.gans@univ-amu.fr

RESULTS

We first investigate the maximum height for a stable column i.e. the maximum height for which the cohesion allows the column to support its own weight. A Mohr-Coulomb criterion predicts a linear expression between this maximum height and the cohesion parameter:

$$H_0 = \frac{2l_c}{\cos\delta(\sin\delta - \mu\cos\delta)}. \tag{1}$$

The experimental results shown in Fig. 1(b) confirm that prediction with a fracture angle $\delta = 53°$. An equivalent numerical configuration has already been studied by Abramian *et al.* [3]

When the collapse occurs, we measure the shape of the final deposit and the final run-out length $L_f = L_i + \Delta L$. As shown by Lajeunesse *et al.* [2], the run-out length ΔL and the final height H_f of a dry granular material are power laws of the aspect ratio a:

$$\frac{\Delta L}{L_i} \propto \begin{cases} a & \text{for } a \leq 3 \\ a^{2/3} & \text{for } a \geq 3 \end{cases} \quad \text{and} \quad \frac{H_f}{L_i} \propto \begin{cases} a & \text{for } a \leq 0.7 \\ a^{1/3} & \text{for } a \geq 0.7 \end{cases} \tag{2}$$

Fig.2 (a) shows that for the non-cohesive case, our results still match the observations of Lajeunesse *et al.* [2]. For the cohesive materials, the power laws are still valid but the pre-factor is affected by the cohesion force. We first propose to introduce a new definition of the aspect ratio $a^* = (H_i - H_0)/L_i$ to account for the the fact that a cohesive column does not fall below a critical height H_0. We also introduce a modified run-out length $L^* = L_f - L_i + H_0 \tan\delta$. This scaling accounts for the observation of a "dead wedge volume" [emphasized by the white arrow on the picture insert of Fig. 2(b)] which does not contribute to the run-out length for an aspect ratio lower than 3. With these new definitions, all the experimental and numerical data follow the same curve governed by a^* as shown in Fig. 2(b). For an aspect ratio larger than 3, the shape of the "dead wedge volume" changes and the influence of the cohesion has not been investigated.

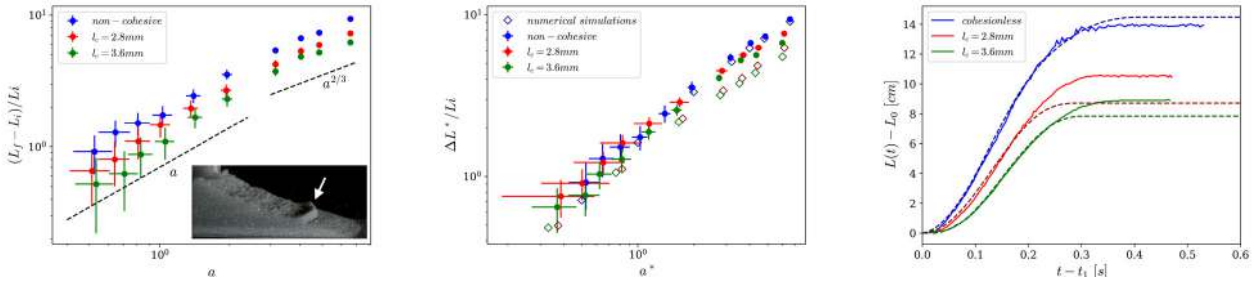

(a) (b) (c)

Figure 2: (a) Run-out length as a function of the aspect ratio for dry and cohesive beads. The power law is the same, but the cohesion changes the pre-factor. (b) Rescaled run-out ΔL^* as a function of the rescaled aspect ratio a^* (c) Position of the front of the falling column over time. The numerical model seems to capture quite well the dynamic of the column

We also investigate the time-evolution of the spreading of the column during the collapse [Fig. 2(c)], and we compare it with numerical simulations. We observe that despite a difference on the final run-out, it seems that the numerical model is able to capture the essential features of the collapse. Further results and explanations will be presented at the conference.

CONCLUSION

Using a cohesion-controlled granular material [1], we investigated the effect of cohesion on the granular collapse of a 2D column. We reported a critical height under which a column will not collapse because of cohesion between grains. This height can be related to the cohesive stress in the media through the cohesive length l_c. We observed that the run-out length of the final deposit depends on the cohesion, and we suggest to use a new definition for the aspect ratio involving the critical height. These experiments provide a first description of the flowing dynamics of cohesion-controlled granular materials.

References

[1] A. Gans, O. Pouliquen, and M. Nicolas. A cohesion-controlled granular material.*Phy. Rev. E.**101.3**,032904 (2020)*
[2] E. Lajeunesse, J. Monnier, and G. Homsy. Granular slumping on a horizontal surface. *Physics of Fluids **17**,103302 (2005)*
[3] Abramian, Anaïs and Staron, Lydie and Lagrée, Pierre-Yves. The slumping of a cohesive granular column: Continuum and discrete modeling. *Journal of Rheology **64.5**,1227-1235 (2020)*
[4] J. Modelland and S.Thuresson. Material composition and method for its manufacturing, Patent WO2008/020800A1 (2008).

COLLISIONS IN NARROW FLUIDIZED BEDS: EXPERIMENTS AND SIMULATIONS

Fernando David Cúñez* [1], Karlo Fernandes Rocha[1,2], and Erick de Moraes Franklin[1]
[1]School of Mechanical Engineering, University of Campinas - UNICAMP, Campinas, Brazil
[2]Federal Institute of Espirito Santo, Cachoeiro de Itapemirim, Brazil

Summary In this work, we investigate experimentally and numerically the behavior of particle collisions in narrow fluidized beds (NFB). For the experiments, the fluidized beds were formed in a 25.4 mm-ID tube and consisted of alumina beads with a diameter of 6mm and a specific gravity of 3.69; thus, the ratio between the tube and the particles was 4.23. We used 3 different arrangements of beds and imposed 2 water flows rates at the bottom of the tube. The fluidized beds were filmed with a high-speed camera and the sound of collisions was recorded using a microphone placed on the tube wall. The numerical simulations were performed using an Eulerian-Lagrangian approach (CFD-DEM). From both the acoustic signal (experiments) and the acceleration of particles (numerical computations), we obtained the characteristic frequencies of different types of collisions.

INTRODUCTION

A narrow fluidized bed (NFB) is a suspension of solid particles (grains) in a vertical tube submitted to an ascending flow, where the ratio between the tube and the particles is less than 10. In this narrow case, the formation of regions of high and low compactness is expected [1]. This kind of fluidized bed is gaining interest in many industrial applications, being found, for example, in bioreactors for biological wastewater treatment, which are employed for both large-scale and domestic treatment of wastewater [2]. For the NFB, the dynamics and instabilities are different because of high confinement effects; therefore, this case is still to be understood. When the fluid is a viscous liquid, the Stokes number, comparing particle inertia to viscous forces, allows to determine if the collisional effects can be considered dominant. Del Pozo et al. [3] made particle collisions measurements in gas and liquid fluidized beds, and observed that the collision frequency is an increasing function of the particle fraction, reaching its maximum at minimum fluidization. Zenit et al. [4] measured the collisional particle pressure in liquid fluidized beds and gravity-driven flows. They quantified the granular pressure and found that it is related to the particle fraction in a non-monotonic way. Following the techniques used in [3, 4], Buffière and Moletta [5], analyzed the effects of the particle fraction and gas velocity in three-dimensional fluidized beds. The authors found that there is an increasing evolution of the collision frequency as a function of the solid fraction with a maximum at about 20%. Finally, Aguilar et al. [6] measured the collision frequency and the coefficient of restitution based on the use of a threshold in the peak of the acceleration of the particles, obtained from experiments using a high-speed camera and optical index matching between the grains and the fluid. They showed that the collision frequency is an increasing function of the particle fraction, and follows a law derived from the kinetic theory for granular flow. For a particle fraction of 0.5, [3, 5, 6], they found that the collision frequency is O (100) Hz.

In this work, we investigate particle-particle and particle-wall collisions in narrow fluidized beds experimentally and numerically, when the fluid is a liquid. From Ref.[1], the formation of granular plugs and liquid bubbles is expected, where particle collisions are usually found inside the plugs, i.e., where the particle fraction is around 0.5, but also outside the plugs, where free-falling particles collide with the tube wall or the top of the next plug, with stronger amplitudes but much smaller frequencies. Therefore, we recorded the sound of collisions in the experiments and tracked every single particle in the numerical simulations in order to obtain the collision frequencies for NFB.

EXPERIMENTAL AND NUMERICAL SETUPS

The experimental setup consisted of a water reservoir, a heat exchanger, a centrifugal pump, a flow meter, a flow homogenizer, a 25.4 mm-ID tube with vertical and horizontal sections, and a return line, being the same of Ref. [1]. Thus, the water flowed in a closed loop in the order described above. The vertical section was a 1.2 m-long, 25.4 mm-ID transparent PMMA (Polymethyl methacrylate) tube, vertically aligned within $\pm 3°$. A visualization box filled with water was mounted around the test section to ensure proper photographic images. The water temperature was maintained at 25°C $\pm$ 3°C by the heat exchanger placed in the water reservoir. Alumina beads with d = 6 mm and ρ_p = 3690 kg/m^3 were used as the solid phase, and three different beds were arranged, each one consisting of 250, 400, 500 particles. Two water flow rates were imposed, Q = 250 and 300 l/h, corresponding to superficial velocities of $\overline{U}$ = 0.137 and 0.164 m/s. The Stokes and Reynolds numbers based on terminal velocities were $St_t = v_t d\rho_p/(9\mu_f)$ = 1650 and $Re_t = \rho_f v_t d/\mu_f$ = 4026, respectively. The NFB was filmed with a high-speed camera with a resolution of 1600 px $\times$ 2560 px at frequencies up to 1400 Hz. LED (low emission diode) lamps were used to provide the necessary light. In all the experiments, the camera frequency was set to between 100 Hz and 200 Hz, and a microphone placed on the tube's wall was used to record the sound of particle collisions. The numerical investigation was conducted with the CFD-DEM method, i.e., the fluid motion is computed with an Eulerian approach, and the granular dynamics with a Lagrangian approach. We considered a 0.45 m long and 25.4 mm-ID vertical tube, filled with alumina beads and water. The bed arrangements and the flow rates were as in the experiments. The simulations were performed with the open source code CFDEM [7], that couples OpenFOAM(CFD) to LIGGGHTS(DEM).

*Corresponding author. E-mail: fernandodcb@fem.unicamp.br

RESULTS

We found the formation of granular plugs and liquid bubbles inside the NFB. These patterns result from a competition between the mechanisms that tend to displace the particles upwards, namely the fluid drag and buoyancy, and downwards, namely the gravity and solid friction between the grains and the wall (this latter being enhanced by the redirection of forces when a granular cluster or plug is pushed upwards). From Fig.1(a), it is possible to observe the good agreement between the experiments and the numerical simulations. Therefore, we tracked every single particle in the simulations to obtain the motion of each particle. We also computed the particle fraction inside the NFB over time and determined that the mean value in the granular plugs is approximately 0.5 [Fig.1(b)]. For all the cases, we found that at least 60% of the particles are exchanged between granular plugs during a period of 5s. To determine the collision frequency from the acoustic signals, we evaluated the energy of the signals applying Fast Fourier Transforms in the time domain; afterwards, by using a high-pass filter, we obtained 2 characteristic frequencies that appear for all cases $f \approx 60$ Hz and $f \approx 120$ Hz [Fig.1(c)]. For the numerical simulations, we computed the instantaneous acceleration of the particles along time and then we used the same technique as Ref.[6], setting a threshold for the peaks of the acceleration and counting the number of peaks above that value. The magnitude of the acceleration is normalized by the acceleration of gravity g and the threshold was $2g$, meaning that we neglected free falling grains between the granular plugs, since they have an acceleration of $\approx 1g$. We observed that the collision frequency of the particles is $f \approx 200$ Hz. The frequencies of particle-wall and particle-plug were identified, and we are currently working on their values and interactions with the different plug regimes.

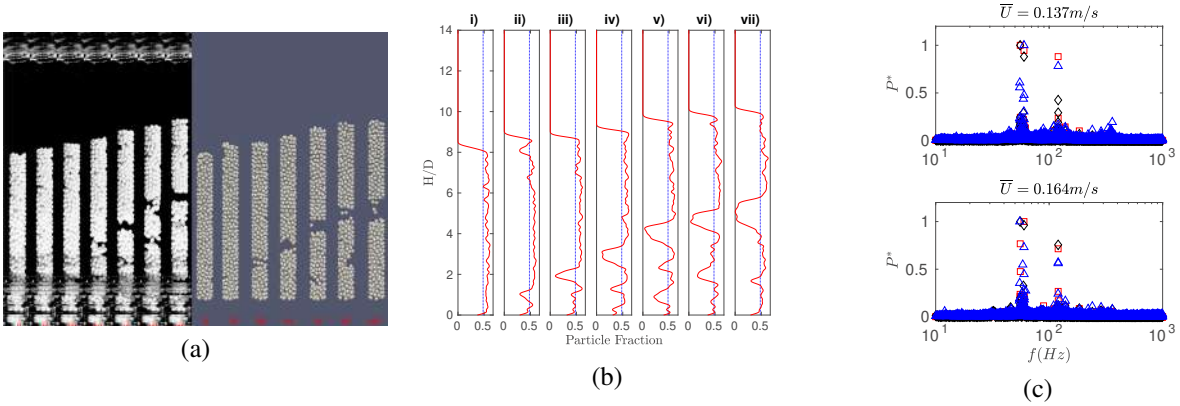

(a) (b) (c)

Figure 1: (a) Instantaneous snapshots for experiments and numerical simulations [1]; (b) Particle fraction; the time step is 0.5s; (c) Dimensionless pressure vs. Characteristic frequencies. Diamonds, squares and triangles correspond to arrangements of 250, 400 and 500 particles, respectively.

CONCLUSIONS

We presented preliminary and novel results about particle collisions in narrow fluidized beds (NFB). The collision frequency was measured in two ways: by obtaining the characteristic frequencies of recorded sounds from the NFB experiments, and analyzing the acceleration of the particles from the numerical simulations. From the results, we could observe that the total frequency has an order of magnitude of 100 Hz. We also noticed that inside the plugs the particle fraction is ≈ 0.5 and does not depend on the fluid velocity, and, in addition, we could identified from the acceleration signal different types of collision (particle-particle, particle-wall and particle-plug).

ACKNOWLEDGMENTS

F. D. C. is grateful to FAPESP (Grant No. 2016/18189-0), K. R. to the IFES-FEM/UNICAMP Dinter, and E. M. F. to FAPESP (Grant No. 2018/14981-7) and to CNPq (Grant No. 400284/2016-2) for the financial support provided.

References

[1] Cúñez F. D., Franklin E. Plug regime in water fluidized beds in very narrow tubes. *Powder Technol.* **345**: 234-246, 2019.
[2] Nelson M. J., Nakhla G., Zhu J. Fluidized-bed bioreactor applications for biological wastewater treatment: A review of research and developments. *Engineering* **3**: 234-246, 2017.
[3] Del Pozo M., Briens C. L., and Wild G. Particle-particle collisions in liquid-solid and gas-liquid-solid fluidized beds. *Chem. Eng. Sci.* **48**: 3313-3319, 1993.
[4] Zenit R., Hunt M.L, Brennen C.E. Collisional particle pressure measurements in solid-liquid flows. *J. Fluid Mech* **353**: 261-283, 1997.
[5] Buffière P., Moletta R. Collision frequency and collisional particle pressure in three-phase fluidized beds. *Chem. Eng. Sci.* **55**: 5555-5563, 2000.
[6] Aguilar-Corona A., Zenit R., and Masbernat O. Collisions in a liquid fluidized bed. *Int. J. Multiphase Flow* **37**: 695-705, 2011.
[7] Goniva C., Kloss C., Deen N. G., Kuipers J. A. M., Pirker S. Influence of rolling friction on single spout fluidized bed simulation. *Particuology* **10**: 582-591, 2012.

O108986 - FS08 - Granular Materials and Flows - Oral

EXTENDED KINETIC THEORY FOR GRANULAR FLOW OVER AND WITHIN AN INCLINED, ERODIBLE BED

Diego Berzi [1], James T. Jenkins [2], and Patrick Richard [3]
[1]Department of Civil and Environmental Engineering, Politecnico di Milano, Milano, Italy
[2]School of Civil and Environmental Engineering, Cornell University, Ithaca, USA
[3]IFSTTAR, site de Nantes, GPEM/MAST, Bouguenais, France

Summary We employ kinetic theory, extended to incorporate the influence of velocity correlations, friction and particle stiffness, and a model for rate-independent, elastic components of the stresses at volume fractions larger than a critical, in an attempt to reproduce the results of discrete-element numerical simulations of steady, fully developed, dissipative, collisional shearing flows over and within inclined, erodible, fragile beds. Numerical solutions of the span-wise averaged differential equations of the theory and the associated boundary conditions are seen to be capable of reproducing profiles of stresses, solid volume fraction, average velocity, and the strength of the particle velocity fluctuations, both in the rapid collisional flow above the bed and in the slower creeping flow within the bed.

INTRODUCTION

Particle flows in nature, such as rock avalanches, occur at length scales that are so large that continuum descriptions must be employed to predict their initiation, flow, and run out. In the search for constitutive relations for the closure of such continuum models in the last fifteen years, two approaches have emerged. One is based on kinetic theory of granular gases [1, 2], extended to include the role of significant contact inelasticity [3], surface friction [4], velocity correlations [5], and particle stiffness [6]; the other is based on a phenomenological relation, the inertial rheology, between the particle shear stress and the shear rate, both made dimensionless using the particle pressure, mass density and diameter [7, 8].

The two approaches offer advantages and disadvantages. Extended Kinetic Theory (EKT) requires as inputs four microscopic, well-defined, parameters, at least in the case of linear contacts, that are also the inputs of discrete element numerical simulations of compliant spheres: the normal and tangential coefficients of restitution, the negative of the ratios of post- to pre-collisional normal and tangential relative velocities between two colliding spheres; the coefficient of sliding friction; and the particle stiffness. On the other hand, EKT introduces a measure of the intensity of the particle velocity fluctuations, the granular temperature, that enters the constitutive relations for the stresses. This additional hydrodynamic variable is governed by a partial differential equation, the balance of fluctuation kinetic energy, that must be solved in addition to the classical mass and momentum balances.

In its simplest incompressible form, the inertial rheology requires three model parameters obtained as fits to experiments or numerical simulations. The rather large number of fitting parameters seems justified, given the simplicity of the approach and its straightforward implementation in already existing mathematical models that employ only mass and momentum balances. However, there are several nonlocal effects that cannot be predicted by the inertial rheology, such as the influence of the boundaries on steady, inclined flows over rigid, rough bases [9] and creep in regions where the stress ratio is less than yield [10]. To deal with this nonlocality, Kamrin and Koval [11] recently suggested the introduction of an additional hydrodynamic field, the granular fluidity, governed by a second-order partial differential equation. This nonlocal model has been successfully employed in a number of flow configurations[12, 13], but at least one additional fitting parameter is necessary. Also, distributions of solid volume fraction and stresses cannot be predicted by the nonlocal model: they have to be known in advanced and treated as inputs.

GOAL

The goal of the present paper is to apply Extended Kinetic Theory to steady, inhomogeneous shearing flows in which the solid volume fraction exceeds the critical value for the development of rate-independent components of the stresses. The flow that we consider is the steady, gravity-driven, free surface flow of frictional, soft spheres over a rigid, bumpy base between flat, frictional sidewalls. When a sufficient number of particles is fed to the system, the flow develops an erodible bed above the rigid base. Above the bed, the spheres interact through collisions, with uncorrelated, binary collisions occurring near the top of the flow and correlated collisions taking place nearer to the bed. Within the bed, the particles creep [14], collisions continue to occur, but ephemeral force chains develop and transfer forces from the bed to the rigid base.

Here, we use EKT for modelling the flow above the bed and propose a model for flow in the bed that combines the rate-dependent mechanism of collisional momentum transfer with the rate-independent elastic transfer of force through a continuous evolving network of chains of particles. The surface of the bed is at the same critical volume fraction at which rate-independent components of the stresses develop in steady, homogeneous shearing flows. However, the force chains that begin at the surface the bed are much weaker that those that span the homogeneous flows [15].

RESULTS

We compare the distributions of various quantities obtained from the solution to the two-point boundary value problem with those measured in DEM simulations of inclined flows of inelastic, frictional spheres between frictional sidewalls. The discrete element method is based on the soft-sphere approach.

EKT can qualitatively and quantitatively reproduce the profiles of velocity (figure 1), both in the collisional flow and in the erodible bed. The well-known exponential decay of the velocity in the erodible bed is notably predicted.

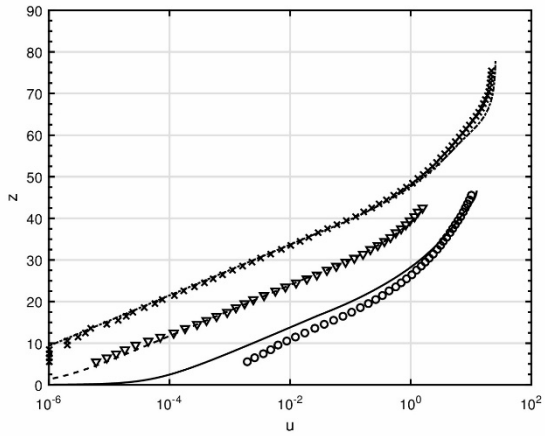

Figure 1. Measured (symbols) and predicted (lines) profiles of velocity for different mass hold-ups, angles of inclination and channel widths.

CONCLUSIONS

We have focused on steady and fully developed, inclined, collisional shearing flows of frictional spheres confined between flat, frictional sidewalls in situations in which the amount of particles in the system is sufficient to develop erodible beds. The bed is the region in which the solid volume fraction exceeds the critical value for the development of rate-independent components of the stresses. Existing results of Discrete Element simulations demonstrate that the flow above the erodible bed is inherently collisional: interactions are essentially binary and stresses originate from momentum exchange in collisions. We have employed the constitutive relations of Extended Kinetic Theory, which accounts for strong collisional inelasticity, friction, velocity correlation at volume fraction larger than the freezing point, and finite duration of particle contacts, to close the balances of momentum and fluctuation energy in the collisional flow.

In the bed, rate-independent stresses proportional to the particle stiffness develop, although much weaker than the rate-independent stresses that would characterize steady and fully developed, homogeneous shearing flows at the same volume fraction.

The comparisons between the numerical solution of the present model and the results of discrete numerical simulations for different values of particle mass per unit basal area, channel widths and inclinations are remarkable. The limited number of physically accessible parameters of the model and its capability of reproducing distributions of stresses, volume fractions, velocity and granular temperature, ranging from dilute to extremely dense conditions, are strong arguments in favor of EKT when dealing with granular flows.

References

[1] Haff P. K. *J. Fluid Mech.* **134**: 401–430, 1983.
[2] Jenkins J. T., Savage S. *J. Fluid Mech.* **130**: 187–202, 1983.
[3] Garzó V., Dufty J. W. *Phys. Rev.* E **59**: 5895–5911, 1999.
[4] Jenkins J. T., Zhang C. *Phys. Fluids* **14**: 1228–1235, 2002.
[5] Jenkins J. T. *Granul. Matter* **10**: 47–52, 2007.
[6] Berzi D., Jenkins J. T. *Soft Matter* **11**: 4799–4808, 2015.
[7] G.D.R. Midi *Eur. Phys. J.* E **14**: 341–65, 2004.
[8] Jop P., Forterre Y., Pouliquen O. *Nature* **441**: 727–730, 2006.
[9] Pouliquen O. *Phys. Fluids* 11: 542–548, 1999.
[10] Koval G., Roux J.-N., Corfdir A., Chevoir F. *Phys. Rev.* E **79**: 021306, 2009.
[11] Kamrin,K., Koval G. *Phys. Rev. Lett.* **108**: 178301, 2012.
[12] Henann D. L., Kamrin K. *PNAS* **110**: 6730–6735, 2013.
[13] Kamrin K., Henann D.L., *Soft Matter* **11**: 179–185, 2014.
[14] Komatsu K., Inagaki S., Nakagawa N., Nasuno S. *Phys. Rev. Lett.* **86**: 1757–1760, 2001.
[15] Berzi D., Jenkins J. T.,. Richard P. *Soft Matter* **15**: 7173–7178, 2019.

GRANULAR DISCHARGE FLOW FROM A CORNER

Pascale Aussillous* [1], Samira Laidaoui [1,2], and Blanche Dalloz1
[1]Aix Marseille Univ, CNRS, IUSTI, Marseille, France
[2]Tahri Mohammed university of Bechar, FIMAS, BP417, Bechar 08000, Algeria

Summary In this work, we study the discharge flow of a granular material from a rectangular silo with an orifice at the corner. We performed experiments where we measure independently the mass flow rate and the velocity profiles, together with continuum simulations with a frictional rheology described by a $\mu(I)$ constitutive law and taking into account the wall friction. We study monolayer flows and 3D flows and we aim to propose an analytical model that predicts the discharge flow rate of particles taking into account the outlet horizontal and vertical size and the silo thickness.

INTRODUCTION

Silos are widely used in the industry. While empirical predictions of the flow rate, based on scaling law, exist for more than a century [1, 2], recently advances have been made on the understanding of the control parameters of the flow. In particular using continuum modelling together with the so-called $\mu(I)$ visco-plastic frictional rheology seem to be successful in predicting the flow rate [3, 4]. Recently Zhou et al [5] have shown experimentally and using continuum simulation that if the outlet, of size D, is located at a lateral position the silo thickness, W, plays a role due to the confinement of the geometry. Indeed they have shown that the parietal friction tends to rotate the streamlines to align them toward the gravity with an angle toward the vertical at the outlet $sin\theta_0 \propto (1+\gamma D/W)^{-1/2}$, whereas the norm of the velocity scales with the aperture size, $U_0 \propto \sqrt{gD}$. Then they predicted that the flow rate follows

$$Q = C_l \rho_p \phi_b W D \frac{\sqrt{gD}}{\sqrt{1+\gamma D/W}} \tag{1}$$

where ϕ_b is the bulk volume fraction, ρ_p the particle density, C_l and γ are fitting parameters. For outlet situated at the bottom of the silo, the central streamline is align with the gravity and the confinement does not play a role leading to the classical Hagen law where $Q \propto WD^{3/2}$. The aim of this study is to predict the discharge flow rate when the outlet is situated both at a lateral and at a bottom position, i.e. a corner, and to identify the role of the confinement.

EXPERIMENTS

As shown in Figure 1a, the experimental setup consists on a rectangular silo (of height $H = 1$ m, width $L = 10$ cm and thickness W which can be varied between 5 and 20 mm) made of two thin vertical glass plates separated on the sides by Plexiglas plates. The outlet is located at the right corner and is defined by its horizontal and vertical size, respectively D_x and D_y. The granular material consists of smooth spherical ceramic beads (density $\rho_p = 6000$ kg.m^{-3}) with different diameters d_p from 190 to 4350 μm (with a dispersion of $\pm 10\%$). Once the silo filled with a mass m_p of particles, the column height h_p is measured, giving the initial bulk particle volume fraction ϕ_b. Then the outlet is quickly opened manually and the grains falling out of the silo are collected in a vessel whose temporal evolution of the mass is recorded using an electronic scale. Each experiment is repeated twice to validate the reproducibility of the process. We observe rapidly a steady-state regime of discharge for all the configurations explored and the steady flow rate Q is obtained by time averaging the instantaneous flow rate during this stationary state. The motion of particles at the front plate is recorded using a high-Speed camera with a spatial resolution of 1024×1024 at a rate higher than 500 frames per second. The test section is located at the bottom of the silo and is ≈ 6 cm wide to permit both good visualisation of the flow around the outlet and good resolution of the particle imaging. Particle velocities are measured by particle image velocimetry (PIV).

CONTINUUM MODELLING

Following [5] we simulate the discharge flow of a granular medium from a rectangular silo with an orifice at the corner considering a non-Newtonian incompressible Navier–Stokes system, averaged across the thickness of the silo:

$$\begin{aligned} \frac{\partial u_i^p}{\partial x_i} &= 0 \\ \rho\left[\frac{\partial u_i^p}{\partial t} + u_j^p \frac{\partial u_i^p}{\partial x_j}\right] &= \frac{\partial \sigma_{ij}^p}{\partial x_j} + \rho g_i + f_{wi}, \end{aligned} \tag{2}$$

where $f_{wi} = -2\frac{\mu_w p^p}{W}\frac{u_i^p}{|u_i^p|}$ represents the depth averaged Coulomb friction on the front and back wall, with a coefficient of friction $\mu_w = 0.1$. The stress tensor of the particle phase $\sigma_{ij}^p = -p^p\delta_{ij} + \tau_{ij}^p$ comes only from direct particle-particle

*Corresponding author. E-mail: pascale.aussillous@univ-amu.fr.

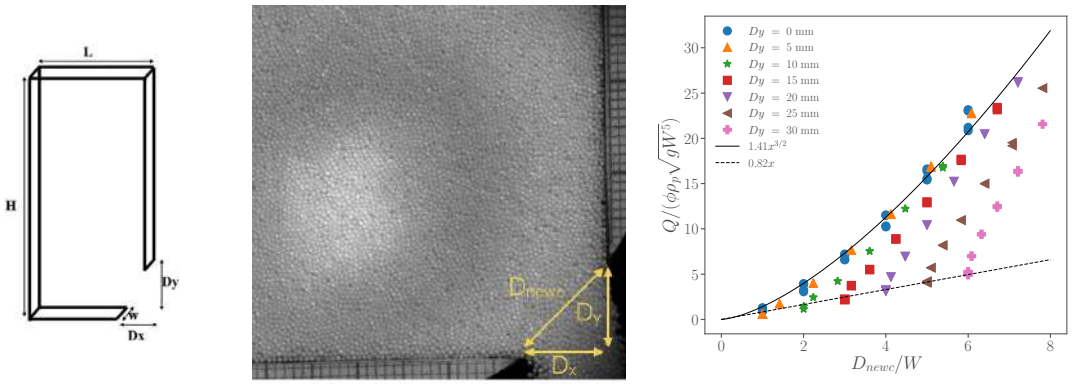

(a) (b) (c)

Figure 1: (a) Experimental set-up. (b) Snapshot of the discharge flow for $d_p = 500\mu$m and $W = 5$mm. (c) Normalised flow rate versus the outlet aspect ratio.

interactions and can be described by a shear-dependant frictional rheology [6], $\tau^p_{ij} = \eta_p(|\dot{\gamma}|, p^p)\dot{\gamma}_{ij}$ with $\eta_p(|\dot{\gamma}|, p^p) = \frac{\mu(I)p^p}{|\dot{\gamma}|}$. We define $I = |\dot{\gamma}|d/\sqrt{p^p/\rho_p}$ where $\dot{\gamma}_{ij} = \partial u^p_i/\partial x_j + \partial u^p_j/\partial x_i$ is the strain-rate tensor and $|\dot{\gamma}| = (0.5\dot{\gamma}_{ij}\dot{\gamma}_{ij})^{0.5}$ its second invariant. For the shear-dependant friction coefficient, we take $\mu(I) = \mu_s + \Delta\mu/(I_0/I + 1)$ with the constant $I_0 = 0.4$, $\mu_1 = 0.4$, and $\mu_2 = 0.68$ [7]. The Navier–Stokes simulations are performed with the free software *Basilisk* which uses a finite-volume projection method and we use a regularisation technique to avoid the divergence of the viscosity.

RESULTS AND DISCUSSION

As shown in Figure 1b, for an aperture at the corner controlled by its horizontal and vertical size we can define the outlet length D_{newc} given by:

$$D_{newc} = (D_x^2 + D_y^2)^{1/2} \tag{3}$$

Figure 1c shows the normalised flow rate $Q/(\rho_p\phi_b\sqrt{gW^5})$ versus the aperture aspect ratio D_{newc}/W for $d_p = 190$ μm and $W = 5$mm. We observe that for an orifice at the bottom, $D_y = 0$, the flow rate is maximum and scales with $(D_{newc}/W)^{3/2}$ corresponding to the classical Hagen law (see the full line). Considering now the case of a lateral orifice with $D_x = 0$, we observe that the flow rate is linear with D_{newc}/W (see the dashed line), corresponding to the asymptotic limit of equation 1 for large D_{newc}/W in good agreement with the experimental and numerical results of Zhou et al. [5]. This shows that D_x and D_y do not play the same role and that the silo thickness is also an important parameter of control of the discharge flow from a corner, due to the friction on the front and rear wall. When D_x and D_y are non-zero values, we observe that all the data are in between these two regimes which suggests that D_{newc}/W is not the correct parameter to describe the discharge flow rate from a corner. To better understand the physical process and the relevant parameters we have performed particle image velocimetry to obtain the velocity fields and in particular the central streamline orientation and the magnitude of the velocity at the outlet. We compare the results with the continuum simulations and propose an empirical law for the discharge flow rate of a granular media from a corner.

References

[1] B. P. Tighe and M. Sperl, Pressure and motion of dry sand: translation of Hagen's paper from 1852, *Granular Mat.* , 9 (2007) 141-144.
[2] W.A. Beverloo, H.A. Leniger and J.V. De Velde, The flow of granular solids through orifices, *Chem. Eng. Sci.* 15 (1961) 260-269.
[3] L. Staron and P.-Y. Lagrée and S. Popinet, The granular silo as a continuum plastic flow: The hour-glass vs the clepsydra, *Phys. Fluids* 24 (2012) 103301.
[4] L. Staron and P.-Y. Lagrée and S. Popinet, Continuum simulation of the discharge of the granular silo, A validation test for the μ(I) visco-plastic flow law, *Eur. Phys. J. E* , 37 (2014) 5.
[5] Y. Zhou, P.-Y. Lagrée, S. Popinet, P. Ruyer, P. Aussillous, Experiments on, and discrete and continuum simulations of, the discharge of granular media from silos with a lateral orifice, *J. Fluid Mech.*, 829 (2017) 459-485.
[6] P. Jop and Y. Forterre and O. Pouliquen, A constitutive law for dense granular flows, *Nature*, 441 (2006) 727-730.
[7] Y. Forterre and O. Pouliquen, Flows of Dense Granular Media, *Annu. Rev. Fluid Mech.*, 40 (2008) 1–24.

FLOW OF WET GRANULAR MATERIALS: EXPERIMENTS AND SIMULATIONS

Abdoulaye Fall[1] and Jean-Noël Roux* [1]
[1]Lab. Navier, Univ. Gustave Eiffel, Ecole Nationale des Ponts et Chaussées, CNRS, Champs-sur-Marne, France

Summary Shear flows of assemblies of wet grains (diameter d) at small liquid saturation (as liquid bridges form near contacts) are investigated with laboratory rheometric experiments and numerical simulations (DEM). Constitutive laws are conveniently expressed in terms of two dimensionless parameters: inertial number I (dimensionless shear rate) and reduced pressure $P^* = \sigma_{22} d^2/F_0$, comparing normal stress σ_{22} in the gradient direction to capillary force F_0. Once the intergranular friction coefficient μ is identified, from the I-dependent rheology of *dry* grains, the simulations quantitatively agree with experiments for $P^* \geq 2$. X-ray tomography is used to probe the 3-phase microstructure. A Mohr-Coulomb cohesion c may be defined in the quasistatic limit, and its microscopic origins are identified. Effects of the liquid viscosity are investigated.

INTRODUCTION

Wet granular materials [1] at small liquid saturations (as liquid menisci join neighboring grains) are interesting both as a particular regime of grain-fluid mixture and as a case of a cohesive granular material for which a quantitative description of interactions is available and numerical simulations can be carried out with well identified models and parameters. We show here that the rheology in shear flow can be measured and its microscopic origins investigated thanks to a combination of rheometry and X-ray visualization in the laboratory, on the one hand, and DEM-type numerical simulations, on the other hand.

MODEL MATERIAL AND RHEOLOGICAL TESTING PROCEDURE

Polystyrene beads of diameter 0.5 mm are mixed with silicone oil, with surface tension $\Gamma \simeq 20.6$ mJ.m^{-2} and contact angle below 5°, varying liquid content $\epsilon = V_l/V_s$ (defined as the liquid to solid volume ratio) in range $0.015 \leq \epsilon \leq 0.075$. The material is tested in normal force-controlled shear flow in a rheometer [2] as sketched in Fig. 1. The top and bottom

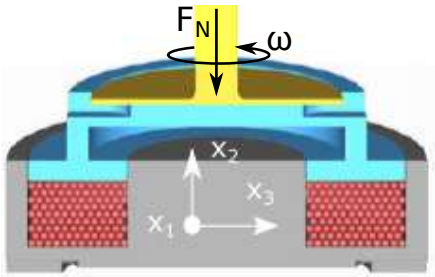

Figure 1: Annular cell (cut by plane containing rotation axis), with controlled normal force F_N on upper wall and varying height h, used in rotatory rheometer.

plates are rough and lateral walls are smooth to enforce as accurately as possible a uniform velocity gradient in the vertical direction. Normal stress σ_{22} and strain rate $\dot{\gamma}$ are respectively deduced from the imposed values of the angular velocity and the normal force, while cell height h in steady flow fixes solid fraction Φ_S and the shear stress is deduced from the measured torque.

Simulations [3] are carried out with standard discrete element modeling of elastic-frictional beads, supplemented by a capillary force model, suitable for small liquid bridges, with contact value $F_0 = \pi \Gamma d$. Elastic properties are irrelevant in flow under ordinary pressure, and the intergranular friction coefficient μ is chosen in order to reproduce the behavior of dry grains in shear flow, as $\mu = 0.09$. The contact laws are described in detail in Refs. [3, 4]. Shear flows are simulated with, typically 4000 beads in a fully periodic cell of variable height [5]. As in experiments, the main macroscopic measurements are those of shear stress σ_{12}, from which the effective macroscopic friction coefficient $\mu^* = |\sigma_{12}/\sigma_{22}|$ is deduced, and of the solid fraction Φ_S.

The material behaviour depends on two dimensionless control parameters: reduced normal stress $P^* = \sigma_{22} d^2/F_0$, comparing cohesive to confining forces, and inertial number $I = \dot{\gamma} d \sqrt{\frac{\rho_S}{\sigma_{22}}}$ (ρ_S denoting the mass density of the solid grains).

*Corresponding author. E-mail:jean-noel.roux@univ-eiffel.fr

MICROTOMOGRAPHIC OBSERVATIONS

A similar rheometric cell was used for microtomographic measurements, consisting of a rotatory plate above a cylindrical cup. This geometry is more favourable for the absorption signal analysis. Images of the corresponding 3-phase morphologies are obtained on assuming they do not change during the necessary time of exposure, and we extract regions where the shear rate is nearly constant during flow. Fig. 2 shows how, for the larger liquid contents, the pendular regime crosses over to a different kind of morphology with menisci merging into larger clusters. Such measurements were also

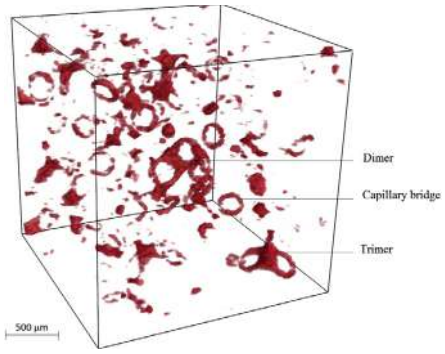

Figure 2: View of liquid menisci within flow, apparent as rings (the liquid layer is too small in meniscus center to be detected). Some are connected to their neighbours, concerning the same grain, forming "clusters" of 3 to 7 rings.

used to check for the absence of global liquid migration – as could be induced by the appearance of narrow shear bands.

MATERIAL RHEOLOGY

Laboratory results for μ^* and Φ_S were shown to be independent of the sample thickness h, ranging from $10d$ to $40d$. Fig. 3 shows the agreement of μ^* and Φ_S, achieved without fitting parameters (once dry quasistatic results are adjusted with $\mu = 0.09$), between simulations and experiments – save perhaps for a somewhat faster increase of μ^* with I at low P^*. We are thus in a good position to exploit the numerical results in the investigation of the microscopic origins of the

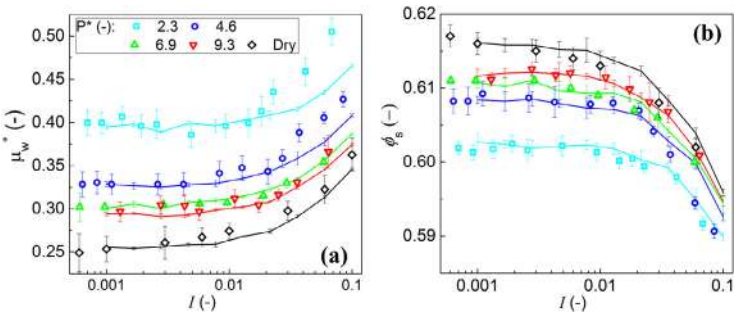

Figure 3: (a) Macroscopic friction coefficient and (b) solid fraction, versus I for different values of P^*. Experimental results are shown as dots, numerical ones as continuous lines.

observed rheology. This was done, e.g., for the observed values of the macroscopic Mohr-Coulomb cohesion [5].

PERSPECTIVES

Some results were obtained for the effects of the liquid viscosity, which causes some increase of μ^*, a decrease of Φ_S and introduced a third influential dimensionless parameters. The influence of liquid content ϵ, quite small in he explored range, will be investigated beyond the pendular regime.

References

[1] N. Mitarai and F. Nori. Wet granular materials. *Advances in Physics*, 55:1, 1–45, 2006.
[2] M. Badetti, A. Fall, D. Hautemayou, S. Rodts, and J.-N. Roux. Rheology and microstructure of unsaturated wet granular materials: Experiments and simulations. *J. of Rheology*, 62:1175–1186, 2018.
[3] S. Khamseh, J.-N. Roux, and F. Chevoir. Flow of wet granular materials: a numerical study. *Phys. Rev. E*, 92:022201, 2015.
[4] V.-D. Than, S. Khamseh, A.-M. Tang, J.-M. Pereira, F. Chevoir, and J.-N. Roux. Basic Mechanical Properties of Wet Granular Materials: A DEM Study. *ASCE Journal of Engineering Mechanics*, 143(SI1):C4016001, 2017.
[5] M. Badetti, A. Fall, F. Chevoir, and J.-N. Roux. Shear strength of wet granular materials: Macroscopic cohesion and effective stress. *European Physical Journal E*, 41:68, 2018.

NUMERICAL INVESTIGATION OF STATISTICAL VARIATION OF RANDOM PACKED BED CHARACTERISTICS

K. Gruszka[1], P. Niegodajew[2] and M. Marek[2]
[2]Czestochowa University of Technology, Department of Physics, Częstochowa, Poland
[1]Czestochowa University of Technology, Department of Thermal Machinery, Częstochowa, Poland

Summary Packings of particles have recently become an object of extensive research. A large number of works is devoted to studies of packed beds characteristics including for instance global and local porosity or orientation distribution of particles. However, despite the random nature of the considered packings, very little attention is devoted to examination whether the number of particles adopted in experiments/simulations is sufficient to get reproducible results. When filling the same container with particles twice, one may expect that the characteristics of the packing structure will not be the same. The reproducibility of packing parameters will depend on a number of factors, in particular, the number of particles (sample size) and ordering effects induced by the confining walls. The purpose of the present study was to analyse the influence of the sample size on the statistical variation of the packed bed characteristics in different realisations of the packing process.

INTRODUCTION

Particles packing is a common problem in a number of engineering applications. One of its applications lies in power industry where the random packing is used in boilers equipped with fluidised beds. The size of particles and their packing density is crucial in particle and heat transport within the boiler. When concerning the pebble bed reactor in nuclear engineering, the graphite reflector life-time is dependent on its efficient cooling, which in turn depends on liquid flow maldistribution within the packed bed. The packing of particles is widely used in chemical industry where heat and mass transfer processes are very common – absorption and stripping may serve as examples.

Mentioned above processes can be improved by intervening, in particular, into the packing geometry. Therefore, a number of works can be found in the literature which focuses on study of such properties as local and global porosity distributions [1], orientation of particles [2] and tortuosity [3] of the pore channels within a packed bed interior. However, very little attention is devoted to study whether the number of particles employed in experiments and simulations is sufficient to get reproducible statistics of packed beds like orientation distribution of particles or local void fraction profiles.

When randomly filling the same space with particles twice, it can be expected that the properties of the resulting packing structure will not be the same. The repeatability of key packaging parameters will depend on many factors, in particular on the size of the population of particles and the ordering effects caused by the bounding walls. In a previous study [4] it was shown that for a very large sample the orientation distribution is almost independent of the packaging procedure. Therefore it is necessary to verify such reproducibility for smaller samples, much more adequate from the point of view of typical experiments [5] or simulations [6]. It is possible that some of the available experimental/numerical results on particle orientation distributions are questionable because of insufficiently large number of particles' used. Hence, the aim of the present work is to analyse the influence of the sample size on the statistical variation of the packed bed characteristics, including particle orientation and porosity (not shown here) in different realisations of the packing process.

NUMERICAL MODEL

In this work, packed bed geometries were generated numerically using of the discrete element method described in detail in the works [7,8]. Such an approach is based on sequentially added particles to the bed. In this procedure, firstly, a single particle is placed above the bed with random location and random orientation. Secondly, the particle motion is due to the gravity force and reaction forces resulting from contact with other particles until reaching the mechanical equilibrium. After this step the particle is incorporated into the bed structure at fixed position until the deposition process is completed. To detect the overlap of particles, each of them is covered with a uniform grid of marker points. Such an approach reduces the problem of calculating the overlap to obtain the immersion distance of the point (marker) in the particle. The direction of reaction force is set to push the marker out of the other particle. An additional force acting in the direction normal to the container axis is included in order increase the packing density and to achieve a more realistic structure with inherent ordering.

SAMPLE RESULTS

From the practical point of view it is preferable to define the sample of interest in the form of its physical dimensions, e.g. the packing height h_B, hence, the results will be presented employing these parameters as independent variables. The number of particles in the sample of a packed bed of height h_B should obviously depend on diameter D_p of the particle and diameter D_c of the column (or ratio D_c/D_p). We obtained results for numerically generated random packed beds of equilateral ($H_p/D_p = 1$) Raschig rings (hollow cylinders, which are commonly used as a packing material in trickle bed reactors) in columns with different aspect ratios D_c/D_p equal to 7, 15 and 30. The inner particle diameter

was set to be $0.8D_p$. Single particle orientation is defined as angle φ ($0 \le \varphi \le 90$ deg) between a column's and particle's symmetry axis. Due to an axisymmetric shape of the container the remaining angles necessary to specify the exact orientation of a particle are not concerned as their probability distribution is uniform.

The first study concerned the evolution of PDF(φ) (Probability Density Function) with increasing distance from the column bottom h_B for D_c/D_p=7 – see Fig. 1a. It can be observed that the PDF(φ) is characterised by relatively large irregularities. These fluctuations are reduced as both the packing height d_B and column particle diameter ratio D_c/D_p increases. This can be expected given that for larger D_c/D_p each layer of particles is more numerous, and therefore the sample size increases faster with h_B.

In order to take a closer look at the reproducibility of the orientation distribution, 10 independent simulations for each considered D_c/D_p ratio were performed. Similarly to the study of PDF(φ), this one was aimed at analysing the impact of packed bed height on variations of PDFs. Figure 1b presents the complementary quantitative results showing the evolution of averaged variability of PDF(φ) defined as:

$$\overline{C_v}^{or} = \frac{1}{n}\sum_{i\in B}\frac{\sigma_i^{or}}{\mu_i^{or}} \tag{2}$$

In the above relation σ_i^{or} and μ_i^{or} are the standard deviation and the mean value of probability determined for i^{th} class (bin) $[\varphi_i, \varphi_{i+1}]$ of orientation angles (the size of each bin was taken as $\varphi_{i+1} - \varphi_i = 5^\circ$, except for the first and last bin of size 2.5°), while n represents number of classes. Figure 1b shows the dependence of the averaged variability of PDF(φ) on the packing height. As can be seen, in general, the averaged variability decreases with the increasing h_B because the number of particles also increases. One should note that with increasing D_c/D_p and h_B the averaged variability decreases, again as the result of increasing sample size.

Regarding the maximum variability it may be of interest to study the contribution of each orientation class to the variability coefficient. For this purpose PDFs of orientations with standard deviation σ_i^{or} of probability marked with bars for D_c/D_p=7 is presented in Fig. 1c for h_B=10. As can be seen different classes of PDF(φ) are characterized by different σ_i^{or}. The most reproducible classes of angles are 0° and 10° whereas the class centred at 50° which is the least reproducible.

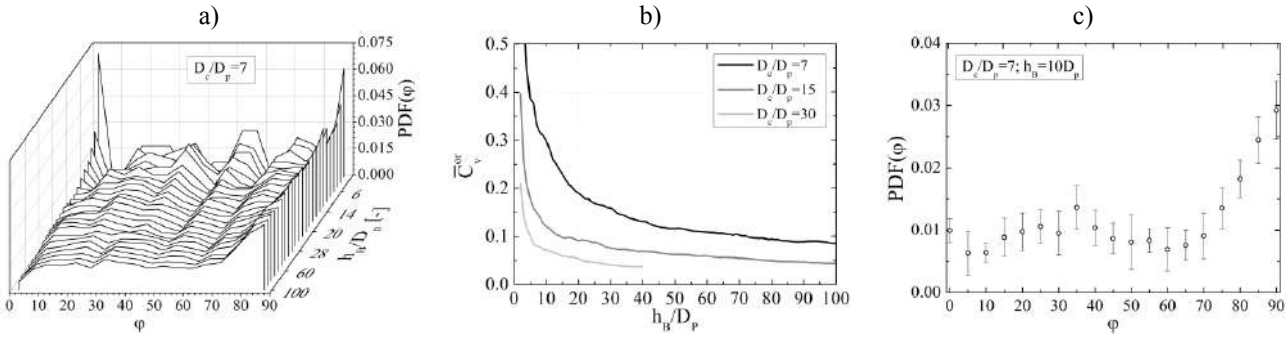

Figure 1. PDFs of orientation distribution – evolution with respect to the increasing h_B for D_c/D_p=7 (a), averaged variability of PDF(φ) as a function of the packing height for D_c/D_p=7, D_c/D_p=15 and D_c/D_p=30 (b) and PDF of orientation with standard deviation bars for D_c/D_p = 7 and h_B = 10 (c)

CONCLUSIONS

We showed that the PDF(φ) strongly depends on the sample size. In particular for slender columns the relative variation of the probability of specific angles can be as high as 50% when the number of layers of the packing is smaller than 10. The statistical variation of orientation angles is influenced not only by the sample size but also by the ordering effects introduced by the column walls or its bottom. The averaged variability of PDF(φ) is not as severe as for single angle classes but can be significant even for larger number of particles in slender columns.

ACKNOWLEDGMENTS

The investigation was supported by National Science Centre, Poland under the Grant No. UMO-2018/31/D/ST8/00199.

References

[1] C.G. du Toit, Nucl. Eng. Des. 238 (2008) 3073–3079.
[2] M. Marek, P. Niegodajew, Powder Technol. 360 (2020) 569–576.
[3] W. Sobieski, Granul. Matter 18: 72 (2016).
[4] P. Niegodajew, M. Marek, Powder Technol. 297 (2016) 193–201.
[5] R. Caulkin, W. Tian, M. Pasha, A. Hassanpour, X. Jia, Comput. Chem. Eng. 76 (2015) 160–169.
[6] J. Kang, Y. Ciou, D. Lin, D.S. Wong, S. Jang, Chem. Eng. Res. Des. 147 (2019) 43–54.
[7] M. Marek, Chem. Process Eng. 34 (2013) 347–359.
[8] M. Marek, Chem. Eng. Sci. 161 (2017) 382–393.

TRANSPORT COEFFICIENTS IN MODERATELY DENSE MULTICOMPONENT GRANULAR SUSPENSIONS

Rubén Gómez González * [1] and Vicente Garzó[1]
[1]Departamento de Física, Universidad de Extremadura, E-06006 Badajoz, Spain

Summary The Enskog kinetic equation for binary granular mixtures in the presence of a bath is considered as a model for multicomponent granular suspensions at moderate densities. As usual, the bath is modeled as a combination of a viscous drag force plus a stochastic Langevin-like term defined in terms of a background temperature. The Enskog equation for the suspension model is solved by means of the Chapman–Enskog method conveniently adapted to dissipative dynamics. To first-order in spatial gradients, the Navier–Stokes transport coefficients are explicitly determined in terms of the parameter space of the problem (masses and sizes, composition, coefficients of restitution, density, and background temperature). A comparison with previous results derived in the dry granular case (no gas phase) shows that in general the impact of the interstitial gas on grains is significant, specially for strong inelasticity.

INTRODUCTION

Kinetic theory tools have been employed in the last few years to get the transport properties of granular matter under rapid flow conditions [1]. Studies have covered not only monodisperse (dry) granular gases but also polydisperse systems where grains have different masses, sizes, and coefficients of restitution. In particular, the Enskog theory has been considered as a reliable model for describing transport at moderate densities. However, although granular matter in nature is generally immersed in a a fluid (like air or water), most of the theoretical and computational works have ignored the influence of the interstitial fluid on the dynamics of grains. Thus, the studies on the application of kinetic theory to gas-solid flows (granular suspensions) are scarcer than those performed so far for dry granular gases.

As usual [2], to model the granular suspension one assumes that the state of the surrounding gas is not affected by the solid particles while the influence of the gas phase on grains is accounted for by means of an external force. This external force is composed by two terms: (i) a viscous drag force proportional to the velocity of the particles and a stochastic force acting on the granular particles. In addition, in the case of a binary system, the drift coefficients γ_i ($i = 1, 2$) appearing in the fluid-solid external forces depend on both partial and global volume fractions and the mechanical properties of grains (masses and sizes).

The objective of this contribution is to determine the Navier–Stokes transport coefficients of the above suspension model. This task is accomplished in two steps. First, in the absence of spatial gradients, the steady state achieved when the energy lost by inelastic collisions and viscous friction is compensated for by the energy injected by the stochastic force is studied. In particular, the partial temperatures T_1 and T_2 (measuring the mean kinetic energy of each component) are explicitly obtained in terms of the parameter space of the problem. The theoretical predictions of these quantities are also shown to be in good agreement with molecular dynamics (MD) simulations. Once the homogeneous steady state is characterized, the set of Enskog equations for the binary mixture is solved by means of the Chapman–Enskog (CE) method. To first-order in spatial gradients, the constitutive equations for the mass, momentum, and heat fluxes are derived with explicit forms for the complete set of relevant Navier–Stokes (NS) transport coefficients.

ENSKOG EQUATION FOR POLIDISPERSE GRANULAR SUSPENSIONS

We consider a granular binary mixture of inelastic smooth hard disks ($d = 2$) or spheres ($d = 3$) immersed in a molecular gas of viscosity η_g. Inelasticity in collisions between particles of the component i with particles of the component j is only characterized by the constant (positive) coefficients of restitution $\alpha_{ij} \leq 1$. In the presence of the gravitational field $\mathbf{g}$, the one-particle velocity distribution function $f_i(\mathbf{r}, \mathbf{v}, t)$ of the component i obeys the Enskog equation

$$\frac{\partial f_i}{\partial t} + \mathbf{v}\cdot\nabla f_i + \mathbf{g}\cdot\frac{\partial f_i}{\partial \mathbf{v}} - \gamma_i \Delta\mathbf{U}\cdot\frac{\partial f_i}{\partial \mathbf{v}} - \gamma_i \frac{\partial}{\partial \mathbf{v}}\cdot\mathbf{V} f_i - \frac{\gamma_i T_{\text{ex}}}{m_i}\frac{\partial^2 f_i}{\partial v^2} = \sum_{j=1}^{2} J_{ij}[f_i, f_j], \quad (i = 1, 2), \tag{1}$$

where $\mathbf{V} = \mathbf{v} - \mathbf{U}$, $\Delta\mathbf{U} = \mathbf{U} - \mathbf{U}_g$, $\mathbf{U}$ and $\mathbf{U}_g$ being the mean flow velocities of the solid and gas phases, respectively. In addition, T_{ex} is the background temperature and $J_{ij}[f_i, f_j]$ is the (inelastic) Enskog collision operator [1]. The drift coefficients γ_i are considered to be proportional to η_g. In such a way, they can be written as $\gamma_i = \gamma_0 R_i$ where $\gamma_0 \propto \eta_g \propto \sqrt{T_{\text{ex}}}$ and the dimensionless quantities R_i are functions of the partial volume fractions ϕ_i, the total volume fraction $\phi = \phi_1 + \phi_2$, and the mass m_1/m_2 and size σ_1/σ_2 ratios. Explicit forms for R_i can be found in the literature for polydisperse gas-solid flows [3].

The balance equations for the densities of mass, momentum, and kinetic energy can be derived exactly from the Enskog equations. These equations are expressed in terms of the mass flux $\mathbf{j}_i$, the pressure tensor P, the heat flux $\mathbf{q}$, and

*Corresponding author. E-mail: ruben@unex.es

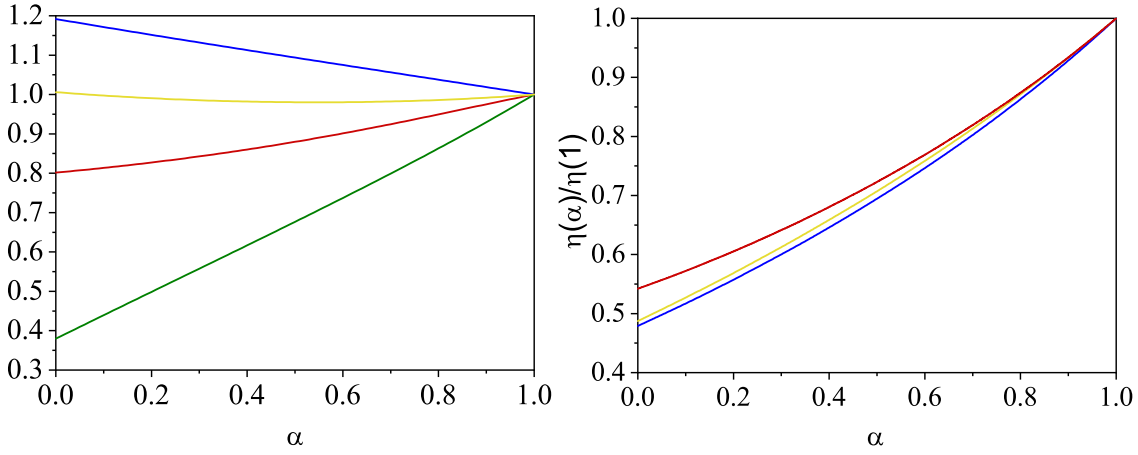

Figure 1: Left panel: Plot of the (reduced) diffusion coefficients $D_{11}(\alpha)/D_{11}(1)$ (green line), $D_{12}(\alpha)/D_{12}(1)$ (yellow line), $D_1^T(\alpha)/D_1^T(1)$ (red line), and $D_1^U(\alpha)/D_1^U(1)$ (blue line) for $m_1/m_2 = 8$. Right panel: Plot of the (reduced) shear viscosity coefficient $\eta(\alpha)/\eta(1)$ for $m_1/m_2 = 0.5$ (red line), $m_1/m_2 = 4$ (blue line), and $m_1/m_2 = 10$ (yellow line). The remaining parameters in both panels are $d = 3$, $T_{\text{ex}}^* \equiv T_{\text{ex}}/(\overline{m}\gamma_0^2\overline{\sigma}) = 0.01$, $x_1 = 0.5$, $\sigma_1/\sigma_2 = 2$, and $\phi = 0.2$. Here, $\overline{m} = \sum_i m_i/2$ and $\overline{\sigma} = \sum_i \sigma_i/2$.

the so-called cooling rate ζ. This latter quantity measures the rate of energy change due to collisions. While the mass flux only contains kinetic contributions, the pressure tensor and the heat flux contain kinetic and collisional contributions.

A simplest situation corresponds to homogeneous steady states where the granular temperature T is obtained from the condition $2\sum_i x_i\gamma_i(T_{\text{ex}} - T_i) - \zeta T = 0$, x_i being the mole fraction of species i. The above equation is coupled to the steady equation for the partial temperature T_i: $2x_i\gamma_i(T_{\text{ex}} - T_i) - \zeta_i T_i = 0$, where ζ_i is the partial cooling rate for the component i. Given that ζ and ζ_i are defined in terms of the distributions f_i, one needs to consider approximate forms for the above distributions. Here, we have considered Maxwellian distributions at different temperatures. In spite of this simplification the theoretical results for the temperature ratio T_1/T_2 compare quite well with MD simulations.

NAVIER–STOKES TRANSPORT COEFFICIENTS

We assume that we slightly perturb the homogenous steady state by small spatial gradients. In this case, we solve the Enskog equation (1) by means of the CE method. For time longer than the mean free time and distance larger than the mean free path, the suspension reaches a hydrodynamic regime where all the space and time dependence of f_i only occurs via a functional dependence on the hydrodynamic fields (*normal* solution). In these conditions, f_i can be expanded in powers of the spatial gradients as $f_i = f_i^{(0)} + f_i^{(1)} + \cdots$ where the approximation $f_i^{(k)}$ is of order k in gradients.

The application of the CE expansion to first-order allows us to obtain the constitutive equations for the fluxes. In particular, the mass flux $\mathbf{j}_i^{(1)}$ and the pressure tensor $P_{\lambda\beta}^{(1)}$ are given by

$$\mathbf{j}_i^{(1)} = -\sum_{j=1}^{2} \frac{m_i\rho_j}{\rho} D_{ij}\nabla \ln n_j - \rho D_i^T \nabla \ln T - D_i^U \Delta \mathbf{U}, \quad P_{\lambda\beta}^{(1)} = -\eta\left(\partial_\lambda U_\beta + \partial_\beta U_\lambda - \frac{2}{d}\delta_{\lambda\beta}\nabla\cdot\mathbf{U}\right) - \delta_{\lambda\beta}\eta_{\text{b}}\nabla\cdot\mathbf{U}, \tag{2}$$

where n_i is the number density of the component i, $\rho_i = m_i n_i$, and $\rho = \sum_i \rho_i$. In addition, in Eq. (2) we have introduced the diffusion transport coefficients D_{ij}, D_i^T, and D_i^U as well as the shear η and bulk η_{b} viscosities. As for molecular hard-sphere mixtures, the above transport coefficients are given in terms of the solution of a set of coupled linear integral equations that can be approximately solved by considering the leading terms in a Sonine (or Laguerre) polynomial expansion. Here, we have obtained explicit forms for these coefficients in terms of the parameters of the system [4]. As an illustration, Fig. 1 shows the dependence of the (reduced) diffusion coefficients (left panel) and the shear viscosity coefficient (right panel) on the (common) coefficient of restitution $\alpha_{ij} = \alpha$ and several systems. Figure 1 highlights the strong influence of inelasticity on the mass and momentum transport, specially in the case of the diffusion coefficients. In addition, a comparison with the results derived for (dry) granular mixtures [1] shows significant differences between both systems (granular suspensions and granular gases). This is clearly indicative that the impact of gas phase on transport properties of solid particles cannot be in general neglected. A more exhaustive discussion on this issue will be developed during the presentation of this work.

References

[1] Garzó, V. Granular Gaseous Flows. Springer Nature Switzerland, Basel, 2019.
[2] Koch D. L., Hill R. J., Inertial effects in suspensions and porous-media flows. *Annu. Rev. Fluid Mech.* **33**: 619-647, 2001.
[3] Yin X., Sundaresan S., Fluid-particle drag in low-Reynolds-number polydisperse gas-solid suspensions. *AIChE* **55**: 1352-1368, 2009.
[4] Gómez González R., Khalil N., Garzó, V., Enskog kinetic theory for multicomponent granular suspensions. *Phys. Rev. E* **101**: 012904(1-23), 2020.

EXPERIMENTAL INVESTIGATION OF MIXING AND SEGREGATION IN A BIDISPERSE GRANULAR MEDIUM IN A VESSEL ROTATING AROUND AN ECCENTRIC STATIC ROD

Kwami Adem MAYEDEN *[1], Evelyne Kolb [2], Stéphanie Deboeuf [3], Pierre Jop [1]
[1]SVI (Surface du Verre et Interfaces), CNRS/SAINT-GOBAIN RESEARCH PARIS, 93300 Aubervilliers, France
[2]PMMH (Physique et Mécanique des Milieux Hétérogènes), UMR 7636, 75005, Paris, France
[3]Institut Jean Le Rond d'Alembert, Place Jussieu 75252 Paris Cedex 05, Paris, France

Summary A bidisperse medium of large glass beads and small sand particles is mixed in a cylindrical vessel that is put in rotational motion around an eccentric static rod. The subsequent segregation occurring in the system is investigated primarily at the free-surface. In order to gain deeper understanding of the intrinsic forces causing the segregation, we also explore the dynamics in the bulk. Average residual bulk displacements fields both vertically and orthoradially could then be measured and show a secondary flow that counteracts the segregation process.

INTRODUCTION

A common problem in mixing granular materials is segregation, mainly size-segregation [1, 2] that often leads to structural mal-performance in industrial products such as glass, abrasives, pills just to name a few.

Even though the dedication of the particles community has allowed to establish theoretical [3], phenomenological [4] and recently numerical laws [5] describing the phenomenon, it has to be noticed that these findings remain solely applicable to classical configurations (rotating drum, heap flow, Couette-flow, etc...) The generalization to complex flows remains an open question. In this paper we experimentally investigate segregation in one of these complex flows generated by the rotation of a cylindrical vessel around a fixed eccentric rod.

EXPERIMENTAL SETUP

The setup (**Fig1.a**) consists in a cylindrical vessel of diameter $D = 14cm$ in which a bidisperse medium of particles is mixed: large glass particles of average diameter $d_l = 600\mu m$ colored in green and white small sand particles ($d_s = 250\mu m$). For the mixing, we use a rod in steel of diameter $d_{rod} = 2cm$ whose center is positioned at $5cm$ from the center of the vessel and whose end-base was kept at $2cm$ from the bottom of the vessel. To mix, the vessel is put in rotational motion at $\omega \approx 1{,}5\ rpm$ while the rod is kept fixed (quasi-static flow regime).

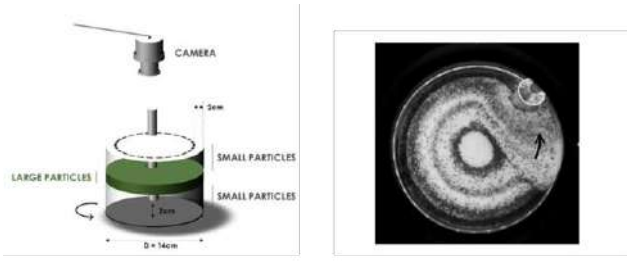

Fig 1: (a) Experimental setup (b) Typical picture of the free-surface after 15 turns with large particles appearing black

We started with a stratified arrangement in which a 4mm layer of large particles is encapsulated between 2 layers of small particles, 3cm at the bottom and 2cm at the top. Once the mixing starts, we use a camera affixed at the top of the vessel to capture 8 bit grayscale images of the free-surface showing how the large particles rise to the surface (**Fig1.b**).

ANALYSIS OF THE SURFACE TO QUANTIFY SEGREGATION

We investigate segregation by processing the successive images that were captured by the camera through time. we define a coverage-ratio $C(t) = \frac{I_0 - I(t)}{I_0 - I_\infty}$ where $I(t)$ is the average grayscale of the surface at time t, I_0 the grayscale at the beginning of the experiment and I_∞ is the grayscale of the free-surface in a hypothetical scenario where the whole surface is covered in black large particles. $C(t)$ is this way, bound between 0 (no large particles at surface) and 1 (full surface saturation with large particles).

RESULTS

Segregation: accumulation at the free-surface

The plotting of $C(t)$ against time shows an overall increase with an exponential relaxation towards a stable regime modulated by repetitive oscillations which represent the successive disappearances and appearances of particles at the

*Corresponding author: kwami.mayeden@saint-gobain.com.

surface (**Fig2.a)**. This rise-and-plunge motion points to the existence a strong recirculation motion that becomes less visible when an equilibrium state is reached in which the repartition of large particles at the surface and the exchanges between bulk and free-surface could be considered as stable. The dynamics observed in the medium through $C(t)$ can then be viewed as a competition between segregation and recirculation currents.

Segregation in the bulk against the normalized distance from the center of the rod

In order to better understand the segregation dynamics in the bulk, a vacuum cleaner is used to remove particles layer by layer after mixing. Pictures of the inside could then be retrieved that show the repartition of particles radially given the depth. From those pictures an average vertical rise could be computed and plotted against the distance from the center of the rod **(Fig 2.b)**. The minimal rise is obtained as expected far away from the rod in the central area of the vessel. The maximal rise on the other hand is obtained at a distance of $\frac{d_{rod}}{2}$ from the outer surface of the rod. If this rise was only due to the amplitude of the shear, one would have expected it to occur close to the rod surface. This result supports the fact that the segregation is not the only mechanism responsible for the movement of the grains. On the wall side, a similar behavior can be observed only with a lower amplitude.

Orthoradial displacement in the bulk against the normalized distance from the center of the rod

As segregation is due to shear which itself stems from displacement, we set up an experiment to retrieve the orthoradial displacement generated by the passage of the rod in the depth of the medium. We encapsulated a thin bar in between the 2 layers of small particles. Vacuuming after mixing allows to retrieve the deformation of the bar stemmed from the passing of the rod. Assuming only an orthoradial displacement we plot the curvilinear displacement $r * \theta$ against the distance from the center of the rod (**Fig2.c**).

On the center-side part of the rod, 2 main regions could be discriminated. A linear model fits the data in the first region whereas an exponential decay satisfyingly fits the curvilinear displacement in the second region (inset **Fig 2.c**). The shear corresponding to this displacement profile should be linked to the segregation and thus to the rise of the grains. Since the curve is monotonous, contrary to the rise curve, this tends to confirm again the existence of another force in the medium that intervenes in the uplifting of the particles: the recirculation current which itself still has to be characterized.

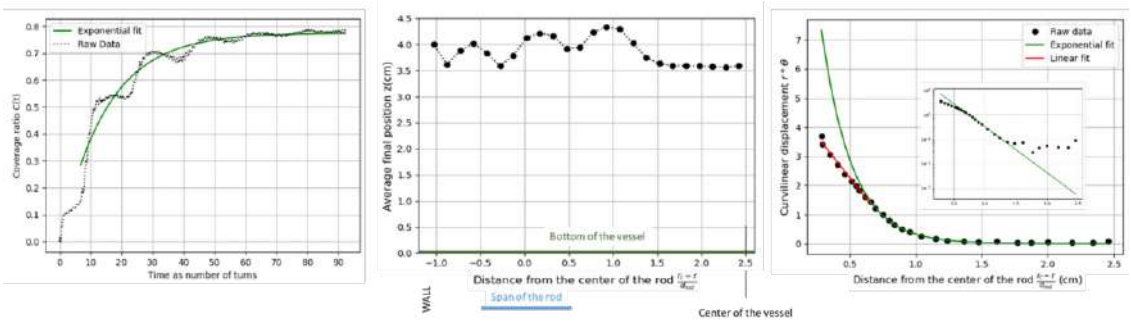

(a) (b) (c)

Fig 2: (a) Evolution of segregation (C(t)) against time for the same parameters as in Fig 1 (b) Average vertical displacement field against normalized distance from the center of the rod after 4 revolutions - the layer of larges particles was initially located at 3cm from the bottom of the vessel (c) Curvilinear displacement against normalized distance from the center of the rod with graph in log space in the inset - r_c being the radial coordinate of the center of the rod

CONCLUSIONS

We investigated segregation dynamics occurring in a bidisperse medium mixed in a cylindrical vessel with an eccentric rod. We showed that the law describing such dynamics has an exponential baseline that is modulated by periodic oscillations which point to the existence of a recirculation current. In the bulk, we studied the rise of particles according to their radial positions. Last, we explored orthoradial displacement field inside the medium generated by the passing of the rod and showed that it follows an exponential law far from the rod. More investigation has to be done especially to understand the downward movement behind the rod and the coupling of recirculation currents with the segregation force.

References

[1] Golick, L.A. and K.E. Daniels, Mixing and segregation rates in sheared granular materials. Phys Rev E Stat Nonlin Soft Matter Phys, 2009. 80(4 Pt 1): p. 042301
[2] Gray, J.M.N.T., Particle Segregation in Dense Granular Flows. Annual Review of Fluid Mechanics, Vol 50, 2018. 50: p. 407-433.
[3] Gray, J.M.N.T. and C. Ancey, Multi-component particle-size segregation in shallow granular avalanches. Journal of Fluid Mechanics, 2011. 678: p. 535-588.
[4] Gajjar, P. and J.M.N.T. Gray, Asymmetric flux models for particle-size segregation in granular avalanches. Journal of Fluid Mechanics, 2014. 757: p. 297-329.
[5] Guillard, F., Y. Forterre, and O. Pouliquen, Scaling laws for segregation forces in dense sheared granular flows. Journal of Fluid Mechanics, 2016. 807

A MULTI-BODY CONTACT MECHANICS FEM METHOD AND ITS APPLICATION TO GRANULAR PHYSICS

Liuchi Li *[1], Mengsu Hu[1], and Jonny Rutqvist[1]
[1]Earth and Environmental Sciences Area, Lawrence Berkeley National Laboratory, Berkeley, California94720, USA

Summary Inter-particle forces in a granular media form spatially heterogeneous force chains. Understanding them is of fundamental significance to various applications in engineering and physics. However, most studies to date have been focusing on granular media composed of mechanically homogeneous grains, leaving the aspect of heterogeneity a rather uncharted area. Here, we specifically investigate how the mechanical property of a constituent grain can alter the amount of force it obtains in a granular media. In pursuit of such knowledge, we first briefly introduce a multi-body contact mechanics FEM implementation and show several verifications. Next, we take this method to simulate stackings of ordered elastic disks. We discuss how the force distribution deviates from the initial homogeneous one under quasi-static uniaxial compression and what role does mechanical property play in this regard.

INTRODUCTION

Any collection of macroscopic solid frictional particles with size greater than 1 μm belong to the family of granular media. They are ubiquitous on earth and are the second most manipulated industrial material. Despite such a unified and simple definition, at the macro-scale, different granular materials can exhibit drastically different mechanical properties and can behave like solids, liquids, gases or even with the aforementioned phases coexisting under different external loading and boundary settings. Such complex macro-scale behavior is closely tied to the heterogeneously distributed filamentary force chains formed by inter-particles forces [1]. Understanding these force chains is therefore of fundamental significance to various applications in engineering [2] and physics [3].Despite the various characteristics a granular media can exhibit, most studies to date have been focusing on granular materials composed of grains with homogeneous mechanical properties [4, 5, 6], leaving the aspect of heterogeneity a rather uncharted area. Here, we specifically investigate an interesting fundamental question inspired by making an analogy to income inequality studied in economics: How the mechanical property of a constituent grain can alter the amount of force it obtains through its collective interactions with neighboring grains? In pursuit of such knowledge, we will first briefly introduce the implementation of a 2D multi-body contact mechanics FEM method and show several verifications and validations [4]. Next, we will take this method to simulate a model granular media as a starting point: collections of ordered mono-disperse disks. By systematically varying the mechanical properties of each disk, we discuss how the force distribution deviates from the initial homogeneous one under quasi-static uniaxial compression and what role does mechanical property play in this regard. In closure, we will briefly outline several inspired future research directions.

A MULTI-BODY CONTACT MECHANICS FEM IMPLEMENTATION

For simplicity, we consider small deformation and assume each grain is made of linear elastic and isotropic materials. In the absence of body force and acceleration, the problem reduces to finding the displacement field that vanishes the divergence of Cauchy stress within each grain under the boundary condition of boundary displacements and tractions (if present), and contact tractions between neighboring grains. This boundary value problem (BVP), under the condition of small deformation and linear elasticity, is linear in the displacement field and can be solved by standard FEM treatment without iteration. However, with the presence of inter-grain contacts, such BVP becomes nonlinear in the displacement field, since contact tractions depend on the displacement field around the contact region (which is unknown *a-priori*).

To solve this non-linear BVP, we implement a Newton-Raphson solver to find the displacement field under the classical penalty formulation accompanied by a regularized Coulomb friction law. At each Newton-Raphson iteration, the inter-grain contact contribution to the Jacobian is computed numerically via finite difference. Considering scenarios with multiple loading steps, at each load step we solve the BVP using the total displacement field, which allows for convenient realization of loading-unloading simulation and future extension to finite deformation. We note that, although certainly feasible, we choose not to augment the penalty formulation with an encapsulating iteration loop for the ease of contact detection, especially in simulating scenarios with continuous loading. Lastly, as a point of departure, we focus on 2D and use the constant strain triangle (CST) elements.

Due to the limitation of length, here we only demonstrate one verification in the case of Hertzian contact where the analytical solution is obtainable [7]. In this example (Figure. 1a), the top surface of the top grain is subjected to a displacement boundary condition in both the x and y direction, while the bottom surface of the bottom grain is fixed. We show the simulated spatial distribution of the normal stress along the y direction (Figure. 1b) with a friction coefficient equaling 0.5. As expected, the stress distributions in two grains are not symmetric with respect to the x direction with

*Corresponding author. E-mail: liuchili@lbl.gov

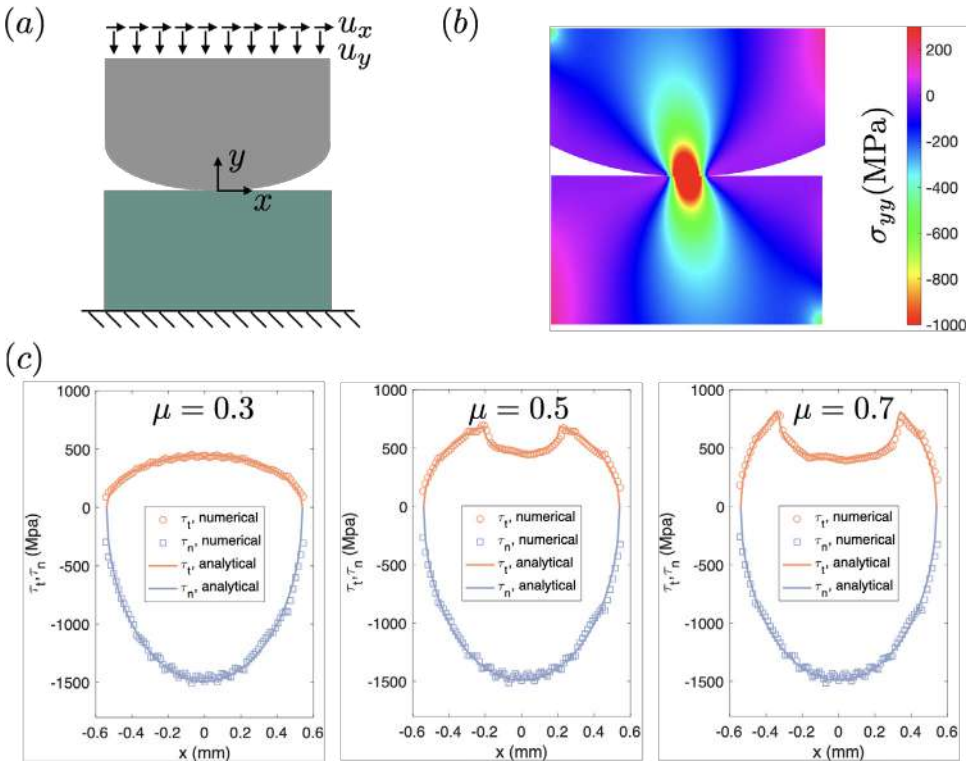

Figure 1: The adopted Hertzian contact example.

mismatched edges, due to the presence of tangent displacement and frictional slip. Further, our implementation also accurately predicts the distributions of both normal and tangent tractions along the contact surface (Figure. 1c) and identifies the slip and stick region for different friction coefficients.

APPLICATIONS TO GRANULAR PHYSICS

We next take this method to analyze the effect of mechanical properties on force chain distributions. Studies are currently under the way, and at the point of the poster presentation, we will discuss, for stackings of ordered disks, how the force distribution deviates from the initial homogeneous one under quasi-static uniaxial compression and what role does mechanical property play in this regard. Besides the fundamental relevance to granular physics, our work can also have practical implications in designing wave-tailoring acoustic devices [8] and tunable mechanical meta-materials [2].

References

[1] Trushant S Majmudar and Robert P Behringer. Contact force measurements and stress-induced anisotropy in granular materials. *Nature*, 435(7045):1079–1082, 2005.

[2] Yifan Wang*, Liuchi Li*, Douglas Hofmann, José Andrade, and Chiara Daraio. Structured textiles with tunable mechanical properties. *Nature, under revision.*

[3] Liuchi Li and José E Andrade. Identifying spatial transitions in heterogeneous granular flow. *Granular Matter*, 22:1–16, 2020.

[4] Ryan Hurley, Eloïse Marteau, Guruswami Ravichandran, and José E Andrade. Extracting inter-particle forces in opaque granular materials: beyond photoelasticity. *Journal of the Mechanics and Physics of Solids*, 63:154–166, 2014.

[5] RC Hurley, SA Hall, JE Andrade, and J Wright. Quantifying interparticle forces and heterogeneity in 3d granular materials. *Physical review letters*, 117(9):098005, 2016.

[6] Liuchi Li, Eloïse Marteau, and José E Andrade. Capturing the inter-particle force distribution in granular material using ls-dem. *Granular Matter*, 21(3):43, 2019.

[7] James R Barber. *Elasticity*. Springer, 2002.

[8] Chiara Daraio, VF Nesterenko, EB Herbold, and Sungho Jin. Strongly nonlinear waves in a chain of teflon beads. *Physical Review E*, 72(1):016603, 2005.

WET ROLLING STONES: GROWTH OF A GRANULAR AGGREGATE

Pierre Jop* [1], Guillaume Saingier[1], and Alban Sauret[2]
[1]Surface du Verre et Interfaces, UMR 125, CNRS/Saint-Gobain, Aubervilliers, France
[2]Department of Mechanical Engineering, University of California, Santa Barbara, CA, USA

Summary Wet granulation processes can be driven from low to high water content. In this study, we consider the model situation of the growth of a single wet aggregate rolling in a dry granular flow inside a rotating drum. We measure the time evolution of its diameter for different grains and liquids, as well as various rotation rates of the drum. Using X-ray tomography, we are able to characterize the internal structure of the granular aggregate at different times during the process. We show that the growth rate of the aggregate can be related to the transport of the liquid inside the granule and the capture of grains. We propose a model to rationalize the maximum size of the aggregate and its growth rate.

INTRODUCTION

Blending dry grains and liquid is a common step of many industrial processes. When the volume of liquid is small compared to the volume of grains, wet aggregates are created. The capillary forces hold the wet grains together, bringing strength to this object. This phenomenon is, for instance, at the base of the wet granulation processes [1]. The wet aggregates interact with the surrounding medium and can collide, break, and exchange grains. In high shear granulators, the kinetic energy of the aggregates is essential. However, in industrial granulation dishes or in rotating drums, the granulation is done at low shear and allows the individual aggregates to preserve their shape and roundness. Depending on the liquid content of the aggregate, different mechanisms can occur. At very low water content, the grains at the surface of the aggregate can be eroded due to the friction of the granular media and to the impact of the dry grains [2]. At very large water content, the flowing dry grains can be captured if they touch a capillary meniscus [3]. In this study, we focus on an isolated wet aggregate during all of its evolution and describe the role of the kinematic and physical properties of the material on its growth.

GROWTH DYNAMICS OF AN AGGREGATE IN A ROTATING DRUM

We use a rotating drum to measure the growth of a single aggregate in a gentle granular flow. The drum is partially filled with sand of diameter $d_g = 60 - 300\ \mu$m and rotates from 3 rpm to 36 rpm. An aggregate is prepared by depositing a drop of aqueous solution of ZnI_2 or glycerol on the surface of the sand before starting the rotation. This method allows us to create an initial aggregate fully saturated with liquid. As shown in Fig. 1(a), the aggregate is then carried by the flow, partially sunk. It can easily be collected after several rotations to characterize its properties, such as its mass.

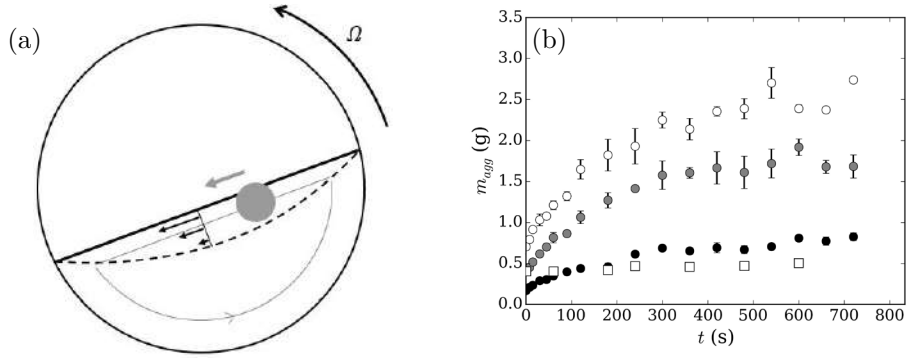

Figure 1: (a) Schematic of the aggregate rolling inside the surface flow of the granular media in a drum. (b) Time evolution of the mass of the aggregates of sand for increasing volumes of the initial droplet of ZnI_2 solution (circles from dark to light) 20 μL, 50 μL, 100 μL and comparison with a buried aggregate in a static media from a 20 μL droplet (squares).

Fig. 1(b) shows the temporal evolution of the mass of the aggregates for different initial volumes of a water solution of ZnI_2. The mass increases with time t, and the growth rate slows down until reaching a saturation. The increase in mass results from the capture of dry grains by the air/liquid menisci at the surface of the aggregate. We do not usually observe clusters of grains detaching from the aggregates. However, at the end of the experiment, a large aggregate can break into several parts. The aggregate then grows by gluing new sand grains on its surface, without releasing them contrary to a recent numerical study [4]. To test if the spontaneous capillary spreading of the liquid toward new dry grains plays a key role, we also report the time evolution of the mass of the same initial aggregate buried in the sand but without flow. We

*Corresponding author. E-mail: pierre.jop@saint-gobain.com

observe that the mass grows by less than 25%. Therefore the capture mechanism of dry grains requires a granular flow and is reminiscent of the growth of wet granular towers [3]. Moreover, as we increase the initial volume of liquid, the mass ratio between the initial and the final aggregate is of the order of 4. This behavior suggests that the evolution of the aggregate can be rescaled by the initial volume of liquid, and the transport of the liquid may be the key parameter.

MODELING OF THE GROWTH DYNAMICS: TRANSPORT OF THE LIQUID

We collect some aggregates at different times and characterize their structure through X-ray tomography, as illustrated in Fig. 2(a)-(d). The solution of ZnI_2 provides a good contrast to observe the liquid distribution in the aggregate. While the pores at the center of the initial aggregate are fully saturated, the local amount of liquid decreases in the outer part. We observe a shell of captured sand grains that are smaller than the initial ones. Moreover, only a fraction of those pores is filled with the liquid. This behavior likely occurs because of the larger probability for the smaller grains, continuously brought to the aggregate by the flow, to get captured. The pore size in the shell is then smaller, and the capillary pressure drops when the liquid starts invading them. As a result, the liquid is pumped out from the core consisting of large pores until it is empty. This hypothesis also explains why the aggregate at rest does not grow: the size distribution of the dry grains in contact with the wet aggregate is the same as the ones inside.

Based on this physical argument and using geometrical assumptions, we can propose a model for the growth rate of this aggregate. We first assume that the core of the aggregate is composed of large grains [inset of Fig. 2(e)] with a shell consisting of smaller grains. Secondly, the volume fraction of the pores is assumed to be constant everywhere. Thirdly, the growth stops when the liquid volume fraction drops below a value that does not allow a continuous path of liquid. The value of this percolation threshold was estimated by Schell *et al* [5] to be of the order of $W = 0.05$, while the initial value for this sand is $W_0 = (1-\phi)/\phi \simeq 0.43$. Finally, the transport of the liquid is governed by a Darcy flow whose pressure gradient is given by the capillary pressure inside the two types of pores. We validate this model using glycerol, which makes stronger aggregates and which wets well the sand grains. We observe a growth of the mass by a factor 10, in quantitative agreement with the prediction of a factor 8.6. Moreover, the model described here provides a growth rate that captures the experimental results, as shown in Fig. 2(e).

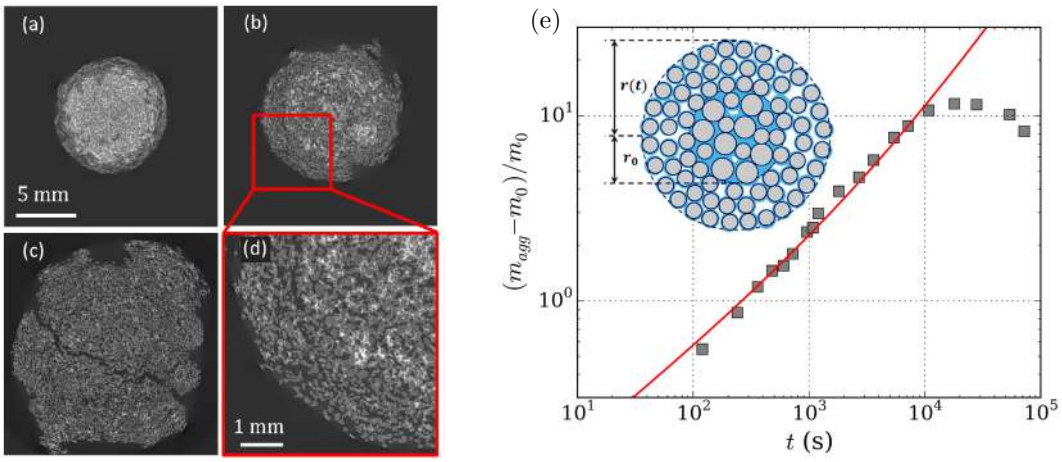

Figure 2: Section of X-ray tomography of aggregates of sand grains at (a) $t = 0$ s, (b) $t = 100$, s, (c) $t = 360$, s and (d) magnification showing the spreading of the liquid. The light area corresponds to the liquid. (e) Time evolution of the mass of the glycerol/sand aggregate (square) and the prediction of the model (line).

CONCLUSIONS

In this study, we characterized the growth of an aggregate, initially saturated in liquid, in a gentle granular flow. We have shown that a shell of smaller grains develops around the core made of larger grains and drives the liquid outside under the effect of capillary pressure. We also presented a model capturing the growth dynamics.

References

[1] Iveson S. M. , Litster J. D., Ennis B. J. Fundamental studies of granule consolidation part 1: Effects of binder content and binder viscosity. *Powder Technology*, **88**:15–20, 1996.
[2] Lefebvre G., Merceron A., Jop P. Interfacial instability during granular erosion. *Physical Review Letters*, 116, 2016.
[3] Saingier G., Sauret A., Jop P. Accretion dynamics on wet granular materials. *Physical Review Letters*, 118, 2017.
[4] Vo T. T., Nezamabadi S., Mutabaruka P., Delenne J.-Y., Izard E., Pellenq R., Radjai F. Agglomeration of wet particles in dense granular flows. *The European Physical Journal E*, **42**(9):127, 2019.
[5] Scheel M., Seemann R., Brinkmann M.D.M.M., Di Michiel M., Sheppard A., Breidenbach B., Herminghaus S. Morphological clues to wet granular pile stability. *Nature materials*, **7**(3):189–193, 2008.

TUNING WAVES IN SOFT PERIODIC POROUS PLATES

Nan Gao[1], Jian Li[1], Ronghao Bao, Weiqiu Chen [1,2], Yueting Wang[3], and Yuesheng Wang[3]
[1]Key Laboratory of Soft Machines and Smart Devices of Zhejiang Province & Department of Engineering Mechanics, Zhejiang University, Hangzhou 310027, China
[2]State Key Lab of CAD & CG, Zhejiang University, Hangzhou 310058, China
[3]School of Mechanical Engineering, Tianjin University, Tianjin 300350, China

Summary Periodic porous plates are a particular type of phononic crystals with structural periodicity, featuring interesting bandgap properties due to the Bragg scattering mechanism. Such porous plates will be further endowed with mechanical tunability when they are made from soft materials. In this work, we focus on two geometric configurations, and show the feasibility to manipulate waves propagating in the periodic porous plate by different means. The first one we examine is a soft plate with arrays of criss-crossed elliptical holes, which takes the buckled configuration of the plate with arrays of circular holes as its initial configuration. We show numerically and experimentally that the wave propagation behaviour can be robustly tuned by tension. The other one is a soft plate with arrays of circular holes, for which we propose to insert hard inclusions into the holes to tune the deformation and wave propagation. Through numerical simulation and experimental study, it is firmly demonstrated that, inserting inclusions into the holes could be a very convenient and also powerful way for manipulating waves in the soft porous plate.

INTRODUCTION

Phononic crystals (PCs) have been a common hot topic in different disciplines including physics, mechanics, materials, devices, etc. for almost 30 years. The particular bandgap properties in PCs induced by Bragg scattering associated with structural periodicity make them perfect candidates for many novel and useful acoustic devices. Bandgap, a frequency range in which waves are prohibited to propagate through the medium, can also be generated by another mechanism, i.e. the local resonance. Materials with local resonant units, which may be arranged in an aperiodic way, are now called metamaterials (MMs). Most of the earlier studies focus on PCs/MMs with a fixed geometry, attempting to find a wide bandgap with a low mid frequency [1].

In 2001, Goffaux and Vigneron suggested to rotate the solid scatterers in an air/solid PC system to tune the bandgaps [2]. Since then, many different ways have been proposed to acquire tunable PnCs/MMs, such as making use of the multifield coupling effects. As regards mechanical means, either prestress or large deformation has been adopted to tune the bandgaps. In particular, Bertoldi and Boyce [3] showed that a soft porous plate with arrays of circular holes in a square pattern will buckle under compression, and the following large postbuckling deformation will greatly affect the bandgap properties.

In this study, we pay our attention to two cases of soft porous plate. In the first case, the soft plate is perforated with arrays of criss-crossed elliptical holes. This topology is identical to the buckled configuration of a soft plate with arrays of circular holes in Ref. [3]. In the second case, we simply consider the same soft porous plate as in Ref. [3], with its holes however possibly inlayed with hard inclusions in a particular filling pattern. Both numerical and experimental investigations are carried out to explore the tunability of wave propagation in these two soft porous plates.

LARGE DEFORMATION AND WAVE PROPAGATION ANALYSES

The soft materials, which can undergo reversible large deformation, are assumed to obey a hyperelastic constitutive law. In this case, the first Piola-Kirchhoff stress tensor $\mathbf{T}$ can be calculated from a strain energy density function $\Omega(\mathbf{F})$ as $\mathbf{T}=\partial\Omega(\mathbf{F})/\partial\mathbf{F}$, with $\mathbf{F}$ being the deformation gradient. We need to carry out the large deformation analysis within the general framework of nonlinear elasticity [4]. For the infinitesimal wave motion superimposed on the pre-deformation, we shall linearize all the governing equations and perform the analysis based on the following linear incremental equations:

$$\mathrm{div}\,\dot{\mathbf{T}}_0 = \rho\partial^2\boldsymbol{u}/\partial t^2 \tag{1}$$

where $\boldsymbol{u}$ is the incremental displacement vector, and the incremental Piola-Kirchhoff stress tensor $\dot{\mathbf{T}}_0 = \boldsymbol{\mathcal{A}}_0 : \mathrm{grad}(\boldsymbol{u})$, with $\boldsymbol{\mathcal{A}}_0$ being the fourth-order effective or instantaneous elastic moduli tensor, which depends on the pre-deformation [4]. Hence, the pre-deformation not only changes the geometry of the structure, but also alters the effective material properties.

For the problems of static large deformation and linear wave propagation, we carry out the finite element modeling based on ABAQUS with respect to either a unit cell or a porous plate of finite size. When a unit cell is employed, we shall impose the Bloch conditions on the boundaries of the unit cell in the wave propagation analysis.

EXPERIMENTS

Shown in Figure 1 is the experimental setup for the soft porous plate with criss-crossed elliptical holes. The plate is first subjected to a uniaxial tension using a very simple machine, and then the wave propagation test is conducted using an electrodynamic shaker to input a plane-wave harmonic force.

Figure 2 indicates the experimental setup for wave propagation test of the soft porous plate with inserted hard inclusions. To reduce the effects of gravity on the in-plane deformation and the in-plane wave propagation, the sample is laid on the metal block. To increase the contact area between the shaker and the sample so as to generate a uniform in-plane wave as far as possible, a PLA (Polylactic acid) block is placed between the shaker and the sample. On the receiving end of the sample, a thin PTFE (Polytetrafluorethylene) block is stuck onto the sample.

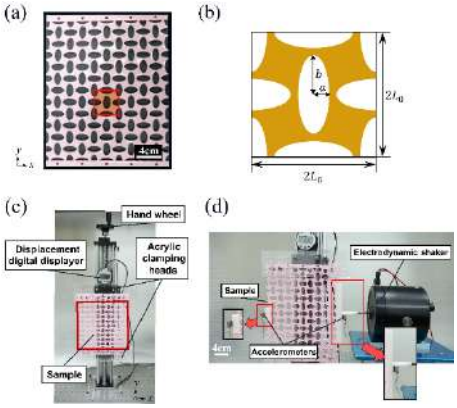

Figure 1. (a) Sample; (b) RVE of (a); (c) Uniaxial tension test; (d) Wave propagation test.

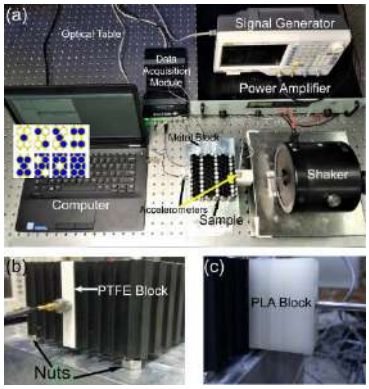

Figure 2. (a) Picture of the experiment; (b) PTFE block; (c) PLA block.

RESULTS

Typical results are given in Figures 2 and 3 for the soft porous plate with criss-crossed elliptical holes subjected to uniaxial tension [5] and for the soft porous plate with its circular holes inserted by hard inclusions in one row in a unit cell (see the specimen in Figure 2(a); different filling patterns are also shown there) [6]. It is seen that both tension and inserting hard inclusions can tune the wave propagation behaviour in soft porous plates effectively. Also, if the theoretical model is appropriate, then the numerical results agree quite well with the experimental observations.

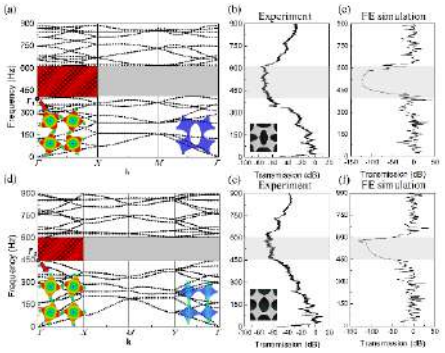

Figure 3 Simulated band diagram, experimental transmission spectrum and simulated transmission spectrum when the uniaxial pre-strain is zero [(a)-(c)] and 0.25 [(d)-(f)], respectively.

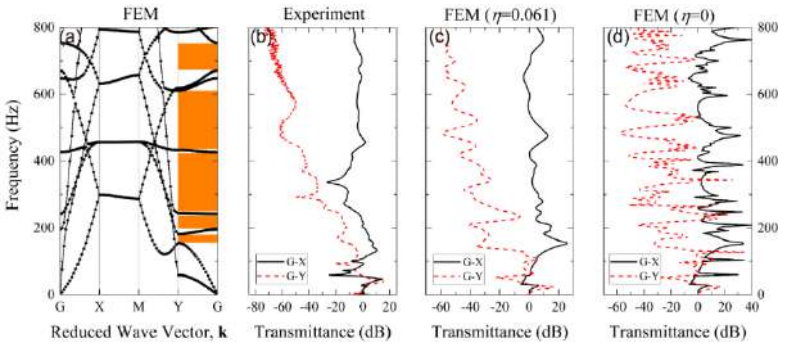

Figure 4 Wave propagation in the G-X and G-Y directions: (a) Band diagram; (b) Experimental transmittance curves; (c) Numerical transmittance curves with damping effect (the loss factor η=0.061); (d) Numerical transmittance curves without damping effect (η=0).

Acknowledgements

The work was supported by the National Natural Science Foundation of China (Nos. 11532001 & 11872329).

References

[1] Deymier P. A. Acoustic Metamaterials and Phononic Crystals. Springer, Berlin, 2013
[2] Goffaux C., Vigneron J. P. Theoretical Study of a Tunable Phononic Band Gap System. *Physical Review B* **64**: 075118, 2001.
[3] Bertoldi K., Boyce M. C. Mechanically Triggered Transformations of Phononic Band Gaps in Periodic Elastomeric Structures. *Physical Review B* **77**: 052105, 2008.
[4] Ogden R. W. Nonlinear Elastic Deformations. Dover, NY, 1997.
[5] Gao N., Li J., Bao R. H., Chen W. Q. Harnessing Uniaxial Tension to Tune Poisson's Ratio and Wave Propagation in Soft Porous Phononic Crystals: An Experimental Study. *Soft Matter* **15**(14): 2921-2927, 2019.
[6] Li J., Wang Y. T., Chen W. Q., Wang Y. S., Bao, R. H. Harnessing Inclusions to Tune Post-buckling Deformation and Bandgaps of Soft Porous Periodic Structures. *Journal of Sound and Vibration* **459**: 11848, 2019.

TRANSITION FROM BENDING-DOMINATED TO STRETCHING-DOMINATED BEHAVIOUR IN TWO-DIMENSIONAL NETWORKS

Harika C. Tankasala * [1], Vikram S. Deshpande[1], and Norman A. Fleck[1]
[1]Department of Engineering, University of Cambridge, Cambridge CB2 1PZ, United Kingdom

Summary The transition in macroscopic response from a compliant, bending-dominated mode to that of a stiff, stretching-dominated mode is explored numerically for two choices of two-dimensional networks: (i) a two-phase regular hexagonal network in-filled with a soft matrix and (ii) a random long fibre network. The effective elastic modulus of these networks is probed under uniaxial tension. It is found that the presence of an infill promotes stretching of the cell walls of the otherwise bending-dominated hexagonal network. In the case of random fibre network, it is the relative depth of the boundary layer to the specimen size that dictates the network stiffness.

INTRODUCTION

It is commonly argued that the existence of a continuous force chain in discrete networks ensures that the macroscopic response is affine. This assumption has formed the basis of several analytical models of biological short fibre networks (such as the actin microstructure in cytosketelon [1]) and long fibre engineering composites [2]. Here, we show that a switch from non-affine to affine response can be achieved by suitable choice of material properties and network geometry.

PROBLEM STATEMENT

A regular hexagonal network and a typical realization of a long fibre random network are both shown in Table 1; the relevant geometric parameters are identified for each case. Boundary conditions to simulate uniaxial tensile loading (in the x_2 direction) of the two networks are summarized in Table 1, along with the choices of material properties and constraints for the overlapping fibres (for the random network).

	Regular hexagonal network	**Random long fibre network**
Geometry	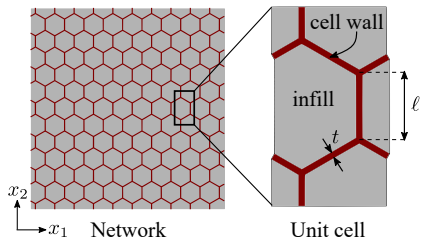	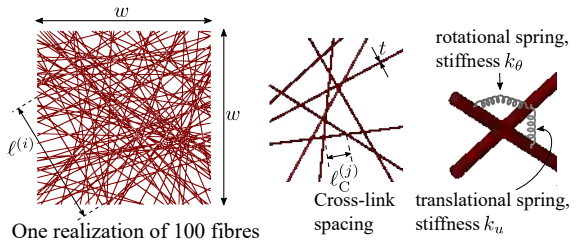
Material properties	Elastic cell wall and elastic infill	Elastic fibres
Fibre-to-fibre constraint	Rigid joint	Two sets of constraints assumed: (i) Rotating joint, $k_u = \infty, k_\theta = 0$ (ii) Rigid joint, $k_u = k_\theta = \infty$
Boundary conditions	Periodic displacements imposed on the boundary of the unit cell: $\Delta u_i = \varepsilon_{ij}^{\infty} \Delta x_j$ with only $\varepsilon_{22}^{\infty}$ specified. (Here $\varepsilon_{ij}^{\infty}$ is the macroscopic nominal strain tensor.)	Three classes considered: **A** Affine displacements prescribed on the boundary: $u_i = \varepsilon_{ij}^{\infty} x_j$ with only $\varepsilon_{22}^{\infty}$ specified. **B** Simple tension test with $u_2 = \varepsilon_{22}^{\infty} w$ prescribed on the top edge; sliding of the top and bottom edges, and lateral contraction of the specimen allowed. **C** Tractions prescribed on the top and bottom edges.

Table 1: Geometry of the networks, assumed material properties, and boundary conditions to simulate uniaxial tensile loading.

The elastic modulus of the cell walls (and fibres) is denoted by E_S. For the hexagonal network, the modulus E_I of the infill is varied between $10^{-4} E_S$ and $0.1 E_S$. Realizations with different number of fibres n are considered for the random network. The effective network modulus E is predicted for varying cell wall (or fibre) volume fraction $\overline{\rho}$ expressed as

$$\overline{\rho} = \frac{2}{\sqrt{3}} \frac{t}{\ell} - \frac{1}{3} \left(\frac{t}{\ell} \right)^2 \text{ for the hexagonal network, and } \overline{\rho} = \frac{t \sum_{i=1}^{n} \ell^{(i)}}{w^2} \text{ for the random network}$$

The relative extent of stretching versus bending in the stiff phase is quantified by the ratio $\phi := W_S / (W_S + W_B)$ where W_S and W_B are the elastic strain energy contributions from axial stretching and bending of the cell walls, respectively. For the random network, we define ϕ for each Gauss point along the fibres. For the hexagonal network, W_S and W_B are the quantities summed over all Gauss points of the lattice phase.

*Corresponding author. E-mail: hct30@cam.ac.uk.

RESULTS AND CONCLUSIONS

Infill promotes cell wall stretching in a regular hexagonal network

A transition from non-affine (i.e. bending-dominated) response to an affine (i.e. stretching-dominated) response of the honeycomb composite is observed with (i) increasing cell wall volume fraction $\overline{\rho}$ for a given infill-to-solid modulus ratio $E_\mathrm{I}/E_\mathrm{S}$, and with (ii) increasing $E_\mathrm{I}/E_\mathrm{S}$ for a given $\overline{\rho}$, see Fig. 1. The mechanical constraint provided by the stiff infill promotes stretching of the cell walls, as seen from the evolution of ϕ with $E_\mathrm{I}/E_\mathrm{S}$ in Fig. 1(a). Likewise, a larger cell wall volume fraction (and thereby a larger t/ℓ) results in an affine response even when the infill is of extremely low stiffness such as $E_\mathrm{I}/E_\mathrm{S} = 10^{-4}$, as shown in Fig. 1(b).

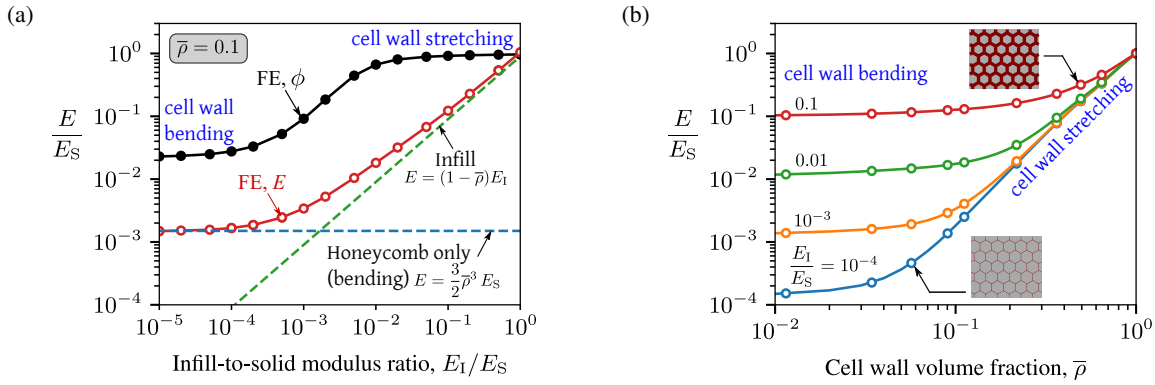

Figure 1: Modulus of the honeycomb composite E as a function of **(a)** infill-to-solid modulus ratio, and **(b)** cell wall volume fraction.

'Structural' non-affine response versus 'material' affine response of a random network

Boundary condition (BC) A gives the Voigt upper bound of the network modulus as $E = (1/3)\overline{\rho}E_\mathrm{S}$, consistent with uniform stretching of all the fibres in the network. BC C corresponds to the Reuss lower bound and is characterised by the bending of fibres such that $E \propto \overline{\rho}^3 E_\mathrm{S}$, see Fig. 2(a). Under simple tension, BC B, the network response switches from a non-affine mode at low $\overline{\rho}$ to an affine mode at high $\overline{\rho}$. This transition correlates with the depth of the compliant boundary layer at the free edges, λ. Denote $\overline{\rho}_\mathrm{T}$ as the transition value of $\overline{\rho}$ such that $E/E_\mathrm{S} = c_1(n)\overline{\rho}_\mathrm{T}^3 = c_2(n)\overline{\rho}_\mathrm{T}$, and $\overline{\ell}_C$ as the mean cross-link spacing of a network. We find from Fig. 2(b)-(d) that at transition, $\lambda \approx w/4 \approx \overline{\ell}_\mathrm{C}/\sqrt{\overline{\rho}_\mathrm{T}}$. The network modulus thus asymptotes between the boundary layer-governed non-affine value and the affine material response.

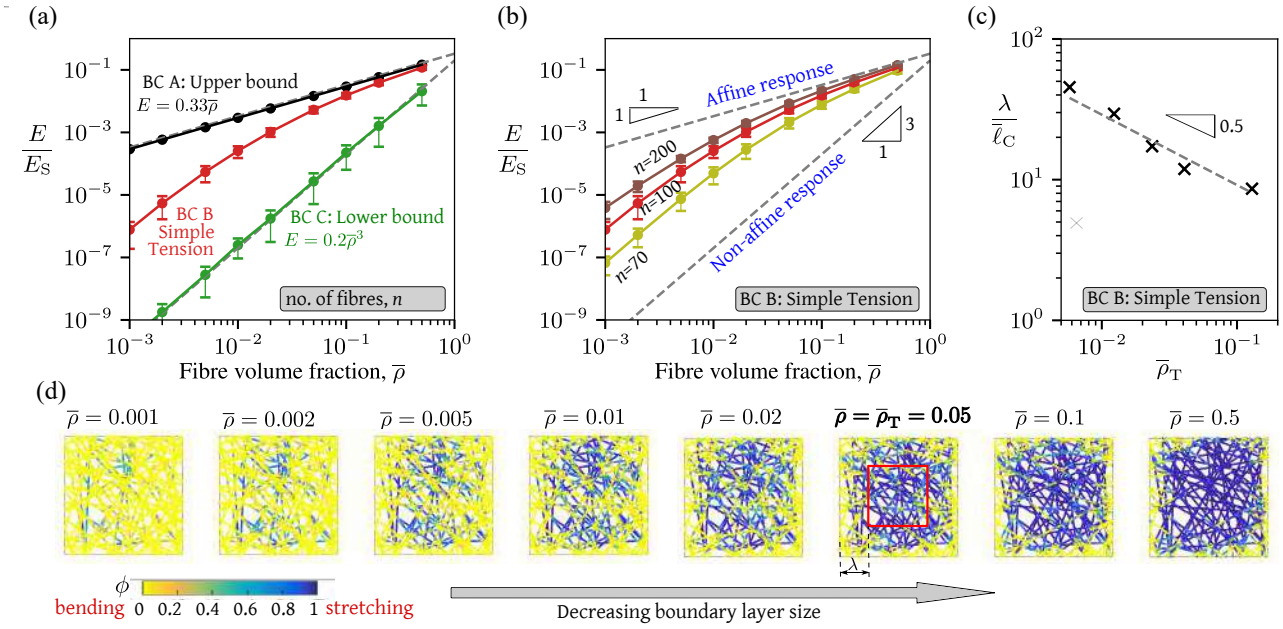

Figure 2: Network modulus E as a function of fibre volume fraction (assuming rotating joints) for **(a)** $n = 100$ and all BCs and **(b)** simple tension BC. The error bars show scatter in E over 20 realizations. **(c)** Depth of the boundary layer λ at transition volume fraction $\overline{\rho}_\mathrm{T}$, and **(d)** contours of ϕ for one realization of $n = 70$: $\phi = 0$ indicates pure bending while $\phi = 1$ indicates pure stretching.

References

[1] Holzapfel G. A. et al. An affine continuum mechanical model for cross-linked F-actin networks with compliant linker proteins. *J.Mech. Beh. Bio. Mater.*, **38**:78-90, 2014

[2] Summerscales J., editor. Microstructural characterisation of fibre-reinforced composites. Woodhead Publishing, 1998

A NEW PARAMETER TO CONTROL THE ANISOTROPY OF PRISMATIC LATTICES

Anastasia Markou and Luc St-Pierre *
Department of Mechanical Engineering, Aalto University, Espoo, Finland

Summary Prismatic lattices, such as the triangular and kagome topologies, have a high specific stiffness and strength. Their in-plane properties are, however, nearly isotropic, which is suboptimal when loading is orientated along a specific direction. Here, we introduce a new parameter to control the degree of anisotropy of a prismatic lattice. This new parameter is the thickness ratio $\bar{t} = t_1/t_2$, where t_1 and t_2 are the thicknesses of bars along different directions. Using the triangular lattice as an example, we have developed new analytical expressions to capture how the elastic modulus and compressive strength vary as a function of this new parameter $\bar{t}$. These equations were then verified by finite element simulations, and found to be in good agreement with experiments performed on 3D printed polymeric lattices.

INTRODUCTION

Lattice materials are among the stiffest and strongest lightweight materials available today. They also possess a unique advantage over fully-dense materials: their mechanical properties can be adjusted by changing their relative density (for a given choice of topology and parent material) [1, 2]. This level of customisation has, however, certain limitations: changing the relative density modifies the density of the lattice and it does not allow to vary the properties along specific loading directions. We propose to alleviate these issues by varying the thickness of the bars along the two in-plane directions of a prismatic lattice, see Fig. 1a. This introduces a new parameter, $\bar{t} = t_1/t_2$, that can be used to control the degree of anisotropy. Considering the triangular lattice as an example, we first derive analytical equations to capture the effect of this new parameter $\bar{t}$ on the elastic modulus and strength of the lattice. These analytical expressions are then verified using finite element simulations and experiments.

ANALYTICAL MODELLING

Consider the triangular lattice shown in Fig. 1a, where the horizontal bars have a thickness t_1 and the diagonal bars, a thickness t_2. All bars have a length l, and are assumed to be made from an elastic perfectly plastic material with a Young's modulus E_s and a yield strength σ_{ys}. Following the same approach used in [1, 2], the elastic modulus of the lattice along x_1 and x_2 can be expressed as:

$$E_1 = \left[\frac{\bar{t}}{\bar{t}+2}\right]\bar{\rho}E_s \qquad \text{and} \qquad E_2 = \frac{9\bar{t}}{(8\bar{t}+1)(\bar{t}+2)}\bar{\rho}E_s, \tag{1}$$

respectively, where the bar thickness ratio $\bar{t} = t_1/t_2$, and the relative density $\bar{\rho} = 2\sqrt{3}(t_1+2t_2)/(3l)$.

When the lattice is compressed, two collapse modes are possible: (i) elastic buckling or (ii) yielding. Elastic buckling occurs when the internal force in a bar reaches the Euler buckling load. With this condition, we find that the elastic buckling strength of the lattice for uniaxial compression along x_1 or x_2 is given by:

$$\sigma_{1,el} = \frac{n^2\pi^2}{16}\left[\frac{\bar{t}}{\bar{t}+2}\right]^3\bar{\rho}^3E_s \qquad \text{and} \qquad \sigma_{2,el} = \frac{3n^2\pi^2}{32}\left[\frac{1}{\bar{t}+2}\right]^3\bar{\rho}^3E_s, \tag{2}$$

respectively. Note that the end constraint factor n varies between 1 and 2 depending on the value of $\bar{t}$. We found the value of n with the method presented in [3, 4], but the procedure is not given here for the sake of brevity.

For high values of relative density, the lattice is expected to collapse by yielding (when the stress in a bar reaches the yield strength of the parent material σ_{ys}). The yield strength of the lattice along x_1 and x_2 directions can be expressed as:

$$\sigma_{1,pl} = \left[\frac{\bar{t}}{\bar{t}+2}\right]\bar{\rho}\sigma_{ys} \qquad \text{and} \qquad \sigma_{2,pl} = \min\left[\frac{3\bar{t}}{(\bar{t}+2)}\bar{\rho}\sigma_{ys}\ ;\ \frac{3}{2(\bar{t}+2)}\bar{\rho}\sigma_{ys}\right], \tag{3}$$

respectively. The expression for $\sigma_{2,pl}$ includes the minimum function because yielding may occur in the horizontal or diagonal bar depending on the value of $\bar{t}$.

RESULTS

The elastic modulus, elastic buckling strength, and yield strength of the lattice are plotted as a function of $\bar{t}$ in Fig. 1b, c, and d, respectively. In all cases, results are given in a non-dimensional form and for both x_1 and x_2 directions.

The results show clearly how $\bar{t}$ can be used to control the degree of anisotropy of the lattice; increasing $\bar{t}$ increases the elastic modulus and strength along x_1, but reduces these properties along x_2. Note, however, that E_1 increases more rapidly than E_2 decreases for $\bar{t} > 0.5$. For example, compare the elastic moduli of a lattice with $\bar{t} = 3$ to those of a conventional lattice with $\bar{t} = 1$. The topology with $\bar{t} = 3$ has a modulus E_1 80% higher than that with $\bar{t} = 1$, whereas the reduction in E_2 is of only 35%. Therefore, the trade-off between E_1 and E_2 can be advantageous. Similar arguments can be made for the elastic buckling and yield strength.

*Corresponding author. E-mail: luc.st-pierre@aalto.fi.

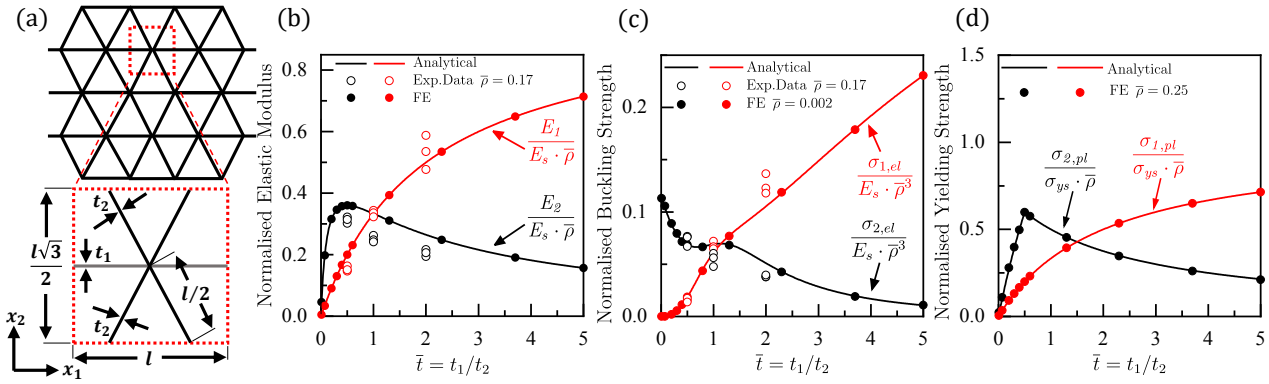

Figure 1: (a) Geometry of the triangular lattice, and its in-plane properties: (b) elastic modulus, (c) elastic buckling strength and (d) yield strength. All properties are given in non-dimensional form, for uniaxial compression along x_1 and x_2 directions, and as a function of the bar thickness ratio $\bar{t}$.

Comparison with finite element simulations

Finite element (FE) simulations were performed to validate the analytical expressions presented above. All simulations were conducted with the implicit solver of the commercial software Abaqus. The calculations were done on a representative unit cell with periodic boundary conditions, and a compressive displacement was prescribed in either x_1 or x_2. Each bar was discretised using 30 beam elements and a geometric imperfection (in the shape of the first eigenvalue and with an amplitude equal to 5% of the bar thickness expected to buckle) was used in all simulations. The material was linear elastic and perfectly plastic, with $E_s = 200\,\text{GPa}$ and $\sigma_{ys} = 250\,\text{MPa}$. Simulations were performed for selected values of $\bar{t}$ ranging from 0.01 to 5, and for two values of relative density $\bar{\rho} = 0.002$ and 0.25. These were selected such that lattices with $\bar{\rho} = 0.002$ collapse by elastic buckling, and those with $\bar{\rho} = 0.25$ fail by yielding.

The elastic modulus, elastic buckling strength and yield strength obtained from FE simulations are compared to our analytical equations in Fig. 1 for both loading directions. In all cases, there is an excellent agreement between FE and analytical results, and this holds true for all values of $\bar{t}$ considered here.

Comparison with experiments

Polymer lattices were produced by additive manufacturing. All samples were made using a Form 2 machine and Clear resin, both provided by Formlabs. Tensile tests, performed on standard dogbone specimens, revealed that the parent material has a Young's modulus $E_s = 2.4\,\text{GPa}$ and a yield strength $\sigma_{ys} = 41\,\text{MPa}$. The lattices manufactured had a bar length $l = 10\,\text{mm}$ with 15 cells along the x_1 direction and 8 cells along x_2 (see Fig. 1a). The relative density was kept constant at $\bar{\rho} = 0.17$, whereas t_1 and t_2 were varied to produce samples with $\bar{t} = 0.5$, 1, and 2.

Compression tests were conducted in both x_1 and x_2 directions. The measured elastic moduli E_1 and E_2 were found to be in reasonable agreement with our analytical predictions as shown in Fig. 1b. For this choice of material and relative density, all specimens collapsed by elastic buckling. The measured compressive strength, along both directions, were also in good agreement with our analytical predictions, see Fig. 1c.

CONCLUDING REMARKS

Prismatic lattices with different bar thicknesses have a significant advantage over those with uniform cell walls: their mechanical properties do not depend only upon their relative density $\bar{\rho}$, but also upon the bar thickness ratio $\bar{t}$. This new parameter $\bar{t}$ allows to control the degree of anisotropy, giving more flexibility to create new materials by design. This concept, demonstrated here with the triangular lattice, is applicable to other topologies and we have extended our investigation to kagome and hexagonal lattices.

References

[1] Ashby M.F., Gibson L.J. Cellular Solids: Structure and Properties. Cambridge University Press, UK 1997.
[2] Wang A.-J., McDowell D.L. In-Plane Stiffness and Yield Strength of Periodic Metal Honeycombs. *J. Eng. Mater. Technol.* **126**: 137-156, 2004.
[3] Fan H., Jin F., Fang D. Uniaxial Local Buckling Strength of Periodic Lattice Composites. *Mater. Des.* **30**: 4136–4145, 2009.
[4] Bažant Z.P., Cedolin L. Stability of Structures – Elastic, Inelastic, Fracture and Damage Theories. Oxford University Press, NY 1991.

IS FRACTURE TOUGHNESS A MATERIAL PROPERTY FOR MICRO-ARCHITECTED SOLIDS?

Angkur Jyoti Dipanka Shaikeea*[1], Huachen Cui[2], M.R.O' Masta[3], Xiaoyu (Rayne) Zheng[4], Vikram S. Deshpande[1]
[1] Department of Engineering, Cambridge University, Cambridge CB2 1PZ, UK (ajds3@cam.ac.uk)
[2] Department of Mechanical Engineering, Virginia Tech, Blacksburg, VA, USA
[3]HRL Laboratories, LLC, 3011 Malibu Canyon Road, Malibu, CA 90265, USA
[4] Mechanical and Aerospace Engineering Department, UCLA, Los Angeles, California 90095, USA

Summary Here we report a combined experimental and numerical study for the fracture of micro-architected cellular solids and develop rules for fracture limited design. We investigated embedded crack geometries resembling penny shape cracks fabricated into specimens with millions of unit cells. Multi-axial loading experiments were conducted in an in-situ X-Ray CT visualisation procedure to monitor the crack tip conditions. These investigations reveal two distinct crack-tip failure modes that are also predicted in full scale FE analysis. Remarkably, fracture for both modes is found to be only function of the remote applied K and T fields. Thus, a simple two-parameter fracture model (K+T) can be adopted for fracture limited engineering design of this emerging class of materials.

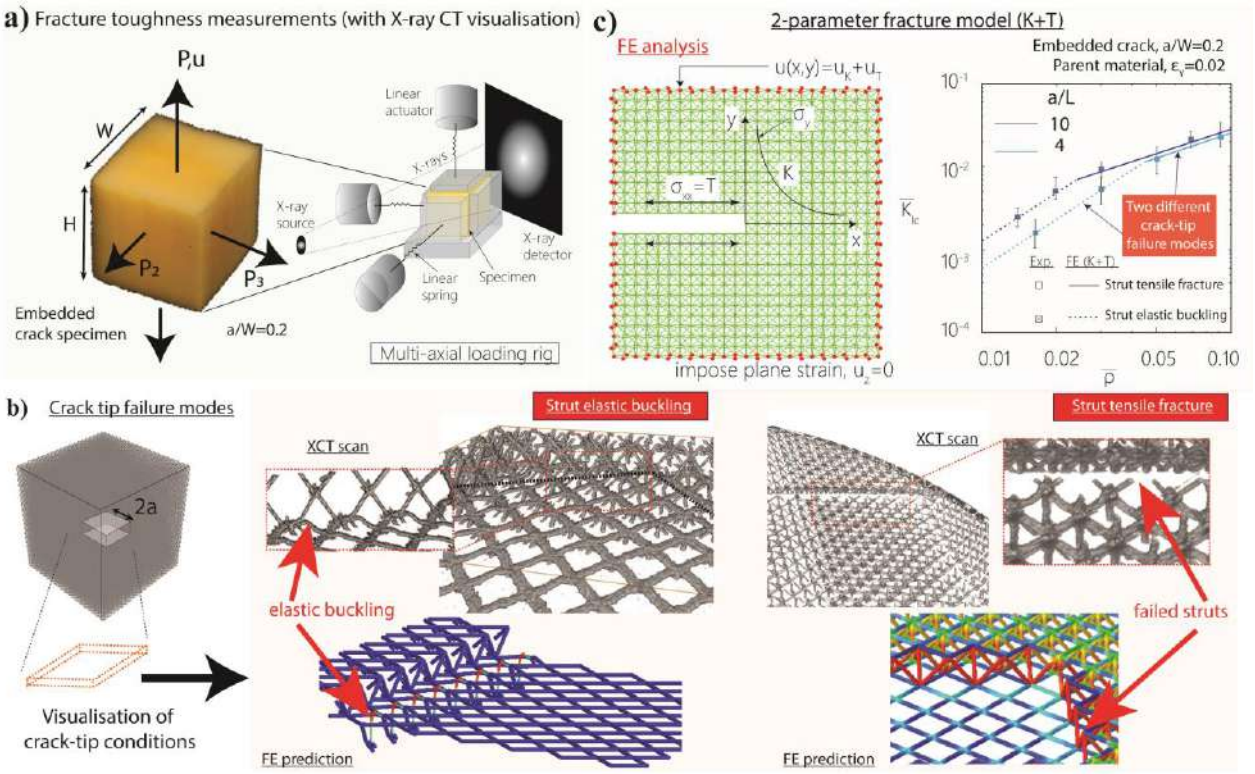

Fig. 1. Fracture toughness of micro-architected cellular solids. (a) Measurement of mode I fracture toughness of the octet truss lattice specimens with an embedded crack (akin to penny shaped crack). The number of unit cells in our specimens ranged from tens of thousands to one million. Specimens with different relative densities (between 0.02 to 0.15) and crack sizes (a/L varied between 4 to 10, where 'a' is crack length and 'L' is unit cell size) were tested in triaxial loadings to understand the significance of crack size effect on toughness. **(b)** Two distinct crack-tip failure modes set the definition of toughness- "elastic buckling" or "tensile yielding" of the crack tip struts. These are captured in FE predictions as well as observed in X-ray CT scans. **(c)** Measured fracture toughness values are in excellent agreement with that predicted from linear elastic FE calculations. Toughness for low density lattices made from soft polymeric materials are knocked down by nearly an order of magnitude in the elastic buckling failure regime. An asymptotic K+T field can generate the same results to show that a simple two parameter (K+T) fracture model can be used to predict failure.

INTRODUCTION

Designing materials as multiscale architected structures has resulted in creation of metamaterials whose properties can be optimised for a plethora of engineering applications. In particular, nano and micro-scale architected cellular materials exhibit properties like enhanced strength, ductility and fracture tolerance [1]. With recent advancements in additive manufacturing techniques such as projection micro-stereolithography [2-4], 3-D micro-architected solids can now be manufactured with 100s of millions of unit cells facilitating a wide spectrum of applications like biomedical implants, nanophotonic devices, energy

*Corresponding author. E-mail:ajds3@cam.ac.uk

storages and even textiles. It is thus important to understand their failure behaviour, or more precisely prescribe failure limits in the presence of flaws. There is a paucity of fracture data in the literature for these materials with data limited to specimens with a few cells [5]. It remains unclear whether traditional fracture mechanics can be applied to this new class of materials. Here we address the question- 'Is fracture toughness a material property for micro-architected solids?'

METHODOLOGY

We began our investigation with a series of mode I fracture toughness measurements on the embedded crack geometry **(Fig. 1a, left)**. To perform valid fracture toughness measurements, the number of unit cells in the truss was increased from a few hundreds of thousands to an excess of one million. To monitor the crack tip condition, experiments were conducted on a custom-built multiaxial loading setup placed inside the X-Ray CT machine **(Fig. 1a, right)**. We developed a procedure to perform in-situ experiments and continuously observed the crack tip conditions in 3D tomographic images while simultaneously measuring the applied loads. Measurements were performed over a wide range of lattice relative densities and loading biaxiality ratios. On the computation side, full scale linear elastic FE calculations were performed to predict the crack-tip failure modes and fracture toughness values**.**

RESULTS

- We found that two modes of failure dictate toughness: (i) tensile strut fracture (ii) strut elastic buckling, even though the remote loading is tensile **(Fig. 1b)**.
- For a given material, these failure modes and toughness values are shown to depend on lattice relative density, biaxiality and normalised crack size (a/L). Thus, toughness can't be defined as a material property using a single parameter K. **(Fig.1c)**
- Interestingly, crack size and loading triaxiality can collapse into a single parameter that is uniquely captured by the "T-stress". Experiments to validate such claim required complicated testing in triaxial loadings and the experimental results are seen to agree with our FE calculations. Thus, a two-parameter (K+T) model can accurately predict toughness values and crack-tip failure modes. This leads to the path for development of failure maps for the fracture limited design of micro-architected cellular solids **(Fig. 2)**.

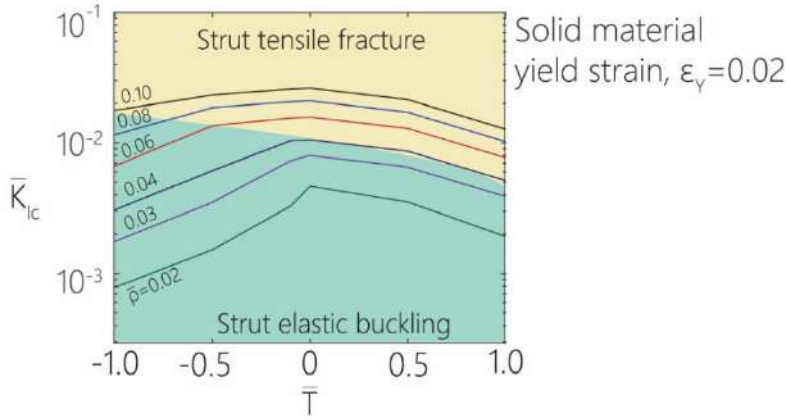

Fig. 2. Design map of failure for the Octet-truss lattice. Contours of the octet truss relative density are shown using axes of normalised toughness, $\overline{K_{Ic}}$ and normalised T-stress, $\bar{T}$.

CONCLUSIONS

In the present study we conclude that fracture toughness can be defined as a material property for micro-architected solids when represented as a 2-parameter (K+T) fracture model. The combined experimental and numerical investigation shows presence of two distinct crack-tip failure modes (strut elastic buckling and strut tensile fracture) across a range of relative densities and applied loading triaxialities. Thus, classical fracture mechanics developed for continuum solids can now be extended to micro-architected solids with the exception that "T-stress" is significant in these solids. Failure maps are generated to aid designing with micro-architected solids.

References

[1] Greer, Julia R., and Vikram S. Deshpande. "Three-dimensional architected materials and structures: Design, fabrication, and mechanical behavior." MRS Bulletin 44.10 (2019): 750-757.
[2] Zheng, Xiaoyu, et al. "Multiscale metallic metamaterials." Nature materials 15.10 (2016): 1100.
[3] Chen, Da, and Xiaoyu Zheng. "Multi-material additive manufacturing of metamaterials with giant, tailorable negative Poisson's ratios." Scientific reports 8.1 (2018): 9139.
[4] Cui, Huachen, et al. "Three-dimensional printing of piezoelectric materials with designed anisotropy and directional response." Nature materials 18.3 (2019): 234.
[5] O'Masta, M. R., et al. "The fracture toughness of octet-truss lattices." Journal of the Mechanics and Physics of Solids 98 (2017): 271-289.

GAS MARBLES: STRENGTH AND GAS PERMEABILITY

Yousra TIMOUNAY[1], Elise LORENCEAU[2], Olivier PITOIS[1], and Florence ROUYER *[1]
[1] Lab Navier, Univ Gustave Eiffel, ENPC, CNRS, F-77454 Marne-la-Vallée, France
[2]Univ. Grenoble Alpes, CNRS, LIPhy, F-38000 Grenoble, France

Summary Introducing solid particles into liquid films drastically changes their properties. Here we demonstrate that the concept of liquid marbles (liquid droplets enwrapped with hydrophobic particles) can be successfully applied for encapsulating and protecting small gas pockets within an air environment. Similarly, to their liquid counterparts, those new soft-matter objects, that we call "gas marbles" can sustain underpressure but the collapse pressure is ten times larger. Moreover, they can resist overpressure. This magnified strength is shown to originate from the strong cohesive nature of the shell. Yet, gas marbles can undergo gas transfer. Our results show that particulate films are less permeable to gas than their pure liquid counterparts because presence of the particles reduces the surface area through which gas diffuses.

INTRODUCTION

In line with the pioneer work of Pickering, we succeeded to produce new objects which can be described as gas pockets in air and are named gas marbles [1]. They are made of gas surrounded by a layer of grains constrained by thin liquid film in gas environment. The exceptional mechanical strength of their granular shell promise them to many applications [2] as the generation of materials with hierarchical porosity as well as gas encapsulation.

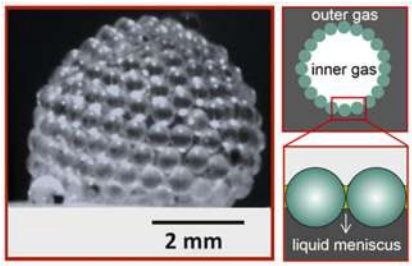

Figure 1. The so-called gas marble elaborated and studied in this work. (a) Image of a gas marble (D_p=590µm and D_b=5mm). (b) Sketch of the cross section revealing the structure of the cohesive granular shell.

MATERIAL and EXPERIMENTAL SET-UP

Gas marbles are created from a granular film by closing over itself after detachment under gravity. The granular film is created by dipping and removing a solid horizontal frame through a particle raft at the interface of a soap solution. The particles are monodisperse polystyrene beads which diameter D_p varies from 140 to 590 µm. The soap solution is a SDS solution at the cmc.

Inserting a needle, connected to a syringe and a pressure sensor, inside the gas marble allows us to study its behaviour during inflation and deflation. The inner pressure P_b is measured by the pressure sensor, and, thanks to a syringe pump, the volume of the syringe is controlled. Increasing the syringe volume results in a decrease of the gas marble inner pressure P_b, and vice versa. Volume variations are performed at a constant flow rate equal to 0.06ml/min during all of our experiments. The inner pressure relative to atmospheric pressure $\Delta P = P_b - P_{atm}$, as a function of the variation of the syringe volume ΔV is recorded while two cameras placed above and on the side allow us to follow the evolution of the shape of gas marbles.

STRENGTH of GAS MARBLES

The strength of gas marbles is characterized by the critical $\Delta P+$ at which the shell fractures (figure 2 top right) and the critical $\Delta P-$ at which the gas marble collapses (figure 2 bottom right). As shown in figure 2 (left), in absolute values these critical pressures are of one order of magnitude larger than the capillary pressure of particle free bubbles. Moreover, $\Delta P-$ and $\Delta P+$ are independent of particle and gas marble size in the range of study. This magnified strength is shown to originate from the strong cohesive nature of the shell.

AIR PERMEABILITY of GAS MARBLES MEMBRANES

To characterize the permeability of gas marble shell, we first increase the inner pressure of gas marbles by a few millibars ($\Delta P < \Delta P+$). Then, we follow the spontaneous evolution of the inner pressure. Figure 3 shows an example of the pressure inside a gas marble relative to the atmospheric pressure $\Delta P = P - Patm$ as a function of time. Considering

*Corresponding author. E-mail: florence.rouyer@u-pem.fr

ideal gas law and gas diffusion though the membrane, one can model the exponential decay of the inner pressure with a characteristic time $\tau = {}^{V}/_{kA}$ where V is the volume of gas inside the marbles, and A and k are respectively the surface and gas permeability of the shell. Experiments with gas marbles of different size and particle sizes show that k is of the order of 0.7 mm/s. One order of magnitude smaller the permeability of a soap bubble. The reduction of gas flow is associated to the area of liquid film reduction due to the hexagonal packing of the spherical particles forming the shell.

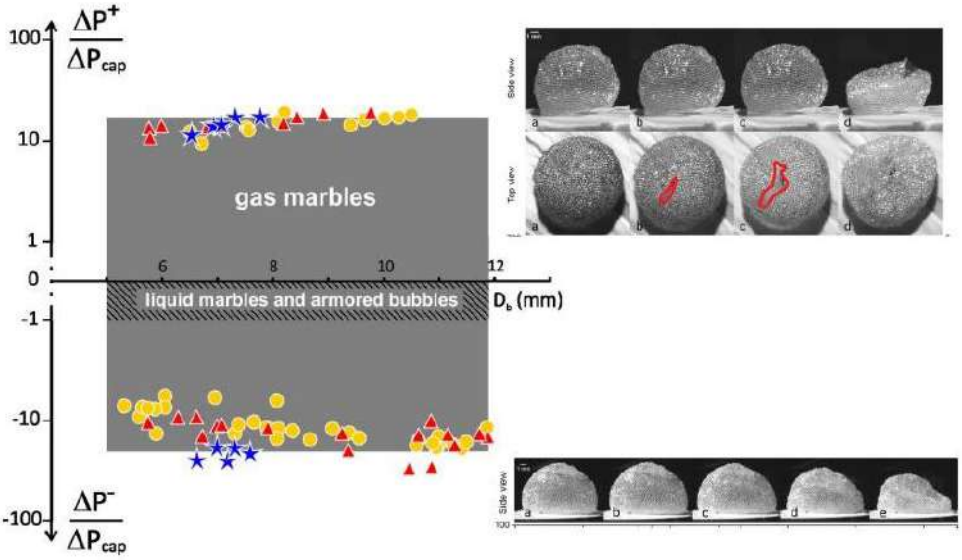

Figure 2. Normalized critical overpressures (ΔP+/ΔPcap) and underpressures (ΔP-/ΔPcap) measured for gas marbles within both inflation and deflation conditions, respectively, as a function of bubble diameter Db. Triangles, stars and circles are data respectively obtained for particles D_p= 250 µm, 315 µm and 590 µm. Laplace pressure ΔPcap= 8γ/D_b is the pressure at equilibrium of the corresponding particle-free bubbles with two interfaces. The stability range of gas marbles is between the two horizontal dashed lines. The images on the right, are successive side and top views during fracturing its granular shell ΔP> ΔP+ (top) and side view of a gas marble after collapsing ΔP< ΔP- (bottom).

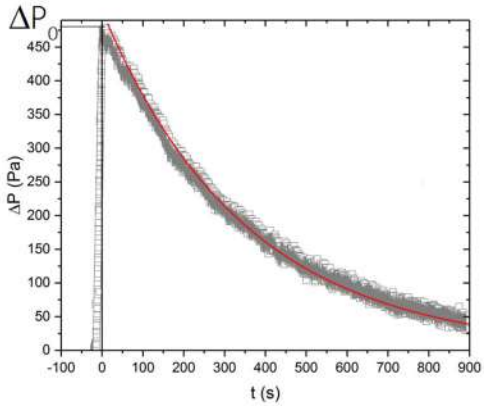

Figure 3. Relative pressure inside a gas marble as a function of time with D_P = 250 µm. The red curve is as fit of the form$\Delta P = \Delta P_0 e^{-t/\tau}$ to the experimental data.

CONCLUSIONS

The strength and low permeability of gas marbles compared to pickering or bare bubbles could be exploited for imprisoning valuable or polluted gases or for designing new aerated materials. Indeed, encapsulation via a liquid membrane - always partially permeable to gases - is metastable and limited by osmotic or capillary gas flows entering or leaving the bubble. The low permeability of the particulate membranes, which ensures slower inflation or deflation of the particle-laden containers, as well as the remarkable strength of the gas marbles' membranes compared to those of pickering bubbles, both ensure a longer lifetime to the gas marbles compared to bare and pickering bubbles. It is therefore the combination of these two properties that makes gas marble an ideal candidate for gas encapsulation.

References

[1] 1. Y. Timounay, O. Pitois, F. Rouyer, *Physical Review Letters,* **118**(22), 228001 (2017).
[2] 2. Y. Timounay, E. Lorenceau, F. Rouyer, *Soft Matter*, **13**, 7717-7720 (2017).

LIGHTWEIGHT AND ULTRA-STRONG PYROLYTIC CARBON NANOLATTICES AND MICROPILLARS

Xuan Zhang[1], Huajian Gao[2], Julia R. Greer[3] and Xiaoyan L*[1]
[1]Centre for Advanced Mechanics and Materials, Applied Mechanic Laboratory, Department of Engineering Mechanics, Tsinghua University, Beijing 100084, China
[2]School of Mechanical and Aerospace Engineering, College of Engineering, Nanyang Technological University, 70 Nanyang Drive, Singapore 639798, Singapore
[3]Division of Engineering and Applied Science, California Institute of Technology, Pasadena, CA, USA

Summary Designing and synthesizing materials that are simultaneously strong and stiff, substantially deformable, and lightweight remains a long-standing and unsolved challenge. Here we fabricated pyrolytic carbon nanolattices and micropillars by a two-step procedure: 3D printing and high-temperature pyrolysis. The pyrolytic carbon nanolattices have a compressive strength of 1.90 GPa at a density of 1.0 g/cm^3, and an average fracture strain of 14.0%-16.7%. The pyrolytic carbon micropillars have an average tensile strength of 1.60 GPa, a compressive strength approaching the theoretical limit of ~13.7 GPa, a substantial elastic limit of 20-30% and a low density of ~1.4 g/cm^3. These unique mechanical properties are attributed to the controlling of characteristic size of materials, and the optimization of structural topology and the selection of constitute materials.

INTRODUCTION

For nearly all structural materials, the trade-offs between high strength and large deformability/ductility and high strength and low density have been recognized as two pairs of inevitable conflicts. For example, metals and alloys are ductile, but their strengths are usually about several hundred MPa. The ceramics have higher strength (up to about several GPa), but their fracture strains are below 5%. Polymers and porous materials like foams are lightweight and deformable, but their strengths are only on the order of ~10 MPa. Existing materials that come close to "optimizing" all three of these properties are Mg alloys, but their ductility is still lower than the requirements of applications for forming and performance of structural components. Designing and synthesizing materials that are simultaneously strong and stiff, substantially deformable (i.e. >10%), and lightweight represents the Holy Grail of materials sciences, and remains a long-standing and unsolved challenge.

PYROLYTIC CARBON NANOLATTICES

We first fabricated pyrolytic carbon nanolattices with stretching-dominated octet- and iso-truss topologies by a two-step procedure: direct laser writing and pyrolysis at high temperature [1]. The unit cells of these nanolattices had the same dimensions of approximately 2 μm, and the diameters of the individual struts in the lattices varied from 261 nm to 679 nm. The smallest characteristic size of the struts approached the limits of resolution of the available three-dimensional lithograph technologies. In situ scanning electron microscopy (SEM) and ex situ compressive testing revealed that these pyrolytic carbon nanolattices have a compressive strength of up to 1.90 GPa at a density below 1.0 g/cm^3. As a result, the pyrolytic carbon nanolattices achieved an exceptional specific strength (i.e., ratio of strength to density) of 1.90 GPa g^{-1} cm3, which is 1-3 orders of magnitude higher than those of nearly all micro/nanolattices reported so far [2,3]. Such specific strength of our nanolattice is about 35% of that (5.60 GPa g^{-1} cm^3) of diamond, which has the highest specific strength of all bulk materials.

Our compression experiments also showed that these octet- and iso-truss nanolattices have the average fracture strains of 14.0% and 16.7%, respectively, which are larger than those of various brittle nanolattices reported previously [1,2]. More remarkably, these nanolattices become insensitive to fabrication-induced defects, allowing them to attain nearly theoretical strength of the constituent material. The combination of ultra-low density, ultra-high strength and specific strength, large fracture strain and flaw insensitivity of these pyrolytic carbon nanolattices are attributed to the miniaturization (nanosized beams) of the overall structure and the optimization of the lattice topology.

PYROLYTIC CARBON MICROPILLARS

We further fabricated a series of pyrolytic carbon micropillars with diameter from 700 nm to 10 μm by using the two-step procedure mentioned above [4]. The atomic-level microstructural characterization showed that these pyrolytic carbon specimens consist of 1-1.5 nm curved graphene layers. The experimental measurements showed the overall density of micro-sized pyrolytic carbon to be 1.4 g/cm^3, which is close to those of some polymers. In-situ SEM nanomechanical experiments revealed an average tensile strength of up to ~1.6 GPa and a compressive strength approaching theoretical limit of 13.7 GPa, with an ultra-large elastic limit of 20-30%. The combination of close-to-theoretical strength and low density of these micron-sized pyrolytic carbon samples points to their ultra-high specific strength of 9.79 GPa cm^3/g, which surpasses the specific strengths of all existing structural materials, including polycrystalline diamond, which has the highest specific strength of ~5.61 GPa cm^3/g in bulk materials reported to date.

*Corresponding author. E-mail: xiaoyanlithu@tsinghua.edu.cn.

Further, pyrolytic carbon samples with diameters below 2.3 μm sustained compressive strains that exceed 50% without catastrophic fracture, deforming like rubber. Large-scale atomistic simulations uncovered the underlying deformation mechanisms, i.e. the compressive deformation is dominated by slipping/shear of the graphene layers and densification of the structure, while the tensile deformation is governed by the nucleation, growth and coalescence of nanoscale cavities or by the extension of initial flaws. These mechanisms enable the unexpected combination of low density, substantial deformability, high elastic limit and high strength of micro-sized pyrolytic carbon samples.

CONCLUSIONS

The excellent mechanical properties of pyrolytic carbon nanolattices and micropillars are attributed to the controlling of characteristic size of materials, and the optimization of structural topology and the selection of constitute materials. The results from our current studies provide potential routes for designing and synthesizing new high-performance carbon materials.

References

[1] Zhang X., Vyatskikh A., Gao H., Greer J. R., Li X. Lightweight, flaw-tolerant, and ultrastrong nanoarchitected carbon. *Proc. Natl. Acd. Sci.* **116**: 6665-6672, 2019.
[2] Zhang X., Wang Y., Ding B., Li X. Design, fabrication, and mechanics of 3D micro-/nanolattices. *Small* 1902842, 2019.
[3] Schwaiger R., Meza L. R., Li X. The extreme mechanics of micro-and nanoarchitected materials. *MRS Bull.* **44**: 758-765, 2019.
[4] Zhang X., Zhong L., Mateos A., Kudo A., Vyatskikh A., Gao H., Greer J. R., Li X. Theoretical strength and rubber-like behaviour in micro-sized pyrolytic carbon. *Nat. Nanotech.* **14**: 762-769, 2019.

CELLULOSE-BASED HIGH-PERFORMANCE FOAM FOR SUSTAINABLE PACKAGING

Teng Li*[1], Shuze Zhu[1], Jian Cheng[1], Liangbing Hu[2], Chaoji Chen[2], Jianwei Song[2]
[1]Department of Mechanical Engineering, University of Maryland, College Park, USA
[2]Department of Materials Science Engineering, University of Maryland, College Park, USA

Summary Most packaging materials are made of plastics, which take 100s years to degrade, leading to severe global pollution. Here, we report a degradable, recyclable, and cost-effective solution to packaging materials based on foam fabricated from graphite and cellulose nanofibers (CNFs) via advanced 3D printing. The CNFs can directly disperse the graphite under the physical sonication without the need for any chemical reaction. The interaction of the CNFs with graphite through the function of the hydrophilic and hydrophobic faces in CNFs renders the dispersion polymer-like rheological properties and a good processability with tunable viscosity for 3D printing. A robust 3D graphite-CNF foam can be printed in large scale, demonstrating a higher mechanical strength, better fire resistance and degradability than commercial packaging foam, representing a sustainable solution to packaging.

BACKGROUND

Packaging materials are in great demand (about 100 million tons per year) in modern society, which are widely used in the food and electronics industries for shock-absorption, storage and heat preservation [1-3]. Most commercial packaging materials are made of plastics such as polystyrene and polyvinyl chloride. These plastics are usually environmentally unfriendly, high-energy consumption, nonrecyclable, and undegradable in the processes of synthesis, molding and disposal, leading to severe environmental issues. Developing environmentally friendly, recyclable, and degradable packaging materials is in urgent need toward a sustainable society.

Natural products are from the nature and most of them are environmentally friendly [4]. Graphite, for example, can be produced from coal formed underground and widely used to produce graphene or as anode materials in rechargeable lithium-ion batteries [5]. Cellulose, as the most abundant natural polymer on earth, has been widely used in a range of applications including energy storage, electronics, structural materials, and water treatment [6].

RESULTS

Here we demonstrate the scalable fabrication of a three-dimensional (3D) graphite-cellulose nanofibers (G-CNF) aerogel as a new generation of cost-effective, environmentally friendly, recyclable, and degradable packaging material via a 3D printing method.

Natural cellulose and graphite are earth abundant, low-cost and accessible, promising large-scale manufacturing. In addition, the G-CNF aerogel can be re-dissolved by water, which makes it recyclable and degradable, representing a sustainable solution to the challenge of white pollution (Figure 1a-c).

As illustrated in Figure 1d, the 3D G-CNF foam with various shapes are 3D printed from the slurry containing graphite and CNF. Note that cellulose can be reused or naturally decomposed into glucose via enzyme-assisted hydrolysis [7], while the chemically inert graphite can be recycled and go back to the carbon cycle, which is naturally environment friendly [8], in sharp comparison with the non-degradable petroleum-based plastics.

Figure 1. Photos and schematics demonstrating the replacement of the white pollution using bagasse and graphite that are recyclable, degradable and printable. (a) The white foam pollution. (b) Digital images of plastic foam and G-CNF foam. (c) Schematic of the recyclability and degradability of the printed G-CNF aerogel made from the plants and graphite mine in nature.

*Corresponding author. E-mail: lit@umd.edu

The resulting G-CNF foam is lightweight and can be supported by a dandelion (Figure 2a). Owing to highly porous structure, the G-CNF foam has an ultra-low density of 0.05 g/cm^3, similar to the density of the commercial plastic foam (Figure 2b). The mechanical properties are important for practical packaging applications. We evaluated these properties of the G-CNF foam and compared with those of the commercial plastic foam, which are shown in Figure 2. The G-CNF foam exhibited an ultimate tensile strength of 3.72 MPa, which is 13 times stronger than the commercial plastic PS foam (Figure 2c). The G-CNF foam also demonstrates a substantially 9 times higher tensile stiffness than the commercial plastic PS foam (27.9 MPa vs. 3.58 MPa). The hydrogen bonding between the graphite and CNF offers the high tensile strength, while there is the weak connection among the PS microspheres of the commercial plastic PS foam. Compressive property is also important for packaging materials. Figure 2d compared the compressive test results of the G-CNF foam and the commercial plastic PS foam. The G-CNF foam showed a higher compressive stiffness of 2.34 MPa than the commercial plastic PS foam. Due to its low density, the specific tensile stiffness and compressive stiffness of the G-CNF foam are as high as 396.8 MPa • cm^3/g and 42.23 MPa • cm^3/g, respectively, both of which are higher than the commercial PS foam.
.

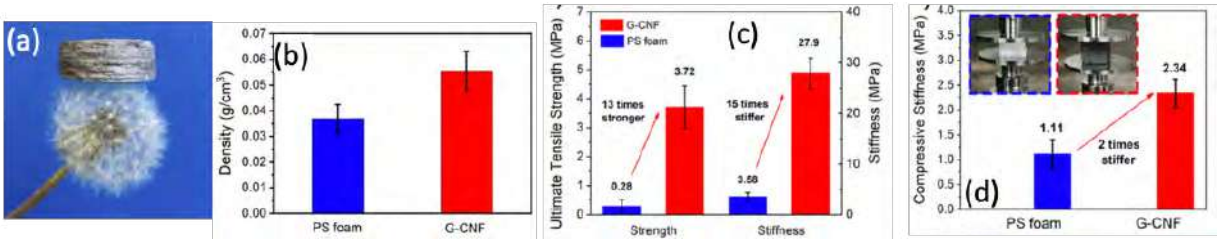

Figure 2. (a) The G-CNF foam supported by a very light dandelion. (b) The density comparison between the G-CNF foam and the commercial plastic foam. (c) The comparison of the ultimate tensile strength and the tensile stiffness between the G-CNF foam and commercial plastic foam. (b) The comparison of the compressive stiffness between the G-CNF foam and commercial plastic foam.

CONCLUSIONS

In conclusion, we develop a degradable, recyclable, and lightweight 3D graphite-cellulose foam as an advanced packaging material via 3D printing method. The graphite powder can be directly dispersed into a uniform and stable slurry by CNF without the need of surfactant or harsh chemicals. The graphite/CNF slurry maintains high apparent viscosity as well as good storage and loss moduli stability, which enables the production of the continuous filaments from slurry to construct 3D architectures. The printed CNF/graphite foam exhibits a 15-times stronger than commercial plastic foam with a high tensile stiffness of 54.9 MPa and 2-times stronger with a high compressive stiffness of 2.34 MPa.

References

[1] Manzione, Louis T, Plastic packaging of microelectronic devices. Van Nostrand Reinhold: 1990.
[2] Weber, C. J.; Haugaard, V.; Festersen, R.; Bertelsen, G., Production and applications of biobased packaging materials for the food industry. *Food Additives & Contaminants* 2002, 19 (sup1), 172-177.
[3] Piringer, Otto G; Baner, Albert Lawrence, Plastic packaging materials for food: barrier function, mass transport, quality assurance, and legislation. John Wiley & Sons.
[4] Klemm, Dieter; Heublein, Brigitte; Fink, Hans-Peter; Bohn, Andreas, Cellulose: Fascinating Biopolymer and Sustainable Raw Material. *Angewandte Chemie International Edition* 2005, 44 (22), 3358-3393.
[5] Pumera, Martin, Graphene-based nanomaterials for energy storage. *Energy & Environmental Science* 2011, 4 (3), 668-674
[6] Leif, Nyholm; Gustav, Nyström; Albert, Mihranyan; Maria, Strømme, Toward Flexible Polymer and Paper-Based Energy Storage Devices. *Advanced Materials* 2011, 23 (33), 3751-3769.
[7] Zhang, Yi-Heng Percival; Lynd, Lee R., Toward an aggregated understanding of enzymatic hydrolysis of cellulose: Noncomplexed cellulase systems. *Biotechnology and Bioengineering* 2004, 88 (7), 797-824.
[8] Zhu, Yongfeng; Ogasawara, Yoshihide, Carbon recycled into deep Earth: Evidence from dolomite dissociation in subduction-zone rocks. *Geology* 2002, 30 (10), 947-950.

MEDIATION OF DEFECTS IN LATTICE MATERIALS BY STRUT TOPOLOGY

Kan Li*[1], Philipp E. Seiler[1], Vikram Deshpande[1], and Norman A. Fleck[1]
[1]Department of Engineering, University of Cambridge, Cambridge, United Kingdom

Summary We make use of the local modification of a lattice in the vicinity of a stress-raiser such as a notch in order to increase the macroscopic strength. Specifically, a spatially non-uniform waviness distribution of sinusoidal shaped struts is assumed in the vicinity of a notch in a hexagonal lattice or a triangular lattice, and the macroscopic tensile response is determined by finite element analysis. Optimal lattice structures are determined that maximise (or minimise) the macroscopic tensile strength. Hexagonal and triangular lattices are studied as they are representative of bending-dominated and stretching-dominated lattices, respectively.

INTRODUCTION

Spatially periodic networks of struts, called lattice materials, are increasingly used in engineering applications, e.g. tower structures in civil engineering, the cores of lightweight sandwich panels, microscopic mechanical filters [1], and soft network materials utilised in bio-integrated electronics [2]. Existing studies mostly focused on the design, fabrication and modelling of spatially uniform lattice materials. However, in practical applications, lattice materials may contain as-designed defects such as holes [3], notches and solid inclusions [4]. In order to modulate the lattice material in the vicinity of the stress-raiser, we ascribe a spatially non-uniform waviness distribution of the struts in the lattice.

METHODS

Parameter study and optimisation of waviness distribution

A periodic representative volume element (RVE) of lattice is studied, as shown in Figure 1(a). The non-uniform distribution of strut waviness of RVE is demonstrated in Figure 1(b). The wavy struts are in sinusoidal shape and their waviness A is defined by a Gaussian distribution

$$A(r) = A_\infty + (A_m - A_\infty) \cdot \exp\left(-\frac{r^2}{R^2}\right)$$

where r is the distance from the centroid of a strut to the centre of RVE, such that $r^2 = x^2 + y^2$. This Gaussian distribution makes use of the 3 parameters A_∞/ℓ, A_m/ℓ and R/ℓ. The dependence of the macroscopic strength and ductility of the lattice upon these 3 parameters was determined by Optimal Latin Hypercube sampling method, using software ISIGHT v2018, in a representatively large design region (A_∞/ℓ, $A_m/\ell \in [0, 0.2]$ and $R/\ell \in [0, 20]$). A Gaussian approximation was employed to assemble these results and to build a design map. Further optimisation is done by choosing the maximum (or minimum) points on the design map.

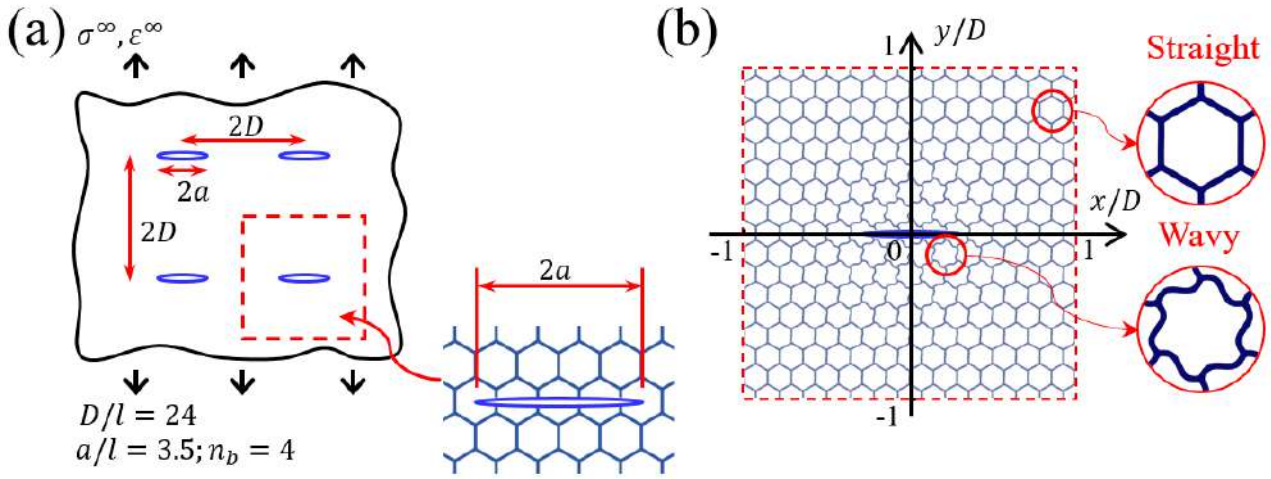

Figure 1. (a) A flaw of length $2a$, consisting of missing cell walls, exists in a periodic RVE of size $D \times D$. (b) A periodic RVE with non-uniform strut waviness distribution.

Finite element modelling

Static finite element simulations are performed using ABAQUS/Standard v2018 to simulate the tensile response of the lattice under uniaxial tension. Periodic boundaries are set by node-to-node equation constraints using a python script

*Corresponding author. E-mail: kl513@cam.ac.uk

interface. Uniaxial loading of the periodic RVE is simulated by imposing a relative displacement between top-most and bottom-most nodes at the boundaries in the y-direction. The finite element mesh of the lattice comprises rectangular elements and quadratic shape functions in plane strain (type CPE8). The elements are of uniform size and each strut has at least 4 elements across its thickness. The material properties are representative of a low carbon steel of Young's modulus $E_S = 210\text{GPa}$, yield strength $\sigma_{YS} = 338\text{MPa}$ and ultimate tensile strength $\text{UTS} = 500\text{MPa}$, as measured from a tensile test on a dog-bone specimen. The macroscopic failure of the lattice is defined by the onset of necking in any strut of the lattice.

RESULTS

Based on the simulations, we plot contours of macroscopic tensile strength of the hexagonal lattice as a function of strut waviness distributions, as shown in Figure 2(a) for the case of a slit with 4 missing cell walls. The normalised tensile strength $\hat{\sigma}$ is defined by

$$\hat{\sigma} = \frac{\sigma_{\text{UTS}}}{\sigma_{\text{UTS}}\left(a; \frac{A_\infty}{\ell} = \frac{A_m}{\ell} = 0\right)}$$

(Similar calculations have been performed for a triangular lattice.) The choice $\frac{A_\infty}{\ell} = \frac{A_m}{\ell} = 0$ corresponds to a lattice with straight struts. The strength of the notched hexagonal lattice is maximised by making the struts wavy within a zone of radius $R = 8\ell$ (Region I), but straight remotely (Region II), as listed in Table 1. Alternatively, the strength is minimised by employing straight struts near the notch (Region I) but wavy remotely (Region II).

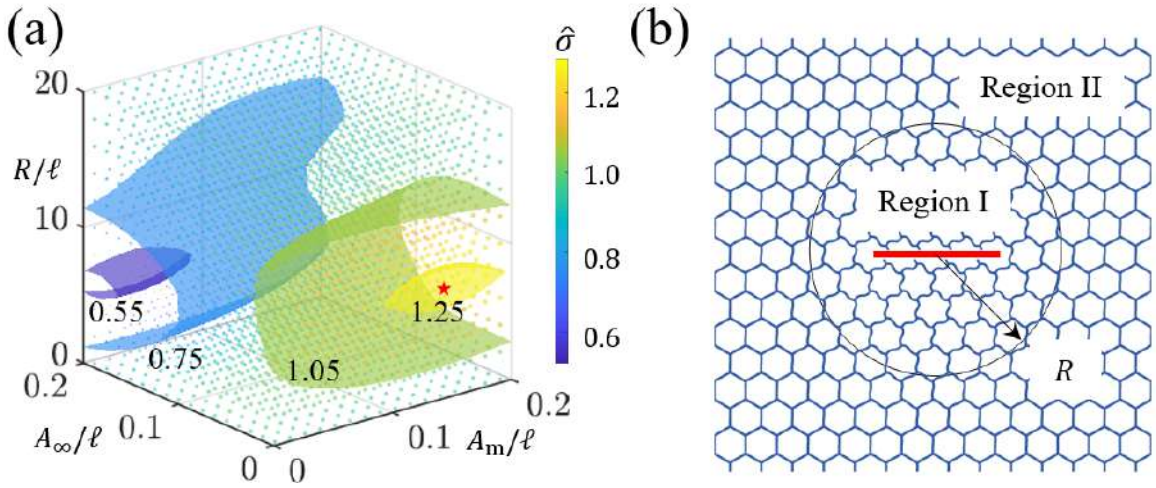

Figure 2. Contours of normalised tensile strength as a function of the strut waviness distributions for a periodic RVE of hexagonal lattice with 4 missing cells. (a) Scattered 3D plot and isosurfaces of normalised tensile strength. (b) Schematic diagram of strut waviness distribution, separating the RVE into two regions by radius R.

	Region I	Region II	$\hat{\sigma}$
$A_\infty/\ell = A_m/\ell = 0$	Straight	Straight	1.00
$A_\infty/\ell = 0, A_m/\ell = 0.15, \quad R/\ell = 8$	Wavy	Straight	Max =1.26
$A_\infty/\ell = 0.2, A_m/\ell = 0, \ R/\ell = 8$	Straight	Wavy	Min = 0.52

Table 1. A summary of the relation between macroscopic tensile strength and the assumed waviness distribution.

References

[1] A. S. Phani, M. I. Hussein, Introduction to Lattice Materials, John Wiley & Sons, Ltd, 2017.
[2] Q. Ma, Y. Zhang, Mechanics of Fractal-inspired Horseshoe Microstructures for Applications in Stretchable Electronics, *Journal of Applied Mechanics*, 1; 83(11):111008, 2016.
[3] J. Liu, H. Song, & Y. Zhang, Toward Imperfection-Insensitive Soft Network Materials for Applications in Stretchable Electronics. *ACS applied materials & interfaces*, 11(39), 36100-36109, 2019.
[4] W. Ronan, V. S. Deshpande, N. A. Fleck, The Tensile Ductility of Cellular Solids: The Role of Imperfections, *International Journal of Solids and Structures*, 0020-7683, 2016.

MULTIAXIAL CRUSHING OF OPEN-CELL FOAMS

Chenglin Yang[1] and Stelios Kyriakides *[1]
[1]Research Center for Mechanics of Solids, Structures & Materials, University of Texas at Austin, Austin, Texas, USA

Summary A true triaxial numerical apparatus is used to crush micromechanically accurate Al-alloy random open-cell foams along radial displacement paths to volume reductions of 70%. For all loading paths the foam traces an initial stiff and stable branch with the foam deforming uniformly. This branch terminates into a stress maximum followed by localized crushing in narrow bands of cells that tend to spread with limited additional effort, while crushed and relatively undeformed cells coexist. The deformation becomes uniform again once the crushing has spread to the whole domain. This work demonstrates that this three-regime behavior can be simulated at the continuum level using a Drucker-Prager type compressible constitutive model calibrated to a stress-strain response with a softening branch over part of the strain history.

INTRODUCTION

It is widely accepted that under uniaxial compression relatively low density foams exhibit a fairly stiff linearly elastic regime that terminates into a load maximum. It is followed by an extended load plateau during which localized cell crushing initiates and gradually spreads throughout the specimen. When most of the cells are crushed, the densified material stiffens again [1]. Uniaxial crushing has been successfully reproduced numerically using micromechanically accurate random foam models [2]. In a recent study a true triaxial apparatus shown in Fig. 1 has been used to crush such foam models under triaxial loading histories [3]. Cubical random foam models with 10^3 cells are crushed between three pairs of rigid orthogonal planes under radial displacement paths in the x-y-z space. It is demonstrated that multiaxial crushing exhibits the same three deformation regimes observed in uniaxial compression. In a first effort to capture this behavior at the continuum setting, a compressible yield function coupled with a material stress-strain response with a softening branch has been proposed. The constitutive model is incorporated in a cubical finite element model with an irregular mesh of solid elements and used to simulate the triaxial crushing loading histories of the random foam. The performance of the homogenized model is evaluated by comparing the calculated responses with those of the random foam.

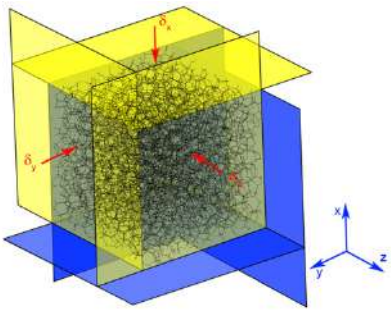

Figure 1. A true triaxial apparatus used to crush random foams under triaxial loadings.

TRIAXIAL CRUSHING OF RANDOM AND HOMOGENIZED MODELS

The true triaxial apparatus shown in Fig. 1 has been used in [3] to crush Al-alloy open-cell foam models with relative density of 0.08 to volume reductions of 70%. The foams start as skeletal versions of monodisperse random foams generated using the Surface Evolver software. They are subsequently assigned the appropriate material distribution along the straight edges of their polyhedral cells, and discretized with shear deformable beam elements as described in [2,3]. Cubical foam models are placed in the triaxial apparatus and crushed along three families of radial displacement paths in the x-y-z space. Here we will outline the results of a representative case crushed along the path $\delta(3,0.5,1)^T$ defined in the inset of Fig. 2. The three recorded true stress-displacement responses are plotted with dashed lines in Fig. 2, and Fig. 3 shows four deformed z-x plane sections from the middle of the domain, which correspond to the numbered bullets on the σ_x - δ_x response. The responses exhibit stiff initial elastic branches that terminate in stress maxima caused by plastic bending of foam ligaments. Descending branches follow during which localizes cell crushing commences starting at the moving platens (e.g., see top of image ①). The crushing continues inwards as shown in images ② and ③, but at different rates and extents in each direction. In the process the stresses trace plateaus (~380 psi–2.62 MPa), an extended one in the x-direction, a shorter one in the z-direction, and an even shorter one in the y-direction. Most importantly, crushed and uncrushed domains coexist up to a volume change of about 60%. For δ_x/H larger than about 0.5, the three stresses trace increasing trajectories that become steeper as the material densifies as shown in image ④ at $\delta_x/H \approx 0.59$. Ref. [3] demonstrates that this three-regime response with two stable branches separated by stress plateaus during which localized crushing spreads was observed in all 18 radial displacements paths considered.

This partially inhomogeneous behavior has been simulated at the continuum level in [4] by adopting a Drucker-Prager type compressible yield function (see also [5]) combined with the partially unstable stress-strain response shown in Fig. 4. A cubical finite element model with an irregular mesh of solid elements is used to simulate the random foam crushing responses of [3]. Included in Fig. 2 are the responses calculated with the continuum model for the $\delta(3,0.5,1)^T$ loading path, and Fig. 5 shows four deformed images of the domain with strain contours superimposed. The responses

*Corresponding author. E-mail: skk@mail.utexas.edu

reproduce the initial stable regime and the limit stresses, and track the subsequent stress plateaus quite well, while the stresses in the densification regime are somewhat underestimated. Since the solid model lacks the microstructure of the random foam, localization is initiated from geometric depressions placed along three of the planes (image [1]). Planar bands of higher deformation then propagate, in this case mainly along two directions, while the stresses remain relatively unchanged. When the whole domain is so deformed the block returns to essentially homogenous deformation. The continuum model performs similarly for the rest of the crushing paths, confirming its veracity.

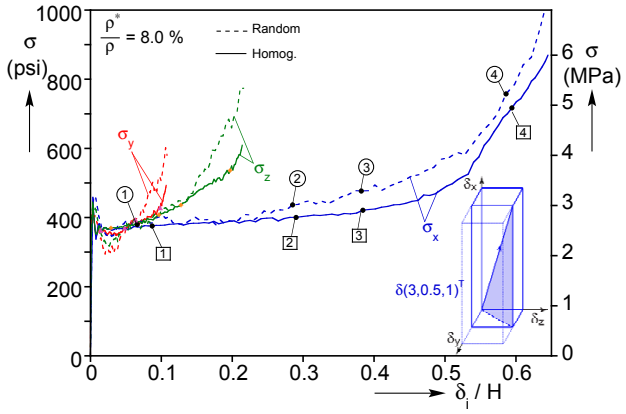

Figure 2. Random and homogenized stress-displacement responses in three directions for a radial triaxial loading.

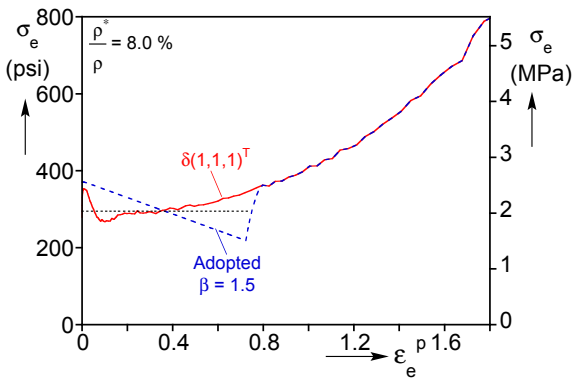

Figure 4. Partially unstable stress-strain response adopted in the homogenized model.

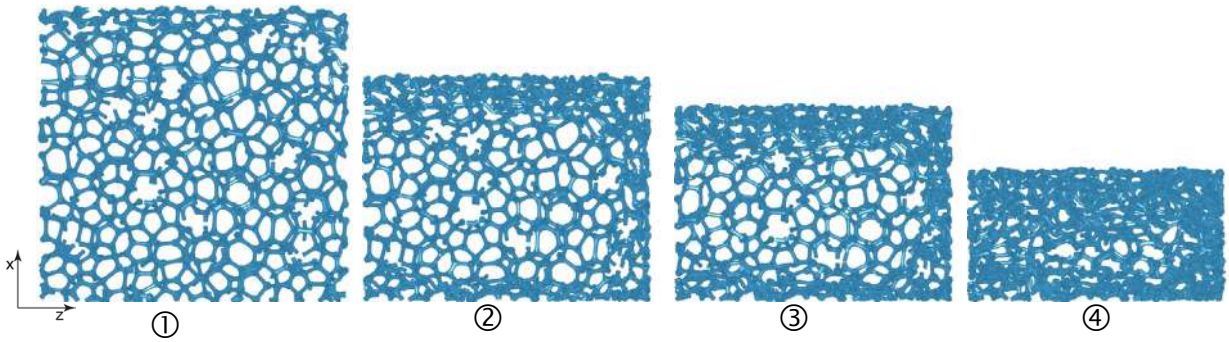

Figure 3. Random foam deformed configurations corresponding to dash line responses in Fig. 2 showing coexisting crushed and uncrushed cells until densification sets in at an increasing stress at ④.

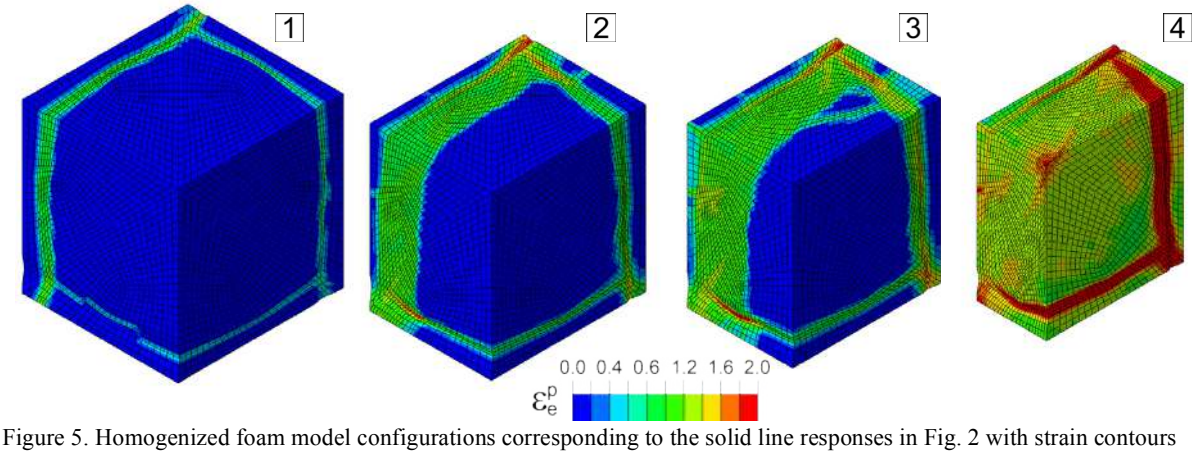

Figure 5. Homogenized foam model configurations corresponding to the solid line responses in Fig. 2 with strain contours superimposed. Observed are zones of high deformation that propagate until the whole domain is affected.

References

[1] Jang, W.-Y., Kyriakides, S. On the Crushing of Aluminum Open-cell Foams: Part I Experiments. *Int'l J. Solids Struct.* **46**, 617-634, 2009.
[2] Gaitanaros S., Kyriakides S., Kraynik A.M. On the Cushing Response of Random Open-cell Foams. *Int'l J. Solids Struct.* **49**, 2733-2743, 2012.
[3] Yang, C., Kyriakides, S. Multiaxial Crushing of Open Cell Foams. *Int'l J. Solids Struct.* **159**, 239-256, 2019.
[4] Yang, C., Kyriakides, S. Continuum Modeling of Crushing of Low Density Foams. *J. Mech. Physics Solids,* in press 2019. https://doi.org/10.1016/j.jmps.2019.103688
[5] Deshpande, V.S., Fleck, N.A. Isotropic Constitutive Models for Metallic Foams. *J. Mech. Phys. Solids* **48**, 1253-1283, 2000.

ELASTICITY OF TWO-DIMENSIONAL SOFT CELLULAR SYSTEMS WITH WEAK DISORDER

Marc Durand* and François Villemot
Matière et Systèmes Complexes (MSC), UMR 7057 CNRS & Université de Paris, Paris, France.

Summary Under small strains, soft cellular matter behaves elastically. We investigate how moderate disorder affects this elastic response. Unlike perfectly regular structure or highly disordered structure, for weakly disordered structures the elastic response depends on the spacial arrangement of topological defects (non hexagonal cells). When defects are generated by large amplitude oscillatory strain, we modelize it as an effective temperature whose impact on the population of defects is numerically investigated. We then relate the effective elastic moduli to the population and spatial arrangement of defects using two independent methods: by direct measurement of the strain energy on one hand, and by studying the interaction between defects on the other hand.

INTRODUCTION

Liquid foams, emulsions, and confluent biological tissues are examples of *soft cellular matter*: They are constituted of highly deformable – yet almost incompressible – units (bubbles, drops, cells,...). When highly compacted, they tile the available space (3D) or plane (2D) perfectly (i.e.; without gaps or overlaps). Interface energy is key to the cohesion and the rigidity of these systems, sometimes constituted solely of fluids. Under small strains, soft cellular matter behaves elastically, with stress proportional to strain and no rearrangements. Above the yield strain, local rearrangements occur and the system deforms plastically. Structural disorder strongly affects the elastic response as well as the yield strain value. We call T1 the elementary neighbor switching event. In a regular (hexagonal) structure, a T1 event corresponds to the creation of paired dislocations (where a dislocation itself is composed of one 5-sided and one 7-sided cells). When the applied shear strain increases, the number of dislocations keeps increasing, and the cellular structure gets more and more disordered. This behavior is reminiscent of that of a two-dimensional crystal submitted to an increasing temperature. This comparison suggests that strain acts as an effective temperature for the cellular structure. To probe further this hypothesis, we study numerically the order-disorder transition driven by an effective temperature.

We then investigate how moderate disorder affects the elastic response of soft cellular matter: under small strain, the displacement field is affine on bubble length scale for both ordered (hexagonal) [1] and highly disordered structures. The mechanical behavior can then be inferred from information on the distribution of size and number of sides in these two limit cases [2]. For moderate disorder however, mechanical response may also depend on the specific spatial arrangement of the topological defects.

NUMERICAL SIMULATIONS

Our simulations are based on the Cellular Potts Model (CPM), which is widely used for simulating cellular systems in various fields of physics or biology. The CPM is a lattice based modeling technique: each cell is represented as a subset of lattice sites sharing the same cell ID. Cellular domains can adopt any shape on the lattice. The system evolves using a recently modified Metropolis algorithm that preserves the integrity of the cellular domains and satisfies the detailed balance equation [3]. This algorithm has also been proved to be more efficient that the standard algorithm used in CPM for a same simulation temperature, allowing us to simulate much larger systems. Energy of a monodisperse cellular system is modeled by the discretized version of the following Hamiltonian:

$$\mathcal{H} = \gamma \sum_{\langle i,j \rangle} L_{ij} + \frac{B}{2A_0} \sum_i \left(A_i - A_0\right)^2 . \tag{1}$$

The first term in Eq. (1) accounts for interfacial effects: the sum is carried over neighboring cells $\langle i,j \rangle$ and L_{ij} is the boundary length between cells i and j. The second term accounts for an effective area elasticity which results from a combination of three-dimensional cell incompressibility and cell bulk elasticity. B is the effective 2D bulk modulus, A_i is the actual area of cell i, and A_0 the preferred cell area. To include shear strain, we extend the Hamiltonian as:

$$\mathcal{H}' = \mathcal{H} + k \sum_{i \in boundaries} \left(x_i - x_i^c(t)\right)^2 , \tag{2}$$

where $x_i^c(t) = \Gamma(t) y_i$ is a slowly varying function of time (compared with the equilibration time), while x_i and y_i are the center coordinates of cell i. The new term corresponds to applying shear strain at the top and bottom boundaries, with Γ corresponding to the applied strain.

*Corresponding author. E-mail: marc.durand@univ-paris-diderot.fr.

RESULTS

Order-disorder transition

We perform extensive numerical simulations of systems of $N = 40,000$ cells with periodic boundary conditions. Figs. 1(a)–1(c) show the equilibrated system at three different temperatures, with non-hexagonal cells that are color-coded. At low temperature [1(a)], the only topological defects are bound dislocation pairs. At intermediate temperature [1(b)], paired and single dislocations coexist. At high temperature [1(c)], most of topological defects are assembled into aggregates.

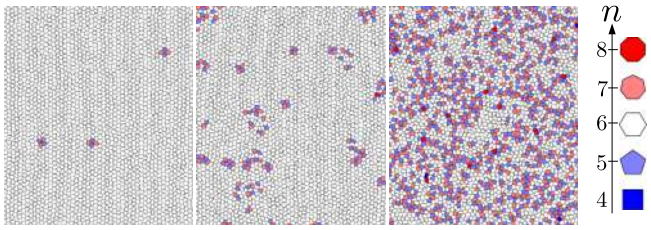

Figure 1: Evolution of defect populations with effective temperature. Only a small portion of the system is shown. Columns from left to right: solid, hexatic, and liquid phases.

By analyzing the evolution of various quantities, including positional and orientational order parameters and the population of defects, we show that the transition follows most of the predictions of Kosterlitz-Thouless-Halperin-Nelson-Young (KTHNY) theory developed for melting of 2D solids. In particular, we show the existence of an intermediate hexatic phase, which preserves the orientational order of the regular hexagonal tiling, but looses its positional order [4].

Elastic behavior of foam with moderate disorder

Our numerical method allows for rigourous simulation of quasistatic shear of cellular systems. After testing its validity with a regular hexagonal foam [1], we show that the spatial distribution of defects deeply affects the small strain response of soft cellular matter. When they are uniformly distributed [Fig. 2a], strain is homogeneous down to the cellular scale and elastic moduli can be evaluated. Their values are recovered independently by analyzing the interaction energy between defects [Fig. 2c]. On the other hand, when defects self-associate into long chains (generated by quenching) the strain is inhomogeneous on length scale comparable with the sample size [Fig. 2b].

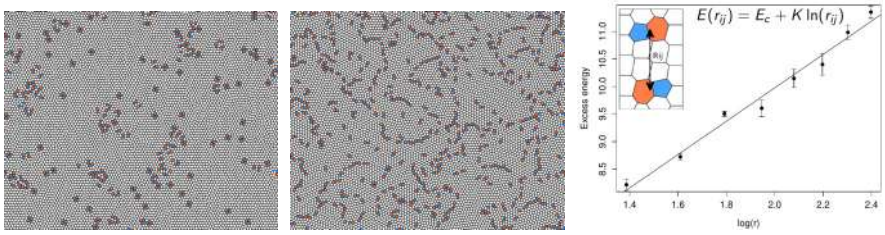

(a) (b) (c)

Figure 2: (a) Cellular system with defects distributed uniformly. (b) Cellular system with defects self-organized into long chains. (c) Semi-log plot of the interaction energy of two dislocations as a function of their distance. Slope allows to extract the effective Young modulus of the medium.

CONCLUSIONS

In summary, we have shown that soft cellular materials under effective thermal agitation follow closely the KTHNY melting scenario, with in particular the existence of an intermediate hexatic phase. Moreover, we have shown that the proportion of n-sided cells within the system, $p(n)$, is not sufficient to capture the mechanical properties of a system with moderated disorder. Spatial correlations of defects must also be accounted for.

References

[1] Princen, H. M. Rheology of foams and highly concentrated emulsions: I. *J. of Coll. and Interf. Sci.* **91**: 160-175, 1983.
[2] Kim S., Hilgenfeldt S. A simple landscape of metastable state energies for two-dimensional cellular matter. *Soft Matter* **15**: 237-242, 2019.
[3] Durand M., Guesnet E. An efficient Cellular Potts Model algorithm that forbids cell fragmentation. *Comp. Phys. Comm.* **208**, 54-63, 2016.
[4] Durand M., Heu J. Thermally driven order-disorder transition in two-dimensional soft cellular systems. *Phys. Rev. Lett.* **123**: 188001, 2019.
[5] Villemot F., Durand M., Elastic behavior of two-dimensional soft material with moderate disorder. *In preparation*.

WATER INDUCED BLISTERING OF CELLULOSE FOAM

Ratul Das *[1], Vikram Deshpande [1], and Norman Fleck [1]
[1]Engineering Department, Cambridge University, Trumpington Street, Cambridge CB2 1PZ, UK

Summary Dry pre-compressed cellulose foam, a biological lattice material, can swell by up to 1500% along one direction when immersed in water. The kinetics of infiltration and swelling are explored by a series of experiments. Specifically, we add a small droplet of water onto the surface of the foam to form a blister. Two successive stages are observed. In Stage I (over the first 0.1s), water infiltrates the foam due to capillary forces, but does not swell the foam. In Stage II, moisture activates swelling of the form and a blister is established within 2s. This study is the first step in developing a micromechanical model for the actuation of foams by moisture uptake.

INTRODUCTION

Dry cellulose swells when moisture is absorbed: this is the underlying mechanism in the swelling of wet wood. Sheets of dry pre-compressed foam (of relative density $\bar{\rho} = 0.45$, with respect to fully dense cellulose) have been obtained from a commercial supplier: the manufacturing route entails the hot compression of wet cellulose foam from an initial state of relative density $\bar{\rho} = 0.03$. The dry as-received foam has structural memory and swells back to its initial state within 2 s upon the addition of water [1]; we shall refer to the swelling direction as the Rise Direction (RD), and note that it is aligned with the compression direction during manufacture of the foam. The swelling occurs in two stages (see Fig. 1(a)). In Stage I, capillary forces [2] suck liquid water into the micron-scale and millimetre-scale pre-existing voids, but initially the water does not swell the foam. Then in Stage II, moisture swells the cellulose cell walls and the millimetre-scale voids open [1,3,4]. Define the moisture content of the damp foam by m_w/m_f where m_w is the mass of water and m_f is the mass of dry compressed foam. Then, a moisture content of at least 50% is needed to fully actuate the dry foam [1]. In our current study, we add a small droplet of water (volume: V_w) onto the surface of pre-compressed foam and form a blister. We then observe the kinetics of liquid absorption and blister growth.

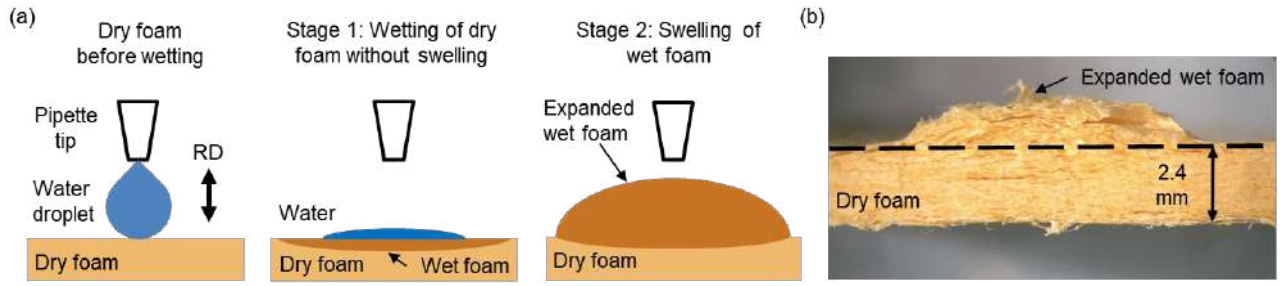

Figure 1. **Wetting of pre-compressed cellulose foam by water and blister formation due to swelling.** (a) Stages of water induced swelling in a pre-compressed foam. RD: Rise Direction (b) Cross-section of a fully formed blister (sectioned along thickness direction of the foam) showing wet expanded foam inside the blister and dry compressed foam underneath it.

MATERIAL AND EXPERIMENT

A droplet of distilled water ($V_w = 0.024$ ml) is added on the surface of a sheet of dry pre-compressed cellulose foam (thickness 2.4 mm). The dry compressed foam has a density of 675 kg/m^3 and can expand approximately 15 times along its thickness direction when wet. Once the droplet touches the surface, the consequent rapid absorption of the water into the sheet and blistering of the foam surface are imaged at a high speed (1000 frames / s) for 19 s; see some of these optical shadowgraphy images in Fig. 2(a). Volumes of the blisters are estimated from the series of high speed images and plotted against time in Fig. 2(b).

OBSERVATIONS

We observe two distinct stages in the experiment:

- In **Stage I** (< 0.1 s), liquid water imbibes into the foam driven by capillary pressure, but does not swell the wet material (see images (i) and (ii) in Fig. 2(a)). Water infiltrates the foam along thickness direction and also spreads radially inside the foam (compare the width of water droplet (ii) and blister (v) in Fig 2(a)). However, the wet foam starts to expand to form a blister before the entire volume of water is absorbed at the end of Stage I. It was

*Corresponding author. E-mail: rd608@cam.ac.uk

not possible to distinguish the liquid water from the wet expanded cellulose foam at the transition from Stage I to Stage II (0.1 s - 0.25 s; see image (iii) in Fig. 2(a)).

- In **Stage II** (> 0.25 s), absorbed water expands the foam and a blister forms on the surface (see images (iv) - (vi) in Fig. 2(a)). The blister volume grows rapidly at a rate of 0.1 ml/s until 1 s, then slows down at times between 1 s and 2 s (see Fig. 2(b)). After 2 s, the blister grows at a slower rate of 0.001 ml/s until the end of experiment.

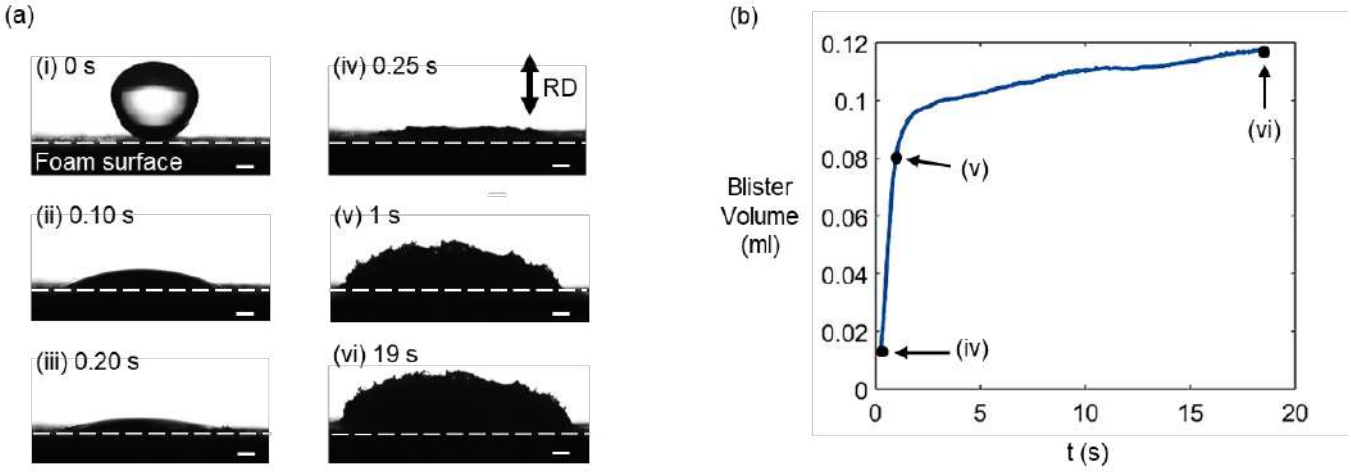

Figure 2. **Kinetics of water induced swelling in a pre-compressed foam** (a) Optical shadowgraphy images of water droplets (i-ii) water mixed with swollen foam (iii), and blisters (iv-vi) during the experiment; scale bars, 1 mm (b) Time evolution of blister volume. Black dots indicate the time and volume of the blister images in (a).

CONCLUDING REMARKS

Controlled actuation of pre-compressed foam is studied by adding a finite volume of water to a pre-compressed foam surface. We observe an initial stage I of water absorption without foam swelling for 0.1 s, and then a second stage of foam swelling between 0.25 s and 19 s. Water infiltration in Stage I is by capillarity action with little to no swelling of foam. In Stage II, moisture activates swelling in foam and forms a blister within 2 s. There is minor additional blistering over 19 s. Further work is needed to determine the mechanism of water transport in the foam in Stage II, and to determine the sensitivity of swelling to a reduced moisture content.

References

[1] Mirzajanzadeh, M., Deshpande, V. S., & Fleck, N. A. (2019). The swelling of cellulose foams due to liquid transport. *Journal of the Mechanics and Physics of Solids*, 103707.
[2] Washburn, E. W. (1921). The dynamics of capillary flow. *Physical review*, *17*(3), 273.
[3] Ha, J., Kim, J., Jung, Y., Yun, G., Kim, D. N., & Kim, H. Y. (2018). Poro-elasto-capillary wicking of cellulose sponges. *Science advances*, *4*(3), eaao7051.
[4] Mirzajanzadeh, M., Deshpande, V. S., & Fleck, N. A. (2019). Water rise in a cellulose foam: By capillary or diffusional flow?. Journal of the Mechanics and Physics of Solids, 124, 206-219.

CFD-MODELLING OF NATURALLY OCCURRING DECAY MECHANISMS AND DESTRUCTION MEASURES IN FOAMS USING THE EULER-EULER APPROACH

Thomas Bernstein *[1], Christoph Gerstenberg[1], Eric Morelle[1], Christopher McHardy[1], and Cornelia Rauh[1]
[1]Institute of Food Technology and Chemistry, Department of Food Biotechnology and Food Process Engineering, Technische Universität Berlin, Berlin, Germany

Summary Foams are complex multiphase systems and experience several dynamically coupled phenomena during its lifetime from formation to decay. This paper deals with the numerical simulation of foam dynamics by the specific adaptation of transport terms in the energy, momentum and mass balance equations. This is done in accordance with current concepts for generalized two-phase flows (GENTOP), using the inhomogeneous Multiple Size Group (iMUSIG) model in the Euler-Euler formulation. The influence of thermal radiation on the superimposed effects of foam decay is shown by the simulation.

INTRODUCTION

Undesired foaming is a frequently observed problem occurring in plants used for the processing and packaging of foods or the refinement of chemicals. During the bottling of non-carbonated beverages, for example, there is a high risk of microbial contamination due to foam reaching systems components, entailing a frequent cleaning procedure of the machines and thus resulting in downtimes and economic losses [1]. Furthermore, severe foaming during distillation of fermented mashes results in additional pressure loss within the distillation column and thus in reduced separation efficiency [2]. So far, foam management measures are limited to (i) usage of anti-foaming agents or (ii) the reduction of throughput.

Spatial extent of foam is the critical variable for process control, resulting from the dynamic balance of foam formation and decay rates [3]. Initially, emergence of foam is driven by volume of entrained gas or gas released by evaporation within the fluid linked to the general foaming capacity of the medium, when gas reaches the surface. Foam decay takes place through the natural ageing processes of drainage, Ostwald ripening and coalescence. These coupled processes extend over different time scales and are of decisive importance for the stability of foams [4]. Design limitations in plants as well as the influence of invasive measurement methods on foam dynamics mostly prevent a complete and realistic process analysis. In order to analyse foam stability, it is therefore necessary to be able to represent different foam formation and decay mechanisms as a function of physical fluid properties and process parameters.

FOAM MODELLING

Due to the continuous increase of available computing power and the drastic price reduction of hardware components, CFD simulations are becoming more and more popular for process analysis and optimization in the engineering sciences. They provide local process information with high resolution, can be flexibly transferred to other plants or material systems and therefore proved to be a useful tool for the analysis of foam formation.

The model approach at hand is able to depict the numerous mechanisms in foam on a macroscopic scale by adapting the terms in the energy, momentum and mass balance equation of the gas and liquid phases [Fig.1]. This is done in accordance with current concepts for generalized two-phase flows (GENTOP), using the inhomogeneous Multiple Size Group (iMUSIG) model in the Euler-Euler formulation [5]. Using this methodology foam modelling and numerical simulation is possible without the need to resolve interfaces of bubbly flows or within foams, but rather by treating the bubble size distribution as a concentration field. Centrepiece of the subsequent model is the definition of a range for the dispersed gas volume fraction from $\alpha_{dg,foam\,min}$ to $\alpha_{dg,foam\,max}$ in which foam is detected by an additional morphological function. This function is denoted by

$$\phi_{foam} = (0.5\tanh(a_l[\alpha_{dg} - \alpha_{dg,foam\,min}] + 0.5) - 0.5\tanh(a_h[\alpha_{dg} - \alpha_{dg,foam\,max}] + 0.5)) \quad (1)$$

wherein a_l and a_h are calibration factors. Source terms within the balance equations are multiplied by the morphological function. Thereby, momentum terms are adapted for specific phases and i.e. capillary forces $\vec{M}_{cap}$ or permeabilities $\vec{M}_{perm}$ are used to describe drainage rates within foams analogous to Darcy's law expressing the liquid flow through porous media. Mass transfer terms between the various bubble size groups can also be adapted when foam is detected. The model switches between well-established models for coalescence by Prince and Blanch [6] or break-up by Luo and Svendsen [7] in bubbly flows and new formulations for changes in bubble size distribution within foams, incorporating coarsening and coalescence rates. Furthermore, experimentally determined thermal conductivities for foams k_{foam}, as well as the absorption and scattering coefficients μ_a and μ_s are available for multiphase-multicomponent radiation transfer within the energy equation. By doing this, natural foam ripening mechanisms as well as the influences of foam destruction measures can be investigated in the simulation. Thermal radiation on the superimposed effects of foam decay is the currently studied destruction measure.

*Corresponding author. E-mail: thomas.bernstein@tu-berlin.de

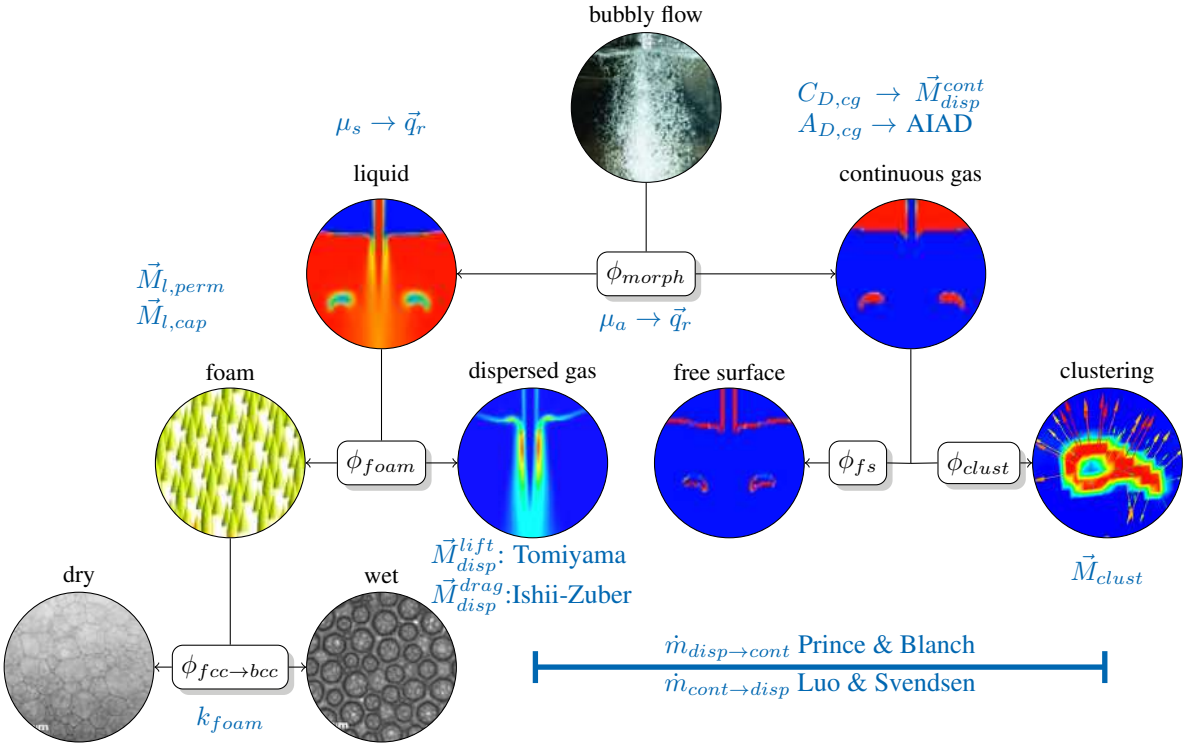

Figure 1: Extension of the GENTOP concept [5] by a foam phase with adapted mass, momentum and energy transfer terms.

EXPERIMENTAL VALIDATION

The main parameters to characterize foams resulting from the simulations are compared with experiments in a test rigs on a laboratory scale. Spatial extent of foam is measured within a Kruess DFA 100. The liquid volume fraction distribution over foam height is measured by electrical conductivity within a specifically designed and constructed foaming device. Bubble size distribution is detected optically and evaluation takes place by convolutional neural networks.

CONCLUSIONS

In the future, the presented model shall offer the possibility to simulate effects of the micro-scale foam dynamics on the macroscopic length scale of production processes. On this basis, characterization of critical plant areas and optimized process windows takes place. If it should emerge, that foam extent can only be controlled by its process parameters entailing performance losses, ideal positioning and operation of thermal actors within process plants can be optimized by the model.

References

[1] McHardy C., Rudolph A., Panckow R., Kostova J., Wegener M., Rauh C. Morphological Characterization of Foams during the Filling of Non-Carbonated Beverages. *In Ruck B., Leder A., Dopheide D. Experimentelle Strömungsmechanik. Proceedings of the Annual Symposium of Experimental Fluid Mechanics GALA e.V.* **26**, 46.1-46.8, 2018.

[2] Senger G. and Wozny G. Impact of Foam to Column Operation. *Technical Transactions* **109**: 209-222, 2012.

[3] Pilon L., Federov A. B., Viscanta A. B. Steady State Thickness of Liquid-Gas Foams. *Journal of Colloid and Interface Science* **242**, 425-436, 2001.

[4] Cohen-Addad S., Höhler R., Pitois O. Flow in Foams and Flowing Foams. *Annual Review of Fluid Mechanics* **45**, 241-267, 2013.

[5] Hänsch S., Lucas D., Krepper E., Höhne T. A Multi-Field Two-Fluid Concept for Transitions between Different Scales of Interfacial Structures. *International Journal of Multiphase Flow* **49**, 171-182, 2012.

[6] Prince M.J., Blanch H.W., Bubble Coalescence and Break-Up in Air-Sparged Bubble Columns. *American Institute of Chemical Engneers Journal* **36** 1485-1499, 1990.

[7] Luo H., Svendsen H.F., Theoretical Model for Drop and Bubble Break-Up in Turbulent Flows. *American Institute of Chemical Engineers Journal* **42**, 1225-1233, 1996.

PREDICTION OF EFFECTIVE ELASTIC MODULUS IN ANY DIRECTIONS OF PERIODIC TRUSS STRUCTURES

Shuheng Wang[1,2], Yongbin Ma[1,2], Zichen Deng[1,2]*
[1]School of Mechanics, Civil Engineering and Architecture, Northwestern Polytechnical University, Xi'an, 710072, PR China
[2]MIIT Key Laboratory of Dynamics and Control of Complex Systems, Northwestern Polytechnical University, Xi'an 710072, PR China

Summary This study develops an analytical formula for the effective elastic modulus of periodic truss structure in any directions. Based on the traditional Representative Volume Element (RVE) method, a displacement matrix equivalent to the strain field is applied as the boundary condition of the unit cell. By expressing the displacement boundary condition as a function of direction, the analytical formula of the effective elastic modulus as a function of direction are obtained by strain energy equivalence. The method presented here can easily optimize the size of the structure to adjust the elastic modulus of the structure. This study takes a simple binary compound truss structure as an example, and utilizes this method to make a reasonable size distribution, so that the optimized structure becomes an elastically-isotropic structure.
Keywords: Periodic truss structures; Effective elastic modulus; Analytical formula.

Introduction

With the rapid development of additive manufacturing technology, lightweight, complex periodic cellular structures with special mechanical properties can be fabricated at a low and declining cost [1]. The microstructure characteristics of the cellular structure govern its macroscopic behaviour, and the cellular structure can obtain unprecedented mechanical properties by designing its microstructure. In the meantime, combining two or more plate- or truss- like structures that exhibit high stiffness in different directions to obtain a compound structure with a higher degree of isotropy in effective elastic modulus has been demonstrated [2-4]. At present, researchers have proposed many homogenization methods to predict the effective mechanical properties of periodic truss structures [5-7]. However, the effective elastic modulus of periodic structure in any directions is not easy to obtain in one calculation, and usually obtained through ABAQUS-Python scripts [7].

In this study, a simple method based on the traditional RVE method is developed to obtained an analytical formula for the effective elastic modulus of periodic truss structure in any directions. The analytical formula can be expressed as a function of the effective elastic modulus of the periodic truss structure with respect to its size and the material property, so the effective elastic modulus of the truss structure can be easily optimized.

Method

The RVE method is to take out some unit cells that can completely contain the material microstructure information from the periodic truss material, and apply the boundary conditions on the boundary of the unit cells, and then obtain the effective elastic modulus of the material based on the strain energy equivalence. The Dirichlet Boundary conditions can be represented by a displacement field $\mathbf{u}(\theta)$ corresponding to the strain field $\boldsymbol{\varepsilon}(\theta)$ as follows:

$$\mathbf{u}(\theta) = \boldsymbol{\varepsilon}(\theta)x, \ \forall x \in \partial\Omega \tag{1}$$

where θ represents the specified direction and $\partial\Omega$ represents the boundary of the unit cell. Then, the strain energy of the unit cell can be obtained as $U_{\text{cell}} = \frac{1}{2}\mathbf{u}(\theta)^{\mathrm{T}}\mathbf{K}\mathbf{u}(\theta)$, where $\mathbf{K}$ is the global stiffness matrix of the unit cell. Regarding the unit cell as an effective homogeneous continuum, and the strain energy of the effective homogeneous continuum can be obtained as $U_{\text{hom}} = \frac{1}{2}\boldsymbol{\varepsilon}(\theta)^2 E(\theta)V$, where $E(\theta)$ is the effective elastic modulus in the specified direction and V is the volume of the unit cell. By considering $U_{\text{cell}} = U_{\text{hom}}$, the analytical formula of the effective elastic modulus with respect to the direction can be obtained as follows:

$$E(\theta) = \mathbf{u}(\theta)^{\mathrm{T}}\mathbf{K}\mathbf{u}(\theta)/\boldsymbol{\varepsilon}(\theta)^2 V \tag{2}$$

Example and results

This study takes a simple binary compound periodic truss structure as an example, the unit cell is taken out from the truss structure and shown in Fig.1(a). The unit cell is composed of two square truss and the corner of the smaller truss is at the midpoint of the edges of the larger truss. Square truss stiff along the edges but highly compliant in other loading directions, e.g. along the diagonal. Therefore, the compound truss structure has a higher degree of isotropy than the square truss. Displacement matrix corresponding to the Dirichlet boundary conditions can be expressed as:

$$\mathbf{u}(\theta) = [u_1\ v_1\ u_2\ v_2\ u_3\ v_3\ u_4\ v_4\ u_5\ v_5\ u_6\ v_6\ u_7\ v_7\ u_8\ v_8]^T \tag{3}$$

where u_i and v_i are the displacement components of the node displacements in the u and v directions after θ is determined, e.g. $u_8 = \varepsilon L\cos\theta\cos\theta$ and $v_8 = \varepsilon L\cos\theta\sin\theta$. Substituting $A = A_1 = \frac{1}{20}$, $L = 1$ and $E = 1$ into Eq.

*Corresponding author: Zichen Deng; E-Mail address: (dweifan@nwpu.edu.cn);

(2), the effective elastic modulus is only determined by θ. Fig. 1 (b) is the polar plot of the effective elastic modulus in different directions.

Fig. 1 (b) shows that the elastic modulus is largest along the edges of the larger square and smallest along its diagonal. When θ is determined, the effective elastic modulus can be optimized by changing the size of the unit cell and the material properties. Due to the symmetry existent in the unit cell, only one-eighth direction needs to be considered. From Eqs. (2,3), $E(0)$ and $E\left(\frac{\pi}{4}\right)$ can be obtained:

$$E(0) = E(\sqrt{2}A_1 + 4A)/2L,\ E\left(\frac{\pi}{4}\right) = E(\sqrt{2}A_1 + A)/L \tag{4}$$

In order to increase the degree of elastic isotropy of the structure, consider leting $E(0) = E\left(\frac{\pi}{4}\right)$ and obtain $A_1 = \sqrt{2}A$. Substituting $A_1 = \sqrt{2}A$ into $E(\theta)$ and it can be find that $E(\theta) = 3EA/2L$, which have nothing to do with θ. Therefore, when $A_1 = \sqrt{2}A$, that is, when the proportions of two square truss structures are equal, the compound structure is elastically isotropic. The optimized structure and its effective elastic modulus in drfferents in shown in Fig. 1 (c, d).

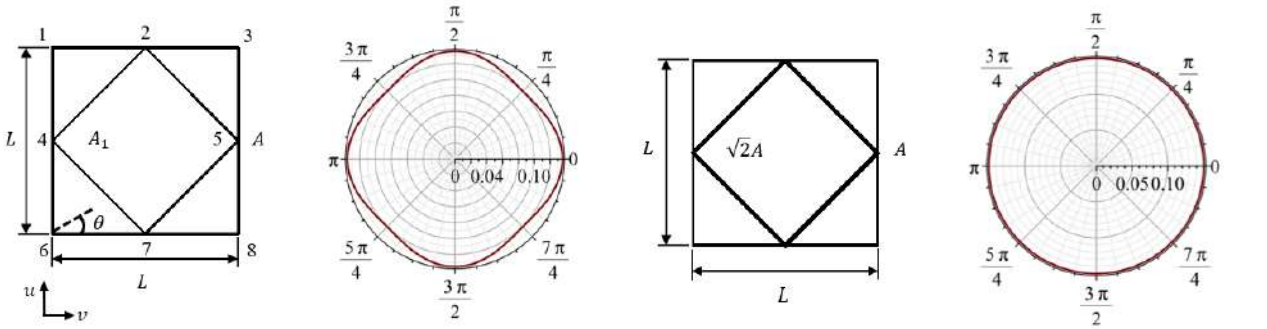

(a) (b) (c) (d)

Figure 1. The size of the unit cells and their effective modulus in different directions.

Conclusion

This study develops an analytical formula for the effective elastic modulus of periodic truss structure in any directions. By using this formula, effective elastic modulus of the truss structure can be easily obtained and optimized through changing the size of the unit cell and material properties. A two-dimensional binary compound periodic truss structure composed of two square trusses is taken as an example to show how the method is implemented and used to optimize the effective elastic modulus of the structure. The method presented in this study can also be used in three-dimensional periodic truss structures.

This work was supported by the National Key R&D Program of China (2017YFB1102801), the National Natural Science Foundation of China (grant numbers: 11602021), and the Graduate Innovation Team Foundation of Northwestern Polytechnical University.

References

[1] Berger J.B., Wadley H.N.G., McMeeking R.M. Mechanical metamaterials at the theoretical limit of isotropic elastic stiffness. *Nature*. **543**, 533–537, 2017.
[2] Zok F.W., Latture R.M., Begley M.R. Periodic truss structures. *J. Mech. Phys. Solids*. **96**, 184–203, 2016.
[3] Latture R.M., Begley M.R., Zok F.W. Design and mechanical properties of elastically isotropic trusses. *J. Mater. Res.* **33(3)**, 249-263, 2018.
[4] Tancogne-Dejean T., Diamantopoulou M., Gorji M.B., et al. 3D Plate-Lattices: An Emerging Class of Low-Density Metamaterial Exhibiting Optimal Isotropic Stiffness. *Adv. Mater*. **1803334**, 1-6, 2018.
[5] Yan J., Cheng G.D., Liu S.T., et al. Comparison of prediction on effective elastic property and shape optimization of truss material with periodic microstructure. *Int. J. Mech. Sci.* **48**, 400-413, 2006.
[6] Arabnejad S., Pasini D. Mechanical properties of lattice materials via asymptotic homogenization and comparison with alternative homogenization methods. *Int. J. Mech. Sci.* **77**, 249-262, 2013.
[7] Liu L., Kamm P., García-Moreno F., et al. Elastic and failure response of imperfect three-dimensional metallic lattices: the role of geometric defects induced by Selective Laser Melting. *J. Mech. Phys. Solids*. **107**, 160-184, 2017.

LOAD CAPACITY COMPARISON OF MULTIFUNCTIONAL SANDWICH PANELS WITH CORRUGATED AND WEB CORES

Shanyouming Sun [1,2], Shangsheng Feng *[3], and Tian Jian Lu *[2]
[1]State Key Laboratory for Strength and Vibration of Mechanical Structures, Xi'an Jiaotong University, Xi'an 710049, PR China
[2]State Key Laboratory of Mechanics and Control of Mechanical Structures, Nanjing University of Aeronautics and Astronautics, Nanjing 210016, PR China
[3]Bioinspired Engineering and Biomechanics Center (BEBC), Xi'an Jiaotong University, Xi'an 710049, PR China

Summary Sandwich panels with web core (namely I core) have recently been found to exhibit superior heat dissipation performance than traditional corrugated sandwich panels [1], and hence it is of significant practical interest to compare their load capacity under different loading conditions. This paper presents a new variegated prismatic core (namely N core) which can be degenerated into the corrugated or web core geometrically, and investigated its compression, bending and shear properties by theoretical modeling and numerical simulation. Results show that under out-of-plane compression and transverse bending, the web core is the best, while under transverse shearing, the corrugated core outperforms the rest. The performance of the three cores is similar under longitudinal bending and shearing.

CORE TOPOLOGIES AND LOAD TYPES

Corrugated cores are extensively used in the packaging and transportation industry [2], while web cores (including I girders or H beams) are widely used in road and bridge construction [3]. In addition to bearing structural load, both corrugated and web cores have fluid through topologies for active cooling applications. Five load types (out-of-plane compression, transverse bending, longitudinal bending, transverse shearing and longitudinal shearing; Table 1) covering almost all the engineering application scenarios are selected to compare the static mechanical properties of corrugated and web cores. A novel variegated corrugated core (namely N core, Table 2) is proposed here by adding ribs at the top angle of corrugated cores. In extreme cases, analytical solutions obtained for the N core under different loading conditions can degenerate into solutions for either corrugated or web core.

Table 1 Load types considered

Out-of-plane compression	Transverse bending	Longitudinal bending	Transverse shearing	Longitudinal shearing
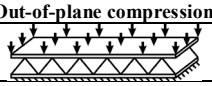	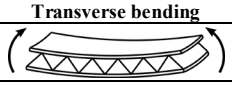	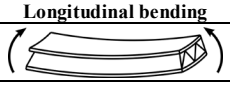	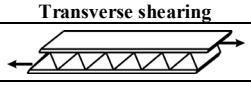	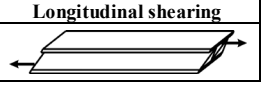

Table 2 Core topologies considered for multifunctional sandwich construction

Corrugated core (V core)	Web core (I core)	N core
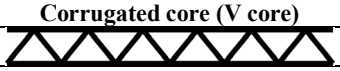	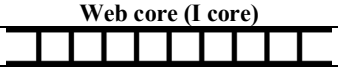	

OUT-OF-PLANE COMPRESSION

A unit cell model (Fig. 1(a)) is used assuming that the stiffness of the facesheet is much greater than that of the core, so that the facesheet only transmits the load, while the core bears axial force, shear force and bending moment [4]. The stress of each strut in the unit cell is obtained by solving their strain energy. The failure modes include elastic buckling and plastic yielding. Corresponding load capacity p of each core can be determined as a function of relative density [5]:

$$p = \min\left\{\sigma_{cb}, \sigma_{cy}, \sigma_{ub}, \sigma_{uy}, \sigma_{db}, \sigma_{dy}\right\} \quad (1)$$

where the first subscript c, u, d indicate the inclined and straight struts, and the second subscript b, y indicate the failure modes. A finite element (FE) model is employed to validate the analysis model, with excellent agreement achieved. The results of Fig. 1(b) demonstrate that the web core is superior to the corrugated core, while the N core is between the two.

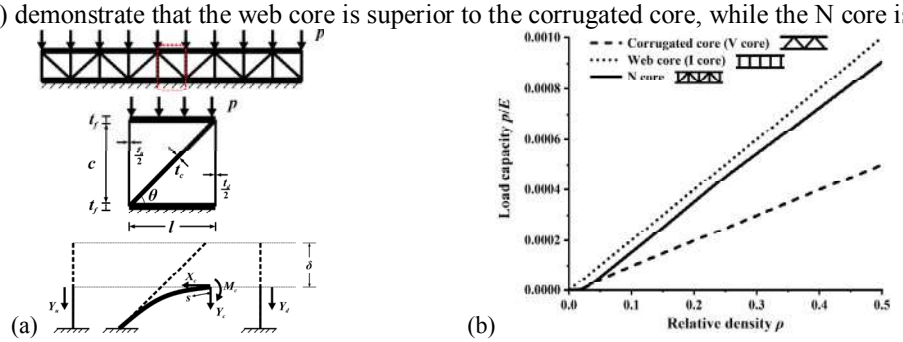

Figure 1. (a) Unit cell analysis of out-of-plane compression for N core; (b) load capacity plotted as a function of relative density under the out-of-plane compression

BENDING

When subjected to bending, one facesheet of the sandwich is in tension while the other is in compression. The core transmits the shear load and bears normal stress to support the facesheet. The maximum bending moment and shear force of the sandwich beam are expressed as M and V, so $\Psi=V/(EM)^{0.5}$ defines a dimensionless load index, and $\chi=M/V$ means the load form (Fig. 2(a)). The failure criterion of elastic buckling is [6]:

* E-mail addresses: shangshengfeng@xjtu.edu.cn (S. Feng), tjlu@nuaa.edu.cn (T. J. Lu)

$$\left(\sigma_i / \sigma_{cr}\right)^2 + \left(\tau_i / \tau_{cr}\right)^2 \le 1 \qquad i = f, c \tag{2}$$

and the failure criterion of plastic yielding is [6]:

$$\sigma_i^2 + 3\tau_i^2 \le \sigma_Y^2 \qquad i = f, c \tag{3}$$

where subscripts f and c denote facesheet and core. It can be seen from Fig. 2(b-c) that under transverse three-point bending, the web core is always the best, while the N core and corrugated core are the weakest at lower (ρ<0.1) and higher (ρ>0.1) relative density, respectively. Under longitudinal three-point bending, the corrugated core and N core outperform the web core, albeit by a small margin.

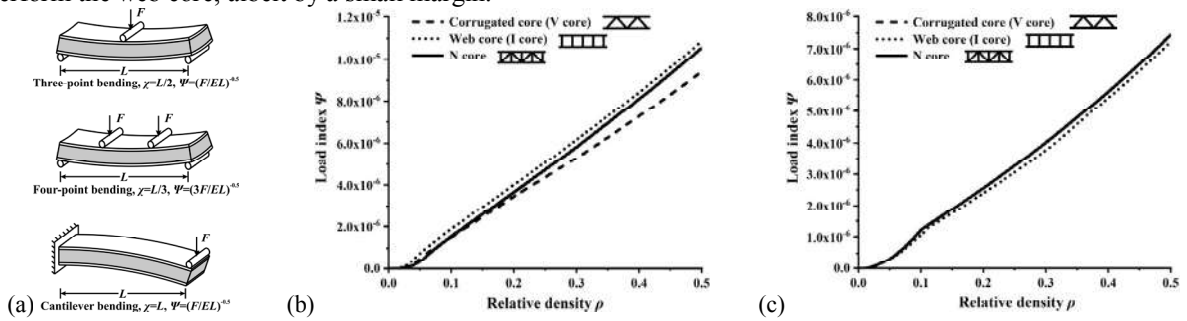

Figure 2. (a) Various bending types of sandwich beams and their corresponding load indices; (b) load capacity plotted as a function of relative density under transverse bending; (c) load capacity plotted as a function of relative density under longitudinal bending

SHEARING

The shearing capacity of corrugated core in its transverse orientation is inferior to its longitudinal orientation [7]. It is assumed that the facesheet is rigid enough and the shear force is distributed to the core. As shown in Fig. 3(a), the compression stress of each strut can also be obtained using a unit cell model. With elastic buckling and plastic yielding assumed as strut failure modes, the corresponding bearing capacity is:

$$\tau = \min\left\{\tau_{cb}, \tau_{cy}, \tau_{ub}, \tau_{uy}, \tau_{db}, \tau_{dy}\right\} \tag{4}$$

It can be seen from Fig. 3(b-c) that under transverse shearing, the performance of the corrugated core is very close to the N core, both better than the web core. Under longitudinal shearing, however, core topology has little influence on the load capacity of the sandwich structure.

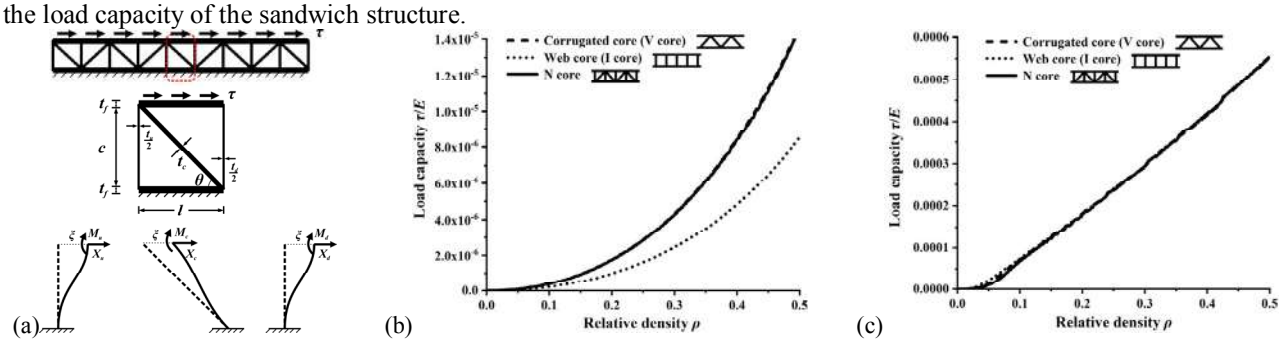

Figure 3. (a) Unit cell analysis of transverse shearing of N core; (b) load capacity plotted as a function of relative density under transverse shearing; (c) load capacity plotted as a function of relative density under longitudinal shearing

CONCLUSIONS

A novel variegated, fluid-through prismatic core topology (namely N core) is presented for sandwich construction for applications requiring simultaneous load-bearing and heat dissipation. Its static load capacity under typical loading conditions is compared with corrugated and web cores by analytical modeling and numerical simulation. It is found that under out-of-plane compression and transverse bending the web core is the best, while under transverse shearing the corrugated core outperforms the rest. The performance of the three cores is similar under longitudinal bending and shearing. Therefore, the thermo-mechanical synergy design of corrugated and web cores needs to be considered comprehensively.

References

[1] Sun S., Feng S., Zhang Q. et al. Forced Convection in Additively Manufactured Sandwich-Walled Cylinders with Thermo-Mechanical Multifunctionality. *Int. J. Heat Mass Transf.* **149**: 119161, 2020.

[2] Nordstrand T., Carlsson L.A., Allen H.G. Transverse Shear Stiffness of Structural Core Sandwich. *Compos. Struct.* **27**: 317-329, 1994.

[3] Tarhini K.M., Frederick G.R. Wheel Load Distribution in I-Girder Highway Bridges. *J. Struct. Eng.* **118(5)**: 1285-1294, 1992.

[4] Cote F., Deshpande V.S., Fleck N.A. et al. The Compressive and Shear Responses of Corrugated and Diamond Lattice Materials. *Int. J. Solids Struct.* **43**: 6220-6242, 2006.

[5] Timoshenko S.P., Gere J.M. Theory of Elastic Stability. McGraw Hill, New York, 1961.

[6] Valdevit L., Hutchinson J.W., Evans A.G. Structurally Optimized Sandwich Panels with Prismatic Cores. *Int. J. Solids Struct.* **41**: 5105-5124, 2004.

[7] Han B., Yu B., Xu Y. et al. Foam Filling Radically Enhances Transverse Shear Response of Corrugated Sandwich Plates. *Mater. Des.* **77**: 132-141, 2015.

CONCURRENT OPTIMIZATION OF EFFECTIVE STRENGTH AND FRACTURE TOUGHNESS OF MULTI-MATERIAL MICRO-ARCHITECTED LATTICES

Padmeya Prashant Indurkar*[1], Angkur Jyoti Dipanka Shaikeea[1], Zhenpeng Xu[2], Huachen Cui[2], Xiaoyu (Rayne) Zheng[2], Vikram S. Deshpande[1]
[1] Department of Engineering, Cambridge University, Cambridge CB2 1PZ, UK (pp522@cam.ac.uk)
[2] Mechanical and Aerospace Engineering Department, UCLA, Los Angeles, California 90095, USA

Summary: This work reports a combined experimental and computational study on the fracture of micro-architected lattices composed of interpenetrating multi-material networks. The double gyroid lattice is an example of such a multi-material lattice. A detailed study on the effective elasto-plastic responses of the double gyroid lattice is conducted as a function of its constituent network properties, such that, one of the networks is elastic-brittle, whereas, the surrounding network possesses high ductility. To probe its effective fracture properties, we first perform boundary layer analysis of cracks subjected to plane strain loading, and secondly, we investigate embedded crack geometries with a surrounding resolution of millions of unit cells. In-situ X-Ray CT visualisation procedure is deployed to monitor crack tip conditions. Our investigations reveal that the network constitutive properties of such multi-material lattices, like the double gyroid, can be efficiently tuned to independently harness both its effective strength and its fracture toughness. Extended investigations into such multi-material lattices will guide the development of lightweight solids concurrently optimized and architected for high-strength and fracture-resistant applications.

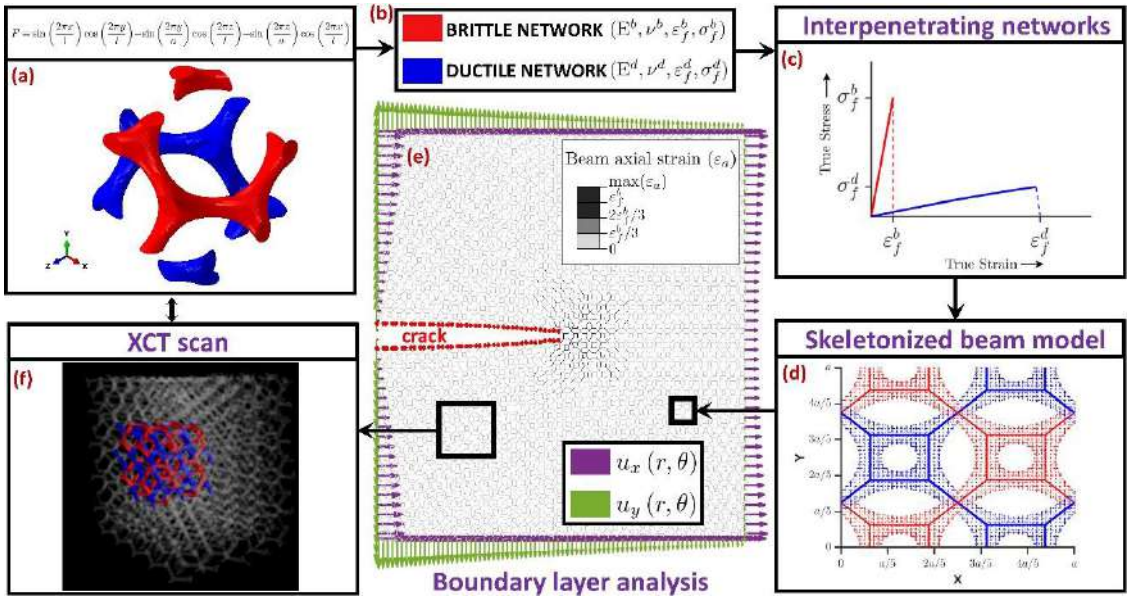

Fig. 1. Methodology for boundary layer analysis of double gyroids. (a) 3D double gyroid comprising of two interpenetrating single gyroids of opposite chirality (coloured red and blue). It is obtained by infilling the space bound by implicit inequalities, $F(x,y,z) - t_0 \leq 0$ and $F(x,y,z) - t_0 \geq 0$ in a cubic domain of edge l, such that t_0 can be tuned to control the total relative density, i.e. $\bar{\rho}$ (volume fraction of the solid material). **(b)** The parameters controlling the constitutive behaviour of the two single gyroids, shown schematically in **(c)**. **(d)** An effective beam skeleton is extracted from the 3D double gyroid in **(a)**, and is discretised in ABAQUS® using 3D Timoshenko beam elements (B31). **(e)** Remote asymptotic boundary displacement fields are applied on the discretized model comprising of ~50X50 unit cells with a central crack (length a) to conduct boundary layer analysis [1]. The plastic zone surrounding the crack can be observed using contours of average beam section strains**. (f)** The 3D printed double gyroids used for experiments, comprising of two networks as shown in **(a)-(d)**.

INTRODUCTION

The mechanical properties of cellular architected materials depend on the topology of the architecture and the constituent materials in the solid phase. Designing such cellular materials with optimised stiffness, strength and ductility is beneficial for a variety of engineering applications like biomedical implants, nanophotonic devices, ballistic armours, energy harnessing, textiles, among many others. The stiffness (E^{lat}) and strength (σ_Y^{lat}) properties of such nano- and micro-scale architected cellular materials have been extensively studied over the past two decades [2]. With recent advancements in additive manufacturing techniques such as projection micro-stereolithography [3-4], 3-D micro-architected solids can now be manufactured with millions of unit cells facilitating their employment in the aforementioned applications. Upper bounds exist on the strength of such solids, e.g. the Hashin-Shtrikman bound [5]. However, the fracture toughness (K_{IC}^{lat}) of such cellular materials is theoretically unbounded, and has been much less investigated. Furthermore, as is the case with continuum solids, it is usually assumed that K_{IC}^{lat} scales inversely with σ_Y^{lat}. This work aims to develop a computational approach to study the fracture toughness of 3D multi-material networked cellular lattices, e.g. the double gyroids, and more importantly, demonstrates that the properties of its constituent networks can be tuned to independently harness the desired K_{IC}^{lat} and σ_Y^{lat}.

*Corresponding author. E-mail:pp522@cam.ac.uk

METHODOLOGY

We begin by creating a beam based topology of the multi-material double gyroid lattices skeletonised from its triply periodic level surface definition **(Figs. 1a-d)**. The red coloured gyroid has elastic-brittle properties (high strength) followed by damage evolution, modelled within ABAQUS®/Explicit using the Johnson-Cook model. The blue coloured gyroid has low strength (10% of the red gyroid), but high strain to failure (ductility), modelled using von Mises plasticity. We first conduct plane-strain boundary layer analysis to map K_{IC}^{lat} as a function of crack growth for different $\bar{\rho}$ and the constituent gyroid properties. Next, we conduct FE calculations of cracks embedded in a 3D RVE with a surrounding resolution of thousands of unit cells. Similar experimental specimens with different material network properties and thousands of unit cells were manufactured **(**a XCT image is shown in **Fig. 1f)**, and the crack tip conditions were monitored using in-situ XCT method.

RESULTS

Fig. 2 briefly reports the results from the boundary layer analysis (**Fig. 1**) for one particular case of $\bar{\rho}$ and gyroid properties.

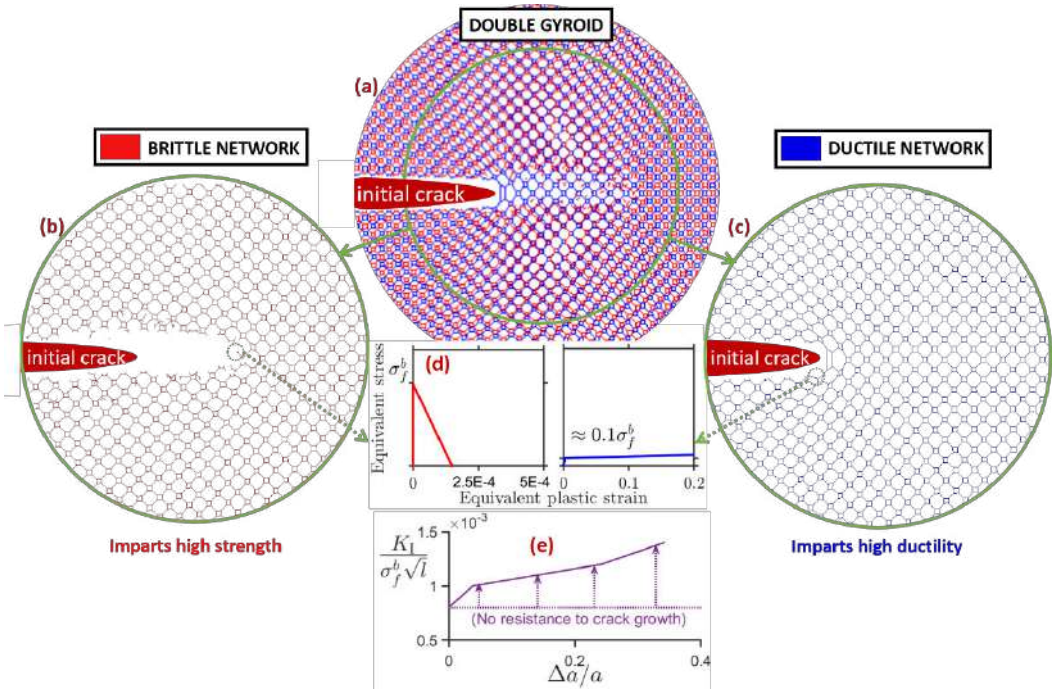

Fig. 2. Results from boundary layer analysis of double gyroids. (a) Crack growth under plane strain asymptotic conditions in double gyroid comprising of two interpenetrating single gyroids (red and blue). **(b)** The brittle network imparts high strength (i.e. σ_f^b), but damage accrued in its struts allows crack growth. **(c)** The ductile network resists crack growth by allowing high plasticity in the crack vicinity, therefore simultaneously allowing the high strength double gyroid structure to attain high strains to failure. **(d)** The equivalent stress-strain curves for the struts that fracture (and are deleted from the FE simulations), and the ones that get highly stretched in the ductile network. **(e)** The evolution of $K_{IC}^{lat}=K_I/(\sigma_f^b\sqrt{l})$ (where K_I is the Mode I stress intensity factor) as a function of crack growth (quantified using $\Delta a/a$). This shows the role played by the ductile gyroid network in prolonging crack growth within such a multi-material networked lattice.

CONCLUSIONS

In this work we present a computational approach to calculate the fracture toughness of multi-material 3D lattices which is then validated with experiments involving thousands of unit cells. We perform boundary layer analysis to map the plastic zone in the vicinity of sharp cracks embedded within these lattices, and measure K_{IC}^{lat} due to a remote crack displacement field. The experimental and numerical investigation of these bending dominated lattices concludes that strength and fracture toughness can be concurrently optimized by tuning the properties of the constituent solid phases, one of which is brittle, while other is highly ductile. This characteristic of such lattices enables us to navigate seamlessly across different domains of the characteristic strength-toughness plot, therefore providing highly optimized cellular architectures for pertinent applications.

References

[1] Sih, G. Co, P. C. Paris, and G. R. Irwin. "On cracks in rectilinearly anisotropic bodies." *International Journal of Fracture Mechanics* 1.3 (1965): 189-203.
[2] Greer, Julia R., and Vikram S. Deshpande. "Three-dimensional architected materials and structures: Design, fabrication, and mechanical behavior." MRS Bulletin 44.10 (2019): 750-757.
[3] Zheng, Xiaoyu, et al. "Multiscale metallic metamaterials." Nature materials 15.10 (2016): 1100.
[4] Chen, Da, and Xiaoyu Zheng. "Multi-material additive manufacturing of metamaterials with giant, tailorable negative Poisson's ratios." Scientific reports 8.1 (2018): 9139.
[5] Hashin, Z. S. H. T. R., and S. Shtrikman. "A variational approach to the theory of the elastic behaviour of polycrystals." *Journal of the Mechanics and Physics of Solids* 10.4 (1962): 343-352.

CONTROLLING FOAM AGEING IN VISCOELASTIC MEDIA

Chiara Guidolin *[1], Emmanuelle Rio [1], and Anniina Salonen [1]
[1]Laboratoire de Physique des Solides - UMR8502, Université Paris-Saclay, 91405 Orsay, France

Summary Foams are dispersions of gas bubbles in a continuous medium. Thanks to their mechanical properties, such systems find application in many industrial fields. However, liquid foams are not stable, as different mechanisms can alter their structure over time, leading to an irreversible foam damage. We probe how the mechanical properties of the continuous phase affect the foam coarsening process. For this purpose, we study foams made of oil-in-water emulsions: at high droplet concentrations, emulsions are elastic and we can vary the elasticity of the foam continuous phase by simply adjusting the emulsion oil fraction. We show that the elasticity of the foam continuous phase strongly slows down the ripening process, but also affects the foam structure, with the appearance of unrelaxed bubble patterns.

INTRODUCTION

Foams are concentrated dispersions of gas bubbles in a continuous medium. Their typical cellular structure lends them lightness and peculiar mechanical properties that are exploited in many different fields, from food industry to cosmetics or even building materials. However, liquid foams are only meta-stable systems, as they usually undergo a competition between different mechanisms which alter their internal structure over time. Gravitational drainage, bubble coalescence and coarsening eventually lead to an irreversible foam damage and thus can be a strong limitation in many industrial processes, such as the design of solid foams with a well-controlled morphology. The desired longevity of a foam clearly depends on the specific applications, which still call for a thorough understanding of foam stability.

We experimentally study how changing the mechanical properties of the foam continuous phase impacts on the coarsening process, in conditions where drainage and coalescence can both be neglected. It has been theoretically shown that the build up of elastic stresses among the bubbles can arrest coarsening and elastically stabilize the entire foam [1] while a halt of coarsening has been experimentally observed in foams made of elastic polymer gels combined with insoluble gas species [2]. But how the rheological properties of the foam continuous phase affect the coarsening rates is still an open question.

We control the mechanical properties of the liquid by using highly concentrated oil-in-water emulsions as the continuous phase of foams, getting what is called a *foamed emulsion*. In fact, at sufficiently high droplet concentrations, emulsions show an elastic behavior, thanks to the storage of interfacial energy from droplet deformations. As this elasticity increases with droplet concentration [3], we can vary the elasticity of the foam continuous phase by simply adjusting the oil volume fraction ϕ of the emulsion. The scale separation between the foam bubbles and the emulsion oil droplets allows us to consider the emulsion as a continuous viscoelastic medium between the gas bubbles, making foamed emulsions a good system for our purpose. We study foamed emulsion coarsening in quasi-2D foam systems, where the bubble pattern evolution can be followed over time through imaging experiments.

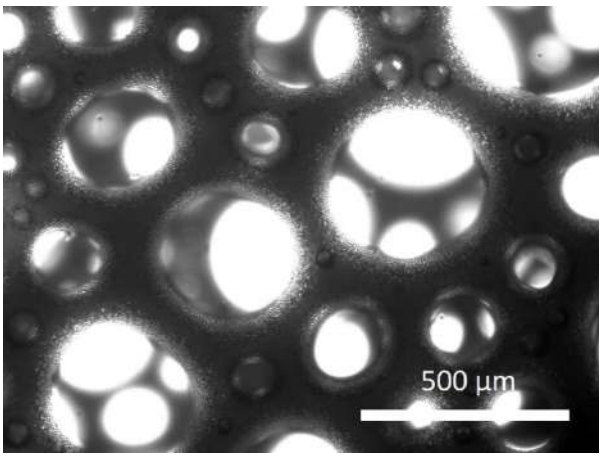

Figure 1. Example of a freshly generated foamed emulsion seen under the microscope.

*Corresponding author. E-mail: chiara.guidolin@universite-paris-saclay.fr.

FOAMED EMULSION COARSENING

Oil-in-water emulsions are prepared by mechanically mixing rapeseed oil and a surfactant solution with the so-called double-syringe method, which ensures a good control of the oil volume fraction ϕ. Emulsions are then foamed with the aid of a planetary kitchen mixer, which allows to incorporate air up to 90% of gas volume fraction. Figure 1 shows how the foams look like under the microscope right after their generation. We then sandwich the freshly generated foamed emulsion between two glass plates and wait for it to coarsen until we get a single layer of bubbles, so that we can visualise and follow the bubble pattern evolution by taking pictures of the quasi-2D foam from the top with a camera. We monitor the coarsening of foamed emulsions having oil fractions ϕ ranging from 65% to 85%. Our experiments show that such systems age very slowly, and that the higher the oil fraction, the lower the mean bubble growth rate. An example of what we observe after several days is shown in figure 2. The picture shows three different samples of foamed emulsions having the same age but increasing oil fraction ϕ from left to right, which means increasing elasticity of the foam continuous phase. One can see how the foam aspect strongly changes as we increase the emulsion oil fraction. While in the first sample on the left at ϕ=70% one can still recognize the typical structure of an aqueous pseudo-2D foam, with approximately polygonal bubbles, as we increase the emulsion elasticity the bubbles are no longer free to rearrange during coarsening, and unrelaxed bubble shapes eventually appear at very high ϕ.

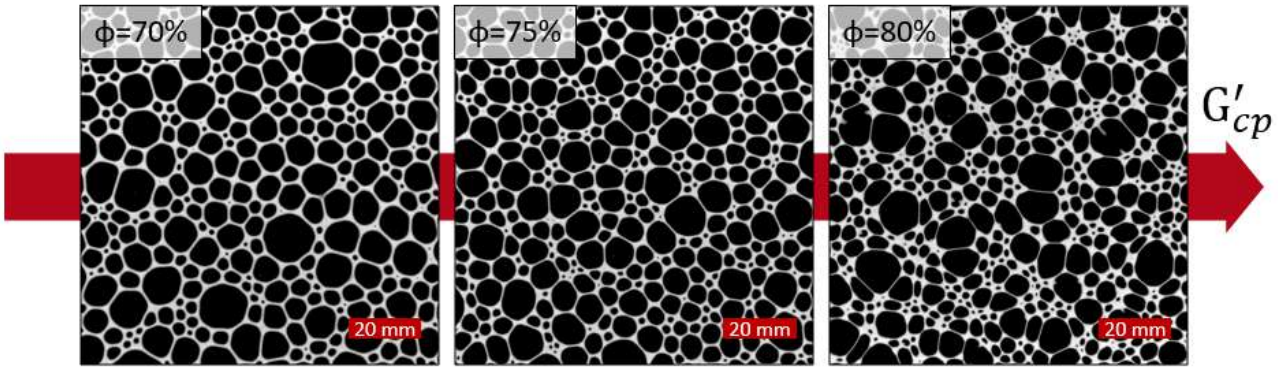

Figure 2. Quasi-2D foamed emulsions at different oil fraction ϕ after 150 hours.

CONCLUSIONS

We show that increasing the elasticity of the foam continuous phase strongly influences the ripening of foamed emulsions, making the coarsening process very slow, with reduced bubble growth rates. Moreover, we show that emulsion viscoelasticity dramatically affects the foam structure, with the appearance of unrelaxed bubble patterns at high oil fractions. The results can lead to a more efficient control of the foam structure and stability.

References

[1] Webster A. J. and Cates M. E., Osmotic Stabilization of Concentrated Emulsions and Foams. *Langmuir* **17**, 3, 595-608, 2001.
[2] Bey H., Wintzenrieth F., Ronsin O., Hohler R., and Cohen-Addad S., Stabilization of foams by the combined effects of an insoluble gas species and gelation, *Soft Matter* **13**, 6816, 2017.
[3] Mason T. G., Bibette J., and Weitz D. A., Elasticity of Compressed Emulsions. *J. Fluid. Mech.* **75**, 2051, 1995.

EMERGING CONCEPTS FOR SMART STRUCTURES IN ADAPTIVE FACADES AND THEIR OPTIMAL DESIGN

Robert J. Zupan[1], Rodrigo Arauz[2], Dale T. Clifford[3], Richard V. Beblo[4], and John C. Brigham *[2,1]
[1]Department of Civil and Environmental Engineering, University of Pittsburgh, Pittsburgh, PA, USA
[2]Department of Engineering, Durham University, Durham, UK
[3]College of Architecture and Environmental Design, California Polytechnic State University, San Luis Obispo, CA, USA
[4]Air Force Research Laboratory, Dayton, OH, USA

Summary Concepts based on both smart materials and emerging smart structural systems for shape-changing façade components for environmentally responsive building facades will be presented. The primary concept considered is a building surface tile fully comprised of a smart material, which can therefore have its intrinsic properties changed on command to facilitate actuating the tile into a variety of different shapes. A numerical representation was experimentally validated and implemented into a computational approach to explore the design space for this adaptive tile to have an effect on the solar irradiance on a building surface. Along with conclusions on this smart material tile concept, present efforts to develop new and complementary strategies incorporating origami and kirigami structural components to achieve adaptivity will be discussed.

BACKGROUND AND MOTIVATION

Energy consumption in the United States is dominated by the commercial building sector at 40% of total energy, and within the commercial building sector the main consumers are lighting and HVAC systems [1]. Due to this, there has been a considerable effort in recent research to reduce energy demand in commercial buildings. Specifically, many of these efforts focus on allowing the building to adapt to internal and external stimuli. Examples of interior building technologies include reducing energy consumption with occupancy sensors for light control [2], or predictive control for ventilation and HVAC systems [3]. Recently, focus has begun to switch to external building technologies, and an example of which is responsive building skins, which change configuration based on an environmental stimulus [4–7].

Responsive building skins have been recently developed to reduce the energy consumption of all main energy consumers within commercial buildings. In an effort to reduce HVAC demand within Media-TIC building in Barcelona an inflatable skin was implemented that inflates portions of the skins based on light sensors to increase insulation [4]. Alternatively the Heliotrace system [4] and the responsive building skin of the Al Bahard towers [5] utilized a series of mechanical apertures to control the flow of light into their respective buildings. Even more recent work has been considering the possibility of including a variety of smart material technologies to further expand the potential capabilities of responsive building skin technologies. The use of smart materials has several potential benefits, due to their controllable (i.e., programmable) intrinsic property changes and the ability to use naturally occurring stimulus (e.g., heat or solar radiation) or minimal supplied energy to elicit these property changes. Utilizing one or both of these smart material capabilities can lead to smart components that have more adaptivity and/or require less energy to achieve the same level of adaptivity, while also potentially eliminating overall system complexity (e.g., removing the need for hinges, etc.).

There are several smart material technologies that have been implemented into external building structures in order to mechanically change the façade to allow the building to positively interact with environmental stimuli. A specific example of a façade component comprised of a smart material was explored in [6] which utilizes hygromorphic materials, which behave similarly to a conifer cone in nature when the relative humidity changes [6]. This allows the façade component to “close” and provide shelter during high moisture loads (i.e., rain) and “open” to allow solar exposure during low moisture loads. Alternatively, Barrett et al. developed a building skin that used bimetal sheet layers that had differing coefficients of thermal expansion in order to curl towards or away from the structure based on the thermal loading in the surrounding environment [7]. The curling behavior of the façade component reduced solar gains by providing shading during high thermal loading and increased insulation during periods of low thermal loading. Alternatively, there has been some focus on creating morphing structures that similarly use intrinsic mechanisms (rather than hinges or multiple mechanical components) to achieve adaptivity, but rather than using smart material, they use structural responses, such as through origami (e.g., bi-stable folding components) or kirigami (e.g., cuts/holes in a component to control deformation). For example, kirigami (i.e., methods based on cutting/removing material) mechanisms have been investigated that can utilize an out-of-plane buckling response to allow portions of the surface to rotate as desired due to in-plane tension or compression [8]. A range of kirigami approaches have been investigated to achieve various structural responses, including parallel cuts, notches, and square cuts.

ADAPTIVE SMART MATERIAL TILE DESIGN CONCEPT

The primary design concept considered herein is an adaptive shape changing “wrinkled” surface tile based upon the prior work developing building surface “cactus tiles” by Clifford [9]. The original cactus tile objective from the previous work was to have static “wrinkled” surface tiles that were both aesthetically pleasing and had functional benefits in terms of self-shading. However, it is envisioned that adding the capability of such tiles to change between

wrinkle patterns, would further enhance the original benefits and potentially include many other functional behaviors. The proposed mechanism to produce a tile that can morph between different wrinkle patterns (i.e., shape changing cactus tile) is envisioned to be controllable localized activation of the smart material comprising the tile (e.g., softening) and mechanical actuation to deform the tile into a desired shape. Localized material activation has been shown to improve the efficiency of a shape-changing structure and is utilized as an additional control variable to increase functionality of the shape-changing building surface tile. Figure 1 shows the apparatus for the benchtop prototype used to test the smart material tiles, validate the numerical representation, and evaluate their morphing capability, including a breakdown of the apparatus components and dimensions.

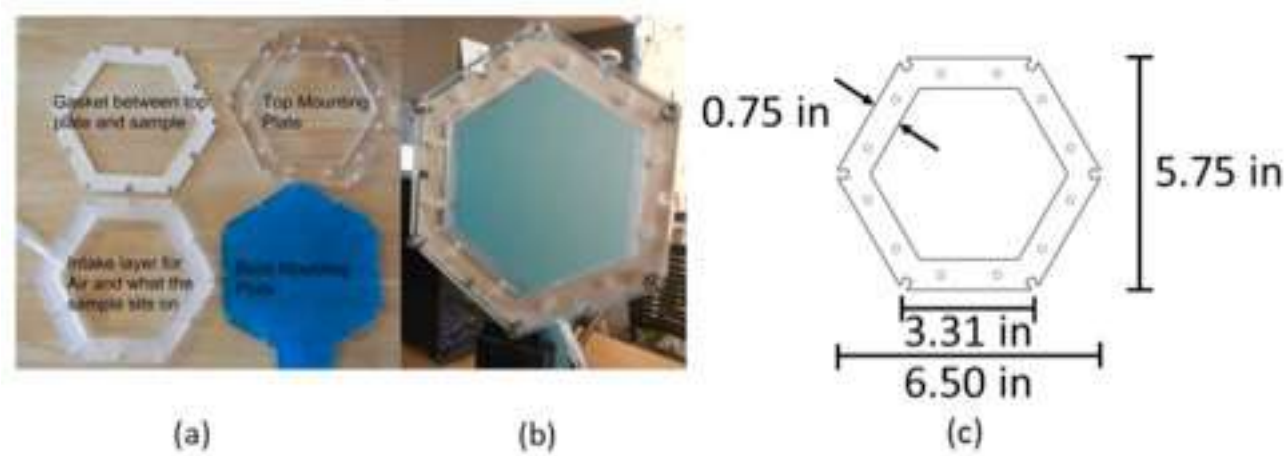

Figure 1. (a) The layers of the apparatus, (b) the fully assembled apparatus, and (c) the dimensions of the apparatus.

RESULTS AND CONCLUSIONS

Several concepts using smart material and smart structural components for creating building surfaces that respond to their environmental conditions have been considered in this work. The particular focus so far has been on a building surface tile entirely composed of a smart material that can be activated and actuated into configurations to reduce solar irradiance on the building surface. The results indicated that the design of the physical tile can be accurately represented by the computational approach and the adaptive tile can change the surface of a structure to considerably improve the structure's interaction with solar irradiance. It was also found that the morphing frequency (i.e., hourly, daily, monthly, etc.) has a significant effect on the area of the tile exposed to solar irradiance. Finally, it was determined that if the tiles are arranged in an array configuration controlling the tiles independently from one another not only leads to less tile area being exposed to solar irradiance but also requires less tile area to be activated. Going forward, concepts utilizing origami and kirigami structural components are being investigated to further enhance energy efficient adaptive façades that can favorably respond to a range of environmental conditions.

References

[1] Renewable Energy. Energy efficiency trends in residential and commercial buildings. 2010.

[2] Marie-Claude Dubois and Ake Blomsterberg. Energy saving potential and strategies for electric lighting in future north european, low energy office buildings: A literature review. Energy and Buildings, 43 (10): 2572–2582, 2011.

[3] Jan Siroky, Frauke Oldewurtel, Jırı Cigler, and Samuel Prıvara. Experimental analysis of model predictive control for an energy efficient building heating system. Applied energy, 88 (9): 3079–3087, 2011.

[4] Y Dewidar, N Mohamed, and Y Ashour. Living skins: A new concept of self active build- ing envelope regulating systems. In Advancing the Green Agenda; Technology, Practices and Policies Conference–BUID, pages 1–8, 2013.

[5] Karen Cilento. Al bahar towers responsive facade/aedas. ArchDaily,September, 5, 2012.

[6] Artem Holstov, Ben Bridgens, and Graham Farmer. Hygromorphic materials for sustainable responsive architecture. Construction and Building Materials, 98: 570–582, 2015.

[7] Ronald M Barrett and Ronald P Barrett. Thermally adaptive building coverings: Theory and application. In ASME 2016 Conference on Smart Materials, Adaptive Structures and Intelli- gent Systems, pages V002T06A001–V002T06A001. American Society of Mechanical Engineers, 2016.

[8] Ahmad Rafsanjani and Katia Bertoldi. Buckling-induced kirigami. *Physical Review Letters*, 118 (8): 084301, 2017.

[9] Robert Joseph Zupan, Dale Clifford, Richard Beblo, and John Brigham. Numerical investigation of capabilities for dynamic self-shading through shape changing building surface tiles. Journal of Facade Design and Engineering, 6 (1), 2018.

TOPOLOGY OPTIMIZATION WITH INEXACT DESIGN SENSITIVITIES

Oded Amir * [1]
[1]Faculty of Civil and Environmental Engineering, Technion – Israel Institute of Technology, Haifa, Israel

Summary We present recent developments of structural topology optimization procedures with inexact design sensitivities. In the nested approach to structural optimization, the vast majority of computational cost is invested in repeated solutions of the state and adjoint equations. These are used in intermediate design iterations solely for computing the design sensitivities that are subsequently used to generate an updated design by solving an approximate convex subproblem. We hereby explore the possibility of relaxing the accuracy requirement in the iterative solution of the state and adjoint problems, based on the predicted accuracy of the sensitivities. Implementation and results for linear-elastic static problems involving compliance and stress functionals are discussed.

INTRODUCTION

Topology optimization is nowadays a mature and widely accepted computational design approach. Manufacturing processes have also progressed and can realize optimized designs with complex geometries. Consequently, topology optimization is pushed towards very high computational resolution so that novel design concepts can be found that bring significant weight reduction and excellent structural performance. Hence there is a growing interest in efficient computational schemes that can generate high-resolution optimized designs using reasonable computational cost.

One evident consequence of the need for high-resolution topology optimization is the increasing popularity of parallel computing where iterative methods are utilized for solving the state and adjoint equations. But top-class hardware and iterative solvers alone are not enough: algorithmic developments are necessary as well in order to achieve significant reduction in computational time. Recent studies demonstrated considerable computational savings by reusing preconditioners and by relaxing the convergence requirements for the iterative solvers [1, 2, 3]. In some cases, up to 80% savings in computational effort were achieved in comparison to a standard implementation.

INEXACT DESIGN SENSITVITIES

Iterative solution of the state and adjoint problems can be terminated prematurely, yielding an approximation of the displacement or adjoint vector at a reduced computational cost. Various criteria for early termination have been investigated in the context of topology optimization, including: naively relaxing the tolerance of the relative force residual; measuring the convergence of the objective or constraint value; relating the tolerance to the accuracy of the finite element approximation [3]; and monitoring the predicted accuracy of the design sensitivities, that are the first-order gradients used for optimization [1, 2].

The aforementioned studies treat the relatively simple case of optimizing compliance versus volume. For the compliance functional, all design sensitivities are negative and their spatial distribution does not change significantly between design iterations. This makes the compliance functional an ideal platform for reusing preconditioners and for relaxing the convergence of the iterative state solver. The more challenging stress functional, that is also more relevant from an industrial perspective, has not been examined so far in the context of efficient computational procedures. Hence the main purpose of the current contribution is to build upon the idea of monitoring the design sensitivities as discussed in [1, 2] and extend its applicability to stress-based problems.

The approximate maximum stress functional $\tilde{\sigma}$ is formulated using a p-norm approximation of the true maximum stress over the entire domain. In the context of approximate procedures, it is more challenging than compliance due to the following aspects: 1) Dominant local contributions; 2) Dependence on two separate (state and adjoint) iterative solves; and 3) Accumulation of errors from the state solve into the assembly of the right-hand-side vector in the adjoint system.

We suggest that termination of the iterative solvers will be determined according to an acceptable convergence of the design sensitivities, rather than based on residual forces. Accordingly, the iterative solution of the state system $\mathbf{K}\left(\overline{\boldsymbol{\rho}}\right)\mathbf{u}=\mathbf{f}$ is terminated based on the evaluation of $\frac{\partial\tilde{\sigma}}{\partial\overline{\boldsymbol{\rho}}}$ and the iterative solution of the adjoint system $\mathbf{K}^T\boldsymbol{\lambda}=-\frac{\partial\tilde{\sigma}}{\partial\mathbf{u}}$ is terminated based on the evaluation of $\boldsymbol{\lambda}^T\frac{\partial\mathbf{K}}{\partial\overline{\boldsymbol{\rho}}}\mathbf{u}$. In each optimization cycle, given the current vector of design variables $\overline{\boldsymbol{\rho}}$ we call a multigrid-preconditioned conjugate gradient (MGCG) solver to approximate the solution of $\mathbf{K}\left(\overline{\boldsymbol{\rho}}\right)\mathbf{u}=\mathbf{f}$. Compared to a standard MGCG solver, the difference is in the stopping criterion, that is based on the evolution (along CG iterations) of the sensitivity term $\frac{\partial\tilde{\sigma}}{\partial\overline{\boldsymbol{\rho}}}$. Once the approximate solve of the displacements has terminated, the right-hand-side vector of the adjoint equation can be evaluated using the approximate stress vector $\boldsymbol{\sigma}_{k+1}$. Then the solution of the adjoint system $\mathbf{K}^T\boldsymbol{\lambda}=-\frac{\partial\tilde{\sigma}}{\partial\mathbf{u}}$ is approximated in another MGCG procedure, that is terminated based on the evolution (along CG iterations) of the sensitivity term $\boldsymbol{\lambda}^T\frac{\partial\mathbf{K}}{\partial\overline{\boldsymbol{\rho}}}\mathbf{u}$.

*Corresponding author. E-mail: odedamir@technion.ac.il

RESULTS

As a demonstrative example, we present the minimum volume optimization of an L-bracket domain, subject to an aggregated p-norm stress constraint. As can be seen in Table 1, the optimized designs are practically identical to the one obtained with exact direct solves. Moreover, the design is not influenced by the value of the convergence tolerance, in the range of $tol = 10^{-2}$ to $tol = 10^{-6}$. Even though the problem is highly nonlinear and non-convex, we obtain very similar convergence curves of the objective and stress constraint, see Figure 1. Remarkably, the first 22 design iterations are practically identical, regardless of the accuracy of the state and adjoint solves. Then parameters are modified according to a continuation scheme and some differences appear. Nevertheless all procedures converge to very similar volumes and satisfy the stress constraint. Computational results are summarized in Table 2. Relaxing the convergence tolerance leads to a reduction of more than 60% in the number of CG iterations performed during the state and adjoint solves. It is important to note that imposing the same tolerances on standard convergence criteria, such as relative residual forces, would not yield the same success. The direct control over the accuracy of the first-order gradients is key to an accurate and efficient optimization outcome.

Table 1: Optimized L-brackets using various design sensitivity tolerances of the iterative solver, compared to the solution with a direct solver. The design is not affected by the inexactness of the design sensitivities.

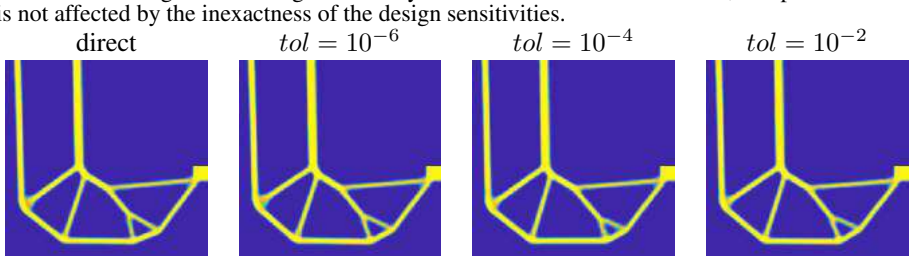

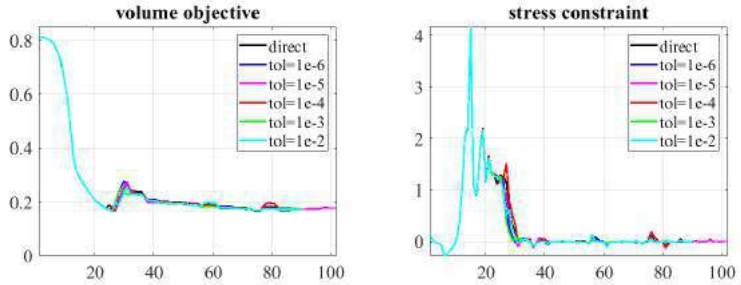

Figure 1: Convergence of the volume objective and stress constraint, for various convergence tolerances of the design sensitivities.

Table 2: L-bracket stress optimization with 31488 finite elements.

tolerance	direct	10^{-6}	10^{-5}	10^{-4}	10^{-3}	10^{-2}
volume	5186	5271	5366	5262	5278	5142
σ_{max}	0.4857	0.4991	0.4949	0.4859	0.4955	0.4906
CG iters., state		1108	1033	695	483	430
CG iters., adjoint		823	682	427	331	295

CONCLUSIONS

A convergence criterion for iterative solves of state and adjoint systems in stress-constrained topology optimization was proposed, based on the predicted accuracy of the design sensitivities. Results show that with this criterion, the number of MGCG iterations—hence the computational cost—is reduced significantly, without compromise on the volume-to-stress trade-off.

References

[1] Amir O., Aage N., Lazarov, B. S. On multigrid-CG for efficient topology optimization. *Structural and Multidisciplinary Optimization*, **49(5)**:815-829, 2014.

[2] Amir O. Revisiting approximate reanalysis in topology optimization: on the advantages of recycled preconditioning in a minimum weight procedure. *Structural and Multidisciplinary Optimization*, **51(1)**:41-57,2015.

[3] Limkilde A., Evgrafov A., Gravesen J. On reducing computational effort in topology optimization: we can go at least this far! *Structural and Multidisciplinary Optimization*, **58(6)**:2481-2492, 2018.

NUMERICAL INVESTIGATION OF STIFFNESS AND BUCKLING RESPONSE OF INFILLED STRUCTURES

Fengwen Wang * [1], Jeroen Peter Groen[1], and Ole Sigmund[1]
[1]Department of Mechanical Engineering, Technical University of Denmark, Kongens Lyngby, Denmark

Summary This study investigates the stiffness and buckling responses of 2D coated MBB beams with orthotropic infills obtained using homogenization-based stiffness optimization and de-homogenization. The considered infills are a reference truss lattice microstructure, and a topology optimized one with enhanced buckling strength. Both linear buckling and post-buckling analyses are employed to predict the structure buckling strength. Numerical results show that 2D coated MBB beams with different infills exhibit close stiffness and that the one with the optimized microstructure possesses higher buckling strength. However, buckling strength enhancement of the optimized microstructure significantly degrades in the 2D coated MBB beam compared with the material prediction.

INTRODUCTION

Additive manufacturing brings a tremendous interest in designing hierarchical structures [1]. Topology optimization methods have been employed to design structures with enhanced stiffness considering 3D printing infill or mapped rank-N laminates [2]. Even though coated structures with infill or de-homogenized rank-2 microstructures do not outperform their solid counterparts regarding stiffness, they may possess an advantage from the buckling strength perspective [3]. Recently, materials with enhanced buckling strength [4] have been systematically designed using topology optimization for different macro-level stress situations. It has been shown that material buckling strength can be significantly enhanced at the cost of decreased stiffness. More recently, the material buckling strength has been further studied when considering the material and geometric nonlinearities and geometrical imperfections [5]. Moreover, stiffness and buckling responses of the simple and optimized periodic infill structures have been numerically investigated for uniaxial compression by the authors [6]. Both studies have shown that the optimized microstructures significantly outperform the reference ones in terms of buckling response at the cost of stiffness.

Until now, however it is an open question, how structures with optimized microstructures as infill perform compared to regular infill structures in terms of stiffness and buckling responses. Based on the work in [6], this study further investigates the stiffness and buckling responses of 2D coated MBB beams with orthotropic infills obtained using homogenization-based stiffness optimization and projection [2]. The considered infills are the reference microstructure (RMS) and the optimized microstructure (OMS) as in [6], see Fig. 1.

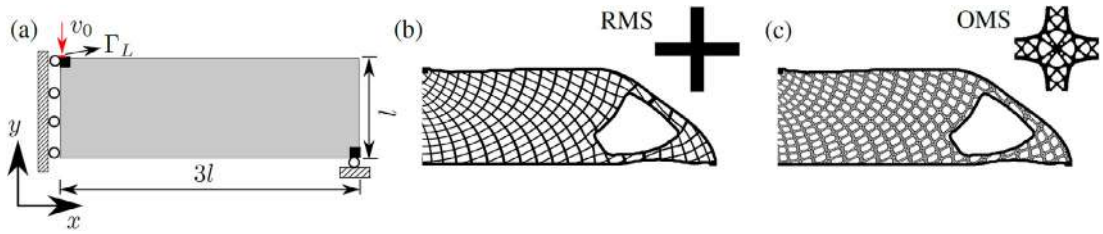

Figure 1: (a) Geometric boundary conditions of the MBB beam. (b) 2D coated MBB beam with RMS. (c) 2D coated MBB beam with OMS.

COMPUTATIONAL METHODS AND NUMERICAL RESULTS

The coated MBB beam is modeled under the plane strain assumptions with a height of $l = 1$ and a thickness of $t = 0.25$. As shown in Fig. 1 (a), the coated MBB beam is subjected to prescribed vertical displacement v_0 on the left upper corner. The length of the loading region Γ_L is 2.4% of the beam height.

Both linear buckling (LB) and post-buckling (PB) analyses are employed to investigate structural performance based on the finite element method. The LB analysis follows the standard linear buckling analysis as described in [7]. In the PB analysis, the total Lagrangian approach is used, and the static equilibrium is solved using the arc-length method for each displacement increment step. The detailed equations for the LB and PB analyses are stated in [6] and will not be repeated here.

The Young's modulus and Poisson's ratio of the base material (in black) are $E_0 = 1$ and $\nu = 0.3$. A modified compressible Neo-Hookean material law [7] is used to describe the material behavior under finite deformations. The corresponding material stored energy density is written as $W = \frac{1}{2}\lambda_0 (J-1)^2 + \frac{\mu_0}{2}(I-3) - \mu_0 \ln(J)$. $\boldsymbol{F}$ is the deformation gradient and $J = \det(\boldsymbol{F})$, $I = \mathrm{trace}(\mathrm{C})$ with $\boldsymbol{C} = \boldsymbol{F}^T\boldsymbol{F}$ being the right Cauchy-Green deformation tensor, and λ_0 and μ_0 are the Lamé parameters of the base material.

*Corresponding author. E-mail: fwan@mek.dtu.dk

In the PB evaluation, the considered geometric imperfections are the equal-weighted first four buckling modes for the LB analysis (see Fig. 2 (a) and (b)), with a maximum perturbation amplitude, $\varphi = 0.0005$. At each equilibrium state, the total reaction force on the displacement loading edge is calculated using $f^{\text{rect}} = \sum_{i \in \Gamma_L} f^{\text{int}}_{y,i}$, where i refers to the nodal number and $f^{\text{int}}_{y,i}$ is the corresponding internal load in the y direction. The buckling point is defined by the state where the structure looses significant stiffness. Here it is defined as the state where the stiffness has decreased to 20% of the initial one.

Fig. 2 shows the structure evaluations using the LB and PB analyses. Fig. 2 (a) and (b) present the first four linear buckling modes with τ_i indicating the ith mode. The LB evaluations show that the 2D coated MBB beam with OMS exhibits 33% higher buckling strength than the one with RMS. Fig. 2 (c) shows the reaction force versus displacement response in the PB analysis with the square symbols indicating buckling points, and final structure deformations. It is seen that the 2D coated MBB beam with OMS exhibits very close stiffness with the one with RMS. Meanwhile, the 2D coated MBB beam with OMS possesses 68% higher buckling strength. Moreover, the buckling strength of both considered structures from the PB analyses is smaller than the corresponding one from the LB analysis due to material and geometric nonlinearity.

Both LB and PB evaluations show that, in the 2D coated MBB beam, buckling strength enhancement of OMS degrades compared with the material prediction in [4, 5] and the evaluations of finite periodic structures under the uniaxial compression in [6].

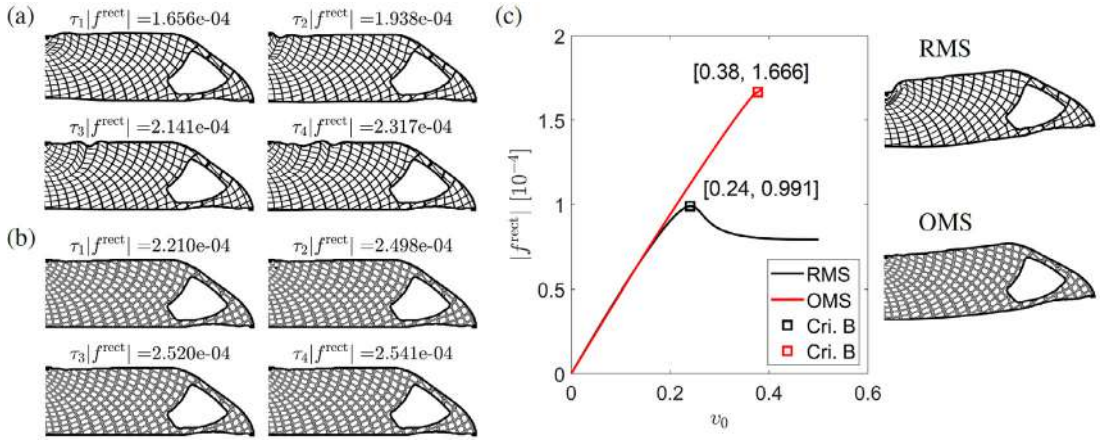

Figure 2: First four buckling modes of the structures with RMS (a) and OMS (b). (c) Post-buckling evaluations and corresponding final structural deformations.

References

[1] Meza L. Zelhofer A. J. Clarke N. et. al. Resilient 3D hierarchical architected metamaterials. *PNAS*, **112(37)**:11502–11507, 2015.

[2] Groen J. P. Wu J. Sigmund O. Homogenization-based stiffness optimization and projection of 2D coated structures with orthotropic infill. *Comput. Methods. Appl. Mech. Eng.*, **349**: 722-742, 2019.

[3] Clausen A. Aage N. Sigmund O. Exploiting additive manufacturing infill in topology optimization for improved buckling load. *Eng.*, **2(2)**:250–257, 2016.

[4] Thomsen C. R. Wang F. Sigmund O. Buckling strength topology optimization of 2D periodic materials based on linearized bifurcation analysis. *Comput. Methods. Appl. Mech. Eng.*, **339**:115–136, 2018.

[5] Bluhm G. L., Sigmund O., Wang F., and Poulios K. Nonlinear compressive stability of hyperelastic 2D lattices at finite volume fractions. *J. Mech. Phys Solids*, (Accepted).

[6] Wang F. Sigmund O. Numerical investigation of stiffness and buckling response of simple and optimized infill structures, *Struct. Multidiscip. Optim.*, (Accepted).

[7] Zienkiewicz O. C. Taylor R. L. The finite element method for solid and structural mechanics. Elsevier Butterworth-Heinemann, Amsterdam; Boston, 2005.

TOPOLOGY OPTIMIZATION OF A SUBWOOFER

Ahmad H. Bokhari1, Martin Berggren1, Daniel Noreland1,2, and Eddie Wadbro*1
[1]Department of Computing Science, Umeå University, SE–901 87 Umeå, Sweden.
[2]The Forestry Research Institute of Sweden (Skogforsk), Uppsala Science Park, SE–751 83 Uppsala, Sweden.

Summary Subwoofers generate the lowest frequency range in loudspeaker systems. Here, we study a so-called band-pass subwoofer enclosure, in which a transducer is mounted in a closed back chamber located inside the subwoofer cabinet, and an output port is placed in the front chamber. To reduce the computational time of simulating the average response for a given subwoofer design, we present a hybrid 3D/2D model that efficiently models the subwoofer's performance. The results of the hybrid model are validated against a full 3D model over a frequency band of interest; the validation confirms that the hybrid model is computationally efficient as well as accurate. We formulate and solve a material distribution based topology optimization problem, to design of the subwoofer's interior cabinet to provide obtain desired transmission properties.

INTRODUCTION

The classical topology optimization problem is to minimize the compliance of a statically loaded elastic structure subject to constraints on the amount of available material. There are well-established techniques to solve this problem [1]. However, techniques for acoustic design optimization are still maturing. Current methods in acoustics focus on optimizing individual components, such as loudspeaker horns and sound mufflers, under idealized conditions. However, real-life acoustic systems consist of many components that affect each other's performance. In this study, we aim to optimize the interior layout of a subwoofer.

HYBRID MODEL

We study a so-called band-pass subwoofer enclosure, in which a transducer is mounted in a closed back chamber located inside the subwoofer cabinet, and an output port is placed in the front chamber. If we discretize the whole system uniformly and consider 3D effects, we obtain a large-scale problem that is computationally intractable. We propose a mathematical model that describes the interaction between the different subwoofer components as interacting modules whose acoustic properties can partly be precomputed. The model is based on time-harmonic linear wave propagation and includes a 3D model of the transducer, an electromechanical circuit model, a 2D model for the subwoofer cabinet's front chamber, whose interior layout is described by a material indicator function, and a 3D model for the exterior wave propagation. The use of a 2D model in planar symmetry for the front chamber drastically reduces the computational cost. The resulting planar design will also be easier to manufacture compared to full 3D design. Due to the long wavelength, it is reasonable with a restriction to 2D wave propagation within the chamber, but not for the transducer or for the exterior, where we rely on 3D models. The results of the hybrid model are validated against a full 3D model over a frequency band of interest. We numerically verify that the hybrid 3D/2D model produces reliable results and that it significantly reduces the computational time compared to a full 3D model. Figure 1 shows two subwoofers with different internal layouts as well as their performance over the interval 20–160 Hz.

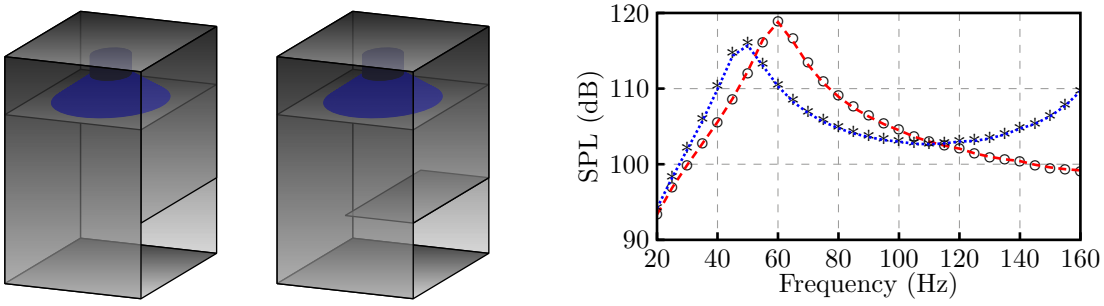

Figure 1: Two subwoofer layouts and their performance evaluated by a full 3D model as well as our proposed hybrid 2D/3D model. The dashed line (hybrid model) and the circles (full 3D model) shows the computed performance of the left subwoofer layout. The right layout has an added internal wall, and its performance is illustrated by the dotted line (hybrid model) and the asterisks (full 3D model).

*Corresponding author. Email: eddiew@cs.umu.se

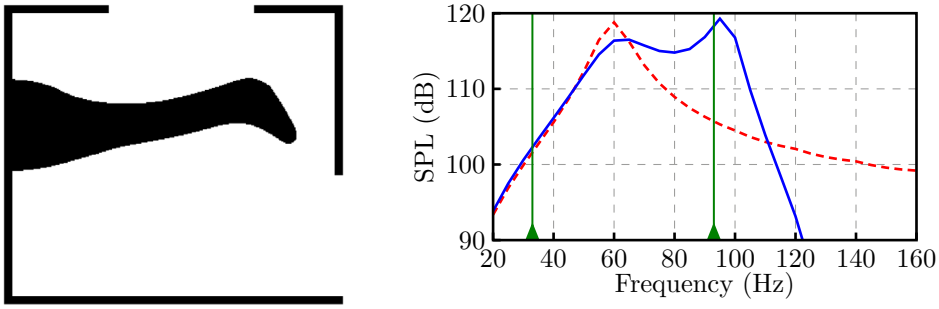

Figure 2: Left: subwoofer optimized for the frequency interval 33–93 Hz, marked by the solid vertical lines. The solid line shows the performance of the optimized subwoofer and the dashed line shows the performance of the of the left subwoofer in Figure 1.

OPTIMIZATION FORMULATION AND RESULTS

We formulate a material distribution topology optimization problem to determine the interior layout of the subwoofer. We use a material indicator function α to determine whether each point in the interior of the subwoofer should be occupied by fluid ($\alpha = 1$) or solid ($\alpha = 0$). To ensure that the resulting interior design (the solid part) has a minimum size, we define α by applying a harmonic-mean based morphology mimicking filter to another function η, which is the function that we optimize over [2, 3, 5].

We mesh the region below the baffle by N elements and in each element, we approximate the material indicator function α and the design η by element-wise constant functions α_h and η_h, respectively. The relation between the vectors $\boldsymbol{\alpha}$ and $\boldsymbol{\eta}$ that hold the element values of α_h and η_h, respectively, can in after discretization be written $\boldsymbol{\alpha} = \mathcal{F}_h(\boldsymbol{\eta})$, where $\mathcal{F}_h$ is a filter operator. The objective of our optimization problem is to find a design so that the output power P is above a certain target P_{target} at given freuencies f_m, $m = 1, \ldots, M$. The topology optimization problem is solved by Svanberg's MMA algorithm, and the adjoint variable method is used to obtain gradients of the objective function with respect to the design variables. Figure 2 shows the cross-sectional internal layout of an optimized subwoofer and its performance together with the performance of the left subwoofer in Figure 1.

References

[1] M. P. Bendsøe and O. Sigmund. Topology Optimization. Theory, Methods, and Applications. Springer, 2003.
[2] L. Hägg and E. Wadbro. On minimum length scale control in topology optimization. Struct. Multidiscip. Optim., 58(3):1015–1032, 2018.
[3] O. Sigmund. Morphology-based black and white filters for topology optimization. Struct. Multidiscip. Optim., 33(4–5):401–424, 2007.
[4] K. Svanberg. The method of moving asymptotes—a new method for structural optimization. Internat. J. Numer. Methods Engrg., 24:359–373, 1987.
[5] K. Svanberg and H. Svärd. Density filters for topology optimization based on the pythagorean means. Struct. Multidiscip. Optim., 48(5):859–875, 2013.

H_∞-NORM DYNAMIC RESPONSE OPTIMIZATION: NUMERICAL AND STRUCTURAL ISSUES

Daniele Boffi[1,2], Lucia Gastaldi[3], and Paolo Venini* [4]
[1]Mathematical and Computer Sciences and Engineering Division, King Abdullah University of Science and Technology, Thuwal 23955-6900, Kingdom of Saudi Arabia
[2]Dipartimento di Matematica "F. Casorati", University of Pavia, Pavia, Italy
[3]Department of Civil, Environmental, Architectural Engineering and Mathematics, University of Brescia, Brescia, Italy
[4]Department of Civil Engineering and Architecture, University of Pavia, Pavia, Italy

Summary An innovative method for structural and topology optimization of dynamic systems is presented. The objective function to be minimized is the H_∞–norm of the input/output transfer function that allows to handle single input-single output as well as multi input-multi output systems. The focus of the paper is twofold: on the one side numerical issues concerning the fast computation of the H_∞–norm and its gradient are addressed; on the other side results of structural and practical interest in broad sense are presented to validate the numerical framework. Ongoing and future extensions are eventually highlighted at the end of the paper.

GENERAL REMARKS

A general dynamic system is considered that depends on a vector of structural parameteres, say $\boldsymbol{p}$, that should be determined so as to satisfy some design requirement. The general *descriptor state–space* form is adopted that encompasses several dynamic systems including structural frames and bi–dimensional plane and plate structures. By doing so, the dynamic equilibrium and output equations respectively read

$$\left\{\begin{array}{rcl} \boldsymbol{E}(\boldsymbol{p})\dot{\boldsymbol{x}} &=& \boldsymbol{A}(\boldsymbol{p})\boldsymbol{x} + \boldsymbol{B}\boldsymbol{w} \\ \boldsymbol{y} &=& \boldsymbol{C}\boldsymbol{x} \end{array}\right., \tag{1}$$

wherein matrices and vectors are defined as

$$\boldsymbol{E}(\boldsymbol{p}) = \begin{bmatrix} \boldsymbol{I} & \boldsymbol{0} \\ \boldsymbol{0} & \boldsymbol{M}(\boldsymbol{p}) \end{bmatrix}, \quad \boldsymbol{A}(\boldsymbol{p}) = \begin{bmatrix} \boldsymbol{0} & \boldsymbol{I} \\ -\boldsymbol{K}(\boldsymbol{p}) & -\boldsymbol{D}(\boldsymbol{p}) \end{bmatrix}, \quad \boldsymbol{B} = \begin{bmatrix} \boldsymbol{0} \\ \tilde{\boldsymbol{B}} \end{bmatrix}, \ \boldsymbol{x} = \begin{bmatrix} d & \boldsymbol{u} \\ & \dot{\boldsymbol{u}} \end{bmatrix}, \tag{2}$$

in which $\boldsymbol{x}$ and $\boldsymbol{y}$ are the state and output vector, respectively, $\boldsymbol{E}$ is the *descriptor* matrix, $\boldsymbol{A}$ is the *state* matrix, $\boldsymbol{B}$ is the *load* matrix that distributes the external action $\boldsymbol{w}$ to the degrees–of–freedom and $\boldsymbol{C}$ is a matrix that allows to specify the entries of the output vector $\boldsymbol{y}$ as linear combinations of the state vector components. Furthermore the state vector $\boldsymbol{x}$ is obtained by piling displacements $\boldsymbol{u}$ and velocities $\dot{\boldsymbol{u}}$ whereas $\boldsymbol{M}(\boldsymbol{p})$, $\boldsymbol{D}(\boldsymbol{p})$ and $\boldsymbol{K}(\boldsymbol{p})$ are the mass, damping and stiffness matrices and $\boldsymbol{0}$ and $\boldsymbol{I}$ are zero and identity matrices of appropriate dimensions. Based on Equation (1), dynamic optimization could be pursued in the time domain (where the problem is differential) for example along the path set in [1]. It is herein preferred to switch to the Laplace domain (eventually to the Fourier domain) taking advantage of algebraic nature of the resulting problem. By taking the Laplace transform of Equation $(1)_1$, plugging the result into the Laplace transform of Equation $(1)_2$ one gets the input/output relation

$$\boldsymbol{Y} = \boldsymbol{G}(s;\boldsymbol{p})\boldsymbol{W}, \tag{3}$$

that is ruled by the transfer function

$$\boldsymbol{G}(s;\boldsymbol{p}) = \boldsymbol{C}(s\boldsymbol{E}(\boldsymbol{p}) - \boldsymbol{A}(\boldsymbol{p}))^{-1}\boldsymbol{B}. \tag{4}$$

If one now recalls that the H_∞–norm of a system transfer function is the peak response computed over all possible input/output channels, the following optimal design problem arises naturally:

$$\left\{\begin{array}{lll} \min\limits_{\boldsymbol{p}} F(\boldsymbol{p}) & = & ||\boldsymbol{G}(i\omega;\boldsymbol{p})||_\infty \\ \text{s.t.} & & \boldsymbol{G}(i\omega;\boldsymbol{p}) = \boldsymbol{C}(\boldsymbol{p})(i\omega\boldsymbol{E}(\boldsymbol{p}) - \boldsymbol{A}(\boldsymbol{p}))^{-1}\boldsymbol{B}(\boldsymbol{p}) \\ & & V(\boldsymbol{p}) \le V_{\max} \\ & & p_{\min} \le \boldsymbol{p} \le p_{\max} \end{array}\right., \tag{5}$$

where the transfer function definition $(5)_2$ is an equality constraint to the overall optimization problem, $(5)_3$ is a *limited resources* constraint and $(5)_4$ is an elementwise size-constraint.

*Corresponding author. E-mail: paolo.venini@unipv.it.

NUMERICAL ISSUES

On the computation of the H_∞-norm

A key for the solution of Problem 5 is the availability of a reliable and possibly fast numerical scheme for the computation of the H_∞–norm of the system transfer function. This is true for a single norm computation but even more for tackling an optimization problem that calls for several (possibly thousands) successive norm computations. A few methods made available in the literature for computing the H_∞–norm of a complex dynamic system, see e.g. [2] and [3], shall be exploited and relevant performances assessed, at least with respect to the structural problems solved numerically. A few heuristic considerations shall also be given concerning possible improvements that may lead to an even faster H_∞-norm computation.

Using reduced–order models

The number of states entering the formulation, i.e. the dimension N of the state-vector $\boldsymbol{x}$, may be extremely large even for systems of moderate complexity. On the other side, using the H_∞-norm as merit function allows to neglect most of the system poles that are located at a remarkable distance from the frequency $\overline{\omega}$ where the peak response is actually attained, i.e. where the H_∞-norm is realized. It may then be convenient to replace the actual system with a reduced-order one that is capable to accurately replicate the system dynamics in the vicinity of $\overline{\omega}$ without caring about high-frequency (numerically expensive) dynamics that are in fact left unmodelled. The time invested in computing the reduced-order model is likely to be largely paid back as time saved in the computation of the H_∞–norm using a system governed by very few states. All these issues shall be investigated in the paper.

STRUCTURAL AND TOPOLOGY OPTIMIZATION

The above approach shall first be applied to the optimization of the dynamic response of steel plane frames undergoing a dynamic load such as earthquakes or strong winds. The scenario is different form the one recently proposed in [4] in that the design variables grouped in vector $\boldsymbol{p}$ are continuous in the case of reinforced-concrete structures (since they typically represent a cross-section size or the like) whereas they are discrete in the case of steel profiles that are allowed to be of commercial type and therefore belong to a finite-dimensional set. This calls for the adoption of "*non-gradient*" numerical optimization methods such as genetic ones that shall be exploited in this investigation.

Bidimensional problems shall also be considered using classical displacement finite elements but also mixed ones. The latter choice allows an easier and more accurate imposition of the stress constraint especially within a truly-mixed setting wherein the stresses are the primary variables. Furthermore the approach may be extended to a time-dependent viscoelastic response that is of considerable importance when base-isoltaed systems are to be modeled.

CONCLUSIONS

A promising approach for structural and topology optimization of dynamic systems has been presented that is based on the H_∞–norm of the input/output transfer function. Numerical and structural issues have been addressed and shall be reported in much detail. Ongoing extensions include applications to 3D systems as well as to structures affected by uncertainties in the apllied loads and/or in structural properties such as the elastic moduli and the mass density.

References

[1] Jensen J. S., Praveen B. N., Tortorelli D. A. On the Consistency of Adjoint Sensitivity Analysis for Structural Optimization of Linear Dynamic Problems. *Struct. Multidisc. Optim.* **49**: 831–837, 2014.

[2] Bruinsma N. A., Steinbuch M. A Fast Algorithm to Compute the H_∞-Norm of a Transfer Function Matrix. *Systems and Control Letters* **14**: 287-293, 1990.

[3] Benner P., Mitchell T. Faster and More Accurate Computation of the H_∞–Norm via Optimization. *SIAM J. Sci. Comput.* **40**(5): A3609–A3635, 2018.

[4] Venini P., Ceresa P. A Rational H_∞–Norm based Approach for the Optimal Design of Seismically Excited Reinforced Concrete Frames. *Earthquake Engng Struct Dyn*. **47**: 1522–1543, 2018.

EFFICIENT AND ROBUST TOPOLOGY OPTIMIZATION OF NONLINEAR FLEXTURES

Fred van Keulen* and Lidan Zhang
Department of Precision and Microsystems Engineering, Delft University of technology, Delft, The Netherlands

Summary Computationally efficient and robust topology optimization schemes are proposed for the design of nonlinear flexure-based mechanisms (flextures). Advanced layouts of flextures can eliminate crosstalk caused by nonlinearities and may lead to compact designs for precision applications. Special attention is on computational efficiency using adaptive reduced-order models and the elimination of spurious instabilities. Different optimization formulations will be demonstrated to address crosstalk phenomena typical for precision applications.

INTRODUCTION

In precision instruments and tools, alignment and positioning components are key system ingredients. To avoid negative effects caused by play, compliant mechanisms are often preferred for precision settings. These compliant systems are either designed as compliant mechanisms, *i.e.* the elastic deformation is mainly concentrated at the elastic hinges, or as leaf-spring-based systems. In both cases, geometric nonlinearities may cause severe difficulties, for example, leading to crosstalk. To avoid geometrically nonlinear side effects, one could restrict the kinematics to very small rotations, leading to systems which are relatively large as compared to the stroke they are designed for. Alternatively, nonlinear effects may be used to counteract each other. Clearly, the latter adds to the complexity of the design process. As an alternative, leaf-spring type components may be designed in such a manner that certain crosstalk effects are eliminated by advanced layout of flexible components. Such a complex layout can be realized using cost-effective laser cutting on thin-walled sheet materials, see, as an example, Figure 1.

Manual design of flextures with complex layout and manufactured from flat or curved sheets is extremely hard because of the geometric nonlinearities. Topology optimization could potentially address this complex design challenge, provided it can handle the nonlinearities and ill-conditioning caused by the thin-walled setting efficiently. In this contribution we propose and evaluate topology optimization schemes which rely on reduced-order modeling and are geared towards thin-walled finite rotation shell problems.

FINITE ROTATION SHELL MODELING

As mentioned above, advanced sheet-based flexture design should take place in a geometrically nonlinear setting, involving finite rotations and deflections but small deformations. We therefore rely on the triangular thin shell element described in [1]. This simple but robust element is based on a combination of the constant strain and the Morley triangle. For the finite rotation formulation, the bending deformations are evaluated using a co-rotational formulation. The very nature of finite rotations requires internal reference vectors to be updated at every step of an incremental-iterative nonlinear analysis. Although the resulting finite-rotation solution is path independent, the internal reference vectors are path dependent.

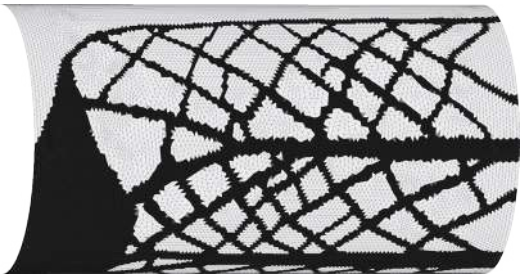

Figure 1: Geometrically nonlinear topology optimization based flexture design on a cylindrical surface. The design is suited for laser cutting.

*Corresponding author. E-mail: A.vanKeulen@tudelft.nl

REDUCED-ORDER MODELING

Topology optimization of geometrically nonlinear structures becomes computationally involved due to the incremental-iterative analyzes involved. For this reason we proposed [2] to use a reduced-order model (ROM), forwhich the degrees of freedom of the finite element model ($\mathbf{u}$) are approximated by $\mathbf{u} \approx \mathbf{R}\mathbf{y}$. Here $\mathbf{y}$ represents a very small set of generalized coordinates and the matrix $\mathbf{R}$ is constructed from a series of carefully selected base vectors Φ_i, *i.e.* $\mathbf{R} = [\Phi_1, \Phi_2, \ldots]$. The base vectors are primarily based on solutions of the full-order model. By measuring the imbalance of a ROM-based solution on the full-order model, an automatic switching between the reduced-order and the full-order model is realized. Moreover, information on the base vectors is used after a design adaptation. Consequently, during an optimization a new analysis may benefit from the ROM basis as developed during previous optimization steps. It was demonstrated that the number of full system solves in a geometrically nonlinear topology optimization could potentially be reduced by one to two orders of magnitude. This ROM formulation is fully compatible with the finite rotation formulation summarized above.

NEARLY INEXTENSIONAL BENDING

Flextures effectively rely on compliant bending modes, whereas extensional modes can be associated with relatively high stiffness. In other words, flexure-based mechanisms exploit nearly inextensional bending. In particularly, for extremely slender structures the correct representation of the bending modes is therefore paramount. Modeling nearly inextensional bending modes incorrectly, may lead to spurious extensions and, consequently, the compliance of the bending modes will be severely underestimated. A careful study of the aforementioned reduced-order model reveals that it suffers from this defect and, therefore is unsuited for the topology optimization of flextures.

To realize a proper ROM-based topology optimization of flexible structures, the ROM basis can be augmented with path-derivative information. A straightforward and inexpensive method to generate path-derivative information is to impose small perturbations of the load level after each full system solve in combination with a modified Newton scheme.

SPURIOUS INSTABILITIES

Geometrically nonlinear topology optimization faces the problems of elements which may, due to severe distortions, "flip" and appearance of spurious instabilities. The latter is especially prominent for thin-walled structures. For flexture design problems, flipping of elements is less prominent. Given the thin-walled nature of flexture designs, spurious instabilities may be anticipated in low density areas.

Different remedies have been proposed to circumvent the above complications. Bruns and Tortorelli [3] proposed to remove the void elements from the model. Yoon and Kim [4] used an element connectivity formulation. Van Dijk *et al.* [5] suggested a scaling of the deformations. Unfortunately, none of these formulations is easy to combine with the co-rotation formulation and/or the ROM scheme being used. Compatible with the ROM scheme at hand is the technique proposed by Wang *et al.* [6], who scale the nonlinearity. In fact, nonlinear elements are converted into linear elements in void areas. A one-to-one application of this method to the co-rotation formulation is not possible. However, given the fact that spurious instabilities are primarily caused by the contributions involving the tangential stress resultants and the membrane deformations are still evaluated via a total-Lagrangian formulation, we opt for a scaling in the spirit of [6], but for the membrane deformations only.

TOPOLOGY OPTIMIZATION OF FLEXTURES

In this presentation, the proposed ROM-based topology optimization schemes with avoidance of spurious instabilities are tested and demonstrated on flexture design problems. The tests are restricted to flextures which can be manufactured from thin sheets (flat or curved) using laser cutting. Different optimization formulations are tested which include crosstalk requirements typical for precision applications. Robustness and efficiency of the proposed methods are demonstrated.

References

[1] Van Keulen F., Booij J. Refined Consistent Formulation of a Curved Triangular Finite Rotation Shell Element. *Int. J. Numer. Meth. Engng.* **39**: 2803–2830, 1996.

[2] Zhang Y., Zhang L., van Keulen F. Topology Optimization of Geometrically Nonlinear Structures *In preparation*, 2020.

[3] Bruns T.E., Tortorelli D.A. An element removal and reintroduction strategy for the topology optimization of structures and compliant mechanisms. *Int. J. Numer. Meth. Engng.* **57**: 1413-1430, 2003

[4] Yoon H.G., Kim, Y.Y. The element connectivity parameterization formulation for the topology design optimization of multiphysics systems. *Int. J. Numer. Meth. Engng.* **64**: 1649–1677, 2005

[5] Van Dijk N., Langelaar M., van Keulen F. Element deformation scaling for robust geometrically nonlinear analyses in topology optimization. *Structural and Multidisciplinary Optimization* **50**, 537-560, 2014.

[6] Wang F., Lazarov B.S., Sigmund O., Jensen J.S. Interpolation Scheme for Fctitious Domain Techniques and Topology Optimization of Fnite Strain Elastic Problems. *Comp. Meth. Appl. Mech. Engng* **276** 453-472, 2014

DESIGN OPTIMIZATION OF LATTICE SUPPORT STRUCTURES TO PREVENT EXCESSIVE THERMAL DEFORMATIONS IN ADDITIVE MANUFACTURING

Mattias Schevenels * [1], Jeroen Pellens[1], Geert Lombaert[2], Manuel Michiels[3], and Tom Craeghs[3]
[1]KU Leuven, Faculty of Engineering Science, Department of Architecture, Leuven, Belgium
[2]KU Leuven, Faculty of Engineering Science, Department of Civil Engineering, Leuven, Belgium
[3]Materialise, Leuven, Belgium

Summary This paper focuses on the design of lattice support structures for 3D printed parts produced by selective laser melting. These support structures are needed to counteract thermal deformations during the printing process, so preventing print failure due to recoater collisions. A method is proposed to minimize the amount of material needed for the lattice support structure. The design is subdivided in a number of printing stages (each combining multiple printed layers), and for each printing stage, constraints are imposed on the upward displacements of the upper side to avoid recoater collisions. In order to predict these displacements, the lattice is modeled as a homogenized medium, and the temperature load is taken into account by means of the inherent strain method. The approach is successfully applied to a number of test problems, both in 2D and in 3D.

INTRODUCTION

Many additive manufacturing techniques involve the generation of heat. This may result in thermal deformations, leading to inaccuracies in the printed part compared to the blueprint design. In the case of selective laser melting, it may also result in complete print failure, as upward displacements due to thermal deformations can give rise to collisions between the recoater (the printer component that deposits new layers of metal powder) and the printed part. Additional support structures that can counteract the thermal deformations are usually foreseen to prevent such recoater collisions. However, these support structures come at a cost, as they involve an increase in material and energy consumption, printing time, and pre- and postprocessing work (to design and to remove the support structure). In this paper, we propose a method to minimize the amount of support structure needed to avoid recoater collisions due to thermal deformations in selective laser melting.

SIMULATION OF THERMAL DEFORMATIONS

Support structures with a lattice layout are often used as they are relatively easy to remove from the printed part. We therefore focus on lattice support structures, and we consider a lattice with the isotruss architecture [1], see figure 1. The isotruss unit cell consists of horizontal and vertical bars with a diameter d and diagonal bars with a diameter $4d/3\sqrt{3}$. This diameter ratio results in isotropic macroscale behavior.

Figure 1: Unit cell of a lattice with the isotruss architecture.

Watts et al. [3] determined approximate polynomial expressions for the homogenized Young's modulus E, Poisson's ratio ν, and bar diameter d of an isotruss lattice in terms of its density ρ. We use these expressions to model the lattice structure as a homogeneous isotropic material.

In order to predict thermal deformations during the printing process, a simulation should be performed for each additional layer. As this is computationally way too expensive due to the large number of layers, a smaller number of printing stages (each consisting of multiple additional layers) is considered instead. For each stage, the inherent strain method is used to model the temperature load. In this method, which has originally been developed for welding [2], initial strains are imposed in the so-called activated layer, or the top layer of the printing stage. The thickness of the activated layer can be chosen freely (e.g. $1\,\mathrm{mm}$); the initial strains must determined from test prints on the same machine where the actual part will be produced, with the same settings, assuming the same activated layer thickness.

The thermal deformations are calculated by means of the finite element method: the design (consisting of the part and the homogenized support structure) is subdivided into finite elements. Each element e of the support structure is assigned a density ρ_e (ranging from 0 for a void element to 1 for a solid element), which determines its elastic properties E_e and ν_e. The element densities ρ_e are collected in a vector $\boldsymbol{\rho}$. Next, the stiffness matrix $\mathbf{K}_i(\boldsymbol{\rho})$ is assembled for each printing stage i, as well as the nodal force vector $\mathbf{f}_i$ that represents the temperature load. Finally, the nodal displacements $\mathbf{u}_i$ for each printing stage i are determined as the solution of the discretized state equation $\mathbf{K}_i\mathbf{u}_i = \mathbf{f}_i$.

*Corresponding author. E-mail: mattias.schevenels@kuleuven.be.

FORMULATION OF THE OPTIMIZATION PROBLEM

The support structure design optimization problem is formulated as follows:

$$\begin{aligned} \min_{\boldsymbol{\rho}} : \quad & V = \sum_e v_e \rho_e \\ \text{s.t.} : \quad & u_{i,j} \leq u_{\max} \quad \forall i,j \\ & \rho_{\min} \leq \rho_e \leq \rho_{\max} \end{aligned} \tag{1}$$

The element densities ρ_e are used as design variables; they are bounded by a minimum value $\rho_{\min}$ and a maximum value $\rho_{\max}$ that depend on the minimum and maximum allowable bar diameter, respectively. The objective is to minimize the total material volume V of the support structure, which depends on the element volumes v_e and densities ρ_e. For each printing stage i, a number of critical nodes on the upper side of the design printed so far is selected, and the vertical displacements of these nodes (denoted by $u_{i,j}$) are restricted to a maximum allowable value $u_{\max}$.

RESULTS

The optimization problem is solved to determine the support structure for a cantilevering part as shown in figure 2a. Two cases are considered: in the first case, a spatially uniform density distribution is adopted for the support structure; i.e. all unit cells of the lattice are identical. In this case, there is only a single design variable, and the optimization problem is solved by means of a bisection algorithm. This leads to the design shown in figure 2b. For this design, $64.3\,\%$ of the material required to produce the component is used to print the support structure.

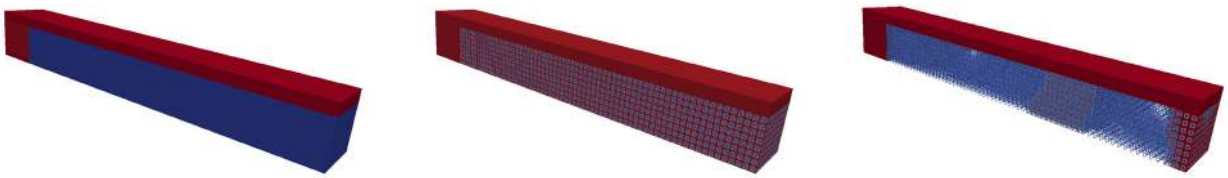

(a) (b) (c)

Figure 2: (a) Part (red) and support structure (blue), (b) minimal support structure with a spatially uniform density distribution, and (c) minimal support structure with a spatially varying density distribution.

In the second case, a spatially varying density distribution is adopted for the support structure; i.e. all unit cells are allowed to vary. In order to ensure manufacturability, the spatial variation of the densities (and hence the bar diameters) is limited by means of a density filter. The optimization problem is solved by means of the method of moving asymptotes. The resulting design is shown in figure 2c. The support structure now concentrates where the largest upward displacements are expected: a vertical strut emerges at the tip of the cantilever. In addition, a shear-resisting structure develops at about two-thirds of the length of the cantilever. This can probably be explained as follows: due to shrinkage of the cantilever, the vertical strut is subjected to bending, resulting in an elongation of its right hand side. This causes an upward displacement of the tip of the cantilever. The shear-resisting structure reduces the shrinkage of the cantilever and thus the upward displacement of the tip. For this design, only $11.6\,\%$ of the material needed is used to print the support structure, which is considerably less than for the spatially uniform design.

CONCLUSION

This paper presents a method for the optimal design of lattice support structures used in selective laser melting to reduce thermal deformations, and so to prevent recoater collisions. The lattice is modeled as a homogenized medium, and the temperature load by means of the inherent strain method. The optimization method leads to considerable material savings compared to a simple spatially uniform design. Future work will focus on the use of bar or beam elements to improve the accuracy of the lattice model and to allow for more design freedom, and on the design of support structures to prevent excessive thermal deformations in parts produced by stereolithography.

References

[1] M.C. Messner. Optimal lattice-structured materials. *Journal of the Mechanics and Physics of Solids*, 96:162–183, 2016.
[2] Y. Ueda, K. Fukuda, and M. Tanigawa. New measuring method of three dimensional residual stresses based on theory of inherent strain. *Transactions of JWRI*, 8(2):249–256, 1979.
[3] S. Watts, W. Arrighi, J. Kudo, D. A Tortorelli, and D.A. White. Simple, accurate surrogate models of the elastic response of three-dimensional open truss micro-architectures with applications to multiscale topology design. *Structural and Multidisciplinary Optimization*, 60(5):1887–1920, 2019.

ELECTROCHEMICAL HEALING OF CELLULAR METALS: IMPLICATIONS FOR MECHANICAL DESIGN AND OPTIMIZATION

Zakaria Hsain[1], Mostafa Akbari[2], Masoud Akbarzadeh[2], and James H. Pikul*[1]
[1]Department of Mechanical Engineering and Applied Mechanics, University of Pennsylvania, Pennsylvania, USA
[2]Polyhedral Structures Laboratory, Weitzman School of Design, University of Pennsylvania, Pennsylvania, USA

Summary Structural materials that can be healed enable new approaches, and remove old constraints, for engineering design and optimization. It has, however, been difficult to heal metal effectively, especially at room temperature and in geometrically complex parts where welding is not possible. This work explains how new advances in electrochemical healing of metal enables new design strategies, as demonstrated by the repair of complex 3-D printed metal parts whose internal geometry prevents repair using conventional technologies.

INTRODUCTION

Modern engineering design follows an approach where a part is optimized to withstand all future loading cases in the part's projected lifetime. This approach has been highly effective, but results in concepts like safety factors, which increase the weight and volume of the part beyond what's necessary in normal loading conditions. Most of this excess material is wasted in a part's lifetime. Additionally, this design approach makes it difficult to transfer parts between different use cases as defects and environmental changes can lead to premature failure. An alternative strategy, however, can be found in biology, such as in bone, where parts are efficiently produced to withstand most loading cases and, when an extreme case is encountered, the parts can be repaired without being replaced. Manmade structural materials that could heal like bone would have several advantages, including increased sustainability by reducing the part mass, which reduces associated CO_2 emissions and environmental pollutants, and by extending part service life, which reduces the need for complex recycling processes [1]. A major challenge, however, has been realizing structural metals that can be effectively healed without an expert (in the case of welding) or without high temperatures which consume lots of energy and degrade nearby materials.

Recently, we have demonstrated a new rapid, effective, low-energy, and room-temperature approach for healing cellular metals using electrochemistry and polymer-coated cellular nickel to mimic the transport-mediated healing of bone (Fig. 1) [2]. The polymer coating enabled selective healing only at the fracture site, electrochemical reactions transported metal ions from a metal source to fractured areas, and the open-cell structure of the metal allowed rapid ion transport to healing sites and effective recovery of strength and toughness when the cellular metal was subjected to scission fracture, tensile failure, and plastic deformation. Using this strategy, fractured samples recovered 100% of their tensile strength in as little as 10 and 4 hours of healing. This electrochemistry-based approach enabled the first demonstration of room-temperature healing of structural metallic materials and required several orders of magnitude less energy than many previously-reported metal healing techniques.

In this work, we will discuss the advantages of electrochemical healing of metals, new design strategies that emerge through the combined optimization of mechanics and electrochemical transport, and how this approach enables the repair of complex metal parts realized from 3-D printing whose internal geometry prevents repair using current technologies.

RESULTS AND DISCUSSION

Figure 1b illustrates our approach for healing cellular nickel at room temperature. First, we conformally coated 5 to 9 µm-thick films of Parylene D (an insulating polymer with excellent barrier properties and chemical stability) onto cellular nickel. The cellular nickel had 250 µm average diameter pores and 3% relative density. Figure 1c shows a fractured nickel strut after straining the cellular nickel in tension. The 10% failure strain of Parylene D was large enough so that only severely damaged nickel was exposed, but lower than the 23% failure strain of the nickel so that fractured nickel was not covered by polymer. Applying a negative potential (-1.8 V) to the fractured cellular nickel, relative to a nickel counter electrode, healed the sample by driving electrons through the conductive nickel to the fracture location and reducing nickel ions in the electrolyte to solid nickel. The open-cell pores enabled rapid ion transport to the fracture site. Nickel electrodeposited on both sides of the fractured strut grew until the growth fronts merged, forming a continuous strut (Figure 1d). Figure 1e shows the typical stress-strain data of Parylene-coated cellular nickel.

This healing strategy is especially effective for geometrically complex parts where conventional repair techniques, such as welding, are impossible due to the difficulty of accessing internal geometric components. Welding also requires high temperatures (~104 K) and consumes large amounts of energy (103 to 106 kJ per mm of crack length healed), which makes it difficult to use in composites with low melting point materials. Figure 2 shows a shellular part [3] designed using 3D optimization to only deform in tension and fabricated with an aluminum alloy using selective laser sintering (SLS). This part has internal surfaces that, if fractured, would be impossible to repair with welding. By applying our electrochemical healing approach to this material, we can repair internal and external fractured surfaces to 100% of their initial strength at room temperature and with low energy. Additionally, we demonstrate that tuning the fracture strain in the polymer coating can optimization healing efficiency.

*Corresponding author. E-mail: pikul@seas.upenn.edu.

CONCLUSIONS

This work is a step forward in optimizing the efficiency of electrochemical healing, as well as demonstrating its superiority over welding in healing geometrically complex metals. Future work will explore the intersection of structural design and electrochemical transport, so that parts can be optimized to achieve both high strength or modulus and fast transport properties so that the healing time and energy can be minimized.

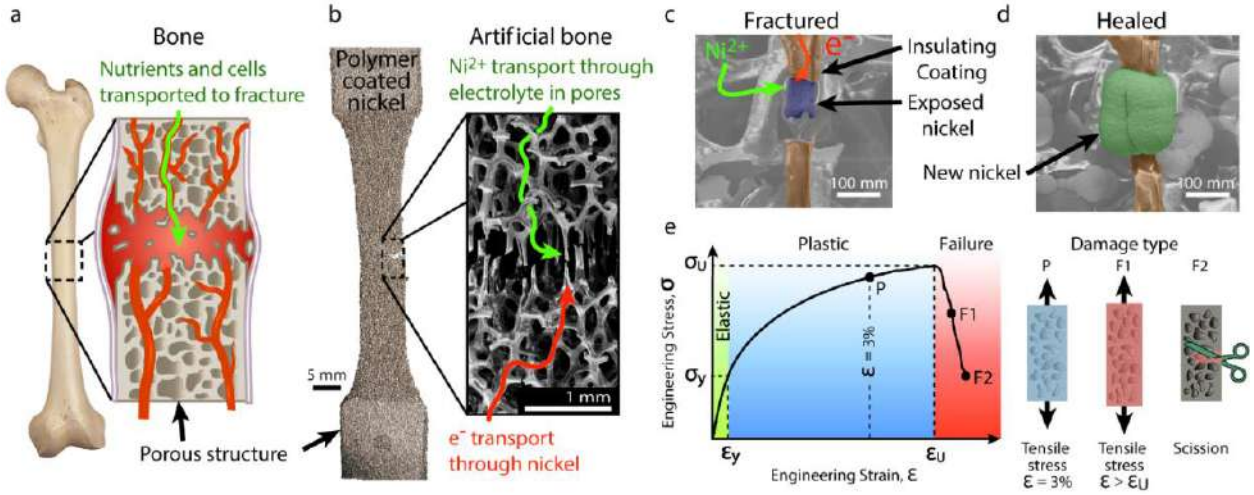

Figure 1. Transport-mediated healing in cellular metals inspired by bone. a) Illustration of hematoma formation during bone fracture. Healing occurs by transporting cells and nutrients through the cellular bone to the fracture location. b) Illustration of our transport-mediated approach for healing polymer-coated cellular nickel. Healing occurs by transporting electrons through the nickel and nickel ions through the electrolyte in the pores to the healing location. The nickel ions electrochemically reduce and new nickel is electrodeposited. c) SEM image of a fractured nickel strut. Exposed nickel and the plastic coating are false-colored with blue and brown, and the background brightened to highlight the strut. d) The same strut in (c) after healing. Electrodeposited nickel is false-colored green. e) Stress-strain data of a cellular nickel sample. We characterized the healing effectiveness of cellular nickel subjected to three damage types: plastic deformation at 3% strain (P), failure beyond the ultimate strain (F1), and local failure by scission (F2).

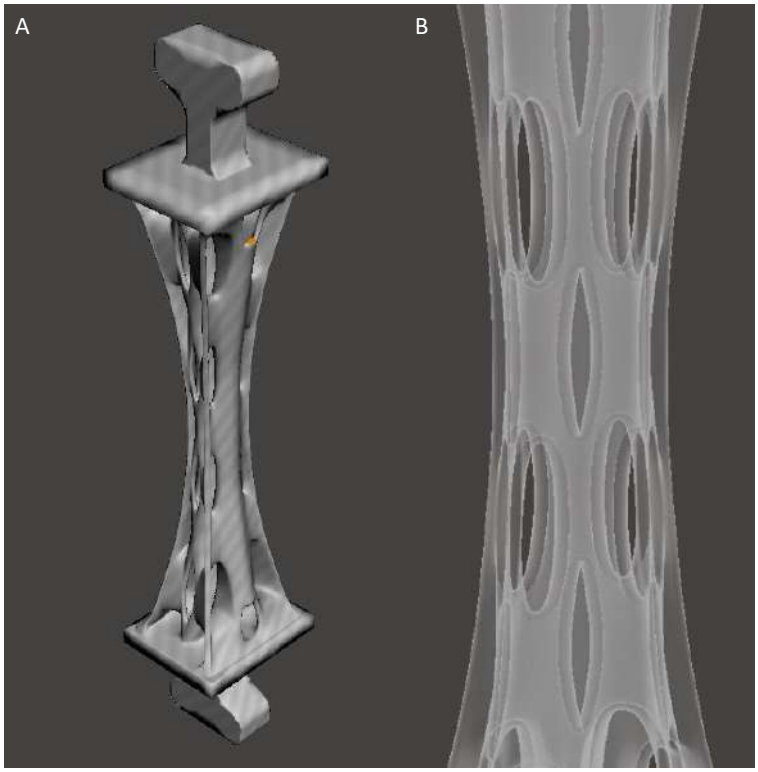

Figure 2. (A) Isomeric view of a 3-D part designed so that all members are strained in tension, without bending. (B) The model has a two-layer structure. A crack in the internal layer is not visible and cannot be healed by welding.

References

[1] Raabe D., Tasan C. C., Olivetti E. A., Strategies for improving the sustainability of structural metals. *Nature*. 575, 64–74, 2019.
[2] Hsain Z., Pikul J.H., Low - Energy Room - Temperature Healing of Cellular Metals. *Adv. Funct. Mater.* 29, 2019.
[3] Han S. C., Lee J. W., Kang K., A New Type of Low Density Material: Shellular. *Adv. Mater.* 27, 5506–5511, 2015.

TOPOLOGY OPTIMIZATION OF IMPERFECT LATTICE MATERIALS ADDITIVELY BUILT

Ahmed Moussa, David Melancon, Asma El Elmi, and Damiano Pasini*
Department of Mechanical Engineering, McGill University, Montreal, Canada

Summary Lattice materials built with current additive technology feature process-induced defects that impact their mechanical properties and optimum design. This work presents a methodology to integrate geometric defects in a gradient-based formulation for topology optimization of additively built lattice materials. The method is of general application, and it is here demonstrated through the application to the Octet-truss unit cell, called to satisfy specific geometric constraints. Validation is performed through the solution of the fixed-beam benchmark problem, assumed to consist of either defect-free or imperfect lattice materials. The results highlight the significance of accounting for geometric defects in topology optimization of additively built lattice materials.

INTRODUCTION

Lattice materials can be designed to feature a range of optimally tuned physical properties, such as stiffness to mass ratio, and mechanical biocompatibility, often superior to those of other existing solids. Once manufactured additively, however, their architecture can deviate from their nominal counterpart due to process-induced defects appearing in both the base material and geometry. The outcome is an undesired shift in mechanical properties [1, 2] and functional performance [3]. To date, however, the impact of additive manufacturing (AM) induced defects on the mechanics and optimized porosity gradient of porous materials has not been studied. This work unveils the role of a set of manufacturing defects and cell orientation on the elastic anisotropy of the unit cell, the optimized gradients of relative density, and the global compliance of optimally graded 3D lattices.

METHODOLOGY

We formulate a gradient-based topology optimization problem that integrates the homogenised properties of imperfect lattice materials. Additively manufactured lattice samples are μCT-reconstructed and morphologically characterized to attain the dispersion of a set of process-induced geometric defects including strut thickness variation and center axis deviation. Their probabilistic distribution is integrated into imperfect-architecture models that can parallel the behavior of as-manufactured lattices.

RESULTS

The geometric discrepancy as well as specific symmetry in elastic properties of the cell have a directional impact on the unit cell response, which also influences the optimized density distribution throughout the entire cellular domain. To capture the moduli dependency on cell orientation with respect to the building direction, Figure 1 illustrates three-dimensional and planar polar plots of the elastic modulus of an illustrative unit cell, the Octet-truss. The responses are given at a representative value of $\rho = 0.4$ (i.e. 60% porosity). Manufacturing defects lead to a shift in symmetry and reduction in elastic moduli of as-built architectures. In the planar plot of the Young's modulus, the maximum discrepancy in the x direction, $\Delta\left(E_{xx}/E_s\right)_{\max}$ between as-designed (nominal) and imperfect models is 25% at 45 degrees rotation angle around z-axis. The impact of these defects can be now integrated into the topology optimization of lattice materials in a benchmark problem.

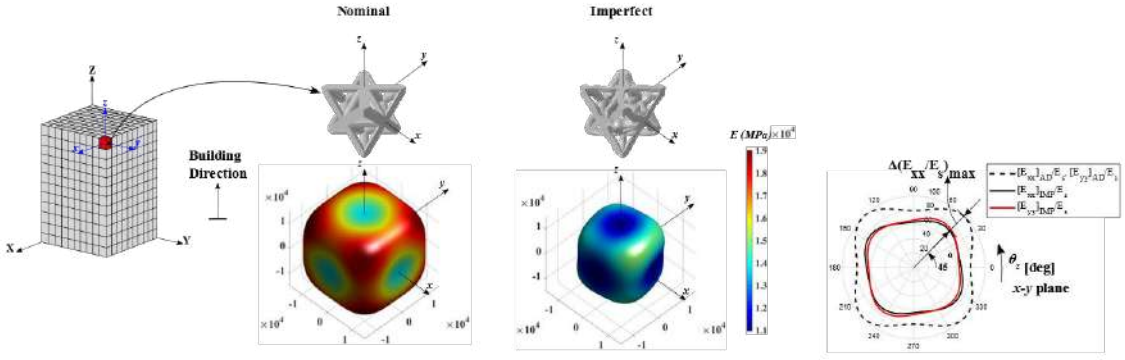

Figure 1. 3D polar plots of Young's moduli, and 2D polar plot of the normalized Young's moduli along *x* and *y* axes at different unit cell orientations, of as-designed and imperfect models, at relative density $\rho = 0.4$.

Figure 2a shows the design domain (L= 6 mm), boundary conditions, and external loads (vertical distributed load F= 1500 N). Heat treated Ti6Al4V alloy (E_s=114 GPa, Poisson's ratio υ_s= 0.342) is used as base material. A design variable filter is applied with a filter radius of 1.5 times the element size. The optimization problem is solved for minimum compliance until convergence is reached for prescribed volume fraction V^*=39% of the solid material. The upper and

*Corresponding author. E-mail: damiano.pasini@mcgill.ca.

lower bounds of the design variable, ρ, are selected as $0.28 \le \rho \le 0.5$, to satisfy manufacturing and pore size constraints here selected in continuity with a previous work [4]. To reduce the computational cost, the effective properties (Figure 1) for both the defect-free and imperfect geometries are used during the optimization process.

Two cell orientations are examined, at rotation angles 0 (top) along the build direction and 45 degrees (bottom) around z-axis. The latter is chosen as a representative value to show the sensitivity to imperfections; in this case it represents the maximum discrepancy in Young's modulus (Figure 1) along the *x* direction ($\Delta\left(E_{xx}/E_s\right)_{\max} = 25\%$). The discrepancy in elastic properties appears in all orientations and along given directions. For example, along the building direction there is approximately 14% difference in Young's modulus E_{xx}, between as-designed (Figure 2b) and imperfect (Figure 2c) models. At both cell orientations, dissimilar relative density distributions are found. For the imperfect models, lower porosity is noticed in the middle region of the fixed beams. In terms of compliance, the imperfect models are typically less stiff than their as-designed counterparts. Their compliance is 32% and 52% higher at unit cell orientations of 0 and 45 degrees respectively. By analyzing the as-designed models at the two cell orientations, we can notice that the density distribution is equivalent with compliance 15% higher at 0 degrees. This result is due to the stiffness of the unit cells at 45 degrees, which is 20% higher than those oriented along the build direction. For the imperfect models, the change in compliance and density distribution is mild. This can be attributed to the small discrepancy present in the elastic modulus between the two orientations ($\Delta\left(E_{xx}/E_s\right) = 6\%$). Process-induced defects also influence the optimized material distribution. Manufacturing defects, which are strongly dependent on the strut orientation [5], are different for both rotation angles. Hence, they alter the density distribution over the fixed beam.

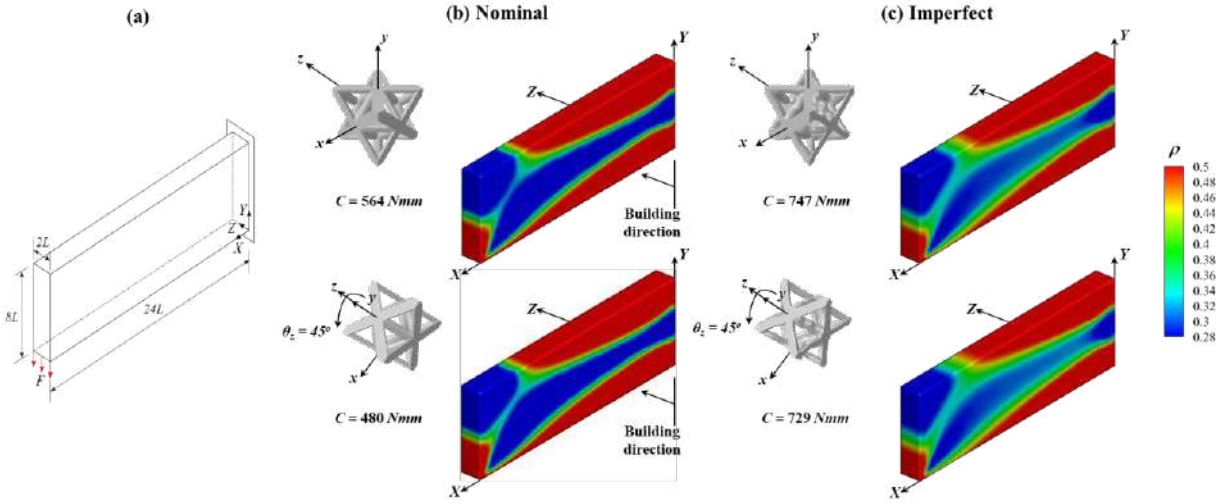

Figure 2. Design domain, boundary conditions, and external loads (a); and optimized relative density distribution for the fixed-beam benchmark problem, of nominal (b) versus imperfect (c) models using the Octet-truss topology. Top: unit cells rotated with an angle 0º, and bottom: unit cells rotated with an angle 45º around the z-axis.

CONCLUSIONS

This work has presented a general framework to assess the role of geometric imperfections on the mechanics and topology optimization of additively built lattice materials. The results have shown the role of cell orientation and manufacturing defects, which impart unit cell anisotropy and impact mechanical properties. As per the influence on the compliance and optimized relative density distribution, the difference within the design domain is shown to be proportional to the discrepancy in elastic properties between as-built and defect-free microarchitecture. The results emphasize the importance of including process-induced defects during the design process, since doing so gives a more realistic assessment of their structural performance.

References

1. Liu, L., P. Kamm, F. García-Moreno, J. Banhart, and D. Pasini, *Elastic and failure response of imperfect three-dimensional metallic lattices: the role of geometric defects induced by Selective Laser Melting.* Journal of the Mechanics and Physics of Solids, 2017. 107: p. 160-184.
2. Wang, P., H. Lei, X. Zhu, H. Chen, and D. Fang, *Influence of manufacturing geometric defects on the mechanical properties of AlSi10Mg alloy fabricated by selective laser melting.* Journal of Alloys and Compounds, 2019.
3. Zhao, L., S. Ha, K.W. Sharp, A.B. Geltmacher, R.W. Fonda, A.H. Kinsey, Y. Zhang, S.M. Ryan, D. Erdeniz, D.C. Dunand, K.J. Hemker, J.K. Guest, and T.P. Weihs, *Permeability measurements and modeling of topology-optimized metallic 3-D woven lattices.* Acta Materialia, 2014. 81: p. 326-336.
4. Melancon, D., Z. Bagheri, R. Johnston, L. Liu, M. Tanzer, and D. Pasini, *Mechanical characterization of structurally porous biomaterials built via additive manufacturing: experiments, predictive models, and design maps for load-bearing bone replacement implants.* Acta Biomaterialia, 2017.
5. Bagheri, Z.S., D. Melancon, L. Liu, R.B. Johnston, and D. Pasini, *Compensation strategy to reduce geometry and mechanics mismatches in porous biomaterials built with Selective Laser Melting.* Journal of the Mechanical Behavior of Biomedical Materials, 2017. 70: p. 17-27.

BIONIAMOTO – THE EFFICIENT NUMERICAL PLATFORM FOR SHAPE AND TOPOLOGY OPTIMIZATION

Michał Nowak *[1], Jan Polak [1]
[1]Department of Virtual Engineering, Poznan University of Technology, Poznan, Poland

Summary The BioniAMoto project based on ideas proven to work in Cosmoprojector software will be presented. It utilizes biomimetic structural optimization algorithm based on trabecular bone remodeling phenomenon. Instead of imposing volume constraint the shapes can be parametrized by the assumed value of the strain energy density. The functional configurations during the process of optimization allows to include size, shape and topology optimization in one numerical procedure. Technically BioniAMoto platform is .Net/C# project designed with Inversion of Control design pattern that provides numerical environment for efficient shape and topology optimization for industrial problems.

INTRODUCTION

The BioniAMoto project is based on ideas proven to work in Cosmoprojector software. It utilizes biomimetic structural optimization algorithm based on trabecular bone remodeling phenomenon. The stiffest design is obtained by adding or removal of material on the structural surface. The assumed value of the strain energy density on the part of the boundary subjected to modification, unlike other topology optimization systems, could be related to the material properties. Change in the assumed value of the strain energy density results in change of the structural form. Instead of imposing volume constraint the shapes can be parametrized by the assumed value of the strain energy density [1].

SHAPE AND TOPOLOGY OPTIMIZATION METHOD BASED ON STRUCTURAL SURFACE MODIFICATION

Due to unique approach to the shape and topology optimization problem, the application has unique features, exceeding existing software on the commercial market. Such features – see Fig.1. - include independence from the design domain, different optimization results for different materials, possible solution of multiple load problem or simultaneous optimisation of size, shape and topology [3].

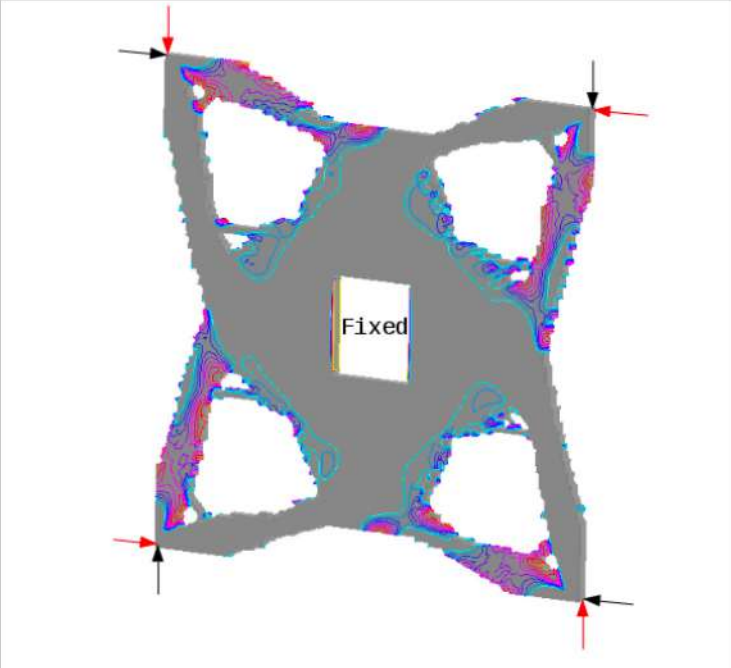

Figure 1. Example of the simultaneous optimization of the shape and topology with use of the presented biomimetic method for multiple load problem. Results are identical to analytical solution [3] (black and red arrows – two different load cases – all loads are of the same magnitude).

Actually BioniAMoto is both growth simulation tool and topological optimization system - the system is based on ideas proven to work in Cosmoprojector software (http://www.cosmoprojector.eu/). It utilizes biomimetic algorithm to optimize shape of input structure using the principles based on bone remodeling phenomenon. Also the bone remodeling process can be simulated for real trabecular structures.

1*Corresponding author. E-mail: Michal.Nowak@put.poznan.pl.

THE EFFICIENT NUMERICAL PLATFORM FOR SHAPE AND TOPOLOGY OPTIMIZATION

In this proven to work approach each iteration of Finite Element Method engine is used to calculate structural strain energy distribution, remodeling (structural evolution) rule is applied and new mesh is constructed. The presented implementation of the BioniAMoto structural optimization system exploits Message Passing Interface support for massive computation. Internally system operates on slices – stack of equally spaced cross-sections of analysed geometry. Application analyzes each slice independently and applies the remodeling rule. Such approach allows to analyze single slice and its neighborhood using small scale and high accuracy approach and then move back to large scale with less details to run structural strain energy distribution calculation. Technically BioniAMoto is .Net/C# project designed with Inversion of Control paradigm design pattern that provides pluggable and extensible platform for both industrial and R&D multi-scale shape and topology optimization. All steps of algorithm are executed by separate components and each can be replaced by custom implementation – see Fig.2. The code uses reactive data flow and is optimized for multithreaded operations.

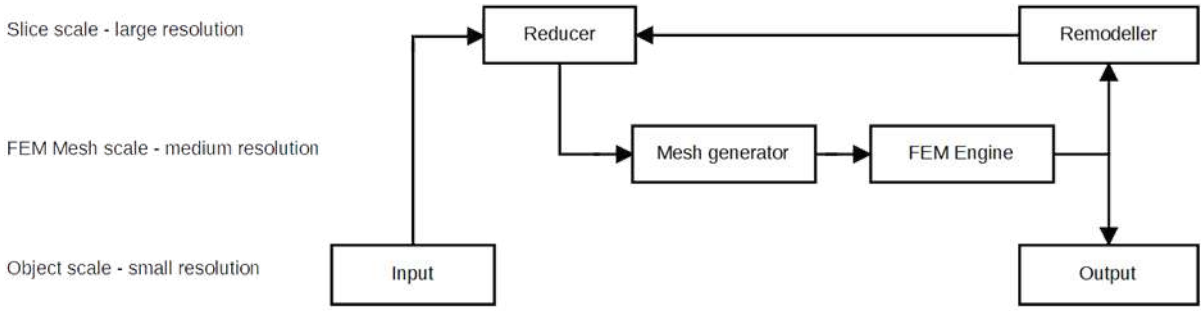

Figure 2. Components of BioniAMoto processing pipeline.

The structural evolution is separated from the Finite Element Method computations and modeled with slices, 2-dimensional images. Each iteration FEM engine is used to calculate stress, remodeling is applied on large resolution model, scale is reduced and new mesh is constructed. FEM engine used for stress calculation is external application, called by BioniAMoto system. Baseline mesh generator creates mesh consisting of tetrahedral elements. Generator was designed to create smooth surfaces to avoid introducing artefacts such as stress concentration at sharp edges. It generates both volume and surface data. Mappings between slices and mesh are maintained so it is possible to find pixels in slices corresponding to mesh points and vice-versa. Multi-scale approach combines precise remodeling on high resolution model with fast structural strain energy distribution calculations with reduced resolution.

CONCLUSIONS

The assumed value of the strain energy density on the part of the boundary subject to modification could be related to the material properties. Change in the assumed value of the strain energy density results in change of the structural form - topology and volume. In this way, the final structural volume results from the optimization procedure. Instead of imposing volume constraint shapes are parametrize by the assumed energy density, which may be quite accurately predicted from the yield criteria. Due to the use of the specific biomimetic approach, the system is particularly suitable for effectively solving the multiple load problem optimization tasks. Project is based on .Net/C# framework, uses multi-scale approach and is optimized for multi-threaded operations. Therefore the structural optimization system is suitable for large problems.

ACKNOWLEDGMENTS

This work was supported by the Polish National Centre for Research and Development under the grant - decision no. DWP/TECHMATSTRATEG-III/136/2020.

References

[1] Nowak M., Sokołowski J., Żochowski A., Justification of a certain algorithm for shape optimization in 3D elasticity, *Struct Multidiscipl Optim.* **57/2**: 721-734, https://doi.org/10.1007/s00158-017-1780-7, 2018.

[2] Rozvany G., Exact analytical solutions for some popular benchmark problems in topology optimization, *Structural optimization.* **15**: 42–48, 1998.

[3] Nowak M., Sokołowski J., Żochowski A., Biomimetic Approach to Compliance Optimization and Multiple Load Cases, *J Optim Theory Appl.* **184**: 210–225, https://doi.org/10.1007/s10957-019-01502-1, 2020.

LEVEL SET TOPOLOGY OPTIMIZATION FOR FLUID-STRUCTURE INTERACTIONS

Andreas Neofytou* [1], Feimi Yu[2], Lucy T. Zhang[2], Jiun-Shyan Chen[3], and H. Alicia Kim[1, 3]
[1]Cardiff School of Engineering, Cardiff University, Cardiff, CF24 3AA, United Kingdom
[2]Department of Mechanical Aerospace and Nuclear Engineering, Rensselaer Polytechnic Institute, Troy, NY, 12180, USA
[3]Structural Engineering Department, University of California San Diego, CA 92093, USA

Summary Topology optimization in a multiphysics environment, e.g. fluid-structure interactions (FSI), poses significant numerical challenges. In this work a level set topology optimization (LSTO) approach is combined with a minimally-intrusive FSI algorithm, the modified immersed finite element method (mIFEM). For the analysis of the solid domain the reproducing kernel particle method (RKPM) is used with the naturally stabilized nodal integration technique (NSNI) for the domain integration. Test cases for flows with a range of Reynolds numbers will be presented in both linear and non-linear problems.

LEVEL SET TOPOLOGY OPTIMIZATION

In the level set topology optimization (LSTO), the structural boundary is defined as the zero level set of an implicit function:

$$\begin{cases} \phi(\mathbf{x}) \geq 0 & \mathbf{x} \in \Omega \\ \phi(\mathbf{x}) = 0 & \mathbf{x} \in \Gamma \\ \phi(\mathbf{x}) < 0 & \mathbf{x} \notin \Omega \end{cases} \tag{1}$$

where ϕ is the level set function, Ω is the structural domain and Γ is the structural boundary. Conventionally, the implicit function is initialized as a signed distance function.

The structural boundary is optimized by iteratively solving the following Hamilton-Jacobi equation

$$\frac{\partial \phi(\mathbf{x}, t)}{\partial t} + |\nabla \phi(\mathbf{x})| \, V_n(\mathbf{x}) = 0 \tag{2}$$

where t is a fictitious time domain for the level set evolution and V_n is the normal velocity.

The velocities required for the level set update are obtained by solving the linearized optimization problem. Details of the level set method can be found in [1]. Key features of the methodology proposed in this paper include the ability to handle multiple constraints in the Hamilton-Jacobi equation based level-set topology optimization method, discretized boundary integrals to estimate function changes and the formulation of an optimization sub-problem to attain the velocity function. This velocity function sub-problem is formulated as a linear program (LP). This level set topology optimization method has been used in the past to solve a variety of problems including stress constraints, aero-elasticity considerations, non-linear thermoelasticity and multiscale material modelling.

REPRODUCING KERNEL PARTICLE METHOD

For the solid domain, the Reproducing Kernel Particle Method (RKPM) [2], is used due to its ability to handle the geometrical changes during the optimization procedure and also large structural deformations without the problems caused by re-meshing as in the finite element method. RKPM is a Galerkin type meshfree method based on the reproducing kernel approximation. For the construction of the approximation no mesh is required. The RK shape function can be expressed as:

$$\Psi = \mathbf{H}^{\mathrm{T}}(\mathbf{0})\mathbf{M}^{-1}(\mathbf{x})\mathbf{H}(\mathbf{x} - \mathbf{x}_I)\mathbf{\Phi}_\alpha(\mathbf{x} - \mathbf{x}_I) \tag{3}$$

where $\mathbf{M}(\mathbf{x}) = \sum_{I=1}^{NP} \mathbf{H}(\mathbf{x} - \mathbf{x_I})\mathbf{H^T}(\mathbf{x} - \mathbf{x_I})\mathbf{\Phi}_\alpha(\mathbf{x} - \mathbf{x_I})$ is the moment matrix and NP is the number of points used in the discretization of the problem domain. $\mathbf{H}(\mathbf{x} - \mathbf{x_I})$ is the vector of monomial basis functions. $\Phi_\alpha(\mathbf{x} - \mathbf{x}_I)$ is the kernel function centered $\mathrm{x_I}$ with support size α. The kernel function controls the locality and smoothness of the approximation, and it is chosen to be the cubic spline function in this work.

*Corresponding author. E-mail: NeofytouA@Cardiff.ac.uk

For a Galerkin type meshfree method domain integration is required. Such a domain integration can be performed either using Gauss quadrature on a background mesh or using nodal integration. In this work, the later approach is adopted. Specifically, the naturally stabilized nodal integration (NSNI) is employed here since it has been shown to overcome the problems associated with direct nodal integration has good computational efficiency and accuracy. An illustration of the capability of RKPM to handle the topological changes within the level set topology optimization framework is shown in Fig. 1 where the objective is to minimize compliance under a volume constraint. In this example a beam is placed within a pressure field governed by the Laplace equation. One-way coupling is achieved by first solving for the pressure and then applying the resulting pressure field on the structural surface to solve for the structure.

(a) (b)

Figure 1: Compliance minimization for leaflet example: (a) Problem definition and (b) Optimum solution

This paper extends this idea into viscous flow, by combining LSTO-RKPM with the modified immersed finite element method.

MODIFIED IMMERSED FINITE ELEMENT METHOD

In conventional immersed methods including the immersed finite element method, the solid displacement is imposed from the fluid velocity rather than being solved from its own governing equations. This may lead to severe solid mesh distortion resulting in the overestimation of the solid deformation especially for high Reynolds number flows. The modified immersed finite element method (mIFEM) [3] changes the formulation so that the imposition of the velocity is reversed. The solid dynamics is solved using its own governing equations and its velocity is imposed onto its overlapping fluid domain. This preserves the solid dynamics and provides more accurate and realistic coupled solutions. An important advantage of the mIFEM is that it allows modularity in the solvers. The interactions between the solid and the fluid are reflected as tractions on the solid boundary, body force and no-slip boundary conditions in the artificial fluid region making the information exchange between the fluid and the solid rather straightforward because the fluid/solid solvers are interfaced to apply Neumann and Dirichlet boundary conditions. The open-source, high performance software OpenIFEM [4] is used in this work for mIFEM.

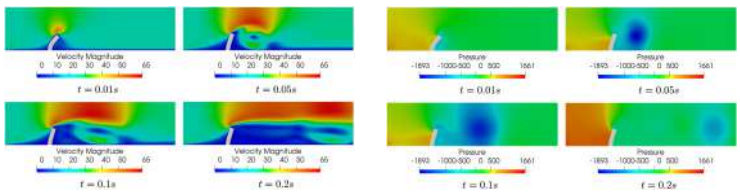

(a) (b)

Figure 2: Leaflet example with OpenIFEM (No optimization): (a) Velocity magnitude in cm/s with contours at different time and (b) Pressure field in $dyne/cm^2$ at different time.

One of the main challenges in topology optimization for FSI is to track the interface. The implicit boundary representation in LSTO can be advantageous for this class of problems. The immersed finite element formulation employs an Eulerian background fluid and in combination with LSTO can provide a framework for solving FSI problems without remeshing for the fluid and the difficulties associated with it. The Lagrangian solid domain sits on top of the fluid. Since the structure continuously changes throughout the optimization process, remeshing for the solid becomes a cumbersome task and the difficulty grows if large deformation problems are to be considered. RKPM is used for the solid in this work, to straightforwardly handle the topological changes. The proposed bridging of the LSTO, mIFEM and RKPM enables the accurate topology optimization in a multiphysics environment and sets the framework for structural topology designs in various multiphysics environments.

References

[1] L O Hedges, H A Kim, and R L Jack. Stochastic level-set method for shape optimisation. *Journal of Computational Physics*, 348:82–107, 2017.
[2] W K Liu, S Jun, and Y F Zhang. Reproducing kernel particle methods. *International Journal for Numerical Methods in Fluids*, 20:1081 – 1106, 1995.
[3] X Wang and L T Zhang. Modified immersed finite element method for fully-coupled fluid–structure interactions. *Comput. Methods Appl. Mech. Engrg.*, 267:150–169, 2013.
[4] J Cheng, F Yu, and L T Zhang. Openifem: A high performance modular open-source software of the immersed finite element method for fluid-structure interactions. *CMES*, 119(1):91–124, 2019.

STRUCTURAL OPTIMIZATION OF ELASTO-PLASTIC FRICTIONAL CONTACT PROBLEMS

Andrzej Myśliński * [1]
[1]Systems Research Institute, Warsaw, Poland

Summary The paper is concerned with the analysis and solution of the shape optimization problems for elasto–plastic rather than elastic structures in bilateral frictional contact with a rigid foundation. The small strain plasticity model with linear hardening and a von Mises effective stress is used. The displacement and stress of this structure are governed by the system of coupled variational inequalities. Using the regularization this original contact problem is replaced by the system of nonlinear equations. The structural optimization problem consists in finding such shape of the domain occupied by the body in contact or its material distribution to minimize the contact stress. The material derivative framework is used to calculate the shape derivative of the cost functional. Generalized Newton as well as the level set method are used to solve numerically the structural optimization problem. The results of computations indicate that the proposed approach generates minimal contact stress topologies.

STRUCTURAL OPTIMIZATION PROBLEM

Consider deformations of an elastic body occupying two–dimensional domain Ω with the smooth boundary Γ [9]. The body is subject to body forces $\mathbf{f}_1(x) = (f_1^1(x), f_2^1(x))$, $x \in \Omega$. The boundary Γ of domain Ω is split into three mutually disjoint parts such that $\Gamma = \bar{\Gamma}_1 \cup \bar{\Gamma}_2 \cup \bar{\Gamma}_3$, $\Gamma_i \cap \Gamma_j = \emptyset$, $i \neq j$, $i,j = 1,2,3$. The body is clamped along the portion Γ_1 of the boundary Γ. The surface tractions $\mathbf{f}_2(x) = (f_1^2(x), f_2^2(x))$, $x \in \Gamma$, are applied on a portion Γ_2 of the boundary Γ. The contact conditions with Tresca friction are prescribed on the portion Γ_3 of the boundary Γ. The domain Ω is filled with a material undergoing elasto-plastic deformation. In the elastic range it obeys Hooke's law [1] governed by a fourth-order tensor $C = (C_{ijkl}(x))$, $i,j,k,l = 1,...2$, $C_{ijkl}(x)$ such that, for any symmetric matrix ζ, $C : \zeta = 2\lambda\zeta + \mu tr(\zeta)\mathbf{I}_d$, where λ and μ are the Lamé constants. Let us also introduce the Cauchy stress tensor σ and the linearized strain tensor $\epsilon(\mathbf{u})$ [1], respectively: $\sigma = \sigma(\mathbf{u}) = \{\sigma_{ij}\}_{i,j=1}^2$ and $\epsilon = \epsilon(\mathbf{u}) = \frac{1}{2}(u_{i,j} + u_{j,i})$ $u_{i,j} = \frac{\partial u_i}{\partial x_j}$, $i,j = 1,...,2$. The summation convention over repeated indices [1] is used throughout the paper. We assume the plastic deformation of the material is governed by the additive small strain plasticity model [1]. In this model the material strain ϵ is sum of the elastic strain ϵ^e and the plastic strain ϵ^p, i.e., $\epsilon(\mathbf{u}) = \epsilon^e(\mathbf{u}) + \epsilon^p(\mathbf{u})$, and the stress tensor satisfies $\sigma(\mathbf{u}) = C : \epsilon^e(\mathbf{u}) = C : (\epsilon(\mathbf{u}) - \epsilon^p(\mathbf{u}))$, and $\epsilon(\mathbf{u}) = C^{-1} : \sigma(\mathbf{u}) + \epsilon^p(\mathbf{u})$.

Under the loading of volume or boundary forces $\mathbf{f}_1$ and $\mathbf{f}_2$ the body material undergoes the deformation. The plastic deformation with the hardening phenomenon is governed by the generalized plastic strain (ϵ^p, ξ) and the generalized stresses (σ, χ). The back stress χ and the internal variable ξ are related in Ω by [1] $\chi = -H : \xi$ where H denotes the hardening tensor. The generalized plastic stress may take values only in a nonempty closed convex set $\mathcal{K}$ of admissible generalized stresses. For a given yield function φ this set is defined as [1] $\mathcal{K} = \{(\sigma, \chi) : \varphi(\sigma, \chi) \leq 0\}$ The evolution of the plastic strain ϵ^p and the internal variable ξ is governed by the associative flow rule [1] stating that the increments $d\epsilon^p$ and $d\xi$ of the plastic strain and the internal variable, respectively, belong to the normal cone N_K to the set K at a point (σ, χ). For the smooth yield function φ it implies the existence of the nonnegative scalar γ and the Kuhn-Tucker complementarity conditions relating γ and the function φ [1]

$$(d\epsilon^p, d\xi) = \gamma \nabla \varphi(\sigma, \chi), \quad \text{and} \quad \gamma \geq 0, \quad \varphi(\sigma, \chi) \leq 0, \quad \gamma\varphi(\sigma, \chi) = 0. \tag{1}$$

The flow rule can also be described using maximal plastic work principle for the generalized stresses [1]. We shall consider the following contact problem: find the generalized stress field (σ, χ), the displacement field $\mathbf{u}$, the generalized strain field (ϵ^p, ξ) satisfying the plasticity condition (1) as well as

$$\text{div}\sigma + \mathbf{f}_1 = 0 \ \text{ in } \ \Omega, \quad \text{div}(\sigma) = \{\sigma_{ij,j}\}, \quad \sigma_{ij,j} = \frac{\partial \sigma_{ij}}{\partial x_j}, \quad i,j = 1,...,2, \tag{2}$$

$$\mathbf{u} = 0 \ \text{ on } \ \Gamma_1 \ \text{ and } \ \sigma_\nu = \mathbf{f}_2 \ \text{ on } \ \Gamma_2, \mathbf{u}_\nu = 0, \ \mid \sigma_\tau \mid \leq \mu_f \tilde{p} \ \text{ on } \ \Gamma_3, \tag{3}$$

$$\mid \sigma_\tau \mid \ < \ \mu_f \tilde{p} \ \Rightarrow \ d\mathbf{u}_\tau = 0 \quad \mid \sigma_\tau \mid \ = \ \mu_f \tilde{p} \ \Rightarrow \ \exists \lambda \geq 0, \ d\mathbf{u}_\tau = -\lambda \sigma_\tau \ \text{ on } \ \Gamma_3. \tag{4}$$

For the unit outward normal vector ν to the boundary Γ normal and tangential components of the displacement field $\mathbf{u}$ (stress σ) are denoted by $\mathbf{u}_\nu$ (σ_ν), and by $\mathbf{u}_\tau$ (σ_τ), respectively. A real constant $\mu_f > 0$ and $\mid \cdot \mid$ denote the friction coefficient and the Euclidean norm, respectively. For a given $\tilde{p} \geq 0$ system (1)-(4) governs the elasto - plastic bilateral contact problem with Tresca friction. Let us introduce the set U_{ad} of admissible domains. This set has the form: $U_{ad} = \{\Omega \ : \Omega \subset D \subset R^2 \ : \ \Omega \text{ is suitable regular, } Vol(\Omega) - Vol^{giv} \leq 0, \ P_D(\Omega) \leq const_1\}$ where $Vol(\Omega) = \int_\Omega dx$ and $P_D(\Omega) = \int_\Gamma dx$. The subset D as well as constants $Vol^{giv}, const_1 > 0$ are given. The set U_{ad} is assumed to be nonempty. Consider the following structural optimization problem: *for a given function* $\eta \in M^{st}$, *find a domain* $\Omega^\star \in U_{ad}$ *such that*

$$J_\eta(\mathbf{u}(\Omega^\star)) = \min_{\Omega \in U_{ad}} J_\eta(\mathbf{u}(\Omega)) \ \text{ where } \ J_\eta(\mathbf{u}(\Omega)) = \int_{\Gamma_2} \sigma_\nu(u)\eta_\nu(x)ds. \tag{5}$$

*Corresponding author. E-mail: myslinsk@ibspan.waw.pl

The set $M^{st} = \{\eta = (\eta_1, \eta_2) : \eta_i \leq 0 \text{ on } D,\ i = 1, 2\}$ and the functional $J_\eta(\cdot)$ approximates the normal contact stress [2, 3]. Structural optimization of elasto-plastic structures has been investigated among others in [4, 5]. Here this approach is extended for elasto-plastic contact problems with friction. For topology optimization of elastic contact problems see [2, 6].

PROBLEM REGULARIZATION

The contact problem (1)–(4) is reformulated in terms of (u, σ, χ) only as a system of two coupled nonlinear equations using von Mises yield function, the regularization of the generalized stress projection on the set of admissible stresses as well as the regularization of friction functional [2, 6, 7]. Shape derivative of the functional (5) with respect to domain perturbation is calculated and the necessary optimality condition is formulated [2, 7].

NUMERICAL IMPLEMENTATION AND RESULTS

Both the state and the adjoint boundary value problems are discretized using bilinear quadrangular finite elements. Ersatz material approach [7] is used to avoid meshing problems with the shapes of domains Ω and singularity of the stiffness matrix. This approach consists in filling the domain $D \setminus \Omega$ with a weak material characterized by law value of Young modulus and mimicking void. The discretized state and adjoint equations are solved numerically using generalized Newton method [2, 7]. Level set method [2, 7, 8, 9] is used to track the domain evolution and find the optimal topology. Fig. 1 presents the optimal domain obtained by solving structural optimization problem (5) in the computational domain D. In a case of elasto-plastic materials the mass of the structure is larger than in a case of elastic model. The algorithm tries to avoid the generation of plastic zones which are less rigid and induce larger displacements. Von Mises effective stress concentration areas appear close to the contact zone (Fig. 2). The obtained normal contact stress is almost constant along the optimal shape boundary and has been significantly reduced comparing to the initial one. The distribution of stresses in elastic and elasto-plastic cases is provided and discussed.

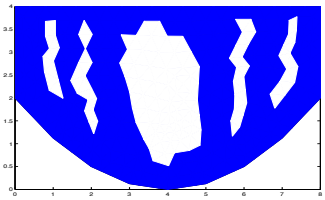

Figure 1: Optimal topology domain $\Omega^\star$.

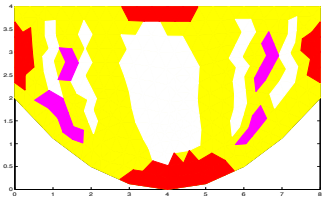

Figure 2: von Mises stress distribution.

CONCLUSION

The obtained results indicate that presented approach based on the application of the level set technique can be applied to solve numerically a topology optimization problem for bodies in bilateral frictional contact where nonlinear small strain elasto-plastic with linear kinematic hardening material model rather than elastic material model is used. It allows to formulate necessary optimality conditions for this type of nonlinear problems and it is capable of finding topologies that generates minimum contact stress. This approach is flexible and can be extended to solve other shape or topology optimization problems for structures governed by nonlinear equations.

References

[1] Han W., Reddy B.D. Plasticity. Mathematical Theory and Numerical Analysis. 2nd edition, Springer, New York 2013.
[2] Myśliński A. Piecewise Constant Level Set Method for Topology Optimization of Unilateral Contact Problems. *Advances in Engineering Software*. **80**:25-32, 2015.
[3] Myśliński A., Wróblewski M. Structural optimization of contact problems using Cahn-Hilliard model. *Computers & Structures*. **180**:52-59, 2017.
[4] Wallin M., Jonsson V., Wingren E. Topology optimization based on finite strain plasticity. *Struct. Multidisc. Optim*. **54**:783-793, 2016.
[5] Werner S., Stingl M., Leugering G. Model-based control of dynamic frictional contact problems using the example of hot rolling. *Comput. Methods Appl. Mech. Engrg*. **319**:442-471, 2017.
[6] De los Reyes J. C. On the optimal control of some nonsmooth distributed parameter systems arising in mechanics. *GAMM-Mitt*. **40**:268-286, 2017.
[7] Maury A., Allaire G., Jouve F. Elasto-plastic shape optimization using the level set method. *SIAM J. on Control Optim*. **56**: 556–581, 2018.
[8] Osher S., Fedkiw R. Level set methods and dynamic implicit surfaces. Springer-Verlag, New York 2003.
[9] van Dijk N.P., Maute K., Langlaar M., van Keulen F. Level-set methods for structural topology optimization: a review. *Struct. Multidisc Optim*. **48**: 437-472, 2013.

RELIABILITY-BASED APPROCHES FOR TOPOLOGY OPTIMIZATION OF ELASTOPLASTIC STRUCTURES

János Lógó *[1], Piotr Tauzowski [2], Bartlomiej Blachowski [2] and Hussien Ismail[1]
[1]Department of Structural Mechanics, Budapest University of Technology and Economics, Hungary
[2]Institute of Fundamental Technological Research, Polish Academy of Sciences, Poland

Summary Plasticity in topology optimization is almost forgotten direction in this popular research area. This paper presents a recently developed elasto-plastic topology optimization procedure extended with reliability constraint. It recalls fundamental concepts from reliability analysis and introduces an algorithm for topology optimization of elasto-plastic structures. In addition to the elasto-plastic constitutive law of the applied material the optimization algorithm includes stress constraints, as well. The presented numerical examples show dependence of the volume fraction on probability of failure.

INTRODUCTION

An important aspect of any optimization process is robustness to variability of structural parameters, either structural (geometry, material) or boundary condition (loading, support location) dependent. The more the structure becomes optimal, the lower the resistance to its parameter changes. One of the possible ways to tackle this issue is to add to the optimization formulation an additional constraint for the probability of failure [2, 5]. The designer will then assure that the optimized structure does not go below the assumed safety level. Since the probability of failure of engineering structures must be small (approximately 0.0001 or smaller), it is possible to obtain a relatively fast estimation of reliability by using first or second order methods [4, 9] or different simulation procedures. Most often, several iterations (finite element solutions) are enough to obtain convergence. Recent advances in probability/reliability based topology problems have been presented in papers by Guest et al. [3] Luo et al. [7], Xia et al. [11], da Silva et al. [8]. The authors of this paper have also several papers in this topic for more than a decade (Logo et al. [5, 6], Blachowski et al. [2]).

Topology optimization is a rather time consuming and discretization dependent computational problem. Due to the complexity of the task it is fundamental to use appropriate topology optimization procedure (Antonietti et al. [1]). In the present paper an iterative topology optimization algorithm together with elasto-plastic material formulation and reliability approach will be shortly described. The formulation based on a recently developed functor-oriented optimization procedure (Tauzowski et al. [10]). Analysis of elasto-plastic structure will be presented on numerical example. All aspects of numerical analysis, finite element formulation, topology optimization as well as reliability analysis library are performed by our own software implemented in MATLAB and C++.

RELIABILITY BASED TOPOLOGY OPTIMIZATION APPROACH

In the case of probabilistic topology optimization random variables vector $\mathbf{r}$ can represent loads or material constants. Shape of the structure is a result of topology optimization therefore random nature of shape parameter is not taken into consideration. In the following the formulation of the elasto-plastic problem of structural analysis as well as the detailed description of the algorithm for topology optimization under reliability constraint is presented briefly. The proposed approach utilizes elastoplastic finite element analysis together with optimality criteria based on sequential removal of the least stressed elements. The whole problem is a standard stress limited topology optimization method extended by a reliability constraint which here is based on a first order reliability method. The stress constrained topology optimization works with an objective function representing the volume of the material required to safely carry the applied loading. The density of the material at a given point in three dimensional space is described by an indicator function $\chi(\mathbf{x})$, taking values 0 or 1. We are looking for a solution to the above problem within a set of kinematically admissible displacement fields V. Additionally, constraints are imposed on stresses $\sigma(\mathbf{x})$ at any the given point of the design domain Ω.

$$\begin{aligned} &\min_{\chi,\mathbf{u}\in V} \quad \int_{\Omega} \chi(\mathbf{x})\mathrm{d}\Omega \\ &\text{s.t.} \quad \int_{\Omega} \chi\boldsymbol{\varepsilon}(\mathbf{u}):\mathbf{D}:\boldsymbol{\varepsilon}(\mathbf{v})\mathrm{d}\Omega - \int_{\Gamma_n} \bar{\mathbf{t}}\cdot\mathbf{v}\mathrm{d}\Gamma = 0\,, \quad \mathbf{v}\in V \\ &\frac{|\sigma(\mathbf{x})|}{\sigma_0} - 1 \le 0, \quad \mathbf{x}\in\Omega_{\mathrm{mat}} \\ &\chi(\mathbf{x}) = \begin{cases} 1, & \mathbf{x}\in\Omega_{\mathrm{mat}} \\ 0, & \mathbf{x}\in\Omega\backslash\Omega_{\mathrm{mat}} \end{cases} \end{aligned} \tag{1}$$

where $\mathbf{u}(\mathbf{x})$, $\mathbf{v}(\mathbf{x})$, $\boldsymbol{\varepsilon}(\mathbf{u})$ represent displacement, virtual displacement and strain fields, respectively. $\mathbf{D}$ is the elasto-plastic material matrix, $\bar{\mathbf{t}}$ is the traction on the boundary, σ_0 is the stress limit and finally Ω_{mat} represents the material domain defined as $\Omega_{\mathrm{mat}} := \{\mathbf{x}\in\Omega \mid \chi(\mathbf{x}) = 1\}$.

*Corresponding author. E-mail: logo@eik.bme.hu

For sake of simplicity the reliability problem is based on a first order reliability method. Probabilistic task is transformed to standard normal space $\mathbf{r} \rightarrow \mathbf{w}$. The most probable point is the closest point to the centre of the coordinate system of this space, which lies on the limit state surface. Therefore determination of this point is optimization problem formulated as follow:

$$\begin{aligned} &\min \quad \|\mathbf{w}^2\| = \mathbf{w} \cdot \mathbf{w}^{\mathrm{T}}, \\ &\text{s. t.} \quad g(\mathbf{w}) = 0. \end{aligned} \tag{2}$$

To tackle this problem Rackwitz and Fiesler [9] proposed the following gradient-based iterative scheme:

$$\mathbf{w}^{(\mathrm{n}+1)} = \frac{1}{\|\nabla g(\mathbf{w}^{(\mathrm{n})})\|^2}\left(\nabla \mathrm{g}\left(\mathbf{w}^{(\mathrm{n})}\right)^{\mathrm{T}}\mathbf{w}^{(\mathrm{n})} - \mathrm{g}\left(\mathbf{w}^{(\mathrm{n})}\right)\right)\nabla \mathrm{g}(\mathbf{w}^{(\mathrm{n})}). \tag{3}$$

In addition to the above formulation the load carrying capacity (P_{Limit}) of the elastoplastic structures is integrated as a first order reliability constraint. The constraint inequality is:

$$P_{\mathrm{FORM}} > P_{\mathrm{Limit}} \tag{4}$$

where $P_{\mathrm{FORM}} = \Phi(-\beta)$ is cumulative distribution function. The reliability procedure above can be interchanged any appropriate formulation (second order reliability method or different simulation techniques).

NUMERICAL RESULTS

To demonstrate the above proposed algorithm the reliability assessment in topological optimization will be illustrated on a simple example shown in Figure 1. The reliability problem is based on a FORM. Regular rectangular mesh composed with four-node Lagrange finite elements is used in the example. The following parameters are used: Young's modulus $E = 71$ GPa, Poisson's ratio $\upsilon = 0.11$, yield stress $\sigma_0 = 260$MPa, thickness $t = 0.22$ units. 10% standard variation is used in case of the Poisson's ratio while the Young's modulus and the yield stress can vary by 5%. Limit state function reflects displacement condition. Unsafe state means the displacement u_c at point c (see Fig. 1.) exceeds permissible value = 0.1 units (l/200). The optimal stress distribution and the topology is shown at right.

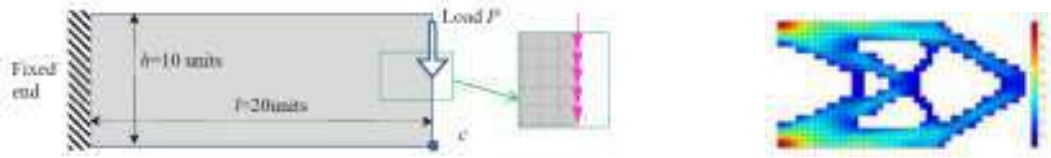

Figure 1. Test problem and the optimal topology with reliability constraint $\mathrm{P_f} = 0.005$.

CONCLUSIONS

In this paper a plasticity based topology optimization procedure with reliability constraint is presented. In the example optimal topology under reliability constraint is shown. Detailed analysis of the results will be discussed and it will be shown that the probability of failure rapidly grows above certain level of volume fraction.

ACKNOWLEDGMENTS

The present study was supported by the National Research, Development and Innovation Office (Grant K 119440, TKP2020 NC, Grant No. BME-NCS) and by the joint grant of the Hungarian and the Polish Academy of Sciences.

References

[1] Antonietti P.F., Bruggi M., Scacchi S., Verani M., On the virtual element method for topology optimization on polygonal meshes: a numerical study. *Computers & Mathematics with Applications*, 74 (5), 1091-1109, 2017.

[2] Blachowski B., Tauzowski P., Logo J., Elasto-plastic topology optimization under stochastic loading conditions, *EngOpt, 6th International Conference on Engineering Optimization*, 2018-09-17/19, Lisbon (PT), 70-79, 2018.

[3] Guest J.K., Igusa T. Structural optimization under uncertain loads and nodal locations. *Computer Methods in Applied Mechanics and Engineering* 198 (1), 116-124, 2009.

[4] Hasofer A.M., Lind N.C. Exact and Invariant Second Moment Code Format. *Journal of the Engineering Mechanics Division* 100, 111–121, 1974

[5] Logo J., Movahedi Rad M.; Knabel J., Tauzowski, P. Reliability based design of frames with limited residual strain energy capacity. *Periodica Polytechnica Civil Engineering*, 55, 1, 13-20, 2011.

[6] Logo J., Balogh B., Pinter E., Topology optimization considering multiple loading, *Computers & Structures*, 207, 233-244, 2018.

[7] Luo Y., Zhou M., Wang M.Y., Deng Z., Reliability based topology optimization for continuum structures with local failure constraints, *Computers & Structures*, 143, 73-84, 2014.

[8] da Silva G.A., Cardoso E.L., Beck A.T. Nonprobabilistic robust continuum topology optimization with stress constraints. *Structural and Multidisciplinary Optimization* , 59, 1181– 1197, 2019.

[9] Rackwitz R., Flessler B. Structural reliability under combined random load sequences, *Computers & Structures*, 9, 5, 489–494, 1978.

[10] Tauzowski, P., Blachowski B., Logo, J. Functor-oriented topology optimization of elasto-plastic structures. *Advances in Engineering Software* 135, 102690, 2019.

[11] Xia H., Wang L., Liu Y., Uncertainty-oriented topology optimization of interval parametric structures with local stress and displacement reliability constraints. *Computer Methods in Applied Mechanics and Engineering* 358, 112644. doi:10.1016/j.cma.2019. 112644., 2020.

INVERSE MEASUREMENT OF EXTERNAL AND BOUNDARY FORCES ON STRUCTURES

Wei Feng[2], Qiaofeng Li [1], Wei Chi[3], and Qiuhai Lu[2]
[1]Department of Mechanical Engineering, Virginia Tech, Blacksburg, 24061, USA
[2]School of Aerospace Engineering, Tsinghua University, Beijing, 100086, China
[3]718 Research Institute of CSIC, Handan, 056027,China

Summary Information on external forces and boundary forces on structures is essential for their damage evaluation and health monitoring. In this paper, we resort to an inverse measurement technique for simultaneous reconstruction of external forces and shock absorber supporting forces on a plate. To solve the inherit ill-posedness in inverse force estimation, a new regularization method, named Element-wise Bayesian regularization, is proposed. A numerical test with two kinds of force profile shows that the proposed method can reconstruct both external forces and shock absorber forces more accurately compared to other existing methods.

INTRODUCTION

Information on external and boundary forces of structures is valuable for response prediction and structural health monitoring. In practice, directly measuring the unknown forces with force transducers is not a reasonable choice due to physical and economic constraints. Inverse methods, i.e., estimating forces based on structural responses, can reconstruct forces at different locations with the same set of sensors, thus offering more flexibility than direct measurements. The inverse problem (force identification) is typically ill-posed and many techniques have been developed to deal with it. The most classic one is Tikhonov regularization which adds a ℓ_2-norm penalty term to stabilize the naive solution (least square method). Another attractive method is ℓ_1 regularzation which produces sparse solutions. However, these methods require precise prior information on the force profile, which is not guaranteed available in practice. The hierarchical Bayesian framework is a promising tool to deal with this problem. It allows a data-driven determination of all unknown variables, relaxing the reliance on prior knowledge of these variables. Aucejo et al. 1 proposed a full Bayesian method to identify multiple forces in frequency domain. Li et al. 2 investigated the influence of shape parameter based on a hierarchical Bayesian formulation with the Markov chain Monte Carlo algorithm. Li et al. 3 proposed an adaptive ℓ_q regularization method to find the appropriate value of shape parameter q. Although promising progress has been continuously made, a stable and accurate method for identification of forces with different types of profile is still strongly demanded. This paper proposes an adaptive method called Element-wise Bayesian Regularization (EWBR) to solve the problem. The method is validated on simultaneous identification of external forces and shock absorber supporting forces on a plate.

HIERARCHICAL BAYESIAN FORMULATION

In Fig. 1, the plate supported by four shock absorbers is assumed as a linear elastic and time invariant system. A response calculation model is established to calculate responses $\mathbf{X}$. Another identification model, i.e., a free plate, is used to calculate the impulse response matrix $\mathbf{H}$ between the external/supporting forces and the response sensors. Denote the excitations as $\mathbf{F}$, and measurement noise as $\mathbf{N}$, we have the following relationship,

$$\mathbf{X}=\mathbf{HF}+\mathbf{N},\quad p\left(\mathbf{F}\left|\mathbf{X}\right.\right)\propto p\left(\mathbf{X}\left|\mathbf{F}\right.\right)p\left(\mathbf{F}\right),\quad p\left(\mathbf{X}\left|\mathbf{F},\tau_n\right.\right)=\left(\frac{\tau_n}{\pi}\right)^{n_s n_t/2}\exp\left(-\tau_n\left\|\mathbf{HF}-\mathbf{X}\right\|_2^2\right) \tag{1}$$

According to Bayes' theorem, the posterior probability distribution function (PDF), which evaluates the distribution of forces given a certain response measurement, is propotional to the product of likelihood function and prior PDF. The likelihood function is equal to the prior PDF of measurement noise which is assumed as a zero-mean Gaussian distribution with precision parameter τ_n. The prior PDF of f_i, i-th element of $\mathbf{F}$, is chosen as a zero-mean Gaussian distribution with the parameter α_i. The components of $\mathbf{F}$ are independent and identically distributed. The proposed method has the ability to deal with multiple forces with different force profile in one reconstruction problem which is very common in engineering condition. Since each element is controlled by their own parameter, no compromise wil be made between the force elements. In the numerical example, the supporting forces are continous profile while the external force (hammer test) is sparse profile.

$$p\left(\mathbf{F}\left|\boldsymbol{\alpha}\right.\right)=\prod_{i=1}^{n_t}\mathcal{N}\left(f_i\left|0,\alpha_i^{-1}\right.\right),\quad p\left(\tau_n\left|a_n,b_n\right.\right)=\frac{{b_n}^{a_n}}{\Gamma\left(a_n\right)}\tau_n^{a_n-1}\exp\left(-b_n\tau_n\right) \tag{2}$$

n_s and n_t are the number of accelerometers and the length of one force history respectively. The precision parameters τ_n and $\boldsymbol{\alpha}$ are also considered as random variables to infer. The prior PDFs of them are assumed as Gamma distribution with small value parameters setting as 1×10^{-16}.

$$p\left(\boldsymbol{\alpha}\right)=\prod_{i=1}^{n_t}p\left(\alpha_i\left|a_f,b_f\right.\right)=\prod_{i=1}^{n_t}\Gamma\left(\alpha_i\left|a_f,b_f\right.\right),\quad \mathbf{F}_{JPM}=\underset{(\mathbf{F},\tau_n,\boldsymbol{\alpha})}{\arg\max}\log p\left(\mathbf{F},\tau_n,\alpha\left|\mathbf{X}\right.\right) \tag{3}$$

*Corresponding author. E-mail: liqiaofeng1990@vt.edu

The hierarchical Bayesian structure is established by repeating Bayes' theorem. The joint posterior mode (JPM) is proposed to estimate $\mathbf{F}$ and all the other unknown variables. The conditional maxmization (CM) algorithm is proposed to solve the JPM.

VALIDATION

A steel plate with four shock absorbers shown in Fig. 1 is used to validate the proposed method. The effect of the four shock absorbers is equivalent to four external forces applying on the free plate. A real external force is exerted vertically on the plate and 7 accelerometers are adopted to measure the responses. Tikhonov regularization with L-curve criterion, ℓ_1 regularization with GIRLS algorithm and Relevance Vector Machine (RVM) are compared with the proposed method. Two cases, sparse-profile and continous-profile for external force, are considered here to validate the proposed method. The reconstructed forces (impact, continous force, and supporting forces of shock absorbers) are illustrated in Fig. 2 and Fig. 3. The measurement noise level is 40dB.

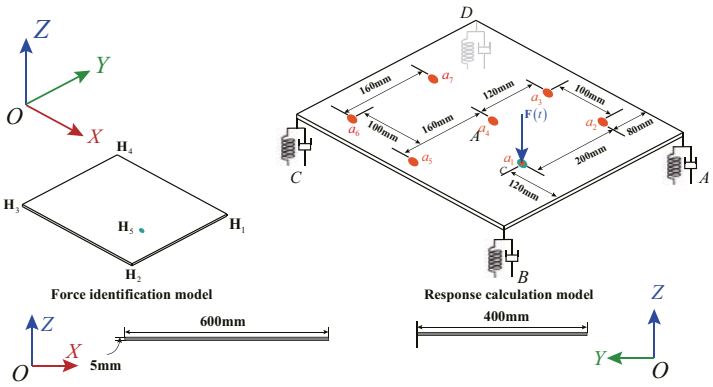

Figure 1: The schematic of the simulated plate.

The result shows that Tikhonov and ℓ_1 regularization can reconstruct the supporting forces successfully in impact case. However, some oscillations appear on the non-force part of the impact with these two methods. RVM is considered as a failure for this reconstruction. EWBR has a great performance in reconstruction of all types of force in both cases compared with other methods. In the continuous force case (Fig. 3), ℓ_1 regularization is invalid since it is sparsity-promoting method.

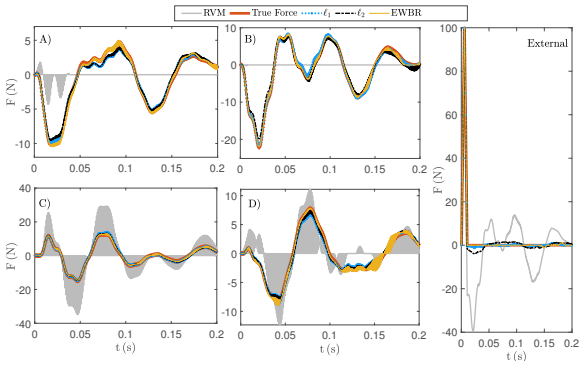

Figure 2: Reconstructed force histories of impact case.

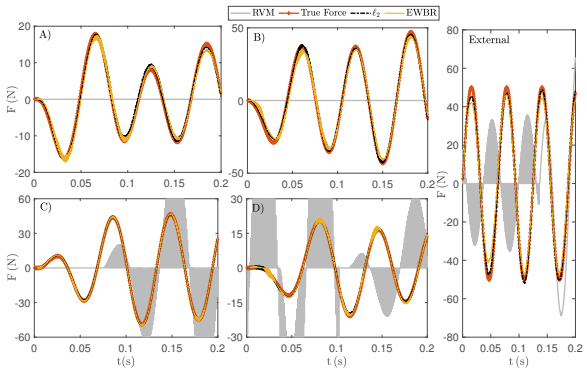

Figure 3: The force histories of continous force case.

CONCLUSIONS

Traditional force identification methods can estimate forces with one type of profile such as sparse or continous. However, forces with different profiles often occur in one reconstruction problem. This paper proposed an Element-wise Bayesian Regularization method based on hierarchical Bayesian formulation for reconstruction of multiple forces with possibly different types of profiles. CM algorithm is adopted for the solution. A numerical validation of a plate is performed to validate the proposed method. The external hammer force, continous sine force, and the supporting forces induced by shock absorbers are identified successfully. Tikhonov regularization, ℓ_1 regularization, and RVM are also applied for this problem. Compared with the traditional methods, EWBR enjoys a more accurate and adaptive merit.

References

[1] Aucejo, M., Olivier De Smet. On a full Bayesian inference for force reconstruction problems. *Mechanical Systems and Signal Processing* 104 (2018): 36-59.

[2] Li Qiaofeng, Qiuhai Lu. A hierarchical Bayesian method for vibration-based time domain force reconstruction problems. *Journal of Sound and Vibration* 421 (2018): 190-204.

[3] Li, Qiaofeng, Qiuhai Lu. Time domain force identification based on adaptive ℓ_q regularization. *Journal of Vibration and Control* 24.23 (2018): 5610-5626.

TOWARDS THE OPTIMAL DESIGN OF TRUSS NETWORKS FABRICATED BY WAAM

Matteo Bruggi[1], Vittoria Laghi*[2], Michele Palermo [2] and Tomaso Trombetti [2]
[1]Department of Civil and Environmental Engineering, Politecnico di Milano, Milano, Italy
[2]Department of Civil, Chemical, Environmental and Materials Engineering, Università di Bologna, Bologna, Italy

Summary A novel approach based on funicular analysis is investigated to cope with the design of spatial truss networks fabricated by Wire-and-Arc Additive Manufacturing (WAAM). The minimization of the horizontal thrusts of networks with fixed plan geometry is stated both in terms of any independent subset of the force densities and in terms of the height of the restrained nodes. Local enforcements are formulated to prescribe lower and upper bounds for the vertical coordinates of the nodes, and to control the stress regime in the branches. Constraints are such that sequential convex programming can be conveniently exploited to handle grids with general topology and boundary conditions. Optimal networks for WAAM are investigated accounting for self-weight, a design-dependent load case.

WIRE-AND-ARC ADDITIVELY MANUFACTURED STRUCTURAL ELEMENTS

Among different Additive Manufacturing (AM) processes, Wire-and-Arc Additive Manufacturing (WAAM) results to be the most suitable for Structural Engineering applications [1]. Indeed, the first demonstrator of the possibilities given by this innovative technology is the MX3D Bridge (Fig.1a) [2], the first metal 3D-printed bridge ever realized, which will be placed in Amsterdam city center by 2020. The WAAM process, which consists of off-the-shelf welding equipment mounted on top of a numerically controlled robotic arm, allows realizing large-scale structural elements up to few meters, without in principle any geometrical constraints in terms of forms and shapes. However, the high velocity required to print real-scale elements induces some non-negligible irregularities in the geometry of the outcome. Moreover, previous studies have confirmed that WAAM-produced metals differ both in the microstructure and in the mechanical response with respect to those traditionally manufactured. Intense research effort has been devoted to the assessment of the main mechanical parameters of WAAM-produced stainless steel elements for structural purposes. The results from the experimental campaign point out high anisotropic response, depending upon the orientation of specimens with respect to the deposition layer of the printing process. Yielding and tensile strength values are comparable to those commonly adopted for stainless steel members, whereas Young's modulus values are highly influenced by the anisotropy of the material, and are on average 40% lower than the standard value for stainless steel adopted in construction. The results are partially presented in [3,4]. Among the available techniques for WAAM, that employing "dot-by-dot" printed stainless steel rods to build spatial truss-like structures is herein considered.

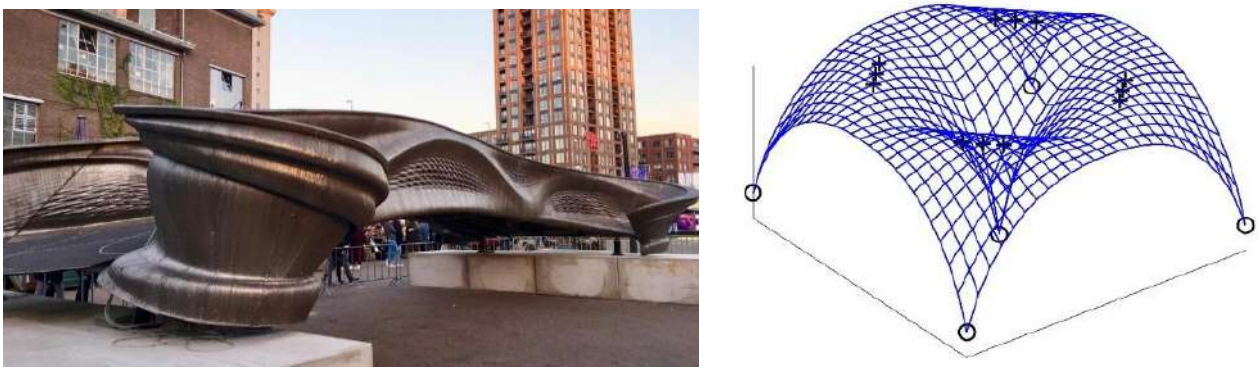

(a) (b)

Figure 1. (a) The MX3D Bridge [2]; (b) Design of a spatial truss network for minimum horizontal reactions under self-weight.

DESIGN OF TRUSS NETWORKS FOR WAAM USING A CONSTRAINED FORCE DENSITY METHOD

Within the above framework, a design approach for WAAM is investigated, by searching among spatial truss networks that fulfil equilibrium. Funicular analysis is extensively adopted to cope with the assessment and design of arcuated structures such as vaults and domes, see in particular [5, 6, 7]. Following this approach, spatial structures such as three-dimensional trusses and shells are modelled as statically indeterminate networks of vertices and edges of given topology. Boundary supports are prescribed at the restrained nodes of the network, whereas unrestrained ones are in equilibrium with the applied vertical and horizontal loads. To assess the safety of an existing structure in the spirit of the lower bound theorem of limit analysis, a funicular network must be found whose vertices lie within its envelope. To design a new one, optimal networks may be sought prescribing lower and upper bounds for the nodal heights. The equilibrium of funicular networks can be conveniently handled through the force density method, i.e. writing the problem in terms of the ratio of force to length in each branch of the network [8]. As investigated in the literature for the case of

vertical loads, independent sets of branches can be detected for networks with fixed plan geometry [9, 10]. However, enforcing the nodes to lie within a prescribed range of heights is not a trivial task from a numerical point of view.

In this contribution an optimization problem is formulated for networks of general shape having fixed plan geometry and loading conditions that may include self-weight. At first, the equations that link dependent and independent branches of the network are found by solving the horizontal equilibrium through the reduced row echelon form of its augmented matrix. A suitable norm of the horizontal thrusts is adopted as objective function of the minimization problem, whereas both the independent force densities and the coordinates of the restrained nodes play as minimization unknowns. A multi-constrained problem is formulated to enforce bounds for the vertical coordinates of the vertices of the network. Constraints on the sign / magnitude of the force density in each branch of the network may be considered as well. Due to its peculiar form, this problem can be efficiently solved through techniques of sequential convex programming that were originally conceived to handle large scale multi-constrained formulations of size optimization for elastic structures [11].

Preliminary numerical simulations are shown investigating the equilibrium of spatial network of trusses to be fabricated by WAAM. Networks that are fully feasible with respect to the local enforcements on the height of the vertices are retrieved in a limited number of iterations, with no need to initialize the procedure with a feasible starting guess. The same algorithm applies to general networks with any type of geometry, loads and restraints. Self-weight, i.e. a design-depend load case, is considered in the optimization, taking full advantage of the direct analytical method to compute sensitivities.

Figure 1b shows the result of a preliminary assessment of the proposed procedure. The design of a spatial truss network for minimum horizontal reactions is investigated. Self-weight is considered, along with constraints enforcing the nodes of the network to lie within a prescribe range of vertical coordinates and all the force densities to be negative. The four corners and the central point of the bay are supported in the vertical direction, whereas symmetry conditions are enforced along each external side of the grid. Restrained nodes are not coplanar. Crosses and circles stand for nodes whose heights match the prescribed upper and lower bounds, respectively. The number of branches in the network is 1248. The independent ones are only 52, meaning that the number of unknowns for the optimization procedure is limited to 57, being 5 the restrained nodes where supports are given.

Constraints prescribing a minimum difference between the height of the nodes of each branch may be additionally considered to account for possible restrictions on the allowable range of truss inclinations. This depends on the features of the adopted WAAM process.

CONCLUSIONS

Wire-and-Arc Additive Manufacturing (WAAM) technology allows realizing metal-based free forms and shapes, introducing very few fabrication constraints. The “dot-by-dot” technique employs stainless steel rods to build spatial truss-like structures with high strength performances, although experimental results point out a more complex mechanical response with respect to those that are traditionally manufactured.

A design approach for “dot-by-dot” WAAM is proposed in this contribution that searches among spatial truss networks fulfilling equilibrium using funicular analysis. The minimization of the horizontal thrusts of a spatial network with given plan geometry is formulated not only in terms of an independent set of force densities, but also in the height of the restrained nodes. Constraints are enforced on the height of the vertical coordinates of the nodes, and on the stress regime in each truss. The former set of enforcements also allows for a straightforward control of the inclination of each branch, as requested by some fabrication processes. Multi-constrained solutions are achieved at a low computational cost using sequential convex programming.

The ongoing research is devoted to endowing the design formulation with local and global buckling constraints.

References

[1] C. Buchanan, L. Gardner, Metal 3D printing in construction: a review of methods, research, applications, opportunities and challenges, Eng. Struct., Vol.180, pp. 332-348, 2019.

[2] MX3D website: **www.mx3d.com**.

[3] V. Laghi, M. Palermo, G. Gasparini, V.A. Girelli, T. Trombetti, Experimental results for structural design of Wire-and-Arc Additive Manufactured stainless steel members, J. Constr. Steel Res, 2019, **https://doi.org/10.1016/j.jcsr.2019.105858**.

[4] V. Laghi, M. Palermo, L. Tonelli, G. Gasparini, L. Ceschini, T. Trombetti, Tensile properties and microstructural features of 304L austenitic stainless steel produced by Wire-and-Arc Additive Manufacturing, Int. J. Adv. Manuf. Tech., 2020, **https://doi.org/10.1007/s00170-019-04868-8**.

[5] D.W. O’Dwyer, Funicular analysis of masonry vaults. Comput. Struct., Vol. 73, pp. 187–197, 1999.

[6] P. Block, J. Ochsendorf, Thrust network analysis: a new methodology for three-dimensional equilibrium, J. Int. Assoc. Shell Spatial Struct., Vol. 48(3), 167–173, 2007.

[7] F. Marmo, L. Rosati, Reformulation and extension of the thrust network analysis, Comput. Struct., Vol. 182, 104-118, 2017.

[8] H.J. Schek, The force density method for form finding and computation of general networks, Comput. Methods Appl. Mech. Eng., Vol. 3, 115-134, 1974.

[9] Cercadillo-Garcıa, C., Fernandez-Cabo, J.L., Analytical and Numerical funicular analysis by means of the Parametric Force Density Method, J. Appl. Res. Technol., 14(2), 108-124, 2016.

[10] Liew, A., Pagonakis, D., Van Mele, T., Block, P., Load-path optimisation of funicular networks, Mecc., 53:1–2, 279–294, 2018.

[11] P. Christensen, A., Klarbring, An Introduction to Structural Optimization, Springer, Berlin, 2009.

DATA-DRIVEN RELIABILITY-BASED DESIGN OPTIMIZATION WITH DIMENSIONALITY REDUCTION

Yoshihiro Kanno* [1]
[1]Mathematics and Informatics Center, The University of Tokyo, Tokyo, Japan

Summary A recently proposed approach to reliability-based design optimization with lack of probabilistic information of uncertain parameters constructs, by using a data sat of samples, a sufficient condition that guarantees the specified target confidence level of structural reliability. This data-driven method, however, often yields a vary overly-conservative structural design, because in general there exists a gap between the constructed sufficient condition and the original confidence-level constraint. By using a dimensionality reduction technique, this paper presents a method that mitigates this gap, especially for a problem involving a large number of uncertain parameters. Numerical experiments demonstrate that the proposed method can drastically reduce over-conservativeness.

INTRODUCTION

Considering uncertainty in design process is indispensable for designing structures with high quality. In structural optimization, *reliability-based design optimization* (RBDO) is one of representative methods handling this issue.

Conventionally, in RBDO we suppose that a probability distribution of uncertain parameters in a structural system is known. However, it is pointed out that, in diverse situations, the input probability distribution is known only imprecisely, due to, e.g., limitation of knowledge, insufficiency of data, etc. Therefore, recent attention has been drawn to RBDO methods addressing uncertainty in the input distribution [1, 2]. Typically, such a method handles the *confidence level*, which is a lower bound for the probability that the structural reliability is no smaller than the target reliability.

As a data-driven approach to RBDO, the method in [3] assumes that a data set of some random samples of uncertain parameters is available, and constructs a robust optimization problem the solution which has the required target confidence level. In this procedure, no information of the input distribution is presumed, and only a given data set is used to guarantee the target confidence level. On the other hand, in general there exists a gap between a sufficient condition used in [3] and the original confidence-level constraint, and this gap often yields an overly-conservative structural design. This paper presents a dimensionality reduction technique to reduce this gap. In other words, the presented method provides an improved approximation. Numerical experiments demonstrate that the proposed method can drastically reduce over-conservativeness of method in [3].

MAIN RESULT

Consider performance constraints $g_i(\boldsymbol{x};\boldsymbol{q}) \le 0$ $(i = 1,\ldots,m)$ in a design optimization problem, where $\boldsymbol{x}$ is a design variable vector and $\boldsymbol{q} \in \mathbb{R}^n$ is a random vector following the joint distribution F. In RBDO, we consider the lower-bound constraint on the probability that the performance constraint is satisfied:

$$\mathrm{P}\{g_i(\boldsymbol{x};\boldsymbol{q}) \le 0\} \ge 1-\epsilon. \tag{1}$$

Here, ϵ $(0 < \epsilon < 1)$ is a constant, and $1-\epsilon$ is the *target reliability*.

When F is known only imprecisely, then the left side of (1) is considered a random variable. Therefore, the inequality (1) is understood only in a probabilistic manner, which leads to a constrain in the form [1, 2]

$$\mathrm{P}_F\left\{\mathrm{P}\{g_i(\boldsymbol{x};\boldsymbol{q}) \le 0\} \ge 1-\epsilon\right\} \ge 1-\delta, \tag{2}$$

where δ $(0 < \delta < 1)$ is a constant, and $1-\delta$ is the *target confidence level*. For instance, if $\epsilon = 0.05$ and $\delta = 0.1$, then (2) means that, with probability at leat 90%, the reliability of design $\boldsymbol{x}$ is no smaller than 95%.

In [3], a sufficient condition for (2) is considered, provided that some independent and identically distributed samples drawn from F are available. For a parameter $\alpha > 0$, define $Q(\alpha) \subset \mathbb{R}^n$ by

$$Q(\alpha) = \{\boldsymbol{q} \in \mathbb{R}^n \mid (\boldsymbol{q}-\bar{\boldsymbol{q}})^\top \Omega (\boldsymbol{q}-\bar{\boldsymbol{q}}) \le \alpha\},$$

where Ω is a positive definite symmetric matrix. For sufficient large α (determined by using the samples), constraint

$$g_i(\boldsymbol{x};\boldsymbol{q}) \le 0, \quad \forall \boldsymbol{q} \in Q(\alpha) \tag{3}$$

serves as a sufficient condition for (2). In the framework of robust optimization, various techniques, e.g., [4, 5], are available to handle the constraint in the form of (3).

*Corresponding author. E-mail: kanno@mist.i.u-tokyo.ac.jp.

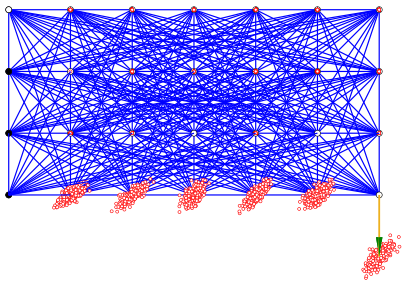

Figure 1: Ground structure and data of external loads.

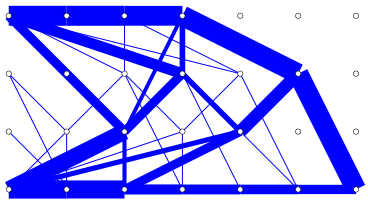

Figure 2: Nominal optimal solution for the mean load.

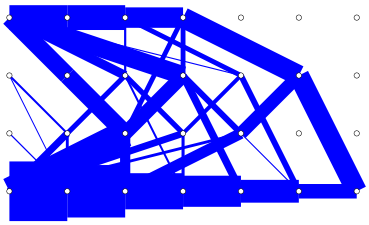

Figure 3: Optimal solution of data-driven RBDO method.

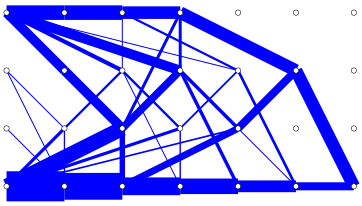

Figure 4: Optimal solution of data-driven RBDO method with dimensionality reduction.

In this paper, we define $Q(\alpha)$ by

$$Q(\alpha) = \{\bar{\boldsymbol{q}} + L\boldsymbol{\theta} \mid \|\boldsymbol{\theta}\| \leq \alpha\}, \tag{4}$$

where $L \in \mathbb{R}^{n\times r}$ $(n > r)$ is a constant matrix obtained by applying the principal component analysis to the given samples. Thus, the dimension of uncertainty parameter is reduced from n to r. If we choose α satisfying

$$\mathrm{P}_F\left\{\mathrm{P}\{\boldsymbol{q} \in Q(\alpha)\} \geq 1-\epsilon\right\} \geq 1-\delta, \tag{5}$$

then a constraint in the form of (3) corresponds to a sufficient condition for (2). To check (5) we use the order statistics of the given samples, in a manner similar to [3]. It is expected that the dimensionality reduction introduced in this paper can mitigate, somewhat, the over-conservativeness of the method in [3].

NUMERICAL EXAMPLES

Consider a truss topology optimization problem outlined in Figure 1. Suppose that the external load vector, denoted $\boldsymbol{f} \in \mathbb{R}^n$, is a random vector, where $n = 48$ is the number of the degrees of the nodal displacements of the ground structure. As a performance requirement, we consider a compliance constraint, $\pi(\boldsymbol{x}; \boldsymbol{f}) \leq \pi^{\mathrm{c}}$, where π^{c} is a specified upper bound.

Small circles in Figure 1 show given samples of $\boldsymbol{f}$, where we suppose that uncertain external forces are applied only at the bottom nodes. For the mean of the samples, denoted $\mathrm{E}(\boldsymbol{f})$, a constraint without considering uncertainty is written as $\pi(\boldsymbol{x}; \mathrm{E}(\boldsymbol{f})) \leq \pi^{\mathrm{c}}$. Under this constraint we minimize the structural volume, which results in the optimal solution shown in Figure 2. Here, the width of each member in the figure is proportional to the member cross-sectional area.

We next consider RBDO with target reliability $1 - \epsilon = 0.95$ and target confidence level $1 - \delta = 0.9$. If the number of available samples is, e.g., 200, then the order statistics guarantees that $Q(\alpha)$ containing 195 samples satisfies (5). Figure 3 shows the optimal solution obtained by the method in [3], i.e., the dimension of uncertainty parameters is $n = 48$. The objective value is 5.588×10^8 mm^3. Figure 4 shows the optimal solution obtained by the method presented in this paper. By using the principal component analysis, the dimension of uncertain parameter is reduced to $r = 5$. The objective value of the solution in Figure 4 is 2.996×10^8 mm^3. Thus, the over-conservativeness of the solution in Figure 3 is drastically mitigated by the presented method.

References

[1] Cho H., Choi K. K., Gaul N. J., Lee I., Lamb D., Gorsich D. Conservative reliability-based design optimization method with insufficient input data. *Structural and Multidisciplinary Optimization*, **54**: 1609–1630, 2016.

[2] Ito M., Kim N. H., Kogiso N. Conservative reliability index for epistemic uncertainty in reliability-based design optimization. *Structural and Multidisciplinary Optimization*, **57**: 1919–1935, 2018.

[3] Kanno Y. A data-driven approach to non-parametric reliability-based design optimization of structures with uncertain load." *Structural and Multidisciplinary Optimization*, textbf60: 83–97, 2019.

[4] Calafiore, G. C., Dabbene, F. Optimization under uncertainty with applications to design of truss structures. *Structural and Multidisciplinary Optimization*, **35**: 189–200, 2008.

[5] Kanno Y., Takewaki I. Sequential semidefinite program for maximum robustness design of structures under load uncertainties. *Journal of Optimization Theory and Applications*, **130**: 265–287, 2006.

TOPOLOGY OPTIMIZATION CONSIDERING MANUFACTURING CONSTRAINTS: NEW CAPABILITIES IN PROJECTION METHODS

Mikhail Osanov[1], Hak Yong Lee[1], Julia Carroll[1], and James K. Guest*[1]
[1]Department of Civil and Systems Engineering, Johns Hopkins University, Baltimore, Maryland, USA

Summary Recent advances in manufacturing have provided tremendous opportunities to re-think design and create novel solutions to complex design problems. Topology optimization offers a systematic computational framework for addressing this new design challenge. This work discusses the integration of topology optimization and manufacturing to create designs that are optimized accounting for the manufacturing process. The approach is based on projection methods, which provide a flexible framework for handling a multitude of manufacturing constraints. Recent advancements in projection methods will be discussed, including new constraint and cost function capabilities, as well as new improvements in computational efficiency. Various examples will be considered, including structural components and architected materials fabricated by additive manufacturing or subtractive processes.

INTRODUCTION

Recent advancements in manufacturing have provided unprecedented opportunities to create complex structures and components, as well as produce materials with defined architecture. Although this has rapidly expanded the design space for engineers, each process, hardware and software has its own restrictions as to what can actually be fabricated, fabricated reliably, and what features tend to add cost and time to the manufacturing process. If these considerations are not accounted for during the design process, proposed designs may go through a re-design where geometric modifications are proposed to address these issues. Subsequent design modifications based on manufacturability then require re-analysis to ensure part performance satisfies design specifications. This re-design process not only increases design cycle time and cost, but also reduces part performance and degrades optimality which was initially sought. These issues strongly motivate the incorporation of manufacturing constraints and metrics within the design process.

This talk will discuss the design tool of topology optimization, a systematic approach to distributing material in a design domain, and explore recent advancements related to the incorporation of manufacturing constraints and metrics into the topology optimization framework. We will focus on projection methods, a class of algorithms that represent design through assembly of manufacturing primitives. These methods have been successful at implementing a number of manufacturing constraints, including minimum feature size for [1], maximum feature sizes [2], machining constraints [3], overhang constraints [4,5], insertion of objects of fixed (or variable) size and shape [6], including those from textile manufacturing [7]. Herein we will focus on recent advancements, including extensions and improvements to existing constraints and development of new functions that enable imposition of strict constraints on features but also relax these features and express them in cost functions.

FORMULATION

The key idea behind projection methods is that physical design variables, typically the relative density of elements ρ^e, are expressed as a function of independent design variables that are related to manufacturing actions. This relation is dictated by the manufacturing process and specifically the manufacturing primitive of a process, defined as the smallest building block that can be deposited in (or removed from) the domain. This is expressed mathematically as:

$$\rho^e = 1 - e^{-\beta \mu^e(\phi)} + \frac{\mu^e(\phi)}{\mu_{max}} e^{-\beta \mu_{max}}$$

where β is the curvature parameter dictating the aggressiveness of the mapping and μ^e is the filtered variables in the neighborhood of element e, the simplest of which is radial with the radius r_{min} dictating the minimum feature size associated with a process [1]. This neighborhood set, when used with the Heaviside projection function above, can be termed the manufacturing primitive, defined as the minimum building block of a manufacturing process.

Different manufacturing constraints can be imposed by changing this primitive shape and size and/or by performing multiple independent or dependent projections. Examples of the former include moving from spherical to short disk-like primitives in three dimensions to mimic the layer-by-layer deposition process or tall cylindrical to mimic the machining process. Examples of multiple projections include building structures

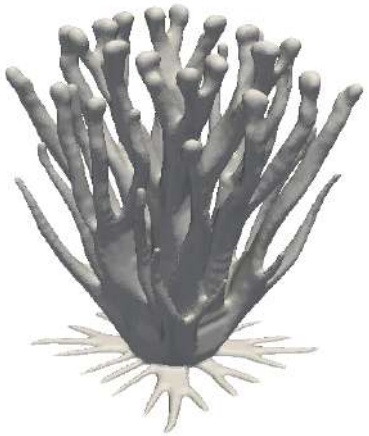

Figure 1. Design of conduction-driven heat sink considering a minimum feature size and overhang constraints of 45 degrees, with the build direction from the bottom up.

*Corresponding author. E-mail: jkguest@jhu.edu.

composed of off-the-shelf inclusions or implementing overhang constraints, defined as a requirement for features to rise at a minimum angle from the build platform, typically associated with the minimum self-supporting angle of a process (e.g., see Figure 1).

In this work we will discuss advancements to the projection approach that include new numerical implementations that provide additional functionality in terms of manufacturing constraints as well as general improvements in computational efficiency. These will include adjustments to existing overhang implementations for topology optimization in additive manufacturing to eliminate enclosed pores and provide specific anchor points for support structures, thereby allowing more convenient access to support structures if they are desired to exist. New cost metrics related to support structures and post-processing costs will also be presenting, culminating in a clear trade-off between material costs (material volume) and post-processing costs of fabricated components. Advancements in topology optimization of subtractive processes will also be presented, including demonstration of an existing machining projection method [3] implemented in a parallel computing framework PETSc for large scale toology optimization [8] (Figure 2). Commonalities between these new methods and future expansions will also be discuss

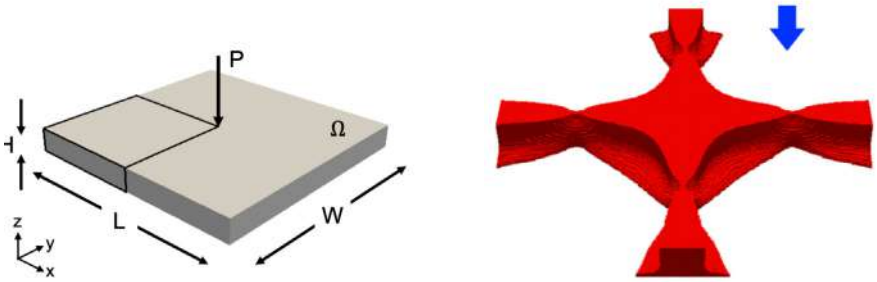

Figure 2. Design of a clamped plate for maximum stiffness using the 2.5 dimension machining projection method from [3].

CONCLUSIONS

Projection methods offer a flexible framework for implementation of manufacturing constraints and considerations in topology optimization. This work demonstrates that with simple modifications to the projection primitives and/or projection functions, that one can implement a wide range of manufacturing constraints and cost functions, including with respect to additive manufacturing (overhang constraints, enclosed pores, feature sizes) and subtractive processes such as machining. These algorithms are demonstrated on structural component design problems as well as for the design of architected materials with optimized combinations of properties.

ACKNOWLEDGEMENTS

The authors acknowledge the support of the National Aeronautics and Space Administration (NASA) under Grant No. 80NSSC18K0428. The opinions, findings, and conclusions or recommendations expressed in this paper are those of the authors and do not necessarily reflect the views of NASA.

References

[1] Guest J.K., Prévost J.H., and Belytschko T. Achieving minimum length scale in topology optimization using nodal design variables and projection functions, *International Journal for Numerical Methods in Engineering*, **61**:238-254, 2004.
[2] Carstensen J.V. and Guest J.K. Projection-based two-phase minimum and maximum length scale control in topology optimization. *Structural and Multidisciplinary Optimization* **58**(5):1845-1860, 2018.
[3] Guest J.K. and Zhu M. Casting and Milling Restrictions in Topology Optimization via Projection-Based Algorithms. *Proceedings of the ASME Design Engineering Technical Conference*, 3 (PARTS A AND B): 913-920, 2012.
[4] Gaynor, A.T., and Guest, J.K. Topology Optimization for Additive Manufacturing: Considering Maximum Overhang Constraint. *Proceedings of the 15th AIAA/ISSMO Multidisciplinary Analysis and Optimization Conference*, Atlanta, GA, 1-8, 2014.
[5] Gaynor A.T. and Guest J.K. Topology optimization considering overhang constraints: Eliminating sacrificial support material in additive manufacturing through design. *Structural and Multidisciplinary Optimization* **54**(5):1157–1172, 2016.
[6] Guest J.K. Optimizing Discrete Object Layouts in Structures and Materials: A Projection-Based Topology Optimization Approach, *Computer Methods in Applied Mechanics and Engineering* **283**: 330-351, *2015*.
[7] Ha S.H., Lee H.Y., Hemker K.J., and Guest J.K. (2019). Topology Optimization of 3D Woven Materials using a Ground Structure Design Variable Representation. *Journal of Mechanical Design, Transactions of the ASME, 141 (6), art. no. 061403*.
[8] Aage N., Andreassen E., and Lazarov B.S. Topology optimization using petsc: An easy-to-use, fully parallel, open source topology optimization framework. *Structural and Multidisciplinary Optimization*, 51: 565–572, 2015.

NEW EFFICIENT MATLAB IMPLEMENTATION OF 2D/3D TOPOLOGY OPTIMIZATION ACCOUNTING FOR BUCKLING

Federico Ferrari * [1], Ole Sigmund[2], and James K. Guest[1]
[1]Department of Civil and Systems Engineering, Johns Hopkins University, Baltimore, MD 21218, USA
[2]Department of Mechanical Engineering, Technical University of Denmark, Lyngby 2400, DK

Summary We present a compact Matlab implementation allowing for the solution of buckling topology optimization problems of an interesting size on a laptop. The code builds on the `top99neo` code [1], and inherits all its basic speedups. The computational burden associated with the setup of the buckling eigenvalue problem and the sensitivity analysis of buckling load factors, which would rapidly become prohibitive when using classical programming approaches in Matlab, is substantially cut by an *ad hoc*, fully vectorized implementation. Some advanced topics, such as the cure of artificial buckling modes and the use of an acceleration strategy are discussed, stressing their easy integration in the basic code.

MOTIVATION

Topology optimization (TO) is rapidly spreading among engineers and researchers from various fields. Its sound mechanical ground and its tendency to highlight mechanical principles and design rules are making it more and more popular among graduate, and even undergraduate engineering students also.

Because TO involves an iterative, redesign procedure containing several ingredients: a finite element analysis, regularization and penalization of the design variables, sensitivity computation and gradient-based variable updates, its programming might be a hurdle to people new to the field. Thus, the well-known `top99` code [2] has certainly the merit of having wrapped up all these procedures in a sharp and short implementation. Then, the `top88` code [3] upgraded the computational efficiency of `top99` exploiting vectorization, allowing users to solve compliance TO problems of an interesting size on a laptop. Recently, Ferrari and Sigmund have shown that also the `top88` had much room left for improvements, and published the new `top99neo`, and its extension to 3D, named `top3D125` [1]. By rethinking some operations and by exploting new routines and functionalities available in Matlab, or developed by independent researchers, the `top99neo` shows speedups ranging from 2 to beyond 6 times compared to the `top88`, on meshes with $3 \cdot 10^4$-$4.8 \cdot 10^5$ elements, and the `top3D125` is the most efficient Matlab implementation for 3D compliance problems to date.

Here we extend the basic codes in [1] to account for buckling, that is a fundamental feature in realistic structural design problems. Our work has been motivated by the lack of any public educational software considering buckling TO and by the fact that both the set up of the buckling analysis and the sensitivity calculation can be potentially highly time consuming operations within a Matlab environment, due to the local nature of the stress stiffness operator.

The new code, named `topBuck250` [4] shares the same neatness and flexibility of the `top99neo` and inherits all its basic speedups: the efficient matrix assembly procedures, the fast implementation of filters and shortcuts in the design update step. Furthermore, by a careful inspection of the stress stiffness operator, we can implement its construction performing extremely cheap matrix operations only, and the same applies for the sensitivity analysis of the buckling load factors (BLFs), introducing major speedups specific for buckling problems. As a result, the proposed code allows the solution of buckling TO problems of a remarkable size ($\approx 10^5$ elements) with a reasonable CPU time.

STATEMENT OF THE OPTIMIZATION PROBLEM

In the standard setting of density-based TO [2] we consider a 2D/3D discretization Ω_h, consisting of m equi-sized elements, and the following single-objective and single-constraint optimization problem

$$\begin{cases} \min\limits_{\mathbf{x}\in[0,1]^m} g_0\left(\hat{\mathbf{x}}\right) \\ \text{s.t.} \quad g_1\left(\hat{\mathbf{x}}\right) \leq 0 \end{cases} \tag{1}$$

The physical densities $\hat{\mathbf{x}}$ are linked to the design variables $\mathbf{x}$ by the relationship $\hat{\mathbf{x}} = \mathcal{H}(H\mathbf{x})$, where H represents the linear density filter and $\mathcal{H}$ the relaxed Heaviside projection.

Either g_0 and g_1 may represent one of the following physical quantities (or the corresponding constraint): volume $V\left(\hat{\mathbf{x}}\right) = \hat{\mathbf{x}}^T \mathbf{1}_m$, compliance $\mathbf{f}^T K^{-1}(\hat{\mathbf{x}})\mathbf{f}$, where $\mathbf{f}$ is a given load vector and $K(\hat{\mathbf{x}})$ is the elastic stiffness matrix, or the buckling load factor $\lambda_1(\hat{\mathbf{x}})$. For this latter we adopt the aggregated measure [5]

$$g_{KS}\left(\lambda_i^{-1}\right) = \lambda_1^{-1} + \frac{1}{\rho} \ln\left(\sum_{i=1}^{q} e^{\rho\left(\lambda_i^{-1} - \lambda_1^{-1}\right)}\right) \tag{2}$$

where λ_i, $1 \ldots q$ are computed by a linearised buckling analysis.

*Corresponding author. E-mail: fferrar3@jhu.edu

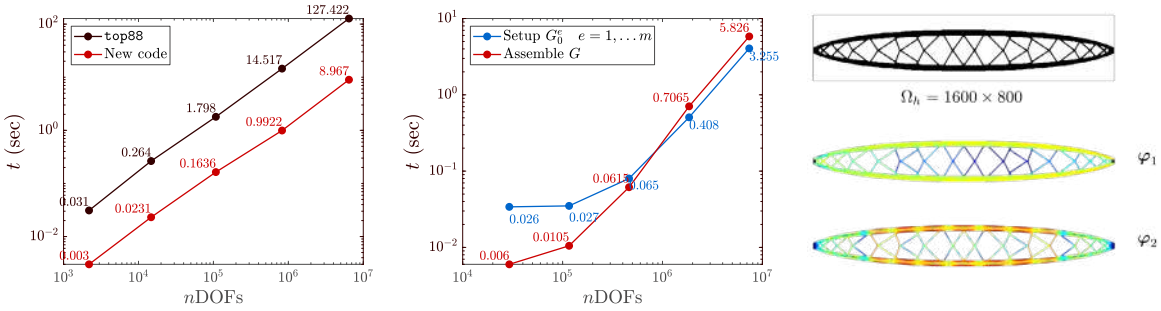

(a) (b) (c)

Figure 1: (a) CPU time for the K matrix assembly, comparing the `top88` approach and the new implementation. (b) CPU time for building all the elemental stress stiffness matrices G^e and global matrix (G) assembly time. (c) example of Topology Optimization for maximising the fundamental buckling load of a 2D simply supported beam

IMPLEMENTATIONS AND SPEEDUPS

The overall structure of the new code follows that of `top99neo`; Problem (1) is dealt with an iterative, nested analysis and design process and the "basic" speedups are due to

- A new assembly strategy for the $K(\hat{\mathbf{x}})$ matrix, taking advantage of the symmetry of the local and global matrices and exploiting the external routine by [6]. Memory requirements are sensibly cut, and the assembly speed improves up to 15 times on large discretizations (see Figure 1(a));
- Implementation of volume-preserving filters and of a bracketing procedure for the Lagrange multiplier, substantially increasing the speed of the redesign step;

Other speedups are more specific to the buckling problem. In particular, the setup of the stress stiffness operator $G(\hat{\mathbf{x}}, \boldsymbol{\sigma})$ could potentially become very expensive since each local matrix ($G^{(e)}$) depends on the elemental stress distribution, and therefore cannot be obtained as a scaling of a constant, pre-computed matrix. However, upon acknowledging the pattern of the independent coefficients $G_{ij}^{(e)}$ and their explicit expression in terms of the elemental stresses, the global stress stiffness matrix can be computed with an efficiency approaching that of the elastic stiffness matrix (see Figure 1(b)), only performing vectorized operations. The same concept is exploited when computing the buckling loads gradients, and we obtain a code for buckling optimizaton which, apart from the eigenvalue solution step [7], is about as efficient as the one for compliance optimization.

Finally, an extension of the Optimality Criterion, working with rather general MMA-like approximations [8], is implemented in a few lines of code and keeping the same efficiency of the basic OC scheme.

CONCLUSIONS

We extend the recent, highly efficient `top99neo` code to account for buckling, keeping the same readability of the basic compliance code and bringing major computational savings to a potentially time-consuming analysis. Several examples that are easily replicable on a laptop will be shown (see Figure 1(c)). Moreover, discussing around some more advanced topics, such as possible remedies to the phenomenon of artificial buckling modes or the use of alternative optimizers and of advanced convergence acceleration strategies, we prove the `topBuck250` to be a helpful and easily extendable tool for spreading the research on buckling TO.

References

[1] F. Ferrari and O. Sigmund. A new generation 99 line matlab code for compliance topology optimization and its extension to 3d. *Structural and Multidisciplinary Optimization*, 62:2211–2228, 2020.
[2] O. Sigmund. A 99 line topology optimization code written in Matlab. *Structural and Multidisciplinary Optimization*, 21(2):120–127, Apr 2001.
[3] Erik Andreassen, Anders Clausen, Mattias Schevenels, Boyan S. Lazarov, and Ole Sigmund. Efficient topology optimization in matlab using 88 lines of code. *Structural and Multidisciplinary Optimization*, 43(1):1–16, Jan 2011.
[4] F. Ferrari, O. Sigmund, and J. K. Guest. Topology optimization with linearized buckling criteria in 250 lines of matlab. Submitted, 2020.
[5] G. Kreisselmeier and R. Steinhauser. Systematic control design by optimizing a vector performance index. *IFAC Proceedings Volumes*, 12(7):113 – 117, 1979. IFAC Symposium on computer Aided Design of Control Systems, Zurich, Switzerland, 29-31 August.
[6] Stefan Engblom and Dimitar Lukarski. Fast matlab compatible sparse assembly on multicore computers. *Parallel Computing*, 56:1–17, 2016.
[7] Federico Ferrari and Ole Sigmund. Towards solving large-scale topology optimization problems with buckling constraints at the cost of linear analyses. *Computer Methods in Applied Mechanics and Engineering*, 363:112911, 2020.
[8] Krister Svanberg. The method of moving asymptotes - A new method for structural optimization. *International Journal for Numerical Methods in Engineering*, 24(2):359–373, 1987.

BAYESIAN INFERENCE OF THE SPATIAL DISTRIBUTIONS OF MATERIAL PROPERTIES

Andrea Vigliotti[1,2], Gábor Csányi[2], and Vikram S. Deshpande * [2]
[1]Innovative Materials Laboratory, Italian Aerospace Research Centre, Capua 81043, Italy
[2]Department of Engineering, University of Cambridge, Trumpington Street, Cambridge CB2 1PZ, UK

Summary The problem of estimating the spatial distributions of material properties from noisy strain measurements is ill-posed and is typically solved by optimisation. Here we employ Bayesian inference and Nested Sampling to identifying the appropriate basis function set and estimate the uncertainty. Complex models generate high likelihood solutions that nevertheless give poor predictions, however, the Bayes' factor peaks for a relatively simple model despite its lower likelihood. Intriguingly, the corresponding maximum likelihood solution still has large errors, but the *mean* of the posterior probability distribution predicts the material properties with significantly higher fidelity. The likelihood landscape is non-Gaussian and can have multiple modes that hinder optimisation methods in such inverse problems.

PROBLEM INTRODUCTION

Estimating the spatial distributions of mechanical properties in a heterogeneous solid body from the measurements of strains or displacements fields has wide ranging applications, including material characterisation, medical diagnosis and civil infrastructure monitoring. For example, there has been a recent burst of activity in the development of smart civil infrastructure and this includes application of strain measurement technologies like fibre optic sensing to monitor the structural health of tunnels (Gue et al., 2015), bridges (Ko and Ni, 2005) and concrete sleepers (Butler et al., 2017), to name a few. In these applications strains are measured at a small number of discrete locations. In some other applications full field measurements of the displacement fields within specimens are available. For example, a technique known as "displacements under applied loading by Magnetic Resonance Imaging" (dualMRI) has been developed to perform in vivo measurements of displacements and strain in musculoskeletal tissues (Chan et al., 2012). In all these cases the spatial distributions of material properties is the information of primary interest but displacement and strain information does not directly describe these material property distributions. The reconstruction of material property maps from noisy (and sometimes sparsely spaced) strain measurements is an ill-posed inverse problem that requires complex modelling approaches.

SOLUTION STRATEGIES

A number of methods have been proposed to identify constitutive parameters from strain/displacement measurements; readers are referred to Avril et al. (2008) for an overview. The most common is the the finite element model updating (FEMU) approach is an optimisation method and involves adjusting the model parameters in order to minimise the difference between computed and measured strains as measured by a likelihood function (Rouger et al., 1991). Various types of regularisations have been proposed to reduce the intrinsic instability of the solutions, but the reconstructed results are inevitably strongly dependent on the choice of the regularisation parameters (Richards et al., 2009). Moreover, the instabilities are aggravated by the presence of measurement noise.

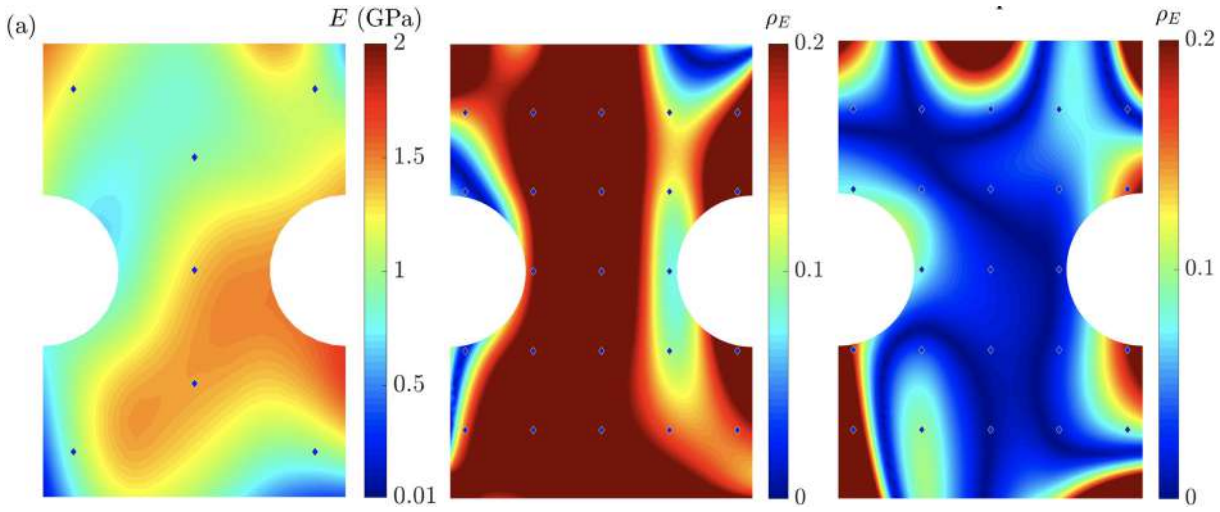

Figure 1: The Young's modulus of our (synthetic) specimen (left), with the error in its prediction by optimisation (middle) and Bayesian inference (right, mean of the posterior).

*Corresponding author. E-mail: vsd20@cam.ac.uk.

Statistical and probabilistic methods are in fact being increasingly used for solutions of ill-posed inverse problems. In particular, the Bayesian approach allows for a full characterisation of all possible solutions, and their relative probabilities, whilst simultaneously addressing the problems associated with the ill-posed problem in a clear and precise fashion. Readers are referred to Stuart (2010) for a detailed discussion of the mathematical basis of Bayesian inference methods. In this study we follow such a Bayesian approach, and in particular we do not use Laplacian or other such approximations for the posterior as in the majority of previous studies, but estimate the entire posterior probability distribution of the material properties using the Nested Sampling method (Skilling, 2006). We quantify the Bayesian evidence in support of particular choices of basis functions, and compare our solutions to those obtained by optimisation.

EXAMPLE

In order to illustrate the method we numerically generated a synthetic specimen with a random spatial distribution of isotropic elastic constants using NURBS functions with grid of 5×5 control weights, the Young's modulus is shown in the left panel of Figure 1. The synthetic strain data was then calculated via the finite element (FE) method. These strains, with and without added measurement noise, were then used as the only available data from which to estimate the spatial distribution of material properties using models with a grid of $p \times p$ control weights. In the presence of measurement noise, the maximum likelihoods increased with increasing p (i.e. increasing model complexity). However, this was a consequence of the complex models overfitting the experimental data, which ultimately resulted in poor predictions of the actual spatial distributions of the material properties. On the other hand, Bayes' factor correctly estimated that a model with a grid of 5×5 control weights best describes the spatial distribution of elastic constants within the specimen and with the lowest uncertainty. Moreover, inference based on Bayes' factor appropriately indicates an increasing uncertainty in model selection with decreasing data and increasing measurement noise. By contrast, inference based purely on likelihood is misleading with the maximum likelihood increasing as the amount of available data decreases. Simpler model selection criteria such as Bayesian information criterion (BIC) were shown to fail for the inverse elasticity problem investigated here and this makes accurate evaluation of the posterior distribution and the associated Bayesian evidence integral (by Nested Sampling or other means) imperative for this class of problems.

Figure 1 also shows the errors in the reconstruction of the spatial distribution of the Young's modulus by optimisation and Bayesian inference. For our parameter settings (number of strain gauges, simulated measurement noise), which are not atypical with respect to a real world scenario, the error in the former is substantial, exceeding 10% over most of the specimen. By contrast, the mean of the posterior obtained by Nested Sampling shows less that 2% error over most of the specimen, except at the edges.

CONCLUSIONS

The numerical results presented above suggest clear advantages of the Bayesian approach over traditional optimisation methods based on maximum likelihood. However, these gains come at the price of considerably higher computational costs and finding ways to reduce these costs is of interest. While Bayesian inference using Nested Sampling has been demonstrated here with the focus on an inverse elasticity problem, the ideas are general and can be readily used for a wide range of high dimensionality problems in mechanics. This includes selection of constitutive models given available (noisy) material data as well as the corresponding estimation of parameters and the associated uncertainty. The key advantages of Bayesian inference over optimisation procedures typically used in these problems include: (i) an in-built Occam's razor that aids in avoiding overfitting both for model selection and parameter estimation; (ii) increased accuracy in predicting material properties for data-poor and high noise regimes; and (iii) a quantification of the uncertainty associated with the estimated parameter values.

References

[1] Gue, C.Y., Wilcock, M., Alhaddad, M.M., Elshafie, M.Z.E.B., Soga, K., Mair, R.J., 2015. The monitoring of an existing cast iron tunnel with distributed fibre optic sensing (DFOS). J. Civil Struct. Health Monit. 5, 573–586.
[2] Ko, J.M., Ni, Y.Q., 2005. Technology developments in structural health monitoring of large-scale bridges. Eng. Struct. 27, 1715–1725.
[3] Butler, L.J., Xu, J., He, P., Gibbons, N., Dirar, S., Middleton, C.R., Elshafie, M.Z.E.B., 2017. Robust fibre optic sensor arrays for monitoring early-age performance of mass-produced concrete sleepers. Struct. Health Monit. Int. J.. https://doi.org/10.1177/1475921717714615.
[4] Chan, D.D., Neu, C.P., 2012. Transient and microscale deformations and strains measured under exogenous loading by noninvasive magnetic resonance. PloS One 7, e33463.
[5] Avril, S., Bonnet, M., Bretelle, A-S, Grédiac, M., Hild, F., Ienny, P., Latourte, F., Lemosse, D., Pagano, S., Pagnacco, E., Pierron, F., 2008. Overview of identification methods of mechanical parameters based on full-field measurements. Exp. Mech. 48, 381.
[6] Rouger, F., Khebibeche, M., Le Govic, C., 1991. Non determined tests as a way to identify wood elastic parameters the finite element approach. In: Mechanical Identification of Composites. Springer, Netherlands, pp. 82–90
[7] Richards, M.S., Barbone, P.E., Oberai, A.A., 2009. Quantitative three-dimensional elasticity imaging from quasi-static deformation: a phantom study. Phys. Med. Biol. 54, 757–779.
[8] Stuart, A.M., 2010. Inverse problems: a Bayesian perspective. Acta Numer. 19, 451–559.
[9] Skilling, J., 2006. Nested sampling for general Bayesian computation. Bayesian Anal. 1, 833–859.

TOPOLOGY OPTIMIZATION WITH 3D PRINTING NOZZLE SIZE RESTRICTIONS

Josephine V. Carstensen *
Department of Civil and Environmental Engineering, MIT, Cambridge MA, USA

Summary This paper presents a density-based topology optimization algorithm that implicitly incorporates the discrete nozzle size constraint associated with material extrusion 3D printing processes. The algorithm uses a projection-based approach such that a discrete number of nozzle passes is enforced on the resulting designs by altering the filtering operation. A standard intermediate density penalization scheme is used and the optimization problem is solved using a mathematical program. The algorithm is demonstrated on 2D benchmark examples.

INTRODUCTION

Recent years has seen a rapid development in manufacturing technologies, including 3D printing. This has raised a need for re-thinking conventional design. Topology optimization offers a means to leverage the new new manufacturing possibilities as it is a free-form design method that does not require a preconceived notion of the final layout. It has been known to achieve new, often complex, solutions that typically outperform conventional low-weight design. It is based on formulating a formal optimization problem and most rigorously solved using a mathematical program.

Although the advances in manufacturing technologies have made it possible to realize increasingly complex designs, there are still constraints associated with fabrication. Most recent research on topology optimization that embeds the constraint and/or possibilities associated with 3D printing has focused on eliminating overhang and designing with multiple base materials (see e.g. overview in [1]). In contrast, this work seeks to address the discrete nozzle size constraint that exists in material extrusion 3D printing processes.

Material extrusion 3D printing processes will in this work refer to manufacturing technologies that use Fused Deposition Modeling (FDM) or a similar fabrication procedure. In most FDM technologies, a 3D object is sliced and printed layer by layer by moving a nozzle that deposits material as illustrated in Fig. 1a. The solid parts of a realized design therefore consists of an integer number of nozzle passes. For example, if a nozzle that deposits material has size $d_{min,c} = 2$ units and is printing along the length of a member, then this member can have thickness $t_{member} = 2$ units, $t_{member} = 4$ units, $t_{member} = 6$ units and so on. It is not possible for the member to have a thickness of e.g. 3 units, since the nozzle cannot pass the member and deposit 1 unit thickness. This constraint is relevant for all FDM processes, but especially important to consider for large scale printing technologies such as concrete 3D printing.

To describe the nozzle constraint, the following assumptions are made about FDM processes; (i) the center part of the extruded material has a discrete member size that cannot be altered or overlap with other nozzle passes, and (ii) a bonding region is present on each side of the non-overlapping center. The bonding region is allowed to overlap with bonding regions created from other passes. The center and bonding regions within the nozzle passes are illustrated in Fig. 1b where the red refers to the non-overlapping part of a nozzle pass whereas green illustrates the bonding regions.

PROJECTION BASED NOZZLE SIZE RESTRICTIONS

This work suggests to implicitly embed discrete nozzle size restrictions in density-based topology optimization using a projection-based approach [2]. The proposed algorithm therefore embeds the manufacturability constraint in the filtering

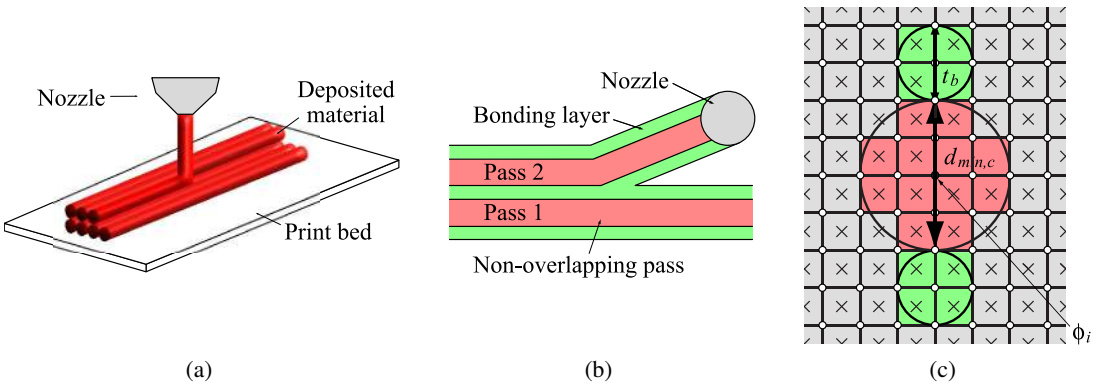

Figure 1: (a) schematic showing the FDM printing process, (b) the two regions herein assumed to be associated with a nozzle pass, and (c) the suggested projection domain that embeds the nozzle size restrictions.

*Corresponding author. E-mail: jvcar@mit.edu.

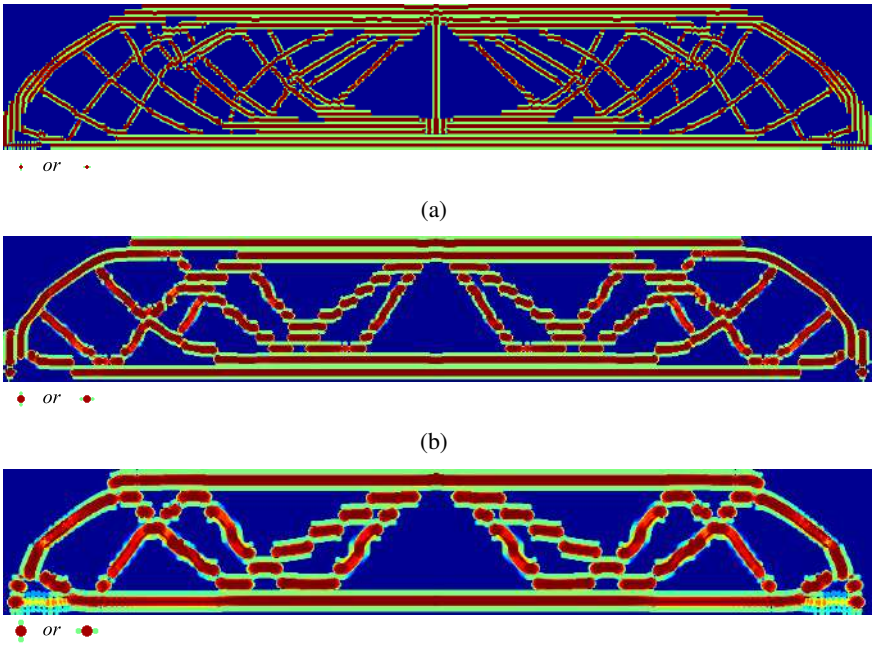

Figure 2: MMB beams designed for minimum compliance with volume constraints of 50% material and nozzle specifications of (a) $d_{min,c} = 0.50$ and $t_b = 0.25$, (b) $d_{min,c} = 1.00$ and $t_b = 0.50$, and (c) $r_{min,c} = 1.50$ and $t_b = 0.75$.

operation and uses a standard intermediate density penalization scheme. In this work, the Solid Isotropic Material with Penalization (SIMP) method [3] is used and the Method of Moving Asymptotes (MMA) [4] is taken as the gradient based optimizer.

To enforce the nozzle size restrictions an altered form of Discrete Object projection [5] is used to create the center and bonding zones. If the printing process is primarily associated with the nozzle moving along a single direction, the bonding layer is placed on each side of the non-overlapping feature along this direction. Figure 1c shows the new projection features for printing processes where the nozzle moves primarily horizontally. Here, the diameter of the circular features $d_{min,c}$ describes the non-overlapping size printed by the nozzle and t_b gives the bonding thickness allowed on each side. To allow horizontally and vertically dominated nozzle movement, an extension is suggested that use nonlinear weighting functions to determine the print direction at each point. The nonlinear weighting functions are taken as in [6].

Benchmark Results

The proposed algorithm is used to solve the standard topology optimization problem of minimum compliance on a range 2D benchmark problems. Figure 2 shows the results obtained for the MBB beam with different nozzle size restrictions and a total material constraint of 50%. As can be seen, the obtained designs depends highly upon the user specified constraints and all designs fulfill the discrete nozzle size requirements.

CONCLUSIONS

A projection based approach can implicitly embed the discrete nozzle size restrictions associated with material extrusion 3D printing processes in topology optimization. The herein suggested algorithm has been demonstrated on 2D examples and is in principal extendable to 3D.

References

[1] Liu J., Gaynor A. T., Chen S., Kang Z., Suresh K., Takezawa, A., Li L., Kato J., Tang J., Wang C. C. L., Chen L., Liang X., To A. C. Current and future trends in topology optimization for additive manufacturing. *Struct. Multidiscipl. Optim.* **57(6)**: 2457-2483, 2018.

[2] Guest J. K., Prévost, J. H., Belytschko, T. Achieving minimum length scale in topology optimization using nodal design variables and projection functions. *Int. J. Numer. Meth. Eng.* **61(2)**: 238-254, 2204.

[3] Bendsøe M. P. Optimal shape design as a material distribution problem. *Struct. Optim.* **1(4)**: 193-202, 1989.

[4] Svanberg K. The method of moving asymptotes: A new method for structural optimization. *Int. J. Numer. Meth. Eng.* **24(2)**: 359-373, 1987.

[5] Ha S.-H., Guest J. K. Optimizing inclusion shapes and patterns in periodic materials using discrete object projection. *Struct. Multidiscipl. Optim.* **50(1)**: 65-80, 2014.

[6] Carstensen J. V., Guest J. K. Projection-based two-phase minimum and maximum length scale control in topology optimization. *Struct. Multidiscipl. Optim.* **58(5)**: 1845-1860, 2018.

GENERATING MULTI-MATERIAL TRUSS-LIKE CELLULAR STRUCTURE DESIGN BASED ON CONTINUOUS/DISCRETE DENSITY MAPPING STRATEGY

Yingchun Bai *, Siqi Li
National Engineering Laboratory for Electric Vehicles, School of Mechanical Engineering, Beijing Institute of Technology, Beijing, China

Summary Multi-material truss-like cellular design can generate high-performance and light-weight structures, however, the design complexities arise from the necessities of material selection and truss cellular design simultaneously. In this work, a continuous/discrete density mapping strategy is proposed in combination with AAP multi-material topology optimizer. A numerical example is tested to demonstrate its effectiveness.

Introduction

With the increasing usage of additive manufacturing (AM), feasibility of fabricating light-weight and high-performance complicated structures makes it extremely urgent to design multi-material truss-like structures. The classical truss-like cellular structure can be designed by using the Ground Structure Approach (GSA) or Size Matching and Scaling (SMS) method, which will bring computational burden when involving multi-material problems. To accelerate the design efficiency, a continuous/discrete density mapping strategy is developed following the continuous multi-material topology optimization solution to generate the truss-like cellular structure, which will balance the computational cost and expected design feature.

Multi-material Relative Density Mapping Strategy (MM-RDM)

Similar as single-material relative density mapping approach, multi-material truss-like cellular structures can be generated by using multi-material relative density mapping strategy (MM-RDM) in combination with multi-material topology optimizer such as alternative active phase (AAP). When multi-material involved, the arising challenges are material selection and geometry size calculation for each member of the background truss structures. Inappropriate mapping strategy may lead to manufactural unfavourable material interface, in which specific material member are isolated within other material members. To handle this issue, we proposed two mapping strategies, namely continuous and discrete mapping strategy, based on which the multi-material truss-like structures can be obtained. The framework of the proposed approach is shown in Fig. 1. The remarkable difference between the continuous and discrete mapping strategies is the material selection method, which will be detailed explained hereafter.

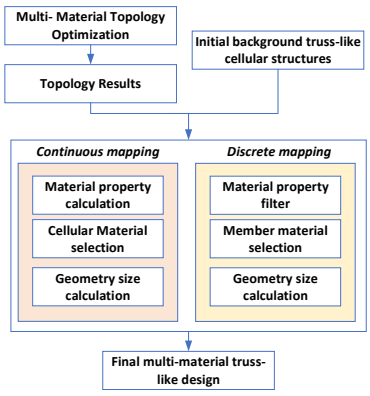

Fig. 1. Framework of the proposed approach

(1) Continuous mapping strategy

Based on the topology optimization results by AAP, a modified projection weight is developed as

$$w_{jm} = \frac{\sum_{i=1}^{n} \rho_{im} SE_i e^{-\frac{r_{ij}}{0.1L}}}{\sum_{i=1}^{n} e^{-\frac{r_{ij}}{0.1L}}} \tag{1}$$

where w_{jm} is the projection weight of mth material for jth truss member; ρ_{im} is the material density of mth material for ith element; SE_i is the strain energy of the ith element of final topology by AAP; r_{ij} is distance between the centroid of ith element and jth truss member; L is the length of the jth truss.

*Corresponding author. E-mail: baiyc@bit.edu.cn.

With the above projection weight, the Young's Modulus E_j of the jth truss member can be calculated by

$$E_j = \frac{\sum_{m=1} E_m w_{jm}}{\sum_{m=1} w_{jm}} \tag{2}$$

where E_m is the Young's Modulus of the mth material. It should be noted that the Young's Modulus E_j may have difference with the actual Young's Modulus of the candidate materials, and it can be further filtered into the Young's Modulus of the candidate materials.

(2) Discrete mapping strategy

Discrete mapping strategy employ a brute-force method to directly compare the projection weight to select the corresponding projection weight. The Young's Modulus E_j of the jth truss member can be calculated by

$$E_j = E_{k \in \max(w_{jm}), m=1,2,\ldots,M_{total}} \tag{3}$$

where $E_{jk \in \max(w_{jm})}$ means assigning the Young's Modulus with the maximal projection weight to jth truss member, and M_{total} is the total number of the candidate materials.

(3) Geometry size calculation

For the above two material selection strategies, the geometry size calculation can be performed using the following formulation

$$Ar_j = \frac{\sum_{m=1} w_{jm} E_m}{E_j} \tag{3}$$

where Ar_j is the cross-section area of jth truss member.

A Demonstrated Numerical Example

A cantilever beam as shown in Fig. 2(a) is provided to demonstrate the effectiveness of the proposed method. The design domain is $80\text{mm} \times 40\text{mm}$. An external force F=1N is applied at the middle point of the right boundary. The Young's Modulus are 3000 Mpa (red material) and 1000Mpa (blue material) for candidate materials, respectively. For the design problem, the target truss volume of each material are 300mm^3 and 300mm^3, respectively.

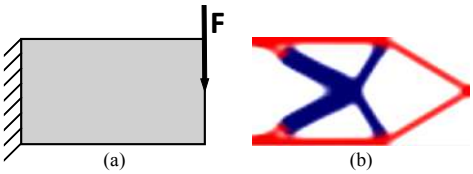

(a) Cantilever example (b) MMTO results

Fig. 2 Design space and MMTO results

The optimization result of the AAP algorithm is shown in Fig.2(b). The result of the continuous mapping method is shown in Fig.3(a), whose displacement of force apply point is 0.21 mm, which costs 47.55s. While the result of the discrete mapping method is shown in Fig.3(b), whose displacement of force apply point is 0.17mm, which costs 44.97s. It can be observed that the proposed strategies can generate manufacturing favourable multi-material truss-like cellular structure.

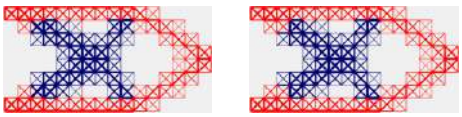

(a) Result of continuous mapping method; (b) Result of discrete mapping method

Fig. 3 Generation of multi-material truss-like structures

CONCLUSIONS

A modified continuous/discrete mapping strategy is proposed for multi-material truss-like structure generation. The numerical example demonstrates that both mapping strategy can generate the manufacturing favourable structures effectively and efficiently. Compared with the continuous approach, the discrete approach shows its advantages in terms of structural performance and computation efficiency.

References

[1] Dorn W, Gomory R, Greenberg H. Automatic design of optimal structures [J]. J Mech, 1964, 3: 25-52.

[2] Graf G C, Chu J, Engelbrecht S, et al. Synthesis methods for lightweight lattice structures[C]//ASME 2009 International design engineering technical conferences and computers and information in engineering conference. American Society of Mechanical Engineers Digital Collection, 2009: 579-589.

[3] Tavakoli R, Mohseni S M. Alternating active-phase algorithm for multi-material topology optimization problems: a 115-line MATLAB implementation[J]. Structural and Multidisciplinary Optimization, 2014, 49(4): 621-642.

[4] Alzahrani M, Choi SK, Rosen DW. Design of truss-like cellular structures using relative density mapping method. Materials and Design, 2015, 85:349-360.

DEMONSTRATION OF THE NEED FOR TRANSIENT TOPOLOGY OPTIMIZATION

Devlin Hayduke*[1], Dr. Daniel Tortorelli [2,3], Dr. Jonathan Wong[3], and Dr. Philip Flater[4]
[1]Materials Sciences LLC, Horsham, PA, USA
[2] University of Illinois at Urbana-Champaign, IL, USA
[3] Lawrence Livermore National Laboratory, Livermore, CA, USA
[4] Air Force Research Laboratory, Munitions Directorate, Eglin AFB, FL, USA

It has been suggested that optimal designs for structures undergoing unsteady, transient loading can be achieved using equivalent static loads [1-4]. However, this approach does not incorporate the structure's force-time history into the optimization process. Consequently, the approach may be suboptimal and, in some cases, may produce designs with decreased performance [5]. A topology optimization (TO) software integrated with a time-resolved, finite element (FE) solver is needed to determine whether the current static TO process is a reasonable cost-effective approach, or whether a more computationally-intensive, time-resolved, TO process is required.

In order to clearly demonstrate this need, Materials Sciences LLC (MSC), Lawrence Livermore National laboratory (LLNL), and the Air Force Research Laboratory (AFRL) are conducting research on the transient topology optimization of structures subjected to dynamic loads and boundary conditions. In particular, the team has focused on the development of a simple benchmark problem that clearly demonstrates that topology optimization via equivalent static loads not only produces a sub-optimal design, but instead produces designs that will fail under the intended transient loading. The presented research will include theoretical analysis of the benchmark problem, development of the static and transient optimizations of the benchmark problem, and experimental verification of the findings. It is believed that the results of this research clearly demonstrate the need for transient topology optimization and provide an experimentally verified benchmark problem to support future algorithm development.

References

1. Choi WS, Park GJ (1999) Transformation of dynamic loads into equivalent static loads based on modal analysis. Int J Numer Methods Eng 46(1):29–43
2. Choi WS, Park GJ (2002) Structural optimization using equivalent static loads at all time intervals. Comput Methods Appl Mech Eng 191:2077–2094
3. Park GJ, Kang BS (2003) Validation of a structural optimization algorithm transforming dynamic loads into equivalent static loads. J Optim Theory Appl 118(1):191–200
4. Shin MK, Park KJ, Park GJ (2007) Optimization of structures with nonlinear behavior using equivalent Comput Methods Appl Mech Eng 196(4–6):1154–1167
5. Stolpe, M., "The Equivalent Static Loads Method for Structural Optimization does not in General Generate Optimal Designs", Structural and Multidisciplinary Optimization, 58, 2018.

*Corresponding author. E-mail: hayduke@materials-sciences.com.

CNN - DRIVEN APPROXIMATE ALGORITHM OF TOPOLOGY OPTIMISATION BASED ON INITIAL STRESS LEARNING

Jun Yan*[1], Qi Zhang[1], Qi Xu[1] , Kun Yan[1]
[1] State Key Laboratory of Structural Analysis for Industrial Equipment, Department of Engineering Mechanics, Dalian University of Technology, Dalian, 116024, China

Summary A new approximate algorithm for topology optimisation is proposed by learning the initial stress, (ISL), which is the principal stress matrix obtained from the finite element analysis in the first iteration of classical topology optimisation. And a new algorithm evaluation method is proposed to optimize the prediction performance by selecting training samples and CNN models. By the established approximate algorithm based on both above, topological prediction results with high prediction accuracy can be produced with no iterations based on a relatively small sample set training. The algorithm is evaluated on cases, obtaining good prediction results.

INTRODUCTION

Recently, machine learning algorithms have developed rapidly. Because the machine learning algorithm requires high calculation costs in its offline training process and the use of trained model requires almost no complex calculations, it is used to achieve the accelerated or instant calculation of complex calculation processes. Currently, scholars have combined topology optimisation with the machine learning algorithm to improve the real-time computing efficiency of topology optimisation. However, existing results primarily include the following drawbacks: (1) The acceleration is incomplete, and the iterative process needs to be performed during online topology optimisation[1]; (2) The optimisation results are not ideal, and a clear load-transferred path cannot be obtained[2]; (3) An extremely large training set is required to train the model to achieve an acceptable approximate accuracy[3], which results in an exorbitant computing cost for training.

Hence, based on the CNN (Convolutional Neural Networks), a new approximate algorithm for topology optimisation is proposed by learning the initial stress, which is the principal stress matrix obtained from the finite element analysis in the first iteration of classical topology optimisation. By learning the relationship between the principal stress matrix of the initial (first iteration) optimisation structure and the final optimisation topology, this algorithm can provide approximate results of topology optimisation with a small number of training samples. Furthermore, a new algorithm evaluation method is proposed herein. Using this evaluation method, a CNN model is set up and trained to verify the feasibility of the algorithm proposed.

FLOW OF TOPOLOGY OPTIMISATION APPROXIMATE ALGORITHM

The flow of the algorithm proposed herein can be divided into three steps: generating dataset, CNN model training, and CNN-based prediction.

In step 1, the algorithm will generate loads according to the given boundary conditions based on certain rules and load types to perform topology optimisation. The specific rules and their effects are introduced in section 4. Based on the data generated using the SIMP method[4] and the optimised topology, the algorithm obtains the principal stress matrix from the finite element analysis in the first iteration of the topology optimisation. Additionally, the final topology optimisation results are required as the labels. These data will be used in step 2 to train the CNN model.

In step 2, the algorithm will train the CNN model according to the data obtained in step 1. The initial principal stress matrix serves as a variable, and the topology optimisation result is the label. To balance the effect of each sample on the training results, the initial principal stress matrix must be normalised (the matrix divided by the largest element) before being imported into the CNN model.

In step 3, the algorithm will predict the topology optimisation results under other load cases according to the trained CNN model obtained in step 2. The prediction requires a finite element calculation based on the topology optimisation problem to be predicted, and the extracted principal stress matrix is input into the trained CNN model. After obtaining the input, the CNN model can output the probability distribution of the final predicted results of topology optimisation of the structure rapidly and convert the distribution into the predicted topology optimisation results.

EVALUATION OF TOPOLOGY OPTIMISATION APPROXIAMATE ALGORTHM

For the algorithm herein, the optimisation formulation of the model optimisation process in traditional concept is as follows:

$$\min \ \frac{\sum_{i=1}^{S} d(\boldsymbol{\rho}^p)}{S}$$
$$d(\boldsymbol{\rho}^p) = \sqrt{\frac{\sum_{i=1}^{m}\sum_{j=1}^{n}(\rho_{ij}^t - \rho_{ij}^p)^2}{N}}, \qquad (1)$$

where m and n are the length and width of the design domain, respectively; $\boldsymbol{\rho}^t$ is the optimised topology matrix composed of ρ_{ij}^t based on the SIMP method; $\boldsymbol{\rho}^p$ is the predicted topology matrix composed of ρ_{ij}^p based on the algorithm; S is the total number of samples in the training set; d is the difference coefficient, which is introduced to represent the effectiveness of the prediction results of the algorithm for a sample. The smaller the $d(\boldsymbol{\rho}^p)$ is, the more similar the predicted topology is to the results obtained by the standard SIMP topology optimisation.

* Corresponding author. Email: yanjun@dlut.edu.cn

The performance evaluation method above is highly effective for most algorithms. However, because the optimisation goal is to minimise the overall difference between the optimised and predicted results, the predicted results of the deep learning model adjusted according to the evaluation method above may exhibit a phenomenon that the deep learning model stops predicting some samples that are difficult to master and only provides ideal or the same predicted results for samples that are easy to master. This may result in algorithm instability. Hence, a prediction accuracy parameter D and a new evaluation method is proposed based on (9):

$$f(\boldsymbol{\rho}_p) = \begin{cases} 0 & if\ \ d(\boldsymbol{\rho}_p) > \alpha \\ 1 & otherwise \end{cases}$$
$$D(\boldsymbol{\rho}_p) = \frac{\sum_{i=1}^{S} f_i(\boldsymbol{\rho}_p)}{S}, \qquad (2)$$

where $f(\boldsymbol{\rho}_p)$ is the similarity discriminant function, which is used to judge whether two structures are similar; α is the critical difference threshold. If the difference coefficient between the optimised and predicted results is greater than this threshold, then the predicted result is not similar to the optimised result; otherwise, it is similar. The smaller the α, the larger is D, and the better is the prediction performance of the model.

THE SINGLE-LOAD EXAMPLE

To verify the validity of the algorithm, a model was designed and trained with 1000 samples in this study. These samples were produced based on load cases in which equidistant sample points were selected and single vertical, horizontal, or 45° unit force was applied to the sample point. Also, a test set with 1000 samples in were set up in which load location and direction are both given randomly. The trained model gives validation accuracy D_v=0.892 on the test set while the critical difference threshold was set as $\alpha = 0.25$. That proves the algorithm proposed herein can effectively predict most single load cases after only 1000 samples of training and provide reasonable approximate results of topology optimisation.

Two load cases are chosen to show the specific prediction result, as shown in **Fig.1**. In case 1, a vertical downward unit load to the lower right corner of the cantilever was applied. In case 2, the load is applied at an upper 45° direction at the centre of the right boundary.

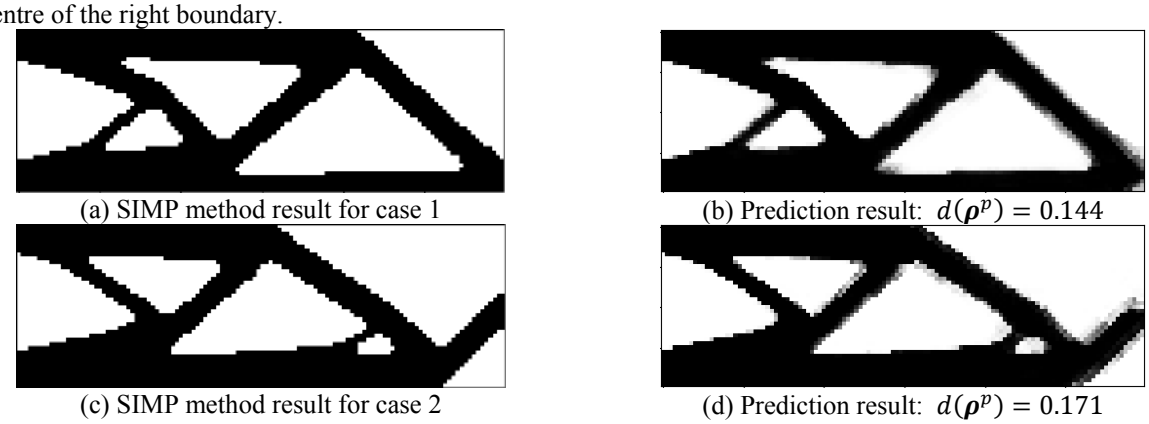

(a) SIMP method result for case 1 (b) Prediction result: $d(\boldsymbol{\rho}^p) = 0.144$

(c) SIMP method result for case 2 (d) Prediction result: $d(\boldsymbol{\rho}^p) = 0.171$

Figure 1 Comparison between topology optimisation and CNN-predicted results of load

CONCLUSIONS

An approximate topology optimisation method with high prediction performance and improved real-time calculation efficiency was proposed. Compared with the published approximate algorithm for machine learning topology optimisation, the algorithm proposed herein reduced the number of learning samples significantly and simultaneously yielded approximate results that were highly similar to those of the standard topology optimisation algorithm. Based on the new algorithm evaluation method proposed herein, a set of CNN model structure and sample selection method are proposed.

ACKNOWLEDGEMENTS

Financial supports for this research were provided by the National Natural Science Foundation of China (nos. 11672057 and U1906233), the 111 project (B14013), the Fundamental Research Funds for the Central Universities (DUT19ZD204).

References

[1]Sosnovik I, Oseledets I. Neural networks for topology optimization[J]. Russian Journal of Numerical Analysis and Mathematical Modelling 2019, 34: 215-223.
[2]Lei X, Liu C, Du Z, et al. Machine learning-driven real-time topology optimization under moving morphable component-based framework[J]. Journal of Applied Mechanics, 2019, 86(1): 011004.
[3]Yu Y, Hur T, Jung J, et al. Deep learning for determining a near-optimal topological design without any iteration[J]. Structural Multidisciplinary Optimization, 2019, 59(3): 787-799.
[4] Andreassen E, Clausen A, Schevenels M, et al. Efficient topology optimization in MATLAB using 88 lines of code[J]. Structural Multidisciplinary Optimization, 2011, 43(1): 1-16.

TWO-DIMENSIONAL (2D) SWIRL TOPOLOGY OPTIMIZATION OF LABYRINTH SEAL FOR METHANE COMPRESSOR APPLICATION: DIODICITY APPROACH

Shahin Ranjbarzadeh*[1], Bruno Caldas[1], Renato Picelli[2], and Emilio Carlos Nelli Silva [1]
[1]Department of Mechanical Engineering, University of Sao Paulo, Sao Paulo, Brazil
[2]Department of Mining and Petroleum Engineering, University of Sao Paulo, Santos, Brazil

Summary Labyrinth seals are the most popular and the oldest mechanical sealing solution in the industry and play a vital role in the prevention and reduction of fluid emission. In the last decades, the improvement of the Labyrinth seal in multi-stage pumps and compressors attracts a great attention. Due to the very high number of geometrical parameters (e.g., seal cavity depth, seal tooth thickness and tooth tip clearance) and difficulties related to determining their effects on labyrinth seal performance, the Topology Optimization is a feasible approach to achieve the best design with the highest efficiency. Thus, this paper presents a Topology Optimization formulation for design the labyrinth seal by using a 2D swirl flow model. The model is developed based on the Navier-Stokes equation to consider an axisymmetric flow with flow rotation around the shaft (fluid flow in labyrinth seal), and an objective function is defined in order to maximize the Diodicity of dissipation energy. Then, the Topology Optimization formulation with a 2D swirl flow model is coupled and implemented in COMSOL Multiphysics (based on the finite element method) and solved using Sparse nonlinear OPTimizer (SNOPT) solver. Post-processed results, e.g. Topology optimization design, fluid flow, and pressure contour, is presented. The results show the improvement in the performance of the labyrinth seal.

INTRODUCTION

Labyrinth seals are the most popular and the oldest mechanical sealing solution in the industry and play a key role in the prevention and reduction of fluid emission. The labyrinth seals have several layouts and because of convenient installation and reasonable efficiency have a wide range of applications in compressors, pneumatic turbines, sodium-cooled fast reactor (SFR), and very high-temperature reactors (VHTR). The fundamental of labyrinth seal mechanism commonly is based on a series of extended surfaces forming chambers between an axis and a fixed part that cause recirculation in the fluid which reduces leakage. The fluid flow through a labyrinth seal can be considered as a flow through a series of mechanical restriction and this fluid is driven by the total pressure gradient between two sides ofthe labyrinth seal. For many years, improving the design and performance of the labyrinth seals attracts great attention and has been a challenge in engineering. Due to the complexity of the labyrinth seal, a few experimental works were conducted to investigate and study the labyrinth seal and stablish an understanding of the flow mechanism in the labyrinth seal

Labyrinth seals being studied with different structures. However, in the context of labyrinth seals optimization, works in literature are limited to parametric assessments, shape optimization, regression optimization, and genetic algorithms. Due to the very high number of geometrical parameters (e.g., seal cavity depth, seal tooth thickness and tooth tip clearance) and difficulties related to determining their effects on labyrinth seal performance, the Topology Optimization is a suitable approach to achieve the best design with the highest efficiency. In recent years, topology optimization has been considered as a powerful computational tool for fluid and structural design. Topology optimization is a mathematical formulation to optimize and distribute the material in the design domain with predefined boundary conditions and constraint.

In order to enhance the performance and efficiency of labyrinth seal, this paper presents a Topology Optimization formulation for design the labyrinth seal by using a 2D swirl flow model. The model is developed based on the Navier-Stokes equation to consider an axisymmetric flow with flow rotation around the shaft (fluid flow in labyrinth seal), and an objective function is defined in order to maximize the energy dissipation. The rotation of the rotor is also taken into consideration in the 2D-Swirl domain to evaluate the shaft rotattion speed influence on the labyrinth seal design. Due to working details of labyrinth seal, it is necessary to keep a gap between labyrinth seal and shaft. Here, we use the diodicity behavior to minimize the leakage in main flow (forward flow) of labyrinth seal using an auxiliary reverse flow to maintain the necessary gap. Then, the Topology Optimization formulation with a 2D swirl flow model with predefined boundary conditions is implemented in COMSOL Multiphysics (based on the finite element method) and optimization was performed using Sparse nonlinear OPTimizer (SNOPT) solver. First, the fluid simulation needs to be performed in both direction, then the output velocities need to be supplied to the sensitivity analysis together with the solution of the adjoint system. Finally, the optimization can take place, calculating the objective function and its gradients, obtaining possible new geometries for the labyrinth seals. The problem constraint is the volume of fluid. To the author's best knowledge, this is the first work that used the topology optimization formulation to improve the labyrinth seal design.

*Corresponding author. E-mail: ranjbarzadeh@usp.br.

NUMERICAL IMPLEMENTATION

The theoretical Multiphysics model has been implemented and subsequently solved numerically in the finite-element software COMSOL Multiphysics. Briefly, the mathematical model consists of the fully coupled fluid and Topology Optimization Method. Fluid implemented with the incompressible Navier-Stokes equations, density model implemented using Darcy model and finally coupled equations solved by Sparse Nonlinear OPTimizaer (SNOPT) solver. The general idea is maximizing diodicity to catch minimum leakage possible at the outlet of labyrinth seal. Figure 1 illustrates the domain and related boundary conditions which is implemented in COMSOL. Here, velocity was chosen at the inlet, ambient pressure (100 kPa) at the outlet and no slip condition applied to the walls. Specified velocity of rotating shaft employed in 2D swirl flow topology optimization simulation.

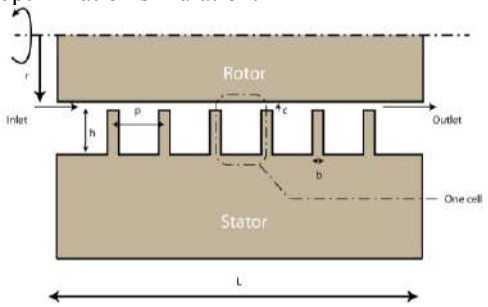

Figure 1. Schematic design of a full labyrinth seal with shaft rotation and key parameters.

PRELIMINARY RESULTS

In this section simulations are performed with focus on full labyrinth seal and topology optimization applied to typical geometry of labyrinth seal consist of inlet, topology domain and the outlet. A labyrinth seal with aspect ratio of 20:3, 40 mm shaft radius, fixed velocity (0.25 m/s) at the inlet and fixed pressure (100 kPa) at the outlet imposed. Simulations here are performed with real properties of CH_4 and 1500 to 6000 rpm rotation. Topology optimized geometry and related fluid velocity profile are demonstrated in figure 2.

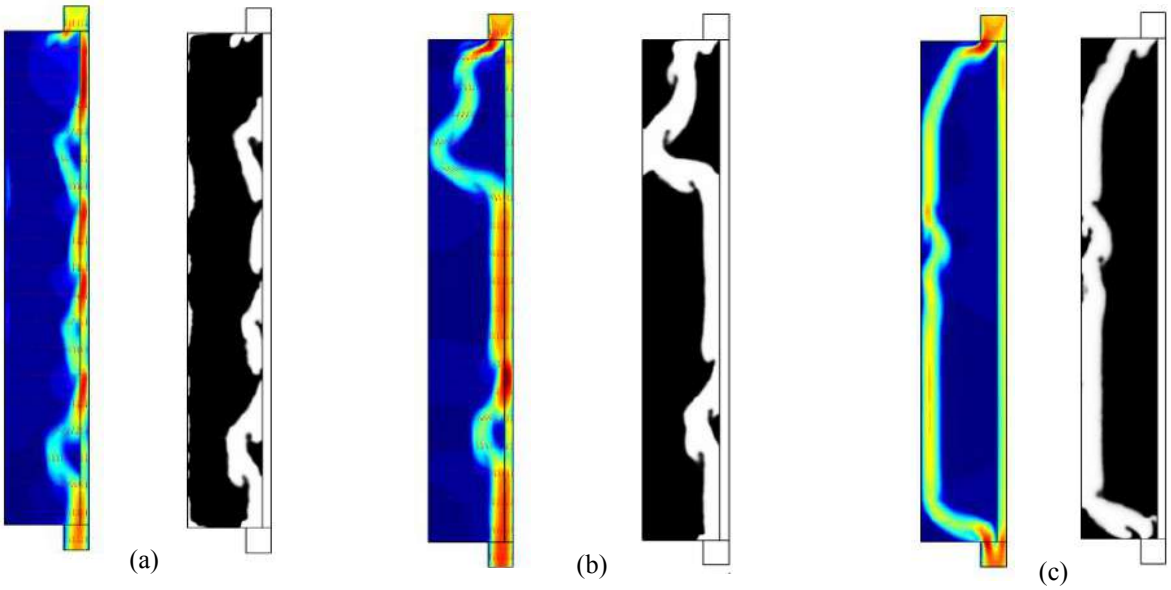

Figure 2. Topology optimized design and related fluid velocity profile obtained for full labyrinth seal with aspect ratio of 20:3, volume constraint < 0.3 and (a)1500 rpm (config. 4), (b) 3000 rpm, and (c) 6000 rpm (config. 5) rotation speed.

References

[1] ALONSO, D. H. et al. Topology optimization applied to the design of 2D swirl flow devices. Structural and Multidisciplinary Optimization, Springer, v. 58, n. 6, p. 2341–2364, 2018.

[2] LIN, S. et al. Topology optimization of fixed-geometry fluid diodes. Journal of Mechanical Design, American Society of Mechanical Engineers, v. 137, n. 8, p. 081402, 2015.

DISCOVERY OF HIGH-PERFORMANCE CU ALLOYS FROM DISCARDED EXPERIMENTS AND PHYSICAL FEATURES: A DATA-DRIVEN METHOD

Qingkun Zhao[1], and Haofei Zhou*[1]
[1]Center for X-mechanics, Department of Engineering Mechanics Zhejiang University, Hangzhou, Zhejiang, PR China

Summary: Copper alloys with high strength and electrical conductivity are ideal candidates for a wide range of civilian and engineering applications. Traditional experiments are costly and time-consuming, leading to the "discarded" experimental data with unsatisfied properties. Herein, an accelerated multi-objective design strategy from the application of machine learning, experimental characterization, genetic algorithm is proposed. The predicted Cu alloys were experimentally characterized, exhibiting superior hardness or electrical conductivity. The physical features of Cu alloys are employed to train effective models, and the impact the features on prediction model is evaluated by a genetic algorithm. Our findings suggest that the data-driven method holds great potential for solving complex optimum problems owing to its ability to consolidate information from multiple sources.

INTRODUCTION

The engineering applications require enhanced mechanical properties of Cu materials such as high strength and hardness while maintaining excellent electrical conductivity. Unfortunately, universal strengthening approaches may cause impurity scattering, leading to the undesirable degradation of electrical conductivity. Conventional "trial-error" exploration of Cu alloys based on a priori knowledge or intuition are lacking robustness, leading to experimental data with undesirable hardness or conductivity. Benefiting from its ability to abstract knowledge from data, the machine learning (ML) tools are used to study the mechanical properties of materials and structures [Wen et al., 2019; Chen et al., 2019; Wang et al., 2019]. Our recent work [Zhao et al., 2021] presents a data-driven method to guide the design of high-performance Cu alloys by learning from the discarded experimental data. The physical features including extra information of the alloys are applied to the small sample training ML models. We successfully synthesized and characterized these optimized alloys, confirming the feasibility of our data mining method in the discovery of high-performance Cu alloys.

MACHINE-LEARNING RESULTS

The discarded experimental data and the physical features are normalized as the inputs of the ML model (Figure 1a). We select the ML algorithms and use the correlation-based feature selection to build an accurate and concise ML model (Figure 1b). The best combination of the experimental data and physical features is selected from all 6.92×10^{18} possible models. Experimental validation and iteration are performed (Figure 1c). In comparison with the original training dataset, the predicted Cu alloys exhibit a maximum of 7% and 12% increases for hardness and electrical conductivity, respectively. Finally, five Cu alloys showing superior overall performance are predicted. The increase of hardness is due to precipitation of second-phase Co-Ti and Fe-Ti compounds during aging, while the rise of electrical conductivity is caused by a purification effect of the precipitates on Cu matrix.

EFFECT OF THE PHYSICAL FEATURES ON ML MODELS

A genetic algorithm is used to quantitively describe the importance of physical features for the ML prediction by counting the survival rate, which is the possibility for a feature to be retained by the algorithm. A feature with survival rate equal to 1 indicates that it is retained in all repeated calculations. Interestingly, the feature named local size mismatch,$D.r = \sum_{i=1}^{n}\sum_{j=1,i\neq j}^{n} C_iC_j * |r_i - r_j|$(where C_i is the molar fraction of compositional element *i* (Cu, Co, Ti, Fe), and r_i is the atomic radius),is reserved in every GA calculation for electrical conductivity prediction. It is generally accepted [Qu et al., 2013] that the contribution of solid solution scattering to electrical resistivity ($\Delta\rho_S$) can be calculated as $\Delta\rho_S = \left(\frac{\Delta\rho}{\Delta x}\right)x$, where x is the element solubility (in Cu), and the coefficient ($\Delta\rho/\Delta x$) depends on the type of element. One possible explanation is that the atomic size bears influence to the coefficient ($\Delta\rho/\Delta x$). The feature related to the modulus mismatch shows the highest survival rate for hardness prediction, can also be explained by solid solution strengthening effect [Wang et al., 2018]. We note that the discovery of these interesting results does not rely on prior knowledge.

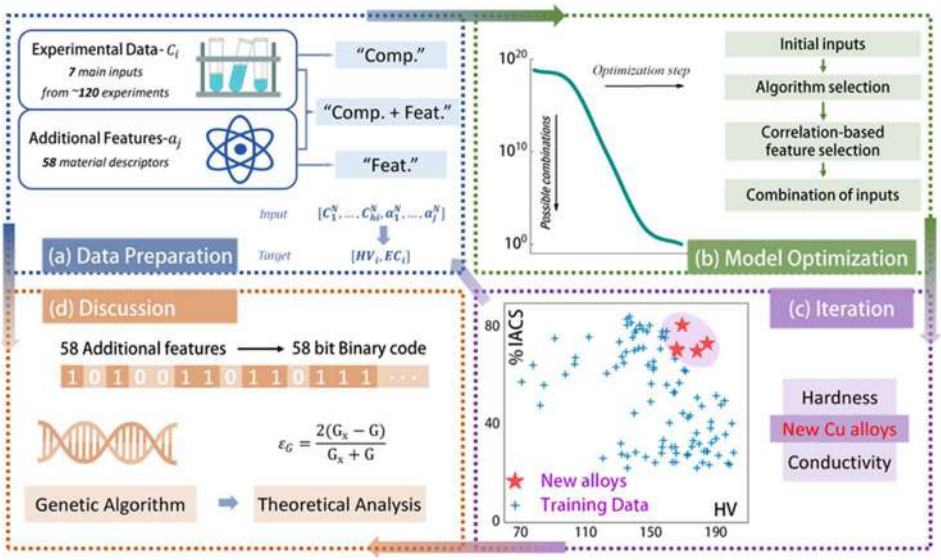

Figure 1. Schematics of the discovery process in high strength and high conductivity Cu alloys.

CONCLUSIONS

In the present study, we proposed a data-driven method to identify the relationship between chemical composition, aging time and target properties (hardness and electrical conductivity) of Cu alloys. The machine learning models were trained by "discarded" experimental data with unsatisfactory properties produced by "trial and error" experiments. The additional features calculated by physical equations were introduced and combined by correlation-based analysis and genetic algorithm, further minimizing the error of prediction and reducing the complexity of the ML models. Through employing the optimized ML model with iteration and experimental validation, better properties of hardness (with an increment of 7%) and electrical conductivity (with an increment of 12%), which are higher than the maximum value in the original training data, were developed in the Cu alloys. Among the five selected Cu alloys showing both high hardness and electrical conductivity, Cu-0.45Co-0.23Ti and Cu-0.44Fe-0.23Ti are chosen for microstructure characterization and property testing. In addition, the impact of additional features on the ML models was analysed by a genetic algorithm and the importance of each feature in the model is quantitatively described. The results indicate that the ML model can predict the hardness and electrical conductivity of Cu alloys with reasonable accuracy, even if the compositional information is removed. Our findings suggest the ML-based method holds great potential for creating high-performance Cu alloys with both high strength and electrical conductivity.

References

[1] Wen C, Zhang U, Wang CX, et al. Machine learning assisted design of high entropy alloys with desired property. *Acta Mater.* **170**: 109-117, 2019.
[2] Chen X, Zhou HF, Li YM. Effective design space exploration of gradient nanostructured materials using active learning based surrogate models. *Mater. Des.* **183**: 108085, 2019.
[3] Wang CS, Fu HD, Jiang L, et al. A property-oriented design strategy for high performance copper alloys via machine learning. *NPJ Comput. Mater.* **5**: 87, 2019.
[4] Zhao QK, Yang HY, Liu JB, et al. Machine learning-assisted discovery of strong and conductive Cu alloys: Data mining from discarded experiments and physical features. *Mater. Des.* **197**: 109248, 2021.
[5] Qu L, Wang EG, Han K, et al. Studies of electrical resistivity of an annealed Cu-Fe composite. *J. Appl. Phys.* **113**: 173708, 2013.
[6] Wang ZP, Fang QH, Li J, et al. Effect of lattice distortion on solid solution strengthening of BCC high-entropy alloys. *J. Mater. Sci. Technol.* **34**: 349-354, 2018.

FILTERING BASED MILLING CONSTRAINTS FOR TOPOLOGY OPTIMIZATION

Lukas C. Høghøj* and Erik A. Träff
Department of Mechanical Engineering, Technical University of Denmark, Kongens Lyngby, Denmark

Summary A PDE-based filtering technique for topology optimization ensuring manufacturability by milling is introduced. The filter is based on the advection-diffusion equation. With the advection term dominating, the equation mimics a cumulative sum in the advection direction. Performing the mapping as a filtering step instead of a cumulative sum allows for a parallel implementation on unstructured grids, using the finite volume method with an upwind difference scheme. Results are obtained on unstructured meshes of up to 64 million elements.

INTRODUCTION

Topology optimization with milling and casting constraints was first introduced by [1], where rows or columns in a structured grid were characterized by a single design variable. The methodology was extended by use of cumulative sums in the milling directions [2]. Arbitrary milling directions were made possible with the approach introduced [3] using cumulative sums and a mapping technique. The mapping technique requires the storage of memory intensive transformation matrices, which also are expensive to assemble. The presented PDE filtering approach mimics the cumulative sum in arbitrary directions, allowing for an efficient implementation on large-scale problems.

FILTER FORMULATION

The milling filter is separated into one shadowing step (mimicking the cumulative sum) for each milling direction. This is seen in Figure 1, where the design field from Figure 1a is shaddowed in two directions, as seen in Figures 1b and 1c, respectively. In the shaddowing process, the density filtered variable is used as source term in the advection-diffusion equation, solved for the respective milling direction. The advection direction is set to the corresponding milling direction, combined with a high Peclet number, ensuring low diffusive effects. The advection-diffusion equation is solved using the Finite Volume Method, implemented with an upstream difference scheme on the advection term, which guarantees numerical stability of the solution. Robin boundary conditions are imposed on free boundaries, which allows for material to be placed adjacent to them. Dirichlet boundary conditions are placed on the boundaries next to passive domains, to ensure the manufacturability of those.

The shadowed fields are agglomerated using a smooth p-norm elementwise minimum function. The agglomerated field is then projected to the physical bounds of the design variable using a smooth Heaviside projection, which yields the final physical field, as seen in Figure 1d.

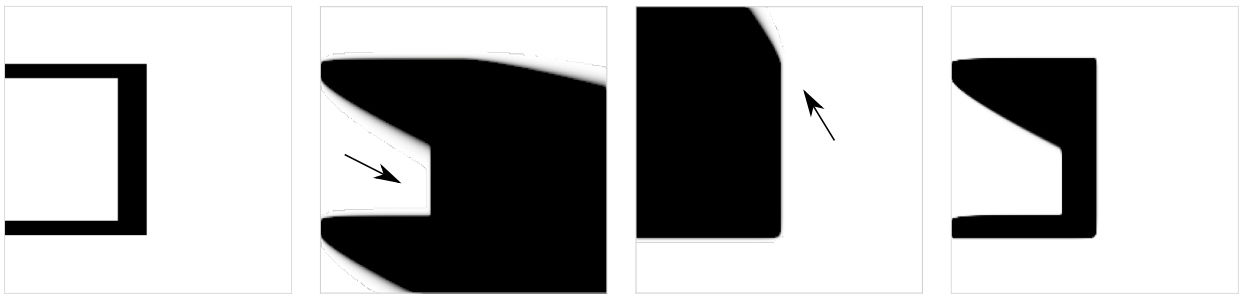

(a) (b) (c) (d)

Figure 1: Example of filtering process for a design field (a). Two shaddowing steps are performed by solving the advection-diffusion PDE (b-c) in the respective milling directions (indicated by the arrows) and are then agglomerated using the soft min and Heaviside projection (d).

The smooth Heaviside projection is performed with a constant projection sharpness to bound the physical field throughout the optimization process. Combined with the general nature of the milling filter, this makes the problem very sensitive. Hence, the Method of Moving Asymptotes (MMA) is used with a tightened initial asymptote setting [4], which alleviates oscilatory behavior.

*Corresponding author. E-mail: luch@mek.dtu.dk.

EXAMPLE

The milling filter is implemented in an in-house parallel three dimensional topology optimization framework [5], operating on unstructured meshes. To illustrate the methodology, the GE aircraft engine bracket [6] is optimized with a single milling direction from the top. The supporting and loaded rings are fixed to be solid, Dirichlet boundary conditions are enforced on the adjacent surfaces of the design domain.

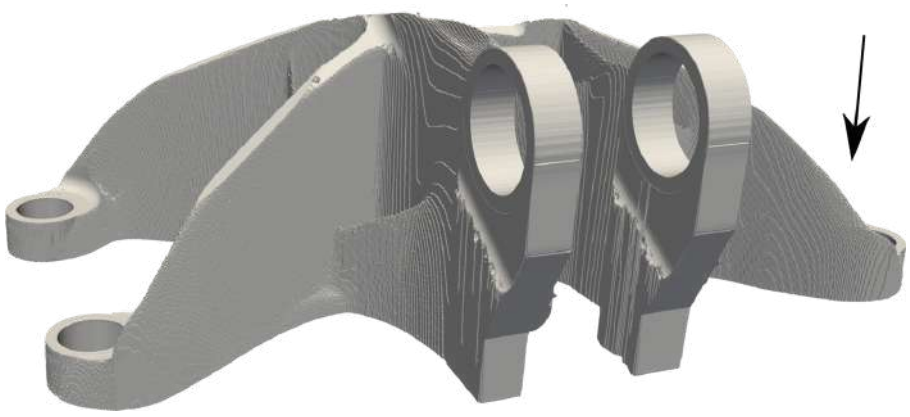

Figure 2: Optimized GE engine bracket, manufacturable with a single milling direction from the top, indicated by the arrow.

The design optimized with the single, from top, milling direction is seen in Figure 2. It is seen that no overhangs, except for the two passive loading rings, are present in the obtained design. The design is hence realizable by milling. The computational effort of the milling filter on the unstructured mesh with 64 million elements on 640 CPU cores is 25s per design iteration (including the projection and two adjoint solutions). In contrast, solving the four linear elasticity loadcases varies from 200s to 600s per design iteration (depending on the change and the contrast of the design).

CONCLUSION

A filtering technique based on the advection-diffusion equation, which ensures manufacturability by milling of the designs, is introduced. Contrary to previous work, the presented methodology allows arbitrary milling directions to be enforced in a parallel setting on unstructured meshes, omitting the need to assemble and store large transformation matrices.

References

[1] Gersborg, A. R., & Andreasen, C. S. (2011). An explicit parameterization for casting constraints in gradient driven topology optimization. Structural and Multidisciplinary Optimization, 44(6), 875–881. https://doi.org/10.1007/s00158-011-0632-0

[2] Guest, J., & Zhu, M. (2012). Casting and Milling Restrictions in Topology Optimization via Projection-Based Algorithms. Proceedings of the ASME Design Engineering Technical Conference, 3. https://doi.org/10.1115/DETC2012-71507

[3] Langelaar, M. (2019). Topology optimization for multi-axis machining. Computer Methods in Applied Mechanics and Engineering, 351, 226–252. https://doi.org/10.1016/j.cma.2019.03.037

[4] Guest, J. K., Asadpoure, A., & Ha, S.-H. (2011). Eliminating beta-continuation from Heaviside projection and density filter algorithms. Structural and Multidisciplinary Optimization, 44(4), 443–453. https://doi.org/10.1007/s00158-011-0676-1

[5] Träff, E. A., Sigmund, O. & Aage, N. (2020). Topology Optimization of Ultra High Resolution Shell Structures. Thin Walled Structures. Accepted.

[6] Carter, W. T. (2014). The GE aircraft engine bracket challenge: An experiment in crowdsourcing for mechanical design concepts. 25th Annual International Solid Freeform Fabrication Symposium an Additive Manufacturing Conference, Sff 2014.

OPTIMIZATION FOR VIBRATING COMPOSITE PLATE BY DISCRETE-CONTINUOUS MODEL AND RESONANT PEAK LIMITATION

Haoqing Ding*[1], Bin Xu[1]
[1]School of Mechanics, Civil Engineering and Architecture, Northwestern Polytechnical University, Xi'an, China

Summary Discrete material model includes many design variables, which cause intensive computational and storage burdens in both frequency response and sensitivity analysis. Even the continuous optimal model can be expected to solve the above problems, local optimal solution is more likely to be obtained due to the model's high non-convex character. Further, resonant peak limitation is also highly significant because of its dominant role in structural vibration. Based on above starting points, this paper develops an efficient optimal model for minimizing composite plate's frequency response by the combination of discrete-continuous parameterization model and the solid isotropic material with penalization scheme. The optimization problem is solved by the method of moving asymptotes and several numerical examples are employed to verify the effectiveness of the proposed model.

INTRODUCTION

Structural vibration suppression gains much attention because many structures in engineering are exposed to dynamic environments and the excessive vibration could have detrimental effects on structural functionality and safety. Integrated optimal design of the damping layer and the host layer is more likely to achieve the best performance of structural vibration reduction. For the optimal design of composite structures, the Discrete Material Optimization (DMO) formulation is considered as one of the effective methods and it has shown its effectiveness in solving both static and dynamic problem [1-3]. However, for complex optimal problems, such DMO technique can also cause heavy computational cost and storage burdens. One effective method to solve this issue is to consider the continuous orientation design. However, the continuous orientation design technique has been proven to be easily obtain a local optimal solution [4-6]. Therefore, the combination of DMO and continuous orientation design may provide a better way to handle the local optimal solution as well as reduce the computational and storage burdens. Besides, using the integration of frequency response as the objective function does not mean the peak value must be reduced. The peak value plays a dominant role in low-frequency vibration. Without limitation of the resonant peak, the structure would vibrate more excessively. Inspired by dynamic topology optimization from other scholars, this paper builds an integrated optimal model for minimizing composite plate's frequency response over a given frequency band and simultaneously considering low-order resonant peak limitation.

OPTIMAL PROBLEM STATEMENT

The optimization model for the laminated plate is formulated as:

$$\begin{aligned}
&\min_{y_i,x_i^l}: && J_d=\int_{\omega_l}^{\omega_u} J(\omega,\mathrm{y}_i,x_i^l,\theta_i^e)d\omega \\
&s.t.: && -\omega^2\mathbf{MU}+\mathbf{KU}=\mathbf{F} \\
&: && G_1=\sum_{i=1}^{N} y_i v_i \,/\sum_{i=1}^{N} v_i - V\le 0 \\
&: && 20\log 10(\left|\mathbf{U}\right|_{\omega=\mathrm{Re}(\omega_i)})\le P_{\lim} \\
&: && 0.001\le y_i\le 1 \\
&: && 0.001\le x_i^l\le 1 \\
&: && \theta_i^e\in[-\frac{\pi}{2n^l},\frac{\pi}{2n^l}]
\end{aligned} \tag{1}$$

where $J(\omega,\mathrm{y}_i,x_i^l,\theta_i^e)=\left|\mathbf{F}^T\mathbf{U}\right|$ represents the dynamic compliance under the excited frequency ω; ω_l and ω_u are the lower and upper bounds of the frequency interval, respectively; V is the maximum allowable volume fraction for the damping material 1; v_i is the volume of the i th finite element; θ_i^e, y_i and x_i^l are the design variables; **M** and **K** are the global mass and stiffness matrix, respectively; $P_{\lim}$ is the resonant peak limitation.

The discrete-continuous model (DCP) is used to obtain the element elastic matrix $\mathbf{Q}_{\theta_i^e}^l$ for the stiffness matrix (i.e. **K**) calculation. It can be stated as:

$$\mathbf{Q}^l=\sum_{i=1}^{n^l}\xi_i\mathbf{Q}_i=\xi_1\mathbf{Q}_1+\xi_2\mathbf{Q}_2+\ldots+\xi_{n^l}\mathbf{Q}_{n^l} \tag{2}$$

$$\mathbf{Q}_{\theta_i^e}^l=\mathbf{T}(\theta_i^e)\ \mathbf{Q}^l(\xi_1,\xi_2,\cdots,\xi_{n^l})\mathbf{T}(\theta_i^e)^T \tag{3}$$

*Corresponding author. E-mail: nwpudhq@163.com

NUMERICAL EXAMPLES

In this numerical example, a three-layer laminated plate with four edges clamped subjected to a harmonic mechanical load is investigated. The amplitude of the load is 100N and it is applied at the central point of the top of the plate. The length, width of the plate and the thickness of each layer are 1 m, 0.5m and 2 mm, respectively. The plate is meshed by 800 (40 × 20) four-node Mindlin laminated plate elements. The material prosperities are shown in **Table 1**. And the optimized results are shown in **Figure 1** and **2**.

Table 1. Material properties

Material	Density(kg/m^3)	Elastic modulus (Gpa)	Poisson's ration	Loss factor
Fiber	1559	$E_x = 165Gpa, E_y = 9Gpa,\ G_{yz} = 4.3Gpa\ , G_{xy} = G_{zx} = 6Gpa,$	$v_{xy} = 0.25$	-
Damping material	1000	2	0.4	0.5
`	200	0.065	0.47	-

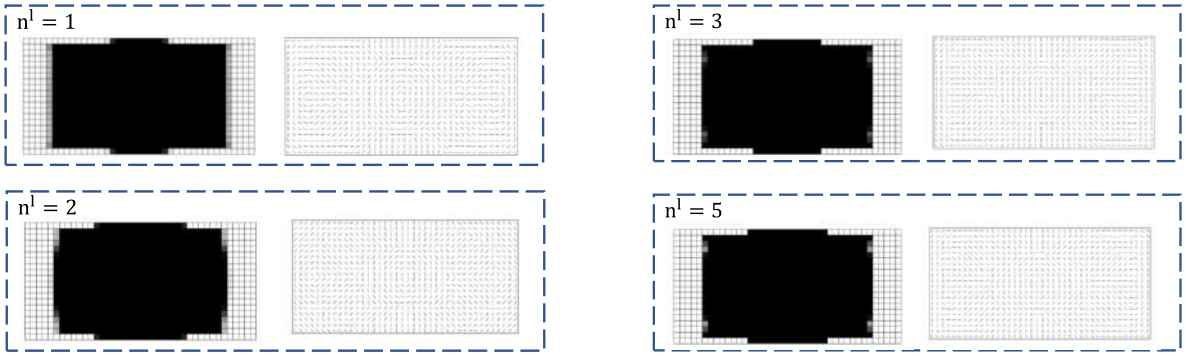

Figure 1 The optimized results for damping layer and fibre layer for different frequency intervals.

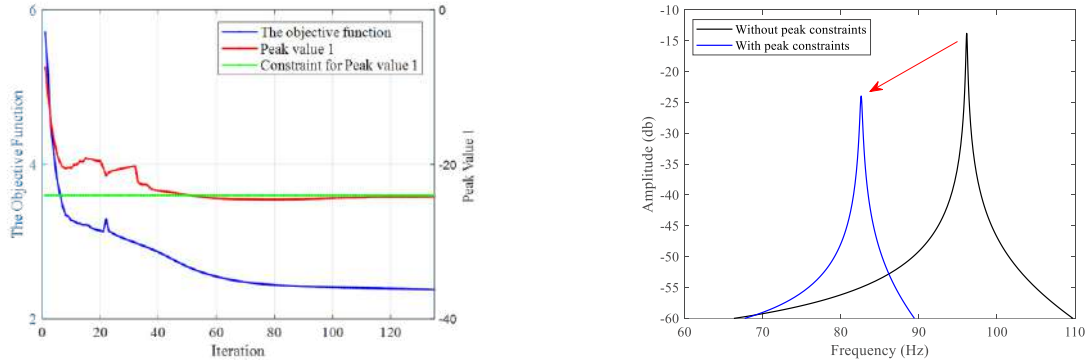

Figure 2. The iteration process and the change of the peak after optimization

CONCLUSIONS

Based on the optimized results in numerical example, a couple of conclusions can be drawn: (1) the DCP model provides a wide and flexible design space and reduces the number of the discrete design variables. Thus, it reduces the computational and storage burdens; (2) the DCP model efficiently reduces the risks of falling into local optimum solution; (3) 2 or 3 subintervals are suggested to efficiently reduce the possibility of falling into local optimum solution;(4) the proposed optimal model with resonant peak limitation is efficient and feasible.

References

[1] Stegmann J, Lund E. Discrete material optimization of general composite shell structures. Int J Numer Methods Eng .62(14): 2009–2027,2005

[2] Lund, E., & Stegmann, J.. Eigenfrequency and Buckling Optimization of Laminated Composite Shell Structures Using Discrete Material Optimization. IUTAM Symposium on Topological Design Optimization of Structures, Machines and Materials. Springer Netherlands.2006.

[3] Niu B, OlhoffN, Lund E, Cheng G. Discrete material optimization of vibrating laminated composite plates for minimum sound radiation. Int J Solids Struct. 47(16):2097–2114, 2010.

[4] Duan Z, Yan J, Zhao G. Integrated optimization of the material and structure of composites based on the Heaviside penalization of discrete material model. Struct Multidiscip Optim. 51(3):721–732, 2015.

[5] Ghiasi H, Fayazbakhsh K, Pasini D, Lessard L. Optimum stacking sequence design of composite materials part ii: variable stiffness design. Compos Struct. 93:1–13, 2010.

[6] Xu Y, Zhu J, Wu Z, Cao Y, Zhao Y, Zhang W. A review on the design of laminated composite structures: constant and variable stiffness design and topology optimization. Adv Compos Hybrid Mater.1:460–77, 2018.

A NOVEL USE OF THE GROUND STRUCTURE TOPOLOGY OPTIMIZATION FOR THE DESIGN OF PRESSURIZED STIFFENED PANELS

Mario Capo, JF Gamache, T. Rochefort-Beaudoin, Aurelian Vadean, Sofiane Achiche
Department of Mechanical Engineering, Polytechnique Montréal, Montréal QC, CANADA

Summary: The Ground Structure method is well-known in the literature for trusses and frames Topology Optimization, but its use in the design of stiffened panel has not been explored. In this work, an original reformulation of the method is proposed. Since beam elements are directly used as the set of candidate reinforcements, this approach ensures an explicit description of the final stiffener's geometry. This eliminates the need for interpreting the resultant material distribution or for imposing any geometric constraint to force the optimization towards manufacturability. The proposed reformulation has been implemented in MATLAB, tested on a benchmark problem and its potential as a design tool is demonstrated on the compliance-based topology optimization of the stiffeners layout of a simplified pressure bulkhead. The optimized design complies with those obtained by using SIMP and MMC methods.

INTRODUCTION

Stiffened panels are commonly used in aircraft structures for their high performance/weight ratio. The design process of such assemblies starts with an a priori choice on the reinforcement configuration (e.g. ortho-grid), mainly based on industrial experience. The use of Topology Optimization (TO) [1] can support this starting phase using a mathematical approach to enhance mechanical properties of stiffened panels from a global point of view.

Early research works proposed to roughly identify rib position optimizing thickness distribution of plates elements [2]. Methodologies based on the use of the SIMP method [3,4], propose to identify the stiffeners layout from the interpretation of high-density regions resulting from the TO. These approaches need the addition of geometric constraints to obtain manufacturable stiffener-like components, and post-processing procedures for the interpretation task [5]. To overcome these issues, new formulations based on the use of topological variables that explicitly control the geometry of the final structure rather than the mechanical properties of the starting mesh have been proposed. Belonging to this category, the MMC approach [6] has been recently applied to composite stiffened panels, where stiffeners are embedded in the plate model using equivalent stiffness method [7]. A major drawback of this method is the need of a very fine mesh to describe the stringers' features. The mesh size has to be at least smaller than the stringer's section width. This renders the use of such a model computationally expensive for large-scale applications.

The idea of a Ground Structure TO, which uses a mesh made of plates and beams comes from two basic considerations:
(1) This modelling strategy is computationally inexpensive and is commonly used in the industry for FEM analysis of large structures composed of stiffened plates, as well as for preliminary sizing of wingbox components. [8]
(2) The Ground Structure method is an easy-to-implement formulation which can deal with the structural members of interest in aircraft constructions. After the removal of vanishing members, the output of the TO contains explicit information on the final geometry without the need for interpretation.

METHODOLOGY

For the proposed formulation, a simple model made of Euler-Bernoulli beams coupled with discrete quadrilateral Kirchhoff plates with isotropic linear elastic material properties is used. In first approximation, one can consider that the two structural elements lie in the same plane and are connected to same nodal grid. Alternatively, to increase the accuracy of the analysis, the nodal points defining the beams must be offset and connected to the plate using rigid connections. Mechanical deformation of the stiffened panel under lateral loads is obtained from a linear static analysis.

An adaptation of the ground structure generation algorithm proposed by [9] is used to automatically superimpose a dense mesh of beam elements on a plate model, with an arbitrary level of connectivity. In the proposed method the topological design variables are the cross-sectional area of each beam elements composing the stiffeners, while the plates properties are kept constant.

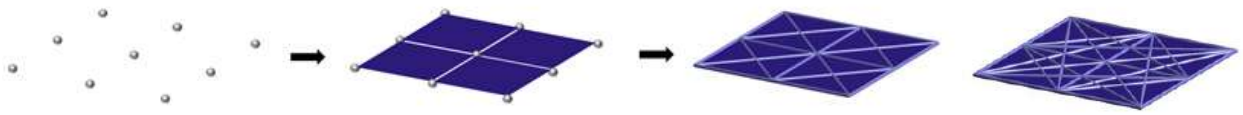

Figure 1. Ground Structure generation with arbitrary level of connectivity.

The formulation of the minimum compliance problem and the pseudo code of the algorithm are summarized in fig.2(a) and fig.2(b). The optimization problem is solved using the Interior Point Method implemented in the MATLAB Optimization Toolbox [10]. Load and nodal displacement vectors $\boldsymbol{f}, \boldsymbol{u}$ are expressed in the global reference system. Vector $\boldsymbol{l}$ contains all beam lengths and v_{max} is the maximum volume allowed for the reinforcement. A benchmark problem faced to test the algorithm is also shown in fig.2(c).

*Corresponding author. E-mail: **mario.capo@polymtl.ca**

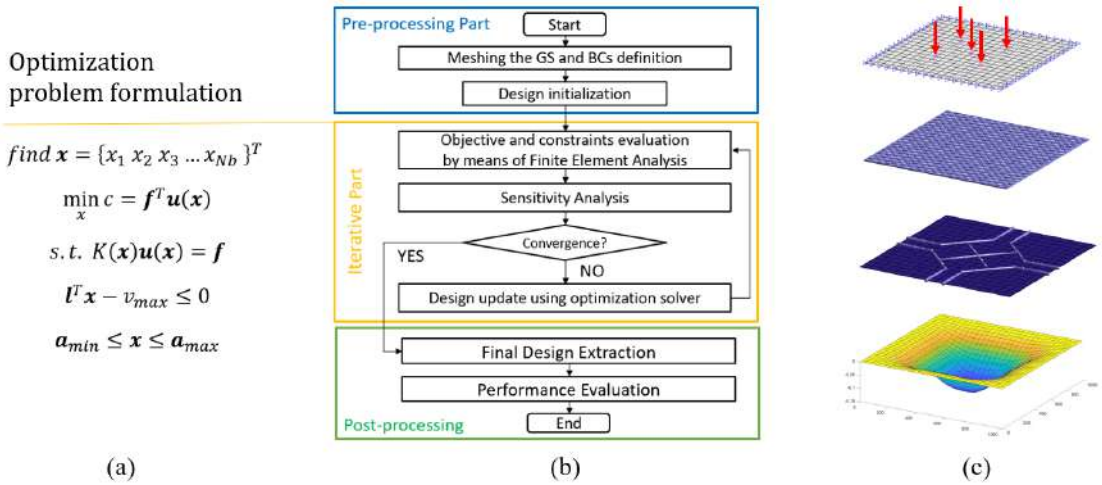

Figure 2. Overview of the method: (a) optimization formulation; (b) pseudo code implemented in MATLAB; (c) a benchmark problem test

A PRACTICAL ENGINEERING APPLICATION

A practical engineering problem is addressed to validate the procedure: the design of a flat pressure bulkhead subject to differential pressure ($0.1\ MPA$). Contour supports are located at equispaced points and simulate a riveting connection. The mechanical properties of Al2024-T4 are used, and geometric parameters are given as follows. A mesh of 40x24 rectangular element discretizes the design domain where $L = 2500\ mm$. This leads to an initial GS of 1984 members. The skin thickness is $1.25mm$, the interval for cross-sectional areas is $a_i \in [10^{-5}, 10^3]mm$, and v_{max} cannot exceed $5.625 \cdot 10^6\ mm^3$. The obtained optimized layout in fig.3 can be compared to those in [4,7].

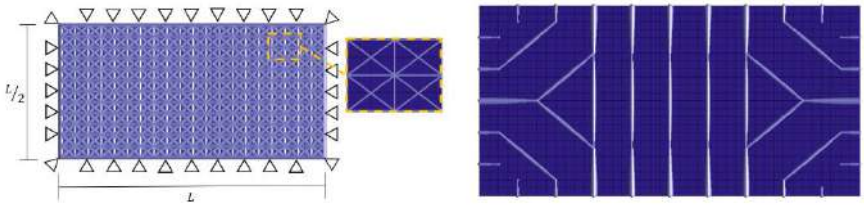

Figure 3. Starting GS and the optimized Stiffeners layout for a flat pressurized bulkhead.

CONCLUSIONS

In this work, a novel reformulation of the ground structure topology optimization is applied to the design of stiffeners layout for pressurized panels. The novelty of the method lies in the hybrid use of plates and beams elements to construct the ground structure, and in the context of application, never explored by the traditional method according to the authors' knowledge [11]. Numerical results indicate that the method can provide a clear stiffener layout for the compliance problem with volume constraints. The structure obtained is sound and one note the lesser involvement of designer during the post-processing procedure and particularly the TO interpretation. Inclusion of stress and buckling criteria, as well as a more complete finite element formulation are promising to be considered in future works.

References

[1] Bendsøe, Martin & Sigmund, Ole. (2004). Topology optimization. Theory, methods, and applications. 2nd ed., corrected printing. 10.1007/978-3-662-05086-6.
[2] Lam, Y.C. & Santhikumar, S.. (2003). Automated rib location and optimization for plate structures. Structural and Multidisciplinary Optimization. 25. 35-45. 10.1007/s00158-002-0270-7.
[3] Krog, L., A. Tucker, Airbus Uk and R. Boyd. "Topology Optimisation of Aircraft Wing Box Ribs." (2004).
[4] Dugré, Alexis & Vadean, Aurelian & Chaussee, Julien. (2016). Challenges of using topology optimization for the design of pressurized stiffened panels. Structural and Multidisciplinary Optimization. 53. 10.1007/s00158-015-1321-1.
[5] Gamache, Jean-François & Vadean, Aurelian & Noirot-Nérin, Emeric & Beaini, Dominique & Achiche, Sofiane. (2018). Image-based truss recognition for density-based topology optimization approach. Structural and Multidisciplinary Optimization.
[6] Zhang, W., Yuan, J., Zhang, J. et al. A new topology optimization approach based on Moving Morphable Components (MMC) and the ersatz material model. Struct Multidisc Optim 53, 1243–1260 (2016).
[7] Sun, Z., Cui, R., Cui, T. et al. An Optimization Approach for Stiffener Layout of Composite Stiffened Panels Based on Moving Morphable Components (MMCs). Acta Mech. Solida Sin. 33, 650–662 (2020).
[8] Megson, Thomas. (2013). Aircraft Structures for Engineering Students / T.H.G. Megson.. Aircraft Structures for Engineering Students
[9] Zegard, T., Paulino, G.H. GRAND — Ground structure based topology optimization for arbitrary 2D domains using MATLAB. Struct Multidisc Optim 50, 861–882 (2014). https://doi.org/10.1007/s00158-014-1085-z
[10] MATLAB and Statistics Toolbox Release 2016b, The MathWorks, Inc., Natick, Massachusetts, United States
[11] Gamache, Jean-François & Vadean, Aurelian & Dodane, Nicolas & Achiche, Sofiane. (2020). Topology Optimization for Stiffened Panels: A Ground Structure Method. 10.1115/DETC2020-22103.

*Corresponding author. E-mail: **mario.capo@polymtl.ca**

TEACHING APPARATUSES FOR MECHANICAL VIBRATIONS

Masato Saeki *[1]
[1]Department of Mechanical Engineering, Shibaura Institute of Technology, Tokyo, Japan

Summary Various apparatuses used in a classroom lecture on mechanical vibrations are presented. In my laboratory, 15 types of apparatus have been developed to reproduce various vibration phenomena such as mechanical resonance and vibration modes. They are used to teach students how to forecast the type of motion that could occur before determining equations of motion for mechanical systems. Their use seems to have a positive educational impact on students.

INTRODUCTION

In a classroom lecture on mechanical vibrations, showing various vibration phenomena in mechanical systems can stimulate the interest of students. Although animated images obtained by numerical simulations are often used in classroom lectures, the use of vibration apparatuses has a positive educational impact on students compared with numerical simulations, because it is more impressive to see live performances. Various demonstrations of physics [1], [2] and structural mechanics [3] have been presented. However, there are not many apparatuses for use in lectures on mechanical vibrations.

In my laboratory, various apparatuses have been developed to reproduce vibration phenomena such as mechanical resonance and vibration modes. They are used to teach students how to forecast the type of motion that could occur before determining equations of motion for mechanical systems. According to the responses to a questionnaire, most students said that the lecture in which teaching apparatuses were used was interesting. All teaching apparatuses have been evaluated by researchers belonging to enterprises and universities and have been improved.

VARIOUS TEACHING APPARATUSES

Figures 1(a) and (b) show two examples of various teaching apparatuses, a vibration conveyor and a device generating transverse vibration of a string, respectively. Although vibration conveyors are widely used in various industries such as food processing and pharmaceuticals, the mechanism of vibration feeding is not well known. Also, most students are not able to move an eraser on a notebook in the horizontal direction by vibration. Therefore, the vibration conveyor shown in Figure 1(a) was developed. In this apparatus, a conveying plate is supported by two leaf springs that are inclined toward the horizontal plane. An eccentric rotating mass vibration motor is attached to the underside of the conveying plate. When the conveying plate is excited by an eccentric rotating mass vibration motor, an object placed on the conveying plate can be conveyed owing to the inertia force acting on the object. Also, the behaviour of the object and the conveying plate can be clearly observed in the images captured by a high-speed camera. As a result, students can understand the mechanism of the vibration conveyor and the purpose of the two inclined leaf springs.

The apparatus shown in Figure 1(b) consists of a motor and a string. The string is fixed at both ends, one of which is excited sinusoidally via a slider-crank mechanism and a motor. When the frequency of the end of the string excited sinusoidally is increased, the first four modes of vibration of the string can be observed.

Figures 2(a) and (b) show a tuned mass damper and a sloshing damper, respectively. In Figure 2(a), apparatus A at the front consists of a primary mass supported by two leaf springs whose ends are located on a linear guideway. The ends of the springs are excited sinusoidally via a slider-crank mechanism. Apparatus B behind A has the same structure as A but a mass-spring system is attached to the primary mass as an auxiliary system. As shown in Figure 2(a), the damping performance of the tuned mass damper can be observed since the amplitude for A is much greater than that for B.

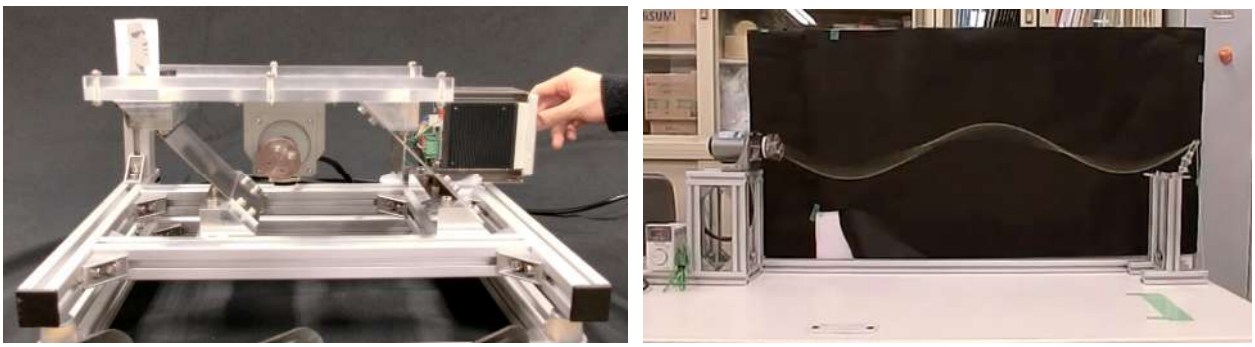

(a) Vibration conveyor (b) Transverse vibration of a string

Figure 1. Two examples of vibration apparatuses.

*Corresponding author. E-mail: saeki@sic.shibaura-it.ac.jp

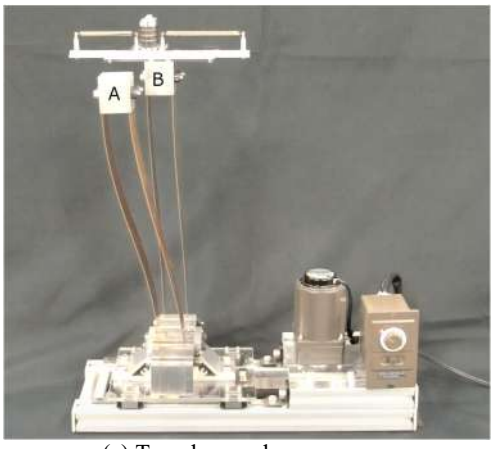

(a) Tuned mass damper

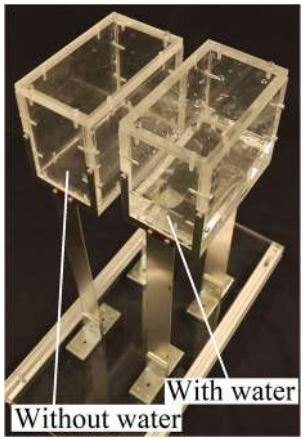

(b) Sloshing damper

Figure 2. Various dampers.

In Figure 2(b), there are two of the same apparatus consisting of a primary mass supported by two leaf springs. As the ends of the springs are fixed to a horizontal plate, two primary masses act as a single-degree-of-freedom system. The primary masses made of acrylic resin are boxlike and a proper amount of water is filled in the primary mass on the right. When the two primary masses are given the same initial displacements and then released suddenly, the primary masses vibrate freely. Since the vibration of the primary mass filled with water stops earlier than that without water, the damping performance of the sloshing damper can be observed.

All of the vibration apparatuses were constructed by the fourth-year students in our laboratory.

EVALUATION AND IMPROVEMENT ACTIVITIES

Figure 3 shows an example of the evaluation of the lecture using teaching apparatuses by the students. As shown in this figure, more than 90% of the students said that the lecture in which the teaching apparatuses were used was interesting. To improve these apparatuses, all teaching apparatuses have also been evaluated by researchers belonging to enterprises and universities.

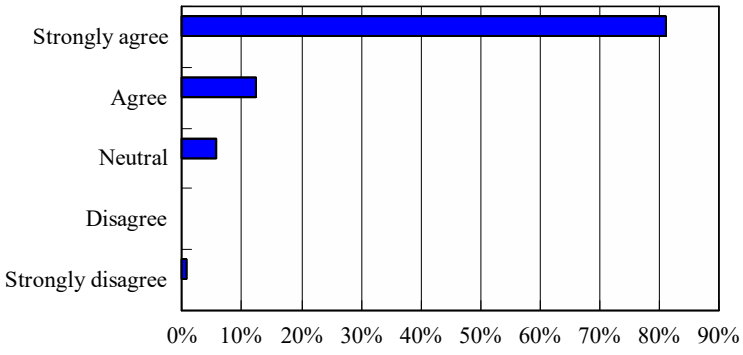

How much do you agree with the following statement?
This lecture using vibration apparatuses was interesting.

Figure 3. Evaluation by students.

CONCLUSIONS

Various apparatuses used in a classroom lecture on mechanical vibrations were presented. The use of vibration apparatuses seemed to have a positive educational impact on students compared with numerical simulations since it is more impressive to see live performances. I would like to develop some apparatuses that reproduce nonlinear phenomena in the future.

References

[1] Lewin W. For the love of physics. Free Press, 2012.
[2] Stern C., Echeverria C. and Porta D. Teaching physics through experimental projects. XXIV ICTAM,3477-3478, 2016.
[3] Bigoni D., Corso F. D. and Misseroni D. Teaching structural mechanics with models. XXIV ICTAM,3471-3472, 2016.

VARIATION OF NATURAL FREQUENCIES OF AXIALLY CONNECTED WOODEN BLOCKS

Vikram Pakrashi[1,2], Eolann Sheehan[3], Jake O'Callaghan[3], Paul Cahill[1,2], Darragh Noble[4], Maria Nogal[5] & Alan O'Connor[4]
[1]Dynamical Systems & Risk Laboratory (DSRL), School of Mechanical and Materials Engineering, University College Dublin, Ireland
[2]SFI MaREI Centre, University College Dublin, Ireland
[3]Department of Civil, Structural and Environmental Engineering, University College Cork, Ireland
[4]Department of Civil, Structural and Environmental Engineering, Trinity College Dublin, Ireland
[5]Department of Materials, Mechanics, Management & Design (M3d), Faculty of Civil Engineering and Geosciences, Technische Universiteit Delft, The Netherlands

Summary: The change of natural frequency of a prestressed beam with increasing prestress has come under significant scrutiny in recent times. Experimental data on both concrete and steel beams tend to indicate that the variation of natural frequency does not monotonically decrease for prestressed beams, despite an intuitive expectation for this to happen. This paper investigates this problem using a desktop experiment with small wooden blocks connected with a central axial force to form a beam and carried out a range of experiments to understand this change. The variation of natural frequencies indicates how the changes are not obvious. Additionally, the experiments raise an important challenge of separating effects of noise from information, when the order of both are similar.

INTRODUCTION

An intuitive estimate of change in natural frequency of a prestressed beam indicates that the natural frequency should monotonically decrease with increased prestressing force on the beam due to reduction in stiffness [1]. However, experimental results on steel and concrete (uncracked and cracked) [2,3,4] indicate that in reality, this answer is more complicated. The changes are not necessarily monotonic with increasing prestressing. While there are several models trying to address this [5,6], none are adequate. This paper presents a simple desk study, with extensive experimental results to present this complex issue in an undergraduate teaching setting. The experiments demonstrate that how even for wooden blocks connected with an axial force, this complex variation exists.

EXPERIMENTAL SETUP

Experimental Design

A tower of individual wooden blocks was connected centrally to form a simple experiment in this regard. The simplicity of the experiment makes it easy to replicate it, especially in an undergraduate framework of Teaching and Learning. Wooden blocks of different geometry were created, and the beam was instrumented with 5 no. LORD Microstrain G-Link LXRS Accelerometers. This can be replaced with any cheaper accelerometer and even by smartphone accelerometers. The data was recorded by a LORD Mircostrain WSDA- Base-LXRS and with Node Commander Software. The accelerometers were attached to the same face of five out of the ten wooden blocks. This was done using a drill and two screws per accelerometer. The base section was bolted firmly to the frame of a table. A cable in then attached to a weight holder by looping one end of the cable through the eye nut and securing it with a bull clip. The threaded bar was then attached to the eye nut and secured with two nuts. A 100x100mm balancing plate was then attached to the other end of the threaded bar and secured with a nut and a 50mm washer either side to keep the plate from tilting. The 'tower' of wooden blocks was placed on top of the bolted down base section, making sure that the accelerometers were on every second block. The 100x100mm steel plate was then placed on the top block. The end of the cable with nothing on it was then passed through the holes in the centre of the beam and secured on top of the steel plate with another bull clip. The base of the system was fixed. Several experiments to estimate the natural frequency were subsequently carried out for varied axial force. Figure 1 presents a setup of this experiment.

Figure 1. *Connected wooden blocks with varying axial force.*

Experimental Procedure

To determine the variations of natural frequencies of the setup, responses due to impulse forces were with 5 accelerometers. A baseline case was initially established for the system in this regard. A wide range of experiments established the experimental variation of estimated natural frequencies of the system.

EXPERIMENTAL RESULTS

The main thought processes currently surrounding the relationship between natural bending frequency and prestress force are as follows:

- Frequency increases with increasing prestress force.
- Frequency decreases with increasing prestress force.
- There is no monotonic relationship between frequency and prestress force.

In the set of experiments carried out it appears that the natural bending frequency overall increased with increasing prestress force. The estimated natural frequency increases with an increase in prestress, but the rate of change of frequency gets smaller and with equal increase in prestressing force. Whether this leads to a limit or if it eventually changes to a decrease (as observed in larger beams in some cases, where the natural frequency decreases after increasing for some time) cannot be established from these experiments. However, the study clearly demonstrates, from a simple desktop experimental study that the answer to this seemingly simply problem is significantly more complex than it appears.

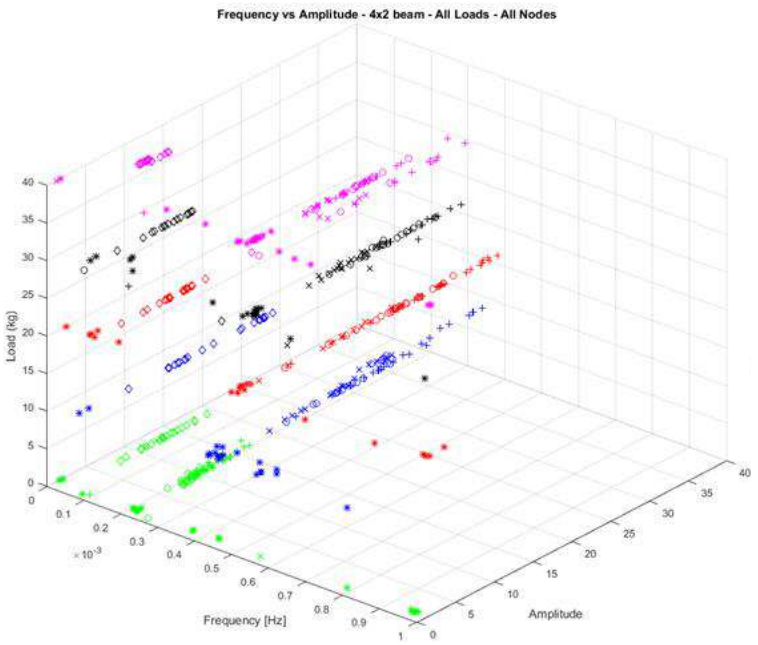

Figure 2. *Variation of Natural Frequencies of the connected wooden blocks for varied axial forces.*

CONCLUSIONS

This paper presents a study on the variation of natural frequency for wooden blocks connected by varied levels of axial forces. In this regard, a simple desktop experiment was created that can be replicated easily in any learning environment. Estimates of natural frequencies for various axial forces provided the variation of such frequencies from extensive experimental study. It was observed that the changes in such frequency are not intuitive, as evidenced by larger experiments in the past. The experiments also indicated the uncertainty due to possible noise and inaccuracies is a challenging problem and extensive work may be required to isolate information from noise, thereby making a obvious interpretation of the variations difficult.

Acknowledgements: Mr. Tony Flaherty, University College Cork, Ireland for setting up part of the experiment.

References

[1] The effect of prestress force magnitude and eccentricity on the natural bending frequencies of uncracked prestressed concrete beams. *J.Sound Vib*. **365**, 22-44.
[2] Noble D, Nogal M, O'Connor AJ and Pakrashi V. (2015). The effect of Post-Tensioning Force Magnitude and Eccentricity on the Natural Bending Frequency of Cracked Post-Tensioned Concrete Beams. *Jnl.Phys:Conf.Series*, **628**(**1**), 012047-1-8.
[3] Noble D, Nogal M, O'Connor A and Pakrashi V. (2015). Dynamic Impact Testing on Post-Tensioned Steel Rectangular Hollow Sections: an Investigation into the "Compression-Softening" Effect. *J.Sound Vib*, **355**, 246-263.
[4] Noble D, Nogal M, O'Connor AJ and Pakrashi V. (2015). Output Only Investigation of the Effect of Post-Tensioning Force on Natural Frequencies of Post-Tensioned Concrete Beams. 6th International Operational Modal Analysis Conference (IOMAC), Gijon, Spain.
[5] Hamed, E. and Frostig, Y. (2006). Natural frequencies of bonded and unbonded prestressed beams–prestress force effects. *J.Sound Vib*, **295**(**1-2**), 28-39.
[6] Saiidi, M., Douglas, B. and Feng, S. (1994). Prestress force effect on vibration frequency of concrete bridges. *Jnl.Struct.Eng*, **120**(**7**), 2233-2241.

AN INTERACTIVE APPROACH TO LEARNING FLUID MECHANICS

Kevin Nolan * [1]
[1]School of Mechanical & Materials Engineering, University College Dublin, Belfield, Dublin 4, Ireland

Summary A new approach to fluid mechanics teaching incorporating interactive and visually engaging media is discussed. A common approach to teaching is via the use of slideware whereby students are required to take notes by filling in gaps in printouts of slides. A challenge in this arrangement is the that students note taking may be interrupted when the next slide is advanced and so they cannot contunue to engage with the material. The use of visually engaging materials and scrolling lecture notes is investigated as a means to build intuition and engagement.

INTRODUCTION

It has been reported that students undertaking introductory fluid mechanics often experience conceptual difficulties when considering ideal fluids. Suarez et al. [9] reports four key observations, (i) students continue to apply hydrostatic reasoning to purely hydrodynamic systems, (ii) students neglect the principe of the conservation of mass when considering flows in vertical pipe configurations (iii) students frequently do not understand the role of pressure and the forces exerted on a fluid element and (iv) that students do not understand the range of validity of Bernoulli's equation.

The literature reports a number of educator interventions to improve student learning in subjects such as fluid mechanics. Of note Fraser et al. [5] eschewed traditional CFD tools in favour of more accessible Excel based computer simulations designed using phenomenographic learning theory to facilitate conceptual understanding. Two of the three simulations evaluated showed good improvement in the student test scores. More recently Barba and Forsyth [1] details an accessible approach to introductory Navier-Stokes using the *Python* programming language and the *Jupyter Notebook* environment with a similar approach used for aerodynamics [2].

The Jupyter (Julia Python Terminal) Notebook environment [8] has a number of advantages that make it useful in engineering education. Jupyter Notebooks are rendered in a web browser and can be navigated in much the same way as a webpage. A typical notebook contains a series of cells that comprise either text (written in the Markdown format with LaTeX equation rendering) or code (in the Julia or Python languages) which can be run interactively. Any generated output such as charts or graphics are displayed inline. Kernels supporting other languages such as Matlab are also available. Notebooks can be run locally on a host machine, or hosted on web server. Hosting can be provided by services such as Nbviewer, Binder and Google CoLab. These services make the notebooks available on any device with a web browser. Jupyter is also extensible and many third-party libraries can be used to increase functionality.

In the field of visual effects, various approaches to fluid flow simulation are employed for a wide range of artistic intent. These methods often lack the accuracy of traditional computational fluid dynamics codes, many methods are not conservative [3], but can visually capture the physical behaviour of complex flows [6] and fluid interactions with objects [4] to a degree suitable for general audiences. Indeed the visual representations of fluids simulated with these methods is often superficiality superior to the visualisations typically produced in CFD studies. The codes also tend to be fast with simulation times on consumer hardware ranging from minutes to several hours.

While Jupyter Notebooks are popular in higher education, the use of sophisticated visual effects tools as a teaching aid has not been explored in the literature to date to the best of the author's knowledge. This work details the use of Jupyter Notebooks and 3D animation of fluid flow to improve engineering student learning and engagement with *Mechanics of Fluids 1* at University College Dublin[7].

INPLEMENTATION

A series of notebooks were compiled on approximately half the course content. The topics included: fluid properties, pressure, hydrostatics, flow kinematics, Bernoulli's equation and control volume analysis. The remainder of the course which comprised the conservation laws, dimensional analysis and internal viscous flow were unchanged. Student feedback and year on year changes in exam performance will be collected and reported.

Each notebook was written in a conversational style with Jupyter cells carefully arranged so that text is broken up with videos and code blocks. This allowed the notebooks to be presented directly to the students with a persistence of content displayed via the scrolling nature of content presented in a web browser avoiding the abrupt nature of slide changes typical of slide ware. This approach was used to directly address prior student feedback.

3D models and animations were created using Blender, an open source 3D content creation suite. Fluid simulations were performed within Blender using a Particle in Cell/Fluid-Implicit Particle (PIC/FLIP) solver. Rendering was performed using the Cycles path tracer in conjunction with the FreeStyle non-photorealistic (NPR) rendering engine to provide emphasis to particular elements. Figure 1 shows snapshots from a number of the videos presented. The blackout line of the manometer tube and the geometry in figure 1(c) and (d) show show the Freestyle result. Videos were exported at 1920×1080 pixels as h.264 in mp4 format which is supported on a wide range of devices.

Shown in figure 1(a) are four streams of fluid each of increasing viscosity. The number indicates the magnitude of the viscosity but no unit is provided. Once the video (and others) are shown and discussed in an attempt to build intuition, the units of viscosity are introduced. In figure 1(b) a similar arrangement of fluids is presented however now only the surface

*Corresponding author. E-mail: kevin.nolan@ucd.ie

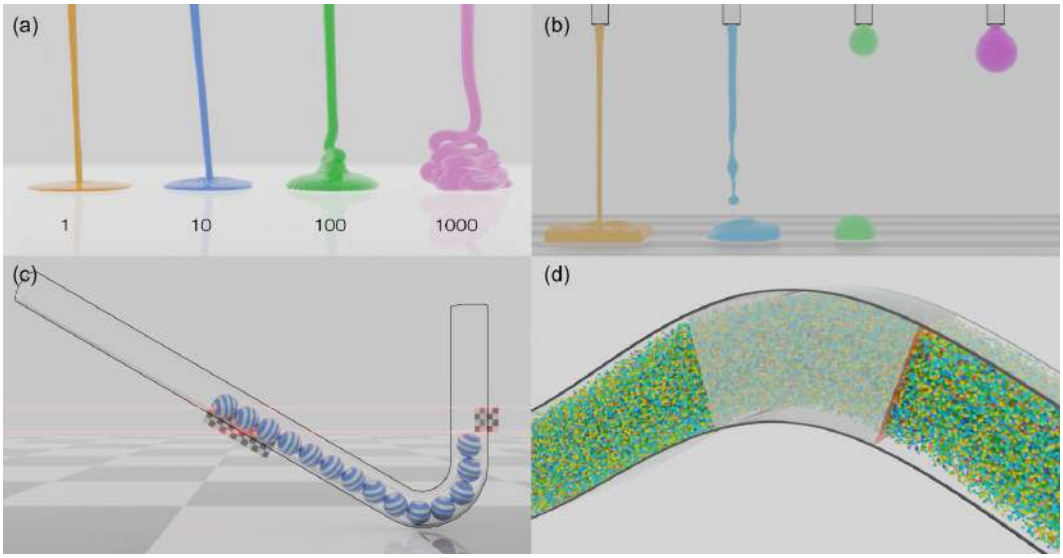

Figure 1: Snapshots of some of the animations used. (a) A demonstration of the effect of increasing viscosity on falling streams of fluid. (b) Demonstration of the effect of increasing surface tension. (c) A simplification of the operation of an inclined manometer with a ball bearing analogy. (d) A colourful introduction to control volume analysis and the difficulties of the Lagrangian frame of reference.

tension of each fluid is varied from zero on the left to some arbitrarily large value on the right. Again this is followed by further examples and a deeper more traditional analysis and discussion of units. Figure 1(c) represents an analogy that was developed to introduce the operation of a manometer whereby a chain of ball bearing represent the gauge fluid. By considering the distribution of ball bearings students can confirm the observed behaviour. This approach also fosters an understanding of role of the fluid weight in this type of problem. Finally in figure 1(d) the flow of a large number of Lagrangian particles is observed to flow through a curved duct. The students are asked to consider the difficulty of tracking each particle in contrast to measuring the amount entering and exiting the translucent control volume.

In addition to the videos, static 3D models depicting concepts such as differential elements were imported as interactive elements into the Jupyter Notebooks. Students are able to rotate, zoom and pan the model as they desire preventing any misintrepretation that may result from a 2D sketch.

Formal student feedback on this new approach is forthcoming and will be presented, however informal feedback from students has been positive. Students report that the visualisations are helpful and the Jupyter approach is gennerall preferred to the slideware approach.

CONCLUSIONS

An approach to teaching fluid mechanics that employs high-quality videos created using visual effects tools is reported. By using the popular Jupyter Notebook environment various types of media can be combined in an easy to use manner. Informal student feedback has been overwhelmingly positive and a statistical analysis of student performance will be performed and formal feedback is forthcoming. The tools used for this work are all open source and straightforward to use with excellent documentation. The teaching materials are available online [7] under an MIT license.

References

[1] L. Barba and G. Forsyth. Cfd python: the 12 steps to navier-stokes equations. *Journal of Open Source Education*, 2 (16):21, 2018.

[2] L. Barba and O. Mesnard. Aero python: classical aerodynamics of potential flow using python. *Journal of Open Source Education*, 2(16):45, 2019.

[3] J. U. Brackbill, D. B. Kothe, and H. M. Ruppel. Flip: a low-dissipation, particle-in-cell method for fluid flow. *Computer Physics Communications*, 48(1):25–38, 1988.

[4] Y. R. Fei, C. Batty, E. Grinspun, and C. Zheng. A multi-scale model for simulating liquid-fabric interactions. *ACM Transactions on Graphics (TOG)*, 37(4):51, 2018.

[5] D. M. Fraser, R. Pillay, L. Tjatindi, and J. M. Case. Enhancing the learning of fluid mechanics using computer simulations. *Journal of Engineering Education*, 96(4):381–388, 2007.

[6] M. Gao, A. Pradhana, X. Han, Q. Guo, G. Kot, E. Sifakis, and C. Jiang. Animating fluid sediment mixture in particle-laden flows. *ACM Transactions on Graphics (TOG)*, 37(4):149, 2018.

[7] K. Nolan. MEEN20010 Mechanics of Fluids 1, 2019. URL `https://github.com/nolankucd/MEEN20010`.

[8] Project Jupyter. Project jupyter, 2020. URL `https://jupyter.org`.

[9] A. Suarez, S. Kahan, G. Zavala, and A. C. Marti. Students' conceptual difficulties in hydrodynamics. *Phys. Rev. Phys. Educ. Res.*, 13:020132, Nov 2017. doi: 10.1103/PhysRevPhysEducRes.13.020132.

TEACHING MECHANICS WITH STRUCTURAL MODELS

Davide Bigoni[1], Francesco Dal Corso[1], Diego Misseroni[1]
[1]Department of Civil, Environmental and Mechanical Engineering, Università di Trento, Trento, Italy

Summary Several models are presented to help teaching solid and structural mechanics, at all levels, to engineering and physics students. The simpler models have been developed to explain the concepts of elastic beam, segmental arch, truss structure, elastic frame, and Euler buckling. More sophisticated models have been designed to introduce advanced concepts such as flutter instability under nonconservative loads, configurational forces generated through bending, and snake locomotion.

INTRODUCTION

In the last fifteen years we have developed physical teaching models to improve the presentation and understanding of scientific results, especially for engineering and physics students (frequenting undergraduate and graduate courses), but also for audiences at all levels, ranging from untrained people to peers in the scientific community.

Digital technology has indisputable merits and is of crucial importance in teaching. However, it tends to reduce physical intuition in students, while for students used to an intuitive approach (such as those involved in engineering studies) it can be difficult to understand how principles are applied in the real world. This is particularly true in mechanical engineering, probably the hardest discipline in engineering studies.

Several mechanical models developed in our laboratory have been shown to be of primary importance (i) as proof-of-concepts of newly discovered phenomena; (ii) as teaching models at different levels, including PhD programs; (iii) as demonstrators at public exhibitions, even for untrained public.

Our models have been conceived, designed, and realized to give tangible, vivid evidence of non-intuitive mechanical phenomena. Some of them have been invented for illustrating results obtained within EU financial schemes, others have been addressed to scientific presentations, and others have been designed to help students in understanding basic and advanced concepts of mechanics.

Our results and findings provide a breakthrough innovation in engineering education, through a simplification in the teaching of mechanics. We will continue developing our methods, thus contributing, through engineering education, to a sustainable and equal opportunities human development.

MODELS FOR STRUCTURAL ANALYSIS

Cross and Morgan wrote in 1932: 'the ability of a designer of continuous structures is measured chiefly by his ability to visualize the deformation of the structure under load. If he cannot form a rough picture of these deformations when he begins the analysis he will probably analyse the structure in some very awkward and difficult way; if he cannot picture these deformations after he has made the analysis, he doesn't know what he is talking about'. This statement remains valid today. However, the visualization of the deformation of a structure is more complex than it may appear and for this reason, teaching models are fundamental to stimulate students' interest and to simplify learning. We have developed several structural models for Civil engineering students, for elastic beam, segmental arch, truss structure [1], elastic frame [2], and Euler's buckling, Fig. 1.

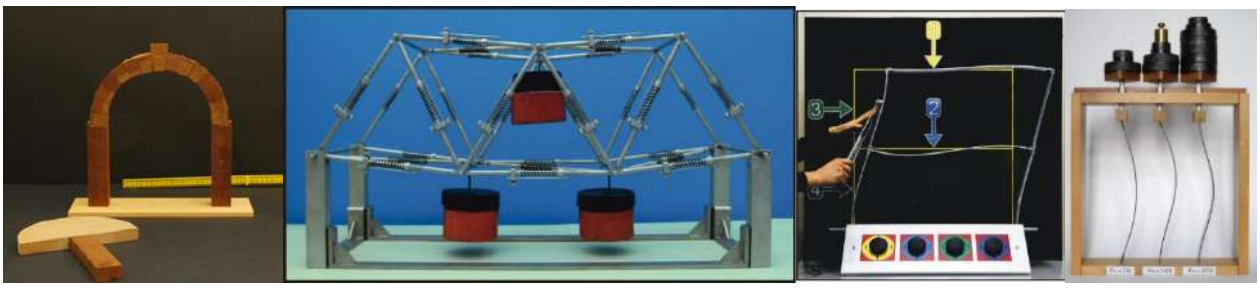

Fig. 1 from left to right, models for: Segmental arch; Truss structure; Elastic frame and Euler's buckling

MODELS FOR NEW PHENOMENA: FLUTTER INSTABILITY & CONFIGURATIONAL FORCES

Proof-of-concept-models have been designed by us to give evidence to previously unknown mechanical phenomena. These include: buckling of an elastic rod under tensile dead load [3], flutter instability induced by dry friction [4], effects of curvature constraint on instability [5], existence of configurational forces [6], effects of configurational forces on instability [7], the elastica arm scale [8], the torsional gun [9], snake locomotion [10], Fig. 2. All these phenomena are so innovative that it is hard to imagine their real-world implications without a working physical model.

Fig. 2 From left to right, models for: Flutter instability; The elastica arm scale; The torsional gun; Snake locomotion

CONCLUSIONS

Usually engineers face the problem of characterizing new materials of unknown properties and this is done using standard testing machines. Our models originate from an 'inverted approach' in which we first develop a theory to describe a phenomenon and then we build a model intended to validate the theory. In this sense, our laboratory is unique: we use our testing machines to fully define the behaviour of our physical models and to see how well it fits the theoretical predictions. We have thus been able to show complex nonlinear instabilities, such as flutter and Hopf bifurcations, which were previously only mathematically demonstrated. We have discovered buckling instability of a bar in tension and the existence of configurational forces. We have invented a new type of elastically deformable arm balance and a torsional actuator, each one with its associated model. We have for the first time tested a model for snake locomotion. These models have been used to engage both our peers and the public in our discoveries. Teaching models of truss structures and frame structures have been developed to enhance teaching at the undergraduate level.

ACKNOWLEDGEMENT

The authors gratefully acknowledge financial support from the ERC Advanced Grant 'Instabilities and nonlocal multiscale modelling of materials' FP7-PEOPLE-IDEAS-ERC-2013-AdG (2014-2019).

References

[1] Bigoni, D., Dal Corso, F., Misseroni D. and Tommasini, M. A teaching model for truss structures. *Eur. J. Phys.* **33**:1179–1186, 2012.
[2] Misseroni D., Bigoni, D. and Dal Corso, F. A model for teaching elastic frames. *J. Materials Education*, **36**:169-174, 2014.
[3] Zaccaria, D., Bigoni, D., Noselli, G. and Misseroni, D. Structures buckling under tensile dead load. *Proc. Royal Soc. A* **467**:1687-1700, 2011.
[4] Bigoni, D, Noselli, G. Experimental evidence of flutter and divergence instabilities induced by dry friction. *J. Mech. Phys. Solids* 59:2208–2226, 2011.
[5] Bigoni, D., Misseroni, D., Noselli, G. and Zaccaria, D. Effects of the constraint's curvature on structural instability: tensile buckling and multiple bifurcations. *Proc. Royal Soc. A* **468**:2191-2209, 2012..
[6] Bigoni, D., Dal Corso, F., Bosi, F. and Misseroni, D. Eshelby-like forces acting on elastic structures: theoretical and experimental proof. *Mech. Materials* **80**: 368–374, 2015.
[7] Bigoni, D., Bosi, F., Dal Corso, F. and Misseroni, D. Instability of a penetrating blade. *J. Mech. Phys. Solids* **64**:411-425, 2014.
[8] Bosi, F., Misseroni, D., Dal Corso, F. and Bigoni, D. An elastica arm scale. *Proc. Royal Soc. A* **470**:20140232, 2014.
[9] Bigoni, D., Dal Corso, F., Misseroni, D. and Bosi, F. Torsional locomotion. *Proc. Royal Soc. A* **470**:20140599, 2014.
[10] Dal Corso, F., Misseroni, D., Pugno, N.M., Movchan, A.B., Movchan, N.V., Bigoni, D. Serpentine locomotion through elastic energy release. J. Royal Soc. Interface, 14, 20170055, 2017.

ELASTICA CATASTROPHE MACHINE FOR TEACHING SNAP INSTABILITIES IN STRUCTURAL MECHANICS

Francesco Dal Corso* , Alessandro Cazzolli, and Diego Misseroni
Department of Civil, Environmental and Mechanical Engineering, University of Trento, Trento, Italy

Summary A new catastrophe machine is proposed to illustrate concepts of snap instabilities in structural mechanics. Differently from the classical catastrophe machines, the present machine is based for the first time on the snapping of a continuous flexible element, namely an elastic rod. In addition to opening new perspectives in the mechanical design for advanced technologies, the developed *elastica catastrophe machine* finds application as a tool for teaching mechanics at different levels, ranging from public exhibitions for untrained public to PhD programs.

René Thom initiated in 1969 the celebrated framework of catastrophe theory [3] to provide interpretation to sudden large changes in the configuration of complex systems as the result of a small variation in the boundary conditions. Over the years, concepts of this theory have been exploited to explain instability phenomena in the mechanics of fluids, solids, and structures, but also in optics, physical chemistry, economics, biology and sociology.

Few years later, Erik Christopher Zeeman invented and realized in 1972 a simple but intriguing mechanical device [4] to illustrate for the first time concepts of catastrophe theory, Fig. 1 (left). The 'Zeeman's catastrophe machine' is a two-spring system composed by two elastic rubber bands tied together through a knot pinned on a disk that can only rotate around its center. The other end of the first elastic band is pinned to a fixed point while that of the second elastic band is held by hand, controlling its position within the plane. The number of equilibrium configurations for the system varies by changing the hand position. More specifically, the physical plane is found to be split in a bistable region inside a closed diamond-shaped curve and a complementary monostable region outside it. The closed curve represents the *catastrophe locus*, because when crossed by the hand position from inside to outside the system may snap.

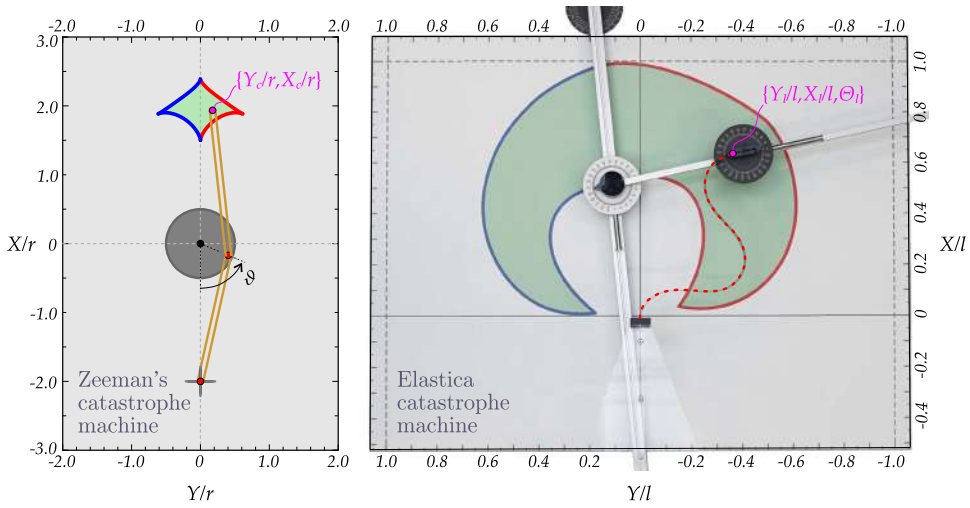

Figure 1: (Left) Sketch of the Zeeman's catastrophe machine and (right) the prototype of the developed *elastica catastrophe machine*. One of the two stable configurations available within the bistable green region is shown for the two rubber bands (left) and for the elastic rod (right).

Based on the recent concept of universal snap surface disclosed for planar elasticae with kinematically controlled ends [1], a catastrophe machine based on an elastic continuous element has been designed and realized for the first time [2], Fig. 1 (right). A general theoretical framework has been developed by extending that of the classical catastrophe machines made up of discrete elastic systems. Similarly to the classical system, the *elastica catastrophe machine* splits the plane in monostable and bistable regions, but now it is a flexible continuous element that displays a snapping mechanism when the controlled end properly crosses the catastrophe locus from inside to outside, Fig. 2. Furthermore, substantial changes in the catastrophe locus properties, such as convexity and number of bifurcation points, are achievable by tuning the design parameters.

In addition to opening new perspectives in the design of cycle mechanisms for actuation and dissipation devices towards energy harvesting, locomotion and wave mitigation, the proposed model finds obvious pedagogical application with reference to catastrophe theory in combination with snapping mechanisms in structural mechanics.

Acknowledgments. FDC gratefully acknowledges financial support from the European Union's Horizon2020 research and innovation programme under the Marie Sklodowska-Curie grant agreement 'INSPIRE - Innovative ground interface concepts for structure protection' PITN-GA-2019-813424-INSPIRE. All authors acknowledge funding from the Italian Ministry of Education, University and Research (MIUR) in the frame of the 'Departments of Excellence' grant L. 232/2016.

*Corresponding author. E-mail: francesco.dalcorso@unitn.it

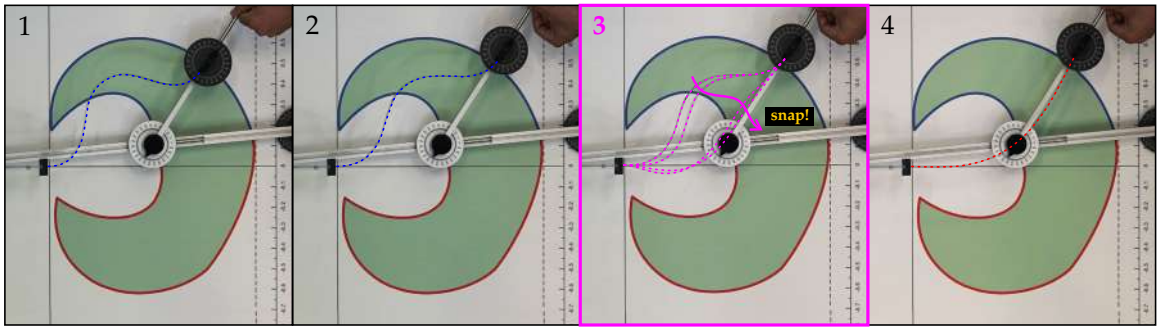

Figure 2: The *elastica catastrophe machine* in action with a carbon fiber rod. Deformed configuration with varying the coordinates of one of its ends. Snapping occurs at crossing the catastrophe locus with the change of the curvature sign at both rod's ends (frame 3, where four snapshots are superimposed).

References

[1] Cazzolli A., Dal Corso F. Snapping of elastic strips with controlled ends. *Int. J. Sol. Struct.*, **162**, 285-303, 2019.

[2] Cazzolli A., Misseroni D., Dal Corso F. (2020). Elastica catastrophe machine: theory, design and experiments. *J. Mech. Phys. Sol.*, https://doi.org/10.1016/j.jmps.2019.103735, 2020.

[3] Thom R. Topological models in biology. *Topology*, **8 (3)**, 313335, 1969.

[4] Zeeman E. C. A catastrophe machine. In *Towards a Theoretical Biology* (C. H.Waddington, ed.). Edinburgh University Press, Edinburgh. Vol. 4, 276282, 1972.

SMART PIV – FLOW VISUALIZATION WITH SMARTPHONES FOR EDUCATION IN FLUID MECHANICS

Christian Cierpka*[1], Constanze Poll[2], Jonas Hüther[2], Sebastian Jeschke[2], Henning Otto[1] and Patrick Mäder[2]
[1]Institute of Thermodynamics and Fluid Mechanics, Technische Universität Ilmenau, Germany
[2] Group for Software Engineering for Safety-Critical Systems, Technische Universität Ilmenau, Germany

Summary Flow visualization is important to understand the underlying non-linearity in fluid mechanics. Students are often astonished encountering surprising effects for example by increasing the Reynolds number in a flow around a cylinder. The SmartPIV app allows them to use their smartphones for the determination of velocity fields on-line in class and export the results for later analysis in lab reports.

INTRODUCTION

Flow visualization is important to understand the underlying non-linearity in fluid mechanics. Students are often astonished encountering surprising effects for example by increasing the Reynolds number in a flow around a cylinder. An advanced optical method to determine the vector field of a flow is particle image velocimetry [1]. In the basic configuration the flow of interest is seeded with so called tracer particles. These tracer particles are illuminated by a thin laser light sheet and their images are recorded by a digital camera. Two images within a very short time span enables to follow the particle displacement, for example by cross correlation or optical flow analysis. With known magnification the velocity can be determined and allows to characterize the instantaneous flow field. However, commercial PIV systems for scientific purposes with double pulse lasers and scientific cameras are very expensive (~100.000 Euro) and very complex. Thus these systems are only seldom used for teaching. Another problem arises that students are very often afraid of using complex and expensive systems.
On the other hand, nowadays students use their smartphones in daily live very intuitively without any reservation. Modern devices incorporate a multitude of sensors and large computational power and are therefore already used for education in physics classes [2,3], as well as for flow visualization by Schlieren techniques [4,5] or for the determination of surface tension [6] and other mechanical properties of fluids [7]. Most smartphones also contain very powerful cameras allowing frame rates of up to 920 Hz and thus very short time distances between images. Therefore these systems are suited for recording PIV images and the comparison with scientific equipment shows that smartphone videos are principally suited for the determination of the velocity field using low cost continuous lasers or LEDs [8]. Aguirre-Pablo et al. [9] even showed the successful application of smartphones for the tomographic reconstruction using pulsed colored LEDs and several smartphones imaging a scene from different angles. However, all these systems use off-line processing of the videos recorded by the smartphone. The aim of the current study was therefore to develop a smartphone app that allows for the on-line evaluation of the images to give a direct feedback for the students in course and to be able to process videos and export the corresponding results for reports of practical lab sessions.

SMART PIV

The app was developed within a student software project in close collaboration between students of engineering and computer science. It is available for Android and IOS in the app stores and can be downloaded and used free of charge. Since the ability for on-line flow visualization was most crucial concerning computer performance also optical flow algorithms were implemented as these request much less resources. On current smartphone the data evaluation time is in the order of ~200 ms for the correlation based algorithm and about ~30 ms for optical flow, which is fast enough for smooth visualization. After choosing the processing parameters (Fig. 1 left) the user can directly process the images from the live preview (Fig. 1, right), record videos or process already stored videos.

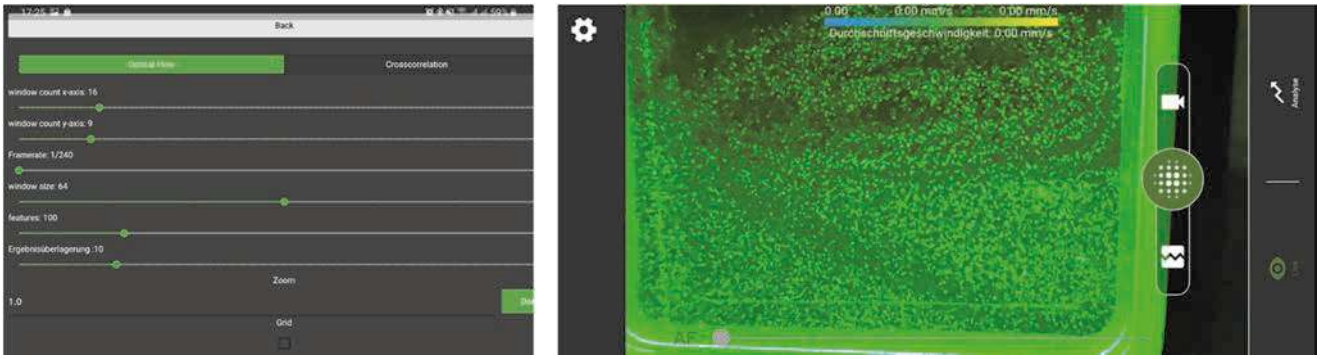

Figure 1. Menu for parameter settings (left) and main preview screen of the smartPIV app (right).

*Corresponding author. E-mail: christian.cierpka@tu-ilmenau.de.

Images as well as videos can also be stored for later export for lab reports. In addition to the images a text file and a csv file will be created that can be used for later analyses for example to test different mean estimators and outlier detection methods that will typically be taught in lab classes. Since for the conversion of the particle image displacement to physical coordinates the knowledge of the optical magnification is necessary a module that allows for a quick calibration using a square white paper with known side length was also included. Since typical fields of view are in the range of 1-20 cm the side length of the calibration target can be adopted to these values. The app can be intuitively controlled by users that are familiar with the video or photo function of their smartphones as the menus are designed very similar. A photograph of the application of smrtPIV for a test flow using a low power continuous laser diode and a fluidic actuator based on surface acoustic waves are shown in Fig. 2.

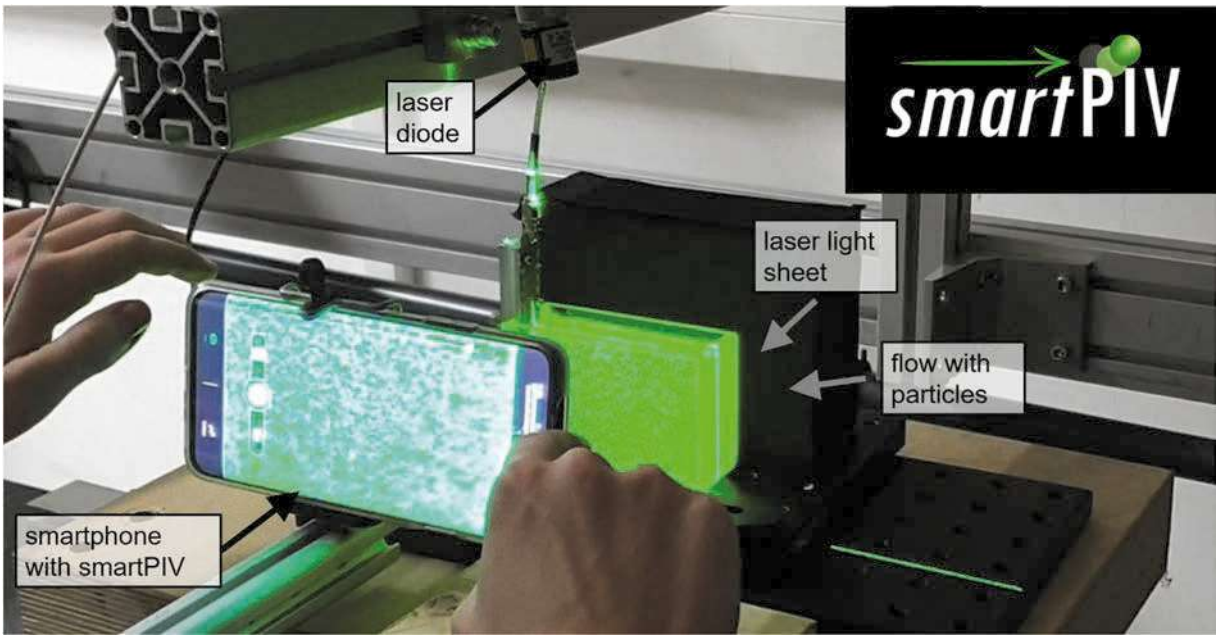

Figure 2. Experimental setup including a continuous laser diode and the smartphone with the preview screen of the smartPIV app.

CONCLUSIONS

The app smartPIV was developed for the velocity determination within lab session based on cross-correlation or optical flow. The app uses the fast camera and computational resources of modern smartphones and can be used in conjunction with a continuous laser to build a low-cost PIV system for educational use. The app also allows for a simple calibration and the storage and export of processed videos for later lab reports. Other than for teaching the app also might be helpful to get a first glimpse on flow velocities in nature or other technical processes even in harsh environments.

ACKNOWLEDGEMENTS

Financial support in the frame of the fellowships for “Innovations for digital teaching” from the Thüringer Ministerium für Wirtschaft, Wissenschaft und Digitale Gesellschaft are gratefully acknowledged. The authors would also like to thank all the students, namely Julia Bruischütz, Teresa Bravo Roger, Jonas Stephan, Jonas Hiese, Marcus Orban, Marcel John, Christian Engelhardt as well as Jörg König for the support in the lab.

References

[1] Kähler, C.J., Astarita, T., Vlachos, P.P., Sakakibara, J., Hain, R., Discetti, S., La Foy, R., Cierpka, C. 2016: Main results of the fourth International PIV Challenge, Experiments in Fluids 57, 97, DOI 10.1007/s00348-016-2173-1, open access
[2] Staacks, S., Heinke, H., Stampfer, C. 2018: Smarte Experimente, Physik Journal 17, 35-38
[3] Dyer, S. 2018: Using Mobile Devices to Improve Engineering Education: A Process Control Laboratory Example, ASEE Conference Boulder, USA, Paper ID 24188
[4] Miller, V.A., Loebner, K.T. 2016, Smartphone Schlieren, arXiv preprint arXiv:1609.04298, 201
[5] Settles, G.S. 2018: Smartphone schlieren and shadowgraph imaging, Optics and Lasers in Engineering 104, 9-21
[6] Goy, N.A., Denis, Z., Lavaud, M., Grolleau, A., Dufour, N., Deblais, A., Delabre, U. 2017: Surface tension measurements with a smartphone, Physics Teacher, American Association of Physics Teachers 55, 498-499
[7] Marshall, K.A., Liedtke, A.M., Todt, A.H., Walker, T. 2017: Extensional rheometry with a handheld mobile device, Experiments in Fluids 58, 69
[8] Cierpka, C., Hain, R., Buchmann, N.A. 2016: Flow visualization by mobile phone cameras, Experiments in Fluids 57, 108
[9] Aguirre-Pablo, A.A., Alarfaj, M.K., Li, E.Q., Hernández-Sánchez, J.F., Thoroddsen, S.T. 2017: Tomographic Particle Image Velocimetry using Smartphones and Colored Shadows, Scientific Reports 7, 3714, DOI 10.1038/s41598-017-03722-9

VIDEO ANALYSIS OF A ROWING KINEMATICS: A CASE STUDY USING OPEN SOURCE TRACKING SOFTWARE AS A TEACHING TOOL

David McKeown[1]
[1]School of Mechanical and Materials Engineering, University College Dublin, Dublin, Ireland

Summary The use of real-life examples in mechanics education can greatly help embed difficult concepts into the minds of students, but a lecture theatre is not real life. Examples from textbooks are generally contrived and limited to sketches capturing only a snapshot in time. Three dimensional animations overcome some of these limitations allowing a time varying representation, but still lack the realism and relatability of real-world examples. Demonstrations in class can be impactful but suffer from reliability, maintainability and are limited due to portability. This paper explores the uses of video analysis of mechanical systems as a teaching aid. The set up required to achieve the automated tracking of features is examined using the case study of a rower's motion captured using a bespoke low-cost tracking system and open source analysis software.

Introduction

The motivation for the cased study was the design of a wrist prosthesis for a 16 year old male rower with a transradial upper limb deficiency. Information about this natural rowing stroke was required implement limits on the range of motion of prosthetic wrist. The project lacked funding or access to a high-end commercial motion tracking system, so I bespoke low cost system was developed. Coloured markers were manufactured from toy rubber balls sliced in half and covered in coloured electrical tape, as shown in Figure 1. These were placed on the body of the rower's joints using double sided adhesive tape. The rower's motion was recorded in a rowing tank. This an indoor training setup where the rower remains stationery and water is pumped around the rower, as shown in Figure 2. This allowed for recording of the rowing stroke using stationary cameras. Four go-pro cameras were set up to record the rower from the left and right sides, from in front and above.

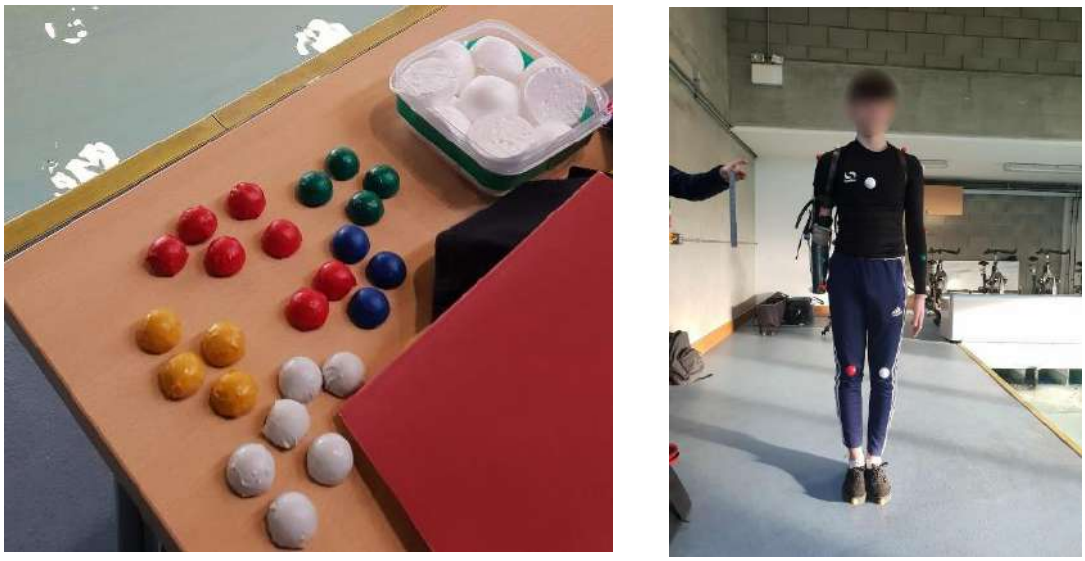

Figure 1. Markers for tracking (left). Rower wearing markers (right)

Software

The ability of track features from one video frame to next is using an automated or semi-automated method is available in a number of software packages. The author found 3 open source software packages, Tracker [1], Kinovea [2] and Mokka [3], which provided this feature. For this study the analysis Tracker was used. It provides automated and manual tracking of features based on matching an updating reference template. The success of this depends on the light conditions and the contrast of the markers with the surroundings. Another limitation is that some markers can become hidden to the camera during parts of the stroke. The video can be annotated with the result of the feature tracking and graphs of the kinematic data automatically produced. If mass and moment of inertia data is assigned to features of force vectors can also be annotated on to the video.

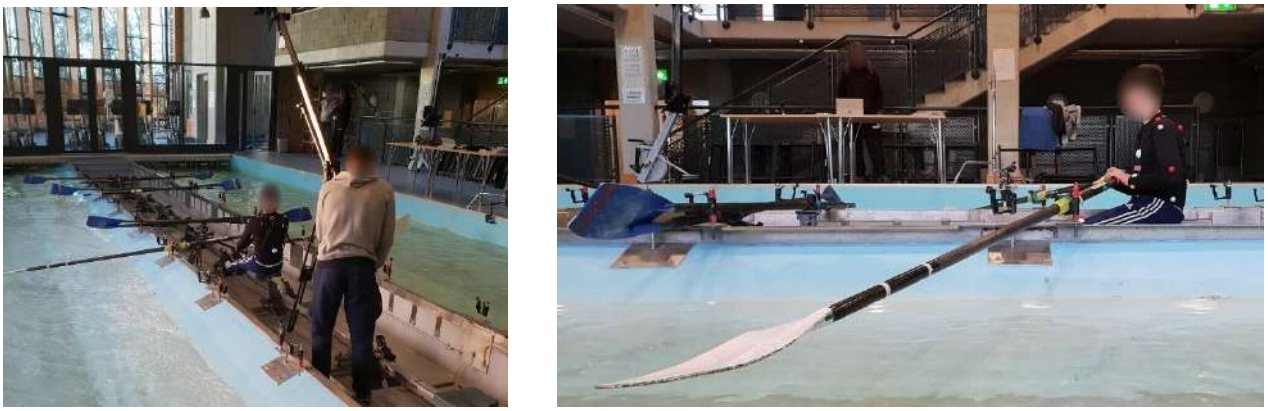

Figure 2. Overhead camera rigging (left). Side on camera (right)

Results.

Figure 3 shows Tracker software sample annotations from the overhead camera. In the figure two joints have been tracked, the left wrist in yellow and the left elbow in cyan. To the right of the video a time series plot of the vertical displacement of the wrist is shown as an output of the automatic marker tracking. Plots of velocity and acceleration (not shown) are also auto generated. The axes (magenta lines) can be aligned to in the direction of motion. The bottom right shows an exportable table of the same data.

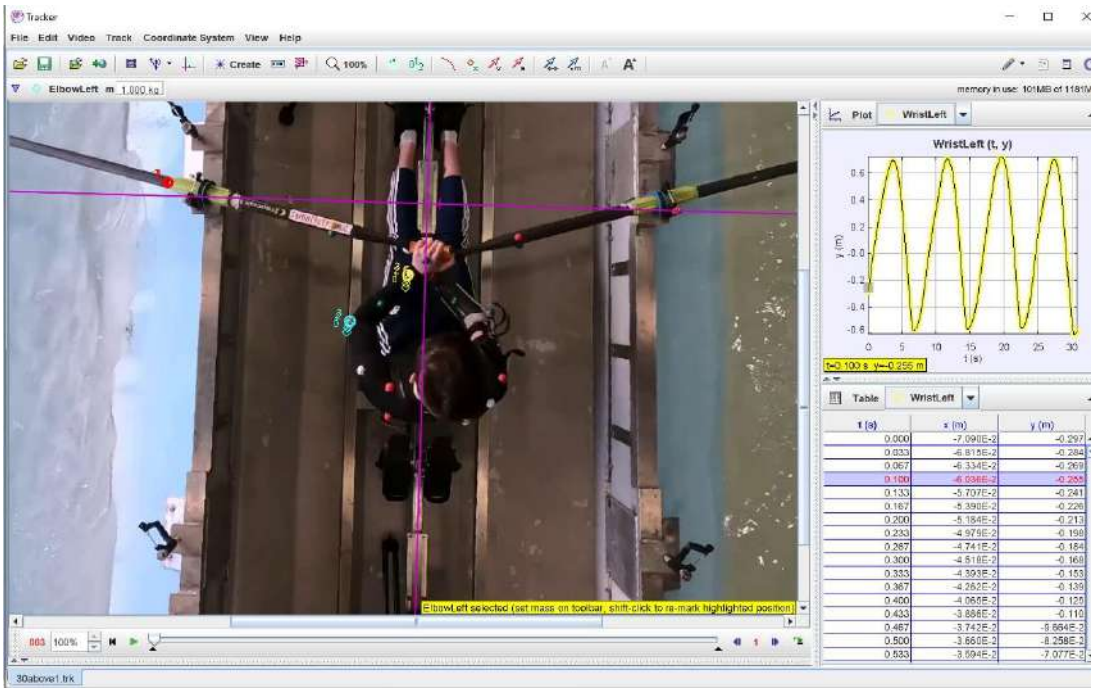

Figure 1. Screenshot of Tracker software. The graphs show the vertical (y-axis) motion of the left wrist marker.

CONCLUSIONS

Software to extract kinematic parameters from videos is powerful and can be relatively simple. It shows good promise as a useable teaching aid especially for reinforcing learning in combination with problem solving through more traditional approaches.

References

[1] Tracker, web site **https://physlets.org/tracker/.**
[2] Kinovea, web site **https://www.kinovea.org/.**
[3] Mokka, web site **https://biomechanical-toolkit.github.io/mokka/**.

METHOD OF ANALOGY FOR A WALKING ROBOT AND A GRIP

Yury Golubev[12] and Elena Melkumova*[1]
[1]Moscow State University, Moscow, Russia
[2]Keldysh Institute of Applied Mathematics, RAS, Moscow, Russia

Summary Theoretical mechanics and mechatronics methods help to solve the walking robot with a grasp problem. We teach our students in Moscow State University by lectures and seminars. These methods are used in statics and dynamics. We consider the problem of a fragile cylinder grasping by the manipulator fingers. Each finger contacts the cylinder in a single supporting point. Using numerical simulations and analytically, possible locations of the contact points on the cylinder, for which there is a kinetostatics problem solution when the cylinder is moved by four fingers, are received. As V.V. Kozlov said, aerobatics are analogies. We use an analogy of the equilibrium of a four-legged robot on a cylinder for the problem of transfer by a manipulator with a four-finger grasp of a fragile rough cylinder. The work was supported by the Russian Foundation for Basic Research (grant No. 19-01-00123 A).

INTRODUCTION

During the teaching we use the book [1] for the lectures and seminars in the Theoretical Mechanics and Mechatronic Chair of the Faculty of Mechanics and Mathematics of Lomonosov Moscow State University. In [2] we continue the series of the manuals devoted to the Theoretical Mechanics methods, issued by our chair. The book is addressed in addition to the students of the Optimal Control, Nonlinear Dynamics System and Control Processes, System Analysis Chairs of the Faculty of Computational Mathematics and Cybernetics of Lomonosov Moscow State University. Basic types of the problems for the first part of the Theoretical Mechanics Course: Kinematics, with expanded solutions are given in the manual. This book is for students and postgraduate students and also for Theoretical Mechanics teachers. The full program of lectures for the Faculty of Computational Mathematics is in our book [2] which is for seminars too.

FORMULATION OF THE PROBLEM

If during driving the car you see the turtle on the road, you save it. But how one robot with a manipulator can help to another. Let the corpus is cylinder. How to hold it. The analytical and the numerical parameter diagrams for two fields of supporting points are shown. A man's hand has five fingers. It is shown in [3-10] that when the number of support points of a walking robot inside a smooth horizontal cylinder increases to two, the support set is divided into two subsets. Similarly in fig. 1. The capture of a tortoise shell by a human hand is shown. One finger on one side and two on the other. In fact, two would have been enough. However, for a more comfortable and confident grip, it is desirable to use four fingers. For more complex surfaces or when changing the capture points are not superfluous, as practice shows, all five fingers.

Figure 1. Division of a reference set into two subsets.

*Corresponding author. E-mail: elena_v_m@mail.ru.

It is assumed that the arms, fingers, and legs of the robot make a predetermined movement relative to the robot body. The kinetic moment of the robot relative to the point is considered. In order for the given motion to be realized, reactions at the fulcrum must satisfy the kinetostatic equations. The first vector equation is responsible for changing the amount of movement of the robot. It is equivalent to the three scalar equations in projection onto the selected axes. The second equation of the system determines a given change in the kinetic moment.

We restrict ourselves to the case when active force $\tilde{\mathbf{\Phi}} \neq 0$ and perpendicular to momentum $\tilde{\mathbf{M}}$. We give the system $\{\tilde{\mathbf{\Phi}}, \tilde{\mathbf{M}}\}$ to the resultant at the point C [11 – 16]. Point C will also be the point of application of the resultant reactions. For example, point C may be the center of mass of the transferred object.

CONCLUSIONS

During the robot motion, one, two and three supporting point phases are changed. And for example the humanoid robot with five arm fingers can hold the object by one and grasp by two, three or four fingers. The reaction distribution problem have a solution in following cases. Let we give some examples. For one-supporting point phase. So the motion existing condition is reaction is equal to force and supporting point and the point C are on the line along the force. And the angle between the force and the normal not exceed friction angle. As for two-supporting point phases. The grasp can be in the cylinder. The point C and the reactions have to be in the plane parallel to the force. If supporting points are on one diameter. When coefficient $E < 0$ [16]. And in some fields with connected set of points, when $E \geq 0$ [17]. Robot can hold the cylinder by two fingers on one diameter. Robot can hold the horizontal cylinder by three fingers. Let one of the points is in vertical plane containing cylinder axis and another are in the plane orthogonal to the axis. Without friction, the cylinder center of mass has to be in the vertical plane that contain the cylinder axis. The supporting points are on the external surface of the lower semi-cylinder and the center mass of the cylinder is in the footholds triangle. If the first supporting point is in the lower semi-cylinder and two another are on the upper, the center of mass has to be out of the footholds triangle. Four fingers can hold the cylinder in two pars symmetric points about the cylinder axis. Or two pairs of points in the rectangular planes. The supporting set is divided into two subsets. For example thumb and the rest except for the little finger. So the robot can transfer the cylinder by one, two, three or four fingers.

References

[1] Golubev Yu. F. Fundamentals of Theoretical Mechanics: Textbook. 3rd ed., Revised and augmented. Publishing House of Moscow State University, Moscow 2019. (In Russian).

[2] Golubev Yu.F., Melkumova E.V. Methods of Theoretical Mechanics. Part 1. Kinematics. Place of publication MAKS Press Moscow, ISBN 978-5-317-05474-8, 60 pp. 2017. (In Russian).

[3] Okhotsimsky D. E., Golubev Yu. F. Mechanics and Motion Control of an Automatic Walking Apparatus. Nauka, Moscow 1984. (In Russian).

[4] Golubev Yu. F., Melkumova E. V. Static Stability Conditions of a Walking Apparatus in a Horizontal Cylinder and on Two Planes // Bulletin of the Russian Academy of Sciences. Theory and control systems. 1999. No. 2. P. 116–122.

[5] Melkumova E. V. Oscillations of a Walking Apparatus Around the Axis of a Smooth Supporting Cylinder-drum // Moscow University Herald. Series 1: Mathematics. Mechanics. 2000. No. 5. P. 47–49.

[6] Golubev Yu. F., Melkumova E. V. Equilibrium of a Biped Robot on a Rough Horizontal Cylinder, Taking into Account Reactions Along its Axis. M .: MAKS Press, 2010.64 s.

[7] Golubev Yu. F., Melkumova E. V. Walking Robot Dynamics on a Rough Inclined Cylinder.//ESMC-2012 - 8th European Solid Mechanics Conference. Graz, Austria, July 9-13, 2012. Book of Abstracts. Ed. Holzapfel G.A. and Ogden R.W.

[8] Golubev Yu. F., Melkumova E. V. Prescribed Motion of a Two-legged Walking Robot on a Rough Cylinder. Proceedings of the 2016 International Conference “Stability and Oscillations of Nonlinear Control Systems” (Pyatnitskiy’s Conference), Moscow, Trapeznikov V.A. Institute of Control Sciences, PP. 1-4.

[9] Golubev Yu. F., Melkumova E. V. The Existence of a Given Robot Movement When Using the Pipe as a Support. In the collection of the VII All-Russian meeting-seminar of the heads of departments and teachers of theoretical mechanics, robotics, mechatronics, universities of the Russian Federation. Makhachkala, 2016, S. 30-33.

[10] Golubev Yu. F., Melkumova E. V. Two-legged Walking Robot Prescribed Motion On a Rough Cylinder // AIP Conference Proceedings, Vol. 1959, 2018, No. 030009, PP. 030009-1-030009-8.

[11] Golubev Yu. F., Melkumova E. V. An Analogy of the Equilibrium of a Two-legged Robot on a Cylinder for the Problem of Transfer by a Manipulator With a Two-finger Grasp of a Cylinder, APM 2018, Proceedings of XLVI Summer School-Conf. "Advanced Problems in Mechanics", June 25–30, St. Petersburg, Russia; Polytech – IPME RAS, PP 117-124.

[12] Golubev Yu. F., Melkumova E. V. Footholds Admissible Areas Structure of a Two-legged Walking Robot on an Inclined Cylinder // Conference Series: Materials Science and Engineering, v. 468, No. 012003, 2018, PP. 1-9.

[13] Golubev Yu. F., Melkumova E. V. Brittle Cylinder Transfer by a Three-finger Grasp // VIII International Conference on Computational Methods for Coupled Problems in Science and Engineering (COUPLED 2019), Sitges (Barcelona), Spain, June 3-5, 2019, https: // congress. cimne.com/coupled2019/frontal/doc/EbookCoupled2019.pdf, PP. 164-175.

[14] Golubev Yu. F., Melkumova E. V. Transfer by a Manipulator with a Three-Finger Grasp of a Brittle Cylinder // APM 2019 Book of Abstracts, XLVII International Conference “Advanced Problems in Mechanics”, June 24-29, 2019, St. Petersburg, Russia, theses, p. 78.

[15] Golubev, Yu. & Melkumova, E. (2019). Transfer of the Fragile Cylinder with a Two-finger Manipulator In the Collection of the XII All-russian Congress on Fundamental Problems of Theoretical and Applied Mechanics. Annotations of Reports, Place of Publication of the RIC of BASHSU UFA, Theses, PP. 62-62.

[16] Golubev, Yu. & Melkumova, E. (2019). Transfer of the Fragile Cylinder with a Three-finger Manipulator In the Collection of the XII All-russian Congress on Fundamental Problems of Theoretical and Applied Mechanics. Annotations of Reports, Place of Publication of the RIC of BASHSU UFA, Theses, PP. 55-55.

STRUCTURAL APPROACH TO TEACHING BASIC COURSES OF MECHANICS OF DEFORMED SOLID

Ekaterina Korovaytseva
Institute of Mechanics, Lomonosov Moscow State University, Moscow, Russia

Summary The work represents methodology of teaching disciplines of mechanics of solids which is based on defining types of problems solved and developing algorithms of solution for each type. Special attention is payed to such disciplines as strength of materials and structural mechanics. Classification of problems considered in mentioned courses is carried out on the basis of unity of mathematical formulations or structural models. The following algorithmization of problems solution includes step-by-step description of doings which reflect either methodical side of solution process or the process of drawing different structural models. Such an approach to teaching leads to significant reducing of content knowledge to be learnt, and at the same time rises generalizing level of knowledge.

In Russia specialty "Dynamics and strength of machines" provides the most complex training of specialists in the field of mechanics of solids. The specialty program supposes, besides humanities, studying of more than thirty general engineering and special disciplines. Instruction is provided mainly on the basis of textbooks of 70^{th}-80^{th} years of the last century, which seems quite reasonable, as mechanics of solids theory hasn't changed through the past 40 years. But in this period computing technology and its role in work of mechanic changed significantly. That's why, in our opinion, the problem of forming contemporary methodology of teaching mechanics of solids courses is still actual. This methodology should connect theoretical disciplines, such as elasticity theory, plasticity theory, plates and shells theory etc. with computing technology using, including both individual programming and using commercial software. Along with this, the most important goal of education process is, besides knowledge transmission, forming a way of thinking which will be required in future work of a specialist.

We distinguish two types of specialists trained in specialty "Dynamics and strength of machines" – scientists (mechanicians) and mechanical engineers. Both types of specialists are taught the same courses by the same methodology, but their purposes in future work are different. The scientists should provide engineering calculations by algorithms, methodology and programs of a high quality, while engineers should be able to use the results of the scientists' work consciously, understanding features of real structures calculation – both properties of the resolving equation systems and properties of calculation process realizing various methodologies or algorithms.

As it is known, "computer multiple times rises level of incompetency of a user". That is why general engineering courses, teaching analytical solution of mechanics of solids problems, are of important value. We developed methodology of strength of materials teaching, the purpose of which is not only knowledge transmission, but also developing skills of finding common patterns, cause-and-effect relations, which allows in future successfully working with large amounts of information when studying individually or in working practice.

Within the framework of this methodology problems of strength of materials are accumulated into 22 types, for each of which solution algorithms are formulated [1]. Problems classification is carried out by the following characteristics:
- type of stress-strain state considered (tension-compression, torsion, bending, combined stress state);
- structure type (rod, beam, plane frame, space frame, shell);
- calculation type (strength, stability, impact).

Also we emphasize unity of different stress-strain types calculation problems from the point of view of mathematical formulation of corresponding problems. For example, structural notation of the rod infinitely small element equilibrium differential equations has the form

$$\frac{dR}{dx} = G(x),$$

where

$$R = \begin{cases} N & \text{for tension-compression} \\ M_к & \text{for torsion} \\ Q_y & \text{for straight transverse bending} \\ M_z & \text{for pure and straight transverse bending} \end{cases} ; \quad G(x) = \begin{cases} q_x(x) & \text{for tension-compression} \\ m_к(x) & \text{for torsion} \\ q_y(x) & \text{for straight transverse bending} \\ Q_y(x) & \text{for pure and straight transverse bending} \end{cases}$$

Structural formulae for calculating maximum stresses, generalized strains and displacements, single for any of four types of elementary stress-strain state, are constructed similarly.

In such a way we develop an ability to find unity or logical connection of problems which seem different at the first site. The students are encouraged to form logic and structural properties of thinking, to be sure in their ability of solving any problems with given structural models.

Using structural approach in strength of materials course allows simply passing to teaching structural mechanics as the most important course for developing skills of carrying out calculations of real structures. We suggest, after introducing the students to theoretical basis of the course, demonstration of unity of the problems considered both in structural mechanics and real calculation practice – unity from the point of view of mathematical formulation. For example, for the course of structural mechanics we suggest introducing three canonical forms of linear boundary

problems of mechanics of deformed solid. These forms can describe behavior of the simplest and complex branched structures as well [2]:
1) two-point boundary value well-posed problems without additional relations (canonical form I);
2) multi-point unbranched boundary value well-posed problems without additional relations (canonical form II);
3) multi-point branched boundary value well-posed problems without additional relations (canonical form III).

Suggested forms can be used for structuring notation of equations of any structure elements deforming. For example, canonical form I includes differential equations

$$\frac{dy}{dx} = \mathbf{A}(x,\mu)y + a(x,\mu), \tag{1}$$

and boundary conditions

$$\mathbf{B}_i(x_i,\mu_i)y_i + b_i(x_i,\mu_i) = 0; \quad i \leftrightarrow e. \tag{2}$$

Here $y(x,\mu)$, $y_i(x_i,\mu_i)$ are vectors of resolving variables, $\mathbf{A}(x,\mu)$, $\mathbf{B}_i(x_i,\mu_i)$ are coefficient matrices, $\mu(x)$, μ_i are vector-function and vector of initial values of the problem parameters, $a(x,\mu)$, $b_i(x_i,\mu_i)$ are vectors of external distributed and concentrated loads correspondingly, i and e are indices denoting values of variables and argument at the initial and end point of integration interval correspondingly. For example, vector of resolving variables y can have the form

$$y = \begin{cases} \{w;\ \vartheta;\ Q_y;\ M_z\}^T & \text{for the beam} \\ \{w;\ \vartheta;\ Qr;\ M_1 r\}^T & \text{for symmetrically loaded round plate} \\ \{u;\ w;\ \vartheta_1;\ T_1;\ Q_1;\ M_1\}^T & \text{for symmetrically loaded shell of revolution} \end{cases}$$

Similar to strength of materials course, for each canonical form we represent an algorithm of corresponding problem solution. Special attention is payed to teaching skills of analyzing considered equation system properties, taking into account features of using this or that numerical method, developing skills of individual constructing problem solution algorithms and further structural programming.

The results of this teaching method are both complex structural way of thinking forming and developing culture of scientific work. This culture is precondition for protecting computer-aided scientific and engineering research from the mistakes of the computer man.

References

[1] Korovaytsev A.V., Korovaytseva E.A., Stolyarchuk V.A. Structural approach in calculations of strength and stability of aircraft structures simplest elements. LENAND, Moscow 2015.

[2] Korovaytsev A.V., Korovaytseva E.A. Universal systematization of one-dimensional linear boundary value problems of mechanics of deformed solid. *Materials of the XVII International symposium "Dynamic and technological problems of mechanics of structures and continuous medium" n.a. A.G. Gorshkov*. **1**: 101-104, 2011.

EFFECTIVE TEACHING OF VECTOR TO MITIGATE TENSOR-PHOBIA IN MECHANICS AND APPLICATION OF EXTERIOR FORM

Ade Akinola * [1], Bolanle Olokuntoye[1], Adebowale Borokinni[1], Odunayo Fadodun[1], and Olawanle Layeni[1]
[1]Department of Mathematics, Obafemi Awolowo University, Ile-Ife, Nigeria

Summary We interrogate the observed proclivity of students of mechanics and engineering and some scientists to nursing phobia towards *Tensor*, known as "*tensor-phobia*" [1-3]. An effective cognitive teaching approach needs urgent attention: to let students see the connection between tensors and vectors, as common invariants. Students are made to carry out simple operations using *invariant/rank* concept. Here, we reveal how the familiar vector operations form synergy with isotropic tensors; and demonsrtate how the *exterior form* behaves as "skew-symmetric tensor". Invoking Poincare's theorem on *differential forms* we reduce the equations of state for plane elasticity to a differential form and show the source of *Airy's Function* deduction. The application of this cognitive principle is used in deriving effective moduli for composites; and on strain-gradient plasticity problem [4].[0]

INTRODUCTION

It is of utmost necessity that most basic engineering designs make ample use of vector concepts [2,3]; and a proper grasp of this is quite imperative [1-3]. But more, any significant modern designs and engineering analysis is unfathomable without proper comprehension of the basics of tensor analysis [3]; particularly so, where it is a *fait accompli* to invoke the concept of continuum mechanics. In fact, in continuum mechanics, without being well grounded in tensor it could be practically quite strenuous interrogating some vital engineering concepts that include: invariants of objects such as stress, strain, material characteristics and others that copiously make use of the Hamilton-Cayley theory; energy function and its tensor derivatives; homogenization theory that enables the delicate navigation through complex relations involved in heterogeneous media and the deduction of effective characteristics of composites.

Observation over the years revealed that while students and researchers in mechanics show some degree of understanding of vector concepts they depict tendency to nurse phobia for tensor, in what is often known to as "*tensor-phobia*" [1]. If this is not properly addressed, it could have a ramifying implication on the development of continuum mechanics and related subject at a later stage. However, the adoption of an appropriate cognitive teaching approach would help mitigate the situation. A potent approach is to let students see early enough the connection between tensor and vectors, for which they already had acquaintance from the secondary or high school. This makes them carry out simple operations, which they were used to, such as *scalar product*, *vector product* and others on vectors, using *invariant/rank* concept. As an illustration, we demonstrate how the already familiar primary vector operations (the *dot* and *cross* products) form synergy with the so-called isotropic tensors. Also, we show how the *exterior form* behaves as skew-symmetric tensor defined on basis, as multiple vector products (now known as *exterior products* or *wedge products*). Then, using the Poincare's theorem on *differential forms* we reduce the equations of state for plane elasticity to a differential form and hence show the basis of *Airy's Function* deduction.

VECTOR OPERATIONS, ISOTROPIC TENSOR, EXTERIOR FORMS

Dot and Cross Vector Product Operations and Isotropic Tensor

Consider, without loss of generality, vectors $\mathbf{a}, \mathbf{b}, \mathbf{c}$ and what we call the rank-2 *isotropic tensor* $\underset{\sim}{\mathbf{I}} = g^{ij}\mathbf{e}_i\mathbf{e}_j = \mathbf{e}^j\mathbf{e}_j$ and rank-3 *isotropic tensor* $\underset{\sim}{\epsilon} = \epsilon^{ijk}\mathbf{e}_i\mathbf{e}_j\mathbf{e}_k$ in the three dimension Euclidean space E^3, $i, j, k = 1, 2, 3$; $\mathbf{e}_i$ and $\mathbf{e}^i$ are the orthogonal covariant and contravariant base vectors respectively. Then recalling from the elementary vector theory, *dot product* is $\mathbf{a}\cdot\mathbf{b} = \mathbf{b}\cdot\mathbf{a}$, *cross product* is $\mathbf{b}\times\mathbf{a} = -\mathbf{a}\times\mathbf{b}$, while the *scalar triple product* is $\mathbf{a}\cdot(\mathbf{b}\times\mathbf{c}) = (\mathbf{a}\times\mathbf{b})\cdot\mathbf{c}$. Now, the cross product of vectors $\mathbf{a}$ and $\mathbf{b}$ can be given with the aid of $\underset{\sim}{\epsilon}$, such that $\mathbf{a}\times\mathbf{b} = \underset{\sim}{\epsilon}\cdot\cdot\,\mathbf{a}\,\mathbf{b}$. In fact,

$$\mathbf{a}\times\mathbf{b} \equiv \begin{vmatrix} \mathbf{k}_1 & \mathbf{k}_2 & \mathbf{k}_3 \\ a_1 & a_2 & a_3 \\ b_1 & b_2 & b_3 \end{vmatrix} = \begin{vmatrix} a_2 & a_3 \\ b_2 & b_3 \end{vmatrix}\mathbf{k}_1 + \begin{vmatrix} a_3 & a_1 \\ b_3 & b_1 \end{vmatrix}\mathbf{k}_2 + \begin{vmatrix} a_1 & a_2 \\ b_1 & b_2 \end{vmatrix}\mathbf{k}_3 = c_m\mathbf{k}_m \equiv \mathbf{c} = \epsilon^{ijk}a_ib_j\mathbf{e}_k = \underset{\sim}{\epsilon}\cdot\cdot\,\mathbf{a}\,\mathbf{b}, \tag{1.1.1}$$

where $m = 1, 2, 3$, c_1, c_2, c_3 are the minor to the orthonormal base vectors $\mathbf{k}_1, \mathbf{k}_2, \mathbf{k}_3$ respectively; and for simplicity, in the cartesian coordinates, the components of $\underset{\sim}{\epsilon}$ become the *Levi Chivita symbols* $e^{ijk} = e_{ijk}$.

*Corresponding author. E-mail: aakinola@oauife.edu.ng

[0]**Prologue:** *Perhaps the best evidence of the remarkable effectiveness of the tensor apparatus in the study of Nature is in the fact that it was possible to include, between the covers of one small volume a large amount of material that is of interest to mathematicians, physicists and engineers. – Sokolnikoff, I. S.*

Cofactor

Further, given any rank-2 tensor $\underset{\sim}{\mathbf{T}}$, its *cofactor tensor* $\underset{\sim}{\mathbf{T}}^c$ can be obtained simply as the *dyad* of vector $\mathbf{e}_i \times \mathbf{e}_j$ and vector $(\underset{\sim}{\mathbf{T}} \cdot \mathbf{e}^i) \times (\underset{\sim}{\mathbf{T}} \cdot \mathbf{e}^j)$ such that

$$\underset{\sim}{\mathbf{T}}^c = [(\underset{\sim}{\mathbf{T}} \cdot \mathbf{e}^i) \times (\underset{\sim}{\mathbf{T}} \cdot \mathbf{e}^j)][\mathbf{e}_i \times \mathbf{e}_j] = \frac{1}{2}\epsilon_{skq}\epsilon^{mnp} T_n{}^k T_p{}^q \mathbf{e}^s \mathbf{e}_m. \tag{1.1.4}$$

Thus, the *1st invariant* $I_1(\underset{\sim}{\mathbf{T}})$ and *2nd invariant* $I_2(\underset{\sim}{\mathbf{T}})$ of tensor $\underset{\sim}{\mathbf{T}}$ can be given through the double dot product:

$$I_1(\underset{\sim}{\mathbf{T}}) = \underset{\sim}{\mathbf{I}} \cdot \cdot \, \underset{\sim}{\mathbf{T}}, \; I_2(\underset{\sim}{\mathbf{T}}) = I_1(\underset{\sim}{\mathbf{T}}^c) = \underset{\sim}{\mathbf{I}} \cdot \cdot \, \underset{\sim}{\mathbf{T}}^c = \frac{1}{2}[I_1^2(\underset{\sim}{\mathbf{T}}) - I_1(\underset{\sim}{\mathbf{T}}^2)]. \tag{1.1.5}$$

This process can be followed to, compute other invariants, obtain the Hamilton-Cayley relation and other tensor functions.

Exterior Form, Differential Form

An *exterior form* $\Phi = \varphi_{i_1 i_2 \ldots i_{m-1} i_m} \mathbf{e}^{i_1} \Lambda \mathbf{e}^{i_2} \cdots \Lambda \mathbf{e}^{i_{m-1}} \Lambda \mathbf{e}^{i_m}, \quad m = 1, 2, 3, \ldots,$ becomes a *differential form* $\omega = a_{i_1 i_2 \ldots i_{m-1} i_m}(x^1, x^2, \ldots, x^{n-1}, x^n) dx^{i_1} \Lambda dx^{i_2} \ldots \Lambda dx^{i_{m-1}} \Lambda dx^{i_m}$ by replacing **(i.)** the base elements *covectors* $\mathbf{e}^{i_k}, k = 1, 2, 3, \ldots$ with the *differentials* dx^k, where **(i.)** the object $\varphi_{i_1 i_2 \ldots i_{m-1} i_m}(x^1, x^2, \ldots, x^{n-1}, x^n)$ in an n-dimensional Euclidean space E^n with the function $a_{i_1 i_2 \ldots i_{m-1} i_m}(x^1, x^2, \ldots, x^{n-1}, x^n) \in C^m(\Omega), \quad m \geq 1, \quad \Omega \subset E^n$, often referred to as the *Cartan's ring of coefficients* and **(ii.)** the base elements *covectors* $\mathbf{e}^{i_k}, k = 1, 2, 3, \ldots$ with the *differentials* dx^k.

Poincare's Theorem:

The second exterior differential of an exterior form is zero,

$$\mathcal{D}\mathcal{D}\omega = 0,$$

where $\mathcal{D}\mathcal{D}\omega = \dfrac{\partial^2 a_{i_1 i_2 \ldots i_{m-1} i_m}}{\partial x^j \partial x^k} dx^k \Lambda dx^j \Lambda dx^{i_1} \Lambda dx^{i_2} \ldots \Lambda dx^{i_{m-1}} \Lambda dx^{i_m}$.

Application of Poincare's Theorem in Plane Elasticity

Theorem: The Airy's function $\phi(x_1, x_2)$ constitutes a *form* describing the state of stress $\sigma_{ij}, i, j = 1, 2,$ equivalent to the elastostatic equations of *plane elasticity* $\frac{\partial \sigma_{11}}{\partial x_1} + \frac{\partial \sigma_{12}}{\partial x_2} = 0; \; \frac{\partial \sigma_{12}}{\partial x_1} + \frac{\partial \sigma_{22}}{\partial x_2} = 0$ only and only if $\sigma_{11} dx_2 - \sigma_{12} dx_1$ and $\sigma_{22} dx_1 - \sigma_{12} dx_2$ respectively is an exact differential - *a form.*

Proof: By Poincare's theorem, ω is an exact differential if $d\omega = 0$. Thus, $\sigma_{11} dx_2 - \sigma_{12} dx_1$ is an exact differential $\Longrightarrow$ $D(\sigma_{11} dx_2 - \sigma_{12} dx_1) = 0$. In deed, we have

$$D(\sigma_{11} dx_2 - \sigma_{12} dx_1) = \frac{\partial}{\partial x_1}(\sigma_{11} dx_2 - \sigma_{12} dx_1) dx_1 + \frac{\partial}{\partial x_2}(\sigma_{11} dx_2 - \sigma_{12} dx_1) dx_2$$

$$= \left(\frac{\partial \sigma_{11}}{\partial x_1} + \frac{\partial \sigma_{12}}{\partial x_2}\right) dx_2 \Lambda dx_1 = 0; \; \text{since } dx_1 \Lambda dx_1 = dx_2 \Lambda dx_2 = 0. \implies \left(\frac{\partial \sigma_{11}}{\partial x_1} + \frac{\partial \sigma_{12}}{\partial x_2}\right) = 0.$$

Conversely: Let $(\frac{\partial \sigma_{11}}{\partial x_1} + \frac{\partial \sigma_{12}}{\partial x_2}) = 0. \implies d(\sigma_{11} dx_2 - \sigma_{12} dx_1) = 0$. Then, $\sigma_{11} dx_2 - \sigma_{12} dx_1$ is an exact differential. $\Longrightarrow \; \exists$ function $P(x_1, x_2)$;

$$\sigma_{11} dx_2 - \sigma_{12} dx_1 = dP(x_1, x_2) = \frac{\partial P}{\partial x_1} dx_1 + \frac{\partial P}{\partial x_2} dx_2; \implies \sigma_{11} = \frac{\partial P}{\partial x_2}, \; \sigma_{12} = -\frac{\partial P}{\partial x_1}.$$

$$\text{Similarly, } \exists\, Q(x_1, x_2); \; \sigma_{22} dx_1 - \sigma_{12} dx_2 = \frac{\partial Q}{\partial x_1} dx_1 + \frac{\partial Q}{\partial x_2} dx_2; \implies \sigma_{22} = \frac{\partial Q}{\partial x_i}, \; \sigma_{12} = -\frac{\partial Q}{\partial x_2}.$$

$$\text{By Poincare}'\text{s theorem } \exists\, \phi; \; \sigma_{11} = \frac{\partial^2 \phi}{\partial {x_2}^2}; \quad \sigma_{22} = \frac{\partial^2 \phi}{\partial {x_1}^2}; \quad \sigma_{12} = -\frac{\partial^2 \phi}{\partial x_2} \partial x_1.$$

CONCLUSIONS

Deep understanding of vector, vector operations and their physical implications, as well as early introduction as a *lower-level invariant* assists to demystify key concepts of tensor, geometry, exterior forms and their applications; which are vital tools for navigating the complex labyrinths of mechanics, application to technology and nature in general.

References

[1] J2kun web site https://jeremykun.com/2014/01/17/how-to-conquer-tensorphobia/
[2] Brillouin, L. Tensor in Mechanics and Elasticity. Masson, Paris 1964.
[3] Dimitrienko, Y. U. Tensor Analysis and Nonlinear Tensor Functions. Springer, 2002.
[4] Borokinni, A. S., Fadodun, O. O., Akinola, A. P. Distortion-Gradient Plasticity for an Isotropic Body in Finite Deformation. *Meccanica* **53**: 3145-3155, Springer, 2018.

AUTHORS' INDEX

C

D

E

F

G

H

I

J

K

L

M

N

O

P

Q

R

S

T

U

V

W

X

Y

Z